JANUARY/FEBRUARY 2004
Volume 15, Number 1

© *Copyright 2004 by the American Chemical Society*

Bioconjugate Chemistry

EDITORIAL

We welcome the following distinguished scientists as *new members* of the Editorial Advisory Board, and we look forward to working with them to take the journal in new directions:

Jackie Barton
California Institute of Technology
Pasadena, CA

Mark E. Davis
California Institute of Technology
Pasadena, CA

Gene M. Dubowchik
Bristol-Myers Squibb
Wallingford, CT

Greg Hermanson
Pierce Chemical Company
Rockford, IL

Donald J. Hnatowich
University of Massachusetts Medical Center
Worcester, MA

Thomas Kissel
Philipps-University of Marburg
Marburg, Germany

Chris Leamon
Endocyte Pharmaceuticals, Inc.
West Lafayette, IN

Helmut R. Maecke
University Hospital Basel
Basel, Switzerland

Oleg Melnyk
Biological Institute of Lille
Lille, France

Sherie L. Morrison
University of California, Los Angeles
Los Angeles, CA

Steven L. Regen
Lehigh University
Bethlehem, PA

P. August Schubiger
Paul Scherrer Institute
Villigen, Switzerland

Paul Selvin
University of Illinois
Urbana, IL

David H. Thompson
Purdue University
West Lafayette, IN

Pierre Vierling
Universite de Nice Sophia-Antipolis
Nice, France

Wynn A. Volkert
University of Missouri
Columbia, MO

We are grateful to the following *outgoing members* of the Editorial Advisory Board for their service during the past years, and we wish them well in their future endeavors.

Maciej Adamczyk
Gary Bignami
Daniel J. Coughlin
Masad Damha
Edith Dellacherie
Jean F. Desreux
Raymond Firestone
Alan Fritzberg
Jean Gariepy
Sidney M. Hecht
Jens Peter Jacobsen
David K. Johnson
John F. W. Keana
Eiichi Kimura
Damon Meyer
Patrick Midoux
Leslie E. Orgel
Mark Reynolds
Kevin G. Rice
Clay Siegall
Cy Stein
Stan Stein
E. Sally Ward
David S. Watt

These scientists have played a significant role in advising, reviewing, and guiding the journal, and the effects of their contributions will persist.

Thanks to Our Reviewers

It is a pleasure to acknowledge the contributions of the reviewers of manuscripts submitted in 2003 for publication in *Bioconjugate Chemistry*. Their unselfish service has been essential in the shaping of the fourteenth volume of the journal.

10.1021/bc030053g CCC: $27.50 © 2004 American Chemical Society
Published on Web 01/21/2004

The scientific community is fortunate that its members are willing to share their time and specialized knowledge in this way. The reviewers are as follows:

Maciej Adamczyk
Steve Alley
Carolyn Anderson
David Andreu
Yasushi Arano
Hidetoshi Arima
Jeffrey Arterburn
Kwamena Baidoo
Craig Beeson
Jean-Paul Behr
Gary Bignami
Alexei A. Bogdanov
Matthew Bogyo
Elijah Bolotin
Jean-Claude Bradley
Merlin Bruening
Art Broom
Donald Buchsbaum
Marvin Caruthers
Chongsu Cho
David Coy
Ben Cravatt
Masad Damha
Gary David
Mark Davis
Mark Distefano
Gene Dubowchik
S. Eremin
Colin Ferguson
Joseph Francisco
Keith Fox
Jean Gariepy
Kieran Geoghegan
Jean Marcus Glomb
David Grainger
Mark Green
Richard Greenwald
Philip R. Hamann
Kevin Hamblett
Kevin Healy
Donald Hnatowich
Hideyoshi Harisima
Richard Haugland
Piet Herdewijn
Greg Hermanson
Ole Hindsgaul
Timothy Hoffman
Ken Houk
Jari Hovinen
R. Hudson
Andres Jaschke
Lee Josephson
Jingyue Ju
Sylvia Jurisson
Alexander Kabanov
Angel Kaifer
Kazunori Kataoka
John Katzenellenbogen
John F. W. Keana
Marc Kirchmeier
Thomas Kissel
Toni Kline
Jindrich Kopecek
Heinz-Bernhard Kraatz
Thomas Krugh
Erika Kullberg
Christopher Leamon
Robert J. Lee
Susan Lever
Michael Lewis
Kai Licha
Shuang Liu
Wen G. Liu
Harri Lonnberg
Gabriel Lopez
Helmut R. Mäcke
Ram Mahato
Charlotte McDonagh
Larry Mclaughlin
Kamran Melikov
Damon Meyer
Dale Miles
Michel Monsigny
John Morley
Russell Mumper
Catherine Murphy
Takeshi Nagasaki
Philippe Neuner
Peter Nielsen
Takuro Niidome
Giovanni Paganelli
Roger Pak
Tae Gwan Park
David Perrin
T. Porter
Lina Prasmickaite
Glenn Prestwich
Michael Przybylski
Martin Read
Michael Reed
Steven L. Regen
Steven Roffler
Buck Rogers
Keith Rose
Roger Schibli
P. August Schubiger
Jonathan Sessler
Yechiel Shai
Lonnie Shea
Dean Sherry
John Shively
Caroline Springer
Patrick Stayton
Diane Stearns
Harald Stover
Francis Szoka Jr.
John-Stephen Taylor
David Thompson
Brian Toki
Eishun Tsuchida
Ching-Hsuan Tung
F. Uchegbu
Ulrich Massing
Ganesan Vaidyanathan
Pierre Vierling
Wynn Volkert
E. Sally Ward
W. Webb
Paul Whetstone
D. Scott Wilbur
Eric Wickstrom
Meir Wilchek
Karen L. Wooley
George Wu
John R. Yates, III
Samuel Zalipsky

Claude F. Meares

Editor-in-Chief

BC030053G

COMMUNICATIONS

Element-Coded Affinity Tags for Peptides and Proteins

Paul A. Whetstone, Nathaniel G. Butlin, Todd M. Corneillie, and Claude F. Meares*

Department of Chemistry, University of California, One Shields Avenue, Davis, California 95616. Received August 26, 2003

Isotope-coded affinity tags (ICAT) represent an important new tool for the analysis of complex mixtures of proteins in living systems [Aebersold, R., and Mann, M. (2003) *Nature, 422*, 198−207]. We envisage an alternative protein-labeling technique based on tagging with different *element-coded* metal chelates, which affords affinity chromatography, quantification, and identification of a tagged peptide from a complex mixture. As proof of concept, a synthetic peptide was modified at a cysteine side chain with either a carboxymethyl group or acetamidobenzyl-1,4,7,10-tetraazacyclododecane-*N*,*N*′,*N*″,*N*‴-tetraacetic acid (AcBD) chelates of terbium or yttrium. A mixture of the three modified peptides in a mole ratio of 100:1.0:0.83 carboxymethyl:AcBD-Tb:AcBD-Y was trypsinized, purified on a new affinity column that binds rare-earth DOTA chelates, and analyzed by LC-MS/MS. Chelate-tagged tryptic peptides eluted cleanly from the affinity column; the tagged peptides chromatographically coeluted during LC-MS analysis, were present in the expected ratio as indicated by MS ion intensity, and were sequence-identified by tandem mass spectrometry. DOTA-rare earth chelates have exceptional properties for use as affinity tags. They are highly polar and water-soluble. Many of the rare earth elements are naturally monoisotopic, providing a variety of simple choices for preparing mass tags. Further, the rare earths are heavy elements, whose mass defects give the masses of tagged peptides exact values not normally shared by molecules that contain only light elements.

INTRODUCTION

The assessment of protein expression profiles is an important tool for understanding many aspects of cell biology, including the effects of drug treatments. One way of comparing protein expression under different conditions involves chemically modifying the proteins in separate samples with isotopically distinct but otherwise identical reagents, followed by enzymatic fragmentation, chromatographic separation, and combination of the samples for mass spectrometric analysis (*1*−*4*). Chemically equivalent, but isotopically discrete, labeled peptides from the combined samples are detected simultaneously in the mass spectrometer, permitting quantitative analysis of expression levels. A well-established enhancement of this approach is isotope-coded affinity tags (ICAT, Scheme 1) in which ^{2}H- or ^{13}C-isotopes are incorporated within a biotinylated tag, permitting affinity capture and enrichment of tagged peptides on avidin columns (*5*−*17*). ICAT is potentially well suited to the study of complex protein mixtures. However, because typical avidin affinity media bind and release some peptides that do not carry the tag, biotin-based ICAT reagents lead to *enrichment* rather than isolation of the tagged peptides and may therefore have limited sensitivity to rare components of the mixture.

Antibody−antigen interactions are often the basis for preparative affinity chromatography. As an alternative to biotin−avidin, we have explored affinity tags based on the interactions between antibody 2D12.5 and the range of ligands that it binds (*18*). These ligands are metal chelates incorporating any of the rare earth metals bound to the macrocycle DOTA.[1] DOTA-rare earth chelates have exceptional properties for use as affinity tags. Unlike biotin, they have no natural analogues that might interfere with affinity purification. They are highly polar and water-soluble. Many of the rare earth elements are naturally monoisotopic, providing a variety of simple choices for preparing mass tags. As shown in Table 1,

Table 1. Mass Differences between Pairs of Naturally Monoisotopic Rare Earths for Use in Element-Coded Affinity Tags

element	^{89}Y	^{139}La	^{140}Ce[a]	^{141}Pr	^{159}Tb	^{165}Ho	^{169}Tm	^{175}Lu
^{89}Y		50	51	52	70	76	80	86
^{139}La			1	2	20	26	30	36
^{140}Ce[a]				1	19	25	29	35
^{141}Pr					18	24	28	34
^{159}Tb						6	10	16
^{165}Ho							4	10
^{169}Tm								6
^{175}Lu								

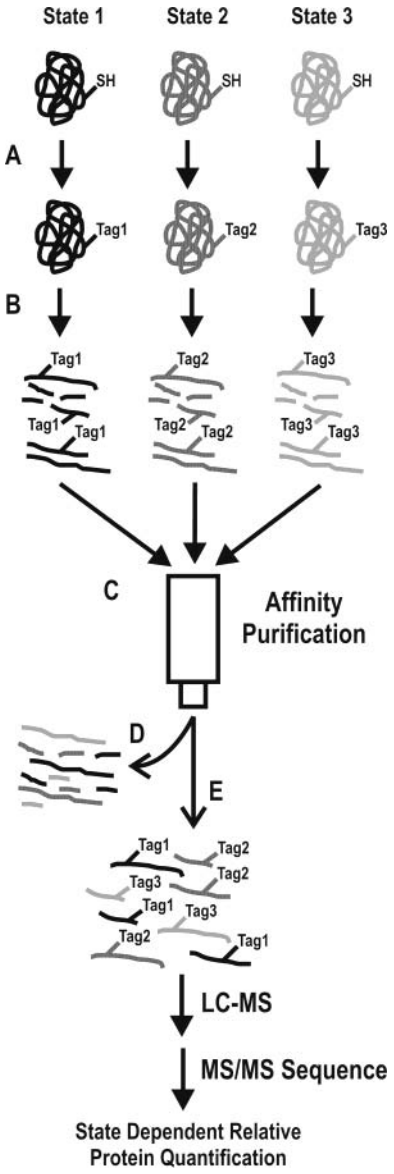
[a] Natural abundance ^{140}Ce (88%) and ^{142}Ce (11%). All other isotopes are naturally >97% monoisotopic.

[1] Abbreviations: BAD, (*S*)-2-(4-(2-bromoacetamido)benzyl)-DOTA; C(AcBD)NSLKLAT-amide, peptide CNSLKLAT-amide with acetamidobenzyl-DOTA group attached to cysteine; C(CM)-NSLKLAT-amide, C(carboxymethyl)NSLKLAT-amide; CID, collision-induced dissociation; CV, column volume; DOTA, 1,4,7,10-tetraazacyclododecane-*N*,*N*′,*N*″,*N*‴-tetraacetic acid; ECAT, element-coded affinity tags; NBD, (*S*)-2-(4-nitrobenzyl)-DOTA.

* Address correspondence to this author. Telephone: 530-752-0936. Fax: 530-752-8938. E-mail: cfmeares@ucdavis.edu.

10.1021/bc034150l CCC: $27.50 © 2004 American Chemical Society
Published on Web 01/03/2004

Scheme 1. Generalized Scheme for ICAT and ECAT[a]



[a] (A) Amino acid side chains such as cysteine sulfhydryls are modified with reactive tag molecules. For ICAT, different tags contain different numbers of ^{2}H or ^{13}C; for ECAT, tags contain different rare earth elements. (B) Tagged protein is digested with a protease: e.g., trypsin. (C) The tryptic fragments from multiple labeling experiments are combined and purified on a tag-specific affinity column. (D) Washing removes untagged peptides from the column. (E) Tagged peptides are eluted from the column and analyzed by LC-MS.

naturally occurring mass tags could be used in combinations differing in mass from 1 to 86 amu. Isotopically enriched elements and non-rare earth elements that bind to DOTA could extend the selection dramatically. Further, the rare earths are heavy elements, whose mass defects give the masses of tagged peptides exact values not normally shared by molecules that contain only light elements (*19*).

It appeared to us that these properties of the rare earths could be advantageous; however, data were not available regarding the suitability of metal chelate mass tags to mass spectrometric analysis. Answers to basic questions regarding the feasibility of element-coded affinity tags (ECAT) are addressed in this communication.

It has already been established that protein-tagging DOTA reagents can be prepared (e.g., *20*−*24*). Besides

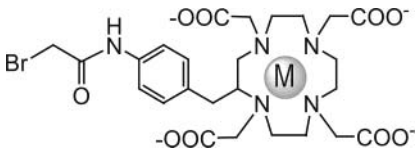


Figure 1. Bromoacetamidobenzyl-DOTA (BAD). Metalation of the chelate with a monoisotopic rare earth (M) provides a unique mass tag. Alkylation of a sulfhydryl group on a protein and protease digestion allow antibody 2D12.5 affinity purification of tagged peptides from complex mixtures, and relative quantification of all tagged peptides in the mixture, as well as sequence identification through tandem mass spectrometric analysis. The bromoacetamido reactive group may be replaced by many others with different chemical properties, e.g., an isothiocyanate that reacts with amines.

demonstrating that these reagents and their protein conjugates are compatible with trypsin digestion conditions, it must be shown that an affinity medium can be prepared, and that the metal chelates are equivalently stable to affinity column binding, washing, and elution. Tagged peptides containing different rare earth elements should also coelute on reverse-phase liquid chromatography. Finally, the tags themselves should not complicate mass spectrometric analysis; preferably, the tags should resist fragmentation under conditions of peptide sequencing by tandem mass spectrometry (MS/MS). We have confirmed these properties, with the results presented below. Experimental details are given in Supporting Information.

Molecules incorporating the macrocyclic polyaminocarboxylate DOTA attached to electrophilic groups can be synthesized by various methods (*20*−*24*). For this work we prepared the reagent BAD[1] (Figure 1). As a trial peptide for tagging, we synthesized the hemagglutinin-based peptide CNSLKLAT-amide using standard solid-phase techniques. Incorporating iodoacetic acid or BAD into the syntheses at appropriate steps led to C(carboxymethyl)-NSLKLAT-amide or C(acetamidobenzyl-DOTA)NSLKLAT-amide. Aliquots of a C(AcBD)NSLKLAT-NH_2 solution were combined with solutions of either $TbCl_3$, YCl_3, or $LuCl_3$ and the chelate-labeled peptides purified.

Metal-labeled C(AcBD)NSLKLAT-NH_2 peptides were examined by LC-MS/MS. Mixed pairs of tagged peptides (chosen from Tb, Y, Lu) were analyzed in triplicate with good reproducibility. In all cases both chelate-labeled peptides in the sample coeluted on reverse phase LC; comparison of relative ion counts yielded expected abundance ratios within 15%. Tandem mass spectrometry of each peptide reproducibly yielded the expected b/y series with no tag fragmentation evident (Figure 2).

A mixture containing carboxymethylated CNSLKLAT-NH_2 peptide as well as Tb- and Y-metalated peptide chelates was prepared in a 100:1.0:0.83 mole ratio. The mixture was completely digested with trypsin (cleaved after the lysine residue) and used to test an affinity column prepared from antibody 2D12.5, which binds all the rare earth−DOTA complexes. The affinity column was prepared using Pierce Amino-link media, and elution protocols were investigated using NBD−rare earth chelates.

To see if the antibody 2D12.5 affinity column could bind different DOTA−rare earth-tagged peptides without significant discrimination while passing untagged peptides, the trypsinized and tagged test peptide mixture was applied to the column, which was washed and eluted. LC-MS analysis of the eluent is shown in Figure 3.

Figure 2 shows that the tags resist fragmentation under conditions of peptide sequencing (MS/MS). Figure

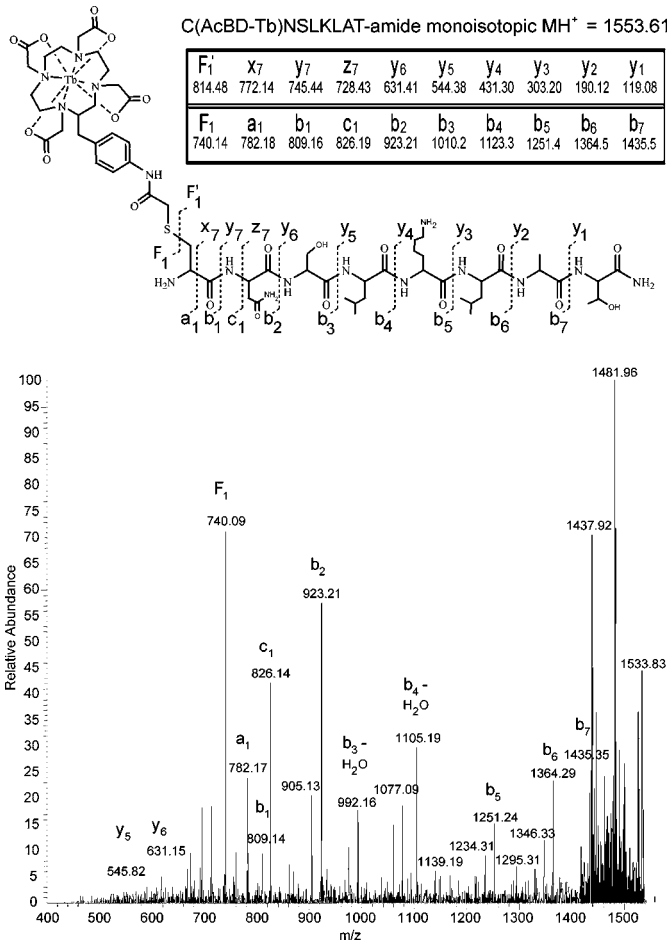


Figure 2. Predicted and observed CID fragment masses of the C(AcBD-Tb)NSLKLAT-NH_2 peptide. Similar results were obtained for peptides with Lu- and Y-metalated mass tags. Because the mass tag is located at the N-terminal end of this peptide, the b-ion series predominates in the observable mass range. Mass spectrometry was performed on an LCQ Deca electrospray ion-trap instrument.

3 shows that tagged peptides containing different rare earth elements coelute by reverse-phase liquid chromatography, and that the affinity column effectively removes untagged peptides. This was confirmed by an additional experiment in which the peptide digest was mixed with a large excess of trypsin-digested human serum albumin before being added to the affinity column; the results were comparable to Figure 3.

Thus element-coded affinity tags based on rare earth−DOTA chelates have the necessary properties for the study of more complicated systems. Element-coded tags also have other properties that may prove useful in applications: all the elements exhibit characteristic X-rays whose energies behave systematically, many have redox potentials accessible under normal conditions, others are paramagnetic or have radioisotopes with useful properties. This alternative to biotin−avidin tags may find applications beyond the study of complex mixtures of proteins.

ACKNOWLEDGMENT

We thank Susan Lee, Sarah Cheal, Carlito Lebrilla, and Nick Young for helpful discussions. This work was supported by Research Grants GM25909 and CA16861 to C.F.M. from the National Institutes of Health. The LCQ mass spectrometer was purchased with support from NIH Shared Instrumentation Grant RR014701.

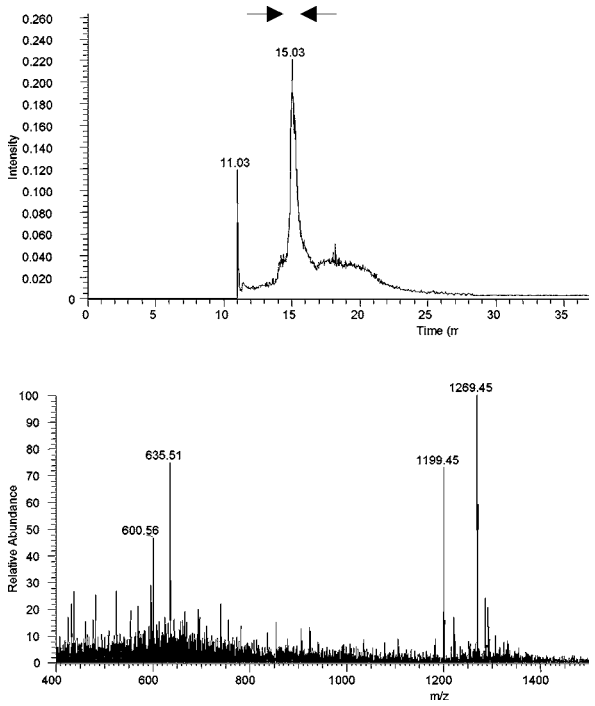


Figure 3. LC-MS of trypsinized, affinity-purified peptide mixture (originally 0.83 Y:1.0 Tb mole ratio in the presence of 100-fold excess untagged peptides, which were removed by the affinity column). The top panel depicts the total ion count versus time; the arrows in the top panel mark the time period over which the one-dimensional mass spectrum in the bottom panel is averaged, indicating that trypsin fragments of the Y- and Tb-labeled peptide, which differ by 70 mass units, coeluted from the LC column. The mass-to-charge ratio (*m*/*z*) of protonated C(AcBD-Tb)NSLK is 1269.45; protonated C(AcBD-Y)NSLK is 1199.45 *m*/*z*. Doubly protonated ions of the Tb- and Y-labeled peptides appear at 635.51 and 600.56 *m*/*z*, respectively.

Supporting Information Available: Experimental details. This material is available free of charge via the Internet at http://pubs.acs.org.

LITERATURE CITED

(1) Chapman, J. R., Ed. (2000) Mass Spectrometry of Proteins and Peptides. In *Methods in Molecular Biology (Totowa, New Jersey)* Vol. 146, pp 1−538, Humana, Totowa, NJ.

(2) Roepstorff, P. (1984) Proposal for a common nomenclature for sequence ions in mass spectra of peptides. *Biomed. Mass Spectrom. 11*, 601.

(3) Hunt, D. F., Yates, J. R., III, Shabanowitz, J., Winston, S., and Hauer, C. R. (1986) Protein sequencing by tandem mass spectrometry. *Proc. Natl. Acad. Sci. U. S. A. 83* (17), 6233−6237.

(4) Shevchenko, A., Chernushevich, I., Ens, W., Standing, K. G., Thomson, B., Wilm, M., and Mann, M. (1997) Rapid 'de Novo' peptide sequencing by a combination of nanoelectrospray, isotopic labeling and a quadrupole/time-of-flight mass spectrometer. *Rapid Commun. Mass Spectrom. 11* (9), 1015−1024.

(5) Ranish, J. A., Yi, E. C., Leslie, D. M., Purvine, S. O., Goodlett, D. R., Eng, J., and Aebersold, R. (2003) The study of macromolecular complexes by quantitative proteomics. *Nat. Genet. 33* (3), 349−355.

(6) Aebersold, R., and Mann, M. (2003) Mass spectrometry-based proteomics [Review]. *Nature 422* (6928), 198−207.

(7) Patterson, S. D., and Aebersold, R. H. (2003) Proteomics: the first decade and beyond [Review]. *Nat. Genet. 33* (Suppl S), 311−323.

(8) Flory, M. R., Griffin, T. J., Martin, D., and Aebersold, R. (2002) Advances in quantitative proteomics using stable isotope tags. *Trends Biotechnol. 20* (12, Suppl.), S23−S29.

(9) Gygi, S. P., Rist, B., Griffin, T. J., Eng, J., and Aebersold, R. (2002) Proteome analysis of low-abundance proteins using multidimensional chromatography and isotope-coded affinity tags. *J. Proteome Res. 1* (1), 47−54.

(10) Goodlett, D. R., Keller, A., Watts, J. D., Newitt, R., Yi, E. C., Purvine, S., Eng, J. K., Von Haller, P., Aebersold, R., and Kolker, E. (2001) Differential stable isotope labeling of peptides for quantitation and de novo sequence derivation. *Rapid Commun. Mass Spectrom. 15* (14), 1214−1221.

(11) Gygi, S. P., Rist, B., Gerber, S. A., Turecek, F., Gelb, M. H., and Aebersold, R. (1999) Quantitative analysis of complex protein mixtures using isotope-coded affinity tags. *Nat. Biotechnol. 17* (10), 994−999.

(12) Smith, R. D., Anderson, G. A., Lipton, M. S., Pasa-Tolic, L., Shen, Y., Conrads, T. P., Veenstra, T. D., and Udseth, H. R. (2002) An accurate mass tag strategy for quantitative and high-throughput proteome measurements. *Proteomics 2* (5), 513−523.

(13) Goshe, M. B., Veenstra, T. D., Panisko E. A., Conrads, T. P., Angell N. H., and Smith, R. D. (2002) Phosphoprotein isotope-coded affinity tags: application to the enrichment and identification of low-abundance phosphoproteins. *Anal. Chem. 74* (3), 607−616.

(14) Goshe, M. B., Conrads, T. P., Panisko, E. A., Angell, N. H., Veenstra, T. D., and Smith, R. D. (2001) Phosphoprotein isotope-coded affinity tag approach for isolating and quantitating phosphopeptides in proteome-wide analyses. *Anal. Chem. 73* (11), 2578−2586.

(15) Conrads, T. P., Alving, K., Veenstra, T. D., Belov, M. E., Anderson, G. A., Anderson, D. J., Lipton, M. S., Pasa-Tolic, L., Udseth, H. R., Chrisler, W. B., Thrall, B. D., and Smith, R. D. (2001) Quantitative analysis of bacterial and mammalian proteomes using a combination of cysteine affinity tags and 15N-metabolic labeling. *Anal. Chem. 73* (9), 2132−2139.

(16) Conrads, T. P., Anderson, G. A., Veenstra, T. D., Pasa-Tolic, L., and Smith, R. D. (2000) Utility of Accurate Mass Tags for Proteome-Wide Protein Identification. *Anal. Chem. 72* (14), 3349−3354.

(17) Yu, L.-R., Johnson, M. D., Conrads, T. P., Smith, R. D., Morrison, R. S., and Veenstra, T. D. (2002) Proteome analysis of camptothecin-treated cortical neurons using isotope-coded affinity tags. *Electrophoresis 23* (11), 1591−1598.

(18) Corneillie, T. M., Whetstone, P. A., Fisher, A. J., and Meares, C. F. (2003) A rare earth-DOTA-binding antibody: Probe properties and binding affinity across the lanthanide series. *J. Am. Chem. Soc. 125* (12), 3436−3437.

(19) Hall, M. P., Ashrafi, S., Obegi, I., Petesch, R., Peterson, J. N. and Schneider, L. V. (2003) 'Mass defect' tags for biomolecular mass spectrometry. *J. Mass Spectrom. 38*, 809−816.

(20) Moi, M. K., Meares, C. F., and DeNardo, S. J. (1988) The Peptide Way to Macrocyclic Bifunctional Chelating Agents: Synthesis of 2-(*p*-Nitrobenzyl)-1,4,7,10-tetraazacyclododecane-*N*,-*N*′,*N*″,*N*‴-tetraacetic Acid and Study of Its Yttrium (III) Complex. *J. Am. Chem. Soc. 110*, 6266−6267.

(21) Meares, C. F., Moi, M. K., Diril, H., Kukis, D. L., McCall, M. J., Deshpande, S. V., DeNardo, S. J., Snook, D., and Epenetos, A. A. (1990) Macrocyclic Chelates of Radiometals for Diagnosis and Therapy. *Br. J. Cancer (Supplement) 62*, 21−26.

(22) McCall, M. J., Diril, H., and Meares, C. F. (1990) Simplified Method for Conjugating Macrocyclic Bifunctional Chelating Agents to Antibodies via 2-Iminothiolane. *Bioconjugate Chem. 1*, 222−226.

(23) Renn, O., and Meares, C. F. (1992) Large-Scale Synthesis of the Bifunctional Chelating Agent 2-(*p*-Nitrobenzyl)-1,4,7,-10-tetraazacyclododecane-*N*,*N*′,*N*″,*N*‴-tetraacetic Acid, and the Determination of Its Enantiomeric Purity by Chiral Chromatography. *Bioconjugate Chem. 3*, 563−569.

(24) Takenouchi, K., Tabe, M., Watanabe, K., Hazato, A., Kato, Y., Shionoya, M., Koike, T., Kimura, E. (1993) Novel Pendant-Type Macrocyclic Bifunctional Chelating Agents. (Carboxymethyl)amino Derivatives of 2-(4-Nitrobenzyl)-1,4,7,10-tetraazacyclo-dodecane-*N*,*N*′,*N*″,*N*‴-tetraacetic Acid and Their Complex Formation with Yttrium(III). *J. Org. Chem. 58* (24), 6895−6899.

BC034150L

Supporting Information for

Element-Coded Affinity Tags for Peptides and Proteins †

Paul A. Whetstone, Nathaniel G. Butlin, Todd M. Corneillie and Claude F. Meares*

Abbreviations: BAD, ((S)-2-(4-(2-bromo-acetamido)-benzyl)-DOTA); C(AcBD)NSLKLAT-amide, peptide CNSLKLAT-amide with acetamidobenzyl-DOTA group attached to cysteine; C(CM)NSLKLAT-amide, C(carboxymethyl)NSLKLAT-amide; CID, collision-induced dissociation; CV, column volume; DIEA, *N,N*-diisopropylethylamine; DOTA, 1,4,7,10-tetraazacyclododecane-*N*,*N*′,*N*″,*N*‴-tetraacetic acid; DTPA, diethylenetriaminepentaacetic acid; HOBt, 1-hydroxybenzotriazole; PyBOP, benzotriazole-1-yl-oxytrispyrrolidinophosphonium hexafluorophosphate; TIS, triisopropylsilane.

Reagents

All reagents and solvents were the purest commercially available and used without further purification. Precautions were taken to minimize contamination with adventitious metal ions. All the laboratory glassware was washed with mixed acid solution and rinsed copiously with 18 MΩ cm H_2O. Trace-metal grade HCl was used for acid washing and as a reagent. All plasticware was washed in 3 M HCl overnight and thoroughly rinsed. Glassware was oven dried overnight and cooled under an argon atmosphere.

All buffer reagents were biochemical grade or higher. Glacial acetic acid (EM Scientific) and trifluoroacetic acid (Acros) were used as received. Triethylamine (EM Scientific), sodium chloride and potassium phosphate mono- and dibasic (Fisher Scientific) were >99.5% and used as received. Antibody 2D12.5, purified from hybridoma cell culture, was a gift from Dr David Goodwin, Palo Alto Veterans Administration Hospital (Palo Alto, CA).

Chelate Synthesis

(S)-2-(p-aminobenzyl)-1,4,7,10-tetraazacyclododecane-N,N',N'',N'''-tetraacetic acid tetra-tertbutyl ester (ABD-tBu$_4$) was synthesized as indicated schematically in Supplementary Scheme 1 according to previously published methods[1-3].

(S)-2-(p-bromoacetamidobenzyl)-1,4,7,10-tetraazacyclododecane- N,N',N'',N'''-tetraacetic acid tetra-tertbutyl ester (BAD-tBu$_4$). To remove adventitious metals, all glassware was soaked in mixed acids overnight and rinsed with double-deionized H_2O.

In a fume hood, 136 μL of bromoacetyl bromide (FW 199.85, 0.682 mmol) was added to 2mL of CH_2Cl_2 in a 25 mL round-bottom flask under an argon atmosphere, and the solution was chilled to 0 °C on ice. Under argon, 250 mg of ABD-tBu_4 (FW 733.50, 0.341 mmol) was dissolved in 5 mL of CH_2Cl_2 and cannulated into a 10 mL addition funnel, to which 107 μL of DIEA (FW 129.15, 0.682 mmol) was added. With stirring, the solution of ABD-tBu_4 was added dropwise over 5 min to the bromoacetyl bromide solution. The mixture was stirred for an additional 5 min and then extracted with an aqueous basic solution (0.1% DIEA in H_2O) until the aqueous fractions remained basic. The CH_2Cl_2 layer was then dried over Na_2SO_4 and solvent was removed under reduced pressure to quantitatively yield 290 mg of BAD-tBu_4 as a light orange solid (ESI-MS *m/z* calc'd (MH+): 854.43, 856.43. Found: 854.42, 856.43.

Peptide Synthesis

Synthesis of the hemagglutinin-based peptide CNSLKLAT-amide was carried out using standard Fmoc-amino acid solid phase techniques [4-10]. Briefly, the peptide was extended on Rink Amide AM resin (NovaBiochem, San Diego, CA) in a batch-wise manner; Fmoc was removed from resin-bound N-terminal amines with a 20% piperidine solution in DMF, and amide couplings were subsequently performed by addition of a solution containing 3 molar equivalents of protected amino acid, HOBt, PyBOP and DIEA in DMF.

The N-terminal cysteine was added with methoxytrityl protection of the sulfhydryl, which was later selectively removed with a 1% CF_3COOH solution in CH_2Cl_2. After sulfhydryl deprotection, the resin was washed, dried and divided into two lots. Each lot

was again pre-swollen in CH_2Cl_2, washed with DMF, and then a solution containing 2 molar equivalents of DIEA and either iodoacetic acid or BAD-tBu_4 in DMF was added. The resin was agitated at room temperature by bubbling argon through the reaction bed; after 2 h, the reaction was deemed complete when an aliquot of resin tested negatively for free sulfhydryl[11-13]. The N-terminal Fmoc was removed, the resin washed, dried, and cleaved at room temperature over 2 h with 95% CF_3COOH, 2.5% TIS, 2.5% H_2O. After CF_3COOH removal under reduced pressure, 2 mL of Et_2O was added to the flask, and the solution was sonicated until it resembled a colloidal suspension. The Et_2O slurry was extracted with H_2O four times; H_2O extracts of each peptide were combined and washed with Et_2O four times. The aqueous portions were then solvent reduced, passed through a 5 μm filter to remove particulate contamination, and purified by reverse phase HPLC to yield C(carboxymethyl)NSLKLAT-amide or C(acetamidobenzylDOTA)NSLKLAT-amide in yields >98%. High-performance liquid chromatography was carried out on a Rainin HPXL system (Rainin Instruments,Woburn, MA) equipped with titanium self-washing pump heads. Solvents were mixed using a Dynamax titanium dual-chamber mixer. UV absorbance was measured at 254 or 280 nm. The HPLC system was controlled by Dynamax software on a Macintosh Plus computer. Analytical reversed-phased HPLC was performed at room temperature at 1 mL/min with an Alltech Altima 4.6 × 250 mm column and 4.6 × 7.5 mm guard column (Alltech Associates, Inc, Deerfield, IL). Preparative RP-HPLC was performed at room temperature at 6mL/min with an Alltech Alltima 22 × 250 mm column. The running solvents were CH_3CN containing 0.075% CF_3COOH and H_2O containing 0.1% CF_3COOH.

Metallation of peptide-chelates

Using a 0.1 M NH_4OAc, pH 6.1 buffer, 100 μL aliquots of a 1 mM solution C(AcBD)NSLKLAT-amide peptide were combined with 10 μL of 100 mM solutions of either $TbCl_3$, YCl_3, $EuCl_3$, or $LuCl_3$. All were incubated at 37 °C for 2 h, after which 10 μL of a 0.1 M solution of DTPA in 0.1 M NH_4OAc, pH 6.1 buffer was added to the solution, incubated 30 min at 37 °C and then purified on SepPak Plus C-18 (Waters, Milford, MA) cartridges. SepPak Plus C18 purification was done according to established protocols. Briefly, cartridges were equilibrated with 10 mL CH_3CN followed by 10 mL 0.1 M NH_4OAc buffer, pH 6.1 at approximate flow-rates of 2 mL/min. Metallated peptide-chelate solutions (in aqueous NH_4OAc) were passed through the cartridge and the cartridge was again washed with 10 mL of NH_4OAc buffer, followed by 10 mL of deionized H_2O. The analytes were eluted with 2 mL of a 1:1 CH_3CN/H_2O solution. Using the reported extinction coefficient of the UV absorption maximum at 244 nm[14], the concentration of each metallated peptide-chelate was measured both before and after application to the SepPak cartridge to verify complete elution. Mass spectrometric analysis was done to verify that the peptide-chelates had been fully metallated.

Trypsinization of peptides

A mixture containing carboxymethylated-peptide as well as Tb- and Y-metallated peptide-chelates was prepared according to Table S1. Solvent was removed under reduced pressure, and the residue was resuspended in 100 μL of 50 mM NH_4HCO_3 buffer, pH 8.0. 10 μg sequencing grade modified porcine trypsin was reconstituted in 10 μL of resuspension buffer (Promega), heated at 30 °C for 15 min, and added to the peptide

mixture. The solution was mixed by pipetting, and incubated at 37 °C for 8 h, at which time mass spectrometry indicated the complete conversion of the carboxymethylated-peptide parent to the expected tryptic fragments.

Table S1 Stoichiometry of peptide mixture trypsinization reaction.

Peptide	nmol	MW	μg
C(AcBD-Tb)NSLKLAT	1.0	1552.6	1.6
C(AcBD-Y)NSLKLAT	0.8	1482.6	1.2
C(CM)NSLKLAT	100.0	906.4	90.6

Mass Spectroscopy

All mass spectrometry was performed on a ThermoFinnigan LCQ Deca electrospray ion-trap instrument. Before LC-MS experiments were performed, the instrument was calibrated according to the manufacturers protocol, and was tuned to maximize signal of the C(CM)NSLKLAT peptide. LC-MS was performed at room temperature at 20 μL/min with a Vydac microbore 218TP51 column. The running solvents were 0.01% CF_3COOH in H_2O and 0.01% CF_3COOH in CH_3CN. Samples were injected at 3%, gradient ramped to 30% over 20 min, with peptide-chelates eluting at 9% CH_3CN.

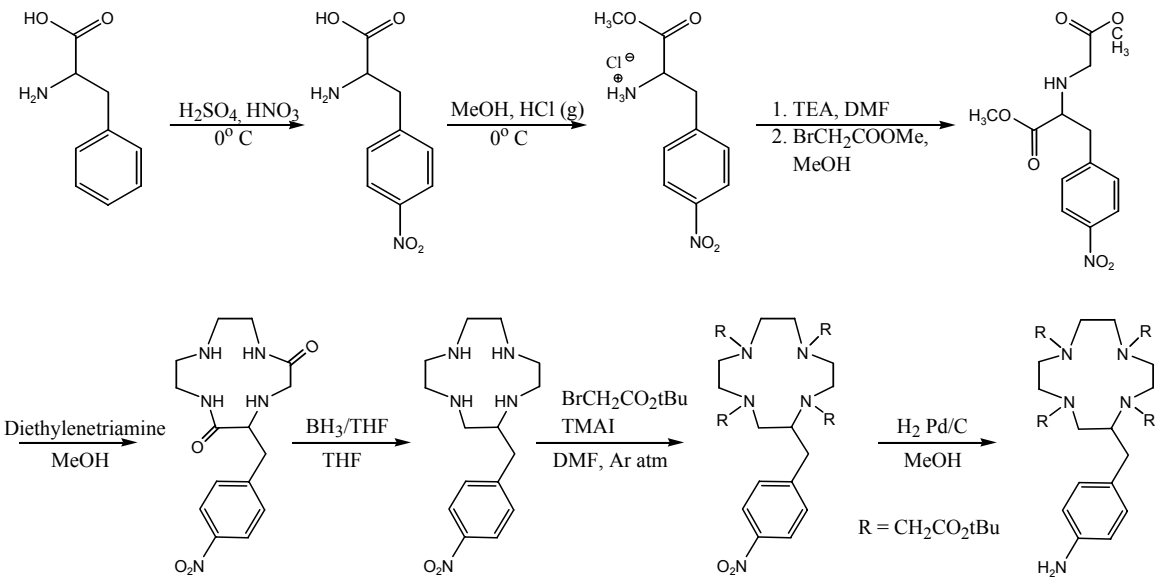
Preparation of 2D12.5 Affinity Column

Antibody 2D12.5 (18 mg) was dialyzed into 3 mL of PBS, pH7.2, and combined with 5 mL of Aminolink slurry (Pierce). The antibody and column material were incubated together overnight at 4 °C with end-over-end rocking. The following morning 200 μL of 5 M $NaCNBH_3$ in 0.01 M NaOH was added to the slurry and incubated for 8 h at 4 °C. The coupled gel was then washed with 5 column volumes of PBS and 3 column volumes of 1.0 M Tris-HCl (pH = 7.4), and incubated and reduced with $NaCNBH_3$ in a similar manner. Coupling efficiency was >90% as determined by A_{280nm} measurements for the

antibody (ε = 1.32 mL/mg). The column material was stored in 10 mM TBS (pH = 7.4) with 0.01% NaN_3 and 1 mM EDTA at 4 °C.

Affinity Purification of Tagged Peptides

All buffer solutions were filter sterilized prior to use with the 2D12.5 affinity media. Digested and tagged test peptide (1 nmol) was resuspended with a trypsin-digested solution of human serum albumin (HSA, 10 nmol). The serine protease inhibitor phenylmethylsulfonyl fluoride (PMSF) was added to a final concentration of 1.0 mM. The peptide solution was loaded onto a 500 µL 2D12.5 minicolumn pre-equilibrated with 10 mM Et_3NHOAc, pH = 7.1 (Buffer A). The minicolumn was washed with 6 column volumes (CVs) of Buffer A, 7 CVs of 1 M NaCl in 10 mM Et_3NHOAc, 1 CV of Buffer A, 7 CVs of 0.5% HOAc (pH = 2.8), 1 CV of Buffer A, 7 CVs of 0.1% Et_3N (adjusted to pH = 10.1 with HOAc), 1 CV of Buffer A, and 7 CVs of 30% CH_3CN v/v in Buffer A. The isolated tagged peptide fragment was eluted in 8 column volumes of aqueous 20% CH_3CN containing 0.1% CF_3COOH. LC-MS analysis of the eluent is shown in Figure 3.



Supplementary scheme 1 Schematic illustration of the synthetic route to *(S)-2-(p-aminobenzyl)-1,4,7,10-tetraazacyclododecane-N,N',N'',N'''-tetraacetic acid tetra-tertbutyl ester.*

1. Moi, M.K., Meares, C.F., and DeNardo, S.J.. (1988) The Peptide Way to Macrocyclic Bifunctional Chelating Agents: Synthesis of 2-(p-Nitrobenzyl)-1,4,7,10-tetraazacyclododecane-N,N',N'',N'''-tetraacetic Acid and Study of Its Yttrium(III) Complex. *Journal of the American Chemical Society* ***110****(18),* 6266-6267.
2. Takenouchi, K., Tabe, M., Watanabe, K., Hazato, A., Kato, Y., Shionoya, M., Koike, T., and Kimura, E. (1993) Novel Pendant-Type Macrocyclic Bifunctional Chelating Agents - (Carboxymethyl)Amino Derivatives of 2-(4-Nitrobenzyl)-1,4,7,10-Tetraazacyclo-Dodecane-N,N',N'',N'''-Tetraacetic Acid and Their Complex Formation with Yttrium(III). *Journal of Organic Chemistry* ***58****(24),* 6895-6899.
3. Corson, D.T. and Meares, C.F. (2000) Efficient multigram synthesis of the bifunctional chelating agent (S)-1-p-isothiocyanatobenzyl-diethylenetetraminepentaacetic acid. *Bioconjugate Chemistry* ***11****(2)*, 292-299.
4. Parker, C.E., and Gould K.G. (1996) Influenza A Virus - A model for Viral Antigen Presentation to Cytotoxic T Lymphocytes [Review]. *Seminars in Virology 7(1),* 61-73.
5. Rajnavolgyi, E., Horvath, A., Gogolak, P., Toth, G.K., Fazekas, G., Fridkin, M. and Pecht, I. (1997) Characterizing Immunodominant and Protective Influenza Hemagglutinin Epitopes by Functional Activity and Relative Binding to Major Histocompatibility Complex Class II Sites. *European Journal of Immunology* ***27****(12),* 3105-3114.
6. Simon, A., Simon, I., and Rajnavolgyi, E. (2002) Modeling MHC class II molecules and their bound peptides as expressed at the cell surface. *Molecular Immunology* ***38****(9),* 681-687.
7. Natarajan, S.K., Assadi, M., and Sadegh-Nasseri, S. (1999) Stable peptide binding to MHC class II molecule is rapid and is determined by a receptive conformation shaped by prior association with low affinity peptides. *Journal of Immunology* ***162****(7),* 4030-4036.

8. *Fmoc solid phase peptide synthesis: a practical approach*. (Chan, W.C. and White, P.D., Ed.) (2000) Oxford University Press, New York.
9. Atherton, E. (1989) *Solid phase peptide synthesis: a practical approach*. IRL Press, New York.
10. Stewart, J.M. and Dillaha, J. (1984) *Solid phase peptide synthesis*. Pierce Chemical Co., Rockford, Ill
11. Walsmley, T., Abernethy, M.H. and Fitzgerald, H.P. (1987) Effects of Daylight on the Reaction of Thiols with Ellman's Reagent. *Clinical Chemistry **33***, 1928-1931.
12. Riddles, P.W., Blakeley, R.L. and Zerner, B. (1983) Reassessment of Ellman's Reagent. *Methods in Enzymology **91***, 49-60.
13. Ellman, G.L. (1959) Tissue Sulfhydryl Groups. *Arch. Biochem. Biophys.* ***82***, 70-77.
14. Yuzuri, T., Wada, H., Suezawa, H. and Hirota, M. (1994) Anomalous Polar Substituent Effect on N-15 NMR Chemical Shifts of Aniline Derivatives - Acylanilides and Related Compounds. *Journal of Physical Organic Chemistry 7(6),* 280-286.

N-(3-Trifluoroethanesulfonyloxypropyl)anthraquinone-2-carboxamide: A New Heterobifunctional Reagent for Immobilization of Biomolecules on a Variety of Polymer Surfaces

P. Kumar, S. K. Agarwal, and K. C. Gupta*

Nucleic Acids Research Laboratory, Institute of Genomics and Integrative Biology, Mall Road, Delhi University Campus, Delhi 110 007, India. Received October 28, 2003

A new heterobifunctional reagent, *N*-(3-trifluoroethanesulfonyloxypropyl)anthraquinone-2-carboxamide (NTPAC) has been developed, useful for making bioconjugates and immobilization of biomolecules, viz., oligonucleotides, peptides, proteins, etc., on a variety of carbon-containing solid surfaces. Its trifluoroethanesulfonate ester group reacts with aminoalkyl or mercaptoalkyl functions present in biomolecules, and the anthraquinone structure reacts with a variety of carbon-containing polymers under ultraviolet irradiation (365 nm). The reagent has been used in two ways. First, the reagent, NTPAC, was first brought in contact with the above said supports and exposed to long wavelength ultraviolet light (365 nm), thereby generating active trifluoroethanesulfonate ester functions on the support, which subsequently react with appropriate mercaptoalkyl- or aminoalkyl-containing biomolecules to fix them on the supports. In another route, the proposed reagent was allowed to react first with proteins or 5′-aminoalkyl- or mercaptoalkyl-modified oligonucleotides to form the appropriate biomolecule−anthraquinone conjugate, which was then brought in contact with a variety of carbon-containing polymers, viz., modified controlled pore glass (CPG), modified glass microslides, cross-linked polystyrene, nylon, cross-linked polysaccharides, polypropylene (PP), polyethylene (PE), etc., and exposed to long wavelength ultraviolet light (365 nm), resulting in immobilization of the conjugates on the support. Both of the routes work satisfactorily and we could successfully immobilize a number of enzymes and modified oligonucleotides on a variety of supports.

INTRODUCTION

A large number of homobifunctional and heterobifunctional reagents (*1*−*7*) are known in the literature to introduce modifications in proteins, nucleic acids, and other biomolecules. In the case of homobifunctional reagents, in almost all cases, the two reactive groups are identical, while the two reactive groups are dissimilar in heterobifunctional reagents. These reagents have been shown to induce cross-linking intramolecularly between two locales within a macromolecule and intermolecularly between two molecules. Intramolecular cross-linking has been used to increase the stability of proteins against thermal and mechanical denaturation, to determine the distances between two reactive groups, and to detect different conformational states. Intermolecular cross-linking has been employed to characterize the nature and extent of protein−protein interactions, to couple two or more different proteins. The unique advantage of heterobifunctional reagents having differential reactivity of the two different functional groups is that cross-linking can be controlled both selectively and sequentially. These reagents find a variety of applications in modern molecular biology. In recent years, the high-density oligonucleotide microarrays have emerged as an important tool for molecular biology studies. Arrays of short synthetic oligonucleotides, peptides, and proteins have been used for various applications (*8*−*14*), viz., drug development, DNA sequencing, medical diagnostics, nucleic acid-ligand binding studies, DNA computing, etc. Basically, two approaches are being followed for the construction of oligonucleotide arrays. In one approach, the oligonucleotides are directly synthesized on the plane surface at a preselected position following conventional chemical methods or photolithography or ink-jet methods (*15*). Another method, which is gaining popularity, is based on fixing prefabricated oligonucleotides, peptides, and proteins on a solid surface (*16*). This method offers great flexibility and can accommodate different chemistries as well as surfaces of choice. Two important factors which affect the quality of microarrays (microchip) fabricated by the latter method depend on the solid surface used and chemistry employed for fixing of oligonucleotides and other biomolecules. A large number of chemical methods (*17*−*20*) and surfaces (*21*−*23*) have been reported for this purpose. Usually, the polymer surface is first modified, to have the desired reactive functional groups, using appropriate reagents, and then peptides or proteins and premodified oligonucleotides are immobilized on the activated surface employing suitable reagents or activators. Thus, one would require a number of steps and reagents to immobilize oligonucleotides or peptides/proteins of choice on a solid surface. We describe here a general method for the immobilization of presynthesized modified oligonucleotides or peptides/proteins on a variety of surfaces, e.g., glass, polypropylene (PP), polyethylene (PE), nylon, and polysaccharide (Sepharose CL-4B), in regioselective fashion using a new heterobifunctional reagent, NTPAC. The reagent has been used in two ways.

* To whom correspondence should be addressed. Tel.: +91 11 27662491; Fax: +91 11 27667471; Email: kcgupta@igib.res.in.

10.1021/bc034198z CCC: $27.50 © 2004 American Chemical Society
Published on Web 12/30/2003

In the first route, the reagent, NTPAC, is brought in contact with a variety of carbon-containing polymers, viz., modified controlled pore glass (CPG), nylon, cross-linked polysaccharides (Sepharose CL-4B), polypropylene (PP), and polyethylene (PE), and exposed to UV light (365 nm), thereby generating the reactive trifluoroethanesulfonate ester functions on the support, enabling them to react with mercaptoalkyl or aminoalkyl group-containing ligands in the subsequent step. In the second route, the anthraquinone−ligand conjugate is formed by allowing the reagent, NTPAC, to react with an appropriate ligand, viz., peptides (having a free α-amino group), proteins, and 5′-aminoalkyl- or mercaptoalkyl-modified oligonucleotides, and the resulting conjugate in the subsequent step reacts with a carbon-containing support under UV irradiation (365 nm). Both of the routes work satisfactorily, and we could successfully immobilize a number of enzymes or modified oligonucleotides on a variety of supports using the proposed heterobifunctional reagent.

EXPERIMENTAL PROCEDURES

Materials. All the reagents used in the present investigation were purified prior to their use. 2,2,2-Trifluoroethanesulfonyl chloride (tresyl chloride), anthraquinone-2-carboxylic acid, 3-aminopropan-1-ol, and dicyclohexylcarbodiimide (DCC) were procured from Aldrich Chemical Co. (St. Louis, MO). FAM-phosphoramidite was obtained from Applied Biosystems, Inc. (Foster City, CA). All other reagents and chemicals were procured locally. All the reactions were carried out in an inert atmosphere unless otherwise specified.

Photochemical Reactions. Photochemical reaction of anthraquinone was carried out in a photochemical chamber (Gautam Enterprises, Delhi, India) attached with long wavelength tubes (365 nm) and a variable energy regulator.

***N*-(3-Hydroxypropyl)anthraquinone-2-carboxamide 2.** To a solution of anthraquinone-2-carboxylic acid (2.0 mmol) **1** and *N*-hydroxysuccinimide (2.5 mmol) in anhydrous *N*,*N*-dimethylformamide (15 mL) was added dicyclohexylcarbodiimide (DCC) (2.5 mmol). The reaction was allowed to stir for 3 h at room temperature. After completion of reaction, 3-aminopropanol (3.0 mmol) and triethylamine (3.0 mmol) were added dropwise at room temperature. The reaction was further allowed to stir for 6 h at room temperature. Then the reaction mixture was filtered to remove dicyclohexylurea and the filtrate concentrated under vacuum to a syrupy mass. The residual mass was dissolved in ethyl acetate (100 mL) and washed with aq 5% sodium bicarbonate (2 × 25 mL), 5% citric acid (2 × 25 mL), and saturated solution of sodium chloride (1 × 25 mL), respectively. The organic phase was collected, dried over anhydrous sodium sulfate, and after filtration, concentrated under vacuum to obtain *N*-(3-hydroxypropyl)anthraquinone-2-carboxamide **2** as solid material in 90% yield. The compound was further characterized by ^{1}H NMR: $CDCl_3$ δ 1.65 (m, 2H, CH_2), 3.2−3.45 (m, 4H, 2 × CH_2), 7.5−8.5 (m, 8H, ArH).

***N*-(3-Trifluoroethanesulfonyloxypropyl)anthraquinone-2-carboxamide (NTPAC) 3.** *N*-(3-Hydroxypropyl)anthraquinone-2-carboxamide (1.0 mmol) **2** was taken up in anhydrous dichloromethane (10 mL) containing triethylamine (1.2 mmol). The reaction mixture was cooled in an ice-bath and 2,2,2-trifluoroethanesulfonyl chloride (tresyl chloride) (1.2 mmol) added dropwise. After 2 h, the solution was filtered in an inert atmosphere to remove suspended ammonium chloride, and the filtrate was concentrated under vacuum and further dried in a desiccator to obtain the title compound **3** in almost quantitative yield as a syrupy material. Attempts were not made to crystallize the syrupy material. The reagent was characterized by its MALDI-TOF (456, M + H^+; matrix: 2,5-dihydroxybenzoic acid).

Oligonucleotides and Their 5′-Modified Analogues. Oligonucleotides, viz., $H_2N(CH_2)_5O-PO_2$-d(ACG TAG CCT TTA GTA CCT TT), $HS(CH_2)_6O-PO_2$-d(ACG TAG CCT TTA GTA CCT TT), and FAM-d(AAA GGT ACT AAA GGC TAC GT), were synthesized on Pharmacia.LKB Gene Assembler Plus at 0.2 μmol scale following standard protocol (*24*). To introduce a mercaptoalkyl or aminoalkyl group at 5′-end of these oligomers, the last coupling was performed with reagent I (*25*) and II (*26*), respectively, in an analogous manner, the normal nucleoside-phosphoramidites were coupled. During the final deprotection step, oligomers with desired functionality were obtained. In case of reagent I, aq ammonium hydroxide containing 0.1 M DTT was used for 16 h at 55 °C. After concentration, the oligomers were dissolved in water (100 μL) and desalted on a reverse phase silica gel column. The oligomers were eluted with 30% acetonitrile and concentrated in a speed vac. Oligomers with free sulfhydryl groups were obtained. Similarly, oligomers with the last coupling performed with reagent II were deprotected in aq ammonium hydroxide (30%), 16 h at 55 °C. Desalting on RP-silica gel gave 5′-aminoalkylated oligonucleotides.

Immobilization of Ligands via Route A. To demonstrate the utility of the proposed reagent **3** for immobilization of biomolecules on a variety of surfaces, a number of enzymes including 5′-modified oligonucleotides were immobilized on a variety of surfaces. In a typical experiment, a few pieces of polypropylene (PP) film (1 cm^2) were dipped in a solution of the reagent **3** (0.5 mL, 0.1 M in dichloromethane). The solvent was evaporated by keeping the reaction vial in air, and the dried pieces of PP film were exposed to UV light (365 nm) for 30 min in a UV chamber. Then the films were washed several times with dry dichloromethane (5 × 5 mL) and dried under vacuum. The activated PP films were then treated with a solution of alkaline phosphatase solution (1 mL) (prepared by dissolving 10 mg enzyme/mL in 0.1 M phosphate buffer, pH 8.0) for 1 h at 37 °C. After the reaction, the films were washed with 0.1 M phosphate buffer, pH 8.0 (3 × 1 mL), and finally with double-distilled water (2 × 1 mL) followed by drying at room temperature under vacuum. These strips were analyzed by treating them with the substrate of alkaline phosphatase (0.001 M *p*-nitrophenyl phosphate disodium salt in 0.1 M Tris buffer, pH 8.0) and subsequently reading the absorbance of the released chromophore (*p*-nitrophenoxide ion) in the solution taking 0.001 M *p*-nitrophenyl phosphate in 0.1 M Tris buffer, pH 8.0, as control followed by determination of activity of the immobilized enzyme. Similarly, other enzymes were immobilized on a variety of solid surfaces and their activities were calculated.

In the case of oligonucleotides (mercaptoalkyl and aminoalkylated), the immobilized oligomers on modified glass beads were hybridized with fluorescent-labeled complementary oligonucleotide. Subsequently, the beads were analyzed under a fluorescent microscope.

Immobilization of Biomolecules via Route B. In this method, the oligomer, d(ACG TAG CCT TTA GTA CCT TT) (2.0 O.D. A_{260}), with aminoalkyl and mercaptoalkyl groups at the 5′-terminus, in 0.1 M phosphate buffer, pH 8.5, was reacted with an excess of the reagent **3** (0.2 μmol) dissolved in dimethylformamide (100 μL). The suspension was agitated at room temperature for 1

Table 1. Immobilization of Ligands on a Variety of Polymeric Surfaces[a]

	support-R + ligand				R-ligand + support			
ligand	PP (u/cm^2)	PE (u/cm^2)	nylon (u/cm^2)	sepharose (u/mg)	PP (u/cm^2)	PE (u/cm^2)	nylon (u/cm^2)	sepharose (u/mg)
peroxidase	0.144	0.165	0.0017	0.53	0.200	0.124	0.0033	0.34
alk. phosphatase	0.0028	0.0034	0.00027	0.0018	0.0041	0.0027	0.0004	0.0021
$NH_2(CH_2)_5$ODMTr	3.7 pmol/cm^2	1.9 pmol/cm^2	–	–	–	–	–	–
$HS(CH_2)_6$ODMTr	4.1 pmol/cm^2	1.8 pmol/cm^2	–	–	–	–	–	–

[a] R = reagent, NTPAC; u = units.

h and then concentrated in a vacuum. The dried residue was dissolved in double-distilled water (25 μL), and the mixture was centrifuged to remove the excess reagent **3**. The decanted solution was charged with lithium chloride to make 0.2 M final concentration and C-8-controlled pore glass beads (500A) (20 mg). Then the suspended beads were kept under UV light (365 nm) for 30 min at room temperature. After being washed with water, the beads were suspended in a solution of complementary oligomer d(AAA GGT ACT AAA GGC TAC GT) (2.0 O.D. A_{260}) labeled with FAM dye at the 5′-terminus dissolved in 0.1 M phosphate buffer, pH 7.1, containing sodium chloride (1 M). The suspension was warmed to 70 °C followed by slow cooling to room temperature and then to 10 °C. Subsequently, the beads were washed several times with 0.1 M phosphate buffer containing 1 M sodium chloride, and the beads were visualized under a fluorescent microscope.

Similarly, enzymes were reacted with the reagent followed by immobilization on a variety of surfaces. Their activity was measured using their respective substrates in solution as described in route A.

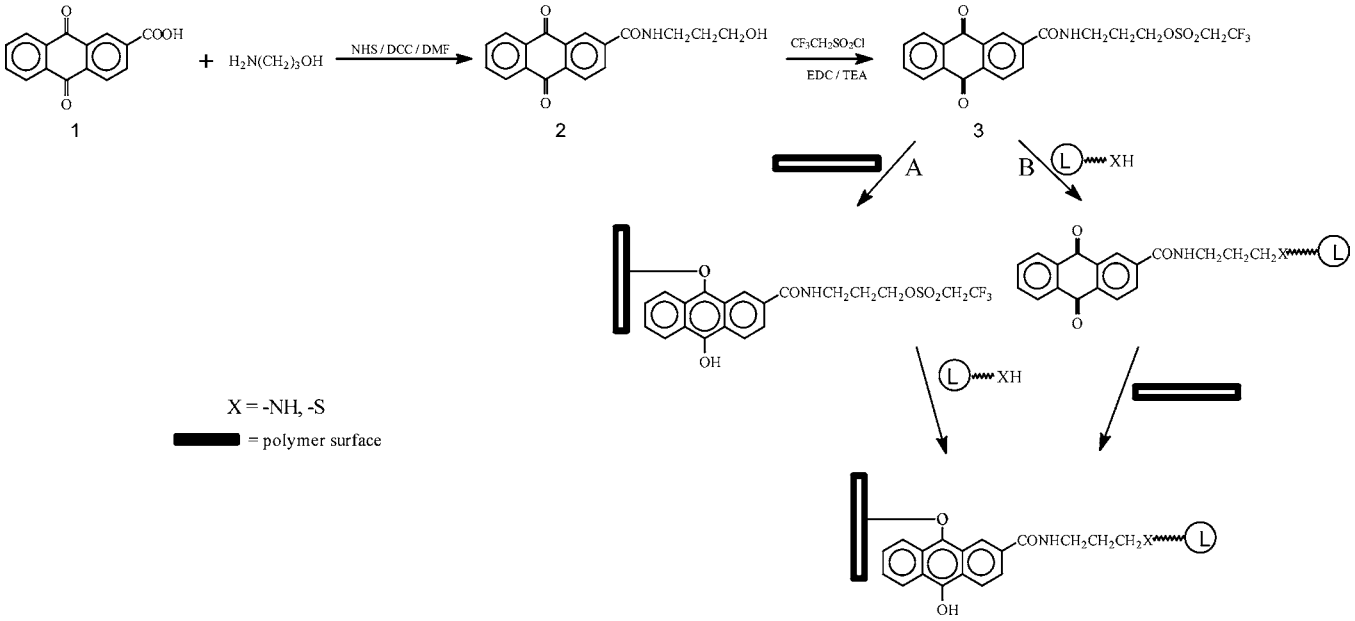
RESULTS AND DISCUSSION

The primary aim of this study was to search for a versatile heterobifunctional reagent useful for immobilization of biomolecules, including modified oligonucleotides, on a variety of solid matrixes. The choice of reactive functional groups in the heterobifunctional reagent was carefully made, keeping in mind that one of the functional groups must have reactivity toward aminoalkyl and mercaptoalkyl functions commonly found in biomolecules such as proteins and peptides and must be easy to introduce in oligonucleotides. The choice for other functional groups is critical, as we wanted it to react with a variety of solid matrixes, viz., polypropylene (PP), polyethylene (PE), nylon, C-8-CPG, and Sepharose. To cover a wide spectrum of polymer supports including the inert supports, we decided to look for a general reactive function which could react with all kinds of polymer supports without undertaking prederivatization of the supports. First we screened a range of chemical functional groups, but we found that they have limited reactivity toward functional groups available on polymer supports and may not cover the whole spectrum of commonly used polymer supports and particularly inert polymer supports. Then we decided to look for photoactivatable functional groups and found that they can cover a wide range of polymer supports including inert ones. On further screening the available photoactivatable moieties, we found that azido, carbenes, and substituted quinones may be the potential candidates (*27*, *28*). However, the azido group leads to generation of nitrenes on photoactivation, which is very reactive and reacts in a nonspecific manner with the substrate as well as with the medium, resulting in loss of efficiency of the reaction. Such reagents may be useful for generating functional groups on inert surfaces. The carbenes also behave in the same way as nitrenes and may not be suitable for our purpose. The use of substituted quinones has been demonstrated for immobilization of biomolecules on solid surfaces. Recently, Koch et al. (*29*) have demonstrated the usefulness of anthraquinone as photoactivatable group for making biochemical conjugates for various studies. The same group has prepared phosphoramidites of anthraquinone derivatives for immobilization of oligonucleotides on solid surface. However, it would require the preparation of phosphoramidite, which is usually very time consuming. The immobilization of biomolecules through photoactivation of anthraquinone proceeds fast, clean, and with high yields. However, it would require several chemical manipulations and use of other coupling reagents for making biomolecule-anthraquinone conjugates before immobilization. This has prompted us to use anthraquinone as one of the reactive functions in the proposed reagent, NTPAC. Being heterobifunctional reagent, NTPAC contains one trifluoroethanesulfonate ester function and one anthraquinone moiety. The trifluoroethanesulfonate ester reacts selectively with aminoalkyl and mercaptoalkyl functions present in biomolecules or modified oligonucleotides to give stable imine and thioether linkages, respectively, and the anthraquinone reacts with almost any polymer support exposing C−H groups under photolight, generating stable covalent bonds. Both of these reactions proceed rapidly under mild conditions. NTPAC has good solubility in organic solvents and particularly in water miscible solvents and hence allows one to use its DMF solution with common buffer solutions containing the ligands (biomolecules).

Design and Synthesis of *N*-(3-Trifluoroethanesulfonyloxypropyl)anthraquinone-2-carboxamide (NTPAC). The synthesis of the reagent NTPAC is depicted in Scheme 1. The synthesis of NTPAC is carried out in a two-step process. In the first step, anthraquinone-2-carboxylic acid (1 equiv) is converted to is *N*-hydroxysuccinimide active ester by its reaction with *N*-hydroxysuccinimide (1.25 equiv) in the presence of dicyclohexylcarbodiimide (1.25 equiv) in *N*,*N*-dimethylformamide. The reaction was allowed to proceed to completion, as checked by TLC. Without isolating the *N*-hydroxysuccinimide active ester, it was allowed to react with 3-aminopropanol (1.5 equiv) in the presence of a tertiary amine, triethylamine (TEA), for 6 h at room temperature. The precipitated dicyclohexylurea was removed by filtration, and the filtrate was concentrated to a syrupy mass, which was taken up in ethyl acetate where successively washed with aq 5% sodium bicarbonate, 5% citric acid, and finally with saturated sodium chloride. The organic phase, after drying over sodium sulfate, was concentrated under vacuum to obtain *N*-(3-hydroxypropyl)anthraquinone-2-carboxamide (NHAC) **2** as solid material in 90% yield.

N-(3-Hydroxypropyl)anthraquinone-2-carboxamide (NHAC) (1 equiv) was converted to NTPAC reagent by its reaction with 2,2,2-trifluoroethanesulfonyl chloride (tresyl chloride) (1.2 equiv) in the presence of triethylamine

Scheme 1. Preparation of Reagent NTPAC and Immobilization of Ligands on Polymeric Surfaces[a]



[a] Abbreviations: NHS, *N*-hydroxysuccinimide; DCC, dicyclohexylcarbodiimide; DMF, *N*,*N*-dimethylformamide; EDC, ethylene dichloride; TEA, triethylamine; L, ligand with aminoalkyl or mercaptoalkyl groups.

(TEA) for 2 h at 4 °C. After the completion of the reaction, the reaction mixture was filtered under inert atmosphere to eliminate ammonium chloride formed during the reaction. The filtrate was concentrated under vacuum to obtain a syrupy mass, which was further dried in a desiccator to obtain the desired reagent, NTPAC **3**, in almost quantitative yield.

Immobilization of Biomolecules. *Immobilization via Route A.* Basically this route of immobilization of biomolecules on a variety of surfaces involves the generation of active trifluoroethanesulfonate ester function on the surface of the polymer matrixes followed by the coupling of aminoalkylated or mercaptoalkylated ligands. The reagent, NTPAC, is brought in contact with the desired surface in dichloromethane; after evaporating the solvent, the dried polymer support is exposed to UV light where through the anthraquinone moiety it gets immobilized on the surface of the matrix with active trifluoroethanesulfonate ester functions on it. The desired ligand, enzyme, or modified oligonucleotide, etc., is then allowed to react with the surface where the trifluoroethanesulfonate ester function reacts with the ligand via their mercaptoalkyl or aminoalkyl functions (*30*). A number of enzymes and oligonucleotides were immobilized following this route successfully on a variety of polymer matrixes. The results are summarized in Table 1. This route is of particular importance in that the reactive functionality, trifluoroethanesulfonate ester, can be generated on a variety of surfaces including the inert ones such as polypropylene (PP), polyethylene (PE), nylon, etc., which are otherwise difficult to functionalize. The schematic diagram of immobilization is depicted in Scheme 1.

Immobilization via Route B. In this route, a conjugate of ligand and the reagent is first formed by mixing the appropriate quantity of the ligand in buffer with an excess of the reagent in dimethylformamide. After a brief period of reaction, the conjugate formed is centrifuged where the unreacted reagent settled as a pellet and the conjugate remained in the solution. The solution of the conjugate is mixed with the desired polymer support and exposed to UV light for about 30 min, allowing the conjugate to fix on the surface through the anthraquinone. 5′-Aminoalkyled and 5′-mercaptoalkylated oligonucleotides and a number of enzymes were immobilized on a variety of surfaces. The results are shown in Table 1.

The reagent NTPAC has also been tried for construction of oligonucleotide arrays on glass slides and polypropylene film and would be communicated shortly. The preliminary account of this work has been communicated elsewhere (*31*).

ACKNOWLEDGMENT

Authors gratefully acknowledge the financial support from CSIR Task Force (NNIOSB) project.

LITERATURE CITED

(1) Chehade, K. A., and Spielmann, H. P. (2000) Facile and efficient synthesis of 4-azidotetrafluoroaniline: a new photoaffinity reagent. *J. Org. Chem. 65*, 4949−4953.
(2) Gaur, R. K., and Gupta, K. C. (1989) A spectrophotometric method for the estimation of amino groups on polymer supports. *Anal. Biochem. 180*, 253−258.
(3) Stalteri, M. A., and Mather, S. J. (1995) A cross-linked monoclonal antibody fragment for improved tumor targeting. *Bioconjugate Chem. 6*, 179−186.
(4) Chen, L. L., Rosa, J. J., Turner, S., and Pepinsky, R. B. (1991) Production of multimeric forms of CD4 through a sugar-based cross-linking strategy. *J. Biol. Chem. 266*, 18237−18243.
(5) Kitagawa, T., Shimozono, T., Aikawa, T., Yoshida, T., and Nishimura, H. (1981) Cross-linking reagent for proteins. *Chem. Pharm. Bull. 29*, 1130−1135.
(6) Hermanson, G. T. (1996) *Bioconjugate Techniques*, pp 239−242, Academic Press, San Diego.
(7) Carlsson, J., Drevin, H., and Axen, R. (1978) Protein thiolation and reverse protein−protein conjugation. N−Succinimidyl 3-(2-pyridyldithio)propionate, a new heterobifunctional reagent. *Biochem. J. 173*, 723−737.
(8) Bednar, M. (2000) DNA microarray technology and application. *Med. Sci. Monit. 6*, 796−800.
(9) Zammatteo, N., Hamels, S., De Longueville, F., Alexandre, I., Gala, J. L., Brasseur, F., and Remacle, J. (2002) New chips for molecular biology and diagnostics. *Biotechnol. Annu. Rev. 8*, 85−101.

(10) Heller, M. J. (2002) DNA microarray technology: devices, systems, and applications. *Annu. Rev. Biomed. Eng. 4*, 129−153.

(11) Panda, S., Sato, T. K., Hampton, G. M., and Hogenesch, J. B. (2003) An array of insights: application of DNA chip technology in the study of cell biology. *Trends Cell Biol. 13*, 151−156.

(12) Vastag, B. (2003) Gene chips inch toward the clinic. *JAMA 289*, 155−156.

(13) McGall, G. H., and Christians, F. C. (2002) High-density genechip oligonucleotide probe arrays. *Adv. Biochem. Eng. Biotechnol. 77*, 21−42.

(14) Southern, E., Mir, K., and Shchepinov, M. (1999) Molecular interactions on microarrays. *Nat. Genet.* (*Suppl.*) *21*, 5−9.

(15) Pease, A. C., Solas, D., Sullivan, E. J., Cronin, M. T., Holmes, C. P., and Fodor, S. P. A. (1994) Light-generated oligonucleotide arrays for rapid DNA sequence analysis. *Proc. Natl. Acad. Sci. U.S.A. 91*, 5022−5026.

(16) Elder, J. K., Johnson, M., Milner, N., Mir, K. U., Sohail, M., and Southern, E. M. (1999) *DNA Microarrays: A Practical Approach* (M. Schena, Ed.) p 77, Oxford Press, New York.

(17) Steel, A., Torres, M., Hartwell, J., Yu, Y.-Y., Ting, N., Hoke, G., Yang H. (2000) *Microarray Biochip Technology* (M. Schena, Ed.) p 87, Eaton Press, Natick,

(18) Pirrung, M. C., Davis, J. D., and Odenbaugh, A. L. (2000) Novel reagents and procedures for immobilization of DNA on glass microchips for primer extension. *Langmuir 16*, 2185−2191.

(19) Joos, B., Kuster, H., and Cone, R. (1997) Covalent attachment of hybridizable oligonucleotides to glass supports. *Anal. Biochem. 247*, 96−101.

(20) Belosludtsev, Y., Iverson, B., Lemeshko, S., Eggers, R., Wiese, R., Lee, S., Powdrill, T., and Hogan, M. (2001) DNA microarrays based on noncovalent oligonucleotide attachment and hybridization in two dimensions. *Anal. Biochem. 292*, 250−256.

(21) Timofeev, E. N., Kochetkova, S. V., Mirzabekov, A. D., and Florentiev, V. L. (1996) Regioselective immobilization of short oligonucleotides to acrylic copolymer gels. *Nucleic Acids Res. 24*, 3142−3148.

(22) Ghosh, S. S., and Musso, G. F. (1987) Covalent attachment of oligonucleotides to solid supports. *Nucl. Acids Res. 15*, 5353−5372.

(23) Strother, T., Hamers, R. J., and Smith, L. M. (2000) *Nucl. Acids Res. 28*, 3535−3541.

(24) Pharmacia. LKB Gene Assembler Plus Manual, Uppsala, Sweden.

(25) Kumar, P., Bhatia, D., Rastogi, R. C., and Gupta, K. C. (1996) Solid-phase synthesis and purification of 5′-mercaptoalkylated oligonucleotides. *BioMed. Chem. Lett. 6*, 683−688.

(26) Gaur, R. K., Sharma, P., and Gupta, K. C. (1989) A simple method for the introduction of thiol group at 5′-termini of oligonucleotides. *Nucleic Acids Res. 17*, 4404.

(27) Yan, M., Cai, S. X., Wybourne, M. N., and Keana, J. F. W. (1993) Photochemical functionalization of polymer surfaces and the production of biomolecule-carrying micrometer-scale structures by deep UV lithography using 4-substituted perfluorophenyl azides. *J. Am. Chem. Soc. 115*, 814−816.

(28) Sigrist, H., Gao, H., and Wegmuller, B. (1992) Light dependent covalent immobilization of biomolecules on inert surfaces. *Biotechnology 10*, 1026−1028.

(29) Koch, T., Jacobsen, N., Fensholdt, J., Boas, U., Fenger, M., and Jacobsen, M. H. (2000) Photochemical immobilization of anthraquinone conjugated oligonucleotides and PCR amplicons on solid surfaces. *Bioconjug. Chem., 11*, 474−483.

(30) Kumar, P., and Gupta, K. C. (2003) A rapid method for the construction of oligonucleotide arrays. *Bioconjug. Chem. 14*, 507−512.

(31) (a) Kumar, P., and K. C. Gupta (2003) Novel heterobifunctional cross-linking reagents useful for attachment of biomolecules on carbon containing surfaces. Ind. Patent application, 63/NF/2003. (b) Kumar, P., Gupta, K. C., and Gandhi, R. P. (2003) UV light-aided immobilization of oligonucleotides on glass surface using N-(3-trifluoroethanesulfonyloxypropyl)anthraquinone-2-carboxamide (NTPAC) and detection of single nucleotide mismatches. *J. Ind. Chem. Soc.*, in press.

BC034198Z

Hybrid Nanoparticles Based on Organized Protein Immobilization on Fullerenes

Pramod Nednoor, Marcello Capaccio, Vasilis G. Gavalas, Mark S. Meier, John E. Anthony, and Leonidas G. Bachas*

Department of Chemistry, University of Kentucky, Lexington, Kentucky 40506-0055. Received August 28, 2003

Nanoscale carbon materials (i.e., fullerenes and nanotubes) are an attractive platform for applications in biotransformations and biosensors. The interesting properties displayed by nanoparticles demand new strategies for the manipulation of these materials on the nanoscale. Controlled modification of their surface with biomolecules is required to fully realize their potential in bionanotechnology. In this work, immobilization of a fullerene derivative with a mutant subtilisin is demonstrated, and the effect of the fullerene on the protein activity is determined. The fullerene-conjugated enzyme had improved catalytic properties in comparison to subtilisin immobilized on nonporous silica. Further, the pH profile of free and fullerene-conjugated subtilisin were almost identical.

Among the exciting possibilities of nanotechnology is the use of nanosized materials as building blocks to construct higher order supramolecular architectures. Nanomaterials that have been proposed to be suitable as building blocks include inorganic nanoparticles, quantum dots, fullerenes, and nanotubes/nanofibers from carbon or inorganic materials (*1*−*4*). Complementing this is the use of biomolecules as connectors between the various building blocks. Additionally, surface functionalization of nanoparticles for selective molecular attachment has facilitated the development of nanosensors, bioprobes, and other devices (*3*,*5*−*7*). Therefore, development of methodologies to prepare hybrid nanoparticles by controlling the interactions between biomolecules and various nanomaterials should enhance the functionality and range of application of nanoparticles. Although methodologies based on attaching nucleic acids to nanoparticles followed by DNA hybridization have appeared in the literature (*8*−*10*), the controlled conjugation of proteins on nanoscale materials has received less attention. We are interested in binding proteins on nanoparticles from a single site on the protein to yield well-defined hybrid nanomaterials with the protein oriented on the surface. For example, we recently demonstrated the preparation of hybrid alumina nanoparticles with phosphorylated pepsin through the interaction of the single phosphoryl group on serine 68 of pepsin with the alumina surface (*11*). Upon attachment to the alumina nanoparticles the enzyme remained active, while its thermal stability was enhanced. Zhang and Cass proposed a different method to orient proteins: a polyhistidine-tagged alkaline phosphatase was oriented on a titanium dioxide film through the interaction of the polyhistidine tail and surface-immobilized Ni^{2+} ions (*12*).

Fullerenes should be useful as building blocks of nanostructured materials because of their rich chemistry, electronic properties, and small dimensions (*13*). Among fullerene derivatives that have found biological applications, a diamido diphenyl fulleroid derivative was used as inhibitor of HIV protease (*14*), a fullerene carboxylic acid was used as a light sensitive biochemical probe (*15*), a C_{60}−PEG conjugate was used for photodynamic tumor therapy (*16*), a vesicular stomatitis virus was photoinactivated with fullerene-conjugated methoxy poly(ethylene glycol) amine (*17*), and a malonic acid derivative was shown to have antiapoptopic activity (*18*). Additionally, it has been recently shown that fullerenes can be used as electron mediators (*19*), or as coatings on piezoelectric quartz crystals to develop biosensors (*20*). Herein, a strategy to couple fullerenes with biomolecules has been explored that involves direct attachment of a site-specifically functionalized protein on the surface of C_{60}.

The approach undertaken involves the introduction of a unique functional group (a single cysteine residue) in the protein sequence using protein engineering. The point of mutation was selected to be away from the protein's active site to avoid deactivation upon coupling to the nanoparticles. Surfaces with maleimides have been previously used for immobilizing site-specifically a variety of proteins and peptides by taking advantage of the presence of a free sulfhydro group in the amino acid cysteine (*21*−*23*). A stable thioether bond is formed when the double bond of maleimide undergoes an alkylation reaction with sulfhydryl groups. Because of the inherent reactivity of maleimides for sulfhydro groups, *N*-(3-maleimidopropionyl)-3,4-fulleropyrrolidine (Figure 1, left), a maleimide-containing functionalized fullerene was synthesized. To obtain this compound, *N*-triphenylmethyl pyrrolidine−C_{60} was initially prepared according to a previously published procedure (*24*, *25*). To this, trifluoroacetic acid was added to obtain an intermediate fullerene pyrrolidine ammonium salt. An amount of 40 mg of the solid containing the protonated amine (fulleropyrrolidinium salt) was suspended by sonication in 15 mL of dry CH_2Cl_2. Anhydrous pyridine (0.6 mL) was added to the suspension followed by maleimidopropionic acid (17.6 mg, 2 equiv). Dicyclohexylcarbodiimide (21.4 mg, 2 equiv) was added at 0 °C, and the mixture was stirred in an ice bath for 30 min and then overnight at room temperature. The reaction mixture was diluted to a final volume of 60 mL with CH_2Cl_2 and filtered

* Corresponding author. E-mail: bachas@uky.edu. Phone: (859) 257-6350. Fax: (859) 323-1069.

10.1021/bc0341526 CCC: $27.50 © 2004 American Chemical Society
Published on Web 12/11/2003

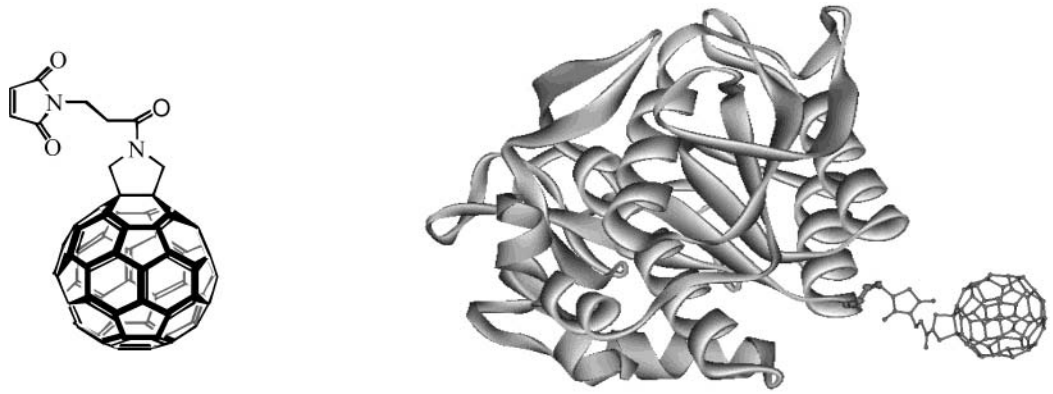


Figure 1. (Left) Structure of *N*-(3-maleimidopropionyl)-3,4-fulleropyrrolidine. (Right) Schematic illustration of the protein conjugated to *N*-(3-maleimidopropionyl)-3,4-fulleropyrrolidine (shown to scale).

through a Büchner funnel. The filtered solution was then washed with water (2 × 60 mL), a saturated solution of $CuSO_4$, and with water again. The organic phase was dried over $MgSO_4$ and evaporated under reduced pressure. The crude product was then purified by column chromatography (eluant CH_2Cl_2) yielding 30.8 mg (65%) of pure *N*-(3-maleimidopropionyl)-3,4-fulleropyrrolidine as a brown solid: ^{1}H NMR ($CDCl_3/CS_2$ 2:1, 200 MHz) 6.78 (s, 2H), 5.46 (s, 2H), 5.38 (s, 2H), 4.14 (triplet, J = 7.2 Hz, 2 H), 3.16 (triplet, J = 7.5 Hz, 2 H); *m/z* (MS−FAB$^-$) 914 (M^-, 45%), 720 (C_{60}, 100%).

Subtilisin is a serine protease secreted by members of the genus *Bacillus* that has high specificity for proteinaceous substrates. Subtilisin BPN′ from *Bacillus amyloliquifaciens* has 275 amino acids without any cysteine residues. For this study, a mutant subtilisin was produced in which a serine to cysteine (S145C) mutation was carried out by oligonucleotide-directed mutagenesis generating a single sulfhydro group per enzyme molecule. This mutant also has a nonspecific G98C mutation as a result of the polymerase chain reaction. Because there is only one attachment site on the maleimidofullerene and only one reactive group on subtilisin, a 1:1 coupling reaction is expected (Figure 1, right). The mutated subtilisin gene was inserted into a plasmid, and the protein was expressed in *Bacillus subtilis*. The plasmid was designed to produce a protein that is secreted into the culture medium (*26*). This helps in the purification of the enzyme, as the culture medium is relatively devoid of other proteins in comparison to whole cell lysate. Subtilisin BPN′ was purified using a BioCAD Sprint perfusion chromatography system (PE Biosystems, Framingham, MA) equipped with a POROS HS cation-exchange column (*26*). A volume of 1 mL of subtilisin solution was loaded to the column, and 1-mL fractions were collected and tested for protein concentration. The protein content was determined with the Micro BCA method (Pierce, Rockford, IL) using bovine serum albumin solutions as standards. The purified protein was dialyzed against phosphate buffer, pH 6.2, and stored after lyophilization at −20 °C.

A Reduce-Imm column (Pierce) was used to reduce any formed intermolecular disulfide bonds and generate the free sulfhydryl group immediately prior to reaction with the maleimidofullerene. The conjugation of maleimidofullerene and subtilisin was performed in phosphate buffer, pH 7.0, a pH that favors the reaction of maleimides with thiols over amines. An amount of 1.6 mg of *N*-(3-maleimidopropionyl)-3,4-fulleropyrrolidine was added to 5 mL of phosphate buffer (pH 7.0) containing 0.06 μmol of mutant subtilisin, and the mixture was vortexed to obtain a homogeneous suspension. The reaction was carried out for 5 h at 4 °C on a rotary shaker. The mixture was centrifuged and rinsed three times with 100 mM Tris-HCl, pH 8.6, buffer to separate the unreacted enzyme. The enzymatic activity was determined in the supernatant and the fullerene-containing solid. The enzyme releases *p*-nitroaniline form the substrate succinyl-Ala-Ala-Pro-Phe-*p*-nitroaniline (SAAPF-pNA) (Sigma, St. Louis, MO). The corresponding increase in absorbance at 412 nm was monitored on a HP 8453 Spectrophotometer. To measure the enzymatic activity, immobilized subtilisin was suspended in the buffer (Tris-HCl, pH 8.6), and aliquots of the suspension were transferred to a cuvette containing the substrate and stirred.

Initially, studies were carried out to investigate whether there is physical adsorption of subtilisin on unmodified C_{60}. For this, an excess of C_{60} (2.5 μmol) was added to the mutant subtilisin (0.05 μmol), and the mixture was shaken in a rotary shaker for 5 h as above. After removing from the rotary shaker, the mixture was centrifuged and washed three times. Activity measurement showed that almost the entire enzyme (92%) was present in the supernatant. No enzyme activity was determined on the fullerene fraction indicating the absence of any nonspecific binding on C_{60}. It should be mentioned that a C_{60} derivative was previously found to inhibit HIV-1 protease by blocking its active site (*14*). Therefore, we also evaluated the inhibitory effect of C_{60} on subtilisin. After adding C_{60} to the enzyme solution, the mixture was vortexed to obtain a homogeneous suspension, which was incubated in a rotary shaker. In this way, C_{60} was made available to the enzyme. The activity of the enzyme did not change in the presence of C_{60} indicating the absence of any kind of inhibition.

Kinetic studies were carried out to compare the K_M and k_{cat} values of free and fullerene-conjugated subtilisin. The amount of enzyme coupled was determined using the Micro BCA protein assay. To determine the K_M and k_{cat} values of the homogeneous and immobilized enzyme, the initial rate of the hydrolysis of the substrate SAAPF-pNA for a range of substrate concentrations was measured (Figure 2). The measurements were carried out in 100 mM Tris-HCl buffer (pH 8.6). The values of K_M and k_{cat} were obtained from Lineweaver−Burk reciprocal plots.

The immobilizeded enzyme demonstrated a higher K_M value than the free enzyme, suggesting that there is an influence of coupling on the affinity of the enzyme for the substrate (Table 1); higher K_M indicates lower affinity. Although this could be explained by the substrate having less access to the active site, it is more likely that the active site conformation is changed slightly upon

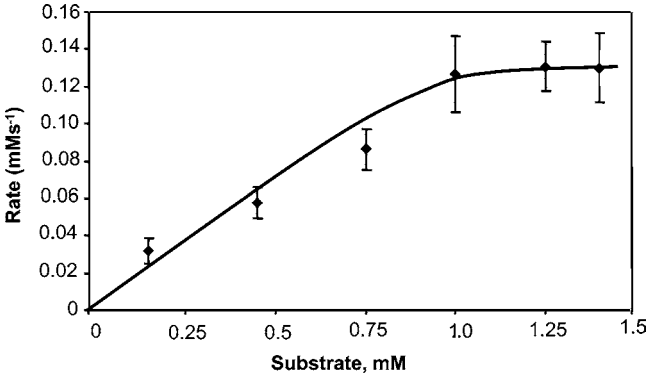


Figure 2. Initial rate (in units of mM of product formed per second) as a function of substrate concentration for the fullerene-conjugated subtilisin. Data shown are average ± standard deviation, $n = 3$. The rates were measured at 25 °C.

Table 1. Comparing the Kinetic Parameters of Free and Conjugated Enzyme

	K_M (mM)	k_{cat} (s^{-1})	k_{cat}/K_M ($M^{-1}\,s^{-1}$)
free subtilisin	0.17 ± 0.01	51 ± 2	$(3.0 \pm 0.2) \times 10^5$
coupled subtilisin with C_{60}	0.76 ± 0.2	37 ± 2	$(4.9 \pm 1.3) \times 10^4$
immobilized subtilisin on derivatized silica (*26*)	0.43 ± 0.02	14 ± 0.4	$(4.2 \pm 0.4) \times 10^4$

coupling to C_{60}. The k_{cat} value of the fullerene-conjugated subtilisin was significantly better when compared to the enzyme immobilized on a nonporous silica support (*26*) from the same amino acid residue. Compared to the free enzyme, the k_{cat} value of the fullerene-conjugated subtilisin was only reduced by 27%, while in the case of the silica support the corresponding reduction was 73%. Both silica and C_{60} are nonporous supports. Despite the hydrophilic nature of silica, which is typically advantageous in immobilized enzyme systems, the silica-conjugated subtilisin had >2.5-fold reduction in activity compared to the fullerene-conjugated subtilisin. C_{60} (0.7 nm) is much smaller in size compared to the silica particles (0.5 μm, average diameter), and it binds to only one enzyme molecule per particle. Thus, crowding effects, which tend to reduce activity at high enzyme loadings (*27*, *28*), are avoided.

The effect of pH on the activity of free and conjugated enzyme was also studied. The enzyme-catalyzed hydrolysis of SAAPF-pNA was investigated at 25 °C under various pH conditions. Buffer solutions composed of 0.0500 M acetic acid and 0.0500 M Bis-Tris propane were adjusted to pH 6.0, 7.0, 8.0, 8.5, and 9.0 with HCl or NaOH solutions. To each of these solutions, a fixed volume of substrate stock solution (40 mM SAAPF-pNA in DMF) was added to reach a concentration of 1 mM. At each pH value, a volume of 2.00 mL of the substrate solution of the corresponding pH was mixed with a fixed amount of the free or immobilized enzyme (60 μL) in a cuvette, and the initial reaction rate (60 s) was determined as described above. Attachment on conventional substrates causes changes in the pH profile of hydrolytic enzymatic reactions that is characterized by a displacement or broadening of the profile toward more acidic or basic values. When either proton exchange groups or diffusional limitation are present, both the limbs of the pH profile can be broadened. It was found that the pH profile curve for the coupled enzyme (Figure 3B) was similar to that of the free enzyme (Figure 3A). This can be explained by the lack of charged groups on the surface of C_{60}. Therefore, there should be no effect of the fullerene surface on the protonation state of the substrate. Broadened pH profiles can also be seen if diffusion on the

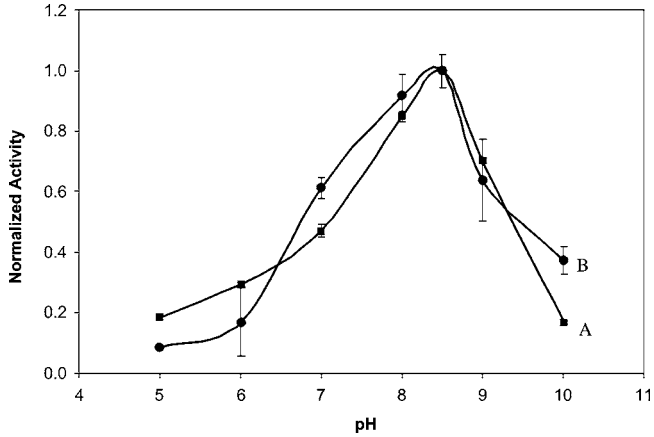


Figure 3. pH profiles of (A) free subtilisin and (B) subtilisin attached to the maleimidofullerene. All measurements were carried out at 25 °C and with a substrate concentration of 1 mM.

substrate to the enzyme is hindered upon immobilization (*29*). The small size of the C_{60} molecule makes the active site of the enzyme accessible to the substrate, and there is no diffusional limitation for the substrate to reach the active site imposed by the C_{60} surface. Thus, with regard to pH sensitivity, the attached enzyme behaves in a similar manner as free enzyme in solution.

In summary, nanotechnology has emerged as a powerful tool in the fabrication of materials having superior and often unique properties. To fully realize the potential of nanotechnology it is essential to control the way by which nanomaterials, such as fullerenes, interact with biomolecules. In this work, a maleimidofullerene was successfully attached to subtilisin through site-specific immobilization. The K_M and k_{cat} values of fullerene-conjugated subtilisin were found to be different from those of the free enzyme, but the k_{cat} was better in comparison to subtilisin immobilized on silica. Thus, the nature of the immobilization support affects the catalytic properties of the enzyme. It was also found that there is a difference in the pH profile of activity between the two supports, which is consistent with the difference in surface ionizable groups.

ACKNOWLEDGMENT

We thank the Office of Naval Research (ONR), National Aeronautics and Space Administration (NASA) and National Science Foundation, Division of Materials Research, under grant no. DMR-9809686 for funding this research. P.N. was partially supported by a training fellowship grant no. P42ES07380 from the National Institute of Environmental Health Sciences, NIH, with funds from HUD.

LITERATURE CITED

(1) Li, Z., Chung, S., Nam, J., Ginger, D. S., and Mirkin, C. A. (2003) Living templates for the hierarchical assembly of gold nanoparticles. *Angew. Chem., Int. Ed. 42*, 2306−2309.

(2) Loweth, C. J., Caldwell, W. B., Peng, X., Alivisatos, A. P., and Schultz, P. G. (1999) DNA-based assembly of gold nanocrystals. *Angew. Chem., Int. Ed. 38*, 1808−1812.

(3) Parak, W. J., Pellegrino, T., Micheel, C. M., Gerion, D., Williams, S. C., and Alivisatos, A. P. (2003) Conformation of oligonucleotides attached to gold nanocrystals probed by gel electrophoresis. *Nano Lett. 3*, 33−36.

(4) Xu, L., Guo, Y., Xie, R., Zhuang, J., and Yang, W. (2002) Three-dimensional assembly of Au nanoparticles using dipeptides. *Nanotechnology 13*, 725−728.

(5) Niemeyer, C. M. (2001) Nanoparticles, proteins, and nucleic acids: Biotechnology meets materials science. *Angew. Chem., Int. Ed. 40,* 4128−4158.
(6) Philip, D., and Stoddart, J. F. (1996) Self-assembly in natural and unnatural systems. *Angew. Chem., Int. Ed. 35,* 1154−1196.
(7) *Perspectives of Fullerene Nanotechnology,* Eiji Osawa, Ed., Kluwer Academic Publishers 2002, pp 155−163.
(8) Alivisatos, A. P., Johnnson, K. P., Peng, X., Wilson, T. E., Loweth, C. J., Bruchez, M. P., and Schultz, P. G. (1996) Organization of nanocrystal molecules using DNA. *Nature 382,* 609−611.
(9) Mucic, R. C., Storhoff, J. J., Mirkin, C. A., and Letsinger, R. L. (1998) DNA-directed synthesis of binary nanoparticle network materials. *J. Am. Chem. Soc. 120,* 12674−12675.
(10) Niemeyer, C. M. (2000) Self-assembled nanostructures based on DNA: Towards the development of nanobiotechnology. *Curr. Opin. Chem. Biol. 4,* 609−618.
(11) Li, J., Wang, J., Gavalas, V. G., Atwood, D. A., and Bachas, L. G. (2003) Alumina-pepsin hybrid nanoparticles with orientation-specific enzyme coupling. *Nano Lett. 3,* 55−58.
(12) Zhang, J. K., and Cass, A. E. G. (2001) A study of His-tagged alkaline phosphatase immobilization on a nanoporous nickel−titanium dioxide film. *Anal. Biochem. 292,* 307−310.
(13) Innocenzi, P., and Brusatin, G. (2001) Fullerene-based organic−inorganic nanocomposites and their applications. *Chem. Mater. 13,* 3126−3129.
(14) Sijbesma, R., Srdanov, G., Wudl, F., Castoro, J. A., Wilkins, C., Friedman, S. H., Decamp, D. L., and Kenyon, G. L. (1993) Synthesis of a fullerene derivative for the inhibition of HIV enzymes. *J. Am. Chem. Soc. 115,* 6510−6512.
(15) Tokuyama, H., Yamago, S., Nakamura, E., Shiraki, T., and Sugiura, Y. (1993) Photoinduced biochemical activity of fullerene carboxylic acid. *J. Am. Chem. Soc. 115,* 7918−7919.
(16) Yasuhiko, T., and Ikada, Y. (1999) Biological functions of fullerene. *Pure Appl. Chem. 71,* 2047−2053.
(17) Hirayama, J., Abe, H., Kamo, N., Shinbo, T., Ohnishi-Yamada, Y., Kurosawa, S., Ikebuchi, K., and Sekiguchi, S. (1999) Photoinactivation of vesicular stomatitis virus with fullerene conjugated with methoxy poly(ethylene glycol) amine. *Biol. Pharm. Bull. 22,* 1106−1109.
(18) Dugan, L., Turetsky, D. M., Du, C.; Lobner, D., Wheeler, M., Almili, C. R., Shen, C. K., Luh, T. Y., Choi, D. W., and Lin, T. S. (1997) Carboxyfullerenes as neuroprotective agents. *Proc. Natl. Acad. Sci., U.S.A. 94,* 9434−9439.
(19) Gavalas, V. G., and Chaniotakis, N. A. (2000) [60]Fullerene-mediated amperometric biosensors. *Anal. Chim. Acta 409,* 131−135.
(20) Chia-Wen, C., and Jeng-Shong, S. (2001) Preparation and application of immobilized C60-glucose oxidase enzyme in fullerene C60-coated piezoelectric quartz crystal glucose sensor. *Sens. Actuators, B 81,* 1−8.
(21) Qian, W., Fang, Y., Song, Z., Liang, B., and Wei, Y. (1998) Site-specific immobilization of Fab′ fragments of goat anti-human IgG on quartz surfaces. *Supramol. Sci. 5,* 701−703.
(22) Reznik, G. O., Vajda, S., Cantor, C. R., and Sano, T. (2001) A streptavidin mutant useful for directed immobilization on solid surfaces. *Bioconjugate Chem. 12,* 1000−1004.
(23) Xiao, S. J., Textor, M., Spencer, N. D., and Sigrist, H. (1998) Covalent attachment of cell-adhesive, (Arg-Gly-Asp)-containing peptides to titanium surfaces. *Langmuir 14,* 5507−5516.
(24) Kurz, A., Halliwell, C. M., Davis, J. J., Hill, H. A., and Canters, G. W. (1998) A fullerene-modified protein. *Chem. Commun.* 433−434.
(25) Prato, M., Maggini, M., Giacometti, C., Scorrano, G., Sandona, G., and Farnia, G. (1996) Synthesis and electrochemical properties of substituted fulleropyrrolidines. *Tetrahedron 52,* 5221−5234.
(26) Wei, H., Wang, J., Bhattacharyya, D., and Bachas, L. G. (1997) Improving the activity of immobilized subtilisin by site-specific attachment to surfaces. *Anal. Chem. 69,* 4601−4607.
(27) Viswanath, S., Wang, J., Bachas, L. G., Butterfield, D. A., and Bhattacharyya, D. (1998) Site-directed and random immobilization of subtilisin on functionalized membranes: Activity determination in aqueous and organic media. *Biotechnol. Bioeng. 60,* 608−616.
(28) Viswanath, S., Watson, C. R., Huang, W., Bachas, L. G., and Bhattacharyya, D. (1997) Kinetic studies of site-specifically and randomly immobilized alkaline phosphatase on functionalized membranes. *J. Chem. Technol. Biotechnol. 68,* 294−302.
(29) Hermanson, G. T., Ed. (1996) *Bioconjugate Techniques,* p 148, Academic Press: San Diego, CA.

BC0341526

ARTICLES

Production of Soluble ScFvs with C-Terminal-Free Thiol for Site-Specific Conjugation or Stable Dimeric ScFvs on Demand

Huguette Albrecht, Patricia A. Burke, Arutselvan Natarajan, Cheng-Yi Xiong, Mark Kalicinsky, Gerald L. DeNardo, and Sally J. DeNardo*

Radiodiagnosis and Therapy, Molecular Cancer Institute, University of California Davis Medical Center, Sacramento, California 95816 Received April 6, 2003; Revised Manuscript Received October 14, 2003

ScFv recombinant antibody fragments can provide specific tumor binding modules for targeting drugs. In the process of building multimeric tumor targeting pharmaceuticals, a prerequisite is the conservation of functional scFv antigen binding domains, thereby excluding scFv random conjugation to a carrier molecule or to another scFv. The pCANTAB 5E phage display/expression vector was genetically engineered to express any scFv gene as scFv with an additional C-terminal cysteine (scFv-Cys) such that the specific conjugation site is removed from the binding domain. Selected scFvs derived from an anti-MUC-1 scFv phage library were expressed in pCANTAB 5E and its modified version pCANTAB 5E Cys vectors, and compared for key characteristics. Production yields of scFv and scFv-Cys in shaker flask and biofermentor were compared. In the absence of a reducing agent, stable dimers (covalent scFv homodimers $(scFv\text{-}Cys)_2$) were the major form of scFv-Cys. These diabodies provided substantial signal enhancement for immunohistochemical staining of tissues. In the presence of a reducing agent, scFv-Cys molecules remained monomeric, with the free SH available for conjugation to a $PEG(maleimide)_2$ scaffold to form immunoreactive $PEG(scFv)_2$ bioconjugates. ScFv expression from pCANTAB 5E Cys allowed for the production of soluble scFv-Cys protein from *E.coli*, either as stable scFv-Cys or $(scFv\text{-}Cys)_2$. ScFv-Cys can be used for conjugation to PEG to form bivalent PEG $(scFv\text{-}Cys)_2$ molecules or used as $(scFv\text{-}Cys)_2$ for increased sensitivity in IHC.

INTRODUCTION

Radiolabeled monoclonal antibodies (mAb)[1] have proven to be effective therapeutic agents (*1*−*3*). However, their large size decreases tumor uptake and penetration (*4*, *5*). Normal tissue binding of the mAb Fc portion contributes to retention in vital organs, resulting in further decrease in tumor to normal tissue radiation or "therapeutic index". The development of single chain Fv antibody fragments (scFv)[1] in combination with phage display technology offers new avenues for tumor-targeted therapy (*6*−*8*). About 1/6 the size of a native antibody, the 25 kDa scFv retains the specificity of an antibody but has a decreased avidity due to its monovalent nature. Pharmacokinetic studies with scFvs have shown that their small size leads to rapid blood clearance by renal glomerular filtration, leaving little opportunity for extravascular tumor targeting (*9*, *10*). However, their use as modules for new targeting multivalent paradigms is under investigation (*11*, *12*).

ScFv fragments are typically stabilized by joining their VH and VL domains with a 15 amino acids flexible linker composed of $(Gly_4Ser)_3$ (*13*). Occasionally, a disulfide bond has been used to stabilize the VH−VL pairing (dsFv) (*14*, *15*). Reduction of the peptide linker length below 12 amino acid residues favors intermolecular VH−VL associations resulting in the formation of noncovalent dimers or diabodies (50 kDa) (*16*, *17*). Covalent dimers or $(scFv')_2$ molecules have been engineered by C-terminal addition of a peptide (*18*) or a cysteine (*10*, *19*−*21*) or by cross-linking with chemical linkers (*22*). Higher scFv multimers, triabodies (75 kDa) and tetrabodies (100 kDa), have been generated by shortening the linker length to less than five amino acid residues (*23*). At high concentrations, in a sequence-dependent manner, spontaneous scFv oligomerization can also occur (*24*).

Our overall objective is to use tumor-specific scFvs as tumor binding modules attached to multiarmed PEG scaffolds, as the initial targeting molecule in pretargeted strategies for cancer therapy. The covalent attachment of PEG to proteins has been used in many pharmaceuticals to extend plasma half-life, reduce immunogenicity, increase solubility, and decrease proteolysis (*25*−*27*). In nonspecific conjugation of appropriately activated PEG polymers to proteins, the usual targets are primary amines of lysine (*28*). Conjugation by random targeting of lysine residues has been satisfactory with large size molecules such as antibodies (*29*). However, site-specific conjugation is more likely to preserve the active binding site on the small scFv protein. In this respect, site-specific

* Corresponding author: Sally J. DeNardo, M.D., Radiodiagnosis and Therapy, Molecular Cancer Institute, University of California, Davis Medical Center, 1508 Alhambra Blvd., Rm. 3100, Sacramento, CA 95816. Telephone: 916-734-3787, Fax: 916-451-2857; E-mail: sjdenardo@ucdavis.edu.

[1] Abbreviations: CDR, complementarity determining region; DTT, dithiothreitol; HRP, horseradish peroxidase; IHC, immunohistochemistry; ITPG, isopropyl β-D-thiogalactopyranoside; mAb, monoclonal antibody; PBS, phosphate-buffered saline; scFv, single chain Fv antibody fragment; TCEP, tris(2-carboxyethyl)phosphine hydrochloride.

10.1021/bc030018+ CCC: $27.50 © 2004 American Chemical Society
Published on Web 12/31/2003

conjugation, based on thiol chemistry, appears to provide an approach that is generally applicable. Most scFvs are primarily stabilized through the intradomain disulfide bridges formed between the two cysteines present in each VH and VL domain. A free SH can be provided by the insertion of an extra cysteine at a location that causes little or no interference with the scFv binding site. Successful site-specific PEGylation via a free thiol has been reported. For example, di- and tri-scFvs were obtained by cross-linking of hinge cysteine residues, introduced at the COOH end of the B72.3 scFv by addition of a cysteine containing hinge region, using maleimide-based di- and trifunctional reagents (*30*). The scFv−immunotoxin LMB-2 molecule was assembled via maleimide conjugation to a free thiol group introduced through a cysteine inserted in the linker joining the scFv to the toxin (*31*).

Here we report the engineering of the generally available pCANTAB 5E, a vector designed for soluble scFv expression in *E. coli*, such that any scFv cloned in this vector will be expressed with an extra cysteine at its carboxy end. This extra cysteine provides a free SH group that can bind to sulfhydryl affinity reagents or resins, facilitating purification, or can participate in disulfide bond formation by mild oxidation, resulting in covalent $(scFv')_2$ homodimers or dimeric scFv molecules, with increased binding avidity. Using scFv clones selected from an anti-MUC-1 immune scFv phage library (*32*), we show improved in vitro targeting of the tumor antigen by dimeric compared to monomeric anti-MUC-1 scFvs, in ELISA and on tissue sections. This stable dimeric scFv product has facilitated evaluation of initial scFv selections on tumor and normal tissue arrays. Toward the development of tumor targeting pharmaceuticals, the effective conjugation of scFv-SH monomers to bivalent PEG is demonstrated.

EXPERIMENTAL PROCEDURES

Mutagenesis on pCANTAB 5E. The anti-MUC1 12E scFv clone in pCANTAB 5E (*44*) was used for mutagenesis. PCR and subsequent cloning were used to create the mutant clone carrying the extra TGT in pCANTAB 5E. The mutagenic ForNotCys primer (5′GCGGCCGCATGTGGTGCGCCGGTGCCGTAT 3′) and the L_{CANT}-3350 primer (5′ TCACCAGTAGCACCATTACCATTAGCAA 3′) (Operon Technologies, Inc., Alameda, CA) were used on the 12E clone to generate a fragment of about 1 Kb using the Pfu Taq polymerase (Stratagene, La Jolla, CA) in the PCR reaction mixture ($V = 100$ μL). Thirty-five cycles of denaturing 94 °C, 30 s; annealing 60 °C, 1 min; extending 72 °C, 1 min, were run. Verification of PCR reaction was confirmed by running 10 μL of the reaction on a 1.3% agarose gel (*33*). The 1 Kb PCR product was cloned into the pCR2.1 vector using the TOPO cloning kit (Invitrogen, Carlsbad, CA). Recombinant plasmids were extracted from positive colonies (white) using the plasmid midi kit (QIAGEN, Valencia, CA) and were sequenced (DBS sequencing facility, UC Davis) to confirm the presence of the extra TGT codon. To obtain the 12E scFv mutant clone (scFv-Cys clone), a recombinant pCR2.1 clone was double digested with NotI and ClaI. The resulting 971 bp NotI/ClaI fragment was gel isolated using a GFX PCR kit (Amersham Biosciences Corp., Piscataway, NJ) and ligated into the NotI/ClaI double digested 12E scFv clone. Transformants were recovered after electroporation of the *E.coli* HB2151 host (K12 Δ (lac-pro), ara, nal^r, thi/F′ [proAB, $lacI^q$, lacZ Δ M15]).

Selection of Mutant Clones. Potential mutant clones were first screened for scFv expression. Clones were grown in 2YT medium (17 g/L bacto-tryptone, 10 g/L bacto-yeast extract, 5 g/L NaCl) containing 2% glucose and 100 μg/mL ampicillin (2YT + AG) in a 96-well microtiter plate overnight (ON) at 30 °C with shaking at 150 rpm. Two replica plates were made by inoculation of 100 μL of 2YT + AG medium with aliquots of the precultures. After 6 h growth at 30 °C with shaking at 150 rpm, one plate was used for induction of scFv expression, and the other plate was stored at −70 °C after addition of 50 μL of 50% glycerol per well. For induction of scFv expression, the bacteria were pelleted by centrifugation at 2000 rpm (Beckman benchtop centrifuge) for 10 min and resuspended in 2YT medium supplemented with ampicillin (100 μg/mL) and isopropyl-β-D-thiogalactopyranoside (ITPG)[1] (USB, Cleveland, OH) at 1 mM final concentration. Following ON induction at 30 °C with shaking at 150 rpm, the cultures were centrifuged for 10 min at 2000 rpm and their supernatants were transferred to a new microtiter plate. Supernatants were tested for the presence of the 12E scFv by immunodetection on western blots using the anti-E Tag mAb (1:2000) conjugated to horseradish peroxidase (HRP)[1]. Enhanced Chemo Luminescence (Amersham Biosciences Corp.) was used to visualize the reactions. Positive clones were sequenced.

Cloning of scFvs into pCANTAB 5E. Other anti-MUC1 scFvs, namely E1 and G1, were selected from our anti-MUC1 phage display library (*48*) on the basis of binding to BSA-MUC1 100 mer synthetic peptide. The scFv fragments were isolated by SfiI/NotI double digestion and ligated into pCANTAB 5E Cys digested by SfiI/NotI digestion. ScFv-Cys clones were recovered following electropration of the HB2151 bacterial host.

ScFv Production in Shaker Flasks. Two liters of 2YT + AG in a 4 L shaker flask were inoculated with 200 mL of preculture grown ON at 30 °C with shaking at 220 rpm in 2YT + AG. After 3 h to 4 h growth at 30 °C with shaking at 220 rpm, the bacteria were pelleted at 6300*g* for 15 min at 4 °C using a Sorval centrifuge with a GSA rotor and resuspended in 2xYT media containing 0.5 mM ITPG and 100 μg/mL of ampicillin for soluble scFv protein production at 30 °C for 16 h.

ScFv Production in the Biofermentor. A 5 L Bioflo 3000 fermentor (New Brunswick Scientific Co., Inc. Edison, NJ) was used to produce scFv on a larger scale. Four liters of medium described previously (*34*), containing ampicillin as the selective agent, was inoculated with preculture of the clone of interest to an initial OD_{630nm} between 0.03 and 0.05.

Growth was carried out under the following conditions: 30 °C, agitation variable between 200 and 800 rpm, pH at 6.9, and constant aeration to maintain the dissolved O_2 level at or above 30%. After 14 to 16 h of growth, when bacteria had reached the stationary phase, scFv production was induced by addition of ITPG to 0.5 mM final concentration. Induction was performed for 8 h.

ScFv Purification and Storage. ScFvs were purified from bacterial periplasms and from culture supernatants. For periplasmic extract preparation, after induction, bacterial cultures were pelleted and resuspended in 3 mL of TES [0.2 M Tris-HCl (pH 8.0), 0.5 mM EDTA, 0.5 M sucrose] per OD_{630} unit, followed by addition of 4.5 mL per OD_{630} unit of 0.2× TES followed. After 30 min incubation on ice with moderate agitation, the bacterial debris and insoluble periplasmic material were pelleted by centrifugation at 12 000 g for 30 min at 4 °C. The

supernatant fraction containing the soluble periplasmic proteins was filtered (0.45 um) and used for scFv purification. For scFv extraction from the bacterial growth medium, the supernatant was filtered (0.45 μm) and a protease inhibitor cocktail (Roche Diagnostics, Mannheim, Germany) was added.

The scFv proteins were affinity purified from the periplasmic extracts and culture supernatants by anti-E Tag affinity column chromatography using the RPAS purification module (Amersham Biosciences Corp.). Centriprep YM-10 (Millipore, Bedford, MA) was used to buffer exchange the purified scFvs into PBS and concentrate them. Purified scFvs in solution at 1 to 2 mg/mL in phosphate-buffered saline pH 7.4 (PBS)[1] (Sigma Aldrich, St Louis, MO) were stored at 4 °C for short-term storage (not exceeding 3 months) or were frozen in liquid nitrogen and kept at −70 °C for long-term storage.

Reduction of SH Groups and Removal of Reducing Agent. Tris(2-carboxyethyl)phosphine hydrochloride (TCEP)[1] (Molecular Probes, Eugene, OR) was used as a reducing agent. TCEP was added to the scFvs in solution in PBS (pH 7.4) in a 2 -fold molar excess, which was the lowest amount required for near 100% reduction in an ON reaction at 4 °C. This was done regularly at the last buffer exchange step in the purification. TCEP was removed from scFv solutions by filtration through a centricon YM-10 (Millipore).

Protein N-Terminal Sequencing. After separation of the scFv forms by nonreducing SDS−PAGE, (∼9.5 and 19 μg of 12E-Cys nonreduced scFv were loaded into two lanes of a 4−12% NuPAge gel (Invitrogen)), the proteins were electroblotted onto a PVDF membrane (Biorad, Hercules, CA) for direct N-terminal sequencing by Edman's degradation. This protein microsequencing was performed on an ABI Procise HT Edman Sequencer System (Perkin-Elmer/Applied Biosystems, Foster City, CA) at the Molecular Structure Facility at UCDavis.

Cell Lines and Cell Lysate Preparation. MUC-1 positive human breast adenocarcinoma MCF-7 cells (American Type Culture Collection (ATCC) Manassas, VA) were grown to 75% confluence in DMEM (Gibco, Invitrogen Corp., Carlsbad, CA) medium supplemented with 5% fetal calf serum (FCS) (Gibco, Invitrogen Corp.). MUC-1-positive DU145 human prostate cancer cells (ATTC) were grown to 100% confluence in RPMI-1640 medium (Gibco, Invitrogen Corp.) supplemented with 10% FCS.

Cell lysates were prepared by hypotonic lysis in a 10 mM Tris, pH 8, 1 mM $MgCl_2$, 1 mM $CaCl_2$ buffer, followed by three cycles of freeze at −70 °C/thaw at room temperature and a final homogenization in a dounce tissue grinder (Wheaton, Milville, NJ).

Protein Quantitation. The Micro BCA protein assay reagent kit (Pierce Chemical Co., Rockford, IL) was used to quantify purified scFvs and total protein content of cell lysates.

ELISA. Pro-Bind ELISA assay plates (Becton Dickinson Labware, Franklin Lakes, NJ) were coated with 100 μL of MCF7 or DU145 cell lysate at 1 mg/mL. The wells were dried by placing the plates at 37 °C ON. Plates not used immediately were stored at −20 °C in the presence of drierite. Nonspecific binding was blocked with 200 μL/well of PBS/0.1% Tween 20 (Sigma Aldrich) containing 3.0% nonfat dry milk (Bio-Rad, Hercules, CA) for 1 h at 37 °C. Anti-MUC-1 scFv proteins at various concentrations in a total volume of 100 μL/well with PBS/0.01% Tween/0.3% nonfat dry milk were incubated at 37 °C for 1 h. Following each incubation, the plates were washed six times with PBS containing 0.01% Tween 20. One hundred microliters of anti-E-Tag-HRP mAb diluted to 1:4000 in PBS/0.1% Tween/0.3% nonfat milk solution was added. Following the last wash step, the 2,2′-amino-bis-3-ethylbenzthiazoline-6-sulfonic acid (ABTS) substrate (Sigma-Aldrich), containing 0.3% H_2O_2, was added. As soon as the colorimetric reaction had developed, the content of each well was transferred to a new plate to prevent the interference of the coating with the readings. Plates were read at $A_{405\ nm}$ (Dynex microplate reader, Chantilly, VA).

Immunohistopathology. Human prostate cancer tissue (Gleason pattern 3), fixed in formalin and embedded in paraffin, was cut into 5 μm sections onto slides. After warming and deparaffinizing, the sections were rehydrated through alchohols and rinsed in PBS. Endogenous peroxidases were blocked by a 15 min incubation in 0.3% H_2O_2 in methanol. After rinsing in PBS, antigen retrieval was performed in 10 mM citrate buffer, pH 6, by microwaving the slides at 600 W three times for 5 min. The slides were rinsed in PBS and blocked for 30 min in 10% goat serum in PBS. The sections were incubated with scFv at 26 μg/mL overnight at 4 °C. ScFv used for tissue staining included one nonbinding control, 12E, 12E-Cys, E1, E1-Cys, G1, and G1-Cys. ScFv staining was compared to staining by mAb BrE−3 (*8*), performed similarly (5 μg/mL) on sections from the same tissue block. After rinsing in PBS, the sections were incubated for 1 h with biotinylated anti-mouse monoclonal antibody (Molecular Probes, Eugene, OR) diluted 1:250. Following PBS rinsing, ABC reagent (Vector Labs, Burlingame, CA) was added and the slides incubated for 30 min. Staining was visualized with 3,3′-diaminobenzidine (DAB), and the sections were rinsed and dipped in Mayer's Modified hematoxylin before dehydration and mounting. All sections were photographed at magnification 400×.

PEG−$(scFv)_2$ Bioconjugate. *Conjugation.* PEG-2-arm *o*-pyridyl disulfide [2 kDa (PEG-$(OPSS)_2$)] and PEG-2-arm maleimide [10 kDa (PEG-$(Mal)_2$)] were obtained from Sun Bio Inc., Anyang City, S. Korea.

12E and 12E-Cys scFvs, PEG-$(OPSS)_2$ and PEG-$(Mal)_2$ were all in solution in PBS, pH 7.4. A 2 molar excess of TCEP was used to maintain the 12E-Cys scFv in its monomeric form and to reduce the intermediate pyridyl disulfide forms to 12E−S−S−PEG-SH. Molar ratios of scFv, PEG$(OPSS)_2$, and PEG-$(Mal)_2$ of 4:5:10, respectively, were combined at room temperature and left to react overnight. The 12E scFv, the control without an extra cysteine, was reacted under the same conditions The conjugation reactions were analyzed by PAGE.

Purification. Conjugation mixture, estimated to contain about 100 μg of scFv protein, was fractionated by size exclusion HPLC chromatography on a calibrated (gel filtration standard, Biorad) 300 × 7.8 mm BioSep-SEC−S 2000 column (Phenomenex, Torrance, CA). The column was preconditioned in 100mM sodium phosphate buffer pH 7.1 and operated at a flow rate of 0.25 mL/min. Fractions of 125 μL were collected.

Immunoreactivity. The concentration of PEG−$(scFv)_2$ bioconjugate was estimated based on the absorbance at 280 nm using a Beckman DU64 spectrophotometer. The absorbance of monomeric scFv-Cys prior to conjugation was compared to the absorbance of the PEG−$(scFv)_2$ bioconjugate for an estimate of bioconjugate concentration. As two scFvs are attached to each PEG molecule, the concentration of PEG−$(scFv)_2$ bioconjugate was estimated as 1/2 the extrapolated concentration. The bioconjugate was diluted to 25 μg/mL in PBS for use on prostate tissue and MUC-1 expressing BT20 cells (*35*). A mixture of the 10 kDa PEG and the 2 kDa PEG linker

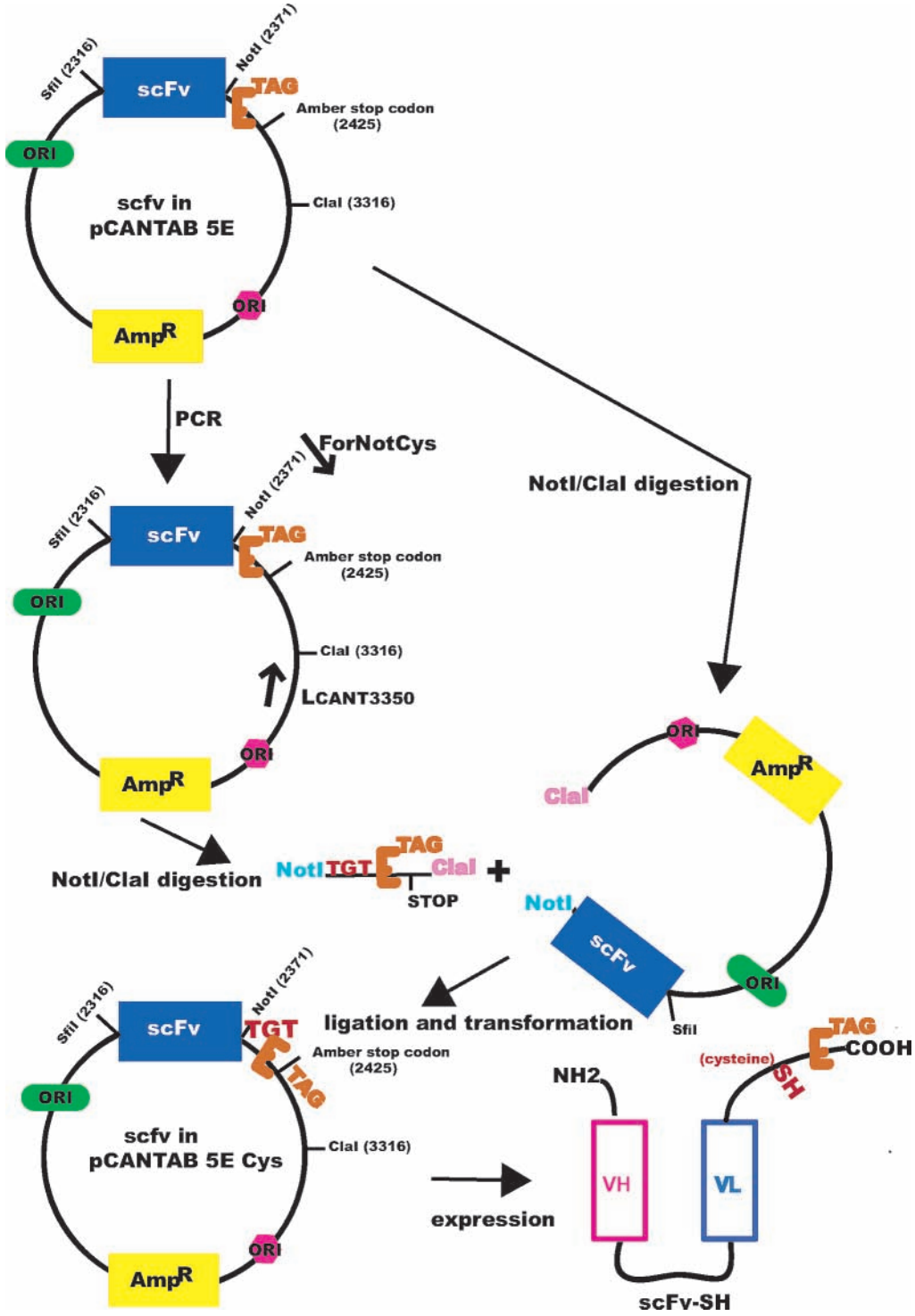


Figure 1. Strategy used to insert a free SH group at the C-terminus of a scFv. PCR on the pCANTAB 5E vector (Amersham Biosciences Inc.); the forward ForNotCys and the reverse $L_{CANT}3350$ primers were used to insert a TGT codon specifying a cysteine, just downstream of the NotI restriction site used for scFv cloning. NotI/ClaI digested PCR fragments and vector were ligated to create the pCANTAB 5E Cys vector. ScFvs expressed from this vector have a cysteine (free SH group) at their C-terminus.

molecules (1:2) was used as a control at the same concentration as in the PEG−$(scFv)_2$ bioconjugate. Prostate tissue slides were treated as described under Immunohistopathology. BT20 cells grown in minimal essential medium with 10% FCS were rinsed, scraped into PBS, and cytospun onto slides. After air-drying, the slides were frozen at −70 °C until use. The cells were fixed for 10 min in 10% buffered formalin and rinsed in PBS. Endogenous peroxidases were quenched by a 15 min incubation in 0.3% H_2O_2 in methanol. After rinsing, PEG−$(scFv)_2$ bioconjugate or control was incubated on cell and tissue slides overnight at 4 °C. After rinsing, slides were treated as described under immunohistopathology. BT20 cells with PEG or PEG−$(scFv)_2$ bioconjugate were photographed at magnification 400×.

RESULTS

Construction of the pCANTAB 5E Cys Vector and Cloning of Other scFvs. PCR site-directed mutagenesis of pCANTAB 5E was used to insert the cysteine-specifying codon at the 3′ end of the scFv gene, downstream of the NotI restriction site and just upstream of the stop

Table 1. Comparison of the Production of Anti-MUC-1 ScFvs in Shaker Flasks and Biofermentor[a]

	anti-MUC-1 scFv	periplasmic extract, mg/L	culture supernatant, mg/L
shaker flask	12E	1.67	not detected
	12E-Cys	0.51	0.57
biofermentor	12E	1.50	not detected
	12E-Cys	2.12	0.69

[a] Shaker flask and biofermentor production yields were determined for the anti-MUC-1 12E and 12E-Cys scFvs. The presence of scFvs in the culture supernatant was determined by immunoblot using the anti-E Tag mAb. ScFvs obtained from bacterial periplasm or culture supernatants were purified and quantified.

codon carried on the vector backbone when NotI is used as a cloning site. From the two codons specifying a cysteine, TGT and TGC, the TGT codon was used in the design of the 30 mer forward mutagenic primer ForNot-Cys with the consideration of the primer T_m. The 28 mer reverse primer, L_{CANT} 3350, hybridizes downstream of the unique ClaI restriction site in pCANTAB 5E and allows for a good size PCR product of 971 bp. As illustrated in Figure 1, the mutation carrying fragment was generated by PCR on the 12E clone in the presence of the proofreading Pfu Taq and subcloned into the pCR2.1 cloning vector. After the presence of the TGT insertion was confirmed by sequencing, the NotI/ClaI mutant fragment was isolated from a recombinant clone and ligated into the 12E clone linearized by NotI/ClaI digestion. Because no unmodified 12E scFv was detected in culture supernatants, we were able to use the secretion of the scFv into the medium as a selection criteria for potential mutant clones. From 32 potential mutant clones tested for their expression by western blot prior to sequence analysis, five expressed scFv in their supernatant at various levels. Sequence analysis of these clones confirmed the presence of the extra TGT codon. The best expressing clone (12E-Cys) was selected for further experiments.

Other selected scFv clones from the anti-MUC-1 scFv library were cloned as SfiI/NotI scFv gene fragments into pCANTAB 5E Cys linearized by SfiI/NotI digestion, e.g. E1-Cys and G1-Cys.

Anti-MUC-1 scFvs Production and Purification. To compare their production yields, both scFv and scFv-Cys were produced in shaker flasks and in a biofermentor. Analyses by western blot were used to test for the distribution of the scFv in the bacterial periplasm and in the culture supernatant. The results, summarized in Table 1, show the distinct behavior of 12E and 12E-Cys scFvs. Whether produced in the shaker flask or the biofermentor, detectable levels of 12E scFv are only present in the bacterial periplasm while 12E-Cys scFv is found in both the periplasm and the culture supernatant. Both scFvs were affinity purified, using the E Tag present at their C-terminus (Figure 1), from periplasmic extracts, and 12E-Cys scFv was also purified from the culture supernatant. Typical yields, shown in Table 1, illustrate that the production of 12E scFv is best in flasks. However, analyses of 12E-Cys scFv indicated that about 1/2 or 1/4 of the total amount of scFv produced was present in the culture supernatant from shaker flask or biofermentor, respectively, and that the production of 12E-Cys scFv was best in the biofermentor.

Other scFv-Cys clones (E1-Cys and G1-Cys) have produced soluble scFvs but secretion into the medium is not a general rule.

Analysis of scFv Expression. PAGE analysis under nonreducing conditions of the purified 12E and 12E-Cys scFvs, illustrated in Figure 2, shows that the two scFvs also have distinct gel profiles. For 12E scFv, shown in lane 1 of Figure 2, two bands were visualized by Coomassie Blue staining. The major band with the highest apparent molecular weight of about 25 kDa corresponds to the monomeric form of the scFv. The 12E-Cys scFv is shown in lane 2 of Figure 2. Two bands are observed with apparent molecular weights of 50 and 25 kDa, corresponding to dimeric and monomeric 12E-Cys scFvs, respectively. Similar profiles were observed for other scFv and scFv-Cys (data not shown).

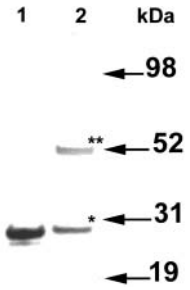


Figure 2. Comparison of the SDS−PAGE profiles of the 12E and 12E-Cys scFvs. Coomassie Blue staining of purified scFvs (8 μg) resolved on a 4−12% gradient polyacrylamide gel by nonreducing SDS−PAGE. The 12E scFv is shown in lane 1 and the 12E-Cys scFv in lane 2. ScFvs monomers (*) and dimers (**) are indicated. Standards for apparent molecular weights are indicated on the right.

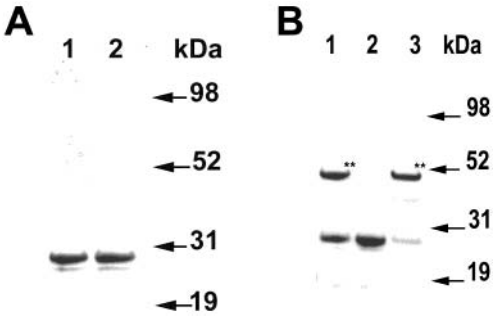
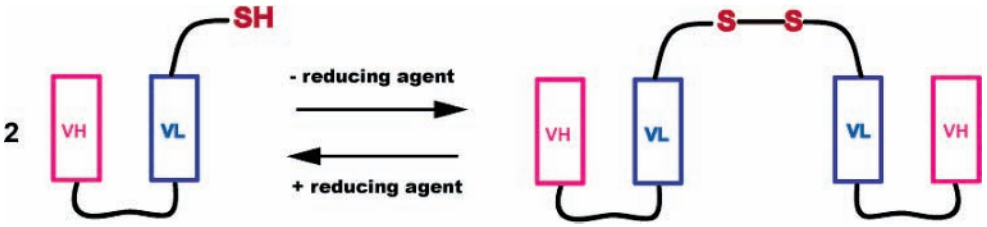


Figure 3. Effect of the reducing agent TCEP on the scFvs forms. Coomassie Blue staining of purified scFvs (8 μg), before and after TCEP treatment and analyzed by 4−12% nonreducing SDS−PAGE is shown. The 12E scFv is illustrated in A and 12E-Cys scFv is shown in B. Lane 1 of Figure 3, A and B, corresponds to untreated scFv. Lane 2 of Figure 3, A and B, illustrates 12E scFv and 12E-Cys scFv, respectively, after addition of a 2-fold molar excess of TCEP. ScFv dimers are indicated by **. Lane 3 of Figure 3B shows the 12E-Cys scFv after removal of TCEP. Standards for apparent molecular weights are indicated on the right.

Reduction of the 12E-Cys Homodimers. Because the extra cysteine is the only difference between the 12E and the 12E-Cys scFvs, the free SH group is most likely involved in the formation of the 12E-Cys dimeric scFv. We used TCEP, a reducing agent which (unlike β-mercaptoethanol and dithiothreitol (DTT)[1]) does not contain any SH group itself and is active in a broad pH range (pH 5 to 8) to compare the scFvs. In the presence of a 2-fold molar excess of TCEP, the 12E-Cys scFv homodimers were reduced to their monomeric counterparts as visualized by nonreducing PAGE analysis (Figure 3B, lane 2). An excess of TCEP was required to observe a reduction near to 100%. Monomeric and dimeric forms, at ~50% each were present in the 12E-Cys scFv control with no TCEP added (Figure 3B, lane 1). Addition of a 2-fold molar excess of TCEP to the 12E scFv left the monomer unchanged (Figure 3A, lane 2) and in comparison to the control without TCEP in lane 1. Removal of

Scheme 1. ScFv-Cys Dual Forms



the reducing agent resulted in the predominance of 12E-Cys scFv dimers (Figure 3B, lane 3). The observation that 12E-Cys scFv homodimers can be reduced is consistent with the free SH involvement in the formation of a covalent dimeric structure. N-Terminal sequencing of both molecular species shows that their N-termini are identical (data not shown). Thus, definite evidence is provided that the protein with an apparent molecular of 50 kDa is formed by dimerization of the protein with an apparent molecular weight of 25 kDa. A schematic representation of the two molecular forms of the 12E-Cys scFv is shown in Scheme 1.

Comparison of scFv and scFv-Cys in Vitro Binding Activities. *ELISA.* Binding of MUC-1 targeting scFvs was tested by ELISA using MCF7 (breast) and DU145 (prostate) cancer cell lysates. 12E-Cys scFv binds 1.4 and 2 times as well, respectively, to these cell lysates compared to 12E scFv (Figure 4, A: MCF7; and B: DU145). Increased binding to MCF7 and DU145 cell lysates was also observed for other anti-MUC-1 scFvs Cys (data not shown).

Immunohistochemistry (IHC)[1]. Binding of the 12E, E1, G1, and 12E-Cys, E1-Cys, and G1-Cys scFvs was compared on sections of malignant prostate tissue (Figure 5). Results show a clear enhancement of specific staining with scFv-Cys compared to unmodified scFvs, consistent with increased avidity associated with the predominance of covalent dimeric scFv form and possible bivalent binding of the second (anti scFv) antibody. In comparison with the negative control (Figure 5A), little or no staining is seen with the 12E and E1 scFvs (Figures 5, C and E), whereas specific tumor cell staining is observed with both scFvs Cys (Figure 5, D and F). G1 scFv staining (Figure 5G) is further enhanced with G1-Cys scFv (Figure 5H). The positive control, with the intact monoclonal anti-MUC1 BrE−3 (*36*), is shown in Figure 5B.

PEG−(scFv)$_2$ Bioconjugate. *Conjugation.* PEGylation in a single reaction mixture and in the presence of TCEP of bifunctional 10 kDa PEG-(Mal)$_2$ and 2 kDa PEG-(OPSS)$_2$ to 12E (without Cys) or 12E-Cys scFvs at respective molar ratios of 4: 5: 10 resulted in three products as visualized by Coomassie Blue staining following nonreducing PAGE (Figure 6A). The product, migrating at about 70 kDa, corresponds to the PEG(10 kDa)−(PEG(2 kDa)−scFv)$_2$ bioconjugate of interest (Figure 6A, lane 4). The broader band at about 50 kDa is thought to represent (PEG(2 kDa)−scFv)$_2$ molecules. Nonconjugated 12E and 12E-Cys scFv monomers are shown in Figure 6A, lanes 1 and 3, respectively. No PEGylated product was visualized with the conjugation control, 12E scFv (without Cys) (Figure 6A, lane 2). Thus, original intramolecular S−S bonds were not available for conjugation to PEG via maleimide.

PEG-(OPSS)$_2$ was added as a spacer between 12E-Cys and PEG-(Mal)$_2$ to increase the reaction yield. Multiple conjugations have confirmed that this approach yields about 40% of PEG(10 kDa)−(PEG(2 kDa)-scFv)$_2$ bioconjugate.

Purification. The PEG−(scFv)$_2$ bioconjugate was isolated from the conjugation mixture (Figure 6A, lane 4) by size exclusion chromatography as illustrated in Figure 6B. Two major peaks were visualized. The first and major peak corresponding to a protein with an apparent molecular weight of 70 kDa was identified as the PEG−(scFv)$_2$ bioconjuagte of interest. The bioconjugate was distributed between four fractions that were pooled and used to test its immunoreactivity. The second peak, with

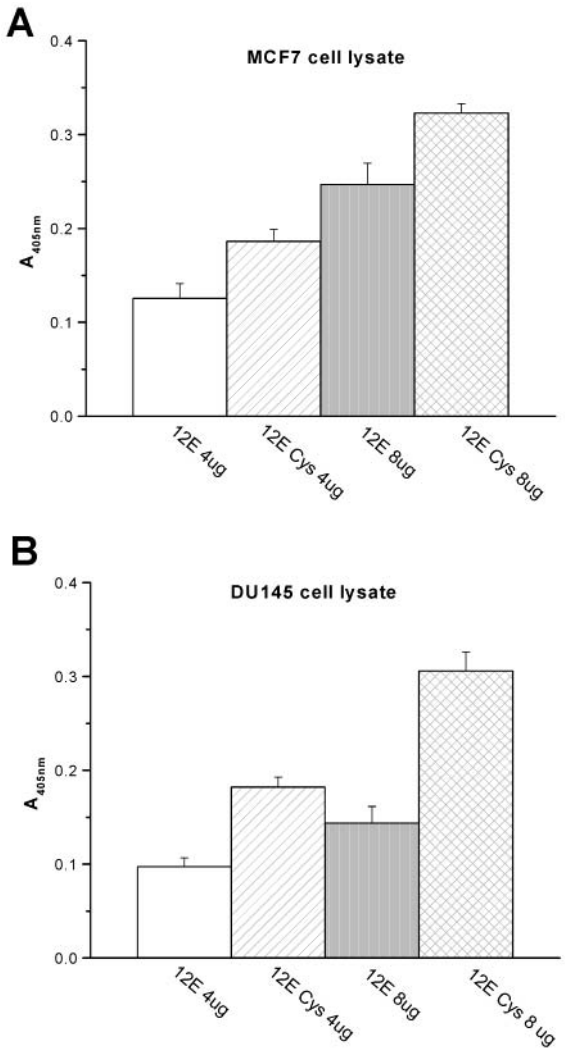


Figure 4. Comparison of MUC-1 binding of 12E and 12E-Cys scFvs to cell lysate. MUC-1 binding 12E and 12E-Cys scFvs, 4 and 8 μg, were tested by ELISA on MCF7 (A) and DU145 (B) cell lysates. Graphs were derived from mean absorbance values normalized to background (no scFv). Corresponding standard errors (SE) from three experiments with triplicates in each experiment are shown. Mean background values and SE were 0.137 (±0.005) for MCF7 cell lysate (A) and 0.154 (±0.010) for DU145 cell lysate (B). 12E-Cys scFv [diagonal (4 μg) and crosshatched (8 μg)] binding was higher compared to 12E scFv [white (4 μg) and gray (8 μg)] on both MCF7 and DU145 cell lysates.

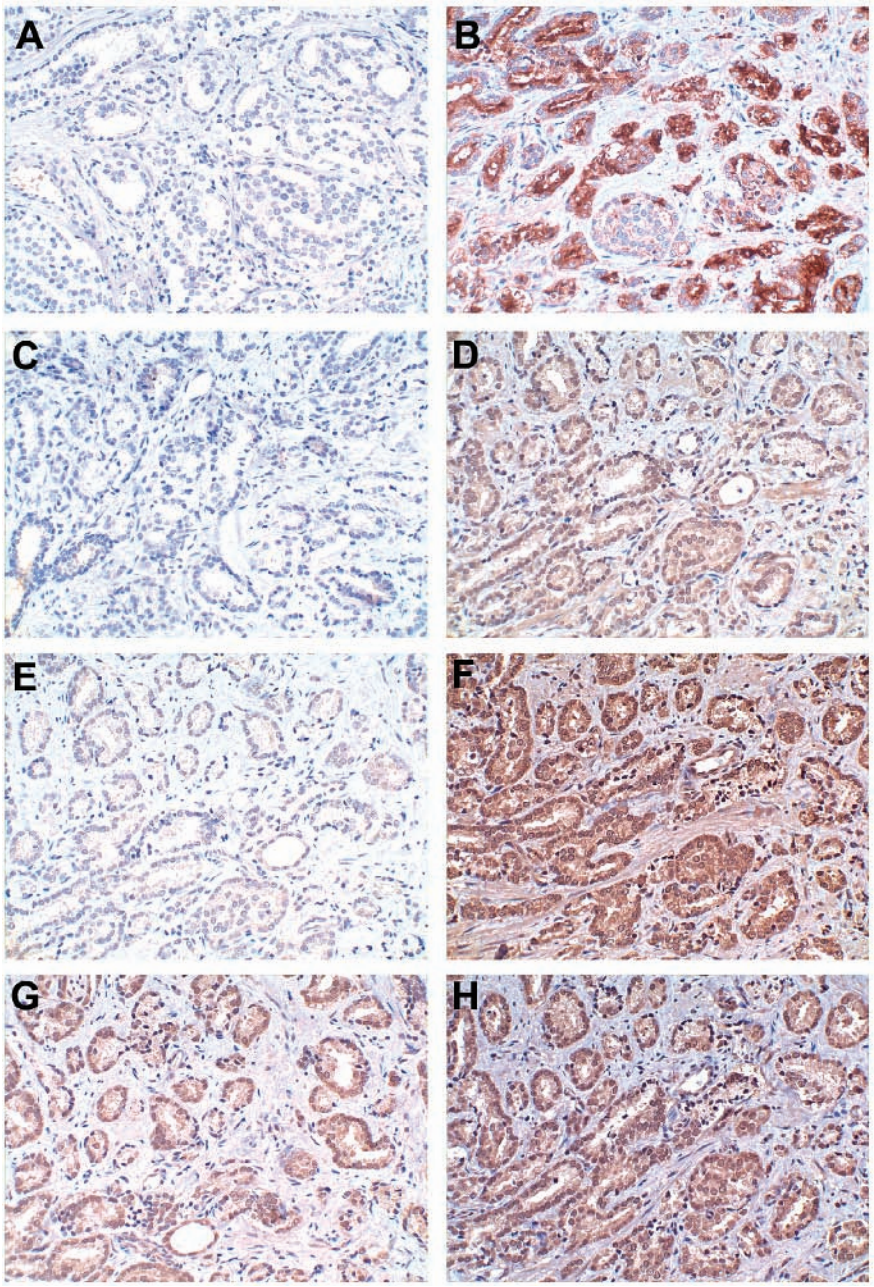


Figure 5. Enhanced specific immunohistochemical staining of MUC-1 on prostate cancer tissue by scFv with extra cysteine. Prostate cancer tissue (Gleason's grade 3) was stained with (A) nonbinding control scFv, (B) mAb BrE−3, (C) scFv 12E, (D) scFv 12E-Cys, (E) scFv E1, (F) scFv E1-Cys, (G) scFv G1, and (H) scFv G1-Cys. The mAb (BrE−3) concentration used was 5 μg/mL, and the scFv concentration used was 26 μg/mL. Tissue was photographed at 400× magnification. The figures illustrate scFv staining of MUC-1 (brown stain) similar to staining by mAb BrE-3, with increased staining observed on tissue stained with scFv containing an extra cysteine (D, F, H) compared to scFv without the additional cysteine (C, E, G), consistent with increased avidity of scFv associated with dimer formation following cysteine insertion.

an apparent molecular weight of 50 kDa, was assumed to represent the scFv-spacer-scFv side product.

Immunoreactivity. Immunoreactivity of the PEG−$(scFv)_2$ bioconjugate was assessed by IHC on MUC-1 expressing cells. The bioconjugate strongly stained MUC-1 expressing BT20 cells (*35*) in comparison to control slides treated with PEG mixture (Figure 6C).

DISCUSSION

The pCANTAB 5E vector was engineered for the addition of a C-terminal cysteine to any scFv expressed from the new pCANTAB 5E Cys vector. Anti-MUC-1 scFvs (*37*) were expressed as scFv-Cys, and production yields, binding activities, and some applications of scFvs with and without a C-terminal cysteine were compared.

The decision to introduce the cysteine at the C-terminus of the scFv was based on several considerations. An initial requirement was to preserve the affinity of antigen binding after conjugation into a larger molecular format. Our 12E anti-MUC-1 scFv 3D model indicated that short N- and C-terminal sequences are flexible and therefore not involved in the structural conformation of the VH and VL domains (*37*). Furthermore, other scFvs with a specific C-terminal cysteine insertion have retained binding activity (*10*, *19*, *20*). Second, the SH group introduced needed to be accessible for intermolecular reactions to facilitate conjugation. Third, the scFvs must be produced in a soluble, properly folded, and active form that can be easily purified. Soluble scFv expression from prokaryotic vectors, such as pCANTAB 5E, involves

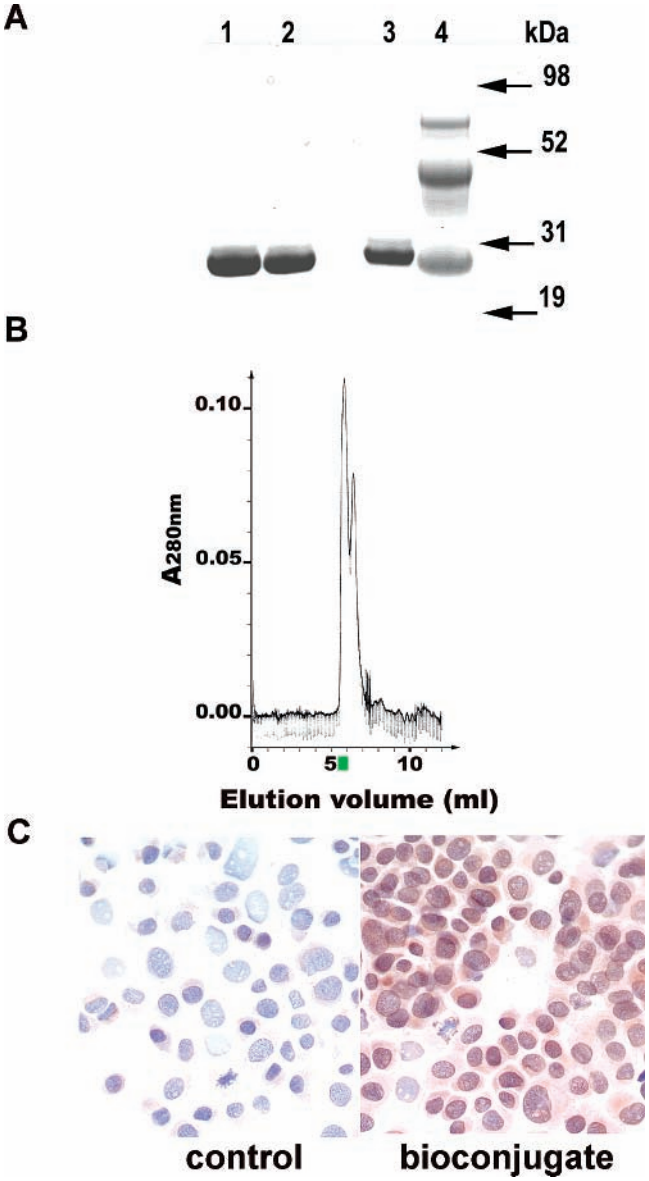


Figure 6. (A) PAGE of the PEG−$(scFv)_2$ bioconjugate. Coomassie blue staining of 12 E (25 μg) and 12E-Cys scFvs (20 μg) in the presence of an excess of TCEP (lanes 1 and 3, respectively), and after conjugation to PEG (lanes 2 and 4 respectively) are shown after separation by nonreducing SDS−PAGE on a 4−12% gradient polyacrylamide gel. Standards for apparent molecular weights are indicated on the right. The (10 kDa)-PEG−(2 kDa)PEG−$(scFv)_2$ product of interest, at ~70 kDa, and the side product of (2 kDa)PEG−$(scFv)_2$, at about 50 kDa, are formed with the 12E-Cys scFv (lane 4) but not with the negative control 12E scFv (lane 3), lacking a free thiol. (B) HPLC purification profile size exclusion HPLC of the PEG−$(scFv)_2$ bioconjugate on a calibrated 300 × 7.8 mm BioSep-SEC−S 2000 column. The column was calibrated in 100 mM sodium phosphate buffer, pH 7.1, and the flow rate was 0.25 mL/min. The fractions corresponding to the PEG−$(scFv)_2$ bioconjugate are underlined in green. (C) Immunoreactivity of the PEG−$(scFv)_2$ bioconjugate MUC-1-expressing BT20 cells were stained with PEG solution (control, left) and the PEG−$(scFv)_2$ bioconjugate (bioconjugate, right), as described in Experimental Procedures. The figure shows staining of BT20 cells incubated with the bioconjugate but not with PEG alone (control), consistent with immunoreactivity of the bioconjugate. Cells were photographed at magnification 400×.

N-terminal maturation of the protein by cleavage of a signal peptide for cytoplasmic export to the periplasm (*38*). Studies of an anti-insulin scFv protein, expressed with a N-terminal cysteine but lacking a signal peptide, demonstrated that it accumulates in inclusion bodies (*39*). Although this provided a useful product, the loss in solubilizing and refolding of the scFvs was substantial. Finally, we did not wish the cysteine addition to be scFv specific; therefore, the modification should be introduced into the vector backbone. This last requirement completely excluded N-terminal addition, as the signal peptide cleavage does not allow for scFv nonspecific modification.

The cysteine specifying codon was added to the vector backbone downstream of the SfiI/NotI restriction sites used for scFv cloning and upstream of the E Tag used for affinity purification.

As illustrated by the yields (50 μg/L to 3 mg/L) obtained for different anti-MUC-1 scFvs produced in shaker flasks and in the biofermentor, scFv production yield was unique to the expressed sequence. An even wider range of scFv production yields, under comparable conditions, have been reported (*40*−*42*). The slightly better biofermentor yields can be accounted for by more optimal growth conditions, achieved by constant aeration, more efficient agitation and pH control of the medium in combination with a shorter induction time. Yields might be increased by changing the linker joining the VH and VL domains (*43*), or by introducing mutations in framework amino acids (*42*, *44*).

Comparison of the shaker flask and biofermentor production yields indicated that the scFv with an extra cysteine (12E-Cys) was produced somewhat better than the original scFv (12E) in the biofermentor. This was unexpected since, according to Blank et al. (*45*), the presence of an unpaired cysteine impairs the periplasmic production of a scFv. Unlike the 12E scFv, the 12E-Cys scFv does not remain exclusively in the periplasmic space but is also released into the culture medium. Thus, even if a negative effect of the unpaired cysteine in the periplasmic space cannot be ruled out, the extra cysteine apparently promoted the secretion of the 12E-Cys scFv into the culture medium. More efficient folding of the 12E-Cys in the bacterial periplasm could be contributing to secretion. The importance of the primary sequence of an antibody is known to play a decisive role in the efficiency of folding in the bacterial environment, and scFv folding in the periplasmic space has also been reported as a limiting factor for its secretion (*44*). Another explanation for the distinct behavior of the 12E-Cys is that, in the oxidizing environment of the periplasm, it engages in an intermolecular disulfide bond. Periplasmic disulfide bond formation was shown to be indispensable for the cellulase secretion by the plant pathogen *Erwinia chrysanthemi* (*46*). Interestingly, as for the scFv-SH, the S−S bond was present in the C-terminal region of the cellulase. However, the formation of such a disulfide bond alone is not enough to account for the 12E-Cys secretion since some of the other scFv-Cys expressed from pCANT-AB 5E Cys remain confined in the periplasmic space (unpublished data). Production and purification from culture supernatant has also been described for scFvs lacking a free C-terminal cysteine (*42*, *47*).

An interesting and important feature of scFv-Cys or scFv-SH, shown here and reported by others (*20*), is its dimerization or stable dimer formation as a result of air oxidation at basic pH. The spontaneous $(scFv')_2$ formation of these scFvs was more efficient than that described by Wang et al. (*20*) for the anti-CD19FVS191 scFv originally produced in an insoluble form. The observation that, by addition in excess or removal of a reducing agent, the homodimers can be reverted to monomers and vice versa, while retaining immunoreactivity, indicates that the SH

group of the extra cysteine is responsible for the formation of a covalent dimer as previously observed for other scFvs (*10*, *19*, *20*). At the concentrations used, the reducing agent (TCEP) reduced the intermolecular disulfide bridge without altering the two intramolecular disulfide bonds, most likely because cysteines were more exposed in complementarity-determining regions (CDR)[1] than they were in the framework regions (*48*). The four native cysteines engaged in intramolecular disulfide bonds in our three anti-MUC-1 scFvs are all part of framework regions, as determined by molecular modeling (*37*), and therefore their inaccessibility might explain why they escape reduction. This conclusion is supported by the identical behavior on PAGE of the 12E scFv (lacking the extra SH) in the absence and presence of TCEP and by the fact that it cannot be PEGylated, even in the presence of TCEP.

The scFv-Cys dual forms have several applications.

In vitro binding of three anti-MUC-1 scFv-Cys, assessed by ELISA or immunohistopathology, showed affinity was not only retained but enhanced, thus supporting the carboxy end choice for the cysteine addition.

The scFv-S−S-scFv dimeric form is useful for immunohistopathological studies of tumor and normal tissues distribution of the scFv antigen target. Undoubtly, the scFv dimerization contributed to improved binding to the MUC-1 antigen. The improved binding of a diabody (antiparallel homodimer), that mimics the higher binding avidity of a bivalent antibody, compared to the univalent scFv is well documented (*49*−*51*). The enhanced immunohistochemical signal observed with the 12E-Cys, E1-Cys, and G1-Cys anti-MUC-1 scFvs was found reproducible with other scFv-Cys (unpublished data). The signal enhancement provided by dimeric scFvs represents the sum of better binding due to the scFv bivalency and of better binding detection since two targets, one on each scFv, are available for the detection antibody. Thus, these scFv-S−S-scFv molecules are a solution to the weak binding signal of monomeric scFvs for scFv binding evaluation on normal and cancer tissues.

The scFv-SH monomeric form provided the free thiol needed for site-specific conjugation to a PEG scaffold, as illustrated here with a biactivated PEG maleimide. The use of PEG-$(OPSS)_2$ as a spacer to boost the PEGylation proved to be beneficial, since a 40% yield was reached for the bioconjugate of interest. The yield was good for a reaction known for its low efficiency. The HPLC-purified ∼70 kDa PEG−$(scFv)_2$ bioconjugate shown here demonstrated binding to MUC-1-expressing BT20 cells. Such a bioconjugate is expected to be a superior in vivo tumor targeting agent compared to monomeric or dimeric svFvs for the following reasons: (i) enhanced bioavailability over the monomeric scFv form should result in increased tumor uptake; (ii) as a consequence of increased molecular size, decreased kidney clearance can be expected since the renal threshold for first pass elimination is about 65 kDa (*52*); (iii) the addition of PEG is likely to prolong circulation time, decrease proteolysis, and lower immunogenicity (*53*).

Finally, the free thiol at the C-terminus of the scFv provides additional choices for affinity purification. For example, the scFv-SH can be directly retained on an activated thiol resin or by avidin or streptavidin after conjugation to maleimide-biotin (*54*). This last bioconjugate can also be used to immobilize scFvs onto a glass surface (*55*) for high-throughput ligand screening.

In conclusion, we have described a way to produce, on demand, a stable dimer or the monomeric form of any scFv expressed from pCANTAB 5E Cys. As shown here, the addition of a cysteine to the C-terminus of a scFv resulted in scFv with improved characteristics for biomedical applications. The scFv-Cys dimer is valuable for in vitro targeting studies, while the scFv-Cys monomer can be conjugated to PEG or other molecules to create tumor targeting pharmaceuticals with improved pharmacokinetics.

ACKNOWLEDGMENT

This work was supported by U.S. Department of Energy Grant DE-FG01-00NE22944, National Cancer Institute Grant PO1 CA47829, Department of Defense Grant DAMD17-01-0177. The authors wish to thank Gary Mirick and Bonnie Bradt for their experimental contributions.

LITERATURE CITED

(1) DeNardo, S. J., DeNardo, G. L., O'Grady, L. F., Macey, D. J., Mills, S. L., Epstein, A. L., Peng, J.-S., McGahan, J. P. (1987) Treatment of a patient with B cell lymphoma by I-131 Lym-1 monoclonal antibodies. *Int. J. Biol. Markers 2*, 49−53.

(2) Juweid, M. E., Stadtmauer, E., Hajjar, G., Sharkey, R. M., Suleiman, S., Luger, S., Swayne, L. C., Alavi, A., Goldenberg, D. M. (1999) Pharmacokinetics, dosimetry and initial therapeutic results with ^{131}I- and ^{111}In-/^{90}Y-labeled humanized LL2 anti-CD22 monoclonal antibody (MAb) in patients with relapsed/refractory non-Hodgkin's lymphoma (NHL). *Clin. Cancer Res. 5*, 3292s−3303s.

(3) Witzig, T. E., White, C. A., Wiseman, G. A., Gordon, L. I., Emmanouilides, C., Raubitschek, A., et al. (1999) Phase I/II trial of IDEC−Y2B8 radioimmunotherapy for treatment of relapsed or refractory CD20+ B-cell non-Hodgkin's lymphoma. *J. Clin. Oncol. 17*, 3793−3803.

(4) DeNardo, G. L., Kroger, L. A., DeNardo, S. J., Miers, L. A., Salako, Q., Kukis, D. L., Fand, I., Shen, S., Renn, O., Meares, C. F. (1994) Comparative toxicity studies of yttrium-90 MX-DTPA and 2-IT-BAD conjugated monoclonal antibody (BrE−3). *Cancer 73*, 1012−1022.

(5) Jain, R. K. (1990) Physiological barriers to delivery of monoclonal antibodies and other macromolecules in tumors. *Cancer Res. 50*, 814s−819s.

(6) Chinn, P. C., Leonard, J. E., Rosenberg, J., Hanna, N., Anderson, D. R. (1999) Preclinical evaluation of 90Y-labeled anti-CD20 monoclonal antibody for treatment of non-Hodgkin's lymphoma. *Int. J. Oncol. 15*, 1017−1025.

(7) DeNardo, S. J., DeNardo, G. L., DeNardo, D. G., Xiong, C. Y., Shi, X. B., Winthrop, M. D., Kroger, L. A., Carter, P. (1999) Antibody phage libraries for the next generation of tumor targeting radioimmunotherapeutics. *Clin Cancer Res. 10*, 3213−3218.

(8) Winter, G., Griffiths, A. D., Hawkins, R. E., Hoogenboom, H. R. (1994) Making antibodies by phage display technology. *Annu. Rev. Immunol. 12*, 433−455.

(9) Adams, G. P. (1998) Improving the tumor specificity and retention of antibody-based molecules. *In Vivo 12*, 11−22.

(10) Adams, G. P., McCartney, J. E., Tai, M. S., Oppermann, H., Huston, J. S., Stafford, W. F., Bookman, M. A., Fand, I., Houston, L. L., Weiner, L. M. (1993) Highly specific in vivo tumour targeting by monovalent and divalent forms of 741F8 anti-c-erbB-2 single-chain Fv. *Cancer Res. 53*, 4026−4034.

(11) Lee, L. S., Conover, C., Shi, C., Whitlow, M., Filpula, D. (1999) Prolonged circulating lives of single-chain Fv proteins conjugated with poly(ethylene glycol): A comparison of conjugation chemistries and compounds. *Bioconjugate Chem. 10*, 973−981.

(12) Wu, A. M. (2001) Tools for pretargeted radioimmunotherapy. *Cancer Biother. Radiopharm. 16*, 103−108.

(13) Huston, J. S., Levinson, D., Mudgett-Hunter, M., Tai, M. S., Novotny, J., Margolies, M. N., Ridge, R. J., Bruccoleri, R. E., Haber, E., Crea, R. (1988) Protein engineering of antibody binding sites: recovery of specific activity in an anti-digoxin

single-chain Fv analogue produced in *Escherichia coli*. *Proc. Natl. Acad. Sci. U. S. A. 85*, 5879−5883.
(14) Brinkmann, U., Reiter, Y., Jung, S. H., Lee, B., Pastan, I. (1993) A recombinant immunotoxin containing a disulfide-stabilized Fv fragment. *Proc. Natl. Acad. Sciences, U. S. A. 90*, 7538−7542.
(15) Glockshuber, R., Malia, M., Pfitzinger, I., Pluckthun, A. (1990) A comparison of strategies to stabilize immunoglobulin Fv-fragments. *Biochemistry 29*, 1362−1367.
(16) Holliger, P., Prospero, T., Winter, G. (1993) 'Diabodies': small bivalent and bispecific antibody fragments. *Proc. Natl. Acad. Sci. U. S. A. 90*, 6444−6448.
(17) Wu, A. M., Williams, L. E., Zieran, L., Padma, A., Sherman, M., Bebb, G. G., Odom-Maryon, T., Wong, T. Y. C., Shively, J. E., Raubitschek, A. A. (1999) Anti-carcinoembryonic antigen (CEA) diabody for rapid tumor targeting and imaging. *Tumor Target. 4*, 1−12.
(18) Pack, P., Pluckthun, A. (1992) Miniantibodies: use of amphipathic helices to produce functional, flexibly linked dimeric Fv fragments with high avidity in *Escherichia coli*. *Biochemistry 31*, 1579−1584.
(19) Kipriyanov, S. M., Dubel, S., Breitling, F., Konterman, R. D., Little, M. (1994) Recombinant single-chain Fv fragments carrying C-terminal cysteine residues: production of bivalent and biotinylated miniantibodies. *Mol. Immunol. 31*, 1047−1058.
(20) Wang, D., Berven, E., Li, Q., Uckun, F., Kersey, J. H. (1997) Optimization of conditions for formation and analysis of anti-CD19 FVS191 single-chain Fv homodimer $(scFv')_2$. *Bioconjugate Chem. 8*, 64−70.
(21) Li, L., Olafsen, T., Anderson, A. L., Wu, A., Raubitschek, A. A., Shively, J. E. (2002) Reduction of kidney uptake in radiometal labeled peptide linkers conjugated to recombinant antibody fragments. Site-specific conjugation of DOTA-peptides to a Cys-diabody. *Bioconjugate Chem. 13*, 985−995.
(22) Cumber, A. J., Ward, E. S., Winter, G., Parnell, G. D., Wawrzynczak, E. J. (1992) Comparative stabilities in vitro and in vivo of a recombinant mouse antibody FvCys fragment and a bisFvCys conjugate. *J. Immunol. 149*, 120−126.
(23) Todorovska, A., Roovers, R. C., Dolezal, O., Kortt, A. A., Hoogenboom, H. R., Hudson, P. J. (2001) Design and application of diabodies, triabodies and tetrabodies for cancer targeting. *J. Immunol. Methods 248*, 47−66.
(24) Desplancq, D., King, D. J., Lawson, A. D. G., Mountain, A. (1994) Multimerization behaviour of single chain Fv variants for the tumor-binding antibody B72.3. *Protein Eng. 7*, 1027−1033.
(25) Nucci, M. L., Shorr, R., Abuchowski, A. (1991) The therapeutic value of poly(ethylene glycol)-modified proteins. *Adv. Drug Deliv. Rev. 6*, 133−151.
(26) Harris, J. M., Chess, R. B. (2003) Effect of pegylation on pharmaceuticals. *Natl. Rev. Drug Discovery 2*, 214−221.
(27) Chapman, A. P. (2002) PEGylated antibodies and antibody fragments for improved therapy: a review. *Adv. Drug Delivery Rev. 54*, 531−545.
(28) Fung, W. J., Porter, J. E., Bailon, P. (1997) Strategies for the preparation and characterization of poly(ethylene glycol) (PEG) conjugated pharmaceutical proteins. *Polym. Prepr. 38*, 565−566.
(29) McCall, M. J., Diril, H., Meares, C. F. (1990) Simplified method for conjugating macrocyclic bifunctional chelating agents to antibodies via 2-iminothiolane. *Bioconjugate Chem. 1*, 222−226.
(30) King, D. J., Turner, A., Farnsworth, A. P. H., Adair, J. R., Owens, R. J., Pedley, B., Baldock, D., Proudfoot, K. A., Lawson, A. D. G., Beeley, N. R. A., Millar, K., Millican, T. A., Boyce, B. A., Antoniv, P., Mountain, A., Begent, R. H. J., Shochat, D., Yarranton, G. T. (1994) Improved Tumor Targeting with Chemically Cross-Linked Recombinant Antibody Fragments. *Cancer Res. 54*, 6176−6185.
(31) Tsutsumi, Y., Onda, M., Nagata, S., Lee, B., Kreitman, R. J., Pastan, I. (2000) Site-specific chemical modification with poly(ethylene glycol) of recombinant immunotoxin anti-TAC-(FV)-PE38 (LMB-2) improves antitumor activity and reduces animal toxicity and immunogenecity. *Proc. Natl. Acad. Sci. U. S. A. 97*, 8548−8553.
(32) Winthrop, M. D., DeNardo, S. J., DeNardo, G. L. (1999) Development of a hyperimmune anti-MUC-1 single chain antibody phage display library for targeting breast cancer. *Clin. Cancer Res. 10*, 3088−3094.
(33) Sambrook, J. (1989) *Molecular cloning: a laboratory manual*. Cold Spring Harbor, New York.
(34) Goshorn, S., Sanderson, J., Axworthy, D., Lin, Y., Hylarides, M., Schultz, J. (2001) Preclinical evaluation of a humanized NR-LU-10 antibody-streptavidin fusion protein for pretargeted cancer therapy. *Cancer Biother. Radiopharm. 16*, 109−123.
(35) Walsh, M. D., Luckie, S. M., Cummings, M. C., Antalis, T. M., McGuckin, M. A. (2000) Heterogeneity of MUC1 expression by human breast carcinoma cell lines *in vivo* and *in vitro*. *Breast Cancer Res. Treatment 58*, 255−266.
(36) Ceriani, R. L., Chan, C. M., Baratta, F. S., Ozzello, L., DeRosa, C. M., Habif, D. V. (1992) Levels of expression of breast epithelial mucin detected by monoclonal antibody BrE−3 in breast-cancer prognosis. *Int. J. Cancer 51*, 343−354.
(37) Winthrop, M. D., DeNardo, S. J., Albrecht, H., Mirick, G. R., Kroger, L. A., Lamborn, K. R., Venclovas, C., Colvin, M. E., Burke, P. A., DeNardo, G. L. (2003) Selection and characterization of Anti-MUC-1 scFvs intended for targeted therapy. *Clin. Cancer Res., in press*.
(38) Skerra, A., Pluckthun, A. (1988) Assembly of a Functional Immunoglobulin Fv fragment in *Escherichia coli*. *Science 240*, 1038−1041.
(39) Zhao, Z. G., Im, J. S., Lam, K. S., Lake, D. F. (1999) Site-specific modification of a single-chain antibody using a novel glyoxylyl-based labeling reagent. *Bioconjugate Chem. 10*, 424−430.
(40) Adams, G. P., Schier, R., McCall, A. M., Crawford, S. M., Wolff, E. J., Weiner, M., Marks, J. D. (1998) Prolonged in vivo tumor retention of a human diabody targeting the extracellular domain of human HER2/neu. *Br. J. Cancer 77*, 1405−1412.
(41) Bayly, A. M., Kortt, A. A., Hudson, P. J., Power, B. E. (2002) Large-scale bacterial fermentation and isolation of scFv multimers using a heat-inducible bacterial expression vector. *J. Immunol. Methods 262*, 217−227.
(42) Kipriyanov, S. M., Moldenhauer, G., Martin, A. C. R., Kupriyanova, O. A., Little, M. (1997) Two amino acid mutations in an anti-human CD3 single chain Fv antibody fragment that affect the yield on bacterial secretion but not the affinity. *Protein Eng. 10*, 445−453.
(43) Turner, D. J., Ritter, M. A., George, A. J. T. (1997) Importance of the linker in expression of single-chain Fv antibody fragments: optimisation of peptide sequence using phage display technology. *J. Immunol. Methods 205*, 43−54.
(44) Knappik, A., Pluckthun, A. (1995) Engineered turns of a recombinant antibody improves its in vivo folding. *Protein Eng. 8*, 81−89.
(45) Blank, K., Diefenbach, B., Pluckthun, A. (2002) Self-Immobilizing recombinant Antibody Fragments for Immunoaffinity Chromatography: Generic, Parallel, and Scalable Protein Purification. *Protein expression and Purification 24*, 313−322.
(46) Bortoli-German, I., Brun, E., Py, B., Chippaux, M., Barras, F. (1994) Periplasmic disulphide bond formation is essential for cellulase secretion by the plant pathogen *Erwinia chrysanthemi*. *Mol. Microbiol. 11*, 545−553.
(47) Ward, E. S., Gussow, D., Griffiths, A. D., Jones, P. T., Winter, G. (1989) Binding activities of a repertoire of single immunglobulin variable domains secreted from *Eschenchi coli*. *Nature 341*, 544−546.
(48) Padlan, E. A. (1994) Anatomy of the antibody molecule. *Mol. Immunol. 31*, 169−217.
(49) Karacay, H., Sharkey, R. M., Govindan, S. V., McBride, W. J., Goldenberg, D. M., Hansen, H. J., Griffiths, G. L. (1997) Development of a streptavidin-anti-carcinoembryonic antigen antibody, radiolabeled biotin pretargeting method for radioimmunotherapy of colorectal cancer. Reagent development. *Bioconjugate Chem. 8*, 585−594.

(50) Wu, A. M., Chen, W., Raubitschek, A., Williams, L. E., Neumaier, M., Fischer, R., Hu, S. Z., Odom-Maryon, T., Wong, J. Y., Shively, J. E. (1996) Tumor localization of anti-CEA single-chain Fvs: improved targeting by noncovalent dimers. *Immunotechnology 2*, 21−36.

(51) Le Gall, F., Kipriyanov, S. M., Moldenhauer, G., Little, M. (1999) Di-, tri-, and tetrameric single chain Fv antibody fragments against human CD19: effect of valency on cell binding. *FEBS Lett. 453*, 164−168.

(52) Maack, T., Johnson, V., Kan, S. T., Figueiredo, J., Sigulem, D. (1979) Renal filtration, transport and metabolism of low molecular weight proteins: a review. *Kidney Int. 16*, 251−270.

(53) Crawford, J. (2002) Clinical uses of pegylated pharmaceuticals in oncology. *Cancer Treatment Rev. 28*, 7−11.

(54) Lind, C., Gerdes, R., Hamnell, Y., Schuppe-Koistinen, I., Brockenhuus van Lowenhielm, H., Holmgren, A., Cotgreave, I. A. (2002) Identification of S-glutathionylated cellular proteins during oxidative stress and constitutive metabolism by affinty purification and proteomic analysis. *Arch. Biochem. Biophys. 406*, 229−240.

(55) Neumann, L., Wohland, T., Whelan, R. j., Zare, R. N., Kobilca, B. K. (2002) Functional Immobilization of a Ligand-Activated G-protein-Coupled Receptor. *ChemBioChem. 3*, 993−998.

BC030018+

Effect of Limited Solid-State Glycation on the Conformation of Lysozyme by ESI-MSMS Peptide Mapping and Molecular Modeling

Faustinus K. Yeboah,*,† Inteaz Alli,‡ Varoujan A. Yaylayan,‡ Konishi Yasuo,† Shafinaz F. Chowdhury,† and Enrico O. Purisima†

Biotechnology Research Institute, 6100 Royalmount Avenue, Montreal, Quebec, Canada H4P-2R2, and Department of Food Science and Agricultural Chemistry, Macdonald Campus, McGill University, 21,111 Lakeshore Road, Ste. Anne de Bellevue, Quebec, Canada H9X 3V9. Received May 16, 2003; Revised Manuscript Received November 26, 2003

Although protein glycation has been implicated in the alteration of protein functionality, both in vivo (in biological systems) and in vitro (in food systems), the effect of the protein-bound glycan moiety on the structure/conformation of proteins that result in the modification of functionality is not clear. In this article, we report a study of the conformational changes of glycated lysozyme using LC-ESI-MSMS peptide mapping, and molecular modeling. A comparison of the RP-HPLC of the tryptic digests of unglycated and glycated lysozyme showed markedly different chromatographic profiles. Analysis of the peptide composition of the chromatographic fractions of the tryptic digests revealed that glycation of lysozyme resulted in the modification of its conformation. Glycation-induced changes in the conformation of lysozyme resulted in the exposure of its active site region to increased proteolytic activity of trypsin. Molecular simulation of triglycated lysozyme also showed that limited glycation of lysozyme caused reorientation of the active site residues (Arg 45, Arg 68, Asn 44, and Trp 62) and increased solvent accessibility into the active site region of the protein. The results of the modeling experiment corroborated the results of the RP-HPLC and ESI-MSMS peptide mapping.

INTRODUCTION

The development of age- and diabetes-related micro- and macrovascular pathologies underlying nephropathy, neuropathy, retinopathy, and sclerosis have been associated, in part, with nonenzymatic glycosylation (glycation) of body proteins and the formation and the accumulation of advanced glycation end products (AGEs) in tissues under chronic hyperglycemia (*1*−*4*). Although the molecular basis of how protein glycation leads to the development of these pathologies is not well understood, it is generally accepted that (1) AGE-modified matrix proteins interact abnormally with other matrix components and with cell surface receptors such as integrins, and (2) age-modified plasma proteins bind to AGE-specific receptors on macrophages and mesangial cells. These interactions induce receptor-mediated production of reactive oxygen species, thereby increasing the oxidative stress status of cells (*4*, *5*).

Alteration of the biological properties of glycated or AGE-modified proteins may derive from changes in their structure and conformation, with a consequent modification to their physicochemical and biochemical properties. The effects of glycation on protein structure and conformation have not been clearly established. Early-stage protein glycation, involving the formation of Amadori rearrangement products, and the initial non-cross-linking reactions of the protein bound sugar moieties, have been reported to enhance the physicochemical properties of several proteins. For example, the emulsifying properties of carp myofibrillar proteins (*6*), whey proteins (*7*), casein (*8*), plasma proteins (*9*), and lysozyme (*10*) have been shown to improve with limited glycation. The gel forming properties of dried egg white (*11*) and bovine serum albumin (*12*) have also been reported to improve with limited glycation. Limited glycation has also been shown to enhance the enzymatic activity of lysozyme (*13*, *14*) and trypsin (*15*). The thermal and conformational stability of several proteins, including bovine β-lactoglobulin (*16*, *17*) and bovine lens Crystallin (*18*) have also been shown to improve with limited glycation. These reports show that the effect of glycation on protein structure and functionality may depend on several factors, including the type of protein, the type of reducing sugar used for glycation, the glycation site on the protein, and the extent of glycation. The reports also suggest that, depending on the protein involved, limited glycation may cause a global conformational change or a localized structural change in the vicinity of the glycation site. Glycation-induced changes in the structure and functional properties of proteins may be due, in part, to the direct covalent attachment of sugar moieties to the basic amino acid residues of proteins, the glyco-oxidative reactions of the protein-bound sugar moieties, and to glycation-induced charge modification of proteins (*19*−*21*). Understanding the nature of the structure and conformational changes that accompany protein glycation will help in elucidating the functional consequences of protein glycation in both food and biological systems. Glycation-induced modification of proteins at the secondary, tertiary, and quaternary structural levels are yet to be elucidated. This paper describes the effect of glycation on conformational changes in the structure of lysozyme.

* Corresponding author. Tel: (514) 496 2593. Fax: (514) 496 5143. e-mail: faustinus.yeboah@nrc.ca.
† Biotechnology Research Institute.
‡ McGill University.

10.1021/bc034083v CCC: $27.50 © 2004 American Chemical Society
Published on Web 01/21/2004

MATERIALS AND METHODS

Materials. Hen egg white lysozyme (LZM)[1] (Sigma cat. # L-6786), D-glucose, D-fructose, and bovine trypsin (Sigma cat. # T-8003) were obtained from Sigma Chemicals (St. Louis, MO). All other chemicals and reagents were of analytical grade from Fisher Scientific (Nepean, ON, Canada). Ultrapure water from the "Nanopure" water purification system (Barnstead, Thermolyne, Dubuque, IA) was used throughout the study.

Protein Glycation. Glycated lysozyme was prepared according to the method described by Yeboah et al. (*23*). Briefly, lyophilized lysozyme or lyophilized mixtures of lysozyme and D-glucose or D-fructose (1:1 molar ratio of ϵ-amino group:sugar carbonyl groups) were incubated at 50 °C and 65% relative humidity. The temperature and humidity condition were chosen to accelerate the rate of glycation. The incubation temperature of 50 °C is below the denaturation temperature of lysozyme (~76 °C) (*22*), so thermal denaturation of lysozyme was not expected to occur in the incubated samples. Samples were incubated for 1, 2, 5, 10, or 14 days. Lyophilized lysozyme was incubated alone (without any reducing sugar) under the same temperature and humidity conditions as a control. After 1, 2, 5, 10, or 14 days of incubation, samples were taken and immediately dialyzed exhaustively against water for 48 h at 4 °C (1 kDa MW cutoff) to remove free unreacted sugar and other low molecular weight reaction products. After dialysis, the samples were lyophilized and stored at −20 °C prior to further analysis.

Tryptic Hydrolysis. Solutions (25 mL) of lysozyme that had been incubated alone for 14 days (LZM) or lysozyme that had incubated with D-glucose (LZM-G) or D-fructose (LZM-F) (100 mg/mL, pH 8.5), and of bovine trypsin (4 mg/mL, pH 8.5) were mixed together (lysozyme:trypsin; 25:1) and incubated at 37 °C. After 6 h incubation, the hydrolysis reaction was terminated by rapidly heating the reaction mixture to boiling. Samples were then cooled over ice, filtered (0.22 μm Millipore syringe filter), and lyophilized. The lyophilized tryptic digests were stored at −20 °C prior to further analysis.

Reversed Phase HPLC. Quantities (5 mg) of the lyophilized tryptic digest of LZM, LZM-G, or LZM-F (prepared as described above) were dissolved in 0.1% aqueous trifluoroacetic acid (TFA) (1 mL), vortexed, and sonicated for 15 min. The resulting solutions were filtered through 0.22 μm syringe filters, and 50 μL of the filtrate was injected for RP-HPLC analysis. RP-HPLC analysis was performed on a Beckman Gold HPLC system, equipped with a UV diode-array detector (Beckman Instruments, Inc., Fullerton, CA). The mobile phase consisted of 0.1% TFA in water (solvent A) and in acetonitrile (solvent B), and the elution gradient was 0% to 60% solvent B in 40 min. Separation was achieved on a reversed phase analytical column (Vydac C_{18} column, 218TP54) at a flow rate of 1 mL/min. Eluting peaks (monitored 220 nm) were collected for electrospray tandem mass spectrometric analysis.

ESI-Mass Spectrometry. Lyophilized HPLC fractions were reconstituted in 70% aqueous acetic acid and analyzed by ESI-MSMS using an API−III MSMS system (SCIEX, Thornhill, Ontario, Canada). Samples were infused into the electrospray ion source through a fused silica capillary (100 μm i.d.) at a rate of 1 μL/min using a low-pressure infusion pump (Model 22, Harvard Apparatus, South Natick, MA). The sequence of tryptic peptides was determined from their collision-induced dissociation (CID) spectrum. The composition of glycoforms of lysozyme in the incubated samples was determined from the area of their corresponding peaks in the electrospray ionization (ESI) mass spectrum. The relative composition of individual glycoforms in the incubation mixture is proportional to the relative area their corresponding peaks. (*23*)

Molecular Modeling of Glycated Lysozyme. The AMBER force field (*24*, *25*) was used to simulate the effect of glycation on the conformation of lysozyme. The parameters had to be supplemented for glycated lysine residues. Missing equilibrium bond and angle parameters of the lysine-bound glucose moiety (Amadori product of lysine in the pyranose for) were obtained from the model compounds in the Cambridge Structural Database (*26*). Force constants were derived from similar atom types in the AMBER force field, and partial charges for glycated lysine were obtained by fitting to the 6-31G* electrostatic potential as calculated in GAMESS (*27*, *28*).

A triglycated model of chicken egg white lysozyme was developed, by replacing Lys-1, Lys-33, and Lys-97 with glucose-derived Amadori-lysine (in the pyranose form) that is glycated at the ϵ-amino group. These three residues were chosen for modification in the glycated lysozyme model because they were the most reactive residues in the protein. Another reason for using a triglycated model of lysozyme in the molecular modeling studies was that the average sugar load, in the form of Amadori product (average number of Amadori-products molecules per molecule of lysozyme) was approximately 2.4, so the next highest whole number was chosen. Molecular models of native lysozyme and of the triglycated lysozyme model were subjected to conjugate gradient energy minimization using a distance-dependent dielectric function ($\epsilon = 4r$) and an 8 Å nonbonded cutoff. Solvation effects were included, using an implicit solvation model with continuum electrostatics (*29*, *30*).

A conformational search using Monte Carlo minimization (*31*−*33*) was carried out to explore the effect of glycation on the structure of lysozyme. The side chain dihedral angles of glycated Lys 1, 33, 97 and of 18 amino acids (Val 2, Arg 21, Phe 34, Asn 37, Gln 41, Thr 43, Asn 44, Arg 45, Asp 52, Gln 57, Trp 62, Trp 63, Arg 68, Leu 75, Ser 81, Ser 86, Val 109, Trp 123) present in and around the active site of lysozyme were searched for a total of 20 000 Monte Carlo-minimization cycles. During minimization, all atoms in the protein were allowed to move. As a control, a similar conformational search was carried out on the same set of amino acids for native enzyme.

RESULTS

Glycation. Incubation of lysozyme with D-glucose or D-fructose resulted in the formation of a mixture of glycoforms of lysozyme. The ESI-mass spectrum of lysozyme incubated alone for 1 day (A), lysozyme incubated with fructose (B), and lysozyme incubated with glucose (C) for 1 day are presented in Figure 1. The mass spectra show the profile of glycoforms of lysozyme formed after 1 day of incubation. Only one peak, corresponding to lysozyme can be observed when lysozyme was incubated alone for 1 day. Incubation of lysozyme with D-fructose resulted in the formation of two glycoforms, mono- and difructated lysozyme (Figure 1B), while the incubation of lysozyme in the presence of glucose resulted

[1] Abrreviations: ESI/MS, electrospray mass spectrometry; ESI/MS/MS, electrospray tandem mass spectrometry; LZM, lysozyme incubated alone; LZM-F, lysozyme glycated by D-fructose; LZM-G, lysozyme glycated by D-glucose; TFA, trifluoroacetic acid.

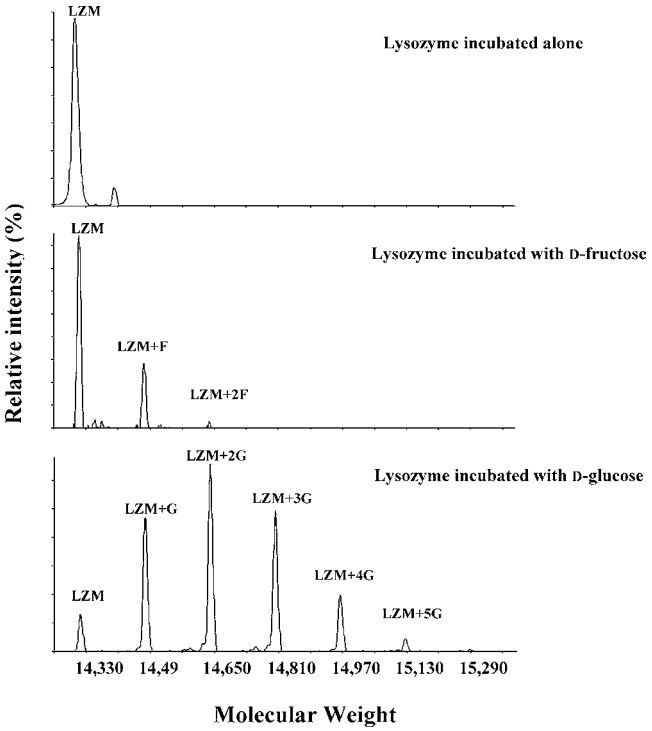


Figure 1. Reconstructed ESI-MS spectra of lysozyme incubated alone for 1 day and of lysozyme incubated with D-fructose and D-glucose for 1 day, showing the distribution of glycoforms of lysozyme formed during incubation.

in extensive glycation, leading to the formation of a mixture of five glycoforms ranging from mono- to pentaglucated lysozyme (Figure 1C). Less than 30% of lysozyme was glycated in the lysozyme−fructose system after the 1st day of incubation, while over 90% of lysozyme was glycated in the lysozyme−glucose system in the same period of incubation. The extent of glycation, determined as the average sugar load per molecule of lysozyme, increased with time of incubation in both sugar systems, but the rate of sugar loading of lysozyme when incubated with glucose was 5 to 6 times higher than when lysozyme was incubated with fructose throughout the incubation period.

Tryptic Digests of Unglycated and Glycated Lysozyme. The chromatographic profiles of the tryptic digest of unglycated and glycated lysozyme are presented in Figures 2 and 3. Figure 2A−D represents the chromatograms of the tryptic digests of lysozyme incubated alone for 14 days, and lysozyme incubated with D-fructose for 1, 5, and 14 days, respectively. Figure 3A−D represents the chromatograms of the tryptic digests of lysozyme incubated alone for 14 days, and lysozyme incubated with D-glucose for 1, 5, and 14 days, respectively. A comparison of the tryptic peptide profile of unglycated lysozyme and that of glycated lysozyme after different periods of incubation reveal marked differences between unglycated and glycated lysozyme. Several peaks (e.g. peaks 3 and 8) that were not observed in the peptide profile of the tryptic digest of unglycated lysozyme appeared in the tryptic digest of glycated lysozyme after only 1 day of incubation with D-fructose. After the 5th day of incubation, other peaks (e.g. peaks 2, 4, and 13) also appeared in the chromatogram in significant amounts. The relative proportion of peaks 7, 12, 14, and 15 decreased sharply after the 1st day of incubation, while at the same time the relative proportions of peaks 5 and 9 increased sharply. The HPLC peptide profile of lysozyme changed progressively with time of incubation. Similar results

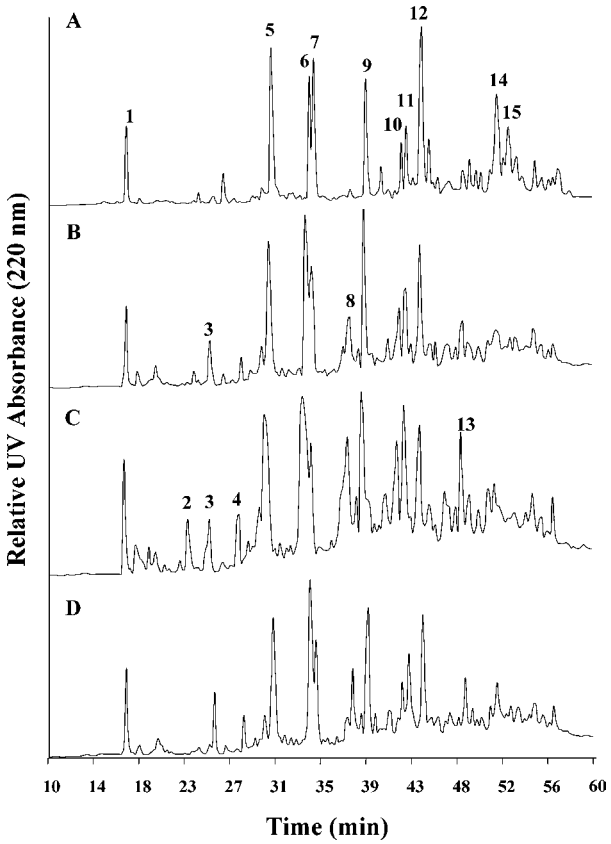


Figure 2. Reversed phase HPLC chromatograms of tryptic digest of unglycated lysozyme incubated alone for 14 days (LZM) (panel A), and lysozyme incubated with D-fructose after 1, 5, and 14 days (panels B, C, and D, respectively), showing peaks (labeled 1 through 15) that were collected and analyzed with ESI-MSMS.

were observed for the tryptic digest of lysozyme glycated with D-glucose as with D-fructose, but the extent of the changes was more pronounced for lysozyme incubated with D-glucose especially after prolonged incubation (Figure 3).

Identification of Tryptic Peptides. Electrospray tandem mass spectrometric was used to identify and sequence the peptide components of the tryptic digests. Table 1A,B shows the m/z $(M + H)^+$ values and the sequence of the peptides identified in the HPLC fractions of the tryptic digests of unglycated and glycated lysozyme after 1, 5, and 14 days of incubation. The symbol "+" or "−" is used to indicated the presence or absence of the designated peptide in the HPLC fraction, and the symbol "++" is used to indicate the major peptide component of an HPLC fraction, if the fraction contains more than one peptide component. The symbol "=" is used to indicate peptide fragments that contain disulfide bonds, and the symbol "*" placed after an amino acid letter code indicates that that amino acid residue is the glycation site. Most of the identified peptides were trypsin-specific peptides (i.e., produced by the cleavage of peptide bonds at the carboxyl end of a lysine or arginine residue). Nontrypsin specific of peptides, such as peptide residues 109−112, 117−123, 97−108, and 98−108 produced by the cleavage of peptide bonds at the carboxyl end of Trp-108 and Trp-123 were also identified.

Residues 117−125 and 98−112, identified in HPLC fractions 12 and 15, respectively, of the tryptic digest of unglycated lysozyme were not detected in the digests of any of the glycated samples. The peptide components of HPLC fractions 2, 3, and 8 of the tryptic digest of glycated

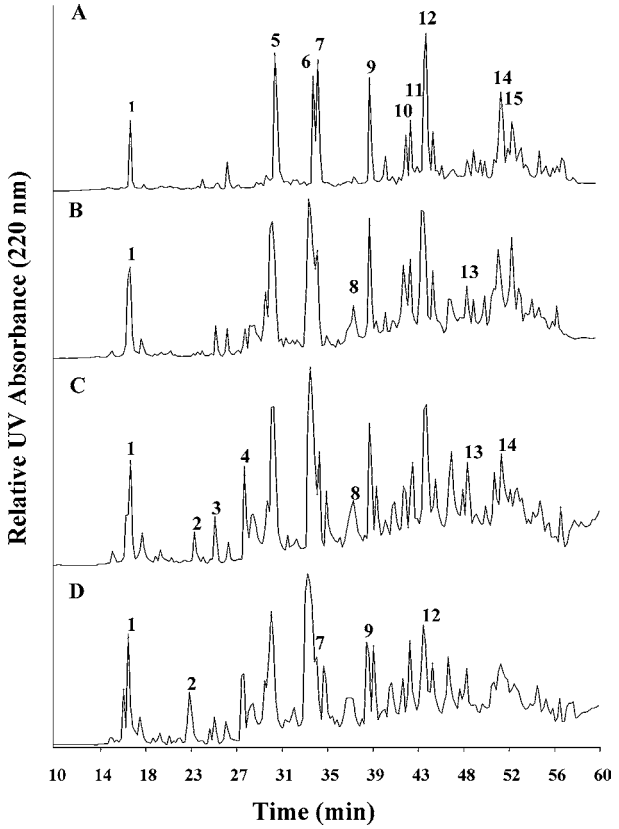


Figure 3. Reversed phase HPLC chromatograms of tryptic digest of unglycated lysozyme incubated alone for 14 days (LZM) (panel A), and lysozyme incubated with D-glucose after 1, 5, and 14 days (panels B, C, and D, respectively), showing peaks (labeled 1 through 15) that were collected and analyzed with ESI-MSMS.

lysozyme (glucated and fructated) were identified as residues 46−53, 35−45, and 60−68, respectively. These peptides were not observed in the tryptic digest of unglycated lysozyme, but they appeared in the digest of glycated lysozyme after the 1st day of incubation. The peptide components of HPLC fraction 13 were identified as residues 22−28, 46−59, 47−61, and 64−84. These peptides were also not released in the digest of unglycated lysozyme. The peptide defined by residues 22−28 was also released in the tryptic digest of glycated lysozyme after the 1st day of incubation in both sugar systems, but residues 46−59, 47−61, and 64−84 were detected in the digest of glucated lysozyme samples after the 5th day of incubation. These peptides were derived by the cleavage of nontrypsin specific bonds.

Glycation of lysozyme with glucose had a more pronounced effect on the peptide composition of the tryptic digest of lysozyme than with fructose. For example, after just 1 day of incubation of LZM with glucose (LZM-G), the peptides defined by residues 1−5, 97−108, 22−23=115−116, 97−112, and 98−112 could not be detected in HPLC fractions 5, 10, 14, and 15, respectively. These peptides were, however, observed in the digest of LZM-F even after the 5th day of incubation. Prolonged incubation of lysozyme with glucose (after 5 days) also resulted in the release of peptides defined by residues 46−59, 47−61, and 64−84 in HPLC fraction 13. These residues were not observed in the tryptic digests of unglycated lysozyme or any of the LZM-F samples. Di- and triglycated peptides ($[M + H]^+ = 936.4$ and 2400.2; see Table 1), and glycated peptides for which the bound sugar moieties had undergone further dehydration (residues with $(M + H)^+ = 750.4$, 1654.8, and 1493) to form deoxyosones were detected in the digests of glycated lysozyme samples (both LZM-F and LZM-G) after the 5th day of incubation. Glycated peptides that had undergone both dehydration and deamination ($[M + H]^+ = 1654.8$ and 1493.6) were only detected in the digest of LZM-G after the 5th day of incubation.

DISCUSSION

Tryptic Peptide Profile. Differences in the chromatographic profile of the tryptic digest of unglycated lysozyme (LZM) and glycated lysozyme (LZM-F or LZM-G) (Figures 2 and 3) suggests that glycation of LZM resulted in changes to its conformation. A comparison of the chromatographic profile of the tryptic digests of unglycated and glycated lysozyme provided information about glycation-induced conformational changes in the structure of lysozyme. Monitoring of the peptide components of chromatographic peaks that appeared only in the tryptic digest of the glycated lysozyme samples also provided information about the regions or domains of unglycated lysozyme that had become more exposed to the proteolytic activity of trypsin after glycation. The peptide profile of peaks that disappeared, or reduced in relative intensity in the chromatogram of the tryptic digest of unglycated lysozyme after glycation provided information about the regions of lysozyme that had become less exposed, or more resistant to the proteolytic activity of trypsin. Information about the glycation sites of lysozyme, and the relative reactivities of the identified glycation sites could also be determined from changes in the chromatographic and peptide profiles of the tryptic digests of lysozyme after glycation.

The detection of peptide residue 46−53, 35−45, 60−68, and 22−28 in HPLC fractions 2, 3, 8, and 13, respectively (Table 1A), of the tryptic digests of glycated lysozyme after the 1st day of incubation indicate that the region(s) or domain(s) of lysozyme that contained these peptide fragments became more exposed to the proteolytic activity of trypsin after limited glycation. An inspection of the 3-D structure of native lysozyme showed that these peptide fragments are all located within or in the vicinity of the active site of lysozyme. A comparison of the chromatographic profile of the tryptic digests (Figures 2 and 3) of unglycated and glycated lysozyme also reveal that the relative chromatographic response of peaks 6, 9, 10, and 11 increased markedly after the 1st day of incubation. The peptide component(s) of these chromatographic fractions were identified as residues 109−112, 117−123, 54−61, and 97−108, respectively. These residues were also found to be located in the vicinity of the active site of lysozyme.

These results show that limited glycation of lysozyme caused an increased exposure of its active site residues to the proteolytic activity of trypsin. It also suggests that limited glycation of lysozyme increased solvent penetration into its active site. This observation may explain the enhanced enzymatic activity of lysozyme after limited glycation (*13, 14*). The active site residues of lysozyme include Phe 34, Glu 35, Ser 36, Asn 37, Asn 44, Asp 52, Leu 56, Gln 57, Trp 62, Trp 63, Leu 75, Asp 101, Asn 103, Ala 107, Trp 108, Val 109, Ala 110, and Arg 114.

The sharp decrease in the relative chromatographic response of peaks 7, 12, 14, and 15 after the 1st day of incubation show that the regions of lysozyme that contain their peptide components had become resistant to the proteolytic activity of trypsin after glycation. The peptide component(s) of fractions 7, 12, 14, and 15 are residues 34−45, 117−125, 97−112, and 98−112 respectively, all

Table 1. Peptide Composition of the Chromatographic Fractions of the Tryptic Hydrolysates of Lysozyme (LZM) and Its Glycated Analogues Lysozyme−Fructose (LZM-F) and Lysozyme−Glucose (LZM-G) after 1, 2, 5, 10, and 14 days of Incubation

					LZM-F			LZM-G		
HPLC fractions	$(M + H)^+$	residues	sequence	LZM	day 1	day 5	day 14	day 1	day 5	day 14
			A. Unglycated Peptides							
1	517.4	69−73	R-TPGSR-N	+	+	+	+	+	+	+
2	872.4	46−53	R-NTDGSTDY-G	-	+	+	+	+	+	+
3	1281.7	35−45	F-ESNFNTQATNR-N	−	+	+	+	+	+	+
5	874.6	15−21	R-HGLDNYR-G	+	++	++	++	++	+	+
5	478.4	2−5	K-VFGR-C	++	+	+	+	+	−	−
5	606.4	1−5	KVFGR-C	+	+	+	−	−	−	−
6	531.6	109−112	W-VAWR-N	+	+	+	+	+	+	+
7	1429.6	34−45	K-FESNFNTQATNR-N	+	+	+	+	+	+	−
7	1474.8	117−129	K-GTDVQAWIRGCRL	−	−	−	−	−	+	−
8	1179.8	60−68	N-SRWWCNDGR-T	−	+	+	+	+	+	
9	776.4	117−123	K-GTDVQAW-I	+	+	+	+	+	+	+
10	900.6	54−61	Y-GILQINSR-W	−	++	+	+	+	+	+
10	1292.6	97−108	K-KIVSDGNGMNAW-V	+	+	−	−	−	−	−
11	1163.6	98−108	K-IVSDGNGMNAW-V	+	+	+	+	+	+	+
12	1045	117−125	K-GTDVQAWIR-G	+	−	−	−	−	−	−
12	1155.6	46−56	R-NTDGSTDYGIL-Q	−	+	+	+	+	+	+
12	1755.2	46−61	R-NTDGSTDYGILQINSR-W	++	++	++	++	++	++	++
13	796.4	22−28	R-GYSLGNW-V	−	+	+	+	+	+	+
13	1510.6	46−59	R-NTDGSTDYGILQIN-S	−	−	−	−	−	+	+
13	2205.8	64−84	W-CNDGRTPGSRNLCNIPCSALL-S	−	−	−	−	−	++	++
14	1517.6	22−33=115−116	R-(GYSLGNMVCAAK)-F=R-(CK)-G	++	++	+	−	−	−	−
14	1805.1	97−112	K-KIVSDGNGMNAWVAWR-N	+	+	−	−	−	−	−
15	1676.7	98−112	K-IVSDGNGMNAWVAWR-N	+	−	−	−	−	−	−
			B. Glycated Peptides							
5	768.6	(1−5)+G	K*VFGR-C	−	−	+	+	+	+	−
5	750.4	(1−5)+G-H_2O	K*VFGR-C	−	−	−	+	−	+	−
5	936.4	(1−5)+2G	K**VFGR-C	−	−	+	+	+	+	−
9	1153.2	(6−14)+G	R-CELAAAMK*R-H	−	−	+	+	−	+	+
10	1454.6	(97−108)+G	K-K*IVSDGNGMNAW-V	−	−	+	+	+	+	+
13	1315.8	(6−14)+2G	R-CELAAAMK**R-H	−	−	−	−	−	+	+
13	1654.8	(46−59)+G-H_2O	R-NTDGSTDYGILQIN-S	−	−	−	−	−	+	+
14	1493.6	(46−59)-NH_3	R-NTDGSTDYGILQIN-S	−	−	−	−	−	+	−
14	2400.2	(1−14=126−128)+3G	(K**VFGRCELAAAMK*R)-H=R-(GCR)-L	−	−	+	+	+	+	−

"+" indicates that peptide was identified in fraction, and "++" is used to indicate the Major peptide component in cases where HPLC fraction contained more than one peptide. "−" indicates that peptide was not identified in fraction or is present below the detectable limit, and "=" is used to indicate disulfied bonds. A. unglycated peptides, and B glycated peptides identified in the HPLC fractions of the hydrolysates of the LZM-F and LZM-G systems.

of which are produced by the cleavage of a peptide bond at the carboxyl end of a lysine residue (Lys-33, -96, -97, and -116). The decreased rates of release of these fragments indicate that the ϵ-amino groups of the respective lysine residues had undergone glycation. This does not mean that every molecule of lysozyme is glycated at all four lysine residues, but that different populations of glycoforms of lysozyme with varying degrees of glycation at Lys-33, -96, -97, and -116 had been formed in the glycation mixture (Figure. 1). The major peptide component of fraction 5 of unglycated lysozyme was residue 2−5, which is formed by the cleavage of peptide bonds at the carboxyl end of Lys-1 and Arg-5. After the 1st day incubation of lysozyme with fructose, the major peptide component of fraction 5 was no longer residue 2−5, but residue 15−21. In addition, peptide fragment 1−5 was not observed in any of the tryptic digests of LZM-G samples, even after only 1 day of incubation, due to the extensive nature of the glycation of lysozyme in the when incubated with glucose. These results indicate the glycation of either the N-terminal α-amino group and/or the ϵ-amino group of Lys-1. The fact that the peptide fragments defined by residues 117−125, and 98−112 could not be detected in the tryptic digest of even the least glycated sample (LZM-F after 1 day incubation) also indicates the glycation of Lys-97 and -116. The results of this study show that all seven lysine residues of lysozyme were involved in the glycation reaction and that Lys-1, -33, and -97 were the most susceptible residues to the glycation reaction. The list of identified glycated peptides (Table 1B) show that diglycation occurred at Lys-1 and -33. The diglycation at Lys-1 could be due to glycation of the N-terminal α-amino and ϵ-amino group or diglycation at the ϵ-amino group. The results of this study are consistent with the report of previous studies (where the lysine residues of lysozyme were modified with acetic anhydride) (*33*), where the order of reactivity of the ϵ-amino groups of the lysine residues of lysozyme was reported as Lys-97 > -33 > -1> -13 > -116 > -96.

Effect of Glycation on the Structure Lysozyme. Changes in the chromatographic profile of the tryptic digest of lysozyme, and in the peptide composition of the HPLC fractions after glycation, show that the glycation of lysozyme resulted in a modification of its structure and conformation. Differences between in the chromatographic and peptide profile of the tryptic digests of lysozyme glycated with glucose and fructose (Figures 2 and 3) can be explained by the differences in the extent of glycation in the two sugar systems. The most dramatic change in the peptide profile of the tryptic digest of lysozyme occurred after the 1st day of incubation with either glucose or fructose. These changes were accompanied by the release of new peptides (residues 46−53, 35−45, 54−61, 46−56, and 22−28) that were not

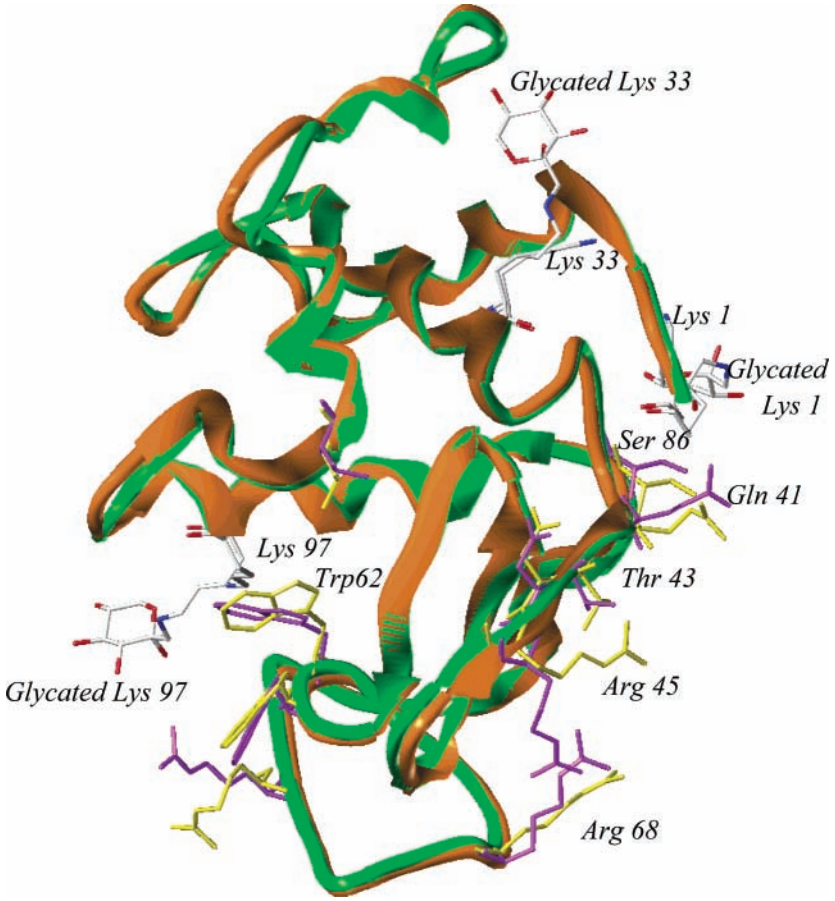


Figure 4. Superimposed structures of native hen egg white lysozyme and its triglycated model. Residues that showed conformational change after glycation are highlighted in yellow (in the glycated model) and purple (in the native enzyme). Secondary structures colored green (in the glycated model) and orange (in the native enzyme) are displayed. Glycated residue Lys 1, Lys 33, and Lys 97 are displayed for clarity.

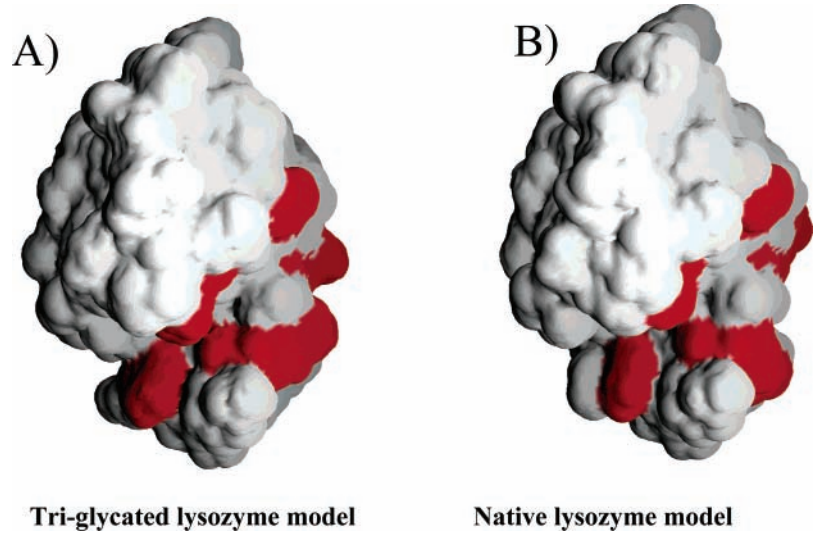


Figure 5. Solvent-accessible surface area of the triglycated model of lysozyme (A) and of the native lysozyme (B). The solvent-accessible surface area of the active site residues is highlighted in red for comparison (see text for detail).

observed in the digest of unglycated lysozyme. The amino acid residue of the peptide fragments defined by residues 46−53, 35−45, 54−61, and 46−56 constitute the active site amino acid residues of lysozyme. The increased rate of release of the peptide fragments from the active site of lysozyme as a result of glycation show that the glycation of lysozyme modified its conformation to expose the active site to the proteolytic activity of trypsin.

It has been reported that reductive methylation of all the ϵ-amino groups of lysozyme resulted in only minor overall structural change of the protein, but caused significant modifications to the surface loops defined by residues 69−72 and 101−103, as well as the C-terminal residues 126−129 (*34*). The minor structural changes effected by the reductive methylation of lysozyme may be due to the small size and hydrophobic nature of the

methyl group. The larger size of D-fructose or D-glucose, with their numerous hydroxyl groups, on the other hand, may cause a more significant change to the structure and hydrodynamic properties of lysozyme as observed in this study.

Modeling. Monte Carlo simulations of models of native and glycated lysozyme were carried out to determine structural perturbation caused by limited glycation, given that limited glycation of lysozyme (after the 1st day of incubation) resulted in significant changes in the chromatographic and peptide profile of the tryptic digest of lysozyme. A superposition of the lowest-energy structures of native lysozyme and a model of triglycated lysozyme is presented in Figure 4. Overall, only minor structural differences were observed between the model of native lysozyme and the triglycated model. However, there was significant reorientation of the side chains of glycated Lys-1, -33, and -97, Gln 41, Thr 43, Asn 44, Arg 45, Arg 68, Trp 62, and Val 109. With the exception of the glycated lysine residues (Lys-1, -33, and -97), the common feature between these amino acid residues is that they are all located in the active site region of lysozyme. A comparison between the solvent-accessible surface area of native lysozyme (6487.11 Å^2) and of the triglycated lysozyme model (6894.38 Å^2) shows a significant net increase of 407.27 Å^2 in the triglycated lysozyme model compared to the native enzyme. The solvent-accessible surface area of the active site region increased from 470 Å^2 in native lysozyme to 550 Å^2 in the triglycated model. This increase of 80 Å^2 is significant, given that it represents ~20% of the total net increase in solvent accessibility of lysozyme (407.27 Å^2), when the contribution of the active site region to the total solvent accessible surface area of native lysozyme is only 7.2%. Figure 5 shows the solvent-accessible surface area of the triglycated lysozyme model (A) and of native lysozyme (B). The solvent-accessible surface area of the active site region is indicated in red for clarity. The reorientation of the side chains of the active site residues, coupled with the increase in the solvent-accessibility of the active site, is consistent with the increased susceptibility of the active site residues in the glycated protein to tryptic digestion.

CONCLUSION

The findings of this study show that limited glycation of lysozyme resulted in conformational changes that increased the susceptibility of its active site region to the proteolytic activity of trypsin. The extent and nature of the conformational change depended on the extent of glycation, as well as the site(s) of glycation. The results also showed that conformational changes could occur at the glycation sites or regions remote from the site of glycation. Although the observed glycation sites of lysozyme in both sugar systems were similar, fructose showed a higher degree of specificity in glycating the ϵ-amino groups of the most reactive lysine residues (Lys-1, -33, and -97) during the early stages of the glycation reaction, due to the lower reactivity of fructose.

The results of this study also show that ESI-MS peptide mapping is a powerful technique for revealing specific and global changes in protein structure due to chemical modifications such as glycation. Glycation-induced changes in the peptide profile of the chromatographic fractions of the tryptic digest of lysozyme at different extends of glycation provided information about the dynamic nature of the changes in the structure and conformation the protein.

LITERATURE CITED

(1) Thorpe, S. R., and Baynes, J. W. (1996) Role of Maillard reaction in diabetes mellitus and diseases of aging. *Drugs Aging 9*, 69−77.

(2) Friedman, E. A. (1999) Advanced glycation end-products in diabetes nephropathy. *Nephrol. Dial. Transplant.. 14* (Suppl. 3), 1−9.

(3) Beisswenger, P. J., Makita, Z., Curphey, T. J., Moore, L. L., Jean, S., Brinck-Johnsen, T., Bucala, R., and Vlassara, H. (1995) Formation of immunochemical advanced glycosylation end products precedes and correlates with early manifestations of renal and retinal disease in diabetes. *Diabetes 44* (7), 824−9.

(4) Brownlee, M. (2001) Biochemistry and molecular cell biology of diabetic complications. *Nature 414* (6865), 813−20.

(5) Gugliucci, A. (2000) Glycation as the glucose link to diabetic complications. *Clin Prac. 100*, 621−634.

(6) Saeki, H. (1997) Preparation of neoglycoprotein from carp myofibrillar protein by Maillard reaction with glucose: biochemical properties and emulsifying properties. *J. Agric. Food Chem. 45*, 680−684.

(7) Nacka, F., Chobert, J. M., Burova, T., Leonil, J., Haertle, T. (1998) Induction of new physicochemical and functional properties by the glycosylation of whey proteins. *J. Protein Chem. 17*, 495−503.

(8) Darewicz, M., Dziuba, J., Mioduszewska, H. (1998) Some physicochemical properties and structural changes of bovine beta-casein upon glycation. *Nahrung 42* (3−4), 213-214.

(9) Matsumodi, N., Inoue, Y., Nakashima, H., Kato, A., Kobayashi, K. (1995) Emulsion stabilization by Maillard-type covalent complex of plasma protein with galactomannan. *J. Food Sci. 60*, 265−268, 283.

(10) Shu, Y. W., Sahara, S., Nakamura, S., and Kato, A. (1996) Effects of the length of polysaccharide chains on the functional properties of the Maillard-type lysozyme -polysaccharide conjugate. *J. Agric. Food Chem. 44*, 2544−2548.

(11) Handa, A., and Kuroda, N. (1999) Functional improvement in dried egg white through the Maillard reaction. *J. Agric. Food Chem. 47*, 1845−1850.

(12) Mat Easa, A., Hill, S. E., Mitchell, J. R., and Taylor, A. J. (1996) Bovine serum albumin gelation as a result of the Maillard reaction. *Food Hydrocoll. 10*, 199−202.

(13) Kato, A., Nakamura, S., Takasaki, H., and Maki, S. (1996) Novel functional properties of glycosylated lysozyme constructed by chemical and genetic modifications. *Macromolecular Interactions in Food Technology* (Parris, N., Kato, A., Creamer, L., and Pearce, J., Eds.) pp 242−256, ACS Symposium Series 650, American Chemical Society: Washington, DC.

(14) Nakamura, S., Kato, A., and Kobayashi, K. (1991) New antimicrobial characteristics of lysozyme−dextran conjugate. *J. Agric. Food Chem. 39*, 647−650.

(15) Kato, Y., Matsuda, T., and Nakamura, R. (1993) Improvement of physicochemical and enzymatic properties of bovine trypsin by non-enzymatic glycation. *Biosci. Biotechnol. Biochem. 57*, 1−5.

(16) Morgan, F., Leonil, J., Molle, D., and Bouhallab, S. (1999) Modification of bovine □-lactoglobulin by glycation in a powdered state or in an aqueous solution: Effect on association behavior and protein conformation. *J. Agric. Food Chem. 47* (1), 83−91.

(17) Chevalier, F., Chobert, J., M.; Popineau, Y., Nicolas, M. G., and Haertle, T. (2001) Improvement of the functional properties of ×e2β-lactoglobulin glycated through the Maillard reaction is related to the sugar nature. *Int. Dairy J. 11*, 145−152.

(18) Liang, J. N., Rossi, M. T. (1990) In vitro non-enzymatic glycation and formation of browning products in the bovine lens alpha-crystallin. *Exp. Eye Res. 50* (4), 367−371.

(19) Takizawa, N., Takada, K., and Ohkawa, K. (1993) Inhibitory effect of nonenzymatic glycation on ubiquitination and ubiquitin-mediated degradation of lysozyme. *Biochem. Biophys. Res. Commun. 192* (2), 700−706.

(20) Winlove, C. P., Parler, K. H., Avery, N. C., and Bailey, A.J. (1996) Interactions of elastin and aorta with sugars in vitro

and their effect on biochemical and physical properties. *Diabetologia 39* (10), 1131−1139.
(21) Coussons, P. J., Jacoby, J., McKay, A., Kelly, S. M., Price, N. C., and Hunt, J. V. (1997) Glucose modification of human serum albumin: a structural study. *Free Radical Biol. Med. 22* (7), 1217−1227.
(22) Elkordy, A. A., Forbes, R. T., and Barry, B. W. (2002) Integrity of crystalline lysozyme exceeds that of a spray-dried form. *Int. J. Pharm. 247* (1−2), 79−90.
(23) Yeboah, F. K., and Yaylayan, V. A. (2001) Analysis of glycated proteins by mass spectrometric techniques: qualitative and quantitative aspects. *Nahrung/Food. 45* (3), 64−171.
(24) Simmering, C., Fox, T., and Kollman, P. A. (1998) Use of Locally Enhanced Sampling in Free Energy Calculations: Testing and Application to the α to *β* Anomerization of Glucose. *J. Am. Chem. Soc. 120*, 5772−5782.
(25) Cornell, W. D. (1995) A Second Generation Force Field for the Simulation of Proteins, Nucleic acids and Organic Molecules. *J. Am. Chem. Soc. 117*, 5179−5197.
(26) Allen, F. H., Davies, J. E., Galloy, J. J,, Johnson, O., Kennard, O., Macrae, C. F., Mitchel, E. M., Mitchel, G. F., Smith, J. M., and Watson, D. G. (1991) The development of version-3 and version-4 of the Cambridge Structural Databse system. *J. Chem. Inf. Comput. Sci. 31*, 187−204.
(27) Cornell, W. D., Cieplak, P., Bayly, C. I., and Kollman, P. A. (1993) Application of RESP Charges to Calculate Conformational Energies, Hydrogen Bond Energies, and Free Energies of Solvation. *J. Am. Chem. Soc., 115*, 9620−9631.
(28) Schmidt, M. W., Baldridge, K. K., Boatz, J. A., Elbert, S. T., Gordon, M. S., Jensen, J. H., Koseki, S., Matsunaga, N., Nguyen, K. A., Su, S., Windus, T. L, Dupuis, M., and Montgomery, J. A., Jr (1993) General Atomic and molecular Electronic Structure System. *J. Comput. Chem. 14*, 1347−1353.
(29) Purisima, E. O., and Nilar, S. H. (1995) A Simple Yet Accurate Boundary Element Method for Continuum Dielectric Calculations. *J. Comput. Chem. 16* (6), 681−689.
(30) Purisima, E. O. (1998) First Summation Boundary Element Method for Calculating Solvation Free Energies of Macromolecules. *J. Comput. Chem. 19* (13), 1494−1505.
(31) Li, Z., and Scheraga, H. A. (1987) Monte Carlo Minimization Approach to the Multiple-Minima Problem in Protein Folding. *Proc. Natl. Acad. Sci. U.S.A. 84*, 6611−6615.
(32) Chowdhury, S. F., Villamor, V. B., Guerrero, R. H., Leal, I., Brun, R., Croft, S. L., Goodman, J. M., Maes, L., Ruiz-Perez, L. M., Pacanowska, D. G., and Gilbert, I. H. (1999) Design, Synthesis, and Evaluation of Inhibitors of Trypanosomal and Leishmanial Dihydrofolate Reductase. *J. Med. Chem. 42*, 4300−4312.
(33) Suckau, D., Mak, M., and Przybylski, M. (1992) Protein surface topology-probing by selective chemical modification and mass spectrometric peptide mapping. *Proc Natl Acad Sci. U.S.A. 89* (12), 5630−5634.
(34) Rypniewski, W. R., Holden, H. M., Rayment, I. (1993) Structural consequences of reductive methylation of lysine residues in hen egg white lysozyme: An X-ray analysis at 1.8-A resolution. *Biochemistry 32*, 9851−9858.

BC034083V

Liposomes with Differential Lipid Components Exert Differential Adjuvanticity in Antigen−Liposome Conjugates via Differential Recognition by Macrophages

Yuriko Tanaka,[†] Michiyuki Kasai,[†] Maiko Taneichi,[†] Seishiro Naito,[†] Hiroshi Kato,[†] Masahito Mori,[‡] Mitsuhiro Nishida,[‡] Naoya Maekawa,[‡] Hiroyuki Yamamura,[‡] Katsutoshi Komuro,[†] and Tetsuya Uchida*[,†]

Department of Safety Research on Blood and Biological Products, National Institute of Infectious Diseases, Tokyo 208-0011, Japan and Drug Delivery System Development Division, Nippon Oil and Fat Corporation, Tokyo 150-6019, Japan. Received July 28, 2003; Revised Manuscript Received November 12, 2003

We previously reported that liposomes having differential lipid components displayed differential adjuvant effects when antigen was coupled with liposomes via glutaraldehyde. In the present study, antigen−liposome conjugates prepared using liposomes having differential lipid components were added to the macrophage culture, and phagocytosis and the antigen digest of liposome-coupled antigen by macrophages were then investigated. Antigen presentation by macrophages to an antigen-specific T-cell clone was further investigated using the same conjugates. Antigen−liposome conjugates which induced higher levels of antibody production in vivo were recognized more often, and the liposome-coupled antigen was digested to a greater degree by macrophages than antigen−liposome conjugates which induced lower levels of antibody production. These results correlated closely with those regarding antigen presentation by macrophages; when antigen was coupled to liposomes showing higher adjuvant effect, macrophages cocultured with antigen−liposome conjugates activated antigen-specific T-cells at a higher degree. The concentration of OVA in the macrophage culture added as antigen−liposome conjugates was approximately 32 μg/mL. However, the extent of T-cell activation was almost equal to that when 800 μg/mL of soluble OVA was added to the culture. The results of the present study demonstrated that the adjuvant activity of liposomes observed primary in vivo correlated closely with the recognition of antigen−liposome conjugates and antigen presentation of liposome-coupled antigen by macrophages, suggesting that the adjuvant effects of liposomes are exerted at the beginning of the immune response, i.e., recognition of antigen by antigen-presenting cells.

INTRODUCTION

Adjuvants play a pivotal role in vaccination, especially when the vaccine antigen itself possesses a weak immunogenicity (*1*−*3*). At present, aluminum adjuvant is the only adjuvant that is clinically in use, although a number of candidate adjuvants have beeen reported and examined in a preclinical study (*3*). However, aluminum adjuvants are known to be effective only for the induction of humoral immunity, not for the induction of cell-mediated immunity. In addition, aluminum adjuvants are also known to induce the production of IgE antibodies, which is a cause of allergic response against the vaccine (*4*−*6*). Consequently, the development of a novel vaccine adjuvant is indispensable. Among the candidates for adjuvants, liposomes have garnered recent attention for their capacity as carriers of vaccines (*7*−*14*).

We previously reported that antigens chemically coupled to the surface of liposomes induced antigen-specific IgG but not IgE antibody production (*15*). This IgE-selective unresponsiveness was induced by antigen−liposome conjugates regardless of the coupling procedure of the antigen and liposomes (*16*), of the antigens used for the coupling with liposomes (*17*), or of the route of inoculation (i.e., intraperitoneal (*15*) or intranasal (*18*)). The inducibility of antigen-specific IgG antibody production by antigen−liposome conjugates varied among the liposome preparations used for the production of antigen−liposome conjugates; the greater the membrane mobility in liposomes, the more antibody production induced by antigen−liposome conjugates (*19*). In fact, alteration of lipid composition has been reported to modulate immune responses (*20*−*26*). The aim of this study is to examine if the differential adjuvant effects displayed among liposomes with different lipid components were due to differential recognition of liposomal antigens by antigen-presenting cells. Antigen−liposome conjugates prepared using liposomes with differential lipid components were added to the culture of macrophages, and recognition and digest of liposomal antigen were compared. Further, antigen presentation by macrophages was investigated after coculture of macrophages with antigen−liposome conjugates made using liposomes having different lipid components.

MATERIALS AND METHODS

Mice. BALB/c mice (8 weeks of age, female) were purchased from Charles River (Yokohama, Kanagawa, Japan).

* To whom correspondence should be addressed: Tetsuya Uchida, Ph.D, Department of Safety Research on Blood and Biological Products, National Institute of Infectious Diseases, 4-7-1 Gakuen, Musashimurayama-city, Tokyo 208-0011, Japan. Tel: +81-42-561-9724; Fax: +81-42-561-9722. E-mail: tuchida@nih.go.jp.

[†] National Institute of Infectious Diseases.

[‡] Nippon Oil and Fat Corporation.

10.1021/bc034134o CCC: $27.50 © 2004 American Chemical Society
Published on Web 12/31/2003

Chemicals. All phospholipids were obtained from NOF Co., Tokyo, Japan. Reagent grades of cholesterol were purchased from Wako Pure Chemical Industries, Osaka, Japan.

Antigens. Ovalbumin (OVA, Grade VII) was purchased from Sigma (St. Louis, MO). For the analysis of the processing of liposome-coupled OVA by macrophages, DQ-OVA, that exhibits green fluorescence upon proteolytic degradation, was purchased from Molecular Probes, Inc. (Eugene, OR).

Fluorescence Labeling of OVA. OVA was labeled with fluorescence using an Alexa Flour 488 protein labeling kit (Molecular Probes, Inc.) following manufacturer's protocol.

Liposomes. Liposomes consisting of two different lipid components were used in this study: "Stearoyl" liposomes composed of distearoyl phosphatidylcholine, distearoyl phosphatidyl ethanolamine, cholesterol, and distearoyl phosphatidyl glycerol acid in 4:3:7:2 molar ratios, and "Oleoyl" liposomes composed of dioleoyl phosphatidylcholine, dioleoyl phosphatidyl ethanolamine, cholesterol, and dioleoyl phosphatidyl glycerol acid in 4:3:7:2 molar ratios. The crude liposome solution was passed through a membrane filter (Nucleopore polycarbonate filter, Coster, Cambridge, MA) with a pore size of 0.2 μm.

Coupling of OVA to Liposomes. Liposomal conjugates with plain OVA, Alexa-labeled OVA, or DQ-OVA were prepared essentially in the same way as described previously (*15*). Briefly, to a mixture of 90 mg of liposomes and 6 mg of OVA in 2.5 mL phosphate buffer (pH 7.2) was added in drops 0.5 mL of 2.5% glutaraldehyde solution. The mixture was stirred gently for 1 h at 37 °C, and then 0.5 mL of 3 M glycine−NaOH (pH 7.2) was added to block excess aldehyde groups. This was followed by incubation overnight at 4 °C. The liposome-coupled OVA and uncoupled OVA in the resulting solution were separated using CL-4B column chromatography (Pharmacia Fine Chemical Co., Upsala, Sweden). The amount of lipid in the liposomal fraction was measured using a Phospholipid-Test-Wako phospholipid content assay kit (Wako Pure Chemical Industries). The OVA−liposome solution was adjusted to 10 mg lipid/mL in RPMI-1640, sterile-filtered using Millex-HA syringe filter unit (0.45 μm, Millipore Corp., Bedford, MA), and kept at 4 °C until use.

Quantification of OVA Coupled to Liposome. For the measurement of OVA coupled to liposome, radiolabeled OVA ([methyl-^{14}C]: purchased from New England Nuclear, Boston, MA) was mixed with cold OVA and used for coupling with liposome and for determining the calibration curve. The radioactivity of the resulting OVA−liposome solution was counted using a calibration curve. The amounts of OVA coupled to "Stealoyl" and "Oleoyl" liposomes were 47.0 and 46.8 μg/mg lipid, respectively.

Immunization. Mice were immunized intraperitoneally (ip) with OVA−liposome at a dose of 2 mg lipid/200 μL/mouse or with 80 μg/200 μL/mouse of plain OVA solution in PBS. Four weeks after primary immunization, mice were boosted in the same manner as that used for primary immunization. For the measurement of serum antibodies, mice were bled from the tail vein.

Measurement of Serum Antibodies. Six weeks after primary immunization, serum anti-OVA IgG and IgG isotypes were determined by ELISA using HRP-labeled goat anti-mouse IgG (Zymed Lab., San Francisco, CA).

Cloned Macrophage Hybridoma. Macrophage hybridoma clone #39, obtained from the fusion of splenic adherent cells from CKB mice and P388D$_1$ (*27*), was used.

Antigen-Specific T-Cell Clone. OVA-specific T-cell clone, 42−6A (*28*), was kindly provided by Dr. T. Kakiuchi, Toho University School of Medicine, Tokyo.

Macrophage Culture. Macrophage hybridoma clone #39 was maintained in RPMI-1640 (Gibco Laboratories, Grand Island, NY) supplemented with 10% heat-inactivated FCS (Hyclone Laboratories, Logan, UT), 100 U/mL of penicillin, and 100 μg/mL of streptomycin (Gibco Laboratories) in a 75 cm^2 flask (No. 3111, Becton Dickinson Labware, Franklin Lakes, NJ).

Flow Cytometry. To investigate the capture of OVA−liposome by macrophages, #39 macrophage clone were incubated for 60 min at 37 °C in the presence of Alexa-labeled OVA−liposome conjugates that contained a final concentration of 4 μg/mL OVA. After the incubation, cells were washed with ice cold PBS. Then they were analyzed on a FACS Calibur flow cytometer (BD Biosciences, Mountain View, CA). The histograms of fluorescence distribution were plotted as the number of cells versus fluorescence intensity on a logarithmic scale.

Confocal Laser Scanning Microscopy To investigate degradation of liposome-coupled OVA by macrophages, #39 macrophage clone were cultured for 18h at 37 °C on eight-hole heavy Teflon-coated slides (Bokusui Brown, New York, NY) and were then incubated with DQ-OVA−liposome conjugates, prepared using "Stearoyl" or "Oleoyl" liposomes, for 60 min at 37 °C. They were washed with MEM and fixed with 4% paraformaldehyde in PBS for 10 min at room temperature. After fixation, they were incubated for 10 min in 0.1 M glycine-HCl, pH 7.0, to block the remaining aldehyde residue. They were then washed two times in PBS. After being washed, these slides were sealed with PBS/glycerin (PBS:glycerin = 1:9). These slides were analyzed under a confocal laser scanning microscope system, LSM410 (Carl Zeiss Co., Germany).

Antigen Presentation by Macrophages Cocultured with OVA−Liposome. OVA−liposome conjugates made using "Stearoyl" or "Oleoyl" liposomes were added to the culture of macrophage clone #39 and incubated overnight. The macrophages were then washed three times in ice-cold media, and 5×10^4 cells were cocultured with 2×10^4 cells of OVA specific T-cell clone, 42−6A, in a 96-well plate (No. 3072, Becton Dickinson Labware). After 18 hours of incubation, IL-2 in the culture supernatants were assayed using a Biotrak mouse ELISA system (Amersham International, Buckinghamshire, UK). The final concentration of OVA−liposome added to the macrophage culture was 800 μg lipid/mL, which included 32 μg OVA/mL. For controls, OVA was added to the macrophage culture continuously at final concentrations of 32 or 800 μg/mL.

RESULTS

Comparison of Anti-OVA Antibody Production in Mice Induced by OVA−Liposome Conjugates Made Using Liposomes of Two Different Lipid Components. Mice were immunized with OVA−liposome conjugates which were made using "Stearoyl" or "Oleoyl" liposomes. Figure 1 shows serum anti-OVA IgG titers six weeks after the primary immunization with OVA−liposome or with plain OVA solution. Levels of anti-OVA IgG antibody production induced by two OVA−liposome conjugates were significantly different; OVA−liposome made using "Oleoyl" liposome induced more than a 10-fold higher level of anti-OVA IgG production than that induced by OVA−liposome made using "Stearoyl" liposome. The same dose of plain OVA solution induced a

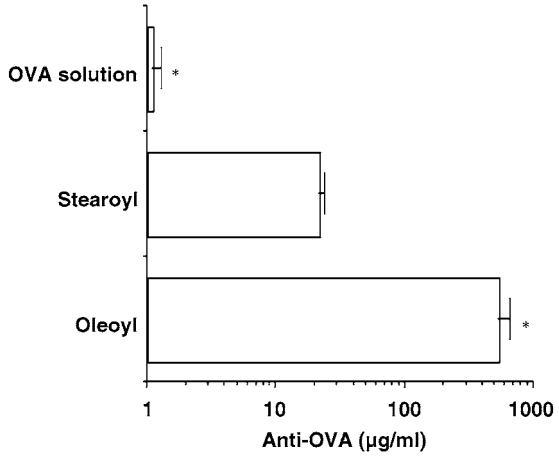


Figure 1. Anti-OVA IgG antibody production in mice immunized with OVA−liposome conjugates. BALB/c mice were immunized with OVA−liposome made using "Stearoyl" or "Oleoyl" liposomes or with plain OVA solution at 0 and 4 weeks. Six weeks after primary immunization, mice were bled from the tail vein, and serum anti-OVA IgG was measured. Data represent mean and SE of five mice per group. Asterisk, significant ($p < 0.01$) difference as compared with "Stearoyl" group.

far lower level of anti-OVA IgG antibody production as compared with that induced by OVA−liposome conjugates.

Phagocytosis of Fluorescence-Labeled OVA by Macrophages. To examine if the differential adjuvant effects between two liposome preparations observed in the above experiment were due to differential recognition of liposomal antigens by antigen-presenting cells, phagocytosis of OVA−liposome by macrophages was investigated by adding fluorescence-labeled OVA coupled with "Stearoyl" or "Oleoyl" liposomes to the macrophage culture. FACS analysis was performed 15, 30, 60, and 120 min after the addition of OVA−liposome conjugates to the macrophage culture, and a maximal incorporation was observed at 60 min. Figure 2a shows the fluorescence intensity of macrophages cultured for 60 min with OVA−liposome conjugates. More OVA was incorporated when OVA was coupled to "Oleoyl" liposomes than when OVA was coupled to "Stearoyl" liposomes. A similar result was observed in the confocal microscopic analysis; more OVA was incorporated by macrophages when OVA coupled to "Oleoyl" liposome was added to the culture (Figure 2b).

Processing of Liposome-Coupled OVA by Macrophages. To compare the processing of OVA coupled either with "Stearoyl" or "Oleoyl" liposomes by macrophages, the fluorescence intensity of the macrophages was investigated by adding DQ-OVA−coupled liposome to the macrophage culture. FACS analysis was performed 15, 30, 60, and 120 min after the addition of OVA−liposome in the macrophage culture, and a maximal processing of OVA was observed at 60 min. Figure 3 shows the results of FACS and confocal microscopic analysis at 60 min after the addition of OVA−liposome in the culture. More OVA appeared to be processed in 60 min by macrophages when OVA was coupled to "Oleoyl" liposome and added to the culture than that when OVA was coupled to "Stearoyl" liposome and added

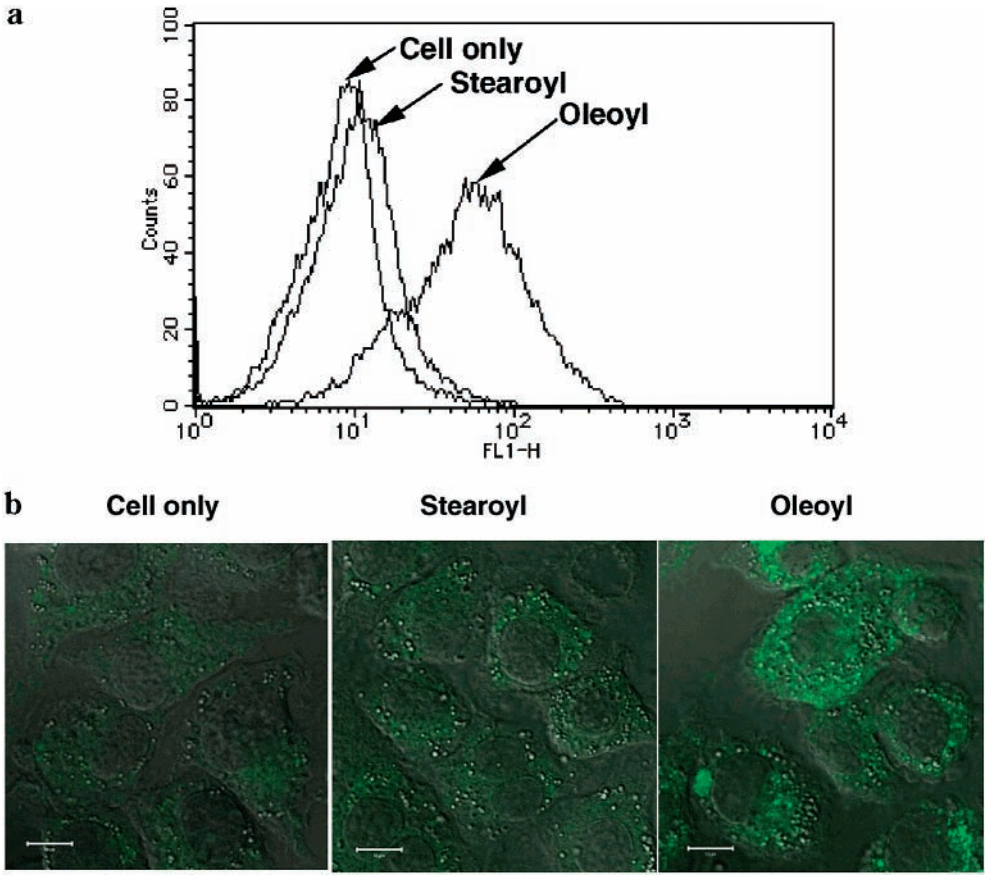


Figure 2. Phagocytosis of OVA−liposome conjugates by macrophages. Fluorescence-labeled OVA was coupled to either "Stearoyl" or "Oleoyl" liposomes and added to the culture of macrophages as described in Materials and Methods. Macrophages recovered from the culture were analyzed using flow cytometry (a) and confocal laser scanning microscopy (b).

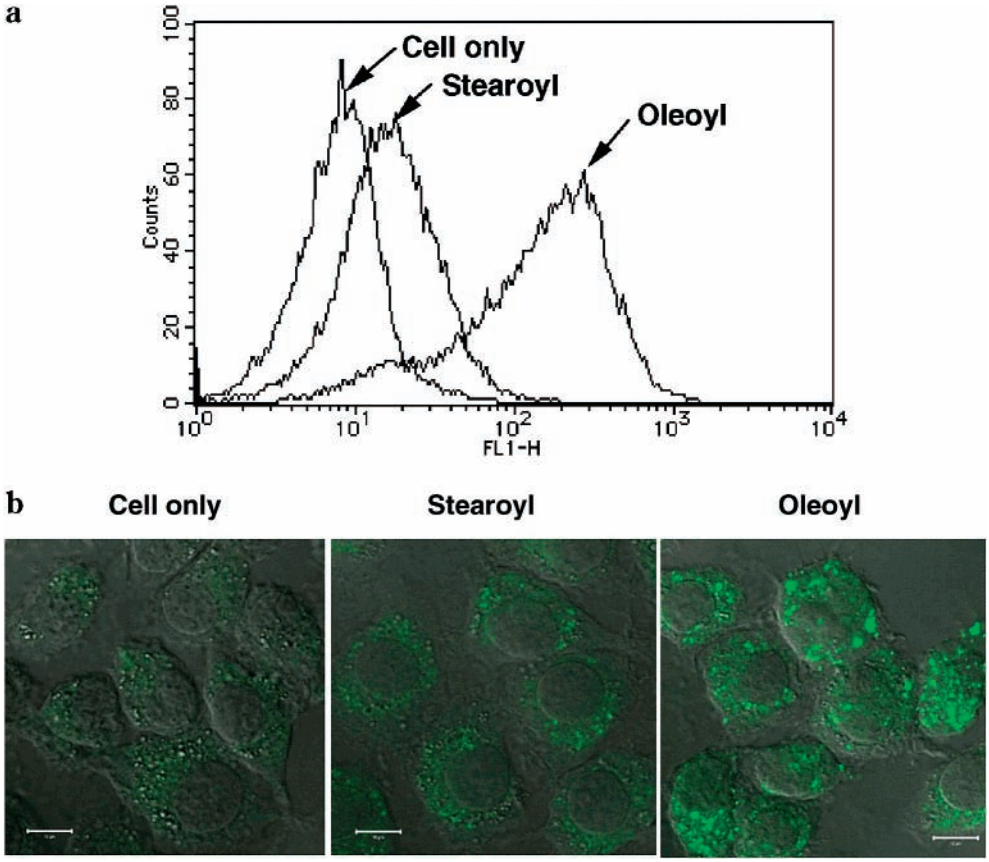


Figure 3. Digestion of liposome-coupled OVA by macrophages. "Stearoyl" or "Oleoyl" liposomes coupled with DQ-OVA were added to the macrophage culture. Sixty minutes after the onset of the culture, macrophages were recovered and analyzed using flow cytometry (a) and confocal laser scanning microscopy (b).

to the culture (Figure 3a). A consistent result was observed by confocal microscopic analysis (Figure 3b).

Antigen-Presentation by Macrophages Cocultured with OVA−Liposome Conjugates. Macrophages were cultured in the presence of OVA−liposome prior to the coculture with OVA-specific T-cell clone, 42−6A, and IL-2 production by the T-cell clone was monitored. Figure 4 shows the amount of IL-2 in the culture supernatant. A significantly high level of IL-2 production was observed when the macrophages were pre-cultured with OVA−liposome made using "Oleoyl" liposomes. The amount of IL-2 was comparable with that when 800 μg/mL of plain OVA was added to the culture. The amount of OVA in the culture to which OVA−liposome conjugates were added was 32 μg/mL. However, the addition of 32 μg of plain OVA to the culture resulted in production of a far lesser amount of IL-2. Although a significant level of IL-2 was produced when macrophages were pre-cultured with OVA−liposome made using "Stearoyl" liposomes, it was more than 10-fold less than that in the "Oleoyl" liposome group.

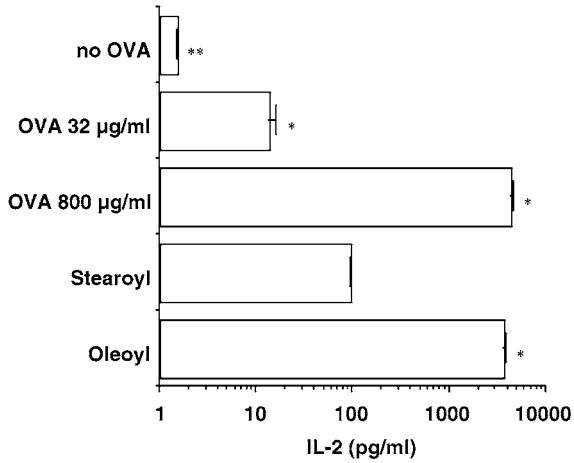


Figure 4. Antigen presentation by macrophages pulsed with OVA−liposomes. Macrophages preincubated with OVA−liposomes were cocultured with OVA−specific T-cell clone as described in Materials and Methods. Data represent mean IL-2 concentration and the SE of the culture supernatant in triplicate cultures. Asterisk, significant ($p < 0.01$) difference as compared with "Stearoyl" group. Two asterisks, significant ($p < 0.01$) difference as compared with the other groups.

DISCUSSION

We previously demonstrated that the adjuvanticity of liposomes in the surface-linked liposomal antigen differs among liposomes of differing lipid compositions (*19*). The results obtained in the present study suggested that the adjuvanticity in liposomes with differential lipid components would correlate with the recognition of liposomal antigens by macrophages, resulting in the differential extent of digestion and antigen presentation. When OVA was coupled to "Oleoyl" liposomes, which expressed high adjuvant activity, OVA was incorporated more efficiently by macrophages than when OVA was coupled to "Stearoyl" liposomes, which expressed lower adjuvanticity. These results further correlated closely with those obtained in the succeeding investigations regarding antigen processing and presentation by macrophages; more OVA was processed in macrophages when OVA was coupled to "Oleoyl" liposomes than when coupled to "Stearoyl" liposomes. Moreover, OVA coupled to "Oleoyl" liposomes was effectively presented to OVA-specific T-cells. When

OVA coupled to "Oleoyl" liposomes was presented to T-cells, the amount of IL-2 released from OVA-specific T-cells was comparable to that when 800 μg/mL of plain OVA was added to the culture, although the amount of OVA added to the culture as OVA−liposome was 32 μg/mL. A significant difference was observed among "Oleoyl"- and "Stearoyl" liposomes in the results, although OVA coupled to "Stearoyl" liposomes was presented even more effectively as compared with that when 32 μg/mL of plain OVA was added to the culture. These results suggest that the adjuvant effect of liposomes correlates well with antigen recognition and presentation by macrophages, at the initiation of immune response.

In the vaccines, adjuvants are indispensable especially for antigens with weak immunogenicity. However, the currently used aluminum adjuvants are known to stimulate only humoral responses (*1*) and are known to induce IgE antibody production, which elicits an allergic response in the vaccinee (*4*). Therefore, the availability of improved adjuvants suitable for clinical use is highly desirable. Among the candidates for adjuvants for novel vaccines, liposomes are garnering attention as antigen carriers (vehicles) because they are known to act as powerful adjuvants when physically associated with a protein antigen (*7*, *10*, *12*, *13*). Most of the liposomal vaccines proposed have been prepared by antigen entrapment within the aqueous lumen of liposomes (*8*). However, it is known that encapsulated and surface-linked liposomal antigens induce differential immune responses in both humoral- (*26*) and cell-mediated (*25*) immunity.

We previously reported that surface-linked liposomal antigen induced IgE-selective unresponsiveness (*15*). The results were consistent even when different procedures for coupling antigen with liposomes (*16*), or for liposomes with different lipid components (*19*), were employed. During the course of an investigation intended to clarify the mechanism of IgE-selective unresponsiveness induced by surface-coupled liposomal antigens, we discovered an alternative approach to regulate the production of IgE, one that is independent of the activity of T-cells (*29*). In the secondary immune response, OVA−liposome enhanced anti-OVA IgG antibody production but it did not enhance ongoing IgE production, suggesting that the IgE-selective unresponsiveness induced by the liposomal antigen involved direct effects on IgE but not IgG switching in vivo. Another advantage of liposomes as an adjuvant is that they are capable of inducing both humoral and cellular immunity. A liposome delivery system could be tailored to induce either a preferential cellular or humoral immune response (*22*, *30*).

The mechanism of action of adjuvants remains unclear. Adjuvants may increase cellular infiltration into the injection site, may directly contribute to the delivery of antigen to the local lymph node, or may directly promote the uptake of antigen into antigen-presenting cells. The results in this study clearly demonstrated that liposomes promote the uptake of liposome-coupled antigen by antigen-presenting cells and enhance antigen presentation to T-cells, which may result in the enhanced induction of systemic immune responses.

ACKNOWLEDGMENT

This work was supported in part by a grant from The Japan Health Sciences Foundation (Research on Health Sciences focusing on Drug Innovation).

LITERATURE CITED

(1) Audibert, F. M., and Lise, D. (1993) Adjuvants: current status, clinical perspectives and future prospects. *Immunol. Today 14*, 281−284.

(2) Gupta, R. K., and Siber, G. R. (1995) Adjuvants for human vaccines − current status, problems and future prospects. *Vaccine 13*, 1263−1276.

(3) O'Hagan, D. T. (2001) Recent developments in vaccine delivery systems. *Curr. Drug Targets − Infect. Disorders 1*, 273−286.

(4) Mark, A., Bjorksten, B., and Granstrom, M. (1995) Immunoglobulin E responses to diphtheria and tetanus toxoids after booster with aluminum-adsorbed and fluid DT-vaccines. *Vaccine 13*, 669−673.

(5) Aggrebeck, H., Wantzin, J., and Heon, I. (1996) Booster vaccination against diphtheria and tetanus in man. Comparison of three different vaccine formulations − III. *Vaccine 14*, 1265−1272.

(6) Nothdurft, H. D., Jelinek, T., Marschang, A., Maiwald, H., Kapaun, A., and Loscher, T. (1996) Adverse reactions to Japanese encephalitis vaccine in travelers. *J. Infect. 32*, 119−122.

(7) Gregoriadis, G. (1990) Immunological adjuvants: a role for liposomes. *Immunol. Today 11*, 89−97.

(8) Gregoriadis, G. (1994) Liposomes as immunoadjuvants and vaccine carriers: antigen entrapment. *ImmunoMethods 4*, 210−216.

(9) Wassef, N. M., Alving, C. R., and Richards, R. L. (1994) Liposomes as carriers for vaccines. *ImmunoMethods 4*, 217−222.

(10) Alving, C. R., Koulchin, V., Glenn, G. M., and Rao, M. (1995) Liposomes as carriers of peptide antigens: induction of antibodies and cytotoxic T lymphocytes to conjugated and unconjugated peptides. *Immunol. Rev. 145*, 5−31.

(11) Green, S., Fortier, J. D., Madsen, J., Swartz, G., Einck, L., Gubish, E., and Nacy, C. (1995) Liposomal vaccines. *Immunology of Proteins and Peptides VIII* (M. Z. Atassi, and G. S. Bixler, Eds.) pp 83−92, Plenum Press, New York.

(12) De Haan, A., Tomee, J. F. C., Huchshorn, J. P., and Wilschut, J. (1995) Liposomes as an immunoadjuvant system for stimulation of mucosal and systemic antibody responses against inactivated measles virus administered intranasally to mice. *Vaccine 13*, 1320−1324.

(13) Gluck, R. (1995) Liposomal presentation of antigens for human vaccines. *Pharm. Biotechnol. 6*, 325−345.

(14) Perrie, Y., Frederik, P. M., and Gregoriadis, G. (2001) Liposome-mediated DNA vaccination: the effect of vesicle composition. *Vaccine 19*, 3301−3310.

(15) Naito, S., Horino, A., Nakayama, M., Nakano, Y., Nagai, T., Mizuguchi, J., Komuro, K., and Uchida, T. (1996) Ovalbumin-liposome conjugate induces IgG but not IgE antibody production. *Int. Arch. Allergy Immunol. 109*, 223−228.

(16) Nakano, Y., Mori, M., Nishinohara, S., Takita, Y., Naito, S., Horino, A., Kato, H., Taneichi, M., Ami, Y., Suzaki, Y., Komuro, K., and Uchida, T. (1999) Antigen-specific, IgE selective unresponsiveness induced by antigen-liposome conjugates. *Int. Arch. Allergy Immunol. 120*, 199−208.

(17) Naito, S., Taneichi, M., Kato, H., Tanaka, Y., Ami, Y., Suzaki, Y., Mori, M., Nakano, Y., Yamamura, H., Morokuma, K., Ohkuma, K., Miyake, H., Kiniwa, M., Komuro, K., and Uchida, T. (2002) Selective inhibition of systemic anti-OVA IgE production in response to oral preadministration with OVA-liposome conjugates. *Int. Arch. Allergy Immunol. 129*, 314−319.

(18) Yoshikawa, T., Uchida, T., Naito, S., Horino, A., Taneichi, M., Kato, H., Komuro, K., Nakano, Y., Mori, M., Nishinohara, S., Chiba, J., Kurata, T., and Tamura, S. (2000) Suppression of IgE antibody response to ovalbumin by intranasal administration of liposome-conjugated ovalbumin. *Int. Arch. Allergy Immunol. 121*, 108−115.

(19) Nakano, Y., Mori, M., Nishinohara, S., Takita, Y., Naito, S., Kato, H., Taneichi, M., Komuro, K., and Uchida, T. (2001) Surface-linked liposomal antigen induces IgE-selective unresponsiveness regardless of the lipid components of liposomes. *Bioconjugate Chem. 12*, 391−395.

(20) Chang, E. Y., Zheng, Y., Holowka, D., and Baird, B. (1995) Alteration of lipid composition modulates FCϵRI signaling in RBL-2H3 cells. *Biochemistry 34*, 4376−4384.

(21) Phillips, N. C., Gagne, L., Ivanoff, N., and Riveau, G. (1996) Influence of phospholipid composition on antibody responses

to liposome encapsulated protein and peptide antigens. *Vaccine 14*, 898−904.
(22) Guan, H. H., Budzynski, W., Koganty, R. R., Krantz, M. J., Reddish, M. A., Rogers, J. A., Longenecker, M., and Samuel, J. (1998) Liposomal formulations of synthetic MUC1 peptides: effects of encapsulation versus surface display of peptide on immune responses. *Bioconjugate Chem. 9*, 451−458.
(23) Hincha, D. K., Oliver, A. E., and Crowe, J. H. (1999) Lipid composition determines the effect of arbutin on the stability of membranes. *Biophys. J. 77*, 2024−2034.
(24) Moody, D. B., Briken, V., Cheng, T.-Y., Roura-Mir, C., Guy, M. R., Geho, D. H., Tykocinski, M. L., Besra, G. S., and Porcelli, S. A. (2002) Lipid length controls antigen entry into endosomal and nonendosomal pathways for CD1b presentation. *Nat. Immunol. 3*, 435−442.
(25) Fortin, A., Shaum, E., Krzystyniak, K., and Therien, HM. (1996) Differential activation of cell-mediated immune functions by encapsulated and surface-linked liposomal antigens. *Cell. Immunol. 169*, 208−217.
(26) Shahum, E., and Therien, H. M. (1988) Immunopotentiation of the humoral response by liposomes: encapsulation versus covalent linkage. *Immunol. 65*, 315−317.
(27) Uchida, T., Ju, S. T., Fay, A., Liu, Y. N., and Dorf, M. E. (1985) Functional analysis of macrophage hybridomas. I. Production and initial characterization. *J. Immunol. 134*, 772−778.
(28) Kakiuchi, T., Watanabe, M., Hozumi, N., and Nariuchi, H. (1990) Differential sensitivity of specific and nonspecific antigen-presentation by B cells to a protein synthesis inhibitor. *J. Immunol. 145*, 1653−1658.
(29) Taneichi, M., Naito, S., Kato, H., Komuro, K., and Uchida, T. (2002) T cell-independent regulation of IgE antibody production induced by surface-linked liposomal antigen. *J. Immunol 169*, 4246−4252.
(30) White, W. I., Cassatt, D. R., Madsen, J., Burke, S. J., Woods, R. M., Wassef, N. M., Alving, C. R., and Koenig, S. (1995) Antibody and cytotoxic T-lymphocyte responses to a single liposome-associated peptide antigen. *Vaccine 13*, 1111−1122.

BC034134O

MicroPET and Autoradiographic Imaging of Breast Cancer α_v-Integrin Expression Using ^{18}F- and ^{64}Cu-Labeled RGD Peptide

Xiaoyuan Chen, Ryan Park, Michel Tohme, Anthony H. Shahinian, James R. Bading, and Peter S. Conti*

PET Imaging Science Center, University of Southern California Keck School of Medicine, Los Angeles, California 90033. Received August 12, 2003

Cell adhesion molecules $\alpha_v\beta_3$ and $\alpha_v\beta_5$ play a pivotal role in tumor angiogenesis and metastasis. Antiangiogenic therapy by using small peptide antagonists of α_v-integrins slows tumor growth and prevents tumor spread. The ability to visualize and quantify integrin expression will enable selection of appropriate patients for clinical trials, following determination of treatment efficacy and development of new potent drugs. We have previously labeled cyclic RGD peptide c(RGDyK) with ^{125}I and ^{18}F and applied the radiotracers to both subcutaneous and orthotopic brain tumor models. Here we conjugated c(RGDyK) with 1,4,7,10-tetraaza-1,4,7,10-tetradodecane-*N*,*N*′,*N*″,*N*‴-tetraacetic acid (DOTA) and labeled the DOTA−RGD conjugate with ^{64}Cu ($t_{1/2}$ = 12.8 h, 19% β^+) in high radiochemical purity and specific activity. The tumor targeting ability and in vivo kinetics of ^{64}Cu-DOTA−RGD was compared with [^{18}F]FB−RGD and ^{125}I-RGD in orthotopic MDA-MB-435 breast cancer model. All three radiotracers revealed fast blood clearance and high tumor-to-blood and tumor-to-muscle ratios. ^{125}I-RGD had higher tumor uptake than the corresponding ^{18}F and ^{64}Cu analogues. [^{18}F]FB−RGD indicated a fast tumor washout rate and an unfavorable hepatobiliary excretion pathway, resulting in significant activity accumulation in gallbladder and intestines. ^{64}Cu-DOTA−RGD had prolonged tumor retention (1.44 ± 0.09 %ID/g at 4 h postinjection) and persistent uptake in the liver. All three tracers revealed receptor specific tumor accumulation which were illustrated by effective blocking via coinjection with a blocking dose of c(RGDyK). Static microPET imaging and whole-body autoradiography showed strong contrast from the contralateral background. In conclusion, overall molecular charge and characteristics of radiolabels have profound effects on tumor accumulation and in vivo kinetics of radiolabeled RGD peptide. Further modification of the RGD peptide and optimization of the tracer for prolonged tumor uptake and improved in vivo kinetics are being explored.

INTRODUCTION

Breast cancer is the most common form of cancer in women (*1*). Despite vigorous efforts to diagnose, treat, and prevent this disease, it remains a leading cause of death among women. To develop new approaches to the treatment of this disease, further knowledge is needed of the basic biology underlying the etiology and progression of the disease. Recent studies have shown that vascularization is significantly higher in node-positive breast tumors than in node-negative tumors, and that a high degree of vascularization is generally associated with a poor prognosis (*2*). This finding has led to the conclusion that inhibition of angiogenesis offers a possible therapeutic modality for a subset of patients (*3*). Antiangiogenic agents that can block the formation of new blood vessels in the body and destroy existing abnormal blood vessels by starving breast tumors and inhibiting the progression of breast tumors have become the new frontiers in the fight against cancer (*4*). Antiangiogenic agents have been shown to increase therapeutic efficacy in conjunction with other chemotherapeutic agents or when used in combination with external radiotherapy (*5*). Since this kind of therapy is primarily cytostatic and not cytotoxic, the established PET imaging criteria based upon metabolic (e.g. FDG) (*6*) or cell proliferation (e.g. FLT) (*7*) tracers for assessing tumor response to chemo- and/or radiotherapy cannot be applied to antiangiogenic therapy (*8*). Molecular imaging of tumor angiogenesis will thus play a pivotal role to visualize and quantify angiogenesis potential and to monitor antiangiogenic treatment efficacy.

Angiogenesis is a complex process involving extensive interplay between cells, soluble factors, and extracellular membrane (ECM) components (*9*). The construction of a vascular network requires different sequential steps including the release of proteases from "activated" endothelial cells with subsequent degradation of basement membrane surrounding the existing vessel, migration of endothelial cells into the interstitial space, endothelial cell proliferation, and differentiation into mature blood vessels. Each of these processes presents a possible target for diagnostic and therapeutic interventions (*10*). We focus here solely on the cell adhesion molecules α_v-integrins, which are responsible for a wide range of cell−extracellular matrix and cell−cell interactions (*11*). Inhibition of α_v-integrins by monoclonal antibodies (mAbs), cyclic RGD peptides, and peptidomimetics has been shown to induce endothelial apoptosis (*12*), to inhibit angiogenesis (*13*−*15*) and to increase endothelial monolayer permeability (*16*). The inhibition of α_v-integrin activity has been associated with decreased tumor growth in breast cancer xenografts (*14*, *17*). Synergy of cylic RGD

* Correspondence should be sent to Peter S. Conti, M. D., Ph.D.; Department of Radiology; University of Southern California; 1510 San Pablo St., Suite 350; Los Angeles, CA 90033. Tel: (323) 442-5940; Fax: (323) 442-3253; E-mail: pconti@usc.edu.

10.1021/bc0300403 CCC: $27.50 © 2004 American Chemical Society
Published on Web 12/30/2003

peptide EMD 121974 with radioimmunotherapy (RIT) has resulted in increased efficacy of therapy in a murine breast cancer model (*15*).

We recently labeled RGD peptide c(RGDyK) with ^{125}I for brain tumor targeting (*18*). This tracer revealed fast blood clearance and rapid tumor uptake; however, the prolonged kidney retention limited the further application of this tracer. The modification of the lysine ϵ-amino group with a monomethoxy poly(ethylene glycol) moiety (mPEG, MW = 2000) found drastically decreased renal uptake, slightly increased liver accumulation and prolonged tumor retention (*18*). Modification of the lysine residue with a sugar moiety revealed increased water solubility and thus improved pharamacokinetics of the tracer (*19*). The same glycosylated RGD peptide c[RGDyK-(SAA)] was further labeled with ^{18}F through a prosthetic labeling moiety 2-[^{18}F]fluoropropionate (*20*) for positron emission tomography (PET) imaging of $\alpha_v\beta_3$ integrin positive tumors. The proof-of-principle experiment demonstrated the feasibility of this tracer for integrin positive tumor targeting and that the tumor uptake is receptor specific since the uptake of the tracer is dose dependent. We labeled c(RGDyK) with ^{18}F through 4-[^{18}F]fluorobenzoyl group and applied this tracer to both subcutaneous U87MG and orthotopic U251T glioblastoma models. The tracer showed very rapid blood clearance and both hepatobiliary and renal excretion. Tumor-to-muscle uptake ratio at 30 min was approximately 5 ± 1 in the subcutaneous U87MG tumor model. MicroPET imaging with the orthotopic U251T brain tumor model revealed very high tumor-to-brain ratio, with virtually no uptake in the normal brain. Successful blocking of tumor uptake of [^{18}F]FB−RGD in the presence of excess amount of c(RGDyK) revealed receptor specific activity accumulation (*21*). Ogawa et al. (*22*) labeled EMD 121974 with ^{18}F via direct electrophilic radiofluorination and revealed very modest tumor uptake in a colon cancer model, probably due to low specific activity of the carrier-added radiotracer. Van Hagen et al. (*23*) substituted the lysine ϵ-amino group on c(RGDyK) with diethylenetriaminepentaacetic acid (DTPA) and labeled the conjugate with ^{111}In to target rat pancreatic CA20948 tumor model. Janssen et al. (*24*) conjugated dimeric RGD peptide E-[c(RGDfK)]$_2$ with 1,4,7,10-tetraazadodecane-*N*,*N*′,*N*″,*N*‴-tetraacetic acid (DOTA) and hydrazinonicotinamide (HYNIC) chelators and labeled the conjugates with ^{111}In/^{90}Y and ^{99m}Tc, respectively, and applied the tracers to NIH:OVCAR-3 sc ovarian carcinoma xenografts. All the metallic radionuclide-labeled RGD peptides revealed significant kidney and liver accumulation. The tracer distribution pattern is markedly affected by the chelator and metal ions. In this study, we conjugated monomeric RGD peptide c(RGDyK) with DOTA and labeled the RGD−DOTA conjugate with ^{64}Cu ($t_{1/2}$ = 12.8 h; 40% β^- (656 keV), 19% β^+ (600 keV), 38% EC) (*25*). The tumor accumulation and in vivo kinetics of this ^{64}Cu-DOTA−RGD is evaluated and compared with ^{125}I-RGD and [^{18}F]-FB−RGD in orthotopic MDA-MB-435 breast cancer xenograft mouse model. In addition, microPET and autoradiographic imaging of breast cancer with ^{64}Cu-DOTA−RGD and [^{18}F]FB−RGD were also assessed.

EXPERIMENTAL PROCEDURES

Materials and Analyses. Cyclic RGD peptide c(RGDyK) was synthetically produced via solution cyclization of fully protected linear pentapeptide H-Gly-Asp(OtBu)-D-Tyr(OtBu)-Lys(Boc)-Arg(Pbf)-OH, followed by trifluoroacetic acid deprotection in the presence of the free radical scavenger triisopropylsilane (*18*, *21*). [^{125}I]-NaI was obtained from Perkin-Elmer Life Sciences Inc. (Boston, MA). No-carrier-added [^{18}F]F$^-$ was produced via the ^{18}O(p,n)^{18}F reaction by bombardment of an isotopically enriched [^{18}O]water target (95% enrichment, Isonics, Golden, CO) with 11 MeV protons using a Siemens RDS-112 negative ion cyclotron. The [^{18}F]F$^-$ was trapped on an anion-exchange resin (Dowex (Cl$^-$) 1X-8, 200−400 mesh), converted to OH$^-$ form and then eluted with K_2CO_3 (0.6 mL 10 mM, 6 μmol) and combined with Kryptofix 2.2.2 (10 mg, 26.6 μmmol). The solvent was evaporated under a stream of argon at 90 °C. Azeotropic drying was repeated twice with 1 mL portions of MeCN. ^{64}Cu was produced on a CS-15 biomedical cyclotron at Washington University School of Medicine by the ^{64}Ni(p,n)^{64}Cu nuclear reaction (*25*).

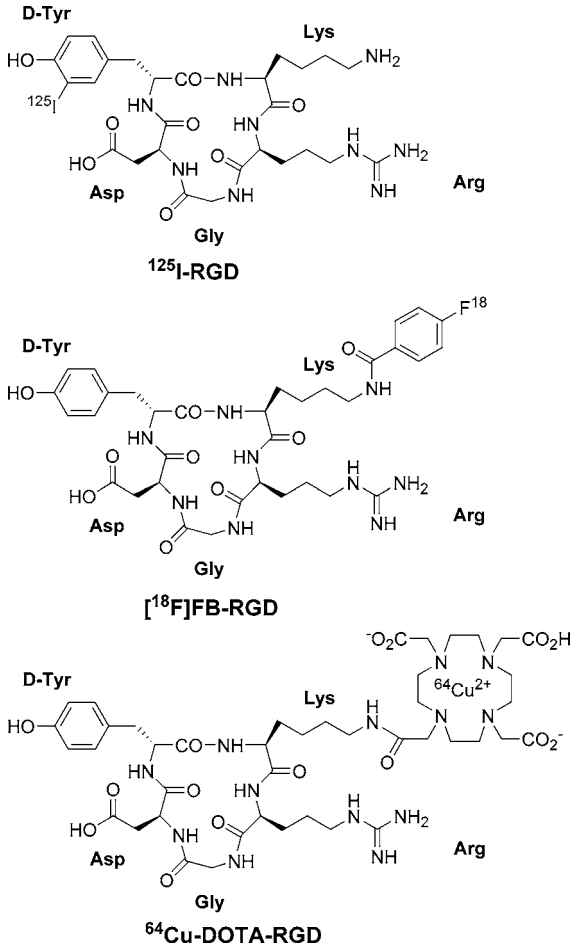


Figure 1. Structures of ^{125}I-RGD, [^{18}F]FB−RGD, and ^{64}Cu-DOTA−RGD.

All reagents, unless otherwise specified, were of analytical grade and commercially available. 1,4,7,10-tetraazadodecane-*N*,*N*′,*N*″,*N*‴-tetraacetic acid (DOTA) was purchased from Macrocyclics, Inc. (Dallas, TX). *N*-hydroxysulfonosuccinimide (SNHS), 1-ethyl-3-[3-(dimethylamino)propyl]carbodiimide (EDC), and Chelex 100 (50−100 mesh) were obtained from Aldrich. 4,7,13,16,21,24-Hexaoxa-1,10-diazabicyclo[8.8.8]hexacosan (Kryptofix 2.2.2) and potassium carbonates (K_2CO_3), as well as sodium phosphate buffer, were obtained from Sigma. Ethyl 4-(dimethylamino)benzoate, methyl trifluoromethanesulfonate, *O*-(*N*-succinimidyl)-*N*,*N*,*N*′,*N*′-tetramethyluronium tetrafluoroborate (TSTU), and tetrapropylammonium hydroxide in water (1.0 M) were from Fluka. Water was distilled and then deionized (18 MΩ/cm^2) by passing through a Milli-Q water filtration system (Millipore Corp., Bedford, MA). Water and all buffers were

passed over a Chelex 100 column (1 × 15 cm) before use in radiolabeling procedures. Dimethyl sulfoxide (DMSO) was distilled from barium oxide, dispensed under N_2 into vials containing activated molecular sieves (4 Å), and stored at 4 °C. Anhydrous acetonitrile (MeCN) from a newly opened flask was stored over activated molecular sieves (4 Å) at room temperature (rt). All other solvents were used without further purification. Radio-TLC was performed using MKC18F plates (Whatman, Clifton, NJ), a Bioscan system 200, and Winscan software, version 2.2. Reversed-phase extraction C-18 SepPak cartridges were obtained from Waters (Milford, MA).

Semipreparative reversed-phase HPLC was accomplished on a Waters 515 chromatography system with a 486 tunable absorbance detector and model 1015-DC−P single channel radiation detector from Carroll & Ramsey Associates (Berkeley, CA). Version 7.2.1 Labtech Notebook/XE software (Andover, MA) was used to record chromatograms. Purification was performed on a Vydac protein and peptide column 218TP510, 5 μm, 250 × 10 mm). The flow was 3 mL/min, with the mobile phase starting from 95% solvent A (0.1% TFA in water) and 5% solvent B (0.1% TFA in acetonitrile) (0−2 min) to 35% solvent A and 65% solvent B at 32 min. The analytical HPLC method was performed with the same gradient system, but with a Vydac 218TP54 column (5 μm, 250 × 4.6 mm) and flow= 1 mL/min. The absorbance was monitored at 218 nm.

Preparation of DOTA−RGD Conjugate. DOTA was activated by EDC at pH 5.5 for 30 min (4 °C), with molar ratio of DOTA:EDC:SNHS = 10:5:4. Typically, 12 mg of DOTA (24 μmol) dissolved in 500 μL of water and 2.3 mg of EDC (12 mmol) dissolved in 130 μL of water were mixed, and 0.1 N NaOH (250 μL) was added to adjust the pH to 5. SNHS (2.1 mg, 9.6 μmol) was then added to the stirring mixture on ice-bath, and 0.1 N NaOH (50 μL) was further added to finalize the pH to 5.5. The reaction was allowed for 30 min at 4 °C. The theoretical concentration of active ester DOTA-OSSu was calculated to be 9.1 mM. Cyclic RGD peptide (1.5 mg, 2.4 μmol) dissolved in 300 μL (5 mg/mL) of water was cooled to 4 °C and added to the DOTA-OSSu reaction mixture, and the pH was adjusted to 8.5 with 0.1 N NaOH (280 μL). The reaction was allowed to incubate for overnight at 4 °C. The DOTA−RGD conjugate was purified by semipreparative HPLC. The peak containing the RGD conjugate was collected, lyophilized, and dissolved in H_2O at a concentration of 1 mg/mL for use in radiolabeling reactions.

Radiolabeling. Cyclic RGD peptide c(RGDyK) was labeled with ^{125}I using the chloramine-T method (*18*). 4-[^{18}F]fluorobenzoyl-RGD ([^{18}F]FB−RGD) was produced by conjugating RGD peptide c(RGDyK) with *N*-succinimidyl 4-[^{18}F]fluorobenzoate ([^{18}F]SFB) under slightly basic condition (*21*). The specific activity of [^{18}F]FB−RGD was estimated to be over 300 GBq/μmol at end of bombardment (EOB)), based on 9.25 GBq (250 mCi) starting [^{18}F]F$^-$ (*21*). DOTA−RGD was labeled with ^{64}Cu by addition of 1−5 mCi of ^{64}Cu (2−5 μg DOTA−RGD per mCi ^{64}Cu) in 0.1 N NaOAc (pH 5.5) buffer followed by 45 min incubation at 50 °C. The reaction was terminated by adding 5 μL of 10 mM EDTA solution and radiochemical yield was determined by Radio-TLC using Whatman MKC18F TLC plates as the stationary phase and 70:30 MeOH:10% NaOAc as the eluent. ^{64}Cu-DOTA−RGD was purified on a C-18 SepPak cartridge, using 85% ethanol as the elution solvent. Radiochemical purity was determined by radio-TLC or radio-HPLC. The ethanol was evaporated and the activity was reconstituted in phosphate-buffered saline and passed through a 0.22 μm Millipore filter into a sterile multidose vial for use in animal experiments.

Animal Models. All animal experiments were performed in compliance with the Guidelines for the Care and Use of Research Animals established by University of Southern California's Animal Studies Committee. MDA-MB-435 estrogen receptor-negative human breast cancer cells were maintained at 37 °C in minimum essential medium (alpha modification) containing 3.7 g of sodium bicarbonate per liter, supplemented with 10% v/v fetal calf serum, in a humidified atmosphere of 5% carbon dioxide. Stock cultures were seeded at a density of 2 × 10^5 cells and allowed to multiply for 48−72 h. Female athymic nude mice (*nu/nu*) obtained from Harlan (Indianapolis, IN) at 4−6 weeks of age were injected orthotopically in the right mammary fat pad with 5 × 10^6 MDA-MB-435 cells suspended in 100 μL of medium. Palpable tumors appeared by the day 10−14 postimplantation. The tumors were allowed to grow 3−4 weeks until 0.5−0.9 g in size.

Biodistribution Studies. When the tumors reached 0.4−0.6 cm in diameter (20 to 25 d after implant), the mice received ^{125}I-RGD (2 μCi), [^{18}F]FB−RGD (20 μCi), or ^{64}Cu-DOTA−RGD (10 μCi). The radiolabeled peptides were injected via the tail vein. Mice (n = 5 per time point) were sacrificed by exsanguinations at different time points postinjection (pi). Blood, tumor and the major organs and tissues were collected, wet-weighed, and counted in a γ-counter (Packard). The percent injected dose per gram (%ID/g) was determined for each sample. For each mouse, radioactivity of the tissue samples was calibrated against a known aliquot of the injectate. Values are quoted as mean ± standard deviation (SD). The receptor-mediated localization of the radiotracers was investigated by determining the biodistribution of radiolabeled peptide in the presence of 15 mg/kg of c(RGDyK). Biodistribution was determined as described above at 1 h pi in 5 mice/group.

MicroPET Imaging. Positron emission tomography (PET) imaging was performed on a microPET R4 rodent model scanner (Concorde Microsystems, Knoxville, TN). The scanner has a computer-controlled bed, 10.8 cm transaxial and 8 cm axial field of view (FOV). The camera has no septa and operates exclusively in 3 D list mode. All raw data were first sorted into 3D sinograms, followed by Fourier rebinning and ordered subsets-expectation maximization (OSEM) reconstruction algorithm using a ramp filter with the Nyquist limit (0.5 cycles/voxel) as the cutoff frequency. For PET imaging of breast cancer tumor-bearing mice, the animal model was injected 200 μCi [^{18}F]FB−RGD or 400 μCi ^{64}Cu-DOTA−RGD via the tail vein. The mouse was then euthanized at 1 h pi and placed near the center of the FOV of the microPET, where the highest image resolution and sensitivity are available. Static imaging was performed for 15 min. To investigated receptor-specific uptake of ^{64}Cu-labeled RGD, one MDA-MB-435 breast cancer-bearing mouse was imaged three times daily apart: (a) without coinjection with c(RGDyK); (b) with 2.5 mg/kg c(RGDyK); and (c) with 7.5 mg/kg c(RGDyK). The mouse was anesthetized with ketamine/xylazine and immobilized in a specially prepared scanner cradle. To assess the tumor uptake of ^{64}Cu-DOTA−RGD, circular regions of interest were placed at the locations of maximum tracer uptake in the tumor and in the corresponding contralateral site (reference region). Relative tracer uptake was expressed as the ratio between mean counts in tumor and the reference region (tumor:background ratio).

Table 1. Radioactivity, Expressed as Percent Injected Dose per Gram Tissue in Different Organs and Tumor of MDA-MB-435 Xenograft Model after Intravenous Injection of 2 μCi of ^{125}I-RGD at 15 min, 30 min, 1, 2, and 1 h Block (with coinjection of 10 mg/kg c(RGDyK)) ($n = 4$)

	15 min	30 min	1 h	2 h	1 h block
blood	2.17 ± 0.37	0.86 ± 0.26	0.33 ± 0.02	0.14 ± 0.01	0.29 ± 0.06
muscle	1.35 ± 0.29	1.33 ± 0.53	1.15 ± 0.31	0.68 ± 0.07	0.87 ± 0.23
tumor	3.65 ± 0.25	3.38 ± 0.10	3.04 ± 0.37	3.02 ± 0.12	0.65 ± 0.36
skin	5.39 ± 0.83	4.31 ± 0.70	3.29 ± 0.58	3.01 ± 0.32	1.68 ± 0.76
bone	2.20 ± 0.21	1.30 ± 0.14	0.99 ± 0.18	1.23 ± 0.16	0.95 ± 0.08
heart	1.75 ± 0.13	1.19 ± 0.03	1.00 ± 0.18	0.62 ± 0.04	0.89 ± 0.13
lung	4.74 ± 0.39	3.11 ± 0.53	2.26 ± 0.22	1.58 ± 0.23	1.94 ± 0.11
liver	4.04 ± 0.36	3.93 ± 0.17	3.29 ± 0.43	2.84 ± 0.51	2.86 ± 0.24
kidney	17.2 ± 1.46	13.1 ± 1.09	10.97 ±1.32	6.48 ± 2.88	8.45 ± 1.08
spleen	3.65 ± 0.65	2.73 ± 1.15	2.13 ± 0.32	2.01 ± 0.38	1.78 ± 0.16
pancreas	1.48 ± 0.08	0.97 ± 0.16	0.91 ± 0.05	0.73 ± 0.16	0.75 ± 0.09
stomach	5.71 ± 0.79	4.88 ± 1.08	3.52 ± 0.35	3.09 ± 0.82	3.89 ± 1.03
intestines	4.51 ± 1.25	8.62 ± 3.78	7.70 ± 2.04	5.31 ± 0.59	5.86 ± 1.44
tumor/blood	1.68 ± 0.45	4.08 ± 1.01	9.24 ± 1.06	20.2 ± 0.80	2.24 ± 0.38
tumor/muscle	2.70 ± 0.64	2.68 ± 0.74	2.79 ± 0.87	4.68 ± 0.59	0.75 ± 0.47

Whole-Body Autoradiography. Autoradiography was performed using a Packard Cyclone Storage Phosphor Screen system (Downers Grove, IL) and a Bright 5030/WD/MR cryomicrotome (Hacker Instruments, Fairfield, NJ). Immediately after microPET scanning, the already killed mice were frozen in a dry ice and isopropyl alcohol bath for 2 min. The bodies were then embedded in a 4% carboxymethyl cellulose (CMC) (Aldrich, Milwaukee, WI) in water mixture using a stainless steel mold. The mold was placed in the dry ice and isopropyl alcohol bath for 5 min and then into a −20 °C freezer for 1 h. The walls of the mold were then removed, and the frozen block was mounted in the cryomicrotome. The block was then cut into 50 μM sections, and desired sections were digitally photographed and captured for autoradiography. The sections were transferred into a chilled autoradiography cassette containing a Super Resolution screen (Packard, Meriden, CT) and kept there overnight at −20 °C. Screens were laser-scanned with the Packard Cyclone.

Statistical Analysis. Statistical analysis was performed using GraphPad Prism 3.0 (GraphPad Software, San Diego, CA). The biodistribution data were analyzed using the one-way ANOVA test. The level of significance was set at $P = 0.05$.

RESULTS

Chemistry and Radiochemistry. The DOTA−RGD conjugate was produced in 79% yield after HPLC purification. Analytical HPLC using conditions described in the Methods section found the retention time to be 11.6 min, whereas cyclic RGD peptide c(RGDyK) eluted at 10.7 min under the same condition. MALDI-TOF-MS: $m/z = 1005.3$ for $[M + H]^+$ ($C_{43}H_{65}N_{13}O_{15}$), 1027.3 for $[M + Na]^+$, and 1043.2 for $[M + K]^+$. ^{64}Cu-DOTA−RGD was labeled in ≥90% radiochemical yield and ≥98% radiochemical purity and was used immediately for in vivo assays. Free ^{64}Cu-acetate remained at the origin of the radio-TLC plate and R_f value of ^{64}Cu-DOTA−RGD was about 0.6. Specific activity of ^{64}Cu-DOTA−RGD ranged from 200 to 500 Ci/mmol (7.4−18.5 GBq/μmol). RGD was labeled with ^{125}I with specific activity of 1700 Ci/mmol (*18*) and conjugation labeled with ^{18}F with specific activity of 6000 Ci/mmol at end of synthesis (EOS) (*21*).

Biodistribution Studies. Summaries of the biodistribution data for ^{125}I-RGD, [^{18}F]FB−RGD, and ^{64}Cu-DOTA−RGD in orthotopic MDA-MB-435 human breast cancer-bearing mice were shown in Table 1, Table 2, and Table 3, respectively. Rapid clearance of the radioactivity from the blood circulation was observed for all three compounds. At any time point examined, the tumor uptake followed the order of ^{125}I-RGD > ^{64}Cu-DOTA−RGD > [^{18}F]FB−RGD. Tumor-to-blood (T/B) and tumor-to-muscle (T/M) ratios increased with time elapsed for both ^{125}I-RGD and [^{18}F]FB−RGD. ^{64}Cu-DOTA−RGD showed highest tumor-to-background ratio at 1 h pi (8.1 ± 0.9 for T/B and 7.1 ± 1.3 for T/M) and the contrast slightly decreased at 2 h (6.9 ± 0.5 for T/B and 6.0 ± 0.6 for T/M) and 4 h (6.0 ± 0.1 for T/B and 6.3 ± 1.3 for T/M) pi ^{125}I-RGD excreted through both renal and hepatobiliary pathways which reflected significant uptake in both liver and kidneys. High and persistent retention in the kidneys may be attributed to the electrostatic interaction between overall positively charged ^{125}I-RGD with negatively charged renal proximal tubular cells, which is responsible for reabsorption of glomerularly filtered peptide into renal cells. Significant accumulation of radioactivity in the stomach was found for ^{125}I-RGD but not for [^{18}F]FB−RGD and ^{64}Cu-DOTA−RGD, demonstrating partial deiodination of the ^{125}I-labeled RGD peptide. The fast tumor washout rate for [^{18}F]FB−RGD was due to the increased lipophilicity of compound upon conjugation labeling through a prosthetic 4-[^{18}F]fluorobenzoyl moiety. The liver, kidneys, and intestines were the only organs to have similar or slightly higher uptake of ^{64}Cu-DOTA−RGD than the tumor. All three tracers revealed receptor-specific tumor accumulation as the uptake was inhibited upon coinjection of c(RGDyK) although the extent of blocking of tumor uptake was different for the three tracers. A detailed comparison of activity accumulation in the blood, tumor, liver, and

Table 2. Radioactivity, Expressed as Percent Injected Dose per Gram Tissue in Different Organs and Tumor of MDA-MB-435 Xenograft Model after Intravenous Injection of 20 μCi of [^{18}F]FB−RGD at 30 min, 1, 2, and 1 h Block (with coinjection of 10 mg/kg c(RGDyK)) ($n = 4$)

	30 min	1 h	2 h	1 h block
blood	0.51 ± 0.07	0.27 ± 0.02	0.08 ± 0.01	0.23 ± 0.04
muscle	0.58 ± 0.11	0.35 ± 0.04	0.17 ± 0.02	0.19 ± 0.08
tumor	1.81 ± 0.26	1.30 ± 0.24	0.98 ± 0.29	0.45 ± 0.13
skin	1.55 ± 0.34	0.98 ± 0.06	0.54 ± 0.05	0.53 ± 0.08
bone	0.60 ± 0.04	0.51 ± 0.01	0.54 ± 0.19	0.59 ± 0.07
heart	0.56 ± 0.06	0.33 ± 0.02	0.17 ± 0.02	0.20 ± 0.03
lung	1.90 ± 0.15	0.76 ± 0.09	0.36 ± 0.07	0.69 ± 0.12
liver	2.49 ± 0.12	1.21 ± 0.21	0.39 ± 0.05	1.77 ± 0.34
kidney	3.21 ± 0.29	1.63 ± 0.32	0.71 ± 0.15	1.42 ± 0.46
spleen	0.77 ± 0.13	0.29 ± 0.04	0.20 ± 0.04	0.30 ± 0.05
pancreas	0.36 ± 0.02	0.26 ± 0.02	0.15 ± 0.02	0.29 ± 0.04
stomach	1.89 ± 0.35	1.48 ± 0.14	1.07 ± 0.45	0.67 ± 0.10
intestines	4.68 ± 0.79	3.59 ± 0.62	0.79 ± 0.08	5.98 ± 0.77
tumor/blood	3.55 ± 0.34	4.81 ± 1.35	12.2 ± 1.25	1.96 ± 0.58
tumor/muscle	3.12 ± 0.29	3.71 ± 0.78	5.76 ± 0.66	2.37 ± 0.44

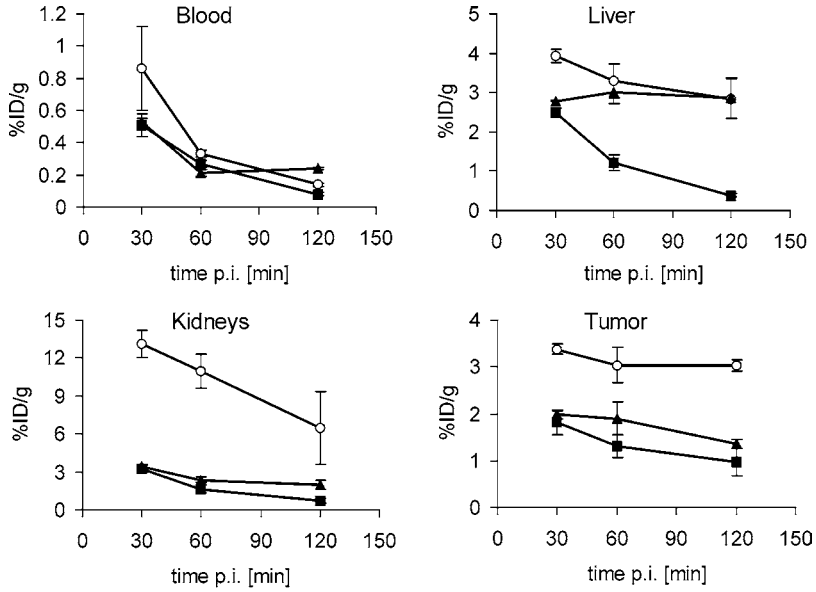


Figure 2. Comparison of biodistribution data of ^{125}I-RGD (○), [^{18}F]FB−RGD (■) and ^{64}Cu-DOTA−RGD (▲) in orthotopic MDA-MB-435 breast cancer-bearing nude mice. Error bars denote SD (n = 5).

Table 3. Radioactivity, Expressed as Percent Injected Dose per Gram Tissue in Different Organs and Tumor of MDA-MB-435 Xenograft Model after Intravenous Injection of 10 μCi [^{64}Cu-DOTA−RGD at 15 min, 30 min, 1, 2, 4, and 1 h Block (with coinjection of 10 mg/kg c(RGDyK)) (n = 4)

	15 min	30 min	1 h	2 h	4 h	1 h block
blood	1.21 ± 0.08	0.53 ± 0.02	0.21 ± 0.02	0.19 ± 0.02	0.24 ± 0.01	0.44 ± 0.01
muscle	0.57 ± 0.04	0.56 ± 0.16	0.26 ± 0.08	0.22 ± 0.02	0.23 ± 0.06	0.13 ± 0.05
tumor	2.02 ± 0.15	1.98 ± 0.10	1.90 ± 0.36	1.36 ± 0.10	1.44 ± 0.09	0.34 ± 0.02
skin	2.74 ± 0.45	2.07 ± 0.01	1.28 ± 0.37	1.20 ± 0.12	1.22 ± 0.09	0.51 ± 0.31
bone	1.02 ± 0.11	0.91 ± 0.14	0.54 ± 0.33	0.50 ± 0.08	0.76 ± 0.28	0.35 ± 0.14
heart	0.88 ± 0.07	0.76 ± 0.03	0.50 ± 0.04	0.54 ± 0.11	0.57 ± 0.01	0.30 ± 0.09
lung	2.04 ± 0.22	1.85 ± 0.38	0.95 ± 0.12	1.04 ± 0.18	1.05 ± 0.21	1.01 ± 0.16
liver	2.91 ± 0.16	2.78 ± 0.01	3.01 ± 0.28	2.87 ± 0.52	2.84 ± 0.17	2.09 ± 0.32
kidney	4.98 ± 0.35	3.45 ± 0.16	2.36 ± 0.23	1.98 ± 0.37	1.98 ± 0.06	1.30 ± 0.21
spleen	1.09 ± 0.04	1.06 ± 0.12	0.78 ± 0.17	0.85 ± 0.09	0.83 ± 0.15	0.42 ± 0.22
pancreas	0.57 ± 0.09	0.50 ± 0.06	0.35 ± 0.03	0.37 ± 0.08	0.33 ± 0.02	0.26 ± 0.17
stomach	2.53 ± 0.28	2.38 ± 0.63	1.48 ± 0.26	1.40 ± 0.14	1.19 ± 0.11	0.53 ± 0.35
intestines	1.09 ± 0.17	2.43 ± 0.50	1.92 ± 0.34	1.64 ± 0.05	1.70 ± 0.04	0.67 ± 0.34
tumor/blood	1.67 ± 0.11	3.72 ± 0.18	8.14 ± 0.88	6.94 ± 0.51	6.00 ± 0.06	0.77 ± 0.06
tumor/muscle	3.54 ± 0.25	3.65 ± 0.85	7.10 ± 1.30	6.02 ± 0.64	6.30 ± 1.28	2.89 ± 1.10

kidneys for the ^{125}I-, ^{18}F-, and ^{64}Cu-labeled RGD peptides were illustrated in Figure 2.

MicroPET and Autoradiographic Imaging. The localization of [^{18}F]FB−RGD in MDA-MB-435 tumor-bearing mouse as determined by microPET imaging followed by whole-body autoradiography was shown in Figure 3. On the left was a coronal imaging (15 min scan) of tumor-bearing mouse, 1 h postadministration of 200 μCi of [^{18}F]FB−RGD. Whole-body autoradiographic section concord with the microPET image was shown on the right. Regions of interest (ROIs) were placed on tumors as well as other organs of interest. The tumor/muscle ratio was 4.6 ± 0.4 (n = 3) from autoradiography and 5.1 ± 0.8 (n = 3) from microPET, in good agreement with that obtained from direct tissue sampling (4.8 ± 1.4) (n = 5).

Static microPET imaging (15 min scan) 120−135 min after iv administration of ^{64}Cu-DOTA−RGD illustrated in a coronal image of an orthotopically implanted MDA-MB-435 tumor-bearing mouse was shown in Figure 4. Tumor was visualized with clear contrast. PET imaging was further validated by whole-body autoradiography in the same animal. Tumor/muscle ratios measured with microPET and autoradiography were 5.6 ± 0.4 and 6.9 ± 0.8, respectively, which again agreed with the biodistribution experiment in a separate group of mice (6.0 ± 0.6; n = 5) (Table 3). As expected, we did not observe any tumor uptake in the brain for any of the three tracers, suggesting that either the tracer does not penetrate the tight blood−brain barrier (BBB) or the normal brain tissue does not express significant amount of α_v-integrins.

The transaxial image of a MDA-MB-435 tumor-bearing mouse acquired at 1 h pi revealed tumor to contralateral background ratio of 7.5 ± 0.6 (Figure 5). Coinjection of ^{64}Cu-DOTA−RGD with different amounts of c(RGDyK) revealed dose-dependent blocking of tumor uptake. The tumor-to-background ratio decreased to 2.3 ± 0.4 [coinjection with 2.5 mg/kg c(RGDyK)] and 1.8 ± 0.5 [coinjection with 7.5 mg/kg c(RGDyK)].

DISCUSSION

Cyclic RGD peptide antagonists of α_v-integrins have been labeled with different isotopes such as ^{125}I, ^{99m}Tc, ^{111}In, ^{90}Y, and ^{18}F for tumor targeting in various preclinical animal models. However, to the best of our knowledge, this is the first report of ^{64}Cu-labeled RGD for tumor angiogenesis imaging. Copper radioistope offers an attractive basis for the development of diagnostic (^{60}Cu, ^{61}Cu, ^{62}Cu, and ^{64}Cu) and therapeutic (^{64}Cu and ^{67}Cu) radiopharmaceuticals (*26*). ^{64}Cu, in particular, has the

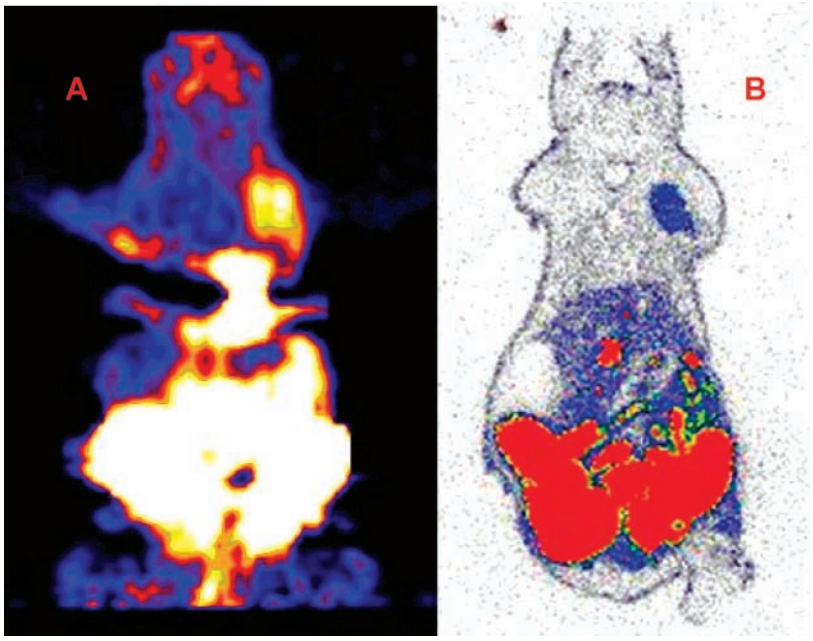


Figure 3. (A) MicroPET scan of mouse administered 200 μCi of [^{18}F]FB−RGD and scanned 60 min after injection (10 min single frame). The mouse carried an orthotopic MDA-MB-435 breast cancer xenograft in the right mammary fat pad. (B) Digital autoradiograph of the section containing tumor after microPET scanning.

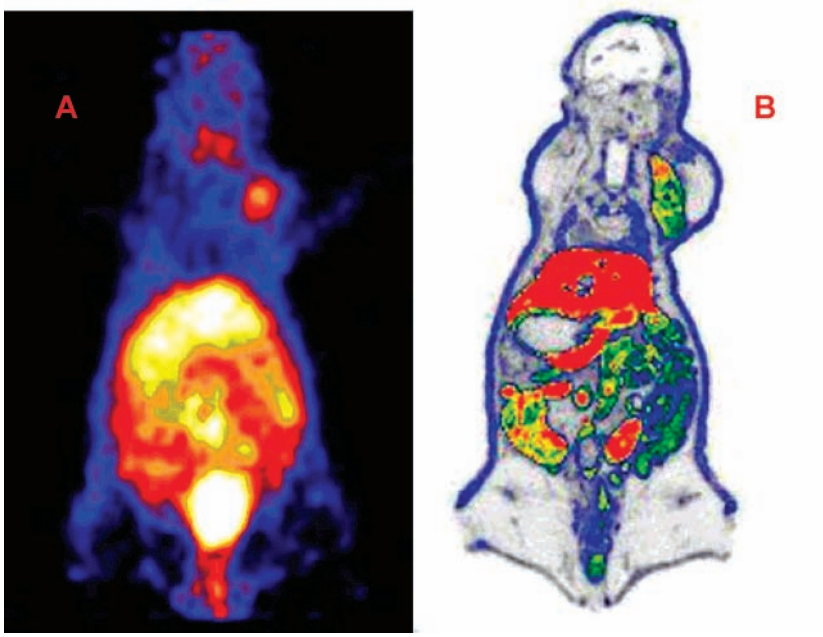


Figure 4. (A) MicroPET scan of mouse administered 400 μCi of ^{64}Cu-DOTA−RGD and scanned 2 h after injection (15 min single frame). The mouse carried an orthotopic MDA-MB-435 breast cancer xenograft in the right mammary fat pad. (B) Digital autoradiograph of the section containing tumor after microPET scanning.

desirable properties for both PET imaging and therapy and can be produced in high yield and high specific activity on a small biomedical cyclotron (*25*, *27*). In this study we would like to compare the tumor targeting ability and in vivo kinetics of ^{125}I-, ^{18}F-, and ^{64}Cu-labeled cyclic RGD peptide c(RGDyK) in murine orthotopic MDA-MB-435 human breast cancer model.

^{125}I-RGD has the highest tumor uptake and slowest tumor washout rate compared to [^{18}F]FB−RGD and ^{64}Cu-DOTA−RGD. The low molecular mass compound c(RGDyK) is optimized in size to fit the binding pocket of the $\alpha_v\beta_3$ integrin receptor. Thus, introduction of any labeling groups is likely to result in a loss of the affinity. Adding ^{125}I label to the ortho-position of the cyclic RGD peptide is expected to have minimal change of geometry and binding characteristics of the peptide and thus allows high receptor-specific tumor uptake. On the other hand, having a bulky 4-[^{18}F]fluorobenzoyl group or ^{64}Cu-DOTA complex (Figure 1) that are not far from the integrin-recognizing RGD moiety decreased receptor binding affinity and specificity of these tracers, which were demonstrated by lowered tumor uptake (Figure 2) and incomplete inhibition of tumor accumulation by applying a blocking dose of c(RGDyK). The blocking experiment indicated tumor-to-muscle ratio of 0.7 ± 0.5, 2.4 ± 0.4, and 2.9 ± 1.1 for ^{125}I-RGD, [^{18}F]FB−RGD, and ^{64}Cu-DOTA−RGD, respectively. Solid-phase receptor binding assay to directly assess the $\alpha_v\beta_3$ and $\alpha_v\beta_5$ integrin binding affinity and specificity of these tracers is needed to further confirm this.

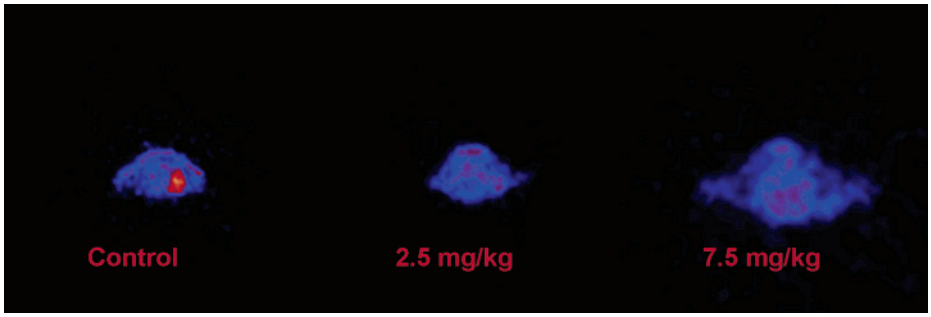


Figure 5. Transaxial microPET images of nude mice bearing MDA-MB-435 xenografts. Images were acquired 60 min after injection of 300 μCi of ^{64}Cu-DOTA−RGD. The three images were obtained from serial ^{64}Cu-DOTA−RGD PET studies on the same mouse. The images illustrate the dose-dependent blockade of tracer uptake by c(RGDyK).

The prolonged liver and blood uptake of ^{64}Cu-DOTA−RGD is problematic for this tracer, suggesting slow dissociation of ^{64}Cu from the DOTA chelator (*28*). It has been demonstrated that ^{64}Cu when bound to DOTA or TETA conjugates tends to transchelate to albumin, superoxide dismutase, ceruloplasmin, and metallothionein, leading to higher blood and liver uptake (*29*−*31*) and that more rapid clearance from the liver is indicative of higher in vivo stability of the ^{64}Cu complex (*32*). Development of more stable chelators for copper radionuclides that have greater kinetic stability and yet fast incorporation rate of ^{64}Cu into the macrocyclic chelating moiety (*32*, *33*) is needed for creation of new copper radiopharmaceuticals for diagnosis and therapy applications. Recent studies to investigate the renal uptake of ^{111}In-DTPA-conjugated octreotide analogues (*34*, *35*) found out that initial kidney uptake is related to the overall molecular charge of the peptide, and that persistent localization of the radioactivity in the kidney would be attributed to the long residence time of the final radiometabolite generated after lysosomal proteolysis in the renal cells. The relatively low renal uptake of ^{64}Cu-DOTA−RGD is probably due to the overall negative charge character of this radiotracer under physiological condition. The sustained low retention of activity in the kidneys may be caused by the metabolites after ^{64}Cu-DOTA-conjugated RGD peptide is internalized, but ^{64}Cu-DOTA−Lys will unlikely be the species which is retained in the lysosomes. Further studies to investigate in vivo transchelation of ^{64}Cu and metabolic stability of the radioconjugate is necessary to fully understand the excretion kinetics of this compound and to further optimize the tracer for potential clinical applications.

MicroPET, a dedicated small animal imaging device, enables real time imaging studies in rodents and forms an invaluable bridge between laboratory and clinical science. The picomolar sensitivity and reasonably good spatial and temporal resolution of microPET makes it play a leading role in molecular imaging (*36*). Depending on the radiotracers used, it allows visualization and quantification of physiological, metabolic, and molecular changes during disease development and upon treatment. Both endogenous protein imaging and exogenous reporter gene imaging are being actively explored. In this study, we demonstrate the feasibility of ^{18}F- and ^{64}Cu-labeled cyclic RGD peptide for breast cancer angiogenesis imaging by targeting cell adhesion molecules, α_v-integrins. Several RGD peptide antagonists have been labeled with ^{111}In and ^{99m}Tc for SPECT imaging of tumor models. Recently Haubner et al. (*20*) labeled a RGD-containing glycopeptide with ^{18}F through a 2-[^{18}F]fluoropropionate moiety for PET imaging of melanoma xenograft. In this study we labeled c(RGDyK) with both ^{18}F and ^{64}Cu for orthotopic breast cancer tumor imaging. MicroPET imaging of [^{18}F]FB−RGD at 1 h postinjection of 200 μCi of activity showed reasonably good tumor-to-background ratio; however, very high uptake in the urinary bladder and intestines was observed, suggesting the unfavorable hepatobiliary excretion pathway due to the lipophilicity of this tracer. This tracer may be able to locate tumors in areas with higher uptake than the liver, such as breast cancer and brain tumors. MicroPET and autoradiographic imaging of ^{64}Cu-DOTA−RGD also gives clear tumor-to-background contrast, but also significant liver and kidney uptake, which correlates well with the distribution pattern found from direct tissue sampling. The successful blocking of tumor uptake of ^{64}Cu-DOTA−RGD in a dose-dependent manner demonstrates that accumulation in the tumor is receptor specific. Further study to correlate the magnitude of tumor uptake with receptor expression level needs to be performed.

High expression and activation of the $\alpha_v\beta_3$ integrin has been correlated with the more metastatic and invasive breast tumors (*37*, *38*). Inhibition of $\alpha_v\beta_3$ integrin activities has been associated with decreased tumor growth in breast cancer xenografts (*14*). The DeNardo group demonstrated increased tumor uptake of ^{90}Y-DOTA−peptide−ChL6 mAb after treatment with cyclic RGD peptide in nude mice bearing HBT 3477 breast cancer xenografts (*39*). The combination of cilengitide and radioimmunotherapy (RIT) significantly increased the efficacy and endothelial cell apoptosis without apparent increase in toxicity, compared with either therapeutic protocol alone (*40*). Recently, Janssen et al. (*24*) labeled DOTA−E[c(RGDfK)]$_2$ with ^{90}Y and applied a therapeutic dose of the radiolabeled compound to a sc ovarian cancer tumor model and induced a significant delay in tumor growth by a single injection. ^{111}In was used as a surrogate for ^{90}Y to obtain dosimetry information. However, the different biodistributions of ^{111}In- and ^{90}Y-labeled compounds may result in inaccurate dosimetry of ^{90}Y-labeled compounds using ^{111}In analogues. A more suitable isotope for accurately imaging the biodistribution of ^{90}Y would be quantitative imaging with the surrogate positron emitter ^{86}Y ($t_{1/2}$ = 14.7 h, 33% β^+) to detect the uptake and dosimetry of ^{90}Y-labeled RGD. Due to the existence of imaging/therapy radionuclide pair (^{64}Cu/^{67}Cu) for diagnosing and treating cancer, ^{64}Cu-DOTA−RGD developed in this study may be able to determine dosimetry and tumor response to the same ligand labeled with therapeutic amounts of ^{67}Cu for $\alpha_v\beta_3$ integrin-mediated internal radiotherapy. Since DOTA-derivatized macrocyclic ligands bind a large number of metal ions with extremely high in vivo stability, the same bioconjugates developed in this study for ^{64}Cu would also be able to bind other imaging radionuclides such as ^{86}Y and therapeutic radionuclides such as ^{90}Y and ^{177}Lu.

CONCLUSIONS

The study presented here demonstrated that [^{18}F]FB−RGD and ^{64}Cu-DOTA−RGD are tracers suitable for PET imaging of α_v-integrin expression in breast cancer. Although the positron emitter-labeled RGD peptide indicated lower tumor uptake than ^{125}I-RGD, they were able to visualize breast cancer tumor in xenograft models with clear contrast and receptor-specific uptake. Unfavorable hepatobiliary excretion and rapid tumor washout rate of [^{18}F]FB−RGD limited its potential clinical applications unless further modification is performed to optimize this tracer. ^{64}Cu-DOTA−RGD, on the other hand, revealed more consistent and sustained blood concentration, prolonged tumor uptake, but also significant amount of liver and kidney retention. The hydrophilicity, overall molecular charge, and characteristics of the radiolabel as well as radiometabolites have profound effects on the tumor targeting and in vivo kinetics of the radiopharmaceuticals derived from cyclic RGD peptides. Modification of the ^{64}Cu-complexing moiety and the systematic investigation of the tethers linking RGD and ^{64}Cu-macrocycle complex will be the future focus to develop a superior ligand for α_v-integrin targeting and for integrin-targeted internal radiotherapy.

ACKNOWLEDGMENT

This work was carried out with partial contributions from NIH grant P20 CA86532 (to P.S.C.), ACS grant ACS-IRG-580007-42 (to X.C.), and the Wright Foundation (to X.C.). The USC cyclotron team, particularly Joseph Cook, is acknowledged for [^{18}F]F$^-$ production. Copper-64 has been provided by Washington University Medical School and partially funded through an NCI grant R24 CA86307.

LITERATURE CITED

(1) Jemal, A. J., Murray, T., Samuels, A., Ghafoor, A., Ward, E., and Thun, M. J. (2003) Cancer statistics, 2003. *CA Cancer J. Clin. 52*, 5−26.

(2) Heimann, R., Ferguson, D., Gray, S., and Hellman, S. (1998) Assessment of intratumoral vascularization (angiogenesis) in breast cancer prognosis. *Breast Cancer Res. Treat. 52*, 147−58.

(3) Sledge, G. W., Jr. (2002) Vascular endothelial growth factor in breast cancer: biologic and therapeutic aspects. *Semin. Oncol. 29*, 104−110.

(4) Jain, R. K. (1998) The next frontier of molecular medicine: delivery of therapeutics. *Nat. Med. 4*, 655−657.

(5) Burke, P. A., and DeNardo, S. J. (2001) Antiangiogenic agents and their promising potential for combined therapy. *Cancer Res. 48*, 7022−7032.

(6) Kubota, K. (2001) From tumor biology to clinical Pet: a review of positron emission tomography (PET) in oncology. *Ann. Nucl. Med. 15*, 471−86.

(7) Barthel, H., Cleij, M. C., Collingridge, D. R., Hutchinson, O. C, Osman, S., He, Q., Luthra, S. K., Brady, F., Price, P. M., and Aboagye, E. O. (2003) 3′-Deoxy-3′-[^{18}F]fluorothymidine as a new marker for monitoring tumor response to antiproliferative therapy in vivo with positron emission tomography. *Cancer Res. 63*, 3791−3798.

(8) Padani, A. R., and Neeman, M. (2001) Challenges for imaging angiogenesis. *Br. J. Radiol. 74*, 886−890.

(9) Jung, Y. D., Ahmad, S. A., Liu, W., Reinmuth, N., Parikh, A., Stoeltzing, O., Fan, F., and Ellis, L. M. (2002) The role of the microenvironment and intercellular cross-talk in tumor angiogenesis. *Semin. Cancer Biol. 12*, 105−12.

(10) Folkman, J. (2002) Role of angiogenesis in tumor growth and metastasis. *Semin. Oncol. (Suppl) 29*, 15−18.

(11) Hynes, R. O. (1992) Integrins: Versatility, modulation and signaling in cell adhesion. *Cell 69*, 577−585.

(12) Brooks, P. C., Montgomery, A. M. P., Rosenfeld, M., Hu, T., Klier, G., and Cheresh, D. A. (1994) Integrin $\alpha_v\beta_3$ antagonists promote tumor regression by inducing apoptosis of angiogenic blood vessels. *Cell 79*, 1157−1164.

(13) Brooks, P. C., Clark, R. A., and Cheresh, D. A. (1994) Requirement of vascular integrin $\alpha_v\beta_3$ for angiogenesis. *Science 264*, 569−571.

(14) Brooks, P. C., Stromblad, S., Klemke, R., Sarkar, F. H., and Cheresh, D. A. (1995) Anti-integrin $\alpha_v\beta_3$ blocks human breast cancer growth and angiogenesis in human skin. *J. Clin. Investig. 96*, 1815−1822.

(15) Buerkle, M. A., Pahernik, S. A., Sutter, A., Jonczyk, A., Messmer, K., and Dellian, M. (2002) Inhibition of the alpha-v integrins with a cyclic RGD peptide impairs angiogenesis, growth and metastasis of solid tumors in vivo. *Br. J. Cancer 86*, 788−795.

(16) Qiao, R., Yan, W., Lum, H., and Malik, A. B. (1995) Arg-Gly-Asp peptide increases endothelial hydraulic conductivity: comparison with thrombin response. *Am. J. Physiol. 269*, C110−C117.

(17) Zhou, Q., Sherwin, R. P., Parrish, C., Richters, V., Groshen, S. G., Tsao-Wei, D., and Markland, F. S. (2000) Contortrostatin, a dimeric disintegrin from Agkistrodon contortrix contortrix, inhibits breast cancer progression. *Breast Cancer Res. Treat. 61*, 249−260.

(18) Chen, X., Park, R., Shahinian, A. H., Bading, J. R., and Conti, P. S. (2003) Pharmacokinetics and tumor retention of ^{125}I-labeled RGD peptide are improved by PEGylation. *Nucl. Med. Biol. 30*, in press.

(19) Haubner, R., Wester, H.-J., Burkhart, F., Senekowitsch-Schmidtke, R., Weber, W., Goodman, S. L., Kessler, H., and Schwaiger, M. (2001) Glycosylated RGD-containing peptides: tracer for tumor targeting and angiogenesis imaging with improved biokinetics. *J. Nucl. Med. 42*, 326−336.

(20) Haubner, R., Wester, H.-J., Weber, W. A., Mang, C., Ziegler, S. I., Goodman, S. L., Senekowitsch-Schmidtke, R., Kessler, H., and Schwaiger M (2001) Noninvasive imaging of $\alpha_v\beta_3$ integrin expression using ^{18}F-labeled RGD-containing glycopeptide and positron emission tomography. *Cancer Res. 61*, 1781−1785.

(21) Chen, X., Park, R., Shahinian, A. H., Tohme, M., Khankaldyyan, V., Bozorgzadeh, M. H., Bading, J. R., Moats, R., and Laug, W. E. (2003) ^{18}F-labeled RGD peptide: initial evaluation for imaging brain tumor angiogenesis. *Nucl. Med. Biol. 30*, in press.

(22) Ogawa, M., Hantaro, K., Oishi, S., Kawasumi, Y., Fuji, N., Kawaguchi, M., Doi, R., Imamura, M., Yamamoto, M., Ajito, K., Mukai, T., Saji, H., and Ito, K. (2003) Direct electrophilic radiofluorination of a cyclic RGD peptide for in vivo $\alpha_v\beta_3$ integrin related tumor imaging. *Nucl. Med. Biol. 30*, 1−9.

(23) Van Hagen, P. M., Breeman, W. A. P., Bernard, H. F., Schaar, M., Mooij, C. M., Srinivasan, A., Schmidt, M. A., Krenning, E. P., and De Jong, M. (2000) Evaluation of a radiolabeled cyclic DTPA-RGD analogue for tumor imaging and radionuclide therapy. *Int. J. Cancer 90*, 186−198.

(24) Janssen, M. L., Oyen, W. J., Dijkgraaf, I., Massuger, L. F., Frielink, C., Edwards, D. S., Rajopadhye, M., Boonstra, H., Corstens, F. H., and Boerman, O. C. (2002) Tumor targeting with radiolabeled $\alpha_v\beta_3$ integrin binding peptides in a nude mouse model. *Cancer Res. 62*, 6146−6151.

(25) McCarthy, D. W., Shefer, R. E., Klinkowstein, R. E., Bass, L. A., Margenau, W. H., Cutler, C. S., Anderson, C. J., and Welch, M. J. (1997) The efficient production of high specific activity Cu-64 using a biomedical cyclotron. *Nucl. Med. Biol. 24*, 35−43.

(26) Anderson, C. J., and Welch, M. J. (1999) Radiometal-labeled agents (non-technetium) for diagnostic imaging. *Chem. Rev. 99*, 2219−2234.

(27) Obata, A., Kasamatsu, S., McCarthy, D. W., Welch, M. J., Saji, H., Yonekura, Y., and Fujibayashi, Y. (2003) Production of therapeutic quantities of ^{64}Cu using a 12 MeV cyclotron. *Nucl. Med. Biol. 30*, 535−539.

(28) Li, W. P., Lewis, J. S., Kim, J., Bugaj, J. E., Johnson, M. A., Erion, J. L., and Anderson, C. J. (2002) DOTA−D-Tyr^1-octreotate: a somatostatin analogue for labeling with metal

and halogen radionuclides for cancer imaging and therapy. *Bioconjugate Chem. 13*, 721−728.
(29) Blower, P. J., Lewis, J. S., and Zweit, J. (1996) Copper radionuclides and radiopharmaceuticals in nuclear medicine. *Nucl. Med. Biol. 23*, 957−980.
(30) Rogers, B. E., Anderson, C. J., Connett, J. M., Guo, L. W., Edwards, W. B., Sherman, E. L. C., Zinn, K. R., and Welch, M. J. (1996) Comparison of four bifunctional chelates for radiolabeleing monoclonal antibodies with copper radioisotopes: Biodistribution and metabolism. *Bioconjugate Chem. 7*, 511−522.
(31) Bass, L. A., Wang, M., Welch, M. J., and Anderson, C. J. (2000) In vivo transchelation of copper-64 from TETA-octreotide to superoxide dismutase in rate liver. *Bioconjugate Chem. 11*, 527−532.
(32) Sun, X., Wuest, M., Weisman, G. R., Wong, E. H., Reed, D. P., Boswell, C. A., Motekaitis, R., Martell, A. E., Welch, M. J., and Anderson, C. J. (2002) Radiolabeling and in vivo behavior of copper-64-labeled cross-bridged cyclam ligands. *J. Med. Chem. 45*, 469−477.
(33) Ma, D., Lu, F., Overstreet, T., Milenic, D. E., and Brechbiel, M. W. (2002) Novel chelating agents for potential clinical applications of copper. *Nucl. Med. Biol. 29*, 91−105.
(34) Akizawa, H., Arano, Y., Mifune, M., Iwado, A., Saito, Y., Mukai, T., Uehara, T., Ono, M., Fujioka, Y., Ogawa, K., Kiso, Y., and Saji, H. (2001) Effect of molecular charges on renal uptake of ^{111}In-DTPA-conjugated peptides. *Nucl. Med. Biol. 28*, 761−768.
(35) Akizawa, H., Arano, Y., Mifune, M., Iwado, A., Saito, Y., Uehara, T., Ono, M., Fujioka, Y., Ogawa, K., Kiso, Y., and Saji, H. (2001) Significance of ^{111}In-DTPA chelate in renal radioactivity levels of ^{111}In-DTPA-conjugated peptides. *Nucl. Med. Biol. 28*, 459−468.
(36) Cherry, S. R., Shao, Y., Silverman, R. W., Meadors, K., Siegel, S., Chatziioannou, A., Young, J. W., Jones, W. F., Moyers, J. C., Newport, D., Boutefnouchet, A., Farquhar, T. H., Andreaco, M., Paulus, M. J., Binkley, D. M., Nutt, R., and Phelps, M. E. (1997) MicroPET: a high-resolution PET scanner for imaging small animals. *IEEE Trans. Nucl. Sci. 44*, 1161−1166.
(37) Gasparini, G., Brooks, P. C., Biganzoli, E., Vermeulen, P. B., Bonoldi, E., Dirix, L. Y., Ranieri, G., Miceli, R., and Cheresh, D. A. (1998) vascular integrin $\alpha_v\beta_3$: a new prognostic indicator in breast cancer. *Clin. Cancer Res. 4*, 2625−2634.
(38) Felding-Habermann, B., O'Toole, T. E., Smith, J. W., Fransvea, E., Ruggeri, Z. M., Ginsberg, M. H., Hughes, P. E., Pampori, N., Shattil, S. J., Saven, A., and Mueller, B. M. (2001) Integrin activation controls metastasis in human breast cancer. *Proc. Natl. Acad. Sci. U.S.A. 98*, 1853−1858.
(39) DeNardo, S. J., Burke, P. A., Leigh, B. R., O'Donnell, R. T., Miers, L. A., Kroger, L. A., Goodman, S. L., Matzku, S., Jonczyk, A., Lamborn, K. R., and DeNardo, G. L. (2000) Neovascular targeting with cyclic RGD peptide (cRGDf-ACHA) to enhance delivery of radioimmunotherapy. *Cancer Biother. Radiopharm. 15*, 71−79.
(40) Burke, P. A., DeNardo, S. J., Miers, L. A., Lamborn, K. R., Matzku, S., and DeNardo, G. L. (2002) Cilengitide targeting of $\alpha_v\beta_3$ integrin receptor synergizes with radioimmunotherapy to increase efficacy and apoptosis in breast cancer xenografts. *Cancer Res. 62*, 4263−4272.

BC0300403

Nanogels for Oligonucleotide Delivery to the Brain

Serguei V. Vinogradov, Elena V. Batrakova, and Alexander V. Kabanov*

College of Pharmacy, Department of Pharmaceutical Sciences, University of Nebraska Medical Center, 986025 Nebraska Medical Center, Omaha, Nebraska 68198-6025 Received September 10, 2003; Revised Manuscript Received October 15, 2003

Systemic delivery of oligonucleotides (ODN) to the central nervous system is needed for development of therapeutic and diagnostic modalities for treatment of neurodegenerative disorders. Macromolecules injected in blood are poorly transported across the blood−brain barrier (BBB) and rapidly cleared from circulation. In this work we propose a novel system for ODN delivery to the brain based on nanoscale network of cross-linked poly(ethylene glycol) and polyethylenimine ("nanogel"). The methods of synthesis of nanogel and its modification with specific targeting molecules are described. Nanogels can bind and encapsulate spontaneously negatively charged ODN, resulting in formation of stable aqueous dispersion of polyelectrolyte complex with particle sizes less than 100 nm. Using polarized monolayers of bovine brain microvessel endothelial cells as an in vitro model this study demonstrates that ODN incorporated in nanogel formulations can be effectively transported across the BBB. The transport efficacy is further increased when the surface of the nanogel is modified with transferrin or insulin. Importantly the ODN is transported across the brain microvessel cells through the transcellular pathway; after transport, ODN remains mostly incorporated in the nanogel and ODN displays little degradation compared to the free ODN. Using mouse model for biodistribution studies in vivo, this work demonstrated that as a result of incorporation into nanogel 1 h after intravenous injection the accumulation of a phosphorothioate ODN in the brain increases by over 15 fold while in liver and spleen decreases by 2-fold compared to the free ODN. Overall, this study suggests that nanogel is a promising system for delivery of ODN to the brain.

INTRODUCTION

Oligonucleotides (ODN) have attracted significant interest as potential diagnostic and therapeutic agents for diseases that currently have no cure. This includes cancer, neurodegenerative disorders (Alzheimer's and Parkinson's disease), and lethal viral infections (*1*−*7*). However, the use of ODN in the body is hindered by the lack of stability of ODN against enzymatic degradation as well as rapid clearance of ODN through renal excretion. Furthermore, the blood−brain barrier (BBB) severely restricts the entry of ODN to the brain from the periphery, which represents a major obstacle for the use of ODN for diagnostics and therapy of disorders of central nervous system (CNS). The need to improve the pharmacological performance of ODN resulted in development of drug delivery systems for ODN (*8*−*12*). In particular, studies involving nanoparticles demonstrated promise in enhancing delivery of ODN to the brain (*13*). Several major features of nanoparticles make them especially useful for this application. First, they represent an injectable drug delivery system with particle size ca. 100 nm or less. Such particles can easily enter brain capillaries and reach the surface of the brain microvascular endothelial cells (BMVEC) forming the BBB. Second, the surface of the nanoparticles, for example, those prepared from poly(lactide-*co*-glycolide) or poly(butylcyanoacrylate), can be modified by poly(ethylene glycol) (PEG) or PEG-containing surfactants. This can prolong the circulation of the nanoparticles in the blood and enhance exposure of the BBB to the modified nanoparticles. Third, the nanoparticles can be further modified with specific targeting molecules that enhance binding of the nanoparticles with the surface receptors of the BMVEC and promote transport of the nanoparticles across the BBB. In particular, Pardridge and collaborators proposed to use for this purpose insulin and transferrin receptors (*14*−*16*). Importantly, the small size of nanoparticles may allow for their receptor-mediated transcytosis in BBB without violating the integrity of the tight junctions of BMVEC, which are impermeable to macromolecules. Various therapeutic agents including ODN, proteins, and peptides can be encapsulated in the nanoparticles. Following the delivery of the nanoparticles to the disease site in the body, the polymer matrix can slowly degrade resulting in sustained release of the encapsulated therapeutic agents. Thus, the nanoparticles have a dual capacity as drug carriers and sustained drug release systems.

However, the currently used nanoparticles have substantial shortcomings including relatively low drug loading capacities and rather complicated preparation and drug formulation procedures. These procedures require exposure to organic solvents and energy input (e.g. sonication), which often result in inactivation of therapeutic macromolecules. One alternative approach, proposed by our group, is to use, as drug carriers, flexible hydrophilic polymer gels of nanoscale size, termed nanogels (NanoGel) (*17*−*20*). Nanogels can be synthesized in the absence of the drug, equilibrated (swollen) in water, and then loaded with the drug. Drug loading occurs spontaneously and results in decrease of the solvent volume, which is followed by the gel collapse and formation of dense nanoscale particles. We have previously described cationic nanogels consisting of covalently cross-linked PEG and polyethylenimine (PEI) chains, nano-PEG-*cross*-PEI (*18*, *20*). Such nanogels can bind and

* Corresponding author. E-mail: akabanov@unmc.edu.

10.1021/bc034164r CCC: $27.50 © 2004 American Chemical Society
Published on Web 12/30/2003

encapsulate spontaneously, through ionic interactions, any type of negatively charged ODN, including antisense ODN, ribozymes, siRNAs, etc. Although the charge neutralization results in condensation of polycation and ODN chains, the loaded nanogels remain stable in aqueous dispersion due to the effect of nonionic PEG chains. A key advantage of nanogels is that they allow for high "payloads" of macromolecules, up to 50 wt %, which usually cannot be achieved with conventional nanoparticles. Nanogels are transported in the cells and can release functionally active antisense ODN, which was shown to produce specific effects on gene expression in the cells (*18*). Furthermore, nanogels can carry ODN across cellular barriers, such as monolayers of human intestine epithelial cells and protect ODN from degradation within these cells (*18*). Previous studies also demonstrated that as a result of modification of nanogels with targeting moieties, such as insulin or transferrin, the modified nanogels undergo receptor-mediated transport in the cells (*18*, *20*).

The objective of the present work is to evaluate whether the nano-PEG-*cross*-PEI nanogels can be useful for delivery of ODN to the brain. We describe the synthesis and characterization of nano-PEG-*cross*-PEI nanogels, modified with insulin and transferrin. We use polarized monolayers of bovine brain microvessel endothelial cells (BBMEC) as an in vitro model of the BBB in the transport studies as well as a mouse model for initial studies of the in vivo biodistribution of nanogels and encapsulated ODN. The results suggest successful delivery of nanogel-encapsulated ODN from the apical to basolateral side of the BBMEC monolayers. Furthermore, the data suggest that nanogel protects ODN from enzymatic degradation in the cells. Finally, the in vivo biodistribution study suggests that following intravenous (iv) administration of nanogel-formulated ODN in mice, substantial amounts of nanogel and ODN accumulate in the brain.

MATERIALS AND METHODS

Materials. PEG (MW 8000), ^{3}H-succinimidyl propionate, 96 mCi/mmol, and ^{3}H-mannitol, 50 mCi/mmol, were purchased from Moravek Radiochemicals (Brea, CA) and DuPont Corp. (Boston, MA), respectively. All other reagents and resins for chromatography were obtained from Sigma-Aldrich Co. (St-Louis, MO). The commercial branched PEI (MW 25 000) was fractionated by gel permeation chromatography on the Sepharose CL-2B column (2.5 × 75 cm) in 0.2 M sodium chloride, 0.025% aqueous ammonia, at elution rate 1 mL min^{-1} with refractive index detection. Polymer fractions containing amines were identified by blue color development following treatment of dried aliquots with a 2% solution of ninhydrin in ethanol. The high molecular mass (>ca. 50 000) and low molecular mass (<ca. 5000) fractions were discarded and the main fraction, ca. 50 wt % of the initial sample, was collected and used for the nanogel synthesis. The carbonyldiimidazole-activated PEG was synthesized from commercial PEG (8000), which was first dried in vacuo at 50 °C overnight and then dissolved in 50 mL of anhydrous acetonitrile and reacted with excess of 1,1′-carbonyldiimidazole under argon atmosphere for 4 h at 40 °C. The product was quantitatively precipitated from anhydrous ether (1 L), collected by centrifugation at 2000*g*, and dried in vacuo. Antisense ODN, 5′GT-CAAGCCAATTTGAATAGC, targeting the MDR1 gene with the 3′-amino (C3) linker (Glen Research, CA) was synthesized using phosphorothioate chemistry on a 1 micromolar scale (UNMC Oligonucleotide Core Facility, Omaha, NE). ODN was used without any additional purification except for ODN precipitation from 0.3 M sodium chloride solution in 2-propanol.

Synthesis of Nano-PEG-*cross*-PEI. Nanogel was synthesized using the emulsification−solvent evaporation method with modifications (*18*). The solution of carbonyldiimidazole-activated PEG (3 g) in dichloromethane (10 mL) was added dropwise to the solution of PEI (1 g) in water (180 mL) upon sonication in a Bransonic ultrasonic bath with ice-cold water. Following complete mixing, the resulting emulsion was sonicated for 20 or 30 min at 40 MHz. After that dichloromethane was quickly removed from the resulting milky solution in vacuo using a Buchi rotary evaporator with water bath set at 30 °C until the solution became clear. After that the solution was stirred for a 24 h period at 25 °C, filtered to separate large debris, and then neutralized by hydrochloric acid. The polymeric product was dialyzed through a SpectraPore membrane with the cutoff 25 000 Da against 0.025% aqueous ammonia for 2 days, concentrated in vacuo, and redissolved in 60 mL of 20% ethanol. Nanogel particles were fractionated by gel permeation chromatography on the Sepharose CL-2B column (2.5 × 75 cm) in 20% ethanol at an elution rate 1 mL min^{-1}. PEG-containing fractions were determined by the colorimetric method (*21*), and the fractions containing amines (PEI) were analyzed using the qualitative ninhydrin reaction. Nanogel fractions, containing both PEG and PEI, were collected and lyophilized. About 65−70% of polymeric material was recovered in the form of nanogel.

Nanogel Characterization. For analysis of PEG/PEI ratio in nanogel preparations, 5% solutions of dried nano-PEG-*cross*-PEI samples in D_2O were prepared and filtered. ^{1}H NMR spectra (with integration) were measured in the range 0−6 ppm at ambient temperature using the Varian 300 MHz spectrometer. Elemental analysis (M−H−W Laboratories, Phoenix, AZ) was used to measure total nitrogen content in nanogel preparations. The amount of ionizable groups in nanogel was determined by potentiometric titration of 1% suspension in 0.15 M solution of sodium chloride with hydrochloric acid. Before analysis, nanogel samples were dialyzed in 2% aqueous ammonia for 24 h and then lyophilized.

Biotin-Conjugated Nanogel. Nanogel (0.2 g) suspension in 2 mL of 0.1 M sodium carbonate buffer, pH 9, was treated with 1% solution of biotin *p*-nitrophenyl ester (0.6 mL) in dimethylformamide (DMF) overnight at 25 °C. Biotinylated nanogel was separated from low molecular weight substances by gel filtration on the Sephadex G-25 column (1 × 20 cm) in 20% ethanol at elution rate 0.5 mL min^{-1}, and fractions containing the product were lyophilized. Content of the covalently attached biotin was determined using 2-anilinonaphthalene-6-sulfonic acid (ANS)−avidin titration assay (*22*).

Rhodamine-Labeled Nanogel. Nanogel (0.2 g) suspension in 2 mL of 0.1 M sodium carbonate buffer, pH 9, was treated with 1% solution of rhodamine isothiocyanate (RITC) (0.2 mL) in DMF overnight at 25 °C. The red fraction of RITC-labeled nanogel was separated from low molecular weight substances by gel filtration on the Sephadex G-25 column (1 × 20 cm) in 20% ethanol at elution rate 0.5 mL min^{-1}, and fractions containing the product were lyophilized. Fluorescent spectral characteristics of the RITC-labeled nano-PEG-*cross*-PEI (λ_{ex} 549 nm and λ_{em} 577 nm) were measured in the phosphate-buffered saline, pH 7.4, using a Shimadzu RF5000 spectrofluorimeter.

Fluorescein-Labeled ODN. Solution of 3′-amino-ODN (10 nmol) in 0.2 mL of 0.1 M sodium carbonate

buffer, pH 9.0, was treated with 0.8 mL of 1% solution of fluorescein isothiocyanate (FITC) in DMF overnight at 25 °C. The green fraction of FITC-labeled OND was separated from low molecular weight substances by gel filtration on the Sephadex G-25 column (1 × 20 cm) in 20% ethanol at elution rate 0.5 mL min^{-1}, and fractions containing the product were lyophilized. Fluorescent spectral characteristics of the FITC-labeled ODN (λ_{ex} 489 nm and λ_{em} 513 nm) were measured in the phosphate-buffered saline, pH 7.4, using a Shimadzu RF5000 spectrofluorimeter.

Tritium-Labeled ODN. ODN bearing a 3′-primary amino group were labeled according to ref 23. The procedure for introduction of tritium label consists of the following steps. First, ODN (10 nmol) was precipitated in the form of cetyltrimethylammonium (CTA) salt, which is soluble in organic solvents, dried in vacuo, and redissolved in DMF. This solution was mixed with ^{3}H-succinimidyl propionate (40 μCi, specific activity 96 Ci/mmol), dissolved in toluene−ethyl acetate, and left to stand overnight at 25 °C. After the volatile organic solvents were removed in the flow of nitrogen, 0.04 mL of 50 mM sodium dodecyl sulfate solution was added to convert labeled ODN from CTAB-salt into sodium salt. Finally, tritium-labeled ODN was precipitated twice from sodium acetate solution in ethanol, washed by 70% ethanol, and dried in vacuo. Radioactivity of the precipitate and solutions was analyzed using Beckman LS6000 IC Liquid Scintillation counter. ODN concentration was determined using UV measurements. Efficiency of the labeling procedure was about 75%, and the specific activity of ODN was 3.3 Ci/mmol.

Preparation of Tritium-Labeled Nanogel. Nanogel (0.2 g) suspension in 2 mL of anhydrous acetonitrile containing 2% (v/v) of triethylamine was treated with a solution of ^{3}H-succinimidyl propionate (150 μCi) in toluene−ethyl acetate mixture overnight at 25 °C. Organic solvents were removed in the flow of nitrogen, and tritium-labeled nanogel was separated from low molecular weight substances by gel filtration on the Sephadex G-25 column (1 × 20 cm) in 20% ethanol at elution rate 0.5 mL min^{-1}. Radioactivity of the fractions was analyzed using Beckman LS6000 IC Liquid Scintillation counter. Fractions containing nanogel were collected and lyophilized. Specific activity of the tritium-labeled nanogel measured in 0.01% aqueous solution was equal to 20 μCi/mg. Efficiency of the labeling procedure was about 80%.

Preparation of Nanogel−ODN Complexes. Nanogel dispersion (1% w/v) in phosphate-buffered saline (PBS) was sonicated for 10−15 min at 25 °C and then filtered through the 0.45 μm filter. Total nitrogen (N) concentration was 66 mM. ODN solution (0.05 mM) in PBS (concentration of phosphate (P) groups 0.95 mM) was used as a stock solution for preparation of the complexes. For example, to prepare complexes containing 5 μM of ODN at N/P ratio 8, 0.2 mL of ODN solution was added dropwise upon stirring to the suspension of biotinylated nanogel (0.023 mL) in 1.78 mL of assay buffer (10 mM HEPES, 122 mM sodium chloride, 25 mM sodium bicarbonate, 10 mM glucose, 3 mM potassium chloride, 1.4 mM calcium chloride, 1.2 mM magnesium sulfate, 0.4 mM dibasic potassium phosphate). The resulting slightly opalescent solution was stirred for 1 h at 25 °C and then filtered through the sterile 0.22 μm filter. This solution could be stored at 4 °C at least for a week without any sign of precipitation. To prepare vectorized carriers, the equal volumes (0.1 mL) of white egg avidin (0.1 mM) and biotinylated bovine insulin (0.1 mM) or biotinylated bovine transferrin (0.1 mM) solutions in PBS were mixed in 1.8 mL of assay buffer upon stirring. After 30 min, this solution was supplemented with 2 mL of the preformed nanogel-ODN dispersion. The final solutions (4 mL) were incubated for at least 2 h at 25 °C, filtered through a 0.45 μm syringe filter, and used in further studies. Freshly prepared insulin and transferrin modified nanogel−ODN complexes were stored without freezing at 4 °C and used next day in the cell transport experiments.

Particle Sizing and ξ-Potential Measurements. The electrophoretic mobility (EPM) measurements of the nanogel−ODN complexes were performed in phosphate buffer, pH 7.4, at various N/P ratios, 25 °C with electrical field strength of 15−18 V cm^{-1} by using 'ZetaPlus' Zeta Potential Analyzer (Brookhaven Instruments, Santa Barbara, CA) with 15 mV solid-state laser operated at a laser wavelength of 635 nm. The ξ-potential of the particles was calculated from the EPM values using manufacturer's software. Effective hydrodynamic diameter of free and the ODN-loaded nanogel particles was measured by photon correlation spectroscopy using the same instrument equipped with the Multi-Angle Option at the angle of 90° and ambient temperature. The instrument was tested by standard suspension of polystyrol latex particles. All solutions were prepared in phosphate buffer, pH 7.4, and filtered through 0.45 μm filter.

To study particle size in the presence of bovine serum albumin (BSA), ODN−nanogel complexes were prepared in 2 mL of phosphate-buffered saline (PBS), incubated 30 min at room temperature, mixed with 0.2 mL of 4% BSA solution, and incubated another 30 or 90 min. Samples were filtered through 0.45 μm filter before measurements.

Cell Culture. BBMEC were isolated according to the method (*24*). BBMEC monolayers for transport studies were grown on the fibronectin- and collagen-coated Transwell polycarbonate membrane inserts (Fisher Scientific, Pittsburgh, PA) in MEM:F12 culture medium supplemented with 10% horse serum, heparin sulfate (100 μg/mL), amphotericin B (2.5 μg/mL), and gentamicin (50 μg mL^{-1}) (Gibco BRL, Grand Island, NY) at 5% CO_2 and 37 °C. The isolated cells formed confluent monolayers following 14 days of incubation. Transepithelial electrical resistance (TEER) values were recorded as indexes of cell viability and monolayer integrity. Under basal conditions, mean resistance was 135 ± 13 Ω/cm^2.

Cytotoxicity. Cytotoxicity of free and ODN-loaded nanogel was assessed by the measurement of IC_{50} value in a standard 3-(4,5-dimethyl-2-thiazolyl)-2,5-diphenyl-2*H*-tetrazolium bromide (MTT) assay (*25*). Briefly, 96-well microtiter plates were seeded with 5000 cells/well and allowed to reattach overnight. Dilutions of the nanogel−ODN dispersion (100 μL) in assay buffer were incubated with the cells for 2 h at 37 °C. Samples were washed three times with 100 μL of Minimum Essential Medium (MEM) and replaced with fresh culture medium (200 μL) daily. After incubation period of 72 h, 25 μL of MTT solution (5 mg/mL) was added to each well and the cells were incubated for 2 h at 37 °C in the dark. Medium and indicator dye were then removed and the cells lysed with 20% sodium dodecyl sulfate in 50% aqueous dimethylformamide (100 μL) overnight at 37 °C. Absorption was measured at 550 nm in Microkinetics reader BT2000, and obtained values were expressed as a percentage of the values obtained for control cells to which no carriers were added. All measurements were repeated eight times.

Transport Experiments. Transport studies were performed as previously described (*26*). Briefly, polycar-

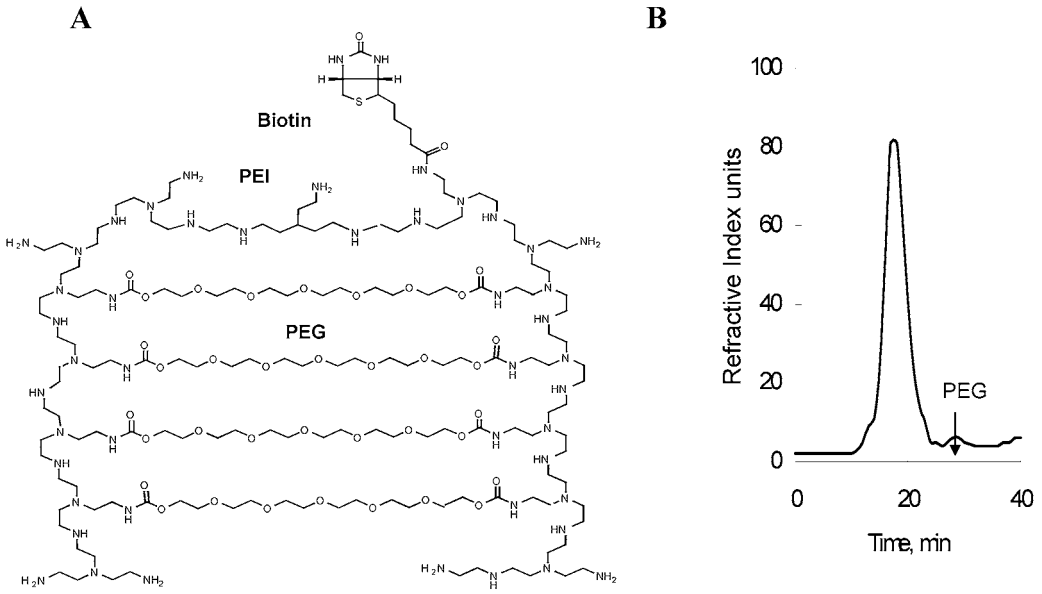


Figure 1. Shematic representing biotinylated nanogel network (A), and the chromatographic profile of GP−HPLC with refractive index (RI) detection of a biotinylated nanogel sample (B). See Material and Methods for chromatography conditions.

bonate membrane inserts with confluent BBMEC monolayers were placed in thermostated Side-By-Side diffusion chambers (Crown BioScientific, Inc.) maintained at 37 °C. Cell monolayers were preincubated for 30 min with the assay buffer added into both donor and receiver chambers. Following the preincubation period, fresh assay buffer was added to the receiver chamber and the buffer in the donor chamber was replaced with nanogel−ODN dispersions containing a paracellular marker for cell monolayers, ^{3}H-labeled mannitol. All experiments were conducted in triplicates. At different time points, solutions in the receiver container were removed and analyzed. Phosphorothioate ODN and nanogel−ODN complexes were quantified by the anion exchange HPLC using Nucleopac PA-100 guard column (0.4 × 5 cm), and gradient elution with buffer A (90% 25 mM Tris, pH 8.0; 10% acetonitrile) and buffer B (90% 2M ammonium chloride in 25 mM Tris, pH 8.0; 10% acetonitrile), at 2 mL min^{-1} and 65 °C with UV detection at 270 nm (*27*). To assess extent of dissociation of the nanogel−ODN complex following the transport across BBMEC monolayer, the samples in receiver chamber were concentrated using Ultrafree-15 Centrifugal Filter Device (5K NMWL, Millipore, Bedford, MA), and then analyzed by the gel permeation HPLC on SigmaChrom GFC-1300 column (0.7 × 30 cm) in 0.1 M sodium phosphate, pH 7.4, at 0.5 mL min^{-1} and 25 °C with UV detection at 270 nm.

Apparent permeability (P_{app}) of the cells with respect to ODN and nanogel−ODN complexes was calculated as follows:

$$P_{app} = (V/AC_o) \times dC/dt \text{ (cm/s)}$$

where $V \times dC/dt$ is the steady-state rate of appearance of ODN at the basolateral side of the monolayers, C_o is the initial ODN concentration at the apical side, and A is the surface area of the membrane.

Confocal Microscopy. Cellular accumulation localization of FITC-labeled ODN, RITC-labeled nanogel, and their complexes was examined using laser confocal fluorescent microscopy. In these studies, BBMEC were grown on chamber slides (Fisher Scientific) and incubated with 0.5 mL of 5 μM ODN or ODN-loaded nanogel for 2 h at 37 °C. After the incubation, cells were washed three times with ice-cold PBS containing 1% bovine serum albumin and scanned with a confocal fluorescence microscopic system ACAS-570 (Meridian Instruments, Okimos, MI) with argon ion laser (excitation wavelength, 488 nm) and corresponding filter set. Digital images were obtained using the CCD camera (Photometrics) and Adobe Photoshop software.

Biodistribution in Mice. All experiments were performed with female FVB wild type mice between 12 and 14 weeks of age (Charles River Laboratories, Wilmington, DE) using procedure analogous to that previously described (*28*). In the initial studies, the nanogel−ODN complex was injected daily in the tail vein to assess tolerated doses. The concentration of the complexes in injected solutions (200 μL) increased daily from 0.5 to 2.5% (w/v) with 0.5% increment. In following experiments, 100 μL of nanogel−ODN (50 μM) complex were injected in the tail vein of FVB mice. In this study we used radioactively labeled compounds, ^{3}H-nanogel or ^{3}H-ODN. There were four animals in each treatment group. Animals were sacrificed 1 h after injection, and their organs (brain, liver, spleen, and lung) were taken and washed with PBS. Blood and organs were weighted, soaked in 4% BSA solution (2 mL g^{-1} of organ), and homogenized. Samples (200 μL) of organ homogenates or 100 μL of blood plasma were added into 4 mL of scintillator solution, and the amount of ^{3}H-nanogel or ^{3}H-ODN was measured using Beckman LS6000 IC liquid scintillation counter. Concentrations of labeled compound in the plasma and brain were expressed as cpm/100 μL of plasma or cpm/200 μL. These concentrations were used to calculate brain/plasma ratios.

RESULTS AND DISCUSSION

Synthesis and Characterization of Nanogel. Figure 1A presents a schematic structure of nano-PEG-*cross*-PEI nanogel synthesized in this work. It was prepared by cross-linking the branched PEI (25 000) with an amino reactive PEG linker (8000), using a modified procedure (*18*). According to this procedure, the solution of the activated PEG in dichloromethane was emulsified in the aqueous solution of PEI by sonication. After completion of the cross-linking reaction, the organic solvent was removed, and nanogel was allowed to maturate in aque-

Table 1. Properties of Nanogel Carriers

batch	PEG/PEI molar ratio	total nitrogen content, μmol/mg	chargeable amino groups, μmol/mg	nanogel effective diameter, nm, and ζ-potential, mV (in brackets)			
				unloaded	N/P = 4	N/P = 8	N/P = 8[a] (+BSA)
batch 1	8.7	6.6	4.0	237 ± 3 (+5)	76 ± 1 (−0.2)	94 ± 2 (+2.3)	54 ± 1
batch 2	8.6	6.9	4.2	148 ± 3 (+4.6)	58 ± 1 (0)	64 ± 2 (+1.9)	50 ± 2

[a] Particle size measured 30 min after addition of 4% BSA solution in phosphate-buffered saline.

ous medium. The maturating stage is important to allow for the completion of the cross-linking reaction, which at high stages of conversion can be decelerated due to the chain entanglements in the forming polymer networks. Nanogel particles of the desired size range were purified using combination of high-speed centrifugation and gel-permeation chromatography. One important modification in the procedure was that we used higher PEG:PEI ratio, 9:1, compared to that reported in our previous studies, 6:1 (*18*). The primary reason for this modification was to increase the stability of nanogel formulations in aqueous dispersion due to increase of the amount of the hydrophilic PEG chains.

We also varied the time of sonication of the dichloromethane−water emulsion during the synthesis of the nanogel and found that this strongly affected the properties of the product, in particular, the particle size. Two major batches of nanogel were obtained following crude fractionation by gel-permeation chromatography: the first one having the particle size 240 nm (sonication time 20 min, "batch 1") and the second one having the particle size 150 nm (sonication time 30 min, "batch 2"). Interestingly, longer sonication time, e.g. 60 min, resulted in formation of macroscopic gel fragments that could not be used in these studies.

The properties of the nanogel batches are listed in Table 1. Generally, 55−70% of the total weight of reacting polymers was recovered in the form of nanogel particles. The absence of the unreacted polymers was verified by gel permeation chromatography with refractive index detection as exemplified in Figure 1B. Contamination of the free PEG (t = 29 min) was less than 5% (the main nanogel peak eluted at t = 17 min). From the NMR data, the proton assignments of nanogel were found to be δ 3.6 ppm (PEG CH_2O) and δ 2.5−3.1 ppm (PEI CH_2NH). The H_{PEG}/H_{PEI} ratios were equal to 2.7 (batch 1) and 2.6 (batch 2), which corresponded to the PEG:PEI molar ratios 8.7 (batch 1) and 8.6 (batch 2). The elemental analysis showed that the total nitrogen content was practically the same for both batches, 6.6−6.9 μmol/mg. The potentiometric titration with hydrochloric acid suggested that approximately 2/3 of the amino groups in nanogel was protonated at pH 4.5, whereas only 1/3 of the amino groups was protonated at pH 7.5. This is typical of branched PEI samples (*29*). We estimated that no more than ca. 3% of amino groups in PEI can be involved in the formation of the cross-links with PEG. Most of the experiments described below (unless stated otherwise) were performed with batch 1.

Biotin-Modified Nanogel. Biotin moiety was introduced in the nanogel (batch 1) by modification of amino groups (1.5% of total) with biotin *p*-nitrophenyl ester. After completion of the reaction, biotin-modified nanogel particles were purified from low-molecular weight products by gel permeation chromatography. The amount of biotin linked to the nanogel was determined by adding the biotin−nanogel to the complex of avidin with a fluorescent probe, ANS. Since biotin has much higher affinity to avidin than ANS, it displaces latter in the complex resulting in the decrease of the probe fluorescence (*22*). The biotin content was found to be equal to 16.5 μg/mg, which is ca. 67% of the theoretical modification degree (24.5 μg/mg) at used reagent combination. The result shows that substantial part of the biotin moieties linked to the nanogel is available for reacting with avidin.

Fluorescent and Radioactive Labeling of the Nanogel. The rhodamine label was introduced into nanogel particles to follow their transport and localization in BBMEC monolayers. For this purpose, the primary amino groups of nanogel were modified with RITC (1% of total amino group). RITC-labeled nanogel was purified by gel permeation chromatography in the dark resulting in a pink-colored dispersion. Spectral characteristics of the labeled carrier were as follows: $\lambda_{excitation}$ = 549 nm, $\lambda_{emission}$ = 577 nm (PBS, pH 7.4). Additionally, a tritium-labeled nanogel was obtained for in vivo biodistribution experiments. The primary amino groups of the nanogel were modified using the ^{3}H-succinimidylpropionate in the presence of 2% triethylamine in anhydrous acetonitrile. ^{3}H-Nanogel with specific activity 20 μCi/mg was separated by gel permeation chromatography on Sephadex G-25. Eighty percent of the radioactive label was found to incorporate into macromolecular fraction.

Complexes of Nanogel and ODN. Mixing of ODN and nanogel solutions in PBS, pH 7.4, resulted in immediate formation of the polyelectrolyte complexes, due to the electrostatic binding of the oppositely charged ODN and PEI chains. This was accompanied by the collapse of the gel and decrease in the particle size. To prepare uniform complexes, ODN solution was typically added to the same volume of stirred nanogel suspension. Although the binding of ODN to nanogel was accompanied by neutralization of electrostatic charges, the overall changes in the ζ-potential of nanogel particles were small. The unloaded nanogel equilibrated in aqueous solution was characterized by low positive ζ-potential values, presumably, because of penetration of the small counterions within the nanogel volume (*30*). Nevertheless, the charge decrease of the nanogel upon binding of ODN was detected. Composition of the polycation−DNA complexes is usually described in terms of N/P ratio, i.e., the ratio of nitrogen (nanogel) to phosphate (ODN) concentrations in the final nanogel and ODN mixture. At N/P = 8 the particles of the complex exhibited small positive charge, while at N/P = 4 these complexes were electroneutral. Table 1 presents the characteristics of unloaded and ODN-loaded nano-PEG-*cross*-PEI nanogels (batches 1 and 2) measured at two N/P ratios, 4 and 8. Binding of ODN to nanogels resulted in 2.6- to 3.1-times size decrease (N/P = 4), which corresponds to ca. 17 to 30 times decrease in the gel volume. Interestingly, the ODN-loaded nanogel formed more uniform particles (polydispersity index 0.05) compared unloaded nanogel, which had much broader particle size distribution (polydispersity index 0.30). Binding of ODN with the RITC-labeled nanogel resulted in almost 10-fold enhancement of the fluorescence (N/P = 4), presumably due to complexation of the charged amino groups of PEI, which, in the absence of ODN, quench the fluorescence.

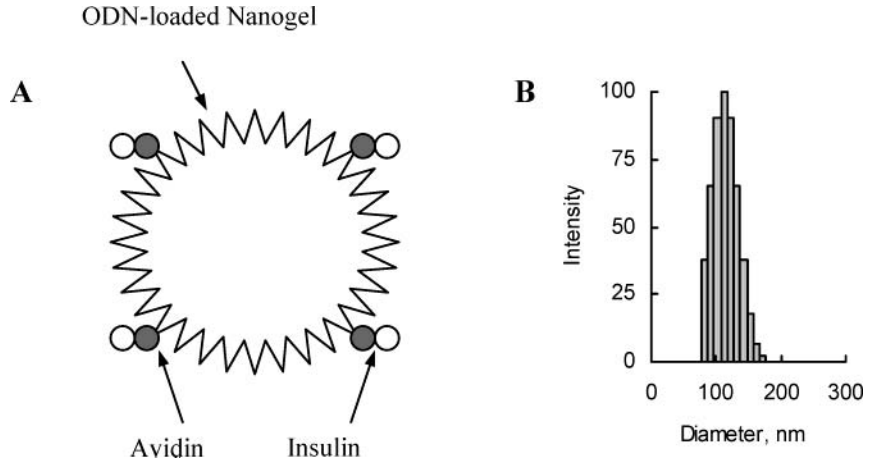


Figure 2. The putative structure (A), and particle size distribution (B) of bovine insulin-vectorized nanogel−ODN complex.

Introduction of BSA into the dispersion of nanogel−ODN complex resulted in an additional 20−40% reduction of the detectable particle size. Although no aggregation was observed following the treatment, stability of the complex might be compromised by extended incubation with the protein. Two hours later both samples of nanogel formed particles with very close mean diameter of 34−39 nm, which showed no more changes. These data could be reasonably explained by the phenomenon of opsonization earlier observed for cationic microcarriers in vivo (*31*).

Modification of ODN-Loaded Nanogel with Insulin and Transferrin. Biotin-modified nanogel was used for further conjugation with transferrin and insulin. First, the biotin-modified nanogel was loaded with ODN at the desired N/P ratio as described above. Second, the ODN-loaded biotin−nanogel complex was reacted with the preformed complex of avidin and biotinylated transferrin or insulin. The schematic showing putative structure of such complex as well as the size distribution diagram of this complex are presented in Figure 2. Importantly, no aggregation of nanogel was observed following the modification procedure, and the particle size increased by only 15% to 20%, e.g., from 94 to 110 nm (N/P = 8). No signs of precipitation have been observed in the formulations for at least 1 day at 4 °C. However, at longer storage periods we observed visible signs of aggregation in these dispersions, most likely induced by interactions of vacant avidin binding sites and excessive biotin residues on vector protein molecules.

Toxicity of Nanogel. Cytotoxicity of nanogel was examined in BBMEC monolayers using MTT assay. Cells were exposed over the period of 2 h to various concentrations of unloaded and ODN-loaded (N/P = 8) nanogel and the cell viability was tested (Figure 3). Nanogel carriers showed little cytotoxicity with respect to the BBMEC. Furthermore, the cytotoxicity was noticeably decreased when the positive charge of nanogel was neutralized by negatively charged ODN. The IC_{50} values were ca. 0.9 mg mL^{-1} and 6 mg mL^{-1} for the free and loaded nanogel, respectively. Nanogel concentrations of about 0.1−0.2 mg mL^{-1} (0.01−0.02%) were relatively nontoxic in both cases, and this concentration range was used in further studies. Preliminary data obtained in animal experiments also revealed no acute toxic effects of nanogel−ODN complexes administered iv in FVB wild-type mice at cumulative dose of up to 15 mg nanogel−ODN per mice.

Transport across BBMEC Monolayers. To evaluate potential effects of nanogel on the delivery of ODN to the brain, we examined ODN permeability using BBMEC monolayers as an in vitro model of BBB. Polarized BBMEC monolayers were grown on membrane filter inserts, which were placed in standard Side-By-Side diffusion chambers. Initial studies characterized the transport of RITC-labeled nanogel from apical (lumenal) to basolateral (ablumenal) side of the monolayers as a function of the composition of the complexes (N/P ratio) as presented in Figure 4. This figure also presents the data on the transport of FITC-labeled ODN for comparison. These data suggest that there is little if any difference in the permeability of unloaded nanogel batches 1 and 2. At the same time the rate of transport of loaded nanogels drastically depended on the composition of the complex. Specifically, the complex prepared at N/P = 8 that displays positive charge (see Table 1) was transported more efficiently than the complex at N/P = 4 having slight negative charge.

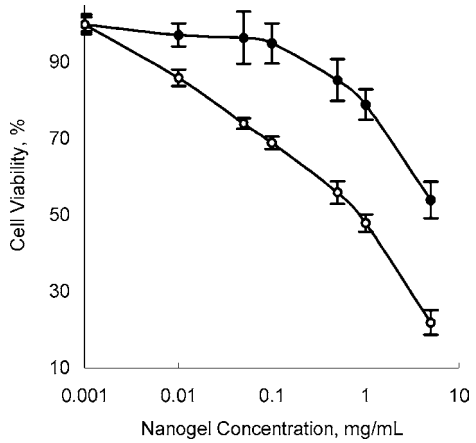


Figure 3. Cell viability based on MTT assay following the incubation of nanogel−ODN complex (black circles), or unloaded nanogel (open circles) with BBMEC monolayers for 2 h at 37 °C. IC_{50} values are equal to 0.9 mg/mL for nanogel alone, and 6 mg/mL for nanogel−ODN complex.

Further study examined whether the ODN transported with nanogel in BBMEC monolayers remains bound to the nanogel or becomes released from it in the receiver chamber. For this purpose the samples from the receiver chamber were analyzed by gel permeation chromatography with UV absorbance at 270 nm. The chromatography profiles are shown in Figure 5. From analysis of the chromatography data it appears that at least ca. 2/3 of ODN detected in the receiver chamber at 2 h time point of the transport study was incorporated in the complex with nanogel (compare peak 3 in Figure 5B with peak 1 in Figure 5A). About 10% appeared to be the free

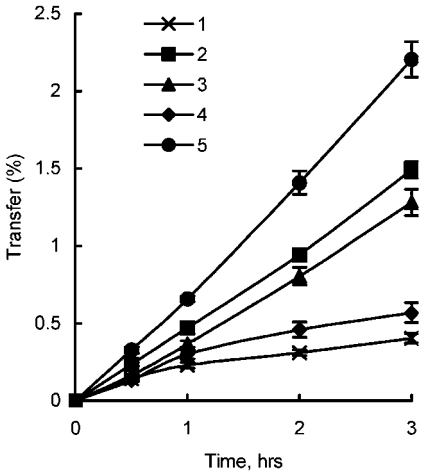


Figure 4. Transport of FITC-labeled ODN and RITC-labeled nanogel particles across BBMEC monolayers: 1, free ODN; 2, unloaded nanogel (batch 1); 3, unloaded nanogel (batch 2); 4, complex of ODN and nanogel (batch 1), N/P = 4; 5, complex of ODN and nanogel (batch 1), N/P = 8. Transport of ODN and nanogel was determined by measuring fluorescence of the corresponding probe (1, FITC; 2−5, RITC) in the receiver chamber. Concentrations of the compounds in the donor chambers were as follows: nanogel, 0.03%, ODN, 2.5−5 μM.

undegraded ODN released from the complex (compare peak 4 in Figure 5B with peak 2 in Figure 5A).

To directly assay the ODN transported through the BBMEC monolayer we used an anion exchange HPLC analysis described previously (*27*). This technique uses highly positively charged chromatography matrix Nucleopac PA-100. When ODN-loaded nanogel particles were applied on the column containing this matrix, the encapsulated ODN was effectively released from the nanogel and eluted with its normal retention time (t = 4.5 min, data not shown). As a result the total ODN in the receiver chamber (both free and nanogel bound) could be easily quantified at the concentrations as low as 5−10 nM. This HPLC technique was used to examine the relative permeability of the free and nanogel−bound ODN in BBMEC monolayers.

Table 2. Permeability Coefficients of ODN and Its Nanogel Formulations in BBMEC Monolayers

ODN formulations	N/P ratio	$P_{app} \times 10^6$, cm s^{-1} [e]
free ODN[a]	−	0.08 ± 0.01
nanogel−ODN[b]	4	0.17 ± 0.02
	8	0.45 ± 0.03
insulin−nanogel−ODN[c]	8	0.96 ± 0.03
transferrin−nanogel−ODN[d]	8	0.86 ± 0.02

[a] ODN concentration was 5 μM in all experiments. [b] Biotinylated nanogel was used at 0.02 wt %, except for N/P = 4, used at 0.01 wt %. [c] Avidin-bovine insulin, 1.25 μM. [d] Avidin-bovine transferrin, 2.5 μM. [e] Data are means ± SEM (n = 3).

In all transport experiment the ODN concentration in the donor chamber was 5 μM. The concentrations of nanogels used in the permeability studies were 0.01−0.02%. A paracellular marker, ^{3}H-mannitol, was also added in the donor chamber to assess possible changes in the integrity of the BBMEC monolayers in the presence of either ODN or its complexes with nanogel. Figure 6 presents the ODN and mannitol permeability data. The ODN permeability coefficients calculated on the base of the transport data are presented in Table 2. Formulation of ODN with nanogel resulted in permeability increases compared to the free ODN. Specifically, at N/P = 4 the permeability increase was only 2-fold (data not shown in Figure 6). At N/P = 8 the increase was almost 6-fold. Therefore, the N/P = 8 was used in experiments to further enhance ODN transport by adding peptide ligands to nanogel formulations. Modification of nanogel with either insulin or transferrin through the avidin−biotin bridges resulted in ca. 11- to 12-fold permeability increases compared to the free ODN. With all ODN formulations used, there were no changes in the permeability of mannitol, which remained the same as its

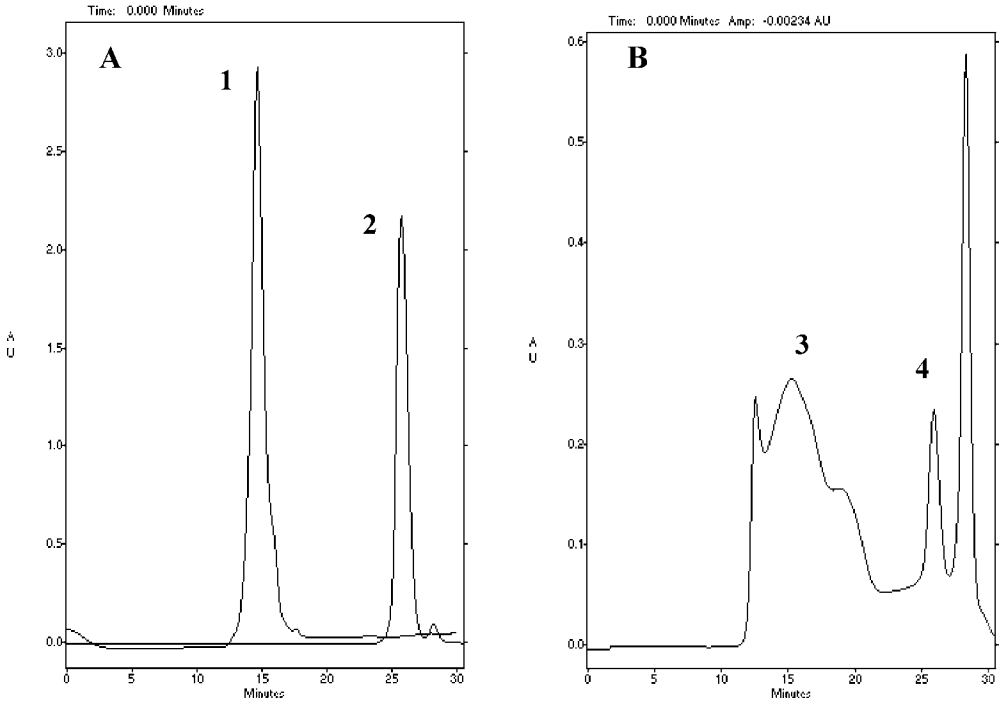


Figure 5. Gel permeation chromatography of ODN and nanogel−ODN complexes. (A) Nanogel−ODN complex (N/P = 8) added in the donor chamber (peak 1) or free ODN added in the donor chamber (peak 2). (B) Nanogel−ODN complex in receiver chamber following transport across the BBMEC monolayers (2 h, 37 °C). The chromatography peaks were assigned as follows: nanogel−ODN complex (peak 3), released ODN (peak 4), last peak relates to UV-absorbing low-molecular weight compounds.

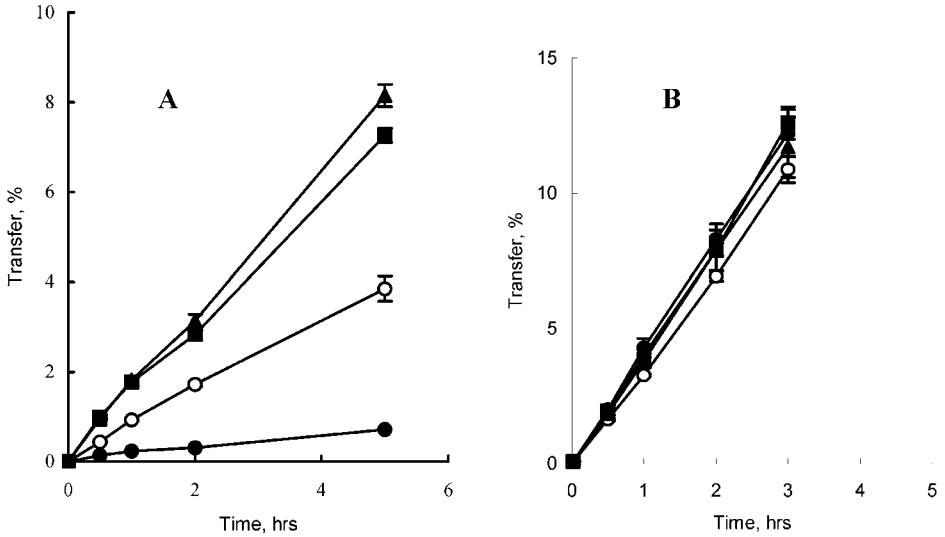


Figure 6. (A) Transport of free ODN and ODN formulated with nanogel across BBMEC monolayers. (B) Transport of paracellular marker, ^{3}H-mannitol, in the presence of the ODN and its formulations with nanogel. The symbols correspond to free ODN (black circles); nanogel−ODN complex (open circles); transferrin-vectorized nanogel−ODN complex ODN (squares); insulin-vectorized nanogel−ODN complex (triangles). All nanogel−ODN complexes are prepared at N/P = 8. Data are means ± SEM (n = 3).

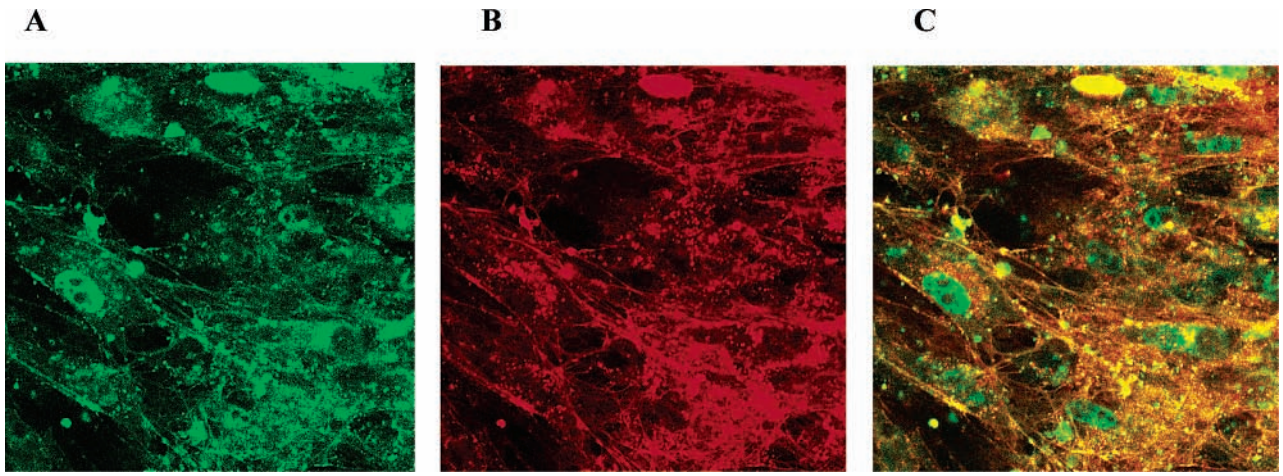


Figure 7. Confocal fluorescent microscopy of BBMEC monolayers after the incubation (2 h) with FITC-labeled ODN loaded into RITC-labeled nanogel. The images were recorded using λ_{ex} 460−500 nm, λ_{ba} 510−560 nm filter for FITC−ODN (A), and λ_{ex} 540−575 nm, λ_{ba} 605−655 nm-filter for RITC-nanogel (B). Panel C is the superposition of images A and B. Magnification ×100.

permeability in the absence of the ODN formulations (2.4×10^{-6}, cm s^{-1}). Therefore, neither free ODN, nor its nanogel formulations, affected the tight junctions in the BBMEC monolayers.

Fluorescence Microscopy Studies. Localization of ODN and nanogel following their uptake in BBMEC monolayers for 2 h was examined by laser confocal fluorescent microscopy. These experiments used FITC-labeled ODN and RITC-labeled nanogel to visualize both components within the cell. Typical micrographs are presented in Figure 7. All three images are recorded from the same sample. Panel A shows the localization of FITC−ODN. Panel B shows the localization of RITC-nanogel. Panel C is the superposition of images A and B displaying localization of both ODN and nanogel. Fluorescein label (ODN) was mainly spread throughout the cells with significant portion displayed in what appears to be cytoplasmic compartments (panel A). Similar cytoplasmic localization was displayed in the case of the rhodamine label (nanogel) (panel B). In the superposed images the areas of colocalization of ODN and nanogel are evident by yellow and orange colors (panel C). However, this panel also clearly shows that in selected cells a portion of fluorescein label is displayed in the nucleus, while practically no rhodamine fluorescence was found in the nucleus.

We have previously speculated that ODN-loaded nanogel can be transported into the cells via endocytosis with some portion crossing the cytoplasmic membrane (*20*). Specifically, despite of the presence of PEO chains, the PEI chains of nanogel are positively charged at endosomal pH, which can destabilize endosomal membrane either by the mechanism similar to that called "proton sponge" (*32*), or by forming cationic patches as a result of interaction of PEI with phospholipid bilayer (*33*). Since ODN chains are relatively short (19 phosphates) and their cooperativity of binding to nanogel is relatively small, some portion of ODN can obviously release in the cytoplasm and then transport into the nucleus through the pores in the nuclear membrane. In contrast, the nanogel particles cannot penetrate through the pores since the size exclusion of these pores is about 20 nm, which is much smaller that even the loaded nanogel particles. (Release of a portion of ODN from nanogel could only result in swelling and increase of the size of the latter). An important result of these studies is that even though a portion of ODN appears to be released in BMVEC a significant portion of it remains bound to the

Table 3. Biodistribution of Free ODN and the Nanogel−ODN Compositions

	radioactivity distribution in tissues, % of injected dose/g[a]				
injected composition	plasma	brain	lung	liver	spleen
nanogel−^{3}H-ODN	3.00 ± 0.16	5.34 ± 0.33	2.26 ± 0.22	4.34 ± 0.28	3.82 ± 0.20
^{3}H-nanogel−ODN	2.81 ± 0.27	2.67 ± 0.13	1.80 ± 0.09	3.80 ± 0.70	3.12 ± 0.16
^{3}H-ODN	2.02 ± 0.26	0.18 ± 0.02	2.50 ± 0.30	7.14 ± 0.55	10.12 ± 0.90

[a] Injected compositions (0.1 mL) contained 50 μM ODN and 0.12% nanogel in PBS (N/P = 8).

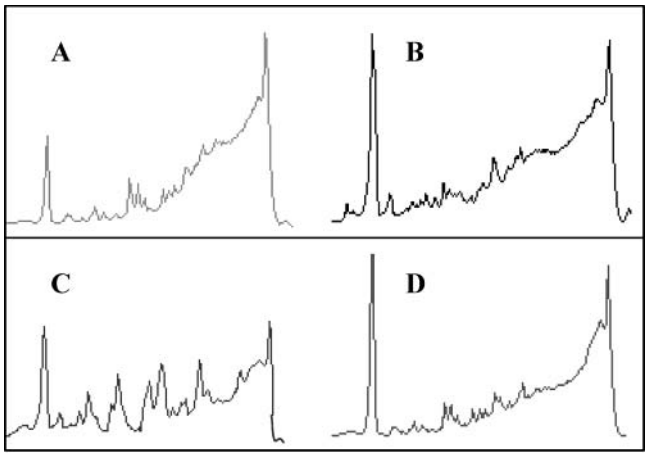


Figure 8. Nuclease resistance of free ODN and ODN incorporated in nanogel in mouse blood serum. The experiment was conducted as follows: Free ODN (5 μM) was added to freshly prepared mouse serum and immediately analyzed by ion-pair reverse phase HPLC (A) or incubated for 1 h at 37 °C and then analyzed by HPLC (C). Similarly, ODN incorporated in nanogel (5 μM, N/P = 8) was added to serum and analyzed immediately (B) or after 1 h incubation (D). In all cases prior to HPLC analysis the samples (200 μL) were mixed with 40 μL of 50 mM sodium dodecyl sulfate solution, proteins were removed by phenol extraction of proteins, and ODN was precipitated by ethanol. The ion-pair reverse phase HPLC was performed on the Spherisorb C18 column (0.4 × 15 cm), elution rate 1 mL/min using 0.2% tetrabutylammonium hydroxide, 50 mM potassium hydrogen phosphate, and 0.1 M sodium chloride in the gradient of acetonitrile 0 to 40%.

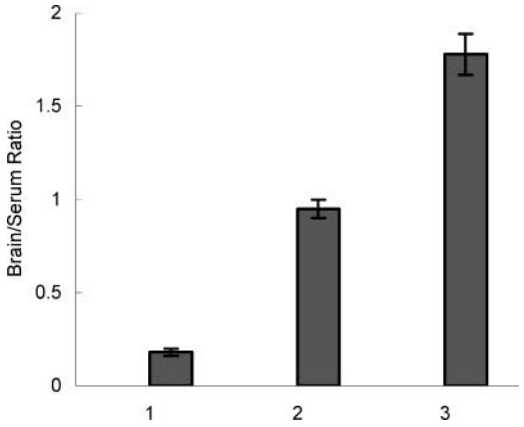


Figure 9. Brain/plasma ratios for the free (1) ^{3}H-ODN and its complexes with nanogel prepared at (2) N/P = 4 and (3) N/P = 8 following iv administration in mice. Animals were sacrificed 1 h after the injection, and the tritium radioactivity in the tissue samples was analyzed. The data represent average values ± SEM (n = 4).

nanogel, a result consistent with the permeability experiments described above.

Stability of Nanogel in Serum. To examine the protection of ODN against nuclease degradation the free ODN or nanogel−ODN complexes were incubated in freshly prepared mouse serum. As is seen in Figure 8 after 1 h incubation in serum substantial amount of free ODN was degraded (compare panels A and C). In contrast ODN incorporated in nanogel displayed little if any degradation (panels B and D).

In Vivo Biodistribution Studies. Finally, in vivo biodistribution of radioactively labeled ODN and nanogel was characterized in mice. The initial studies were conducted using complexes of ODN with ^{3}H-labeled nanogel injected iv. The injected dose contained 120 μg of nanogel. Following 1 h after injection, only 2.8% of injected dose (3.4 μg) of nanogel was detected in 1 g of blood. Significant portion of the injected dose was distributed in the organs (Table 3).

We further used ^{3}H-labeled ODN to assess its biodistribution after iv injection in a free form or as nanogel−ODN formulation. Previous studies reported that the highest levels of ODN are found in liver and spleen, with significantly smaller quantity of ODN accumulating in the brain (~0.3%) (*34*−*36*). As is seen in Table 3, our data for the free ODN were consistent with these observations. However, for nanogel−ODN complexes the amount of the radioactivity in the brain was greatly increased compared to the free ODN. At the same time the accumulation of the radioactivity in the liver and spleen was significantly decreased while plasma and lungs displayed relatively less changes. It was shown that the tritium label introduced into phosphorothioate ODN using the same technique is metabolically stable in blood in vivo for at least 2 h after injection (*23*). Therefore, the results of our experiments strongly suggest that formulation of ODN with nanogel leads to increased brain and decreased liver and spleen accumulations compared to the free phosphorothioate ODN. This effect in the brain is further illustrated in Figure 9 presenting brain/plasma ratios for free ODN and nanogel−ODN formulations 1 h after iv injection. This ratio for the nanogel−ODN formulation increased by as much as 1 order of magnitude compared to the free ODN. It also appears from this study that nanogel formulation at N/P = 8 was more efficacious in brain delivery of ODN than the formulation at N/P = 4.

On the basis of these studies, it appears that nanogel carriers can protect ODN from rapid clearance by peripheral tissues and increase ODN transport to the brain. It was demonstrated that iv-injected phosphorothioate ODNs strongly bind to albumin and other plasma proteins (*37*). Encapsulation of ODN in nanogels may have protective effect reducing the nonspecific interactions. It could also decrease the renal clearance of ODN because the molecular mass of nanogel−ODN complexes exceeds the renal clearance threshold (*38*). However, to fully address this issue, further studies of the in vivo properties of nanogel carriers need to be done.

CONCLUSIONS

A novel ODN delivery system based on positively charged nanosized hydrogel particles, nano-PEG-*cross*-PEI, has been developed. The ODN-loaded nanogel remains stable in dispersion due to the solubilizing effect of nonionic hydrophilic PEG chains resulting in a formation of nanosized particles. Nanogel structure enables easy attachment of vector groups for targeted delivery.

In particular, nanogel carriers vectorized with insulin and transferrin molecules were shown to efficiently deliver antisense ODN across BBB as demonstrated using a cell model, BBMEC. Following transport across the brain microvessel endothelial cells a significant portion of ODN remained associated with nanogel. Nanogel carriers have low toxicity, especially in the loaded form, and show no adverse toxic effect being injected intravenously in mice. Further studies in vivo should reveal the potential for the use of the vectorized nanogel carriers for systemic delivery of antisense ODN into the brain.

ACKNOWLEDGMENT

The studies were supported in parts by grants from National Science Foundation (BES 9986393) and National Institutes of Health (NS 366229) awarded to A.V.K.. NanoGel is a trademark of Supratek Pharma Inc. (Montreal, Canada), who supported part of the work on synthesis of the nanogel material. A.V.K. is a cofounder and consultant for this company. The authors would like to acknowledge the technical assistance of Shu Li in performing of the transport studies on BBMEC monolayers.

LITERATURE CITED

(1) Boado, R. J., Tsukamoto, H., and Pardridge, W. M. (1998) Drug delivery of antisense molecules to the brain for treatment of Alzheimer's disease and cerebral AIDS. *J. Pharm. Sci. 87*, 1308−1315.

(2) Seidman, S., Eckstein, F., Grifman, M., and Soreq, H. (1999) Antisense technologies have a future fighting neurodegenerative diseases. *Antisense Nucleic Acid Drug Dev. 9*, 333−340.

(3) Field, A. K. (1999) Oligonucleotides as inhibitors of human immunodeficiency virus. *Curr. Opin. Mol. Ther. 1*, 323−331.

(4) Ho, S. P., and Hartig, P. R. (1999) Antisense oligonucleotides for target validation in the CNS. *Curr. Opin. Mol. Ther. 1*, 336−343.

(5) McCarthy, M. M., Auger, A. P., Mong, J. A., Sickel, M. J., and Davis, A. M. (2000) Antisense oligodeoxynucleotides as a tool in developmental neuroendocrinology. *Methods 22*, 239−248.

(6) Wang, H., Prasad, G., Buolamwini, J. K., and Zhang, R. (2001) Antisense anticancer oligonucleotide therapeutics. *Curr Cancer Drug Targets 1*, 177−196.

(7) Dias, N. and Stein, C. A. (2002) Potential roles of antisense oligonucleotides in cancer therapy. The example of Bcl-2 antisense oligonucleotides. *Eur. J. Pharm. Biopharm. 54*, 263−269.

(8) Broaddus, W. C., Prabhu, S. S., Wu-Pong, S., Gillies, G. T. and Fillmore, H. (2000) Strategies for the design and delivery of antisense oligonucleotides in central nervous system. *Methods Enzymol. 314*, 121−135.

(9) Matsuo, H., Okamura, T., Chen, J., Takanaga, H., Ohtani, H., Kaneda, Y., Naito, M., Tsuruo, T. and Sawada, Y. (2000) Efficient introduction of macromolecules and oligonucleotides into brain capillary endothelial cells using HVJ-liposomes. *J. Drug Target. 8*, 207−216.

(10) Merdan, T., Kopecek, J. and Kissel, T. (2002) Prospects for cationic polymers in gene and oligonucleotide therapy against cancer. *Adv Drug Delivery Rev. 54*, 715−758.

(11) Brigger, I., Dubernet, C. and Couvreur, P. (2002) Nanoparticles in cancer therapy and diagnosis. *Adv Drug Deliv. Rev. 54*, 631−651.

(12) Pardridge, W. M. (2002) Drug and gene targeting to the brain with molecular Trojan horses. *Nat Rev Drug Discovery 1*, 131−139.

(13) Kreuter, J. (2001) Nanoparticulate systems for brain delivery of drugs. *Adv Drug Delivery Rev 47*, 65−81.

(14) Pardridge, W. M., Eisenberg, J., and Yang, J. (1985) Human blood-brain barrier insulin receptor. *J Neurochem. 44*, 1771−1778.

(15) Pardridge, W. M., Eisenberg, J., and Yang, J. (1987) Human blood-brain barrier transferrin receptor. *Metabolism 36*, 892−895.

(16) Zhang, Y., Jeong Lee, H., Boado, R. J., and Pardridge, W. M. (2002) Receptor-mediated delivery of an antisense gene to human brain cancer cells. *J Gene Med. 4*, 183−194.

(17) Kabanov, A. V. and Vinogradov, S. V. (2001), Supratek Pharma, Inc., US.

(18) Vinogradov, S. V., Batrakova, E. V., and Kabanov, A. V. (1999) Poly(ethylene glycol)-polyethyleneimine NanoGel particles: novel drug delivery systems for antisense oligonucleotides. *Coll. Surf. B: Biointerfaces 16*, 291−304.

(19) Lemieux, P., Vinogradov, S. V., Gebhart, C. L., Guerin, N., Paradis, G., Nguyen, H. K., Ochietti, B., Suzdaltseva, Y. G., Bartakova, E. V., Bronich, T. K., St-Pierre, Y., Alakhov, V. Y., and Kabanov, A. V. (2000) Block and graft copolymers and NanoGel copolymer networks for DNA delivery into cell. *J. Drug Target. 8*, 91−105.

(20) Vinogradov, S. V., Bronich, T. K., and Kabanov, A. V. (2002) Nanosized cationic hydrogels for drug delivery: preparation, properties and interactions with cells. *Adv Drug Delivery Rev 54*, 135−147.

(21) Nag, A., Mitra, G., and Ghosh, P. C. (1996) A colorimetric assay for estimation of poly(ethylene glycol) and poly(ethylene glycol)ated protein using ammonium ferrothiocyanate. *Anal. Biochem 237*, 224−231.

(22) Mock, D. M., Lankford, G., and Horowitz, P. (1988) A study of the interaction of avidin with 2-anilinonaphthalene-6-sulfonic acid as a probe of the biotin binding site. *Biochim Biophys Acta 956*, 23−29.

(23) Ledoan, T., Auger, R., Benjahad, A., and Tenu, J. P. (1999) High specific radioactivity labeling of oligonucleotides with 3H-succinimidyl propionate. *Nucleosides Nucleotides 18*, 277−289.

(24) Miller, D. W., Audus, K. L.. and Borchardt, R. T. (1992) Application of cultured bovine brain endothelial cells of the brain microvasculature in the study of the blood-brain barrier. *J. Tissue Cult. Methods 14*, 217−224.

(25) Ferrari, M., Fornasiero, M. C.. and Isetta, A. M. (1990) MTT colorimetric assay for testing macrophage cytotoxic activity in vitro. *J Immunol Methods 131*, 165−172.

(26) Batrakova, E. V., Li, S., Miller, D. W.. and Kabanov, A. V. (1999) Pluronic P85 increases permeability of a broad spectrum of drugs in polarized BBMEC and Caco-2 cell monolayers. *Pharm. Res. 16*, 1366−1372.

(27) Bourque, A. J.. and Cohen, A. S. (1993) Quantitative analysis of phosphorothioate oligonucleotides in biological fluids using fast anion-exchange chromatography. *J Chromatogr. 617*, 43−49.

(28) Batrakova, E. V., Miller, D. W., Li, S., Alakhov, V. Y., Kabanov, A. V.. and Elmquist, W. F. (2001) Pluronic P85 enhances the delivery of digoxin to the brain: in vitro and in vivo studies. *J. Pharmacol. Exp. Ther. 296*, 551−557.

(29) Vinogradov, S. V., Bronich, T. K. and Kabanov, A. V. (1998) Self-assembly of polyamine-poly(ethylene glycol) copolymers with phosphorothioate oligonucleotides. *Bioconjugate Chem. 9*, 805−812.

(30) Bronich, T., Vinogradov, S. and Kabanov, A. V. (2001) Interaction of nanosized copolymer networks with oppositely charged amphiphilic molecules. *Nano Lett. 1*, 535−540.

(31) Ogris, M., Brunner, S., Schuller, S., Kircheis, R., Wagner, E. (1999) PEGylated DNA/transferrin-PEI complexes: reduced interaction with blood components, extended circulation in blood and potential for systemic gene delivery. *Gene Ther. 6*, 595−605.

(32) Boussif, O., Lezoualc'h, F., Zanta, M. A., Mergny, M. D., Scherman, D., Demeneix, B. and Behr, J. P. (1995) A versatile vector for gene and oligonucleotide transfer into cells in culture and in vivo: polyethylenimine. *Proc. Natl. Acad. Sci U. S. A. 92*, 7297−7301.

(33) Helander, I. M., Latva-Kala, K. and Lounatmaa, K. (1998) Permeabilizing action of polyethyleneimine on *Salmonella*

typhimurium involves disruption of the outer membrane and interactions with lipopolysaccharide. *Microbiology 144 (Pt 2)*, 385−390.

(34) Banks, W. A., Farr, S. A., Butt, W., Kumar, V. B., Franko, M. W. and Morley, J. E. (2001) Delivery across the blood-brain barrier of antisense directed against amyloid beta: reversal of learning and memory deficits in mice overexpressing amyloid precursor protein. *J. Pharmacol. Exp. Ther. 297*, 1113−1121.

(35) Geary, R. S., Yu, R. Z. and Levin, A. A. (2001) Pharmacokinetics of phosphorothioate antisense oligodeoxynucleotides. *Curr. Opin. Investig. Drugs 2*, 562−573.

(36) Wu, D., Boado, R. J. and Pardridge, W. M. (1996) Pharmacokinetics and blood-brain barrier transport of [3H]-biotinylated phosphorothioate oligodeoxynucleotide conjugated to a vector-mediated drug delivery system. *J. Pharmacol. Exp. Ther. 276*, 206−211.

(37) Srinivasan, S. K., Tewary, H. K. and Iversen, P. L. (1995) Characterization of binding sites, extent of binding, and drug interactions of oligonucleotides with albumin. *Antisense Res. Dev. 5*, 131−139.

(38) Sawai, K., Miyao, T., Takakura, Y. and Hashida, M. (1995) Renal disposition characteristics of oligonucleotides modified at terminal linkages in the perfused rat kidney. *Antisense Res. Dev. 5*, 279−287.

BC034164R

[^{18}F]Galacto-RGD: Synthesis, Radiolabeling, Metabolic Stability, and Radiation Dose Estimates

Roland Haubner,*,‡ Bertrand Kuhnast,‡ Christian Mang,§ Wolfgang A. Weber,‡ Horst Kessler,§ Hans-Jürgen Wester,‡ and Markus Schwaiger‡

Department of Nuclear Medicine, Technische Universität München, 81675 München, Germany, and Institute of Organic Chemistry and Biochemistry, Technische Universität München, 85747 Garching, Germany.
Received September 18, 2003

It has been demonstrated in various murine tumor models that radiolabeled RGD-peptides can be used for noninvasive determination of $\alpha v\beta 3$ integrin expression. Introduction of sugar moieties improved the pharmacokinetic properties of these peptides and led to tracer with good tumor-to-background ratios. Here we describe the synthesis, radiolabeling, and the metabolic stability of a glycosylated RGD-peptide ([^{18}F]Galacto-RGD) and give first radiation dose estimates for this tracer. The peptide was assembled on a solid support using Fmoc-protocols and cyclized under high dilution conditions. It was conjugated with a sugar amino acid, which can be synthesized via a four-step synthesis starting from pentaacetyl-protected galactose. For radiolabeling of the glycopeptide, 4-nitrophenyl-2-[^{18}F]fluoropropionate was used. This prosthetic group allowed synthesis of [^{18}F]Galacto-RGD with a maximum decay-corrected radiochemical yield of up to 85% and radiochemical purity >98%. The overall radiochemical yield was 29 ± 5% with a total reaction time including final HPLC preparation of 200 ± 18 min. The metabolic stability of [^{18}F]Galacto-RGD was determined in mouse blood and liver, kidney, and tumor homogenates 2 h after tracer injection. The average fraction of intact tracer in these organs was approximately 87%, 76%, 69%, and 87%, respectively, indicating high in vivo stability of the radiolabeled glycopeptide. The expected radiation dose to humans after injection of [^{18}F]Galacto-RGD has been estimated on the basis of dynamic PET studies with New Zealand white rabbits. According to the residence times in these animals the effective dose was calculated using the MIRDOSE 3.0 program as 2.2×10^{-2} mGy/MBq. In conclusion, [^{18}F]Galacto-RGD can be synthesized in high radiochemical yields and radiochemical purity. Despite the time-consuming synthesis of the prosthetic group 185 MBq of [^{18}F]Galacto-RGD, a sufficient dose for patient studies, can be produced starting with approximately 2.2 GBq of [^{18}F]flouride. Moreover, the fast excretion, the suitable metabolic stability and the low estimated radiation dose allow to evaluate this tracer in human studies.

INTRODUCTION

Integrins are heterodimeric glycoproteins consisting of an α- and a β-subunit, which are involved in cell/cell and cell/matrix interactions (*1*). They possess large extracellular and short cytoplasmatic domains. The C-terminal end of the β-subunit is connected via cytoplasmatic proteins such as talin, vinculin, and α-actinin with the actin filament of the cytoskeleton. This connection allows inside out as well as outside in signaling. Thus, integrins are not only adhesion receptors linking cells with proteins of the extracellular matrix, but are also involved in signal transduction pathways (*2*).

One of the most prominent members of this receptor class is the $\alpha v\beta 3$ integrin which is involved in several pathological processes such as osteoporosis (*3*), restenosis (*4*), inflammation (*5*), rheumatoid arthritis (*6*), metastasis (*7*), and tumor-induced angiogenesis (*8*). Thus, great efforts are being made to develop $\alpha v\beta 3$ antagonists for several therapeutic approaches (*9*, *10*). First, cyclic pentapeptides (*11*, *12*) were introduced which contain the tripeptide sequence arginine-glycine-aspartic acid (RGD[1] in single letter amino acid code). This is a recognition motif used by several extracellular matrix proteins, like fibronectin and vitronectin, to bind to a variety of integrins including $\alpha v\beta 3$ (*13*). It has been demonstrated in model systems that cyclo(-Arg-Gly-Asp-D-Phe-Val-), one member of this peptide class, can block tumor-induced angiogenesis. For example, it has been shown in a chick chorioallontoic membrane model that this RGD-peptide inhibits tumor induced formation of new blood vessels without affecting already existing adjacent vessels (*14*).

Initial clinical trials evaluating the use of $\alpha v\beta 3$ antagonists as antiangiogenic therapy in patients with various malignant tumors have been initiated (*15*) (e.g. Cilengitide, a derivative of cyclo(-Arg-Gly-Asp-D-Phe-Val-) where valine is replaced by NMeVal, is in clinical phase

* To whom requests for reprints should be addressed, at Department of Nuclear Medicine, Klinikum rechts der Isar, Technische Universität München, Ismaninger Str. 22, D-81675 München, Germany. Phone: +49-89-41406332; FAX: +49-89-41404841. E-mail: R.Haubner@lrz.tum.de.

‡ Department of Nuclear Medicine.

§ Institute of Organic Chemistry and Biochemistry.

[1] Abbreviations: EOB, end of bombardment; ESI-MS, electrospray ionization mass spectroscopy; [^{18}F]FDG, 2-[^{18}F]fluoro-deoxyglucose; FP, 2-fluoropropionyl; NMeVal, N^{α}-methylated valine; PET, positron emission tomography; RGD, single letter code for the amino acids arginine (R), glycine (G), and aspartate (D); SAA, sugar amino acid; SSTR, somatostatin receptor; TEMPO, 2,2,6,6-tetramethylpiperidine-1-yloxy.

10.1021/bc034170n CCC: $27.50 © 2004 American Chemical Society
Published on Web 12/13/2003

II studies (*16*)). Thus, radiolabeled RGD-peptides may be of advantage to document $\alpha v\beta 3$ expression of the tumors prior to administration of $\alpha v\beta 3$ antagonists allowing appropriate selection of patients entering clinical trials and determination of the optimal dose of $\alpha v\beta 3$ antagonists. Moreover, $\alpha v\beta 3$ expression has been reported to be an important factor determining the invasiveness and metastatic potential of malignant tumors in experimental tumor models as well as in patient studies (*17*, *18*). Therefore, noninvasive imaging of $\alpha v\beta 3$ expression using radiolabeled RGD-peptides and positron emission tomography may provide a unique means of characterizing the biological aggressiveness of a malignant tumor in an individual patient.

On the basis of cyclo(-Arg-Gly-Asp-D-Phe-Val-), several radiohalogenated and radiometalated RGD-peptides have been synthesized during the past few years (for review see ref 19). First tracers resulted from radioiodination of cyclo(-Arg-Gly-Asp-D-Tyr-Val-) and cyclo(-Arg-Gly-Asp-D-Phe-Tyr-) (*20*). These compounds showed high $\alpha v\beta 3$-affinity and selectivity in vitro and receptor specific tumor uptake in vivo. However, due to their lipophilic character, high activity concentration was found in the liver. To reduce the lipophilicity of the tracer, the peptide was modified allowing conjugation with a sugar amino acid. The resulting radioiodinated glycopeptide Gluco-RGD showed higher initial retention in the blood, higher uptake in the tumor and clearly reduced activity concentration in the liver (*21*). On the basis of these results, a ^{18}F-labeled glycopeptide was synthesized using 4-nitrophenyl-2-[^{18}F]fluoropropionate as prosthetic group. It has already been demonstrated that this compound allows noninvasive determination of $\alpha v\beta 3$-expression in a murine tumor model using a dedicated small animal PET scanner (*22*). Here we describe the detailed synthesis of the precursor including synthesis of the corresponding sugar amino acid, the optimization of the labeling strategy, the metabolic stability, and first radiation dose estimates on [^{18}F]Galacto-RGD.

MATERIALS AND METHODS

All chemicals were used as supplied without further purification. 9-Fluorenylmethoxycarbonyl (Fmoc) amino acids were purchased from Bachem (Heidelberg, Germany) or Novabiochem (Bad Soden, Germany). The trityl chloride polystyrene (TCP) resin was purchased form PepChem (Tübingen, Germany). 1-Hydroxybenzotriazole (HOBt), *O*-(1*H*-benzotriazol-1-yl)-*N*,*N*,*N*′,*N*′-tetramethyluronium tetrafluoroborate (TBTU), and diphenyl phosphorazidate (DPPA) were purchased from Aldrich (Steinheim, Germany) or Alexis (Grünberg, Germany). 1-Hydroxy-7-azabenzotriazole (HOAt) and *O*-(7-azabenzotriazol-1-yl)-1,1,3,3-tetramethyluronium hexafluorophosphate (HATU) were purchased from PerSeptive Biosystems (Hamburg, Germany). All other organic reagents were purchased from Merck (Darmstadt, Germany), Aldrich, or Fluka (Neu-Ulm, Germany). Human M21 melanoma cells were a kind gift of D. A. Cheresh, Departments of Immunology and Vascular Biology, The Scripps Research Institute, La Jolla, CA.

Mass spectra were recorded on the LC-MS system LCQ from Finnigan (Bremen, Germany) using the Hewlett-Packard series 1100 HPLC system. NMR-spectra were recorded on a Bruker AC 250 or Bruker AMX 500 (Karlsruhe, Germany) at 300 K. For all experiments, the solvent signal was used for calibration.

Analytical reversed-phase high-performance liquid chromatography (RP-HPLC), using several acetonitrile/water gradients with 0.1% trifluoroacetic acid, was performed on Sykam equipment (Gilching, Germany) using columns with YMC−Pack ODS-A (5 μm, 250 × 4 mm) (YMC Co., Ltd, Kyoto, Japan). For radioactivity monitoring, the outlet of the UV detector was connected to a well-type NaI(Tl) detector from EG&G (München, Germany). Preparative RP-HPLC was performed with the same system using a YMC−Pack J'sphere H80 (4 μm, 150 × 20 mm) column.

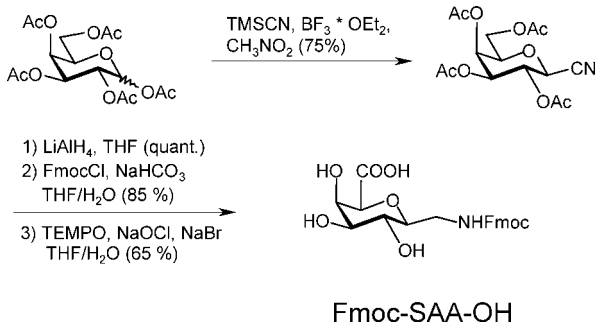


Figure 1. Synthesis of the Fmoc-protected sugar amino acid (Fmoc-SAA-OH). Synthesis starts with the transformation of the anomeric acteyl group of the pentaacetyl-protected galactose into a cyanide group using trimethylsilyl cyanide (TMSCN) under Lewis acidic conditions. The nitrile group is reduced to an aminomethylene unit using lithiumaluminum hydride. Subsequently, Fmoc-protection via standard protocols was carried out. Finally, the primary hydroxyl group is oxidized using a TEMPO-catalyzed oxidation.

Synthesis of the Fmoc-Protected Sugar Amino Acids (Fmoc-SAA-OH) (Figure 1). *2,3,4,6-Tetra-O-acetylgalactosyl-β-D-pyranosyl Cyanide (Ac$_4$GalCN).* Synthesis of the protected pyranosyl cyanide was carried out using a slightly modified protocol compared with literature (*23*). Briefly, to a solution of 42.8 g of penta-*O*-acetylgalacto-β-D-pyranose (110 mmol) in 200 mL of nitromethane were consecutively added 15 mL of trimethylsilyl cyanide (110 mmol) and 3 mL of boron trifluoride etherate (0.33 mmol, 0.3 equiv). After stirring at room temperature for 1 h, an additional 10 mL of trimethylsilyl cyanide (55 mmol, 0.5 equiv) and 2 mL of boron trifluoride etherate (22 mmol, 0.15 equiv) were added. After stirring for a further 30 min, the solvent was evaporated and the residue was dissolved in acetyl acetate (EtOAc). The solution was consecutively washed with a saturated $NaHCO_3$ solution, H_2O, and brine and dried over Na_2SO_4. Evaporation of the solvent and crystallization from EtOAc yielded 32.4 g (83%). R_f (hexane/EtOAc 2:1) = 0.3; ESI-MS: m/z = 710 (2M − HCN + Na^+), 737 (2M + Na^+); Analysis ($C_{15}H_{19}NO_9$) C, H, N; calcd C 50.42, H 5.36, N 3.92; found C 50.39, H 5.14, N 4.05; ^{1}H NMR ($CDCl_3$, 250 MHz): 5.5 (t, 1H, H2); 5.42 (dd, 1H, $^3J_{3,4}$ = 3.3 Hz, $^3J_{4,5}$ = 1.1 Hz, H4); 4.95 (dd, 1H, $^3J_{2,3}$= 10.1 Hz, $^3J_{3,4}$ = 3.3 Hz, H3); 4.15 (d, 1H, $^3J_{1,2}$ = 10.2 Hz, H1), 4.08 (d, 2H, $^3J_{5,6}$ = 6.3 Hz, H6 und H6′); 3.93 (td, 1H, $^3J_{4,5}$ = 1.1 Hz, $^3J_{5.6}$ = 6.3 Hz, H5); 2.12−1.92 (4s, 12H, acetyl-CH_3); ^{13}C NMR (DMSO-d_6, 62.5 MHz): 169.9, 169.8, 169.3, 169.1 (Acetyl-*C*O); 115.6 (CN); 74.5 (C1); 69.7 (C2); 67.3 (C3); 65.9 (C4); 65.0 (C5); 61.6 (C6); 20.5, 20.3, 20.24, 20.19 (acetyl-*C*H$_3$)

β-D-Galactopyranosylmethylamine (GalCH$_2$NH$_2$). Gal-CH_2NH_2 was synthesized according to BeMiller et al. (*24*) using a modified workup procedure. Briefly, to a suspension of 20 g of $LiAlH_4$ (527 mmol, 3.8 equiv) in 100 mL of dry tetrahydrofuran (THF) was slowly added a saturated solution of 50 g of Ac$_4$GalCN (140 mmol) in dry THF. After completion of addition, the resulting suspension was stirred for 3 h at RT. Ethanol was added dropwise

until no further hydrogen evolution was detectable. Subsequently, 100 mL concentrated NH_3 solution was slowly added, and the suspension was stirred for 1.5 h. The suspension was centrifuged, and the remaining solid was washed five times with water. The following steps can be accomplished without further purification although the solid contains large amounts of inorganic salts. ESI-MS: m/z = 194.2 ($M + H^+$); 200.1 ($M + Li^+$)

N-(Fluorenylmethyloxycarbonyl)-β-D-galactopyranosylmethylamine. To a solution of 4.7 g of $GalCH_2NH_2$ (24 mmol) in 70 mL of a 10% $NaHCO_3$ solution was added a solution of 6.93 g FmocCl (26.8 mmol, 1.1 equiv) in 40 mL of THF. After stirring for 1.5 h at RT, the pH of the solution was adjusted to 2 using cationic ion-exchange resin (Amberlyst 15, H^+ form). The resin was filtrated off and washed thoroughly with THF. The organic solvents were removed in vacuo and the remaining emulsion was extracted twice with hexane and five times with EtOAc. The combined EtOAc-fractions were evaporated to dryness and coevaporated with toluene. The resulting crude product (9.6 g) can be used without further purification. R_f (chloroform/methanol 9:1) = 0.45; ESI-MS: m/z = 416.2 ($M + H^+$)

Fmoc-SAA-OH. The reaction was accomplished using a procedure published by de Nooy et al. (*25*). For the workup, the pH of the reaction mixture was adjusted to 1.5 using cationic ion-exchange resin (Amberlyst 15, H^+ form), then the resin was filtered off and washed thoroughly with water. The filtrate was saturated with NH_4Cl and extracted five times with EtOAc. The collected organic layers were evaporated, then coevaporated twice with toluene. The product was purified by crystallization from methanol. Nine grams of *N*-(fluorenylmethyloxycarbonyl)-β-D-galactopyranosyl-methylamine yield 6.7 g (72%) of Fmoc-SAA-OH as white crystalls. R_f (chloroform/methanol 9:1) = 0.15; ESI-MS: m/z = 429.9 ($M + H^+$); 452.2 ($M + Na^+$); 663.6 ($3M + K^+ + Na^+/2$); 858.8 ($2M + H^+$); 880.9 ($2M + Na^+$); 897.0 ($2M + K^+$); 1309.6 ($3M + Na^+$); 1326.7 ($3M + K^+$); ^{1}H NMR (DMSO-d_6, 500 MHz): 7.87 (d, 2H, $^3J_{HH}$ = 7.5 Hz, Fmoc-CH); 7.69 (d, 2H, $^3J_{HH}$ = 7.5 Hz, Fmoc-CH); 7.4 (t, 2H, $^3J_{HH}$ = 7.9 Hz, Fmoc-CH); 7.3 (m, 2H, Fmoc-CH); 7.23 (t, br, 1H, NH); 5.0−4.65 (m, 3H, OH); 4.32 (d, 2H, $^3J_{HH}$ = 6.7 Hz, Fmoc-CHCH_2), 4.24 (t, 1H, $^3J_{HH}$ = 6.6 Hz, Fmoc-CHCH$_2$); 4.05 (s, 1H, H2); 3.97 (s, br, 1H, H3); 3.55 (dd, 1H, $^3J_{HH}$ = 4.4 Hz, $^3J_{HH}$ = 12.7 Hz, H7); 3.38 (m, 1H, H4); 3.30 (m, 1H, H5); 3.19 (m, 1H, H6); 3.05 (m, 1H, H7′); ^{13}C NMR (DMSO-d_6, 125 MHz): 170.2 (COOH); 156.2 (Fmoc-CO); 143.9−120.1 (arom-C); 78.2 (C6); 77.1 (C2); 73.8 (C4); 70.2 (C3); 67.9 (Fmoc-CH_2); 65.4 (C5); 46.8 (Fmoc-CH); 42.2 (C7).

Glycopeptide Synthesis (Figure 2). *Cyclo(-Arg(Pbf)-Gly-Asp(OtBu)-D-Phe-Lys-).* Loading of the TCP-resin, synthesis of the peptide, subsequent cyclization, and selective deprotection of the lysine moiety were carried out following the protocols described elsewhere (*20*, *21*, *26*). Side chain protection was 2,2,4,6,7-pentamethyldihydrobenzofuran-5-sulfonyl (Pbf) for arginine, benzyloxycarbonyl (Z) for lysine, and *tert*-butyl (tBu) for aspartic acid. ESI-MS: $(M + H)^+$ = 912; RP-HPLC: t_R = 13.8 min, K' = 7.6 (30−80% MeCN; 30 min).

Cyclo(-Arg(Pbf)-Gly-Asp(OtBu)-D-Phe-Lys(Fmoc-SAA)-). After dissolving 0.08 mmol cyclo(-Arg(Pbf)-Gly-Asp(OtBu)-D-Phe-Lys-) and 0.24 mmol Fmoc-SAA-OH in 6 mL dimethylformamide (DMF), 0.24 mmol HATU and 0.24 mmol HOAt were added. The pH was adjusted to 8 using *N*-ethyldiisopropylamine. After stirring the solution for 1 h at ambient temperature, the solvent was reduced in vacuo, the residue was triturated with water and the crude peptide was isolated by centrifugation. ESI-MS: $(M + H)^+$ = 1323; RP-HPLC: t_R = 33.0 min, K' = 11.7 (0−80% MeCN; 30 min).

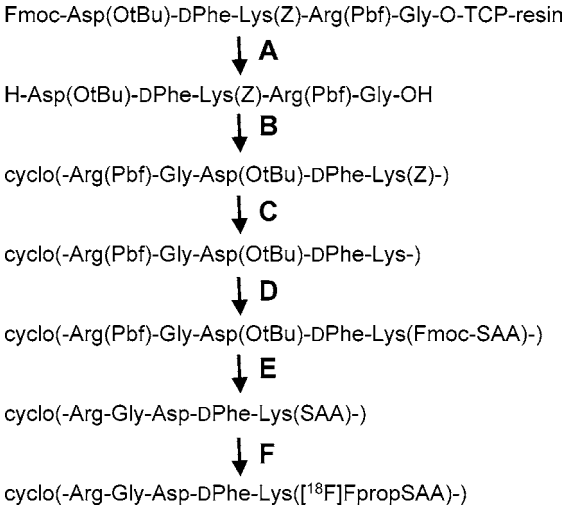


Figure 2. Schematic presentation of the synthesis of the ^{18}F-labeled glycosylated RGD-peptide. The protected linear peptide was assembled on a trityl chloride resin. (A) Removal from the resin. (B) Cyclization of the side chain protected peptide. (C) Selective deprotection of the lysine ϵ-amino function. (D) Conjugation with Fmoc-SAA-OH. (E) Complete deprotection of the glycopeptide. (F) Labeling with [^{18}F]NFP.

Table 1. Analytical Data for the Labeling Precursor c(RGDfK(SAA)) (0−80% MeCN in 20 min) and the Reference Compound [^{19}F]Galacto-RGD (0−50% MeCN in 30 min)

peptide	formula	MW [g/mol]	HPLC-MS $(M + H)^+$	t_R [min]	K'
c(RGDfK(SAA))	$C_{34}H_{52}N_{10}O_{12}$	792.85	794	10.8	5.0
[^{19}F]Galacto-RGD	$C_{37}H_{55}N_{10}O_{13}F$	866.90	868	23.5	6.8

Cyclo(-Arg(Pbf)-Gly-Asp(OtBu)-D-Phe-Lys(SAA)-). The Fmoc-protected glycopeptide was dissolved in 5 mL of 20% piperidine in DMF and stirred for 20 min at ambient temperature. After concentration of the solvent in vacuo, the glycopeptide was precipitated with diethyl ether. The crude product was isolated by centrifugation and washed 3 times with diethyl ether. ESI-MS: $(M + H)^+$ = 1101; RP-HPLC: t_R = 16.7 min, K' = 6.0 (30−80% MeCN; 30 min).

Cyclo(-Arg(Pbf)-Gly-Asp(OtBu)-D-Phe-Lys(SAA-(FP))-). After dissolving 0.01 mmol cyclo(-Arg(Pbf)-Gly-Asp(OtBu)-D-Phe-Lys(SAA)-) and 0.02 mmol 2-fluoropropionate in 1 mL of DMF, 0.02 mmol of HATU, and 0.02 mmol of HOAt were added. *N*-Ethyldiisopropylamine was used to adjust the pH to 8.5. After stirring the solution for 1 h at ambient temperature, the solvent was reduced in vacuo, and the residue was triturated with water. The crude product was isolated by centrifugation and dried in vacuo. ESI-MS: $(M + H)^+$ = 1174; RP-HPLC: t_R = 19.2 min, K' = 9.1 (30−80% MeCN; 30 min).

Removal of the Side Chain Protection Groups of the Glycopeptides. Glycopeptides were treated with 20 mL of a solution of 95% trifluoroacetic acid (TFA), 2.5% water, and 2.5% triisobutylsilane for 24 h at ambient temperature. The mixture was filtered if necessary, evaporated in vacuo, triturated with diethyl ether, filtered, and washed several times with diethyl ether.

The crude, cyclic glycopeptides were purified by RP-HPLC. Analytical data are given in Table 1.

[^{18}F]Fluoride Production. No carrier added [^{18}F]-fluoride was produced on a RDS-112 cyclotron (Siemens/

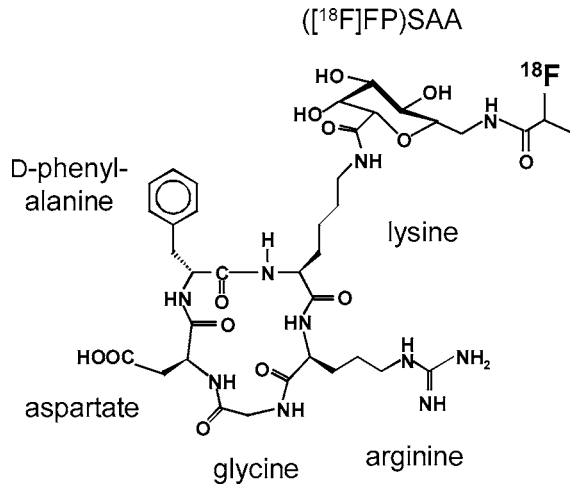


Figure 3. Schematic structure of [^{18}F]Galacto-RGD. Labeling with [^{18}F]NFP was carried out via acylation of the aminomethyl group at the C1-position of the sugar moiety. (This figure is reproduced with permission from the American Association for Cancer Research, Inc.; see ref 22).

CTI, Knoxville, TN) by irradiation of a water target using an 11 MeV proton beam on isotopically enriched [^{18}O]-water (Rotem, Beersheva, Israel). At end of bombardment, the enriched water containing [^{18}F]fluoride was passed through an anion-exchange resin (Dowex, AG1 × 8, 40 mg). The [^{18}F]fluoride was eluted from the resin using 200 to 300 μL of a 5.7 mg/mL aqueous $K_2CO_3 \cdot 1.5H_2O$ solution and collected in a 5 mL conical vial closed with a septum containing 10 mg of Kryptofix 222 in 500 μL of dry MeCN (acetonitrile for DNA synthesis). The resulting solution was concentrated to dryness at 100 °C in vacuo. The azeotropic drying was repeated at least twice with 500 μL portions of acetonitrile.

Synthesis of 4-Nitrophenyl-2-[^{18}F]fluoropropionate. Synthesis of 2-[^{18}F]fluoropropionate was prepared according to literature (*27*−*29*).

Synthesis of [^{18}F]Galacto-RGD. The glycopeptide (0.01−5.0 mg) was dissolved in 200 μL of dimethyl sulfoxide (DMSO) and added to the polypropylene vial containing 4-nitrophenyl-2-[^{18}F]fluoropropionate (185−370 MBq). The reaction mixture was allowed to remain for different times at different temperatures (for details see Figure 4). Purification of the [^{18}F]Galacto-RGD (Figure 3) was performed using RP-HPLC with an acetonitrile/water gradient containing 0.1% trifluoroacetic acid (10−50% acetonitrile in 30 min; flow 10 mL/min, t_R = 11.6 min, K' = 5.1). For animal experiments the solvent was removed in vacuo, and the residue was dissolved in phosphate-buffered saline (PBS) pH 7.4.

Octanol/Water Partition Coefficient. Approximately 2.5 kBq [^{18}F]Galacto-RGD in 10 μL PBS was diluted with 490 μL of PBS and added to 500 μL of octanol in an Eppendorf tube. After vigorous mixing of the suspension for 3 min at room temperature, the caps were centrifuged (10 300 g; 6 min) and 100 μL aliquots of both layers were counted in a gamma counter. The experiment was repeated six times.

Metabolic Stability. *Tumor Xenografts.* Metabolic stability of [^{18}F]Galacto-RGD was evaluated in mice using a xenotransplanted human melanoma model. It has previously been demonstrated that this tumor model shows high expression of the $\alpha v\beta 3$ integrin (*20*, *30*). Human M21 melanoma cells (*30*) were cultured in a humidified atmosphere with 5% CO_2. The cell culture medium was RPMI 1640 (Seromed Biochrom, Berlin, Germany) supplemented with 10% fetal calf serum and gentamycine. Tumor xenografts were obtained by subcutaneous injection 5×10^6 cells. Mice bearing tumors weighing 300−400 mg were used for the studies.

Metabolic Stability. Nude mice bearing tumor xenografts of human melanoma M21 were intravenously injected with 3.7 MBq of [^{18}F]Galacto-RGD. The animals were sacrificed and dissected 120 min after tracer injection. Blood, liver, kidney, and tumor were removed. Blood was immediately centrifuged for 5 min at 1200 g. Organs were frozen with liquid nitrogen, homogenized using a Mikro Dismembranator II (B. Braun, Melsungen, Germany), suspended in 1 mL of PBS pH 7.4, and centrifuged for 3 min at 15 600*g*. After removal of the supernatants, the pellets were washed with 500 μL of PBS. For each sample supernatants of both centrifugation steps were combined and passed through Sep-Pak C18 cartridges. The cartridges were washed with 2 mL of water and eluted with 2 mL of acetonitrile containing 0.1% TFA. Before analysis with RP-HPLC, the acetonitrile was removed in vacuo, and the residues were dissolved in 500 μL of PBS. Aliquots of 350 μL were injected onto a RP-HPLC (Sykam, Gilching, Germany; 150 × 10 mm Multosphere 100 RP-18, 5 μm column, CS Chromatographie Service GmbH, Langerwehe, Germany) using a flow of 3 mL/min (gradient: 10−50% acetonitrile, 20 min). Radioactivity was monitored using a flow scintillation analyzer (Radiomatic 500 TR Series, Packard Canberra Company, Meriden, CT). HPLC analysis was carried out in duplicate and extraction efficiency determination in triplicate.

To verify if the peak eluting approximately 1.5 min before [^{18}F]Galacto-RGD (designated as metabolite 2) is a metabolite of [^{18}F]Galacto-RGD and not [^{18}F]Galacto-RGD in a different protonation status, both peaks were sampled and aliquots were reinjected onto the HPLC. In addition, coinjection of both fractionated samples was carried out.

Dynamic PET Study and Dose Estimates. Anesthetized New Zealand white rabbits underwent dynamic PET studies using a Simens ECAT HR+ scanner (Siemens/CTI, Knoxville, Tennessee). Tracer distribution was followed for 60 min after injection of 18.5 MBq of [^{18}F]Galacto-RGD. Residence times were calculated by monoexponential extrapolation of the time activity curves for the various organ systems. According to the residence times radiation doses were calculated for an adult female patient using the MIRDOSE 3.0 program.

RESULTS

Radiosynthesis. ^{18}F-Fluorination of Galacto-RGD was carried out using 4-nitrophenyl-2-[^{18}F]fluoropropionate. Synthesis of the prosthetic group follows the protocol previously published (*27*−*29*) and resulted in a radiochemical yield of 45.2 ± 10.6% (n = 20) with an average reaction time of 126 ± 10 min. As shown in Figure 3, radiolabeling of the glycopeptide was performed via acylation of the amino methyl group at the C1-position of the sugar moiety. This led to a ^{18}F-labeled glycopeptide with an even more hydrophilic character than found for radioiodinated Gluco-RGD (21) (log P([^{125}I]Gluco-RGD) = −2.45 vs log P([^{18}F]Galacto-RGD) = −3.17).

The dependence of the radiochemical acylation yield on peptide concentration, temperature, and reaction time was investigated (for details see Figure 4). The maximum yield for the acylation step was approximately 85%. This can be reached by either using 0.5 mg of peptide at 70 °C within 10 min, 1 mg of peptide at 45 °C within 10 min, or 1 mg of peptide at 70 °C within 2.5 min. At least

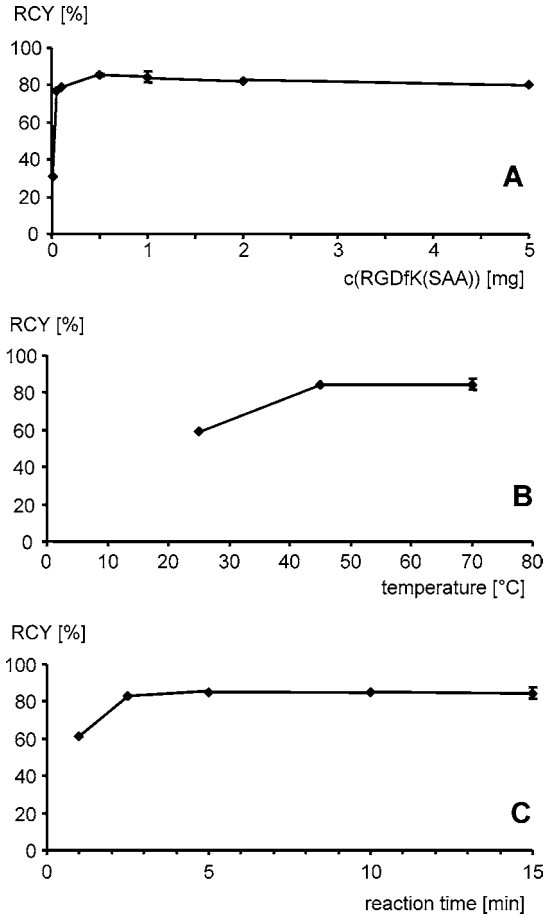


Figure 4. Dependence of the radiochemical acylation yield from (A) peptide concentration (70 °C, 10 min), (B) reaction temperature (6.3 mM peptide, 10 min), and (C) reaction time (6.3 mM peptide, 70 °C).

76% can be reached using 0.5 mg Galacto-RGD at 45 °C within 2.5 min. Final RP-HPLC with a semipreparative column allows preparation of [18F]Galacto-RGD with radiochemical purities >98% and with specific activities ranging from 40 to 100 TBq/mmol. The total radiochemical yield was 29.5 ± 5.1% (EOB) with a total reaction time of 200 ± 18 min including final HPLC purification (calculation based on 1.0 mg of peptide, 70 °C, and 10 min reaction time ($n = 6$)). Typically, starting with 2200 MBq of [18F]F$^-$, 185 MBq of [18F]Galacto-RGD was prepared in a synthesis time compatible with the half-life of 18F-fluorine.

Metabolism of [18F]Galacto-RGD. The metabolic stability of [18F]Galacto-RGD was determined in mouse blood and liver, kidney, and tumor homogenates 2 h after tracer injection. For all organs extraction efficiency was between 60% and 93% (Table 2). The lowest extraction efficiency was found for the liver homogenates and highest was found for the kidneys. Between 2 and 8% of the total activity could not be fixed on the C-18 cartridges, which can correspond with very hydrophilic metabolites or protein bound activity.

HPLC analysis of the soluble fraction of the different samples (Figure 5) allowed detection of two radiolabeled metabolites in tumor, liver, and kidney homogenates. The retention times of metabolite 1 (met 1) and metabolite 2 (met 2) were ~4.0 min and ~9.5 min, respectively. The retention time for [18F]Galacto-RGD was ~11.0 min. In blood samples only one metabolite, corresponding with met 2 in the other samples, was found. Detailed HPLC-analysis of met 2 and [18F]Galacto-RGD showed that both

Table 2. Extraction Efficiency and Data from the HPLC Analysis of the Soluble Fraction of the Organ Homogenates and the Blood Samples 120 min after Tracer Injection

	blood	liver	kidneys	tumor
Extraction Efficiency [%] ($n = 3$)				
unsoluble fraction	25.7 ± 3.8	34.1 ± 6.7	5.3 ± 3.1	19.8 ± 5.9
nonretained fraction[a]	7.8 ± 2.3	5.8 ± 0.1	1.7 ± 0.7	5.4 ± 1.1
soluble fraction[b]	66.6 ± 2.3	60.2 ± 6.9	93.0 ± 3.7	74.8 ± 6.6

	blood	liver	kidneys	tumor
HPLC Analysis [%] ($n = 2$)				
met 1	n.d.[c]	2.4 ± 0.4	3.5 ± 1.3	0.7[d]
met 2	14.4 ± 5.1	21.9 ± 1.8	27.8 ± 1.3	12.3 ± 1.7
intact tracer	85.6 ± 5.2	75.8 ± 2.2	68.7 ± 2.5	87.4 ± 2.2

[a] Amount of activity, which could not be fixed on the C-18 cartridge. [b] Amount of activity, which was eluted from the C-18 cartridge using acetonitrile with 0.1% trifluoroacetic acid. [c] Not detectable. [d] Detectable only in one sample.

peaks represent two different radiolabeled species and not [18F]Galacto-RGD in different protonated forms. The average fraction of intact tracer was between 70% and 87% (Table 2). The average amount of met 1 was between 1% and 4% and of met 2 between 12% and 28%. Highest metabolic stability of [18F]Galacto-RGD was found in tumor (87% intact tracer) and blood (86% intact tracer).

PET Study and Dose Estimates. The dynamic PET study of two New Zealand white rabbits showed fast renal elimination of the tracer with low activity accumulation in almost all organs of the rabbit (Figure 6). One minute after injection of 18.5 MBq of [18F]Galacto-RGD, highest activity concentration was found in heart, kidneys, liver, and large blood vessels. At 15 min pi, most activity could be detected in kidneys and at 60 min pi in the urinary bladder. Calculation of time activity curves demonstrated that there is no tracer retention in any of the investigated organs (Figure 7).

The expected radiation dose to an adult female patient after injection of [18F]Galacto-RGD has been estimated to be of 2.2×10^{-2} mGy/MBq. Only slightly different results were obtained from radiation dose calculations based on the biodistribution data in mice (biodistribution data can be found in (*22*)). An effective radiation dose of 3.8×10^{-2} mGy/MBq was calculated on the basis of the mouse data. The highest radiation doses were found for the urinary bladder wall and the small intestine (1.5×10^{-1} mGy/MBq and 2.2×10^{-1} mGy/MBq, respectively). In rabbits the radiation dose for the gallbladder wall and the small intestine were lower than in the mouse model, probably reflecting slower excretion kinetics in larger animals. Table 3 shows the expected radiation dose for the individual organ systems.

DISCUSSION

It has been shown that sugar derivatives can improve several pharmacological properties of peptides such as bioavailability (*31*), increased stability toward enzymatic degradation (*32*), and solubility under physiological conditions (*33*). Recently, radiolabeled octreotide and octreotate derivatives conjugated with glucose, maltose or maltotriose have been described (*29*, *34*−*36*). These glycosylated tracers showed reduced liver and increased tumor uptake resulting in excellent tumor-to-background ratios which allows imaging of SSTR-positive tumors with high contrast.

We used a similar approach to improve the pharmacokinetic behavior of our first generation compounds and conjugated sugar amino acids with cyclo(-Arg-Gly-Asp-D-Tyr-Lys-) (*21*). An advantage of sugar amino acids,

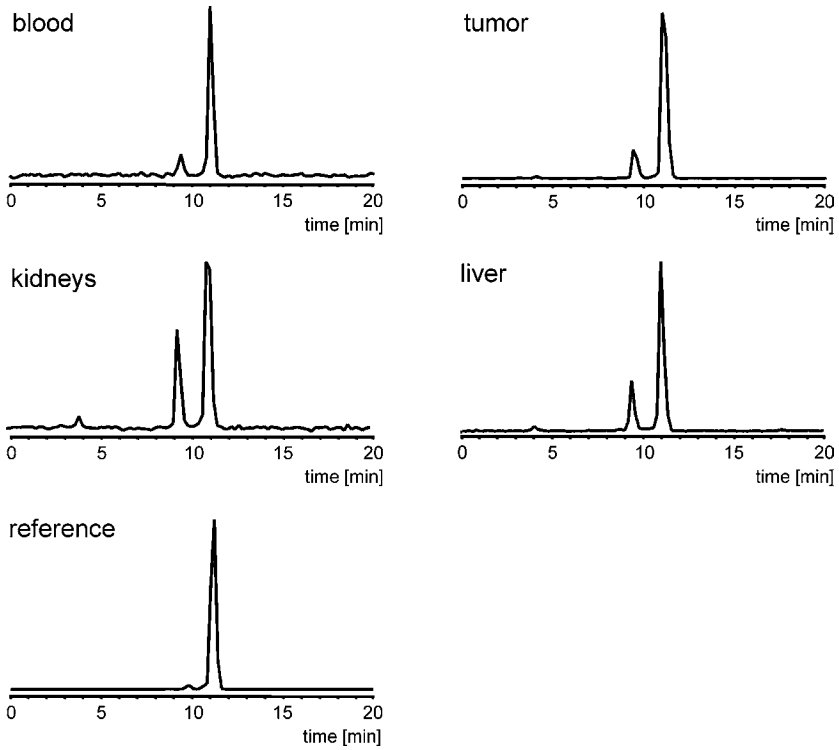


Figure 5. Representative HPLC profiles of the reference compound, and the soluble fraction of blood samples, tumor, kidney, and liver homogenates collected 120 min after tracer injection.

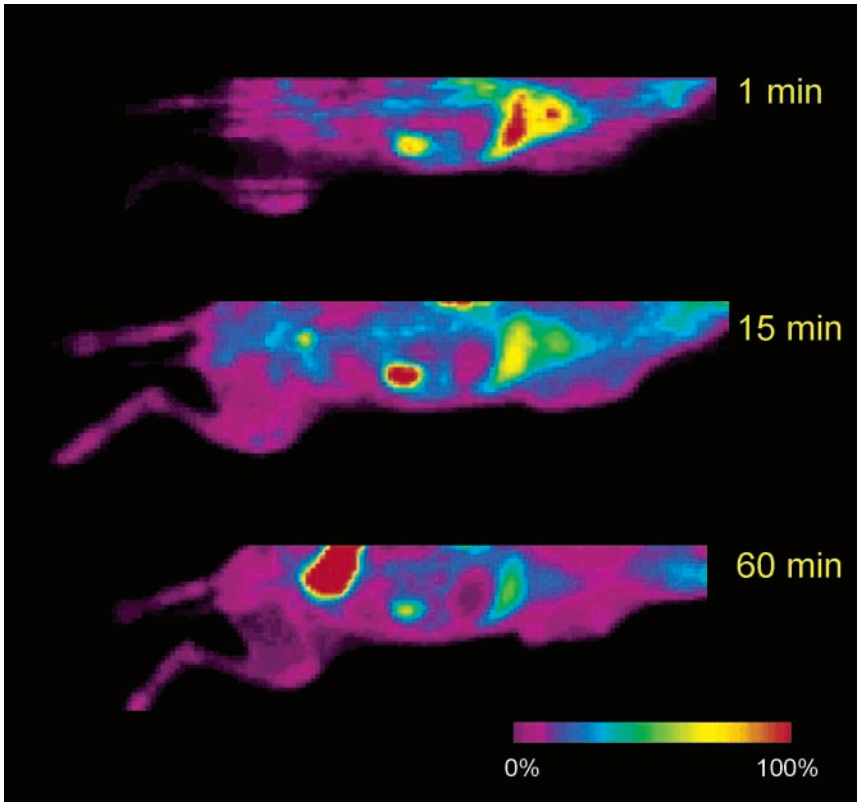


Figure 6. Dynamic PET study of a New Zealand white rabbit over 60 min after injection of [^{18}F]Galacto-RGD. The image 1 min after tracer injection shows blood-pool activity in the heart, liver, right kidney, and large blood vessels. In the image 15 min pi there is accumulation of the tracer in the right kidney and clearance of blood-pool activity. Furthermore, activity is found in the bladder. At 60 min pi the tracer has accumulated in the bladder. Liver and right kidney are only faintly visible. Please note that some parts of the left side of the rabbit including the left kidney were not in the field of view of the PET scanner.

which are sugar derivatives with an amino and a carboxylic function (*37*), is that they can easily be used with standard peptide synthesis protocols. Moreover, due to the carbon−carbon bond at the anomeric center, the resulting glycopeptides are expected to be very stable toward metabolic degradation. For the synthesis of the first radioiodinated glycopeptide, a sugar amino acid based on glucose was used. The resulting radioiodinated

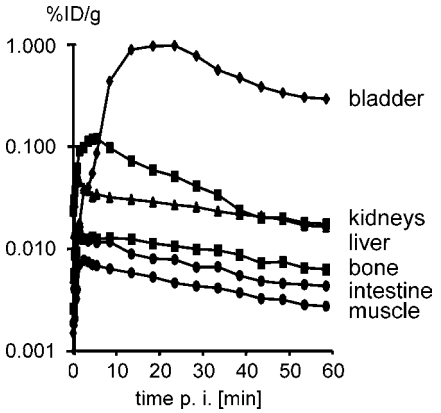


Figure 7. Time activity curves derived from the dynamic PET study shown in Figure 6.

Table 3. Estimated Radiation Doses for a Female Adult Patient after Intravenous Injection of [18F]Galacto-RGD, as Derived from Melanoma-Bearing Nude Mice and New Zealand White Rabbits

	radiation dose [mGy/MBq]	
target organ	mouse data	rabbit data
adrenals	8.87×10^{-3}	1.59×10^{-2}
brain	1.29×10^{-4}	1.42×10^{-2}
breast	8.05×10^{-4}	1.24×10^{-2}
gallbladder wall	2.21×10^{-2}	1.72×10^{-2}
large intestine	8.19×10^{-2}	2.78×10^{-2}
small intestine	2.19×10^{-1}	1.85×10^{-2}
stomach	1.06×10^{-2}	1.60×10^{-2}
heart wall	2.11×10^{-3}	1.58×10^{-2}
kidneys	2.04×10^{-2}	2.56×10^{-2}
liver	1.03×10^{-2}	1.63×10^{-2}
lungs	1.69×10^{-3}	1.00×10^{-2}
muscle	6.40×10^{-3}	8.60×10^{-3}
ovaries	3.98×10^{-2}	1.92×10^{-2}
pancreas	8.34×10^{-3}	1.68×10^{-2}
red marrow	8.79×10^{-3}	1.41×10^{-2}
bone	4.31×10^{-3}	1.51×10^{-2}
skin	2.17×10^{-3}	1.14×10^{-2}
spleen	6.92×10^{-3}	1.55×10^{-2}
thymus	4.66×10^{-3}	1.51×10^{-2}
thyroid	3.13×10^{-4}	1.39×10^{-2}
urinary bladder wall	1.50×10^{-1}	1.04×10^{-1}
uterus	3.47×10^{-2}	2.22×10^{-2}
total body	9.09×10^{-3}	4.47×10^{-2}
effective dose	3.78×10^{-2}	2.16×10^{-2}

Gluco-RGD showed promising improved pharmacokinetics and increased activity retention in the tumor (*21*). For ^{18}F-labeling with prosthetic groups, another sugar amino acid based on galactose was introduced (*22*) allowing acylation at the amino function at the C1-position of the sugar moiety.

This Fmoc-protected sugar amino acid (Fmoc-SAA-OH, Figure 1) can be synthesized in four steps starting from pentaacetyl protected galactose. The reaction starts with the transformation of the anomeric acetyl into a cyanide group by reaction of the protected galactose with trimethylsilyl cyanide under Lewis acidic conditions. The nitrile group is then reduced to an aminomethylene unit using lithiumaluminum hydride and the newly formed amino group is subsequently Fmoc-protected via standard protocols. In the last step the primary hydroxyl group is oxidized using a TEMPO-catalyzed oxidation which yields the carboxylic acid moiety that enables fast and efficient glycosylation of the partially protected cyclo(-Arg-Gly-Asp-D-Phe-Lys-) via the ϵ-amino function of the lysine. The final deprotection of the peptide side chain functions, as well as the primary amino function at the sugar moiety, offers a RGD-containing glycopeptide which can be labeled with ^{18}F-fluorine by prosthetic groups, such as succinimidyl-4-[^{18}F]fluorobenzoate ([^{18}F]-SFB) (*38*) and 4-nitrophenyl-2[^{18}F]-fluoropropionate ([^{18}F]-NFP) (*27*). To minimize the negative effect of hydrophobic prosthetic groups, such as [^{18}F]SFB, on the optimized hydrophilicity of sugar-conjugated tracer, [^{18}F]NFP was chosen for labeling. Acylation of the glycopeptide with this prosthetic group resulted in the radiolabeled compound with high radiochemical purity and radiochemical yield. By using a peptide concentration of 0.32 mM, radiochemical acylation yields of approximately 76% can already be reached at 45 °C within 2.5 min. Moreover, it is not necessary to add any additional base during the acylation step when the amino function of the sugar is in the deprotonated form. This can be carried out by adding 1 equiv sodium carbonate and subsequent removal of the solvent in vacuo. Although the synthesis of [^{18}F]NFP is a time-consuming three step procedure necessary to be improved, the discussed synthesis route allows the production of [^{18}F]Galacto-RGD in amounts sufficient for clinical trials.

In murine tumor models it has already been demonstrated that [^{18}F]Galacto-RGD shows receptor specific accumulation in the tumor with good tumor-to-background ratios and allows noninvasive determination of $\alpha v\beta 3$-expression using a small animal scanner (*22*). The dynamic PET study using a New Zealand white rabbit confirmed the data from biodistribution studies with tumor-bearing mice indicating fast predominantly renal excretion of the tracer. The radiation dose estimates using the MIRDOSE program resulted in values very similar to that found for [^{18}F]FDG, indicating low radiation doses for patients. The studies concerning the metabolic stability showed that there remains between 5 and 35% of the injected activity in the unsoluble fraction, which could be due to coprecipitation, or especially for the blood sample, also due to some binding to cells. However, this was not verified in more detail in this study. Nevertheless, between 65 and 90% of the tracer in the soluble fraction remains intact during the time frame essential for ^{18}F-PET studies. Especially in tumor and blood, even 2 h after tracer injection more than 85% of the activity found correspond with the intact tracer, indicating that the resulting signal mainly reflects tracer accumulation.

In conclusion, glycosylation of RGD-peptides using a sugar amino acid is easy to accomplish via standard peptide chemistry protocols. Subsequently, radiolabeling with [^{18}F]NFP results in [^{18}F]Galacto-RGD in high radiochemical yields and radiochemical purity. Introduction of the sugar moiety in combination with this prosthetic group leads to a hydrophilic tracer with fast predominantly renal excretion and suitable metabolic stability in vivo which allows noninvasive determination of $\alpha v\beta 3$-expression in different murine tumor models. The route described enables production of a standard amount of [^{18}F]Galacto-RGD sufficient for patient studies, starting with approximately 2.2 GBq of [^{18}F]fluoride. The estimated radiation dose is in the same range as found for [^{18}F]FDG.

ACKNOWLEDGMENT

This work was supported by a grant from the Sander Foundation (grant no. 96.017.3). Wolfgang Linke, Claudia Bodenstein, Gitti Dzewas, and Burghard Cordes are acknowledged for excellent technical assistance and Amy R. Claus for carefully reading the manuscript. We thank

the RDS-cyclotron team, and especially Michael Herz, for providing the ^{18}F-fluorine and initial training at the hot cells. We acknowledge David A. Cheresh, The Scripps Research Institute, La Jolla, CA, for supplying us with M21 melanoma cells. The rabbit was kindly provided by Ivo Buschmann and Emanuelle K. Chorianopoulos, University of Freiburg, Germany.

LITERATURE CITED

(1) Cox, D., Aoki, T., Seki, j., Motoyama, Y., and Yoshida, K. (1994) The pharmacology of integrins. *Med. Res. Rev. 14*, 192−228.

(2) Hynes, R. O. (1992) Integrins: versatility, modulation, and signaling in cell adhesion. *Cell 69*, 11−25.

(3) Teitelbaum, S. L. (2000) Bone resorption by osteoclasts. *Science 289*, 1504−1508.

(4) Bishop, G. G., McPherson, J. A., Sanders, J. M., Hesselbacher, S. E., Feldman, M. J., McNamara, C. A., Gimple, L. W., Powers, E. R., Mousa, S. A., and Sarembock, I. J. (2001) Selective alpha(v)beta(3)-receptor blockade reduces macrophage infiltration and restenosis after balloon angioplasty in the atherosclerotic rabbit. *Circulation 103*, 1906−1911.

(5) Albelda, S. M., Smith, C. W., and Ward, P. A. (1994) Adhesion molecules and inflammatory injury. *FASEB J. 8*, 504−512.

(6) Storgard, C. M., Stupack, D. G., Jonczyk, A., Goodman, S. L., Fox, R. I., and Cheresh, D. A. (1999) Decreased angiogenesis and arthritic disease in rabbits treated with an alpha-(v)beta(3) antagonist. *J. Clin. Invest. 103*, 47−54.

(7) Clezardin, P. (1998) Recent insights into the role of integrins in cancer metastasis. *Cell Mol. Life Sci. 54*, 541−548.

(8) Eliceiri, B. P., and Cheresh, D. A. (1999) The role of alpha-(v) integrins during angiogenesis: insights into potential mechanisms of action and clinical development. *J. Clin. Invest. 103*, 1227−1230.

(9) Ranieri, G., and Gasparini, G. (2001) Angiogenesis and angiogenesis inhibitors: a new potential anticancer therapeutic strategy. *Curr. Drug Targets Immune Endocr. Metabol. Disord. 1*, 241−253.

(10) Kerr, J. S., Slee, A. M., and Mousa, S. A. (2002) The alpha-(v) integrin antagonists as novel anticancer agents: an update. *Expert Opin Investig Drugs 11*, 1765−1774.

(11) Aumailley, M., Gurrath, M., Muller, G., Calvete, J., Timpl, R., and Kessler, H. (1991) Arg-Gly-Asp constrained within cyclic pentapeptides. Strong and selective inhibitors of cell adhesion to vitronectin and laminin fragment P1. *FEBS Lett. 291*, 50−54.

(12) Gurrath, M., Muller, G., Kessler, H., Aumailley, M., and Timpl, R. (1992) Conformation/activity studies of rationally designed potent anti- adhesive RGD peptides. *Eur. J. Biochem. 210*, 911−921.

(13) Ruoslahti, E., and Pierschbacher, M. D. (1987) New perspectives in cell adhesion: RGD and integrins. *Science 238*, 491−497.

(14) Brooks, P. C., Montgomery, A. M., Rosenfeld, M., Reisfeld, R. A., Hu, T., Klier, G., and Cheresh, D. A. (1994) Integrin alpha(v)beta(3) antagonists promote tumor regression by inducing apoptosis of angiogenic blood vessels. *Cell 79*, 1157−1164.

(15) Brower, V. (1999) Tumor angiogenesis—new drugs on the block. *Nat. Biotechnol. 17*, 963−968.

(16) Dechantsreiter, M. A., Planker, E., Matha, B., Lohof, E., Holzemann, G., Jonczyk, A., Goodman, S. L., and Kessler, H. (1999) *N*-Methylated cyclic RGD peptides as highly active and selective alpha(V)beta(3) integrin antagonists. *J. Med. Chem. 42*, 3033−3040.

(17) Felding-Habermann, B., Mueller, B. M., Romerdahl, C. A., and Cheresh, D. A. (1992) Involvement of integrin alpha(v) gene expression in human melanoma tumorigenicity. *J. Clin. Invest. 89*, 2018−2022.

(18) Gasparini, G., Brooks, P. C., Biganzoli, E., Vermeulen, P. B., Bonoldi, E., Dirix, L. Y., Ranieri, G., Miceli, R., and Cheresh, D. A. (1998) Vascular integrin alpha(v)beta(3): a new prognostic indicator in breast cancer. *Clin. Cancer Res. 4*, 2625−2634.

(19) Haubner, R., Wester, H. J., Weber, W. A., and Schwaiger, M. (2003) Radiotracer-based strategies to image angiogenesis. *Quat. J. Nucl. Med. 47*, 189−199.

(20) Haubner, R., Wester, H. J., Reuning, U., Senekowitsch-Schmidtke, R., Diefenbach, B., Kessler, H., Stocklin, G., and Schwaiger, M. (1999) Radiolabeled alpha(v)beta(3) integrin antagonists: a new class of tracers for tumor targeting. *J. Nucl. Med. 40*, 1061−1071.

(21) Haubner, R., Wester, H. J., Burkhart, F., Senekowitsch-Schmidtke, R., Weber, W., Goodman, S. L., Kessler, H., and Schwaiger, M. (2001) Glycosylated RGD-containing peptides: tracer for tumor targeting and angiogenesis imaging with improved biokinetics. *J. Nucl. Med. 42*, 326−336.

(22) Haubner, R., Wester, H. J., Weber, W. A., Mang, C., Ziegler, S. I., Goodman, S. L., Senekowitsch-Schmidtke, R., Kessler, H., and Schwaiger, M. (2001) Noninvasive imaging of alpha-(v)beta(3) integrin expression using ^{18}F-labeled RGD-containing glycopeptide and positron emission tomography. *Cancer Res. 61*, 1781−1785.

(23) de las Heras, F. G., and Fernandez-Resa, P. (1982) Synthesis of Ribosyl and Arabinosyl Cyanides by Reaction of 1-O−Acyl Sugars with Trimethylsilyl Cyanide. *J. Chem. Soc., Perkin Trans. 1* 903−907.

(24) BeMiller, J. N., Yadav, M. P., Kalabokis, V. N., and Myers, R. W. (1990) N-Substituted beta-D-galactopyranosylmethylamines, and C-beta-D-galactopyranosylformamides, and related compounds. *Carbohydr Res. 200*, 111−126.

(25) de Nooy, A. E. J., Besemer, A. C., and van Bekkum, H. (1995) Highly selective nitroxyl radical-mediated oxidation of primary alcohol groups in water soluble glucans. *Carbohydr Res. 269*, 89−98.

(26) Haubner, R., Gratias, R., Diefenbach, B., Goodman, S. L., Jonczyk, A., and Kessler, H. (1996) Structural and Functional Aspects of RGD-Containing Cyclic Pentapeptides as Highly Potent and Selective Integrin alpha(v)beta(3) Antagonists. *J. Am. Chem. Soc. 118*, 7461−7472.

(27) Guhlke, S., Coenen, H. H., and Stöcklin, G. (1994) Fluoroacylation Agents Based on Small nca [^{18}F]Fluorocarboxylic Acids. *Appl. Radiat. Isot. 45*, 715−727.

(28) Wester, H. J., Brockmann, J., Rösch, F., Wutz, W., Herzog, H., Smith-Jones, P., Stolz, B., Bruns, C., and Stöcklin, G. (1997) PET-pharmacokinetics of 18F-octreotide: A comparison ^{67}Ga-DFO-octreotide and ^{86}Y-DTPA-octreotide. *Nucl. Med. Biol. 24*, 275−286.

(29) Wester, H. J., Schottelius, M., Scheidhauer, K., Meisetschlager, G., Herz, M., Rau, F. C., Reubi, J. C., and Schwaiger, M. (2003) PET imaging of somatostatin receptors: design, synthesis and preclinical evaluation of a novel ^{18}F-labeled, carbohydrated analogue of octreotide. *Eur. J. Nucl. Med. Mol. Imaging 30*, 117−122.

(30) Cheresh, D. A., and Spiro, R. C. (1987) Biosynthetic and functional properties of an Arg-Gly-Asp-directed receptor involved in human melanoma cell attachment to vitronectin, fibrinogen, and von Willebrand factor. *J. Biol. Chem. 262*, 17703−17711.

(31) Albert, R., Marbach, P., Bauer, W., Briner, U., Fricker, G., Bruns, C., and Pless, J. (1993) SDZ CO 611: a highly potent glycated analogue of somatostatin with improved oral activity. *Life Sci. 53*, 517−525.

(32) Marastoni, M., Spisani, S., and Tomatis, R. (1994) Synthesis and biological activity of d-glycopyranosyl peptide T derivatives. *Arzneimittelforschung/Drug Res. 44*, 984−987.

(33) Michael, K., Wittmann, V., König, W., Sandow, J., and Kessler, H. (1996) S- and C-glycopeptide derivatives of an LH−RH agonist. *Int. J. Pept. Protein Res. 48*, 59−70.

(34) Leisner, M., Kessler, H., Schwaiger, M., and Wester, H. J. (1999) Synthesis of Na-D-Phe1-Amadori Derivatives of Tyr^3-Octreotide: Precursor for ^{123}I−/^{18}F-Labeled SSTR−Binding SPECT/PET Tracers with Improved Biodistribution. *J. Labelled Compd. Radiopharm. 42 (Suppl.)*, S549−S551.

(35) Schottelius, M., Wester, H. J., Reubi, J. C., Senekowitsch-Schmidtke, R., and Schwaiger, M. (2002) Improvement of

Pharmacokinetics of Radioiodinated Tyr3-Octreotide by Conjugation with Carbohydrates. *Bioconjugate Chem. 13,* 1021−1030.

(36) Wester, H. J., Schottelius, M., Scheidhauer, K., Reubi, J. C., Wolf, I., and Schwaiger, M. (2002) Comparison of radioiodinated TOC, TOCA and Mtr-TOCA: the effect of carbohydration on the pharmacokinetics. *Eur. J. Nucl. Med. Mol. Imag. 29,* 28−38.

(37) Gruner, S. A., Locardi, E., Lohof, E., and Kessler, H. (2002) Carbohydrate-based mimetics in drug design: sugar amino acids and carbohydrate scaffolds. *Chem. Rev. 102,* 491−514.

(38) Wester, H. J., Hamacher, K., and Stöcklin, G. (1996) A Comparative Study of N.C.A. Fluorine-18 Labeling of Proteins via Acylation and Photochemical Conjugation. *Nucl. Med. Biol. 23,* 365−372.

BC034170N

Structure Property Analysis of Pentamethine Indocyanine Dyes: Identification of a New Dye for Life Science Applications

Oliver Mader,[§] Knut Reiner,[#] Hans-Joachim Egelhaaf,[†] Rainer Fischer,[§] and Roland Brock*[,§]

Institute for Cell Biology, University of Tübingen, Auf der Morgenstelle 15, 72076 Tübingen, Germany, and Institute of Physical and Theoretical Chemistry, University of Tübingen, Auf der Morgenstelle 8, 72076 Tübingen, Germany, and FEW Chemicals GmbH, ChemiePark Bitterfeld Wolfen, Areal A - Technikumstrasse 1, 06766 Wolfen, Germany. Received October 16, 2003; Revised Manuscript Received November 27, 2003

A collection of nine pentamethine indocyanine dyes was synthesized, and the photophysical characteristics relevant to applications in cell biology and single molecule detection were analyzed in detail. Substituents at the aromatic system covering the auxochromic series and substitutions in the polymethine chain were investigated with respect to absorption and emission spectra, fluorescence lifetimes, fluorescence quantum yields, and fluorescence autocorrelations. Substitutions in the polymethine chain increased the nonradiative energy dissipation of the excited singlet state and decreased the fluorescence quantum yield, relative to the unsubstituted compound. For substituents at the aromatic rings the fluorescence quantum yield negatively correlates with the position of the substituents in the auxochromic series $-SO_3^-$, -H, -F, $-CH_3$. Compounds with sulfonic acid groups or halogen atoms attached to the indolenine systems had the highest fluorescence quantum yields. The compound S0387 had nearly 70% of the quantum yield of Cy5 and comparable photostability. The free carboxylic acid of S0387 was attached to peptides in high yield and purity by established procedures of solid-phase synthesis. The dye-labeled peptides did not aggregate or bind to tissue culture cells and proteins unspecifically. The indocyanine dye S0387 is therefore an attractive new fluorophore for in vitro and cell-based detection of receptor ligand interaction at nanomolar concentrations by flow cytometry, fluorescence correlation spectroscopy, and laser scanning microscopy.

INTRODUCTION

Over the past decade, fluorescence has become one of the key detection principles in life sciences and drug discovery. The sensitivity of fluorescence-based detection systems has enabled the miniaturization of assay formats in high-throughput screening for new drug candidates, greatly reducing the consumption of costly assay reagents (*1*).

Spectrally resolved detection modalities, such as fluorescence anisotropy decay, detection of fluorescence lifetimes, and simultaneous detection of different wavelengths (*2*), have greatly increased the information per assay. Depending on the fluorophore used, the spectral characteristics provide valuable information on the chemical environment of a fluorophore (*3*), molecular interactions (*4*), or enzymatic turnover (*5*).

The suitability of a fluorophore for life science applications is determined by its photophysical characteristics and the chemical compatibility with the respective biological application. The key photophysical parameters of a fluorophore are the compatibility of the excitation and emission spectra with available instrumentation, the fluorescence quantum yield, the dependence of the photophysical characteristics on the chemical environment, and its photostability. Moreover, the chemical stability of the fluorophore to labeling conditions, minimum interference with biological activity of the labeled molecules, and the solubility in aqueous buffers are essential prerequisites for applications (*6*).

Detection techniques based on fluorescence emitted from single molecules are gaining significance in miniaturized drug screening and biophysical research. Fluorophores employed for such detection modalities should be free of any tendency to aggregate. In addition, the quantum yield for the transition into electronic states with long lifetimes, such as triplet state transitions, should be minimal for techniques based on the time-resolved analysis of fluorescence fluctuations.

Applications of fluorophores in life sciences include the labeling of small synthetic molecules and of large biomolecules such as proteins in screening applications for drug development, of antibodies for immunofluorescence (*7*), of nucleotides in DNA sequencing (*8*), and of oligonucleotides or proteins as probes in DNA and protein microarrays (*9*). The requirements of chemical stability depend on the molecules to be labeled. To label proteins, an active ester or maleimido group is usually attached to a free carboxyl group of the fluorophore (*10*, *11*). These groups react with primary amines or thiol groups in aqueous buffers and at mildly basic pH, conditions affecting neither the biomolecule nor the dye. In solid-phase synthesis (SPS)[1] (*12*), the in situ activation of carboxylic acids provides a more efficient and cheaper way to label compounds (*13*) than preactivation. Using

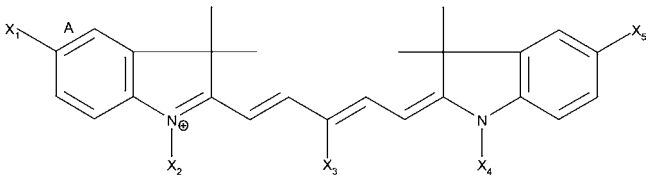
* To whom correspondence should be addressed. Roland Brock, Institute for Cell Biology, University of Tübingen, Auf der Morgenstelle 15, 72076 Tübingen, Germany. Ph.: +49-7071-2977629. Fax: +49-7071-295359. E-mail: roland.brock@uni-tuebingen.de, oliver.mader@uni-tuebingen.de.

[§] Institute for Cell Biology, University of Tübingen.

[†] Institute of Physical and Theoretical Chemistry, University of Tübingen.

[#] FEW Chemicals GmbH.

10.1021/bc034191h CCC: $27.50 © 2004 American Chemical Society
Published on Web 01/21/2004



S0438	S0436	S0430	S0428	S0387
X_1: SO_3^-	X_1: H	A : Aryl	X_1: SO_3^-	X_1: H
X_2: $(CH_2)_6COOH$	X_2: $(CH_2)_4SO_3^-$	X_2: $(CH_2)_4SO_3^-$	X_2: $(CH_2)_5COOH$	X_2: $(CH_2)_4SO_3^-$
X_3: CH_3	X_3: H	X_3: H	X_3: Cl	X_3: H
X_4: $(CH_2)_6COOH$	X_4: $(CH_2)_5COOH$	X_4: $(CH_2)_6COOH$	X_4: $(CH_2)_6COOH$	X_4: $(CH_2)_5COOH$
X_5: SO_3Na	X_5: H	X_5: H	X_5: SO_3Na	X_5: SO_3Na

S0301	S0223	S0694	S0693	Cy5
A : Aryl	X_1: H	X_1: F	X_1: CH_3	X_1: SO_3^-
X_2: $(CH_2)_4SO_3^-$	X_2: CH_3	X_2: $(CH_2)_4SO_3^-$	X_2: $(CH_2)_4SO_3^-$	X_2: CH_2CH_3
X_3: H	X_3: H	X_3: H	X_3: H	X_3: H
X_4: CH_2CH_3	X_4: $(CH_2)_5COOH$	X_4: $(CH_2)_5COOH$	X_4: $(CH_2)_5COOH$	X_4: $(CH_2)_5COOH$
X_5: CH_2COOH	X_5: H + Br^-	X_5: SO_3Na	X_5: SO_3Na	X_5: SO_3Na

Figure 1. Structures of the pentamethine indocyanine dyes investigated in this work.

dye and coupling reagents in excess, complete formation of the labeled products can be achieved. Unreacted dye can be removed easily by washing the solid-phase resin. However, relatively harsh chemical conditions may be encountered during further on-resin labeling of compounds, such as strong acid for the cleavage of these compounds from the resin. Thus, the reactivity of a fluorophore to the conditions encountered in a particular SPS protocol needs to be evaluated in detail.

Compounds based on the indocyanine scaffold are widely used as fluorophores for labeling biomolecules (*14*−*18*). The spectral characteristics of these compounds depend primarily on the length of the polymethine chain linking the two aromatic systems. As a rule-of-thumb, the wavelength of the excitation and emission maxima shifts to the red by 100 nm with every vinylene unit, rendering the $n = 0$ dyes (n is the number of vinylene units in the polymethine chain) compatible with excitation with argon-ion lasers at 488 nm, the $n = 1$ dyes compatible with excitation by helium−neon lasers at 543 nm, and the $n = 3$ dyes compatible with excitation by helium−neon lasers at 633 nm (*19*, *20*). Dyes with $n = 2$ or $n = 3$ have maximum quantum yields (*21*). A major factor reducing the fluorescence quantum yield of the polymethine dyes is the photoinduced trans−cis isomerization of the polymethine chain. This process, which occurs via a twisted excited singlet state (*22*), leads to a nonradiative dissipation of absorbed energy (Figure 2) (*23*).

Efforts to improve the photophysical characteristics of fluorophores based on a number of different scaffolds have identified sulfonic acid groups and halogen atoms as substituents increasing water solubility (*17*) and fluorescence quantum yield and decreasing the dependence of the fluorescence on the chemical environment. The results of these efforts are exemplified by the difluorinated fluorescein derivatives Oregon Green 488 and Oregon Green 514 (*24*). Early analyses of the structure property relationship of substituted polymethine dyes in benzene solution demonstrated a sensitive dependence of the photophysical properties on the substituents on the aryl rings (*25*). Groups with strong −I effects, e.g., trifluoromethyl groups, increase the fluorescence quantum yield compared with the unsubstituted analogues (*25*).

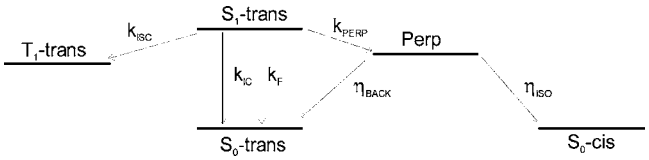


Figure 2. Processes contributing to the dissipation of energy from the excited singlet state. The fluorescence rate constant k_F describes the dissipation by emission of light, k_{ISC} intersystem crossing to the triplet state, k_{IC} internal conversion to the ground state, and k_{PERP} the transition to the partially twisted transition state from where the isomerization or the dissipation to the ground state occurs with efficiencies η_{ISO} and $\eta_{BACK} = 1 - \eta_{ISO}$, respectively.

To assess the effect of substitutions on the photophysical characteristics of pentamethine indocyanines in more detail and to identify new fluorophores for life science applications, a collection of nine pentamethine indocyanine dyes was synthesized and the photophysical properties were determined in aqueous buffers, methanol, and glycerol. Two of these compounds bear a methyl or a chlorine substituent in the polymethine chain to investigate the effect of such substitutions on the tendency to undergo photoinduced trans−cis isomerization.

Absorption, excitation, and emission spectra were recorded and fluorescence lifetimes and quantum yields were measured for each of the new derivatives. Fluorescence correlation spectroscopy (FCS) was employed to assess the suitability of these compounds for single molecule detection. In FCS, information on molecular interactions and molecular concentrations is derived from temporal autocorrelations of time-resolved fluorescence measurements (*26*, *27*). The autocorrelation function responds sensitively to the presence of fluorescent aggregates. Moreover, photophysical transitions into long-lived dark states manifest themselves in the autocorrelation function (*28*). A detailed analysis of the photoinduced trans−cis isomerization of Cy5 by FCS was presented in 2000 (*23*). The compound S0387 had about 70% of the quantum yield of Cy5, had comparable photostability, and did not show any aggregation. For this reason, this compound was further characterized with respect to life science applications. A major histocompatibility complex (MHC) class I binding epitope (SIINFEKL) (*29*, *30*) was labeled with this fluorophore and tested for MHC binding by confocal laser scanning microscopy and flow cytometry. In another experiment, the interaction of an S0387 labeled c-myc peptide (*31*) with a peptide binding antibody was detected by FCS (*32*).

MATERIALS AND METHODS

Synthesis of Fluorophores. *S0387.* (A) 2-(4-Acetanilino-1,3-butadienyl)-3,3-dimethyl-1-(4-sulfobutyl)-indolium inner salt: A mixture of 1-(4-sulfobutyl)-2,3,3-trimethylindolium inner salt (4.75 g, 50 mmol) and malonaldehyde dianil hydrochloride (13.2 g, 51 mmol) in 80 mL of acetic acid anhydride was allowed to react for 1 h at a temperature of 120 °C. After cooling to room temperature, the

[1] Abbreviations: Aca, aminocaproic acid; ACN, acetonitrile; Boc_2O, di-*tert*-butyl dicarbonate; DCM, dichloromethane; Dde, 1-(4,4-dimethyl-2,6-dioxocyclohexylidene)ethyl; DIC, *N*,*N*′-diisopropyl carbodiimide; DIPEA, *N*,*N*′-diisopropylethylamine; DMF, *N*,*N*′-dimethylformamide; DMSO, dimethyl sulfoxide; FCS, fluorescence correlation spectroscopy; Fmoc, 9-fluorenylmethoxycarbonyl; fwhm, full width at half-maximum; HBS, HEPES-buffered saline; HeNe, helium−neon; HEPES, *N*-2-hydroxyethylpiperazine-*N*′-2-ethanesulfonic acid; HOBt, 1-hydroxybenzotriazol; HPLC, high-performance liquid chromatography; MALDI-MS, matrix-assisted laser desorption ionization-mass spectrometry; MeOH, methanol; MHC, major histocompatibility complex; NMR, nuclear magnetic resonance; PBS, phosphate buffered saline; RP, reversed phase; SPPS, solid-phase peptide synthesis; SPS, solid-phase synthesis; tBuOH, *tert*-butyl alcohol; TFA, trifluoroacetic acid; TIS, triisopropylsilane.

reaction mixture was diluted with 300 mL of ethyl acetate. The crude solid was boiled with acetonitrile. Yield: 19.4 g.

(B) 1-(5-Carboxypentyl)-2,3,3-trimethyl-indolium-5-sulfonate: The sodium salt of 2,3,3-trimethyl-indoleninium-5-sulfonate (2.61 g, 10 mmol) and 6-bromohexanoic acid (2.1 g, 11 mmol) were mixed and heated at 110 °C for 2 h with constant stirring. The reaction mixture was cooled to room temperature, and the residue was boiled with acetone until a powder was obtained. Yield: 2.58 g.

^{1}H NMR (DMSO-d_6): δ (ppm) 7.94 (s, 1H, arom. CH), 7.65 (dd, 1H, arom. CH), 7.46 (d, 1H, arom. CH), 4.43 (t, 2H, NCH_2), 2.83 (s, 3H, CH_3), 2.21 (t, 2H, CH_2), 1.84 (b, 2H, CH_2), 1.54(s, 3H, CH_3), 1.32−1.61 (b, 4H, CH_2)

(C) 2-[5-[1-(5-Carboxypentyl)-1,3-dihydro-3,3-dimethyl-5-sulfo-2H-indol-2-ylidene]-penta-1,3-dienyl]-3,3-dimethyl-1-(4-sulfobutyl)-3H-indolium inner salt, sodium salt: Compound A (2.33 g, 5 mmol) and compound B (1.77 g, 5 mmol) were dissolved in 20 mL of ethanol. After sodium acetate (0.82 g, 10 mmol) was added to the sample, the mixture was heated for 20 min to reflux. The solution was cooled to 5−8 °C, and the crude product was collected by filtration and washed with ethyl acetate. After air-drying the crude dye was chromatographed on silica gel (Kieselgel 60, Merck, Darmstadt, Germany) using a methanol/chloroform (4:9, v/v) mixture as eluent. Yield: 0.81 g, λ_{max} (methanol): 646 nm, ϵ = 187 000 M^{-1} cm^{-1}.

^{1}H NMR (DMSO-d_6): δ (ppm) 8.35 (m, 2H, CH), 7.81 (d, 1H, arom. CH), 7.64 (d, 2H, arom. CH), 7.48(m, 1H, arom. CH), 7.30 (m, 2H, arom. CH), 6.62 (t, 1H, CH), 6.36 (q, 2H, CH), 4.08 (b, 4H, NCH_2), 2.55 (b, CH_2), 2.14 (t, 2H, CH_2), 1.75 (b, CH_2), 1.69 (s, 12H, CH_3), 1.55 (b, CH_2), 1.37 (b, CH_2), HPLC: 97.3%.

S0693. (D) 2,3,3,5-Tetramethyl-1-(4-sulfobutyl)-indolium hydroxide inner salt: 2,3,3,5-tetramethylindolenine (8.65 g, 0.05 mol) and 1,4-butanesulfone (9.0 g, 0,06 mol) were mixed and heated to 120 °C for 2 h. The reaction mixture was cooled and triturated with acetone until a purple colored powder was obtained. Yield: 8.1 g.

^{1}H NMR (DMSO-d_6): δ (ppm) 7.91 (d, 1H, arom. CH), 7.66 (s, 1H, arom. CH), 7.43 (d, 1H, arom. CH), 4.76 (t, 2H, NCH_2), 2.83 (s, 3H, CH_3), 2.54 (m, 2H, CH_2), 2.45 (s, 3H, CH_3), 1.98 (m, 2H, CH_2), 1.73 (m, 2H, CH_2), 1.52 (s, 6H, CH_3).

(E) 2-(4-Acetanilino-1,3-butadienyl)-3,3,5-trimethyl-1-(4-sulfobutyl)-indolium inner salt: This compound was prepared by reacting compound D with malonaldehyde dianil hydrochloride following the procedure for compound A. Yield: 15.7 g.

(F) 2-[5-[1-(5-Carboxypentyl)-1,3-dihydro-3,3-dimethyl-5-sulfo-2H-indol-2-ylidene]-penta-1,3-dienyl]-3,3,5-trimethyl-1-(4-sulfobutyl)-3H-indolium inner salt, sodium salt: This dye was prepared by condensing intermediates E and B following the procedure for compound C. Yield: 0.58 g, λ_{max} (methanol): 651 nm, ϵ = 163000 M^{-1} cm^{-1}.

^{1}H NMR (DMSO-d_6): δ (ppm) 8.33 (m, 2H, CH), 7.80 (d, 1H, arom. CH), 7.63 (d, 1H, arom. CH), 7.48 (m, 1H, arom. CH), 7.39 (d, 1H, arom. CH), 7.26 (m, 2H, arom. CH), 6.59 (t, 1H, CH), 6.43 (d, 1H, CH), 6.24 (d, 1H, CH), 4.10 (b, 4H, NCH_2), 2.60 (b, CH_2), 2.39 (s, 3H, CH_3), 2.22 (t, 2H, CH_2), 1.76 (b, CH_2), 1.69 (s, 12H, CH_3), 1.56 (b, CH_2), 1.39 (b, CH_2), HPLC: 95.8%.

S0694. (G) 5-Fluoro-2,3,3,-trimethyl-1-(4-sulfobutyl)-indolium hydroxide inner salt: The compound was prepared following the procedure for compound D. Yield: 13.7 g.

^{1}H NMR (DMSO-d_6): δ (ppm) 8.23 (q, 1H, arom. CH), 7.86 (d, 1H, arom. CH), 7.50 (t, 1H, arom. CH), 4.51 (t, 2H, NCH_2), 2.86 (s, 3H, CH_3), 2.54 (m, 2H, CH_2), 1.99 (m, 2H, CH_2), 1.76 (m, 2H, CH_2), 1.56 (s, 6H, CH_3).

(H) 2-(4-Acetanilino-1,3-butadienyl)-5-fluoro-3,3,-dimethyl-1-(4-sulfobutyl)-indolium inner salt: This compound was prepared by reacting compound G with malonaldehyde dianil hydrochloride following the procedure for compound A. Yield: 16.1 g.

(I) 2-[5-[1-(5-Carboxypentyl)-1,3-dihydro-3,3-dimethyl-5-sulfo-2H-indol-2-ylidene]-penta-1,3-dienyl]-5-fluoro-3,3-dimethyl-1-(4-sulfobutyl)-3H-indolium inner salt, sodium salt: This dye was prepared by condensing intermediates H and B following the procedure for compound C. Yield: 0.41 g, λ_{max} (methanol): 646 nm, ϵ = 140 000 M^{-1} cm^{-1}.

^{1}H NMR (DMSO-d_6): δ (ppm) 8.34 (m, 2H, CH), 7.81 (d, 1H, arom. CH), 7.68 (m, 2H, arom. CH), 7.49 (m, 1H, arom. CH), 7.29 (m, 2H, arom. CH), 6.60 (t, 1H, CH), 6.36 (q, 2H, CH), 4.14 (b, 4H, NCH_2), 2.58 (b, CH_2), 2.07 (t, 2H, CH_2), 1.78 (b, CH_2), 1.71 (s, 12H, CH_3), 1.56 (b, CH_2), 1.35 (b, CH_2), HPLC: 88.1%.

S0436. (J) 2-[5-[1-Carboxypentyl-1,3-dihydro-3,3-dimethyl-2H-indol-2-ylidene]-penta-1,3-dienyl]-3,3-dimethyl-1-(4-sulfobutyl)-3H-indolium hydroxide inner salt: The dye was prepared according to the synthesis of compound C by the reaction of 1-(5-carboxypentyl)-2,3,3-trimethyl-indoleninium bromide with compound A; λ_{max} (methanol): 643 nm, ϵ = 160 000 M^{-1} cm^{-1}.

^{1}H NMR (DMSO-d_6): δ (ppm) 8.35 (m, 2H, CH), 7.63 (d, 2H, arom. CH), 7.39 (m, 4H, arom. CH), 7.23 (m, 2H, arom. CH), 6.60 (t, 1H, CH), 6.33 (q, 2H, CH), 4.09 (b, 4H, NCH_2), 2.57 (b, CH_2), 2.05 (t, 2H, CH_2), 1.76 (b, CH_2), 1.67 (s, 12H, CH_3), 1.52 (b, CH_2), 1.38 (b, CH_2), HPLC: 98.2%.

S0430. (K) 3-Carboxypentyl-2-[5-(1,3-dihydro-3,3-dimethyl-1-(4-sulfobutyl)-2H-indol-2-ylidene)-penta-1,3-dienyl]-1,1-dimethyl-1H-benzo[*e*]indolium hydroxide inner salt: The dye was prepared according to the synthesis of compound C by the reaction of 1-(5-carboxypentyl)-2,3,3-trimethyl-indoleninium bromide with 2-(4-acetanilino-1,3-butadienyl)-1,1-dimethyl-3-(4-sulfobutyl)-H-benzo[*e*]indolium hydroxide inner salt, λ_{max} (methanol): 663 nm, ϵ = 162 000 M^{-1} cm^{-1}.

^{1}H NMR (DMSO-d_6): δ (ppm) 8.43 (t, 1H, arom. CH), 8.33 (t, 1H, arom. CH), 8.22 (d, 1H, arom. CH), 8.05 (dd, 2H, CH), 7.78 (d, 1H, arom. CH), 7.67 (t, 1H, arom. CH), 7.58 (d, 1H, arom. CH), 7.49 (t, 1H, arom. CH), 7.35 (m, 2H, arom. CH), 7.19 (m, 1H, arom. CH), 6.61 (t, 1H, CH), 6.45 (d, 1H, CH), 6.24 (d, 1H, CH), 4.25 (b, 2H, NCH_2), 4.05 (b, 2H, NCH_2), 2.57 (b, CH_2), 2.04 (t, 2H, CH_2), 1.91 (s, 3H, CH_3), 1.81 (b, CH_2), 1.67 (s, 12H, CH_3), 1.55 (b, CH_2), 1.35 (b, CH_2), 1.27 (b, CH_2), HPLC: 95.8%.

S0223. (L) 2-[5-[1-(5-Carboxypentyl)-1,3-dihydro-3,3-dimethyl-2H-indol-2-ylidene]-penta-1,3-dienyl]-1,3,3-trimethyl-3H-indolium bromide: The dye was prepared according to the synthesis of compound C by the reaction of 1-(5-carboxypentyl)-2,3,3-trimethyl-indoleninium bromide with 2-(4-acetanilino-1,3-butadienyl)-1,3,3-trimethyl-indolium bromide; λ_{max} (methanol): 640 nm, ϵ = 184 000 M^{-1} cm^{-1}.

^{1}H NMR (DMSO-d_6): δ (ppm) 8.09 (t, 2H, CH), 7.50−7.00 (b, 8H, arom. CH), 6.85 (t, 1H, CH), 6.36 (d, 2H, CH), 6.30 (d, 1H, CH), 4.06 (t, 2H, NCH_2), 3.68 (s, 3H, CH_3), 2.41 (t, 2H, CH_2), 2.08 (t, 2H, CH_2), 1.73 (s, 12H, CH_3), 1.35 (b, CH_2), HPLC: 95.3%.

The symmetrical dyes S0438 and S0428 were prepared following the procedures described in earlier publications (*33*, *34*). The unsymmetrical dye S0301 was synthesized using a procedure described in the literature (*35*). The purity of all dyes was confirmed using a Merck-Hitachi analytical high performance liquid chromatography

Table 1. Photophysical Characteristics of Pentamethine Indocyanine Derivatives[a]

	$\lambda_{max\ abs}$ [nm] in MeOH	$\lambda_{max\ em}$ [nm] in MeOH	ϵ ($\lambda_{max\ abs}$) [$M^{-1}\ cm^{-1}$] in MeOH	[ns] τ_F in PBS	Φ_F in PBS	k_F [$10^9\ s^{-1}$]	k_{NR} [$10^9\ s^{-1}$]	[ns] τ_R in PBS	r in PBS
Cy5	648	670	250000[b]	1.00[d]	0.27[c]	0.27	0.73	0.58	0.14
	649[b]	670[b]							
S0693	651	675	163000	0.45	0.10	0.22	2.00	0.62	0.22
S0694	646	668	140000	0.60	0.14	0.23	1.43	0.54	0.18
S0223	640	665	184000	0.56	0.12	0.21	1.57	0.37	0.15
S0301	666	692	203000	0.50	0.08	0.16	1.84	0.56	0.20
S0387	646	669	187000	0.70	0.18	0.26	1.17	0.47	0.15
S0428	653	669	240000	0.50	0.12	0.24	1.76	0.56	0.20
S0430	663	688	162000	0.50	0.08	0.16	1.84	0.50	0.19
S0436	643	667	160000	0.67	0.15	0.22	1.27	0.39	0.14
S0438	647	665	270000	0.46	0.11	0.24	1.94	0.57	0.21

[a] The molar extinction coefficients were determined for fluorophores dissolved in methanol at a concentration of 10 mg/L. The fluorescence lifetime τ_F, the fluorescence quantum yield Φ_F, the rate constant of fluorescence k_F, the nonradiative rate constant k_{NR}, as well as the anisotropy r and the rotational correlation time τ_R were determined as described in the materials and methods section. [b] Values were adopted from ref *17*. [c] Value in PBS was obtained from Amersham Bioscience. [d] Agrees very well with reported lifetime of Cy5 (1.0 ns) (*45*).

(HPLC) unit, equipped with a Purospher RP18e column (Agilent, Waldbronn, Germany) with acetonitrile/water (1:1, v/v) as eluent.

Peptide Synthesis. The SIINFEKL (MHC class I epitope) and EQKLISEEDL (myc-tag) peptides were synthesized using solid-phase Fmoc-chemistry on an automated peptide synthesizer for multiple peptide synthesis (RSP5032, Tecan, Hombrechtlikon, Switzerland). Fmoc-protected amino acids were purchased from Novabiochem (Läufelfingen, Switzerland). Standard chemicals for peptide chemistry were obtained from Fluka (Deisenhofen, Germany) and Merck (Darmstadt, Germany), solvents were p. a. grade. The SIINFEKL peptide was synthesized on Fmoc-Leu preloaded 2-chloro trityl resin (capacity 0.5 mmol/g; Senn Chemicals, Dielsdorf, Switzerland) using Fmoc-Lys(Dde)-OH as an orthogonally deprotectable building block. To protect the N-terminus from the reaction with dye, the resin bound peptide SIINFEK(Dde)L (15 μmol) was reacted with Boc_2O (39.3 mg, 180 μmol) and DIPEA (31 μL, 180 μmol) in DMF for 32 h. The Dde protecting group at the ϵ-amino group of lysine was cleaved off using 2% hydrazine hydrate in DMF (3 × 5 min). S0387 was covalently attached to the deprotected ϵ-amino group using 5 equiv of DIC (11.7 μL, 75 μmol), 5 equiv of HOBt (11.5 mg, 75 μmol) and 1.5 equiv of S0387 (15.9 mg, 22,5 μmol) in DMF twice for 16 h. The peptide was cleaved off the resin by treatment with 92.5% TFA, 2.5% TIS, 2.5% ethanedithiol, and 2.5% H_2O twice for 2 h, each. The crude peptide was precipitated by adding cold diethyl ether (−20 °C). Finally, the peptide was dissolved in tBuOH/H_2O 4:1 and lyophilized.

The c-myc peptide Aca-EQKLISEEDL-Aca-K−NH_2 was synthesized on Rink amide resin (Rapp Polymere, Tübingen, Germany). The dye S0387 was attached to the N-terminus. Coupling conditions as well as cleavage off the resin were performed as described for the SIINFEKL peptide.

The identity and purity of the peptides was determined using Maldi-TOF-MS (G2025A, Hewlett-Packard, Waldbronn, Germany) and by analytical RP-HPLC using a H_2O (0.1% TFA, solvent A)/ACN (0.1% TFA, solvent B) gradient on a Waters 600 System (Eschborn, Germany) with detection at 214 nm. The samples were analyzed on an analytical column (Nucleosil 100, 250 × 2 mm, C18 column, 5 μm particle diameter; Grom, Herrenberg, Germany), using a linear gradient from 10% B to 100% B within 30 min (flow rate: 0.3 mL/min). The calculated masses were 1631.1 and 2222.1 Da, experimental masses 1631.8 and 2222.8 Da [M+H^+] for SIINFEK(S0387)L and S0387-Aca-EQKLISEEDL-Aca-K-NH_2 respectively. The respective purities were >63 and >66%. The peptides were purified using preparative RP-HPLC (Nucleosil 300 C18 column, 10 μm particle diameter, 250 × 20 mm; Grom, Herrenberg, Germany) using H_2O (0.1% TFA)/ACN (0.1% TFA) gradient on a Waters 600 Multisolvent Delivery System (HPLC: >98%).

Photophysical Characterization. Fluorescence spectra were recorded on an LS50B (Perkin-Elmer, Rodgau-Jügesheim, Germany) and a SPEX Fluorolog 222 spectrofluorometer (Jobin Yvon Horiba, Edison, NJ). The spectra were corrected for the sensitivity of the detection system. Absorption spectra were measured with an Ultrospec 2000 (Pharmacia Biotech, Cambridge, UK).

Fluorescence lifetimes were measured on a SPEX Fluorolog 112 fluorometer. Fluorescence was excited by a stabilized HAMAMATSU C4725 diode laser, which provides pulse widths (full width at half-maximum, fwhm) of 64 ps at the excitation wavelength 653 nm. Fluorescence was detected with an R928 photomultiplier tube (Hamamatsu Photonics, Shizuoka, Japan). The resulting signals were fed into an ORTEC 457 time-to-amplitude converter via an ORTEC 454 timing filter amplifier and an ORTEC 937 picosecond timing discriminator (AMETEK, Meerbusch, Germany). The fwhm of the resulting instrument response was Δt = 600 ps. Fluorescence decay times were obtained by fitting the decay curves to single exponential decays. Fitting to sums of exponentials did not improve the quality of the fits.

The quantum yields Φ_{sample} of the dyes in PBS were determined using eq 1

$$\Phi_{sample} = \Phi_{reference} \frac{I_{sample}}{I_{reference}} \frac{[1 - 10^{-E_{reference}}]}{[1 - 10^{-E_{sample}}]} K \quad (1)$$

where E_{sample} and E_{ref} are the absorbencies of sample and reference, respectively. I_{sample} and I_{ref} are the integral fluorescence intensities. K is a correction factor accounting for the difference in the steady-state fluorescence anisotropies of sample and reference, r_{sample} and r_{ref}, respectively (Table 1). K is given by eq 2, where G is the ratio of the sensitivities of the detection system for vertically and horizontally polarized light, $G = S_v/S_h$. A is the ratio of the quantum fluxes of horizontally and vertically polarized components in the exciting light, $A = I_{exc,h}/I_{exc,v}$.

$$K = \frac{r_{\text{ref}}\left[\frac{3G}{1+A} - (G+1)\right] + (G+1)}{r_{\text{sample}}\left[\frac{3G}{1+A} - (G+1)\right] + (G+1)} \qquad (2)$$

Cy5 in PBS served as the reference with $\Phi_{\text{reference}} = 0.27$ (Amersham Bioscience Europe, Freiburg, Germany). Measurements were performed at room temperature (20 °C) under magic angle conditions (polarizer vertical, analyzer at 54.7° from vertical), i.e., $A \approx 0$ and $G = 2G'$, where $G' = 0.30$ is the value obtained without polarizer in the detection system.

Relative photostabilities were determined by irradiating 10 nM dye solutions in closed capillary tubes using the 633 nm HeNe Laser of a ConfoCor2 fluorescence correlation microscope (Carl Zeiss, Jena, Germany). The fluorescence quantum yields of Cy5 and S0387 in glycerol were measured immediately after preparation of the solutions, because both absorbance and fluorescence intensity of the solutions decreased quickly, even in the dark.

Fluorescence Correlation Spectroscopy. FCS measurements were carried out on a ConfoCor2. For excitation, the light of a 633 nm HeNe-laser was reflected into the sample via an HFT633 main beam-splitter, and fluorescence was detected using an LP650 emission filter. The dyes were dissolved in methanol to a concentration of 300 μM and further diluted to working concentrations of 10 nM either in methanol or PBS, pH 7.4. Twenty autocorrelation functions were recorded over 10 s each. The prebleach time was set to zero to include initial photobleaching in the count-trace and the laser power was 84 kW/cm^2. Autocorrelation functions not affected by initial photobleaching were fitted from autocorrelation times of 1 μs to 3.4 s with an algorithm describing one diffusing molecule (*28*) using the ConfoCor2 software (eq 3).

$$G(\tau) = 1 + \frac{1}{N_{\text{App}}} \cdot \frac{1 - T + Te^{-\tau/\tau_{tr}}}{(1-T)} \cdot \frac{1}{\left(1 + \frac{\tau}{\tau_{\text{D}}}\right)\sqrt{1 + \left(\frac{\omega_{xy}}{\omega_z}\right)^2 \frac{\tau}{\tau_{\text{D}}}}} \qquad (3)$$

N_{App} is the apparent number of molecules affected by scattered light, τ_{D} is the diffusional autocorrelation time, and ω_{xy} and ω_z are the radii of the detection volume in the optical plane and along the optical axis, respectively (defined by the isocontour of e^{-2} detection efficiency relative to the center of the confocal detection volume). T denotes the equilibrium molar fraction of fluorophores in a transient nonfluorescent ("dark") state (assumed, to a first approximation, equal for bound and unbound dye-labeled peptide (see below)) and τ_{T} is the triplet lifetime of the dark state. In this work, T and τ_T account for the sum of all intramolecular deactivation processes which lead to a dark state.

Peptide antibody interactions were measured with 8.5 nM c-myc peptide (S0387-Aca-EQKLISSEDL-Aca-K-NH_2) and 260 nM of the monoclonal anti-c-myc antibody (clone 9E10, Dianova, Hamburg, Germany) in HBS using 384-well glass bottom microplates (MMI, Glattburg, Switzerland). To prevent unspecific binding of peptide and antibody, before use every well was blocked with 1% BSA (Sigma, Taufkirchen, Germany) in HBS for 12 h on ice followed by washing with HBS containing 0.2% BSA. The concentration of the antibody was derived from information provided by the supplier. The FCS data obtained for peptide antibody interactions were fitted with an algorithm describing independent species of freely diffusing molecules, assuming that all fluorescent molecules have the same fluorescence efficiency (eq 4).

$$G(\tau) = 1 + \frac{1}{N_{\text{App}}} \cdot \frac{1 - T + Te^{-\tau/\tau_{tr}}}{(1-T)} \cdot \left(\sum_j Y_j \frac{1}{\left(1 + \frac{\tau}{\tau_{\text{D},j}}\right)\sqrt{1 + \left(\frac{\omega_{xy}}{\omega_z}\right)^2 \frac{\tau}{\tau_{\text{D},j}}}} \right) \qquad (4)$$

Y_j is the contribution of the jth fluorescent molecule and $\tau_{D,j}$ is the respective diffusional autocorrelation time.

MHC Peptide Binding. Murine RMA-S cells expressing the H-2k^b MHC class I molecule (obtained from S. Stevanović) (*36*) were grown in a 5% CO_2 humidified atmosphere at 37 °C in RPMI 1640 medium (PAN Biotech, Aidenbach, Germany), supplemented with 10% fetal calf serum (PAN Biotech), 100 U/mL penicillin, and 0.1 mg/mL streptomycin (Biochrom, Berlin, Germany). Cells were passaged every third to fourth day by a 1:5 dilution with fresh medium.

To determine peptide binding to MHC class I molecules, cells were seeded at a density of 40 000 per well in 96-well plates (Nunc, Wiesbaden, Germany) and kept 16 h at room temperature (25 °C) in RPMI 1640 medium containing fetal calf serum to allow the accumulation of peptide free MHC class I molecules on the plasma membrane (*37*, *38*). Cells were then incubated for 1 h with the S0387-labeled SIINFEKL peptide (SIINFEK-(S0387)L) at concentrations of 1 and 10 nM and, alternatively, with a mixture of the labeled peptide and a 100-fold excess of unlabeled peptide in serum free RPMI medium. Cells were washed four times with PBS followed by confocal laser scanning microscopy and flow cytometry. Confocal fluorescence images were recorded on an inverted LSM510 laser scanning microscope (Carl Zeiss, Göttingen, Germany). S0387 was excited with a helium−neon laser at 633 nm and fluorescence detected with an LP650 long-pass filter. Flow cytometry was performed on a FACSCalibur flow cytometer (Becton Dickinson, Heidelberg, Germany) using a 633 nm HeNe-laser for excitation. Vital cells were gated based on forward light and side scatter. Cells, not incubated with any peptide, were used to set the sensitivity of the fluorescence detector to the appropriate level (histogram peak in the first decade of the 4 decade log scale).

RESULTS AND DISCUSSION

Synthesis and General Characterization. The synthesis of the substituted pentamethine indocyanines (Figure 1) followed published protocols with modifications. A quaternary indolium salt having an acidic methyl group was reacted with malonaldehyde dianil hydrochloride followed by condensation of the intermediate with a second indolium salt under basic conditions in ethanol. Two of the compounds were symmetrical (S0428 and S0438), while the remaining dyes were unsymmetrical with respect to the substituents of the indolenine groups. For the asymmetric indocyanines, the second step resulted in the formation of a mixture of the symmetric indocyanine and the desired product which was purified by column chromatography on silica gel. The purity of all compounds was confirmed by analytical HPLC, and

the structures of the dyes were verified using ^{1}H NMR spectroscopy. Except for S0694 (purity, 88%), the purity of all other compounds exceeded 95%. All compounds except S0223 were readily soluble in methanol and no precipitation occurred upon dilution of the methanol stock solutions into water or PBS.

To render these compounds compatible with the labeling of biomolecules, each derivative contained at least one carboxyl group for covalent attachment to primary amines. All compounds except S0223 were substituted with at least one sulfonic acid group to increase water solubility. The compounds S0387, S0436, S0693, and S0694 were synthesized to assess the dependence of the photophysical characteristics on substitutions of the aromatic system with substituents of the auxochromic series. Compounds S0428 and S0438 were prepared to address the effect of substitutions at the meso-position of the pentamethine chain on isomerization. Rotation around one of the bonds of the pentamethine chain is known as an effective mechanism of radiationless loss of excitation energy of the pentamethine compounds. With S0301 and S0430 the effect of extensions of the aromatic systems were investigated.

Photophysical Characteristics. *Absorption, Excitation, and Emission Spectra.* The absorption maxima of the dyes were in a range of 640−666 nm around the absorption maximum of Cy5 at 648 nm (Table 1). Replacement of both sulfonic acid groups on the aryl rings by hydrogen atoms (S0436) led to a hypsochromic shift of 5−8 nm compared to Cy5. Substitution of only one sulfonic acid group by hydrogen (S0387) or fluorine (S0694) caused a weak hypsochromic shift by 2 nm, while substitution by a methyl group (S0693) led to a small bathochromic shift by 3 nm. Introduction of a methyl group at the X_3 position in the polymethine chain (S0438) caused a slight hypsochromic shift, while a significant bathochromic shift was observed for a chlorine substituent (S0428). The extension of the aromatic system shifted the absorption and emission maxima to the red by about 15 nm (S0301 and S0430). The Stokes shifts of all compounds were in the range between 16 and 26 nm, the smallest values being obtained for the dyes that carry a substituent in the X_3 position.

Fluorescence Quantum Yields and Lifetimes. After excitation of the indocyanine dyes to the excited singlet state, deactivation by fluorescence competes with nonradiative dissipation of energy (Figure 2). Internal conversion to the ground state with the rate constant k_{IC}, intersystem crossing to the triplet state (with rate constant k_{ISC}), and transition into a partially twisted transition state with rate constant k_{PERP} (*39*) from where trans−cis isomerization occurs are possible mechanisms for nonradiative deactivation (*23*, *40*) that occurs with the rate constant k_{NR} (eq 5). k_{ISC} is negligible in carbocyanines without heavy atoms ($\Phi_{ISC} < 10^{-3}$) (*40*, *41*).

$$k_{NR} = k_{IC} + k_{PERP} + k_{ISC} \quad (5)$$

The dyes with extended aromatic systems (S0301 and S0430) had the lowest fluorescence quantum yields ($\Phi_F = 0.08$), and S0387 and Cy5 had the highest ones with $\Phi_F = 0.18$ and $\Phi_F = 0.27$, respectively (Table 1). The latter two compounds also had the longest fluorescence lifetimes τ_F of 0.70 and 1.0 ns.

To get a deeper insight into the relationship of structure and photophysics of the dyes, the radiative rate constants k_F and the rate constants of nonradiative deactivation k_{NR} were calculated from the fluorescence quantum yields Φ_F and the fluorescence lifetimes τ_F according to eqs 6 and 7, respectively (Table 1).

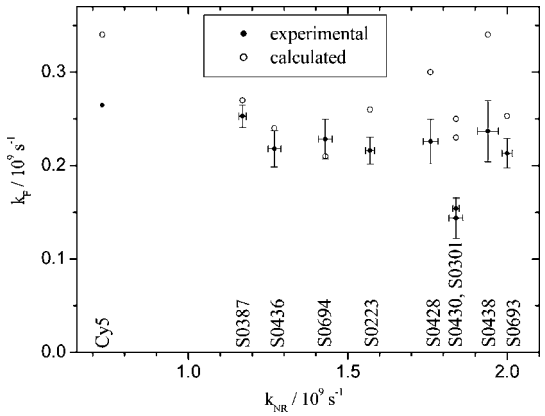


Figure 3. Radiative and nonradiative rate constants for the cyanine dyes in PBS. Experimental values were obtained from fluorescence quantum yields and lifetimes (Table 1) using eqs 6 and 7. Calculated values were obtained from absorption spectra using the Strickler−Berg equation (eq 8).

$$k_F = \frac{\Phi_F}{\tau_F} \quad (6)$$

$$k_{NR} = \frac{1 - \Phi_F}{\tau_F} \quad (7)$$

A plot of k_F vs k_{NR} revealed that the differences in fluorescence quantum yields and decay times between the dyes were mainly due to the variations in k_{NR}, while k_F varied only very little (Figure 3). The values of k_{NR} span a range between 0.73×10^9 and 2.0×10^9 s^{-1}, with Cy5 showing the lowest nonradiative rate constant of all dyes followed by S0387.

To identify the specific nonradiative process leading to this variation in k_{NR}, the effect of solvent viscosity on fluorescence quantum yields and lifetimes of Cy5 and S0387 was investigated. The increase of the viscosity from 1 cPoise in PBS to 1340 cPoise in glycerol should strongly reduce k_{PERP}, the rate constant of photoinduced twisting about the bonds in the polymethine chain (*42*, *43*). In glycerol, the fluorescence quantum yields increased to $\Phi_F = 0.60$ and $\Phi_F = 0.59$ for Cy5 and S0387, respectively. For the fluorescence lifetimes $\tau_F = 1.93$ ns and $\tau_F = 1.90$ ns were obtained. While the radiative rate constants increased less than 20% with respect to the values obtained in PBS (Table 1), the nonradiative rate constants decreased by more than 70% to $k_{NR} = 0.21 \times 10^9$ s^{-1} and $k_{NR} = 0.22 \times 10^9$ s^{-1} for Cy5 and S0387, respectively. From the almost identical values of k_{NR} for both dyes in glycerol, we concluded that the difference in k_{NR} of Cy5 and S0387 in PBS was mainly due to the different rates k_{PERP} of bond twisting in the excited state. Assuming that k_{PERP} in glycerol is negligible for both dyes, values of $k_{PERP} = 5.3 \times 10^8$ s^{-1} and $k_{PERP} = 9.6 \times 10^8$ s^{-1} were calculated for Cy5 and S0387 in PBS, respectively.

This result has important consequences for the application of these dyes. In environments of high viscosity, as they are encountered for fluorophores conjugated to proteins, the differences between the photophysical properties of Cy5 and S0387 are negligible.

In summary, our results provide information on the effect of substitution pattern on k_{NR} for three types of substitutions: (i) k_{NR} increases in the series Cy5 < S0387 < S0436 < S0694 < S0693. Obviously, k_{NR} increases with the position of X_1- and X_5-substituents in the auxochromic

series along $-SO_3^- < -H < -F < -CH_3$. This finding agrees with the results obtained on indocarbocyanine derivatives by Murphy and Schuster (*25*), who found decreasing k_{PERP} values with increasing -M-effect of the terminal substituents as quantified by their Hammett parameters. Originally sulfonic acid groups were introduced into cyanine dyes to increase the water solubility of these compounds (*17*). Our results show that in addition to increasing the solubility these substituents also improve the fluorescent properties by decreasing k_{NR}. (ii) Extension of the aromatic system by annellation of benzene rings increases the nonradiative rate constants. (iii) Introduction of substituents into the polymethine chain at the X_3 position (S0428, S0438) resulted in relatively high nonradiative rate constants of $k_{NR} \geq 1.76 \times 10^9\ s^{-1}$, independent of the auxochromic effect of the substituent. This increase in k_{NR} is propably caused by the enhancement of bond torsion due to steric crowding as described by Khimenko et al. (*40*).

The radiative rate constants k_F of most of the dyes were in the relatively small range between $0.21 \times 10^9\ s^{-1}$ and $0.27 \times 10^9\ s^{-1}$ (Figure 3). Only for the aryl substituted dyes S0430 and S0301 significantly smaller values of $k_F = 0.16 \times 10^9\ s^{-1}$ were obtained. To elucidate the reasons for this anomaly, the radiative rate constants k_F (calc) were calculated from the absorption spectra using the Strickler−Berg relationship (eq 8) and compared with the experimental values.

$$k_F\,(\text{calc}) = 2.8825 \times 10^{-9} \text{cm}^2\ \text{s}^{-1}\text{mol}^{-1} \cdot n^2 \cdot \langle \tilde{\nu}_F^{-3} \rangle^{-1} \cdot \int \epsilon(\tilde{\nu}) d\ln\tilde{\nu} \quad (8)$$

where n is the refractive index of the solution, $\tilde{\nu}_F$ is a wavenumber of the fluorescence spectrum, and $\epsilon(\tilde{\nu})$ is the extinction coefficient.

For most compounds the Strickler−Berg equation resulted in radiative rate constants larger than those determined experimentally. For S0387, S0436, and S0694, the deviation was close to or within the margin of error. For S0223 and S0693, the deviation was less than 20%. Significantly larger deviations were found for the dyes with extended aromatic systems (S0301 and S0430), with substituents in the polymethine chain (S0428 and S0438) and for Cy5. The k_F values calculated for S0301 and S0430 were in the range of most of the other compounds, whereas the values calculated for S0428 and S0438 exceeded those of all other compounds, due to the large extinction coefficients of the X_3-substituted dyes.

The most likely explanation for the discrepancies between calculated and experimental k_F values are fast conformational changes upon excitation of the dyes, which are not accounted for by eq 8. However, although care was taken to avoid any aggregation and adsorption effects in the determination of the fluorescence quantum yields, the presence of nonfluorescent aggregates as another possible reason for this discrepancy cannot be excluded completely. The large difference between the experimental and calculated rate constants of fluorescence observed for Cy5 may be due to a too large extinction coefficient provided by the supplier.

Rotational Diffusion. The rotational correlation times τ_R were calculated from the fluorescence lifetime τ_F and the steady-state anisotropy r according to eq 9.

$$\tau_R = \frac{\tau_F}{\frac{r_0}{r} - 1} \quad (9)$$

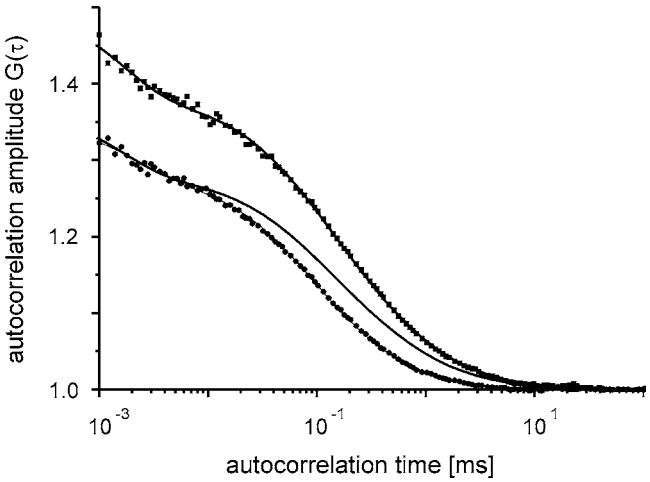


Figure 4. Autocorrelation functions and fits for an S0387 labeled c-myc peptide in the absence (bottom curve, fit for one diffusing species) and presence of an anti-myc-tag antibody (top curve, fit for two diffusing species). Center curve: Fit to the autocorrelation function in the presence of antibody, normalized to the amplitude of the autocorrelation function in the absence in order to better illustrate the shift of the diffusional autocorrelation time. The laser power was 84 kW/cm^2.

where the value observed in glycerol, $r = 0.38$, was inserted for the limiting anisotropy, r_0. The values of τ_R for the free dyes in PBS were in a narrow range of 0.37 ns for S0223 and 0.61 ns for Cy5. They were mainly determined by the hydrodynamic volume of the substituents in the X_1 and X_5 positions.

Applications in FCS, Fluorescence Microscopy, and Flow Cytometry. *Fluorescence Correlation Spectroscopy.* To determine the suitability of the dyes for single molecule detection, fluorescence correlation spectroscopy was applied to fluorophores dissolved in methanol and diluted with PBS. For S0223, aggregates interfered with the acquisition of autocorrelation functions. For all other dyes the autocorrelations could be fitted with a function containing one diffusion term and one exponential term, the latter accounting for the formation of nonfluorescent states by all intramolecular deactivation processes, e.g., intersystem crossing (data not shown). Due to the limited temporal resolution of our instrument, no detailed analysis of this fast process was possible as presented by Widengren and Schwille (*23*). Autocorrelation functions with low noise were obtained for Cy5, S0693, S0694, S0387, S0428, and S0438. In contrast, for S0301, S0430, and S0436 the acquisition of the autocorrelation functions was complicated by the low molecular brightness. An important requirement for the application of fluorescent dyes in fluorescence microscopy and FCS is a high photostability. Therefore, the photostability of S0387 was compared to the photostability of Cy5. Aqueous solutions of both dyes in glass capillaries were illuminated with a focused HeNe laser at 633 nm and fluorescence was recorded over time (data not shown). Both dyes had comparable photostabilities.

Due to its favorable photophysical properties, S0387 was further characterized as a reporter group in biochemical and cellular applications. First S0387 was used in the detection of molecular interactions in vitro by FCS measurements of an S0387 labeled c-myc peptide (S0387-Aca-EQKLISEEDL-Aca-K-NH_2) incubated with an anti-c-myc antibody (Figure 4). From the autocorrelation curve of S0387 and c-myc-S0387 a diffusion coefficient of $1.3 \times 10^{-6}\ cm^2\ s^{-1}$ was calculated for the dye-labeled peptide, assuming a diffusion coefficient of $2.5 \times 10^{-6}\ cm^2\ s^{-1}$ (*44*)

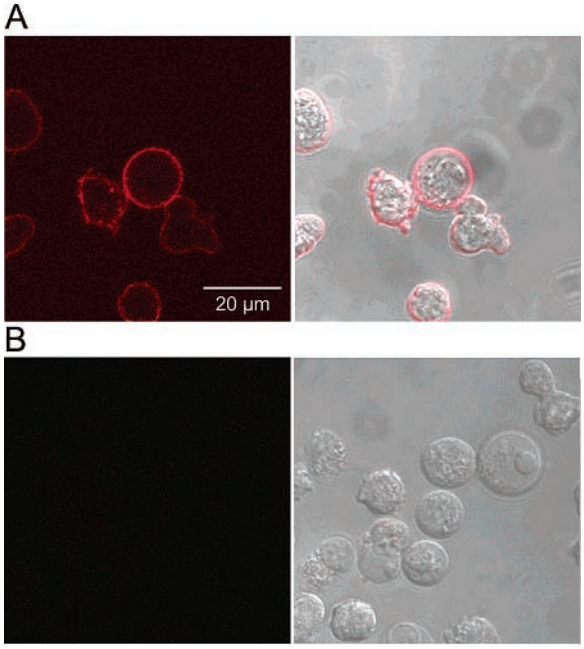


Figure 5. Receptor binding of an S0387 labeled peptide. (A) RMA-S cells were incubated with 10 nM S0387 labeled SIINFEKL for 1 h followed by intensive washing with PBS. Images were acquired by confocal laser scanning microscopy. (B) Cells incubated with 10 nM S0387 labeled SIINFEKL peptide in the presence of a 100-fold excess of unlabeled SIINFEKL peptide. One confocal section is shown in each case.

for the free dye molecule. After incubation of the free c-myc-S0387-peptide with anti-c-myc antibodies, an equilibrium between free and antibody-bound peptide was observed. The antibody bound peptide was detected as a second diffusive component in the autocorrelation function with a longer diffusion time compared to the unbound peptide resulting in a diffusion coefficient of 3.5 $\times$ 10^{-7} cm^2 s^{-1}.

Flow Cytometry and Fluorescence Microscopy. Nonspecific binding of fluorophores to proteins and cellular components is a major concern in the development of new fluorophores for life science applications. The fluorophore was attached to the MHC class I binding peptide SIINFEKL (SIINFEK(S0387)L) by solid-phase chemistry after selective deprotection of the ϵ-amino-group of the lysine side chain. The activation of the carboxyl group was carried out in situ using DIC and HOBt. Complete turnover of the amino group was achieved by coupling twice with only 1.5 times excess of dye. The fluorophore was fully resistant to the acidic conditions during the cleavage of the peptide from the resin and workup procedure. Incubation of RMA-S cells expressing empty MHC class I molecules (H-$2k^b$) on the cell surface with S0387-labeled SIINFEKL resulted in a fluorescence confined to the cell surface (Figure 5). Using flow cytometry fluorescence could be detected from cells incubated in the presence of as little as 1 nM peptide (data not shown). Incubation in the presence of a 100-fold excess of unlabeled competitor peptide reduced the fluorescence to background levels.

ACKNOWLEDGMENT

We thank Günther Jung for excellent facilities in peptide chemistry and instrumental analytics, Nicole Sessler for expert technical assistance in peptide synthesis, Lisa Neumann for proofreading the manuscript, and Manfred Claassen for technical assistance in FCS measurements. R.B. acknowledges financial support from the Volkswagen-Foundation (Conformational Control of Biomolecular Function, Nachwuchsgruppen an Universitäten).

LITERATURE CITED

(1) Eigen, M., and Rigler, R. (1994) Sorting single molecules: Application to diagnostics and evolutionary biotechnology. *Proc. Natl. Acad. Sci. U.S.A. 91*, 5740−5747.

(2) Fernandes, P. B. (1998) Technological advances in high-throughput screening. *Curr. Opin. Chem. Biol. 2*, 597−603.

(3) Madge, D., Rojas, G. E., and Seybold, P. G. (1999) Solvent dependence of the fluorescence lifetimes of xanthene dyes. *Photochem. Photobiol. 70*, 737−744.

(4) Heyduk, T., and Niedziela-Majka, A. (2002) Fluorescence resonance energy transfer analysis of *Escherichia coli* RNA polymerase and polymerase-DNA complexes. *Biopolymers 61*, 201−213.

(5) Cummings, R. T., Salowe, S. P., Cunningham, B. R., Wiltsie, J., Park, Y. W., Sonatore, L. M., Wisniewski, D., Douglas, C. M., Hermes, J. D., and Scolnick, E. (2002) A peptide-based fluorescence resonance energy transfer assay for Bacillus anthracis lethal factor protease. *Proc. Natl. Acad. Sci. U.S.A. 99*, 6603−6606.

(6) Kawamura, A. (1969) *Fluorescent Antibody Techniques and Their Applications*, University Park Press, Baltimore.

(7) Lansdorp, P. M., Smith, C., Safford, M., Terstappen, L. W. M. M., and Thomas, T. E. (1991) Single laser three color immunofluorescence staining procedures based on energy transfer between phycoerythrin and cyanine 5. *Cytometry 12*, 723−730.

(8) Sauer, M., Angerer, B., Han, K.-T., and Zander, C. (1999) Detection and identification of single dye labeled mononucleotide molecules released from an optical fiber in a microcapillary: First steps towards a new single molecule DNA sequencing technique. *Phys. Chem. Chem. Phys. 1*, 2471−2477.

(9) Kodadek, T. (2002) Development of protein-detecting microarrays and related devices. *Trends Biochem. Sci. 27*, 295−300.

(10) Staros, J. V., Wright, R. W., and Swingle, D. M. (1986) Enhancement by N-hydroxysulfosuccinimide of water-soluble carbodiimide-mediated coupling reactions. *Anal. Biochem. 156*, 220−222.

(11) Wang, Y.-L. (1989) Fluorescent analog cytochemistry: Tracing functional protein components in living cells. *Methods Cell Biol. 29*, 1−12.

(12) Jung, G., and Beck-Sickinger, A. G. (1992) Multiple peptide synthesis methods and their applications. *Angew. Chem., Int. Ed. Engl. 31*, 367−486.

(13) Weber, P. J. A., Bader, J. E., Folkers, G., and Beck-Sickinger, A. G. (1998) A fast and inexpensive method for N-terminal fluorescein-labeling of peptides. *Bioorg. Med. Chem. Lett. 8*, 597−600.

(14) Ernst, L. A., Gupta, R. K., Mujumdar, R. B., and Waggoner, A. S. (1989) Cyanine dye labeling reagents for sulfhydryl groups. *Cytometry 10*, 3−10.

(15) Mujumdar, R. B., Ernst, L. A., Mujumdar, S. R., and Waggoner, A. S. (1989) Cyanine dye labeling reagents containing isothiocyanate groups. *Cytometry 10*, 11−19.

(16) Southwick, P. L., Ernst, L. A., Tauriello, E. W., Parker, S. R., Mujumdar, R. B., Mujumdar, S. R., Clever, H. A., and Waggoner, A. S. (1990) Cyanine dye labeling reagents-Carboxymethylindocyanine succinimidyl esters. *Cytometry 11*, 418−430.

(17) Mujumdar, R. B., Ernst, L. A., Mujumdar, S. R., Lewis, C. J., and Waggoner, A. S. (1993) Cyanine dye labeling reagents: Sulfoindocyanine succinimidyl esters. *Bioconjugate Chem. 4*, 105−111.

(18) Mishra, A., Behera, R. K., Behera, P. K., Mishra, B. K., and Behera, G. B. (2000) Cyanines during the 1990s: A review. *Chem. Rev. 100*, 1973−2011.

(19) Kuhn, H. (1949) A quantum-mechanical theory of light absorption of organic dyes and similar compounds. *J. Chem. Phys. 17*, 1198−1212.

(20) Gordon, P. F., and Gregory, P. (1983) *Organic Chemistry in Colour*, Springer-Verlag, Heidelberg.
(21) Mostovnikov, V. A., Rubinov, A. N., Al'perovich, M. A., Avdeeva, V. I., Levkoev, I. I., and Loiko, M. M. (1974) Dependence of the luminescence and generation properties of solutions of polymethine dyes on their structure. *Zh. Prikl. Spektr. 20*, 42−47.
(22) Chibisov, A. K. (1976) Triplet states of cyanine dyes and reactions of electron transfer with their participation. *J. Photochem. 6*, 199−214.
(23) Widengren, J., and Schwille, P. (2000) Characterization of photoinduced isomerization and back-isomerization of the cyanine dye Cy5 by fluorescence correlation spectroscopy. *J. Phys. Chem. A 104*, 6416−6428.
(24) Sun, W.-C., Gee, K. R., Klaubert, D. H., and Haugland, R. P. (1997) Synthesis of fluorinated fluoresceins. *J. Org. Chem. 62*, 6469−6475.
(25) Murphy, S., and Schuster, G. B. (1995) Electron relaxation in a series of cyanine dyes: Evidence for electronic and steric control of the rotational rate. *J. Phys. Chem. 99*, 8516−8518.
(26) Magde, D., Elson, E. L., and Webb, W. W. (1972) Thermodynamic fluctuations in a reacting system − Measurement by fluorescence correlation spectroscopy. *Phys. Rev. Lett. 29*, 705−708.
(27) Magde, D., Elson, E. L., and Webb, W. W. (1974) Fluorescence correlation spectroscopy − An experimental realization. *Biopolymers 13*, 29−61.
(28) Widengren, J., Mets, Ü., and Rigler, R. (1995) Fluorescence correlation spectroscopy of triplet states in solution: A theoretical and experimental study. *J. Phys. Chem. 99*, 13368−13379.
(29) Falk, K., Rötzschke, O., Stevanovic, S., Jung, G., and Rammensee, H.-G. (1991) Allele-specific motifs revealed by sequencing of self-peptides eluted from MHC molecules. *Nature 351*, 290−296.
(30) Rötzschke, O., Falk, K., Stevanovic, S., Jung, G., Walden, P., and Rammensee, H.-G. (1991) Exact prediction of a natural T cell epitope. *Eur. J. Immunol. 21*, 2891−2894.
(31) Fuchs, P., Breitling, F., Little, M., and Dübel, S. (1997) Primary structure and functional scFv antibody expression of an antibody against the human protooncogen c-myc. *Hybridoma 16*, 227−233.
(32) Tetin, S. Y., Swift, K. M., and Matayoshi, E. D. (2002) Measuring antibody affinity and performing immunoassay at the single molecule level. *Anal. Biochem. 307*, 84−91.
(33) Reiner, K., Ernst, S., and Mustroph, H. (2000) DE 10018199 A1, German patent.
(34) Reiner, K., Ernst, S., and Mustroph, H. (1999) DE 19957001 A1, German patent.
(35) Mank, A. J. G., van der Laan, H. T. C., Lingeman, H., Gooijer, C., Brinkman, U. A. T., and Velthorst, N. H. (1995) Visible diode laser-induced fluorescence detection in liquid chromatography after precolumn derivatization of amines. *Anal. Chem. 67*, 1742−1748.
(36) Ljunggren, H.-G., and Kärre, K. (1985) Host resistance directed selectively against H-2-deficient lymphoma variants. *J. Exp. Med. 162*, 1745−1759.
(37) Ljunggren, H.-G., Stam, N. J., Öhlén, C., Neefjes, J. J., Höglund, P., Heemels, M. T., Bastin, J., Schumacher, T. N. M., Townsend, A., Kärre, K., and Ploegh, H. L. (1990) Empty MHC class I molecules come out in the cold. *Nature 346*, 476−480.
(38) Townsend, A., Öhlén, C., Bastin, J., Ljunggren, H.-G., Foster, L., and Kärre, K. (1989) Association of class I major histocompatibility heavy and light chains induced by viral peptides. *Nature 340*, 443−448.
(39) Rulliére, C. (1976) Laser action and photoisomerization of 3,3′-diethyl oxadicarbocyanine iodide (DODCI): Influence of temperature and concentration. *Chem. Phys. Lett. 43*, 303−308.
(40) Khimenko, V., Chibisov, A. K., and Görner, H. (1997) Effects of alkyl substituents in the polymethine chain on the photoprocesses in thiacarbocyanine dyes. *J. Phys. Chem. A 101*, 7304−7310.
(41) Chibisov, A. K., and Görner, H. (1997) Singlet versus triplet photoprocesses in indodicarbocyanine dyes and spiropyran-derived merocyanines. *J. Photochem. Photobiol. B 105*, 261−267.
(42) Horng, M.-L., Gardecki, J. A., and Maroncelli, M. (1997) Rotational dynamics of coumarin 153: Time-dependent friction, dielectric friction, and other nonhydrodynamic effects. *J. Phys. Chem. A 101*, 1030−1047.
(43) Buschmann, V., Weston, K. D., and Sauer, M. (2002) Spectroscopic study and evaluation of red-absorbing fluorescent dyes. *Bioconjugate Chem. 14*, 195−204.
(44) Hansen, R. L., Zhu, X. R., and Harris, J. M. (1998) Fluorescence correlation spectroscopy with patterned photoexcitation for measuring solution diffusion coefficients of robust fluorophores. *Anal. Chem. 70*, 1281−1287.
(45) Sauer, M. (1995) Entwicklung effizienter Fluoreszenzfarbstoffe für den hochempfindlichen Nachweis von Biomolekülen unter Einsatz zeitaufgelöster LIF−Spektroskopie, Dissertation, University of Heidelberg.

BC034191H

Noninvasive Imaging of Quantum Dots in Mice

Byron Ballou,*[,†,‡] B. Christoffer Lagerholm,[†] Lauren A. Ernst,[†] Marcel P. Bruchez,[§] and Alan S. Waggoner[†,‡]

Molecular Biosensor and Imaging Center, and Department of Biological Sciences, Carnegie Mellon University, 4400 Fifth Avenue, Pittsburgh, Pennsylvania 15213 and Quantum Dot Corporation, 26118 Research Road, Hayward, California 94545. Received August 29, 2003; Revised Manuscript Received November 23, 2003

Quantum dots having four different surface coatings were tested for use in in vivo imaging. Localization was successfully monitored by fluorescence imaging of living animals, by necropsy, by frozen tissue sections for optical microscopy, and by electron microscopy, on scales ranging from centimeters to nanometers, using only quantum dots for detection. Circulating half-lives were found to be less than 12 min for amphiphilic poly(acrylic acid), short-chain (750 Da) methoxy-PEG or long-chain (3400 Da) carboxy-PEG quantum dots, but approximately 70 min for long-chain (5000 Da) methoxy-PEG quantum dots. Surface coatings also determined the in vivo localization of the quantum dots. Long-term experiments demonstrated that these quantum dots remain fluorescent after at least four months in vivo.

INTRODUCTION

Quantum dots (QDs) are stable, bright fluorophores that, under ideal conditions, can have high quantum yields, narrow fluorescence emission bands, high absorbency, very long effective Stokes shifts, high resistance to photobleaching, and can provide excitation of several different emission colors using a single wavelength for excitation (*1*). Because QDs have size-tunable narrow emission bands, in addition to single-wavelength excitation, QDs are suitable for detecting multiple ligands in a single experiment. Multiplexing using several colors and intensities of quantum dots to code assay supports ("barcoding") would allow the detection of many distinct ligands in single experiments (*2*−*4*). Moreover, QDs may be readily imaged using two-photon microscopy in vitro and in vivo (*5*). However, commercially available materials do not yet offer many of the potential advantages of QDs. The chief hindrances to routine use have been difficulties in reproducible production of QDs in quantity and the lack of suitable surface coatings that maintain high quantum yields, confer stability in aqueous solution, and can be chemically manipulated for biological applications.

Bruchez et al. (*6*) and Chan and Nie (*7*) first reported the use of quantum dot conjugates for labeling biological specimens. In these experiments, QDs were coated with silica and mercaptoacetic acid layers, respectively. Both groups showed specific labeling by covalent coupling of ligands to these surfaces. Subsequently, several authors have shown labeling of whole cells and tissue sections using several different surface modifications of QDs (*1*, *8*−*11*). A variety of colors of Qdot conjugates for immunospecific labeling are now available commercially from Quantum Dot Corporation (www.qdots.com).

* To whom correspondence should be addressed. E-mail: bbal@andrew.cmu.edu.

[†] Molecular Biosensor and Imaging Center, Carnegie Mellon University.

[‡] Department of Biological Sciences, Carnegie Mellon University.

[§] Quantum Dot Corporation.

Quantum dot preparations reported to date have not been optimized for in vivo studies. For in vivo imaging, QDs must have adequate circulating lifetime, must show minimal nonspecific deposition, and must retain their fluorescence for a sufficiently long time. We report that QDs coated using an amphiphilic poly(acrylic acid) polymer are stable in vivo, that changing surface chemistry prolongs circulating lifetime and reduces nonspecific deposition in vivo, that targeting to tissues may be observed by noninvasive whole body fluorescence, and that QDs may be visualized in tissue sections by light and electron microscopy many weeks after injection.

MATERIALS AND METHODS

Quantum Dots. Quantum dots were supplied by Quantum Dot Corporation, Hayward, CA 94545. Core−shell zinc sulfide-cadmium selenide QDs emitting at 606, 635, 645, and 655 nm were coated with an amphiphilic poly(acrylic acid) polymer (amp QDs (*9*)) or the same coating conjugated with methoxy- or carboxy-terminated poly(ethylene glycol) amine (mPEG-750 QDs, mPEG-5000 QDs, COOH−PEG-3400 QDs). Quantum dots have spectra that exhibit an absorption peak at a wavelength slightly shorter than the emission wavelength ("longest wavelength peak.") At wavelengths shorter than this peak, absorbance first declines, then rises steeply at shorter wavelengths, with no definite peak. Absorption and excitation spectra are nearly identical; thus QD's may be excited at any wavelength shorter than the emission maximum (e.g., (*6*)). QD concentration was determined by absorbance using appropriate extinction coefficients (for example, 800 000 M^{-1} cm^{-1} at 638 nm for the 655 materials and 650 000 M^{-1} cm^{-1} at the longest wavelength peak for the 605 materials). These values agree with concentrations measured by a variety of distinct techniques including elemental analysis, stoichiometric gel shift assays, and fluorescence correlation spectroscopy.

Quantum Yield Determination. Quantum yields were measured by comparing integrated fluorescence intensity of absorbance matched solutions in an intensity

10.1021/bc034153y CCC: $27.50 © 2004 American Chemical Society
Published on Web 12/30/2003

Table 1. Optical Properties and Circulating Half-Lives of Surface-Modified QDs. See Methods for Details

	QD surface coating			
	amp	mPEG-750	COOH−PEG-3400	mPEG-5000
molar extinction, 450 nm[a]	4.5×10^6	4.1×10^6	4.6×10^6	6.8×10^6
emission maximum, nm	655	645	655	655
quantum yield	0.52	0.28	0.38	0.89
circulating half-life, imaging (min)	ND	6.1 ± 2.9[b]	ND	141 ± 45
circulating half-life, venipuncture (min)	4.6 ± 1.0	3.2 ± 0.6	12.6 ± 4.9	71 ± 20

[a] See the discussion of QD optical properties at http://www.qdots.com. These data are from the QD preparations used in this paper and are not corrected for scatter. [b] Weighted average of two-exponential fits to data; in the original fits, the fast component was 2.2 ± 2.5 min; the slow component was 9.8 ± 9.1 min.

calibrated Ocean Optics S2000 fluorimeter. The absorbance of the solutions was fixed at 0.03 ± 0.003 AU at the excitation wavelength. Red QDs (576−655) were compared to Rhodamine 101 in methanol (QY 0.95) with excitation at 530 nm. The integrated fluorescent intensities were scaled according to the absolute absorbance of the sample and the standard, and the ratio of these values multiplied by the reported standard quantum yield gives the absolute sample quantum yield. Properties of the quantum dots used in this paper are shown in Table 1.

PEG Conjugation. Poly(ethylene glycol) derivatives were acquired from Shearwater Polymers Corp (Huntsville, AL 35806; COOH−PEG-3400-amine, mPEG-5000-amine) and from Sigma-Aldrich (Milwaukee, WI 53201; mPEG-750-amine). Other reagents were supplied by Sigma. These reactions have been carried out at a variety of scales, but the 5 mL scale reaction is described here for the mPEG-750 amine. Quantum dots were dispersed at 1.0 uM in 50 mM sodium borate, pH 8.0, with a molar ratio of 2000:1 of PEG-amine (7.5 mg). These materials were then reacted with a 1500:1 molar ratio of *N*-dimethylaminopropyl-*N*′-ethylcarbodiimide (EDC, 1.4 mg) for 2 h followed by purification using a 100 kDa centrifugal ultrafiltration device (Vivascience, Edgewood, NY).

The number of PEG-amine molecules coupled to each quantum dot was determined by conducting the coupling reaction in the presence of an excess of PEG-amine, then reacting the residual amines with fluorescamine reagent. This reagent produced a blue fluorescent species that was monitored at 490 nm and compared to the signal produced from the materials without EDC activation. The % retained signal corresponds to the remaining excess amine that did not react with the quantum dots. The difference was assumed to have completely reacted with the quantum dots, so the concentration of consumed amines (initial concn × (final signal/initial signal)) divided by the concentration of quantum dots yielded the number of amines reacted per quantum dot.

For all PEG-substituents, we attempted to saturate available carboxyl groups. The levels of substitution were approximately 300 residues/QD for mPEG-750, and 100 residues/QD for COOH−PEG-3400 and mPEG-5000.

The final materials were filtered through a 0.2 μm filter unit and prepared at an appropriate concentration for tail vein injection prior to use. Each dose was adjusted to 0.14 M NaCl by addition of 1.4 M NaCl just prior to use.

Mice. Balb/C and athymic nude mice were obtained from Harlan Sprague Dawley (Indianapolis, IN, 46229); mice were used at ages from 6 to 12 weeks without any noticeable effect of age. For all results shown in this paper, QDs (360 pmol) in 200 μL normal saline were injected into the tail veins of mice (typically 18 g; thus 180 nM QD, 20 pmol QD/g animal weight). In other experiments, doses ranging from 50 to 500 pmol in 50−200 μL normal saline were administered, with no significant dose effect on circulating time or distribution. Mice were anesthesized for imaging either by pentobarbital intraperitoneally to effect, or by inhalation anesthesia using isofluorane (*12*). For timed measurements, animals were first anesthetized, then injected while under the camera. To compare whole-blood lifetimes to lifetimes derived from images, mice were bled by saphenous venipuncture (*13*). All operations on animals were in accord with institutional animal use and care regulations.

Macro Imaging. Whole body images were acquired on a Photometrics (Tucson, AR) C258 cooled CCD camera equipped with a custom filter holder and lens adapter (Bioptechs, Butler, PA 16002). Animals were illuminated using four 250-W quartz-halogen illuminators (Cuda Products, Jacksonville, FL 32217) equipped with half-inch fiber optic bundles terminating in filter holders (Edmund Industrial Optics, Barrington, NJ 08007). Excitation filters were 460/50 nm, and emission filters were 20 nm wide band-pass filters, centered on the emission maxima of the QDs. All filters were provided by Chroma Technologies (Brattleboro, VT. 05301). Imaging times varied with time postinjection and were adjusted on the fly to give maximum dynamic range, but were typically 0.5 s; for time series, three images were acquired in rapid succession at 1-min intervals; acquisition times of 0.2, 1.0, and 5 s were normally used to bracket the large range in intensities between different sites of deposition.

Microscopy. Light and fluorescence images were acquired on an inverted Zeiss Axiovert 135TV microscope (Zeiss, Thornwood, NY 10594) equipped with a Hamamatsu ORCA II cooled CCD camera (Hamamatsu, Bridgewater, NJ 08807). Fluorescence images of quantum dots were acquired with a 440/20 nm excitation filter and appropriately selected 20 nm wide band-pass emission filters, centered on the emission maxima of the quantum dots.

Tissue samples for light microscopy were 10 μm frozen sections. Sections were cut on a cryostat, fixed for 10 s in methanol, dipped for 1 min in Gill's 2X hematoxylin, briefly rinsed and then developed in Scott's solution.

Electron Microscopy. Tissue specimens were fixed in 2% glutaraldehyde buffered with 0.1 M sodium cacodylate, pH 7.4. The tissue was washed with 3 changes of 0.1 M sodium cacodylate buffer, pH 7.4, and postfixed for 1 h in a solution containing 1% OsO4 buffered with 0.1 M sodium cacodylate, pH 7.4, then washed in three changes of dH_2O and dehydrated in EtOH. Propylene oxide was used as a transitional solvent. The tissue was infiltrated overnight in a 1:1 mixture of Epon-Araldite and propylene oxide. The following day, the 1:1 mixture was removed and replaced with 100% Epon-Araldite. The specimens were infiltrated an additional 8 h, placed in embedding capsules, and polymerized for 48 h at 60 °C.

The embedded specimens were thin sectioned (0.1 μm), then stained with 1% uranyl acetate and Reynolds lead citrate. The sections were viewed on a Hitachi H-7100 TEM operating at 50 kV. Digital images were obtained using an AMT Advantage 10 CCD Camera System and NIH Image software.

Image Analysis. All image analysis was performed in ImageJ (http://rsb.info.nih.gov/ij/) while curve fitting was done using Mathematica (Wolfram Research, Champaign, IL; 61820; http://www.wolfram.com/). To analyze circulating lifetimes from bleeds, macro fluorescence images were acquired using ~20 μL blood samples in 1 mm × 0.1 mm bore rectangular glass capillary tubes (VitroCom, Mountain Lakes, NJ 07046). Fluorescence intensity was measured using a rectangular region of interest over the body of the capillaries; background was determined using an identical region of interest over an adjacent noncapillary area. The mean fluorescence intensity was determined and the resulting background corrected data was curve fit to single exponentials.

To obtain circulating lifetimes by whole mouse imaging, mice were imaged at 1 min intervals postinjection for 1−3 h (Figure 1). Lifetime data were then generated by selecting nine 2 × 2 pixel regions of interest per mouse, where the regions of interest were selected to coincide with conspicuous blood vessels, and by tracking them through time. Background due to intrinsic fluorescence was normally negligible; subtraction of fluorescence in adjacent tissue made little or no difference to the slope of the intensity versus time plot. The resulting background-corrected data was fitted to one- and two-exponential curves with the two-exponential curve providing a better fit for mPEG-750 QDs, as evidenced by F-statistics. However, mPEG-5000 QD data showed no improvement using a two-exponential fit as compared to a one-exponential fit.

RESULTS

Core−shell cadmium selenide−zinc sulfide quantum dots having maximum emission wavelengths at 606, 630, 645, and 655 nm were supplied by Quantum Dot Corporation. The core−shell size (and hence emission wavelengths) of the QDs had no significant effects on tissue deposition or circulating lifetimes. Four different surface coatings were used: an amphiphilic poly(acrylic acid) primary coat (amp) that stabilizes the quantum dots in aqueous solution (*9*), and quantum dots having the amp coating further coupled to methoxy-terminated poly(ethylene glycol), molecular weight 750 (mPEG-750), carboxy-terminated poly(ethylene glycol), molecular weight 3400 (COOH−PEG-3400), or methoxy-terminated poly(ethylene glycol), molecular weight 5000 (mPEG-5000).

We compared the amp-QDs to the three differently substituted PEG-QDs by noninvasive imaging and repetitive bleeds to determine whether PEG-substitution would affect the circulating lifetime. Immediately after intravenous injection, fluorescence from all QD emission wavelengths and surface coatings is easily seen in the superficial vasculature. Subsequently, QDs are seen to deposit in liver, skin, and bone marrow in a surface coating dependent manner. By 1 h postinjection, QDs having amp-, mPEG-750-, and COOH-PEG-3400 coatings are cleared from the circulation, while mPEG-5000 QDs remain visible in circulation for at least 3 h (Figures 1 and 2, and see Supporting Information, which includes a Quicktime movie of in vivo distribution of the mPEG-750 and mPEG-5000 quantum dots). Circulating lifetimes (Table 1) were 12 min or less for the amp, mPEG-750, and COOH-PEG-3400 QDs, while the mPEG-5000 QDs had a much longer circulating lifetime (50−100 min by venipuncture, 140 min by imaging). There was no statistically significant difference between nude and normal mice in the circulating lifetime of QDs. The circulating lifetime obtained by noninvasive imaging of whole animals was consistently longer than that obtained by venipuncture; this is caused mostly by the presence of extravasated QD's in surrounding tissue (data not shown.) Due to an erratic pattern of early deposition in the skin by amp and COOH−PEG-3400 QDs, only early lifetime data (<5 min) could be derived from images. Deposition in the skin was initially punctate, then spread over most of the surface. Most of the skin fluorescence disappeared by 24 h postinjection.

Necropsy at 24 h corroborated and extended the localization of mPEG-750 (Figure 3) and mPEG-5000 (Figure 4) quantum dots seen by noninvasive imaging. Figures 3A and 4A show noninvasive fluorescence images of living mice, which, compared to the short-term images in Figure 1, show increased deposition in lymph nodes and bone marrow relative to the liver; intestinal contents also show significant fluorescence due mainly to excretion of QDs from the liver. Figure 3 also shows two stages of necropsy (B,C). In addition to sites seen by noninvasive imaging, major sites of fluorescence include the deep lymph nodes and the spleen. Figure 4B,C shows a similar necropsy of an animal injected using mPEG-5000 QDs. The most striking difference from Figure 3 is the very low labeling of the lymph nodes, compared to the liver, spleen, and bone marrow. These results suggest that the longer circulating lifetime of the higher molecular weight mPEG-substituted QDs may be due to lesser uptake by the lymph nodes as well as to the lower rate of uptake by the liver. Uninjected animals showed no comparable fluorescence in any organs.

To determine the long-term stability and tissue deposition of QDs in vivo, a set of normal Balb/C mice were intravenously injected using mPEG-750 QDs. Animals were imaged during necropsy at 15 min, 1 day, 3 days, 7 days, 28 days, and 133 days (>four months) postinjection. QDs remained for at least one month in liver, lymph nodes, and bone marrow. By one month, fluorescence was substantially decreased, but the overall distribution of fluorescence remained similar to that at 24 h after injection. In follow-up experiments at 133 days postinjection, QD fluorescence was still visible on necropsy, though background fluorescence from intestinal contents was now higher than that in lymph nodes. The liver had no grossly visible fluorescence; however, QD's were still grossly visible in lymph nodes and bone marrow (Figure 5), and visible by fluorescence microscopy in liver, lymph nodes, and spleen (data not shown).

Cellular sites of uptake were identified by microscopy of tissue sections. Imaging of whole spleen by fluorescence 24 h postinjection of mPEG-750 QDs showed a freckled pattern of dark centers having bright haloes. Figure 6 shows one frozen section from a spleen taken 24 h postinjection, stained using hematoxylin and visualized in white light and by fluorescence. Deposition is perifollicular, with no accumulation in germinal centers. The QDs are concentrated in internal vacuoles of phagocytic cells. Sections of lymph nodes showed a similar pattern. QDs were further localized by electron microscopy. Figure 7 shows transmission electron microscope images of a mouse spleen cell 24 h postinjection. Localization in endosomes is confirmed by these images, which also demonstrate that QDs deposited in tissues may be imaged easily using standard electron microscopic meth-

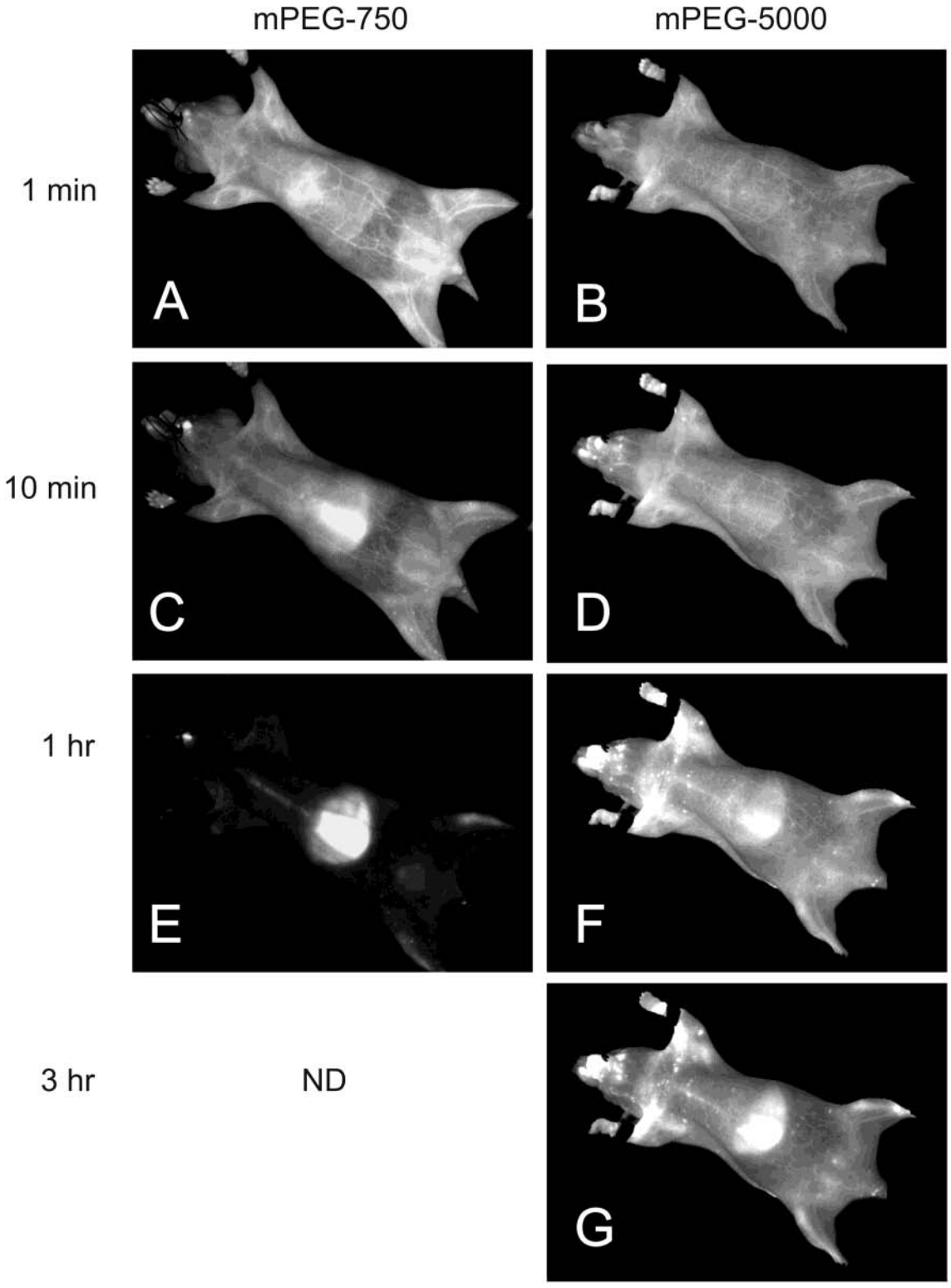


Figure 1. Noninvasive imaging using 645 nm mPEG-750 QDs (left, A, C, E) and 655 nm-emitting mPEG-5000 QDs (right, B, D, F, G). Nude mice were imaged at 1min (A, B), 10 min (C, D) 1 h (E, F), and 3 h (G) postinjection. Note that even at 1 min, significant liver uptake is visible using mPEG-750 QDs (A), while even at 10 min there is little or no visible liver uptake using mPEG-5000 QDs (D). At 1 h, the difference between mPEG-750 QDs (E) and mPEG-5000 QDs is even more marked, with PEG-750 QDs completely cleared from the circulation, while mPEG-5000 QDs persist (F); even 3 h postinjection, mPEG-5000 QDs remain in circulation (G). Since essentially all fluorescence is cleared from the circulation by 1 h, imaging of mPEG-750 QDs was terminated at 1 h after injection. In other experiments, we found that the pattern of deposition of mPEG-750 QDs seen at 1 h remained stable for at least 24 h.

ods. At one month postinjection, electron microscope images show subcellular localization in the spleen similar to that seen 24 h postinjection. Whether QDs remain in the cells that originally took them up is not yet known.

DISCUSSION

We have shown that quantum dots are well suited for fluorescence visualization in whole animals. Because of

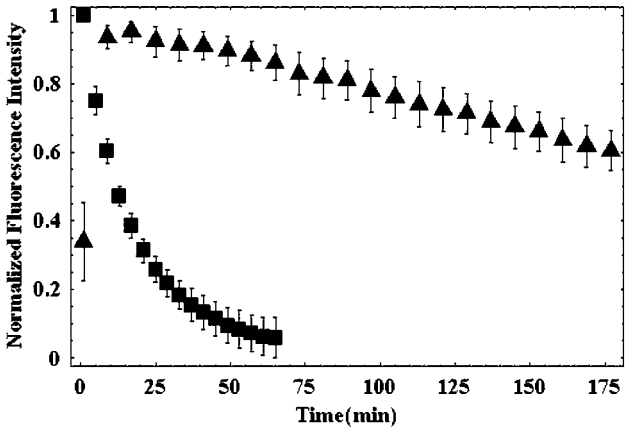


Figure 2. Regions of interest (2 × 2 pixels) over several different surface vessels of the animals in Figure 1 were used to determine the circulating lifetime of the QDs. Mean fluorescence intensities from nine regions of interest on each animal were measured, normalized to maximum initial values, and plotted versus time after injection (triangles, mPEG-5000 QDs; squares, mPEG-750 QDs.) Bars indicate standard deviations. Exponential fits of the fluorescence intensities as a function of time yielded average circulating half-lives of 6.1 ± 2.9 min for mPEG-750 QDs and 141 ± 45 min for mPEG-5000 QDs (Table 1).

their high quantum yields and high absorbency, the fluorescence of QDs in the superficial vasculature was readily visible to the naked eye just after injection; even the orange 605 nm-emitting QDs can be imaged noninvasively in liver and bone marrow. QDs in tissue can be imaged on scales that range from the whole animal to the electron microscope level. Moreover, the QDs used in these experiments are stable and fluorescent in vivo for at least four months. Microscopy showed no signs of localized necrosis at the sites of deposition, and there was no obvious sign of breakdown of the QDs as seen by electron microscopy. This stability is presumably due to the amp coating, which preserves fluorescence and protects the QDs from degradation in vivo. We cannot exclude the possibility that some QDs are no longer fluorescent after prolonged residence in tissue, but their structure is preserved as revealed by electron microscopy.

QDs can be excited by any light wavelength shorter than their emission wavelength. We used blue excitation because of the higher absorbency of QDs in the blue, and the ability to use QDs with emission wavelengths from green through infrared with a single excitation wavelength. Red light excitation should improve visualization and resolution at increased tissue depth, at some cost in efficiency of excitation. Because of the resistance of QDs to photobleaching, higher intensity illumination or a long integration time should make up for any decrease in absorbency in the red. However, in our hands, blue excitation with a wideband filter proved quite satisfactory in mice, and use of red laser illumination produced no significant improvement.

The small size of QDs and their conjugates should allow efficient tissue perfusion and good targeting to specific sites in tissues, provided that the QDs remain in circulation long enough. For many uses in vivo, reducing Qdot uptake by the reticuloendothelial system and increasing circulating lifetime will be essential. PEGylation of nanoparticles and liposomes to prolong serum lifetime and aid in targeting is an area of active research; second-generation PEG derivatives may offer longer lifetimes and enhanced tissue perfusion (*14*−*24*.) Our results recall those of Gref et al. (*23*) and Mosqueria et al. (*24*), who found that increasing PEG density and chain length-reduced nanoparticle binding to cells and

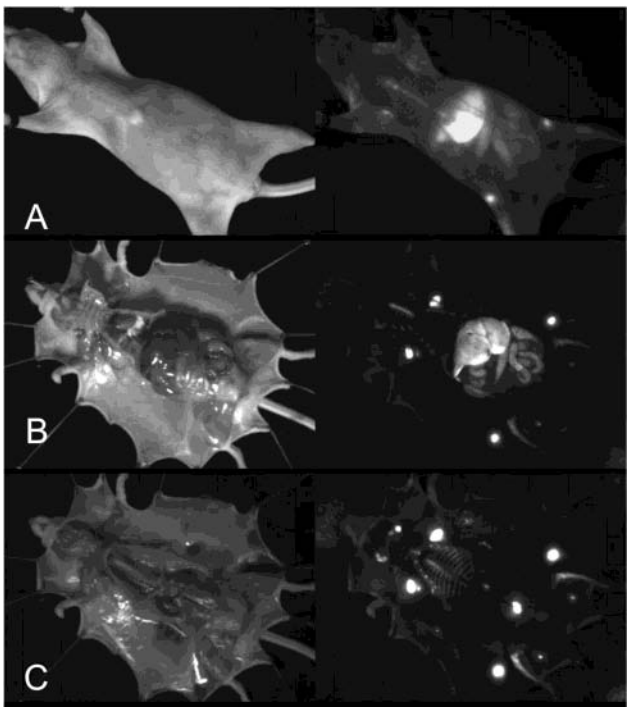


Figure 3. Mouse imaged 24 h postinjection of 645 nm mPEG-750 QDs. Left, light images; Right, fluorescence images. A, whole animal; B, skin and peritoneum removed, sternum pinned back showing marrow staining, but concealing cervical nodes. C, sternum, heart, lungs, liver, and digestive tract removed. Note the visibility of axillary and inguinal lymph nodes through the skin (A), and the retention of QDs by bone marrow as well as by lymph nodes and liver (B, C).

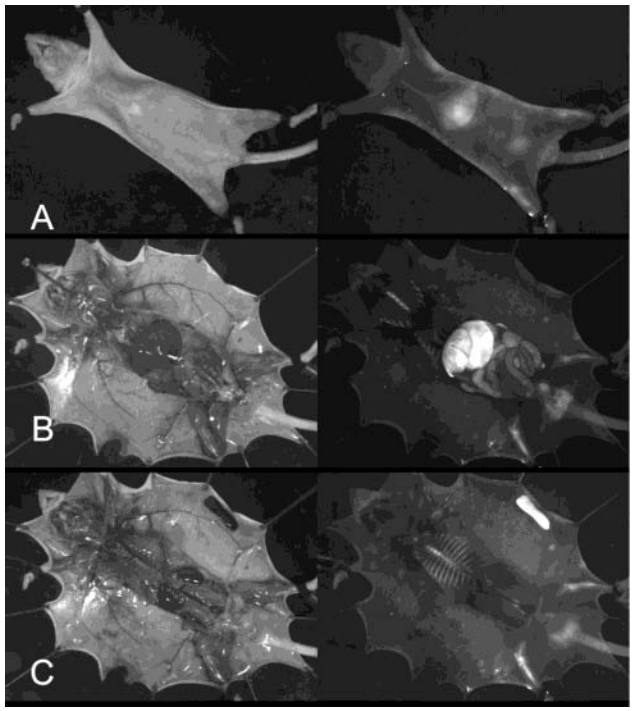


Figure 4. Mouse imaged 24 h postinjection of 655 nm mPEG-5000 QDs. Left, light images; Right, fluorescence images. A, whole animal; B, skin and peritoneum removed, sternum pinned back showing marrow staining, but concealing cervical nodes. C, sternum, heart, lungs, liver, and digestive tract removed. Note the minimal labeling of lymph nodes compared to mPEG-750 (Figure 3). Note the high relative brightness of the spleen, displayed on the upper right of the dissection (C).

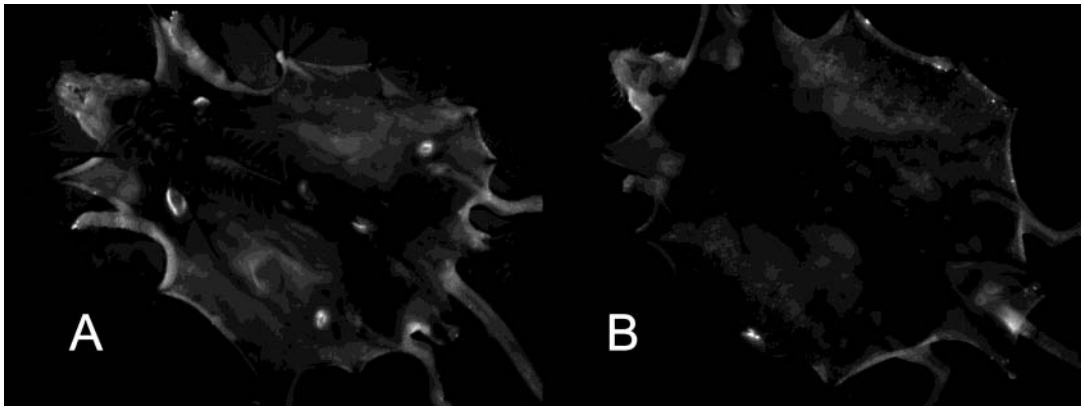


Figure 5. Long-term retention of QD fluorescence in vivo. A. Mouse imaged 133 days postinjection of 360 pmol of 655 nm mPEG-750 QDs. The mouse was dissected, and most internal organs were removed to show continuing fluorescence of axillary, inguinal, and lumbar lymph nodes as well as weak fluorescence of bone marrow. B. Same dissection of control (uninjected) mouse. Mice were imaged under identical conditions, and images are displayed using identical brightness functions.

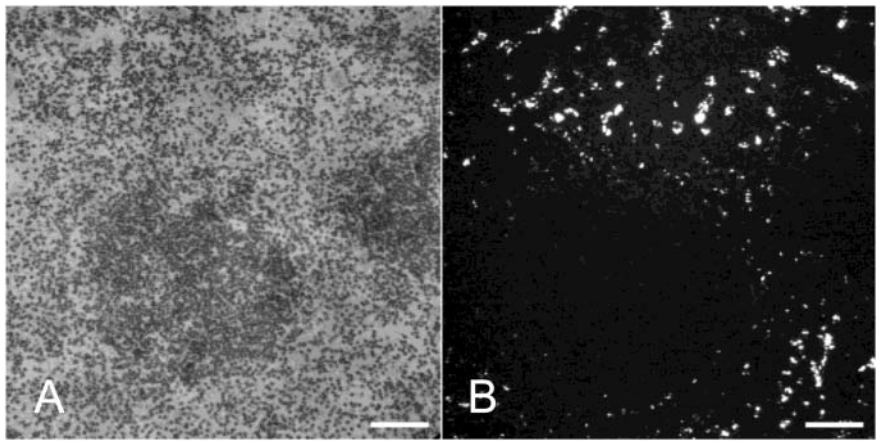


Figure 6. Spleen, frozen section 24 h postinjection of 630 nm-emitting mPEG-750 QDs. A. Section stained using Gill's hematoxylin, white light image; B. Fluorescence image of A. Note concentration of QDs in perifollicular areas, but not in germinal centers. Bar = 200 μm.

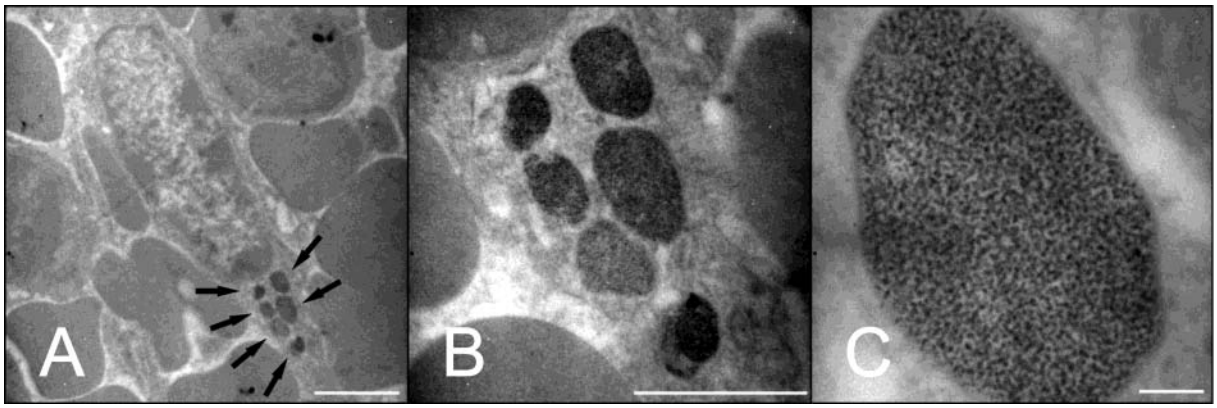


Figure 7. mPEG-750 QDs in mouse spleen imaged by electron microscopy 24 h postinjection. A. Perifollicular cell, presumably macrophage, bar = 10 μm; arrows indicate endosomes. B. Same cell, bar = 1 μm. C, Enlarged single endosome, showing individual QDs, bar = 100 nm. Glutaraldehyde fixation, Epon embedding, osmium stain.

plasma components and increased circulating lifetime. We anticipate that circulating lifetimes will be further improved by adjusting the surface composition of QDs.

Other groups have used QDs in vivo. Dubertret et al. (*25*) microinjected QDs enclosed in PEG-conjugated lecithin micelles; these QDs persisted in Xenopus embryos from blastula at least until tadpole stage, with little or no indication of toxicity. Akerman et al. (*26*) explored the deposition of peptide conjugated and PEGylated QDs in mice using fluorescence microscopy of tissue sections rather than whole-body visualization. By using a high level of PEG-substitution on QD−peptide conjugates directed to vascular and tumor targets, this group found that uptake in RES sites could be reduced, while selective targeting to organ-specific vasculature and to tumors could be achieved. These results, taken with ours, demonstrate the usefulness of QDs for targeting in vivo and whole-body visualization.

Several groups, including ours, have investigated organic fluorochromes as labels for targeting in vivo; all have concluded that far-red and near-infrared fluorophores are more effective than shorter wavelengths (*27*−

33). For good visualization through a significant thickness of tissue (>1 mm), stable near-infrared-emitting QDs will be necessary (*34*). Difficulties in the manufacture and stabilization of infrared-emitting QDs are being resolved; this should enable visualization in whole animals at greater depth and with increased sensitivity.

That QD surfaces can control serum lifetime and pattern of deposition suggests many medical uses. Rapid deposition in the reticuloendothelial system is potentially useful for defining some tumor types and detecting sentinel lymph nodes. Tumor targeting by QD conjugates is an exciting prospect, as tumor sites and margins could be readily imaged during surgery (*26*), provided that heavy-metal toxicity due to the QD's can be appropriately limited or controlled. As with antibody conjugates, the key to good targeting in vivo is the use of surface coatings that reduce nontargeted uptake. We have shown considerable increase in circulating lifetimes and reduction in nonspecific uptake of QDs by the use of long-chain PEG surfaces. At this point, the serum lifetime of mPEG-5000 QDs is similar to that of some of our cyanine fluorochrome antibody conjugates that were successfully used for tumor labeling (*28*, *29*). Finally, thanks to the high stability of amp-coated QDs, experiments using molecules and cells tagged with QDs and injected into animals may permit analysis of antigen trafficking and cellular migration over very long time scales, with unprecedented sensitivity and resolution.

ACKNOWLEDGMENT

We thank Joseph P. Suhan (Department of Biological Sciences, Carnegie Mellon University) for excellent technical assistance in electron microscopy, Joyce Horner and Lisa McGaw (Department of Biological Sciences, Carnegie Mellon University) for assistance with animal handling and anesthesia. This work was supported by NIH grant number R01 EB 000364. The work at Quantum Dot Corporation was partly funded by NIST-ATP 70NANB0H3000.

Supporting Information Available: A Quicktime movie showing fluorescence images of whole animal distribution of the mPEG-750 and mPEG-5000 quantum dots directly after injection. This material is available free of charge via the Internet at http://pubs.acs.org.

NOTE ADDED IN PROOF

Hanaki et al. have demonstrated that QD fluorescence can persist for days in endosomes (Hanaki, K., Momo, A., Oku, T., Komoto, S., Maenosono, Y., Yamaguchi, Y., and Yamamoto, K. (2003) Semiconductor quantum dot/albumin complex is a long-life and highly stable photostable endosome marker. *Biochem. Biophys. Res. Commun. 302*, 496−501).

LITERATURE CITED

(1) Watson, A., Wu, X., and Bruchez, M. (2003) Lighting up cells with quantum dots. *Biotechniques 34*, 296−303.

(2) Gao, X., Chan, W. C., and Nie, S. (2002) Quantum-dot nanocrystals for ultrasensitive biological labeling and multicolor optical encoding. *J. Biomed. Opt. 7*, 532−537.

(3) Chan, W. C., Maxwell, D. J., Gao, X., Bailey, R. E., Han, M., and Nie, S. (2002) Luminescent quantum dots for multiplexed biological detection and imaging. *Curr. Opin. Biotechnol. 13*, 40−46.

(4) Xu, H., Sha, M. Y., Wong, E. Y., Uphoff, J., Xu, Y., Treadway, J. A., Truong, A., O'Brien, E., Asquith, S., Stubbins, M., Spurr, N. K., Lai, E. H., and Mahoney, W. (2003) Multiplexed SNP genotyping using the Qbead system: a quantum dot-encoded microsphere-based assay. *Nucleic Acids Res. 31*, e43.

(5) Larson, D. R., Zipfel, W. R., Williams, R. M., Clark, S. W., Bruchez, M. P., Wise, F. W., Webb, W. W. (2003) Water-soluble quantum dots for multiphoton fluorescence imaging in vivo. *Science 300*, 1434−1436.

(6) Bruchez, M., Jr., Moronne, M., Gin, P., Weiss, S., and Alivisatos, A. P. (1998) Semiconductor nanocrystals as fluorescent biological labels. *Science 281*, 2013−2016.

(7) Chan, W. C., and Nie, S. (1998) Quantum dot bioconjugates for ultrasensitive nonisotopic detection. *Science 281*, 2016−2018.

(8) Rosenthal, S. J., Tomlinson, I., Adkins, E. M., Schroeter, S., Adams, S., Swafford, L., McBride, J., Wang, Y., DeFelice, L. J., Blakely, R. D. (2002) Targeting cell surface receptors with ligand-conjugated nanocrystals. *J. Am. Chem. Soc. 124*, 4586−4594.

(9) Wu, X., Liu, H., Liu, J., Haley, K. N., Treadway, J. A., Larson, J. P., Ge, N., Peale, F., and Bruchez, M. P. (2003) Immunofluorescent labeling of cancer marker Her2 and other cellular targets with semiconductor quantum dots. *Nat. Biotechnol. 21*, 41−46.

(10) Dubertret, B., Skourides, P., Norris, D. J., Noireaux, V., Brivanlou, A. H., and Libchaber, A. (2002) In vivo imaging of quantum dots encapsulated in phospholipid micelles. *Science 298*, 1759−1762.

(11) Jaiswal, J. K., Mattoussi, H., Mauro, J. M., and Simon, S. M. (2003) Long-term multiple color imaging of live cells using quantum dot bioconjugates. *Nat. Biotechnol. 21*, 47−51.

(12) Flecknell P. (2000) *Laboratory Animal Anesthesia*, London, Academic Press.

(13) Hem, A., Smith, A. J., and Solberg, P. (1998) Saphenous vein puncture for blood sampling of the mouse, rat, hamster, gerbil, guinea pig, ferret and mink. *Lab. Anim. 32*, 364−368.

(14) Harris, J. M., and Chess, R. B. (2003) Effect of pegylation on pharmaceuticals. *Nat. Rev. Drug Discovery 2*, 214−221.

(15) Maruyama, K. (2002) PEG-immunoliposome. *Biosci Rep 22*, 251−266.

(16) Sharpe, M., Easthope, S. E., Keating, G. M., and Lamb, H. M. (2002) Poly(ethylene glycol)-liposomal doxorubicin: a review of its use in the management of solid and haematological malignancies and AIDS-related Kaposi's sarcoma. *Drugs 62*, 2089−2126.

(17) Molineux, G. (2002) Pegylation: engineering improved pharmaceuticals for enhanced therapy. *Cancer Treat. Rev. 28 Suppl A*, 13−16.

(18) Harrington, K. J., Mubashar, M., and Peters, A. M. (2002) Poly(ethylene glycol) in the design of tumor-targetting radiolabeled macromolecules - - lessons from liposomes and monoclonal antibodies. *Q. J. Nucl. Med. 46*, 171−180.

(19) Chapman, A. P. (2002) PEGylated antibodies and antibody fragments for improved therapy: a review. *Adv. Drug Delivery Rev. 54*, 531−545.

(20) Greenwald, R. B. (2001) PEG drugs: an overview. *J Controlled Release 74*, 159−171.

(21) Moghimi, S. M., Hunter, A. C., and Murray, J. C. (2001) Long-circulating and target-specific nanoparticles: theory to practice. *Pharmacol. Rev. 53*, 283−318.

(22) Brigger, I., Dubernet, C., and Couvreur, P. (2002) Nanoparticles in cancer therapy and diagnosis. *Adv. Drug Delivery Rev. 54*, 631−651.

(23) Gref, R., Luck, M., Quellec, P., Marchand, M., Dellacherie, E., Harnisch, S., Blunk, T., and Muller, R. H. (2000) 'Stealth' corona-core nanoparticles surface modified by poly(ethylene glycol) (PEG): influences of the corona (PEG chain length and surface density) and of the core composition on phagocytic uptake and plasma protein adsorption. *Colloids Surf. B: Biointerfaces 18*, 301−313.

(24) Mosqueira, V. C., Legrand, P., Morgat, J. L., Vert, M., Mysiakine, E., Gref, R., Devissaguet, J. P., Barratt, G. (2001) Biodistribution of long-circulating PEG-grafted nanocapsules in mice: effects of PEG chain length and density. *Pharm. Res. 18*, 1411−1419.

(25) Dubertret, B., Skourides, P., Norris, D. J., Noireaux, V., Brivanlou, A. H., and Libchaber, A. (2002) In vivo imaging

of quantum dots encapsulated in phospholipid micelles. *Science 298*, 1759−1762.
(26) Akerman, M. E., Chan, W. C., Laakkonen, P., Bhatia, S. N., and Ruoslahti, E. (2002) Nanocrystal targeting in vivo. *Proc. Natl. Acad. Sci. U. S. A. 99*, 12617−12621.
(27) Becker, A., Hessenius, C., Licha, K., Ebert, B., Sukowski, U., Semmler, W., Wiedenmann, B., and Grotzinger, C. (2001) Receptor-targeted optical imaging of tumors with near-infrared fluorescent ligands. *Nat. Biotechnol. 19*, 327−331.
(28) Ballou, B., Fisher, G. W., Hakala, T. R., and Farkas, D. L. (1997) Tumor detection and visualization using cyanine fluorochrome-labeled antibodies. *Biotechnol. Prog. 13*, 649−658.
(29) Ballou, B., Fisher, G. W., Deng, J. S., Hakala, T. R., Srivastava, M., and Farkas, D. L. (1998) Cyanine fluorochrome-labeled antibodies in vivo: assessment of tumor imaging using Cy3, Cy5, Cy5.5, and Cy7. *Cancer Detect. Prev. 22*, 251−257.
(30) Licha, K., Riefke, B., Ebert, B., and Grotzinger, C. (2002) Cyanine dyes as contrast agents in biomedical optical imaging. *Acad. Radiol. 9 Suppl 2*, S320−322.
(31) Ebert, B., Sukowski, U., Grosenick, D., Wabnitz, H., Moesta, K. T., Licha, K., Becker, A., Semmler, W., Schlag, P. M., and Rinneberg, H. (2001) Near-infrared fluorescent dyes for enhanced contrast in optical mammography: phantom experiments. *J. Biomed. Opt. 6*, 134−140.
(32) Lin, Y., Weissleder, R., and Tung, C. H. (2002) Novel near-infrared cyanine fluorochromes: synthesis, properties, and bioconjugation. *Bioconjugate Chem. 13*, 605−610.
(33) Folli, S., Westerman, P., Braichotte, D., Pelegrin, A., Wagnieres, G., van den Bergh, H., and Mach, J.-P. (1994) Antibody-indocyanin conjugates for immunophotodetection of human squamous cell carcinoma in nude mice. *Cancer Res. 54*, 2643−2649.
(34) Lim, Y Taik, Kim, Sungjee, Nakayama, Akira, Stott, Nathan E., Bawendi, Moungi G., and Frangioni, John V. (2003) Selection of quantum dot wavelengths for biomedical assays and imaging. *Mol. Imag. 2*, 50−64.

BC034153Y

Persubstituted Cyclodextrin-Based Glycoclusters as Inhibitors of Protein−Carbohydrate Recognition Using Purified Plant and Mammalian Lectins and Wild-Type and Lectin-Gene-Transfected Tumor Cells as Targets†

Sabine André,*,‡ Herbert Kaltner,‡ Tetsuya Furuike,§ Shin-Ichiro Nishimura,*,|| and Hans-Joachim Gabius‡

Institute of Physiological Chemistry, Faculty of Veterinary Medicine, Ludwig-Maximilians-University Munich, Veterinärstr. 13, D-80539 Munich, Germany, and Laboratory for Glycocluster Project, Japan Bioindustry Association, Graduate School of Science, Hokkaido University, Sapporo 060-0810, Japan, and Division of Biological Sciences, Graduate School of Science, Hokkaido University, Kita-10 Nishi-8, Kitaku, Sapporo 060-0810, Japan. Received May 1, 2003; Revised Manuscript Received October 15, 2003

Multivalent glycoclusters have the potential to become pharmaceuticals by virtue of their target specificity toward clinically relevant sugar receptors. Their application can also provide fundamental insights into the impact of two spatial factors on binding, i.e., topologies of ligand (branching mode, cluster presentation) and carbohydrate recognition domains in lectins. Persubstituted macrocycles derived from nucleophilic substitution of iodide from heptakis 6-deoxy-6-iodo-β-cyclodextrin by the unprotected sodium thiolate of 3-(3-thioacetyl propionamido)propyl glycosides (galactose, lactose and *N*-acetyllactosamine) were prepared. The produced glycoclusters were first tested as competitive inhibitors in solid-phase assays. A plant toxin from mistletoe and an immunoglobulin G fraction from human serum were markedly susceptible. A nearly 400-fold increase in inhibitory potency of each galactose moiety in the heptavalent form relative to free lactose (217-fold relative to free galactose) was detected. Thus, these glycoclusters can efficiently interfere, for example, with xenoantigen-dependent hyperacute rejection. Among the tested galectins selected from this family of adhesion- and growth-regulatory endogenous lectins, the substituted β-cyclodextrins acted as sensors to delineate topological differences between the two dimeric prototype proteins. The relatively strong reactivity with chimera-type galectin-3, a mediator of tumor metastasis, disclosed selectivity for glycocluster binding among galectins. Equally important, the geometry of ligand display (maxiclusters, bi- or triantennary N-glycans) made its mark on the inhibitory potency. To further determine the sensitivity of a distinct galectin presented on the cell surface and not in solution, we established a stably transfected tumor cell clone. We detected a significant response to presence of the multivalent inhibitor. This type of chemical scaffold with favorable pharmacologic properties might thus be exploited for the design of galectin- and ligand-type-selective glycoclusters.

INTRODUCTION

The emergence of the concept of the sugar code entails an increasing interest in the activities of endogenous lectins (Winterburn and Phelps, 1972; Laine, 1997; Reuter and Gabius, 1999; Rüdiger et al., 2000; Gabius et al., 2002; Kilpatrick, 2002). On account of cell surface presentation and capacity for endocytosis, medical applications are being examined for several C-type lectins (Gabius, 1991, 1997; Rice, 1997; Yamazaki et al., 2000, 2001; Davis and Robinson, 2002), by exploiting glycoligands as a postal code in vectorized drug delivery. Acting as role models for this purpose, the hepatic and macrophage asialoglycoprotein receptors and the tandem-repeat mannose macrophage receptor have already served as proof-of-principle. In fact, the design of multivalent ligands matching the rather rigid topological display of these lectins' carbohydrate recognition domains was the basis for achieving astounding affinity enhancements of custom-made glycoclusters relative to their monovalent form, termed the glycoside cluster effect (Lee and Lee, 1994; Biessen et al., 1996; Grandjean et al., 2001; East and Isacke, 2002; Weigel and Yik, 2002). A similarly impressive example for how rational design of the ligand display accomplishes complementarity to fixed geometry of receptor sites is afforded by starfish and modularly prepared pentavalent inhibitors for bacterial AB_5 toxins (Schengrund, 2003). Thus, there is already ample reason to conclude that the combination of synthetic chemistry with lectin research promises insights into receptor functionality and a clinical perspective (Lee and Lee, 1994; Bovin and Gabius, 1995; Roy, 1996, 2002; Kiessling

* To whom correspondence should be addressed. S.A.: Fax: +49-89-2180-2508; e-mail: Sabine.Andre@lmu.de. S.N.: Fax: +81-11-706-3435; e-mail: shin@glyco.sci.hokudai.ac.jp.

† Dedicated in respect and thankful commemoration to Prof. Dr. F. Cramer who recently deceased three months before his 80th birthday.

‡ Ludwig-Maximilians-University Munich.

§ Laboratory for Glycocluster Project, Hokkaido University.

|| Division of Biological Sciences, Hokkaido University.

[1] Abbreviations: ASF, asialofetuin; CD, cyclodextrin; Gal, galactose; IgG, immunoglobulin G; Lac, lactose; Lac-BSA, lactosylated bovine serum albumin; LacNAc, *N*-acetyllactosamine; SAP, serum amyloid P component; VAA, *Viscum album* L. agglutinin.

10.1021/bc0340666 CCC: $27.50 © 2004 American Chemical Society
Published on Web 11/22/2003

et al., 2000; Gabius, 2001a; Cloninger, 2002; Houseman and Mrksich, 2002).

Presently, a major challenge in this area is to figure out how spatial factors and binding avidity toward soluble lectins are correlated. Model studies revealed that sugar surface density is a crucial factor for selectivity of binding, rate of cluster formation, and their stoichiometry (Horan et al., 1999; Cairo et al., 2002). However, increases in epitope density in neoglycoconjugates do not necessarily entail improved capacity as competitive inhibitors in model systems (Zanini and Roy, 1997a,b; Ashton et al., 1998; André et al., 1999a, 2001). Thus, systematic studies are warranted. After the chemistry to graft bioactive carbohydrates onto synthetic/natural scaffolds had been mastered, first studies on molecular interactions were nearly exclusively performed with plant lectins. Of note, the behavior of endogenous lectins cannot be reliably deduced on this experimental basis. As study objects, we consequently included mammalian proteins from a lectin family with adhesion/growth-regulatory activity on normal and malignant cells, i.e., the galectins (Gabius, 1997; Hirabayashi, 1997; Ohannesian and Lotan, 1997; Kaltner and Stierstorfer, 1998; André et al., 1999b; Brewer, 2002; Danguy et al., 2002; Rabinovich et al., 2002). For comparison, we also worked with a galactoside-specific plant lectin with potent signaling activity and—at increased concentration—toxicity on mammalian cells (Endo, 1989; Timoshenko et al., 1999; Gabius, 2001b) and an affinity-purified human immunoglobulin G fraction, a model for auto- or xenoreactive carbohydrate-binding antibodies in serum. Similar to galectins, these two sugar receptors are also cross-linking modules (Gupta et al., 1996). Persubstituted β-cyclodextrins maintaining their C_n-symmetry were chosen as test substance owing to several favorable properties for potential applications.

Cyclodextrins are nonimmunogenic natural macrocycles with inherently low pharmacological activity and high biocompatibility, the capacity to host pharmaceuticals in their truncated cone-shaped hydrophobic cavity coming along as added value. Functionalization with carbohydrate derivatives was accomplished with the long-term aim to devise an "intelligent" drug delivery system (Fulton and Stoddart, 2001a; Houseman and Mrksich, 2002; Ortiz Mellet et al., 2002). Having developed the facile synthesis of persubstituted β-cyclodextrins with galactose (Gal), lactose (Lac), or *N*-acetyllactosamine (LacNAc) as headgroup (Furuike et al., 2000), these glycoclusters (for schematic illustration, please see Figure 1) were introduced to assays with galectins. These endogenous lectins harbor marked intrafamily complexity. It encompasses different modes of spatial orientations of the carbohydrate recognition domains and cross-linking capacity, leading to functional divergence in disease mechanisms such as tumor invasion and spread (Kopitz et al., 2001; Lahm et al., 2001; Brewer, 2002; Camby et al., 2002; Cooper, 2002; Nangia-Makker et al., 2002; Nagy et al., 2003). For this study, we selected two related prototype proteins (galectins-1 and -7) and the chimera-type galectin-3. Because sugar density and topology are emerging as crucial factors modulating lectin binding, we systematically tested the glycoclusters' capacity to inhibit lectin binding to a panel of surface-presented ligands. Toward this end, (neo)glycoproteins presenting either lactose maxiclusters, bi- or triantennary N-glycans, or a complex mixture of N- and O-glycans were used for establishing the model surface. Last but not least, our study design accounted for another parameter of importance: the potency to interfere with multivalent interactions can vary with the nature of the test system (Mann et al., 1998). To address this issue properly, we performed solid-phase, haemagglutination, and cell binding assays. In these experimental settings the lectins were invariably present in solution. To be able to probe galectin behavior when presented on a cell surface, we generated a stable galectin-1-overexpressing colorectal cancer cell clone by transfection as a test model. The presented data reveal (a) efficiency of the substituted cyclodextrins to abolish receptor binding, (b) differential sensitivity of the tested galectins, (c) the improtance of ligand topology, and (d) of lectin presentation either in solution or on the cell surface.

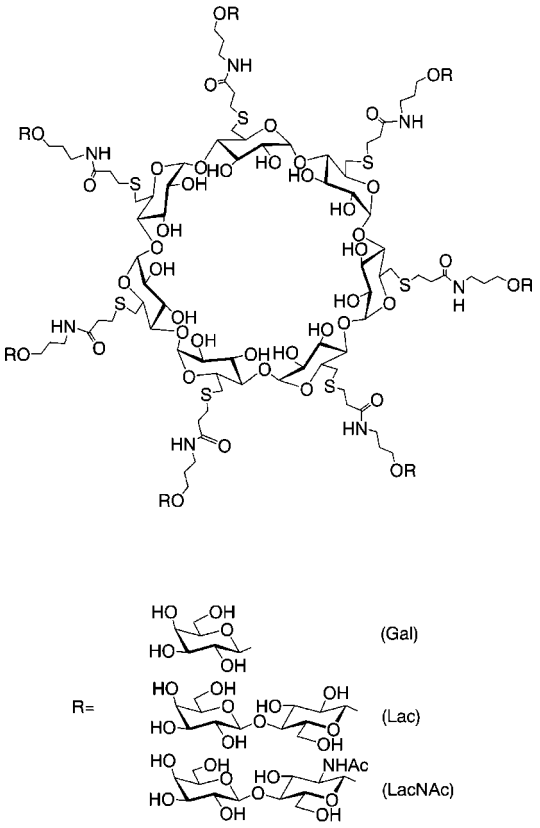


Figure 1. Structural illustration of the perglycosylated β-cyclodextrin derived from coupling 3-(3-thioacetyl propionamido)-propyl glycosides after de-O,S-acetylation to yield unprotected glycosides with a terminal sodium thiolate to heptakis 6-deoxy-6-iodo-β-cyclodextrin.

EXPERIMENTAL PROCEDURES

Reagents. The persubstituted glycoclusters with galactose, lactose, and *N*-acetyllactosamine as headgroup (please see Figure 1 for structural details) were prepared by conjugation of the respective sodium thiolate derived from treatment of 3-(3-thioacetyl propionamido)propyl sugars with NaOMe to heptakis 6-deoxy-6-iodo-β-cyclodextrin at 70 °C for 24 h, as described (Furuike et al., 2000). Following gel filtration on Sephadex G25, concentration of peak fractions, washing of the crude solid and lyophilization analytical procedures (optical rotation, ^{1}H and ^{13}C NMR spectroscopy, and matrix-assisted laser desorption ionization time-of-flight mass spectrometry) checked structure and purity of the products prior to the inhibition studies. Galectin-1 from bovine heart, murine galectin-3 (using the plasmid prCBP35s and *E. coli* JA 221 cells; a kind gift of Dr. J. L. Wang), and human galectin-7 (using the plasmid pQE−60/hGal-7 and *E. coli* M15[pREP4] cells; a kind gift of Dr. F.-T. Liu), the

Table 1. Determination of the IC_{50} Values and the Inhibitory Capacity (relative potency, rel pot.) of Gal-, Lac-, and LacNAc-Containing β-Cyclodextrins Relative to the Univalent Inhibitor Lactose in a Solid-Phase Assay

inhibitor	sugar content/ molecule	Lac−BSA		SAP		ASF		laminin	
		IC_{50} (μM)	rel pot.	IC_{50} (μM)	rel pot.	IC_{50} (μM)	rel pot.	IC_{50} (μM)	rel pot.
A. With Surface-Immobilized (Neo)glycoproteins and VAA in Solution[a]									
D-gal	1	2500	0.4	20000	0.38	5000	0.6	900	0.56
lactose	1	1000	1	7500	1	3000	1	500	1
Gal−CD	7	4.9	204 (29.1)[b]	48.7	154 (22.0)	122	24.6 (3.5)	36.5	13.7 (2.0)
Lac−CD	7	0.45	2222 (317)	181	41.4 (5.9)	2.3	1304 (186)	2.7	185 (26.4)
LacNAc−CD	7	25.5	39.2 (5.6)	255	17.6 (2.5)	212 = 44% inhib	<14.5 (<2.1)	53.1	9.4 (1.3)
B. With Surface-Immobilized (Neo)glycoproteins and Lactoside-Binding IgG in Solution[c]									
D-gal	1	100000	0.03	200000	1	55000	1.8		
lactose	1	3000	1	200000	1	100000	1		
Gal−CD	7	6.1	492 (70.3)[d]	183	1093 (156)	36.5	2740 (391)		
Lac−CD	7	15.8	190 (27.1)	904 = 22.8% inhib	<221 (<31.6)	452	221 (31.6)		
LacNAc−CD	7	6.4	469 (67.0)	425	471 (67.3)	12.8	781 (112)		

[a] The assays were performed at the following combinations of lectin and (neo)glycoprotein concentration: VAA/Lac-BSA (1.5 μg/mL/0.05 μg), VAA/SAP (1.5 μg/mL/0.5 μg), VAA/ASF (1.5 μg/mL/1μg), VAA/laminin (3 μg/mL/0.5 μg/mL). [b] The numbers in parentheses denote the relative potency of each sugar unit in the heptavalent cyclodextrin compared to carrier-free lactose set as internal quality standard [c] The assays were performed at the following combinations of IgG and (neo)glycoprotein concentration: Lac-IgG/Lac-BSA (1 μg/mL/0.05 μg), Lac-IgG /SAP (10 μg/mL/0.5 μg), Lac-IgG /ASF (10 μg/mL/1μg); laminin was not tested as matrix. [d] The numbers in parentheses denote the relative potency of each sugar unit in the heptavalent cyclodextrin compared to carrier-free lactose set as internal quality standard.

galactoside-specific agglutinin from *Viscum album* L. (VAA) and the lactoside-binding immunoglobulin G fraction of human serum, subfractionated by removing any α-galactoside-binding activity, were isolated and their purity was checked by one- and two-dimensional gel electrophoresis as described (Gabius, 1990; André et al., 1997). Biotinylation was performed under optimized activity-preserving conditions, and the binding partners for the sugar receptors, i.e., lactosylated bovine serum albumin with an average ligand density of 28 moieties per carrier molecule, human serum amyloid P component, and bovine asialofetuin, were prepared, as described previously (André et al., 2001). Murine Engelbreth-Holm-Swarm laminin was a kind gift by Dr. R. Timpl.

Quaternary Structure Analysis. Aliquots of 100 μg of galectin were run over a prepacked Superose 12 HR 10/30 column (24 mL bed volume) connected to a HPLC system (Hitachi-Merck, Darmstadt, Germany) with 50 mM phosphate-buffered saline (pH 7.2) without/with 100 mM lactose at a flow rate of 0.7 mL/min. Commercial standard proteins (BioRad, Munich, Germany) were used for calibration.

Inhibition Assays. The solid-phase assays were performed in microtiter plate wells (Microlon; Greiner, Nürtingen, Germany). Surface coating of the (neo)-glycoproteins was carried with an optimal concentration based on initial systematic testing (please see Table 1 and Table 2 for details) with 50 μL of 20 mM phosphate-buffered saline (pH 7.2) overnight at 4 °C. Thorough washing, blocking of remaining protein-binding sites with 100 μL of buffer solution containing 1% carbohydrate-free bovine serum albumin for 1 h at 37 °C and again thorough washing preceded the incubation step with the biotinylated sugar receptor in the absence/presence of glycocluster for 1 h at 37 °C. This mixture had been preincubated for 30 min at 37 °C without visible precipitate formation. Signal generation by streptavidin-peroxidase and *o*-phenylenediamine/H_2O_2 and its quantitation followed, as described in detail (André et al., 1997). Carbohydrate-dependent haemagglutination of trypsin-treated, glutaraldehyde-fixed rabbit erythrocytes by lectins was monitored with increasing concentrations of glycoinhibitor to determine the minimal inhibitory concentration, as described (Gabius et al., 1984). Flow cytofluorimetric analysis of binding of labeled galectins or lactosylated neoglycoprotein to tumor cell surfaces (human colon adenocarcinoma line SW480 obtained from the American Type Culture Collection, Rockville, MD, and human B-lymphoblastoid line Croco II established and propagated as described by Gabius et al., 1991) used standard FACScan instrumentation (Becton-Dickinson, Heidelberg, Germany, equipped with the software package CellQuest Pro) and fluorescent streptavidin-*R*-phycoerythrin (Sigma, Munich, Germany) as signal-generating reagent, as described (Kojima et al., 1997).

Generation of Stable Galectin-1-Overexpressing Transfectants. Cells of the human colorectal adenocarcinoma line DLD-1 (American Type Culture Collection, Rockville, MD) were grown in RPMI 1640 medium with 10% fetal calf serum (Biochrom, Berlin, Germany), 2 mM L-glutamine, 100 U/mL penicillin, and 100 μg/mL streptomycin. For transfection full-length cDNA for human galectin-1, kindly provided in the pH14Gal vector by Dr. J. Hirabayashi, was subcloned into the Kpn I restriction site of the pcDNA3.1(+) vector (Invitrogen/Life Technologies, Karlsruhe, Germany). Using 60−80% confluent cultures and the SuperFect reagent (Qiagen, Hilden, Germany; 10 μL/100 μL serum-free medium × 2 μg vector DNA) the cells were transfected and selection with G418 (600 μg/mL) initiated. Mock transfection with insert-free (null) vector was performed in parallel.

Characterization of Stable Transfectants. Insertion of the cDNA-carrying vector into genomic DNA was verified by PCR. Pellets from 2×10^6 cells were treated with 600 μL of nuclear lysis solution (Promega, Mannheim, Germany) and RNase. Following precipitation of proteins the genomic DNA in solution was pelleted by addition of 2-propanol and centrifugation. A 0.5 μg amount of this material was subjected to PCR analysis using the following pair of sense (5′-CGCTAGGGTAC-CATGGCTTGTGGTCTGGTCG-3′) and antisense (5′-CG-TACGGGTACCTCAGTCAAAGGCCACACA-3′; KpnI site underlined) sequences. In parallel, actin gene amplification was run. For the RT-PCR analysis total RNA was extracted with the RNAeasy kit reagents (Quiagen, Hilden, Germany) and reverse transcription used 200 U Superscript II RNase H^- Reverse Transcriptase (Invitrogen/Life Technologies, Karlsruhe, Germany). Western blotting analysis from total cell extracts with non-cross-reactive anti-galectin-1 antibody (1 μg immunoglobulin G/ml) was performed, as described (Gabius et al., 1986; Kaltner et al., 2002). Specifically bound antibody was visualized with an horseradish peroxidase/goat anti-rabbit immunoglobulin G conjugate (0.2 μg/mL) and a

Table 2. Determination of the IC_{50} Values and the Inhibitory Capacity (relative potency, rel pot.) of Gal-, Lac-, and LacNAc-Containing β-Cyclodextrins Relative to the Univalent Inhibitor Lactose in a Solid-Phase Assay

inhibitor	sugar content/ molecule	Lac-BSA		SAP		ASF		laminin	
		IC_{50} (μM)	rel pot.	IC_{50} (μM)	rel pot.	IC_{50} (μM)	rel pot.	IC_{50} (μM)	rel pot.
A. With Surface-Immobilized (Neo)glycoproteins and Galectin-1 in Solution[a]									
D-gal	1	40000	0.03	200 mM = 20% inhib		70000	0.06	200 mM = 6% inhib	
lactose	1	1100	1	180000	1	4000	1	300000	1
Gal−CD	7	30.5	36.1 (5.2)[b]	1218 = 0% inhib		609 = 11% inhib	< 6.6 (<0.9)	1218 = 32.2% inhib	
Lac−CD	7	54.2	20.3 (2.9)	904 = 8.7% inhib		226 = 33% inhib	< 17.7 (<2.5)	904 = 0% inhib	
LacNAc−CD	7	63.8	17.2 (2.5)	850	212 (30.3)	425	9.4 (1.3)	850 = 0% inhib	
B. With Surface-Immobilized (Neo)glycoproteins and Galectin-3 in Solution[c]									
D-gal	1	60000	0.01	30000	0.03	55000	0.02	15000	0.03
lactose	1	500	1	800	1	1000	1	400	1
Gal−CD	7	1218 = 0% inhib	<0.4 (<0.1)[d]	609 = 8.9% inhib	<1.3 (<0.2)	1218 = 37.1% inhib	<0.82 (<0.1)	609 = 36.3% inhib	<0.7 (<0.1)
Lac−CD	7	9.0	55.6 (7.9)	13.6	58.8 (8.4)	181	5.5 (0.8)	113	3.5 (0.5)
LacNAc−CD	7	149	3.4 (0.5)	53.1	15.1 (2.2)	85	11.8 (1.7)	34.0	11.8 (1.7)
C. With Surface-Immobilized (Neo)glycoproteins and Galectin-7 in Solution[e]									
D-gal	1	35000	0.14	95000	0.06	4500	0.18	15000	0.13
lactose	1	5000	1	6000	1	800	1	2000	1
Gal−CD	7	1218 = 37% inhib	<0.8 (<0.1)[f]	1218 = 4.8% inhib	<4.9 (<0.7)	1218 = 34% inhib	0.66 (0.1)	1218 mM = 5.7% inhib	<1.6 (<0.2)
Lac−CD	7	452	2.2 (0.3)	904	6.6 (0.9)	181	4.4 (0.6)	452	4.4 (0.6)
LacNAc−CD	7	425	2.4 (0.3)	850 =36.9% inhib	<7.1 (<1.0)	383	2.1 (0.3)	850 = 38.1% inhib	<2.4 (<0.3)

[a] The assays were performed at the following combinations of lectin and (neo)glycoprotein concentration: galectin-1/Lac-BSA (10 μg/mL/1 μg), galectin-1/SAP (15 μg/mL/0.5 μg), galectin-1/ASF (10 μg/mL/1μg), galectin-1/laminin (10 μg/mL/0.5 μg/mL). [b] The numbers in parentheses denote the relative potency of each sugar unit in the heptavalent cyclodextrin compared to carrier-free lactose set as internal quality standard. [c] The assays were performed at the following combinations of lectin and (neo)glycoprotein concentration: galectin-3/Lac-BSA (5 μg/mL/0.25 μg), galectin-3/SAP (10 μg/mL/0.5 μg), galectin-3/ASF (5 μg/mL/1μg), galectin-3/laminin (20 μg/mL/0.5 μg/mL). [d] The numbers in parentheses denote the relative potency of each sugar unit in the heptavalent cyclodextrin compared to carrier-free lactose set as internal quality standard. [e] The assays were performed at the following combinations of lectin and (neo)glycoprotein concentration: galectin-7/Lac-BSA (30 μg/mL/0.05 μg), galectin-7/SAP (30 μg/mL/0.5 μg), galectin-7/ASF (30 μg/mL/1μg), galectin-7/laminin (30 μg/mL/0.5 μg/mL). [f] The numbers in parentheses denote the relative potency of each sugar unit in the heptavalent cyclodextrin compared to carrier-free lactose set as internal quality standard.

chemiluminescence kit system (Amersham/Pharmacia Biotech, Freiburg, Germany). In a second round of probing actin was detected on the same blots by a polyclonal anti-actin antibody (Sigma, Munich, Germany; 3 μg/mL). Cell growth kinetics was analyzed for 10 days starting with a cell density of 10^4 cells/ml in 24-well culture plates loaded with 1 mL at 24 h intervals using an improved Neubauer chamber. Flow cytofluorimetric detection of cell surface galectin-1 was carried out, as described above for cell binding of lectins and lactosylated neoglycoprotein using a goat anti-rabbit immunoglobulin G FTC-conjugate (Sigma, Munich, Germany; 1:100 dilution of commercial solution).

RESULTS

Quaternary Galectin Structure. The three tested mammalian galectins belong to different subgroups within this family of endogenous lectins. Galectins-1 and -7 are prototype family members. They are characterized by the presence of a protomer harboring one carbohydrate recognition domain. In principle, it may or may not associate noncovalently to a dimeric cross-linking module. Galectin-3, in contrast, is the only known chimera-type family member. Its C-terminal carbohydrate recognition domain is linked to a collagenase-sensitive tandem-repeat region and a short N-terminal stretch. To ascertain the quaternary structure of these preparations of galectins-1 and -3 in solution, we performed molecular weight analysis by analytical gel filtration. Using a Superose matrix containing galactose and 3,6-anhydro-*L*-galactose in its repeating unit (agarobiose), the elution profile for galectin-1 confirmed its complete dimerization, whereas galectin-3 was retarded considerably in relation to the expected position (Figure 2, upper panel). Recalling binding capacity of galectin-3 to both nonreducing terminal and internal LacNAc sequences (Ahmad et al., 2002), a weak carbohydrate-specific interaction with the matrix was a reasonable and testable explanation. We therefore repeated the analysis in the presence of 100 mM lactose to block it. Indeed, the elution peak of galectin-3 was shifted to the position of the monomer (calculated MW: 27,384 Da) as predicted (Figure 2, bottom panel). This result underscored the necessity for rigorous specificity controls in the binding assay especially for galectin-3 (please see below).

With these two positions in the elution profile extending the set of molecular weight markers, we next addressed the question on the quaternary structure of human galectin-7. To preclude that weak and transient binding to the matrix might erroneously intimate presence of a monomer, this analysis was likewise performed in the absence and presence of lactose. Irrespective of altering this parameter galectin-7 eluted exclusively at the position of the dimer like galectin-1 (Figure 2). This result is in accord with recent mass spectrometric assessment (Kopitz et al., 2003). Galectin-7 is thus a dimeric prototype galectin in solution. It is noteworthy that its retention time (18.8 min) was longer than that for galectin-1 (16.52 min) despite a molecular weight difference of 546 Da in favor of galectin-7. Evidently, the shape of the two prototype galectins differed in solution. This intragroup variation is a strong argument to include members of the same subclass into our investigation whether and to what extent the tested multivalent inhibitors will affect lectin binding. Two principal types of inhibition assay were performed to answer this ques-

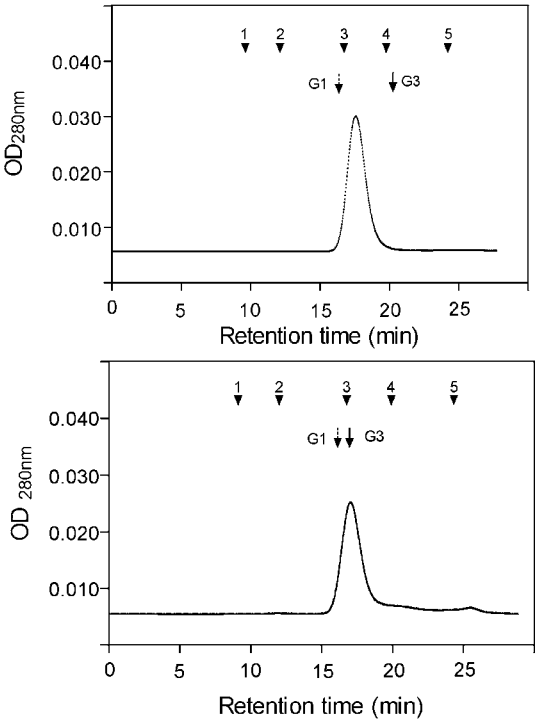


Figure 2. Determination of the molecular weight under native conditions for bovine galectin-1 (G1, arrow), murine galectin-3 (G3, arrow), and human galectin-7 (elution profile) with a Superose 12 HR 10/30 column. The analysis was performed in running buffer without addition of lactose (top) and in the presence of 100 mM lactose (bottom). Positions of molecular weight markers for calibration are given by arrowheads: bovine immunoglobulin (1) at 159 kDa, bovine serum albumin (2) at 66 kDa, carbonic anhydrase (3) at 29 kDa, cytochrome *c* (4) at 12.4 kDa, and aprotinin (5) at 6.5 kDa.

tion: a.) solid-phase binding to a matrix of biochemically defined (neo)glycoproteins mimicking a standardized cell surface and b.) cell-based binding using erythrocytes as laboratory models as well as cultured tumor cells and a lectin-overexpressing cell clone after gene transfection for clinical relevance. We tested persubstituted cyclodextrins to assess their potency to interfere with the protein-carbohydrate interactions.

Cyclodextrins as Inhibitors of Binding to (Neo)-glycoproteins. The adsorption of (neo)glycoproteins to the surface of ELISA plate wells established a matrix with ligand properties of a cell surface. The way the persubstituted β-cyclodextrins meddle with lectin binding to the glycans of the artificial glycocalyx can thus be considered as model situation to measure their influence on extracellular lectin activities. In the first step, the sugar dependence of the interaction between the surface-immobilized (neo)glycoproteins and the sugar receptors was ascertained. Invariably, binding for all sugar receptors was saturable and sensitive to presence of the haptenic sugar but not mannose. We performed our measurements with lactosylated albumin, presenting rather widely spaced ligand sites (maxiclusters), and three glycoproteins with known differences in glycan features: the human pentraxin serum amyloid P component (SAP) with a single complex-type biantennary N-glycan at Asn32 per protomer which -convenient for interaction studies − extends outward from the subunits, asialofetuin with preferentially triantennary N-glycans at its three N-glycosylation sites and murine laminin harboring a complex array of especially bi- and triantennary N-glycans including poly(*N*-acetyllactosamine) elongations distributed over 73 sites for N-glycosylation.

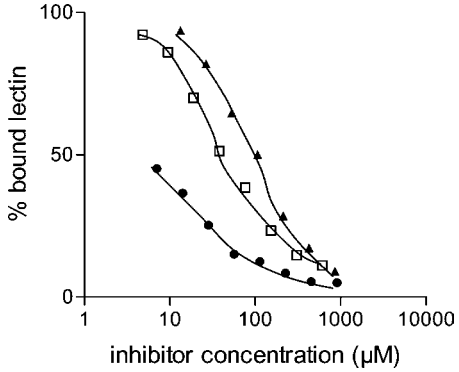


Figure 3. Inhibition curves of binding of biotinylated galactoside-specific *Viscum album* L. agglutinin to surface-immobilized murine laminin using the β-cyclodextrin-based glycoclusters with derivatives of D-galactose (□), lactose (●) and *N*-acetyllactosamine (▲) as headgroup.

Thus, this set enabled us to relate inhibitory capacity to the lectin and also to a defined glycan display, the latter parameter so far not thoroughly evaluated. To exclude that the cyclooligosaccharide carrier itself impaired receptor binding, we performed assays to figure out as to whether presence of unsubstituted β-cyclodextrins affected extent of binding of the biotinylated markers. Even at the very high concentration of 3.52 mM no or only minor (up to 15%) inhibitory activity could generally be picked up under the standard assay conditions. Looking at the data reported in the first section of Results, an expectable exception was galectin-3, with this concentration for example reaching 43.4% inhibition of binding to SAP. Because functionalization improved the inhibitory capacity of the cyclooligosaccharide by up to 2 orders of magnitude, these effects could yet be considered to be minor. Maintaining the overall symmetric geometry of their presentation, we attached three different headgroups to the carrier scaffold, i.e., Gal, Lac, and LacNAc via the same linker structure. Thus, we could determine exclusively the influence of headgroup tailoring under otherwise identical conditions. β-Cyclodextrin-based glycoclusters were then tested as competitive inhibitors to matrix binding of the sugar receptors kept in solution.

By raising the concentration of the glycocluster in the individual experimental series, the percentage of surface-bound receptor was reduced to varying extents, as exemplarily shown in Figure 3. Conjugation of the carbohydrate derivatives to the cyclodextrin scaffold thus did not harm binding properties of the headgroups to lectins and immunoglobulins. To calculate the glycoclusters' efficiency, we set an internal standard by running assays with galactose and lactose as reference substances in parallel. Tables 1 and 2 present the data for the five receptor types and the four (neo)glycoproteins as IC_{50} values. The measurements revealed that the glycoclusters had pronounced activities, the immunoglobulin G fraction and the plant lectin being markedly responsive (Tables 1a,b). Importantly, the topological display of the glycans (maxicluster, bi- or triantennary N-glycan chains) of the surface-presented ligand mattered. Plant lectin binding to maxiclusters and triantennary glycans was preferentially sensitive to glycocluster presence (Table 1a). Galactose-presenting scaffolds impaired binding of the serum immunoglobulin G fraction, too, especially in the presence of triantennary N-glycans of ASF in the artificial glycocalyx (Table 1b). Further synthetic manipulations of the glycoclusters by adding a glucose moiety and then a *N*-acetyl group were apparently not beneficial in this case. Regarding the galectins, there is

Table 3. Determination of the Minimal Inhibitory Concentration (MIC) and the Relative Inhibitory Capacity of Glycosubstances in Lectin-Mediated Haemagglutination

	VAA (0.1 μg/mL)		galectin-1 (1 μg/mL)		galectin-3 (100 μg/mL)	
inhibitor	MIC [μM]	relative potency	MIC [μM]	relative potency	MIC [μM]	relative potency
D-galactose	25000	0.5	6250	0.1	50000	0.06
lactose	12500	1	625	1	3000	1
ASF	10.5	1190 (132)[a]	2.5	250 (27.8)	105	28.6 (3.2)
β-CD	no inhibition up to 3500 μM	<3.6	no inhibition up to 3500 μM	<0.18	no inhibition up to 3500 μM	<0.86
Gal−CD	305	41.0 (5.9)	1218	0.5 (0.07)	no inhibition up to 1218 μM	< 2.5
Lac−CD	452	27.7 (4.0)	226	2.8 (0.4)	452	6.6 (0.9)
LacNAc−CD	850	14.7 (2.1)	106	5.9 (0.8)	106	28.3 (4)

[a] The numbers in parentheses denote the relative potency of each sugar unit in the heptavalent cyclodextrin compared to carrier-free lactose set as internal quality standard.

a general trend that headgroup extension improved the inhibitory efficiency (Table 2a−c). However, the overall sensitivity did often not reach the high level of inhibition detected for the other two sugar receptors. Among the galectins, galectin-3 showed the comparatively best responsiveness (Table 2b). In comparison, the two prototype proteins were generally not very reactive with these glycoclusters, although interindividual differences were apparent between galectins-1 and -7 (Table 2a−c). The inhibition of galectin-3 binding to maxiclusters and biantennary N-glycans showed a stronger dependence on inhibitor multivalency than that to the other two glycoproteins (Table 2b vs Table 2a,c). When calculating the relative potency of each carbohydrate unit of the cyclic glycoclusters, rather modest increases were obtained for the prototype galectins, depending on the nature of the ligand tested, relative to the other two sugar receptor types (Tables 1a,b, Tables 2a,c). Because a potential field of application will entail blocking binding to cell surfaces, not a matrix established by a single (neo)glycoprotein, we next tested the glycoclusters in assays using different cell types.

Cyclodextrins as Inhibitors of Binding to Cells. In the first test system we determined the extent of inhibition of lectin-mediated haemagglutination using trypsin-treated, glutaraldehyde-fixed rabbit erythrocytes as popular cell model. The agglutination was sugar dependent and not affected by the unsubstituted cyclodextrin up to 3.5 mM, as shown by controls (Table 3). The glycoclusters were clearly inhibitory, especially for the plant lectin. In this case, their design led to an improvement of the inhibitory capacity on the level of the individual sugar molecule by the factor of 11.8 in direct comparison to free galactose (Table 3). Corroborating the results of the solid-phase assays, the bridging activity of galectins was also inhibited by the functionalized macrocycles, especially with LacNAc as headgroup. Relative to the plant lectin, their activity toward the tested prototype galectin again was less pronounced. On the other hand, galectin-3, a weak haemagglutinin due to the requirement of aggregation when surface bound as it is monomeric in solution (please see Figure 1), was a rather suitable target (Table 3). To address the issue as to whether the assay design using cell agglutination and not cell binding as endpoint might influence the results, we performed flow cytofluorimetric measurements with two tumor cell lines (the B-lymphoblastoid line Croco II and the colon carcinoma line SW480). We tested the glycoclusters as inhibitors of lectin binding to the cell surface.

The results clearly showed that both assay types monitoring cell binding (haemagglutination or surface binding of labeled lectin) yielded comparable results. As shown in Figure 4 for the Croco II cells, the functionalized β-cyclodextrin was a potent inhibitor for the plant lectin relative to the monovalent sugar (top panel). The inhibition of galectin-3 binding by the Lac/LacNAc-bearing glycoclusters was significant and in the same favorable range, which had been monitored in haemagglutination, compared to the free sugar (middle and bottom panels). Up to this point, the assays were designed with a ligand-exposing surface to which the receptor coming from solution associates. The inhibitor and the receptor were thus both in solution. This situation simulated extracellular activities of galectins. In addition and equally important, they can also exert functions from the cell surface. To further define the extent to which the glycoclusters inhibit interactions mediated by cell surface lectins, it was thus essential to determine their influence on blocking galectin functionality on the cell surface. At this site, the lectin such as galectin-1 can act as a signal sensor or as a cell migration/adhesion molecule directing transient or firm adhesion to other cells and/or extracellular matrix glycoproteins, a step crucial for metastasis. To assign inhibitory potency of the glycoclusters on binding of glycans to a distinct galectin of the cell surface, a tumor cell line with strong surface expression of a certain galectin was required. The two tumor lines used above produce a set of four galectins, namely types 1, 3, 8, and 9 (Gabius et al., 1991; Lahm et al., 2001), confounding the interpretation. For this purpose, we generated a clone by gene transfection, using the human colorectal cancer line DLD-1 and galectin-1 as models.

Stable gene transfection by a galectin-1-cDNA-bearing expression vector and ensuing galectin-1 overexpression on the mRNA and protein levels were verified by PCR analysis of genomic DNA, RT-PCR monitoring, and Western blotting (Figure 5). The primer sequences were chosen to yield an amplification product of 408 bp from the vector-based cDNA in the genomic DNA and the mRNA. The length of the amplification product from the regular galectin-1 gene in the genomic DNA is 8142 bp. Highly efficient reverse transcription and Western blotting revealed traces of galectin-1-specific products in wild-type cells, signal absence in mock-transfected cells, and very strong expression in the sense-transfected cells. The morphological appearance of the three cell populations was rather similar (Figure 6), excluding a detrimental effect caused by this genetic manipulation. Also, the cell growth kinetics of the cell populations gave no indications for a markedly altered behavior with impaired membrane functions (Figure 7). Of interest for our study was the measurement of cell surface presentation of galectin-1. Relative to the control value the anti-galectin-1 antibody binding to the cell surface was clearly increased for the stably transfected cells (Figure 8). Using fluorescent

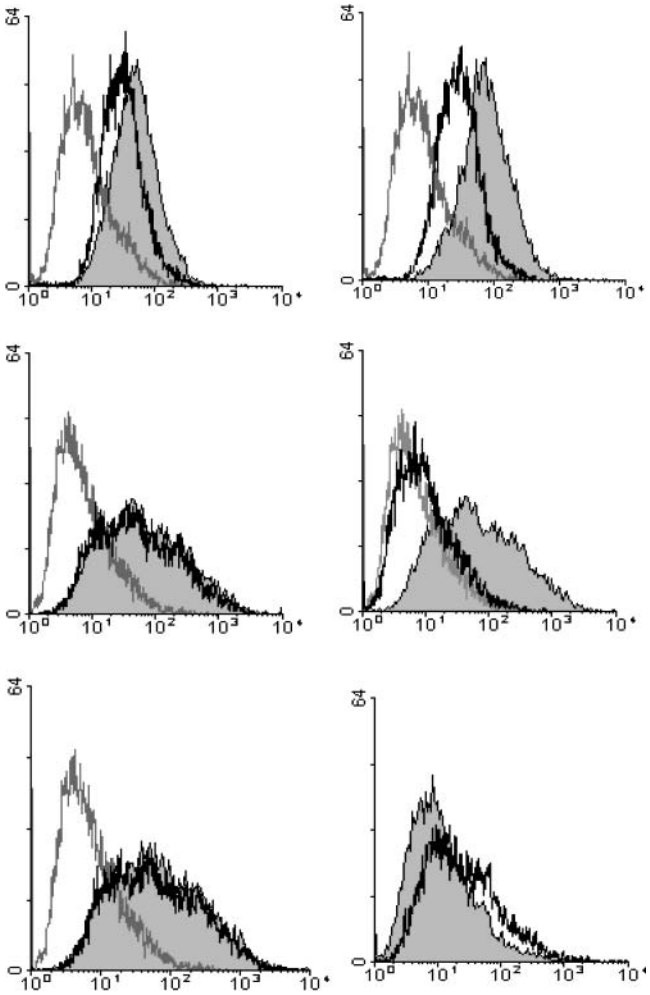


Figure 4. Semilogarithmic representation of fluorescent staining of the surface of human B-lymphoblastoid Croco II cells by biotinylated lectins in the absence and in the presence of glycoinhibitors using streptavidin R-phycoerythrin as second-step reagent. Top panel: cell staining after incubation with the second-step reagent only (gray line), with 0.5 μg mistletoe lectin/ml in the absence of any inhibitor (gray area; left) and in the presence of 6.4 mM lactose (black line; left), 3.5 mM β-cyclodextrin (gray area; right) and 0.9 mM lactose-presenting β-cyclodextrin (equivalent of 6.3 mM lactose in the heptavalent glycoclusters (black line; right)). Middle and bottom panels: cell staining after incubation with the second-step reagent only (gray line), with 10 μg galectin-3/ml in the absence of any inhibitor (gray area; middle panel) and in the presence of 2.2 mM D-galactose (black line in middle panel; left), 1.6 mM lactose (black line in middle panel; right), 180 μM substituent-free β-cyclodextrin and 61 μM galactose-presenting β-cyclodextrin (gray area and black line in bottom panel; left) as well as 43 μM *N*-acetyllactosamine- and lactose-presenting β-cyclodextrin (gray area and black line in bottom panel, right).

lactosylated albumin as probe, the inhibition of its cell surface association by lactose and lactose-bearing β-cyclodextrin was compared in FACScan analysis. Notably, the maxiclusters on the neogycoprotein enabled multivalent contacts to the surface-presented lectin, as already shown for several tumor cell lines and neoglycoenzymes as probes (Gabius et al., 1990). With the lactose concentration set at 6.4 mM, the percentage of positive cells was decreased to 70.5% relative to the control. The β-cyclodextrin derivative used at the same concentration also reduced binding of the neoglycoprotein to the cells, 59.5% of the cells remaining positive. Remarkably, even an increase of the free lactose concentration to 200 mM did not reach this level of competition with multivalent binding. The same tendency was apparent for the mean fluorescence intensity of cells. This result indicates that this galectin was more responsive to the multivalent inhibitor when presented on the cell surface than when in solution.

DISCUSSION

A general feature of protein−carbohydrate interactions is the requirement for establishment of several contacts to generate a sufficiently high affinity for biological activities. Therefore, carbohydrate recognition domains in lectins are often clustered, as recently summarized and illustrated for mammalian lectins (Gabius et al., 2002). A panel of structural motifs gives rise to diverse ways for the relative orientation of the binding sites. "Intelligent" blocking reagents or drug-delivery systems will capitalize on this factor to selectively home in on their targets. Advances in synthetic chemistry to solve problems of convenient carrier functionalization have made it possible to move from the preparative phase to testing the custom-made glycoclusters. In the case of heptaantennated β-cyclodextrins, plant lectins have so far served as model receptors. Respective measurements led to the conclusions that multivalency triggered nonuniform responses for various agglutinins in inhibition assays and that an increase in sugar density will not necessarily entail linear enhancement of inhibitory capacity.

In detail, galactosyl clusters interacted with the peanut lectin leading to a 16-fold increased association constant relative to the monovalent analogue but the individual ligands in two forms of persubstituted β-cyclodextrins (i.e. heptakis[6-*S*-β-D-galactopyranosyl-6-thio]cyclomaltoheptaose and heptakis[6-amino-6-deoxy-6-N−(β-D-galactopyranosyl-1-thiomethyl-carbonyl]cyclomaltoheptaose) failed to retain the level of inhibitory activity of a galactose moiety as internal standard in a solid-phase assay (García-López et al., 1999; Yasuda et al., 2000). The same inhibitor design gave reactivity for the pea lectin, the *Griffonia simplicifolia* I and wheat germ agglutinins but not the lectin from *Galanthus nivalis* (Ichikawa et al., 2000; Yasuda et al., 2000). Wheat germ agglutinin was also found to be remarkably responsive, whereas the dimeric *Erythrina corallodendron* lectin showed a reduced level of sensitivity (Furuike et al., 2000). Interestingly, studies with this lectin or its closely related variant from *Erythrina cristagalli* had not detected a strong effect of multivalency in dendrimers or neoglycopolymers (Zanini and Roy, 1997a; Pohl and Kiessling, 1999). This body of evidence discourages prediction of a priori potent activity of glycoclusters on lectins, although they harbor more than one binding site (Rüdiger and Gabius, 2001; Loris, 2002). It rather advises consideration of systematic experimental work as mandatory. Moving from hepta- to tetradeca-antennated glycoclusters, the apparent binding affinity to concanavalin A was not improved and, of relevance for drug targeting approaches, the ability of the cyclodextrin carrier to form an inclusion complex with 2-naphthalenesulfonate was harmed (Ortega-Caballero et al., 2001). This behavior is evocative of the eventual decrease in inhibitory capacity of Tris-branched dendritic wedges attached by 1,3,5-trisubstitution to a benzenoid core by increasing the number of headgroups from nine, then 18 to finally 36 carbohydrate residues (Ashton et al., 1998). The way the nature of the linker can even drastically influence the inhibition profile was illustrated in the case of heptasubstitution of primary hydroxyls with mannopyranosylthioureido moieties which fail to bind to concanavalin A (Baussanne et al., 2001; Ortiz

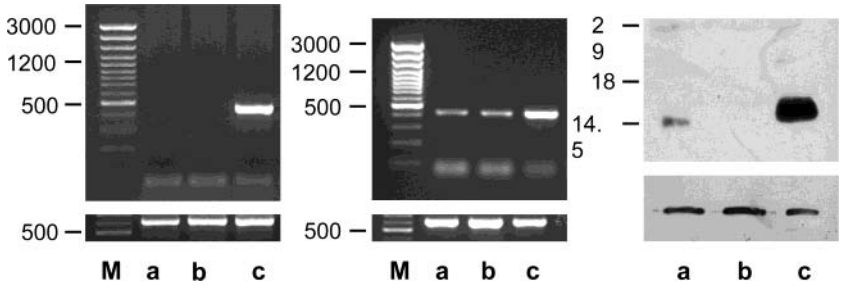


Figure 5. Detection of presence of galectin-1-specific cDNA in genomic DNA (left), of galectin-1-specific mRNA by RT-PCR analysis (middle) and of galectin-1 by Western blotting (right) in material obtained from human colorectal adenocarcinoma DLD-1 cells (a = wild type, b: mock-transfected cells, c: galectin-1 sense transfectant). Numbers on the left side of each panel indicate length of markers (M) or molecular weight of standard proteins. Actin-related parameters were determined as positive quality control (bottom panel).

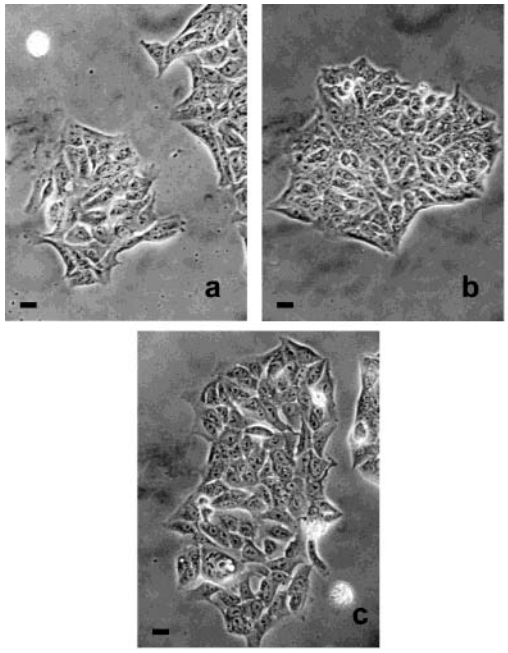


Figure 6. Light micrographs from populations of human wild-type colorectal adenocarcinoma DLD-1 cells (a), a mock-transfected variant clone (b) and the galectin-1 sense transfectant clone (c); bar = 20 μm.

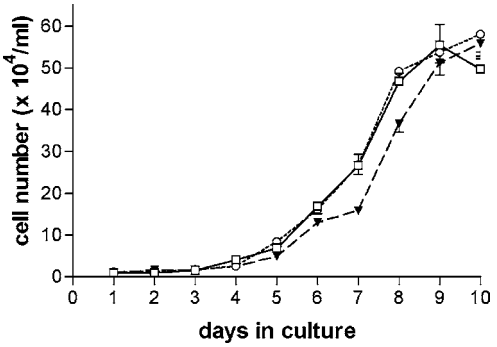


Figure 7. Determination of cell growth of DLD-1 wild-type cells (□), a mock-transfected variant clone (○), and the galectin-1 sense transfectant clone (▼).

Mellet et al., 2002). When extending the linker's length to give the supposedly required degree of conformational freedom, as for example documented by García-López et al. (1999), it should not be overlooked that long alkyl spacer arms might find access to the hydrophobic cavity and that carbohydrates might form interresidual hydrogen bonds, impairing their accessibility for lectins (Fulton and Stoddart, 2001b). The strong preference of the

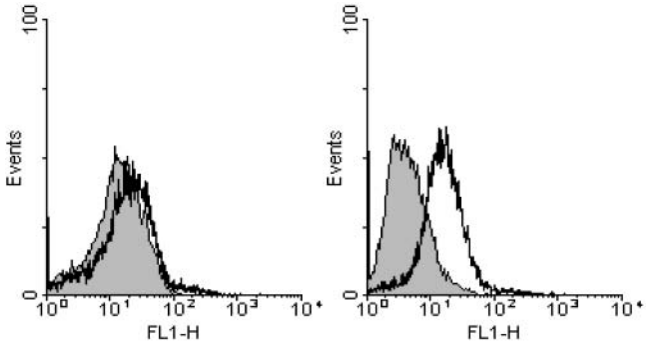


Figure 8. Detection of expression of galectin-1 on the surface of wild-type (left) and sense-transfected DLD-1 cells (right) by flow cytofluorimetry (black line) relative to antigen-independent staining by the fluorescent second-step reagent (gray area) as control.

mistletoe lectin for lactose relative to *N*-acetyllactosamine despite rather similar binding properties in inhibition assays and isothermal titration calorimetry appears to indicate occurrence of such unfavorable events (Lee et al., 1992; Galanina et al., 1997; Bharadwaj et al., 1999). On the other hand, galectin-1, where presence of the *N*-acetyl group accounts for a 0.7 kcal/mol increase of $-\Delta G$ relative to lactose binding (300 K), preferred this ligand in contrast to galectin-7, ΔG in this case decreasing from -4.6 for lactose to -4.4 kcal/mol for LacNAc (Ahmad et al., 2002). With this background, Fulton and Stoddart (2001a) stated that "it is probably fair to conclude that, in the area of saccharide-branched cyclodextrins, and indeed saccharide-branched macrocycles, the research carried out to date only begins to scratch the surface of understanding the subtleties of the relative spatial orientation of carbohydrate ligands, relative to their scaffolds and to each other."

In comparison between the presented reactivity profiles, the plant lectin with its double trefoil structure (Niwa et al., 2003) was prominent for its sensitivity toward glycoinhibitor multivalency. Mitogenic effects on immune and, notably, tumor cells in the ng/mL-range and toxicity at doses above this concentration, seen in vitro for cultured and for peripheral blood cells as well as histotypic tumor cultures (Hajto et al., 1990; Gabius et al., 2001), can thus be abrogated swiftly by these inhibitiors. A similar result can be expected for other plant AB toxins such as ricin. Similarly, the natural β-galactoside-specific immunoglobulin G fraction from human serum was efficiently blocked by hepta-galactosylated β-cyclodextrin. The relative potency on the level of the individual carrier-attached moiety reached the factor of 391 compared to lactose as internal standard. The remarkable sensitivity of the immunoglobulin to these

glycoclusters and also to starburst/wedgelike glycodendrimers and neoglycopolymers might find practical application to protect patients from antibody-dependent hyperacute rejection originating from the immunoreactivity of carbohydrate xenoantigens (André et al., 1999a, 2001; Wang et al., 1999; Baek and Roy, 2002).

In contrast to these two sugar receptors, the prototype galectins with their binding sites on opposing sides of the dimer at a distance of close to 50 Å were less reactive. This result is in line with previous measurements assaying divalent ligands connected by varying linker lengths as well as starburst and wedgelike glycodendrimers (Lee et al., 1990; André et al., 1999a, 2001, 2003). However, our measurements with the gene-transfected cell clone revealed that cell surface presentation can render the prototype galectin-1 more susceptible to a multivalent ligand compared to its behavior in solution. As the k_{off}-rates from *p*-aminophenyl lactoside differed only slightly between the plant lectin and galectin-1 in plasmon resonance monitoring (Dettmann et al., 2000), the impact of the topological aspect is underscored. Also, the differential activity of the substituted β-cyclodextrins against the two prototype galectins, which are both dimeric, can be interpreted to be a sensitive sensor for slight differences in their shape. They might have a bearing on galectin functionality by ligand cross-linking and thus contribute to explain differences in the biological response profile of related galectins (Camby et al., 2001; Kopitz et al., 2001; Sheikholeslam-Zadeh et al., 2001; Brewer, 2002; Cao et al., 2002; Nagy et al., 2002, 2003; Timoshenko et al., 2003). It is thus useful to have a reliable marker in hand to probe these characteristics comparatively.

The most notable difference between the galectins concerned galectin-3 relative to galectins-1 and -7. Monomeric in solution, the chimera-type galectin can form aggregates via its N- and C-terminal domain which are responsive toward multivalent ligands (André et al., 2001 and references therein). The relative potency of the substituted β-cyclodextrins to galectin-3 distinguished this family member from the prototype galectins, a clear indication for subgroup selectivity. This result is in line with the activity profile of wedgelike glycodendrimers, especially after spacer rigidification (André et al., 2001; Vrasidas et al., 2003). The answer to the question as to whether persubstitution is indispensable for this feature can be figured out by testing less than hepta-antennated products obtained by running conjugation with a subsaturating concentration of the carbohydrate derivative. Combining these topological factors, i.e., ligand display and spacer properties, with exploitation of the differences in carbohydrate fine-specificity, among others the 12-fold difference of inhibitory capacity of α2,6-sialylated diLacNAc to galectin-3 vs galectin-1 (Ahmad et al., 2002; Hirabayashi et al., 2002), the discriminatory power is sure to be further enhanced. In this area, combinatorial synthesis of carbohydrates and mimetics thereof is likely to be instrumental to extend the panel of structures, efficiently homing in on a certain lectin (Nishimura, 2001; Ramström et al., 2002).

A further salient finding of this report is the influence of the topology of the lectin's binding partner on the inhibitory profile. To avoid missing this "topological" specificity, it will be essential to routinely test more than one biochemically defined ligand. By using (neo)glycoproteins with precisely known glycan profile (maxiclusters, bi- and/or triantennary N-glycans), we obtained a nonuniform response to the substituted β-cyclodextrins for each tested sugar receptor. Thus, we can in fact conclude that the characteristics of the ligand population (cluster formation, status of branching) matter more than currently appreciated for receptors in solution. Avidity of binding to branched and/or clustered ligands encompasses both a contact and a topology dimension. With chemoenzymatically synthesized glycan chains becoming available, systematic studies of this aspect are clearly warranted. The way the natural N-glycan substitution by core fucosylation modulates lectin affinity to the galactoside termini of complex-type biantennary N-glycans has recently set a precedent for further efforts in this respect (Unverzagt et al., 2002).

In conclusion, this report proves that hepta-antennated β-cyclodextrins present their carbohydrate appendages in bioactive form for galactoside-specific plant and, notably, mammalian lectins as well as immunoglobulin G. Furthermore, discriminatory potency of these glycoclusters between two prototype and between prototype vs chimera-type galectins was evidenced. Beside the topological aspect of binding site arrangement in the receptor part, the geometry of the ligand structure was shown to exert a considerable influence, a result with evident biological implications. In more general terms, our results provide a promising example that substituted β-cyclodextrins, owing to their favorable pharmacologic properties, have potential to find their place in the design of "intelligent" blocking reagents.

ACKNOWLEDGMENT

The skilfull technical assistance of B. Hofer, the kind gifts of reagents from Drs. J. Hirabayashi, F.-T. Liu, R. Timpl, and J. L. Wang, the helpful advice from Drs. B. B. and S. Namirha, and the generous financial support of the Wilhelm Sander-Stiftung (Munich, Germany) are gratefully acknowledged.

LITERATURE CITED

(1) Ahmad, N., Gabius, H.-J., Kaltner, H., André, S., Kuwabara, I., Liu, F.-T., Oscarson, S., Norberg, T., and Brewer, C. F. (2002) Thermodynamic binding studies of cell surface carbohydrate epitopes to galectins-1, -3 and -7: evidence for differential binding specificities. *Can. J. Chem. 80*, 1096−1104.

(2) André, S., Unverzagt, C., Kojima, S., Dong, X., Fink, C., Kayser, K., and Gabius, H.-J. (1997) Neoglycoproteins with the synthetic complex biantennary nonasaccharide or its α2,3/α2,6-sialylated derivatives: their preparation, assessment of their ligand properties for purified lectins, for tumor cells in vitro, and in tissue sections, and their biodistribution in tumor-bearing mice. *Bioconjugate Chem. 8*, 845−855.

(3) André, S., Ortega, P. J., Perez, M. A., Roy, R., and Gabius, H.-J. (1999a) Lactose-containing starburst dendrimers: influence of dendrimer generation and binding-site orientation of receptors (plant/animal lectins and immunoglobulins) on binding properties. *Glycobiology 9*, 1253−1261.

(4) André, S., Kojima, S., Yamazaki, N., Fink, C., Kaltner, H., Kayser, K., and Gabius, H.-J. (1999b) Galectins-1 and -3 and their ligands in tumor biology. *J. Cancer Res. Clin. Oncol. 125*, 461−474.

(5) André, S., Pieters, R. J., Vrasidas, I., Kaltner, H., Kuwabara, I., Liu, F.-T., Liskamp, R. M. J., and Gabius, H.-J. (2001) Wedgelike glycodendrimers as inhibitors of binding of mammalian galectins to glycoproteins, lactose maxiclusters, and cell surface glycoconjugates. *ChemBioChem 2*, 822−830.

(6) André, S., Liu, B., Gabius, H.-J., and Roy, R. (2003) First demonstration of differential inhibition of lectin binding by synthetic tri- and tetravalent glycoclusters from cross-coupling of rigidified 2-propynyl lactoside. *Org. Biomol. Chem. 1*, 3909−3916.

(7) Ashton, P. R., Hounsell, E. F., Jayaraman, N., Nilsen, T. M., Spencer, N., Stoddart, J. F., and Young, M. (1998)

Synthesis and biological evaluation of α-D-mannopyranoside-containing dendrimers. *J. Org. Chem. 63*, 3429−3437.
(8) Baek, M.-G., and Roy, R. (2002) Synthesis and protein binding properties of T-antigen containing glycoPAMAM dendrimers. *Bioorg. Med. Chem. 10*, 11−17.
(9) Baussanne, I., Benito, J. M., Ortiz Mellet, C., García Fernández, J. M., and Defaye, J. (2001) Dependence of concanavalin A binding on anomeric configuration, linkage type, and ligand multiplicity for thiourea-bridged mannopyranosyl-β-cyclodextrin conjugates. *ChemBioChem 2*, 777−783.
(10) Bharadwaj, S., Kaltner, H., Korchagina, E. Y., Bovin, N. V., Gabius, H.-J., and Surolia, A. (1999) Microcalorimetric indications for ligand binding as a function of the protein for galactoside-specific plant and avian lectins. *Biochim. Biophys. Acta 1472*, 191−196.
(11) Biessen, E. A. L., Noorman, F., van Teijlingen, M. E., Kuiper, J., Barrett-Bergshoeff, M., Bijsterbosch, M. K., Rijken, D. C., van Berkel, and T. J. (1996) Lysine-based cluster mannosides that inhibit ligand binding to the human mannose receptor at nanomolar concentration. *J. Biol. Chem. 271*, 28024−28030.
(12) Bovin, N. V., and Gabius, H.-J. (1995) Polymer-immobilized carbohydrate ligands: versatile chemical tools for biochemistry and medical sciences. *Chem. Soc. Rev. 24*, 413−421.
(13) Brewer, C. F. (2002) Binding and cross-linking properties of galectins. *Biochim. Biophys. Acta 1572*, 255−262.
(14) Cairo, C. W., Gestwicki, J. E., Kanai, M., and Kiessling, L. L. (2002) Control of multivalent interactions by binding epitope density. *J. Am. Chem. Soc. 124*, 1615−1619.
(15) Camby, I., Belot, N., Rorive, S., Lefranc, F., Maurage, C.-A., Lahm, H., Kaltner, H., Hadari, Y., Ruchoux, M.-M., Brotchi, J., Zick, Y., Salmon, I., Gabius, H.-J., and Kiss, R. (2001) Galectins are differentially expressed in supratentorial pilocytic astrocytomas, astrocytomas, anaplastic astrocytomas and glioblastomas, and significantly modulate tumor astrocyte migration. *Brain Pathol. 11*, 12−26.
(16) Camby, I., Belot, N., Lefranc, F., Sadeghi, N., de Launoit, Y., Kaltner, H., Musette, S., Darro, F., Danguy, A., Salmon, I., Gabius, H.-J., and Kiss, R. (2002) Galectin-1 modulates human glioblastoma cell migration into the brain through modifications to the actin cytoskeleton and levels of expression of small GTPases. *J. Neuropathol. Exp. Neurol. 61*, 585−596.
(17) Cao, Z., Said, N., Amin, S., Wu, H. K., Bruce, A., Garate, M., Hsu, D. K., Kuwabara, I., Liu, F.-T., and Panjwani, N. (2002) Galectins-3 and -7, but not galectin-1, play a role in re-epithelialization of wounds. *J. Biol. Chem. 277*, 42299−42305.
(18) Cloninger, M. J. (2002) Biological applications of dendrimers. *Curr. Opin. Chem. Biol. 6*, 742−748.
(19) Cooper, D. N. W. (2002) Galectinomics: finding themes in complexity. *Biochim. Biophys. Acta 1572*, 209−231.
(20) Danguy, A., Camby, I., and Kiss, R. (2002) Galectins and cancer. *Biochim. Biophys. Acta 1572*, 285−293.
(21) Davis, B. G., and Robinson, M. A. (2002) Drug delivery systems based on sugar-macromolecule conjugates. *Curr. Opin. Drug Discovery Dev. 5*, 279−288.
(22) Dettmann, W., Grandbois, M., André, S., Benoit, M., Wehle, A. K., Kaltner, H., Gabius, H.-J., and Gaub, H. E. (2000) Differences in zero-force and force-driven kinetics of ligand dissociation from β-galactoside-specific proteins (plant and animal lectins, immunoglobulin G) monitored by plasmon resonance and dynamic single molecule force microscopy. *Arch. Biochem. Biophys. 383*, 157−170.
(23) East, L., and Isacke, C. (2002) The mannose receptor family. *Biochim. Biophys. Acta 1572*, 364−386.
(24) Endo, Y. (1989) Mechanism of action of ricin and related toxic lectins on the inactivation of eukaryotic ribosomes. *Adv. Lectin Res. 2*, 60−73.
(25) Fulton, D. A., and Stoddart, J. F. (2001a) Neoglycoconjugates based on cyclodextrins and calixarenes. *Bioconjugate Chem. 12*, 655−672.
(26) Fulton, D. A., and Stoddart, J. F. (2001b) Synthesis of cyclodextrin-based carbohydrate clusters by photoaddition reactions. *J. Org. Chem 66*, 8309−8319.
(27) Furuike, T., Aiba, S., and Nishimura, S.-I. (2000) A highly practical synthesis of cyclodextrin-based glycoclusters having enhanced affinity with lectins. *Tetrahedron 56*, 9909−9915.
(28) Gabius, H.-J. (1990) Influence of type of linkage and spacer on the interaction of β-galactoside-binding proteins with immobilized affinity ligands. *Anal. Biochem. 189*, 91−94.
(29) Gabius, H.-J. (1991) Detection and functions of mammalian lectins − with emphasis on membrane lectins. *Biochim. Biophys. Acta 1071*, 1−18.
(30) Gabius, H.-J. (1997) Animal lectins. *Eur. J. Biochem. 243*, 543−576.
(31) Gabius, H.-J. (2001a) Glycohistochemistry: the why and how of detection and localization of endogenous lectins. *Anat. Histol. Embryol. 30*, 3−31.
(32) Gabius, H.-J. (2001b) Probing the cons und pros of lectin-induced immunomodulation: case studies for the mistletoe lectin and galectin-1. *Biochimie 83*, 659−666.
(33) Gabius, H.-J., Engelhardt, R., Rehm, S., and Cramer, F. (1984) Biochemical characterization of endogenous carbohydrate-binding proteins from spontaneous murine rhabdomyosarcoma, mammary adenocarcinoma and ovarian teratoma. *J. Natl. Cancer Inst. 73*, 1349−1357.
(34) Gabius, H.-J., Engelhardt, R., Rehm, S., Barondes, S. H., and Cramer, F. (1986) Presence and relative distribution of three endogenous β-galactoside-specific lectins in different tumor types of rat. *Cancer J. 1*, 19−22.
(35) Gabius, S., Schirrmacher, V., Franz, H., Joshi, S. S., and Gabius, H.-J. (1990) Analysis of cell-surface sugar receptor expression by neoglycoenzyme binding and adhesion to plastic-immobilized neoglycoproteins for related weakly and strongly metastatic cell lines of murine tumor model systems. *Int. J. Cancer 46*, 500−507.
(36) Gabius, S., Joshi, S. S., Gabius, H.-J., and Sharp, J. G. (1991) Establishment, characterization and determination of cell surface sugar receptor (lectin) expression by neoglycoenzymes of a human myeloid marker-expressing B-lymphoblastoid cell line. *Anticancer Res. 11*, 793−800.
(37) Gabius, H.-J., Darro, F., Remmelink, M., André, S., Kopitz, J., Danguy, A., Gabius, S., Salmon, I., and Kiss, R. (2001) Evidence for stimulation of tumor proliferation in cell lines and histotypic cultures by clinically relevant low doses of the galactoside-binding mistletoe lectin, a component of proprietary extracts. *Cancer Invest. 19*, 114−126.
(38) Gabius, H.-J., André, S., Kaltner, H., and Siebert, H.-C. (2002) The sugar code: functional lectinomics. *Biochim. Biophys. Acta 1572*, 165−177.
(39) Galanina, O. E., Kaltner, H., Khraltsova, L. S., Bovin, N. V., and Gabius, H.-J. (1997) Further refinement of the description of the ligand-binding characteristics for the galactoside-binding mistletoe lectin, a plant agglutinin with immunomodulatory potency. *J. Mol. Recogn. 10*, 139−147.
(40) García-López, J. J., Hernández-Mateo, F., Isac-Garciá, J., Kim, J. M., Roy, R., Santoyo-González, F., and Vargas-Berenguel, A. (1999) Synthesis of per-glycosylated β-cyclodextrins having enhanced lectin binding affinity. *J. Org. Chem. 64*, 522−531.
(41) Grandjean, C., Angyalosi, G., Loing, E., Adriaenssens, E., Melnyk, O., Pancre, V., Auriault, C., and Gras-Masse, H. (2001) Novel hyperbranched glycomimetics recognized by the human mannose receptor: quinic or shikimic acid derivatives as mannose bioisosteres. *ChemBioChem 2*, 747−757.
(42) Gupta, D., Kaltner, H., Dong, X., Gabius, H.-J., and Brewer, C. F. (1996) Comparative cross-linking activities of lactose-specific plant and animal lectins and a natural lactose-binding immunoglobulin G fraction from human serum. *Glycobiology 6*, 843−849.
(43) Hajto, T., Hostanska, K., Frei, K., Rordorf, C., and Gabius, H.-J. (1990) Increased secretion of tumor necrosis factor-α, interleukin-1, and interleukin-6 by human mononuclear cells exposed to the galactoside-specific lectin from clinically applied mistletoe extract. *Cancer Res. 50*, 3322−3326.
(44) Hirabayashi, J., Ed. (1997) Recent topics on galectins. *Trends Glycosci. Glycotechnol. 9*, 1−180.
(45) Hirabayashi, J., Hashidate, T., Arata, Y., Nishi, N., Nakamura, T., Hirashima, M., Urashima, T., Oka, T., Futai, M., Müller, W. E. G., Yagi, F., and Kasai, K.-i. (2002) Oligosac-

charide specificity of galectins: a search by frontal affinity chromatography. *Biochim. Biophys. Acta 1572*, 232−254.
(46) Horan, N., Yan, L., Isobe, H., Whitesides, G. M., and Kahne, D. (1999) Nonstatistical binding of a protein to clustered carbohydrates. *Proc. Natl. Acad. Sci. U.S.A. 96*, 11782−11786.
(47) Houseman, B. T., and Mrksich, M. (2002) Model systems for studying polyvalent carbohydrate binding interactions. *Top. Curr. Chem. 218*, 1−44.
(48) Ichikawa, M., Woods, A. S., Mo, H., Goldstein, I. J., and Ichikawa, Y. (2000) Simple preparation of multivalent cyclodextrin-carbohydrate conjugates. *Tetrahedron: Asymmetry 11*, 389−392.
(49) Kaltner, H., and Stierstorfer, B. (1998) Animal lectins as cell adhesion molecules. *Acta Anat. 161*, 162−179.
(50) Kaltner, H., Seyrek, K., Heck, A., Sinowatz, F., and Gabius, H.-J. (2002) Galectin-1 and galectin-3 in fetal development of bovine respiratory and digestive tracts. *Cell Tissue Res. 307*, 35−46.
(51) Kiessling, L. L., Gestwicki, J. E., and Strong, L. E. (2000) Synthetic multivalent ligands in the exploration of cell-surface interactions. *Curr. Opin. Chem. Biol. 4*, 696−703.
(52) Kilpatrick, D. C. (2002) Animal lectins: a historical introduction and overview. *Biochim. Biophys. Acta 1572*, 187−197.
(53) Kojima, S., André, S., Korchagina, E. Y., Bovin, N. V., and Gabius, H.-J. (1997) Tyramine-containing poly(4-nitrophenylacrylate) as iodinatable ligand carrier in biodistribution analysis. *Pharmaceut. Res. 14*, 879−886.
(54) Kopitz, J., von Reitzenstein, C., André, S., Kaltner, H., Uhl, J., Ehemann, V., Cantz, M., and Gabius, H.-J. (2001) Negative regulation of neuroblastoma cell growth by carbohydrate-dependent surface binding of galectin-1 and functional divergence from galectin-3. *J. Biol. Chem. 276*, 35917−35923.
(55) Kopitz, J., André, S., von Reitzenstein, C., Versluis, K., Kaltner, H., Pieters, R. J., Wasano, K., Kuwabara, I., Liu, F.-T., Cantz, M., Heck, A. J. R., and Gabius, H.-J. (2003) Homodimeric galectin-7 (p53-induced gene 1) is a negative growth regulator for human neuroblastoma cells. *Oncogene 22*, 6277−6288.
(56) Lahm, H., André, S., Hoeflich, A., Fischer, J. R., Sordat, B., Kaltner, H., Wolf, E., and Gabius, H.-J. (2001) Comprehensive galectin fingerprinting in a panel of 61 human tumor cell lines by RT-PCR and its implications for diagnostic and therapeutic procedures. *J. Cancer Res. Clin. Oncol. 127*, 375−386.
(57) Laine, R. A. (1997) The information-storing potential of the sugar code. In *Glycosciences: Status and Perspectives* (H.-J. Gabius and S. Gabius, Eds.) pp 1−14, Chapman & Hall, London.
(58) Lee, R. T., and Lee, Y. C. (1994) Enhanced biochemical affinities of multivalent neoglycoconjugates. In *Neoglycoconjugates. Preparation and Applications* (Y. C. Lee and R. T. Lee, Eds.) pp 23−50, Academic Press, San Diego.
(59) Lee, R. T., Ichikawa, Y., Allen, H. J., and Lee, Y. C. (1990) Binding characteristics of galactoside-binding lectin (galaptin) from human spleen. *J. Biol. Chem. 265*, 7864−7871.
(60) Lee, R. T., Gabius, H.-J., and Lee, Y. C. (1992) Ligand binding characteristics of the major mistletoe lectin. *J. Biol. Chem. 267*, 23722−23727.
(61) Loris, R. (2002) Principles of structures of animal and plant lectins. *Biochim. Biophys. Acta 1572*, 198−208.
(62) Mann, D. A., Kanai, M., Maly, D. J., and Kiessling, L. L. (1998) Probing low affinity and multivalent interactions with surface plasmon resonance: ligands for concanavalin A. *J. Am. Chem. Soc. 120*, 10575−10582.
(63) Nagy, N., Bronckart, Y., Camby, I., Legendre, H., Lahm, H., Kaltner, H., Hadari, Y. R., Van Ham, P., Yeaton, P., Pector, J.-C., Zick, Y., Salmon, I., Danguy, A., Kiss, R., and Gabius, H.-J. (2002) Galectin-8 expression decreases in cancer compared with normal and dysplastic human colon tissue and acts significantly on human colon cancer cell migration as a suppressor. *Gut 50*, 392−401.
(64) Nagy, N., Legendre, H., Engels, O., André, S., Kaltner, H., Wasano, K., Zick, Y., Pector, J.-C., Decaestecker, C., Gabius, H.-J., Salmon, I., and Kiss, R. (2003) Refined prognostic evaluation in colon cancer using immunohistochemical galectin fingerprinting. *Cancer 97*, 1849−1858.
(65) Nangia-Makker, P., Hogan, V., Honjo, Y., Baccarini, S., Tait, L., Bresalier, R., and Raz, A. (2002) Inhibition of human cancer cell growth and metastasis in nude mice by oral intake of modified citrus pectin. *J. Natl. Cancer Inst. 94*, 1854−1862.
(66) Niwa, H., Tonevitsky, A. G., Agapov, I. I., Saward, S., Pfüller, U., and Palmer, R. A. (2003) Crystal structure at 3 Å of mistletoe lectin I, a dimeric type-II ribosome-inactivating protein, complexed with galactose. *Eur. J. Biochem. 270*, 2739−2749.
(67) Nishimura, S.-I. (2001) Combinatorial syntheses of sugar derivatives. *Curr. Opin. Chem. Biol. 5*, 325−335.
(68) Ohannesian, D. W., and Lotan, R. (1997) Galectins in tumor cells. In *Glycosciences: Status and Perspectives* (H.-J. Gabius and S. Gabius, Eds.) pp 459−469, Chapman & Hall, London.
(69) Ortega-Caballero, F., Giménez-Martínez, J. J., García-Fuentes, L., Ortiz-Salmerón, E., Santoyo-González, F., and Vargas-Berenguel, A. (2001) Binding affinity properties of dendritic glycosides based on a β-cyclodextrin core toward guest molecules and concanavalin A. *J. Org. Chem. 66*, 7786−7795.
(70) Ortiz Mellet, C., Defaye, J., and García Fernández, J. M. (2002) Multivalent cyclooligosaccharides: versatile carbohydrate clusters with dual role as molecular receptors and lectin ligands. *Chem. Eur. J. 8*, 1982−1990.
(71) Rabinovich, G. A., Rubinstein, N., and Toscano, M. A. (2002) Role of galectins in inflammatory and immunomodulatory processes. *Biochim. Biophys. Acta 1572*, 274−284.
(72) Ramström, O., Bunyapaiboonsri, T., Lohmann, S., and Lehn, J.-M. (2002) Chemical biology of dynamic combinatorial libraries. *Biochim. Biophys. Acta 1572*, 178−186.
(73) Reuter, G., and Gabius, H.-J. (1999) Eukaryotic glycosylation: whim of nature or multipurpose tool? *Cell. Mol. Life Sci. 55*, 368−422.
(74) Rice, K. G. (1997) Glycoconjutate-mediated drug targeting. In *Glycosciences: Status and Perspectives* (H.-J. Gabius and S. Gabius, Eds.) pp 471−483, Chapman & Hall, London.
(75) Roy, R. (1996) Blue-prints, synthesis and applications of glycopolymers. *Trends Glycosci. Glycotechnol. 8*, 79−99.
(76) Roy, R. (2002) Designing novel multivalent glycotools for biochemical investigations related to sialic acid. *J. Carbohydr. Chem. 21*, 769−798.
(77) Rüdiger, H., Gabius, H.-J. (2001) Plant lectins. *Glycoconjugate J. 18*, 589−613.
(78) Rüdiger, H., Siebert, H.-C., Solís, D., Jiménez-Barbero, J., Romero, A., von der Lieth, C.-W., Díaz-Mauriño, T., and Gabius, H.-J. (2000) Medicinal chemistry based on the sugar code: fundamentals of lectinology and experimental strategies with lectins as targets. *Curr. Med. Chem. 7*, 389−416.
(79) Schengrund, C.-L. (2003) "Multivalent" saccharides: development of new approaches for inhibiting the effects of glycosphingolipid-binding pathogens. *Biochem. Pharmacol. 65*, 699−707.
(80) Sheikholeslam-Zadeh, R., Decaestecker, C., Delbrouck, C., Danguy, A., Salmon, I., Zick, Y., Kaltner, H., Hassid, S., Gabius, H.-J., Kiss, R., and Choufani, G. (2001) The levels of expression of galectin-3, but not of galectins-1 and -8, correlate with apoptosis in human cholesteatomas. *Laryngoscope 111*, 1042−1047.
(81) Timoshenko, A. V., Gorudko, I. V., Kaltner, H., and Gabius, H.-J. (1999) Dissection of the impact of various intracellular signaling pathways on rat thymocytes after initial lectin-dependent cell association using a plant lectin as model and target-selective inhibitors. *Mol. Cell. Biochem. 197*, 137−145.
(82) Timoshenko, A. V., Gorudko, I. V., Maslakova, O. V., André, S., Kuwabara, I., Liu, F.-T., Kaltner, H., and Gabius, H.-J. (2003) Analysis of selected blood and immune cell responses to carbohydrate-dependent surface binding of proto- and chimera-type galectins. *Mol. Cell. Biochem. 259*, 139−149.
(83) Unverzagt, C., André, S., Seifert, J., Kojima, S., Fink, C., Srikrishna, G., Freeze, H., Kayser, K., and Gabius, H.-J. (2002) Structure−activity profiles of complex biantennary glycans with core fucosylation and with/without additional α2, 3/α2,6-sialylation: synthesis of neoglycoproteins and their

properties in lectin assays, cell binding and organ uptake. *J. Med. Chem. 45*, 478−491.
(84) Vrasidas, I., André, S., Valentini, P., Böck, C., Lensch, M., Kaltner, H., Liskamp, R. M. J., Gabius, H.-J., and Pieters, R. J. (2003) Rigidified multivalent lactose molecules and their interactions with mammalian galectins: a route to selective inhibitors. *Org. Biomol. Chem. 1*, 803−810.
(85) Wang, J.-Q., Chen, X., Zhang, W., Zacharek, S., Chen, Y., and Wang, P. G. (1999) Enhanced inhibition of human anti-gal antibody binding to mammalian cells by synthetic α-gal epitope polymers. *J. Am. Chem. Soc. 121*, 8174−8181.
(86) Weigel, P. H., and Yik, J. H. N. (2002) Glycans as endocytosis signals: the cases of the asialoglycoprotein and hyaluronan/chondroitin sulfate receptors. *Biochim. Biophys. Acta 1572*, 341−363.
(87) Winterburn, P. J., and Phelps, C. F. (1972) The significance of glycosylated proteins. *Nature 236*, 147−151.
(88) Yamazaki, N., Kojima, S., Bovin, N. V., André, S., Gabius, S., and Gabius, H.-J. (2000) Endogenous lectins as targets in drug delivery. *Adv. Drug Delivery Rev. 43*, 225−244.
(89) Yamazaki, N., Jigami, Y., Gabius, H.-J., and Kojima, S. (2001) Preparation and characterization of neoglycoprotein-liposome conjugates: a promising approach to developing drug delivery materials applying sugar chain ligands. *Trends Glycosci. Glycotechnol. 13*, 319−329.
(90) Yasuda, N., Aoki, N., Abe, H., and Hattori, K. (2000) Per-C-6 oligosaccharide-branched cyclodextrin interacting with both the lectin and drug. *Chem. Lett. 6*, 706−707.
(91) Zanini, D., and Roy, R. (1997a) Chemoenzymatic synthesis and lectin binding properties of dendritic *N*-acetyllactosamine. *Bioconjugate Chem. 8*, 187−192.
(92) Zanini, D., and Roy, R. (1997b) Synthesis of new α-thiosialodendrimers and their binding properties to the sialic acid specific lectin from *Limax flavus*. *J. Am. Chem. Soc. 119*, 2088−2095.

BC0340666

Synthesis and Physicochemical Characterization of Gd−DTPA−B(sLe^x)A, a New MRI Contrast Agent Targeted to Inflammation

Sophie Laurent, Luce Vander Elst, Yanjun Fu,† and Robert N. Muller*

NMR Laboratory, Department of Organic Chemistry, University of Mons-Hainaut, B-7000 Mons, Belgium. Received July 8, 2003; Revised Manuscript Received October 8, 2003

A new magnetic resonance imaging (MRI) contrast agent designed to mimic sialyl Lewis X (sLe^X) and to target inflammation has been synthesized and characterized. The evolution of its proton longitudinal relaxivity as a function of the magnetic field (NMRD) and temperature has been studied. The exchange rate of the water coordinated to the metal has been assessed by oxygen-17 relaxometry. The transmetalation by zinc(II) ions and the noncovalent binding to human serum albumin have been evaluated. The results show no limitation by the residence time of the coordinated water molecule above room temperature, a higher stability of the complex versus transmetalation by zinc(II) ions than a parent complex, the clinically used Gd-DTPA-BMA, and negligible interaction with human serum albumin.

INTRODUCTION

The interaction between E-selectin of endothelial cells and sialyl Lewis^x (sLe^x), an oligosaccharide located on the surface of monocytes, neutrophils, basophils, eosinophils, and a specific subset of T lymphocytes, occurs early after tissue injury and leads to inflammation (*1*, *2*). Blocking the sLe^x/selectin interaction has thus been considered as an efficient way to treat inflammatory disease (*3*). Although sLe^x has demonstrated antiinflammatory action, its large-scale synthesis, like that of other oligosaccharides, is difficult. Therefore, efforts to produce mimetics have been attempted. The conformation of sLe^x in solution and the three-dimensional structure of the human E-selectin have been determined (*4*−*7*). Six functional groups of the sLe^x molecule, the 2-, 3- and 4-hydroxyl groups of L-fucose, the 4- and 6-hydroxyl groups of galactose, and the carboxylate group of the sialic acid, are essential for the recognition by E-selectin (*8*, *9*). Compounds containing these functional groups and mimicking the active conformation of sLe^x have been recently designed and synthesized (*10*−*15*).

For the purpose of developing a novel contrast agent targeted to inflammation, we have described a successful and original synthesis of a new DTPA ligand conjugated to a sialyl Lewis^X mimetic, a 3-(2-α-D-mannopyranosyloxyphenyl)phenylacetic acid moiety which is a potent inhibitor for sLe^x-selectin binding (*16*). DTPA was chosen as metal chelator because of its high thermodynamic equilibrium constant with stable paramagnetic or radioactive ions such as gadolinium (*17*, *18*). The coupling of DTPA to the sialyl Lewis^X mimetic is performed through its bicyclic bisanhydride form (*19*, *20*). The DTPA ligand has been subsequently complexed with gadolinium, an ion commonly used as the paramagnetic core of MRI contrast agents (*21*, *22*). In the present work, the specific MRI contrast agent Gd−DTPA−B(sLe^x)A has been submitted to a classical physicochemical characterization encompassing the study of its relaxivity as a function of the magnetic field and temperature, stability in the presence of Zn(II) ions, and the assessment of noncovalent binding to albumin and the determination of water residence time by oxygen-17 relaxometry.

* Corresponding author. Tel/Fax: +32 65 37 35 20, e-mail: robert.muller@umh.ac.be.

† Present address: Center for Pharmaceutical and Molecular Imaging, Department of Radiology, Box 0628, UCSF, San Francisco, CA 94143.

EXPERIMENTAL PROCEDURES

Chemicals. Gd−DTPA (Magnevist) was obtained from Schering AG (Berlin, Germany), and Gd−DTPA−BMA (Omniscan) from Amersham-Nycomed (Oslo, Norway). $GdCl_3$ and $ZnCl_2$ were purchased from Aldrich (Bornem, Belgium). Phosphate buffer pH 7 was from Merck (Overijse, Belgium).

Mass Spectrometry. The mass spectrum was obtained on a Q-tof II mass spectrometer (Micromass, Manchester, UK). Compound (0.5 mg) was dissolved in 1 mL of a mixture MeOH/H_2O (50/50) and infused in the source at a debit of 5 μL/min.

Chromatography. Reverse-phase HPLC was carried out on a system consisting of a Waters 600 controller and a Waters 996 photodiode array detector equipped with a Novapak C18 column for analytical runs (i.d. 4.56 mm × 150 mm) and for semiprep runs (i.d. 25 mm × 100 mm) (Waters, Milford, MA). A gradient of 95:5 to 50:50 (S1/S2, v/v) solvent was run over 20 min at a flow rate of 0.7 mL/min for analysis or 9.0 mL/min for preparation (solvent S1, 5% aqueous CH_3CN with 0.3 mM HCl; solvent S2, 95% aqueous CH_3CN with 0.3 mM HCl). Addition of HCl was necessary to decrease the adsorption of samples on the column materials. UV adsorption of the effluent was monitored at 254 nm.

Dialysis. Dialysis was carried out against deionized water using a cellulose ester tube with cutoff molecular weight of 500 (Spectra/PorCE, diameter 20 mm).

Relaxometry. Proton nuclear magnetic relaxation dispersion (NMRD) profiles were recorded at different temperatures on an IBM Research Field Cycling Relaxometer working between 0.02 and 40 MHz. The samples

10.1021/bc034114m CCC: $27.50 © 2004 American Chemical Society
Published on Web 11/22/2003

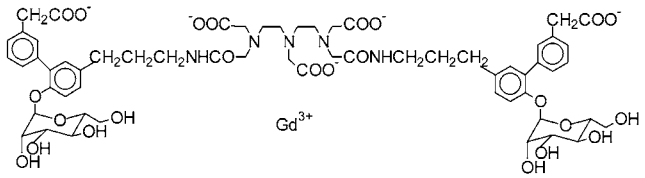


Figure 1. Structure of the Gd−DTPA−B(sLe^x)A.

(0.6 mL) were contained in 10 mm o.d. tubes. The temperature was controlled with a precision of 0.1 °C. Additional points at 20, 40, and 300 MHz were respectively obtained on Minispec systems PC-20 and PC-40 and on an AMX 300 spectrometer (Bruker, Germany). Fitting of the ^{1}H NMRD curves was performed with a previously described software using minimization routines (Minuit, CERN Library) (*23*, *24*), according to the theoretical innersphere (*25*, *26*) and outersphere models (*27*). T_1 measurements at 7.05 T were performed with the inversion recovery Fourier transform technique and a subsequent three parameters fit of the peak height.

The oxygen-17 measurements (*28*) were carried out on 2 mL samples contained in 10 mm o.d. tubes on a Bruker AMX-300 spectrometer equipped with a broadband probe and with a Bruker BVT-2000 unit for temperature control. The temperature was regulated by air or nitrogen flow. Diamagnetic transverse relaxation times of ^{17}O water (pH ≈ 6.5) were measured at natural abundance using a Carr−Purcell−Meiboom−Gill sequence and a two-parameter fit of the data points. ^{17}O transverse relaxation times of water (natural abundance) in solutions containing paramagnetic complexes were calculated directly from the line width measurement. All ^{17}O NMR spectra were proton decoupled. The evaluation of the exchange rate of the water coordinated to the Gd ion was carried out by analyzing the temperature dependence of the oxygen-17 resonance line width in the range of 280−350 K.

Transmetalation. Transmetalation by zinc ions was evaluated by the decrease of the water longitudinal relaxation rate at 310 K and 20 MHz (Bruker Minispec) of buffered phosphate solutions containing 2.5 mM of the gadolinium complex and 2.5 mM of Zn (*29*).

Synthesis. Gadolinium (III) complex, Gd−DTPA−B(sLe^X)A: A solution of $GdCl_3 \cdot 6H_2O$ (0.196 mmol, 72.8 mg) in distilled water (5 mL) was added slowly to the ligand DTPA−B(sLe^X)A solution (0.196 mmol). The complexation was performed at pH 6−6.5 by adding diluted NaOH. The mixture was stirred at 50 °C for 3 h and then submitted to an exhaustive dialysis (membrane cutoff: 500 Da, 4 × 300 mL, 4 × 18 h). The dialyzate, in which the absence of free Gd^{3+} ions was assessed by the arsenazo III test (*30*), was lyophilized to give 230 mg of chromatographically pure complex as a slightly yellow solid. Analytical reverse-phase HPLC: retention time 4.94 min, semiprep HPLC: retention time: 12.14 min. ESI: Gd-isotopes m/z = 1446−1455 $(M + H)^+$. Anal. ($C_{60}H_{72}N_5O_{24}GdNa_2 \cdot 6H_2O$): calcd (found): C 46.21 (46.01); H 5.4 (5.25); N 4.49 (4.45).

RESULTS AND DISCUSSION

The Gd−DTPA−B(sLe^x)A complex obtained by mixing an equimolar amount of ligand (*16*) and gadolinium chloride hexahydrate is shown in Figure 1.

Residence Time of the Coordinated Water Molecule. The possible influence of the residence time of the coordinated water molecule, τ_M, on proton relaxation was evaluated by measuring the proton longitudinal relaxivity r_1 of the Gd complexes at 0.47 T over a temperature range extending from 5 to 45 °C (Figure 2). The continuous increase of r_1 when temperature decreased shows that no drastic limitation of the relaxivity of the complex occurs at low temperatures, even if by comparison to the data obtained for Gd−DTPA there is evidence of a slight limitation at low temperatures.

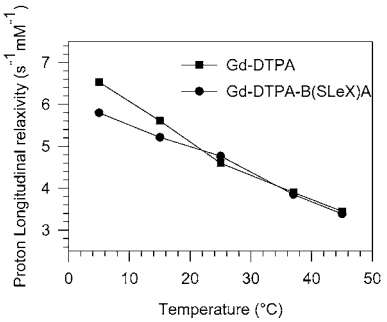


Figure 2. Temperature dependence of the proton longitudinal relaxivity of Gd−DTPA−B(sLe^x)A and Gd−DTPA at 20 MHz.

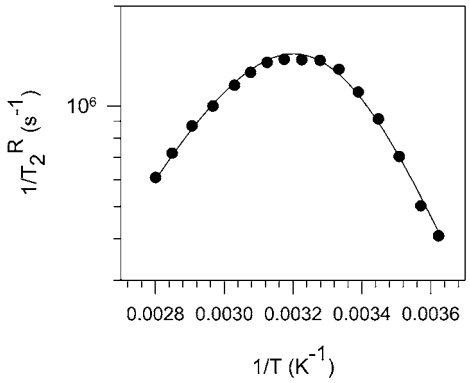


Figure 3. Temperature dependence of the oxygen-17 reduced transverse relaxation rate of Gd−DTPA−B(sLe^x)A (26.3 mM).

The quantitative determination of the residence time of water molecules in the first coordination sphere of the gadolinium complexes (τ_M) was performed as described previously (*28*) by analysis of the temperature dependence of the paramagnetic oxygen-17 transverse relaxation rate of a 26.3 mM solution of the complex (Figure 3). From the theoretical fitting of the data, several parameters are obtained: first, the hyperfine coupling constant between the oxygen-17 nucleus and the electronic spin of Gd^{3+} ($A/\hbar$); second, the parameters related to the electronic relaxation times of the gadolinium ion τ_{S1} and τ_{S2}, i.e., τ_V, the correlation time for the modulation of the zero field splitting, E_V, the activation energy for this process, and B, which depends on the trace of the square of the zero field splitting tensor (Δ^2) and on the electron spin S ($B = \Delta^2\{4S(S + 1) - 3\}/25$); and, third, the parameters of the water exchange rate, i.e., the enthalpy ($\Delta H^{\ddagger}$) and the entropy ($\Delta S^{\ddagger}$) of activation. By analogy with other derivatives of Gd−DTPA, the number of coordinated water molecules (q) was assumed to be equal to one. The theoretical fitting of the reduced transverse relaxation rates ($1/T_2^R = \{1/T_2^{obs} - 1/T_2^{dia}\} \times 55.55/$ [Gd complex]) obtained over a temperature range extending from 276 to 357 K gives a τ_M^{298} value of 525 ± 57 ns. This value is somewhat larger than that reported for Gd−DTPA ($\tau_M^{298} = 331 \pm 60$ ns) (*31*) but much shorter than that of Gd−DTPA−BMA ($\tau_M^{298} = 2130 \pm 80$ ns) (*32*) or other Gd−DTPA bisamides substituted by alkyl chains (*32*). The fitted parameters are shown in Table 1 (the values obtained for Gd−DTPA−BMA are shown for com-

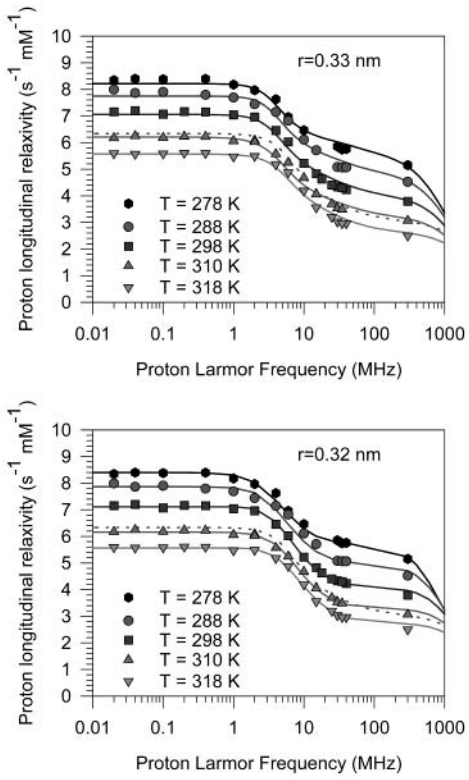


Figure 4. Experimental NMRD profiles of Gd−DTPA−B(sLe^x)A (1.18 mM) in water at different temperatures. Top graph: the lines correspond to the theoretical fitting performed with outer-sphere and inner-sphere interactions. Bottom graph: the lines correspond to the theoretical fitting performed with inner-sphere and second-sphere interactions. Dotted line: Gd−DTPA at 310 K.

Table 1. Parameters Obtained from the Fitting of the Reduced Transverse Relaxation Rate of Oxygen-17

	Gd−DTPA−B(sLe^x)A	Gd−DTPA	Gd−DTPA−BMA
B (10^{20} s^{-2})	1.96 ± 0.64	2.60 ± 0.06	2.04 ± 0.06
τ_V^{298} (ps)	18.5 ± 5.6	12.3 ± 0.3	21.2 ± 0.6
$A/\hbar$ (10^6 rad s^{-1})	−3.0 ± 0.1	−3.4 ± 0.1	−3.2 ± 0.1
$\Delta H^{\ddagger}$(kJ/mol)	42.7 ± 0.1	51.5± 0.3	48.0 ± 0.1
$\Delta S^{\ddagger}$(J/mol K)	18.7 ± 0.5	52.1 ± 0.6	24.9 ± 0.2
E_V (kJ/mol)	15.4 ± 2.2	4.5 ± 4.2	15.0 ± 10.9
τ_M^{310} (ns)	259 ± 27	143 ± 26	967 ± 36

parison). The value obtained for the hyperfine coupling constant confirms the presence of one coordinated water molecule.

The τ_M^{310} value is short enough to enable a fast exchange between coordinated and bulk water molecules. However, at low temperatures, a slight limitation of the inner-sphere proton relaxivity by the water residence time is responsible for the lower relaxivity of Gd−DTPA−B(sLe^x)A as compared to that of Gd−DTPA.

Relaxivity at Various Magnetic Fields and Temperatures. The proton NMRD profiles recorded at five temperatures are shown in Figure 4.

Despite the larger molecular weight of the Gd−DTPA−B(sLe^x)A complex (MW = 1449), its proton relaxivity at 310 K is comparable to that of Gd−DTPA (MW = 547) (*31*) over the whole proton Larmor frequency range. The fittings of the proton NMRD profiles were performed as described in the Experimental Section and include both inner-sphere and outer-sphere interactions (*23*−*27*). The following parameters were fixed during the fitting procedure: *d*, the distance of closest approach for the outersphere contribution which was set at 0.36 nm (*28*, *31*), τ_M values which were those obtained by ^{17}O NMR, and *q*, the number of water molecules in the first coordination sphere of Gd^{3+}, which was set to one. The parameters describing the electronic relaxation times, τ_V and τ_{SO} (the electronic relaxation time at zero field), were optimized for the outer-sphere and the inner-sphere contributions simultaneously. The distance *r* between the protons of the coordinated water molecule and the Gd ion is usually set to 0.3 or 0.31 nm for Gd−DTPA derivatives unsubstituted on the carbon backbone (*32*, *33*, *34*). The rotational correlation time of the complex, τ_R, could not be estimated by the analysis of the deuterium relaxation rates due to the hydrolysis of the amide bonds during the labeling of the α-carbons of carbonyl groups. Its estimation by the Stokes−Einstein law, assuming that the molecular volume is roughly proportional to the molecular weight and that the complex rotates as a rigid structure, gives a value of approximately 145 ns at 310 K. This value and a distance *r* equal to 0.31 nm did not allow a proper fitting of the experimental data. Reasonable fits were obtained either by decreasing the value of τ_R to values even lower than those of Gd−DTPA, which seems unrealistic, or by increasing the distance *r*. In a first approach, this last solution was chosen. The fitting performed with an *r* value of 0.33 nm results in a τ_R^{310} of 93 ps. This value of τ_R seems acceptable since internal motion could lower the effective rotational correlation time. The fittings were thus performed for the five temperatures with this value of *r*. The resulting parameters are given in Table 2.

Table 2. Parameters Obtained from the Fitting of the Proton NMRD Data of Gd−DTPA-B(sLe^x)A

Inner-Sphere and Outer-Sphere Contributions with r = 0.33 nm

temperature	D (10^{-9} m^{2}s^{-1})[a]	τ_R (ps)	τ_{so}[b] (ps)	τ_v (ps)	τ_M (ns)
278 K	1.5	194	95	33	1945
288 K	1.9	146	94	34	988
298 K	2.5	116	97	32	525
310 K	3.3	93	97	24	259
318 K	3.7	71	97	27	166

Inner-Sphere and Second-Sphere Contributions with r = 0.32 nm[c]

temperature	τ_R (ps)	τ_{so}[b] (ps)	τ_v (ps)	τ_M (ns)	τ_{ss} (ps)[d]
278 K	261	119	40	1945	44
288 K	168	104	40	988	35
298 K	120	93	40	525	30
310 K	90	82	30	259	25
318 K	75	85	33	166	20

[a] The relative translational diffusion coefficient was set to the averaged value measured on a series of lanthanum analogues (*37*). [b] τ_{SO} is the electronic relaxation time at very low magnetic field. [c] The number of water molecules in the second sphere was set to 6, and the distance for this second sphere interaction was fixed at 0.4 nm. [d] τ_{ss} is the correlation time modulating the second-sphere interaction.

In a second approach, the hypothesis of a reduced outer-sphere contribution was also considered. With such a hypothesis, good agreement between theoretical and experimental points was found only for frequencies lower than 1 MHz or larger than 40 MHz. Moreover, for an *r* value of 0.31 nm and a τ_R value equal to 92 ps at 310 K, this fitting implies a much larger value of the distance of closest approach (d = 0.85 nm), a value which is quite unrealistic.

In a third approach, given the presence of several hydroxyl groups in the vicinity of the gadolinium ion, a second sphere contribution was included in the fittings (*35*). In this case, the outer-sphere contribution was

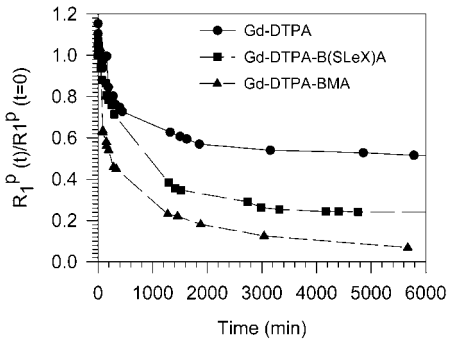


Figure 5. Evolution of the ratio $R_1^p(t)/R_1^p$ ($t = 0$) as a function of time for Gd−DTPA−B(sLe^x)A, Gd−DTPA, and Gd−DTPA−BMA.

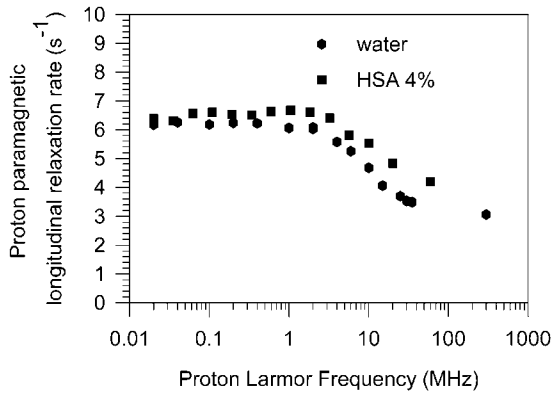


Figure 6. Paramagnetic proton longitudinal relaxation rate of 1 mM solutions of Gd−DTPA−B(sLeX)A in pure water and in a 4% HSA solution.

neglected, the distance *r* for the inner-sphere interaction was set to 0.32 nm, the number of water molecules in the second sphere was fixed to 6, and the distance of interaction for these water molecules was set to 0.4 nm. The results are shown in Table 2.

The first and the third approaches give similar fits. The choice of one fitting procedure is difficult but, based on the recent report of Caravan et al. stating that the distance *r* must be equal to 0.31 ± 0.1 nm (*36*), the model including inner- and second-sphere interactions seems to be better. An accurate determination of the distance *r* would be needed to select the best model.

Kinetics of Transmetalation. Transmetalation was assessed by the time-evolution of the paramagnetic proton longitudinal relaxation rate (R_1^p) of a phosphate buffer solution (pH 7) containing 2.5 mM of the gadolinium complex and 2.5 mM of $ZnCl_2$ (*29*). When transmetalation takes place, the released gadolinium ions form an insoluble complex with phosphate ions. Consequently, the paramagnetic relaxation rate decreases. The measurements were performed at 0.47 T and 310 K. After 5000 min, the paramagnetic relaxation rate had decreased by 90% for Gd−DTPA−BMA, by 48% for Gd−DTPA, and by 76% for Gd−DTPA−B(sLe^x)A (Figure 5). Gd−DTPA−B(sLe^x)A is thus more stable than the commercial bisamide Gd−DTPA−BMA but, as the other bisamide complexes (*29*), less stable than the parent pentacarboxylic compound Gd−DTPA.

Interaction with Albumin. The possible interaction of the complex with human serum albumin was studied through the comparison of the proton paramagnetic relaxation rate of an aqueous 1 mM solution of the complex in the absence and in the presence of 4% of HSA. If an interaction with the protein occurs, a significant increase of the proton paramagnetic relaxation is expected. The ratio of the paramagnetic relaxation rates observed in the presence and in the absence of HSA was equal to 1.3 at 20 MHz and 310 K. The NMRD profiles of the paramagnetic relaxation rate of this solution and of a 1 mM solution in pure water are very similar except at frequencies larger than 10 MHz, where the values of the HSA solution are slightly higher (Figure 6). This behavior is similar to that of Gd−DTPA that does not interact with albumin and markedly different from that of other gadolinium complexes known for their interaction with albumin and for which significant increase of the paramagnetic relaxation rate at low and high magnetic fields are observed. These data agree thus with the absence of marked interaction between the complex and the protein.

CONCLUSION

The new contrast agent potentially targeting inflammation is characterized by an unexpected low proton relaxivity as compared to Gd−DTPA despite a larger molecular weight. This feature does not result from a limitation by the water residence time at and above room temperature, as shown by the τ_M values obtained from the analysis of the oxygen-17 transverse relaxation rate data. Rather, it seems that this peculiarity can be explained by a slightly larger distance between the gadolinium ion and the protons of the coordinated water molecule. The stability of the complex versus transmetalation by zinc(II) ions is larger than that of the commercial contrast agent Gd−DTPA−BMA, and no significant interaction with serum albumin is observed. The study of its efficacy as a contrast agent for the in vivo detection by MRI of pathologies characterized by inflammation is currently under progress. The preliminary results show a prolonged contrast enhancement of blood vessels in livers submitted to fulminant hepatitis (*38*).

ACKNOWLEDGMENT

The authors thank Mrs Patricia de Francisco for her help in preparing the manuscript. This work was supported by the ARC Program (contracts number 95/00-194 and 00-05/258) of the French Community of Belgium.

LITERATURE CITED

(1) Rosen, S. D., Bertozzy, and C. R. (1994) The selectins and their ligands. *Curr. Opin. Cell. Biol. 6,* 663−673.

(2) Lasky, L. A. (1995) Selectin-carbohydrate interactions and the initiation of the inflammatory response. *Annu. Rev. Biochem. 64,* 113−139.

(3) Buerke, M., Weyrich, A. S., Zheng, Z., Gaeta, F. C. A., Forrest, M. J., and Lefer, A. M. (1994) Sialyl Lewis x-containing oligosaccharide attenuates myocardial reperfusion injury in cats. *J. Clin. Invest. 93* (3), 1140−1148.

(4) Lin, Y. C., Hummel, C. W., Huang, D.-H., Ichikawa, Y., Nicolaou, K. C., and Wong, C. H. (1992) Conformational studies of sialyl Lewis X in aqueous solution. *J. Am. Chem. Soc. 114* (13), 5452−5454.

(5) Ichikawa, Y., Lin, Y. C., Dumas, D. P., Shen, G. J., Garcia-Junceda, E., Williams, M. A., Bayer, R., Ketcham, C., Walker, L. E., Paulson, J. C., and Wong, C. H. (1992) Chemical-enzymic synthesis and conformational analysis of sialyl Lewis X and derivatives. *J. Am. Chem. Soc. 114* (24), 9283−9298.

(6) Ball, G. E., O'Neill, R. A., Schultz, J. E., Lowe, J. B., Weston, B. W., Nagy, J. O., Brown, E. G., Hobbs, C. J., and Bednarski, M. D. (1992) Synthesis and structural analysis using 2-D NMR of sialyl Lewis X (SLex) and Lewis X (Lex) oligosaccharides: ligands related to E-selectin [ELAM-1] binding. *J. Am. Chem. Soc. 114* (13), 5449−5451.

(7) Graves, B. J., Crowther, R. L., Chandran, C., Rumberger, J. M., Li, S., Huang, K. S., Presky, D. H., Familletti, P. C., Wolitzky, B. A., and Burns, D. K. (1994) Insight into E-selectin/ligand interaction from the crystal structure and mutagenesis of the lec/EGF domains. *Nature 367*, 532−538.
(8) Brandley, B. K., Kiso, M., Abbas, S., Nikrad, P., Srivasatava, O., Foxall, C., Oda, Y., and Hasegawa, A. (1993) Structure−function studies on selectin carbohydrate ligands. Modifications to fucose, sialic acid and sulfate as a sialic acid replacement. *Glycobiology 3* (6), 633−641.
(9) Ramphal, J. Y., Zheng, Z. L., Perez, C., Walker, L. E., DeFrees, S. A., and Gaeta, F. C. (1994) Structure−activity relationships of sialyl Lewis x-containing oligosaccharides. 1. Effect of modifications of the fucose moiety. *J. Med. Chem. 37* (21), 3459−3463.
(10) Monzavi-Karbassi, B., Cunto-Amesty, G., Luo, P., Shamloo, S., Blaszcyk-Thurin, M., and Kieber-Emmmons, T. (2001) Immunization with a carbohydrate mimicking peptide augments tumor-specific cellular responses. *Int. Immunol. 13* (11), 1361−1371.
(11) De Vleeschauwer, M., Vaillancourt, M., Goudreau, N., Guindon, Y., and Gravel, D. (2001) Design and synthesis of a new sialyl Lewis X mimetic: how selective are the selectin receptors? *Bioorg. Med. Chem. Lett. 11* (9), 1109−1112.
(12) Cheng, X., Khan, N., and Mootoo, D. R. (2000) Synthesis of the C-glycoside analogue of a novel sialyl Lewis X mimetic. *J. Org. Chem. 65* (8), 2544−2547.
(13) Thoma, G., Kinzy, W., Bruns, C., Patton, J. T., Magnani, J. L., and Banteli, R. (1999) Synthesis and biological evaluation of a potent E-selectin antagonist. *J. Med. Chem. 42* (23), 4909−4913.
(14) Huwe, C. M., Woltering, T. J., Jiricek, J., Weitz-Schmidt, G., and Wong, C. H. (1999) Design, synthesis and biological evaluation of aryl-substituted sialyl Lewis X mimetics prepared via cross-metathesis of C-fucopeptides. *Bioorg. Med. Chem. 7* (5), 773−788.
(15) Ida, Y., Satoh, Y., Katsumata, M., Nagasao, M., Hirai, Y., Kajimoto, T., Katada, N., Yasuda, M., and Yamamoto, T. (1998) Two novel oleanic acid saponins having a sialyl Lewis X mimetic structure from Achyranthes fauriei root. *Bioorg. Med. Chem. Lett. 8* (18), 2555−2558.
(16) Fu, Y., Laurent, S., and Muller, R. N. (2002) Synthesis of a sialyl Lewis X mimetic conjugated with DTPA, potential ligand of new contrast agents for medical imaging. *Eur. J. Org. Chem*. 3966−3973.
(17) Paul-Roth, C., and Kenneth, N. R. (1995) Amide functional group contribution to the stability of gadolinium (III) complexes: DTPA derivatives. *Inorg. Chem. 34*, 1408−1412.
(18) Jasanada, F., Urizzi, P., Souchard, JP., Le Gaillard, F., Favre, G., Boneu, A., and Nepveu, F. (1996) Indium-111 labeling of low-density lipoproteins with the DTPA-bis-(stearylamide): evaluation as a potential radiopharmaceutical for tumor localization. *Bioconjugate Chem. 7*, 72−81.
(19) Maisano, F., Gozzini, L., and De Haën, C. (1992) Coupling DTPA to proteins: a critical analysis of the cyclic dianhydride method in the case of insulin modification. *Bioconjugate Chem. 3*, 212−217.
(20) Hnatowich, D. J., Layne, W. W., and Childs, R. L. (1982) The preparation and labeling of DTPA- coupled albumin. *J. Appl. Radiat. Isot. 33*, 327−332.
(21) Muller, R. N. (2000) Contrast agents in magnetic resonance: operating mechanisms, Methods in Biomedical Magnetic Resonance Imaging and Spectroscopy. Vol I, pp 698−705, J. Wiley & Sons, Chichester, UK.
(22) Caravan, P., Ellison, J. J., McMurry, T. J., and Lauffer, R. B. (1999) Gadolinium (III) chelates as MRI contrast agents: structure, dynamics and applications. *Chem. Rev. 99*, 2293−2352.
(23) Muller, R. N., Declercq, D., Vallet, P., Giberto, F., Daminet, B., Fischer, H. W., Maton, F., and Van Haverbeke, Y. (1990) Implementation and operation of an integrated and comprehensive relaxometric data bank. Proceedings of the ESMRMB, 7th Annual Congress, Strasbourg, p 394.
(24) Vallet, P. (1992) *Relaxivity of nitroxide stable free radicals. Evaluation by field cycling method and optimisation*, Ph.D. Thesis, University of Mons-Hainaut, Belgium.
(25) Solomon, I. (1955) Relaxation processes in a system of two spins. *Phys. Rev. 99*, 559−565.
(26) Bloembergen, N. (1957) Proton relaxation times in paramagnetic solutions. *J. Chem. Phys. 27*, 572−573.
(27) Freed, J. H. (1978) Dynamic effects of pair correlation functions on spin relaxation by translational diffusion in liquids. II. Finite jumps and independent T_1 processes. *J. Chem. Phys. 68*, 4034−4037.
(28) Vander Elst, L., Maton, F., Laurent, S., Seghi, F., Chapelle, F., and Muller, R. N. (1997) A multinuclear MR study of Gd-EOB-DTPA: an example of comprehensive preclinical characterization of an organ specific MRI contrast agent. *Magn. Reson. Med. 38*, 604−614.
(29) Laurent, S., Vander Elst, L., Copoix, F., and Muller R. N. (2001) Stability of MRI paramagnetic contrast media. A proton relaxometric protocol for transmetalation assessment. *Invest. Radiol. 36*, 115−122.
(30) Budesinsky, B. (1968) Structure of metal chelates of arsonazo III, phosphonazo III and sulphonazo III. *Talanta 15*, 1063−1068.
(31) Laurent, S., Vander Elst, L., Houzé, S., Guérit, N., and Muller, R. N. (2000) Synthesis and characterization of various benzyl diethylenetriaminepentaacetic acids (DTPA) and their paramagnetic complexes: potential organ specific contrast agents for MRI. *Helv. Chim. Acta 83*, 394−406.
(32) Botteman, F., Nicolle, G. M., Vander Elst, L., Laurent, S., Merbach, A. E., and Muller, R. N. (2002) Synthesis, variable temperature and pressure NMR ^{17}O study of water exchange kinetics of bisalkylamide derivatives of Gd-DTPA. A study of the substitution effect. *Eur. J. Inorg. Chem*., 2686−2693.
(33) Powell, D. H., Gonzalez, G., Tissieres, V., Micskei, K., Brucher, E., Helm, L., and Merbach, A. E. (1994) Gd^{3+} chelates of interest in magnetic resonance imaging (MRI): studies using ^{17}O NMR and EPR at several magnetic fields. *J. Alloys Compd., 207/208*, 20−24.
(34) Micskei, K., Helm, L., Brucher, E., and Merbach, A. E. (1993) Oxygen-17 NMR study of water exchange on gadolinium polyaminopolyacetates $[Gd(DTPA)(H_2O)]^{2-}$ and $[Gd(DOTA)(H_2O)]^{-}$ related to NMR imaging. *Inorg. Chem. 32*, 3844−3850.
(35) Aime, S., Botta, M., Fedeli, F., Gianolio, E., Terreno, E., and Anelli, P. (2001) High-relaxivity contrast agents for magnetic resonance imaging based on multisite interactions between a β-cyclodextrin oligomer and suitably functionalized Gd^{III} chelates. *Chem. Eur. J. 7*, 5262−5269.
(36) Caravan, P., Astashkin, A. V., and Raitsimring, A. M. (2003) The gadolinium(III)-water hydrogen distance in MRI contrast agents. *Inorg. Chem. 42*, 3972−3974.
(37) Sessoye, A. (2002) *Study of the molecular diffusion of lanthanide complexes by proton NMR spectrometry.* B.Sc. thesis, University of Mons-Hainaut, Belgium.
(38) Boutry, S. (2001) *Contribution to the development of a specific contrast agent for MRI. Study of Gd-DTPA-B(sLe^x)A, a potential marker for inflammation.* B.Sc. thesis, University of Mons-Hainaut, Belgium.

BC034114M

Potential and Practical Adrenomedullary PET Radiopharmaceuticals as an Alternative to *m*-Iodobenzylguanidine: *m*-(ω-[^{18}F]Fluoroalkyl)benzylguanidines

Byung Chul Lee,[†] Jin-Young Paik,[‡] Dae Yoon Chi,*[,†] Kyung-Han Lee,*[,‡] and Yearn Seong Choe*[,‡]

Department of Chemistry, Inha University, 253 Yonghyundong Namgu, Inchon 402-751, Korea, and Department of Nuclear Medicine, Samsung Medical Center, Sungkyunkwan University School of Medicine, 50 Ilwon-dong Kangnam-ku, Seoul 135-710, Korea. Received July 8, 2003; Revised Manuscript Received October 26, 2003

To investigate adrenomedullary radiopharmaceuticals for positron emission tomography (PET), we have developed no-carrier-added *m*-(ω-[^{18}F]fluoroalkyl)benzylguanidines. *m*-(ω-[^{18}F]Fluoroalkyl)benzylguanidines were prepared in two steps starting from *N*,*N*′-bis(*tert*-butyloxycarbonyl)-*N*″-(ω-methanesulfonyloxyalkyl)benzylguanidines in 20−30% radiochemical yields (decay corrected for 100 min) and with high radiochemical purity (>97%) and shown to be stable (>90%) in an in vitro metabolic stability assay. The binding of *m*-(3-[^{18}F]fluoropropyl)benzylguanidine (**[^{18}F]3**) to SK-N-SH human neuroblastoma cells was temperature dependent, and binding levels at 4 °C were reduced to half of that at 37 °C, which was similar to the reduction rate observed for [^{123}I]MIBG. Tissue distribution studies in mice showed the highest uptake in the adrenals (%ID/g = 27.2 ± 5.0%) with relatively high uptake in the myocardium (%ID/g = 9.3 ± 0.5%). The results suggest that this radiotracer holds promise as a useful adrenomedullary radiopharmaceutical for PET imaging.

INTRODUCTION

m-Iodobenzylguanidine (MIBG) is a structural analogue of the adrenergic-neuron-blocking agent guanethidine and a functional analogue of the neurotransmitter norepinephrine (*1*, *2*). MIBG shares the same uptake and release mechanism as norepinephrine in neuroendocrine tumors and in myocardial sympathetic nerve endings (*3*, *4*). Radiolabeled [^{123}I]MIBG and [^{131}I]MIBG, therefore, are widely used for the localization and therapy of neuroendocrine tumors such as pheochromocytoma and neuroblastoma, and [^{123}I]MIBG is also applied for assessing the cardiac adrenergic system in cardiomyopathy and myocardial infarction (*5*−*10*). Many laboratories have shown an interest in MIBG analogues for PET, which can probe altered biochemical pathways and can be used to access metabolic levels quantitatively (*11*−*14*). Although MIBG analogues labeled with ^{18}F, ^{124}I, and ^{76}Br have been synthesized, none of them are practically useful as clinical PET tracers, because of either impractical synthetic routes or difficulties in availabilities of radionuclides (*12*−*17*).

On the other hand, fluorine-18 is the most desirable PET radionuclide due to its ideal physical properties (511 keV, $t_{1/2}$ = 110 min) (*18*, *19*). Three fluorine-18-labeled analogues of MIBG have been developed: *para*- and *m*-[^{18}F]fluorobenzylguanidine ([^{18}F]PFBG, [^{18}F]MFBG) and (4-[^{18}F]fluoro-3-iodobenzyl)guanindine ([^{18}F]FIBG) (*12*−*14*, *17*). The synthesis of [^{18}F]PFBG was more facile than that of [^{18}F]MFBG, but [^{18}F]MFBG gave better in vitro cell binding results. Nevertheless both compounds have lower binding affinities than MIBG, which may derive from their low lipophilicities. It is believed that lipophilic aromatic substituents can enhance neuron-blocking potency (*20*). By fluoride ion displacement reaction of the sulfonate group on the side chain of the aromatic system, [^{18}F]fluoroalkyl aromatics could be synthesized very efficiently in short reaction time with good radiochemical yield (*21*). In this report, we describe the preparation and evaluation of 3-(ω-[^{18}F]fluoroalkyl)-benzylguanidines.

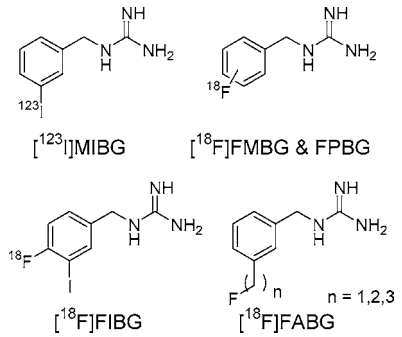


Figure 1. Structures of [^{123}I]MIBG, [^{18}F]FMBG, [^{18}F]FPBG, [^{18}F]FIBG, and [^{18}F]FABG.

MATERIALS AND METHODS

General. Solvents and reagents were purchased from the following commercial sources: Aldrich, Kanto, and Acros. ^{1}H NMR spectra were obtained on a Varian Gemini-200 and 400 (200 and 400 MHz) spectrometer (Palo Alto, CA) and ^{13}C NMR at 50 or 100 MHz. Chemical shifts were reported in parts per million (ppm, δ units) and coupling constants in units of hertz (Hz). Electron impact (EI) and chemical ionization (CI) mass spectra were obtained on a GC/MS QP5050A spectrometer (Shimadzu, Kyoto, Japan). Fast atom bombardment (FAB) mass spectra were obtained on a JMS 700 (JEOL Ltd.,

* To whom correspondence should be addressed. Telephone: +82-32-860-7686. Fax: +82-32-867-5604. E-mail: dychi@inha.ac.kr.
[†] Inha University.
[‡] Sungkyunkwan University School of Medicine.

10.1021/bc034115e CCC: $27.50 © 2004 American Chemical Society
Published on Web 12/13/2003

Tokyo, Japan). [^{18}F]Fluoride ion was produced from [^{18}O]-H_2O (Rotem Industries, Ltd., Israel) by a cyclotron (GEMS, Uppsala, Sweden). High performance liquid chromatography (HPLC) was carried out on a Thermo Separation Products System (Fremont, CA) with a semi-preparative column (Alltech Econosil C18 silica gel, 10 μm, 10 × 250 mm) and analytic column (Alltech Enonosil C18 silica gel, 5 μm, 4.6 × 250 mm). The eluant was simultaneously monitored by a UV detector (215 nm) and a NaI(Tl) radioactivity detector. Thin-layer chromatography (TLC) was performed on Merck F_{254} silica gel or C-18 silica gel plates and analyzed on a Bioscan radio-TLC scanner (Washington DC). In vitro incubation was carried out at 37 °C using a block heater (Digi-Block Laboratory Device Inc., Holliston, MA). Radioactivity was measured in a dose calibrator. All animal experiments were performed in compliance with the rules of Samsung Medical Center Laboratory Animal Care based on NIH guidelines. [^{123}I]MIBG was prepared at the Korea Cancer Center Hospital, Seoul, Korea (The radiochemical purity, over 95%; the activity concentration, about 473.6 MBq/mL; specific activity, 220 GBq/μmol).

General Procedure for the Synthesis of 4a,b. To a mixture of 3-bromobenzonitrile (1.00 g, 5.49 mmol) and lithium chloride (1.67 g, 39.6 mmol) in dry THF (25 mL) under nitrogen atmosphere was added tetrakis(triphenylphosphine)palladium(0) (100 mg, 1.6 mol %). The mixture was stirred at room temperature. After 40 min, a colorless solution was generated and to this was added allyltributyltin (1.87 mL, 6.03 mmol). This mixture was heated at 75 °C for 12 h. The reaction mixture was cooled to room temperature and diluted with ethyl acetate (20 mL), and the LiCl·Pd(II) complex was removed by filtration. The filtrate was washed with 10% NaOH (aq 2 × 15 mL), and the organic layer was dried over Na_2SO_4. After the solvents were removed by vacuum, the residue was purified by silica gel flash column chromatography (hexane/EtOAc =19:1) gave **4b** (634 mg, 81%) as a colorless oil: **3-Allylbenzonitrile (4b).** ^{1}H NMR (200 MHz, $CDCl_3$) δ 7.51−7.35 (m, 4H, Ar), 6.03−5.83 (m, 1H, CH), 5.17−5.05 (m, 2H, CH_2), 3.42 (d, J = 6.6 Hz, 2H, CH_2); ^{13}C NMR (50 MHz, $CDCl_3$) δ 141.38, 135.70, 133.08, 132.02, 129.80, 129.08, 118.77, 117.05, 112.43, 39.46; MS (CI) m/z 144 (M^+ + H). HRMS calcd for $C_{10}H_{10}N$ 144.0813, found 144.0818.

3-Vinylbenzonitrile (4a). Colorless oil in 81% yield; ^{1}H NMR (200 MHz, $CDCl_3$) δ 7.65−7.38 (m, 4H, Ar), 6.74 (dt, J = 17.6, 10.6 Hz, 1H, CH), 5.63 (d, J = 17.6 Hz, 1H, CH_2), 5.56 (d, J = 15.0 Hz, 1H, CH_2); ^{13}C NMR (50 MHz, $CDCl_3$) δ 138.53, 134.60, 130.80, 130.44,129.47, 129.15, 118.44, 116.37, 112.58; MS (CI) m/z 130 (M^+ + H). HRMS calcd for C_9H_8N 130.0657, found 130.0656.

3-Cyanobenzyl Alcohol (5a). To a solution of 3-cyanobenzaldehyde (1.00 g, 7.62 mol) in 15 mL of ethanol was added sodium borohydride (346 mg, 9.15 mmol). After 1 h, the reaction was quenched by a piece of ice and diluted with ethanol. The ethanol was evaporated under reduced pressure, and then water was poured into the reaction mixture. The resulting mixture was extracted with dichloromethane (2 × 25 mL). The combined extracts were dried over Na_2SO_4. After removal of the solvent, silica gel flash column chromatography (hexane/EtOAc = 3:2) gave **5a** (993 mg, 98%) as a colorless oil: ^{1}H NMR (200 MHz, $CDCl_3$) δ 7.60−7.40 (m, 4H, Ar), 4.67 (s, 2H, CH_2), 3.70 (bs, 1H, OH); ^{13}C NMR (50 MHz, $CDCl_3$) δ 142.36, 130.95, 130.76, 129.87, 129.02, 118.67, 111.79, 63.28; MS (EI) m/z 133 (M^+). Anal. (C_8H_7NO) calcd: C, 72.16; H, 5.30; N, 10.52. found: C, 71.99; H, 5.43; N, 10.74.

General Procedure for the Synthesis of 5b,c. To a stirred solution of **4b** (350 mg, 2.44 mmol) in dry tetrahydrofuran (7 mL) at 0 °C under a nitrogen atmosphere was added 1 M borane−tetrahydrofuran complex (2.92 mL, 2.92 mmol). After 1 h, water (2 mL) was added cautiously to decompose excess hydride. Oxidation was carried out by adding 2.6 mL of 4 N sodium hydroxide, followed by addition of 3.5 mL of 28% hydrogen peroxide. The reaction mixture was stirred for 40 min. The crude product was extracted by EtOAc (3 × 5 mL). The organic layer was dried over Na_2SO_4. After the organic layer was removed by vacuum, the product was obtained by silica gel flash column chromatography (hexane/EtOAc = 7:3) gave **5c** (295 mg, 75%) as a colorless oil: **3-(3-Hydroxypropyl)benzonitrile (5c).** ^{1}H NMR (200 M MHz, $CDCl_3$) δ 7.50−7.34 (m, 4H, Ar), 3.66 (t, J = 6.3 Hz, 2H, CH_2), 2.76 (t, J = 7.7 Hz, 2H, CH_2), 2.42 (bs, 1H, OH), 1.95−1.82 (m, 2H, CH_2); ^{13}C NMR (50 MHz, $CDCl_3$) δ 143.28, 133.01, 131.82, 129.51, 129.03, 118.844, 112.10, 61.32, 33.53, 31.45; MS (CI) m/z 162 (M^+ + H). HRMS calcd for $C_{10}H_{12}NO$ 162.0919, found 162.0918.

3-(2-Hydroxyethyl)benzonitrile (5b). Colorless oil with 45% yield: ^{1}H NMR (200 MHz, $CDCl_3$) δ 7.53−7.36 (m, 4H, Ar), 3.85 (t, J = 7.2 Hz, 2H, CH_2), 2.88 (t, J = 6.4 Hz, 2H, CH_2), 2.39 (bs, 1H, OH); ^{13}C NMR (50 MHz, $CDCl_3$) δ 140.43, 133.56, 132.41, 129.94, 129.08, 118.76, 112.18, 62.632; MS (EI) m/z 147 (M^+). HRMS calcd for C_9H_9NO 147.0684, found 147.0656.

General Procedure for the Synthesis of 6a−c, 11a−c. To a stirred solution of **5a** (1.16 g, 8.71 mmol) and triethylamine (1.33 mL, 9.58 mmol) in 25 mL of methylene chloride was added methanesulfonyl chloride (674 μL, 8.71 mmol) at 0 °C dropwise. After 30 min, the reaction was quenched by the addition of saturated sodium bicarbonate. The resulting mixture was extracted with dichloromethane (3 × 20 mL). The organic layer was dried over Na_2SO_4. After the organic layer was removed by vacuum, the product was obtained by silica gel flash column chromatography (hexane/EtOAc = 3:2) gave **6a** (1.69 g, 92%) as a colorless oil: **3-(Methanesulfonyloxymethyl)benzonitrile (6a).** ^{1}H NMR (200 MHz, $CDCl_3$) δ 7.73−7.55 (m, 4H, Ar), 5.27 (s, 2H, CH_2), 3.06 (s, 3H, CH_3); ^{13}C NMR (50 MHz, $CDCl_3$) δ 135.15, 132.57, 132.51, 131.61, 126.66, 117.99, 112.92, 69.22, 36.47; MS (CI) m/z 212 (M^+ + H). HRMS calcd for $C_9H_{10}NO_3S$ 212.0381, found 212.0382.

3-(2-Methanesulfonyloxyethyl)benzonitrile (6b). Colorless oil with 93% yield: ^{1}H NMR (200 MHz, $CDCl_3$) δ 7.55−7.41 (m, 4H, Ar), 4.40 (t, J = 6.6 Hz, 2H, CH_2), 3.06 (t, J = 6.6 Hz, 2H, CH_2), 2.91 (s, 3H, CH_3); ^{13}C NMR (50 MHz, $CDCl_3$) δ 137.84, 133.47, 132.30, 130.65, 129.38, 118.48, 112.38, 69.10, 37.16, 34.84; MS (CI) m/z 226 (M^+ + H). HRMS(FAB) calcd for $C_{10}H_{11}NO_3SNa$ 248.0357, found 248.0399.

3-(3-Methanesulfonyloxypropyl)benzonitrile (6c). Colorless oil with 97% yield: ^{1}H NMR (200 MHz, $CDCl_3$) δ 7.55−7.41 (m, 4H, Ar), 4.25 (t, J = 6.0 Hz, 2H, CH_2), 3.03 (s, 3H, CH_3), 2.81 (t, J = 7.7 Hz, 2H, CH_2), 2.16−2.02 (m, 2H, CH_2); ^{13}C NMR (50 MHz, $CDCl_3$) δ 141.82, 132.99, 131.87, 130.12, 129.38, 118.67, 112.72, 68.43, 37.46, 31.19, 30.37; MS (FAB) m/z 240 (M^+ + H). HRMS calcd for $C_{11}H_{14}NO_3S$ 240.0694, found 240.0651.

***N,N′*-Bis(*tert*-butyloxycarbonyl)-*N″*-3-(methanesulfonyloxymethyl)benzylguanidine (11a).** Colorless oil with 98% yield; ^{1}H NMR (200 MHz, $CDCl_3$) δ 11.56 (s, 1H, NH), 8.63 (s, 1H, NH), 7.40−7.30 (m, 4H, Ar), 5.24 (s, 2H, CH_2), 4.65 (d, J = 5.0 Hz, 2H, CH_2), 2.92 (s, 3H, CH_3), 1.51 (s, 9H, $3CH_3$), 1.49 (s, 9H, $3CH_3$); ^{13}C NMR (50 MHz, $CDCl_3$) δ 167.40, 156.07, 153.10, 137.80, 133.84,

129.21, 128.62, 127.92, 127.85, 83.21, 79.31, 71.04, 44.37, 38.25, 28.17, 27.93; MS (FAB) *m/z* 458 ($M^+ + H$). HRMS calcd for $C_{20}H_{32}N_3O_7S$ 458.1961, found 458.1962.

***N,N′*-Bis(*tert*-butyloxycarbonyl)-*N″*-3-(2-methanesulfonyloxyethyl)benzylguanidine (11b).** Colorless oil with 98% yield: ^{1}H NMR (200 MHz, $CDCl_3$) δ 11.54 (s, 1H, NH), 8.59 (s, 1H, NH), 7.31−7.14 (m, 4H, Ar), 4.61 (d, J = 2.5 Hz, 2H, CH_2), 4.41 (t, J = 6.8 Hz, 2H, CH_2), 3.05 (t, J = 6.9 Hz, 2H, CH_2), 2.84 (s, 3H, CH_3), 1.51 (s, 9H, $3CH_3$), 1.48 (s, 9H, $3CH_3$); ^{13}C NMR (50 MHz, $CDCl_3$) δ 163.49, 156.04, 153.13, 137.77, 136.84, 129.10, 128.41, 128.26, 126.53, 83.22, 79.43, 70.10, 44.68, 37.25, 35.43, 28.20, 27.98; MS (FAB) *m/z* 472 ($M^+ + H$). HRMS calcd for $C_{21}H_{34}N_3O_7S$ 472.2117, found 472.2096.

***N,N′*-Bis(*tert*-butyloxycarbonyl)-*N″*-3-(3-methanesulfonyloxypropyl)benzylguanidine (11c).** Colorless oil with 97% yield: ^{1}H NMR (200 MHz, $CDCl_3$) δ 11.55 (s, 1H, NH), 8.58 (s, 1H, NH), 7.33−7.10 (m, 4H, Ar), 4.61 (d, J = 5.0 Hz, 2H, CH_2), 4.23 (t, J = 6.2 Hz, 2H, CH_2), 3.00 (s, 3H, CH_3), 2.76 (t, J = 7.5 Hz, 2H, CH_2), 2.15−2.01 (m, 2H, CH_2) 1.52 (s, 9H, $3CH_3$), 1.48 (s, 9H, $3CH_3$); ^{13}C NMR (50 MHz, $CDCl_3$) δ 163.53, 156.05, 153.148, 140.78, 137.67, 128.92, 127.89, 127.65, 125.70, 83.12, 79.28, 68.96, 44.84, 37.30, 31.41, 30.48, 28.25, 27.99; MS (FAB) *m/z* 486 ($M^+ + H$). HRMS calcd for $C_{22}H_{36}N_3O_7S$ 486.2274, found 486.2271.

General Procedure for the Synthesis of 7a−c. To a stirred solution of **6a** (1.63 g, 7.72 mmol) in 25 mL of acetonitrile was added tetra-*n*-butylammonium flouride hydrate (2.43 g, 7.72 mmol) at 130 °C. After 40 min, the acetonitrile was evaporated under reduced pressure. The product was obtained by silica gel flash column chromatography (hexane/EtOAc = 19:1) gave **7a** (920 mg, 91%) as a colorless oil: **3-(Fluoromethyl)benzonitrile (7a).** ^{1}H NMR (200 MHz, $CDCl_3$) δ 7.68−7.52 (m, 4H, Ar), 5.42 (d, J = 47.2 Hz, 2H, CH_2); ^{13}C NMR (50 MHz, $CDCl_3$) δ 139.80 (d, J = 17.8 Hz), 132.05 (d, J = 2.3 Hz), 131.10 (d, J = 6.1 Hz), 130.28 (d, J = 6.8 Hz), 129.43, 118.26, 112.74, 82.93 (d, J = 168.4 Hz); MS (CI) *m/z* 136 ($M^+ + H$). HRMS calcd for C_8H_7NF 136.0563, found 136.0566.

3-(2-Fluoroethyl)benzonitrile (7b). Colorless oil with 15% yield: ^{1}H NMR (200 MHz, $CDCl_3$) δ 7.58−7.26 (m, 4H, Ar), 4.65 (dt, J = 46.8, 6.1 Hz, 2H, CH_2), 3.04 (dt, J = 26, 6.0 Hz, 2H, CH_2); ^{13}C NMR (100 MHz, $CDCl_3$) δ 138.88, 133.51, 132.45, 130.45, 129.30, 118.72, 112.58, 83.19 (d, J = 168.3 Hz), 36.36 (d, J = 19.7 Hz); MS (CI) *m/z* 149 ($M^+ + H$). HRMS calcd for C_9H_8NF 149.0641, found 149.0629.

3-(3-Fluoropropyl)benzonitrile (7c). Colorless oil with 65% yield: ^{1}H NMR (200 MHz, $CDCl_3$) δ 7.47−7.35 (m, 4H, Ar), 4.44 (dt, J = 46.8, 5.7 Hz, 2H, CH_2), 2.78 (t, J = 7.7 Hz, CH_2), 2.13−1.86 (m, 2H, CH_2); ^{13}C NMR (50 MHz, $CDCl_3$) δ 140.88, 131.38, 130.27, 128.22, 127.59, 117.14, 110.91, 80.87 (d, J = 165.0 Hz), 29.91 (d, J = 20.0 Hz), 29.32 (d, J = 5.0 Hz); MS (CI) *m/z* 164 ($M^+ + H$). HRMS calcd for C_8H_7NF 164.0876, found 164.0873.

General Procedure for the Synthesis of 8a−c. A mixture of **7a** (1.4 g, 10.7 mmol) and 1 M borane−THF complex (40 mL, 40.6 mmol) in dry THF (15 mL) under nitrogen atmosphere was stirred at 75 °C for 12 h. The mixture was diluted with ethanol. After the solvent was removed using an evaporator, the crude mixture was extracted from the aqueous layer with EtOAc (3 × 15 mL). The crude product was dried over sodium sulfate. The solvent was evaporated under reduced pressure. The mixture was dissolved in tetrahydrofuran, and then 1 N HCl in tetrahydrofuran (50 μL) was added dropwise. Filtration of the generated solid gave **8a** (880 mg, 47%) as a granular solid: **3-(Fluoromethyl)benzylamine Hydrochloride (8a).** mp, 149.4−153.5 °C; ^{1}H NMR (200 MHz, CD_3OD) δ 7.49−7.46 (m, 4H, Ar), 5.41 (d, J = 47.6 Hz, 2H, CH_2), 4.10 (s, 2H, CH_2); ^{13}C NMR (50 MHz, CD_3OD) δ 139.20 (d, J = 17.1 Hz), 135.55, 130.60, 130.36 (d, J = 2.7 Hz), 129.22 (d, J = 5.7 Hz), 129.11 (d, J = 4.6 Hz), 85.18 (d, J = 164.3 Hz), 44.40; MS (EI) *m/z* 138 ($M^+ - H$). HRMS calcd for C_8H_9NF 138.0719, found 138.0727.

3-(2-Fluoroethyl)benzylamine Hydrochloride (8b). White solid with 55% yield: mp, 143.8−144.9 °C; ^{1}H NMR (200 MHz, CD_3OD) δ 7.45−7.33 (m, 4H, Ar), 4.64 (dt, J = 47.2, 6.2 Hz, 2H, CH_2), 4.11 (s, 2H, CH_2), 3.04 (dt, J = 25.0, 6.4 Hz, 2H, CH_2); ^{13}C NMR (50 MHz, CD_3OD) δ140.52, 134.79, 131.09, 130.81, 130.53, 128.28, 85.01 (d, J = 166.9 Hz), 44.45, 37.87 (d, J = 20.5 Hz); MS (EI) *m/z* 152 ($M^+ - H$). HRMS calcd for $C_9H_{11}NF$ 152.0876, found 152.0857.

3-(3-Fluoropropyl)benzylamine Hydrochloride (8c). White solid with 61% yield: mp, 105.3−107.1 °C; ^{1}H NMR (200 MHz, CD_3OD) δ 7.41−7.25 (m, 4H, Ar), 4.44 (dt, J = 47.2, 6.0 Hz, 2H, CH_2), 4.07 (s, 2H, CH_2), 2.78 (t, J = 8.4 Hz, 2H, CH_2), 2.14−1.91 (m, 2H, CH_2); ^{13}C NMR (50 MHz, CD_3OD) δ 143.97, 135.47, 130.45, 130.35, 130.14, 127.66, 84.06 (d, J = 163.5 Hz), 44.65, 33.37 (d, J = 19.7 Hz), 32.35 (d, J = 5.3 Hz); MS (EI) *m/z* 167 (M^+). HRMS calcd for $C_{10}H_{14}NF$ 167.1110, found 167.1083.

General Procedure for the Synthesis of 9a−c. To a solution of **8a** (200 mg, 1.40 mmol) in 2.50 mL of dimethylformamide was stirred at 0 °C. To the stirred mixture was added *N,N′*-bis(*tert*-butyloxycarbonyl)-2-methylthiourea and triethylamine. After 5 min, mercury chloride was added. The reaction mixture was stirred at 0 °C for 1 h and then diluted with EtOAc (5 mL). The precipitate was filtered through Celite. The filtrate was washed with saturated ammonium chloride (2 × 10 mL) and aqueous sodium bicarbonate (2 × 10 mL). The organic layer was dried over Na_2SO_4. The product was obtained by silica gel flash column chromatography (hexane/EtOAc = 4:1) gave **9a** (416 mg, 78%) as a white solid: ***N,N′*-Bis(*tert*-butyloxycarbonyl)-*N″*-3-(fluoromethyl)benzylguanidine (9a).** mp, 113.0−114.9 °C; ^{1}H NMR (200 MHz, $CDCl_3$) δ 11.53 (bs, 1H, NH), 8.58 (bs, 1H, NH), 7.39−7.29 (m, 4H, Ar), 5.34 (d, J = 48.0 Hz, 2H, CH_2), 4.62 (d, J = 5.2 Hz, 2H, CH_2), 1.49 (s, 9H, $3CH_3$), 1.45 (s, 9H, $3CH_3$); ^{13}C NMR (50 MHz, $CDCl_3$) δ 163.47, 156.07, 153.13, 137.85, 136.72 (d, J = 17.1 Hz), 128.93, 128.03 (d, J = 2.7 Hz), 126.72 (d, J = 6.1 Hz), 126.51 (d, J = 6.1 Hz), 84.17 (d, J = 165. 8 Hz), 83.14, 79.26, 44.64, 28.22, 27.96; MS (FAB) *m/z* 382 ($M^+ + H$). HRMS calcd for $C_{19}H_{29}N_3O_4F$ 382.2143, found 382.2148.

***N,N′*-Bis(*tert*-butyloxycarbonyl)-*N″*-3-(2-fluoroethyl)benzylguanidine (9b).** White solid with 82% yield: mp, 81.0−82.7 °C; ^{1}H NMR (200 MHz, $CDCl_3$) δ 11.54 (bs, 1H, NH), 8.57 (bs, 1H, NH), 7.29−7.13 (m, 4H, Ar), 4.61 (dt, J = 47.0, 6.4 Hz, 2H, CH_2), 4.60 (d, J = 5.2 Hz, 2H, CH_2), 3.00 (dt, J = 23.2, 6.6 Hz, 2H, CH_2), 1.51 (s, 9H, $3CH_3$), 1.47 (s, 9H, $3CH_3$); ^{13}C NMR (50 MHz, $CDCl_3$) δ 163.56, 156.06, 153.14, 137.57, 137.47, 128.91, 128.51, 128.21, 126.14, 83.87 (d, J = 168.0 Hz), 83.12 79.32, 44.85, 35.75 (d, J = 20.5 Hz), 28.25, 28.00; MS (FAB) *m/z* 396 ($M^+ + H$). HRMS calcd for $C_{20}H_{31}N_3O_4F$ 396.2299, found 396.2273.

***N,N′*-Bis(*tert*-butyloxycarbonyl)-*N″*-3-(3-fluoropropyl)benzylguanidine (9c).** White solid with 75% yield: mp, 97.9−98.8 °C; ^{1}H NMR (200 MHz, $CDCl_3$) δ 11.55 (bs, 1H, NH), 8.58 (bs, 1H, NH), 7.28−7.11 (m, 4H, Ar), 4.69 (d, J = 5.2 Hz, 2H, CH_2), 4.46 (dt, J = 47.6, 5.9 Hz, 2H, CH_2), 2.74 (t, J = 7,7 Hz, 2H, CH_2), 2.10−1.90 (m, 2H, CH_2), 1.52 (s, 9H, $3CH_3$), 1.48 (s, 9H, $3CH_3$); ^{13}C

NMR (50 MHz, $CDCl_3$) δ 163.61, 156.09, 153.20, 141.62, 137.54, 128.83, 128.02, 127.74, 125.51, 83.12, 82.99 (d, J = 164.0 Hz), 79.30, 44.97, 31.90 (d, J = 19.8 Hz), 31.21 (d, J = 5.7 Hz), 28.31, 28.04; MS (FAB) m/z 410 (M^+ + H). HRMS calcd for $C_{21}H_{33}N_3O_4F$ 410.2455, found 410.2459.

General Procedure for the Synthesis of 10a−c. A solution of **5a** (151 mg, 1.14 mmol) and lithium borohydride (40 mL, 40.6 mmol) in dry tetrahydrofuran (15 mL) under nitrogen atmosphere was stirred at 75 °C for 12 h. The reaction was quenched with ethanol carefully. After the solvent was removed under reduced pressure, the crude mixture dissolved in dichloromethane (50 mL) was washed with water. The crude product in organic layer was dried over sodium sulfate. The solvent was evaporated under reduced pressure. This crude mixture dissolved in 2.50 mL of dimethylformamide and stirred at 0 °C. To the stirred mixture were added *N*,*N*′-bis(*tert*-butyloxycarbonyl)-2-methylthiourea and triethylamine. After 5 min, mercury chloride was added. The reaction mixture was stirred at 0 °C for 1 h and then diluted with EtOAc (5 mL). The precipitate was filtered through Celite. The filtrate was washed with saturated ammonium chloride (2 × 10 mL) and aqueous sodium bicarbonate (2 × 10 mL). The organic layer was dried over Na_2SO_4. The product was obtained by silica gel flash column chromatography (hexane/EtOAc = 3:2) gave **10a** (335 mg, 78%) as colorless oil: ***N*,*N*′-Bis(*tert*-butyloxycarbonyl)-*N*″-3-(hydroxymethyl)benzylguanidine (10a).** ^{1}H NMR (200 MHz, $CDCl_3$) δ 11.53 (bs, 1H, NH), 8.57 (bs, 1H, NH), 7.36−7.20 (m, 4H, Ar), 4.65 (s, 2H, CH_2), 4.59 (d, J = 5.0 Hz, 2H, CH_2), 2.58 (bs, 1H, OH), 1.51 (s, 9H, $3CH_3$), 1.47 (s, 9H, $3CH_3$); ^{13}C NMR (50 MHz, $CDCl_3$) δ 163.45, 156.02, 153.07, 141.54, 137.43, 128.82, 126.83, 126.31, 126.10, 83.12, 79.33, 64.80, 44.84, 28.22, 27.97; MS (FAB) m/z 380 (M^+ + H). HRMS calcd for $C_{19}H_{30}N_3O_5$ 380.2185, found 380.2189.

***N*,*N*′-Bis(*tert*-butyloxycarbonyl)-*N*″-3-(2-hydroxyethyl)benzylguanidine (10b).** Colorless oil with 75% yield: ^{1}H NMR (200 MHz, $CDCl_3$) δ 11.47 (bs, 1H, NH), 8.53 (bs, 1H, NH), 7.27−7.07 (m, 4H, Ar), 4.54 (d, J = 2.6 Hz, 2H, CH_2), 3.79 (t, J = 6.5 Hz, 2H, CH_2), 2.80 (t, J = 6.6 Hz, 2H, CH_2), 1.45 (s, 9H, $3CH_3$), 1.41 (s, 9H, $3CH_3$); ^{13}C NMR (100 MHz, $CDCl_3$) δ 163.47, 156.01, 153.09, 139.06, 137.44, 128.85, 128.48, 128.25, 125.80, 83.11, 79.33, 63.41, 44.83, 38.98, 28.19, 27.95; MS (FAB) m/z 394 (M^+ + H). HRMS calcd for $C_{20}H_{32}N_3O_5$ 394.2342, found 394.2363.

***N*,*N*′-Bis(*tert*-butyloxycarbonyl)-*N*″-3-(3-hydroxypropyl)benzylguanidine (10c).** Colorless oil with 81% yield: ^{1}H NMR (200 MHz, $CDCl_3$) δ 11.53 (bs, 1H, NH), 8.57 (bs, 1H, NH), 7.30−7.10 (m, 4H, Ar), 4.59 (d, J = 4.8 Hz, 2H, CH_2), 3.65 (t, J = 6.4 Hz, 2H, CH_2), 2.70 (t, J = 8.0 Hz, 2H, CH_2), 1.94−1.80 (m, 2H, CH_2), 1.52 (s, 9H, $3CH_3$), 1.47 (s, 9H, $3CH_3$); ^{13}C NMR (50 MHz, $CDCl_3$) δ 163.53, 156.02, 153.15, 142.33, 137.30, 128.71, 127.96, 127.64, 125.22, 83.10, 79.28, 61.87, 44.96, 33.95, 31.86, 28.25, 27.99; MS (FAB) m/z 408 (M^+ + H). HRMS calcd for $C_{21}H_{34}N_3O_5$ 408.2498, found 408.2497.

General Procedure for the Synthesis of 1−3. To a stirred solution of **9a** (50 mg, 0.236 mmol) in EtOAc was added 3 M HCl in EtOAc (4 mL) carefully. The reaction mixture was heated at 65 °C for 30 min, and then solvent was removed under reduced pressure. The crude mixture was dissolved with water (200 μL), loaded on C-18 silica gel in a disposable pipet, and washed with water (2 mL) and ethanol (2 mL) successively. The ethanol rinse contained the product. Removal of solvent under reduced pressure gave **1** (38 mg, 91%) as a pale yellow oil: **3-(Fluoromethyl)benzylguanidine (1).** ^{1}H NMR (200 MHz, CD_3OD) δ 7.48−7.33 (m, 4H, Ar), 5.39 (d, J = 47.6 Hz, 2H, CH_2), 4.66 (s, 1H, NH), 4.44 (s, 2H, CH_2); ^{13}C NMR (100 MHz, DMSO-d_6) δ 158.73, 140.13, 138.80 (d, J = 17.5 Hz), 130.21, 128.62, 128.12 (d, J = 6.1 Hz), 127.57 (d, J = 6.0 Hz), 85.20 (d, J = 163.7 Hz), 46.58; MS (FAB) m/z 182 (M^+ + H). HRMS calcd for $C_9H_{13}N_3F$ 182.1094, found 182.1107.

3-(2-Fluoroethyl)benzylguanidine (2). Colorless oil with 95%: ^{1}H NMR (200 MHz, CD_3OD) δ 7.38−7.20 (m, 4H, Ar), 4.62 (dt, J = 47.0, 6.2 Hz, 2H, CH_2), 4.40 (d, J = 6.0 Hz, 2H, CH_2), 3.01 (dt, J = 25.0, 6.6 Hz, 2H, CH_2); ^{13}C NMR (50 MHz, CD_3OD) δ 159.32, 149.63, 137.79, 130.08, 129.74, 129.11, 126.60, 84.98 (d, J = 166.9 Hz), 46.07, 37.80 (d, J = 20.2 Hz); MS (FAB) m/z 196 (M^+ + H). HRMS calcd for $C_{10}H_{15}N_3F$ 196.1250, found 196.1227.

3-(3-Fluoropropyl)benzylguanidine (3). Colorless oil with 97%: ^{1}H NMR (200 MHz, DMSO-d_6) δ 7.31−7.14 (m, 4H, Ar), 4.43 (dt, J = 47.2, 5.8 Hz, 2H, CH_2), 4.26 (s, 2H, CH_2), 2.64 (t, J = 8.0 Hz, 2H, CH_2), 1.81−2.01 (m, 2H, CH_2); ^{13}C NMR (50 MHz, DMSO-d_6) δ 157.31, 141.65, 137.95, 128.87, 127.64, 127.42, 125.03, 81.34 (d, J = 161.2 Hz), 43.99, 31.9, 31.7 (d, J = 19.4 Hz), 30.96; MS (FAB) m/z 210 (M^+ + H). HRMS calcd for $C_{11}H_{17}N_3F$ 210.1407, found 210.1405.

General Procedure for the Labeling of [^{18}F]1−3. [^{18}F]Fluoride was produced in a cyclotron by the ^{18}O-(p,n)^{18}F reaction. A volume of 100−200 μL of [^{18}F]fluoride (18.5−370 MBq) in water was added to a vacutainer containing n-Bu_4NHCO_3 (40% aq, 2.70 μL, 3.65 μmol). The azeotropic distillations were carried out each time with 200 μL aliquots of CH_3CN at 85 °C under a stream of nitrogen. A fluorine-18 ion displacement reaction of **11c** (2 mg, 4.1 μmol) with n-Bu_4N[^{18}F]F in acetonitrile (200 μL) was carried out in a reaction vial at 75−80 °C for 10 min. After the reaction, the vial was cooled in an ice bath. The solvent was removed under a gentle stream of nitrogen at room temperature. To deprotect two Boc groups, the residue was treated with 3 M HCl in EtOAc (200 μL) at 65 °C for 10 min. The solvent was removed with a gentle stream of nitrogen. The crude compound was injected onto reverse phase HPLC with the help of 5% methanol in 0.2 M $(NH_4)H_2PO_4$ (1 mL) and purified. The desired compound was collected from HPLC (t_R = 23 min; C18 silica gel, 10 μm, 10 × 250 mm; 0.2 M $(NH_4)H_2PO_4/CH_3CN$ = 70:30 (v/v); 215 nm; 1.5 mL/min), and the HPLC solvent was removed on water bath (75−80 °C) using a gentle stream of nitrogen. The resulting residue was further treated with ethanol and passed through a Celite plug for the desalting. After the ethanol was evaporated, 3-(3-[^{18}F]fluoropropyl)benzylguanidine (**[^{18}F]3**) was used for biological study. For the identification of the radioproduct, the collected HPLC fraction was matched with the cold compound. The labeling of **[^{18}F]-1−2** was followed with the same procedure. The total labeling time of **[^{18}F]1−3** was 100 min, and the overall decay-corrected radiochemical yield was about 20−30%. Specific activity at the end of synthesis was calculated by relating radioactivity to the mass associated with the UV absorbance (215 nm) peak of cold compound. Specific radioactivity of **[^{18}F]1−3** (**[^{18}F]1**; 59 GBq/μmol, **[^{18}F]2**; 47 GBq/μmol, **[^{18}F]3**; 51 GBq/μmol) was obtained after purification on HPLC column.

In Vitro Metabolic Stability Studies. Mouse hepatic microsomes (0.5 mg/mL) were placed in five test tubes containing 0.1 M phosphate buffer (pH 7.4, 3 mL) and radiotracer (0.074−0.74 MBq) dissolved in ethanol (50 μL). After each test tube was preincubated at 37 °C for 3 min, the reaction was initiated by addition of NADPH

(0.25 mM), and the mixture was incubated at 37 °C. The volume per sample in the in vitro stability was 500 μL. At the indicated time points (1, 5, 15, 30, and 60 min), the sample was picked out and passed through a Celite plug (2 cm) using 2 mL of absolute ethanol. The obtained mixture was developed on TLC and was analyzed by radio-TLC (*33*).

Cells and Culture Conditions. The human neuroblastoma cells SK-N-SH was obtained from Seoul National University, Seoul, Korea (J. J. Kim, MD). Cells were cultured in RPMI-1640 media supplemented with 10% FBS, glutamine, and antibiotics. Cells that has been seeded into 12-well plates (1×10^5 cells in 1 mL medium per well) 24 h prior to experiments were either 0.74 MBq/well of (**[^{18}F]3**) or [^{123}I]MIBG in paired format to allow comparison. To investigate the effect of temperature on cell binding levels, cells were incubated with the radiotracers at either 4 °C or 37 °C for 30 min or 2 h.

Comparison of [^{18}F]3 and [^{123}I]MIBG Uptake in SK−N−SH Human Neuroblastoma Cells. Cells were incubated with either **[^{18}F]3** (0.74 MBq/well) or [^{123}I]-MIBG for 30 and 120 min at 37 °C. To investigate the effect of temperature on radiotracer uptake, another set of cells were incubated with the radiotracers at 4 °C for 30 and 120 min (*32*). At the end of incubation, media was removed and the cells were washed twice with PBS. The cell bound activity was counted along with standards using a high energy gamma counter.

Inhibition of [^{18}F]3 Binding to SK−N−SH Cells by Graded Preincubation Time with Desipramine. **[^{18}F]3** (0.74 MBq/well) uptake measured in SK-N-SH cells after preincubation with 50 μM desipramine for indicated duration of times. At desired time, the medium was removed and cell bound activity was counted after PBS washing.

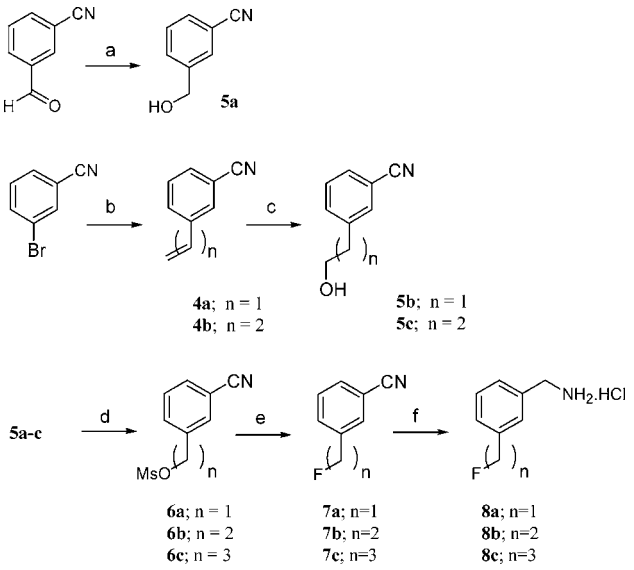
Tissue Distribution in Normal Mice. Tissue distribution was performed in male ICR mice (n = 3, 26−30 g) with tail vein administration of **[^{18}F]3** (1.1 MBq/mouse) dissolved in phosphate buffered saline to a final volume of 150 mL. After 2 h postinjection, mice were sacrificed by cervical dislocation, and tissues of interest were isolated, weighed, and counted for radioactivity. The injected dose was calculated from standards prepared from the injection solution. The data were expressed as percent injected dose per gram of tissue (%ID/g).

RESULTS AND DISCUSSION

The unlabeled 3-(ω-fluoroalkyl)benzylguanidines (**1**−**3**) were synthesized as shown in Schemes 1 and 2. 3-Cyanobenzyl alcohol (**5a**) was prepared from 3-cyanobenzaldehyde by reduction using sodium borohydride in ethanol in over 96% yield. Stille reaction (*22, 23*) of 3-bromobenzonitrile with either tributylvinyltin or allyltributyltin in the presence of tetrakis(triphenylphosphine palladium(0)) and lithium chloride followed by hydroboration (*24*) provided homologated alcohols **5b**,**c**. Mesylation of the alcohols and subsequent fluorination using tetra-*n*-butylammonium fluoride (TBAF) gave **7a**−**c** in 93, 15, 65% yields, respectively. The big differing yields of fluorinations of three compounds came from the intrinsic properties of aliphatic displacement reactions at benzylic, phenethylic, or plain aliphatic position.

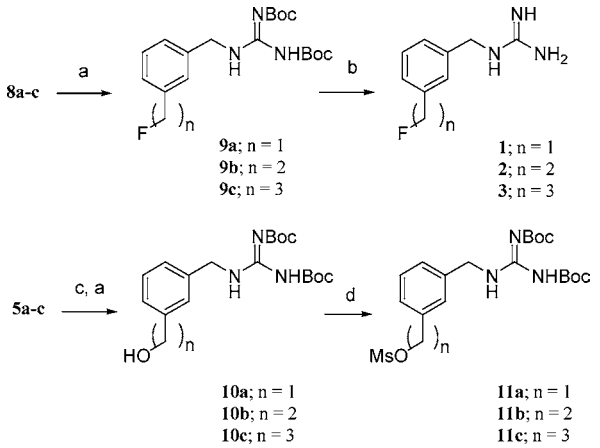
In the case of fluorination of **6b**,**c**, elimination and hydrolyzed byproducts were formed using TBAF in which fluoride was considered as a base. We have developed a new aliphatic fluorination using KF (*25*) as well as [^{18}F]-fluoride (*26*) in ionic liquid, which is expected to provide high yields of fluoroalkyl (especially fluoroethyl) aromatics during the synthesis of **7b**,**c**. Reduction of the nitrile group in **7a**−**c** to aminomethyl moiety was achieved by the treatment with borane−tetrahydrofuran complex. When lithium borohydride was used instead of borane−tetrahydrofuran complex, 3-alkylbenzylamine was obtained as a major product. In the synthesis of **8a** from **7a**, the ratio of **8a** to 3-methylbenzylamine was 2:8. Due to the difficulty of purification of 3-(ω-fluoroalkyl)benzylamines, **8a**−**c** were isolated as HCl salts. Authentic target compounds **1**−**3**, were prepared from **8a**−**c** with *N*,*N*′-bis(*tert*-butyloxycarbonyl)-2-methylthiourea in good yield under mild condition (*27*−*30*) as shown in Scheme 2, followed by deprotection of Boc groups. Parenthetically, we synthesized guanidine from benzylamine using 2-methyl-2-thio-pseudourea sulfate or cyanamide but in very low yield and with difficulty due to its high polarity. The reduction of the nitrile of **5a**−**c** by BH_3-THF did not give good yields, consequently requiring the more powerful reducing reagent. With the use of lithium borohydride (*31, 32*), 3-(ω-hydroxyalkyl)benzylamines were synthe-

Scheme 1[a]



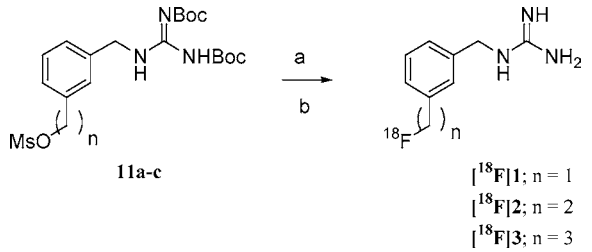
[a] Reagents: (a) $NaBH_4$, EtOH, rt, 40 min; (b) $Pd(PPh_3)_4$, LiCl, tributylvinyl(or allyl)tin, THF, 80 °C, 12 h; (c) (1) 1 M BH_3·THF, 0 °C, 1 h; (2) 4 N NaOH, H_2O_2, 0 °C, 40 min; (d) MsCl, Et_3N, CH_2Cl_2, 0 °C, 30 min; (e) n-Bu_4NF, CH_3CN, 80 °C, 2 h; (f) (1) 1 M BH_3·THF, THF, 80 °C, 12 h, (2) 1 N HCl in THF, 30 min.

Scheme 2[a]



[a] Reagents: (a) *N*,*N*′-bis(*tert*-butyloxycarbonyl)-2-methylthiourea, $HgCl_2$, DMF, Et_3N, 0 °C, 1 h; (b) 3 M HCl in EtOAc, 65 °C, 30 min; (c) $LiBH_4$, THF, 80 °C, 12 h; (d) MsCl, Et_3N, CH_2Cl_2, 0 °C, 30 min.

Scheme 3[a]



11a-c

[**^{18}F]1**; n = 1
[**^{18}F]2**; n = 2
[**^{18}F]3**; n = 3

[a] Reagents: (a) *n*-$Bu_4N^{18}F$, CH_3CN, 75−80 °C, 10 min; (b) 3 M HCl in EtOAc, 65 °C, 10 min.

Table 1. Yields of the Fluorine-18 Incorporation of 11a−c and the Yields of Deprotection of Boc Groups

compound	1st step:[a] fluorine-18 radiolabeling yields,[c] %	2nd step:[b] deprotection of Boc guanidine,[c] %
11a	35.7 ± 2.1	>90
11b	30.3 ± 3.5	>89
11c	38.1 ± 4.2	>95

[a] An appropriate amount of radioactivity was placed in a Vacutainer containing *n*-Bu_4NHCO_3 (40% aq, 2.70 μL, 3.65 μmol), and three azeotropic distillations were carried out each time with 200 μL aliquots of CH_3CN at 85 °C under a stream of N_2. The resulting *n*-$Bu_4N[^{18}F]F$ was delivered to a reaction vial with CH_3CN. The reaction was heated at 75−80 °C for 10 min. [b] Deprotection was carried out using 3 M HCl in EtOAc (200 μL) at 65 °C for 10 min. [c] Progress of the reaction was analyzed by radio-TLC (1st; hexane/EtOAc = 9: 1 on silica TLC, 2nd; 0.2 M $(NH_4)H_2PO_4/CH_3CN$ = 7:3 on C18 TLC).

sized in about 80% yields. Either BH_3−THF or $LiBH_4$ was used for selective reduction of compounds containing a nitrile group such as **7a−c** and **5a−c**. Because 3-(ω-hydroxyalkyl)benzylamine was unstable when dissolved in solvents, it was difficult to isolate the product by flash column chromatography. After reduction of **5a−c** with $LiBH_4$, the crude mixture was treated with *N*,*N*′-bis(*tert*-butyloxycarbonyl)-2-methylthiourea and mercuric chloride under mild condition to provide **10a−c**. Mesylated products **11a−c** were used as the precursor for the synthesis of [**^{18}F]1−3**.

The process for preparation of 3-(ω-[^{18}F]fluoroalkyl)-benzylguanidines contains only two steps: the displacement of [^{18}F]fluoride and the deprotection of two Boc groups as shown in Scheme 3. The results of the fluoride-18 incorporation and deprotection steps for the preparation of [**^{18}F]1−3** are summarized in Table 1. Based on the analysis by radio-TLC, the radiochemical yields of the Boc-protected compounds [**^{18}F]9a−c** decreased gradually after 10 min. While there was a big difference of chemical yields in the aliphatic nucleophilic fluorination of cold **9a−c**, we have obtained [**^{18}F]9a−c** in 35.7, 30.3, and 38.1% yields, respectively. After deprotection with 3 M HCl, the radiolabeled product was purified by HPLC.

We expected the fluoroalkylated compounds **1−3** to have similar lipophilicities to MIBG. Using retention time on HPLC (5 μm, 4.6 × 250 mm; C18 column; 215 nm; 0.1 M ammonium dihydrogen phosphate:acetonitrile = 50:50 (v/v); 1.0 mL/min), the lipophilicity of each compound is assessed by the capacity factor value which was correlated to the level of binding to SK-N-SH neuroblastoma cells expressed as % binding relative to that of [**^{18}F]-3**. The capacity factor ($k' = (t_R - t_0)/t_0$) of each compound was compared to that of MIBG (k' = 4.26), and cell binding assays were carried out using SK-N-SH human neuroblastoma cells to compare the relative level of cell binding for [**^{18}F]3** (Table 2). The capacity factor of **3** was similar to that of MIBG and [**^{18}F]3** also demonstrated

Table 2. Comparison of Lipophilicities and in Vitro SK-N-SH Human Neuroblastoma Cells of *m*-(ω-[^{18}F]Fluoroalkyl)benzylguanidines

compound	capacity factors (k')[a]	% binding of input activity	% cell binding ratio vs [**^{18}F]3**[b]
[**^{18}F]1**	2.36	3.0 ± 0.4	56 ± 6.7
[**^{18}F]2**	3.23	4.2 ± 0.2	81 ± 1.3
[**^{18}F]3**	3.57	5.3 ± 0.7	100

[a] Using retention time on HPLC (C18 column; 215 nm; 0.1 M ammonium dihydrogen phosphate:acetonitrile = 50:50), the capacity factors were calculated. [b] Measured by γ-counter.

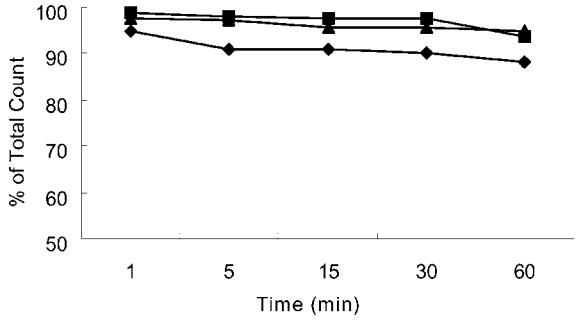


Figure 2. In vitro metabolic stability study of [**^{18}F]1**, [**^{18}F]2**, and [**^{18}F]3**. Using rat hepatic microsomes the radiotracer (0.074−0.74 MBq) was incubated at 37 °C and the obtained mixture was analyzed by radio-TLC at 1, 5, 15 30, and 60 min, respectively. ◆ [**^{18}F]1**; ■ [**^{18}F]2**; ▲ [**^{18}F]3**.

higher binding levels to SK-N-SH cells compared to the other tracers. On the basis of these results, [**^{18}F]3** was used for the remaining in vitro and in vivo studies.

The prospective metabolites of fluoroalkyl compounds would be formed by defluorination, *N*-dealkylation, and hydroxylation. We developed an easy method to check the formation of metabolites by hepatic microsomes (*33*). These polar metabolites could be differentiated by a TLC developing system (0.2 M $(NH_4)H_2PO_4/CH_3CN$ = 7:3 on C18 silica gel TLC). Using a radio-TLC scanner, [**^{18}F]1** (R_f = 0.62), [**^{18}F]2** (R_f = 0.57), and [**^{18}F]3** (R_f = 0.55) were retained with 88, 97, and 95%, respectively (Figure 2), and only a single unknown peak appeared at the starting point on the TLC developed for 60 min. The single unknown peak was matched with free fluorine-18 on C18 silica gel TLC. This demonstrates that the fluoropropyl and fluoroethyl compounds are more stable than the fluoromethyl compound in an in vitro metabolic environment, and that these radiotracers are expected to be highly stable in an in vivo. Magata et al. reported the study of defluorination metabolism of ^{18}F-labeled benzyl fluorides in vivo (*34*), and Welch et al. proposed the mechanism of in vivo stability of fluoroethyl and fluoropropyl group (*35*).

Cell binding assays were carried out using SK-N-SH human neuroblastoma cells in a paired format to compare [**^{18}F]3** and [^{123}I]MIBG uptake. In the in vitro cell uptake study, [**^{18}F]3** and [^{123}I]MIBG showed comparable results as shown in Figure 3. To confirm energy-dependence of uptake, tracer uptake was evaluated by incubation at 37 °C and 4 °C. Incubation at 4 °C decreased cellular binding of [**^{18}F]3** to 44.6 ± 7.0% and 62.4 ± 7.6% of levels obtained at 37 °C, repectively. This result was similar to the change shown for [^{123}I]MIBG uptake (35.9 ± 4.6% and 42.8 ± 5.5%).

The inhibition of [**^{18}F]3** binding to SK-N-SH cells was performed at a increasing preincubation time with 50 μM of desipramine. The time dependent result was shown in Figure 4. After 48 h of incubation with desipramine, uptake in SK-N-SH cell was 24.6 ± 2.8% (p = 0.00114)

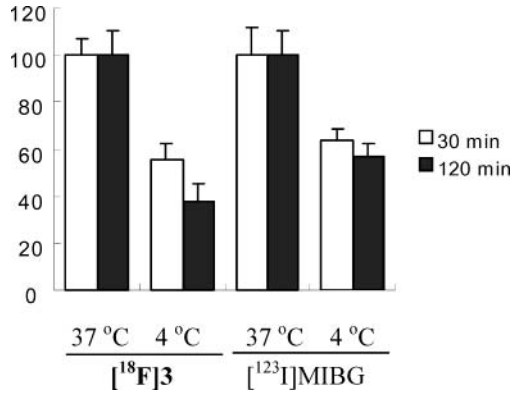


Figure 3. Comparison of temperature-dependent uptake of **[18F]3** and [123I]MIBG in SK-N-SH human neuroblastoma cells. The level of binding to SK-N-SH neuroblastoma cells expressed as % cell binding at 4 °C relative to that of 37 °C. (□) The incubation time is 30 min; (■) the incubation time is 120 min.

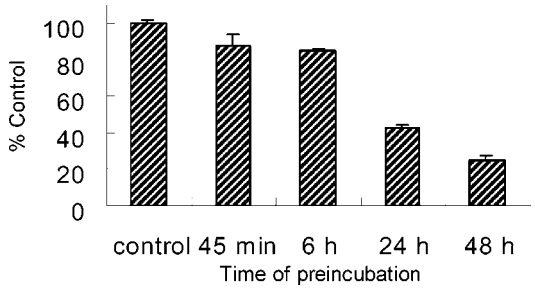


Figure 4. Inhibition of **[18F]3** binding SK-N-SH cell by graded incubation time of desiparamine.

Table 3. Tissue Distribution of nca [18F]3[a] in Normal Mice

tissue	%ID/g:[b] 2 h postinjection
blood	1.6 ± 0.4
heart	9.3 ± 0.5
lung	10.6 ± 1.0
liver	12.1 ± 3.5
spleen	9.7 ± 2.0
pancreas	12.3 ± 4.0
muscle	4.4 ± 1.4
adrenal	27.2 ± 5.2
kidney	4.7 ± 0.9

[a] Tracer **[18F]3** was dissolved in saline and injected into normal ICR mice The normal dose per mouse was 1.1 MBq via tail vein. [b] Percent injected dose per gram of tissue; mean ± SD (n = 3).

relative to control levels. However, longer durations of inhibition were required and the magnitude of inhibited binding was smaller than previous reports on desipramine inhibition of MIBG uptake. It thus appears that **[18F]3** has limitations compared to MIBG with respect to specificity of binding, and part of the cellular binding of **[18F]3** may be mediated by systems other than the neuronal pump. This demonstrated that tracer accumulated through the uptake-1 mechanism.

Tissue distribution of **[18F]3** in mice was performed to evaluate whether the radiotracer undergoes an in vivo uptake mechanism similar to that of MIBG. The tissue distribution results of **[18F]3** in mice are summarized in Table 3. After 2 h postinjection, tissue distribution studies showed the uptake of **[18F]3** to be highest in the adrenals (%ID/g = 27.2 ± 5.0%), followed by the myocardium (%ID/g = 9.3 ± 0.5%). The distribution of **[18F]3** in most of the major organs were comparable to previously reported distribution for [125I]MIBG in normal mice, although myocardial uptake levels were somewhat lower for **[18F]3** (*17*).

CONCLUSION

In conclusion, *m*-(*ω*-[18F]fluoroalkyl)benzylguanidines were prepared in two steps with good yields and high stability in vivo. Cell studies of SK-N-SH human neuroblastoma cells and biodistribution data suggest that **[18F]-3** may have potential as a useful PET radiopharmaceutical agent for evaluating adrenomedullary tissue.

ACKNOWLEDGMENT

This work was supported by National Research Laboratory Program and the Health Planning Technology Research Grant #01-PJ1-PG3-20500-0143 from the Ministry of Health and Welfare, Korea.

LITERATURE CITED

(1) Wieland, D. M., Brown, L. E., Rogers, W. L., Worthington, K. C., Wu, J.-L., Clinthrone, N. H., Otto, C. A., Swanson, D. P., and Beierwaltes, W. H.(1981) Myocardial imaging with a radioiodinated norepinephrine storage analogue. *J. Nucl. Med. 22*, 22−31.

(2) Ackery, D. M., Tippett, P. A., Condon, B. P., Sutton, H. E., and Wyeth, P. (1984) New approach to the localization of phaeochromocytoma: imaging with iodine-131-metaiodobenzylguanidine. *Br. Med. J. 288*, 1587−1591.

(3) Wieland, D. M., Wu, J.-l., Brown, L. E., Mangner, T. J., Swanson, D. P., and Beierwaltes, W. H. (1980) Radiolabeled adrenergic neuron-blocking agents: adrenomedullary imaging with [131I]iodobenzylguanidine. *J. Nucl. Med. 21*, 349−353.

(4) Tobes, M. C., Jacques, S., Jr., Wieland, D. M., and Sisson, J. C. (1985) Effect of uptake-one inhibitor on the uptake of norepinephrine and metaiodobenzylguanidine. *J. Nucl. Med. 26*, 897−907.

(5) McGhie, A. I., Corbett, J. R., Akers, M. S., Kulkarni, P., Sills, M. N., Kremers, M., Buja, L. M., Durant-Reville, M., Parkey, R. W., and Willerson, J. T.(1991) Regional cardiac adrenergic function using I-123 meta-iodobenzylguanidine tomographic imaging after acute myocardial infarction. *Am. J. Cardiol. 67*, 236−242.

(6) Feldman, J. M., Blinder, R. A., Lucas, K. J., and Cloeman, R. E. (1986)Iodine-131 metaiodobenzylguanidine scintigraphy of carcinoid tumors. *J. Nucl. Med. 27*, 1691−1696.

(7) McEwan, A. J., Shapiro, B., Sission, J., Beierwaltes, W. H., and Ackery. D. M. (1985) Radioiodobenzylguanidine for the scintigraphic location and therapy of adrenergic tumor. *Semin. Nucl. Med. 15*, 132−153.

(8) Wakasugi, S., Wada, A., Hasegawa, Y., Nakano, S., and Shibata, N. (1992) Detection of abnormal cardiac adrenergic neuron activity in adriamycin-induced cardiomyopathy with iodine-125-metaiodobenzylguanidine. *J. Nucl. Med. 33*, 208−214.

(9) Stanton, M. S., Tuli, M. M., Radtke, N. L., Heger, J. J., Miles, W. M., Mock, B. H., Burt, R. W., Wellman, H. N., and Zipes, D. P.(1988) Regional sympathetic denervation after myocardial infarction in humans detected noninvasively using 123I-metaiodobenzylguanidine. *J. Am. Coll. Cardiol. 14*, 1519−1529.

(10) Shapiro, N., and Gross, M. D. (1987) Radiochemistry, biochemistry and kinetics of 131I-metaiodobenzylguanidine (MIBG) and 123I-MIBG: clinical implications of the use of 123I-MIBG. *Med. Pediatr. Oncol. 15*, 170−177.

(11) Wieland, D. M., Mangner, T. J., Inbasekaran, M. N., Brown, L. E., and Wu, J.-L. (1984) Adrenal medulla imaging agents: a structure-distribution relationship study of radiolabeled aralkylguanidines. *J. Med. Chem. 27*, 149−155.

(12) Chen, W. L., Yu, M. D., Liu, R. S., and Yeh, S. H. (1993) A novel synthesis of [F-18]metafluorobenzylguanidine for PET studies. *J. Nucl. Med.* 238P.

(13) Garg, P. K., Garg, S., and Zalutsky, M. R. (1994) Synthesis of perliminary evaluation of *para*- and *meta*-[18F]fluorobenzylguanidine. *Nucl. Med. Biol. 21*, 97−103.

(14) Vaidyanathan, G., Affleck, D. J., and Zalutsky, M. R. (1994) (4-[^{18}F]Fluoro-3-iodobenzyl)guanidine, a potential MIBG analogue for Positron Emission Tomography. *J. Med. Chem. 37*, 3655−3662.

(15) Loc′h, C., Mardon, K., Valette, H., Brutesco, C., Merlet, P., Syrota, A., and Maziere, B. (1994) Preparation and pharmacological characterization of [^{76}Br]-*meta*-bromobenzylguanidine ([^{76}Br]MBBG). *Nucl. Med. Biol. 21*, 49−55.

(16) Valette, H., Loc'h, C., Mardon, K., Bendriem, B., Merlet, P., Fuseau, C., Sabry, S., Raffel, D., Mazière, B., and Syrota, A. (1993) Bromine-76-meta-bromobenzylguanidine: A PET radiotracer for mapping sympathetic nerves of the heart. *J. Nucl. Med. 34*, 1739−1744.

(17) Vaidyanathan, G., Affleck, D. J., and Zalutsky, M. R. (1995) Validation of 4-[fluorine-18]fluoro-3-iodobenzylguanidine as a positron-emitting analogue of MIBG. *J. Nucl. Med. 36*, 644−650.

(18) Kilboun, M. R. (1990) *Fluorine-18 labeling of radiopharmaceuticals*, National Academy Press, Washington, DC.

(19) Berridge, M. S., and Tewson, T. J. (1986) Chemistry of fluorine-18 radiopharmaceuticals, *Appl. Radiat. Isot. 37*, 685−693.

(20) Short, J. H., and Darby, T. D. (1967) Sympathetic nervous system blocking agents. 3. Derivatives of benzylguanidine. *J. Med.* Chem. *10*, 833−840.

(21) Lee, K. C., and Chi, D. Y. (1999) An efficient synthesis of (fluoromethyl)pyridylamines for labeling with fluorine-18. *J. Org. Chem. 64*, 8576−8581.

(22) Milstein, D., and Still,J. K. (1979) Palladium-catalyzed coupling of tetraorganotin compound with aryl and benzyl halides. Synthetic utility and mechanism. *J. Am. Chem. Soc. 101*, 4992−4998.

(23) Scott, W. J., Crisp, G. T., and Still, J. K. (1984) Palladuim-catalyzed coupling of vinyl triflates organostannanes. a short synthesis of pleralysillin-1. *J. Am. Chem. Soc. 106*, 4630−4632.

(24) Brown, H. C., and Unni, M. K. (1968) The hydroboration of 3-butenyl derivatives containing representative substitutions. *J. Am. Chem. Soc. 90*, 2902−2905.

(25) Kim, D. W., Song, C. E., and Chi, D. Y. (2002) New method of fluorination using potassium fluoride in ionic liquid: significantly enhanced reactivity of fluoride and improved selectivity. *J. Am. Chem. Soc. 124*, 10278−10279.

(26) Kim, D. W., Choe, Y. S., and Chi, D. Y. (2003) A new nucleophilic fluorine-18 labeling method for aliphatic mesylates: reaction in ionic liquids shows tolerance for water. *Nucl. Med. Biol. 30*, 345−350.

(27) Michael, A. P., Edwin, I., Joyce, A. R., James, L., and Zhengxiang, G. (1992) A mild and efficient method for the preparation of guanidines. *Tetrahedron* Lett. *33*, 5933−5936.

(28) Bernatowicz, M. S., Wu, Y., and Matsueda, G. R. (1993) Urethane protected derivatives of 1-guanylpyrazole for the mild and efficient preparation of guanidines. *Tetrahedron Lett. 34*, 3389−3392.

(29) Kim, K. S. and Qian, L.(1993) Improved method for the preparation of guanidines. *Tetrahedron Lett. 34*, 7677−7680.

(30) Michael, S., Feichtinger, C., Zapf, C., Sings, H. L., and Goodman, M. (1998) Diprotected triflylguanidines: A new class of guanidinylation reagents. *J. Org. Chem. 63*, 3804−3805.

(31) Soai, K., and Ookawa, A. (1986) Mixed solvents containing methanol as useful reaction media for unique chemoselective reduction with lithium borohydride. *J. Org, Chem. 51*, 4000−4005.

(32) Brown, H. C., Narasimhan, S., and Choi, Y. M. (1982) Selective reduction. 30. Effect of cation and solvent on the reactivity of saline borohydrides for reduction of carboxylic esters. Improved procedures for the conversion of esters to alcohols by metal borohydrides. *J. Org. Chem. 47*, 4702−4708.

(33) Lee, S. Y., Choe, Y. S., Kim, D. H., Park, B. N., Kim, S. E., Choi, Y., Lee, K. H., Lee, J., and Kim, B.-T. (2001) A simple and efficient in vitro method for metabolism studies of radiotracer. *Nucl. Med. Biol. 28*, 391−395.

(34) Magata, Y., Lang, L., Kiesewetter, D. O., Jagoda, E. M., Channing, M. A., and Eckelman, W. C. (2000) *Nucl. Med. Biol. 27*, 163−168.

(35) Welch, M. J., Katzenellenbogen, J. A., Mathias, C. J., Brodack, J. W., Carlson, K. E., Chi, D. Y., Dence, C. S., Kilbourn, M. R., Perlmutter, J. S., Raichle, M. E., and Ter-Pogossian, M. M. (1988) *N*-(3-[^{18}F]Fluoroalkyl)-spiperone: the preferred ^{18}F-labeled spiperone analogue for positron emission tomographic studies of the dopamine receptor. *Nucl. Med. Biol. 15*, 83−97.

BC034115E

A Comparative Study of Different Presentation Strategies for an HIV Peptide Immunogen

Luis J. Cruz,*[,†] Enrique Iglesias,[‡] Julio C. Aguilar,[‡] Luis J. González,[‡] Osvaldo Reyes,[‡] Fernando Albericio,[†,§] and David Andreu[||]

Barcelona Institute of Biomedical Research, Barcelona Science Park, 08028 Barcelona, Spain, Centro de Ingeniería Genética y Biotecnología, Cubanacán, Habana 10600, Cuba, Department of Organic Chemistry, University of Barcelona, 08028 Barcelona, Spain, and Department of Experimental and Health Sciences, Pompeu Fabra University, 08003 Barcelona, Spain. Received July 10, 2003; Revised Manuscript Received October 17, 2003

Different strategies have been used to increase the immunogenicity of an antigenic HIV peptide as a vaccine candidate. The selected B-cell epitope comprises 15 amino acids (317−331) of the V3 region of HIV-1, JY1 isolate (subtype D), in tandem with a T-helper epitope corresponding to the 830−844 region of tetanus toxoid. Several presentations, including oligomerization, multiple antigenic peptide dendrimers, and conjugation to dextran beads or to other macromolecular carriers, have been synthesized and evaluated. Murine sera from the different presentations of the V3 epitope have been compared with regard to antibody titers and cross-reactivity with heterologous HIV subtypes. The dendrimer version of the peptide conjugated to HBsAg protein was a better immunogen than the dendrimer alone and showed a higher immunogenicity than other multimeric presentations or than the peptide alone conjugated to dextran. The dendrimer version, either alone or conjugated to HBSAg, enhanced cross-reactivity toward heterologous V3 sequences relative to monomeric peptide. In addition, fine epitope mapping of the entire JY1 sequence by sera from the different immunization groups was performed by the spot synthesis technique. Results showed that the amino acids involved in molecular recognition were LXQXXY or LXQXLY, with particularly strong recognition of the C-terminal region LGQALY. However, cross-reactivity toward the heterologous sequences did not completely correlate with recognition of particular amino acids in the primary sequences. These results can find application in the development of HIV vaccine candidates.

INTRODUCTION

Although vaccines are widely regarded as the ideal solution for the control of infectious diseases, only a handful of them are currently available and a pressing demand is felt for improvements on existing ones, with particular emphasis on higher efficiency and undisputed safety profiles. In recent years, considerable attention has been focused on the development of peptide-based vaccines as an alternative to conventional formulations. Peptide vaccines have obvious advantages such as high safety, low cost, and easy handling and storage. In contrast to classical vaccines, they can be tailor-made against specific targets including antigenic sites not easily accessible to the immune system. However, they suffer also from limitations such as the usually low immunogenicity of small peptides and the vulnerability to proteolytic degradation. Many of these problems can be addressed by improved forms of presentation of the synthetic epitope to the immune system, including formulations such as multiple antigen peptide systems (MAPs[1]) (*1*), dendrimers (*2*), lipopeptides (*3, 4*), polymerization (*5, 6*), conjugation to carriers such as proteins or synthetic polymers (*7, 8*) or association to particulate systems such as liposomes (*9*), or immunostimulating complexes such as ISCOMs (*10*). Combined approaches such as coupling of MAPs to carrier proteins (*11*) have also been shown to enhance peptide immunogenicity and to induce protective or neutralizing antibody responses for parasitic and viral pathogens.

In HIV-1 infection, the V3 loop is the primary target for neutralizing antibodies (*12, 13*) and is involved in other aspects of infectivity. Thus, sequence changes in V3 can affect chemokine receptor usage and therefore modulate which cell types are infected (*14*). This V3 region includes both T-helper and CTL epitopes (*15*). Antibodies against the principal neutralizing domain (PND) of V3 appear to exert some control over the viral load (*16*−*18*). For the HIV-1 MN (subtype B) isolate, a

* Corresponding author. David Andreu, Department of Experimental and Health Sciences, Pompeu Fabra University, Doctor Aiguader 80, 08003 Barcelona, Spain. david.andreu@upf.edu.

[†] Barcelona Institute of Biomedical Research.

[‡] Centro de Ingeniería Genética y Biotecnología.

[§] University of Barcelona.

[||] Pompeu Fabra University.

[1] Abbreviations: AAA, amino acid analysis; AcOH, acetic acid; Boc, *tert*-butyloxycarbonyl; Bzl, benzyl; BSA, bovine serum albumin; CFA, complete Freund's adjuvant; DIPC, 1,3-diisopropylcarbodiimide; DTT, dithiothreitol; DCM, dichloromethane; DMF, *N*,*N*-dimethylformamide; DIPEA, diisopropylethylamine; EDTA, ethylenediaminetetraacetic acid; EDAC, 1-ethyl-3-(dimethylaminopropyl)carbodiimide; Fmoc, 9-fluorenylmethyloxycarbonyl; HBsAg, hepatitis B surface antigen; HF, hydrogen fluoride; HOBt, 1-hydroxybenzotriazole; HPLC, high-performance liquid chromatography; IFA, incomplete Freund's adjuvant; MAP, multiple antigenic peptides; MALDI-TOF, matrix-assisted laser desorption ionization with time-of-flight analysis; MS, mass spectrometry; PBS, phosphate-buffered saline; RP, reverse phase; TFA, trifluroacetic acid; TBTU, 2-(1*H*-benzotriazol-1-yl)-1,1,3,3-tetramethyluronuim tetrafluoroborate.

10.1021/bc034119j CCC: $27.50 © 2004 American Chemical Society
Published on Web 12/11/2003

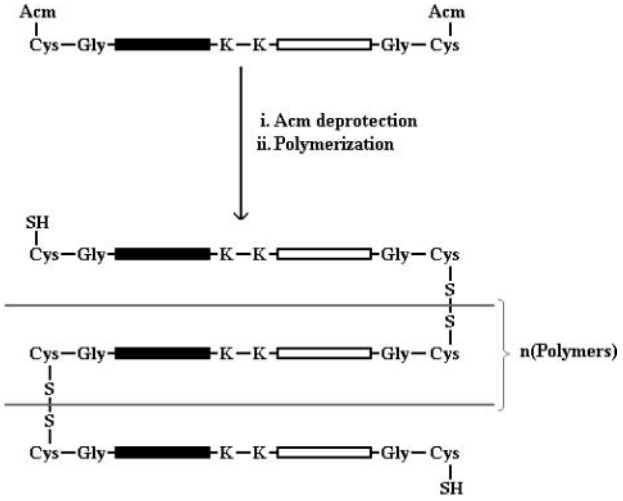


Figure 1. Reaction scheme for the polymerization of a peptide containing the JY1 epitope (filled box) in tandem with a T-epitope of tetanus toxoid (empty box) separated by a cathepsin cleavage site insert. Deprotection of both N- and C-terminal Cys residues gives a dithiol that polymerizes under basic conditions.

high titer against V3 has been correlated to slow progression rates in seropositive hemophilic Japanese patients (*19*). All these findings highlight the immunological relevance of the V3 loop, which has been included in a number of HIV-1 vaccine candidates (*20*). They also underscore the significance of studying how different ways of presentation of the synthetic peptide epitope affect the quality of the immune response.

In the present work we have investigated several presentation strategies for the V3 epitope, with a view to enhance its immunogenicity. Our selected B-cell epitope comprises 15 residues (317−331) of the V3 region from HIV-1 JY1 isolate (*21*), linked through a Lys-Lys cathepsin-like cleavage site (*6*) to a helper T-cell epitope (residues 830−844) from tetanus toxoid (*22*). We have evaluated the anti-peptide antibody response of these presentations and their cross-reactivity toward other V3 sequences and have fine-mapped their recognition of the entire JY1 epitope sequence.

EXPERIMENTAL PROCEDURES

Chemicals and Biologicals. Fmoc- and Boc- protected amino acids were purchased from Bachem (Switzerland). Solvents for peptide synthesis (dichloromethane, 2-propanol, *N*,*N*′-dimethylformamide) were obtained from Merck (Germany). Dextran beads cross-linked with epichlorhydrin (Sephadex G 150) were from Pharmacia Biotech (Sweden). Succinic anhydride and other chemicals were from Sigma (St. Louis, MO). Recombinant hepatitis B virus surface antigen (rHBsAg) and TAB9 protein, a multiepitope polypeptide (MEP) including the V3 region from six divergent HIV-1 isolates (LR150, JY1, RF, MN, BRVA, and IIIB, in this order) fused to the amino terminus (47 amino acids) of P64K protein from *N. meningitidis*, were obtained from CIGB (Cuba).

Synthetic Peptide Antigens and Conjugates. *Peptide Synthesis.* The monomeric form of the immunogen [C(Acm)GRQSTPIGLGQALYTTKKQYIKANSKFIGITELGC(Acm)] (Figure 1) was synthesized by the Boc/Bzl strategy on 4-methylbenzhydryl-amine (MBHA) resin (100−200 mesh, 0.7 mmol/g, Fluka) using the tea bag method (*23*). Side chain protecting groups were acetamidomethyl (Acm) for Cys, benzyl ether for Ser and Thr, benzyl ester for Asp and Glu, tosyl for Arg, dichlorobenzyl for Tyr, and 2-chlorobenzyloxycarbonyl for Lys. Coupling

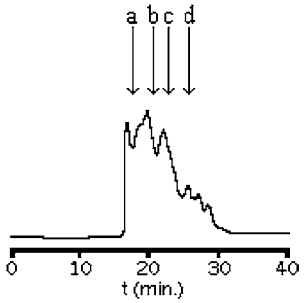


Figure 2. HPLC analysis of the polymerization reaction by gel filtration on TSK G 2000SW in 10% acetonitrile in water. Arrows a−d indicate, respectively, the elution volumes of bovine serum albumin (M_r 67 000), chymotrypsinogen A (M_r 25 000), lysozyme (M_r 14 000), and the monomer peptide (M_r 4000).

of the amino acids was achieved by activation with 1,3-diisopropylcarbodiimide and was monitored by the Kaiser test (*24*). Side-chain deprotection [except for Cys (Acm)] and cleavage from the resin was performed by the low-high HF procedure, using HF-DMS−*p*-cresol (25:65:10) for 2 h at 0 °C followed by HF−DMS−anisole−thiocresol (79.8:10:10:0.2) for 1 h at 0 °C (*25*). The resin was subsequently washed with diethyl ether and dried off under vacuum. The crude peptide was extracted from the resin with 30% acetic acid, diluted with water, and lyophilized.

Polymerization via S-Acm Deprotection/Oxidation with Iodine. The above peptide, with its Cys residues protected with Acm, was dissolved at 25 mmol/L in AcOH/H_2O (3:2, v/v), and 1.5 equiv of 80 mM aqueous HCl and 10 equiv of iodine in DMF were added. The polymerization reaction was stopped after 30 min by addition of L-ascorbic acid. The reaction mixture was purified on a PD10 Sephadex G-25 column (1.5 × 10 cm) equilibrated and eluted with 1% AcOH, to remove excess reagents and to prevent precipitation of polymers. After exhaustive dialysis against 1% AcOH, the solution was lyophilized. The polymer was characterized by HPLC gel filtration using a TSK G 2000SW column (8 × 300 mm) equilibrated and eluted with 10% MeCN (+0.05% TFA) in water (+0.1% TFA). Lysozyme, chymotrypsinogen A, and bovine serum albumin were used as molecular weight markers.

MAP Synthesis. The MAP version of the V3 peptide (see Figure 3 for details) was assembled by stepwise Boc solid-phase methods (*23*), using the protection scheme described above, except that Cys residue at the C-terminus was protected with the 4-methoxybenzyl (Mob) group. The Lys residues responsible for branching (one in the tetravalent, three in the octavalent versions of the MAP, respectively) were incorporated as Boc-Lys(Boc)-OH and coupled with TBTU/DIEA activation. Double couplings with 10-fold excess of Boc-amino acids and DIEA/HOBt were used for most residues of the V3 epitope. When required by the Kaiser test, capping steps were performed with 4% acetic anhydride and 1% DIEA in DMF. After low-high HF cleavage and deprotection as above, the MAPs were extracted into 0.1 M Tris-HCl, pH 8.0, containing 8 M urea, and dimerization of the MAP monomer by disulfide bond formation was allowed to proceed and monitored by the Ellman test (*26*). The homodimeric MAPs were dialyzed against 2 M urea in 0.1 M Tris-HCl buffer, pH 8.0 for 24 h, then dialyzed against 1 M AcOH, to remove all the urea and lyophilized.

Reduction and S-Carboxymethylation. The lyophilized homodimeric MAPs were dissolved at a concentration of 5 mg/mL in 0.3 M Tris.HCl, 6 M guanidinium chloride,

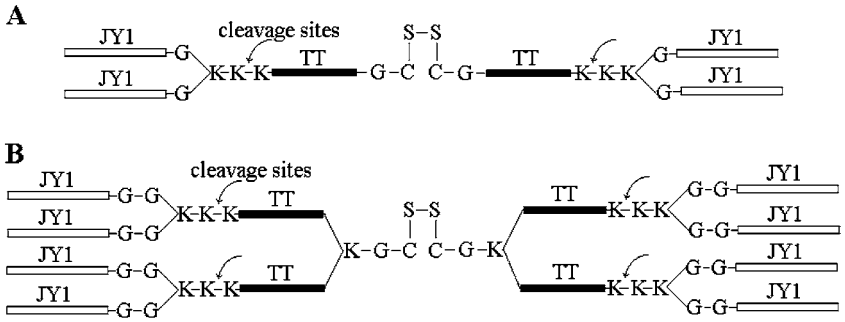


Figure 3. The JY1-MAP4 (A) and JY1-MAP8 (B) dendrimeric immunogens are disulfide dimers of lysine-branched constructs containing the JY1 and TT epitopes in a 2:1 ratio linked through a cathepsin cleavage site.

3 mM EDTA buffer, pH 8.5. A 20-fold molar excess of DTT over Cys residues was added, and the solution was flushed with nitrogen and incubated for 2 h at 37 °C. A 2-fold molar excess of iodoacetic acid over DTT was next added, and the solution was kept at room temperature for 1 h in the dark. Modified MAPs were characterized by RP-HPLC and mass spectrometry as described above.

Assembly of Peptides on Dextran Beads. The dried dextran beads were chemically modified to introduce anchor functions suitable for peptide synthesis. Thus, 1 g of dextran beads was treated for 24 h with 4 mL of a 0.4 M Fmoc-β-alanine solution (activated with 0.48 M DIPC and 0.8 M NMI in DMF) to modify the hydroxyl groups into amine functions. Unreacted hydroxyl sites were acetylated by treatment with 20% acetic anhydride/10% DIPEA/10% NMI in DMF for 30 min. Peptide synthesis was subsequently carried out using Fmoc/tBu chemistry (*27*). Side chain protecting groups were *tert*-butyl for Glu, Thr, Ser, and Tyr; trityl for Gln and Asn; Boc for Lys and 2,2,5,7,8-pentamethylchroman-6-sulfonyl for Arg. Fmoc deprotection was done with 20% piperidine in DMF for 20 min, and the resulting Fmoc-piperidine adduct was quantitated spectrophotometrically to determine resin substitution. Couplings were carried out with 200 μmol each of Fmoc-amino acid, HOBt, and DIPC in DMF for 1 h and monitored by the bromophenol blue (*28*) and Kaiser ninhydrin tests (*24*). When required, recouplings were performed with 300 μmol each of Fmoc-amino acid, TBTU, and HOBt, in the presence of 900 μmol of DIEA, in DMF. Systematic capping after each coupling step was performed with 4% (v/v) acetic anhydride and 1% (v/v) DIEA in DMF.

After the sequence assembly was completed, side chain protecting groups were removed with 50% (v/v) TFA in DCM containing 1% phenol, 2% ethanedithiol, 2% thiophenol, and 2% water (all v/v) for 2 h. Peptide−dextran beads were next washed (4× each) with DCM, DMF, and methanol. Finally, the peptide was cleaved from the dextran beads with 0.1 M NaOH for 15 min, neutralized, and analyzed by RP-HPLC. The main peak was collected and characterized by AAA and mass spectrometry.

Conjugation of Peptides and MAP to Carrier Proteins. Peptides and MAP were coupled to HBsAg as described by Deen et al. (*29*). Briefly, 5 mg of HBsAg was dissolved in 5 mL of 0.2 M K_2HPO_4, pH 8.0, solid succinic anhydride (1 mg) was added, and the solution was stirred until all anhydride was dissolved, adding 3 M NaOH dropwise as required to keep the pH at 8−8.5. The activated protein was next exhaustively dialyzed against dilute HCl (pH 4.5), treated with 7 mg 1-ethyl-3-(dimethylaminopropyl) carbodiimide (EDAC), and stirred for 10 min at 25 °C. Then, 5 mg of peptide or MAP dissolved in 1 mL of 3 M guanidine hydrochloride in PBS was added and the mixture gently stirred for 3 h at 25 °C. The conjugates were purified by gel filtration through Sephadex CL-4B (Pharmacia) eluted with PBS. The front-eluting fractions were pooled and quantitated by the Coomassie method (*30*).

Chromatography. Soluble peptides and MAPs were analyzed by RP-HPLC on Vydac C_{18} (100 × 4.6 mm) and Baker C_8 wide-pore (100 × 4.6 mm) columns, respectively, in a Pharmacia-LKB (Sweden) model 2150 dual pump chromatograph coupled to a Knauer (FRG) variable wavelength UV detector. Linear gradients of acetonitrile (+0.05% TFA) into water containing (+0.1% TFA) were used for the separation, at a 0.8 mL/min flow rate. Optical density was monitored at 226 nm. Data were processed with the BioCrom program (CIGB, Cuba).

Amino Acid Analysis. Samples of S-carboxymethylated MAPs were hydrolyzed with 6 M HCl containing 0.1% phenol and 0.1% 2-mercaptoethanol for 24 h in vacuum-sealed ampules. After evaporation, amino acids in the hydrolyzate were determined in an Alpha Plus 4151 (Pharmacia-LKB, Sweden) analyzer using a sodium buffer system and *o*-phthalaldehyde derivatization for fluorescence detection. All samples were analyzed in triplicate.

Mass Spectrometry. The FAB mass spectrum was recorded in a JMS HX-110HF double-focusing two-sector spectrometer (JEOL, Japan) equipped with a FAB gun, a collision cell, and a DMA-5000 data analysis system, as previously reported (*31*).

Electrospray MS was performed in a hybrid quadrupole-time-of-flight (Q-TOF) instrument (Micromass, UK) fitted with a Z-spray nanoflow ion source (*32*). The mass spectrometer was operated with a source temperature of 80 °C and a drying gas flow rate of 50 L/h. Peptides, polymers, peptides cleaved off dextran beads, and MAP purified by RP-HPLC were dissolved in a 50% (v/v) water/acetonitrile solution containing 1% acetic acid, to an approximate concentration of 5 pmol/μL. The peptide solution was infused at 3 μL/min into the mass spectrometer using a syringe pump (Harvard Apparatus, Holliston, MA). The capillary and cone voltage were set to 3 kV and 35 V, respectively. Data acquisition and processing were performed with the Micromass MassLynx package.

Immunizations. Female Balb/c mice 6−8 weeks old (CENPALAB, Cuba) were inoculated subcutaneously on days 0, 14, 28, and 56 with 100 μL with 40 μg of antigen emulsionated in either CFA (day 0) or IFA (other days) (Sigma). Animals were bled 10 days after the fourth dose. A summary of immunization schedules is shown in Table 1.

Enzyme-Linked Immunosorbent Assay against Synthetic Peptides. ELISA of anti-peptide sera was done as previously described (*33*). Briefly, 96-well polystyrene plates (High binding, Costar) were coated with

Table 1. Summary of Immunization Schedules

groups	doses (μg)	adjuvant	mice
JY1-MAP8	40	CFA-IFA	8
JY1-MAP4	40	CFA-IFA	8
Polymer	40	CFA-IFA	8
peptide	40	CFA-IFA	8
peptide-dextran	40	PBS	8
HBsAg−JY1-peptide	10	CFA-IFA	8
HBsAg−JY1-MAP4	10	CFA-IFA	8
HBsAg−JY1-MAP8	10	CFA-IFA	8
negative control	-	CFA-IFA	4

100 μL of BSA-coupled V3 peptides (Table 2) at 10 μg/mL and incubated overnight at 4 °C. After three washings with 0.05% Tween 20 in distilled water, plates were blocked with 2% milk in PBS (blocking solution) for 1 h at 37 °C. Samples were diluted with 0.05% Tween 20 and 5% sheep serum in blocking solution and incubated for 2 h at 37 °C. After four washings, an anti-mouse IgG peroxidase conjugate (Amersham, UK) was added and incubated for 1 h at 37 °C. The color reaction with *o*-phenylenediamine was allowed to develop for 10 min and then stopped with 3 M H_2SO_4 solution (50 μL), and the absorbance at 492 nm was determined in a SensIdent Scan (Merck, FRG). Results were expressed as log titer, determined by interpolation of OD values at fixed serum dilutions into a standard curve of a serum with known titer. Titer was defined as the log of the highest dilution giving twice the absorbance of negative control sera. Titers are given as the geometric mean ± SD of the titers of individual sera.

Peptide Synthesis on Cellulose Membranes for Epitope Mapping. Fifteen 15-residue peptides corresponding to the Ala scan of the RQSTPIGLGQALYTT sequence were synthesized as spots on a cellulose membrane. Twenty-five other paper-bound peptides, seven and five residues long, were also synthesized for epitope mapping. The spot synthesis method of Frank et al. (*34*) was used. Functionalition of the paper (Whatman 540) was carried out by esterification of an Fmoc-β-Ala-OH residue, using DIPC and *N*-methylimidazole in DMF. The remaining residues were incorporated by paper synthesis-adapted Fmoc/tBu chemistry (*34*). All peptides were acetylated at the N-terminus at the end of the synthetic program.

Paper-Based Peptide Enzyme Immunoassay. Washing steps and incubations were performed at 25 °C with Tris-buffered saline (TBS) containing 0.05% Tween-20 (T-TBS). Blocking of free binding sites was performed by overnight incubation with 5% skim milk in TBS. Incubation times were 3 h for sera and 2 h for alkaline phosphatase-conjugated anti-mouse IgG (Sigma). Detection of bound antibody was achieved by incubation with 5-bromo-4-chloro-3-indolyl phosphate (Sigma) in substrate buffer (0.1 M Tris, 0.1 M NaCl, 2 mM $MgCl_2$, pH, 8.9). Washing with PBS stopped staining. The peptide-bearing cellulose sheets were regenerated and prepared for the next run as described by Frank (*34*).

Statistical Analysis. Statistical analyses were conducted using Microsoft Excel software. Averages, variance, and standard deviations (SDs) were determined using standard functions. All ELISA OD values were transformed to the natural logarithm to get a normal distribution in the immunized groups. An *F*-test was performed to assess variance homogeneity among groups and a Student's *t*-test was done ($p < 0.05$ was considered statistically significant).

Table 2. V3 Peptides from Different HIV-1 Isolates[a]

isolates	clades	amino acid sequences
JY1	D	RQSTPIGLGQALYTT
BRVA	B	RKRITMGPGRVYYTT
IIIB	B	SIRIQRGPGRAFVTI
MN	B	RKRIHIGPGRAFYTT
LR150	B	SRGIRIGPGRAILAT
RF	B	RKSITKGPGRVIYAT

[a] Sequence alignments using Clustal X software.

Table 3. Amino acid Compositions of Antigenic Peptides[a]

amino acid	peptide	polymer	JY1-MAP4	JY1-MAP8	peptide on dextran
Asx	1.3 (1)	1.1 (1)	1.1 (1)	2.5 (2)	1.1 (1)
Thr	3.6 (4)	3.4 (4)	6.4 (7)	11.7 (14)	3.6 (4)
Ser	1.7 (2)	1.9 (2)	2.3 (3)	5.6 (6)	1.6 (2)
Glx	4.5 (4)	4.2 (4)	6.7 (6)	12.2 (12)	3.8 (4)
Gly	5 (3)	4.1 (3)	8.7 (8)	16.3 (19)	3.2 (3)
Ala	1.8 (2)	2 (2)	2.7 (3)	5.4 (6)	2.0 (2)
Val	-	-	-	-	-
Met	-	-	-	-	-
Ile	4.1 (4)	4.5 (4)	5.2 (5)	9.7 (10)	4.1 (4)
Leu	2.8 (3)	3.1 (3)	4.1 (4)	7.8 (8)	3.0 (3)
Tyr	2 (2)	1.8 (2)	3.3 (3)	5.9 (6)	2.7 (2)
Phe	1.1 (1)	1.4 (1)	0.9 (1)	3.1 (2)	1.2 (1)
His	-	-	-	-	-
Lys	4.5 (4)	4.3 (4.0)	6.2 (6)	13.7 (11)	3.9 (4)
Arg	0.8 (1)	0.6 (1)	2.1 (2)	4.6 (4)	0.7 (1)
L-Cys	-	2.3 (2)	1.1 (1)	1.1 (1)	-

[a] Data are expressed as number of residues per molecule. Experimental values represent the mean of three independent determinations. Theoretical values are given in parentheses. Asx: aspartic acid plus asparagines; Glx: glutamic acid plus glutamine. Proline was not detected.

RESULTS AND DISCUSSION

Synthesis of Immunogens. *Free and Oligomeric Versions of the JY1 Peptide.* The primary structure of the monomeric form of the immunogen is shown in Figure 1. It consisted of the JY1 epitope (RQSTPIGLGQALYTT) in tandem with the T-cell epitope of tetanus toxoid (TT, residues 830−844, QYIKANSKFIGITEL), with an intervening Lys pair designed as a cathepsin-like cleavage site and with flanking Cys-Gly and Gly-Cys residues at each end to promote oligomerization. The peptide was synthesized by stepwise solid-phase methods, with the two Cys residues protected with the HF-stable Acm group. After cleavage and characterization, the Acm-protected monomer was treated with iodine to remove the two Acm groups and oligomerization was performed in AcOH:H_2O (3:2, v:v), where the monomer was highly soluble. The reaction proceeded quickly, and a high conversion to oligomer was observed by gel filtration HPLC (Figure 2). ESI-MS analysis of the main fractions of the oligomerization mixture allowed identification of the tetra-, tri-, and dimeric species. In addition, as expected, the monomer underwent intramolecular cyclization. Attempts to reduce the extent of this relatively undesired side reaction by varying the initial concentration of monomer were unsuccessful. Small levels of peptides with masses consistent with the cyclic disulfide forms of the oligomers were also detected. A summary of these findings is shown in Table 3.

Multiple Antigenic Peptide System. Two multivalent (MAP-like) dendrimeric presentations of the JY1 peptide with defined composition and varying number of B- and T-cell epitopes were also designed and synthesized (Figure 3). The JY1-MAP4 immunogen, containing four B and two Th epitopes (Figure 3A), resulted from dimerization of a monomer with a single Lys branching

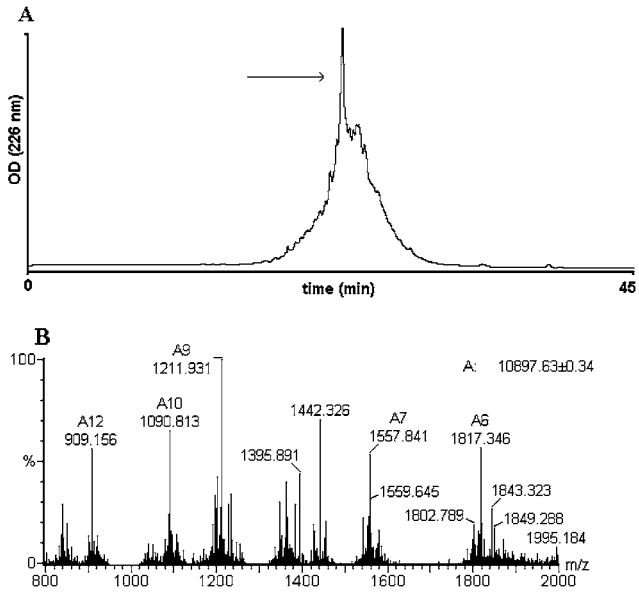


Figure 4. Analytical characterization of JY1-MAP8. A: HPLC analysis after reduction and carboxymethylation; B. ES-MS spectrum of the main HPLC fraction (labeled with an arrow in panel A).

point, while the JY1-MAP8, with eight and four epitopes, respectively (Figure 3B), contained three Lys branching units in each monomer. The monomers were prepared by Boc/benzyl solid-phase chemistry and dimerized as above. To evaluate the quality of each synthesis, an aliquot of each final dimer was reduced and *S*-carboxymethylated and characterized by reverse phase HPLC (Figure 4). The divalent monomer (JY1-MAP2 precursor) was less clean than the tetravalent monomer (JY1-MAP4 precursor), probably due to the use of a resin with too high substitution. In both cases, however, the main fraction of each HPLC profile was identified by ESI-MS as the expected species (Table 4). In conclusion, the dendrimeric approach allowed the preparation of a high molecular weight immunogen of defined composition in a more reproducible form than oligomerization.

Peptide on Dextran Beads. Cross-linked dextran beads were chemically modified with a substoichiometric amount of Fmoc-βAla to give an amine-functionalized support suitable for solid-phase peptide synthesis. The remaining hydroxyl functions of the polymer were blocked by acetylation to avoid the formation of deletion sequences and reduce the substitution to convenient levels. A β-Ala loading of ca. 30 μmol/g of dry resin was determined by spectrophotometric titration of the Fmoc group. On this dextran support, the JY1-LysLys-TT sequence (as in Figure 1, but without the flanking Gly and Cys residues) was assembled by Fmoc chemistry, using HOBt- and DIPC-mediated couplings with relatively high excess of all components (10 equiv) in DMF. Most residues required double couplings with TBTU activation and prolonged reaction times (2 h) until a negative Kaiser test was observed. For additional safety, a capping step with acetic anhydride was performed after incorporation of each residue. The quality of the dextran-bound peptide was evaluated by RP-HPLC analysis of an aliquot cleaved from the support by alkaline hydrolysis (Figure 5). The main product of the chromatogram was satisfactorily characterized as the target peptide by ESI-MS (Table 4).

Table 4. Mass Spectrometry of V3 Antigenic Peptides

antigen	theory (Da)	experimental (Da)
linear peptide	4031.5	4031.9[a]
cyclized monomer	3887.50	3887.02
cyclized dimer	7774.01	7773.11
cyclized trimer	11659.57	11659.67
cyclized tetramer	15546.06	15546.03
JY1-MAP2	5500.10	5498.84
JY1-MAP4	10898.55	10897.63
peptide on dextran beads	3754.3	3754.4[a]

[a] Determined by fast atom bombardment mass spectrometry (FAB-MS).

Peptide and MAP Conjugates. To further enhance the immunogenicity of the anti-peptide response, both the monomeric and the two dendrimeric versions of the JY1-TT peptide were conjugated to recombinant HBsAg protein. HBsAg is a polymeric protein of about 2000 kDa. The 25 kDa monomer contains 14 cysteines which form an uncertain number of intra- and intermolecular disulfide bridges, giving rise to particles of 22 nm average diameter, each containing approximately 100 monomer units (*35*). Our choice of HBsAg was based on its high molecular weight, proven stability, and high immunogenicity and because it is known to act as an effective and safe vaccine in humans.

The conjugations of JY1-TT monomer and JY1-MAP4 and JY1-MAP8 dendrimers to HBsAg were done by means of succinic anhydride, a homobifunctional reagent that allows cross-linking of amino groups. The first step was succinylation of HBsAg under mildly alkaline conditions, followed by dialysis to remove excess succinic anhydride and thus avoid unwanted MAP−MAP and/or

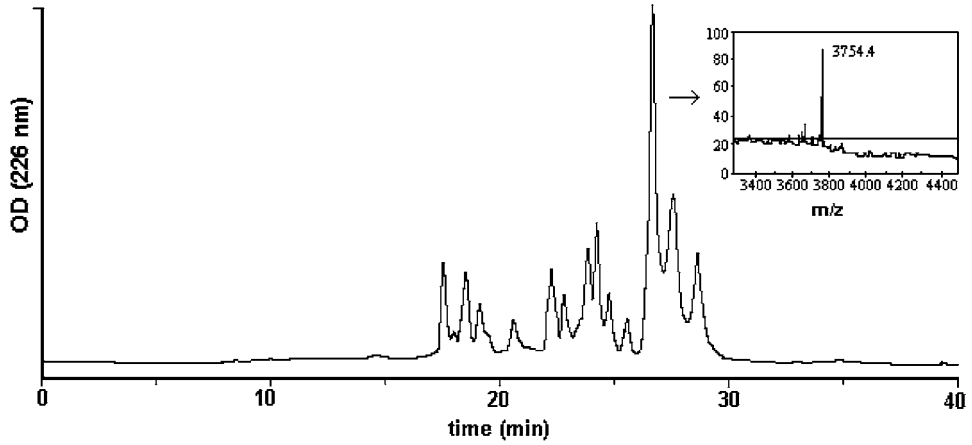


Figure 5. HPLC analysis of crude (after base cleavage) RQSTPIGLGQALYTTKKQYIKANSK-FIGITEL-βAla$_2$ synthesized on dextran beads. The peak labeled with an arrow corresponds to the correct sequence. Inset: FAB-MS of HPLC fractions corresponding to the arrow-labeled peak (see also Table 4).

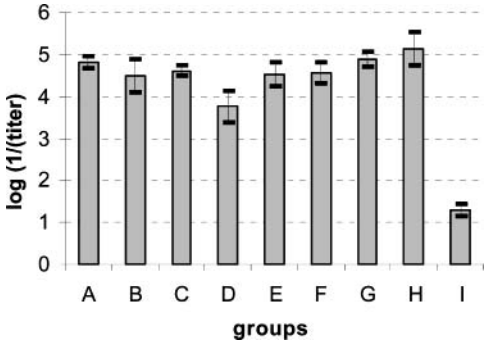


Figure 6. Antibody titers of mice after immunization with four doses of: A, JY1-MAP8, 40 μg; B, JY1-MAP4, 40 μg; C, polymer, 40 μg; D, peptide monomer, 40 μg; E, peptide on dextran beads, 40 μg; F, HBsAg−JY1-peptide, 10 μg; G, HBsAg−JY1-MAP4, 10 μg; H, HBsAg−JY1-MAP8, 10 μg; I, PBS negative control. Titer is defined as the log of the highest dilution giving twice the absorbance of negative control. Titers are the geometric mean ± SD corresponding to eight mice antisera.

peptide−peptide cross-linking. The carboxyl groups on the modified HBsAg were next activated with EDAC (a soluble carbodiimide) and allowed to react with the free amino groups of either linear monomer or JY1-MAP4 or JY1-MAP8. The conjugates were purified by gel filtration to avoid aggregation. For this purpose a Sephadex S300 matrix was selected. This matrix allowed a quick and efficient separation of those conjugates from byproducts such as carbodiimide and MAPs in excess.

Comparison of the Antibody Response in Mice Immunized with Different Presentations of JY1 Peptide. Groups of eight Balb/c mice were inoculated subcutaneously with different presentations of the JY1 peptide antigen and their anti-peptide antibody responses after four doses of the epitope were evaluated by ELISA. Figure 6 shows the titers obtained for the different immunization groups. As can be seen, both HBsAg−JY1-MAP4 and HBsAg−JY1-MAP8 conjugates elicited the highest titers against JY1. The superior immunogenicity of these conjugates may be attributed to the combination of large size and epitope multiplicity, plus the known T-cell response of the carrier protein. The importance of epitope multiplicity was evinced by the fact that the anti-peptide titers elicited by monomeric JY1 conjugated to HBsAg (group F) were significantly lower ($p < 0.01$) than when presented as a MAP dendrimer (groups G and H).

Epitope multiplicity, however, did not provide a simple, uniform pattern in the immune response against JY1. Thus, octameric JY1-MAP8 (group A) was significantly ($p < 0.05$) more immunogenic than monomeric JY1 conjugated to HBSAg (group F), but a similar effect was not observed for tetrameric JY1-MAP4 (group B; $p = 0.893$). On the other hand, the responses to HBsAg−JY1-MAP4 and HBsAg−JY1-MAP8, while the highest among all immunization groups, did not vary significantly ($p = 0.107$) despite the 2-fold difference in multiplicity, nor were there substantial differences between JY1-MAP8 and JY1-MAP4 immunization groups ($p = 0.055$), in contrast to previous results (*36*). In earlier studies, the MAP system has been shown to be more immunogenic than the peptide conjugated to a carrier protein (*37*−*39*). However, the opposite result has also been observed (*40*), a phenomenon that can be related to the nature of the carrier molecule.

The antibody responses generated by immunization with the linear polymer (group C) were significantly lower than those of the JY1-MAP8 dendrimer ($p < 0.05$). However, no significant difference was observed between the linear polymer and the JY1-MAP4 ($p = 0.468$). As for the peptide−dextran conjugate, its anti-JY1 titers were not statistically different from those of the MAP versions or the linear polymer. Finally, as expected, antibody responses of any conjugated or multiple presentation of JY1 were significantly superior to those obtained with the monomeric version.

Analysis of Cross-Reactivity. Pooled sera corresponding to the different immunization groups under study (Table 1) were diluted to an anti-JY1 titer of ca. 10^{-5} and compared with a panel of several V3 peptides from gp 120 HIV-1 (Table 2) for their ability to cross-react. In this experiment, the TAB9 protein, which integrates a number of V3 peptides, was used as a positive control. Results showed that at least three epitopes, MN, IIIB, and JY1, were readily accessible (*36*). As can be seen in Figure 7, the group immunized with the JY1-TT peptide did not exhibit cross-reactivity with other V3 epitopes even after four doses of immunogen. A similar result was found for the same peptide attached to dextran beads, and only marginal recognition was detected for the oligomerized versions of the epitope. On the contrary, when the JY1 sequence was presented as a MAP dendrimer, significant levels of cross-reactivity with the other epitopes were observed after four doses. Similar patterns of cross-reactivity were found for the most immunogenic conjugates HBsAg−JY1-MAP4 and HBsAg−JY1-MAP8. Thus, four 10-μg doses of. the former immunogen sufficed to achieve cross-reactivity with all the variant peptides. Since a substantial proportion of these 10 μg corresponds (in weight) to the HBSAg, not the JY1-MAP4, this means that the carrier has a

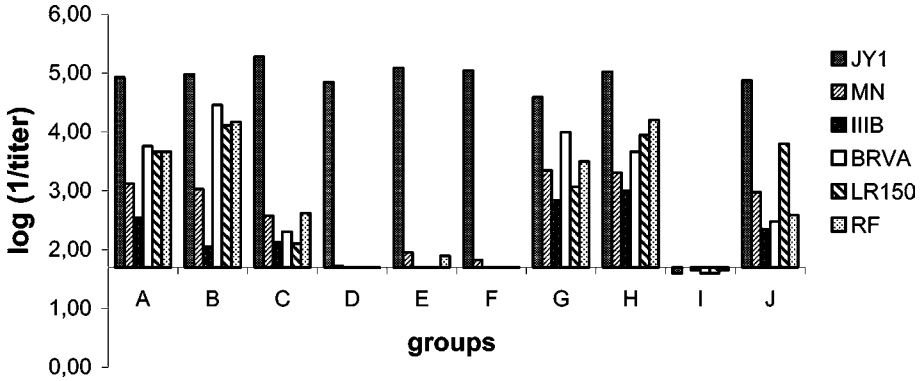


Figure 7. Cross-reactivity of pooled sera from different immunization groups after the fourth inoculation against heterologous V3 sequences. A, JY1-MAP8 B, JY1-MAP4; C, polymer; D, peptide monomer; E, peptide on dextran beads; F, HBsAg−JY1-peptide; G, HBsAg−JY1-MAP4; H, HBsAg−JY1-MAP8; I, negative control; J, positive control (TAB9 protein). The heterologous V3 sequences are shown in Table 1. Plates were coated with BSA-V3 conjugate as specified in the text.

SPOT	PEPTIDE SEQUENCE	A	B	C	D	E	F	G	H	I	J
1	RQSTPIGLGQALYTT										
2	**A**QSTPIGLGQALYTT										
3	R**A**STPIGLGQALYTT										
4	RQ**A**TPIGLGQALYTT										
5	RQS**A**PIGLGQALYTT										
6	RQST**A**IGLGQALYTT										
7	RQSTP**A**GLGQALYTT										
8	RQSTPI**A**LGQALYTT										
9	RQSTPIG**A**GQALYTT										
10	RQSTPIGL**A**QALYTT										
11	RQSTPIGLG**A**ALYTT										
12	RQSTPIGLGQ**A**AYTT										
13	RQSTPIGLGQAL**A**TT										
14	RQSTPIGLGQALY**A**T										
15	RQSTPIGLGQALYT**A**										
16	RQSTPIG										
17	QSTPIGL										
18	STPIGLG										
19	TPIGLGQ										
20	PIGLGQA										
21	IGLGQAL										
22	GLGQALY										
23	LGQALYT										
24	GQALYTT										
25	RQSTP										
26	QSTPI										
27	STPIG										
28	TPIGL										
29	PIGLG										
30	IGLGQ										
31	GLGQA										
32	LGQAL										
33	GQALY										
34	QALYT										
35	ALYTT										

Figure 8. Alanine scan (first 15 sequences) and fine epitope mapping (20 sequences) of peptide JY1using the spot synthesis technique. Pooled sera from different immunization groups (after fourth dose) were diluted 1:100 and tested against the peptides. Columns A to J, as in Figure 7. Boxes are coded as follows: white, no recognition; light gray, weak recognition; dark gray, intermediate recognition; black, strong recognition.

significant role in the generation of broadly reactive antibodies. It is important to note that, in most cases, recognition of the heterologous peptides was more than 10 times lower than that of the homologous JY1 peptide. This means that only a minor subset of antibodies were able to react with at least another peptide. Those subsets of antibodies emerged only after repetitive immunizations (data not shown).

To further analyze the cross-reactivity, an alignment analysis of all V3 peptide sequences (Table 2) was performed. The sequence closest to JY1 was MN, with 53.3% homology, followed by RF and BRVA, with 40% homology; LR150 with 33.3%; and the less related IIIB sequence with 26.7%. The ELISA data were in good agreement with this homology. Our results also agreed with previous findings that antibodies for a specific V3 variant provide cross-neutralization for different HIV-1 field isolates (*41*, *42*).

In conclusion, our experiment demonstrated that a certain potential for cross-reactivity is associated to the V3 peptide sequence, but that its intensity strongly depends on the presentation of the epitope to the immune system.

Epitope Mapping. We also examined the effect of the different strategies of immunopeptide presentation on the antibody response to individual residues of the linear JY1 epitope. Our goal was to determine which amino acids in that sequence were more directly involved in the antigen−antibody interaction. For this purpose, we performed fine epitope mapping and an alanine scan of the whole JY1-peptide using the spot synthesis technique.

For epitope mapping, twenty seven- and five-residue peptides covering the JY1 sequence were prepared by simultaneous spot synthesis, as shown in Figure 8. For the alanine scan, fifteen 15-residue peptides with a systematic Ala replacement at each position of the JY1 sequence were similarly synthesized. The cellulose-bound peptides were then assayed by the above protocols against 1:100 dilutions of pooled sera from each immunization group.

The alanine scan (Figure 8) showed that the LXQXXY or LXQXLY sequences were involved in the immune recognition by all sera. This was in good agreement with fine epitope mapping results, in which sera from all immunization groups strongly recognized the C-terminal region (LGQALY) of the JY1-sequence. In addition, mice immunized with either free peptide, peptide oligomers, or MAP also showed weak recognition of the N-terminal region of the JY1-epitope. This region was not recognized when the epitopes were presented as carrier protein

conjugates. On the other hand, this analysis of the antibody response against the linear JY1 epitope did not provide any clues on the different cross-reactivity patterns observed in the above experiments.

SUMMARY AND CONCLUSIONS

In this paper we have described different approaches to improve the immunogenicity of JY1 peptide epitope presentations. These include (i) the JY1-TT construct, where the JY1 epitope is presented in tandem with a well-known T-cell epitope, (ii) oligomeric, disulfide-linked versions of this chimeric sequence, with sizes between 8 and 16 kDa, iii) dendrimeric, MAP-type presentations of the B- and T-cell epitopes, with well-defined structures and masses in the 11−21 kDa range. These immunogens were administered either free or conjugated to HBsAg, an effective carrier protein. In addition, the JY-TT peptide was also administered immobilized on dextran beads, an inexpensive, biocompatible, and biodegradable natural polysaccharide which holds promise as an attractive adjuvant for peptide vaccination (*43*).

This is, as far as we know, one of very few comparative studies on presentation of peptide epitopes to the immune system. We have observed the highest anti-peptide titers in animal groups immunized with MAP−carrier protein conjugates. All dendrimeric versions of the immunogens elicited antibodies that cross-reacted with other V3 HIV-1 sequences. Furthermore, we have shown that cross-recognition can be enhanced by conjugation to a carrier protein, with the advantage that less amount of immunogen is required to achieve a broadly reactive antibody response. This phenomenon of cross-reactivity toward variable regions such as the V3 loop is highly desirable in designing new vaccine candidates against VIH-1. In addition, this approach may be valuable to generate bivalent vaccines when the carrier protein is per se a vaccine immunogen like the HBsAg.

ACKNOWLEDGMENT

This work was supported by the Center for Genetic Engineering and Biotechnology, Havana, Cuba. Work at Barcelona was supported by Spanish CICYT grants (PB97-0873 and BIO2002-04091-C03-01 to D.A., BQ2000-0235 to F.A.), by AECI (Spanish-Cuban cooperation, to D.A.), and by CERBA, Generalitat de Catalunya (to F.A. and D.A.).

LITERATURE CITED

(1) Tam, J. P. (1988) Synthetic peptide vaccine design: synthetic and properties of a high-density multiple antigenic peptide system. *Proc. Natl. Acad. Sci. U.S.A. 85*, 5409−5413.

(2) Tomalia, D. A., Baker, H., Dewald, J., Hall, M., Kallos, G., and Martin, S (1985) A new class of polymers: Starburst-dendritic macromolecules. *Polym. J. 17*, 117−132.

(3) Volpina, O. M., Yarov, A. V., Zhmak, M. N., Kuprianova, M. A., Chepurkin, A. V., Toloknov, A. S., and Ivanov, V. T (1996) Synthetic vaccine against foot-and-mouth disease based on a palmitoyl derivate of the VP_1 protein 135−159 fragment of the A_{22} virus strain. *Vaccine 14*, 1375−1380.

(4) BenMohamed, L., Wechsler. S. L., and Nesburn, A. B. (2002) Lipopeptide vaccines−yesterday, today, and tomorrow. *Lancet Infect Dis. 2*, 425−431.

(5) Lindner, W., and Robey, F. A. (1987) Automated synthesis and use of N− chloroacetyl- modified peptides for the preparation of synthetic peptide polymers and peptide−protein immunogens. *Int J Pept. Protein Res. 30*, 794−800.

(6) Borras-Cuest, F., Fedon, Y., and Pellit-Camordan, A. (1988) Enhancement of peptide immunogenicity by linear polymerization. *Eur J Immunol. 18*, 199−202.

(7) Defoort, J. P., Nardelli, B., Huang, W., and Tam, J. P. (1992) A rational designo f synthetic peptide vaccine wiht a built-in adjuvant. A modular approach for unambiguity. *Int. J. Pept. Protein Res. 40*, 214−221.

(8) Singh, M., Li, X. M., Wang, H., McGee, J. P., Zamb, T., Koff, W., Wang, C. Y., and O′Hagan, D. T. (1998) Controlled release microparticles as a single dose diphtheria toxoid vaccine: immunogenicity in small animal models. *Vaccine 16*, 346−352.

(9) Gregoriadis, G. (1994) Liposomes as immunoadjuvants and vaccine carriers: antigen entrapment. *Immunomethods 4*, 210−216.

(10) Lovgren, K., and Larsson, M. (1994) Conjugation of synthetic peptides to carrier iscoms: factors affecting the immunogenicity of the conjugate. *J. Immunol. Methods 173*, 237−243.

(11) Cruz, L. J., Iglesias, E., Aguilar, J. C., Quintana, D., Garay, H. E., Duarte, C., and Reyes, O. (2001) Study of different coupling agents in the conjugation of a V3-based synthetic MAP to carrier proteins. *J. Pept. Sci. 7*, 511−518.

(12) Moore, J. P., and Nara, P. L., (1991) The role of the V3 loop in HIV infection. *AIDS 5*, 521−533.

(13) Nara, P. L., Garrity, R. R., and Goudsmit, J. (1991) Neutralization of HIV-1: a paradox of humoral properties. *FASEB J. 5*, 2437−2455.

(14) Speck, R. F., Wehrly, K., Platt, E. J., Atchison, R. E., Charo, I. F., and Kabat, D. (1997) Selctive employment of chemokine receptors as human immunodeficiency virus type 1 coreceptors determined by individual amino acids within the envelope V3 loop. *J. Virol. 71*, 7136−7139.

(15) Berzofsky, J. A. (1991) Development of artificial vaccines against HIV using defined epitopes. *FASEB J. 5*, 2412−2418.

(16) Schreiber, M., Wachsmuth, C., Muller, H., Hagen, C., Schmitz, H., and Van-Lunzen, J. (1996) Loss of antibody reactivity directed against the V3 domain of certain human immunodeficiency virus type 1 variants during disease progression. *J. Gen. Virol. 77*, 2403−2414.

(17) Rubinstein, A., Goldstein, H., Pettoello-Mantovani, M., Mizrachi, Y., Bloom, B. R., Furer, E., Althaus, B., Que, J. U., Hasler, T., and Cryz, S. J. (1995) Safety and immunogenicity of a V3 loop synthetic peptide conjugated to purified protein derivative in HIV-seronegative volunteers. *AIDS 9*, 243−251.

(18) Letvin, N. L., Robinson, S., Rohne, D., Axthelm, M. K., Fanton, J. W., Bilska, M., Palker, T. J., Liao, H. X., Haynes, B. F., and Montefiori, D. C. (2001) Vaccine-elicited V3 loop-specific antibodies in rhesus monkeys and control of a simian-human immunodeficiency virus expressing a primary patient human immunodeficiency virus type 1 isolate envelope. *J Virol. 75*, 4165−4175.

(19) Yamanaka, T., Fujimura, Y., Ishimoto, S., Yoshioka, A., Konishi, M., Naritam, N., Mimaya, J., Meguro, T., Nakasone, T., Okamoto, Y., Yoshizaki, H., Yamada, K., and Honda, M. (1997) Correlation of titer of antibody to principal neutralizing domain of HIVMN strain with disease progression in Japanese hemophiliacs seropositive for HIV type 1. *AIDS Res. Hum. Retroviruses 4*, 317−326.

(20) Esparza, J., Osmanov, S., and Heyward, W. I. (1995) HIV Preventive Vaccines. Progress to date. *Drugs 50*, 792−804.

(21) Yourno, J., Josephs, S. F., Reitz, M., Zagury, D., F., Wong-Staal, R., and Gallo, C. (1988) Nucleotide sequences analysis of the env gene of a new Zairian isolate of HIV-1. *AIDS Res. Hum. Retroviruses 4*, 165−173.

(22) Panina-Bordingnon, P., Tan, G., Termijtelen, A., Demotz, S., Corradin, G., and Lanzavecchia, A. (1989) Universally immunogenic T-cell epitopes: promiscuous binding to human MHC class II and promiscuous recognition by T-cells. *Eur. J. Immunol. 19*, 2237−2247.

(23) Houghten, R. A., Graw, S. T., and Bray, M. K., (1986) Simultaneous multiple peptide synthesis: The rapid preparation of large numbers of discrete peptides for biological, immunological and methodological studies. *BioTechniques 4*, 522−526.

(24) Kaiser, E., Colescott, R. L., Bossinger, C. D., and Cook, P. I. (1970) Color test for detection of free terminal amino groups in solid-phase synthesis of peptides. *Anal.Biochem. 34*, 595−598.

(25) Houghten, R. A., Bray, M. K., Degraw, S. T., and Kirby, C. J. (1986) Simplified procedure for carrying out simultaneous multiple hydrogen fluoride cleavages of peptides resins. *Int. J. Pept. Protein Res. 27*, 673−678.

(26) Ellman, G. L. (1959) Tissue sulfhydryl groups.*Arch. Biochem. Biophys. 82*, 70−77.

(27) Fields, G. B., and Noble, R., L. (1990) Solid-phase peptide synthesis utilizing 9- fluorenylmethoxycarbonyl amino acids. *Int. J. Pept. Protein Res. 35*, 161−214.

(28) Krchnak, V., Maly, A., and Flegel, M. (1988) Solid-phase synthesis of a nonadecapeptide coded for by the v-myb oncogene. *Int. J. Pept. Protein Res. 2*, 239−244.

(29) Deen, C., Claassen, E., Gerritse, K., Zegers, N. D., and Boersma, W. J. A. (1990) A novel carbodiimide coupling method for synthetic peptides: Enhanced antipeptide antibody responses. *J. Immunol. Methods 129*, 119−125.

(30) Bradford, M. M. (1976). A rapid and sensitive method for the quantitation of microgram quantities of proteins utilizing the principle of protein-dye binding. *Anal. Biochem. 72*, 248−254.

(31) Gonzalez, J., Besada, V., Garay, H., Reyes, O., Padron, G., Tambara, Y., Takao, T., and Shimonishi, Y. (1996) Effect of the position of a basic amino acid on C-terminal rearrangement of protonated peptides upon collision-induced dissociation. *J. Mass. Spectrom. 31*, 150−158.

(32) Mo, W., Sakamoto, H., Nishikawa, A., Kagi, N., Langridge, J. I., Shimonishi Y., and Takao, T. (1999) Structural characterization of chemically derivatized oligosaccharides by nanoflow electrospray ionization mass spectrometry. *Anal. Chem. 71*, 4100−4106.

(33) Gómez, C. E., López-Campistrous, A. E., and Duarte, C. A. (1998) An immunoassay with bovine serum albumin coupled peptides for the improved detection of anti V3 antibodies in HIV-1 + Human sera. *J. Virol. Methods 71*, 7−16.

(34) Frank, R. (1992) Spot-Synthesis: An easy technique for the positionally addressable, parllel chemical synthesis on a membrane support. *Tetrahedron 48*, 9217−9232.

(35) Hardy, E., Martinez, E., Diago, D., Diaz, R., Gonzalez, D., and Herrera, L. (2000)Large-scale production of recombinant hepatitis B surface antigen from *Pichia pastoris*. *J. Biotechnol. 77*, 157−167.

(36) Cruz, L. J., Quintana, D., Iglesias, E., García, Y., Huerta, V., Garay, H. E., Duarte, C., and Reyes, O. (2000) Immunogenicity Comparison of a Multi-antigenic Peptide Bearing V3 Sequences of the Human Immunodeficiency Virus Type 1 with TAB9 Protein in Mice. *J. Pept. Sci. 6*, 217−224.

(37) Chai, S. K., Clavijo, P., Tam, J. P., and Zavala, F. (1992) Immunogenic properties of multiple antigen peptide systems containing defined T and B epitopes. *J. Immunol. 149*, 2385−2390.

(38) McLean, G. W., Owsianka, A. M., Subak-Sharpe, J. H., and Marsden, H. S. (1991) Generation of anti-peptide and anti-protein sera. Effect of peptide presentation on immunogenicity. *J. Immunol. Methods 137*, 149−157.

(39) Kanda, P., Fritz, D. A., Gage, D. A., and Shuler, K. R. (1995) Dependence of the murine antibody response to an anti-CDR2 VH peptide on immunogen formulation. *Mol. Immunol. 32*, 1319−1328.

(40) Helling, F., and Livingston, P. O. (1994) Ganglioside conjugate vaccines. Immunotherapy against tumors of neuroectodermal origin. *Mol. Chem. Neuropathol. 21*, 299−309.

(41) Wang, C. Y, Looney, D. J, Li, M. L., Walfield, A. M., Ye, J., Hosein, B., Tam, J. P., and Wong-Staal, F. (1991) Long-term high-titer neutralizing activity induced by octameric synthetic HIV-1 antigen. *Science 254*, 285−288.

(42) Zhang, P. F., Bouma, P., Park, E. J., Margolick, J. B., Robinson, J. E., Zolla-Pazner, S., Flora, M. N., and Quinnan, G. V. (2002)Peng Fei Zhang. A variable region 3 (V3) mutation determines a global neutralization phenotype and CD4-independent infectivity of a human immunodeficiency virus type 1 envelope associated with a broadly cross-reactive, primary virus-neutralizing antibody response. *J. Virol. 76*, 644−655.

(43) Diwan, M., Misra, A., Khar R. K., and Talwar, G. P. (1997) Long-term high immune response to diphtheria toxoid in rodents with diphtheria toxoid conjugated to dextran as a single contact point delivery system.*Vaccine 15*, 1867−1871.

BC034119J

8-Cyclopentadienyltricarbonyl ^{99m}Tc 8-Oxooctanoic Acid: A Novel Radiotracer for Evaluation of Medium Chain Fatty Acid Metabolism in the Liver

Byung Chul Lee,[†,‡] Yearn Seong Choe,[†,*] Dae Yoon Chi,[‡] Jin-Young Paik,[†] Kyung-Han Lee,[†] Yong Choi,[†] and Byung-Tae Kim[†]

Department of Nuclear Medicine, Samsung Medical Center, Sungkyunkwan University School of Medicine, 50 Ilwon-dong, Kangnam-ku, Seoul 135-710, Korea and Department of Chemistry, Inha University, 253 Yonghyundong, Namgu, Inchon 402-751, Korea. Received July 19, 2003

8-Cyclopentadienyltricarbonyl ^{99m}Tc 8-oxooctanoic acid (^{99m}Tc−CpTTOA; **1a**) was synthesized for evaluation of medium chain fatty acid metabolism in the liver. ^{99m}Tc−CpTTOA was prepared in high radiochemical yield (50−63%) by a double ligand transfer reaction of methyl 8-ferrocenyl-8-oxooctanoate and $Na^{99m}TcO_4$ in the presence of $CrCl_3$ and $Cr(CO)_6$, followed by hydrolysis. This radiotracer was shown to be stable (>90% at 6 h) when incubated with human serum. Aqueous extraction of the radioactivity from the liver and blood samples of mice suggested that ^{99m}Tc−CpTTOA was mainly metabolized via β-oxidation in the liver, and the radioactivity was retained longer in CCl_4-treated mice than in control mice, possibly due to impaired β-oxidation in the former. Planar images of rats injected with ^{99m}Tc−CpTTOA showed accumulation of the radioactivity in the liver, kidneys, and bladder with rapid hepatic clearance as a function of time. Analysis of the metabolites from the liver and urine samples of rats further supported that ^{99m}Tc−CpTTOA was metabolized to 4-cyclopentadienyltricarbonyl ^{99m}Tc 4-oxobutanoic acid (^{99m}Tc−CpTTBA; **1c**) via β-oxidation. The results suggested that this radiotracer might be of valuable use in the evaluation of fatty acid metabolism in the liver.

INTRODUCTION

Fatty acids are important substrates for energy metabolism, particularly in the heart and liver. In the normal state, glucose and fatty acids are utilized as energy substrates in ATP production. On the other hand, in the fasted state, glucose is synthesized from amino acids (gluconeogenesis) and the rate of fatty acid oxidation is enhanced (*1*, *2*). Therefore, the β-oxidation of fatty acid can be a marker for energy metabolism of the heart and liver. Long chain fatty acids are not only metabolized via β-oxidation but also stored as triglycerides, while medium chain fatty acids are predominantly metabolized via β-oxidation that degrades the fatty acid by the removal of two-carbon units (*3*, *4*). Fatty acid is taken up in many organs, enters the mitochondria, and is metabolized. Unlike long chain fatty acid, medium chain fatty acid enters the mitochondria without the use of carnitine shuttle system (*5*). For past decades, fatty acids were radiolabeled with ^{11}C, ^{18}F, ^{123}I, and ^{99m}Tc (*3*−*4*, *6*−*14*) and utilized for evaluation of fatty acid metabolism using positron emission tomography (PET) and single photon emission computed tomography (SPECT). Among the radionuclides, single photon emitting ^{99m}Tc is desirable due to its ideal physical properties (141 keV, $t_{1/2}$ = 6 h) (*15*, *16*) and ready availability. Therefore, efforts were made to develop ^{99m}Tc-labeled fatty acid analogues (*4*, *7*−*12*). Early attempts included preparation of ^{99m}Tc-labeled fatty acid analogues containing strong chelating groups such as DTPA and EDTA, and these radiotracers were poorly accumulated in the myocardium (*7*, *8*). In other cases, ^{99m}Tc cores such as ^{99m}Tc−N_2S_2 and ^{99m}Tc−N_3S ligand were successfully coordinated to long chain fatty acid analogues, but the radiolabeled analogues showed poor uptake in the myocardium that may be partly due to relatively large size of the ^{99m}Tc cores or inappropriate lipophilicity and thus are not recognized as fatty acids. ^{99m}Tc-labeled iminodiacetic acid was rapidly taken up to the liver and the biliary system and thus applied for hepatobiliary imaging (*11*, *12*). As a same token, radiolabeled medium chain fatty acids have been studied for evaluation of the liver function, based on their rapid accumulation in the liver (*17*). *p*-[^{123}I]Iodophenylenanthic acid and *p*-[^{123}I]iodophenylvaleric acid were studied for assessment of hepatic viability. The results showed that they were taken up to and cleared from the liver rapidly. [1-^{11}C]Octanoate showed the similar pattern of the liver uptake and clearance to other medium chain fatty acid analogues. This radiotracer along with *p*-[^{123}I]-iodophenylenanthic acid were metabolized by β-oxidation in the liver with slower hepatic clearance in CCl_4-treated mice than in control mice due to impaired β-oxidation (*3*, *6*). The results demonstrated that both are promising diagnostic agents for assessment of the liver function. [^{99m}Tc]MAMA−hexanoic acid, a ^{99m}Tc-labeled medium chain fatty acid analogue, was also rapidly accumulated in the liver, and the metabolism via β-oxidation was confirmed by detection of the radiometabolite, [^{99m}Tc]-MAMA−butyric acid (*4*). [^{99m}Tc]MAG−hexanoic acid, a polar analogue, however, showed poor accumulation in the liver and was immediately excreted from the kidneys to the bladder, because of its low lipophilicity. Recent preparation of cyclopentadienyltricarbonyl ^{99m}Tc (^{99m}Tc−CpTT) extended its utilization to the preparation of the various ^{99m}Tc complexes (*18*−*20*). This small lipophilic core is attractive, because the ferrocene with various

* Corresponding author. Tel: +82-2-3410-2623, Fax: +82-2-3410-2639, E-mail: yschoe@samsung.co.kr.
† Sungkyunkwan University School of Medicine.
‡ Inha University.

10.1021/bc0341268 CCC: $27.50 © 2004 American Chemical Society
Published on Web 12/30/2003

substituents can be readily prepared via Friedel−Crafts acylation, and thus biomolecules can be efficiently labeled with ^{99m}Tc−CpTT. Small size of the core is also expected to minimize the perturbation of biological activity of the fatty acid.

In this work, we prepared ^{99m}Tc−CpTTOA (**1a**) by facile incorporation of ^{99m}Tc−CpTT into a medium chain fatty acid analogue. Its metabolism in the liver was evaluated and the metabolite was identified using the proposed radiometabolites, 6-cyclopentadienyltricarbonyl ^{99m}Tc 6-oxohexanoic acid (^{99m}Tc−CpTTHA; **1b**) and ^{99m}Tc−CpTTBA (**1c**).

EXPERIMENTAL SECTION

Materials and Methods. Solvents and reagents were purchased from the following commercial sources: Sigma-Aldrich Company (Milwaukee, WI) and Acros Organics (Geel, Belgium). ^{1}H NMR were obtained on Varian Gemini-200 and 400 (Palo Alto, CA) and a JEOL JNM-LA 300 spectrometer, and ^{13}C NMR at 50 and 100 MHz. Chemical shifts were reported in parts per million (ppm, δ units). Electron impact (EI) and chemical ionization (CI) mass spectra were obtained on a GC/MS QP5050A spectrometer (Shimadzu, Kyoto, Japan). Fast atom bombardment (FAB) mass spectra were obtained on a JMS 700 (JEOL Ltd., Tokyo, Japan). Elemental analyses were performed at the Inha University (CE instrument, Italy). HPLC was carried out on a Thermo Separation Products System (Fremont, CA) with a semipreparative column (Alltech Econosil silica gel, 10 μm, 10 × 250 mm) and an analytical column (YMC C18, 5 μm, 4.6 × 250 mm). The eluant was simultaneously monitored by a UV detector (254 nm) and a NaI(Tl) radioactivity detector. TLC was performed on Merck F_{254} silica plates and analyzed on a Bioscan radio-TLC scanner (Washington DC). $Na^{99m}TcO_4$ was eluted on a daily basis from ^{99}Mo/^{99m}Tc generators (DuPont Pharmaceuticals Co., Wilmington, DE, and Daiichi Radioisotope Labs., Chiba, Japan). Images of rats were obtained on a gamma camera (Trionix Research Lab. Inc., Twinsburg, OH) using a pinhole collimator.

Synthesis of Methyl 8-Ferrocenyl-8-oxooctanoate (3a). The flask was charged with ferrocene (150 mg, 0.806 mmol), methyl 8-chloro-8-oxooctanoate (114 μL, 0.806 mmol), and CH_2Cl_2 (1.5 mL). The solution was then chilled thoroughly in an ice bath. To this solution was added anhydrous aluminum chloride (113 mg, 0.846 mmol) carefully for 20 min using a spatula under N_2. The reaction mixture, which turned to deep violet color, was allowed to stir for 30 min in an ice-bath and for another 2 h at room temperature. At the end of the reaction, the flask was placed again in an ice bath, and water (2 mL) was slowly added. The resulting two-phase mixture was stirred vigorously for 30 min. The organic layer was dried over anhydrous sodium sulfate, and the solvent was removed in vacuo. The residue was purified by flash column chromatography (15:85 ethyl acetate−hexane) to afford **3a** (244 mg, 85%) as a red oil: ^{1}H NMR (300 MHz, $CDCl_3$) δ 4.78 (t, J = 2.0 Hz, 2H, −Fe−Cp-H (α)), 4.49 (t, J = 2.0 Hz, 2H, −Fe−Cp-H (β)), 4.19 (s, 5H, Cp-H), 3.67 (s, 3H, OCH_3), 2.70 (t, J = 7.3 Hz, 2H, CH_2), 2.33 (t, J = 7.6 Hz, 2H, CH_2), 1.74−1.62 (m, 4H), 1.40−1.37 (m, 4H); ^{13}C NMR (50 MHz, $CDCl_3$) δ 202.030, 171.746, 76.694, 69.669, 67.279, 66.862, 49.020, 37.132, 31.572, 26.694, 26.565, 22.355, 21.907; MS (EI) m/z 356 (M^+). Anal. ($C_{19}H_{24}O_3Fe$) C, H.

Methyl 6-Ferrocenyl-6-oxohexanoate (3b). The flask was charged with ferrocene (500 mg, 2.688 mmol), adipoyl chloride (390 μL, 2.688 mmol), and CH_2Cl_2 (20 mL). The solution was then chilled thoroughly in an ice bath. To this solution was added anhydrous aluminum chloride (394 mg, 2.955 mmol) carefully for 20 min using a spatula under N_2. The reaction mixture, which turned to deep violet color, was allowed to stir for 40 min in an ice-bath and for another 30 min at room temperature. Without further purification, the reaction mixture was heated at 90 °C for 1 h after slow addition of methanol (9 mL) and triethylamine (2 mL). At the end of the reaction, the solvents were removed in vacuo, and the residue was purified by flash column chromatography (20:80 ethyl acetate−hexane) to afford **3b** (389 mg, 44%) as a red oil: ^{1}H NMR (200 MHz, $CDCl_3$) δ 4.76 (t, J = 1.8 Hz, 2H, Fe−Cp-H (α)), 4.48 (t, J = 1.8 Hz, 2H, Fe−Cp-H (β)), 4.18 (s, 5H, Cp-H), 3.67 (s, 3H, OCH_3), 2.72 (t, J = 7.0 Hz, 2H, CH_2), 2.37 (t, J = 7.0 Hz, 2H, CH_2) 1.75−1.68 (m, 4H); ^{13}C NMR (50 MHz, $CDCl_3$) δ 203.976, 173.918, 78.950, 72.145, 69.717, 69.247, 51.532, 39.181, 33.901, 24.729, 23.848; MS (CI) m/z 329 ($M + H)^+$. Anal. ($C_{17}H_{20}O_3Fe$) C, H.

Methyl 8-Ferrocenyl-8-oxobutanoate (3c). A red oil: ^{1}H NMR (200 MHz, $CDCl_3$) δ 4.79 (t, J = 1.8 Hz, 2H, −Fe−Cp-H (α)), 4.49 (t, J = 1.8 Hz, 2H, −Fe−Cp-H (β)), 4.23 (s, 5H, Cp-H), 3.71 (s, 3H, OCH_3), 3.07 (t, J = 6.6 Hz, 2H, CH_2), 2.68 (t, J = 6.4 Hz, 2H, CH_2); ^{13}C NMR (50 MHz, $CDCl_3$) δ 202.027, 173.516, 78.312, 72.167, 69.869, 69.118, 51.767, 34.143, 27.611; MS (CI) m/z 301 ($M + H)^+$. Anal. ($C_{15}H_{16}O_3Fe$) C, H.

Synthesis of 8-Ferrocenyl-8-oxooctanoic Acid (4). A solution of the ester **3a** (70 mg, 0.197 mmol) in 1.5 mL of ethanol and 1.5 mL of 20% NaOH (aq) was heated under reflux for 1 h. The reaction mixture was cooled and acidified with 5 mL of 20% HCl in an ice bath and then stirred vigorously for a few minutes to make free acid from the sodium salt. The product was collected by suction filtration at room temperature, washed with 10 mL of water, and dried. Pure 8-ferrocenyl-8-oxooctanoic acid (**4**) was obtained in 90% yield (60 mg) as a red solid: mp 80.2 °C; ^{1}H NMR (300 MHz, $CDCl_3$) δ 4.78 (t, J = 2.0 Hz, 2H, −Fe−Cp-H (α)), 4.49 (t, J = 2.0 Hz, 2H, −Fe−Cp-H (β)), 4.19 (s, 5H, Cp-H), 2.70 (t, J = 7.4 Hz, 2H, CH_2), 2.38 (t, J = 7.6 Hz, 2H, CH_2), 1.74−1.62 (m, 4H), 1.30−1.22 (m, 4H); ^{13}C NMR (50 MHz, $CDCl_3$) δ 204.628, 179.450, 79.079, 72.145, 69.733, 69.346, 39.570, 33.942, 29.102, 28.904, 24.527, 24.360; MS(FAB) m/z 342 ($M + H)^+$. Anal. ($C_{18}H_{22}O_3Fe$) C, H.

Synthesis of Methyl 8-Cyclopentadienyltricarbonylrhenium-8-oxooctanoate (5a). A mixture of the ester **3a** (52.8 mg, 0.147 mmol), NH_4ReO_4 (13 mg, 0.047 mmol), $Cr(CO)_6$ (58 mg, 0.265 mmol), and $CrCl_3$ (15 mg, 0.094 mmol) was placed in a 4 mL reaction vial containing a magnetic stir bar. Dry methanol (300 μL) was added to the vial that was sealed and heated at 160 °C for 1 h. At the end of the reaction, the mixture was cooled in an ice bath for 15 min and the solvent was removed in vacuo. Flash column chromatography (1:4 ethyl acetate−hexane) of the crude mixture afforded **5a** (26 mg, 35%) as a gray solid: mp 70.2 °C; ^{1}H NMR (300 MHz, $CDCl_3$) δ 5.99 (t, J = 2.4 Hz, 2H, Re−Cp-H (α)), 5.40 (t, J = 2.3 Hz, 2H, Re−Cp-H (β)), 3.67 (s, 3H, OCH_3), 2.58 (t, J = 7.3 Hz, 2H, CH_2), 2.31 (t, J = 7.5 Hz, 2H, CH_2), 1.71−1.61 (m, 4H), 1.38−1.33 (m, 4H); ^{13}C NMR (50 MHz, $CDCl_3$) δ 194.993, 191.777, 174.063, 96.337, 87.765, 85.094, 51.367, 38.645, 33.919, 28.783, 28.631, 24.671, 24.110; MS (FAB) m/z 507 ($M + H)^+$; HRMS calcd for $C_{17}H_{20}O_6{}^{187}$Re 507.0818, found 507.0812.

Methyl 6-Cyclopentadienyltricarbonylrhenium-6-hexanoate (5b). A pale yellow oil: ^{1}H NMR (400 MHz,

$CDCl_3$) δ 5.97 (t, J = 2.0 Hz, 2H, Re−Cp-H (α)), 5.39 (t, J = 2.0 Hz, 2H, Re−Cp-H (β)), 3.66 (s, 3H, OCH_3), 2.61 (t, J = 7.2 Hz, 2H, CH_2), 2.35 (t, J = 7.0 Hz, 2H, CH_2), 1.73−1.64 (m, 4H); ^{13}C NMR (100 MHz, $CDCl_3$) δ 194.689, 191.778, 173.766, 95.786, 87.886, 85.195, 51.590, 38.309, 33.684, 24.239, 23.557; MS (FAB) m/z 479 $(M + H)^+$; HRMS calcd for $C_{15}H_{16}O_6{}^{187}$Re 479.0505, found 479.0515.

Methyl 4-Cyclopentadienyltricarbonylrhenium-4-oxobutanoate (5c). A pale yellow oil: ^{1}H NMR (400 MHz, $CDCl_3$) δ 6.03 (t, J = 2.4 Hz, 2H, Re−Cp-H (α)), 5.40 (t, J = 2.4 Hz, 2H, Re−Cp-H (β)), 3.69 (s, 3H, OCH_3), 2.92 (t, J = 6.8 Hz, 2H, CH_2), 2.31 (t, J = 6.4 Hz, 2H, CH_2); ^{13}C NMR (100 MHz, $CDCl_3$) δ 193.241, 191.710, 172.857, 95.156, 87.977, 85.217, 51.961, 33.366, 27.635; MS (FAB) m/z 451 $(M + H)^+$; HRMS calcd for $C_{13}H_{12}O_6{}^{187}$Re 451.0192, found 451.0188.

Synthesis of 8-Cyclopentadienyltricarbonylrhenium-8-oxooctanoic Acid (2a). A solution of **5a** (100 mg, 0.197 mmol) in 3 mL of 20% NaOH (aq) and ethanol (1:1) was heated at 80 °C for 1 h. The solution was cooled and acidified with 5 mL of 0.1 N HCl in an ice bath. The reaction mixture was extracted with CH_2Cl_2, and the organic layer was dried over anhydrous sodium sulfate and concentrated. The crude product was purified by flash column chromatography (60:40 ethyl acetate−hexane) to give **2a** (79 mg, 82%) as a pale yellow oil: ^{1}H NMR (200 MHz, $CDCl_3$) δ 5.99 (t, J = 2.4 Hz, 2H, Re−Cp-H (α)), 5.40 (t, J = 2.4 Hz, 2H, Re−Cp-H (β)), 2.59 (t, J = 7.2 Hz, 2H, CH_2), 2.36 (t, J = 7.3 Hz, 2H, CH_2), 1.73−1.62 (m, 4H), 1.39−1.26 (m, 4H); ^{13}C NMR (100 MHz, $CDCl_3$) δ 195.136, 191.816, 179.453, 96.149, 87.863, 85.142, 38.597, 33.715, 28.681, 28.590, 24.391, 24.034; MS (FAB) m/z 493 $(M + H)^+$; HRMS calcd for $C_{16}H_{18}O_6{}^{187}$Re 493.0662, found 493.0616.

6-Cyclopentadienyltricarbonylrhenium-6-oxohexanoic Acid (2b). A pale yellow oil: ^{1}H NMR (400 MHz, $CDCl_3$) δ 5.99 (t, J = 2.4 Hz, 2H, Re−Cp-H (α)), 5.40 (t, J = 2.2 Hz, 2H, Re−Cp-H (β)), 2.62 (t, J = 7.0 Hz, 2H, CH_2), 2.39 (t, J = 7.2 Hz, 2H, CH_2), 1.77−1.62 (m, 4H); ^{13}C NMR (100 MHz, $CDCl_3$) δ 194.765, 191.816, 179.316, 95.686, 87.939, 85.255, 38.263, 33.707, 23.966, 23.443; MS (FAB) m/z 465 $(M + H)^+$; HRMS calcd for $C_{14}H_{14}O_6{}^{187}$Re 465.0348, found 465.0356.

4-Cyclopentadienyltricarbonylrhenium-4-oxobutanoic Acid (2c). A pale yellow oil: ^{1}H NMR (400 MHz, $CDCl_3$) δ 6.03 (t, J = 2.4 Hz, 2H, Re−Cp-H (α)), 5.41 (t, J = 2.4 Hz, 2H, Re−Cp-H (β)), 2.90 (t, J = 6.4 Hz, 2H, CH_2), 2.74 (t, J = 6.4 Hz, 2H, CH_2); ^{13}C NMR (100 MHz, $CDCl_3$) δ 195.580, 191.717, 179.305, 94.966, 88.053, 85.263, 33.123, 27.635; MS (FAB) m/z 437 $(M + H)^+$; HRMS calcd for $C_{12}H_{10}O_6{}^{187}$Re 437.0035, found 437.0055.

Radiochemical Synthesis of ^{99m}Tc−CpTTOA (1a). A solution of $Na^{99m}TcO_4$ eluted from a generator was placed in a glass tube and was concentrated to dryness under a stream of N_2 at 75−80 °C. The resulting residue was treated with methanol, and the fraction soluble in methanol was collected in a pressure tube. To this were added the ester **3a** (3 mg, 8.42 μmol), $Cr(CO)_6$ (3.3 mg, 15.16 μmol), and $CrCl_3$ (0.8 mg, 5.39 μmol). The reaction mixture was heated at 160 °C for 1 h. At the end of the reaction, the mixture was cooled in an ice bath and methanol was removed under a stream of N_2. The residue was dissolved in CH_2Cl_2, passed through a short silica plug, and the solvent was removed. The residue was redissolved in methanol (150 μL) and treated with 0.4 N NaOH (50 μL) at 80 °C for 10 min. The solution was cooled, acidified with 50 μL of 0.5 N HCl, and extracted with CH_2Cl_2. ^{99m}Tc−CpTTOA (**1a**) was purified by HPLC at a flow 4 mL/min using a 91:9:0.09 mixture of hexane:methanol:acetic acid. ^{99m}Tc−CpTTOA collected from HPLC was concentrated, redissolved in ethanol, and diluted in saline to give a final solution of 10% ethanol in saline. A portion of the sample was treated with bovine serum albumin to give 5% of the total volume. An aliquot was analyzed by reversed phase HPLC at a flow 1 mL/min using a 70:30 mixture of methanol-0.1% acetic acid (aq). ^{99m}Tc−CpTTHA (**1b**) and ^{99m}Tc−CpTTBA (**1c**) were prepared as in the synthesis of **1a**.

In Vitro Stability Studies. An aliquot (18.5 MBq) of ^{99m}Tc−CpTTOA in 10% ethanol−saline was added to human serum (1 mL) and incubated at 37 °C, and the solution was analyzed at 30, 60, 240, and 360 min by radio-TLC using ethyl acetate−hexane (7:3) as the developing solvents.

Animals. A group of mice (ICR, male, 28 g) was orally administered 30% CCl_4 (1 mL CCl_4/kg) in olive oil after 6 h-long fast, whereas control mice were administered the same volume of olive oil under the same conditions (*3*, *21*). These two groups were fasted for another 2 h and then fed ad libitum for 15 h.

Biological Studies. Control and CCl_4-treated mice were fasted for another 3 h before administration of ^{99m}Tc−CpTTOA (1.5 MBq/mouse) via tail vein. At 2, 30, 60, and 120 min postinjection, both groups of mice (n = 3/time point) were sacrificed by cervical dislocation, and samples of blood and liver were isolated, weighed, and counted. The injected dose was calculated from standards prepared from the injection solution. The data were expressed as percent injected dose per gram of tissue (%ID/g). The 30 min samples of the serum and the liver were homogenized, extracted with a 2:1:1 mixture of $CHCl_3$/MeOH/0.001 N NaOH, and centrifuged (3000 rpm, 30 min) (*22*). The resulting chloroform and aqueous layers (1 mL each) were counted, respectively.

^{99m}Tc−CpTTOA was injected to 6-h-long fasted SD rats and planar images were obtained at 5, 30, and 60 min postinjection. Two sets of experiment were carried out, one with the radiotracer in 10% ethanol−saline and the other with additional 5% bovine serum albumin. In another set of experiment, SD rats (n = 2/time point) were injected with ^{99m}Tc−CpTTOA, and samples of the liver and the bladder were collected at 30 and 60 min postinjection. The liver samples were homogenized and centrifuged as previously, whereas urine samples were filtered through a membrane (MW cutoff 10 000). The samples were analyzed by both HPLC at a flow rate of 1 mL/min using a 70:30 mixture of methanol and 0.1% acetic acid (aq) as the eluants and radio-TLC using a 50:50 mixture of methanol and 0.2% acetic acid (aq) as the developing solvents.

RESULTS AND DISCUSSION

Synthesis of 8-Cyclopentadienyltricarbonylrhenium-8-oxooctanoic Acid (2a). The ester **3a** was prepared by Friedel−Crafts acylation from ferrocene and methyl 8-chloro-8-oxooctanoate in the presence of $AlCl_3$ (*23*). A double ligand transfer reaction of the ester **3a** and NH_4ReO_4 using $CrCl_3$ and $Cr(CO)_6$ was carried out to provide Re compound **5a**. This reaction was well described by Spradau and Katzenellenbogen (*18*), in that ReO_4^- is reduced and carbonylated, which undergoes a Cp ligand transfer reaction with the ferrocenyl precursor. The optimal reaction solvent was methanol among various solvents studied. Hydrolysis of the resulting compound in 0.4 N NaOH (aq) and methanol (1:3) afforded 8-cyclopentadienyltricarbonylrhenium-8-oxooctanoic acid

Table 1. Comparison of Radiochemical Yields Depending on Precursors and Solvents in the Double Ligand Transfer Reaction

precursor	solvent[a]	yield[b] (no. of reacion)
3	methanol	58−82 (8)
4	THF	NR[c] (3)
4	2-propanol	12−15 (2)

[a] A total volume was 200 μL. [b] Yield was based on radio-TLC data. [c] NR: no reaction.

(**2a**). A double ligand transfer reaction of the carboxylic acid **4** in methanol gave the **5a** instead of the **2a** (2−5% yield), possibly due to methyl ester formation of the carboxylic acid by methanol. The ester **3b** was prepared from ferrocene and methyl 6-chloro-6-oxohexanoyl chloride in the presence of $AlCl_3$, followed by methyl ester formation in methanol in the presence of triethylamine. Re complexes **2b** and **2c** were prepared as the synthesis of **2a**.

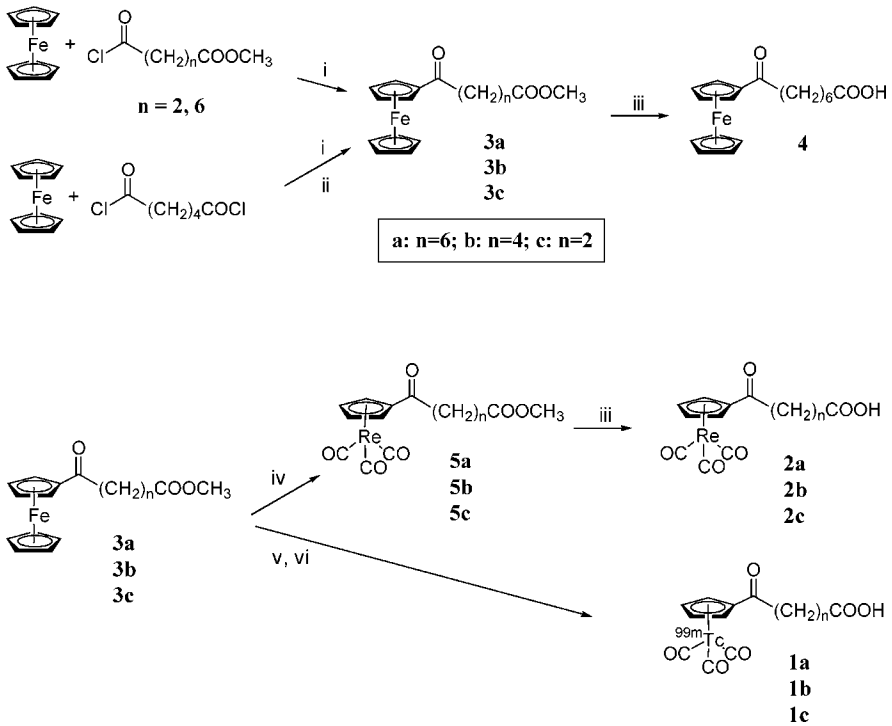
Radiochemical Synthesis of ^{99m}Tc−CpTTOA (1a). ^{99m}Tc−CpTTOA was synthesized via the same route as the preparation of Re-fatty acid **2a** (*18*−*20*). The ester **3a** was reacted with $^{99m}TcO_4^-$ in the presence of $CrCl_3$ and $Cr(CO)_6$ at 160 °C for 1 h. When either the acid **4** was used as the precursor or THF (or 2-propanol) as the solvent, the radiochemical yield of **1a** was low as shown in Table 1 and some unknown radioactive peaks appeared on radio-TLC. Therefore, the ester **3a** and methanol were employed to produce **1a** as shown in Scheme 1. Hydrolysis of the ^{99m}Tc-labeled compound was attempted in 20% NaOH (aq) and ethanol (*24*) as described for the hydrolysis of the **5a**, but unknown radioactive compounds were detected upon analysis by radio-TLC. Although the unknown peaks were not identified, they were likely to be derived from cleavage of the ^{99m}Tc core. Therefore, hydrolysis conditions were varied to give a maximal yield of the desired product and to minimize the production of the unknown radiochemical impurities. As shown in Table 2, hydrolysis of the methyl ester of ^{99m}Tc−CpTTOA in a 1:3 mixture of 0.4 N NaOH and methanol gave the highest yield (72−77%). The reaction mixture was then purified by HPLC, and the retention time of ^{99m}Tc−CpTTOA was 12.5 min using a 91:9:0.09 mixture of hexane:methanol:acetic acid as the eluants. An aliquot was analyzed by reversed phase HPLC, and ^{99m}Tc−CpTTOA and Re−CpTTOA were eluted at 16.9 and 14.4 min, respectively. Although they were not coeluted on HPLC, ^{99m}Tc−CpTTOA was identified based on the similar chemical properties between Tc and Re complexes. The different retention times of Tc and Re complexes on HPLC have been also reported in other cases (*20*). Synthesis of ^{99m}Tc−CpTTOA gave higher yield than the corresponding Re complex, due to higher reactivity of ^{99m}Tc than Re. Overall radiochemical yield of ^{99m}Tc−CpTTOA was 50−63% (decay-corrected) and radiochemical purity was higher than 99% as determined by HPLC and radio-TLC. ^{99m}Tc−CpTTHA (**1b**) and ^{99m}Tc−CpTTBA (**1c**) were prepared as in the synthesis of **1a** and used as the radiometabolite standards of **1a**. HPLC retention times of **1b** and **1c** were 11.1 and 8.2

Table 2. Comparison of Hydrolysis Conditions of the Methyl Ester of ^{99m}Tc−CpTTOA (1a)

reagent	NaOH/ methanol[a]	ratio of unknown peak to **1a**[b]
20% NaOH/ethanol	1:1	NR[c]
0.1 N NaOH/methanol	1:1	4/1
0.2 N NaOH/methanol	1:1	3/1
0.4 N NaOH/methanol	1:1	3.3/1
0.4 N NaOH/methanol	1:3	1/3
0.5 N NaOH/methanol	1:1	9/1
0.7 N KOH/methanol	1:1	8/1

[a] The reaction was carried out in a total volume of 200 μL (80 °C, 10 min). [b] Measured by radio-TLC. [c] NR: no reaction.

Scheme 1[a]



[a] Reaction conditions: (i) $AlCl_3$, CH_2Cl_2, 0 °C, 3 h; (ii) MeOH, Et_3N, 90 °C, 1 h; (iii) 20% NaOH (aq)−ethanol (1:1), 80 °C, 1 h; (iv) NH_4ReO_4, $CrCl_3$, $Cr(CO)_6$, CH_3OH, 160 °C, 1 h; (v) $Na^{99m}TcO_4$, $CrCl_3$, $Cr(CO)_6$, CH_3OH, 160 °C, 1 h; (vi) 0.4 N NaOH (aq)−CH_3OH (1:3), 80 °C, 10 min.

Table 3. In Vitro Stability of ^{99m}Tc−CpTTOA (1a) in Human Serum

time (min)	% of ^{99m}Tc−CpTTOA[a]
30	98
60	98
240	94
360	92

[a] ^{99m}Tc−CpTTOA was incubated with human serum at 37 °C for 6 h and the percentage of the remaining radiotracer was analyzed by radio-TLC.

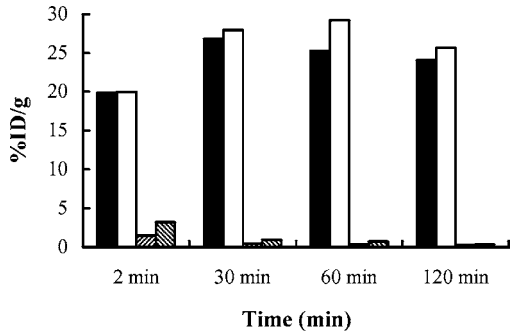


Figure 1. Measurement of the radioactivity in liver and blood samples of control and CCl_4-treated mice. Both groups of mice were injected with ^{99m}Tc−CpTTOA, and the liver and blood were collected at 2, 30, 60, and 120 min postinjection and counted. The injected dose was calculated from standards prepared from the injection solution. The data were expressed as percent injected dose per gram of tissue (%ID/g). Closed bar: liver sample from control mice; open bar: liver sample from CCl_4-treated mice; right-handed striped bar: blood sample from control mice; left-handed striped bar: blood sample from CCl_4-treated mice.

min, respectively, when analyzed in a 70:30 mixture of methanol-0.1% acetic acid (aq) at a flow rate of 1 mL/min.

In Vitro Stability Studies. Percentage of the remaining ^{99m}Tc−CpTTOA was 98% after 1 h and over 90% even after 6 h when the radiotracer was incubated with human serum at 37 °C and analyzed by radio-TLC, indicating high in vitro stability of the radiotracer (Table 3).

Measurement of the Radioactivity in the Liver and Blood Samples of Control and CCl_4-Treated Mice. Control and CCl_4-treated mice were fasted for 3 h before injected with ^{99m}Tc−CpTTOA. Initial uptake of the radioactivity in CCl_4-treated mice was similar to that in control mice at 2 min postinjection of ^{99m}Tc−CpTTOA, as shown in Figure 1. In contrast, the amounts of radioactivity in the liver of CCl_4-treated mice were higher than those of control mice at 30, 60, and 120 min postinjection, reaching a maximum at 60 min. The radioactivity in the samples of blood was slightly higher in CCl_4-treated mice. This was also the case when [1-^{11}C]-octanoate was evaluated in the control and CCl_4-treated mice (*3*), although the difference in the liver uptake of the radioactivity between the two groups of mice was more profound in [1-^{11}C]octanoate than in ^{99m}Tc−CpTTOA. This result demonstrated that the ^{99m}Tc−CpTTOA underwent slower hepatic clearance in CCl_4-treated mice compared to the control mice, probably due to impaired β-oxidation caused by CCl_4 that is known to induce the hepatotoxicity (*21*).

Solubility of the Radioactivity in the Liver and Blood Samples of Control and CCl_4-Treated Mice. Most of the radioactivities obtained from the blood and liver at 30 min postinjection in control and CCl_4-treated mice were extracted into the aqueous layer rather than into the organic layer, indicating that the metabolites are water-soluble (Table 4). The radioactivities produced by esterification should be extracted into chloroform layer. The results therefore indicated that the ^{99m}Tc−CpTTOA was predominately metabolized by β-oxidation in the liver and not esterified as triglycerides, which was consistent with the results of other medium chain fatty acid analogues such as *p*-[^{123}I]iodophenylenanthic acid, *p*-[^{123}I]iodophenylvaleric acid, and [1-^{11}C]octanoate in the liver (*3*, *6*).

Table 4. Solubility of the Radioactivity in Liver and Blood Samples of Control and CCl_4-Treated Mice at 30 min after Administration of ^{99m}Tc−CpTTOA (1a)

	tissue	organic[a]	aqueous[a]
control	liver	1.7	98.3
	serum	14.5	85.5
CCl_4-treated	liver	1.6	98.4
	serum	8.9	91.1

[a] Mean average of three mice.

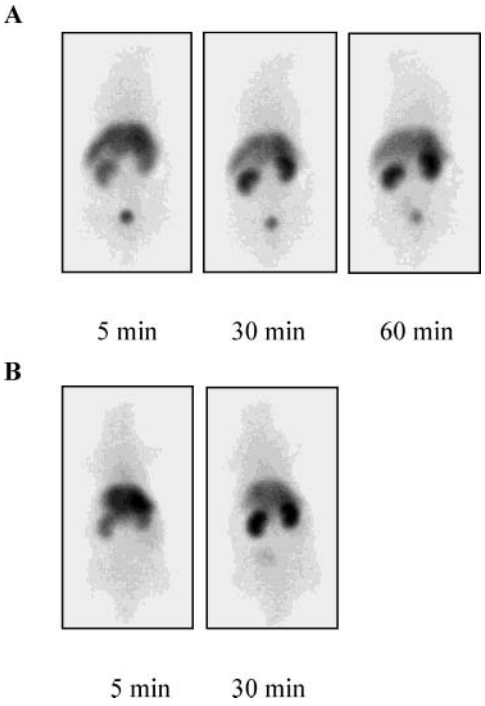


Figure 2. Planar images of ^{99m}Tc−CpTTOA (**1a**) in rats. The radiotracer (11 MBq) was administered to SD rats via tail vein and planar images were obtained at 5, 30, and 60 min postinjection, respectively (A). Another sets of planar images were obtained at 5 and 30 min after administration of the radiotracer containing 5% bovine serum albumin (B).

Imaging Studies. Since fatty acids are predominantly metabolized in the fasted state, the animals were fasted for 6 h prior to the experiments. Planar images of the rats injected with ^{99m}Tc−CpTTOA showed rapid uptake of the radioactivity in the liver, kidneys and bladder at 5 min postinjection with rapid elimination of the radioactivity from the liver as a function of time (Figure 2A). Within 60 min, most of the radioactivity was observed in the kidneys and bladder. This rapid hepatic clearance indirectly suggested that this fatty acid analogue was not esterified, unlike long chain fatty acid. Uptake pattern of the ^{99m}Tc−CpTTOA was not significantly affected by the presence of 5% bovine serum albumin (Figure 2B), even though bovine serum albumin is known to facilitate the penetration of the fatty acid through the cell membranes (*25*). There was no significant uptake in the thyroid or salivary gland, indicating that ^{99m}Tc pertechnetate was not regenerated during the time of the study.

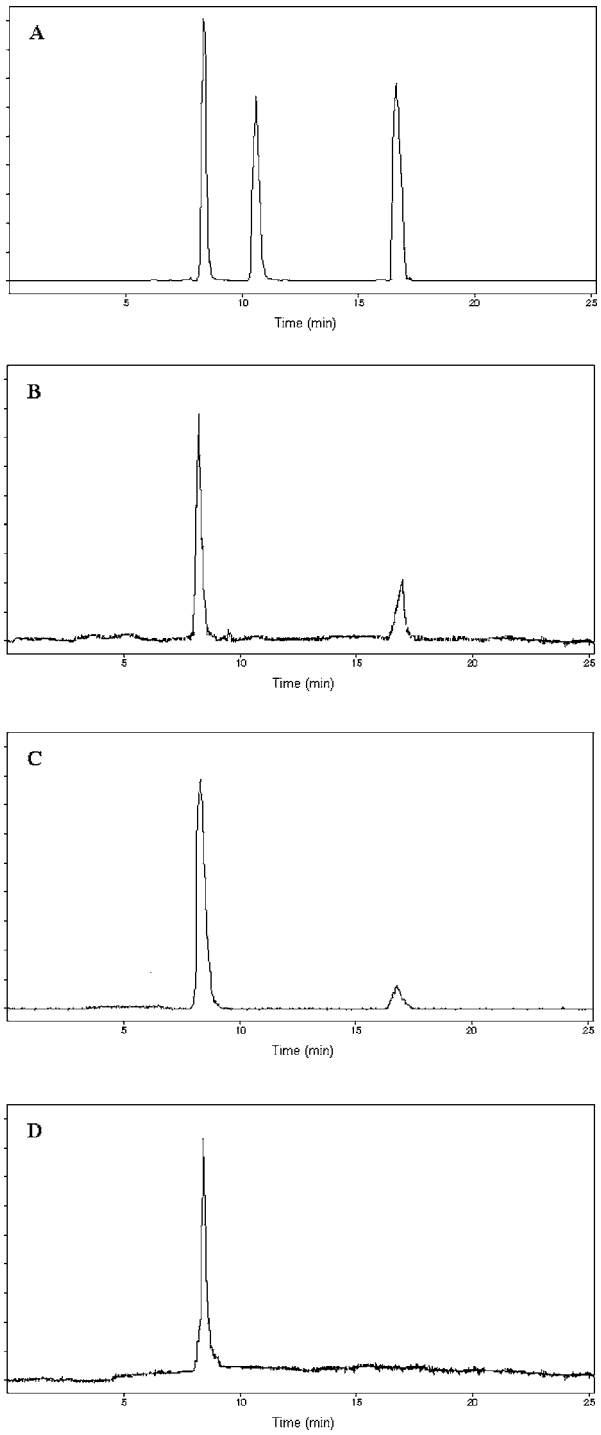


Figure 3. HPLC profile of the standards. (A); t_R = 8.2 min (**1c**), 11.1 min (**1b**), 16.9 min (**1a**). HPLC analysis of the liver and urine samples of the rats injected with ^{99m}Tc−CpTTOA (**1a**); (B): liver, 30 min, (C): urine 30 min, and (D): urine 60 min.

It is likely that the lipophilic properties of ^{99m}Tc−CpTT contributed to rapid uptake of this fatty acid analogue to the liver because medium chain fatty acid does not use carnitine shuttle step when enters the mitochondria, whereas a polar [^{99m}Tc]MAG−hexanoic acid was hardly accumulated in the liver (*4*). Although ^{99m}Tc−CpTT is smaller than ^{99m}Tc−N_2S_2 core, difference in the size of the cores did not significantly affect on the biological activity of the corresponding medium chain fatty acid analogue.

Analysis of Metabolites. When the samples of the liver and urine of rats were analyzed, the sole radiometabolite appeared at the retention time of 8.2 min on HPLC and was identified as ^{99m}Tc−CpTTBA on both radio-TLC and HPLC (Figure 3). ^{99m}Tc−CpTTHA, the metabolite after one cycle of β-oxidation of ^{99m}Tc−CpTTOA, was not detected (Figure 3B-D). Ratios of peak area under ^{99m}Tc−CpTTBA to ^{99m}Tc−CpTTOA were 77:23 and 90:10 in 30 min samples of the liver and urine, respectively (Figure 3B and C). The 60 min samples of the liver were not analyzed because of the insufficient radioactivity. The parent was completely converted to the metabolite in the 60 min sample of the urine (Figure 3D). This indicated that ^{99m}Tc−CpTTOA was metabolized to ^{99m}Tc−CpTTBA via β-oxidation in the liver and excreted to the kidneys and bladder, which was similar to the metabolism of [^{99m}Tc]MAMA−hexanoic acid in the liver (*4*).

CONCLUSION

The labeling method using ^{99m}Tc−CpTT was advantageous, because the precursor was readily prepared by Friedel−Crafts acylation from ferrocene and fatty acid analogue, and ^{99m}Tc labeling via a double ligand transfer reaction was easily achievable. A novel radiotracer, ^{99m}Tc−CpTTOA, was metabolized via β-oxidation in the liver, which supported that the β-oxidation was the main metabolic pathway of this medium chain fatty acid analogue. The results suggest that ^{99m}Tc−CpTTOA may be useful for evaluation of fatty acid metabolism in the liver. This is the first example of the medium chain fatty acid analogue containing ^{99m}Tc−CpTT.

ACKNOWLEDGMENT

This work was supported in part by a grant of Nuclear R & D Program, Korea Ministry of Science and Technology (M20204-190027-02A0701-00150). We thank Mr. S. Y. Kim and S. W. Choi for their technical assistance.

Supporting Information Available: Combustion analysis data. This material is available free of charge via the Internet at http://pubs.acs.org.

LITERATURE CITED

(1) Burt, A. D., and James, O. F. W. (1994) Pathophysiology of the Liver. *Pathology of the Liver* (MacSween, R. N. M., Anthony, P. P., Scheuer, P. J., Burt, A. D., and Portmann, B. C., Eds.) pp 51−81, Churchill Livingstone, New York.

(2) Zakim, D. (1996) Metabolism of Glucose and Fatty Acids by the Liver. *Hepatology. A Textbook of Liver Disease* (Zakim, D., and Boyer, T. D., Eds.) pp 58−92, Saunders, Philadelphia.

(3) Yamamura, N., Magata, Y., Kitano, H., Konishi, J., and Saji, H. (1998) Evaluation of [1-^{11}C]octanoate as a new radiopharmaceutical for assessing liver function using positron emission tomography. *Nucl. Med. Biol. 25*, 467−472.

(4) Yamamura, N., Magata, Y., Arano, Y., Kawaguchi, T., Ogawa, K., Konishi, J., and Saji, H. (1999) Technetium-99m-labeled medium-chain fatty acid analogues metabolized by β-oxidation: radiopharmaceutical for assessing liver function. *Bioconjugate Chem. 10*, 489−495.

(5) Bennett, M. J. (1994) The enzymes of mitochondrial fatty acid oxidation. *Clin. Chim. Acta 226*, 211−224.

(6) Yamamura, N., Magata, Y., Konishi, J., and Saji, H. (1999) Evaluation of radioiodinated medium chain fatty acids as new diagnostic agents for the determination of hepatic viability. *Eur. J. Nucl. Med. 26*, 1597−1605.

(7) Eckelman, W. C., Karesh, S. M., and Reba, R. C. (1975) New compounds: fatty acid and long chain hydrocarbon derivatives containing a strong chelating agent. *J. Pharma. Sci. 64*, 704−706.

(8) Karesh, S. M., Eckelman, W. C., and Reba, R. C. (1977) Biological distribution of chemical analogues of fatty acids

and long chain hydrocarbons containing a strong chelating agent. *J. Pharm. Sci. 86*, 225−228.
(9) Mach, R. H., Kung, H. F., Jungwiwattanaporn, P., and Guo, Y. Z. (1991) Synthesis and biodistribution of a new class of ^{99m}Tc-labeled fatty acid analogues for myocardial imaging. *Nucl. Med. Biol. 18*, 215−226.
(10) Jones, G. S., Elmaleh D. R., Strauss, H. W., and Fischman, A. J. (1994) Synthesis and biodistribution of a new ^{99m}technetium fatty acid. *Nucl. Med. Biol. 21*, 117−123.
(11) Loberg, M. D., Cooper, M., Harvey, E., Callery, P., and Faith, W. (1976) Development of new radiopharmaceuticals based on N-substituted iminodiacetic acid. *J. Nucl. Med. 17*, 633−638.
(12) Ryan, J., Cooper, M., Loberg, M., Harvey, E., and Sikorski, S. (1977) Technetium-99m-labeled N−(2,6-dimethylphenylcarbamoylmethyl) iminodiacetic acid (Tc-99m HIDA): a new radiopharmaceutcial for hepatobiliary imaging studies. *J. Nucl. Med. 18*, 997−1004.
(13) Eisenhut, M. (1982) Simple labeling of omega-phenylfatty acids by iodine isotope exchange. *Int. J. Appl. Radiat. Isot. 33*, 499−504.
(14) Ambrose, K. R., Owen, B. A., Goodman, M. M., and Knapp, F. F., Jr. (1987) Evaluation of the metabolism in rat hearts of two new radioiodinated 3-methyl-branched fatty acid myocardial imaging agents. *Eur. J. Nucl. Med. 12*, 486−491.
(15) Schwochau, K. (1994) Technetium radiopharmaceuticals. Fundamentals, synthesis, structure, and development. *Angew. Chem., Int. Ed. 33*, 2258−2267.
(16) Jurisson, S., Berning, D., Jia, W., and Ma, D. S. (1993) Coordination compounds in nuclear medicine. *Chem. Rev. 93*, 1137−1156.
(17) Gholson, C. F., Provenza, J. M., and Bacon, B. R. (1990) Hepatological considerations in patients with parenchymal liver disease undergoing surgery. *Am. J. Gastroenterol. 85*, 487−496.
(18) Spradau, T. W. and Katzenellenbogen, J. A. (1998) Preparation of cyclopentadienyltricarbonylrhenium complexes using a double ligand transfer reaction. *Organometallics 17*, 2009−2017.
(19) Cesati, R. R., III, Tamagnan, G., Baldwin, R. H., Zoghbi, S. S., Innis, R. B., and Katzenellenbogen, J. A. (1999) Synthesis of cyclopentadienyl tricarbonyl technetium phenyl-tropane derivatives by direct double ligand transfer with ferrocene precursors. *J. Labelled Compd. Radiopharm. 42*, S150−152.
(20) Skaddan, M. B., Wust, F. R., Jonson, S., Syhre, R., Welch, M. J., Spies, H., and Katzenellenbogen, J. A. (2000) Radiochemical synthesis and tissue distribution of Tc-99m-labeled 7α-substituted estradiol complex. *Nucl. Med. Biol. 27*, 269−278.
(21) Hjelle, J. J., Grubbs, J. H., Beer, D. G., and Petersen, D. R. (1983) Time course of the carbon tetrachloride-induced decrease in mitochondrial aldehyde dehydrogenase activity. *Toxicol. Appl. Pharmacol. 67*, 159−165.
(22) Forch, J., Less, M., and Sloane-Stanley, G. H. (1957) A simple method for the isolation and purification of total lipids from animal tissues. *J. Biol. Chem. 226*, 497−509.
(23) Reeves, P. C. (1963) Carboxylation of Aromatic Compound: Ferrocenecarboxylic Acid. *Organic Syntheses* (Mrowca, J. J., Borecki, M. M., and Sheppard, W. A., Eds.) Coll. Vol. VI, pp 625−627, John Wiley & Sons, New York.
(24) Burness, D. M. (1963) 3-Methyl-2-Furoic Acid and 3-Methylfuran. *Organic Syntheses* (Cason, J., and Hutchinson, R. B., Eds.) Coll. Vol. IV, pp 628−630, John Wiley & Sons, New York.
(25) Hamilton, J. A. (1989) Medium-chain fatty acid binding to albumin and transfer to phospholipid bilayers. *Proc. Natl. Acad. Sci. U.S.A. 86*, 2663−2667.

BC0341268

A New Strategy for the Preparation of Peptide-Targeted Radiopharmaceuticals Based on an Fmoc-Lysine-Derived Single Amino Acid Chelate (SAAC). Automated Solid-Phase Synthesis, NMR Characterization, and in Vitro Screening of fMLF(SAAC)G and fMLF[(SAAC−Re(CO)$_3$)$^+$]G

Karin A. Stephenson,[†] Jon Zubieta,[‡] Sangeeta Ray Banerjee,[‡] Murali K. Levadala,[‡] Linda Taggart,[†] Lorna Ryan,[†] Nicole McFarlane,[†] Douglas R. Boreham,[†] Kevin P. Maresca,[§] John W. Babich,[§] and John F. Valliant*[,†]

Department of Chemistry and The Medical Physics and Applied Radiation Sciences Unit, McMaster University, Hamilton, ON, Canada L8S 4M1, Department of Chemistry, Syracuse University, Syracuse, New York 13244-4100, and Molecular Insight Pharmaceuticals Inc., Cambridge, Massachusetts 02142. Received July 21, 2003; Revised Manuscript Received October 12, 2003

A tridentate single amino acid chelate (SAAC) derived from N-α-Fmoc-L-lysine was incorporated within a short peptide sequence using an automated peptide synthesizer. Novel derivatives of the chemotactic peptide fMLF were prepared such that the SAAC and its Re complex were selectively placed between a terminal glycine amino acid and the targeting fMLF sequence. The products, which were synthesized in parallel, were characterized by mass spectrometry and multi-NMR spectroscopy. The latter technique demonstrated that the structures of the targeting portions of the peptides are the same in the SAAC and Re−SAAC derivatives. The affinities of the reported compounds for the formyl peptide receptor were subsequently determined using flow cytometry and were found to be comparable to that of the parent peptide. The results of this work demonstrate the feasibility and numerous benefits of using the SAAC system to prepare peptide-targeted Tc(I) and Re(I) radiopharmaceuticals.

INTRODUCTION

Small peptides have proven to be one of the most effective means of targeting radionuclides to specific receptors (*1*). The success of peptides as biological vectors for radioisotopes is a result of their receptor specificity, ease of preparation and modification, ability to target receptors, and clearance from nontarget tissues in a time frame that correlates with the half-life of clinically useful radionuclides such as ^{99m}Tc, ^{111}In, and ^{18}F.

It has been well-documented that several factors influence the receptor binding affinity and biodistribution of technetium-labeled peptides (*2*). These include the site of derivatization, the presence and type of a spacer group between the ligand−metal complex and the peptide, and the nature of the Tc−ligand complex (charge, size, lipophilicity, etc.). As a means of identifying optimal combinations of these factors several groups have begun to employ solid-phase synthesis (SPS) strategies. SPS is attractive because it is a convenient means of preparing analogues of a particular peptide−ligand bioconjugate in parallel (*3*).

The most common SPS strategy used to prepare peptide-targeted Tc radiopharmaceuticals has been to append Tc ligands to the N-termini of peptides bound to a polymeric support. Hoffman et al., for example, reported the synthesis of a series of bombesin derivatives in which a N_3S triamide chelate and its Re complex were linked to the resin-bound peptide through a variety of different spacer groups (*4*). Gariépy and co-workers described a related solid-phase synthesis method for adding a diaminedithiol ligand to the N-terminus of short peptides (*5*). Blower and co-workers recently described a novel SPS approach in which a hydrazinonicotinyl acid (HYNIC) derivative of Fmoc-lysine was used as a metal-binding amino acid analogue (*6*, *7*). The N-protected HYNIC derivative was successfully incorporated within a bioactive peptide using standard Fmoc solid-phase peptide chemistry.

The above-mentioned SPS methods have some limitations including one or more of the following: a lack of flexibility in terms of changing the site of derivatization, the need to employ additional protecting groups on the ligand donor atoms, the inability to prepare the corresponding Re or ^{99}Tc complexes on the solid support and/or in solution and the need to use HPLC to obtain products of sufficient purity. The ideal SPS strategy should be based on a ligand system that forms stable and/or inert complexes with Tc/Re and, like the HYNIC system reported by Blower et al., is able to be incorporated into a peptide at any position using conventional SPS methods. The SPS strategy should also allow the ligand to be incorporated into the peptide without the need for additional protecting groups and isolation of the bioconjugate should be accomplished without the need for extensive HPLC purification. The Re (or ^{99}Tc) complex of the ligand should be sufficiently stable and well-defined to permit the synthesis of the metal complex of

* To whom correspondence should be addressed: Tel: 905-525-9140 ext. 23303 (J.F.V.); FAX: 905-522-2509; E-mail: valliant@mcmaster.ca.

[†] McMaster University, Hamilton, Ontario, Canada.

[‡] Syracuse University, Syracuse, NY.

[§] Molecular Insight Pharmaceuticals Inc., Cambridge, MA.

10.1021/bc034128s CCC: $27.50 © 2004 American Chemical Society
Published on Web 11/22/2003

the peptide using the same solid-phase synthetic methodology used to prepare the ligand. At present, Re and ^{99}Tc complexes are often prepared separately for characterization purposes, in vitro screening experiments and to verify the nature of products produced at the tracer level. To consider using combinatorial chemistry and high throughput screening methods as a means of identifying novel radiopharmaceuticals, a viable SPS method should allow for the Re and/or ^{99}Tc peptide complex to be prepared in parallel with the free ligand.

The ability to meet these criteria depends greatly upon the choice of ligand. Zubieta and co-workers recently described the synthesis and structural characterization of a series of Re(I) complexes of tridentate chelates containing two pyridine and one tertiary amine donor groups (*8*). The ligands and their Re(I) complexes, which were prepared in high yield, are stable to a wide range of reaction conditions making them ideal synthons for solid-phase peptide synthesis. With this in mind, an analogous ligand was prepared from Fmoc-lysine, which is herein referred to as a single amino acid chelate (SAAC). The SAAC is a unique Re(I)/Tc(I)-binding amino acid mimic, which has the potential to be incorporated into a peptide at any position using standard automated synthetic protocols. The corresponding Re complex, owing to its stability, inertness, and well-defined structure, should similarly be capable of being incorporated into a peptide using the same basic synthetic procedure. We report herein, the preparation, characterization, and in vitro screening studies of SAAC and Re−SAAC-peptide derivatives prepared using a convenient automated solid-phase synthesis methodology.

EXPERIMENTAL PROCEDURES

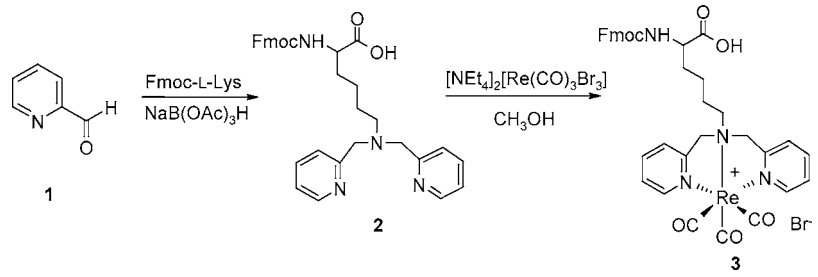
Materials. Unless otherwise stated, all reagents and solvents were ACS grade or higher and used without further purification from commercial suppliers. Polystyrene-based *N*-α-9-fluorenylmethoxycarbonyl (Fmoc)-glycine loaded SASRIN resin (0.69 mmol g-1, 1% divinylbenzene, 200−400 mesh) was obtained from Bachem Inc. Fmoc-protected amino acids were purchased from NovaBiochem Inc., Bachem Inc., and Advanced ChemTech Inc. Fluorescein-labeled fNLFNTK was purchased from Molecular Probes Inc. (product # F-1314).

Instrumentation. All peptides were prepared on an Advanced ChemTech 348 Ω Peptide Synthesizer using a 40 well reaction vessel. Peptides were analyzed by electrospray mass spectrometry using a Micromass Quattro Ultima instrument in positive ion mode. Samples were dissolved in 50/50 ACN/H_2O prior to analysis. FTIR spectra were acquired on a Bio-Rad FTS-40 FTIR spectrometer. NMR experiments were performed using a Bruker Avance DRX-500 NMR spectrometer. Proton spectra were acquired at 500.13 MHz using a 5-mm broadband inverse probe with triple axis gradient capability. Spectra were obtained in eight scans in 32K data points over a 6.775 kHz spectral width (2.418 s acquisition time). Proton COSY 2-D NMR spectra were recorded in the absolute value mode using the pulse sequence 90°−t1−45°-acq and included pulsed field gradients for coherence selection. During 2-D Fourier transformation a sine-bell squared window function was applied to both dimensions. The transformed data were then symmetrized. Carbon-13 NMR spectra were recorded at 125.771 MHz using the 5 mm broadband inverse probe with triple axis gradient capability. The spectra were acquired over a 28.986 kHz spectral width in 32K data points (0.565 s acquisition time). Inverse detected ^{1}H−^{13}C 2-D chemical shift correlation spectra were acquired in the phase-sensitive mode using the pulsed field gradient version the HSQC pulse sequence. Inverse detected ^{1}H−^{13}C 2-D chemical shift correlation spectra through two- and three-bond coupling interactions were acquired in the absolute value mode using the pulsed field gradient version of the HMBC pulse sequence. ROESY 2-D spectra were acquired in the phase sensitive mode. The data were acquired in 16 scans for each of the 256 FIDs that contained 2K data points in the F2 dimension over a 3.931 kHz spectral width. Zero-filling in the F1 dimension produced a 1K × 1K data matrix with a digital resolution of 3.839 Hz/point in both dimensions. During the real 2-D Fourier transformation, a sine-bell squared window function shifted by $\pi/2$ was applied to both dimensions. The transformed data were not symmetrized. The ROESY 2-D spectrum was plotted displaying negative contours only. Selective 1-D TOCSY ^{1}H NMR spectra were recorded over a 4.006 kHz spectral width in 32K data points (4.089 s acquisition time). Gaussian-shaped pulses were defined by 256 data points with the pulse being truncated at 1% of the maximum pulse amplitude.

Analytical HPLC was performed using a Varian Pro Star model 330 PDA detector, model 230 solvent delivery system and a C-18 Microsorb column (4.6 × 250 mm, 300 Å-5 μm). Semipreparative HPLC was carried out using a Varian Pro Star HPLC fitted with a model 320 UV-detector, a model 215 solvent delivery system and a C-18 Microsorb column (10 × 250 mm, 300 Å-5 μm). The elution protocol for both analytical and semipreparative experiments was a linear gradient of 25% acetonitrile containing 0.1% TFA to 75% acetonitrile containing 0.1% TFA over 15 min. The flow rates were 1.0 mL min^{-1} and 4.2 mL min^{-1} for the analytical and semipreparative experiments, respectively. All analytical HPLC experiments were monitored at $\lambda = 254$ and 214 nm.

Solid-Phase Peptide Synthesis. Fmoc-glycine-loaded SASRIN resin (300 mg, 0.69 mmol/g) was added to two wells of the reaction vessel, suspended in DMF (2 mL/well) and shaken at 900 rpm for 1 min. The wells were subsequently filtered, suspended in THF (2 mL/well), shaken at 900 rpm for 1 min, and drained for 90 s. The THF wash was repeated two more times. The DMF wash was then repeated a final two times to complete the general wash cycle. This procedure was used between every deprotection and coupling step. Fmoc deprotection was brought about through the addition of 25% v/v piperidine−DMF solution to the active vessels (2 mL/well) and shaking for 5 min at 900 rpm. Following filtration, the process was repeated, shaking for 10 min. The deprotected resin-bound amino acid was washed using the general wash procedure and subsequently coupled to the next Fmoc-protected amino acid using a standard HBTU coupling technique. Coupling reactions initially involved adding DMF (200 μL) to the active vessels followed by the addition of a 4-fold excess of the protected amino acid as a 0.5 M solution in DMF. Four equivalents of HBTU as a 0.5 M solution in DMF was then added followed by a 8-fold excess of DIPEA as 2.0 M solution in DMF. The reaction block was subsequently shaken for 80 min at 900 rpm. Following filtration, the resin was washed using the general washing procedure prior to the start of the next cycle. Peptides were cleaved from the resin support using a TFA cocktail containing EDT (2%), water (2%), and TIS (2%). The cleavage cocktail, cooled to 0 °C, was added to the resin and the mixture allowed to warm to room temperature over 60 min. The suspension was filtered into cold diethyl ether and the resulting heterogeneous solution centrifuged at

Scheme 1. Preparation of SAAC (2) and [SAAC−Re(CO)$_3$]$^+$ (3)



3000 rpm and −5 °C for 10 min. The resulting pellet was washed with cold diethyl ether (3 × 25 mL), dissolved in distilled−deionized water, and lyophilized yielding a white solid for both compounds **6** and **8** (Schemes 2 and 3). Compound **6** showed: FT-IR (KBr, cm^{-1}): 1540 (C═O), 1670 (C═O), 2927 (C−H), and 3069 (N−H); ESMS 805 [M + H]$^+$. Compound **8** showed: FT-IR (KBr, cm-^{1}): 1538 (C═O), 1927 and 2032 (C≡O), 2926 (C−H); ESMS 1075 [M + H]$^+$.

Leukocyte Preparation. Whole human blood (10−15 mL) was collected in vacutainer tubes (Becton Dickinson) containing sodium heparin. The red blood cells were lysed using a modified ammonium chloride method (1 part whole blood to 23 parts 0.145 M ammonium chloride solution containing 1.5 mM potassium bicarbonate and 0.1 mM EDTA). Tubes were incubated at room temperature for 15 min and then centrifuged in a Beckman Coulter Allegra 6R centrifuge at 900 rpm (400 g) for 7 min at 5 °C. The supernatant was removed and the pellet of leukocytes subsequently resuspended in HBSS containing 0.1% BSA, 10 mM HEPES, and 1.5 mM $CaCl_2$ (HBSS+). The cells were spun for 7 min at 400*g* at 5 °C, the supernatant removed, and the pellet resuspended in HBSS+. Cell counts were performed using a hemacytometer and a Beckman Coulter Z2 Coulter Particle Count and Size Analyzer. Cell concentrations were adjusted to 2 × 10^6 mL^{-1}.

Flow Cytometry. Samples were run on a Beckman Coulter EPICS XL, equipped with an argon laser (488 nm excitation wavelength). Fluorescence was measured using a 525 ± 15 nm band-pass filter. The flow cytometer was calibrated with fluorescein isothiocyanate (FITC)-labeled beads (Quantum 26 Beads, Bangs Laboratories, Inc, Fishers, IN) prior to sample analysis. The fluorescence intensity of the standard was provided by the manufacturer in units of Molecules of Equivalent Soluble Fluorochrome (MESF) and ranged from 5300 to 468 800. A linear fit of MESF versus mean channel number of the beads was used to convert all subsequent mean channel values to MESF values.

Equilibrium Binding Assay. The equilibrium-binding assay was used to determine the number of formyl peptide receptors (FPRs) on the surface of the neutrophils and the dissociation constant (K_d) of the fluorescein-labeled fNLFNTK (Molecular Probes) (1.0 nM) by preparing a saturated binding curve of peptide concentrations verses fluorescence intensity. Peptide stock solutions were made by dissolving the peptide derivatives **6** and **8** in DMSO and then diluting with HBSS+ to the desired concentrations, ensuring the concentration of DMSO was less than 0.1%. Cells at 1 × 10^6 mL^{-1} were equilibrated with 0.25, 0.50. 1.0, 3.0, 5.0, 10.0, and 20.0 nM solutions of the peptide derivatives (U) in duplicate. The samples were incubated for 2 h at 0 °C in the dark and then run on the flow cytometer. Neutrophils were gated on the basis of forward and side scatter parameters using Expo 32 ADC software (Beckman Coulter). All samples were repeated in the presence of 30 μM fMLF to account for nonspecific binding. The number of receptor−ligand complexes per cell (*B*) was determined using the following equation, where *Q* is a normalization factor used by Waller et al. (*14*) and *F* is the total fluorescence per cell:

$$B(\text{in ligand bound per cell}) = F\left(\frac{\text{MESF}}{\text{cell}}\right) \times Q$$

The level of nonspecific binding did not vary significantly with concentration of labeled peptide, thus an average value of nonspecific binding was subtracted from the total fluorescence per cell, *F*, when determining the number of receptor−ligand complexes. The total number of *N*-formyl peptide receptors, R_{tot}, and the equilibrium dissociation constant, K_d, were evaluated by minimizing the squared residual of the equilibrium solution using a one-site binding model (see the following equation). The values of R_{tot} and K_d for each donor were solved simultaneously.

$$[\text{LR}] = \frac{R_{tot}[\text{L}]}{[\text{L}] + K_d}$$

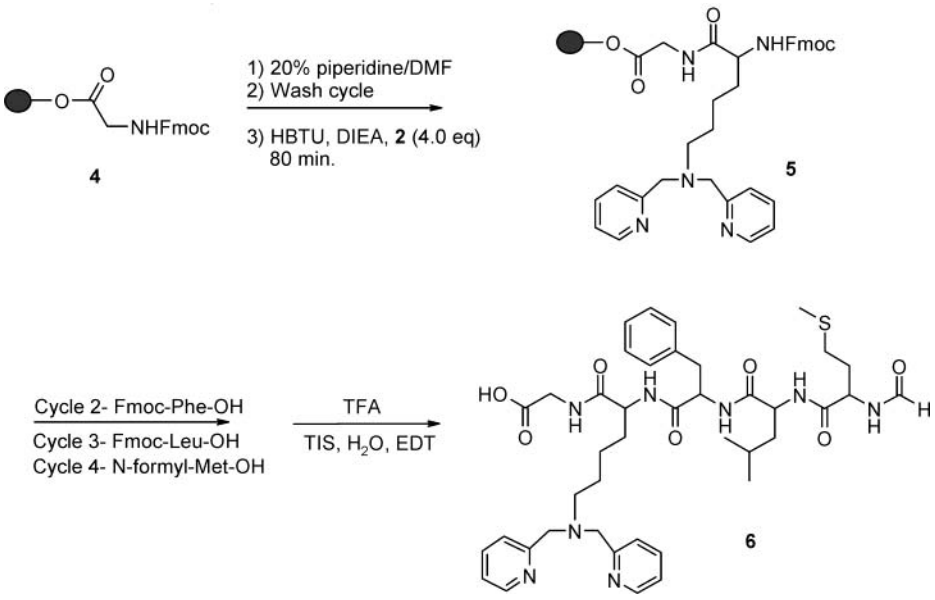
RESULTS

SAAC Synthesis. The synthesis of the Fmoc-protected single amino acid chelate **2** (Scheme 1) will be described elsewhere (*9*). Briefly, Fmoc-L-lysine was reacted with 2-pyridinecarboxaldehyde **1** in the presence of sodium triacetoxyborohydride. The resulting product was isolated in good yield and there was no epimerization of the lysine α proton. The Re complex was prepared in quantitative yield by adding a stoichiometric amount of [NEt$_4$]$_2$[Re(CO)$_3$Br$_3$] in methanol to compound **2**. Using these methods it is possible to produce multigram quantities of the amino acid analogue and its Re complex.

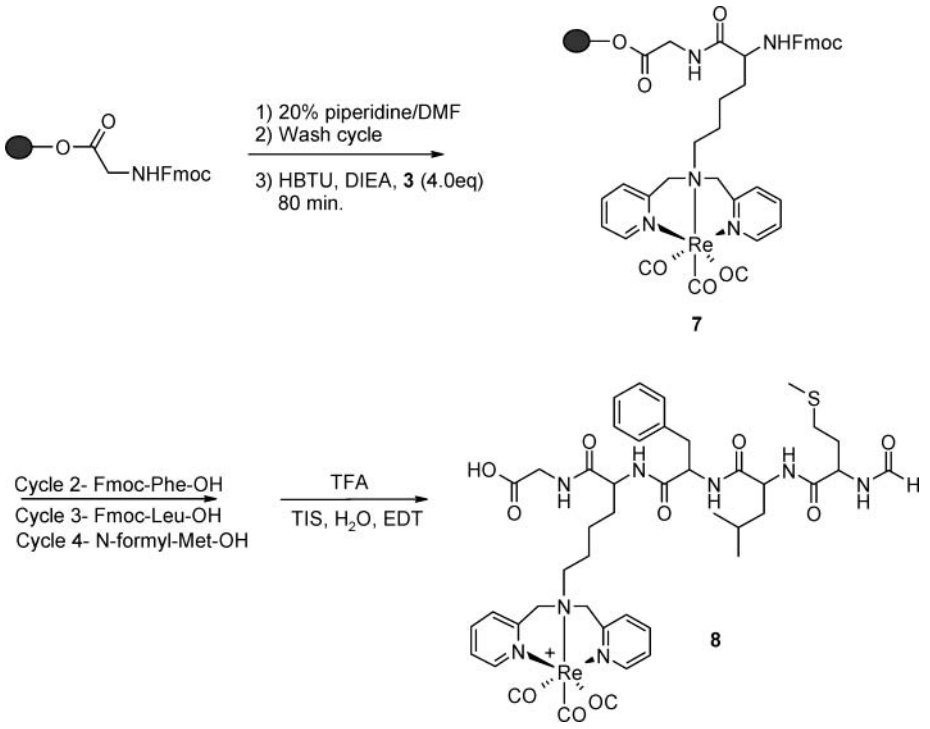
Peptide Synthesis and Characterization. Peptides were prepared on an Advanced ChemTech 348 Ω Peptide Synthesizer using HBTU as the coupling agent (Schemes 2 and 3) (*10*−*12*). The Fmoc protected dipyridyl chelate **2** and its Re complex **3**, as the bromide salt, were dissolved in DMF and coupled to the growing peptide chain using a 4-fold excess of ligand. The duration of the coupling steps to afford complete conversion to compounds **5** and **7** were determined by exposing samples of resin taken from the reaction mixtures to a solution containing ninhydrin (*13*). The time to complete conversion of the amine to the amide in both cases was identical to the conditions used for natural amino acid derivatives. As a result, modification of standard peptide coupling protocols was not necessary.

Peptides were cleaved from the resin using a TFA solution containing ethanedithiol (EDT, 2%), water (2%), and triisopropylsilane (TIS, 2%). Because of the presence of methionine, exclusion of oxygen and the use of freshly

Scheme 2. Solid-Phase Synthesis of fMLF(SAAC)G, 6



Scheme 3. Solid-Phase Synthesis of fMLF[(SAAC−Re(CO)$_3$)$^+$]G, 8



distilled EDT were necessary to avoid oxidation of the thioether to the sulfoxide. Precipitation of the peptide TFA salts was brought about by trituration with cold ether. The resulting solids were collected by centrifugation and washed with cold ether. Following dissolution in distilled water and lyophilization, compounds **6** and **8** were collected as white solids.

LCMS analysis of the crude peptide **6** showed two peaks in a 3:1 ratio. Both peaks exhibit the same *m*/*z* value (805), which corresponds to the mass of the protonated form of the desired peptide. The two components were readily separated by semipreparative HPLC and the analytical trace of the major product is shown in Figure 1a.

HPLC analysis of the crude Re complex **8** similarly showed two peaks possessing the same *m*/*z* value in the electrospray mass spectrum. Semipreparative HPLC again enabled isolation of the major product (Figure 1b), which was a colorless solid. IR analysis of **8** exhibited two distinct metal−CO stretches (1927 and 2032 cm^{-1}) which is consistent with the proposed geometry of the metal complex and similar to the values reported for the Re complex **3**.

NMR Characterization of fMLF(SAAC)G and fMLF[(SAAC−Re(CO)$_3$)$^+$]G. The ^{1}H NMR of HPLC purified **6** was run in 50/50 CF_3CO_2D−CD_3CN at 500 MHz. The spectrum (Figure 2a) shows a downfield singlet at 8.22 pm which is consistent with the presence of the formamide proton. A series of multiplets in the aromatic region were apparent, arising from the protons on the pyridine rings and the phenylalanine aryl group. The α protons of the amino acids, which appear between 4 and 5 ppm, and the side chain residues were readily assigned through the use of COSY and selective TOCSY experi-

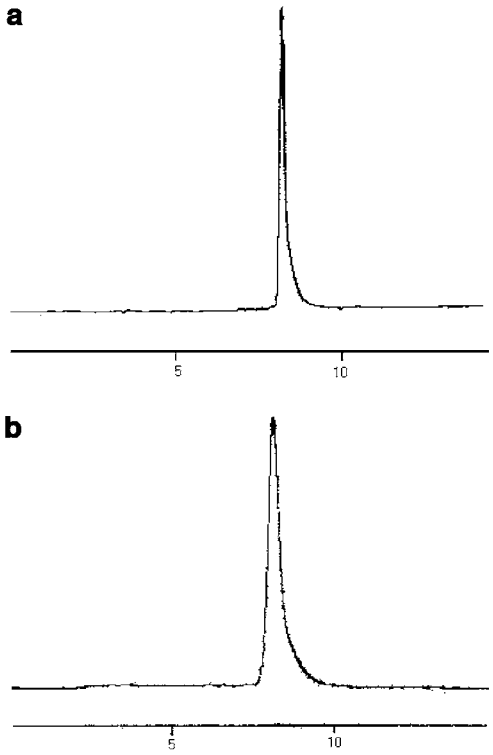


Figure 1. (a) Analytical HPLC of fMLF(SAAC)G, **6**. (b) Analytical HPLC of fMLF[(SAAC−$Re(CO)_3)^+$]G, **8**.

ments (Table 1). The α proton of the dipyridyl chelate appears at 4.37 ppm.

A comparison of the ^{1}H NMR of the Re complex (Figure 2b) with that for compound **6** shows that only the protons associated with the SAAC chelate are influenced by the presence of the Re(I) core. H-23, H-24, H-25, and H-26 shifted downfield with the latter proton moving more than one ppm (Table 1). The protons on the pyridine rings were readily assignable and shifted on average by 0.6 ppm compared to **6** with the exception of H-32 whose chemical shift, somewhat surprisingly, remained unchanged.

The ^{13}C NMR of **6** exhibited the expected number of carbonyl peaks (six) with the formamide carbon appearing at 166.1 ppm. There were numerous signals in the aromatic region corresponding to the pyridine groups and the aryl group of phenylalanine. The remainder of the peptide backbone was assigned using HSQC and HMBC spectra (Table 2).

The ^{13}C NMR of **8** showed two additional peaks downfield at 196.2 and 196.9 ppm arising from the metal−CO ligands. Two peaks are expected given the local symmetry of the complex. The remaining carbonyl groups, which are associated with the amide and acid groups of the peptide backbone, showed no major changes from that for compound **6**. Only the carbon atoms in close proximity to the Re center exhibited significant shifts. C-26 and C-27, for example, were shifted downfield to a similar degree. The carbon atoms on the pyridine groups, not surprisingly, also exhibited significant changes in chemical shift. C-30/36 shifted upfield as did C-29/35 while C-28/34 moved downfield from 154.1 to 161.3 ppm.

In Vitro Screening Studies Using Flow Cytometry. Peptides **6** and **8** were screened on a flow cytometer using a competitive binding assay (*14*−*16*) where the concentration of the competitor was allowed to vary while maintaining the concentration of the fluorescent peptide. Competitive binding data was obtained on the same day using the same blood donor as for the equilibrium binding data, to minimize variability in the number of receptors. Cells at 10^6 mL^{-1} were incubated with 1.0 nM fluorescent peptide (L) and 0.25, 0.5, 1.0, 3.0, 5.0, 10.0, and 15.0 nM competitor (U) in duplicate for 2 h at 0 °C in the dark. Flow cytometry was used to quantify the fluorescence per cell after the incubation. Neutrophils were gated on the basis of forward and side scatter parameters using Expo 32 ADC software (Beckman Coulter). The average value for nonspecific binding, obtained from the equilibrium-

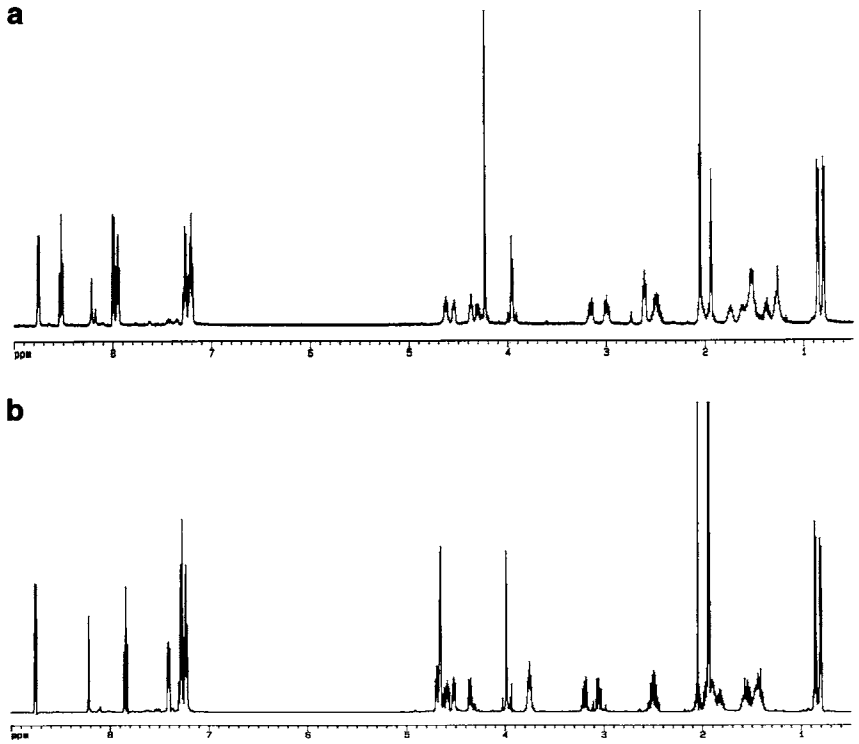
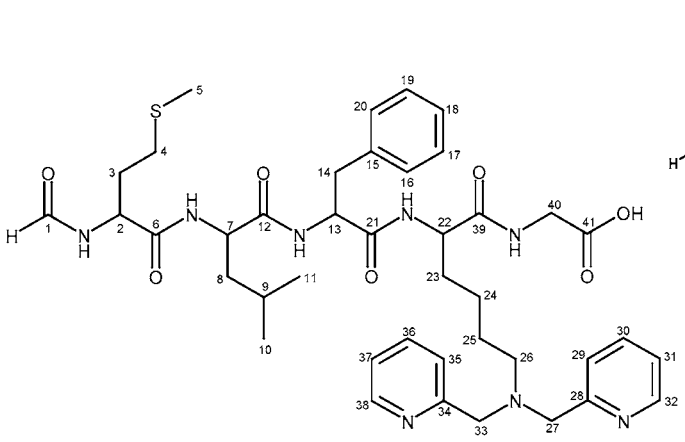
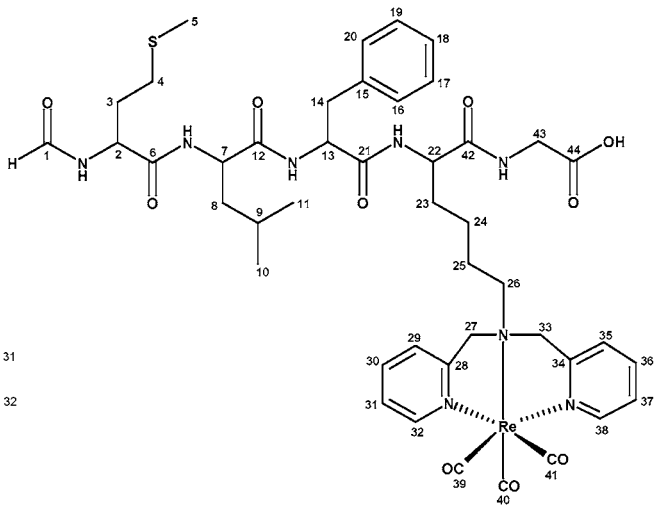


Figure 2. (a) ^{1}H NMR (500 MHz) of fMLF(SAAC)G, **6**. (b) ^{1}H NMR (500 MHz) of fMLF[(SAAC−$Re(CO)_3)^+$]G, **8**.

Table 1. ^{1}H NMR Assignments and Coupling Constants for fMLF(SAAC)G and fMLF[(SAAC−Re(CO)$_3$)$^+$]G





compound **6**			compound **8**		
atom label	^{1}H chemical shift (ppm)	coupling constant (Hz)	atom label	^{1}H chemical shift (ppm)	coupling constant (Hz)
1	8.220		1	8.219	
2	4.544	$^3J_{(2,3')} = 8.3$ $^3J_{(2,3'')} = 8.6$	2	4.585	$^3J_{(2,3')} = 8.6$ $^3J_{(2,3'')} = 8.7$
3′	1.951	$^2J_{(3',3'')} = -14.6$	3′	2.006	$^2J_{(3',3'')} = -11.8$
3″	2.030		3″	2.056	
4	2.484		4	2.498	
5	2.043		5	2.047	
7	4.302	$^3J_{(7,8')} = 10.4$ $^3J_{(7,8'')} = 10.2$	7	4.355	$^3J_{(7,8')} = 10.4$ $^3J_{(7,8'')} = 10.1$
8′	1.363	$^2J_{(8',8'')} = -9.2$	8′	1.424	$^2J_{(8',8'')} = -9.4$
8″	1.384		8″	1.562	
9	1.533	$^3J_{(9,10)} = 6.4$ $^3J_{(9,11)} = 6.4$	9	1.562	$^3J_{(9,10)} = 6.0$ $^3J_{(9,11)} = 6.4$
10	0.795		10	0.811	
11	0.861		11	0.904	
13	4.628	$^3J_{(13,14')} = 8.6$ $^3J_{(13,14'')} = 8.6$	13	4.697	$^3J_{(13,14')} = 5.9$ $^3J_{(13,14'')} = 5.7$
14′	2.986	$^2J_{(14',14'')} = -16.2$	14′	3.098	$^2J_{(14',14'')} = -14.0$
14″	3.155		14″	3.240	
16, 20	7.237		16−20	7.263	
17−19	7.212				
22	4.372	$^3J_{(22,23')} = 6.5$ $^3J_{(22,23'')} = 7.4$	22	4.521	$^3J_{(22,23')} = 8.6$ $^3J_{(22,23'')} = 8.4$
23′	1.528	$^2J_{(23',23'')} = -14.0$	23′	1.888	$^2J_{(23',23'')} = -9.3$
23″	1.734		23″	1.869	
24	1.271		24	1.443	
25	1.637		25	1.914	
26	2.629		26	3.753	
27/33	4.231		27/33	4.661	
29/35	7.995	$^3J_{(29,30)} = 8.0$	29/35	7.407	$^3J_{(29,30)} = 7.9$ $^3J_{(29,31)} = 3.1$
30/36	8.522	$^3J_{(30,31)} = 7.3$	30/36	7.844	$^3J_{(30,31)} = 7.9$
31/37	7.950	$^3J_{(31,32)} = 6.3$	31/37	7.263	$^3J_{(31,32)} = 5.5$
32/38	8.753		32/38 (2H)	8.759	
40	3.956	$^3J_{(40',40'')} = -5.5$	43	3.987	$^3J_{(43',43'')} = -3.0$

binding assay, was subtracted from the total fluorescence per cell when determining the ligand bound per cell. The equilibrium dissociation constant for the competing unlabeled ligand, K_d, was determined following literature procedures by fitting the specific ligand bound data to the same one-site binding model. The peptide, fMLF was used as a reference standard. Its K_d value was in good agreement with the value reported in the literature (*15*). The K_d values for fMLF and compounds **6** and **8** are given in Table 3.

DISCUSSION

To probe the utility of the single amino acid chelate (SAAC) system, derivatives of the well-studied fMLF peptide were prepared on a commercial automated peptide synthesizer. The fMLF sequence has been used to target a range of different radionuclides, including ^{99m}Tc and ^{111}In, to formyl peptide receptors (FPR) found on the surface of neutrophils as a means of imaging sites of infection and inflammation (*17*−*26*). The traditional approach to preparing these compounds has been to prepare fMLF or fMLFK sequences and to then append, in solution, a Tc ligand to the C-terminus or lysine ϵ-amine groups, respectively. In this study, the SAAC was specifically placed between a terminal glycine amino acid and the fMLF targeting sequence.

The Fmoc-dipyridyl chelate **2** and the Re complex **3** were readily incorporated into the growing peptide linked

Table 2. ^{13}C NMR Assignments for fMLF(SAAC)G and fMLF[(SAAC−Re(CO)$_3$)$^+$]G

compound 6		compound 8	
atom label	^{13}C chemical shift (ppm)	atom label	^{13}C chemical shift (ppm)
1	166.1	1	165.9
2	53.4	2	53.0
3	31.9	3	31.6
4	30.8	4	30.4
5	15.5	5	15.1
6	173.9	6	173.5
7	54.1	7	53.7
8	40.8	8	40.5
9	25.7	9	25.3
10	21.7	10	21.1
11	23.3	11	22.9
12	175.5	12	175.2
13	56.4	13	56.2
14	38.1	14	37.7
15	137.5	15	137.0
16, 20	129.9	16/17, 19/20	130.2, 129.6
17−19	130.5, 128.4	18	128.0
21	173.9	21	173.7
22	54.8	22	54.3
23	32.1	23	31.9
24	23.8	24	25.4
25	32.1	25	25.1
26	55.8	26	71.1
27/33	56.6	27/33	68.5
28/34	154.1	28/34	161.3
29/35	128.8	29/35	124.3
30/36	148.8	30/36	141.3
31/37	127.9	31/37	126.6
32/38	143.1	32/38	153.0
39	174.8	39/40/41	196.9, 196.2
40	42.2	42	174.4
41	171.8	43	41.8
		44	171.3

Table 3. Dissociation Constants

peptide	K_d (nM)
fMLF	32 ± 2.8
fMLF(SAAC)	19 ± 3.4
fMLF[(SAAC−Re(CO)$_3$)$^+$]G	9 ± 0.8

to a SASRIN resin, using standard peptide synthesis protocols. Two products were produced in each synthesis. ^{1}H NMR showed that the minor byproducts were the result of epimeriation of the methionine α protons. To determine if the epimerization was caused by the dipyridyl ligand, the peptide was prepared using N-α-Fmoc-N-ϵ-Boc-lysine in place of compounds **2** and **3**. ^{1}H NMR again showed two sets of signals associated with the protons in the methionine backbone. Formation of the second isomer is therefore not related to the incorporation of the ligand or its Re complex but due to the ease with which *N*-formyl amino acid derivatives epimerize (*27*). When the synthesis was repeated using Fmoc-methionine in place of the *N*-formyl derivative, only one product, MLF(SAAC)G, was produced.

As the epimerization issue described previously clearly demonstrates, LCMS studies alone are not always sufficient for characterizing peptide-targeted radiopharmaceuticals. Consequently multi-NMR spectroscopy was used to fully characterize compounds **6** and **8** and to investigate the impact of Re coordination on the structure of the peptide. The ^{1}H and ^{13}C spectra of the peptide−ligand and corresponding Re complex were readily assigned using standard 2-D and selective TOCSY NMR experiments. A comparison of the ^{1}H and ^{13}C spectra for compounds **6** and **8** revealed that metal coordination does not alter the structure of the peptide backbone. The only resonances to undergo significant changes are directly associated with the SAAC. These observations suggest that radiolabeling of **6** will not cause significant structural changes. This hypothesis is supported by the in vitro studies, which showed that compound **6** and **8** have similar affinities for the FPR receptor.

Traditional radioligand displacement methods, which are not particularly suited for evaluating libraries of compounds, are typically used to screen fMLF conjugates. In this study, flow cytometric studies were undertaken as a means of evaluating ligand−receptor interactions. The advantages of using flow cytometry over traditional screening methods are that studies can be performed in real time on single cells (*14*). Flow cytometry also affords the opportunity to look at the binding of ligands to specific subpopulations. The screening studies reported here show that compounds **6** and **8** bind to granulocytes with affinities that are greater than the parent fMLF peptide, which was used as a reference standard. In light of the K_d values, compound **6** is a promising agent for targeting ^{99m}Tc to FPR receptors. Biodistribution studies in animal models of infection are currently underway.

Despite the unavoidable epimerization issue, in a single synthesis run, sufficient quantities of compounds **6** and **8** were produced to carryout characterization studies, including detailed NMR experiments, and in vitro screening studies in parallel. The chelate **2** and its Re complex behaved as typical Fmoc-amino acids and can therefore be incorporated regioselectively into any peptide using commercial peptide synthesizers. The SAAC chelate did not require any additional protecting groups beyond the N-α-Fmoc group, and its metal complex was stable to the conditions used to prepare the peptide and cleave it from the support. The ability to prepare macroscopic quantities of the metal complex, which exists as a single isomer, offers a tremendous advantage over other more commonly employed Tc ligand systems such as HYNIC where purification and detailed characterization of the ^{99}Tc and Re complexes are habitually problematic.

The commercial viability of the [Tc(CO)$_3$]$^+$ core as a synthon for the preparation of radiopharmaceuticals has been queried recently (*28*). Despite the numerous benefits of working with Tc(I), which have been elegantly summarized by Alberto (*29*) and highlighted throughout this paper, intellectual property issues and the increasing clinical use of PET in the United States have brought into question as to whether a clinically useful agent based on the Tc-carbonyl motif will ever be realized.

The current widespread use of technetium in nuclear medicine is not driven solely by the advantages of working with ^{99m}Tc, but by the clinical usefulness of ^{99m}Tc radiopharmaceuticals. The discovery of new imaging agents will determine the future role of ^{99m}Tc in diagnostic nuclear medicine, as is the case for all radionuclides, which places considerable importance on developing new methods that can improve the efficiency of the radiopharmaceutical discovery process. It should also be noted that the opportunity to prepare complementary (i.e. isostructural) Re radiotherapy agents based on ^{186}Re and ^{188}Re will further enhance the future demand for new Tc radiopharmaceuticals.

To develop new Tc and Re radiopharmaceuticals in a reasonable time frame and in a cost-effective manner, researchers must shift to more contemporary drug discovery techniques, like the strategy reported here. Because the Tc(I) and Re(I) core is highly versatile and much more amenable to modern drug discovery techniques than existing Tc/Re (or other radiometal) synthons, commercial matters aside, there is a high prob-

ability that clinically viable diagnostic and/or therapeutic agent based on the Tc(I) or Re(I) carbonyl cores will be discovered.

CONCLUSIONS

The single amino acid chelate used in this study affords the opportunity to incorporate a Tc(I)/Re(I) binding ligand into peptides using standard solid-phase synthesis methods. The derivatization strategy is flexible in that it allows for the chelate to be incorporated at any position in the peptide as an additional amino acid or in place of an existing amino acid that is not involved in receptor binding. In the present study, novel derivatives of a simple chemotactic peptide were prepared and screened using flow cytometry. The use of flow cytometry as a screening strategy creates the opportunity to rapidly identify compounds that are capable of selectively targeting specific types of granulocytes. The focus of our current efforts is to build upon the reported synthesis and screening methods to develop and screen combinatorial libraries of compounds that are capable of targeting specific cell populations that accumulate at sites of infection and inflammation.

ACKNOWLEDGMENT

We thank The Canadian Foundation for Innovation (CFI) and The Ontario Innovation Trust (OIT) and McMaster University for providing the infrastructure used in this project and NSERC of Canada for a scholarship for K.A.S..

Supporting Information Available: HPLC, ESMS, ^{1}H and ^{13}C NMR, FT-IR data, and competetive binding data. This material is available free of charge via the Internet at http://pubs.acs.org.

LITERATURE CITED

(1) Liu, S., and Edwards, D. S. (1999) ^{99m}Tc-Labeled small peptides as diagnostic radiopharmaceuticals. *Chem. Rev. 99*, 2235−2268.

(2) Fischman, A. J., Babich, J. W., and Strauss, H. W. (1993) A ticket to ride: peptide radiopharmaceuticals. *J. Nucl. Med. 34*, 2253−2263.

(3) Valliant, J. F., Riddoch, R. W., Hughes, D. W., Roe, D. G., Fauconnier, T. K., and Thornback, J. R. (2001) The solid-phase synthesis and NMR spectroscopy of a ^{99}Tc chelate-bombesin derived peptide conjugate. *Inorg. Chim. Acta 325*, *155*-163.

(4) Smith, C. J., Gali, H., Sieckman, G. L., Higginbotham, C., Volkert, W. A., and Hoffman, T. J. (2003) Radiochemical investigations of ^{99m}Tc−N_3S−X-BBN[7−14]NH_2. An in vitro/in vivo structure−activity relationship study where $X = 0$, 3, 5, 8, and 11-carbon tethering moieties. *Bioconjugate Chem. 14*, 93−102.

(5) Gariépy, J., Rémy, S., Zhang, X., Ballinger, J. R., Bolewska,-Pedyczak, E., Rauth, M., and Bisland, S. K. (2002) A simple two-step approach for introducing a protected diaminedithiol chelator during solid-phase assembly of peptides. *Bioconjugate Chem. 13*, 679−684.

(6) Greenland, W. E. P., Howland, K., Hardy, J., Fogelman, I., and Blower, P. J. (2003) Solid-phase synthesis of peptide radiopharmaceuticals using Fmoc-N-ϵ-(HYNIC−Boc)-lysine, a technetium-binding amino acid: application to Tc-99m-labeled salmon calcitonin. *J. Med. Chem. 46*, 1751−1757.

(7) Hunter, D. H., and Luyt, L. G. (2000) Lysine conjugates for the labeling of peptides with technetium-99m and rhenium. *J. Labelled Compd. Radiopharm. 43*, 403−412.

(8) Banerjee, S. R., Levadala, M. K., Lazarova, N., Wei, L., Valliant, J. F., Stephenson, K. A., Babich, J. W., Maresca, K. P., and Zubieta, J. (2002) Bifunctional single amino acid chelates (SAAC) for labeling of biomolecules with $\{Tc(CO)_3\}^{+1}$ and $\{Re(CO)_3\}^{+1}$ cores. The crystal and molecular structures of $[ReBr(CO)_3(H_2NCH_2C_5H_4N)]$, $[Re(CO)_3\{X(Y)NCH_2CO_2-CH_2CH_3\}]Br$, (X ═Y= 2-pyridylmethyl; X = 2-pyridylmethyl, Y = 2-(1-methylimidazolyl)methyl; X ═Y= 2-(1-methylimidazolyl)methyl, $[ReBr(CO)_3\{(C_5H_4NCH_2)NH(CH_2C_4H_3S)]$ and $[Re(CO)_3\{(C_5H_4NCH_2)N(CH_2C_4H_3S)CH_2CO_2)]$. *Inorg. Chem. 41*, 6417−6425.

(9) Levadala, M. K, Banerjee, S. R., Babich, J. W., and Zubieta, J. Sodium triacetoxyborohydride: A robust reagent for direct reductive alkylation of amino acids. Applications for the synthesis of bifunctional chelates for nuclear imaging. Unpublished results.

(10) Chan, W. C., and White, P. D. *FMOC Solid-Phase Peptide Synthesis, A Practical Approach*; Oxford University Press: New York, 2000.

(11) Fields, G. B., and Noble, R. L. (1990) Solid-phase peptide synthesis utilizing 9-fluorenylmethoxycarbonyl amino acids. *Int. J. Pept. Protein. Res. 35*, 161−214.

(12) Fields, C. G., Lloyd, D. H., Macdonald, R. L., Otteson, K. M., and Noble, R. L. (1991) HBTU Activation for automated Fmoc solid-phase peptide synthesis. *Pept. Res. 4*, 95−101.

(13) Sarin, V. K., Kent, S. B., Tam, J. P., and Merrifield, R. B. (1981) Quantitative monitoring of solid-phase peptide synthesis by the ninhydrin reaction. *Anal. Biochem. 117*, 147−157.

(14) Waller, A., Pipkorn, D., Sutton, J. L., Linderman, J. L., and Omann, G. M. (2001) Validation of flow cytometric competitive binding protocols and characterization of fluorescently labeled ligands. *Cytometry 45*, 102−114.

(15) Fay, S. P., Posner, R. G., Swann, W. N., and Sklar, L. A. (1991) Real-Time analysis of the assembly of ligand, receptor, and G protein by quantitative fluorescence flow cytometry. *Biochemistry 30*, 5066−5075.

(16) Hoffman, J. F., Keil, M. L., Riccobene, T. A., Omann, G. M., and Linderman, J. L. (1996) Interconverting receptor states at 4 °C for the neutrophil N-formyl peptide receptor. *Biochemistry 35*, 13047−13055.

(17) Babich, J. W., Graham, W., Barrow, S. A., Dragotakes, S. C., Tompkins, R. G., Rubin, R. H., and Fischman, A. J. (1993) Technetium-99m-labeled Chemotactic Peptides: Comparison with indium-111-labeled white blood cells for localizing acute bacterial infection in the rabbit. *J. Nucl. Med. 34*, 2176−2181.

(18) Van Der Laken, C. J., Boerman, O. C., Oyen, W. J. G., Van Der Ven, M. T. P., Edwards, D. S., Barrett, J. A., Van Der Meer, J. W. M., and Corstens, F. H. M. (1997) Technetium-99m-labeled chemotactic peptides in acute infection and sterile inflammation. *J. Nucl. Med. 38*, 1310−1315.

(19) Edwards, D. S., Liu, S., Ziegler, M. C., Harris, A. R., Crocker, A. C., Heminway, S. J., Barrett, J. A., Bridger, G. J., Abrams, M. J., and Higgins, J. D., III. (1999) RP463: A stabilized technetium-99m complex of a hydrazino nicotinamide derivatized chemotactic peptide for infection imaging. *Bioconjugate. Chem. 10*, 884−891.

(20) Babich, J. W., Coco, W. G., Barrow, S., Fischman, A. J., Femia, F. J., and Zubieta, J. (2000) 99mTc-labeled chemotactic peptides: influence of coligand on distribution of molecular species and infection imaging properties. Synthesis and structural characterization of model complexes with the $\{Re(^2\text{-}HNNC_5H_4N)(^1\text{-}NNC_5H_4N)\}$ core. *Inorg. Chim. Acta 309*, 123−136.

(21) Babich, J. W., Graham, W., Barrow, S. A., and Fischman, A. J. (1995) Comparison of the infection imaging properties of a ^{99m}Tc labeled chemotactic peptide with ^{111}In IgG. *Nucl. Med. Biol. 22*, 643−648.

(22) Fischman, A. J., Pike, M. C., Kroon, D., Fucello, A. J., Rexinger, D., TenKate, C., Wilkinson, R., Rubin, R. H., and Strauss, H. W. (1991) Imaging focal sites of bacterial infection in rats with indium-111-labeled chemotactic peptide analogs. *J. Nucl. Med. 32*, 483−491.

(23) Rennen, H. J., Corstens, F. H., Oyen, W. J., and Boerman, O. C. (2001) New concepts in infection/inflammation imaging. *Quart. J. Nuc. Med. 45*, 167−173.
(24) Verbeke, K., Verbeke, A., Vanbilloen, H., and Verbruggen, A. (2002) Preparation and preliminary evaluation of ^{99m}Tc-EC−For-MLFK. *Nucl. Med. Biol. 29*, 585−592.
(25) Baidoo, K. E., Scheffel, U., Stathis, M., Finley, P., Lever, S. Z., Zhan, Y., and Wagner, H. N., Jr. (1998) High-affinity no-carrier-added ^{99m}Tc-labeled chemotactic peptides for studies of inflammation in vivo. *Bioconjugate Chem. 9*, 208−217.
(26) Babich, J. W., Solomon, H., Pike, M. C., Kroon, D., Graham, W., Abrams, M. J., Tompkins, R. G., Rubin, R. H., and Fischman, A. J. (1993) Technetium-99m-labeled hydrazino nicotinamide derivatized chemotactic peptide analogues for imaging focal sites of bacterial infection. *J. Nucl. Med. 34*, 1964−1974.
(27) Greathouse, D. V., Goforth, R. L., Crawford, T., Van der Wel, P. C., and Killian, J. A. (2001) Optimized aminolysis conditions for cleavage of N-protected hydrophobic peptides from solid-phase resins. *J. Pept. Res. 57*, 519−527.
(28) Welch, M. J., and Lewis, J. S. (2003) $[Tc(CO)_3]^+$ chemistry: a promising new concept for SPECT? *Eur. J. Nucl. Med. 30*, 1302−1304.
(29) Alberto, R. (2003) $[Tc(CO)_3]^+$ chemistry: a promising new concept for SPET? *Eur. J. Nucl. Med. 30*, 1299−1302.

BC034128S

Synthesis, Characterization, and Evaluation of Ferrocene−Theophylline Conjugates for Use in Electrochemical Enzyme Immunoassay

Nigel J. Forrow,* Nicola C. Foulds, Jane E. Frew, and John T. Law

MediSense (UK) Ltd., Abbott Laboratories, 14/15 Eyston Way, Abingdon, Oxon OX14 1TR, UK. Received July 22, 2003; Revised Manuscript Received October 20, 2003

A series of 8-(ferrocenylalkyl)theophylline conjugates were synthesized for evaluation in a homogeneous, competitive electrochemical immunoassay for theophylline with amperometric detection of the ferrocene label at +320 mV. The electrical signal was amplified via redox cycling with the glucose oxidase/glucose system. The resulting catalytic current was strongly inhibited upon binding of the conjugates to anti-theophylline antibodies such that a large excess of theophylline was required to achieve complete reversal leading to an assay with poor sensitivity in the clinical range. A study of the nonspecific interaction of the antibodies with various ferrocene derivatives indicated that this was reduced when a charged functional group was present on the metallocene ring. Consequently, a conjugate was synthesized with a quaternary ammonium group which when incorporated into the assay resulted in improved sensitivity.

INTRODUCTION

Many different types of immunoassays have been developed that avoid the use of radioisotopic labels with their associated problems of short shelf life, disposal, and safety. Fluorescent and chemiluminescent markers along with enzymes have received the most attention as alternative labels for nonisotopic assay systems (*1*). The use of metal complexes as probes was first reported by Cais et al. who described the principle of metalloimmunoassay (MIA) in which, for example, steroid antigens were labeled with ferrocene with detection by flameless atomic absorption spectroscopy (*2*). Recently, this type of immunoassay has been expanded to include the use of metal carbonyl labels which can be detected by Fourier transform infrared spectroscopy (FT-IR). The term carbonylmetalloimmunoassay (CMIA) has been suggested for this class of assay (*3, 4*). Metal complexes, in particular ferrocene, are also of interest for use as electrochemical tracers in immunoassays. Here, the wide variety of substituted derivatives of ferrocene makes it an attractive label for conjugation to antigens. The relative ease of synthesis of ferrocene-labeled molecules, coupled with reversible electrochemistry and the ability to alter redox potential if desired, has led to ferrocene being the first choice for use in electrochemical sensing systems. Thus, ferrocene has also found widespread use as an electrochemical label for oligonucleotides (*5*−*9*) in DNA probes and for host molecules (*10*, *11*) in the detection of neutral and charged guest species. Also, ferrocene−peptide conjugates have been suggested to be useful in electrochemical sensors for the detection of proteins (*12*, *13*).

The use of electrochemical detection offers the possibility of cheap, miniature devices capable of performing rapid assays in cloudy test samples. For example, commercial biosensor devices such as the hand-held MediSense Precision QID glucose meter incorporate a ferrocene derivative in a mass-produced enzyme electrode for use by diabetics to determine their sugar levels in whole blood (*14*).

The potential of ferrocene as an electrochemical label in immunoassays was first explored by Weber and Purdy (*15*) who prepared a ferrocene−morphine conjugate and demonstrated that its electrochemistry was perturbed on binding to the antibody so that a homogeneous competitive assay could, in principle, be configured in which separation of free and antibody-bound label was unnecessary. This procedure has been enhanced using enzyme amplification by exploiting the known (*16*, *17*) ability of ferrocene derivatives to act as electron-transfer mediators to glucose oxidase (GOx). An amperometric immunoassay for lidocaine has been configured using this approach (*18*). Also, brief reports have appeared in a patent application (*19*) and a book (*20*) describing its use for an electrochemical theophylline assay. Here, a detailed report of the synthesis and characterization of some ferrocene−theophylline conjugates and the problems associated with configuring an immunoassay based on them are described.

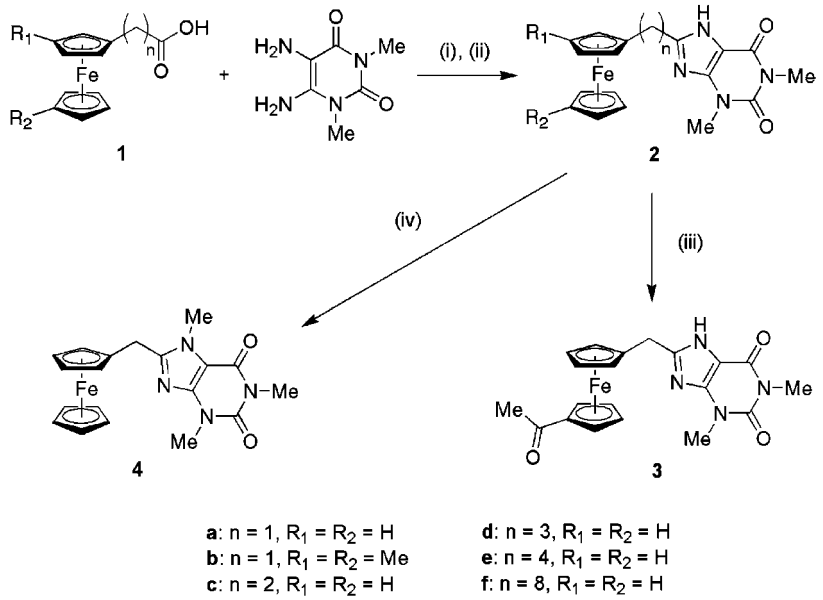
RESULTS AND DISCUSSION

Synthesis of 8-(Ferrocenylalkyl)theophylline Conjugates. 8-Phenyl and 8-benzyl derivatives of theophylline have been previously prepared by condensation of 5,6-diamino-1,3-dimethyluracil with the respective carboxylic acids in refluxing $POCl_3$ followed by cyclization with NaOH (*21*). The preparation of 8-(ferrocenylmethyl)-theophylline **2a** from ferrocenylacetic acid **1a** using an adaptation of this method has been briefly reported (*19*, *20*). A high boiling solvent, *N*,*N*-dimethylaniline (DMA), is used in place of $POCl_3$. The Experimental Procedures section of this article provides a detailed description of the reaction conditions for the synthesis of **2a** and further applies them to the preparation of a series of ferrocene−theophylline conjugates **2b**−**f** from the corresponding

* Corresponding author. Telephone: +44 (0)1235 542122. Fax: +44 (0)1235 467640. E-mail: nigel.forrow@abbott.com.

10.1021/bc034131b CCC: $27.50 © 2004 American Chemical Society
Published on Web 12/11/2003

Scheme 1. Synthesis of Ferrocene−Theophylline Conjugates[a]



[a] (i) Δ, DMA; (ii) NaOH; (iii) **2a**, Ac_2O, $AlCl_3$, CH_2Cl_2; (iv) **2a**, MeI, Na_2CO_3, DMF.

ferrocene carboxylic acids **1b**−**f** (Scheme 1). No identifiable conjugate was produced from the reaction of ferrocene carboxylic acid **1** ($n = 0$, $R_1 = R_2 = H$) or ferrocene dicarboxylic acid with 5,6-diamino-1,3-dimethyluracil.

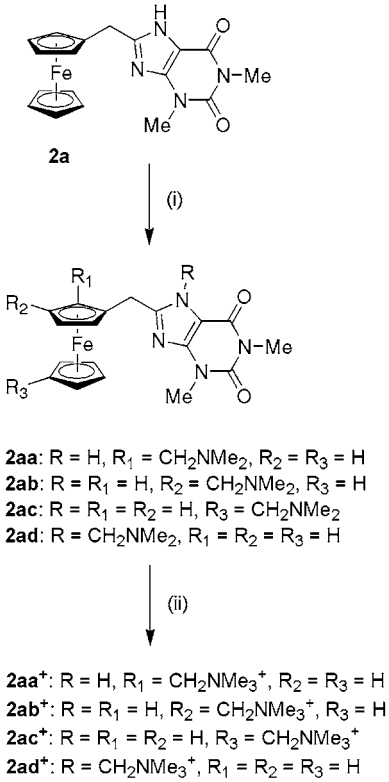
The synthesis of substituted ferrocene−theophylline conjugates was of interest for a number of reasons. In the first instance, the introduction of electron-donating substituents such as methyl groups into the ferrocene cyclopentadienyl rings will alter the redox potential of the conjugate such that a lower operating potential is required in an electrochemical assay. This is advantageous for test media, such as blood or plasma, which may contain oxidizable species. Here, the dimethyl-substituted conjugate **2b** can be synthesized from the readily available (1,1′-dimethylferrocenyl)acetic acid **1b**. However, apart from **1b**, substituted ferrocene carboxylic acids are not easily accessible for use as starting materials in the synthesis of ferrocene−theophylline conjugates.

Direct substitution of a ferrocene ring in a conjugate was explored for the introduction of electron-donating substituents. Here, functional groups of this type were attractive for modifying the hydrophobic nature of the ferrocene−theophylline conjugates. For example, the conjugates **2a**−**f** were almost completely insoluble in aqueous buffer solutions. As such, a carboxylate or amino substituent might be effective in enhancing the aqueous solubility of the conjugates as well as modulating the strength of their binding with anti-theophylline antibodies.

The Friedel−Crafts acetylation of conjugate **2a** proceeded remarkably cleanly to afford the acetyl derivative **3** in moderate yield (Scheme 1). Acetylation was observed to occur only in the unsubstituted ferrocene ring. It was hoped that the acetyl group could be further elaborated into a carboxylate group. However, known procedures for effecting this transformation in acetylated ferrocene derivatives using $NaOH/Br_2$ (*22*) or I_2/pyridine then NaOH (*23*) failed for the conjugate **3**.

The Mannich reaction was considered to be a possible direct route to a tertiary amino derivative of conjugate **2a** which could then be converted simply to a hydrophilic quaternary ammonium compound by alkylation. It appeared feasible that alkylation could be confined to the tertiary amine group since reaction at N-7 of theophylline required the additional use of base to obtain the caffeine conjugate **4** from the corresponding theophylline compound **2a** (Scheme 1). However, we were aware that aminomethylation of **2a** could result in reaction at three different ferrocene ring positions [cf. methylferrocene (*24*)] to yield the isomers **2aa**, **2ab**, **2ac** and also at the N-7 position of theophylline (*25*) to give **2ad** (Scheme 2).

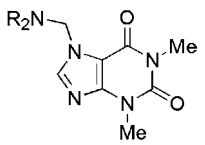
Scheme 2. Aminomethylation of Ferrocene-Labeled Conjugate 2a[a]



[a] (i) Δ, $(Me_2N)_2CH_2$, H_3PO_4, AcOH; (ii) MeI, MeOH.

Initially, we successfully repeated the known (*25*) Mannich reaction of theophylline itself using Et_2NH/HCHO to yield the unstable 7-(diethylaminomethyl)-

theophylline **5** which displayed a signal at δ 5.2 for the N-7 methylene group in the ^{1}H NMR spectrum. No reac-



5: R = Et
6: R = Me

tion was observed when we applied the exact same reaction conditions to the ferrocene–theophylline conjugate **2a**. This result was encouraging in that it seemed that the ferrocenylmethyl substituent in the 8-position of theophylline had the effect of reducing the acidity of the N-7 hydrogen of **2a** such that it might be possible to restrict aminomethylation to the ferrocene rings of the conjugate. Next, we carried out an aminomethylation reaction on **2a** with the reagents used for methylferrocene (*24*) and ferrocene (*26*), i.e., bis(dimethylamino)methane in the presence of phosphoric acid as a catalyst with glacial acetic acid as the solvent. A brown, water-soluble, oily product was obtained in low yield. The ^{1}H NMR spectrum demonstrated that substitution had occurred at ferrocene to yield **2aa**/**2ab**/**2ac** rather than at theophylline since the expected signal at approximately δ 5 for the N-7 aminomethylene group of **2ad** was not observed. Further examination of the spectrum indicated that only two ferrocene ring isomers were present. These are presumed to be **2aa** and **2ab** by analogy with the isomer distribution seen for aminomethylated methylferrocene (*24*). Latterly, we did note that it was also possible to effect N-7 aminomethylation of theophylline using bis(dimethylamino)methane to afford 7-(dimethylaminomethyl)theophylline **6**. Here, compound **6** displayed a methylene signal at δ 5.1 in the ^{1}H NMR spectrum.

Methylation of **2aa**/**2ab** with MeI proceeds readily at NMe_2 to afford the quaternary ammonium salt **2aa**$^+$/**2ab**$^+$ (Scheme 2) as expected from standard ferrocene chemistry (*24*, *26*). Further support for ferrocene ring substitution was indicated by the apparent stability of **2aa**$^+$/**2ab**$^+$. Thus, attempts to form the quaternary ammonium salt of 7-(dimethylaminomethyl)theophylline **6** resulted only in the isolation of theophylline. No such decomposition to the starting conjugate was observed during the quaternization of the aminomethylated products of conjugate **2a**. Also, it was noted earlier in this article that N-7 methylation of the theophylline unit with MeI to produce a caffeine derivative does not occur in the absence of base.

Despite poor yields and limited characterization data, the water soluble salt **2aa**$^+$/**2ab**$^+$ was nonetheless included in further studies as the only example of a hydrophilic ferrocene–theophylline conjugate. The structural assignments for **2aa**$^+$/**2ab**$^+$ and **2aa**/**2ab** were considered to be sound based on a combination of ^{1}H NMR data and comparative reactions carried out on theophylline itself for the purpose of eliminating N-7 in favor of ferrocene ring substitution.

Electrochemistry of Ferrocene–Theophylline Conjugates. The conjugates **2a**–**f** are practically insoluble in aqueous buffer solution. Polyoxyethylene 9-lauryl ether (5%) was therefore employed to enhance the solubility of **2a**–**f** such that their aqueous electrochemistry could be easily studied by cyclic voltammetry. In contrast, the aminomethylated methiodide conjugate

Table 1. Electrochemical Data for Ferrocene–Theophylline Conjugates

conjugate[a]	no.	$E_{1/2}$, mV[b]
Fc-CH_2–Theo	**2a**	+235
		+220[c]
Me_2Fc-CH_2–Theo	**2b**	+135
Fc-$(CH_2)_2$–Theo	**2c**	+225
Fc-$(CH_2)_3$–Theo	**2d**	+205
Fc-$(CH_2)_4$–Theo	**2e**	+220
Fc-$(CH_2)_8$–Theo	**2f**	+235
Fc-CH_2–Caff	**4**	+265
Theo-CH_2–Fc-$CH_2NMe_3^+$	**2aa**$^+$/**2ab**$^+$	+220[d]

[a] Fc = ferrocene, Me_2Fc = 1,1′-dimethylferrocene, Theo = theophylline, Caff = caffeine. [b] Unless otherwise stated, electrochemical data was obtained in 0.15 M phosphate/0.2 M NaCl buffer (pH 7.0), containing 5% polyoxyethylene 9-lauryl ether. [c] 0.1 M BES/0.15 M NaCl (pH 7.0), containing 1% THF. [d] 0.15 M phosphate/0.2 M NaCl buffer (pH 7.0), no polyoxyethylene 9-lauryl ether.

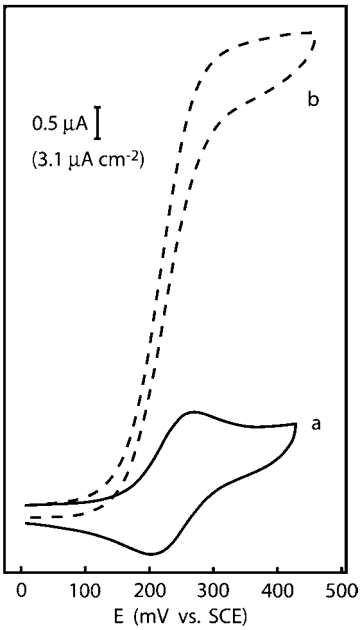


Figure 1. (a) Cyclic voltammogram (at 5 mV s^{-1}) of **2a** (0.25 mM) in a 0.6 mL of 0.15 M phosphate/0.2 M NaCl buffer (pH 7.0), containing 5% polyoxyethylene 9-lauryl ether, at a gold electrode (area 0.16 cm^2); (b) as for a but with the addition of 100 μL of stock glucose oxidase solution at a final concentration of 2.1 μM.

2aa$^+$/**2ab**$^+$ is water soluble. Reversible redox waves due to the ferrocene/ferrocenium couple with midpoint potentials $E_{1/2}$ in the range +135 to +265 mV were recorded for **2a**–**f** and **2aa**$^+$/**2ab**$^+$ (Table 1). In addition, conjugate **2aa**$^+$/**2ab**$^+$ displayed a broad wave in the range +500 to +600 mV due to the oxidation of iodide. This provides further support for the assignment of **2aa**$^+$/**2ab**$^+$ as a methiodide salt. A typical cyclic voltammogram for a ferrocene–theophylline conjugate is displayed in Figure 1a.

As expected from previous work (*17*) on the aqueous electrochemistry of ferrocene derivatives, the dimethyl-substituted conjugate **2b** was observed to have an $E_{1/2}$ value 100 mV lower than the corresponding unsubstituted compound **2a**. There was no clear trend in $E_{1/2}$ value on increasing the number of methylene groups in the ferrocene–theophylline linker from one in **2a** to eight in **2f**. Here, $E_{1/2}$ varied over a narrow range of +205 to +235 mV. The $E_{1/2}$ value for the caffeine conjugate **4** is 30 mV higher than the corresponding to theophylline compound **2a**. The use of 1% THF in place of 5%

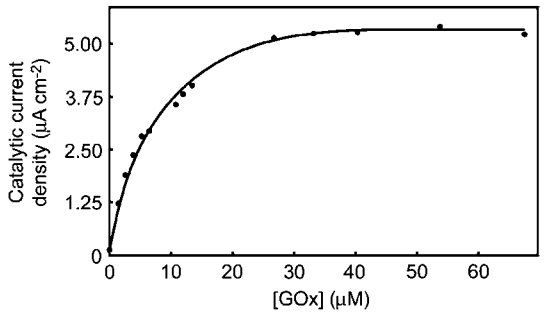


Figure 2. Variation of the catalytic current with glucose oxidase concentration as measured by chronoamperometry. Different amounts of enzyme were added to conjugate **2a** (2 μM) in a cell containing glucose (0.1 M) in BES buffer.

polyoxyethylene 9-lauryl ether did not result in a large shift in the $E_{1/2}$ value for the conjugate **2a**.

Redox mediation of Ferrocene−Theophylline Conjugates with Glucose Oxidase. An enhanced catalytic wave was observed during cyclic voltammetry of the conjugates **2a**−**f** in the presence of glucose oxidase and a nonlimiting excess amount (0.1 M) of glucose substrate. Figure 1b displays a typical voltammogram for **2a** recorded under these conditions. Here, the oxidized ferrocenium form of the conjugate mediated the transfer of electrons from reduced glucose oxidase, produced during oxidation of glucose by the enzyme, to the electrode. This is basis of the signal generation in the proposed immunosensor.

Chronoamperometry is an appropriate electrochemical technique for the exploitation of this signal generation mechanism. A fixed potential ($> E_{1/2}$) was applied to an electrode such that the ferrocenium form of the conjugate was initially generated and then recycled upon reduction by reduced glucose oxidase thereby amplifying the signal. A poise potential of +320 mV was found to be suitable in this respect for the conjugates **2a**−**f**. Each of the compounds **2a**−**f** yielded similar maximum catalytic currents in the region of 0.8 μA (5.0 μA cm^{-2}) for 2 μM solutions in the presence of 0.1 M glucose and a minimum of 35 μM of glucose oxidase (Figure 2).

Inhibition of Conjugate Catalytic Current in the Presence of Antiserum. The redox mediation reaction of conjugates **2a**−**f** with glucose oxidase was inhibited by the anti-theophylline antiserum. For example, this is clearly demonstrated for **2a** in Figure 3a, which was obtained by incubating a fixed amount of conjugate (2 μM) with increasing quantities of undiluted antiserum followed by performing chronoamperometry on the mixture in the presence of glucose oxidase and glucose to determine the catalytic current. Here, it is presumed that the conjugate binds to the antibody and is thereby prevented from interacting with the flavin cofactor inside the active site of glucose oxidase due to the large size of the conjugate−antibody complex. This effect has been reported previously for a ferrocene−lidocaine conjugate in the presence of anti-lidocaine antiserum (*18*). Furthermore, a clear analogy can be drawn with cyclodextrin inclusion complexes of ferrocene derivatives, which are also known not to mediate with glucose oxidase (*27*).

Partial reversal of the inhibition of the catalytic current was achieved upon addition of theophylline to the mixture of conjugate, antiserum, glucose, and glucose oxidase. This is illustrated in Figures 3b and 3c for **2a** for different amounts of theophylline. Here, theophylline competed with the ferrocene−theophylline conjugates

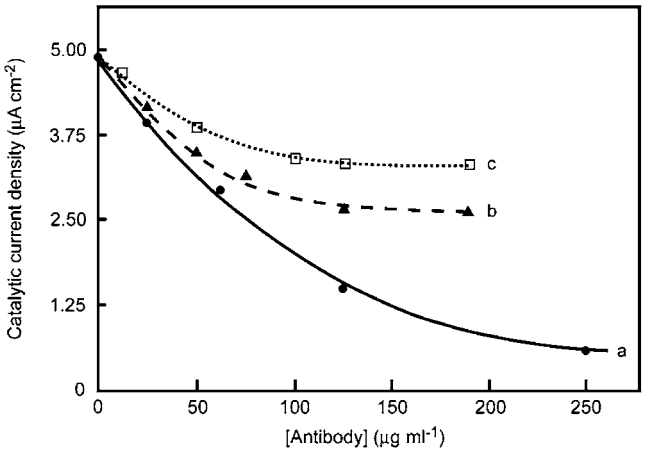


Figure 3. (a) Inhibition of the catalytic current on addition of varying volumes of undiluted anti-theophylline antisera to conjugate **2a** (2 μM) in the presence of glucose (0.1 M) and glucose oxidase (35 μM); (b) as for a but with the addition of theophylline at a final concentration of 25 μM; (c) as for a but with the addition of theophylline at a final concentration of 50 μM.

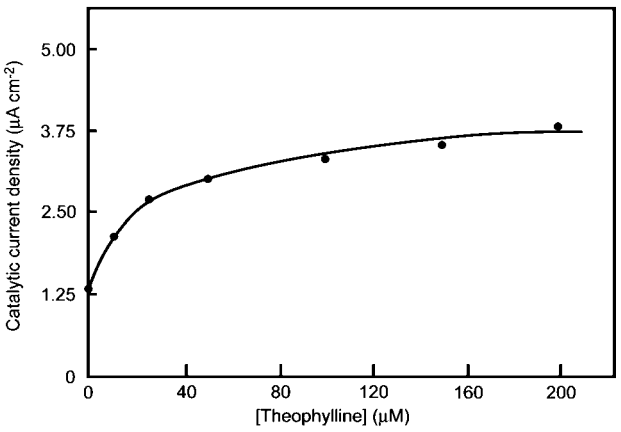


Figure 4. Theophylline calibration curve for electrochemical immunoassay mediated by conjugate **2a** and using an antibody concentration of 125 μg mL^{-1}.

2a−**f** for binding with the antibodies thereby releasing more electroactive label for redox mediation with glucose oxidase. The antibody interaction with the conjugates could not be reversed completely even in the presence of a large excess of theophylline. In this respect, **2a** appeared to be the least antigenic and therefore further work was confined to this particular conjugate. Figure 4 displays a calibration curve for theophylline using **2a**; this spans the therapeutic range for theophylline of 55−100 μM. However, the assay has a low sensitivity in the clinical range due to the poor reversibility of the binding of **2a** with the antibodies.

The Influence of Antiserum on the Redox Mediation of Ferrocene Derivatives with Glucose Oxidase. It appeared unlikely that the ferrocene−theophylline conjugates were more antigenic toward the antiserum than theophylline itself. The nature of the interaction of ferrocene with proteins is unknown but other authors (*13*) have also commented on its strength. In the present system, a possible explanation might be that the hydrophobic nature of the ferrocene group in **2a** leads to nonspecific interactions with the antibody. In this respect, we decided to investigate the influence of anti-theophylline antibodies on the redox mediation of charged

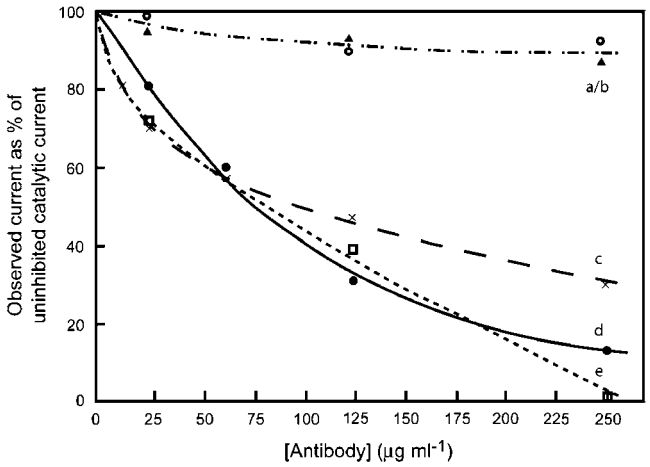
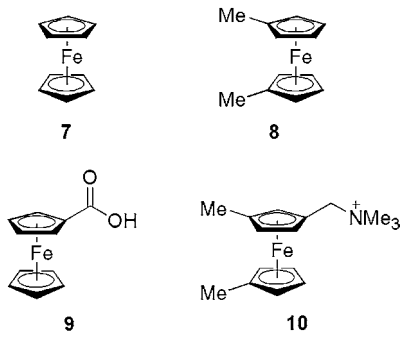


Figure 5. Inhibition of the catalytic current on addition of varying volumes of undiluted anti-theophylline antisera to various ferrocene derivatives (2 μM) in the presence of glucose (0.1 M) and glucose oxidase (35 μM): (a/b) ferrocene carboxylic acid **9** (▲) and dimethylaminomethyl-1,1′-dimethylferrocene methiodide **10** (○); (c) ferrocene **7** (×); (d) conjugate **2a** (●) (for comparison); (e) 1,1′-dimethylferrocene **8** (□).

and uncharged ferrocenes **7**, **8**, **9**, and **10** with glucose oxidase in comparison with the conjugate **2a**.



In a fashion similar to the conjugates **2a**−**f**, the ability of the uncharged ferrocenes **7** and **8** to mediate with glucose oxidase was markedly inhibited in the presence of antiserum (Figures 5c and 5e). Even the addition of an excess (100 μM) of theophylline had no significant effect upon the observed decrease in catalytic current. In contrast, the charged ferrocene derivatives **9** and **10** displayed no such inhibition (Figure 5a/b). These results support the hypothesis that nonspecific hydrophobic interactions between the ferrocene moiety of conjugates **2a**−**f** and the antibody contribute to the observed inhibition.

Attempts to Reduce Nonspecific Interactions in the Assay System. In light of the above results, the charged conjugate **2aa**$^+$/**2ab**$^+$ was synthesized since the ability of the ferrocene quaternary ammonium salt **10** to mediate with glucose oxidase was not inhibited by the presence of antiserum. Nonspecific interactions between the ferrocene unit and anti-theophylline antibodies should then, in theory, be reduced to a minimum. However, as for the uncharged **2a**, the catalytic activity of the charged conjugate **2aa**$^+$/**2ab**$^+$ with glucose oxidase was inhibited by antisera (Figure 6). Complete reversal of this inhibition could only be achieved through the addition of a 50-fold excess of theophylline over **2aa**$^+$/**2ab**$^+$. Therefore, although reducing the hydrophobic nature of the ferrocene moiety of the conjugate improves the reversibility of the inhibition, the sensitivity of the assay over the clinical range remains unsatisfactory (Figure 7).

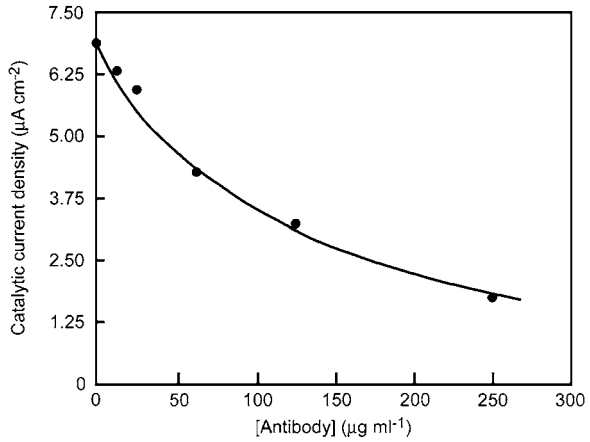


Figure 6. Inhibition of the catalytic current on addition of varying volumes of undiluted anti-theophylline antisera to conjugate **2aa**$^+$/**2ab**$^+$ (2 μM) in the presence of glucose (0.1 M) and glucose oxidase (35 μM).

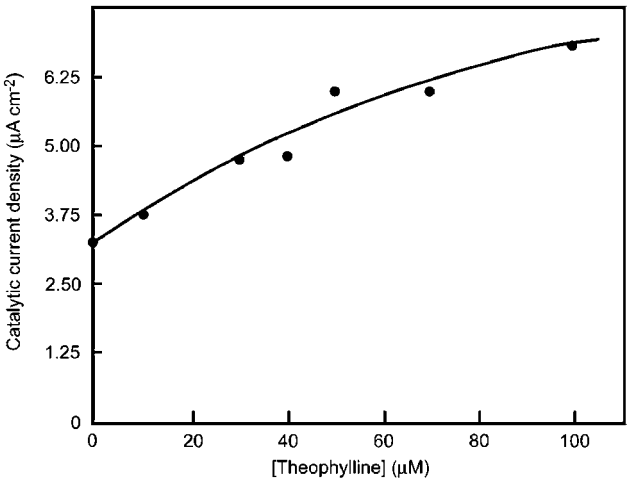


Figure 7. Theophylline calibration curve for electrochemical immunoassay mediated by conjugate **2aa**$^+$/**2ab**$^+$ and using an antibody concentration of 125 μg ml^{-1}.

CONCLUSION

8-(Ferrocenylalkyl)theophylline conjugates, with a range of linker arm chain lengths, were readily synthesized from the corresponding ferrocenylalkanoic acid and 5,6-diamino-1,3-dimethyluracil in moderate yield. However, the conjugates were discovered to bind more strongly to anti-theophylline antibodies than theophylline itself. The resulting competitive, homogeneous immunoassay displayed poor sensitivity in the therapeutic range for theophylline. The nonspecific interaction of the ferrocene moiety with the antibodies was found to be reduced by introducing a charged functional group into the metallocene ring of one conjugate. The assay sensitivity using the modified conjugate was improved but remains unsatisfactory for development into a viable electrochemical immunoassay for theophylline. This work indicates that, unless nonspecific interactions with antibodies can be overcome, ferrocene may be an unsuitable electrochemical label for general use in immunoassays.

EXPERIMENTAL PROCEDURES

Materials. All reactions were carried out under an atmosphere of nitrogen. Anhydrous solvents (Sure Seal grade; Aldrich) were used for reactions when required. All reagents and starting materials for reactions were purchased from Aldrich except for 1,1′-dimethylferrocene

8 (Strem) and were used without further purification. Literature methods were used for the preparation of dimethylaminomethyl-1,1′-dimethylferrocene methiodide **10** (*24*), ferrocenylacetic acid **1a** (*28*), 3-ferrocenylpropanoic acid **1c** (*29*, *30*), 4-ferrocenylbutanoic acid **1d** (*31*), 5-ferrocenylpentanoic acid **1e** (*31*), and 9-ferrocenylnonanoic acid **1f** (*32*, *33*). Dimethylaminomethyl-1,1′-dimethylferrocene methiodide **10** was used as a mixture of the 2- and 3-isomers. Theophylline and polyoxyethylene 9-lauryl ether were obtained from Sigma. Rabbit anti-theophylline antiserum Travenol H113, containing 2.5 mg/mL antibody, was purchased from Clinical Assays.

Glucose oxidase (EC 1.1.3.4 from *Aspergillus niger*) was supplied by Rhodia. The commercial dilute enzyme was concentrated, using tangential flow filtration (30 kDa size exclusion membrane, Millipore), to a protein level of ca. 250 mg/mL (1.5 mM) in 0.2 M BES buffer pH 7.5. The concentration of glucose oxidase was expressed in terms of catalytically active FAD determined spectrophotometrically at 450 nm. A molar extinction coefficient of 1.31×10^4 M^{-1} cm^{-1} was used (*34*). The BES buffer solution of 0.1 M BES (with 0.15 M NaCl as supporting electrolyte), pH 7.0, and containing 0.1 M D-glucose was prepared using AnalaR reagents from VWR in deionized water. The solution was stored overnight at 4 °C prior to use to allow equilibration of the α- and β-anomers. The phosphate buffer (0.15 M, with 0.2 M NaCl), pH 7.0, and containing 0.1 M D-glucose was also prepared employing AnalaR reagents (VWR).

Proton NMR spectra were recorded on Brüker WH 300 (300 MHz) or AM 500 (500 MHz) (external NMR service, University of Oxford) and Hitachi R-24B (60 MHz) instruments. Spectra were referenced internally to either the solvent or $SiMe_4$. Microanalyses were performed by C. H. N. Analysis Ltd., Leicester and Butterworth Laboratories, Teddington. Mass spectra (electron impact) were obtained via the external mass spectrometry service at the University of Oxford.

8-(Ferrocenylmethyl)theophylline (2a). Ferrocenylacetic acid **1a** (20.0 g, 82.3 mmol) and 5,6-diamino-1,3-dimethyluracil hydrate (16.7 g, 88.7 mmol) were dissolved in *N*,*N*-dimethylaniline and refluxed for 5 h using a Dean−Stark water separator. After cooling, NaOH solution (8% w/v, 400 mL) was added and the mixture was stirred for 18 h. The *N*,*N*-dimethylaniline was then removed by steam distillation. A heavy yellow precipitate was observed which partially dissolved upon acidification to pH 3−4 with 6 M HCl. The product was separated from the deep red solution by filtration, and then washed with acetonitrile followed by Et_2O to afford **2a** as an analytically pure yellow powder (11.9 g, 38%). Mp 270−272 °C (dec). Anal. Found: C, 56.93; H, 4.84; N, 14.78%; M^+ 378. $C_{18}H_{18}N_4O_2Fe$ requires C, 57.16; H, 4.80; N, 14.81%; M 378. IR (Nujol, cm^{-1}): 1700, 1650 (υ_{CO}); ^1H NMR (500 MHz; $CDCl_3$): 3.43 (s, 3H, NMe), 3.62 (s, 3H, NMe), 3.94 (s, 2H, CH_2), 4.19 (s, 5H, C_5H_5), 4.21 (m, 2H, C_5H_4), 4.25 (m, 2H, C_5H_4).

8-(Ferrocenylmethyl)caffeine (4). To a mixture of 8-(ferrocenylmethyl)theophylline **2a** (1.25 g, 3.31 mmol) and Na_2CO_3 (0.53 g, 5.0 mmol) in DMF (100 mL) was added iodomethane (0.25 mL). After stirring for 3 d at room temperature, the reaction mixture was filtered and evaporated to dryness. The yellow residue was dissolved in CH_2Cl_2 and then filtered to remove inorganic salts. Removal of the solvent yielded **4** as a yellow solid (1.23 g, 95%). Mp 182−184 °C. ^1H NMR (500 MHz; $CDCl_3$): 3.42 (s, 3H, NMe), 3.62 (s, 3H, NMe), 3.90 (s, 2H, CH_2), 3.92 (s, 3H, NMe), 4.18 (s + m, 9H, C_5H_5 + C_5H_4).

(1,1′-Dimethylferrocenyl)acetonitrile. Dimethylaminomethyl-1,1′-dimethylferrocene methiodide (10.0 g, 24 mmol) was suspended in water (100 mL), and KCN (7.87 g, 121 mmol) was added. The mixture was then refluxed for 2 h. A brown oil separated on cooling. The aqueous layer was decanted from the oil and washed with Et_2O. The oil and the ether extracts were combined and dried ($MgSO_4$). Removal of the solvent in vacuo gave the crude nitrile as an orange oil (6.10 g, 100%). IR (liquid film, cm^{-1}): 2250 (υ_{CN}).

(1,1′-Dimethylferrocenyl)acetic Acid (1b). Unpurified (1,1′-Dimethylferrocenyl)acetonitrile (6.10 g, 24 mmol) was dissolved in EtOH (50 mL), and a solution of KOH (14.0 g, 25 mmol) in water (200 mL) was added. The mixture was refluxed for 7 h. After cooling, the reaction mixture was washed twice with Et_2O before being acidified with 6 M HCl to pH 1. A dark yellow oil was obtained. The oil was dissolved in CH_2Cl_2 (250 mL) and dried ($MgSO_4$). The crude product **1b** was obtained as a brown oil (4.76 g, 73%) after evaporation of the chlorinated solvent. IR (liquid film, cm^{-1}): 1700 (υ_{CO}).

8-[(1,1′-Dimethylferrocenyl)methyl]theophylline (2b). Unpurified (1,1′-Dimethylferrocenyl)acetic acid **1b** (4.76 g, 17.5 mmol) was dissolved in *N*,*N*-dimethylaniline (150 mL), and 1,3-dimethyl-5,6-diamino uracil hydrate (3.57 g, 19 mmol) was added. The reaction mixture was refluxed for 5 h using a Dean−Stark water separator. NaOH solution (8% w/v, 50 mL) was added, and the mixture was stirred for 18 h. *N*,*N*-Dimethylaniline was then removed by steam distillation. Upon cooling, a solid precipitated and this was collected by filtration. The filtrate was acidified with glacial acetic acid to pH 4−5 affording a yellow precipitate. The crude product was dissolved in CH_2Cl_2 and dried ($MgSO_4$). An orange-yellow solid (3.10 g) was thus obtained which was subjected to column chromatography (Florisil). Elution with Et_2O−Me_2CO−MeOH (8:1:1) gave a yellow band from which the product **2b** was obtained as a yellow-green solid (1.46 g, 21%). Mp 220 °C (dec). Anal. Found: C, 59.02; H, 5.44; N, 13.80%; M^+ 378. $C_{20}H_{22}N_4O_2Fe$ requires C, 59.13; H, 5.46; N, 13.79%. ^1H NMR (60 MHz; $CDCl_3$): 1.90 (br m, 6H, C_5H_4*Me* + C_5H_3*Me*), 3.45 (br s, 3H, NMe), 3.55 (br s, 3H, NMe), 3.80 (9H, br m, CH_2 + C_5H_4Me + C_5H_3Me).

Preparation of Ferrocene−Theophylline Conjugates (2c−f). The above procedure for the synthesis of 8-[(1,1′-dimethylferrocenyl)methyl]theophylline **2b** was followed substituting the appropriate ferrocenylalkanoic acid **1c−f** for (1,1′-dimethylferrocenyl)acetic acid **1b**. After column chromatography, the desired ferrocene−theophylline conjugates **2c−f** were isolated as yellow solids in 20−30% yield.

8-(2-Ferrocenylethyl)theophylline (2c). Mp > 200 °C (dec). Anal. Found: C, 58.27; H, 4.55; N, 14.14%. $C_{19}H_{20}N_4O_2Fe$ requires C, 58.18; H, 5.14; N, 14.28%. IR (Nujol, cm^{-1}): 1720, 1630 (υ_{CO}); ^1H NMR (300 MHz; $CDCl_3$): 2.88 (t, J(HH) 6.9 Hz, 2H, CH_2), 3.08 (t, J(HH) 6.9 Hz, 2H, CH_2), 3.48 (s, 3H, NMe), 3.67 (s, 3H, NMe), 4.01 (m, 4H, C_5H_4), 4.11 (s, 5H, C_5H_5), 12.64 (s, 1H, NH).

8-(3-Ferrocenylpropyl)theophylline (2d). Mp 210−212 °C (dec). Anal. Found: C, 58.90; H, 5.50; N, 13.70%. $C_{20}H_{22}N_4O_2Fe$ requires C, 59.13; H, 5.46; N, 13.79%. IR (Nujol, cm^{-1}): 1710, 1640 (υ_{CO}); ^1H NMR (300 MHz; $CDCl_3$): 2.07 (m, J(HH) 7.6 Hz, J(HH) 7.6 Hz, 2H, CH_2), 2.44 (t, J(HH) 7.6 Hz, 2H, CH_2), 2.90 (t, J(HH) 7.6 Hz, 2H, CH_2), 3.44 (s, 3H, NMe), 3.65 (s, 3H, NMe), 4.05 (m, 4H, C_5H_4), 4.09 (s, 5H, C_5H_5), 12.61 (s, 1H, NH).

8-(4-Ferrocenylbutyl)theophylline (2e). Mp 192−194 °C (dec). Anal. Found: C, 59.70; H, 6.22; N, 12.71%.

$C_{21}H_{24}N_4O_2Fe$ requires C, 60.01; H, 5.76; N, 13.33%. IR (Nujol, cm^{-1}): 1710, 1625 (υ_{CO}); ^1H NMR (300 MHz; $CDCl_3$): 1.59 (m, J(HH) 7.6 Hz, J(HH) 7.6 Hz, 2H, CH_2), 1.88 (m, J(HH) 7.6 Hz, J(HH) 7.6 Hz, 2H, CH_2), 2.38 (t, J(HH) 7.6 Hz, 2H, CH_2), 2.90 (t, J(HH) 7.6 Hz, 2H, CH_2), 3.47 (s, 3H, NMe), 3.64 (s, 3H, NMe), 4.02 (m, 4H, C_5H_4), 4.07 (s, 5H, C_5H_5), 12.74 (s, 1H, NH).

8-(8-Ferrocenyloctyl)theophylline (2f). Mp 157−158 °C. Found: C, 63.63; H, 6.82; N, 11.82%. $C_{25}H_{32}N_4O_2Fe$ requires C, 63.03; H, 6.77; N, 11.76%. IR (Nujol, cm^{-1}): 1710, 1625 (υ_{CO}); ^1H NMR (300 MHz; $CDCl_3$): 1.30 (br m, 8H, CH_2), 1.48 (br m, 2H, CH_2), 1.84 (m, J(HH) 7.6 Hz, J(HH) 7.0 Hz, 2H, CH_2), 2.30 (t, J(HH) 7.7 Hz, 2H, CH_2), 2.87 (t, J(HH) 7.7 Hz, 2H, CH_2), 3.48 (s, 3H, NMe), 3.64 (s, 3H, NMe), 4.04 (m, 4H, C_5H_4), 4.09 (s, 5H, C_5H_5), 12.66 (s, 1H, NH).

8-(1′-Acetyl-ferrocenylmethyl)theophylline (3). 8-(Ferrocenylmethyl)theophylline **2a** (3.78 g, 10 mmol) was dissolved in CH_2Cl_2 (600 mL). $AlCl_3$ (6.65 g, 50 mmol) was added followed by the dropwise addition of acetic anhydride (0.94 mL, 1.02 g, 10 mmol). The reaction mixture was stirred for 4 d and then quenched with water. The orange organic layer was separated and dried ($MgSO_4$). Filtration and removal of the solvent afforded an orange solid which was chromatographed (SiO_2). Elution with $Me_2CO-CH_2Cl_2$ (1:4) yielded a small amount of starting material **2a** as a yellow band. The red product band was eluted with $MeOH-CH_2Cl_2$ (1:19) and evaporated to dryness to provide **3** as an orange solid (2.43 g, 58%). Mp 219−220 °C (dec). Anal. Found: C, 57.58; H, 4.88; N, 13.37%. $C_{20}H_{20}N_4O_3Fe$ requires C, 57.16; H, 4.80; N, 13.33%. ^1H NMR (500 MHz; $CDCl_3$): 2.35 (s, 3H, CH_3-CO), 3.46 (s, 3H, NMe), 3.59 (s, 3H, NMe), 3.78 (s, 2H, CH_2), 4.12 (m, 2H, C_5H_4), 4.23 (m, 2H, C_5H_4), 4.41 (t, 2H, C_5H_4), 4.61 (t, 2H, C_5H_4).

8-(2/3-Dimethylaminomethyl-ferrocenylmethyl)-theophylline (2aa/2ab). 8-(Ferrocenylmethyl)theophylline **2a** (1.0 g, 2.65 mmol) was added to a well-stirred solution of bis(dimethylamino)methane (0.51 g, 5 mmol) and H_3PO_4 (10 g) in 100 mL of glacial acetic acid. The resulting mixture was heated for 5 h in an oil bath maintained at 100 °C. A dark amber solution was obtained. This was diluted with water (100 mL) and then extracted with CH_2Cl_2 to remove the starting conjugate **2a**. The aqueous layer was adjusted to pH7 with NaOH pellets and then extracted with CH_2Cl_2. The organic layer was dried (Na_2SO_4), filtered then evaporated to yield a brown oil soluble in $CHCl_3$, CH_2Cl_2, EtOH and water. This oil was passed through a short column of basic Al_2O_3, eluting with $MeOH/CH_2Cl_2$ (1:9), to provide **2aa**/**2ab** as an oil (0.1 g, 9%). ^1H NMR (500 MHz; $CDCl_3$): 2.31 (s, 6H, NMe_2), 3.40 (s, 3H, NMe), 3.58 (s, 3H, NMe), 3.9−4.3 (12H, ferrocene ring protons + 2 × CH_2).

8-(2/3-Dimethylaminomethyl-ferrocenylmethyl)-theophylline Methiodide ($2aa^+/2ab^+$). Crude aminomethylated conjugate **2aa**/**2ab** (0.1 g, 0.23 mmol) from the above reaction was dissolved in MeOH. Iodomethane (0.5 mL) was added and the resulting mixture was stirred for 2 h. After evaporation of the solvent, the residue was redissolved in the minimum volume of MeOH. The methiodide $\mathbf{2aa}^+/\mathbf{2ab}^+$ was precipitated from this solution by the addition of Et_2O. The precipitate was collected, washed with Et_2O and dried to afford 0.11 g (83%) of a beige powder.

Aminomethylation of Theophylline. *(a) Reaction with Diethylamine/Formaldehyde* (*24*). Formaldehyde solution (37%, 0.9 mL, 10 mmol) was added to a well-stirred solution of diethylamine (10 mmol) and theophylline (1.80 g, 10 mmol) in EtOH (30 mL). After 15 min, undissolved starting material was filtered off. The filtrate was evaporated to dryness to yield 7-(diethylaminomethyl)theophylline **5** as a white crystalline solid. The ^1H NMR spectrum of **5** in $CDCl_3$ displayed a singlet at δ 5.2 for the methylene protons.

(b) Reaction with Bis(dimethylamino)methane. Theophylline (1.80 g, 10 mmol) was added to a mixture of bis(dimethylamino)methane (2.04 g, 2.72 mL, 20 mmol), H_3PO_4 (10 g), and glacial acetic acid (150 mL). This mixture was heated at 100 °C on an oil bath for 5 h. Upon cooling, the reaction mixture was diluted with 200 mL of water and then made alkaline with NaOH pellets. Extraction with CH_2Cl_2 followed by separation, drying ($MgSO_4$), and filtration of the organic layer gave a colorless solution. Removal of the solvent provided 7-(dimethylaminomethyl)theophylline **6** as a white solid (0.5 g, 21%). ^1H NMR (500 MHz; $CDCl_3$): 2.45 (s, 6H, NMe_2), 3.37 (s, 3H, NMe), 3.56 (s, 3H, NMe), 5.12 (s, 2H, CH_2).

(c) Attempted Formation of the Methiodide. 7-(Dimethylaminomethyl)theophylline **6** (0.5 g, 1.14 mmol) was dissolved in MeOH and a large excess of iodomethane (1 mL) was added. The resulting solution was stirred for 2 h. Addition of Et_2O produced no precipitate so the solvent was removed under reduced pressure to give a white solid which was washed with CH_2Cl_2. A white solid remained and this was identified as theophylline by ^1H NMR spectroscopy.

Apparatus. Cyclic voltammetry and chronoamperometry experiments were carried out in a two-chamber glass cell of working volume 0.5 cm^3. The cell contained a 1 cm^2 platinum gauze counter electrode and a KCl-saturated calomel electrode as reference. All potentials are referred to SCE. The working electrode was a 4 mm diameter gold disk. An Oxford Electrodes potentiostat was employed.

Solutions of Ferrocene Conjugates. The ferrocene derivatives were only sparingly soluble in the aqueous BES and phosphate buffer solutions. The solubility of the conjugates was enhanced through the use of either 1% tetrahydrofuran (THF) or 5% polyoxyethylene 9-lauryl ether. Generally, THF was employed in chronoamperometry experiments involving anti-theophylline antiserum whereas polyoxyethylene 9-lauryl ether was used during cyclic voltammetry of the conjugates. In the former case, concentrated solutions (0.2 mM) of the ferrocene derivatives were prepared by first dissolving them in THF then mixing with the BES buffer to the desired concentration (2 μM). In the latter case, concentrated solutions (0.25 mM) of the ferrocene derivatives were prepared by first dissolving them in warmed liquid polymer then mixing with the phosphate buffer to the desired percentage (5%). The aminomethylated methiodide conjugate $\mathbf{2aa}^+/\mathbf{2ab}^+$ is water soluble so the use of either THF or polyoxyethylene 9-lauryl ether was unnecessary in the preparation of solutions for electrochemical experiments.

Procedure. Solutions (2 μM) of ferrocene derivatives, including ferrocene−theophylline conjugates, were freshly prepared in the BES buffer solution containing a high level (0.1 M) of D-glucose such that the kinetics of glucose oxidase was saturated. The buffer solution of ferrocene derivative was added to the cell followed by rabbit anti-theophylline antiserum (0−100 μL) and theophylline (0−300 μM). All concentrations are final ones obtained in a total assay volume of 1 mL. The mixture was then stirred for 5 min at room temperature. Finally, glucose oxidase (35 μM) was added then the working electrode was replaced in the cell. A potential of +320 mV was applied and current−time transients were recorded. Catalytic

currents were measured after 3 min and were corrected by subtraction of the background current obtained in the absence of enzyme and antisera.

ACKNOWLEDGMENT

The authors thank MediSense and Abbott Laboratories for permission to publish this article.

LITERATURE CITED

(1) Mayer, A., and Neuenhofer, S. (1994) Luminescence labels − an alternative to radioisotopes? *Angew. Chem., Int. Ed. Engl. 33,* 1044−1072.

(2) Cais, M., Slovin, E., and Snarsky, L. (1978) Metalloimmunoassay II. Iron-metallohaptens from estrogen steroids. *J. Organomet. Chem. 160,* 223−230.

(3) Salmain, M., Vessières, A., Brossier, P., Butler, I. S., and Jaouen, G. (1992) Carbonylmetalloimmunoassay (CMIA), a new type of nonradioisotopic immunoassay. I. Principles and application to phenobarbital assay. *J. Immunol. Methods 148,* 65−75.

(4) Vessières, A., Kowalski, K., Zakrzewski, J., Stepien, A., Grabowski, M., and Jaouen, G. (1999) Synthesis of CpFe(CO)-(L) Complexes of Hydantoin Anions (Cp = η^5-C_5H_5, L = CO, PPh_3), and the Use of the 5,5-Diphenylhydantoin Anion Complexes as Tracers in the Nonisotopic Immunoassay CMIA of this Antiepileptic Drug. *Bioconjugate Chem. 10,* 379−385.

(5) Beilstein, A. E., and Grinstaff, M. W. (2001) Synthesis and characterization of ferrocene-labeled oligodeoxynucleotides. *J. Organomet. Chem. 637−639,* 398−406.

(6) Yu, C. J., Wang, H., Wan, Y., Yowanto, H., Kim, J. C., Donilon, L. H., Tao, C., Strong, M., and Chong, Y. (2001) 2′-Ribose-ferrocene oligonucleotides for electronic detection of nucleic acids. *J. Org. Chem. 66,* 2937−2942.

(7) Yu, C. J., Wang, H., Wan, Y., Yowanto, H., Lie, J., Tao, C., James, M. D., Tan, C. L., Blackburn, G. F., and Meade, T. J. (2001) 2′-Ribose-ferrocene oligonucleotides for electronic detection of nucleic acids. *J. Am. Chem. Soc. 123,* 11155−11161.

(8) Brazill, S. A., Kim, P. H., and Kuhr, W. G. (2001) Capillary gel electrophoresis with sinusoidal voltammetric detection: a strategy to allow four-"color" DNA sequencing. *Anal. Chem. 73,* 4882−4890.

(9) Uto, Y., Kondo, H., Abe, M., Suzuki, T., and Takenaka, S. (1997) Electrochemical analysis of DNA amplified by the polymerase chain reaction with a ferrocenylated oligonucleotide. *Anal. Biochem. 250,* 122−124.

(10) Beer, P. D., Chen, P. A., and Zheng, G. (1999) Mechanisms of electrochemical recognition of cations, anions and neutral guest species by redox-active receptor molecules. *Coord. Chem. Rev. 185−186,* 3−36.

(11) Beer, P. D., and Gale, P. A. (2001) Anion recognition and sensing: The state of the art and future perspectives. *Angew. Chem., Int. Ed. Engl. 40,* 486-516.

(12) Xu, Y., and Kraatz, H.-B. (2001) Efficient synthesis of unsymmetrically disubstituted ferrocenes: towards electrochemical dipeptide-Fc-biosensors. *Tetrahedron Lett. 42,* 2601−2603.

(13) Plumb, K., and Kraatz, H.-B. (2003) Interaction of a ferrocenyl-modified peptide with papain: toward protein-sensitive electrochemical probes. *Bioconjugate Chem. 14,* 601−606.

(14) Lehmann, R., Kayrooz, S., Greuter, H., and Spinas, G. A. (2001) Clinical and technical evaluation of a new self-monitoring blood glucose meter: assessment of analytical and user error. *Diabetes Res. Clin. Pract. 53,* 121−128.

(15) Weber, S. G., and Purdy, W. C. (1979) Homogeneous voltammetric immunoassay: a preliminary study. *Anal. Lett. 12,* 1−9.

(16) Cass, A. E. G., Davis, G., Francis, G. D., Hill, H. A. O., Aston, W. J., Higgins, I. J., Plotkin, E. V., Scott, L. D. L., and Turner, A. P. F. (1984) Ferrocene-mediated enzyme electrode for amperometric determination of glucose. *Anal. Chem. 56,* 667−671.

(17) Forrow, N. J., Sanghera, G. S., and Walters, S. J. (2002) The influence of structure in the reaction of electrochemically generated ferrocenium derivatives with reduced glucose oxidase. *J. Chem. Soc., Dalton Trans.* 3187−3194.

(18) Di Gleria, K., Hill, H. A. O., McNeil, C. J., and Green, M. J. (1988) Homogeneous ferrocene-mediated amperometric immunoassay. *Anal. Chem. 58,* 1203−1205.

(19) Hill, H. A. O. (1984) Assay techniques utilizing specific binding agents. *Eur. Pat. Appl.* 0,125,139.

(20) Foulds, N. C., Frew, J. E., and Green, M. J. (1990) Immunoelectrodes. *Biosensors*: *A Practical Approach* (A. E. G. Cass, Ed.) pp 97−124, IRL Press, Oxford.

(21) Hager, G. P., and Kaiser, C. (1954) Bifunctional theophylline derivatives and corresponding imidazolines. *J. Am. Pharm. Assoc. 43,* 148−155.

(22) Sonoda, A., and Moritani, I. (1971) Reactions of ferrocenylcarbene. IV. Synthesis of [3]-ferrocenophan-2-one tosylhydrazone and the thermal decomposition of its sodium salt. *J. Organomet. Chem. 26,* 133−140.

(23) Rinehart, Jr., K. L., Motz, K. L., and Moon, S. (1957) Organic chemistry of ferrocene. I. The acetylation of dialkylferrocenes. *J. Am. Chem. Soc. 79,* 2749−2754.

(24) Pauson, P. L., Sandhu, M. A., Watts, W. E., Haley, R. C., and Knox, G. R. (1967) Ferrocene derivatives. Part XVIII. The aminomethylation of methyl- and dimethyl-ferrocene. *J. Chem. Soc. (C)* 1851−1853.

(25) Burckhalter, J. H., and Dill, D. R. (1959) Theophylline in the Mannich reaction. *J. Am. Chem. Soc. 24,* 562−564.

(26) Lednicer, D., and Hauser, C. R. (1973) N,N-Dimethylaminomethylferrocene methiodide. *Organic Syntheses,* Collect. Vol. V, pp 434−437, Wiley: New York.

(27) Ryabov, A. D., Tyapochlein, E. M., Varfolomeev, S. D., and Karyakin, A. (1990) Ferrocenes inside cyclodextrin cavities do not mediate electron transport between glucose oxidase and an electrode. *Bioelectrochem. Bioenerg. 24,* 257−262.

(28) Lednicer, D., Lindsay, J. K., and Hauser, C. R. (1958) Reaction of the methiodide of N,N-dimethylaminomethylferrocene with potassium cyanide to form ferrocylacetonitrile. *J. Org. Chem. 23,* 653−655.

(29) Hauser, C. R., and Lindsay, J. K. (1957) Certain alkylations with the methiodide of N,N-dimethylaminomethylferrocene. Synthesis of an α-amino acid having the ferrocene group. *J. Org. Chem. 22,* 1246−1247.

(30) Anne, A., Blanc, B., and Moiroux, J. (2001) Synthesis of the first ferrocene-labeled dideoxynucleotide and its use for 3′-redox end-labeling of 5′-modified single-stranded oligonucleotides. *Bioconjugate Chem. 12,* 396−405.

(31) Rinehart, K. L., Jr., Curby, R. J., Jr., and Sokol, P. E. (1957) Organic chemistry of ferrocene. II. The preparation of ω-ferrocenyl aliphatic acids. *J. Am. Chem. Soc. 79,* 3420−3424.

(32) Salisova, M., Solcaniova, E., and Toma, S. (1980) Attempts on internal Michael addition of the 1-(ω-anisoylalkyl)-1′-cinnamoylferrocenes. *Acta Fac. Rerum Nat. Univ. Comenianae, Chim. 28,* 103−126.

(33) Salisova, M., Toma, S., and Solcaniova, E. (1980) Acylation of anisole with ω-ferrocenylalkanoyl chlorides. *Chem. Zvesti 34,* 497−506.

(34) Duke, F. R., Weibel, M., Page, D. S., Bulgrin, V. G., and Luthy, J. (1969) Glucose oxidase mechanism. Enzyme activation by substrate. *J. Am. Chem. Soc. 91,* 3904−3909.

BC034131B

A Glycopolymer Chaperone for Fibroblast Growth Factor-2

Ran Guan,[†] Xue-Long Sun,[†] Sijian Hou,[†] Peiyi Wu,[†] and Elliot L. Chaikof*[,†,‡]

Departments of Surgery and Biomedical Engineering, Emory University School of Medicine, Atlanta, Georgia 30322, and School of Chemical Engineering, Georgia Institute of Technology, Atlanta, Georgia 30332. Received August 5, 2003; Revised Manuscript Received November 19, 2003

Mono- and disaccharide-containing glycopolymers were synthesized by cyanoxyl-mediated polymerization of acrylamide with acrylate-derivatized mono- and disaccharides. We demonstrate that a glycopolymer bearing pendant, fully sulfated lactose units effectively replaces heparin and heparan sulfate as a molecular chaperone for fibroblast growth factor-2 (FGF-2). Specifically, a compound was identified that protects FGF-2 from proteolytic, acid, and heat-induced degradation, while selectively promoting growth factor and receptor dimerization. Significantly, the capacity of this heparin-mimic to promote an FGF-2 specific proliferative cell response was confirmed and suggests potential applications for this compound and related derivatives in areas related to therapeutic angiogenesis.

INTRODUCTION

Heparan sulfates (HS) influence regenerative responses by acting as cofactors for a variety of cytokines (*1, 2*). For example, heparan sulfates bind fibroblast growth factors (e.g. FGF-1, FGF-2, FGF-7), heparin binding-epidermal growth factor (HB-EGF), platelet-derived growth factor (PDGF), and vascular endothelial growth factor (VEGF), all of which promote endothelial and/or smooth muscle cell motility and proliferation (*3*−*5*). Significantly, the interaction of heparin-binding cytokines and growth factors with heparan sulfates serves to protect these molecules from heat, pH, and protease-related degradation mechanisms, establish high concentration storage sites and may, at times, assist in their appropriate presentation to specific cell-signaling receptors by promoting oligomerization or by altering cytokine or receptor conformation (*6*−*8*). For example, FGF-2 sequestration, dimerization, and stimulation of cell proliferation is dramatically reduced in extracellular matrix produced from chlorate treated cells that are unable to produce fully sulfated glycosaminoglycans (GAG) (*9*).

The diverse biological properties of heparin and heparan sulfate combined with the inherent difficulty associated with the synthesis of these chemically complex natural products have motivated efforts to generate simpler structural mimics as component biomaterials for a variety of applications. In the past five years, significant advances in the synthesis of polymers with pendent saccharides, also known as "glycopolymers", offer one such biomimetic strategy (*10*−*13*). For example, vinyl-, acrylate-, or norbornene-containing saccharide derivatives can be polymerized to yield glycopolymers with biologically active hydrophilic saccharides in the side chains. Moreover, the backbone structure may be altered to modulate both polymer biostability and processability. Significantly, the carbohydrate density of the polymer chain, which appears to affect both ligand binding affinity, as well as polymer physiochemical properties, can be controlled through the choice of polymerizable saccharide, associated comonomers, and dictated chain size. Overall, the potential to stably link bioactive oligosaccharide ligands is an important feature of the glycopolymer approach and presents an opportunity to create GAG mimicking structures that facilitate optimized sequestration and controlled local release of bioactive protein species.

In prior reports, we have examined the applicability of cyanoxyl (•OC≡N)-mediated free-radical polymerization in the synthesis of model glycopolymers from unprotected alkene- and acrylate-derivatized sulfated and unsulfated glycomonomers consisting of a variety of mono- and disaccharide species (*14*−*17*). Significantly, we observed that this polymerization technique can be conducted in aqueous solution, is tolerant of a broad range of functional groups (OH, NH_2, COOH, and OSO_3^-), yields low-polydispersity polymers (PDI < 1.50) with high saccharide content, and can be applied to the synthesis of block and graft copolymers. We have used this approach to generate glycopolymers with pendant monosaccharides, as well as HS- and non-HS-related disaccharides. In this report, we demonstrate that this strategy can yield a novel HS-mimetic that acts as an effective *macromolecular chaperone* for a pro-angiogenic protein growth factor (FGF-2), sequestering and protecting FGF-2 from proteolytic, acid, or heat-induced degradation. In addition, this glycopolymer selectively promotes the interaction of FGF-2 with its receptor, fibroblast growth factor receptor-1 (FGFR-1), as well as the dimerization of both FGF-2 and the FGF-2/FGFR-1 complex. Significantly, all of these features are necessary for receptor activation. The capacity of this glycopolymer to uniquely promote a FGF-2-specific proliferative cell response is confirmed.

MATERIALS AND METHODS

Materials. All solvents and reagents for monomer or polymer synthesis were purchased from commercial sources and were used as received, unless otherwise noted. Deionized water with a resistivity of 18 MΩ·cm was used as a solvent in all polymerization reactions. FGF-2 (human recombinant, 17.2 kDa) was obtained

* Address correspondence to Elliot L. Chaikof, M.D., Ph.D. 1639 Pierce Dr., Rm. 5105, Emory University, Atlanta, GA 30322. Phone (404) 727-8413. Fax: (404) 727-3660. E-mail: echaiko@emory.edu.

[†] Emory University School of Medicine.

[‡] Georgia Institute of Technology.

10.1021/bc034138t CCC: $27.50 © 2004 American Chemical Society
Published on Web 01/03/2004

from Pepro Tech Inc (Rocky Hill, NJ), ^{125}I-FGF-2 was purchased from NEN (Boston, MA). Silver stain reagent was obtained from BioRad (Hercules, MA) and disuccinimidyl suberate (DSS) from Pierce (Rockford, IL). RPMI-1640 media, penicillin−streptomycin, L-glutamine, and G418 were all obtained from Mediatech Inc. (Herndon, VA) and bovine calf serum from Hyclone (Logan, UT). Sodium heparin from porcine intestinal mucosa (MW between 12 000 and 20 000, lot 30K0572), heparin sulfate (MW ∼7000, lot 41K1130), and sodium dextran sulfate (MW 5000, 10 000, and 500 000) were obtained from Sigma (St. Louis, MO). Sucrose octasulfate potassium salt was aquired from Toronto Research Chemicals Inc. (Toronto, Canada), and β-mercaptoethanol, protein A sepharose, and [methyl-^{3}H]-thymidine (5 Ci/mmol) were purchased from Amersham Pharmacia Biotech (Piscataway, NJ). FGFR-1 antibody raised against the carboxy terminus of FGFR-1 of human origin (identical to the corresponding mouse sequence) was purchased from Santa Cruz.

General Synthetic Methods. Thin-layer chromatography (TLC) was performed on Whatman silica gel aluminum-backed plates of 250 μm thickness on which spots were visualized with UV light or by charring the plate after dipping in 10% H_2SO_4 in methanol. Mass spectra (MS/FAB) were obtained at an ionizing voltage of 70 eV. ^{1}H NMR spectra were recorded at room temperature with a Varian INOVA 400 spectrometer (magnetic field strengths of 400 and 100 MHz for ^{1}H and ^{13}C NMR analyses, respectively). The size-exclusion chromatography (SEC) equipment comprised a Waters model 510 HPLC pump, a Waters Ultrahydrogel 250 column, and a Wyatt Technology Optilab 903 refractometer. The eluent consisted of a 0.1 mol/L $NaNO_3$ deionized water solution containing 0.05 wt % sodium azide at a flow rate of 0.7 mL/min. The actual molar masses of the glycopolymer samples were determined from the response of the Dawn EOS (Wyatt Technology) multiangle laser light-scattering (LLS) detector that was connected to the outlet of the SEC apparatus.

2-*O*-Acryoylethoxyl-2-acetylamino-3,4,6-trisulfoxy-β-D-glucopyranoside (4) and 2-*N*-Acryoylaminoethoxyl 4-*O*-(2,3,4,6-Tetrasulfoxy-β-D-galatopyranosyl)-2,3,6-trisufoxy-β-D-glucopyranoside (5) were synthesized as previously reported (*14*, *16*).

Homopolymerization of Acrylamide-Derived Glycomonomers Initiated by $ClC_6H_4N{\equiv}N^+BF_4^-$/NaOCN. In a three-neck flask, 3 mg (2.45×10^{-5} mol) of *p*-chloroaniline was reacted with 7 mg of HBF_4 (48 wt % aqueous solution, 3.67×10^{-5} mol) in 2 mL of water at 0 °C and under an Ar atmosphere. The diazonium salt $ClC_6H_4N^+{\equiv}NBF_4^-$ was generated by adding 2 mg (2.93×10^{-5} mol) of $NaNO_2$ to the reaction medium. After 30 min, a degassed mixture of 390 mg (1.22×10^{-3} mol) of glycomonomer **5** (or **4**) and 2 mg (2.45×10^{-5} mol) of sodium cyanate (NaOCN) dissolved in 0.5 mL of water was introduced into the flask containing the arenediazonium salt. The polymerization solution was then heated to 50 °C for 16 h. By varying the [M]/[I] ratio and reaction times resulting glycopolymers **7a** and **7b** (or **6a** and **6b**) were isolated by precipitation in a 10-fold excess of cold methanol and dried to yield white cotton wool-like materials.

Copolymerization of Acylamide-Derived Glycomonomers Initiated by $ClC_6H_4N{\equiv}N^+BF_4^-$/NaOCN. In a three-neck flask, 8 mg (6.03×10^{-5} mol) of *p*-chloroaniline was reacted with 17 mg of HBF_4 (48 wt % aqueous solution, 9.04×10^{-5} mol) in 2 mL of water at 0 °C and under an Ar atmosphere. The diazonium salt $ClC_6H_4N^+{\equiv}NBF_4^-$ was then generated by adding 5 mg (7.2×10^{-5} mol) of sodium nitrite ($NaNO_2$) to the reaction medium. After 30 min, a degassed mixture of 225 mg (6.03×10^{-4} mol) of glycomonomer **5** (or **4**), 171 mg (2.41×10^{-3} mol) of acrylamide, and 4 mg (6.03×10^{-5} mol) of NaOCN dissolved in 1 mL of water were introduced into the flask containing the diazonium salt. The polymerization solution was then heated to 50 °C. The statistical copolymers **7c** and **7d** (or **6c**−**e**) formed after 16 h of reaction were isolated by precipitation in a 10-fold excess of cold methanol and dried. The conversions were determined by weight of the resultant glycopolymer.

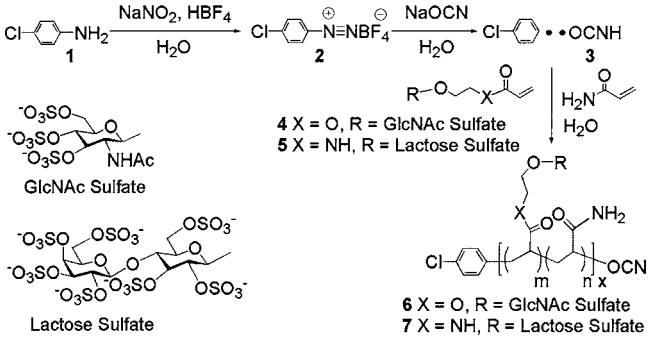
Cell Culture. BaF3-FR1C-11 mouse lymphoma cells were kindly provided by Dr. D. Ornitz (Washington University, St. Louis, MO) and were cultured in RPMI 1640 media supplemented with 10% bovine calf serum, 10% WEHI-3 conditioned medium, 100 u/mL penicillin, 100 μg/mL streptomycin, 4 mM L-glutamine, 0.0035% β-mercaptoethanol, and 600 μg/mL G418. FR1C-11 cells were derived from the BaF3 line and have been transfected with a mouse cDNA encoding the 3Ig domain form of FGFR1-IIIc (*18*).

Proliferation Assay. BaF3-FR1C-11 mouse lymphoma cells were washed twice with RPMI 1640 media lacking IL-3 and plated at a concentration of 2.2×10^4 cells/well in a 96-well plate in the presence of 3 ng/mL FGF-2 and increasing concentrations of heparin or various test compounds in a total volume of 150 μL of media (RPMI 1640−10% fetal calf serum without IL-3). After a 36 h incubation period, 1 μCi of ^{3}H-thymidine was added to each well in a volume of 50 μL of RPMI media (without FGF or IL3). Cells were incubated for an additional 5 h and harvested onto glass fiber filters with a TOMTEC cell harvester (Tomtec Co., Orange, CT). Incorporated ^{3}H-thymidine was determined by liquid scintillation counting. Each compound concentration was tested in triplicate.

Dimerization of FGF-2 and FGFR-1. Compound-induced FGF-2 dimerization was assessed, as detailed elsewhere (*19*). Briefly, ^{125}I-FGF-2 (20 ng/mL) was incubated for 1 h at room temperature in the presence and absence of heparin (25 μg/mL) or various concentrations of test glycopolymer in 20 μL buffer containing 150 mM NaCl and 25 mM Hepes, pH 7.5. DSS was then added to a final concentration of 0.3 mM, and the mixture was incubated for an additional 20 min. The cross-linking reaction was quenched with 10 mM ethanolamine-HCl, pH 8.0, for 20 min and diluted with 2 × SDS−PAGE loading buffer. The protein was analyzed on a 15% SDS−PAGE gel, and cross-linked FGF-2 was visualized by autoradiography on XAR film (Eastman Kodak Co., Rochester, NY).

For FGFR cross-linking studies, 10^6 cells were washed with binding buffer (RPMI 1640), 1 mg/mL of bovine serum albumin (BSA), and 20 mM *N*-2-hydroxyethylpiperazine-*N*′-2-ethanesulfonic acid (HEPES, pH 7.5) and incubated with 3 ng/mL ^{125}I-FGF-2 in the absence or presence of either heparin or HS-mimetic compound at 4 °C for 5 h. After three washes with ice cold PBS with 1 mg/mL of BSA, cells were resuspended and incubated in 250 μL of cross-linking solution (PBS, 0.2 mM DSS, 1 mg BSA/mL) for 45 min at room temperature. The reaction was quenched with 500 μL of TN buffer (50 mM tris, pH 7.4, 150 mM NaCl), washed twice with TN, and solubilized in RIPA buffer (PBS, 0.5% deoxycholic acid, 1% Triton X-100, 1 mM EDTA, 1 mM phenylmethylsulfonyl fluoride, 10 μg aprotinin per mL). After 10 min on ice, the nuclei were removed by centrifugation and the supernatants were analyzed by electrophoresis through

Scheme 1. Cyanoxyl-Mediated Free-Radical Copolymerization of Sulfated Glycomonomer with Acrylamide



a 6% SDS−PAGE gel. The cross-linked FGF-2-FGFR was visualized by autoradiography on XAR film (Eastman Kodak Co., Rochester, NY) (*20*).

Proteolytic Digestion of FGF-2. Trypsin-mediated digestion of FGF-2 in the presence of test compound was evaluated as described by Coltrini et al. (*21*). Briefly, 1-μg aliquots of the growth factor were incubated at 37 °C for 5 min in 5 mM Tris/HCl pH 7.6, in the presence of increasing concentrations of the test compound. This was followed by the addition of 100 ng of trypsin with incubation at 37 °C for 3 h. Samples were then supplemented with SDS−PAGE reducing sample buffer, heated to 100 °C for 5 min, and then electrophoresed on a SDS−PAGE (15%) gel. The amount of undigested protein in a given lane was determined by densitometric analysis of silver-stained gels (*21*, *22*).

Acid and Heat Treatment of FGF-2. FGF-2 (100 μg/mL) in 5 mM Tris (pH 7.6) was combined with heparin or test compound and then incubated for 2 h at room temperature in the presence of trifluoroacetic acid (TFA) diluted in water. TFA at a final concentration of 0.05, 0.1, 0.25, 0.5,1, 2.5, and 5% corresponds to a pH of 3.4, 2.37, 1.5, 1.08, 0.4, 0.2, and 0, respectively, which was unaffected by the addition of heparin, test compound, or FGF-2. The reaction mixture was further diluted as indicated with RPMI 1640−10% fetal calf serum. The final pH was neutral, as indicated by a phenol red indicator (*23*). To define the capacity of test compound to protect FGF-2 from heat inactivation, FGF-2 was incubated with heparin or test compound and then heated at 65 °C for 5 min. In both assays, residual FGF-2 activity was determined by measuring the proliferation of BaF3-FR1C-11 cells in response to 1 μL of reaction mixture.

RESULTS AND DISCUSSION

Synthesis of Sulfated Glycopolymers. Polyacrylamide-based neoglycoconjugates have been used as diagnostic reagents, such as in the inhibition of hemagglutination by pathogens (*24*) or as solid-phase coatings in enzyme-linked immunosorbent assays (ELISA) (*25*, *26*). Our prior investigations have confirmed that cyanoxyl (OCN)-mediated free-radical polymerization of acryl-derivatized glycomonomers is a convenient tool to produce water-soluble glycopolymers. In this reaction, cyanoxyl radicals were generated by an electron-transfer reaction between cyanate anions ($^-OC{\equiv}N$), from a NaOCN aqueous solution, and *p*-chlorobenzene-diazonium salts ($ClC_6H_4N{\equiv}N^+BF_4^-$), that were previously prepared in situ through a diazotization reaction of *p*-chloroaniline in water (Scheme 1). In addition to cyanoxyl persistent radicals, aryl-type active radicals were simultaneously produced, and only the latter species is capable of initiating chain growth. As summarized in Tables 1 and 2, cyanoxyl-mediated homopolymerization of sulfated *N*-acetylglucosamine glycomonomer **4** or lactose heptasulfate monomer **5** generated the expected sulfated glycopolymers **6** or **7** in good conversion yield (60−80%) and with relatively low polydispersity ($1.13 < M_w/M_n < 1.62$), respectively. Polymers of varying molecular weight were prepared by altering either monomer conversion or the initial ratio of monomer to initiator concentrations ($[M]_o/[I]_o$). Similarly, copolymers were prepared by copolymerization of sulfated glycomonomer **4** or **5** with acrylamide in low-polydispersity ($1.15 < M_w/M_n < 1.57$). The resultant glycopolymers were characterized by NMR spectroscopy as well as by SEC coupled with both refractive index and multiangle laser-scattered detectors.

Table 1. Sulfated Monosaccharide-Based Glycopolymers

monomer ratio GM/AM (mol)	polymer composition (mol)	glucosamine content (wt %)[a]	M_n (g/mol)	M_w/M_n SEC	glycopolymer
1/0	1/0	100	9900	1.13	**6a** (**SM1**)
1/0	1/0	100	20 800	1.49	**6b** (**SM2**)
1/1	1/9	47	5400	1.15	**6c** (**SM3**)
1/1	1/12	40	21 700	1.20	**6d** (**SM4**)
1/1	1/4	66	48 000	1.45	**6e** (**SM5**)
1/4	1/9	42	115 600	1.57	**6f** (**SM6**)

[a] Mass content of monosaccharide was determined by ^{1}H NMR analysis.

Table 2. Sulfated Disaccharide-Based Glycopolymers

monomer ratio GM/AM (mol)	polymer composition (mol)	lactose content (wt %)[a]	M_n (g/mol)	M_w/M_n SEC	glycopolymer
1/0	1/0	100	7500	1.19	**7a** (**SL5**)
1/0	1/0	100	114 000	1.62	**7b** (**SL7**)
1/1	1/10	57	9300	1.46	**7c** (**SL3**)
1/1	1/11	56	33 400	1.47	**7d** (**SL4**)

[a] Mass content of disaccharide was determined by ^{1}H NMR analysis.

Glycopolymers Bearing Lactose Heptasulfate Dissacharides Stimulate FGF-2-Mediated Cell Proliferation. The capacity of selected glycopolymers to potentiate FGF-2 mitogenic activity was measured by [^{3}H]-thymidine incorporation into BaF3-FR1C-11 cells, which express the FGF receptor, FGFR-1, but not cell surface heparan sulfate. In the absence of exogenous heparin or heparan sulfate, FGF-2 is incapable of eliciting cell proliferation. Cells were treated with 3 ng/mL of FGF-2 and increasing concentrations of indicated oligosacharides. Test compounds include a series of glycopolymers ranging in molecular weight, pendant group type, and density, as well as corresponding monomers, sucrose octasulfate (SOS), heparin, and heparan sulfate (Figure 1).

The synthesis of sulfated glycopolymers did not ensure the generation of compounds that mimicked heparin's ability to stimulate FGF-2-dependent cell proliferation. For example, glycopolymers **6** (**SM1**−**SM6**) carrying fully sulfated NAcGlc pendant groups were ineffective in promoting FGF-2-dependent cell proliferation (Figure 1A). However, glycopolymers **7** (**SL3**, **SL4**, **SL5,** and **SL7**) bearing sulfated lactose residues were able to elicit a range of proliferative activity depending upon the structural features of the polymer (Figure 1B−D). Of note, a high level of bioactivity was demonstrated by a glycopolymer designated **SL3** (MW 9300, PDI 1.46) that was a copolymer of sulfated lactose monomers (GM) and acrylamide (AM) (molar ratio AM:GM 1:10, lactose

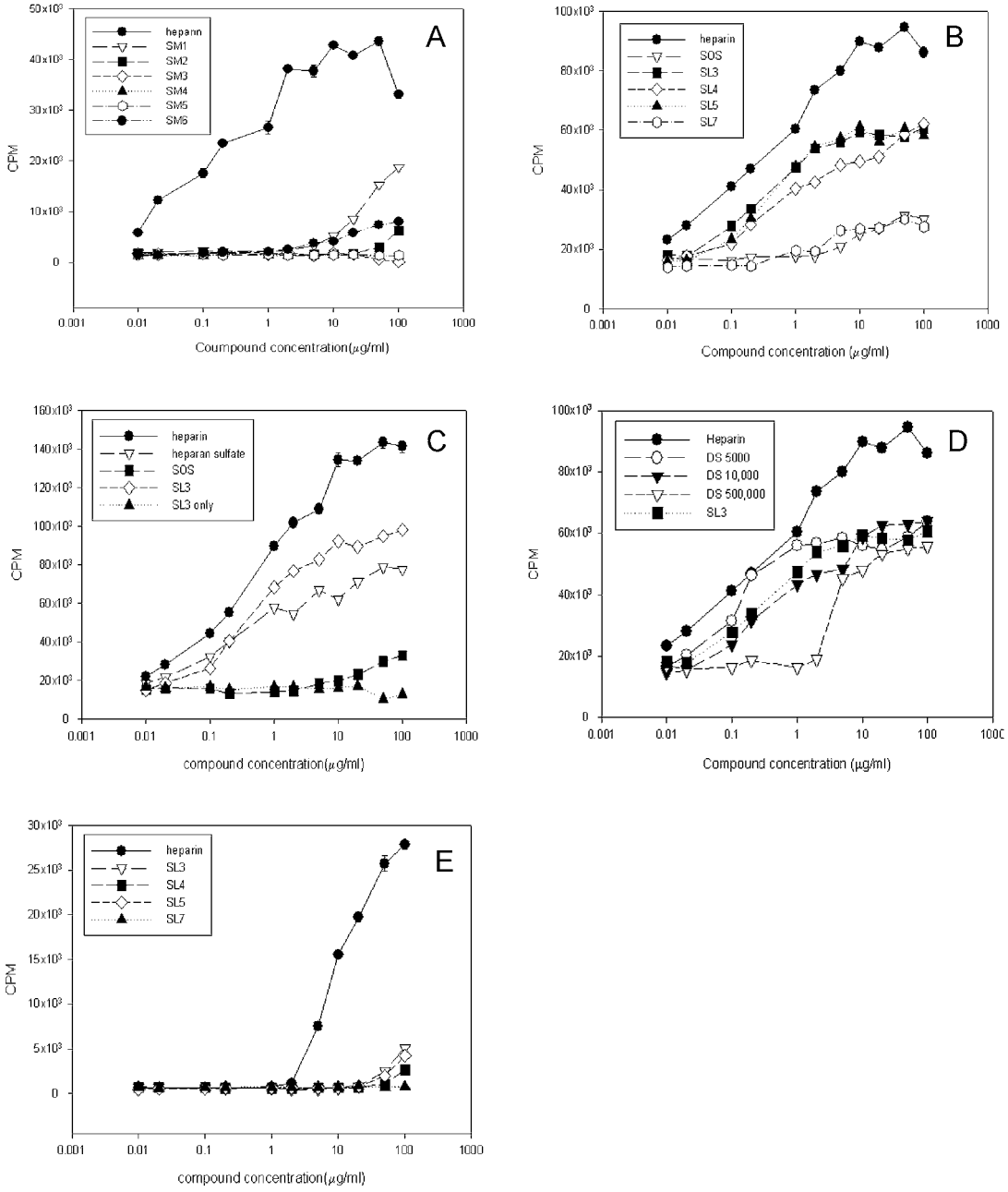


Figure 1. Mitogenic activity of natural and synthetic carbohydrate-based compounds. Activation of FGF mitogenic activity as measured by [^{3}H]-thymidine incorporation into BaF3-FR1C-11 cells treated with 3 ng/mL FGF-2 and increasing concentrations of the indicated compound. (A) Mitogenic activity of glycopolymers (**SM1**−**SM6**) in the presence of FGF-2. (B) Comparison of mitogenic activity of glycopolymers (**SL3**−**SL7**) with SOS and heparin. (C) Comparison of mitogenic activity of glycopolymer **SL3** with **SL3** monomer, SOS, and heparan sulfate. (D) Comparison of mitogenic activity of glycopolymer **SL3** with dextran sulfate 5000, 10 000, and 500 000. (E) Mitogenic activity of synthetic glycopolymers in the presence of FGF-1. Activation of FGF-1 mitogenic activity as measured by [^{3}H]-thymidine incorporation into BaF3-FR1C-11 cells treated with 4 ng/mL FGF-1 and increasing concentrations of the indicated compound.

content 57 wt %). **SL3**-mediated proliferative responses to FGF-2 exceeded those observed with heparan sulfate, as well as SOS and free **SL3** monomer **5**. Of interest, the **SL3** effect is selective in that it was not capable of initiating a proliferative response to FGF-1 (Figure 1E).

FGF-2 and FGFR-1 Dimerization Is Mediated by the Mitogenic Glycopolymer SL3. Characteristically, FGF-2 is sequestered in the ECM in a dimerized form only when matrix-producing cells produced fully sulfated GAGs. Significantly, dimerization of both FGF-2 and FGFR-1 are essential for an optimized biological response. To examine the capacity of **SL3** to mediate FGF-2 dimerization, 20 ng/mL of ^{125}I-FGF-2 was incubated with either heparin or **SL3** for 1 h at room temperature. After disuccinimidyl suberate cross-linking, the samples were resolved by electrophoresis and visualized by autoradiography (Figure 2). **SL3** was as effective as heparin in mediating FGF-2 dimerization. Likewise, **SL3**-mediated FGFR-1 dimerization was investigated by incubating BaF3-FGFR-1C-11 cells with ^{125}I-labeled FGF-2 in the presence or absence of either heparin or **SL3**. Cells were treated with disuccinimidyl suberate to cross-link FGF-2 to its receptor. Cross-linked proteins were electrophoresed on an SDS−6% polyacrylamide gel and detected by autoradiography (Figure 3). **SL3** was as effective as heparin in mediating FGFR-1 dimerization.

Glycopolymer SL3 Protects FGF-2 from Protein Degradation Induced by Trypsin, Acidic Condi-

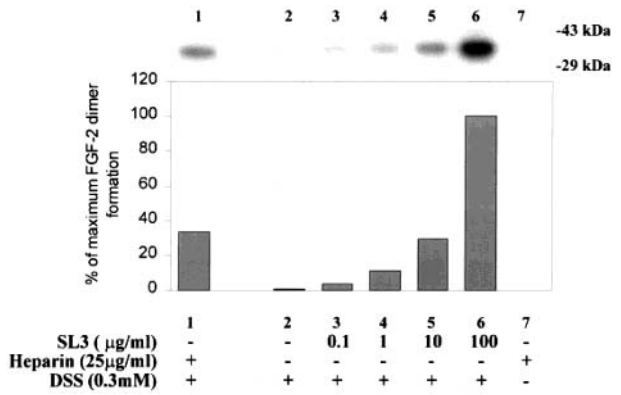


Figure 2. Dimerization of FGF-2 in the presence of **SL3**. ^{125}I-FGF-2 20 (ng/mL) was incubated with either heparin or **SL3** for 1 h at room temperature. After disuccinimidyl suberate cross-linking, samples were resolved by electrophoresis and visualized by autoradiography.

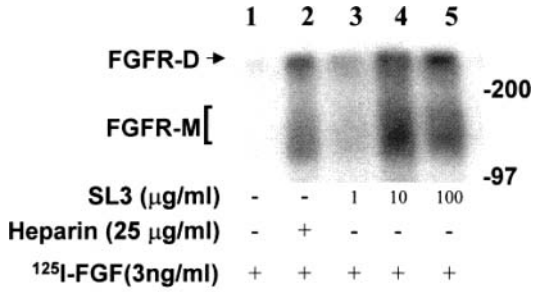


Figure 3. Cross-linking of ^{125}I-FGF-2 to FGFR-1. BaF3-FGFR-1C-11 cells were incubated with ^{125}I -labled FGF-2 in the presence or absence of either heparin or **SL3** and subsequently treated with disuccinimidyl suberate to cross-link FGF to the FGFR-1 receptor. Cross-linked proteins were electrophoresed on an SDS−6% polyacrylamide gel and detected by autoradiography.

tions, and Heat. It has been suggested that once soluble proteins, such as FGF-2, are released into the ECM, their sequestration by heparan sulfate proteoglycans is essential for preservation of bioactivity. In principle, complexation with HS chains should protect heparin-binding proteins from heat-, pH-, and protease-related degradation mechanisms. To assess protection from proteolysis, FGF-2 (1 μg) was incubated with trypsin for 3 h at 37 °C in the presence or absence of 25 μg/mL of heparin or decreasing concentration of glycopolymer **SL3**. Samples were then analyzed by SDS−PAGE and undigested FGF-2 was estimated by densitometry (Figure 4). **SL3** was as effective as heparin in protecting FGF-2 from proteolytic degradation. Protection from acidic conditions was determined by incubation of FGF-2 with or without heparin or glycopolymer **SL3** (25 μg/mL) in varying concentrations of trifluoroacetic acid (0.05 to 5%), corresponding to a pH range of 0 to 3.4. After 2 h incubation at room temperature, samples were diluted 20-fold with RPMI 1640 and incubated with heparin deficient cells (BaF3-FGFR-1) expressing the FGF receptor (FGFR-1). ^{3}H-Thymidine incorporation was determined as an indicator of retained FGF-2 activity (Figure 5). Preservation of biological activity upon heat-treatment of FGF-2 was measured by incubation of FGF-2 at 65 °C for 5 min with or without heparin or glycopolymer **SL3** (25 μg/mL). Samples were diluted in RPMI 1640 and incubated with BaF3-FGFR-1 cells, and ^{3}H-thymidine incorporation was determined (Figure 6). Both heparin and the heparin-mimetic glycopolymer **SL3** provided substantial protection of FGF-2 from trypsin, heat, and acidic conditions.

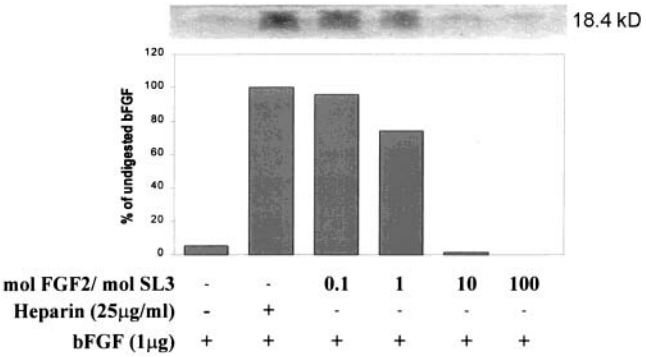


Figure 4. SL3 protects FGF-2 from trypsin digestion. Aliquots (1 μg) of recombinant FGF-2 were incubated at 37 °C with trypsin in the absence or presence of 25 μg/mL heparin or decreasing concentration of **SL3**. Samples were then analyzed by SDS−PAGE and visualized by silver staining. Undigested FGF-2 in each lane of the gel was estimated by densitometry.

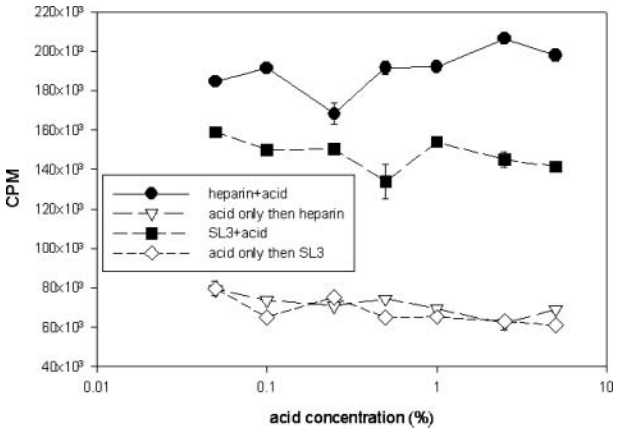


Figure 5. SL3 protects FGF-2 on exposure to acidic conditions. A stock solution of FGF-2 (100 μg/mL in 5 mM tris, pH 7.6) in the presence or absence of either heparin or **SL3** was diluted 10-fold with TFA ranging in concentration from 0.05 to 5%. After 2 h incubation at room temperature, the samples were further diluted 20-fold with RPMI 1640−10% FCS without IL-3 (final FGF-2 concentration 0.5 μg/mL) and added to BaF3-FGFR-1C-11 cells. Heparin or SL3 was added to those test samples that were incubated in TFA in the absence of either compound. The final FGF-2 concentration was 3.3 ng/mL, while that of heparin or SL3 was 25 μg/mL. After 36 h, 1 μCi of [^{3}H]-thymidine was added to each sample. The cells were incubated for an additional 5 h and incorporated thymidine determined by liquid scintillation counting.

Despite recent advances in achieving sustained local delivery of protein growth factors through the use of synthetic or native macromolecules as controlled delivery vehicles, significant limitations remain in achieving optimal control over the degree of growth factor sequestration and maximum preservation of growth factor activity during and after release. For example, while the addition of MgOH to polylactide/glycolide (PLGA) microspheres have led to improvements in protein stabilization during material processing and polymer degradation, the risk of protein inactivation due to proteolytic, thermal, or other mechanisms that are operative at the depot site in the body remains (*27*−*30*). All of this necessitates the delivery of increased quantities of growth factor, with significant added cost, to compensate for its reduced bioavailability. Moreover, variability in the nature, extent, and magnitude of those physiochemical processes, which may degrade or denature protein growth factors, further complicates the goal of predictable uniform drug delivery.

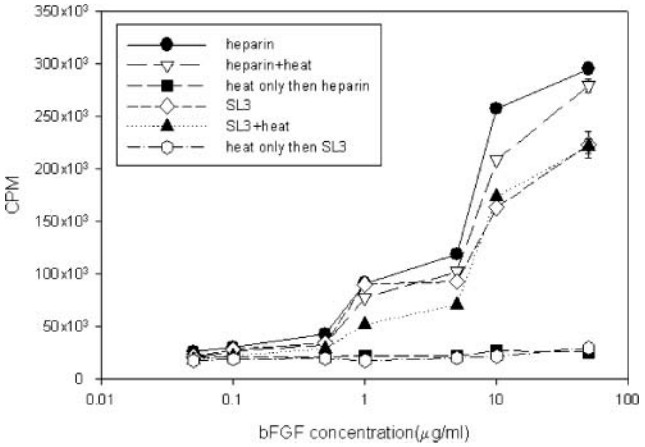


Figure 6. SL3 protects FGF-2 from thermal denaturation. A stock solution of FGF-2 (100 μg/mL, in 5.0 mM tris, pH 7.6) was diluted 10-fold in PBS with or without **SL3** or heparin and heat inactivated. An aliquot was added to BaF3-FGFR-1C-11 cells such that the final FGF-2 concentration was 3.3 ng/mL, while that of heparin or **SL3** was 25 μg/mL. After 36 h, 1 μCi of [^{3}H]-thymidine was added to each sample. The cells were incubated for an additional 5 h and incorporated thymidine determined by liquid scintillation counting.

In this report, we postulate that heparan sulfate proteoglycans, which act as reservoirs for heparin-binding growth factors and cytokines, establishes a useful biomimetic paradigm for the generation of biomaterials for the controlled delivery of proangiogenic proteins or other growth factors. The diverse biological properties of heparin and heparan sulfate combined with the inherent difficulty associated with the synthesis of these chemically complex natural products have motivated efforts to generate simpler structural mimics as component biomaterials for a variety of applications. For example, Cooper et al. (*31*, *32*), and Ito et al. (*33*, *34*) and Onishi (*35*) have all produced sulfonate-functionalized polymers with promising anticoagulant-like properties. Of particular interest have been the efforts of Jozenfowicz and colleagues who have prepared dextrans derivitized with carboxymethyl, carboxymethylbenzamide, and carboxymethylbenzylamide sulfonate functional groups (*36*−*39*). The biological features of these polysaccharides are related to the number and distribution of chemical groups randomly attached along the dextran chain. Indeed, several of these polymers exhibit anticoagulant and anticomplement properties, and in some cases mimic heparin's inhibitory effect on smooth muscle cell growth (*9*, *40*−*41*). Other variants potentiate the activities of FGF-1 and FGF-2 and appear to stimulate the healing responses of a variety of tissue types in vitro and in vivo (*38*, *39*). In this report, we demonstrate that a glycopolymer bearing pendant fully sulfated lactose units effectively replaces heparin and heparan sulfate as a molecular chaperone for FGF-2. A compound was identified that protects FGF-2 from proteolytic, acid, and heat-induced degradation, while selectively promoting its dimerization and interaction with its receptor. Significantly, the capacity of this heparin-mimic to promote an FGF-2 specific proliferative cell response suggests potential applications in areas related to therapeutic angiogenesis, including wound healing, myocardial or lower extremity revascularization, as well as in tissue engineering.

ACKNOWLEDGMENT

This work was supported by grants from the NIH. The authors acknowledge the Emory University NMR and Mass Spectrometry Centers for their facilities. They are also indebted to Dr. Suri Iyer for kind technical assistance.

LITERATURE CITED

(1) Casu, B., and Lindahl, U. (2001) Structure and biological interactions of heparin and heparan sulfate. *Adv. Carbohydr. Chem. Biochem. 57*, 159.

(2) Iozzo, R. V., and San Antonio, J. D. (2001) Heparan sulfate proteoglycans: Heavy hitters in the angiogenesis arena. *J. Clin. Invest. 108*, 349.

(3) Gallagher, J. T. (1995) Heparan sulphate and protein recognition: Binding specificities and activation mechanisms. *Adv. Exp. Med. Biol. 376*, 125.

(4) Higashiyama. S., Abraham, J. A., and Klagsburn, M. (1993) Heparin-binding EGF-like growth factor stimulation of smooth muscle cell migration: Dependence on interactions with cell surface heparn sulphate. *J. Cell Biol. 122*, 933.

(5) Rapraeger, A. C., Krufka, A., and Olwin, B. B. (1991) Requirement of heparin sulphate for bFGF-mediated fibroblast growth and myoblast differentiation. *Science 252*, 1705.

(6) Gallagher, J. T. (2001) Heparan sulfate: Growth control with a restricted sequence menu. *J. Clin. Invest. 108*, 357.

(7) Vlodavsky, I., Miao, H. Q., Medalion, B., Danagher, P., and Ron, D. (1996) Involvement of heparan sulfate and related molecules in sequestration and growth promoting activity of fibroblast growth factor. *Cancer Metastasis Rev. 15*, 177.

(8) Ye, S., Luo, Y., Lu, W., Jones, R. B., Linhardt, R. J., and Capila, I., et al. (2001) Structural basis for interaction of FGF-1, FGF-2, and FGF-7 with different heparan sulfate motifs. *Biochemistry 40*, 14429.

(9) Miao, H. Q., Ishai-Michaeli, R., Atzmon, R., Peretz, T., and Vlodavsky, I. (1996) Sulfate moieties in the subendothelial extracellular matrix are involved in basic fibroblast growth factor sequestration, dimerization, and stimulation of cell proliferation. *J. Biol. Chem. 271*, 4879.

(10) Miyata, T., and Nakamae, K. (1997) Polymers with pendent saccharides—'glycopolymers'. *Trends Polym. Sci. 5*, 198.

(11) Tsuchida, A., Kobayashi, K., Matsubara, N., Muramatsu, T., Suzuki, T., and Suzuki, Y. (1998) Simple synthesis of sialyllactose-carrying polystyrene and its binding with influenza virus. *Glycoconjugate J.* 15, 1047.

(12) Vetere, A., Donati, I., Campa, C., Semeraro, S., Gamini, A., and Paoletti, S. (2002) Synthesis and characterization of a novel glycopolymer with protective activity toward human anti-alpha-Gal antibodies. *Glycobiology 12*, 283.

(13) Owen, R. M., Gestwicki, J. E., Young, T., and Kiessling, L. L. (2002) Synthesis and applications of end-labeled neoglycopolymers. *Org. Lett. 4*, 2293.

(14) Sun, X.-L., Grande, D., Baskaran, S., Hanson, S. R., and Chaikof, E. L. (2002) Glycosaminoglycan-mimetic biomaterials 4. Synthesis of sulfated lactose-based glycopolymers that exhibit anticoagulant activity. *Biomacromolecules 3*, 1065.

(15) Baskaran, S., Grande, D., Sun, X.-L., Yayon, A., and Chaikof, E. L. (2002) Glycosaminoglycan-mimetic biomaterials. 3. Glycopolymers prepared from alkene-derivatized mono- and disaccharide-based glycomonomers. *Bioconjugate Chem. 13*, 1309.

(16) Grande, D., Baskaran, S., and Chaikof, E. L. (2001) Glycosaminoglycan-mimetic biomaterials. 2. Alkene- and acrylate-derivatized glycopolymers by cyanoxyl-mediated free-radical polymerization. *Macromolecules 34*, 1640.

(17) Grande, D., Baskaran, S., Baskaran, C., and Chaikof, E. L. (2000) Glycosaminoglycan-mimetic biomaterials. 1. Non-sulfated and sulfated glycopolymers by cyanoxyl-mediated free-radical polymerization. *Macromolecules 33*, 1123.

(18) Ornitz, D. M., Xu, J., and Colvin, J. S. (1996) McEwen DG. MacArthur CA. Coulier F. Gao G. Goldfarb M. Receptor specificity of the fibroblast growth factor family. *J. Biol. Chem. 271*, 15292.

(19) Miao, H.-Q., Ornitz, D. M., Aingorn, E., Ben-Sasson, S. A., and Vlodavsky, I. (1997) Modulation of fibroblast growth factor-2 receptor binding, dimerization, signaling, and angiogenic activity by a synthetic heparin-mimicking polyanionic compound. *J. Clin. Invest. 99*, 1565.

(20) Wang, J.-K., Gao, G., and Goldfarb, M. (1994) Fibroblast growth factor receptors have different signaling and mitogenic potentials. *Mol. Cell. Biol. 14*, 181.

(21) Coltrini, D., Rusnati, M., Zoppetti, G., Oreste, P., Isacchi, A., Caccia, P. Bergonzoni, L., and Presta, M. (1993) Biochemical bases of the interaction of human basic fibroblast growth factor with glycosaminoglycans. New insights from trypsin digestion studies. *Eur. J. Biochem. 214*, 51.

(22) Sandra, L., Daria, L., Johan, N., Robert, E., Marco, R., Patrizia, D., Prabhat, C., Erik, C., and Marco, P. (1999) Modulation of fibroblast growth factor-2 receptor binding, signaling, and mitogenic activity by heparin-mimicking polysulfonated compounds. *Mol. Pharmacol. 56*, 204.

(23) Gospodarowicz, D., and Cheng, J. (1986) Heparin protects basic and acidic FGF from inactivation. *J. Cell. Physiol. 128*, 475.

(24) Sigal, G. B., Mammen, M., Dahmann, G., and Whitesides, G. M. (1996) Polyacrylamides Bearing Pendant α-Sialoside Groups Strongly Inhibit Agglutination of Erythrocytes by Influenza Virus: The Strong Inhibition Reflects Enhanced Binding through Cooperative Polyvalent Interactions. *J. Am. Chem. Soc. 118*, 3789.

(25) Roy, R., Tropper, F. D., and Romanowska, A. (1992) A New strategy in glycopolymer synthesis. Preparation of antigenic water-soluble poly(acrylamide-*co*-p-acrylamidophenyl beta-lactoside). *Bioconjugate Chem. 3*, 256.

(26) Bovin, N. V. (1998) Polyacrylamide-based glycoconjugates as tools in glycobiology. *Glycoconjugate J. 15*, 431.

(27) Zhu, G., Mallery, S. R., and Schwendeman, S. P. (2000) Stabilization of proteins encapsulated in injectable poly-(lactide-*co*-glycolide). *Nat. Biotechnol 18*, 52−7.

(28) Burke, P. A. (2000) Controlled release protein therapeutics: Effect of process and formulation on stability. *Handbook of Pharmaceutical Controlled Release Technology* (D. L. Wise, Ed.) Marcel Dekker: New York.

(29) Topp, E. M., Song, Y., Wilson, A., Li, R., Hagmen, M. J., and Schowen, R. L. (2000) Solid-state chemical stability of peptides and proteins: Applications to controlled release formulations. *Handbook of Pharmaceutical Controlled Release Technology* (D. L. Wise, Ed.) pp 693−724, Marcel Dekker: New York.

(30) Brannon-Peppas, L., and Vert, M. (2000) Polylactic and polyglycolic acids as drug delivery vehicles. *Handbook of Pharmaceutical Controlled Release Technology* (D. L. Wise, Ed.) pp 99−130, Marcel Dekker: New York.

(31) McCoy, T. J., Wabers, H. D., and Cooper, S. L. (1990) Series shunt evaluation of polyurethane vascular graft materials in chronically AV-shunted canines. *J. Biomed. Mater. Res. 24*, 107.

(32) Grasel, T. G., and Cooper, S. L. (1989) Properties and biological interactions of polyurethane anionomers: Effect of sulfonate incorporation. *J. Biomed. Mater. Res. 23*, 311.

(33) Ito, Y., Iguchi, Y., Kashiwagi, T., and Imanishi, Y. (1991) Synthesis and nonthrombogenicity of polyetherurethaneurea film grafted with poly(sodium vinyl sulfonate). *J. Biomed. Mater. Res. 25*, 1347.

(34) Ito, Y., Iguchi, Y., and Imanishi, Y. (1992) Synthesis and nonthrombogenicity of heparanoid polyurethanes. *Biomaterials 13*, 131.

(35) Onishi, M., Miyashita, Y., Motomura, T., Yamashita, S., Sakamoto, N., and Akashi, M. (1998) Anticoagulant and antiprotease activities of a heparinoid sulfated glucoside-bearing polymer. *J. Biomater. Sci. Polym. Ed. 9*, 973.

(36) Crepon, B., Maillet, F., Kazatchkine, M. D., and Jozefonvicz, J. (1987) Molecular weight dependency of the acquired anticomplementary and anticoagulant activities of specifically substituted dextrans. *Biomaterials 8*, 248.

(37) Thomas, H., Maillet, F., Letourneur. D., Jozefonvicz, J., and Kazatchkine, M. D. (1995) Effect of substituted dextran derivative on complement activation in vivo. *Biomaterials 16*, 1163.

(38) Tardieu, M., Gamby, C., Avramoglou, T., Jozefonvicz, J., and Barritault, D. (1992) Derivatized dextrans mimic heparin as stabilizers, potentiators, and protectors of acidic or basic FGF. *J. Cell. Physiol. 150*, 194.

(39) Letourneur, D., Machy, D., Pelle, A., Marcon-Bachari, E., D'Angelo, G., and Vogel, M., et al. (2002) Heparin and nonheparin-like dextrans differentially modulate endothelial cell proliferation: in vitro evaluation with soluble and cross-linked polysaccharide matrixes. *J. Biomed. Mater. Res. 60*, 94.

(40) Whitelock, J. M., Murdoch, A. D., Iozzo, R. V., and Underwood, P. A. (1996) The degradation of human endothelial cell-derived perlecan and release of bound basic fibroblast growth factor by stromelysin, collagenase, plasmin, and heparanases. *J. Biol. Chem. 271*, 10079.

(41) Kato, M., Wang, H., Kainulainen, V., Fitzgerald, M. L., Ledbetter, S., Ornitz, D. M., et al. (1998) Physiological degradation converts the soluble syndecan-1 ectodomain from an inhibitor to a potent activator of FGF-2. *Nat. Med. 4*, 691.

BC034138T

Factors Influencing the Ability of Nuclear Localization Sequence Peptides To Enhance Nonviral Gene Delivery

K. Helen Bremner,[†] Leonard W. Seymour,*[,‡] Ann Logan,[§] and Martin L. Read[§]

Cancer Research UK Institute for Cancer Studies, University of Birmingham, Birmingham, B15 2TH, UK, Department of Clinical Pharmacology, University of Oxford, Oxford, OX2 6HE, UK, and Department of Medicine, University of Birmingham, Birmingham, B15 2TH, UK. Received August 8, 2003; Revised Manuscript Received November 6, 2003

Nonviral gene delivery is limited by inefficient transfer of DNA from the cytoplasm to the nucleus. Nuclear localization sequence (NLS) peptides have been widely used to exploit intracellular transport mechanisms and promote nuclear uptake of DNA. However, the exact conditions to successfully utilize the properties of NLS peptides are still unclear. In the present study a panel of NLS peptides that bind different transport receptors were compared for their ability to enhance nonviral gene transfer. Several factors such as method of incorporating the NLS peptide, type of NLS peptide, DNA morphology, and proper characterization of NLS peptide/DNA conjugates were identified as important considerations in utilizing NLS peptides to enhance gene transfer. In particular, it was shown that a peptide derived from human T cell leukaemia virus type 1 (HTLV) was able to effectively condense DNA into discrete particles and mediate levels of transgene expression up to 32-fold greater than polylysine-based polyplexes. This is the first study to demonstrate efficient transfection mediated by an importin β-binding peptide based on the HTLV sequence. Promising results were also achieved with a 7-fold increase in gene expression using a NLS peptide/DNA conjugate formed by site-specific linkage of an extended SV40 peptide via a peptide nucleic acid (PNA) clamp. Altogether, the results from this study should help to define the requirements for successful NLS-enhanced transfection.

INTRODUCTION

Gene therapy has tremendous potential as either a standalone treatment or adjuvant therapy for many forms of disease such as cancer (*1*). The most efficient methods of delivering genes are those based on viral vectors such as adenovirus and retroviruses. However, safety issues relating to inflammatory and immune responses to adenoviral proteins and malignant transformation due to insertional mutagenesis with retroviral delivery have raised concerns over the use of these vectors (*2*, *3*). A safer alternative is to use nonviral (or synthetic) vectors such as polyplexes and lipoplexes for gene transfer. At present, however, the low levels of gene expression typically observed in vivo restrict the usefulness of nonviral vectors compared to viral vectors. Inefficient transfer of DNA from the cytoplasm to the nucleus has been identified as a major reason for this, particularly in postmitotic and quiescent cells where there is no periodic breakdown of the nuclear membrane (*4*, *5*).

By comparison, cellular and viral proteins enter the nucleus efficiently by means of nuclear localization sequences (NLS[1]), stretches of amino acids that bind to intracellular transport receptors such as importins and facilitate transfer through the nuclear pore. Early experiments showed that NLSs retain their activity when conjugated as a synthetic peptide to otherwise nonnuclear proteins such as bovine serum albumin and transferrin (*6*). The application of NLS peptides for nonviral gene transfer has since been widely investigated (*7*) and results to date have indicated the potential of this approach to improve nuclear delivery of DNA. For example, coupling of streptavidin−NLS conjugates to biotinylated DNA enabled linear DNA fragments of between 310 and 1500 bp to enter the nuclei of digitonin permeabilized cells by an active transport process (*8*). Significant increases in gene expression were also observed following ligation of an oligonucleotide-NLS conjugate to one or both termini of a linear DNA molecule, although no conclusive localization or mechanistic data was given in this study (*9*).

Results have been encouraging using linear DNA fragments but the type of chemistry used to conjugate peptides to circular plasmid DNA often results in loss of transcriptional capability. Two recent studies, for example, used either a photoactivation reaction (*10*) or a cyclopropapyrroloindole group (*11*) to couple NLSs at random locations on the DNA molecule. Sebestyen et al. demonstrated nuclear import in digitonin-permeabilized HeLa cells when >100 NLS peptides were attached to each plasmid, but transgene expression was completely

* To whom correspondence should be addressed. Phone: 44-1865-224986. Fax: 44-1865-224538. E-mail: Len.Seymour@clinpharm.ox.ac.uk.

[†] Cancer Research UK Institute for Cancer Studies. Present address: Department of Pathology, Columbia University, 630 W. 168th St. P&S 15-410, New York, NY 10032.

[‡] Department of Clinical Pharmacology.

[§] Department of Medicine.

[1] Abbreviations: DOTAP, 1,2-dioleoyl-3-(trimethylammonio)-propane; DTT, dithiothreitol; EtBr, ethidium bromide; FITC, fluorescein isothiocyanate; GST, glutathione S-transferase; HEPES, *N*-(2-hydroxyethyl)piperazine-*N*′-2-ethanesulfonic acid; HTLV, human T cell leukaemia virus type 1; Impα1, importin α1; Impβ1, importin β1; NLS, nuclear localization sequences; PEI, polyethylenimine; PLL, polylysine; PNA, peptide nucleic acid; PNA-b, PNA-biotin; PNA-m, PNA-maleimide; RPC, reducible polycation; SV40p, SV40 promoter; Tn1, transportin 1; TX-Red Mal, Texas Red maleimide.

10.1021/bc034140k CCC: $27.50 © 2004 American Chemical Society
Published on Web 12/13/2003

abolished (*11*). More encouragingly, Ciolina et al. found no decrease in expression until modification reached the level of 43 peptides per plasmid; however, despite binding of the conjugates to importin α, no increase in gene expression was observed (*10*).

A strategy to prevent loss of gene expression is to attach NLS peptides to DNA at specific locations using peptide nucleic acid (PNA) molecules that have a repeating polyamide backbone rather than a repeating sugar−phosphate backbone and hybridize to DNA in a high-affinity and sequence specific manner (*12*). Branden et al. recently demonstrated the utility of this approach with an 8-fold increase in transfection using PNA-NLS and 25-kDa PEI (*13*). The interaction between DNA and mono PNA is weakened under physiological conditions but has been recently overcome by the use of a homopyrimidine J-base containing bis PNA clamp that forms $(PNA)_2$DNA triplexes in a highly stable, pH-independent manner (*14*). PNA clamps have so far been used to label DNA with fluorophores, but there is potential in this approach to attach a wide range of ligands to DNA to provide specific functions without compromising transcriptional capability (*15*).

The exact conditions to successfully utilize the properties of NLS peptides to enhance nonviral gene transfer are, however, still not clear. It is unknown, for example, what type or length of NLS peptide is best suited for this application and NLS sequences that bind to a range of transport receptors, including importin β1 or transportin 1, have not been thoroughly investigated. The aim of the present study was to help define the requirements for successful NLS-enhanced transfection by comparing the ability of a panel of NLS peptides to enhance nonviral gene delivery. Two different strategies for incorporating NLS peptides in nonviral vectors were evaluated. In the first, NLS peptides were linked to DNA in a site-specific manner via an intracellularly stable thioether bond formed between a maleimide-labeled PNA clamp and a cysteine residue at the carboxy terminal of each peptide. The ability of NLS peptide-PNA/DNA conjugates to bind to their intracellular transport receptor and promote levels of gene expression was then examined. In the second strategy, the cationic nature of NLS peptides was utilized by investigating their ability to condense plasmid DNA into discrete particles and mediate transfection.

EXPERIMENTAL PROCEDURES

Materials. Peptides were synthesized by Severn Biotech Ltd (Kidderminster, UK) using standard fmoc chemistry with the following sequences: PKKKRKVEDPYC (SV40 T NLS) and SSDDEATADSQHSTPPKKKRKVEDPYC (Ext SV40 T NLS) containing the wild-type SV40 large T NLS, PKTKRKVEDPYC (mSV40 T NLS) and SSDDEATADSQHSTPPKTKRKVEDPYC (Ext mSV40 T NLS) containing a mutant SV40 large T NLS, MPKTRRRPRRSQRKRPPTPWAHFPGFGQSLC (HTLV) from the human T cell leukaemia virus type 1 Rex protein, GNQSSNFGPMKGGNFGGRSSGPYGGGGQYFAKPRNQGGYC (M9) from heterogeneous ribonucleoprotein A1, and a scrambled version SPGNRMGAGYFKGSGNKSGFQGRNPGSGQGYGPNQGFYGC (Scr M9). Oligonucleotides containing either one, three, or five copies of the PNA binding site (AGAGAGAG) were purchased from Alta Bioscience (University of Birmingham, Birmingham, UK) and inserted into the KpnI-MluI cloning site of pGL3con (Promega). The sequence of oligonucleotides containing PNA-binding sites for pGL3con constructs were 5′-CGATATCCAGCTGTCTCTCTCTCA-3′ (one site), 5′-CGATATCCTTAAGCTCTCTCTCTCTCTCTCTCTCTCTA-3′ (three sites), and 5′-CGATATCCTTAAGCTCTCTCTCTCTCTCTCTCTCTCTCTCTCTCTCTCTA-3′ (five sites). A bis PNA clamp of sequence TCTCTCTC−O−O−O-JTJTJTJT covalently attached at the amino terminus to biotin or maleimide was purchased from Gene Therapy Systems (San Diego, CA). J represents a pseudoisocytosine that is placed in the strand parallel to the DNA forming the "Hoogsteen strand", and O represents an 8-amino-3,6-dioxaoctanoic acid linker.

Preparation of Importin- and Transportin-GST Fusion Proteins. Importin α-GST and importin β-GST were grown from pGEX-2T plasmids (kindly provided by Y. Yoneda, Osaka University, Japan) and transportin 1 from a pGEX-5X plasmid (a kind gift from G. Dreyfuss, University of Pennsylvania) as previously described (*16*, *17*). Proteins were expressed in BL21 (DE3) cells and induced with 1 mM IPTG for 18 h at 20 °C (importins) or 17 °C (transportin 1). Cells were harvested by centrifugation and disrupted by freeze thawing followed by sonication. Fusion proteins were recovered from cleared bacterial lysate using glutathione−sepharose (Pharmacia) according to the manufacturer's instructions. Purified proteins were dialyzed against 20 mM HEPES−NaOH pH 7.3, 100 mM potassium acetate, 2 mM DTT containing 0.5 μg/mL protease inhibitor cocktail (Sigma). Purity of proteins was assessed by Coomassie staining following SDS−PAGE and Western blotting using an anti-GST antibody (Pharmacia).

Interaction of NLS Peptides with Transport Receptors. Binding of NLS peptides to transport receptors was measured by ELISA similar to that previously described (*17*). Maxisorp 96-well plates were coated with peptide (41.9 pmol for SV40 peptide, 41.8 pmol for Ext SV40 peptide, 33.5 pmol for HTLV peptide, and 30.9 pmol for M9 peptide) in 50 mM $NaHCO_3$ pH 9.8 at 4 °C overnight. After blocking with intracellular buffer (IB; 110 mM KCl, 5 mM $NaHCO_3$, 5 mM $MgCl_2$, 1 mM EGTA, 0.1 mM $CaCl_2$, 20 mM HEPES−NaOH pH 7.4, 1 mM DTT, 5 μg/mL protease inhibitor cocktail) containing 5% BSA, plates were incubated at 4 °C overnight with 12.5 nM transport receptor-GST or GST alone in IB/1% BSA. After washing the plate three times, the primary antibody goat anti-GST was applied for 2 h at 1/1000 dilution in IB/1% BSA. The plate was again washed three times and incubated with HRP-labeled rabbit anti-goat antibody (1/1000 in IB/1% BSA) for 2 h. After a further three washes, the plates were incubated with OPD substrate for 20 min and the reaction stopped by addition of 50 μL of 4 M sulfuric acid. The absorbance at 490 nm was measured using a Victor multilabel plate reader and background readings subtracted.

Preparation and Analysis of PNA/DNA Conjugates. PNA-biotin was vortexed for 2 min and heated at 55 °C for 15 min then added to plasmid DNA in PNA binding buffer (10 mM sodium phosphate buffer pH 7, 1 mM EDTA, 20 mM NaCl) and incubated at 37 °C for 24 h. Conjugate formation was assessed using streptavidin-Texas Red (Molecular Probes) to probe for bound PNA-biotin. In brief, PNA-biotin/DNA conjugates were restricted with KpnI and HindIII, purified using Sephadex G-25 spin columns (Pharmacia) and incubated with a 10-fold molar excess of streptavidin-Texas Red in the presence of 200 mM NaCl at room temperature for 30 min. Following gel electrophoresis on a 1.6% agarose gel in ethidium bromide-free conditions, the presence of Texas Red-labeled DNA was detected using a Typhoon gel scanner (Molecular Dynamics, λ_{ex} 633 nm, λ_{em} 610 nm, 800 V). Gels were also stained in ethidium bromide

solution (0.5 μg/mL) for 20 min and DNA fragments visualized using the Typhoon gel scanner (λ_{ex} 532 nm, λ_{em} 526 nm, 550 V). The signal intensity of particular bands was quantified using ImageQuant software. PNA-maleimide was conjugated to plasmid DNA by incubating at 37 °C for 2 h in PNA binding buffer.

Characterization of NLS Peptides. Cysteine-terminated NLS peptides were incubated with Texas-Red maleimide for 3 h in the dark, and reaction products analyzed on 16.5% Tris-Tricine SDS PAGE. Samples (0.5−20 μg of peptide) were loaded in sample buffer (2% SDS, 10% glycerol, 62.5 mM Tris.-HCl pH 6.8, 0.05% bromophenol blue) and were not heated prior to loading. Gels were scanned to detect Texas Red fluorescence using the Typhoon gel scanner (λ_{ex} 633 nm, λ_{em} 610 nm, 800 V).

Preparation of NLS Peptide-PNA/DNA Conjugates and Binding to Transport Receptors. PNA-maleimide/DNA conjugates were purified using Sephacryl S-500HR spin columns and incubated with a 20-fold molar excess of cysteine-terminated NLS peptides in 1 M NaCl for 1 h at room temperature followed by 2 h at 4 °C. The NLS peptide-PNA/DNA conjugates were then purified by ethanol precipitation and resuspended in water, and the amount of DNA was quantified by a fluorimetric assay using Hoechst dye (Sigma). Linear DNA conjugates were prepared by restriction digest using the enzymes KpnI and BamHI and purified by ethanol precipitation, and the amount of DNA was quantified using the Hoechst dye assay.

Binding of NLS/DNA conjugates to transport receptor-GST was measured using an in vitro binding assay similar to that described previously (*10*), whereby transport receptor-GST was immobilized on glutathione−sepharose and the extent of NLS peptide-PNA/DNA binding measured. Briefly, 20 μL of glutathione−sepharose slurry was washed three times in 100 μL of binding buffer (20 mM HEPES−NaOH pH 6.8, 150 mM potassium acetate, 2 mM magnesium acetate, 1 mM EGTA, 5 mM $MgCl_2$) containing 100 μg/mL BSA and incubated with 25 nmol transport receptor-GST in a total volume of 100 μL for 2 h at room temperature with end-over-end rotation. Beads were washed three times in binding buffer containing 1% BSA and then incubated with 0.5 μg of NLS peptide-PNA/DNA or DNA in binding buffer containing 1% BSA, again in a total volume of 100 μL for 2 h at room temperature with rotation. After washing three times, the beads in a volume of 100 μL of binding buffer/1% BSA were assayed for the presence of DNA by addition of 100 μL of PicoGreen (Molecular Probes, 1 in 200 dilution in TE buffer (10 mM Tris-HCl pH 8, 1 mM EDTA)) to samples in 96-well plates. After 2−5 min incubation in the dark, the fluorescence was measured using the Victor plate reader (λ_{ex} 485 nm, λ_{em} 535 nm for 10 s). A DNA standard curve, also containing glutathione−sepharose beads, was included and the amount of DNA bound to the transport receptor was calculated for each sample.

Formation of NLS Peptide/DNA Polyplexes. NLS peptide/DNA polyplexes were formed in water by the addition of the appropriate amount of NLS peptide to 20 μg/mL DNA, mixed and incubated at room temperature for 20 min prior to use. The ethidium bromide condensation and agarose gel retardation assays were used to assess polyplex formation. Briefly, fluorescence of a 10 μg/mL DNA solution with 400 ng/mL ethidium bromide added was measured at λ_{ex} 532 nm, λ_{em} 610 nm using a fluorimeter (PerkinElmer, LS-50B). NLS peptides were added in small increments and the fluorescence measured. Background fluorescence from ethidium bromide alone was subtracted and the N:P ratio of NLS peptide to DNA was plotted as a percentage of the fluorescence in the absence of peptide. In the gel retardation assay DNA was incubated with NLS peptide or PLL in the range N:P of 0 to 10 prior to analysis by agarose gel electrophoresis in the presence of 50 μg/mL ethidium bromide.

Maintenance and Passage of Mammalian Cells in Culture. The human cervical carcinoma cell line HeLa was grown in RPMI containing 1 mM glutamine, glucose (1 g/L) and 10% foetal calf serum (FCS). The PC-3 human prostatic carcinoma cell line was grown in DMEM supplemented with 1 mM glutamine, glucose (1 g/L) and 10% FCS.

Transfection Studies. Cells were seeded at 30 000 cells per well in 48-well plates 24 h prior to transfection. In some experiments, NLS peptide/DNA polyplexes at a N:P ratio of between 1:1 and 10:1 were used to transfect cells and in others, a reducible polycation (RPC) was used in combination with the lipid DOTAP as the transfection agent as previously described (*18*). Briefly, the RPC was added to 50 μg/mL DNA solution at an N:P ratio of 2:1 and incubated at room temperature for 20 min. DOTAP was added at a (w/w) ratio of 5:1 to DNA in 7.5 mM HEPES−NaOH pH 7.4 and complexes incubated at room temperature for a further 30 min before use. Unless stated otherwise, 0.5 μg of DNA was added per well. Cells were incubated in serum-free medium at 37 °C for 2.5 h in the presence or absence of 100 μM chloroquine. The media was replaced with media containing 10% FCS, and the cells were cultured for a total of 8−24 h prior to analysis of reporter gene expression.

Analysis of Reporter Genes. Luciferase expression following transfection was measured by a luminescence assay using cell lysates. The culture media was discarded, and cell lysates were harvested after freeze−thawing cells in 100 μL of lysis buffer. The lysate was gently vortexed, and 20 μL diluted into 100 μL of luciferase reaction buffer (20 mM glycylglycine, 1 mM $MgCl_2$, 0.1 mM EDTA, 3.3 mM DTT, 0.5 mM ATP, 0.27 mM coenzyme A lithium salt). The luminescence was integrated over 10 s on a Lumat LB9507 (Berthold Instruments, UK), and the results were expressed as relative light units (RLU) per mg of cell protein, as determined using the Advanced Protein Assay (Totam Biologicals, Northampton, UK).

MTS Assay for Cell Viability. Cells were seeded at 5000 per well in a flat-bottomed 96-well plate 24 h prior to the experiment. Following transfection (0.25 μg of DNA per well), the medium was changed and 20 μL of MTS reagent (Promega) added per well. Plates were incubated at 37 °C for 5 h prior to measuring the absorbance at 490 nm. Background absorbance was subtracted, and the results were plotted as percentage cell viability.

RESULTS

NLS Peptides Used in Study. Three different types of NLS peptides were used in this study. Peptides SV40 and Ext SV40 were derived from the SV40 T antigen sequence that binds to importin α1, while control peptides mSV40 and Ext mSV40 contained the K128T mutation reported to abolish NLS function (*19*, *20*). The HTLV peptide is a 31 amino acid sequence from the amino terminus of the HTLV Rex posttranscriptional regulatory protein that has previously been identified as mediating nuclear import by direct interaction with importin β1 (*21*). The 38 amino acid peptide M9 was

Table 1. NLS Peptides Used in Study

Peptide	Sequence
SV40	PKK KRK VED PYC
mSV40	PKT KRK VED PYC
Ext SV40	SSD DEA TAD SQH STP PKK KRK VED PYC
Ext mSV40	SSD DEA TAD SQH STP PKT KRK VED PYC
HTLV	MPK TRR RPR RSQ RKR PPT WAH FPG FGQ GSL C
M9	GNQ SSN FGP MKG GNF GGR SSG PYG GGG QYF AKP RNQ GGY C
Scr M9	SPG NRM GAG YFK GSG NKS GFQ GRN PGS GQG YGP NQG FYG C

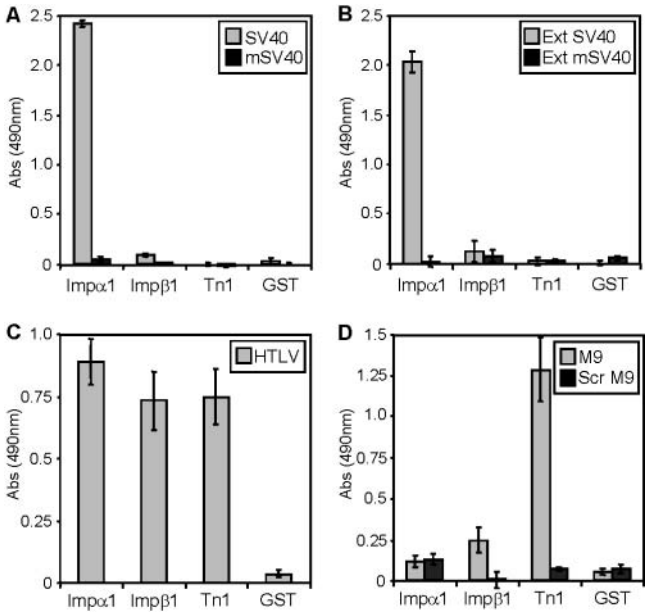


Figure 1. Binding of NLS peptides to transport receptors. 96-well plates were coated with 30−40 pmol/well of the (A) SV40 peptide, (B) Ext SV40 peptide, (C) HTLV peptide, or (D) M9 peptide in 50mM $NaHCO_3$ at 4 °C overnight. After blocking with intracellular buffer containing 5% BSA, plates were incubated with 12.5 nM transport receptor-GST or with GST alone. The presence of the transport receptor was detected using goat anti-GST antibody, HRP-labeled anti-goat and OPD substrate. The absorbance at 490 nm was measured and background subtracted. In panels A, B, and D binding of mutated (mSV40, Ext mSV40) and scrambled (Scr M9) peptides to transport receptors were also determined. Results are shown as a mean and standard deviation from at least three samples.

derived from heterogeneous ribonucleoprotein A1 reported to bind transportin 1, and a scrambled version of this peptide was used as a control peptide. The amino acid sequences of these peptides are shown in Table 1. For all peptides a cysteine residue was included at the carboxy terminus to enable attachment to PNA-maleimide/DNA conjugates.

Binding of NLS Peptides to Intracellular Transport Receptors. The nature of the interaction of NLS peptides with a range of intracellular transport receptors was determined using an ELISA-based assay with purified GST fusion proteins and an anti-GST antibody. Significant binding to importin α1 was observed with the SV40 (Figure 1A) and Ext SV40 (Figure 1B) peptides but not the M9 peptide or the control peptides mSV40 and Ext mSV40. Unexpectedly, the HTLV peptide bound at similar levels to importin α1, importin β1 and transportin 1 (Figure 1C). However, the HTLV peptide bound only weakly to GST alone, indicating some degree of specificity for the interaction. The M9 peptide exhibited a strong interaction with transportin 1, its known receptor, whereas

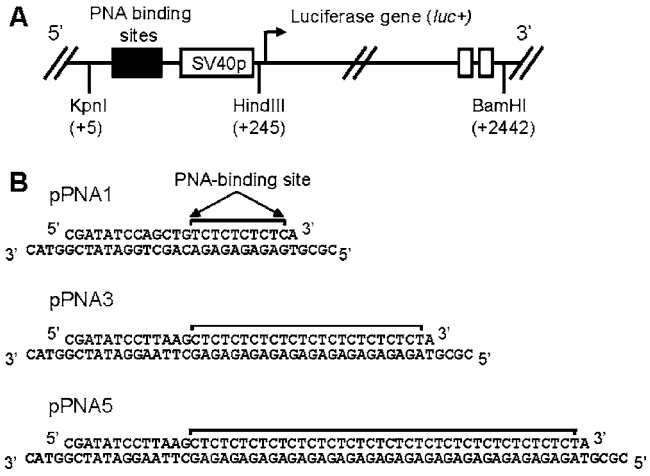


Figure 2. Schematic showing PNA binding sites used in study. (A) Relative location of oligonucleotides containing PNA binding sites inserted into the luciferase expression vector pGL3con (Promega). The relative positions of the SV40 promoter (SV40p), transcription start point and three restriction sites (Kpn1, HindIII, and BamH1) are indicated. (B) Sequences of oligonucleotides containing between one and five PNA binding sites used in study. The sequence of the PNA binding site within each oligonucleotide is highlighted and the name of the resultant plasmid DNA construct given (pPNA1, pPNA3 and pPNA5).

the scrambled peptide control, Scr M9, did not bind (Figure 1D). A significant interaction was also observed between the M9 peptide and importin β1 ($p < 0.05$), although at 5-fold lower than with transportin-1. These data demonstrates that the NLS peptides are capable of binding to intracellular transport receptors in vitro with different degrees of interaction and specificity. The ability of these NLS peptides to enhance delivery of plasmid DNA was therefore next investigated.

Characterization of PNA/DNA Conjugates. In the first strategy to utilize NLS peptides for gene delivery, PNA/DNA conjugates were prepared and characterized prior to attachment of NLS peptides. The requirements for efficient binding of the PNA to DNA were examined using constructs based on the plasmid pGL3con containing one, three, or five copies of the PNA binding sequence AGAGAGAG inserted immediately upstream of the SV40 promoter. Figure 2 shows the relative location and sequence of PNA binding sites inserted into pGL3con. These constructs were incubated with PNA-biotin and the presence of bound PNA-biotin probed using Texas-Red labeled streptavidin. Comigration of streptavidin Texas-Red with DNA following electrophoresis demonstrated significant binding of PNA-biotin to constructs containing three or five copies of the PNA binding site (Figure 3A). By comparison, there was no significant binding of PNA-biotin to DNA without any binding sites (Figure 3A) or to constructs containing only one binding site (data not shown). The interaction between PNA and plasmid DNA was investigated in more detail by restriction of PNA-biotin/DNA conjugates with KpnI and HindIII, generating DNA fragments of either 277 bps (containing three PNA sites) or 293 bps (containing five PNA sites). Probing for PNA-biotin with streptavidin Texas-Red showed that PNA-biotin bound specifically to the PNA binding site, as only short DNA fragments (<300 bps) were labeled with Texas-Red and not the rest of the plasmid DNA (>5 kb) without any known PNA-binding site (data not shown). Binding of streptavidin Texas-Red to PNA-biotin also resulted in retardation of the shorter DNA fragments producing discrete bands. For example, addition of streptavidin Texas-Red to the DNA

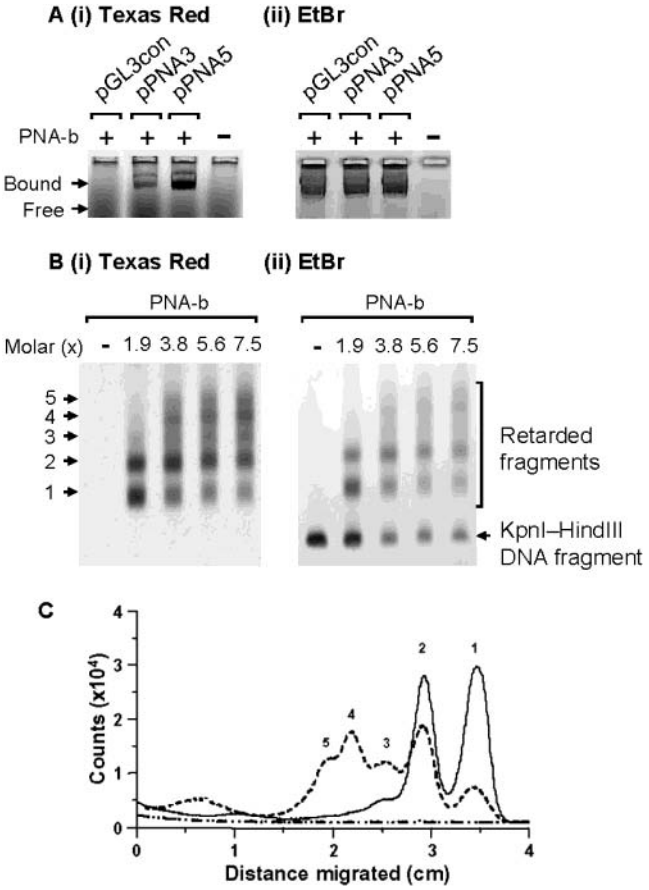


Figure 3. Characterization of PNA/DNA conjugates. (A) PNA-biotin (PNA-b) was added to pGL3con (Lane 1), pPNA3 (Lane 2), and pPNA5 (Lane 3) at a 7.5−12.5 molar excess, incubated at 37 °C for 24 h, and a 10-fold molar excess of streptavidin Texas-Red added in 200 mM NaCl for 30 min. Samples were run on a 0.8% ethidium bromide (EtBr)-free agarose gel and conjugate formation assessed by scanning for (i) Texas Red fluorescence on a Typhoon fluorimager. The gel was then stained in (ii) 50 μg/mL EtBr and scanned for the presence of DNA. Lane 4 (−) contains streptavidin-Texas Red alone with no DNA present. (B) The PNA-b/pPNA5 conjugate was prepared as in (A) using 1.9 to 7.5 molar excess of PNA-b and restricted with KpnI and HindIII prior to addition of streptavidin-Texas Red. Samples were run on a 1.6% agarose gel for 3 h and visualized for (i) Texas Red and (ii) EtBr fluorescence as in (A). Restriction fragment of 293 bp is shown only. (C) Analysis of agarose gel from (B) using ImageQuant software with image density plotted as a function of distance migrated. The peaks numbered 1 to 5 are indicated, and the lines represent using PNA-b at a molar excess of 1.9 (intact) and 7.5 (dashed).

fragment containing five copies of the PNA binding site produced five distinct bands with reduced electrophoretic mobility (Figure 3B and 3C). Similarly, plasmids containing three copies of the PNA binding site gave three retarded bands in the presence of streptavidin Texas-Red (data not shown). These retarded bands most likely indicate that an increasing number of PNA-biotin molecules are bound to each plasmid.

The amount of PNA-biotin used correlated with the intensity of Texas-Red fluorescence in retarded bands, reflecting the level of PNA-biotin bound to the DNA. For example, two major retarded bands were observed using the DNA fragment containing five PNA-binding sites with PNA-biotin at a molar excess of 1.9, whereas five distinct bands of reduced intensity were observed using 4-fold more PNA-biotin (Figures 3B and 3C). The proportion of DNA bound by PNA-biotin was determined by quantifying the ethidium bromide fluorescence of free DNA (Table 2). These results indicated that approximately 80% of plasmid DNA containing five PNA binding sites was bound by PNA-biotin when 7.5 molar excess was used. In contrast, only 25% of plasmid DNA containing three PNA binding sites was bound to PNA-biotin at a molar excess of 12.5. Altogether these results indicate that while PNA bound specifically to plasmids containing three copies of the PNA binding site, at least five binding sites were required to achieve an appropriate level of PNA/DNA conjugation that might prove useful for gene delivery applications.

Table 2. Efficiency of PNA Binding to DNA

construct	PNA-b[a]	%DNA bound[b]
pPNA1	37.5	1.7
pPNA3	3.13	12.1
pPNA3	12.5	18.0
pPNA5	1.88	15.7
pPNA5	7.5	79.4

[a] Molar excess of PNA-biotin added to DNA. [b] Percentage of DNA bound by PNA-b determined by measuring ethidium bromide fluorescence of free DNA.

Preparation and Characterization of NLS Peptide-PNA/DNA Conjugates. To determine the reactivity of terminal cysteine residues the SV40 and Ext mSV40 peptides were incubated with Texas-Red maleimide and reaction products analyzed by Tris-Tricine SDS-PAGE. Two major bands were observed corresponding to the fluorescently labeled NLS peptide and free Texas-Red maleimide (Figure 4A, lane 2i,ii). Increasing the amount of peptide used from 1 to 20-fold molar excess (Figure 4A, lanes 2−4i,ii) resulted in complete loss of free Texas-Red maleimide and more labeled NLS peptide. Similar results were obtained with all of the cysteine terminated NLS peptides (data not shown). On the basis of these results a 20-fold molar excess of NLS peptide to PNA-maleimide was subsequently used in conjugation reactions.

The next step was to attach NLS peptides directly to the PNA/DNA conjugates. However, the NLS peptides used in this study are cationic, containing lysine and arginine residues, and are capable of binding nonspecifically to DNA by electrostatic interaction. To overcome this problem NLS peptide-PNA-maleimide/DNA conjugates were prepared by incubating PNA-maleimide/DNA conjugates with a 20-fold molar excess of each NLS peptide in 1M NaCl. Unreacted peptide was then removed by ethanol precipitation. To verify conjugate formation and removal of free peptide, PNA-maleimide/DNA conjugates were labeled with an N-terminal FITC-labeled HTLV peptide and restricted to release a 293 base pair fragment. Analysis of the restriction fragments by gel electrophoresis demonstrated that fluorescence of the NLS peptide was only associated with DNA fragments containing the PNA binding sites and not with the rest of the plasmid (Figure 4B). Using an agarose gel-based assay to generate a peptide standard curve with FITC-labeled HTLV peptide, it was estimated that on average 1.26 NLS peptides were bound to each plasmid (data not shown). However, as the PNA was bound to 80% of the DNA, this figure was recalculated to an average of 1.6 copies of the NLS peptide bound to 80% of the DNA. These results demonstrate that site-specific conjugation between NLS peptides and the PNA-maleimide/DNA conjugates was achieved.

In Vitro Biological Activity of NLS Peptide-PNA/DNA Conjugates. The biological activity of NLS peptide-PNA/DNA conjugates was evaluated by their ability to bind to intracellular receptors and transfection activity

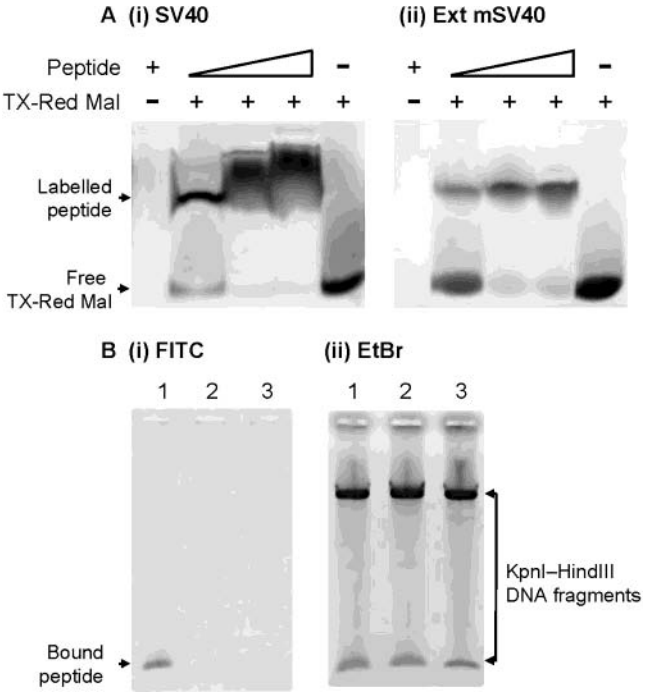


Figure 4. Conjugation of NLS peptides to PNA/DNA. (A) NLS peptides (i) SV40 and (ii) Ext mSV40 were incubated with Texas-Red maleimide (TX-Red mal) for 3 h, analyzed on a 16.5% Tris-Tricine SDS−PAGE gel and scanned using a Typhoon fluorimager at λ_{ex} 633 nm, λ_{em} 610 nm. NLS peptides were added at 1-, 10-, and 20-fold molar excess. Positions of labeled peptides and free TX-Red mal are indicated. (B) NLS peptide-PNA/DNA conjugates were prepared as previously described using either PNA-maleimide (lane 1), PNA-biotin (lane 2) or no PNA (lane 3), and a FITC-tagged HTLV peptide. The conjugates were then restricted with KpnI and HindIII and samples run on a 1.6% ethidium bromide (EtBr)-free agarose gel. The peptide was detected by scanning for (i) FITC using a Typhoon fluorimager at λ_{ex} 532 nm, λ_{em} 526 nm. The gel was stained in (ii) 50 μg/mL EtBr and scanned for the presence of DNA at λ_{ex} 532 nm, λ_{em} 610 nm. Specific conjugate formation was indicated by comigration of the peptide with the DNA fragment containing PNA-binding sites.

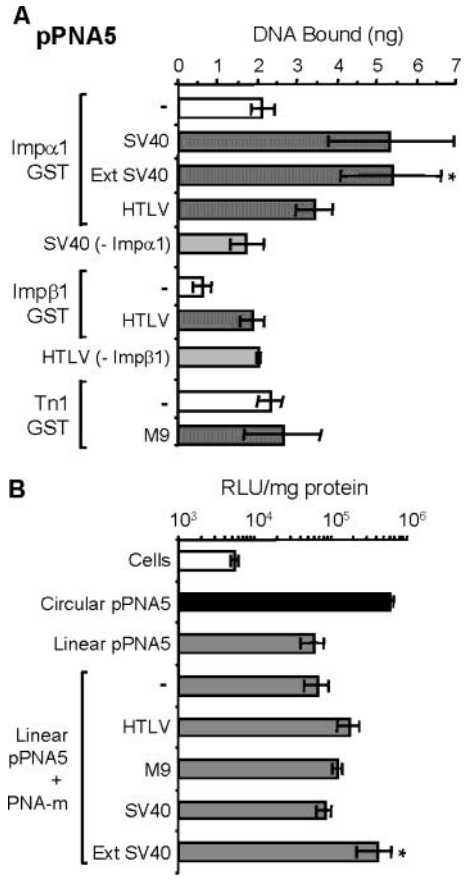


Figure 5. Biological activity of NLS peptide-PNA/DNA conjugates. (A) Binding to intracellular transport receptors. Glutathione−sepharose beads were incubated with 25 nmol of transport receptor-GST (Impα1-importin α1, Impβ1-importin β1, and Tn1-transportin 1) as indicated for 2 h, washed in NLS buffer/1% buffer, and incubated with 0.5 μg of NLS peptide-PNA-maleimide/pPNA5 for 2 h at room temperature. The picogreen assay was used to determine the amount of DNA bound to beads. In control experiments the transport receptor-GST was omitted (−) as indicated. Significant difference was observed between Ext SV40−PNA/DNA conjugates and DNA alone (*p < 0.05). (B) Transfection activity of linear NLS peptide-PNA/pPNA5 conjugates. HeLa cells were transfected with 0.25 μg of 2491 bp linear DNA fragments generated from NLS peptide-PNA/DNA conjugates using RPC/DOTAP as delivery vector. Luciferase expression was assayed after 24 h and normalized to protein concentration. Significant difference was observed between Ext SV40−PNA/DNA conjugates and DNA alone (*p < 0.035). Results are shown as a mean and standard deviation from at least three samples.

in HeLa cells. Using an in vitro binding assay based on GST-receptor fusion proteins bound to glutathione−sepharose beads, approximately 5 ng of SV40 and Ext SV40−PNA/DNA conjugates (p < 0.05) and 3.5 ng of the HTLV−PNA/DNA conjugate (p = 0.0123) bound to importin α1-GST, compared to 2 ng with DNA alone (Figure 5A). In contrast, there was no significant binding observed with the HTLV−PNA/DNA conjugate to importin β1 or the M9-PNA/DNA conjugate to transportin 1-GST. Previous studies have indicated that NLS peptides attached to linear DNA molecules enhance nuclear delivery (*9*). Therefore, NLS peptide-PNA/DNA conjugates were restricted with KpnI and BamHI to generate linear DNA molecules of 2491 base pairs prior and their transfection ability assessed. Transfection of HeLa cells using 0.25 μg of DNA with a reducible polycation/DOTAP delivery system (*18*) showed that reporter gene expression of unmodified linear DNA was 10-fold less than intact circular DNA after 24 h (Figure 5B). Attachment of the Ext SV40 peptide to the PNA/DNA conjugate mediated a significant 7-fold increase in transgene expression (p = 0.035) compared to linear DNA and PNA/DNA controls. There were no significant improvements in gene expression observed using any of the other NLS peptides. These results indicate that biological activity of linear DNA can be enhanced by linkage of NLS peptides using PNA technology but it is dependent on the type of NLS peptide used.

Polyplex Formation Using NLS Peptides. A second strategy to enhance gene delivery was investigated using NLS peptides to condense plasmid DNA into discrete particles and mediate transfection in mammalian cells. The ability of NLS peptides to condense DNA was examined using the ethidium bromide condensation and agarose gel retardation assays. Two different controls were used, an oligolysine peptide consisting of 18 lysine residues (K18) and a 7.5 kDa PLL polymer (PLL). K18 was of similar molecular weight to the smaller NLS peptides such as the SV40 peptide, whereas PLL was used as a control for larger peptides resulting from any dimerization of NLS peptides via disulfide bridges between the terminal cysteine residues. Plasmid DNA was efficiently condensed by PLL (Figure 6A) and K18 (data not shown) with an almost complete loss of fluorescence (~90%) at an N:P ratio of between 1 and 2. The HTLV

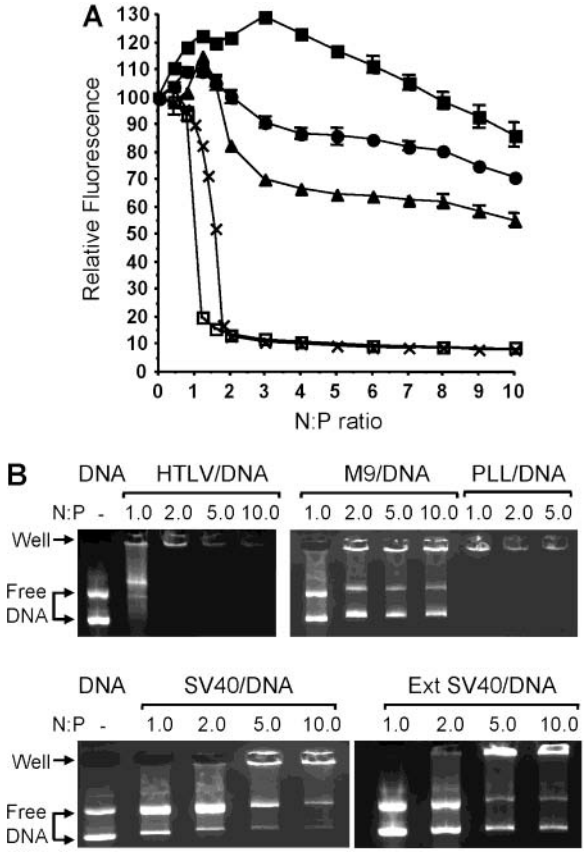


Figure 6. Polyplex formation using NLS peptides. (A) EtBr condensation assay with the following peptides: M9 (filled squares), Ext SV40 (filled circles), SV40 (filled triangles), HTLV (crosses), and PLL 7.5kDa (empty squares). Results are shown as a mean and standard deviation from at least three samples. (B) Agarose gel electrophoresis of plasmid DNA complexed with the indicated NLS peptide at N:P ratios of 1.0, 2.0, 5.0, and 10.0. The control lane (−) contains plasmid DNA alone. The relative locations of wells and free DNA are indicated.

peptide also produced a similar reduction in fluorescence at an N:P ratio of 2 to 3. In contrast, the SV40, Ext SV40 and M9 peptides were relatively poor at condensing DNA with only a 15−40% reduction in fluorescence at an N:P ratio of between 5 and 10. Similar trends were observed using the agarose gel retardation assay where DNA was retained in the wells at an N:P ratio of 1 to 2 with PLL (Figure 6B), K18 (data not shown), and HTLV peptides (Figure 6B), whereas free DNA was still observed with the SV40, Ext SV40, and M9 peptides even at an N:P ratio of 10. These results indicate that the HTLV peptide was the only NLS peptide capable of fully condensing DNA. Photon correlation spectroscopic analysis provided additional evidence that the HTLV peptide efficiently condensed plasmid DNA with polyplexes observed less than 90 nm in diameter at an N:P ratio of 10 (data not shown).

Transfection Activity of NLS Peptide/DNA Polyplexes. PC-3 cells were transfected with NLS peptide/DNA polyplexes formed at an N:P ratio of 10 and luciferase gene expression assayed after 24 h to determine transfection activity (Figure 7A). No significant gene expression was observed using polyplexes formed with the SV40, Ext SV40, or M9 peptides in the presence of 100 μM chloroquine compared to cells alone (Figure 7A). This result was most likely due to the inability of these peptides to condense DNA. In contrast, HTLV/DNA polyplexes mediated levels of gene expression (1.4×10^6 RLU/mg protein) that were approximately 186-fold higher

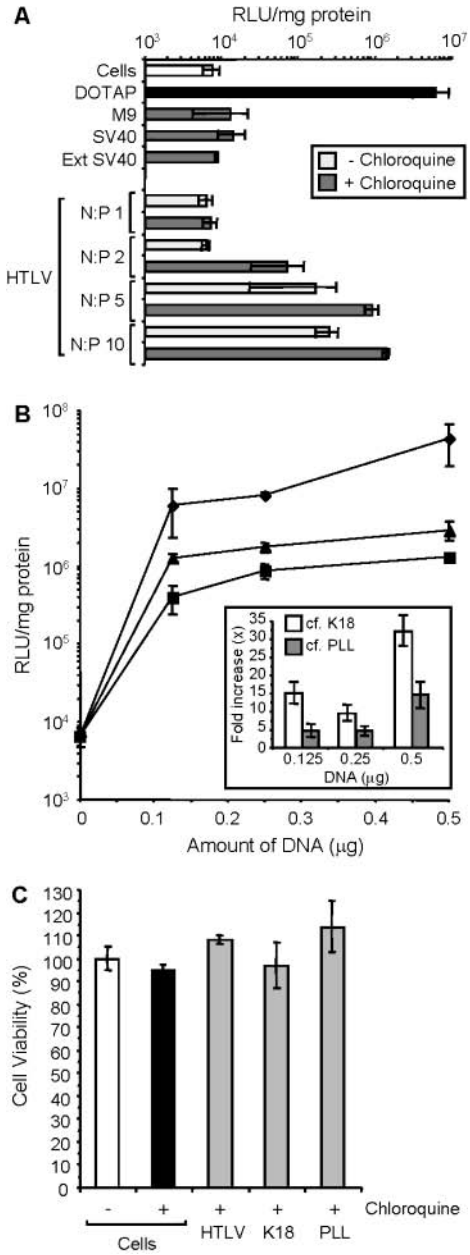


Figure 7. Transfection activity of NLS peptide-based polyplexes. (A) PC-3 cells were transfected with 0.5 μg pGL3con complexed with M9, SV40, Ext SV40, and HTLV peptides at an N:P ratio of 10, unless otherwise indicated, in the absence (light gray bars) or presence (dark gray bars) of 100 μM chloroquine. DOTAP/DNA complexes (black bar) were used as the positive control. (B) PC-3 cells were transfected with either 0, 0.1, 0.25, or 0.5 μg of pGL3con complexed with HTLV peptide (filled diamonds), PLL 7.5 kDa (filled triangles), and K18 (filled squares) at an N:P ratio of 10 in the presence of 100 μM chloroquine. The fold differences in levels of expression achieved using the HTLV peptide compared to PLL (grey bars) or K18 (empty bars) are shown in the inset. Luciferase expression was assayed 24 h after transfection and normalized to protein concentration as in (A). (C) Cytotoxicity of NLS peptide-based polyplexes. PC-3 cells were incubated for 5 h with 0.5 μg of pGL3con complexed with the HTLV peptide, K18, and PLL 7.5 kDa at an N:P ratio of 10 in the presence of 100 μM chloroquine. MTS reagent was then added to the cells and the absorbance at 490 nm measured. Results are shown as a mean and standard deviation from at least three samples.

than cells alone. In the absence of chloroquine, significant levels of reporter gene expression (2.5×10^5 RLU/mg protein) were still observed but were 5.6-fold lower indicating the requirement for the endoosmolytic reagent.

Similar levels of expression were observed using HTLV/DNA polyplexes formed at an N:P ratio of 5. However, no transgene expression was observed at an N:P ratio of 1, reflecting the incomplete condensation of DNA at this N:P ratio.

The transfection activity of HTLV/DNA polyplexes was also compared against those formed with K18 and PLL, which are both capable of condensing DNA efficiently. Measurement of luciferase expression 24 h after transfection demonstrated that the HTLV peptide mediated levels of transgene expression approximately 4.7−14.7-fold greater than PLL and 9.6−32.3-fold greater than K18 depending on the amount of DNA used (Figure 7B). This difference was not due to cellular toxicity as viability assays showed that there was no toxicity observed using any of the NLS peptides (Figure 7C). Altogether these results indicate that HTLV-based polyplexes mediate efficient transfection of cells at levels that are significantly higher than those achieved with polyplexes based on PLL of similar molecular weight.

DISCUSSION

A number of cellular barriers restrict transgene expression but inefficient transfer of DNA from the cytoplasm to the nucleus has been identified as the major contributory factor with only 0.1% of naked DNA or 1% of polyplex DNA reaching the nucleus following microinjection into the cytoplasm (*22*). A common strategy to enhance nuclear delivery of DNA has been to incorporate synthetic NLS peptides into gene delivery vectors that bind intracellular transport receptors, such as importin α, and utilize the highly efficient physiological protein nuclear import pathways. Many of these approaches have however met with limited success (*10*, *11*, *23*, *24*), although one study reported a 10−1000-fold increase in gene expression (*9*). The aim of the present study was to facilitate the development of NLS-based vectors by helping to identify the requirements for NLS-enhanced transfection, including the type of NLS peptide, morphology of DNA and method of incorporating the NLS peptide.

Two different strategies using a range of NLS peptides were evaluated in order to enhance nonviral gene delivery. In the first approach we inserted PNA-binding site oligonucleotides into the plasmid pGL3con and demonstrated site-specific conjugation of NLS peptides via a PNA-maleimide clamp. A major advantage of this approach was that, unlike a number of previous studies (*10*, *11*), NLS peptide-modified DNA did not have diminished transcriptional capacity. In addition, we were able to show in vitro binding of the Ext SV40−PNA/DNA conjugate to an importin α1-GST fusion protein and a corresponding 7-fold increase in reporter gene expression using linear DNA. This increase in gene expression was comparable to the 2−8-fold increases observed in the majority of related studies (*8*, *13*). Whereas, there was no significant improvement in gene expression observed using other NLS peptides such as HTLV or M9.

The number of NLS peptides required to enhance nuclear delivery of DNA, whether circular or linear, is the subject of controversy with some researchers favoring a single NLS and others preferring as great a number of peptides as possible. It has been proposed that a single or cluster of NLS peptides attached to one end of linear DNA is sufficient for nuclear import and that more may actually hinder the process (*8*, *9*). This hindrance could in principle occur through multiple NLSs causing docking of the DNA to several nuclear pore complexes and has been calculated to be physically possible with DNA over 1 kb in size (*25*). In this study, a mixed population of NLS peptide-PNA/DNA conjugates was produced containing a cluster of different numbers of the NLS peptide, and it was estimated using a fluorescently tagged HTLV peptide that on average 1.26−1.6 NLS peptides were bound to each plasmid. Enhanced transfection was only observed, however, when the Ext SV40 peptide was conjugated to DNA, indicating that the type and length as well as the number of NLS peptides play an important role in promoting nuclear delivery.

Initial binding studies demonstrated a strong interaction between the NLS peptides with their corresponding intracellular receptors. In the case of the SV40 and Ext SV40 peptides, for example, this interaction was highly specific as a single mutation from a K to T residue abolished binding. Surprisingly, the HTLV peptide bound with a similar affinity to all of the receptors examined, which may have been a nonspecific interaction as this peptide is highly positively charged. Transportin 1, however, has 24% sequence homology with importin β1 (*26*) and possesses two distinct, nonoverlapping cargo-binding sites, one for M9-like sequences, and one for more basic sequences (*27*). The HTLV peptide may have therefore bound to the second cargo site on transportin 1.

A likely explanation for the lack of NLS activity observed with the HTLV and M9 peptides was their apparent loss in ability to interact with transport receptors following conjugation to DNA. There was also relatively weak binding observed between the Ext SV40−PNA/DNA conjugate and importin α1-GST fusion protein. This lack of binding was most likely due to electrostatic interaction between the negatively charged phosphate groups of DNA with the cationic NLS peptides. The positive charges of the lysine and arginine residues of many NLS peptides are critical for interaction with transport receptors, and their neutralization would likely hinder cargo recognition. Possible ways to overcome this problem include increasing the spacer length separating the NLS peptide from the DNA or to increase the number of NLS peptides attached to the DNA. Ciolina et al., for example, showed that increasing the number of SV40 NLS peptides attached to DNA from 45 to 100 also resulted in enhanced binding of DNA to importin α1-GST (*10*). An advantage of the PNA technology used in this study is the possibility to increase the number of NLS peptides attached to the DNA by insertion of additional PNA-binding sites. However, it is likely that to achieve maximum NLS-mediated transfection a balance will be required between improving the interaction of NLS peptide/DNA conjugates to transport receptors and the proposed hindrance of binding to multiple nuclear pore complexes (*9*).

An important consideration throughout this study was to fully characterize and purify NLS peptide-PNA/DNA conjugates prior to biological evaluation. The presence of unconjugated NLS peptides, for instance, may compete for binding to transport receptors. NLS peptides were therefore attached to PNA/DNA conjugates in the presence of high salt conditions to avoid nonspecific interactions and unreacted peptides removed by ethanol precipitation of the DNA. A fluorescence-based assay was also developed to analyze binding of PNA to DNA indicating that at least five binding sites were required for efficient PNA binding (>80% of DNA bound). No significant PNA binding was observed with plasmids containing just one site or to linear DNA (data not shown). Although some short PNAs can interact stably with their complementary sequence (*28*), weaker binding of PNA to linear DNA compared to circular DNA has been

previously observed by up to two to 3 orders of magnitude (*29*). In addition, secondary structure of the plasmid may hinder binding of PNA to DNA which is dependent on the exact sequence of the plasmid DNA used (*30*).

The morphology of the DNA used was also observed to be an important factor in this study to influence NLS-enhanced transfection. Initial transfection results showed a modest 2-fold increase in gene expression using the SV40 peptide attached to PNA/circular DNA (data not shown). However, the level of gene expression was enhanced to 7-fold compared to unmodified DNA when the NLS peptide-PNA/DNA conjugate was restricted with the enzymes KpnI and BamHI to produce a linear DNA molecule with the cluster of NLS peptides at one end. This is in agreement with previous studies that have shown enhanced gene expression using linear DNA with NLS peptides following ligation of an oligonucleotide−NLS conjugate (*9*) or incorporation of a modified nucleotide for chemical linkage of the NLS peptide (*8*). It is also still not clear what delivery vectors should be used with NLS peptide/DNA conjugates to properly exploit the NLS-transport pathways. Previous studies have observed enhanced gene expression with NLS peptide/DNA conjugates using cationic lipids and PEI (*9*). However, the intracellular trafficking and location of DNA release from these types of vectors are thought to differ greatly, with cationic lipids releasing DNA into the cytoplasm and PEI/DNA polyplexes remaining largely intact (*31*, *32*). PEI might even be expected to hinder NLS activity by masking the peptide and preventing interaction with transport receptors. In this study we used a reducible polycation/lipid combination that has recently been shown to facilitate release of nucleic acids into the cytoplasm and is therefore likely to promote availability of NLS peptides for interaction with transport receptors (*18*).

In the second approach we examined the ability of NLS peptides to condense DNA and mediate transfection. Of all the NLS peptides examined, the HTLV peptide was the most efficient at condensing DNA and mediated transfection at levels 5−32-fold higher than control polyplexes formed with PLL of similar molecular weight. Chloroquine potentiated the transfection activity of HTLV/DNA polyplexes by 5−10-fold, an expected result, as the HTLV peptide does not contain any lytic sequences known to mediate endosomal escape. This is the first study to the best of our knowledge that has demonstrated efficient transfection mediated by a peptide based on the HTLV sequence. The inability of the SV40 and M9 peptides to mediate transfection is probably due to the lack of positively charged amino acids in their sequence since a minimum length of six to eight cationic amino acids are known to be required to compact DNA into structures active in gene delivery (*33*). It still remains to be investigated whether the increased level of transfection observed using the HTLV peptide is NLS-mediated or due to some other mechanism. The arginine-rich sequence of the HTLV peptide is similar to many protein transduction domains (PTDs), such as that in HIV TAT (*34*), which mediate cross-membrane transfer and are also thought to have nuclear homing capacity (*35*). Therefore, it is possible that the HTLV peptide used in this study is functioning as a nuclear homing PTD.

CONCLUSION

Based on these results, a number of factors were identified that directly influence the ability of NLS peptides to enhance nonviral gene transfer. These included the type of NLS peptide, morphology of DNA, and method used to incorporate NLS peptides into nonviral vectors. Highly cationic NLS peptides such as the HTLV sequence were most effective at condensing DNA and enhanced levels of gene expression compared to polylysine controls. Peptides based on the SV40 but not the M9 and HTLV sequences were able to promote gene expression when attached to the ends of linear DNA. Proper characterization of NLS peptide/DNA conjugates was also an important consideration in evaluating the transfection capability of NLS-modified vectors. Further development of NLS-modified vectors is required before they can be used routinely; however, these results help to define the requirements for NLS-modified vector design and construction. It may also prove necessary to include additional components used by viruses to achieve effective nuclear delivery, such as the triple-stranded DNA flap for HIV-1 genome nuclear import (*36*), before more efficient nonviral delivery systems can be developed.

ACKNOWLEDGMENT

We express our gratitude to Dr. Y. Yoneda (Osaka University, Japan) for the pGEX-2T plasmids, Dr. G. Dreyfuss (University of Pennsylvania) for the pGEX-5X plasmid and Dr. L. Haynes (University of Birmingham, UK) for the GST protein. We also thank Dr. R. Grand (University of Birmingham, UK), Dr. G. McNab (University of Birmingham, UK), and Dr. D. Jans (Monash University, Australia) for useful discussions. This work was supported by grants from the Biotechnology and Biological Sciences Research Council (BBSRC) and Cancer Research UK.

Supporting Information Available: Western blot analysis of receptor GST fusion proteins. Sequence data demonstrating insertion of oligonucleotides into pGL3con. Tris-Tricine SDS-PAGE analysis demonstrating reactivity of NLS peptides with maleimide-Texas Red. Characterization of NLS peptides by HPLC analysis and mass spectroscopy. This material is available free of charge via the Internet at http://pubs.acs.org.

LITERATURE CITED

(1) Read, M. L., and Bremner, K. H. (2002) Antisense strategies and nonviral gene therapy for cancer. *Expert Opin. Ther. Pat. 12*, 379−391.

(2) Buckley, R. H. (2002) Gene therapy for SCID−a complication after remarkable progress. *Lancet 360*, 1185−6.

(3) (2003) French gene therapy group reports on the adverse event in a clinical trial of gene therapy for X-linked severe combined immune deficiency (X-SCID). *J. Gene Med. 5*, 82−84.

(4) Zabner, J., Fasbender, A. J., Moninger, T., Poellinger, K. A., and Welsh, M. J. (1995) Cellular and molecular barriers to gene transfer by a cationic lipid. *J. Biol. Chem. 270*, 18997−9007.

(5) Brunner, S., Sauer, T., Carotta, S., Cotten, M., Saltik, M., and Wagner, E. (2000) Cell cycle dependence of gene transfer by lipoplex, polyplex and recombinant adenovirus. *Gene Ther. 7*, 401−7.

(6) Lanford, R. E., Kanda, P., and Kennedy, R. C. (1986) Induction of nuclear transport with a synthetic peptide homologous to the SV40 T antigen transport signal. *Cell 46*, 575−82.

(7) Bremner, K. H., Seymour, L. W., and Pouton, C. W. (2001) Harnessing nuclear localization pathways for transgene delivery. *Curr. Opin. Mol. Ther. 3*, 170−7.

(8) Ludtke, J. J., Zhang, G., Sebestyen, M. G., and Wolff, J. A. (1999) A nuclear localization signal can enhance both the nuclear transport and expression of 1 kb DNA. *J. Cell Sci. 112* (Pt 12), 2033−41.

(9) Zanta, M. A., Belguise-Valladier, P., and Behr, J. P. (1999) Gene delivery: a single nuclear localization signal peptide is sufficient to carry DNA to the cell nucleus. *Proc. Natl. Acad. Sci. U.S.A. 96*, 91−6.

(10) Ciolina, C., Byk, G., Blanche, F., Thuillier, V., Scherman, D., and Wils, P. (1999) Coupling of nuclear localization signals to plasmid DNA and specific interaction of the conjugates with importin alpha. *Bioconjugate Chem. 10*, 49−55.

(11) Sebestyen, M. G., Ludtke, J. J., Bassik, M. C., Zhang, G., Budker, V., Lukhtanov, E. A., Hagstrom, J. E., and Wolff, J. A. (1998) DNA vector chemistry: the covalent attachment of signal peptides to plasmid DNA. *Nat. Biotechnol. 16*, 80−5.

(12) Nielsen, P. E., Egholm, M., Berg, R. H., and Buchardt, O. (1991) Sequence-selective recognition of DNA by strand displacement with a thymine-substituted polyamide. *Science 254*, 1497−500.

(13) Branden, L. J., Mohamed, A. J., and Smith, C. I. (1999) A peptide nucleic acid-nuclear localization signal fusion that mediates nuclear transport of DNA. *Nat. Biotechnol. 17*, 784−7.

(14) Zelphati, O., Liang, X., Hobart, P., and Felgner, P. L. (1999) Gene chemistry: functionally and conformationally intact fluorescent plasmid DNA. *Hum. Gene Ther. 10*, 15−24.

(15) Zelphati, O., Liang, X., Nguyen, C., Barlow, S., Sheng, S., Shao, Z., and Felgner, P. L. (2000) PNA-dependent gene chemistry: stable coupling of peptides and oligonucleotides to plasmid DNA. *Biotechniques 28*, 304−10, 312−4, 316.

(16) Imamoto, N., Shimamoto, T., Takao, T., Tachibana, T., Kose, S., Matsubae, M., Sekimoto, T., Shimonishi, Y., and Yoneda, Y. (1995) In vivo evidence for involvement of a 58 kDa component of nuclear pore-targeting complex in nuclear protein import. *EMBO J. 14*, 3617−26.

(17) Imamoto, N., Shimamoto, T., Kose, S., Takao, T., Tachibana, T., Matsubae, M., Sekimoto, T., Shimonishi, Y., and Yoneda, Y. (1995) The nuclear pore-targeting complex binds to nuclear pores after association with a karyophile. *FEBS Lett. 368*, 415−9.

(18) Read, M. L., Bremner, K. H., Oupicky, D., Green, N. K., Searle, P. F., and Seymour, L. W. (2003) Vectors based on reducible polycations facilitate intracellular release of nucleic acids. *J. Gene Med. 5*, 232−45.

(19) Lanford, R. E., and Butel, J. S. (1984) Construction and characterization of an SV40 mutant defective in nuclear transport of T antigen. *Cell 37*, 801−13.

(20) Kalderon, D., Richardson, W. D., Markham, A. F., and Smith, A. E. (1984) Sequence requirements for nuclear location of simian virus 40 large-T antigen. *Nature 311*, 33−8.

(21) Palmeri, D., and Malim, M. H. (1999) Importin beta can mediate the nuclear import of an arginine-rich nuclear localization signal in the absence of importin alpha. *Mol. Cell Biol. 19*, 1218−25.

(22) Pollard, H., Remy, J. S., Loussouarn, G., Demolombe, S., Behr, J. P., and Escande, D. (1998) Polyethylenimine but not cationic lipids promotes transgene delivery to the nucleus in mammalian cells. *J. Biol. Chem. 273*, 7507−11.

(23) Neves, C., Escriou, V., Byk, G., Scherman, D., and Wils, P. (1999) Intracellular fate and nuclear targeting of plasmid DNA. *Cell Biol. Toxicol. 15*, 193−202.

(24) Roulon, T., Helene, C., and Escude, C. (2002) Coupling of a targeting peptide to plasmid DNA using a new type of padlock oligonucleotide. *Bioconjugate Chem 13*, 1134−9.

(25) Maul, G. G., and Deaven, L. (1977) Quantitative determination of nuclear pore complexes in cycling cells with differing DNA content. *J. Cell Biol. 73*, 748−60.

(26) Pollard, V. W., Michael, W. M., Nakielny, S., Siomi, M. C., Wang, F., and Dreyfuss, G. (1996) A novel receptor-mediated nuclear protein import pathway. *Cell 86*, 985−94.

(27) Jakel, S., and Gorlich, D. (1998) Importin beta, transportin, RanBP5 and RanBP7 mediate nuclear import of ribosomal proteins in mammalian cells. *EMBO J. 17*, 4491−502.

(28) Datta, B., and Armitage, B. A. (2001) Hybridization of PNA to structured DNA targets: quadruplex invasion and the overhang effect. *J. Am. Chem. Soc. 123*, 9612−9.

(29) Bentin, T., and Nielsen, P. E. (1996) Enhanced peptide nucleic acid binding to supercoiled DNA: possible implications for DNA "breathing" dynamics. *Biochemistry 35*, 8863−9.

(30) Kushon, S. A., Jordan, J. P., Seifert, J. L., Nielsen, H., Nielsen, P. E., and Armitage, B. A. (2001) Effect of secondary structure on the thermodynamics and kinetics of PNA hybridization to DNA hairpins. *J. Am. Chem. Soc. 123*, 10805−13.

(31) Godbey, W. T., Wu, K. K., and Mikos, A. G. (1999) Tracking the intracellular path of poly(ethylenimine)/DNA complexes for gene delivery. *Proc. Natl. Acad. Sci. U.S.A. 96*, 5177−81.

(32) Xu, Y., and Szoka, F. C., Jr. (1996) Mechanism of DNA release from cationic liposome/DNA complexes used in cell transfection. *Biochemistry 35*, 5616−23.

(33) Plank, C., Tang, M. X., Wolfe, A. R., and Szoka, F. C., Jr. (1999) Branched cationic peptides for gene delivery: role of type and number of cationic residues in formation and in vitro activity of DNA polyplexes. *Hum. Gene Ther. 10*, 319−32.

(34) Frankel, A. D., and Pabo, C. O. (1988) Cellular uptake of the tat protein from human immunodeficiency virus. *Cell 55*, 1189−93.

(35) Efthymiadis, A., Briggs, L. J., and Jans, D. A. (1998) The HIV-1 Tat nuclear localization sequence confers novel nuclear import properties. *J. Biol. Chem. 273*, 1623−8.

(36) Zennou, V., Petit, C., Guetard, D., Nerhbass, U., Montagnier, L., and Charneau, P. (2000) HIV-1 genome nuclear import is mediated by a central DNA flap. *Cell 101*, 173−85.

BC034140K

Dendritic Polyglycerol Sulfates as New Heparin Analogues and Potent Inhibitors of the Complement System

Holger Türk,[†] Rainer Haag,*[,†] and Susanne Alban*[,‡]

Freiburg Materials Research Center, Albert-Ludwigs-University of Freiburg, Stefan-Meier-Strasse 21, 79104 Freiburg, Germany, and Pharmaceutical Institute, Christian-Albrechts-University of Kiel, 24118 Kiel, Germany. Received March 26, 2003; Revised Manuscript Received October 20, 2003

Due to several limitations of heparin, a widely used antithrombotic drug, there is large interest to develop alternatives. The aim of the presented study was to produce fully synthetic highly branched heparin mimetics. For this purpose, a new type of 'treelike' polysulfated polymers based on dendritic polyglycerol was synthesized. An efficient synthetic approach has been chosen to prepare several polyglycerol sulfates with different molecular weights as well as a polyglycerol carboxylate analogue and to evaluate them for their anticoagulant and anticomplementary activities. In contrast to the nonderivatized and the carboxylated polyglycerols, the polyglycerol sulfates prolong the activated partial thromboplastin time (APTT) and thrombin time (TT) and inhibit both the classical (CCA) and alternative complement activation (ACA). Whereas their anticoagulant activity in the APTT and in the TT amounts to 5.7−8.1% and 15.7−33.6%, respectively, of that of unfractionated heparin (UFH), their CCA and ACA inhibitory activity is 13.4−23.9 and 2.7−3.7 times, respectively, higher. In contrast to sulfated polysaccharides, the activities are not clearly dependent on the molecular weight, which might be due to the globular 3D-structure of the dendritic molecules. Due to the coherence between coagulation, complement activation and inflammation in the pathophysiology of numerous diseases, polyglycerol sulfates with both anticoagulant and anticomplementary activities represent promising candidates for the development of potential drugs.

INTRODUCTION

Although the glycosaminoglycan *heparin* has been the drug of choice in the prevention and treatment of thromboembolic disorders for nearly 70 years, there is large interest to find alternatives to both unfractionated heparin (UFH[1]) and low molecular weight heparins (LMWH). Beside well-documented clinical limitations (*1*), some disadvantages of heparin are based on its natural origin (*2*). It still has to be isolated from mammalian organs, which implies a potential risk of contamination with pathogens such as prions. Because of the increased use of heparin, especially LMWH, there is a growing shortage of the raw material. Moreover, heparin is a polydisperse mixture of molecules with different chain length and chemical structure (*3*, *4*). Numerous parameters, ranging from the animals providing heparin up to the last purification step of the product, influence its respective composition resulting in wide chemical and thus also activity variations between different heparin preparations.

Recent developments such as fondaparinux (*5*), the first selective synthetic factor Xa inhibitor, and ximelagatran (*6*), the first orally available direct thrombin inhibitor, circumvent many problems related to heparin. However, these specifically acting new antithrombotics lack the other biological activities, which are characteristic for heparin and other natural sulfated polysaccharides, e.g., complement inhibiting (*7*), antiinflammatory (*8*, *9*), antiangiogenic (*10*), antimetastatic (*11*), antiatherosclerotic (*12*), antiproliferative (*13*), antiadhesive (*14*), and antiviral effects (*15*). These additional actions can contribute to the overall therapeutic benefit of heparin in some cases (*11*). For example, heparin-coated cardiopulmonary bypass circuits have an improved biocompatibility showing better clinical outcomes (*16*).

Therefore, heparin analogues with a similar or even improved action profile, but lacking the disadvantages of this animal product, are of interest. Beside partial synthetic sulfated linear polysaccharides (*17*), fully synthetic sulfated linear polymers (*18*), which are produced independently of any suitable starting carbohydrate, may represent promising heparin mimetics. Recently, a new type of polysulfated heparin analogue based on branched polysaccharides has been described to possess a much higher anticoagulant activity than their linear counterparts (*19*). However, the accessibility of branched polysaccharides is problematic due to limited natural sources. In the present study, we describe a new synthetic approach to highly branched polysulfated heparin analogues based on dendritic polyglycerol (*20*−*22*). Several polyglycerol sulfates with different molecular weights as

* To whom correspondence should be addressed. R.H.: e-mail rainer.haag@uni-dortmund.de. S.A.: e-mail salban@pharmazie.uni-kiel.de.

[†] Albert-Ludwigs-University of Freiburg. Present address: Department of Chemistry, University of Dortmund, Otto-Hahn-Str. 6, 44227 Dortmund, Germany. Fax: +49-231-755-6148. E-mail: rainer.haag@uni-dortmund.de. Internet: www.polytree.de.

[‡] Pharmaceutical Institute, Christian-Albrechts-University of Kiel.

[1] Abbreviations: ACA, alternative complement activation; APTT, activated partial thromboplastin time; CCA, classical complement activation; DC, concentration for doubling the baseline coagulation time; dc, degree of carboxylation; DMF, *N*,*N*-dimethylformamide; ds, degree of sulfation; IC_{50}, inhibitory concentration 50%; LMWH, low molecular weight heparins; PG, polyglycerol; PPP, citrated human platelet poor pool plasma; TT, thrombin time; UFH, unfractionated heparin.

10.1021/bc034044j CCC: $27.50 © 2004 American Chemical Society
Published on Web 12/06/2003

Table 1. Characterization of Polyglycerol Sulfates 2a−c and Polyglycerol Carboxylate 3

polyglycerol derivative	polymer core	DP_n	M_n of the polymer core[a] [g/mol]	degree of functionalization[b] [%]	M_n of the polyglycerol derivative[c] [g/mol]
sulfate **2a**	**1a**	32	2500	85	5500
sulfate **2b**	**1b**	66	5000	79	10 500
sulfate **2c**	**1c**	133	10 000	84	21 700
carboxylate **3**	**1d**	106	8000	26	10 300

[a] Determined from NMR and/or GPC (DMF). [b] **2a−c**: Degree of sulfation (ds) obtained from elemental analysis; **3**: degree of carboxylation (dc) obtained from titration (see Experimental Procedures and Supporting Information). [c] Calculated using the M_n of the polyglycerol core and the experimental degree of functionalization.

well as a polyglycerol carboxylate analogue have been prepared and evaluated for their anticoagulant and anticomplementary activities.

EXPERIMENTAL PROCEDURES

Materials. Polyglycerols (PG) **1a** (M_n = 2500 g/mol, M_w/M_n = 1.6), **1b** (M_n = 5000 g/mol, M_w/M_n = 1.6), **1c** (M_n = 10 000 g/mol, M_w/M_n = 1.8) and **1d** (M_n = 8000 g/mol, M_w/M_n = 2.0) were prepared as described previously, using 1,1,1-tris(hydroxymethyl)propane (TMP) as initiator (*22*). SO_3/pyridine complex and sodium chloroacetate were purchased from Fluka (Buchs, Switzerland). Both reagents were used without further purification. The solvent *N*,*N*-dimethylformamide (DMF, p.a. quality, purchased from Roth, Karlsruhe, Germany) was dried over CaH_2 and stored over molecular sieve 4 Å prior to use. Dialysis (regenerated cellulose tubing, SpectraPore 6/Roth) in distilled water was performed in a 5 L beaker, changing the solvent three times over a period of 48 h.

Unfractionated heparin (UFH) of porcine mucosal origin (147 USP−U/mg, purchased from Sigma, Deisenhofen, Germany) was used as reference substance in the coagulation and complement assays.

Analysis. ^{1}H NMR and ^{13}C NMR spectra were recorded in D_2O at concentrations of 100 mg/mL on a Bruker ARX 300 spectrometer operating at 300 and 75.4 MHz, respectively. IR measurements were performed on a Bruker IFS 88 FT-IR spectrometer using a KBr disk.

The degree of sulfation (ds) (Table 1) of compounds **2a−c** was determined by elemental analysis. The amount of carboxylate groups in compound **3** was determined by a common titration method (*23*): 50 mg polyglycerol carboxylate (dried over P_2O_5) dissolved in 20 mL of distilled water was stirred with 2 g of Lewatit K1131 (H^+) resin. The solution of the polyglycerol carboxylic acid was filtered and subsequently titrated with 0.01 N NaOH (1 mL steps), and the pH was recorded by conductivity measurements. The equivalence point was evaluated by extrapolation of the two branches of the titration curve. The degree of carboxylation (dc) (Table 1) was then calculated using the following eq 1 (for derivation, see Supporting Information):

$$dc = \frac{(A \cdot M_n)/(m - AB)}{DP_n + f_c} \times 100\ (\%) \qquad (1)$$

with A = consumption of NaOH (mmol) corresponding to the inflection point; M_n = average molecular weight of the polyglycerol core; m = dry weight of the polyglycerol carboxylate (50 mg); B = equiv weight corresponding to one additional C_2HO_2Na unit (80.02 g/mol); DP_n = degree of polymerization of the polyglycerol core; f_c = functionality of the initiator molecule TMP (f_c = 3).

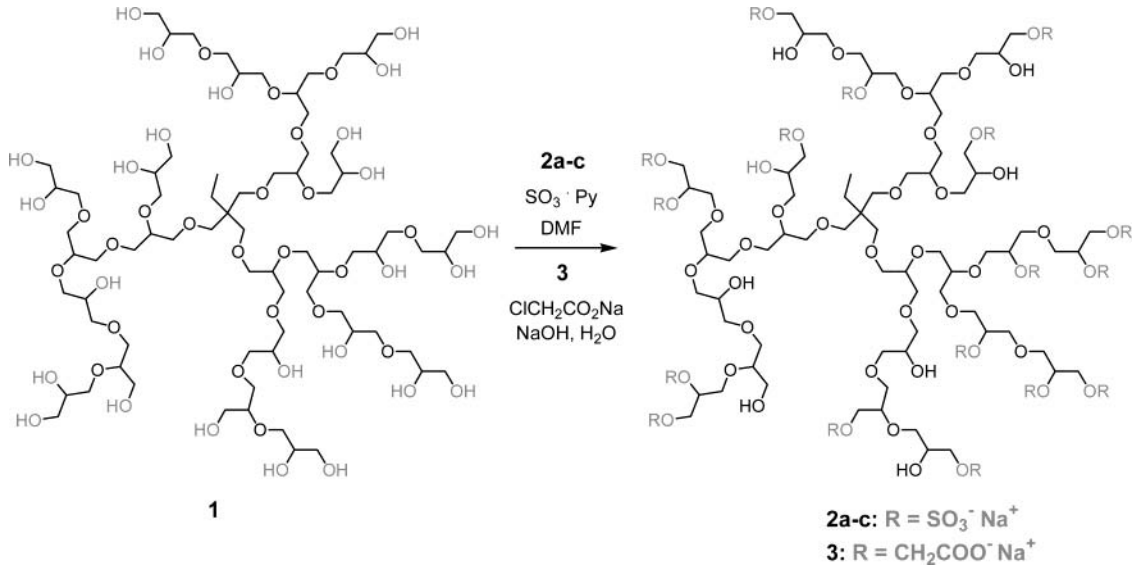
Synthesis of Polyglycerol Sulfates 2a−c. The sulfation of the polyglycerols was performed according to the method described by Alban et al. (*24*). To a stirred solution of 5.0 g of polyglycerol (**1a**, **1b**, **1c**) (67.5 mmol OH-groups) in 25 mL DMF was added dropwise a solution of 10.75 g (67.5 mmol) SO_3/pyridine complex in 67.5 mL of DMF over 4 h at 60 °C under an argon atmosphere. After the reaction mixture was stirred for additional 2 h at 60 °C and 18 h at room temperature, 50 mL of distilled water was added. To the aqueous solution was added 1 M NaOH immediately until a pH of 11 was reached. Concentration in vacuo gave the crude product which was further purified by dialysis in water. After evaporation of the solvent, the polyglycerol sulfates **2a−c** were obtained as pale yellow solids which were further dried over P_2O_5. Yields: 7.49 g (**2a**); 8.96 g (**2b**); 7.01 g (**2c**). ^{1}H NMR (300 MHz, D_2O): δ (ppm) 0.98 [t, 3H, C*H*$_3$CH$_2$C(CH$_2$O)$_3$-PG-OSO$_3$Na], 1.48 [m, 2H, CH$_3$C*H*$_2$C-(CH$_2$O)$_3$-PG-OSO$_3$Na], 3.40−4.00 [m, CH$_3$CH$_2$C(C*H*$_2$O)$_3$-*PG*-OSO$_3$Na], 4.19, 4.33, 4.38 [*PG*-OSO$_3$Na], 4.72 [PG-OCH$_2$CH(OSO$_3$Na)C*H*$_2$OSO$_3$Na]. ^{13}C NMR (D_2O, 75.4 MHz): δ (ppm) 66.9, 67.6, 68.2, 69.4, 70.3, 75.8, 77.2, 78.3 [*PG*-OSO$_3$Na]. IR (KBr): ν (cm^{-1}) 3470 [OH], 2930 [CH], 1260 [S=O], 780 [C−O−S]. Sulfur content from elemental analysis: **2a**: 15.38% S, **2b**: 14.28% S, **2c**: 15.20% S.

No degradation of the polyglycerol core could be observed by ^{1}H NMR spectroscopy (see Supporting Information).

Synthesis of Polyglycerol Carboxylate 3. To a stirred solution of 23.0 g of polyglycerol **1d** (310.5 mmol OH-groups) in 124.2 g of 30 wt % NaOH (931.5 mmol NaOH) was added dropwise a solution of 108.5 g (931.5 mmol) sodium chloroacetate in 130 mL of distilled water over 30 min. The reaction mixture was heated to 80 °C for 16 h and then cooled to room temperature, neutralized with 2 N hydrochloric acid and concentrated in vacuo. The crude product was purified by dialysis in distilled water. Upon evaporation of the solvent, 12.2 g of the polyglycerol carboxylate **3** were obtained as a colorless solid which was then dried over P_2O_5. ^{1}H NMR (D_2O, 300 MHz): δ (ppm) 0.89 [t, 3H, C*H*$_3$CH$_2$C(CH$_2$O)$_3$-PG-CH$_2$-CO$_2$Na], 1.39 [m, 2H, CH$_3$C*H*$_2$C(CH$_2$O)$_3$-PG-CH$_2$CO$_2$Na], 3.35−3.90 [m, *PG*-CH$_2$CO$_2$Na], 3.98, 4.09 [s, 2H, PG-O$_{prim}$-C*H*$_2$CO$_2$Na, PG-O$_{sec}$-C*H*$_2$CO$_2$Na]. ^{13}C NMR (D_2O, 75.4 MHz): δ (ppm) 60.9, 62.7, 68.9, 70.3, 72.2, 78.0, 79.5 [*PG*-CH$_2$CO$_2$Na], 77.1 [PG-*C*H$_2$CO$_2$Na], 177.8 [PG-CH$_2$*C*O$_2$-Na]. IR (KBr): ν (cm^{-1}) 3500 [OH], 2870 [CH], 1610 [C(=O)O$^-$], 1110 [C−O−C]. Titration of carboxylic acid groups with 0.01 N NaOH (consumption corresponds to the inflection point): 13.7 mL (mean value, which corresponds to a dc of 26%).

Anticoagulant Activity. The anticoagulant activity of the polyglycerol derivatives was evaluated by classical coagulation assays. All assays were performed using citrated human platelet poor pool plasma (PPP) pooled from at least eight healthy adults. PPP was obtained according to the guidelines for preparing citrated plasma for hemostaseological analyses (*25*) and stored at −70 °C until use. Freshly thawed PPP was supplemented with dilution series of the polyglycerols **1**, the polyglycerol derivatives **2**, **3** and UFH in 0.9% sodium chloride resulting in final concentrations ranging between 0.1 and 100 μg/mL. The clotting times in seconds were recorded with a Kugel coagulometer KC 10 (Amelung, Lemgo, Germany). All assays were performed in duplicate and repeated at least three times on different days (n = 6). For comparison with the standard UFH, the concentrations needed for doubling the baseline coagulation time (DC) were determined.

Scheme 1. Synthesis of Polyanionic Polyglycerol Derivatives (sulfates 2a-c, Carboxylate 3)[a]



[a] The depicted structures have a degree of branching of ca. 60% and are only small idealized fragments of the large dendritic polymer cores **1a**−**d**.

Activated Partial Thromboplastin Time (APTT). An amount of 100 μL of supplemented plasma was incubated with 100 μL of Pathromtin (Dade Behring, Marburg, Germany) for 120 s at 37 °C. The coagulation was started by adding 100 μL of 0.025 M calcium chloride solution (Dade Behring, Marburg, Germany).

Thrombin Time (TT). An amount of 100 μL supplemented plasma and 100 μl diethylbarbiturate−acetate buffer solution (pH 7.6) (Dade Behring, Marburg, Germany) was incubated at 37 °C for 60 s. The coagulation was started by adding 100 μL of 3.0 IU/mL Test-Thrombin (bovine) in diethylbarbiturate−acetate buffer solution (pH 7.6) (Dade Behring, Marburg, Germany).

Anticomplementary Activity. The influence of the polyglycerol derivatives on both classical complement activation (CCA) and alternative complement activation (ACA) was determined by complement-induced hemolysis assays using a microtiter plate technique as recently described by Alban et al. (*26*). The assay principle is based on the lysis of antibody-sensitized sheep (for the classical complement activation) and rabbit erythrocytes (for the alternative complement activation) by the remaining active complement proteins contained in human pooled serum and the photometric measurement of the released hemoglobin. All assays were performed in triplicate and repeated at least one time on a different day ($n = 6$). For comparison with the standard UFH, the concentrations reducing the baseline (i.e., in the absence of test compounds) hemolysis by 50% (IC_{50}) were determined.

RESULTS AND DISCUSSION

A. Synthesis and Characterization of Dendritic Polyanions. Polyglycerol **1** is a readily available well-defined polymer with dendritic (treelike) branching obtained by controlled anionic polymerization of glycidol (*20*−*22*). The degree of branching of **1** (60%) is lower than that of perfect glycerol dendrimers (100%) (*27*). Nevertheless, the physicochemical properties are very similar (*28b*). The molecular weight (1000−30 000 g mol^{-1}) and hence the degree of polymerization (DP) can be easily tailored by the monomer/initiator ratio and narrow polydispersities are obtained (typically < 2.0) (*22*). Due to the biocompatible properties of the aliphatic polyether polyols in general (e.g., polysaccharides, poly(ethylene glycol)s), similar properties are expected for polyglycerol (*21*). In addition, oligoglycerols (2−10 monomer units) have been studied in detail with respect to their toxicological properties and have been approved as food and pharma additives (*28, 29*). Dendritic polyglycerol **1** should therefore be well suited as a highly functional support for drugs and for the generation of dendritic polyanions (polysulfates and polycarboxylates) as highly branched heparin analogues.

The synthesis of the polyglycerol sulfates was carried out by modifying a method established for the sulfation of β-1,3-glucans (*24*) using dendritic polyglycerols (*20*) with different molecular weights (**1a**−**c**) as core polymers and the SO_3/pyridine complex as sulfation reagent in dry DMF as solvent (Scheme 1). For all examples the concentration of the SO_3/pyridine complex in DMF as well as its molar ratio (SO_3 per OH groups) were kept constant. The polyglycerol sulfates (**2a**−**c**) were obtained in good yields (50−75%) and high purities (>98% according to ^{1}H NMR) after dialysis in distilled water. Using a SO_3/pyridine concentration equimolar to the OH groups, about 85% of all the free OH groups have been sulfated (Table 1). This high degree of sulfation shows that polyglyerols are much more accessible to sulfation than polysaccharides (*24*).

The synthesis of the polyglycerol carboxylate was performed using the well-known preparation of carboxymethylcellulose from cellulose (*30*). In close analogy to this method, polyglycerol **1d** was treated with aqueous sodium hydroxide solution and the reagent sodium chloroacetate at elevated temperature (80 °C) in order to obtain polyglycerol carboxylate **3** (Scheme 1). Although 3-fold excess of sodium chloroacetate was used, only a moderate carboxylate content (26%) could be achieved (Table 1). However, for biological evaluation this should be sufficient, since most of these carboxylate groups will be on the terminal groups of the dendritic macromolecule.

Detailed analysis (see experimental procedures) of all starting materials **1a**−**d** and products **2a**−**c**, **3** by NMR, IR, elemental analysis, and titration confirmed the structure and degree of functionalization of these dendritic polyanionic heparin analogues. The molecular weights of the unfunctionalized polyglycerols have been

Table 2. Anticoagulant and Anticomplementary Activities of the Polyglycerol Derivatives

polyglycerol derivative	M_n (theoret) [g/mol]	anticoagulant activity, DC [μg/mL][a]		anticompelementary activity, IC_{50} [μg/mL][b]	
		APTT	TT	CCA	ACA
UFH		0.99	1.21	33.9	406
1b	5000	inactive[c]	inactive[c]	inactive[c]	inactive[c]
2a	5500	17.3	7.70	2.53	110
2b	10 500	12.3	3.60	1.42	116
2c	21 700	14.9	5.10	1.56	149
3	10 300	inactive[c]	inactive[c]	inactive[c]	inactive[c]

[a] DC [μg/mL] corresponds to the concentration doubling the baseline coagulation time in the APPT and TT assay. [b] IC_{50} [μg/mL] corresponds to the concentration reducing the baseline hemolysis by 50%. [c] Inactive = not determinable due to missing activity up to 100 μg/mL in APTT and TT and up to 250 μg/mL in CCA and ACA.

calculated from ^{1}H NMR data after precipitation (see Supporting Information). The obtained values agreed with the theoretical adjusted MW in this pseudo-living anionic ring-opening polymerization process (see ref 22). Molecular weights of these highly branched polyglycerols obtained from GPC are systematically lower due to the use of linear calibration standards (e.g. poly(ethylene oxide)). During sulfation, no depolymerization of the polyglycerol backbone has been observed as demonstrated by 2-fold dialysis and ^{1}H NMR analysis of the product **2a**. By comparison of the relative integrals of incorporated starter unit and polyglycerol backbone identical proton ratios were observed as in the starting material **1a** (see Supporting Information). This allowed us to calculate the molecular weight of the products **2a**−**c** and also **3** (degradation is not possible under alkalic reaction conditions) with the functionalization data of elemental analysis or titration measurements, respectively (cf. Table 1).

B. Biological Evaluation (APTT, TT, CCA, ACA). The anticoagulant activity of the polyglycerol derivatives was investigated by the classical coagulation assays APTT and TT using UFH as reference compound. The APTT determines the intrinsic coagulation, i.e., an influence on Factor XIIa, XIa, IXa, VIIIa, kallikrein, and high molecular weight kininogen. Further, effects on FVa and FXa, and moderately also on thrombin and fibrinogen can be detected. The thrombin time, i.e., the coagulation time after adding an excess of thrombin, is the assay for the last step of coagulation, i.e., the thrombin-mediated fibrin formation. Whereas the unfunctionalized polyglycerols (**1a**−**d**) as well as the polyglycerol carboxylate **3** did not influence the coagulation time, the three polyglycerol sulfates **2a**, **2b**, and **2c** concentration-dependently prolonged both APTT and TT. As determined from their DC (Table 2), their APTT-activities amounted to 5.7% (**2a**), 8.1% (**2b**), and 6.6% (**2c**) of that of UFH (Figure 1). Regarding their relative TT-activities of 15.7% (**2a**), 33.6% (**2b**), and 23.7% (**2c**), it appears that the polyglycerol sulfates interfere rather with the last coagulation step than with the intrinsic coagulation activation. However, further studies will be needed to identify their detailed mode of anticoagulant action.

Comparing the three compounds, which actually differ only in their molecular weight, especially in the TT assay, the activity of **2b** with a medium molecular weight is significantly the highest, followed by **2c** and finally **2a** with the lowest molecular weight. These findings are in contrast to the correlation between the anticoagulant activity and the molecular weight of sulfated polysaccharides (*31*−*34*). This might be due to the different

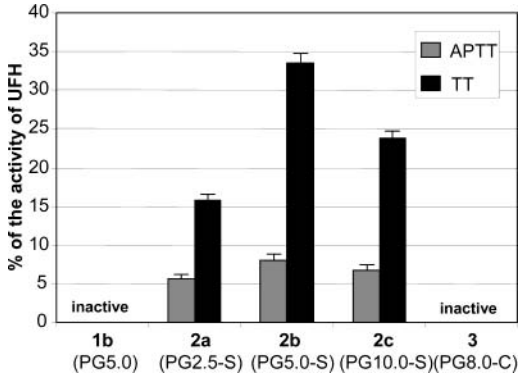


Figure 1. Anticoagulant activities of the polyglycerol derivatives in the APTT and TT assay in relation to UFH as calculated from the DC [μg/mL]. The activity of UFH corresponds to 100%.

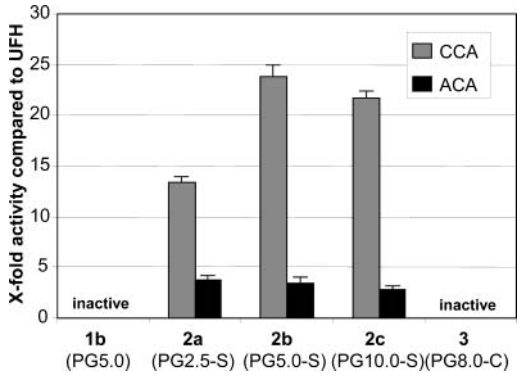


Figure 2. Anticomplementary activities of the polyglycerol derivatives in the CCA and ACA assay in relation to UFH as calculated from the IC_{50} [μg/mL]. The activity of UFH corresponds to 1.0.

three-dimensional structure and the higher density of sulfate groups; whereas a longer chain length of flexible polysaccharide molecules increases the probability of interactions with biomolecules, the globular conformation of polyglycerols may be hindering above a certain size. On the other hand, as demonstrated by **2a**, already a relatively low molecular weight is sufficient for pronounced activity, which is supposed to be advantageous with respect to a potential in vivo application.

Similar to the coagulation assays, both the unfunctionalized polyglycerols **1a**−**d** and the polyglycerol carboxylate **3** were completely inactive in the complement-induced hemolysis assays. They also did not show any complement activating effect as it is known for numerous unsulfated polysaccharides (*26*). All three polyglycerol sulfates, however, concentration-dependently inhibited the hemolysis induced by classical (CCA) as well as alternative (ACA) complement activation. Like some sulfated polysaccharides (*35*), they turned out to be superior to UFH particularly in the CCA assay (Table 2). As calculated from the IC_{50} values, they were 13 (**2a**), 24 (**2b**), and 22 times (**2c**) more active than UFH (Figure 2). In the ACA assay, the factor ranged only between 2.7 and 3.7. In view of the inactivity of polyglycerol carboxylate **3** in both the CCA and ACA assay, sulfate groups are essential to any effect and cannot be replaced by other negatively charged residues (i.e., carboxylates).

In the CCA assay, there is again no clear molecular weight dependency of the activities of **2a**, **2b**, and **2c**, whereby in contrast to the anticoagulant activity **2b** is only slightly more active than **2c**. But in the ACA assay, the inverse order of activities applies: **2c** with the highest molecular weight revealed a considerable weaker effect

than **2b** and **2a**. Consequently, the biological effects of polyglycerol sulfates on diverse biological systems, e.g., CCA and ACA, seem to be favored by different structural characteristics.

In relation to UFH, whose ratio of the anticomplementary to the anticoagulant activity is set to 1.0, the ratio of the anticomplementary- (CAA) to the anticoagulant activity (APTT or TT) of the polyglycerol sulfates amounts to about 300 or 80, respectively. The therapeutic utilization of the relatively weak anticomplementary activity of UFH is limited by the potential bleeding risk (*7*). Referring to this, polyglycerol sulfates exhibit an improved efficacy−risk ratio so that efficient anticomplementary doses may be combined with moderate anticoagulant activities, which do not induce bleeding.

CONCLUSIONS

For the development of synthetic heparin alternatives without the characteristic disadvantages of this animal-derived product, but having a similar activity profile, dendritic polyglycerols have been functionalized with negatively charged sulfate and carboxylate groups. A major advantage of these fully synthetic polyglycerol sulfates is their straightforward preparation, which can be easily scaled up. In contrast to inactive nonderivatized and carboxylated polyglycerols, polyglycerol sulfates turned out to exhibit both anticoagulant and anticomplementary activities. Whereas their anticoagulant activity is lower than that of heparin, they show manyfold stronger anticomplementary effects. A clear molecular weight dependence could not be detected with this limited set of accessible polymer sizes, but the respective activities turned out to depend on the individual structure. Consequently, it should be possible to produce compounds with specific action profiles. Due to the cross-linking between coagulation and inflammation (including complement activation) in the pathophysiology of, for example, sepsis or cardiovascular diseases (*36*, *37*), polyglycerol sulfates with both anticoagulant and antiinflammatory activities represent promising candidates for the development of corresponding drugs. To evaluate the therapeutic potential of this new class of heparin analogues, further studies on the structure−activity-relationships and investigations of the complete action profile and the mechanisms of actions are in progress.

ACKNOWLEDGMENT

H.T. and R.H. would like to acknowledge Prof. Rolf Mülhaupt for his generous support and thank Dr. Béla Oláh, Bernhard Siegel, and Katrin Armbruster for their synthetic support in this project. S.A. is grateful to Gabriele Brunner for her excellent technical assistance at the testing of the compounds. R.H. is indebted to the Deutsche Forschungsgemeinschaft, the Fonds der chemischen Industrie, and Dr. Otto-Röhm Gedächtnisstiftung for financial support.

LITERATURE CITED

(1) Hirsh, J., Warkentin, T. E., Shaughnessy, S. G., Anand, S. S., Halperin, J. L., Raschke, R., Granger, C., Ohman, E. M., and Dalen, J. E. (2001) Heparin and Low-Molecular-Weight Heparin: Mechanisms of Action, Pharmacokinetics, Dosing, Monitoring, Efficacy, and Safety. *Chest 119*, 64S-94S.

(2) Demir, M., Iqbal, O., Dietrich, C. P., Hoppensteadt, D., Ahmad, S., Daud, A. N., and Fareed, J. (2001) Anticoagulant and antiprotease effects of a novel heparinlike compound from shrimp (Penaeus brasiliensis) and its neutralization by heparinase I. *Clin. Appl. Thromb. Hemostasis 7*, 44−52.

(3) Linhardt, R. J., Loganathan, D., Al-Hakim, A., Wang, H.-M., Walenga, J. M., Hoppensteadt, D., and Fareedt, J. (1990) Oligosaccharide Mapping of Low Molecular Weight Heparins: Structure and Activity Differences. *J. Med. Chem. 33*, 1639−1645.

(4) Capila, I., and Linhardt, R. J. (2002) Heparin-Protein-Wechselwirkungen. *Angew. Chem. 114*, 426−450.

(5) Petitou, M., Duchaussoy, P., Herbert, J.-M., Duc, G., El Hajji, M., Branellec, J.-F., Donat, F., Necciari, J., Cariou, R., Bouthier, J., and Garrigou, E. (2002) The Synthetic Pentasaccharide Fondaparinux: First in the Class of Antithrombotic Agents that Selectively Inhibit Coagulation Factor Xa. *Semin. Thromb. Hemostasis 28*, 393−402.

(6) Hopfner, R. (2002) Ximelagatran. *Curr. Opin. Investig. Drugs 3*, 246−251.

(7) Weiler, J. M., Edens, R. E., Linhardt, R. J., and Kapelanski, D. P. (1992) Heparin and modified heparin inhibit complement activation in vivo. *J. Immunol. 148*, 3210−3215.

(8) Winkelhake, J. L. (1991) Will complex carbohydrate ligands of vascular selectins be the next generation of non-steroidal anti-inflammatory drugs? *Glycoconjugate J. 8*, 381−386.

(9) Arfors, K.-E., and Ley, K. (1993) Sulfated polysaccharides in inflammation. *J. Lab. Clin. Med. 121*, 201−202.

(10) Linhardt, R. J., and Toida, T. (1997) Heparin oligosaccharides: New analogues development and applications. *Carbohydrates in Drug Design* (Witczak, Z. J., and Nieforth, K. A., Eds.) pp 277−341, Marcel Dekker, New York.

(11) Zacharski, L. R., and Ornstein, D. L. (1998) Heparin and cancer. *Thromb. Haemostasis 80*, 10−23.

(12) Engelberg, H. (1991) Heparin, nonheparin glycosaminoglycans, and heparinoids: an overview of their application in atheroscerosis. *Semin. Thromb. Hemostasis 17*, 5−8.

(13) Garg, H. G., Thompson, B. T., and Hales, C. A. (2000) Structural determinants of antiproliferative activity of heparin on pulmonary artery smooth muscle cells. *Am. J. Physiol. Lung Cell. Mol. Physiol. 279*, L779-L789.

(14) Ley, K., Cerrito, M., and Arfors, K.-E. (1991) Sulfated polysaccharides inhibit leukocyte rolling in venules by protamin and sulfated polysaccharides. *Am. J. Physiol. Heart Circ. Physiol. 260*, H1667−H1673.

(15) DeClercq, E. (1993) Anti-HIV activity of sulfated polysaccharides. *Carbohydrates and Carbohydrate Polymers, Analysis, Biotechnology, Modification, Antiviral, Biomedical and other Application* (Yalpani, M., Ed.) pp 87−100, ATL Press, Shrewsbury.

(16) Hsu, L. C. (2001) Heparin-coated cardiopulmonary bypass circuits: current status. *Perfusion 16*, 417−428.

(17) Alban, S., and Franz, G. (2001) Partial synthetic glucan sulfates as potential new antithrombotics. *Biomacromolecules 2*, 354−361.

(18) Gunay, N. S., and Linhardt, R. J. (1999) Heparinoids: Structure, Biological Activities and Therapeutic Applications. *Planta Med. 65*, 301−306.

(19) Alban, S. (1997) Carbohydrates with anticoagulant and antithrombotic properties. *Carbohydrates in Drug Design* (Witczak, Z. J., and Nieforth, K. A., Eds.) pp 209−276, Marcel Dekker, New York.

(20) Sunder, A., Mülhaupt, R., Haag, R., and Frey, H. (2000) Hyperbranched Polyether Polyols: A Modular Approach to Complex Polymer Architectures. *Adv. Mater. 12*, 235−239.

(21) Frey, H., and Haag, R. (2002) Dendritic polyglycerol: a new versatile biocompatible material. *Rev. Mol. Biotech. 90*, 257−267.

(22) Sunder, A., Hanselmann, R., Frey, H., and Mülhaupt, R. (1999) Controlled Synthesis of Hyperbranched Polyglycerols by Ring-Opening Multibranching Polymerization. *Macromolecules 32*, 4240−4246.

(23) Casu, B., and Gennaro, U. (1975) A conductometric method for the determination of sulphate and carboxyl groups in heparin and other mucopolysaccharides. *Carbohydr. Res. 39*, 168−176.

(24) Alban, S., Kraus, J., and Franz, G. (1992) Synthesis of Laminarin Sulfates with Anticoagulant Activity. *Arzneim.-Forsch./Drug Res. 42*, 1005−1008.

(25) Witt, I., Beeser, H., and Müller-Berghaus, G. (1995) Minimalanforderungen zur Gewinnung von Citratplasma für hämostaseologische Analysen. *Laboratory Medicine 19*, 143−145.
(26) Alban, S., Classen, B., and Blaschek, W. (2002) Differentiation between the complement modulating effects of an arabinogalactan-protein from Echinacea purpurea and of heparin. *Planta Med. 68*, 1118−1124.
(27) Haag, R., Sunder, A., and Stumbé, J.-F. (2000) An Approach to Glycerol Dendrimers and Pseudo-Dendritic Polyglycerols. *J. Am. Chem. Soc. 122*, 2954−2955.
(28) Wilson, R., Van Schie, B. J., and Howes, D. (1998) Overview of the Preparation, Use and Biological Studies on Polyglycerol Polyricinoleate (PGPR). *Food Chem. Toxicol. 36*, 711−718.
(29) Howes, D., Wilson, R., and James, C. T. (1998) The Fate of Ingested Glyceran Esters of Condensed Castor Oil Fatty Acids [Polyglycerol Polyricinoleate (PGPR)] in Rat. *Food Chem. Toxicol. 36*, 719−738.
(30) Gait, M. J., Jones, A. S., and Walker, R. T. (1974) Synthetic Analogues of Polynucleotides. Part XII. Synthesis of Thymidine Derivatives containing an Oxyacetamido- or an Oxyformamido-linkage instead of a Phosphodiester Group. *J. Chem. Soc., Perkin Trans. 1* 1684−1686.
(31) Oshima, G. (1989) The molecular-mass dependence of dextran sulfate enhancement of inactivation of thrombin and fibrinogen and on factor Xa neutralization by antithrombin III. *Biol. Chem. 370*, 715−721.
(32) Alban, S., and Franz, G. (1994) Anticoagulant activity of β-1,3-glucan sulfates in dependence on their molecular weight. *Pure Appl. Chem. 66*, 2403−2406.
(33) Mauray, S., De Raucourt, E., Chaubet, F., Maiga-Revel, O., Sternberg, C., and Fischer, A. M. (1998) Comparative anticoagulant activity and influence on thrombin generation of dextran derivatives and of a fucoidan fraction. *J. Biomater. Sci. Polym. Ed. 9*, 373−387.
(34) Chevolot, L., Foucault, A., Chaubet, F., Kervarec, N., Sinquin, C., Fisher, A. M., and Boisson-Vidal, C. (1999) Further data on the structure of brown seaweed fucans: relationships with anticoagulant activity. *Carbohydr. Res. 319*, 154−165.
(35) Yvin, J.-C., Alban, S., and Franz, G. (2002) Antiinflammatory and healing medicine based on laminarin sulphate. PCT Int. Appl. Patent WO 2002036132.
(36) Levi, M., ten Cate, H., and van der Poll, T. (2002) Endothelium: interface between coagulation and inflammation. *Crit. Care Med. 30*, S220−S224.
(37) Black, P. H., and Garbutt, L. D. (2002) Stress, inflammation and cardiovascular disease. *J. Psychosom. Res. 52*, 1−23.

BC034044J

Synthesis and Characterization of Hapten−Protein Conjugates for Antibody Production against Small Molecules

K. V. Singh, Jasdeep Kaur, Grish C. Varshney, Manoj Raje, and C. Raman Suri*

Institute of Microbial Technology, Sector 39-A, Chandigarh 160 036, India. Received September 5, 2003; Revised Manuscript Received November 4, 2003

For the generation of antibodies against small hapten molecules, the hapten is cross-linked with some carrier protein to make it immunogenic. However, the formation of such conjugates is not always reproducible. This may lead to inconsistent hapten−protein stoichiometries, resulting in large variations in the generation of the desired antibodies. In the study described here the hapten (mercaptopropionic acid derivative of atrazine) was coupled to carrier protein at five different molar ratios. The hapten−protein conjugates prepared were characterized thoroughly by spectrophotometric absorption, fluorescence, matrix-assisted laser desorption ionization (MALDI), and gel electrophoresis methods, before being used for the immunization and assay purposes. Electrophoresis and fluorescence methods were very useful in detecting hapten−protein cross-linking while MALDI-MS and spectrophotometric detection provided qualitatively comparable hapten density. The production of specific antibodies was sought following the generation of appropriate hapten−protein conjugates. A high antibody titer with moderate antibody specificity was obtained with hapten density around 15 molecules per carrier protein. The study proved useful for monitoring the course of hapten−protein conjugation for the production of specific antibodies against small molecules.

INTRODUCTION

Small molecules such as pesticides, drugs, etc. are usually nonimmunogenic and hence do not elicit an immune response unless coupled with some macromolecules such as proteins. It is, therefore, required to modify these small substances (hapten) for coupling with macromolecules (carrier) so as to make a stable carrier−hapten complex. Synthesis of hapten for linking with carrier proteins is the most important aspect of specific antibody generation against small molecules for immunoassay applications (*1*−*3*). The functional group of the hapten governs the selection of the conjugation method to be employed. Common procedures use amine, carboxylic acid, hydroxyl, or sulfhydryl groups on the hapten and the protein (*4*). The most frequently used carrier proteins for conjugation are bovine serum albumin (BSA), ovalbumin (OVA), conalbumin (CONA), thyroglobulin (TG), immunoglobulin (Ig), fibrinogen, or keyhole limpet hemocyanin (KLH). Hapten−protein conjugates made with serum albumin are more frequently used than conjugates of γ-globulin or other carrier proteins. The hapten−protein conjugates of bovine, rabbit, and human serum albumin were found to be soluble above pH 5.5. However, similar conjugates made of γ-globulin and egg albumin precipitated out of solution during preparation (*5*). KLH, even though consisting of a large number of available lysines for hapten conjugation, its use as a carrier protein is restricted because of the problem of its solubility in various buffers due to its high molecular size.

There has been significant progress in recent years in protein−hapten conjugates for the generation of anti-hapten antibodies with applications in immunoassays for environmentally hazardous pollutants (*6*−*8*). An improved method for the microscale preparation and characterization of hapten−protein conjugates for nonchromophore hydroxylated haptens was demonstrated by Naar and co-workers (*9*). In another study, a solid-phase conjugation method utilizing carrier protein bound to an ion exchange matrix was developed, and the conjugation ratio was determined by acid hydrolysis and amino acid analysis (*10*). Verification of the coupling reaction and determination of the hapten density can be accomplished spectrophotometerically, mainly by evaluating the available free amino groups before and after conjugation (*11*, *12*), by matrix-assisted laser desorption ionization mass spectrometry (MALDI-MS) to determine the mass change before and after conjugation (*13*, *14*) or by radiolabeled haptens (*15*). To prepare an effective hapten−protein conjugate for the desired immune response, it is important to characterize the resulting hapten−protein conjugates to determine the hapten density on carrier protein. The higher ratio of hapten usually increases the strength and specificity of the immune response. However, there is a risk that a high degree of substitution could adversely affect the activity and specificity of antibodies produced (*16*). Besides, the formations of protein−hapten conjugates are not always reproducible, even in best experimental conditions. This may lead to inconsistent hapten−protein stoichiometries resulting large variation in desired antibodies generation. Careful selection of hapten density for hapten−protein conjugation is therefore an important aspect of antibody generation. In the present study, the binding efficiency of hapten−carrier conjugate (number of hapten molecules per protein molecule) was optimized by taking different hapten: carrier molar ratios. Mercaptopropionic acid derivative of atrazine (MPAD) was synthesized in our laboratory for coupling with carrier protein. Five molar ratios of hapten were used to make hapten−protein conjugates for immunization purpose. The optimum molar ratio of hapten to protein to produce conjugates

* Corresponding author; Tel.: +91-172-695215; Fax: +91-172-690632; E-mail: Raman@imtech.res.in.

10.1021/bc034158v CCC: $27.50 © 2004 American Chemical Society
Published on Web 12/23/2003

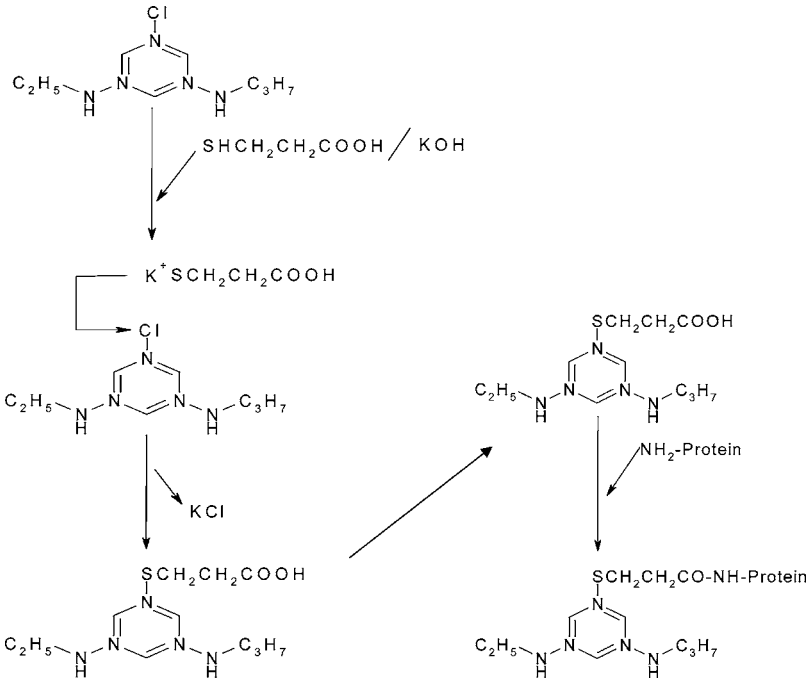


Figure 1. Synthesis and conjugation of MPAD derivative of atrazine with protein.

for immunization was determined according to a balance between good antibody titers and specific antibodies generated.

MATERIALS AND METHODS

Reagents. Bovine serum albumin (BSA), dicyclohexyl carbodiimide (DCC), *N*-hydroxysuccinimide (NHS) ester, 3-mercaptopropionic acid, 2,4,6-trinitrobenzene 1-sulfonic acid (TNBS), fluorescein isothiocyanate (isomer 1), peroxidase conjugated goat anti-rabbit immunoglobulin, normal anti-rabbit immunoglobulin, and 3,5-dimethoxy-4-hydroxycinnamic acid (Sinapinic acid) were purchased from Sigma Chemical Co., St. Louis, MO. Technical grade atrazine was purchased from Supelco. Peroxidase (POD) and 3,3′,5,5′-tetramethylbenzidine (TMB) substrate were obtained from Bangalore-Genei, India. Affi-gel-102 was purchased from Bio-Rad. All chemicals, reagents, and solvents used in this study were of high purity analytical grade. Buffers were made in Milli-Q double distilled water.

Synthesis of Atrazine Derivative. Mercaptopropionic acid derivative of atrazine (MPAD) was synthesized in our laboratory by the method described by Goodrow and co-workers (*2*). Briefly, in a solution of 5.01 mmol of atrazine (Tech. Grade) in 50 mL of ethanol was added slowly, under constant stirring, a solution of 3-mercaptopropionic acid (5.5 mmol) and 85% KOH (10.8 mmol) in 10 mL of ethanol. The mixture was refluxed for 6 h, and then the solvent was evaporated under reduced pressure. The residue was taken up in 25 mL of 5% $NaHCO_3$ and washed three times with 10 mL of chloroform. The aqueous layer of the solution was acidified (pH 2.0) with 6 N HCl, causing the acidic derivative to precipitate immediately. The supernatant was decanted, and the derivative was dried under mild vacuum. The precipitate was further dissolved in 1 mL of ethanol and then allowed under reduced pressure at 37 °C to form MPAD crystals. The product was stored in a tightly sealed bottle for further use.

Conjugation of Hapten with Protein. Conjugates of atrazine (MPAD derivative) with protein (BSA) at five different molar ratios of protein−hapten (1:5, 1:10, 1:20, 1:40, and 1:100, M1-M5) were prepared. The stock solution of protein (10 mg/mL; 0.15 μmol) was made in pH 9.0 borate buffer, and the final reaction volume of the protein−hapten conjugates was kept constant at 1 mL for each preparation. Stock solution of haptens was made by adding 50 μmol of MPAD derivative of atrazine in 1 mL of DMF along with 125 μmol of DCC and 125 μmol of NHS. The mixture was incubated for 4 h at RT and then centrifuged for 5 min at 10 000 rpm to remove the urea precipitate. The reaction mechanism of MPAD−protein conjugation method is shown in Figure 1. The supernatant was used to prepare conjugates with protein by adding different amounts of hapten to a fixed amount of protein (10 mg) in a final volume of 1 mL to make protein−hapten conjugates of different molar ratios as shown in Table 1. The conjugates were passed through P10 gel filtration column (Pharmacia, Sweden). The fractions with maximum protein concentration were collected, pooled, and checked for the final concentration of protein (hapten−protein) with UV spectrophotometer at 280 nm.

Table 1. Different Molar Ratios of Protein−Hapten Used for Making Conjugates M1 to M5

protein concentration	hapten concentration	protein−hapten ratio
0.15 μmol (10 mg)	0.75 (15 μL)	1:5 (M1)
0.15 μmol (10 mg)	1.50 (30 μL)	1:10 (M2)
0.15 μmol (10 mg)	3.00 (60 μL)	1:20 (M3)
0.15 μmol (10 mg)	6.00 (120 μL)	1:40 (M4)
0.15 μmol (10 mg)	15.0 (300 μL)	1:100 (M5)

Characterization of Conjugates. Protein−hapten conjugates were characterized by following physical techniques to determine the extent of conjugation.

(a) Spectrophotometric Analysis. The available groups of surface lysine present in carrier proteins before and after conjugation (made at different molar ratios of hapten−protein) were determined using 2,4,6-trinitrobenzene-1-sulfonic acid (TNBS) reagent. The amount of amino groups present in the carrier protein before and after coupling with carboxylated hapten was directly quantitated with a UV/vis spectrophotometer (Shimadzu 1601) at 335 nm. Different conjugates were prepared at

Table 2. Determination of Hapten Density on BSA−MPAD Conjugates Using Chemical TNBS and Physical MALDI−TOFF Mass Spectrometric Method[a]

conjugate	carrier−hapten molar ratio used for preparation of conjugates	chemical TNBS method		mass spectrometry MALDI−TOFF		
		% amino groups consumed	approximate no. of amino groups used	observed mass[b] (kDa)	change in mass (ΔM)	$\Delta M/M_h$ (hapten density[c])
control	1:0	0.0	0.0 (0)	67221.0	0	0
M1	1:5	6.0	3.48 (3)	67744.9	523.9	1.84 (2)
M2	1:10	8.0	4.64 (5)	68293.8	1072.8	3.76 (4)
M3	1:20	18.0	10.44 (10)	70288.7	3067.7	10.75 (11)
M4	1:40	24.0	13.92 (14)	71720.8	4499.8	15.77 (16)
M5	1:100	29.0	16.82 (17)	*d*	–	–

[a] The number of lysine groups on protein being utilized for conjugates M1 to M5 before and after conjugation are given in brackets. [b] Mass of hapten (MPAD) $M_h = 285.4$. [c] Number of hapten molecules per BSA molecule. [d] Did not fly.

a concentration of 1 mg/mL and were reacted with 0.1% TNBS solution under alkaline conditions to determine the percentage of NH_2 groups used during conjugation in different conjugates. An amount of 200 μL of conjugate solution was taken and mixed with 200 μL of 4% $NaHCO_3$ solution. An amount of 200 μL of 0.1% TNBS solution was added to the mixture and incubated for 1 h at 37 °C. The color of the solution was read at 335 nm. The amount of NH_2 groups used during conjugation of pesticide residues to the BSA molecules was determined from the difference between the O.D. of the control and the conjugate.

(b) Fluorescence Spectra. The emission spectra of hapten−protein conjugates (M1-M5) were taken in the range of 300−450 nm after excitation at 290 nm (tryptophan excitation) using Kontron spectrofluorometer (SFM 25). The conjugates were also excited at 270 nm to see the effects of both tyrosine and tryptophan amino acids on the conjugates. Spectra were obtained using 1 nm excitation and emission slits, and were recorded at a scan rate of 5 nm s^{-1}.

(c) Gel Electrophoresis. The native and SDS−PAGE of the conjugates (different hapten−protein molar ratio) was performed using Bio-Rad electrophoresis apparatus according to method developed by Laemmli (*17*). Solutions of the conjugates were prepared in SDS−PAGE sample buffer (10 mM Tris, 1 mM EDTA, 2.5% SDS, and 5% mercaptoethanol, pH 8.0) to 1 mg/mL and heated to 100 °C for 5 min. Gels were loaded with 5 μL of sample and run under denaturing conditions for 90 min at 120 V. Coomassie blue staining was done using a standard developing protocol supplied by the manufacturer. The gel was washed three times in Milli-Q water, followed by staining for 1 h with stain reagent followed by washing in Milli-Q water.

(d) MALDI-TOF. The mass analysis of hapten−protein conjugates was done with MALDI spectrometer (Kratos Analytical Systems). Sinapinic acid solution was prepared at a concentration of 15 mg/mL in acetonitrile. Protein conjugates dialyzed against distilled water were used at a concentration of 1.5 mg/mL. The conjugate samples and matrix solution were mixed in equal amounts (1 μL each) and added on the stainless steel probe having 0.5 μL of TFA solution (0.1%). The samples were allowed to dry at room temperature and then kept in the system for MASS analysis. The data were acquired with 50 shots per sample in the linear mode at 30 kV and analyzed using the software provided with the system.

Antibody Generation. The hapten−protein conjugates were used to immunize mice and rabbits subcutaneously by taking 25 μg and 250 μg of each conjugate, respectively, emulsified with Freund's complete adjuvant. This was followed by three secondary boosters of same dose with incomplete Freund adjuvant at intervals of 21 days. The mice and rabbits were bled on the 5th day after the each boost, and the antibody titer was determined. After the confirmation of good titers (checked by ELISA), sufficient amount of sera were prepared and the immunoglobulin fraction was purified using a protein A-sepharose column (Amersham-Pharmacia Biotech). The relative functional affinity of the antibodies was measured by diethylamine dependent displacement of antigen−antibody interaction. Results were expressed as the logarithmic increase in antibody concentration required to obtain the same level of O.D. at 50% of saturation in the absence of diethylamine (*18*).

ELISA Procedure. ELISA plates (96-well polystyrene from Imperial Biomed, India) were coated with 100 μL of each conjugate (25 μg/mL) made in carbonate buffer (pH 9.6) and incubated overnight at 4 °C. After being coated, the plates were washed thoroughly with phosphate buffer saline (50 mM, pH: 7.2). Unbound sites of the plates were blocked with 5% defatted skim milk in PBS for 2 h at 37 °C. The plates were washed three times with PBS containing 0.05% Tween-20 (PBST) and finally with PBS. Primary antibodies (serum) incubation was done for 3 h at 37 °C by adding 100 μL of antibody solution in each well at a dilution of 1:1000 in PBS. After incubation, the plates were thoroughly washed three times with PBST and finally with PBS. The plates were then incubated with 100 μL of HRP conjugated goat anti-mouse immunoglobulin (1:5000 dilution) for 1 h at 37 °C. The plates were washed as before, and the color was developed by adding 100 μL of TMB/H_2O_2 solution. The reaction was stopped with 50 μL of 1 N H_2SO_4. Optical density at 450 nm was measured using an ELISA plate reader (Molecular Devices).

RESULTS

Analysis of Conjugates. TNBS Method. Covalent attachment of carboxylic acid haptens to protein (BSA) via available surface amino groups on BSA (26 surface L-lysine) was confirmed by reacting all the prepared conjugates (M1−M5) with TNBS reagent. The number of amino groups present in the carrier protein before and after conjugation was quantitated with UV/vis spectrophotometer (Shimadzu 1601) at 335 nm and shown in Table 2. The gradual decrease in the available surface lysine on protein after reaction with different molar ratios of hapten confirms the increase in conjugation density (number of hapten molecules per protein molecule) with increasing hapten−protein molar ratio.

Fluorescence Method. The fluorescence emission spectra for each hapten−protein conjugate in the range of 300−450 nm after excitation at 290 nm (excitation of tryptophan residues only) are shown in Figure 2. The combined effects of both tyrosine and tryptophan amino acids in conjugates were also checked by exciting the samples at 270 nm and monitoring the spectra between

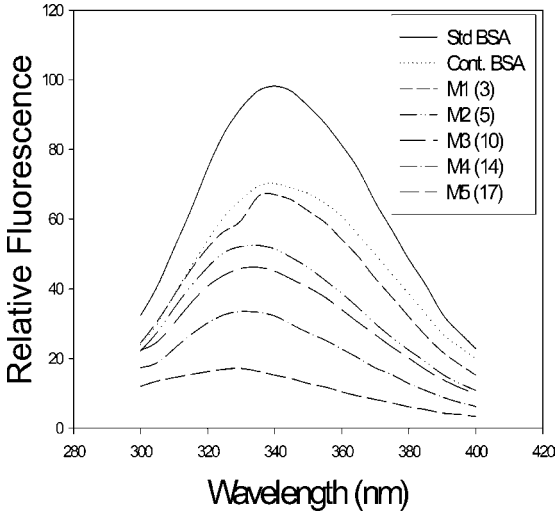


Figure 2. The fluorescence emission spectra (λ_{ex} at 290 nm) of hapten−protein conjugates M1, M2, M3, M4, and M5 having average hapten densities of 3, 5, 10, 14, and 17, respectively.

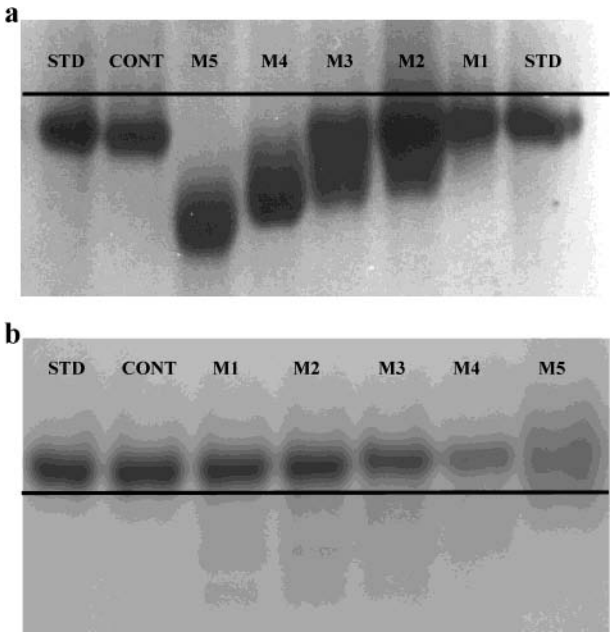


Figure 3. Gel electrophoresis of conjugates (a) native gel and (b) SDS−PAGE. Different BSA-atrazine conjugates M1, M2, M3, M4, and M5 were prepared by reacting activated hapten (MPAD) in molar excess of 1:5, 1:10, 1:20, 1:40, and 1:100, respectively.

300 and 450 nm. No significant change in fluorescent intensity was observed at 270 and 290 nm excitation for the hapten conjugated with protein. The fluorescence spectrum analysis was therefore performed at 290 nm excitation wavelength. Conjugates with increasing molar ratios of protein−hapten (M1−M5) showed linear decrease in fluorescence intensity. The fluorescence intensity of M5 conjugate having protein−hapten molar ratio 1:100 showed almost zero fluorescence intensity.

Gel Electrophoresis and MALDI-MS Analysis. SDS−PAGE and native gel electrophoresis of conjugates are shown in Figure 3. The use of pure protein (BSA) and conjugates made by using different molar ratio of hapten as generated by native gel showed well-defined bands with gradual increments for each hapten with increase in molar ratio (Figure 3a). For the SDS−PAGE (Figure 3b), it was observed that the BSA molecules with higher conjugation density moved further, as this conjugate is more negatively charged in comparison to conjugates prepared with low molar ratio. The SDS−PAGE results correspond to the mass pattern obtained by MALDI-TOF spectrometer. Conjugation density for each hapten in increasing molar ratio (M1−M5) resulted in a detectable increase in the molecular weight of the conjugate as determined by observing the peak shift of mass spectrum (Table 2). The molecular weight of each conjugate was calculated from the peak centroid of the peaks. The incremental change in molecular weight due to incorporation of hapten molecules to protein corresponds to the number of hapten molecules per protein molecule. Apparent coupling efficiency for the MPAD to BSA, at different molar ratios, was nearly same.

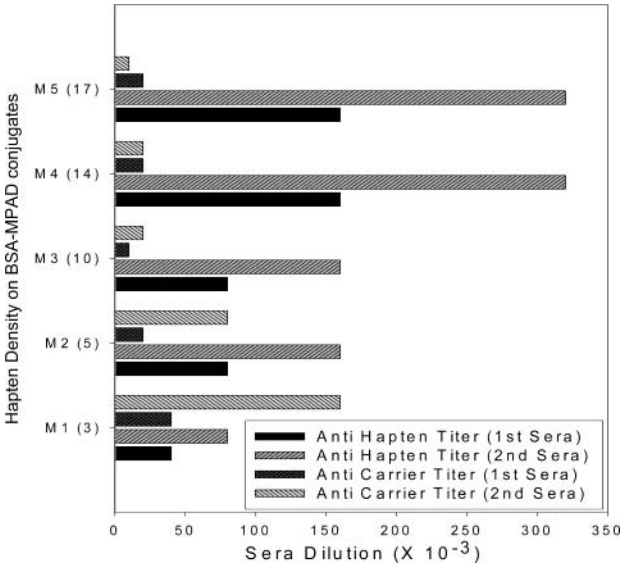


Figure 4. The titer of anti-hapten (atrazine) and anti-carrier (BSA) antibodies in antisera. Rabbits were immunized with various BSA−atrazine conjugates (M1 to M5) having average hapten densities of 3, 5, 10, 14, and 17, respectively.

ELISA Results. All conjugates were tested for their immunogenicity by checking the antibody titers in serum after immunization. The titer of the serum was defined as the dilution giving 50% maximal response by ELISA. Immunization of mice with conjugates (M1 to M5) produced different amount of antibody titers when tested by ELISA (Figure 4). A relatively good titer of anti-hapten antibodies was obtained with M4 conjugate (hapten: protein ratio 1:40). The further increase in conjugational density, i.e., conjugates with hapten−protein ratio of 1:100 (M5), did not show any increase in specific anti-hapten antibodies.

Antibody Characterization. To characterize the antibodies generated against different conjugates, ELISA was done to determine the sensitivity of generated antibodies. The antibody obtained against M4 conjugate, as determined by standard dilution curve analysis, showed very good sensitivity up to the level of ng/mL (Figure 5).

DISCUSSION

For the generation of specific antibodies against small molecules, these molecules are synthesized and conjugated with carrier proteins in such a way that they mimic the structure of the compound and contain a reactive group that can form a covalent linkage with the carrier proteins. The functional group of the hapten governs the selection of the conjugation method to be employed. The method used in this study utilized carbodiimide method

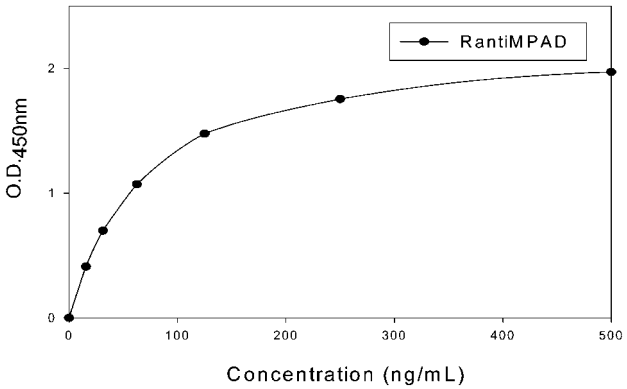


Figure 5. Standard dilution curve for antibody obtained against conjugate M4. Antibody was tested for its sensitivity by dilution curve analysis of data obtained between 12.5 ng/mL to 500 ng/mL of antibody concentration.

(*19*) for carboxy acid haptens (atrazine derivative) to link with BSA. This approach ensured stable cross-linking of haptens with protein along with *N*-acylurea formation. The optimum use of high grade of reagents along with thorough dialysis to remove unbound hapten and *N*-acylurea resulted in good coupling efficiency of haptens to protein as shown by SDS−PAGE and native gel electrophoresis results (Figure 3a,b). Each conjugate generated well-defined bands with low diffusibility. In native gel analysis, the gradual movement of bands with an increase in hapten density is due to a change in net charge of the conjugates, since for each lysine on protein utilized for the conjugation with hapten, one positive charge is lost. Thus, conjugates with more haptens per protein become relatively more negative and move farther than native BSA. Although the electrophoresis analyses of conjugation could not give definite information about the degree of hapten density, its main advantage was in detecting the course of cross-linked conjugation (*21*). In MALDI analysis, the relative increase in the molecular weight of the conjugates is apparent by gradual mass peak shift (Table 2). This corresponds to an increase in hapten density of conjugates, thus determining accurately the number of haptens per protein molecule. A BSA molecule with molecular weight of 66 531 Da (from the manufacturer's data sheet) showed a gradual shift in mass peaks with conjugates made with different molar ratios of hapten (MPAD derivative of atrazine). BSA with 26 available surface lysines can theoretically bind up to 26 hapten molecules. However, the estimated number of hapten molecules linked to BSA could not be more than 17, even at the highest hapten density, i.e., hapten−protein ratio of 1:100. The reason for a lower binding limit of haptens to the protein might be the protein conformational changes induced by haptens. This has also been observed in our analysis of fluorescence spectra for different conjugates (Figure 2) where tryptophan intensity of the hapten−protein conjugates shift toward the blue region for conjugates with higher hapten density, respectively. Due to this compactness of the protein, some surface lysine might actually be in the buried region of the protein, thus allowing fewer lysine groups for linking with the hapten.

The fluorescence spectra for different hapten−protein conjugates showed a linear decrease in fluorescence intensity with increase in hapten−protein molar ratio. The fluorescence signal at 290 nm excitation and 340 nm emission is mainly due to a number of tryptophan residues being available in the protein. The decrease in fluorescence intensity at this wavelength is due to quenching of tryptophan intensity with increase in hapten density, i.e., increase in the number of amide bonds formed between the surface lysine groups of the protein and carboxylated hapten (atrazine derivative). This gradual shift in the fluorescence signal or quenching of tryptophan intensity with different conjugates thus confirms the course of hapten−protein conjugation.

The hapten density of the conjugate is an important parameter which generally defines the quality and quantity of antibody produced. A good antibody titer with higher specificity could be generated with an optimum number of haptens per protein molecule. Higher substitution resulted in an IgM response exceeding that of IgG and produced antibodies of lower affinity. Similar observations have been reported by some other groups (*20*−*21*). It is assumed that high antibody titers with moderate antibody affinities are usually obtained with hapten density of 15−30 molecules per carrier protein while a lower hapten density induces a slower immune response with higher affinity antibodies.

In conclusion, we have characterized different conjugates for getting an optimum molar ratio of protein−hapten conjugate for immunization purposes. The spectrophotometric method using trinitrobenzenesulfonic acid (TNBS) and MALDI-MS were able to quantify the hapten−protein conjugation density accurately. A new fluorescence method has been developed to confirm the course of conjugation by monitoring the relative shift in fluorescence intensity of conjugates. However, the role of many parameters, such as hapten polarity, type of solvent, and the nature of quenching, on the fluorescence signal have to be studied before this method can be used for quantitative determination of conjugation efficiency. This work is undergoing in our laboratory.

ACKNOWLEDGMENT

The authors are thankful to Dr. P. R. Patnaik for the critical review of the manuscript. We also acknowledge financial support from the SDC (Switzerland) and DBT (India) under their ISCB research grant.

LITERATURE CITED

(1) Van Emon, J. M., Sciber, J. N., and Hammock, B. D. (1985) *ACS Symp. Ser. 276*, 307−316.

(2) Goodrow, M. H., Harrison, R. O., and Hammock, B. D. (1990). Hapten synthesis, antibody development, and competitive inhibition enzyme immunoassay for *s*-Triazine herbicides. *J. Agric. Food Chem. 38*, 990−996.

(3) Szurdoki, F., Szekacs, A., Le, H. M., and Hammock, B. D. (2002). Synthesis of haptens and protein conjugates for the development of immunoassays for the insect growth regulator fenoxycarb. *J. Agric. Food Chem. 50*, 29−40.

(4) Hill, A. S., McAdam, D. P., Edward, S. L., and Skerritt, J. H. (1993). Quantitation of bioresmethrin, a synthetic pyrethroid grain protectant, by enzyme immunoassay. *J. Agric. Food Chem. 41*, 2011−2018.

(5) Harrison, R. O., Goodrow, M. H., and Hammocks, B. D. (1991). Competitive inhibition ELISA for the s-triazine herbicides: assay optimization and antibody characterization. *J. Agric. Food Chem. 39*, 122−128.

(6) Kramer, P. M. (1996) Biosensors for measuring pesticides residues in the environment: Past, Present and Future. *J. AOAC 79*, 1245−54.

(7) Lee, G. U., Ahn, K. C., Park, O. S., Kang, S. Y., and Hammock, B. D. (2001). Development of an ELISA for the detection of the residues of the insecticides imidacloprid in agriculture and environment samples. *J. Agric. Food Chem. 49*, 2159−2167.

(8) Sazurdoki, F., Szekacs, A., Le H. M., and Hammock, B. D. (2002). Synthesis of haptens and protein conjugates for the development of immunoassay for the insect growth regulator fenoxycarb. *J. Agric. Food Chem. 50*, 29−40.
(9) Naar, J., Branaa, P., Chinain, M., and Pauillac S. (1999). An improved method for the microscale preparation and characterization of hapten−protein conjugates: the use of cholesterol as a model for nonchromophore hydroxylated haptens. *Bioconjugate Chem. 10*, 1143−1149.
(10) Houen, G., Olsen, D. T., Hansen, P. R., Petersen, K. B., and Barkholt, V. (2003). Preparation of bioconjugates by solid-phase conjugation to ion exchange matrix-adsorbed carrier proteins. *Bioconjugate Chem. 14*, 75−79.
(11) Habeeb, A. F. S. A. (1966). Determination of free amino groups in protein by TNBS. *Anal. Biochem. 14*, 328−336.
(12) Sashidhar, R. B., Capoor, A. K., and Ramana, D. (1994). Quantitation of epsilon-amino group using amino acids as reference standards by trinitrobenzene sulfonic acid. A simple spectrophotometric method for the estimation of hapten to carrier protein ratio. *J. Immunol. Methods 167*, 121−127.
(13) Keough, T., Lacey, M. P., Trakshel, G. M., and Asquith, T. N. (1997). The use of MALDI mass spectrometry to characterize synthetic protein conjugates. *Int. J. Mass Spectrom.Ion Processes 169/170*, 201−215.
(14) Hillenkamp, F. (1992). Determination of the hapten density of immunoconjugates by MALDI-Mass Spectrometry. *Anal. Lett. 25*, 1983−1997.
(15) Rinder, D. F., and Fleeker, J. R. (1981). A radioimmunoassay to screen for 2,4-D and 2,4-T in surface water. *Bull. Environm. Contam. Toxicol. 26*, 375−380.
(16) Marco, M., Gee, S., and Hammock, B. D. (1995). Immunochemical techniques for environmental analyisII. Antibody production and immunoassay development. *Trends Anal. Chem. 14*, 415−425.
(17) Laemmli, U.K. (1970). Cleavage of structural proteins during the assembly of the head of bacteriophage T4. *Nature 227*, 680−685.
(18) Hudson, L., and Hay, F. C. (1989) *Practical immunology*, 3rd ed.; Blackwell Scientific Pub.: London, p 224.
(19) ten Hoeve, W., Wynberg H., Jones, W. T., Harvey, D., Ryan, G. B., and Reynolds, P. H. (1997). Syntheses of haptens containing dioxaphosphorinan methoxyacetic acid linker arms for the production of antibodies to organophosphate pesticides. *Bioconjugate Chem. 8*, 257−66.
(20) Adamczyk, M., Gebler, J. C., and Mattingly, P. G. (1996). Characterization of protein−hapten conjugates. 2. Electrospray mass spectrometry of bovine serum albumin-hapten conjugates. *Bioconjugate Chem. 7*, 475−481.
(21) Malaitsev, V. V., and Azhipa, O. Y. (1993). Influence of epitope density on immunogenic properties of hapten−protein conjugates. *Bull. Exp. Biol. Med. 115*, 726−728.

BC034158V

Preparation of Azacrown-Functionalized 2′-*O*-Methyl Oligoribonucleotides, Potential Artificial RNases

Teija Niittymäki, Ulla Kaukinen, Pasi Virta, Satu Mikkola, and Harri Lönnberg*

Department of Chemistry, University of Turku, FIN-20014 Turku, Finland. Received September 15, 2003

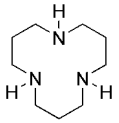
An improved synthesis for 3-(3-aminopropyl)- and 3-(3-mercaptopropyl)-1,5,9-triazacyclododecane has been developed and alternative methods for their conjugation to oligonucleotides have been described. Accordingly, the 3-aminopropyl azacrown and its *N*-(3-aminopropanoyl)-3-aminopropyl analogue have been tethered to the 3′-terminus of a 2′-*O*-methyloligoribonucleotide by aminolytic cleavage of the thioester linker utilized for the chain assembly. Studies on a monomeric model compound verify that the reaction proceeds solely by the attack of the primary amino group. 5′-Conjugation has been achieved by introducing a 2-benzylthio-2-oxoethyl group to the 5′-terminus as a phosphoramidite reagent and cleaving the thioester bond with the 3-aminopropyl azacrown. For intrachain conjugation, a phosphoramidite reagent derived from 1-deoxy-1-(2-benzylthio-2-oxoethyl)-*β*-D-*erythro*-pentofuranose has been inserted in a desired position within the chain and subjected to on-support aminolysis with the 3-aminopropyl azacrown or its *N*-(3-aminopropanoyl)-3-aminopropyl and *N*-(6-aminohexanoyl)-3-aminopropyl analogues. The 3-mercaptopropyl-derivatized azacrown has been tetherd by a disulfide bond to a 3′-(3-mercaptoalkyl)phosphate-tailed oligonucleotide. The 3′- and intrachain-tethered conjugates have been shown to cleave as their Zn(II) chelate complementary oligoribonucleotide sequences.

INTRODUCTION

Oligonucleotide conjugates that sequence selectively cleave complementary RNA targets have received attention as catalytic antisense oligonucleotides, i.e. as chemical agents with which the expression of a desired gene could be efficiently inhibited in cell lines or even in vivo (*1*−*6*). Unmodified oligodeoxyribonucleotides and their phosphorothioate analogues when hybridized with a complementary mRNA sequence activate an intracellular enzyme, RNase H, which depolymerizes the RNA strand of the duplex leaving the deoxynucleotide strand intact (*7*, *8*). Accordingly, the antisense effect of these oligonucleotides exhibits catalytic turnover. Most of the structurally modified oligonucleotides prepared for antisense purposes do not, unfortunately, have this property. On attempting to increase biological half-life, hybridization efficiency, and cellular uptake by extensive structural modifications, the ability to activate RNase H is often lost (*9*) and the antisense effect is based only on stoichiometric arresting. One may hope that tethering a catalytically active moiety to such an antisense oligonucleotide allows chemical degradation of the target RNA and leads to RNase H-independent turnover. In fact, positive indications of the feasibility of this approach have recently been obtained by in vitro studies on cell lines (*10*, *11*).

The artificial ribonucleases described so far fall in three different categories: (i) oligonucleotide conjugates of redox active chelates or organic molecules that cleave the target RNA by radical induced degradation of a sugar moiety (*12*−*14*), (ii) conjugates of metal ion chelates that catalyze the hydrolysis of a phosphodiester bonds in the target RNA chain (*15*−*30*), and (iii) conjugates of peptidelike oligomers that catalyze the phosphodiester hydrolysis (*31*−*39*). While many of these constructs will undoubtedly find applications as research tools for molecular biology, they do not meet all the requirements of a chemotherapeutic agent and, hence, a wider variety of potential cleaving agents is still desirable. Conjugates cleaving their targets by a radical mechanism, for example, exhibit a reasonably high catalytic activity, but diffusion of radicals creates a risk for deleterious side reactions. It is also worth noting that radical reactions degrade DNA more readily than RNA (*40*). Among the metal ion-dependent nucleases that catalyze the phosphodiester hydrolysis by a polar mechanism, those derived from cationic lanthanide ion chelates are most efficient (*15*−*24*), but they may suffer from leakage of lanthanide ions. The Cu(II) and Zn(II) complexes of aromatic nitrogen bases constitute another group of cleaving agents which deserves attention as a source of drug candidates (*25*−*30*). Also with these cleaving agents, the stability of the chelates may turn out to be the critical parameter. Purely organic conjugates would undoubtedly form the most solid basis for drug development (*31*−*39*). However, only few such conjugates are known and their catalytic activity is low compared to that of the metal ion-dependent cleavers.

Macrocyclic polyamines, the so-called azacrowns, are known to form exceptionally stable complexes with 3d transition metal ions, the log *K* values ranging from 8 to 16 (*41*, *42*), and their chelates have been extensively studied as artificial enzymes (*43*). Among these chelates, the complexes of 1,5,9-triazacyclododecane ([12]aneN$_3$; **1**) have been shown to cleave rather efficiently both mono-



1

* To whom correspondence should be addressed. E-mail: harlon@utu.fi.

10.1021/bc034166b CCC: $27.50 © 2004 American Chemical Society
Published on Web 12/23/2003

meric (*44*, *45*) and oligomeric (*46*−*48*) phosphodiesters. It is, hence, quite surprising that no azacrown-functionalized oligonucleotides, with the exception of a [12]aneN$_3$ conjugate of a short oligo(T) (*49*), have been prepared, and no such conjugate has been tested as an artificial RNase. We now report on a solid-phase synthesis of 2′-*O*-methyl oligoribonucleotides bearing a 1,5,9-triazacyclododec-3-yl group at the 3′- or 5′-terminus or within the chain has been described. For the attachment of the conjugate group to the oligonucleotide, two different linker chemistries, viz. a peptide and disulfide bond formation, have been applied. Preliminary results on the cleaving activity show that these conjugates really are viable candidates for further development of biocompatible artificial ribonucleases.

EXPERIMENTAL PROCEDURES

General. The NMR spectra were recorded on a JEOL JNM-GX 400 or Bruker 200 NMR spectrometer. The chemical shifts are given in ppm from internal TMS. The mass spectra of small molecular compounds were recorded on a 7070E VG mass spectrometer and those of oligonucleotides and their conjugates on a Finnigan MAT Lasermat, Sciex ABI 365 Triple Quadrupole or ABI Mariner ESI-TOF spectrometer. The 2′-*O*-methylribo oligonucleotides used for conjugation with the functionalized azacrowns and the chimeric 2′-*O*-methylribo/ribo oligonucleotides used as targets in the cleavage experiments were assembled in 1.0 μmol scale on an Applied Biosystems 392 DNA synthesizer from commercially available 5′-*O*-dimethoxytritylated 2′-*O*-methyl- and 2′-*O*-triisopropylsilyloxymethyl ribonucleoside 3′-(2-cyanoethyl)-*N*,*N*-diisopropylphosphoramidites having the base moiety amino groups benzoylated. The HEPES buffer, zinc nitrate, and sodium nitrate used in the cleavage experiments were of reagent grade.

1-Bromo-3-trityloxypropane (2). Trityl chloride (20 g, 72 mmol) was added to a stirred solution of 3-bromo-1-propanol (10 g, 72 mmol) in THF (150 mL). Triethylamine (10 mL, 72 mmol) was slowly added to the mixture, which was allowed to stir in dark for 2 days at room temperature. Volatiles were removed under reduced pressure, and CH_2Cl_2 (250 mL) was added to the residue. The mixture was washed with water and brine, dried over Na_2SO_4, and evaporated to dryness. The crude reaction mixture was purified by silica gel chromatography (50% pentane in CH_2Cl_2) to yield 23 g (82%) of **2** as white solid flakes. MS (EI): *m*/*z* 243 (100%) Tr^+, 380 and 382 (20% and 20%) M^+. ^{1}H NMR (200 MHz, $CDCl_3$): δ = 7.49−7.24 (m, 15H, Tr), 3.58 (t,2H, J = 6.8 Hz, CH_2Br), 3.22 (t, 2H, J = 5.8 Hz, TrOCH_2), 2.13 (m, 2H, CH_2CH$_2$Br). ^{13}C NMR (50 MHz, $CDCl_3$): δ = 144.1, 128.6, 127.8, 127.0, 86.5, 61.2, 33.5, 30.7.

Diethyl 2-(3-Trityloxypropyl)malonate (3). Diethyl malonate (28 g, 0.17 mol) was dissolved in ethanolic NaOEt (0.12 mol in 200 mL), tritylated 3-bromopropanol **2** (23 g, 59 mmol) was added, and the mixture was refluxed overnight. Volatiles were removed under reduced pressure, CH_2Cl_2 (250 mL) was added, and the organic phase was washed with water and brine, dried over Na_2SO_4, and evaporated to dryness. The residual oil was purified by silica gel chromatography (50 to 10% pentane in CH_2Cl_2) to yield 23 g (85%) of **3** as a colorless oil. MS (EI): *m*/*z* 383 (100%) $[M - Ph]^+$, 460 (35%) M^+. ^{1}H NMR (200 MHz, $CDCl_3$): δ = 7.46−7.22 (m, 15H, Tr), 4.18 (q, 4H, J = 7.1 Hz, 2 × OCH_2CH$_3$), 3.32 [t, 1H, J = 7.5 Hz, CH(COOEt)$_2$], 3.32 (t, 2H, J = 6.3 Hz, TrOCH_2), 1.94−2.05 (m, 2H, TrOCH$_2$CH_2), 1.72−1.57 [m, 2H, TrO(CH$_2$)$_2$CH_2], 1.26 (t, 6H, J = 7.1 Hz, 2 × OCH$_2$CH_3). ^{13}C NMR (50 MHz, $CDCl_3$): δ = 169.4, 144.3, 128.7, 127.7, 126.9, 86.4, 62.9, 61.3, 51.8, 27.7, 25.7, 14.1.

2-(3-Trityloxypropyl)propane-1,3-diol (4). $LiAlH_4$ (7.0 g, 0.18 mol) was added portionwise to a stirred and cooled solution (−20 °C) of **3** (23 g, 50 mmol) in diethyl ether (100 mL). The mixture was allowed to warm to room temperature, and the stirring was continued for additional 2 h. The reaction was carefully quenched by water, which caused slow refluxing. The mixture was concentrated, CH_2Cl_2 (500 mL) was added, and the organic phase was washed several times with water, resulting in formation of an abundant gray precipitation. After this, the organic phase was dried over Na_2SO_4 and evaporated to dryness. The residue was purified by silica gel chromatography (0 to 7% MeOH in CH_2Cl_2) to yield 15 g (79%) of **4** as a colorless oil. MS (EI): *m*/*z* 299 (100%) $[M - Ph]^+$, 376 (6%) M^+. ^{1}H NMR (200 MHz, $CDCl_3$): δ = 7.45−7.21 (m, 15H, Tr), 3.78−3.44 [m, 5H, CH(CH_2-OH)$_2$], 3.06 (t, 2H, J = 6.4 Hz, TrOCH_2), 2.64 (br, 2H, 2 × OH), 1.57−1.78 (m, 2H, TrOCH$_2$CH_2), 1.35−1.24 [m, 2H, TrO(CH$_2$)$_2$CH_2]. ^{13}C NMR (50 MHz, $CDCl_3$): δ = 144.3, 128.6, 127.7, 126.9, 86.4, 66.2, 63.6, 41.8, 27.6, 24.3.

1,3-Ditosyloxy-2-(3-trityloxypropyl)propane (5). Alcohol **4** (15 g, 40 mmol) was dissolved in pyridine (70 mL), *p*-toluenesulfonyl chloride (23 g, 0.12 mol) was added, and the reaction was allowed to stir at room temperature for 5 h. Volatiles were removed under reduced pressure, and CH_2Cl_2 (200 mL) was added to the residue. The organic phase was washed with saturated $NaHCO_3$ and brine, dried over Na_2SO_4, and evaporated to dryness. The residue was purified by silica gel chromatography (20 to 0% pentane in CH_2Cl_2) to yield 18 g (66%) of **5** as colorless oil. MS (EI): *m*/*z* 442 (100%) $[M - Tr]^+$, 607 (89%) $[M - Ph]^+$, 685 (30%) M^+. ^{1}H NMR (400 MHz, $CDCl_3$): δ = 7.69−7.72 (m, 4H, Ts), 7.19−7.36 (m, 19 H, Ts and Tr), 3.93 [dd, 2H, J = 4.9 and 2.2 Hz, CH(CHHOTs)$_2$], 3.87 [dd, 2H, J = 4.9 and 3.1 Hz, CH(CHHOTs)$_2$], 2.94 (t, 2H, J = 3.0 Hz, TrOCH_2), 2.41 (s, 6H, Ts), 1.92 [m, 1H, CH(CH$_2$OTs)$_2$], 1.39−1.46 (m, 2H, TrOCH$_2$CH_2), 1.29−1.35 [m, 2H, TrO(CH$_2$)$_2$CH_2]. ^{13}C NMR (100 MHz, $CDCl_3$): δ = 145.0, 144.1, 132.4, 129.9, 128.6, 127.9, 127.8, 126.9, 86.4, 68.6, 62.8, 37.7, 26.7, 23.8, 21.7.

2-(3-Trityloxypropyl)hexahydro-1*H*,4*H*,7*H*-3a,6a,9a-triazaphenalene (6). TBD (7.4 g, 53 mmol) was added portionwise to a stirred solution of **5** (18 g, 26 mmol) in DME (50 mL). The stirring was continued for 48 h, the mixture was diluted to 100 mL with DME, and $NaBH_4$ (8.0 g, 0.21 mol) was added. The mixture was allowed to stir at ambient temperature overnight. The reaction was carefully quenched with MeOH (100 mL). Volatiles were removed under reduced pressure after the foaming had ceased, and the residue was dissolved in CH_2Cl_2 (150 mL). The resulting organic phase was washed with saturated $NaHCO_3$, dried over Na_2SO_4, and evaporated to dryness. The residue was purified by silica gel chromatography (5% MeOH and 0.5% Et_3N in CH_2Cl_2) to yield 10 g (79%) of **6** as a colorless oil. MS (EI): *m*/*z* 236 (8%) $[M - Tr]^+$, 480 (100%) M^+. ^{1}H NMR (400 MHz, $CDCl_3$): δ = 7.40−7.43 (m, 6H, Tr), 7.19−7.30 (m, 9H, Tr), 3.02 (t, 2H, J = 6.7 Hz, TrOCH$_2$), 2.78−2.82 and 1.90−2.14 [m, 6H and m, 7H, 2×CH$_2$(CH_2N)$_2$ and CH$_2$CH(CH_2N)$_2$], 2.25 (br, 1H, CHN$_3$), 1.75 and 1.60 [m, 2H and m, 2H, 2×CH_2(CH$_2$N)$_2$], 1.41 (m, 2H, TrOCH$_2$CH_2), 1.15 [m, 2H, TrO(CH$_2$)$_2$CH_2]. ^{13}C NMR (100 MHz, $CDCl_3$): δ = 144.4, 128.6, 127.7, 126.8, 99.8, 86.3, 63.7, 60.1, 53.7, 53.6, 33.0, 28.3, 27.1, 24.1.

1,5,9-Tris(*tert*-butoxycarbonyl)-3-(3-chloropropyl)-1,5,9-triazacyclododecane (7). Orthoamide **6** (2.4 g, 5 mmol) was refluxed overnight in a mixture of concd aq HCl and dioxane (1:1, *v*/*v*, 30 mL). Volatiles were removed, and the aqueous phase was washed with CH_2Cl_2 and evaporated to dryness. Aqueous HCl (6 mol L^{-1}, 30 mL) was added to the residue. The mixture was refluxed again overnight and evaporated to dryness, and NaOH (1.2 g, 30 mmol) in aq acetonitrile (1:1, *v*/*v*, 60 mL) was added. Bis(*tert*-butyl) dicarbonate (5.5 g, 25 mmol) was added, and the reaction was allowed to stir at room temperature overnight. Volatiles were removed under reduced pressure, and the residue was purified by silica gel chromatography (3% MeOH and 0.5% Et_3N in CH_2Cl_2) to yield 0.85 g (31%) of the desired chloride **7** and 1.2 g (46%) of the corresponding alcohol **8**. **7:** MS (EI): *m*/*z* 57 (100%) *t*Bu^+, 246 (30%) [M − 3×Boc]$^+$, 346 (29%) [M − 2×Boc]$^+$, 446 (22%) [M − Boc]$^+$, 547 (7%) M^+. ^{1}H NMR (200 MHz, $CDCl_3$): δ = 3.45−3.84 and 2.83−3.02 [m, 4H and m, 4H, 2×CH_2(CH_2N)$_2$], 3.48 (t, 2H, J = 6.5 Hz, $ClCH_2$), 3.30 [d, 4H, J = 7.1 Hz, CH_2CH(CH_2N)$_2$], 2.14 [m, 1H, CH_2CH(CH_2N)$_2$], 1.71−2.04 [m, 8H, $ClCH_2$-(CH_2)$_2$ and 2×CH_2(CH_2N)$_2$], 1.44 [s, 27H, 3×C(CH_3)$_3$]. ^{13}C NMR (50 MHz, $CDCl_3$): δ = 156.4, 156.2, 79.8, 79.7, 49.2, 47.6, 45.2, 43.8, 36.3, 29.6, 28.8, 28.7.

1,5,9-Tris(*tert*-butoxycarbonyl)-3-(3-hydroxypropyl)-1,5,9-triazacyclododecane (8). Compound **8** was obtained in 89% yield when orthoamide **6** was hydrolyzed in aq HCl (6 mol L^{-1}) without treatment with concd aq HCl in dioxane. MS (EI): *m*/*z* 57 (100%) *t*Bu^+, 228 (25%) [M − 3×Boc]$^+$, 328 (28%) [M − 2×Boc]$^+$, 428 (25%) [M − Boc]$^+$, 529 (6%) M^+. ^{1}H NMR (200 MHz, $CDCl_3$): δ = 3.54−3.75 and 2.84−2.97 (m, 4H and m, 4H, 2×CH_2-(CH_2N)$_2$], 3.29 [d, 4H J = 7.0 Hz, CH_2CH(CH_2N)$_2$], 1.40−2.00 [m, 9H, (CH_2)$_2$CH(CH_2N)$_2$ and 2×CH_2(CH_2N)$_2$], 1.43 [s, 27H, 3×C(CH_3)$_3$]. ^{13}C NMR (50 MHz, $CDCl_3$): δ = 156.3, 79.8, 62.8, 53.7,47.7, 43.8, 36.5, 29.9, 28.7, 27.1.

3-(3-Acetylthiopropyl)-1,5,9-tris(*tert*-butoxycarbonyl)-1,5,9-triazacyclododecane (9). Potassium thioacetate (0.82 g, 7.2 mmol) and a catalytic amount of NaI were added to a solution of **7** (0.85 g, 1.6 mmol) in DMF (5.0 mL). The reaction mixture was allowed to stir overnight at 70 °C, and volatiles were then removed under reduced pressure. CH_2Cl_2 (70 mL) was added, and the resulting organic phase was washed with saturated $NaHCO_3$ and brine, dried over Na_2SO_4, and evaporated to dryness. The residue was purified by silica gel chromatography (20 to 30% EtOAc in petroleum ether) to yield 0.71 g (78%) of **9** as colorless oil. MS (EI): *m*/*z* 57 (100%) *t*Bu^+, 287 (23%) [M − 3×Boc]$^+$, 387 (28%) [M − 2×Boc]$^+$, 487 (27%) [M − Boc]$^+$, 588 (5%) M^+. ^{1}H NMR (200 MHz, $CDCl_3$): δ = 3.57−3.70 and 2.81−2.96 [m, 4H and m, 4H, 2×CH_2(CH_2N)$_2$], 3.28 [d, 2H, J = 7.0 Hz, CH_2CH(CH_2N)$_2$)], 2.82 (t, 2H, J = 7.2 Hz, AcSCH_2), 2.30 (s, 3H, AcS), 1.34−2.00 [m, 9H, (CH_2)$_2$CH(CH_2N)$_2$ and 2×CH_2(CH_2N)$_2$], 1.45 [s, 27H, 3×C(CH_3)$_3$]. ^{13}C NMR (50 MHz, $CDCl_3$): δ = 191.5, 156.2, 79.7, 49.3, 47.6, 43.6, 36.4, 30.6, 29.8, 29.3, 28.4, 26.7.

1,5,9-Tris(*tert*-butoxycarbonyl)-3-(3-mercaptopropyl)-1,5,9-triazacyclododecane (10). A mixture of **9** (0.80 g, 1.4 mmol) and MeONa (30 mmol) in MeOH (30 mL) was stirred at room temperature overnight. The mixture was neutralized with acetic acid, and volatiles were removed under reduced pressure. CH_2Cl_2 (70 mL) was added, and the organic phase was washed with water and brine, dried over Na_2SO_4, and evaporated to dryness. The residue was purified by silica gel chromatography to yield 0.69 g (93%) of **10** as colorless oil. MS (EI): *m*/*z* 57 (100%) *t*Bu^+, 244 (6%) [M − 3×Boc]$^+$, 344 (6%) [M − 2×Boc], 444 (14%) [M − Boc]$^+$, 544 (17%) M^+. ^{1}H NMR (200 MHz, $CDCl_3$): δ = 3.63−3.70 and 2.87−2.98 [m, 4H and m, 4H, 2×CH_2(CH_2N)$_2$], 3.32 [d, 4H, J = 6.2 Hz, CH_2CH(CH_2N)$_2$)], 2.62 (t, 2H, J = 7.0 Hz, HSCH_2), 1.26−2.09 [m, 9H, (CH_2)$_2$CH(CH_2N)$_2$ and 2×CH_2(CH_2N)$_2$], 1.46 [s, 27H, 3×C(CH_3)$_3$]. ^{13}C NMR (50 MHz, $CDCl_3$): δ = 156.4, 156.2, 79.8, 49.4, 47.8, 43.7, 38.9, 36.6, 30.4, 29.9, 28.5, 26.3.

3-(3-Mercaptopropyl)-1,5,9-triazacyclododecane trihydrochloride (11). Compound **10** (0.67 g, 1.2 mmol) was dissolved in a mixture of EtOH (50 mL) and concd aq HCl (10 mL). The mixture was stirred for 3h at room temperature, and it was then evaporated to dryness. The crude reaction product (0.44 g, a quantitative amount) obtained as a white hygroscopic solid was used without purification for the preparation of the disulfide-tethered oligonucleotide conjugates. MS (EI): *m*/*z* 36 (100%) HCl, 212 (12) [M − SH]$^+$, 245 (10%) M^+. ^{1}H NMR (200 MHz, D_2O): δ = 3.16−3.20 (m, 12H, 6×CH_2N), 2.60 (t, 2H, J = 6.4 Hz, HSCH_2), 2.20 [m, 1H, CH_2CH(CH_2N)$_2$], 2.07 [m, 4H, 2×CH_2(CH_2N)$_2$], 1.66 (m, 2H, HSCH_2CH_2), 1.47 [m, 2H, HS(CH_2)$_2$CH_2]. ^{13}C NMR (50 MHz, D_2O): δ = 42.6, 39.8, 37.3, 34.2, 29.2, 25.8, 22.6, 15.8.

1,5,9-Tris(*tert*-butoxycarbonyl)-3-(3-phthalimidopropyl)-1,5,9-triazacyclododecane (12). DEAD (0.56 mL, 3.6 mmol) was added dropwise to a stirred mixture of **8** (1.7 g, 3.3 mmol), phthalimide (0.49 g, 3.3 mmol), and triphenylphosphine (0.87 g, 3.3 mmol) in THF (15 mL). The mixture was refluxed for 72 h, volatiles were removed under reduced pressure, and CH_2Cl_2 was added. The organic phase was washed two times with saturated $NaHCO_3$, dried over Na_2SO_4, and evaporated to dryness. The crude reaction mixture was purified by silica gel chromatography (50% EtOAc in petroleum ether) to yield 1.92 g (88%) of **12**. MS (EI): *m*/*z* 57 (100%) *t*Bu^+, 357 (27%) [M − 3×Boc]$^+$, 457 (35%) [M − 2×Boc]$^+$, 557 (40%) [M − Boc]$^+$, 658 (5%) M^+. ^{1}H NMR (200 MHz, $CDCl_3$): δ = 7.84 (q, 2H, J = 3.1 and 5.3 Hz, *o*-Pht), 7.72 (q, 2H, J = 3.1 and 5.6 Hz, M − Pht), 3.66 and 2.97−2.87 [m, 6H and m, 4H, CH_2NPht and 2×CH_2(CH_2N)$_2$], 3.30 [d, 4H, J = 6.9 Hz, CH_2CH(CH_2N)$_2$], 2.05−0.93 [m, 9H, (CH_2)$_2$CH-(CH_2N)$_2$ and 2×CH_2(CH_2N)$_2$], 1.44 [s, 27H, 3xC(CH_3)$_3$]. ^{13}C NMR (50 MHz, $CDCl_3$): δ = 167.3, 155.2, 132.9, 131.2, 124.6, 78.8, 73.9, 48.5, 46.6, 42.8, 37.1, 35.5, 28.8, 27.5, 24.7.

3-(3-Aminopropyl)-1,5,9-tris(*tert*-butoxycarbonyl)-1,5,9-triazacyclododecane (13). Compound **12** (1.8 g, 2.7 mmol) was dissolved in EtOH (10 mL), hydrazine hydrate (0.66 mL, 14 mmol) was added, and the reaction mixture was stirred overnight at room temperature. Volatiles were removed under reduced pressure, and CH_2Cl_2 was added. The resulting organic phase was washed with saturated $NaHCO_3$, dried over Na_2SO_4, and evaporated to dryness. The crude product was purified by silica gel chromatography (10% MeOH and 0.5% Et_3N in CH_2Cl_2) to yield 1.0 g (70%) of **13** as white foam. MS (EI): *m*/*z* 57 (100%) *t*Bu^+, 227 (10%) [M − 3×Boc]$^+$, 327 (8%) [M − 2×Boc]$^+$, 427 (6%) [M − Boc]$^+$, 528 (21%) M^+. ^{1}H NMR (400 MHz, $CDCl_3$): δ = 3.61−3.54 and 2.88−2.85 [m, 4H and m, 4H, 2×CH_2(CH_2N)$_2$], 3.26 [d, 4H, J = 6.2 Hz, CH_2CH(CH_2N)$_2$], 2.62 (m, 2H, $CH_2CH_2NH_2$), 1.93 [m, 4H, 2xCH_2(CH_2N)$_2$], 1.77−1.85 [m, 1H, CH_2CH-(CH_2N)$_2$], 1.41 [s, 27H, 3×C(CH_3)$_3$], 1.25−1.31 (m, 2H, $CH_2CH_2CH_2NH_2$), 1.06−1.12 [m, 2H, CH_2(CH_2)$_2$$NH_2$]. ^{13}C NMR (100 MHz, $CDCl_3$): δ = 156.2, 79.6, 49.2, 47.7, 46.0, 43.6, 42.5, 36.5, 30.5, 29.9, 28.4.

3-(3-Aminopropyl)-1,5,9-triazacyclododecane (14). Compound **13** (0.85 g, 1.6 mmol) was dissolved in MeOH (5 mL), and aq HCl (6 mol L^{-1}, 5 mL) was added. The

mixture was stirred for 2 h at room temperature and then evaporated to dryness. The product was converted to the free base by passing it through a Dowex 2 × 8 resin (50/100 mesh, OH^- form) using water as an eluent. Water was removed to yield 0.89 g (80%) of **14** as colorless oil. MS (EI): *m/z* 228 (29%) M^+. ^1H NMR (200 MHz, D_2O): δ = 2.35−2.86 (m, 14H, 6×CH_2N, CH_2NH_2), 1.46−1.62 [m, 5H, 2×CH_2(CH_2N)$_2$ and CH_2CH(CH_2N)$_2$], 1.27−1.38 (m, 2H, C$H_2CH_2NH_2$), 1.03−1.21 [m, 2H, CH_2(CH_2)$_2NH_2$]. ^{13}C NMR (50 MHz, D_2O): δ = 49.5, 44.5, 44.0, 38.4, 32.7, 26.8, 25.6, 22.5.

***N*-{3-[1,5,9-Tris(*tert*-butoxycarbonyl)-1,5,9-triazacyclododec-3-yl]propyl}-3-(*tert*-butoxycarboxamido)-propanamide (15).** *N-tert*-Butoxycarbonyl-β-alanine (0.10 g, 0.50 mmol) and 1-hydroxybenzotriazole (70 mg, 0.50 mmol) were dissolved in 1,4-dioxane (6 mL), *N,N′*-dicyclohexylcarbodiimide was added, and the mixture was stirred for 30 min at room temperature. Compound **13** (0.26 g, 0.50 mmol) was added, and the reaction was allowed to stir for 22 h. Dicyclohexylurea formed was filtered off, and volatiles were removed under reduced pressure. The residue was dissolved in CH_2Cl_2 and washed with saturated $NaHCO_3$, 0.5 M citric acid, and brine. The organic phase was dried over Na_2SO_4 and evaporated to dryness. The crude reaction mixture was purified by silica gel chromatography (10% MeOH and 0.5% Et_3N in CH_2Cl_2) to yield 0.30 g (86%) of **15**. MS (EI): *m/z* 57 (100%) tBu$^+$, 298 (4%) [M − 4×Boc]$^+$, 398 (6%) [M − 3×Boc]$^+$, 498 (8%) [M − 2×Boc]$^+$, 599 (13%) [M − Boc]$^+$, 699 (3%) M^+. ^1H NMR (200 MHz, $CDCl_3$): δ = 3.58−2.80 (m, 16H, 6×CH_2N and BocNHCH_2CH_2-CONHCH_2), 2.20 (t, 2H, J = 7.3 Hz, BocNHCH_2CH_2CO), 1.90−1.11 [m, 9H, CH_2CH(CH_2N)$_2$, 2×CH_2(CH_2N)$_2$ and BocNH(CH_2)$_2$CONHCH_2(CH_2)$_2$], 1.39 [s, 36H, 4×C(CH_3)$_3$]. ^{13}C NMR (50 MHz, $CDCl_3$): δ = 170.0, 155.4, 78.7, 52.0, 48.8, 47.2, 45.5, 43.0, 36.7, 35.7, 29.4, 28.1, 24.4.

***N*-{3-[1,5,9-Tris(*tert*-butoxycarbonyl)-1,5,9-triazacyclododec-3-yl]propyl}-6-(*tert*-butoxycarboxamido)-hexanamide (16).** Compound **13** was conjugated with *N-tert*-butoxycarbonyl-6-aminohexanoic acid to obtain **16**, as described above for the preparation of **15**. Silica gel chromatography (0 to 10% MeOH and 0.5% Et_3N in CH_2Cl_2) gave 0.30 g (58%) of **16**. MS (EI): *m/z* 57 (100%) tBu$^+$, 340 (6%) [M − 4×Boc]$^+$, 440 (8%) [M − 3×Boc]$^+$, 540 (12%) [M − 2×Boc]$^+$, 641 (20%) [M − Boc]$^+$, 741 (2%) M^+. ^1H NMR (400 MHz, DMSO-d_6): δ = 3.49−3.66 and 2.92−3.05 [m, 4H and m, 4H, 2×CH_2(CH_2N)$_2$], 3.08−3.31 [m, 8H, CH_2CH(CH_2N)$_2$ and BocNHCH_2(CH_2)$_4$CONHCH_2], 2.17 [t, 2H, J = 7.5 Hz, BocNH(CH_2)$_4$CH_2], 1.79−2.01 and 1.29−1.37 [m, 10H, BocNHCH_2(CH_2)$_3$CH_2CONHCH_2-(CH_2)$_2$], 1.60−1.68 [m, 1H, CH_2CH(CH_2N)$_2$], 1.46 [s, 36H, 4×C(CH_3)$_3$].

***N*-{3-[1,5,9-Triazacyclododec-3-yl]propyl}-3-amino-propanamide (17).** Compound **15** (0.30 g, 0.43 mmol) was added to a mixture of TFA (5 mL) and CH_2Cl_2 (5 mL). After 1.5 h stirring at room temperature, the mixture was evaporated to dryness and the amino functionalized azacrown was converted to the free base by passing it through a Dowex 2 × 8 resin (50/100 mesh, OH^- form) using water as an eluent. Evaporation of the appropriate fractions gave 0.11 g (85%) of **17**. MS (EI): *m/z* 255 (25%) [M − $H_2NCH_2CH_2$]$^+$, 299 (100%) M^+. ^1H NMR (200 MHz, D_2O): δ = 2.98 [m, 2H, H_2N(CH_2)$_2$-CONHCH_2], 2.63 (m, 12H, 6xCH_2N), 2.39 (m, 2H, H_2NCH_2), 2.14 (m, 2H, $H_2NCH_2CH_2CO$), 1.49 [m, 5H, CH_2CH(CH_2N)$_2$ and 2×CH_2(CH_2N)$_2$], 1.32 [m, 2H, H_2N-(CH_2)$_2$CONHCH_2CH_2], 1.01 [m, 2H, H_2N(CH_2)$_2$CONH-(CH_2)$_2$CH_2]. ^{13}C NMR (50 MHz, D_2O): δ = 171.9, 49.4, 44.6, 44.3, 36.5, 36.1, 34.9, 32.3, 25.2, 23.3, 22.2.

***N*-{3-[1,5,9-Triazacyclododec-3-yl]propyl}-6-amino-hexanamide (18).** Compound **16** was converted to **18** (0.12 g, 91%), as described above for the conversion of **15** to **17**. MS (EI): *m/z* 255 (41%) [M − $H_2N(CH_2)_5$]$^+$, 341 (100%) M^+. ^1H NMR (200 MHz, D_2O): δ = 2.97 (t, 2H, J = 6.4 Hz, CONHCH_2), 2.54−2.79 (m, 12H, 6×CH_2N), 2.43 (m, 2H, H_2NCH_2), 2.04 (t, 2H, J = 7.2 Hz, CH_2CONH), 1.53 [m, 5H, CH_2CH(CH_2N)$_2$ and 2×CH_2(CH_2N)$_2$], 1.23−1.44 (m, 6H, $H_2NCH_2CH_2CH_2CH_2CH_2CONHCH_2CH_2$), 1.04−1.19 [$H_2N(CH_2)_2CH_2(CH_2)_2CONH(CH_2)_2CH_2$]. ^{13}C NMR (50 MHz, D_2O): δ = 173.9, 49.4, 44.7, 44.3, 38.5, 37.6, 36.4, 33.0, 32.2, 26.6, 25.2, 23.3, 22.6, 22.1.

Disulfide-Tethered Oligonucleotide 3′-Conjugate (22). A 13-mer 2′-*O*-methyl oligoribonucleotide, 5′-UUU CCG CAA UUU U-3′, was assembled by the conventional phosphoramidite chemistry on a polystyrene-anchored disulfide linker, **19**, prepared as described previously. The base moiety protections were removed by normal ammonolysis (concd aq NH_3, 55 °C, 8 h). The deprotected oligonucleotide was then cleaved from the support as a 3′-(3-mercaptopropyl)phosphate (**20**) with slightly alkaline aq dithiotreitol (DTT, 0.5 mol L^{-1}) by using a double-syringe method (Scheme 2) (*50*). The support was washed with water and MeCN, and the solution was evaporated to dryness. DTT was removed by precipitating **20** from EtOH. The terminal mercapto function was activated by conversion to 2-pyridyl disulfide (**21**) with aq bis(2-pyridyl) disulfide (*51*). The activated oligonucleotide (**21**) was purified by RP HPLC (Hypersil ODS, 10 × 250 mm, 5 μm), desalted, and evaporated to dryness. The 3-mercaptopropyl-functionalized azacrown **11** (4.0 mg, 10 μmol), triethylamine (5.7 μL, 40 μmol), and **21** were dissolved in water (1.0 mL), the reaction was allowed to proceed overnight at room temperature, and the mixture was then neutralized with acetic acid. The disulfide-tethered oligonucleotide conjugate **22** was purified by RP HPLC (Hypersil ODS, 10 × 250 mm, 5 μm; 5 min H_2O and then from 0 to 70% MeCN in 20 min, flow rate 1.0 mL min^{-1}, t_R 15−17 min). MS(MALDI): 4579.1 [M + H]$^+$, 2289.8 [(M + 2H)/2]$^+$. M_{calcd} 4578.8.

Amide Bond-Tethered Oligonucleotide 3′-Conjugates (24, 25). Two 13-mer 2′-*O*-methyl oligoribonucleotides, 5′-GGG UAG AGU GCG G-3′ and 5′-UUU CCG CAA UUU U-3′, were assembled from commercial 2′-*O*-methylated building blocks on a LCAA-CPG-supported thioester linker (*52*) (**23** in Scheme 3) using standard phosphoramidite RNA-coupling strategy. Upon completion of the chain assembly, the thioester linker was cleaved by shaking the support in 0.5 mol L^{-1} aq solution of the appropriate azacrown derivative, **14** or **17**, overnight at room temperature. To remove the remaining base protections, the solution phase was diluted with concd aq ammonia and kept 8.5 h at 55 °C. All volatile materials were evaporated under reduced pressure, the residue was dissolved in water, and the pH was adjusted to 7 with acetic acid. The oligonucleotide conjugates (**24**, **25**) obtained were purified by ion exchange chromatography on a SynChropak AX-300 column [4.6 × 250 mm, 6.5 μm; buffer A: 0.05 M KH_2PO_4 in 50% aq formamide, pH 5.6; buffer B: buffer A + 0.6 M $(NH_4)_2SO_4$; flow rate: 1 mL min^{-1}; a linear gradient from 10 to 70% B in 35 min] and desalted by RP HPLC (Hypersil ODS, 10 × 250 mm, 5 μm) by applying gradient elution from water to 50% (v/v) aq acetonitrile. The oligonucleotides were characterized by mass spectrometry. The overall isolated yield of both **24** and **25** was about 20%. The authenticity of the conjugates was verified by ESI-MS. MS(ESI) for **24**: *m/z* 685.6 (100%) [M − 7H]$^{7-}$, 800.1 (60%) [M − 6H]$^{6-}$, 960.3 (40%) [M − 5H]$^{5-}$, 1200.6 (31%) [M − 4H]$^{4-}$,

1601.1 (14%) $[M - 3H]^{3-}$. M_{obs} 4806.4, M_{calcd} 4805.0. MS(ESI) for **25**: *m/z* 574.4 (23%) $[M - 8H]^{8-}$, 656.6 (71%) $[M - 7H]^{7-}$, 766.1 (100%) $[M - 6H]^{6-}$, 919.7 (54%) $[M - 5H]^{5-}$, 1149.8 (38%) $[M - 4H]^{4-}$, 1532.9 (22%) $[M - 3H]^{3-}$. M_{obs} 4602.9, M_{calcd} 4604.2.

Amide Bond-Tethered Oligonucleotide 5′-Conjugate (28). The 5′-tethered azacrown conjugate (**28**) of a 13-mer 2′-*O*-methyl oligoribonucleotide, 5′-GGC GUG AGA UGG G-3′, was prepared by the normal phosphoramidite chemistry using a thioester phosphoramidite reagent **26** (0.6 mol L^{-1} in MeCN; coupling time 600 s) in the last coupling cycle to obtain conjugate **27** and cleaving the thioester bond with the 3-aminopropyl derivatized azacrown **14** (Scheme 4). The conjugate was isolated and purified as described above for conjugate **24**.

Amide Bond-Tethered Oligonucleotide Intrachain Conjugates (31−33). A 17-mer 2′-*O*-methyloligoribonucleotide (**30**), 5′-CUC UCC XGC AAG CUU CG-3′, was assembled by the conventional phosphoramidite strategy (Scheme 5). In the sequence, X stands for the abasic building block **29**, which was prepared as described previously (*49*). Upon completion of the oligonucleotide chain assembly, the protected oligonucleotide was treated with an azacrown derivative, either **14**, **17**, or **18** (0.5 mol L^{-1} solution of the free base in water), and then with concd aq ammonia, as described above, to afford the intrachain conjugates **31**, **32**, and **33**, respectively. The conjugates were isolated, purified by ion exchange HPLC and desalted as described above for conjugates **24** and **25.** The overall isolated yields ranged from 7 to14% (10−20 OD). The auhtenticity of the conjugates was verified by ESI-MS. MS(ESI) for **31**: *m/z* 565.7 (28%) $[M - 10H]^{10-}$, 628.7 (88%) $[M - 9H]^{9-}$, 707.6 (96%) $[M - 8H]^{8-}$, 808.4 (100%) $[M - 7H]^{7-}$, 943.7 (31%) $[M - 6H]^{6-}$, 1132.4 (38%) $[M - 5H]^{5-}$, 1415.6 (22%) $[M - 4H]^{4-}$. M_{obs} 5667.2, M_{calcd} 5664.9. MS(ESI) for **32**: *m/z* 572.9 (28%) $[M - 10H]^{10-}$, 636.5 (71%) $[M - 9H]^{9-}$, 716.3 (100%) $[M - 8H]^{8-}$, 818.6 (95%) $[M - 7H]^{7-}$, 955.1 (63%) $[M - 6H]^{6-}$, 1146.2 (55%) $[M - 5H]^{5-}$, 1433.3 (32%) $[M - 4H]^{4-}$, 1912.1 (4%) $[M - 3H]^{3-}$. M_{obs} 5737.7, M_{calcd} 5736.0. MS(ESI) for **33**: *m/z* 577.1 (29%) $[M - 10H]^{10-}$, 641.3 (80%) $[M - 9H]^{9-}$, 721.7 (100%) $[M - 8H]^{8-}$, 824.6 (88%) $[M - 7H]^{7-}$, 962.3 (55%) $[M - 6H]^{6-}$, 1154.9 (49%) $[M - 5H]^{5-}$, 1443.8 (29%) $[M - 4H]^{4-}$, 1925.9 (8%) $[M - 3H]^{3-}$. M_{obs} 5780.3, M_{calcd} 5778.1.

Thymidine 3′-(2-Cyanoethyl, 2-benzylthio-2-oxoethyl)phosphate (34). Carefully dried benzylthio ester of glycolic acid (92 mg, 0.50 mmol) and 5′-*O*-(4,4′-dimethoxytrityl)thymidine 3′-[*O*-(2-cyanoethyl)-*N*,*N*-diisopropyl]phosphoramidite (250 mg, 0.34 mmol, Glenn Research) were dissolved in dry acetonitrile (180 mL), 1*H*-tetrazole (1.36 mmol, 3.0 mL of 0.45 mol L^{-1} solution in acetonitrile) was added, and the mixture was stirred for 2 h at room temperature. The reaction mixture was concentrated under reduced pressure, and 9.5 mL of 0.1 mol L^{-1} solution of iodine in a mixture of THF and water (2:1) was added. After 35 min at room temperature, an aq $NaHCO_3/CH_2Cl_2$ workup was carried out, and the product was treated for 50 min with a mixture of CH_2Cl_2, dichloroacetic acid, and EtOH (10 mL, 85:5:1, v/v) to remove the dimethoxytrityl protection. The crude product obtained by an aq $NaHCO_3/CH_2Cl_2$ workup was purified by silica gel chromatography (5% MeOH in CH_2Cl_2) yielding **34** as a yellow foam (130 mg, 71%). MS(ESI): *m/z* 225.4 (94%) $[Thd\text{-}OH]^+$, 316.1 (100%) $[NC(CH_2)_2OP(OH)_2OCH_2COSBn]^+$, 540.4 (81%) $[MH]^+$, 1079.6 (36%) $[2MH]^+$. ^1H NMR (400 MHz; $CDCl_3$): $\delta = 9.25$ (1H, br s, N*H*), 7.39 (1H, s, *H*6), 7.25 (5H, m, Phe), 6.11 (1H, t, $J =$ 7.5 Hz, *H*1′), 5.18 (1H, m, *H*3′), 4.69 (2H, d, $J = 10.2$ Hz, OCH_2COSBn), 4.30 (2H, m, OCH_2CH_2CN), 4.17 (1H, m, *H*4′), 4.13 (2H, s, SCH_2Ph), 3.82 (2H, m, *H*5′ and *H*5″), 3.14 (1H, br s, 5′-O*H*), 2.73 (2H, t, $J = 6.8$ Hz, OCH_2CH_2CN), 2.47 (2H, m, *H*2′ and *H*2″), 1.83 (3H, s, CH_3). ^{31}P NMR (162 MHz; $CDCl_3$): $\delta = -3.47$ ppm.

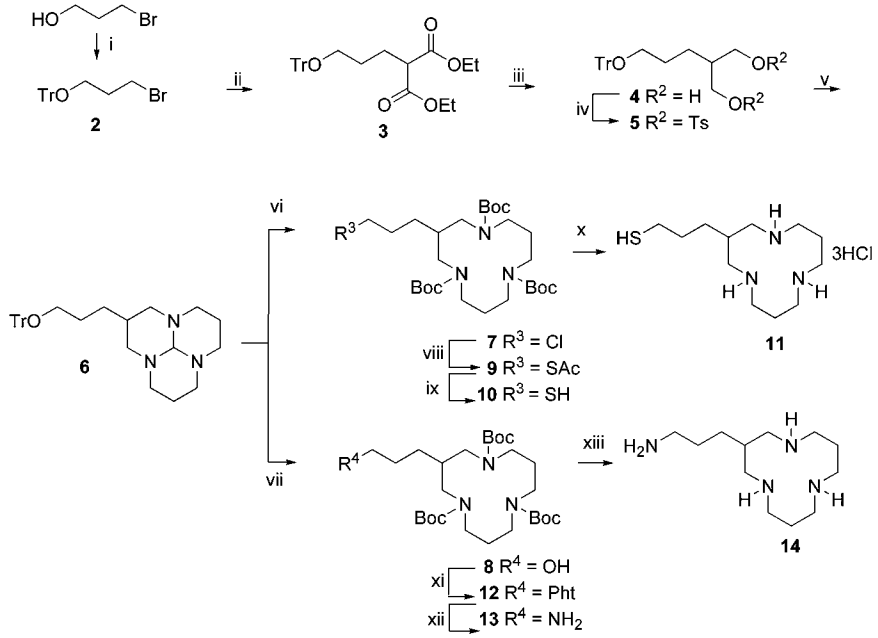
Thymidine 3′-{2-[3-(1,5,9-Triazacyclododec-3-yl)-propylamino]-2-oxoethyl}phosphate (35). Equal volumes of a 3.0 mmol L^{-1} solution of **34** in MeCN and a 0.5 mol L^{-1} aq solution of **14** as a free base were mixed. The progress of the reaction was followed by HPLC-ESI-MS on a LiChroCART ODS column (4 × 250 mm, 5 μm) using a gradient elution: isocratic elution with an acetic acid/sodium acetate buffer (pH 3.4) for 5 min was followed by linear increase of the MeCN content from 0% to 100% in 25 min. The starting material **34** disappeared almost immediately, and two products, the desired azacrown derivative **35** and the hydrolysis product of **34** (thymidine 3′-carboxymethyl phosphate), were formed. The retention times were at a flow rate 1 mL min^{-1} 11.3 (*m/z* 589.6) and 14.7 min (*m/z* 379.0), respectively. Compound **35** was isolated on a semipreparative LiChroCART RP-18 column (10 × 250 mm, 5 μm) and characterized by ^1H NMR spectroscopy. MS(ESI): *m/z* 589.6 (100%) M^-. ^1H NMR (500 MHz; CD_2HOD): 7.83 (1H, s, *H*6), 6.28 (1H, dd, $J =$ 7.8 and 6.2 Hz, *H*1′), 4.87 (1H, m, *H*3′), 4.35 (2H, d, $J =$ 9.1 Hz, OCH_2CONH), 4.13 (1H, m, *H*4′), 3.79 (2H, m, *H*5′ and *H*5″), 3.30 (2H, m, $CONHCH_2$), 3.01−3.26 (12H, m, *H*2,*H*4,*H*6,*H*8,*H*10,*H*12 of [12]aneN$_3$), 2.43 (1H, m, *H*2′), 2.31 (1H, m, *H*2″), 2.05 (5H, m, *H*3,*H*7,*H*11 of [12]aneN$_3$), 1.89 (3H, s, CH_3), 1.63 (2H, m, $OCH_2CONHCH_2CH_2$), 1.40 (2H, m, $OCH_2CONHCH_2CH_2CH_2$).

Cleavage Assays. The reactions were carried out in small seal-cap vials immersed in a water bath, the temperature of which was maintained at 35.0 ± 0.1 °C. The volume of the reaction mixture was 200 μL. The pH was adjusted to 7.3 with a HEPES buffer (0.1 mol L^{-1}, $I =$ 0.1 mol L^{-1} with $NaNO_3$). Zinc ions were added as nitrates in 20% excess compared to the azacrown functionalized oligonucleotide, the concentration of which was 4.5 μmol L^{-1} with **22** and 18 μmol L^{-1} with **25**, **32**, and **33**. The concentration of the target was double compared to that of the cleaving agent. *p*-Toluenesulfonate or *p*-nitrobenzenesulfonate ion was used as an internal standard. Aliquots of 20 μL were withdrawn at suitable intervals and immediately cooled to 0 °C. The reaction was quenched by adding aqueous hydrogen chloride (1.0 μL of 1.0 mol L^{-1} solution). The samples were analyzed immediately by capillary zone electrophoresis (CZE; Hewlett-Packard ^{3}DCE or Beckman Coulter P/ACE MDQ CE system) using a fused silica capillary, inverted polarity, and a citrate buffer (0.2 M, pH 3.2) as a background electrolyte. The voltage applied was −30 kV. The temperature of the capillary was kept at 25 °C. Hydrodynamic injection and UV detection were applied.

RESULTS AND DISCUSSION

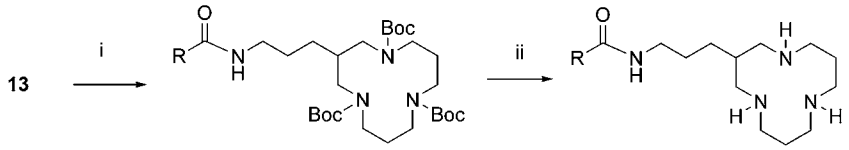
Preparation of the Functionalized Azacrowns. Azacrowns are usually functionalized for conjugation by attachment of an appropriate sidearm to one of the ring nitrogens. Alkylation of one of the donor atoms may, however, be expected to reduce the binding ability of the relatively small triaza crown (1) employed in the present work. For comparison, methylation of all the nitrogen atoms of 1,4,8,11-tetraazacycotetradecane destabilizes the Zn^{2+} complex by 5 orders of magnitude (*53*). Accordingly, tethering through a carbon atom appears more attractive. Preparation of 3-(3-aminopropyl)-1,5,9-triazacyclododecane (**14**) starting from commercially available

Scheme 1[a]



[a] Reagents and conditions: (i) TrCl, Et_3N, THF; (ii) diethyl malonate, NaOEt, EtOH; (iii) $LiAlH_4$, Et_2O; (iv) TsCl, Py; (v) 1. TBD, DME, 2. $NaBH_4$, DME; (vi) 1. concd aq HCl, dioxane, 2. 6 M aq HCl, 3. Boc_2O, NaOH, H_2O, MeCN; (vii) 1. 6 Mol L^{-1} aq HCl, 2. Boc_2O, NaOH, H_2O, MeCN; (viii) KSAc, NaI, DMF; (ix) 1 mol L^{-1} NaOMe, (x) concd HCl, EtOH; (xi) DEAD, PhtH, Ph_3P, THF; (xii) NH_2NH_2, EtOH; (xiii) 1. 6 mol L^{-1} aq HCl, MeOH, 2. Dowex 2 × 8, OH^-.

Scheme 2[a]



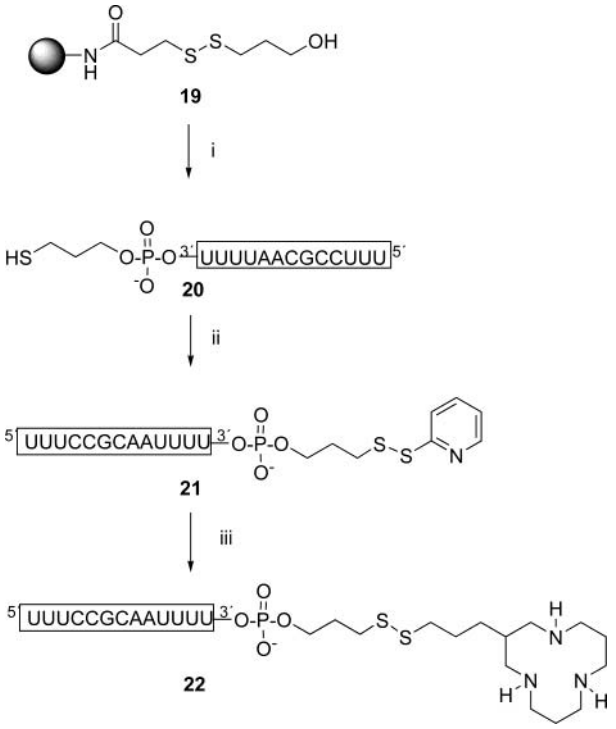
[a] Reagents and conditions: (i) DCC, HOBt, and $BocNH(CH_2)_nCOOH$ (n = 2 or 5) in dioxane, (ii) 1. TFA, CH_2Cl_2, 2. Dowex 2 × 8, OH^-.

diethyl 2-(2-cyanoethyl)malonate has been described previously (*54*). Scaling up of the reported synthesis is, however, difficult since the first step, viz. reduction of the cyano group to an amino group with borane−dimethyl sulfide, yields the desired 2-(3-aminopropyl)-1,3-propanediol as a minor component (34%), the corresponding monoethyl ether being the major product (59%). A reaction that necessitated a careful chromatographic separation at an early stage of a multistep synthesis proved inconvenient in our hands and, hence, the synthesis was modified to the form depicted in Scheme 1. Accordingly, diethyl 2-(3-trityloxypropyl)malonate (**3**) obtained by alkylation of 3-trityloxypropyl bromide (2) with diethyl malonate carbanion was used as the starting material. $LiAlH_4$ reduction to a diol (**4**) and conversion to a ditosylate (**5**) allowed introduction of the azacrown structure by a nucleophilic displacement with TBD, as originally shown by Alder et al. (*55*) and Kim et al. (*56*) and also utilized in the previous synthesis. Acid-catalyzed hydrolysis of the resulting orthoamide (**6**) and removal of the trityl group in a single step followed by introduction of Boc-protection on the ring nitrogen atoms gave the 3-(3-hydroxypropyl)-functionalized azacrown (**8**). The hydroxy function was displaced with a phthaloyl group by a Mitsunobu reaction **12**, and the amino group was exposed (**13**) by a hydrazine treatment. The Boc-protections were finally removed with aq hydrogen chloride and the product obtained as a hydrochloride salt was converted to a free base (**14**) by passing it through a strong anion-exchange resin (Dowex 2 × 8) in a hydroxy ion form. All the reactions proceeded in a good yield, typically around 80% without optimization, giving the final product in a 15% overall yield.

The 3-(3-mercaptopropyl) derivatized azacrown (**11**) was prepared from the same orthoamide (**6**) as its 3-aminopropyl counterpart. When **6** was treated with concd aq hydrogen chloride in dioxane, the 3-(3-chloropropyl) azacrown (**7**) was obtained in a 31% yield, besides the corresponding alcohol (**8**). Displacement of the chloro substituent with a thioacetate ion (**9**), followed by removal of the acetyl- and Boc-protections by a base-catalyzed transesterification and acid-catalyzed hydrolysis, respectively, gave 3-(3-mercaptopropyl)-1,5,9-triazacyclododecane as a hydrochloride salt in a 73% yield.

The pendant group of 3-(3-aminopropyl)-1,5,9-triazacyclododecane was elongated by acylating the primary amino group of 13 with *N*-Boc-protected *β*-alanine and 6-aminohexanoic acid (Scheme 2). A conventional DCC/HOBt-coupling was applied. Removal of the Boc groups from the products (**15**, **16**) and conversion to a free base gave the *N*-(3-aminopropanoyl)-3-aminopropyl (**17**) and *N*-(6-aminohexanoyl)-3-aminopropyl (**18**) azacrowns in a 73% and 53% yield, rescectively.

Scheme 3[a]



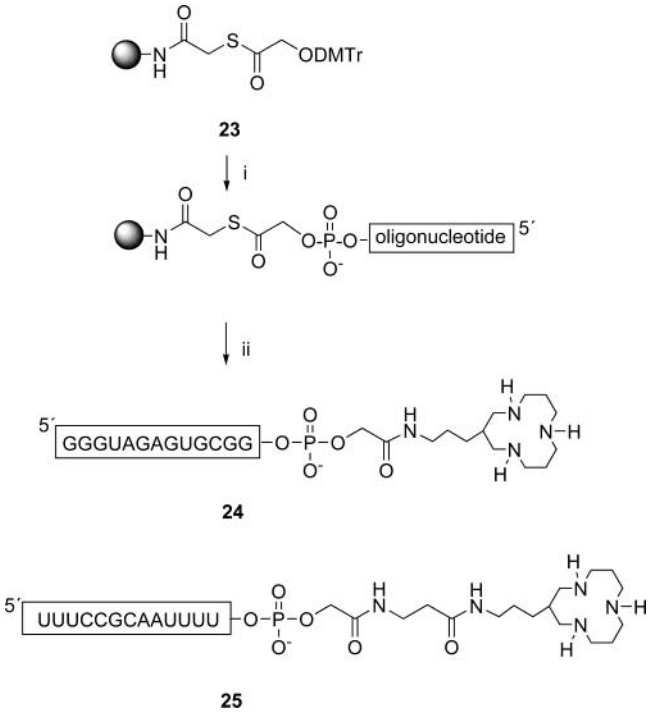
[a] Reagents and conditions: (i) 1. Oligonucleotide synthesis 2. concd aq NH_3, 3. DTT, aq; (ii) PySSPy; (iii) **11**, Et_3N, H_2O.

Preparation of the disulfide-tethered oligonucleotide conjugate. Conjugation of the 3-(3-mercaptopropyl) azacrown (**11**) to the 3′-terminus of a 13-mer 2′-*O*-methyl oligoribonucleotide is outlined in Scheme 3. Accordingly, the oligonucleotide was first assembled by the conventional phosphoramidite chemistry on a polystyrene-anchored disulfide linker (19), prepared as described previously (*50*). The acyl protections of the base moieties were removed by normal ammonolysis, and the oligonucleotide was then cleaved from the support with slightly alkaline aq dithiotreitol and purified by precipitation from EtOH, as also shown earlier. The terminal mercapto function of the 3′-(3-mercaptopropyl)-tailed oligonucleotide (**20**) was activated by conversion to a 2-pyridyl disulfide (**21**) and reacted with the mercapto-functionalized azacrown (**11**) in silightly basic aq solution. The disulfide-tethered conjugate (**22**) was purified by RP-HPLC and characterized by MALDI-MS.

Preparation of the Amide Bond-Tethered Oligonucleotide Conjugates. The previously developed thioester approach was applied to obtain the oligonucleotide conjugates having the azacrown tethered via an amide bond. Accordingly, the 3′-tethered conjugates were prepared by assembling the desired 2′-*O*-methyl oligoribonucleotide on a LCAA-CPG-supported thioester linker **23** (Scheme 4) and the linker was cleaved by using an appropriate azacrown derivative, viz. **14** or **17**, as the attacking nucleophile. The deprotection of the conjugates (**24**, **25**) was completed by ammonolysis in solution and the conjugates were then purified by ion-exchange HPLC, desalted by RP-HPLC, and characterized by ESI-MS.

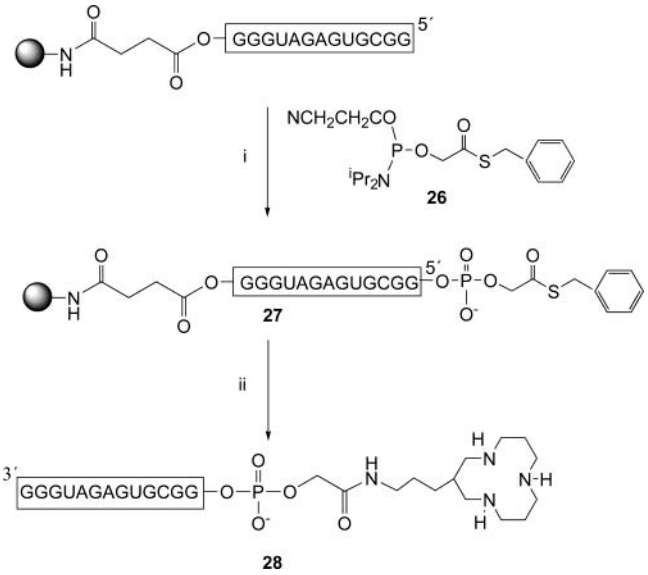
Conjugation to the 5′-terminus was achieved by assembling the chain on a standard succinyl-linker using a nonnucleosidic thioester phosphoramidite reagent (26) in the last coupling cycle (Scheme 5). The azacrown derivative (**14**) was then introduced upon the aminolytic cleavage of the conjugate (**27**) from the support, and the

Scheme 4[a]



[a] Reagents and conditions: (i) Oligonucleotide synthesis; (ii) 1. **14**, aq, 2. concd aq NH_3.

Scheme 5[a]

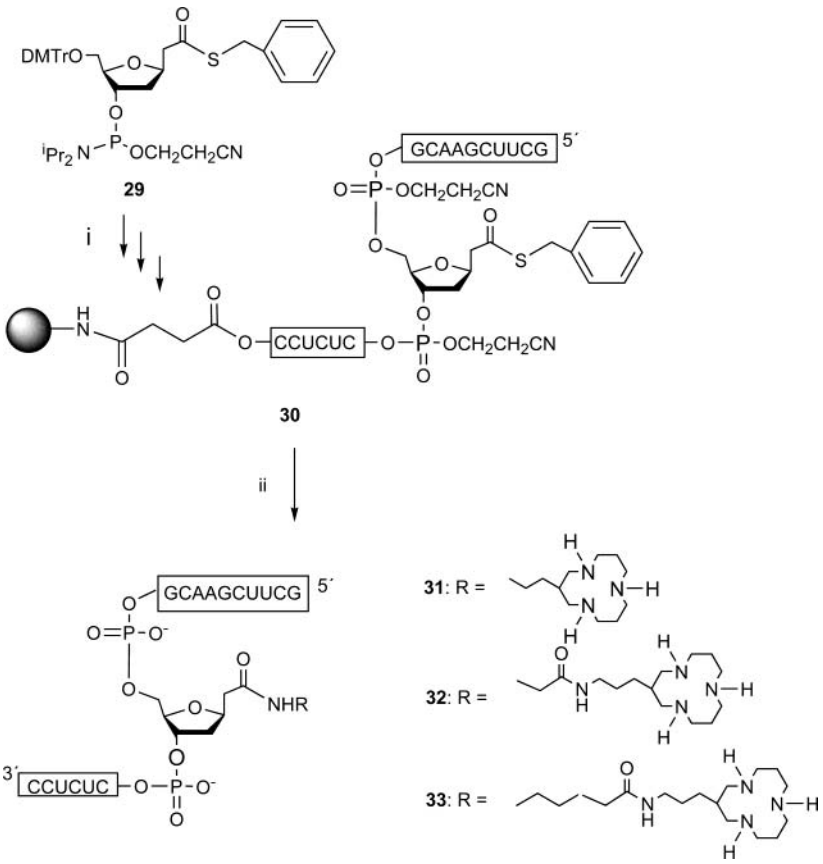


[a] Reagents and conditions: (i) **26**, MeCN, tetrazole; (ii) 1. **14**, aq, 2. concd aq NH_3.

deprotected oligonucleotide conjugate (**28**) was purified and characterized as the 3′-conjugates.

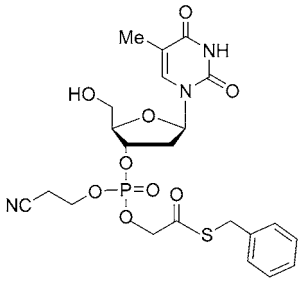
Conjugation to an intrachain position was performed with the aid of an abasic *C*1-(2-benzylthio-2-oxoethyl) building block (**29**) prepared as described previously (*49*). Upon insertion of this unit in a desired position within the chain and completion of the chain assembly to obtain the solid-supported oligonucleotide **30**, the thioester bond was cleaved with three different azacrown derivatives, **14**, **17**, or **18**, bearing 4-, 8-, and 11-atom long pendant aromatics, respectively (Scheme 6). The intrachain conjugates obtained (**31**−**33**) were ammonolyzed, purified, desalted, and characterized as described above the 3′-conjugates.

Scheme 6[a]



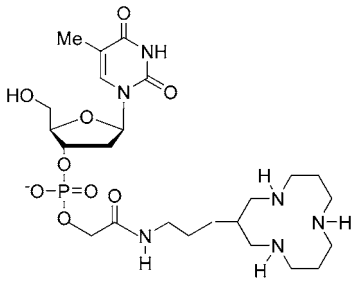
[a] Reagents and conditions: (i) Oligonucleotide synthesis; (ii) 1. **14**, **17**, or **18**, aq, 2. concd aq NH_3.

Since the thioester bonds were cleaved with fully deprotected azacrown derivatives (**14**, **17**, **18**), the ring nitrogen atoms could in principle compete with the primary amino group as nucleophiles. To verify that the difference between the nucleophilicity of the primary and secondary amino groups was sufficient to warrant the formation of a single product, the cleavage reaction was studied in more detail with a monomeric model compound (**34**) prepared from a commercial thymidine 3′-phos-



34

phoramidite building block and benzylthio ester of glycolic acid (*52*) by the conventional phosphoramidite chemistry in solution. This compound was treated with 0.5 mol L^{-1} solution of the 3-aminopropyl-functionalized azacrown (**14**) in a 1:1 mixture of water and MeCN and the progress of the reaction was followed by HPLC-ESI-MS. Rapid disappearance of the starting material (**34**) was accompanied by formation of two products, the desired azacrown derivative (**35**; *m*/*z* 589.6) and thymidine 3′-carboxymethyl phosphate (*m*/*z* 379.0), the hydrolysis product of **34**. Compound **35** was isolated by



35

semipreparative RP-HPLC and characterized by NMR spectroscopy. In the heteronuclear multibond correlation spectrum (HMBC), the carbonyl carbon of the amide bond (170 ppm) was coupled to the methylene protons (3.30 ppm) of C3 of the sidearm of the azacrown moiety consistent with bonding to the primary amino group.

Cleavage Experiments. The ability of the 3′-tethered conjugates (**22**, **25**) to cleave, as their Zn^{2+} chelates, a complementary chimeric 2′-*O*-methylribo/ribo oligonucleotide (**36**) was studied. The reactions were carried

3′-**AAA GGC GUU** AAA AUC UUC AU-5′

(2′-*O*-Me-ribonucleosides indicated with

bold and ribonucleosides with normal letters)

36

out in a HEPES buffer (0.1 mol L^{-1}, $I = 0.1$ mol L^{-1} with $NaNO_3$) at 35.0 ± 0.1 °C. The initial concentrations of conjugates **22** and **25** were 4.5 and 18 μmol L^{-1}, respectively. The concentration of the target was double com-

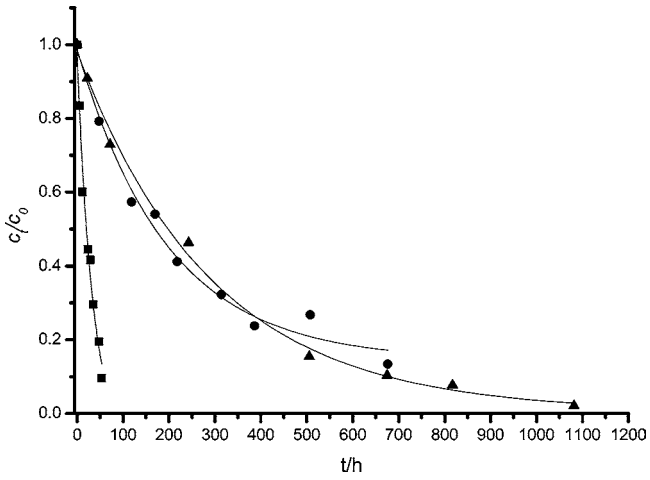


Figure 1. Cleavage of chimeric 2′-*O*-methylribo/ribo oligonucleotides by 2′-*O*-methyl oligoribonucleotides functionalized with the Zn(II) chelate of 1,5,9-triazacyclododecane. Notation: $T = 35.0$ °C, $I = 0.1$ mol L^{-1} with $NaNO_3$. Filled squares refer to target **36** cleaved by conjugate **22**, filled circles to target **36** cleaved by conjuagate **25**, and filled triangles to target **37** cleaved by conjugate **32**.

pared to that of the conjugate. *p*-Toluenesulfonate or *p*-nitrobenzenesulfonate ion was used as an internal standard. The progress of the reactions was followed by analyzing the content of the aliquots withdrawn at suitable intervals by capillary zone electrophoresis with UV-detection. Both conjugates cleaved the target sequence. The disappearance of the signal of the target was in both cases accompanied by appearance of two product signals. On using **22** as a cleaving agent and a 102 cm capillary, the signal at 21.8 min disappeared and those at 20.5 and 30.5 min appeared, while on using **25** and a 50 cm capillary, the signal at 9.8 min disappeared and those at 10.7 and 11.1 min appeared. Both conjugates also showed turnover without any indication of product inhibition. In other words, the disappearance of the target was complete, and it obeyed first-order kinetics throughout a kinetic run (Figure 1), although the concentration of the target was double compared to that of the cleaving agent. Since the complementary region in duplexes **22**/**36** and **25**/**36** is only 13 nucleotides long and contains only 4 CG pairs, it appears likely that the conjugate remains largely unhybridized under the experimental conditions and, hence, the effective concentration of the cleaving agent remains constant during a kinetic run. Quite unexpectedly, the disulfide-tethered conjugate (**22**) turned out to cleave the target 8 times as fast as the amide bond-tethered conjugate (**25**), although the length of the linker is almost equal, viz. 10 and 12 atoms between the 3′-terminal oxygen atom and *C*3 of the azacrown. Either, the cleaving ability is very susceptible to the length of the linker, or the amide bond present in the linker interacts with the chelated Zn^{2+} ion reducing its catalytic activity. One should also bear in mind that the results obtained with **22** and **25** refer to different concentrations of the cleaving agent, 4.5 and 18 μmol L^{-1}, respectively. Accordingly, the possibility that the cleaving agent tends at higher concentrations to become deactivated by aggragation cannot be excluded. The disulfide-tethered conjugate (**22**) turned out to be an approximately as efficient cleaving agent as the previously reported Zn^{2+}-based artificial RNases. The half-life for the disappearance of the target is about 20 h at 35 °C, while a nuclease derived from a Zn^{2+}/2,9-dimethylphenantroline chelate has been reported to cleave 50% of the target in 60 h at 37 °C (*30*) and a nuclease bearing a dinuclear *N*,*N*,*N*′,*N*′-tetrakis(2-pyridylmethyl)-3,5-bis(aminomethyl)phenoxy chelate 5% of the target in 3 h at 37 °C (*29*).

Conjugates **32** and **33** bearing a Zn^{2+}/[12]aneN_3 in an intrachain position cleaved target **37**, having a trinucleotide bulge opposite to cleaving agent (Figure 1). Again the cleavage reaction obeyed nicely first-order kinetics. Conjugate **32**, having a shorter linker, turned out to be a more efficient cleaving agent than conjugate **33**. The cleaving activity was comparable to that of the corresponding 3′-tethered conjugate **25**. By contrast, the 5′-tethered conjugate **28** did not show any cleaving activity during 100 h under the same conditions.

3′-**GAG AG**G AAA CGU **UCG AAG C**-5′

(2′-*O*-Me-ribonucleosides indicated with

bold and ribonucleosides with normal letters)

37

ACKNOWLEDGMENT

The authors wish to thank Ms. Susanna Virpi, B. Sc., for her skilful help in the preparation of the functionalized aza crowns. Financial aid from the Academy of Finland is gratefully acknowledged.

LITERATURE CITED

(1) Travick, B. N., Daniher, A. T., and Bashkin, J. K. (1998) Inorganic mimics of ribonucleases and ribozymes: from random cleavage to sequence-specific chemistry to catalytic antisense drugs. *Chem. Rev. 98*, 939−960.

(2) Oivanen, M., Kuusela, S., and Lönnberg, H. (1998) Kinetics and mechanisms for the cleavage and isomerization of the phosphodiester bonds of RNA by Brönsted acids and bases. *Chem. Rev. 98*, 961−990.

(3) Häner, R., Hall, J., Pfützer, A., and Hüsken, D. (1998) Development of artificial nucleases. *Pure Appl. Chem. 70*, 111−116.

(4) Komiyama, M., Sumaoka, J., Kuzuya, A., and Yamamoto, Y. (2001) Sequence-selective artificial ribonucleases. *Methods Enzymol. 341*, 455−468.

(5) Cowan, J. A. (2001) Chemical Nucleases. *Curr. Opin. Chem. Biol. 5*, 634−642.

(6) Häner, R. (2001) Artificial ribonucleases. *Chimia 55*, 1035−1037.

(7) Agrawal, S., Mayrand, S. H., Zamecnik, P. C., and Pederson, T. (1990) Site-specific excision from RNA by RNase H and mixed-phosphate-backbone oligodeoxynucleotides. *Proc. Natl. Acad. Sci. U.S.A. 87*, 1401−1405.

(8) Chiang, M. Y., Chan, H., Zounes, M. A., Freier, S. M., Lima, W. F., and Bennett, C. F. (1991) Antisense oligonucleotides inhibit intercellular adhesion molecule 1 expression by two distinct mechanisms. *J. Biol. Chem. 266*, 18162−18171.

(9) For structurally modified antisense oligonucleotides that activate RNaseH, see Mangos, M. M., Min, K.-L., Viazovkina, E., Galarneau, A., Elzagheid, M. I., Parniak, M. A., and Damha, M. J. (2003) Efficient RNase H-directed cleavage of RNA promoted by antisense DNA or 2′F-ANA constructs containing acyclic nucleotide inserts. *J. Am. Chem. Soc. 125*, 654−661, and references therein.

(10) Ushijima, K., Shirakawa, M., Kagoshima, K., Park, W.-S., Miyano-Kurosaki, N., and Takaku, H. (2001) Anti-HIV-1 activity of an antisense phosphorothioate oligonucleotide bearing imidazole and primary amine groups. *Bioorg. Med. Chem. 9*, 2165−2169.

(11) Baker, B. F., Lot, S. S., Kringel, J., Cheng-Flournoy, S., Villiet, P., Sasmor, H. M., Siwskowski, A. M., Chappel, L. L., and Morrow, J. M. (1999) Oligonucleotide -europium complex conjugate designed to cleave the 5′-cap structure of the ICAM-1 transcript potentiates antisense activity in cells, *Nucleic Acids Res. 27*, 1547−1551.

(12) Sigman, D. S., Mazumder, A., and Perrin, D. M. (1993) Chemical nucleases. *Chem Rev. 93*, 2295−2316.

(13) Sigman, D. S., Bruice, T. W., Mazumder, A., and Sutton, C. L. (1993) Targeted chemical nucleases. *Acc. Chem. Res. 26*, 98−104.

(14) Duarte, V., Sixou, S., Favre, G., Pratviel, G., and Meunier, B. (1997) Oxidative damage on RNA mediated by cationic metalloporphyrin antisense oligonucleotide conjugates. *J. Chem. Soc., Dalton Trans. 21*, 4113−4118.

(15) Hall, J., Hüsken, D., Pieles, U., Moser, H. E., and Häner, R. (1994) Efficient sequence-specific cleavage of RNA using novel europium complexes conjugated to oligonucleotides. *Chem. Biol. 1*, 185−190.

(16) Hall, J., Hüsken, D., and Häner, R. (1996) Towards artificial ribonucleases: the sequence specific cleavage of RNA in a duplex. *Nucleic Acids Res. 24*, 3522−3526.

(17) Häner, R., and Hall, J. (1997) The sequence-specific cleavage of RNA by artificial chemical ribonucleases. *Antisense Nucleic Acid Drug Dev. 7*, 423−430.

(18) Hall, J., Husken, D., and Häner, R. (1997) Sequence-specific cleavage of RNA using macrocyclic lanthanide complexes conjugated to oligonucleotides: a structure−activity study. *Nucleosides Nucleotides 16*, 1357−1368.

(19) Canaple, L., Hüsken, D., Hall, J., and Häner, R. (2002) Artificial ribonucleases: efficient and specific in vitro cleavage of human *c-raf-1* RNA. *Bioconjugate Chem. 13*, 945−951.

(20) Magda, D., Miller, R. A., Sessler, J. L., and Iverson, B. L. (1994) Site-specific hydrolysis of RNA by europium(III) texapyrin conjugated to a synthetic oligodeoxyribonucleotide. *J. Am. Chem. Soc. 116*, 7439−7440.

(21) Magda, D., Wright, M., Crofts, S., Lin, A., and Sessler, J. L. (1997) Metal complex conjugates of antisense DNA which display ribozyme-like activity. *J. Am. Chem. Soc. 119*, 6947−6948.

(22) Magda, D., Crofts, S., Lin, A., Miles, D., Wright, M., and Sessler, J. (1997) Synthesis and kinetic properties of ribozyme analogues prepared using phosphoramidite derivatives of dysprosium(III) texapyrin. *J. Am. Chem. Soc. 119*, 2293−2294.

(23) Huang, L., Chappell, L. L., Iranzo, O., Baker, B. F., and Morrow, J. R. (2000) Oligonucleotide conjugates of Eu(III) tetraazamacrocycles with pendent alcohol and amide groups promote sequence-specific RNA cleavage. *J. Biol. Inorg. Chem. 5*, 85−92.

(24) Matsumura, K., Endo, M., and Komiyama, M. (1994) Lanthanide complex-oligo-DNA hybrid for sequence-selective hydrolysis of RNA. *J. Chem. Soc., Chem. Commun.* 2019−2020.

(25) Bashkin, J. K., Frolova, E. I., and Sampath, U. (1994) Sequence-specific cleavage of HIV mRNA by a ribozyme mimic. *J. Am. Chem. Soc. 116*, 5981−5982.

(26) Trawick, B. N., Osiek, T. A., and Bashkin, J. K. (2001) Enhancing sequence-specific cleavage of RNA within a duplex region: incorporation of 1,3-propanediol linkers into oligonucleotide conjugates of serinol-terpyridine. *Bioconjugate Chem. 12*, 900−905.

(27) Putnam, W. C., Daniher, A. T., Trawick, B. N., and Bashkin, J. K. (2001) Efficient new ribozyme mimics: direct mapping of molecular design principles from small molecules to macromolecular, biomimetic catalysis. *Nucleic Acids Res. 29*, 2199−2204.

(28) Sakamoto, A., Tamura, T., Furukawa, T., Komatsu, Y., Ohtsuka, E., Kitamura, M., and Inoue, H. (2003) Highly efficient catalytic RNA cleavage by the cooperative action of two Cu(II) complexes embodied within an antisense oligonucleotide. *Nucleic Acids Res. 31*, 1416−1425.

(29) Matsuda, S., Ishikubo, A., Kuzuya, A., Yashiro, M., and Komiyama, M. (1998) Conjugates of a dinuclear zinc(II) complexes and DNA oligomers as novel sequence-selective artificial ribonucleases. *Angew. Chem., Int. Ed. 37*, 3284−3286.

(30) Åström, H., Williams, N. H., and Strömberg, R. (2003) Oligonucleotide based artificial nuclease (OBAN) systems. Bulge size dependence and positioning of catalytic group in cleavage of RNA-bulges. *Org. Biomol. Chem. 1*, 1461−1465.

(31) Reynolds, M. A., Beck, T. A., Say, P. B., Schwartz, D. A., Dwyer, B. P., Daily, W. J., Vaghefi, M. M., Metzler, M. D., Klem, R. E., and Arnold, L. J., Jr. (1996) Antisense oligonucleotides containing an internal nonnucleotide-based linker promote site-specific cleavage of RNA. *Nucleic Acids Res. 24*, 760−765.

(32) Komiyama, M., and Inokawa, T. (1994) Selective hydrolysis of tRNA by ethylenediamine bound to a DNA oligomer. *J. Biochem. 116*, 719−720.

(33) Endo, M., Azuma, Y., Saga, Y., Kuzuya, A., Kawai, G., and Komiyama, M. (1997) Molecular design for a pinpoint RNA scission. Interposition of oligoamines between two DNA oligomers. *J. Org. Chem. 62*, 846−852.

(34) Vlassov, V., Abramova, T., Godovikova, T., Giege, R., and Silnikov, V. (1997) Sequence-specific cleavage of yeast $tRNA^{Phe}$ with oligonucleotides conjugated to a diimidazole construct. *Antisense Nucleic Acid Drug Dev. 7*, 39−42.

(35) Beloglazova, N. G., Silnikov, V. N., Zenkova, M. A., and Vlassov, V. V. (2000) Cleavage of yeast $tRNA^{Phe}$ with complementary oligonucleotide conjugated to a small ribonuclease mimic. *FEBS Lett. 481*, 277−280.

(36) Beloglazova, N. G., Epanchintsev, A. Yu., Silnikov, V. N., Zenkova, M. A., and Vlassov, V. V. (2002) Highly efficient site-directed RNA cleavage by imidazole-containing conjugates of antisense oligonucleotides. *Mol. Biol. 36*, 581−588.

(37) Ushijima, K., Gouzu, H., Hosono, K., Shirakawa, M., Kagosima, K., Takai, K., and Takaku, H. (1998) Site-specific cleavage of tRNA by imidazole and/or primary amine groups bound at the 5′-end of oligodeoxyribonucleotides. *Biochim. Biophys. Acta 1379*, 217−223.

(38) Verheijen, J. C., Deiman, B. A. L. M., Yeheskiely, E., van der Marel, G. A., and van Boom, J. H. (2000) Efficient hydrolysis of RNA by a PNA-diethylenetriamine adduct. *Angew. Chem., Int. Ed. 39*, 369−372.

(39) Verbeure, B., Lacey, C. J., Froeyen, M., Rozenski, J., and Herdewijn, P. (2002) Synthesis and cleavage experiments with oligonucleotide conjugates with a diimidazole-derived catalytic center. *Bioconjugate Chem. 13*, 333−350.

(40) Thorp, H. H. (2000) The importance of being r: greater oxidative stability of RNA compared with DNA. *Chem. Biol. 7*, R33−R36.

(41) Zompa, L. J. (1978) Metal complexes of cyclic triamines. 2. Stability and electronic spectra of nickel(II), copper(II), and zinc(II) complexes containing nine- through twelve-membered cyclic triamine ligands. *Inorg. Chem. 17*, 2531−2536.

(42) Kodama, M., and Kimura, E. (1977) Equilibria and kinetics of complex-formation between zinc(II), lead(II), and cadmium(II), and 12-membered, 13-membered, 14-membered and 15-membered macrocyclic tetra-amines. *J. Chem. Soc., Dalton Trans.* 2269−2276.

(43) Kimura, E. (2001) Model studies for molecular recognition of carbonic anhydrase and carboxypeptidase. *Acc. Chem. Res. 34*, 171−179.

(44) Kuusela, S. and Lönnberg, H. (1992) Metal ion promoted hydrolysis of uridine 2′,3′-cyclic monophosphate: effect of metal chelates and uncomplexed aquo ions. *J. Phys. Org. Chem. 5*, 803−811.

(45) Kuusela, S. and Lönnberg, H. (1993) Metal ions that promote the hydrolysis of nucleoside phosphoesters do not enhance the intramolecular phosphate migration. *J. Phys. Org. Chem. 6*, 347−356.

(46) Kuusela, S. and Lönnberg, H. (1994) Metal ion promoted hydrolysis of polyuridylic acid. *J. Chem. Soc., Perkin Trans. 2*, 2301−2306.

(47) Zagorowska, I., Kuusela, S., and Lönnberg, H. (1998) Metal ion-dependent hydrolysis of RNA phosphodiester bonds within hairpin loops. A comparative kinetic study on chimeric ribo/2′-*O*-methylribo oligonucleotides. *Nucleic Acids Res. 26*, 3392−3396.

(48) Kaukinen, U., Bielecki, L., Mikkola, S., Adamiak, R. W., and Lönnberg, H. (2001) The cleavage of phosphodiester bonds within small RNA bulges in the presence and absence of metal ion catalysts: towards artificial RNases. *J. Chem. Soc., Perkin Trans. 2* 1024−1031.

(49) Hovinen, J. and Salo, H. (1997) *C*-Glycoside phosphoramidite building block for versatile functionalization of oligonucleotides. *J. Chem. Soc., Perkin Trans. 1*, 3017−3020.
(50) Salo, H., Guzaev, A., and Lönnberg, H. (1998) Disulfide-tethered solid supports for synthesis of photoluminescent oligonucleotide conjugates: hydrolytic stability and labeling on the support. *Bioconjugate Chem. 9*, 365−371.
(51) Azhayeva, E., Azhayev, A., Guzaev, A., Hovinen, J., and Lönnberg, H. Looped oligonucleotides form stable hybrid complexes with a single-stranded DNA. *Nucleic Acids Res. 23*, 1170−1176.
(52) Hovinen, J., Guzaev, A., Azhayeva, E., Azhayev, A., and Lönnberg, H. (1995) Imidazole-tethered oligodeoxyribonucleotides: synthesis and RNA cleaving activity. *J. Org. Chem.* **1995**, *60*, 2205−2209.
(53) Nakani, B. S., Welsh, J. J. B., and Hancock, R. D. (1983) Formation constants of some complexes of tetramethylcyclam. *Inorg. Chem. 22*, 2956−2958.
(54) Hovinen, J. (1998) Synthesis of carbon-3-substituted 1,5,9-triazacyclododecanes, RNA cleavage agents suitable for oligonucleotide tethering. *Bioconjugate Chem. 9*, 132−136.
(55) Alder, R. W., Mowlam, R. W., Vachon, D. J., and Weisman, G. R. (1992) New synthetic routes to macrocyclic triamines, *J. Chem. Soc. Chem. Commun.* 507−508.
(56) Kim, R. D. H., Wilson, M., and Haseltine, J. (1994) Simple preparation of tricyclic orthoamides and macrocyclic triamines, *Synth. Commun. 24*, 3109−3014.

BC034166B

Site-Specific Conjugation of Boron-Containing Dendrimers to Anti-EGF Receptor Monoclonal Antibody Cetuximab (IMC-C225) and Its Evaluation as a Potential Delivery Agent for Neutron Capture Therapy

Gong Wu,[†] Rolf F. Barth,[†,*] Weilian Yang,[†] Madhumita Chatterjee,[‡] Werner Tjarks,[‡] Michael J. Ciesielski,[§] and Robert A. Fenstermaker[§]

Department of Pathology and College of Pharmacy, The Ohio State University, Columbus, Ohio 43210 and Department of Neurosurgery, Roswell Park Cancer Institute, Buffalo, New York 14263. Received September 15, 2003; Revised Manuscript Received October 29, 2003

The gene encoding EGFR often is amplified in human gliomas, and the receptor itself has been considered as a potential target for the specific delivery of therapeutic agents to brain tumors. The purpose of the present study was to investigate the use of the chimeric MoAb cetuximab (IMC-C225), which is directed against EGFR and EGFRvIII, as a boron delivery agent for neutron capture therapy (NCT) of brain tumors. As determined by ^{125}I-cetuximab radioligand binding assays, F98 rat glioma cells, which had been transfected with the gene encoding EGFR ($F98_{EGFR}$), expressed $1.60 \pm 0.13 \times 10^5$ receptor sites/cell with a $K_a = 1.64 \pm 0.32 \times 10^8$ M^{-1}. F98 cells transfected with the gene encoding a mutant form of EGFR, designated the $F98_{EGFRvIII}$ glioma, expressed $1.07 \pm 0.10 \times 10^5$ receptor sites/cell with a $K_a = 2.18 \pm 0.54 \times 10^9$ M^{-1} compared to background levels expressed on F98 wild-type cells ($F98_{WT}$). A heavily boronated, fifth generation polyamidoamine (PAMAM or "starburst") dendrimer, G5-B_{1100}, was linked to oligosaccharide moieties, which were distant from antigen binding sites of cetuximab, by means of the heterobifunctional reagents *N*-succinimidyl 3-(2-pyridyldithio)-propionate (SPDP) and *N*-(k-maleimidoundecanoic acid) hydrazide (KMUH). The resulting bioconjugate, designated C225-G5-B_{1100}, was separated from the unconjugated dendrimer using a Sephacryl S-300 column. On the basis of the relative concentration ratios of boron and protein, there were ~1100 boron atoms per molecule of cetuximab with only a slight reduction of K_a. The localization of C225-G5-B_{1100} or G5-B_{1100} in rats bearing intracerebral implants of either $F98_{EGFR}$ or $F98_{WT}$ gliomas was determined 24 h following direct intratumoral (i.t.) injection at which time 92.3 ± 23.3 μg B/g tumor was localized in $F98_{EGFR}$ gliomas versus 36.5 ± 18.8 μg B/g tumor in $F98_{WT}$ gliomas and 13.4 ± 6.1 μg in normal brain. In contrast, only 6.7 ± 3.6 μg B/g tumor of G5-B_{1100} was localized in $F98_{EGFR}$ gliomas following i.t. injection, thereby demonstrating specific molecular targeting of EGFR. Based on these data, BNCT studies will be initiated in $F98_{EGFR}$ glioma bearing rats to evaluate C225-G5-B_{1100} for the treatment of intracerebral brain tumors.

INTRODUCTION

Malignant gliomas are fast growing, highly invasive brain tumors that usually lead to death within 12−18 months following diagnosis (*1*). Despite intensive research over the past several decades, high grade gliomas still are extremely resistant to all current forms of therapy, including surgery, chemotherapy, and radiotherapy (*2*). The long term survival of patients, which is almost 0 % at 5 years, has remained unchanged, and depending upon a number of factors, the 2 year survival is usually less than 10% (*1*). However, significant advances have been made in understanding the molecular genetic events leading to the development and progression of gliomas, and this hopefully will lead to the development of new molecular therapeutic agents designed to specifically inhibit tumor cell proliferation and invasion (*3*, *4*).

The epidermal growth factor receptor (EGFR)[1] or its mutant isoform EGFRvIII are attractive targets for the

* To whom correspondence should be addressed: Rolf F. Barth, M.D., The Ohio State University, Department of Pathology, 165 Hamilton Hall, 1645 Neil Ave., Columbus, OH 43210. Tel: (614) 292−2177. Fax: (614) 292-7072. E-mail: barth.1@osu.edu.

[†] Department of Pathology, The Ohio State University.

[‡] College of Pharmacy, The Ohio State University.

[§] Department of Neurosurgery, Roswell Park Cancer Institute.

[1] Abbreviations: BBB, blood−brain barrier; BNCT, boron neutron capture therapy; BSA, bovine serum albumin; BSD, boronated starburst dendrimer; CED, convection enhanced delivery; DCP-AES, direct current plasma-atomic emission spectroscopy; DMEM, Dulbecco's Modified Eagle's Medium; DMSO, dimethyl sulfoxide; DTT, dithiothreitol; EDTA, ethylenediamine tetraacetic acid; EGF, epidermal growth factor; EGFR, epidermal growth factor receptor; G, generation; G5-B_{1100}, ethylenediamine core boronated (1100 boron atoms/dendrimer) fifth generation PAMAM dendrimer; FBS, fetal bovine serum; % ID, % injected dose; i.t., intratumoral; KMUH, *N*-[κ-maleimidoundecanoic acid] hydrazide; LET, linear energy transfer; MW, molecular weight; MWCO, molecular weight cut off; MoAb, monoclonal antibody; NCT, neutron capture therapy; PAMAM, poly-amidoamine; PBS, phosphate buffered saline; SD, standard deviation; SPDP, *N*-succinimidyl 3-(2-pyridyldithio)-propionate; TCA, trichloracetic acid; TGF-α, transforming growth factor-alpha; Tris, tris(hydroxymethyl)aminoethane or Trisamine; UV/vis, ultraviolet/visible.

10.1021/bc0341674 CCC: $27.50 © 2004 American Chemical Society
Published on Web 12/10/2003

treatment of gliomas since they frequently are overexpressed in brain tumors (*5*, *6*). A number of drugs (*7*−*10*) and monoclonal antibodies (*11*−*13*) have been developed to target the EGFR and its signaling pathways (*14*, *15*). Among these is the MoAb cetuximab (IMC-C225), which has been produced by ImClone Systems, Inc., New York, NY. Cetuximab is a chimeric MoAb directed against both wild-type EGFR, and its mutant isoform, EGFRvIII (*16*). This antibody can block the binding of both EGF and TGF-α to their receptors (*16*,*17*), thereby interfering with cell signaling pathways (*14*, *15*) and producing cell cycle arrest and apoptosis (*17*). Phase I clinical trials have shown that cetuximab is well tolerated (*18*, *19*) and preclinical studies (*17*, *18*, *20*), as well as Phase II trials in patients with EGFR positive cancers, have demonstrated that cetuximab had a synergistic effect when administered together with ionizing radiation (*20*, *21*), and cytoreductive chemotherapeutic agents such as cisplatin (*22*), doxorubicin (*23*), gemcitabine (*24*), and docetaxel (*25*).

We previously have reported on the use of heavily boronated "PAMAM" (starburst) dendrimers linked to MoAbs (*26*−*28*) or EGF (*29*) as potential boron delivery agents for neutron capture therapy. Using several different approaches, Carlsson and co-workers have produced a variety of other boron-containing EGF targeting vehicles for boron neutron capture therapy (*30*−*32*). BNCT is based on the nuclear capture and fission reactions that occur when ^{10}B is irradiated with low energy (<0.025 eV) thermal neutrons to produce high LET α particles and recoiling ^{7}Li nuclei, which have path lengths of ∼9 μm and ∼5 μm, respectively. In order for BNCT to be successful for the treatment of brain tumors, ^{10}B concentrations in the tumor should be in the range of 15−20 μg/g, and concomitantly, levels in normal brain should be low. These requirements have been discussed in detail in several recent reviews and monographs (*33*−*36*), and this has been the subject of a recent issue of a neuro-oncology journal (*37*). The use of cetuximab as a boron delivery agent for NCT of gliomas is particularly attractive since not only would the boronated bioconjugate kill tumor cells as a result of the high LET particles produced following neutron irradiation, but it also could block the binding of EGF and TGF-α to EGFR, thereby interfering with critical signal transduction pathways and acting synergistically with BNCT.

We recently have reported on the use of boronated EGF as a molecular targeting agent for BNCT of the F98 rat glioma that had been transfected with the gene encoding human EGFR (*38*). In the present report we describe the preparation and in vitro and in vivo evaluation of cetuximab, which has been site specifically linked to a boronated fifth generation PAMAM dendrimer. This bioconjugate has the capacity to deliver twice the amount of boron compared to that of a previously described (*29*) fourth generation dendrimer/EGF bioconjugate with a minimal reduction in its binding affinity and favorable biodistribution following i.t. delivery.

EXPERIMENTAL PROCEDURES

General Synthetic/Analytical Methods and Materials. A fifth generation PAMAM dendrimer, containing 128 reactive terminal amine groups, was purchased from Sigma-Aldrich Corp., St. Louis, MO; $Na(CH_3)_3NB_{10}H_8NCO$ was prepared from $(CH_3)_3NB_{10}H_8CO$ (Katchem Ltd., Prague, Czech Republic), as previously described (*39*). *N*-Succinimidyl 3-(2-pyridyldithio)propionate and *N*-(κ-maleimidoundecanoic acid) hydrazide both were purchased from Pierce, Rockford, IL. Other chemicals were of reagent grade and were purchased from a number of chemical supply companies. Cetuximab was generously provided by Dr. Daniel Hicklin, ImClone Systems Inc. (New York, NY). Millipore Stirred Cell/Ultrafiltration Membrane (MWCO 100 000) was purchased from Fisher Scientific, Pittsburgh, PA. PD-10 disposable columns, Sephadex G25 and Sephacryl S-300 were purchased from Amersham Pharmacia Biotech, Piscataway, NJ. UV measurements were carried out by means of a Beckman DU6 recording spectrophotometer (Beckman, Fullerton, CA). The protein concentrations of unmodified cetuximab were determined by UV absorption spectrometry at 280 nm, and those of boronated cetuximab were determined at 595 nm using a Coomassie protein assay reagent (Pierce, Rockford, IL). All measurements were made against known concentrations of cetuximab as a reference standard. The concentrations of SPDP in the SPDP-G5-B_{1100} conjugate were determined by UV spectrometry at 343 nm following cleavage of the disulfide bond by DTT. Boron was quantified by means of direct current plasma-atomic emission spectroscopy, using a Spectraspan VB spectrometer (Applied Research Laboratories, La Brea, CA), as previously described by us (*40*). Briefly, 10 μL of the boron containing sample were diluted to 1.0 mL with 0.1 M phosphate buffer, pH 7.5, and the boron concentrations were determined by DCP-AES at 249 nm. The instrument was calibrated using standard boron solutions (VHG Labs, Manchester, NH).

Oxidation of Cetuximab and Conjugation to G5-B_{1100}. A schematic representation of the conjugation chemistry that was used is shown in Figure 1. $NaIO_4$ (**2**, 2.14 mg, 10 μmol) was added to a 1.0 mL of cetuximab (**1**, 2 mg, 13 nmol) in 0.1 M acetate buffer (pH 4.5), and the reaction mixture was kept in the dark for 2 h at ambient temperature. The oxidized cetuximab (C225-CHO, **3**) was desalted on a PD-10 column by elution with 50 mM phosphate buffer (pH 7.4). G5 (**4**, 1.15 g, 5% w/w in methyl alcohol, 2 μmol) and SPDP (**5**, 3.12 mg, 10 μmol) were incubated in 1.0 mL of 0.1 M PBS (pH 7.5) at ambient temperature for 2 h and then applied to a PD-10 column, and the intermediate (SPDP-G5, **6**) was eluted with 0.1 M carbonate buffer (pH 9.0). The number of SPDP molecules linked to G5 was determined by UV spectrometry, as described in a preceding section. The introduction of boron clusters into SPDP-G5 was carried out with minor modifications, as previously described (*39*). Briefly, SPDP-G5 (58 mg, 2 μmol) (**6**) and $Na(CH_3)_3NB_{10}H_8NCO$ (**7**, 117 mg, 250 μmol) were reacted in 1.0 mL of 0.1 M carbonate/bicarbonate buffer, pH 9.0, at ambient temperature for 24 h to yield SPDP-G5-B_{1100} (**8**). The low molecular components of the mixture were separated from SPDP-G5-B_{1100} by PD-10 column chromatography using 50 mM phosphate buffer (10% DMSO, pH 7.5) as the mobile phase. The number of the boron clusters in SPDP-G5-B_{1100} was estimated by comparing the boron concentrations before and after passage through a PD-10 desalting column. The disulfide bond of SPDP-G5-B_{1100} subsequently was cleaved by exposing the bioconjugate to DTT (7.7 mg, 50 μmol) (**9**) in 0.1 M phosphate buffer (pH 7.5) containing 10% DMSO, for 30 min at ambient temperature. Low molecular weight contaminants were removed by passing the mixture through a PD-10 column using the same buffer system. The resulting sulfhydryl-containing HS-G5-B_{1100} bioconjugate (**10**) was mixed with 100 μL solution of KMUH (2.95 mg, 10 μmol) (**11**) in DMSO at a molar ratio of 1:5. The mixture was incubated for 2 h at ambient temper-

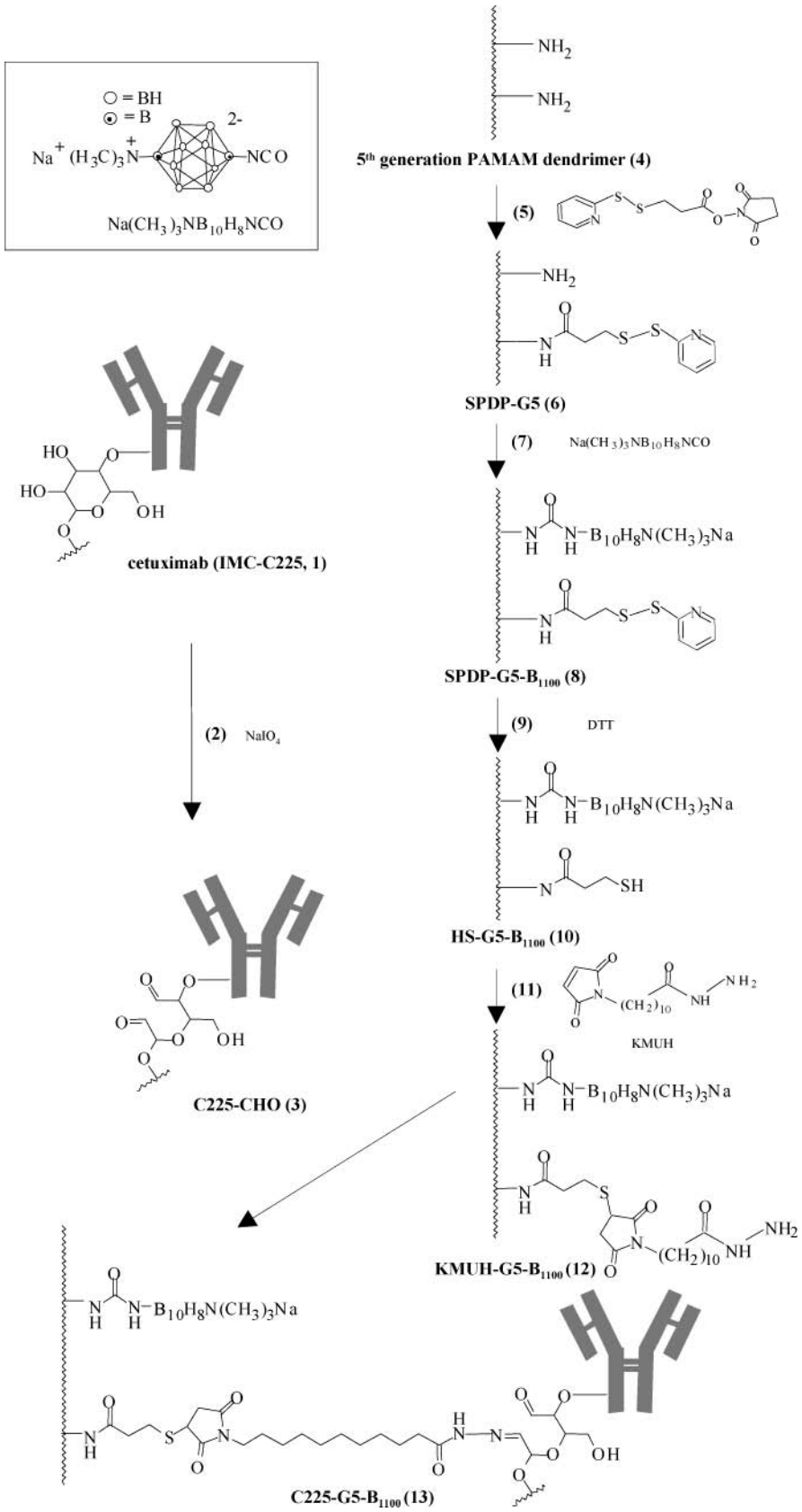


Figure 1. Conjugation scheme for the linkage of boron-containing dendrimer to cetuximab.

ature and then separated from unreacted KMUH by passage through a PD-10 column using PBS as the mobile phase. Following this, the conjugated KMUH-G5-B_{1100} (**12**) was added to the oxidized cetuximab at a molar ratio of 2:1 and mixed overnight at ambient temperature. The final bioconjugate, C225-G5-B_{1100} (**13**), was concentrated to 1−2 mL by ultrafiltration and then applied onto a Sephacryl S-300 gel filtration column, which had been preequilibrated and then eluted with 50 mM phosphate buffer (pH 7.5) containing 10% DMSO. Those fractions containing *both* cetuximab and boron were collected, pooled, and concentrated by ultrafiltration (MWCO, 10K).

Cell Culture. The parental (wild-type) F98 glioma cell line ($F98_{WT}$) has been extensively used by us for studies relating to BNCT (*41*). The $F98_{EGFR}$ glioma cell was produced by transfecting parental F98 glioma cells with an expression vector containing human EGFR cDNA and its production recently has been described by us in detail (*38*). Cells were maintained and propagated in DMEM containing 100 units/mL penicillin, 100 μm/mL streptomycin, 200 mg/mL of G418 and 10% fetal bovine serum (Life Technologies, Inc., Rockville, MD). The $F98_{WT}$ cells were cultured as monolayers in the same media lacking G418 at 37 °C in a humidified atmosphere containing 5% CO_2.

Radiolabeling of Bioconjugate. Radiolabeling of cetuximab with ^{125}I was carried out using IODO-GEN precoated iodination tubes according to the procedure described by the manufacturer (Pierce, Rockford, IL). Briefly, 10 μL (1.0 mCi) of carrier-free $Na^{125}I$ (ICN Biomedicals Inc, Costa Mesa, CA) and 100 μL of 25 mM phosphate buffer (pH 7.5, 0.1 M NaCl) were added to the precoated tubes. After incubation for 6 min at ambient temperature, the activated iodide was removed and added to the antibody solution (50 μg/50μL) and then incubated for an additional 6−9 min. Radiolabeled cetuximab was purified on a Bio-Spin 30 TRIS column (Bio-Rad Laboratories, Hercules, CA) by elution with 25 mM phosphate buffer, pH 7.5. Protein-bound and free ^{125}I were determined by precipitation with TCA and γ-scintillation counting using a well counter (TM Analytic, Des Plaines, IL), as previously described (*29*).

Determination of K_a and Competitive Binding Assay. $F98_{WT}$, $F98_{EGFR}$ and $F98_{EGFRvIII}$ cells were seeded into T-150 flasks and cultured for 3 days to establish a confluent monolayer. Cells were washed 2× with PBS and then harvested by incubating them with 0.5 mM EDTA at 37 °C for 10 min. Following removal of EDTA, 10^6 cells were added to 1.5 mL tubes to which varying amounts of ^{125}I radiolabeled cetuximab or C225-G5-B_{1100} in 0.1% BSA had been added, and these were incubated at 4 °C for 90 min. The cells then were washed 3× with PBS, the cell bound and free radiolabeled antibody or bioconjugate were separated by centrifugation, and radioactivity was determined by γ-scintillation counting. The K_a and the number of receptor sites were derived by nonlinear regression analysis. For the competitive binding assay, $F98_{EGFR}$ cells were incubated at 4 °C for 90 min with 110 ng of ^{125}I-cetuximab and varying amounts of either unmodified cetuximab or C225-G5-B_{1100}. The cells then were washed 3× with PBS, and the cell bound ^{125}I-cetuximab was separated from free ^{125}I-cetuximab by centrifugation following which radioactivity was determined by γ-scintillation counting.

Assay To Detect Internalization of Cetuximab. The procedure of Reist et al. (*42*) was used to determine if cetuximab was internalized following exposure of cells to the antibody. $F98_{EGFR}$ cells were incubated with an excess of ^{125}I-cetuximab for 1 h at 4 °C, following which they were washed 3× with cold PBS (pH 7.4) containing 1% BSA to remove unbound antibody. Then aliquots containing 10^6 cells per/mL were dispensed into 1.5 mL Eppendorf tubes containing DMEM, supplemented with 10% FBS, and incubated at 37 °C for 0, 1, 2, 4, 8, and 24 h. At each time point, cells were sedimented and the supernatants were saved for γ-scintillation counting. Cell pellets were acid washed twice with a solution containing 1% BSA, the pH of which had been adjusted to 2.0 by the addition of HCl in order to remove cell surface bound antibody. Radioactivity of the original supernatants, the acid washes, and the cell pellets was determined by γ-scintillation counting.

Tumor Model and Biodistribution of C225-G5-B_{1100} and G5-B_{1100}. Fischer rats were purchased from the Animal Production Branch, National Cancer Institute, Frederick Research Laboratory, Frederick, MD. Procedures to minimize discomfort, pain, and distress were in accord with guidelines issued by the American Association for Accreditation of Laboratory Animal Care. One million $F98_{WT}$ or $F98_{EGFR}$ cells were stereotactically implanted into the right caudate nucleus of Fischer rats, as previously described by us (*38*). Biodistribution studies were initiated 12 to 14 days following i.t. injection of C225-G5-B_{1100} or G5-B_{1100} via the central entry port of a plastic screw, which had been embedded into the skull at the time of tumor implantation. Rats received an i.t. injection of either C225-G5-B_{1100} or G5-B_{1100}, containing 50 μg of boron/animal, and were euthanized 24 h later. Ten microliters of the test agent were injected over 2 min using a 20 μL Hamilton syringe fitted with a 27 gauge needle. Tumor, normal brain, blood, liver, kidneys, and skin samples were taken, and biodistribution was determined by means of DCP-AES (*40*). Five animals were used per group and the %ID/g was calculated.

RESULTS

Conjugation and Characterization of Boronated Bioconjugate. The bioconjugation scheme, which was used to boronate a fifth generation PAMAM dendrimer, is shown in Figure 1. The heterobifunctional reagent SPDP was easily linked to the dendrimer under mild conditions in aqueous solution and the protected thiol group, which had been introduced, later was cleaved by reduction with DTT. Using a 5:1 molar ratio of SPDP to G5 (**4**), approximately four molecules of SPDP were attached to G5, as determined by measurement of the absorbance of pyridine-2-thione at 343 nm, which was released upon reduction. Boron clusters were conjugated to SPDP-G5 (**6**) via the reaction of a primary amine with an isothiocyanate, which was carried out overnight in carbonate buffer (pH 9.0) and noncovalently associated clusters were removed by PD-10 column chromatography. As determined by quantitation of boron by means of DCP-AES prior to and following PD-10 column chromatography, the amount of boron attached to the dendrimer was ∼1100 boron atoms per molecule of G5 (**4**). The boronated dendrimer (SPDP-G5-B_{1100}, **8**) then was incubated with 50 mM DTT for 30 min. The free sulfhydryl groups, which had been introduced (HS-G5-B_{1100}, **10**), then were reacted with KMUH (**11**), another heterobifunctional reagent that linked aldehyde and sulfhydryl groups with a spacer length of ∼19 Å. The resulting bioconjugate, KMUH-G5-B_{1100} (**12**), then was separated from unreacted KMUH by Sephadex-G25 column chromatography. Different ratios of oxidized cetuximab (C225-CHO, **3**) and boronated dendrimer (KMUH-G5-B_{1100}, **12**) used for the final conjugation of C225-G5-B_{1100} (**13**) have been tested, and as determined from the Sephacryl S-300 elution profile (Figure 2), there were two peaks containing both boron and protein suggesting that either two or more boronated dendrimers were linked to one cetuximab molecule or alternatively, that two or more cetuximab molecules were linked to one molecule of dendrimer. The shift in boron and protein concentrations at the second peak indicated the presence of a small amount of free cetuximab. The contamination of the bioconjugate with free cetuximab was minimized by collecting fractions with high boron to protein concentration ratios.

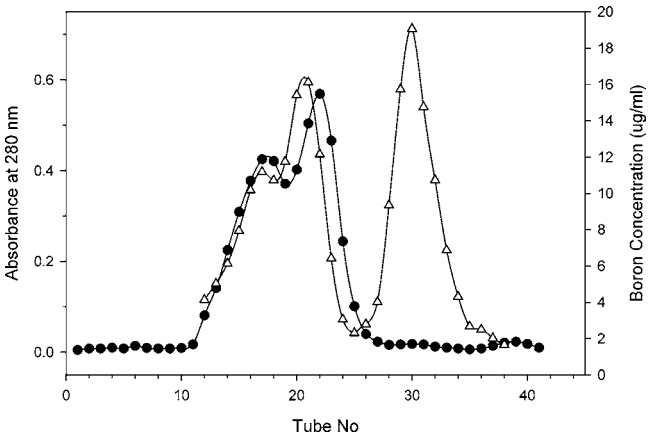


Figure 2. Elution profiles of protein and boron content of samples following completion of the conjugation procedure. The final reaction mixture was concentrated by ultrafiltration and loaded on to a Sephacryl S-300 column and eluted with 50 mM phosphate buffer, pH 7.5 (10% DMSO). Flow rate was 0.5 mL/min. Each fraction contained 1.0 mL. The protein content was measured by UV (●), and the boron concentration was determined by DCP-AES (△).

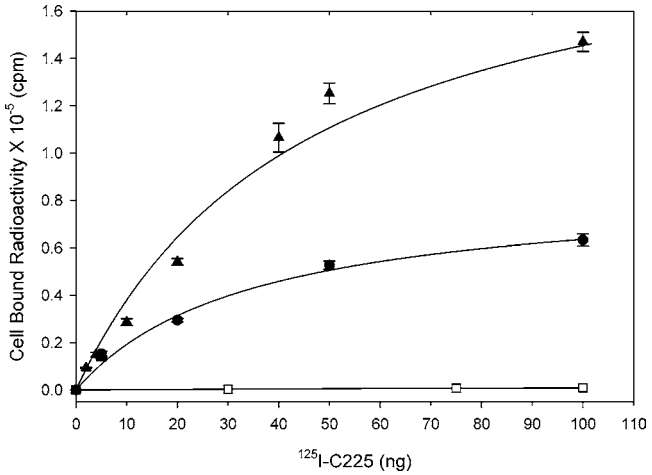


Figure 3. Cellular binding of cetuximab. Varying amounts of ^{125}I-cetuximab ranging from 5 ng to 100 ng were incubated at 4 °C for 90 min with cells expressing wild-type EGF receptors ($F98_{EGFR}$) (▲), mutant EGFRvIII receptors ($F98_{EGFRvIII}$) (●), and receptor negative parental cells ($F98_{WT}$) (□). Cell bound radioactivity was determined by γ-scintillation counting. Mean values ±SD are shown.

Determination of Receptor Sites and Affinity Constants. The binding of cetuximab or the C225-G5-B_{1100} bioconjugate to EGFR was determined by incubating either $F98_{EGFR}$, $F98_{EGFRvIII}$, or $F98_{WT}$ cells with ^{125}I labeled, unmodified MoAb or the bioconjugate. Data from ligand saturation experiments are shown in Figures 3 and 4. The ^{125}I-cetuximab had a very low binding affinity with $F98_{WT}$ cells indicating that the expression of EGFR on F98 wild-type cell was negligible. In contrast, as determined by the binding of ^{125}I-cetuximab, $F98_{EGFR}$ cells expressed $1.60 \pm 0.13 \times 10^5$ receptor sites per cell, as determined from the apparent binding site concentration (B_{max}). The affinity constants (K_a) were $1.64 \pm 0.32 \times 10^8$ M^{-1} for cetuximab and $2.00 \pm 0.22 \times 10^8$ M^{-1} for C225-G5-B_{1100}, respectively, and these also were confirmed by means of a competitive binding assay. The binding of C225-G5-B_{1100} to $F98_{EGFR}$ cells was comparable to that of cetuximab, although the IC_{50} (i.e. the amount required to produce a 50% inhibition of unmodified cetuximab) of C225-G5-B_{1100} was 1.44 nM, which was 2.6-fold greater than that of cetuximab (Figure 5). $F98_{EGFRvIII}$ cells

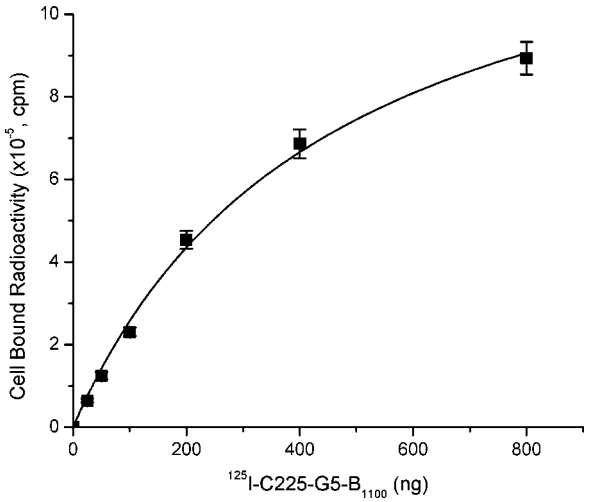


Figure 4. Cellular binding of the conjugate C225-G5-B_{1100}. Varying amounts of ^{125}I-C225-G5-B_{1100} ranging from 25 ng to 800 ng were incubated with $F98_{EGFR}$ cells at 4 °C for 90 min. Cell bound radioactivity was determined by γ-scintillation counting.

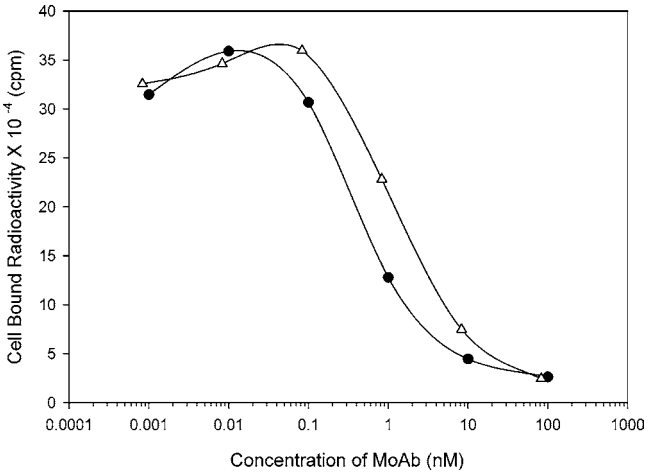


Figure 5. Competitive binding assay. $F98_{EGFR}$ cells were incubated with ^{125}I-cetuximab and varying amounts of nonradiolabeled cetuximab (●) or C225-G5-B_{1100} (△) at 4 °C for 90 min. Cell bound radioactivity was determined by γ-scintillation counting.

expressed $1.07 \pm 0.10 \times 10^5$ receptor sites per cell and the affinity constants (K_a) was $2.18 \pm 0.54 \times 10^9$ M^{-1}, as determined by competitive binding studies with radiolabeled cetuximab.

Internalization of Cetuximab. As shown in Figure 6, the percent cell surface associated radioactivity declined as a function of time from 76.26 ± 1.03% to 48.54 ± 0.88% while the corresponding values in the supernatants increased concomitantly from 12.28 ± 0.07% to 43.96 ± 1.45%. Intracellular radioactivity decreased over the first 8 h from 11.46 ± 0.80% to 3.64 ± 0.34% and then increased over the next 16 h to 7.51 ± 0.16% at 24 h, demonstrating that cetuximab was continuously internalized at the same time as it was being released from the cells.

Biodistribution Following Intratumoral Injection. To determine if C225-G5-B_{1100} could be used to specifically target to EGFR in $F98_{EGFR}$ glioma bearing rats, the bioconjugate was injected i.t. via the entry port of a plastic screw that had been embedded in the calvarium of rats bearing either $F98_{WT}$ or $F98_{EGFR}$ gliomas. After 24 h boron concentrations in tumor and normal brain were measured by DCP-AES. As shown in

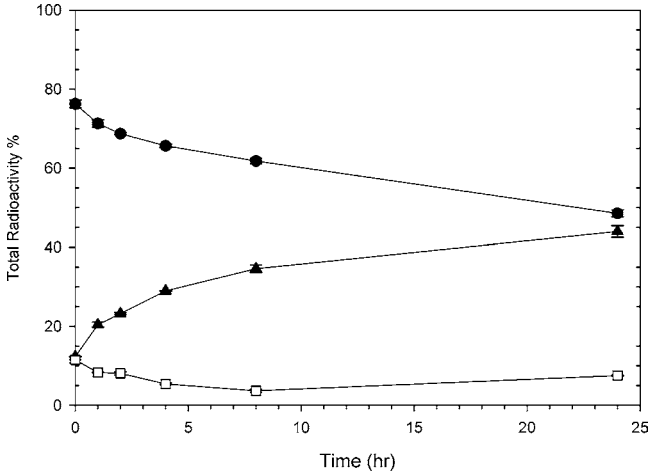


Figure 6. Internalization of cetuximab by $F98_{EGFR}$ cells. Radioactivity was determined by γ-scintillation counting for that associated with the cell culture supernatant before acid wash (▲), and after acid wash (□) and the supernatant from the acid wash (●).

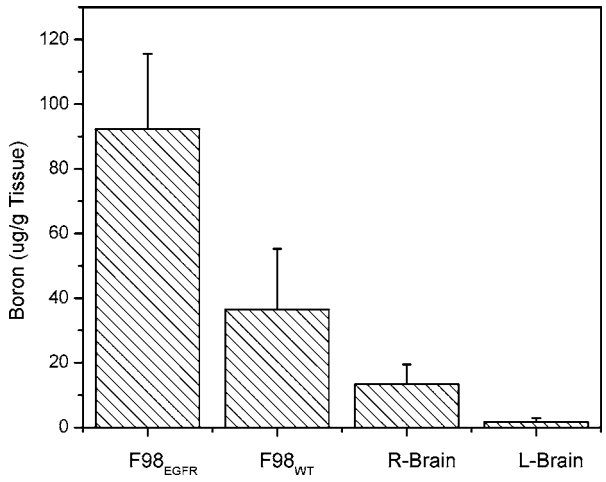


Figure 7. Biodistribution of C225-G5-B_{1100} following i.t administration to rats bearing intracerebral implants of $F98_{EGFR}$ or $F98_{WT}$ gliomas. Animals were euthanized 24 h after injection, the brains were removed and processed for boron determination by means of DCP-AES, the tumor was dissected, and the concentrations of boron in tumor and right (R brain) and left (L brain) cerebral hemispheres was quantified by DCP-AES. Mean values ±SD are shown.

Figure 7, the mean boron concentration was 92.3 ± 23.3 μg/g tumor in rats (n = 4) bearing $F98_{EGFR}$ gliomas compared with 36.5 ± 18.8 μg/g tumor in rats bearing $F98_{WT}$ gliomas. The corresponding boron concentrations of normal brain from the tumor bearing right (ipsilateral) and left (contralateral), nontumor bearing cerebral hemispheres were 13.4 ± 6.1 and 1.7 ± 1.2 μg/g tissue, respectively. Blood, liver, kidneys, spleen, and skin all had nondetectable levels of boron (<0.5 μg/g tissue). Specificity of uptake was further established by injecting either C225-G5-B_{1100} i.t. or nontargeted G5-B_{1100} into rats bearing $F98_{EGFR}$ tumors. As shown in Figure 8, the boronated dendrimer alone without the cetuximab targeting moiety was cleared and the tumor boron content was 6.7 ± 3.6 μg/g at 24 h, which was 13.8-fold less than the cetuximab targeted boronated dendrimer.

DISCUSSION

In the present study, we have site specifically linked a boronated fifth generation PAMAM dendrimer to

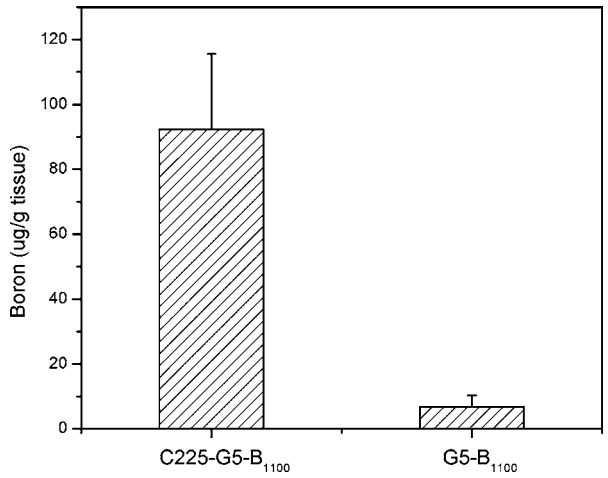


Figure 8. Biodistribution studies of targeted and untargeted conjugates. C225-G5-B_{1100} and untargeted boronated dendrimer G5-B_{1100} were i.t. injected into rats bearing $F98_{EGFR}$ brain tumors and sacrificed 24 h after the injection. Tumor boron concentrations were determined by DCP-AES. Mean values ±SD are shown.

oligosaccharide moieties located in the F_c region of cetuximab. This minimized the loss of binding activity since the covalent linkage sites were specific and distal to the antigen binding site. With minor modifications, this conjugation procedure was based on a recently reported one in which boronated polylysine was linked to an anti-TSH antibody (*43*). Using the improved procedure described in the present report, one reaction step with the antibody was eliminated, but the specific linkage site at the F_c region of the antibody molecule was preserved and the final product was the same. As shown in Figure 1, the maleimide of KMUH first was reacted with SH groups of the boronated fifth generation PAMAM dendrimer, which created stable thioether linkages. After purification, the hydrazide groups of KMUH were reacted with oxidized cetuximab to produce the final bioconjugate by forming hydrazone linkages.

As determined by a binding assay with radiolabeled cetuximab, $F98_{EGFR}$ cells expressed 1.6 ± 0.13 × 10^5 EGFR sites per tumor cell, while the parental $F98_{WT}$ cells expressed <1% of that of $F98_{EGFR}$ cells. The larger number of receptor sties (5.0 × 10^5) determined using the ligand EGF (*38*) may have been due to steric hindrance of the antibody molecule (MW = 150 000Da), whose size was 25× greater that that of EGF (6000 Da), and this also may explain the lower K_a of cetuximab (1.64 × 10^8 M^{-1}), which was 5.7× less than that of EGF (9.1 ± 3.3 ×10^8 M^{-1}) (*38*). Following direct i.t injection, the amount of boron retained in $F98_{EGFR}$ gliomas was 2.5× greater than that of $F98_{WT}$ tumors and 13.8× greater than the nonspecific retention of G5-B_{1100} in $F98_{EGFR}$ gliomas. Boron uptake following administration of C225-G5-B_{1100} was 92.3 μg/g tumor, which was 4.5× higher than the 21.1 μg/g tumor, that we previously reported using EGF-boronated starburst dendrimer as the bioconjugate (*38*). The increased boron uptake and retention, in part, could have been due to the higher generation of the dendrimer that was used to prepare the bioconjugate in the present study. A fifth generation PAMAM dendrimer has 128 amine groups compared to 64 groups in a fourth generation dendrimer. Each molecule of C225-G5-B_{1100} that bound to an EGF receptor had twice the amount of boron than that of the EGF−BSD bioconjugate that we previously have used for in vivo molecular targeting (*38, 44*). Another explanation for the higher tumor retention of C225-G5-B_{1100} could

have been its slower diffusion within the tumor and its prolonged clearance time due to its increased molecular size compared to that of the EGF−BSD bioconjugates. On the basis of the present results, a lower dose of the bioconjugate could be administered to achieve the same therapeutic concentration of boron in the tumor with concomitantly lower boron concentrations in normal brain. It is particularly noteworthy that cetuximab was continuously internalized following receptor binding. This could result in cellular accretion of larger amounts of boronated dendrimer than would have been predicted on the basis of the number of EGFR sites alone.

Approximately 10 years ago, we reported that "starburst", or as they are now referred to, PAMAM dendrimers, could be linked to a MoAb and used as a carrier of ^{10}B for NCT (*26*). These dendrimers are branched, spherical polymers with a unique number of primary amino groups on their surface, which is dependent upon their generation (*45*). They are highly soluble in aqueous solution, which makes them excellent drug carriers because of their high loading capacity (*45*, *46*). They can be precisely synthesized, based on either ammonia as a trivalent initiator core or ethylenediamine as a tetravalent core (*45*). With each new layer or generation, the number of surface amino groups doubles. A fourth generation dendrimer with an ethylenediamine core, such as that which we previously have used (*38*), has a molecular weight of 14215 Da and 64 reactive terminal amino groups. A fifth generation dendrimer, which was used in the present study, has a molecular weight of 28826 Da and the number of reactive functional groups is 128. Their defined structure and large number of surface amine groups recently have led to the use of dendrimers for the delivery of methotrexate (*47*) and 5-flourouracil (*48*). Kobayashi and co-workers (*49*−*51*) have produced indium-111, yttrium-88, and gadolinium-153 dendrimer−monoclonal antibody bioconjugates directed against either Tac (*49*) or murine alkaline phosphatase (*50*) for targeted radioimmunotherapy, Gd NCT, or as an MRI contrast agent (*51*). They were able to attach 49× more ^{111}In and ^{153}Gd atoms to the antibody molecule than was possible using conventional labeling procedures with a minimal loss of immunoreactivity against antigen-expressing tumor cells and with good tumor-localizing properties (*50*). Using an alternative approach, a sixth generation PAMAM dendrimer was biotinylated, chelated, and then reacted with ^{153}Gd citrate, to produce a bioconjugate that had 254 atoms of ^{153}Gd (*51*). This bioconjugate had high in vivo tumor-localizing properties when injected following the i.p. administration of avidin to nude mice bearing i.p. ovarian carcinoma cells, and it was internalized and accumulated within tumor cells in amounts sufficient for Gd NCT.

Very recently, several reports have been published describing drug or radionuclide cetuximab bioconjugates (*23*, *52*, *53*), but dendrimers were not used as the drug carrier. Safavy et al. have directly linked paclitaxel to cetuximab through amide bond formation (*52*). The resulting bioconjugate had increased in vitro cytotoxicity against several EGFR (+) epidermoid carcinoma cell lines compared to cetuximab or paclitaxel alone or a mixture of the two agents. However, there was no difference in the in vivo antitumor activity of the bioconjugate and free paclitaxel, and it was suggested that this might have been due to either the relatively low dose of the bioconjugate that was delivered or a problem relating to its release. On the basis of the data described in the present report, linkage of the drug to a dendrimer might obviate both of these problems. Wen et al. have linked ^{111}In to cetuximab via a pegylated chelator, diethylenetriaminepentacetic acid (*53*). The resulting bioconjugate had better imaging properties than that of its nonpegylated counterpart, and it was concluded that this was a promising strategy to optimize delivery. Since in our study the cetuximab bioconjugate was administered by direct i.t. injection, little would be gained by pegylating it. Finally, and most directly related to what we have described in the present report, Vega et al. have site specifically linked cetuximab to the terminus of a doxorubicin-bound coploymer, poly(L-glutamic acid)-*co*-poly(ethylene glycol) (*23*). The use of this polymer, in a manner similar to that which we have used a fifth generation dendrimer, enhanced the drug payload capacity of the antibody. The resulting bioconjugate had a greater in vitro inhibitory effect on the growth of an EGFR (+) squamous cell carcinoma than that of the free drug. These data, as well as our own, provide a strong argument for using a macromolecular species to enhance the carrying capacity of cetuximab.

The $F98_{EGFR}$ rat glioma that was used in the present study and another F98 transfectant expressing EGFRvIII ($F98_{EGFRvIII}$) are excellent models for investigating localization and in vivo retention of targeting agents (*38*). We recently have established *proof of principle* for the efficacy of BNCT following molecular targeting of EGFR using a fourth generation boronated dendrimer linked to EGF (*38*). To achieve a concentration of ^{10}B capable of producing a lethal $^{10}B(n,\alpha)^{7}Li$ reaction at the cellular level, $\sim 10^9$ boron atoms must be delivered to each tumor cell, or $\sim$15 μg boron/g tumor. Twenty-four hours following i.t injection of the bioconjugate (60 μg ^{10}B/15 μg EGR) to Fischer rats bearing intracerebral implants of $F98_{EGFR}$ cells, the boron concentration was 21.1 ± 4.2 μg/g tumor and the normal brain value was 5.6 ± 1.6 μg/g and blood was <0.5 μg/mL. Based on these data, therapy studies were initiated in $F98_{EGFR}$ glioma bearing rats using boronated EGF either alone or in combination with boronophenylalanine as delivery agents. Following BNCT, the percent increased life span of $F98_{EGFR}$ rats was triple that of animals bearing EGFR negative $F98_{WT}$ gliomas (*38*).

We would like to make some comment concerning our choice of direct i.t. delivery of cetuximab. The major limitation of using anti-EGFR MoAbs, clinically to treat brain tumors, has been that extraordinarily small amounts of the antibody reach the tumor following systemic administration (*54*−*56*). This is attributable to a combination of their rapid clearance by the reticoloendothelial system and the blood−brain barrier, which prevents the passage of hydrophilic agents with a MW in excess of $\sim$250 Da, unless there is an active transport system (*56*). Direct intracerebral delivery will bypass the BBB, minimize toxicity associated with systemic administration, and reduce by orders of magnitude the amount of the agent that would have to be administered by systemic injection. Our previous studies with systemically administered boronated EGF (*57*, *58*) have shown that the amount of the bioconjugate localizing in the tumor following i.v. injection was 0.06% ID/g at 24 h, which was insufficient to deliver the requisite amount of ^{10}B to the tumor. On the other hand, direct i.t. injection resulted in >20 μg of boron/gm tumor, which was therapeutically effective (*38*). Our recent studies indicate that the tumor boron uptake can be further improved by means of convection enhanced delivery (*59*). CED is an innovative method to increase the uptake and distribution of both low and high molecular weight agents to the central nervous system by applying a pressure gradient to

establish bulk flow during interstitial infusion (*60*−*62*). The tumor uptake of ^{125}I-labeled boronated EGF was increased 1.4× following administration by CED compared to i.t. injection (*63*).

We recently have reported preliminary data (*63*) on the potential use of MoAb L8A4 as a boron delivery agent for BNCT using the $F98_{EGFRvIII}$ glioma model. MoAb L8A4 specifically recognizes the EGFRvIII mutant isoform of the receptor (*13*). EGFRvIII has an in frame deletion of 801 base pairs of the coding sequence, which constitutively activates the receptor independent of ligand binding (*64*, *65*). The number of EGFRvIII sites expressed on $F98_{EGFRvIII}$ glioma cells, as determined by a receptor binding assay using cetuximab, was equivalent to that determined with L8A4 ($1.07 \pm 0.10 \times 10^5$ versus $1.20 \pm 0.08 \times 10^5$). However, since cetuximab can target both EGFR and EGFRvIII, it potentially could have significant advantages over either boronated EGF or L8A4 as a receptor targeting agent for BNCT.

Since gliomas contain a heterogeneous population of tumor cells, including EGFR or EGFRvIII (+) and (−) cells, the combination of high molecular weight EGFR targeting agents, administered intracerebrally, together with systemic administration of the low-molecular weight drugs boronophenylalanine (*66*−*69*) and sodium borocaptate (*70*), both of which have been used clinically for BNCT of brain tumors (*37*), would provide a way for targeting the heterogeneous population of cells that are found within glioblastomas. Experimental studies to evaluate this approach using boronated cetuximab, administered by CED, and BPA administered systemically, will be carried out.

ACKNOWLEDGMENT

This work was supported in part by United States Department of Energy grant DE-FG02 98ERG2595 and National Institutes of Health grant 1R01 CA098945-01. We thank Dr. Daniel Hicklin, ImClone Systems, Inc., New York, NY, for a generous gift of cetuximab and Dr. John Mendelsohn, M.D. Anderson Cancer Center, Houston, TX, for facilitating this. We thank Michelle Smith for secretarial assistance in the preparation of this manuscript and Michele R. Smith for technical assistance.

LITERATURE CITED

(1) Davis, F. G., Freeks, S., Grutsch, J., Barlas, S., and Brem, S. (1998) Survival rates in patients with primary malignant brain tumors stratified by patient age and tumor histological type: and analysis based on surveillance, epidemiology and end results (SEER) data 1973−1991. *J. Neurosurg. 88*, 1−10.

(2) Gutin, P. H., and Posner, J. B. (2000) Neuro-oncology: Diagnosis and management of cerebral gliomas − past, present, and future. *Neurosurgery 47*, 1−8.

(3) Mischel, P. S., Cloughesy, T. F. (2003) Targeted molecular therapy of GBM. *Brain Pathol. 13*, 52−61.

(4) Tremont-Lukats, I. W., and Gilbert, M. R. (2003) Advances in molecular therapies in patients with brain tumors. *Cancer Control 10*, 125−137.

(5) Sauter, G., Maeda, T., Waldman, F. M., Davis, R. L., and Feuerstein, B. G. (1996) Patterns of epidermal growth factor receptor amplification in malignant gliomas. *Am. J. Pathol. 148*, 1047−1053.

(6) Schwechheimer, K., Huang, S., and Cavenee, W. K. (1995) EGFR gene amplification-rearrangement in human glioblastoma. *Int. J. Cancer 62*, 145−148.

(7) Bonomi, P. (2003) Clinical studies with non-Iressa EGFR tyrosine kinase inhibitors. *Lung Cancer 41*, Suppl 1: S43−48.

(8) Anido, J., Matar, P., Albanell, J., Guzman, M., Rojo, F., Arribas, J., Averbuch, S., and Baselga, J. (2003) ZD1839, a specific epidermal growth factor receptor (EGFR) tyrosine kinase inhibitor, induces the formation of inactive EGFR/HER2 and EGFR/HER3 heterodimers and prevents heregulin signaling in HER2-overexpressing breast cancer cells. *Clin. Cancer Res. 9*, 1274−1283.

(9) Grunwald, V., and Hidalgo, M. (2003) Developing inhibitors of the epidermal growth factor receptor for cancer treatment. *J. Natl. Cancer Inst. 95*, 851−67.

(10) Ciardiello, F. (2000) Epidermal growth factor receptor tyrosine kinase inhibitors as anticancer agents. *Drugs 62, Suppl 1*, 25−32.

(11) Modjtahedi, H., Hickish, T., Nicolson, M., Moore, J., Styles, J, Exxles, S., Jackson, E., Salter, J., Sloane, J., Spencer, L., Priest, K., Smith, I., Dean, C., and Gore, M. (1996) A phase I trial and tumour localisation of the anti-EGFR antibody ICR62 in head and neck or lung cancer. *Br. J. Cancer 73*, 228−235.

(12) Yang, X. D., Jia, X. C., Corvalan, J. R., Wang, P., Davis, C. G., and Jakabovits, A. (1999) Eradication of established tumors by a fully human monoclonal antibody to the epidermal growth factor receptor without concomitant chemotherapy. *Cancer Res. 59*, 1236.

(13) Wikstrand, C. J., Cokgor, I., Sampson, J. H., and Bigner, D. D. (1999) Monoclonal antibody therapy of human gliomas: current status and future approaches. *Cancer Metastasis Rev. 18*, 451−64.

(14) Nagane, M., Lin, H., Cavenee, W. K., and Huang, H. J. (2001) Aberrant receptor signaling in human malignant gliomas: mechanisms and therapeutic implications. *Cancer Letter 162, Suppl*, S17−S21.

(15) Arteaga, C. L. (2002) Overview of epidermal growth factor receptor biology and its role as a therapeutic target in human neoplasia. *Semin Oncol. 29, Suppl 14*, 3−9.

(16) Mendelsohn, J. (2002) Targeting the epidermal growth factor receptor for cancer therapy. *J. Clin. Oncol. 20*, 1s−13s.

(17) Huang, S. M., Bock, J. M., and Harari, P. M. (1999) Epidermal growth factor receptor blockade with C225 modulates proliferation, apoptosis, and radiosensitivity in squamous cell carcinomas of the head and neck. *Cancer Res. 59*, 1935−1940.

(18) Milas, L., Mason, K., Hunter, N., Petersen, S., Yamakawa, M., Ang, K., Mendelsohn, J., and Fan, Z. (2000) In vivo enhancement of tumor radioresponse by C225 antiepidermal growth factor receptor antibody. *Clin. Cancer Res. 6*, 701−708.

(19) Needle, M. N. (2002) Safety experience with IMC-C225, an anti-epidermal growth factor receptor antibody. *Semin. Oncol. 29*, 55−60.

(20) Bianco, C., Bianco, R., Tortora, G., Damiano, V., Guerrieri, P., Montemaggi, P., Mendelsohn, J., De Placido, S., Bianco, A. R., and Ciardiello, F. (2000) Antitumor activity of combined treatment of human cancer cells with ionizing radiation and anti-epidermal growth factor receptor monoclonal antibody C225 plus type 1 protein kinase A antisense oligonucleotide. *Clin. Cancer Res. 6*, 4343−4350.

(21) Harari, P. M., and Huang, S. M. (2002) Head and neck cancer as a clinical model for molecular targeting of therapy: combining EGFR blockade with radiation. *Int. J. Radiat. Oncol. Phys. 49*, 427−433.

(22) Shin, D. M., Donato, N. J., Perez-Soler, R., Shin, H. J., Wu, J. Y., Zhang, P., Lawhorn, K., Khuri, F. R., Glisson, B. S., Myers, J., Clayman, G., Pfister, D., Falcey, J., Waksal, H., Mendelsohn, J., and Hong, W. K. (2001) Epidermal growth factor receptor-targeted therapy with C225 and cisplatin in patients with head and neck cancer. *Clin. Cancer Res. 7*, 1204−1213.

(23) Vega, J., Ke, S., Fan, Z., Wallace, S., Charsangavej, C., and Li, C. (2003) Targeting doxorubicin to epidermal growth factor receptors by site-specific conjugation of C225 to poly(L-glutamic acid) through a poly(ethylene glycol) spacer. *Pharm. Res. 20*, 826−832.

(24) Bruns, C. J., Harbison, M. T., Davis, D. W., Portera, C. A., Tsan, R., McConkey, D. J., Evans, D. B., Abbruzzese, J. L.,

Hicklin, D. J., and Radinsky, R. (2000) Epidermal growth factor receptor blockade with C225 plus gemcitabine results in regression of human pancreatic carcinoma growing orthotopically in nude mice by antiangiogenic mechanisms. *Clin. Cancer Res. 6*, 1936−1948.

(25) Herbst, R. S., and Langer, C. J. (2002) Epidermal growth factor receptors as a target for cancer treatment: the emerging role of IMC-C225 in the treatment of lung and head and neck cancers. *Semin. Oncol. 29*, 27−36.

(26) Barth, R. F., Adams, D. M., Soloway, A. H., Alam, F., and Darby, M. V. (1994) Boronated starburst dendrimer-monoclonal antibody immunoconjugates: evaluation as a potential delivery system for neutron capture therapy. *Bioconjugate Chem. 5*, 58−66.

(27) Liu, L., Barth, R. F., Adams, D., Soloway, A. H., and Reisfeld, R. A. (1995) Bispecific antibodies as targeting agents for boron neutron capture therapy of brain tumors. *J. Hematother. 4*, 477−483.

(28) Liu, L., Barth, R. F., Adams, D. M., Soloway, A. H. and Reisfeld, R. A. (1996): Critical evaluation of bispecific antibodies as targeting agents for boron neutron capture therapy of brain tumors. *Anticancer Res. 16*, 2581−2588.

(29) Capala, J., Barth, R. F., Bendayan, M., Lauzon, M., Adams, D. M., Soloway, A. H., Fenstermaker, R. A., and Carlsson, J. (1996) Boronated epidermal growth factor as a potential targeting agent for boron neutron capture therapy of brain tumors. *Bioconjugate Chem. 7*, 7−15.

(30) Carlsson, J., Gedda, L., Grönvik, C., Hartman, T., Lindström, A., Lindström, P., Lundqvist, H., Lövqvist, A., Malmqvist, J., Olsson, P., Essand, M., Pontén, J., Sjöberg, S., Westermark, B. (1994) Strategy for boron neutron capture therapy against tumor cells with overexpression of the epidermal growth factor receptor. *Int. J. Radiat. Oncol. Biol. Phys. 30*, 105−115.

(31) Olsson, P., Gedda, L., Goike, H., Liu, L, Collins, V. P., Pontén, J., and Carlsson, J. (1998) Uptake of a boronated epidermal growth factor-dextran conjugate in CHO xenografts with and without homan EGF-receptor expression. *Anticancer Drug Des. 13*, 279−289.

(32) Carlsson, J., Kullberg, E. B., Capala, J., Sjöberg, S., Edwards, K., and Gedda, L. (2003) Ligand liposomes and boron neutron capture therapy. *J. Neuro-Oncology 62*, 47−59.

(33) Soloway, A. H., Tjarks, W., Barnum, B. A., Rong, F.-G., Barth, R. F., Codogni, I. M., and Wilson, J. G. (1998) The chemistry of neutron capture therapy. *Chem. Rev. 98*, 1515−1562.

(34) Barth, R. F., Soloway, A. H., Goodman, J. H., Gahbauer, R. E., Gupta, N., Blue, T. E., Yang, W., and Tjarks, W. (1999) Boron neutron capture therapy of brain tumors: an emerging therapeutic modality. *Neurosurgery 44*, 433−451.

(35) Coderre, J. A., and Morris, G. M. (1999) The radiation biology of boron neutron capture therapy. *Radiat. Res. 151*, 1−18.

(36) Sauerwein, W., Moss, R., and Wittig, A., Eds. (2002) *Research and development in neutron capture therapy*, Monduzzi Editore S.p. A., International Proceedings Division, Bologna, Italy.

(37) Barth, R. F. (2003) A critical assessment of boron neutron capture therapy: An overview. *J. Neuro-Oncol. 62*, 1−5.

(38) Barth, R. F., Yang, W., Adams, D. M., Rotaru, J. H., Shukla, S., Sekido, M., Tjarks, W. Fenstermaker, R. A., Ciesielski, M., Nawrocky, M. M., and Coderre, J. A. (2002) Molecular targeting of the epidermal growth factor receptor for neutron capture therapy of gliomas. *Cancer Res. 62*, 3159−3166.

(39) Shukla, S., Wu, G., Chatterjee, M., Yang, W., Sekido, M., Diop, L. A., Muller, R., Sudimack, J. J., Lee, R. J., Barth, R. F., and Tjarks, W. (2003) Synthesis and biological evaluation of folate receptor-targeted boronated PAMAM dendrimers as potential agents for neutron capture therapy. *Bioconjugate Chem. 14*, 158−167.

(40) Barth, R. F., Adams, D. M., Soloway, A. H., Mechetner, E. B., Alam, F., and Anisuzzaman, A. K. (1991) Determination of boron in tissues and cells using direct-current plasma atomic emission spectroscopy. *Anal. Chem. 63*, 890−893.

(41) Barth, R. F., Yang, W., and Coderre, J. A. (2003) Rat brain tumor models to assess the efficacy of boron neutron capture therapy: a critical evaluation. *J. Neuro-Oncol. 62*, 61−74.

(42) Reist, C. J., Garg, P. K., Alston, K. L., Bigner, D. D., and Zalutsky, M. R. (1996) Radioiodination of internalizing monoclonal antibodies using N-succinimidyl 5-iodo-3-pyridinecarboxylate. *Cancer Res. 56*, 4970−4977.

(43) Novick, S., Quastel, M. R., Marcus, S., Chipman, D., Shani, G., Barth, R. F., and Soloway, A. H. (2002) Linkage of boronated polylysine to glycoside moieties of polyclonal antibody; boronated antibodies as potential delivery agents for neutron capture therapy. *Nucl. Med. Biol. 29*, 159−67.

(44) Yang, W., Barth, R. F., Adams, D. M., and Soloway, A. H. (1997) Intratumoral delivery of boronated epidermal growth factor for neutron capture therapy of brain tumors. *Cancer Res. 57*, 4333−4339.

(45) Esfand, R., and Tomalia, D. A. (2001) Poly(amidoamine) (PAMAM) dendrimers: from biomimicry to drug delivery and biomedical applications. *Drug Discov. Today 6*, 427−436.

(46) Chow, H.-F., Mong, T. K. K., Nongrum, M. F., and Wan, C.-W. (1998) The synthesis and properties of novel functional dendritic molecules. *Tetrahedron 54*, 8543−8660.

(47) Quintana, A., Raczka, E., Piehler, L., Lee, I., Myc, A., Majoros, I., Patri, A. K., Thomas, T., Mulé, J., and Baker, Jr. J. R. (2002) Design and function of a dendrimer-based therapeutic nanodevice targeted to tumor cells through the folate receptor. *Pharm. Res. 19*, 1310−1316.

(48) Zhou, R. X., Du, B., and Lu, Z. R. (1999) In vitro release of 5-flourouracil with cyclic core dendritic polymer. *J. Controlled Resease 57*, 249−257.

(49) Kobayashi, H., Wu, C., Kim, M. K., Paik, C. H., Carrasquillo, J. A., and Brechbiel, M. W. (1999) Evaluation of the in vivo biodistribution of indium-111 and yttrium-88 labeled dendrimer-1B4M-DTPA and its conjugation with anti-Tac monoclonal antibody. *Bioconjugate Chem. 11*, 103−111.

(50) Kobayashi, H., Sato, N., Saga, T., Nakamoto, Y., Ishimori, T., Toyama, S., Togashi, K., Konishi, J., and Brechbiel, M. W. (2000) Monoclonal antibody-dendrimer conjugates enable radiolabeling of antibody with markedly high specific activity with minimal loss of immunoreactivity. *Eur. J. Nucl. Med. 27*, 1334−1339.

(51) Kobayashi, H., Kawamoto, S., Saga, T., Sato, N., Ishimori, T., Konishi, J., Ono, K., Togashi, K., and Brechbiel, M. W. (2001) Avidin-dendrimer-(1B4M-Gd)254: A tumor-targeting therapeutic agent for gadolinium neutron capture therapy of intraperitoneal disseminated tumor which can be monitored by MRI. *Bioconjugate Chem. 12*, 587−593.

(52) Safavy, A., Bonner, J. A., Waksal, H. W., Buchbaum, D. J., Gillespie, G. Y., Khazaeli, M. B., Arani, R., Chen, D.-T., Carpenter, M., and Raisch, K. P. (2003) Synthesis and biological evaluation of paclitaxel-c225 conjugate as a model for targeted drug delivery. *Bioconjugate Chem. 14*, 302−310.

(53) Wen, X., Wu, Q.-P., Lu, Y., Fan, Z., Charnsagavej, C., Wallace, S., Chow, D., and Li, Ch. (2001) Poly(ethylene glycol)-conjugated anti-EGF receptor antibody C225 with radiometal chelator attached to the termini of polymer chains. *Bioconjugate Chem 12*, 545−553.

(54) Snelling, L., Miyamoto, C. T., Bender, J., Brady, L. W., Stepewski, Z., Class, R., Emrich, J., and Rackover, M. A. (1995) Epidermal growth factor receptor 425 monoclonal antibodies radiolabeled with iodine-125 in the adjuvant treatment of high-grade astrocytomas. *Hybridoma 14*, 111−114.

(55) Faillot, T., Magdelenat, H., Mady, E., Stasiecki, P., Fohanno, D., Gropp, P., Poisson, M., and Delattre, J. Y. (1996) A phase I study of an anti-epidermal growth factor receptor monoclonal antibody for the treatment of malignant gliomas. *Neurosurgery 39*, 478−483.

(56) Greig, N. H. (1994) Drug delivery to the brain by blood-brain barrier circumvention and drug modification, in *Implication of the blood-brain barrier and its manipulation* (E. A. Neuwelt, Ed.) Vol. 1, pp 311−367, Plenum Press, New York.

(57) Yang, W., Barth, R. F., Adams, D. M., and Soloway, A. H. (1997) Intratumoral delivery of boronated epidermal growth

factor for neutron capture therapy of brain tumors. *Cancer Res. 57*, 4333−4339.
(58) Yang, W., Barth, R. F., Leveille, R., Adams, D. M., Capala, J., Ciesielski, M., and Fenstermaker, R. A. (2001) Evaluation of systemically administered radiolabeled epidermal growth factor as a brain tumor targeting agent. *J. Neuro-Oncol. 55*, 19−28.
(59) Yang, W., Barth, R. F., Adams, D. M., Ciesielski, M. J., Fenstermaker, R. A., Shukla, S., Tjarks, W., and Caliguri, M. A. (2002) Convection enhanced delivery of boronated epidermal growth factor for molecular targeting of EGFR positive gliomas. *Cancer Res. 62*, 6552−6558.
(60) Lieberman, D. M., Laske, D. W., Morrison, P. F., Bankiewicz, K. S., and Oldfield, E. H. (1995) Convection-enhanced distribution of large molecules in gray matter during interstitial drug infusion. *J. Neurosurg. 82*, 1021−1029.
(61) Laske, D. W., Youle, R. J., Morrison, P. F., Governale, L. S., and Oldfield, E. H. (1997) Tumor regression with regional distribution of the targeted toxin TF−CRM107 in patients with malignant brain tumors. *Nature Med. 3*, 1362−1368.
(62) Groothuis, D. R., Ward, S., Itskovich, A. C., Dobrescu, C., Allen, C. V., Dills, C., and Levy, R. M. (1999) Comparison of ^{14}C-sucrose delivery to brain by intravenous, intraventricular, and convection-enhanced intracerebral infusion. *J. Neurosurg. 90*, 321−331.
(63) Yang, W., Barth, R. F., Adams, D. M., Fenstermaker, R. A., Ciesielski, M. J., Shukla, S., Sekido, M., Tjarks, W., and Wikstrand, C. J. (2002) Molecular targeting of EGFRvIII positive gliomas: Convection enhanced delivery vs intratumoral injection of boronated monoclonal antibody L8A4, in *Research and Development in Neutron Capture Therapy.* (W. Sauerwein, R. Moss, and A. Wittig, Eds.) Monduzzi Editore S.p. A., pp 841−844, International Proceedings Division, Bologna, Italy.
(64) Kuan, C. T., Wikstrand, C. J., and Bigner, D. D. (2001) EGF mutant receptor VIII as a molecular target in cancer therapy. *Endocr. Relat. Cancer 8*, 83−96.
(65) Pederson, M. W., Meltorn, M., Damstrup, L., and Poulsen, H. S. (2001) The type III epidermal growth factor receptor mutation. Biological significance and potential target for anticancer therapy. *Ann. Oncol. 12*, 745−760.
(66) Diaz, A. Z. (2003) Assessment of the results from the Phase I/II boron neutron capture therapy trials at the Brookhaven National Laboratory from a clinician's point of view. *J. Neuro-Oncol. 62*, 101−109.
(67) Busse, P. M., Harling, O. K., Palmer, M. R., Kiger, W. S., Kaplan, J., Kaplan, I., Chuang, C. F., Goorley, J. T., Riley, K. J., Newton, T. H, Santa Cruz, G. A., Lu, X.-Q., and Zamenhof, R. G. (2003) A critical examination of the results from the Harvard-MIT NCT program phase I clinical trial of neutron capture therapy for intracranial disease. *J. Neuro-Oncol. 62*, 111−121.
(68) Joensuu, H., Kankaanranta, L., Seppälä, T., Auterinen, I., Kallio, M., Kulvik, M., Laakso, J., Vähütalo, J,. Kortesniemi, M,. Kotilutot, P., Serén, T., Karila, J., Brander, A., Järviluoma, E., Ryynänen, P., Paetau, A., Ruokonen, I., Minn, H., Tenhunen, M., Jääskeläinen, J., Färkkilä, M., and Savolainen, S. (2003) Boron neutron capture therapy of brain tumors: Clinical trials at the Finnish facility using boronophenylalanine. *J. Neuro-Oncol. 62*, 123−134.
(69) Capala, J., H.-Stensam, B., Sköld, K., af Rosenschöld, P. M., Giusti, V., Persson, C., Wallin, E., Brun, A., Franzen, L., Carlsson, J., Salford, L., Ceberg, C., Persson, B., Oerittieli, L., and Henriksson, R. (2003) Boron neutron capture therapy for glioblastoma multiforme: Clinical studies in Sweden. *J. Neuro-Oncol. 62*, 135−144.
(70) Nakagawa, Y., Pooh, K., Kobayashi, T., Sakurai, Y., Kageji, T., Uyama, S., Matsumura, A., Yamamoto, T., and Kumada, H. (2003) Clinical review of the Japanese experience with boron neutron capture therapy and a proposed strategy using epithermal neutron beams. *J. Neuro-Oncol. 62*, 87−99.

BC0341674

Preparation of No-Carrier-Added Technetium-99m Complexes via Metal-Assisted Cleavage from a Solid Phase

Stefan Mundwiler, Lukas Candreia, Pascal Häfliger, Kirstin Ortner, and Roger Alberto*

Department of Inorganic Chemistry, University of Zürich,
CH-8057 Zürich, Switzerland Received September 18, 2003; Revised Manuscript Received November 7, 2003

A novel method for the preparation of no-carrier-added (nca) complexes [^{99m}Tc(CO)$_3$L] (L = diethylenetriamine or picolylamine-*N*-acetic acid) is described. The ligands were covalently bound to a solid support of organic polymers via formation of a tertiary amine from the chelating unit. This C−N bond to the solid phase is selectively cleaved during the formation of the technetium complexes by intramolecular nucleophilic attack of a remaining hydroxy ligand to the α-carbon. The complex [^{99m}Tc(CO)$_3$L] is released into solution while uncomplexed ligand and uncleaved complex remain solid-phase bound. High specific activity technetium complexes can then be isolated by simple filtration. Cleavage yield depends on temperature, pH, and ligand. Up to 50% release from the solid phase could be achieved under optimized conditions. Corresponding to the ^{99m}Tc concentration, free ligand is present in concentrations lower than 10^{-7} M. If a targeting vector is conjugated to these ligands, no-carrier-added radiopharmaceuticals can be prepared in that way.

INTRODUCTION

For the application of radiolabeled receptor binding biomolecules it is highly desirable that only "hot" compounds are administered. This avoids receptor saturation in vivo or toxic side effects from the cold compounds and gives better resolved images (scintigrams) and, thus, allows a clear diagnosis. High specific activity in a normal homogeneous labeling procedure demands the lowest possible amount (concentration) of chelator−biomolecule conjugate still resulting in quantitative labeling. Depending on chelator and complex precursor, these concentrations are often relatively high since the rate of labeling is slow and accompanied by decomposition of ligand or ^{99m}Tc precursor.

Physical separation of cold from hot compound could conveniently be achieved with solid-phase technology, if the ligand−biomolecule conjugate attached to a solid-phase selectively cleaves during complex formation. Examples for such metal-assisted cleavage from solid phases are rare although solid-phase bound metal complexes are frequently applied in heterogeneous catalysis (*1*) or as artificial peptidases (*2*). In the context of radiopharmaceuticals, it has recently been shown that thiols release the protecting group after coordination to a Tc=O center (*3*). On the basis of this observation, Roe et al. bound a tetradentate chelator via thioether bond to a gold surface. Upon coordination of Tc(V) to the sulfur donor in this ligand the ^{99m}Tc-complex was *selectively* released after S−Au-bond break (*4*). More recently, Ballinger et al. described a similar method. The chelator functionalized with biotin was attached to an organic polymeric support by a covalent C−S bond. This bond cleaved concomitantly to the Tc−S bond formation, affording a labeled biotin derivative with very high specific activity (*5*). Another interesting approach was described by Arterburn et al. (*6*). An estradiol derivative, bound to a solid support via an acetyl hydrazine anchor, was reacted with [ReOCl$_3$(PPh$_3$)$_2$] to selectively release the labeled compound via formation of an organoimido-Re complex.

In this paper, we extend the possibilities for the preparation of very high specific activity radiopharmaceuticals to low valent carbonyl complexes containing the "*fac*-[Tc(CO)$_3$]$^+$" moiety (*7*). This novel method employs highly Lewis acidic [^{99m}Tc(OH$_2$)$_3$(CO)$_3$]$^+$ for selective hydrolytic cleavage of a C−N bond in a tertiary amine.

Tridentate chelators comprising mutual combinations of aliphatic and aromatic amines and carboxylate groups as donors are excellent ligands for complex formation with [^{99m}Tc(OH$_2$)$_3$(CO)$_3$]$^+$ even at very low ligand concentration. Biomolecules can easily be conjugated to this ligands via, i.e., formation of a secondary or tertiary amine. We found that biomolecules conjugated through a tertiary amine cleaved from the chelator during complex formation in variable amounts (*8*). Cleavage did not occur in the absence of ^{99m}Tc; thus, is clearly mediated by the Lewis acidity of the Tc(I) center in *fac*-[Tc(CO)$_3$]$^+$. In this work we present a basic study to use this uncommon cleavage for the preparation of nca ^{99m}Tc complexes. The ligand is attached to a solid-phase resin. During complex formation with [^{99m}Tc(OH$_2$)$_3$(CO)$_3$]$^+$, the labeled product is released from the solid phase and can be separated from cold ligand by simple filtration (Scheme 1). Ligands investigated for this purpose are depicted in Chart 1.

EXPERIMENTAL PROCEDURES

Materials and Methods. TentaGel S AC resin (90 μm, 0.24 mmol/g) was purchased from Rapp-Polymere, Tübingen, Germany, other chemicals were from Merck, Dietikon (CH), Aldrich, or Fluka, Buchs (CH). Chemicals were of reagent grade and used without further purification. The precursors (NEt$_4$)$_2$[ReBr$_3$(CO)$_3$] and (NEt$_4$)$_2$-[^{99}TcCl$_3$(CO)$_3$] were synthesized according to a previously published method (*9*). Ligand **2** and complexes **5** and **6** were prepared as previously described (*7*).

* Corresponding author. Roger Alberto, University of Zürich, Institute of Inorganic Chemistry, Winterthurerstrasse 190, 8057 Zürich, Switzerland. Phone: + 41 1 635 46 54/31. Fax: + 41 1 635 68 03. E-mail: ariel@aci.unizh.ch.

10.1021/bc034171f CCC: $27.50 © 2004 American Chemical Society
Published on Web 12/16/2003

Scheme 1. Preparation of No-Carrier-Added ^{99m}Tc Compounds

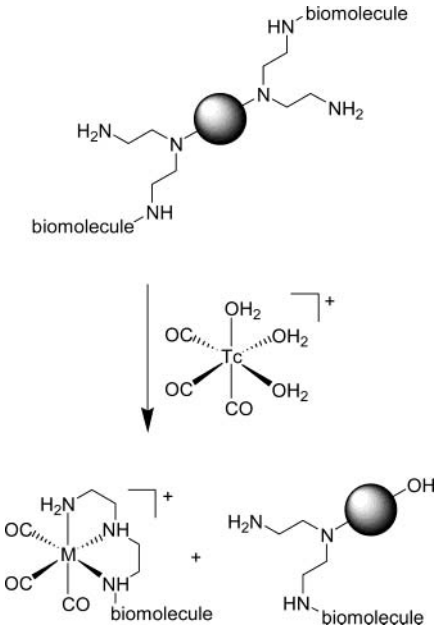
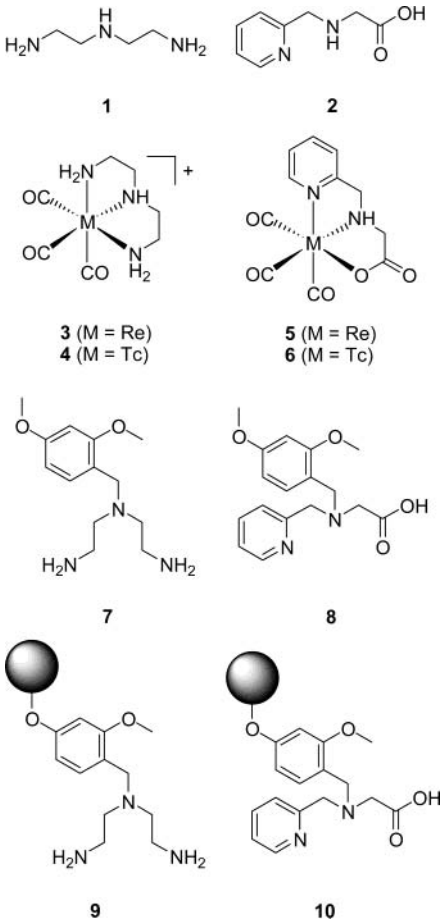


Chart 1. Tridentate Ligands 1,5-Diamino-3-azapentane (diethylenetriamine, diene, 1) and Picolylamine-*N*-acetic Acid (pama, 2), the Corresponding Tc and Re Complexes 3−6, Model Compounds 7 and 8, and Their Solid-Phase Bound Analogues 9 and 10



HPLC analyses were performed on a Merck-Hitachi L-7000 system equipped with a EG&G Berthold LB 508 radiometric detector, using a C-18ec RP column (5 μm particle size, 100 Å pore size, 250 × 3 mm) for separation. HPLC solvents are trifluoroacetic acid, 0.1% in water (A) and methanol (B). Gradient: 0−3 min 100% A, 3.1−9 min 75% A, 9.1 min 66% A, 9.1−20 min 66% A → 0% A, 20−25 min 0% A; 0.5 mL/min. Cleavage yields were calculated by comparing the areas of the product peaks and the corresponding peak of the starting material [^{99m}Tc-$(OH_2)_3(CO)_3]^+$. The activity of the filtered liquids as well as of the resins was measured by a Veenstra Dose Calibrator VDC-304. Semipreparative HPLC separations were performed on LDC Analytical system using a Merck LiChroSpher C-18 reversed-phase column (5 μm particle size, 100 Å pore size, 250 × 10 mm). Electrospray ionization mass spectra (ESI-MS) were recorded on a Merck Hitachi M-8000 spectrometer, GC-MS measurements on a Varian Chrompack Saturn 2000 GC/ion trap MS with splitless injection (1:1) and a CP−Sil 8 CN column. The flow rate was 1 mL/min, the temperature was 70 °C for 5 min, followed by a linear gradient up to 300 °C within 11.5 min, then remaining at 300 °C for 10 min. Free amino groups on the solid-phase resins were visualized by color tests: bromophenol blue solution in water for primary and secondary amino groups and trinitrotoluenesulfonic acid (in DMF/diisopropylethylamin 10:1) and Kaiser's reagent exclusively for primary amines. The loading of chelator to the resins was calculated from the N-content of the resins as determined by elementary analyses.

$[Re(CO)_3$(diethylenetriamine)$]^+(CF_3COO)^-$ (3). An aqueous solution (5 mL) of $(NEt_4)_2[ReBr_3(CO)_3]$ (200 mg, 0.26 mmol) and diethylenetriamine (**1**) (28.3 μL, 0.26 mmol) was refluxed for 12 h. After removal of the solvent, the resulting white powder was purified by preparative HPLC. Subsequent lyophilization yielded 96 mg (76%) of complex **3**. Crystals were obtained by slow diffusion of diethyl ether in a methanolic solution of the Re complex. ^{1}H NMR (D_2O, 300 MHz): δ 2.94−3.05 (*m*, 2H), 2.88 (*p*, 4H, 5.4 Hz), 2.71−2.79 (*m*, 2H).^{13}C NMR (D_2O, 75 MHz): δ, 194.2, 192.9, 50.1, 40.7. ESI-MS: *m*/*z* 372.6 $[M]^+$.

The corresponding ^{99}Tc-complex **4** was formed by mixing solutions of **1** (76 μL, 31 mM in water), [^{99}Tc-$(OH_2)_3(CO)_3]^+$ (1 mL, 2.4 mM in water) and phosphate buffer pH 7.4 (0.1 mL, 1 M), followed by stirring at 90 °C for 30 min (*10*).

***N*′-(2,4-Dimethoxybenzyl)diethylenetriamine (7).** A mixture of 2,4-dimethoxybenzaldehyde (196 mg, 1.18 mmol), *N*,*N*″-bis(*tert*-butyloxycarbonyl)diethylenetriamine (*11*) (357 mg, 1.18 mmol), and sodium triacetoxyborohydride (349 mg, 1.65 mmol) was stirred in dichloromethane (10 mL) for 23 h at room temperature. Excess of sodium triacetoxyborohydride was destroyed by adding aqueous $NaHCO_3$. The BOC-protected intermediate was isolated by extraction into ethyl acetate and purified by column chromatography (silica, methanol/dichloromethane 3:97) to give a viscous, colorless oil (520 mg, 97%). ^{1}H NMR (300 MHz, acetone-d_6): δ 7.21 (d, ^3J = 8.4, 1H); 6.55 (d, ^3J = 2.4, 1H); 6.46 (dd, ^3J = 8.4, ^3J = 2.4, 1H); 5.75 (br s, 2H); 3.87 (s, 3H), 3.78 (s, 3H); 3.53 (s, 2H); 3.13 (td, ^3J = 6.0, ^3J = 6.0, 4H); 2.52 (t, ^3J = 6.0, 4H); 1.40 (s, 18H). ESI-MS: *m*/*z* = 454.4 $[M + H]^+$, *m*/*z* = 150.9 [2,4-dimethoxytoluene]$^+$. Anal. (including one equivalent of acetone) ($C_{26}H_{45}N_3O_7$) C, H, N.

Standard methods for removing of the BOC protecting groups using triflouroacetic acid in dichloromethane or water failed due to the instability of the substrate under these conditions. Deprotection was achieved by stirring a solution of the BOC-protected intermediate (97 mg, 0.21 mmol), chlorotrimethylsilane (230 mg, 2.1 mmol), and phenol (600 mg, 6.4 mmol) in dichloromethane (2.1 mL) for 2.5 h at room temperature. Product **7** was isolated

by extraction into water and purified by semipreparative HPLC to give a colorless, viscous oil (63 mg, 45%), containing traces of water. ^{1}H NMR (300 MHz, Et_2O-d_{10}): δ 7.18 (d, ^3J = 8.1, 1H); 6.59 (s, 1H); 6.52 (d, ^3J = 8.1, 1H); 3.84 (s, 3H), 3.79 (s, 3H); 3.74 (s, 2H); 3.13 (t, ^3J = 6.0, 4H); 2.86 (t, ^3J = 6.0, 4H). ESI-MS: m/z = 253.9 $[M + H]^+$.

***N*-(2,4-Dimethoxybenzyl)-*N*-(2-picolyl)glycine (8).** A mixture of 2,4-dimethoxybenzaldehyde (85 mg, 0.50 mmol), *N*-picolylamineacetic acid ethyl ester (**16**) (99 mg, 0.51 mmol), and sodium triacetoxyborohydride (150 mg, 0.70 mmol) was stirred in dichloromethane (6 mL) for 19 h at room temperature. Excess of sodium triacetoxyborohydride was destroyed by adding aqueous sodium bicarbonate. The ethyl ester intermediate was isolated by extraction into ethyl acetate to give a viscous, colorless oil (171 mg, 97%). ^{1}H NMR (300 MHz, acetone-D_6): δ 8.45 (d, ^3J = 4.8, 1H); 7.73 (dd, ^3J = 8.7, ^3J = 7.8, 1H); 7.63 (d, ^3J = 7.8, 1H); 7.30 (d, ^3J = 8.7, 1H); 7.19 (dd, ^3J = 4.8, ^3J = 7.8, 1H); 6.5 (m, 2H); 4.11 (q, ^3J = 7.2, 2H); 3.94 (s, 2H); 3.7 (m, 8H); 3.33(s, 2H); 1.22 (t, ^3J = 7.2, 3H). ESI-MS: m/z = 344.3 $[M]^+$, m/z = 150.8 [2,4-dimethoxytoluene]$^+$.

The ethyl ester-protected intermediate (111 mg, 0.32 mmol) was stirred in a mixture of ethanol (1 mL), water (3 mL) and aqueous sodium hydroxide (1 M, 0.48 mL) for 24 h at room temperature under a nitrogen atmosphere. Removing of the solvent in vacuo gave the acid **8**. It was used without further purification from the excess of sodium hydroxide.

Preparation of the Solid-Phase Bound Chelator 9. *N*,*N*′′-Bis(1-(4,4-dimethyl-2,6-dioxocyclohexyliden)ethyl)diethylenetriamine (**15**) (101.8 mg, 235.9 μmol) was dissolved in DMF (5 mL), resin **14** (196.6 mg, 47.2 mol) was added, and the mixture was gently stirred at room temperature for 22 h. The reaction mixture was filtered, and the resin was washed with DMF (three times), DMF and methanol (three times alternating), and DMF (five times). The protecting groups were removed by washing the resin 10 times with a solution of hydrazine hydrate, 2% in DMF (1 mL) for 5 min. The reaction mixture was filtered, and the resin was washed with DMF (three times), DMF and methanol (five times alternating), DMF (three times), and diethyl ether (three times). The resin was dried at high vacuum to give product **9** in an yield of 192.3 mg (97.8%; loading 0.236 mmol/g, coupling efficiency 100%).

Preparation of the Solid-Phase Bound Chelator 10. *N*-Picolylamineacetic acid ethyl ester (**16**) (54 mg, 280 μmol) was dissolved in DMF (3 mL), and resin **14** (280 mg, 67 μmol) was added. The mixture was gently stirred at room temperature for 15 h, the reaction mixture was filtered, and the resin was washed with DMF (three times), methanol (three times alternating), and diethyl ether (three times). The protecting groups were removed by gently stirring the resin in a mixture of water (5 mL) and 1 M sodium hydroxide (0.30 mL) for 28 h. Filtration of the resin, washing with DMF (three times), DMF and methanol (three times alternating), DMF (three times), and diethyl ether (three times) and drying at high vacuum gave product **10** in an yield of 268 mg (96%; loading 0.209 mmol/g, coupling efficiency 87.1%).

$[Re(CO)_3$(*N*′-(2,4-dimethoxybenzyl)diethylenetriamine)$]^+Br^-$ (11). Ligand **7** (36 mg, 54 μmol) and $(NEt_4)_2[ReBr_3(CO)_3]$ (50 mg, 65 μmol) were dissolved in water (5 mL), and aqueous $NaHCO_3$ was added until the pH-value reached 8.5. The reaction mixture was stirred at room temperature for 2 h under a nitrogen atmosphere, and a crude product was separated by extraction into dichloromethane. Purification by semipreparative HPLC gave **11** as a white solid in a yield of 16 mg (57%). ^{1}H NMR (300 MHz, Et_2O-D_{10}): δ 7.26 (d, 1H, ^3J = 8.1); 6.58 (s, 1H); 6.55 (d, 1H, ^3J = 8.1); 5.1 (*m*, 2H); 4.50 (s, 2H); 3.8 (*m*, 2H); 3.75 (s, 6H); 3.06 (*m*, 6H); 2.5 (*m*, 2H). ESI-MS: m/z = 523.6 $[M]^+$, m/z = 150.8 [2,4-dimethoxytoluene]$^+$. The corresponding ^{99}Tc-complex **12** was formed by mixing solutions of **7** (1 mL, 2 mM in water), $[^{99}Tc(OH_2)_3(CO)_3]^+$ (0.82 mL, 2.4 mM in water), and phosphate buffer pH 7.4 (0.1 mL, 1 M), followed by stirring at room temperature for 26 h.

Table 1. Homogeneous Reaction of 7 with $[^{99m}Tc(OH_2)_3(CO)_3]^+$: Yield of Cleavage as a Function of Conditions

temp, °C	reaction time, min	pH	[**7**], μM	[Tc], μM	conversion of $[Tc(OH_2)_3(CO)_3]^+$, %	yield of **4**, %	yield of **12**, %
82	30	7.5	1000	0.04	100	11	87
82	37	8.5	10	0.0068	100	12	79
82	37	8.5	100	0.0062	100	16	78
78	60	8.5	250	0.0082	100	34	57

***N*,*N*′′-Bis(1-(4,4-dimethyl-2,6-dioxocyclohexylidene)ethyl)diethylenetriamine (15).** 2-Acetyl-5,5-dimethyl-1,3-cyclohexanedione (695 mg, 3.81 mmol) was dissolved in ethanol (5 mL). Diethylenetriamine (0.197 mL, 1.82 mmol) was added, and the solution was stirred at room temperature for 3 h. The solvent was removed in vacuo, and the crude product was purified by column chromatography (silica, dichloromethane/methanol 92.5: 7.5) to give **15** as a colorless oil. Yield: 714 mg, 90.9%. ^{1}H NMR (300 MHz, $CDCl_3$): δ 3.60 (m, 4H); 3.02 (t, ^3J = 6.2, 4H); 2.56 (s, 6H); 2.32 (s, 8H); 1.00 (s, 12H). ^{13}C NMR (75 MHz, $CDCl_3$): δ 198.1, 173.7, 108.0, 52.7, 47.6, 43.3, 29.9, 28.1, 18.0. ESI-MS: m/z = 431.6 $[M]^+$.

Labeling Procedure. $Na[^{99m}TcO_4]$ was eluted from a ^{99}Mo/^{99m}Tc generator (Mallinckrodt, Petten, The Netherlands) using 0.9% saline. Solutions of the precursor $[^{99m}Tc(OH_2)_3(CO)_3]^+$ were prepared out of $[^{99m}TcO_4]^-$ (1 mL eluate) using a borocarbonate kit containing $K_2CO_2BH_3$ (4 mg), disodium tartrate dihydrate (7 mg), and Borax decahydrate (7 mg). After stirring the mixture for 20 min at 95 °C, it was cooled, neutralized with 1 M HCl, and buffered with phosphate buffer 0.1 M, pH 7.4 (1−6 mL) (*12*).

Of the soluble chelators, 0.01 M solutions in aqueous 0.1 M phosphate buffer, pH 7.4, were prepared. 0.10 mL of this solutions were added to 1 mL of the freshly prepared $[^{99m}Tc(OH_2)_3(CO)_3]^+$ solution. The reaction mixture was stirred at 82 °C for 30 min and cooled in an ice bath. HPLC analyses with γ-detection was performed to quantify the conversion of the ^{99m}Tc. Reaction time, concentrations, and temperature were varied. Typical results are given in Table 1.

Of the solid-phase bound chelators, 1 mg (0.2 mmol) was given to the $[^{99m}Tc(OH_2)_3(CO)_3]^+$ solution (1 mL), the mixture was shortly sonicated and then heated to 82 °C for 30 min. The solution was separated from the solid-phase resin by filtration through a 45μm syringe filter and analyzed by HPLC with γ-detection. The pH value of the reaction mixture was varied by adding 1 M HCl or 1 M NaOH. Reaction time, concentrations, and temperature were also varied. Typical yields are given in Table 2.

RESULTS AND DISCUSSION

Complexation of $[Tc(OH_2)_3(CO)_3]^+$ under concomitant cleavage of the tertiary C−N bond to the solid phase was found for the ligands depicted in Chart 1 and Scheme 1, yielding a secondary amine coordinated to the Tc-center.

Table 2. Labeling Experiments with Solid-Phase Bound Chelators 9 and 10: Reaction Conditions, Conversion of $[Tc(OH_2)_3(CO)_3]$, and Yield of Products and Side Products in Solution of Some Typical Reactions

resin	temp, °C	reaction time, min	pH	[resin], μM	[Tc], μM	conversion of $[Tc(OH_2)_3(CO)_3]^+$, %	product yield of **4**[a] or **6**[b], %	intermediate yield, %
9	70	90	8.5	100	0.074	100	13[a]	19
9	82	30	8.5	250	0.068	98	23[a]	13
9	82	37	8.5	1000	0.007	100	10[a]	8.2
10	43	400	8.5	250	0.098	63	32[b]	15
10	56	260	8.5	250	0.021	96	21[b]	10
10	70	120	8.5	250	0.021	100	42[b]	5.1
10	82	37	7.5	250	0.032	100	45[b]	8.3
10	82	60	8.5	250	0.130	100	51[b]	1.4
10	82	102	8.5	250	3.000	100	45[b]	0

[a] Compound **4.** [b] Compound **6**.

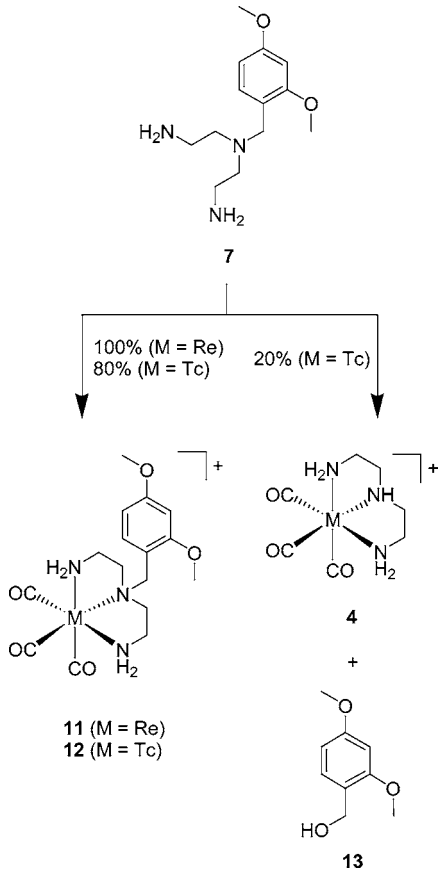
To quantify cleavage, we have chosen two structural frameworks of essential ligands as model compounds. Ligand **1** is a linear triamine and ligand **2** is picolylamine-*N*-acetic acid (pama). Both ligands can potentially be attached to a biomolecule. They form cationic and hydrophilic [M(diethylenetriamine)$(CO)_3]^+$ (**3**: M = Re, **4**: M = Tc) and neutral [M(pama)$(CO)_3$] (**5**: M = Re, **6**: M = Tc) respectively in quantitative yields. For homogeneous studies, **1** and **2** were alkylated at the secondary amine with the same side group as later present on the solid-phase resin. These derivatives **7** and **8** allow studies in homogeneous solution under varying conditions, and possible mechanisms can then be deduced from analytical characterization of the cleavage products. For the heterogeneous studies, **1** and **2** were resin bound to yield **9** and **10** as shown in Chart 1.

Ligand **7** reacted with $(Et_4N)_2[ReBr_3(CO)_3]$ in water to form the corresponding complex [Re(*N*′-(dimethoxybenzyl)-diethylenetriamine)(CO_3)]Br (**11**). It should be emphasize at this point that cleavage never occurred with Re under the conditions where cleavage with $^{99(m)}$Tc was observed. This seems to be one of the rare examples in which Re and Tc behave principally different. The reaction of 4 mM aqueous solutions of $[^{99}Tc(OH_2)_3(CO)_3]^+$ with **7** gave [Tc-(*N*′-(dimethoxybenzyl)-diethylenetrimanine)(CO_3)]Br (**12**) in 80% yield. Two additional peaks in the HPLC were assigned to the cleavage products **4** and 2,4-dimethoxybenzyl alcohol (**13**). This assignment was confirmed by coinjection with the corresponding reference compounds (Scheme 2). To further assess the nature of the two new peaks, they were separatly collected from the HPLC and analyzed by ESI-MS. The M^+ signal of one peak confirmed complex **4**. GC-MS of the second peak showed the mass of methylated **13**. Methylation occurred during the HPLC separation in methanolic solution as confirmed with commercially available 2,4-dimethoxybenzyl alcohol.

The presence of **13** as the primary cleavage product underlines the hypothesis of hydrolytically induced cleavage of the C−N bond. Intermolecular reaction between free hydroxide (or solvent water) and **12** could not be excluded at this stage. Extended reaction time did not improve the yield, and intact complex **12** prepared under mild conditions did not cleave at all. This rationalizes an intramolecular mechanism at a time where not all three coordination sites are occupied by the tridentate chelator. Again, reaction with $[Re(OH_2)_3(CO)_3]^+$ showed no cleavage. Similar experiments with **8** were not possible on the ^{99}Tc level due to complete insolubility of [M$(CO)_3$**8**] (M = Re, Tc) in water.

Homogeneous reaction of **7** with $[^{99m}Tc(OH_2)_3(CO)_3]^+$ confirmed the experimental results found with macroscopic amounts of ^{99}Tc. The yields depend on the conditions and typical cleavage is shown in Table 1.

Scheme 2. Reaction of Ligand 7 with $(Et_4N)_2[ReBr_3(CO)_3]$ and $[^{99}Tc(OH_2)_3(CO)_3]^+$



Complexes **3** and **5**, the rhenium analogues of the cleavage products **4** and **6**, were prepared and the X-ray structure of **3** was elucidated. An ORTEP presentation of the cation is given in Figure 1. The structure has no unusual features but the high hydrophilicity of the complex is worthwhile to mention. The amine donors are not deprotonated. CCDC 219290 contains the supplementary crystallographic data for this paper. These data can be obtained free of charge via www.ccdc.cam.ac.uk/conts/retrieving.html (or from the CCDC, 12 Union Road, Cambridge CB2 1EZ, UK; fax: +44 1223 336033; e-mail: deposit@ccdc.cam.ac.uk).

Cleavage from the Solid Support. The two ligands **1** and **2** were covalantly conjugated to the solid-phase resin in order to show that cleavage does not only occur in a homogeneous reaction. The choice of the solid-phase material is crucial since it has to be stable up to 90 °C and to swell in water to allow diffusion of the Tc-species. The polystyrene/poly(ethylene glycol) resin TentaGel S

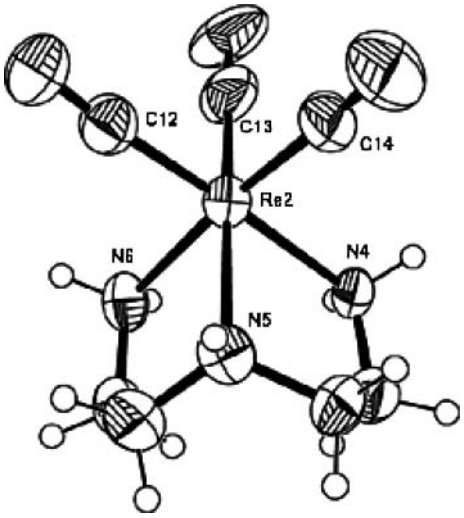
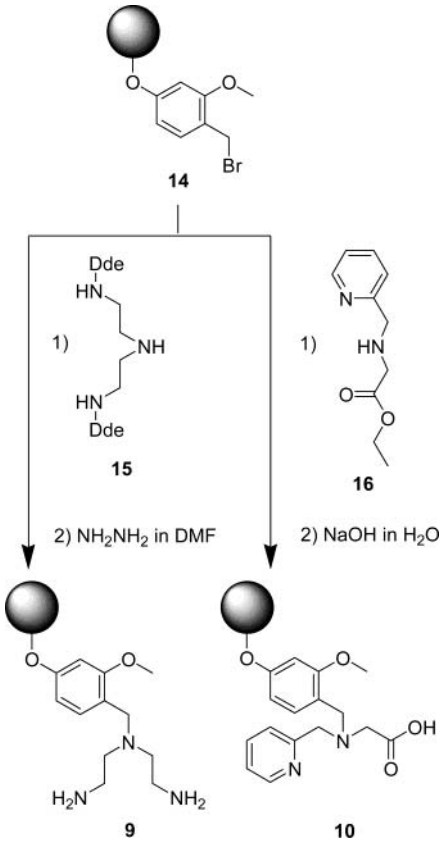


Figure 1. ORTEP drawing of one of the two complexes **3** in the asymmetric unit. Re(2)−C(12), 1.924(13) Å; Re(2)−C(13), 1.934(18) Å; Re(2)−C(14), 1.956(15) Å; Re(2)−N(4), 2.241(9) Å; Re(2)−N(5), 2.215(11) Å; Re(2)−N(6), 2.226(10) Å.

Scheme 3. Synthesis of the Solid-Phase Bound Chelators 9 and 10



AC is appropriate since its active site, a benzyl alcohol derivative (Scheme 3), can be converted into the bromide **14** (*13*). Alkylation with terminal N-protected dien **15** gave after deprotecting the solid-phase bound chelator **9**. Analogously, a biomolecule derivatized ligand could be bound to the support. Reaction of **14** with **16** produced solid-phase bound ligand **10** after ester hydrolysis. The nitrogen contents of compounds **9** and **10** were determined by elemental analysis. Accordingly, the capacity of the resins in mmols of chelating units per gram of solid-phase material was 0.24 mmol/g for **9** and 0.21 mmol/g for **10**, respectively, corresponding to coupling efficiency of 100% and 88%.

The capacity of resin **9** was also verified by the reaction with $[^{99}Tc(OH_2)_3(CO)_3]^+$. The Tc concentration in solution decreased to an extent as expected from elemental analysis. HPLC analyses confirmed that no cleavage from the solid phase occurred under mild conditions. The resin, once loaded with ^{99}Tc, was heated at 80 °C for 5 h in phosphate buffer pH 7.5. As in case of **12**, only minor amounts (<3%) of ^{99}Tc-complex were released into solution. This is much less than the 11% found when the loading reaction was directly carried out with $[^{99}Tc(OH_2)_3(CO)_3]^+$ at 80 °C for 30 min.

For the heterogeneous reaction with the solid phases **9** and **10**, 1 mL of $[^{99m}Tc(OH_2)_3(CO)_3]^+$ was prepared as recently described (*12*), buffered to pH 8.5, and mixed with 1 mg of the solid-phase resins (corresponds to 0.24 mM in ligand). Short ultrasonication ensured good swelling of the resin. The mixtures were incubated for 30 min at 82 °C and cooled to 0 °C, and the solution was separated from the solid-phase resins by filtration. The activities on the solid phase and in solution were measured separately by a γ-counter. Complex **4** was cleaved from the resin **9** in yields up to 23%. During the process, HPLC analysis revealed that an intermediate appeared in strongly condition-dependent amounts. After 30 min it reached 13% but converted completely into product **4** after a further 1 h at 82 °C. This increased the total yield of **4** to 46%. The radiochemical purity after full conversion was >99%, and no $[^{99m}TcO_4]^-$ was observed.

Cleavage of complex **6** from resin **10** and $[^{99m}Tc(OH_2)_3(CO)_3]^+$ was more efficient compared to **4** from **9**. Up to 51% was released at pH 8.5, 82 °C, and after 1 h. The formation of **6** was confirmed by HPLC and coinjection with separately produced **6**. On the nca level it was possible to confirm M^+ of 399 by ESI-MS for the main product which corresponds to $[^{99m}Tc(OH_2)(CO)_2(pama)]^+$. One CO ligand was replaced by water during ionization. As in the case of resin **9**, an intermediate was observed which also converted to **6** after 1 h at 82 °C. The yield as a function of reaction conditions is given in Table 2.

To confirm metal-assisted cleavage from the solid-phase resin, ^{99m}Tc-loaded resin **10** was repeatedly washed with phosphate buffer and reacted with a blank solution as used for the preparation of $[^{99m}Tc(OH_2)_3(CO)_3]^+$ for 1 h and at 82 °C but without any technetium. This afforded less than 2.4% complex release which confirms cleavage takes place during coordination. Subsequently, the resin was reacted again with $[^{99m}Tc(OH_2)_3(CO)_3]^+$, and a yield of 24% was found. Obviously, the predominant process is $[^{99m}Tc(OH_2)_3(CO)_3]^+$-mediated cleavage.

Reaction temperature, pH value, and time were varied to further improve the cleavage yield. Complete conversion of $[^{99m}Tc(OH_2)_3(CO)_3]^+$ and formation of one single product in solution are required for application without the need of purification. The cleavage yield of **6** from resin **10** is strongly pH dependent and ranges from 4% at pH 6 to 52% at pH 8.5. At higher pH the yield decreases again and is about 22% at pH 11. The rest of the activity remains quantitatively bound to the polymer. A strong temperature dependence was observed. At rt, quantitative complex formation on the resin but no cleavage was found. At 45 °C, minor amounts of cleaved products appeared and only at 70 °C did yields increase to 40%. At 85 °C, a maximal yield of 50% was achieved. Stability of the solid-phase resin and of attached biomolecules limits the maximal temperature. For the TentaGel S

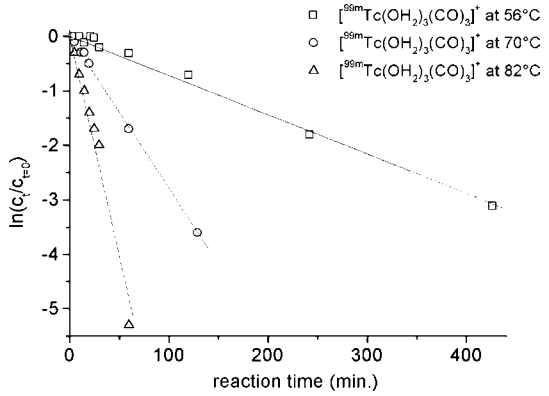


Figure 2. Kinetics of $[^{99m}Tc(OH_2)_3(CO)_3]^+$ conversion at different temperatures, [resin] = 0.25 mM.

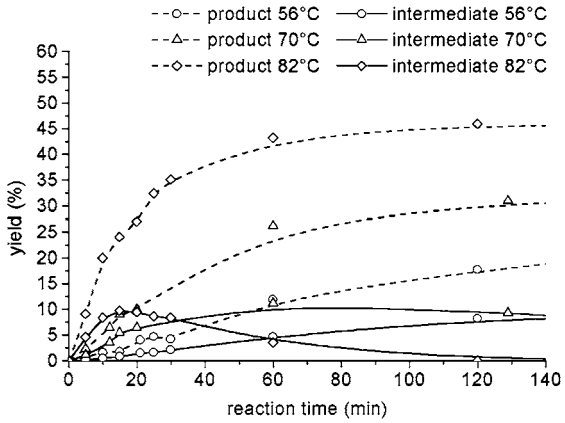


Figure 3. Formation of **6** and the intermediate at 56 °C, 70 °C, and 82 °C.

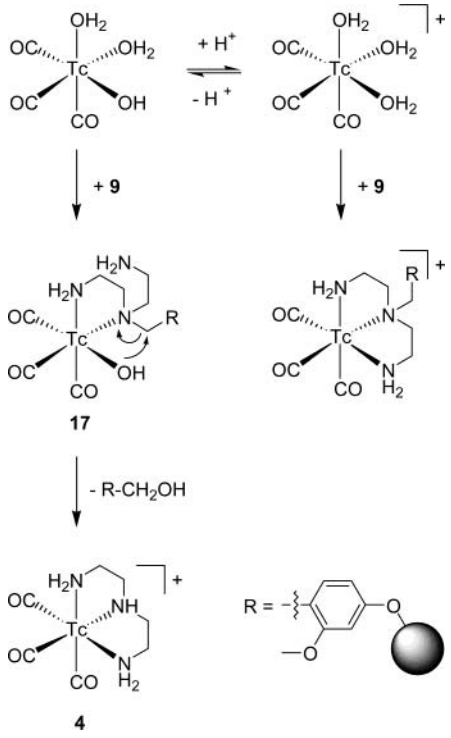
resin, temperatures between 70 °C to 90 °C are preferential to yield radiochemically pure product in good yields.

To get additional insight into the mechanism, the reaction of resin **10** with $[^{99m}Tc(OH_2)_3(CO)_3]^+$ was analyzed at distinct time points by HPLC analysis. The amount of $[Tc(OH_2)_3(CO)_3]^+$ was monitored at 56 °C, 70 °C and 82 °C (pH 8.5, [**10**] 0.25 M). Typical curves are shown in Figure 2. From linearization, second-order rate constants for the conversion of $[Tc(OH_2)_3(CO)_3]^+$ were calculated to be 0.48 L mol^{-1} s^{-1} at 56 °C, 1.85 L mol^{-1} s^{-1} at 70 °C, and 5.36 L mol^{-1} s^{-1} at 82 °C. This transforms into an activation energy of the rate-determining step of about 90 kJ mol^{-1} and a preexponential factor of 7.8×10^{13} L mol^{-1} s^{-1}.

In these experiments, the formation of **6** and the above-mentioned intermediate were monitored as well. Typical concentrations as a function of time are depicted in Figure 3. At 82 °C and after 2 h, $[Tc(OH_2)_3(CO)_3]^+$ completely disappeared and the intermediate fully converted into product **6**. At 70 °C after 2 h, no $[^{99m}Tc(OH_2)_3(CO)_3]^+$ was left but the concentration of the intermediate was still high. Conversion was complete after another 2 h. Reaction rates at 56 °C finally are not practical since the intermediate converts too slowly. For all conditions, the "second product" goes through a maximum and is steadily converted into product **6**, clearly showing its intermediate nature rather than a side product. As obvious from Figure 3, only a minor amount of the product is formed through this intermediate; the direct pathway to product formation is still dominant.

The ratio between ^{99m}Tc and ^{99}Tc complex, already present in the eluate, gives the specific activity. More

Scheme 4. Proposed Mechanism of the C−N Bond Cleavage Reaction

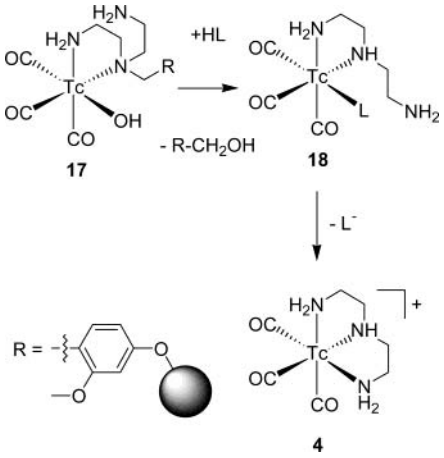


practically for application, the specific activity is defined as the ratio between labeled and unlabeled material. Concentrations of ^{99m}Tc-complex after cleavage can be determined from the activity and was typically between 10^{-8} M and 10^{-7} M (depending on the generator). ^{99}Tc "contamination" can be calculated, and the ratio $[^{99}Tc]/[^{99m}Tc]$ is about three 24 h after elution. Due to the very low ligand concentrations expected, the quantification of free chelator is not routine. We developed a radiochemical method in which the yield of complex formation at ligand concentrations between 10 nM and 1000 nM of **2** served as a scale. Filtered solutions of cleavage reactions of **10** were kept in a freezer until complete ^{99m}Tc decay and were then labeled again. Comparison of the yield with the calibration curve then gives an approximate amount of free ligand. It was found for all experiments that the ligand concentration was in the range of the original technetium concentration, confirming no-carrier-added specific activity. Thus, the specific activity of the complex or the labeled bioconjugate is at least between 10 and 100 times higher than what can be obtained in homogeneous labeling procedures under comparable conditions.

Preliminary studies with bioconjugates are currently going on to prove the principle of labeling targeting vectors. Biomolecules of interest to be labeled at very high specific activity are peptides, brain receptor ligands, or other small molecules. We showed previously that pyrene (a DNA intercalator) can be coupled to solid-phase bound **1**, and that the corresponding ^{99m}Tc complex is released in solution in 5−10% yield in very high specific activity (*14*). Cleavage experiments with peptides and biotin coupled to the ligand **1** and bound to the solid phase show that comparable yields can be achieved; however, the synthetic preparation of the solid phase is rather demanding (*15*).

Proposed Mechanism. The proposed mechanism is depicted in Scheme 4. The observation that the free ligands and the fully coordinated complexes are not susceptible for C−N bond cleavage implies an intramo-

Scheme 5. Formation of the Side Product 18



lecular cleavage mechanism during complex formation. Since the ratio between cleaved and resin retained complex is temperature dependent, two competing reactions must occur. The cleavage must have the higher activation energy barrier. The pH dependence is similar as found in enzyme kinetics and implies that deprotonation of $[^{99m}Tc(OH_2)_3(CO)_3]^+$ to $[^{99m}Tc(OH_2)_2(OH)(CO)_3]$ (pK_s for the rhenium analogue: 7.5) (*16*) is relevant for cleavage. The tridentate ligand initially replaces two aquo ligands in $[^{99m}Tc(OH_2)_2(OH)(CO)_3]$, and $[TcL(OH)(CO)_3]$ (**17**) is formed. The strong Lewis acid Tc activates the tertiary amine and the adjacent CH_2 group, respectively, by the formation of a kind of quaternary amine. Then, as the key step, an intramolecular nucleophilic attack of the hydroxo ligand to this methylene group occurs inducing the C−N-bond cleavage and formation of **4** and **13**. The pathway has a counterpart in the Hoffman degradation of tertiary amines. This mechanism is evident from the intramolecular reaction, the pH-dependence, and the hydroxylation of the leaving group. The nucleophilic attack of a hydoxy ligand rationalizes why cleavage occurs exclusively at tertiary aliphatic amines whereas primary and secondary N−C bonds are stable. Unsaturated residues additionally activate nucleophilic substitution. Indeed, benzylic amines cleave much more readily than aliphatic amines which are much less reactive. Metal-bound hydroxo ligands are known as strong nucleophiles in many hydrolytically active enzymes. Solid-phase bound enzyme models with hydroxide ligands coordinating to cobalt, acting as intramolecular nucleophiles, have been described by Suh et al.(*17*). An example of a rhenium-bound hydroxy ligand which acts as a nucleophile was recently described by Pérez et al. (*18*).

The intermediates which converted into **4** or **6** are probably the complexes in which the tridentate ligand is only bidentately bound. After the nucleophilic attack, one coordination site is available. The third donor group of the tridentate might be in a sterically unfavored position for coordination, enabeling a halide to coordinate (Scheme 5). The intermediates already contain the incompletely bound chelator and Tc. The structure is likely to be $[Tc(CO)_3LX]$ **18** where L is the bidentately coordinated ligand and X an additional monodentate ligand, probably Cl^-.

CONCLUSION

A convenient method for the preparation of complexes containing the $^{99m}Tc(CO)_3$ core with very high specific activity has been described. The chelator is bound to a solid-phase support from which the complex cleaves. Uncoordinated ligand and fully coordinated complex remain linked to the solid support. Since exclusively labeled complex is released, very high specific activities can be produced. Although herein shown only with model ligands, biomolecules can be conjugated to the chelators which will allow the production of nca targeting radiopharmaceuticals. Clearly, the bioconjugates must resist relatively high temperatures, but this is not a problem with small molecules such as central nervous system receptor targeting molecules or even peptides. Further studies with bioconjugates bound to the described solid-phase resins are under investigation.

ACKNOWLEDGMENT

We thank Mallinckrodt Inc. for financial support of this work.

Supporting Information Available: X-ray crystallographic data for compound **3**. This material is available free of charge via the Internet at http://pubs.acs.org.

LITERATURE CITED

(1) Leadbeater, N. E., and Marco, M. (2002) Preparation of polymer-supported ligands and metal complexes for use in catalysis. *Chem. Rev. 102*, 3217−3273.

(2) Suh, J., and Moon, S. J. (2001) Artificial peptidase with an active site comprising a Cu(II) center and a proximal guanidinium ion. A carboxypeptidase a analogue. *Inorg. Chem. 40*, 4890−4895.

(3) Fritzberg, A. R., Kasina, S., Eshima, D., and Johnson, D. L. (1986) Synthesis and Biological Evaluation of Tc-99m Mag3 as a Hippuran Replacement. *J. Nucl. Med. 27*, 111−116.

(4) Pollak, A., Roe, D. G., Pollock, C. M., Lu, L. F. L., and Thornback, J. R. (1999) A convenient method of preparing high specific activity technetium complexes using thiol-containing chelators adsorbed on gold. *J. Am. Chem. Soc. 121*, 11593−11594.

(5) Dunn-Dufault, R., Pollak, A., Fitzgerald, J., Thornback, J. R., and Ballinger, J. R. (2000) A solid-phase technique for preparation of no-carrier-added technetium-99m radiopharmaceuticals: Application to the streptavidin/biotin system. *Nucl. Med. Biol. 27*, 803−807.

(6) Arterburn, J. B., Rao, K. V., and Perry, M. C. (2000) Solid-supported hydrazine substrate for labeling estradiol ligands with rhenium. *Angew. Chem., Int. Edit. 39*, 771.

(7) Schibli, R., La Bella, R., Alberto, R., Garcia-Garayoa, E., Ortner, K., Abram, U., and Schubiger, P. A. (2000) Influence of the denticity of ligand systems on the in vitro and in vivo behavior of $^{99m}Tc(I)$-tricarbonyl complexes: A hint for the future functionalization of biomolecules. *Bioconjugate Chem. 11*, 345−351.

(8) Mundwiler, S., and Alberto, R. (2001) Thymidine Derivatives with Tridentate Metal-chelating Units and their Labeling with a $[^{99m}Tc(OH_2)_3(CO)_3]^+$-kit. *J. Labelled Compd. Radiopharm. 44*, S494−S495.

(9) Alberto, R., Schibli, R., Schubiger, P. A., Abram, U., and Kaden, T. A. (1996) Reactions with the technetium and rhenium carbonyl complexes $(NEt_4)_2[MX_3(CO)_3]$. Synthesis and structure of $[Tc(CN\text{-}^tBu)_3(CO)_3](NO_3)$ and $(NEt_4)[Tc_2(\mu\text{-}SCH_2CH_2OH)_3(CO)_6]$. *Polyhedron 15*, 1079−1089.

(10) Alberto, R., Schibli, R., Egli, A., Schubiger, A. P., Abram, U., and Kaden, T. A. (1998) A novel organometallic aqua complex of technetium for the labeling of biomolecules: Synthesis of $[^{99m}Tc(OH_2)_3(CO)_3]^+$ from $[^{99m}TcO_4]^-$ in aqueous solution and its reaction with a bifunctional ligand. *J. Am. Chem. Soc. 120*, 7987−7988.

(11) Adamczyk, M., Fishpaugh, J. R., and Heuser, K. J. (1998) Chemoselective synthesis of protected polyamines and facile synthesis of polyamine derivatives using O-alkyl-O′-(N-succinimidyl) carbonates. *Org. Prep. Proced. Int. 30*, 339−348.

(12) Alberto, R., Ortner, K., Wheatley, N., Schibli, R., and Schubiger, A. P. (2001) Synthesis and properties of boranocarbonate: A convenient in situ CO source for the aqueous preparation of $[^{99m}Tc(OH_2)_3(CO)_3]^+$. *J. Am. Chem. Soc. 123*, 3135−3136.

(13) Ngu, K., and Patel, D. V. (1997) Preparation of acid-labile resins with halide linkers and their utility in solid-phase organic synthesis. *Tetrahedron Lett. 38*, 973−976.

(14) Mundwiler, S., Candreia, L., and Alberto, R. (2002) No Carrier Added Preparation of ^{99m}Tc-$(CO)_3$-complexes by Solid-Phase Techniques via Metal Assisted Cleavage from the Solid Support. *Technetium, Rhenium and other Metals in Chemistry and Nuclear Medicine* (Nicolini, M., and Mazzi, U., Eds.) Vol. 6, pp 167−169, SGEdotoriali, Padova.

(15) Alberto, R., and Mundwiler, S. (2003) Preparation of $M(CO)_3$ − complexes by solid-phase techniques via metal assisted cleavage from the solid support. Eur. Pat. Appl. 2002078743.8.

(16) Egli, A., Hegetschweiler, K., Alberto, R., Abram, U., Schibli, R., Hedinger, R., Gramlich, V., Kissner, R., and Schubiger, P. A. (1997) Hydrolysis of the organometallic aqua ion factriaquatricarbonylrhenium(I). Mechanism, pK_a, and formation constants of the polynuclear hydrolysis products. *Organometallics 16*, 1833−1840.

(17) Jeung, C. S., Kim, C. H., Min, K., Suh, S. W., and Suh, J. (2001) Hydrolysis of plasmid DNA catalyzed by Co(III) complex of cyclen attached to polystyrene. *Bioorg. Med. Chem. Lett. 11*, 2401−2404.

(18) Gerbino, D. C., Hevia, E., Morales, D., Clemente, M. E. N., Perez, J., Riera, L., Riera, V., and Miguel, D. (2003) A new reactivity pattern of low-valent transition-metal hydroxo complexes: straightforward synthesis of hydrosulfido complexes via reaction with carbon disulfide. *Chem. Commun.* 328−329.

BC034171F

Reagents for Astatination of Biomolecules: Comparison of the in Vivo Distribution and Stability of Some Radioiodinated/Astatinated Benzamidyl and *nido*-Carboranyl Compounds

D. Scott Wilbur,*,† Ming-Kuan Chyan,† Donald K. Hamlin,† Brian B. Kegley,† Reudi Risler,† Pradip M. Pathare,† Janna Quinn,‡ Robert L. Vessella,‡ Catherine Foulon,§ Michael Zalutsky,§ Timothy J. Wedge,# and M. Frederick Hawthorne#

Departments of Radiation Oncology, and Urology, University of Washington, Seattle, Washington 98195, Department of Radiology, Duke University, Durham, North Carolina 27710, and Department of Chemistry and Biochemistry, University of California, Los Angeles, California. Received September 26, 2003; Revised Manuscript Received November 21, 2003

An investigation has been conducted to assess the in vivo stability of a series of astatinated benzamides and astatinated *nido*-carborane compounds in mice. It was hypothesized that the higher bond strength of boron−astatine bonds in the *nido*-carboranes might provide increased stability toward in vivo deastatination. Four tri-*n*-butylstannylbenzamides were prepared for radiohalogenation and evaluation in vivo. Those compounds were *N*-propyl-4-(tri-*n*-butylstannyl)benzamide **1a**, *N*-propyl-3-(tri-*n*-butylstannyl)benzamide **2a**, ethyl 4-tri-*n*-butylstannylhippurate **3a**, and 4-tri-*n*-butylstannyl-hippuric acid **4a**. Seven mono-*nido*-carboranyl derivatives were prepared for radiohalogenation and in vivo evaluation. Four of the seven mono-carboranyl derivatives (**5a**, **6a**, **7a**, **13a**) contained a 3-(*nido*-carboranyl)propionamide functionality, and the remaining compounds (**8a**, **8g**, **10a**) contained a 4-(*nido*-carboranyl)aniline functionality. Two additional derivatives (**11a**, **12a**) were prepared that contained bis-(*nido*-carboranylmethyl)benzene moieties (also referred to as Venus flytrap complexes (VFCs). All benzamide and *nido*-carborane compounds underwent facile iodination and radiohalogenation, except a 4-(*nido*-carboranyl)aniline derivative, **8a**. Iodination of **8a** resulted in a mixture, of which the desired iodinated product was a minor component. Therefore, radiohalogenation was not attempted. It is believed that the mixture of products is due to the presence of a thiourea bond. Previous studies have shown that thiourea bonds can interfere with halogenation reactions. In vivo comparisons of the compounds were conducted by co-injection of dual labeled ($^{125/131}$I and ^{211}At) compounds. Tissue distribution data were obtained at 1 and 4 h postinjection of the radiolabeled compounds, as that was sufficient to determine if astatine was being released. Stability of the astatinated compound was assessed by the difference in concentration of radioiodine and astatine in lung and spleen. All of the benzamides were found to undergo rapid deastatination in vivo. The *nido*-carborane derivatives appeared to be slightly more stable to in vivo deastatination; however, they had long blood residence times. The surprising finding was that the VFC derivatives did not release ^{211}At in vivo, even though they rapidly localized to liver. This finding provides encouragement that stable conjugates of ^{211}At may be attained if appropriate modifications of the VFC can be made to redirect their excretion through the renal system.

INTRODUCTION

Astatine-211 is one of only a few α-particle emitting radionuclides that have properties suitable for application to targeted radionuclide therapy (TRT)[1] of cancer (*5*−*7*). TRT using α-emitting radionuclides (α-TRT) is of particular interest for treatment of micrometastatic disease, cancer contained in compartmental spaces (e.g., ovarian cancer), and cancer that is resistant to other forms of radiation (e.g., melanoma). Aside from the therapeutic radionuclide, a key component in TRT is the cancer cell targeting agent. Fortunately, a large number of cancer cell selective monoclonal antibodies (mAbs) applicable to TRT have been developed (*8*−*12*). In addition to mAbs, there is a rapidly expanding number of other cancer cell targeting agents being identified that might be used in TRT (*13*, *14*). Importantly, to take advantage of the cancer cell targeting provided by mAbs or other agents, the α-emitting radionuclide, e.g., ^{211}At,

* Address correspondence to D. Scott Wilbur, Ph.D., Department of Radiation Oncology, University of Washington, 2121 N. 35th Street, Seattle, WA 98103-9103. Phone: 206-685-3085. FAX: 206-685-9630. E-mail: dswilbur@u.washington.edu.

† Department of Radiation Oncology.

‡ Department of Urology, University of Washington.

§ Duke University.

University of California.

[1] Abbreviations: BSA, bovine serum albumin; CDI, 1,1′-carbonyldiimidazole; ChT, chloramine-T; cpm, counts per minute; DCC, 1,3-dicyclohexylcarbodiimide; DTPA, diethylenetriaminepentaacetic acid; EDC, 1-(3-dimethylaminopropyl)-3-ethylcarbodiimide; mAb, monoclonal antibody; NCS, *N*-chlorosuccinimide; %ID/g, percent injected dose/g; PBS, phosphate buffered saline; pi, postinjection; rt, room temperature; tBoc, *tert*-butoxycarbonyl; TCDI, 1,1′-thiocarbonyldiimidazole; TFA, trifluoroacetic acid; TFP, 2,3,5,6-tetrafluorophenyl; TFP-OH, 2,3,5,6-tetrafluorophenol; TFP-OTFA, 2,3,5,6-tetrafluorophenyl trifluoroacetate; VFC, "Venus flytrap complex".

10.1021/bc034175k CCC: $27.50 © 2004 American Chemical Society
Published on Web 12/30/2003

must be coupled to the carrier molecule in a manner that is stable toward release of the radionuclide in vivo. Therefore, the method by which a radionuclide is attached to the carrier molecule is of paramount importance in the development of agents used for TRT of cancer.

Direct astatination of the cancer targeting carrier molecule is often problematic. Unlike radioiodine, direct reaction of electrophilic ^{211}At with tyrosine moieties of proteins or peptides does not work well (*15*, *16*), and results in labeled molecules that are not stable to in vivo deastatination (*17*, *18*). To circumvent this problem, deactivated aryl compounds (e.g., benzoates) have been investigated as pendant groups for attaching ^{211}At to carrier molecules (*19*−*23*). Although some biomolecules labeled with astatinated deactivated aryl groups have been found to be stable to in vivo deastatination, other biomolecules labeled using benzoate pendant groups have been found to undergo extensive deastatination in vivo. It is not presently known why large differences in stability are observed, but it may be due to factors such as the rate, or mode, of metabolism of the carrier molecule. Most importantly, the in vivo instability limits the potential for ^{211}At in cancer therapy as it limits which cancer targeting carrier molecules can be used.

The observed in vivo instability of astatinated benzoate conjugated biomolecules prompted investigation of alternate pendant groups to attain higher in vivo stability. Vaidyanathan, Affleck, and Zalutsky (*24*) and Yordanov et al. (*1*) indicated that modifications in the aryl ring of antibody conjugates did not provide high stability,[2] so a very different pendant group was sought. The only criterion set for the pendant group was that it react rapidly and efficiently with ^{211}At as do the organometallic intermediates used for labeling the nonactivated aryl pendant groups (*25*−*27*). This high reactivity was sought so that only a small portion of the ^{211}At ($t_{1/2}$ = 7.2 h) would be lost due to decay during preparation of the radiopharmaceutical. In prior studies by Hawthorne et al. (*28*, *29*), a radioiodinated isothiocyanatophenyl-*nido*-carborane pendant group was used for labeling mAbs. This unique labeling approach involving radioiodinated *nido*-carboranes[3] appeared to have potential for use with ^{211}At. Importantly, radioiodination studies of *nido*-carboranes demonstrated that they could be rapidly and efficiently labeled, and the products were stable to in vivo deiodination (*30*). It was hypothesized that astatinated *nido*-carboranes might be more stable toward in vivo deastatination than the astatinated benzoate derivatives as boron−halogen bonds are generally stronger than carbon−halogen bonds (*31*). On the basis of that hypothesis, an investigation that examined the in vivo stability of four astatinated benzamide derivatives and nine astatinated *nido*-carborane derivatives was conducted. In addition to compounds containing a single *nido*-carboranyl moiety, compounds containing two *nido*-carboranyl moieties, also referred to as Venus flytrap complexes (VFCs) (*32*−*34*), were included in the investigation. To determine the stability of the astatinated compounds, they were labeled with both ^{211}At and radioiodine. Since radioiodinated nonactivated aryl compounds and *nido*-carboranes have previously been shown to be stable in vivo, the differences between the concentrations of ^{211}At and radioiodine in tissues that localize ^{211}At (e.g., lung and spleen) were used to estimate the in vivo stability of the ^{211}At label. Small radiolabeled molecules were employed in this investigation so that stability would be readily determined. The results obtained from the investigation are reported herein.

EXPERIMENTAL PROCEDURES

General. Chemicals purchased from commercial sources were analytical grade or better, and were used without further purification except where noted. 4-Aminobenzyldiethylenetriaminepentaacetic acid (**12d**) was purchased from Macrocyclics (Dallas, TX). 4-Pentynoic acid was obtained from Lancaster (Windham, NC) or Farchan Laboratories (Gainesville, FL). Decaborane was obtained from Alfa Aesar (Ward Hill, MA). Chloramine-T (ChT) and phosphate buffered saline (PBS) were obtained from Sigma (St. Louis, MO). Iodobenzoic acid and most other chemicals were obtained from Aldrich Chemical Co. (Milwaukee, WI). Solvents for HPLC analysis were obtained as HPLC grade and were filtered (0.2 μm) prior to use. Tetrafluorophenyl trifluoroacetate (TFP−OTFA) was prepared as previously described (*35*).

Radioactivity. Initial ^{211}At labeling studies (involving **5a**) were conducted at Duke University, with later studies being conducted at the University of Washington. All radioactive materials were handled according to approved protocols at Duke University and at the University of Washington. Astatine-211 production at Duke University involved the ^{209}Bi(α,2n)^{211}At reaction, where natural bismuth was irradiated with 28 MeV α-particles on the Duke University Medical Center cyclotron. The ^{211}At activity was distilled from the bismuth target into a cooled $CHCl_3$ trap as previously described (*36*). Production of ^{211}At was also carried out at the University of Washington on a Scandatronix MP-50 cyclotron using the same conditions described above. At the University of Washington, distillation and labeling with ^{211}At were conducted in a glovebox (Innovative Technologies, Inc., radioisotope glovebox) in which the exhaust passes through a charcoal filter. The ^{211}At was distilled from the irradiated bismuth targets into a 0.05 N NaOH solution using the dry distillation apparatus previously described (*37*).

All radiohalogenation reactions were conducted in vials capped with Teflon-coated septa, within a radioactivity approved fume hood. The reaction vials were vented through a 10-mL charcoal filled syringe. Additions of reagents to, or removal of materials from, radiohalogenation vessels were conducted by passing a syringe needle through the septa. All radiohalogenation reactions at the University of Washington were conducted in a charcoal-filtered Plexiglas enclosure (radioiodine fume hood, 20 × 24 × 36 in., Biodex Medical Systems Inc., Shirley, NY) within a radiochemical fume hood.

Na[^{125}I]I was purchased from Perkin-Elmer Life and Analytical Sciences (formerly NEN/Dupont, Billerica,

[2] Interestingly, application of a succinyl-phenethylamide moiety provided increased stability for protein labeling (*1*), and *m*-astatobenzylguanidine ([^{211}At]MABG) displayed a much higher stability in vivo than aryl groups not having the benzyl guanidine moiety (*2*, *3*).

[3] The term "carborane" is used to describe a boron cage moiety that has carbon and boron atoms. There are two carbon atoms in the carborane moieties in these studies. The icosahedral carborane cage moiety containing two carbon atoms and 10 boron atoms is also named as 1,2-dicarba-*closo*-dodecaborane (*4*). The term "*nido*-" (or nest like) signifies a carborane cage molecule that has a boron atom removed from its apex, which is opposed to the "*closo*" (or closed) form of the carborane cage molecule. *nido*-Carboranes are anionic and thus are salts containing cationic counterions. The term *nido*-carboranyl as used herein is simplified from 7-substituted dodecahydro-7,8-dicarba-*nido*-undecaborate(−1).

MA) as a high concentration/high specific activity radioiodide in 0.1 N NaOH. Measurement of ^{125}I, ^{131}I, and ^{211}At was accomplished in one of three dose calibrators. Measurements at Duke University were accomplished on a Capintec CRC-7 Radioisotope calibrator (Ramsey, NJ). To count ^{211}At on that instrument, the ^{133}Xe setting was used with a multiplication factor of 2.4. Measurements at the University of Washington were conducted on either a Capintec CRC-15R or a Capintec CRC-6A Radioisotope calibrator using calibration #44 (designated by Capintec Technical Services). Tissue samples containing these radionuclides were counted in a LKB 1282 gamma counter (Wallac, Turku, Finland) with the following window settings: channels 35−102 (20−90 keV) and channels 165−185 (300−450 keV) when ^{125}I and ^{131}I were counted together. Spillover of ^{131}I into the ^{211}At window was estimated to be 13.5% and the data were corrected for this. Tissue samples containing ^{211}At and ^{125}I were counted in a Wallac 1480 Wizard gamma counter (EG & G, Wallac, Turku, Finland). In this latter case, the tissue samples were initially counted to obtain both ^{211}At and ^{125}I counts, then they were recounted after 3−5 days (0.1% or less ^{211}At remaining) to obtain ^{125}I counts. Radioactivity counts were imported into an Excel Spreadsheet (Microsoft Corp., Redmond, WA) where calculations were made. The ^{211}At counts were obtained by subtracting ^{125}I counts from total counts. Individual tissue counts for ^{211}At were corrected for decay from the time of counting the first standard (at the beginning of the tissue counting process).

Spectroscopic Data. ^{1}H NMR spectra were obtained on either a Bruker AC-200 (200 MHz), Bruker AF-301 (300 MHz), or AM-500 (500 MHz) instrument. The chemical shifts are expressed as ppm using tetramethylsilane as an internal standard ($\delta = 0.0$ ppm). ^{11}B NMR were obtained at 160 MHz (500 MHz for ^{1}H), and 96 MHz (300 MHz for ^{1}H). The spectra are referenced ($\delta = 0.0$ ppm) to $BF_3{\cdot}O(Et)_2$ as an external standard (insert) in the NMR tube. ^{11}B NMR included ^{1}H coupled and decoupled spectra for all samples examined. Only ^{1}H decoupled resonances are reported. All ^{11}B resonances were split in the coupled spectra except in iodinated samples where one proton was not coupled. IR data were obtained on a Perkin-Elmer 1420 infrared spectrophotometer. Mass spectra were obtained for all new compounds, except for **2f** where several attempts were unsuccessful. Mass spectral data were obtained on a VG 70SEQ mass spectrometer with 11250J data system. Fast atom bombardment (FAB^+) mass spectral data were obtained at 8 kV using a matrix of 90% thioglycerol, 9% DMSO and 1% TFA (DMIX) or propylene glycol 600 containing thioglycolate.

Analytical Chromatography. All reactions were monitored by HPLC. Nonradioactive samples were assessed on a system that contained a Hewlett-Packard quaternary 1050 gradient pump, a variable wavelength UV detector (254 nm), and a Varex ELSD MKIII evaporative light-scattering detector. Analysis of the HPLC data were conducted on Hewlett-Packard HPLC ChemStation software. Reversed-phase HPLC chromatography was carried out on an Alltech Altima C-18 column (5 μm, 250 × 4.5 mm) using a gradient solvent system at a flow rate of 1 mL/min. The gradient mixture was composed of MeOH (eluant A), 0.1% aqueous HOAc (eluant B) or 0.05 M, pH 5.5 aqueous triethylammonium acetate (eluant C). Two gradient methods were employed: [Method A] This gradient started with 40% MeOH and 60% eluant B for 2 min; then the % MeOH was increased linearly to 100% over a 10 min period; following this the elution continued with 100% MeOH for an additional 8 min. [Method B] This gradient started with 40% MeOH and 60% eluant C for 2 min; then the % MeOH was increased linearly to 100% over a 13 min period; following this the elution continued with 100% MeOH for an additional 5 min. All compounds were evaluated using method A except for compounds **5a**, **5b**, and **7f**, which were evaluated using method B. Retention times (t_R) are provided with the experimental for each compound.

Radioiodinated and astatinated compounds were evaluated for identity and purity, and isolated for animal studies, using reversed-phase radio-HPLC. All radioiodinated compounds were characterized by correlation with nonradioactive standards on the HPLC. Astatinated compounds generally had a slightly longer retention time on reversed-phase HPLC. Radioactive samples were assessed on one of two gradient systems. One system (Duke University) was used for analysis of [^{131}I]**5b**/[^{211}At]-**5c** had two LKB model 2150 pumps, a LKB 2152 controller, a LKB 2138 UV (254 nm), a Beckman 170 Radioisotope detector and PC running Nelson Analytical Data − Chromatography software (v. 3.5) with a 760 interface. A gradient for the elution of the *nido*-carboranes used 50 mM triethylammonium acetate (TEAA) and MeOH. The gradient began with 60% TEAA/40% MeOH and increased to 95% MeOH over 15 min. The second system (University of Washington), used for all other radiolabeled compounds, consisted of two Beckman model 110B pumps (or a HP 1050 quaternary pump), a Beckman 420 controller, a Beckman model 153 UV detector (254 nm), and a Beckman model 170 radioisotope detector. Analysis of the HPLC data were conducted on a PC running Hewlett-Packard HPLC ChemStation software. Reversed-phase HPLC chromatography was carried out on an Alltech Altima C-18 column (5 μm, 250 × 4.5 mm) using a gradient solvent system at a flow rate of 1 mL/min. Retention times (t_R) are provided with the experimental for each compound.

Preparation of the following compounds was conducted as previously described: 4-iodobenzoic acid TFP ester, **1e** (*38*); 4-(tri-*n*-butylstannyl)benzoic acid TFP ester **1f** (*38*); *tert*-butyldimethylsilyl-1,2-dicarba-*closo*-dodecaborane, **11e** (*39*); 1,2-bis-(*tert*-butyldimethylsilylcarboranylmethyl)benzene, **11f** (*39*); bis-(carboranyl-methyl)-benzene, **11g** (*39*). Iodinated derivatives of compounds containing a *nido*-carborane structure used for HPLC standards were obtained as mixtures containing no iodine, one iodine, or a chlorine (from *N*-chlorosuccinimide); therefore, they were isolated from HPLC and identified by mass spectral analysis only.

***N*-Propyl-4-(tri-*n*-butylstannyl)benzamide, 1a.** A solution containing 0.50 g (0.89 mmol) **1f**, 63 mg (1.07 mmol) of *n*-propylamine and 5 mL of anhydrous DMF was stirred at room temperature for 30 min. The volatile materials were evaporated under vacuum and the residue was purified by silica gel column (30 g), eluting with 10% ethyl acetate/hexanes, to yield 0.30 g (74%) of **1a** as a colorless oil; ^{1}H NMR ($CDCl_3$, 200 MHz) δ 0.88 (t, J = 8.0, 7.3 Hz, 9H), 0.97 (t, J = 7.3, 7.3 Hz, 3H), 1.07 (t, J = 7.7, 8.1 Hz, 6H), 1.16−1.41 (m, 7H), 1.46−1.72 (m, 7H), 3.41 (q, J = 6.6, 7.0, 6.6 Hz, 2H), 6.24 (s, 1H), 7.53 (d, J = 7.7 Hz, 2H), 7.69 (d, J = 7.7 Hz, 2H); HRMS $(ES)^+$ calcd for $C_{22}H_{40}NOSn$ $(M+H)^+$ 454.2132, found 454.2140. HPLC: t_R = 18.5 min.

4-Iodo-*N*-propylbenzamide, 1b. A 0.09 g quantity (1.51 mmol) of *n*-propylamine in 1 mL of anhydrous DMF was added to a solution containing 0.50 g (1.26 mmol) of **1e** in 4 mL of anhydrous DMF. The solution was stirred at room temperature for 30 min and the DMF was

removed under vacuum. The residue was purified by silica gel column (30 g, 10% ethyl acetate/hexanes) to yield 0.31 g of (85%) of **1b** as a colorless solid, mp 119−120 °C; ^{1}H NMR ($CDCl_3$, 200 MHz) δ 0.98 (t, J = 7.3, 7.7 Hz, 3 H), 1.54−1.73 (m, 2 H), 3.40 (q, J = 6.6, 7.0, 6.6 Hz, 2 H), 6.16 (s, 1 H), 7.48 (d, J = 8.4 Hz, 2 H), 7.77 (d, J = 8.4 Hz, 2 H); HRMS (ES)$^+$ calcd for $C_{10}H_{13}INO$ $(M+H)^+$ 290.0042, found 290.0040. HPLC: t_R = 11.8 min.

3-Iodobenzoic Acid TFP Ester, 2e. A 11.62 g (44.35 mmol) quantity of 2,3,5,6-tetrafluorophenyl trifluoroacetate (TFP−OTFA) was added dropwise over 5 min to a solution containing 10 g (40.32 mmol) of 3-iodobenzoic acid, **2d**, Et_3N (6.74 mL, 48.38 mmol) and 30 mL of anhydrous DMF at ice−water temperature. After the addition was completed, the reaction mixture was stirred for 30 min, and the volatile materials were evaporated under vacuum. The crude product was purified by silica gel column (100 g) eluting with 5% ethyl acetate/hexanes to give 13.92 g (87%) of **2e** as a colorless solid, mp 67−68 °C; ^{1}H NMR ($CDCl_3$, 200 MHz) δ 7.06 (m, 1 H), 7.30 (t, J = 7.7, 8.1 Hz, 1 H), 8.03 (d, J = 8.1 Hz, 1 H), 8.18 (d, J = 7.7 Hz, 1 H), 8.54 (s, 1 H); HRMS (ES)$^+$ calcd for $C_{13}H_5F_4IO_2$ $(M)^+$ 395.9270, found 395.9283. HPLC: t_R = 15.6 min.

3-Tri-*n*-butylstannylbenzoic Acid TFP Ester, 2f. To a solution containing 1.0 g (2.52 mmol) of **1e** in 30 mL of anhydrous toluene was added 2.55 mL (5.04 mmol) of bis(tributyltin) followed by 29 mg (0.025 mmol) of tetrakis(triphenylphosphine)palladium(0). The reaction mixture was heated to reflux for 4 h, then cooled to room temperature, and the toluene was evaporated under vacuum. The resultant thick oil was purified by silica gel column (40 g, 5% ethyl acetate−hexanes) to give 1.22 g (86%) of **2f** as a colorless oil; ^{1}H NMR ($CDCl_3$, 300 MHz) δ 0.90 (t, J = 7.3 Hz, 9H), 1.12 (t, J = 8.0 Hz, 6H), 1.28−1.41 (m, 6H), 1.51−1.61 (m, 6H), 6.98−7.09 (m, 1H), 7.48 (t, J = 7.3 Hz, 1H), 7.78 (d, J = 7.3 Hz, 1H), 8.13 (d, J = 8.3 Hz, 1H), 8.28 (s, 1H); HPLC: t_R = 17.1 min.

***N*-Propyl-3-(tri-*n*-butylstannyl)benzamide, 2a.** A 25 mg (0.43 mmol) quantity of *n*-propylamine in 1 mL of anhydrous DMF was added dropwise to a solution containing 200 mg (0.36 mmol) of **2f** in 3 mL of anhydrous DMF. The reaction mixture was stirred at room temperature for 30 min, and was then triturated with water. The water was decanted, the oily product was washed with additional water, then dried under vacuum to yield 154 mg (95%) of **2a** as a colorless oil; ^{1}H NMR ($CDCl_3$, 300 MHz) δ 0.88 (t, J = 7.3 Hz, 9H), 0.99 (t, J = 7.3 Hz, 3H), 1.08 (t, J = 7.8, 8.3 Hz, 6H), 1.27−1.39 (m, 6H), 1.48−1.71 (m, 14H), 3.39−3.46 (m, 2H), 6.16 (br s, 1H), 7.36 (t, J = 7.8, 7.3 Hz, 1H), 7.57 (d, J = 7.3 Hz, 1H), 7.63 (d, J = 7.8 Hz, 1H), 7.86 (s, 1H); HRMS (ES)$^+$ calcd for $C_{22}H_{40}NOSn$ $(M+H)^+$ 454.2132, found 454.2131. HPLC: t_R = 18.1 min.

3-Iodo-*N*-propylbenzamide, 2b. To a solution containing 0.50 g (1.26 mmol) of **2e** in 4 mL of anhydrous DMF at room temperature was added dropwise 0.09 g of (1.51 mmol) *n*-propylamine in 1 mL of anhydrous DMF. The reaction mixture was stirred at room temperature for 30 min, then DMF was removed under vacuum. The residue was purified by silica gel column (30 g) eluting with 10% ethyl acetate/hexanes to yield 0.24 g (66%) of **2b** as a colorless solid, mp 86−87 °C; ^{1}H NMR ($CDCl_3$, 200 MHz) δ 0.98 (t, J = 7.7, 7.3 Hz, 3 H), 1.64 (m, 2 H), 3.41 (q, J = 6.6, 7.0, 6.6 Hz, 2 H), 6.15 (s, 1 H), 7.16 (t, J = 8.1, 7.7 Hz, 1 H), 7.71 (d, J = 8.1 Hz, 1 H), 7.81 (d, J = 7.7 Hz, 1 H), 8.09 (s, 1 H); HRMS (FAB$^+$) calcd for $C_{10}H_{12}INO$ $(M)^+$ 288.9963, found 288.9958. HPLC: t_R = 12.7 min.

4-Tri-*n*-butylstannylhippuric Acid Ethyl Ester, 3a. A 0.15 g (1.07 mmol) quantity of glycine ethyl ester hydrochloride was added slowly to a solution containing 0.50 g (0.89 mmol) of **1f** and 0.19 mL (1.34 mmol) of Et_3N in 5 mL of anhydrous DMF at room temperature. The reaction mixture was stirred at room temperature for 30 min, then the volatile materials were removed under vacuum. The crude residue was purified by silica gel column (30 g, 5% ethyl acetate/hexanes) to yield 0.39 g (88%) of **3a** as a colorless oil; ^{1}H NMR ($CDCl_3$, 300 MHz) δ 0.88 (t, J = 7.3 Hz, 9H), 1.08 (t, J = 7.8, 8.3 Hz, 6H), 1.26−1.39 (m, 9H), 1.48−1.64 (m, 6H), 4.23−4.30 (m, 4H), 6.68 (br s, 1H), 7.55 (d, J = 7.8 Hz, 2H), 7.74 (d, J = 7.8 Hz, 2H); HRMS (ES)$^+$ calcd for $C_{23}H_{40}NO_3Sn$ $(M+H)^+$ 498.2030, found 498.2028. HPLC: t_R = 17.5 min.

4-Iodohippuric Acid Ethyl Ester, 3b. To a solution containing 0.50 g (1.26 mmol) of **1e** and 0.21 g (1.51 mmol) of glycine ethyl ester hydrochloride in 5 mL of anhydrous DMF at room temperature was added 0.26 mL (1.89 mmol) of Et_3N dropwise. The resultant solution was stirred at room temperature for 30 min. The volatile materials were removed under vacuum, then the residue was purified by silica gel column (30 g) eluting with 10% ethyl acetate/hexanes to yield 0.37 g (88%) of **3b** as a colorless solid**,** mp = 123−124 °C; ^{1}H NMR ($CDCl_3$, 300 MHz) δ 1.32 (t, J = 7.3, 6.7 Hz, 3 H), 4.21−4.30 (m, 4 H), 6.70 (s, 1 H), 7.53 (d, J = 8.3 Hz, 2 H), 7.79 (d, J = 8.3 Hz, 2 H); HRMS (ES)$^+$ calcd for $C_{11}H_{13}NO_3I$ $(M+H)^+$ 333.9940, found 333.9938. HPLC: t_R = 11.8 min.

4-Tri-*n*-butylstannylhippuric Acid, 4a. A 0.30 g quantity (0.60 mmol) of **3a** was dissolved in 5 mL of methanol, then 0.10 g (1.81 mmol) of KOH in 5 mL of water was added. The reaction mixture was stirred at 60 °C for 1 h, then allowed to cool to room temperature. A 60 mL quantity of water was added and the resulting solution was acidified with 3 mL of 1 N HCl. After stirring of the sample at room temperature for additional 10 min, the solution was filtered and washed with 200 mL of water. The remaining oily product (isolated on filter paper) was dissolved in 20 mL of EtOAc, and the EtOAc was evaporated under vacuum to yield 0.26 g (92%) of **4a** as a colorless oil; ^{1}H NMR ($CDCl_3$, 300 MHz) δ 0.88 (t, J = 7.3, 7.3 Hz, 9 H), 1.07 (t, J = 7.8, 8.3 Hz, 6 H), 1.25−1.41 (m, 6 H), 1.47−1.68 (m, 6 H), 4.19 (d, J = 5.2 Hz, 1 H), 6.30 (br s, 1 H), 6.98 (s, 1 H), 7.53 (d, J = 7.8 Hz, 2 H), 7.73 (d, J = 7.8 Hz, 2 H); HRMS (ES)$^+$ calcd for $C_{21}H_{36}NO_3Sn$ $(M+H)^+$ 470.1717, found 470.1737. HPLC: t_R = 16.8 min.

4-Iodohippuric Acid, 4b. A reaction mixture containing 0.20 g (0.60 mmol) of **3b** and 0.10 g (1.81 mmol) of KOH in a mixture of 5 mL of methanol and 5 mL of H_2O was stirred at 60 °C for 1 h. After the solution cooled to room temperature, 60 mL of H_2O and 3 mL of 1 N HCl were added respectively with stirring. The resulting mixture was stirred at room temperature for 10 min, filtered, washed with 500 mL of water, then dried under high vacuum to yield 0.16 g (87%) of **4b** as a colorless solid, mp = 188−189 °C; ^{1}H NMR (CD_3OD, 300 MHz) δ 4.08 (s, 1 H), 7.60 (d, J = 8.3 Hz, 2 H), 7.85 (d, J = 8.3 Hz, 2 H); HRMS (ES)$^+$ calcd for $C_9H_8INO_3$ $(M+Na)^+$ 327.9447, found 327.9448. HPLC: t_R = 10.1 min.

4-Pentynoic Acid TFP Ester, 5e. A 10 g (102 mmol) quantity of 4-pentynoic acid, **5d**, was dissolved in 350 mL of THF. To this solution was added 32 g (155 mmol) of DCC, then shortly thereafter 34 g (205 mmol) of 2,3,5,6-tetrafluorophenol (TFP-OH). A precipitate began forming immediately after the addition of the TFP-OH and the mixture turned light brown. The reaction mixture was stirred overnight at room temperature and 0.5

mL of HOAc was added. This mixture was stirred for 1 h, the precipitate was filtered, then washed with THF. The solvent was removed under vacuum, and the residue was dissolved in 400 mL of hexanes. The resulting precipitate was filtered and washed with 50 mL of hexanes. The hexane was removed under vacuum and the resulting residue was dissolved in 5 mL of EtOAc/120 mL of hexane. That solution was washed 5× with 100 mL of 10% $NaHCO_3$. The hexane solution was dried with $MgSO_4$ and evaporated under vacuum to yield 20.5 g (82%) of **5e**. An analytical sample was prepared by sublimation in a Kugelrohr apparatus to yield a colorless solid, mp 47−49 °C; ^{1}H NMR (CD_3OD, 500 MHz) δ 2.36 (t, J = 2.5 Hz, 1H), 2.60−2.63 (m, 2H), 2.95 (t, J = 7.1 Hz, 2H), 7.40−7.47 (m, 1H); LRMS (EI$^+$) calcd for $C_{11}H_6F_4O_2$ (M)$^+$ 246, found, 246. HPLC: t_R = 13.4 min.

3-(*closo*-Carboranyl)propionate TFP Ester, 5f. A 5.0 g (39.0 mmol) quantity of decaborane was dissolved in 40 mL of CH_3CN and refluxed for 30 min. To that solution was added 9.6 g (40.9 mmol) of **5e**, then the reaction mixture was stirred at reflux for 25 h. The mixture was allowed to cool to room temperature and a 2 g quantity of silica gel was added. That mixture was stirred for 1 h and filtered and the CH_3CN was removed under vacuum. The crude product was sublimed (170 °C) on a Kugelrohr apparatus to yield 7.2 g (50%) of **5f** as a colorless solid, mp 135−136 °C; ^{1}H NMR (CD_3OD, 500 MHz) δ 1.46−2.72 (m, 10H), 2.76 (t, J = 7.4 Hz, 2H), 3.00 (t, J = 7.4 Hz, 2H), 7.39−7.46 (m, 1H); ^{11}B NMR (CD_3OD, decoupled, 160.46 MHz) δ −0.91 (1B), −4.12 (1B), −7.85 (2B), −10.03 (4B), −11.26 (2B) (all peaks split in ^{1}H coupled spectrum); LRMS (EI)$^+$ Calcd for $C_{11}H_{16}B_{10}O_2F_4$ (M)$^+$ 364, found 364; HPLC: t_R = 15.2 min.

3-(*closo*-Carboranyl)propionic Acid, 5g. A 2.5 g (6.9 mmol) quantity of **5f** was added to a mixture containing 2.5 g (44.6 mmol) of KOH in 25 mL of EtOH. The resultant mixture was stirred at room temperature for 1 h, and the EtOH was removed under vacuum. The residue was dissolved in H_2O and 1 N HCl was added until a pH of 4 was obtained. The precipitate was filtered, washed with H_2O, and dried over P_2O_5 under high vacuum to yield 1.4 g (94%) of **5g** as a colorless solid, mp 148−149 °C; ^{1}H NMR (CD_3OD, 500 MHz) δ 1.53−2.91 (m, 10H), 2.49−2.53 (m, 2H), 2.57−2.61 (m, 2H), 4.56 (s, 1H); ^{11}B NMR (CD_3OD, decoupled, 160.46 MHz) δ −1.96 (1B), −5.25 (1B), −9.01 (2B), −11.21 (4B), −12.37 (2B) (all peaks split in ^{1}H coupled spectrum); HRMS (EI)$^+$ calcd for $C_5H_{15}B_{10}O_2Na_2$ (M−H+2Na)$^+$ 263.1798, found 263.1798; HPLC: t_R = 13.6 min.

3-(*nido*-Carboranyl)propionic Acid, 5a. A 350 mg quantity (1.62 mmol) of **5g** was dissolved in 1 mL of pyrrolidine at 0 °C, then allowed to come to room temperature. The mixture bubbled vigorously. After stirring of the sample for 30 min at room temperature, the pyrrolidine was removed under vacuum. The pyrrolidine salt was dissolved in H_2O/MeOH and was eluted on an Amberlite IR-120 ion exchange column (2.5 × 15 cm; pretreated with saturated NaCl, washed with H_2O, then MeOH). The effluent was collected and 10 mL of 25% Me_4NCl was added. The MeOH was removed and the precipitate was collected and dried to yield 292 mg (88%) of **5a** as the Me_4N salt, mp 291 °C (dec); ^{1}H NMR (CD_3OD, 500 MHz) δ 0.82−2.29 (m, 13H), 2.47−2.59 (m, 1H), 3.49 (t, J = 6.8 Hz, 1H), 3.68−3.87 (m, 2H); ^{11}B NMR (CD_3OD, decoupled, 160.46 MHz) δ −10.83 (1B), −11.42 (1B), −13.25 (1B), −15.25 (1B), −18.06 (1B), −19.31 (1B), −20.62 (1B), −32.64 (1B), −36.91 (1B) (all peaks split in ^{1}H coupled spectrum); HRMS (EI)$^-$ calcd for $C_5H_{15}B_9O_2$ 206.2024 (M)$^-$, found 206.2039; HPLC: t_R = 11.7 min.

3-(Iodo-*nido*-carboranyl)propionic Acid, 5b. A 20 mg quantity of **5a** (0.116 mmol) was dissolved into 2 mL of 1% HOAc/MeOH. To that solution was added 17 mg (0.114 mmol) of NaI and 17.5 mg (0.131 mmol) of *N*-chlorosuccinimide (NCS) and the reaction mixture was stirred for 5 min. The MeOH was then removed and the crude product was taken up into 4 mL of EtOAc. The organic layer was washed with water (2 × 4 mL), concentrated, and dried under vacuum to yield 28 mg (86%) of **5b** as a tacky solid. ^{1}H NMR (CD_3OD, 500 MHz) δ 1.23 (s, 1H), 1.87−2.23 (m, 6H), 2.67 (t, J = 6.7 Hz, 2H), 3.53−3.62 (m, 1H), 3.68−3.77 (m, 1H), 3.89−3.96 (m, 2H); ^{11}B NMR (CD_3OD, decoupled, 160.46 MHz) δ −6.77 (1B), −13.99 (1B), −16.02 (1B), −17.39 (1B), −20.74 (1B), −23.75 (1B), −29.76 (1B), −36.68 (2B); LRMS (EI)$^-$ calcd for $C_5H_{20}B_9IO_5$ [M+3(H_2O)] 386, found 386; HPLC: t_R = 13.3 min.

3-(*nido*-Carboranyl)-*N*-propyl-propionamide, 6a. To a solution containing 0.20 g (0.55 mmol) of **5f** in 2 mL of anhydrous DMF at room temperature was added dropwise a solution containing 0.09 mL (1.10 mmol) of *n*-propylamine in 1 mL of anhydrous DMF. After the reaction was stirred at room temperature for 30 min, the solution was triturated with H_2O (100 mL), then stirred for additional 10 min. The H_2O was decanted, the residue was washed with water (2 × 100 mL), and subsequently dried under vacuum to yield a residue containing **6d.** The isolated residue was used directly in the subsequent step.

A 5 mL quantity of pyrrolidine was added to dissolve the residue, and the resultant solution was stirred at room temperature for 30 min. Pyrrolidine was evaporated at room temperature under a stream of argon, and the residue was dried under vacuum to yield 150 mg (86%) of **6a** as a tacky solid (pyrrolidine salt). ^{1}H NMR (CD_3OD, 300 MHz) δ 0.92 (t, J = 7.3 Hz, 3H), 1.47−1.59 (m, 2H), 1.66−1.93 (m, 6H), 1.96−2.00 (m, 4H), 2.29 (t, J = 7.8 Hz, 2H), 3.10 (t, J = 7.3 Hz, 2H), 3.18−3.22 (m, 4H); ^{11}B NMR (CD_3OD, decoupled, 96.3 MHz) δ −10.72 (2B), −13.18 (1B), −16.28 (1B), −18.13 (2B), −21.19 (1B), −32.80 (1B), −36.83 (1B); HRMS (ES$^-$) calcd for $C_8H_{23}B_9NO$ (M)$^-$ 248.2617, found 248.2618. HPLC: t_R = 8.1 min.

3-(Iodo-*nido*-carboranyl)-*N*-propyl-propionamide, 6b. A 2.7 mg (0.02 mmol) quantity of *N*-chlorosuccinimide in 0.5 mL of MeOH was added to a mixture containing 3.1 mg (0.02 mmol) of NaI and 6.3 mg (0.02 mmol) of **6a** in 5 mL of 5% HOAc/MeOH. The resulting solution was stirred at room temperature for 30 s, then 3.9 mg (0.02 mmol) of sodium metabisulfite in 0.5 mL of H_2O was added to quench the reaction (HPLC indicated ∼100% yield). As this compound was used only as an HPLC standard, an analytical sample of **6b** was obtained by HPLC purification. HRMS (ES$^-$) calcd for $C_8H_{22}B_9INO$ (M)$^-$ 374.1584, found 374.1579. HPLC: t_R = 10.8 min.

***N*-(3-Aminophenyl)-3-(*closo*-carboranyl)propionamide, 7d.** A 1.0 g (2.72 mmol) quantity of **5f** was dissolved in 20 mL of DMF. In a separate flask, 0.59 g (5.43 mmol) of 1,3-phenylenediamine was dissolved in 20 mL of DMF. The solution containing **5f** was then added dropwise to the solution of 1,3-phenylenediamine over a 1 h period. After addition was complete, reaction was allowed to stir for 2.5 h. The DMF was removed on a Kugelrohr apparatus under vacuum at 50 °C. The residue was dissolved into 50 mL of ether and washed by 1% HOAc/H_2O (2 × 25 mL), then with H_2O (1 × 25 mL). Ether was removed under vacuum, and was dried under vacuum to yield 0.79 g (95%) of **7d** as a colorless solid, mp 105−108 °C; ^{1}H NMR ($CDCl_3$, 500 MHz) δ 1.54−2.81 (m, 10H), 2.18 (s, 2H), 2.57 (t, J = 7.1 Hz, 2H), 2.68 (t, J

= 7.1 Hz, 2H), 3.51 (s,1H), 6.4 (dd, J = 1.8, 8.0 Hz, 1H), 6.5−6.6 (m, 1H), 6.6 (d, J = 8.0 Hz, 1H), 7.0 (t, J = 8.0 Hz, 2H), 7.0 (t, J = 1.8 Hz, 2H), 7.1 (s, 1H); ^{11}B NMR (CD_3OD, decoupled, 160.46 MHz) δ −2.0(1B), −5.2(1B), −9.1(2B), −10.9(4B), −12.3(2B); all peaks split in ^{1}H coupled spectrum; HRMS (ES^+) calcd for $C_{11}H_{22}B_{10}N_2ONa$ $(M+Na)^+$ 331.2560, found 331.2562; HPLC: t_R = 13.5 min.

***N*-(3-Aminophenyl)-3-(*nido*-carboranyl)propionamide, 7e.** A 600 mg (1.95 mmol) quantity of **7d** was dissolved in neat pyrrolidine (2.9 mL) and stirred for 1 h. Excess pyrrolidine was evaporated under a stream of air and the residue was washed with ether (2 × 50 mL), decanting the ether after each washing. Residue was dissolved a minimal amount of H_2O/CH_3CN/MeOH (5:4:1) and that solution was loaded onto preequilibrated ion exchange columns. In the column preparation, two Alltech IC−H ion exchange columns (IC−H, Alltech Associates, Inc.) were connected in series and washed with 10 mL of 1 N NaOH, then with water until the column reached neutral pH, and finally with 20 mL of eluants (H_2O/CH_3CN/MeOH; 5:4:1). The column was eluted in 1 mL fractions of eluant (20×). Fractions containing **7e** were collected and volatile solvents were removed under vacuum. The remaining aqueous solution was washed with CH_2Cl_2 (2 × 25 mL), and then a saturated solution of $(CH_3)_4NCl$ was added. The colorless precipitate was collected by filtration and dried under vacuum to yield 205 mg (36%) of **7e** as the $(CH_3)_4N$ salt: mp 28−30 °C; ^{1}H NMR (CD_3OD, 500 MHz) δ 1.5−2.2 (m, 9H) 2.46 (m, 3H), 3.1 (s, 12H), 3.3 (m, 1H), 6.4 (dd, J = 1.2, 8.0 Hz, 1H), 6.8 (dd, J = 1.2, 8.0 Hz, 1H), 7.0 (t, J = 8.0 Hz, 2H); ^{11}B NMR (CD_3OD, decoupled, 160.46 MHz) −10.2(2B), −12,8(1B), −15.8(1B), −17.5(1B), −18.1(1B), −20.8(1B), −32.4(1B), −36.4(1B); all peaks split in ^{1}H coupled spectrum; HRMS $(ES)^-$ calcd for $C_{11}H_{21}B_9N_2O$ $(M)^-$ 296.2487, found 296.2481; HPLC: t_R = 8.5 min.

3-(*nido*-Carboranyl)-*N*-(3-isothiocyanatophenyl)-propionamide, 7f. A 50 mg (0.16 mmol) quantity of **7e** was dissolved in 2 mL of DMF and 24.3 mg (0.16 mmol) of 1,1-thiocarbonyldiimidazole was added. The reaction was stirred for 0.5 h and the DMF was removed under vacuum. The residue was dissolved in a minimal amount of MeOH, then loaded onto a preparative TLC plate (60 F_{254}, 20 cm × 20 cm × 2 mm, EM Science). The plate was eluted with hexanes/ethyl acetate (9:1). The silica at the origin was removed and washed with MeOH. The MeOH was removed under vacuum and the remaining solid was dried under high vacuum to yield 49 mg (87%) of **7f** as a tacky brown solid, mp 22−24 °C; ^{1}H NMR (CD_3OD, 500 MHz) δ 1.45−1.75 (m, 2H), 1.83 (s, 1H), 1.92−2.00 (m, 2H), 2.03−2.09 (m, 2H), 2.12−2.22 (m, 1H), 2.37−2.49 (m, 1H), 2.52−2.62 (m, 4H), 3.27 (s, 12H), 6.56 (dd, J = 2.2, 8.0 Hz, 1H), 6.91 (d, J = 8.0 Hz, 1H), 7.11 (t, J = 8.0 Hz, 1H), 7.13 (s, 1H); ^{11}B NMR (CD_3OD, decoupled, 160.46 MHz) −7.8(2B), −12.3(1B), −15.2(1B), −17.1(1B), −17.8(1B), −20.3(1B), −31.9(1B), −35.9(1B); all peaks split in ^{1}H coupled spectrum; LRMS $(ES)^-$ calcd for $C_{12}H_{19}B_9N_2OS$ $(M)^-$ 338.2, found 338.3; HPLC: t_R = 14.8 min.

3-(*nido*-Carboranyl)-*N*-[3-(3-propylthioureido)-phenyl]propionamide, 7a. To a solution containing 48 mg (0.16 mmol) of **7e** in 2 mL of anhydrous DMF at room temperature was added 35 mg (0.20 mmol) of 1,1′-thiocarbonyldiimidazole. The resulting mixture was stirred at room temperature for 30 min, then 28 μL (0.34 mmol) of *n*-propylamine was added and the solution was stirred for another 10 min. A 30 mL quantity of diethyl ether was added to the reaction solution, which was stirred for an additional 30 min at room temperature. The solvents were decanted, the residue was washed with diethyl ether (2 × 30 mL), then dried under high vacuum to yield 60 mg (93%) of **7a** as a colorless tacky solid. ^{1}H NMR (CD_3OD, 300 MHz) δ 0.92 (t, J = 7.3, 7.8 Hz, 3H), 1.18 (t, J = 6.7, 7.3 Hz, 2H), 1.56−1.73 (m, 2H), 1.82−2.30 (m, 6H), 2.49 (t, J = 7.8 Hz, 1H), 2.86−2.95 (m, 1H), 3.29−3.32 (m, 4H), 3.39−3.75 (m, 4H), 7.27 (d, J = 1.0 Hz, 2H), 7.30−7.39 (m, 1H), 8.19 (s, 1H); ^{11}B NMR (CD_3OD, decoupled, 96.3 MHz) δ −10.82 (2B), −13.46 (1B), −16.45 (1B), −18.46 (2B), −21.60 (1B), −33.46 (1B), −37.42 (1B); HRMS $(ES)^-$ calcd for $C_{15}H_{28}B_9N_3OS$ $(M)^-$ 397.2791, found 397.2801. HPLC: t_R = 9.6 min.

3-(Iodo-*nido*-carboranyl)-*N*-[3-(3-propylthioureido)phenyl]propionamide, 7b. To a stirred solution containing 9.3 mg (0.02 mmol) of **7a** in 5 mL of 5% HOAc/MeOH, was added 3.1 mg (0.02 mmol) of NaI and 2.7 mg (0.02 mmol) of *N*-chlorosuccinimide, respectively. The reaction mixture was stirred at room temperature for 30 s, then 3.9 mg (0.02 mmol) of sodium metabisulfite was added to quench the reaction (HPLC indicated that a yield of 41% was obtained). As this compound was used only as an HPLC standard, an analytical sample of **7b** was obtained by HPLC purification; t_R = 11.0 min. HRMS $(ES)^-$ calcd for $C_{15}H_{28}B_9IN_3OS$ $(M)^-$ 524.1835, found 524.1824.

1-Phenylcarborane, 8d. (A modified procedure from that previously reported (*40*) was used.) To 5.0 g (41 mmol) of decaborane in 60 mL of anhydrous CH_3CN was added 4.18 g (41 mmol) of phenylacetylene slowly over a period of 3 h. The resulting solution was refluxed for 24 h. After cooling the samples to room temperature, the CH_3CN was removed and the residue was sublimed to give 6.4 g (71%) of **8d** as a colorless solid, mp = 67−69 °C. HPLC: t_R = 15.3 min.

4-Carboranyl-1-nitrobenzene, 8e. (A modified procedure from that previously reported (*40*) was used.) A 1.50 g (6.81 mmol) quantity of **8d** in 30 mL of CH_2Cl_2 was added to a stirred solution of 15% concentrated HNO_3 in concentrated H_2SO_4. The resultant reaction mixture was stirred at room temperature for 20 h. The CH_2Cl_2 portion was separated and washed with H_2O (2 × 50 mL), dried over anhydrous Na_2SO_4, then evaporated to a solid residue. The crude residue was crystallized from CCl_4 three times to yield 0.83 g (46%) of **8e** as a light yellow solid, mp = 165−167 °C (reported 167−168 °C (*40*)). HPLC: t_R = 15.2 min.

4-Carboranylaniline, 8f. A solution containing 0.5 g (1.88 mmol) **8e** in 30 mL of EtOH was stirred with 50 mg of 10% Pd/C catalyst under 40 psi H_2 pressure (Parr Hydrogenation apparatus) for 16 h at room temperature. After removal of the remaining H_2 and filtration of the catalyst, the EtOH was removed under vacuum to yield 0.42 g (95%) **8f** as a colorless solid, mp = 102−104 °C (reported 104−105 °C (*40*)). HPLC: t_R = 14.3 min.

4-(*nido*-Carboranyl)aniline, 8g. A 100 mg (0.42 mmol) quantity of **8f** was dissolved in 3 mL of neat pyrrolidine and the resultant solution was stirred at room temperature for 30 min. The pyrrolidine was removed under vacuum to yield 125 mg (100%) of **8g** as a light yellow tacky solid (pyrrolidine salt) (reported mp = 155−156 °C as the Me_4N salt (*28*)). HPLC: t_R = 8.3 min.

1-(4-*nido*-Carboranylphenyl)-3-propylthiourea, 8a. A 44.6 mg (0.25 mmol) quantity of 1,1′-thiocarbonyldiimidazole was added to a stirred solution containing 50 mg (0.17 mmol) of **8g** (pyrrolidine salt) in 3 mL of anhydrous DMF, then the reaction mixture was allowed to be stirred at room temperature for 30 min. The 4-(*nido*-

carboranyl)phenylisothiocyanate, **8h**, formed was used without purification in the next reaction step.

A 28 μL (0.34 mmol) quantity of *n*-propylamine was added to the crude reaction mixture containing **8h**, and that resultant mixture was stirred for another 10 min at room temperature. After that time, 30 mL of diethyl ether was added to the reaction mixture, and it was stirred for an additional 30 min. The solvents were decanted, the residue was washed with diethyl ether (2 × 30 mL), and the residue was dried under high vacuum to yield 57 mg (85%) of **8a** as a colorless tacky solid. ^{1}H NMR (CD_3OD, 300 MHz) δ 0.90 (t, J = 7.3 Hz, 2H), 1.01 (t, J = 7.3 Hz, 3H), 1.52−1.74 (m, 6H), 2.17 (s, 1H), 6.98 (d, J = 8.3 Hz, 2H), 7.21 (d, J = 8.8 Hz, 2H); ^{11}B NMR (CD_3OD, decoupled, 96.3 MHz) δ −8.70 (1B), −10.34 (1B), −13.36 (1B), −16.38 (1B), −17.80 (1B), −19.42 (1B), −22.44 (1B), −32.65 (1B), −35.79 (1B); HRMS (ES)$^-$ calcd for $C_{12}H_{24}B_9N_2S$ (M)$^-$ 327.2498, found 327.2535. HPLC: t_R = 8.7 min.

1-(Iodo-4-*nido*-carboranylphenyl)-3-propylthiourea, 8b. A 7.9 mg (0.02 mmol) quantity of **8a** and 3.1 mg (0.02 mmol) of NaI were dissolved in 5 mL of 5% HOAc/MeOH at room temperature. To that solution was added 2.7 mg (0.02 mmol) of *N*-chlorosuccinimide in 0.5 mL of methanol. After the addition was complete, the reaction solution was stirred at room temperature for 30 s, then 3.9 mg (0.02 mmol) of sodium metabisulfite in 0.5 mL of H_2O was added to quench the reaction. The reaction mixture had several products by HPLC analysis with only 35% yield in the peak identified as **8b** by mass spectral analysis. An analytical sample of **8b** was obtained by HPLC purification. HRMS (ES)$^-$ calcd for $C_{12}H_{23}B_9IN_2S$ (M)$^-$ 453.1464, found 453.1476. HPLC: t_R = 11.8 min.

4-(Iodo-*nido*-carboranyl)aniline, 9b. A 5.9 mg (0.02 mmol) quantity of **8g** and 3.1 mg (0.02 mmol) of NaI were dissolved at room temperature in 5 mL of 5% HOAc in MeOH, then 2.7 mg (0.02 mmol) of *N*-chlorosuccinimide in 0.5 mL of MeOH was added. Following the additions, the reaction mixture stirred at room temperature for 30 s, then 3.9 mg (0.02 mmol) of sodium metabisulfite was added to quench the reaction. A quantitative yield was obtained. As this compound was used only as an HPLC standard, an analytical sample of **9b** was obtained by HPLC purification. HRMS (ES)$^-$ calcd for $C_8H_{16}B_9IN$ (M)$^-$ 352.1165, found 352.1180. HPLC: t_R = 10.7 min.

1-(4-*closo*-Carboranylphenyl)-3-propylurea, 10e. To a solution containing 40 mg (0.17 mmol) of **8f** in 2 mL of $CHCl_3$ was added 55 mg (0.34 mmol) of 1,1′-carbonyldiimidazole. The reaction solution was stirred at room temperature for 2 h and 5 mL of H_2O was added. The reaction mixture was stirred for an additional 10 min, then the $CHCl_3$ layer was separated. A 28 μL (0.34 mmol) quantity of *n*-propylamine was added to the crude isocyanate (**10d**) solution, and it was stirred at room temperature for 30 min. The $CHCl_3$ and excess *n*-propylamine were evaporated under a stream of argon, and the crude product was purified on silica gel (12 g) eluted with 30% ethyl acetate−hexanes to provide 45 mg (83%) of colorless solid, mp 101−102 °C. ^{1}H NMR (CD_3OD, 300 MHz) δ 0.94 (t, J = 7.3 Hz, 3H), 1.47−1.59 (m, 2H), 1.71−3.02 (m, br, 10H), 3.14 (t, J = 7.3 Hz, 2H), 7.34 (d, J = 8.8 Hz, 2H), 7.42 (d, J = 8.8 Hz, 2H); ^{11}B NMR (CD_3OD, decoupled, 96.3 MHz) δ −1.75 (1B), −2.36 (1B), −8.16 (2B), −8.85 (2B), −10.14 (3B), −12.01 (1B); HRMS (ES$^+$) calcd for $C_{12}H_{25}B_{10}N_2O$ (M+H)$^+$ 323.2897, found 323.2892. HPLC: t_R = 14.8 min.

1-(4-*nido*-Carboranylphenyl)-3-propylurea, 10a. A 20 mg (0.062 mmol) quantity of **10e** was dissolved in 2 mL of neat pyrrolidine and that solution was stirred at room temperature for 1 h. The pyrrolidine was evaporated under a stream of argon. The residue containing crude *nido*-carborane was washed with diethyl ether (2 × 20 mL), dried under vacuum to give **10a** as a light-yellow tacky solid (pyrrolidine salt). Yield 24 mg (∼100%). ^{1}H NMR (CD_3OD, 300 MHz) δ 0.93 (t, J = 7.3, 7.8 Hz, 3H), 1.48−1.58 (m, 2H), 1.86−1.90 (m, 4H), 2.00−2.28 (m, 4H), 2.87−2.92 (m, 1H), 3.03−3.14 (m, 6H), 3.30 (s, 2H), 3.40−3.71 (m, 3H), 7.04 (d, J = 8.8 Hz, 2H), 7.08 (d, J = 8.8 Hz, 2H); ^{11}B NMR (CD_3OD, decoupled, 96.3 MHz) δ −8.87 (1B), −10.29 (1B), −13.11 (1B), −16.17 (1B), −18.00 (2B), −21.88 (1B), −32.19 (1B), −35.59 (1B); HRMS (ES)$^-$ calcd for $C_{12}H_{24}B_9N_2O$ (M)$^-$ 311.2726, found 311.2725. HPLC: t_R = 10.5 min.

1-(Iodo-4-*nido*-carboranylphenyl)-3-propylurea, 10b. An 83 μL (6.2 μmol) aliquot of a 10 mg/mL solution of *N*-chlorosuccinimide in MeOH was added with stirring to a vial containing 300 μL of a MeOH/5% HOAc solution containing 2.4 mg (6.2 μmol) of **10a** and 10 μL (6.2 μmol) of a solution containing 100 mg/mL NaI in H_2O. After the reaction mixture was stirred at room temperature for 30 s, 119 μL (6.2 μmol) of a 10 mg/mL sodium metabisulfite in H_2O was added to quench the reaction. Pure **10b** was collected from HPLC; t_R = 14.1 min. HRMS (ES)$^-$ calcd for $C_{12}H_{23}B_9IN_2O$ (M)$^-$ 437.1693, found 437.1693.

Bis-(*nido*-Carboranylmethyl)benzene, 11a. [C_6H_4-*bis*-(CH_2-7,8-$C_2B_9H_{10}$)$_2$]$^{2-}$ 2($N(CH_3)_3H$)$^+$, (11a). To a solution containing 3.60 g (9.10 mmol) of **11g** in 85 mL of 95% ethanol was added 3.10 g (54.7 mmol) of KOH pellets. The solution was heated at reflux overnight followed by cooling to ambient temperature and subsequent addition of 4.10 g (93.0 mmol) CO_2. The carbonate was filtered and the solids were washed with 95% ethanol (3 × 100 mL). The extracts were combined and concentrated under vacuum. The crude solids were dissolved in 30 mL water and added to an aqueous solution containing 1.90 g (20.1 mmol) Me_3NHCl. The solids were collected by filtration and dried to give 3.60 g (7.30 mmol) of **11a** (80% yield). IR (Nujol, cm^{-1}) 3139 (s), 3072 (w), 2926 (s), 2505 (s), 1413 (w), 1315 (w), 1256 (w), 1075 (w), 1028 (m), 976 (s), 804 (w), 762 (m), 735 (m); ^{1}H NMR ((CD_3)$_2$CO, 200.13 MHz) δ 8.38 (s, br, 2H), 7.16 (m, 4H), 4.25 (s, 2H), 3.09 (s 18H), 2.88 (m, 4H); ^{13}C NMR ((CD_3)$_2$-CO, 50.32 MHz) δ 141.4, 129.7, 125.8, 46.1, 42.7; ^{11}B NMR ((CH_3)$_2$CO, 160.46 MHz) δ −9.39 (d, 2B), −10.57 (d, 2B), −13.08 (d, 2B), −15.78 (d, 2B), −18.40 (d, 2B), −19.73 (d, 2B), −32.81 (d, 2B), −36.33 (d, 2B); LRMS (FAB$^-$) calcd for $C_{12}H_{30}B_{18}$, 368.97, found 368.34.

[Iodo-bis-(*nido*-Carboranylmethyl)]benzene, 11b. To 4.2 mg (4.9 μmol) of **11a** dissolved in 4.2 mL of 5% HOAc/MeOH, was added 7.3 μL of a 100 mg/mL in H_2O solution of NaI (4.9 μmol), then 65 μL of a 10 mg/mL in MeOH solution of *N*-chlorosuccinimide (4.9 μmol). After the reaction mixture was stirred at room temperature for 30 s, 93 μL of a 10 mg/mL in H_2O solution of sodium metabisulfite was added to quench the reaction. Yield was ∼100%. An analytical sample of **11b** was obtained by collection from HPLC. LRMS (ES)$^-$ calcd for $C_{12}H_{26}B_{18}I$ (M-2H)$^-$ 495.3, found 495.3. HPLC: t_R = 13.6−13.8 min.

3,4-Bis-(*closo*-carboranylmethyl)nitrobenzene, 11h; *m*-NO_2-C_6H_3-*bis*-(CH_2-1,2-$C_2B_{10}H_{11}$)$_2$, (11h). To a solution of 35.1 g (89.8 mmol) of **11g** in 1 L of CH_2Cl_2 was added a mixture of concentrated H_2SO_4 (380 mL) and HNO_3 (70 mL) at 0° C. This solution warmed to ambient temperature and was stirred for 2 days. The aqueous layer was decanted off and extracted with CH_2Cl_2 (3 × 400 mL). The organic phases were combined and con-

centrated under vacuum. The crude product was purified by column chromatography on silica gel with diethyl ether/hexane (1:3) as the eluting solvent. The collected fractions afforded 36.8 g (84.6 mmol) of **11h** as a yellow solid (94% yield), mp 110−112° C. IR (Nujol, cm^{-1}) 3056 (s), 2941 (s), 2570 (s), 1620 (w), 1590 (w), 1513 (s), 1370 (w), 1330 (m), 1090 (w), 1065 (w), 1020 (m), 830 (m), 788 (s), 766 (m), 735 (m), 720 (w); ^{1}H NMR ($(CD_3)_2CO$, 200.13 MHz) δ 8.25 (d, J = 6.5 Hz, 1H), 8.24 (s, 1H), 7.70 (d, J = 9.3 Hz, 1H), 4.98 (s, 1H), 4.89 (s, 1H), 4.02 (s, 2H), 4.00 (s, 2H); ^{13}C NMR ($(CD_3)_2CO$, 50.32 MHz) δ 148.3, 142.0, 137.0, 134.6, 127.7, 123.8, 75.0, 74.7, 63.4, 63.2, 39.9; ^{11}B NMR ($(CH_3)_2CO$, 160.46 MHz) δ −2.18 (d, 2B), −4.98 (d, 2B), −9.00 (d, 4B), −11.34 (d, 8B), −12.24 (d, 4B); LRMS (EI) calcd for $C_{12}H_{29}B_{20}NO_2$, 435.59, found 435.43.

3,4-Bis-(*closo*-carboranylmethyl)aniline, 11i; *m*-NH_2-C_6H_3-*bis*-$(CH_2$-1,2-$C_2B_{10}H_{11})_2$, (11i). To a solution of 26.0 g (59.6 mmol) of **11h** in 1 L of methanol was added 80 mL of concentrated HCl and 14.9 g of (126 mmol) tin metal. The reaction mixture was heated at reflux for 10 h, followed by stirring at ambient temperature overnight. The solvent was removed under vacuum, and to the residue was added 100 mL of diethyl ether. The pH of the mixture was neutralized by slow addition of aqueous sodium bicarbonate. An additional 400 mL of diethyl ether was added and the two-phase mixture was transferred to a separatory funnel. The layers were separated and the aqueous layer was extracted with diethyl ether (2 × 300 mL). The organic phases were combined and dried over $MgSO_4$. The yellow solution was filtered and concentrated under vacuum affording 16.1 g (39.7 mmol) of **11i** as a yellow solid (67% yield), mp 150−152° C. IR (Nujol, cm^{-1}) 3390 (w), 3056 (w), 2951 (s), 2577 (s), 1621 (s), 1583 (s), 1513 (w), 1331 (w), 1291 (w), 1018 (m), 816 (w), 725 (s); ^{1}H NMR ($(CD_3)_2CO$, 200.13 MHz) δ 6.96 (d, J = 8.2 Hz, 1H), 6.62 (dd, J = 8.2 Hz, 2.4 Hz, 2H), 6.55 (d, J = 2.3 Hz, 1H), 4.63 (s, 1H), 4.60 (s, 1H), 3.61 (s, 2H), 3.59 (s, 2H); ^{13}C NMR ($(CD_3)_2CO$, 50.32 MHz) δ 149.1, 135.3, 133.6, 122.6, 117.7, 115.1, 77.2, 76.1, 62.0, 61.9, 40.8, 40.2; ^{11}B NMR ($(CH_3)_2CO$, 160.46 MHz) δ −2.30 (d, 2B), −5.47, (d, 2B), −9.30 (d, 4B), −11.19 (d, 8B), −12.50 (d, 4B); LRMS (EI) calcd for $C_{12}H_{31}B_{20}N$, 405.61, found 406.00.

3,4-Bis-(*nido*-carboranylmethyl)aniline, 11j; [*m*-NH_2-C_6H_3-*bis*-$(CH_2$-7,8-$C_2B_9H_{10})_2]^{2-}$ $2Cs^+$, (11j). To a solution of 24.0 g (59.2 mmol) of **11i** in 550 mL of 95% ethanol was added 20.0 g (357 mmol) of KOH pellets. The solution was heated at reflux overnight followed by cooling to ambient temperature and subsequent addition of 20.0 g (455 mmol) of CO_2. The carbonate was filtered and the solids were washed with 95% ethanol (3 × 100 mL). The extracts were combined and concentrated under vacuum. The crude solids were dissolved in 75 mL of water and that solution was added to an aqueous solution containing 21.0 g (125 mmol) of CsCl. The solids were collected by filtration, dried, and recrystallized from hot water to give 30.8 g (47.4 mmol) of **11j** (80% yield), mp > 200° C (decomposes). IR (Nujol) 3340 (w), 3035 (w), 2951 (s), 2508 (s), 1604 (s), 1070 (w), 1028 (m), 724 (m); ^{1}H NMR (CD_3CN), 200.13 MHz) δ 7.04 (dd, J = 7.0, 1.3 Hz, 1H), 6.74 (s, 1H), 6.67 (dd, J = 8.1, 2.4 Hz, 1H), 2.80 (m, 4H), 1.70 (s, 2H); ^{13}C NMR (CD_3CN), 50.32 MHz) δ 142.9, 140.6, 140.5, 134.8, 134.7, 131.2, 131,1, 119.3, 119.2, 115.6, 60.5, 48.1, 42.6, 41.9; ^{11}B NMR ($(CH_3)_2CO$, 160.46 MHz) δ −9.03 (d, 2B), −10.20 (d, 2B), −12.66 (d, 2B), −15.21 (d, 2B), −17.02 (d, 4B), −20.97 (d, 2B), −32.44 (d, 2B), −35.94 (d, 2B); LRMS (negative ion FAB) calcd for $C_{12}H_{31}B_{18}N$, 383.99, found 384.53.

4-{[3,4-bis-(*nido*-carboranylmethyl)phenyl]ureido}-benzyl-DTPA, 12a. A 7.0 mg (0.043 mmol) of quantity of 1,1′-carbonyldiimidazole was added to a solution containing 20 mg (0.040 mmol) of **11j** $(NMe_3H)_2$ in 2 mL of anhydrous CH_3CN. The reaction mixture was stirred at room temperature for 1 h, and the CH_3CN was evaporated under a stream of argon. The residue containing the isocyanato derivative **11k** was redissolved in 2 mL of anhydrous DMF. To that solution was added 20 mg (0.031 mmol) of 4-aminobenzyl-diethylenetriaminepentaacetic acid hydrochloride salt and 20 μL of anhydrous pyridine, respectively. The resultant reaction mixture was stirred at room temperature for 16 h, and the volatile materials were evaporated under vacuum. The crude **12a** was redissolved in 2 mL of 1 N $NaHCO_3$ and purified by Sephadex G-15 gel column, eluting with water to afford 26 mg (58%) of **12a** as a colorless solid (Na salt). ^{1}H NMR (D_2O, 200 MHz) δ 1.97 (s, 2H), 2.91−2.94 (m, 1H), 3.07 (d, J = 1.8 Hz, 1H), 3.18 (s, 18H), 3.26−3.36 (m, 6H), 3.50−3.71 (m, 6H), 3.87−4.32 (m, 8H), 4.36 (s, 1H), 7.38−7.46 (m, 3H), 7.50 (d, J = 2.2 Hz, 1H), 7.55−7.64 (m, 2H), 7.67 (d, J = 2.2 Hz, 1H); ^{11}B NMR (D_2O, 160.46 MHz) d −12.20 (2B), −13.19 (2B), −15.06 (1B), −18.36 (2B), −20.83 (2B), −22.64 (1B), −34.48 (4B), −38.49 (4B); LRMS (MALDI$^-$) calcd for $C_{34}H_{59}B_{18}N_5O_{11}$ $(M)^-$ 911.6, found 911.7. HPLC: t_R = 9.1−9.3 min.

4-{[3,4-Bis-(iodo-*nido*-carboranylmethyl)phenyl]-ureido}benzyl-DTPA, 12b. A 100 μL (4.4 μmol) quantity of a 10 mg/mL aqueous solution of chloramine-T was added to a solution containing 5 mg (4.4 μmol) of **12a**, 6.6 μL (4.4 μmol) of a 100 mg/mL aqueous solution of NaI, and 5 mL of a 5% HOAc/ H_2O solution. The reaction mixture was stirred at room temperature for 30 s, and 84 μL (4.4 μmol) of a 10 mg/mL aqueous solution of sodium metabisulfite was added to quench the reaction. Pure **12b** was collected from HPLC. Yield was ∼100%. LRMS (MALDI$^-$) calcd for $C_{34}H_{57}B_{18}IN_5O_{11}$ $(M - H)^-$ 1036.5, found 1036.9. HPLC: t_R = 10.9−11.3 min.

3-(*closo*-Carboranyl)-*N*-{3-[(3-benzyl-DTPA)ureido]-phenyl}propionamide, 13e. 1,1′-Carbonyldiimidazole (5.3 mg, 0.033 mmol) was added to a solution containing *N*-(3-aminophenyl)-3-(*closo*-carboranyl)propionamide **7d** (10 mg, 0.033 mmol) and anhydrous chloroform (1 mL), and then the reaction mixture was stirred at room temperature for 1 h. After chloroform was evaporated with a stream of argon, the crude isocyanate **13d** was redissolved in anhydrous DMF (1 mL). 4-Aminobenzyl-diethylenetriaminepentaacetic acid hydrochloride salt (10 mg, 0.016 mmol) and pyridine (20 μL) were added, respectively, and the reaction solution was stirred at room temperature for 16 h. The solution was triturated with $CHCl_3$ (20 mL), filtered, washed with additional $CHCl_3$, and dried under high vacuum to afford **13e** as a colorless solid (57%). ^{1}H NMR (CD_3OD, 200 MHz) δ 2.57 (s, 10H), 2.96−3.34 (m, 6H), 3.39−3.80 (m, 8H), 4.49 (s, 1H), 7.13 (m, 3H), 7.29 (t, J = 8.0 Hz, 1H), 7.46 (s, 2H), 7.67 (m, 1H), 8.76 (s, 1H); ^{11}B NMR (CD_3OD, decoupled, 160.4 MHz) δ −1.11 (1B), −4.32 (1B), −8.05 (2B), −10.13 (4B), −11.37 (2B); LRMS (MALDI$^+$) calcd for $C_{33}H_{50}B_{10}N_6O_{12}Na$ $(M+Na)^+$ 855.5, found 855.5. HPLC: t_R = 12.6 min.

3-(*nido*-Carboranyl)-*N*-{3-[(3-benzyl-DTPA)ureido]-phenyl}propionamide, 13a. 20 mg (0.024 mmol) of **13e** was dissolved in neat pyrrolidine (2 mL) and stirred at room temperature for 1 h. After pyrrolidine was evaporated by a stream of argon, the residue was washed with ethyl acetate (2 × 20 mL), and dried under vacuum to give **13a** as a light-yellow tacky solid (quantitative yield). ^{1}H NMR (CD_3OD, 200 MHz) δ 1.96−2.00 (m, 8H), 2.46−

2.53 (m, 1H), 2.89−3.04 (m, 1H), 3.21−3.25 (m, 10H), 3.29−3.32 (m, 4H), 3.36−3.78 (m, 4H), 3.83 (d, J = 3.6 Hz, 1H), 7.19−7.29 (m, 5H), 7.42 (d, J = 8.3 Hz, 2H), 7.64 (s, 1H); ^{11}B NMR (CD_3OD, decoupled, 96.3 MHz) δ −10.62 (1B), −13.23 (1B), −16.10 (1B), −17.92 (1B), −20.86 (1B), −32.80 (2B), −37.04 (2B); LRMS $(ES)^-$ calcd for $C_{33}H_{50}B_9N_6O_{12}$ $(M)^-$ 821.5, found 821.5. HPLC: t_R = 9.7 min.

3-(Iodo-*nido*-carboranyl)-*N*-[3-(3-benzyl-DTPA)-ureido)phenyl]propionamide, 13b. To a solution of **13a** (8.9 mg, 0.01 mmol) in 5% HOAc-MeOH (2.5 mL) sodium iodide (1.5 mg, 0.01 mmol) and *N*-chlorosuccinimide (1.3 mg, 0.01 mmol) were added, respectively, with stirring. After the reaction mixture was stirred at room temperature for 30 s, sodium metabisulfite (1.9 mg, 0.01 mmol) was added to quench the reaction. A quantitative yield was estimated by HPLC. Pure **13b** was collected from HPLC and dried under vacuum to give a light-yellow tacky solid. LRMS ($MALDI^-$) calcd for $C_{33}H_{49}B_9IN_6O_{12}$ $(M-H)^-$ 947.3, found 947.7. HPLC: t_R = 10.8 min.

Radiohalogenation of Arylstannanes. A. (Labeling with ^{211}At) To a solution containing 100 μL of 1 mg/mL of arylstannane **1a**, **2a**, **3a**, or **4a** in MeOH/5% HOAc was added 10 μL of Na[^{211}At]astatide in 0.05 N NaOH, or 100 μL of Na[^{211}At]At (100−800 μCi) in MeOH with 10% 0.05N NaOH. To the resultant solution was added 20 μL of a 1 mg/mL solution of *N*-chlorosuccinimide (NCS) in MeOH. The reaction was quenched after 30 s to 2 min with 20 μL of a 1 mg/mL solution of sodium metabisulfite in H_2O. Following the reaction, the bulk of the mixture was injected onto a reversed-phase HPLC column and the peak at the retention time just following the iodo-standard was collected. Radiochemical yields for astatinated compounds were as follows: [^{211}At]**1c**, 55%; [^{211}At]-**2c**, 38%; [^{211}At]**3c** 33%; [^{211}At]**4c**, 42% (yields not optimized).

B. (Labeling with ^{125}I or ^{131}I): The radioiodination reactions were conducted as described for ^{211}At labeling, with the following changes in reagent quantities: Na[*I]I, 1−5 μL of a 0.1 N NaOH solution; NCS, 10 μL; and sodium metabisulfite, 10 μL. Radiochemical yields for radioiodinated compounds ([^{125}I]**1b**, [^{125}I]**2b**, [^{125}I]**3b**, [^{125}I]-**4b**) ranged from 90 to 98%.

Radiohalogenation of *nido*-Carboranyl Compounds. A. (Labeling with ^{211}At): To a solution containing 100 μL of 1 mg/mL of *nido*-carboranyl compound (**5a, 6a, 7a, 8g, 10a, 11a, 12a**, and **13a**) in either H_2O/5%HOAc or 50:50 MeOH/H_2O/5%HOAc, depending on compound solubility, was added 100 μL of Na[^{211}At]At (100−800 μCi) in 0.05 N NaOH. To this solution was added 20 μL of a 1 mg/mL solution of chloramine-T (ChT) in H_2O. The reaction was quenched after 30 s to 2 min with 20 μL of a 1 mg/mL solution of sodium metabisulfite in H_2O. Following the reaction, the bulk of the reaction mixture was injected onto a reversed-phase HPLC column and the peak at the retention time just following the iodo-standard was collected. Radiochemical yields for astatinated compounds were as follows: ([^{211}At]**5c**, 71%; [^{211}At]**6c**, 39%; [^{211}At]**7c**, 61%; [^{211}At]**9c,** 49%; [^{211}At]**10c**, 86%; [^{211}At]**11c**, 72%; [^{211}At]**12c**, 63%; [^{211}At]**13c**, 39% (yields were not optimized).

B. (Labeling with ^{125}I or ^{131}I): The radioiodination reactions were conducted as described for ^{211}At labeling of *nido*-carboranes, with the following changes in reagent quantities. The quantity of Na[*I]I used was 1−5 μL of a 0.1 N NaOH solution; 10 μL of ChT solution; and 10 μL of sodium metabisulfite solution. Radiochemical yields for radioiodinated compounds ([^{131}I]**5b**, [^{125}I]**6b**, [^{125}I]**7b**, [^{125}I]**9b**, [^{125}I]**10b**, [^{125}I]**11b**, [^{125}I]**12b**, [^{125}I]**13b**) ranged from 28 to 95%.

Biodistribution Studies. Animal use and procedures were approved by Duke University's Animal Care Committee or the University of Washington's Institutional Animal Care and Use Committee depending on where the study was conducted. In all studies, animal care and use were conducted in accordance with the NIH guidelines.[4] A biodistribution was conducted at Duke University to compare [^{131}I]**5b** and [^{211}At]**5c** in BALB/c mice. All other biodistribution studies were conducted at the University of Washington using BALB/c nu/nu mice. All reagents were administered to mice in a total volume of approximately 100 μL (injectate weighed) via the lateral tail vein. Injections and euthanasia of the animals were done at predetermined times. Blood samples were obtained by cardiac puncture immediately before killing. Urine samples were obtained by syringe bladder tap at the time the tissues were excised. The tissues excised included muscle, lung, kidney, spleen, liver, intestines, neck (with thyroid), and stomach. Excised tissues were blotted free of blood, weighed, and counted. Calculation of the percent injected dose (%ID) and percent injected dose per gram (% ID/g) of radioactivity in the tissues was based on internal standards containing 1 μL of the injected dose. The counts obtained were corrected for decay, and where dual radionuclide counting was required, the ^{125}I counts were corrected for spillover counts from ^{131}I activity. Total blood volume was estimated to be 8% of body weight. The data obtained are provided in Tables 1−13 in Supporting Information. The amount of $^{125/131}$I and ^{211}At administered to mice, and the average mouse weight, in each biodistribution are provided in the table legends.

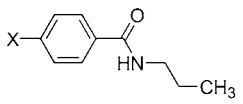
RESULTS

Design and Synthesis of Target Compounds. The goal of this investigation was to prepare and evaluate a series of astatinated benzamide and *nido*-carboranyl compounds to help identify structural features which maximize in vivo stability of an astatine label on a targeting carrier molecule. The compounds prepared for the investigation are shown in Figure 1. Initially, the compounds targeted were simple molecules. However, results obtained during the study led to synthesis of more complex molecules, which incorporated functional groups intended to increase renal excretion and decrease binding with blood components. In a majority of compounds prepared, biomolecule (amine) reactive groups were conjugated with *n*-propylamine to provide simple conjugates, which might be expected to be metabolized readily. Small rapidly metabolized molecules were chosen as they seemed the best candidates to test in vivo stability of the ^{211}At label, and in some cases represented structures that could be useful as prosthetic groups for labeling biomolecules.

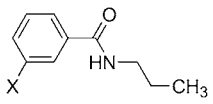
To incorporate the radiohalogens into the nonactivated aryl groups, tri-*n*-butylstannyl derivatives were prepared as reactive intermediates. The compounds containing the *nido*-carboranyl functionality were very reactive with radiohalogens, so they were reacted directly with radiohalogens. For evaluation purposes, the prepared compounds have been placed into three groups based on the type of radiohalogenation moiety and on the functional groups conjugated with that moiety. The three groups

[4] NIH guidelines are described in NIH Publication 86-23: "Guide for the Care and Use of Laboratory Animals."

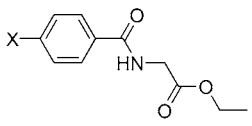
Benzamides



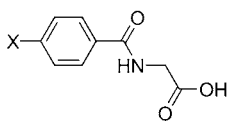
1a: X = $SnBu_3$
1b: X = I, I-125
1c: X = At-211



2a: X = $SnBu_3$
2b: X = I, I-125
2c: X = At-211

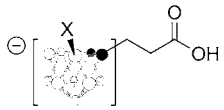


3a: X = $SnBu_3$
3b: X = I, I-125
3c: X = At-211

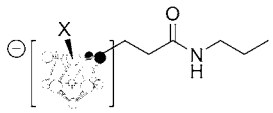


4a: X = $SnBu_3$
4b: X = I, I-125
4c: X = At-211

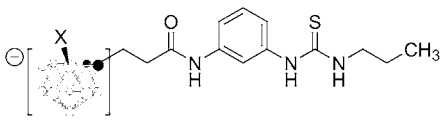
***nido*-Carboranes**



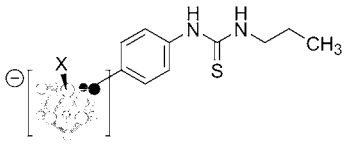
5a: X = H
5b: X = I, I-131
5c: X = At-211



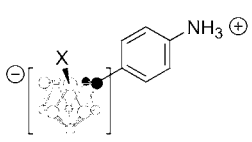
6a: X = H
6b: X = I, I-125
6c: X = At-211



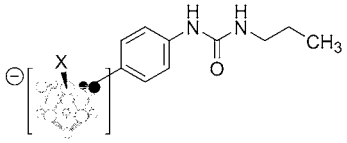
7a: X = H
7b: X = I, I-125
7c: X = At-211



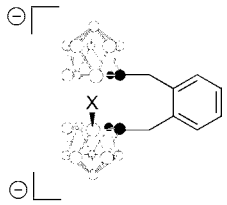
8a: X = H
8b: X = I, I-125
8c: X = At-211



8g: X = H
9b: X = I, I-125
9c: X = At-211

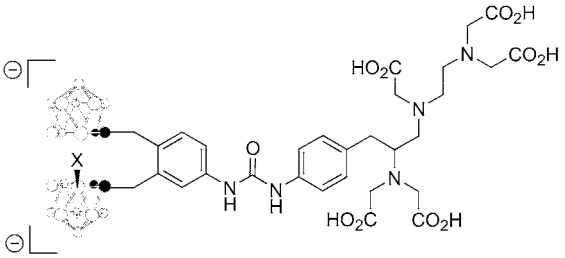


10a: X = H
10b: X = I, I-125
10c: X = At-211

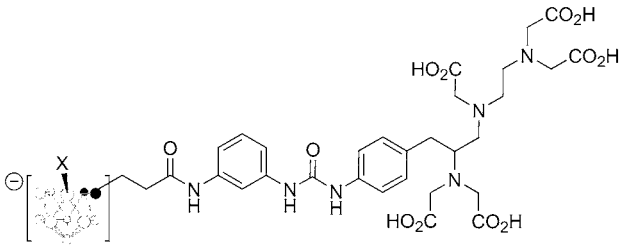


11a: X = H
11b: X = I, I-125
11c: X = At-211

***nido*-Carboranes conjugated with DTPA**



12a: X = H
12b: X = I, I-125
12c: X = At-211



13a: X = H
13b: X = I, I-125
13c: X = At-211

Figure 1. Aryl- and *nido*-carboranyl-compounds and their radiohalogenation derivatives prepared for evaluation in the studies. (Note that for simplicity, carborane cage hydrogen atoms, and possible halogenated *nido*-carboranyl regioisomers, are not shown.)

were benzamides, *nido*-carboranes, and *nido*-carboranes conjugated with DTPA. In all compounds studied, nonradioactive iodo derivatives were prepared as HPLC standards. The iodo derivatives were used for comparison of both radioiodinated and astatinated derivatives as there are no nonradioactive astatine nuclides, and the longest lived astatine radionuclide (^{210}At) has a half-life of only 8.3 h.

The *nido*-carborane structures and the structures of their radiohalogenated products shown in Figure 1 and in the synthetic schemes are simplified in that they do not include all of the possible halogenated positional isomers. Some of the possible positional isomers of substituted *nido*-carboranes [i.e., 7-substituted dodecahydro-7,8-dicarba-*nido*-undecaborate(-1)[3]] are shown in Figure 2. While other halogenated positional isomers are possible (i.e., substitution on other cage boron atoms), the positional isomers depicted in Figure 2, where the halogen atom is substituted on the boron atom adjacent to a carbon atom on the rim of the open icosahedron face, seem most likely based on the crystal structures of iodinated *nido*-carboranes previously reported by Hawthorne et al. (*28*, *41*). The figures and schemes have been simplified by not including positional isomers or show carborane cage protons for clarity. It is, however, important to appreciate the fact that the presence of isomers complicates interpretation of the NMR spectra, and can be observed as separate peaks on the HPLC chromato-

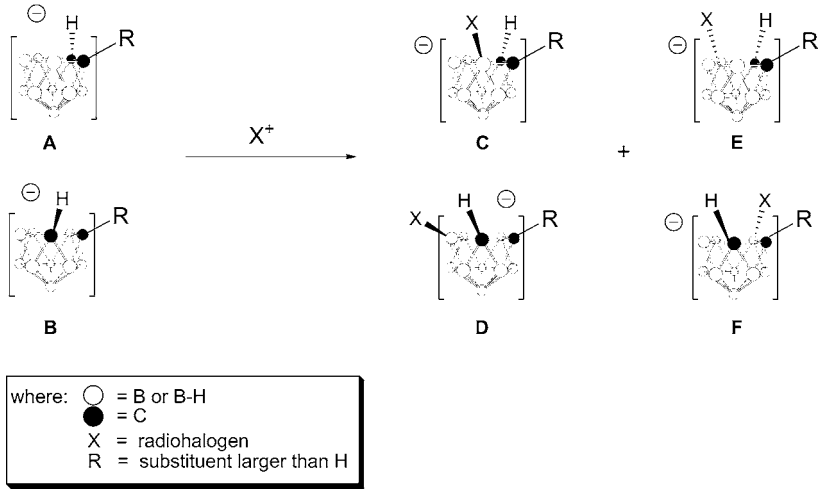
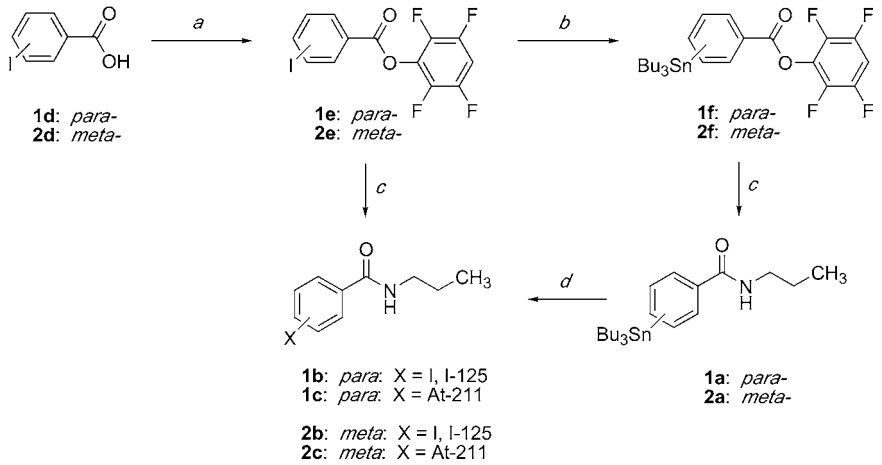


Figure 2. Positional isomers of halogenated C-substituted *nido*-carboranes. (Isomers shown (**C**−**F**) have the halogen on a boron adjacent to a carbon atom.)

Scheme 1. Synthesis and Radiohalogenation of *N*-Propyl-*meta*/*para*-Tri-*n*-butylstannylbenzamides, 1a and 2a[a]



[a] (a) EtOAc, EDC, TFP-OH, rt, 16−24 h (or) TFP-OTFA, Et_3N, DMF, 0−4 °C, 30 min, 87%; (b) toluene, $(Bu_3Sn)_2$, $[(C_6H_5)_3P]_4Pd(0)$, Δ, 4−6 h, 73−86%; (c) *n*-propylamine, DMF, rt, 30 min, 74−95%; (d) NCS, NaX (X = I, ^{125}I or ^{211}At), MeOH/5% HOAc, rt, 30 s, 38−98%.

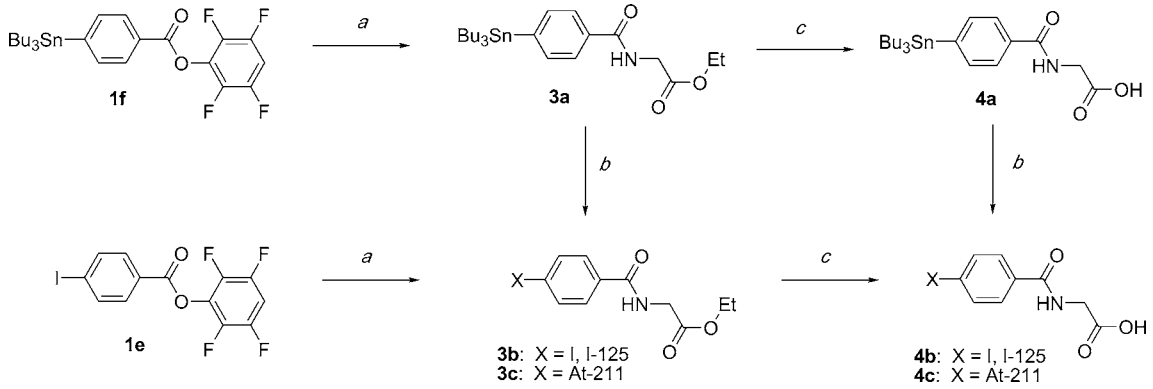
grams in cases in which diastereomeric pairs of isomers are formed.

Benzamide Derivatives. N-Hydroxysuccinimide esters of *p*-astatobenzoic acid and *m*-astatobenzoic acid have been utilized extensively for labeling proteins (*26*, *42*), so benzamide derivatives of these reagents were included in the investigation. The syntheses of the *para*- and *meta*-stannylbenzamides **1a** and **2a**, which are reactive intermediates for the preparation of the [^{211}At]-astatobenzamides **1c** and **2c**, and the iodinated *para*- and *meta*-iodobenzamides **1b** and **2b**, are shown in Scheme 1. The tetrafluorophenyl (TFP) ester of the iodobenzoates, **1e** and **2e**, were readily prepared using 1-(3-dimethylaminopropyl)-3-ethylcarbodiimide (EDC) and tetrafluorophenol (TFP-OH) in EtOAc (*38*), or by using tetrafluorophenyl trifluoroacetate (TFP-OTFA) in anhydrous DMF. Conversion of the iodobenzoate TFP esters to their tri-*n*-butylstannyl derivatives, **1f** and **2f**, was also readily accomplished using hexabutylditin and tetrakis-triphenylphosphine palladium(0) in refluxing toluene. The benzoate TFP esters were reacted with propylamine to provide the targeted stannylbenzoates **1a** and **2a** and the iodobenzoates **1b** and **2b**.

The *para*-astatohippuryl ester **3c** was included in the investigation as previous reports indicated that protein conjugates of an iodohippuryl ester were excreted almost exclusively as the free iodohippuric acid (*43*, *44*). The thought was that rapid renal excretion may decrease the in vivo deastatination. For comparison, *para*-astatohippuric acid **4c** was also prepared and tested. Synthesis of the requisite stannylhippurates **3a/4a** and iodohippurates **3b/4b** is shown in Scheme 2. Reaction of the benzoate TFP esters **1e** and **1f** with glycine ethyl ester provided the targeted hippuryl esters **3a** and **3b**, and base hydrolysis of those compounds gave the targeted hippuric acids **4a** and **4b**.

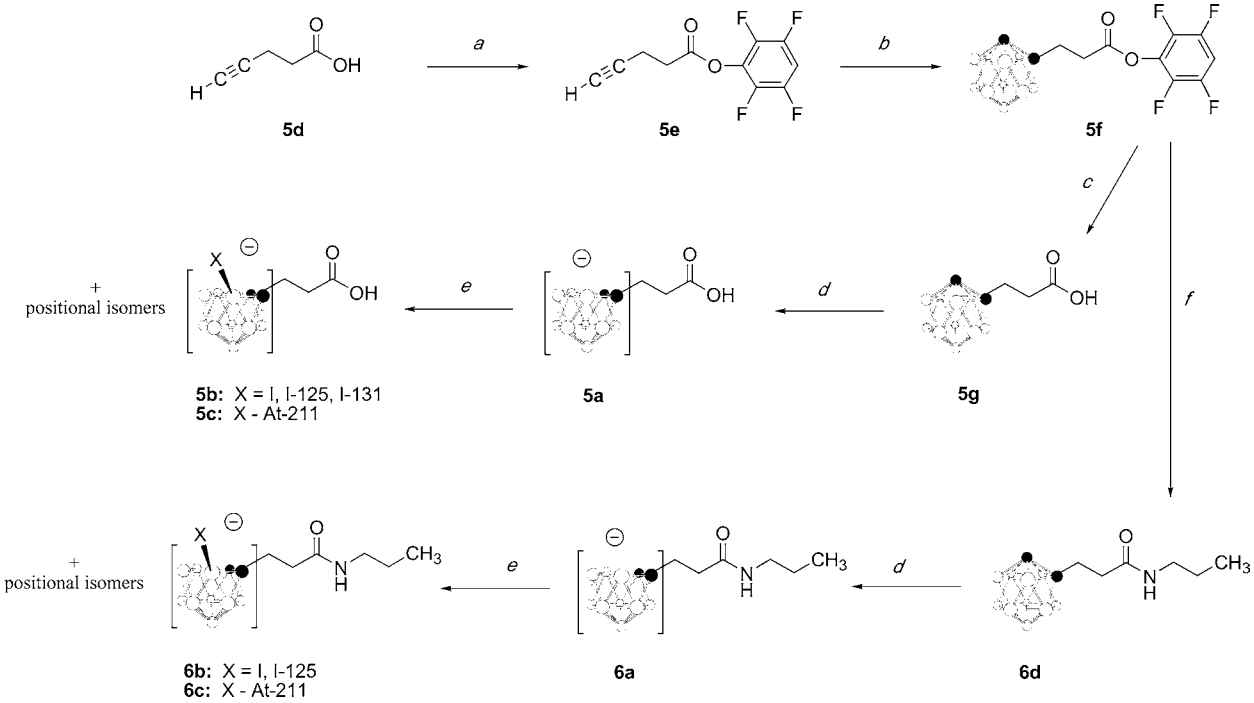
***nido*-Carborane Derivatives.** Initial studies of *nido*-carboranes involved preparation of *nido*-carboranylpropionic acid **5a** and its propylamine adduct **6a**. The synthesis of these compounds and their astatinated and iodinated derivatives is shown in Scheme 3. In the synthesis, 4-pentynoic acid TFP ester **5e** was prepared using 1,3-dicyclohexylcarbodiimide (DCC) and TFP-OH in THF. The resulting propynoic tetrafluorophenyl (TFP) ester **5e** was reacted with decaborane in refluxing acetonitrile to provide the *closo*-carboranylpropionic acid TFP ester **5f**. Hydrolysis of the TFP ester using KOH in EtOH provided **5g**, which was subsequently treated with pyrrolidine to prepare the *nido*-carborane derivative **5a**. Iodination of **5a** with 0.75 equiv of *N*-chlorosuccinimide (NCS) and NaI in MeOH/1% HOAc provided the monoiodo derivative **5b** (as positional isomers). The adduct **6a**

Scheme 2. Synthesis and Radiohalogenation of *para*-Tri-*n*-butylstannylhippuric Acid, 4a, and Its Ethyl Ester, 3a[a]



[a] (a) Glycine ethyl ester, Et_3N, DMF, rt, 30 min, 88%; (b) NCS, NaX (X = I, ^{125}I or ^{211}At), MeOH/5% HOAc, rt, 30 s, 18−90%; (c) MeOH, KOH, 60 °C, 1 h.

Scheme 3. Synthesis and Radiohalogenation of 3-(*nido*-Carboranyl)propionic Acid, 5a, and Its *n*-Propylbenzamide Adduct, 6a[a]



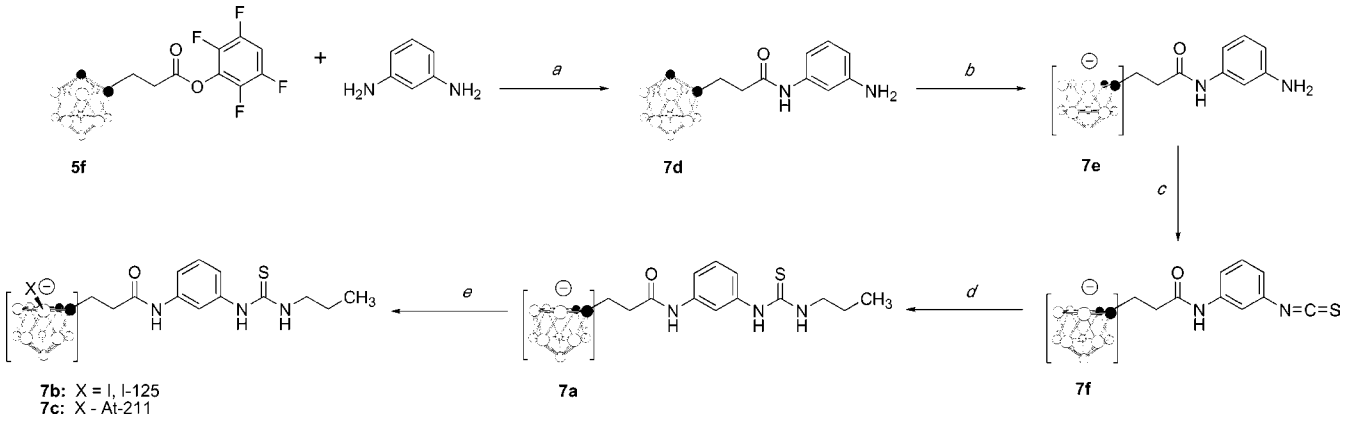
[a] In carborane structures, open circles represent boron or B−H atoms and closed circles represent carbon or C−H atoms. (a) THF, DCC, TFP-OH, rt, 16−24 h, 82%; (b) $B_{10}H_{14}$, CH_3CN, Δ, 25 h, 50%; (c) EtOH, KOH, rt, 1 h, 94%; (d) pyrrolidine, rt, 30 min, 86−88%; (e) NCS, NaX (X = I, ^{125}I or ^{211}At), MeOH/5% HOAc, rt, 30 s − 5 min, 35−39%; (f) *n*-propylamine, DMF, rt, 30 min (not isolated).

and its iodinated derivative **6b** were prepared by reaction of the TFP ester **5f** with propylamine, followed by reaction of pyrrolidine as in the preparation of **5a**. Iodination of **6a** to obtain **6b** employed the same conditions as used to prepare **5b**.

On the basis of the results obtained with the radiohalogenated 3-(*nido*-carboranyl)propionate derivatives **5b/c** and **6b/c**, an additional *nido*-carboranylpropionate derivative **7a**, which incorporated a diaminobenzene moiety, was prepared and evaluated. The thought was that the more complex molecule may have a slower metabolism, and thus decrease the rate of ^{211}At release in vivo. The synthesis of **7a** is shown in Scheme 4. Reaction of an excess of 1,3-diaminobenzene provided the adduct **7d** in high yield. Conversion of **7d** to its *nido*-carborane structure **7e** was accomplished using neat pyrrolidine. The amine reactive isothiocyanate **7f** was readily formed from **7e** by reaction with thiocarbonyldiimidazole (TCDI). Reaction of **7f** with *n*-propylamine gave the targeted 3-(*nido*-carboranyl)propylphenyl derivative **7a**. Iodination of **7a** was accomplished using NCS/NaI in 5% HOAc/MeOH solution to provide the HPLC standard **7b**.

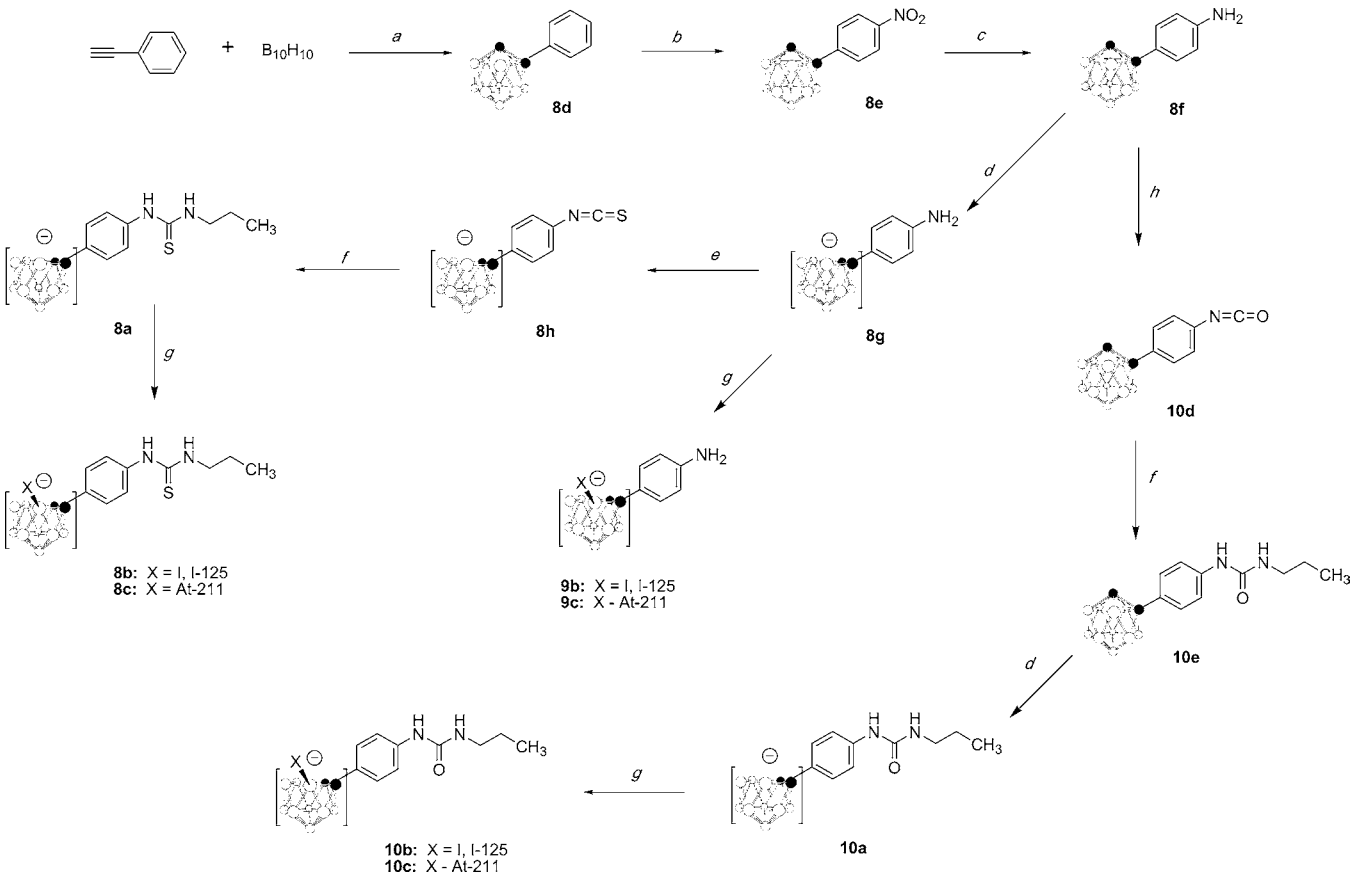
Three compounds that have a phenyl ring bonded the *nido*-carborane structure, **8a**, **8g**, and **10a**, were synthesized in the studies. Synthesis of these compounds and their iodinated and astatinated derivatives is shown in Scheme 5. Compound **8a** was initially targeted for synthesis and evaluation. This compound was included in the investigation to determine if having a phenyl group directly bonded to the *nido*-carborane altered the radiolabeling yields and/or improved the in vivo stability of the astatinated derivative relative to the 3-(*nido*-carboranyl)propionate moiety (e.g., **6a**). Hawthorne et al. had previously reported the synthesis of isothiocyanatophenyl-*nido*-carborane **8h**, and demonstrated that it could be radioiodinated and conjugated with proteins (*28*, *29*). In these studies, reaction of **8h** with *n*-propylamine provided **8a** for radiohalogenation. Iodination of **8a** using

Scheme 4. Synthesis and Radiohalogenation of 3-(*nido*-Carboranyl)-*N*-[3-(3-propylthioureido)-phenyl]propionamide, 7a[a]



[a] In carborane structures, open circles represent boron or B−H atoms and closed circles represent carbon or C−H atoms. (a) DMF, rt, 3.5 h, 95%; (b) pyrrolidine, rt, 1 h, 36%; (c) TCDI, DMF, rt, 30 min, 87%; (d) *n*-propylamine, DMF, rt, 40 min, 93%; (e) NCS, NaX (X = I, ^{125}I or ^{211}At), MeOH/5% HOAc, rt, 30 s − 5 min, 28−61%.

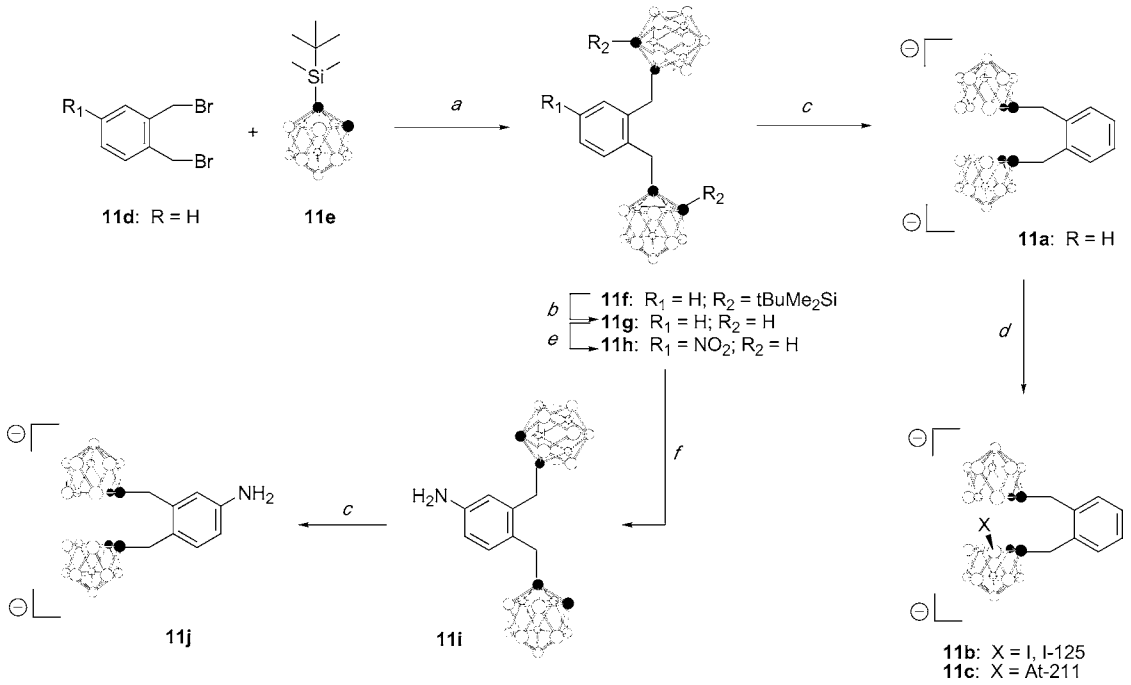
Scheme 5. Synthesis and Radiohalogenation of 1-(4-*nido*-Carboranylphenyl)-3-propylthiourea, 8a, 4-(*nido*-Carboranyl)aniline, 8g, and 1-(4-*nido*-Carboranylphenyl)-3-propylurea, 10a[a]



[a] In carborane structures, open circles represent boron or B−H atoms and closed circles represent carbon or C−H atoms). (a) CH_3CN, Δ, 24 h, 71%; (b) HNO_3/H_2SO_4, CH_2Cl_2, rt, 20 h, 46%; (c) EtOH, Pd/C, H_2, rt, 16 h, 95%; (d) pyrrolidine, rt, 30 min, 100%; (e) TCDI, DMF, rt, 30 min, (not isolated); (f) *n*-propylamine, rt, 30 min, 83−85%; (g) ChT, NaX (X = I, ^{125}I or ^{211}At), rt, 30 s, 49−95%; (h) CDI, $CHCl_3$, rt, 2 h (not isolated).

chloramine-T in water gave a mixture of products, of which **8b** was obtained in low yield. The structurally similar **7a** provided higher iodination yields under the same reaction conditions, but also was present in a mixture of compounds by HPLC analysis. This is not surprising as we have previously observed that compounds with thiourea moieties can interfere with radiohalogenation reactions (*45*, *46*). As an alternative, compound **8g** which does not contain an isothiocyanate functionality was iodinated to form **9b**, astatinated to prepare **9c**, and tested in vivo. The fact that **8g** iodinated readily suggested that the difficulty with iodination of **8a** was due to the isothiocyanate functionality. Another phenyl-*nido*-carborane, which did not contain a thiourea functionality, **10a**, was also targeted for synthesis. Initially, the conversion of the aniline derivative **8g** to the isocyanate derivative was studied. However, unlike the phenylisothiocyanate **8h**, the phenylisocyanate was unstable, so another synthetic route was sought. The successful synthesis of **10a** began with the in situ

Scheme 6. Synthesis and Radiohalogenation of Bis-*nido*-carborane Derivatives (Venus Flytrap Complexes), 11a and 11j[a]



[a] In carborane structures, open circles represent boron or B−H atoms and closed circles represent carbon or C−H atoms). (a) C_6H_6/Et_2O, 35 °C, 24 h, 74% [39]; (b) THF, $^nBu_4NF$, −76 to 0 °C, 20 min, 71% [39]; (c) KOH, EtOH, H_2O, Δ, 80%; (d) ChT, NaX (X = I, ^{125}I or ^{211}At), rt, 30 s, 72−80%; (e) concentrated H_2SO_4, HNO_3, 0 °C − rt, 2 days, 94%; (f) MeOH, HCl, Sn, Δ, 10 h, 67%.

generation of the phenylisocyanate **10d** by reaction of **8f** with carbonyldiimidazole (CDI) in $CHCl_3$. Subsequent reaction of **10d** with *n*-propylamine yielded the *closo*-carboranylphenylpropylurea **10e**. Reaction of **10e** with pyrrolidine provided the targeted **10a**. Iodination of **10a** with NCS/NaI in MeOH/HOAc solution gave a high yield of one major product. It is important to note that the structure of **10a** is identical to that of **9a** except it contains a urea functionality rather than a thiourea functionality. This result further supports the observations that thiourea functionalities can interfere with halogenation reactions.

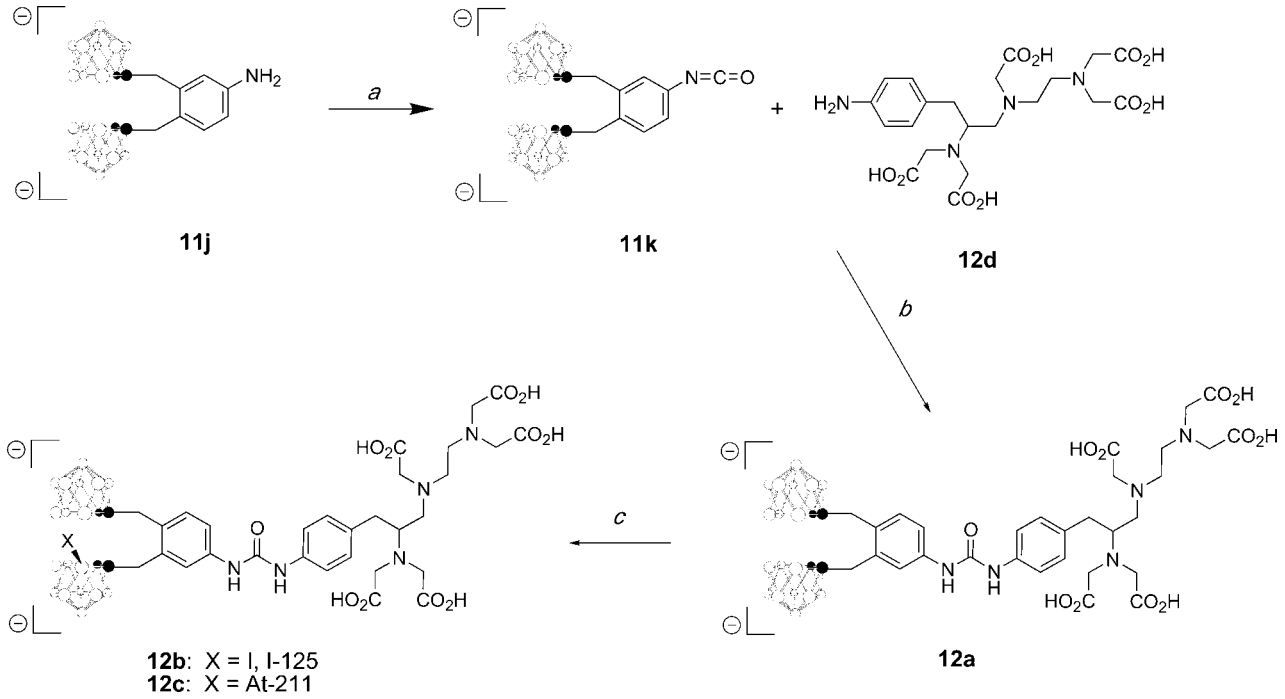
The seventh *nido*-carborane to be synthesized and evaluated, **11a**, contains two *nido*-carborane functionalities. This structure has been termed a "Venus flytrap complex" by Hawthorne et al., and similar complexes have been used for incorporating radiometals (*34*). Syntheses of **11a** and the iodinated HPLC standard **11b** were accomplished as shown in Scheme 6. Synthesis of the **11a** began with reaction of lithiated *tert*-butyldimethylsilyl-*ortho*-carborane **11e** with 1,2-bis(bromomethyl)benzene as previously described (*39*). Removal of the *tert*-butyldimethylsilyl group to obtain **11g** was accomplished by reaction of **11f** with tetra-butylammonium fluoride in THF. Degradation of the *closo*-carborane cages in **11f** to form the bis-*nido*-carborane **11a** was accomplished by reaction of KOH in EtOH at reflux. Iodination of **11a** to prepare the HPLC standard **11b** was accomplished by reaction with *N*-chlorosuccinimide and NaI in MeOH/HOAc for 30 s at room temperature.

***nido*-Carborane-DTPA Adducts.** In vivo results obtained with the radiohalogenated VFC **11a** led to a decision to prepare an adduct of DTPA. This decision was based on the hypothesis that the radiolabeled VFC was binding with plasma proteins, which increased the serum half-life and led to hepatobiliary excretion. Binding with plasma proteins can cause a radiolabeled compound to be excluded from renal filtration and elimination. DTPA is used to measure renal function when chelated with a radiometal (*47*); thus, we believed that an adduct with the VFC might decrease the serum protein binding (i.e., decrease blood residence time) and increase the renal excretion of the astatinated VFC. Synthesis of a DTPA derivative of the VFC is shown in Schemes 6 and 7. In the synthesis, bis-(1,2-*closo*-carboranylmethyl)benzene, **11g**, was nitrated using concentrated sulfuric and nitric acid to provide the nitro derivative **11h**. Reduction of the nitro group using Sn/HCl in MeOH provided the anilino derivative **11i**, and conversion of **11i** to the bis-*nido* derivative **11j** was accomplished using KOH in EtOH at reflux overnight. The choice was made to avoid incorporation of a thiourea moiety in the targeted compound, **12a** (Scheme 7), to eliminate the possibility that it would interfere with the radiohalogenation reactions. Thus, the bis-*nido*-carboranylaniline, **11j**, was converted to the isocyanate derivative **11k**. Subsequent reaction of the isocyanate **11k** with aminobenzyl-DTPA, **12d**, provided the targeted compound **12a**. Iodination of **12a** was facile using chloramine-T and NaI in H_2O.

As a comparison, a mono-(*nido*-carboranyl)-DTPA derivative **13a** was also prepared as depicted in Scheme 8. The 1,3-diaminobenzene adduct of *closo*-carboranylpropionic acid, **7d**, was converted to the isocyanato derivative **13d**. Again, the isothiocyanate was avoided so that the target compound would not have a thiourea functionality in it. Reaction of **13d** with aminobenzyl-DTPA, **12d**, provided the *closo*-carboranyl adduct **13e**. Neat pyrrolidine was used to prepare the *nido*-carboranyl-DTPA adduct, **13a**. The iodinated HPLC standard was prepared by reaction of **13a** with NCS and NaI in MeOH/HOAc.

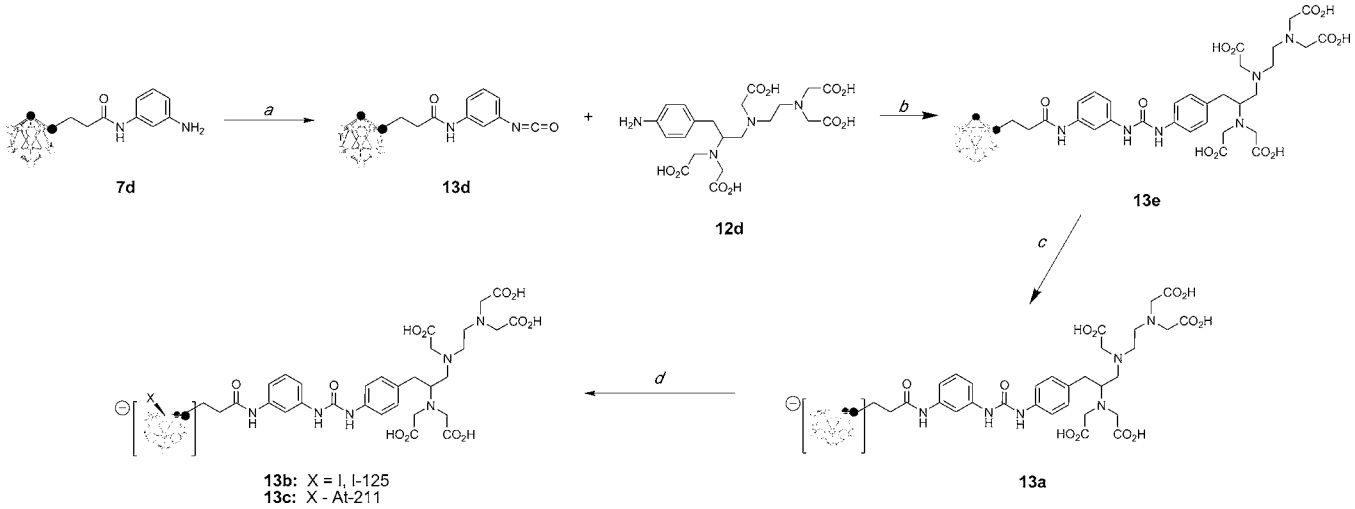
Radioiodination and Astatination Reactions of Aryl and *nido*-Carborane Derivatives. Radiohalogenation reactions of arylstannanes have proven to be very facile, and this was found to be the case for reactions with **1a**, **2a**, **3a**, and **4a**. The low aqueous solubility of aryl

Scheme 7. Synthesis and Radiohalogenation of Bis-*nido*-carborane Derivative (Venus Flytrap Complex) with Coupled Benzyl-DTPA, 12a[a]



[a] In carborane structures, open circles represent boron or B−H atoms and closed circles represent carbon or C−H atoms). (a) CDI, CH_3CN, rt, 1 h, (not isolated); (b) pyridine, DMF, rt, 16 h, 58%; (c) ChT, NaX (X = I, ^{125}I or ^{211}At), rt, 30 s, 63−76%.

Scheme 8. Synthesis and Radiohalogenation of *nido*-Carborane Derivative Which Has a Benzyl-DTPA Moiety Attached, 13a[a]



[a]In carborane structures, open circles represent boron or B−H atoms and closed circles represent carbon or C−H atoms. (a) CDI, $CHCl_3$, rt, 1 h, (not isolated); (b) DMF, pyridine, rt, 16 h, 57%; (c) pyrrolidine, rt, 1 h, 100%; (d) ChT, NaX (X = I, ^{125}I or ^{211}At), rt, 30 s, 39−70%.

stannanes makes it favorable to conduct the radiohalogenation reactions in MeOH. To offset the addition of base in the radionuclide solution, 5% HOAc was added to the solvent. The astatinations were conducted using the same reaction conditions as used for radioiodinations. The astatination yields (33−55%) were considerably lower than the radioiodination yields (90−95%) under the conditions studied. The reason for this difference has not been established, but it is possible that the amount of H_2O introduced with the Na[^{211}At]At caused the lower yields. Previous studies had demonstrated that a maximum of 10% water was tolerated in radioiodination reactions using the same reaction conditions, and that as the percentage of water increased, the radiochemical yields decreased. It should be noted that none of the radiohalogenation reaction conditions were optimized. It is important to note that free astatide did not elute from the reversed-phase HPLC column under the eluant conditions used. Thus, the yields reported represent the percentages of radioactivity that were isolated as the desired astatinated products from a measured amount of radioactivity (reaction mixture) injected. After isolation, the MeOH and HOAc were removed under a stream of nitrogen (vented through charcoal containing syringe).

Radiohalogenation reactions with *nido*-carboranyl derivative **5a** were conducted in MeOH/HOAc using NCS as oxidant; however, it was more convenient to conduct the reactions in aqueous solution using chloramine-T as the oxidant. Radioiodination and astatination of *nido*-carboranes **6a**, **7a**, **8g**, **10a**, **11a**, **12a**, and **13a** were

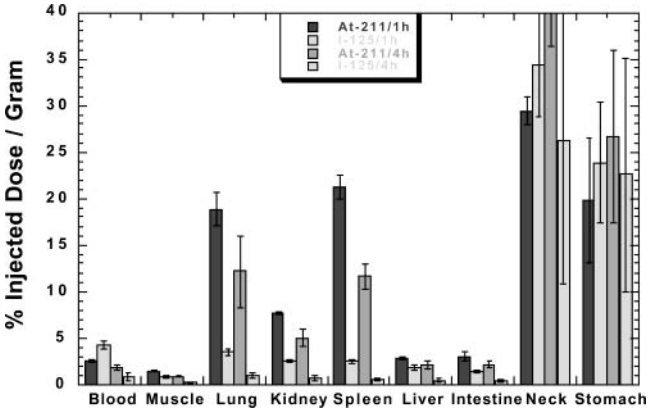


Figure 3. Graph depicting ^{211}At and ^{125}I concentrations (% injected dose/g) in blood and selected tissues of athymic mice at 1 and 4 h postinjection. (Numerical data and additional information on the study are provided in Table 1 of Supporting Information.)

conducted using chloramine-T and Na[^{125}I]I or Na[^{211}At]-At in H_2O for 30 s to 2 min. Radiolabeling of **8a** was not attempted due to the observation that the reaction with stable iodide resulted in a mixture of products using the same reaction conditions. In most reactions, the astatination and radioiodination yields obtained with *nido*-carborane derivatives were similar, with radioiodination yields ranging from 28 to 95**%** and astatination yields ranging from 39 to 72%. Due to the propensity of the *nido*-carborane compounds to adhere to glass surfaces, plastic vials were used for isolating the products. This adherence to glass surfaces appeared to increase with time and with removal of solvent. The radiohalogenated *nido*-carborane derivatives employed in animal studies were diluted with a solution of 1% BSA in PBS to keep the labeled material from adhering to the syringe.

Biodistributions of Radiolabeled Aryl and *nido*-Carborane Derivatives. Our previous studies of astatinated compounds provided data that suggested the best method for determining the in vivo stability of astatinated compounds was to conduct co-injected dual-label experiments with radioiodine. Stability of an astatinated compound can be inferred from the differences in [^{211}At]-astatide and [$^{125/131}$I]iodide concentrations in the tissues where astatide naturally localizes. Although there are literature reports comparing [^{211}At]astatide and [$^{125/131}$I]-iodide, we chose to conduct our own experiment to determine the tissue localization of the free radionuclides by co-injecting them into athymic mice. The biodistribution data from that study are provided in Table 1 in Supplemental Information, and are depicted graphically in Figure 3. As in previous reports involving other animal models (*48*), the primary tissues where [^{211}At]astatide localizes are lung, spleen, neck, and stomach. Importantly, unlike the neck (thyroid) and stomach, low concentrations of iodide are found in the lung and spleen, making the difference between concentrations of ^{211}At and radioiodine in these tissues good indicators of the quantity of free astatide, and thus, the stability of the astatinated compound.

Twelve biodistribution studies were conducted in mice to evaluate the in vivo distributions and stability of the astatinated compounds. All studies, except the one conducted at Duke University, were conducted in athymic mice to provide a baseline for comparison to future studies of astatinated biomolecules in mice bearing human tumor xenografts. The biodistribution study of astatinated *nido*-carborane [^{211}At]**5c** was conducted at Duke University. That study evaluated the distributions of co-injected [^{211}At]**5c** and [^{131}I]**5b** at three time points (1, 3, and 24 h pi). In all other studies, biodistribution data were obtained at 1 and 4 h postinjection as previous studies had shown that instability of ^{211}At could be readily noted during this time period (*23*, *49*). Complete biodistribution data obtained in the investigation are included as tables in Supporting Information (Tables 2−13). Graphs depicting the concentration of astatinated and radioiodinated benzamidyl- and *nido*-carboranyl-derivatives, **1b/c** to **7b/c** and **9b/c** to **13b/c**, are provided as Figures 4A,B and 5A−D. Data from concentration of radionuclides in selected tissues at 4 h postinjection are plotted in pairs of two compounds with similar structures for ease of comparison. All graphs have the same axis values for comparison purposes.

Due to the high stability toward in vivo deiodination of radioiodinated benzamides and *nido*-carboranyl compounds, the concentration of radioiodine in a tissue is indicative of the concentration of the radiolabeled compound(s) in that tissue. However, the concentration of astatine in tissues can be indicative of free astatide, astatinated molecule(s), or a mixture of these due to the lower stability of astatinated molecules in vivo. In molecules that are stable to deastatination, the distribution of ^{211}At and $^{125/131}$I should be very similar. Thus, large differences in tissue concentrations of radionuclides, particularly in lung, spleen, and neck are likely due to release of astatine.

Concentrations (% injected dose/g of tissue) of ^{211}At and ^{125}I in selected tissues of mice at 4 h postinjection of radiolabeled benzamide derivatives **1**−**4** are depicted in Figure 4A,B. As expected, the iodobenzamides **1b**−**4b** are rapidly cleared from the mice, resulting in very low concentrations of radioiodine in tissues by 4 h postinjection. In comparison, a fair amount of astatine is observed in tissues where free astatide localizes. Indeed, comparison of the tissue ^{211}At activity in Figure 4A,B with that in Figure 3 leads to the conclusion that most, if not all, of the ^{211}At observed is present as free astatide. These results, and the data obtained at 1 h postinjection, indicate that the astatinated benzamides studied are unstable, undergoing rapid deastatination in vivo.

Concentrations of ^{211}At and $^{125/131}$I in selected tissues of mice at 4 h postinjection of radiolabeled *nido*-carborane derivatives **5**−**7** and **9**−**13** are depicted in Figure 5A−D. The tissue concentrations of radioactivity for the *nido*-carboranylpropionic acid derivative **5** and its *N*-propylamine adduct **6** are shown in Figure 5A. Large differences in the ^{211}At and ^{131}I or ^{125}I concentrations can be noted in the tissues where astatide localizes (i.e., lung, spleen and thyroid/neck). These data indicate that astatinated structurally simple *nido*-carboranes coupled by a C-alkyl bond are also unstable to in vivo deastatination. Tissue concentrations of the more structurally complex *nido*-carboranylpropionamide derivatives **7** and **13** are provided in Figure 5B. Much higher blood concentrations are noted for this pair of compounds versus the structurally simpler compounds, **5** and **6**. Inspection of the differences in ^{211}At and ^{125}I concentrations in lung, spleen, and neck for compound **7** indicates that this compound undergoes deastatination similar to, but perhaps slower than **6**. Interestingly, conjugation of the benzyl-DTPA appears to greatly diminish the differences in concentration of ^{211}At and ^{125}I in lung, spleen, and neck, suggesting less deastatination occurred. It is unclear why this is the case, but the higher concentrations in blood and lower

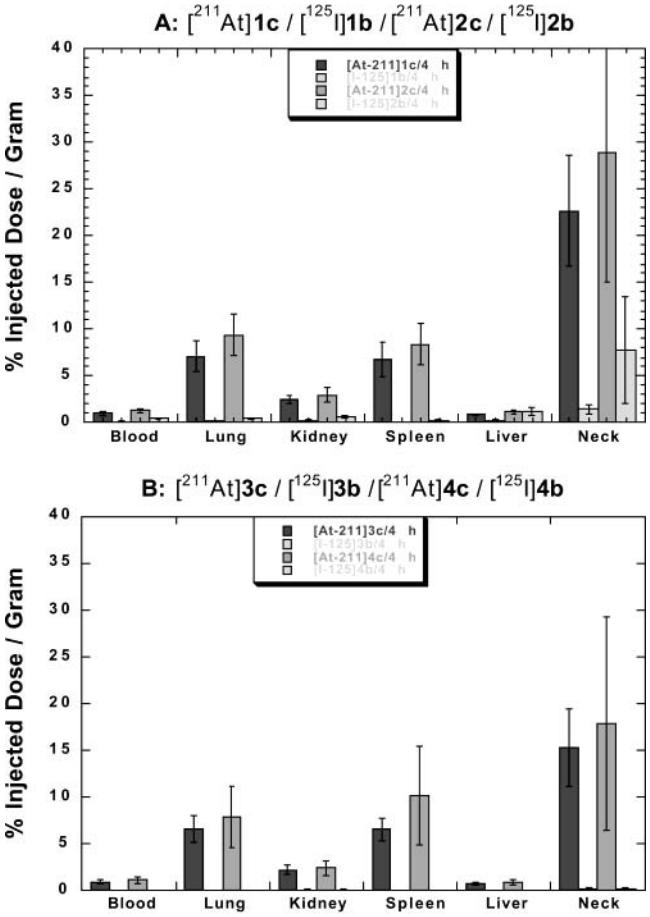


Figure 4. Graphs showing ^{211}At and ^{125}I concentrations (% injected dose/g) of radiolabeled benzamides (**1**−**4**) in selected tissues of athymic mice at 4 h postinjection (Numerical biodistribution data and additional information for the astatinated and iodinated compounds are provided in Tables 2−5 in Supporting Information). Data from two sets of dual labeled compounds are plotted in each panel. Identification of the radiolabeled compound represented by each bar (in the correct order) is provided at the top of the graph with the panel designation (A or B).

concentrations in kidney and liver of **13** may indicate that the difference is simply due to a slower rate of metabolism.

Concentrations of ^{211}At and ^{125}I in selected tissues of mice for the *nido*-carborane derivatives with a phenyl group directly attached to the cage are provided in Figure 5C. It is interesting to note that the zwitterionic derivatives **9b** and **9c** have quite high blood concentrations at 4 h postinjection. Conjugation of the anilino-amine to form **10b** or **10c** results in a dramatic decrease in the blood concentration. Interestingly, inspection of the differences in concentration of radionuclides in lung, spleen, and neck for **9b/c** and **10b/c** suggests that the two molecules are deastatinated at similar rates. Indeed, both are deastatinated, suggesting that there is little difference in stability toward deastatination between the alkyl- and aryl-substituted *nido*-carboranes.

Concentrations of ^{211}At and ^{125}I in selected tissues of mice for the bis-*nido*-carboranyl derivatives **11** and **12** are provided in Figure 5D. In most tissues examined, the concentrations of ^{211}At and ^{125}I are nearly the same. For compounds **11** and **12**, most of the differences between ^{211}At and ^{125}I concentrations in tissues were not significant as measured by a paired Student-t test (see Tables 11 and 12 in Supporting Information). In contrast to this, the differences observed in tissues for the other compounds were highly significant for most tissues when examined in the same analysis. Inspection of the concentrations of ^{211}At and ^{125}I in lung, spleen, and neck leads one to believe that both of these compounds may be quite stable to in vivo deastatination. No differences in concentrations of radionuclides are noted in the spleen. For compound **12**, no significant differences are seen in lung and spleen, but a significant difference is observed in neck. This was also true for data from the 1 h time point. While this may indicate that there is some deastatination, it is likely to be very small quantity as significant differences in the lung and spleen might be expected otherwise. No significant differences were found for concentrations of ^{211}At and ^{125}I in lung, spleen, and neck for compound **12**. Although the difference between the ^{211}At and ^{125}I concentrations in lung for compound **12** appears to be significant by inspection, the difference was not significant when evaluated in the Student-t test. The apparent high stability of the bis-*nido*-carboranyl derivatives **11** and **12** is particularly surprising in that there is a rapid localization to liver and transit to the intestines.

DISCUSSION

The potential for using the alpha-particle emitting radionuclide ^{211}At in TRT of cancer was mentioned in the literature a half-century ago (*50*), and has been the focus of many literature reviews in more recent years (*7*, *51*−*54*). While it is not clear whether alpha-particle emitting radionuclides will be of value in the therapy of solid tumors, their high cytotoxicity and short path length (e.g., 50−80 μm) make them particularly well suited for therapy of metastatic disease, disease in compartmental spaces (e.g., ovarian carcinoma), and cancer cells remaining in surgical tumor resection margins. It is important to note that ^{211}At is one of only a few alpha-emitting radionuclides that are considered appropriate for clinical use (*5*). Although the half-life of ^{211}At is short ($t_{1/2}$ = 7.2 h), there are many cancer cell targeting agents and approaches that are potentially compatible with it. But a key factor in the development and evaluation of ^{211}At-labeled cancer targeting agents is its stability toward deastatination in vivo. Release of ^{211}At from the cancer targeting molecule can be expected to result in accumulation in lung, spleen, stomach, and thyroid as documented previously in mice, rats, and monkeys (*48*, *55*, *56*), and as shown in Figure 3. Dependent on the extent of deastatination, such nontarget tissue localization could completely negate the beneficial effects of the cancer therapy. Therefore, it is imperative that chemical methods for attaching ^{211}At to cancer targeting agents provide high stability in vivo. Without such stability, the application of ^{211}At will be limited.

Since astatine is a member of the halogen group of elements, the chemistry of its nearest neighbor, iodine, is often used to predict astatine chemistry. However, studies have shown that its chemistry can vary significantly from that of iodine (*57*). This difference has been particularly noteworthy when radiolabeling molecules for use in vivo. Early studies of ^{211}At labeled proteins demonstrated that, unlike radioiodine counterparts, direct labeling of proteins with ^{211}At resulted in products that were unstable to deastatination in serum (*17*, *18*). Subsequent investigations found that use of astatinated nonactivated aryl compounds as conjugates for labeling proteins resulted in stabilizing them toward both in vitro and in vivo deastatination (*19*, *20*). Studies in our laboratories, and several other laboratories, have dem-

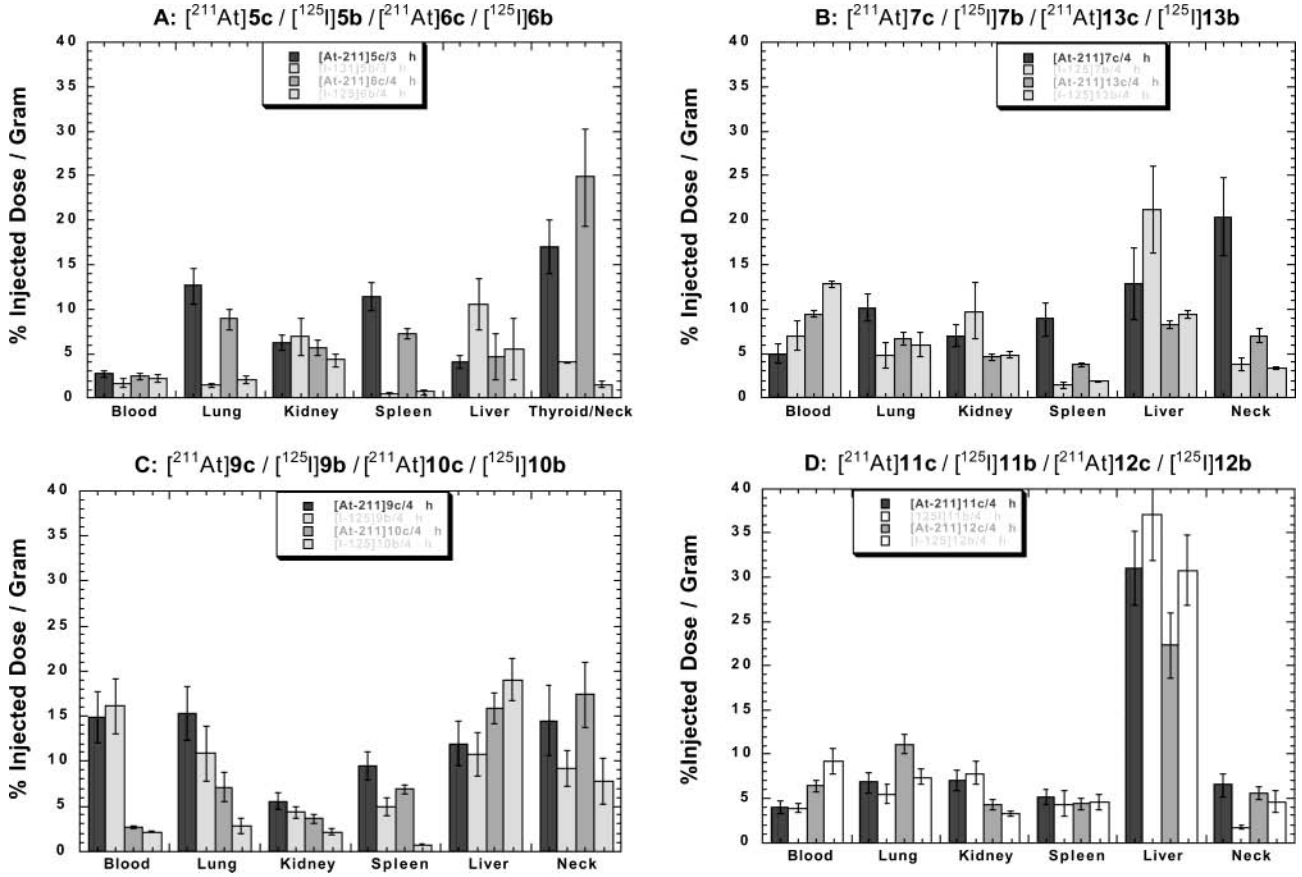


Figure 5. Graphs showing ^{211}At and ^{125}I concentrations (% injected dose/g) of radiolabeled *nido*-carborane derivatives (**5**−**7** and **9**−**13**) in selected tissues of athymic mice at 4 h postinjection (Numerical biodistribution data and additional information for the astatinated and iodinated compounds are provided in Tables 6−12 in Supporting Information). Data from two sets of dual labeled compounds are plotted in each panel. Identification of the radiolabeled compound represented by each bar (in the correct order) is provided at the top of the graph with the panel designation (A−D).

onstrated that astatinated benzoic acid conjugates with reactive functional groups provided a rapid and relatively high yielding method to label monoclonal antibodies (mAbs) for in vivo application (*1*, *22*, *23*, *36*, *37*). In those investigations, it was demonstrated that intact mAbs, and some F(ab′)$_2$ fragments, labeled with ^{211}At were relatively stable to in vivo deastatination. However, the 7.21 h half-life of ^{211}At did not match well with the biological half-lives of the intact mAb and F(ab′)$_2$ fragments, such that most of the radionuclide decayed before good tumor targeting was obtained. To improve in vivo pharmacokinetics, astatinated Fab fragments were evaluated. Even though the ^{211}At was bonded to a stabilizing benzoate derivative, it was not stable to in vivo deastatination when coupled to the more rapidly metabolized Fab fragments (*23*). This was surprising as examination of the in vitro stability of the astatinated Fab indicated that it was quite stable in serum. Thus, it appears that the release of ^{211}At from mAb Fab fragments results from enzymes or other conditions that are present during metabolism of the protein.

Given the fact that the instability of aryl-astatine bond appears to be facilitated by metabolic degradation of the carrier molecule, we hypothesized that there may be two methods of stabilizing astatine on carriers used for in vivo targeting. The first method is to utilize astatinated molecules that are excreted intact, avoiding the metabolic degradation. Because metabolic pathways can vary greatly with the nature of the biomolecule involved, it seems that this approach would not be applicable to most carrier molecules. The second method is to find alternative bonding structures that are not deastatinated under metabolic conditions. On the basis of the expectation that a boron astatine bond might be more stable than the aryl-astatine bond, we became interested in boron cage molecules, and particularly *nido*-carboranes, as pendant groups for astatine labeling. Hawthorne et al. had previously demonstrated that a *nido*-carborane conjugate could be used in the radioiodination of antibodies (*34*). *nido*-Carboranes were also investigated as hydrophilic pendant groups for attaching radionuclides of iodine to biomolecules (*30*). Those investigations showed that *nido*-carborane containing molecules were radioiodinated rapidly (<10 s) in high radiochemical yields (85−99%), and the resultant radioiodinated *nido*-carboranes were stable to in vivo deiodination. Reports of the astatination of *closo*-dodecaborate(2-) have been published (*58*, *59*). However, no previous investigations of astatinated *nido*-carborane derivatives have been reported, so we focused our studies in that area.

The primary goals of the investigation reported herein were to determine if astatinated *nido*-carboranes are more stable to in vivo deastatination than some simple aryl astatine compounds, and to examine the astatinated compounds distribution in vivo to determine if the pendant groups had properties that alter their in vivo characteristics. In addition to those goals, we were interested in (a) determining whether there were differences in the in vivo stability of *meta*- or *para*-substituted benzamide derivatives; (b) comparing the in vivo stability of a *nido*-carboranyl derivative which has a phenyl group attached to a carbon atom on the carborane cage molecule

with a similar *nido*-carborane molecule that has a methylene group attached to the carborane cage, and (c) determining if having two *nido*-carboranyl moieties held in close proximity (e.g., VFCs) would provide increased stability over astatinated compounds that had only one *nido*-carborane moiety. When planning the studies, simple in vitro assays were not included since our previous studies, and studies in other laboratories, had demonstrated that ^{211}At-labeled compounds were generally quite stable in serum and when challenged with a variety of reagents. In vitro assays that mimic organs, such as incubation of astatinated compounds with liver homogenates, were considered as they represented potential methods to predict in vivo ^{211}At stability with a minimal use of animals. However, those in vitro assays did not appear to be practical due to limitations on synthesis of compounds studied and the quantity of ^{211}At produced, which limited the preparation to only one ^{211}At labeled compound at a time. Further, in vitro analyses could not provide information on the differences in tissue distribution that was sought. Thus, we chose to conduct in vivo studies on each astatinated compound. To address the study goals, we decided to examine the biodistributions and in vivo stability of potential astatinated pendant groups by evaluation of simple derivatives that might be readily metabolized. The salient point is that we anticipate pendant groups that are stable to deastatination as simple derivatives will likely be stable in more complex molecules.

The studies conducted required the synthesis and radiolabeling of a number of benzoate and *nido*-carborane derivatives (Figure 1 and Schemes 1−8). The aryl stannanes and aryl halides were readily synthesized as depicted in Schemes 1 and 2 using methods previously described in the literature. Fortunately, the 1,2-carborane derivatives were also readily prepared as depicted in Schemes 3−8 using standard organic synthetic methods. Both the aryl stannanes and the *nido*-carboranes reacted very rapidly with electrophilic astatine to provide good labeling yields under mild conditions. The animal studies conducted were designed to provide limited biodistribution data, which based on previous studies would also provide information on the in vivo stability of astatinated compounds.

The determination of the in vivo stability of astatinated molecules toward deastatination was greatly facilitated by the propensity of astatide to localize to lung and spleen. Examining the tissue distribution data for ^{211}At alone (Figure 4) could lead to the conclusion that the astatinated benzoate derivatives provide the most favorable in vivo characteristics due to the high liver and intestine concentrations of the astatinated *nido*-carborane derivatives. However, dual label experiments provide data (tables in Supporting Information and Figure 5) that indicate the astatinated benzoates are deastatinated rapidly making them unfavorable as pendant groups. Indeed, the large difference between the concentration of ^{211}At- and ^{125}I-labeled benzamides in lung and spleen at 1 and 4 h postinjection (Figure 5) suggests that deastatination is very rapid. We had anticipated that the boron−astatine bond might be more stable toward deastatination than an aryl−astatine bond. While it appears that astatinated *nido*-carboranes are slightly more stable than the benzamides, it is not possible to state that unequivocally. Indeed, the difference in stability is not as large as had been anticipated. Further, the *nido*-carborane containing compounds have long retention in the blood, which could affect biomolecules when they are conjugated. Interestingly, comparison of the in vivo data from **7c** and **10c** indicates that there is very little difference between an astatinated *nido*-carborane containing an alkyl substituent or an aryl substituent. We had anticipated that a larger difference would be obtained based on steric and electronic differences in the *nido*-carborane cages.

The data obtained for the astatinated bis-*nido*-carborane derivatives **11c** and **12c** indicate that they provide high stability toward in vivo deastatination as (relatively) small molecule adducts. However, their propensity to localize to liver is problematic in their use as astatinated pendant groups. Interestingly, the radiohalogenated VFCs do not seem to adhere to glass and syringe needles to the extent that mono-*nido*-carborane derivatives do. This is encouraging as it may be possible through modification of the VFC to diminish the hepatobiliary excretion. It is interesting to consider possible explanations for the differences in stability between the astatinated mono-*nido*-carboranyl derivatives and bis-*nido*-carboranyl derivatives. Although the explanation is unknown, it might be speculated that the ^{211}At could bind with both *nido*-carborane moieties to bridge them. Such a bonding structure would require a higher oxidation state of ^{211}At, but the astatination is conducted under oxidative conditions and the halonium bridged structure would be similar to the well-known iodonium salt structures (*60*, *61*).

The benzyl-DTPA derivatives **12** and **13** were specifically prepared to decrease blood concentrations by inducing a more rapid renal clearance. However, the results indicate that the DTPA adducts did not reduce the blood concentrations; rather, an increased blood concentration was obtained. We had anticipated that the DTPA adducts would be metalated in vivo, which would have increased their hydrophilicity. In future studies, it may be better to chelate the DTPA prior to injection. While the addition of a DTPA did not decrease the blood concentration, it either resulted in more clearance by the renal system or more rapid passage through the liver. Unfortunately, the very high concentrations in liver of the bis-*nido*-carborane (VFC) did not appear to be altered appreciably by the addition of a benzyl-DTPA moiety.

In conclusion, we have prepared a series of astatinated and radioiodinated benzoate and *nido*-carboranyl compounds to examine their in vivo properties. The studies have demonstrated that there are large differences in the in vivo blood concentrations and tissue distributions. However, most of the small molecules labeled with ^{211}At were found to release free astatide via some unknown deastatination process. The exception to this were the astatinated "VFC" containing compounds, which were found to be quite stable to in vivo deastatination. Unfortunately, the VFC containing compounds are highly excreted by the hepatobiliary tract, making them unsuitable as biomolecule conjugates unless they are modified to decrease this propensity.

ACKNOWLEDGMENT

We thank Duke University investigators Susan Slade and Bent Schoultz for their technical assistance in the studies, and Dr. Roy H. Larsen for his discussions on the experiments conducted there. We thank the Department of Energy (DE-FG01-00NE22946) for funding the majority of the studies presented. Some portions of the studies were supported by NIH (CA42324) and the Department of Energy, Medical Applications and Biophysical Research Division, Office of Health and Environmental Research under Grant Number DE-FG06-95ER62029.

Supporting Information Available: Complete tissue distribution data (Tables 1−13). HPLC chromatograms, ^{1}H NMR spectra, and mass spectra for new compounds (**1a, 1b, 2a, 2b, 2e, 2f, 3a, 3b, 4a, 4b, 5a, 5b, 5e−5g, 6a, 6b, 7a, 7b, 7d−7f, 8a, 8b, 9b, 10a, 10b, 10e, 12a, 12b, 13a, 13b, 13e**) prepared in the research described in this paper. This material is available free of charge via the Internet at http://pubs.acs.org.

LITERATURE CITED

(1) Yordanov, A. T., Garmestani, K., Zhang, M., Zhang, Z., Yao, Z., Phillips, K. E., Herring, B., Horak, E., Beitzel, M. P., Schwarz, U. P., Gansow, O. A., Plascjak, P. S., Eckelman, W. C., Waldmann, T. A. and Brechbiel, M. W. (2001) Preparation and in vivo evaluation of linkers for ^{211}At labeling of humanized anti-Tac. *Nucl. Med. Biol. 28*, 845−856.

(2) Vaidyanathan, G., and Zalutsky, M. R. (1992) 1-(*m*-[^{211}At]-Astatobenzyl)guanidine: Synthesis via Astato Demetalation and Preliminary in Vitro and In Vivo Evaluation. *Bioconjugate Chem. 3*, 499−503.

(3) Vaidyanathan, G., Friedman, H. S., Keir, S. T. and Zalutsky, M. R. (1996) Evaluation of *Meta*-[^{211}At]Astatobenzylguanidine in an Athymic Mouse Human Neuroblastoma Xenograft Model. *Nucl. Med. Biol. 23*, 851−856.

(4) Grimes, R. N. (1970) Structures and Bonding. In *Carboranes*, pp 5−22, Academic Press, New York.

(5) Feinendegen, L. E., and McClure, J. J. (1997) Alpha-Emitters for Medical Therapy − Workshop of the United States Department of Energy. *Radiat. Res. 148*, 195−201.

(6) Wilbur, D. S. (1991) Potential use of alpha emitting radionuclides in the treatment of cancer. *Antibody, Immunoconjugates, Radiopharm. 4*, 85−97.

(7) Zalutsky, M. R., and Bigner, D. D. (1996) Radioimmunotherapy With α-Particle Emitting Radioimmunoconjugates. *Acta Oncol. 35*, 373−379.

(8) Breitz, H. B., Weiden, P. L., and Beaumier, P. L. (2000) Radioimmunotherapy of Solid Tumors. In *Radioimmunotherapy of Cancer* (P. G. Abrams, and A. R. Fritzberg, Eds.) pp 265−307, Marcel Dekker, Inc., New York.

(9) Kairemo, K. J. A. (1996) Radioimmunotherapy of Solid Cancers. *Acta Oncol. 35*, 343−355.

(10) DeNardo, S. J., Kroger, L. A., and DeNardo, G. L. (1999) A new era for radiolabeled antibodies in cancer? *Curr. Opin. Immunol. 11*, 563−569.

(11) Goldenberg, D. M. (2002) Targeted therapy of cancer with radiolabeled antibodies. *J. Nucl. Med. 43*, 693−713.

(12) von Mehren, M., Adams, G. P., and Weiner, L. M. (2003) Monoclonal antibody therapy for cancer. *Annu. Rev. Med. 54*, 343−369.

(13) Reubi, J. C. (1997) Regulatory peptide receptors as molecular targets for cancer diagnosis and therapy. *Q. J. Nucl. Med. 41*, 63−70.

(14) Heppeler, A., Froidevaux, S., Eberle, A. N., and Maecke, H. R. (2000) Receptor targeting for tumor localisation and therapy with radiopeptides. *Curr. Med. Chem. 7*, 971−994.

(15) Vaughan, A. T. M., and Fremlin, J. H. (1977) The Preparation of Astatotyrosine. *Int. J. Appl. Radiat. Isot. 28*, 595−598.

(16) Visser, G. W. M., Diemer, E. L., and Kaspersen, F. M. (1979) The Preparation and Stability of Astatotyrosine and Astato-iodotyrosine. *Int. J. Appl. Radati. Isot. 30*, 749−752.

(17) Vaughan, A. T. M., and Fremlin, J. H. (1978) The Preparation of Astatine Labeled Proteins Using an Electrophilic Reaction. *Int. J. Nucl. Med. Biol. 5*, 229−230.

(18) Visser, G. W. M., Diemer, E. L., and Kaspersen, F. M. (1981) The Nature of the Astatine-Protein Bond. *Int. J. Appl. Radiat. Isot. 32*, 905−912.

(19) Friedman, A. M., Zalutsky, M. R., Wung, W., Buckingham, F., Harper, P. V., Scherr, G. H., Wainer, B., Hunter, R. L., Appelman, E. H., Rothberg, R. M., Fitch, F. W., Stuart, F. P., and Simonian, S. J. (1977) Preparation of a Biologically Stable and Immunologically Competent Astatinated Protein. *Int. J. Nucl. Med. Biol. 4*, 219−224.

(20) Vaughan, A. T. M. (1979) Labeling of Proteins with ^{211}At using an Acylation Reaction. *Int. J. Appl. Radiat. Isot. 30*, 576−577.

(21) Harrison, A., and Royle, L. (1984) Preparation of a ^{211}At−IgG Conjugate which is Stable in vivo. *Int. J. Appl. Radiat. Isot. 35*, 1005−1008.

(22) Zalutsky, M. R., and Narula, A. S. (1988) Astatination of Proteins using an *N*-Succinimidyl Tri-*n*-Butylstannyl Benzoate Intermediate. *Appl. Radiat. Isot. 39*, 227−232.

(23) Hadley, S. W., Wilbur, D. S., Gray, M. A., and Atcher, R. W. (1991) Astatine-211 labeling of an antimelanoma antibody and its Fab fragment using N-succinimidyl *p*-[^{211}At]astatobenzoate: comparisons in vivo with the *p*-[^{125}I]iodobenzoyl conjugate. *Bioconjugate Chem. 2*, 171−179.

(24) Vaidyanathan, G., Affleck, D., and Zalutsky, M. R. (1994) Monoclonal Antibody F(ab′)$_2$ Fragment Labeled With N-Succinimidyl 2,4-Dimethoxy-3-halobenzoates: In Vivo Comparison of Iodinated and Astatinated Fragments. *Nucl. Med. Biol. 21*, 105−110.

(25) Coenen, H. H., Moerlein, S. M., and Stöcklin, G. (1983) No−Carrier-Added Radiohalogenation Methods with Heavy Halogens. *Radiochim. Acta 34*, 47−68.

(26) Wilbur, D. S. (1992) Radiohalogenation of proteins: An overview of radionuclides, labeling methods and reagents for conjugate labeling. *Bioconjugate Chem. 3*, 432−470.

(27) Kabalka, G. W., and Varma, R. S. (1989) The Synthesis of Radiolabeled Compounds Via Organometallic Intermediates. *Tetrahedron 45*, 6601−6621.

(28) Mizusawa, E. A., Thompson, M. R., and Hawthorne, M. F. (1985) Synthesis and Antibody-Labeling Studies with the *p*-Isothiocyanatobenzene Derivatives of 1,2-Dicarba-*closo*-dodecaborane(12) and the Dodecahydro-7,8-dicarba-*nido*-undecaborate(1-) Ion for Neutron-Capture Therapy of Human Cancer. Crystal and Molecular Stucture of Cs+[*nido*-7-(*p*-C_6H_4NCS)-9-I-7,8-$C_2B_9H_{11}$]. *Inorg. Chem. 24*, 1911−1916.

(29) Varadarajan, A., Sharkey, R. M., Goldenberg, D. M., and Hawthorne, M. F. (1991) Conjugation of Phenyl Isothiocyanate Derivatives of Carborane to Antitumor antibody and in Vivo Localization of Conjugates in Nude Mice. *Bioconjugate Chem. 2*, 102−110.

(30) Wilbur, D. S., Hamlin, D. K., and Srivastava, R. R. (1994) Radioiodinations of *nido*-Carboranes. Potential Hydrophilic Pendant Groups for Radiohalogenation of Biological Molecules. *J. Labelled Compd. Radiopharm. 35*, 199−201.

(31) Kerr, J. A. (1993) Strengths of Chemical Bonds. In *CRC Handbook of Chemistry and Physics* (D. R. Lide, Ed.) pp 9-123−9-145, CRC Press, Boca Raton.

(32) Paxton, R. J., Beatty, B. G., Hawthorne, M. F., Varadarajan, A., Williams, L. E., Curtis, F. L., Knobler, C. B., and Shively, J. E. (1991) A Transition metal complex (Venus flytrap cluster) for radioimmunodetection and radioimmunotherapy. *Proc. Natl. Acad. Sci. U.S.A. 88*, 3387−3391.

(33) Varadarajan, A., Johnson, S. E., Gomez, F. Z., Chakrabarti, S., Knobler, C. B., and Hawthorne, M. F. (1992) Synthesis and Structural Characterization of Pyrazole-Bridged Metalla-Bis(dicarbollide) Derivatives of Cobalt, Nickel, Copper, and Iron: Models for Venus Flytrap Cluster Reagents. *J. Am. Chem. Soc. 114*, 9003−9011.

(34) Hawthorne, M. F., and Maderna, A. (1999) Applications of radiolabeled boron clusters to the diagnosis and treatment of cancer. *Chem. Rev. 99*, 3421−3434.

(35) Gamper, H. B., Reed, M. W., Cox, T., Virosco, J. S., Adams, A. D., Gall, A. A., Scholler, J. K., and Meyer, R. B. (1993) Facile Preparation of Nuclease Resistant 3′ Modified Oligodeoxynucleotides. *Nucleic Acids Res. 21*, 145−150.

(36) Zalutsky, M. R., Garg, P. K., Friedman, H. S., and Bigner, D. D. (1989) Labeling monoclonal antibodies and F(ab′)$_2$ fragments with the α-particle-emitting nuclide astatine-211: Preservation of Immunoreactivity and in vivo localizing capacity. *Proc. Natl. Acad. Sci. U.S.A. 86*, 7149−7153.

(37) Wilbur, D. S., Vessella, R. L., Stray, J. E., Goffe, D. K., Blouke, K. A., and Atcher, R. W. (1993) Preparation and evaluation of *para*-[^{211}At]astatobenzoyl labeled anti-renal cell carcinoma antibody A6H F(ab′)$_2$. In vivo distribution comparison with *para*-[^{125}I]iodobenzoyl labeled A6H F(ab′)$_2$. *Nucl. Med. Biol. 20*, 917−927.

(38) Wilbur, D. S., Hamlin, D. K., Pathare, P. M., and Weerawarna, S. A. (1997) Biotin reagents for antibody pretargeting. Synthesis, radioiodination and in vitro evaluation of water soluble, biotinidase resistant biotin derivatives. *Bioconjugate Chem. 8*, 572−584.

(39) Gomez, F. A., Johnson, S. E., and Hawthorne, M. F. (1991) A Versatile Protecting Group for 1,2-Dicarba-*closo*-dodecaborane(12) and the Structure of a Silylcarborane Derivative. *J. Am. Chem. Soc. 113*, 5915−5917.

(40) Heying, T. L., Ager, J. W., Clark, S. L., Mangold, D. J., Goldstein, H. L., Hillman, M., Polak, R. J., and Szymanski, J. W. (1963) A New Series of Organoboranes. I. Carboranes from the Reaction of Decaborane with Acetylenic Compounds. *Inorg. Chem. 2*, 1089−1092.

(41) Olsen, F. P., and Hawthorne, M. F. (1965) Halodicarbaundecaborate(II) Ions. *Inorg. Chem. 4*, 1839−1840.

(42) Zalutsky, M. R., and Vaidyanathan, G. (2000) Astatine-211-labeled radiotherapeutics: an emerging approach to targeted alpha-particle radiotherapy. *Curr. Pharm. Des. 6*, 1433−1455.

(43) Arano, Y., Wakisaka, K., Ohmomo, Y., Uezono, T., Mukai, T., Motonari, H., Shiono, H., Sakahara, H., Konishi, J., Tanaka, C., and Yokoyama, A. (1994) Maleimidoethyl 3-(Tri-*n*-butylstannyl)hippurate: A Useful Radioiodination Reagent for Protein Radiopharmaceuticals to Enhance Target Selective Radioactivity Localization. *J. Med. Chem. 37*, 2609−2618.

(44) Arano, Y., Wakisaka, K., Mukai, T., Uezono, T., Motonari, H., Akizawa, H., Kairiyama, C., Ohmomo, Y., Tanaka, C., Ishiyama, M., Sakahara, H., Konishi, J., and Yokoyama, A. (1996) Stability of a Metabolizable Ester Bond in Radioimmunoconjugates. *Nucl. Med. Biol. 23*, 129−136.

(45) Wilbur, D. S., Hamlin, D. K., Kegley, B. B., Chyan, M. K., Pathare, P. M., and Wan, F. (2001) Studies Which Indicate That Thiourea Bonds Interfere With Radioiodination Reactions. *J. Labelled Compd. Radiopharm. 44*, S973−S975.

(46) Wilbur, D. S., Chyan, M. K., Hamlin, D. K., Kegley, B. B., Nilsson, R., Sandberg, B. E., and Brechbiel, M. (2002) Trifunctional conjugation reagents. Reagents that contain a biotin and a radiometal chelation moiety for application to extracorporeal affinity adsorption of radiolabeled antibodies. *Bioconjugate Chem. 13*, 1079−1092.

(47) Trejtnar, F., and Laznicek, M. (2002) Analysis of renal handling of radiopharmaceuticals. *Q. J. Nucl. Med. 46*, 181−194.

(48) Hamilton, J. G., Asling, C. W., Garrison, W. M., and Scott, K. G. (1953) The Accumulation, Metabolism and Biological Effects of Astatine in Rats and Monkeys. *Univ. Calif. Publ. Pharmacol. 2*, 283−343.

(49) Garg, P. K., John, C. S., and Zalutsky, M. R. (1995) Preparation and Preliminary Evaluation of 4-[^{211}At]Astato-N-piperidinoethyl Benzamide. *Nucl. Med. Biol. 22*, 467−473.

(50) Hughes, W. L., and Gitlin, D. (1955) Astatinated (At^{211}) Organic Compounds for Production of Highly Localized Radiobiological Effects. *Am. Soc. Biol. Chem. 14*, 229.

(51) Friedman, A. M. (1978) Radioastatine: Possible Uses of a Heavy Halogen. In *Therapy in Nuclear Medicine* (R. P. Spencer, Ed.) pp 139−144, Grune & Stratton, New York.

(52) Brown, I. (1987) Astatine: Its Organonuclear Chemistry and Biomedical Applications. *Adv. Org. Chem. 31*, 43−88.

(53) Brown, I. (1986) Astatine-211: Its Possible Applications in Cancer Therapy. *Appl. Radiat. Isot. 37*, 789−798.

(54) Wilbur, D. S. (1991) Potential use of alpha-emitting radionuclides in the treatment of cancer. *Antibody, Immunoconjugates, Radiopharm. 4*, 85−97.

(55) Visser, G. W. M., Diemer, E. L., Vos, C. M., and Kaspersen, F. M. (1981) The Biological Behaviour of Some Organic Astatine Compounds in Rats. *Int. J. Appl. Radiat. Isot. 32*, 913−917.

(56) Garg, P. K., Harrison, C. L., and Zalutsky, M. R. (1990) Comparative Tissue Distribution in Mice of the α-emitter ^{211}At and ^{131}I as Labels of a Monoclonal Antibody and $F(ab')_2$ Fragment. *Cancer Res. 50*, 3514−3520.

(57) Berei, K., and Vasáros, L. (1983) Organic chemistry of astatine. *The Chemistry of Functional Groups, Supplement D* (S. Patai, and Z. Rappoport, Eds.) pp 405−440, John Wiley & Sons Ltd, New York.

(58) Orlova, A., Lebeda, O., Tolmachev, V., Sjoberg, S., Carlsson, J., and Lundqvist, H. (2000) *Closo*-dodecaborate (2-) anion as a potential prosthetic group for attachment of astatine to proteins. Aspects of the labeling chemistry with Chloramine-T. *J. Labelled Compd. Radiopharm. 43*, 251−260.

(59) Orlova, A., Lebeda, O., Tolmachev, V., Sjoberg, S., Carlsson, J., and Lundqvist, H. (1999) Astatination of *Closo*-Dodecaborate(2-) Anion. *J. Labelled Compd. Radiopharm. 42*, S735−S737.

(60) Varvoglis, A. (1992) Iodonium Salts. In *The Organic Chemistry of Polycoordinated Iodine*, pp 207−306, VCH Publishers, Inc.,

(61) Zhdankin, V. V., and Stang, P. J. (2002) Recent Developments in the Chemistry of Polyvalent Iodine Compounds. *Chem. Rev. 102*, 2523−2584.

BC034175K

TECHNICAL NOTES

Efficient Synthesis of Isotopically Pure Isotope-Coded Affinity Tagging Reagents

Anupama Patel and David M. Perrin*

Department of Chemistry, 2036 Main Mall, University of British Columbia, Vancouver, B. C. V6T 1Z1 Canada, and PENCE Inc. (Protein Engineering Network of Centers of Excellence), 750 Heritage Medical Research Center, Edmonton, Alberta T6G-2S2 Canada. Received June 3, 2003; Revised Manuscript Received July 23, 2003

Synthesis of an isotopically pure d_8-ICAT linker, *N*-[(5,5,6,6,8,8,9,9-^{2}H)-13-biotinamido-4,7,10-trioxatridecanyl] *tert*-butyloxy carbamide (**12**), has been achieved in seven steps with an overall yield of 33%. Conjugation of exchange-inert d_4-starting materials by classic etherification reaction yielded a pure synthon, carrying eight deuteriums that remained exchange-inert throughout subsequent reactions. This modified synthesis constitutes a significant improvement to the reported syntheses of "heavy" ICAT reagent in terms of expense, yield, and isotopic retention. This synthesis is easily adapted to incorporate additional deuterium atoms and is equally applicable for incorporation of either ^{13}C and/or ^{18}O. In addition, this synthesis allows for the introduction of different orthogonal functionalities and provides for a high yielding series of differentially encoded ICAT tags.

INTRODUCTION

Proteomics is an exciting field in the study of proteins and particularly the study of complex systems involving multiple proteins where each may exert a subtle effect that synergistically gives rise to an identifiable global cellular or physiological state or process. The multiplicity of proteins and effectors increases the difficulty of assigning the cellular and physiological functions to individual proteins as well as complicates the process of drug discovery and target validation. In this growing research field of proteomics, various new approaches have become available to facilitate the identification of many of the proteins in a cell and to generate data that more closely correlate with protein activity levels. However, compared to genomics, proteomics studies face formidable technical challenges due to the structural complexity, the temporal nature of regulation, function, and abundance as well as vast structural variation of different proteins in a cell. To permit a global characterization of the proteome with more rapid and more detailed interrogation, various new strategies are being developed in the research field of proteomics (*1*−*8*). In this context, Aebersold described a creative alternative method dubbed isotope-coded affinity tagging (ICAT)[1] methodology (*9*).

Instead of relying on 2D PAGE and protein-staining methods for quantification, the ICAT method involves utilization of isotopically labeled chemical probes, (ICAT, Figure 1) (*9*) for the quantitative comparison of protein abundances between complex proteomes. Ultimately, this analysis is achieved by some form of mass spectrometry that is being interfaced with robotics and automated sample analysis so as to streamline the discovery process and eliminate human error.

* To whom correspondence should be addressed. Phone: 001 604 822 0567; Fax: 001 604 822 2847; E-mail: dperrin@chem.ubc.ca.

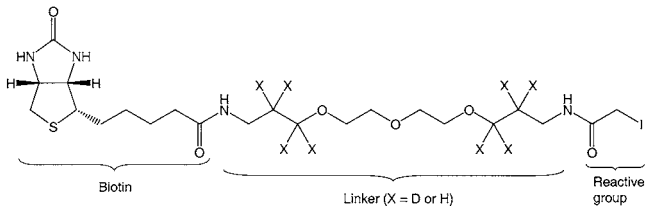


Figure 1. Cysteine-speciic ICAT-reagents for quantitative proteomics studies.[9]

Conceptually, the ICAT reagent is a trifunctional molecule, composed of (a) a specific reactive group capable of reacting covalently with an active site nucleophile (e.g. iodoacetamide for covalent attachment to a cysteinyl thiol); (b) an isotopically coded linker that occurs in a deuterated (isotopically "heavy", X = D) or nondeuterated (isotopically "light", X = H) form and provides the basis for accurate quantification; and (c) a biotin group that enables the isolation of the tagged peptides from complex peptide mixtures via avidin affinity chromatography. This approach makes use of the principle of isotope dilution for analysis. For the quantitative comparison between two proteomes in two different states (e.g. normal and disease state), the 'light' (nondeuterated) ICAT reagent is used to covalently tag proteins of one proteome and the 'heavy' (deuterated) ICAT reagent is used to covalently tag proteins of a second proteome. The two proteomes are then combined for quantitative analysis. Analysis often involves further steps such as digestion of the mixture with a protease (e.g. trypsin), isolation of the ICAT-labeled peptides by affinity purification on avidin, and analysis of the isolated labeled peptide mixture by liquid chromatography−mass spectrometry (LC/MS). Prior mixing of proteins that have been labeled with either light or heavy ICAT reagents eliminates much of the potential experimental error associated with postlabeling analysis. Since the two different physiologi-

10.1021/bc0300293 CCC: $27.50 © 2004 American Chemical Society
Published on Web 12/30/2003

cal states are correlated with differential labeling, proteins that are present at very different levels in the two cell states will yield a pair of signals of unequal intensity in the LC-MS (each signal pair differing in mass by the number of deuterium atoms incorporated). Searching for peptide pairs of unequal intensity, followed by tandem MS sequencing, identifies proteins whose levels change as a consequence of the disease.

Although many reports have highlighted the utility of the ICAT methodology for proteomic profiling (*9*−*16*), few have discussed the synthetic methodologies for generating 'heavy' ICAT reagents with respect to the isotopic purity and the cost of the synthesis. As initially reported for the synthesis of the 'heavy' ICAT reagent (*9*, *17*), the d_8-diamine linker was synthesized in two steps: first by Michael addition of diethylene glycol-d_2 (i.e. $O(CH_2CH_2OD)_2$) on the expensive d_3-acrylonitrile, in the presence of catalytic NaOD solution in D_2O, and then subsequent nitrile reduction using Raney nickel, providing an octadeuterodiamine linker. Reacting an excess molar equivalent of the d_8-diamine linker with biotin-pentafluorophenyl ester (*18*) afforded the biotinylated d_8- linker-monoamine, which was then treated with iodoacetic anhydride to give rise to the "heavy" ICAT reagent (Figure 1, X = D).

The problems associated with the reported synthesis of "heavy" ICAT reagent (*9*, *17*) are as follows. (a) The Michael addition reaction results in significant (about 10%) loss of deuterium due to exchange with protium at the carbon α to the nitrile group. Consequently, d_7 and d_6 derivatives contaminate the desired d_8-linker. This gives rise to an inseparable mixture of octa-, hepta-, and hexadeuterodinitrile linkers. (b) The subsequent nitrile reduction to amine groups using Raney nickel results in an increase in the percentage of d_7 and d_6 derivatives due to considerable exchange of the deuteriums with protiums at the α-carbon to the nitrile group. In addition, the yield in this step is very low due to a notable retro-Michael type reaction (*12*). (c) The subsequent amide coupling reaction with biotin pentafluorophenyl ester necessarily requires a large molar excess of d_8-diamine linker (*9*, *12*) to ensure mono-biotinylation and avoid bis-biotinylation. The excess of unreacted diamine, being polar, is difficult to recover from the reaction mixture and results in a significant loss of the diamine. Recently Gelb and co-workers addressed these concerns, as they have described a different reaction strategy that improved the yield of the d_8-diamine linker with respect to deuterium exchange (*12*). However, their process involves a larger number of steps, still requires the use of d_3-acrylonitrile, and moreover does not address the problem of the loss of the diamine in the amide coupling reaction with biotin or other capture ligands. Addressing this problem not only applies to the deuterium-labeled approach, but to other, more recent approaches involving ^{13}C-labeled linkers.

EXPERIMENTAL SECTION

General. Methods And Materials. Flash chromatography was carried out using silica gel 60, 230−400 mesh, supplied by E. Merck Co. TLC was performed on silica gel 60 F_{254} on aluminum sheets (E. Merck, type 5554), and detection was carried out by staining with 8% ammonium molybdate tetrahydrate (Fluka) in 2 M sulfuric acid solution in methanol, and under UV light and by iodine adsorption when applicable. Nuclear magnetic resonance spectra (^1H and ^{13}C) were recorded at 298 K, at 400 MHz (for ^1H) and 100.67 MHz for (^{13}C NMR) using a Bruker AV-400 instrument. Chemical shifts are given in ppm values relative to internal standard TMS (0.00 ppm). Solvent, signal multiplicity, coupling constants (in Hz), and integration ratios are indicated in the experimental procedures. Two-dimensional $^1H-^1H$ and $^1H-^{13}C$ COSY (HMQC) experiments were performed for complete signal assignments wherever necessary. ESI MS spectra were obtained on a Bruker Esquire-LC instrument. HRMS spectra were obtained for final compound **12** in the mass spectrometry laboratory of the Chemistry Department, UBC. Palladium hydroxide (20 wt. %), Raney nickel, *n*-Bu_4NBr, formic acid, anhydrous DMF (99.8%), and DIPEA were purchased from Aldrich, and biotin from Sigma. Toluene was dried over Na metal, DIPEA was distilled over CaH_2, and anhydrous DMF was stored on activated molecular sieves prior to use. Tetradeuterated precursors **1** (*19*) and **2** (*20*) were synthesized from the commercially available (Aldrich) and inexpensive compounds ethylene-d_4 glycol and 2-bromoethanol-1,1,2,2-d_4 according to a known literature procedure. Also following a literature procedure, compound **5** (*22*) from 3-chloropropylamine hydrochloride (Aldrich) and biotin pentaflourophenyl ester (*18*) from biotin have been prepared. As described in the following experimental procedures, all the compounds were easily purified by flash chromatographic methods, and structure of each compound has been characterized and confirmed by NMR and mass spectrometry.

Synthesis. (1,1,2,2,4,4,5,5-^{2}H)-5-Benzyloxy-1-tetrahydropyranyloxy-3-oxapentane (3). (1,1,2,2-^{2}H)-2-Benzyloxyethylene glycol (**1**) (1.1 g, 7.05 mmol) was suspended in NaOH solution (20 mL, 1 g/mL in H_2O) containing *n*-Bu_4NBr (0.1 g, 0.7 mmol) and heated at 80 °C for 30 min. To the hot reaction mixture (1,1,2,2-^{2}H)-1-tetrahydropyranyloxy-2-bromoethanol (**2**) (1.8 g, 8.46 mmol) was added, and the reaction mixture was further stirred at 80 °C for 3 h. Then the reaction mixture was cooled to room temperature and diluted with water (10 mL). The crude product was extracted with diethyl ether (2 × 15 mL) and ethyl acetate (10 mL). The organic layer was successively washed with water and brine and then dried over anhydrous Na_2SO_4. After filtration, the solvent was concentrated in vacuo, and the crude product obtained was purified by flash chromatography (petroleum ether−ethyl acetate, 6:1) to afford the title compound (**3**, 1.9 g, 6.6 mmol, 94%) as a colorless syrup. TLC (petroleum ether−ethyl acetate, 4:1): $R_f = 0.35$ (UV, blue stain in ammonium molybdate). ^1H NMR (400 MHz, $CDCl_3$): δ = 7.35−7.20 (m, 5H, 5 aryl-H), 4.61 (m_c, 1H, OCHO), 4.55 (s, 2H, OCH_2Ph), 3.85 (m_c, 1H, OCH_a), 3.47 (m_c, 1H, OCH_b), 1.91−1.40 (m, 6H, $3CH_2$) ppm; ^{13}C NMR (100.61 MHz, $CDCl_3$): δ = 138.92 (aryl *t*-C), 128.97, 128.89, 128.26, 128.10 (5 aryl-C), 99.47 (OCHO), 73.74 (OCH_2Ph), 70.29, 69.41, 66.43 (3 weak multiplets, 4 OCD_2), 62.75 (OCH_2), 31.14, 26.0, 20.04 (3 CH_2) ppm. ESI-MS: m/z = 311.21 $[M + Na]^+$, 327.21 $[M + K]^+$ observed for $C_{16}H_{16}D_8O_4$ (288.22).

(1,1,2,2,4,4,5,5-^{2}H)-5-Benzyloxy-3-oxapentan-1-ol (4). A solution of **3** (1.8 g, 6.25 mmol) in MeOH (10 mL) was treated with HCl solution (10% in MeOH, 0.5 mL) at 0 °C for 1 h. The acidic reaction mixture was neutralized with aqueous $NaHCO_3$ solution and concentrated in vacuo. The crude product was purified by flash chromatography (petroleum ether−ethyl acetate, 7:3) to afford the alcohol derivative, (**4**, 1.15 g, 5.63 mmol, 90%) as colorless syrup. TLC (petroleum ether−ethyl acetate, 2:1): $R_f = 0.1$ (UV, blue stain in ammonium molybdate). ^1H NMR (400 MHz, $CDCl_3$): δ = 7.35−7.20 (m, 5H, 5 aryl-H), 4.54 (s, 2H, OCH_2Ph), 2.35 (bs, 1H, OH) ppm;

^{13}C NMR (100.61 MHz, $CDCl_3$): δ = 137.98 (aryl *t*-C), 128.39, 127.74 (5 aryl-C), 73.23 (OCH_2Ph), 69.79, 68.28, 60.95 (3 weak multiplets, 4 OCD_2) ppm. ESI-MS: *m*/*z* = 205.18 $[M + H]^+$, 227.20 $[M + Na]^+$ observed for $C_{11}H_8D_8O_3$ (204.16).

***N*-[(5,5,6,6,8,8,9,9-^{2}H)-9-Benzyloxy-4,7-dioxanonanyl]-*tert*-butyloxycarbamide (6).** Following the similar experimental procedure as in case of compound **3**, the title compound **6** was prepared by reacting **4** (1.01 g, 4.95 mmol) and *N*-(3-chloropropyl)-*tert*-butyloxycarbamide (**5**) (1.92 g, 9.92 mmol) in NaOH solution (10 mL, 1 g/mL in H_2O) containing *n*-Bu_4NBr (0.1 g, 0.7 mmol) at 80 °C for 1 h. The crude product obtained was purified by flash chromatography (petroleum ether−ethyl acetate, 4:1) to afford the corresponding conjugate (**6**, 1.31 g, 3.62 mmol, 73%) as colorless syrup. TLC (petroleum ether−ethyl acetate, 2:1): R_f = 0.3 (UV, blue stain in ammonium molybdate). ^{1}H NMR (400 MHz, $CDCl_3$): δ = 7.36−7.20 (m, 5H, 5 aryl-H), 4.92 (bs, 1H, NHBoc), 4.55 (s, 2H, OCH_2Ph), 3.52 (t, *J* = 5.87 Hz, 2H, OCH_2), 3.20 (m_c, 2H, C*H*$_2$NHBoc), 1.72 (m, 2H, OCH_2CH_2), 1.41 (s, 9H, *t*-Bu) ppm; ^{13}C NMR (100.61 MHz, $CDCl_3$): δ = 156.32 (CONH), 138.56 (aryl *t*-C), 128.63, 128.0, 127.86 (5 aryl-C), 79.17 (*C*(CH_3)), 73.46 (OCH_2Ph), 69.81 (OCH_2, weak multiplet for 4 OCD_2), 38.90 (CH_2NHBoc), 29.92 (OCH_2CH_2), 28.73 (C(*C*H_3)) ppm. ESI-MS: *m*/*z* = 362.29 $[M + H]^+$, 384.3 $[M + Na]^+$, 400.3 $[M + K]^+$ observed for $C_{19}H_{23}D_8NO_5$ (361.27).

***N*-[(5,5,6,6,8,8,9,9-^{2}H)-9-Hydroxy-4,7-dioxanonanyl]-*tert*-butyloxycarbamide (7).** A mixture of **6** (1.14 g, 3.15 mmol) and $Pd(OH)_2$ (20% on charcoal, 50 mg) in ethyl acetate (10 mL) was hydrogenated under atmospheric pressure for 3 h at RT. Then the reaction mixture was filtered through a thin Celite bed, and the residue was washed with MeOH (10 mL). The filtrate was concentrated in vacuo, and the residue was subjected to flash chromatographic purification on silica gel using neat ethyl acetate as the eluent, yielding the alcohol derivative (**7**, 0.74 g, 2.73 mmol, 87%) as a colorless syrup. For flash column chromatographic purification, neat ethyl acetate was needed to obtain the desired product **7** in pure form. The increased polarity of **7** may be accounted to the free hydroxyl group resulting from the hydrogenolysis. TLC (petroleum ether−ethyl acetate, 1:1): R_f = 0.5 (white patch in ammonium molybdate). ^{1}H NMR (400 MHz, $CDCl_3$): δ = 5.10 (bs, 1H, NHBoc), 3.52 (t, *J* = 5.86 Hz, 2H, OCH_2), 3.20 (t, *J* = 6.37 Hz, 2H, C*H*$_2$NHBoc), 2.78 (bs, 1H, OH), 1.71 (m, 2H, OCH_2CH_2), 1.41 (s, 9H, *t*-Bu) ppm; ^{13}C NMR (100.61 MHz, $CDCl_3$): δ = 156.30 (CONH), 79.31 (*C*(CH_3)), 69.73 (OCH_2, weak multiplet for 3 OCD_2), 61.18 (weak multiplet, CD_2OH), 38.71 (CH_2NHBoc), 29.90 (OCH_2CH_2), 28.69 (C(*C*H_3)) ppm. ESI-MS: *m*/*z* = 294.3 $[M + Na]^+$, 310.25 $[M + K]^+$ observed for $C_{12}H_{17}D_8NO_5$ (271.22).

***N*-[(5,5,6,6,8,8,9,9-^{2}H)-12-Cyano-4,7,10-trioxadidecanyl]-*tert*-butyloxycarbamide (10).** To a suspension of **7** (0.67 g, 2.47 mmol) and solid NaOH (10 mg, 0.24 mmol) in anhydrous toluene (10 mL) was added acrylonitrile (0.21 mL, 3.21 mmpl) under nitrogen atmosphere, and the reaction mixture was stirred for 3 h at RT in the dark. Then the reaction mixture was diluted with ethyl acetate and successively washed with water (5 mL) and brine. After drying over anhydrous Na_2SO_4, the organic layer was filtered and concentrated in vacuo. Purification of the crude product by flash chromatography (petroleum ether−ethyl acetate, 1:1) afforded the nitrile adduct (**10**, 0.77 g, 2.37 mmol, 96%) as colorless syrup. TLC (petroleum ether−ethyl acetate, 1:1): R_f = 0.1 (iodine, white patch in ammonium molybdate). ^{1}H NMR (400 MHz, $CDCl_3$): δ = 4.90 (bs, 1H, NHBoc), 3.70 (t, *J* = 6.44 Hz, 2H, OCH_2), 3.52 (t, *J* = 5.97 Hz, 2H, OCH_2), 3.18 (m_c, 2H, C*H*$_2$NHBoc), 2.58 (t, *J* = 6.45 Hz, 2H, CH_2CN), 1.73 (m, 2H, OCH_2CH_2), 1.41 (s, 9H, *t*-Bu) ppm; ^{13}C NMR (100.61 MHz, $CDCl_3$): δ = 155.97 (CONH), 117.79 (CN), 78.93 (*C*(CH_3)), 69.46 (OCH_2, weak multiplet for 4 OCD_2), 65.86 (OCH_2), 38.68 (CH_2NHBoc), 29.63 (OCH_2CH_2), 28.41 (C(*C*H_3)), 18.84 (CH_2CN) ppm. ESI-MS: *m*/*z* = 325.26 $[M + H]^+$, 347.31 $[M + Na]^+$, 363.31 $[M + K]^+$ observed for $C_{15}H_{20}D_8N_2O_5$ (324.25).

***N*-[(5,5,6,6,8,8,9,9-^{2}H)-13-Amino-4,7,10-trioxatridecanyl]-*tert*-butyloxycarbamide (11).** A mixture of **10** (0.58 g, 1.79 mmol) and Raney nickel (30 mg) in MeOH (8 mL) was hydrogenated under atmospheric pressure for 12 h at RT. Then the reaction mixture was filtered through a thin Celite bed, and the filtrate was concentrated in vacuo which afforded the pure amine derivative **11** (0.6 g) as a colorless oil, in quantitative yield. After filtration of the catalyst, compound **11** was obtained in pure form without any further need for chromatographic purification. TLC (CH_2Cl_2−MeOH, 9:1): R_f = 0.1 (iodine, white patch in ammonium molybdate). ^{1}H NMR (400 MHz, d_4-MeOH): δ = 3.51 (t, *J* = 6.1 Hz, 2H, OCH_2), 3.46 (t, *J* = 6.2 Hz, 2H, OCH_2), 3.08 (t, *J* = 6.76 Hz, 2H, C*H*$_2$NHBoc), 2.52 (t, *J* = 6.82 Hz, 2H, CH_2NH_2), 1.78−1.60 (m, 4H, 2 OCH_2CH_2), 1.38 (s, 9H, *t*-Bu) ppm; ^{13}C NMR (100.61 MHz, d_4-MeOH): δ = 158.45 (CONH), 79.84 (*C*(CH_3)), 70.36 (OCH_2, weak multiplet for 4 OCD_2), 69.81 (OCH_2), 40.10 (CH_2NHBoc), 38.71 (CH_2NH_2), 33.55, 30.92 (2 OCH_2CH_2), 28.80 (C(*C*H_3)) ppm. ESI-MS: *m*/*z* = 329.32 $[M + H]^+$, 351.33 $[M + Na]^+$ observed for $C_{15}H_{24}D_8N_2O_5$ (328.28).

***N*-[(5,5,6,6,8,8,9,9-^{2}H)-13-Biotinamido-4,7,10-trioxatridecanyl]-*tert*-butyloxycarbamide (12).** To a solution of **11** (obtained from the previous reaction without further purification, 0.6 g) in anhydrous DMF (5 mL) was added a solution of the biotin pentaflourophenyl ester (1.12 g, 2.74 mmol) in anhydrous DMF (5 mL) followed by DIPEA (0.3 mL, 1.61 mmol) addition under nitrogen atmosphere. Then the reaction mixture was stirred at RT for 12 h. The reaction mixture was concentrated in vacuo, and the crude product was purified by flash chromatography (CH_2Cl_2−MeOH, 19:1) using neutral silica gel that afforded the pure biotinylated derivative (**12**, 0.64 g, 1.15 mmol, 64% overall yield for two steps) in the form of a white solid (hygroscopic). Compound **12**, being polar due to the presence of amide linkages, could not be purified on commercially available silica gel because of its slightly acidic nature. However, performing the flash column chromatography on neutral silica gel, compound **12** was obtained in pure form with out any loss. To neutralize the commercially available silica gel (230−400 mesh), it was loaded onto a column and washed with CH_2Cl_2 (300 mL), containing 0.1% triethylamine, prior to loading of the crude reaction mixture onto the same column. Then a solvent mixture of CH_2Cl_2 and MeOH in the ratio 19 to 1, without containing any triethylamine, was used for the chromatographic purification of **12**. TLC (CH_2Cl_2−MeOH, 9:1): R_f = 0.6 (iodine, blue stain in ammonium molybdate). ^{1}H NMR (400 MHz, d_4-MeOH): δ = 4.45 (m_c, 1H, CH_2CHNH), 4.26 (dd, J_1 = 4.47 Hz, J_2 = 7.87 Hz, 1H, $CHCHNH$), 3.51−3.42 (m, 4H, 2 OCH_2), 3.20 (t, *J* = 6.8 Hz, 2H, C*H*$_2$CONH), 3.15 (m_c, 1H, SCH), 3.06 (t, *J* = 6.76 Hz, 2H, C*H*$_2$NHBoc), 2.88 (dd, J_1 = 4.99 Hz, J_2 = 12.74 Hz, 1H, SCH_a), 2.66 (d, *J* = 12.72 Hz, 1H, SCH_b), 2.16 (t, *J* = 7.35 Hz, 2H, C*H*$_2$NHCO), 1.77−1.50 (m, 6H, OCH_2CH_2, 2 CH_2), 1.46−1.30 (m, 2H, CH_2), 1.40 (s, 9H, *t*-Bu) ppm; ^{13}C NMR (100.61 MHz, d_4-MeOH): δ = 175.93

($CH_2NHCOCH_2$), 166.07 (NHCONH), 158.44 ($NHCO_2t$-Bu), 79.85 ($C(CH_3)$), 69.88 (OCH_2, weak multiplet for 4 OCD_2), 69.82 (OCH_2), 63.37, 61.62 (2 CH), 56.99 (SCH), 41.03 (SCH_2), 38.73 (CH_2NHBoc), 37.83 (CH_2CONH), 36.85 (CH_2NHCO), 30.94, 30.43, 29.80, 29.50, 28.81 (5 CH_2), 26.87 ($C(CH_3)$) ppm. ESI-MS: $m/z = 555.37$ $[M + H]^+$, 577.39 $[M + Na]^+$, 593.38 $[M + K]^+$ observed for $C_{25}H_{38}D_8N_4O_7S$ (554.36); HRMS: found 555.3668 $[(M + H)^+]$, $C_{25}H_{39}D_8N_4O_7S$ requires 555.3659.

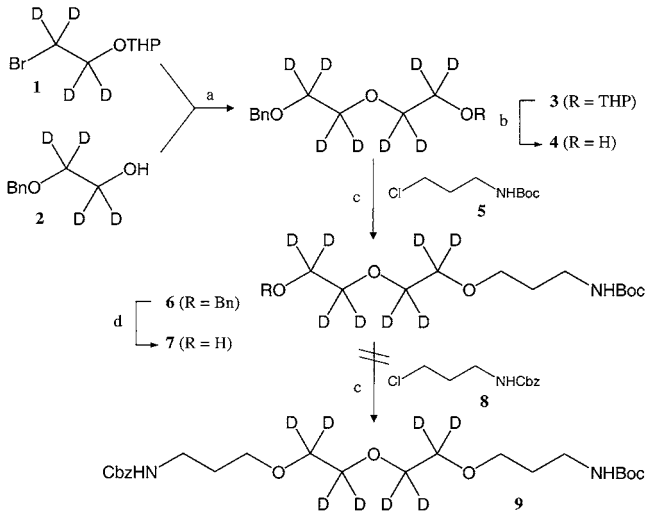
RESULTS AND DISCUSSION

To overcome all the problems associated with the synthesis of heavy-ICAT linker as discussed in the Introduction, as well as to expand the chemical functionality that may be introduced into ICAT reagents, here we describe an efficient synthesis of the "heavy" ICAT reagent. We contend that the synthesis reported herein is less expensive, facile, and high yielding with no loss of incorporated deuteriums throughout all the subsequent reaction conditions. The synthesis began with the conjugation of the two tetradeutero-precursors **1** (*19*) and **2** (*20*), by classical etherification reaction (*21*) at 80 °C using aqueous NaOH solution and phase-transfer catalyst (n-Bu_4NBr), that gave rise to the orthogonally protected d_8-diethylene glycol (**3**) in 94% yield with no loss of deuterium. Along with ^1H NMR characterization, further evidence for the structure of **3** was obtained by ESI MS that showed signals at $m/z = 311.21$ and 327.21 for $[M + Na]^+$ and $[M + K]^+$, respectively. In the ^{13}C NMR spectrum of **3** instead of singlets, four multiplets with lower intensity have been observed for the four OCD_2 groups arising due to the lack of ^1H broad-band decoupling experiment. Unlike the reported literature method involving simultaneous introduction (*9*), this orthogonally protected glycol linker (**3**) provides for successive introduction of propylamine fragments by chemoselective deprotection of THP and benzyl groups. Thus, chemically differentiable functionalities, including at least one amine, could be further achieved for successive introduction of biotin and a chosen reactive group without the enormous loss of the precious d_8-diamine linker.

The THP group was hydrolyzed in the presence of the acid-stable benzyl group using mild acidic reaction conditions (methanolic HCl solution, 10%) to give the alcohol derivative **4** in 90% yield (Scheme 1). Another etherification reaction between **4** and *N*-(3-chloropropyl)-*tert*-butyloxycarbamide (**5**) (*22*) under similar reaction conditions as used for **3**, provided the Boc derivative **6** in 73% yield, thus installing a propylamine fragment on one end of the linker. In the ^1H and ^{13}C NMR spectra of compound **6**, additional signals due to the extended chain were observed. In the ^{13}C NMR spectrum of **6**, the weak multiplets arising from the four OCD_2 groups were still detectable even though they coincided with the strongly visible singlet corresponding to the newly introduced OCH_2 group. To install the other propylamine fragment, compound **6**, was subjected to hydrogenolysis to give the free alcohol **7** in high yield (87%). In the ^{13}C NMR spectrum of **7**, an upfield shift of the CD_2OH signal (61.18 ppm) was observed, whereas the remaining OCD_2 and OCH_2 signals resonated together at 69.73 ppm.

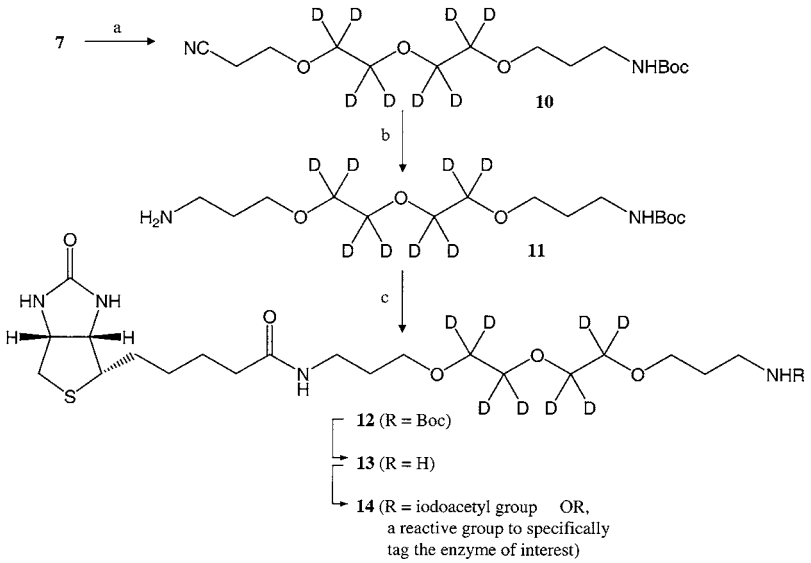
With an eye to preparing an orthogonally protected d_8-diamine linker **9**, *N*-(3-chloro-propyl)-benzyloxy carbam-

Scheme 1[a]



[a] Reagents and conditions: (a) aq NaOH, TBABr, 80 °C, 2 h, 94%; (b) HCl−MeOH (10%), RT, 1 h, 90%; (c) **5**, aq NaOH, TBABr, 80 °C, 1 h, 73%; (d) $Pd(OH)_2$, H_2, ethyl acetate, 3 h, 87%.

Scheme 2[a]



[a] Reagents and conditions: (a) acrylonitrile, NaOH cat., absol toluene, RT, 3 h, 96%; (b) Ra/Ni, MeOH, RT, 12 h, quant.; (c) Biotin pfP ester, DIPEA, DMF, RT, 12 h, 64% overall yield for steps b and c.

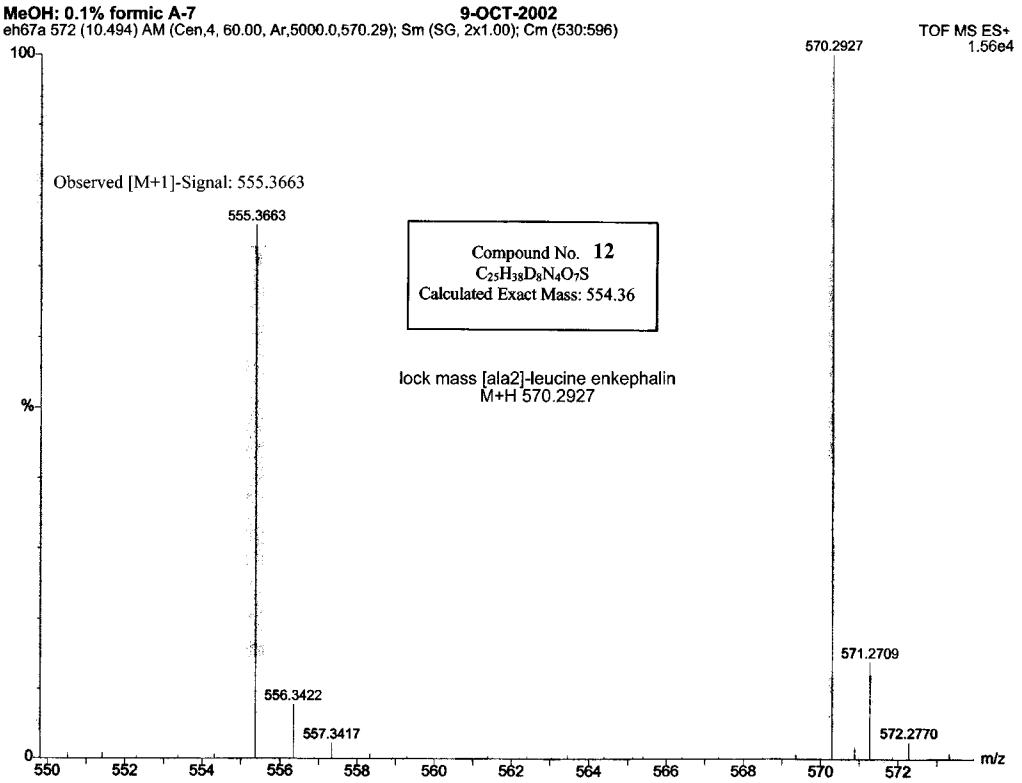


Figure 2. High-resolution mass spectrum of the d_8-ICAT linker, *N*-[(5,5,6,6,8,8,9,9-^{2}H)-13-biotinamido-4,7,10-trioxatridecanyl]-*tert*-butyloxycarbamide (**12**).

ide (**8**) (*23*) was chosen for the etherification reaction with compound **7**, which would then allow selective cleavage of the Cbz and the Boc groups successively in order to introduce biotin for the affinity purification on avidin and a reactive group to covalently tag the enzyme under study, respectively. Initially, the attempted etherification reaction led to the decomposition of the Cbz functionality in **9** due to the strongly basic medium and high reaction temperature. Thus a different approach was chosen wherein first, Michael addition on **7** gave the nitrile derivative **10** in 96% yield. NMR spectra of **10** showed additional signals corresponding to the newly introduced propylnitrile chain (at 117.79 ppm for CN carbon and a triplet at 2.58 ppm for CH_2CN protons) and in the ^{13}C NMR spectrum the OCD_2 signals appeared as one broad multiplet and overlapping with one of the two OCH_2 signals. Subsequently, Raney nickel reduction of the nitrile to amine **11** was achieved in greater than 80% yield (Scheme 2). A triplet corresponding to the newly formed CH_2NH_2 group at 2.52 ppm in the ^1H NMR spectrum along with ESI mass spectrometry (m/z = 329.32 and 351.33 for $[M + H]^+$ and $[M + Na]^+$) confirmed the amine formation. In this reaction we did not experience yield reduction due to formation of any side products resulting from the retro-Michael type reaction as reported by Gelb and co-workers (*12*).

The monoamine linker **11**, without further purification, was directly coupled to biotin using the activated biotin pentafluorophenyl ester in anhydrous DMF in the presence of DIPEA to give **12** in 64% overall yield for both steps (reduction and biotin coupling). New signals at 4.45 and 4.26 ppm, due to the CH protons of biotin, were well separated from all other signals in the ^1H NMR spectrum of compound **12** and clearly confirmed the introduction of biotin moiety. As observed before, the ^{13}C NMR spectrum revealed weak multiplets corresponding to OCD_2 groups that overlapped one of the two OCH_2 signals. An additional proof of structure and purity of **12** was obtained by HRMS which showed an $[M + H]^+$ signal at m/z = 555.3668 with a deviation of only −0.8 ppm from the required value (Figure 2).

Having established the viability of this synthetic procedure, we envision utility for developing ICAT reagents of high isotopic purity. For instance, the d_8-linker **12** can be readily elaborated into a cysteine specific d_8-ICAT reagent (Figure 1) by deprotection of the Boc group, followed by acylation of the resulting free amine with iodoacetic anhydride. Similarly, any similar d_8-ICAT reagent (**14**, Scheme 2) can be prepared by introducing the reactive group of choice that can specifically tag an enzyme of interest.

Unlike in the previously reported procedures, we incorporated eight deuteriums on the ICAT reagent within the diethylene glycol region in the very first step with no loss of deuteriums through etherification reaction of isotopically pure tetradeutero precursors **1** and **2**. Those incorporated deuteriums are stable throughout the subsequent reaction conditions. Thus, the d_8-ICAT reagent **12** was obtained in 100% isotopic purity and with 33% overall yield. The resultant d_8-ICAT reagent **12** carries deuterium in different positions of the ICAT reagent and is a structural isoform of the original d_8-ICAT reagent (Figure 1). The slight compositional differences between the ICAT linker **12** reported herein, and previously reported ICAT reagents, should not affect the efficiency of the isotopically encoded protein quantification obtained in the ICAT method.

CONCLUSION

In conclusion, we have described an inexpensive and high yielding synthetic strategy to prepare a d_8-ICAT reagent with 100% isotopic purity. A salient aspect of this synthesis is that it allows the synthesis of a wide range of deuterated diamine linkers carrying at least four and potentially any multiple of four deuteriums as the

etherification steps can be repeated to generate longer linkers with a substantially higher isotopic differential. Moreover, this work also enables the synthesis of a class of "heavy, medium, and light" reagents that might be useful for simultaneously probing three cell-based systems; for example (i) uninfected, (ii) infected without treatment, and (iii) infected with treatment. Longer linkers may easily give up to five differentially encoded tags.

Whereas the work herein employed deuterated precursors, other isotopes can be introduced instead of deuterium with minimal alteration to the overall synthetic routes if desired. Indeed, recent reports have underscored slight, yet significant, chromatographic differences due to replacement of protium with deuterium (*24*). Consequently, other stable isotopes, namely ^{13}C, have now been used instead of deuterium. These recent approaches have used ^{13}C-labeled acrylonitrile to address this problem along with undesired exchange of D for H during Michael addition and hydrogenation. The synthetic strategy reported herein can be adapted for (^{13}C or ^{18}O) labeled ICAT reagents by using ^{13}C- or ^{18}O-labeled starting materials (*25*) in the etherification steps. Moreover, *both* carbon *and* oxygen isotopes could be used in tandem to generate an even higher isotopic differential on a relatively shorter linker arm.

In general, this work suggests a modular approach to achieving a high-yielding synthesis of ICAT linkers to give defined isotopic mass differences. Finally, nitrile hydrolysis of **10** with appropriate amine protection, or alternately, Michael addition of **7** to acrylic acid esters is readily envisioned to generate "amino acid" ICAT linkers (carrying an amine at one end and a carboxylic acid at the other end) compatible with automated solid-phase peptide synthesis. Furthermore, Michael addition of **7** to acrolein would give the corresponding aldehyde that could be alternately conjugated to amines, hydrazines, and oximes. In summary, (a) the orthogonal protection strategy obviates extensive loss or tedious recovery steps, (b) allows for effective economy at the level of monobiotinylation, (c) provides options for the introduction of a carboxylate/carbonyl functionality that can be handily converted to an activated ester for the direct attachment to amines, and (d) allows for multiple isotopic labelings through the simultaneous use of ^{13}C or ^{18}O to obtain shorter linkers with higher isotopic density if so desired.

ACKNOWLEDGMENT

We thank PENCE (Protein Engineering Network of Centers of Excellence of Canada) for financial support.

LITERATURE CITED

(1) Corthals, G. L., Wasinger, V. C., Hochstrasser, D. F., and Sanchez, J. C. (2000) The dynamic range of protein expression: a challenge for proteomic research. *Electrophoresis 21*, 1104−1115.

(2) Gygi, S. P., Corthals, G. L., Zhang, Y., and Aebersold, R. (2000) Evaluation of two-dimensional gel electrophoresis-based proteome analysis technology. *Proc. Natl. Acad. Sci. U.S.A. 97*, 9390−9395.

(3) Cravatt, B. F., and Sorensen, E. J. (2000) Chemical strategies for the global analysis of protein function. *Curr. Opin. Chem. Biol. 4*, 663−668.

(4) Gerber, S. A., Scott, C. R., Turecek, F., and Gelb, M. H. (2001) Direct profiling of multiple enzyme activities in human cell lysates by affinity chromatography/electrospray ionization mass spectrometry: application to clinical enzymology. *Anal. Chem. 73*, 1651−1657.

(5) Turecek, F. (2002) Mass spectrometry in coupling with affinity capture-release and isotope-coded affinity tags for quantitative protein analysis *J. Mass Spectrom. 37*, 1−14.

(6) Chelius, D., and Bondarenko, P. V. (2002) Quantitative profiling of proteins in complex mixtures using liquid chromatography and mass spectrometry *J. Proteom. Res. 1*, 317−323.

(7) Zhou, H., Ranish, J. A., Watts, J. D., and Aebersold, R. (2002) Quantitative proteome analysis by solid-phase isotope tagging and mass spectrometry. *Nat. Biotechnol. 19*, 512−515.

(8) Sechi, S. (2002) A method to identify and simultaneously determine the relative quantities of proteins isolated by gel electrophoresis. *Rapid Commun. Mass Spectrom. 16*, 1416−1424.

(9) Gygi, S. P., Rist, B., Gerber, S. A., Turecek, F., Gelb, M. H., and Aebersold, R. (1999) Quantitative analysis of complex protein mixtures using isotope-coded affinity tags. *Nat. Biotechnol. 17*, 994−999.

(10) Han, D. K., Eng, J., Zhou, H., and Aebersold, R. (2001) Quantitative profiling of differentiation-induced microsomal proteins using isotope-coded affinity tags and mass spectrometry. *Nat. Biotechnol. 19*, 946−951.

(11) Gerber, S. A., Scott, C. R., Turecek, F., and Gelb, M. H. (1999) Analysis of rates of multiple enzymes in cell lysates by electrospray ionization mass spectrometry *J. Am. Chem. Soc. 121*, 1102−1103.

(12) Gerber, S. A., Turecek, F., and Gelb, M. H. (2001) Design and synthesis of substrate and internal standard conjugates for profiling enzyme activity in the sanfilippo syndrome by affinity chromatography/electrospray ionization mass spectrometry. *Bioconjugate Chem. 12*, 603−615.

(13) Lee, H., Griffin, T. J., Gygi, S. P., Rist, B., and Aebersold, R. (2002) Development of a multiplexed microcapillary liquid chromatography system for high-throughput proteome analysis. *Anal. Chem. 74*, 4353−4360.

(14) Yu, L.-R., Johnson, M. D., Conrads, T. P., Smith, R. D., Morrison, R. S., and Veenstra, T. D. (2002) Proteome analysis of camptothecin-treated cortical neurons using isotope-coded affinity tags. *Electrophoresis 23*, 1591−1598.

(15) Shiio, Y., Donohoe, S., Yi, E. C., Goodleyy, D. R., Aebersold, R., and Eisenman, R. N. (2002) Quantitative proteomic analysis of Myc oncoprotein function. *EMBO J. 21* (19), 5088−5096.

(16) Borisov, O. V., Goshe, M. B., Conrads, T. P., Rakov, V. S., Veenstra, T. D., and Smith, R. D. (2002) Low-energy collision-induced dissociation fragmentation analysis of cysteinyl-modified peptides. *Anal. Chem. 74*, 2284−2292.

(17) Ashikaga, K., Ito, S., Yamamoto, M., and Nishijima, Y. (1988) Intramolecular end-to-end reactions of photoactive terminal groups linked by poly(oxyethylene) chains. *Bull. Chem. Soc. Jpn. 61*, 2443−2450.

(18) Schön, I., Nyéki, O., and Demeter, Á. (2000) Synthesis of biotinylated thymocartins. *J. Labelled Compd. Radiopharm. 43* (4), 309−322.

(19) Bird, I., and Farmer, P. B. (1988) The synthesis of deuterium labeled 2-bromoethanol, acrylonitrile, acrylamide, 2-aminoethanol, 2-bromoethylamine hydrobromide and 1-bromo-2-chloroethane. *J. Labelled Compd. Radiopharm. XXVII* (2), 199−216.

(20) Kondareddiar, R., and Woodward, R. W. (1986) Synthesis and ^1H NMR of deuterium labeled D, L.-Homoserine lactone hydrochlorides. *J. Labelled Compd. Radiopharm. XXIV* (4), 369−376.

(21) Nouguier, R. M., and Mchich, M. (1985) Alkylation of Pentaerythritol and trimethylolpropane, two very hydrophilic polyols, by phase-transfer catalysis. *J. Org. Chem. 50*, 3296−3298.

(22) Barros, M. T., and Siñeriz, F. (2000) Total Synthesis of Saturated and Unsaturated di-trans-N-substituted Cyclam-based Macrocycles Through a Versatile Intermediate. *Tetrahedron 56* (27), 4759−4764.

(23) Murakata, M., Yamada, K., and Hoshino, O. (1998) Studies on synthesis of araplysillins via oxidative cyclization of o-phenolic oxime-acid derivatives using phenyliodonium diacetate. *Heterocycles 47* (2), 921−931.

(24) Zhang, R., and Regnier, F. E. (2002) Minimizing resolution of isotopically coded peptides in comparative proteomics. *J. Proteome Res. 1*, 139−47.

(25) ^{13}C-Labeled **1** and **2** are commercially available. ^{18}O-Labeled **1** and **2** can be prepared by reaction of $H_2{}^{18}O$ with dibromoethane under solvolytic conditions.

(26) Abbreviations: ICAT, isotope coded affinity tagging; DIPEA, diisopropylethylamine; DMF, dimethylformamide; n-Bu_4NBr, tetrabutylammonium bromide; THP, tetrahydropyran.

BC0300293

MARCH/APRIL 2004
Volume 15, Number 2

© *Copyright 2004 by the American Chemical Society*

Bioconjugate Chemistry

COMMUNICATIONS

A Novel Method for the N-Terminal Modification of Native Proteins

Marzena Lewinska,[†] Christian Seitz,[†] Arne Skerra,[‡] and Franz P. Schmidtchen*[,†]

Institut für Organische Chemie und Biochemie, Technische Universität München, 85747 Garching, Germany, and Center of Life Science Weihenstephan, Munich Institute of Technology, D- 85350 Freising-Weihenstephan.
Received May 18, 2003

The formation of structurally defined bioconjugates of proteins hinges on their regioselective modification. Toward this goal a novel method is described here using the commercial IgA protease to attach a nonnatural peptidic moiety to the N-terminus of predisposed proteins by means of a kinetically controlled reverse proteolysis in water. The process requires an H-Ala-Pro N-terminal sequence and then furnishes a selectively modified conjugate under nondenaturing and nondestructive conditions in acceptable yield. The method lends itself to the N-terminal introduction of orthogonal moieties that may be elaborated further.

The regioselective decoration of native proteins with nonnatural structural elements poses an eminently attractive goal, because many possibilities for the tailored modification of their functional properties would be opened which hitherto cannot be implemented by current biological or artificial methods. Particularly interesting options encompass the introduction of atomic markers (isotopes or heavy atoms), reporter groups or therapeutic compounds at well defined positions, the covalent attachment of other biomolecules to form conjugates, the mutually site-selective immobilization to solid supports, or the addition of hydrophobic residues necessary for membrane anchoring. While the chemistry required in manipulation of native proteins is available in quite a variety (*1*−*3*), the major obstacle in the realization of this catalog emerges from the paucity of methods capable to regioselectively address target epitopes in the folded proteins. In principle, two general strategies can be distinguished here. One incorporates the uniquely addressable moiety at the stage of protein synthesis. Peptide segment condensation (*4*−*6*) and protein in vitro biosynthesis (*7*, *8*) provide successful examples using this route. They must, however, rely on the unpredictable chance that the nonnatural moiety does not affect the correct folding pattern.

Alternatively, one can try to regioselectively modify the mature protein in its native folded state, requiring the differentiation of a respectable number of functional groups of quite similar reactivity. Chemical methods in general are devoid of the necessary selectivity unless the reactivity of a certain epitope stands out among all others and thereby paves the way to selective modification (e.g. affinity labels) (*9*, *10*). Better chances may be expected employing protein-modifying enzymes acting in their native role. This approach, however, is blocked by the unavailability of the biocatalyst as well as by their

* To whom correspondence should be addressed. Fax: ++49-89-289-14698. E-mail: schmidtchen@ch.tum.de.
[†] Institute of Organic Chemistry and Biochemistry.
[‡] Center of Life Science Weihenstephan.

10.1021/bc034085f CCC: $27.50 © 2004 American Chemical Society
Published on Web 02/21/2004

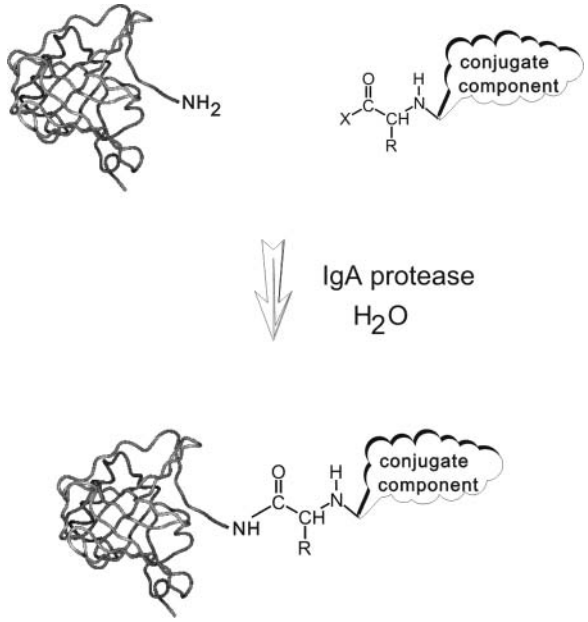


Figure 1. N-Terminal covalent extension of native proteins using the sequence specific restriction endoprotease IgA-protease.

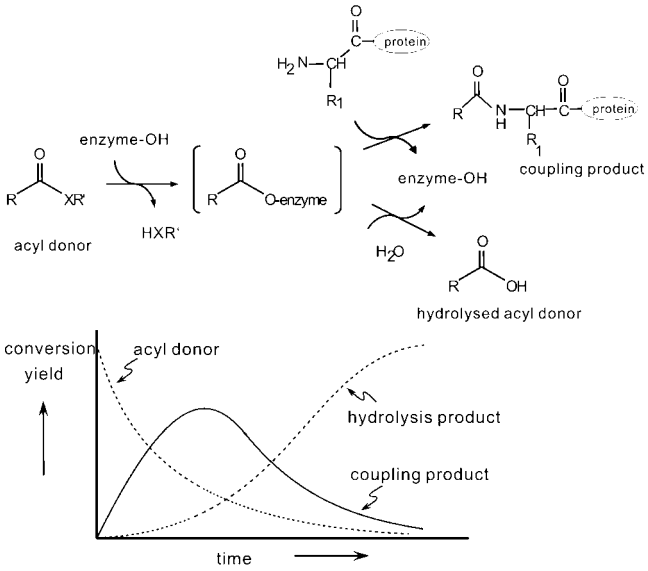


Figure 2. Reverse proteolysis in aqueous buffer depends on the kinetic branching at the stage of a covalent enzyme intermediate between hydrolysis and transamidation. The time dependence of coupling product formation (diagram) shows a maximum at which the reaction must be stopped to obtain an optimal yield (i.e. kinetic control).

substrate specificity that limits the variety of nonnatural groups attachable to the target epitope and undermines generality.

Here, we describe the use of the commercially available protease IgA-Protease to regioselectively elongate the N-terminus of native proteins and peptides with synthetically accessible nonnatural tetrapeptide esters (Figure 1). The novel approach in combination with organometallic aqueous catalyses (*11*) opens a way to introduce a variety of biogenic and abiotic moieties by directed covalent attachment to the N-terminus under nondenaturing conditions without retreat to protective strategies. Conceptually, our method applies a variant of kinetically controlled reverse proteolysis schemes (*12*, *13*). Since all enzymes catalyze the approach to the equilibrium state from the substrate as well as from the product side, proteases will not only cleave but also make peptide bonds. For reactions in water, this facet is invisible, because the position of the equilibrium largely favors the cleavage product. However, shifting of the equilibrium by lowering the water activity (i.e. employing nonaqueous conditions) or avoiding equilibration in total may result in the head-to-tail coupling of peptides subject to the specificity determinants of the enzyme (Figure 2). The kinetic control refers to the exact tuning of the quench process that will stop the enzyme catalysis when the yield of the coupling product arising from the kinetic distribution of an enzyme-bound covalent intermediate between coupling and hydrolysis reaches maximum.

To apply this scheme to the covalent modifications of proteins, serine or cysteine proteases have to be found that do not randomly degrade proteins but will only act on certain primary sequence motifs. One candidate resembling the restriction nucleases in selectivity is the bacterial IgA-protease (*14*−*16*), which recognizes a stretch of at least seven amino acids (*17*) and contains the scissile peptide bond in the middle of the recognition sequence: X-(Ser, Pro) (Arg, Thr) Pro Pro↓(Ala, Gly, Ser) Pro (Ser, Trp, Tyr).

This specificity determinant rarely occurs in globular proteins, thus minimizing the risk of unspecific hydrolysis of protein substrates. For IgA-protease-catalyzed peptide bond formation to occur, two peptidic components are needed: An amino nucleophile representing the N-terminus of the protein to be modified, containing a mandatory proline residue in the penultimate position and preferably an alanine, glycine, or serine residue at the N-terminus. The second component functions as the acyl donor by virtue of its carboxy-terminal ester group that readily acylates the active-site serine residue of IgA-protease, provided at least a tetrapeptide with the correct primary sequence is offered as a substrate. Within generous limits, the chemical nature of the nonnatural group X is uncritical to the success of the reaction (*17*) making this position a good place to implant the desired abiotic moiety.

The principal viability of the approach was probed by peptide fragment coupling of BOC−Pro-Arg-Pro-Pro-OCH_3 as the acyl donor produced by nonmonotonic solution synthesis and carbohydrate-structure-mimicking-peptide, CSMP (H_2N-Ala-Pro-Trp-Leu-Tyr-Gly-Pro-Ala-OH), a commercial octapeptide possessing the mandatory N-terminal sequence and a fluorogenic tryptophane residue that eases the quantitative analysis. The kinetic course of the reverse proteolysis using these substrates under physiological conditions was monitored by HPLC (Figure 3) and revealed the clean formation of a fluorescent product peak in the initial stages of the reaction. Isolation and MALDI-TOF analysis confirmed the identity of the expected coupling product. In continuation of the reaction, this product peak decreases and finally vanishes, completely refurnishing the starting nucleophilic CSMP-peptide, corroborating that IgA-protease strictly follows the assigned specificity pattern. The yield of coupled product at the maximum of its formation is almost 70% based on the CSMP-peptide.

Visualizing the individuality of proteins, the conditions and even the overall outcome of the procedure successful with oligopeptides may not be transferable to the modification of folded proteins. On purpose, we had selected the N-terminus for modification since this epitope is likely to belong to the least structured regions in proteins and in most cases is accessible to enzymatic action from solution because it has been processed by trimming

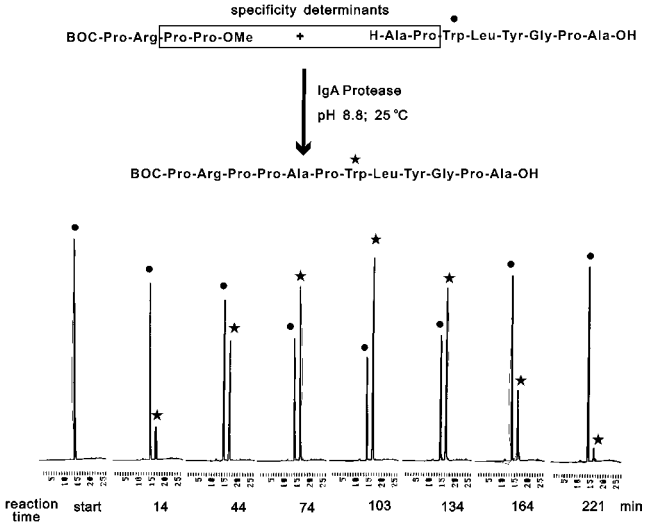


Figure 3. Monitoring peptide fragment coupling of BOC-Pro-Arg-Pro-Pro-OMe with CSMP (●) in aqueous buffer by HPLC fluorescence detection. Only Trp-containing compounds are observable. The formation of the coupling product (★) reaches maximum after 100 min corresponding to a 67% product yield.

enzymes before (cleavage of signal peptides or formylmethionine).

To demonstrate the applicability of our method to native proteins we selected the anticalin FluA (*18*, *19*), a stable, genetically engineered 174-amino acid residue β-barrel protein capable to selectively bind fluorescein with nanomolar affinity. FluA does not contain a sequence motif that would make it susceptible to degradation by IgA-protease, and this inference was fully corroborated by experiment. However, to function as a nucleophile in IgA-protease-catalyzed N-terminal strand extension, the primary sequence had to be altered to include the penultimate Pro residue. Based on the specificity screening (*17*), an Ala-Pro-Ser-Trp tetrapeptide sequence was inserted at the junction of the signal peptide that is lost in the mature FluA-protein and the native N-terminus by established gene-recombinant methods. Expression of the engineered FluA-gene in *E. coli* coding this N-terminally elongated variant furnished the correctly processed FluA protein (H_2N-IgAP1-OH) as proven by MALDI-TOF mass spectral analysis and Edman amino acid sequencing.

IgA-protease-mediated N-terminal elongation of IgAP1 employed the BOC-protected tetrapeptide ester as the unnatural acyl donor that was already used in CSMP-modification. The reaction conditions largely corresponded to those elaborated with the oligopeptides except for the 7-fold lower concentration of the protein nucleophile IgAP1 due to its limited solubility in the reaction medium. The protein modification could be followed by reversed-phase HPLC using fluorescence detection, and the corresponding kinetics are depicted in Figure 4. After 3 h about 30% of the IgAP1 protein was converted into a derivative, and contrary to the analogous experiments with oligopeptides, the yield did not decrease with time again, most likely because the IgA-protease was totally deactivated. The characterization of the product peak after preparative HPLC isolation revealed the correct molecular mass expected from the BOC-tetrapeptide-appended IgAP1 protein. In addition, deblocking the novel N-terminus by treatment with trifluoroacetic acid followed by standard Edman degradation of the initial six amino acids residues unequivocally confirmed that protein modification had occurred in the prospected

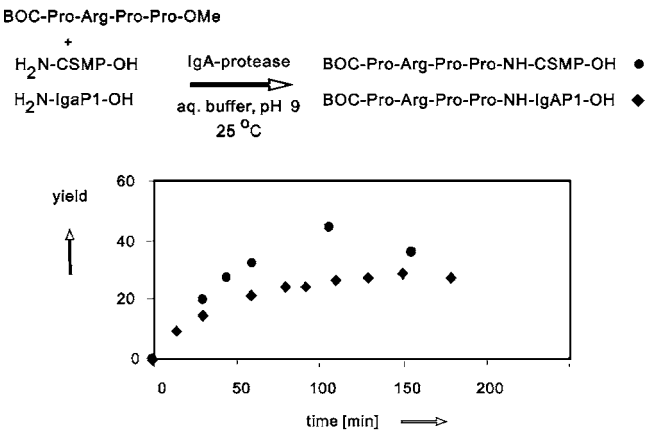


Figure 4. Comparative kinetic runs of the N-terminal modification of CSMP (●) and H_2N-IgaP1-OH (◆) under identical concentration relations. The coupling yield is based on the HPLC-fluorimetric analysis, applying internal standardization. For conditions, see the experimental details.

fashion. To further elucidate the influence imposed by the folded protein structure on the IgA-protease-catalyzed strand extension, IgAP1 and CSMP were compared under identical conditions. The kinetic pattern (Figure 4) shows that the general time course for both substrates is very much alike, but CSMP hits a much higher maximum yield. Since both substrates are very similar in their specificity determining N-terminal sequences, we attribute the difference in derivatization yield to the steric congestion of IgAP1 binding to IgA-protease caused by the bulky 3D-structure of the protein substrate. For the improvement of modification yields, it should be helpful to prolong the N-terminus of the protein to be derivatized rather liberally to arrive at a good substrate for IgA-protease.

The IgA-protease-catalyzed modification of native proteins opens new routes to protein bioconjugates, which are not yet accessible by genetic engineering. Thus, our method (*20*, *21*) complements recombinant methods to generate proteins with a regioselective covalent decoration that may prove vital to their function and use.

Supporting Information Available: MALDI-TOF spectra. This material is available free of charge via the Internet at http://pubs.acs.org.

NOTE ADDED AFTER ASAP POSTING

The Supporting Information paragraph omitted in the manuscript posted February 21, 2004, was added and the manuscript reposted March 4, 2004.

LITERATURE CITED

(1) Tawfik, D. S. (2002) Side chain selective chemical modifications of proteins. *Protein Protocol Handbook* (Walker, J. M., Ed.) 2nd ed., p 465ff, Humana Press, Totowa, NJ.

(2) Hamachi, I., and Shinkai, S. (1999) Chemical Modification of the Structures and Functions of Proteins by the Cofactor Reconstitution Methodology. *Eur. J. Org. Chem.* 539−549.

(3) Tyagi, R., and Gupta, M. N. (1998) Chemical modification and chemical cross-linking for protein/enzyme stabilisation. *Biochemistry (Moscow) 63*, 334−344.

(4) Miyazawa, T., Ensatsu, E., Hiramatsu, M., Yanagihara, R., and Yamada, T. (2002) α-Chymotrypsin-catalysed segment condensation *via* the kinetically controlled approach using carbamoylmethyl esters as acyl donors in organic media. *J. Chem. Soc., Perkin Trans. 1*, 396−401.

(5) Canne, L. E., Botti, P., Simon, R. J., Chen, Y., Dennis, E. A., and Kent, S. B. H. (1999) Chemical Protein Synthesis by

Solid-Phase Ligation of Unprotected Peptide Segments. *J. Am. Chem. Soc. 121*, 8720−8727.
(6) Muir, T. W., and Cowburn, D. (2001) Segmental isotopic labeling using expressed protein ligation. *Methods Enzymol. 339*, 41−54.
(7) Eisenhauer, B. M., and Hecht, S. M. (2002) Site-Specific Incorporation of (Aminooxy)acetic Acid into Proteins. *Biochemistry 41*, 11472−11478.
(8) Chamberlin, A. R., Gilmore, M. A., and Steward, L. E. (1999) Incorporation of noncoded amino acids by in-vitro protein biosynthesis. In *Implementation and redesign of catalytic function in proteins* (Schmidtchen, F. P., Ed.) Topics in Current Chemistry, vol. 202, pp 77−99, Springer, Heidelberg.
(9) Baltzer, L., Nilson, H., and Nilson, J. (2001) De novo design of proteins.-What are the rules? *Chem. Rev. 101*, 3153−3163.
(10) Pool, C. T., and Thompson, T. E. (1999) Methods for dual, site-specific derivatization of bovine pancreatic trypsin inhibitor: Trypsin protection of lysine-15 and attachment of fatty acids or hydrophobic peptides at the N-terminus. *Bioconjugate Chem. 10*, 221−230.
(11) Dibowski, H., and Schmidtchen, F. P. (1998) Bioconjugation of peptides by Palladium-catalyzed C−C cross-coupling in Water. *Angew. Chem., Int. Ed. 37*, 476−478.
(12) Schellenberger, V., and Jakubke, H.-D. (1991) Protease catalysed kinetically controlled peptide synthesis. *Angew. Chem., Int. Ed. Engl. 30*, 1437−1449.
(13) Liu, C.-F., and Tam, J. P. (2001) Subtilisin-catalyzed synthesis of amino acid and peptide esters. application in a two-step enzymatic ligation strategy. *Org. Lett. 3*, 4157−4159.
(14) Plaut, A. G., and Bachovchin W. W. (1994) IgA-specific prolyl endopeptidases: serine type. *Methods Enzymol. 244*, 137−151.
(15) Poulsen, S. K., Reinhodt, J., Jespersgaard, C., Boye, K., Brown, T. A., Hange, M., and Killian, M. (1998) A comprehensive genetic study of streptococcal immunoglobulin A1 proteases: Evidence for recombination within and between species. *Infect. Immunol. 66*, 181−190.
(16) Pohlner, J., Langenberg, U., Wölk, U., Beck, S. C., and Meyer, T. F. (1995) Uptake and nuclear transport of Neisseria IgA1 protease-assosiated α-proteins in human cells. *Mol. Microb. 17*, 1073−1083.
(17) Seitz, C. (1995) Kupplung von Peptidfragmenten durch kinetisch kontrollierte Proteolyse unter Verwendung von Restriktionsproteasen, Dissertation TU München.
(18) (a) Skerra, A. (2002) Anticaline −Neuartige Bindungsproteine mit massgeschneiderten Liganden-Erkennungseigenschaften durch evolutives Protein-Design. *BIOforum 25*, 227−229.
(19) Beste, G., Schmidt, F. S., Stibora, T., and Skerra, A. (1999) Small antibody-like proteins with prescribed ligand specificities derived from the lipocalin fold. *Proc. Natl. Acad. Sci. U.S.A. 96*, 1898−1903.
(20) Experimental: To a mixture of the IgA-P1 substrate protein (∼100 μM) and acyl donor peptide BOC-Pro-Arg-Pro-Pro-OMe (70 mM) in 100 mM bicine buffer, pH 8.9, containing 2 mM of EDTA and 20 vol % of glycerol was added preconditioned recombinant IgA-protease to make a final concentration of 85 U/100 μL (*11*). The reaction was allowed to proceed at 25 °C for 3 h while adding three 20 μL aliquots of a saturated solution of the acyl donor in the reaction buffer after 20, 50, and 90 min, respectively, to compensate for hydrolysis. Reaction progress was followed by HPLC using a RP-8 column (300 Å, 5 μm) and an acetonitrile/0.1% trifluoroacetic acid gradient at 60 °C (linear from 25% to 45% in 50 min) for elution using fluorescence detection (λ_{ex} = 280 nm; λ_{em} = 350 nm). At the concentration maximum of the product after 3 h, the reaction was quenched by acidification and the product was isolated by HPLC and analyzed by MALDI-TOF mass spectroscopy and Edman degradation.
(21) Recombinant IgA-protease was purchased from MoBiTec, Göttingen, Germany. The enzyme is quite sensitive and was preconditioned in the reaction buffer for 1 h after thawing from the frozen state. The activity was standardized using the hydrolysis of BOC-Pro-Arg-Pro-Pro-*p*-nitroanilide (to be published). According to our procedure, commercial samples of IgA-protease contained 2.5−6 U/μg protein.

BC034085F

ARTICLES

^{90}Y and ^{111}In Complexes of a DOTA-Conjugated Integrin $\alpha_v\beta_3$ Receptor Antagonist: Different but Biologically Equivalent

David C. Onthank, Shuang Liu,* Paula J. Silva, John A. Barrett,† Thomas D. Harris, Simon P. Robinson, and D. Scott Edwards

Discovery R & D, Bristol-Myers Squibb Medical Imaging, 331 Treble Cove Road, North Billerica, Massachusetts 01862. Received June 26, 2003; Revised Manuscript Received December 15, 2003

^{90}Y-TA138 is a ^{90}Y-labeled nonpeptide integrin $\alpha_v\beta_3$ receptor antagonist that binds with high affinity and specificity to integrin $\alpha_v\beta_3$ receptors overexpressed on both endothelial and tumor cells. ^{90}Y-TA138 has demonstrated significant therapeutic effects in several preclinical tumor-bearing animal models. Since ^{90}Y is a pure β-emitter, ^{111}In-TA138 has been chosen as the imaging surrogate for dosimetry determination of ^{90}Y-TA138. This report describes the synthesis of ^{111}In-TA138 and biological evaluations of both ^{111}In-TA138 and ^{90}Y-TA138 in the c-neu Oncomouse model. The HPLC data shows that ^{111}In-TA138 is more hydrophilic with the retention time ~4.5 min shorter than that of ^{90}Y-TA138 under identical chromatographic conditions. Since the only difference between ^{111}In-TA138 and ^{90}Y-TA138 is the metal ion, the HPLC retention time difference strongly suggests that indium and yttrium chelates do not share the same coordination sphere in solution even though they are coordinated by the same DOTA conjugate. Despite their differences in lipophilicity and solution structure, biodistribution data in the c-neu Oncomouse model clearly showed that ^{111}In-TA138 and ^{90}Y-TA138 are biologically equivalent with respect to their uptake in tumors and other major organs. Therefore, ^{111}In-TA138 is useful as an imaging surrogate for ^{90}Y-TA138 and should be able to predict the radiation dosimetry of ^{90}Y-TA138, a therapeutic radiopharmaceutical for treatment of rapidly growing tumors.

INTRODUCTION

There is currently a considerable interest in radiolabeled biomolecules (BM) as target-specific radiopharmaceuticals for diagnosis and treatment of cancers (*1*−*10*). DOTA and its analogues have been used as bifunctional chelators (BFCs) for the radiolabeling of a variety of biomolecules, including antibodies (*11*−*17*) and small peptides (*18*−*24*). While ^{90}Y-labeled DOTA−BM conjugates are used for tumor radiotherapy, ^{111}In-labeled DOTA−BM conjugates are often used as imaging surrogates for the purpose of dosimetry determination. This is largely based on the assumption that ^{90}Y- and ^{111}In-labeled DOTA−BM conjugates are chemically and biologically equivalent. However, results from recent literature have shown differences in biological properties between ^{90}Y- and ^{111}In-labeled BFC−BM conjugates (*25*−*27*). This causes some concerns about the validity of using ^{111}In-labeled BFC−BM conjugates as imaging surrogates for their ^{90}Y analogues.

We have been interested in developing diagnostic and therapeutic radiopharmaceuticals based on radiolabeled integrin $\alpha_v\beta_3$ receptor antagonists (*23*, *24*, *28*−*33*). In our previous communication (*32*), we reported synthesis of the ^{90}Y complex of a DOTA-conjugated nonpeptide integrin $\alpha_v\beta_3$ receptor antagonist (Figure 1: TA138). ^{90}Y-TA138 has been evaluated as a therapeutic radiopharmaceutical in preclinical tumor-bearing animal models (e.g. c-neu Oncomouse, HCT116, and HT460 xenografts). In all cases, tumor growth was significantly inhibited in mice treated with ^{90}Y-TA138 (30 mCi/kg) on day 7 and 11 after subcutaneous implantation of tumor cells in mice (*33*). As a continuation of these studies, we now present the synthesis of ^{111}In-TA138. To demonstrate the validity of ^{111}In-TA138 as the imaging surrogate for ^{90}Y-TA138, we have evaluated biodistribution characteristics of ^{111}In-TA138 and ^{90}Y-TA138 in the same c-neu Oncomouse model. Results from this study clearly demonstrated that ^{111}In-TA138 and ^{90}Y-TA138 are biologically equivalent with respect to their uptake in tumors and other major organs despite their differences in lipophilicity and solution structures.

EXPERIMENTAL SECTION

Materials. Ammonium acetate, diethylenetriaminepentaacetic acid (DTPA), and sodium gentisate were purchased from Sigma-Aldrich (St. Louis, MO) and were used as received. $^{90}YCl_3$ and $^{111}InCl_3$ (in 0.05 N HCl) were purchased from Perkin-Elmer Life Sciences, North Billerica, MA. Synthesis of TA138 (3-sulfon-*N*-[[4,7,10-tris(carboxymethyl)-1,4,7,10-tetraaza-cyclododec-1-yl]-acetyl]-L-alanyl-*N*-[2-[4-[[[(1*S*)-1-carboxy-2[[[1,4-dihydro-7-[(1*H*-imidazol-2-ylamino]methyl]-1-methyl-4-oxo-3-quinolinyl]carbonyl]amino]ethyl]amino]sulfonyl]-3,5-

* To whom correspondence should be addressed. Current address: Department of Industrial and Physical Pharmacy, School of Pharmacy, Purdue University, 575 Stadium Drive, West Lafayette, IN 47907-2051. Phone: 765-494-0236 (S. L.); Fax 765-496-3367; E-mail: lius@pharmacy.purdue.edu.

† Current address: EPIX Medical Inc., 71 Rogers St., Cambridge, MA 02142-1118.

10.1021/bc034108q CCC: $27.50 © 2004 American Chemical Society
Published on Web 02/17/2004

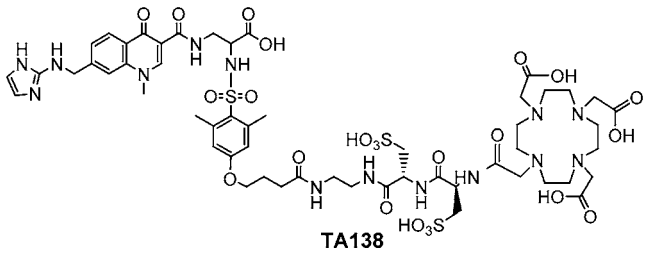


Figure 1. Structure of the DOTA-conjugated integrin $\alpha_v\beta_3$ receptor antagonist TA138.

dimethylphenoxy]-1-oxobutyl]amino]ethyl]-3-sulfo-L-alaninamide) has been described in our previous communication (*32*).

Analytical Methods. The radio-HPLC method used a HP-1100 HPLC system with an UV/visible detector (λ = 230 nm), an IN−US radio-detector, and a Zorbax C_{18} column (4.6 mm × 250 mm, 80 Å pore size). The flow rate was 1 mL/min with a gradient mobile phase starting from 92% solvent A (25 mM ammonium acetate buffer, pH 6.8) and 8% solvent B (acetonitrile) to 90% solvent A and 10% solvent B at 18 min. The mobile phase was isocratic using 40% of solvent A and 60% solvent B from 19 to 25 min. The TLC method used the C_{18} reverse phase glass plates and a mobile phase containing methanol, acetone, and saline (2:1:1 = v:v:v). By this method, both ^{90}Y-TA138 and ^{111}In-TA138 migrate to the solvent front while unchelated radiometal remains at the origin. The corrected radiochemical purity was calculated by subtracting the percentage of unchelated radiometal obtained by TLC from that obtained by radio-HPLC.

Synthesis of ^{90}Y-TA138. To a clean 10 mL vial containing 775 μg of TA138 were added 15.2 mg sodium gentisate and 7.6 mL of ammonium acetate buffer (0.5 M, pH = 6.0). The solution was immediately degassed under vacuum (<1.0 mmHg) for ~2 min. Upon addition of 175 μL of $^{90}YCl_3$ (~150 mCi) in 0.05 N HCl, the reaction mixture was heated at 95 °C for 5 min. After radiolabeling, a sample of the resulting solution was first diluted 40-fold with the 1.0 mM DTPA solution containing sodium gentisate (10 mg/mL) and was then analyzed by radio-HPLC and TLC. The radiochemical purity was 99.0% for ^{90}Y-TA138. The dose for animal studies was made by diluting part of the kit formulation to a concentration of ~50 μCi/mL with saline.

Synthesis of ^{111}In-TA138. TA138 (100 μg) and sodium gentisate (1.0 mg) were dissolved in 1.5 mL of ammonium acetate buffer (0.5 M, pH = 6.0). The resulting solution was immediately degassed under vacuum (<1 mmHg) for ~2 min. Upon addition of $^{111}InCl_3$ solution (2.2 mCi) in 0.05 N HCl, the reaction mixture was heated at 100 °C for 5 min. After cooling to room temperature, a sample of the resulting solution was analyzed by radio-HPLC and TLC. The radiochemical purity was 99.5% for ^{111}In-TA138. The dose for animal studies was made by diluting the solution above to a concentration of ~15 μCi/mL with saline.

In Vivo Biodistribution Study. The c-neu Oncomouse is a spontaneous tumor-bearing model that carries an activated c-neu oncogene driven by a mouse mammary tumor virus (MMTV) promoter. Transgenic mice uniformly expressing the MMTV/c-neu gene develop mammary adenocarcinomas (4 to 8 months postpartum) that involve the entire epithelium in each gland. The mice used in this study were obtained through an in-house breeding program and were anesthetized intramuscularly with 0.1 mL of a ketamine/acepromazine mixture (1.8 mL saline, 1.0 mL ketamine, and 0.2 mL acepromazine) prior to dosing and tissue sampling. Equal volumes of ^{90}Y-TA138 (50 μCi/mL) and ^{111}In-TA138 (15 μCi/mL) solutions were mixed before injection. The final concentration was 25 μCi/mL for ^{90}Y-TA138 and 7.5 μCi/mL for ^{111}In-TA138. Doses (0.1 mL) were drawn into 0.5 mL insulin syringes for injection.

Eighteen mice (~25 g) were divided into three groups according to the biodistribution time (2, 24, and 48 h) postinjection. Each group had six mice, and each mouse was administered a mixture (0.1 mL) containing ^{90}Y-TA138 at a dose of 2.5 μCi/mouse and ^{111}In-TA138 at a dose of 0.75 μCi/mouse in a single tail vein injection. Biodistributions were performed at the assigned time points (2, 24, and 48 h). Blood, eye, muscle, liver, kidney, bile, spleen, heart, lung, urine, stomach, colon, uterus, bone marrow, bone, and tumors were sampled and assayed for radioactivity. Since the c-neu Oncomouse spontaneously develops tumors in the mammary glands, most mice have more than one tumor. To assess the amount of uptake in the tumors, each tumor was sampled and counted separately. Subsequently, the activity was averaged to obtain an overall representation of tumor uptake. All tissue samples and injected dose aliquots were dissolved in 1 mL of Solvable (Packard Instrument Co., Meriden, CT) and incubated overnight at 37 °C. Each sample was then counted for 15 min on a calibrated Cobra gamma counter (Packard, Instrument Co., Meriden, CT) with dual window settings for counting each isotope. Raw radioactivity data was corrected for background and tested for quantitation limits according to the literature method (*34*). Results are shown in Figures 3−6 and are reported as a percent of the injected dose per gram of the tissue (%ID/g).

Data Analysis. Comparison of ^{90}Y-TA138 and ^{111}In-TA138 tissue uptake was evaluated for bioequivalence based on the 2002 bioequivalence guidance document adopted by the FDA. Briefly, this method describes the estimation of the difference between the means of the logarithms of the data, calculation of the 90% confidence interval for the mean difference, and taking the anti-logs of the limits of the 90% confidence interval. The test compounds are considered bioequivalent if the 90% confidence interval for the ratio of the means is between 0.8 and 1.25. ^{90}Y-TA138 and ^{111}In-TA138 were administered concurrently enabling the ratios of the tissue uptake (%ID/g) to be determined using paired-data analyses. For those organs that only had a single time point available (blood, muscle, bile, bone marrow, and bone), the comparison used the %ID/g. For those organs that had more than one time point available, the comparison used the area under the %ID/g versus time curve (AUC). In the single time point analyses, the paired-difference, log(%ID/g ^{111}In-TA138) − log(%ID/g ^{90}Y-TA138), was calculated for each animal. The mean paired-difference and the 90% confidence limits for the mean were calculated and the antilogarithms obtained to provide the mean and 90% confidence limits for the ratio %ID/g (^{90}Y-TA138)/%ID/g (^{111}In-TA138). The antilog data was necessary in order to express the data on the original scale of measurement. AUCs were estimated using trapezoidal approximations for the multiple time point analyses. The paired-difference, log[AUC(^{90}Y-TA138)] − log[AUC(^{111}In-TA138)], was calculated for each animal. The mean paired-difference and the 90% confidence limits for the mean were calculated and the antilogarithms obtained to provide the mean and 90% confidence limits for the ratio AUC (^{90}Y-TA138)/^{111}In-TA138).

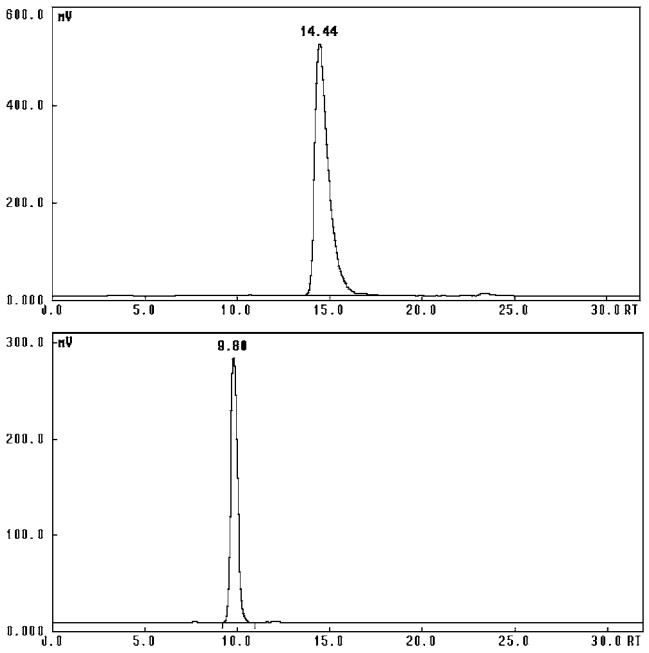


Figure 2. Radio-HPLC chromatograms of ^{90}Y-TA138 (top) and ^{111}In-TA138 (bottom) using a gradient mobile phase (8−10% B over 18 min, A = 25 mM ammonium acetate, B = acetonitrile).

RESULTS

Synthesis of ^{90}Y-TA138 and ^{111}In-TA138. ^{90}Y-TA138 was readily prepared in high yield (RCP > 98%) according to the procedure described in our previous communication (*32*). ^{111}In-TA138 was prepared using a similar procedure with slight modification. In both cases, exclusion of oxygen is required for successful radiolabeling and can be achieved either by degassing under vacuum or by bubbling nitrogen through the mixture before the addition of radiometal. Sodium gentisate was used as a radiolytic stabilizer to prevent radiolysis during the radiolabeling and HPLC analysis. In this study, we used ∼100 μg of TA138 for 20 mCi of $^{90}YCl_3$ (TA138:^{90}Y ∼170:1) for the synthesis of ^{90}Y-TA138, and 2.25 mCi of $^{111}InCl_3$ for preparation of ^{111}In-TA138. The corrected radiochemical purity for ^{90}Y-TA138 and ^{111}In-TA138 was >98% with minimal radiometal colloid formation.

HPLC Characterization of ^{90}Y-TA138 and ^{111}In-TA138. ^{90}Y-TA138 and ^{111}In-TA138 were analyzed by the same reversed phase HPLC method using a gradient mobile phase (8−10% B over 18 min, solvent A = 25 mM ammonium acetate buffer, solvent B = acetonitrile). Figure 2 shows typical radio-HPLC chromatograms of ^{90}Y-TA138 (top) and ^{111}In-TA138 (bottom). There are some small peaks (the void-volume peak at ∼3.0 min and the wash-peak at ∼23 min) due to radioimpurities in ^{90}Y-TA138 and ^{111}In-TA138 preparations. Since these radioimpurities are less than 1.0%, no further characterization was performed. The retention time of ^{111}In-TA138 is ∼4.5 min shorter than that of ^{90}Y-TA138, suggesting that ^{90}Y-TA138 is more lipophilic than that of ^{111}In-TA138. We also tried other reversed phase HPLC methods. It was found that the HPLC retention time difference for ^{90}Y-TA138 and ^{111}In-TA138 depends on the gradient of the mobile phase. Under isocratic conditions (7% B over 30 min, solvent A = 25 mM ammonium acetate buffer, solvent B = acetonitrile), the HPLC retention time difference between ^{90}Y-TA138 and ^{111}In-TA138 was ∼10 min.

Biodistributions of ^{90}Y-TA138 and ^{111}In-TA138 in the c-neu Oncomouse Model. ^{90}Y-TA138 and ^{111}In-TA138 showed rapid blood clearance (Figure 3) primarily via the renal system, and very similar biodistribution patterns (Figures 4−6) in the c-neu Oncomouse model over 48 h postinjection. At 2 h postinjection, the tumor uptake was ∼10% ID/g for ^{90}Y-TA138 and ^{111}In-TA138. The uptake in the eye and bile were below the limit of quantification at 2 h postinjection. Activity levels of ^{90}Y-TA138 and ^{111}In-TA138 were also below the limit of quantification in the blood, muscle, bone, and bone marrow at 24 h postinjection while the uptake in other

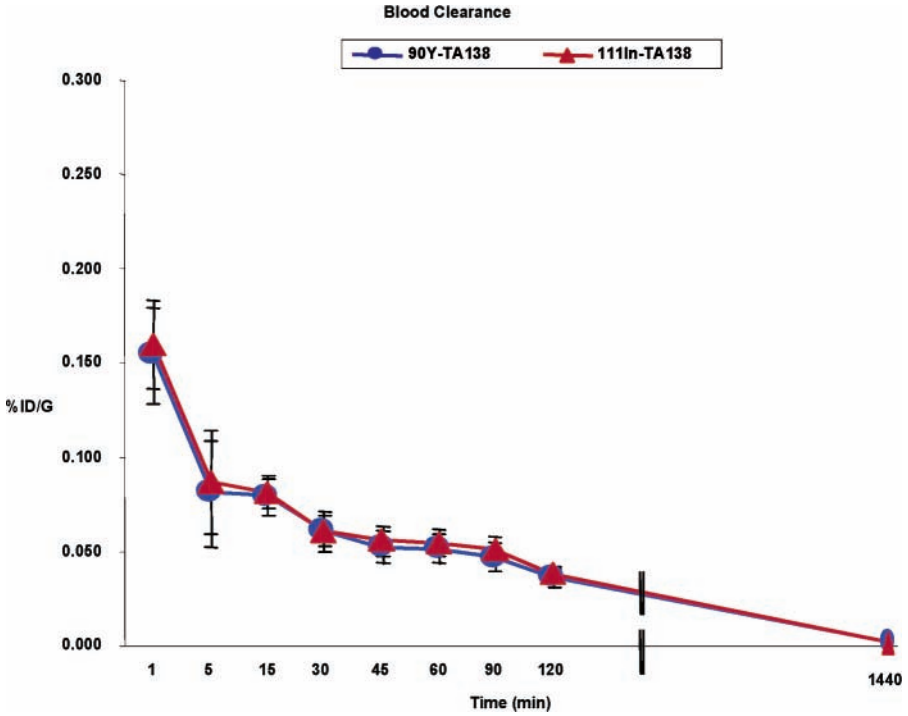


Figure 3. Blood clearance curve for ^{90}Y-TA138 and ^{111}In-TA138 in the c-neu Oncomouse model at 0−24 h postinjection. Each time point is the average ± the standard error of the mean (SEM) (n = 6).

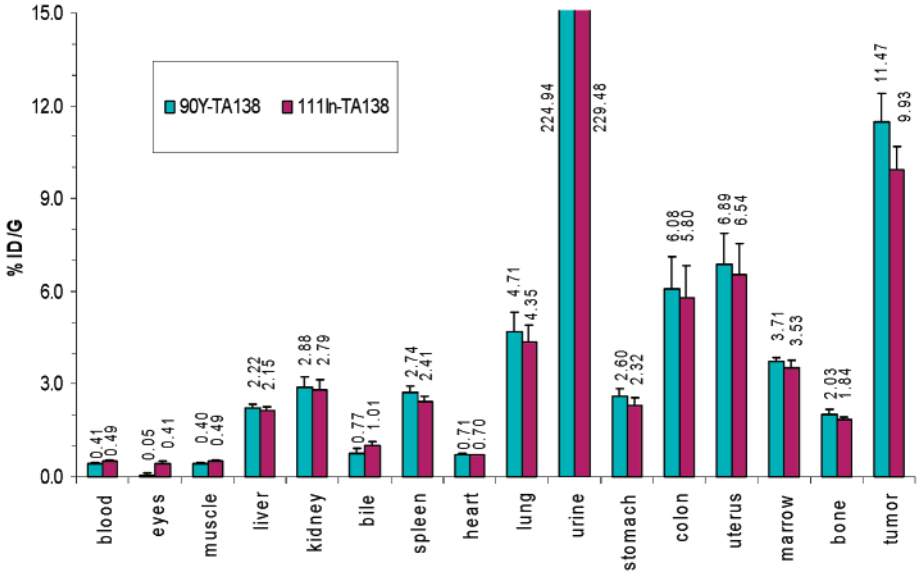


Figure 4. Biodistribution data for ^{90}Y-TA138 (left) and ^{111}In-TA138 (right) in the c-neu Oncomouse model at 2 h postinjection. Each histogram is the average ± the standard error of the mean (SEM) ($n = 6$). The data are decay corrected.

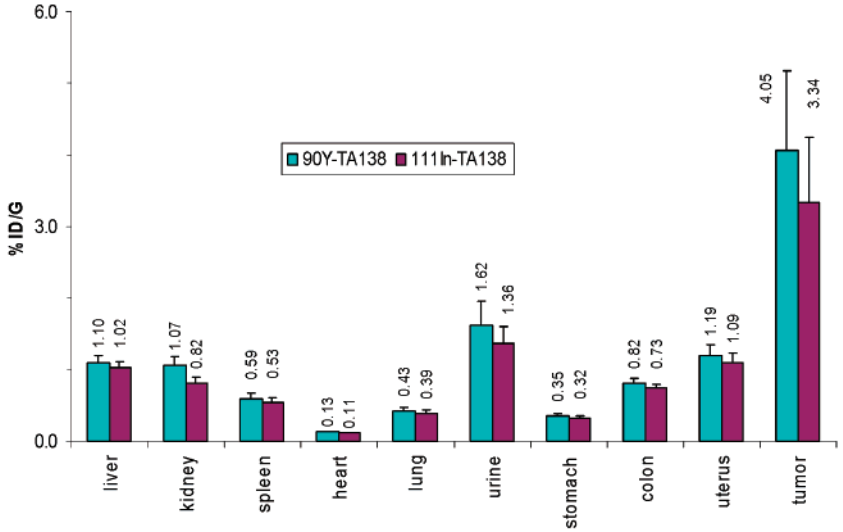


Figure 5. Biodistribution data for ^{90}Y-TA138 (left) and ^{111}In-TA138 (right) in the c-neu Oncomouse model at 24 h postinjection. Each histogram is the average ± the standard error of the mean (SEM) ($n = 6$). The data are decay corrected.

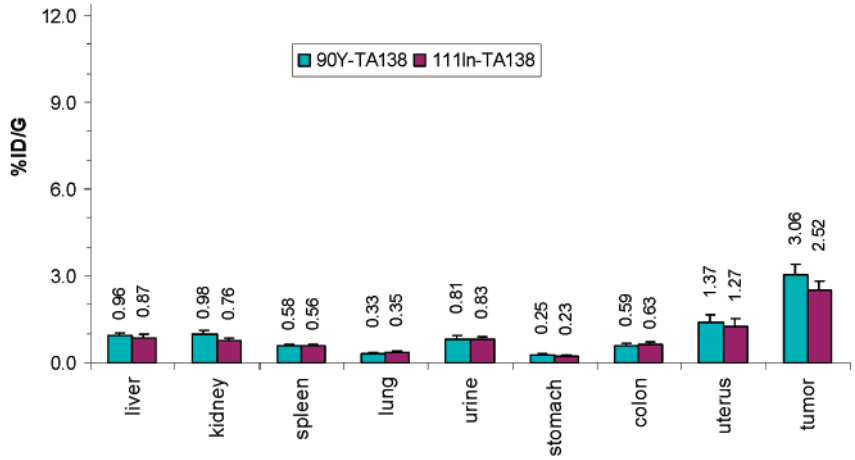


Figure 6. Biodistribution data for ^{90}Y-TA138 (left) and ^{111}In-TA138 (right) in the c-neu Oncomouse model at 48 h postinjection. Each histogram is the average ± the standard error of the mean (SEM) ($n = 6$). The data are decay corrected.

organs were less than 2% ID/g, except the tumor uptake of 3−4%ID/g. At 48 h postinjection, the uptake in all organs except tumor (2−3%) and uterus (1−2%) were less than 1% for ^{90}Y-TA138 and ^{111}In-TA138. At all the time points, there was no significant difference between ^{90}Y-TA138 and ^{111}In-TA138 with respect to their uptake in all organs of interest. HPLC analysis of blood and urine samples at 2 and 24 h postinjection showed no significant metabolism for both ^{90}Y-TA138 and ^{111}In-TA138.

DISCUSSION

^{90}Y-TA138 has demonstrated significant therapeutic effects in several preclinical tumor models, including c-Neu oncomouse, HCT116, and HT460 xenografts (*33*). Since ^{90}Y is a pure β-emitter, ^{111}In-TA138 was chosen as the imaging surrogate for biodistribution and dosimetry determination. Is ^{111}In-TA138 chemically and biologically equivalent to ^{90}Y-TA138? Can ^{111}In-TA138 be used to accurately predict the biodistribution and dosimetry of ^{90}Y-TA138 in animal models? With these questions in mind, we carried out the experiments described in this report.

Difference in Lipophilicity between ^{90}Y-TA138 and ^{111}In-TA138. Radio-HPLC has become a routine method for the characterization of radiolabeled compounds. It is also a powerful tool to compare lipophilicity of two closely related radiolabeled compounds. In this study, we used a reversed phase HPLC method with a gradient mobile phase. It was found that the retention time of ^{111}In-TA138 is ∼4.5 min shorter than that of ^{90}Y-TA138 by the same HPLC method (Figure 2). Similar results were obtained for ^{90}Y and^{111}In complexes of DOTA-BA (BA = benzylamine), a model compound for DOTA−biomolecule conjugates (*35*). Since the only difference in ^{111}In-TA138 and ^{90}Y-TA138 is the metal ion, different retention times strongly suggest that indium and yttrium chelates do not share the same coordination sphere even though they are coordinated by the same DOTA conjugate. If indium and yttrium chelates were to share the same coordination sphere, ^{111}In-TA138 would have had the same retention time as that of ^{90}Y-TA138 under identical chromatographic conditions.

Structural Differences between Y and In Chelates in Solid State. Recently, Mäcke and co-workers (*18*, *36*) described the crystal structures of complexes M(DOTA-D-Phe-NH_2) (M = Y and In) and found that both indium and yttrium in these complexes are eight-coordinated with four amine-nitrogen, one carbonyl-oxygen, and three carboxylate-oxygen atoms bonding to the metal center (*18*, *36*). The difference between these two structures arises from the different conformation of ethylenic bridges and the orientation of sidearms. Y(DOTA-D-Phe-NH_2) exists in solid state as the m-isomer (traditionally designated as the minor isomer) while In(DOTA-D-Phe-NH_2) is observed as the M (major isomer) isomer. The same M isomer is also seen in In(DOTA-AA) (AA = *p*-aminoanilide) (*37*). Since the metal chelate is only one-third of the radiolabeled TA138, the slight difference in solid-state structures of yttrium and indium chelates hardly explains retention time differences between ^{90}Y-TA138 and ^{111}In-TA138 and is not consistent with solution dynamics of In(DOTA-BA) and In(DOTA-AA) as observed in our previous communication (*35*, *37*).

Structural Differences between Y and In Chelates in Solution. The size of Y^{3+} (ionic radius = 0.87 Å) fits perfectly to the coordination cavity of the DOTA-monoamide chelator. It is not surprising that most yttrium complexes of DOTA derivatives are able to maintain their rigid eight-coordinated structure in solution (*18*, *35*, *38*−*41*). In^{3+} has an ionic radius of 0.75 Å, which is smaller than that of Y^{3+} (*42*). As a result, the coordination number for In^{3+} is typically 6 or 7 (*43*−*46*). Only a few eight-coordinated In^{3+} complexes are known (*36*, *37*, *47*−*49*). Due to its smaller size, In^{3+} does not fit to the coordination cavity of the DOTA-monoamide chelator. Although In^{3+} is eight-coordinated in the solid state of In(DOTA-monoamide), the carbonyl-oxygen may become dissociated in solution. This is particularly true for ^{111}In-TA138 at the tracer level (10^{-9} to 10^{-8} M). This explanation is consistent with the HPLC retention time differences between ^{90}Y-TA138 and ^{111}In-TA138, and the fluxionality of In(DOTA-BA) and In(DOTA-AA) in solution (*35*, *37*).

Bioequivalence between ^{90}Y-TA138 and ^{111}In-TA138. There are several factors influencing the bioequivalence of ^{90}Y-TA138 and ^{111}In-TA138. These include solution structures and dissociation kinetics of radiometal chelates, specific activity of radiometals, and the amount of unlabeled TA138 injected into each animal. Since DOTA and its derivatives form eight-coordinated In(III) and Y(III) chelates with extremely high thermodynamic stability and kinetic inertness (*18*, *38*−*41*), the dissociation kinetics may not contribute to the difference, if there is any, in biological properties of ^{90}Y-TA138 and ^{111}In-TA138. In this study we chose to administer ^{90}Y-TA138 and ^{111}In-TA138 concurrently into each animal so that we can eliminate the effect of specific activity and amount of unlabeled TA138 on biodistribution properties of ^{90}Y-TA138 and ^{111}In-TA138. In this way, the only remaining factor that can influence biodistribution properties of ^{90}Y-TA138 and ^{111}In-TA138 would be their structural differences between ^{90}Y and ^{111}In chelates in solution.

In the c-neu Oncomouse model, ^{90}Y-TA138 and ^{111}In-TA138 showed almost identical biodistribution patterns (Figures 4−6) over 48 h. Both ^{90}Y-TA138 and ^{111}In-TA138 are excreted rapidly from blood circulation (Figure 3) via the renal system. There was no significant difference between ^{90}Y-TA138 and ^{111}In-TA138 with respect to their uptake in tumor and other major organs of interest over 48 h postinjection. These results clearly demonstrated that ^{111}In-TA138 and ^{90}Y-TA138 are biologically equivalent despite their differences in solution structure and lipophilicity.

CONCLUSION

This report describes the synthesis and HPLC characterization of ^{111}In-TA138. The HPLC data showed that ^{111}In-TA138 is more hydrophilic, with the retention time being ∼4.5 min shorter than that ^{90}Y-TA138. Since the only difference between ^{111}In-TA138 and ^{90}Y-TA138 is the metal ion, the HPLC retention time difference strongly suggests that indium and yttrium chelates do not share the same coordination sphere in solution even though they are coordinated by the same DOTA conjugate. Despite their differences in lipophilicity and solution structure, biodistribution data in the c-neu Oncomouse model clearly demonstrated that ^{111}In-TA138 and ^{90}Y-TA138 are biologically equivalent with respect to their uptake in tumors and other major organs. Therefore, ^{111}In-TA138 is useful as an imaging surrogate for ^{90}Y-TA138 and should be able to accurately predict the radiation dosimetry of ^{90}Y-TA138, which has the potential as a new therapeutic radiopharmaceutical for the treatment of rapidly growing solid tumors.

LITERATURE CITED

(1) Reubi, J. C. (1997) Regulatory peptide receptors as molecular targets for cancer diagnosis and therapy. *Quart. J. Nucl. Med. 41*, 63−70.

(2) Volkert, W. A. and Hoffman, T. J. (1999) Therapeutic radiopharmaceuticals. *Chem. Rev. 99*, 2269−2292.

(3) Kwekkeboom, D., Krenning, E. P., and de Jong, M. (2000) Peptide receptor imaging and therapy. *J. Nucl. Med. 41*, 1704−1713.

(4) Boerman, O. C., Oyen, W. J. G., and Corstens, F. H. M. (2000) Radiol-labeled receptor-binding peptides: A new class of radiopharmaceuticals. *Semin. Nucl. Med. 30*, 195−208.

(5) Liu, S., and Edwards, D. S. (2001) Bifunctional chelators for target specific therapeutic lanthanide radiopharmaceuticals. *Bioconjugate Chem. 12*, 7−34.

(6) Signore, A., Annovazzi, A., Chianelli, M., Coretti, F., Van de Wiele, C., Watherhouse, R. N., and Scopinaro, F. (2001) Peptide radiopharmaceuticals for diagnosis and therapy. *Eur. J. Nucl. Med. 28*, 1555−1565.

(7) Liu, S., and Edwards, D. S. (2002) Fundamentals of receptor-based diagnostic metalloradiopharmaceuticals. *Topics Curr. Chem. 222*, 259−278.

(8) Jong, M., Kwekkeboom, D., Valkema, R., and Krenning, E. P. (2003) Radiolabeled Peptides for tumor therapy: current status and future directions. *Eur. J. Nucl. Med. 30*, 463−469.

(9) Fichna, J., and Janecka, A. (2003) Synthesis of target-specific radiolabeled peptides for diagnostic imaging. *Bioconjugate Chem. 14*, 3−17.

(10) Liu, S., Robinson, S. P., and Edwards, D. S. (2003) Integrin $\alpha_v\beta_3$ directed radiopharmaceuticals for tumor imaging. *Drugs Future 28*, 551−564.

(11) Moi, M. K., Meares, C. F., McCall, M. J., Cole, W. C., and DeNardo, S. J. (1985) Copper chelates as probes of biological systems: stable copper complexes with macrocyclic bifunctional chelating agent. *Anal. Chem. 148*, 249−253.

(12) Moi, M. K., and Meares, C. F. (1988) The peptide way to macrocyclic bifunctional chelating agents: synthesis of 2-(*p*-nitrobenzyl)-1,4,7,10-tetraazacyclododecane-N,N′N″,N‴-tetraacetic acid and study of its yttrium(III) complex. *J. Am. Chem. Soc. 110*, 6266−6267.

(13) Kline, S. J., Betebenner, D. A., and Johnson, D. K. (1991) Carboxymethyl-substituted bifunctional chelators: preparation of aryl isothionate derivatives of 3-(carboxymethyl)-3-azapentanedioic acid, 3, 12-bis(carboxymethyl)-6,9-dioxa-3,12-diazatetradecanedioic acid, and 1, 4,7,10-tetraazacyclododecane-N,N′N″,N‴-tetraacetic acid for use as protein labels. *Bioconjugate Chem. 2*, 26−31.

(14) Li, M., and Meares, C. F. (1993) Synthesis, metal chelate stability studies, and enzyme digestion of a peptide-linked DOTA derivative and its corresponding radiolabeled immunoconjugates. *Bioconjugate Chem. 4*, 275−283.

(15) Lewis, M. R., Raubitschek, A., and Shively, J. E. (1994) A facile, water soluble method for modification of proteins with DOTA. Use of elevated temperature and optimized pH to achieve high specific activity and high chelate stability in radiolabeled immunoconjugates. *Bioconjugate Chem. 5*, 565−576.

(16) Kulis, D. L., DeNardo, S. J., DeNardo, G. L., O'Donnell, R. T., and Meares, C. F. (1998) Optimized conditions for chelation of yittrium-90-DOTA immunoconjugates. *J. Nucl. Med. 39*, 2105−2110.

(17) Lewis, M. R., and Shively, J. E. (1998) Maleimidocycteine-amido-DOTA derivatives: New reagents for radiometal chelate conjugation to antibody sulfhydryl groups undergo pH-dependent cleavage reactions. *Bioconjugate Chem. 9*, 72−86.

(18) Heppler, A., Froidevaux, S., Mäcke, H. R., Jermann, E., Béhé, M., Powell, P., and Hennig, M. (1999) Radiometal-labeled macrocyclic chelator-derived somatostatin analogue with superb tumor-targeting properties and potential for receptor-mediated internal therapy. *Chem. Eur. J. 5*, 1974−1981.

(19) De Jong, M., Bakker, W. H., Bernard, B. F., Valkema, R., Kwekkeboom, D. J., Reubi, J.-C., Srinivasan, A., Schmidt, M., and Krenning, E. P. (1999) Internalization of radiolabelled [DTPA°]octreotide and [DOTA°, Tyr^3]octreotide: peptides for somatostatin receptor-targeted scintigraphy and radionuclide therapy. *J. Nucl. Med. 40*, 2081−2087.

(20) Reubi, J. C., Waser, B., Schaer, J. C., Laederach, U., Erion, J., Srinivasam, A., Schmidt, M. A., and Bugaj, J. E. (1998) Unsulfated DTPA- and DOTA-CCK analogs as specific high affinity ligands for CCK−B receptor-expressing human and rat tissues in vitro and in vivo. *Eur. J. Nucl. Med. 25*, 481−490.

(21) Behr, T. M., Jenner, N., Béhé, M., Angerstein, C., Gratz, S., Raue, F., and Becker, W. (1999) Radiolabeled peptides for targeting cholecystokinin-B-gastrin receptor-expressing tumors. *J. Nucl. Med. 40*, 1029−1040.

(22) Behr, T. M., Jenner, N., Béhé, M., Angerstein, C., Gratz, S., Raue, F., and Becker, W. (1999) Cholecystokinin-B-gastrin receptor binding peptides: preclinical development and evaluation of their diagnostic and therapeutic potential. *Clin. Cancer Res. 5*, 3124s−3138s.

(23) Liu, S., Cheung, E., Rajopadyhe, M., Ziegler, M. C., Edwards, D. S. (2001) ^{90}Y-and ^{177}Lu-labeling of a DOTA-conjugated vitronectin receptor antagonist for tumor therapy. *Bioconjugate Chem. 12*, 559−568.

(24) Liu, S., and Edwards, D. S. (2001) Stabilization of ^{90}Y-labeled DOTA-biomolecule conjugates using gentisic and ascorbic acid. *Bioconjugate Chem. 12*, 554−558.

(25) Carrasquillo, J. A., White, J. D., Paik, C. H., Raubitschek, A., Le N., Rotman, M., Brechbiel, M. W., Gansow, O. A., Top, L. E., Perentesis, P., Reynolds, J. C., Nelson, D. L., and Waldmann, T. A. (1999) Similarities and differences in ^{111}In- and ^{90}Y-labeled 1B4M-DTPA antiTac monoclonal antibody distribution. *J. Nucl. Med. 40*, 268−276.

(26) Canera, L., Kinuya, S., Garmestani, K., Brechbiel, M. W., Wu, C., Pai, L. H., McMurry, T. J., Gansow, O. A., Pastan, I., Paik, C. H., and Carrasquillo, J. A. (1994) Comparative biodistribution of indium- and yttrium-labeled B3 monoalonal antibody conjugated to either 2-(p-SCN−Bz)-6-methyl-DTPA (1B4M-DTPA) or 2-(p-SCN−Bz-)-1,4,7,10-tetraazacyclododecane tetraacetic acid (2B-DOTA). *Eur. J. Nucl. Med. 21*, 640−646.

(27) Rösch, F., Herzog, H., Stolz, B., Brockmann, J., Köhle, M., Mühlensiepen, H., Marbach, P., and Müller-Gärtner, H.-W. (1999) Uptake kinetics of the somatostatin receptor ligand [^{86}Y]DOTA-$_D$Phe^1-Tyr^3-octreotide ([^{86}Y]SMT487) using positron emission tomography in nonhuman primates and calculation of radiation doses of the ^{90}Y-labeled analogue. *Eur. J. Nucl. Med. 26*, 358−366.

(28) Liu, S., Edwards, D. S., Ziegler, M. C., Harris, A. R., Hemingway, S. J., and Barrett, J. A. (2001) ^{99m}Tc-Labeling of a hydrazinonictotinamide-conjugated vitronectin receptor antagonist. *Bioconjugate Chem. 12*, 624−629.

(29) Liu, S., Cheung, E., Rajopadyhe, M., Williams, N. E., Overoye, K. L. and Edwards, D. S. Isomerism and solution dynamics of ^{90}Y-labeled DTPA- biomolecule conjugates. *Bioconjugate Chem.* **2001**, *12*, 84−91.

(30) Liu, S., and Edwards, D. S. (2001) Synthesis and characterization of two ^{111}In labeled DTPA-peptide conjugates. *Bioconjugate Chem. 12*, 630−634.

(31) Janssen, M., Oyen, W. J. G., Massuger, L. F. A. G., Frielink, C., Dijkgraaf, I., Edwards, D. S., Rajopadyhe, M., Corsten, F. H. M., and Boerman, O. C. Tumor targeting with radiolabeled alpha(v)beta(3) integrin binding peptides in nude mouse model. *Cancer Res* **2002**, *62*, 6146−6151.

(32) Liu, S., Harris, T. D., Ellars, C., and Edwards, D. S. (2003) Anaerobic ^{90}Y- and ^{177}Lu-labeling of a DOTA-conjugated nonpeptide vitronectin receptor antagonist. *Bioconjugate Chem. 14*, 1030−1037.

(33) Harris, T. D., Kalogeropoulos, S., Nguyen, T., Liu, S., Bartis, J., Ellars, C. E., Edwards, D. S., Onthank, D., Yalamanchili, P., Robinson, S. P., Lazewatsky, J., and Barrett, J. A. (2003) Design, synthesis and evaluation of radiolabeled integrin $\alpha_v\beta_3$ antagonists for tumor imaging and radiotherapy. *Cancer Biother. Radiopharm. 18*, 627−641.

(34) Currie, L. A. (1968) Limits for qualitative detection and quantitative determination. *Anal. Chem. 40*, 586−593.

(35) Liu, S., Pietryka, J., Ellars, C. E., and Edwards, D. S. (2002) Comparison of yttrium and indium complexes of

DOTA-BA and DOTA-MBA: models for ^{90}Y- and ^{111}In-labeled DOTA-biomolecule conjugates. *Bioconjugate Chem. 13*, 902−913.

(36) Maeke, H., Scherer, G., Heppeler, A., and Henig, M. (2001) Is In-111 an ideal surrogate for Y-90? If not, why? *Eur. J. Nucl. Med. 28*, 967 (abstract no. OS-27).

(37) Liu, S., He, Z.-J., Hsieh, W.-Y., and Fanwick, P. E. (2003) Synthesis, characterization, and crystal structure of In(DOTA-AA) (AA = *p*-aminoanilide): a model compounds for ^{111}In-labeled DOTA-biomolecule conjugates. *Inorg. Chem. 42*, 559−568.

(38) Aime, S., Botta, M., and Ermodi, G. (1992) NMR study of solution structures and dynamics of lanthanide(III) complexes of DOTA. *Inorg. Chem. 31*, 4291−4299.

(39) Aime, S., Anelli, P. L., Botta, M., Fedeli, F., Ermondi, G., Grandi, M., Paoli, P., and Uggeri, F. (1992) Synthesis, characterization, and *1*/*T*1 NMRD profiles of gadolinium(III) complexes of monoamide derivatives of DOTA-like ligands. X-ray structure of the 10-[2-[[2-hydroxy-1-(hydroxymethyl)-ethyl]amino]-1-(phenylmethoxy)methyl]2-oxoethyl]-1,4,7,10-tetraazacyclododecane-1,4,7-triacetic acid-gadolinium(III) complex. *Inorg. Chem. 31*, 2422−2428.

(40) Aime, S., Botta, M., Ermondi, G., Terreno, E., Anelli, P. L., Dedeli, F., and Uggeri, F. (1996) Relaxometric, structural, and dynamic NMR studies of DOTA-like Ln(III) complexes (Ln = La, Gd, Ho, Yb) containing a *p*-nitrophenyl substituent. *Inorg. Chem. 35*, 2726−2736.

(41) Kumar, K., Chang, C. A., Francesconi, L. C., Dischino, D. D., Malley, M. F., Cougoutas, J. Z., and Tweedle, M. F. (1994) Synthesis, stability, and structure of gadolinium(III) and yttrium(III) macrocyclic poly(amino carboxylates). *Inorg. Chem. 33*, 3567−3575.

(42) Shannon, R. D. (1976) Revised effective ionic radii and systemic studies of interatomic distances in halides and chalogenides. *Acta Crystallogr. A32*, 751−767.

(43) Yang, L.-W., Liu, S., Wong, E., Rettig, S. J., and Orvig, C. (1995) Lanthanide complexes of potentially heptadentate (N_4O_3) schiff base and aminephenol ligands: influence of rigidity and preorganization of ligands on compound structure. *Inorg. Chem. 34*, 2164−2178.

(44) Liu, S., Wong, E., Rettig, S. J., and Orvig, C. (1993) Hexadentate N_3O_3 amine phenol ligands for group 13 Metal Ions: Evidence for intrastrand and interstrand hrdrogen bonds in polydentate amine phenols. *Inorg. Chem. 32*, 4268−4276.

(45) Liu, S., Wong, E., Karunaratne, V., Rettig, S. J., and Orvig, C. (1993) Highly flexible chelating ligands for group 13 metals. Design, synthesis and characterization of hexadentate (N_3O_3) tripodal amine phenol ligand complexes of aluminum, gallium and indium. *Inorg. Chem. 32*, 1756−1765.

(46) Liu, S., Rettig, S. J., and Orvig, C. (1992) Polydentate ligand chemistry of group 13 metals: Effects of the size and donor-selectivity of metal ions on structures and properties of aluminum, gallium and indium complexes with potentially heptadentate (N_4O_3) amine phenol ligands. *Inorg. Chem. 31*, 5400−5407.

(47) Riesen, A., Kaden, T. A., Ritter, W., and Mäcke, H. R. (1989) Synthesis and X-ray structural characterization of seven coordinate macrocyclic In^{3+} complexes with relavance to radiopharmaceutical applications. *J. Chem. Soc., Chem. Commun.* 460−462.

(48) Mäcke, H. R., Riesen, A., and Ritter, W. (1989) The molecular structure of indium-DTPA. *J. Nucl. Med. 30*, 1235−1239.

(49) Malyrick M. A., Ilyhin, A. B., and Petrosyans, S. P. (1994) Seven- and eight-coordinate complexes of indium(III) with nitrilotriacetic acid. *Main Group Metal Chem. 17*, 707−717.

BC034108Q

A Dual Fluorochrome Probe for Imaging Proteases

Moritz F. Kircher, Ralph Weissleder, and Lee Josephson*

Center for Molecular Imaging Research, Massachusetts General Hospital and Harvard Medical School, Charlestown, Massachusetts 02129. Received August 27, 2003; Revised Manuscript Received December 12, 2003

Near-infrared fluorescence (NIRF) optical probes have been able to provide a noninvasive assessment of enzyme activity for a number of different enzymes and types of pathology. Here we describe a dual fluorochrome enzyme-activatable probe featuring one NIRF fluorochrome that is activated by protease activity and a second fluorochrome that is protease resistant and serves as an internal standard. The probe was prepared by attaching Cy7 directly to an amino-CLIO, an amine functional cross-linked iron oxide (CLIO) nanoparticle carrier, in a protease resistant manner. Cy5.5 was attached to a protease sensitive polyarginine peptide spacer, also attached to amino-CLIO. In vitro and in vivo the ratio of the Cy5.5 to Cy7 fluorescence was increased by protease, reflecting the increase in Cy5.5 fluorescence by protease in the vicinity of the probe. In vitro and in vivo the absolute values of the Cy5.5 and Cy7 fluorescence reflected lesion size and the distance of lesions from the surface, while the ratio of Cy5.5 to Cy7 fluorescence obtained was constant and independent of lesion size and depth. The dual fluorochrome probe, and related dual wavelength imaging method, represents a novel approach for imaging protease activity in vivo.

INTRODUCTION

In recent years a variety of so-called "smart" probes have been designed that respond to the presence of molecules in their environment with a change in signal. These include calcium indicators (*1*, *2*), sensors of β-galactosidase activity (*3*), and fluorogenic substrates for a variety of hydrolytic enzymes (*4*). Recently, high molecular weight near-infrared fluorescent (NIRF) molecules have been synthesized which are quenched until activated by proteases, and these have been used to image protease activity in vivo (*5*, *6*). These probes consist of a high molecular weight carrier, a cleavable peptide spacer or "stalk" attached through a C-terminal cysteine, and a fluorochrome attached to the N-terminus. These features of probe design are shown in Figure 1. Probes of this design have been used to visualize a variety of proteases including cathepsin D (*7*), MMP-2 (*8*), and thrombin (*9*). The high molecular carrier can be a graft copolymer or a magnetic nanoparticle, the latter serving as combined NIRF/optical and water relaxation enhancing/MR agent, a feature that is sometimes termed a multimodal imaging capability (*10*).

Use of such probes to measure foci of enzyme activity in vivo was initially achieved with surface reflectance-based instrumentation (*11*), but more recent tomographic methods have been used to obtain tissue concentrations of the fluorochrome released as a product of protease activity (*12*). However, the absolute value of fluorescence obtained is a function of the intensity of incident light and the depth and size of the lesion. In addition, the amount of enzyme product produced by protease reflects not only the enzyme activity but also the delivery of substrate (substrate concentration).

We previously reported on a dual probe-based imaging method where an optical probe originally designed for use as a single enzyme-activated probe (*10*) was used together with a second, nondegradable probe employing a second, optically distinct fluorochrome (see ref 13). The nondegradable probe served as a standard for internalization by macrophages; macrophages expressing cathepsin B phagocytosed both probes similarly but could only activate one probe, while macrophages without cathepsin B could not activate either probe. Hence, the ratio of fluorescence provided a measure of cathepsin B activity corrected for variable levels of macrophage internalization. These results indicated the feasibility of using dual fluorochrome ratio imaging methods for the improved

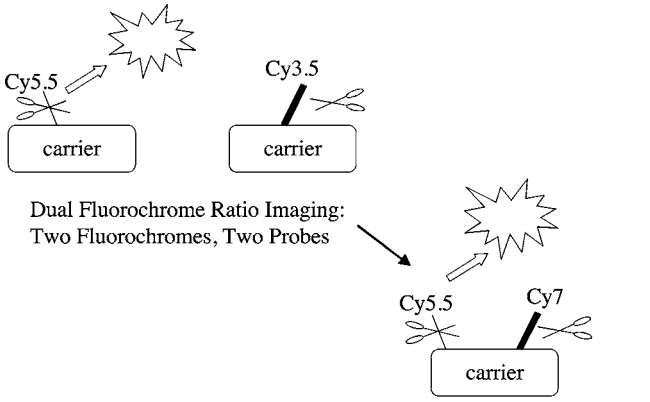


Figure 1. Dual fluorochrome imaging strategies. Dual fluorochrome ratio imaging methods began with two probes with peptide stalks of different proteolytic susceptibility (*13*). Proteolytic cleavage of a peptide by an enzyme (scissors)-activated fluorescence. Here the dual fluorochrome probe consists of a single probe and two fluorochromes. One fluorochrome (Cy5.5) is activatable (cleaved by scissors), while a second (Cy7) serves as an internal standard. The probe is denoted Cy5.5−R4−Cy7−CLIO where the peptide "stalk" is the L-arginyl peptide "R4" and the carrier is amino-CLIO.

* Corresponding author: Lee Josephson, Ph.D., Center for Molecular Imaging Research, Massachusetts General Hospital, Bldg. 149 13th Street, #5406, Charlestown, MA 02129. Tel.: (617)726 6478. Fax: (617)726 5708. E-mail: ljosephson@partners.org.

10.1021/bc034151d CCC: $27.50 © 2004 American Chemical Society
Published on Web 02/28/2004

quantification of enzyme activity, but the method required the synthesis of two probes and their use as a mixture.

Here we report on an improvement of our previous dual fluorochrome, dual probe method consisting of a single probe that features two fluorochromes. A schematic representation of these different approaches to dual fluorochrome probes is shown in Figure 1. We attached one fluorochrome (Cy5.5) via a cleavable peptide linker while a second fluorochrome (Cy7) was attached directly to a macromolecular carrier and was resistant to proteolytic activation. The amino-CLIO nanoparticle (CLIO = cross-linked iron oxide) was employed as a carrier. The ratio of Cy5.5 to Cy7 fluorescence reflected activation by protease and could be used to correct for differences in the size and depth of a target lesions.

MATERIAL AND METHODS

The dual fluorochrome probe was synthesized by first attaching Cy7 directly to the amino-CLIO carrier and then by attaching Cy5.5 to the N-terminus of a proteolytically cleavable L-polyarginine peptide ("R4"). The probe is denoted Cy5.5−R4−Cy7−CLIO. Attachment of the peptide R4 (R-R-R-R-G-C) to the nanoparticle is through the thiol of the C-terminal cysteine and was accomplished by use of the bifunctional agent succinimidyl iodoacetate (SIA). Cy5.5 is attached to the N-terminal arginine. A more complete synthetic scheme of the probe Cy5.5−R4−CLIO, a probe identical to that used here but lacking the Cy7 attached to the CLIO, has been provided; see refs 10 and 13.

Synthesis of Cy7−CLIO. Amino-CLIO, a magnetic nanoparticle with a coating of cross-linked dextran and primary amino groups was prepared as described (*14*, *15*). To 1 mL of amino-CLIO (10 mg Fe/mL) was added 100 μL of 10x PBS and 2.5 μL 0.5 M EDTA. The mixture was added to one Cy7 dye tube (1 mg) (Amersham-Pharmacica, Piscataway, NJ) and incubated for 1 h at room temperature and then overnight at 4 °C. Unbound Cy7 was then removed by spin-separation over a PD-10 column (Amersham) equilibrated with PBS, 1.25 mM EDTA.

Synthesis of the Peptide−Nanoparticle, R4−Cy7−CLIO. The L-arginyl peptide R-R-R-R-G-C ("R4") was synthesized as described previously (*13*, *14*). To 1 mL Cy7−CLIO (10 mg Fe/mL) were added 330 μL of 0.1 M Na_2HPO_4 and 330 μL of 150 mM succinimidyl iodoacetate in DMSO. The mixture was allowed to sit for 1 h at room temperature and the addition of succinimidyl iodoacetate repeated. Iodoacetyl-CLIO was separated from iodoacetic acid using a Sephadex G-25 column equilibrated with 0.025 M citrate pH 6.5 run at 4 °C. To the void volume (3 mL) was added 10 mg of R4 peptide, and the reaction was incubated overnight at room temperature. Unreacted peptide was removed by dialysis against 3 L of 0.02 M citrate pH 8.2 using a 14 kDa cutoff membrane.

Synthesis of the Dual Fluorochrome Probe, Cy5.5−R4−Cy7−CLIO. To attach Cy5.5, 140 μL of 1 M NaHCO3 (pH 8.3) was added to 3 mL of R4−Cy7−CLIO. The mixture was then distributed to 6 tubes of Cy5.5. After 2 h at room temperature, the tubes were pooled and 10% volume of 1.5 M hydroxylamine was added. The mixture was allowed to sit for an additional 2 h at room temperature and separated using PD-10 columns (equilibrated with 0.02 M citrate buffer, pH 8.2) run in a spin separation mode. One milliliter of sample was added to columns that were spun at 830*g* for 5 min.

Physical Properties of Cy5.5−R4−Cy7−CLIO. Spectra of conjugates were taken using a Hitachi 3500 spectrophotometer. The number of Cy5.5 and Cy7 dyes present was determined spectrophotometrically, using an extinction coefficient of 250 000 M^{-1} cm^{-1} at 675 nm for Cy5.5, and 200 000 M^{-1} cm^{-1} at 747 nm for Cy7. Iron concentration was determined spectrophotometrically (*14*). The ratio of fluorochromes to nanoparticles was obtained assuming 2064 iron atoms per crystal (*16*). R1 and R2 relaxivities were measured using a 0.47T MR relaxometer (*14*). Size was determined by laser light scattering using a Zetasizer 1000 (Malvern, Worcestershire, UK).

Activation of Fluorescence by Trypsin. Cy5.5−R4−Cy7−CLIO fluorescence was determined in a microtiter plate with 0.01 M Na_2HPO_4, pH 7.4, 50 μg Fe/mL of Cy5.5−R4−Cy7−CLIO, and 10 μg/mL trypsin. The plate was incubated at room temperature and Cy7 and Cy5.5 fluorescence determined (ex 747, em 777 and ex 645, em 695, respectively) using a fluorescent microtiter plate reader (SpectraMAXGeminiXS, Molecular Devices, Sunnyvale, CA).

Optical Imaging. To examine the ability of the dual fluorochrome probe to correct for lesion size, a homogenate prepared from the liver from a mouse injected with Cy5.5−R4−Cy7−CLIO was used. Magnetic nanoparticle based probes are internalized by the liver with activation of their fluorescence (*10*, *13*). C57BL/6 mice (National Cancer Institute, Bethesda, MD) were injected via tail vein with 10 mg Fe/mL of Cy5.5−R4−Cy7−CLIO, and 24 h later mice were sacrificed and the livers excised and homogenized. Volumes of homogenate containing activated probe were transferred to 384-well plates to serve as models of enzyme activated "lesions" in vivo. To mimic lesions of different sizes, volumes were chosen to yield wells containing between 2 mm and 10 mm high volumes of homogenate. To demonstrate the ability of the dual fluorochrome probe to correct for lesion depth, liver from a noninjected mouse was transferred to a 384-well plate to achieve heights of 0 to 7 mm in 1 mm increments. Subsequently, 15 μL of 1% agarose containing 10 μg of Cy5.5−R4−Cy7−CLIO was added to each well with liver samples.

To demonstrate the ability of the dual fluorochrome probe to correct for lesion size and depth, the 9L rat gliosarcoma cell line stably transfected to express green fluorescence protein (GFP) (*17*) was cultured at 37 °C in a humidified 5% CO_2 atmosphere in Dulbecco's modified eagle medium (DMEM) supplemented with 10% fetal bovine serum, 1% penicillin and streptomycin and 500 μg/mL geniticine G418 (all products from Cellgro, Herndon, VA). 9L gliosarcomas were induced by means of bilateral injection of 9L glioma cells deep into the mammary fat pad of nude mice ($n = 3$, Charles River, Wilmington, MA). To obtain tumors of different sizes, 0.5×10^6 cells were implanted on the right, and 2×10^6 cells in the left mammary fat pad. After 12 days, animals were anesthetized (ketamine/xylazine, 65/10 mg/kg) and 10 mg Fe/kg body weight Cy5.5−R4−Cy7−CLIO injected by tail vein. Twenty-four hours later, mice were imaged, euthanized by halothane inhalation, and underwent progressive dissection and further NIRF imaging.

Optical imaging of the plates and mice was performed using a whole mouse imaging system as described (*11*). Cy5.5 fluorescence was obtained with an excitation band-pass filter at 630 ± 15 nm (630RDF30; Omega Optical, Brattleboro, VT) and emission band-pass filter at 700 ± 20 nm (700DF40; Omega Optical). Cy7 fluorescence was obtained with an excitation band-pass filter at 736 ± 20 (736AF40; Omega Optical) and emission band-pass filter at 800 ± 20 (800AF40; Omega Optical). Images were

Table 1. Physical Properties of Cy5.5−R4−Cy7−CLIO

size (nm)	R1 (s^{-1} mM^{-1})	R2 (s^{-1} mM^{-1})	Cy5.5 fluorochromes per particle	Cy7 fluorochromes per particle
28	16	45	2.3	2.5

acquired using a cooled CCD camera with 800 × 600-pixel resolution (SenSys; Photometrics, Tucson, AZ). Kodak Digital Science 1D Software (Eastman Kodak; Rochester, NY) was used for acquisition and data analysis.

RESULTS

Properties of the Dual Fluorochrome Probe Cy5.5−R4−Cy7−CLIO. The physical properties of Cy5.5−R4−Cy7−CLIO are summarized in Table 1. The probe uses a thioether linkage and an enzyme-cleavable L-arginine peptide (*10*, *13*). Figure 2A shows the absorption spectrum of Cy5.5−R4−Cy7−CLIO, with a characteristic absorption of the iron oxide in the ultraviolet region of the spectrum and with the absorption maxima of Cy5.5 and Cy7 at 674 and 748 nm, respectively. Figure 2B shows the absorption spectra of Cy5.5−R4−Cy7−CLIO in relation to the excitation and emission filters used. Also shown are the emission maxima for Cy5.5 (694 nm) and Cy7 (737 nm). As shown in Figure 2C an excellent separation of fluorescent signals from Cy5.5 and Cy7 was obtained with the optical imaging system used in this study.

Enzyme Activation of Cy5.5−R4−Cy7−CLIO. Figure 3 shows the effect of treating Cy5.5−R4−Cy7−CLIO with trypsin. Trypsin cleaved the R4 peptide, producing a 700% increase in the Cy5.5 fluorescence after 60 min and 850% increase after 24 h (data not shown). In contrast, Cy7 fluorescence was nearly constant, as expected, because of the direct attachment of Cy7 to the cross-linked dextran coating of CLIO and inability to undergo enzymatic cleavage. The small increase of about 20% in Cy7 fluorescence may reflect a small quenching effect resulting from slight interaction between the two fluorochromes when in close physical proximity to each other (on the same probe). We next performed a series of experiments to determine whether the light associated with Cy5.5 fluorescence and Cy7 fluorescence would be attenuated (or transmitted) similarly in biological tissues. If Cy5.5 fluorescence and Cy7 fluorescence are attenuated similarly, the ratio of their fluorescence should reflect the activation of the probe and be independent of size and depth of the fluorescent lesion.

Imaging with Cy5.5−R4−Cy7-CLIO in Vitro. To assess whether the ratio of Cy5.5 to Cy7 fluorescence depended on the size or magnitude of the fluorescence, we imaged phantoms consisting of a 384-well plate containing variable amounts of liver homogenate (Figure 4). A mouse was injected with 10 mg Fe/kg Cy5.5−R4−Cy7−CLIO and liver homogenate containing probe plus a mixture of naturally occurring proteins and light absorbing materials, was placed in the wells of the plate at different heights (Figure 4A). The fluorescence from Cy5.5 and Cy7 and the ratio of Cy5.5 to Cy7 fluorescence was obtained as shown in Figures 4B and 4C. Cy5.5 and Cy7 fluorescence intensities increased with increasing amounts of homogenate, however, for both fluorochromes fluorescence tended to plateau at higher amounts of homogenate. This reflects the fact that the NIRF signal obtained is strongly surface weighted with this type of instrumentation. However, the ratio of Cy5.5 to Cy7 fluorescence was nearly constant over a 7-fold change in

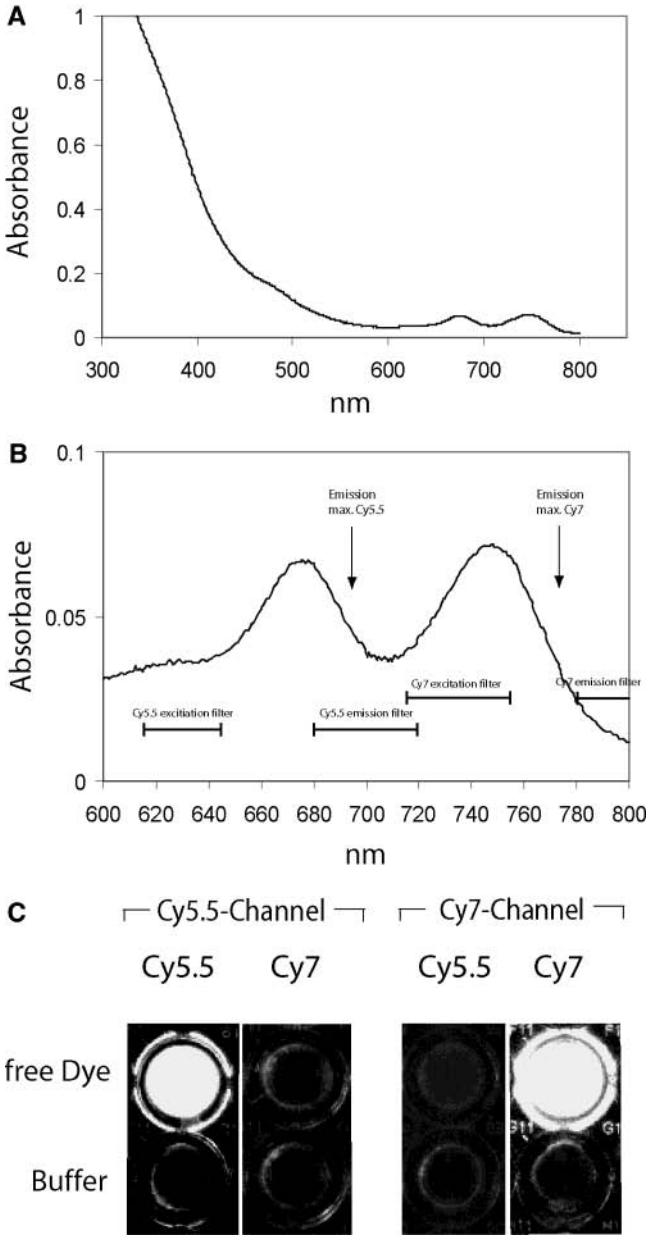


Figure 2. (A) Absorption spectra of Cy5.5−R4−Cy7−CLIO. (B) Magnification of (A) with indication of emission and excitation filters used in the imaging experiments. (C) Spectral separation of imaging channels. Images of a 96-well plate containing free Cy5.5, free Cy7, or buffer only, respectively. Note the clear channel separation despite high fluorochrome concentration.

homogenate height (Cy5.5/Cy7 = 6.43 at 1 mm versus 6.13 at 7 mm). With the liver homogenate the dual fluorochrome probe and ratio imaging method yielded a value of Cy5.5/Cy7 fluorescence of 6 to 7 which was characteristic of the activated probe in vitro, see Figure 3.

We next assessed whether the ratio of Cy5.5 to Cy7 fluorescence could correct for a constant lesion at variable depths from the surface. For this purpose, a constant amount of agar containing unactivated Cy5.5−R4−Cy7−CLIO was placed on top of variable amounts of liver tissue from a noninjected animal (Figure 5A). Figures 5B and 5C show that Cy5.5 and Cy7 fluorescence decreased with increasing depths of liver. However, the ratio of Cy5.5 to Cy7 fluorescence was nearly constant when light passed through 1 to 10 mm of liver (Cy5.5/Cy7 = 1.70 at 1 mm versus 1.64 at 10 mm). The Cy5.5/Cy7 ratio of

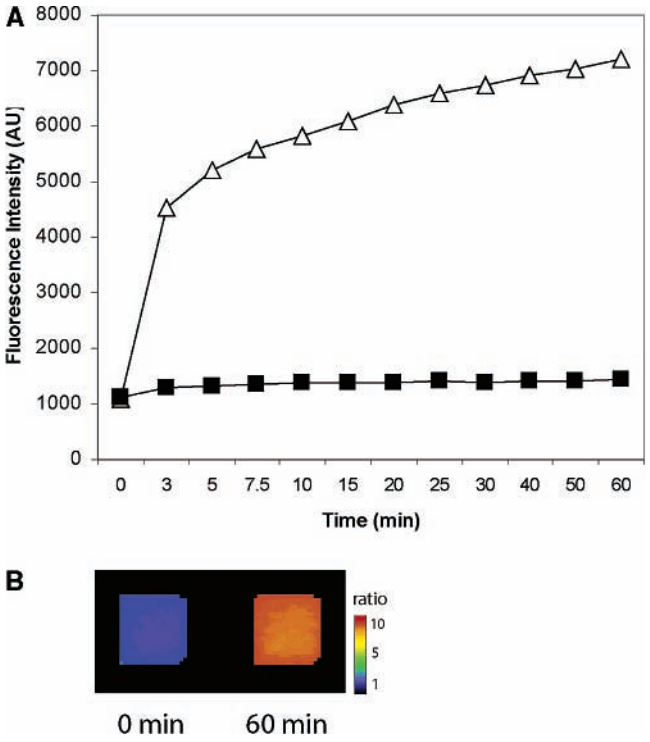


Figure 3. Activation of the dual fluorochrome probe Cy5.5−R4−Cy7−CLIO by trypsin. (A) Time-course measured with fluorescent plate reader. Cy5.5 fluorescence (Δ), Cy7 fluorescence (■). (B) Images representing ratio Cy5.5/Cy7 at 0 and 60 min of activation by trypsin. Orange color corresponds to probe activation or to a Cy5.5/Cy7 fluorescence ratio of about 7. Cy5.5 fluorescence is increased by proteolytic cleavage while Cy7 fluorescence is nearly constant.

about 1.7 was slightly higher than the ratio of native probe (1.0−1.2, see Figure 2). The slight probe activation presumably results from mixing at the interface between native probe (clear solution) with enzymes in liver tissue (brown tissue).

Imaging with Cy5.5−R4−Cy7−CLIO in Vivo. We next tested the ability of the dual fluorochrome probe to correct for differences in tumor size and depth in vivo. Nude mice bearing 9L GFP expressing gliosarcomas of different sizes (Figure 6) were injected with Cy5.5−R4−Cy7−CLIO. Cy5.5 and Cy7 fluorescence from tumors were then determined, where tumor borders (regions of interest) were defined by tumor GFP fluorescence using our previously described technique (*18*). Figure 6 shows white light, fluorescent, and Cy5.5/Cy7 ratio images for an intact animal with tumors of different size as dissection progressed. With the intact animal, the Cy5.5 and Cy7 fluorescence intensities of the two tumors were markedly different, a difference which was not seen on the ratio of Cy5.5/Cy7 image (top row, right image). The ratio of Cy5.5 to Cy7 fluorescence for the two tumors (12 mg and 195 mg) was further independent of dissection level. Results with variable tumor size were similar to in vitro results obtained with variable amounts of homogenate (Figure 4).

DISCUSSION

Here we report on a novel type of multimodal probe that features two fluorochromes covalently linked to an MRI detectable carrier (amino-CLIO), in which each fluorochrome responds differently to proteases. While we have utilized only the optical properties of the Cy5.5−R4−Cy7−CLIO probe, the superparamagnetic iron oxide core of the CLIO nanoparticle has potent relaxation enhancing properties and can be used in conjunction with MRI to determine probe location (*14*, *15*). The feasibility of optical- or magnetic resonance-based imaging in vivo using a probe similar to Cy5.5−R4−Cy7−CLIO but lacking Cy7 has been shown (*10*).

We have shown that fluorescent activation occurs, not by direct interaction between proteases or reducing agents and the fluorochrome, but with the transfer of the fluorochrome from the local environment of the nanoparticle to the bulk solvent (*10*). Cleavage of the bond between a fluorochrome and a nanoparticle has been achieved with proteases such as trypsin or with DTT (dithiothreitol). Use of the latter reagent requires disulfide-linked fluorochromes, synthesized by use of the bifunctional cross-linking agent *N*-succinimidyl 3-(2-pyridyldithio)propionate (SPDP), in contrast to the bifunctional agent succinimidyl iodoacetate (SIA) used in the current study. DTT could not activate fluorescence when a thioether linkage was used to attach the fluorochrome to the nanoparticle (see Figure 3 of ref 10), and proteases could not activate fluorescence when protease resistant D-arginyl peptides were used to couple the fluorochrome to the nanoparticle (*13*). The activation of Cy5.5 fluorescence by trypsin of (700%, Figure 3A) therefore results from the proteolytic cleavage of the R4 peptide, which transfers Cy5.5 from the local environment of the nanoparticle to the bulk solvent. The much lower activation of Cy7 fluorescence (about 20% Figure 3A) reflects Cy7's direct attachment to the nanoparticle, its resistance to proteolysis, and the inability of the protease to affect a transfer to the bulk solvent.

A second feature of fluorescence quenching by nanoparticles is that when fluorochromes with widely different optical properties (fluorescein, Cy5.5, or Cy3) are attached to CLIO nanoparticles, significant quenching results (see ref 10 and Josephson, unpublished observations). Fluorescence quenching also occurs when fluorochromes are attached to colloidal gold (*19*). In the case of CLIO nanoparticles, quenching reflects two types of effects: interactions between fluorochromes on the nanoparticle, and interactions between fluorochromes and the nanoparticle itself. The effects of quenching due to fluorochrome/nanoparticle interaction, rather than fluorochrome/fluorochrome interaction, were evident from the synthesis of nanoparticles with as little as 0.14 fluorochromes (average per nanoparticle). Such probes still showed greater than 200% activation of fluorescence when treated by DTT, and the fluorochrome was transferred to the bulk solvent (*10*). For colloidal gold and the colloidal CLIO nanoparticle, a major mechanism of quenching is the interaction between the fluorochrome and the nanoparticles, which may reflect collisions of the dye against the nanoparticle surface (collisional or dynamic quenching) (*19*).

The value of the dual fluorochrome probe and related imaging methods is not related to the specific protease(s) responsible for fluorescence activation. As noted above, probes of this general design (high molecular weight carrier, linker peptide, fluorochrome) have been designed to image a wide variety of proteases by varying the structure of the linker peptide. Several factors suggest that the activation of the Cy5.5−R4−Cy7−CLIO probe described here results from cathepsin B activity. First, using specific protease inhibitors and macrophages in vitro, we have shown that the protease activating Cy5.5−R4−CLIO, the single fluorochrome version of the dual fluorochrome probe of the current study, was cathepsin B (*13*). Second, as noted, a nanoparticle probe made with

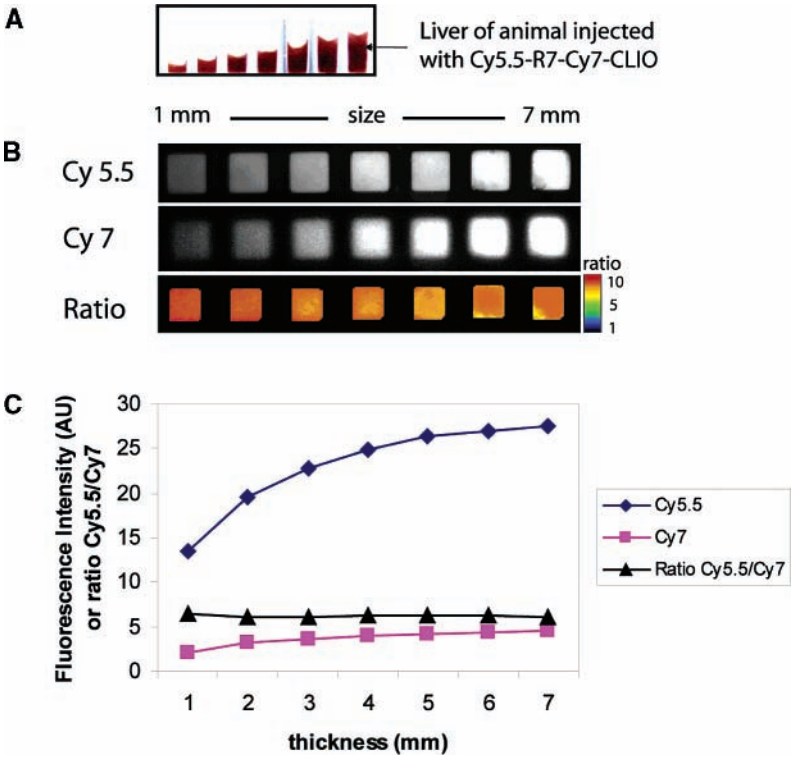


Figure 4. Dual fluorochrome probe imaging with different amounts of liver homogenate. (A) White light image of wells containing different amounts of liver homogenate. Liver is from mouse injected with Cy5.5−R4−Cy7−CLIO. (B) NIRF images of wells in A in the Cy5.5 and Cy7 channels and resulting ratio Cy5.5/Cy7 image (color-coded). Orange color corresponds to a Cy5.5/Cy7 ratio of about 7, which is characteristic of the activated probe. (C) Values of fluorescence intensity and the ratio of Cy5.5/Cy7 fluorescence obtained by region of interest analysis from images in B.

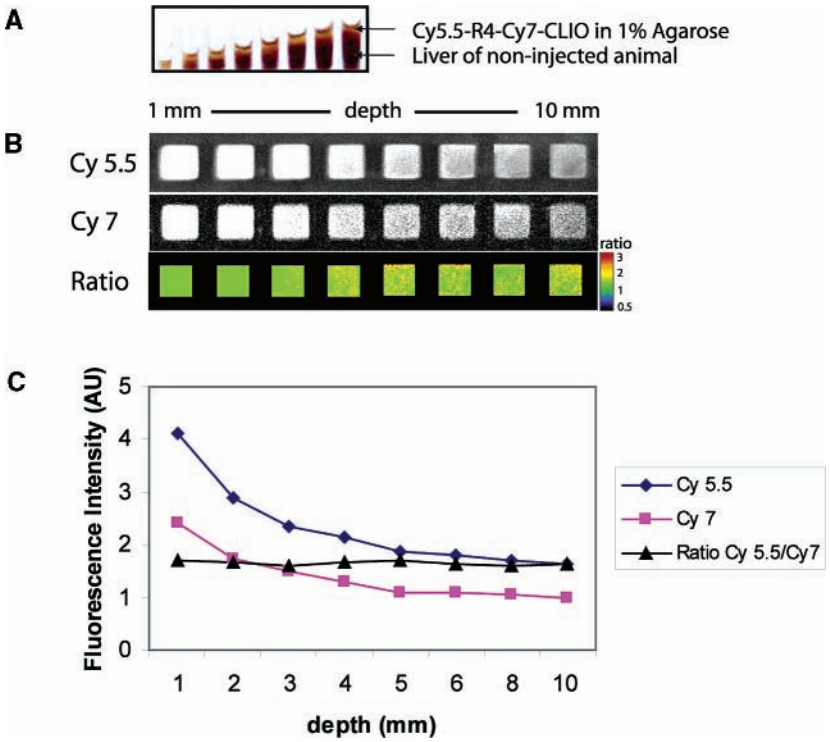


Figure 5. Dual fluorochrome probe imaging through different depths of liver tissue. (A) White light image of wells containing liver from a noninjected animal overlayed with a constant amount of Cy5.5−R4−Cy7−CLIO in 1% agar. (B) NIRF images of wells in A in the Cy5.5 and Cy7 channels and resulting ratio Cy5.5/Cy7 image (color-coded). (C) Values of fluorescence intensity and ratio of Cy5.5/Cy7 fluorescence obtained from images in B.

noncleavable D-arginine peptide spacer could not be activated by macrophages (*13*). Third, macrophages including Kupffer cells of the liver are high in cathepsin B (*20*−*22*). After injection, CLIO nanoparticles are removed by phagocytosis and are concentrated in high cathepsin B activity containing macrophages (*17*, *23*, *24*). Finally, cathepsin B hydrolyzes peptides with arginine in the S2 or S1 subsites of the protease, which are provided by L-polyarginine peptides used to couple the Cy5.5 due to the nanoparticle (*25*, *26*).

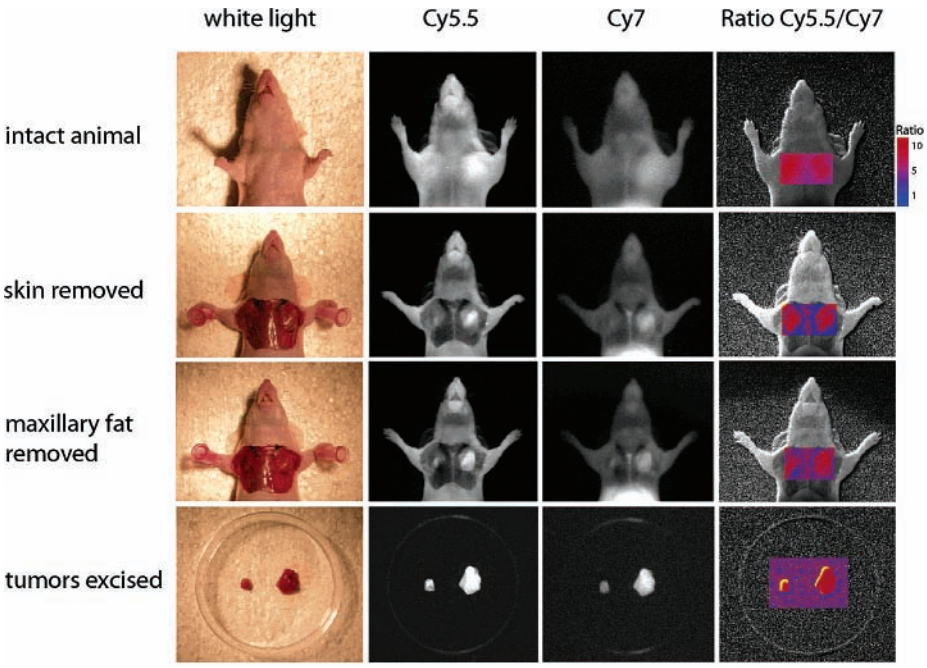


Figure 6. Dual fluorochrome ratio imaging of implanted 9L GFP expressing gliosarcoma tumors. A nude mouse bearing tumors of different sizes (12 mg (left) and 195 mg (right), respectively) implanted in the mammary fat pads was injected with Cy5.5−R4−Cy7−CLIO. From left to right are shown the white light image, the Cy5.5 fluorescent image, the Cy7 fluorescence image and the ratio of Cy5.5 to Cy7 fluorescence (color-coded). Note that despite the variation in signal intensity caused by the differences in tumor size and differences in dissection level (depth), the resulting ratio is similar reflecting the ability of the intenal standard Cy7 to correct for size and depth.

The optical properties of the Cy5.5 (ex 675, em 694) and Cy7 (ex 747, em 777) were found to be well suited to their use in dual fluorochrome probes. First, the fluorescence from each fluorochrome was detected without significant interference from each other (Figure 2). Second, the interaction between the two fluorochromes when attached to the probe was minimal. Proteolytic cleavage and transfer of Cy5.5 to the bulk solvent was associated with a 700% increase in fluorescence, while the increase in Cy7 fluorescence was only about 20% (Figure 3A), which presumably reflects interactions between Cy5.5 and Cy7. If Cy5.5 and Cy7 interacted strongly to quench each other, then both would be dequenched by proteolytic cleavage of either. Third, the ratio of Cy5.5 to Cy7 fluorescence reflected probe activation both in vitro and in vivo. Thus a value of 1 was characteristic of the probe before exposure to proteases but increased to 7 in the presence of protease (Figure 1). A similar value was obtained in liver homogenates after iv injection of the probe (Figure 4). Fourth, the ratio of Cy5.5 to Cy7 fluorescence was independent of sample size (Figures 4 and 6) and tissue depth (Figure 5).

The dual fluorochrome multimodal probe using the Cy5.5/Cy7 fluorochrome pair, and related dual fluorochrome imaging, may permit use of this type of probe to gather a new type of information with in vivo imaging, in addition to the corrections for lesion size and depth demonstrated here. Currently the interaction of a probe with a molecular target, such as a protease, can reflect both the activity of the molecular target enzyme in a specific tissue, and the transport and concentration of the probe in the vicinity of the molecular target. Factors affecting probe transport include blood flow, capillary permeability, capillary blood volume, and other physiological factors. In these studies the dual fluorochrome probe and imaging method provided information on probe activation that is independent of the absolute value of Cy5.5 fluorescence, which depended on parameters such as lesion size and depth. Hence with the dual fluorochrome probe design used here, the Cy7 fluorescence might provide an internal standard for determining probe concentration, allowing Cy5.5 fluorescence to be corrected for variable levels of probe transport. However, proof of this hypothesis that Cy7 fluorescence can yield probe concentration in vivo will require determination of probe concentrations by a suitable reference "gold standard" bioanalytical method. Such studies now appear warranted based on the properties of the Cy5.5−R4−Cy7−CLIO probe described here.

ACKNOWLEDGMENT

This study was funded by the NIH grants P50 CA8635 and R01 EB 001872. M.F.K. was supported by the German Research Foundation (DFG). We thank Edward E. Graves for assistance in computing ratio images.

LITERATURE CITED

(1) Takahashi, A., Camacho, P., Lechleiter, J. D., and Herman, B. (1999) Measurement of intracellular calcium. *Physiol. Rev. 79*, 1089−125.

(2) Li, W. H., Parigi, G., Fragai, M., Luchinat, C., and Meade, T. J. (2002) Mechanistic studies of a calcium-dependent MRI contrast agent. *Inorg. Chem. 41*, 4018−24.

(3) Louie, A. Y., Huber, M. M., Ahrens, E. T., Rothbacher, U., Moats, R., and Jacobs, R. E., et al. (2000) In vivo visualization of gene expression using magnetic resonance imaging. *Nat. Biotechnol. 18*, 321−5.

(4) Haugland, R. P. (1995) Detecting enzymatic activity in cells using fluorogenic substrates. *Biotech Histochem. 70*, 243−51.

(5) Weissleder, R., and Ntziachristos, V. (2003) Shedding light onto live molecular targets. *Nat. Med. 9*, 123−8.

(6) Weissleder, R., Tung, C. H., Mahmood, U., and Bogdanov, A., Jr. (1999) In vivo imaging of tumors with protease-activated near-infrared fluorescent probes. *Nat. Biotechnol. 17*, 375−8.

(7) Tung, C. H., Bredow, S., Mahmood, U., and Weissleder, R. (1999) Preparation of a cathepsin D sensitive near-infrared

fluorescence probe for imaging. *Bioconjugate Chem. 10*, 892−6.
(8) Bremer, C., Tung, C. H., and Weissleder, R. (2001) In vivo molecular target assessment of matrix metalloproteinase inhibition. *Nat. Med. 7*, 743−8.
(9) Jaffer, F. A., Tung, C. H., Gerszten, R. E., and Weissleder, R. (2002) In vivo imaging of thrombin activity in experimental thrombi with thrombin-sensitive near-infrared molecular probe. *Arterioscler. Thromb. Vasc. Biol. 22*, 1929−35.
(10) Josephson, L., Kircher, M. F., Mahmood, U., Tang, Y., and Weissleder, R. (2002) Near-infrared fluorescent nanoparticles as combined MR/optical imaging probes. *Bioconjugate Chem. 13*, 554−560.
(11) Mahmood, U., Tung, C. H., Bogdanov, A. Jr., and Weissleder, R. (1999) Near-infrared optical imaging of protease activity for tumor detection. *Radiology 213*, 866−70.
(12) Ntziachristos, V., Tung, C. H., Bremer, C., and Weissleder, R. (2002) Fluorescence molecular tomography resolves protease activity in vivo. *Nat. Med. 8*, 757−60.
(13) Kircher, M. F., Josephson, L., and Weissleder, R. (2002) Ratio imaging of enzyme activity using dual wavelength optical reporters. *Mol. Imaging 1*, 89−95.
(14) Josephson, L., Tung, C. H., Moore, A., and Weissleder, R. (1999) High-efficiency intracellular magnetic labeling with novel superparamagnetic-Tat peptide conjugates. *Bioconjugate Chem. 10*, 186−91.
(15) Josephson, L., Perez, J. M., and Weissleder, R. (2001) Magnetic nanosensors for the detection of oligonucleotide sequences. *Angew. Chem., Int. Ed. 40*, 3204−3206.
(16) Shen, T., Weissleder, R., Papisov, M., Bogdanov, A., Jr., and Brady, T. J. (1993) Monocrystalline iron oxide nanocompounds (MION): physicochemical properties. *Magn. Reson. Med. 29*, 599−604.
(17) Moore, A., Weissleder, R., and Bogdanov, A., Jr. (1997) Uptake of dextran-coated monocrystalline iron oxides in tumor cells and macrophages. *J. Magn. Reson. Imaging 7*, 1140−5.
(18) Petrovsky, A., Schellenberger, E., Josephson, L., Weissleder, R., and Bogdanov, A., Jr. (2003) Near-infrared fluorescent imaging of tumor apoptosis. *Cancer Res. 63*, 1936−42.
(19) Dubertret, B., Calame, M., and Libchaber, A. J. (2001) Single-mismatch detection using gold-quenched fluorescent oligonucleotides. *Nat. Biotechnol. 19*, 365−70.
(20) Ii, K., Hizawa, K., Kominami, E., Bando, Y., and Katunuma, N. (1985) Different immunolocalizations of cathepsins B, H, and L in the liver. *J. Histochem. Cytochem. 33*, 1173−5.
(21) Lesser, M., Chang, J. C., and Orlowski, M. (1985) Cathepsin B and D activity in stimulated peritoneal macrophages. *Mol. Cell Biochem. 69*, 67−73.
(22) Crocker, J., Burnett, D., and Jones, E. L. (1984) Immunohistochemical demonstration of cathepsin B in the macrophages of benign and malignant lymphoid tissue. *J. Pathol. 142*, 87−94.
(23) Wunderbaldinger, P., Josephson, L., and Weissleder, R. (2002) Tat Peptide Directs Enhanced Clearance and Hepatic Permeability of Magnetic Nanoparticles. *Bioconjugate Chem. 13*, 264−268.
(24) Weissleder, R., Heautot, J. F., Schaffer, B. K., Nossiff, N., Papisov, M. I., and Bogdanov, A., Jr., et al. (1994) MR lymphography: study of a high-efficiency lymphotrophic agent. *Radiology 191*, 225−30.
(25) Melo, R. L., Barbosa Pozzo, R. C., Alves, L. C., Perissutti, E., Caliendo, G., and Santagada, V., et al. (2001) Synthesis and hydrolysis by cathepsin B of fluorogenic substrates with the general structure benzoyl-X-ARG-MCA containing non-natural basic amino acids at position X. *Biochim Biophys Acta 1547*, 82−94.
(26) Bromme, D., Bonneau, P. R., Lachance, P., and Storer, A. C. (1994) Engineering the S2 subsite specificity of human cathepsin S to a cathepsin L- and cathepsin B-like specificity. *J. Biol. Chem. 269*, 30238−42.

BC034151D

Long-Term Expression with a Cationic Polymer Derived from a Natural Polysaccharide: Schizophyllan†

Takeshi Nagasaki,*,‡ Masaya Hojo,‡ Atsushi Uno,‡ Taku Satoh,‡ Kazuya Koumoto,§ Masami Mizu,§ Kazuo Sakurai,§ and Seiji Shinkai||

Department of Applied & Bioapplied Chemistry, Graduate School of Engineering, Osaka City University, Sugimoto, Sumiyoshi, Osaka 558-8585, Japan, Department of Chemical Process & Enviroments, The University of Kitakyushu, Hibikino, Kitakyushu, Fukuoka 808-0135, Japan, and Department of Chemistry & Biochemistry, Graduate School of Engineering, Kyushu University, Hakozaki, Fukuoka 812-8581, Japan. Received September 30, 2003; Revised Manuscript Received December 23, 2003

Among the various synthetic gene carriers based on biomaterials, cationic polymers with polysaccharide backbones have long been studied as nonviral vectors due to their low immunogenicity and high water solubility. Schizophyllan, a β-(1,3)-glucan, is one of the various polysaccharides that are clinically administered. Furthermore, its safety in the human body has already been confirmed. Various functional groups can be selectively introduced into the side chain, not into the main chain of schizophyllan. Therefore, we have synthesized various oligoamine conjugates from schizophyllan. It was confirmed that their in vitro transfection efficiencies are superior to that of polyethylenimine by adjusting the molecular weight and the degree of amination of cationic schizophyllan. While it was possible to reduce cytotoxicity by adjusting the amount of DNA complex per cell, as seen with poly-L-lysine, polyethylenimine, and chitosan, PEGylation was the most effective means of reducing toxicity. Furthermore, using cationic schizophyllan carriers, it was also possible to express a reporter protein for a long period of time due to a long residence time of plasmid DNA in cells.

INTRODUCTION

Of the various ways of transferring exogenous genes into mammalian cells, biological techniques utilizing viral infectivity are advantageous in terms of high gene transfection efficiency and expression, but disadvantageous in terms of cost, immunogenicity, pathological infection, cancerization, and other virus-related safety issues (*1*). Therefore, safer nonviral vectors are being examined and studied more closely. Nonviral vectors can be roughly divided into two groups: cationic lipids and cationic polymers. In liposome-based gene transfection systems, liposomes are often formed from lipids associated with biological membranes in order to facilitate interactions with cell membranes and organelles, and the degree of antigenicity is low. However, liposome-based gene transfection systems are not suitable for repeated use due to high cytotoxicity. Although it has been reported that using PEGylated liposomes can reduce the degree of cytotoxicity, PEGylation decreases transfection efficiency (*2*). Toxicity is a major obstacle to using cationic lipids in gene therapy, and as a result, the level of interest in cationic polymer-based nonviral vectors shown by researchers is increasing. Research is actively being conducted on the use of dendritic structures (*3*−*6*) and polyethyleneimine (PEI) (*7*−*9*).

However, the transfection efficiency of cationic polymers is generally lower than that of cationic lipids and much lower than that of viral vectors. Moreover, the problem of toxicity is not completely resolved with cationic polymers (*10*), and studies on poly-L-lysine have reported that transfection efficiency and cell membrane toxicity exhibit a positive correlation (*11*). Therefore, when designing cationic polymers, strategies that use biocompatible or biodegradable materials and take cytotoxicity and degradation into account are often employed (*12*, *13*). Of the various biopolymers, cationic polymers with polysaccharide backbones have long been studied as nonviral vectors due to their low immunogenicity and high water solubility (*14*, *15*). However, the cytotoxicity of one such polymer, DEAE−dextran, is very high (*16*). In chitosan, DNA complexation occurs only under certain conditions, and a large amount of DNA is needed to achieve a sufficient level of gene expression (*17*, *18*). Furthermore, the transfection efficiency of chitosan, including chitosan derivatives, is insufficient (*19*).

Schizophyllan (SPG), a β-(1,3)-glucan, is one of the various polysaccharides that are clinically administered by the intramuscular route. The safety of this polysaccharide in the human body has already been confirmed: SPG has been injected intramuscularly as an adjuvant in the treatment of gynecological cancer for over 20 years (*20*, *21*). Moreover, its affinity to antigen-presenting cells in the immune system has been documented (*22*, *23*). Recently, Sakurai and Shinkai discovered that schizophyllan, naturally existing as a triple helix, can form a hetero-triple helix with a single chain of certain nucleotides when it is dissociated into a single chain (*24*, *25*). This characteristic also applies to other β-(1,3)-glucans: for example, molecular weight-dependent single-chain nucleotide affinity has been also confirmed with Curdlan, which does not have a glucose side chain (*26*). Further-

* To whom correspondence should be addressed. Phone: +81-6-6605-2696. FAX: +81-6-6605-2785. E-mail: nagasaki@bioa.eng.osaka-cu.ac.jp.

† This is the 24th paper in the series of "polysaccharide−polynucleotide complexes".

‡ Osaka City University.

§ The University of Kitakyushu.

|| Kyushu University.

10.1021/bc034178x CCC: $27.50 © 2004 American Chemical Society
Published on Web 02/26/2004

more, by utilizing this triple helix complex formation, β-(1,3)-glucans have been used as oligonucleotide carriers (*27*).

Schizophyllan is a β-(1,3)-glucan in which various functional groups can be selectively introduced into the side chain, but not into the main chain at all. In the present study, the usefulness of this polysaccharide as a backbone of a transfection agent of mammalian cells was investigated by introducing oligoamines into the side chain to increase the amount of its cationic charge, thus enhancing its affinity toward plasmid DNA.

EXPERIMENTAL PROCEDURES

Materials. Triple strand SPG with weight-average molecular weight (M_w) of 1.5×10^5 and the number of repeating units of 231, respectively, was kindly supplied from Taito Co. Ltd., (Kobe, Japan). Methoxy-polyethylenglycol succinimidyl propionates (m-PEG-SPA; M_w 2000 and 5000) were purchased from Shearwater (Huntsville, AL). PEI with molecular weight of 2.5×10^4 was purchased from Aldrich. *N*,*N*′-Bis(3-aminopropyl)-1,3-propanediamine, spermidine, and spermine were purchased from Across Organics (Geel, Belgium), sodium borohydride, 2-aminoethanol, and dextran (M_w 40000) were from Tokyo Kasei Kogyo Co., Ltd. (Tokyo, Japan), and sodium periodate was from Wako Pure Chemical Industries, Ltd. (Osaka, Japan), respectively. Cell counting kit-8 containing WST-8 and 1-methoxyphenazinium methosulfate was purchased from Dojindo (Kumamoto, Japan). The fetal bovine serum (FBS), nonessential amino acids, and penicillin/streptomycin were purchased from Gibco/BRL. Dulbecco's modified Eagle's medium (DEMEM) and RPMI1640 were obtained from Nissui Pharmaceutical Co. Ltd (Tokyo, Japan). Other reagents and solvents were purchased from Aldrich or Wako Pure Chemical Industries, Ltd. (Osaka, Japan).

Plasmids and Cells. pGL3-control was purchased from Promega (Madison, WI). pCMV^{tk}Luc was obtained from the American Type Culture Collection (Manassas, VA). pEGFP-Endo was purchased from Clonetech (Palo Alto, CA). Plasmid DNAs were amplified in *Escherichia coli* and purified by EndoFree Plasmid Kit (Qiagen, Hilden, Germany). Rhodamine-labled pGL3-control was prepared as described in the protocol of Label IT Rhodamine Nucleic Acid Labeling Kit (Mirus, Madison, WI). COS-1, CHO-K1, and HeLa cells were from the American Type Culture Collection. COS-1 and HeLa cells were cultured in DMEM containing 10% FBS, 100 units/mL penicillin, 100 μg/mL streptomycin without or with 0.1 mM nonessential amino acid, respectively. CHO-K1 cells were cultured in Ham's F12K medium, and the other conditions were the same as those of COS-1. The cell incubation was always carried out at 37 °C in a fully humidified air containing 5% CO_2.

Preparation of SPG Having Various Molecular Weights. Hydrolysis of SPG(150K) was carried out in 90% formic acid, and the resultant hydrolyzed mixture was purified by fractionate precipitation according to the reported method (*28*). The molecular weight of the samples obtained by fractionate precipitation was evaluated by gel permeation chromatography (GPC) on an AsahipackGS320-220 column (Asahi Kasei Co., Japan) at a flow rate of 1.0 mL/min in water. The molecular weight was calibrated by a pullulun standard (Hayashibara Biochemical Laboratories, Inc., Okayama, Japan). The molecular weight of the SPG was estimated to be 12000 (12K), 34000 (34K), and 80000 (80K), respectively.

Preparation of Various Amine-Conjugated SPGs. The general synthetic scheme is shown in Chart 1. To 100 mg of SPG(34K) sample dissolved in 100 mL of water was added 165 mg of sodium periodate (5 equiv for the repeating unit of SPG) in 2 mL of water. The mixture was stirred for 2 days at 4 °C. After dialysis with distilled water, the solution was lyophilized. The white solid thus obtained, and 2 mL of *N*,*N*′-bis(3-aminopropyl)-1,3-propanediamine was added into 20 mL of dimethyl sulfoxide and stirred for 2 days. After the reaction mixture became clear, 100 mg of sodium borohydride was added to the mixture to reduce the Schiff base formed. Excess sodium borohydride was quenched by acetic acid, and the solution was dialyzed with acidic water, basic water, and distilled water. After the removal of insoluble slug by centrifugation, the supernatant was lyophilized. Thus, we obtained APPD-SPG(34K). The degree of the introduced amine was evaluated as the amount of nitrogen% that determined by elemental analysis. The elemental analysis was carried out at least three times after thoroughly drying with phosphorus oxide, and the degree of amination was estimated to be 40.7 ± 1.2 mol %. Ethanolamine, spermidine, and spermine-conjugated derivatives were synthesized with similar method as mentioned above.

Table 1. Chemical Characterization of SPG Derivatives Conjugated with Various Oligoamines

conjugates	oligoamine	*M*w of SPG	N% (found)	μmol/mg (N)	modified %
AE58(34K)	AE	34000	2.38	1.70	58
SPD47(34K)	SPD	34000	5.24	3.74	47
SP49(34K)	SP	34000	6.74	4.81	49
APPD37(12K)	APPD	12000	5.42	3.87	37
APPD3(34K)	APPD	34000	0.51	0.365	3
APPD9(34K)	APPD	34000	1.48	1.06	9
APPD18(34K)	APPD	34000	2.86	2.04	18
APPD28(34K)	APPD	34000	4.26	3.04	28
APPD41(34K)	APPD	34000	5.91	4.22	41
APPD46(80K)	APPD	80000	6.50	4.64	46
APPD45(150K)	APPD	150000	6.39	4.56	45

Preparation of SPG with Various Degrees of Amination. When conjugating *N*,*N*′-bis(3-aminopropyl)-1,3-propanediamine to SPG with a molecular weight of 34000 Da, the amount of sodium periodate in relation to the glucose side chain was adjusted to 10, 40, 80, 150, or 500 mol %, and the subsequent reductive amination resulted in derivatives with a degree of amination of 3, 9, 18, 28, and 41%, respectively (Table 1). Degree of amination was assessed by an elemental analysis with an assumption that two amine molecules were introduced to the glucose side chain and was defined as the ratio of aminated glucose.

Preparation of Amine-Conjugated Dextran Derivative. To 200 mg of dextran dissolved in 200 mL of water was added 530 mg of sodium periodate (2.0 equiv for the glucose residue) in 2 mL of water. The mixture was stirred for 2 days at 4 °C. After dialysis with distilled water at 4 °C, the solution was lyophilized. The white solid thus obtained, and 2 mL of *N*,*N*′-bis(3-aminopropyl)-1,3-propanediamine was added into 20 mL of dimethyl sulfoxide and stirred for 2 days at 20 °C. After the reaction mixture became clear, 100 mg of sodium borohydride was added to the mixture to reduce the Schiff base formed. Excess sodium borohydride was quenched by acetic acid in the ice bath, and the solution was dialyzed with acidic water, basic water, and distilled water at 4 °C. After the removal of insoluble slug by centrifugation, the supernatant was lyophilized. Thus, we obtained APPD-DEX. The degree of the introduced amine was evaluated as the amount of nitrogen% that determined by elemental analysis. The elemental analysis was carried out at least three times after thoroughly

Chart 1. Syntheses of Various Oligoamine-Conjugated SPG

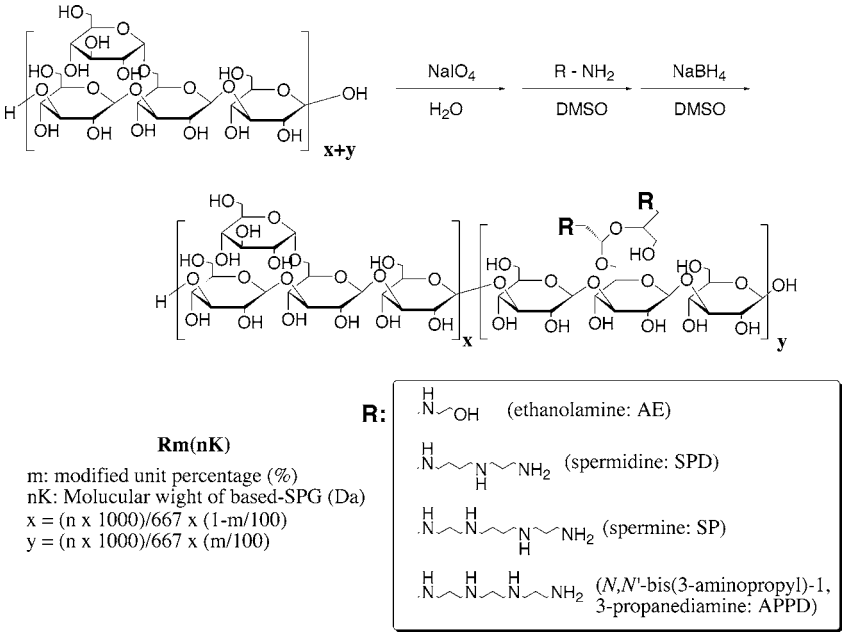


Table 2. Chemical Characterization of PEGlyated Derivatives

conjugates	*M*w of PEG	N% (found)	μmol/mg (protonable N)
2KPEG-APPD46(80K)	2000	3.93	2.21
5KPEG-APPD46(80K)	5000	1.22	0.71
5KPEG-APPDDEX	5000	1.87	1.08

drying with phosphorus oxide, and the degree of amination was estimated to be 34.3 ± 1.3 mol %.

PEGylation of Cationic SPG and Dextran. *N*,*N*′-Bis(3-aminopropyl)-1,3-propanediamine-conjugated polysaccharides (APPD46(80K) and APPD34DEX; 20 μmol of protonable nitrogen atom) were mixed with methoxy-poly(ethylen glycol) succinimidyl propionates (m-PEG-SPA; M_w 2000 or 5000, 2.5 mol % to protonable nitrogen atom) in dry DMSO (1 mL) (Scheme 1). After being gently shaken at room temperature for 24 h, the reaction mixture was poured into Milli-Q (5 mL). PEGylated compounds were purified with ultrafiltration Centricon Plus-20 (nominal molecular weight limit = 10 kDa, Millipore, Bedford, MA) followed by lyophilization. Products were characterized by elemental analyses (Table 2). The yield of 2KPEG-APPD46(80K), 5KPEG-APPD46-(80K), and 5KPEG-APPDDEX was 89%, 81%, and 77%, respectively. The degree of modification of primary amino groups of introduced amine residues of oligoamine-conjugated schizophyllan can be determined by a ninhydrin assay in a manner similar to Wagner's report (*29*). We have confirmed no decrease in free primary amino groups.

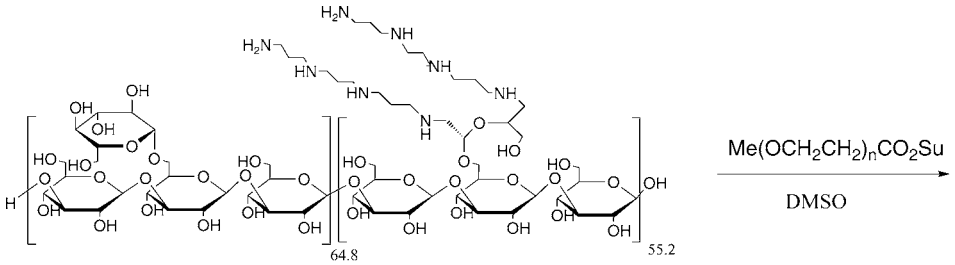
Transfection. In general, COS-1 cells (3×10^4 cells for an each well) were grown to just before confluence in a 24-wells culture plates (Techno Plastic Products, Trasadingen, Switzerland) in DMEM with 10% FBS and 100 U/mL penicillin and 100 μg/mL streptomycin in an atmosphere of 5% CO_2 at 37 °C and washed twice with 0.5 mL of PBS. 10% PBS was prepared by dilution of PBS with Milli-Q water to decrease the ionic strength. Transfection was performed with 1 μg plasmid DNA for each well. Basic protocol includes 3 h of transfection time and 48 h of post-transfection time. Luciferase assays were performed as described in the protocol of Steady-Glo Luciferase Assay System (Promega, Madison, WI). Luciferase relative light units (RLU) were analyzed by luminometer Fluoroskan Ascent-FL (Thermo Labsystems, Finland). The protein concentrations of the cell lysates were measured as described in the protocol of NanoOrange Protein Quantitation Kit (Molecular Probes, Eugene, OR) using bovine serum albumin as a standard. The measurement of transfection efficiency was performed in triplicate. To evaluate the effect of backbone on long-term expression, COS-1 cells (1×10^4 cells for an each well) were plated in 12-well culture plates (Techno Plastic Products, Trasadingen, Switzerland), and then the luciferase assay was performed with 4, 7, 14, 21, and 28 days of post-transfection time.

Cytotoxicity. Cells (6×10^3 cells for each well) were seeded in 96-well plates (Techno Plastic Products, Trasadingen, Switzerland) and allowed to attach to the plate for overnight. In the following day, the medium was changed for a fresh medium, and cells were treated with same conditions as transfection. After change of medium, cells were incubated for 48 h before measurement of the cell viability. The viable cell number was estimated by use of Cell Counting Kit-8, called WST assay. WST assays were performed as described in the protocol of Cell Counting Kit-8. Plates were read on microplate reader Multiskan Acent (Thermo Labsystems, Finland). The absorbance was measured at 450 nm. The protein concentrations of the cell lysates were measured as described previously. The measurement of cell viability was performed in sextuplicate.

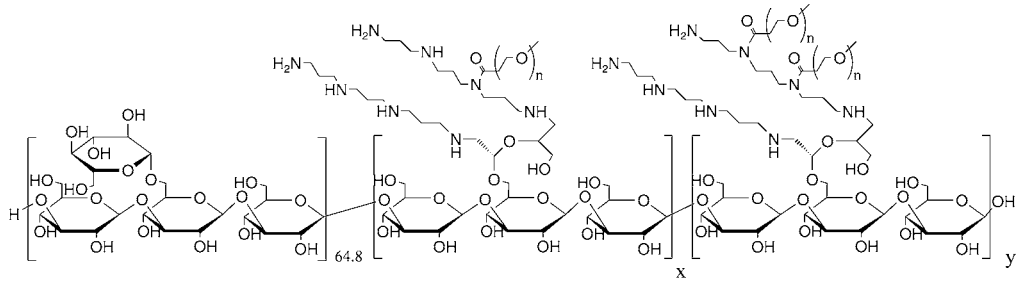
Agarose Gel Retardation Assay. Plasmid DNA binding was studied by mean of agarose gel retardation assays. Plasmid DNA (1 μg) and increasing amounts of cationic polymer were each diluted in 20 μL of 100 mM NaCl and mixed for complexation in which the amino groups/phosphate groups ratios (N/P ratio) were 0, 0.5, 1, 1.5, 2, 2.5, 3, and 5, respectively. After 20 min of incubation at room temperature, samples (10 μL) with the gel loading buffer (2μL) were electrophoresed through 1% agarose gel for 40 min at 100V. TBE (45 mM Tris-borate and 1 mM EDTA, pH8.0) buffer was used as an electrophoresis buffer. DNA was visualized after ethidium bromide staining.

Ethidium Bromide Competitive Binding Assay. The efficiency of DNA compaction mediated by cationic

Scheme 1. Synthetic Scheme of PEGylated *N,N′*-Bis(3-aminopropyl)-1,3-propanediamine-Conjugated SPG with a Molecular Weight of 80000



APPD46(80K)



2KPEG-APPD46(80K): (x, y) = (16.6, 38.6)
5KPEG-APPD46(80K): (x, y) = (27.6, 27.6)

polymers was evaluated using fluorescence quenching method. It is based on the use of ethidium bromide, a DNA-intercalating agent; its fluorescence is importantly enhanced upon binding to DNA and quenched by the dissociation of complex. Increasing amounts of cationic polymers based on SPG or PEI were added to the complex of 2 μg DNA with 2 μg of ethidium bromide. The fluorescence (λ_{ex} = 485 nm and λ_{em} = 590 nm) is reported relative to the value obtained in the absence of the carrier (after subtraction of the inherent fluorescence of ethidium bromide) using by a fluorescence spectrometer RF-5000 (Shimazu, Kyoto, Japan).

Intracellular Trafficking of Internalized DNA Complex. COS-1 cells were plated at a density of 5 × 10^3 cells/150 μL on a 10-mm glass-bottom dish (Matsunami Glass, Kishiwada, Japan) and cultured overnight to attain complete adhesion. In the first step, COS-1 cells were transfected with 1 μg of pEGFP-Endo gene for 3 h. In the next step, after 12 h of post-transfection period, 1 μg of rhodamine-labled pGL3-control complex with APPD46(80K) at N/P ration of 10 was prepared and added to cells. After 1.5 h of incubation at 37 °C in a 5% CO_2 incubator, the cells were then washed twice with PBS (125 μL), fixed with 4% HCHO (80 μL), and 1 wt% DAPI/methanol (20 μL) at 4 °C for 15 min, and examined by confocal fluorescent microscopy. Images of the samples were collected by fluorescence microscopy on IX-70 (Olympus, Tokyo, Japan), attaching a confocal scan unit CSU-10 (Yokogawa, Tokyo, Japan) with ORCA-ER CCD Camera (Hamamatsu Photonics, Hamamatsu, Japan) using a 40 × Uapo/340 objective with NA 0.9.

Residence Time Measurement of Intact Plasmid in COS-1 Cells. Transfected COS-1 cells with 1 μg of pCMVtkLuc in 12-well plates for long-term expression were used to isolate intact plasmid DNA remaining after long post-transfection time. After 2, 7, 14, 21, and 28 days of post-transfection time, COS-1 cells were trypsinized and collected in microtubes. Isolation of intact plasmid DNA from cell pellets was performed with a QIAprep Spin Plasmid Kit (Quagen, Hilden, Germany) (*30*). Yields of intact plasmid DNA isolated were compared by transforming *E. coli* strain as follows. Isolated plasmid DNA was dissolved in 10 μL of Milli-Q and transformed into 100 μL competent cells of *E. coli JM109* (Nippongene, Toyama, Japan) with a heat shock method. The number of transformants was compared. The measurement of remaining intracellular plasmid DNA was performed in triplicate.

RESULTS

Structural Influence of Amines Introduced into the Side Chain. Schizophyllan has a β-(1,3)-glycoside bond as its backbone and three glucose residues as repeating units. The second residue of the repeating units binds with the glucose side chain via β-(1,6)-glycoside. Periodate oxidation only affects the 1,2-diol groups in the side chain, and as a result, aldehyde groups can be introduced only to the side chain, leaving the main chain intact (*31*, *32*). Furthermore, since various amines can be introduced by reductive amination, it is possible to prepare various amine-modified cationic schizophyllans (*33*). In the present study, amine-conjugated SPG carriers were prepared using the following amines: ethanolamine, spermidine, spermine, and *N,N′*-bis(3-aminopropyl)-1,3-propanediamine (Chart 1, Table 1). Compounds are denoted with the code that represents structure of amine by capital letters, the degree of amination of side chain by percentage, and molecular weight of original SPG in parentheses, in this order. Each amine-conjugated SPG derivative was synthesized according to Chart 1. The transfection efficiency and cytotoxicity of each of these SPG derivatives were assessed (Figure 1). To achieve maximum amination to one part of the glucose side chain, 5 parts of sodium periodate and 100 parts of amine compounds were added as reported previously (*33*). The products were identified by various spectroscopic

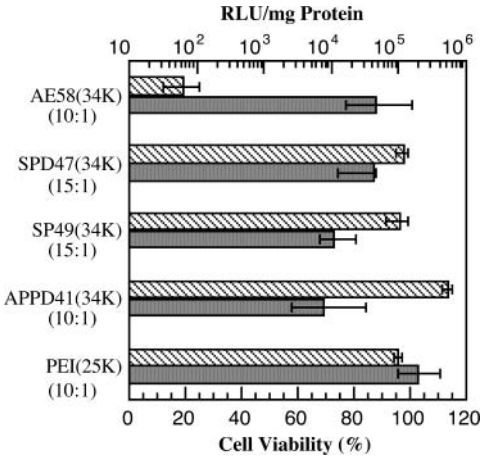


Figure 1. Comparison of transfection efficiency and cytotoxicity of DNA complexes with various oligoamine-conjugated SPG in COS-1 cells at selected N/P ratios. Slashed bars indicate the relative transfection efficiency and shaded bars indicate the cell viability. Relative transfection efficiency is shown as relative light units (RLU)/mg of protein on the upper ordinate. Cell viability is shown as percentage of living cells on the lower ordinate.

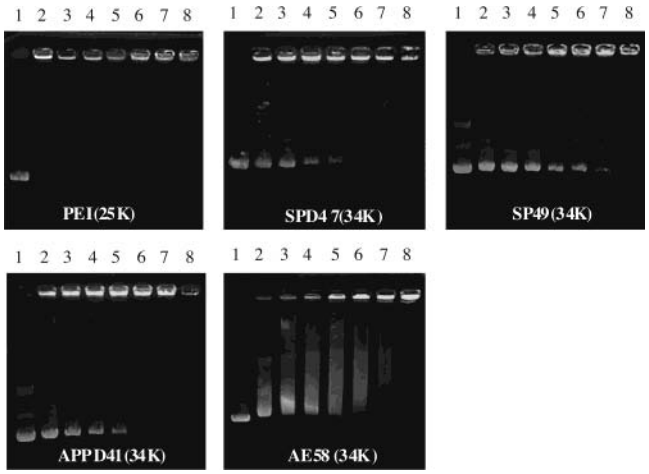


Figure 2. DNA binding was studied by means of an agarose gel retardation assay. Plasmid DNA (1 μg) and increasing amounts of cationic polymer were each diluted in 20 μL of 100 mM NaCl and mixed. After a period of 15 min, samples (10 μL) were electrophoresed through a 1% agarose gel. Lanes 1 to 8: (1) naked DNA, (2−8) cationic polymer/DNA complexes at N/P ratios equal to 0.5, 1, 1.5, 2, 2.5, 3, and 5, respectively.

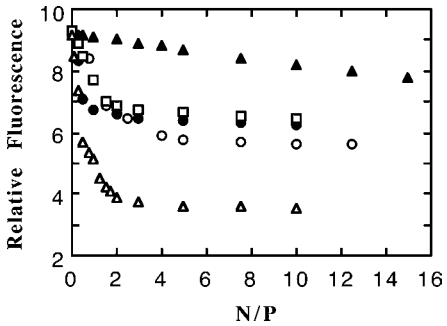


Figure 3. Competitive binding of ethidium bromide toward plasmid DNA in poplyplex with AE58(34K) (closed triangle), APPD41(34K) (open square), SPD47(34K) (closed circle), SP49-(34K) (open circle), and PEI (open triangle). Increasing amounts of cationic polymer were added to 2 μg DNA and to the resulting 2 mL of complex in PBS was added 2 μg of ethidium bromide.

methods. The content of amino groups was estimated with elemental analyses as summarized in Table 1. The results of in vitro transfection efficiency of amine-conjugated SPG showed that when compared to branched PEI with a molecular weight of 25000, a commercially available polycation with high transfection efficiency (*7*), transfection efficiency of the ethanolamine derivative (AE58(34K)) was lower, but those of the oligoamine derivatives, spermidine (SPD47(34K)), spermine (SP49-(34K)), and *N*,*N*′-bis(3-aminopropyl)-1,3-propanediamine (APPD41(34K)), were comparable or higher. In particular, the transfection efficiency of APPD41(34K) was about five times greater than that of PEI. We can suppose that all of amino groups are not necessarily protonated at physiological pH. Therefore, we can denote the N/P ratio as the number polymer nitrogen per DNA phosphate and not as a charge ratio. Transfection efficiency was dependent on N/P ratio, with carriers having SPG as the backbone exhibiting the highest transfection efficiency with N/P ratios of 10−15. Under this transfection condition, cytotoxicity was assessed in terms of cell viability with the WST assay (*34*). The results showed that the number of viable cells was high for the ethanolamine derivative, which had low transfection efficiency (about 0.01% of that for APPD41(34K)). Hence, one can recognize the general tendency that the greater the transfection efficiency, the lower the cell viability.

So the question arises: how does the amine structure affect the physical properties of polymers to improve transfection efficiency? To find an answer for this, we examined the affinity of each cationic SPG derivative toward plasmid DNA by agarose gel electrophoresis and ethidium bromide competitive binding. The results of electrophoresis (agarose gel retardation assay) showed the level of DNA affinity to be highest for PEI, followed by SPD47(34K), APPD41(34K), SP49(34K), and AE58-(34K), in this order (Figure 2). Nonetheless, under the transfection conditions with N/P of 10−15, all derivatives formed DNA complexes. Ethidium bromide competitive binding assay can assess plasmid compaction, which reflects polycation and polyanion binding (*35*). The degree of decrease in the fluorescence intensity of ethidium bromide was greatest for PEI, followed by SP49(34 K), SPD47(34 K), APPD41(34 K), and AE58(34 K), in this order (Figure 3). Hence, there was no clear correlation with transfection efficiency.

Molecular Weight Dependence of the SPG Backbone. Using the *N*,*N*′-bis(3-aminopropyl)-1,3-propanediamine derivative, we attained the highest transfection efficiency among the different amine derivatives, so that the effects of the molecular weight of the SPG backbone on transfection efficiency and cytotoxicity were investigated with these homologues (Figure 4). Derivatives having backbones with a molecular weight of 12000, 34000, 80000, or 150000 Da were subjected to the maximum amination. The results showed that the transfection efficiency of the APPD37(12K) and APPD45(150K) is lower than that of PEI, while that of the APPD41(34K) and APPD46(80K) is greater than that of PEI. In particular, the transfection efficiency of APPD46(80K) was about eight times greater than that of PEI. Hence, the existence of an optimal range of molecular weight for transfection efficiency was clarified. When cytotoxicity was investigated under the transfection conditions, the tendency appeared that the greater the transfection efficiency, the lower the cell viability: cytotoxicity was the highest for the APPD46(80K), followed by the APPD41(34K), APPD45(150K), and APPD37(12K), in this order, thus confirming the relationship between transfection efficiency and cytotoxicity as reported with poly-L-lysine (*11*).

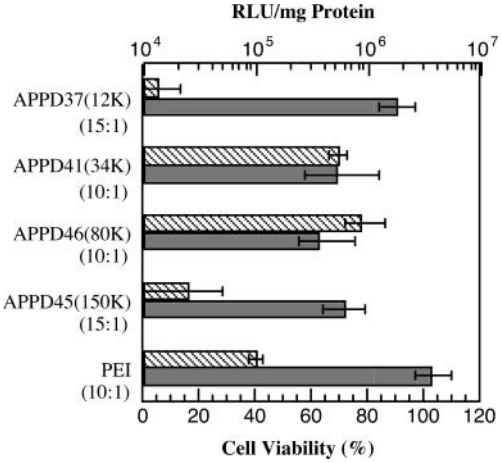


Figure 4. Comparison of transfection efficiency and cytotoxicity of DNA complexes with various molecular weights of based SPG in COS-1 cells at selected N/P ratios. Slashed bars indicate the relative transfection efficiency and shaded bars indicate the cell viability. Relative transfection efficiency is shown as relative light units (RLU)/mg of protein on the upper ordinate. Cell viability is shown as percentage of living cells on the lower ordinate.

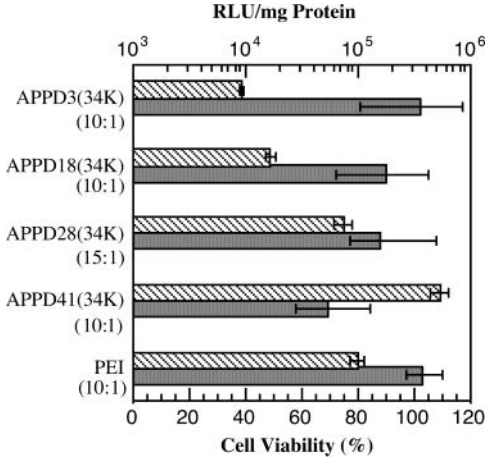
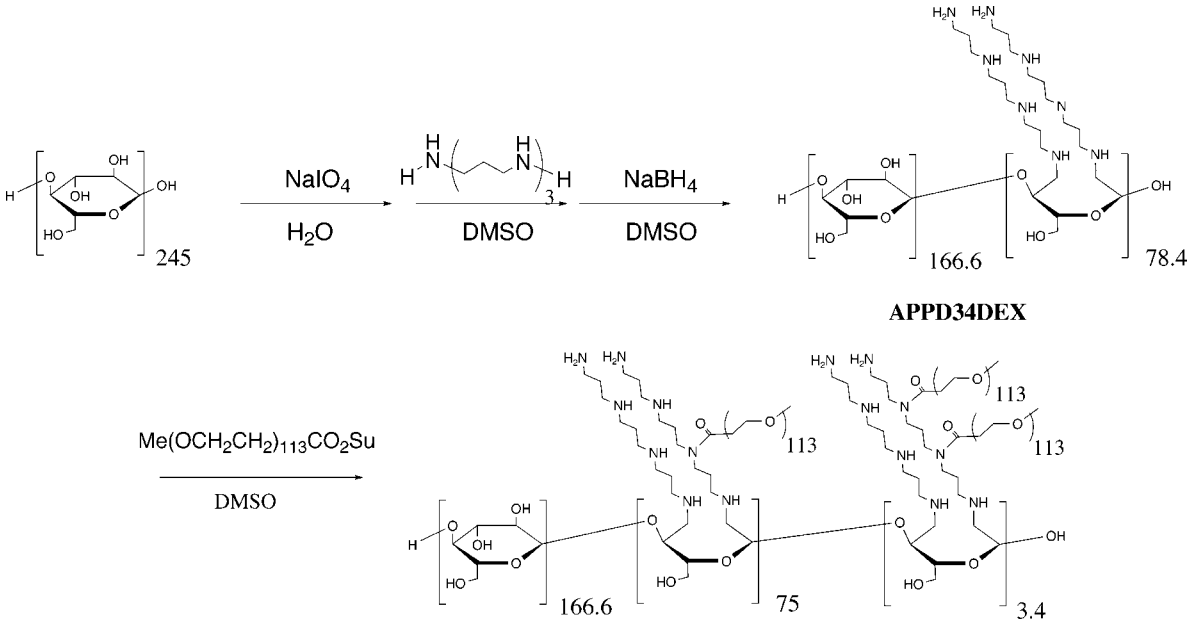


Figure 5. Comparison of transfection efficiency and cytotoxicity of DNA complexes with various degree of amination of side chain of SPG with a molecular weight of 34000 in COS-1 cells at selected N/P ratios. Slashed bars indicate the relative transfection efficiency and shaded bars indicate the cell viability. Relative transfection efficiency is shown as relative light units (RLU)/mg of protein on the upper ordinate. Cell viability is shown as percentage of living cells on the lower ordinate.

Influence of Amination Degree. Concerning the influence of the amine structure on transfection efficiency, oligoamine derivatives exhibited greater transfection efficiency than monoamine derivatives, thus suggesting the importance of cation density. The amination degree in the side chain was therefore adjusted by varying the amount of periodic acid, to ascertain the effects of amination on transfection efficiency and cytotoxicity (Figure 5). Degree of amination was assessed by elemental analysis with an assumption that two amine groups were introduced into the glucose side chain and was defined as the ratio of aminated glucose. When conjugating *N*,*N*′-bis(3-aminopropyl)-1,3-propanediamine to SPG with a molecular weight of 34000 Da, the amount of sodium periodate with respect to the glucose side chain was adjusted to 10, 40, 80, 150, or 500%, and the subsequent reductive amination resulted in derivatives with a degree of amination of 3, 9, 18, 28, and 41%, respectively (Table 1). The tendency observed here was that the greater the degree of amination, the greater the transfection efficiency. In other words, transfection efficiency for the derivative with 41% amination (APPD41-(34K)) was the highest and was about five times greater than that of PEI. Furthermore, cytotoxicity was assessed under the transfection conditions. The results again showed the tendency that the greater the transfection efficiency, the lower the cell viability.

Comparison to Carriers Possessing a Dextran Backbone. Domb and colleagues synthesized cationic polysaccharides made of dextran, arabinogalactan, or pullulan (*15*), but not schizophyllan, by subjecting the main chain to periodate oxidation and introducing many

Scheme 2. Synthetic Scheme of PEGylated *N*,*N*′-Bis(3-aminopropyl)-1,3-propanediamine-Conjugated Dextran with a Molecular Weight of 40000



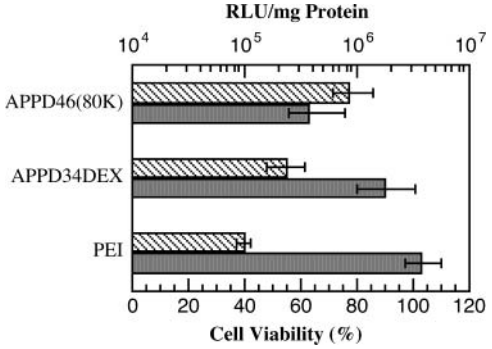


Figure 6. Comparison of transfection efficiency and cytotoxicity of DNA complexes with cationic polymer possessing a backbone consisting of SPG or detran in COS-1 cells at an N/P ratio of 10:1. Slashed bars indicate the relative transfection efficiency and shaded bars indicate the cell viability. Relative transfection efficiency is shown as relative light units (RLU)/mg of protein on the upper ordinate. Cell viability is shown as percentage of living cells on the lower ordinate.

oligoamines by reductive amination. They reported that transfection efficiency was high when oligoamines were introduced into dextran. Therefore, in the present study, we compared transfection efficiency between dextran, which has mainly α-(1,6)-glycoside bonds and oligoamines introduced into the main chain, and schizophyllan, which has β-(1,3)-glycoside bonds and oligoamines introduced into the side chain. According to Domb et al., a dextran derivative with ca. 11% N amination with *N*,*N*′-bis(3-aminopropyl)-1,3-propanediamine was able to maximize transfection efficiency. So, we synthesized *N*,*N*′-bis(3-aminopropyl)-1,3-propanediamine-conjugated dextran according with Scheme 2. The results (Figure 6) showed that when compared to this dextran derivative (APPD34-DEX), transfection efficiency of APPD46(80K) was greater although the cytotoxicity of the schizophyllan derivative was higher.

Conditions for DNA Complexation. The particle size of cationic polymer/DNA complexes usually increased with time (*36*). In addition, a close correlation has been documented between the transfection efficiency of cationic polymers and the particle size of DNA complexes (*37*). Therefore, to ascertain the effects of the duration of DNA complexation on the transfection efficiency of APPD46(80K), which exhibited the highest transfection efficiency, the duration of DNA complexation was set at 30 min or 12 h. With PEI, the transfection efficiency of the longer complexation times was markedly lower (80% decrease), but with APPD46(80K), that of the longer complexation times (12 h) was only slightly decreased (10% decrease).

The complexation of a polyamine compound with polyanionic plasmid DNA is due to polyion complexation based on electrostatic interactions. Therefore, the complexation is largely influenced by the dielectric constant of the medium. Furthermore, solvents used for complexation could contribute to cytotoxicity. Hence, the influence of complexation solvents was examined. The results showed that the transfection efficiency for complexation using 10% PBS without any organic solvent such as DMSO or glycerol was higher than that for complexation using organic solvents. Also, the transfection efficiency of complexation using PBS with a high ionic strength was lower than that for complexation using 10% PBS.

In Vitro Transfection Conditions. Using a 24-well plate, the number of cells per well was increased from the conventional number of 30000 to 50000, 70000, or 90000 in order to reduce cytotoxicity by lowering the

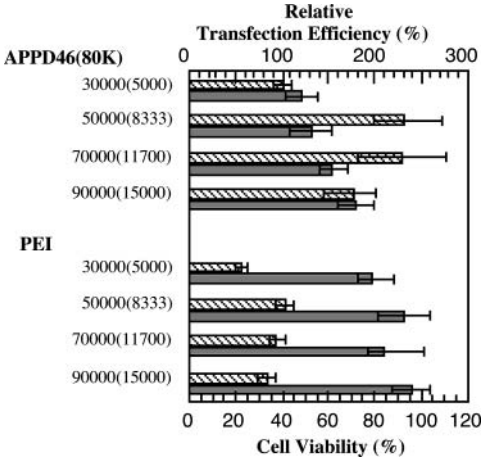


Figure 7. Comparison of transfection efficiency and cytotoxicity of DNA complexes with APPD46(80K) and PEI in COS-1 cells at an N/P ratio of 10:1 and different number of cells per well. Slashed bars indicate the relative transfection efficiency and shaded bars indicate the cell viability. Relative transfection efficiency is reported to the efficiency at the number of 30000 (=100%) on the upper ordinate. Cell viability at various numbers in parentheses is shown as percentage of living cells on the lower ordinate.

amount of cations per cell. Also, in a WST assay on toxicity using a 96-well plate, 5000, 8333, 11700, or 15000 cells were placed in each well. As a carrier possessing a schizophyllan backbone, APPD46(80K) was used owing to its high transfection efficiency. The results (Figure 7) showed the tendency that the greater the number of cells, the higher the cell viability under the transfection conditions. However, the level of luciferase expression per unit protein was the highest for 50000 cells.

Furthermore, in transfection, serum proteins such as albumin and globulins strongly interact with cationic compounds. In addition, the presence of serum generally lowers the transfection efficiency of nonviral vectors. However, serum has beneficial effects on cell viability, thus affecting cytotoxicity. Therefore, the influence of serum on transfection was assessed. As expected, the level of cytotoxicity was higher without serum; however, the presence of serum did not markedly lower the transfection efficiency (5% decrease). Moreover, the optimal P/N ratio for transfection with serum was 10, whereas without serum less cation was required (P/N ratio = 5).

Plasmid and Cell Types. In COS-1 cells infected with the SV-40 virus, when pGL3-control possessing an SV-40 promoter is used as an expression vector, the plasmid is replicated inside the cells (*38*), thus making it possible to prepare a more sensitive experimental system. However, a good plasmid vector is one that can efficiently transfer various genes to many different cells. Hence, a comparison was made with the pCMV^{tk}Luc plasmid (*39*), which has a cytomegalovirus promoter, using COS-1, CHO-K1, and HeLa cells (Figure 8). The results showed that the present transfection conditions (N/P ratio, complexation time, solvent usage, plasmid usage, transfection time, and post-transfection time) were optimal for transfecting COS-1 cells with pGL3-control, and that the transfection efficiency is highest for COS-1 cells. Regardless of the plasmid types, the transfection efficiency of APPD46(80K) was higher than that of PEI for COS-1 cell. However, the results varied among the different cell lines, thus clarifying that transfection efficiency is largely dependent on cell/plasmid combinations.

Cellular Uptake Mechanism. It is known that the positively charged polyplexes electrostatically interact

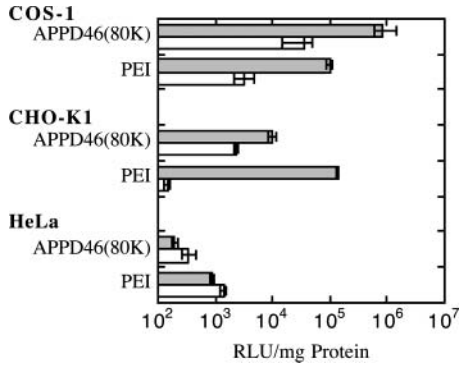


Figure 8. Comparison of transfection efficiency and cytotoxicity of DNA complexes with APPD46(80K) and PEI in various cells at an N/P ratio of 10:1. Gray bars indicate the relative transfection efficiency using pGL3-cntrol and white bars indicate that of pCMV^{tk}Luc. Relative transfection efficiency is shown as relative light units (RLU)/mg of protein.

with negatively charged proteoglycans of the plasma membrane (*40*). Then, endocytosis is generally involved in the cellular uptake of plasmid DNA using nonviral vectors without ligands exhibiting affinity to certain receptors, and this also applied to the cellular uptake of cationic SPG carriers. Therefore, we have confirmed the mechanism of cellular uptakes by previously reported method (*41*). The intracellular trafficking of internalized plasmid DNA was directly observed by confocal fluorescence microscopy. In the first step, COS-1 cells were transfected with pEGFP-Endo gene. It is known that expressed RhoB-fused green fluorescent proteins localize in endosome since RhoB has an endosomal localization signal (*42*). At transfected COS-1 cells, therefore, the lipid membrane of endocytic vesicles can be visualized green. In the next step, a rhodamine-labled DNA complex with APPD46(80K) was prepared and added to cells. As was the case with the transfection, after 1.5 h of incubation, the cells were fixed and examined by confocal fluorescent microscopy. The result in Figure 9 represented that the localization of the red fluorescence for administered plasmid DNA mostly matched the green fluorescence for the lipid membrane of endocytic vesicles. This finding indicates the internalization of the DNA complex by endocytosis.

Reduced Toxicity Due to PEG Modification. The relationship between cytotoxicity and transfection efficiency has been investigated using many cationic polymers, and the tendency that higher transfection efficiency is associated with higher cytotoxicity has been recognized (*11*). One of the important factors for transfection efficiency is cytoplasmic transport of DNA complexes. Carriers with high transfection efficiency is first adsorbed electrostatically to a cell membrane, and their cell membrane toxicity causes instability in the membrane structure, thus increasing the cellular uptake. As a result, the subsequent research has been directed toward the reduction of cytotoxicity by shielding cationic charges with poly(ethylene glycol) chains (*29*, *35*).

In the present study, after PEGylation of the amino groups of cationic schizophyllan and dextran, cytotoxicity and transfection efficiencies were estimated (Schemes 1 and 2, Table 2, Figure 10). When a poly(ethylene glycol) chain with a molecular weight of 2000 or 5000 was introduced into APPD46(80K), cytotoxicity was reduced as expected, but transfection efficiency was also decreased. Nonetheless, the cytotoxicity of the derivative with 5000 Da PEG (5KPEG-APPD46(80K)) was almost nonexistent, and its transfection efficiency was still greater than that for PEI and PEGlyated dextran derivative (5KPEG-APPDDEX).

Long-Term Expression. One of the factors influencing the expression efficiency of nonviral vectors is intracellular DNA release. If a carrier is biodegradable, DNA release should occur efficiently (*43*−*45*). The backbone of cationic schizophyllan carriers is β-(1,3)-glucan; however, β-(1,3)-glucanase does not exist in animal cells (*46*). In other words, β-(1,3)-glucan is decomposed simply by hydrolysis, and as a result, the rate of decomposition is expected to be much slower than those catalyzed by enzymes. In the present study, the expression of a reporter protein was measured by extending the length of the post-transfection period from 2 days to 7, 14, 21, and 28 days in order to assess long-term protein expression.

In relation to the level of luciferase expression at 2 days after transfection, those at 7 14, 21, and 28 days after transfection were determined for each carrier (Figure 11). When compared to dextran derivatives (PEG-APPDDEX) which are biodegraded enzymatically in animal cells (*47*), the transfection efficiency of PEG-APPD46(80K) was obviously higher for 7−28 days after transfection, thus clarifying the ability of SPG carriers to express a target protein for a long period of time.

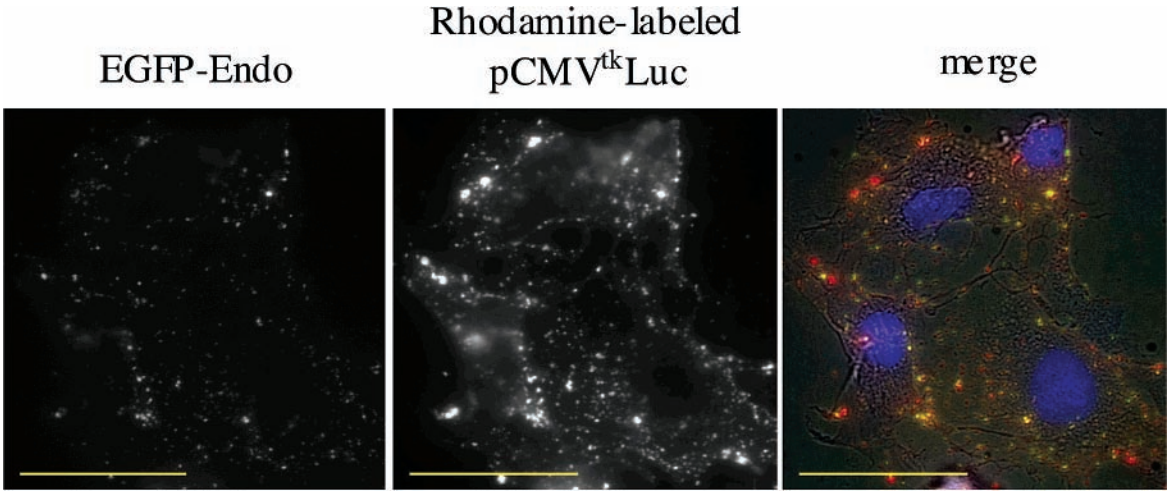


Figure 9. Rhodamine-labeled pCMV^{tk}Luc DNA (red) was internalized with APPD46(80K) into COS-1 cells transfected with pEGFP-Endo. Nuclei are post-stained with DAPI (blue) and endocytic vesicles are visualized by membrane-localized EGFP (green). Bar: 50 μm.

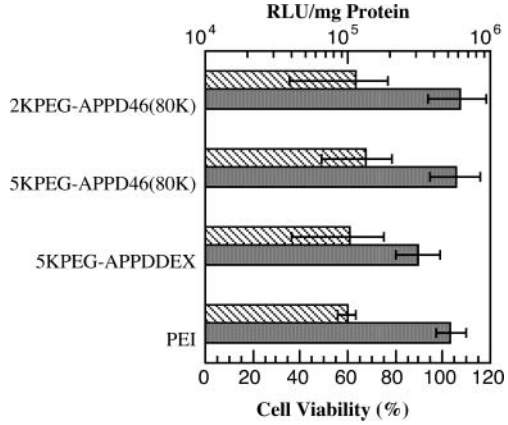


Figure 10. Comparison of transfection efficiency and cytotoxicity of DNA complexes with PEGlyated cationic polymers in COS-1 cells at an N/P ratio of 10:1. Slashed bars indicate the relative transfection efficiency and shaded bars indicate the cell viability. Relative transfection efficiency is shown as relative light units (RLU)/mg of protein on the upper ordinate. Cell viability is shown as percentage of living cells on the lower ordinate.

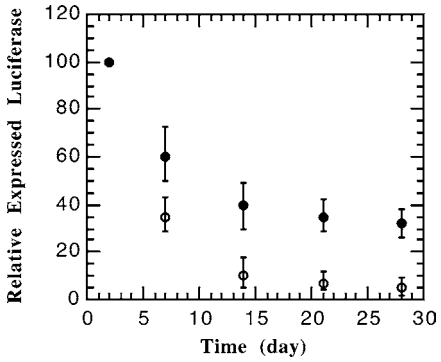


Figure 11. Comparison of long-term transfection efficiency in COS-1 cells at an N/P ratio of 10:1 with PEG-APPD46(80K) (closed circle) and PEG-APPD-DEX (open circle). Relative transfection efficiency is reported to the amounts of expressed luciferase with post-transfection time of 2 days (=100%).

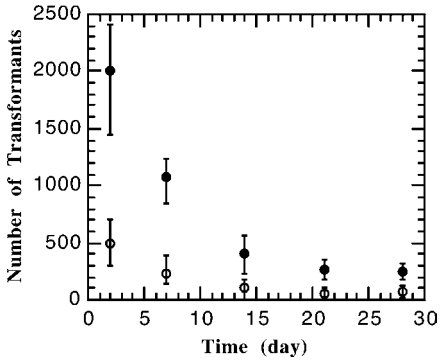


Figure 12. Comparison of the number of transformants using long-residence time plasmid DNA in COS-1 cells (1×10^4) transfected with pCMV^{tk}Luc (1 μg) complexes with PEG-APPD46(80K) (closed circle) and PEG-APPD-DEX (open circle).

Residence Time Measurement of Intact Plasmind in COS-1 Cells. We determined the time course of remaining intracellular plasmid DNA in transfected COS-1 cells with 1 μg of pCMVtkLuc (Figure 12). Number of transformants due to isolated plasmid DNA after long-term post-transfection indicated that amounts of remaining plasmid DNA decreased rapidly with dextran derivatives (PEG-APPD-DEX). In contrast, when compared to this dextran derivative, more than 4-fold amount of plasmid DNA remained intact with PEG-APPD46(80K) after 4 weeks of post-transfection time.

DISUCUSSION

Of the various polyamines, the transfection efficiency for PEI is higher than that for PAMAM dendrimers (*48*). With PEI, genes can be efficiently transferred to various cells both in vitro and in vivo (*7*−*9*). In PEI, nitrogen accounts for one in every three main-chain atoms, and the polyamine consists of 25% primary amine, 50% secondary amine, and 25% tertiary amine. Furthermore, PEI forms homogeneous and condensed DNA complexes, thus contributing to efficient cellular uptake (*8*). The proton sponge hypothesis has been proposed to explain the high gene expression exhibited by PEI (*7*, *49*); however, while escape of DNA from lysosomal DNA decomposition might play a role, no conclusive evidence has been found. In any case, it appears certain that in PEI the high cation charge density (5.3 μmol N/mg) plays an important role. Therefore, when developing a polyamine transfection agent, it is important to increase the amount of protonable nitrogen atoms. In the present study, among the derivatives with a molecular weight of 34000 Da, the degree of modification of the glucose side chain was high (58%) for AE58(34K), an ethanolamine (monoamine) derivative, but its nitrogen content was not particularly high at 1.7 μmol of nitrogen atom per mg. An agarose gel retardation assay showed that, under the transfection condition (N/P = 10), all DNA fragments formed complexes with AE58(34K), but their ion pair formation was very loose, and a competitive binding assay using ethidium bromide suggested the absence of compaction. On the other hand, with oligoamines such as spermidine, spermine, and *N*,*N*′-bis(3-aminopropyl)-1,3-propanediamine, the nitrogen content was high at 3.7, 4.8, and 4.2 μmol N/mg, respectively, and these figures were closer to that for PEI. In addition, the transfection efficiency for these derivatives was high. Interestingly, of the various derivatives with a molecular weight of 34000 Da, the transfection efficiency was highest for the APPD41(34K) derivative. The result of an ethidium bromide competitive binding assay showed that the degree of compaction with DNA for this derivative was not so high as that observed for PEI. After entering the nucleus in the form of a DNA complex, strong complexation is disadvantageous for transcription. This could explain the higher transfection efficiency for APPD41-(34K) with respect to PEI. The correlation between amination and transfection efficiency confirms the correlation between nitrogen contents and transfection efficiency.

As far as the molecular weight of the backbone was concerned, transfection efficiency was low with both low and high molecular weights, thus confirming that the transfection efficiency of cationic polymers is high within a certain range of molecular weight. Using poly-L-lysine, it has been confirmed that the size and particle distributions of DNA complexes are dependent on the molecular weight of the polymer (*11*). Hence, the difference in the characteristics of DNA complexes influences transfection efficiency, and transfection efficiency thus becomes higher in the polymers with certain molecular weights.

In the present study, internalized DNA complexes with cationic polymers made from a schizophyllan backbone and a side chain modified by oligoamines localized in endocytic vesicles. This indicates that the cellular uptake of cationic polymer/DNA complexes is mediated by en-

docytosis. In other words, the interaction between a DNA complex and a cell membrane is the first step of cellular uptake. However, a strong interaction leads to high cytotoxicity. Of the various carriers prepared in the present study, polyamine carriers with high transfection efficiency exhibited higher degrees of cytotoxicity: in fact, APPD46(80K) demonstrated both the highest transfection efficiency and the highest cytotoxicity. The cytotoxicity of polymeric carriers thus appears to be based on cell membrane instability. While it was possible to reduce cytotoxicity by adjusting the amount of DNA complex per cell, as seen with poly-L-lysine (*50*, *51*), PEI (*35*), and chitosan (*19*), PEGylation was the most effective means of reducing toxicity. It appears that increased water solubility of DNA complexes and shielding of cation charge reduce the level of interaction with the cell membrane.

The transfection efficiency of APPD46(80K) without FBS was not much higher than that with FBS, and while the optimal N/P for the transfection without FBS was 10, that for the transfection with FBS was lower (at 5). Without FBS, DNA complexes do not interact with serum proteins, and as a result, efficient transfection can be achieved with a smaller amount of DNA complexes.

In the present study, cationic schizophyllan carriers with a chemically modified glucose side chain and an intact main chain of β-(1,3)-glucan showed higher transfection efficiency than cationic dextran carriers with a chemically modified backbone of α-(1,6)-glucan. Furthermore, the most important characteristic of the β-(1,3)-glucan backbone is its usefulness in long-term expression. In animal cells, β-(1,3)-glucanase does not exist and β-(1,3)-glucan might be degraded slowly by hydrolysis at a speed much slower than enzymatic degradation. Hence, cationic polymers could be gradually degraded over a long period of time, and DNA is released slowly to achieve long-term protein expression. In fact, the long residence time of plasmid DNA in cells supports this phenomenon.

In conclusion, it was possible to achieve transfection efficiency superior to that of PEI by adjusting the molecular weight and amination of cationic schizophyllan with a chemically modified glucose side chain. We also succeeded in the reduction of cytotoxicity and the development of a safe schizophyllan-based gene carrier by the modification with poly(ethylene glycol) chains. Furthermore, using the cationic schizophyllan carrier, it was possible to express a reporter protein for a long period of time due to the long residence time of plasmid DNA in cells. Cationic schizophyllan-based carriers with a natural β-(1,3)-glucan backbone will be useful in certain forms of gene therapy where it is necessary to safely express a particular therapeutic protein over a long period of time. We are now proceeding to evaluate the transfection efficiency and the safty of cationic schizophyllan carriers in vivo.

ACKNOWLEDGMENT

We gratefully acknowledge the financial support by SORST program in Japan Science and Technology Corporation. We also greatly appreciate the kindly gift of SPG samples from Taito Co. Ltd..

Supporting Information Available: Experimental details. This material is available free of charge via the Internet at http://pubs.acs.org.

LITERATURE CITED

(1) Marshall, E. (2002) What to do when clear success comes with an unclear risk? *Science 298*, 510−511.

(2) Filion, M. C., and Phillips, N. C. (1998) Major limitation in the use of cationic liposomes for DNA delivery. *Int. J. Pharm 162*, 159−170.

(3) Tang, M. X., and Szoka, F. C., Jr. (1996) In vitro gene delivery by degraded polyamidoamine dendrimer. *Bioconjugate Chem. 7*, 703−714.

(4) Osaki, M., Okuda, T., Wada, A., Hirayama, T., Niidome, T., and Aoyagi, H. (2002) In vitro transfection using dendritic poly(L-lysine). *Bioconjugate Chem. 13*, 510−517.

(5) Kihara, F., Arima, H., Tsutsumi, T., Hirayama, F., and Uekama, K. (2002) Effect of structure of polyamidoamine dendrimer on gene transfer efficiency of the dendrimer conjugate with α-cyclodextrin. *Bioconjugate Chem. 13*, 1211−1219.

(6) Wang, Y., Boros, P., Liu, J., Qin, L., Bai, Y., Bielinska, A. U., Kukowska-Latallo, J. F., Baker, J. R. Jr., and Bromberg, J. S. (2000) DNA/Dendrimer complexes mediate gene transfer into murine cardiac transplants ex vivo. *Mol. Ther. 2*, 602−608.

(7) Boussif, O., Lezoulc'h, F., Zanta, M. A., Mergny, M. D., Scherman, D., Demeneix, B., and Behr, J. P. (1995) A versatile vector for gene and oligonucleotide transfer into cells in culture and in vivo: Polyethylenimine. *Proc. Natl. Acad. U.S.A. 92*, 7297−7301.

(8) Coll, J. L., Chollet, P., Brambilla, E., Desplaques, D., Behr, J. P., and Favrot, M. (1999) In vivo delivery to tumors of DNA complexed with linear polyethylenimine. *Hum. Gene Ther. 10*, 1659−1666.

(9) Zou, S. M., Erbacher, P., Remy, J. S., and Behr, J. P. (2000) Systemic linear polyethylenimine(L-PEI)-mediated gene delivery in the mouse. *J. Gene Med. 2*, 128−134.

(10) Tan, Y., and Huang, L. (2002) Overcoming the inflammatory toxicity of cationic gene vectors. *J. Drug Target. 10*, 153−160.

(11) Wolfert, M. A., and Seymour, L. W. (1996) Atomic force microscopic analysis of the influence of the molecular weight of poly(L)lysine on the size of polyelectrolyte complexes formed with DNA. *Gene Ther. 3*, 269−273.

(12) Han, S.-O., Mahato, R. I., Sung, Y. K., and Kim, S. W. (2000) Development of biomaterials for gene therapy. *Mol. Ther. 2*, 302−317.

(13) Ochiya, T., Nagahara, S., Sano, A., Itoh, H., and Terada, M. (2001) Biomaterials for gene delivery: aterocollagen-mediated controlled release of molecular medicines. *Curr. Gene Ther. 1*, 31−52.

(14) Yamaoka, T., Hamada, N., Iwata, H., Murakami, A., and Kimura, Y. (1998) Effect of cation content of polycation-type gene carriers on in vitro gene transfer. *Chem. Lett. 27*, 1171−1172.

(15) Azzam, T., Eliyahu, H., Shapira, L., Linial, M., Barenholz, Y., and Domb, A. J. (2002) Polusaccharide-olgoamine based conjugates for gene delivery. *J. Med. Chem. 45*, 1817−1824.

(16) Lopata, M. A., Cleveland, D. W., and Soller-Webb, B. (1984) High level trasient expression of a chloramphenicol acetyl transferase gene by DEAE-dextran mediated DNA transfection coupled with a dimethyl sulfoxide or glycerol shock treatment. *Nucleic Acids Res. 12*, 5707−5717.

(17) MacLaughlin, F. C., Mumper, R. J., Wang, J., Tagliaferri, J. M., Gill, I., Hinchcliffe, M., and Rolland, A. P. (1998) Chitosan and depolymerized chitosan oligomers as condensing carriers for in vivo plasmid delivery. *J. Controlled Release 56*, 259−272.

(18) Ishii, T., Okahata, Y., and Sato, T. (2001) Mechanism of cell transfection with plasmid/chitosan complexes. *Biochim. Biophys. Acta 1514*, 51−64.

(19) Mao, H.-Q., Roy, K., Troung-Le, V. H., Janes, K. A., Lin, K. Y., Wang, Y., August, J. T., and Leong, K. W. (2001) Chitosan-DNA nanoparticles as gene carrier: synthesis, characterization and transfection efficiency. *J. Controlled Release 70*, 399−421.

(20) Shimizu, Y., Chen, J.-T., Hasumi, K., and Masubuchi, K. (1990) Augmentative effect of sizofiran (SPG) on immune responses of patients with gynecologic malignancy. *Biotherapy 4*, 1390−1399.

(21) Shimizu, Y., Hasumi, K., and Masubuchi, K. (1992) Augmentative effect of sizofiran on the immunofunction of regional lymph nodes in cervical cancer. *Cancer 69*, 1184−1194.
(22) Okamura, K., Suzuki, M., Chihara, T., Fujiwara, A., Fukuda, T., Goto, S., Ichinohe, K., Jimi, S., Kasamatsu, T., and Kawai, N, et al. (1986) Clinical evaluation of schizophyllan combined with irradiation in patients with cervical cancer. A randomized controlled study. *Cancer 58*, 865−872.
(23) Hasegawa, K., Nishimura, R., Kinugasa, M., Okamura, M., Kimura, A., Ohtsu, F., Takeuchi, K, and Mizuhara, V. (1990) Electron microscopic and immunological studies concerning the effect on the antitumor activity of sizofiran (SPG) combined with radiotherapy for cervical cancer. *Nippon Gan Chiryo Gakkai Shi 25*, 2549−2561.
(24) Sakurai, K., and Shinkai, S. (2000) Molecular recognition of adenine, cytosine, and uracil in a single-strand RNA by a natural polysaccharide: schizophyllan. *J. Am. Chem. Soc. 122*, 4520−4521.
(25) Sakurai, K., Mizu, M., and Shinkai, S. (2001) Polysaccharide-polynucleotide complexes. 2. Complementary polynucleotide mimic behavior of a natural polysaccharide: schizophyllan in the macromolecular complex with a single strand RNA: poly(C). *Biomacromolecules 2*, 641−650.
(26) Koumoto, K., Kimura, T., Kobayashi, H., Sakurai, K., and Shinkai, S. (2001) Chemical modification of Curdlan to induce an interaction with poly(C). *Chem. Lett. 30*, 908−909.
(27) Mizu, M., Koumoto, K., Kimura, T., K. Sakurai, Nagasaki, T., and Shinkai, S. Polysaccharide-polynucleotide complexes. Part 13. Enhanced antisense effect by preventing the antisense oligonucleotide from binding to proteins in the culture medium. Submitted to *Bull. Chem. Soc. Jpn*.
(28) Tabata, K., Ito, W., Kojima, T., Kawabata, S., and Misaki, A. (1981) Ultrasonic degradation of schizophyllan, an antitumor polysaccharide produced by *Schizophyllum commune* Fries. *Carbohydr. Res. 89*. 121−35.
(29) Ogris, M., Brunner, S., Schuller, S., Kirccheis, R., and Wagner, E. (1999) PEGylated DNA/transferring-PEI complexes: reduced interaction with blood components, extended circulation in blood and potential for systemic gene delivery. *Gene Ther. 6*, 595−605.
(30) Siebenkotten, G., Leyendeckers, H., Christine, R., and Radbruch, A. (1995) Isolation of plasmid DNA from mammalian cells with QIAprep. *Quagen News 1*, 11−12.
(31) Koumoto, K., Kimura, T., Kobayashi, H., Sakurai, K., and Shinkai, S. (2001) Chemical modification of schizophyllan by introduction of a cationic charge into the side chain which enhance the thermal stability of schizophyllan/poly(C) complexes. *Chem. Commun*. 1692−1693.
(32) Koumoto, K., Kimura, T., Mizu, M., Kunitake, T., Sakurai, K., and Shinkai, S. (2002) Polysaccharide-polynucleotide complexes. Part 12. Enhanced affinity for various polynucleotide chains by site-specific chemical modification of schizophyllan. *J. Chem. Soc., Perkin Trans. 1* 2477−2484.
(33) Numata, M., Matsumoto, T., Umeda, M., Koumoto, K., Sakurai, K., and Shinkai, S. (2003) Polysaccharide-polynucleotide complexes (15): thermal stability of schizophyllan (SPG)/poly(C) triple strands is controllable by a-amino acid modification. *Bioorg. Chem. 31*, 163−171.
(34) Ishiyama, M., Miyazono, Y., Sasamoto, K., Ohkura, Y., and Ueno, K. (1997) A highly water-soluble disulfonated tetrazolium salt as a chromogenic indicator for NADH as wellas cell viability. *Talanta 44*, 1299−1305.
(35) Kichler, A., Chillón, M., Leborgne, C., Danos, O., and Frisch, B. (2002) Intranasal gene delivery with a polyethylenimine-PEG conjugate. *J. Controlled Release 81*, 379−388.
(36) Okuda, T., Kidoaki, S., Ohsaki, M., Koyama, Y., Yoshikawa, K., Niidome, T., and Aoyagi, H. (2003) Time-dependent complex formation of dendritic poly(L-lysine) with plasmid DNA and correleation with in vitro transfection efficiencies. *Org. Biomol. Chem. 1*, 1270−1273.
(37) Emi, N., Kidoaki, S., Yoshikawa, K., and Saito, H. (1997) Gene transfer mediated by polyarginine requires a formation of big carrier-complex of DNA aggregate. *Biochem. Biophys. Res. Commun. 231*, 421−424.
(38) Gluzman, Y. (1981) SV40-transformed simian cells support the replication of early SV40 mutants. *Cell 23*, 175−182.
(39) Altschmied, J., and Duschl, J. (1997) Set of optimized luciferase reporter gene plasmids compatible with widely used CAT vectors. *Biotechniques 23*, 436−438.
(40) Erbacher, P., Remy, J.-S., and Behr, J.-P. (1999) Gene transfer woth synthetic virus-like particles via the integrin-mediated endocytosis pathway. *Gene Ther. 6*, 138−145.
(41) Nagasaki, T., Taniguchi., A., and Tamagaki, S. (2003) Photoenhancement of transfection efficiency using novel cationic lipids having a photocleavable spacer. *Bioconjugate Chem. 14*, 513−516.
(42) Ellis, S., and Mellor, H. (2000) Regulation of endocytic traffic by rho family GTPases. *Trends Cell Biol. 10*, 85−88.
(43) Lynn, D. M., Anderson, D. G., Putnam, D., and Langer, R. (2001) Accelated discovery of synthetic transfection vectors: Parallel synthesis and screening of a degradable polymer library. *J. Am. Chem. Soc. 123*, 8155−8156.
(44) Wang, J., Mao, H.-Q., and Leong, K. W. (2001) A novel biodegradable gene carrier based on polyphosphoester. *J. Am. Chem. Soc. 123*, 9480−9481.
(45) Petersen, H., Merdan, T., Kunath, K., Fischer, D., and Kissel T. (2002) Poly(ethylenimine-*co*-L-lactamide-*co*-succinamide): A Biodegradable polyethylenimine derivative with an advantageous pH-dependent hydrolytic degradation for gene delivery. *Bioconjugate Chem. 13*, 812−821.
(46) Piavaux, A. (1977) Distribution and localization of the digestive laminarinases in animals. *Biochem. System. Ecol. 5*, 231−239.
(47) Gray, I. (1953) Metabolism of plasma expanders studied with carbon-14-labled dextran. *Am. J. Physiol. 174*, 462−466.
(48) Remy, J. S., Abdallah, B., Zanta, M. A., Boussif, O., Behr, J. P., and Demeneix, B. (1998) Gene transfer with lipospermines and polyethylenimines. *Adv. Drug Delivery Rev. 30*, 85−95.
(49) Thomas, M., and Klibanov, A. M. (2002) Enhancing polyethylenimine's delivery of plasmid DNA into mammalian cells. *Proc. Natl. Acad. U.S.A. 99*, 14640−14645.
(50) Katayose, S., and Kataoka, K. (1997) Water-soluble polyion complex associates of DNA and poly(ethylene glycol)-poly(L-lysine) block copolymer. *Bioconjugate Chem. 8*, 702−707.
(51) Toncheva, V., Wolfert, M. A., Dash, P. R., Oupicky, D., Ulbrich, K., Seymour, L. W., and Schacht, E. H. (1998) Novel vectors for gene delivery formed by self-assembly of DNA with poly(L-lysine) grafted with hydrophilic polymers. *Biochim. Biophys. Acta 1380*, 354−368.

BC034178X

NMR Structure Determination of a Modified DNA Oligonucleotide Containing a New Intercalating Nucleic Acid

Christina B. Nielsen,*,† Michael Petersen,† Erik B. Pedersen,† Poul Erik Hansen,‡ and Ulf B. Christensen†

Nucleic Acid Center, Department of Chemistry, University of Southern Denmark, DK-5230 Odense M, Denmark, and Department of Life Science and Chemistry, University of Roskilde, P.O. Box 260, DK-4000, Denmark.
Received October 22, 2003; Revised Manuscript Received February 3, 2004

The intercalating nucleic acid (INA) presented in this paper is a novel 1-*O*-(1-pyrenylmethyl)glycerol DNA intercalator that induces high thermal affinity for complementary DNA. The duplex examined contained two INA intercalators, denoted X, inserted directly opposite each other: d($C_1T_2C_3A_4A_5C_6$-$\mathbf{X_7}C_8A_9A_{10}G_{11}C_{12}T_{13}$):d($A_{14}G_{15}C_{16}T_{17}$-$T_{18}G_{19}\mathbf{X_{20}}G_{21}T_{22}T_{23}G_{24}A_{25}G_{26}$). Unlike most other nucleotide analogues, DNA with INA inserted has a lower affinity for hybridizing to complementary DNA with an INA inserted directly opposite than to complementary unmodified DNA. In this study we used two-dimensional ^{1}H NMR spectroscopy to determine a high-resolution solution structure of the weak INA−INA duplex. A modified ISPA approach was used to obtain interproton distance bounds from NOESY cross-peak intensities. These distance bounds were used as restraints in molecular dynamics (rMD) calculations. Twenty final structures were generated for the duplex from a B-type DNA starting structure. The root-mean-square deviation (RMSD) of the coordinates for the 20 structures of the complex was 1.95 Å. This rather large value, together with broad lines in the area of insertion, reflect the high degree of internal motion in the complex. The determination of the structure revealed that both intercalators were situated in the center of the helix, stacking with each other and the neighboring nucleobases. The intercalation of the INAs caused an unwinding of the helix in the insertion area, creating a ladderlike structure. The structural changes observed upon intercalation were mainly of local character; however, a broadening of the minor groove was found throughout the helix.

INTRODUCTION

There has been a long search for new oligonucleotide analogues having different properties than natural DNA and RNA. This search has resulted in a very large selection of nucleotide analogues such as PNA (*1*), LNA (*2*), α-L-LNA (*3*), HNA (*4*), ANA (*5*), CNA (*6*), and CeNA (*7*). For a recent review see Leumann (*8*). Many of these analogues bind with improved affinity to DNA and/or RNA, but all of them bind even stronger to a complementary strand of the same type of analogue, i.e., they have a high affinity for self-hybridization. This is a large problem if you want to target both strands of a DNA duplex or a secondary structure of RNA like a hairpin (*9*, *10*). To overcome this problem there has been an intensive search for analogues that bind preferentially to the target and not to the analogue itself, which has resulted in a few new analogues (*11*, *12*).

In this paper we present a novel intercalating nucleotide analogue (INA). The concept of intercalation was proposed in 1961 by Lerman (*13*) and have since been subject for intense investigation (*14*). Some intercalators can be used as fluorescent labels and are applied universally in biology, biotechnology, and medicine (*15*−*17*). The pyrene moiety is one of the most heavily investigated molecules in terms of base stacking, thermal stabilization, and fluorescent abilities in DNA oligonucleotides (*18*−*27*). It has been suggested as an artificial nucleobase in DNA (*28*), attached to modified nucleotides such as LNA (*29*), and inserted in DNA with a glycerol backbone (*30*). These investigations showed a loss of stability upon hybridization except for the last example where a minor stabilization was observed when hybridized to DNA.

Pyrene has also been tested as an intercalator covalently attached to the O2′ in a uracil nucleotide through a methylene linker. The investigations showed a promising stabilization when inserted in and hybridized to DNA whereas hybridization to RNA caused destabilization (*31*). Insertion in RNA caused destabilization when hybridized to both RNA and DNA (*32*).

Recently, very promising results were presented, for a new intercalating nucleic acid (INA), consisting of a 1-*O*-(1-pyrenylmethyl)glycerol (*33*, *34*) (Scheme 1). These results showed that when INA is inserted as a bulge and hybridized to DNA, large thermal stabilizations are observed, whereas hybridization to RNA gives minor destabilizations. This makes INA highly promising as one of a few modifications that are able to discriminate between DNA and RNA. Fluorescent measurements show a decrease in fluorescence emission upon excitation at 340 nm after hybridization (*33*). This indicates that the pyrene moiety intercalates into the DNA double helix (*27*, *35*).

* To whom correspondence should be addressed. E-mail: cbn@chem.sdu.dk.

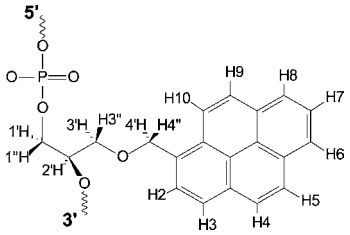
† University of Southern Denmark.

‡ University of Roskilde.

[1] Abbreviations: DQF−COSY, double quantum-filtered correlation spectroscopy; dsDNA, double-stranded DNA.; ssDNA, single-stranded DNA.; EDTA, ethylenediaminetetraacetic acid; INA, intercalating nucleic acid; NOE, nuclear Overhauser effect; NOESY, nuclear Overhauser effect spectroscopy; rMD, restrained molecular dynamics; RMSD, root-mean-square deviation; ISPA, isolated spin pair approximation; TOCSY, total correlation spectroscopy.

10.1021/bc0341932 CCC: $27.50 © 2004 American Chemical Society
Published on Web 03/02/2004

Scheme 1. A Schematic Drawing of the Intercalating Pseudo Nucleotide (INA), with Numbering of Protons Included



Scheme 2. Numbering Scheme for the Four Duplexes Investigated[a]

	1	2	3	4	5	6	7	8	9	10	11	12	13	
5'-	C	T	C	A	A	C	X_1	C	A	A	G	C	T	-3'
3'-	G	A	G	T	T	G	X_2	G	T	T	C	G	A	-5'
	26	25	24	23	22	21	20	19	18	17	16	15	14	

Duplex nr.	X_1	X_2
1	-	-
2	-	INA
3	INA	-
4	INA	INA

[a] "INA" indicates that an INA pesudo nucleotide has been incorporated and "−" indicates a normal DNA strand with no insertions.

In the present investigation, the objective was to explore the structural implications of two INAs placed directly opposite each in a dsDNA duplex and to determine whether INAs possess highest affinity for self-hybridization or for hybridization to complementary DNA.

EXPERIMENTAL PROCEDURES

Sample Preparation. Samples of duplex **1** and **4** were prepared for NMR investigations (Scheme 2). The two modified strands were synthesized as described elsewhere (*33*). The unmodified oligonucleotides were purchased from DNA Technology, Århus, Denmark. The samples were made by dissolving the two single strands in equivalent amounts in 0.5 mL of 10 mM sodium phosphate buffer (pH 7.0), 100 mM NaCl, and 0.05 mM EDTA. The samples were heated to 80 °C and slowly cooled to achieve hybridization. The final concentrations of the duplexes were 1.9 mM. For experiments in D_2O, the solid sample was lyophilized three times from D_2O and redissolved in 99.96% D_2O (Cambridge Isotope Laboratories). For experiments involving exchanging protons, the sample was dissolved in 90% H_2O and 10% D_2O. The numbering scheme used for the duplexes is shown in Scheme 2.

Thermal Stability Studies. The thermal stability was measured of duplexes **1**−**4** (Scheme 2). The thermal stability was determined spectrophotometrically on a Perkin-Elmer spectrophotometer equipped with a thermoregulated Peltier element. Hybridization mixtures were prepared by dissolving equimolar amounts (2.5−3.5 μM) of the oligonucleotides in 10 mM $Na_2HPO_4 \cdot H_2O$ (pH 7.0), 140 mM NaCl, and 1 mM EDTA. Measurements were done at pH ranging from 4 to 10 in steps of one unit. The pH was regulated using NaOH and HCl. The melting temperature was monitored while the temperature was changed linearly from 20 to 70 °C (1 °C min^{-1}) and then back to 20 °C. The melting temperatures were obtained as the average between the maxima/minima of the first derivatives of the melting curves.

NMR Experiments. The NMR experiments were performed on a Varian INOVA 600 spectrometer at 25 °C unless otherwise stated. For duplex **1**, a NOESY spectrum in D_2O was acquired using 2048 complex points in t_2 and a spectral width of 6000 Hz. A total of 512 t_1 experiments were recorded using the States phase cycling scheme. The residual signal of HOD was removed by low-power presaturation. A NOESY spectrum in H_2O was obtained using the watergate pulse sequence. The spectrum was acquired with 2048 complex points in t_2 and a spectral width of 12000 Hz. A total of 512 t_1 experiments were recorded using the States phase cycling. A DQF−COSY spectrum and TOCSY spectra with mixing times of 30 and 70 ms were obtained using the States phase cycling scheme.

For duplex **4**, two NOE buildup curves were obtained, one in D_2O and one in H_2O. In D_2O, the NOESY spectra were acquired using 2048 complex points in t_2 and a spectral width of 6000 Hz. A total of 512 t_1 experiments were recorded using the States phase cycling scheme. The NOESY spectra with mixing times of 50, 100, 150, and 200 ms were obtained sequentially without removing the sample from the magnet. 64 scans were acquired for each t_1 value with a repetition delay of 4.0 s between each scan. The residual signal of HOD was suppressed by low-power presaturation. In H_2O, the watergate-NOESY spectra were acquired using 2048 complex points in t_2 and a spectral width of 12000 Hz. A total of 680 t_1 experiments were recorded using the States phase cycling scheme. Spectra with mixing times of 100, 200, and 300 ms were obtained sequentially without removing the sample from the magnet. 64 scans were acquired for each t_1 value with a repetition delay of 2.0 s between each scan. A DQF−COSY spectrum and TOCSY spectra with mixing times of 30 and 70 ms were obtained using the States phase cycling scheme. An inversion recovery experiment was recorded to estimate the T_1 relaxations rates.

All the acquired data were processed using FELIX (Version 98, MSI, San Diego, CA). All spectra were apodized by a skewed sinebell squared in F1 and F2. The four spectra used in the D_2O NOE build up were linear predicted in F1 from 340 up to 400 points and baseline-corrected in F2 using the Flatt algorithm. The three spectra used in the build up in H_2O were linear-predicted in F1 from 420 up to 600 points and baseline corrected using the Flatt algorithm in F2.

Distance Restraints. The upper and lower diagonal part of each of the four NOESY buildup spectra in D_2O were separately integrated with FELIX, yielding a total of eight peak intensity sets which were corrected for minor saturation effects using the T_1 relaxations rates determined. A modified ISPA approach, as suggested by Wijmenga and Van Buuren, was used to calculate inter-proton distance bounds from the eight intensity sets (*36*). Bound widths were set to ±10% of the distances obtained. The same procedure was used for the buildup spectra in H_2O, but here the bounds were set to ±15% of the distances. Base planarity restraints and backbone torsion angle restraints were added for the two terminal base pairs: C1:G26, T2:A25, C12:G15, and T13:A14. The values of the 27 backbone angles included were: $-90° < \alpha < -30°$, $-210 < \beta < -150°$, $30° < \gamma < 90°$, $150° < \epsilon < 210°$, and $-150 < \zeta < -90°$. These values encompass both A- and B-type duplex structures.

Restrained molecular Dynamics. Two starting structure for the structure calculations were generated: an A-type and a B-type duplex. These were built with the *nucgen* and *nukit* modules of AMBER 6 (*37*). The INA nucleotides were added using the *xleap* module and

Table 1. Melting Temperatures of INA and DNA Duplexes Measured at Different pH Values[a]

	strand		pH						
duplex	1	2	4.2	5.0	6.1	7.0	8.0	9.0	10.0
1	DNA	DNA	30.6	43.6	47.8	47.2	49.1	49.6	43.3
2	DNA	INA	-	49.7	54.7	54.5	55.7	54.1	51.1
3	INA	DNA	-	45.4	51.9	52.5	54.7	52.1	46.4
4	INA	INA	-	36.1	46.0	46.5	48.5	46.5	40.9

[a] The measurements were done in 1 mM EDTA, 10 mM $Na_2HPO_4 \cdot H_2O$, and 140 mM NaCl.

atomic charges for the INA nucleotides were calculated using the RESP procedure as described by Bayly *et al.*, (*38*).

All distance restraints were incorporated into an rMD procedure for structure refinement. An initial energy minimization was followed by 28 ps of restrained molecular dynamics: at 600 K for 4 ps, followed by cooling to 200 K in 50 K steps of 3 ps each. The final structure was then energy minimized to a final derivative of 0.01 Å. A distance dependent dielectric constant ($\epsilon = r$) was employed to account for solvent effects. The pseudo-energy term used to enforce the distance restraints was:

$$E_{NOE} = \begin{cases} k_1(r - r_1)^2 & \text{when } r_1 > r \\ 0 & \text{when } r_2 \geq r \leq r_1 \\ k_2(r - r_2)^2 & \text{when } r_{2>} r \end{cases}$$

r_1 and r_2 are the lower and upper distance bounds, and k_1 and k_2 are the force constants. A force constant of 50 kcal mol^{-1} $Å^{-2}$ for lower and upper bounds was assigned to all distance restraints.

Helix parameters were calculated with the program CURVES 5.2 (*39*, *40*).

RESULTS

Thermal Stability. The thermal stabilities of the four duplexes shown in Scheme 2 were determined and compared (Table 1). Sharp monophasic transitions were obtained with hypochromicities of 1.1−1.2. No indications of biphasic transitions were detected. The measurements were performed at different pH values to investigate the pH dependency of INAs thermostability, and it can be noted that both DNA and INA duplexes are most stable in slightly basic environments.

Incorporation of one INA modification in either of the strands (duplex **2** and **3**) creates an increase in melting temperature of up to 6.6 °C. The difference in melting temperature reveals a small sequence dependency of the stabilization created by INA. Incorporation of INA modifications in both strands (duplex **4**) creates a decrease in melting temperature of up to 7.2 °C compared to the duplexes with INA in one only of the strands (duplexes **2** and **3**) and 0.6 °C compared to the unmodified duplex (duplex **1**). These results suggest that INA does *not* have a high affinity for self-hybridization; on the contrary, insertion of two INAs directly opposite each other creates a significant thermal destabilization of the duplex compared to when one INA is inserted in one of the strands. The degree of destabilization when INA modifications are inserted opposite each other is increasing when going to acidic pH values.

Spectral Analysis. The 1D ^1H NMR spectrum of the INA:INA duplex exhibits only lines from the expected duplex, and there were no signs of alternative hybridizations. The NOESY spectra of the INA:INA duplex exhibit the characteristic features of right-handed dsDNA sequential connectivities. The assignment of the nonexchangeable DNA protons in the INA:INA duplex was performed using standard methods (*41*−*44*). Both aromatic (H6, H8, and H2) and sugar protons (H1′, H2′, H2″, H3′, H4′, H5′, and H5″) were assigned. The NOESY spectrum recorded with short mixing time (50 ms) allowed unambiguous assignments of the H2′ and H2″ resonances. The H6/H8−H1′ cross-peaks were all weak, suggesting that the glycosidic angle is in the anti-position. The assignment of the exchangeable protons was obtained from the NOESY spectra in H_2O (*45*). The chemical shift values and the NOE connectivity pattern of the imino protons observed were in accordance with normal Watson−Crick base pairing. The unmodified duplex was assigned using the same strategy as for the INA:INA duplex; all determined chemical shift values of the unmodified DNA duplex indicated a canonical B-type helix structure. A selection of the chemical shift values of the DNA nucleotides in the INA:INA duplex are given in Table 2 and compared to the corresponding values of the unmodified duplex.

The assignment of the INA protons was performed using NOESY, DQF−COSY, and TOCSY spectra. The NOESY spectra showed that both INA nucleotides are intercalated, resulting in a large number of NOEs involving both of the aliphatic linkers and the pyrene moieties. The lines arising from INA and from the neighboring nucleotides are broader than other DNA lines, indicating more dynamics in the insertion area. The chemical shift values of the INA intercalators are given in Table 3.

Structure Calculations. More than 1000 NOE cross-peaks were observed in the NOESY spectra obtained with a 200 ms mixing time in D_2O. The accuracy of the integration of some cross-peaks was hampered by spectral overlap. These cross-peaks were not included in the modified ISPA calculations. The integration of the cross-peaks in the four buildup spectra was done separately for each side of the diagonal, resulting in two times four sets of 406 and 415 NOE cross-peaks intensities, respectively. This gives a total of 3284 integrated cross-peaks intensities used in the modified ISPA calculation. Cross-peak intensities that correspond to covalently fixed distances in the dsDNA were used for internal calibration and were therefore not converted into distance restraints. As the number of covalently fixed distances in DNA is rather limited, some internal sugar distances that are fairly independent of the sugar conformation were used for calibration as well. There are 19 internal proton−proton distances in a deoxyribose; these distances were determined at five different pseudorotation angles in the area of the two low energy conformations C3′-endo and C2′endo. In each of the 10 sets, NOESY cross-peaks corresponding to 77 deoxyribose distances and 19 covalently fixed distances were observed and thus yielded 96 distances used in calibration of unknown distances. The final bounds used in the rMD calculations were the average distances from the 10 distance sets ± 10%. The calculations returned 443 interproton distances; of those, 39 involved an INA proton.

Evaluation of the NOESY spectra in H_2O showed normal Watson−Crick bonding in the DNA parts of the duplex except between A9:T18, justifying inclusion of 28 hydrogen bond distance restraints. Three hydrogen bonds were included for each of the six GC base pairs and two hydrogen bonds for each of the five AT base pairs with upper and lower bounds of 1.74 and 2.10 Å, respectively. From the NOESY buildup in H_2O, a total of 36 distance restraints were determined using the same method as in D_2O. But here only covalent fixed distances were used

Table 2. A Selection of Chemical Shifts (in ppm) for the DNA Nucleotides in the INA:INA Duplex[a]

	H1′	H2′	H2″	H3′	H6/H8	H5/H2/CH_3	H1/H3	H4	H4
C1	5.86	2.24	2.57	4.64	7.88	5.95			
	(5.91)	(2.25)	(2.60)	(4.68)	(7.92)	(6.00)			
T2	6.12	2.19	2.52	4.88	7.59	1.66	13.82		
	(6.15)	(2.22)	(2.57)	(4.90)	(7.61)	(1.70)	(13.86)		
C3	5.34	1.98	2.26	4.82	7.48	5.64		8.53	6.80
	(5.43)	(2.01)	(2.32)	(4.85)	(7.51)	(5.74)		(8.61)	(6.84)
A4	5.72	2.70	2.77	5.01	8.16	7.15		7.73[b]	6.28[b]
	(5.87)	(2.78)	(2.89)	(5.06)	(8.26)	(7.24)		(−)	(−)
A5	5.89	2.39	2.60	4.98	7.92	7.36		7.18[b]	5.59[b]
	(6.10)	(2.61)	(2.83)	(5.00	(8.11)	(7.63)		(−)	(−)
C6	5.49	2.02	2.14	4.85	6.80	4.82		6.82	5.86
	(5.71)	(1.91)	(2.35)	(4.70)	(7.16)	(5.15)		(8.05)	(6.39)
X7									
C8	5.13	1.97	2.15	4.72	7.55	5.75		7.48	6.36
	(5.37)	(1.92)	(2.28)	(4.89)	(7.37)	(5.48)		(8.42)	(6.58)
A9	5.63	2.75	2.79	5.02	8.19	7.00		-	-
	(5.82)	(2.73)	(2.87)	(5.03)	(8.20)	(7.22)		(−)	(−)
A10	5.93	2.61	2.79	5.01	8.03	7.45		-	-
	(5.98)	(2.62)	(2.81)	(5.04)	(8.05)	(7.50)		(−)	(−)
G11	5.69	2.44	2.58	4.91	7.56		12.72		
	(5.74)	(2.45)	(2.60)	(4.92)	(7.57)		(12.77)		
C12	6.02	2.16	2.44	-	7.39	5.32		8.16	6.51
	(6.06)	(2.20)	(2.46)	(4.75)	(7.42)	(5.33)		(8.20)	(6.51)
T13	6.24	2.28	2.28	4.54	7.55	1.71	-		
	(6.26)	(2.30)	(2.30)	(4.56)	(7.59)	(1.74)	(−)		
A14	5.97	2.47	2.63	4.83	8.00	7.92		-	-
	(5.99)	(2.64)	(2.81)	(4.84)	(8.01)	(−)		(−)	(−)
G15	5.84	2.69	2.69	4.98	7.87		12.80		
	(5.98)	(2.22)	(2.45)	(−)	(7.57)		(12.83)		
C16	6.01	2.07	2.51	4.74	7.43	5.30		8.01	6.46
	(6.04)	(1.65)	(2.57)	(4.65)	(7.36)	(5.25)		(8.05)	(6.51)
T17	5.98	2.02	2.41	4.82	7.37	1.57	13.90		
	(6.08)	(2.15)	(2.58)	(−)	(7.46)	(1.61)	(14.06)		
T18	5.51	1.48	2.84	4.72	7.00	1.58	-		
	(5.81)	(2.06)	(2.46)	(4.89)	(7.31)	(1.69)	(13.82)		
G19	5.20	2.52	2.60	4.97	7.48		11.00[b]		
	(5.70)	(2.71)	(2.75)	(5.00)	(7.86)		(12.61)		
X20									
G21	5.91	2.77	2.77	5.00	8.07		10.61		
	(5.95)	(2.54)	(2.75)	(4.90)	(7.64)		(12.77)		
T22	5.67	1.96	2.28	4.72	7.16	1.30	13.33		
	(6.00)	(2.06)	(2.54)	(4.85)	(7.24)	(1.29)	(13.82)		
T23	5.59	1.87	2.24	4.76	7.16	1.58	13.71		
	(5.75)	(1.96)	(2.34)	(4.86)	(7.27)	(1.66)	(13.80)		
G24	5.37	2.69	2.69	4.96	7.86		12.54		
	(5.43)	(2.71)	(2.71)	(4.99)	(7.91)		(12.59)		
A25	6.09	2.63	2.88	5.01	8.08	7.73		7.95[b]	6.04[b]
	(6.12)	(2.66)	(2.90)	(5.03)	(8.12)	(7.78)		(−)	(−)
G26	5.97	2.24	2.37	4.60	7.61		-		
	(6.01)	(2.39)	(2.39)	(4.62)	(7.64)		(−)		

[a] The values of the unmodified duplex are given in parentheses. The values are measured at 25 °C relative to water unless otherwise stated. [b] Measured at 5 °C relative to water.

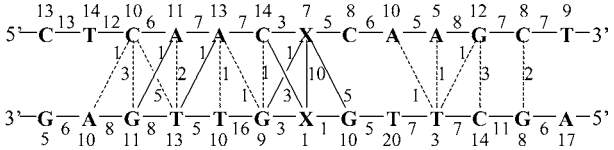
Table 3. Chemical Shift Values (ppm) of the INA Nucleotides[a]

	X7	X20
H2	6.67	7.21
H3	6.93	6.98
H4	7.30	7.14
H5	7.38	7.20
H6	7.37	7.07
H7	7.22	6.81
H8	7.14	6.72
H9	7.58	7.53
H10	7.55	7.36
H1′1/H1′2	4.09/4.16	4.20/4.29
H2′	4.47	4.61
H3′1/H3′2	3.79/3.84	3.86/3.98
H4′1/H4′2	4.84/4.84	4.30/4.54

[a] The values are given at 25 °C relative to water.

for calibration, and bounds were set to the average distances ±15%. None of the restraints from the spectra acquired in H_2O involved an INA proton. Thus, a total

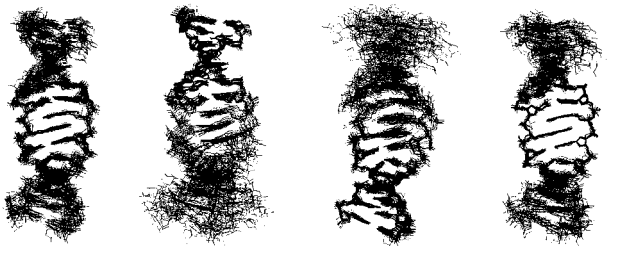
Scheme 3 Dispersion of the Distance Restraints Used in the RMD Calculations[a]



[a] Dashed lines are distances derived from NOESY spectra in H_2O; solid lines are distances from NOESY spectra in both D_2O and H_2O.

of 479 interproton restraints were used in the rMD calculations. The dispersion of the distance restraints used in the rMD calculation is shown in Scheme 3.

Twenty final structures starting from both A- and B-type starting structures, respectively, were generated. All the structures converged to one family of conformations, but the RMSD between structures generated from A- and B-types were slightly larger than internally in each of the two families. Since no A-type properties are



Ensemble	A	B	C	D
residues superimposed	[1-13;14-26]	[1-6;21-26]	[8-13;14-19]	[5-9;18-22]
RMSD	1.95	0.91	0.86	0.75

Figure 1. Four different views of 20 superimposed structures. (A) All residues are superimposed. (B) Residues [1−6;21−26] are superimposed. (C) Residues [8−13;14−19] are superimposed. (D) Residues [5−9;18−21] are superimposed. Hydrogens have been omitted for clarity.

observed in the final structure, only the 20 structures generated from the B-type structure are further analyzed. Four different views of the duplex are shown in Figure 1, with the RMSD for each ensemble indicated. The average all atom RMSD of the coordinates of the 20 B-type structures was 1.95 Å (Figure 1A). This rather high value, along with line broadening of the INA protons as well as the protons from the neighboring nucleotides, reflects the dynamics of the duplex. Segments of the duplex all had RMSDs below 1.0 Å (Figure 1B−D). The average sum of violations was 12.9 Å for the B-type starting structure. Just eight violations greater than 0.2 Å were observed and none greater than 0.3 Å.

The reliability of the structure calculation was carefully evaluated. rMD calculations were performed with distance restraints force constants changed to either 25 or 100 kcal mol^{-1} $Å^{-2}$, respectively. The generated structures all converged to the same family of structures as with the force constants set to 50 kcal mol^{-1} $Å^{-2}$. The structure obtained is not strongly dependent on the exclusion of any of the restraints. In particular, calculations performed without the Watson−Crick restraints yielded the same structure but with a slightly larger RMSD.

Helix Parameters. Helical parameters for the 20 final structures were analyzed with the program CURVES 5.2 (*39*, *40*). Plots of some global helical parameters for the INA:INA duplex are shown in Figure 5. The coordinates for the twenty final structures are deposited in the RSCB Protein Data Bank under pdb ID 1S88 (*46*).

DISCUSSION

Spectral Data. The NOESY cross-peaks shows that the duplex has a right-handed helix conformation with all nucleotides in the anti conformation. The sequential pathway is broken at the INA modifications due to their unusual backbone. The H6/H8−H1′ region of the 200 ms NOSEY spectrum is shown in Figure 2. It shows some of the sequential connectivities, and examples of INA−DNA cross-peaks.

The chemical shift values displayed in Table 2 demonstrate a close agreement between the modified and the unmodified duplex except for the protons near the INA modifications. The differences in chemical shift are primarily displayed at C6, C8, T18, G19, and G21. The changes in chemical shift can largely be explained by enhanced ring current effects induced by the pyrene moieties. It is difficult to make a pattern in the changes in chemical shifts observed, but it seems as if the nucleotides on the 5′-site of the intercalators (G6 and G19) obtains an upfield shift whereas the nucleotides on the 3′-site (C8 and G21) shift downfield. The chemical shifts of the intercalators are rather difficult to discuss,

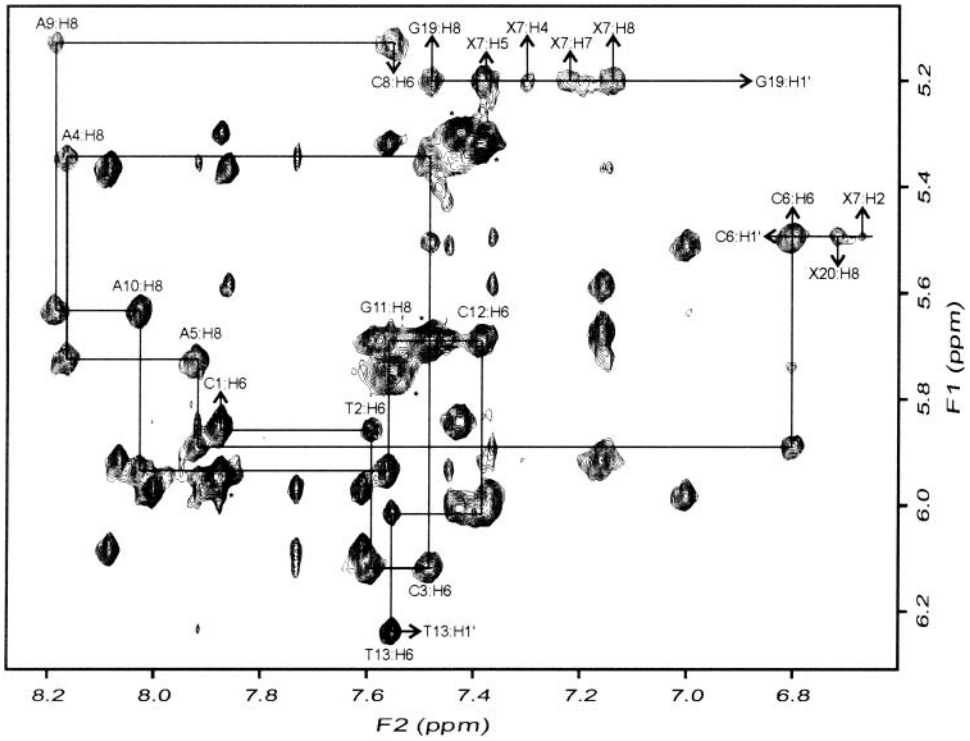


Figure 2. A section of the 200 ms NOESY spectrum displaying the H6/H8−H1′ region. The sequential connectivities for the C1−T13 strand are shown. Note that the connectivity is broken between C6 and C8, due to the missing sugar ring in INA. Cross-peaks between the DNA protons C6:H1′ and C19:H1′ and some of the aromatic protons on the intercalators, X7 and X20, are shown. Cytosine H6−H5 cross-peaks are marked with an asterisk. The C6:H6−C6:H5 cross-peak is not present, due to an upfield shift of C6:H5 induced by the pyrene moiety of X20.

but compared to pyrene, the aromatic protons in the pyrene moieties are shifted approximately 1 ppm upfield. This is probably due to ring current effects from one INA to the other and vice versa, indicating that both pyrene moieties are intercalated. These findings are supported by calculations of ring current effects, which display a similar trend (*47*, *48*)

The imino protons of G19 and G21 are shifted upfield 1.61 and 2.16 ppm, respectively. Such a dramatic upfield shift has been observed before in the literature for imino protons in guanines stacking with pyrenyl ring systems (*21*). Upfield shift of imino protons can be caused by two things: imino protons, with sharp and narrow lines, shifted upfield indicate significant ring current effects due to stacking interactions, whereas, imino protons,with broad lines due to rapid exchange, indicate disruption of the base pair hydrogen bonding (*21*). The reason for the dramatic upfield shift observed for G19:H1 and G21:H1 are probably a combination of the two. They have broad lines and G21:H1 can only be observed in the NOESY spectrum in H_2O at 5 °C, but the characteristic cross-peaks defining Watson−Crick hydrogen bonding are present in the spectra, indicating that base pairing does occur between G19:C8 and G21:C6. The broad lines are presumably due to internal motion rather than disruption of the base paring.

It is interesting that the chemical shift changes observed at T18 are greater than at G19, especially T18: H2′ is shifted 0.58 ppm upfield. Also no Watson−Crick base pairing is observed in the base pair A9:T18. This could be due to necessary structural compensations induced by the intercalation of the INA modfications. The reason it occurs at the A9:T18 base pair rather than at one of the flanking G:C base pairs is that A:T base pairs are more prone to disruption than G:C base pairs. This could explain why the chemical shift changes at T18 are greater than at G19, even though G19 is a neighbor to the intercalator ×20.

Description of the Structure. Qualitatively, the NOESY spectra of the INA:INA duplex indicate that it adopts a right-handed B-type helix conformation, with all the bases in the anti conformation and all forming normal Watson−Crick base pairs. However, Figure 3A reveals that even though the ends of the duplex looks like normal right-handed B-type helixes, some major changes occur in the area of the inserted intercalators. One obvious consequence of the intercalators is a dramatic unwinding of the helix in the insertion area creating a ladderlike structure. Unwinding of the helix as a consequence of intercalation is a common phenomenon for noncovalent bound intercalators (*49*). However, in this case where the INA nucleotide provides its own backbone, unwinding was not necessarily expected.

INA is designed to intercalate in the opposite strand, but Figure 4 reveals that when two INA are inserted opposite to each other they prefer to stack with each other, and X7 is therefore intercalated in the opposite strand as expected whereas X20 intercalates more or less in the strand where it is inserted. Thus both pyrene moieties stack in the same DNA strand, creating good stacking between G19, X7, X20, and G21, whereas stacking with C6 and C8 is less predominant. This shows that INA prefers to stack with G rather than C, due to the larger aromatic system of guanine. Due to the difference in intercalation, the conformation of the linker of the two INA nucleotides is different. The linker of X7 is quite extended whereas the linker of X20 is rather compact. Figure 4 shows that both intercalators are oriented the same way in the duplex relative to the strand direction. This could indicate that the pyrene moieties of the INA nucleotides have a preferred orientation when they intercalate.

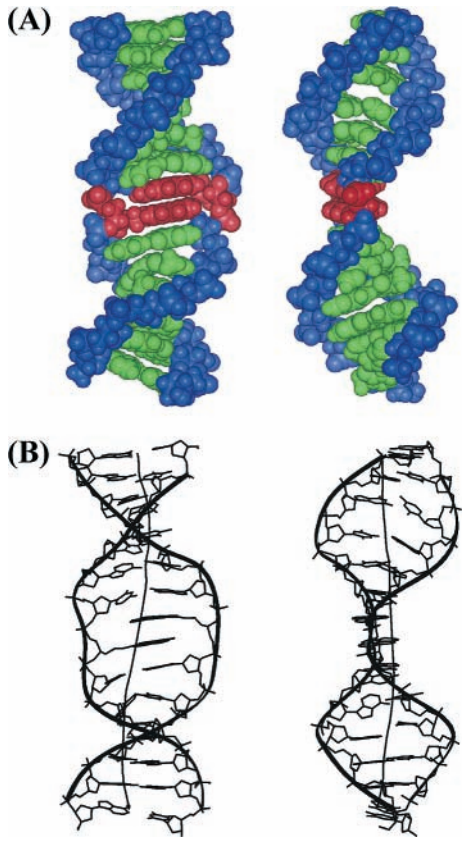


Figure 3. (A) Space-filling representations of the structure viewed from the minor groove (left) and turned 90° (right). (B) Stick representations of the structure. The helix axis calculated with CURVES is shown, and a ribbon has been added to emphasize the backbone. Hydrogens have been omitted for clarity.

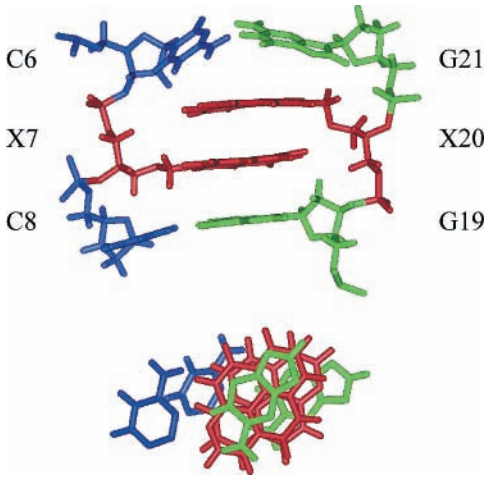


Figure 4. Top: Base pair stacking in the central part of the INA:INA duplex viewed from the major groove. Bottom: Same picture viewed along the helix axis, the backbone is not shown. There seems to be good stacking between G19, X7, X20, and G21, whereas the stacking of the pyrenes with C6 and C8 is rather limited.

Dynamic Considerations. The structure of the INA:INA duplex (duplex **4**) shows that both pyrene moieties are intercalated. This observation is supported by chemical shift values observed for the protons in the pyrene moiety. They are shifted approximately 1 ppm compared to pyrene, indicating ring current effects from one pyrene

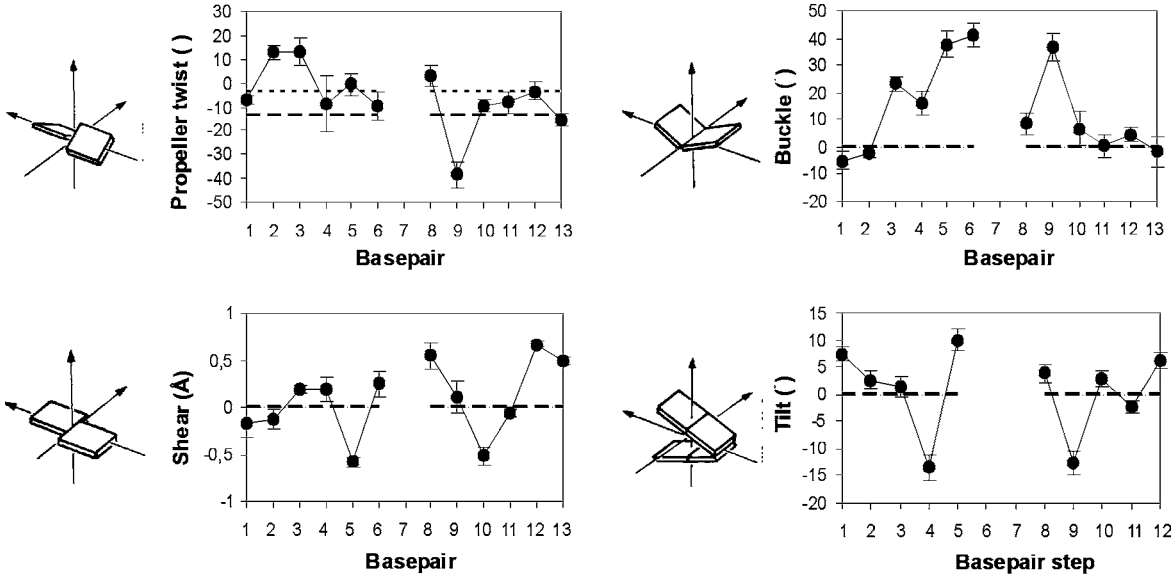


Figure 5. A selection of the helix parameters calculated for the INA:INA duplex. The parameters were calculated using CURVES 5.2 and are compared to values of canonical A-type duplex (- ─ -) and B-type duplex (- ─ -) parameters. No values are calculated for the intercalators X7 and X20.

moiety affecting the other and vice versa. However, all INA protons, as well as the protons from the neighboring nucleotides, have line widths broader than normal, indicating intermediate dynamics in this area. These dynamics have to occur on a fast time scale since only one set of peaks can be observed in any of the acquired spectra.

The observed dynamics of the duplex could have its origin in several different patterns of movement by the pyrenes. They could be intercalated alternately and only briefly be intercalated both at the same time, they could simultaneously move in and out of the helix, or they could be sliding on top of each other either sideways or back and forth. Considering the amount of cross-peaks identified between X7 and X20, the two first models do not seem likely. If the pyrenes only were stacking with each other for a short time, the number of cross-peaks and their intensities would probably be lower. To distinguish between the two other possibilities is more problematic, but since the minor groove has been shown to be extensively widened in the duplex, the last option where the two pyrene moieties are sliding back and forth does seem more appealing. Unfortunatly, no definitive answer can be given.

Helix Parameters. There are three major categories of helical parameters: axis-base pair, intrabase pair and interbase pair parameters (*50*). For the INA:INA duplex some of these parameters are shown in Figure 5. However, no data are available for the intercalators, and the data for the terminal base pairs are probably less reliable due to dynamic processes and a lower density of restraints and are only included for completeness.

The global helix axis is fairly straight (Figure 3B), but it should be noted that the axis does not pass through the intercalators, as they seem to be shifted toward the minor groove. The width of the minor groove, measured as the shortest interstrand phosphorus distance (reduced by 5.8 Å to account for the van der Waals radius of two phosphate groups), is reported in Figure 6. For classical B-type helices, a value of approximately 5.7 Å is expected (*51*), but in the INA structure, a remarkable widening of the minor groove is observed throughout the duplex. The widening is most dramatic in the insertion area where enlargements up to 10.1 Å are observed. This remarkable



Figure 6. The minor groove width measured as the smallest distance between two interstrand phosphorus atoms reduced by 5.8 Å to account for the van der Waals radius of two phosphate groups. A greatly enlarged minor groove width in the central part of the helix is observed.

result indicates that even though the two INAs seemingly are stacking well, they also push the two strands of the duplex apart and hence have a pronounced influence on the minor groove width of the entire duplex.

The calculated values of the intrabase pair parameters shear, buckle, and propeller twist all deviate from normal A- and B-type DNA in the central part of the helix. Changes in buckle have been reported earlier to be connected to changes in the sugar conformations (*52*, *53*), but values of the pseudorotation angle show a majority of S-type conformation in all nucleotides except C6 (results not shown). Even though propeller twist for structures of oligonucleotides determined by NMR normally are more negative than for canonical B-type helixes

(*54*−*57*), the large negative value for the A9:T18 base pair is noteworthy. Together with the large positive buckle, it explains why no Watson−Crick hydrogen bonding could be observed for this base pair. The unusually large positive values of buckle and the large changes in shear, combined with the large changes in the interbase pair parameter tilt in the insertion area, demonstrate the dramatic adaptations the structure has to perform due to the insertion of the two INAs.

Stability of INA Duplexes. The thermal stability measurements displayed in Table 1 shows that one INA nucleotide inserted in either of the strands increases the affinity for the complementary ssDNA. This increase in melting temperature was expected from previous results (*33*). We have shown that even though INA has the very high affinity for its target DNA, it has a lower affinity for complementary INA, when the two INA insertions are placed opposite each other. By adjusting pH to 5.0 (see Table 1), it is possible to optimize the difference in thermal stability between the INA:DNA hybrid and the INA:INA duplex to 13.6 °C. However, thermal stability measurements of duplexes with INA molecules inserted in each strand, displaced with one to three base pairs, show a stabilizing effect of up to 7.0 °C, indicating that INA in general have a high affinity for other sequences with INA inserted (unpublished results).

Even though the intercalation of the two pyrene moieties makes a severe pertubation to the duplex structure, the thermostability of the INA:INA duplex is only slightly lower than that of the unmodified dsDNA duplex. One possible explanation of this could be that even though two intercalators inserted directly opposite each other distort the duplex, they also create an area with an increased flexibility due to the greater mobility of the backbone of the intercalators compared to a normal nucleotide. This enables the duplex to make major changes in the insertion area without having to rearrange the rest of the duplex, thereby creating independent helixes on each side of the intercalators. Another factor minimizing the degree of destabilization is the strong stacking of the INAs, contributing to the stability of the duplex, an effect observed previously with bipyridyl C-nucleotides (*58*). This enhanced stacking in the duplex induced by the pyrene moieties is probably the reason insertion of INAs displaced by one to three base pairs stabilizes the duplex. Such an INA arrangement would intuitively destabilize the duplex even further because the structural adaptations necessary to fit both intercalators in the helix would spread over a greater part of in the duplex. However, due to the enhanced stacking abilities of the pyrene moieties compared to the natural nucleobases, insertion of INAs creates an enhanced stacking in the duplex in a larger area, thereby stabilizing the duplex.

One of the conclusions obtained in this investigation is that insertion of two INA intercalators opposite each other creates a minor thermal destabilization of the duplex. This destabilization is founded in an unwinding of the helix in the insertion area, where the pyrene moieties exhibit good stacking abilities but also push the two strands apart, creating an extensively widened minor groove. Thermal stability measurements suggest that the destabilizing effect of inserting INA in both strands is specific for the case where they are inserted directly opposite each other; otherwise insertion of INA in both strands have a stabilizing effect. The measurements also show that by adjusting pH it is possible to optimize INA affinity for a complementary DNA target over a complementary INA target.

Intercalating nucleic acid is thus one of the first nucleotide analogues that have reduced affinity for hybridization to a complementary strand of its own kind, while still processing a highly increased affinity for hybridizing to its complementary DNA strands, making targeting of both of the complementary strands of a DNA duplex possible. On the basis of the high-affinity, high specificity and low self-affinity, we believe that INA can be used with great advantage in a versatile range of applications where hybridization to single- as well as double-stranded targets is desired.

ACKNOWLEDGMENT

We would like to thank Professor Michael P. Williamson at the University of Sheffield for calculating the ring current values for the duplexes. We thank the Danish National Research Foundation, The Danish Natural Science Research Foundation, and the Danish Technical Research Foundation for financial support.

LITERATURE CITED

(1) Nielsen, P. E., and Haaima, G. (1997) Peptide nucleic acid (PNA). A DNA mimic with a pseudopeptide backbone. *Chem. Soc. Rev. 26*, 73−78.

(2) Koshkin, A. A., Singh, S. K., Nielsen, P., Rajwanshi, V. K., Kumar, R., Meldgaard, M., Olsen, C. E., and Wengel, J. (1998) LNA (Locked Nucleic Acids): Synthesis of the adenine, cytosine, guanine, 5-methylcytosine, thymine and uracil bicyclonucleoside monomers, oligomerisation, and unprecedented nucleic acid recognition. *Tetrahedron 54*, 3607−3630.

(3) Rajwanshi, V. K., Hakansson, A. E., Dahl, B. M., and Wengel, J. (1999) LNA stereoisomers: xylo-LNA (beta-D-xylo configured locked nucleic acid) and alpha-L-LNA (alpha-L-ribo configured locked nucleic acid). *Chem. Commun.* 1395−1396.

(4) Van Aerschot, A., Verheggen, I., Hendrix, C., and Herdewijn, P. (1995) 1,5-Anhydrohexitol Nucleic-Acids, A New Promising Antisense Construct. *Angew. Chem., Int. Ed. Engl. 34*, 1338−1339.

(5) Allart, B., Khan, K., Rosemeyer, H., Schepers, G., Hendrix, C., Rothenbacher, K., Seela, F., Van Aerschot, A., and Herdewijn, P. (1999) D-Altritol nucleic acids (ANA): Hybridisation properties, stability, and initial structural analysis. *Chem.-Eur. J. 5*, 2424−2431.

(6) Maurinsh, Y., Rosemeyer, H., Esnouf, R., Medvedovici, A., Wang, J., Ceulemans, G., Lescrinier, E., Hendrix, C., Busson, R., Sandra, P., Seela, F., Van Aerschot, A., and Herdewijn, P. (1999) Synthesis and pairing properties of oligonucleotides containing 3-hydroxy-4-hydroxymethyl-1-cyclohexanyl nucleosides. *Chem.-A Eur. J. 5*, 2139−2150.

(7) Wang, J., Verbeure, B., Luyten, I., Lescrinier, E., Froeyen, M., Hendrix, C., Rosemeyer, H., Seela, F., Van Aerschot, A., and Herdewijn, P. (2000) Cyclohexene nucleic acids (CeNA): Serum stable oligonucleotides that activate RNase H and increase duplex stability with complementary RNA. *J. Am. Chem. Soc. 122*, 8595−8602.

(8) Leumann, C. J. (2002) DNA analogues: from supramolecular principles to biological properties. *Bioorg. Med. Chem. 10*, 841−854.

(9) Cheng, S., Van Houten, B., Gamper, H. B., Sancar, A., and Hearst, J. E. (1988) Use of psoralen-modified oligonucleotides to trap three-stranded RecA-DNA complexes and repair of these cross-linked complexes by ABC excinuclease. *J. Biol. Chem. 263*, 15110−15117.

(10) Lohse, J., Dahl, O., and Nielsen, P. E. (1999) Double duplex invasion by peptide nucleic acid: a general principle for sequence-specific targeting of double-stranded DNA. *Proc. Natl. Acad. Sci. U.S.A 96*, 11804−11808.

(11) Kutyavin, I. V., Rhinehart, R. L., Lukhtanov, E. A., Gorn, V. V., Meyer, R. B., Jr., and Gamper, H. B., Jr. (1996) Oligonucleotides containing 2-aminoadenine and 2-thiothymine act as selectively binding complementary agents. *Biochemistry 35*, 11170−11176.

(12) Woo, J. S., Meyer, R. B., and Gamper, H. B. (1996) G/C-modified oligodeoxynucleotides with selective complementarity: Synthesis and hybridization properties. *Nucleic Acids Res. 24*, 2470−2475.

(13) Lerman, L. S. (1961) Structural Considerations in Interaction of Dna and Acridines. *J. Mol. Biol. 3*, 18−30.

(14) Johnson, D. S., and Boger, D. L. (1996) DNA binding Agents. In *Supramolecular Reactivity and Transport: Bioorganic Systems* (Atwood, J. L., Davies, J. E. D., MacNicol, D. D., Vögtle, F, Murakami, Y., Eds.) Chapter 3, Pergamon, Exeter, UK.

(15) Brana, M. F., Cacho, M., Gradillas, A., Pascual-Teresa, B., and Ramos, A. (2001) Intercalators as anticancer drugs. *Curr. Pharm. Design 7*, 1745−1780.

(16) Mayer, A., and Neuenhofer, S. (1994) Luminescent Labels − More Than Just An Alternative to Radioisotopes. *Angew. Chem., Int. Ed. Engl. 33*, 1044−1072.

(17) Zimmer, M. (2002) Green fluorescent protein (GFP): Applications, structure, and related photophysical behavior. *Chem. Rev. 102*, 759−781.

(18) Filichev, V. V., and Pedersen, E. B. (2003) Intercalating nucleic acids (INAs) with insertion of N-(pyren-1-ymethyl)−(3R,4R)-4-(hydroxymethyl)pyrrolidin-3-ol. DNA (RNA) duplex and DNA three-way junction stabilities. *Org. Biomol. Chem. 1*, 100−103.

(19) Strassler, C., Davis, N. E., and Kool, E. T. (1999) Novel nucleoside analogues with fluorophores replacing the DNA base. *Helv. Chim. Acta 82*, 2160−2171.

(20) Paris, P. L., Langenhan, J. M., and Kool, E. T. (1998) Probing DNA sequences in solution with a monomer−excimer fluorescence color change. *Nucleic Acids Res. 26*, 3789−3793.

(21) Geacintov, N. E., Cosman, M., Hingerty, B. E., Amin, S., Broyde, S., and Patel, D. J. (1997) NMR solution structures of stereoisomeric covalent polycyclic aromatic carcinogen-DNA adducts: Principles, patterns, and diversity. *Chem. Res. Toxicol. 10*, 111−146.

(22) Puri, N., Zamaratski, E., Sund, C., and Chattopadhyaya, J. (1997) Synthesis of 5′-polyarene-tethered oligo-DNAs and the thermal stability and spectroscopic properties of their duplexes and triplexes. *Tetrahedron 53*, 10409−10432.

(23) Yamana, K., Kumamoto, S., and Nakano, H. (1997) Homopyrimidine oligonucleotides modified by a pyrenylmethyl group at the terminal position: Enhanced fluorescence upon binding to double helical DNA. *Chem. Lett. 11*, 1173−1174.

(24) Li, Y., Bevilacqua, P. C., Mathews, D., and Turner, D. H. (1995) Thermodynamic and activation parameters for binding of a pyrene-labeled substrate by the Tetrahymena ribozyme: docking is not diffusion-controlled and is driven by a favorable entropy change. *Biochemistry 34*, 14394−14399.

(25) Tong, G., Lawlor, J. M., Tregear, G. W., and Haralambidis, J. (1995) Oligonucleotide−Polyamide Hybrid Molecules Containing Multiple Pyrene Residues Exhibit Significant Excimer Fluorescence. *J. Am. Chem. Soc. 117*, 12151−12158.

(26) Yamana, K., Gokota, T., Ozaki, H., Nakano, H., Sangen, O., and Shimidzu, T. (1992) Enhanced Fluorescence in the Binding of Oligonucleotides with A Pyrene Group in the Sugar Fragment to Complementary Polynucleotides. *Nucleosides Nucleotides 11*, 383−390.

(27) Telser, J., Cruickshank, K. A., Morrison, L. E., and Netzel, T. L. (1989) Synthesis and characterization of DNA oligomers and duplexes containing covalently attached molecular labels: Comparison of biotin, fluorescein, and pyrene labels by thermodynamic and optical spectroscopic measurements. *J. Am. Chem. Soc. 111*, 6966−6976.

(28) Matray, T. J., and Kool, E. T. (1998) Selective and stable DNA base pairing without hydrogen bonds. *J. Am. Chem. Soc. 120*, 6191−6192.

(29) Babu, B. R., and Wengel, J. (2001) Universal hybridization using LNA (locked nucleic acid) containing a novel pyrene LNA nucleotide monomer. *Chem. Commun.* 2114−2115.

(30) Yamana, K., Takei, M., and Nakano, H. (1997) Synthesis of oligonucleotide derivatives containing pyrene labeled glycerol linkers: Enhanced excimer fluorescence on binding to a complementary DNA sequence. *Tetrahedron Lett. 38*, 6051−6054.

(31) Yamana, K., Iwase, R., Furutani, S., Tsuchida, H., Zako, H., Yamaoka, T., and Murakami, A. (1999) 2′-Pyrene modified oligonucleotide provides a highly sensitive fluorescent probe of RNA. *Nucleic Acids Res. 27*, 2387−2392.

(32) Yamana, K., Zako, H., Asazuma, K., Iwase, R., Nakano, H., and Murakami, A. (2001) Fluorescence detection of specific RNA sequences using 2′-pyrene-modified oligoribonucleotides. *Angew. Chem., Int. Ed. 40*, 1104−1106.

(33) Christensen, U. B., and Pedersen, E. B. (2002) Intercalating nucleic acids containing insertions of 1-O−(1-pyrenylmethyl)-glycerol: stabilisation of dsDNA and discrimination of DNA over RNA. *Nucleic Acids Res. 30*, 4918−4925.

(34) Christensen, U. B., and Pedersen, E. B. (2003) Intercalating nucleic acids with pyrene nucleotide analogues as next-nearest neighbours for excimer fluorescence detection of single point mutations under nonstringent hybridisation conditions. *Helv. Chim. Acta*, accepted.

(35) Haralambidis, J., Angus, K., Pownall, S., Duncan, L., Chai, M., and Tregear, G. W. (1990) The Preparation of Polyamide-Oligonucleotide Probes Containing Multiple Nonradioactive Labels. *Nucleic Acids Res. 18*, 501−505.

(36) Wijmenga, S. S., and van Buuren, B. N. M. (1998) The use of NMR methods for conformational studies of nucleic acids. *Prog. Nuclear Magn. Reson. Spectrosc. 32*, 287−387.

(37) Case, D. A., Pearlman, D. A., Caldwell, J. W., Cheatham, T. E., III, Ross, W. S., Simmerling, C. L., Darden, T. A., Merz, K. M., Stanton, R. V., Cheng, A. L., Vincent, J. J., Crowley, M., Tsui, V., Radmer, R. J., Duan, Y., Pitera, J., Massova, I., Seibel, G. L., Singh, U. C., Weiner, P. K., and Kollman, P. A. *AMBER 6*, University of California, San Francisco, 1999.

(38) Bayly, C. I., Cieplak, P., Cornell, W. D., and Kollman, P. A. (1993) A Well-Behaved Electrostatic Potential Based Method Using Charge Restraints for Deriving Atomic Charges − the Resp Model. *J. Phys. Chem. 97*, 10269−10280.

(39) Lavery, R., and Sklenar, H. (1989) Defining the Structure of Irregular Nucleic-Acids − Conventions and Principles. *J. Biomol. Struct. Dyn. 6*, 655−667.

(40) Lavery, R., and Sklenar, H. (1988) The Definition of Generalized Helicoidal Parameters and of Axis Curvature for Irregular Nucleic-Acids. *J. Biomol. Struct. Dyn. 6*, 63−91.

(41) Hare, D. R., Wemmer, D. E., Chou, S. H., Drobny, G., and Reid, B. R. (1983) Assignment of the Non-Exchangeable Proton Resonances of D(C−G- C−G-A−A-T−T-C−G-C−G) Using Two-Dimensional Nuclear Magnetic- Resonance Methods. *J. Mol. Biol. 171*, 319−336.

(42) Scheek, R. M., Russo, N., Boelens, R., and Kaptein, R. (1983) Sequential Resonance Assignments in Dna H-1-Nmr Spectra by Two-Dimensional Noe Spectroscopy. *J. Am. Chem. Soc. 105*, 2914−2916.

(43) Feigon, J., Leupin, W., Denny, W. A., and Kearns, D. R. (1983) Two-Dimensional Proton Nuclear Magnetic-Resonance Investigation of the Synthetic Deoxyribonucleic-Acid Decamer D(Atatcgatat)2. *Biochemistry 22*, 5943−5951.

(44) Wüthrich, K. (1986) *NMR of Proteins and Nucleic Acids*, John Wiley & Sons, New York.

(45) Boelens, R., Scheek, R. M., Dijkstra, K., and Kaptein, R. (1985) Sequential Assignment of Imino-Proton and Amino-Proton Resonances in H-1-Nmr Spectra of Oligonucleotides by Two-Dimensional Nmr-Spectroscopy − Application to A Lac Operator Fragment. *J. Magn. Reson. 62*, 378−386.

(46) Berman H. M., Westbrook, J., Feng, Z., Gilliland, G., Bhat, T. N., Weissig, H., Shindyalov, I. N., and Bourne P. E. (2000) *Nucleic Acids Res. 28*, 235−242.

(47) Williamson, M. P., and Asakura, T. (1993) Empirical Comparisons of Models for Chemical-Shift Calculation in Proteins. *J. Magn. Reson. Ser. B 101*, 63−71.

(48) Asakura, T., Taoka, K., Demura, M., and Williamson, M. P. (1995) The Relationship Between Amide Proton Chemical-Shifts and Secondary Structure in Proteins. *J. Biomol. NMR 6*, 227−236.

(49) Searle, M. S. (1993) Nmr-Studies of Drug-Dna Interactions. *Prog. Nuclear Magn. Reson. Spectrosc. 25*, 403−480.
(50) Dickerson, R. E., Bansal, M., Calladine, C. R., Diekmann, S., Hunter, W. N., Kennard, O., von Kitzing, E., Lavery, R., Nelson, H. C. M., Olson, W. K., Saenger, W., Shakked, Z., Sklenar, H., Soumpasis, D. M., Tung, C. S., Wang, A. H. J., and Zhurkin, V. B. (1989) Definitions and Nomenclature of Nucleic-Acid Structure Parameters. *EMBO J. 8*, 1−4.
(51) Saenger, W. (1984) *Principles of Nucleic Acid Structure,* Springer-Verlag, New York.
(52) Nielsen, K. E., Singh, S. K., Wengel, J., and Jacobsen, J. P. (2000) Solution structure of an LNA hybridized to DNA: NMR study of the d(CT(L)GCT(L)T(L)CT(L)GC): d(GCA-GAAGCAG) duplex containing four locked nucleotides. *Bioconjugate Chem. 11*, 228−238.
(53) Nielsen, C. B., Singh, S. K., Wengel, J., and Jacobsen, J. P. (1999) The solution structure of a locked nucleic acid (LNA) hybridized to DNA. *J. Biomol. Struct. Dyn. 17*, 175−191.
(54) Baleja, J. D., Pon, R. T., and Sykes, B. D. (1990) Solution Structure of Phage-Lambda 1/2-Operator Dna by Use of Nmr, Restrained Molecular-Dynamics, and Noe-Based Refinement. *Biochemistry 29*, 4828−4839.
(55) Mujeeb, A., Kerwin, S. M., Kenyon, G. L., and James, T. L. (1993) Solution structure of a conserved DNA sequence from the HIV-1 genome: restrained molecular dynamics simulation with distance and torsion angle restraints derived from two-dimensional NMR spectra. *Biochemistry 32*, 13419−13431.
(56) Schmitz, U., Sethson, I., Egan, W. M., and James, T. L. (1992) Solution Structure of A Dna Octamer Containing the Pribnow Box Via Restrained Molecular-Dynamics Simulation with Distance and Torsion Angle Constraints Derived from 2-Dimensional Nuclear- Magnetic-Resonance Spectral Fitting. *J. Mol. Biol. 227*, 510−531.
(57) Weisz, K., Shafer, R. H., Egan, W., and James, T. L. (1992) The Octamer Motif in Immunoglobulin Genes − Extraction of Structural Constraints from 2-Dimensional NMR Studies. *Biochemistry 31*, 7477−7487.
(58) Brotschi, C. and Leumann, C. J. (2003) DNA with Hydrophobic Base Substitutes: A Stable, Zipperlike Recognition Motif Based On Interstrand-Stacking Interactions. *Angew. Chem., Int. Ed 42*, 1655−1658.

BC0341932

Antigenic Prenylated Peptide Conjugates and Polyclonal Antibodies To Detect Protein Prenylation

Xiao-hui Liu,[†] Dae-Yeon Suh,[†] Jeffrey Call,[‡] and Glenn D. Prestwich*[,†]

Department of Medicinal Chemistry and the Center for Cell Signaling, The University of Utah, 419 Wakara Way, Suite 205, Salt Lake City, Utah 84108-1257, and Biotechnology & Genomic Research Center, Utah State University, 4700 Old Main Hill, Logan, Utah 84322. Received October 30, 2003

Posttranslational modification of proteins with farnesyl and geranylgeranyl groups is a required modification for signaling proteins that includes the small GTPases in the Ras, Rho, and Rab families, heterotrimeric G proteins, and nuclear lamin proteins. To develop antibodies capable of detecting and distinguishing prenylated proteins, we synthesized two antigens, succinylglycine-(geranylgeranyl)-cysteine methyl ester (SuccG-(gg)CMe, **1**) and succinylglycine-(farnesyl)cysteine methyl ester (SuccG-(f)CMe, **2**). These prenylated peptides were covalently coupled to bovine serum albumin (BSA) and to keyhole limpet hemocyanin (KLH) to produce polyvalent, immunogenic bioconjugates. Immunization of rabbits with these immunogens generated polyclonal antisera that contained significant titers of anti-geranylgeranyl and anti-farnesyl antibodies. The selectivity of the polyclonal antisera was examined using ELISA and dot blotting methods. The anti-farnesyl and anti-geranylgeranyl antisera crossreacted with both antigens. Attempts to purify the polyclonal antisera by either positive or negative immunoaffinity selection protocols failed to produce selective anti-geranylgeranyl and anti-farnesyl antibodies. Moreover, both crude antisera and purified antibodies also crossreacted with myristoylated and palmitoylated BSA conjugates. Immunofluorescence staining of EYFP-CVLL or EYFP-CVIM transfected CHO-K1 cells with rabbit polyclonal antisera showed colocalized membrane fluorescence. Thus, an important caveat for the use of antibodies raised against aliphatic antigens is that extensive controls must be performed to determine selectivity.

INTRODUCTION

Antibodies are synthesized predominantly by plasma cells, which are terminally differentiated cells of the B-lymphocyte lineage and constitute a crucial line of defense against foreign antigens (*1*). The unique specificities of the antibodies have made them indispensable tools in cell and developmental biology, therapeutic medicine, and pathology (*2*). While the majority of antigens used for immunization are proteins, peptides, nucleic acid, carbohydrates, or cell-surface antigens, small molecules can be immunogenic if delivered in a polyvalent form with an appropriate adjuvant. This often requires covalent linkage to a carrier protein such as keyhole limpet hemocyanin (KLH), bovine serum albumin (BSA), or thyroglobulin. Recent studies revealed that some antigenic nonpeptide molecules can stimulate a strong T-cell response in humans and in mouse models. These molecules include aliphatic glycolipids, phosphoantigens, aromatic glycolipids, alkylamines, and lipids (*3*−*11*).

Some anti-lipid antibodies can occur naturally. For example, anti-phospholipid antibodies (αPL) are an important clinical problem (*12*), occurring in autoimmune diseases (e.g., lupus erythematosus) and in infectious diseases such as tuberculosis, hepatitis, Lyme disease, malaria, and bacterial septicemia (*13*). Stereospecific antibodies against phosphatidylserine have been generated using liposomes (*14*) and acyl-linked antigens (*15*); these antigens have been employed for immunolocalization in human placenta (*16*) and other tissues (*17*). In recent studies of lipid signaling, selective antibodies against the phosphoinositides PI(4,5)P_2 and PI(3,4,5)P_3 have been developed (*18, 19*) and used to visualize changes in subcellular phosphoinositides in stimulated cells and in tissue sections (*20*).

Prenylation is a required posttranslational modification of most small GTPases and a variety of other proteins (*21*−*26*). In particular, Ras, Rho, and Rab proteins play important roles in cell proliferation and signal transduction. Aberrant signaling is responsible for the growth and proliferation of cancer cells. Each of these mature small GTPases have isoprenyl moieties (farnesyl or geranylgeranyl) linked to a common cysteine methyl ester via a thioether bond. Proteins are prenylated by the transfer of a farnesyl (C-15) or geranylgeranyl (C-20) unit from farnesyl diphosphate (FPP) or geranylgeranyl diphosphate (GGPP) to the cysteine of a C-terminal motif. Three carboxyl terminal motifs specify the type of prenylation: CA_1A_2X, CC, and CAC, where A is an aliphatic amino acid and X is any amino acid. Generally, the CA_1A_2X (X = Ser, Met, Ala or Gln) sequence is a substrate for farnesylation unless X = Leu or Phe, in which case geranylgeranylation occurs. The CC and CAC sequences are substrates for bisgeranylgeranylation and are found exclusively in the Rab family of small GTPases.

Two groups have reported a polyclonal anti-farnesyl antibody to identify farnesylated proteins in cells (*27, 28*), developed using *N*-acetyl-*S*-farnesyl-L-cysteine, which was coupled to KLH using carbodiimide chemistry. However, the reported polyclonal antibodies crossreacted

* To whom correspondence should be addressed. Phone: 801-585-9051; fax: 801-585-9053; E-mail: gprestwich@deans.pharm.utah.edu.

[†] The University of Utah.

[‡] Utah State University.

10.1021/bc0342027 CCC: $27.50 © 2004 American Chemical Society
Published on Web 02/18/2004

with geranylgeranyl moieties. Since selective anti-geranylgeranyl and anti-farnesyl antibodies could be very useful tools for the study of prenylated proteins in cells, we designed and synthesized two new antigens: SuccG-(gg)CMe **1** and SuccG-(f)CMe **2**. (To avoid confusion with single letter amino acid abbreviations, geranylgeranyl is abbreviated as "gg" and farnesyl as "f".) The introduction of a succinylglycine spacer was selected to enhance immunogenicity and to increase the likelihood of obtaining prenyl selective antibodies. Antisera that contained polyclonal antibodies were obtained from immunized rabbits. Antibodies were purified by affinity and size exclusion chromatography and were characterized using ELISA, dot blots, and immunofluorescence.

EXPERIMENTAL PROCEDURES

General. All reactions were conducted using oven-dried glassware. Column chromatography was performed on silica gel (60 Å, 240−400 mesh ASTM) from Whatman Co. BSA and KLH were from Sigma. Affigel-10 was from Bio-Rad. Dot blotting and western blotting reagents were from Amersham. Myristoyl-Gly was from BACHEM, and all other organic reagents were from Sigma-Aldrich Chemical Co. CHO-K1 cells were from ATCC. Lipofectamine and cell culture medium were from Invitrogen Life Technologies. G418 (Geneticin) was from Gibco. L-(Trityl)-Cys **3** was prepared from L-cysteine as described (*29*). The synthetic compounds were visualized on TLC with anisaldehyde−H_2SO_4−AcOH solution.

Vector pcDNA3.1 encoding YFP-KMSKDGKKKKK-KSKTKCVIM was the generous gift of Dr. Tamas Balla (Endocrinology and Reproduction Research Branch, National Institutes of Health). EYFP-CVLL was constructed by site-directed mutagenesis from the EYFP-CVIM, using QuickChange mutagenesis kit (Invitrogen). The mutagenesis primers were sense, 5′-ACAAAGTGTGTACT-TCTTTAAAGATCTCGG-3′; antisense, 5′-CCGAGATCTT-TAAAGAAGTACACACTTTGT-3′. The PCR conditions were 95 °C for 45 s, followed by 18 cycles at 95 °C for 45 s, 55 °C for 1 min, and 68 °C for 13 min.

2-Amino-3-(tritylsulfanyl)propionic Acid Methyl Ester (L-(trityl)-CysMe, 4). A mixture containing concentrated HCl (1.25 mL) and L-(trityl)-Cys **3** (1 g, 2.75 mmol) in 20 mL of methanol was heated to reflux for 15 h. Then the solution was diluted with water, neutralized with Na_2CO_3, and extracted with EtOAc. The organic layer was concentrated and then purified on SiO_2 (EtOAc) to afford a thick colorless oil, 560 mg (54%). ^{1}H NMR ($CDCl_3$, 400 MHz) δ 7.41−7.44 (m, 6H, ArH), 7.19−7.31 (m, 9H, ArH), 3.66 (s, 3H, OCH_3), 3.21 (br s, CH), 2.62 (m, 1H, CHS), 2.52 (m, 1H, CHS), 1.71 (br s, NH_2).

2-(2-(*tert*-Butoxycarbonylamino)acetylamino)-3-(tritylsulfanyl)propionic Acid Methyl Ester (Boc-Gly-(trityl)-CysMe, 5). A solution of L-(trityl)-CysMe **4** (377 mg, 1 mmol), *N*-(*tert*-butoxycarbonyl)glycine (210 mg, 1.2 mmol), and DCC (247 mg, 1.2 mmol) in CH_2Cl_2 (50 mL) was stirred at room temperature for 3 h. The mixture was filtered and concentrated. Chromatography on SiO_2 (EtOAc/hexanes 3:2) afforded 480 mg (90%) of a white solid. ^{1}H NMR ($CDCl_3$, 400 MHz) δ 7.39−7.36 (m, 5H, ArH), 7.31−7.20 (m, 10H, ArH), 5.01 (br s, 1H, NH), 6.38 (d, J = 7.6 Hz, 1H, NH), 4.54 (m, 1H, CH), 3.76 (m, 2H, CH_2), 3.71 (s, 3H, OCH_3), 2.66 (m, 2H, CH_2), 2.04 (s, 1H, CH), 1.48 (s, 9H, $3CH_3$). ^{13}C NMR ($CDCl_3$, 400 MHz) δ 170.8, 169.2, 144.4, 129.7, 128.2, 127.1, 67.2, 60.6, 52.9, 51.3, 33.8, 28.5. EI-MS *m*/*z* 478, 434.1, 316.1, 243, 239, 165, 101, 57. HRMS (EI) (*m*/*z*) calcd for $C_{30}H_{34}SN_2O_5$ (M^+) 534.66744; found 534.2176.

2-(2-Aminoacetylamino)-3-(tritylsulfanyl)propionic Acid Methyl Ester (Gly-(trityl)-Cys-Me, 6). A solution of Boc-Gly-(trityl)-CysMe **5** (400 mg, 0.748 mmol) in 4 mL of TFA/CH_2Cl_2 (1:1) was stirred at room temperature for 1 h. The mixture was concentrated and evaporated 3× with ether. Filtration with ether afforded 494 mg of a white solid. ^{1}H NMR (CD_3OD, 400 MHz) δ 7.38−7.20 (m, 15H, 3Ph), 3.86 (s, 2H, CH_2), 3.61 (s, 3H, OCH_3), 2.69−2.51 (m, 3H), 2.00 (4H, $2CH_2$). ^{13}C NMR (CD_3OD, 400 MHz) δ 170.8, 166, 144, 129.5, 127.9, 126.9, 110, 52.2, 51.8, 40.2, 33.2. EI-MS *m*/*z* 434, 357, 309.8, 243, 239, 165, 117.9, 68.9, 44.9. HRMS (EI) (*m*/*z*) calcd for $C_{25}H_{26}SN_2O_3$ (M^+) 434.55162; found 434.1663.

***N*-[(1-(Methoxycarbonyl)-2-(tritylsulfanyl)ethylcarbamoyl)methyl]succinamic Acid (Succ-Gly-(trityl)-CysMe, 7).** A mixture containing Gly-(trityl)-CysMe **6** (420 mg, 0.966 mmol) and succinic anhydride (146 mg, 1.45 mmol) in 25 mL of HOAc was stored at room temperature for 2 days. The mixture was concentrated under vacuum and purified on SiO_2 (EtOAc/HOAc 100:3). Pale yellow oil (414 mg, 80%) was obtained. ^{1}H NMR (CD_3OD, 400 MHz) δ 7.38−7.20 (m, 15H, 3Ph), 3.86 (s, 2H, CH_2), 3.61 (s, 3H, OCH_3), 2.69−2.51 (m, 3H), 2.00 (4H, $2CH_2$). ^{13}C NMR (CD_3OD, 400 MHz) δ 175.2, 174.0, 173.9, 171.8, 170.8, 170.4, 144.6, 129.5, 127.8, 126.8, 67.0, 60.4, 52.0, 51.7, 42.1, 33.2, 30.3, 29.0, 19.7, 19.6, 13.3. FAB-MS *m*/*z* 533, 470, 437, 356.9, 311.1, 291, 275, 239, 205, 183, 167, 113. HRMS (FAB) (*m*/*z*) calcd for $C_{29}H_{30}SN_2O_6$ $(M-1)^+$ 533.17463; found 533.17565

***N*-[(2-Mercapto-1-(methoxycarbonyl)ethylcarbamoyl)methyl]succinamic Acid (Succ-Gly-CysMe, 8).** To a solution of Succ-Gly-(trityl)-CysMe **7** (55 mg, 102.8 μmol) in 4 mL of 50% TFA/CH_2Cl_2 was added triethylsilane (66 μL, 411 μmol). The mixture was stored at room temperature overnight. After evaporation to remove solvent, the residue was purified on SiO_2 (EtOAc/MeOH 4:1) to afford 57.7 mg (71%) of Succ-Gly-CysMe **8**. ^{1}H NMR (CD_3OD, 400 MHz) δ 3.90 (s, 2H, CH_2), 3.73 (s, 3H, OCH_3), 2.67−2.50 (m, 3H), 2.00 (4H, $2CH_2$). ^{13}C NMR (CD_3OD, 400 MHz) δ 174.3, 171.9, 170.6, 60.4, 55.0, 51.8, 42.4, 30.2, 29.0, 19.7, 19.6, 13.2. EI-MS *m*/*z* 244, 207, 167, 165, 152, 115, 91, 71, 57.

***N*-{[2-(3,15-Dimethylhexadeca-2*E*,6*E*,10*E*,14-tetraenylsulfanyl)-1-(methoxycarbonyl)ethylcarbamoyl]methyl}succinamic Acid (SuccG-(gg)CMe, 1).** A solution that contained geranylgeranyl chloride (35 mg, 113 μmol), Succ-Gly-CysMe **8** (33 mg, 113 μmol), and $Zn(OAc)_2{\cdot}2H_2O$ (37 mg, 169 μmol) in 4 mL of DMF/CH_3CN/0.025% TFA (2:1:1) was stirred at 0 °C and then brought to room-temperature overnight. The mixture was concentrated and purified on SiO_2 (EtOAc/HOAc 100:3) to afford 36.7 mg (57.5%) of pale yellow oil. ^{1}H NMR (CD_3OD, 400 MHz) δ 5.20 (m, 1H), 5.12 (m, 2H), 4.64 (m, 1H), 3.90 (d, J = 2 Hz, 2H), 3.7 (s, 3H, OCH_3), 3.24 (m, 1H), 3.13 (m, 1H), 2.95 (m, 1H), 2.74 (m, 1H), 2.63 (t, J = 6.4 Hz, 2H), 2.50 (t, J = 6.4 Hz, 2H), 2.14−1.98 (m, 18H), 1.69, 1.66, 1.60, 1.59 (5s, 15H). ^{13}C NMR (CD_3OD, 400 MHz) δ 174.2, 139.5, 124.3, 120.2, 52.4, 51.7, 42.2, 39.7, 32.0, 30.3, 29.1, 26.6, 26.2, 19.6, 15.0.

***N*-{[1-Methoxycarbonyl-2-(3,7,11-trimethyl-dodeca-2*E*,6*E*,10-trienylsulfanyl)ethylcarbamoyl]methyl}-succinamic Acid (SuccG-(f)CMe, 2).** A solution containing farnesyl bromide (29 mg, 97.5 μmol), Succ-Gly-CysMe **8** (57 mg, 195 μmol), and $Zn(OAc)_2{\cdot}2H_2O$ (66 mg, 292.5 μmol) in 4 mL of DMF/CH_3CN/0.025% TFA (2:1:1) was stirred at 0 °C overnight. The mixture was condensed and purified on SiO_2 (EtOAc) to afford 56 mg (∼100%) of pale yellow oil. ^{1}H NMR (CD_3OD, 400 MHz) δ 5.21 (m,

1H), 5.11 (m, 2H), 4.62 (m, 1H), 3.90 (d, $J = 2$ Hz, 2H), 3.71 (s, 3H, OCH_3), 3.22 (m, 1H), 3.12 (m, 1H), 2.78 (m, 1H), 2.65 (t, $J = 6.8$ Hz, 2H), 2.53 (t, $J = 6.8$ Hz, 2H), 2.13−1.96 (m, 8H), 1.69, 1.66, 1.60, 1.59 (4s, 12H). ^{13}C NMR (CD_3OD, 400 MHz) δ 222.0, 163.9, 124.3, 123.9, 120.2, 72.6, 52.4, 51.8, 42.2, 39.7, 39.6, 36.0, 32.0, 30.6, 30.3, 29.0, 26.6, 26.2, 24.8, 19.6, 16.6, 15.1, 15.0. FAB-MS *m*/*z* 497.1, 416.8, 354.9, 336.9, 304.9, 69. HRMS (FAB) (*m*/*z*) calcd for $C_{25}H_{40}SN_2O_6$ $(M - 1)^+$ 495.24288; found 495.25174.

2-[2-(2,5-Dioxopyrrolidin-1-yl)acetylamino]-3-(3,7,-11,15-tetramethylhexadeca-2,6,10,14-tetraenylsulfanyl)propionic Acid Methyl Ester (Succinimide-G-(gg)CMe, 11). SuccG-(gg)-CMe **1** (36.7 mg, 65 μmol), SDPP (33 mg, 97.4 μmol), and triethylamine (37 μL, 260 μmol) were dissolved in 10 mL of CH_3CN. The mixture was stored at room temperature for 16 h and then concentrated and purified on SiO_2 (EtOAc) to afford 14.7 mg (41%) of oil. ^{1}H NMR ($CDCl_3$, 400 MHz) δ 6.52 (s, 1H), 5.19 (t, $J = 8$ Hz, 1H), 5.09 (s, $J = 6$ Hz, 2H), 4.76 (m, 1H), 4.23 (m, 2H), 3.76 (s, 3H, OCH_3), 3.2−2.97 (m, 2H), 2.97−2.78 (m, 6H), 2.09 (m, 8H), 1.98(m, 4H), 1.67, 1.65 (2s, 6H, $2CH_3$), 1.59 (s, 9H, $3CH_3$). ^{13}C NMR ($CDCl_3$, 400 MHz) δ 176.4, 170.9, 169.1, 168.2, 165.5, 165.2, 140.2, 135.4, 134.9, 131.2, 126.1, 124.4, 124.2, 123.7, 120.3, 119.4, 52.7, 52.0, 41.1, 39.7, 39.6, 33.2, 30.0, 28.2, 26.7, 26.6, 26.4, 25.7, 25.6, 25.3, 17.7, 17.5, 16.1, 16.0.

2-[2-(2,5-Dioxopyrrolidin-1-yl)acetylamino]-3-(3,7,-11-trimethyldodeca-2,6,10-trienylsulfanyl)propionic Acid Methyl Ester (Succinimide-G-(f)CMe, 12). SuccG-(f)-CMe **2** (47 mg, 94.6 μmol), SDPP (47.7 mg, 142 μmol), and triethylamine (53 μL, 378 μmol) were dissolved in 10 mL of CH_3CN. The mixture was stored at room temperature for 4 h and then concentrated and purified on SiO_2 to afford 10 mg (22%) of a colorless oil. ^{1}H NMR ($CDCl_3$, 400 MHz) δ 5.19 (t, $J = 8.4$ Hz, 1H), 5.09 (t, $J = 6$ Hz, 2H), 4.77 (m, 1H), 4.23 (m, 2H), 3.77 (s, 3H, OCH_3), 3.2−3.0 (m, 2H), 2.98−2.86 (m, 2H), 2.80 (s, 4H, $2CH_2$), 2.10−1.95 (m, 8H), 1.68, 1.66, 1.60, 1.54 (4s, 12H, $4CH_3$). ^{13}C NMR ($CDCl_3$, 400 MHz) δ 184.4, 176.7, 171.1, 165.4, 140.4, 135.6, 131.5, 130.0, 126.3, 124.5, 123.9, 120.5, 120.4, 119.6, 60.6, 52.9, 52.3, 41.3, 39.9, 39.8, 33.5, 30.3, 28.4, 26.9, 26.4, 25.9, 25.5, 17.9, 16.3, 16.2.

***N*-(2-Methoxyethyl)succinamic Acid (13).** A solution containing 2-methoxyethylamine (100 mg, 1.33 mmol) and succinic anhydride (134 mg, 1.33 mmol) in HOAc (2 mL) was stored at room temperature overnight. The solvent was evaporated, and the residue was recrystallized in EtOAc to afford needles, 185 mg (79%). ^{1}H NMR ($CDCl_3$, 400 MHz) δ 6.18 (br s, NH), 3.46 (m, 4H), 3.36 (s, 3H), 2.70 (m, 2H), 2.53 (m, 2H).

1-(2-Methoxyethyl)pyrrolidine-2,5-dione (14). To a solution of acid **13** (5 mg, 28.5 μmol) in 0.5 mL of CH_3CN were added SDPP (14.2 mg, 28.5 μmol) and triethylamine (16 μL). The reaction was allowed to proceed overnight, and the residue was purified on SiO_2 (EtOAc) to give 2 mg of succinimide. ^{1}H NMR ($CDCl_3$, 400 MHz) δ 3.74 (m, 2H), 3.56 (m, 2H), 3.32 (s, 3H), 2.72 (s, 4H).

2-Amino-3-(3,7,11-trimethyldodeca-2,6,10-trienylsulfanyl)propionic Acid Methyl Ester (Farnesyl-CysMe, 20). A solution containing farnesyl bromide (30 mg, 105 μmol), L-cysteine methyl ester hydrochloride (36 mg, 210 μmol), and $Zn(OAc)_2 2H_2O$ (71.4 mg, 315 μmol) in 6 mL of DMF/CH_3CN/ 0.025%TFA (2:1:1) was stirred at 0 °C for 2 h. The mixture was concentrated and purified on SiO_2 (EtOAc) to afford 57.8 mg (91.6%) of pale yellow oil. ^{1}H NMR (CD_3OD, 400 MHz) δ 5.24 (t, $J = 7.2$ Hz, 1H), 5.13 (m, 2H), 3.78 (s, 3H, OCH_3), 3.16 (m, 1H), 3.03 (m, 1H) 2.82 (m, 1H), 2.16−2.04 (m, 8H), 1.96 (m, 2H), 1.70 (m, 3H), 1.66 (s, 3H), 1.61 (s, 3H), 1.59 (s, 3H). ^{13}C NMR (CD_3OD, 400 MHz) δ 172.8, 141.1, 135.6, 131.5, 124.5, 123.9, 119.1, 53.6, 53.4, 39.9, 34.3, 29.6, 26.9, 26.7, 25.9, 17.9, 16.6, 16.2, 14.3.

2-(Acetylamino)-3-(hexadecanoylsulfanyl)propionic Acid (Palm-AcCysOH, 21). A mixture containing *N*-acetylcysteine (16.3 mg, 0.1 mmol), palmitoyl chloride (36.4 μL, 0.12 mmol), and DIEA (52 μL, 0.3 mmol) in 1 mL of DMF was stirred at room temperature overnight. The product was purified with silica gel (EtOAc/HOAc 100:2) to afforded 8.88 mg (21.4%) of Palm-AcCysOH. ^{1}H NMR ($CDCl_3$, 400 MHz) δ 7.20 (s, 1H), 6.72 (m, 1H), 4.62 (m, 1H), 4.14 (m, 2H), 3.37 (m, 1H), 2.85 (s, 2H), 2.05 (s, 3H), 1.90−1.30 (m, 30H).

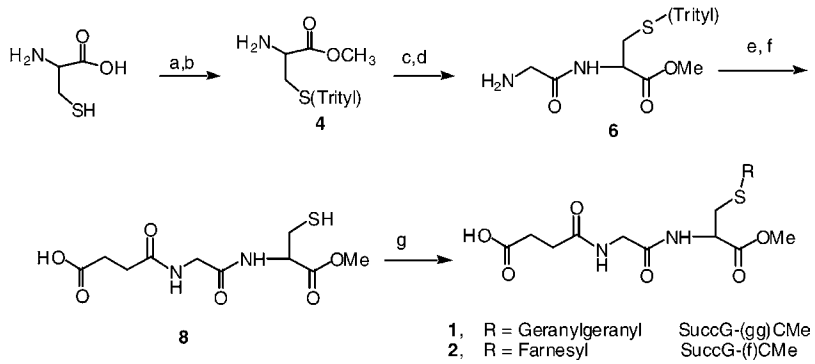
Coupling of SuccG-(gg)-CMe 1, SuccG-(f)-CMe 2, (gg)-CysMe 19, (f)-CysMe 20, Palm-AcCysOH 21, and Myr-GlyOH to BSA with EDCI. To a solution of haptens (1.2 μmol, 33 equiv to BSA) and BSA (0.36 μmol) in 30% DMSO buffer (10 mM NaH_2PO_4, 200 mM NaCl, pH 7.2) was added EDCI (4.5 mg, 23.4 μmol). The mixture was stirred at room temperature for 2 h and then purified (Sephadex G-25) by elution with 10 mM NaH_2PO_4, 200 mM NaCl, pH 7.2. Sample concentrations were measured using the Bradford reagent.

Coupling of SuccG-(gg)-CMe 1, SuccG-(f)-CMe 2 to KLH with EDCI. To a solution containing prenylated peptides **1** and **2** (0.8 μmol, 833 eq. to KLH) and KLH (0.96 μmol) in 30% DMSO buffer (31 mM NaH_2PO_4, 0.96 M NaCl, pH 7.4) was added EDCI (2 mg, 10.4 μmol). The mixture was stirred at room temperature for 2 h and then purified (Sephadex G-25) by elution with with 10 mM NaH_2PO_4, 200 mM NaCl, pH 7.2. Sample concentrations were measured using the Bradford reagent.

ELISA. A Maxisorp plate (Nunc) was washed twice with PBS 200 μL/well and then coated with BSA−SuccG-(gg/f)CMe 1 μg/well in the amount of 50 μL and incubated at room temperature for 1 h. The plate was rinsed 3× with 100 μL/well of PBS. Blocking solution (100 μL/well, 5% BSA/TBST) was added, and the plate was shaken for 1 h at room temperature. Blocking solution was removed, and the plate was washed 3× with 100 μL/well of TBST. Next, 50 μL/well of primary antibody (1:300) was added to the plate and shaken at room temperature for 1 h. The plate was washed 4× with 100 μL/well of TBST. Then 50 μL/well of anti-rabbit IgG-HRP at 1:2000 in TBST was applied and shaken for 1 h at room temperature. Antibodies were removed and washed 4× with 100 μL/well of TBST; TMB (Sigma) was added (100 μL/well). The plate was placed in a dark drawer for 15−20 min as the blue color developed. The reaction was stopped with 50 μL/well of 0.5 M H_2SO_4 to yield a yellow color. Absorbance at 430 nm was measured by a UV spectrometer.

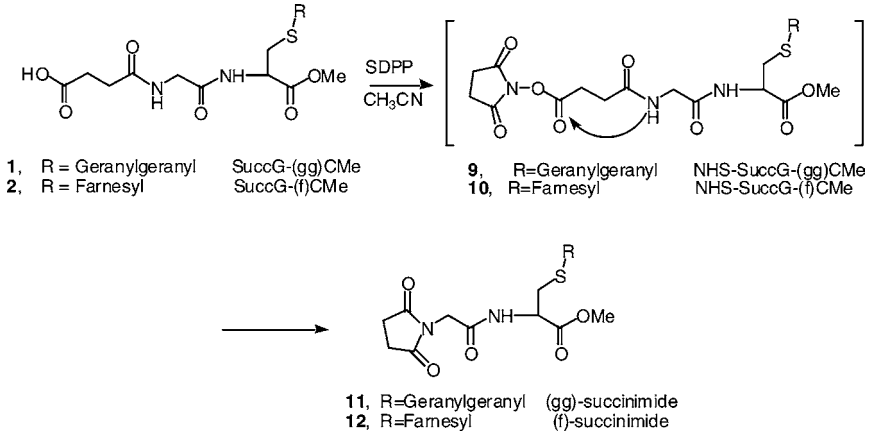
CHO-K1 Cell Culture and Transfection. CHO-K1 epithelial cells (1×10^5) were seeded in a 6-well plate and incubated at 37 °C for 19 h to reach 30% confluence. Vector EYFP-CVLL (6 μg) was dissolved in 60 μL of serum-free medium. Lipofectamine (30 μL) was dissolved into 180 μL of serum-free medium, mixed at room temperature for 30 min, and then diluted with 1.6 mL of serum-free medium. Cells were treated with 1 mL of this mixture after aspiration of the original medium. The transfection continued for 6 h at 37 °C and was stopped by addition of medium containing G418 (0.5 mg/mL). The transfected cells were visualized by fluorescence microscopy. In the blank cell cultures, most cells were killed with G 418 antibiotic by day 9. Cell colonies could be seen in the Petri dishes.

Scheme 1. Synthesis of Farnesylated and Geranylgeranylated Cysteine Haptens[a]



[a] Reagents and conditions: (a) $(Ph)_3COH$, TFA, 75%; (b) concentrated HCl, MeOH, 54%; (c) *N*-Boc-glycine, DCC, CH_2Cl_2, 90%; (d) TFA/CH_2Cl_2; 100%; (e) succinic anhydride, HOAc, 80%; (f) $(Et)_3SiH$, TFA/CH_2Cl_2; 71%; (g) farnesyl bromide or geranylgeranyl chloride, $Zn(OAc)_2 \cdot 2H_2O$, $DMF/CH_3CN/TFA$.

Scheme 2. Side Product Succinimides 11 and 12 in the Attempted Synthesis of NHS Esters 9 and 10



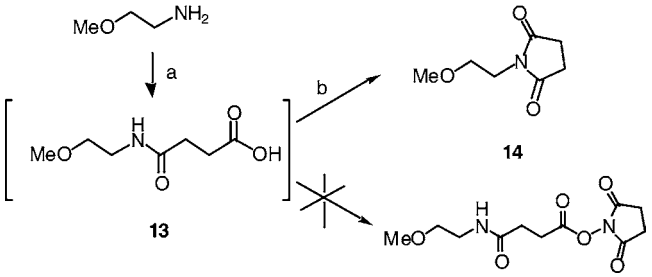
Purification of Anti-gg/f from Rabbit Sera with Positive Immunoaffinity Chromatography. Rabbit antisera (1 mL, 26.7 mg/mL, serum-15, immunized with KLH−SuccG-(gg)CMe **15**) was diluted in 4 mL of NaOAc (60 mM, pH 4.0). Caprilic acid (125 μL) was added dropwise, and the mixture was stirred gently at room temperature for 30 min. The mixture was centrifuged to remove precipitate at 10 000 × *g* at room temperature for 30 min. The supernatant was dialyzed against 20 mM Tris-Cl (pH 7.5) overnight (protein concentration was 1.01 mg/mL, total 6.5 mg). Affigel-10 (Bio-Rad, 0.3 mL) was mixed with 0.5 mL of BSA−(gg)CMe **22** (0.54 mg/mL) or BSA−(f)CMe **23** (0.79 mg/mL) and incubated at 4 °C overnight. The Affigel beads were centrifuged at 5000 × *g*. The beads were washed twice with 0.4 mL of 10 mM Na_3PO_4/200 mM NaCl (pH 7.0) and then incubated with 0.2 mL of 7 M urea/1 M NaCl at room temperature for 1 h. The beads were further washed 3× with 0.4 mL of 10 mM Na_3PO_4/200 mM NaCl (pH 7.0) and then once with 0.4 mL of 0.2 M glycine, pH 7.2. Next, the beads were washed 3× with 0.4 mL of 10 mM Na_3PO_4/200 mM NaCl (pH 7.0) and then incubated with 0.4 mL of pretreated antibody solution at room temperature for 1 h. The beads were washed 3× with 0.4 mL of 10 mM Na_3PO_4/200 mM NaCl (pH 7.0). The beads were transferred to a column and eluted with 0.2 M glycine buffer (pH 2.0), and 150 μL of each fraction was collected into 150 μL of 2 M Tris-Cl, pH 8.8. The diluted antibodies were dialyzed against PBS and concentrated to about 1 mg/mL by ultrafiltration.

Fluorescence Imaging of CHO-K1 and EYFP-CVLL CHO-K1 Cells with Rabbit Antiserum. Cells were seeded on cover slips for 10 h to reach ~30% confluence. The localization of EYFP was visualized by fluorescence microscopy. The medium was aspirated, and then cells were washed with 2 × 1 mL of PBS. The cells were fixed with 4% paraformaldehyde for 10 min at room temperature. The cells were washed with 2 × 1 mL of PBS and permeabilized by addition of 0.8 mL of 0.2% Triton X-100 in PBS for 5 min at room temperature. The cells were washed with 3 × 1 mL of 0.2% Triton X-100 in PBS. The cover slips were blocked with 3% BSA/0.2% Triton X-100 in PBS 25 μL/each for 0.5 h. After adding serum-15 (1:150, 25 μL, 3% BSA/0.2% Triton X-100 in PBS), incubation continued for 1 h. The cells were washed with 3 × 1 mL of 0.2% Triton X-100 in PBS, 5 min/each and then incubated with 25 μL of anti-rabbit IgG-Texas Red (1:500, 3% BSA/0.2% Triton X-100 in PBS) for 1 h. Next, the cells were washed with 3 × 1 mL of 0.2% Triton X-100 in PBS, 5 min/each, followed by dehydration with 2 × 1 mL of ethanol, and 10 mL of xylene. Cover slips were mounted on glass slides.

RESULTS AND DISCUSSION

The haptens for coupling to BSA or KLH were synthesized from L-cysteine (Scheme 1). The free thiol of L-cysteine was protected with triphenylmethanol, and the S-protected cysteine was then converted to the methyl ester and coupled to *N*-Boc glycine (*29*, *30*). Subsequent removal of the Boc group afforded dipepetide **6**, which was converted to compound **8** by reaction with succinic anhydride, followed by deprotection of the trityl group (*31*, *32*). Compound **8** is a common intermediate used to synthesize the desired farnesylated and geranylgeranylated haptens SuccG-(gg)CMe **1** and SuccG-(f)CMe **2** (*33*).

Scheme 3. Model Reaction To Form Succinimide[a]



[a] Reagents and conditions: (a) Succinic anhydride, HOAc, 79%; (b) SDPP, CH_3CN.

Table 1. Haptens, Carrier Proteins, and Immunogens for Preparation and Characterization of Anti-Isoprenyl Antibodies

haptens	carrier	conjugates
SuccG-(gg)CMe **1**	KLH	KLH−SuccG-(gg)CMe **15**
SuccG-(f)CMe **2**	KLH	KLH−SuccG-(f)CMe **16**
SuccG-(gg)CMe **1**	BSA	BSA−SuccG-(gg)CMe **17**
SuccG-(f)CMe **2**	BSA	BSA−SuccG-(f)CMe **18**
(gg)-CMe **19**	BSA	BSA−(gg)CMe **22**
(f)-CMe **20**	BSA	BSA−(f)CMe **23**
Palm-AcCys **21**	BSA	BSA−Palm-AcCys **24**
Myr-Gly	BSA	BSA−Myr-Gly **25**

Originally, we planned on using the *N*-hydroxysuccimidyl (NHS) esters **9** and **10** of compounds **1** and **2** as active haptens ready for coupling to BSA or KLH (Scheme 2). Pure products were obtained when **1** and **2** were treated with SDPP in CH_3CN (*34*). However, immunization of chickens with their BSA or KLH conjugates did not produce any anti-isoprenyl reactivity in the IgY fractions. After careful examination of the chemistry of the immunogen preparation, we discovered an unexpected side reaction. When SDPP is added to SuccG-(gg)CMe **1** or SuccG-(f)CMe **2**, the NHS esters **9** and **10**, respectively, appear to form as unstable intermediates that rapidly undergo intramolecular cyclization to the more stable succinimide side products **11** and **12**. To confirm this hypothesis, a model reaction using methoxyethylamine was conducted, and 1-(2-methoxyethyl)-pyrrolidine-2,5-dione **14** was isolated as the main product (Scheme 3).

Successful preparation of immunogens was achieved by conjugation of SuccG-(gg)CMe **1** or SuccG-(f)CMe **2** to BSA and KLH using EDCI (Table 1) (*35*). The reactions were complete in 2 h as determined by TLC. Longer reaction times resulted in the formation of the succinimide byproducts. Four immunogens, KLH−SuccG-(gg)-CMe **15**, KLH−SuccG-(f)CMe **16**, BSA−SuccG-(gg)CMe **17**, and BSA−SuccG-(f)CMe **18** were obtained and then used to immunize both rabbits and mice. Six weeks later the animals were bled and sacrificed to collect antisera.

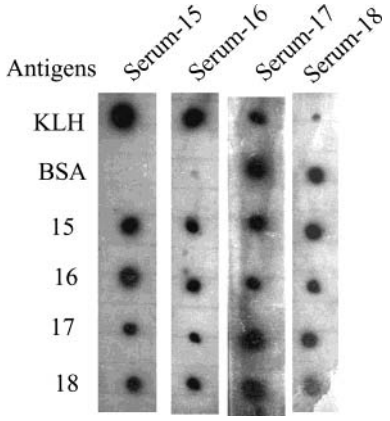


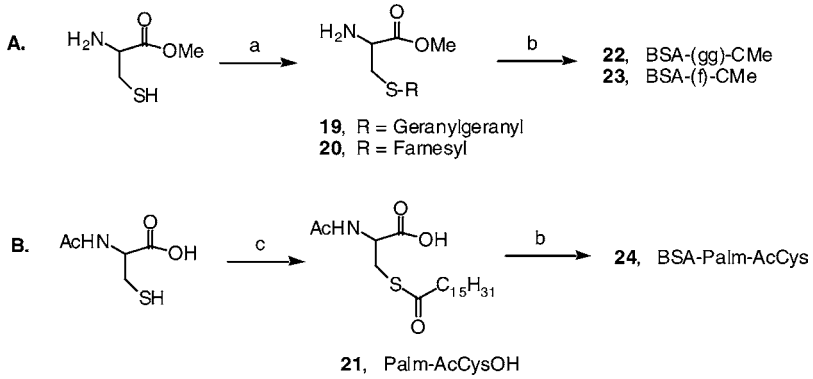
Figure 1. Dot blotting of antisera from rabbits; dilution 1:500.

Rabbit and mouse antisera containing polyclonal antibodies were checked with dot blotting. Figure 1 shows that the rabbit antisera contained antibodies against all four immunogens (**15**, **16**, **17**, **18**). None of the mouse-derived antisera contained sufficiently high titers of either anti-farnesyl or antigeranylgeranyl antibodies to allow us to proceed further with fusion and cloning (data not shown). Antisera from rabbits immunized with KLH−SuccG-(gg)CMe **15** (designated serum-15) or KLH−SuccG-(f)CMe **16** (serum-16) had the same patterns and did not recognize unmodified BSA. In contrast, antisera from rabbits immunized with BSA−SuccG-(gg)CMe **17** (serum-17) and BSA−SuccG-(f)CMe **18** (serum-18) were similar and showed a cross reaction with KLH. We thus selected serum-15 as the starting material for subsequent studies using BSA conjugates.

To determine whether serum-15 could recognize (gg)-CMe and (f)CMe epitopes, two additional immunogens, BSA−(gg)-CMe **22** and BSA−(f)-CMe **23**, were synthesized from geranygeranylated or farnesylated cysteine methyl esters **19** and **20** (Scheme 4A) (*36*). ELISA on Maxisorp plate (Figure 2) further showed that serum-15 recognized both farnesylated and geranylgeranylated immunogens (**17**, **18**, **22**, **23**) and that the selectivity was low.

We also asked whether, given the lack of selectivity between the farnesyl and geranylgeranyl groups, the serum-15 antibodies could distinguish prenylation from simple fatty acid modifications such as *S*-palmitoylation and *N*-terminal myristoylation. To test this hypothesis, first, we synthesized BSA−Palm-AcCys **24** and BSA−

Scheme 4. Synthesis of Immunogens for Characterization of Polyclonal Antibodies[a]



[a] Reagents and conditions: (a) farnesyl bromide or geranylgeranyl chloride, $Zn(OAc)_2 \cdot 2H_2O$, DMF/CH_3CN/TFA; (b) EDCI; (c) palmitoyl chloride, Et_3N, 21%.

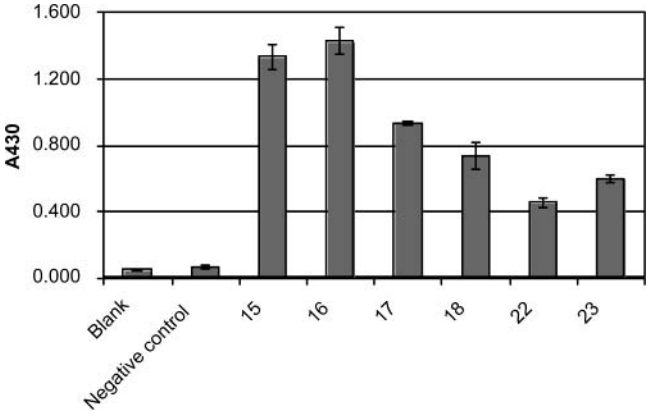


Figure 2. ELISA of rabbit serum-15 on Maxisorp plate. Immunogens (1 μg/well) were added to 96-well plate. In the negative control, no antiserum was added. See text for experiment details.

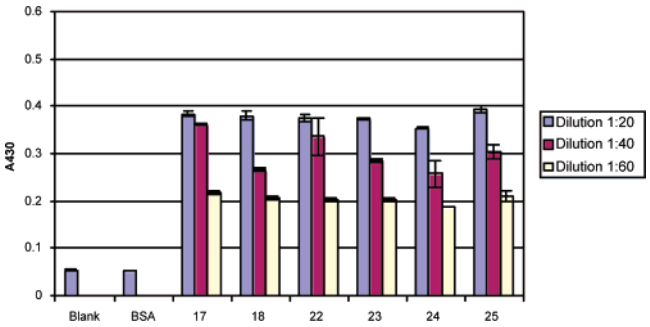


Figure 3. ELISA of BSA conjugates (**17**, **18**, **22**, **23**, **24**, and **25**) using immunoaffinity purified anti-gg antisera in a series of concentration (anti-f antisera gave similar results). Aliquots (1 μg) of BSA and BSA conjugates were added into each well on 96-well plate.

Myr-Gly **25** (Scheme 4B and Table 1). Second, we attempted to obtain selective polyclonal anti-gg or anti-f antibodies from serum-15 by positive immunoaffinity chromatography. Thus, BSA−SuccG-(gg)CMe (**17**) or BSA−SuccG-(f)CMe (**18**) was coupled to Affigel-10, and these resins were then incubated with pretreated serum-15 to bind the desired specific antibodies. After washing the resin beads with sodium phosphate buffer, followed by elution with glycine buffer, pH 2.0, putative anti-gg- or anti-f-containing fractions were collected in Tris-Cl buffer (2 M, pH 8.8). To our surprise, both the anti-gg and the anti-f fractions showed strong cross-reactivity with these aliphatic modifications as well (Figure 3).

It is apparent that rabbit polyclonal antibodies poorly distinguish aliphatic-modified peptides. One future opportunity will be exploring the use of these antibodies as "universal" detectors of lipidated proteins in cells for a proteomic approach to identify differentially expressed lipidated proteins in cells (*37*−*40*).

To address whether serum-15 could be used to stain isoprenylated proteins in cells, we transfected CHO-K1 cells with EYFP-CVLL (*41*−*43*), a fluorescent protein with a C-terminal CAAX sequence for geranylgeranylation. In the G1 phase of the cell cycle, tranasfected cells overexpressed and geranylgeranylated EYFP-CVLL, thus facilitiating movement of the EYFP transport to cell plasma membrane (Figure 4A). When the cells were fixed and treated with serum-15 followed by anti-rabbit IgG-Texas Red, red fluorescence was observed, which indicated colocalization with EYFP in the cell plasma membrane (Figure 4B). As a control, staining of native CHO-K1 cells with the same protocols gave dim red fluorescence in cytosol (Figure 4C). When the cells were treated with lovastatin, which blocks HMG CoA reductase and thus stops the production of FPP and GGPP, EYFP-CVLL could not be geranylgeranylated and thus remained localized in cytosol (Figure 4D) (*44*−*48*). Only dim red fluorescence could be observed in transfected and native CHO-K1 cells (Figure 4E, 4F). Taken together, these results demonstrate that serum-15 could be used to visualize overexpressed isoprenylated proteins in cells. The background fluorescence can be attributed either to nonspecific binding or to low-abundance of naturally occurring prenylated proteins.

In summary, the synthetic immunogens KLH−SuccG-(gg)CMe (**15**), KLH−SuccG-(f)CMe (**16**), BSA−SuccG-(gg)CMe (**17**), and BSA−SuccG-(f)CMe (**18**) stimulated strong immune responses in rabbits, affording antisera containing high titers of polyclonal anti-lipid antibodies. The lack of selectivity of these antisera suggest that distinguishing among specific lipidated proteins in cells would not be feasible. However, the antisera can visualize overexpressed isoprenylated cell proteins localized to the cell membrane, suggesting that perhaps a more universal

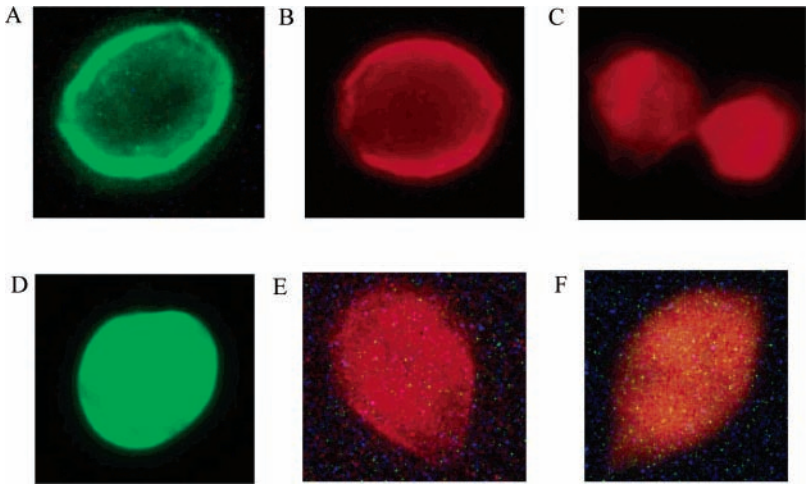


Figure 4. Immunofluorescence of EYFP-CVLL CHO-K1 cells and native CHO-K1 cells. Panel A: EYFP-CVLL cell, 10 h after seeding; Panel B: EYFP-CVLL cells stained with serum-15 (1:150), 10 h after seeding; Panel C: Native CHO-K1 cells stained with serum-15 (1:150), 10 h after seeding; Panel D: EYFP-CVLL cells was treated with 20 μM lovastatin for 24 h; Panel E: EYFP-CVLL cells were treated with 20 μM lovastatin for 24 h and then stained with serum-15 1:150; Panel F: Native CHO-K1 cells were treated with 20 μM lovastatin for 24 h and then stained with serum-15 (1:150).

tool for identification of electrophoretically separated lipidated proteins could be developed (*37*−*40*).

ACKNOWLEDGMENT

Vector pcDNA3.1 encoding EYFP-CVIM was the generous gift provided by Dr. Tamas Balla (Endocrinology and Reproduction Research Branch, National Institutes of Health). Mr. Hyo-Young Chung helped to prepare EYFP-CVLL vectors. This work was supported by the Center for Cell Signaling and NIH grant GM 44836 to G.D.P.

LITERATURE CITED

(1) Delves, P. J. (1997) *Antibody Production*. Essential techniques series (Rickwood, D., Ed.) VII vols., John Wiley & Sons, Oxford.

(2) Harlow, E., and Lane, D. (1999) *Using Antibodies − A Laboratory Manual*. 11 vols., Cold Spring Harbor Laboratory Press, Woodbury, NY.

(3) Lafont, V., Liautard, J., Sable-Teychene, M., Sainte-Marie, Y., and Favero, J. (2001) Isopentenyl pyrophosphate, a mycobacterial nonpeptidic antigen, triggers delayed and highly sustained signaling in human gamma delta T lymphocytes without inducing down-modulation of T cell antigen receptor. *J. Biol. Chem. 276*, 15961−15967.

(4) Allison, T., Winter, C., Fournie, J., Bonneville, M., and Garboczi, D. (2001) Structure of a human gamma delta T-cell antigen receptor. *Nature 411*, 820−824.

(5) Steele, C., Oppenheim, D., and Hayday, A. (2000) Gamma (delta) T cells: Nonclassical ligands for nonclassical cells. *Curr. Biol. 10*, R282−285.

(6) Morita, C., Lee, H., Leslie, D., Tanaka, Y., Bukowski, J., and Marker-Hermann, E. (1999) Recognition of nonpeptide prenyl pyrophosphate antigens by human gamma delta T cells. *Microbes Infect. 1*, 175−186.

(7) Bukowski, J., Morita, C., and Brenner, M. (1999) Human gamma delta T cells recognize alkylamines derived from microbes, edible plants, and tea: Implications for innate immunity. *Immunity 11*, 57−65.

(8) Belmant, C., Espinosa, E., Halary, F., Apostolou, I., Sicard, H., Peyrat, M., Vercellone, A., Kourilsky, P., Gachelin, G., Poupot, R., Bonneville, M., and Fournie, J. (1999) Conventional and nonconventional recognition of non-peptide antigens by T lymphocytes. *C. R. Acad. Sci. III 322*, 919−924.

(9) Tanaka, Y., Sano, S., Nieves, E., De Libero, G., Rosa, D., Modlin, R., Brenner, M., Bloom, B., and Morita, C. (1994) Nonpeptide ligands for human gamma delta T cells. *Proc. Natl. Acad. Sci. U.S.A. 91*, 8175−8179.

(10) Yokota, S., Ohtsuka, H., Kohzuki, T., and Noguchi, H. (1996) A polyreactive human anti-lipid A monoclonal antibody having cross reactivity to polysaccharide portions of *Pseudomonas aeruginosa* lipopolysaccharides. *FEMS Immunol. Med. Microbiol. 14*, 31−38.

(11) Helmerhorst, E., Maaskant, J., and Appelmelk, B. (1998) Anti-lipid A monoclonal antibody Centoxin (HA-1A) binds to a wide variety of hydrophobic ligands. *Infect. Immun. 66*, 870−873.

(12) Alarcon-Segovia, D., and Cabral, A. (1996) The antiphospholipid/cofactor syndromes. *J. Rheumatol. 238*, 1319−1321.

(13) McNeil, H., Chesterman, C., and Krilis, S. (1991) Immunology and clinical importance of antiphospholipid antibodies. *Adv. Immunol. 49*, 193−280.

(14) Umeda, M., Igarashi, K., Nam, K., and Inoue, K. (1989) Efffective production of monoclonal antibodies against phosphatidylserine: Stereospecific recognition of phosphatidylserine by monoclonal antibody. *J. Immunol. 143*, 2273−2279.

(15) Diaz, C., Balasubramanian, K., and Schroit, A. (1998) Synthesis of disulfide-containing phospholipid analogues for the preparation of headgroup-specific lipid antigens: generation of phosphatidylserine antibodies. *Bioconjugate Chem. 9*, 250−254.

(16) Katsuragawa, H., Rote, N., Inoue, T., Narukawa, S., Kanzaki, H., and Mori, T. (1995) Monoclonal anti-PS antibody reactivity against human first-trimester placental trophoblasts. *J. Obstet. Gynecol. 172*, 1592−1597.

(17) Maneta-Peyret, L., Bessoule, J., Geffard, M., and Cassagne, C. (1988) Demonstration of high specificity antibodies against phosphatidylserine. *J. Immunol. Methods 108*, 123−127.

(18) Thomas, C., Steel, J., Prestwich, G., and Schiavo, G. (1999) Generation of phosphatidylinositol-specific antibodies and their characterization. *Biochem. Soc. Trans. 27*, 648−652.

(19) Chen, R., Kang, V., Chen, J., Shope, J., Torabine, J. J., DeWald, D., and Prestwich, G. (2002) A monoclonal antibody to visualize PtdIns(3,4,5)P(3) in cells. *J. Histochem. Cytochem. 50*, 697−708.

(20) Prestwich, G. D., Chen, R., Feng, L., Ozaki, S., Ferguson, C. G., Drees, B. E., Neklason, D. W., Mostert, M. J., Porter-Gill, P. A., Kang, V. H., Shope, J. C., Neilsen, P. O., and DeWald, D. B. (2002) In situ detection of phospholipid and phosphoinositide metabolism. *Adv. Enzyme Regul. 42*, 19−38.

(21) Sinensky, M. (2000) Functional aspects of polyisoprenoid protein substituents: Roles in protein−protein interaction and trafficking. *Biochim. Biophys. Acta 1529*, 203−209.

(22) Sinensky, M. (2000) Recent advances in the study of prenylated proteins. *Biochim. Biophys. Acta 1484*, 93−106.

(23) Zhang, F., and Casey, P. (1996) Protein prenylation: molecular mechanisms and functional consequences. *Annu. Rev. Biochem. 65*, 241−269.

(24) Ridley, A. (2001) Rho family proteins: coordinating cell responses. *Trends Cell Biol. 11*, 471−477.

(25) Ridley, A. (2001) Rho GTPases and cell migration. *J. Cell Sci. 114*, 2713−2722.

(26) Ridley, A. (2001) Rho proteins: linking signaling with membrane trafficking. *Traffic 2*, 303−310.

(27) Lin, H., Hsu, S., Wu, J., Sheen, I., Yan, B., and Syu, W. (1999) Localization of isoprenylated antigen of hepatitis delta virus by anti-farnesyl antibodies. *J. Gen. Virol. 80*, 91−96.

(28) Baron, R., Fourcade, E., Lajoie-Mazenc, I., Allal, C., Couderc, B., Barbaras, R., Favre, G., Faye, J., and Pradines, A. (2000) RhoB prenylation is driven by the three carboxyl-terminal amino acids of the protein: evidenced in vivo by an anti-farnesyl cysteine antibody. *Proc. Natl. Acad. Sci. U.S.A. 97*, 11626−11631.

(29) Wolfe, S., and Jokinen, M. G. (1979) Total synthesis of δ-(L-α-aminoadipyl)-L-cysteinyl-D-valine (ACV), a biosynthetic precursor of penicillins and cephalosporins. *Can. J. Chem. 57*, 1388−1396.

(30) Joseph, J. T., Elmore, J. D., and Wong, J. L. (1990) Comparative sulfhydryl reaction pathways of chlorooxirane and chloroacetaldehyde. *J. Org. Chem. 55*, 471−474.

(31) Boeckler, C., Frisch, B., and Schuber, F. (1998) Design and synthesis of thiol-reactive lipopeptides. *Bioorg. Med. Chem. Lett. 8*, 2055−2058.

(32) Pearson, D. A., Blanchette, M., Baker, M. L., and Guindon, C. A. (1989) Trialkylsilanes as scavengers for the trifluoroacetic acid deblocking of protecting groups in peptide synthesis. *Tetrahedron Lett. 30*, 2739−2742.

(33) Xue, C. B., Becker, J. M., and Naider, F. (1992) Efficient regioselective isoprenylation of peptides in acidic aqueous solution using zinc acetate as catalyst. *Tetrahedron Lett. 33*, 1435−1438.

(34) Luo, Y., and Prestwich, G. D. (1999) Synthesis and selective cytotoxicity of a hyaluronic acid−antitumor bioconjugate. *Bioconjugate Chem. 10*, 755−763.

(35) Hermanson, G. T. (1996) *Bioconjugate Techniques*, Academic Press, San Diego.

(36) Liu, X., and Prestwich, G. (2002) Didehydrogeranylgeranyl (ΔΔGG): A fluorescent probe for protein prenylation. *J. Am. Chem. Soc. 124*, 20−21.

(37) Alban, A., David, S., Bjorkesten, L., Andersson, C., Sloge, E., Lewis, S., and Currie, I. (2003) A novel experimental design for comparative two-dimensional gel analysis: Two-dimensional difference gel electrophoresis incorporating a pooled internal standard. *Proteomics 3*, 36−44.

(38) Von, E. F., Gawriljuk, A., Fiedler, W., Ernst, G., Claussen, U., Klose, J., and Romer, I. (2001) Fluorescent dual colour 2D-protein gel electrophoresis for rapid detection of differ-

ences in protein pattern with standard image analysis software. *Int. J. Mol. Med. 8*, 373−377.
(39) Yan, J., Devenish, A., Wait, R., Stone, T., Lewis, S., and Fowler, S. (2002) Fluorescence two-dimensional difference gel electrophoresis and mass spectrometry based proteomic analysis of *Escherichia coli*. *Proteomics 2*, 1682−1698.
(40) Nishihara, J., and Champion, K. (2002) Quantitative evaluation of proteins in one- and two-dimensional polyacrylamide gels using a fluorescent stain. *Electrophoresis 23*, 2203−2215.
(41) Choy, E., Chiu, V., Silletti, J., Feoktistov, M., Morimoto, T., Michaelson, D., Ivanov, I., and Philips, M. (1999) Endomembrane trafficking of ras: The CAAX motif targets proteins to the ER and Golgi. *Cell 98*, 69−80.
(42) Apolloni, A., Prior, I., Lindsay, M., Parton, R., and Hancock, J. (2000) H-ras but not K-ras traffics to the plasma membrane through the exocytic pathway. *Mol. Cell Biol. 20*, 2475−2487.
(43) Michaelson, D., Silletti, J., Murphy, G., D'Eustachio, P., Rush, M., and Philips, M. (2001) Differential localization of Rho GTPases in live cells: Regulation by hypervariable regions and RhoGDI binding. *J. Cell Biol. 152*, 111−126.
(44) Jones, K., Couldwell, W., Hinton, D., Su, Y., He, S., Anker, L., and Law, R. (1994) Lovastatin induces growth inhibition and apoptosis in human malignant glioma cells. *Biochem. Biophys. Res. Commun. 205*, 1681−1687.
(45) Keyomarsi, K., Sandoval, L., Band, V., and Pardee, A. (1991) Synchronization of tumor and normal cells from G1 to multiple cell cycles by lovastatin. *Cancer Res. 51*, 3602−3609.
(46) Wu, J., and Gilbert, D. (2000) Lovastatin arrests CHO cells between the origin decision point and the restriction point. *FEBS Lett. 484*, 108−112.
(47) Jakobisiak, M., Bruno, S., Skierski, J., and Darzynkiewicz, Z. (1991) Cell cycle-specific effects of lovastatin. *Proc. Natl. Acad. Sci. U.S.A. 88*, 3628−3632.
(48) Martinez-Botas, J., Ferruelo, A., Suarez, Y., Fernandez, C., Gomez-Coronado, D., and Lasuncion, M. (2001) Dose-dependent effects of lovastatin on cell cycle progression. Distinct requirement of cholesterol and nonsterol mevalonate derivatives. *Biochim. Biophys. Acta 1532*, 185−194.

BC0342027

Dimers of D-*myo*-Inositol 1,4,5-Trisphosphate: Design, Synthesis, and Interaction with Ins(1,4,5)P_3 Receptors

Andrew M. Riley,[†] Alex J. Laude,[‡] Colin W. Taylor,[‡] and Barry V. L. Potter*[,†]

Wolfson Laboratory of Medicinal Chemistry, Department of Pharmacy and Pharmacology, University of Bath, Claverton Down, Bath BA2 7AY, UK, and Department of Pharmacology, Tennis Court Road, University of Cambridge, CB2 1PD, UK. Received November 18, 2003; Revised Manuscript Received January 23, 2004

The design and synthesis of dimeric versions of the intracellular signaling molecule D-*myo*-inositol 1,4,5-trisphosphate [Ins(1,4,5)P_3] are reported. Ins(1,4,5)P_3 dimers in a range of sizes were constructed by conjugation of a partially protected 2-*O*-(2-aminoethyl)-Ins(1,4,5)P_3 intermediate with activated oligo- and poly(ethylene glycol) (PEG) tethers, to give benzyl-protected dimers with amide or carbamate linkages. After deprotection, the resulting water-soluble Ins(1,4,5)P_3 dimers were purified by ion-exchange chromatography. The interaction of the Ins(1,4,5)P_3 dimers with tetrameric Ins(1,4,5)P_3 receptors was explored, using equilibrium [^{3}H]Ins(1,4,5)P_3-binding to membranes from cerebellum, and $^{45}Ca^{2+}$-release from permeabilized hepatocytes. The results showed that dimers, even when they incorporate large PEG tethers, interact potently with Ins(1,4,5)P_3 receptors, and that the shorter dimers are more potent than Ins(1,4,5)P_3 itself. A very small dimer, consisting of two Ins(1,4,5)P_3 motifs joined by a short *N*,*N*′-diethylurea spacer, was synthesized. Preliminary studies of $^{45}Ca^{2+}$ release from the intracellular stores of permeabilized hepatocytes showed this shortest dimer to be almost as potent as adenophostin A, the most potent Ins(1,4,5)P_3 receptor ligand known. Possible interpretations of this result are considered in relation to the recently disclosed X-ray crystal structure of the type 1 Ins(1,4,5)P_3 receptor core binding domain.

INTRODUCTION

D-*myo*-inositol 1,4,5-trisphosphate [Ins(1,4,5)P_3, **1**, Figure 1] is a hydrophilic intracellular signaling molecule that mediates the release of Ca^{2+} from intracellular stores by binding to Ins(1,4,5)P_3-gated Ca^{2+} channels [Ins(1,4,5)P_3 receptors, InsP_3Rs] located on the endoplasmic reticulum (*1*). Two naturally occurring glyconucleotides, adenophostins A and B (Figure 1), have been shown to activate InsP_3Rs with higher potency than Ins(1,4,5)P_3 itself (*2*, *3*), and work with synthetic adenophostin analogues suggests that this property is directly related to the presence of the aromatic base, which may interact with residues close to the Ins(1,4,5)P_3-binding site (*2*−*5*). An alternative approach to the development of novel and potent InsP_3R ligands may be to exploit the possibility of multivalent binding. InsP_3Rs are tetramers, composed of four subunits, each with a single Ins(1,4,5)P_3-binding site, surrounding the central ion channel, and this oligomeric structure of InsP_3Rs suggests that it may be possible to construct multivalent InsP_3R ligands that could simultaneously occupy more than one Ins(1,4,5)P_3-binding site in the tetramer.

Multivalent binding can lead to enhanced affinity and selectivity for the target protein (*6*, *7*); successful applications of this approach in recent years include multivalent inhibitors of selectins (*8*) and bacterial toxins (*9*), and the development of highly potent and selective inhibitors for the proteasome (*10*), *β*-tryptase (*11*), and glutathione *S*-transferases (*12*) using bivalent ligands. In addition, multivalent InsP_3R ligands could potentially be used as tools with which to study the relationship between Ins(1,4,5)P_3-binding and activation of InsP_3Rs (*13*).

In the first attempt to develop multivalent ligands for InsP_3Rs, bivalent and tetravalent clustered disaccharide analogues related to the adenophostins were synthesized (*13*) in which two or four molecules of a synthetic carbohydrate-based Ins(1,4,5)P_3 mimic were directly attached to a small hydrophobic hub (Figure 1). Although these analogues showed Ca^{2+}-releasing potencies comparable to Ins(1,4,5)P_3, no significant enhancement of binding affinity for InsP_3Rs was found when the multivalent ligands were compared with their monomeric equivalent, suggesting that only monovalent binding occurred (*13*). As electron microscopy studies (*14*−*18*) have shown that InsP_3Rs are large (about 20 nm across) and the locations of the Ins(1,4,5)P_3-binding sites are unknown, we considered that a more promising and versatile approach might be to use bivalent ligands with polymeric tethers in a wide range of lengths. This strategy has been successfully employed to produce super-potent dimeric ligands for tetrameric cyclic nucleotide gated (CNG) channels of photoreceptor and olfactory neurons by using a series of dimers of the 8-thio derivative of the natural ligand (cGMP) linked by poly(ethylene glycol) (PEG) chains of various lengths (*19*). Here we describe the design, synthesis, and biological activities of Ins(1,4,5)P_3 dimers containing poly- and oligo(ethylene glycol) tethers, and of a novel dimeric analogue containing two Ins(1,4,5)P_3 motifs joined by a short *N*,*N*′-diethylurea spacer. Some of this work has previously been reported in preliminary form (*20*), and

* To whom correspondence should be addressed. Tel: +44 (0)1225 826639. Fax: +44(0) 1225 826114. E-mail B.V.L.Potter@bath.ac.uk.
[†] University of Bath.
[‡] University of Cambridge.

10.1021/bc034214s CCC: $27.50 © 2004 American Chemical Society
Published on Web 02/21/2004

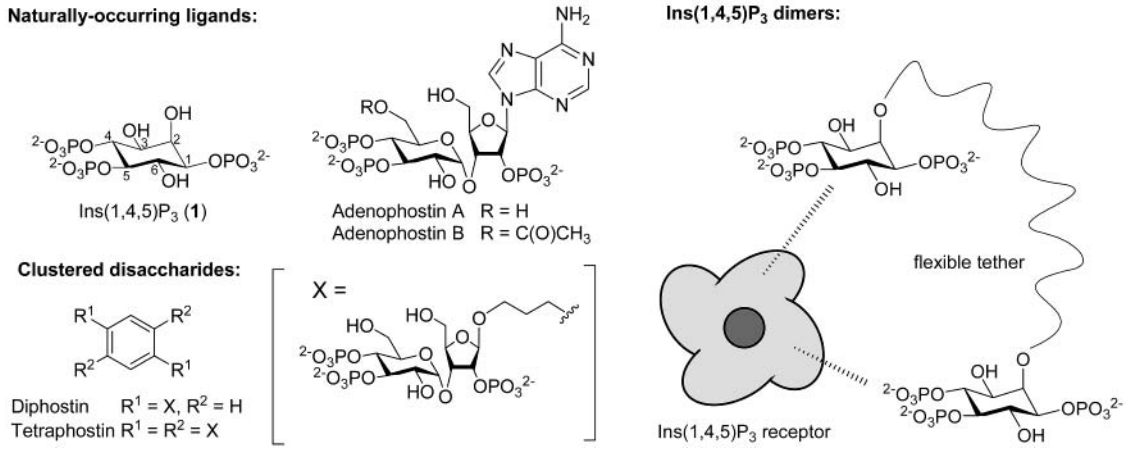


Figure 1. Structures of InsP_3R ligands: D-*myo*-inositol 1,4,5-trisphosphate (**1**), adenophostins A and B, clustered disaccharide analogues diphostin and tetraphostin, and Ins(1,4,5)P_3 dimers.

we have reported in depth on the first findings of biological activity (*21*).

MATERIALS AND METHODS

General Methods. Tetrahydrofuran (THF) was distilled from sodium and benzophenone under a nitrogen atmosphere. Dimethylformamide (DMF), acetonitrile, dichloromethane, and *N*,*N*-diisopropylethylamine (DIPEA) were purchased in anhydrous form and used without further purification. Poly(ethylene glycol)s (PEGs) were dried under vacuum at 60 °C or by azeotropic distillation from toluene prior to use. PEG3350 bis(4-nitrophenyl carbonate) was obtained from Sigma and used without further purification. "NH_4OH" refers to an approximately 28% w/w solution of NH_3 in water. Thin-layer chromatography (TLC) was performed on precoated plates (Merck TLC aluminum sheets silica 60 F_{254}) with detection by UV light or with phosphomolybdic acid in methanol or alkaline aqueous $KMnO_4$, followed by heating. Flash chromatography was carried out on silica gel (particle size 40−63 μm). Ion-exchange chromatography was performed on an LKB−Pharmacia medium-pressure ion exchange chromatograph using Q-Sepharose Fast Flow resin and gradients of triethylammonium bicarbonate (TEAB) as eluent. Quantitative analysis of phosphate was performed using a modification of the Briggs phosphate assay (*22*) or the Ames phosphate assay (*23*). ^{31}P NMR shifts were measured in ppm relative to external 85% phosphoric acid and are positive when downfield from this reference. FAB mass spectra were recorded at the University of Bath using 3-nitrobenzyl alcohol (NBA) as the matrix. Microanalysis was carried out by the Microanalysis Service, University of Bath. Melting points (uncorrected) were determined using a Reichert-Jung hot stage microscope apparatus.

Biological Assays. Equilibrium competition binding assays using [^{3}H]Ins(1,4,5)P_3 (New England Nuclear, 30 Ci/mmol) and membranes prepared from rat cerebellum were performed in medium (50 mM Tris, 1 mM EDTA, pH 8.3 at 2 °C) and using a final concentration of 1.5 nM [^{3}H]Ins(1,4,5)P_3 as previously described (*21*). Functional assays measured the effects of the Ins(1,4,5)P_3 analogues on release of $^{45}Ca^{2+}$ from the intracellular stores of permeabilized rat hepatocytes loaded with $^{45}Ca^{2+}$ in a cytosol-like medium. The methods were reported previously (*21*). The analogues were added (with 1 μM thapsigargin to inhibit further Ca^{2+} uptake) to cells loaded to steady-state with $^{45}Ca^{2+}$, and their effects on the $^{45}Ca^{2+}$ content of the stores were assessed after a further 60 s incubation.

Molecular Docking of Dimer 18. This was carried out using GOLD (*24*) (Version 2.0) running on a Silicon Graphics Octane2 workstation, and the X-ray crystal structure of the Ins(1,4,5)P_3-binding core of mouse type 1 InsP_3R in complex with Ins(1,4,5)P_3 [1N4K, (*25*)] according to methods previously described (*5*). Briefly, a docking protocol was first established that accurately reproduced the crystallographically observed position and conformation of Ins(1,4,5)P_3 in the site. This required that some of the crystallographically observed water molecules involved in the interactions of the 4,5-bisphosphate of Ins(1,4,5)P_3 with the binding site were included in the docking experiments. A model of dimer **18** was then built using Sybyl 6.8 (Tripos Associates) molecular modeling software and docked using the same protocol. Docked solutions were scored using the GoldScore (*24*) fitness function. In the highest scoring "fittest" solutions found, one Ins(1,4,5)P_3 component of **18** interacted with the Ins(1,4,5)P_3-binding site in a similar way to that revealed by the crystal structure, while the second Ins(1,4,5)P_3 interacted with residues close to the Ins(1,4,5)P_3-binding site. However, it was not possible to identify a definitive binding mode for **18**.

(2′*S*,3′*S*)-D-3,6-Di-*O*-benzyl-4,5-*O*-(2′,3′-dimethoxybutane-2′,3′-diyl)-1-*O*-(4-methoxybenzyl)-*myo*-inositol (4). To a solution of diol **3** (*26*) (4.00 g, 8.43 mmol) in MeOH (150 mL) was added dibutyltin oxide (2.12 g, 8.52 mmol). The suspension was heated at reflux for 16 h with removal of formed water using a Soxhlet apparatus containing 3 Å molecular sieves. The resulting clear solution was allowed to cool and then concentrated to dryness by evaporation under reduced pressure. CsF (2.56 g, 16.9 mmol, previously dried in vacuo over P_2O_5), was added, and the flask was fitted with a rubber septum and nitrogen line. Anhydrous DMF (30 mL) was injected, followed by 4-methoxybenzyl chloride (1.45 mL, 10.7 mmol), and the mixture was stirred at 50 °C under N_2 for 5 h, after which time TLC (chloroform/acetone 30:1) showed almost total conversion of diol (R_f 0.15) into a product (R_f 0.40). The solvents were removed by evaporation in vacuo at 50 °C, and the residue was taken up in Et_2O (200 mL) and washed with water (200 mL). The organic layer was dried over $MgSO_4$, filtered through Celite, and concentrated by evaporation under reduced pressure to give an oily residue. Purification by flash chromatography (Et_2O/hexane 1:2, then 1:1) gave the

alcohol **4** as a colorless oil which became a white foam on drying overnight in vacuo (4.22 g, 84%); $[\alpha]^{20}_D = +69$ ($c = 1.3$, $CHCl_3$); ^{1}H NMR ($CDCl_3$, 270 MHz) δ 1.36 (s, 3H, CH_3), 1.38 (s, 3H, CH_3), 2.51 (br s, 1H, D_2O exch. 2-OH), 3.30 (s, 3H, OCH_3), 3.33 (s, 3H, OCH_3), 3.30−3.36 (m, 1H, buried, 1/3-H), 3.42 (dd, 1H, $J = 10.1$, 2.9 Hz, 1/3-H), 3.62 (dd, 1H, $J = 10.1$, 9.9 Hz, 5-H), 3.80 (s, 3H, OCH_3), 3.96 (dd, 1H, $J = 9.5$, 9.5 Hz, 4/6-H), 4.16 (br s, 1H, D_2O exch. gives dd, $J = 2.9$, 2.9 Hz, 2-H), 4.19 (dd, 1H, $J = 9.9$, 9.9 Hz, 4/6-H), 4.58−4.95 (m, 6H, AB systems of CH_2Ar), 6.81−6.88 (m, 2H, *meta*-H of PMB), 7.22−7.41 (m, 12H, ArH); ^{13}C NMR ($CDCl_3$, 68 MHz) 17.76 (2 × CH_3), 47.83, 47.92 (2 × OCH_3), 55.22 ($C_6H_4OCH_3$), 69.13, 69.30, 71.29 (C-2, C-4 and C-5), 72.77, 73.21, 75.65 (3 × OCH_2Ar), 76.55, 78.31, 79.47 (C-1, C-3 and C-6), 99.20, 99.28 (2 × BDA quaternary C), 113.73 (*meta*-C of PMB), 127.45, 127.55, 127.94, 128.20, 128.28, 129.48 (aromatic CH), 130.11 (*ipso*-C of PMB), 138.45 and 139.03 (2 × *ipso*-C of Ph), 159.24 (*para*-C of PMB); MS *m*/*z* (+ve ion FAB, relative intensity); 617 [$(M + Na)^+$, 64%], 593 [$(M - H)^+$, 40%], 563 [$(M - CH_3O)^+$, 16%], 121 (100), 91 [$(C_7H_7)^+$, 44%]; MS *m*/*z* (−ve ion FAB, relative intensity); 1188 (80), 747 [$(M + NBA)^-$, 100%], 593 [$(M - H)^-$, 64%]; Anal. ($C_{34}H_{42}O_9$) C, H.

(2′*S*,3′*S*)-D-3,6-Di-*O*-benzyl-2-*O*-cyanomethyl-4,5-*O*-(2′,3′-dimethoxybutane-2′,3′-diyl)-1-*O*-(4-methoxybenzyl)-*myo*-inositol (5). To a solution of **4** (2.63 g, 4.42 mmol) in dry acetonitrile (15 mL) was added sodium hydride (0.90 g of a 60% dispersion in mineral oil, 23 mmol). The suspension was stirred under N_2 at room temperature for 1 h and then cooled to −30 °C. Bromoacetonitrile (2.0 mL, 29 mmol) was added dropwise, and stirring was continued at −40 °C to −20 °C for 5 h. The suspension was then allowed to warm to room temperature, and stirring was continued overnight. The resulting brown liquid was concentrated by evaporation under reduced pressure, and the residue was suspended in water (100 mL) and extracted with Et_2O (2 × 100 mL). The combined organic extracts were dried over $MgSO_4$ and concentrated to give a brown residue. Purification by flash chromatography (Et_2O/hexane 2:3) gave the product **5** as a white solid (2.33 g, 83%); mp 120−121 °C (from ethyl acetate/hexane); $[\alpha]^{18}_D = +56$ ($c = 1.0$, $CHCl_3$); ^{1}H NMR ($CDCl_3$, 270 MHz) δ 1.35 (s, 3H, CH_3), 1.37 (s, 3H, CH_3), 3.295 (s, 3H, OCH_3), 3.30 (s, 3H, OCH_3), 3.30−3.36 (m, 1H, buried, 1/3-H), 3.47 (dd, 1H, dd, $J = 10.3$, 2.6 Hz, 1/3-H), 3.62 (dd, 1H, $J = 9.9$, 9.9 Hz, 5-H), 3.86 (s, 3H, s, OCH_3), 3.89 (dd, 1H, $J = 9.5$, 9.5 Hz, 4/6-H), 4.07 (dd, 1H, $J = 2.6$, 2.6 Hz, 2-H), 4.11 (dd, 1H, $J = 10.1$, 9.9 Hz, 4/6-H), 4.52−4.93 (m, 8H, 4 × AB systems of OCH_2), 6.83−6.89 (m, 2H, *meta*-H of PMB), 7.24−7.40 (m, 12H, ArH); ^{13}C NMR ($CDCl_3$, 68 MHz) 17.74 (2 × CH_3), 47.84 and 47.94 (2 × OCH_3), 55.22 ($C_6H_4OCH_3$), 57.38 (CH_2CN), 69.57 and 71.45 (C-4 and C-5), 73.45, 73.85, 75.70 (3 × OCH_2Ar), 77.10, 77.41, 78.36, 79.47 (C-1, C-2, C-3 and C-6), 99.35, 99.41 (2 × BDA quaternary C), 113.81 (*meta*-C of PMB), 127.50, 127.66, 127.94, 128.22, 128.38, 129.72 (aromatic CH), 129.82 (*ipso*-C of PMB), 138.29 and 138.90 (2 × *ipso*-C of Ph), 159.34 (*para*-C of PMB); MS *m*/*z* (+ve ion FAB, relative intensity); 656 [$(M + Na)^+$, 50%], 632 [$(M - H)^+$, 76%], 602 [$(M - CH_3O)^+$, 16%], 394(76), 121 (100), 91 [$(C_7H_7)^+$, 54%]; MS *m*/*z* (−ve ion FAB, relative intensity); 786 [$(M + NBA)^-$, 100%], 679 (40), 512 (40); Anal. ($C_{36}H_{43}NO_9$) C, H, N.

D-3,6-Di-*O*-benzyl-2-*O*-[2-(2,2,2-trifluoroacetylamino)ethyl]-*myo*-inositol (6). To a solution of $LiAlH_4$ in THF (3.5 mL of a 1 M solution, 3.5 mmol) under N_2 at room temperature was added a solution of **5** (2.00 g, 3.16 mmol) in dry THF (5 mL) dropwise over 10 min. The reaction was stirred at room temperature for a further 1 h and then quenched by careful addition of water. Aqueous 15% NaOH (50 mL) was added, and the resulting solution was extracted with CH_2Cl_2 (3 × 50 mL). The combined organic extracts were dried ($MgSO_4$) and concentrated to give the crude amine (∼2 g) as a colorless oil. The crude amine was taken up in dry THF (10 mL), and ethyl trifluoroacetate (0.5 mL, 4.2 mmol) was added. The solution was stirred at room temperature with exclusion of moisture overnight and then concentrated by evaporation under reduced pressure to give an oil, which was redissolved in CH_2Cl_2 (10 mL). Aqueous trifluoroacetic acid (95%, 10 mL) was added, and the solution was stirred at room temperature for 30 min. The solvents were removed by evaporation under reduced pressure, and the residue was purified by flash chromatography (EtOAc/hexane 2:1) to give triol **6** as a white solid (1.22 g, 77% yield over three steps); mp 130−131 °C (from ethyl acetate/hexane); $[\alpha]^{18}_D = +3$ ($c = 1.0$, $CHCl_3$); ^{1}H NMR ($CDCl_3$, 400 MHz) δ 2.85 (br s, 1H, D_2O exch. OH), 2.97 (br s, 1 H, D_2O exch. OH), 2.98 (br s, 1 H, D_2O exch. OH), 3.21 (dd, 1 H, $J = 9.8$, 2.4 Hz, 3-H), 3.33−3.48 (m, 3H, 1-H, 5-H, OCH_2CHCHN), 3.50−3.57 (m, 1 H, OCH_2CHCHN), 3.61 (dd, 1H, $J = 9.8$, 9.3 Hz, 6-H), 3.65 (ddd, 1 H, $J = 11.2$, 7.8, 2.9 Hz, $OCHCHCH_2N$), 3.81−3.87 (m, 2H, 2-H, 4-H), 3.96 (ddd, 1H, $J = 11.2$, 5.9, 3.4 Hz, $OCHCHCH_2N$), 4.65, 4.69 (AB, 2H, $J_{AB} = 11.7$ Hz, OCH_2Ph), 4.71, 4.97 (AB, 2H, $J_{AB} = 11.2$ Hz, OCH_2Ph), 7.28−7.38 (m, 10H, Ph), 8.08 (br s, 1H, NH); ^{13}C NMR ($CDCl_3$, 100 MHz) δ 40.38 ($CH_2CH_2NHC(O)CF_3$), 71.56 ($CH_2CH_2NHC(O)CF_3$), 71.74, 72.99 and 74.93 (C-1, C-4 and C-5), 73.13, and 75.27 (2 × OCH_2Ph), 78.46, 79.66 and 81.05 (C-2, C-3 and C-6), 115.99 ($^1J_{CF} = 289$ Hz, CF_3), 128.00, 128.03, 128.11, 128.38, 128.67, 128.75 (Ph CH), 137.23 and 138.29 (2 × *ipso*-C of Ph), 157.31 ($^2J_{CF} = 36.8$ Hz, C=O); MS *m*/*z* (+ve ion FAB, relative intensity); 500 [$(M + H)^+$, 76%], 498 (50), 408 (20), 320 (48), 91 [$(C_7H_7)^+$, 100%]; MS *m*/*z* (−ve ion FAB, relative intensity); 652 [$(M + NBA)^-$, 36%], 498 [$(M - H)^-$, 100%]; Anal. ($C_{24}H_{28}F_3NO_7$) C, H, N.

D-3,6-Di-*O*-benzyl-2-*O*-[2-(2,2,2-trifluoroacetylamino)ethyl]-*myo*-inositol 1,4,5-Tris(dibenzyl phosphate) (7). To a suspension of 1*H*-tetrazole (588 mg 8.39 mmol) and triol **6** (700 mg, 1.40 mmol) in dry CH_2Cl_2 (10 mL) under N_2 was added bis(benzyloxy)diisopropylaminophosphine (2.18 g, 6.31 mmol). The mixture was stirred at room temperature for 1.5 h and then cooled to −78 °C, before MCPBA (57%, 2.5 g, 8.3 mmol) was added in portions over 1 min. The mixture was allowed to warm to room temperature and then diluted with CH_2Cl_2 (100 mL). The clear solution was washed with 10% aq Na_2SO_3 solution (100 mL), dried over $MgSO_4$, and concentrated by evaporation under reduced pressure. The residue was purified by flash chromatography eluting with EtOAc/hexane 1:1 then 2:1 to give the title compound as an oil which slowly crystallized (1.72 g, 96%); mp 85−87 °C (from diisopropyl ether); $[\alpha]^{20}_D = -6$ ($c = 1.0$, $CHCl_3$); ^{1}H NMR ($CDCl_3$, 400 MHz, COSY) δ 3.33−3.42 (m, 3H, 3-H and OCH_2CH_2NH), 3.64−3.74 (m, 2H, OCH_2CH_2NH), 3.96−4.02 (m, 2H, 2-H and 6-H), 4.16 (ddd, 1H, $J = 9.4$, 6.6 and 2.3 Hz, 1-H), 4.39, 4.59 (AB, $J_{AB} = 11.3$ Hz, OCH_2Ph), 4.45 (ddd, 1H, $J = 9.8$, 9.4 and 9.4 Hz, 5-H), 4.62−5.04 (m, 15H, 4-H and 7 × CH_2Ph), 6.94−6.98 (m, 2H, Ph), 7.06−7.32 (m, 38H, Ph), 7.64 (br t, 1H, $J \sim 5$ Hz, OCH_2CH_2NH); ^{13}C NMR ($CDCl_3$, 100 MHz) δ 39.83 (OCH_2CH_2NH), 69.03−69.46 (with couplings, 6 × $OPOCH_2Ph$), 70.78, 73.21 and 74.47 (OCH_2), 76.10 and 77.33 (inositol ring *C*H), 77.35−78.51 (with $^2J_{CP}$ cou-

plings, inositol ring *C*H), 115.62 ($^1J_{CF}$ = 287 Hz, CF_3), 126.72 and 126.95 (Ph *C*H), 127.52−128.46 (Ph *C*H), 134.90−135.64 (*ipso-C* of $POCH_2$*Ph*), 136.37 and 137.68 (*ipso*-C of Ph), 156.99 ($^2J_{CF}$ = 36 Hz, C=O); ^{31}P NMR ($CDCl_3$, 109 MHz) δ −1.17 (1P), −0.95 (1P) and −0.77 (1P); MS *m/z* (+ve ion FAB, relative intensity); 1280 [$(M + H)^+$, 90%], 91 [$(C_7H_7)^+$, 100%]; Anal. ($C_{66}H_{67}F_3NO_{16}P_3$) C, H, N.

D-2-*O*-(2-Aminoethyl)-3,6-di-*O*-benzyl-*myo*-inositol 1,4,5-Tris(dibenzyl phosphate) (2). To a solution of **7** (300 mg, 0.234 mmol) in THF (4 mL) was added a solution of $LiOH·H_2O$ (98 mg, 2.34 mmol) in MeOH (4 mL) and water (2 mL). The mixture was stirred at room temp for 1 h, after which TLC (CH_2Cl_2−MeOH−NH_4OH, 200:20:1) showed complete conversion of starting material (R_f 0.90) into a more polar product (R_f 0.36). The mixture was then diluted with Et_2O (40 mL) and washed with brine (40 mL). The organic layer was dried over $MgSO_4$ and concentrated to give crude **2** as an oil (266 mg, >90% pure by TLC, >86%); ^{1}H NMR ($CDCl_3$, 270 MHz) δ 2.74 (t, 2H, J = 5.0 Hz, $OCH_2CH_2NH_2$), 3.39 (dd, 1H, J = 9.7, 2.3 Hz, 3-H), 3.60−3.75 (m, 2H, OCH_2-CH_2NH), 4.05 (dd, 1 H, J = 9.7, 9.4 Hz, 6-H), 4.12 (dd, 1H, J = 2.3, 2.3 Hz, 2-H), 4.20 (ddd, 1H, J = 9.7, 7.9, 2.3 Hz, 1-H), 4.45−5.08 (m, 18H, 4-H, 5-H and 8 × CH_2Ph), 6.94−7.00 (m, 2H, Ph), 7.06−7.38 (m, 38H, Ph). Amine **2** was found to be unstable, and in subsequent experiments it was freshly prepared from **7**, immediately before use.

Dimer 9. To a solution of crude amine **2** (277 mg, 0.236 mmol) in dry DMF (1 mL) under N_2 was added a solution of **8** (*27*) (33 mg, 0.079 mmol) in dry DMF (1 mL). The solution was stirred at under N_2 at room temperature for 16 h. The solvents were removed by evaporation under reduced pressure, and the residue was purified by flash chromatography (CH_2Cl_2/MeOH 30:1). This procedure removed excess amine and *N*-hydroxysuccinimide, but the product was only ∼60 to 80% pure as judged by TLC. The crude product was taken up in MeOH (20 mL), and deionized water (5 mL) was added, followed by Pd−C (10%, 50% water, 200 mg). The mixture was shaken in a Parr hydrogenator under H_2 (50 psi) for 20 h. The catalyst was removed by filtration through a PTFE syringe filter and 1.0 M TEAB (1 mL) was added. The solvents were removed by evaporation under reduced pressure, and the residue was purified by ion-exchange chromatography on Q-Sepharose Fast Flow resin eluting with a gradient of TEAB (0 to 2 M). Fractions containing the target compound were identified by a modification of the Briggs phosphate test (*22*). The combined fractions were concentrated by evaporation in vacuo, and methanol was repeatedly added and evaporated, eventually leaving the triethylammonium salt of **9** as a colorless glass, which was accurately quantified using a modification of the Briggs phosphate assay (*22*) (15.4 μmol, 19%); $[\alpha]^{20}_D$ = −16 (c = 0.5, MeOH); ^{1}H NMR (D_2O, 400 MHz, COSY) δ 3.26−3.38 (m, 4H, OCH_2CH_2N), 3.58 (dd, 2H, J = 9.7, 2.3 Hz, 3-H), 3.62 (br s, 8H, 2 × OCH_2CH_2O), 3.62−3.68 (m, 2H, $OCHCH_2N$), 3.75 (dd, 2H, J = 9.7, 9.7 Hz, 6-H), 3.80−3.94 (m, 8H, 1-H, 2-H, 5-H and $OCHCH_2N$), 3.96 (br s, 4H, $NHC(O)CH_2O$), 4.14 (ddd, 2H, J = 9.1, 9.1, 9.1 Hz, 4-H); ^{31}P NMR (D_2O, 100 MHz) δ 0.31 (2P), 1.17 (2P), 1.55 (2P); MS *m/z* (−ve ion FAB, relative intensity); 1111 [M^-, 100%]; Accurate mass FAB− calcd for $C_{24}H_{49}N_2O_{35}P_6^-$, 1111.0548; found 1111.0542.

Hexa(ethylene glycol) Bis(4-nitrophenyl carbonate) (10a). To a solution of hexa(ethylene glycol) (564 mg, 2.00 mmol) in dry DMF (10 mL) under N_2 was added bis(4-nitrophenyl) carbonate (1.83 g, 6.00 mmol) followed by DIPEA (1.0 mL, 5.7 mmol). The solution was stirred at room temperature for 20 h, and the solvents were removed by evaporation in vacuo. The residue was purified by flash chromatography on silica gel (EtOAc/hexane 2:1 then EtOAc) to give **10a** as a pale yellow oil (1.17 g, 96%); ^{1}H NMR ($CDCl_3$, 270 MHz) δ 3.67 (br s, 8H, 4 × OCH_2), 3.69 (m, 8H, 4 × OCH_2), 3.78−3.84 (m, 4H, OCH_2CH_2OCO) 4.42−4.48 (m, 4H, OCH_2CH_2OCO), 7.36−7.42 (m, 4H, 2-H and 6-H of 4-nitrophenyl), 8.25−8.31 (m, 4H, 3-H and 5-H of 4-nitrophenyl); MS *m/z* (+ve ion FAB, relative intensity); 613 [$(M + H)^+$, 70%], 210 (100); Anal. Calcd for ($C_{26}H_{32}N_2O_{15}$) C, H, N.

PEG1450 Bis(4-nitrophenyl carbonate) (10b). Synthesized as for **10a** from PEG1450 (1.45 g, approximately 1.0 mmol) using bis(4-nitrophenyl) carbonate (1.83 g, 6.00 mmol) and DIPEA (1.0 mL, 5.7 mmol) in dry DMF (10 mL). Purification by flash chromatography (CH_2Cl_2, then CH_2Cl_2/MeOH 20:1) gave **10b** as a pale yellow waxy solid (1.09 g, 61%); δ 3.60−3.82 (m, approximately 130H, PEG-CH_2), 3.80−3.86 (m, 4H, OCH_2CH_2OCO) 4.40−4.50 (m, 4H, OCH_2CH_2OCO), 7.41 (d, 4H, J = 9.2 Hz, 2-H and 6-H of 4-nitrophenyl), 8.24 (d, 4H, J = 9.2 Hz, 3-H and 5-H of 4-nitrophenyl).

PEG8000 Bis(4-nitrophenyl carbonate) (10d). Synthesized as for **10a** from PEG8000 (4.0 g, approximately 0.5 mmol) using bis(4-nitrophenyl) carbonate (915 mg, 3.00 mmol) and DIPEA (0.5 mL, 2.9 mmol) in dry DMF (40 mL, heating initially required to dissolve). Purification by flash chromatography (CH_2Cl_2, then CH_2Cl_2/MeOH 50:1 to 5:1) gave **10d** as a white solid (2.06 g, 49%) δ 3.50−3.85 (m, approximately 700H, PEG-CH_2), 4.42−4.48 (m, 4H, OCH_2CH_2OCO), 7.40 (d, 4H, J = 9.2 Hz, 2-H and 6-H of 4-nitrophenyl), 8.29 (d, 4H, J = 9.2 Hz, 3-H and 5-H of 4-nitrophenyl).

Methoxyhexa(ethylene glycol) 4-Nitrophenyl Carbonate (12). To a solution of methoxyhexa(ethylene glycol) (**11**) (*28*) (550 mg, 1.86 mmol) in dry DMF (5 mL) under N_2 was added bis(4-nitrophenyl) carbonate (913 mg, 3.00 mmol) followed by DIPEA (0.5 mL, 2.9 mmol). The solution was stirred at room temperature for 20 h, and the solvents were removed by evaporation in vacuo. The residue was purified by flash chromatography (EtOAc/hexane 1:1; then EtOAc) to give **12** as a pale yellow oil (710 mg, 83%); ^{1}H NMR ($CDCl_3$, 400 MHz) δ 3.37 (s, 3H, OMe), 3.53−3.57 (m, 2H, CH_2OMe), 3.62−3.72 (m, 18H, 9 × OCH_2), 3.79−3.82 (m, 2H, OCH_2CH_2OCO), 4.43−4.45 (m, 2H, OCH_2CH_2OCO), 7.37−7.42 (m, 2H, 2-H and 6-H of 4-nitrophenyl), 8.26−8.31 (m, 2H, 3-H and 5-H of 4-nitrophenyl); MS *m/z* (+ve ion FAB, relative intensity); 462 [$(M + H)^+$, 100%], 210 (50), 103(30); Anal. ($C_{20}H_{31}NO_{11}$) C, H, N.

Benzyl-Protected Dimer 13a. To a solution of **7** (300 mg, 0.234 mmol) in THF (4 mL) was added a solution of $LiOH·H_2O$ (98 mg, 2.34 mmol) in MeOH (4 mL) and water (2 mL). The mixture was stirred at room temp for 1 h and then diluted with Et_2O (40 mL). The resulting suspension was washed with brine (40 mL). The organic layer was separated, dried over $MgSO_4$, and concentrated to give amine **2**, which was further dried by addition and evaporation of DMF (3 × 5 mL). Dry DMF (2 mL) was then added under N_2, followed by a solution of **10a** (36 mg, 0.059 mmol) in dry DMF (1 mL). The mixture was stirred under N_2 at room temperature for 16 h. TLC (EtOAc) showed a product at R_f 0.58, and 4-nitrophenol at R_f 0.66. TLC (CH_2Cl_2/MeOH/NH_4OH, 200:20:1) confirmed the presence of excess unreacted amine **2**. Water (2 mL) was added, and the mixture was stirred for a further 1 h, before the solvents were removed by evaporation in vacuo. The residue was purified by flash

chromatography, eluting with CH_2Cl_2/MeOH 50:1 to give **13a** as a colorless oil (93 mg, 58% yield); ^{1}H NMR ($CDCl_3$, 400 MHz) δ 3.24−3.30 (m, 4H, OCH_2CH_2N), 3.38 (dd, 2H, J = 10.0, 2.1 Hz, 3-H), 3.50−3.70 (m, 24H, 10 × OCH_2 and OCH_2CH_2N), 4.00 (dd, 2H, J = 9.7, 9.4 Hz, 6-H), 4.04 (br s, 2H, 2-H), 4.10−4.16 (m, 4H, 2 × $CH_2OC(O)NH$), 4.18 (ddd, 2H, J = 9.7, 7.3, 2.3 Hz, 1-H), 4.48 (ddd, 2H, J = 9.4, 9.4, 9.1 Hz, 5-H), 4.47, 4.57 (AB_q, 4H, J_{AB} = 11.7 Hz, 2 × OCH_2Ph), 4.62−4.68 (0.5 of AB_q with $^3J_{HP}$ coupling, 2H, J_{AB} 11.7 Hz, J_{HP} 8.5 Hz, $POCH_2Ph$), 4.74−5.07 (m, 28H, 4-H and 6.5 AB systems of OCH_2Ph), 5.60 (br t, 2H, J = 5.3 Hz, NH), 6.96−6.98 (m, 4H, Ph), 7.08−7.36 (m, 76H, Ph); ^{31}P NMR ($CDCl_3$, 162 MHz) δ −0.56 (2P), −0.60 (2P), −0.63 (2P).

Benzyl-Protected Dimer 13b. Synthesized as for **13a** from **7** (300 mg) and **10b** (112 mg, 0.063 mmol) in dry DMF (3 mL). Purification by flash chromatography CH_2Cl_2/MeOH (50:1 then 30:1 and finally 10:1) gave the product **13b** as a colorless glass (147 mg, 0.038 mmol, 60% based on linker); ^{1}H NMR ($CDCl_3$, 400 MHz) was almost identical to that for **13a** except δ 3.55−3.70 (m, approx 130H, CH_2 of PEG); ^{31}P NMR ($CDCl_3$, 162 MHz) δ −0.63 (broad, 4P), −0.59 (broad 2P).

Benzyl-Protected Dimer 13c. Synthesized as for **13a** from **7** (300 mg) and **10c** (Sigma, 248 mg, 0.067 mmol) in dry DMF (4 mL). Purification by flash chromatography using a gradient of CH_2Cl_2/MeOH (20:1 then 10:1 and finally 5:1) gave the product **13c** as a colorless glass (191 mg, 0.033 mmol, 49% based on linker); ^{1}H NMR ($CDCl_3$, 270 MHz) was almost identical to that for **13a** except δ 3.55−3.70 (m, approx 300H, CH_2 of PEG); ^{31}P NMR ($CDCl_3$, 109 MHz) δ approximately −0.9 (broad).

Benzyl-Protected Dimer 13d. Synthesized as for **13a** from **7** (300 mg) and **10d** (450 mg, 0.055 mmol) in dry DMF (5 mL). Purification by flash chromatography eluting with a gradient of CH_2Cl_2/MeOH (20:1 then 10:1 and finally 5:1) to give the product **13d** as a colorless glass (180 mg, 0.017 mmol, 31% based on linker). ^{1}H NMR ($CDCl_3$, 270 MHz) was almost identical to that for **13a** except δ 3.55−3.70 (m, approx 700H, CH_2 of PEG); ^{31}P NMR ($CDCl_3$, 109 MHz) δ approximately −0.9 (broad).

Dimer 14a. To a solution of **13a** (28 mg, 10 μmol) in MeOH (20 mL) and water (5 mL) was added Pd−C (10%, 50% water, 200 mg). The mixture was shaken in a Parr hydrogenator under H_2 (50 psi) for 48 h. The catalyst was removed by filtration through a PTFE syringe filter, and 1.0 M TEAB (1 mL) was added. The solvents were removed by evaporation under reduced pressure, and the residue was purified by ion-exchange chromatography on Q-Sepharose Fast Flow resin, eluting with a gradient of TEAB (0 to 2 M). Fractions containing the target compound were identified by a modification of the Briggs phosphate test (*22*). The combined fractions were concentrated by evaporation in vacuo, and methanol was repeatedly added and evaporated, eventually leaving the triethylammonium salt of **14a** as a colorless glass, which was accurately quantified using the Ames total phosphate assay (*23*) (5.2 μmol, 52%); ^{1}H NMR (CD_3OD, 400 MHz) δ ~3.3 (m, 4H, (buried), OCH_2CH_2N), 3.61−3.70 (m, 22H, 3-H and 10 × OCH_2), 3.77−3.85 (m, 2H, $OCHHCH_2N$), 3.92−4.00 (m, 6H, 5-H, 6-H and $OCHHCH_2N$), 4.01−4.06 (m, 4H, 1-H and 2-H), 4.14−4.20 (m, 4H, 2 × $CH_2OC(O)NH$), 4.32 (ddd, 2H, J = 9.4, 8.9, 8.6 Hz, 4-H); ^{31}P NMR (CD_3OD, 162 MHz) δ 2.06 (2P), 3.19 (2P) and 3.66 (2P); MS *m*/*z* (−ve ion FAB, relative intensity); 1281 (90), 1259 [M^-, 80%], 97 [$H_2PO_4^-$, 100]; Accurate mass FAB− calcd for $C_{30}H_{61}N_2O_{39}P_6^-$, 1259.1277; found 1259.1221.

Dimer 14b. Hydrogenolysis of **13b** (147 mg, 38 μmol) and purification as for **14a** gave the triethylammonium salt of **14b** as a colorless glass which crystallized on standing (21 μmol, 55%). ^{1}H NMR (CD_3OD, 400 MHz) was similar to that for **14a** except δ 3.62−3.66 (m, approx 130H, CH_2 of PEG); ^{31}P NMR (CD_3OD, 109 MHz) δ 1.53 (2P) 2.36 (2P) and 2.85 (2P).

Dimer 14c. Hydrogenolysis of **13c** (191 mg, 33 μmol) and purification as for **14a** gave the triethylammonium salt of **14c** as a colorless glass which crystallized on standing (21 μmol, 64%). ^{1}H NMR (CD_3OD, 400 MHz) was similar to that for **14a** except δ 3.5−3.7 (m, approx 300H, CH_2 of PEG); ^{31}P NMR (CD_3OD, 109 MHz) δ 1.41 (2P) 2.18 (2P) and 2.67 (2P).

Dimer 14d. Hydrogenolysis of **13d** (180 mg, 17 μmol) and purification as for **14a** gave the triethylammonium salt of **14d** as a colorless glass which crystallized on standing (11 μmol, 65%). ^{1}H NMR (CD_3OD, 400 MHz) was similar to that for **14a** except δ approximately 3.5−3.7 (m, approx 700H, CH_2 of PEG); ^{31}P NMR (CD_3OD, 109 MHz) δ 2.02 (2P), 2.70 (2P) and 3.20 (2P).

Benzyl-Protected Methoxyhexa(ethylene glycol)−Ins(1,4,5)P$_3$ Conjugate 15. To a solution of the crude amine **2** (90 mg, 76 μmol, prepared from **7** as in the synthesis of **13a**) in dry DMF (1 mL) under N_2 was added a solution of **12** (115 mg, 250 μmol) in DMF (1 mL). The yellow solution was stirred at room temperature for 16 h and then concentrated by evaporation under reduced pressure. The residue was taken up in THF (5 mL), and NH_4OH (5 drops) was added to destroy excess **12**. After 20 min, the solvents were removed by evaporation under reduced pressure, and the residue was purified by flash chromatography ($CHCl_3$/MeOH 100:1 then 50:1) to give **15** as a colorless oil (67 mg, 58%). ^{1}H NMR ($CDCl_3$, 400 MHz) δ 3.24−3.30 (m, 2H, OCH_2CH_2N), 3.37 (s, 3H, OMe), 3.38 (dd, 1H, partially buried, 3-H), 3.50−3.70 (m, 24H, 11 × OCH_2 and OCH_2CH_2N), 4.01 (dd, 1H, J = 9.7, 9.8 Hz, 6-H), 4.04 (br s, 1H, 2-H), 4.10−4.16 (m, 2H, $CH_2OC(O)NH$), 4.18 (ddd, 1H, J = 9.7, 7.3, 2.3 Hz, 1-H), 4.48 (ddd, 1H, J = 9.4, 9.4, 9.1 Hz, 5-H), 4.47, 4.57 (AB_q, 2H, J_{AB} = 11.7, OCH_2Ph), 4.62−4.68 (0.5 of AB_q with $^3J_{HP}$ coupling, 1H, J_{AB} = 11.7 Hz, J_{HP} = 8.5 Hz, $POCH_2Ph$), 4.73−5.06 (m, 14H, 4-H and 6.5 AB systems of OCH_2Ph), 5.60 (br t, 1H, J ~ 5.3 Hz, NH), 6.95−6.98 (m, 2H, Ph), 7.08−7.36 (m, 38H, Ph); ^{31}P NMR ($CDCl_3$, 162 MHz) δ −0.59 (1P), −0.63 (2P); MS *m*/*z* (+ve ion FAB, relative intensity); 1507 [$(M + H)^+$, 80%], 181 (10), 91 (100); *m*/*z* (−ve ion FAB, relative intensity); 1659 [$(M + NBA)^-$, 40%], 1415 [$(M - C_7H_7)^-$, 90%], 277 (100); accurate mass FAB^+ calcd for $C_{78}H_{95}NO_{23}P_3^+$, 1506.5508; found 1506.5552.

Methoxyhexa(ethylene glycol)−Ins(1,4,5)P$_3$ Conjugate 16. Hydrogenolysis of **15** (47 mg, 31 μmol), and purification by ion exchange chromatography on Q-Sepharose Fast Flow resin eluting with a gradient of TEAB (0 to 1 M) gave the triethylammonium salt of **16** as a colorless glass (29 μmol, 94%). ^{1}H NMR (CD_3OD, 400 MHz) δ ~3.3 (m, 2H, (buried), OCH_2CH_2N), 3.35 (s, 3H, OMe), 3.51−3.56 (m, 2H, PEG CH_2OMe), 3.57−3.70 (m, 21H, 3-H and 10 × CH_2 of PEG), 3.76−3.83 (m, 1H, $OCHHCH_2N$), 3.92−4.08 (m, 5H, 1-H, 2-H, 5-H, 6-H and $OCHHCH_2N$), 4.13−4.17 (m, 2H, CH_2 of PEG), 4.34 (ddd, 1H, J = 9.4, 8.9, 8.6 Hz, 4-H); ^{31}P NMR (CD_3OD, 162 MHz) δ 1.86, 2.65 and 3.10; MS *m*/*z* (−ve ion FAB, relative intensity); 1569 [(2M−H)-, 80%], 784 (M^-, 100%); accurate mass FAB− calcd for $C_{22}H_{45}NO_{23}P_3^-$, 784.1995; found 784.1603.

Benzyl-Protected Dimer 17. To a solution of the crude amine **2** (205 mg, 0.173 mmol, freshly prepared

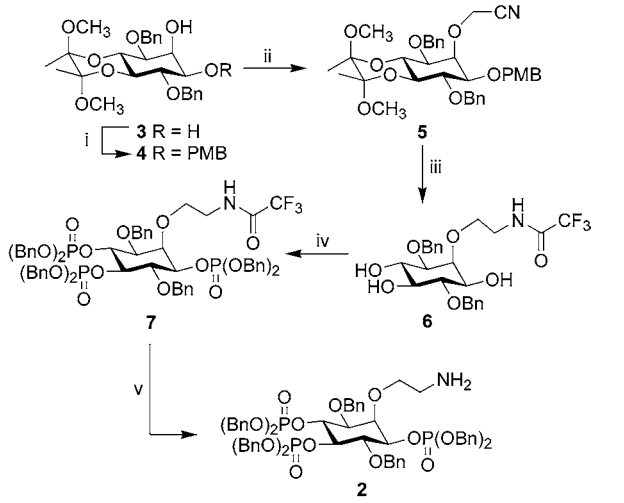
from **7** as in the synthesis of **13a**) in dry DMF (3 mL) under N_2 was added bis(4-nitrophenyl) carbonate (recrystallized from CH_2Cl_2/hexane, 24 mg, 0.079 mmol). The mixture was stirred overnight at room temp. The solvents were removed by evaporation in vacuo to give a residue, which was purified by flash chromatography (CH_2Cl_2 then CH_2Cl_2/MeOH 100:1 to 30:1) to give **17** as a colorless oil (134 mg, 56.0 μmol 71%); ^{1}H NMR ($CDCl_3$, 400 MHz) δ 3.21−3.43 (m, 6H, OCH_2CH_2N and H-3), 3.65−3.72 (m, 2 H, $OCHCH_2N$), 3.72−3.80 (m, 2H, $OCHCH_2N$), 4.04 (dd, 2H, J = 9.8, 9.4 Hz, 6-H), 4.10 (br s, 2H, 2-H), 4.18 (ddd, 2H, J = 9.8, 9.4, 1.6 Hz, 1-H), 4.42−4.51 (m, 6H, OCH_2Ph and 5-H), 4.57−4.63 (0.5 of AB_q with $^3J_{HP}$ coupling, 2H, J_{AB} = 11.7, J_{HP} = 8.6 Hz, $POCHHPh$), 4.70−5.02 (m, 28H, 4-H and 6.5 AB systems of OCH_2Ph), 5.99 (br t, 2H, J = 5.3 Hz, NHC(O)), 6.90−6.94 (m, 4H, Ph), 7.02−7.34 (m, 76H, Ph); ^{13}C NMR ($CDCl_3$, 100 MHz) δ 40.15 (OCH_2CH_2NH), 68.99−69.35 (with $^3J_{CP}$ couplings, $OPOCH_2Ph$), 72.14, 73.40 and 74.44 (OCH_2CH_2NH and OCH_2Ph), 75.38 (inositol ring *C*H), 77.19−78.53 (with J_{CP} couplings, inositol ring *C*H), 126.80−128.23 (Ph *C*H), 135.11−135.59 (*ipso-C* of $POCH_2Ph$), 136.62 and 137.85 (*ipso*-C of Ph), 158.29 (urea C=O); ^{31}P NMR (CD_3Cl_3, 162 MHz) δ −0.69 (2 P), −0.52 (2 P), −0.46 (2 P). MS *m/z* (+ve ion FAB, relative intensity); 2394 [$(M + H)^+$, 80%], 181 (100).

Dimer 18. Hydrogenolysis of **17** (48 mg, 20 μmol) and purification as for **14a** gave the triethylammonium salt of **18** as a colorless glass (12.5 μmol, 63%); $[\alpha]^{20}_D$ = −14 (*c* = 0.40, MeOH); ^{1}H NMR (CD_3OD, 400 MHz) δ ~3.3 (m, 4H, (buried), OCH_2CH_2N), 3.60 (dd, 2H, J = 9.8, 2.3 Hz, 3-H), 3.80−3.87 (m, 2H, $OCHCH_2N$), 3.88−3.96 (m, 2H, $OCHCH_2N$), 3.96−4.07 (m, 8H, 1-H, 2-H, 5-H and 6-H), 4.35 (ddd, 2H, J = 9.4, 9.09, 8.6 Hz, 4-H); ^{31}P NMR (CD_3OD, 162 MHz) δ 2.08 (2P), 3.42 (2P) and 3.79 (2P); MS *m/z* (−ve ion FAB, relative intensity); 951 (M^-, 100%), accurate mass FAB− calcd for $C_{17}H_{37}N_2O_{31}P_6^-$, 950.9806; found 950.9789.

RESULTS

Synthetic Strategy. Structure−activity studies using synthetic Ins(1,4,5)P_3 analogues (*29*, *30*) have demonstrated that large groups can be attached to the axial 2-oxygen atom of Ins(1,4,5)P_3 with minimal reduction in affinity for InsP_3Rs. This suggested that, at the Ins(1,4,5)P_3-binding sites of InsP_3Rs, this area may be open to solvent. This hypothesis has subsequently been confirmed with the publication of the X-ray crystal structure of the Ins(1,4,5)P_3-binding core (*25*). We therefore envisaged a strategy in which a 2-*O*-aminoalkyl-modified Ins(1,4,5)P_3 headgroup would be conjugated with a range of linkers to give dimers of Ins(1,4,5)P_3. These dimers would then be used to conduct a distance scan to identify the separation of Ins(1,4,5)P_3-binding sites. If bivalent binding to InsP_3Rs could be achieved then this should be signaled by an increase in potency for dimers with a particular range of lengths. The same Ins(1,4,5)P_3 headgroup could then be conjugated with more rigid spacers or scaffolds in the appropriate size range. For the linkers, we chose activated derivatives of PEGs and their shorter oligo(ethylene glycol) equivalents. While highly flexible linkers such as PEG may not be ideal in terms of enhancement of potency (*6*), the facts that PEGs are water-soluble irrespective of size, and available in a range of lengths make them an attractive starting point when the locations of the binding sites are unknown and their separation is possibly large, as in the case of InsP_3Rs. For installation of the Ins(1,4,5)P_3 headgroups, we identified **2** (Scheme 1) as a key intermediate. In **2**, a selectively protected derivative of Ins(1,4,5)P_3, the phosphate monoesters and hydroxyl groups are masked with benzyl groups, leaving a primary amine group exposed for reaction with electrophilically activated linkers. A major advantage of this approach, as opposed to using a simple aminoalkyl derivative of Ins(1,4,5)P_3 itself, is that the coupling reactions can be carried out in organic solvents under anhydrous conditions, and the product can be purified to homogeneity by chromatography on silica gel before a final deprotection step. This strategy avoids any hydrolysis of reactive end-groups on the spacer and minimizes the possibility of contamination of the final product with monomeric linker-Ins(1,4,5)P_3 conjugates.

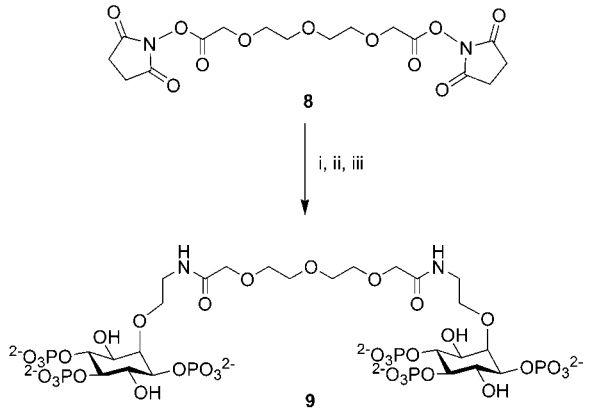
Scheme 1. Preparation of Protected 2-*O*-(2-Aminoethyl)-Ins(1,4,5)P_3 (2)[a]



[a] Reagents and conditions: i, (*a*) Bu_2SnO, MeOH, reflux, 16 h; (*b*) PMBCl, CsF, DMF, 50 °C, 5 h, ii, NaH, $BrCH_2CN$, CH_3CN, −20 °C to −40 °C 5 h then room temp, 16 h; iii, (*a*) $LiAlH_4$, THF, room temp, 1 h, (*b*) ethyl trifluoroacetate, THF, room temp, 1 h, (*c*) TFA/CH_2Cl_2/H_2O 19:20:1, room temp, 30 min; iv, $(BnO)_2PNPr^i_2$, 1*H*-tetrazole, CH_2Cl_2, room temp, 1 h, then MCPBA, −78 °C to room temp, 30 min; v, LiOH·H_2O (10 equiv) in THF/MeOH/H_2O 2:2:1, room temp, 1 h. Bn = benzyl, PMB = 4-methoxybenzyl.

Preparation of a Selectively Protected 2-*O*-(2-Aminoethyl)−Ins(1,4,5)P_3 for Cross-Linking. The required amine **2** was synthesized from diol **3** (*26*) (Scheme 1). Regioselective stannylene-mediated alkylation of the equatorial 1-OH group with 4-methoxybenzyl chloride gave the alcohol **4** in 80% yield. Alkylation of the free 2-OH group in **4** with bromoacetonitrile and sodium hydride at reduced temperatures in acetonitrile (*31*) then gave the crystalline 2-*O*-cyanomethyl derivative **5** in 83% yield. Higher temperatures and alternative solvents gave much-reduced yields. The nitrile group of **4** was smoothly reduced with $LiAlH_4$ in THF to give the primary amine, which was not isolated but temporarily protected as the trifluoroacetamide. This was conveniently achieved by reaction of the crude amine, after standard aqueous workup, with ethyl trifluoroacetate in THF (*32*). Finally, the acid-labile butanediacetal (BDA) and PMB protecting groups were cleaved using TFA, exposing the hydroxyl groups at positions 1, 4, and 5. The trifluoracetyl protection was not affected under these conditions, and the crystalline triol **6** was obtained in 77% overall yield over three steps from **5**. Phosphitylation using bis(benzyloxy)diisopropylaminophosphine and 1*H*-tetrazole followed by in situ oxidation with MCPBA gave crystalline **7** in 96% yield.

Scheme 2. Synthesis of a Short Oligo(ethylene glycol)-Linked Ins(1,4,5)P_3 Dimer[a]



[a] Reagents and conditions: i, **2**, DMF, room temp, 16 h; ii, H_2, Pd−C, MeOH/H_2O, 50 psi, room temp, 16 h; iii, Ion-exchange chromatography on Q Sepharose Fast Flow resin.

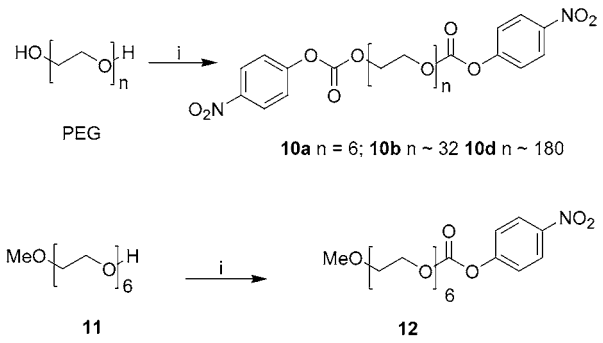
It was now necessary to expose the primary amine by selective removal of the trifluoroacetyl group from **7**. Treatment of **7** with methanolic ammonia or K_2CO_3 in aqueous methanol was only partially successful; long reaction times were required, leading to the formation of various polar products, presumably from partial cleavage of benzyl phosphate esters. However, it was found that the trifluoroacetyl group could cleanly be removed by treatment using LiOH in THF/MeOH/H_2O (*33*) for 1 h. Within this time there was little effect on the benzyl phosphate groups. Amine **2** was found to be an unstable oil and was therefore prepared freshly for each cross-linking reaction from **7**, which can conveniently be stored in crystalline form at room temperature for at least a year without deterioration.

Synthesis of a Small Oligo(ethylene glycol)-Linked Ins(1,4,5)P_3 Dimer. Our first attempt at cross-linking molecules of **2** employed the disuccinimidyl ester **8** (*27*) of 3,6,9-trioxaundecane-1,11-dioic acid (Scheme 2). The reaction of **8** with 3 equiv of **2** gave a complex mixture of products, but after careful chromatography on silica it was possible to obtain the required benzyl-protected dimeric intermediate with amide linkages in about 60 to 80% purity as judged by TLC. The mixture was deprotected by hydrogenolysis over Pd−C, and the product was purified by ion-exchange chromatography on Q Sepharose Fast Flow resin, eluting with a gradient of TEAB buffer. Phosphate-containing fractions were identified by a modification of the Briggs phosphate test (*22*), and the pure triethylammonium salt of the target dimer **9** was isolated in low overall yield. The dimeric structure of **9** was clearly apparent from integration of signals in its ^{1}H NMR spectrum, and from its FAB mass spectrum.

The reaction of **2** with longer PEG diacid linkers activated as disuccinimidyl esters was less satisfactory. The coupling reactions were difficult to follow, and the highly reactive disuccinimidyl esters had to be synthesized from their respective PEG diacids immediately before use to avoid the possibility of partial hydrolysis on storage, which could lead to complications from the formation of monomeric conjugates. Although we successfully isolated a longer Ins(1,4,5)P_3 dimer of this type, with a PEG600 spacer (*21*) in low yield (details not shown), we decided to investigate an alternative strategy for cross-linking of **2**.

Synthesis of Homobifunctional PEG−Carbonate Linkers. As an alternative to the disuccinimidyl esters, we now explored the use of activated carbonate esters of PEGs, which would give carbamate rather than amide linkages on reaction with **2**. Activated carbonate esters are more stable than their activated carboxylic ester equivalents and also have the advantage that they can be prepared directly from commercially available PEGs (*34*). We found that either succinimidyl carbonates (*35*, *36*) or 4-nitrophenyl carbonates were suitable, but we eventually chose 4-nitrophenyl carbonates because the coupling reactions were more easily followed by TLC (see below). The PEG−bis(4-nitrophenyl carbonate) esters were easily prepared by reaction of the appropriate PEG with bis(4-nitrophenyl) carbonate, and they could be purified to homogeneity by flash chromatography on silica. Thus, reaction of hexa(ethylene glycol) with bis-(4-nitrophenyl) carbonate in DMF in the presence of DIPEA (Scheme 3) gave the required bis(4-nitrophenyl carbonate) ester **10a** in 96% yield after chromatography, and similar reactions between PEG1450 and PEG8000 gave the corresponding homobifunctional linkers. The bis(4-nitrophenyl carbonate) ester of PEG3350 (**10c**) is commercially available. The mono(4-nitrophenyl carbonate) ester **12**, for use in the construction of a monofunctional version of **10a** was also synthesized in a similar way from methoxyhexa(ethylene glycol) **11** (*28*).

Scheme 3. Synthesis of Homobifunctional Linkers 10a, 10b, and 10d and Mono(4-nitrophenyl carbonate) Ester 12[a]

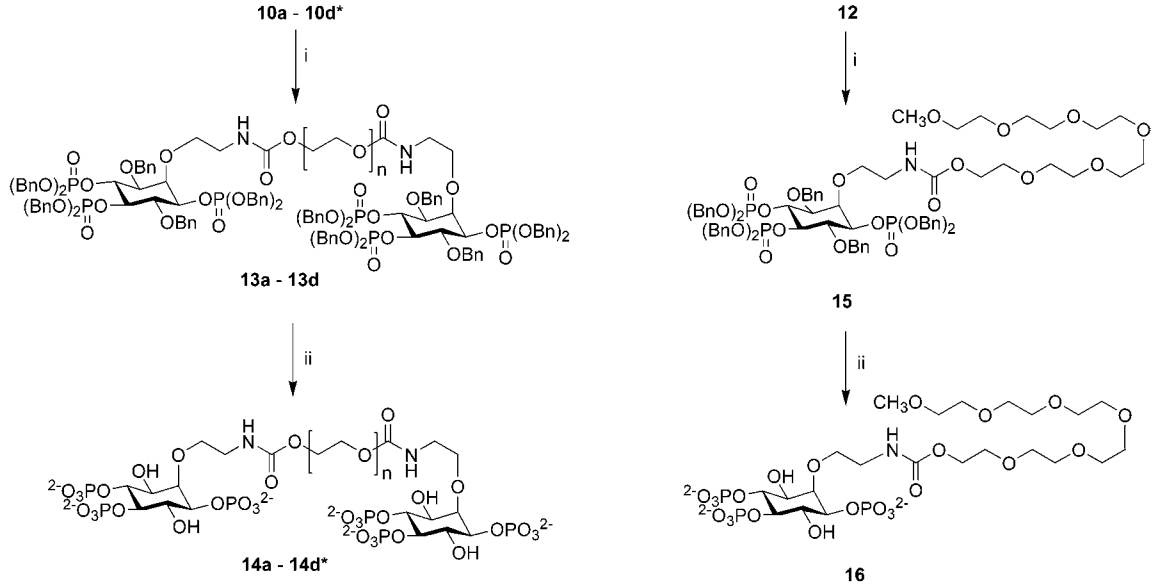


[a] Reagents and conditions: i, Bis(4-nitrophenyl)carbonate, DMF, DIPEA, 20 h.

Synthesis of PEG−Ins(1,4,5)P_3 Conjugates with Carbamate Linkages to PEG. The reaction of **10a** with an excess of freshly prepared **2** (Scheme 4) proceeded smoothly, and the benzyl-protected dimer **13a** was isolated in 58% yield after flash chromatography on silica. The reaction could conveniently be monitored using TLC by the appearance of 4-nitrophenol (yellow, UV-active spot) and the disappearance of amine (polar, UV-active spot, stains with phosphomolybdic acid) and activated PEG (UV-active spot, stains yellow on heating) and the concomitant appearance of the required product **13a** (UV-active, no yellow on heating, stains with phosphomolybdic acid). The ^{1}H NMR spectrum of **13a** showed a characteristic signal (broad triplet, ^3J = 5.3 Hz) at 5.60 ppm corresponding to the two carbamate NH protons, while the ^{31}P spectrum of **13a** showed three well-resolved signals, each corresponding to two equivalent phosphorus atoms of the protected Ins(1,4,5)P_3 headgroups. Hydrogenolytic deprotection as in the synthesis of **9**, followed by purification as before, gave pure **14a**, isolated as its triethylammonium salt.

The much larger protected dimeric intermediates **13b−d** were now synthesized by reaction of homobifunctional linkers **10b−d** with freshly prepared amine **2**, and in each case, the protected dimeric intermediate was isolated by flash chromatography on silica. For these

Scheme 4. Synthesis of PEG-Linked Ins(1,4,5)P_3 Dimers 14a to 14d, with Carbamate Linkages to PEG, and of a Monomeric Control (16)[a]



[a] Reagents and Conditions: i, **2**, DMF, room temp, 16−24 h; ii, H_2, Pd−C, MeOH/H_2O, 50 psi, room temp, 24 h, then ion-exchange chromatography on Q Sepharose Fast Flow resin. ***a**, $n = 6$; **b**, n ∼ 32; **c**, n ∼ 75; **d**, n ∼ 180. Bn = benzyl.

larger PEG-linked dimers, the ^{1}H NMR spectra of intermediates **13b**−**d** were invaluable in confirming the structures of the dimers. Because each molecule of **13a**−**d** contains 16 benzyl groups, the large aromatic proton signal in the ^{1}H NMR spectrum of each intermediate (integrating to eighty protons) could be accurately integrated and compared with the PEG-CH_2 signal at approximately 3.5 to 3.7 ppm, allowing the dimeric structure to be verified in each case. This was particularly important for the two largest dimers, whose ^{1}H NMR spectra after deprotection were dominated by the PEG-CH_2 signal. Signals in the ^{31}P NMR spectra of the protected dimeric intermediates became broader with increasing PEG size, and for **13c** and **13d**, they coalesced into a single broad peak. Hydrogenolytic deprotection of **13b** to **13d** and purification of the products by ion exchange chromatography as before gave dimers **14b** to **14d**, each of whose ^{31}P NMR spectra in CD_3OD showed three well-resolved signals, irrespective of PEG size. Finally, a monomeric version of **14a** was synthesized for use as a control in biological experiments. Thus, the reaction of **2** with excess methoxyhexa(ethylene glycol) 4-nitrophenyl carbonate ester **12** (Scheme 4) gave the protected mPEG-Ins(1,4,5)P_3 conjugate **15**, isolated in 58% yield after flash chromatography. Deprotection and purification as before gave pure **16**.

Binding of Ins(1,4,5)P_3 Dimers to Cerebellar Membranes. Equilibrium competition binding studies of the monomeric conjugate **16** using cerebellar membranes showed that the oligo(ethylene glycol) structure alone slightly reduced binding affinity (Table 1 and ref 21); the K_d for **16** (23.6 ± 2 nM) was slightly higher than that for Ins(1,4,5)P_3 (11.52 ± 1.98 nM). However, similar experiments using the equivalent dimer **14a** showed that the K_d of **14a** (3.17 ± 0.08 nM) was three to four times *lower* than that of Ins(1,4,5)P_3. The fact that the affinity of **14a** for cerebellar InsP_3Rs was more than 7-fold higher than its monomeric equivalent **16**, confirmed that the enhanced affinity of the short oligo(ethylene glycol)-linked dimers resulted from the second molecule of Ins(1,4,5)P_3 and was not related to the presence of the oligo(ethylene glycol) tether. The short dimer with amide linkages (**9**) showed activity close to that of the similarly sized dimer **14a**, with a K_d some 6-fold lower than that measured for Ins(1,4,5)P_3. The longer dimers **14b** and **14c** bound with affinities slightly higher than Ins(1,4,5)P_3 itself, but lower than the short dimers, although the longest dimer (**14d**) also appeared to show a significant gain in binding affinity relative to Ins(1,4,5)P_3 (*21*). The demonstration that even dimers with very large tethers (PEG8000 in **14d**) can bind to InsP_3Rs with high affinity confirmed our expectation that, at the Ins(1,4,5)P_3-binding site, the area close to the 2-oxygen atom of Ins(1,4,5)P_3 must be open to solvent.

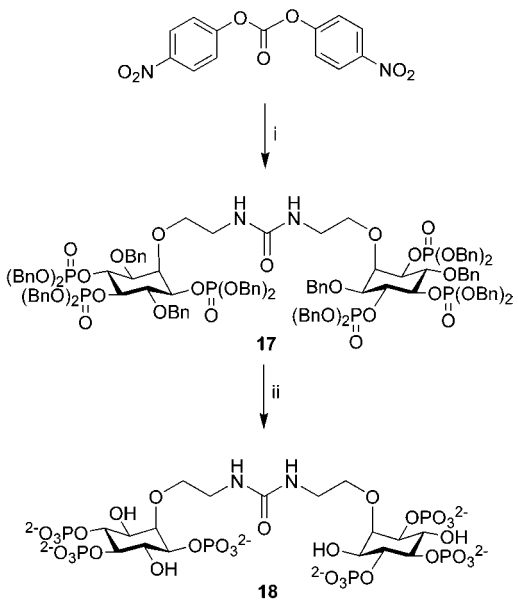
Table 1. Effects of Ins(1,4,5)P_3 Dimers on Ca^{2+} Release from Permeabilized Hepatocytes and [^{3}H]Ins(1,4,5)P_3 Binding to Membranes from Cerebellum[a]

	EC_{50} relative to Ins(1,4,5)P_3 (hepatocytes)	K_d relative to Ins(1,4,5)P_3 (cerebellum)
Ins(1,4,5)P_3	1	1
adenophostin A	13.3 ± 2.5	6.44 ± 1.06
16 (monomer)	ND	0.49 ± 0.09[b]
9	2.9 ± 0.4[b]	6.19 ± 1.24[b]
14a	3.8 ± 0.6[b]	3.64 ± 0.63[b]
14b	0.9 ± 0.1[b]	1.76 ± 0.45[b]
14c	1.7 ± 0.4[b]	1.41 ± 0.41[b]
14d	1.4 ± 0.3[b]	3.67 ± 0.64[b]
18	12.7 ± 4.9	ND

[a] Results (means ± SE from at least three experiments) show the ability of the analogues to stimulate $^{45}Ca^{2+}$ release from permeabilized hepatocytes (EC_{50}) and to displace specific binding of [^{3}H]Ins(1,4,5)P_3 from cerebellar membranes (K_d). In both cases, results are expressed relative to the effect of Ins(1,4,5)P_3 measured in parallel, with numbers greater than unity denoting analogues with greater potency (or affinity) than Ins(1,4,5)P_3. ND, not determined. At maximally effective concentrations, each analogue displaced all specifically bound [^{3}H]Ins(1,4,5)P_3 and released a similar fraction of the intracellular Ca^{2+} stores as that released by Ins(1,4,5)P_3 (54 ± 3%, $n = 20$). [b] Calculated from data published in (*21*).

Synthesis of a Short, Urea-Linked Ins(1,4,5)P_3 Dimer. As the equilibrium binding experiments showed that dimers with short linkers had the highest affinities for InsP_3Rs, a further logical step was to synthesize a

Scheme 5. Synthesis of Urea-Linked Ins(1,4,5)P_3 Dimer 18



[a] Reagents and Conditions: i, **2**, DMF, room temp, 16h; ii, H_2, Pd−C, MeOH/H_2O, 50 psi, 24 h, then ion-exchange chromatography on Q Sepharose Fast Flow resin. Bn = benzyl.

dimer having the shortest possible (one carbon) linker. It has previously been demonstrated that reaction of bis(4-nitrophenyl) carbonate with amines provides a convenient method for the synthesis of ureas (*37*), and we found that this method could be applied to the dimerization of amine **2**. Thus, the reaction of 3 equiv of **2** with pure bis(4-nitrophenyl) carbonate (recrystallized from CH_2Cl_2/hexane) in DMF gave the benzyl-protected symmetrical urea-linked dimer **17**, which could be isolated by flash chromatography in 71% yield (Scheme 5).

The ^{1}H NMR spectrum of **17** in $CDCl_3$ showed a signal at 5.99 ppm (broad triplet, ^3J approximately 5 Hz) corresponding to the two urea NH protons, and the ^{13}C NMR spectrum of **17** showed the signal of a quaternary carbon atom resonating at 158.3 p.p.m, corresponding to the urea carbonyl carbon atom. The ^{31}P NMR spectrum showed three signals corresponding to the three pairs of equivalent phosphorus atoms in the symmetrical molecule. Total deprotection of **17** as for the PEG-linked dimers gave the divalent Ins(1,4,5)P_3 analogue **18** as its triethylammonium salt, which, like the PEG-linked dimers, was freely soluble in water or methanol.

Stimulation of Ca^{2+} Release from Permeabilized Hepatocytes. When tested for their ability to release Ca^{2+} from the intracellular stores of permeabilized hepatocytes, all the dimers potently stimulated the release of intracellular Ca^{2+}, with maximally effective concentrations of each dimer releasing similar fractions of the intracellular Ca^{2+} stores. In agreement with the results from equilibrium binding experiments in cerebellum (see above), all the dimers had EC_{50} values similar to, or lower than that of Ins(1,4,5)P_3, with the shorter dimers showing the lowest EC_{50} values (Table 1 and ref 21). Surprisingly, the new urea-linked dimer **18**, in which the two Ins(1,4,5)P_3 motifs are held closest together, was by far the most potent of the series, with an EC_{50} value more than 12-fold lower than Ins(1,4,5)P_3 (Table 1 and Figure 2). The potency of **18** in these experiments approached that of adenophostin A (Table 1) the most potent known agonist of InsP_3Rs.

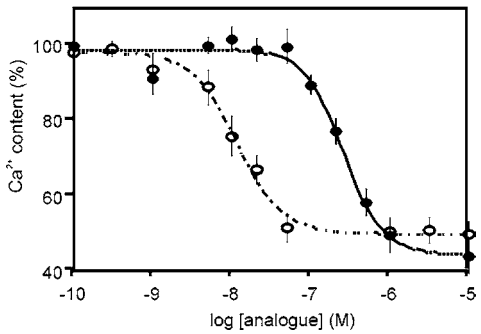


Figure 2. The effects of the indicated concentrations of Ins(1,4,5)P_3 (filled circles) or **18** (open circles) on the intracellular stores of permeabilized hepatocytes. Results are means ± SE from 10 [Ins(1,4,5)P_3] or 19 (**18**) independent experiments.

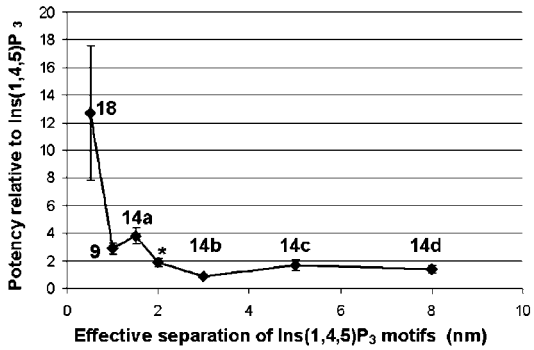


Figure 3. Relative potencies of Ins(1,4,5)P_3 dimers in evoking Ca^{2+} release from permeabilized hepatocytes plotted as a function of effective (rms) separation of the two component Ins(1,4,5)P_3 structures in each dimer. *Measured using an Ins(1,4,5)P_3 dimer synthesized from PEG600 diacid in a similar way to dimer **9** (*21*).

DISCUSSION

To estimate the separation of the two Ins(1,4,5)P_3 structures in each dimer, we followed the approach described by Kramer and Karpen (*19*) in which the effective separation is taken as the average (rms) length of the flexible PEG linker. The rms length can be calculated from previous determinations of the lengths of specific PEGs (*38*) assuming that the rms length is proportional to the square root of the number of ethylene glycol monomers. This method predicts rms lengths of approximately 1 and 1.5 nm, respectively, for the linkers in the two smallest oligo(ethylene glycol)-linked dimers (**9** and **14a**), increasing to 8 nm for the largest dimer (**14d**). It should be remembered, however, that more extended conformations of the longer dimers are capable of spanning much greater distances than 8 nm. This method of estimating separation is difficult to apply to the very short dimer **18**, in which the PEG is replaced by a single atom linker. However, molecular models show that even in the most extended conformations of **18**, the distance between the two O-2 atoms of the two Ins(1,4,5)P_3 motifs cannot be greater than 1 nm. For **18**, the linker between Ins(1,4,5)P_3 motifs contains only six rotatable bonds, and its rigidity relative to the other dimers may also be an important factor, even though the effective separation of its two component Ins(1,4,5)P_3 structures may be only slightly less than the rms separation in **9**. Figure 3 compares the Ca^{2+}-releasing potencies of the dimers in permeabilized hepatocytes measured relative to that of Ins(1,4,5)P_3, plotted as a function of the effective (rms) separation of the two component Ins(1,4,5)P_3 motifs in each dimer. Clearly the potency decreases steeply as effective separation increases, falling

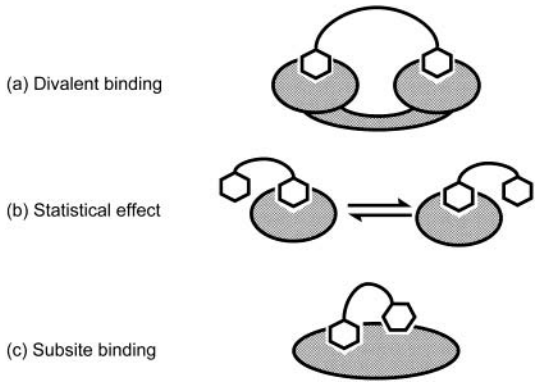


Figure 4. Schematic representations of three possible modes of interaction of Ins(1,4,5)P_3 dimers with binding sites of InsP_3Rs.

to Ins(1,4,5)P_3-like levels beyond an effective separation of around 2 nm.

We have suggested elsewhere (*21*) that dimers **9** and **14a** may be able to bridge equivalent Ins(1,4,5)P_3 binding sites within tetrameric InsP_3Rs. This interpretation is supported by more detailed experiments, which showed that long (**14d**) and short (**9** and **14a**) dimers bound to monomeric Ins(1,4,5)P_3-binding domains with similar affinities to Ins(1,4,5)P_3, so that high-affinity binding for **9** and **14a** (Table 1) appears to require that the receptors are in the tetrameric state. We also suggested that the increased affinity of the longest dimer (**14d**) for cerebellar membranes, where the receptors are densely packed, may result from the linked Ins(1,4,5)P_3 molecules binding to sites on adjacent receptors, because **14d** binds to purified tetrameric cerebellar receptors with similar affinity to Ins(1,4,5)P_3 (*21*). However, the unexpectedly high potency of the very short dimer **18** may be difficult to reconcile with either explanation (intratetramer or intertetramer binding).

Three possible explanations for the high potency of **18** are summarized schematically in Figure 4:

(a) Divalent binding (Figure 4a). In this explanation, the two Ins(1,4,5)P_3 structures in **18** can occupy equivalent Ins(1,4,5)P_3-binding sites. However, molecular models show that even in the most extended conformations of **18**, the distance between the two O-2 atoms of the two Ins(1,4,5)P_3 motifs cannot be greater than 1 nm. It seems very unlikely that the Ins(1,4,5)P_3-binding sites could be so close, little more than the width of a single Ins(1,4,5)P_3 molecule.

(b) A statistical effect (Figure 4b). The high local concentration of the Ins(1,4,5)P_3 motif in **18** may favor rebinding (*39*−*41*) and thereby enhance apparent affinity for InsP_3Rs. Against this analysis, however, it has been shown that the small clustered disaccharide analogues (Figure 1) did not show enhanced affinity for InsP_3Rs over their monomeric equivalent (*13*). It is not obvious why a statistical effect, arising from a simple effect on local concentration, could enhance the affinity of **18**, but not the affinities of diphostin and tetraphostin (Figure 1) for InsP_3Rs, although **18** is likely to be smaller and more rigid than the clustered disaccharides.

(c) Subsite binding (Figure 4c). This interpretation is based on the idea that elements of the second Ins(1,4,5)P_3 motif in **18** may be able to interact with residues close to the Ins(1,4,5)P_3-binding site to enhance binding of the dimer. While this work was nearing completion, the X-ray crystal structure of the core binding domain (residues 224−604) of the mouse type 1 receptor (InsP_3R1) was reported (*25*). This allowed us to explore the possibility of subsite binding for **18** using a molecular modeling approach.

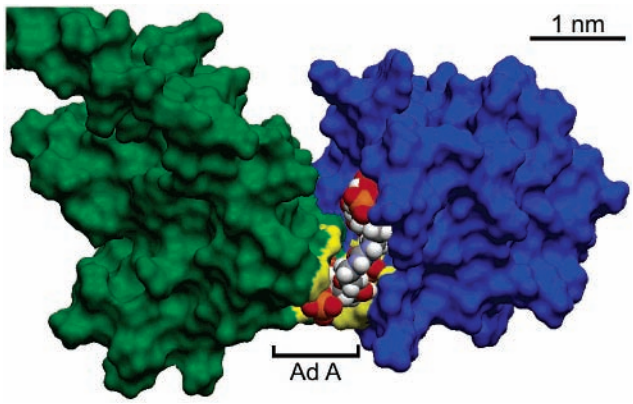


Figure 5. Representative result from molecular docking experiments of **18** and the X-ray crystal structure (*25*) of the type 1 InsP_3R Ins(1,4,5)P_3-binding core. While one Ins(1,4,5)P_3 motif occupies the Ins(1,4,5)P_3-binding site (colored yellow), components of the second motif could interact with other residues elsewhere within the cleft between the α-domain (green) and *β*-domain (blue). The proposed subsite for interaction with the adenosine component of adenophostin A (*5*) is indicated by a bracket.

In the X-ray structure, the bound molecule of Ins(1,4,5)P_3 occupies one end of a deep cleft between two domains. As expected, the area of the binding site around the 2-hydroxyl group of the bound Ins(1,4,5)P_3 molecule is open to solvent. This validates our choice of the 2-oxygen atom of Ins(1,4,5)P_3 for the attachment of linkers in the design of the dimers (see above) and is in agreement with the high affinity of the dimers for the InsP_3Rs of cerebellum, which are primarily type 1. Although the Ca^{2+}-release experiments described here were carried out using hepatocytes, which express mainly type 2 InsP_3Rs, the high homology between the Ins(1,4,5)P_3-binding domains of InsP_3R1 and InsP_3R2 in the Ins(1,4,5)P_3-binding region justifies our use of the InsP_3R1 crystal structure in the analysis of the Ca^{2+}-release results. We therefore carried out molecular docking experiments using **18** and this structure. In the highest-scored docking results, one Ins(1,4,5)P_3 motif of **18** consistently docked into the Ins(1,4,5)P_3-binding site in a similar way to the crystallographically observed position of bound Ins(1,4,5)P_3, while the second motif interacted with other residues within the cleft (Figure 5). It was not possible to identify a single definitive binding mode for **18** because different positions were observed for the second Ins(1,4,5)P_3 according to the details of the docking procedure used, and different residues were involved. Nevertheless, these experiments support the idea that the surprisingly high potency of **18** could result from subsite binding.[1]

[1] After this manuscript was submitted, a three-dimensional electron microscopy study (*44*) was published in which the cytosolic domains of type 1 InsP_3Rs were sometimes observed to be in head-to-head contact such that analogous regions of each might be in close proximity. This led the authors to suggest that our short dimers (**9** and **14a**) may be linking the Ins(1,4,5)P_3-binding domains of different receptors, and that the longest dimer (**14d**) may link Ins(1,4,5)P_3-binding domains within a receptor. While it is not impossible for the two Ins(1,4,5)P_3 motifs in the new dimer **18** to span two Ins(1,4,5)P_3 binding sites in this head-to head mode, we still consider that subsite binding is the most likely explanation for the high potency of **18**. Further investigations are underway.

Adenophostin A, the most potent known agonist of $InsP_3Rs$, has also been proposed to interact with residues close to the Ins(1,4,5)P_3-binding site (Figure 5) (*5*). It would be particularly interesting if **18** could derive its similar enhanced potency by accessing a different subsite, as proposed here. Further investigations to identify the mode of action of **18** are in progress. If **18** does achieve its higher potency by a nonspecific interaction of one Ins(1,4,5)P_3 motif with residues close to the Ins(1,4,5)P_3-binding site then it is likely that only some elements of this second Ins(1,4,5)P_3 component are involved, and also that the interactions involved are not optimal. In that case it might be possible to create even more potent ligands by replacing the second Ins(1,4,5)P_3 motif in **18** with other structures. This suggests a new, divergent strategy for synthesizing potent Ins(1,4,5)P_3 analogues by conjugating 2-*O*-(2-aminoethyl)-Ins(1,4,5)P_3 with a range of molecular fragments chosen to interact with other regions of the $InsP_3R$ that lie close to the Ins(1,4,5)P_3-binding site.

In conclusion, we have presented a synthetic strategy for the construction of divalent analogues of Ins(1,4,5)P_3, examined the effects of Ins(1,4,5)P_3 dimers on Ins(1,4,5)P_3 receptors, and discussed possible interpretations of the results. The synthetic approach described here is equally applicable to the synthesis of multivalent forms of other inositol phosphates. Modular phosphoinositide binding domains such as PH (*42*) and FYVE (*43*) domains may form oligomers, for example, and these small proteins could be attractive targets for synthetic multivalent inositol phosphate ligands. In some cases the appropriate size of linker could be estimated directly from available X-ray structures, allowing rigid scaffolds of well-defined geometry and size to be employed in place of flexible PEG tethers where necessary. Finally, the short urea-linked Ins(1,4,5)P_3 dimer **18** is the most potent inositol-based $InsP_3R$ ligand yet identified, providing a basis for the development of a potential new class of high-affinity synthetic probes for $InsP_3Rs$.

ACKNOWLEDGMENT

We thank the Wellcome Trust for Programme Grant support (0060554 to B.V.L.P. and 039662 to C.W.T.).

LITERATURE CITED

(1) Berridge, M. J., Lipp, P., and Bootman, M. D. (2000) The versatility and universality of calcium signaling. *Nature Rev. Mol. Cell Biol. 1*, 11−21.

(2) Takahashi, M., Tanzawa, K., and Takahashi, S. (1994) Adenophostins, newly discovered metabolites of *Penicillium brevicompactum*, act as potent agonists of the inositol 1,4,5-trisphosphate receptor. *J. Biol. Chem. 269*, 369−372.

(3) Morris, S. A., Nerou, E. P., Riley, A. M., Potter, B. V. L., and Taylor, C. W. (2002) Determinants of adenophostin A binding to inositol trisphosphate receptors. *Biochem. J. 367*, 113−120.

(4) Hotoda, H., Murayama, K., Miyamoto, S., Iwata, Y., Takahashi, M., Kawase, Y., Tanzawa, K., and Kaneko, M. (1999) Molecular recognition of adenophostin, a very potent Ca^{2+} inducer, at the D-*myo*-inositol 1,4,5-trisphosphate receptor. *Biochemistry 38*, 9234−9241.

(5) Rosenberg, H. J., Riley, A. M., Laude, A. J., Taylor, C. W., and Potter, B. V. L. (2003) Synthesis and Ca^{2+}-mobilizing activity of purine-modified mimics of adenophostin A: a model for the adenophostin-Ins(1,4,5)P_3 receptor interaction. *J. Med. Chem. 46*, 4860−4871.

(6) Mammen, M., Choi, S.-K., and Whitesides, G. M. (1998) Polyvalent interactions in biological systems: implications for design and use of multivalent ligands and inhibitors. *Angew. Chem., Int. Ed. Engl. 37*, 2754−2794.

(7) Portoghese, P. S. (2001) From models to molecules: opioid receptor dimers, bivalent ligands, and selective opioid receptor probes. *J. Med. Chem. 44*, 2259−2269.

(8) Gordon, E. J., Gestwicki, J. E., Strong, L. E., and Kiessling, L. L. (2000) Synthesis of end-labeled multivalent ligands for exploring cell-surface-receptor−ligand interactions. *Chem. Biol. 7*, 9−16.

(9) Fan, E., Zhang, Z., Minke, W. E., Hou, Z., Verlinde, C. L. M. J., and Hol, W. G. J. (2000) High-affinity pentavalent ligands of *Escherichia coli* heat-labile enterotoxin by modular structure-based design. *J. Am. Chem. Soc. 122*, 2663−2664.

(10) Loidl, G., Groll, M., Musiol, H.-J., Huber, R., and Moroder, L. (1999) Bivalency as a principle for proteasome inhibition. *Proc. Natl. Acad. Sci. U.S.A. 96*, 5418−5422.

(11) Schaschke, N., Matschiner, G., Zettl, F., Marquardt, U., Bergner, A., Bode, W., Sommerhoff, C. P., and Moroder, L. (2001) Bivalent inhibition of human β-tryptase. *Chem. Biol. 8*, 313−327.

(12) Lyon, R. P., Hill, J. J., and Atkins, W. M. (2003) Novel class of bivalent glutathione *S*-transferase inhibitors. *Biochemistry 42*, 10418−10428.

(13) de Kort, M., Correa, V., Valentijn, A. R. P. M., van der Marel, G. A., Potter, B. V. L., Taylor, C. W., and van Boom, J. H. (2000) Synthesis of potent agonists of the D-*myo*-inositol 1, 4, 5- trisphosphate receptor based on clustered disaccharide polyphosphate analogues of adenophostin A. *J. Med. Chem. 43*, 3295−3303.

(14) Chadwick, C. C., Saito, A., and Fleischer, S. (1990) Isolation and characterization of the inositol trisphosphate receptor from smooth muscle. *Proc. Natl. Acad. Sci. U.S.A. 87*, 2132−2136.

(15) Katayama, E., Funahashi, H., Michikawa, T., Shiraishi, T., Ikemoto, T., Iino, M., Hirosawa, K., and Mikoshiba, K. (1996) Native structure and arrangement of inositol-1,4,5-trisphosphate receptor molecules in bovine cerebellar Purkinje cells as studied by quick-freeze deep-etch electron microscopy. *EMBO J. 15*, 4844−4851.

(16) Hamada, K., Miyata, T., Mayanagi, K., Hirota, J., and Mikoshiba, K. (2002) Two-state conformational changes in inositol 1,4,5-trisphosphate receptor regulated by calcium. *J. Biol. Chem. 277*, 21115−21118.

(17) da Fonseca, P. C. A., Morris, S. A., Nerou, E. P., Taylor, C. W., and Morris, E. P. (2003) Domain organisation of the type 1 inositol 1,4,5-trisphosphate receptor as revealed by single-particle analysis. *Proc. Natl. Acad. Sci. U.S.A. 100*, 3936−3941.

(18) Serysheva, I. I., Bare, D. J., Ludtke, S. J., Kettlun, C. S., Chiu, W., and Mignery, G. A. (2003) Structure of the type 1 inositol 1,4,5-trisphosphate receptor revealed by electron cryomicroscopy. *J. Biol. Chem. 278*, 21319−21322.

(19) Kramer, R. H., and Karpen, J. W. (1998) Spanning binding sites on allosteric proteins with polymer-linked ligand dimers. *Nature 395*, 710−713.

(20) Riley, A. M., and Potter, B. V. L. (2000) Poly(ethylene glycol)-linked dimers of D-*myo*-inositol 1,4,5-trisphosphate. *Chem. Commun.* 983−984.

(21) Riley, A. M., Morris, S. A., Nerou, E. P., Correa, V., Potter, B. V. L., and Taylor, C. W. (2002) Interactions of inositol 1,4,5-trisphosphate (IP3) receptors with synthetic poly(ethylene glycol)-linked dimers of IP3 suggest close spacing of the IP3-binding sites. *J. Biol. Chem. 277*, 40290−40295.

(22) Lampe, D., Liu, C., and Potter, B. V. L. (1994) Synthesis of selective non-Ca^{2+}-mobilizing inhibitors of D-*myo*-inositol 1,4,5-trisphosphate 5-phosphatase. *J. Med. Chem. 37*, 907−912.

(23) Ames, B. N., and Dubin, D. T. (1960) The role of polyamines in the neutralization of bacteriophage deoxyribonucleic acid. *J. Biol. Chem. 235*, 769−775.

(24) Jones, G., Willett, P., Glen, R. C., Leach, A. R., and Taylor, R. (1997) Development and validation of a genetic algorithm for flexible docking. *J. Mol. Biol. 267*, 727−748.

(25) Bosanac, I., Alattia, J.-R., Mal, T. K., Chan, J., Talarico, S., Tong, F. K., Tong, K. I., Yoshikawa, F., Furuichi, T., Iwai, M., Michikawa, T., Mikoshiba, K., and Ikura, M. (2002) Structure of the inositol 1,4,5-trisphosphate receptor binding core in complex with its ligand. *Nature 420*, 696−700.
(26) Riley, A. M., Correa, V., Mahon, M. F., Taylor, C. W., and Potter, B. V. L. (2001) Bicyclic analogues of D-*myo*-inositol 1,4,5-trisphosphate related to adenophostin A: synthesis and biological activity. *J. Med. Chem. 44*, 2108−2117.
(27) Wittmann, V., Takayama, S., Gong, K. W., Weitz-Schmidt, G., and Wong, C.-H. (1998) Ligand recognition by E- and P-selectin: chemoenzymatic synthesis and inhibitory activity of bivalent sialyl Lewis x derivatives and sialyl Lewis x carboxylic acids. *J. Org. Chem. 63*, 5137−5143.
(28) Yamashita, K., Janout, V., Bernard, E. M., Armstrong, D., and Regen, S. L. (1995) Micelle/monomer control over the membrane-disrupting properties of an amphiphilic antibiotic. *J. Am. Chem. Soc. 117*, 6249−6253.
(29) Hirata, M., Yanaga, F., Koga, T., Ogasawara, T., Watanabe, Y., and Ozaki, S. (1990) Stereospecific recognition of inositol 1,4,5-trisphosphate analogues by the phosphatase, kinase, and binding proteins. *J. Biol. Chem. 265*, 8404−8407.
(30) Potter, B. V. L., and Lampe, D. (1995) Chemistry of inositol lipid-mediated cellular signaling. *Angew. Chem., Int. Ed. Engl. 34*, 1933−1972.
(31) Malet, C., and Hindsgaul, O. (1996) Versatile functionalization of carbohydrate hydroxyl groups through their *O*-cyanomethyl ethers. *J. Org. Chem. 61*, 4649−4654.
(32) Xu, D., Prasad, K., Repic, O., and Blacklock, T. J. (1995) Ethyl trifluoroacetate − a powerful reagent for differentiating amino-groups. *Tetrahedron Lett. 36*, 7357−7360.
(33) Baker, R., and Castro, J. L. (1990) Total synthesis of (+)-macbecin-I. *J. Chem. Soc., Perkin Trans. 1* 47−65.
(34) Zalipsky, S. (1995) Functionalized poly(ethylene glycol) for preparation of biologically relevant conjugates. *Bioconjugate Chem. 6*, 150−165.
(35) Miron, T., and Wilchek, M. (1993) A simplified method for the preparation of succinimidyl carbonate poly(ethylene glycol) for coupling to proteins. *Bioconjugate Chem. 4*, 568−569.
(36) Morpurgo, M., Bayer, E. A., and Wilchek, M. (1999) *N*-hydroxysuccinimide carbonates and carbamates are useful reactive reagents for coupling ligands to lysines on proteins. *J. Biochem. Biophys. Methods 38*, 17−28.
(37) Izdebski, J., and Pawlak, D. (1989) A new convenient method for the synthesis of symmetrical and unsymmetrical *N*,*N*′-disubstituted ureas. *Synthesis* 423−425.
(38) Knoll, D., and Hermans, J. (1983) Polymer-protein interactions. Comparison of experiment and excluded volume theory. *J. Biol. Chem. 258*, 5710−5715.
(39) Kiessling, L. L., Gestwicki, J. E., and Strong, L. E. (2000) Synthetic multivalent ligands in the exploration of cell-surface interactions. *Curr. Opin. Chem. Biol. 4*, 696−703.
(40) Gestwicki, J. E., Cairo, C. W., Strong, L. E., Oetjen, K. A., and Kiessling, L. L. (2002) Influencing receptor−ligand binding mechanisms with multivalent ligand architecture. *J. Am. Chem. Soc. 124*, 14922−14933.
(41) Pohl, N. L., and Kiessling, L. L. (1999) Scope of multivalent ligand function: lactose-bearing neoglycopolymers by ring-opening metathesis polymerization. *Synthesis*, 1515−1519.
(42) Lemmon, M. A., and Ferguson, K. M. (2000) Signal-dependent membrane targeting by pleckstrin homology (PH) domains. *Biochem. J. 350*, 1−18.
(43) Stenmark, H., Aasland, R., and Driscoll, P. C. (2002) The phosphatidylinositol 3-phosphate-binding FYVE finger. *FEBS Lett. 513*, 77−84.
(44) Hamada, K., Terauchi, A., and Mikoshiba, K. (2003) Three-dimensional rearrangements within inositol 1,4,5-trisphosphate receptors by calcium. *J. Biol. Chem. 278*, 52881−52889.

BC034214S

Cellular Uptake of Antisense Morpholino Oligomers Conjugated to Arginine-Rich Peptides

Hong M. Moulton,* Michelle H. Nelson, Susie A. Hatlevig, Muralimohan T. Reddy, and Patrick L. Iversen

AVI BioPharma, Inc., Corvallis, Oregon 97333. Received December 5, 2003; Revised Manuscript Received January 14, 2004

Although the sequence specificity, biostability, and low toxicity of PMO (phosphorodiamidate morpholino oligomers) make them good antisense agents to study gene function, their limited ability to cross cell membranes limits their use in cell culture. In this paper we show that conjugation to arginine-rich peptides significantly enhanced the cellular uptake of PMO. The factors that affect the conjugate's cellular uptake and its antisense activity toward a targeted mRNA were investigated. Factors studied include the number of arginines in the peptide, the choice of cross-linker, the peptide conjugation position, the length of the PMO, and the cell culture conditions. Delivery of PMO to the cell nucleus and cytosol required conjugation rather than complexation of peptides to PMO. R_9F_2C was best suited to deliver a PMO to its target RNA resulting in the strongest antisense effect. By simply adding the R_9F_2C−PMO conjugate into the cell culture medium at low μM concentration, missplicing of pre-mRNA was corrected. This particular peptide-conjugated PMO was more effective than the PMO conjugated to the transmembrane transport peptides of HIV-1 Tat protein, *Drosophila* antennapedia protein, or to peptides with fewer arginines. Length of PMO did not affect a peptide's delivery efficacy, but all other factors were important. R_9F_2C peptide provided a simple and efficient delivery of PMO to a RNA target. Conjugation of peptide to PMO enhances the opportunities to evaluate gene functions in cell cultures.

INTRODUCTION

Phosphorodiamidate morpholino oligomers (PMO) (*1*, *2*) are antisense molecules that inhibit gene expression by preventing translation or interfering with pre-mRNA splicing. The antisense specificity and efficacy of PMO have been well demonstrated in cells and in embryos (*3*−*12*). PMO are similar to DNA with two major structural differences: the negatively charged phosphorodiester internucleoside linkage in DNA is replaced by the neutral phosphorodiamidate linkage; the five-membered ring of deoxyribose in DNA is replaced by the six-membered ring of morpholine (Figure 1). The uncharged and hydrophilic PMO are highly resistant to enzymes and biological fluids (*13*).

To bind to an RNA target, PMO must access the cytoplasm and/or nucleus. The typical length for a PMO to achieve effective antisense activity is between 18 and 25 bases. However, at this size, passive diffusion through cell membranes is slow. When using PMO to study gene function in cultured cells, delivery techniques such as scrape-loading (*14*) and using cationic lipid complexed with heteroduplexes of PMO/DNA (*15*) are generally required. Peptide-based delivery systems offer an attractive alternative to current delivery methods, being much simpler and relevant to in vivo applications.

Some naturally occurring proteins, such as *Drosophila* antennapedia (Ant) and HIV-1 Tat, easily transport macromolecules into cells. The motifs within the transport proteins responsible for membrane "penetration" have been identified and characterized as cationic in nature (*16*−*19*). The cationic transport peptides are especially useful for delivering uncharged antisense oligomers due to lack of the problematic electrostatic interactions which may occur with anionic antisense oligomers. The electrostatic interactions between cationic peptides and anionic oligomers mask the positive charges of the peptide that are important for its delivery ability, subsequently decreasing the delivery efficacy of the peptide. Tat or Ant peptides have been used to deliver uncharged peptide nucleic acids (PNA) (*19*−*22*). PTD4 is an analogue of pTat peptide and was designed to have

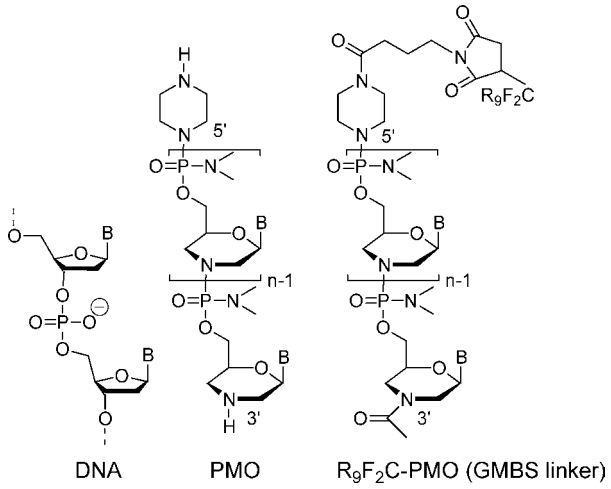


Figure 1. Structure of DNA, PMO, and R_9F_2C−PMO conjugate. The structure of the conjugate is shown with R_9F_2C peptide conjugated at the 5′-end of PMO by the GMBS linker. "B" represents a base.

* Corresponding author: Hong M. Moulton, Ph.D., AVI BioPharma, Inc., 4575 SW Research Way, Suite 200, Corvallis, OR 97333. Phone: (541) 753-3635. Fax: (541) 754−3545. E-mail: moulton@avibio.com.

10.1021/bc034221g CCC: $27.50 © 2004 American Chemical Society
Published on Web 02/28/2004

Table 1. Peptides and PMO: Nomenclatures and Sequences

names	sequence	length
	Peptides[a]	
pTat	NH_2-CYGRKKRRQRRR-$CONH_2$	12
PTD4	NH_2-YARAAARQARAC-$CONH_2$	12
pAnt	NH_2-DRQIKIWFQNRRMKWKKC-$CONH_2$	18
R_9F_2C	NH_2-RRRRRRRRRFFC-$CONH_2$	12
R_6F_2C	NH_2-RRRRRRFFC-$CONH_2$	9
R_5F_2C	NH_2-RRRRRFFC-$CONH_2$	8
	Antisense Oligomers[b]	
705[c]	CCT CTT ACC TCA GTT ACA-acetyl	18
705-FL[d]	CCT CTT ACC TCA GTT ACA-fluorescein	18
705(12)-FL	CTT ACC TCA GTT-fluorescein	12
705(24)-FL	CCT CTT ACC TCA GTT ACA ATT TAT-fluorescein	24

[a] The sequences of peptides are written using the standard one letter amino acid symbols from N to C terminus. [b] PMO sequences are written using the standard genetic code from 5′ to 3′-end. [c] The antisense PMO was targeted to a mutant splice site at the nucleotide 705 of human β-globin intron 2. [d] 705 had carboxylfluorescein attached at the 3′-end.

more α helical structure than pTat to improve cellular uptake (*23*). It has been reported that Jurkat cells take up the fluorescein-tagged PTD-4 33 times more than fluorescein-tagged pTat (*23*). We have previously shown that Tat peptide enhances cellular uptake of PMO in cultured cells (*24*) as well. But this requires high μM concentration to achieve antisense activity. Therefore, a more effective delivery peptide than the Tat peptide is needed.

We designed a peptide containing nine arginines (R), two phenylalanines (F), and one cysteine (C) with the sequence of NH_2-RRRRRRRRRFFC-$CONH_2$ (R_9F_2C). Arginine residues in the Tat peptide are found to be crucial for the cell delivery; substitution of nonarginine residues in the Tat peptide sequence with arginines increases the cellular uptake of a fluorescein tag (*25*). We added two phenylalanines to R_9 to increase hydrophobicity, enhancing interaction with cell membranes and improving purification by reverse phase chromatography. Adding a hydrophobic moiety onto an arginine-rich peptide has also been shown to increase uptake of the cargo (*26*, *27*). A final cysteine residue provided a sulfhydryl group for conjugation to PMO.

The effectiveness of a peptide to deliver PMO to the targeted mRNA was tested using a positive readout assay rather than conventional "knockdown" assays. Traditionally, decreasing gene expression of cells treated with antisense oligomers has been interpreted as the result of the antisense activity; however, other potential causes of decreased expression must be considered. For example, general suppression of gene expression in the target cells may result if an oligomer causes toxicity, if its degradation products are toxic, or if a delivery method causes toxicity. The toxicity may be misinterpreted as the antisense effect. To remedy these problems, an approach based on the ability of steric-blocking oligomers to alter mRNA splice site selection has been developed to evaluate antisense activity (*28*−*30*).

Sensitive assays that give positive readout of antisense action, in the form of production of functional reporter protein, have been devised in both cell culture (*31*, *32*) and in mice (*33*). These assays exploit mutations in intron 2 of human β-globin pre-mRNAs that lead to missplicing. The mutated intron cannot be properly excised resulting in an in-frame stop codon in the luciferase coding sequence. Two conditions must be met to produce the functional reporter protein at 37 °C. First, an antisense oligomer must enter the cell nucleus to block the mutated splice site, thus restoring normal splicing and read through of the reporter message. The result is mRNA-encoding functional reporter protein. Second, but equally important, the cells must be viable to carry out RNA processing and translation so that reporter protein activity is produced.

Using the splice correction assay, we assessed the necessity of covalent attachment verses complexation of the peptide and PMO and compared the effectiveness of R_9F_2C to other peptides for delivery of PMO to the targeted pre-mRNA. We further determined the effects of conjugation chemistry, conjugation position, length of PMO, and cell culture conditions on the cellular uptake and antisense activity of peptide−PMO conjugates. The linker effects on intracellular distribution and concentration of the peptide conjugated PMO were also examined by fluorescent microscopy and flow cytometry. The cellular toxicity of the conjugates was evaluated.

EXPERIMENTAL PROCEDURES

Peptides, PMO, and Cross-Linkers. The nomenclature and the sequences of peptides and PMO are listed in Table 1. All peptides were synthesized by Global Peptide Services (Ft. Collins, CO) and purified to >90% purity. PMO were synthesized at AVI BioPharma as described elsewhere (*1*, *34*). Cross-linkers: Sulfo-EMCS (*N*-[ϵ-maleimidocaproyloxyl]sulfosuccinimide ester) was obtained from Molecular Bioscience (Boulder, CO). GMBS (*N*-[γ-maleimidobutyryloxy]succinimide ester), sulfo-KMUS (*N*-[κ-maleimidoundecanoyloxy]sulfosuccinimide ester), SBAP (succinimidyl 3-[bromoacetamido]propionate), SPDP (*N*-succinimidyl 3-[2-pyridyldithio]propionate), and sulfo-LCSPDP (sulfosuccinimidyl 6-[3′-(2-pyridyldithio)propionamido]hexanoate were acquired from Pierce (Rockford, IL).

3′-End Acetylated or Fluoresceinated PMO. Acetic anhydride (0.1 M), dissolved in *N*-methyl-2-pyrrolidinone (NMP) containing 1% *N*-ethylmorpholine (v:v) was added to PMO while the oligomer was still attached to the synthesis resin via the 5′-end. The PMO was incubated at 25 °C for 90 min, washed with NMP, cleaved off from the synthesis resin, and purified as described previously (*24*). The product was analyzed by MALDI time-of-flight mass spectrometry (MALDI TOF MS) and high-pressure liquid chromatography (HPLC). Seventy percent of the product corresponded to full-length sequence with acetyl at its 3′-end and a piperazine group at the 5′-end. 5-(and 6-) Carboxyfluorescein was attached to the 3′-end of PMO as described previously (*24*).

Addition of a Cross-Linker to 5′-End of PMO. A cross-linker (Figure 2) predissolved in 50 μL of DMSO was mixed with a PMO (2−5 mM) dissolved in sodium phosphate buffer (50 mM, pH 7.2) containing 20% CH_3-CN at 1:2 PMO:cross-linker molar ratio. The mixture was

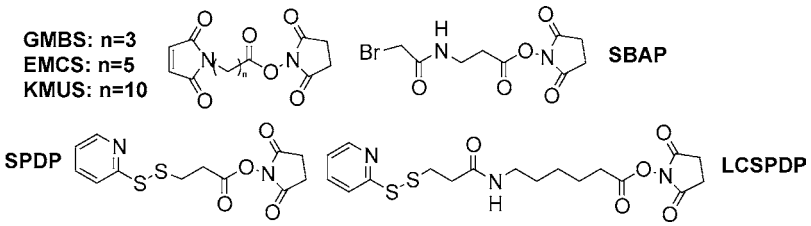


Figure 2. Names and structures of the bifunctional cross-linkers.

stirred at 25 °C in the dark for 30 min, and the product was precipitated in 30-fold excess of cold acetone. The PMO−linker was lyophilized and analyzed by MALDI-TOF MS and HPLC. The conversion from PMO to PMO−linker was >90%.

Peptide and PMO Conjugation. PMO−linker (2−5 mM) was dissolved in sodium phosphate buffer (50 mM, pH 6.5, 5 mM EDTA) containing 20% CH_3CN. The peptide was added to the PMO−cross-linker solution at 2:1 peptide:PMO molar ratio. The reaction was stirred at 25 °C in the dark for 2 h. The conjugate was purified first by CM-sepharose (Sigma, St. Louis, MO) ion exchange chromatography to remove unconjugated PMO and then by reverse phase chromatography (HLB, Waters, Milford, MA) and lyophilized. The concentration calculation used for all conjugates was based on the total absorbance at 260 nm of a sample. As analyzed by MALDI-TOF MS and capillary electrophoresis, the final product contained about 60% peptide conjugated to the full length PMO with the balance composed of conjugates of shorter PMO, a small amount of unconjugated full, and shorter length PMO, and about 2% of unconjugated peptide.

Conjugating a Peptide onto 3′-End of PMO. Addition of a cross-linker and conjugation to a peptide to 3′-end of PMO is described previously (*24*).

Cell Culture. HeLa pLuc705 (*32*) cell line was obtained from Gene Tools (Philomath, OR). NIH3T3 cells were obtained from ATCC (Manassas, VA). Both cell lines were cultured in RPMI 1640 supplemented with 2mM glutamine, 100 μg/mL streptomycin, 100 U/mL penicillin, and 10% fetal bovine serum (FBS) (Hyclone, Ogden, UT) unless specified in the figure legends. Cell lysis buffer contained 10 mL of cell lysis reagent (Promega, Madison, WI) and one proteinase inhibitor cocktail tablet (Roche Diagnostics, Mannheim, Germany).

Fluorescent Microscopy. Exponentially growing cells were plated in a 48-well plate. The next day the conditioned medium was removed, and a test substance, in fresh medium, was added to the well. After a designated time, the cells were washed with phosphate-buffered saline (PBS) three times and imaged directly in the culture medium with a Nikon Diaphot 300 inverted microscope. Images were captured with an Olympus digital camera connected to a computer using MagnaFire software (Optronics, Goleta, CA). Dihydroethidium, a nucleic acid stain, was obtained from Molecular Probes (Eugene, OR).

Flow Cytometry. HeLa pLuc705 cells, plated at 80 000 cells per well in a 24-well plate 20 h before the treatment, were treated with medium containing a test substance for various times at a specified concentration. After each treatment, cells were washed with PBS three times. To measure the internalized conjugate, the membrane-bound conjugate was removed by trypsinization (*21*, *35*). Trypsin (100 μL) (0.25%, Hyclone, Logan, UT) was added to each well and incubated for 6 min at 37 °C, followed by addition of 300 μL of culture media. The cells were spun down and washed with PBS one time then resuspended in 200 μL of a buffer containing PBS, 1% FBS, and 0.2% NaN_3. The flow data (10 000 events) was collected using a BD FACSCalibur cytometer, and data was analyzed using FCS Express 2 (De Novo Software, Thornhill, Ontario, Canada).

Correction of Misspliced Pre-mRNA. HeLa pLuc705 cells, plated in a 48-well plate 20 h before the treatment, were treated with medium containing a test substance at a specified concentration. At designated times, the cells were washed with PBS twice and the cell lysate was collected. Luciferase produced was determined by mixing 30 μL of cell lysate and 50 μL of luciferase assay reagent (Promega, Madison,WI) followed by measuring the light production using the Flx 800 microplate fluorescence/luminescence reader (Bio-tek, Winooski, Vermont). The relative light units were normalized to μg of protein determined by the bicinchoninic acid method following the manufacturer's procedure (Pierce, Rockford, IL).

Cytotoxicity. Cell viability was determined by an MTT (methylthiazoletetrazolium, Sigma, MO) assay. HeLa pLuc705 cells were incubated with or without a test substance for 24 h in a 96-well plate, the conditioned medium in each well was replaced with 100 μL of fresh medium containing 500 μg/mL MTT, and the cells were incubated for 4 h. The medium was removed, and DMSO was added to each well and mixed thoroughly. The absorbance was measured at 540 nm. The percent cell viability was calculated by normalizing absorbance of treated cells to the untreated cells.

Statistical Analysis. Data were plotted and analyzed using GraphPad Prism 3.0 software (GraphPad Software, San Diego, CA).

RESULTS AND DISCUSSION

Peptide−PMO Conjugates. The chemical structures of DNA, PMO, and R_9F_2C−705 conjugate are shown in Figure 1. The nomenclature, the linkers used, conjugation position, and calculated and observed mass and purity are tabulated (Table 2). Peptides and PMO were conjugated by bifunctional cross-linkers. The structures of cross-linkers are illustrated in Figure 2. The conjugate with the GMBS linker is designated as peptide−PMO, otherwise the name of a specific linker is included in the nomenclature. For example, the conjugate of R_9F_2C and 705-FL by GMBS or SPDP linker are designated as R_9F_2C−705-FL or R_9F_2C−SPDP−705-FL, respectively.

Conjugation to R_9F_2C Peptide Was Required To Deliver PMO to the Targeted mRNA. The effect of R_9F_2C peptide on delivering PMO was first determined by comparing fluorescent images of HeLa pLuc705 and NIH3T3 cells treated with a fluorescein tagged PMO (705-FL), a mixture of free R_9F_2C and 705-FL (R_9F_2C +705-FL), and the conjugate of R_9F_2C and 705-FL (R_9F_2C−705-FL). To avoid artifacts that may be caused by cell fixation techniques (*21*, *35*), all fluorescent images were taken of live cells where no fixative agent or mounting medium was used. Very little fluorescence was

Table 2. Peptide−PMO Conjugates: Nomenclatures, Linkers, and the Calculated and Observed Mass and Purity

name	linker	calcd average mass	obsd average protonated mass[a]	% purity of full length conjugate
pTat−705	GMBS	7857	7858	60
PTD4−705	GMBS	7616	7617	65
pAnt−705	GMBS	8558	8559	60
R_9F_2C−705	GMBS	8015	8014	59
R_9F_2C−705-FL	GMBS	8330	8330	60
R_9F_2C−EMCS−705-FL	EMCS	8360	8359	61
R_9F_2C−KMUS−705-FL	KMUS	8430	8431	67
R_9F_2C−SPDP−705-FL	SPDP	8255	8253	60
R_9F_2C−LCSPDP−705-FL	LCSPDP	8433	8442	64
R_9F_2C−SBAP−705-FL	SBAP	8276	8277	50
R_6F_2C−705	GMBS	8015	8015	61
R_5F_2C−705	GMBS	7391	7391	60
R_9F_2C−705(12)-FL	GMBS	6375	6377	64
R_9F_2C−705(24)-FL	GMBS	10330	10331	67
705−R_9F_2C[b]	GMBS	8310	8311	62

[a] Observed mass accuracy ± 0.05% of calculated protonated mass. [b] All peptides were added to the PMO 5′-end except for 705−R_9F_2C for which R_9F_2C was added to the 3′-end of PMO.

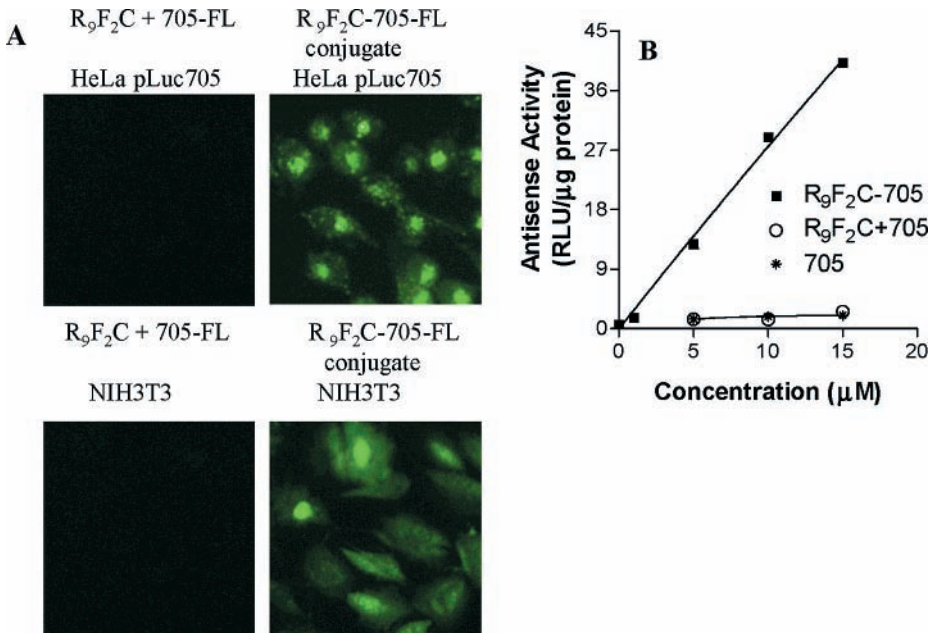


Figure 3. Conjugation to R_9F_2C peptide was required to deliver PMO to the targeted mRNA. (A) Fluorescent images (200× magnification) of live HeLa pLuc705 or NIH3T3 cells treated with test substance at 10 μM for 20 h. The test substances, as indicated above the images, were a mixture of free R_9F_2C peptide and fluorescein tagged 705 (R_9F_2C + 705-FL) (1:1 molar ratio) and R_9F_2C−705-FL conjugate. (B) R_9F_2C−705 conjugate corrected misspliced pre-mRNA and upregulated the expression of luciferase reporter gene while R_9F_2C + 705 (1:1 molar ratio) or 705 alone did not. HeLa pLuc705 cells were treated with the test substance at indicated concentrations in medium containing 10% FBS for 24 h. Antisense activity is represented by luciferase activity, expressed as the relative light units (RLU) per μg protein. Each data point is an average ± the range of means of two independent experiments each consisting of a triplicate sample.

observed with 705-FL (image not shown) or R_9F_2C + 705-FL (Figure 3A). Mixed diffused/punctate cytosolic and nuclear fluorescence was seen in 100% of the cells treated with the R_9F_2C−705-FL conjugate (Figure 3A), suggesting successful delivery of PMO to the cytosol and nucleus in both cell lines.

The necessity of the covalent attachment of R_9F_2C to PMO was evaluated in the splice correction assay, which measures antisense activity of PMO in the nucleus and gives a positive luciferase reporter signal using the HeLa pLuc705 cell line. This cell line (*32*) is stably transfected with a plasmid carrying the luciferase coding sequence interrupted by a mutated human β-globin intron 2. Cells treated with PMO (705) alone or with a mixture of free R_9F_2C and 705 showed the same level of luciferase as cells treated with vehicle control (H_2O). However, cells treated with the R_9F_2C−705 conjugate produced luciferase in a dose-dependent manner (Figure 3B), indicating successful nuclear delivery of PMO. The results show that conjugation of R_9F_2C peptide to PMO was required for delivery to the nucleus.

R_9F_2C Was More Effective in Delivering PMO Than pTat, PTD4, pAnt, and Peptides with Fewer Arginines. Using the splice correction assay and flow cytometry, we compared the effectiveness of R_9F_2C to pTat, PTD4, and pAnt to deliver PMO to the nucleus. PMO conjugated to R_9F_2C corrected splicing 4, 14, or 19 times more effectively than the PMO conjugated to pTat, pAnt, or PTD4, respectively (Figure 4A). Cells treated with R_9F_2C−705-FL had 3, 12, or 17 times more fluorescence than the ones treated with pTat−705-FL, pAnt−705-FL, or PTD4−705-FL (Figure 4B), respectively.

R_9F_2C, pTat, and PTD4 are peptides with the same length but differ in their sequences and number of arginines. pTat, pAnt, or PTD4 contains six, three, or three arginines, respectively, while R_9F_2C has nine

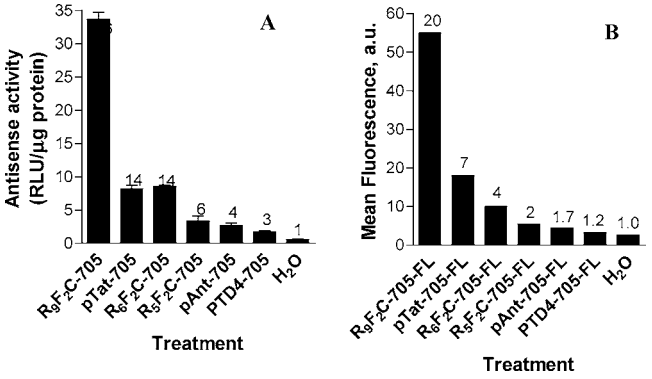


Figure 4. R_9F_2C was more effective to deliver PMO than pTat, PTD4, pAnt, and peptides with fewer arginines. (A). Luciferase activity of HeLa pLuc705 cells treated with the 705 conjugated to R_9F_2C, pTat, R_6F_2C, R_5F_2C, pAnt, or PTD4 by the GMBS linker at 15 μM in the medium containing 10% FBS for 24 h. Each data point is an average ± the range of means of two independent experiments each consisting of a triplicate sample. (B). Flow cytometry measurement of mean fluorescence of HeLa pLuc705 cells treated with 2 μM of a conjugate for 3 h. The antisense activity or mean fluorescence of each conjugate relative to the vehicle control (H_2O) is quantified above each bar.

arginines (Table 1). It has been suggested that arginine-rich peptides with different primary and secondary structures have a similar uptake mechanism (*36*). The number of arginines appears to be more important (*25*), and the structural variations have less effect on cellular uptake (*37*, *38*). These reports are based on studies using fluorescein-tagged peptides; a quantitative comparison using a functional assay has not yet been reported until this study.

To directly verify whether reducing the number of arginines decreases the peptide's delivery efficacy, the cellular uptake of R_9F_2C−705-FL was compared to R_6F_2C−705-FL and R_5F_2C−705-FL by both flow cytometry and the splice correction assay. The mean fluorescence decreased as the number of arginines decreased (Figure 4B). Relative to the vehicle control (H_2O) treated cells, the cells treated with R_9F_2C−705, R_6F_2C−705, or R_5F_2C−705 gave 56, 14, or 5.6-fold increase in luciferase production, respectively (Figure 4A). Lower mean fluorescence given by the conjugates with fewer arginines indicated less PMO delivered by the peptide, which correlated well with their lower antisense activity. We show here, for the first time by an antisense functional assay, that the number of arginines greatly influences the delivery effectiveness of the peptide.

Antisense Activity Was Affected by Linker Length and Not by the Conjugation Chemistry. We examined the effects of linker length (bond length) and connectivity between PMO and R_9F_2C on PMO antisense activity. All linkers used in this study (Figure 2) were bifunctional cross-linkers, containing an amine-reactive *N*-hydroxysuccinimide (NHS) and a sulfhydryl-reactive moiety. To have a meaningful comparison of the linkers, the PMO or R_9F_2C peptide used was from one synthesis batch. The 5′-end of the PMO was conjugated at one end of a cross-linker through NHS chemistry. The opposite end of the cross-linker was conjugated to the sulfhydryl group of R_9F_2C by maleimide, bromoacetyl, or pyridyl disulfide chemistry.

The effect of the linker length was determined by the splice correction assay, and the results are summarized in Table 3. The effect was explored by comparing R_9F_2C−705-FL, R_9F_2C−EMCS−705-FL, and R_9F_2C−KMUS−705-FL and by comparing R_9F_2C−SPDP−705-FL to

Table 3. Effect of the Linker and Linking Chemistry on the Antisense Activity of the R_9F_2C and 705-FL Conjugates[a]

treatment	linker type	linker spacer (Å)	antisense activity RLU/μg protein (range)
vehicle control (H_2O)	N/A	N/A	1 (0.1)
R_9F_2C−705-FL	thiomaleimide	6.8	102 (4.9)
R_9F_2C−EMCS−705-FL	thiomaleimide	9.4	141 (4.3)
R_9F_2C−KMUS−705-FL	thiomaleimide	15.7	171(14.3)
R_9F_2C−SMPB−705-FL	thiomaleimide	11.6	123 (2.1)
R_9F_2C−SMCC−705-FL	thiomaleimide	11.6	86 (1.4)
R_9F_2C−SBAP−705-FL	thioether	6.2	98 (3.2)
R_9F_2C−SPDP−705-FL	disulfide	6.8	109 (2.9)
R_9F_2C−LCSPDP−705-FL	disufide	15.6	181 (7.8)

[a] HeLa pLuc705 cells were treated with 10 μM of an indicated conjugate in the serum free medium for 6 h. The antisense activity was indicated by luciferase activity, expressed as RLU/μg protein. Each data point is an average ± range of means from two independent experiments each consisting of a triplicate sample.

R_9F_2C−LCSPDP−705-FL. The first three conjugates contained a thiomaleimide bond, but differed in spacing between the peptide and PMO. R_9F_2C−KMUS−705-FL (15.7 Å spacer) and R_9F_2C−EMCS−705-FL (9.7 Å) had 1.7 or 1.4-fold higher antisense activity, respectively, than R_9F_2C−705-FL (6.8 Å) (Table 3). The pyridyl disulfide chemistry was used to make R_9F_2C−SPDP−705-FL and R_9F_2C−LCSPDP−705-FL, resulting in each conjugate containing a disulfide bond. LCSPDP (15.6 Å spacer) is about 8.8 Å longer than the SPDP (6.8 Å) linker, and R_9F_2C−LCSPDP−705-FL was almost twice as effective in splice correction as R_9F_2C−SPDP−705-FL. Overall, the conjugates with longer linker length had greater antisense activity.

The effect of conjugation chemistry was determined by comparing three conjugates, R_9F_2C−SBAP−705-FL, R_9F_2C−705-FL, and R_9F_2C−SPDP−705-FL, in the splice correction assay. The three conjugates each had the same linker spacing but differed in linking chemistry: thioether in R_9F_2C−SBAP−705-FL, thiomaleimide in R_9F_2C−705-FL and disulfide in R_9F_2C−SPDP−705-FL. These conjugates had the same antisense activity despite their difference in conjugation chemistry.

The above results show that the antisense activity of the PMO was increased with longer linkers but not affected by the conjugation chemistry. Increasing the backbone and side chain flexibility (*37*) of an arginine-rich peptide or an addition of a hydrophobic moiety (*26*, *27*) onto a peptide have both shown to give better delivery of a fluorescein cargo. The higher antisense activity of the conjugates with longer chains of $(CH_2)_n$ moieties may be the result of their greater flexibility and/or hydrophobicity than those with shorter linkers. It is also possible that a longer linker reduces steric interference for PMO binding to the targeted pre-mRNA.

Effect of Linker Type on Intracellular Distribution and Concentration of the Peptide−PMO Conjugates. The intracellular distribution of the fluorescein-tagged PMO (705-FL), conjugated to R_9F_2C via different linkers, was determined by fluorescent microscopy. All conjugates containing thiomaleimide or thioether bonds gave a similar fluorescent pattern: a bright fluorescent spot in addition to a dimmer diffused fluorescence throughout the cells, as represented by the image of cells treated with R_9F_2C−705-FL (Figure 5A). Green and red dual fluorescence staining (Figure 5B and 5C) reveals that the bright fluorescent spot was located outside of the nucleus as shown by cotreatment of cells with the conjugate and dihydroethidium, a cell-permeable nucleic stain that fluoresces red upon DNA intercalation. This

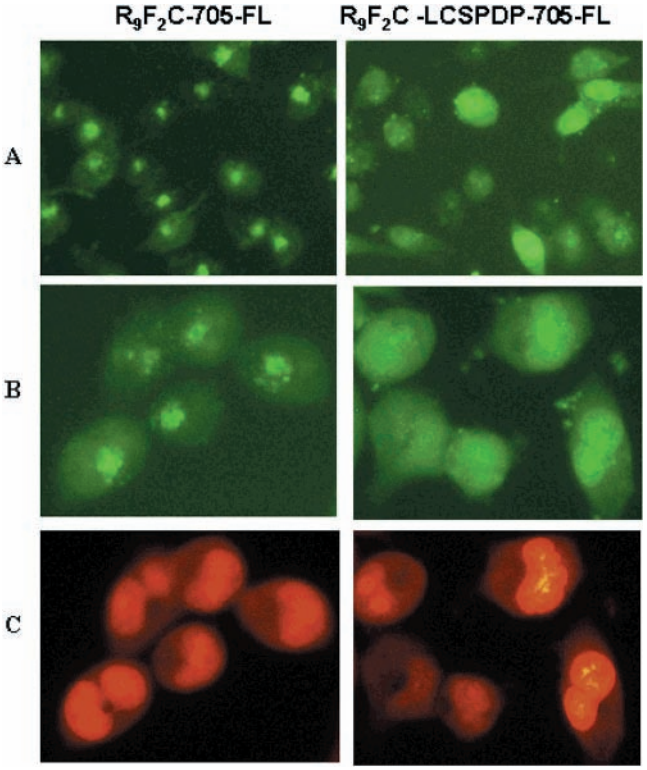


Figure 5. Effect of the linker type on intracellular distribution of the peptide−PMO conjugates. (A). Fluorescent image (200× magnification) of live HeLa pLuc705 cells treated with 10 μM of R_9F_2C−705FL or R_9F_2C−LCSPDP−705-FL for 20 h in RPMI with 10% FBS medium. (B and C). Dual fluorescence staining of HeLa pLuc705 cells treated with 2 μM of either R_9F_2C−705-FL or R_9F_2C−LCSPDP−705-FL in opti-MEM medium for 24 h. 10 μM of dihydroethidium, a nucleic acid stain, was added to the cells during the last 90 min incubation period of the conjugate. The same field image of cells was taken (400× magnification) through the green channel (B) or the red channel (C) of the microscope.

bright fluorescent spot seen using R_9F_2C−GMBS−705-FL was not observed with either disulfide-containing conjugates, R_9F_2C−LCSPDP−705-FL (Figure 5A and 5B) or R_9F_2C−SPDP−705-FL. Instead, the latter conjugates gave dimmer but more diffused fluorescence throughout the cytoplasm and nucleus than the thiomaleimide- or thioether-containing conjugates.

The effect of thiomaleimide or disulfide linker on cellular uptake was measured quantitatively by flow cytometry. Cells treated with R_9F_2C−KMUS−705-FL exhibited significantly higher fluorescence than R_9F_2C−LCSPDP−705-FL (Figure 6). Uptake of R_9F_2C−LCSPDP−705-FL was comparable to R_9F_2C−KMUS−705-FL at the 30 min timepoint but did not increase with longer treatment as did R_9F_2C−KMUS−705-FL. This could be explained by the intrinsic instability of the disulfide bond of R_9F_2C−LCSPDP−705-FL in the serum and/or the cleavage of the disulfide bond by glutathione at the cell surface (*39*). Cleavage of PMO from the peptide outside of the cell membrane would decrease the amount of PMO delivered.

Despite the significant difference in intracellular concentration between R_9F_2C−KMUS−705-FL and R_9F_2C−LCSPDP−705-FL, both conjugates gave nearly identical antisense activities (Table 3) in a dose dependent manner (data not shown). This suggests that the amount of internalized PMO available for the targeted pre-mRNA in the cell nucleus was similar. These interesting results can be analyzed in light of the difference in their linker types. R_9F_2C−LCSPDP−705-FL contained a disulfide bond that can be cleaved by cellular reducing agents such as glutathione in the golgi apparatus (*39*, *40*), releasing PMO from the peptide. R_9F_2C−KMUS−705-FL contained a thiomaleimide bond that does not have known cleavage enzymes and so the PMO likely remained bonded to the peptide. If this is the case, the positive charges of R_9F_2C may make it easier for R_9F_2C−KMUS−705-FL to bind anionic cellular components other than the targeted pre-mRNA. The result would be a decrease in effective PMO concentration, despite its higher intracellular concentration than that of R_9F_2C−LCSPDP−705-FL.

The above explanation was supported by fluorescent images (Figure 5A and 5C). PMO delivered by the peptide with the disulfide linker diffused throughout the cells, similar to the distribution of scrape-loaded unconjugated PMO (*14*). PMO delivered by the peptide with the thiomaleimide linker gave more distinct and localized fluorescence outside nucleus (Figure 5A), similar to the fluorescent image of fluorescein-tagged R_9F_2C (data not shown). These results indicate that the delivery peptide had greater influence on subcellular distribution of PMO with a noncleavable linker compared to a cleavable linker.

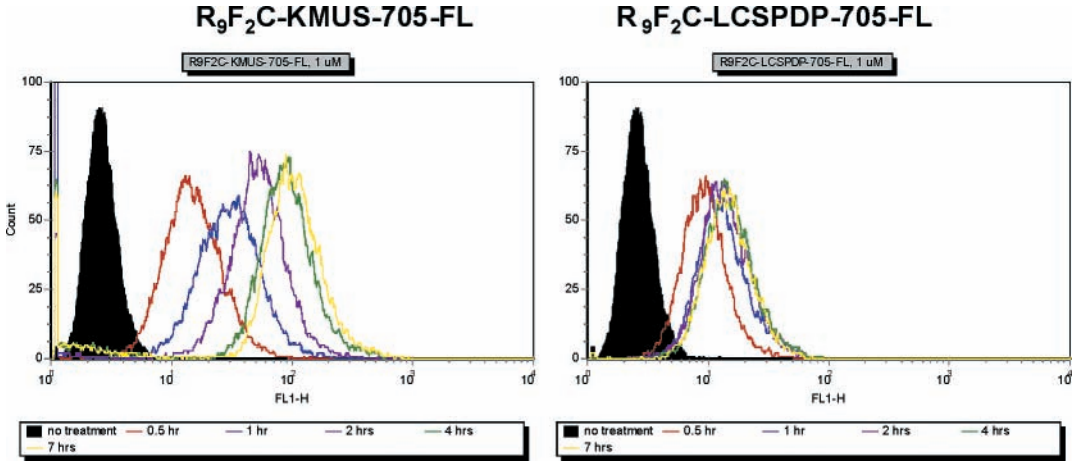


Figure 6. Effect of the linker type on intracellular concentration of the peptide−PMO conjugates. Flow cytometry diagram of the Hela pLuc705 cells treated with 1 μM of R_9F_2C−KMUS−705FL or R_9F_2C−LCSPDP−705-FL for 0.5 (red line), 1 (blue line), 2 (purple line), 4 (green line), or 7 (yellow line) h. The black filled histogram represented the background fluorescence of vehicle control (H_2O) treated cells.

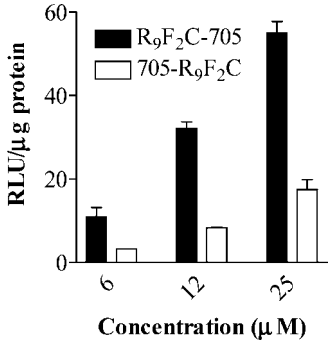


Figure 7. PMO with R_9F_2C at its 5′-end had greater antisense activity than PMO with R_9F_2C at its 3′-end. Luciferase activity of HeLa pLuc705 cells treated with the 705 conjugated to R_9F_2C either at the 5′-end (R_9F_2C−705) or the 3′-end (705-R_9F_2C) at indicated concentrations in the medium containing 10% FBS for 24 h. Each data point is an average ± the range of means of two independent experiments each consisting of a triplicate sample.

PMO with R_9F_2C at the 5′-End Had Higher Antisense Activity Than the PMO with R_9F_2C at the 3′-End. Either the 3′-end or the 5′-end of the PMO can be conjugated to the peptide. The effect of position of the peptide on PMO was determined by comparing two conjugates of 705 with R_9F_2C either at the 3′-end (705−R_9F_2C) or at the 5′-end (R_9F_2C−705). R_9F_2C−705 produced nearly four times as much as luciferase as 705−R_9F_2C (Figure 7).

The data indicate that the 5′-end of PMO is preferred for conjugation and can be understood in terms of PMO−RNA binding. PMO interrupt mRNA processes by steric blocking the access of other biomolecules to the target region (*2*). Addition of bulky moieties such as carboxylfluorescein or cholesterol to the 3′-end of a PMO decreases its antisense activity (data not shown), probably due to steric interference of the PMO/mRNA binding. We hypothesize that the positively charged linear peptide at the 3′-end may have a similar effect.

Length of PMO Did Not Affect Delivery Ability of R_9F_2C but Affects the Antisense Activity of PMO. Tat peptide has been used to deliver various-sized cargos, ranging from small fluorescein (*41*) to large magnetic beads (*42*). The effect of cargo size on cellular delivery by an arginine-rich peptide has not been determined quantitatively. The effect of PMO length on delivery of R_9F_2C conjugate was determined by flow cytometry and splice correction assay. PMO 705(12)-FL, 705-FL and 705(24)-FL are fluorescein-tagged and consist of 12, 18, and 24 bases (Table 1), respectively. R_9F_2C was conjugated to the 5′-end of each PMO using the GMBS linker.

HeLa pLuc/705 cells treated with R_9F_2C−705 (12)-FL, R_9F_2C−705 -FL or R_9F_2C−705 (24)-FL exhibited identical fluorescence (Figure 8A), indicating the same amount of PMO was delivered to the cells. However, the antisense activity of the three conjugates increased with the length of PMO (Figure 8B). A longer PMO is known to have greater antisense activity than shorter ones (*2*), and the higher activity of longer PMO is most likely due to its higher RNA binding affinity, rather than uptake differences. To verify this, each free PMO was delivered into cells by scrape-loading, which is a mechanical method that creates transient pores in the cell membrane, allowing extracellular macromolecules to enter into the cytoplasm directly (*14*). The result from scrape-loading showed a similar trend as R_9F_2C-mediated delivery (Figure 8C) with higher antisense activity for longer PMO. Taken together, the results indicate that the length of PMO does not affect the delivery effectiveness of the R_9F_2C peptide but affects the antisense activity.

Culture Conditions Affected the Cellular Uptake of R_9F_2C−PMO Conjugate. The effect of cell density, type of medium, and the serum concentration within the medium were examined by the splice correction assay. All were found to greatly influence the uptake of the conjugates. Cells treated with R_9F_2C−705 at cell confluence of 40−50%, 70−80%, or 90−100% produced 52, 40, or 28 RLU/μg protein, respectively (Figure 9A). Therefore, lower cell density was ideal when testing the peptide−PMO conjugates. The choice of culture media was examined by adapting the HeLa pLuc705 cells in RPMI, DME/F12, or MEM media for at least two weeks prior to treatment with the R_9F_2C−705 conjugate. Cells treated with the conjugate in RPMI medium had the highest luciferase production (40 RLU/μg protein) compared to those treated in DME/F12 (28 RLU/μg protein) or MEM (11 RLU/μg protein) (Figure 9B). The type and concentration of components vary among these culture media. Therefore, the difference in cellular uptake of the conjugate may be the result of differential interaction between the positively charged conjugate and components of the medium.

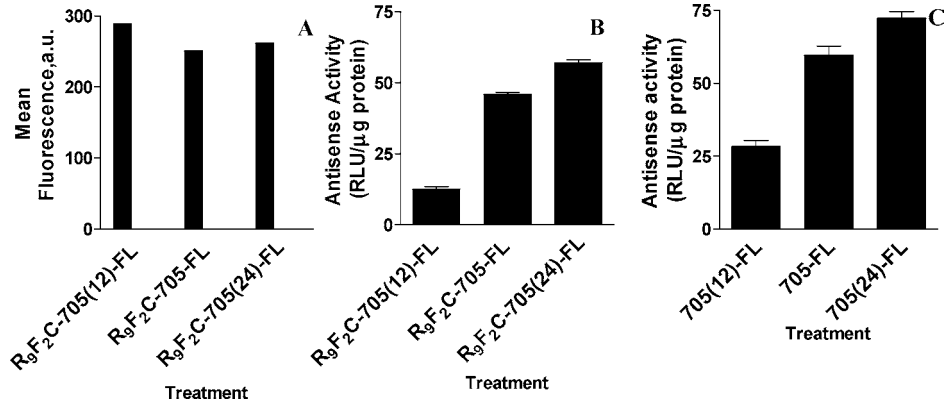


Figure 8. Length of PMO did not affect the delivery ability of R_9F_2C but affects the antisense activity. (A). Mean fluorescence of HeLa pLuc705 cells treated with 1 μM R_9F_2C conjugated to fluorescein-tagged PMO with 12 bases (R_9F_2C−705(12)-FL), 18 bases (R_9F_2C−705-FL), or 24 bases (R_9F_2C−705(24)-FL), determined by flow cytometry. The cells were treated with the test substance for 7 h in serum-free medium. (B). Luciferase activity of cells treated with the 1 μM conjugate for 7 h in serum-free RPMI medium. (C). Luciferase activity of cells treated with the 5 μM unconjugated PMO for 7 h. The unconjugated PMO was delivered by the scrape-loading method (*14*). Each data point is an average ± the range of means of two independent experiments and each consisting of a triplicate sample.

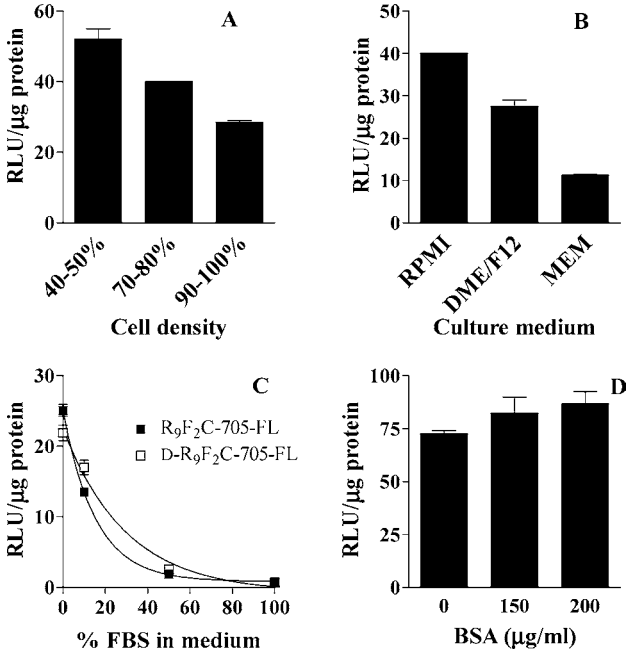


Figure 9. Cell culture conditions affected the cellular uptake of R_9F_2C-PMO conjugate. Luciferase activity of HeLa pLuc705 cells treated with the test substances. Each data point represents the mean of a triplicate sample ± SEM. (A). Cells at indicated cell density treated with 10 μM R_9F_2C-705 for 24 h in RPMI medium with 10% FBS. (B). Cells treated with 10 μM R_9F_2C-705 in indicated culture medium for 24 h in 10% FBS. (C). Cells treated with 5 μM of R_9F_2C-705-FL or D-R_9F_2C-705-FL for 24 h in RPMI medium containing indicated % of FBS. (D). Cells treated with 10 μM R_9F_2C-705 for 6 h in RPMI medium containing 1% FBS and indicated amount of additional BSA.

The effect of serum concentration in the culture medium was determined by incubating the cells with concentrations of FBS from 0% to 100%. Cells produced less luciferase as the concentration of FBS increased. Luciferase production was near background when the percentage of serum in the cultured media was >50% (Figure 9C). Positively charged molecules are known to bind to serum components. R_9F_2C is a highly positively charged peptide made of L-amino acids and may bind to serum components and/or be cleaved by proteinases in the serum. These two factors would decrease the peptide's delivery effectiveness resulting in decreased antisense activity.

To explore whether serum binding and/or serum proteinases were the cause of a decrease in antisense activity, a R_9F_2C peptide made of D-amino acids (D-R_9F_2C) was used in a side-by-side experiment against R_9F_2C. D-R_9F_2C cannot be degraded by FBS proteinase. The result from D-R_9F_2C-705 conjugate was nearly identical to that from R_9F_2C-705 (Figure 9C), indicating that the FBS proteinases did not affect the antisense activity. This points to the binding of serum components as the main cause for reduced antisense activity of a conjugate. Bovine serum albumin (BSA) is one of the major serum proteins. Whether it inhibits cellular uptake of the conjugate was examined in the splice correction assay. The splice correction was not inhibited by addition of BSA to the medium (Figure 9D), showing BSA is not the component that inhibits the function of the conjugate.

Cellular Toxicity. The conjugates of arginine-rich peptide and PMO exhibited dose-dependent toxicity (data not shown). The degree of toxicity depended on cell-type and was influenced by the number of arginines, with

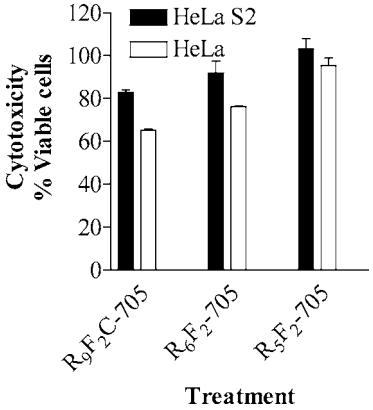


Figure 10. Cellular toxicity of the conjugate. Percentage viable HeLa S2(HeLa pLuc705) or HeLa cells treated with the indicated conjugate at 10 μM for 24 h, determined by MTT assay. Each data point represents the mean of a triplicate sample ± SEM.

greater number of arginines being more toxic (Figure 10). The difference in cellular toxicity was seen even within the subtypes of the HeLa cell line. The HeLa S2 cells (HeLa pLuc705) or HeLa cells treated with 10 μM of R_9F_2C-705 exhibited 83% (±1.4 SEM) or 65% (±0.61 SEM) cell viability (Figure 10). Increasing serum concentrations in the media decreases cellular toxicity of the conjugate (data not shown). The nature of this cytotoxicity is not well understood. Formation of transmembrane pores is not the cause of the toxicity because cells treated with the conjugate did not have elevated extracellular lactate dehydrogenase levels (data not shown). It is observed that adherent cells treated with the conjugate at high concentrations detached more readily from the culture wells compared to untreated cells.

In summary, the conjugation of R_9F_2C peptide to a PMO provided a simple and efficient delivery of the PMO to the RNA target. The length of PMO did not affect the delivery efficacy of the peptide while other factors did. When using the conjugate to study gene function in cell culture, the 5′-end of PMO is the preferred end for conjugation and a flexible linker of 15 Å was the best length of these tested. We have found that R_9F_2C peptide delivers PMO effectively into many different cell lines; however, the cell culture conditions greatly affect the antisense activity of the conjugate. Cell density, type of medium, and serum concentration along with their relationships with cytotoxicity in the specific cell type studied are important considerations when using the conjugate of an arginine-rich peptide and an uncharged antisense oligomer to study gene function in cell culture.

ACKNOWLEDGMENT

We thank Drs. Bruce Geller and Jon Moulton for editing this paper. We are grateful to Candace Lovejoy for synthesizing the PMO used in this study.

LITERATURE CITED

(1) Summerton, J., and Weller, D. (1997) Morpholino antisense oligomers: design, preparation, and properties. *Antisense Nucleic Acid Drug Dev. 7,* 187−195.

(2) Summerton, J. (1999) Morpholino antisense oligomers: the case for an RNase H-independent structural type. *Biochim. Biophys. Acta 1489,* 141−158.

(3) Taylor, M. F., Paulauskis, J. D., Weller, D. D., and Kobzik, L. (1996) In vitro efficacy of morpholino-modified antisense

oligomers directed against tumor necrosis factor-alpha mRNA. *J. Biol. Chem. 271*, 17445−17452.

(4) Taylor, M. F., Paulauskis, J. D., Weller, D. D., and Kobzik, L. (1997) Comparison of efficacy of antisense oligomers directed toward TNF-alpha in helper T and macrophage cell lines. *Cytokine 9*, 672−681.

(5) Taylor, M. F., Weller, D. D., and Kobzik, L. (1998) Effect of TNF-alpha antisense oligomers on cytokine production by primary murine alveolar macrophages. *Antisense Nucleic Acid Drug Dev. 8*, 199−205.

(6) Summerton, J., Stein, D., Huang, S. B., Matthews, P., Weller, D., and Partridge, M. (1997) Morpholino and phosphorothioate antisense oligomers compared in cell-free and in-cell systems. *Antisense Nucleic Acid Drug Dev. 7*, 63−70.

(7) Hudziak, R. M., Summerton, J., Weller, D. D., and Iversen, P. L. (2000) Antiproliferative effects of steric blocking phosphorodiamidate morpholino antisense agents directed against c-myc. *Antisense Nucleic Acid Drug Dev. 10*, 163−176.

(8) Stein, D. A., Skilling, D. E., Iversen, P. L., and Smith, A. W. (2001) Inhibition of Vesivirus infections in mammalian tissue culture with antisense morpholino oligomers. *Antisense Nucleic Acid Drug Dev. 11*, 317−325.

(9) Nasevicius, A., Larson, J., and Ekker, S. C. (2000) Distinct requirements for zebrafish angiogenesis revealed by a VEGF-A morphant. *Yeast 17*, 294−301.

(10) Heasman, J., Kofron, M., and Wylie, C. (2000) Beta-catenin signaling activity dissected in the early Xenopus embryo: a novel antisense approach. *Dev. Biol. 222*, 124−134.

(11) Howard, E. W., Newman, L. A., Oleksyn, D. W., Angerer, R. C., and Angerer, L. M. (2001) Sp*K*rl: a direct target of beta-catenin regulation required for endoderm differentiation in sea urchin embryos. *Development 128*, 365−375.

(12) Kos, R., Reedy, M. V., Johnson, R. L., and Erickson, C. A. (2001) The winged-helix transcription factor FoxD3 is important for establishing the neural crest lineage and repressing melanogenesis in avian embryos. *Development 128*, 1467−1479.

(13) Hudziak, R. M., Barofsky, E., Barofsky, D. F., Weller, D. L., Huang, S. B., and Weller, D. D. (1996) Resistance of morpholino phosphorodiamidate oligomers to enzymatic degradation. *Antisense Nucleic Acid Drug Dev 6*, 267−272.

(14) Ghosh, C., and Iversen, P. L. (2000) Intracellular delivery strategies for antisense phosphorodiamidate morpholino oligomers. *Antisense Nucleic Acid Drug Dev. 10*, 263−274.

(15) Morcos, P. A. (2001) Achieving efficient delivery of morpholino oligos in cultured cells. *Genesis 30*, 94−102.

(16) Fawell, S., Seery, J., Daikh, Y., Moore, C., Chen, L. L., Pepinsky, B., and Barsoum, J. (1994) Tat-mediated delivery of heterologous proteins into cells. *Proc. Natl. Acad. Sci. U. S. A. 91*, 664−668.

(17) Derossi, D., Joliot, A. H., Chassaing, G., and Prochiantz, A. (1994) The third helix of the Antennapedia homeodomain translocates through biological membranes. *J. Biol. Chem. 269*, 10444−10450.

(18) Vives, E., Brodin, P., and Lebleu, B. (1997) A truncated HIV-1 Tat protein basic domain rapidly translocates through the plasma membrane and accumulates in the cell nucleus. *J. Biol. Chem. 272*, 16010−16017.

(19) Pooga, M., Soomets, U., Hallbrink, M., Valkna, A., Saar, K., Rezaei, K., Kahl, U., Hao, J. X., Xu, X. J., Wiesenfeld-Hallin, Z., Hokfelt, T., Bartfai, T., and Langel, U. (1998) Cell penetrating PNA constructs regulate galanin receptor levels and modify pain transmission in vivo. *Nat. Biotechnol. 16*, 857−861.

(20) Koppelhus, U., Awasthi, S. K., Zachar, V., Holst, H. U., Ebbesen, P., and Nielsen, P. E. (2002) Cell-dependent differential cellular uptake of PNA, peptides, and PNA-peptide conjugates. *Antisense Nucleic Acid Drug Dev. 12*, 51−63.

(21) Richard, J. P., Melikov, K., Vives, E., Ramos, C., Verbeure, B., Gait, M. J., Chernomordik, L. V., and Lebleu, B. (2003) Cell-penetrating peptides. A reevaluation of the mechanism of cellular uptake. *J. Biol. Chem. 278*, 585−590.

(22) Villa, R., Folini, M., Lualdi, S., Veronese, S., Daidone, M. G., and Zaffaroni, N. (2000) Inhibition of telomerase activity by a cell-penetrating peptide nucleic acid construct in human melanoma cells. *FEBS Lett. 473*, 241−248.

(23) Ho, A., Schwarze, S. R., Mermelstein, S. J., Waksman, G., and Dowdy, S. F. (2001) Synthetic protein transduction domains: enhanced transduction potential in vitro and in vivo. *Cancer Res. 61*, 474−477.

(24) Moulton, H. M., Hase, M. C., Smith, K. M., and Iversen, P. L. (2003) HIV Tat peptide enhances cellular delivery of antisense morpholino oligomers. *Antisense Nucleic Acid Drug Dev. 13*, 31−43.

(25) Wender, P. A., Mitchell, D. J., Pattabiraman, K., Pelkey, E. T., Steinman, L., and Rothbard, J. B. (2000) The design, synthesis, and evaluation of molecules that enable or enhance cellular uptake: peptoid molecular transporters. *Proc. Natl. Acad. Sci. U. S. A. 97*, 13003−13008.

(26) Futaki, S., Ohashi, W., Suzuki, T., Niwa, M., Tanaka, S., Ueda, K., Harashima, H., and Sugiura, Y. (2001) Stearylated arginine-rich peptides: a new class of transfection systems. *Bioconjugate Chem. 12*, 1005−1011.

(27) Chen, L., Wright, L. R., Chen, C. H., Oliver, S. F., Wender, P. A., and Mochly-Rosen, D. (2001) Molecular transporters for peptides: delivery of a cardioprotective epsilonPKC agonist peptide into cells and intact ischemic heart using a transport system, R(7). *Chem. Biol. 8*, 1123−1129.

(28) Kole, R. (1998) Modification of pre-mRNA splicing by antisense oligonucleotides. In *Applied Antisense Oligonucleotides Technology* (Stein, C. A. M., Ed.) pp 451−469, Wiley-Liss, Inc., New York.

(29) Sierakowska, H., Sambade, M. J., Agrawal, S., and Kole, R. (1996) Repair of thalassemic human beta-globin mRNA in mammalian cells by antisense oligonucleotides. *Proc. Natl. Acad. Sci. U. S. A. 93*, 12840−12844.

(30) Lacerra, G., Sierakowska, H., Carestia, C., Fucharoen, S., Summerton, J., Weller, D., and Kole, R. (2000) Restoration of hemoglobin A synthesis in erythroid cells from peripheral blood of thalassemic patients. *Proc. Natl. Acad. Sci. U. S. A. 97*, 9591−9596.

(31) Sazani, P., Kang, S. H., Maier, M. A., Wei, C., Dillman, J., Summerton, J., Manoharan, M., and Kole, R. (2001) Nuclear antisense effects of neutral, anionic and cationic oligonucleotide analogs. *Nucleic Acids Res. 29*, 3965−3974.

(32) Kang, S. H., Cho, M. J., and Kole, R. (1998) Up-regulation of luciferase gene expression with antisense oligonucleotides: implications and applications in functional assay development. *Biochemistry 37*, 6235−6239.

(33) Sazani, P., Gemignani, F., Kang, S. H., Maier, M. A., Manoharan, M., Persmark, M., Bortner, D., and Kole, R. (2002) Systemically delivered antisense oligomers upregulate gene expression in mouse tissues. *Nat. Biotechnol. 20*, 1228−1233.

(34) Summerton, J., and Weller, D. (1991). Uncharged morpholino-based polymers having phosphorus containing chiral intersubunit linkages. US Patent 5185444.

(35) Moulton, H. M., and Moulton, J. D. (2003) Peptide-assisted delivery of steric-blocking antisense oligomers. *Curr. Opin. Mol. Ther. 5*, 123−132.

(36) Suzuki, T., Futaki, S., Niwa, M., Tanaka, S., Ueda, K., and Sugiura, Y. (2002) Possible existence of common internalization mechanisms among arginine-rich peptides. *J. Biol. Chem. 277*, 2437−2443.

(37) Rothbard, J. B., Kreider, E., VanDeusen, C. L., Wright, L., Wylie, B. L., and Wender, P. A. (2002) Arginine-rich molecular transporters for drug delivery: role of backbone spacing in cellular uptake. *J. Med. Chem. 45*, 3612−3618.

(38) Futaki, S., Nakase, I., Suzuki, T., Youjun, Z., and Sugiura, Y. (2002) Translocation of branched-chain arginine peptides through cell membranes: flexibility in the spatial disposition of positive charges in membrane-permeable peptides. *Biochemistry 41*, 7925−7930.

(39) Feener, E. P., Shen, W. C., and Ryser, H. J. (1990) Cleavage of disulfide bonds in endocytosed macromolecules. A processing not associated with lysosomes or endosomes. *J. Biol. Chem. 265*, 18780−18785.

(40) Mandel, R., Ryser, H. J., Niaki, B., Ghani, F., and Shen, W. C. (1991) Isolation of variants of Chinese hamster ovary

cells with abnormally low levels of GSH: decreased ability to cleave endocytosed disulfide bonds. *J. Cell Physiol. 149*, 60−65.

(41) Schwarze, S. R., Ho, A., Vocero-Akbani, A., and Dowdy, S. F. (1999) In vivo protein transduction: delivery of a biologically active protein into the mouse. *Science 285*, 1569−1572.

(42) Lewin, M., Carlesso, N., Tung, C. H., Tang, X. W., Cory, D., Scadden, D. T., and Weissleder, R. (2000) Tat peptide-derivatized magnetic nanoparticles allow in vivo tracking and recovery of progenitor cells. *Nat. Biotechnol. 18*, 410−414.

BC034221G

Molecular Binding Behavior of Pyridine-2,6-dicarboxamide-Bridged Bis(*β*-cyclodextrin) with Oligopeptides: Switchable Molecular Binding Mode

Yu Liu,* Guo-Song Chen, Yong Chen, Fei Ding, Tao Liu, and Yan-Li Zhao

Department of Chemistry, State Key Laboratory of Elemento-Organic Chemistry, Nankai University, Tianjin 300071, P. R. China. Received December 20, 2003; Revised Manuscript Received January 30, 2004

Bridged bis(*β*-cyclodextrin) **1** with a pyridine-2,6-dicarboxamide linker was synthesized, and its inclusion complexation behavior with some aliphatic oligopeptides was investigated in aqueous buffer solution of pH 2.0 and 7.2 at 25 °C by means of circular dichroism, fluorescence, and 2D NMR techniques. The results show that the resulting inclusion complexes of **1** with oligopeptides adopt a cooperative "cyclodextrin−guest−cyclodextrin" sandwich binding mode in a neutral media, but a "guest−linker−cyclodextrin" coinclusion binding mode in an acidic media. These switchable binding modes consequently rationalize the binding ability of bis(*β*-cyclodextrin) **1** at different pH values; that is, **1** shows the stronger association with oligopeptides in a neutral media. Because of the simultaneous contributions of hydrophobic, hydrogen bond, and electrostatic interactions, bis(*β*-cyclodextrin) **1** affords length-selectivity up to 4.7 for the Gly-Gly/Gly-Gly-Gly pair at pH 2.0 and sequence-selectivity up to 4.2 for the Gly-Leu/Leu-Gly pair at pH 7.2. These phenomena are discussed from the viewpoint of the size−fit concept and the multipoint recognitions between host and guest.

INTRODUCTION

Cyclodextrins are a class of cyclic oligosaccharides consisting, for the most common representatives, of six to eight D-glucose units linked by α-1,4-glucose bonds. They are well-known to encapsulate various organic guests within their hydrophobic cavities to afford host−guest complexes or supramolecular species in aqueous solution (*1*). This fascinating property enables them to be successfully utilized as drug carriers (*2*−*4*), separation reagents (*5*), enzyme mimics (*6*), and photochemical sensors (*7*), etc. Bis-cyclodextrin derivatives can greatly enhance the original binding ability and molecular recognition of parent cyclodextrins through the cooperative binding of two adjacent hydrophobic cavities. In addition, the functional linker group introduced in bridged bis-cyclodextrins can not only adjust the distance and orientation of two cyclodextrin cavities in cyclodextrin dimers to affect the penetration depth of guest molecules but also supply additional binding ability toward accommodated guest upon inclusion complexation. Owing to these potential advantages, a variety of dimeric cyclodextrins with different functional linkers have been designed and synthesized to understand the multiple recognition mechanisms of cyclodextrin dimers and to mimic the "multimode, multipoint" binding often observed in the biological systems (*8*−*10*). Among the various families of organic and biological guests for these studies, oligopeptides have attracted considerable interest because they represent an intermediate step toward the recognition of protein surfaces, and the short peptide sequences are themselves worthwhile targets for recognition due to their potential applications in separation, diagnostic, or biological areas (*11*, *12*). Recently, a number of works on the recognition and separation of peptides by cyclodextrins have been published (*13*−*16*). Schneider reported a detailed analysis on the inclusion complexation of some di- and tripeptides with amino cyclodextrins, demonstrating the simultaneous presence of complexes with a peptide phenyl unit approaching from both the narrow and the wide side of the cyclodextrin cavity (*17*). Breslow et al. reported a series of elegant works on the molecular recognition of oligopeptides by cyclodextrin cavities, which showed that the cyclodextrin dimers could strongly associate with the oligopeptides through the cooperative binding of two hydrophobic cavities (*18*). Inoue et al. reported the chiral recognition thermodynamics of dipeptides with native *γ*-cyclodextrin and discussed the effects of the length, size, and flexibility of the tether connecting the two aromatic moieties in a peptide on the molecular recognition (*19*). More recently, synthetic receptors bearing a 2,6-disubstituted pyridine group were proven to be one type of effective host compound for the recognition of peptide guests with a carboxylic acid terminus, since the pyridine unit can specifically bind to the carboxylic acid fragment of the peptide (*20*, *21*). However, most of the studies on the molecular recognition of peptides by cyclodextrins are carried in the neutral media, and the corresponding investigations in the acidic media are less involved (*17*, *22*). Herein, we wish to report the synthesis of a bis(*β*-cyclodextrin) with a fluorescent pyridine-2,6-dicarboxamide linker (Chart 1) and its inclusion complexation behavior with six aliphatic oligopeptides at different pH values. These studies will help us to gain a deeper insight into the recognition process of peptides in different biological environments, such as serum (pH ca. 7.3) or gastric acid (pH ca. 1.5), and consequently meet their potential applications as drug carriers.

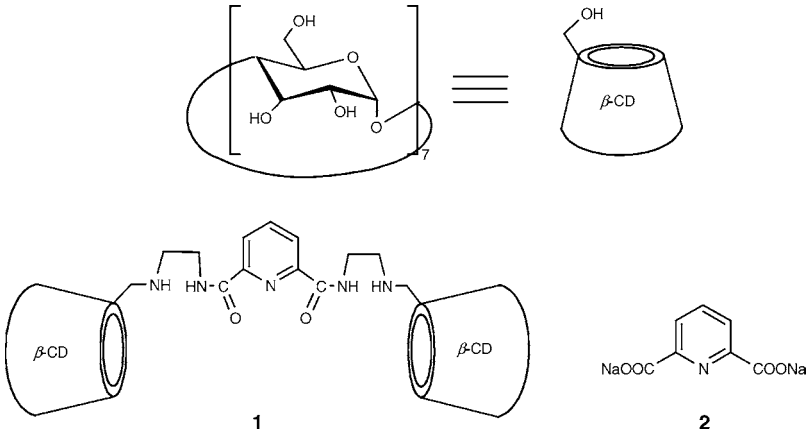
EXPERIMENTAL PROCEDURES

Materials. All guest oligopeptides, i.e., Glu-Glu, Gly-Gly, Gly-Leu, Leu-Gly, Met-Met, and Gly-Gly-Gly (Chart 2), were commercially available and used without further

* Author for correspondence. Tel: +86-022-23503625; fax: +86-022-23503625 (or 4853). E-mail: yuliu@public.tpt.tj.cn.

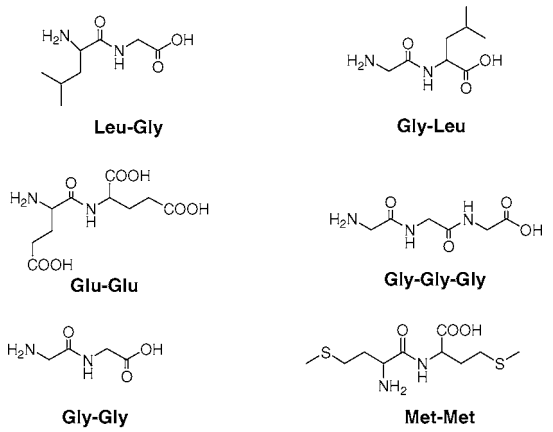
10.1021/bc034230p CCC: $27.50 © 2004 American Chemical Society
Published on Web 02/26/2004

Chart 1



1 2

Chart 2



purification. Pyridine-2,6-dicarboxylic acid was purchased from Alfa Aesar. β-Cyclodextrin of reagent grade was recrystallized twice from water and dried in vacuo at 95 °C for 24 h prior to use. *N*,*N*-Dimethylformamide (DMF) was dried over calcium hydride for 2 days and then distilled under reduced pressure prior to use. Mono-[6-*O*-(*p*-toluenesulfonyl)]-β-cyclodextrin (6-OTs-β-cyclodextrin) was prepared by the reaction of tosyl chloride with β-cyclodextrin in an alkaline aqueous solution according to the literature reports (*23*). Then, 6-OTs-β-cyclodextrin was converted to mono[6-(2-aminoeythylamino)-6-deoxy]-β-cyclodextrin in 70% yield on heating in excess ethylenediamine at 70 °C for 7 h (*24*).

Measurements. Elemental analyses were performed on a Perkin-Elmer-2400C instrument. NMR spectra were recorded on a Varian Mercury VX300 instrument. UV and circular dichroism (CD) spectra were performed on a Shimadzu UV 2401 spectrophotometer and a JASCO J-715S spectropolarimeter, respectively. Fluorescence spectra were measured in a conventional rectangular quartz cell (10 × 10 × 45 mm) at 25 °C on a JASCO FP-750 spectrometer equipped with a constant-temperature water bath, with the excitation and emission slits width of 10 nm. In the spectral measurements, disodium hydrogen phosphate dodecahydrate (25.79 g) and sodium dihydrogen phosphate dihydrate (4.37 g) were dissolved in 1000 mL of deionized water to make a 0.10 M aqueous phosphate buffer solution of pH 7.2, whereas 20 mM potassium chloride was adjusted to pH 2.0 with 1 M hydrochloric acid to give an acidic buffer solution (*25*), which were used as solvent for all measurements.

Synthesis of Pyridine-2,6-dicarboxamide-Bridged Bis(β-cyclodextrin) (1). To a solution of DMF (50 mL) containing 2.6 g of mono[6-(2-aminoeythylamino)-6-deoxy]-β-cyclodextrin and 1.24 g of dicyclohexylcarbodiimide (DCC) was added 0.16 g of pyridine-2,6-dicarboxylic acid in the presence of a small amount of 4 Å molecular sieves. The reaction mixture was stirred for 3 d in an ice bath and another 4 d at room temperature. The precipitate was removed by filtration, and the filtrate was poured into 300 mL of acetone. The white precipitate was collected and subsequently purified on a Sephadex G-25 column with deionized water as eluent. After drying in vacuo, a pure sample was obtained in 4% yield. ^{1}H NMR (D_2O, TMS, ppm) δ 2.5−3.0 (m, 8H), 3.1−4.0 (m, 84H), 4.9 (m, 14H), 7.9 (m, 3H); FT-IR (KBr) ν/cm^{-1} 3330, 3064, 2928, 1702, 1615, 1573, 1434 1368, 1301, 1239, 1155, 1079, 1031, 945, 847, 757, 707, 580, 529, 504, 411. Anal. Calcd for $C_{95}H_{153}O_{70}N_5 \cdot 8H_2O$: C, 43.40; H, 6.48; N, 2.66. Found: C, 43.53; H, 6.27; N, 2.94.

RESULTS AND DISCUSSION

Conformational Analysis. Over the past decades, circular dichroism (CD) spectrometry has become a convenient and widely employed method for the elucidation of the absolute conformation of chiral compounds (*26*). Moreover, achiral compounds can also show the induced circular dichroism (ICD) signal in the corresponding transition band in cases where there is a chiral microenvironment. Possessing an inherent chiral cavity, cyclodextrins can certainly provide such a microenvironment for the attached achiral moiety. In this context, we have measured the CD spectra of **1** at 1.0 × 10^{-4} mol dm^{-3} concentration in aqueous buffer solutions (Figure 1) to investigate the conformation of this β-cyclodextrin dimer with a chromophoric pyridine linker.

As shown in Figure 1a, host **1** displays quite different CD spectra in the two buffer solutions of different pH values considered in this study, which indicates that there should exist significant but different degrees of interaction between the linker group and the cyclodextrin cavity. The CD spectrum of **1** shows a strong positive Cotton effect peak around 213 nm ($\Delta\epsilon$ = 3.91 dm^3 mol^{-1} cm^{-1}) in a pH 7.2 buffer but displays a moderate negative Cotton effect peak around 220 nm ($\Delta\epsilon$ = −1.54 dm^3 mol^{-1} cm^{-1}) and a weak negative Cotton effect peak around 270 nm ($\Delta\epsilon$ = −0.14 dm^3 mol^{-1} cm^{-1}) in a pH 2.0 buffer. In the control experiment, the UV spectrum of the reference compound **2**, disodium pyridine-2,6-dicarboxylate, shows a peak around 272 nm and a shoulder around 220 nm, while the CD spectrum of **2** only exhibits a weak positive Cotton effect peak around 219 nm ($\Delta\epsilon$ = 0.1 dm^3 mol^{-1} cm^{-1}) assigned to the ^1L_a transition of the pyridine chromophore. According to the empirical rule proposed

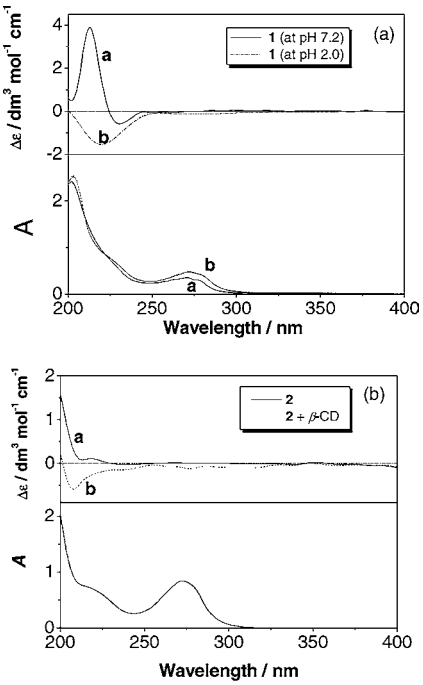


Figure 1. (a) Circular dichroism and UV spectra of host **1** (1.0×10^{-4}mol dm^{-3}) in the pH 7.2 and 2.0 buffers at 25 °C. (b) Circular dichroism and UV spectra of **2** (1×10^{-4}mol dm^{-3}) in the absence and presence of β-cyclodextrin (20 equiv.) in the pH 7.2 buffer at 25 °C.

by Kajtár (*27*), and Harata (*28*), the sign of ICD signal depends on the orientation of the transition dipole moment of the chromophore with respect to the dipole moment of the cyclodextrin. For the chromophore located inside the cyclodextrin cavity, its electronic transition parallel to the cyclodextrin axis gives a positive ICD signal, whereas the perpendicular transitions gives a negative signal, but this situation is reversed for the chromophore located outside the cyclodextrin cavity. So we can deduce that the pyridine group in the linker of host **1** may be located outside the cyclodextrin cavity in a pH 7.2 buffer, where the transition moment of ^1L_a band around 213 nm is nearly perpendicular to the cyclodextrin axis and thus induces the positive CD signal. On the other hand, in a pH 2.0 buffer, the pyridine chromophore may be shallowly included in the cyclodextrin cavity, where both the ^1L_a and ^1L_b transition moments around 220 and 270 nm are nearly perpendicular to the cyclodextrin axis, resulting in the two negative Cotton effect peaks. As a good reference system, the CD spectrum of **2** in the presence of excess amount of β-cyclodextrin is also measured. As can be seen in Figure 1b, compound **2** displays similar, but weak, CD signals to those of bis(β-cyclodextrin) **1** in a pH 7.2 buffer. However, in the presence of β-cyclodextrin, the CD spectrum of **2** shows two negative Cotton effect peaks around 208 and 277 nm, respectively, which is like the spectrum of **1** in a pH 2.0 buffer. In addition, the fluorescence spectra of **1** in the pH 7.2 and 2.0 buffers also provide some useful information. As can be seen in Figure 2, bis(β-cyclodextrin) **1** emits stronger fluorescence in a pH 2.0 buffer than in a pH 7.2 buffer, which indicates that the pyridine chromophore in **1** is certainly located in a more hydrophobic environment in the pH 2.0 buffer. The results of the CD and fluorescence experiments jointly indicate that there exist some interactions between the pyridine chromophore in the linker group and the cyclodextrin cavity, which consequently supports our hypothesis about the self-inclusion conformation of **1** in an acidic media.

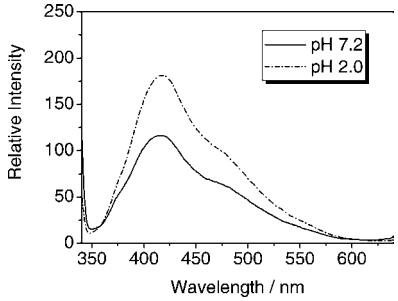


Figure 2. Fluorescence spectra of **1** (1.0×10^{-4} mol dm^{-3}) in the pH 7.2 and 2.0 buffers.

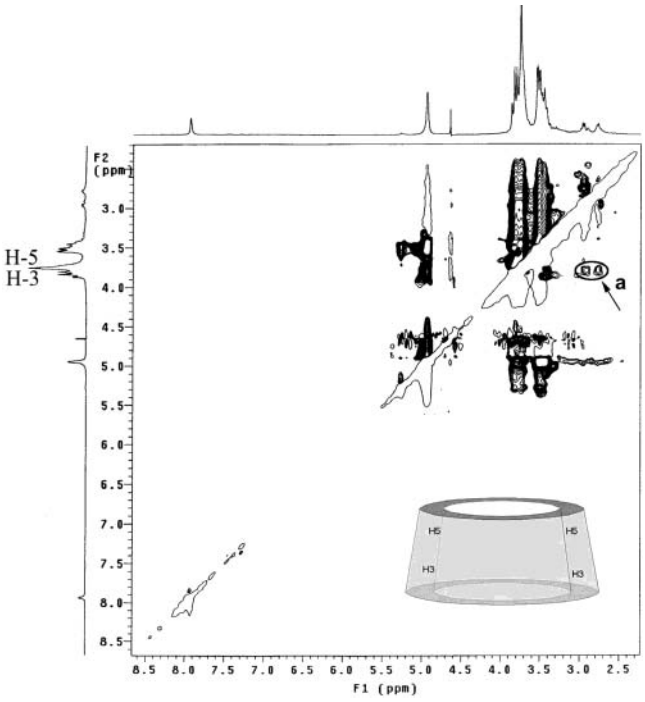


Figure 3. 2D ROESY spectra of host **1** (5 mM) in pD 7.2 buffer at 298 K with a mixing time of 400 ms.

2D NMR experiment provides reliable information about the conformation of bis(β-cyclodextrin) **1** in a pH 7.2 buffer. As illustrated in Figure 3, the ROSEY spectrum of **1** displays clear NOE cross-peaks between the H-5 protons of cyclodextrin and the ethylene protons of the linker group (peaks a). On the other hand, no NOE correlations between the inner protons (H-3 and H-5) of the cyclodextrin moieties and the pyridine protons can be observed. These phenomena indicate that only the ethylene unit of the linker group is shallowly embedded in the cyclodextrin cavity, but the pyridine group is located at the exterior. From the above CD, fluorescence, and NMR results, we can draw the conclusion that the conformation of **1** switches according to the pH value of the buffer solution as represented in Figure 4. Unfortunately, the ROSEY signals of **1** at pD 2.0 are too ambiguous to examine the NOE correlations between the pyridine unit and the H-3/H-5 protons of cyclodextrin, which may be due to the protonation of the pyridine unit, although the mechanism is still unclear. However, we can still get some useful information about the self-inclusion conformation of host **1** at pH 2.0 from the ^{1}H NMR spectra. Seen from the structure of host **1**, one can deduce that its self-inclusion conformation at pH 2.0 should result in the existence of a degenerated chemical-exchange process, i.e. the pyridinium ring included in one or the other cyclodextrin cavity, which would result in

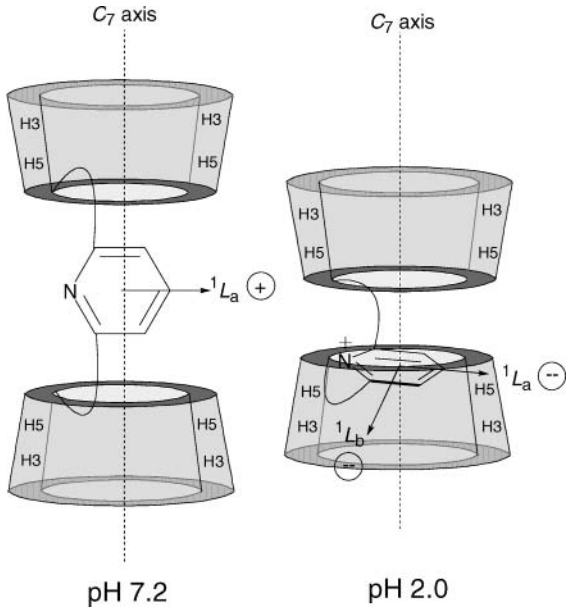


Figure 4. Possible conformation of bis(β-cyclodextrin) **1** in pH 7.2 and 2.0 buffers.

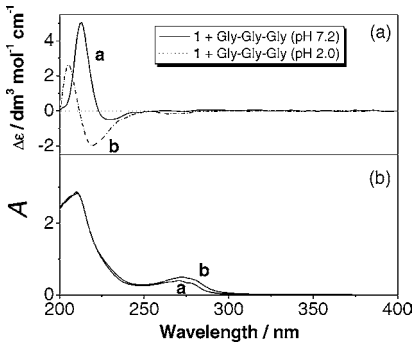


Figure 5. Circular dichroism (a) and UV (b) spectra of host **1** (1.0×10^{-4} mol dm^{-3}) in the presence of Gly-Gly-Gly (6.0×10^{-4} mol dm^{-3}) in the pH 7.2 and 2.0 buffers at 25 °C.

the significant line broadening in the ^{1}H NMR spectra unless this exchange is very rapid. Therefore, the obvious line broadening of the pyridinium protons in **1** at pD 2.0 clearly indicates the self-inclusion conformation of **1** in the acidic media.

Binding Mode. In our previous researches, we found that bridged bis(β-cyclodextrin) hosts could adopt different binding modes upon cooperative association with a given guest molecule, leading to either a sandwich or a coinclusion complex (*29*). In this work, we examine the CD spectra of bis(β-cyclodextrin) **1** in the presence of Gly-Gly-Gly to investigate its binding mode at different pH values. The reason for choosing Gly-Gly-Gly as guest molecule is that it displays no appreciable CD signals in the range of 200−400 nm. As seen from Figure 5, in either the pH 7.2 or the pH 2.0 buffer, the CD spectrum of **1** remains unchanged upon addition of Gly-Gly-Gly, but the Cotton effect intensities increase significantly. The enhanced Cotton effects ($\Delta\Delta\epsilon = 1.13$ dm^3 mol^{-1} cm^{-1} for pH 7.2 buffer and $\Delta\Delta\epsilon = 0.43$ dm^3 mol^{-1} cm^{-1} for pH 2.0 buffer) indicate that **1** has associated with Gly-Gly-Gly to form a host−guest complex. The fact that **1** exhibits similar pH dependent CD signals in the absence and in the presence of Gly-Gly-Gly supports that it adopts binding modes upon inclusion complexation that are compatible with the above-discussed host conformations. In a pH 7.2 buffer, bis(β-cyclodextrin) **1** may adopt a sandwich binding mode, where the guest molecule is cooperatively bound by two cyclodextrin cavities (Figure 6). However, in a pH 2.0 buffer, bis(β-cyclodextrin) **1** probably adopts a coinclusion binding mode; that is, the linker group is partly self-included in one of the hydrophobic cavities, while the guest molecule penetrates into the other cavity (Figure 6).

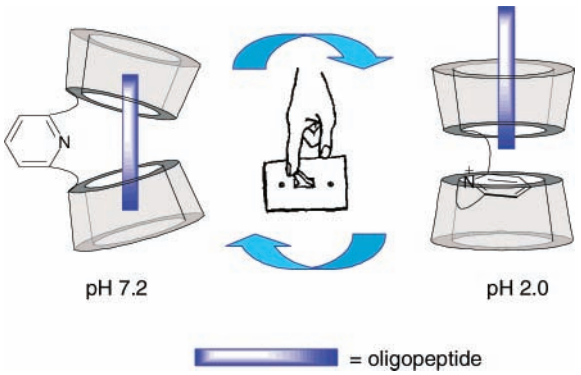


Figure 6. Possible binding mode of bis(β-cyclodextrin) **1** with oligopeptides.

The NMR data further reveal these binding modes in more detail. Since the chemical shifts of the isopropyl protons in Leu fragment are distant from those of the protons in bis(β-cyclodextrin) **1** and can be easily recognized in NMR spectra, we select Gly-Leu as guest to examine the binding geometry of the bridged bis(cyclodextrin) **1** with the guest oligopeptides. As illustrated in Figure 7, the ROESY spectrum of an equimolar mixture of **1** with Gly-Leu displays clear NOE cross-peaks between the H-3 protons of cyclodextrin and the methyl protons (H-5′) in Gly-Leu (peak a) as well as those between the H-5 protons of cyclodextrin and the methine proton (H-4′) of Gly-Leu (peak b). In addition, the initial strong correlation between the ethylene protons in the linker group of bis(cyclodextrin) **1** and the H-5 protons of cyclodextrin (peak a in Figure 3) disappears after the addition of guest oligopeptide. These results jointly indicate that the guest Gly-Leu is accommodated in the cyclodextrin cavity and the linker group is entirely driven out after the guest inclusion, which confirms the cooperative sandwich binding mode between host and guest. On the other hand, the appreciable line broadening of the pyridinium protons in **1** at pD 2.0 in the presence of Gly-Leu indicates that the pyridinium group is still self-included in the cyclodextrin cavity even after host−guest complexation, which consequently verifies the coinclusion binding mode as illustrated in Figure 6.

Spectral Titration. Quantitative investigation of the complexation behavior of **1** with the selected oligopeptides has been examined at pH 7.2 and 2.0 by means of titration fluorimetry. The fluorescence intensity of **1** gradually increases with the stepwise addition of oligopeptides (Figure 8). As expected, all of the continuous variation (Job) plots show the maximum at a molar fraction of 0.5, confirming the formation of 1:1 host−guest inclusion complexes for either the sandwich or the coinclusion binding mode. (Figure 9)

Using a nonlinear least squares curve-fitting method (*30*), we obtain the complexation stability constant for each host−guest combination. The excellent curve fits support the reliability of the stability constants obtained. The stability constant (K_s) and Gibbs free energy change ($-\Delta G°$) for the inclusion complexation of host bis(β-cyclodextrin) **1** with a series of oligopeptide guests are listed in Table 1.

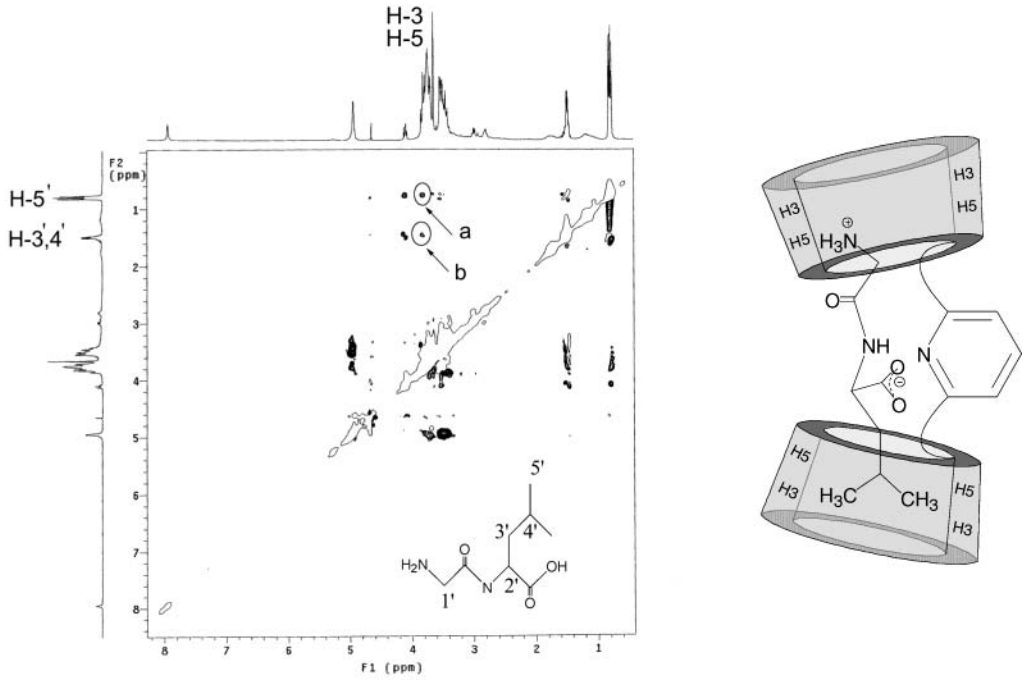


Figure 7. (left) 2D ROESY spectrum of mixture of host **1** (5 mM) and Gly-Leu (5 mM) in pD 7.2 buffer at 298 K with a mixing time of 400 ms, (right) possible binding mode of host **1** with Gly-Leu.

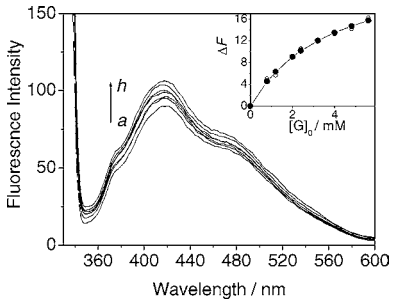


Figure 8. Fluorescence spectral changes bis(*β*-cyclodextrin) **1** (0.08 mM) upon addition of guest Gly-Gly-Gly (0−5.6 mM from *a* to *h*) at pH 7.2 and the nonlinear least-squares analysis (inset) of the differential intensity (Δ*F*) to calculate the complex stability constant (K_s). The excitation wavelength is 330 nm.

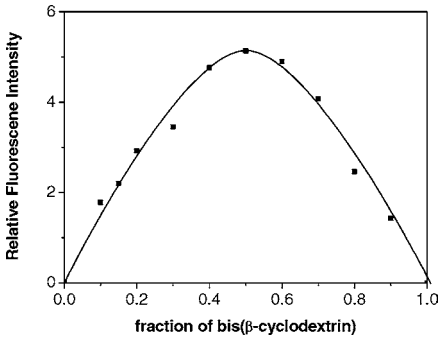


Figure 9. Continuous variation plot of the **1**/Gly-Gly system ([bis(*β*-cyclodextrin)] + [Gly-Gly] = 1.0×10^{-4} mol dm^{-3}) in a pH 2.0 buffer.

Molecular Binding Ability and Molecular Selectivity. It is well-known that several weak interactions, including van der Waals, hydrophobic, and hydrogen bond interactions, simultaneously contribute to the inclusion complexation of cyclodextrins with guest molecules. Additionally, other intermolecular interactions, such as electrostatic interaction and electron transfer, can also affect the binding behavior of cyclodextrins to some extent. In the present case, we find that the host−guest size/shape matching and induced fit dominate the stability of the complexes formed between host **1** and the assayed oligopeptides.

Table 1. Complex Stability Constant (K_s) and Gibbs Free Energy Change ($-\Delta G°$) for 1:1 Inclusion Complexation of Host 1 with Various Oligopeptide Guests in Aqueous Buffer Solution (pH 7.2 and 2.0) at 25 °C

pH	oligopeptide	Ks/M^{-1}	log K_s	$-\Delta G°$/kJ mol^{-1}
7.2	Glu-Glu	320 ± 10	2.50	14.3
2.0	Glu-Glu	153 ± 3	2.18	12.5
7.2	Gly-Gly	832 ± 30	2.92	16.7
2.0	Gly-Gly	339 ± 10	2.53	14.4
7.2	Gly-Leu	1208 ± 40	3.08	17.6
2.0	Gly-Leu	517 ± 20	2.71	15.5
7.2	Leu-Gly	356 ± 10	2.55	14.6
2.0	Leu-Gly	330 ± 10	2.52	14.4
7.2	Met-Met	700 ± 30	2.84	16.2
2.0	Met-Met	641 ± 20	2.81	16.0
7.2	Gly-Gly-Gly	263 ± 10	2.42	13.8
2.0	Gly-Gly-Gly	72 ± 3	1.86	10.6

From Table 1, we can see that the corresponding K_s value for a given oligopeptide guest at pH 7.2 is higher than that at pH 2.0. This observation is consistent with the cooperative contributions of two cyclodextrin cavities on binding with one guest. On the other hand, for the coinclusion mode, the guest molecule is only bound by one cyclodextrin, which will inevitably lead to weaker interactions between host and guest. Among the guest oligopeptides, bis(*β*-cyclodextrin) **1** displays the strongest binding ability toward Gly-Leu and Met-Met, both of which possess a carboxyl group located in the middle of the peptide chain. It is known that the diamidopyridine group can interact with the carboxyl group and thus effectively recognizes complementary peptide guests (*20*, *31*). In our case, this interaction rationalize not only the strong associations of bis(*β*-cyclodextrin) **1** with guest Gly-Leu and Met-Met but also the high sequence selectivity of **1** for Gly-Leu as compared with Leu-Gly ($K_s^{Gly-Leu}/K_s^{Leu-Gly} = 4.2$ at pH 7.2). On the other hand, although Glu-Glu has a similar structure to Met-Met, its poor hydrophobicity arising from the presence of three hydrophilic carboxyl groups in the molecule reduces the

hydrophobic interactions upon complexation with the cyclodextrin cavities and thus results in the moderate K_s value. Another interesting point is that, although possessing a relatively long linker group, bis(β-cyclodextrin) **1** exhibits a higher K_s value for the shorter Gly-Gly than for the longer Gly-Gly-Gly ($K_s^{Gly-Gly}/K_s^{Gly-Gly-Gly} = 4.7$ at pH 2.0), which may be attributed to the size−fit relationship between host and guest. That is, for a coinclusion mode in which the guest is only associated with one cyclodextrin cavity, the shorter guest Gly-Gly (skeleton length 7.246 Å, estimated by MM2) is fits better to the height of the cyclodextrin cavity (7.9 Å) than Gly-Gly-Gly (skeleton length 10.87 Å, estimated by MM2).

Protonation Effect. Because of the relatively low pK_a value of the pyridine group (pK_a ca. 5.4) and the ethylenediamino group (pK_a ca. 3.2), all of the N atoms in the linker group of **1** should be protonated in a pH 2.0 buffer. On the other hand, for the selected guest oligopeptides, the pK_a values of the carboxyl groups are around 3 (*22a*), while the corresponding values for the amino terminus are around 8 (*32*), which indicates that the C-terminals of the guests should exist as COOH the N-terminals as NH_3^+ at pH 2.0. That is to say, in an acidic media (pH 2.0), both host **1** and oligopeptide are positively charged, which will inevitably lead to unfavorable electrostatic repulsions between host and guest. However, this negative contribution will be partly compensated by the hydrogen bonds between the carboxyl, amino, and/or sulfydryl groups of guest peptides and the hydroxyl groups of the cyclodextrin. As a cumulative result of the hydrophobic, electrostatic and hydrogen bond interactions, the differential Gibbs energy changes for the complexation of bis(β-cyclodextrin) at different pH values ($\Delta\Delta G° = \Delta G°_{pH\ 7.2} - \Delta G°_{pH\ 2.0}$) vary in a narrow range (0.2−3.2 kJ/mol). This phenomenon indicates that the protonation effect can only affects the binding ability of bis(β-cyclodextrin) **1** with oligopeptides to a limited extent.

ACKNOWLEDGMENT

This work was supported by NNSFC (No. 90306009 and 20272028), which are gratefully acknowledged.

LITERATURE CITED

(1) (a) Szejtli, J. (1998) Introduction and General Overview of Cyclodextrin Chemistry. *Chem. Rev. 98*, 1743−1754. (b) Saenger, W. (1980) Cyclodextrin inclusion compounds in research and industry. *Angew. Chem., Int. Ed. Engl. 19*, 344−362. (c) Wenz, G. (1994) Cyclodextrins as building blocks for supramolecular structures and functional units. *Angew. Chem., Int. Ed. Engl. 33*, 803−822.

(2) Szejtli, J. (1988) *Cyclodextrin Technology*, Kluwer, Dordrecht.

(3) (a) Uekama, K., Hirayama, F., and Irie, T. (1998) Cyclodextrin Drug Carrier Systems. *Chem. Rev. 98*, 2045−2076. (b) Loftsson, T., and Järvinen, T. (1999) Cyclodextrins in ophthalmic drug delivery. *Adv. Drug Delivery Rev. 36*, 59−79.

(4) Ortiz Mellet, C., Defaye, J., and García Fernández, J. M. (2002) Multivalent Cyclooligosaccharides: Versatile Carbohydrate Clusters with Dual Role as Molecular Receptors and Lectin Ligands. *Chem. Eur. J. 8*, 1982−1990.

(5) Li, S., and Purdy, W. C. (1992) Cyclodextrins and their applications in analytical chemistry *Chem. Rev. 92*, 1457−1470.

(6) Breslow, R., and Dong, S. D. (1998) Biomimetic Reactions Catalyzed by Cyclodextrins and Their Derivatives *Chem. Rev. 98*, 1997−2011.

(7) Ueno, A., (1996) Fluorescent Cyclodextrin for Molecule Sensing. *Supramol. Sci. 3*, 31−36.

(8) (a) Nelissen, H. F. M., Kercher, M., de Cola, L., Feiters, M. C., and Nolte, R. J. M. (2002) Photoinduced Electron Transfer between Metal-Coordinated Cyclodextrin Assemblies and Viologens. *Chem. Eur. J. 8*, 5407−5414. (b) Venema, F., Nelissen, H. F. M., Berthault, P., Birlirakis, N., Rowan, A. E., Feiters, M. C., and Nolte, R. J. M. (1998) Synthesis, Conformation, and Binding Properties of Cyclodextrin Homo- and Heterodimers Connected through Their Secondary Sides. *Chem. Eur. J. 4*, 2237−2250.

(9) (a) von Bommel, K. J. C., de Jong, M. R., Metselaar, G. A., Verboom, W., Huskens, J., Hulst, R., Kooijman, H., Spek, A. L., and Reinhoudt, D. N. (2001) Complexation and (Templated) Synthesis of Rhenium Complexes with Cyclodextrins and Cyclodextrin Dimers in Water. *Chem. Eur. J. 7*, 3603−3616. (b) de Jong, M. R., Engbersen, J. F. J., Huskens, J., and Reinhoudt, D. N. (2000) Cyclodextrin Dimers as Receptor Molecules for Steroid Sensors. *Chem. Eur. J. 6*, 4034−4040. (c) Michels, J. J., Huskens, J., and Reinhoudt, D. N. (2004) Noncovalent Binding of Sensitizers for Lanthanide(III) Luminescence in an EDTA-bis(β-cyclodextrin) Ligand. *J. Am. Chem. Soc. 124*, 2056−2064.

(10) Baugh, S. D. P., Yang, Z., Leung, D. K., Wilson, D. M., and Breslow, R. (2001) Cyclodextrin Dimers as Cleavable Carriers of Photodynamic Sensitizers. *J. Am. Chem. Soc. 123*, 12488−12494.

(11) Peczuh, M. W., and Hamilton, A. D. (2000) Peptide and Protein Recognition by Designed Molecules. *Chem. Rev. 100*, 2479−2494.

(12) Tsubaki, K., Kusumoto, T., Hayashi, N., Nuruzzaman, M., and Fuji, K. (2002) Sequence-Selective Visual Recognition of Nonprotected Dipeptides. *Org. Lett. 4*, 2313−2316.

(13) Schaschke, N., Fiori, S., Weyher, E., Escrieut, C., Fourmy, D., Müller, G., and Moroder, L. (1998) Cyclodextrin as Carrier of Peptide Hormones. Conformational and Biological Properties of β-Cyclodextrin/Gastrin Constructs. *J. Am. Chem. Soc. 120*, 7030−7038.

(14) Ueoka, R., Matsumoto, Y., Harada, K., Akahoshi, H., Ihara, Y., and Kato, Y. (1992) Cyclodextrin-mediated deacylation of peptide esters with marked stereoselectivity. *J. Am. Chem. Soc. 114*, 8339−8340.

(15) Fukahori, T., Ugawa, T., and Nishikawa, S. (2002) Molecular Recognition Kinetics of Leucine and Glycyl-Leucine by β-Cyclodextrin in Aqueous Solution in Terms of Ultrasonic Relaxation *J. Phys. Chem. A 106*, 9442−9445.

(16) (a) Hossain, M. A., Mihara, H., and Ueno, A. (2003) Novel Peptides Bearing Pyrene and Coumarin Units with or without β-cyclodextrin in Their Side Chains Exhibit Intramolecular Fluorescence Resonance Energy Transfer. *J. Am. Chem. Soc. 125*, 11178−11179. (b) Matsumura, S., Sakamoto, S., Ueno, A., and Mihara, H. (2000) Construction of α-Helix Peptides with β-Cyclodextrin and Dansyl Units and Their Conformational and Molecular Sensing Properties. *Chem. Eur. J. 6*, 1781−1788. (c) Furukawa, S., Mihara, H., and Ueno, A. (2003) Sensing Behavior of Fluorescent Cyclodextrin/Peptide Hybrids Bearing a Macrocyclic Metal Complex. *Macromol. Rapid Commun. 24*, 202−206.

(17) Hacket, F., Simova, S., and Schneider, H. J. (2001) The complexation of peptides by aminocyclodextrins. *J. Phys. Org. Chem. 14*, 159−170.

(18) (a) Maletic, M., Wennemers, H., McDonald, Q. D., Breslow, R., and Still, W. C. (1996) Selective Binding of Dipeptides L-Phe-D-Pro and D-Phe-L-Pro to β-Cyclodextrin. *Angew. Chem., Int. Ed. 35*, 1490−1492. (b) Breslow, R., Yang, Z., Ching, R., Trojandt, G., and Odobel, F. (1998) Sequence Selective Binding of Peptides by Artificial Receptors in Aqueous Solution. *J. Am. Chem. Soc. 120*, 3536−3537. (c) Wilson, D., Perlson, L., and Breslow, R. (2003) Helical Templating of Oligopeptides by Cyclodextrin Dimers. *Bioorg. Med. Chem. 11*, 2649−2653. (d) Leung, D. K., Yang, Z., and Breslow, R. (2000) Selective Binding of Dipeptides L-Phe-D-Pro and D-Phe-L-Pro to β −Cyclodextrin. *Proc. Natl. Acad. Sci. U.S.A. 97*, 5050−5053. (e) R. Breslow, and B. Zhang, (1992) Very fast ester hydrolysis by a cyclodextrin dimer with a catalytic linking group. *J. Am. Chem. Soc. 114*, 5882−5883.

(19) Rekharsky, M., Yamamura, H., Kawai, M., and Inoue, Y. (2003) Complexation and Chiral Recognition Thermodynam-

ics of γ-Cyclodextrin with *N*-Acetyl- and N-Carbobenzyloxy-dipeptides Possessing Two Aromatic Rings. *J. Org. Chem. 68*, 5228−5235.

(20) Braxmeier, T., Demarcus, M., Fessmann, T., McAteer, S., and Kilburn, J. D. (2001) Identification of Sequence Selective Receptors for Peptides with a Carboxylic Acid Terminus. *Chem. Eur. J. 7*, 1889−1898, and references therein.

(21) Botana, E., Ongeri, S., Arienzo, R., Demarcus, M., Frey, J. G., Piarulli, Potenza, U. D., Gennari, C., and Kilburn, J. D. (2001) Enantioselective binding of dipeptides using acyclic receptors. *Chem. Commun.* 1358−1359.

(22) (a) Süss, F., Popptiz, W., Sänger-van de Griend, C. E., and Scriba, G. K. E. (2001) Influence of the amino acid sequence and nature of the cyclodextrin on the separation of small peptide enantiomers by capillary electrophoresis using randomly substituted and single isomer sulfated and sulfonated cyclodextrins. *Electrophoresis 22*, 2416−2423. (b) Süss, F., Kahle, C., Holzgrabe, U., and Scriba, G. K. E. (2002) Studies on the chiral recognition of peptide enantiomers by neutral and sulfated β-cyclodextrin and heptakis-(2,3-di-O-acetyl)-β-cyclodextrin using capillary electrophoresis and nuclear magnetic resonance. *Electrophoresis 23*, 1301−1307.

(23) (a) Petter, R. C., Salek, J. S., Sikorski, C. T., Kumaravel, G., and Lin, F.-T. (1990) Cooperative binding by aggregated mono-6-(alkylamino)-β-cyclodextrins. *J. Am. Chem. Soc. 112*, 3860−3868. (b) Vitzitiu, D., Walkinshaw, C. S., Gorin, B. I., and Thatcher, G. R. (1997) Synthesis of Monofacially Functionalized Cyclodextrins Bearing Amino Pendent Groups. *J. Org. Chem. 62*, 8760−8766.

(24) (a) Tabushi, I., and Shimizu, N. (1978) *Jpn. Kodai Tokkyo Koho* 78102985, [Tabushi, I., and Shimizu, N. (1979) *Chem. Abstr. 90*, 39196b]. (b) May, B. L., Kean, S. D., Easton, C. J., and Lincoln, S. F. (1997) Preparation and characterization of 6^A-polyamine-monosubstituted β−cyclodextrins. *J. Chem. Soc., Perkin Trans. 1* 3157−3160.

(25) Zhu, X., and Lever, S. Z. (2002) Formation kinetics and stability studies on the lanthanide complexes of 1,4,7,10-tetraazacyclododecane-N,N′,N″,N‴-tetraacetic acid by capillary electrophoresis. *Electrophoresis 23*, 1348−1356.

(26) Lightner, D. A., and Gurst, J. E. (2000) *Organic Conformational Analysis and Stereochemistry from Circular Dichroism Spectroscopy*, Wiley-VCH, New York.

(27) Kajtár, M., Horvath-Toro, C., Kuthi, E., and Szejtli, J. (1982) A simple rule for predicting circular dichroism induced in aromatic guests by cyclodextrin hosts in inclusion complexes. *Acta Chim. Acad. Sci. Hung. 110*, 327−355.

(28) Harata, K., and Uedaira, H. (1975) The circular dichroism spectra of the β-cyclodextrin complex with naphthalene derivatives. *Bull. Chem. Soc. Jpn. 48*, 375−378.

(29) (a) Liu, Y., Chen, Y., Liu, S.-X., Guan, X.-D., Wada, T., and Inoue, Y. (2001) Unique Fluorescence Behavior of Rhodamine B upon Inclusion Complexation with Novel Bis(β-cyclodextrin-6-yl) 2, 2′-Bipyridine-4,4′-dicarboxylate. *Org. Lett. 3*, 1657−1660. (b) Liu, Y., Song, Y., Wang, H., Zhang, H.-Y., Wada, T., and Inoue, Y. (2003) Selective Binding of Steroids by 2,2′-Biquinoline-4,4′-dicarboxamide-Bridged Bis(β-cyclodextrin): Fluorescence Enhancement by Guest Inclusion. *J. Org. Chem. 68*, 3687−3690.

(30) Liu, Y., Li, B., Wada, T., and Inoue, Y. (1999) Novel *o*-phenylenediseleno-Bridged bis(β-cyclodextrin)s complexes with platinum(IV) and palladium(II) Ions. *Supramol. Chem. 10*, 279−285.

(31) (a) Fessmann, T., and Kilburn, J. D. (1999) Identification of Sequence-Selective Receptors for Peptides with a Carboxylic Acid Terminus. *Angew. Chem., Int. Ed. 38*, 1993−1996.

(32) Sänger-van de Griend, C. (1999) Enantiomeric separation of glycyl dipeptides by capillary electrophoresis with cyclodextrins as chiral selectors. *Electrophoresis 20*, 3417−3423.

BC034230P

Peptide−Protein Microarrays for the Simultaneous Detection of Pathogen Infections

Xavier Duburcq,[†,‡] Christophe Olivier,[‡] Frédéric Malingue,[‡] Rémi Desmet,[§] Ahmed Bouzidi,[‡] Fenhling Zhou,[‡] Claude Auriault,[†] Hélène Gras-Masse,[‡] and Oleg Melnyk*[,§]

UMR CNRS 8527, Biological Institute of Lille, 1 Rue du Pr Calmette, 59021 Lille, France, Sedac-Therapeutics, Le Galénis, Bât. B, 85 Rue Nelson Mandela, 59120 Loos, France, and UMR CNRS 8525, Biological Institute of Lille, 1 Rue du Pr Calmette, 59021 Lille, France. Received July 10, 2003; Revised Manuscript Received December 12, 2003

We describe novel peptide−protein microarrays, which were fabricated using semicarbazide glass slides that permitted the immobilization of glyoxylyl peptides by site-specific ligation and the immobilization of proteins by physisorption. The arrays permitted the simultaneous serodetection of antibodies directed against hepatitis C virus (HCV core p21 15−45 peptide, NS4 1925−1947 peptide, core, NS3, NS4, and mixture of core, NS3, NS4, and NS5 antigens), hepatitis B virus (HBc, HBe, and HBs), human immunodeficiency virus (Gp41 and Gp120 for HIV-I and Gp36 for HIV-II), Epstein−Barr virus (VCAp18 153-176 peptide), and syphilis (rTpN47 and rTpN17) antigens using an immunofluorescence assay. Peptide−protein microarrays displayed high signal-to-noise ratios, sensitivities, and specificities for the detection of antibodies as revealed by the analysis of a collection of human sera referenced against these five pathogens.

INTRODUCTION

The parallel detection of different antibodies in complex biological samples have a wide range of potential applications in the diagnosis of allergies and autoimmune and infectious diseases, as well as in epitope mapping studies and the development of vaccines (*1*−*3*). Actually, the detection of antibodies is usually performed using ELISA-based assays, which are time-consuming and require large quantities of both reagents and biological samples. These limitations have stimulated the development of high-throughput screening systems based on microfabricated analytical devices.

Several reports have demonstrated that peptide microarrays could be utilized for the detection of antibodies (*4*, *5*). On the other hand, the application of protein microarrays in this context has lagged because of poor stability, cross-reactivities, complex coupling chemistries and low sensitivities (*6*−*10*).

Very recently, we have shown that peptide microarrays fabricated by site-specific ligation of glyoxylyl peptides onto semicarbazide glass slides (Figure 1) displayed high levels of sensitivity and specificity for the detection of antibodies in human sera. The detection, based on an immunofluorescent assay, required very small blood samples from infected individuals (typically 1 μL) (*11*). Encouraged by these detection results, we examined the possibility of extending the methodology to the fabrication of protein or of peptide−protein microarrays.

We show in this article that proteins can be efficiently immobilized on semicarbazide glass slides by physisorption, whereas formation of a covalent bond between small peptidic antigens and the surface was found to be necessary to prevent the loss of material. Interestingly, the printing step and the whole process used for peptide microarrays in an antibody detection experiment were found to be applicable to proteins. Thus, peptide−protein microarrays could be prepared and used to detect antibodies directed against viral or bacterial antigens. In particular, we used antigens derived from HCV (core p21 15−45 peptide (*12*), NS4 1925−1947 peptide (*13*), core, NS3, NS4 and mixture of core, NS3, NS4, and NS5 antigens), HBV (HBc, HBe, and HBs), HIV (Gp41 and Gp120 for HIV-I and Gp36 for HIV-II), EBV (VCA p18 153−176 peptide (*14*)), and *Treponema pallidum* (rTpN47 and rTpN17 (*15*)). The performance of this miniaturized assay in terms of sensitivity and specificity was examined using a collection of sera referenced against HIV (245 sera), HCV (300 sera), HBV (220 sera), EBV (90 sera), or *Treponema pallidum* (30 sera) with commercially available tests. The possibility of detecting simultaneously HCV, HBV, HIV, and EBV antibodies with a high level of sensitivity and specificity was demonstrated using a collection of 90 sera referenced against these 4 pathogens.

In the accompanying article, we report other interesting properties of semicarbazide glass slides (chemical

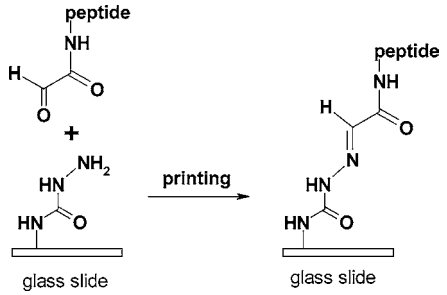


Figure 1. α-Oxo semicarbazone site-specific ligation of glyoxylyl peptides onto semicarbazide functionalized glass slides.

* To whom correspondence should be addressed. Phone: 33-(0)3 20 87 12 14. Fax: 33(0)3 20 87 12 35. E-mail: oleg.melnyk@ibl.fr.

† UMR CNRS 8527, Biological Institute of Lille.

‡ Sedac-Therapeutics.

§ UMR CNRS 8525, Biological Institute of Lille.

10.1021/bc034226d CCC: $27.50 © 2004 American Chemical Society
Published on Web 02/28/2004

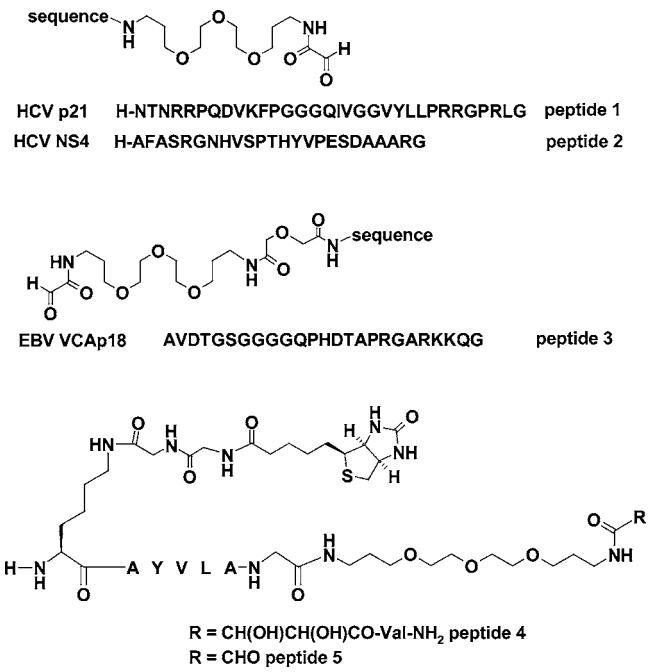


Figure 2. Synthetic peptides used in this study.

stability of the functional layer, stability of printed antigens, reproducibility), which complement the data presented here and confirm the usefulness of semicarbazide microarrays.

MATERIALS AND METHODS

Peptide Synthesis. HCV core p21 15−45, HCV NS4 1925−1947, and EBV VCA p18 153−176 glyoxylyl peptides (Figure 2) were synthesized in an automated peptide synthesizer (model Pioneer, Perseptive Biosystems Inc., MA) using the Fmoc/*tert*-butyl strategy (*16*). The synthesis of these peptides was already described elsewhere (*17*−*19*).

Proteins. HBc (10 mg/mL), HBs (5 mg/mL), HBe (10 mg/mL), HCV core (1.5 mg/mL), HCV NS3 (0.5 mg/mL), HCV NS4 (0.4 mg/mL), HCV mixture of core, NS3, NS4, and NS5 antigens (1/1/1/1 by weight, 2 mg/mL overall), HIV-I Gp120 (0.5 mg/mL), HIV-I Gp41 (2 mg/mL), HIV-II Gp36 (1 mg/mL), syphilis rTpN47 (1 mg/mL), and rTpN17 (1 mg/mL) were purchased from Beijing Hepatitis Research Institute or from Henan Lily Bio-Products Company (Beijing, China). All these proteins were dissolved in a pH 9.6 0.05 M carbonate/bicarbonate buffer.

Printing of the Arrays. The preparation of semicarbazide glass slides was reported in detail elsewhere (*20*). The slides were printed using a 4-pin Affymetrix 417 arrayer (MWG, Santa Clara, CA) or a 32-pin manual arrayer (Microarray Printer XMM 47832, Xenopore, Hawthorne). Similar results were obtained using these two printing methods. The printed slides were incubated overnight at 37 °C in a humid chamber (60% relative humidity) and stored until use at room temperature. The number of replicates is indicated in the figures and tables.

Glyoxylyl peptides were printed in 0.1 M pH 5.5 sodium acetate buffer, whereas proteins were printed in the buffer used for their storage (pH 9.6 0.05 M carbonate/bicarbonate buffer).

Human Sera. Sera were collected from the clinical laboratory of the Centre Hospitalier Régional (Lille, France).

HCV. The reactivity of HCV referenced sera was determined with the AxSYM HCV version 3.0 Abbott ELISA kit (30 HCV-negative and 100 HCV-positive individuals). For some sera an additional RIBA HCV 3.0 SIA test (Ortho-Clinical Diagnostics) or a DECISCAN HCV PLUS test (BIORAD) was performed.

HBV. The reactivity of HBc referenced sera (40 HBc-negative and 60 HBc-positive individuals) was determined with the BIORAD MONOLISA anti-HBc PLUS test. The reactivity of HBe referenced sera (16 HBe-negative and 16 HBe-positive individuals) was determined with the BIORAD MONOLISA anti-HBe PLUS test. The reactivity of HBs referenced sera (40 HBs-negative and 60 HBs-positive individuals) was determined with the BIORAD MONOLISA anti-HBs PLUS test.

HIV. The reactivity of HIV referenced sera (90 HIV-positive and 20 HIV-negative individuals) was determined with DADE BEHRING Enzygnost HIV Integral and with BIORAD GENSCREEN PLUS HIV tests. The positivity was confirmed with BIORAD New Lav Blot I and II.

EBV. The reactivity of EBV referenced sera (70 EBV-positive and 20 EBV-negative individuals) was determined using an immunofluorescence assay (anti-VCA IFA, Immunoconcept).

Panels and Required Specifications. Panels used in this study (HIV 24+/20−, HCV 40+/40−, and syphilis 10+/20−) were from the National Institute for Drugs and Bio-products Quality Control (Beijing, China). The composition of the panels was as following.

HCV: 40 positive sera and 40 negative sera (anti-HCV and anti-HIV negative). Required ELISA specifications for HCV: less than one false positive and less than two false negatives.

HIV: 20 HIV positive sera (P1−20), 4 HIV-I positive sera with a concentration of anti-Gp41 antibodies close to the detection limit (S21−24), and 20 HIV negative sera (N1−20). Required ELISA specifications for HIV: (1) no false negative; (2) at least three S21−24 sera must be detected as positive; (3) less than two false positives.

Syphilis: 10 positive and 20 negative sera. Required ELISA specifications for syphilis: no false positives or negatives.

Detection of Antibodies. The phosphate-buffered saline (PBS) used for the preparation of the saturation, incubation, and washing solutions was 0.01 M, pH 7.2. PBS-A contained 0.1% of Tween 20 (by volume) and 2.5% of half-fat milk (by weight). PBS-B contained 0.05% of Tween 20 (by volume).

The saturation of the printed slides was performed under sonication in PBS-A during 60 min. After four washings with PBS-B, 1 μL of human serum diluted in 49 μL of PBS-A was incubated for 45 min at 37 °C under cover-glass. After four washings with PBS-B, 50 μL of tetramethylrhodamine-conjugated goat antibodies to human IgG-A-M (Jackson ImmunoResearch Laboratories, Baltimore, MD) diluted $^1/_{100}$ in PBS-A were incubated for 45 min at 37 °C under cover-glass. The slides were then washed three times with PBS-B, with distilled water, and with absolute ethanol (ACROS Organics, Geel, Belgium), and dried in air.

Data Collection and Analysis. The slides were scanned with an Affymetrix 418 array scanner (MWG, Santa Clara, CA). The scanner sensitivity is indicated in the figures and tables. The data were analyzed using the Scanalyse software (Stanford University, CA) or the Affymetrix Jaguar software (MWG, Santa Clara, CA). The background was subtracted from the spot fluores-

cence intensity. This subtraction was performed automatically by the Affymetrix Jaguar software. For all HCV, HIV, and EBV antigens except HCV mixture, the spots after incubation with negative sera were found to be indistinguishable from the background and led to a zero output value. In this case, the cutoff value of positivity was set to zero. For the HCV mixture and HBV and *Treponema pallidum* antigens, the cutoff value of positivity was calculated as the mean of negative sera fluorescence values ± 3 SD.

RESULTS AND DISCUSSION

The development of a microarray for the serodiagnostic of multiple pathogen infections requires a collection of epitopes allowing the highly sensitive and specific detection of antibodies directed against the selected pathogens. However, if there is no doubt about the interest of synthetic peptides for the detection of antibodies, some epitopes of diagnostic value can hardly be represented by linear synthetic peptides and necessitate the whole protein antigen. In this context, the possibility of combining linear synthetic peptidic epitopes and recombinant proteins was found to be attractive. Thus, we engaged in a project devoted to the fabrication of peptide−protein microarrays. The semicarbazide glass slide surface was selected owing to its usefulness for peptide microarray preparation (*11*).

Peptide and Protein Immobilization. The peptidic antigens used in this study are presented in Figure 2 and are derived from HCV (HCV core p21 15−45 (*12*) antigen for peptide **1**, HCV NS4 1925−1947 (*13*) antigen for peptide **2**) or EBV (VCA p18 153−176 (*14*) antigen for peptide **3**) pathogens. The glyoxylyl group was easily generated by periodate oxidation of an N-terminal seryl precursor in solution as described by Geoghegan et al. (*21*) for the EBV VCA p18 peptide or of an isopropylidene tartrate based linker on a solid support for HCV p21 and NS4 peptides (Figure 2) (*18*, *19*). In this latter case, the glyoxylyl group was situated at the C-terminus and separated from the backbone by a flexible spacer. The peptides were dissolved in a pH 5.5 acetate buffer to favor the site-specific ligation to the surface.

For peptides, the presence of a glyoxylyl group is important to avoid the loss of probe during the different incubation or washing steps. This aspect was easily demonstrated using biotinylated peptides **4** and **5**, which were synthesized as described elsewhere (*20*). Peptides **4** and **5** were printed at different concentrations (10^{-3}−10^{-6} M) in acetate buffer, and the slides were incubated with tetramethylrhodamine labeled goat antibiotin antibodies with a competitor for nonspecific adsorption (5% BSA). As shown in Figure 3, the signal displayed by the glyoxylyl peptide **5** at 10^{-4} M was about 7-fold higher than those given by the control peptide **4**.

On the other hand, the chemical modification of proteins by aldehyde groups without altering their recognition properties can be a difficult task and can lead to the loss of material and to additional costs. Thus, we examined the possibility of immobilizing proteins on semicarbazide glass slides by physisorption, as has been done by Haab and co-workers on amine-type cationic surfaces (*9*). Indeed, and to the contrary of small peptides, proteins can adsorb strongly on various surfaces because they are able to establish multiple interactions with accessible functional groups (*22*).

In a first approach, protein A was selected as a model protein for the physisorption studies and was printed at 1 mg/mL on semicarbazide glass slides using a pin-and-ring type printing robot. The microarrays were stored overnight at room temperature and then incubated with diluted human sera. Detection of antibodies captured through interaction with Fc (*23*) was performed following incubation with tetramethylrhodamine-labeled goat antihuman antibodies as described in Figure 4. The microarrays were analyzed using the Cy3 channel of a confocal fluorescence scanner. Figure 5 shows the results for five human sera. For the control experiment without human serum, the protein A spots were found to be indistinguishable from the background of the slide, showing that the high fluorescence observed with human sera was due to captured human antibodies. These data demonstrate that the semicarbazide surface can be used for the immobilization of proteins by simple adsorption.

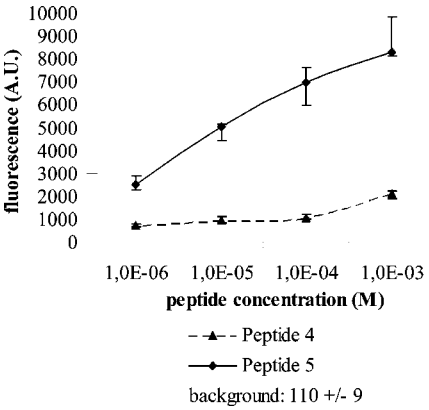


Figure 3. Printing of peptides **4** and **5** on semicarbazide slides and incubation of the arrays with tetramethylrhodamine labeled goat anti-biotin antibodies (10^{-2} mg/mL). Incubations were performed in the presence of 5% (w/v) BSA, using an Affymetrix 418 scanner, Cy3 channel, L35, PMT50. The fluorescence is expressed in arbitrary units (AU). The data were analyzed using ScanAlyse Sofware (Stanford University). The data represent the median and the interquartile range (n = 6).

We next examined the possibility of adsorbing HBs glycoprotein antigen and of using the arrays for the detection of anti-HBs antibodies in human sera. In this experiment, we have printed also HBs protein oxidized with periodate. Indeed, the polysaccharide moieties of HBs can be oxidized with sodium periodate using well-established protocols for generating aldehyde groups on the surface of glycoproteins (*24*). These aldehyde groups are able to react with the semicarbazide moieties to give a covalent semicarbazone linkage (*25*). Thus, this experiment allowed us to compare the physisorption and the covalent immobilization of the same protein antigen on the semicarbazide surface. As shown in Figure 6, similar results were obtained for these two immobilization methods. The largest difference in fluorescence intensity between oxidized and unmodified HBs proteins was found to be 8% (serum 11 in Figure 6B). These results confirm that proteins can be immobilized efficiently on semicarbazide slides by physisorption without the need for chemical modifications.

Peptide−Protein Antigen Microarrays, HCV Serodetection. The possibility of preparing peptide−protein microarrays useful for the serodiagnostic of pathogen infections was first examined with HCV antigens. The antigens used in this study were core p21 15−45 peptide, NS4 1925−1947 peptide, recombinant core, NS3 and NS4 protein antigens, and a mixture of core, NS3, NS4, and NS5 antigens (HCV mixture). Detection of antibodies was performed again as described in Figure 4 using adapted protocols from ref 11.

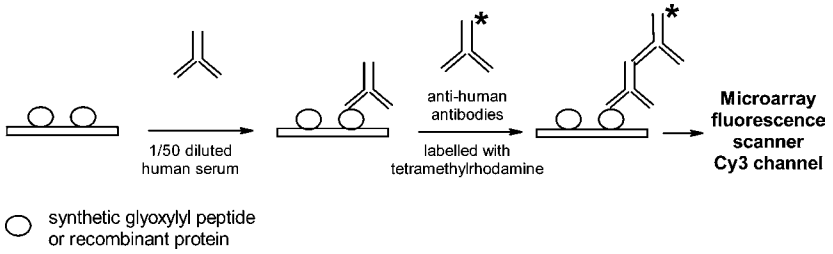


Figure 4. Detection of antibodies using the peptide−protein microarrays. Glyoxylyl peptides were immobilized by site-specific α-oxo semicarbazone ligation. Recombinant protein antigens were immobilized by simple adsorption.

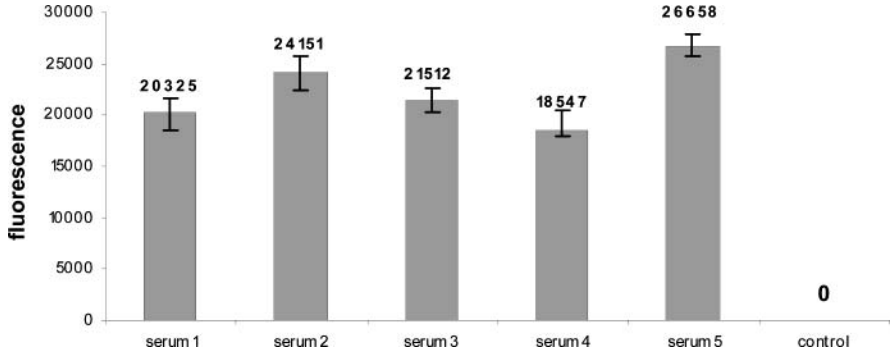


Figure 5. Detection of antibodies captured by protein A (1 mg/mL, $n = 12$) printed on semicarbazide glass slides. Five human sera were used in this experiment. The control experiment was performed by incubating one printed slide with the buffer. The slides were analyzed with an Affymetrix 418 scanner, Cy3 channel, sensitivity L35, PMT50. The fluorescence is expressed in arbitrary units. The data represent the median and the interquartile range.

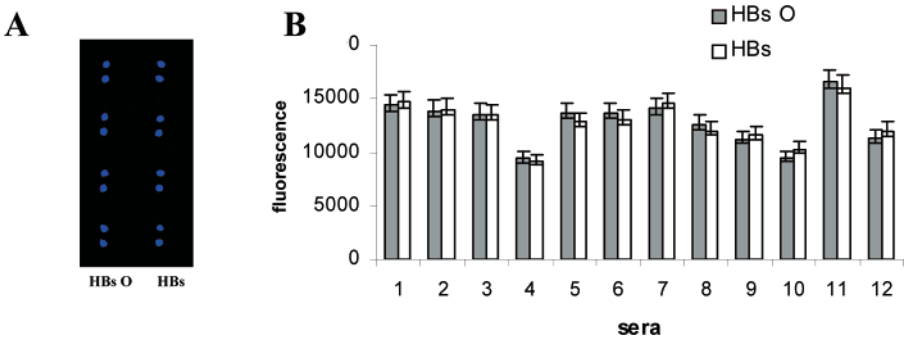


Figure 6. Detection of specific antibodies with physisorbed or oxidized HBs glycoprotein antigen on semicarbazide slides. Oxidized HBs (HBs, ○) and nonoxidized HBs were printed at 0.1 mg/mL: (A) image obtained with serum 11; (B) fluorescence data values for 12 HBs ELISA positive sera, using L35, PMT50. The data represent the median and the interquartile range ($n = 8$).

Table 1. HCV Serodetection Results Using HCV Mixture

entry	no. of sera	ELISA[a]	HCV mixture[b]	Western blot[c]	remarks
1	94	+	+	nd	
2	6	+	−	−	false positive ELISAs
3	30	−	−	nd	

[a] 130 ELISA referenced sera (100+/30−, AxSYM HCV version 3.0 Abbott ELISA). [b] HCV mixture is core/NS3/NS4/NS5, 1/1/1/1, by weight, 0.5 mg/mL (n=6). [c] RIBA HCV 3.0 SIA test. Scanner sensitivity L35, PMT50. Cutoff value of positivity (mean ± 3 SD of the 30 negative sera presented in entry 3) was 115. nd: not determined.

The collection of 30 HCV sera allowed us to determine the cutoff of positivity for all the HCV antigens (mean fluorescence ± 3 SD of negative sera). For the mixture of HCV antigens, a low signal arising from nonspecific binding could be observed and resulted in a cutoff of 115 at L35, PMT50 scanner sensitivity. For comparison, the lowest fluorescence signal observed with this mixture of antigens for an HCV positive serum was 331 (Table 2, group 4, serum 36). Table 1 describes the serodetection results obtained with this HCV mixture for 130 HCV sera referenced with a commercially available ELISA test (100 HCV+, 30 HCV−). Microarrays and ELISA assays were in agreement for 94 HCV+ and 30 HCV− sera. A Western blot assay recognized as the most specific assay for HCV antibodies detection was carried out for the six sera where discrepancies were observed (Table 1, entry 2). The Western blot assays were negative and thus in accord with the microarray data. In such a situation where ELISA tests are positive and Western blot assays negative, the sera are considered as false positive (*26*). At this stage, our results demonstrated that at least for the collection of tested sera microarrays displayed high levels of sensitivity and specificity.

These data in hand, we next examined the specificity and sensitivity of HCV serodetection using the different peptide or protein antigens considered separately. A collection of sera composed of the 6 previous false positive ELISA (Table 1, entry 2) and 34 new sera (HCV positive ELISA) were analyzed using a recombinant immunoblot assay that permitted the detection of specific antibodies directed against HCV core, NS3, and NS4 antigens.

Western blot negative sera are collected in group 1 of Table 2. The first six sera (sera 1−6) corresponded to the

Table 2. Sensitivity and Specificity Results Obtained with 40 HCV Positive ELISA[b] Sera

						microarrays[c]					
							core antigen			NS4 antigen	
		Western-blot[a]					HCV	peptide	NS3 antigen	HCV	peptide
group	serum no.	core	NS3	NS4	NS5	mix-HCV	core	p21	HCV NS3	NS4	NS4
1	1	−	−	−	−	25	0	0	0	0	0
	2	−	−	−	−	42	0	0	0	0	0
	3	−	−	−	−	29	0	0	0	0	0
	4	−	−	−	−	36	0	0	0	0	0
	5	−	−	−	−	47	0	0	0	0	0
	6	−	−	−	−	28	0	0	0	0	0
	7	−	−	−	−	51	0	0	0	0	0
	8	−	−	−	−	39	0	0	0	0	0
2	9	+++	++	++		11254	17854	15214	13215	6254	4658
	10	+++	++	++		14251	21542	22542	20135	12352	10684
	11	+++	++	++		17548	23215	29854	21524	17548	13654
	12	++	+++	+++		15429	29584	25145	16548	12496	9854
	13	+++	+++	+++		17859	28964	29854	19548	15421	13654
	14	+++	++	+++		21524	31250	34125	20482	19854	14985
	15	+++	+++	+		19854	28546	30489	17458	5485	4695
	16	+++	+++	++		18549	25348	21897	17965	8549	4685
	17	+++	++	++		21549	29846	31245	22304	14528	10238
	18	+++	+++	+++		16325	24065	20547	16524	11248	9584
	19	+++	+++	+++		25639	29032	31284	21468	15486	11278
	20	+++	+++	++		21025	25584	23654	15421	12495	10319
	21	+++	+++	+++		24569	29548	19874	14025	18542	15497
	22	+++	+++	+++		19854	21024	25421	9587	112445	9703
	23	++	+	+		8547	15421	13524	9584	5985	3958
	24	++	+	++		14582	18546	17954	15468	13250	10854
3	25	−	+++	+++		11245	0	0	21514	10545	7985
	26	−	++	+		10524	0	0	8954	5214	4625
	27	−	+++	+++		14521	0	0	15462	11245	8547
	28	−	++	−		456	0	0	452	0	0
	29	−	++	+		5684	0	0	6895	4632	3958
	30	++	++	−		12045	18546	15874	4325	0	0
	31	+++	+	−		15421	20135	21547	2154	0	0
	32	−	+	−	0.5+	1524	0	0	1095	0	0
4	33	−	0.5+	−	0.5+	495	0	0	568	0	0
	34	0.5+	−	−		925	4162	2958	0	0	0
	35	0.5+	+	0.5+		512	456	213	325	651	428
	36	−	−	0.5+	0.5+	331	0	0	0	312	115
	37	+++	++	0.5+		10254	21452	19854	7548	2154	1654
	38	+++	++	0.5+		15214	21549	14528	12415	542	384
	39	+++	+++	0.5+		9602	11542	13879	5695	598	258
	40	+++	+++	0.5+		12542	14201	16547	5698	354	215
cutoff[d]						115	0	0	0	0	0

[a] Western blot assay: RIBA HCV 3.0 SIA test or DECISCAN HCV PLUS test. [b] AxSYM HCV version 3.0 Abbott ELISA. [c] NS3 antigen (1 mg/mL), NS4 antigen (0.4 mg/mL), HCV mixture (0.5 mg/mL), p21 and NS4 HCV peptides (10^{-4} M). [d] Cutoff = mean ± 3 SD of 30 HCV ELISA negative sera, scanner sensitivity L35, PMT50, $n = 6$.

false positive ELISA of Table 1. Two sera (sera 7 and 8) among the 34 new sera were found to be also false positive ELISA. Interestingly, the sera of group 1 were also found to be negative for all the HCV antigens in the microarray format. Western blot core, NS3, and NS4 positive sera are collected in group 2. In this case, all the microarray HCV antigens displayed high fluorescence signals. Group 3 includes the sera that displayed one or two Western blot negative reactivities. The same sensitivity and specificity were observed with the arrayed antigens. Group 4 collects the sera, which displayed at least one Western blot 0.5+ intensity for core, NS3, or NS4 antigens. These sera were particularly useful because they permitted us to evaluate the performance of peptide−protein microarrays in a context where the limit of sensitivity of the Western blot was attained for at least one antigen. Interestingly, antibodies that led to a Western blot 0.5+ intensity were easily detected using the corresponding microarray HCV antigens, illustrating the ability of the miniaturized device to detect specifically low levels of antibodies in human sera.

HBV and HIV Serodetection. These encouraging results obtained with HCV antigens led us to examine the possibility of detecting antibodies directed against other pathogens such as HBV (HBc, HBe and HBs antigens) and HIV (Gp41 and Gp120 antigens).

For the HBV serodetection study, a collection of sera referenced against HBc, HBs, or HBe by ELISA was used to document the sensitivity and specificity of the microarrays (Figure 7). As for the HCV mixture of antigens described above, some nonspecific binding could be observed with these antigens. The cutoff values for the three antigens corresponded to about 10-fold the background of the slides. Nevertheless, all the ELISA positive sera were detected without difficulty. The lowest positive signal observed with HBc, HBs, or HBe antigens corresponded to 12-, 6.5-, or 5.9-fold the cutoff of positivity, respectively. Alternatively, all the ELISA negative sera gave a fluorescence value below the cutoff of positivity. Taken together, these data highlight the utility of semicarbazide antigen microarrays for the sensitive and specific detection of antibodies directed against HBc, HBe, and HBs.

For the HIV serodetection study, we used a collection of 110 sera referenced against Gp120 and Gp41 antigens by ELISA. Here, as for HCV core, NS3 and NS4 recom-

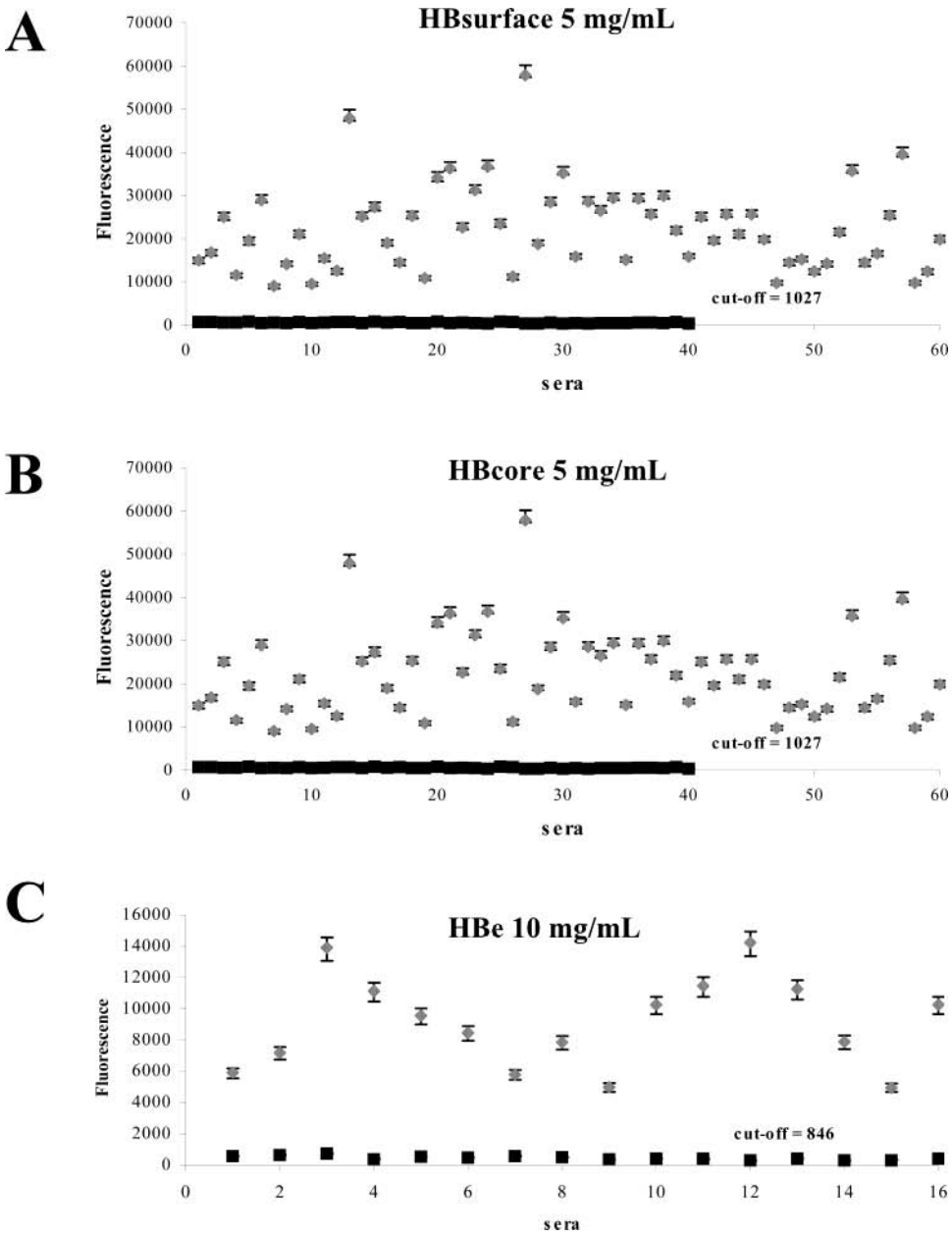


Figure 7. HBV serodetection study. The data were obtained after incubation of the microarrays with ELISA positive (open squares) or ELISA negative (filled squares) sera for (A) HBs 60+/40−, (B) HBc 60+/40−, (C) HBe 16+/16−. The fluorescence values (arbitrary units) represent the median and the interquartile range for six spots at L35, PMT 50 scanner sensitivity.

binant antigens and Gp41 and Gp120 spots were found to be indistinguishable from the background of the slide for all negative referenced sera, leading to a cutoff value of positivity equal to zero. No false positive sera were observed whatever the concentration tested (Gp120 0.5−0.01 mg/mL, Gp41 2−0.1 mg/mL). Both Gp41 and Gp120 antigens displayed 100% of sensitivity for the concentrations above 0.05 mg/mL. The printing of Gp120 at 0.01 mg/mL resulted in a loss of sensitivity (89%). Figure 8 details the fluorescence data obtained for the highest Gp120 or Gp41 concentrations.

These encouraging results led us to evaluate the performance of the device in a simultaneous serodetection study of multiple pathogen infections.

Simultaneous Detection of Multiple Pathogen Infections. Model Study with HCV, HBV, HIV, and EBV Antigens. For this study, the antigens selected for HCV serodetection were core p21 15−45 and NS4 1925−1947 peptides, the HCV mixture, and NS3 recombinant protein. For HIV, we used Gp120 and Gp41. HBc was selected for HBV serodetection, and finally EBV VCAp18 153−176 peptide was used for the serodetection of EBV infections. Protein A was printed as a positive control.

Ninety sera referenced against these four pathogens were used in this study. Twenty sera were negative for all the pathogens (entry 1), whereas 70 sera were positive for one (entry 2), two (entries 3−6), three (entries 7−9), or all pathogens (entry 10). The data collected in Table 3 show that there was usually a good correspondence between the reference tests and the microarray serodetection results except for entries 2 and 6, which corresponded to HCV false positive ELISAs, as confirmed by the Western blot assays. These sera were found to be HCV negative using the microarrays. No cross-reactivity was observed in this study. Figure 9 shows microarray images obtained using a serum positive (Figure 9A) or negative (Figure 9B) for all the pathogens.

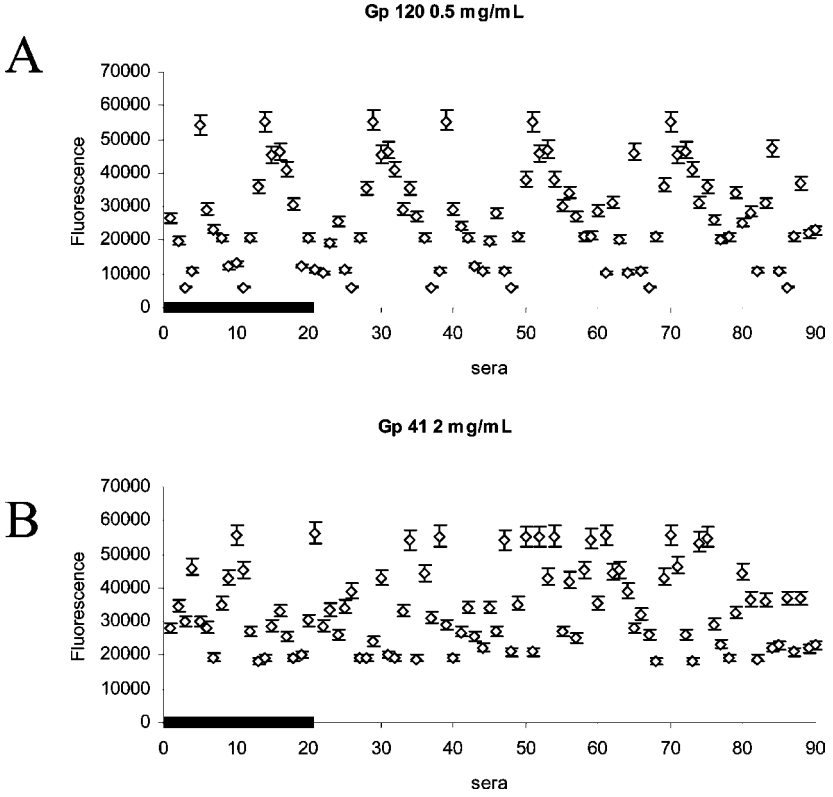


Figure 8. HIV serodetection study. The data were obtained after incubation of the microarrays with ELISA positive (open squares) or ELISA negative (filled squares) sera for (A) Gp120 90+/20− and (B) Gp41 90+/20−. The fluorescence values (arbitrary units) represent the median and the interquartile range for six spots at L35, PMT 50 scanner sensitivity.

Table 3. Simultaneous Detection of Infections by HCV, HBV, HIV, and EBV

			HCV		HBV		HIV		EBV	
entry	no. of infections	no. of sera	arrays[a]	ref test[b]	arrays[a]	ref test[b]	arrays[a]	ref tests[c]	arrays[a]	ref test[d]
1	0	20	−	−	−	−	−	−	−	−
2	1	4	−[e]	+	−	−	−	−	+	+
3	2	10	+	+	−	−	−	−	+	+
4	2	21	−	−	+	+	−	−	+	+
5	2	19	−	−	−	−	+	+	+	+
6	2	1	−[e]	+	−	−	+	+	+	+
7	3	11	+	+	+	+	−	−	+	+
8	3	1	+	+	−	−	+	+	+	+
9	3	2	−	−	+	+	+	+	+	+
10	4	1	+	+	+	+	+	+	+	+
total		90	23+ 67−	28+ 62−	35+ 55−	35+ 55−	24+ 66−	24+ 66−	70+ 20−	70+ 20−

[a] Peptide−protein microarrays: HBV (HBV core 5 mg/mL), HCV (mixture of HCV core-NS3-NS4-NS5 antigens, 0.5 mg/mL), HIV (Gp41 1 mg/mL, Gp120 0.5 mg/mL), and EBV (10^{-4} M). [b] ELISA. [c] ELISA and Western blot. [d] Immunofluorescence assay. [e] Negativity confirmed by Western blot. Scanner sensitivity L35, PMT50, $n = 4$.

Screening of HCV, HIV, and Syphilis Panels. To confirm the utility of semicarbazide microarrays for the serodiagnostic of pathogen infections, HCV, HIV, and syphilis panels of referenced sera from the Chinese National Institute for Drugs and Bio-products Quality Control were studied. These panels, combining sera with low levels of antibodies or sera known to give cross-reactivity problems, are used to select ELISA tests that are sensitive and specific enough to merit further evaluation. The microarray data will be discussed in light of ELISA specifications (see Materials and Methods) because no specifications were available for microarray-based serodiagnostic assays.

For the three panels (Figures 10−12), microarrays displayed 100% of specificity and sensitivity. For HCV (Figure 10B), the lowest positive signal was 3.8-fold the cutoff value of positivity. For the HIV panel (Figure 11), the specifications were imposed to detect at least three S21−24 sera, which contained low levels of antibodies and were close to the detection limit in ELISA. Interestingly, these four sera were detected as positive. Taken together, these results highlight the high sensitivity and specificity of peptide−protein microarrays on semicarbazide glass slides for the parallel detection of antibodies in complex biological samples.

CONCLUSION

In conclusion, we have described in this article a peptide−protein microarray methodology that was found to be useful for the serodetection of antibodies directed against different pathogens. Microarrays were prepared using semicarbazide functionalized glass slides. Peptidic antigens were functionalized by a glyoxylyl group and anchored to the glass surface by site-specific α-oxo

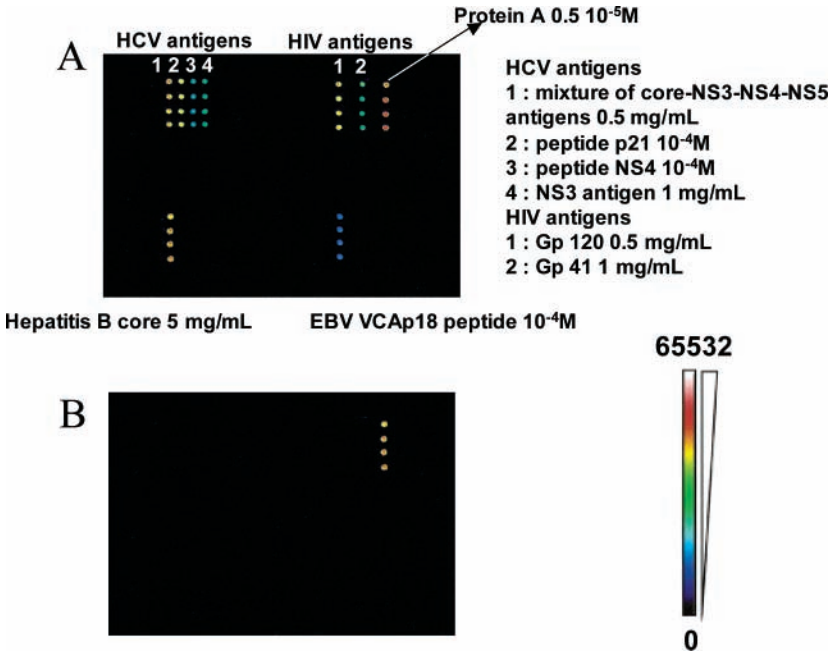


Figure 9. Microarray images obtained during the multiple serodetection study of HIV, HBV, HCV, and EBV infections: (A) referenced serum positive for all the pathogens; (B) referenced serum negative for all the pathogens. Scanner sensitivity was L35, PMT50. Protein A was used as a positive control.

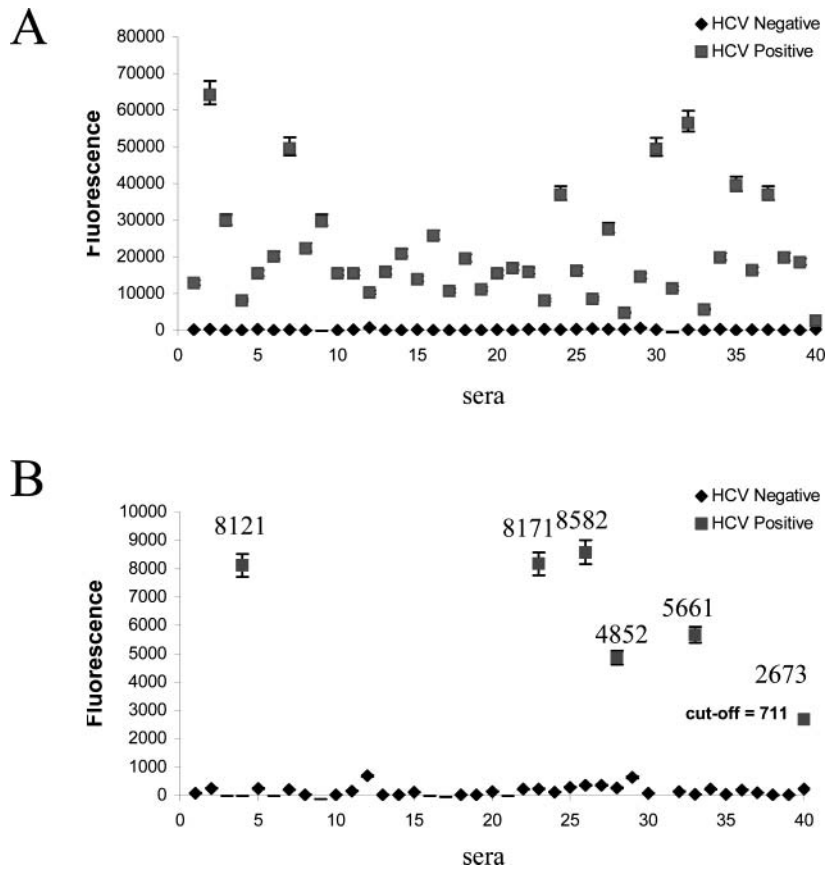


Figure 10. HCV serodetection results using the mixture of HCV core-NS3-NS4 and NS5 antigens, 1.5 mg/mL overall: (A) whole HCV panel; (B) sera that displayed the lowest fluorescence signals. The fluorescence values (arbitrary units) represent the median and the interquartile range for nine spots at L35, PMT 50 scanner sensitivity.

semicarbazone ligation, whereas recombinant proteins were adsorbed on the substrate. The microarrays, used in an immunofluorescence assay, displayed high levels of sensitivity and specificity for the detection of antibodies directed against HIV, HCV, HBV, and EBV pathogens. The performance of the device was further confirmed using referenced HIV, HCV, and syphilis panels. These promising results open the way for further validation studies on a larger scale. In the accompanying paper, we present a comparative study with amine glass slides and other data concerning the characterization of semicarbazide microarrays using chemical and physical methods.

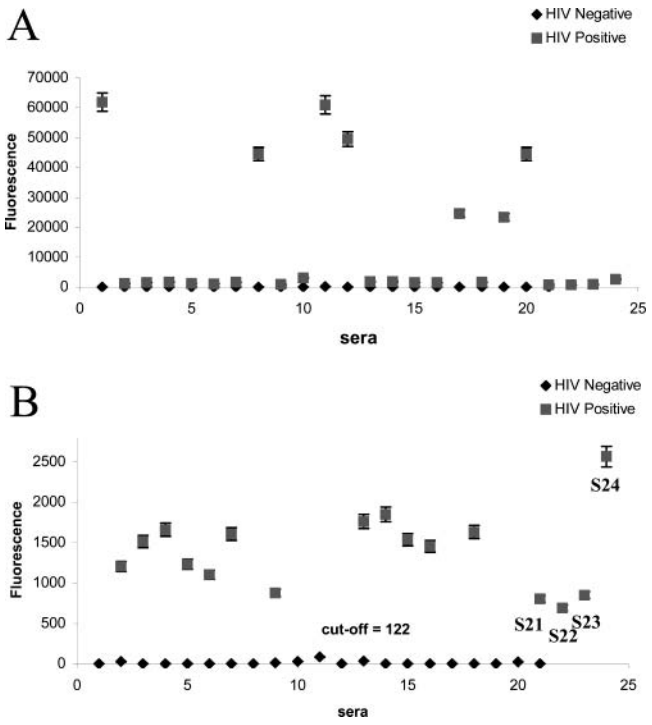


Figure 11. HIV serodetection results using the mixture of HIV antigens, 1 mg/mL overall: (A) whole panel; (B) sera that displayed the lowest fluorescence signals. The fluorescence values (arbitrary units) represent the median and the interquartile range for four spots at L35, PMT 50 scanner sensitivity.

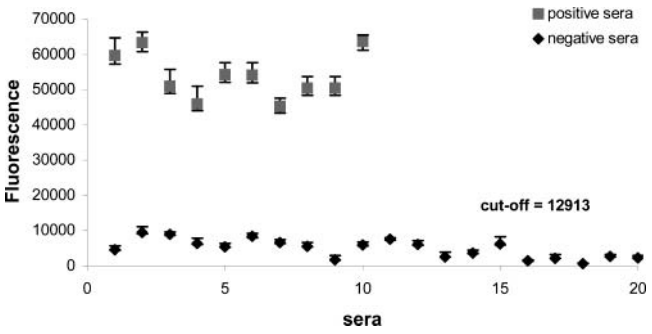


Figure 12. Syphilis serodetection results obtained with the mixture of rTpN antigens, 1 mg/mL overall. The fluorescence values (arbitrary units) represent the median and the interquartile range for nine spots at L35, PMT 50 scanner sensitivity.

ACKNOWLEDGMENT

We thank CNRS, Université de Lille 2, Institut Pasteur de Lille, and Sedac-Therapeutics for financial support, Eric Diesis for technical assistance, and David Hot, Ludovic Huot, and Erwan Levillain for fluorescence measurements. We thank Pr Yves Lemoine for giving us an access to the Affymetrix 418 array scanner and Affymetrix 417 arrayer.

LITERATURE CITED

(1) Templin, M. F., Stoll, D., Schrenk, M., Traub, P. C., Vöhringer, C. F., Joos, T. O. (2002) Protein microarray technology. *Drug Discovery Today 7*, 815−822.

(2) Talapatra, A., Rouse, R., Hardiman, G. (2002) Protein microarrays: challenges and promises. *Pharmacogenomics 3*, 527−536.

(3) Ryan, T. E., Patterson, S. D. (2002) Proteomics: drug target discovery on an industrial scale. *Trends Biotechnol. 20*, S45−S51.

(4) Lesaicherre, M.-L., Uttamchandani, M., Chen, G. Y. J., Yao, S. Q. (2002) Developing site-specific immobilization strategies of peptides in a microarray. *Bioorg. Med. Chem. Lett. 12*, 2085−2088.

(5) Falsey, J. R., Renil, M., Park, S., Li, S., Lam, K. S. (2001) Peptide and small molecule microarray for high throughput cell adhesion and functional assays. *Bioconjugate Chem. 12*, 346−353.

(6) MacBeath, G., Schreiber, S. L. (2000) Printing proteins as microarrays for high-throughput function determination. *Science 289*, 1760−1763.

(7) Lueking, A., Horn, M., Eickhoff, H., Büssow, K., Lehrach, H., Walter, G. (1999) Protein microarrays for gene expression and antibody screening. *Anal. Chem. 270*, 103−111.

(8) Joos, T. O., Schrenk, M., Höpfl, P., Kröger, K., Chowdhury, U., Stoll, D., Schörner, D., Dürr, M., Herick, K., Rupp, S., Sohn, K., Hämmerle, H. (2000) A microarray enzyme-linked immunosorbent assay for autoimmune diagnostics. *Electrophoresis 21*, 2641−2650.

(9) Haab, B. B., Dunham, M. J., Brown, P. O. (2001) Protein microarrays for highly parallel detection and quantitation of specific proteins and antibodies in complex solutions. *Genome Biol. 2*, Research 0004.

(10) Mezzasoma, L., Bacarese-Hamilton, T., Di Cristina, M., Rossi, R., Bistoni, F., Crisanti, A. (2002) Antigen microarrays for serodiagnosis of infectious diseases *Clin. Chem. 48*, 121−30.

(11) Melnyk, O., Duburcq, X., Olivier, C., Urbès, F., Auriault, C., Gras-Masse, H. (2002) Peptide arrays for highly sensitive and specific antibody-binding fluorescence assays. *Bioconjugate Chem. 13*, 713−720.

(12) Jolivet-Reynaud, C., Dalbon, P., Viola, F., Yvon, S., Paranhos-Baccala, G., Piga, N., Bridon, L., Trabaud, M, A., Battail, N., Sibai, G., Jolivet, M. (1998) HCV core immunodominant region analysis using mouse monoclonal antibodies and human sera: characterization of major epitopes useful for antigen detection. *J. Med. Virol. 56*, 300−309.

(13) Longombardo, G., Ferri, C., Marchi, S., Costa, F., Lombardini, F., Vacri, L., Bombardieri, S., Migliorini P. (1998) Immune response to an epitope of the NS4 protein of hepatitis C virus in HCV-related disorders. *Clin. Immunol. 87*, 124−129.

(14) Van Grunsven, W. M. J., Spaan, W. S. M., Middeldorp, J. M. (1994) Localization and diagnostic application of immunodominant domains of the BFRF3-encoded Epstein−Barr virus capsid protein. *J Infect. Dis. 170*, 13−19.

(15) Sambri, V., Marangoni, A., Eyer, C., Reichhuber, C., Soutschek, E., Negosanti, M., D'Antuono, A., Cevenini, R. (2001) Evaluation of recomWell Treponema, a novel recombinant antigen-based enzyme-linked immunosorbent assay for the diagnosis of syphilis. *Clin. Diagn. Lab. Immunol.* 8, 534−539.

(16) Fields, G. B., Noble, R. L. (1990) Solid-phase peptide synthesis utilizing 9-fluorenylmethoxycarbonyl amino acids. *J. Pept. Protein Res. 35*, 161−214.

(17) Melnyk, O., Fruchart, J.-S., Grandjean, C., Gras-Masse, H. (2001) Tartric acid-based linker for the solid-phase synthesis of C-terminal peptide α-oxo aldehydes *J. Org. Chem. 66*, 4153−4160.

(18) Fruchart, J.-S., Gras-Masse, H., Melnyk, O. (1999) Tartric acid-based linker for the solid-phase synthesis of C-terminal peptide alpha-oxo aldehydes *Tetrahedron Lett. 40*, 6225−6228.

(19) Urbès, F., Fruchart, J.-S., Gras-Masse, H., Melnyk, O. (2002) C-Terminal glyoxylyl peptides for densitive enzyme linked immunosorbent assays. *Lett. Pept. Sci. 8*, 253−258.

(20) Olivier, C., Hot, D., Huot, L., Ollivier, N., El-Mahdi, O., Gouyette, C., Huynh-Dinh, T., Gras-Masse, H., Lemoine, Y., Melnyk, O. (2003) α-Oxo Semicarbazone Peptide or Oligodeoxynucleotide Microarrays. *Bioconjugate Chem. 14*, 430−439.

(21) Geoghegan, K. F., Stroh, J. G. (1992) Site-directed conjugation of nonpeptide groups to peptides and proteins via periodate oxidation of a 2-amino alcohol. Application to modification at N-terminal serine. *Bioconjugate Chem. 3*, 138−146.

(22) Tertykh, V. A., Yanishpolskii, V. (2000) *Surf. Sci. Ser. 90*, 523−564.

(23) Alonzo, D. V. D., Daggett, V. (2000) Staphylococcal protein A: Unfolding pathways, unfolded states, and differences between the B and E domains. *Proc. Natl. Acad. Sci. U.S.A. 97,* 2300−2305.

(24) Wolfe, C.-A.-C., Hage, D. S. (1995) Studies on the rate and control of antibody oxidation by periodate. *Anal. Biochem. 231,* 123−130.

(25) Melnyk, O., Duburcq, X., Olivier, C., Urbès, F., Auriault, C., Gras-Masse, H. *Proceedings of 7th International Symposium on Solid Phase, Synthesis & Combinatorial Chemical Libraries*; Epton, R., Ed.; Mayflower Scientific Ltd.: U.K., 2001; pp 18−22.

(26) Gebo, K. A, Bartlett, J. G. *Management of hepatitis C: A Review of the NIH Consensus Development Conference*; Hopkins HIV Report; September 2002; Volume 14, Issue 5, Supplements i−iv, Johns Hopkins University Press, Baltimore, MD.

BC034226D

Polypeptide Semicarbazide Glass Slide Microarrays: Characterization and Comparison with Amine Slides in Serodetection Studies

Xavier Duburcq,[†,‡] Christophe Olivier,[‡] Rémi Desmet,[§] Matej Halasa,[§] Olivier Carion,[§] Bruno Grandidier,[#] Thomas Heim,[#] Didier Stiévenard,[#] Claude Auriault,[‡] and Oleg Melnyk*[,§]

UMR CNRS 8527, Biological Institute of Lille, 1 Rue du Pr Calmette 59021 Lille, France, Sedac-Therapeutics, Le Galénis, Bât. B, 85 Rue Nelson Mandela 59120 Loos, France, UMR CNRS 8525, Biological Institute of Lille, 1 Rue du Pr Calmette 59021 Lille, France, and IEMN, Cité Scientifique, Avenue Poincaré, 59652 Villeneuve d'Ascq Cedex, France. Received July 10, 2003; Revised Manuscript Received December 12, 2003

We have described in the accompanying article the preparation of peptide−protein semicarbazide microarrays and their use for the simultaneous serodetection of antibodies directed against different pathogens. Here, we present a comparative study between semicarbazide and amine glass slides in an immunofluorescent serodetection assay using HIV (Gp120, Gp41), HCV (mix-HCV, core, NS3, and NS4), and HBV (HBs) recombinant antigens. Amine and semicarbazide surfaces displayed the same sensitivity for antibodies detection just after printing. However, the reactivity of protein antigens changed rapidly upon aging on amine slides but not on semicarbazide slides. Peptide or protein semicarbazide microarrays were found to be remarkably stable for months. Additional data concerning the characterization of the semicarbazide surface (homogeneity of the slides, chemical stability, contact angle measurements, atomic force microscopy studies, reproducibility of serodetection results) are also presented and discussed.

INTRODUCTION

The parallel detection of antibodies in complex biological samples have a wide range of potential applications in the diagnosis of allergies, autoimmune, and infectious diseases as well as in epitope mapping studies and vaccines development. The need for high-throughput screening systems have stimulated the development of microfabricated analytical devices.

In the preceding paper, we have described the preparation of novel peptide−protein microarrays based on the utilization of glass slides functionalized by a semicarbazide layer. This surface can be used for the site-specific immobilization of glyoxylyl-peptidic antigens through α-oxo semicarbazone ligation or for the immobilization of recombinant proteins through physisorption. These peptide−protein arrays could be used for the capture of antibodies in the sera of infected individuals using an immunofluorescent assay. Owing to the miniaturization, very small quantities of antigens, of sera (1 μL), and of tetramethylrhodamine labeled secondary antibodies (1 μg) could be used. The microarrays displayed high levels of sensitivity and specificity for the detection of HIV, HCV, HBV, EBV, and syphilis antibodies as revealed by the screening of a collection of sera referenced against these pathogens.

We disclose in this article a comparative study between semicarbazide and amine microarray glass slides, the later surface being often used for the preparation of protein microarrays (*1*, *2*). In particular, we have examined the performance of the two surfaces in the serodetection of HBV, HIV, and HCV infections and the evolution of the serodetection results during an accelerated aging of the arrays. The reproducibility of antibody detection with semicarbazide microarrays was documented. We have also carried out contact angle measurements with reference liquids to determine the sensitivity of both surfaces to air pollution. Finally, the semicarbazide glass slides were analyzed by atomic force microscopy to give a picture of the surface topography and to measure the height of the silane layer.

MATERIALS AND METHODS

Peptide Synthesis. HCV core p21 15−45, HCV NS4 1925−1947, and EBV VCA p18 153−176 glyoxylyl peptides were synthesized in an automated peptide synthesizer (Pioneer, Perseptive Biosystems Inc., MA) using the Fmoc/*tert*-butyl strategy (*3*) and an isopropylidene tartrate based linker (*4*−*6*) as described elsewhere (*7*).

Proteins. HCV core (1.5 mg/mL), HCV NS3 (0.5 mg/mL), HCV NS4 (0.4 mg/mL), HCV mixture of core, NS3, NS4, and NS5 antigens (1/1/1/1 by weight, 2 mg/mL overall), HIV-I Gp120 (0.5 mg/mL), and HIV-I Gp41 (2 mg/mL) were purchased from Beijing Hepatitis Research Institute or from Henan Lily Bio-Products Company (Beijing, China). All these proteins were supplied in a pH 9.6 0.05 M carbonate/bicarbonate buffer. HBs antigen (1 mg/mL) was purchased from Advanced ImmunoChemical (Long Beach, CA) and was supplied in a 0.01 M pH 7.2 PBS solution. All these proteins were diluted before printing in the buffer used for their storage.

Protein A (51 mg/mL) was purchased from Sigma-Aldrich (Saint Quentin Fallavier, France) and was supplied in water. Protein A was diluted with a 0.1 M pH 5.5 sodium acetate buffer before printing.

* To whom correspondence should be addressed. Phone: 33-(0)3 20 87 12 14. Fax: 33(0)3 20 87 12 35. E-mail: oleg.melnyk@ibl.fr.

[†] UMR CNRS 8527, Biological Institute of Lille.

[‡] Sedac-Therapeutics.

[§] UMR CNRS 8525, Biological Institute of Lille.

[#] IEMN.

10.1021/bc034118r CCC: $27.50 © 2004 American Chemical Society
Published on Web 02/28/2004

Table 1. Contact Angle Measurements on Semicarbazide or Amine Glass Slides

	contact angle, deg (standard error)			γ,[a] mJ/m^2					
	w	dim	fad	tot	LW	acid	base	ΔG_{sws},[b] mJ/m^2	ΔG_{sw},[c] mJ/m^2
semicarbazide	36.3(0.5)	30.9(0.2)	15.6(0.9)	56.4	43.9	1.2	33.9	4.6	−131.5
amine	33.1(0.5)	31.5(0.6)	21.5(0.7)	54.0	43.8	0.7	39.8	13.7	−133.7

[a] The surface tension parameters of diiodomethane (dim), water (w), and formamide (fad) were taken from the literature (*20*). [b] Interfacial interaction free energy of the surface in water. [c] Free energy of binding of water to the surface.

Preparation of the Glass Slides. Amine Glass Slides. Microscope slides (ESCO precleaned microslide, frosted) were cleaned using a freshly prepared piranha solution (H_2SO_4/H_2O_2, 1/1 by volume, overnight). The slides were washed with water (3 × 3 min) and methanol (3 min) and treated with 3% 3-aminopropyltrimethoxysilane in methanol/water, 95/5 by volume (30 min, under sonication). The slides were then washed with methanol, water (two times), and methanol and annealed for 15 min at 110 °C.

Semicarbazide glass slides were prepared and characterized as described elsewhere (*8*). Rapidly, the amine slides prepared as described above were treated with triphosgen/diisopropylethylamine in 1,2-dichloroethane and then Fmoc-$NHNH_2$ (*9*) in DMF containing 1% EtOH (by volume) to install the semicarbazide functions. Finally, removal of the Fmoc groups was performed with piperidine/1,8-diaza-bicyclo[5.4.0]undec-7-ene (DBU) in *N*,*N*-dimethylformamide (DMF, 30 min). Four slides were used for the quality control. Three slides were immersed for 1 h at 37 °C in a 10^{-4} M solution of Rho-Lys-Arg-NH-$(CH_2)_3$NH-CO-CHO (synthesized according to refs 7 and 8, where Rho is (5)-6-carboxytetramethylrhodamine). One slide was treated with the control peptide Rho-Lys-Arg-NH_2. The fluorescence intensity of the slides was quantified using an Affymetrix 418 array scanner (MWG, Santa Clara, CA). Amine and semicarbazide slides were stored at room temperature in air in a closed box.

Printing of the Arrays. The slides were printed using a 4-pin Affymetrix 417 arrayer (MWG, Santa Clara, CA) or a 32-pin manual arrayer (Microarray printer XMM 47832, Xenopore, Hawthorne). The printed slides were incubated overnight at 37 °C in a humid chamber (60% relative humidity) and stored until use at room temperature. The number of replicates is indicated in the figures or tables.

Human Sera. Sera were collected from the clinical laboratory of the Centre Hospitalier Régional (Lille, France).

HCV. The reactivity of HCV referenced sera was determined with the AxSYM HCV version 3.0 Abbott ELISA kit (30 HCV-negative and 100 HCV-positive individuals). For some sera an additional RIBA HCV 3.0 SIA test (Ortho-Clinical Diagnostics) or a DECISCAN HCV PLUS test (BIORAD) was performed.

HIV. The reactivity of HIV referenced sera (90 HIV-positive and 20 HIV-negative individuals) was determined with DADE BEHRING Enzygnost HIV Integral and with BIORAD GENSCREENPLUS HIV tests. The positivity was confirmed with BIORAD New Lav Blot I and II.

HBs. The reactivity of HBs referenced sera (40 HBs-negative and 60 HBs-positive individuals) was determined with the BIORAD MONOLISA anti-HBs PLUS test.

Detection of Antibodies. The phosphate-buffered saline (PBS) used for the preparation of the saturation, incubation, and washing solutions was 0.01 M pH 7.2. PBS-A contained 0.1% of Tween 20 (by volume) and 2.5% of half-fat milk (by weight). PBS-B contained 0.05% of Tween 20 (by volume).

The saturation of the printed slides was performed under sonication in PBS-A during 60 min. After four washings with PBS-C, 1 μL of human serum diluted in 49 μL of PBS-A was incubated during 45 min at 37 °C under cover-glass. After four washings with PBS-B, 50 μL of tetramethylrhodamine-conjugated goat antibodies to human IgG-A-M (Jackson ImmunoResearch Laboratories, Baltimore, MD) diluted $^1/_{100}$ in PBS-A were incubated for 45 min at 37 °C under cover-glass. The slides were then washed three times with PBS-B, with distilled water, and with absolute ethanol (ACROS Organics, Geel, Belgium) and dried in air.

Data Collection and Analysis. The slides were scanned with an Affymetrix 418 array scanner (MWG, Santa Clara, CA). The scanner sensitivity is indicated in the figures or tables. The data were analyzed using the Affymetrix Jaguar software (MWG, Santa Clara, CA).

Statistical Analyses. Statistical analyses were performed using the nonparametric Mann−Whitney U-test (two samples) or the Kruskal−Wallis test for more than two samples (*10*).

Contact Angle Measurements. Contact angle measurements were performed at 20 °C with a Digidrop goniometer (GBX, Romans sur Isère, France) and water, formamide, and diiodomethane as reference liquids. For each liquid, at least nine drops of 1 μL were used for the determination of the angle (median, interquartile range). The Lifshitz−van der Waals and Lewis acid and base surface tension parameters (van Oss theory (*22*); see Table 1) were determined using the Young's equation. The interfacial interaction free energy between the surface in water (ΔG_{sws}) and the free energy of binding of water to the surface (ΔG_{sw}) were calculated as described in ref 22.

AFM Studies. The thickness of the amine or semicarbazide silane layer was obtained by local reactive ion etching of the surface followed by atomic force microscopy (AFM) analysis of the step between the silicon oxide and semicarbazide regions.

Reactive Ion Etching (RIE). A 200 nm layer of polystyrene was first deposited on the glass surfaces by spin-coating (v = 3000 rpm, acc = 2500 rpm/s during 10 s). The samples were dried by a rapid thermal annealing (120 °C, 1 min) and covered with a 1.6 μm photolithographic resin layer (S18S18, Chimie Tech Service, Anthony, France). The irradiation of the resin by a UV light (365 nm, 5 mW/cm^2, 12 s) was performed through an optical mask with square-shaped patterns with lateral dimensions of 9 μm. The irradiated regions were removed by a MF319 solution (Chimie Tech Service, Anthony, France). The polystyrene layer in the square-shaped pattern was decomposed with an oxygen plasma (Plasmalab 80 plus, Oxford instrument; 0.1 Torr; 20 sccm; 100 W) during 7 min. The engraving speeds for S18S18 and for polystyrene thickness were 200 and 170 nm/min, respectively (the silicon oxide substrate was not affected by the oxygen plasma). Finally, the samples were soaked with

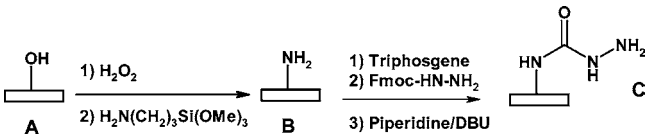


Figure 1. Fabrication of amine and semicarbazide functionalized glass slides used in this study.

sonication in a series of solvents to remove the unreacted parts (toluene, isopropyl alcohol, and water, 10 min each).

AFM Measurements. AFM (atomic force microscopy) was carried out with a Nanoscope IIIa controller (Digital Instrument) using intermittent contact mode at room temperature under ambient conditions. Processing of the AFM images was achieved by removing only local planes to the images. The height of the silane layer was measured from averaged profiles (so-called profile line) obtained along lines that run through the square-shape patterns. To characterize the substrate homogeneity, the root-mean-squared surface roughness (R_{rms}) was measured in the different layers.

RESULTS AND DISCUSSION

Preparation of the Glass Slides. The functionalization of glass slides by a semicarbazide sol−gel layer was discussed in detail elsewhere and is rapidly described in Figure 1 (*8*). Commercially available glass slides were silanized with 3-aminopropyltrimethoxysilane. The amine groups were treated successively with triphosgene and Fmoc protected hydrazine to install the semicarbazide functions. The correct functionalization of the slides is controlled using a glyoxylyl probe labeled with tetramethylrhodamine, which is able to react chemoselectively with the surface through the formation of an α-oxo semicarbazone linkage. This aspect will be discussed later, since this quality control was used to document the chemical stability of the semicarbazide glass slides upon aging.

Amine glass slides used for the comparative study were the same as those utilized for the synthesis of semicarbazide glass slides (Figure 1).

Fabrication of Protein Microarrays on Semicarbazide or Amine Glass Slides. Comparison in a Serodetection Study. The preparation of protein microarrays by adsorption of proteins on surfaces is an appealing strategy because no chemical modification of the proteins is required. As shown in the accompanying paper, recombinant proteins were found to adsorb efficiently on semicarbazide glass slides. The corresponding microarrays permitted the highly sensitive and specific detection of antibodies in human sera and were used for the simultaneous serodetection of multipathogen infections. Alternatively, proteins are known to adsorb on amine-modified surfaces. For this reason, amine glass slides were often utilized for the preparation of protein microarrays (*11*, *12*). For example, Mezzasoma et al. have recently described the fabrication of antigen microarrays for the serodiagnosis of infectious diseases using aminosilane-derivatized slides (*13*). Robinson et al. have printed antigens or antibodies on poly-L-lysine for the detection of their cognate ligands (*14*).

Both semicarbazide and amine glass slides present NH_2 groups on the surface. However, the pK_a values of semicarbazide and alkylamines are completely different (*15*). Indeed, the pK_a of semicarbazide is 3.65 at 25 °C, whereas the pK_a of methylamine is 10.65 at 25 °C. Thus, the semicarbazide surface is expected to be uncharged at physiological pH, whereas in the same conditions amine slides are protonated and thus cationic surfaces. Given the different physicochemical properties of these

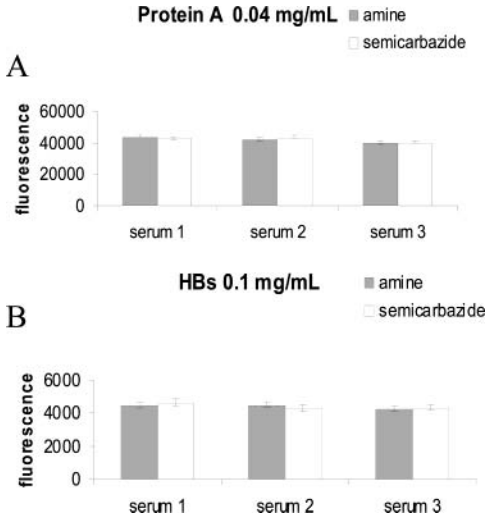


Figure 2. Adsorption of protein A (A) or HBs antigen (B) on amine or semicarbazide slides. For protein A, the arrays were incubated 1 h with a human serum (diluted $^1/_{50}$). For HBs, the arrays were incubated 2 h with a HBs positive referenced serum (diluted $^1/_{50}$). Detection of captured antibodies was performed with tetramethylrhodamine labeled goat antihuman IgG-A-M antibodies. $n = 6$, L35, PMT50. The interquartile range is indicated at the top of the bar (median).

surfaces, we have decided to print recombinant proteins on both surfaces in a microarray format and to evaluate their ability to detect antibodies in sera. In addition, we have studied the stability of the printed arrays upon accelerated aging. Despite the importance of this aspect for the development of protein microarrays, no long-term stability studies have been reported to our knowledge.

In a preliminary study, we have printed protein A and the surface antigen of hepatitis B virus (HBs) at 0.04 and 0.1 mg/mL, respectively (Figure 2). Each printed slide was incubated first with a human serum (ELISA referenced HBV positive serum for HBs microarrays) and then with goat antihuman secondary antibodies labeled with tetramethylrhodamine. The arrays were analyzed using the Cy3 channel of a fluorescence microarray scanner. As shown in Figure 2, both proteins behaved similarly on the two surfaces, both in term of signal intensity and background level. These results show that adsorption of proteins occurs similarly on amine and semicarbazide surfaces, even if the mechanism of immobilization is probably different.

These preliminary data in hand, we have selected other antigens derived from HCV to confirm the previous observations. We used recombinant core, NS3, and NS4 antigens and a mixture of core, NS3, NS4, and NS5 antigens named mix-HCV antigen. The HCV antigen microarrays were incubated with a collection of ELISA referenced HCV sera (16+, 4−) just after the printing step. The determination of the cutoff values of positivity is described in detail elsewhere (*16*). As shown in Figure 3, both types of microarrays displayed 100% of sensitivity and specificity with this collection of sera. Usually, the signal displayed by amine slides was equal or superior to the signal obtained with semicarbazide supports. However, for mix-HCV and core antigens, some sera led to higher signals on semicarbazide slides.

Stability Study of Amine and Semicarbazide Microarrays, Protein Antigens. These data set the stage for the stability study, which was performed using both surfaces. We used the previous HCV antigen microarrays and HIV antigen microarrays composed of two HIV recombinant proteins Gp 120 (0.5−0.05 mg/mL) and

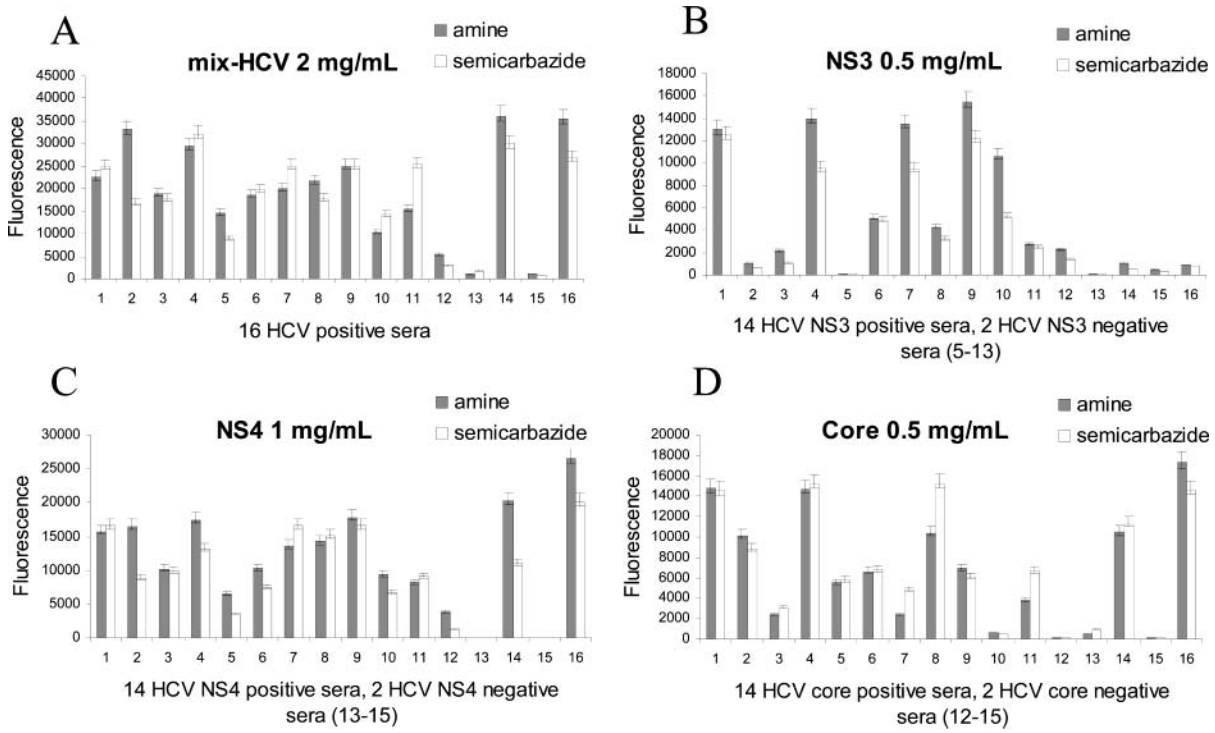


Figure 3. Detection of antibodies using amine or semicarbazide slides and HCV core, NS3, NS4, and mix-HCV antigens. HCV referenced sera (for ELISA, AxSYM HCV version 3.0, Abbott; for Western blot, RIBA, CHIRON RIBA HCV 3.0 SIA, Ortho-Clinical Diagnostics). The cutoff values of positivity (mean ± 3 SD) were determined using a collection of 30 HCV ELISA negative sera. The normality of the distribution was verified using the Shapiro−Wilk test. (A) mix-HCV, cutoff: 161 ± 36. (B) NS3 recombinant protein, cutoff: 28 ± 8. (C) NS4 recombinant protein, cutoff: 31 ± 9. (D) Core recombinant protein, cutoff: 23 ± 7. $n = 6$, L35, PMT50. The interquartile range is indicated at the top of the bar (median).

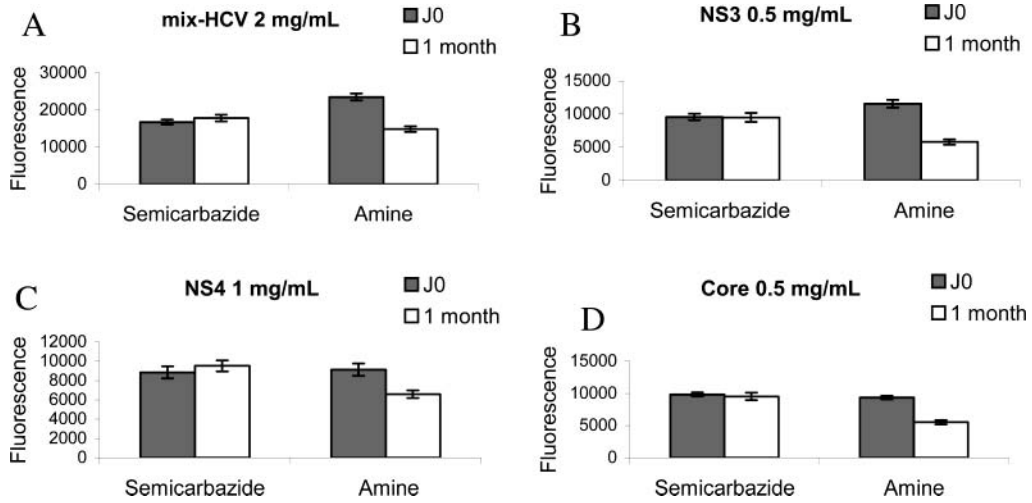


Figure 4. Stability of HCV core, NS3, NS4, and mix-HCV antigens on amine or semicarbazide surfaces. HCV referenced positive serum (for ELISA, AxSYM HCV version 3.0, Abbott; for Western blot, RIBA, CHIRON RIBA HCV 3.0 SIA, Ortho-Clinical Diagnostics). The microarrays were stored at 38 °C in a humid chamber. $n = 9$, L35, PMT50. The interquartile range is indicated at the top of the bar (median).

Gp41 (2−0.1 mg/mL). For each study, one ELISA referenced positive serum was selected. A series of microarrays were used for antibody detection just after printing. The other slides were placed in a humid chamber (60% relative humidity) at 38 °C to accelerate the aging.

The data corresponding to the HCV stability study are presented in Figure 4. The specificity of antibody detection was verified using HCV ELISA negative sera (data not shown). After 1 month, the fluorescence signal was found to drop significantly for all the tested antigens on amine slides: −37% for mix-HCV, −50% for NS3, −16% for NS4, and −44% for core. Alternatively, the largest variation observed with semicarbazide slides was +7.5% for NS4. Interestingly, the signals displayed by NS3 or core antigens were found to be stable on the semicarbazide surface (−0.8% and +2.7%, respectively, nonsignificant at $p < 0.05$), whereas the loss of reactivity on amine slides upon aging was as high as 45−50%. This high difference in stability was confirmed with other sera (data not shown).

The data corresponding to the HIV study are collected in Figures 5 and 6. For amine microarrays (Figure 5), the signals displayed by Gp120 and Gp41 antigens changed significantly ($p < 0.05$) upon aging for all the tested concentrations. The figure for Gp41 was complex and depended on both concentration and time of aging

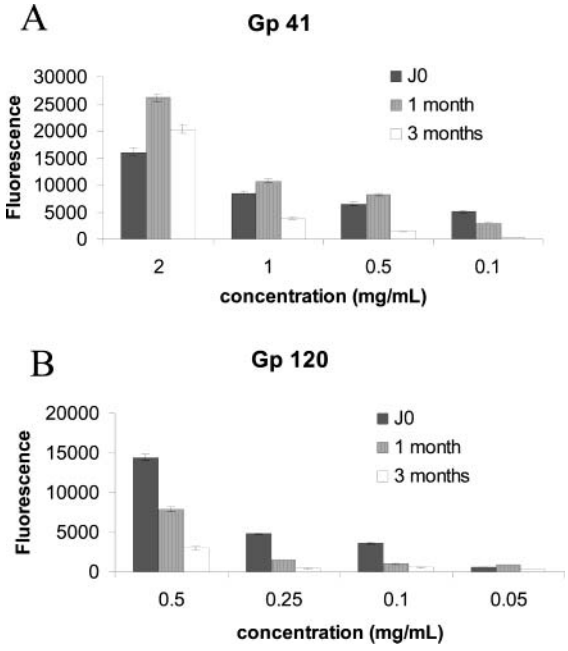


Figure 5. Stability of HIV Gp41 (A) and Gp120 (B) antigens on amine surfaces. HIV positive referenced serum, $n = 9$, L35, PMT 50. The confidence interval ($p = 0.05$, $t = 2.26$) is indicated at the top of the bar (mean).

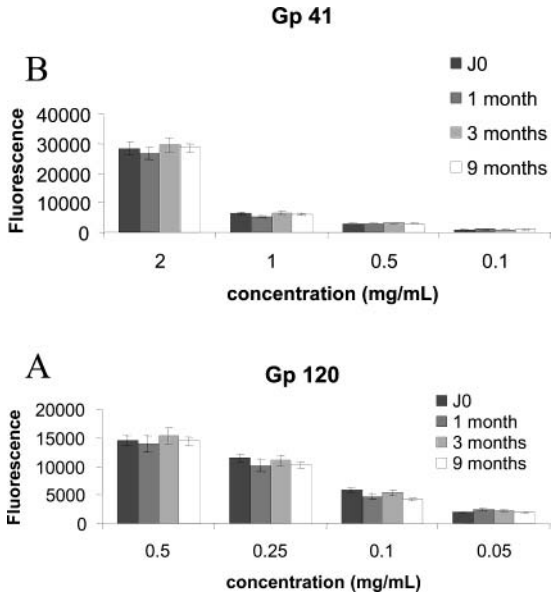


Figure 6. Stability of HIV Gp41 (A) and Gp120 (B) antigens on semicarbazide surfaces. HIV positive referenced serum, $n = 9$, L35, PMT 50. The confidence interval ($p = 0.05$, $t = 2.26$) is indicated at the top of the bar (mean).

(Figure 5A). For the highest concentrations (0.5−2 mg/mL), the signal increased after 1 month and then decreased after 3 months, whereas for the lowest concentration (0.1 mg/mL) the signal always decreased. For Gp120 (Figure 5B), the signal was found to drop for the three highest concentrations. After 3 months, the signal represented only 20% of the initial value at 0.5 mg/mL and 10% at 0.25 mg/mL.

In the meantime, Gp41 and Gp120 antigens were found to be stable on the semicarbazide surface (Figure 6). Thus, the stability study was continued up to 9 months. In the accompanying paper, we show that the highest concentrations used here for Gp41 and Gp120 (2 and 0.5 mg/mL, respectively) permitted the sensitive and

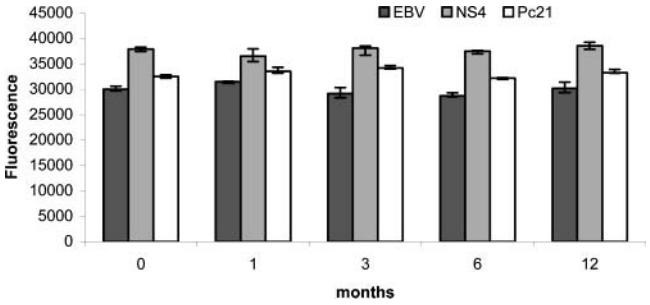


Figure 7. Stability of peptide arrays on semicarbazide slides. HCV P21 and NS4 peptides, EBV VCA p18 peptide, HCV and EBV positive referenced sera. Peptides were printed at 10^{-4} M. $n = 6$, L35, PMT50. The interquartile range is indicated at the top of the bar (median).

specific detection of antibodies against HIV. Interestingly, for these concentrations, the largest variation of the fluorescence intensity relative to the reference data obtained just after printing did not exceed 7%, illustrating the very good stability of both protein antigens on semicarbazide glass slides.

Stability Study of Semicarbazide Microarrays, Peptide Antigens. In the accompanying paper, we have described the utility of semicarbazide glass slides for the fabrication of peptide−protein microarrays. Thus, it is also important to document the stability of the peptide probes during aging.

The covalent attachment of small peptides to the glass surface through the formation of an α-oxo semicarbazone bond is important to avoid the loss of probe during the washing and incubation steps. The stability of the α-oxo semicarbazone linkage toward hydrolysis is expected to have a profound impact upon the results of the aging study. HCV core p21 15−45 (*17*), HCV NS4 1925−1947 (*18*), and EBV VCA p18 153−176 glyoxylyl peptides (*19*) were printed on semicarbazide slides. Figure 7 presents the evolution of the fluorescence intensity for these three peptidic antigens upon a 12-month stability study. For the three peptides, the differences were not found to be significant ($p < 0.05$), thus demonstrating the good stability of peptide α-oxo semicarbazone arrays.

Reproducibility. Another important aspect of microarray technologies is the ability to reach a high level of reproducibility inside a slide and between slides of the same batch or of different batches. We have examined the reproducibility of semicarbazide microarray fabrication and antibodies detection using again Gp120 and 41 HIV antigens.

The variation coefficients for Gp120 (5.0%) and Gp41 (5.5%) inside a slide were determined using 64 spots. These values are close to the variation coefficient obtained for the HCVcore p21 15−45 peptide ($n = 600$).

Next, two batches were tested (five slides per batch). The data presented in Figure 8 show that for a given antigen, the differences between the slides of a batch or between the two batches were not significant at $p < 0.05$, thus showing the good reproducibility of the assay. These results can be attributed to a quality control of the semicarbazide glass slides and to the simplicity of the microarray preparation and use.

Chemical Stability of Semicarbazide Glass Slides. Recently, we have described a method allowing the control of the semicarbazide layer reactivity. This quality control utilized two peptides labeled with (5)-6-carboxytetramethylrhodamine. One peptide Rho-Lys-Arg-NH-$(CH_2)_3$NH-CO-CHO (Rho-COCHO) was modified by a glyoxylyl group and thus was able to react chemoselec-

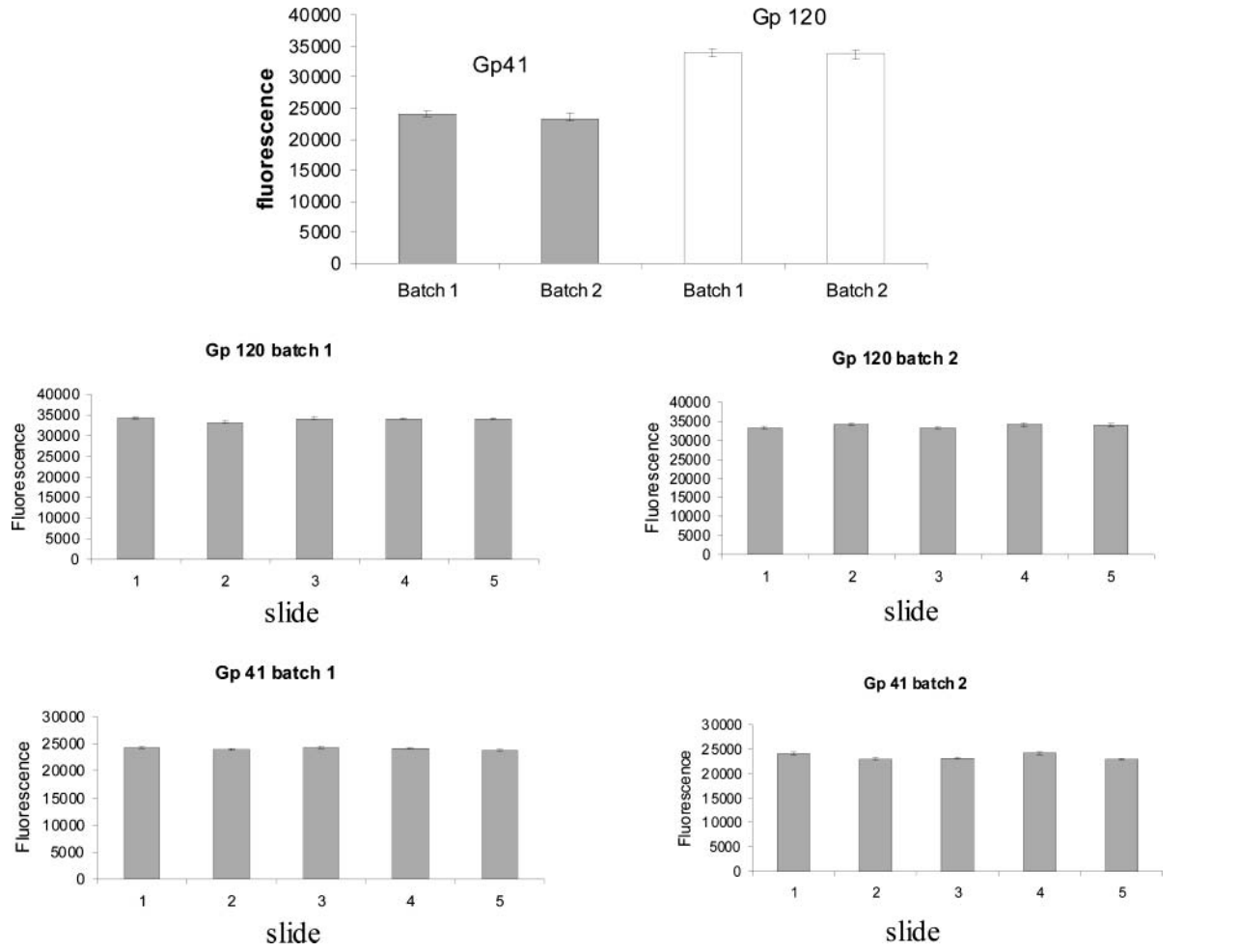


Figure 8. Reproducibility study. The semicarbazide slides were printed with Gp41 (2 mg/mL) and Gp120 (0.5 mg/mL) and used for the detection of anti-HIV antibodies in a diluted human serum ($^1/_{50}$). $n = 6$, L35, PMT50. The interquartile range is indicated at the top of the bar (median).

tively with the accessible semicarbazide groups on the surface, whereas the other peptide Rho-Lys-Arg-NH_2 (Rho-$CONH_2$) was a control lacking the glyoxylyl group for anchorage.

The quality control was performed by immersing one slide 1 h at 37 °C in a 0.1 mM solution of Rho-COCHO and another slide in a solution of the control Rho-$CONH_2$. Both slides were washed to remove the excess of peptide and analyzed using a fluorescence scanner. A large difference in fluorescence intensity between the two slides is indicative of a high level of surface functionalization. The variation coefficient of the fluorescence gives an indication of the homogeneity of the slide.

This method of characterization was used to document the chemical stability of the semicarbazide slides upon aging. The slides of the same batch were analyzed just after preparation or following 3 months of storage at room temperature in a closed chamber. The data presented in Figure 9 show that the fluorescence intensity of the slides did not change over a 3-month period for both labeled peptides ($p < 0.05$). The variation coefficient of the fluorescence intensity was also unaffected in this experiment (4−8% for Rho-COCHO and 4−7% for Rho-$CONH_2$). Thus, the chemical properties of the semicarbazide slides are conserved at least 3 months even if some air pollution could be detected after 30 days of storage by contact angle measurements (see later).

Characterization of the Semicarbazide Surface by Contact Angle Measurements. In the previous section, we have described a chemical method allowing a quality control of the semicarbazide surface reactivity. An interesting aspect of this method is the possibility characterizing the homogeneity of the surface viewed through the reactivity of solvent-accessible semicarbazide groups. A complementary method allowing the rapid, simple, and cheap characterization of surfaces is

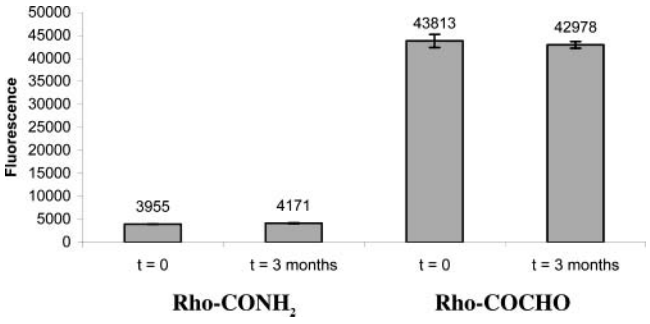


Figure 9. Chemical stability of semicarbazides slides. The slides were analyzed after synthesis or after 3 months of storage in air using glyoxylyl Rho-COCHO or amide Rho-$CONH_2$ peptides labeled with (5)-6-carboxytetramethylrhodamine as described elsewhere. The slides were scanned at L25, PMT40 using an Affymetrix 418 array scanner (MWG, Santa Clara, CA), and the data were analyzed with the Scanalyze software (Stanford University). Thirty measurements were performed per slide. The grid covered about 70% of the glass surface. The bars represent the mean and the confidence interval ($p = 0.05$).

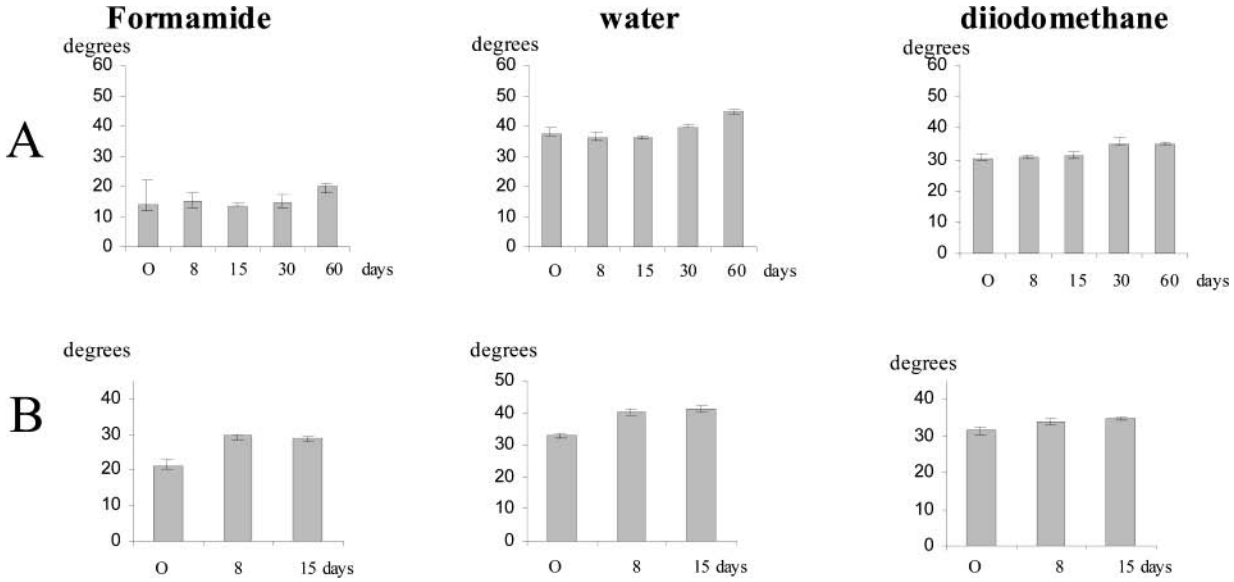


Figure 10. Stability studies on semicarbazide (A) or amine (B) glass slides using contact angle measurements with formamide, water, or diiodomethane, 20 °C. The interquartile range is indicated at the top of the bar (median).

to perform contact angle measurements with liquids whose surface tension is well-known.

α-Bromonaphthalene, dimethyl sulfoxide, and ethylene glycol were found to spread on semicarbazide slides. Diiodomethane, water, and formamide were found to be useful referenced liquids. Contact angle measurements performed just after the preparation of the surfaces can be considered as reference data for a quality control. These contact angles determined for amine and semicarbazide glass slides are collected in Table 1. The use of the Young's equation permitted the determination of the Lifshitz−van der Waals (LW) and Lewis acid and base surface tension parameters according to the van Oss theory (Table 1) (*20*). In addition, we have calculated the interfacial interaction free energy of the surface in water (ΔG_{sws}) and the free energy of binding of water to the surface (ΔG_{sw}), which are a good indication of the hydrophilicity of a surface (*21*, *22*).

The contact angle of diiodomethane was found to be similar on both surfaces ($p < 0.05$, Table 1). The Lifshitz−van der Waals surface tensions of the surfaces were close to 44 mJ/m^2, a typical γ^{LW} value for a large number of substances (*22*). The contact angle of water was found to be slightly greater on the semicarbazide surface ($p < 0.05$, Table 1), but the angle of formamide was found to be similar on both surfaces ($p < 0.05$, Table 1). Thus, the polar surface tension parameters for the two surfaces were also found to be similar. Taken together, it seemed that the amine and semicarbazide surfaces could not be distinguished by this technique. The fact that semicarbazide and amine surfaces have similar surface tension parameters could explain why proteins were found to adsorb similarly on both surfaces, at least if only interfacial interactions are considered.

If we consider now the interfacial interaction free energy between the surfaces in water ΔG_{sws}, both surfaces displayed a positive value (Table 1). In addition, the free energy of binding of water to the surface ΔG_{sw} was found to be inferior to −113 mJ/m^2, a value below which a substance is usually considered as hydrophilic (*22*).

Evolution of Contact Angles on Semicarbazide or Amine Glass Slide upon Aging. Another interesting application of contact angle measurements is to follow the evolution of the surface upon aging. The silane layer covering the glass slide surface can be the subject of changes due to chemical transformation of surface functional groups (for example, air oxidation) or to the deposition of air contaminants. Air pollution of amine surfaces has been well studied (*23*). Contact angle measurements on amine surfaces obtained by silanization with 3-aminopropyltrimethoxysilane demonstrated a rapid pollution of the surface by air impurities. Thus, we have studied the evolution of the contact angles of the three referenced liquids diiodomethane, water, and formamide on both surfaces (Figure 10). The stability study was performed during 15 days for amine and 2 months for semicarbazide glass slides.

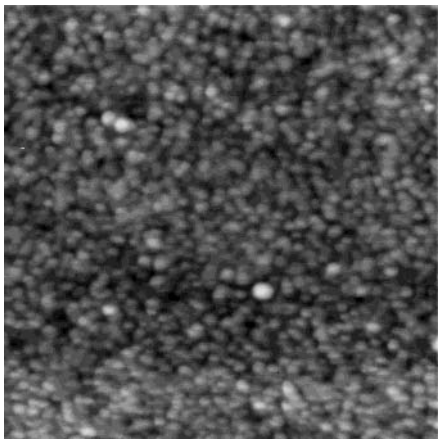


Figure 11. Intermittent contact mode AFM image image (500 × 500 nm^2) of the semicarbazide glass slide surface in air. The gray scale ranges from 0 (black) to 7 nm (white). The mean roughness Ra and the rms roughness were found to be 0.75 and 0.98 nm, respectively.

In agreement with previous studies (*23*), the amine surface was found to be very sensitive to aging, as shown by the data obtained for the three referenced liquids and nonparametric statistical analysis ($p < 0.05$). The major change was observed during the first 8 days of aging.

For semicarbazide glass slides, a significant change in the contact angles was observed after 30 days of aging for diiodomethane and 60 days for water ($p < 0.05$), thus suggesting that the semicarbazide glass slides are more stable toward air pollution than amine glass slides. Interestingly, pollution of the semicarbazide surface by

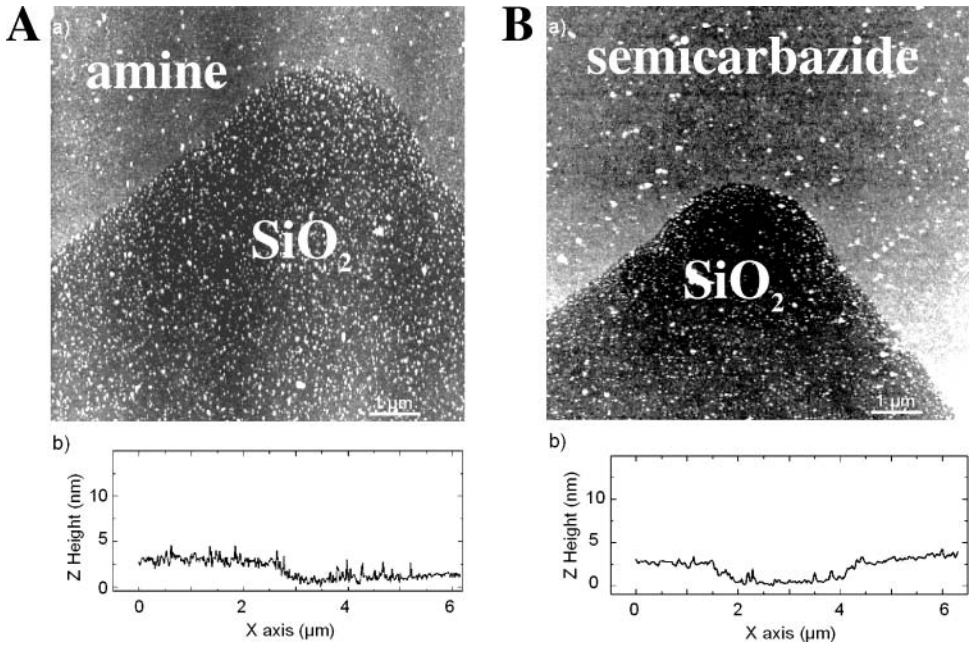


Figure 12. Determination of the amine (A) and semicarbazide (B) layer thickness by reactive ion etching and tapping mode AFM analysis. AFM images showing a dark area, where the silane layer was removed by RIE from the glass surface. The white spots corresponded to contaminants resulting from the cutting procedure of the glass slide. The curves below the AFM images show a representative line cut through the silane and the glass layers. The height of the step separating the two regions was 1.8−2.2 nm for both surfaces.

air contaminants did not alter the reactivity of the layer as shown previously in a 3 months of chemical stability study.

AFM Characterization of Semicarbazide Glass Slides. Glass slides were cleaned using a piranha solution and silanized with 3-(aminopropyl)trimethoxysilane as described elsewhere. Some amine slides were used directly for AFM studies, and the others were treated as usual to install the semicarbazide groups. Thus, AFM measurements were performed on amine or semicarbazide slides coming from the same silanization bath.

Figure 11 gives a typical aspect of a semicarbazide glass slide surface. The mean roughness Ra and the rms roughness were found to be, respectively, 0.75 and 0.98 nm. Similar results were obtained for the amine surface (data not shown).

The thickness of the layer was determined by removing a defined region of the glass surface by reactive ion etching to get the original silicon oxide substrate. The height of the step at the frontier between the silicon oxide and semicarbazide surface was determined by AFM. As shown in Figure 12B, the thickness of the layer was ranging from 1.8 to 2.2 nm, a value superior to the length of one silane unit (about 1 nm in an extended conformation) (*23*). The same results were obtained for the amine surface (Figure 12A).

These AFM studies demonstrate that the amine and semicarbazide layers are very similar in term of rugosity and thickness. We have shown previously that the two surfaces could not be distinguished by contact angle measurements. Nevertheless, the evolution of antigen reactivity on both surfaces was found to be drastically different. Additional studies are necessary to understand these differences.

CONCLUSION

We have demonstrated in this article that semicarbazide functionalized glass slides allow the adsorption of proteins as efficiently as amine slides, with the important advantage of giving stable antibodies detection results. In addition, semicarbazide glass slides were found to be less sensitive to air pollution than amine surfaces and chemically stable. Peptide microarrays prepared by α-oxo semicarbazone site-specific ligation were also found to give stable antibodies detection results, leading to the possibility of preparing high-quality peptide−protein microarrays. Both surfaces could not be distinguished by contact angle measurements or AFM studies. Thus, more experiments are needed to identify the origin of these large differences.

ACKNOWLEDGMENT

We thank CNRS, Université de Lille 2, Institut Pasteur de Lille, and Sedac-Therapeutics for financial support, Eric Diesis for technical assistance, and David Hot, Ludovic Huot, and Erwan Levillain for fluorescence measurements. We thank Pr Yves Lemoine for giving us an access to the Affymetrix 418 array scanner and Affymetrix 417 arrayer.

LITERATURE CITED

(1) Templin, M. F., Stoll, D., Schrenk, M., Traub, P. C., Vöhringer, C. F., Joos, T. O. (2002) Protein microarray technology. *Drug Discovery Today 7*, 815−822.

(2) Lin, S. C., Tseng, F. G., Huang, H. M., Chieng, C. C. (2001) Microsized 2D protein array immobilized by micro-stamps and micro-wells for disease diagnosis and drug screening. *Fresenius J. Anal. Chem. 371*, 202−208.

(3) Fields, G. B., Noble, R. L (1990) Solid phase peptide synthesis utilizing 9-fluorenylmethoxycarbonyl amino acids. *Int. J. Pept. Protein Res. 35*, 161−214.

(4) Melnyk, O., Fruchart, J.-S., Grandjean, C., Gras-Masse, H. (2001) Tartric acid-based linker for the solid-phase synthesis of C-terminal peptide α-oxo aldehydes. *J. Org. Chem. 66*, 4153−4160.

(5) Fruchart, J.-S., Gras-Masse, H., Melnyk, O. (1999) A new linker for the synthesis of C-terminal peptide α-oxo aldehydes. *Tetrahedron Lett. 40*, 6225−6228.

(6) Urbès, F.; Fruchart, J.-S.; Gras-Masse, H.; Melnyk, O. (2002) C-Terminal glyoxylyl peptides for densitive enzyme linked immunosorbent assays. *Lett. Pept. Sci. 8*, 253−258.

(7) Melnyk, O., Duburcq, X., Olivier, C., Urbès, F., Auriault, C., Gras-Masse, H. (2002) Peptide arrays for highly sensitive and specific antibody-binding fluorescence assays. *Bioconjugate Chem. 13*, 713−720.

(8) Olivier, C., Hot, D., Huot, L., Ollivier, N., El-Madhi, O., Gouyette, C., Huynh-Dinh, T., Gras-Masse, H., Lemoine, Y., Melnyk, O. (2003) α-Oxo semicarbazone peptide or oligodeoxynucleotide microarrays. *Bioconjugate Chem. 14*, 430−439.

(9) Zhang, R. E., Cao, Y. L., Hearn, M. W. (1991) Synthesis and application of Fmoc-hydrazine for the quantitative determination of saccharides by reversed-phase high-performance liquid chromatography in the low and subpicomole range. *Anal. Biochem. 195*, 160−167.

(10) Miller, J. C., Miller, J. N. *Statistics for Analytical Chemistry*, 3rd ed.; Ellis Horwood PTR Prentice Hall: New York, 1993.

(11) Gurova, K. V., Roklin, O. W., Krivokrysenko, V. I., Chumakov, P. M., Cohen, M. B., Feinstein, E., Gudkov, A. V. (2002) Expression of prostate specific antigen (PSA) is negatively regulated by p53. *Oncogene 1*, 153−157.

(12) Bogatskii, A. V., Davidenko, T. I., Chuenko, A. V., Ianishpol'skii, V. V., Tertykh, V. A. (1979) Pronase E and P immobilization on aminoorganosilica surface. *Ukr. Biokhim. Zh. 51*, 315−318.

(13) Mezzasoma, L., Bacarese-Hamilton, T., Di Cristina, M., Rossi, R., Bistoni, F., Crisanti, A. (2002) Antigen microarrays for serodiagnosis of infectious diseases. *Clin. Chem. 48*, 121−130.

(14) Robinson, W. H., DiGennaro, C., Hueber, W., Haab, B. B., Kamachi, M., Dean, E. J., Fournel, S., Fong, D., Genovese, M. C., de Vegvar, H. E., Skriner, K., Hirschberg, D. L., Morris, R. I., Muller, S., Pruijn, G. J., van Venrooij, W. J., Smolen, J. S., Brown, P. O., Steinman, L., Utz, P. (2002) Autoantigen microarrays for multiplex characterization of autoantibody responses. *Nat. Med. 8*, 295−301.

(15) Patai, S., Ed. *The Chemistry of the Hydrazo, Azo, and Azoxy Groups*; John Wiley & Sons: New York, 1975; pp 161.

(16) Duburcq, X., Olivier, C., Malingue, F., Desmet, R., Bouzidi, A., Zhou, F., Auriault, C., Gras-Masse, H., Melnyk, O. (2004) Peptide−protein microarrays for the simultaneous detection of pathogen infections. *Bioconjugate Chem. 15*, 307−316.

(17) Jolivet-Reynaud, C., Dalbon, P., Viola, F., Yvon, S., Paranhos-Baccala, G., Piga, N., Bridon, L., Trabaud, M. A., Battail, N., Sibai, G., Jolivet, M. (1998) HCV core immunodominant region analysis using mouse monoclonal antibodies and human sera: characterization of major epitopes useful for antigen detection. *J. Med. Virol. 56*, 300−309.

(18) Longombardo, G., Ferri, C., Marchi, S., Costa, F., Lombardini, F., Vacri, L., Bombardieri, S., Migliorini P. (1998) Immune response to an epitope of the NS4 protein of hepatitis C virus in HCV-related disorders. *Clin. Immunol. Immunopathol. 87*, 124−129.

(19) Van Grunsven, W. M. J., Spaan, W. S. M., Middeldorp, J. M. (1994) Localization and diagnostic application of immunodominant domains of the BFRF3-encoded Epstein−Barr virus capsid protein. *J. Infect. Dis. 170*, 13−19.

(20) van Oss, C. J., Chaudhury, M. K., Good, R. J. (1987) Monopolar surfaces. *Adv. Colloid Interface Sci. 28*, 35−64.

(21) van Oss, C. J., Good, R. J. (1988) Orientation of the water molecules of hydration of human serum albumin. *J. Protein Chem. 20*, 179−183.

(22) van Oss, C. J. *Forces Interfaciales en Milieu Aqueux* (Interfacial Forces in Aqueous Media), 1st ed.; Masson: Paris, 1996.

(23) Siqueira, R. D., Petri, D. F., Wenz, G., Schunk, P., Schimmel, T. (1999) An Improved Method for the Assembly of Amino-Terminated Monolayers on SiO_2 and the Vapor Deposition of Gold Layers. *Langmuir 15*, 4520−4523.

BC034118R

Gene Transfer into Human Hepatoma Cells by Receptor-Associated Protein/Polylysine Conjugates

Tae-Gyun Kim,[†] Seog-Youn Kang,[†] Ju-Hye Kang,[†] Mi-Young Cho,[†] Joo-Il Kim,[†] Seung-Hee Kim,[†] and Jin-Seok Kim*[,‡]

Department of Pharmacology, National Institute of Toxicological Research, Korea Food and Drug Administration, Seoul 122−704, Republic of Korea, and College of Pharmacy, Sookmyung Women's University, Seoul 140−742, Republic of Korea. Received February 24, 2003; Revised Manuscript Received January 19, 2004

Receptor-associated protein (RAP) is a ligand for all members of low-density lipoprotein (LDL) receptor families. RAP is internalized into cells via receptor-mediated endocytic trafficking, making it an attractive mechanism for efficient gene delivery. In this study, we have developed a gene delivery system using RAP as a targeting ligand. A RAP cDNA lacking a C-terminal heparin-binding domain was amplified by polymerase chain reaction (PCR) from a human liver cDNA library and was reamplified by using a primer containing a cysteine codon at its carboxyl end to facilitate its conjugation to polylysine (polyK). RAP was purified using a bacterial expression system and coupled to poly-D-lysine (PDL) or poly-L-lysine (PLL) of average MW 50 kDa via the heterobifunctional cross-linker SPDP. Using fluorescence-labeled RAP ligand, cellular uptake of the transfection complexes into HepG2 cells was shown to be highly efficient and more specific to PDL-conjugated RAP compared with PLL-conjugated one. Plasmid DNA containing a luciferase reporter gene was condensed with either RAP−PDL or RAP−PLL. In vitro transfection into HepG2 cells with RAP−PDL conjugate resulted in significantly higher luciferase expression levels in comparison to either nonconjugated PDL, or RAP−PLL, or LipofecAMINE/DNA complexes in the presence of 10% fetal bovine serum. Luciferase expression was inhibited by the addition of excess RAP. Treatment of the cells with Lovastatin, which inhibits HMG-Co reductase and increases expression of LDL receptor, stimulates luciferase expression, suggesting that the gene delivery is specifically mediated by LDL receptor. Thus, RAP−PDL conjugates have the potential to be used as a new nonviral gene delivery vector.

INTRODUCTION

Receptor-mediated endocytosis (RME) represents a highly efficient internalization pathway (*1*) and offers an efficient cellular route for the delivery of gene therapy vectors. A number of gene transfer systems have been developed to deliver foreign DNA via RME using specific ligands such as asialoglycoprotein (*2*), transferrin (*3*), or anti-CD3 antibody (*4*). Gene transfer using these ligands has been accomplished by synthetic vectors termed molecular conjugates, which consist of two linked functional domains: a ligand domain and a DNA-binding domain to achieve binding and incorporation of the transgene into the vector complex. For many of these approaches, polylysine (polyK) provides a DNA-condensing carrier function, and chemical linkage methods are used to achieve linkage between the polyK and the ligand domain of the complex (*5*). For some cell types, receptor-mediated transport of DNA is a highly effective and physiological means of introducing DNA into the cells (*3, 4, 6*).

The low density lipoprotein (LDL) receptor gene family is a large family of endocytic receptors that bind and internalize various ligands, which include several apolipoproteins that are involved in cholesterol homeostasis (*7*). This receptor family is ubiquitously expressed in many tissues such as liver and brain (*8*). Moreover, LDL receptor activities are elevated in malignant cells, which have high LDL requirements as do rapidly dividing cells (*9*). The receptor-associated protein (RAP) is a specialized folding chaperone/escort protein that is associated with newly synthesized receptors in the endoplasmic reticulum (*10*) and can bind with high affinity to the members of the LDL receptor family such as the LDL receptor-related protein (LRP), the very low-density lipoprotein (VLDL) receptor, and megalin (gp330) (*8*). Exogenously added RAP binds to receptors on the cell surface in vitro and antagonizes all known ligand interactions with the receptors (*10, 11*). Interestingly, RAP is internalized into cells via receptor-mediated endocytic trafficking (*12, 13*), which is an attractive mechanism for efficient gene delivery.

In this study, we explore the use of RAP as a targeting ligand for receptor-mediated gene transfer into human hepatoma cells (HepG2). The interaction, uptake, and gene expression of the transfection complexes were found to be due to the specific function of RAP ligand. As with other ligand-dependent gene delivery systems, we find that transfected gene expression is decreased by addition of unconjugated RAP ligand in the transfection medium and enhanced by treatment of Lovastatin, which inhibits cholesterol biosynthesis and increases the expression of

* To whom correspondence should be addressed. Tel: +82-2-710-9574; Fax: +82-2-712-0032; E-mail: jskim@sdic.sookmyung.ac.kr.

[†] National Institute of Toxicological Research.

[‡] Sookmyung Women's University.

[1] Abbreviations: RAP, receptor-associated protein; polyK, polylysine; PDL, poly-D-lysine; PLL, poly-L-lysine; RME.; receptor-mediated endocytosis; ILU, integrated light unit; LDL, low-density lipoprotein; LRP, LDL receptor-related protein; SPDP, 3-(2-pyridyldithio)propionic acid *N*-hydroxysuccinimide ester.

10.1021/bc0340262 CCC: $27.50 © 2004 American Chemical Society
Published on Web 02/28/2004

LDL receptor (*14, 15*). Because LRP and LDL receptors are abundant on hepatoma cells, RAP-mediated gene delivery systems may be useful for the delivery of therapeutic genes into this cell type.

EXPERIMENTAL PROCEDURES

Materials. Human liver cDNA library and LA Taq with GC buffer kit were purchased from TaKaRa Shuzo Company (Shiga, Japan). Pinpoint Xa protein purification system, pPinPoint Xa-3 vector, factor Xa protease, pRL-CMV, and Dual-Luciferase reporter assay kit were from Promega (Madison, WI). Reagents including LB medium, ampicillin, *N*-[2-hydroxyethyl]piperazine-*N*′-[2-ethanesulfonic acid] (HEPES), 3-(2-pyridyldithio)propionic acid *N*-hydroxysuccinimide ester (SPDP), fetal bovine serum (FBS), streptavidin-fluorescene isothiocyanate (FITC), poly-D-lysine hydrobromide (PDL, molecular weight 30 000−70 000) and poly-L-lysine hydrobromide (PLL, molecular weight 30 000−70 000) were from Sigma Chemical Company (St. Louis, MO). PCR primers, restriction enzymes, isopropyl β-D-thiogalactopyranoside (IPTG), dithiothreitol (DTT), Eagle's minimal essential medium (EMEM), LipofecAMINE reagent, and Opti-MEM medium were purchased from Life Technologies (Rockville, MD). Biotin, Sephacryl S-100 column, and Sepadex G-25 superfine were from Amersham Pharmacia Biotech (UK). Centriplus YM-10 filter device was from Millipore, Co. (Bedford, MA). BCA protein assay kit was from Pierce (Rockford, IL). QIAquick gel extraction kit, EndoFree plasmid Maxi kit, and column were from Qiagen (Germany). Lovastatin was kindly supplied by Choongwae Pharmaceutical Co. (Korea). Deionized−distilled water was produced by using Milli-Q water purification system (Millipore) and FI−STREEM III Bi-Distiller system (Barnstead, Dubuque, IA). All other chemicals and reagents were of tissue culture grade.

Construction and Expression of RAP. The cDNA for partial RAP_{1-260} was amplified in polymerase chain reaction (PCR) from human liver cDNA library with a 5′ primer, GGAGAAGAACCAGCCCAAGC, and a 3′ primer, GCGCAGCCGCTCGCCCCAGGC. The RAP cDNA was reamplified with a 5′ primer containing a *BamH* I restriction site to facilitate its ligation and a 3′ primer containing a *Kpn* I site and an additional cysteine codon preceding a stop codon to facilitate its conjugation to polyK (*6*). The PCR product was cloned into *BamH* I-*Kpn* I-digested pPinPoint Xa-3, a bacterial expression vector with N-terminally biotin-tagged sequence. The plasmid structure was confirmed by DNA sequence analysis with ABI prism 3700 (Applied Biosystems), transformed into *E. coli*/JM109 cells, and expressed according to the manufacturer's instructions.

Purification and Reduction of RAP. RAP expressed with biotin tag was purified using PinPoint Xa protein purification system and digested with factor Xa protease in Xa buffer (20 mM Tris-HCl pH 7.4, 100 mM NaCl). The solution of digested RAP was incubated with avidin resin to remove the biotin tag and passed through Sephacryl S-100 column to remove factor Xa protease. Eluent fractions were concentrated with a centrifugal filter device (Centriplus YM-10). Purified RAP was analyzed using SDS−PAGE and assayed for protein concentration by BCA protein assay kit. A cysteine residue in the C-terminal of recombinant RAP was reduced by dithiothreitol (DTT) to generate free sulfhydryl groups. Briefly, to 1 mg of RAP in 0.8 mL of HEPES-buffered saline (HBS; 150 mM NaCl, 10 mM HEPES pH 7.4) was added 8 μL (4 μmol) of 0.5 M DTT solution. The solution was kept under argon for 1 h, and the pH was adjusted to 5.2 by adding 3 M sodium acetate buffer. After gel filteration (Sepadex G-25 superfine), a solution of reduced RAP for preparing RAP-polyK conjugates was obtained (*3*).

Preparation of RAP−polyK Conjugates. Two kinds of polyK were used to conjugate recombinant RAP; poly-D-lysine (PDL) and poly-L-lysine (PLL), both of which have an average molecular weight of 50 kDa. Purified RAP was conjugated to each polyK, using a heterobifunctional cross-linker, 3-(2-Pyridyldithio)propionic acid *N*-hydroxysuccinimide ester (SPDP) (*3*). Briefly, each polyK, consisting of approximate 400 lysine residues, was mixed with SPDP at a molar ratio of 1:20 in PBS. After incubation for 1 h at room temperature, the reaction mixture was dialyzed against deionized−distilled water for 48 h to remove excess unreacted SPDP. This reaction theoretically yielded a polyK molecule with about 5% SPDP modification of its lysine residues. Each SPDP-polyK was then mixed with RAP and incubated for 24 h at room temperature. These RAP−PDL or RAP−PLL conjugates were used for preparing transfection complexes.

Plasmid Vector. pRL-CMV (4079 bp), a plasmid expression vector containing a cDNA encoding *Renilla reniformis* (sea pansy) luciferase driven by the cytomegalovirus (CMV) promoter, was grown in *E. coli* DH5α cells in LB medium containing ampicillin (100 μg/mL) and was purified using EndoFree plasmid Maxi kit and column.

Gel Retardation Assay. The RAP−PDL/DNA complexes were prepared by adding various amounts of RAP−PDL conjugate, ranging from 0 to 14 μg, in 20 μL of HBS to 1 μg of pRL-CMV DNA in 20 μL of HBS. The RAP−PDL solution was slowly added to the DNA solution and mixed gently. The reaction mixture was incubated for 30 min at room temperature and applied to a 0.8% agarose gel in Tris acetate EDTA buffer, pH 7.6, with 0.5 μg/mL ethidium bromide. Electrophoresis was carried out at 5 V/cm for 50 min.

Cell Line. The human hepatoma cells (HepG2) were obtained from the American Type Culture Collection. HepG2 cells were maintained in T-75 culture flask with vented cap containing EMEM supplemented with heat inactivated 10% fetal bovine serum (FBS), penicillin (100 units/ml), streptomycin (100 μg/mL), 4 mM L-glutamine, and 1.0 mM sodium pyruvate at 37 °C, 5% CO_2.

Preparation of RAP-polyK/DNA Complexes and Transfection. Cells were plated in 24-well culture plates at 5×10^4 cells/well density and incubated for 24 h prior to transfection, by which time the cells were ∼30% confluent. One microgram of plasmid DNA and the various amounts of RAP−PDL were diluted to a final volume of 100 μL with HBS. The RAP−PDL solution was added to the DNA solution, gently mixed, and incubated at room temperature. RAP−PDL/DNA complexes were formed at various weight ratios, which were calculated as molar ratios of the charge of PDL nitrogen to DNA phosphate (N:P); 1 μg of PDL for a N:P ratio of 1.3:1, 3 μg of PDL for 3.8:1, 6 μg of PDL for 7.5:1, 9 μg of PDL for 11.3:1, and 12 μg of PDL for 15:1. Charge ratios were calculated as described (*16*). After 30 min incubation, the solutions of gene transfer complexes (200 μL) were mixed with 1.5 mL of 10% serum-containing medium and added to the cells ($n = 4$). Forty-eight hours after incubation with transfection medium, the medium was removed and luciferase activity was assayed, by which time the cells were ∼90% confluent. RAP−PLL/DNA and PDL/DNA complexes were prepared in an identical manner as with

RAP−PDL/DNA complexes. For the transfection by LipofecAMINE reagent, pRL-CMV DNA (1 μg) in Opti-MEM medium was mixed with an equal volume of LipofectAMINE (14 μg) diluted appropriately in Opti-MEM medium. Complexes were incubated for 30 min at room temperature before addition to cells. Cells were transfected in the presence of 10% FBS.

Assay for Luciferase. Cell lysates were prepared by the addition of 100 μL of lysis buffer (Dual-Luciferase reporter assay kit) and incubation with agitation for 20 min at room temperature. After centrifugation at 12 000 g for 10 min, 10 μL of the supernatant of cell lysates were analyzed for luciferase activity using a Clinilumat LB9502 instrument (Berthold, Germany). These data were normalized for protein content assayed by BCA protein assay kit. Results shown are expressed as integrated light units (ILU)/mg of protein unless otherwise indicated.

Detection of Internalized Gene Transfer Complexes. Complexes containing streptavidin−FITC were formed as follows: RAP containing N-terminal biotin tag was conjugated with PDL or PLL as described above. Ten micrograms of the conjugates was diluted with 100 μL of HBS and incubated with 5 μg of streptavidin−FITC for 10 min with occasional mixing. Plasmid DNA diluted in 100 μL of HBS was added to the mixture and incubated for 30 min at room temperature. Each complex was then diluted in medium containing 10% serum and added to the cells as above. Twenty-four hours after transfection, cellular uptake of FITC-labeled RAP-polylysine/DNA complexes was analyzed with fluorescence microscopy (Olympus IX).

Competitive Inhibition by Free RAP. A competitive inhibition assay using free RAP was performed to confirm the specificity of RAP ligand-dependent gene delivery. Briefly, 10^5 HepG2 cells (24-well plate) were incubated with free recombinant RAP (0.2, 0.5, and 1 mg/mL in 1.5 mL of the medium) for 10 min in CO_2 incubator, followed by the addition of gene transfer complexes in the presence of free RAP, which consisted of 1 μg of pRL-CMV and 9 μg of RAP−PDL with 200 μL of HBS. Transfection medium was removed after 24 h incubation, and luciferase activity of cell lysates was measured as described above.

Treatment with Lovastatin. To further confirm receptor-mediated gene delivery, transfection efficiency of RAP−PDL conjugate was measured after treatment with Lovastatin, which inhibits a rate-limiting enzyme for cholesterol biosynthesis, hydroxymethylglutaryl-coenzyme A (HMG-CoA) reductase (K_i = 0.6 nM). The transfection and luciferase assay were performed as described in the above competition experiment except that Lovastatin was added to the medium with the transfection complexes simultaneously.

RESULTS

Cloning and Expression of Recombinant RAP. We amplified a partial cDNA of the RAP gene (amino acids 1−260) lacking its C-terminal heparin-binding domain by PCR from human liver cDNA library. The PCR product was reamplified with primers that contain restriction sites for cloning and a C-terminal cysteine residue for conjugation (*6*) and then cloned into a bacterial expression vector. DNA sequencing analysis revealed that the cloned RAP gene showed 99.6% homology with the previously reported RAP gene (accession number: NM_002337, GI: 4505020) (*17*), and the predicted protein sequence was identical (data not shown).

Purification and Reduction of Recombinant RAP. Recombinant RAP was produced in the form of a 47 kDa fusion protein that is biotinylated in the N-terminal tag (Figure 1, lane 4), of which approximated 10 mg was recovered using 30 mL of avidin resin. This purified fusion protein was digested with factor Xa protease for 10 h at 37 °C. Coomassie staining revealed a 30 kDa band corresponding to RAP; however, biotin tag (17 kDa) and factor Xa protease (44 kDa) contaminants were present (Figure 1, lane 5). To improve the purity, the solution of digested fusion protein was incubated with avidin resin (Figure 1, lane 6). After further purification by Sephacryl S-100 column chromatography, pooled fractions containing recombinant RAP displayed a single band at 30 kDa (Figure 1, lane 7), and the solution was concentrated. Approximately 500 μg of RAP was obtained from one liter of bacterial culture. The single cysteine residue at the C-terminal end of the purified RAP was reduced by DTT treatment and used in the following experiments.

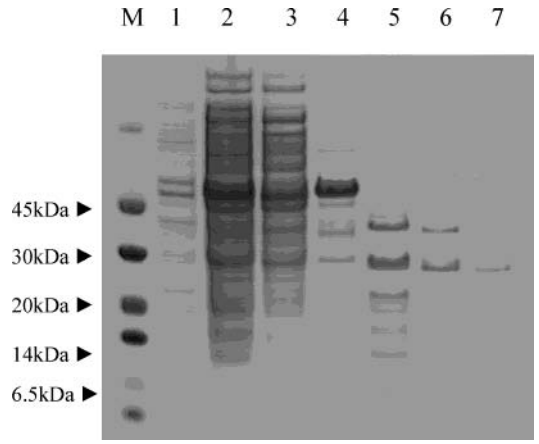


Figure 1. Expression and purification of RAP. The cell lysates of RAP fusion protein expressing *E. coli* and purified RAP were analyzed by 4−20% gradient SDS-polyacrylamide gel and Coomassie staining. Lanes: 1, *E. coli* cell lysate before induction of the fusion protein; 2, lysate after induction; 3, lysate after binding with avidin resin; 4, eluant RAP with biotin tag (47 kDa); 5, RAP and biotin tag fragment incubated with factor Xa for 10 h; 6, RAP and factor Xa after incubaion with avidin resin; 7, purified RAP after column chromatography (30 kDa).

Synthesis of RAP−polyK Conjugates. A heterobifunctional cross-linker, SPDP, was used to introduce a dithiopyridine linker into polyK, where the NHS ester group of SPDP reacted with ϵ-amino groups of polyK to form an amide linkage (*18*). Ziady et al. reported that reaction with 20× molar excess of SPDP modifies 3.5% of the lysine residues in a polyK molecule with dithiopyridine linkers (*19*). These linkers will readily react with sulfhydryl groups of RAP, yielding disulfide linkages between RAP and polyK (*6*). Purified RAP−PDL or RAP−PLL displayed reduced electrophoresis in SDS gradient polyacrylamide gel because of the basic amino acids in each polyK. We did not detect a significant amount of unconjugated free RAP in the reaction product (data not shown).

Gel Retardation Assay. To determine the optimal RAP−PDL/DNA ratio by measuring the effect of complex formation and charge neutralization, agarose gel electrophoresis was performed (*2*). As shown in Figure 2, electrophoretic mobility of the RAP−PDL/DNA complex decreased gradually with increasing amounts of RAP−PDL conjugates. DNA band retardation occurs due to the neutralization of DNA negative charges by the positive charges of RAP−PDL conjugates. At a weight ratio of 1 μg DNA:8 μg PDL coupled to RAP, plasmid DNA showed complete retardation, indicating that the DNA negative

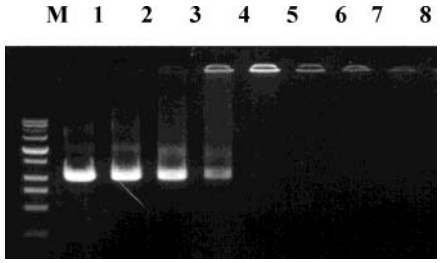


Figure 2. Gel retardation assay of DNA complexed with RAP−PDL. Lanes: M, size marker (1 kbp ladder); 1, plasmid DNA alone (1 μg); 2−8, DNA mixed with 2, 4, 6, 8, 10, 12, or 14 μg of PDL conjugated with RAP, respectively.

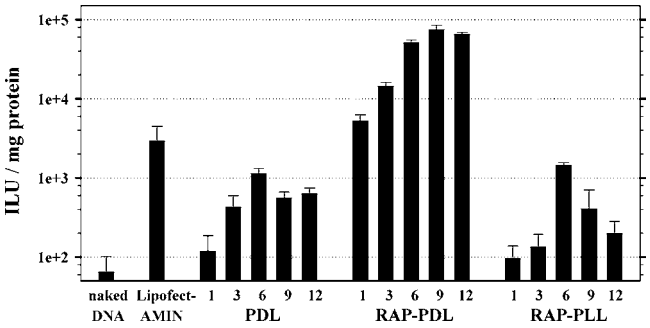


Figure 3. Transfection efficiency of RAP−polylysine/DNA complexes with human HepG2 hepatoma cells. The increasing amounts (μg) of polylysines shown on the ordinate (1, 3, 6, 9, 12) were used to complex 1 μg of DNA (pRL-CMV; 4079 bp). Each DNA complex (in 0.2 mL HBS) was mixed with 1.5 mL of culture medium (EMEM containing 10% FBS) and added to 5 $\times$ 10^4 cells per well in 24-well plates. After 48 h, the transfection medium was removed and cells were harvested. Luciferase activity is shown as means ± SD (n = 4). Transfection efficiency of naked DNA (1 μg), LipofectAMINE-DNA (14 μg) and unconjugated PDL is shown for comparison.

charge was neutralized or slightly positively charged with RAP−PDL conjugate at this weight ratio (Figure 2, lane 5).

Formulation Optimization of RAP−polyK/DNA Complexes. The RAP ligand-dependent transfection efficiencies of the complexes in five different weight ratios of polyK to DNA are shown in Figure 3. To detect gene expression, cells were transfected with particles containing the plasmid pRL-CMV, a vector with a luciferase reporter gene insert driven by the cytomegalovirus (CMV) promoter/enhancer. Plasmid DNA (1 μg) was either complexed with PDL alone, with RAP conjugated to PDL (RAP−PDL), or with RAP conjugated to PLL (RAP−PLL). Plasmids complexed with RAP−PDL showed the highest transfection efficiencies (Figure 3, RAP−PDL). In addition to ligand specificity, transfection efficiencies were dependent on the cation:anion ratio. A weight ratio of 1 μg DNA:9 μg RAP−PDL yielded the highest luciferase expression level (up to 65-fold higher than those obtained with unmodified PDL and up to 25-fold higher than with LipofectAMINE, a commercial cationic lipid formulation). At the highest weight ratio (1 μg:12 μg), the viability of the cells was not significantly affected (viability ≥95%, data not shown) and the transfection efficiency decreased slightly (less than 14%). This decrease was observed in a previous study using polyK coupled to anti-CD3 antibody (*4*) and could be due to excess polyK relative to the amount of DNA used (1 μg). Interestingly, compared to their effectiveness at high cation:anion ratios, RAP−PDL/DNA complexes were more effective at lower cation:anion ratios than were ligand-free PDL/DNA complexes. Transfection efficiencies

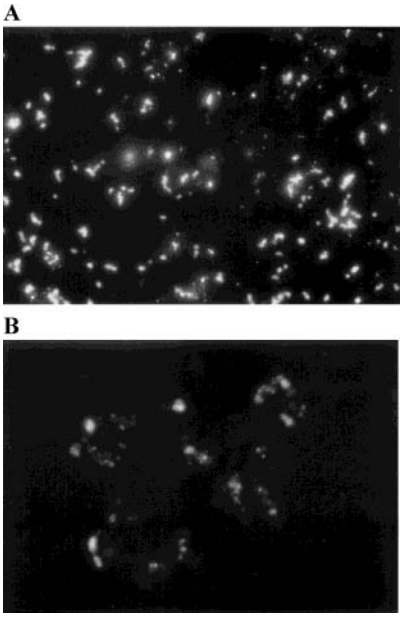


Figure 4. Cellular uptake of fluorescence-labeled RAP−polyK/DNA complexes into HepG2 cells. RAP fusion protein expressed with biotin tag was coupled to PDL or PLL, as described in Materials and Methods, and incubated with equal amounts of streptavidin−FITC. Twenty-four hours after addition of each fluorescence-labeled conjugate/DNA complex (9 μg:1 μg), endocytosed particles were visualized with fluorescence microscopy. The internalized gene transfer complexes of RAP−PDL (A) and RAP−PLL (B).

of RAP−PLL/DNA complexes were similar to those of ligand-free PDL/DNA complexes over all cation:anion ratios.

Cellular Uptake of Fluorescence-Labeled RAP−polyK/DNA Complexes. The uptake of RAP−PDL gene transfer complexes into HepG2 cells was assessed by using fluorescence microscopy (Figure 4). RAP components of the complexes were labeled with streptavidin−FITC. Following transfection with FITC-labeled RAP−PDL/DNA, almost 100% of HepG2 cells contained endocytosed gene transfer particles. In each transfected cell, several FITC-labeled RAP−PDL/DNA complexes were observed (Figure 4A). In contrast, following transfection with FITC-labeled RAP−PLL/DNA complexes, only about 30% of the cells contained observable internalized gene transfer particles distributed in intracellular vesicles (Figure 4B). The number of fluorescent particles per cell was also lower in transfection with RAP−PLL/DNA complexes, and the morphology of intracellular particles appeared to be more diffused than that of RAP−PDL/DNA complexes. Endocytosed particles were only detected using RAP−PDL/DNA or RAP−PLL/DNA complexes; in cells incubated with the complexes containing unconjugated PDL, distinct internalized gene transfer particles were not detectable.

Competitive Inhibition with Free RAPs. To confirm the specific interaction of RAP−PDL conjugates with hepatoma cells, competitive inhibition experiments were performed with excess free RAP, which was added to the cell culture medium during transfection (Figure 5). The addition of soluble RAP ligand at three concentrations decreased transfection efficiencies of RAP−PLD/DNA complexes by 10−30%. RAP concentrations of 0.2, 0.5, and 1 mg/mL were approximately 2, 5, and 10 molar equiv in excess of conjugated RAP. In transfections with unconjugated PDL/DNA complexes, coincubation with excess free RAP did not affect reporter gene expression in cells. These results indicate that the cell interaction,

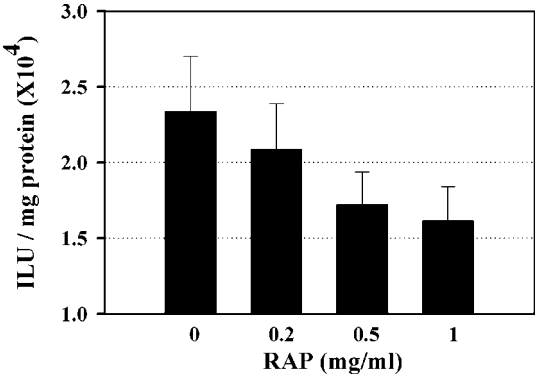


Figure 5. Free RAP competition experiment. Nine micrograms of RAP−PDL were used to complex 1 μg of DNA. DNA complexes in 200 μL of HBS were added to HepG2 cells (10^5 cells per well in 24-well plates) in 1.5 mL of EMEM containing 10% FBS in the absence or presence of the free RAP at three concentrations as indicated. The cells were harvested 24 h after transfection. Luciferase activity was measured as described in Materials and Methods and shown as means ± SD (n = 4).

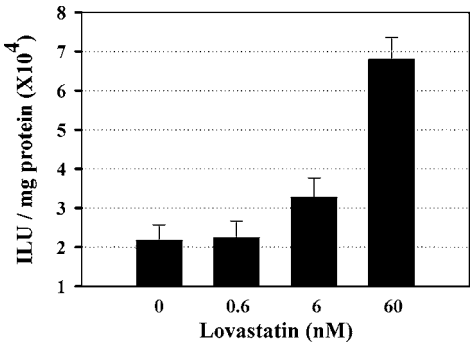


Figure 6. Enhanced transfection efficiencies of RAP−PDL conjugates by the treatment of Lovastatin, an inhibitor of HMG CoA reductase. The experiment was performed as described in the legend of Figure 5, except that transfections were carried out in the absence or presence of three concentrations of Lovastatin as indicated.

uptake, and gene expression of the RAP−PDL/DNA complexes in HepG2 cells is due to the specific interaction of the RAP−PDL conjugate with its receptor(s).

The Effect of Lovastatin on RAP-Mediated Gene Transfer. Lovastatin (Mevinolin) is a potent competitive inhibitor of a rate-limiting enzyme of cholesterol biosynthesis, HMG-CoA reductase (K_i = 0.6 nM) (*20*). Lovastatin activates LDL receptor gene expression in HepG2 cells (*15*). The presence of Lovastatin in RAP−PDL/DNA (1 μg:9 μg) transfections augmented reporter gene expression in a dose-dependent manner (Figure 6). The addition of 60 nM Lovastatin together with gene transfer complexes increased the transfection efficiency of RAP-mediated gene delivery by a factor of 100 relative to that of Lovastatin nontreated cells.

Duration of Transgene Expression. The time-course of luciferase expression in HepG2 cells is shown in Figure 7. Cells were transfected when they were 20−30% confluent and continued to grow for 2 days post-transfection, at which time the transfected cells approached confluence. The maximum level of luciferase activity was detected 2 days posttransfection. Luciferase activity decreased to ∼10% by the fifth day posttransfection. The degree of luciferase expression steeply declined 3 days after transfection and persisted for at least 5 days.

A potential concern of gene transfer using RAP−PDL conjugates is the influence of cell proliferation. To assess

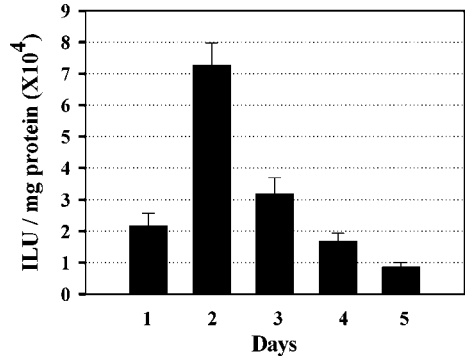


Figure 7. Duration of transgene expression. The experiment was performed as described in the legend of Figure 5, except that luciferase activity was measured 1, 2, 3, 4, and 5 days after transfection. Data represented are a mean of four independent experiments.

Table 1. Effects of Serum on the Transfection Efficiency of RAP−PDL/DNA Complexes[a]

transfection conditions	luciferase activity: (ILU × 10^{-4}/mg cell protein)
without serum	0.1 ± 0.3
5% serum	1.8 ± 0.5
10% serum	2.3 ± 0.7
25% serum	2.5 ± 0.4
50% serum	2.6 ± 0.7

[a] Note: HepG2 cells were transfected with RAP−PDL/DNA complexes (9 μg:1 μg). The experiment was performed as described in the legend of Figure 5, except that the complexes were diluted in medium with different amounts of fetal bovine serum, as indicated. Data are expressed as ILU × 10^{-4}/mg cell protein. Results shown are mean values ± SD (n = 4).

this potential influence, cells were retransfected at day 3 with the same complexes. This second transfection yielded marginal increases (∼5%) in gene expression levels at days 4 and 5 posttransfection. This result suggests that RAP-mediated gene delivery and expression may depend on cell proliferation.

Effects of Serum on Transfection. Effects of serum on the transfection of RAP−PDL complexes was also investigated by comparing the expression level of reporter gene following transfection in the presence (final concentration 50%) or absence of serum (Table 1). Addition of fetal bovine serum (FBS) to the transfection medium slightly increased reporter gene expression. In the absence of FBS, the transfection efficiency was ∼25-fold lower than that in 10%, 25%, or 50% FBS.

DISCUSSION

The development of a safe and efficient method for the delivery of transgenes to target cells and tissues still represents a major challenge. It has been reported that polycation conjugated with ligand for asialoglycoprotein receptor (*2*), transferrin receptor (*3*), c-kit receptor (*21*), or EGFR receptor (*22, 23*) resulted in specific gene delivery to cells expressing these receptors. The LDL receptor gene family is well-characterized. LDL-receptor−ligand interactions lead to endocytosis, providing an attractive mechanism for gene transfer. The LDL receptor is abundant in liver tissue, which is the principle organ of several genetic, acquired, and viral diseases amenable to gene therapy (*24*). Furthermore, all actively dividing cells require cholesterol which is taken up by the cells as a ligand−lipoprotein complex through receptor-mediated endocytosis (RME) (*8*). The expression of LDL receptors is particularly high on proliferating malignant cells as compared with the corresponding normal

tissues (*25, 26, 27*), making the LDL receptor an attractive target for cancer therapy.

For this reason, there are many studies on the selective delivery of cytotoxic compounds to cancer cells using LDL as a vehicle through the RME pathway (*9*). However, very few studies on gene transfer through LDL receptor-mediated endocytosis have been reported. Sipehia et al. developed a new method for DNA transfection of cultured endothelial cells using apolipoprotein E (Apo E) adsorbed lipofection reagent−DNA complexes (*28*). The transfection efficiencies with this method was found to be more efficient than conventional methods including calcium phosphate precipitation and lipofection. Furthermore, Kim et al. demonstrated another gene delivery vehicle (Terplex DNA) that is generated through electrostatic and hydrophobic interactions between LDL, stearyl-PLL, and DNA (*29*). However, receptor-mediated gene delivery of ligand−polycation conjugates via LDL receptor gene family members has not been reported previously.

To exploit this ubiquitous and efficient transport mechanism for introducing transgene into cells, human RAP was purified at high yields using a bacterial expression system and was conjugated with a DNA-binding polycation, polyK. The affinity of RAP for LDL receptor gene family is equivalent to that of apolipoprotein E, a high affinity ligand for the receptors (*7*). The intact 39-kDa RAP (323 amino acids) contains several structural and functional domains (*7*). In this study, we used a truncated version of RAP (N-terminal 260 amino acids), which contains at least two high affinity binding domains for LDL receptor gene families (*30, 31*) but does not contain RAP's C-terminal heparin binding domain. Because this truncated RAP lacks a cysteine residue, we engineered our recombinant RAP to contain a C-terminal cysteine residue. RAP-containing complexes were prepared by coupling SPDP-polyK to the cysteine residue of recombinant RAP. Recently, Gupta et al. (*6*) developed a similar recombinant ligand for receptor-mediated gene delivery: a single chain Fv of a monoclonal antibody (directed against human polymeric immunoglobulin receptor [plgR]), containing a C-terminal cysteine residue conjugated to polyK.

We chose two DNA-binding polycations for conjugating to RAP that had previously been used in the RME-based gene transfer system: PLL (*2*−*4, 32*) and PDL (*33*). The results of in vitro experiments clearly showed that the conjugation of the targeting ligand RAP to PDL results in a 65-fold increase in the transfection efficiency in HepG2 cells (Figure 3). For the RAP−PDL/DNA complexes, the best transfection efficiency was found at a ratio of 1 μg DNA:9 μg RAP−PDL. Corresponding results indicated complete retardation of the complexes at a ratio of 1 μg DNA:8 μg in a gel retardation assay (Figure 2). The increase of transfection efficiency was blocked by addition of free RAP (Figure 5), indicating that RAP ligand dependent uptake of the transfection complex is responsible for the higher transfection efficiency. This result is consistent with previous reports of receptor-mediated gene delivery (*4, 6*). Uptake of gene transfer particles into HepG2 cells via RAP−PDL is highly efficient: almost all cells contained several endocytosed particles following transfer of the FITC-avidin labeled complexes (Figure 4).

In contrast to the RAP−PDL system, transfection efficiencies of RAP−PLL/DNA complexes were similar to that of ligand-free PDL/DNA complexes (Figure 3). These data (both Figures 3 and 4) indicate that the PDL complex is more stable than the PLL complex in a lysosomal environment as well as in transfection media. Furthermore, the transfection of fluorescence-labeled RAP−PLL/DNA complexes showed that the internalized fluorescence particles, which had a diffused morphology (Figure 4), could be observed in about 30% of the cells. In a study of the endocytic trafficking of RAP/gp330, a member of the LDL receptor gene family, RAP dissociated from the receptor complex in late endosomes and was then rapidly delivered to lysosomes and degraded (*13*). The data from our study show that a portion of the endocytosed RAP−PLL/DNA complexes might remain unstable and be degraded in lysosomal compartments, whereas RAP−PDL is resistant to such degradation and released into the cytoplasm, entering the nucleus. Thus, media instability and lysosomal degradation of PLL and DNA may explain why, as observed in the PLL-based system, inclusion of membrane-active agents such as adenovirus capsid or membrane-active compounds into the gene transfer complexes greatly enhances transfection efficiency (*22, 34, 35*).

DNA encoding the luciferase gene complexed to RAP−PDL conjugate was specifically and efficiently transfected into HepG2 cells bearing LDL receptor and LRP. Gene transfer by this method is ligand dependent and receptor mediated. DNA complexes containing RAP were shown to be effectively internalized into HepG2 cells by ligand−receptor interaction. HepG2 cells, which are abundant in LRP and LDL receptor, were efficiently transfected with the RAP−PDL/DNA complexes in a ligand-dependent manner. Nontargeted complexes that lacked the RAP ligand did not efficiently transfect HepG2 cells. Transfection of a luciferase reporter gene by the RAP−PDL conjugate could be inhibited by addition of an excess of free RAP. Although we did not test competition by the other ligands for the receptors such as Apo E or Apo B, they are likely to compete for the following reason: The transfection efficiency of the conjugates into HepG2 cells was greatly enhanced in the presence of Lovastatin (a cholesterol biosynthesis inhibitor), which results in the overexpression of the LDL receptors in HepG2 cells. The transfection efficiencies of RAP−PDL conjugates in Lovastatin treated cells increased up to 100-fold relative to that in nontreated cells.

In addition to enhancing transfection efficiency, the incorporation of ligands offers the opportunity for specific targeting of gene delivery. Since rapidly dividing cells express the LDL receptor at a high level, RAP is a promising ligand in cancer gene therapy when proliferating cells such as malignant cells are to be targeted. However, specificity of target tissue and/or organ may be difficult to achieve using RAP due to the broad expression of the RAP binding receptor, the LDL receptor gene family, in the human body. This difficulty may be overcome by incorporating a tissue specific enhancer and/or promoter sequence in the expression vector.

In conclusion, we have developed a novel gene delivery system via the RME pathway using RAP conjugated with PDL as a gene delivery vector. Gene delivery using PDL itself or RAP−PLL was not efficient. Our data demonstrate that synthetic RAP−PDL is an effective reagent facilitating formation of DNA-ligand complexes for subsequent receptor-mediated gene transfer. RAP−PDL is thus a promising tool for enabling targeted transfer of genes in vivo.

LITERATURE CITED

(1) Schwartz, A. L. (1995) Receptor cell biology: Receptor-mediated endocytosis. *Pediatr. Res. 38,* 835−843.

(2) Wu, G. Y., and Wu, C. H. (1987) Receptor-mediated in vitro gene transformation by a soluble DNA carrier system. *J. Biol. Chem. 262*, 4429−4432.
(3) Wagner, E., Zenke, M., Cotton, M., Beug, H., and Birnstiel, M. L. (1990) Transferrin-polycation conjugates as carriers for DNA uptake into cells. *Proc. Natl. Acad. Sci. U.S.A. 87*, 3410−3414.
(4) Buschle, M., Cotton, M., Kirlappos, H., Mechtler, K., Schaffner, G., Zauner, W., Birnstiel, M. L., and Wagner, E. (1995) Receptor-mediated gene transfer into human T lymphocytes via binding of DNA/CD3 antibody prticles to the CD3 T cell receptor complex. *Hum. Gene Ther. 6*, 753−761.
(5) Cristiano, R. J., and Curiel, D. T. (1996) Strategies to accomplish gene delivery via the receptor-mediated endocytosis pathway. *Cancer Gene Ther. 3*, 49−57.
(6) Gupta, S., Eastman, J., Silski, C., Ferkol, T., and Davis, P. B. (2001) Single chain Fv: a ligand in receptor-mediated gene delivery. *Gene Ther. 8*, 586−592.
(7) Gliemann, J. (1998) Receptors of the low density lipoprotein (LDL) receptor family in man. Multiple functions of the large family members via interaction with complex ligands. *Biol. Chem. 379*, 951−964.
(8) Hussain, M. M., Strickland, D. K., and Bakillah, A. (1999) The mammalian low-density lipoprotein receptor family. *Annu. Rev. Nutr. 19*, 141−172.
(9) Firestone, R. A. (1994) Low-density lipoprotein as a vehicle for targeting antitumor compounds to cancer cells. *Bioconjugate Chem. 5*, 105−113.
(10) Bu, G. (1998) Receptor-associated protein: a specialized chaperone and antagonist for members of the LDL receptor gene family. *Curr. Opin. Lipidol. 9*, 149−155.
(11) Willnow, T. E. (1998) Receptor-associated protein (RAP): A specialized chaperone for endocytic receptors. *Biol. Chem. 379*, 1025−1031.
(12) Willnow, T. E., and Herz, J. (1994) Genetic deficiency in low density lipoprotein receptor-related protein (LRP) confers cellular resistance to pseudomonas exotoxin A − evidence that LRP is required for uptake and degradation of multiple ligands. *J. Cell Sci. 107*, 719−726.
(13) Czekay, R., Orlando, R. A., Woodward, L., Lundstrom, M., and Farquhar, M. G. (1997) Endocytic trafficking of megalin/RAP complexes: Dissociation of the complexes in late endosomes. *Mol. Biol. Cell 8*, 517−532.
(14) Traber, M. G., and Kayden, H. J. (1984) Inhibition of cholesterol synthesis by mevinolin stimulates low-density lipoprotein receptor activity in human monocyte-derived macrophages. *Atherosclerosis 52*, 1−11.
(15) Qin, W., Infante, J., Wang, S. R., and Infante, R. (1992) Regulation of HMG-CoA reductase, apoprotein-B and LDL receptor gene expression by the hypocholesterolemic drugs simvastatin and ciprofibrate in HepG2, human and rat hepatocytes. *Biochim. Biophys. Acta 1127*, 57−66.
(16) Felgner, P. L., Barenholz, Y., Behr, J. P., Cheng, S. H., Cullis, P., Huang, L., Jessee, J. A., Seymour, L., Szoka, F., Thierry, A. R., Wagner, E., and Wu, G. (1997) Nomenclature for synthetic gene delivery systems (editorial). *Hum. Gene Ther. 8*, 511−512.
(17) Furukawa, T., Ozawa, M., Huang, R. P., and Muramatsu, T. (1990) A heparin binding protein whose expression increase during differentiation of embryonal carcinoma cells to parietal endoderm cells: cDNA cloning and sequence analysis. *J. Biochem. 108*, 297−302.
(18) Hermanson, G. T. (1996) *Bioconjugate Techniques*, pp 64−65, Academic Press, San Diego, CA.
(19) Ziady, A., Ferkol, T., Gerken, T., Dawson, D. V., Perlmutter, D. H., and Davis, P. B. (1998) Ligand substitution of receptor targeted DNA complexes affects gene transfer into hepatoma cells. *Gene Ther. 5*, 1685−1697.
(20) Alberts, A. W., Chen, J., Kuron, G., Hunt, V., Huff, J., Hoffman, C., Rothrock, J., Lopez, M., Joshua, H., Harris, E., Patchett, A., Monaghan, R., Currie, S., Stapley, E., Albers-Schonberg, G., Hensens, O., Hirshfield, J., Hoogsteen, K., Liesch, J., and Springer, J. (1980) Mevinolin: a highly potent competitive inhibitors of hydroxymethylglutaryl-coenzyme A reductase and a cholesterol-lowering agent. *Proc. Natl. Acad. Sci. U.S.A. 77*, 3957−3961.
(21) Schwarzenberger, P., Spence, S. E., Gooya, J. M., Michiel, D., Curiel, D. T., Ruscetti, F. W., and Keller, J. R. (1996) Targeted gene transfer to human hematopoietic progenitor cell lines through the c-kit receptor. *Blood 87*, 472−478.
(22) Chen, J., Gamou, S., Takayanagi, A., and Shimizu, N. (1994) A novel gene delivery system using EGF receptor-mediated endocytosis. *FEBS Lett. 338*, 167−169.
(23) Lee, T. K., Han, J., Fan, S., Liang, Z., Tian, P., Gu, J., and Ng, I. O. (2001) Gene delivery using a receptor-mediated gene transfer system targeted to hepatocellular carcinoma cells. *Int. J. Cancer 93*, 393−400.
(24) Ledley, F. D. (1993) Hepatic Gene therapy: Present and Future. *Hepatology 18*, 1263−1273.
(25) Rudling, M. J., Stahle, L., Peterson, C. O., and Skoog, L. (1986) Content of low-density lipoprotein receptors in breast cancer tissue related to survival of patients. *Br. Med. J. 292*, 580−582.
(26) Niendorf, A., Nagele, H., Gerding, D., Meyer-Pannwitt, U., and Gebhardt, A. (1995) Increased LDL receptor mRNA expression in colon cancer is correlated with a rise in plasma cholesterol levels after curative surgery. *Int. J. Cancer 61*, 461−464.
(27) Juliusson, G., and Vitols, S. (1988) Impaired low-density lipoprotein receptor activity in chronic B-lymphocytic leukemia cells. *Eur. J. Hematol. 40*, 18−24.
(28) Sipehia, R., and Martucci, G. (1995) High-efficiency transformation of human endothelial cells by Apo E-mediated transfection with plasmid DNA. *Biochem. Biophys. Res. Commun. 214*, 206−211.
(29) Kim, J., Maruyama, A., Akaike, T., and Kim, S. W. (1997) In vitro gene expression on smooth muscle cells using a terplex delivery system. *J. Controlled Release 47*, 51−59.
(30) Orlando, R. A., and Farquhar, M. G. (1994) Functional domains of the receptor-associated protein (RAP). *Proc. Natl. Acad. Sci. U.S.A. 91*, 3161−3165.
(31) Rall, S. C., Ye, P., Jr., Bu, G., and Wardell, M. R. (1998) The domain structure of human receptor-associated protein: Protease sensitivity and guanidine HCl denaturation. *J. Biol. Chem. 273*, 24152−24157.
(32) Perales, J. C., Ferkol, T., Molas, M., and Hanson, R. W. (1994) An evaluation of receptor-mediated gene transfer using synthetic DNA-ligand complexes. *Eur. J. Biochem. 226*, 255−266.
(33) Hisayasu, S., Miyauchi, M., Akiyama, K., Gotoh, T., Satoh, S., and Shimada, T. (1999) In vivo targeted gene transfer into liver cells mediated by a novel galactosyl-D-lysine/D-serine copolymer. *Gene Ther. 6*, 689−693.
(34) Gao, L., Wagner, E. O., Cotton, M., Agarwal, S., Harris, C., Romer, M., Miller, L., Hu, P. C., and Curiel, D. (1993) Direct in vivo gene transfer to airway epithelium employing adenovirus-polylysine-DNA complexes. *Hum. Gene Ther. 4*, 17−24.
(35) Plank, C., Oberhauser, B., Mechtler, K., Koch, C., and Wagner, E. (1994) The influence of endosome-disruptive peptides on gene transfer using synthetic virus-like gene transfer systems. *J. Biol. Chem. 17*, 12918−12924.

BC0340262

Immobilization of a Novel Antibacterial Agent on Solid Phase and Subsequent Isolation of EF-Tu

Martin R. Deibel, Jr.,* Alice L. Bodnar, Anthony W. Yem, Cindy L. Wolfe, Charlotte L. Heckaman, Michael J. Bohanon, W. Rodney Mathews, Michael T. Sweeney, Gary E. Zurenko, Keith R. Marotti, Timothy P. Boyle, and Atli Thorarensen*

Pharmacia, Kalamazoo, Michigan 49001-0199. Received April 21, 2003;
Revised Manuscript Received December 11, 2003

Screening of our compound collection identified PNU-92560, a 2-[1,3,4]thiadiazolo[3,2-*a*]pyrimidine-6-carboxamide, as a novel antibacterial agent. Extensive analogue development identified that the 2-position of the thiadiazole could be functionalized with a linker that would allow the compound to be attached to a solid support. The extreme insolubility of the analogues prevented the mechanism of action for these compounds to be determined utilizing traditional methodology. The solid-supported compounds were utilized as affinity columns to identify elongation factor Tu (EF-Tu) as a putative target for this class of compounds. The activity of the compounds in a metabolic labeling experiments and in translation assay supports the identity of the target for these compounds to be EF-Tu.

INTRODUCTION

Bacterial resistance is a significant problem in the treatment of bacterial infections (*1*−*3*). This emerging resistance has fueled a continuous search for new antibiotics, resulting in numerous commercially available products. A key limitation of existing antibiotics is that they constitute a narrow range of structural diversity, and bacterial resistance has been shown in some cases to encompass entire structural classes, thus rendering all agents from that class ineffective. Moreover, the microorganisms have the ability to acquire resistance against new members of an antibiotic class relatively quickly. This ability of the organism to rapidly adapt fuels the search for novel antibiotics.

Recent advances in biology and automation have resulted in an impressive rate of discovery of new bacterial targets (*4*). These approaches may employ both genomics and whole cell-based high throughput screening (*5*). Current efforts at Pharmacia have utilized a combination of genomics for the identification of novel mechanistic targets essential for bacterial survival with whole cell screening of the compounds against the microorganism *Staphylococcus aureus*. Such assays have been used for screening of the Research Compound Collection (RCC). In addition, several mechanistic screens have been performed which identified potential templates for evaluation. We have previously reported our effort in the identification of a novel peptidyl deformylase (PDF) inhibitor as well as the identification of antibacterial potentiators (*6*).

An alternative approach to antibiotic drug discovery is to search for potent antibacterial agents without prior knowledge of their mechanism. This approach is complementary to the mechanism-based approach and has the attractive feature that the identified bacterial agents already have whole-cell activity. Given that the lack of whole-cell activity can be the major hurdle in working with mechanism-based leads, the cellular activity of screening leads can be a key advantage. Historically this approach has been utilized in the search for new antibiotics, and the literature has a plethora of examples where new natural products have been identified due to their antibacterial activity. The identification of vancomycin, its commercialization, and subsequent elucidation of its mechanism of action serves as an illustrative example of the success of this approach (*7*, *8*). The inherent disadvantage of the latter approach is that the mechanism is unknown and the reason for the cellular activity of the compounds may simply be nonspecific toxicity. Therefore it is imperative to couple the chemical optimization of such leads with intensive biological efforts, devoted to the identification of their mechanism of action.

One such method for identifying molecular targets of small molecular agents has been immobilization followed by affinity chromatography. Immobilization has been successfully applied in the past in combination with molecular biology to unravel several fascinating aspects of how small molecules interact with large biomolecules. This strategy was successfully explored by Schreiber for the identification of the FK506 binding protein FKBP12 using an immobilized rapamycin (*9*), as well as by Yem for the identification of the FK506 binding proteins immunophilin hsp56 (FKBP52), and a chicken homologue of the human protein (*10*). Further, this approach was recently applied to a membrane protein target, resulting in the identification of a 36-kDa microfibril-associated glycoprotein protein as the potential target of tranilast (*11*). An important advantage of this affinity method is that the drug concentration can be set at levels significantly above the binding constants for target receptors, particularly if such receptors exist as a family with variable binding constants. A disadvantage of the bound ligand approach relates to the requirement for using cell homogenates, under which increased nonspecific interactions are possible (i.e. higher background noise). Ad-

* Corresponding authors. Chemistry current address: Pfizer Global R&D, Medicinal Chemistry, 700 Chesterfield Parkway West − BB-4G, Chesterfield, MO 63017, Tel.: +1-636-247-3962; e-mail: atli.thorarensen@pfizer.com. Biology current address: Proteos; Southwest Michigan Innovation Center; 4717 Campus Dr., Kalamazoo, MI 49008; e-mail: mrdeibel@proteos.net.

10.1021/bc034060g CCC: $27.50 © 2004 American Chemical Society
Published on Web 02/19/2004

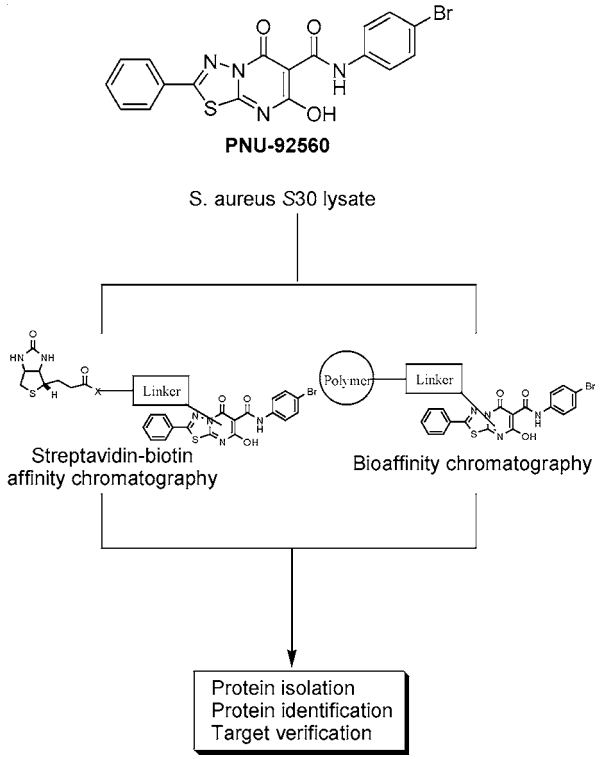


Figure 1. Schematic drawing presenting the parallel approach using soluble (left side) and polymer-supported (right side) affinity reagents envisioned to identify potential targets for the novel pyrimidine carboxamide antibacterial agent PNU-92560.

ditionally, in such an environment, the probability of finding low abundance receptor proteins is diminished. A related affinity approach relies on the use of biotin as part of the linker connected to the pharmacophore. In this technique, streptavidin Sepharose can be utilized to affinity bind to the biotinylated drug and any accompanying biochemical targets. This approach has benefits in that the drug can be delivered to a target bacterial cell, thereby decreasing the chances for nonspecific interactions. A major disadvantage of this approach is that the drug of interest must have good solubility. There are several additional approaches available to elucidate the mechanism of action of compounds, such as photoaffinity labeling. There are drawbacks to each method, such as handling of radiolabeled material, solubility of reagents, etc. (*12*).

We have previously disclosed our initial evaluation of potent enols as antibacterial agents with an unknown mechanism of action (*13*). In this paper we disclose the discovery of a novel pyrimidine carboxamide antibacterial agent with potent broad-spectrum antibacterial activity. In addition, the subsequent immobilization of potent analogues in an attempt to identify the mechanism of action of this promising antibacterial template will be described. Figure 1 highlights our two strategies for identifying the molecular target of PNU-92560, a potent antibacterial agent.

MATERIAL AND METHODS

All reactions were performed under an atmosphere of nitrogen with the exception of the reactions performed in water or otherwise explicitly stated. Brine refers to a saturated solution of sodium chloride. Solvents utilized for reactions or chromatography were HPLC grade and were used as is with the exception of when the following solvents were utilized for reactions: tetrahydrofuran (THF) (distilled Na/benzophenone), toluene (Na), and CH_2Cl_2 (distilled P_2O_5). Reactions were monitored by thin-layer chromatography on Analtech 10 × 20 cm (250 μm) silica gel GF glass plates. Visualization was achieved with ultraviolet light, phosphomolybdic acid, or anisaldehyde solution. Silica gel chromatography was performed on Biotage Flash 15−40 utilizing cartridges with KP-SIL (32−63 μm) silica gel. Melting points were performed in open capillary tubes on a Thomas-Hoover melting point apparatus and are uncorrected. NMR spectra were recorded on Brucker Model AM-300 spectrometer and chemical shifts (δ) are reported in parts per million relative to tetramethylsilane. Spectra were referenced relative to tetramethylsilane as an internal standard or the chemical shift of the appropriate NMR solvent. Other physical data, such as IR, MS, and elemental analysis were performed by the Structural, Analytical and Medicinal Chemistry Unit.

Dimethyl 2-[(4-Bromoanilino)carbonyl]malonate, 1. In a 1 L round-bottom flask were placed THF (500 mL), dimethyl malonate (14.86 mL, 126.3 mmol, 1.00 equiv), and potassium *tert*-butoxide (14.15 g, 126.3 mmol, 1.00 equiv). This was stirred vigorously for 10 min upon which time 4-bromophenyl isocyanate (25.00 g, 126.3 mmol, 1.00 equiv) was added and stirred vigorously for 2 h. The THF was removed in vacuo and diluted with water. Acidification with concentrated HCl caused precipitation of the product, which was collected by filtration, rinsed well with water, and dried on high vacuum to provide 37.13 g (89%) of crude material. Recrystallization from EtOAc/heptane yielded 19.299 g (46%) of **1**. ^{1}H NMR (DMSO-d_6) δ 10.52 (s, 1 H), 7.52 (s, 4 H), 4.79 (s, 1 H), 3.73 (s, 6 H). ^{13}C NMR (DMSO-d_6) δ 165.1, 161.2, 137.6, 131.8, 121.0, 115.6, 59.7, 52.9.

***N*-(4-Bromophenyl)-7-hydroxy-5-oxo-2-sulfanyl-5*H*-[1,3,4]thiadiazolo[3,2-*a*]pyrimidine-6-carboxamide Dimethylamine Salt, 3.** In a 250 mL round-bottom flask were placed 2-amino-5-thio-1,3,4-thiadiazole (2.00 g, 15.04 mmol, 1.00 equiv), diester amide 1 (5.38 g, 15.04 mmol, 1.00 equiv), *o*-xylene (150 mL), and DMF (0.8 mL). The mixture was refluxed for 16 h. After cooling to room temperature, a precipitate formed which was collected by filtration and rinsed with acetone to provide 4.042 g (67%) of the desired product as the dimethylamine salt. The brown product was decolorized to a tan by further rinsing with acetone to finally provide 2.863 g of **3** (48%). Mp 235−237 °C ^{1}H NMR (TFA) δ 7.95 (d, J = 8.7 Hz, 2 H), 7.76 (d, J = 8.7 Hz, 2 H), 3.32 (t, J = 5.7 Hz, 6H). ^{13}C NMR (DMSO-d_6) δ 173.5, 170.2, 168.3, 166.3, 156.4, 136.3, 131.9, 122.6, 116.5, 88.5, 34.4. IR (drift) 3061 (b), 2753, 2499 (w), 2378 (w), 2097 (w), 1675, 1608, 1542 (s), 1507 (s), 1487 (s), 1465, 1429, 1403 (s), cm^{-1} MS (FAB) m/z (rel intensity) 399 (MH^+, 2), 202 (5), 200 (28), 129 (4), 127 (6), 118 (10), 74 (4), 47 (5), 46 (99), 44 (5), 39 (14). HRMS (FAB) calcd for $C_{12}H_7BRN_4O_3S_2$+H_1 398.9221, found 474.9211. HRMS (FAB) calcd for $C_{12}H_7BRN_4O_3S_2$+C_2H_8N 443.9800, found 443.9796.

2-{[4-(Acetylamino)benzyl]sulfanyl}-*N*-(4-bromophenyl)-7-hydroxy-5-oxo-5*H*-[1,3,4]thiadiazolo-[3,2-*a*]-pyrimidine-6-carboxamide, 4a. In a 10 mL two-neck round-bottom flask were placed DMSO (anhyd, 6 mL) and NaH (60% with mineral oil, 0.055 g, 1.38 mmol, 1.10 equiv) and stirred for 10 min. **3** (0.500 g, 1.25 mmol, 1.00 equiv) was then added in one portion and stirred until the solution was clear, about 20 min. 4-Acetamidobenzyl chloride (0.211 g, 1.25 mmol, 1.00 equiv) was then added and stirred for 1 h. The reaction mixture was then diluted with EtOAc and a small amount of acetone/heptane. The resulting precipitate was collected by filtration to provide

the product **4a** as a brown solid (0.442 g, 65%). Mp 204−206 °C. ^{1}H NMR (DMSO-d_6) δ 11.10 (s, 1 H), 7.62 (d, J = 8.9 Hz, 2 H), 7.56 (d, J = 8.5 Hz, 2 H), 7.41 (d, J = 6.0 Hz, 2 H), 7.40 (d, J = 6.0 Hz, 2 H), 4.45 (s, 2 H), 2.03 (s, 3 H). ^{13}C NMR (TFA) δ 176.2, 168.4, 165.0, 164.2, 135.3, 134.0, 133.2, 130.7, 124.8, 124.1, 122.4, 37.5, 21.3. IR (drift) 2350 (w), 1675 (s), 1626, 1602, 1586, 1550 (s), 1532 (s), 1516 (s), 1488, cm^{-1}. MS (FAB) *m*/*z* (rel intensity) 546 (MH$^+$, 25), 570 (57), 568 (59), 397 (48), 148 (99), 106 (59), 69 (71), 67 (50), 57 (60), 55 (73), 43 (48). HRMS (FAB) calcd for $C_{21}H_{16}BrN_5O_4S_2$+Na 567.9725, found 567.9733.

Methyl 4-[({6-[(4-Bromoanilino)carbonyl]-7-hydroxy-5-oxo-5*H*-[1,3,4]thiadiazolo[3,2-*a*]pyrimidin-2-yl}sulfanyl)methyl]benzoate, 4b. In a 10 mL two-neck round-bottom flask were placed DMSO (anhyd, 6 mL) and NaH (60% with mineral oil, 0.055 g, 1.38 mmol, 1.10 equiv) and stirred for 10 min. **3** (0.500 g, 1.25 mmol, 1.00 equiv) was then added in one portion and stirred until the solution was clear, about 20 min. Methyl 4-(bromomethyl)benzoate (0.286 g, 1.25 mmol, 1.00 equiv) was then added and stirred for 1 h. The reaction mixture was then diluted with EtOAc and a small amount of acetone/heptane. The resulting precipitate was collected by filtration to provide 0.381 g (56%) of the product **4b** as a brown solid. Mp > 250 °C. ^{1}H NMR (DMSO-d_6) δ 7.94 (d, J = 8.3 Hz, 2 H), 7.64 (d, J = 8.3 Hz, 2 H), 7.61 (d, J = 8.9 Hz, 2 H), 7.41 (d, J = 8.8 Hz, 2 H), 4.58 (s, 2 H), 3.84 (s, 3 H). ^{13}C NMR (DMSO-d_6) δ 170.7, 166.2, 165.8, 157.1, 141.7, 139.2, 131.2, 129.6, 129.3, 128.8, 121.0, 90.1, 52.1, 35.9. IR (drift) 2350 (w), 1931 (w), 1720, 1676, 1626, 1610, 1551 (s), 1531 (s), 1517 (s), cm^{-1}. MS (FAB) *m*/*z* (rel intensity) 547 (MH$^+$, 41), 593 (69), 591 (67), 569 (37), 549 (41), 547 (41), 342 (41), 149 (35), 72 (73), 39 (43), 23 (99). HRMS (FAB) calcd for $C_{21}H_{15}BrN_4O_5S_2$+Na 568.9566, found 568.9585. Anal. Calcd for $C_{21}H_{15}BrN_4O_5S_2$: C, 46.08; H, 2.76; N, 10.23; Br, 14.60; S, 11.71. Found: C, 45.70; H, 2.77; N, 10.49.

2-{[3-(Acetylamino)propyl]sulfanyl}-*N*-(4-bromophenyl)-7-hydroxy-5-oxo-5*H*-[1,3,4]thiadiazolo[3,2-*a*]pyrimidine-6-carboxamide, 4c. In a 15 mL two-neck round-bottom flask were placed THF (5.5 mL), pyridine (0.5 mL), 3-bromopropylamine hydrobromide (274 mg, 1.25 mmol), and acetic anhydride (0.12 mL, 1.25 mmol, 1.00 equiv) and stirred for 1 h. In a separate 15 mL two-neck round-bottom flask were placed DMSO (6 mL) and NaH (60% with mineral oil, 0.055 g, 1.38 mmol, 1.10 equiv) and stirred for 5 min. **3** was then added in one portion and stirred until the solution cleared to a deep orange. This solution was then transferred by syringe into the first flask and stirred for 3 h. Water was added, and the resulting precipitate was collected by filtration to provide a mixture (0.309 g). Purification by silica gel chromatography provided the desired product **4c** as a brown solid (0.037 g, 6%). Mp 251−254 °C. ^{1}H NMR (DMSO-d_6) δ 7.96 (bs, 1 H), 7.67−7.59 (m, 4 H), 3.3 (m, 2 H), 3.18 (q, J = 6.1 Hz, 2 H), 1.94−1.85 (m, 2 H), 1.83 (s, 3 H).^{13}C NMR (DMSO-d_6) δ 169.2, 156.7, 131.9, 122.7, 89.0, 41.1, 37.0, 30.6, 28.5, 22.5. IR (drift) 2350 (w), 2339 (w), 1667, 1627 (w), 1600, 1568, 1550, 1536, 1531, 1508 (s), 1481 (s), cm^{-1}. MS (FAB) *m*/*z* (rel intensity) 498 (MH$^+$, 88), 502 (12), 501 (24), 500 (99), 499 (47), 498 (88), 497 (26), 327 (27), 100 (79), 57 (14), 30 (12). HRMS (FAB) calcd for $C_{17}H_{16}BrN_5O_4S_2$+H 497.9906, found 497.9918.

3-[({6-[(4-Bromoanilino)carbonyl]-7-hydroxy-5-oxo-5*H*-[1,3,4]thiadiazolo[3,2-*a*]pyrimidin-2-yl}sulfanyl)methyl]benzoic Acid, 4d. 3 (200 mg, 0.449 mmol) and 3-(chloromethyl)benzoic acid (151 mg, 0.890 mmol, 2.0 equiv) were dissolved in DMF (2.5 mL) and stirred at room temperature overnight (or until precipitation). The reaction was then filtered, and the resulting solid was washed with cold DMF followed by cold EtOH to afford 216 mg (90%) of **4d** as a white solid. ^{1}H NMR (300 MHz, DMSO-d_6) δ 11.56 (s, 1 H), 8.12 (s, 1 H), 7.90−7.79 (m, 2 H), 7.66−7.58 (m, 4 H), 7.53−7.48 (m, 1 H), 4.68 (s, 2 H). ^{13}C NMR (75 MHz, DMSO-d_6) δ 171.31, 167.77, 166.86, 165.43, 159.38, 156.71, 136.33, 135.90, 133.72, 131.87, 131.09, 130.01, 128.85, 128.68, 122.80, 116.84, 88.99, 35.97. IR (drift) 2351 (w), 2338 (w), 1921 (w), 1916 (w), 1718, 1685 (s), 1599, 1551 (s), 1532 (s), 1519 (s), 1482 (s), 1418, 1157, 828, 764, cm^{-1}. MS (FAB) *m*/*z* (rel intensity) 533 (MH$^+$, 86), 535 (99), 534 (61), 533 (86), 532 (21), 362 (32), 170 (11), 147 (10), 135 (44), 118 (57), 59 (10). HRMS (FAB) calcd for $C_{20}H_{13}BRN_4O_5S_2$+H 532.9589, found 532.9586. % Water (KF): 0.11. Anal. Calcd for $C_{20}H_{13}BrN_4O_5S_2$: C, 45.04; H, 2.46; N, 10.50; Br, 14.98; S, 12.02. Found: C, 44.54; H, 2.55; N, 10.69.

4-[({6-[(4-Bromoanilino)carbonyl]-7-hydroxy-5-oxo-5*H*-[1,3,4]thiadiazolo[3,2-*a*]pyrimidin-2-yl}sulfanyl)methyl]benzoic Acid, 6. In a 100 mL two-neck round-bottom flask were placed **3** (1.625 g, 3.65 mmol, 1.00 equiv) and DMSO (anh., 36 mL) and stirred until dissolved. NaH (60% with mineral oil, 0.146 g, 3.65 mmol, 1.00 equiv) was added with vigorous bubbling noted. This was stirred until the solution was clear, and then 4-(chloromethyl)benzoic acid (0.624 g, 3.65 mmol, 1.00 equiv) was added and stirred at room temperature for 16 h. The reaction was diluted with EtOAc until no more precipitation was noted (about 1 L) and the solid collected by filtration to provide 0.681 g (35%) of crude material highly complexed to sodium, as evidenced by elemental analysis. The crude material was dissolved in DMSO (10 mL), and 1.0 N HCl/Et$_2$O (3.8 mL, 3 equiv) was added and stirred, capped, for 2 h. A precipitate slowly came of solution. Collection by filtration provided a white solid (0.142 g, 7%) as the pure product **6** as a very hygroscopic material. ^{1}H NMR (DMSO-d_6) δ 11.53 (s, 1 H), 7.90 (d, J = 8.3 Hz, 2 H), 7.65−7.56 (m, 6 H), 4.65 (s, 2 H). MS (FAB) *m*/*z* (rel intensity) 533 (MH$^+$, 21), 1463 (19), 557 (26), 555 (23), 535 (23), 533 (21), 362 (19), 200 (33), 135 (19), 118 (27), 46 (99). HRMS (FAB) calcd for $C_{20}H_{13}BrN_4O_5S_2$+H 532.9589, found 532.9582.

6-Affigel 102 Column. 6 (300 mg, 0.561 mmol) was dissolved in DMSO (67 mL) followed by the addition of NaH (60%, 45 mg, 1.12 mmol, 2.0 equiv). The resulting mixture was stirred at room temperature for 1 h. A volume of 50 mL (packed) of Affigel 102 (Bio-Rad) were washed on a glass filter with water and then with 50% DMSO (v/v). The resin suspension along with the compound in solution were mixed in a 500 mL flask. Since a slight turbidity was noted, an additional 130 mL of DMSO were added to improve solubility. The pH was checked at this time and found to be 8.3. EDAC [1-ethyl-3-(3-dimethylaminopropyl)carbodiimide] was added in small increments, creating some turbidity over time. An additional volume of DMSO was then added (85 mL) resulting in clearance. The suspension of resin and compound/EDAC solution was stirred for 16 h at room temperature. The product (**6**-Affigel 102) was obtained by removal of the noncoupled compound and carbodiimide byproducts by scintered glass filtering. The resin was washed with 250 mL of DMSO, followed by 500 mL of ethanol and 500 mL of water. The resin was collected and mixed with 50% glycerol for storage at −20 °C, or was dried down by Savant vacuum centrifugation and stored as a powder. The yield of immobilized **6** was determined by elemental analysis (bromine content). The final concentration of the compound was 2.6 mM (where

mM is measured as mmoles of compound per liter of resin). Observed elemental bromine analysis wt % Br (**6**-affigel resin) 0.05−0.35; (Affigel control) 0.0

Preparation of *S. aureus* S30 Lysates. The procedure for making *S. aureus* S30 extracts was followed according to Mahmood, R. et al. with some modifications (*14*). Six liters of BHI media were inoculated with 250 mL of a *S. aureus* overnight culture and grown at 37 °C for 4−5 h to an OD600 of 2−4. Cells were washed successively with 500 mL of cold S30−Buffer A (10 mM Tris-acetate, pH 8.0, 14 mM Mg-acetate, 1 mM DTT) containing 1 M KCl and then 250 mL of Buffer A containing 50 mM KCl. Cell pellets (∼50 gm wet weight) were stored at −70 °C. Frozen cell pellets were thawed on ice for 30−60 min. The slurry was resuspended up to a final volume of 99 mL of Buffer B (10 mM Tris-acetate, pH 8.0, 20 mM Mg-acetate, 50 mM KCl, 1 mM DTT). 1.5 mL of 0.8 mg/mL lysostaphin in Buffer B was added to the bottom of three precooled, 35 mL polyallomer SS-34 centrifuge tubes. 33 mL of cell slurry each was transferred to the three tubes containing lysostaphin solution (35 ug/mL final), capped, and gently but extensively mixed by inversion. Incubation was at 37 °C for 45−60 min. The tubes were inverted periodically. After incubation, 150 μL of 0.5 M DTT is added to each tube and mixed gently by inversion. The lysed cells were spun at 4 °C in an SS-34 rotor (16000 rpm; 30000*g*) for 30 min. The supernatant was removed, and the cell pellet was spun under the same conditions. For prolonged storage of the S30 lysate, it is mixed with an equal volume of glycerol and stored at −20 °C.

Bioaffinity Chromatography of S30 Lysates Using Immobilized 6-Affigel. *S. aureus* S30 lysate was diluted 100× with buffer (50 mM Tris HCl, pH 8.0) and mixed with 1 mL of **6**-Affigel 102 matrix that had been equilibrated with buffer. The mixture was incubated for 30−40 min on a mechanical rocker at 8 °C. The resin was then washed with 25 mL of low ionic buffer (50 mM Tris HCl, pH 8.0). This was followed by a high ionic buffer wash (2 M NaCl, 50 mM Tris HCl, pH 8.0) and a deionized water wash. These stringent washing steps were installed to limit nonspecific binding of proteins onto the affinity column. The deionized water wash elutes protein that may be binding to the affinity column or to proteins through hydrophobic interactions alone. This step facilitates the final TFA (trifluoroacetic acid) (1%) elution of the remaining bound protein on the column. This type of elution has been described previously (*10*). To concentrate the eluted protein(s), the elute was freeze-dried on a Speed-vac (Savant) system and was analyzed by SDS polyacrylamide gel electrophoresis (SDS PAGE). Affinity elution or competitive displacement of bound proteins with **6** was impossible due to the insoluble nature of the compound. A freeze-dried sample was also provided for mass spectral analysis (proteomics). The affinity matrix tends to lose its capacity to bind and retain protein after several uses for an unknown reason. This demanded that new column resin had to be used for each experiment. Possible explanations for the loss of function include compound tautomerization, metal binding, or actual chemical changes. To address this issue, a Br analysis was completed on new vs one time used resin. The latter resin had lost the capacity to bind to the protein target(s). The Br analysis showed that the same level of Br was present, indicating that the compound itself was still on the matrix, but somehow changes physically after a single experiment.

SDS Polyacrylamide Gel Electrophoresis (1D). Protein samples were analyzed by 15% polyacrylamide gel electrophoresis. Precision Protein Standard (BioRad) marker proteins were used for size referencing. Samples were treated with sample denaturing buffer (2% SDS, 5% 2-mercaptoethanol) at 100 °C for 2−3 min. For record keeping, each gel was transferred onto a PVDF matrix using a semidry electroblot system (Polyblot) run according to the manufacturer's instructions. Proteins transferred to the blot were visualized by Coomassie Blue R250 staining followed by destaining with 30% ethanol to remove background staining. Storage of the blots was possible after air-drying.

C4 Reverse Phase Chromatography of Proteins Bound to 6-Affigel 102. Eluted protein collected from the immobilized **6**-affinity column (in 0.1% trifluoroacetic acid (TFA)) was injected onto a C4 column (SMART System, Pharmacia). The column was developed with a linear gradient of 0−55% acetonitrile in 1% TFA over 60 min. A large protein peak was detected after the gradient with an 80% acetonitrile/0.1% TFA elution. The peak was collected for tryptic digestion, and the peptide fragments were analysis by mass spectroscopy. The protein was positively identified as elongation factor-Tu (EF-Tu).

Trypsin Digest. HPLC fractions were taken to dryness in a vacuum centrifuge and reconstituted in digestion buffer, 50 mM ammonium bicarbonate pH 8.5. Following the addition of trypsin the solution was incubated overnight at 37° C. Aliquots of the protein digest solution were analyzed by MALDI-Tof and nanoLC/MS/MS as described below.

MALDI-Tof Mass Spectrometry. Matrix-assisted laser desorption ionization time-of-flight (MALDI-Tof) analysis was performed on a Applied Biosystems Voyager STR mass spectrometer operated in the reflector mode with delayed extraction. Typical instrument operating conditions were: total accelerating voltage 20 kV; grid voltage, 73%; guide wire, 0−0.02%; and delay time, 225 ns. An aliquot of the trypsin digest was mixed with MALDI matrix (α-cyano-4-hydrozycinnamic acid), spotted to the MALDI target, and analyzed. Typically 256 laser shots were acquired and averaged for each spectra. The resulting spectra were internally calibrated using the autocatalyzed trypsin peaks at *m/z* 842.51, 1045.56, and 2211.10. A local copy of the database search program MS-Fit (prospector.ucsf.edu) was used to search against the Human Genome Sciences (HGS) database for protein identification.

Liquid Chromatography Tandem Mass Spectrometry (LC-MS/MS). Samples were analyzed by LC-MS/MS on a Finnigan LCQ (San Jose, CA) with a New Objectives PicoView (Cambridge, MA) nanospray adapter and a New Objectives tip coated PicoTip needle (360 mm OD × 20 mm ID × 10 mm tip diameter). LC was performed with a LC Packings Ultimate (San Francisco, CA) pump and a LC Packings Famos autoinjector. The Ultimate was operated at a flow rate of 300 nL/min. A sample volume of 2 to 5 μL was injected and concentrated onto an LC Packings PepMap precolumn (300 mm ID × 5 mm) by flow of 0.1% formic acid at 40 μL/min produced by auxiliary Gilson 305 pump (Gilson Medical Electronics, Middleton, WI). After 3 min of washing, samples were directed to a Fusica II column (75 mm ID × 150 mm) with 5 mm Vydac C18 stationary phase (LC Packings). The mobile phases used to elute the peptides were (A) 0.1% formic acid and (B) 90% acetonitrile, 0.1% formic acid. The peptides were eluted with a gradient of 5−75% B in 10 min. The following are instrumental parameters for the LCQ: heated capillary temperature, 230 °C; needle voltage, 1.60 kV. The LCQ MS spectra were acquired in data dependent mode. The MS/MS spectra

were selected and submitted to a local copy of Sequest (Thermoquest, San Jose, CA) for protein identification using the HGS database.

Metabolic Labeling Experiments. Drugs are tested at a series of 2-fold dilutions surrounding the reported MIC value: 4×, 2×, 1×, 0.5×, 0.25× MIC. In some instances, using the reported MIC value did not yield a profile that exhibited the expected dose−response type of curve, especially in the case of some of the standards. In such cases, the MIC value used was adjusted such that a dose−response type of curve was obtained. Typically, a 10 mM stock solution of drug is made in 100% DMSO, and the appropriate dilution is performed to obtain 200 mL of a 4× stock. Subsequently, 2-fold serial dilutions are made to obtain the other stock solutions. If the 4× MIC stock is greater than 10 mM, then the original stock solution must be adjusted accordingly. An aliquot of 5 mL of the appropriate concentration is added to each well, into a final volume of 150 mL; the 4× stock must take this aliquot size into account to obtain the correct final concentration. A Microsoft Excel file has been designed that performs all the necessary calculations for resuspending and diluting the compound to obtain the correct concentrations. Once all the stock solutions of drug are made, aliquots are transferred into a sterile round-bottom microtiter dish (Falcon 3918). Drug concentrations are run in quadruplicates; thus, a total of 24 wells are needed per macromolecular synthesis assayed. Radiolabeled substrates are ^{14}C-leucine, ^{14}C-uridine, ^{14}C-thymidine (50 mCi/ml, Amersham), and ^{14}C-D-alanine (100 mCi/ml, American Radiolabeled Chemicals) to assay for protein synthesis, RNA synthesis, DNA synthesis, or cell wall synthesis, respectively. ^{14}C-leucine is used neat; the other three substrates are used diluted 1:4. Typically, a repeating pipettor is used for dispensing, so an excess of substrate needs to be made. An aliquot of 5 mL is added to each well containing drug or vehicle. *Staphylococcus aureus* strain 31552 is used (UC9218). For the assay, 2 mL of an overnight culture of sa31552 are added to 18 mL of LB in a 50 mL conical tube and incubated at 37 °C for 45 min, 250 rpm. Using a multichannel pipet, 140 mL of this culture is added to each well previously aliquotted with drug/vehicle and ^{14}C-labeled substrate. A lid is placed on the microtiter plate and it is incubated at 37 °C at 1000 rpm for 1.5 h in an Eppendorf Thermomixer. Near the end of the incubation, a Millipore filterplate, type MAHV, is prepared. Each well receives a 50 mL aliquot of cold 25% TCA. After about 10 min, the TCA is filtered using the manifold apparatus designed for the filterplate. Each well of the filterplate then receives 100 mL of 50% ice cold TCA; the filterplate is kept on ice to keep the TCA cold. After 1.5 h of incubation, 100 mL of the incubation culture are removed from each well using a multichannel pipet and put into the corresponding wells containing 50% TCA. The filterplate is shaken on the Thermomixer for 1 min at 800 rpm and then placed at 0−4 °C for 1 h. After 1 h, the filterplate is placed into the vacuum manifold, and a low vacuum is applied to the unit. The filterplate is washed four times with 245 mL of 10% ice-cold TCA per well each time. The filterplate is then separated from its underdrain backing and blotted onto a paper towel. Finally, the filterplate is suspended in the hood such that airflow underneath the bottom thoroughly dries the filters, about 15−25 min. A Multiscreen Liner (EG&G Wallac) is fitted onto the underside of the filterplate. An aliquot of 25 mL of SuperMix scintillation fluid is added to each well, and a sealing tape is placed over the top of the wells. The filterplate assembly is then placed into a Wallac 1450−106 cassette. The plate is allowed to rest on the bench for at least 1 h before being counted in a Wallac Tri-Lux counter. Sample counts of 5 min per well are performed, and results are normalized against a ^{14}C control. Results are reported in CPM.

Immobilization of 3 onto UltraLink Iodoacetate. Ultralink iodoacetyl (5 mL, Pierce Chemical Co.) was washed with 25 mL of coupling buffer (50 mM Tris HCl, 5 mM EDTA (Na), pH 8.5). The resin was transferred to a flask after the immediate supernatant was removed. Compound **3** (30 mg) dissolved in DMSO was added to the moist resin. An additional amount of DMSO was then added (15 mL). The suspension was stirred slowly at room temperature for 1 h. The solution phase was then removed by gravity filtration. At this stage, the solution did not exhibit a positive reaction with Ellman's reagent, indicating that the reaction was likely quantitative. The resin was washed with 25 mL of DMSO, followed by washing with buffer alone. At this point, 25 mL of buffer containing 5 mg of cysteine was added (pH adjusted) to block remaining active substituents. This suspension was incubated for an additional 30 min at room temperature. After several washing steps, the resin was ready to use. Some of the conjugated resin was dried in vacuo and was submitted for bromine analysis. Observed elemental bromine analysis wt % Br (**3**−Ultralink resin) 0.88−1.07; (Ultralink control) 0.0.

Bioaffinity Chromatography of S30 Lysates Using Immobilized 3-Ultralink. *S. aureus* S30 lysate was diluted 100× with buffer (50 mM Tris HCl, pH 8.0) and mixed with 1 mL of **3** matrix that had been equilibrated with buffer. The mixture was incubated for 30−40 min on a mechanical rocker at 8 °C. The resin was then washed with 25 mL of low ionic buffer (50 mM Tris HCl, pH 8.0). This was followed by a high ionic buffer wash (2 M NaCl, 50 mM Tris HCl, pH 8.0) and a deionized water wash. These stringent washing steps were incorporated to limit nonspecific binding of proteins onto the affinity column. The deionized water wash elutes proteins that may be binding either to the affinity column or to other bound proteins through hydrophobic interactions alone. This step facilitates the final TFA (trifluoroacetic acid) (1%) elution of the remaining bound protein on the column. Alternatively, the bound specific protein was eluted with **3**. To concentrate the eluted protein(s), the elute was freeze-dried on a Speed-vac (Savant) system and was analyzed by SDS polyacrylamide gel electrophoresis (SDS PAGE). A new column resin was used for each experiment.

SDS Polyacrylamide Gel Electrophoresis (1D). Protein samples were analyzed by 15% polyacrylamide gel electrophoresis. Precision Protein Standard (BioRad) marker proteins were used for size referencing. Samples were treated with sample denaturing buffer (2% SDS, 5% 2-mercaptoethanol) at 100 °C for 2−3 min. For record keeping, each gel was transferred onto a PVDF matrix using a semidry electroblot system (Polyblot) run according to the manufacturer's instructions. Proteins transferred to the blot were visualized by Coomassie Blue R250 staining followed by destaining with 30% ethanol to remove background staining. Storage of the blots was possible after air-drying.

Cloning and Expression of *S. aureus* EF-Tu in *E. coli*. Using polymerase chain reaction (PCR), we amplified the region of *S. aureus* EF-Tu beginning with the start codon at nucleotide 51 and ending at 1232 just before the natural stop codon. *S. aureus* genomic DNA (RN4220) was used as a template. BamHI sites were introduced on either end of the EF-Tu in this PCR

reaction using oligonucleotide primers EF-1: 5′-GCG ATC GGA TCC ATG GCA AAA GAA AAA TTC G-3′ and EF-2: 5′-GCG CTC GGA TCC TTT AAT GAT TTC AGT AAT-3′. We chose to ligate the EF-Tu into the *E. coli* expression vector pQE60 which would code for the EF-Tu with a C-terminal hexa-histidine (His6) tag. PQE60 was first linearized with BamHI, dephosphorylated with calf intestinal alkaline phosphatase (CIAP), and gel purified. After digestion of the ends of the EF-Tu PCR product with BamHI and gel purification of the DNA, we ligated it into the BamHI sites of pQE60 using Pharmacia Biotech's T4 DNA ligase Ready-to-go kit. Resulting plasmids were transformed into Promega competent JM109 *E. coli*. Restriction mapping revealed that although we had obtained clones of the EF-Tu insert in pQE60, all were in the reverse orientation. EF-Tu insert purified from one such reverse clone was ligated back into pQE60 and produced clones, which contained the EF-Tu insert in the correct orientation. DNA sequence analysis confirmed that although one nucleotide change was detected, this change did not affect our desired amino acid sequence for the EF-Tu followed by a C-terminal His6 tag.

Purification of His-Tagged Recombinant *S. aureus* EF-Tu Expressed in *E. coli*. Four liters of *E. coli* expressing *S. aureus* EF-Tu were grown in M9 media and harvested after 2 h of ITPG induction. The cell pellet was resuspended in ∼160 mL of 50 mM Tris HCl, pH 8.0 buffer. One milliliter of an inhibitor cocktail (Boehringer Mannheim) was prepared according to the manufacturer's recommendation and added to the cell mixture. This suspension was placed in an ice bath and sonicated at maximum gain (Branson) for 15 s/min over a period of 6 min. The mixture was clarified by centrifugation (SS-34 rotor, Sorvall 205000 rpm for 40 min at 6 °C) and the supernatant collected was mixed with 15 mL of Ni−NTA (Qiagen) affinity matrix that had been pre-equilibrated with Tris buffer as described. The affinity-attached rEF-Tu was competed off from the column with 200 mM imidazole. The protein was further purified and desalted by Superose-12 (Pharmacia) gel filtration column chromatography. The final protein purified was roughly 90% pure and was stored at −20 °C in 50% glycerol after YM-10 ultrafiltration concentration.

In Vitro Susceptibility Test. Minimum inhibitory concentration (MIC) values were determined by standard broth microdilution methods (*15*).

RESULTS

Identification of Lead Structure. Our compound collection was screened for compounds with whole cell antibacterial activity, and the compounds that exhibited good potency were further evaluated. The potency of the compounds in this initial set was confirmed, leading to the identification of a handful of compounds with good potency. Rigorous evaluation of these initial leads based on their chemical tractability resulted in the emergence of PNU-92560, Figure 2. Related compounds have been previously described in the literature as antihelmintic agents (*16*). PNU-92560 had broad-spectrum antibacterial activity against a panel of important pathogenic Gram-positive and Gram-negative bacteria. One of our initial evaluations of this template relied on inspection of its historical activity in our HTS screens. Gratifyingly, while this compound had been screened in a variety of assays, nonspecific broad ranging activity was not noted (*17*). Furthermore, testing of this compound against a range of cell lines indicated that this compound was surprisingly nontoxic. For example, screening against a broad panel of fungi revealed that this compound was inactive with all MIC values >32 μg/mL. Subsequently, when we evaluated the pharmacokinetic properties of PNU-92560, it demonstrated 44% bioavailability, and it appeared to have no adverse effects on the animals. Extensive searches of the literature indicated that pyrimidines having a substructure of PNU-92560 had been reported as inhibitors of tumor growth (*18*). Testing of this compound in a metabolic assay was hampered by its poor solubility, thus providing no useful information regarding potential mechanism of action. While hampered by poor solubility, given the importance of identifying this compound's mechanism of action, we decided to employ an affinity-based technique in an effort to identify its bacterial target.

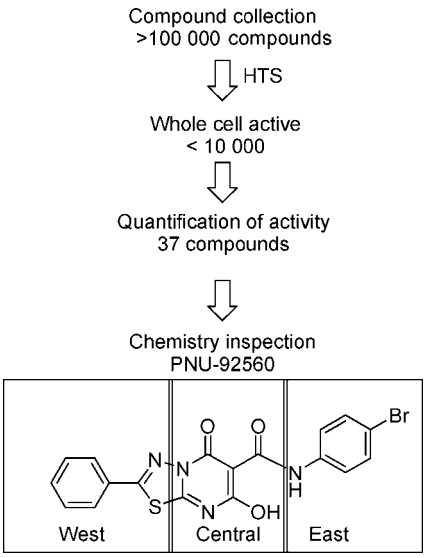
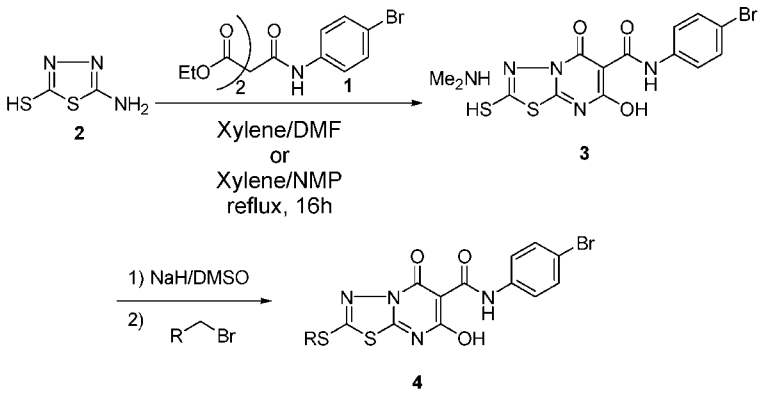
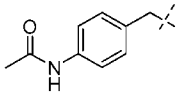
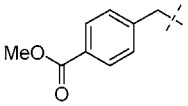
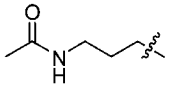
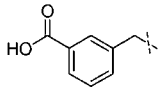


Figure 2. This schematic representation illustrates the stepwise process that resulted in the identification of PNU-92560 as a viable lead for chemistry optimization and detailed biology evaluation. MIC (μg/mL) values for PNU-92560 were *S. aureus* 0.125; *E. faecalis* 0.25; *S. epidermidis* 0.5; *S. pneumoniae* 2; *H. influenzae* 4; *E. coli* >128; *K. pneumoniae* >128; *P aeruginosa* >128.

Identification of Linker Attachment to PNU-92560. To implement our strategy to use bioaffinity isolation of potential targets, there were several chemistry requirements necessary for the approaches described above to be successful. These included (1) identification of an appropriate linker site, (2) identification of a suitable linker, (3) preparation of compounds for immobilization followed by actual immobilization, and (4) the selection of appropriate controls. To address these issues, we sought to identify a fully functionalized molecule with a protected form of the linker that exhibited comparable antibacterial activity to PNU-92560. After the identification of the linker, the compound would be attached to the affinity matrix. An extensive chemistry effort was initiated to evaluate the structure−activity relationships on PNU-92560, and it identified that only the western portion (Figure 2) of the molecules tolerated attachment of linkers (*19*). We therefore turned our attention toward identifying a suitable linker attached to PNU-92560 analogues. These molecules were easily prepared by the condensation of tricarbonyl compound **1** with the appropriate thiadiazole derivative **2** at elevated temperature in DMF or NMP/xylene mixtures. The thiol salt **3** was easily obtained in large quantities and could be easily functionalized with alkyl halides. The initial set of analogues provided some interesting observations,

Table 1. Evaluation of Various Tethers



R	Number	Yield %	MIC (μg/mL)					
			SAUR[a]	EFAE[b]	SEPI[c]	SPNE[d]	HINF[e]	ECOL[f]
Ph	**92560**	-	0.25	1	0.25	0.5	>128	>128
H*NHMe$_2$	**3**	67	>128	>128	>128	128	>128	>128
	**4a**	65	0.5	0.5	0.5	2	ND	>128
	**4b**	56	0.125	0.25	0.25	2	>128	>128
	**4c**	6	8	8	8	16	ND	>128
	**4d**	90	>128	>64	8	8	>128	>128

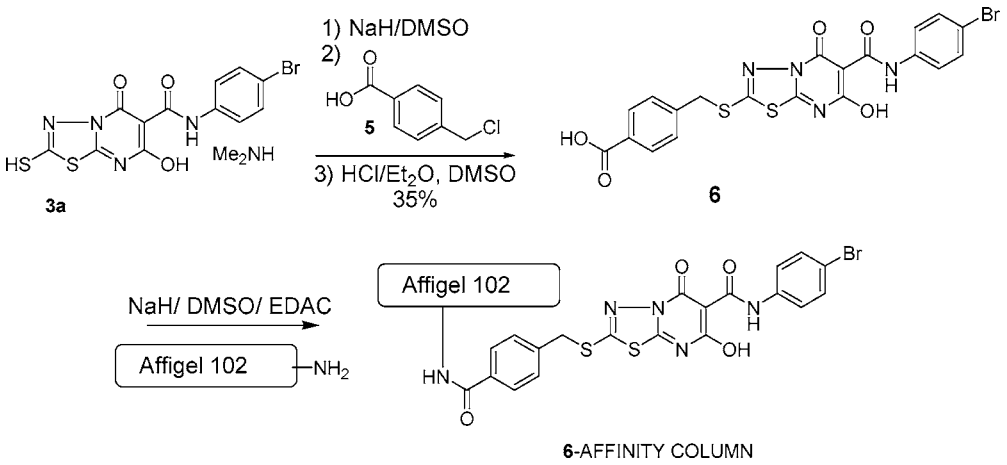
[a] Staphylococcus aureus UC 9218. [b] *Enterococcus faecalis* UC 9217. [c] *Staphylococcus epidermidis* UC 12084. [d] *Streptococcus pneumoniae* UC 9912. [e] *Haemophilus influenzae* UC 30063. [f] *Escherichia coli* UC 6674.

including that *S*-alkyl-substituted analogues were equipotent to the corresponding alkyl-substituted analogues (**4a**/**4b** vs PNU-92560). In addition, alkyl substituent **4c** could replace the aryl ring found in PNU-92560 with some loss of potency. Our attempt to identify a suitable linker as in **4d** with the attaching unit unprotected was unsuccessful since the compound had very poor activity. Gratifyingly, we identified **4a** and **4b** with significant activity containing an embedded linker.

First Generation Affinity Matrix. The advantage of using a soluble affinity matrix is that the conjugate might retain solubility for use on living bacterial cells. In this approach, the biotinylated compound could be delivered to *S. aureus* cells in culture using serum free media, thereby allowing targeting to the intracellular space where contact with a receptor could occur. A biotin analogue was prepared through a multistep synthesis, but immediate concerns related to compound solubility emerged. The compound was only partially soluble in DMSO stock solution, so that when dilutions were made into the cell lysate solution, precipitation occurred readily. Nevertheless, after incubation in S30 lysate solution, the solution was passed over a streptavidin Sepharose column. Unfortunately, no protein signals were detected using this approach.

In an effort to circumvent this solubility problem, attention was turned next to a solid-phase affinity matrix approach. The corresponding fully functionalized compound ready for immobilization was easily prepared on large scale by an S-alkylation. The acid was then coupled to Affi-gel 102 resin. This coupling was found to be difficult to achieve, since only low amounts of the compound actually reacted with the amino group on the resin in the presence of the carbodiimide, EDAC. This difficulty hampered a reproducible coupling onto the resin. After extensive experimentation, it was found that deprotonation of **6** with 2 equiv of NaH in DMSO was optimal to achieve a consistent loading on the column. It is thought that solubility of the compound was enhanced using the latter method, enabling the coupling reaction to occur (Scheme 1). The actual yield of coupling was determined by elemental analysis of the bromine content of the resin. The amount of bromine (i.e., representing **6**) was on average in the millimolar range (mmoles of compound per liter volume of resin) when the NaH method was utilized, but appreciably lower when other coupling methods were employed. The resulting affinity matrix was washed sufficiently with neat DMSO in order to remove noncoupled compound which may resist washes in aqueous solution due to its insolubility.

Scheme 1



Affinity Isolation. The use of the immobilized **6**-Affigel 102 as an affinity matrix was examined under conditions which would clearly represent compound concentrations well above the binding constant for any possible receptor (i.e., 1−5 mM). With this approach, the binding interactions with proteins and nucleic acids in the solution phase would be favored, compared to the extremely low concentrations of biotinylated compound used in experiments described above. *S. aureus* S30 lysates were incubated with the resin as described in Materials and Methods. After a short period of time, the nonbound fraction was collected. The resin was then washed with incubation buffer to remove nonspecifically bound protein, followed by a wash with 2 M NaCl to displace those proteins bound to the resin through weakly ionic interactions. After a water wash step to remove proteins bound through hydrophobic interactions, the protein(s) bound to the column was eluted with trifluoroacetic acid (TFA) and evaporated to dryness. Importantly, in this process the development of binding and washing conditions for specific receptors to immobilized compounds is a time-consuming venture. Careful analysis must follow since nonspecific interactions may occur at higher levels than specific interactions. Generally, our approach was to use a control matrix lacking the coupled compound, but exposed to the same conditions needed to generate the experimental resin. Any proteins found from the latter column are considered to be nonspecific proteins.

In the **6**-Affigel 102 experiment, the protein(s) eluted from the column were next analyzed by 1D electrophoresis (see Figure 3). As shown in Figure 3, a principle band was observed at about 53 kD, along with other minor bands. Of particular interest was the observation that this band was almost completely removed from the starting lysate (as shown in the nonbound fraction). This result provides a point of reference for the analysis using proteomics technology. This latter approach involves separation and identification of proteins selectively retained by the affinity column. The proteins of interest, which may be a subset of the total proteins separated and quantified, are identified by mass spectrometry. For these experiments, the most abundant protein was

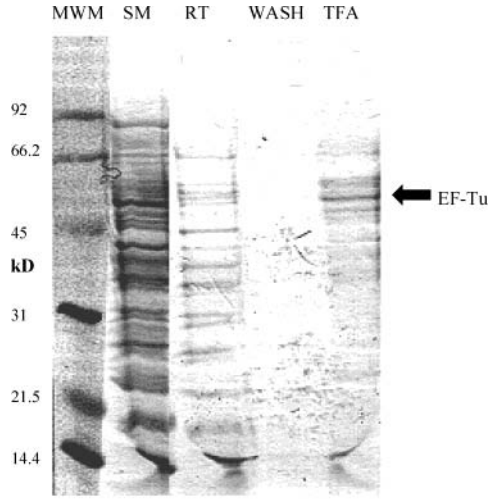


Figure 3. 1D polyacrylamide gel electrophoresis analysis of the eluant from a **6**-Affigel 102 column treated with *S. aureus* S30 lysate. The experimental procedures are described in Materials and Methods. Lanes from left to right are MWM, molecular weight marker proteins (with kD indications on the left *Y*-axis); SM, starting material (S30 lysate) used for the bioaffinity experiment; RT, the pool of material which was not bound to the column; WASH, a series of steps to include both high and low salt; and TFA, the protein eluted by dilute trifluoroacetic acid. The arrow indicates the position of what was determined to be an EF-Tu band.

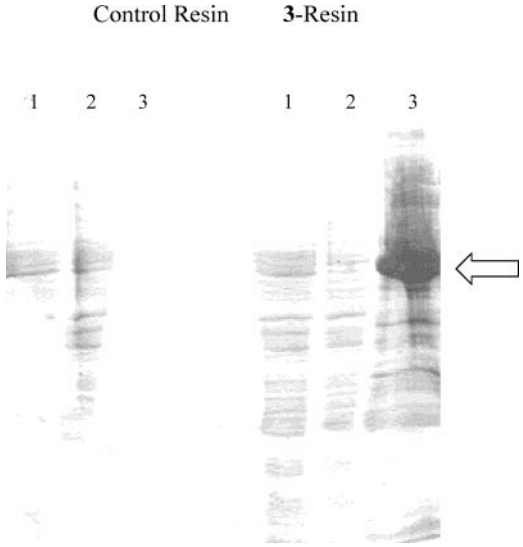


Figure 4. The binding of *S. aureus* S30 lysate protein to a control (no drug)-UltraLink resin column versus a **3**−UltraLink column resin. Lane 1, column starting material (S30 lysate from *S. aureus*); Lane 2, nonbound protein; Lane 3, elution by 5 mM **3** in 50 mM Tris-HCl, pH 8.0. The gel was run with an equal volume of the starting material and run through, and for the eluted fractions, i.e., 5 mM **3** or 0.1% TFA, with an aliquot of sample concentrated by freeze-drying.

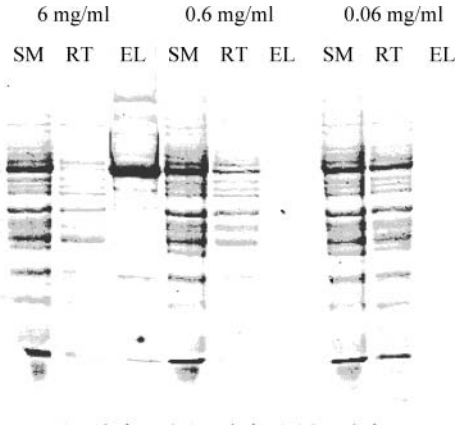


Figure 5. Effect of the concentration of immobilized **3** on binding of protein. Different amounts of **3** were immobilized on UltraLink iodoacetic acid (Pierce) in three concentrations: 6, 0.6, and 0.06 mg/mL. Only at 6 mg/mL or higher was the observed protein interaction displayed. At 0.6 and 0.06 mg/mL drug, no binding was observed.

selected for identification. The proteins retained by the affinity column were eluted by 0.1% TFA and resolved on a C4 reverse phase column. The major peak was digested with trypsin and analyzed by MALDI-Tof mass spectrometry. The experimentally determined masses of the tryptic peptides (referred to as the peptide mass fingerprint of the protein) were used to search the HGS sequence database using the software program MS-fit. The results of the database search resulted in the sequence of EF-Tu being identified as the major component being retained by the column.

Second Generation Affinity Matrix. The Affigel columns employed in the above experiments did not allow a careful control of compound density on the matrixes. We were able to circumvent this problem by preparing an alternative affinity matrix by reacting **3** in a DMSO solution with Ultralink iodoacetyl resin. Using this second generation approach, we were able to control the loading as judged by elemental bromine analysis. This resin appeared to have very similar affinity to EF-Tu as the affigel resin as depicted in Figure 4. The protein targets captured by bioaffinity chromatography were identified using proteomics techniques as described above. To define the nature of the affinity of the proteins to **3**, the effect of variation of compound concentration was examined with **3** immobilized at three different concentrations, all differing by one log. The resulting affinity eluted materials were analyzed by SDS PAGE (Figure 5). Only the highest concentration (roughly 6 mg/mL) was shown to bind protein (i.e., EF-Tu) (Figure 5, top)

Relevance of EF-Tu as a Molecular Target. Using the immobilization method, we have identified EF-Tu as a putative molecular target in *S. aureus* for these compounds. Results from metabolic labeling experiments indicate that **4b** acts via inhibition of bacterial protein synthesis, which is consistent with EF-Tu as the mechanistic target (Figure 6). Metabolic labeling experiments allow for a determination of the effect drugs have on the four major pathways in bacteria: DNA synthesis, RNA synthesis, protein synthesis, and cell wall synthesis. Compounds are analyzed by serial dilutions around the reported MIC value (4×, 2×, 1×, 0.5×, 0.25× MIC). Radiolabeled substrates ^{14}C-leucine, ^{14}C-uridine, ^{14}C-thymidine, and ^{14}C-D-alanine are used to monitor protein synthesis, RNA synthesis, DNA synthesis, or cell wall synthesis, respectively. Control antibiotics do demonstrate a complete inhibition of protein synthesis at 32× the MIC. However, the compounds reported in this study have very limited solubility and actually readily precipitate out in the growth medium so that even though the amount of compound added to the bacterial culture is 32× the MIC, in reality, only a small portion of that is in solution. In these and other experiments in which several PNU-92560 analogues were analyzed, the data clearly support the conclusion that PNU-92560 compounds primarily affect protein synthesis, but not DNA synthesis. We have evaluated a range of these compounds in a transcription/translational assay (*20*). In this assay several of the compounds display significant inhibition (at 100 μM, **3** had inhibition of 72% and **4b** had inhibition of 21%) despite the difficulties encountered due to insolubility of the compounds (*21*, *22*).

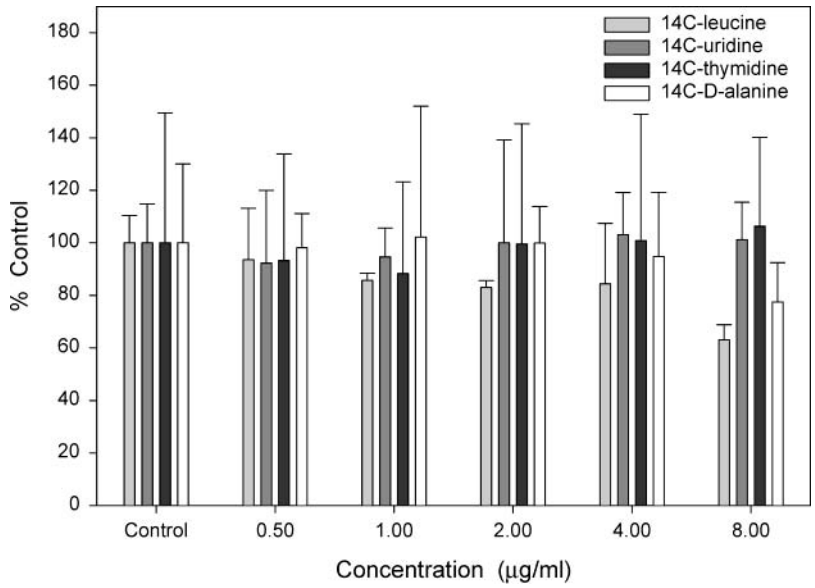


Figure 6. Metabolic labeling experiments of *S. aureus* with **4b**. Results from metabolic labeling experiments indicate that PNU-92560 acts via the inhibition of bacterial protein synthesis, which is consistent with EF-Tu as the mechanistic target. Metabolic labeling experiments allow for a determination of the effect drugs have on the four major pathways in bacteria: DNA synthesis, RNA synthesis, protein synthesis, and cell wall synthesis.

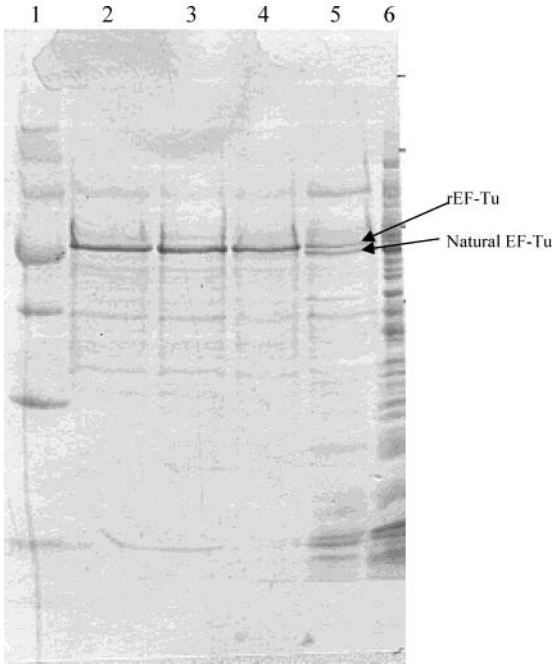


Figure 7. A demonstration that **6**-Affigel 102 binds to native and recombinant EF-Tu. Lane 1: Molecular size markers; Lane 2, rEF-Tu loaded onto a **6**-Affigel 102 column; Lane 3, Flow through containing rEF-Tu, indicating that the binding sites on the column were saturated with rEF-Tu; Lane 4, protein bound to the column (tested as a control); Lane 5, the effect of competition by an S30 lysate, allowing natural EF-Tu to compete with the rEF-Tu from the column; Lane 6 is the S30 lysate.

To validate whether EF-Tu is a target of these compounds, a recombinant form of *S. aureus* EF-Tu was cloned, expressed, and purified in an *E. coli* expression system as described in Materials and Methods. The EF-Tu protein system has been well characterized, particularly in *E. coli* (*23*). The recombinant protein has been crystallized and its structure solved in the presence and absence of several antibiotics (*24*). In our attempts to express the *S. aureus* rEF-Tu in *E. coli*, we were successful in obtaining the purified protein. We examined the interaction of the protein with **3** as shown in Figure 7. The affinity matrix could be shown to bind to the recombinant EF-Tu and also to directly compete with natural EF-Tu from S30 lysates of *S. aureus* (Figure 7, lane 5).

DISCUSSION

In this report, it has been shown that bioaffinity chromatography combined with proteomics can be used to identify an unknown receptor of a compound having a biologically measurable activity. Two important lessons can be learned in this set of experiments: (1) the choice of a compound and how it is covalently attached to a solid support is critical to the success of the project; and (2) the biochemical methods, including the ability to utilize intact living cells versus the necessity of using cellular lysates, can be crucial in the success of identifying a target. For the latter, two biochemical methods are described which have widely different impacts. The first approach involves the use of a ligand attached to the compound, which provides an enhanced method for bioaffinity purification. Most commonly, the ligand used is biotin, since it can be readily removed, along with bound targets, by streptavidin Sepharose. For this method it is possible to use intact living cells to allow the biotinylated compound to internalize and bind to appropriate targets. Unfortunately this approach failed due to the significant insolubility of the compounds in both organic (including DMSO) and aqueous solutions. The second approach involves the use of immobilization of a compound onto a solid support such that concentrations exceeding all binding constants for likely receptors are achieved. Importantly, in most cases, the compound concentration presented on a Sepharose resin far exceeds the possible solution-phase solubility of the compound. This improves the likelihood of a truly insoluble compound of being able to select out protein targets. The negative side of such experiments is the need to use cell extracts or lysates, rather than intact whole cells, and the necessity for the use of detergent-solubilized cell extracts if one expects a membrane protein. Unfortunately, if such action causes the loss of function of a protein target, binding to an immobilized compound may not occur. We have determined that **3** binds to EF-Tu by affinity chromatography. In addition, **3** has been successfully used to displace bound EF-Tu from **3**−UltraLink in an apparently competitive manner. Finally, the interaction of the compounds with EF-Tu was studied using purified recombinant EF-Tu. In this case, the recombinant protein was able to bind to the immobilized compound columns as well as compete for binding effectively with the natural EF-Tu present in the *S. aureus* lysate. It is therefore logical to conclude that the interaction of this class of compounds with EF-Tu does occur, although the precise mechanism governing this interaction is not known at present. The next challenges will be to determine where the drug binds to EF-Tu and a relative binding affinity. Competition with known EF-Tu inhibitors might offer an approach to this problem. Additional experiments are underway to better define the role of EF-Tu as a putative target of this novel class of antibacterials. The plan is to raise resistance mutants to the compounds, map the gene, and sequence the mutant gene to definitively identify the mechanism of action. In addition, we will overexpress the EF-Tu gene to demonstrate that overexpression will result in an increase in the MIC in the presence of our compounds. Nevertheless, results, including those from the metabolic labeling experiments, which show that protein synthesis is inhibited, are consistent with the concept of EF-Tu as the mechanistic target.

CONCLUSION

In this paper we have reported the discovery of a novel antibacterial agent PNU-92560. Subsequently a site on this compound was identified where a linker could be attached for affinity isolation of putative targets. The affinity chromatography identified EF-Tu as the major component obtained from the columns. Additional work such as metabolic labeling, activity in a transcription/translation assay, and affinity for recombinant EF-Tu supports the relevance of this protein as a target for this class of compounds. Additional work will be necessary to unravel the details of the affinity of these compounds for EF-Tu, as well as to discover the binding site on the protein and the general mechanism of inhibition of protein translation afforded by these compounds.

ACKNOWLEDGMENT

We are grateful to Ping Gao for formulation of PNU-92560 and Wei-Zhu Zhong for the pharmacokinetic evaluation of PNU-92560. We acknowledge the people in the Structural, Analytical and Medicinal chemistry unit for their fine analytical services. We are particularly

appreciative for the help of Jack Kreling and Jack DeZwaan for determination of the bromine content of the immobilized compound resins. We also acknowledge the help of Robert Murray who provided us with *S. aureus* S30 lysate, and Jerry Slightom and colleagues for DNA sequence support (recombinant EF-Tu). Finally, we thank Jeffrey A. Pfefferkorn and Dr. Jeffrey for critical reading of this manuscript.

LITERATURE CITED

(1) Cohen, M. L. (1992) Epidemiology of drug resistance: Implication for a post-antimicrobial era. *Science 257*, 1050.

(2) (a) Allen, N. E. (1995) Biochemical mechanism of resistance to noncell wall antibacterial gents. In *Progress in Medicinal Chemistry* (Ellis, G. P., and Luscombe, D. K., Eds.) vol. 32, Chapter 4, pp 157−238, Elsevier Science, New York. (b) Hayes, J. D.; Wolf, C. R. (1990) Molecular mechanism of drug resistance. *Biochem. J. 272*, 281. (c) Spratt, B. G. (1994) Resistance to antibiotics mediated by target alterations. *Science 264*, 388. (d) Nikaido, H (1994) Prevention of drug access to bacterial targets: permeability barriers and active efflux. *Science 264*, 382.

(3) Russell, A. D. (1998) Mechanisms of bacterial resistance to antibiotics and biocides. In *Progress in Medicinal Chemistry (*Ellis, G. P., Luscombe, D. K., and Oxford, A. W., Eds.) vol. 35, Chapter 4, Elsevier Science, New York. (b) Fuchs, T. M. (1998) Molecular mechanism of bacterial pathogenicity. *Naturwissenschaften 85*, 99−108. (c) Cunha, B. A. Antibiotic resistance. (1998) *Drugs Today 34*, 691−698.

(4) Setti, E. L., and Micetich, R. G. New trends in antimicrobial development (1998) *Curr. Med. Chem. 5*, 101−113. (b) Katz, L., Chu, D, T., and Reich, K. **(**1997) Bacterial genomics and the search for novel antibiotics *Annu. Rep. Med. Chem. 32*, 121. (c) Gelbert, L. M., and Gregg, R. E. **(**1997) Will genetics really revolutionize the drug discovery process? *Curr. Opin. Biotechnol. 8*, 669. (d) Andrade, M. A., and Sander, C. (1997) Bioinformatics**:** from genome data to biological knowledge *Curr. Opin. Biotechnol. 8*, 675.

(5) (a) Chopra, I. (1997) Approaches to antibacterial drug discovery *Exp. Opin. Invest. Drugs 6*, 1019−1024. (b) Isaacson, R. E. (1997) Novel targets for antibiotics-an update *Exp. Opin. Invest. Drugs, 6*, 1010−1018.

(6) (a) Thorarensen, A., Deibel, M. R., Rohrer, D. C., Vosters, A. F., Yem, A. W., Marshall, V. D., Lynn, J. C., Bohanon, M. J., Tomich, P. K., Zurenko, G. E., Sweeney, M. T., Jensen, R. M., Nielsen, J. W., Seest, E. P., and Dolak, L. A. (2001) Identification of novel potent hydroxamic acid inhibitors of peptidyl deformylase and the importance of the hydroxamic acid functionality on inhibition *Bioorg. Med. Chem. Lett. 11*, 1355. (b) Thorarensen, A.; Presley-Bodnar A. L., Marotti, K. R., Boyle, T. P., Heckaman, C. L., Bohanon, M. J., Tomich, P. K., Zurenko, G. E., Sweeney, M. T., and Yagi, B. H. (2001) 3-Arylpiperdines as potentiators of existing antibacterial agents. *Bioorg. Med. Chem. Lett. 11*, 1903.

(7) McCormick, M. H., Stark, W. M., Pittenger, G. E., Pittenger, R. C., and McGuire, J. M. (1955−56) Vancomycin, A new antibiotic I. Chemical and biological properties. *Antibiot. Annu.* 606.

(8) Williams, D. H., and Bardslay, B. (1999) The Vancomycin group of antibiotics and the fight against resistant bacteria. *Angew. Chem., Int. Ed. 38*, 1173.

(9) Fretz, H., Albers, M. W., Galat, A., Standeart, R. F., Lane, W. S., Burakoff, S. J., and Schreiber, S. L. (1991) Rapamycin and FK506 binding proteins (immunophilins). *J. Am. Chem. Soc. 113*, 1409.

(10) (a) Yem, A. W., Tomasselli, A. G., Heinrikson, R. L., Zurcher-Neely, H., Ruff, V. A., Johnson, R. A., and Deibel, M. R., Jr. (1992) The "hsp56" component of steroid receptor complexes binds to immobilized FK506 and shows homology to FKBP-12 and FKBP-13. *J. Biol. Chem. 267*, 2868−71. (b) Yem, A. W., Reardon, I. M., Leone, J. W., Heinrikson, R. L., and Deibel, M. R., Jr. (1993) An active FK506-binding domain of 17000 daltons is isolated following limited proteolysis of chicken thymus HSP56. *Biochemistry 32*, 12571−6.

(11) Furuichi, H., Yamashita, K., Okada, M., Toyoshima, T., Hata, Y., Suzuki, S., Itano, T., Shishibori, T., Tokumitsu, H., and Kobayashi, R. (2000) Identification of tranilast-binding protein as 36kDa microfibril-associated glycoprotein by drug affinity chromatography, and its localization in human skin. *Biochem. Biophys. Res. Commun. 270*, 1002.

(12) Fleming, S. A. (1995) Chemical reagents in photoaffinity labeling *Tetrahedron 51*, 12479.

(13) Thorarensen, A., Zurenko, G. E., Sweeney, M. T., Marotti, K. R., and Boyle, T. P. (2001) Enols as potent antibacterial agents *Bioorg. Med. Chem. Lett. 11*, 2931.

(14) Mahmood, R., Compagnone-Post, P., and Khan, S. A. (1991) An in vitro coupled transcription-translation system from *Staphylococcus aureus. Gene 106*, 29.

(15) National Committee for Clinical Laboratory Standards. (1997) *Methods for dilution antimicrobial susceptibility tests for bacteria that grow aerobically* (Approved Standard) 4th ed., NCCLS Document M7-A4, NCCLS, Wayne, PA.

(16) Lee, B. H., Clothier, M. F., Dutton, F. E., Conder, G. A., and Johnson, S. S. (1998) Antihelmintic β-Hydroxyketoamides (BKAS). *Bioorg. Med. Chem. Lett. 8*, 3317.

(17) PNU-92560 had been screened against 93 different targets and only demonstrated initial activity in three of those screens but not of sufficient magnitude to warrant further work.

(18) Brewer, A. D. (1990) Barbituric acid derivatives and their use in treatment of leukemia and tumors. Patent US 4920126; *Chem. Abstr.* **1990**, 565414 and references therein.

(19) The extensive structure activity relationship will be disclosed in due course. Preliminary disclosure: Wakefield, B. D., Bodnar, A. L., Yem, A. W., Deibel, M. R., Zurenko, G. E., Sweeney, M. T., Marotti, K. R., Boyle, T. P., Tomich, P. K., Bohanon, M. J., and Thorarensen, A. (2002) The promising antibacterial lead PNU-92560: Exploration of the exocyclic phenyl region in search of enhanced physical and biological properties. *Abstracts of Papers*, 224th American Chemical Society National Meeting, Boston, MA, Aug 18−22, 2002.

(20) Murray, R. W., Melchior, E. P., Hagadorn, J. C., and Marotti, K. R. (2001) Staphylococcus aureus cell extract transcription-translation assay: firefly luciferase reporter system for evaluating protein translation inhibitors. *Antimicrob. Agents Chemother. 45*, 1900.

(21) (a) Mahmood R., Compagnone-Post P., and Khan, S. A. (1991) An in vitro coupled transcription-translation system from Staphylococcus aureus. *Gene 106*, 29−34. (b) Murray, R. W., Melchior, E. P., Hagadorn, J. C., and Marotti, K. R. (2001) Staphylococcus aureus cell extract transcription-translation assay: firefly luciferase reporter system for evaluating protein translation inhibitors. *Antimicrob. Agents Chemother. 45*, 1900.

(22) Compound **3** is a zwitterionic analogue and zwitterionic nature of the compound is assumed to prevent the compound from penetrating the bacterial cell, resulting in lack of MIC activity. The zwitterionic nature of the compound does not prevent it from inhibiting protein synthesis in a cell free translation assay.

(23) (a) Krab, I. M., and Parmeggiani, A. (1998) EF-Tu, a GTPase odyssey. *Biochim. Biophys. Acta 1443*, 1−22. (b) Hogg, T., Mesters, J. R., and Hilgenfeld, R. (2002) Inhibitory mechanism of antibiotics targeting elongation factor Tu. *Curr. Protein Pept. Sci. 3*, 121−131.

(24) (a) Mui, S., Delaria, K., and Jurnak, F. (1990) Preliminary crystallographic analysis of a complex between tetracycline and the trypsin-modified form of Escherichia coli elongation factor Tu. J. *Mol. Biol. 212*, 445−7. (b) Jurnak, F., Heffron, S. E., Schick, B., and Delaria, K. (1990) 3-Dimensional Models of the GDP and GTP forms of the guanine-nucleotide domain of Escherichia coli elongation factor Tu. *Biochim. Biophys. Acta 1050*, 209−14. (c) Heffron, S. E., and Jurnak, F. (2000) Structure of an EF-Tu complex with a thiazolyl peptide antibiotic determined at 2.35 angstrom resolution: Atomic basis for GE2270A inhibition of EF-Tu. *Biochemistry 39*, 37−45.

BC034060G

Preparation of Bionanoreactor Based on Core−Shell Structured Polyion Complex Micelles Entrapping Trypsin in the Core Cross-Linked with Glutaraldehyde

Montree Jaturanpinyo, Atsushi Harada,† Xiaofei Yuan, and Kazunori Kataoka*

Department of Materials Engineering, Graduate School of Engineering, The University of Tokyo, 7-3-1 Hongo, Bunkyo-ku, Tokyo 113-8656, Japan. Received August 26, 2003; Revised Manuscript Received January 20, 2004

Recently, the polyion complex (PIC) micelle has been suggested as a promising carrier system for peptide and proteins. However, its utilities are limited by its sensitivity to the environment such as dilution and ionic strength of the solution. In this study, to overcome these obstructions, PIC micelles prepared from an anionic block copolymer, poly(ethylene glycol)−poly(α,β-aspartic acid), and a cationic protein, trypsin, were cross-linked with glutaraldehyde through the Schiff base formation. On the basis of a light scattering technique, the results revealed an efficient resistance of the cross-linked PIC micelle to a high salt concentration, which was a key parameter controlling the structure of the PIC micelles. Moreover, the stability of trypsin after cross-linking was remarkably improved. Evidently, as a bionanoreactor and/or bionanoreservoir, the PIC micelles entrapping protein molecules in the cross-linked core reveal an improved stability, allowing their wide application in the fields of biotechnology and pharmaceutical sciences.

INTRODUCTION

Peptides and proteins are now available in sufficient quantities to provide new utilities in the fields of biotechnology and pharmaceutical sciences. However, their use is still limited by their own sensitive characteristics and various environmental factors (*1*−*3*). Recently, a novel bioconjugating system, polyion complex (PIC) micelles, which are formed through the driving force of the electrostatic interaction between a pair of oppositely charged block copolymers, has emerged (*4*−*7*). On the basis of the charged properties of the protein, egg white lysozyme having an isolectric point of 11 was first examined for incorporation into the core of the PIC micelles using an anionic block copolymer, poly(ethylene glycol)−poly(α,β-aspartic acid) block copolymer [PEG-P(Asp)] (*8*, *9*). Not only the achievement of a stable PIC micelle formation was easily obtained but also the apparent enzymatic activity of the lysozyme entrapped in the cores of the PIC micelles was increased (*10*, *11*). Additionally, this system revealed valuable advantages including a narrow size distribution on a mesoscopic scale, total water solubility, and biocompatibility due to the core−shell architecture having a water-insoluble protein−polyelectrolyte complex core completely protected from an undesirable environment by the PEG shell. With such properties, PIC micelles entrapping protein in the core may be one of fulfilling systems for improving the stability and activity of proteins.

As is widely known, the stability and characteristics of micelles, including PIC micelles, are influenced by various factors involving their chemical compositions and their vicinity. In particular, for PIC micelles, the ionic strength of solution is a key parameter for the stability because of the shielding effect of ionic species on the Coulombic interactions. Consequently, the feasibility of controlling the activity and enhancing the stability of proteins through the core−shell structure of PIC micelle seems to be obstructed. To date, some approaches have been reported, which include the stabilization of micelles by cross-linking the shell (*12*−*14*) and the core (*15*, *16*). The structures of the micelles are locked and efficiently prevent any dissociation from the fluctuating environment. Therefore, for application in both biotechnology and pharmaceutical sciences, one solution to overcome this obstruction of salt stability may be to cross-link the core of the PIC micelle.

Glutaraldehyde has been introduced as a powerful fixative reagent for electron microscopy for many decades (*17*). Recently, the interest in glutaraldehyde used as a protein cross-linking reagent has significantly increased, making it often used to immobilize and stabilize proteins for many purposes (*18*, *19*). Because of its fairly small size, glutaraldehyde rapidly penetrates into tissues to thoroughly cross-link proteins. The nature of the cross-linkage is the formation of imines (Schiff base) between the aldehyde groups of glutaraldehyde and the primary amino groups of the protein.

The aim of this study is to introduce a novel approach for maintaining the activity of proteins through the stabilization of the PIC micelle, which is composed of an anionic segment, P(Asp), and trypsin having a pI of 10.5 (*20*), by cross-linking in the core (Figure 1). The stability of cross-linked PIC micelle entrapping protein in the core under high ionic strength is examined by light scattering measurements. Furthermore, the enzymatic activity of trypsin entrapped in the cores after cross-linking is evidenced by using L-lysine *p*-nitroaniline as a substrate. This new prototype might have a practical utility acting as a bionanoreactor and/or bionanoreservoir in the fields of biotechnology and pharmaceutical sciences.

* To whom correspondence should be addressed. Phone: +81-3-5841-7138. Fax: +81-3-5841-7139. E-mail: kataoka@bmw.t.u-tokyo.ac.jp

† Present address: Department of Applied Materials Science, Graduate School of Engineering, Osaka Prefecture University, 1-1 Gakuen-cho, Sakai, Osaka 599-8531, Japan.

10.1021/bc034149m CCC: $27.50 © 2004 American Chemical Society
Published on Web 02/18/2004

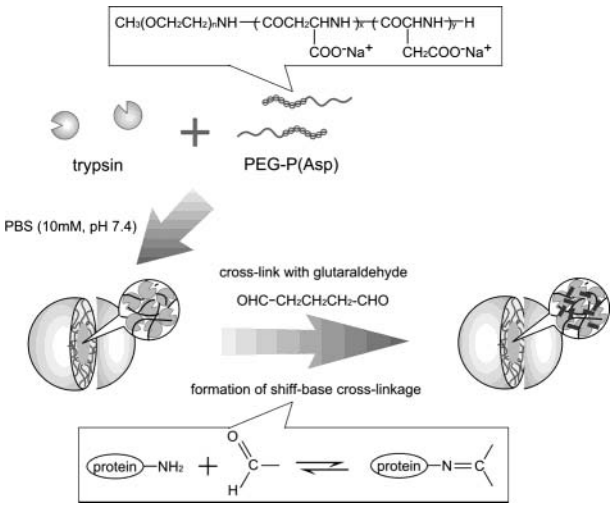


Figure 1. Schematic concept and preparation of PIC micelles entrapping trypsin in the core cross-linked with glutaraldehyde.

EXPERIMENTAL SECTION

Materials. The poly(ethylene glycol)−poly(α,β-aspartic acid) block copolymer [PEG-P(Asp), 12 000 g/mol of PEG M_w, 63 polymerization degree of P(Asp)] was synthesized as already described (*8*). Bovine pancreas trypsin (M_w = 23 800) and L-lysine *p*-nitroaniline were purchased from Sigma (St. Louis, MO) and used without further purification. $Na_2HPO_4 \cdot 12H_2O$, $NaH_2PO_4 \cdot 2H_2O$, and 70% glutaraldehyde were reagent grade and were purchased from Wako Pure Chemical Industries (Osaka, Japan).

Preparation of Polyion Complex Micelles Entrapping Trypsin in the Core. Given amounts of trypsin and PEG-P(Asp) were separately dissolved in phosphate buffer solution (PBS, 10 mM, pH 7.4) at ambient temperature. The solutions were mixed at the optimum mixing ratio of PIC micelle formation from trypsin and PEG-P(Asp), in which the ratio of the number of Asp residues in PEG-P(Asp) to the total number of Lys and Arg residues in trypsin is 0.75. The solution was stored at 4 °C overnight before further use or evaluation.

Preparation of Cross-Linked PIC Micelles Entrapping Trypsin in the Core with Glutaraldehyde. To introduce cross-linking to the core of the PIC micelles, the PIC micelles entrapping trypsin in the core were treated with various amounts of 70% glutaraldehyde solutions, which were calculated on the basis of the glutaraldehyde cross-linking ratios (GR) defined as the total number of aldehyde groups in the glutaraldehyde solution versus the total number of Lys residues in trypsin of 10, 50, 100, 500, and 1000. The cross-linked PIC micelle solutions were then kept at 4 °C for 24 h to ensure the completion of the cross-linking process.

Characterization of PIC Micelles Entrapped Trypsin in the Core. The characteristics of the cross-linked PIC micelles were investigated by light scattering measurements at a wavelength of 488 nm from an Ar ion laser at 25 °C using a DLS-7000 spectrometer (Otsuka Electronics Co., Ltd., Japan).

Synthesis of ω-Acetyl-PEG-P(Asp). Poly(ethylene glycol)−poly(β-benzyl-L-aspartate) block copolymer [PEG−PBLA, 12 000 g/mol of PEG M_w, 60 polymerization degree of PBLA], which is a precursor of PEG-P(Asp) and prepared by the ring-opening polymerization of β-benzyl-L-aspartate *N*-carboxyanhydride initiated from the terminal amino group of α-methoxy-ω-aminopoly(ethylene glycol) (*8*), was dissolved in distilled DMF at 50 mg/mL. To this solution was added 10 equiv of acetic anhydride to the ω-amino group of PEG−PBLA. After the reaction at 40 °C for 2 h under an Ar atmosphere, the polymer was precipitated into a mixture of ethyl acetate and hexane (40/60 v/v). The acetylation of the ω-amino group of PEG−PBLA was confirmed by ^{1}H NMR in DMSO-d_6. The degree of acetylation of the end group of the block copolymer was determined to be 91% from the peak intensity ratio of methyl protons of the acetyl group (CH_3CO-, 1.8 ppm) and ethylene protons of PEG (CH_2CH_2O, 3.7 ppm). The benzyl group of the obtained ω-acetyl-PEG−PBLA was removed in 0.5 N NaOH to obtain ω-acetyl-PEG-P(Asp) [PEG-P(Asp)-$NHCOCH_3$]. No change in the acetylation degree of the end group of ω-acetyl-PEG-P(Asp) as well as the polymerization degree of the P(Asp) segment through the deprotection procedure was confirmed by ^{1}H NMR measurement in D_2O.

Transmittance Measurement. The time course of transmittance at 800 nm for the cross-linked PIC micelles at GR100 after the addition of NaCl solutions at various concentrations were monitored using a V550 spectrophotometer (Jasco, Japan) at 25 °C.

Enzymatic Activity. The cross-linked PIC micelles prepared at GR 100 were dialyzed against PBS in order to remove excess glutaraldehyde. Complete removal of the excess glutaraldehyde was confirmed using 3-methyl-2-benzothazolinone hydrazone (*21*). The enzymatic activity of trypsin was evaluated using L-lysine *p*-nitroaniline as the substrate (*22*). The reaction rate was determined by monitoring the change in absorbance at 410 nm; at this wavelength, the extinction coefficient of *p*-nitroaniline is 8800 cm^{-1} M^{-1}.

RESULTS AND DISCUSSION

Cross-Linked PIC Micelles Entrapping Trypsin in the Core with Glutaraldehyde. In 10 mM PBS (pH 7.4), trypsin and PEG-P(Asp) spontaneously associated to form PIC micelles through the driving force of electrostatic interaction. On the basis of a DLS measurement, the PIC micelles incubated at 25 °C for 30 min had an average diameter of ca. 70 nm and a polydispersity index of less than 0.1, suggesting that there was a well-defined structure and no secondary aggregation. The obtained PIC micelles had a trypsin/P(Asp) complex core surrounded by a PEG shell layer. However, this system was quite unstable even in the medium with low ionic strength such as 10 mM PBS.

As seen in Figure 2, the relative light intensity as well as cumulant diameter of the un-cross-linked PIC micelles in 10 mM PBS (closed circle) rapidly decreased as a function of time. The complete dissociation was observed after incubating the sample at 25 °C for 2.5 h. As is widely known, trypsin is a proteolytic enzyme, which cleaves a peptide bond next to the basic amino acids, Lys and Arg, in the peptide chain. Thus, it also digests itself, which is called self-digestion or autolysis. Time-dependent decrease in the stability of the un-cross-linked PIC micelles is most likely to be correlated with this autolysis of trypsin. Indeed, there was no change in the relative scattering intensity of un-cross-linked micelles with time in the presence of 8.0 M urea (closed square in Figure 2a), a condition that enzymatic activity of trypsin is completely inhibited (*23*). Note that the enzymatic activity of trypsin, examined by using L-lysine *p*-nitroaniline as a model substrate, suggests that the rate of autolysis is even accelerated in the micelle system compared with free trypsin, which might be due to the condensation of trypsin molecules in the core, and eventually, this accelerated autolysis results in an abrupt disintegration of the un-cross-linked PIC micelles.

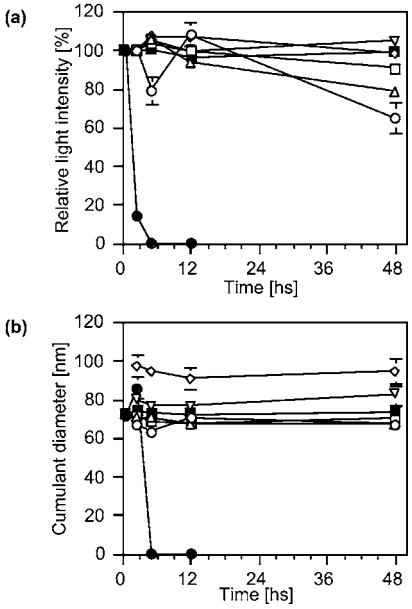


Figure 2. Time-dependent change in relative light scattering intensities (a) and cumulant diameters (b) of PIC micelles entrapping trypsin in the core cross-linked with glutaraldehyde at various ratios (GR = 0 (●), 10 (○), 50 (△), 100 (□), 500 (▽), and 1000 (◇) in the absence of urea and GR = 0 (■) in the presence of 8.0M urea) measured by SLS and DLS at a detection angle of 90° and temperature of 25 °C. The plots are presented as the average of three experiments ± SEM. Error bars for some data points were smaller than the size of symbols and are not visible in the figures.

Cross-linked cores entrapping trypsin are simply established by just adding glutaraldehyde to the previously prepared PIC micelle solution. The cross-linking reaction was carried out at 4 °C in order to suppress the autolysis of trypsin. After treatment with glutaraldehyde, no precipitation was observed in the micelle solution at all the glutaraldehyde ratios, compared with free trypsin, which gradually aggregated and thus precipitated from the entire solution. This result indicates that the core of the PIC micelle serves as a nanoscopic domain for the cross-linking reaction. Note the high reproducibility of the cross-linked PIC micelle preparation from the error bar being very small for all the plots. Furthermore, the cross-linked proteins are completely protected from aggregation by the steric stabilization effect of the PEG shell layer. DLS measurements reveal no difference in the initial cumulant diameter ($t = 0$) between the cross-linked micelles and un-cross-linked PIC micelles (Figure 2b). Consequently, the cross-linking process has no significant influence on the structure of the micelles. In addition, the unimodality of the representative histogram of the PIC micelles cross-linked with glutaraldehyde at GR 100 as shown in Figure 3 and the polydispersity index, less than 0.1, confirm that there is no aggregation and alteration of the structure of the micelles by the cross-link reaction. The slight changes in the diameters of cross-linked PIC micelles at GR 500 and 1000 might be explained by the influence of excess glutaraldehyde on the viscosity of the solvent involving the Stokes−Einstein equation used to calculate the hydrodynamic diameter in the DLS measurements. Furthermore, the association number of trypsin and PEG-P(Asp) was calculated from the micellar mass prepared at GR = 0 and 100, which was determined by Debye plots of SLS. The micellar mass of GR = 0, i.e., un-cross-linked micelle, was determined to be 2 100 000, and the association numbers of trypsin and PEG-P(Asp) were then calculated

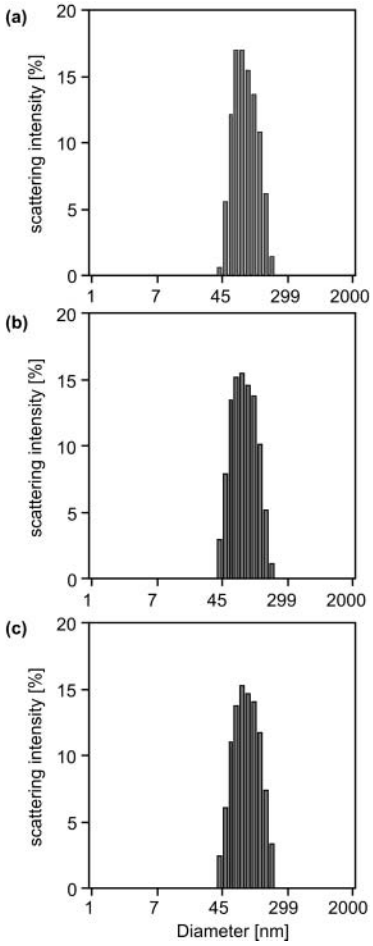


Figure 3. Size distributions of PIC micelles entrapping trypsin in the core without cross-linking (a), PIC micelles entrapping trypsin in the core cross-linked with glutaraldehyde at GR 100 before adding NaCl (b), and that after adding NaCl (0.15M) (c) determined by DLS (histogram method) at a detection angle of 90° and temperature of 25 °C.

to be 77 and 15. The cross-linked micelle at GR = 100 had similar micellar mass (2 300 000) compared with un-cross-linked micelle. The association numbers of trypsin and PEG-P(Asp) were calculated by disregarding the amount of glutaraldehyde and were found to be 84 and 16, respectively. The small difference in the micellar mass as well as the association number between un-cross-linked and cross-linked micelles indicates that the cross-linking could be constructed with the core−shell structure maintained.

The time-dependent relative light intensities and diameters of the cross-linked PIC micelles at varying GRs in Figure 2 obviously indicate that the cross-linked PIC micelles are much more stable than the un-cross-linked PIC micelles. This might be due to the immobilization of the entrapped trypsin by cross-linkages, thus retarding the autolysis through the interaction of trypsin molecules in the core. At GRs 10 and 50, the relative light scattering intensities of the cross-linked micelles are slightly decreased with time despite no change in their diameters. This suggests that even for the condition with a relatively low GR the micelle structure can be maintained by fixation of the cross-linked core although the un-cross-linked fraction of the trypsins may be partially self-digested.

Stability of Cross-Linked PIC Micelles against NaCl. Basically, the electrostatic interaction in the core of the PIC micelle is shielded by increasing the NaCl

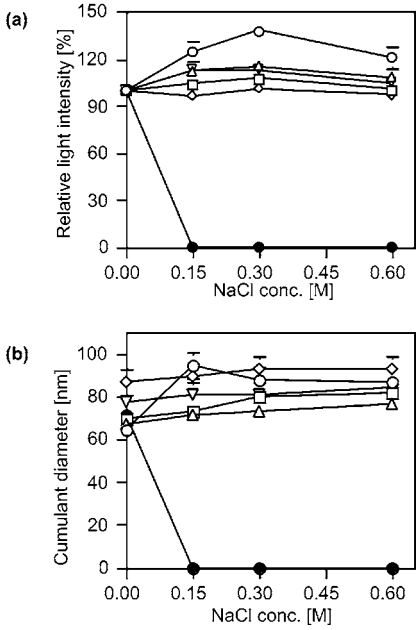


Figure 4. Changes in relative light scattering intensities (a) and cumulant diameters (b) with NaCl concentrations of PIC micelles entrapping trypsin in the core cross-linked with glutaraldehyde at various ratios (GR = 0 (●), 10 (○), 50 (△), 100 (□), 500 (▽), 1000 (◇)) obtained from SLS and DLS at a detection angle of 90° and temperature of 25 °C. The plots are presented as the average of three experiments ± SEM. Error bars for some data points were smaller than the size of symbols and are not visible in the figures.

concentration, thus leading to dissociation. Preliminary results of the cross-linked PIC micelles at GR 0.00−4.00 demonstrated that they were unable to resist NaCl concentrations greater than the physiological conditions (0.15 M). From GR 0.00 to 1.00, the PIC micelles rapidly dissociated, whereas at GR 2.00 and 4.00, they gradually precipitated from the solution. The precipitation may be caused by an incomplete cross-linking between trypsin and the primary amino group of the ω-end group of PEG-P(Asp), resulting in the secondary aggregation of the cross-linked trypsin molecules after the PEG-P(Asp) chains are removed from the core−shell structure by an increased shielding effect. The effect of the end group of the block copolymer on the stabilization of the micelle structure will be discussed later.

Figure 4 illustrates the relative light scattering intensities and cumulant diameters of the cross-linked PIC micelles against NaCl at various concentrations. Obviously, the cross-linked PIC micelles at all GRs greater than 10 have an improved stability against a high salt concentration despite the observation that the diameters of the cross-linked PIC micelles tend to increase at all GRs, especially at GR 10 ($p < 0.05$ for 0−0.15 M NaCl; $p < 0.05$ for 0−0.30 M NaCl; $p < 0.05$ for 0−0.60 M NaCl), as a result of shielding of the electrostatic interaction in the core. Additionally, the representative histogram in Figure 3c at GR 100 after increasing the NaCl concentration to 0.15 M is still unimodal, confirming the high resistance of the cross-linked PIC micelle structure to the change in the ionic strength of the solution.

One aspect that should be mentioned here is that the structure of the micelle can still exist in a medium with an appreciably high ionic strength without any electrostatic interaction between PEG-P(Asp) and trypsin. It might be explained by two possibilities that include the physical entrapment of polymer chains being entangled in the cross-linked cores and the formation of a cross-

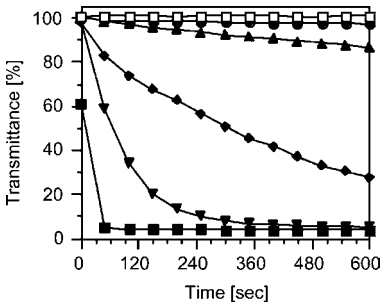


Figure 5. Time course of change in transmittance for GR100-NH2 at 0.1 M NaCl (□) and GR100-NHCOCH3 at various NaCl concentrations (0.01 M (●), 0.02 M (▲), 0.03 M (◆), 0.04 M (▼), 0.1 M (■)): trypsin concentration = 3.2 mg/mL, ratio of glutaraldehyde GR = 100, monitor weavelength = 800 nm, temperature = 25 °C.

linkage between the primary amino groups at the ω-end of the P(Asp) segments and aldehyde groups in glutaraldehyde. To evaluate the importance of the cross-linking between trypsin and PEG-P(Asp), another type of trypsin-entrapped PIC micelle at GR 100 (GR100-$NHCOCH_3$) was prepared using the PEG-P(Asp)-$NHCOCH_3$. The change in the transmittance after NaCl addition was monitored to compare the stabilities of these two kinds of PIC micelles against the change in ionic strength in the solutions, and the obtained result is shown in Figure 5. With an increase in the NaCl concentration, the transmittance of the GR100-$NHCOCH_3$ micelles immediately decreased because of the precipitation of the solutes, especially at NaCl concentrations over 0.04 M. It might be reasonably considered that the precipitates were mainly composed of the secondary aggregation of the cross-linked trypsins after partial or entire PEG-P(Asp)-$NHCOCH_3$ chains are removed from the core−shell structure by the shielding effect of NaCl. The transmittance of the GR100-NH_2 micelle at 0.1 M NaCl showed no change in the monitored time period as shown in Figure 5, and the GR100-NH_2 micelles also showed no change in relative scattering intensity and cumulant diameter even at 0.6 M NaCl as shown in Figure 4. Such a difference in the stability against the change in ionic strength between the GR100-$NHCOCH_3$ and GR100-NH_2 micelles was induced by the presence of the end reactive group, the primary amino group, in the block copolymer. Consequently, it was concluded that the cross-linkages of not only protein−protein but also protein−polymer were required for the preparation of stable cross-linked micelles.

Enzymatic Activity of Cross-Linked Trypsin Entrapped in the Core of PIC Micelles. The enzymatic activity of trypsin entrapped in the core of the PIC micelles was examined using L-lysine *p*-nitroaniline. It was selected as a substrate because of the low molecular weight, which was small enough to penetrate into the core to react with the entrapped trypsin. Before measurement of the enzymatic activity of the cross-linked trypsin, the sample was dialyzed against PBS in order to remove excess glutaraldehyde, which interferes with enzymatic reaction by a possible reactivity toward the primary amino group of the substrate.

In Figure 6, free trypsin and un-cross-linked trypsin entrapped in the PIC micelle dramatically lose their activities within a week by self-digestion. In contrast, after 1 week, the cross-linked trypsin entrapped in the core of the PIC micelles (GR = 100) significantly reveals a remaining catalysis rate of 4.76×10^{-7} M/s, which is approximately twice as great as that of the freshly prepared free trypsin. Worth noticing is that the activity

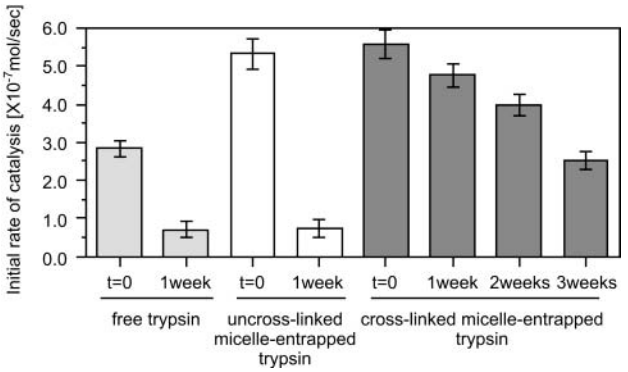


Figure 6. Catalytic activity of free trypsin and trypsin entrapped in un-cross-linked and cross-linked PIC micelles incubated at 25 °C for 1−3 weeks compared to that of freshly prepared free trypsin. The data are presented as the average of three experiments ± SEM.

of the entrapped trypsin cross-linked by glutaraldehyde still remained at the same level as the freshly prepared free trypsin even after 3 weeks, although it slowly decreased. The change in the apparent enzymatic activity of trypsin entrapped in cross-linked PIC micelles was explained by the substrate condensation, and the details of this effect will be reported elsewhere (*24*). These results clearly indicate that the stability of trypsin was improved in a controllable manner by its entrapment in the cross-linked core of the PIC micelles.

CONCLUSION

The stability of the PIC micelles entrapping proteins in the core was significantly improved by introducing cross-linking in the core with glutaraldehyde through a Schiff base formation of the protein−protein and protein−block copolymer. Not only stable cross-linked PIC micelles were obtained with a well-defined structure and narrowly distributed size on a mesoscopic scale but also trypsin entrapped in the cores still retained appreciable activity for small substrate molecules and was much more stable than the native one. These results provide a novel concept in the design of a bionanoreactor and/or bionanoreservoir potentially useful as protein delivery systems, including enzyme prodrug therapy, and as bioengineered production systems.

ACKNOWLEDGMENT

This study was supported by the Industrial Technology Research Grant Program from New Energy and Industrial Technology Development Organization (NEDO) of Japan. M.J. is thankful for the fellowship from the Ministry of Education, Culture, Sports, Science and Technology (MEXT), Japan.

LITERATURE CITED

(1) Humphrey, M. J., and Ringrose, P. S. (1986) Peptides and related drugs—A review of their absorption, metabolism, and excretion. *Drug Metab. Rev. 17*, 283−310.

(2) Lee, V. H. L., and Yamamoto, A. (1990) Penetration and enzymatic barriers to peptide and protein absorption. *Adv. Drug Delivery Rev. 4*, 171−207.

(3) Cholewinski, M., Luckel, B., and Horn, H. (1996) Degradation pathways, analytical characterization and formulation strategies of a peptide and a protein. Calcitonin and human growth hormone in comparison. *Pharm. Acta Helv. 71*, 405−419.

(4) Harada, A., and Kataoka, K. (1995) Formation of polyion complex micelles in an aqueous milieu from a pair of oppositely-charged block copolymers with poly(ethylene glycol) segments. *Macromolecules 28*, 5294−5299.

(5) Harada, A., and Kataoka, K. (1999) Chain length recognition: Core−shell supramolecular assembly from oppositely charged block copolymers. *Science 283*, 65−67.

(6) Kabanov, A. V., Vinogradov, S. V., Suzdaltseva, Y. G., and Alakhov, V. Y. (1995) Water-soluble block polycations as carriers for oligonucleotide delivery. *Bioconjugate Chem. 6*, 639−643.

(7) Kabanov, A. V., Bronich, T. K., Kabanov, V. A., Yu, K., and Eisenberg, A. (1996) Soluble stoichiometric complexes from poly(*N*-ethyl-4-vinylpyridinium) cations and poly(ethylene oxide)-block-polymethacrylate anions. *Macromolecules 29*, 6797−6802.

(8) Harada, A., and Kataoka, K. (1998) Novel polyion complex micelles entrapping enzyme molecules in the core: Preparation of narrowly-distributed micelles from lysozyme and poly(ethylene glycol)−poly(aspartic acid) block copolymer in aqueous medium. *Macromolecules 31*, 288−294.

(9) Harada, A., and Kataoka, K. (1999) Novel polyion complex micelles entrapping enzyme molecules in the core. 2. Characterization of the micelles prepared at nonstoichiometric mixing ratios. *Langmuir 15*, 4208−4212.

(10) Harada, A., and Kataoka, K. (1999) On−off control of enzymatic activity synchronizing with reversible formation of supramolecular assembly from enzyme and charged block copolymers. *J. Am. Chem. Soc. 121*, 9241−9242.

(11) Harada, A., and Kataoka, K. (2001) Pronounced activity of enzymes through the incorporation into the core of polyion complex micelles made from charged block copolymers. *J. Controlled Release 72*, 85−91.

(12) Butun, V., Billingham, N. C., and Armes, S. P. (1998) Synthesis of shell cross-linked micelles with tunable hydrophilic/hydrophobic cores. *J. Am. Chem. Soc. 120*, 12135−12136.

(13) Stewart, S., and Liu, G. J. (1999) Hollow nanospheres from polyisoprene-block-poly(2-cinnamoylethyl methacrylate)-block-poly(*tert*-butyl acrylate). *Chem. Mater. 11*, 1048−1054.

(14) Thurmond, K. B., II, Kowalewski, T., and Wooley, K. L. (1996) Water-soluble knedel-like structures: The preparation of shell-cross-linked small particles. *J. Am. Chem. Soc. 118*, 7239−7240.

(15) Guo, A., Liu, G., and Tao, J. (1996) Star polymers and nanospheres from cross-linkable diblock copolymers. *Macromolecules 29*, 2487−2493.

(16) Kakizawa, Y., Harada, A., and Kataoka, K. (1999) Environment-sensitive stabilization of core−shell structured polyion complex micelle by reversible cross-linking of the core through disulfide bond. *J. Am. Chem. Soc. 121*, 11247−11248.

(17) Sabatini, D. D., Bensch, K., and Barrnett, R. J. (1963) Cytochemistry and electron microscopy. The preservation of cellular ultra-structure and enzymatic activity by aldehyde fixation. *J. Cell Biol. 17*, 19−58.

(18) Marquie, C. (2001) Chemical reactions in cottonseed protein cross-linking by formaldehyde, glutaraldehyde, and glyoxal for the formation of protein films with enhanced mechanical properties. *J. Agric. Food Chem. 49*, 4676−4681.

(19) Gerrard, J. A., Brown, P. K., and Fayle, S. E. (2002) Maillard crosslinking of food proteins I: The reaction of glutaraldehyde, formaldehyde and glyceraldehydes with ribonuclease. *Food Chem. 79*, 343−349.

(20) Buck, F., Vithayathil, A., Bier, M., and Nord, F. (1962) On the mechanism of enzyme action. LXXIII. Studies on trypsin from beef, sheep and pig pancreas. *Arch. Biochem. Biophys. 97*, 417−424.

(21) Sawicki, E., Hauser, T. R., Stanley, T. W., and Elbert, W. (1961) 3-Methyl-2-benzothiazolinone hydrazone test. Sensitive new methods for the detection, rapid estimation, and determination of aliphatic aldehydes. *Anal. Chem. 33*, 93−96.

(22) Erlanger, B. F., Kokowsky, N., and Cohen, W. (1961) The preparation and properties of two new chromogenic substrates of trypsin. *Arch. Biochem. Biophysics 96*, 271−278.

(23) Viswanatha, T., and Liener, I. E. (1955) The inhibition of trypsin III. Influence of urea. *J. Biol. Chem. 215*, 777−785.

(24) Harada, A., Kawamura, A., Kono, K., Takagishi, T., and Kataoka, K. Manuscript in preparation.

BC034149M

Synthesis of Novel, Multivalent Glycodendrimers as Ligands for HIV-1 gp120

Richard D. Kensinger,[†] Brian C. Yowler,[†] Alan J. Benesi,[‡] and Cara-Lynne Schengrund*[,†]

Department of Chemistry, The Pennsylvania State University, 152 Davey Laboratory, University Park, Pennsylvania 16802, and Department of Biochemistry and Molecular Biology H171, The Pennsylvania State University College of Medicine, 500 University Drive, Hershey, Pennsylvania 17033. Received September 3, 2003; Revised Manuscript Received December 18, 2003

Multivalent neoglycoconjugates are valuable tools for studying carbohydrate−protein interactions. To study the interaction of HIV-1 gp120 with its reported alternate glycolipid receptors, galactosyl ceramide (GalCer) and sulfatide, galactose- and sulfated galactose-derivatized dendrimers were synthesized, analyzed as ligands for rgp120 by surface plasmon resonance, and tested for their ability to inhibit HIV-1 infection of CXCR4- and CCR5-expressing indicator cells. Four different series of glycodendrimers were made by amine coupling spacer-arm derivatized galactose residues, either sulfated or nonsulfated, to poly(propylenimine) dendrimers, generations 1−5. One series of glycodendrimers was prepared from the ceramide saccharide derivative of purified natural GalCer, and another was from chemically synthesized 3-(*β*-D-galactopyranosylthio)propionic acid. Synthesis of 3-sulfogalactopyranosyl-derivatized dendrimers was accomplished using the novel compound, 3-(*β*-D-3-sulfogalactopyranosylthio)propionic acid. The fourth series was made by random sulfation of the 3-(*β*-D-galactopyranosylthio)propionic acid functionalized dendrimers. Structures of the carbohydrate moieties were confirmed by NMR, and the average molecular weights and polydispersities of the different glycodendrimers were determined using MALDI-TOF MS. Surface plasmon resonance studies found that rgp120 IIIB bound to the derivatized dendrimers tested with nanomolar affinity, and to dextran sulfate with picomolar affinity. In vitro studies of the effectiveness of these compounds at inhibiting infection of U373-MAGI−CCR5 cells by HIV-1 Ba-L indicated that the sulfated glycodendrimers were better inhibitors than the nonsulfated glycodendrimers, but not as effective as dextran sulfate.

INTRODUCTION

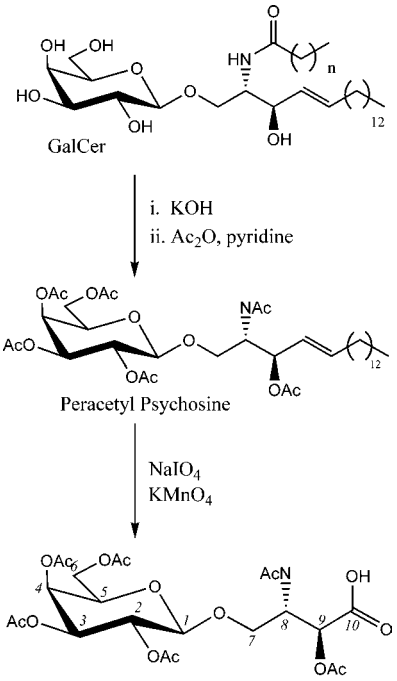
The primary protein receptors for HIV-1 are the cell surface CD4 molecules (*1*). Interaction of viral envelope glycoprotein, gp120, with CD4 results in a conformational change within gp120 that allows it to interact with a chemokine coreceptor (*1*, *2*). This results in formation of a 'fusion pore' which leads to fusion of viral and cellular membranes (*2*−*4*). In the absence of CD4, however, it is believed that the cell surface glycosphingolipids (GSLs), GalCer and its 3′-sulfated derivative, sulfatide (SGalCer), act as alternate receptors for HIV-1 gp120 (*5*−*10*). It has been shown that gp120 has distinct binding sites for GalCer and CD4 (*5*, *11*, *12*), and that the GalCer binding site has a nanomolar affinity for GalCer (*8*, *13*, *14*)—which is on the order of that reported for the affinity of gp120 for CD4 (*15*−*17*). The fact that the GalCer binding site is distinct and of relatively high affinity has made it a target for the development of GalCer and SGalCer mimetics as potential inhibitors of the interaction of HIV-1 with its target cells. Support for this idea is provided by a number of studies of the effectivieness of GalCer analogues as ligands for gp120 or as inhibitors of HIV infectivity (*18*−*25*).

Cell surface GSLs are involved in membrane trafficking, cell adhesion, cell morphogenesis, and signal transduction (*26*−*29*). In addition to these functions, GSLs in lipid rafts are used by a variety of pathogens for cellular entry (*30*, *31*). GSLs consist of a ceramide (*N*-acylated sphingosine) backbone and a carbohydrate moiety *β*-linked to the terminal hydroxyl group of the sphingosine. The ceramide portion intercalates into the phospholipid bilayer of the cell membrane, and the carbohydrate moiety extends outward from the membrane surface. Although the role of the ceramide portion in bacterial and viral adhesion is debatable (*13*, *23*, *24*), the consensus is that it is necessary for the positioning of the saccharide moiety such that it is available as a ligand for the pathogen (*13*, *32*). It is interesting that the carbohydrate moieties of GSLs function as receptors for various pathogens, since individual carbohydrate−protein interactions are often of low affinity (*33*−*35*). This is counterintuitive for biological processes that require high specificity and avidity. Nature has overcome this problem of innately weak monosaccharide interactions by clustering carbohydrate ligands together on the cell surface to yield a 'cluster' or 'multivalency' effect, that results in much stronger interactions (*35*−*38*). In some cases, the cluster effect has been observed to result in affinities that are greater than would be expected based on the sum of the total individual carbohydrate−protein interactions themselves—a cooperative affinity greater than that of valency (*36*, *38*). The clustering of GSLs in cell surface lipid rafts or 'detergent insoluble membranes' is a good example of the natural clustering of carbohydrate residues (*29*, *39*). Lipid rafts have been shown to serve as docking sites for

* To whom correspondence should be sent. Telephone (717) 531-8048. Fax (717) 531-7072. E-mail cxs8@psu.edu.
[†] Department of Biochemistry and Molecular Biology.
[‡] Department of Chemistry.

10.1021/bc034156a CCC: $27.50 © 2004 American Chemical Society
Published on Web 02/27/2004

Scheme 1. Formation of Peracetylated GalCer Ceramide Saccharide (1). Numbering System for NMR Analysis Is Shown

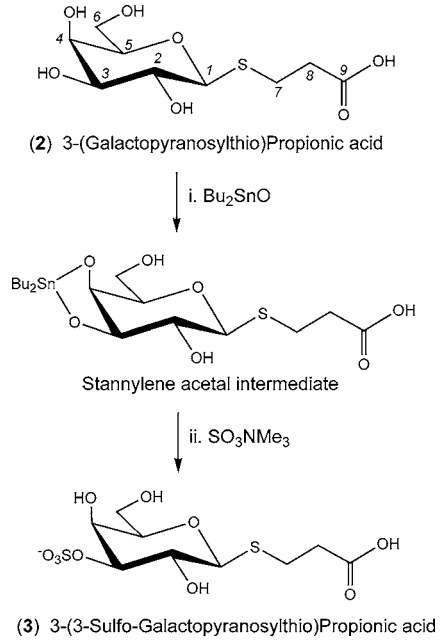


(1) Peracetyl GalCer Ceramide Saccharide

various bacterial toxins and viruses (*31*). Therefore, it is reasonable to hypothesize that a successful inhibitor of the binding of trimers of gp120 found on the surface of HIV-1 to GalCer/SGalCer would need to mimic the natural clustering of the carbohydrate moieties found in lipid rafts.

Multivalent neoglycoconjugates have been found to be useful mimetics of the natural clustering of carbohydrate residues (*40*, *41*). Glycodendrimers (*42*−*44*) are particularly effective due to their propensity to form spherical nano-cellular decoys (*33*, *36*). Effective ligands for influenza virus (*33*), cholera toxin (*45*), and various lectins (*37*, *46*) have been successfully prepared by conjugating cell surface carbohydrate ligands to spherical hyperbranched dendrimers. To study the interaction of HIV-1 gp120 with GalCer and SGalCer, and to develop potential carbohydrate-based inhibitors of this interaction, we synthesized several series of novel glycodendrimers of increasing size as multivalent mimetics of GalCer and SGalCer. This was accomplished by chemically isolating the saccharide portions of GalCer (compound **1**, see Scheme 1) and SGalCer and then using amine coupling to conjugate the "ceramide saccharide" (*47*) to polypropylenimine (DAB-Am) dendrimers. DAB-AM dendrimers were also functionalized with 3-(*β*-D-galactopyranosylthio)-propionic acid (compound **2**, Scheme 2) and 3-(*β*-D-3-sulfogalactopyranosylthio)propionic acid (compound **3**, Scheme 2). Failure to obtain efficient linkage of the 3-sulfated, spacer-arm derivatized galactose molecule to the DAB-Am dendrimer cores led us to randomly sulfate dendrimers derivatized with compound **2**. NMR was used to confirm synthesis of the various saccharides, and the average molecular weights and polydispersities of the glycodendrimers were determined by MALDI-TOF MS. Surface plasmon resonance (SPR) was used for kinetic analysis of the interaction of HIV-1 rgp120 IIIB with the different glycodendrimers, and dextran sulfate (DxS)—a known potent binding inhibitor of HIV-1. Last, the effectiveness of the glycodendrimers at blocking HIV-1 infection of cultured indicator cells was ascertained.

Scheme 2. Synthesis of 3-(3-Sulfo-*β*-D-glacto-pyranosylthio)propionic Acid (3). Numbering System for NMR Analysis Is Shown



(3) 3-(3-Sulfo-Galactopyranosylthio)Propionic acid

EXPERIMENTAL PROCEDURES

Abreviations. Bu_2SnO, dibutyltin oxide; BF_3Et_2O, borontriflouride dietherate; COSY, correlated spectroscopy; DCM, dichloromethane; DCE, dichloroethane; DIPEA, diisopropylethylamine; DxS, dextran sulfate; DAB-Am, poly(propylene imine) dendrimers; DMF, dimethylformamide; Et_3N, triethylamine; GalCer, galactosyl ceramide; HATU, *N*,*N*,*N*′,*N*′-tetramethyl-*O*-(7-azabenzotriazol-1-yl)uronium hexafluorophosphate; HMBC, heteronuclear multiple bond correlation; HMQC, heteronuclear multiple quantum correlation; HPTLC, high performance thin-layer chromatography; IAA, *trans*-3-indoleacrylic acid; $KMnO_4$, potassium permangenate; k_a, association rate constant; k_d, dissociation rate constant; K_D, equilibrium dissociation constant; kDa, kilodaltons; M_n, number-average molecular weight; M_w, weight-average molecular weight; MALDI-TOF MS, matrix-assisted laser desorption ionization time-of-flight mass spectrometry; MTS, 3-(4,5-dimethylthiazol-2-yl)-5-(3-carboxymethoxyphenyl)-2-(4-sulfophenyl)-2*H*-tetrazolium, inner salt; NaOMe, sodium methoxide; PD, polydispersity; PMS, phenazine methosulfate; SO_3NMe_3, sulfur trioxide trimethylamine complex; SGalCer, sulfatide; SPR, surface plasmon resonance; R_{max}, maximum binding capacity in RUs; RU, resonance unit (change in surface concentration of ∼1 pg of protein/mm^2); THAP, trihydroxyacetophenone.

Materials. GalCer, SGalCer, lyso-sulfatide, and psychosine standards were purchased from Matreya, Inc (Pleasant Gap, PA). GalCer and SGalCer for ceramide saccharide syntheses were purified from bovine brain white matter as previously described (*48*). Recombinant HIV-1 IIIB gp120 was obtained from Immunodiagnostics, Inc (Woburn, MA), DAB-Am dendrimers were from Aldrich (Milwaukee, WI), and silica gel 60 HPTLC plates were from Merck (Germany). Unless designated otherwise, all other materials were commercially available, and used without further purification.

Preparation of Peracetylated GalCer Ceramide Saccharide (1). GalCer was deacylated to form psychosine using reaction conditions described by Radin and by Dubois et al. for the removal of the fatty acid side-chain

from GSLs (*49*, *50*). The ceramide saccharide derivative of GalCer was made from pyschosine according to procedures published by Mylvaganum and Lingwood (*51*). MALDI-TOF MS *m/z* 548 $[M - H]^-$: $C_{22}H_{31}NO_{15}$ (549).

3-(β-D-Galactopyranosylthio)propionic Acid (2). 3-Mercaptopropionic acid (10.5 mL, 120 mmol) was added with stirring to a solution of galactose-β-pentaacetate, 11.7 g (30 mmol), in 60 mL of anhydrous DCM. This was followed by the addition of 5.7 mL (45 mmol) of $BF_3 \cdot Et_2O$ (*52*, *53*). The reaction was stirred at room temp and followed by TLC ($BuOH:CH_3OH:H_2O$; 2:1:1, v/v/v). Upon completion (~5 h), the reaction mixture was poured into ice water in a separatory funnel. The lower organic phase was removed, and the aqueous phase was rinsed 3× with DCM. The combined organic phases were washed with water, treated with anhydrous sodium sulfite, filtered over Celite, and dried by rotary evaporation. Peracetylated galactothiopropionic acid was isolated from the resulting viscous oil on a silica gel column and eluted with a step gradient of $DCM:CH_3OH$ of increasing polarity. It was recovered as a colorless oil in 80% yield. For NMR analysis and regioselective sulfation, a portion of the peracetylated galactothiopropionic acid was deacetylated using NaOMe in anhydrous CH_3OH. After stirring overnight at room temp, it was neutralized using DOWEX 50W $[H^+]$. ^1H NMR (400 MHz, D_2O, 25 °C): $\delta = 2.50$ (t, $J_{7A,8} \approx 7$ Hz, $J_{7B,8} \approx 7$ Hz, 2H, H-8), 2.90 (m, $J_{7A,8} \approx 7$ Hz, $J_{7B,8} \approx 7$ Hz, 2H, H-7), 3.52 (t, $J_{1,2} = 9.72$ Hz, $J_{2,3} = 9.6$ Hz,1H, H-2), 3.61 (dd, $J_{2,3} = 9.6$ Hz, $J_{3,4} = 3.4$ Hz, 1H, H-3), 3.66 (m, 1H, H-6B), 3.67 (m, $J_{4,5} = 0.2$ Hz, 1H, H-5), 3.72 (m, 1H, H-6A), 3.93 (d, $J_{3,4} = 3.36$ Hz, $J_{4,5} = 0.2$ Hz, 1H, H-4), 4.46 (d, $J_{1,2} = 9.72$ Hz, 1H, H-1). ^{13}C NMR (D_2O, 25 °C): $\delta = 27.3$ (C-7), 38.6 (C-8), 61.7 (C-6), 69.5 (C-4), 70.3 (C-2), 74.55 (C-3), 79.6 (C-5), 86.65 (C-1), 181.4 (C-9). MALDI-TOF MS *m/z* 291 $[M + Na]^+$: $C_9H_{16}O_7S$ (268).

3-(3-Sulfo-β-D-galactopyranosylthio)propionic Acid (3). Compound **3** was prepared because the carbohydrate moiety of sulfatide (SGalCer) is galactose-3-sulfate, and the hypothesis was that it would probably be the best mimetic for sulfatide. Galactothiopropionic acid, 5.86 g (21.87 mmol), and Bu_2SnO, 5.99 g (1.1 equiv, 24.05 mmol), were refluxed in 200 mL of anhydrous CH_3OH for 4 h at 90 °C (*54*, *55*). The resulting translucent yellow solution was dried by rotary evaporation, taken up in 150 mL of DMF, and 3.42 g SO_3NMe_3 (1.2 equiv, 24.6 mmol) was added. The mixture was sonicated (~1 min) and stirred at room temp for 30 h (*54*, *55*). The reaction was quenched with CH_3OH, dried by rotary evaporation using an oil vacuum pump, and purified on a silica gel column eluted with a $CHCl_3:CH_3OH$ step gradient. ^1H NMR (400 MHz, D_2O, 25 °C): $\delta = 2.68$ (t, $J_{7A,8} \approx 7$ Hz, $J_{7B,8} \approx 7$ Hz, 2H, H-8), 2.97 (m, $J_{7A,8} \approx 7$ Hz, $J_{7B,8} \approx 7$ Hz, 2H, H-7), 3.70 (dd, $J_{1,2} = 9.90$ Hz,1H, H-2), 3.72 (m, 1H, H-6B), 3.75 (m, 1H, H-5), 3.75 (m, 1H, H-6A), 4.32 (s, 1H, H-4), 4.33 (dd, 1H, H-3), 4.60 (d, $J_{1,2} = 9.90$ Hz, 1H, H-1). ^{13}C NMR (D_2O, 25 °C): $\delta = 26.4$ (C-7), 36.9 (C-8), 61.6 (C-6), 67.9 (C-4), 68.3 (C-2), 79.25 (C-5), 82.1 (C-3), 86.3 (C-1), 179.0 (C-9). MALDI-TOF MS *m/z* 347 $[M]^-$: $C_9H_{15}O_{10}S_2^-$ (347).

Conjugation of Functionalized Saccharides to Polypropylenimine Dendrimers. The peracetylated derivative of compound **1**, **2**, or **3**, 50 to 100 mg (1.5 equiv per dendrimer terminal primary amine), was taken up in CH_3CN (10 mg/mL). One equivalent of HATU (Aldrich, Milwaukee, WI) in CH_3CN (10 mg/mL) and 1 equiv of DIPEA were added to each sample to activate the terminal carboxyl group (*56*). After 5−10 min, the appropriate amount of DAB-AM dendrimer at a concentration of 10 mg/mL in DCM was added dropwise to the stirring mixture. Reactions were adjusted to 1:1, DCM:CH_3CN, and allowed to incubate at room temperature with stirring overnight. Product formation was monitored by TLC ($BuOH:CH_3OH:H_2O$; 2:1:1, v/v/v). Free amino groups were visualized using ninhydrin spray and sugar residues using 5% sulfuric acid in ethanol. Upon completion, the mixture was dried under vacuo and the product deacetylated with $Et_3N:CH_3OH:H_2O$ (2:6:10; v/v/v) at a final concentration of 0.5 mg/mL. After being stirred at 37 °C for 4 h, the reaction was dried, washed with 10 m*M* HCl in 90% EtOH (*51*), dried again, and purified on a BioGel P2 column. Fractions were spotted on TLC plates, and carbohydrate-containing conjugates were visualized with 5% H_2SO_4 in EtOH. Fractions containing the purified glycodendrimers were pooled, dried, and lyophilized. Once dried, the average molecular weights of the glycodendrimers were determined by MALDI-TOF MS. Glycodendrimers that were built by conjugating **1** to DAB-Am dendrimers, generations 1−5, are referred to as glycodendrimers, **1a**−**e**, where **1a** is the 4-mer glycodendrimer and **1e** is the 64-mer. Likewise, glycodendrimers made from compounds **2** and **3** are referred to as glycodendrimers **2a**−**e** and **3c**−**e**.

Direct Sulfation of Dendrimers Derivatized with 3-(β-D-Galactopyranosylthio)propionic Acid (2c, 2d, and 2e). Random sulfation of **2c**, **2d**, and **2e** was done in order to make sulfated 3-(β-D-galactopyranosylthio)-propionic acid-derivatized dendrimers. 30 mgs of **2c**, **2d**, or **2e** were taken up in 30 mL of DMF, prior to the addition of SO_3NMe_3 (2 equiv per hydroxyl group). The reaction mixture was refluxed with stirring at 60 °C for 30 h and then dried by rotary evaporation under reduced pressure supplied by an oil vacuum pump. Dried films were taken up in 2 mL of 1 M NaCl, and **4c**, **4d**, and **4e** were purified by size-exclusion chromatography on a BioGel P2 column, using water as the eluate.

Matrix-Assisted Laser Desorption Ionization Time-of-Flight (MALDI-TOF) Mass Spectrometry. MALDI-TOF MS was done on a Perseptive Biosystems Voyager DE-PRO spectrometer. Spectra (100) of negatively charged sugars were generated in linear, negative ion mode using THAP matrix, or in linear, positive ion mode using IAA. Glycodendrimer spectra (200) were generated in linear, positive ion mode using an IAA matrix (20 mg/mL in DMF, diluted 11:1 with a 1 mM aqueous solution of glycodendrimer to yield a matrix-to-analyte ratio of ~1000:1) (*57*). In some instances, negative ion mode was used to detect the sulfated glycodendrimers. Average molecular weights and polydispersities of the glycodendrimers were calculated using Data Explorer version 4.0 (Applied Biosystems). Macros within this software allow for the calculation of M_n (the number-average molecular weight), M_w (the weight-average molecular weight), and the polydispersity (PD) from the ratio of M_w to M_n according to the following equations:

$$M_n = \sum(N_i M_i)/\sum N_i$$

$$M_w = \sum(N_i M_i^2)/\sum N_i M_i$$

where N_i and M_i represent signal intensity and mass at point *i*, respectively (*58*, *59*).

Nuclear Magnetic Resonance (NMR) Analyses. All spectra were obtained on a Bruker DRX-400 NMR spectrometer operating in the quadrature mode at 25.0 °C using a triple-axis-gradient broadband inverse probe. ^1H chemical shifts were referenced indirectly to TMS (0

ppm) via DSS (sodium-2,2-dimethyl-2-silapentane-5-sulfonate), a secondary reference. ^{13}C chemical shifts were referenced indirectly to TMS (0 ppm) via acetone (30.89 and 215.9 ppm), a secondary reference. All samples were dissolved in D_2O. One bond $^1H-^{13}C$ correlation 2D spectra were obtained using the gradient-selected version of the phase-sensitive HMQC experiment. Long range (2 and 3 bond) $^1H-^{13}C$ correlation 2D spectra were obtained using the gradient-selected version of the magnitude-mode HMBC experiment. When necessary for assignment purposes, gradient-selected Double-Quantum-Filtered COSY experiments were used to verify $^1H-^1H$ couplings.

Surface Plasmon Resonance. SPR experiments were done at 25 °C using a Biacore 3000 system and CM5 sensor chips (Biacore, Uppsala, Sweden). Glycodendrimers **1c**−**e** and **2c**−**e** were amine-coupled to the sensor chip according to the manufacturer's protocol, using the free amines that were not functionalized on the glycodendrimers. To obtain a low-density surface suitable for affinity analysis, 350−500 RUs of each glycodendrimer were immobilized. Varying concentrations of rgp120 (62.5−0.98 nM) were injected simultaneously over a blank control surface and the immobilized glycodendrimers at a flow rate of 30 μL/min for 3 min in HBS-EP buffer (10 mM HEPES, 150 mM NaCl, 3 mM EDTA, 0.005% P-20 surfactant, pH 7.4). Following the injection, the dissociation of the rgp120-glycodendrimer complex was measured for 10 min. Any remaining bound rgp120 was removed by a 1 min injection of 4 M KCl. This regeneration step prepared the surface for the next injection of rgp120. Each concentration of rgp120 was injected in duplicate over the immobilized glycodendrimer, with a representative sensorgram chosen for analysis.

The sulfated glycodendrimers, **4c**−**e**, did not couple to the CM5 chip, presumably due to repulsion of the negatively charged sulfate groups by the negatively charged carboxyl groups on the carboxymethylated dextran matrix. Therefore, approximately 3000 RUs of rgp120 was amine-coupled to the CM5 sensor chip and the potential ligand used as analyte. DxS (50 kDa, 12.5−0.39 nM), **4c**, **4d**, or **4e** (89−0.36 nM) were injected simultaneously over a blank control surface and the immobilized rgp120 at a flow rate of 30 μL/min, for 3 min. Dissociation of the complex was measured for 10 min, followed by a 1 min injection of 4 M KCl to regenerate the rgp120 surface. Nonspecific binding was accounted for by subtraction of the blank control surface from each of the test surfaces. Subtracted sensorgrams were then analyzed by fitting the data to a 1:1 (Langmuir) binding model and kinetic constants determined using the BiaEvaluation 3.2 software.

Cell Culture. U373-MAGI-CCR5 cells were obtained from the AIDS Reagent Program #3597. Cells were propagated in 'Selection Media' consisting of DMEM supplemented with 10% FCS, 0.4 mg/mL L-glutamine, penicillin and streptomycin (0.08 mg/mL each), 0.05% sodium bicarbonate, 0.2 mg/mL G418, 0.1 mg/mL hyrgromycin B, and 1.0 ug/mL puromycin. 'Culture Media' for virus inhibition assays consisted of DMEM with 10% FCS and 0.05% sodium bicarbonate. Cells were grown at 37 °C in an atmosphere of 95% air/5% CO_2.

Viral Inhibition Assays. Cells, in Selection Media, were plated in 96-well tissue culture plates at a density of 1.0×10^4 cells per well. One day later, commercially available (Advanced Biotechnologies, Columbia, MD), concentrated cell-free viral preparations of HIV-1 Ba-L (R5) were diluted 1:400 in 'Culture Media'. Glycodendrimer and DxS stock solutions were made up in culture media and serially diluted with culture media in separate sterile V-bottom 96-well microtiter plates, to a final volume of 30 μL per well. This was followed by the addition of 30 μL of the diluted virus and incubation at 37 °C for ∼ 20 min. Selection Media was then removed from the plated cells, and 50 μL of virus or virus plus potential inhibitor was added to the plated cells. The virus- or virus plus inhibitor-exposed cells were then incubated at 37 °C in an atmosphere of 95% air/5% CO_2 for 2 h. After the absorption period, 200 μL of Culture Media was added to the wells, and the cells were allowed to grow for an additional 40−48 h. Cells treated with culture media served as negative controls, and cells treated with virus only were positive controls. All measurements were done in quadruplicate.

After the 48 h incubation, culture media was removed from the wells, the cells were washed with 200 μL of PBS, and β-galactosidase activity was measured using the Galacto-Star β-Galactosidase Reporter Gene Assay System from Applied Biosystems (Foster City, CA), according to the manufacturer's instructions. Briefly, after the cells were washed with PBS, 10 μL of lysis solution was added to each well and the plate incubated for 10 min at 37 °C. The Galacto-Star substrate was diluted 1:50 and 100 μL added to each well containing cell lysate. Well contents were mixed and 90 μL were removed and added to a 96-well opaque luminometer plate. One hour after the Galacto-Star substrate was added, luminescence was determined using a luminometer. Percent inhibition was determined as $[(L_{\text{no inhibitor}} - L_{\text{inhibitor}})/L_{\text{no inhibitor}}] \times 100$. The effective concentration that inhibited 50% of viral infectivity (EC_{50}) was determined by plotting the percent inhibition versus the log of the concentration of the potential inhibitor.

Cytotoxicity. The effect of the glycodendrimers and control compounds on cell viability was determined using the CellTiter 96 AQ_{ueous} Cell Proliferation Assay (Promega, Madison, WI). In this viability assay, mitochondrial dehydrogenases in metabolically active cells catalyze the conversion of MTS into a formazan product. The absorbance of formazan is read at 490 nm and is directly proportional to the number of viable cells. Assays were performed according to the manufacturer's instructions.

Replicate 96-well plates of each of the HIV infection inhibition assay plates were set up and treated identically, with the exception that no virus was added to the cells. After the 48 h incubation, the cell culture media was removed, cells were washed with PBS, and 100 μL of culture media was added to each well. The MTS reagent was mixed with the electron coupling reagent PMS according to the instructions, and 100 μL of the mixture was added to the cells. The 96-well replicate plates were incubated for 3 h at 37 °C, in an atmosphere of 95% air/5% CO_2, and absorbance was read on an ELISA plate reader at 490 nm. Cell viability indices were calculated by dividing the average absorbance of nontreated cells (negative control wells) into the average absorbance obtained for each concentration of each compound tested. Therefore, nontreated cells would have a viability index of 1.0 while that for cells exposed to cytotoxic compounds would be less than 1.0. The index obtained for each concentration of a compound was then used to correct for inhibition due to cell death induced by a potential inhibitor.

RESULTS

Synthesis of Spacer-Arm Derivatized Saccharides. To build multivalent GalCer and SGalCer derivatized dendrimers, the saccharide moiety of GalCer and

Table 1. ^{1}H and ^{13}C NMR Chemical Shifts of Compounds 2 and 3. Also Shown Are the Chemical Shifts Relative to 2

compound	H-1	H-2	H-3	H-4	H-5	H-6A	H-6B
2	4.46	3.52	3.61	3.93	3.67	3.72	3.66
3	4.60	3.70	4.33	4.32	3.75	3.75	3.72
	(+0.14)	(+0.18)	(+0.72)	(+0.39)	(+0.08)	(+0.03)	(+0.06)
	C-1	C-2	C-3	C-4	C-5	C-6	
2	86.65	70.3	74.55	69.5	79.6	61.7	
3	86.3	68.3	82.1	67.9	79.25	61.6	
	(−0.35)	(−2.00)	(+7.55)	(−1.60)	(−0.35)	(−0.1)	

SGalCer (galactose and galactose-3-sulfate, respectively), containing a portion of the sphingosine moiety, were isolated from the natural GSLs (Scheme 1). Techniques described by Mylvaganum and Lingwood, for the preparation of glycolipid ceramide saccharides for neoglycoconjugation (*51*), were used for the synthesis of the peracetylated ceramide saccharides directly from GalCer (**1**) and SGalCer. This was achieved by deacylation of the GSL followed by its acetylation to block vicinal hydroxyls prior to oxidative cleavage of the double bond of the sphingosine to obtain the acetylated "ceramide saccharide" (Scheme 1). The carboxyl group of the *N*-acetylated butyric acid provided the reactive group needed to link the sugar to a primary amine on the dendrimer core. The yield of ceramide saccharide derivative of SGalCer obtained was very low (<20%), and the resulting product did not conjugate to the DAB-Am dendrimers efficiently. Also, according to MALDI-TOF MS, deacetylation of the peracetyl SGalCer ceramide saccharide resulted in the loss of approximately 40% of the sulfate residues (data not shown). Therefore, this approach was not pursued.

These results led to a search for a more efficient method of making galactopyranosyl and 3-sulfogalactopyranosyl derivatized dendrimers. The method described by Ashton et al. for the synthesis of 3-(*β*-D-galactopyranosylthio)propionic acid (**2**) was used to derivatize the sugars with a spacer arm that could be used to link them to the DAB-Am dendrimers (*60*). This method was efficient, with the yield of derivatized galactose molecules greater than 80%. While **2** was not made directly from natural GSLs, its structure is similar to **1**, and it may actually be better suited for synthesis of neoglycoconjugates because the thioglycosidic linkage is more resistant to cleavage by endogenous glycosidases than the corresponding *O*-glycosides (*61*).

To make a spacer-arm derivatized galactose-3-sulfate molecule, the novel 3′-sulfated derivative of **2** was made according to methods described by Lubineau and Lemoine, and Guilbert et al. for the regioselective sulfation of dibutylstannylene acetals (*54*, *62*). In this technique, dibutyltin oxide was used to form stannylene acetal complexes between cis diols, C-3 and C-4 on compound **2** (63) (Scheme 2). The C-3 was then preferentially sulfated by reacting the complex with SO_3NMe_3 in DMF for 30 h at 60 °C. After purification, novel **3** was obtained in ∼70% yield. NMR data shown in Table 1 confirmed that sulfation occurred at position C-3. The chemical shifts obtained agree with those published by Ikami et al. (1997) for compounds they synthesized as sulfatide mimetics (*64*). HPTLC (Figure 1) indicated that the precursors used and the compounds synthesized (**1**, **2**, and **3)** contained no visible contaminants. It can be seen that the less polar GalCer (Figure 1, lane a), peracetylated psychosine (lane c), and galactose-*β*-D-pentaacetate (lane e) migrated closest to the solvent front while the more polar compounds **2** (lane g) and **3** (lane h) had the slowest mobilities.

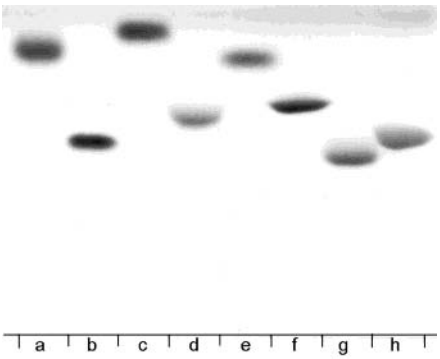


Figure 1. HPTLC showing the relative mobilities of functionalized carbohydrates and their precursors. (a) GalCer; (b) psychosine; (c) peracetylated psychosine; (d) GalCer ceramide saccharide (**1**); (e) galactose-*β*-D-pentaacetate; (f) peracetylated 3-(*β*-D-galactopyranosylthio)propionic acid; (g) 3-(*β*-D-galactopyranosyl-thio)propionic acid (**2**); (h) 3-(3-sulfo-*β*-D-galactopyranosylthio)propionic acid (**3**). The plate was chromatographed in 2:1:1 BuOH:CH_3OH:H_2O (v/v/v), and compounds visualized by charring with 5% H_2SO_4 in EtOH.

Conjugation of Derivatized Saccharides to DAB-Am Dendrimers. Compounds **1**, **2**, and **3** were conjugated to DAB-Am dendrimers, generations 1−5, by amine-coupling the terminal carboxyl groups on the derivatized saccharides to the terminal primary amines on the DAB-Am dendrimers. The carboxyl activator, HATU, commonly used in peptide synthesis, was used to activate the peracetylated derivatized saccharides. In this manner glycodendrimers **1a**−**e, 2a**−**e,** and **3c**−**e** were built; where the designations **a**−**e** correspond to DAB-Am generations 1−5, respectively (Figure 2). MALDI-TOF MS was used to determine the average number of saccharide residues incorporated onto the DAB-Am dendrimers. To calculate the average number of residues incorporated, the theoretical molecular weight of the starting DAB-Am dendrimer was subtracted from the M_w of the functionalized dendrimer and the difference divided by the weight of one derivatized saccharide, minus 18 Da to account for the loss of a H_2O molecule during formation of the amide bond. Table 2 shows the average molecular weights (M_w), polydispersities (PD), and average number of incorporated sugars for glycodendrimers **1a**−**e**, **2a**−**e**, and **3c**−**e**.

MALDI-TOF MS analysis revealed that less than 50% of the dendrimer arms were derivatized with **3**. Failure to fully link **3** to the DAB-Am dendrimers may have been due to the lack of solubility of the sulfated products formed during the reaction, or due to steric hindrance enhanced by electrostatic repulsion between sulfate groups. Regardless, attempts to build a fully functionalized gal-3-sulfate derivatized dendrimer by directly coupling **3** to a DAB-Am dendrimer core were unsuccessful. Therefore, regioselective sulfation of the C-3 position on the galactose moieties of galactose-derivatized dendrimers **2a**−**e**, via the stannylene acetal intermediate was tried. However, this approach was also unsuccessful, presumably due to the solubility differences between the dibutyltin oxide reagent and the glycoden-

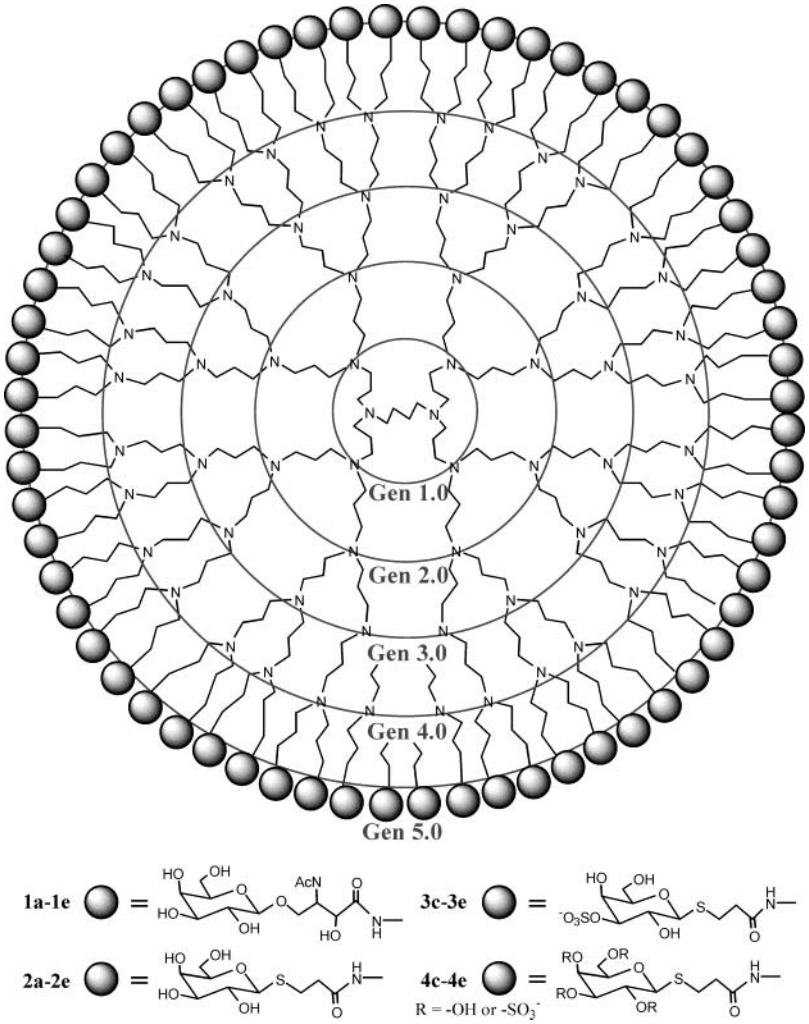


Figure 2. Schematic representation of the glycodendrimers synthesized. The generation circles indicate where one generation ends, and the next begins. Glycodendrimers are labeled according to their functionalized compounds **1**, **2**, **3**, or **4** followed by the generation of dendrimer, where generations 1−5 correspond to a−e, respectively.

Table 2. MALDI-TOF MS Analysis of the Glycodendrimers

compound	theoretical molecular wt	M_N	M_W	PD	avg no. sugars	avg no. sulfates	theorectical % incorporation
1a GC-4mer	1600	1454	1478	1.02	3.6	−	90
1b GC-8mer	3341	3073	3100	1.01	7.2	−	90
1c GC-16mer	6823	4978	5189	1.04	10.9	−	68
1d GC-32mer	13786	10138	10342	1.02	21.2	−	66
1e GC-64mer	27712	20508	20778	1.01	42.4	−	66
2a Gal-4mer	1316	1341	1342	1.00	4.0	−	100
2b Gal-8mer	2773	2634	2642	1.00	7.5	−	94
2c Gal-16mer	5687	5043	5062	1.00	13.5	−	84
2d Gal-32mer	11514	9722	9761	1.00	25.0	−	78
2e Gal-64mer	23168	19031	19143	1.01	47.9	−	75
3c 3-sulfo-16mer	6951	3867	4004	1.04	7.0	5.7	44
3d 3-sulfo-32mer	14042	5989	6184	1.03	8.1	6.5	25
3e 3-sulfo-64mer	28224	10767	10954	1.02	11.5	9.3	18
4c SGal-16mer	−	6938	7010	1.01	13.5	12.2	−
4d SGal-32mer	−	13336	13484	1.01	25.0	23.3	−
4e SGal-64mer	−	19425	24581	1.01	47.9	34.2	−

drimers **2a**−**e**. Therefore, glycodendrimers **2c**, **2d**, and **2e** were randomly sulfated using a 2-fold excess of SO_3NMe_3 per hydroxyl group. This gave the sulfated galactose-derivatized dendrimers **4c**, **4d**, and **4e** (Figure 2). Subtraction of the starting molecular weights of **2c**, **2d**, and **2e** from the respective sulfated products **4c**, **4d**, and **4e**, followed by division of the molecular weight of one sulfate−pyridine salt minus 1 H^+ (158), gave the average number of sulfate groups incorporated (Table 2). MALDI-TOF MS analysis indicated that on average 12, 23, and 34 sulfate groups were added to the glycodendrimers **4c**, **4d**, and **4e**, respectively (Table 2). Proton NMR analysis of the randomly sulfated **4d** glycodendrimer showed broad, overlapping peaks for the H-2 through H-6 protons, suggesting that different hydroxyls were sulfated (data not shown). While the relative amount of sulfation of each hydroxyl was not determined, reports in the literature indicate that sulfation most likely occurred at C-6 followed by C-4 and C-3 (*62*, *65*).

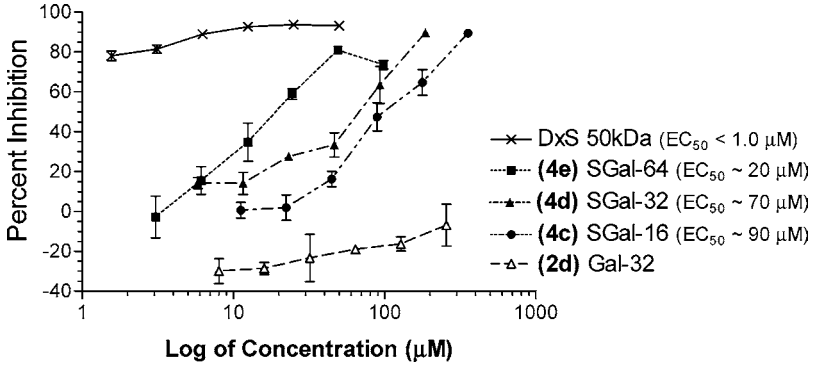


Figure 3. Inhibition of HIV-1 BaL infection of U373-MAGI−CCR5 cells by glycodendrimers, **4c**−**e** and **2d**, and by DxS (50 kDa).

Table 3. Rate and Equilibrium Constants for the Interaction of Rgp120 IIIB with √ the Derivatized Dendrimers, 1c-1e, 2c-2e, and 4c-4e, and DxS

compound	k_a	k_d	K_D (M)
GC-16mer, **1c**	1.73×10^5	1.03×10^{-3}	5.94×10^{-9}
GC-32mer, **1d**	3.70×10^5	5.61×10^{-4}	1.52×10^{-9}
GC-64mer, **1e**	1.42×10^5	9.60×10^{-4}	6.78×10^{-9}
Gal-16mer, **2c**	4.46×10^4	1.35×10^{-3}	3.02×10^{-8}
Gal-32mer, **2d**	1.89×10^5	1.43×10^{-3}	7.57×10^{-9}
Gal-64mer,**2e**	1.86×10^5	1.15×10^{-3}	6.18×10^{-9}
SGal-16mer, **4c**	9.56×10^4	3.09×10^{-4}	3.23×10^{-9}
SGal-32mer, **4d**	6.27×10^5	1.18×10^{-4}	1.89×10^{-10}
SGal-64mer, **4e**	5.11×10^5	9.04×10^{-4}	1.77×10^{-9}
DxS (50 kDa)	2.83×10^6	6.49×10^{-5}	2.29×10^{-11}

Kinetic Analysis of the Interaction between rgp120 IIIB and the Synthesized Glycodendrimers. SPR was used to study the binding kinetics of rgp120 to the different derivatized dendrimers. Sensorgrams were analyzed by fitting the data to a 1:1 (Langmuir) binding model and kinetic constants determined using the BiaEvaluation 3.2 software. Rate constants and affinity constants for the interaction of rgp120 with each of the glycodendrimers and DxS are shown in Table 3. Overall, the affinities of rgp120 for the various glycodendrimers were in the nanomolar range, with the SGal-derivatized denrimers (**4c**−**e**) displaying somewhat stronger affinities than their Gal-derivatized dendrimer counterparts (**2c**−**e**). Gp120 had the greatest affinity for DxS, with an equilibrium dissociation constant (K_D) of 2.29×10^{-11}.

Inhibition of HIV-1 Ba-L Infection of Cultured Glioblastoma Indicator Cells. Glycodendrimers **1c**−**e**, **2c**−**e,** and **4c**−**e**, and DxS 50 kDa, were tested for their ability to inhibit HIV-1 BaL (R5-tropic) infection of U373-MAGI−CCR5 cells and their affect on cell viability. The 4- and 8-mer derivatized dendrimers were not tested due to preliminary results that indicated that the larger molecules were better inhibitors. The observed EC_{50s} for the sulfated glycodendrimers **4c**, **4d**, and **4e** were 90μM, 70μM, and 20μM, respectively (Figure 3). While the increase in inhibition seen with increasing size of the sulfated glycodendrimers was small, it was reproducible. DxS was a potent inhibitor of infection by HIV-1 BaL with an EC_{50} lower than that of the lowest concentration tested, 1.6 μM. The galactose functionalized glycodendrimers (**1c**−**e** and **2c**−**e**) showed little or no inhibitory effect. The 50% inhibition level was not reached at concentrations of galactose-derivatized dendrimer as high as 2.5 mg/ml (see Figure 3 for data for **2d**). Neither **4c**−**e**, **2d**, nor DxS were cytotoxic to the cultured indicator cells at the highest concentrations tested (2.5 mg/ml).

DISSCUSSION

SPR is a powerful technique for examining the association of two biological molecules; however, to correctly interpret the data, certain experimental conditions must be met. For the SPR studies reported here, two control experiments were done to determine the validity of the binding data and the 1:1 model used. The first was a mass transfer control experiment. This was done to determine whether the association rate was limited by the transport of analyte from the bulk solution to the immobilized ligand on the sensor chip surface. For each of the nonsulfated glycodendrimers, a single concentration of analyte (gp120) was injected over the ligand at three different flow rates (5, 15, and 75 μL/min). The association phases were then overlaid to determine whether binding was increased by the increased flow rate. In each case, this was not observed, indicating that binding was not limited by mass transport. The second control experiment was to determine whether the association and dissociation steps occurred in a single phase. Again, for each glycodendrimer tested, a single concentration of analyte was injected over the ligand at a constant flow rate, but for different lengths of time (1, 3, and 20 min). The dissociation phases were then overlaid to determine whether there were any differences. Typically, if binding is biphasic, a more stable complex will form over time. This complex will then dissociate more slowly than the less stable complex. For example, if the binding was biphasic, a 20 min injection would most likely allow for the formation of a more stable complex and give a slower dissociation rate than a 1 min injection. For each sample studied, no differences in the dissociation phases were observed, which indicated that the binding in each case was monophasic.

Another variable that must be accounted for is the goodness of fit of the binding model applied to the data. An indication of the goodness of fit of a model to the data is the residual plot (shown in Supporting Information). The residuals are simply the difference between the data and the fitted model. Residuals should be less than 5% of the experimental R_{max} (maximum binding response). For each of the fits reported here, the residuals were generally less than 5% of the experimental R_{max}. Another indication of the goodness of fit of the model to the data is the χ^2 value. The χ^2 is a numerical representation of the goodness of fit, the sum of the squared residuals (see Supporting Information). The χ^2 value should be less than 5% of the experimental R_{max}. Each of the χ^2 values reported here was less than 5% of the R_{max}.

Although the glycodendrimers are multivalent ligands, the results from the SPR data indicated that the 1:1 (Langmuir) binding model accurately described the interaction of rgp120 with both DxS and each of the glycodendrimers tested. This model assumes that each analyte binds independently, in one step, to a single site on the immobilized ligand. Control experiments were

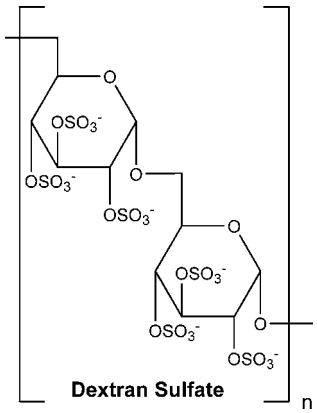


Figure 4. Structure of DxS. All hydroxyls are shown as sulfated.

performed to determine the presence of mass transfer limitations or multiphasic binding. No clear deviations from a 1:1 interaction were observed for the glycodendrimers or DxS. Additionally, the chi square (χ^2), an indication of the goodness of fit of the data to the model, was less than 5% of R_{max} for each of the fits reported. Therefore, the fits meet the requirements for acceptable SPR kinetic data.

The observation that rgp120 contains a single high affinity binding site for the GalCer mimetic glycondendrimers agrees with the affinities reported for gp120 binding to GalCer (8,13). It was interesting to note, however, that despite the observed nanomolar affinity of gp120 for the GalCer mimetic glycodendrimers (**1c**−**e** and **2c**−**e**), no inhibition of HIV-1 Ba-L infection was seen (Figure 3). In contrast, the SGal glycodendrimers (**4c**−**e**), which were also bound by rgp120 with nanomolar affinity, were able to inhibit HIV-1 Ba-L infection of the cultured indicator cells with micromolar EC_{50s} (corresponding to ∼0.5 mg/mL). Interestingly, the affinity of rgp120 IIIB for DxS was much greater than that for the derivatized dendrimers. However, DxS is a known potent binding antagonist of HIV infection in vitro, and the EC_{50} of DxS observed in Figure 3A was lower than the lowest concentration tested (1.6 μM or 80 μg/mL), which may reflect the picomolar affinity of gp120 for DxS. Therefore, for the sulfated glycodendrimers and DxS, it appears as though the SPR data is a good indication of inhibition of HIV infectivity. We hypothesize that the lack of inhibition by the nonsulfated glycodendrimers reflects their inability to block the interaction of the positively charged V3-loop of gp120 with the negatively charged, sulfated-tyrosine residues of the N-terminus of the chemokine coreceptors (*66*). The fact that DxS was reported to bind gp120 at the V3-loop, thus preventing interaction with the chemokine co-receptors (*67*), and the fact that GalCer was also reported to bind at or near the V3-loop (*7*, *9*, *68*), supports this hypothesis. Despite its binding to the V3-loop, GalCer apparently does not inhibit the interaction of the V3-loop with the sulfated-amino terminus of the chemokine coreceptors (CXCR4 and CCR5); and therefore, does not prevent the formation of the fusion pore complex.

The affinity and infectivity differences observed for the glycodendrimers and DxS are likely due to structural differences. DxS consists of repeating, branched glucose units linked (β1−6). It is made up of approximately 17% sulfur, which corresponds to approximately 2.3 sulfate groups per repeating glucosyl residue (Figure 4). Therefore, the degree of sulfation for DxS is more than twice that of the sulfated glycodendrimers **4c**−**e**, which had on average less than 1 sulfate group per galactose residue. Division of the average molecular weight of DxS (50 kDa) by the MW of one glucosyl residue with 2.3 sulfates, and multiplication of that value by 2.3 results in an estimation of 387 sulfate groups per molecule of DxS. In contrast, glycodendrimer **4e** had only 34 sulfate groups per molecule. The observation that rgp120 bound to glycodendrimer **4e** with a K_D of 1.9×10^{-9} and to DxS with a K_D of 2.34×10^{-11} allows the hypothesis that the incorporation of another one or two sulfate groups per galactose residue of compounds **4c**−**e** might result in their being bound with greater affinity by rgp120. The fact that sulfate groups on DxS are found on C-2, C-3, and C-4 of its repeating glucosyl residues, combined with the likelihood that the sulfates on glycodendrimers **4c**−**e** are on C-6, and then C-4 and C-3, permits the hypothesis that addition of a sulfate to the C-3 position of the galactosyl residues on **4c**−**e** might increase their ability to function as ligands for gp120 IIIB. In conclusion, the randomly sulfated galactose-derivatized dendrimers described are good ligands for rgp120 IIIB and may serve as the basis for the development of a novel class of HIV-1 binding antagonists.

ACKNOWLEDGMENT

We thank Dr. Mary Cloninger for her helpful conversations and for the MADLI-TOF glycodendrimer protocol, Dr. Bruce Stanley for his teaching and instruction regarding the use of the MALDI-TOF mass spectrometer, and Dr. Samir Qamar for his help with purifying and deacylating GalCer. We also thank our collaborators, Dr. Brian Wigdahl, Dr. Fred Krebs, and Dr. Bradley Cantalone, for their input into the HIV inhibition and cytotoxicity experiments. This work was supported in part by Public Health Service grants RO1 NS40231 to C-L.S. and F31 NS11184-01 to R.D.K. from the National Institute of Neurological Disorders and Stroke.

Supporting Information Available: NMR spectra for compounds **1**, **2**, and **3**, representative SPR data fit for compound **2d**, and MALDI-TOF MS traces. This material is available free of charge via the Internet at http://pubs.acs.org.

LITERATURE CITED

(1) Wyatt, R., and Sodroski, J. (1998) The HIV-1 envelope glycoproteins: fusogens, antigens, and immunogens. *Science 280*, 1884−1888.

(2) Jones, P. L., Korte, T., and Blumenthal, R. (1998) Conformational changes in cell surface HIV-1 envelope glycoproteins are triggered by cooperation between cell surface CD4 and co-receptors. *J. Biol. Chem. 273*, 404−409.

(3) Monck, J. R., and Fernandez, J. M. (1996) The fusion pore and mechanisms of biological membrane fusion. *Curr. Opin. Cell Biol. 8*, 524−533.

(4) Munoz-Barroso, I., Durell, S., Sakaguchi, K., Appella, E., and Blumenthal, R. (1998) Dilation of the human immunodeficiency virus-1 envelope glycoprotein fusion pore revealed by the inhibitory action of a synthetic peptide from gp41. *J. Cell Biol. 140*, 315−323.

(5) Fantini, J., Cook, D. G., Nathanson, N., Spitalnik, S. L., and Gonzalez-Scarano, F. (1993) Infection of colonic epithelial cell lines by type 1 human immunodeficiency virus is associated with cell surface expression of galactosylceramide, a potential alternative gp120 receptor. *Proc. Natl. Acad. Sci. U.S.A. 90*, 2700−2704.

(6) Furuta, Y., Eriksson, K., Svennerholm, B., Fredman, P., Horal, P., Jeansson, S., Vahlne, A., Holmgren, J., and Czerkinsky, C. (1994) Infection of vaginal and colonic epithelial cells by the human immunodeficiency virus type 1 is neutralized by antibodies raised against conserved epitopes

in the envelope glycoprotein gp120. *Proc. Natl. Acad. Sci. U.S.A. 91*, 12559−12563.
(7) Hammache, D., Pieroni, G., Yahi, N., Delezay, O., Koch, N., Lafont, H., Tamalet, C., and Fantini, J. (1998) Specific interaction of HIV-1 and HIV-2 surface envelope glycoproteins with monolayers of galactosylceramide and ganglioside GM3. *J. Biol. Chem. 273*, 7967−7971.
(8) Harouse, J. M., Bhat, S., Spitalnik, S. L., Laughlin, M., Stefano, K., Silberberg, D. H., and Gonzalez-Scarano, F. (1991) Inhibition of entry of HIV-1 in neural cell lines by antibodies against galactosyl ceramide. *Science 253*, 320−323.
(9) Harouse, J. M., Collman, R. G., and Gonzalez-Scarano, F. (1995) Human immunodeficiency virus type 1 infection of SK−N-MC cells: domains of gp120 involved in entry into a CD4-negative, galactosyl ceramide/3′ sulfo-galactosyl ceramide-positive cell line. *J. Virol. 69*, 7383−7390.
(10) Yahi, N., Baghdiguian, S., Moreau, H., and Fantini, J. (1992) Galactosyl ceramide (or a closely related molecule) is the receptor for human immunodeficiency virus type 1 on human colon epithelial HT29 cells. *J. Virol. 66*, 4848−4854.
(11) Bhat, S., Mettus, R. V., Reddy, E. P., Ugen, K. E., Srikanthan, V., Williams, W. V., and Weiner, D. B. (1993) The galactosyl ceramide/sulfatide receptor binding region of HIV-1 gp120 maps to amino acids 206−275. *AIDS Res. Hum. Retroviruses 9*, 175−181.
(12) Cook, D. G., Fantini, J., Spitalnik, S. L., and Gonzalez-Scarano, F. (1994) Binding of human immunodeficiency virus type I (HIV-1) gp120 to galactosylceramide (GalCer): relationship to the V3 loop. *Virology 201*, 206−214.
(13) Conboy, J. C., McReynolds, K. D., Gervay-Hague, J., and Saavedra, S. S. (2002) Quantitative measurements of recombinant HIV surface glycoprotein 120 binding to several glycosphingolipids expressed in planar supported lipid bilayers. *J. Am. Chem. Soc. 124*, 968−977.
(14) Bhat, S., Spitalnik, S. L., Gonzalez-Scarano, F., and Silberberg, D. H. (1991) Galactosyl ceramide or a derivative is an essential component of the neural receptor for human immunodeficiency virus type 1 envelope glycoprotein gp120. *Proc. Natl. Acad. Sci. U.S.A. 88*, 7131−7134.
(15) Lundin K, N. A., Arthur LO, Robey WG, Morein B, Ramstedt U, Gidlund M, Wigzell H. (1987) A specific assay measuring binding of 125I-Gp 120 from HIV to T4+/CD4+ cells. *J. Immunol. Methods 97*, 93−100.
(16) Lasky, L. A., Nakamura, G., Smith, D. H., Fennie, C., Shimasaki, C., Patzer, E., Berman, P., Gregory, T.; Capon, D. J. (1987) Delineation of a region of the human immunodeficiency virus type 1 gp120 glycoprotein critical for interaction with the CD4 receptor. *Cell 50*, 975−985.
(17) Smith, D. H., Byrn, R. A., Marsters, S. A., Gregory, T., Groopman, J. E., and Capon, D. J. (1987) Blocking of HIV-1 infectivity by a soluble, secreted form of the CD4 antigen. *Science 238*, 1704−1707.
(18) Faroux-Corlay, B., Greiner, J., Terreux, R., Cabrol-Bass, D., Aubertin, A. M., Vierling, P., and Fantini, J. (2001) Amphiphilic anionic analogues of galactosylceramide: synthesis, anti- HIV-1 activity, and gp120 binding. *J. Med. Chem. 44*, 2188−2203.
(19) Faroux-Corlay, B., Clary, L., Gadras, C., Hammache, D., Greiner, J., Santaella, C., Aubertin, A. M., Vierling, P., and Fantini, J. (2000) Synthesis of single- and double-chain fluorocarbon and hydrocarbon galactosyl amphiphiles and their anti-HIV-1 activity. *Carbohydr. Res. 327*, 223−260.
(20) Rico-Lattes, I., Gouzy, M. F., Andre-Barres, C., Guidetti, B., and Lattes, A. (1998) Synthetic neoglycolipids for biological applications: correlation between their structures and their interactions with membrane proteins. *Biochimie 80*, 483−487.
(21) Fantini, J., Hammache, D., Delezay, O., Yahi, N., Andre-Barres, C., Rico-Lattes, I., and Lattes, A. (1997) Synthetic soluble analogues of galactosylceramide (GalCer) bind to the V3 domain of HIV-1 gp120 and inhibit HIV-1-induced fusion and entry. *J. Biol. Chem. 272*, 7245−7252.
(22) Fantini, J. (2000) Synthetic soluble analogues of glycolipids for studies of virus- glycolipid interactions. *Methods Enzymol. 311*, 626−638.
(23) Gu, Y, L. R., O'Brien, D. F., Saavedra, S. S. (2001) Quantitative Studies of Binding between Synthetic Galactosyl Ceramide Analogues and HIV-1 Gp120 at Planar Membrane Surfaces. *Angew. Chem., Int. Ed. 40*, 29−47.
(24) LaBell, R. Y., Jacobsen, N. E., Gervay-Hague, J., and O'Brien, D. F. (2002) Synthesis of novel glycolipids that bind HIV-1 Gp120. *Bioconjugate Chem. 13*, 143−149.
(25) McReynolds, K. D., Bhat, A., Conboy, J. C., Saavedra, S. S., and Gervay-Hague, J. (2002) Non-Natural glycosphingolipids and structurally simpler analogues bind HIV-1 recombinant Gp120. *Bioorg. Med. Chem. 10*, 625−637.
(26) Kasahara, K., and Sanai, Y. (2000) Functional roles of glycosphingolipids in signal transduction via lipid rafts. *Glycoconjugate J. 17*, 153−162.
(27) Hakomori, S. I. (2000) Cell adhesion/recognition and signal transduction through glycosphingolipid microdomain. *Glycoconjugate J. 17*, 143−151.
(28) Simons, K., and Toomre, D. (2000) Lipid rafts and signal transduction. *Nat. Rev. Mol. Cell Biol. 1*, 31−39.
(29) Simons, K., and Ikonen, E. (1997) Functional rafts in cell membranes. *Nature 387*, 569−572.
(30) Harder, T. (2001) Raft membrane domains and immunoreceptor functions. *Adv. Immunol. 77*, 45−92.
(31) Fivaz, M., Abrami, L., and van der Goot, F. G. (1999) Landing on lipid rafts. *Trends Cell Biol. 9*, 212−213.
(32) Kawakami, K., Ahmed, K., Utsunomiya, Y., Rikitomi, N., Hori, A., Oishi, K., and Nagatake, T. (1998) Attachment of nontypable Haemophilus influenzae to human pharyngeal epithelial cells mediated by a ganglioside receptor. *Microbiol. Immunol. 42*, 697−702.
(33) Reuter, J. D., Myc, A., Hayes, M. M., Gan, Z., Roy, R., Qin, D., Yin, R., Piehler, L. T., Esfand, R., Tomalia, D. A., and Baker, J. R., Jr. (1999) Inhibition of viral adhesion and infection by sialic-acid-conjugated dendritic polymers. *Bioconjugate Chem. 10*, 271−278.
(34) Roy, D. Z. a. R. (1998) Practical Synthesis of Starburst PAMAM−Thiosialodendrimers for Probing Multivalent Carbohydrate-Lectin Binding Properties. *J. Org. Chem. 63*, 3486-3491.
(35) Fulton D, S. J. (2001) Neoglycoconjugates Based on Cyclodextrins and Calizarenes. *Bioconjugate Chem. 12*, 655−672.
(36) Borman, S. (2000) Multivalency: Strength in Numbers. *C&EN* 48−53.
(37) Page, D., and Roy, R. (1997) Synthesis and Biological Properties of Mannosylated Starburst Poly(amidoamine) Dendrimers. *Bioconjugate Chem. 8*, 714−723.
(38) Lundquist, J. J., and Toone, E. J. (2002) The cluster glycoside effect. *Chem. Rev. 102*, 555−578.
(39) Brown, D. A., and London, E. (2000) Structure and function of sphingolipid- and cholesterol-rich membrane rafts. *J. Biol. Chem. 275*, 17221−17224.
(40) Turnbull, W. B., Pease, A. R., and Stoddart, J. F. (2000) Toward the synthesis of large oligosaccharide-based dendrimers. *Chembiochem. 1*, 70−74.
(41) Peerlings H, N. S., Stoddart J, Meijer E. (1998) Synthesis of Spacer-Armed Glucodendrimers Based on the Modification of Poly(propyene Imine) Dendrimers. *Eur. J. Org. Chem.* 1879−1886.
(42) Andre, S., Ortega, P. J., Perez, M. A., Roy, R., and Gabius, H. J. (1999) Lactose-containing starburst dendrimers: influence of dendrimer generation and binding-site orientation of receptors (plant/animal lectins and immunoglobulins) on binding properties. *Glycobiology 9*, 1253−1261.
(43) Turnball, W. B., S. J. (2002) Design and synthesis of glycodendrimers. *Rev. Mol. Biotechnol. 90*, 231−255.
(44) Bezouska, K. (2002) Design, functional evaluation and biomedical applications of carbohydrate dendrimers (glycodendrimers). *J. Biotechnol. 90*, 269−290.
(45) Thompson, J. P., and Schengrund, C. L. (1997) Oligosaccharide-derivatized dendrimers: defined multivalent inhibitors of the adherence of the cholera toxin B subunit and the heat labile enterotoxin of E. coli to GM1. *Glycoconjugate J. 14*, 837−845.
(46) Dam, T. K., Roy, R., Page, D., and Brewer, C. F. (2002) Thermodynamic binding parameters of individual epitopes of multivalent carbohydrates to concanavalin a as determined

by "reverse" isothermal titration microcalorimetry. *Biochemistry 41*, 1359−1363.
(47) Mylvaganam, M., Meng, L., and Lingwood, C. A. (1999) Oxidation of glycosphingolipids under basic conditions: synthesis of glycosyl "serine acids" as opposed to "ceramide acids". Precursors for neoglycoconjugates with increased ligand binding affinity. *Biochemistry 38*, 10885−10897.
(48) Schengrund, C. L., and Ringler, N. J. (1989) Binding of Vibrio cholera toxin and the heat-labile enterotoxin of *Escherichia coli* to GM1, derivatives of GM1, and nonlipid oligosaccharide polyvalent ligands. *J. Biol. Chem. 264*, 13233−13237.
(49) Radin, N. S. (1974) Preparation of psychosines (1-O-hexosyl sphingosine) from cerebrosides. *Lipids 9*, 358−360.
(50) Dubois, G., Zalc, B., Le Saux, F., and Baumann, N. (1980) Stearoyl[1−14C]sulfogalactosylsphingosine ([14C]sulfatide) as substrate for cerebroside sulfatase assay. *Anal. Biochem. 102*, 313−317.
(51) Mylvaganam, M., and Lingwood, C. A. (2000) Oxidation of aglycone of glycosphingolipids: serine and ceramide acid precursors for soluble glycoconjugates. *Methods Enzymol. 312*, 473−487.
(52) Manusson, G, N. G., Dahmen, J., Frejd, T., and Lave, T. (1981) BF_3-Etherate Induced Formation of 2, 2, 2,-Trichloroethyl Glycopyranosides. Selective Visualization of Carbohydrate Derivatives on TLC Plates. *Acta Chemica Scand. B 35*, 213−216.
(53) Elofsson, M. W. B., Kihlberg, J. (1991) Building blocks for glycopeptide synthesis: glycosylation of 3-mercaptopropionic acid and Fmoc amino acids with unprotected carboxyl groups. *Tetrahedron Lett. 32*, 7613−7616.
(54) Guilbert, B, D. N., Pearce, M., Aplin, R., and Flitsch, S. (1994) Dibutylstannylene acetals: Useful intermediates for the regioselective sulfation of glycosides. *Tetrahedron: Asymmetry 5*, 2163−2178.
(55) Nishida, Y., Uzawa, H., Toba, T., Sasaki, K., Kondo, H., and Kobayashi, K. (2000) A facile synthetic approach to L- and P-selectin blockers via copolymerization of vinyl monomers constructing the key carbohydrate modules of sialyl LewisX mimics. *Biomacromolecules 1*, 68−74.
(56) Poirot, E., Zhang, X., Whittaker, N. F., and Kovac, P. (2001) Syntheses of the L-manno and some other analogues of the terminal determinants of the O−PS of *Vibrio cholerae* O: 1. *Carbohydr Res. 330*, 7−20.
(57) Woller, E. K., and Cloninger, M. J. (2001) Mannose functionalization of a sixth generation dendrimer. *Biomacromolecules 2*, 1052−1054.
(58) Zhu, H., Yalcin, T., and Li, L. (1998) Analysis of the Accuracy of Determining Average Molecular Weights of Narrow Polydispersity Polymers by Matrix-Assisted Laser Desorption Ionization Time-of-Flight Mass Spectrometry. *Am. Soc. Mass Spectrom. 9*, 275−281.
(59) Zhu, T., Mo, H., Wang, N., Nam, D. S., Cao, Y., Koup, R. A., and Ho, D. D. (1993) Genotypic and phenotypic characterization of HIV-1 patients with primary infection. *Science 261*, 1179−1181.
(60) Ashton, R, B. S., Brown, C., Nepogodiev, S., Meijer, E., Peerlings, H., and Stoddart, J. (1997) Synthesis of Glycodendrimers by Modification of Poly(propylene imine) Dendrimers. *Chem. Eur. J. 3*, 974−984.
(61) Driguez, H. (1997) Thiooligosaccharides in glycobiology. *Topics Curr. Chem. 187*, 85−116.
(62) Lubineau, A., and Lemoine, R. (1994) Regioselective sulfation of galactose derivatives through the stannylene procedure. New synthesis of the 3′-O'sulfated Lewis trisaccharide. *Tetrahedron Lett. 35*, 8795−8796.
(63) David, S., and Hanessian, S. (1985) Regioselective Manipulation of Hydroxyl Groups Via Organotin Derivatives. *Tetrahedron 41*, 643−663.
(64) Ikami, T., Hamajima, H., Usui, T., Mitani, T., Ishida, H., Kiso, M., and Hasegawa, A. (1997) Synthetic Studies on Selectin Ligands/Inhibitors: One-Pot Synthesis of the Mono- and Oligo-Sulfated 2-(Tetradecyl)Hexadecyl β-D-Galacto- and Lactopyranosides as the Sulfatide Mimetics. *J. Carbohydr. Chem. 16*, 859−875.
(65) Guilbert, B, D. N., and Flitsch, S. (1994) Regioselective Sulfation of Disaccharides Using Dibutylstannylene Acetals. *Tetrahedron Lett. 35*, 6563−6566.
(66) Farzan, M., Mirzabekov, T., Kolchinsky, P., Wyatt, R., Cayabyab, M., Gerard, N. P., Gerard, C., Sodroski, J., and Choe, H. (1999) Tyrosine sulfation of the amino terminus of CCR5 facilitates HIV-1 entry. *Cell 96*, 667−676.
(67) Callahan, L. N., Phelan, M., Mallinson, M., and Norcross, M. A. (1991) Dextran sulfate blocks antibody binding to the principal neutralizing domain of human immunodeficiency virus type 1 without interfering with gp120-CD4 interactions. *J. Virol. 65*, 1543−1550.
(68) Yahi, N., Sabatier, J. M., Baghdiguian, S., Gonzalez-Scarano, F., and Fantini, J. (1995) Synthetic multimeric peptides derived from the principal neutralization domain (V3 loop) of human immunodeficiency virus type 1 (HIV-1) gp120 bind to galactosylceramide and block HIV-1 infection in a human CD4- negative mucosal epithelial cell line. *J. Virol. 69*, 320−325.

BC034156A

A Novel, High-Affinity, Fluorescent Progesterone Receptor Antagonist. Synthesis and in Vitro Studies

Claudia Hödl,[†] Wolfgang S. L. Strauss,[‡] Reinhard Sailer,[‡] Christoph Seger,[§] Rudolf Steiner,[‡] Ernst Haslinger,[†] and H. Wolfgang Schramm*[,†]

Institute for Pharmaceutical Chemistry and Pharmaceutical Technology, Karl-Franzens-University, Universitätsplatz 1, A-8010 Graz, Austria, Institut für Lasertechnologien in der Medizin und Messtechnik an der Universität Ulm, Helmholtzstrasse 12, D-89081 Ulm, Germany, and Institute of Pharmacy, Department of Pharmacognosy, Leopold-Franzens-University, Innrain 52, A-6020 Innsbruck, Austria. Received September 16, 2003; Revised Manuscript Received February 3, 2004

The present paper describes the chemical synthesis and in vitro characterization of a novel, high-affinity, fluorescent progesterone receptor (PR) antagonist. The three-step synthesis was carried out starting from mifepristone. After demethylation with calcium oxide, the methylamino group was alkylated with 6-bromohexanol, and the resulting compound was reacted with fluorescein 5-isothiocyanate, yielding the fluorescein−mifepristone conjugate. Interaction of the conjugate as well as of its precursors with PR was determined in cell culture (alkaline phosphatase assay and transactivation assay). Antiprogestagenic activity of the intermediates were comparable to that of the parent compound. Even after attachment of the bulky fluorescein moiety, considerable antiprogestagenic activity was maintained. Microscopic studies revealed that fluorescence of the conjugate was almost confined to the nuclei of steroid hormone receptor-positive cells, whereas the nuclei of steroid hormone receptor-negative cells remained unstained. To our knowledge, this is the first report on a fluorescent ligand for PR suitable for studies in living cells. It is proposed that the present fluorescent PR antagonist might serve as a lead compound for the development of contrast agents for PR imaging, e.g., by near-infrared optical imaging.

INTRODUCTION

The progesterone receptor (PR)[1] is a ligand-activated transcription factor that belongs to the nuclear receptor superfamily, which includes the steroid hormone receptors as well as thyroid, vitamin D, and retinoic acid receptors. It contains conserved functional domains, including the N-terminus, a centrally located DNA binding domain (DBD), and the C-terminal ligand binding domain (LBD). The human PR exists as two isoforms (A and B) in most PR-expressing cells, which arise from a single gene located in the region 11q22-q23 of chromosome 11. The isoform A (PRA) is a 164 amino acid N-terminally truncated variant of the isoform B (PRB). Although both isoforms have similar DNA and ligand binding properties, they have distinct functional properties. Current knowledge of the ligand−receptor interaction at the molecular level mainly relies on the crystal structure of the LBD of the PR complex formed after binding of progesterone (*1*) as well as on results of site-directed mutagenesis experiments (*2*) and classical molecular dynamics simulations (*3*). According to the physiological role of its natural ligand, i.e., establishment and maintenance of pregnancy, high PR levels are found in the female reproductive system. Current development of drugs interacting with the PR comprise (1) selective PR antagonists (*4, 5*) expected to be useful for the treatment of chronic conditions, e.g., endometriosis or leiomyomas, and (2) radioligands (*6*−*8*) to enable determination of PR levels in vivo for assessing the hormone responsiveness of breast cancer without tissue biopsy.

During the past decade, optical imaging using near-infrared (NIR) light has emerged as a new diagnostic modality, in particular for breast tissue (*9*). Since contrast and image resolution is limited by multiple scattering of the photons, reliable tissue characterization based on intrinsic absorption and scattering inhomogeneities is often difficult, in particular with respect to distinguish between benign and malignant lesions (*10, 11*). Similar to other clinical imaging modalities, it is likely that sensitivity and specificity of optical imaging will be improved by contrast agents. Considering photophysical properties, cyanine dyes are one of the most promising classes of compounds suitable as contrast agents for NIR optical imaging (*12, 13*). Recently, indocyanine green has been successfully applied to detect breast cancer probing tumor vascularization and vessel permeability (*14*). In addition to tumor targeting by such unspecific mechanisms, contrast agents which specifically target receptors overexpressed in tumor cells (*15*−*18*), or which are activated by tumor-associated enzymes (*19*−*23*), have recently been developed, thus enabling molecular imaging.

PR status of breast cancer was found to be an independent predictive factor for benefit from adjuvant

* Corresponding author: phone +43/316/380-538; fax+43/316/380-9846; e-mail: wolfgang.schramm@uni-graz.at.

[†] Karl-Franzens-University.

[‡] Institut für Lasertechnologien in der Medizin und Messtechnik an der Universität Ulm.

[§] Leopold-Franzens-University.

[1] Abbreviations: CH, cyclohexane; DMF, *N*,*N*-dimethylformamide; DMSO, dimethyl sulfoxide; EtOAc, ethyl acetate; FCS, fetal calf serum; FITC, fluorescein isothiocyanate; MeCN, acetonitrile; MeOH, methanol; MMTV, mouse mammary tumor virus; NIR, near-infrared; PBS, phosphate-buffered saline; PR, progesterone receptor; THF, tetrahydrofuran.

10.1021/bc034169o CCC: $27.50 © 2004 American Chemical Society
Published on Web 02/26/2004

endocrine therapy. Patients with steroid hormone receptor-positive tumors, expressing estrogen receptor as well as PR, have the most favorable prognosis (*24*). Therefore, reliable and noninvasive determination of PR levels in breast cancer, preferentially with high sensitivity and without harmful radiation, i.e., by NIR optical imaging, seem to be highly desirable. However, no appropriate PR-binding contrast agent is known, so far. In the present paper, synthesis and in vitro studies of a novel, high-affinity, fluorescent PR antagonist is reported, which might serve as lead compound for the development of PR-binding contrast agents for NIR optical imaging.

EXPERIMENTAL PROCEDURES

Materials and Chemical Methods. (11β,17β)-17-Hydroxy-11-[4-(dimethylamino)phenyl]-17-(1-propynyl)-estra-4,9-dien-3-one (**1**) and fluorescein 5-isothiocyanate (FITC, isomer I) were obtained from Sigma-Aldrich. All other reagents for syntheses were purchased from either Sigma-Aldrich or Merck and were used without further purification. Reagent-grade solvents were obtained from Merck and were purified and dried using standard methods. Solvents of analytical and spectroscopic grade and deuterated NMR solvents were purchased from Merck and Uetikon, respectively.

UV/vis spectra were recorded on a Shimadzu UV-160A spectrometer. Absorption maxima λ_{max} are given in nm. Fluorescence spectra were measured using a Kontron Instruments spectrofluorometer. Excitation and emission maxima λ_{max} are given in nm. IR spectra were recorded on a Perkin-Elmer FTIR 2000 spectrometer. Absorption maxima ν_{max} are given in cm^{-1} and are referred to as s (strong), m (medium), w (weak), and br (broad). EI-mass spectra were measured with a Finnigan MAT 212 or Varian MAT 312 spectrometer at 70 eV ionizing voltage. Intensities are given in % of the base peak. NMR spectra were recorded at 300 K on a Varian Unity Inova 400 NMR spectrometer equipped with a tunable broad band probe. Inverse detected gradient selected 2D experiments (gCOSY, HSQC, HMBC) were performed using standard pulse sequence programs. HMBC experiments were optimized for a long range-coupling constant of 8 Hz. Spectra were referenced internally using tetramethylsilane. Chemical shifts δ are given in ppm. Coupling constants (*J* values) are expressed in Hz, and multiplicities are referred to as s (singlet), d (dublet), t (triplet), q (quartet), m (multiplet), and br (broad).

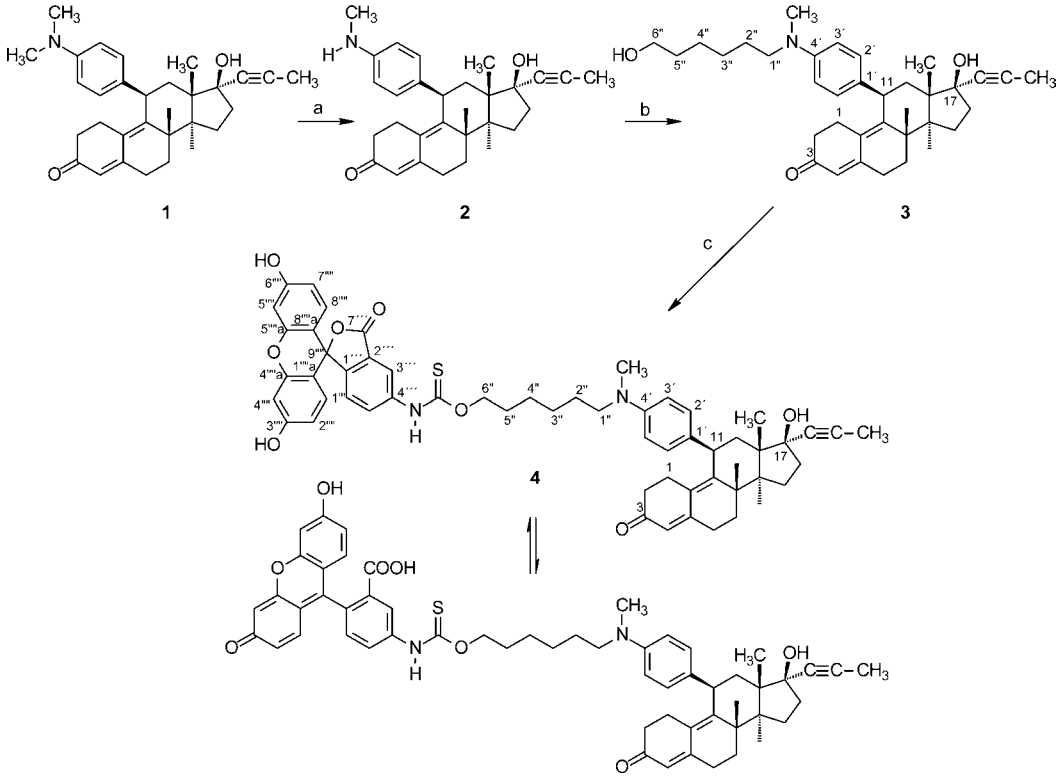
TLC analyses were performed on Merck F_{254} silica gel plates. Spots were visualized either by UV absorbance at 254 nm or fluorescence emission excited at 366 nm. Column chromatography was carried out on Merck silica gel 60, 70−230 mesh, using EtOAc:cyclohexane (CH) (3:2) as eluent. Preparative RP-HPLC was performed using a Labomatic HD-200 pump equipped with a Labocord-700 UV/vis detector.

(11β,17β)-17-Hydroxy-11-[4-(methylamino)phenyl]-17-(1-propynyl)estra-4,9-dien-3-one (2). (11β,17β)-17-Hydroxy-11-[4-(dimethylamino)phenyl]-17-(1-propynyl)-estra-4,9-dien-3-one (**1**) (500 mg, 1.164 mmol) was dissolved in a 1:1 mixture of MeOH and THF (7.0 mL), and freshly calcined CaO (555 mg, 9.897 mmol) was added. I_2 (739 mg, 2.912 mmol) dissolved in the same solvent (1.5 mL) was added dropwise at 0 °C. The reaction mixture was stirred at 0 °C for 1 h. After CaO removal, it was diluted with 10% $Na_2S_2O_3$ and extracted with CH_2Cl_2. The combined organic layers were washed with water and brine and dried over Na_2SO_4. The solvent was evaporated after filtration, and the crude product was purified by column chromatography. Fractions containing the steroidal compounds **1** and **2** were further purified by HPLC (ProntoSIL 120−5-C18H, 5 μm, 200 × 20 mm, MeCN:H_2O = 84:16, 23 mL/min, λ = 254 nm) to afford compound **2** as a white solid (135 mg, 28%) after lyophilization, t_R = 3.4 min. Educt **1** was recovered (130 mg, 26%), t_R = 4.3 min. TLC (EtOAc:CH = 3:2): R_f = 0.5; TLC (CH_2Cl_2:MeOH = 9:1): R_f = 0.71. UV/vis (MeOH): 209.0, 250.0, 303.5; UV/VIS (MeCN): 254.0, 295.5. IR (KBr): 3387 (m (br), N−H, O−H); 2929 (s, C−H); 2870 (m, C−H); 2250 (w, C≡C); 1654 (s (br), C═O), 1615 (s, C═C). MS (*m*/*z*): 415 (M^+, 100); 397 (7); 331 (11); 266 (71); 213 (23); 120 (47); 107 (76); 91 (54); calculated for $C_{28}H_{33}NO_2$, 415. ^{1}H NMR ($CDCl_3$): 0.50 (s, 3H, H-18); 1.40 (m, 1H, H-16); 1.42 (m, 1H, H-7); 1.68 (m, 2H, H-14, H-16); 1.84 (s, 3H, H-21); 1.89 (td, *J* = 11.4, *J* = 3.2, 1H, H-15); 1.98 (m, 1H, H-7); 2.16 (m, 1H, H-15); 2.21 (m, 1H, H-12); 2.29 (m, 4H, H-1, 2x(H-2), H-12); 2.42 (dd, *J* = 10.4, *J* = 0.8, 1H, H-8); 2.52 (m, 2H, H-6); 2.73 (m, 1H, H-1); 2.86 (s, 3H, NCH_3); 4.31 (d, *J* = 6.4, 1H, H-11); 5.52 (s, 1H, H-4); 6.61 (m, 2H, H-3′, H-5′); 6.97 (m, 2H, H-2′, H-6′). ^{13}C NMR ($CDCl_3$): 3.7 (q, C-21); 13.6 (q, C-18); 23.2 (t, C-16); 25.6 (t, C-1); 27.2 (t, C-7); 31.0 (t, C-6); 36.7 (t, C-2); 38.8 (t, C-12, C-15); 39.0 (d, C-8); 39.4 (d, C-11); 40.5 (q, NCH_3); 46.7 (s, C-13); 49.7 (d, C-14); 79.9 (s, C-17); 82.0 (s, C-20/C-19); 82.4 (s, C-19/C-20); 112.7 (d, C-3′, C-5′); 122.5 (d, C-4); 127.3 (d, C-2′, C-6′); 128.8 (s, C-10); 132.0 (s, C-1′); 146.8 (s, C-9); 148.4 (s, C-4′); 156.9 (s, C-5); 199.5 (s, C-3).

(11β,17β)-17-Hydroxy-11-(4-[(6-hydroxyhexyl)methylamino]phenyl)-17-(1-propynyl)estra-4,9-dien-3-one (3). Compound **2** (200 mg, 0.481 mmol) and freshly distilled 6-bromohexanol (500 mg, 2.760 mmol) were dissolved in anhydrous DMF (4.0 mL) and stirred in the presence of dry K_2CO_3 (80 mg, 0.579 mmol) at 65 °C for 18 h. The solvent was removed in vacuo, and the residue was purified by column chromatography, yielding 134 mg (54%) of compound **3** as a white solid. For biological studies 25 mg of compound **3** were additionally purified by HPLC (YMC−Pack ODS-A (C18), 10 μm, 250 × 20 mm, MeCN:H_2O = 2:3, 12 mL/min, λ = 264 nm), t_R = 9.3 min. After lyophilization 13.5 mg (54%) were recovered. TLC (EtOAc:CH = 3:2): R_f = 0.3; TLC (CH_2Cl_2:MeOH = 9:1): R_f = 0.87. UV/vis (MeOH): 208.5, 263.5, 303.5. IR (KBr): 3421 (m, O−H); 2934 (s, C−H); 2861 (m, C−H); 2250 (w, C≡C); 1653 (s, C═O), 1611 (s, C═C). MS (*m*/*z*): 515 (M^+, 100), 475 (12), 428 (83), 388 (17), 366 (12), 120 (18); calculated for $C_{34}H_{45}NO_3$, 515. ^{1}H NMR ($CDCl_3$): 0.53 (s, 3H, H-18); 1.34 (m, 1H, H-16); 1.42 (m, 1H, H-7); 1.46 (m, 6H, H-3″, H-4″, H-5″); 1.55 (m, 2H, H-2″); 1.70 (m, 2H, H-14, H-16); 1.87 (s, 3H, H-21); 1.88 (td, *J* = 12.0, *J* = 3.2, 1H, H-15); 2.00 (m, 1H, H-7); 2.24 (m, 3H, 2x(H-12), H-15); 2.39 (m, 4H, H-1, 2x(H-2), H-8); 2.55 (m, 2H, H-6); 2.75 (m, 1H, H-1); 2.86 (s, 3H, NCH_3); 3.24 (m, 2H, H-1″); 3.61 (br, 2H, H-6″); 4.32 (d, *J* = 6.8, 1H, H-11); 5.73 (s, 1H, H-4); 6.57 (m, 2H, H-3′, H-5′); 6.97 (m, 2H, H-2′, H-6′). ^{13}C NMR ($CDCl_3$): 3.8 (q, C-21); 13.7 (q, C-18); 23.3 (t, C-16); 25.6 (t, C-2″); 25.8 (t, C-1); 26.7 (t, C-3″/C-4″); 26.9 (t, C-4″/C-3″); 27.4 (t, C-7); 31.1 (t, C-6); 32.7 (t, C-5″); 36.9 (t, C-2); 38.2 (q, NCH_3); 38.8 (t, C-12/C-15); 38.9 (t, C-15/C-12); 39.1 (d, C-8); 39.5 (d, C-11); 46.8 (s, C-13); 49.8 (d, C-14); 52.9 (t, C-1″); 62.8 (t, C-6″); 80.2 (s, C-17); 82.3 (s, C-19/C-20); 82.5 (s, C-20/C-19); 112.2 (d, C-3′, C-5′); 123.6 (d, C-4); 127.6 (d, C-2′, C-6′); 129.0 (s, C-10); 131.3 (s, C-1′); 146.9 (s, C-9); 147.3 (s, C-4′); 157.0 (s, C-5); 199.7 (s, C-3).

***O*-(6-[*N*-Methyl-*N*-(4-[(11β,17β)-17-hydroxy-3-oxo-17-(1-propynyl)estra-4,9-dien-11-yl]phenyl)amino]-hexyl)-*N*-(3′,6′-dihydroxy-3-oxospiro[isobenzofuran-1(3*H*),9′-[9′*H*]xanthen]-5-yl)-carbamothioate (4).** Com-

Scheme 1: Synthesis of Conjugate 4 and Its Precursors 2, 3[a]



[a] (a) CaO/I_2/MeOH/THF; (b) $BrCH_2(CH_2)_4CH_2OH$/DMF; (c) FITC (isomer I)/DMF.

pound **3** (120 mg, 0.234 mmol) and fluorescein 5-isothiocyanate (136 mg, 0.349 mmol) were dissolved in anhydrous DMF (5.0 mL) and stirred at 70 °C for 5 h. It was diluted with ice/H_2O to give a brownish precipitate. The crude product was extracted with EtOAc, washed with H_2O, and dried over Na_2SO_4. The solvent was evaporated after filtration, and the residue was purified by column chromatography. HPLC purification (YMC−Pack ODS-A (C18), 10 μm, 250 × 20 mm, MeOH: H_2O = 4:1, 12 mL/min, λ = 220 nm) was applied to afford conjugate **4** as a yellow solid (18.5 mg, 8.6%) after lyophilization, t_R = 5.3 min. TLC ($CHCl_3$:MeOH = 4:1): R_f = 0.63. UV/vis (MeOH): 220.5, 284.0, 454.5, 480.5. IR (KBr): 3430 (s, O−H); 2934 (m, C−H); 2861 (m, C−H); 1737 (w, C═O, lactone); 1636 (s, C═O), 1612 (s, C═C). MS (*m*/*z*): 905 (M^+, 13), 887 (14), 597 (5), 408 (19), 390 (90), 374 (76); 348 (100); calculated for $C_{55}H_{56}N_2O_8S$, 905. ^{1}H NMR (acetone-d_6): 0.56 (s, 3H, H-18); 1.36 (m, 1H, H-16); 1.41 (m, 3H, H-7, 2x(H-3″/H-4″)); 1.51 (m, 2H, H-4″/H-3″); 1.58 (m, 2H, H-2″); 1.68 (m, 1H, H-16); 1.74 (m, 1H, H-14); 1.77 (m, 2H, H-5″); 1.82 (s, 3H, H-21); 1.89 (m, 1H, H-15); 2.04 (m, 1H, H-7); 2.11 (m, 1H, H-15); 2.20 (m, 1H, H-1); 2.28 (m, 1H, H-12); 2.29 (m, 2H, H-2); 2.37 (m, 1H, H-12); 2.49 (m, 1H, H-8); 2.61 (m, 2H, H-6); 2.78 (m, 1H, H-1); 2.87 (s, 3H, NCH_3); 3.31 (t, J = 6.8, 2H, H-1″); 4.08 (m, 2H, H-6″); 4.36 (d, J = 6.8, 1H, H-11); 4.55 (s, 1H, OH-17); 5.63 (s, 1H, H-4); 6.70 (m, 6H, H-3′, H-5′, H-1‴, H-2‴, H-7‴, H-8‴); 6.75 (d, J = 2.0, 2H, H-4‴, H-5‴); 7.02 (m, 2H, H-2′, H-6′); 7.23 (m, 1H, H-6‴); 9.00 (s (br), 2H, OH-3‴, OH-6‴); 10.40 (s (br), 1H, NH). ^{13}C NMR (acetone-d_6): 3.4 (q, C-21); 14.3 (q, C-18); 23.9 (t, C-16); 26.5 (t, C-1); 27.2 (t, C-3″/C-4″); 27.3 (t, C-2″); 27.4 (t, C-4″/C-3″); 28.5 (t, C-7); 29.1 (t, C-5″); 31.6 (t, C-6); 37.5 (t, C-2); 38.3 (q, NCH_3); 39.7 (t, C-12/C-15); 39.8 (t, C-15/C-12); 40.1 (d, C-8); 40.3 (d, C-11); 47.7 (s, C-13); 50.7 (d, C-14); 53.1 (t, C-1″); 60.5 (t, C-6″); 80.1 (s, C-17); 81.4 (s, C-19/C-20/C-9‴); 83.7 (s, C-20/C-9‴/C-19); 84.2 (s, C-9‴, C-19, C-20); 103.3 (d, C-4‴, C-5‴); 111.5 (s, C-1‴a, C-8‴a); 113.1 (d, C-3′, C-5′/C-2‴, C-7‴); 113.3 (d, C-2‴, C-7‴/C-3′, C-5′); 117.3 (d, C-3‴); 123.0 (d, C-4); 125.2 (d, C-6‴); 128. 5 (d, C-2′, C-6′); 129.6 (s, C-10); 130.1 (d, C-1‴, C-8‴); 132.7 (s, C-1′); 140.8 (s, C-2‴); 147.7 (s, C-4′); 148.2 (s, C-9); 149.7 (s, C-4‴); 153.3 (s, C-4‴a, C-5‴a); 157.1 (s, C-5); 160.3 (s, C-3‴, C-6‴); 169.0 (s, C-7‴); 189.4 (s, CS); 198.6 (s, C-3).

Cell Culture and Media. T47-D cells (breast cancer, human, steroid hormone receptor-positive) were obtained from American Type Culture Collection (ATCC number HTB-133 (*25*)) and OV2774 cells (ovarian cancer, human, steroid hormone receptor-negative) were kindly provided by Prof. D. G. Kieback, Department for Obstetrics and Gynecology, Maastricht University Medical Center, The Netherlands. T47-D-Cl24 cells stably expressing luciferase under control of hormone responsive mouse mammary tumor virus (MMTV) promoter (*26*) were generated. Vectors ΔMa-Luc (generous gift of Prof. R. Schüle, Department of Obstetrics and Gynecology, University Hospital Freiburg, Germany) and pcDNA6/HisA (invitrogen) were cotransfected into T47-D cells using Rotifect (Roth) as recommended by the supplier. Stable transfectants were selected with blasticidin (2.5 μg/mL), and individual colonies were picked and cultured separately. Clones were screened for luciferase expression after incubation with progesterone (10^{-6} mol/L). Clone 24 was chosen considering level and dynamic range of luciferase expression after progesterone incubation (10^{-11} to 10^{-6} mol/L). T47-D and T47-D-Cl24 cells were maintained in RPMI 1640 medium (invitrogen) supplemented with 10% fetal calf serum (FCS, Biochrom) and antibiotics (penicillin (100.000 U/L), streptomycin (100.000 μg/L), invitrogen) and cultured in a humidified atmosphere containing 5% CO_2 at 37 °C. Twenty-four hours prior to the experiments cells were seeded at a density of 100 cells per mm^2 in 96-well plates (Nunc) or on microscope slides (Marienfeld) and were cultivated in RPMI 1640 medium

(without phenol red) supplemented with 5% dextran charcoal stripped FCS (DCS) and antibiotics at 5% CO_2 and 37 °C. Incubation media were made up by adding an appropriate volume of the stock solutions of compounds **1**−**4** and progesterone (prepared in dimethyl sulfoxide (DMSO) and stored at −20 °C) to RPMI 1640 medium (without phenol red, plus 5% DCS and all other supplements). In each case, the final DMSO concentration in the incubation medium was 0.1% (v/v). Incubations were performed after washing the cultures with phosphate-buffered saline (PBS).

Alkaline Phosphatase Assay. T47-D cells were coincubated with increasing concentrations of either compound **1** (reference antagonist) or test compounds **2**, **3**, or **4** (10^{-11} to 10^{-7} mol/L) and progesterone (10^{-9} mol/L). The alkaline phosphatase assay was performed as reported previously (*27*, *28*) with some minor modifications. Briefly, after 48 h incubation cells were washed with 0.9% saline and stored at −80 °C for at least 30 min.. After thawing cells were incubated with 50 μL *p*-nitrophenyl phosphate (5 mM, Fluka) dissolved in aqueous diethanolamine (1 M, supplemented with 0.5 mM magnesium chloride and 20 μM zinc sulfate, and adjusted to pH 9.8) for 2−5 h in the dark at room temperature. Absorbance of *p*-nitrophenolate was measured in a Lucy 1 multimode plate reader (anthos labtec instruments) at 405 nm (vs 690 nm as reference). For each compound, at least four independent experiments (with six data points each) were carried out. After background subtraction (absorbance of cells without hormonal treatment), absorbance was normalized to the absorbance resulting from the progesterone incubation. Median (central tendency) ± median absolute deviation (variability) were calculated. IC_{50} values were determined from dose−response curves and are given in nmol/L.

Transactivation Assay. T47-D-Cl24 cells were coincubated with increasing concentrations of compound **1** (reference antagonist) or test compounds **2**, **3**, or **4** (10^{-12} to 10^{-8} mol/l) and progesterone (10^{-9} mol/L). After 24 h incubation, luciferase activities were measured by the Reporter Gene Luciferase Assay, Constant Light Signal (Roche Diagnostics) as recommended by the supplier in the Lucy 1 reader. For each compound, four independent experiments (with six data points each) were carried out using white 96-well plates. Luciferase activity is given as normalized response value relative to the luciferase activity produced by progesterone. Median (central tendency) ± median absolute deviation (variability) were calculated. IC_{50} values were determined from dose−response curves and are given in nmol/L.

Fluorescence Microscopy. T47-D and OV2774 cells were incubated with either compound **4** or fluorescein (Riedel-de Haen) for 5−7 h at 37 °C. Incubation concentrations were varied between 10^{-8} mol/L and 10^{-6} mol/L. After incubation, cells were washed twice with PBS. Fluorescence images were obtained with an upright Axioplan I microscope (Zeiss) equipped with a highly sensitive CCD camera (ST138 (Princeton Instruments) equipped with a thermoelectrically cooled CCD-512EFT chip (EEV)) at 40× magnification (oil immersion NA 1.3). Fluorescence was excited in the blue spectral region (band-pass filter: 450−490 nm) and detected above 520 nm (dichroic mirror: 510 nm, long-pass filter: 520 nm). For both compounds, an identical exposure time of 1 s was applied to minimize photobleaching. Image acquisition was performed using WinView 32 (Princeton Instruments). Images were stored as TIFF files, and contrast and brightness were adjusted manually (Adobe Photoshop 6.0, Adobe Systems, Inc.).

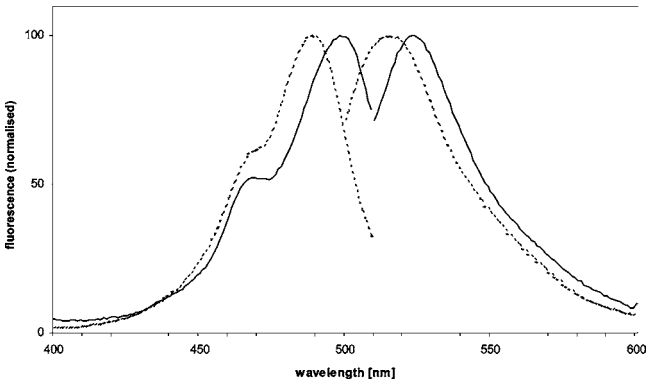


Figure 1. Fluorescence excitation and emission spectra of conjugate **4** (solid lines) and fluorescein (dotted lines) in PBS (supplemented with 10% FCS). Excitation spectra were recorded at the emission maxima (515 nm (fluorescein) and 524 nm (conjugate **4**)), and emission spectra were recorded at the excitation maxima of each compound (488 and 498 nm) at a concentration of 10^{-6} mol/L.

Table 1. Antiprogestagenic Activity of Conjugate 4, Intermediates 2, 3, and Parent Compound 1

	alkaline phosphatase assay[a]		transactivation assay[b]	
compound	IC_{50} values[c]	rel potency[d]	IC_{50} values[c]	rel potency[d]
1	0.045	1	0.021	1
2	0.170	0.26	0.073	0.29
3	0.063	0.71	0.071	0.30
4	1.5	0.03	0.550	0.04

[a] Inhibition of progesterone-induced (10^{-9} mol/L) alkaline phosphatase activity in T47-D cells. [b] Inhibition of progesterone-induced (10^{-9} mol/L) transcriptional activity in T47-D-Cl24 cells. [c] IC_{50} values are were determined from dose−response curves and are given in nmol/L. [d] Relative potency is defined as the ratio of IC_{50} (**1**) to IC_{50} (x) with x = **2**, **3**, **4**.

RESULTS

Chemistry. Synthesis of the conjugate **4** was carried out starting from the antiprogestin **1**, mifepristone (RU486), which was converted to intermediate **2** by treating with calcium oxide and iodine in methanol/tetrahydrofuran (*29*). Alkylation of the methylamino group of **2** with 6-bromohexanol in anhydrous dimethylformamide in the presence of potassium carbonate resulted in intermediate **3**, which was reacted with FITC in dry dimethylformamide (*30*), yielding compound **4** as yellow crystals. The synthetic pathway of conjugate **4** is depicted in Scheme 1. The colorless, nonfluorescent lactone form of conjugate **4** was prevalent in the aprotic NMR solvent, whereas an aqueous environment as used in biological studies caused spontaneous conversion into its quinoid, fluorescent form. Fluorescence excitation and emission spectra of fluorescein and conjugate **4** are quite similar (Figure 1), although a bathochromic shift of about 10 nm was observed for excitation and emission maxima (488 nm vs 498 nm and 515 nm vs 524 nm).

Antiprogestagenic Activity. Antagonistic activity of conjugate **4** and intermediates **2** and **3** was determined in cell culture using the alkaline phosphatase assay in T47-D cells and a transactivation assay in T47-D-Cl24 cells stably transfected with the luciferase gene linked to the hormone responsive MMTV promoter. Inhibition of progesterone-induced increase of either alkaline phosphatase or luciferase activity was found for all compounds. IC_{50} values determined from dose−response curves and the relative potencies (defined as the ratio of the IC_{50} value of the reference antagonist **1** to the IC_{50} value of the individual test compound) are summarized in Table 1. Antiprogestagenic activity of the intermedi-

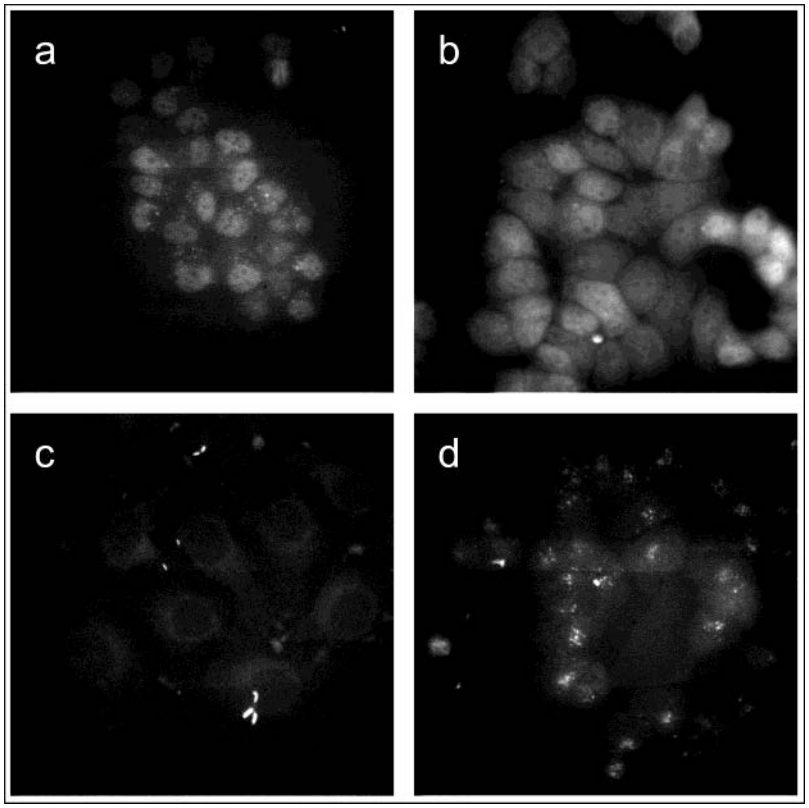


Figure 2. Fluorescence images (40× magnification) of conjuagte **4** in steroid hormone receptor-positive T47-D breast cancer cells at incubation concentrations of 10^{-8} mol/L (A) and 10^{-7} mol/L (B) as well as in steroid hormone receptor-negative OV2774 ovarian cancer cells (C, 10^{-7} mol/L), and fluorescence image of fluorescein in T47-D cells (D, 10^{-7} mol/L). Incubations were carried out 5−7 h prior to microscopy at 37 °C.

ates **2** and **3** were 3- to 4-fold lower than that of the reference antagonist **1**. Conjugate **4** exhibited considerable antiprogestagenic activity with IC_{50} values in the nanomolar range, although the relative potency of conjugate **4** was approximately 30-fold lower as compared with the parent compound **1**.

Fluorescence Microscopy. Subcellular distribution of conjugate **4** was examined by fluorescence microscopy. For steroid hormone receptor-positive T47-D cells, fluorescence of conjugate **4** was almost confined to the cell nuclei (without staining the nucleoli) at the lowest incubation concentration of 10^{-8} mol/L. Predominantly diffuse fluorescence arising from the cytoplasm was barely above background (intrinsic cell fluorescence) (Figure 2a). When incubation concentration was increased to 10^{-7} mol/L or 10^{-6} mol/L, fluorescence was distributed more homogeneously within the whole cell, and cell nuclei were stained prominently only in selected cases (Figure 2b). In contrast, fluorescence of conjugate **4** could not be detected in the cell nuclei of steroid hormone receptor-negative OV2774 cells independently of the incubation concentration. Cells exhibited a weak fluorescence with sometimes a distinct pattern within the cytoplasm at an incubation concentration of 10^{-7} mol/L (Figure 2c), whereas fluorescence intensity was close to intrinsic cell fluorescence at 10^{-8} mol/L. Control experiments performed with fluorescein in T47-D cells revealed diffuse fluorescence within the cytoplasm together with fluorescent granules in the perinuclear region, which is exemplified for an incubation concentration of 10^{-7} mol/L in Figure 2d.

DISCUSSION

Conjugate **4** was obtained in a three-step synthesis. After demethylation of mifepristone to intermediate **2** (step 1), the methylamino group was alkylated with 6-bromohexanol, resulting in intermediate **3** (step 2), which was reacted with FITC, yielding the desired conjugate **4** (step 3). Oxidative demethylation of 4-substituted *N*,*N*-dimethylanilines (*31*) has previously been applied to obtain intermediate **2** and a related antiprogestin (*29*). Alternatively, intermediate **2** could also be obtained by reacting **1** with iodobenzene diacetat (*32*). The other two steps were performed following standard procedures. Structures of all compounds were confirmed by NMR spectroscopy, and clean spectra were obtained in all cases. Although the protons at positions 3‴ and 5‴ as well as the carbon atoms 1‴ and 5‴ of conjugate **4** could not be resolved at the applied magnetic field strength, the NMR spectra clearly confirm the prevalence of the lactone form of conjugate **4** in the aprotic solvent. Several protolytic forms of fluorescein are known. The neutral species can be obtained as a solid as a colorless lactone, yellow zwitterion or red quinoid (*33*). Since covalent attachment of fluorescein does not perturb the protolytic transitions of the chromophore (*34*), the dianion form of conjugate **4** is the predominant fluorescent species in an aqueous environment at near neutral pH values (*33*, *34*).

To demonstrate ligand−receptor interaction of conjugate **4** and intermediates **2** und **3** in cell culture, antiprogestagenic activity of all compounds was determined using two independent assays, which was compared with that of the parent compound **1**, mifepristone, as reference antagonist. Compounds **1**−**3** exhibited antiprogestagenic activity in the same order of magnitude. Even after attachment of the bulky fluorescein moiety to intermediate **3**, considerable antiprogestagenic acitivity was maintained. Although the interactions of conjugate **4** and the intermediates **2** and **3** with other steroid hormone recep-

tors were not evaluated, it is likely that all three compounds display a similar receptor interaction profile as the parent compound **1**, e.g., considerable antiglucocorticoid activity (*35*). Since functional activity is roughly in agreement with receptor binding affinity (RBA) (*36*), considerable affinity of conjugate **4** to PR is supposed.

Specific binding of the conjugate **4** to PR is strongly supported by fluorescence microscopy. Nuclear localization was observed solely in steroid hormone receptor-positive T47-D cells, whereas nuclei of steroid hormone receptor-negative OV2774 cells remained unstained. Moreover, coincubation of conjugate **4** with a 10-fold excess of the antiprogestin **1** prevented nuclear staining (R. Sailer et al., unpublished data). Fluorescence microscopy of conjugate **4** is concordant to findings obtained recently with chimeras of PR and green fluorescent protein (GFP). Binding of either agonist (17,21-dimethyl-19-nor-pregn-4,9-diene-3,20-dione, promegestone, a synthetic progestin) or antagonist (compound **1**) to either GFP−PRA or GFP−PRB chimeras caused import of the receptors into the nucleus, but excluding the nucleoli (*37*). The different fluorescence intensity of conjugate **4** in the nuclei of different cells demonstrates the heterogeneity in PR expression, which varies during the cell cycle (*38*, *39*). Accumulation of conjugate **4** within the cytoplasm at higher incubation concentration is most likely to result from unspecific accumulation or binding to other proteins after saturation of the specific PR binding sites.

So far, efforts to develop fluorescent ligands with high affinity for PR resulted in the synthesis of a nitrobenzoxadiazole derivative of a 11β-substituted 19-nor-steroid ((11β,17β)-17-hydroxy-11-(4-[(7-nitro-4-benzofurazanyl)-amino-methyl]phenyl]-17-(1-propynyl)estra-4,9-dien-3-one (*40*)). This compound exhibits high affinities for PR as well as glucocorticoid receptor (*40*, *41*) and high fluorescence quantum yield in hydrophobic solvents (*41*). Although fluorescence was maintained after unspecific binding to proteins, the ligand became nonfluorescent after specific binding to PR (*41*). Since ligand−receptor interaction is not severely impaired after attachment of either the nitrobenzoxadiazole fluorophore or fluorescein to a 11β-substituted 19-nor-steroid, the distance between the fluorophore and the steroid moiety might be important to obtain a fluorescent PR complex. To our knowledge, this is the first report on a fluorescent ligand for PR suitable for studies in living cells. However, it should be mentioned that fluorescence polarization might be used to determine ligand−steroid hormone receptor interaction (Fluormone, Invitrogen; PCT International Application (*32*), Boehringer Ingelheim) in homogeneous systems. But it remains to be elucidated, whether the ligands used in these assays are also fluorescent in viable cells.

To summarize, conjugate **4** is a novel, high-affinity, fluorescent PR antagonist, which might serve as a lead compound for the development of PR-binding contrast agents for NIR optical imaging. It is anticipated that fluorescein can be replaced by an appropriate NIR dye (*12*, *13*) without further compromising ligand−PR interaction. However, further development of a contrast agent for PR imaging should consider (1) receptor binding profile and (2) tissue distribution. Ligand specificity is likely to be increased, when the conjugate is assembled with a highly selective antiprogestin (*4*, *5*, *42*, *43*), thus minimizing binding to other steroid hormone receptors. Minimizing the uptake of the conjugate into nontarget tissues is more challenging as outlined for several receptor-specific small-molecule radiopharmaceuticals (*44*).

ACKNOWLEDGMENT

This work was supported by the Austrian Cancer Aid/Styria (grant no. 03/2001) and the Bundesministerium für Bildung und Forschung (BMBF), Germany (grants no. 01KS9605/2 and 13N8490). The authors want to especially thank Eva Winkler, Institut für Lasertechnologien in der Medizin und Messtechnik an der Universität Ulm, for perfect technical assistance.

LITERATURE CITED

(1) Williams, S. P., and Sigler, P. B. (1998) Atomic structure of progesterone complexed with its receptor. *Nature 393*, 392−396.

(2) Letz, M., Bringmann, P., Mann, M., Mueller-Fahrnow, A., Reipert, D., Scholz, P., Wurtz, J.-M., and Egner, U. (1999) Investigation of the binding interaction of progesterone using muteins of the human progesterone receptor ligand binding domain designed on the basis of a three-dimensional protein model. *Biochim. Biophys. Acta 1429*, 391−400.

(3) Mordasini, T., Curioni, A., Bursi, R., and Andreoni, W. (2003) The binding mode of progesterone to its receptor deduced from molecular dynamics simulations. *ChemBioChem 4*, 155−161.

(4) Fuhrmann, U., Hess-Stumpp, H., Cleve, A., Neef, G., Schwede, W., Hoffmann, J., Fritzemeier, K.-H., and Chwalisz, K. (2000) Synthesis and biological activity of a novel, highly potent progesterone receptor antagonist. *J. Med. Chem. 43*, 5010−5016.

(5) Sathya, G., Jansen, M. S., Nagel, S. C., Cook, C. E., and McDonnell, D. P. (2002) Identification and characterization of novel estrogen receptor-β-sparing antiprogestins. *Endocrinology 143*, 3071−3082.

(6) Buckman, B. O., Bonasera, T. A., Kirschbaum, K. S., Welch, M. J., and Katzenellenbogen, J. A. (1995) Fluorine-18-labeled progestin 16 alpha, 17 alpha-dioxolanes: development of high-affinity ligands for the progesterone receptor with high in vivo target site selectivity. *J. Med. Chem. 38*, 328−337.

(7) Vijaykumar, D., Mao, W., Kirschbaum, K. S., and Katzenellenbogen, J. A. (2002) An effective route for the preparation of a 21-fluoro progestin-16α, 17α-dioxolane, a high affinity ligand for PET imaging of the progesterone receptor. *J. Org. Chem. 67*, 4904−4910.

(8) Wüst, F., Skaddan, M. B., Leibnitz, P., Spies, H., Katzenellenbogen, J. A., and Johannsen, B. (1999) Synthesis of novel progestin−rhenium conjugates as potential ligands for the progesterone receptor. *Bioorg. Med. Chem. 7*, 1827−1835.

(9) Ntziachristos, V., and Chance, B. (2001) Probing physiology and molecular function using optical imaging: applications to breast cancer. *Breast Cancer Res. 3*, 41−46.

(10) Troy, T. L., Page, D. L., and Sevick-Muraca, E. M. (1996) Optical properties of normal and diseased breast tissue: prognosis for optical mammography. *J. Biomed. Opt. 1*, 342−355.

(11) Moesta, K., Fantini, S., Jess, H., Totkas, S., Franceschini, M., Kaschke, M., and Schlag, P. (1998) Contrast features of breast cancer in frequency-domain laser scanning mammography. *J. Biomed. Opt. 3*, 129−136.

(12) Licha, K., Riefke, B., Ntziachristos, V., Becker, A., Chance, B., and Semmler, W. (2000) Hydrophilic cyanine dye as contrast agents for near-infrared tumor imaging: synthesis, photophysical properties and spectroscopic in vivo characterization. *Photochem. Photobiol. 72*, 392−398.

(13) Lin, Y., Weissleder, R., and Tung, C.-H. (2002) Novel near-infrared cyanine fluorochromes: synthesis, properties and bioconjugation. *Bioconjugate Chem. 13*, 605−610.

(14) Ntziachristos, V., Yodh, A. G., Schnall, M., and Chance, B. (2000) Concurrent MRI and diffuse optical tomography of breast after indocyanine green enhancement. *Proc. Natl. Acad. Sci. U.S.A. 97*, 2767−2772.

(15) Bugaj, J. E., Achilefu, S., Dorshow, R. B., and Rajagopalan, R. (2001) Novel fluorescent contrast agents for optical imaging of in vivo tumors based on a receptor-targeted dye-peptide conjugate platform. *J. Biomed. Opt. 6*, 122−133.

(16) Becker, A., Hessenius, C., Licha, K., Ebert, B., Sukowski, U., Semmler, W., Wiedenmann, B., and Grötzinger, C. (2001) Receptor-targeted optical imaging of tumors with near-infrared fluorescent ligands. *Nat. Biotechnol. 19*, 327−331.

(17) Licha, K., Hessenius, C., Becker, A., Henklein, P., Bauer, M., Wisniewski, S., Wiedenmann, B., and Semmler, W. (2001) Synthesis, characterization, and biological properties of cyanine-labeled somatostatin analogues as receptor-targeted fluorescent probes. *Bioconjugate Chem. 12*, 44−50.

(18) Tung, C.-H., Lin, Y., Moon, W. K., and Weissleder, R. (2002) A receptor-targeted near-infrared fluorescence probe for in vivo tumor imaging. *ChemBioChem 8*, 784−786.

(19) Weissleder, R., Tung, C. H., Mahmood, U., Bogdanov, A. (1999) In vivo imaging of tumors with protease-activated near-infrared fluorescent probes. *Nat. Biotechnol. 17*, 375−378.

(20) Bremer, C., Tung, C.-H., Bogdanov, A., and Weissleder, R. (2002) Imaging of differential protease expression in breast cancers for detection of aggressive tumor phenotypes. *Radiology 222*, 814−818.

(21) Tung, C.-H., Mahmood, U., Bredow, S., and Weissleder, R. (2000) In vivo imaging of proteolytic enzyme activity using a novel molecular reporter. *Cancer Res. 60*, 4953−4958.

(22) Bremer, C., Tung, C.-H., and Weissleder, R. (2001) In vivo molecular target assessment of matrix metalloproteinase inhibition. *Nat. Med. 7*, 743−748.

(23) Bremer, C., Bredow, S., Mahmood, U., Weissleder, R., and Tung, C.-H. (2001) Optical imaging of matrix metalloproteinase-2 activity in tumors: feasibility study in a mouse model. *Radiology 221*, 523−529.

(24) Bardou, V. J., Arpino, G., Elledge, R. M., Osborne, C. K., and Clark, G. M. (2003) Progesterone receptor status significantly improves outcome prediction over estrogen receptor status alone for adjuvant endocrine therapy in two large breast cancer databases. *J. Clin. Oncol. 21*, 1973−1979.

(25) Keydar, I., Chen, L., Karby, S., Weiss, F. R., Delarea, J., Radu, M., Chaitcik, S., and Brenner, H. J. (1979) Establishment and characterization of a cell line of human breast carcinoma origin. *Eur. J. Cancer 15*, 659−670.

(26) Cato, A. C., Skroch, P., Weinmann, J., Butkeraitis, P., and Ponta, H. (1988) DNA sequences outside the receptor-binding sites differently modulate the responsiveness of the mouse mammary tumour virus promoter to various steroid hormones. *EMBO J. 7*, 1403−1410.

(27) Di Lorenzo, D., Albetini A., and Zava D (1991) Progestin Regulation of alkaline phosphatase in the human breast cancer cell line T47-D. *Cancer Res. 51*, 4470−4475.

(28) Markiewicz, L., and Gurpide, E. (1994) Estrogenic and progestagenic activities coexisting in steroidal drugs: Quantitative evaluation by in vitro bioassays with human cells. *J. Steroid Biochem. Mol. Biol. 48*, 89−94.

(29) Rao, P. N., Acosta, C. K., Cessac, J. W., Bahr, M. L., and Kim, H. K. (1999) Synthesis of N-desmethyl derivatives of 17α-acetoxy-11β-(4-N,N-dimethylaminophenyl)-19-norpregna-4,9-diene-3, 20-dione and mifepristone. Substrates for the synthesis of radioligands. *Steroids 64*, 205−212.

(30) Schramm, H. W. (1991) Über Synthese und Struktur von 3-Arylimidazolidin-2,4-dionen. *Sci. Pharm. 59*, 115−122.

(31) Acosta, K., Cessac, J. W., Rao, P. N, and Kim, H. K (1994) Oxidative demethylation of 4-substituted N, N-dimethylanilines with iodine and calcium oxide in the presence of methanol. *J. Chem. Soc., Chem. Commun.*, 1985−1986.

(32) Goldrick, S. E., Nelson, R. M., Crute, J. J., Wasti, R. C., Nabozny, G. H., Proudfoot, J. R. and Thomson, D. S. (2002) Methods and labeled molecules for determining ligand binding to steroid receptors. PCT Int. Appl. WO 02/95354 A2.

(33) Sjöback, R., Nygren, J., and Kubista, M. (1995) Absorption and fluorescence properties of fluorescein. *Spectrochim. Acta A 51*, L7-L21.

(34) Klonis, N., and Sawyer, W. H. (2003) The thiourea group modulates the fluorescence emission decay of Fluorescein-labeled molecules. *Photochem. Photobiol. 77*, 502−509.

(35) Busso, N., Collart, M., Vassalli, J. D., and Belin, D. (1987) Antagonist effect of RU 486 on transcription of glucocorticoid-regulated genes. *Exp. Cell Res. 173*, 425−430.

(36) Schoonen, W. G., Dijkema, R., de Ries, R. J., Wagenaars, J. L., Joosten, J. W., de Gooyer, M. E., Deckers, G. H., and Kloosterboer, H. J. (1998) Human progesterone receptor A and B isoforms in CHO cells. II. Comparison of binding, transactivation and ED50 values of several synthetic (anti)-progestagens in vitro in CHO and MCF-7 cells and in vivo in rabbits and rats. *J. Steroid Biochem. Mol. Biol. 64*, 157−170.

(37) Lim, C. S., Baumann, C. T., Htun, H., Xian, W., Irie, M., Smith, C. L., and Hager, G. L. (1999) Differential localization and affinity of the A- and B-forms of the human progesterone receptor using green fluorescent protein chimeras. *Mol. Endocrinol. 13*, 366−375.

(38) Cassanelli, S., Guillaud, P., Louis, J., and Seigneurin, D. (1991) Image Cytometry of progesterone receptor expression during the cell cycle in the MCF-7 cell line. *J. Histochem. Cytochem. 39*, 1713−1718.

(39) Graham II, M. L., Bunn Jr., P. A., Jewett, P. B., Gonzalez-Aller, C., and Horwitz, K. B. (1989) Simultaneous measurement of progesterone receptors and DNA indices by flow cytometry: characterization of an assay in breast cancer cell lines. *Cancer Res. 49*, 3934−3942.

(40) Teutsch, G., Klich, M., Bouchoux, F., Cerede, E., and Philibert, D. (1994) Synthesis of a fluorescent steroid derivative with high affinities for the glucocorticoid and progesterone receptors. *Steroids 59*, 22−26.

(41) Carlson, K. E., Coppey, M., Magdelenat, H., and Katzenellenbogen, J. A. (1989) Receptor binding of NBD-labeled fluorescent estrogens and progestins in whole cells and cell-free preparations. *J. Steroid Biochem. 32*, 345−355.

(42) Kloosterboer, H. J., Deckers, G. H., de Gooyer, M. E., Dijkema, R., Orlemans, E. O., and Schoonen, W. G. (1995) Pharmacological properties of a new selective antiprogestagen: Org 33628. *Ann. N Y Acad. Sci. 761*, 192−201.

(43) Wagner, B. L., Pollio, G., Giangrande, P., Webster, J. C., Breslin, M., Mais, D. E., Cook, C. E., Vedeckis, W. V., Cidlowski, J. A., and McDonnell, D. P. (1999) The novel progesterone receptor antagonists RTI 3021−012 and RTI 3021−022 exhibit complex glucocorticoid receptor antagonist activities: implications for the development of dissociated antiprogestins. *Endocrinology 140*, 1449−1458.

(44) Hom, B. K., and Katzenellenbogen, J. A. (1997) Technetium-99m-labeled receptor-specific small-molecule radiopharmaceuticals: recent developments and encouraging results. *Nucl. Med. Biol. 24*, 485−798.

BC034169O

Optimized Conjugation of a Fluorescent Label to Proteins via Intein-Mediated Activation and Ligation

Robert J. Wood, David D. Pascoe, Zoë K. Brown, Emma M. Medlicott, Marco Kriek, Cameron Neylon, and Peter L. Roach*

School of Chemistry, University of Southampton, Highfield, Southampton, Hampshire, U.K. SO17 1BJ
Received September 19, 2003

Intein-mediated ligation provides a site-specific method for the attachment of molecular probes to proteins. The method is inherently flexible with regard to either the protein sequence or the attached probe, but practical difficulties have limited the widespread use of this valuable labeling system for the attachment of small- to medium-sized molecules. We report herein studies to improve the efficiency and practical application of these reactions, including the assembly of plasmids for the expression of target−intein fusion proteins and the analysis of their reaction with a fluorescent cysteine derivative under a range of conditions. Optimal ligation of the fluorophore to the target protein is critically dependent on the degree of oxidation of the fluorescent cysteine derivative. Efficient ligation has been achieved with freshly prepared fluorescent cysteine derivative under rigorously anaerobic conditions. Similar ligation yields have also been achieved using more practically convenient conditions including anaerobic reaction with addition of thiophenol, or aerobic reaction with the further addition of tricarboxyethylphosphine.

INTRODUCTION

Studies of a wide range of proteins and enzymes could potentially benefit from the site-specific attachment of molecular probes to the protein of interest. Recently, intein-mediated activation of the C-terminus of a protein domain has been shown to provide a general method for attaching a wide range of molecules, including proteins (*1*), peptides (*2*), fluorescent labels (*3*), carbohydrates (*4*), oligonucleotides (*5*), and affinity tags and metal chelators (*6*). Intein-mediated ligation has also been used for the assembly of selectively labeled proteins for NMR studies (*7, 8*) and to prepare cyclic peptides and proteins (*9, 10*).

Intein-mediated labeling reactions require two protein domains: the N-terminal domain which contains the protein sequence to be labeled (the target domain) and a C-terminal domain containing the intein (the intein domain). These domains are usually joined in a single fusion protein containing both the intein and target domains [a target−intein fusion protein Figure 1, **1**]. For those intein domains beginning with an N-terminal cysteine residue, the molecular basis of intein-mediated activation is a spontaneous reversible N → S transacylation step forming thioester (**2**) that occurs at this cysteine residue (Figure 1, **1** → **2**). The ligation of probes to target domains has been achieved using a range of cysteine derivatives (**4**) under appropriate conditions (*2*). Although the thioester (**2**) is more reactive toward nucleophiles than a backbone amide, direct reaction with peptides containing an N-terminal cysteine residue was unsuccessful, a result that has been rationalized in terms of steric hindrance from the bulky intein domain (*2*). The use of several thiols including thiophenol [195 mM (*2*)], ethanethiol [0.49 M (*11*)], or MESA[1] [30 mM (*6*)] has been reported to enhance intein-mediated ligation reactions, presumably by trans-thioesterification to the less hindered intermediate (**3**). Under these conditions, cysteine derivatives (**4**) are thought to form the kinetic product (**5**), then rearrange to the thermodynamically more stable amide (**6**) (*2, 12*).

Another potential problem with intein-mediated ligation chemistry is the possible oxidation of both the activating thiol reagent and the modified cysteine derivative to disulfides. The use of thiol reducing agents such as DTT is not possible, as these compounds effectively cleave and derivatize the target domain. This problem has been circumvented by the use of the water soluble phosphine TCEP (*3*), which efficiently reduces disulfides to thiols (*13*).

Since our initial attempts to utilize intein-mediated ligation for the fluorescent labeling of proteins gave disappointing and variable yields of labeled protein, we set out to identify the factors that are important in achieving efficient and consistent labeling. Herein we report the efficient expression and purification of target−intein fusion proteins and studies to determine the optimal conditions for ligation reactions.

EXPERIMENTAL PROCEDURES

Cloning and expression vectors pBAD TOPO and pBAD/HisA and TOP10 competent cells were obtained from Invitrogen (Groningen, NL). The plasmid pTYB1 from the IMPACT-CN system was obtained from New England Biolabs (Herts., UK). DNA was isolated from cultures or agarose gels using commercially available kits following the manufacturers' instructions. Fluorescein isothiocyanate (isomer I, 90%), Supelclean LC-18 reverse phase columns (60 mL), and HPLC solvents (Riedel-de Haën, chromasolv HPLC grade) were obtained from

* Author for correspondence. Telephone: +44 (0)23 80595919, fax: +44 (0)23 80596805. E-mail: plr2@soton.ac.uk.

[1] Abbreviations: MESA, 2-mercaptoethanesulfonic acid; FTEC, *N*-[2-[[[(fluorescein-5-yl)amino]thioxomethyl]amino]ethyl]-L-cysteinamide; TCEP, tricarboxyethylphosphine; CDI, carbonyldiimidazole; TFA, trifluoroacetic acid.

10.1021/bc0341728 CCC: $27.50 © 2004 American Chemical Society
Published on Web 01/30/2004

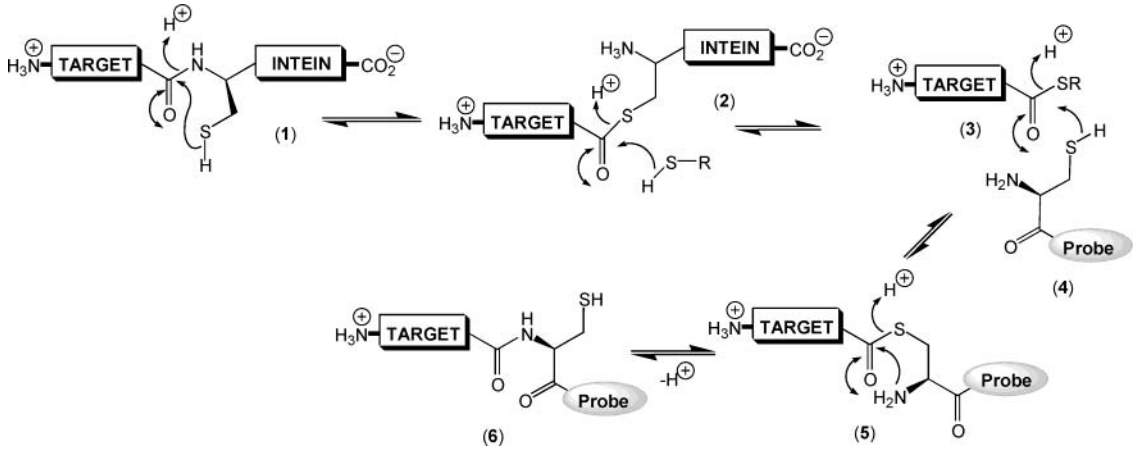


Figure 1. The mechanism of intein-mediated protein labeling. Acyl transfer of the target−intein fusion protein (**1**) from the α amino group to the thiol of the reactive cysteine yields thioester (**2**), which is attacked by a small molecule thiol to give the less hindered thioester (**3**). Attack of a cysteine based labeling reagent (**4**) yields thioester (**5**), which rearranges to give the thermodynamic amide product (**6**).

Sigma-Aldrich (Poole, UK). NMR spectra were recorded on Brucker AC300 or AC400 spectrometers. Electrospray ionization mass spectra were recorded on a Micromass Platform 2 single quadrupole MS, HP1050, in positive mode from methanol solutions. IR spectra were recorded on a BioRad FT-IR.

***N*-Boc-*S*-Trityl-*N*-2-aminoethyl-L-cysteinamide (8).** *N*-Boc-*S*-trityl-L-cysteine [1.0 g, 2.16 mmol, **7**] was dissolved in DMF (10 mL), and solid carbonyl diimidazole (420 mg, 2.6 mmol) was added. After 30 min, ethylenediamine (1.4 mL, 21.6 mmol) was added in a single portion and the reaction stirred at room temperature for a further 2 h. The DMF was then removed in vacuo and the residue dissolved in dichloromethane (50 mL). The solution was washed with water (5 × 50 mL) and saturated brine (50 mL) and dried with anhydrous magnesium sulfate. The solvent was reduced to ∼10 mL in vacuo, yielding **8** as a white crystalline solid which was collected by filtration and dried in vacuo (980 mg, 90%). Mp 76−80 °C; ^{1}H NMR (300 MHz, $CDCl_3$): δ 7.29 (6H, d, J = 8.1 Hz), 7.21 (9H, m), 6.65 (1H, t, J = 5.2 Hz), 4.89 (1H, d, J = 7.4 Hz), 3.85 (1H, dd, J = 12.5, 6.6 Hz), 3.25 (2H, ddd, J = 11.4, 4.7, 1.5 Hz), 2.78 (2H, t, J = 5.88 Hz), 2.71 (1H, m), 2.54 (1H, dd, J = 12.5, 5.15 Hz), 1.42 (9H, s). ESMS 506.3 (MH^+).

***N*-Boc-*S*-Trityl-*N*-[2-[[[(fluorescein-5-yl)amino]-thioxomethyl]amino]ethyl]-L-cysteinamide (10).** Compound **8** (500 mg, 0.99 mmol) was dissolved in methanol (20 mL) and a solution of fluorescein isothiocyanate [424 mg, 1.09 mmol, **9**] in methanol (30 mL) added dropwise. The reaction was stirred under nitrogen for 20 h. The solvent was removed in vacuo to yield an orange residue which was redissolved in 80% MeOH/20% water (20 mL). The solution was applied to a Supelclean LC-18 reverse phase column (60 mL) that had been preequilibrated in 80% MeOH/20% water and the compound eluted in the same solvent. The purest fractions were combined and the solvent removed in vacuo to afford the slightly unstable **10** as an orange solid (815 mg, 92% yield). Mp 184−190 °C; IR (neat) 3256, 2918, 2849, 1667, 1592, 1487, 1443, 1249, 1158, 840 cm^{-1}; ^{1}H NMR (400 MHz, CD_3OD), δ 8.0 (1H, s), 7.58 (1H, d, J = 8.0 Hz), 7.3−7.0 (15H, m), 6.97 (1H, d, J = 8.5 Hz), 6.66 (2H, d, J = 9 Hz), 6.6 (2H, d, J = 2 Hz), 6.44 (2H, dd, J = 8.8, 2.0 Hz), 3.88 (1H, m), 3.6−3.8 (2H, m), 3.37 (2H, t, J = 5.15 Hz), 2.48 (2H, d, J = 6.6 Hz), 1.31 (9H, s); ^{13}C NMR (100 MHz, CD_3OD) δ 182.8, 174.0, 173.3, 171.2, 157.0, 154.7, 146.0, 145.6, 141.5, 130.4, 129.5, 128.7, 128.6, 127.7, 127.6, 127.4, 126.4, 120.9, 114.8, 112.0, 103.3, 80.7, 67.7, 64.1, 55.0, 45.0, 39.9, 35.0, 28.4; ESMS 917.5 (MNa^+), 895.5 (MH^+).

***N*-[2-[[[(Fluorescein-5-yl)amino]thioxomethyl]amino]ethyl]-L-cysteinamide (11, FTEC).** Water (100 μL), triisopropylsilane (92 μL, 0.448 mmol), and TFA (4 mL) were added to **10** (100 mg, 0.112 mmol) under nitrogen. The reaction mixture was stirred at room temperature for 30 min. The solvent was removed in vacuo to afford a crude oily orange residue that was triturated with diethyl ether (5 mL). The resultant orange solid was collected by filtration and washed with a further portion of diethyl ether (10 mL) to afford **11** as an orange solid (55 mg, 89% yield). Mp 190−195 °C; IR (neat) 3263, 3061, 2933, 1665, 1585, 1535, 1175, 1115 cm^{-1}; ^{1}H NMR (400 MHz, CD_3OD) δ 8.21 (1H, d, J = 2.0 Hz), 7.79 (1H, dd, J = 8.1, 2.0 Hz), 7.20 (1H, d, J = 8.1 Hz), 6.80 (2H, d, J = 8.1 Hz), 6.77 (2H, d, J = 2.0 Hz), 6.62 (2H, dd, J = 8.1, 2.0 Hz), 4.07 (1H, dd, J = 6.6, 5.1 Hz), 3.95−3.80 (2H, m), 3.62−3.49 (2H, m), 3.11−3.03 (2H, m); ^{13}C NMR (100 MHz, CD_3OD) δ 182.4, 169.9, 167.8, 161.5, 153.8, 147.0, 141.2, 130.9, 129.7, 128.3, 125.3, 120.0, 113.3, 111.0, 102.5, 65.9, 55.2, 43.8, 39.3, 25.3; ESMS 553.2 (MH^+).

HPLC Analysis of FTEC. The extent to which FTEC had oxidized to its disulfide was assessed by reverse phase HPLC using a Gilson System Workcenter and a Phenomenex Prodigy 5 μm ODS-2 (150 × 4.6 mm) column. HPLC Buffer A was 0.1% TFA in water; HPLC buffer B was 0.1% TFA in acetonitrile. The following conditions were used during the separation with linear gradients between time points: flow rate 0.8 mL/min; detector wavelength λ = 480 nm; detector wavelength 2, 280 nm; t = 0 min, 95% A, 5% B; t = 5.0 min, 95% A, 5% B; t = 40.0 min, 10% A, 90% B. The following retention times were recorded: FTEC, 19.7 min; FTEC disulfide, 21.3 min.

Construction of Plasmids for the Expression of Target−Intein Fusions. DNA manipulations were carried out using standard protocols (*14*). The desired genes were amplified by PCR from *E. coli, Sulfolobus sulfotaricus* genomic DNA, or from the plasmid pTYBI (New England Biolabs, Hertfordshire) as required, using *Pfu* Turbo polymerase and oligonucleotide primers as follows: *pfbioB* 5′-*ccatgg*ctcaccgcccacgc; *prbioB* 5′-*ggatcc*ttactcgagtaatgctgccgcgttgtaatattcg; *pfint* 5′-*ctcgag***ggc**tgctttgccaagggt; *print* 5′-*gaattc*tca**gtggtggtggtggtggtg**ttgaagctgccacaaggcaggaacgt; *pffpr* 5′-*ccatgg*ctgattgggtaacaggc; *prfpr* 5′-ttagcc*ctcgag*ccagtaatgctccgctgt;

pflipA 5′-*ccatgg*agaaaaaagttcaaattgc; *prlipA* 5′-ggatcct-ca*ctcgag*actatgattcttagcattttcaatcgcc. DNA encoding the VMAI intein−chitin binding protein fusion was amplified from pTYBI using primers *pfint* and *print* which add a *Xho*I site (italics) and a glycine codon (bold) to the 5′ end of the amplified gene and DNA encoding a His_6 tag (bold) and an *Eco*RI site (italics) to the 3′ end. The PCR amplification product was purified and inserted into pBAD TOPO according to the manufacturer's instructions, and the resultant plasmids were transformed into competent TOP10 cells. Ampicillin resistant colonies were screened by PCR for plasmids containing the correct insert and plasmid DNA isolated. The *Xho*I-*Eco*RI fragment containing the modified intein gene was inserted between the unique *Xho*I and *Eco*RI sites of pBAD/HisA to yield plasmid pRJW2960/82.

The *bioB* gene was amplified from *E. coli* genomic DNA using primers *pfbioB* and *prbioB* which added a 5′ *Nco*I site (italics), removed the native stop codon, and added a 3′ *Xho*I site (italics) to the wild-type DNA sequence. The PCR product was then inserted into pBAD TOPO, the resultant plasmid transformed into TOP10 cells, and plasmid DNA containing the desired insert isolated. The *Nco*I-*Xho*I fragment containing *bioB* was ligated to the large *Nco*I-*Xho*I fragment of pRJW2960/82 to give plasmid pRJW2960/89. Plasmids pRJW2960/88 and pRJW3104/40 were constructed in similar fashion from pRJW2960/82 by inserting the *E. coli fpr* and *Sulfolobus sulfataricus lipA* sequences amplified from genomic DNA. Primers *pffpr* and *prfpr* were used to construct pRJW2960/88 for expression of Fpr−intein fusion protein and primers *pflipA* and *prlipA* were used to construct pRJW3104/40 for expression of LipA−intein fusion protein. The overall design of the constructs is shown in Figure 3.

Expression and Purification of Target−Intein Fusion Proteins. All purification steps were carried out at 4 °C. Cell pastes and purified proteins were stored at −80 °C. Liquid and solid growth media contained ampicillin (100 mg/L) as required. Protein purity was judged by SDS−PAGE with Coomassie staining. *E. coli* BL21(DE3) (*15*) was transformed with plasmid pRJW2960/89, ampicillin resistant transformants were isolated on 2YT agar, and single colonies were grown for strain storage (*14*). 2YT medium (100 mL) was inoculated from stored strains and grown overnight in a shaking incubator at 37 °C, 220 rpm. This overnight culture was used as 1% innocula into fresh medium (4 × 1250 mL) and grown until the OD_{600} reached 0.6. The cultures were induced by addition of arabinose (20% w/v filter sterilized solution, 10 mL/L), and growth was continued at 27 °C for 4 h. Cells were harvested by centrifugation (10000*g*, 4 °C, 10 min), and the cell paste was stored at −80 °C until required.

The BioB−intein fusion protein was purified from cell paste (∼25 g) resuspended in 4 mL/g Lysis Buffer (50 mM Tris/HCl, 10% w/v glycerol, 0.2 mg/mL lysozyme, 50 U/mL benzonase, pH 8.1). The suspension was stirred (30 min) and then sonicated (10 × 30 s bursts) and the lysate cleared by centrifugation (22000*g*, 4 °C, 30 min). The supernatant was applied to a nickel charged Chelating Sepharose FF column previously equilibrated in Buffer A (50 mM Tris/HCl, 500 mM NaCl, pH 7). The column was washed with Buffer A (200 mL), and the proteins were eluted with Buffer B (Buffer A plus 500 mM imidazole). The purest fractions were pooled, concentrated to 25 mg/mL, and applied to a Superdex 200 column (33 mm ID × 80 cm) previously equilibrated in Buffer A. The column eluate was collected in fractions (9 mL), and the purest fractions stored to yield BioB−intein (150 mg from ∼25 g of cell paste).

The Fpr−intein fusion protein (180 mg from ∼ 95 g cell paste) was purified by a similar method from *E. coli* strain 821 (*16*) transformed with pRJW2960/88 except that (i) all buffers were adjusted to pH 8.1; (ii) Buffer A contained imidazole (50 mM); (iii) the gel filtration chromatography used Buffer C (50 mM Tris/HCl, 500 mM NaCl, pH 8.1). The LipA−intein fusion protein (140 mg from ∼50 g of cell paste) was purified from *E. coli* C43 (DE3) (*17*) transformed with pRJW3104/40 by the method used for the Fpr−intein fusion protein.

General Conditions for Cleavage and Fluorescent Labeling Reactions. Reagents were added to reactions as required to the following final concentrations: BioB−intein fusion protein (0.7 mg/mL), LipA−intein fusion protein (0.64 mg/mL), Fpr−intein fusion protein (1.3 mg/mL), thiols (thiophenol, 2-aminobenzenethiol, 2-methoxythiophenol, MESA, or 4-fluorobenzenethiol, 25 mM), TCEP (20 mM), FTEC (2.3 mM), Tris/HCl buffer (50 mM, pH 8.1). Reactions were stopped by rapid freezing to −80 °C. Protein samples (10 μL) were denatured in Gel Loading Buffer (5 μL) for 5 min at 80 °C (*14*) and analyzed by SDS−PAGE on 10% gels. Gels were visualized under UV illumination and after Coomassie staining using a Syngene GeneGenius imager. The images were analyzed using GeneTools software (Syngene, Cambridge, UK). Where required a sample of fluorescently labeled BioB was applied to the gel to provide a fluorescence intensity calibration. Where noted, reactions were maintained under anaerobic conditions using a glovebox (Belle Technology, Portesham, UK) maintained at 20 °C under nitrogen at <0.2 ppm O_2. Buffers for these experiments were introduced into the glovebox and allowed to deoxygenate overnight, then used to prepare the solutions of reagents. Aliquots of protein (100 μL) were allowed to deoxygenate for 1 h before use.

Comparison of Aerobic and Anaerobic Cleavage Reactions with Various Thiols. Cleavage reactions contained BioB−intein, Tris/HCl buffer, and one of five thiols: thiophenol, 2-aminobenzenethiol, 2-methoxythiophenol, MESA, or 4-fluorobenzenethiol. The reactions were incubated either aerobically at room temperature or anaerobically for 24 h and analyzed.

Assay of Thiol Dependent Fluorescent Labeling. Labeling reactions contained target−intein, FTEC, Tris/HCl buffer, and one of four thiols: thiophenol, 2-methoxythiophenol, MESA, or 4-fluorobenzenethiol. The reactions were incubated anaerobically for 24 h and analyzed.

Comparing the Progress of Labeling Reactions under Various Conditions. Anaerobic labeling reactions, with an initial total volume of 500 μL, contained BioB−intein fusion protein, FTEC, Tris/HCl buffer, and where indicated, TCEP and/or thiophenol. Aliquots (40 μL) were withdrawn and stored at −80 °C after 1, 2, 3, 4, 5, 6, 8, 10, 14, and 27 h. The aliquots were then thawed and immediately analyzed.

Effect of Thiophenol Concentration on Labeling Reactions. Labeling reactions (100 μL) contained BioB−intein, Tris/HCl buffer, and thiophenol at the following concentrations: 0, 0.5, 5, 10, 12.5, 25, 50 mM. The reactions were maintained under anaerobic conditions for 16 h and analyzed.

RESULTS AND DISCUSSION

Intein-mediated ligation appears to provide a general solution to the problem of site specifically attaching

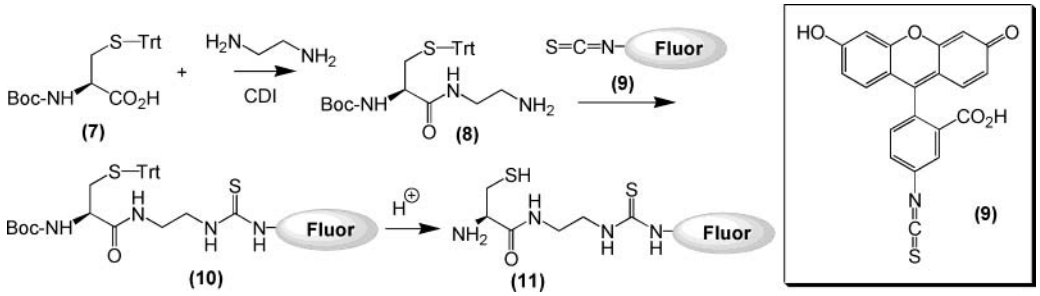


Figure 2. Synthesis of *N*-[2-[[[(fluorescein-5-yl)amino]thioxomethyl]amino]ethyl]-L-cysteinamide (FTEC, **11**).

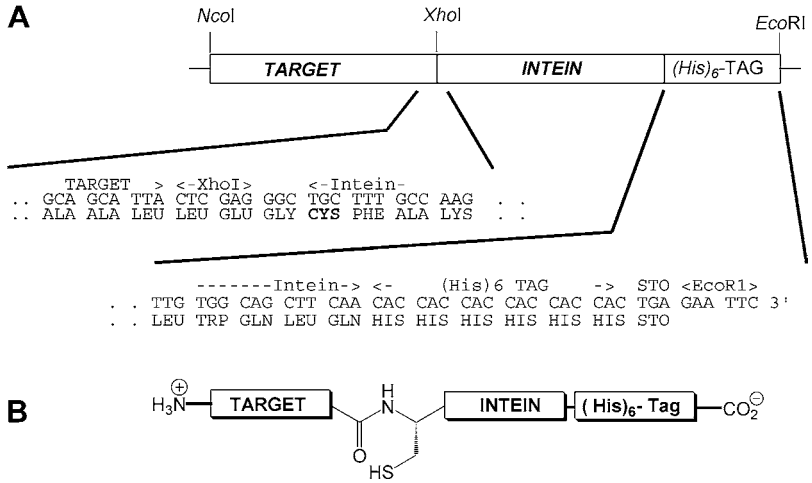


Figure 3. Design of plasmids (A) for the expression of target−intein fusion proteins (B). The target protein gene sequence is extended using PCR to remove the stop codon and incorporate a *Xho*I restriction site. A glycine codon was incorporated between the *Xho*I restriction site and the VMAI intein sequence from pTYB1. DNA encoding a $(His)_6$ affinity tag was introduced to the C-terminus of the intein domain. The domain labeled intein includes DNA encoding intein and chitin binding domains from pTYB1.

small- or medium-sized molecules to proteins under mild conditions (*18*). A variety of methods for intein-mediated ligation have been reported, with reaction under aerobic conditions in the presence of thiophenol (*2*) or MESA (*19*) being the most commonly used. However, a systematic analysis of the important factors for achieving efficient ligation using these fusion proteins has not been reported. We therefore set out to identify the optimal conditions for efficient and convenient fluorescent labeling using three model target−intein fusions. We have developed an efficient synthesis of a water soluble fluorescent labeling reagent and flexible plasmids for the expression of target−intein fusions and determined the optimal conditions for the labeling reaction.

Preparation of FTEC (11). The synthetic strategy (Figure 2) was to prepare a protected cysteine derivative (**8**) which is suitable for reaction with a diverse range of activated fluorescent reagents (*6*). Thus, reaction of **8** with fluorescein isothiocyanate (**9**) gave the fully protected derivative (**10**) in good yield (92%) after low-pressure reverse phase chromatography (**10** is not stable to silica flash chromatography).

As a precaution against the eventuality of FTEC disulfide formation, it is convenient to deprotect **10** in small aliquots (∼50 mg) for immediate use in labeling reactions. This simple three-step route to FTEC (**11**) has been completed in an overall yield of 74%.

Plasmids for the Expression of Target−Intein Fusion Proteins. Plasmid pRJW2960/82 was constructed to allow the straightforward assembly of vectors for the expression of target−intein fusion proteins under the control of an arabinose-inducible promotor (*20*). The plasmid contains an *Nco*I site for the insertion at the start codon of the gene for the target protein and a unique *Xho*I site for insertion in frame with the downstream gene encoding the intein domain. An inserted triplet encodes a glycine residue N-terminal of the splice site cysteine residue, a modification that has been demonstrated to allow efficient transacylation (*21*). DNA encoding a His_6 tag has been added at the 3′ end of the construct to allow purification of target−intein fusion proteins by metal affinity chromatography. The pTYBI-derived DNA also encodes a chitin binding protein domain as an alternative affinity purification tag. Finally a unique *Eco*RI site at the 3′ end of the construct allows the insertion of alternative intein domains as *Xho*I-*Eco*RI fragments if desired. Plasmids pRJW2960/89, pRJW2960/88, and pRJW3104/40 were constructed from pRJW2960/82 for the expression of *E. coli* BioB−, Fpr−, and *Sulfolobus sulfataricus* LipA−intein fusion proteins, respectively. The overall design of the constructs is shown in Figure 3.

Expression and Purification of Target−Intein Fusion Proteins. Fusion proteins were successfully expressed at high levels from each of the expression plasmids in a variety of *E. coli* strains. Protein isolated after nickel affinity chromatography always contained a mixture of the full-length fusion protein and intein domain (Figure 4), presumably as a result of in vivo cleavage by abundant intracellular thiols such as glutathione. While the selection of the optimal expression strain remains empirical, it may be significant that the proportion of full-length fusion protein could usually be increased by expression in *E. coli* 821 cells (data not shown), a mutant strain unable to produce glutathione (*16*). After preliminary small scale expression experiments, satisfactory yields of full-length proteins were obtained from BL21(DE3) for BioB−intein fusion, *E. coli*

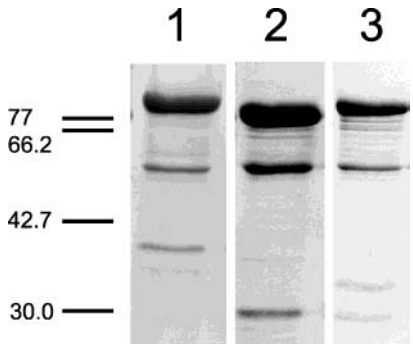


Figure 4. Coomassie-stained SDS−PAGE analysis of purified target−intein fusion proteins. Lanes: 1, BioB−; 2, Fpr−; 3, LipA−intein fusions. Molecular weights (kDa) are indicated on the left-hand side.

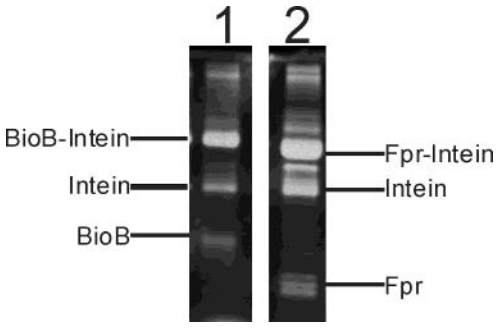


Figure 5. Fluorescent derivatization of target−intein fusion under nonreducing conditions. Thiophenol was not added to the labeling reaction and the sample was prepared for SDS−PAGE analysis with DTT-free Gel Sample Buffer. Lane 1, BioB−intein, lane 2 Fpr−intein. Bands as indicated were identified by comparison to Coomassie-stained gels.

821 for Fpr−intein fusion, and C43(DE3) for LipA−intein fusion (*17*).

Conditions for SDS−PAGE Analysis of Intein-Mediated Fluorescent Labeling Reactions. The conditions (5 min at 80 °C) used to prepare samples for SDS−PAGE were selected to allow efficient denaturation and reduction of disulfide bonds, without inducing extensive DTT dependent cleavage of the target−intein fusion protein. The use of Gel Loading Buffer without DTT resulted in nonspecific labeling (Figure 5), which presumably arises from disulfide bond formation between FTEC and cysteine residues in the proteins.

Comparison of Aerobic and Anaerobic Thiol Dependent Cleavage Reactions. Preliminary experiments with FTEC and BioB−intein fusion protein resulted in poor incorporation of the label, despite the use of large excesses of FTEC. In an attempt to resolve this problem, a range of thiols was investigated to assess their potential for aerobic cleavage of the target−intein fusion protein to yield the α-thioester (**3**). Aminobenzenethiol is effective at cleaving the fusion protein but is difficult to use as it forms an emulsion. 4-Fluorobenzenethiol showed the largest extent of cleavage under these conditions (Figure 6, compare lanes 1−6).

In reactions with thiophenol and 2-methoxybenzenethiol, a white precipitate was observed to form within 5 min, presumably as a result of oxidation of the thiol to the disulfide (*11*). In the case of 2-methoxythiophenol, this causes coprecipitation of some protein (Figure 6, lane 4). The poor performance of the thiols under aerobic conditions led us to explore the potential of rigorously anaerobic cleavage conditions (<0.2 ppm O_2). In each case, the extent of reaction was significantly enhanced and precipitation of the disulfide was avoided. Under

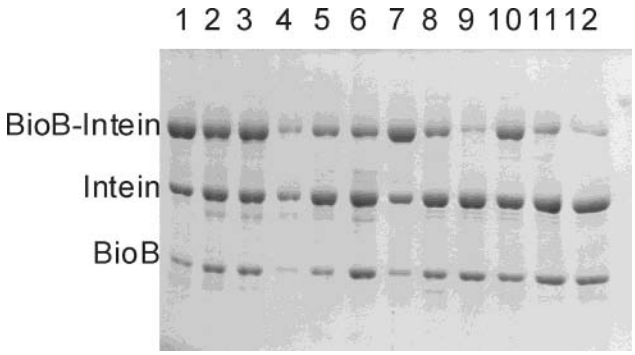


Figure 6. Cleavage of BioB−intein fusion protein by various thiols. Lanes 1−6, aerobic; lanes 7−12, anaerobic. Lanes 1 and 7, no thiol; lanes 2 and 8, thiophenol; lanes 3 and 9, 2-aminobenzenethiol; lanes 4 and 10, 2-methoxybenzenethiol; lanes 5 and 11, MESA; lanes 6 and 12, 4-fluorobenzenethiol.

these conditions, 2-amino- and 4-fluorobenzene thiols are most effective at cleaving the BioB−intein fusion protein (Figure 6, compare lanes 7−12) to yield the α-thioester intermediate (**3**).

Assay of Thiol-Activated Fluorescent Labeling. The anaerobic ligation of FTEC to target proteins was investigated, including the effect of thiol reagents and the target protein domain. Reactions conducted in the absence of thiols resulted in a variable extent of labeling (for example, estimated at less than 20% from the Coomassie-stained SDS PAGE gel, Figure 7, Fpr, lane 2) and could result in no labeling (Figure 7, BioB and LipA, lanes 2). The addition of thiols increased the cleavage of the target−intein fusion protein (Figure 7, lower panels) and the yield of fluorescently labeled protein (Figure 7, upper panels). The experiments showed that thiophenol and MESA were most efficient at promoting the introduction of the fluorescent label.

Comparing the Progress of Labeling Reactions under Various Conditions. The extent of fluorescent labeling could be quantified by integrating the fluorescent band intensity. Thus, by analyzing aliquots withdrawn from a labeling reaction at different time points, the progress of the reaction could be followed (Figure 8a). Moreover, by including a fluorescent standard on each gel to act as a calibrant (e.g. Figure 8a, lanes C), it was possible to directly compare data obtained from different gels. This allowed comparison of the kinetics of fluorescent labeling under different conditions. A plot of the fluorescence intensity of each band against time (Figure 8b) confirmed that the reaction proceeded most efficiently under anaerobic conditions in the presence of thiophenol. The data could be fitted to a single exponential to give an observed pseudo-first-order rate constant of 0.30 ± 0.04 hour^{-1}. A similar rate constant could be fitted to data obtained from a labeling reaction under aerobic conditions with added thiophenol and TCEP [$k = 0.23 \pm 0.04$)]. In multiple experiments, these rate constants consistently fell in the range 0.1−0.3 h^{-1}, a rate of reaction similar to that observed by Muir (*11*). In the case of an aerobic labeling experiment with thiophenol but no TCEP, while the reaction shows a similar initial rate to the previous examples, it did not proceed to completion, presumably as a result of thiophenol disulfide formation. Reactions under other conditions showed little fluorescent labeling (<10%). It is interesting to note that the most efficient cleavage reagents (2-amino- and 4-fluorobenzenethiols) are not the most efficient in promoting fluorescent labeling. This probably reflects the different rate-determining steps of cleavage and labeling reactions.

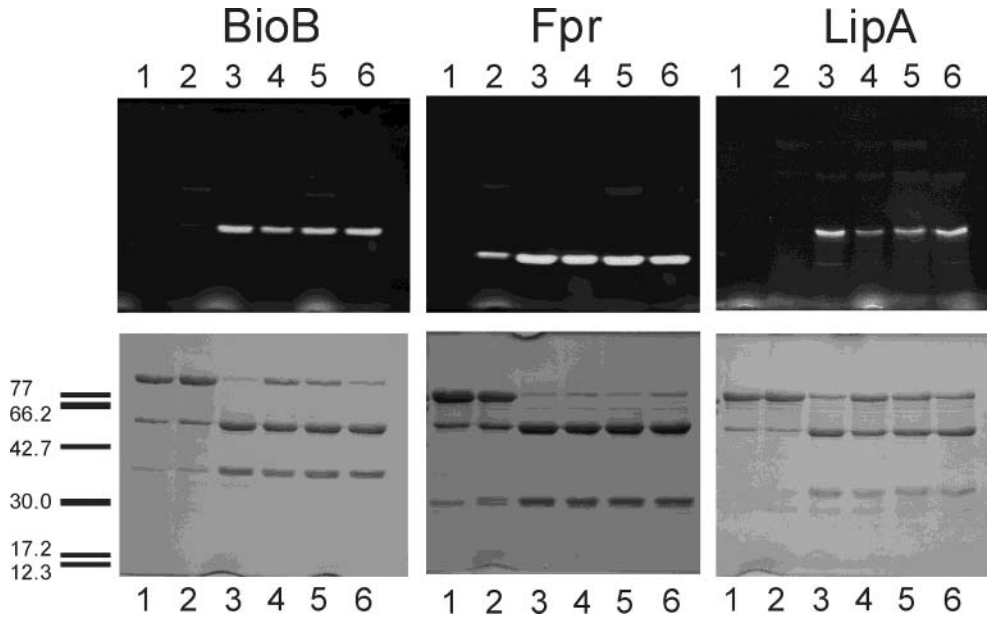


Figure 7. SDS−PAGE analysis of fluorescent labeling reaction with BioB−, Fpr−, and LipA−intein fusions in the presence of a variety of thiols (each 25 mM). Top panels are fluorescence images, lower panels are Coomassie stained. In each case: lane 1, no thiol, no FTEC; 2, FTEC only; 3, FTEC plus thiophenol; 4, FTEC plus 2-methoxybenzenethiol; 5, FTEC plus 4-fluorobenzenethiol; 6, FTEC plus MESA.

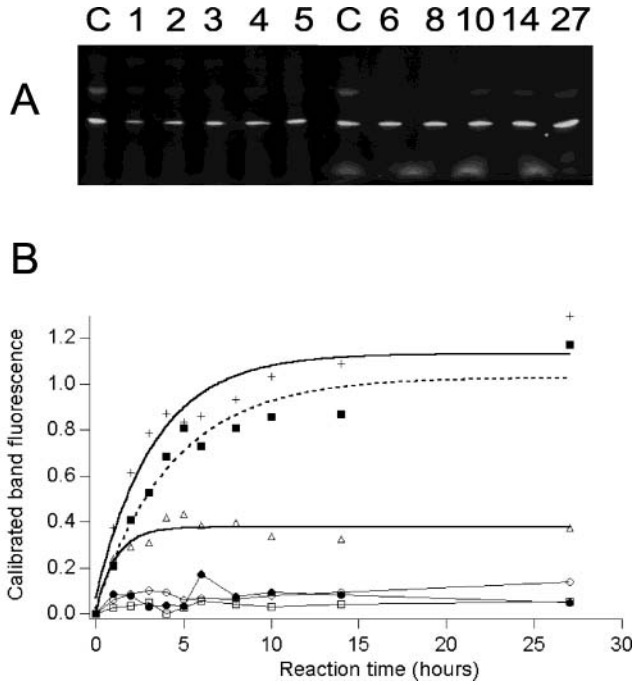


Figure 8. Time course of fluorescent labeling reaction with BioB−Intein fusion protein. (A). Gel showing timecourse of anaerobic labeling in the presence of thiophenol. Lanes marked C contain a previously prepared sample of fluorescent BioB used as a calibrant. Other lanes contain samples taken from the labeling reaction at the times (h) indicated. (B). Graph showing time course of fluorescent labeling under various conditions. The following conditions were compared: (□) aerobic; (●) aerobic plus phosphine; (△) aerobic with thiophenol; (■) aerobic with phosphine and thiophenol; (○) anaerobic; (+) anaerobic with thiophenol. Data for reactions with thiophenol and for aerobic reaction in the presence of thiophenol and TCEP were fitted to a first-order exponential. For the remaining slow reactions, data cannot be fitted and the points are connected to indicate the general trend.

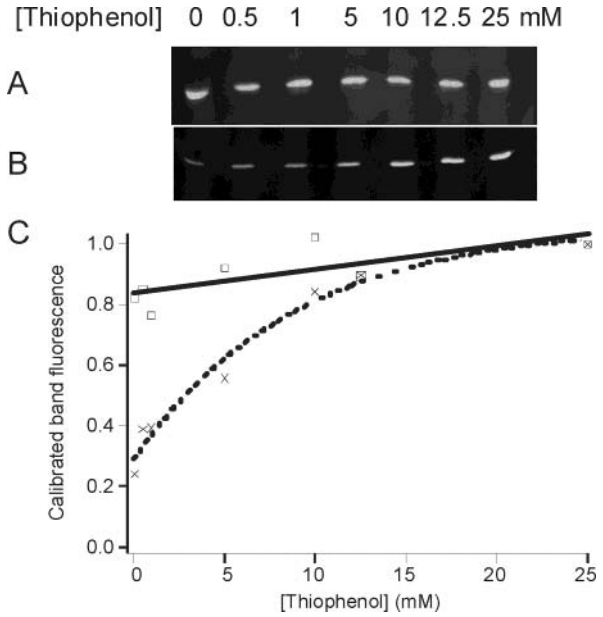


Figure 9. Examples of two fluorescent labeling reactions of BioB. (A and B) Two different samples of FTEC (2.3 mM) in the presence of increasing concentrations of thiophenol as shown. (C) Graph showing yield of fluorescent protein at various thiophenol concentrations: (□) A; (×) B. Data are fit to a straight line (A) and exponential curve (B).

Effect of Thiophenol Concentration on Labeling Reactions. While thiophenol has been reported to be essential in intein-mediated ligation reactions (*22*), it is a toxic and highly reactive compound. For example, thiophenol might react with the labile Fe−S cluster redox centers present in proteins such as LipA and BioB (*23, 24*). For these, and other delicate proteins, labeling reactions would ideally omit thiophenol or other small activating thiol. It is therefore of interest to determine the minimum concentration of thiophenol required for efficient fluorescent labeling.

In experiments where no thiophenol was added, the extent of target protein labeling was observed to be variable (e.g. Figure 9). The underlying reason for this variability has yet to be determined; however, it may simply be due to the oxidation of FTEC to the disulfide,

a process observed by HPLC analysis to occur in solution at pH 8.1, even under the low oxygen tension within the glovebox (<0.2 ppm O_2). The concentration of thiophenol required for consistent efficient labeling under anaerobic conditions was investigated (Figure 9). Over a wide range of experiments, it was found that a concentration of 10 mM thiophenol ensured efficient labeling within 16 h.

These observations suggest that thiophenol may have a 2-fold function in the labeling reactions, first to form a thioester intermediate (**5**) and second that it may be important in maintaining FTEC in a reduced and hence reactive state. In these relatively complex reactions, it is difficult to deconvolute the relative importance of these roles; indeed, the function of the thiophenol in efficient labeling may also depend on the anaerobicity of the reaction, the presence of other efficient reductants (such as TCEP), and the steric constraints of the target−intein junction.

CONCLUSIONS

Practical conditions for intein-mediated attachment of fluorescent labels to protein domains have been determined:

(a) Using FTEC and rigorously anaerobic reaction conditions to achieve labeling without the addition of either thiophenol or TCEP; however, these conditions should be used with caution, as the yield can be variable.

(b) For routine aerobic labeling reactions, the addition of thiophenol (10 mM) and TCEP to ensure a high yield of the fluorescently labeled derivative after 24 h of reaction.

(c) In our hands, reaction under anaerobic conditions with the addition of thiophenol (10 mM) consistently achieves the highest levels of label incorporation, and these conditions are suitable for labeling a wide range of proteins for biophysical studies.

ACKNOWLEDGMENT

This work was supported by grants from the Royal Society (P.L.R.), the EPSRC (M.K. and R.J.W.) and the Wellcome Trust (Z.K.B.). We thank John Langley, Julie Herniman, Joan Street, and Neil Wells for their expert assistance in obtaining spectroscopic data.

LITERATURE CITED

(1) Evans, T. C., Benner, J., and Xu, M. Q. (1999) The in vitro ligation of bacterially expressed proteins using an intein from Methanobacterium thermoautotrophicum. *J. Biol. Chem. 274*, 3923−3926.

(2) Muir, T. W., Sondhi, D., and Cole, P. A. (1998) Expressed protein ligation: A general method for protein engineering. *Proc. Natl. Acad. Sci. U.S.A. 95*, 6705−6710.

(3) Mukhopadhyay, J., Kapanidis, A. N., Mekler, V., Kortkhonjia, E., Ebright, Y. W., Ebright, and R. H. (2001) Translocation of sigma(70) with RNA polymerase during transcription: Fluorescence resonance energy transfer assay for movement relative to DNA. *Cell 106*, 453−463.

(4) Macmillan, D., and Bertozzi, C. R. (2000) New directions in glycoprotein engineering. *Tetrahedron 56*, 9515−9525.

(5) Lovrinovic, M., Seidel, R., Wacker, R., Schroeder, H., Seitz, O., Engelhard, M., Goody, R. S., and Niemeyer, C. M. (2003) Synthesis of protein-nucleic acid conjugates by expressed protein ligation. *Chem. Commun.* 822−823.

(6) Tolbert, T. J., and Wong, C. H. (2000) Intein-mediated synthesis of proteins containing carbohydrates and other molecular probes. *J. Am. Chem. Soc. 122*, 5421−5428.

(7) Camarero, J. A., Shekhtman, A., Campbell, E. A., Chlenov, M., Gruber, T. M., Bryant, D. A., Darst, S. A., Cowburn, D., and Muir, T. W. (2002) Autoregulation of a bacterial sigma factor explored by using segmental isotopic labeling and NMR. *Proc. Natl. Acad. Sci. U.S.A. 99*, 8536−8541.

(8) Xu, R., Ayers, B., Cowburn, D., and Muir, T. W. (1999) Chemical ligation of folded recombinant proteins: Segmental isotopic labeling of domains for NMR studies. *Proc. Natl. Acad. Sci. U.S.A. 96*, 388−393.

(9) Iwai, H., Lingel, A., and Pluckthun, A. (2001) Cyclic green fluorescent protein produced in vivo using an artificially split PI−PfuI intein from Pyrococcus furiosus. *J. Biol. Chem. 276*, 16548−16554.

(10) Abel-Santos, E., Scott, C. P., and Benkovic, S. J. (2003) Use of Inteins for the In Vivo Production of Stable Cyclic Peptide Libraries in E. coli. *Methods Mol. Biol. 205*, 281−294.

(11) Ayers, B., Blaschke, U. K., Camarero, J. A., Cotton, G. J., Holford, M., and Muir, T. W. (1999) Introduction of unnatural amino acids into proteins using expressed protein ligation. *Biopolymers 51*, 343−354.

(12) Dawson, P. E., Muir, T. W., Clarklewis, I., and Kent, S. B. H. (1994) Synthesis of Proteins by Native Chemical Ligation. *Science 266*, 776−779.

(13) Burns, J. A., Butler, J. C., Moran, J., and Whitesides, G. M. (1991) Selective Reduction of Disulfides by Tris(2- Carboxyethyl)Phosphine. *J. Org. Chem. 56*, 2648−2650.

(14) Sambrook, J., Fritsch, E. E., and Maniatis, T. *Molecular Cloning: A laboratory manual*; Cold Spring Harbor laboratory: Cold Spring Harbor, NY, 1989.

(15) Studier, F. W., and Moffat, B. A. (1986) Use of bacteriophage T7 RNA polymerase to direct high-level selective expression of cloned genes. *J. Mol. Biol. 189*, 113−130.

(16) Apontoweil, P., and Behrends, W. (1975) Isolation and initial characterisation of glutathione-deficient mutants of *Escherichia coli* K12. *Biochem. Biophys. Acta 399*, 10−12.

(17) Miroux, B., and Walker, J. E. (1996) Over-production of proteins in *Escherichia coli*: Mutant hosts that allow synthesis of some membrane proteins and globular proteins at high levels. *J. Mol. Biol. 260*, 289−298.

(18) Hofmann, R. M., and Muir, T. W. (2002) Recent advances in the application of expressed protein ligation to protein engineering. *Curr. Opin. Biotechnol. 13*, 297−303.

(19) Evans, T. C., Benner, J., and Xu, M. Q. (1998) Semisynthesis of cytotoxic proteins using a modified protein splicing element. *Protein Sci. 7*, 2256−2264.

(20) Guzman, L. M., Belin, D., Carson, M. J., and Beckwith, J. (1995) Tight Regulation, Modulation, and High-Level Expression by Vectors Containing the Arabinose P−Bad Promoter. *J. Bacteriol. 177*, 4121−4130.

(21) Chong, S., Williams, K. S., Wotkowicz, C., and Xu, M. Q. (1998) Modulation of Protein Splicing of the *Saccharomyces cerevisiae* Vacuolar Membrane ATPase Intein. *J. Biol. Chem. 273*, 10567−10577.

(22) Severinov, K., and Muir, T. W. (1998) Expressed protein ligation, a novel method for studying protein−protein interactions in transcription. *J. Biol. Chem. 273*, 16205−16209.

(23) Kriek, M., Peters, L., Takahashi, Y., and Roach, P. L. (2003) Effect of iron−sulfur cluster assembly proteins on the expression of *Escherichia coli* lipoic acid synthase. *Protein Express. Purif. 28*, 241−245.

(24) Ollagnier-De Choudens, S., Sanakis, Y., Hewitson, K. S., Roach, P., Baldwin, J. E., Munck, E., and Fontecave, M. (2000) Iron−sulfur center of biotin synthase and lipoate synthase. *Biochemistry 39*, 4165−4173.

BC0341728

Production of [F-18]Fluoroannexin for Imaging Apoptosis with PET

John R. Grierson,*,† Kevin J. Yagle,† Janet F. Eary,† Jonathan F. Tait,‡ Don F. Gibson,‡ Barbara Lewellen,† Jeanne M. Link,† and Kenneth A. Krohn†

Departments of Radiology and Laboratory Medicine, University of Washington, Seattle, Washington 91895.
Received September 19, 2003; Revised Manuscript Received January 27, 2004

Recombinant human-annexin-V was conjugated with 4-[F-18]fluorobenzoic acid (FBA) via its reaction with the *N*-hydroxysuccinimidyl ester (FBA-OSu) at pH 8.5. A series of reactions using varying amounts of annexin-V, unlabeled FBA-OSu, and time produced products with different conjugation levels. Products were characterized by mass spectrometry and a cell-binding assay to assess the effect of conjugation. In each case, the conjugated protein was a mixture of proteins with a range of conjugation. Annexin-V could be conjugated with an average of two FBA mole equivalents without decreasing its affinity for red blood cells (K_d 6−10 nM) with exposed phosphatidylserine. An average conjugation of 7.7 (range 3−13) diminished the binding 3-fold. Large-scale production and purification of [F-18]-FBA-OSu from [F-18]fluoride was accomplished within 90 min and in 77% radiochemical yield (decay-corrected to the end of cyclotron bombardment). The conjugation reaction of annexin with [F-18]FBA-OSu was studied with respect to activity level, protein mass, and concentration. Under the most favorable conditions, >25 mCi [F-18]fluoroannexin (FAN) was isolated in 64% yield (decay-corrected for a 22 min conjugation process) from labeling 1.1 mg of annexin-V. A pilot PET imaging study of [F-18]fluoroannexin in normal rats showed high uptake in the renal excretory system and demonstrated sufficient clearance from most other internal organs within 1 h. [F-18]Fluoroannexin should prove useful in imaging targeted apoptosis.

INTRODUCTION

Apoptosis is a normal physiological process of programmed cell death that plays a key role in maintaining constant cell density in tissues undergoing cell proliferation. It also provides a defense mechanism for eliminating abnormal cells with damaged DNA. As such, apoptosis plays an important role in cancer biology and cancer treatment. Cancer can result from a failure of apoptosis to balance cell proliferation, either by under-expressing genes that promote apoptosis or by overexpressing genes that inhibit it. In addition to genetic mutations that lead to unregulated cell proliferation, other mutations that affect the cell's ability to undergo apoptosis can also be part of the progress toward uncontrolled growth. For example, the *bcl-2* oncogene appears to contribute to the development of lymphoma by inhibiting apoptosis, without affecting cell proliferation (*1*). Furthermore, chemotherapy and radiation therapy generally kill cells by activating apoptosis. In this context, a sensitive method for imaging apoptosis in vivo should prove useful for monitoring cancer treatment.

In contrast to normal cells, high levels of phosphatidylserine are exposed on the outer membrane leaflet of apoptotic cells. This provides a selective and accessible target for molecular imaging. Annexin-V (36 kDa) is an endogenous protein ligand with a high affinity (K_d ~10 nM) for phosphatidylserine (PS) (*2*). Consequently, it has been adapted for use as a radiopharmaceutical after labeling it with technetium-99m (*3*−*5*). Studies with [Tc-99m]annexin-V have demonstrated that apoptosis imaging is feasible in animal models of induced apoptosis and with human subjects (*6*−*8*). This success prompted us to develop a fluorine-18-labeled annexin-V analogue for quantitative 3-D imaging with PET. We were also attracted by the potential application of combining [F-18]-fluoroannexin-V and [C-11]thymidine in the same imaging session to investigate the balance between cell death and growth rates in tumors.

In this report we show that annexin-V can be effectively labeled using the *N*-hydroxysuccinimidyl ester of [F-18]fluorobenzoic acid (Figure 1) and that the biological activity of the acylated product, [F-18]fluoroannexin (FAN), is equivalent to that of annexin-V. Exploratory PET imaging of [F-18]FAN in normal rats showed rapid blood clearance and low background activity in organs other than the kidneys and bladder, which are involved in clearance of the protein.

EXPERIMENTAL PROCEDURES

Materials and Methods. (a) Chemicals. Reagent chemicals were obtained from Aldrich Chemical Co. (Milwaukee, WI) and were used as received. The labeling precursor for [F-18]FBA-OSu:ethyl 4-trimethylammonium benzoate trifluoromethanesulfonate salt was prepared according to Haka et al. (*9*) and stored in the cold. Unlabeled 4-fluorobenzoic acid *N*-hydroxysuccinimide ester (FBA-OSu) was prepared using standard peptide methods with 4-fluorobenzoic acid, *N*-hydroxysuccinamide, and dicyclohexylcarbodiimide in ether. The isolated solid was recrystallized twice from ether (mp 110−112 °C). Anhydrous dimethyl sulfoxide (DMSO), contained in break-seal ampules, was used for labeling experiments. Enriched (95%-atom) [O-18]water was obtained from Isonics Corp. (Golden, CO). AG 1-X8 ion-exchange resin, for separating [F-18]fluoride from [O-18]water, was obtained from Rio-Rad (Hercules, CA). C18-Plus SepPak

* Corresponding author. E-mail: grierson@u.washington.edu. Ph: 206-598-6247. Fax: 206-598-4192.
† Department of Radiology.
‡ Department of Laboratory Medicine.

10.1021/bc0300394 CCC: $27.50 © 2004 American Chemical Society
Published on Web 02/27/2004

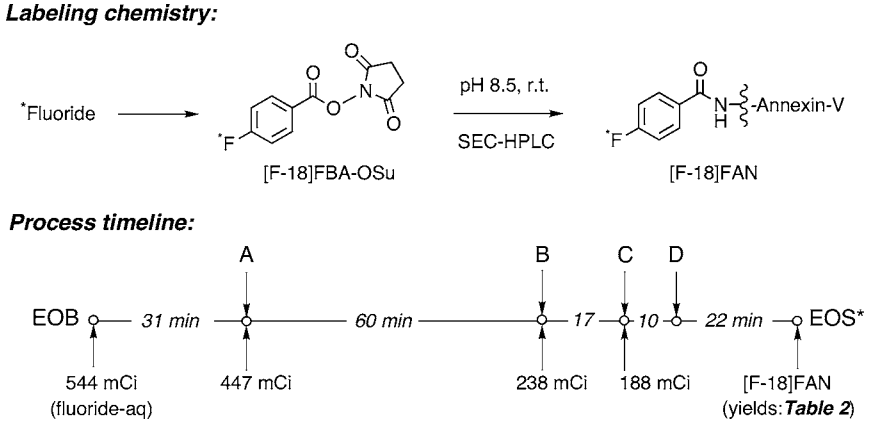


Figure 1. Radiolabeling scheme and timeline for the synthesis of [F-18]fluoroannexin. EOB (end of cyclotron bombardment); A (end of label incorporation rxn); B (end of FBA-OSu purification); C (isolation of FBA-OSu in dry ether); D (solvent-free FBA-OSu isolated).

Table 1. Mass Spectrometry (ES^+) Study of Annexin-V Acylation by Cold FBA-NHS

stoichiometry: FBA-OSu/annexin	rxn time (min)	FBA conjugations: annexin:(*x*) (% distribution)						average: FBA/annexin	IC_{50} (nM)
		(0)	(1)	(2)	(3)	(4)	(5)		
1:1	15	97	3					0.03	12 ± 1
2:1	15	89	11					0.11	9 ± 1
4:1	15	79	21					0.21	10 ± 2
8:1	15	69	26	5				0.37	8 ± 2
16:1	15	42	34	17	7			0.89	10 ± 2
32:1	15	12	26	27	23	9	5	2.06	8 ± 2

cartridges were obtained from the Waters Corporation (Milford, MA).

(b) Annexin-V Protein. Laboratory grade recombinant (*E. coli*) human annexin-V (*rh*-annexin-V) was purified as described by Wood et al. (*10*). Stock protein solutions (1.0, 7.6, or 8.7 mg/mL) were prepared with 10 mM NaH_2PO_4 pH 7.4 buffer containing 140 mM sodium chloride and stored frozen (−15 °C) until used. Clinical grade *rh*-annexin-V was provided (1.0 mg/mL, 10 mM NaH_2PO_4 pH 7.4 buffer, 140 mM NaCl) as a gift from the Theseus Imaging Corporation (Worcester, MA) and stored at −80 °C until used.

(c) Buffers. HNKGB buffer (10 mM HEPES pH 7.4, 136 mM NaCl, 2.7 mM KCl, 5 mM glucose, 1 mg/mL fatty acid free bovine serum albumin) was prepared as needed. Sodium chloride (0.9%, USP) was obtained from Baxter (Deerfield, IL) and used for the size exclusion HPLC purification of [F-18]fluoroannexin. For animal work, pH 7.4 PBS was used. Borate buffers (0.025 M and 0.50 M, pH 8.5) were prepared from sodium tetraborate decahydrate (Borax, 99.999%) and hydrochloric acid. The more concentrated buffer solution (9.52 g Borax + 2.53 mL concentrated HCl/50 mL) must be prepared with heating to dissolve the salt. The solution (rt) was used before recrystallization initiated (∼30 min).

(d) Chromatography Systems and Detectors. Purifications were performed using a Thermo-Separation Products (Riviera Beach, FL) Constametric 4100 HPLC pump, Rheodyne (Cotati, CA) 7125 and 7725i injectors and flow-through radiation detector systems from Beckman (Fullerton, CA; model 170) or Carroll & Ramsey Associates (Berkeley, CA; model 105-S). For studies with unlabeled annexin a variable wavelength V^4-UV absorbance detector from ISCO (Lincoln, NE) was used. HPLC columns were obtained from Phenomenex (Torrance, CA): column-A (LUNA-5 μm C18(2)) 250 × 10 mm i.d.; column-B (BioSep SEC−S 2000) 300 × 7.8 mm i.d.; column-C (LUNA-5 μm C18(2)) 250 × 4.6 mm i.d.. Radioactivity >100 μCi was measured using an ion chamber Capintec CRC-12 Radioisotope Calibrator (Pittsburgh, PA) and <0.1 μCi measurements were made with a Packard Auto-Gamma 500 series instrument (Downers Grove, IL).

(e) Reactions of Unlabeled FBA-OSu and Annexin-V with Varied Stoichiometry and Time. A series of FBA-OSu/annexin-V conjugation reactions with mole ratios of 4:1, 8:1, 16:1, and 32:1, and reaction times of 15, 30, and 60 min, was performed. In each case, 150 μg of annexin-V (150 μL, 1 mg/mL, 10 mM PBS, 140 mM NaCl) was reacted with FBA-OSu in pH 8.5 borate buffer (150 μL, 0.025 M) and acetonitrile (32 μL). The buffer was added to the acetonitrile/FBA-OSu reagent solution followed by the protein solution. After incubation for the required time at room temperature, the reaction was terminated using size-exclusion HPLC (Column-B eluted with PBS at 2 mL/min). The conjugation product was collected in an elution volume characteristic for the elution of annexin-V. UV-detection at 267 nm was used, and the chromatographic profiles of the purifications mimicked those seen during the radiosynthesis of [F-18]-fluoroannexin. In each case, the chromatography revealed the presence of some unreacted FBA-OSu that eluted late from the column. Selected purified products were analyzed by mass spectrometry, as described in section-k, to determine the extent of conjugation on individual annexin-V protein molecules and their population within the product mixture. Individual product solutions were stored frozen for up to 3 days before mass analysis was performed. Results from these reactions are presented in Table 1.

(f) Radiolabeling and Purification of *O*-(*N*-Hydroxysuccinimidyl)[F-18]fluorobenzoate (FBA-OSu). Our radiosynthesis modifies the original report by Wester et al. (*11*). Our adaptations substituted the previously described solid-phase extraction media with standard SepPak (C-18) cartridges. We have also included a HPLC purification and isolation of the active ester prior to its

reaction with *rh*-annexin-V. A timeline for the process is presented in Figure 1.

Enriched [O-18]water (95%) was bombarded with 11 MeV protons in a pressurized silver target (1.25 mL) using a CTI (Knoxville, TN) RDS-111 cyclotron. Post-irradiation, [F-18]fluoride was separated from target water by passing the solution through a short plug of anion-exchange resin (12−15 mg, OH^- form, 200−400 mesh) using the method reported by Schlyer (*12*). Resin-bound fluoride was eluted with 0.1 M potassium carbonate (250 μL) and collected in a borosilicate test tube (100 × 16 mm i.d., Kimax 51) containing Kryptofix [2.2.2] (19 mg, 50 μmol). The tube was placed in a dry-block at 100 °C, and water was removed by azeotropic distillation with MeCN (4 × 1 mL) under a rapid stream of argon. Typically, 350−400 mCi of dried [F-18]KF/carbonate/Kry-[2.2.2] complex was produced within 30 min after the end-of-bombardment (EOB). The residue was treated with ethyl 4-trimethylammonium benzoate trifluoromethanesulfonate salt (15.5 mg, 43 μmol) in DMSO (300 μL) at 100 °C for 7 min, and then 1 N KOH (100 μL) was added to saponify the ester group. After 7 min, the mixture was acidified with 0.1 N HCl (10 mL) and the solution was pulled through a C-18 SepPak. A water rinse (4 mL) of the reaction vessel was also extracted. The retained 4-[F-18]fluorobenzoic acid was eluted from the SepPak with MeOH into a test tube (100 × 16 mm) containing tetramethylammonium hydroxide (25 wt % in MeOH, 10 μL). The resultant solution was concentrated at 100 °C under a rapid stream of argon, and the residue (ca. 100 μL) was azeotropically dried with MeCN (2 × 1 mL).

Solid *O*-(*N*-succinimidyl)-*N*,*N*,*N*′*N*′-tetramethyluronium tetrafluoroborate (30 mg, 73 μmol) was added to the residual film of tetramethylammonium 4-[F-18]fluorobenzoate, and then dry MeCN (400 μL) was used to wash down the tube wall. The reaction mixture was heated at 100 °C for 3 min and then quenched with 5% acetic acid (8 mL). The acidic solution was pulled into an intervening septum-sealed vial (10 mL) and then forced (60 psi air) through a 0.2 μm self-venting filter (Braun: Bethlehem, PA; PFE−2000) attached to the HPLC injector port. The injector was fitted with a precolumn that substituted for a regular sample injection loop. The precolumn was made from an empty 50 × 4.6 mm (i.d.) guard column filled with C-18 SepPak media and was conditioned with EtOH (4 mL) and then water (6 mL) before use. Concentration of the sample on the precolumn was followed by a water (3 mL) rinse. The retained active ester was eluted with 45% MeCN−water at 6 mL/min and purified using Column-A. The product fraction was collected in ∼6 mL after 8 min. A representative chromatogram is shown in Figure 2. The collected product solution was diluted with water (20 mL) and then pulled through a tandem pair of C-18 SepPaks at ∼5 mL/min. The SepPaks were washed with brine (4 mL) and then eluted with ether (4 mL). The coeluted brine (∼0.5 mL) was removed before adding anhydrous magnesium sulfate (0.1 g) to the collected ether solution. The dried solution and a rinse (2 mL) were filtered using a 10-mm platform 0.2 μm ceramic micron filter (Anotop: Alltech, Deerfield, IL). The precautions taken with drying and filtering are recommended to standardize the quality of [F-18]FBA-OSu and provide consistent annexin-V labeling yields. Drying is designed to minimize ester hydrolysis during temporary storage or while concentrating solutions to residual films for reaction. Filtration is designed to eliminate small amounts of high surface area particles that always shed from eluted SepPaks and which may interfere with protein labeling or recovery.

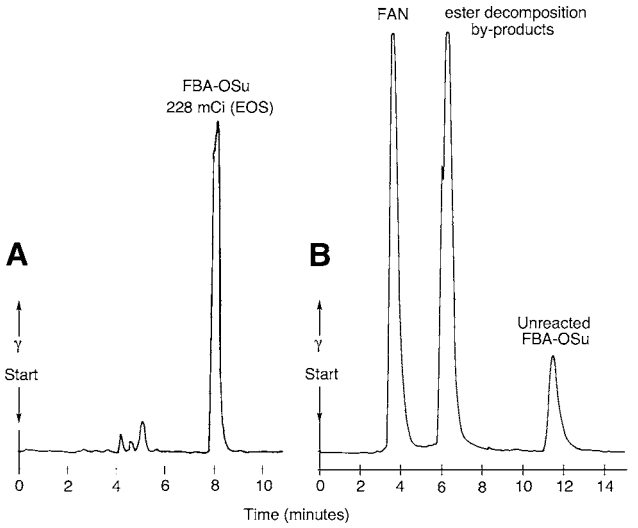


Figure 2. Typical HPLC-radiochromatograms for [F-18]FBA-OSu and [F-18]fluoroannexin purifications. Trace A: C18 column eluted with 45% MeCN-water. Trace B: Size exclusion column eluted with 0.9% saline.

(g) Radiosynthesis of 4-[F-18]Fluorobenzoyl *rh*-Annexin-V. The purified active ester in dry ether was concentrated at room temperature in a 100 × 16 mm test tube under a rapid stream of argon. To the residual colorless film was added stock annexin-V and then pH 8.5 borate buffer solution (see Table 2 for protein mass and reaction volumes), and the labeling mixture was incubated at room temperature, with periodic agitation. Labeled [F-18]fluoroannexin was isolated using a silica-based semipreparative size-exclusion chromatography (SEC) column (Column-B) eluted at 2 mL/min with 0.9% saline for studies involving K_d determinations, or with PBS for animal experiments. Characteristically, [F-18]-fluoroannexin is the first component eluted from the column and is collected in a ∼3 mL fraction starting at 3.8 min. A representative chromatogram is shown in Figure 2. A timeline for the process, along with typical activity levels and yields, also appears in Figure 1. The fraction of activity lost to the reaction tube wall can be high (>30%) if the active ester is not concentrated to a small area prior to its reaction. To minimize the problem we evaporated the stock aliquot (∼4 mL) to dryness and then used a small volume of ether (400 μL) to wash down the tube wall, followed by gentle evaporation to a final residual film.

(h) Cell Binding Assay for Labeled Annexin. A previously developed cell-binding assay (*5*) was used to determine the affinity of labeled annexin samples to a standard preparation of human red blood cells with externalized (PS+) phosphatidylserine. The assay was conducted in the absence and presence of calcium, which is essential for annexin binding. Briefly, labeled annexin at a final concentration of 10 nM (the approximate K_d of annexin-V) was incubated for 15 min at rt in HNKGB buffer (total volume 1 mL) containing either 2.5 mM Ca^{2+} or 5 mM EDTA, and 100 μL of PS+ cells (∼4 × 10^8 erythrocytes). The specific binding (1-[cpm (Ca^{2+})/cpm total]) was measured after pelleting cells by centrifugation at 10 000*g* (Eppendorf model 5415D; Hamburg, Germany) for 3 min. Typically, the specific binding ranged from 80 to 90%, and this value was used to correct for nonbinding annexin in the determinations of K_d (section-j).

(i) Determining Unlabeled Fluoroannexin-V Inhibition Concentration (IC_{50}) Relative to FITC-

Table 2. Radiochemical Yields and Product Analysis for [F-18]Fluoroannexin-V Production

	labeling reaction variables					[F-18]fluoroannexin production			
entry	reaction activity, mCi	FBA-OSu batch	protein mass, μg	buffer volume, μL	reaction volume, μL	F-annexin-V activity (EOS), mCi	yield (SOS) vs FBA-OSu, %	specific activity (EOS), μCi/μg	protein recovery, %
1	24.5	A	150	150	300	1.39	7	16	59
2	50.7	B	150	150	300	2.82	6	31	59
3	18.3	A	1140	150	300	4.63	29	4	86
4	138.4	C	1140	150	300	33.9	28	36	84
5	48.1	D	1140	15	165	26.7	64	29	83
6	41.3	E	1305	15	165	22.8	64	23	76
7	44.7	E	150	15	165	6.0	17	76	53
8	44.2	E	300	15	315	6.7	19	29	79

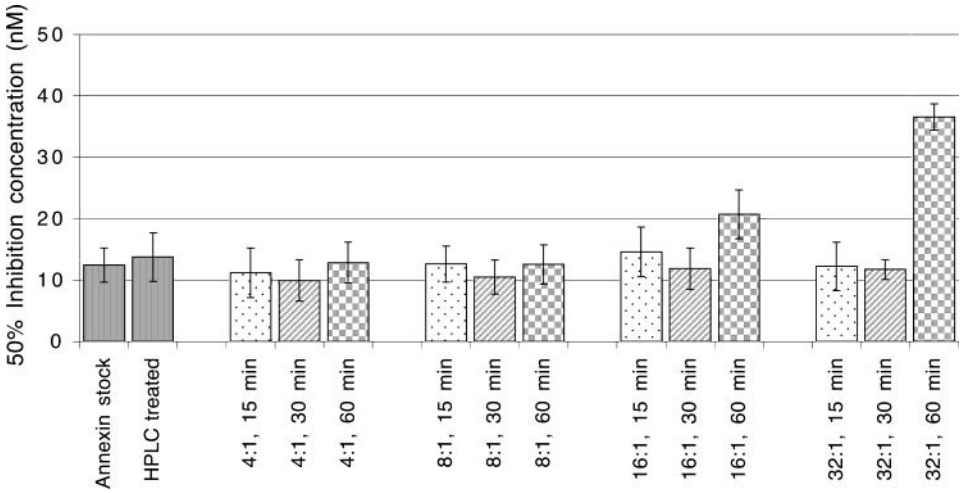


Figure 3. Fluoroannexin IC_{50} values vs reaction conditions for fluoroannexin syntheses. Product protein IC_{50} values were determined using a competitive binding assay with FITC-annexin as described in section-i; error bars (2 × SD).

Annexin-V Binding to PS+ (phosphatidylserine) Red Blood Cells. The concentration of purified fluoroannexin protein samples was first assayed by the Bradford method (*13*) using reagents from BioRad (Hercules, CA) with BSA fraction-V (Pierce, Rockford, IL) as a standard. Fluoroannexin samples were added at concentrations from 2 to 100 nM to a reaction tube containing 5 nM fluorescein-labeled annexin-V (FITC-annexin) (*5*) and 8×10^6 PS+ erythrocytes in HNKGB buffer, in a final volume of 1 mL. After incubating for 15 min at room temperature, cells were pelleted by centrifugation at 10 000*g* for 3 min. The supernatant was removed to a separate tube, and the FITC-annexin-V bound to the pellet was released by adding 950 μL of 5 mM EDTA/HNKGB. The sample was recentrifuged, and 800 μL of supernatant was assayed for FITC-annexin-V content by fluorometric analysis using an Abbott TDX analyzer (Abbott Park, IL). The results from these inhibition experiments are shown in Figure 3.

(j) Determining the Apparent K_d for [F-18]Fluoroannexin Bound to PS+ Red Blood Cells. Quantitative titrations were used to determine the dissociation constant, as described previously (*5*). Briefly, labeled fluoroannexin (2−300 nM) was added to 10^7 PS+ erythrocytes in HNKGB buffer (250 μL total volume) with either 2.5 mM Ca^{2+} or 5 mM EDTA. After incubation at room temperature for 15−30 min, bound and free fluoroannexin were separated by centrifugation through 40 μL of DC550 silicone oil (Dow Chemical, Midland, MI) in 0.3 mL small-tipped microtubes (Sarstedt; Nuembrecht, Germany) at 10 000*g* for 3 min. After cutting off the tube tip to isolate the pellet, the bound fluoroannexin in the cell pellet was counted. Counts were converted to molecules bound/cell using the known specific activity of the protein. The concentration of free annexin was determined by measuring activity remaining in the supernatant and correcting for nonbindable fluoroannexin, as determined using the method described in section-h. A typical data set is shown in Figure 4. K_d and B_{max} values were calculated using a nonlinear least-squares analysis (Microsoft Excel) to fit data to a model of noncooperative binding to homogeneous sites.

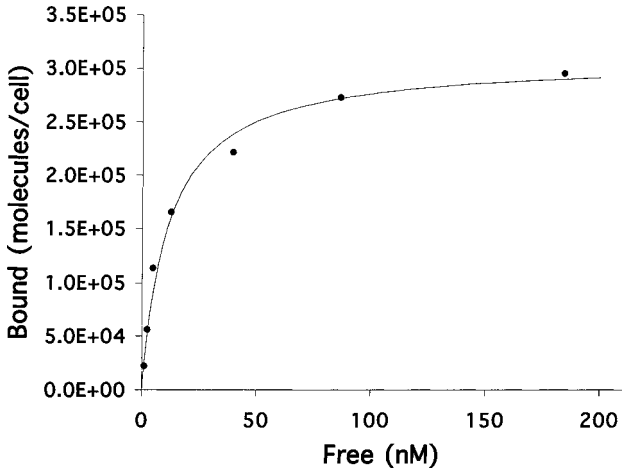


Figure 4. PS^+-red blood cell binding data for [F-18]fluoroannexin.

(k) Mass Spectrometry. A Micromass (Manchester, UK) Quattro II Tandem Quadrupole Mass Spectrometer, that has unit resolution over a 4000 *m*/*z* range, was used with electrospray ionization (ESI^+) for analysis of fluoroannexin samples containing mixed levels of protein conjugation with 4-fluorobenzoic acid. Samples were desalted by HPLC prior to their infusion into the electrospray source. The chromatographic method used a

Poros RP1 packed column (150 × 2.1 mm, wide pore cross-linked polystyrene media supplied by Applied Biosystems Inc, Foster City, CA) and a Shimadzu (Columbia, MD) LC-10AD pump. The RP1 column was eluted at 300 μL/min using mixtures of mobile phase: A = water−0.05% trifluoroacetic acid (TFA) and B = MeCN−0.05%TFA. The mobile phase profile was 90:10 (A/B) between 0 and 5 min, followed by a linear gradient to 5:95 (A/B) between 5 and 20 min, and a final isocratic elution to 30 min. Micromass MassLynxNT 3.2 software was used to control the HPLC, the spectrometer, and data acquisition. The column eluate flow was diverted from the electrospray source for 2 min with a VICI Valco Instruments (Houston, TX) six-port injection valve. After 15 min of programmed elution, the fluoroannexin proteins eluted unseparated over a 4-min period. The spectrometer scan-time was 3.5 s between 500 and 2000 Da, with an interscan period of 0.1 s. MaxEnt, a statistical software package within the MassLynx operating system, was used to deconvolute complex multiple-charge-state mass spectral envelopes. A uniform Gaussian width-at-half-height of 2 Da was applied for mass peak recognition. An example data set and analysis is provided as Supporting Information.

(m) PET Imaging. Normal male Sprague−Dawley rats (260−280 g) were purchased from Animal Technologies Ltd. (Kent, WA). Animals were housed according to institutional guidelines, and all procedures were approved by the University of Washington Institutional Animal Care and Use Committee (IACUC). Prior to imaging, rats were anesthetized with ketamine (68 mg/kg) and xylazine (4.4 mg/kg) by iv injection. Anesthesia was maintained by booster injections of ∼7 mg/kg ketamine every 20 min. PET images were obtained using a GE (Waukesha, WI) Advance PET system. Image data was collected for 3 h, in 10 min time bins, starting 30 s after tail vein injection of [F-18]fluoroannexin (1−1.5 mCi). The specific activity was 13 μCi/μg at the time of injection. Data were collected in 2D-mode and reconstructed using the attenuated weighted OSEM algorithm (2 iterations, 28 subsets) with a 4 mm Gaussian postfilter. The reconstructed field of view was 20 cm.

RESULTS AND DISCUSSION

[F-18]Fluoroannexin (FAN) was prepared by adapting a general protein labeling protocol developed by Wester et al. (*11*). The method uses the *N*-hydroxysuccinimidyl ester of 4-fluorobenzoic acid (FBA-OSu). Our choice was based on initial success with labeling FBA-OSu and the previous claim that, in vivo, protein−(fluoro)benzamide conjugation was more stable than protein−(fluoro)alkylamide conjugation (*11*). We have further investigated the production of [F-18]FBA-OSu and evaluated its potential for labeling annexin-V. The basic scheme is illustrated in Figure 1. The issue of fluorobenzoic acid (FBA) conjugate load was addressed with experiments using unlabeled FBA-OSu and annexin-V.

Study of Annexin-V Conjugation. Annexin-V has 22 lysine residues and a free amino terminus that provide potential sites for fluorobenzoic acid (FBA) conjugation. Prior to this work, no information was available on how many FBA conjugations could be tolerated before the characteristic PS-binding of the parent protein (K_d 10 nM) was compromised. This issue was addressed by a series of experiments that varied the stoichiometry (1:1 to 32:1 FBA-OSu/annexin) of 15 min−pH 8.5−room temperature reactions. Fluoroannexin reaction products were purified by size exclusion HPLC and analyzed by mass spectrometry to determine the distribution of annexin molecules with different numbers of FBA groups. Table 1 lists annexin-xFBA distributions within each sample and the associated IC_{50} values (50% inhibitory concentration) that measure the ability of protein samples to competitively displace FITC-annexin (K_d 10 nM) bound to PS+ cell membranes. The data showed that even a 32:1 molar ratio yields quite a low (2.1) average FBA substitution level and that the reaction protocol could yield adequate specific activity without loss of phosphatidylserine binding. The average level of FBA conjugation with annexin-V was linearly related (r^2 = 0.99) to the offering ratio up to the highest ratio tested, 32:1. Extended reaction times (30 and 60 min) with a 32:1 mole ratio were also examined to test the limits of conjugation. These experiments are summarized in Figure 3, which indicated that only an extended reaction time and a high FBA-OSu:annexin molar ratio (60 min, 32:1) yields a protein conjugate with significantly compromised binding to PS+ membranes. The two control samples were stock annexin solution and a stock sample that was purified by SEC. The product from the most heavily treated reaction was analyzed by mass spectrometry to determine how many FBA/annexin were present. The range of conjugation was 3−13, and the average was 7.7 (Supporting Information). Collectively, these data showed that it should be possible to prepare [F-18]fluoroannexin with high protein specific activity and maintain competitive binding.

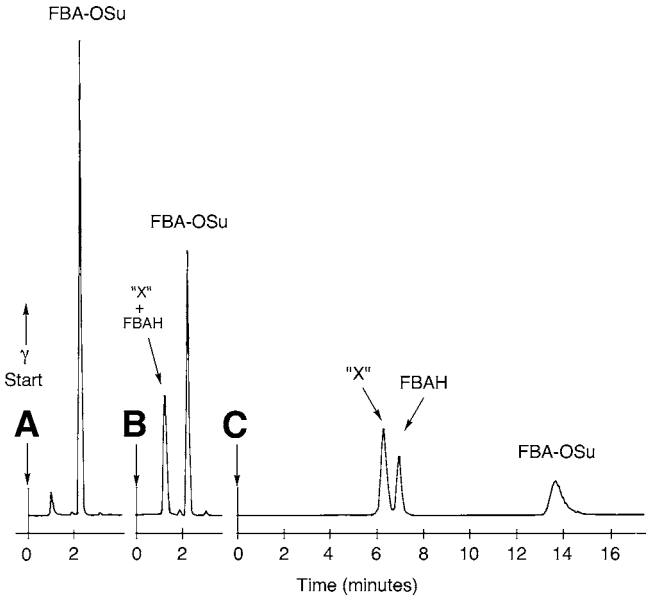


Figure 5. Radiochromatographic study of [F-18]FBA-OSu stability. Injection-A and -B: C18 column eluted with 60% MeCN−water; Injection-C: size exclusion column eluted with 0.9% saline.

Radiolabeling FBA-OSu and Annexin-V. The production of [F-18]FBA-OSu was accomplished in 77% radiochemical yield (EOB). We chose to include a HPLC purification of FBA-OSu to circumvent potential problems with protein labeling and to eliminate unlabeled or labeled impurities that might interfere with the [F-18]-FAN bioassay. Using the pure ester offered better quality control for evaluating the protein-conjugation reaction. The extra time taken to purify and isolate the ester in dry ether may be optional, but we have demonstrated that large quantities of the ester can be made. A typical timeline for the process is shown in Figure 1. Time points B and C mark, respectively, the collection of the ester from the HPLC column (91 min) and its subsequent

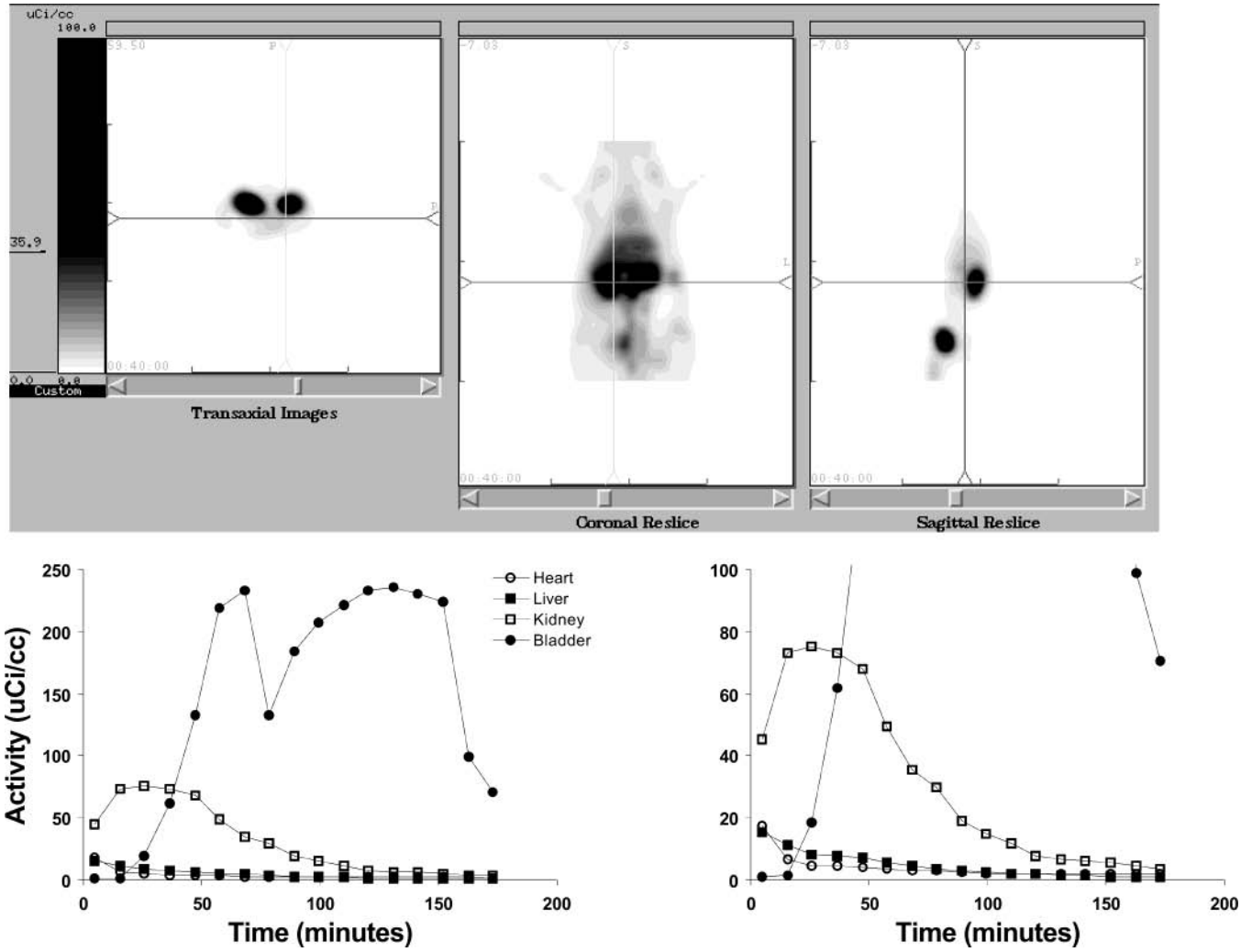


Figure 6. PET image of a male rat injected with [F-18]fluoroannexin and tissue TAC's. PET image set (top); tissue TAC: full scale (left); expanded scale (right).

reformulation in dry ether (108 min, 35% radiochemical yield, not decay corrected). Isolation of the ester in dry ether minimized its decomposition and provided a convenient solvent for rapidly evaporating aliquots. Figure 2 illustrates a set of HPLC radiochromatographic profiles for FBA-OSu and FAN purifications. Initial attempts with FBA-OSu production gave a 25% (not decay corrected) radiochemical yield (55%, decay corrected to the end of cyclotron bombardment (EOB)) on a >350 mCi scale. With practice, however, the yields steadily increased to 44% (not decay corrected) for collecting FBA-OSu off the HPLC column, requiring 90 min overall.

Figure 5 is a series of radiochromatograms that demonstrate the stability of FBA-OSu. Chromatogram-A shows a sampling of FBA-OSu in dry ether after the solution was allowed to stand for 2 h (initial activity 80 mCi/6 mL). Clearly the ester has good stability in ether. Another stability test of FBA-OSu at pH 8.5 mimicked the labeling conditions with annexin-V. An aliquot of ester stock solution was evaporated and treated with a 16% solution of acetonitrile in 0.025 M borate buffer (150 μL). Chromatogram-B represents a sample after 15 min at room temperature. Assuming FBA-OSu decomposes by hydrolysis or attack by other ambient species at the active ester site, a crude estimate of FBA-OSu decomposition gives a first order kinetic half-time of 32 min. This value acceptable compared to the 15 min labeling protocol. The identity of the FBA-OSu decomposition byproducts in chromatogram-B was partially clarified using the size exclusion HPLC method involved with FAN purification. Chromatogram-C identified 4-fluorobenzoic acid (verified by coinjection) and an unidentified component "x". Considering the composition of the test mixture, "x" is likely derived from acetonitrile decomposition byproducts that become labeled. This implicated fluorobenzamide or *N*-fluorobenzoylacetamide, but the issue was not pursued further.

Table 2 lists selected fluoroannexin labeling results using [F-18]FBA-OSu. [F-18]FAN activity values are referenced to the end-of-synthesis (EOS) to reflect the quantities typically encountered with the 22 min reaction and purification process. In some cases (1, 2, and 7) radiochemical yields were influenced by low protein recovery.

The poor yields (6%) seen for reactions 1 and 2 showed that a 1 mg/mL protein concentration diluted (1:1) with pH 8.5 buffer was impractical. By comparison, the higher protein stock concentration (7.4 mg/mL) used in reactions 3 and 4 improved the yields through gains in protein recovery and labeling efficiency. Protein recovery showed a practical limit of ~85% when the protein content was above 1.1 mg (reactions 3−6). In these cases, unrecovered activity was accounted for by the reaction vessel residue and transfer loss to the HPLC column. Further improvement in yield (2.3-fold) was realized (e.g. reaction 5 vs 4) when the buffer volume was reduced 10-fold (15 μL vs

150 μL). A supersaturated borate buffer (0.5 M) was used. Less concentrated buffers may be as effective but were not tested. The 64% yield for reactions 5 and 6 appears to be the limit, considering transfer losses in the process and the competing FBA-OSu decomposition. Overall, the final protein concentration in the reaction was the most important factor that determined the percent conjugation of FBA with annexin-V.

Reactions 6−8 used a common batch of FBA-OSu and comparable amounts of activity and protein. This series also evaluated clinical grade (1.0 mg/mL) *rh*-annexin-V. Reaction 6 used the same research grade *rh*-annexin-V as reactions 1−5. In comparison to the yield for reaction 1, the yield for reaction 7 is higher than expected. This could be ascribed to differences in FBA-OSu batches A and E at the start of the labeling reaction. The specific activities in FBA-OSu batches A−D were not measured. However, fluoride activity levels for all batches were comparable (average 478 mCi, range 335−535 mCi). FBA-OSu specific activity for batch E (2 Ci/μmol) was determined indirectly by performing mass spectrometry on the FAN product from reaction 7. The value was calculated by dividing the protein specific activity (88 μCi/μg decay corrected to SOS) by the average number of FBA conjugations per FAN protein molecule (1.6). The FAN−*x*FBA distribution frequency was 0-FBA(13%), 1-FBA-(37%), 2-FBA(32%), 3-FBA(12%), 4-FBA(3%), and 5-FBA-(3%), and the FBA-OSu/annexin ratio for reaction 7 was 5.3:1. Figure 4 shows rbc-binding profile for FAN from reaction 7. The apparent K_d and B_{max} values (±2SD) for the protein were 10.8 ± 5.0 nM and 3.04 + 0.35 × 10^5/cell, respectively, as calculated from a nonlinear least-squares fit. The apparent K_d values compare favorably with the reported K_d for annexin V, which is between 6 and 10 nM at this Ca^{2+} concentration (2.5 mM) (*5*). From a collection of similarly prepared samples (n = 8) the average K_d; B_{max} values were 9.6 nM (± 20%) and 3.1 × 10^5/cell (± 13%), respectively.

PET Imaging. Our goal is to use [F-18]fluoroannexin to image apoptosis in humans. As a preliminary step, normal rats were injected with [F-18]fluoroannexin and imaged to study which organs had the highest uptake and how rapidly the activity was cleared from tissues. Figure 6 shows the first PET images obtained with FAN in a normal rat. This series of 10-min frames centered on 45 min postinjection demonstrates the high uptake in the renal excretory system. The heart and liver are discernible above the kidneys, and the ureters are even visible. This figure also illustrates tissue time−activity curves (TAC) for heart, liver, kidney, and bladder. The graph on the right-hand side uses an expanded scale for activity values in order to better display the lower valued curves. It is clear from these curves and the image set that there is sufficiently rapid clearance of [F-18]fluoro-annexin so that only modest activity remains in most internal organs after 1 h. The clearance characteristics of [F-18]fluoroannexin should prove useful for early imaging of apoptosis. We are currently investigating the use of [F-18]fluoroannexin in imaging apoptosis in animal models.

ACKNOWLEDGMENT

Financial support was provided by the National Institutes of Health (CA42045). We thank William Howald and Ross Lawrence for their assistance with protein mass measurements. We also thank Theseus Imaging Corporation for the gift of clinical grade *rh*-annexin-V

Supporting Information Available: Mass spectral ion data and its deconvolution for a fluoroannexin sample. This material is available free of charge via the Internet at http://pubs.acs.org/BC.

LITERATURE CITED

(1) Rantanen, S., Monni, O., Joensuu, H., Franssila, K., and Knuutila, S. (2001) Causes and consequences of BCL2 over-expression in diffuse large B-cell lymphoma. *Leuk. Lymphoma 42*, 1089−1098.

(2) Thiagarajan, P., and Tait, J. F. (1990) Binding of annexin V/placental anticoagulant protein I to platelets. Evidence for phosphatidylserine exposure in the procoagulant response of activated platelets. *J. Biol. Chem. 265*, 17420−3.

(3) Tait, J. F., and Gibson, D. (1994) Measurement of membrane phospholipid asymmetry in normal and sickle- cell erythrocytes by means of annexin V binding. *J. Lab. Clin. Med. 123*, 741−8.

(4) Stratton, J. R., Dewhurst, T. A., Kasina, S., Reno, J. M., Cerqueira, M. D., Baskin, D. G., and Tait, J. F. (1995) Selective uptake of radiolabeled annexin V on acute porcine left atrial thrombi. *Circulation 92*, 3113−21.

(5) Tait, J. F., Brown, D. F., Gibson, D. F., Blankenberg, F. G., and Strauss, H. W. (2000) Development and characterization of annexin-V mutants with endogenous chelation sites for ^{99m}Tc. *Bioconjugate Chem. 11*, 918−925.

(6) Blankenberg, F. G., Katsikis, P., Tait, J. F., Davis, R. E., Naumovski, L., Ohtsuki, K., Kopiwoda, S., Abrams, M. J., Darkes. M., Robbins, R. C., Maecker, H. T., and Strauss, H. W. (1998) In vivo detection and imaging of phosphatidylerine expression during programmed cell death. *Proc. Natl. Acad. Sci. U.S.A. 95*, 6349−6354.

(7) Blankenberg, F. G., Katsikis, P. D., Tait, J. F., Davis, R. E., Naumovski, L., Ohtsuki, K., Kopiwoda, S., Abrams, M. J., and Strauss, H. W. (1999) Imaging of apoptosis (programmed cell death) with ^{99m}Tc annexin V. *J. Nucl. Med. 40*, 184−191.

(8) Belhocine, T., Steinmetz, N., and Hustinx, R., et al. (2002) Increased uptake of the apoptosis-imaging agent 99mTc recombinant human annexin-V in human tumors after one course of chemotherapy as a predictor of tumor response and patient prognosis. *Clin. Cancer Res. 8*, 2766−2774.

(9) Haka, M. S., Kilbourn, M. R., Watkins, G. L., and Toorongain S. A. (1989 Aryltrimethylammonium trifluoromethanesulfonates as precursors to aryl[F-18]fluorides: Improved synthesis of [F-18]GBR-13119. *J. Label. Comput. Radiopharm. 27*, 823.

(10) Wood, B. L., Gibson, D. F., and Tait, J. F. (1996) Increased erythrocyte phosphatidylserine exposure in sickle cell disease: flow-cytometric measurement and clinical associations. *Blood 88*, 1873−1880.

(11) Wester, H. J., Hamacher, K., and Stocklin, G. (1996) A comparative study of the nca fluorine-18 labeling of proteins via acylation and photochemical conjugation. *Nucl. Med. Biol. 23*, 365−372.

(12) Schlyer, D. J., Batos, M., and Wolf, A. P. (1987) A rapid quantitative separation of fluorine-18 from oxygen-18 water. *J. Nucl. Med. 40*, 25P.

(13) Bradford, M. M. (1976) A rapid and sensitive method for the quantitation of microgram quantities of protein utilizing the principle of protein-dye binding. *Anal. Biochem. 72*, 248−254.

BC0300394

Design and Synthesis of Visible Isotope-Coded Affinity Tags for the Absolute Quantification of Specific Proteins in Complex Mixtures

Patricia Bottari,[†] Ruedi Aebersold,[§] Frantisek Turecek,*[,†] and Michael H. Gelb*[,†,||]

Departments of Chemistry and Biochemistry, University of Washington, Seattle, Washington 98195, and Institute for Systems Biology, Seattle, Washington 98103-8904. Received September 22, 2003; Revised Manuscript Received December 18, 2003

Identification of proteins in complex mixtures by mass spectrometry is most useful when quantitative data is also obtained. We recently introduced isotope-coded affinity tags (ICAT reagents) for the relative quantification of proteins present in two or more biological samples. In this report, we describe a new generation of ICAT reagents that contain the following additional features: (1) a visible tag that allows the electrophoretic position of tagged peptides during separation to be easily monitored; (2) a photocleavable linker that allows most of the tag to be removed prior to mass spectrometric analysis; (3) an isotope tag that contains carbon-13 and nitrogen-15 atoms instead of deuterium to ensure precise comigration of light and heavy tagged peptides by reverse-phase HPLC. These reagents contain an iodoacetyl group that selectively reacts with peptide cysteine residues. Peptide modification chemistry is also reported that allows tagging of peptides that are devoid of cysteine. The synthesis of these visible isotope-coded affinity tags (VICAT reagents), and their reaction with peptides are described in this report. VICAT reagents containing a carbon-14 visible probe or an NBD fluorophore are described. These reagents are most useful for the determination of the absolute quantity of specific target proteins in complex protein mixtures such as serum or cell lysates.

INTRODUCTION

Mass spectrometry has emerged as one of the most useful techniques for the detection of proteins and protein-derived peptides. Since mass spectrometry often depends on internal standards for quantification, there have been recent efforts to develop novel chemical reagents that, when combined with mass spectrometry, provide protein abundance information on a quantitative level (*1*−*3*). Most of these methods involve the use of an internal standard, that is a compound identical to the analyte whose level is desired but is distinguished by different molecular mass due to heavy isotopic substitution. Along these lines, we have developed a reagent called the isotope-coded affinity tag (ICAT) and first applied this reagent to detect changes in the relative levels of specific proteins in yeast in response to changes in growth conditions (*4*). This is an example of a survey-type method in which abundance information is obtained on as many proteins as possible in a complex protein mixture (*5*, *6*). ICAT reagents are used to selectively tag the SH groups of peptide cysteine residues, with the introduction of a light and heavy isotope tag and a biotin residue for selective enrichment of tag peptides. Another cysteine peptide enrichment and isotope tagging scheme has been developed by Johnson and co-workers (*7*).

There is also a clear need for the development of reagents that allow a specific set of known proteins to be detected in complex mixtures and their absolute abundance determined. Detection of specific proteins in a complex mixture is usually carried out by one or more immunological methods including immunoblotting (western blotting) and ELISA. Although these methods are routinely used and provide valuable information, they have a number of limitations as discussed previously (*8*). For example, it often requires ∼1 year of work at a substantial cost to develop a highly specific antibody required for an ELISA-based detection of low levels of a specific protein in a complex biological fluid such as serum. Thus, it is not practical for a single laboratory to develop an immunological assay of a set of say 10−20 proteins, for example to evaluate the levels of proteins discovered by other techniques such as nucleic acid microarrays.

When the sequence of the peptide derived from the protein of interest is known, the mass spectrometer can be used to selectively monitor the particular parent ion mass of the target peptide of interest. Additional selective monitoring is provided by tandem mass spectrometry, in which a specific fragment ion or ions derived from the peptide parent ion is detected (specific or multiple reaction monitoring). Typically this type of experiment is done by separation of the peptide mixture on a reverse-phase, microbore HPLC column, which is interfaced directly with an electrospray ionization mass spectrometer. However, HPLC separation combined with specific reaction monitoring is probably not generally sufficient to detect specific peptides in complex peptide mixtures such as a trypsin digest of a eukaryotic cell lysate. This is because such tryptic digests may contain hundreds of thousands of distinct peptides, and the peptide of interest may be present in relatively small amounts compared to highly abundant peptides. For example, sequential separation is employed in the AQUA method (*9*), which makes use of protein electrophoresis (Laemmli gel) prior to

* Corresponding authors. M.H.G.: phone (206) 543-7142; fax (206) 685-8665; e-mail gelb@chem.washington.edu. F.T.: phone (206) 685-2041; fax (206) 685-8665; e-mail turecek@chem.washington.edu.

[†] Department of Chemistry.

[||] Department of Biochemistry.

[§] Institute for Systems Biology.

10.1021/bc034174s CCC: $27.50 © 2004 American Chemical Society
Published on Web 02/21/2004

combined HPLC/multiple reaction monitoring via tandem mass spectrometry for the absolute quantification of specific proteins in cell lysates.

In the present study, we describe the design and synthesis of modified ICAT reagents that contain a visible probe that allows tagged peptides to be detected by methods independent of mass spectrometry. These visible isotope-coded affinity tag reagents (VICAT reagents) are designed to be used in a analytical scheme in which peptides tagged with VICAT reagents are first resolved by isoelectric focusing (IEF) on a commercial gel strip containing an immobilized pH gradient. The presence of the visible probe allows the precise position of the desired tagged peptide to be immediately determined following one-dimensional separation by IEF. The desired region of the IEF gel strip is then excised, and eluted peptides are analyzed by combined reverse-phase, microbore HPLC/electrospray ionization tandem mass spectrometry. The visible probe also allows the absolute amount of the target peptide to be quantified at all steps in the process from postpeptide tagging to quantification in the mass spectrometer. This is an important feature since losses of analyte are inevitable in any multistep process.

In the present paper, we report the first phase of our development of VICAT reagents, the full experimental details for their synthesis and a demonstration of their reactivity with peptides and subsequent transformation prior to chromatographic separation and quantification by mass spectrometry. We also describe a peptide modification sequence, which allows tagging with ICAT and VICAT reagents of peptides that lack cysteine residues. In a subsequent, more biologically oriented study (*8*), we demonstrate the use of VICAT reagents for the absolute quantification of specific target proteins in eukaryotic cell lysates.

EXPERIMENTAL PROCEDURES

General Procedures. The structures of the VICAT reagents are shown in Figure 1, and their syntheses is outlined in Figures 2 and 4. Tetrahydrofuran (THF) was distilled from sodium/benzophenone under Ar, and methylene chloride (CH_2Cl_2) and triethylamine (TEA) were distilled from CaH_2 under Ar. Anhydrous dimethylformamide (DMF), pyridine, [^{13}C,^{15}N]-potassium cyanide, and 1,2-[$^{13}C_2$]-dibromoethane were purchased from Aldrich. Unless otherwise noted, all other compounds are reagent grade and were used as received. Unless otherwise noted, all nonaqueous reactions were carried out under Ar with oven-dried glassware. Electrospray ionization mass spectrometry (ESI-MS) was carried out on a Bruker Daltonics Esquire ion trap mass spectrometer, and MALDI data was obtained on a Applied Biosystems 4700 Proteomics Analyzer. Silica gel flash chromatography was performed using 230−400 mesh silica gel 60 (Merck, Darmstadt, Germany). Thin-layer chromatography was performed on aluminum-backed silica 60 plates with F254 indicator (Merck). Unless otherwise noted, reverse-phase HPLC separations were performed using a Vydac (Hisperia, CA) semipreparative column (up to 5 mg total loading, 10 μm packing, 10 mm × 250 mm, catalog no 218TP1010) at 4 mL/min, or a preparative column (up to 300 mg total loading, 10 μm packing, 20 mm × 250 mm, catalog no 218TP1022), or an a large preparative column (up to 1 g total loading, 10−15 μm packing, 5 × 25 cm, catalog no 218TP101550).

Synthesis of Sulfhydryl-Specific VICAT Reagents ($VICAT_{SH}$). *Biotin Tetrafluorophenyl Ester (**1**).* (+)-Biotin (4.5 g, 18.4 mmol) was dissolved in warm anhydrous DMF (90 mL). After the solution was cooled to room temperature, TEA (4.7 mL, 33.8 mmol) was added, followed by dropwise addition of tetrafluorophenyl trifluoroacetate (7.3 g, 27.4 mmol, (*10*)). After being stirred for 30 min at room temperature, the solvent was removed under reduced pressure. The residue was triturated with dry diethyl ether, and the product was filtered. The solid was dried under vacuum to afford 6.2 g (86%) of a white solid. ^1H NMR (300 MHz, d_6-DMSO) δ 7.9 (m, 1H); 6.4 (d, 2H); 4.35 (t, 1H); 4.15 (t, 1H); 3.2 (m, 1H); 2.75−2.9 (m, 3H), 2.6 (d, 1H); 1.4−1.8 (m, 6H).

*Biotin 2′-Aminoethylamide (**2**).* To a round-bottom flask containing ethylenediamine (8.5 g, 141.7 mmol) at 0 °C was transferred via cannula a solution of **1** (5 g, 12.8 mmol) in dry DMF (100 mL), also at 0 °C. After the mixture was stirred for 2 h at 0 °C, ethyl ether (100 mL) was added, and the solid was filtered and washed with ether. The white solid was left under vacuum overnight, and 3.15 g (86%) of the product was obtained. ^1H NMR (300 MHz, d_6-DMSO) δ 7.75 (bs, 1H); 6.4 (d, 2H); 4.35 (t, 1H); 4.15 (t,1H); 3.1 (m, 1H); 3.0 (q, 2H); 2.85 (dd, 1H); 2.5 (m, 3H); 2.0 (t, 2H), 1.2−1.7 (m, 6H). ESI-MS $(M + H^+)^+$: 287.0, $(2M + H^+)^+$: 573.0.

*Biotin 2′-(2″-Methylcarbonyl-1″-nitro-4″-phenylamino)-ethylamide (**3**).* To a round-bottom flask containing a solution of compound **2** (2.4 g, 8.4 mmol) in dry DMF (72 mL) and diisopropylethylamine (DIPEA) (2.9 mL, 16.7 mmol) at 0 °C was slowly added a solution of 5-bromomethyl-2-nitroacetophenone (*11*, *12*) (2.4 g, 9.3 mmol) in dry DMF (24 mL). After stirring for 3 h at 0 °C, the pH was adjusted to ∼5 with concentrated HCl (moist pH paper), and the solvent was removed in vacuo. The product was purified on a silica column packed with 5:1 CH_2Cl_2:MeOH. The column was developed with the same solvent, and the product was obtained in 64% yield (2.5 g). ^1H NMR (300 MHz, d_4-MeOH) δ 8.0 (d, 1H, J = 8.3 Hz); 7.75 (m, 2H); 4.45 (dd, 1H); 4.25 (dd,1H); 4.1 (s, 2H); 3.4 (t, 2H); 3.2 (m, 1H); 2.95 (m, 3H); 2.85 (d, 1H); 2.55 (s, 3H); 2.1 (t, 2H), 1.25−1.8 (m, 6H). ESI-MS $(M + H^+)^+$: 464.2, $(M + Na^+)^+$: 486.1.

*Compound **4**.* To a round-bottom flask containing a solution of compound **3** (2.5 g, 5.4 mmol) in MeOH (100 mL) and TEA (750 μL, 5.4 mmol) was added di-*tert*-butyl dicarbonate (1.3 g, 6.0 mmol). The mixture was stirred at 50 °C for 2 h and then cooled to room temperature. Sodium borohydride (650 mg,16.2 mmol) was added, and the reaction was stirred for an additional 1 h. Solvent was removed under reduced pressure and the residue resolubilized in CH_2Cl_2 (80 mL). The resulting solution was washed with water (40 mL) and brine (40 mL) and dried over anhydrous Na_2SO_4. Solvent was removed under reduced pressure to afford the product in 78% overall yield (2.4 g). ^1H NMR (300 MHz, $CDCl_3$) δ 7.8 (d, 1H, J = 8.4 Hz); 7.75 (bs, 1H); 7.2 (m, 1H); 6.9 (d, 1H); 5.9 (d, 1H); 5.35 (m, 1H); 4.4 (m, 3H); 4.25 (m,1H); 4.1 (d, 1H); 3.0−3.4 (m, 5H); 2.8 (dd, 1H); 2.65 (d, 1H); 2.1 (m, 2H); 1.8 (bs, 1H), 1.20−1.75 (m, 18H). ESI-MS $(M + Na^+)^+$: 588.5.

*N-(2-Aminoethyl)carbamate of **4** (**5**).* To a round-bottom flask containing a solution of compound **4** (224 mg, 0.4 mmol) in dry CH_2Cl_2 (4 mL) was added a solution of carbonyl diimidazole (CDI) (97.2 mg, 0.6 mmol) in dry CH_2Cl_2 (10 mL). After the mixture was stirred 2 h at room temperature in the presence of 4 Å molecular sieves, ethylenediamine (53.4 μL, 0.8 mmol) was added. After 1 h, the solvent was removed in a Speed-Vac (Savant Instruments). The residue was purified by HPLC: preparative C_{18} column, λ = 240 nm, 6 mL/min, solvent A = H_2O with 0.08% trifluoroacetic acid (TFA), solvent B =

CH_3CN with 0.08% TFA, gradient: 0′−20′: 0−20% B; 20′−70′: 20−70% B. The TFA salt of the product (244 mg, 79.7%) eluted between 38.7 and 44.3% B. ^{1}H NMR (300 MHz, d_4-MeOH) δ 7.9 (d, 1H); 7.5 (m, 1H); 7.35 (dd, 1H); 6.2 (m, 1H); 4.6 (bd, 2H); 4.45 (dd, 1H); 4.3 (m,1H); 3.25−3.5 (m, 6H); 3.2 (m, 1H); 3.0 (m, 2H); 2.8 (dt, 1H); 2.65 (dd, 1H); 2.2 (m, 2H); 1.25−1.8 (m, 18H). ESI-MS $(M + H^+)^+$: 652.4, $(M + Na^+)^+$: 674.3.

*Compound **6***. To a vial containing compound **5** (244 mg, 0.32 mmol) in dry THF (8 mL) in the presence of 4 Å molecular sieves was added DIPEA (112 μL, 0.64 mmol), followed by a solution of iodoacetic anhydride (170 mg, 0.48 mmol) in dry THF (2 mL). After the mixture was stirred 1.5 h at room temperature, the pH was adjusted to ∼5 with TFA (moist pH paper). The solvent was removed under reduced pressure and the residue purified by HPLC. Preparative C_{18} column, $\lambda = 240$ nm, 6 mL/min, gradient: 0′−20′: 0−20% B; 20′−80′: 20−70% B. The product (160 mg, 61%) eluted between 50.5 and 52% B. ^{1}H NMR (300 MHz, d_4-MeOH) δ 7.95 (d, 1H); 7.55 (m, 1H); 7.35 (dd, 1H); 6.2 (m, 1H); 4.55 (bs, 2H); 4.45 (dd, 1H); 4.25 (dd,1H); 3.65 (bs, 2H); 3.1−3.45 (m, 9H); 2.9 (dd, 1H); 2.65 (dd, 1H); 2.2 (m, 2H); 1.25−1.8 (m, 18H). ESI-MS $(M + Na^+)^+$: 842.2.

*Deprotection of **6** (**7**)*. To a vial containing a solution of compound **6** (160 mg, 0.2 mmol) in $CHCl_3$ (0.5 mL) was added TFA (200 μL). The reaction mixture was stirred for 1.5 h at room temperature. Solvent was removed in a Speed-Vac. MeOH was added, and the resulting solution was concentrated in a Speed-Vac. This procedure was repeated three times to remove excess TFA. The TFA salt of the product was obtained in 98.5% yield (160 mg). ^{1}H NMR (300 MHz, d_4-MeOH) δ 8.0 (d, 1H); 7.8 (bs, 1H); 7.6 (dd, 1H); 6.1 (m, 1H); 4.5 (m, 1H); 4.4 (bd, 2H); 4.3 (dd, 1H); 4.25 (dd,1H); 3.7 (bs, 2H); 3.55 (m, 2H); 3.0−3.45 (m, 7H); 2.9 (dd, 1H); 2.65 (dd, 1H); 2.2 (t, 2H); 1.25−1.8 (m, 9H). ESI-MS $(M + H^+)^+$: 720.

^{14}C-VICAT$_{SH}$(−28). To an Eppendorf tube containing a solution of compound **7** (7.34 mg; 8.8 μmol) in MeOH (272 μL) was added 1% [^{14}C]formaldehyde in water (v/v, 51 μL, 17.6 μmol, 1 mCi, specific activity 56 Ci/mol, Perkin-Elmer) followed by 1.2 M methanolic $NaCNBH_3$ (15 μL, 17.6 μmol) and 1.2 M methanolic DIPEA (22 μL, 26.4 μmol). The capped Eppendorf tube was placed in a shaker at 168 rpm for 6 h. The pH was adjusted to ∼5 (moist pH paper) with a 1.2 M aqueous solution of TFA (20 μL). The mixture was diluted with 30% CH_3CN in water and injected on to the HPLC column. Preparative C_{18} column, $\lambda = 240$ nm, 6 mL/min, gradient: 0′−20′: 0−20% B; 20′−80′: 20−70% B. The product (4.6 mg, 0.19 mCi) eluted between 34.4 and 36.7% B.

*N-(4-Aminobutyl)carbamate of **4** (**8**)*. To a round-bottom flask containing a solution of compound **4** (2.0 g, 3.54 mmol) in dry CH_2Cl_2 (20 mL) was added a solution of carbonyl diimidazole (860 mg, 5.31 mmol) in dry CH_2Cl_2 (20 mL). After the mixture was stirred 2 h at room temperature in the presence of 4 Å molecular sieves, 1,4-diaminobutane (putrecine) (623 mg, 7.08 mmol) was added. After an additional 2 h, the solvent was removed in a Speed-Vac. The residue was solubilized in water and the pH adjusted to ∼5 with TFA. The solution was injected onto the HPLC column. Large preparative C_{18} column, $\lambda = 240$ nm, 50 mL/min, gradient: 0′−10′: 20% B; 10′−60′: 70% B. The product as the TFA salt (2.15 g, 77%) eluted between 37 and 41.7% B. ^{1}H NMR (300 MHz, d_4-MeOH) δ 7.9 (d, 1H); 7.5 (m, 1H); 7.35 (dd, 1H); 6.2 (m, 1H); 4.6 (bd, 2H); 4.45 (dd, 1H); 4.3 (m,1H); 3.25−3.5 (m, 4H); 3.2 (m, 1H); 3.1 (m, 2H); 2.95 (m, 3H); 2.8 (dd, 1H); 2.2 (m, 2H); 1.25−1.8 (m, 22H). ESI-MS $(M + H^+)^+$: 680.5.

*N-(4-Iodoacetamidobutyl)carbamate of **4** (**9**)*. To a vial containing compound **8** (1.0 g, 1.26 mmol) in dry THF (15 mL) in the presence of 4 Å molecular sieves was added DIPEA (440 μL, 2.52 mmol), followed by a solution of iodoacetic anhydride (670 mg, 1.89 mmol) in dry THF (5 mL). After the mixture was stirred 1.5 h at room temperature, the pH was adjusted to ∼5 with TFA (moist pH paper). The solvents were removed under reduced pressure, and the residue was purified by HPLC. Large preparative C_{18} column, $\lambda = 240$ nm, 50 mL/min, gradient: 0′−10′: 20% B; 10′−80′: 70% B. The product (657 mg, 61%) eluted at 46.6% B. ^{1}H NMR (300 MHz, d_4-MeOH) δ 8.0 (d, 1H, $J = 8.3$ Hz); 7.6 (m, 1H); 7.4 (d, 1H, $J = 8.3$ Hz); 6.15 (m, 1H); 4.55 (d, 2H); 4.5 (dd, 1H); 4.3 (dd,1H); 3.65 (bs, 2H); 3.1−3.45 (m, 9H); 2.95 (dd, 1H); 2.75 (dd, 1H); 2.2 (t, 2H); 1.25−1.8 (m, 22H). ESI-MS $(M + H^+)^+$: 848.0; $(M + Na^+)^+$: 870.5.

*Deprotection of **9** (**10**)*. To a vial containing a solution of compound **9** (603 mg, 0.71 mmol) in $CHCl_3$ (3 mL) was added TFA (1.2 mL). The reaction mixture was stirred for 2 h at room temperature. Solvent was removed using in a Speed-Vac. MeOH was added, and the resulting solution was concentrated in the Speed-Vac. This procedure was repeated three times to remove excess TFA. The TFA salt of the product was obtained in 100% yield (611 mg). ^{1}H NMR (300 MHz, d_4-MeOH) δ 8.0 (d, 1H); 7.8 (bs, 1H); 7.6 (dd, 1H); 6.1 (m, 1H); 4.5 (m, 1H); 4.4 (bd, 2H); 4.3 (dd, 1H); 4.25 (dd,1H); 3.65 (bs, 2H); 3.55 (m, 2H); 3.1−3.35 (m, 7H); 2.95 (dd, 1H); 2.65 (dd, 1H); 2.25 (t, 2H); 1.4−1.8 (m, 13H). ESI-MS $(M + H^+)^+$: 748.4

^{14}C-VICAT$_{SH}$. To an Eppendorf tube containing a solution of compound **10** (7.54 mg; 8.8 μmol) in MeOH (272 μL), was added 1% [^{14}C]formaldehyde in water (v/v, 59 μL, 17.6 μmol, 1 mCi, 49.5 Ci/mole) followed by 1.2 M methanolic $NaCNBH_3$ (15 μL, 17.6 μmol) and 1.2 M methanolic DIPEA (22 μL, 26.4 μmol). The capped Eppendorf tube was placed in a shaker at 168 rpm for 6 h. The pH was adjusted to ∼5 (moist pH paper) with a 1.2 M aqueous solution of TFA (20 μL). The reaction was diluted with 30% CH_3CN:water and injected on to the HPLC column. Preparative C_{18} column, $\lambda = 240$ nm, 6 mL/min, gradient: 0′−10′: 0−20% B; 10′−70′: 20−70% B. The product (3.5 mg, 0.162mCi) eluted between 36.8 and 39.3% B.

VICAT$_{SH}$. The nonradioactive reaction was carried out as for ^{14}C-VICAT$_{SH}$ using compound **10** (1.09 g, 1.27 mmol), 37% formaldehyde in water (207 μL, 2.54 mmol), $NaCNBH_3$ (168 mg, 2.54 mmol), MeOH (50 mL) and DIPEA (662 μL, 3.81 mmol). The compound was purifed on the large preparative C18 column, $\lambda = 240$ nm, 50 mL/min, gradient: 0′−10′: 0−20% B; 10′−60′: 20−70% B. The product (900 mg, 81.8%) eluted at 32% B. ^{1}H NMR (300 MHz, d_4-MeOH) δ 8.0 (d, 1H); 7.8 (s, 1H); 7.6 (dd, 1H); 6.1 (m, 1H); 4.5 (dd, 1H); 4.25 (dd,1H); 3.65 (bs, 2H); 3.6 (m, 2H); 3.1−3.45 (m, 9H); 2.95 (m, 4H); 2.65 (dd, 1H); 2.25 (t, 2H); 1.25−1.8 (m, 13H). ESI-MS $(M + H^+)^+$: 762.3.

*[$^{15}N_2$,$^{13}C_4$]butanedinitrile (**11**)*. Potassium [^{13}C, ^{15}N]-cyanide (176.3 mg, 2.63 mmol) and [1,2-$^{13}C_2$]-dibromoethane (0.5 g, 2.63 mmol) were refluxed for 5 h in 70% ethanol (2 mL). The reaction mixture was cooled to room temperature and passed through a silica plug with benzene. The solvent was removed under reduced pressure to afford the product in 80% yield (90 mg). ^{1}H NMR (300 MHz, $CDCl_3$) δ 3.0 (m, 2H); 2.55 (m, 2H).

*[$^{14}N_2$,$^{13}C_4$]-1,4-Butanediamine dihydrochloride (**12**)*. Compound **11** (137.1 mg, 1.59 mmol) and a 1 M solution of

borane in dry THF (16 mL, 15.9 mmol) were refluxed for 24 h. After the reaction was cooled to room temperature, anhydrous ethanol (18 mL) was added. The reaction was stirred for 24 h, and HCl gas was bubbled through the solution for 10 min, or until saturation. The di-chloride salt was filtered, washed with anhydrous ethanol, and dried under vacuum to afford 146.5 mg (55.2%) of a white solid. ^{1}H NMR (300 MHz, D_2O) δ 3.5 (m, 2H); 2.75 (m, 2H); 2.15 (m, 2H); 1.75 (m, 2H).

*N-([$^{14}N_2$,$^{13}C_4$]aminobutyl)carbamate of **4** (**13**).* A solution of compound **12** (30 mg, 0.18 mmol), and TEA (368 μL, 2.62 mmol) in DMSO (1 mL) was heated at 80 °C for 2 h. In another round-bottom flask containing a solution of compound **4** (25.4 mg, 0.045 mmol) in dry CH_2Cl_2 (1 mL) was added a solution of carbonyl diimidazole (10.9 mg, 0.067 mmol) in dry CH_2Cl_2 (0.5 mL). The reaction was stirred at room temperature for 2 h, and transferred to the DMSO solution that was being heated. The resulting reaction was kept at the same temperature for 1.5 h. The pH was adjusted to ~5 with TFA (moist pH paper), and the CH_2Cl_2 was evaporated under reduced pressure. The residue was diluted with water and injected on to the HPLC column. Preparative C_{18} column, λ = 240 nm, 6 mL/min, gradient: 0′−10′: 0−20% B; 10′−70′: 20−70% B. The product as the TFA salt (26.8 mg74.7%) eluted between 43.8% B. ^{1}H NMR (300 MHz, d_4-MeOH) δ 7.9 (d, 1H); 7.5 (m, 1H); 7.35 (dd, 1H); 6.2 (m, 1H); 4.6 (bd, 2H); 4.45 (dd, 1H); 4.3 (m,1H); 3.1−3.45 (m, 7H); 2.9 (m, 3H); 2.75 (dd, 1H); 2.2 (m, 2H); 1.25−1.8 (m, 22H). ESI-MS $(M + H^+)^+$: 686.3.

*Compound **14**.* The same procedure as described for compound **9** was used. The following amounts were used: Compound **13** (37.5 mg, 0.047 mmol); iodoacetic anhydride (25 mg, 0.07 mmol), DIPEA (16.3 μL, 0.094 mmol), and dry THF (0.6 mL). The product was purified by HPLC. Preparative C_{18} column, λ = 240 nm, 6 mL/min, gradient: 0′−10′: 0−20% B; 10′−70′: 20−70% B. The product (compound **16**) (24.5 mg, 61.3%) eluted between 50.8 and 53% B. ESI-MS $(M + H^+)^+$: 854.5; $(M + Na^+)^+$: 876.5.

*Compound **15**.* The same procedure as described for compound **10** was used. The following amounts were used: Compound **14** (24.5 mg, 0.029 mmol); TFA (160 μL), and $CHCl_3$ (240 μL). The TFA salt of the product was obtained in 94.8% yield (23.6 mg). ^{1}H NMR (300 MHz, d_4-MeOH) δ 8.0 (d, 1H); 7.8 (bs, 1H); 7.6 (dd, 1H); 6.1 (m, 1H); 4.5 (m, 1H); 4.4 (bd, 2H); 4.3 (dd, 1H); 3.65 (bs, 2H); 3.55 (m, 2H); 3.15−3.35 (m, 7H); 2.95 (dd, 2H); 2.70 (m, 1H); 2.65 (dd, 1H); 2.25 (t, 2H); 1.4−1.8 (m, 13H). ESI-MS $(M + H^+)^+$: 754.4.

VICAT$_{SH}$(+6). The same procedure as described for VICAT$_{SH}$ was used. The following amounts were used: Compound **15** (23.6 mg, 0.027 mmol); 1% aqueous solution of formaldehyde (83 μL; 0.054 mmol); 1.2 M methanolic $NaCNBH_3$ (23 μL; 0.054 mmol); 1.2 M methanolic DIPEA (34 μL; 0.081 mmol); and MeOH (800 μL). The reaction was diluted with 30% CH_3CN in water, and injected on to the HPLC column. Preparative C_{18} column, λ = 240 nm, 6 mL/min, gradient: 0′−10′: 0−20% B; 10′−70′: 20−70% B. The product (14.8 mg, 70.8%) eluted between 36.2 and 39% B. ^{1}H NMR (300 MHz, d_4-MeOH) δ 8.0 (d, 1H); 7.8 (s, 1H); 7.6 (dd, 1H); 6.15 (m, 1H); 4.45 (dd, 1H); 4.30 (dd,1H); 3.65 (bs, 2H); 3.6 (m, 2H); 3.1−3.5 (m, 7H); 2.9−3.0 (m, 6H); 2.6 (dd, 1H); 2.2 (t, 2H); 1.2−1.8 (m, 13H). ESI-MS $(M + H^+)^+$: 768.4; $(M + Na^+)^+$: 790.3.

^{14}C-VICAT$_{SH}$(+6). This compound was made using a variation of the procedure used to make ^{14}C-VICAT$_{SH}$. To a vial with a Teflon septum-lined screw cap containing a solution of compound **15** (17.3 mg; 20 μmol) in MeOH (765 μL) was added 1 M aqueous sodium acetate, pH 6.7 (139 μL). To a tube containing 60 μL of 0.33 M formaldehyde in water (19.8 μmol, prepared by diluting reagent grade 37% (w/v) formaldehyde with water), was added 49 μL of an aqueous solution of [^{14}C]formaldehyde in water (25 mCi/mL, 1.23 mCi, 21.9 μmol, 56 mCi/mmol, Perkin-Elmer). This mixture was transferred to the reaction vial. To the vial was added 1.2 M methanolic $NaCNBH_3$ (105 μL, 40 μmol). After the mixture was stirred for 30 min at room temperature, most of the solvent was removed with a stream of N_2. The residue was diluted with 100 μL of water containing 0.08% TFA, and the solution was injected onto the HPLC column. Preparative C18 column, λ = 240 nm, 6 mL/min, gradient: 0′−10′: 0−20% B; 10′−70′: 20−70% B. The TFA salt of the product (12.4 mg, 70.4% yield) eluted between 36.5 and 40% B. The compound was characterized by its HPLC retention, which matched that of the nonradiolabeled VICAT$_{SH}$(+6).

The specific radioactivity of ^{14}C-VICAT$_{SH}$(+6) was determined by accurately weighing several milligrams of the HPLC-purified material (after three rounds of evaporation to dryness in a Speed-Vac followed by dissolution in 0.4 mL of MeOH and drying in vacuo to constant weight), dissolving the compound in 1 mL of CH_3CN, and submitting a 5 μL aliquot to scintillation counting. The counter was calibrated using a vial of ^{14}C standard. Final specific activity is 22.0 mCi/mmol.

*Compound **16**.* To a vial containing a solution of compound **10** (5 mg; 5.81 mmol) in MeOH (179 μL) was added 1 M sodium acetate pH 6.7 (76 μL), followed by a 1.2 M methanolic solution of *tert*-butyl *N*-(2-oxyethyl)-carbamate (19.3 μL, 23.2 mmol, Aldrich) and a 1.2 M methanolic solution of $NaCNBH_4$ (19.3 μL, 23.2 mmol). The reaction was stirred at room temperature for 1 h. The solvent was partially removed, a mixture of 20% acetonitrile in water was added, and the reaction mixture was injected onto the HPLC column. Preparative C18 column, λ = 240 nm, 6 mL/min, gradient: 0′−20′: 0−20% B; 20′−80′: 20−100% B. The TFA salt of product **16** (5.8 mg, 92.6% yield) eluted between 53.8 and 58% B. ^{1}H NMR (300 MHz, d_1-$CHCl_3$/d_4-MeOH) δ 7.9 (d, 1H); 7.85 (m, 1H); 7.55 (m, 1H); 6.1 (m, 1H); 4.45 (m, 3H); 4.2 (m, 1H); 3.6 (s, 2H); 2.9−3.4 (m, 13H); 2.8 (dd, 1H); 2.6 (d, 1H); 2.2 (t, 2H); 1.25−1.65 (m, 22H). ESI-MS $(M + H^+)^+$: 891.0; $(M + Na^+)^+$: 913.5.

*Compound **17**.* To a vial containing a solution of **16** (5 mg, 5.07 mmol) in $CHCl_3$ (30 μL) was added TFA (12 μL). The reaction mixture was stirred for 1.5 h at room temperature. Solvent was removed using a Speed-Vac. MeOH was added, and the resulting solution was concentrated in the Speed-Vac. This procedure was repeated three more times to remove excess TFA. The TFA salt of the product (compound **17**) was obtained in 95.6% yield (4.3 mg) as an oil. ^{1}H NMR (300 MHz, acetone-d_6) δ 7.9 (d, 1H); 7.7 (s,1H); 7.5 (d, 1H); 6.1 (m, 1H); 4.6 (m, 1H); 4.4 (m, 1H); 3.9 (m, 2H); 3.7 (s, 2H); 3.4−2.9 (m, 12H); 2.7 (m, 3H); 2.2 (t, 2H); 1.4−1.8 (13H, m). ESI-MS $(M + H^+)^+$: 791.5; (M + Na+)+: 813.5.

NBD-VICAT$_{SH}$. To a vial containing **17** (4.2 mg, 4.64 mmol) was added a solution of NBD-F (2.86 mg, 15.6 mmol, 70% pure, Dojindo Molecular Technologies) in DMF (220 μL), followed by DIPEA (3.15 μL, 18.1 mmol). After being stirred for 2 h at room temperature, the solvent was partially removed in a Speed-Vac. The residue was solubilized in 20% acetonitrile in water and injected onto the HPLC. Preparative C18 column, λ = 500 nm, 6 mL/min, gradient: 0′−20′: 0−20% B; 20′−

80′: 20−100% B. The orange solid product (3.5 mg, 81.4%) eluted between 61.3 and 69.7% B. ^{1}H NMR (300 MHz, CD_3CN) δ 8.43 (d, 1H); 7.65 (d, 1H); 7.6 (bs, 1H); 7.4 (d, 1H); 6.0 (m, 2H); 4.4 (m, 1H); 4.25 (m, 1H); 3.75 (d, 2H); 3.6 (s, 2H); 2.9−3.2 (m, 12H); 2.65 (m, 3H); 2.22 (t, 2H); 1.35−1.8 (m, 13H). ESI-MS $(M + H^+)^+$: 954.5, $(M + Na^+)^+$: 976.4.

NBD-VICAT$_{SH}$(−28). This compound was prepared from **7** as described for the preparation of NBD-VICAT$_{SH}$ starting from **10**. HPLC Preparative C18 column, $\lambda = 500$ nm, 6 mL/min, gradient: 0′−20′: 0−20% B; 20′−80′: 20−100% B. The product as an organge solid (4.6 mg, 43.8%) eluted at 51% B. ^{1}H NMR (500 MHz, CD_3CN) δ 8.43 (d, 1H); 7.7 (bs, 1H); 7.6 (bs, 1H); 7.4 (bs, 1H); 6.16 (bs, 1H); 6.05 (bs, 1H); 4.4 (m, 1H); 4.25 (m, 1H); 3.8 (m, 2H); 3.65 (s, 2H); 2.9−3.2 (m, 12H); 2.7 (m, 3H); 2.22 (t, 2H); 1.35−1.9 (m, 9H). ESI-MS $(M + H^+)^+$: 926.6, $(M + Na^+)^+$: 948.7.

Peptide Modification Reactions. *Conversion of Peptide Amines into Thioacetamido Groups*. The reaction sequence is shown in Figure 5. To a 1.5 mL Eppendorf tube was added 280 μL of DMF:0.1 M Hepes, pH 8.0 (1:1) (pH adjusted before DMF added), followed by 20 μL of 1 mM angiotensin I peptide in water (DRVYIHPFHL, Sigma) and then 100 μL of *N*-succinimidyl S-acetylthioacetate (SATA, Pierce, 40 mM in dry DMF, freshly prepared). After incubation for 2 h at room temperature, 40 μL of deacetylation solution (0.5 M NH_2OH, 25 mM EDTA, 50 mM sodium phosphate, pH 7.5, store at 4 °C) was added, and the mixture was incubated for 2 h at room temperature. Then 150 μL of tris(2-carboxylethyl)-phosphine (TCEP, Aldrich, 0.2 M in water, store at −20 °C) was added followed by a 1 h incubation at 37 °C. The pH was dropped to 3−4 by adding 50 μL of 2% TFA, and the mixture was loaded onto a C18 reverse-phase, solid-phase extraction cartridge (500 mg resin, Varian) previously washed with 80% CH_3CN/0.1% TFA and then equilibrated with 0.1% TFA. The cartridge was washed with 0.1% TFA (2 × 1 mL) and then with 5% CH_3CN/0.1% TFA (4 × 1 mL), and peptide was eluted into a new tube with 1 mL of 80% CH_3CN/0.1% TFA. The solution was concentrated to dryness (Speed-Vac) in an Eppendorf tube.

Conjugation of Thioacetylated Peptide with VICAT$_{SH}$. All steps involving VICAT$_{SH}$ reagents were carried out in normal room light (fluorescent overhead lights) and away from windows exposed to bright sunlight. The residue from the previous step was resuspended in 50 μL of 20% CH_3CN. Buffer (4.8 μL of 0.5 M sodium phosphate, 0.5 M sodium borate, pH 8.4) was added, followed by 5.2 μL of VICAT$_{SH}$ stock (22.9 mM in CH_3CN, stored at −20 °C). The tube was wrapped with foil to exclude light and left for 12 h at room temperature. The reaction was examined by HPLC by adding 100 μL of 2% TFA and injecting the solution onto the column (Vydac 218TP52) previously equilibrated with 0.08% TFA (solvent A). The column was developed as follows: 0−15 min, 0% B (CH_3CN/0.08% TFA); 15−20 min, 0−10% B; 20−60 min, 10% B, 60−110 min, 10−80% B. The flow rate was 0.2 mL/min, and the absorbance at 217 nm was monitored. Peak fractions were examined by ESI-MS and MALDI.

Photocleavage of VICAT$_{SH}$-Tagged Peptides. The desired peptide conjugate HPLC fraction (see above) was concentrated to dryness (Speed-Vac) in an Eppendorf tube and the residue dissolved in 100 μL of 20% CH_3CN/0.1% TFA. Neat 2-mercaptoethanol (1 μL) was added, and the tube was shaken in an Eppendorf vibrating rack mixer at room temperature with irradiation for 20 min at room temperature from a UV lamp (Black-Ray long wave ultraviolet lamp model 100AP, VWR) with the bulb face held 10 cm from the tube. The intensity of the lamp was routinely checked with a UV light meter (Mannix UV340, Professional Equipment, Inc.). The reaction mixture was examined by HPLC (same column as above) using a solvent program of 0−60 min, 0−70% B. Fractions were examined by ESI-MS and MALDI.

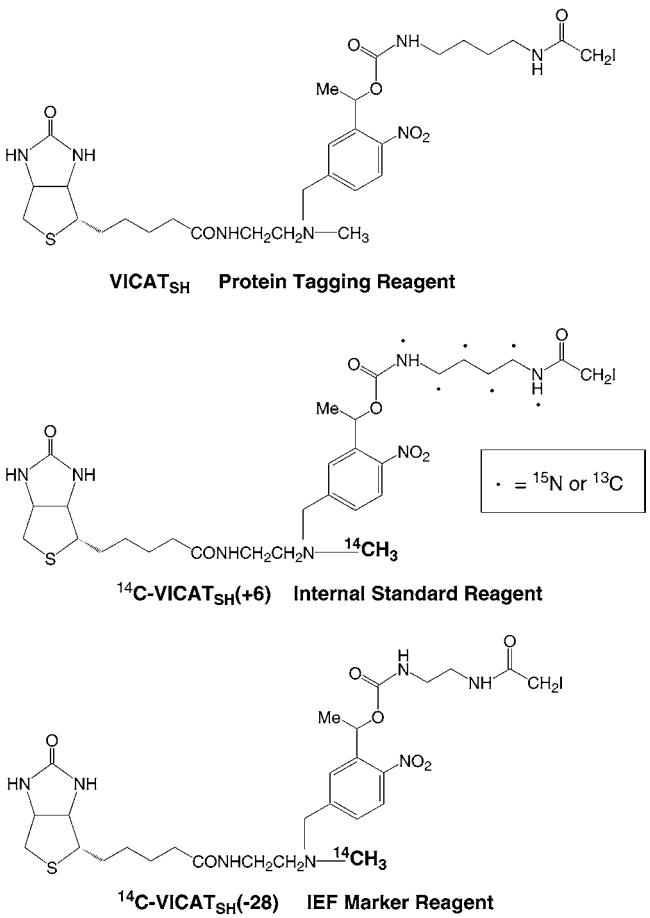


Figure 1. VICAT$_{SH}$ reagents.

The photocleavage of bead-bound peptide conjugate was also carried out. A 50 μL aliquot of beads (streptavidin-Agarose, 1:1 suspension in buffer as supplied by the manufacturer, Sigma) was pelleted in an Eppendorf tube (1 min full speed spin in a microfuge), and the pellet was washed twice with 1 mL portions of phosphate-buffered saline and resuspended in 1 mL of the same buffer. The peptide−VICAT$_{SH}$ conjugation reaction mixture (see above) was added to the bead suspension. The tube was placed on a rocking platform for 1 h at room temperature. The beads were pelleted and washed twice with 1 mL portions of water and resuspended in 100 μL of 20% CH_3CN/0.1% TFA. 2-Mercaptoethanol (1 μL) was added, and the tube was irradiated with UV light as described above. A 2 μl aliquot was analyzed by MALDI.

RESULTS AND DISCUSSION

VICAT Reagents. The present paper describes the design and synthesis of VICAT reagents and their reaction with peptides. In a subsequent study we will illustrate the usefulness of these reagents to determine the absolute quantity of specific target proteins in complex protein mixtures (*8*). The set of three VICAT reagents is shown in Figure 1. These reagents contain an iodoacetyl group and thus react specifically with the

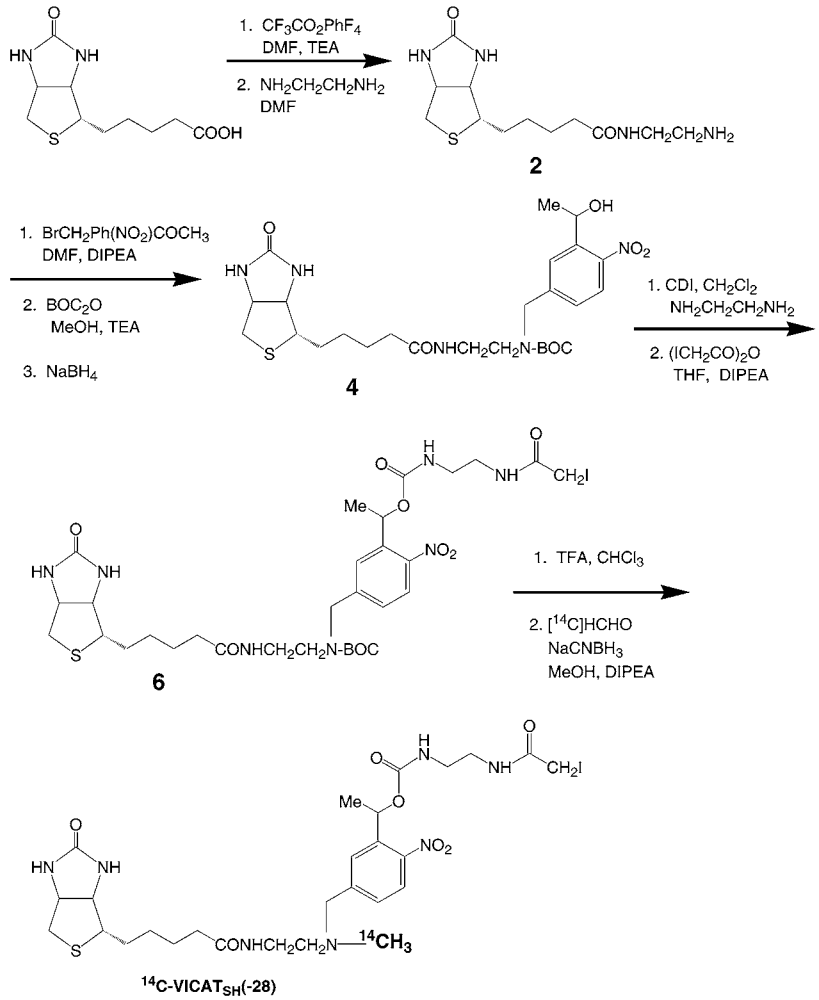


Figure 2. Synthesis of ^{14}C-VICAT$_{SH}$(−28).

SH group of cysteine-containing peptides. Thus we refer to these as VICAT$_{SH}$ reagents. We also show below that peptides without cysteine can be modified to contain an SH group which can be reacted with VICAT reagents. The VICAT reagents are used for (1) derivatization of SH-containing peptide fragments derived from all of the proteins in the sample including the target protein of interest, (2) preparation of an internal standard suitable for absolute quantification of the target protein of interest, and (3) preparation of a marker suitable for locating the tagged peptide derived from the target protein of interest following separation on an IEF gel strip. The VICAT-derivatized peptides are distinguished by the different masses of the tag introduced into the peptide as shown below.

The first reagent, VICAT$_{SH}$, is the "protein tagging" reagent as it is used to tag the SH groups present in peptides generated by proteolytic digestion of all of the proteins present in the biological sample to be analyzed. This reagent contains a 1,4-diaminobutane linker attached to the iodoacetyl group (Figure 1).

The second reagent, VICAT$_{SH}$(+6) is chemically identical to VICAT$_{SH}$ except for the presence of four ^{13}C and two ^{15}N labels in the diaminobutane linker (Figure 1). VICAT$_{SH}$(+6) is used as the "internal standard" reagent to tag the authentic synthetic peptide (prepared by solid-phase peptide synthesis) whose sequence is identical to the tryptic peptide derived from the target protein of interest. The mass difference of 6 Da between the sample-derived and internal standard peptides is sufficient for the distinction of both singly and doubly charged ions produced by electrospray ionization. A precise amount of the VICAT$_{SH}$(+6)−peptide conjugate is added to the sample and serves as an internal standard that is differentiated in the mass spectrometer from the protein sample-derived, tagged peptide. Integration of the ion chromatogram peaks, observed by mass spectrometry, from the sample-derived and internal standard conjugates in the mass spectrometry analysis provides the absolute abundance of the former and thus the absolute abundance of the specific protein in the complex protein mixture. We also prepared ^{14}C-VICAT$_{SH}$(+6), which can also be used to prepare the internal standard. This reagent is radiolabeled and of known specific activity and thus offers the ability to readily determine the absolute quantity of purified internal standard by scintillation counting.

The third reagent, ^{14}C-VICAT$_{SH}$(−28), contains the radioactive label and functions as the "IEF marker" for peptide visualization on the IEF strip. This reagent is used to derivatize the same synthetic peptide used to prepare the internal standard. ^{14}C-VICAT$_{SH}$(−28) contains a shorter (two-carbon) diamine linker that is attached to the iodoacetyl group (Figure 1). The purpose of using a shorter linker is 2-fold. First, the tagged peptide formed after photocleavage (see below) is more polar than the tagged peptides derived from the other VICAT$_{SH}$ reagents and is expected to have a slightly shorter reverse-phase HPLC retention time than the internal standard and sample protein-derived tagged

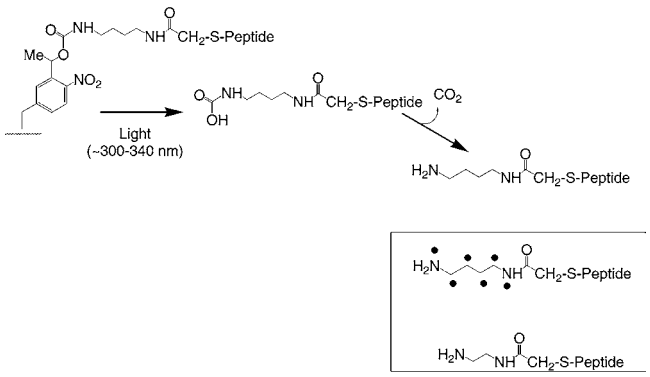


Figure 3. Photocleavage of VICAT$_{SH}$-tagged peptide. Shown is the photocleavage of the peptide tagged with VICAT$_{SH}$, which generates the carbamic acid, which spontaneously decarboxylates to give the peptide derived from the sample protein of interest bearing a tag with the diaminobutane linker. Shown in the box are the tagged peptides resulting from photocleavage of the internal standard and IEF marker, respectively. The black dots on the internal standard tag designate ^{15}N and ^{13}C labels.

peptides, both of which have a four-carbon linker in their tags. Second, the tag left on the IEF marker peptide is 28 Da lighter than the tag left on the sample protein-derived peptide and 34 Da higher than the tag left on the internal standard and so is readily distinguished by mass spectrometry. Both factors are important for achieving a high dynamic range in the detection of peptides from low-level sample proteins in the presence of a substantially larger (10−1000-fold) amount of the visible marker applied to the IEF strip.

Following IEF, peptides are eluted from the appropriate region of the IEF gel strip using the IEF marker as a guide (*8*). The biotinyl moiety of these VICAT$_{SH}$ reagents is used for affinity capture of tagged peptides using streptavidin−agarose. Peptides are then released from the solid phase by photocleavage as shown in Figure 3. This has the advantage that the impurities in the sample after IEF, including soluble ampholytes, are not carried forward to the next step. Note that a small isotope tag remains on the peptides after photocleavage (Figure 3). This allows differentiation between the sample-derived and internal standard peptides in the mass spectrometer. The use of ^{15}N and ^{13}C present in VICAT$_{SH}$(+6) is advantageous over substitution with deuterium since the latter sometimes causes a slight change in the reverse-phase HPLC retention time of the isotope tagged peptide relative to that of the peptide tagged with the light isotope. The lack of precise coelution of heavy and light tagged peptides complicates the accurate integration of ion peaks observed in the mass spectrometer. Note that the peptide derived from the IEF marker bears a tag that is two methylene groups shorter than the tags left on the sample-derived and internal standard peptides (Figure 3). The IEF marker is typically used in much larger quantities than the internal standard because mass spectrometry is more sensitive than ^{14}C radiometric analysis. Since the IEF marker-derived peptide is 28 Da lighter than the sample-derived peptide, it is easily excluded during selective ion monitoring with the mass spectrometer. The use of a relatively large amount of IEF marker actually offers the important advantage of serving as a carrier to minimize nonspecific losses of trace amounts of sample-derived and internal standard peptides present throughout the analytical process. Such nonspecific losses can be severe when analyzing femtomole amounts of material.

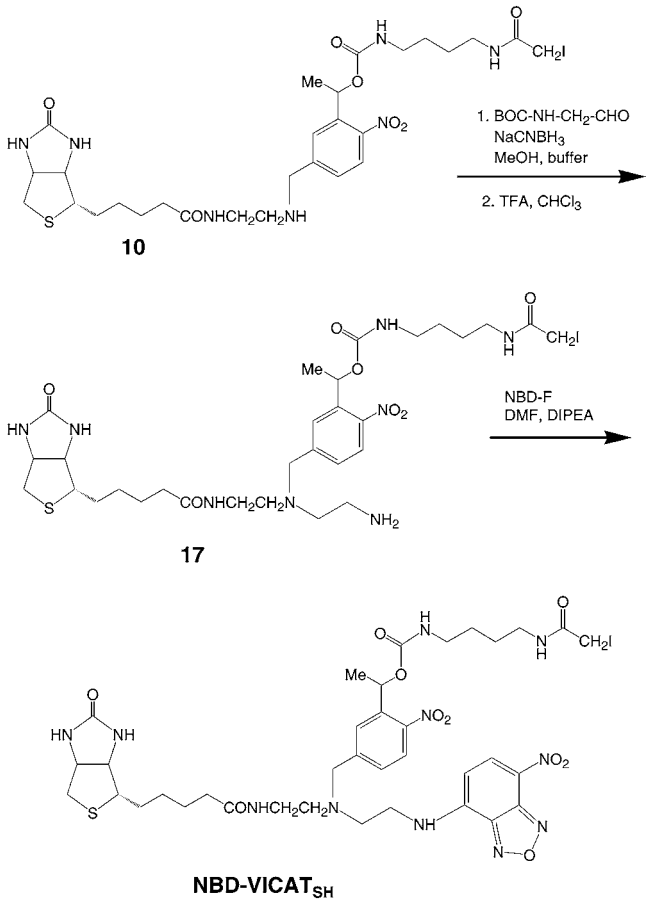


Figure 4. Synthesis of NBD-VICAT$_{SH}$.

Synthesis of VICAT$_{SH}$ Reagents. A highly efficient synthesis of VICAT$_{SH}$ reagents was developed as shown in Figure 2. This scheme allows the radiolabel of ^{14}C-VICAT$_{SH}$(−28) to be introduced in the last synthetic step using readily available ^{14}C-H_2CO. All of the steps proceed in acceptable yields. The heavy atom substituted 1,4-diaminobutane used to prepare VICAT$_{SH}$(+6) was readily prepared by a simple two-step scheme starting from the relatively inexpensive heavy isotopic materials [^{13}C,^{15}N]-potassium cyanide and 1,2-[$^{13}C_2$]-dibromoethane.

Using this scheme, we have been able to prepare gram quantities of VICAT$_{SH}$ reagent, sufficient for tens of thousands of VICAT$_{SH}$-based analyses. The other two reagents, ^{14}C-VICAT$_{SH}$(+6) and ^{14}C-VICAT$_{SH}$(−28), are required in relatively small amounts since each VICAT$_{SH}$-based analysis requires femtomole amounts of internal standard and nanomole amounts of IEF marker.

We have also designed a variant of VICAT$_{SH}$ reagents in which the visible probe is an NBD fluorophore rather than a radiolabel. As shown in Figure 4, intermediate **10** can be reductively aminated with commercially available BOC-NHCH$_2$CHO. Removal of the BOC group provides primary amine **17**, which can be reacted with a variety of different amine-reactive fluorophores including NBD-F as shown in Figure 4. Thus, both radioactive and fluorescent VICAT$_{SH}$ reagents can be prepared from a common synthetic intermediate. The availability of VICAT$_{SH}$ reagents bearing a fluorophore as the visible probe is advantageous in laboratories that are not approved for use of radioisotopes. The use of these fluorimetric reagents for the absolute quantification of specific proteins in complex protein mixtures is being currently developed in our laboratories. In cases were ^{14}C-VICAT$_{SH}$ is used, it may be noted that the carbon-14

Table 1. Thioacetylation of Peptide Amino Groups

peptide[a]	product	yield[b]
DRVYIHPFHL	(thioacetyl)DRVYIHPFHL	quantitative
pyroELYENKPRRPYIL	pyroELYENK(thioacetyl)PRRPYIL	quantitative
HDMNKVLDL	(thioacetyl)HDMNK(thioacetyl)VLDL	quantitative
ALEPPEPKKSRRCVLL	(thioacetyl)ALEPPEPK(thioacetyl)K(thioacetyl)SRRCVLL	quantitative

[a] pyroE is pyroglutamic acid. [b] Yields were determined by inspection of the HPLC trace (absorbance at 214 nm) and by MALDI mass spectrometry.

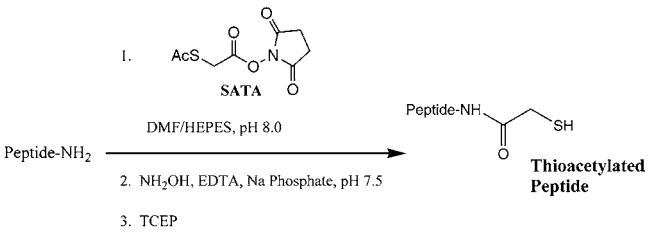


Figure 5. Thioacetylation of amino groups in peptides and reaction with $VICAT_{SH}$ reagents.

remains bound to the solid-phase streptavidin−agarose following photocleavage; thus, radioisotopes do not come in contact with the mass spectrometer.

Introduction of the SH Group into Peptides That Lack Cysteine. The use of ICAT and $VICAT_{SH}$ reagents to selectively tag cysteine-containing peptides has the advantage that complex mixtures of peptides, such as those derived from a cell lysate, are greatly simplified. However, in some cases it is desirable to tag peptides that lack cysteine, i.e., to quantify a protein that lacks cysteine or to quantify a protein segment that contains a post-translational modification and that also lacks cysteine. Thus, we desired a simple and quantitative method to introduce SH groups into peptides lacking cysteine. We chose the modification of amino groups since every tryptic peptide will contain an N-terminal amino group (except for the N-terminal peptide of N-terminally modified proteins), and those that have a lysine at the C-terminus will also have an ϵ-amino group. It is possible to design peptide-tagging reagents that contain a functional group such as an acylating agent that reacts with peptide amino groups. However, agents such as active esters that efficiently acylate amino groups also undergo hydrolysis in water, and thus an excess of tagging reagent is required, which is not desirable when using isotopically substituted tagging reagents. Thus, we desired a simple method for the conversion of peptide amino groups into sulfhydryl groups using inexpensive reagents and prior to tagging with $VICAT_{SH}$ reagents. This has the advantage that a large excess of acylating agent can be used to drive the amino group modification to completion and that the same ICAT and $VICAT_{SH}$ reagents can be used for peptides that contain or lack cysteine.

The previously described reagent *N*-succinimidyl-S-acetylthioacetate (SATA) is known to react with the amino group to give the amide which can be treated with hydroxylamine, resulting in the replacement of the amino group with a 2-sulfhydryl-acetamido group (Figure 5) (*13*). We examined this reaction sequence with a variety of peptides containing one or two amino groups (Table 1). A concentration of SATA of 10 mM was found to give quantitative acylation of peptide amino groups after 2 h at room temperature. Acylation studies at pH 6−9 revealed incomplete reaction at pH 6 (presumably due to protonation of the peptide amino groups) and at pH 9 (presumably due to hydrolysis of SATA). Addition of NH_2OH in slight excess over the amount of SATA led to incomplete deacylation; thus, a large excess (>100 mM) was optimal. It was found that after deacylation, a significant amount of the disulfide peptide-$NHCOCH_2$-$SSCH_2COOH$ was detected by MALDI and HPLC. Thus, the reaction mixture was treated with tricarboxylethylphosphine (TCEP), which led to quantitative reduction to the free thiol.

Using the optimized conditions, we obtained quantitative thioacetylation of amino groups in the peptides shown in Table 1. Thioacetylated peptides were examined by reverse phase HPLC, and single symmetrical product peaks were observed in all cases (not shown). Furthermore, MALDI mass spectrometry analysis of the HPLC product fraction showed only the desired product, with no trace of starting material or side products (not shown). The peptides in Table 1 have one to three amino groups, which were fully thioacetylated in all cases. Amino acids with nucleophile-containing side chains other than the amino group, Arg, Asp, Cys, Glu, His, Ser, and Tyr were not thioacetylated (any acylation of these nucleophiles during reaction with SATA would be reversed during treatment with NH_2OH).

Reaction of Peptides with $VICAT_{SH}$ Reagents. Thioacetylated angiotensin I peptide [(thioacetyl)DRVYIHPFHL] was desalted by solid-phase extraction on a C18 reverse-phase cartridge and then subjected to tagging with $VICAT_{SH}$. Conjugation of peptide SH group with $VICAT_{SH}$ reagent (~6 equiv based on peptide SH groups) was carried out in 20% CH_3CN/aqueous buffer to ensure good solubility of most peptides and tagging reagent and at pH 8.4, which is standard for reaction of peptide SH groups with iodoacetamido reagents. Reverse-phase HPLC analysis of the reaction mixture (not shown) showed the desired tagged peptide (confirmed by ESI-MS and MALDI), remaining $VICAT_{SH}$ reagent (confirmed by ESI-MS and MALDI), a trace amount of $VICAT_{SH}$-TCEP adduct (ESI-MS and MALDI gave $m/z = 884$), and a trace amount of $VICAT_{SH}$ cyclization product (ESI-MS and MALDI analyses show a m/z of 634, which is presumed to result from an intramolecular reaction of the tertiary amine of $VICAT_{SH}$ with the iodoacetyl group). No other HPLC peaks were observed, and spiking the reaction mixture with nontagged thioacetylated angiotensin I peptide confirmed that peptide tagging went to completion.

Thioacetylated angiotensin I tagged with $VICAT_{SH}$ was subjected to solution phase photocleavage or to affinity capture with streptavidin−agarose followed by on-resin photocleavage. HPLC analysis (not shown) of both reaction mixtures revealed only two peaks, one due to the desired photocleavage product, NH_2-$(CH_2)_4$−$NHCOCH_2SCH_2CONH$-peptide, and the other due to the photofragmented $VICAT_{SH}$ reagent containing the 2-nitrosoacetophenone moiety (products confirmed by ESI-MS and MALDI). Only these two products were seen when both photocleavage reaction mixtures were examined by MALDI prior to HPLC (not shown). This indicates that the $VICAT_{SH}$-tagged peptide undergoes quantitative photocleavage to the desired peptide containing the isotope tag (see above).

Application of VICAT$_{SH}$ Reagents and Future Prospects. There are numerous examples where the use of VICAT$_{SH}$ reagents will be useful. A major advantage of VICAT$_{SH}$ reagents is that they permit the absolute quantification of specific proteins in complex mixtures (*8*). In contrast, immunological methods require the lengthy and costly production of highly specific antibodies. Furthermore, immunoblot analyses (western blots) provide only qualitative data. Microarray nucleic analysis of changes in gene expression often need to be validated at the protein level. Furthermore, the search for markers in readily available biological fluids such as serum that have diagnostic value for human diseases will require a method for the absolute quantification of specific proteins. Microarray analyses often suggest tens if not hundreds of proteins that might be upregulated in human tumors for example. The validation of these candidate proteins using immunological methods is probably not practical, especially for a single laboratory effort.

The tagging of cysteine SH groups by VICAT$_{SH}$ reagents offers an important simplification of the peptide mixture in that many peptides will be removed following the purification of tagged peptides with streptavidin−agarose. Nevertheless, in some cases it will be beneficial to tag peptides that lack cysteines with VICAT reagents. A simple and efficient method to introduce SH groups into peptides lacking cysteine has been developed, and such peptides may be tagged with the same VICAT$_{SH}$ reagents used to modify cysteine-containing peptides. In a subsequent study (*8*), we will illustrate the usefulness of these reagents to determine the absolute quantity of specific target proteins in complex protein mixtures.

During the completion of the present study, the AQUA method was introduced for obtaining the absolute quantity of proteins in complex mixtures (*9*). The availability of two methods is beneficial, especially since it seems unlikely that a single method will provide useful data in every attempted experiment. It may be noted that with both the AQUA and VICAT$_{SH}$ methods, the amount of added internal standard should be within an order of magnitude of the amount of sample-derived peptide, given the issues of dynamic range in the mass spectrometry analysis. A detailed comparison of the AQUA and VICAT$_{SH}$ methods will be presented (*8*). VICAT$_{SH}$ reagents are available from the authors upon request.

ACKNOWLEDGMENT

This work was supported by NIH grant DK67859 (M.H.G. and F.T.) and by the National Heart, Lung, and Blood Institute, NIH, under contract no. NO1-HV-28179 (R.A.).

LITERATURE CITED

(1) Gygi, S. P., and Aebersold, R. (2000) Mass spectrometry and proteomics. *Curr. Opin. Chem. Biol. 4*, 489−494.

(2) Mo, W., and Karger, B. L. (2002) Analytical aspects of mass spectrometry and proteomics. *Curr. Opin. Chem. Biol. 6*, 666−675.

(3) Turecek, F. (2002) Mass spectrometry in coupling with affinity capture-release and isotope-coded affinity tags for quantitative protein analysis. *J. Mass Spectrom. 37*, 1−14.

(4) Gygi, S. P., Rist, B., Gerber, S. A., Turecek, F., Gelb, M. H., and Aebersold, R. (1999) Quantitative analysis of complex protein mixtures using isotope-coded affinity tags. *Nat. Biotechnol. 17*, 994−999.

(5) Aebersold, R., and Mann, M. (2003) Mass spectrometry-based proteomics. *Nature 422*, 198−207.

(6) Liu, H., Lin, D., and Yates, J. R. r. (2002) Multidimensional separations for protein/peptide analysis in the post-genomic era. *Biotechniques 32*, 898−902.

(7) Shen, M., Guo, L., Wallace, A., Fitzner, J., Eisenman, J., Jacobson, E., and Johnson, R. S. (2003) Isolation and Isotope Labeling of Cysteine- and Methionine-containing Tryptic Peptides: Application to the Study of Cell Surface Proteolysis. *Mol. Cell Proteomics 2*, 315−324.

(8) Lu, Y., Bottari, P., Turecek, F., Aebersold, R., and Gelb, M. H. (2003) Visible Isotope-Coded Affinity Tags for the Absolute Quantification of Specific Proteins in Complex Mixtures. *Anal. Chem.*, submitted.

(9) Gerber, S. A., Rush, J., Stemman, O., Kirschner, M. W., and Gygi, S. P. (2003) Absolute quantification of proteins and phosphoproteins from cell lysates by tandem MS. *Proc. Natl. Acad. Sci. U.S.A. 100*, 6940−6945.

(10) Gamper, H. B., Reed, M. W., Cox, T., Virosco, J. S., Adams, A. D., Gall, A. A., Scholler, J. K., and Meyer, R. B. (1993) Facile preparation of nuclease resistant 3′ modified oligodeoxynucleotides. *Nucleic Acids Res. 21*, 145−150.

(11) Doppler, T., Schmid, H., and Jurgen, H. (1979) On the Photochemistry of 2,1-Benzisoxazoles (Anthraniles) and on the Thermal and Photochemical Decomposition of 2-Azidoacylbenzenes in Strong Acidic Solution. *Helv. Chim. Acta 62*, 271.

(12) Senter, P. D., Tansey, M. J., Lambert, J. M., and Blattler, W. A. (1988) Novel photocleavable protein cross-linking reagents and their use in the preparation of antibody-toxin conjugates. *Photochem. Photobiol. 42*, 231−237.

(13) Duncan, R. J. S., and Weston, P. D. (1983) A new reagent which may be used to introduce sulfhydryl groups into proteins, and its use in the preparation of conjugates for immunoassay. *Anal. Biochem. 132*, 68−73.

BC034174S

A Tc-99m-Labeled Long Chain Fatty Acid Derivative for Myocardial Imaging

Yasuhiro Magata,*[,†,‡] Takayoshi Kawaguchi,[†] Misa Ukon,[†] Norio Yamamura,[†] Tomoya Uehara,[||] Kazuma Ogawa,[†] Yasushi Arano,[||] Takashi Temma,[†] Takahiro Mukai,[§] Eiji Tadamura,[§] and Hideo Saji[†]

Laboratory of Genome Bio-Photonics, Photon Medical Research Center, Hamamatsu University School of Medicine, Hamamatsu, Japan, Department of Patho-Functional Bioanalysis, Graduate School of Pharmaceutical Sciences, Kyoto University, Kyoto, Japan, Department of Molecular Imaging and Radiotherapy, Graduate School of Pharmaceutical Sciences, Chiba University, Japan, and Department of Nuclear Medicine and Diagnostic Imaging, Graduate School of Medicine, Kyoto University, Kyoto, Japan. Received October 15, 2003; Revised Manuscript Received December 16, 2003

C-11- and I-123-labeled long chain fatty acid derivatives have been reported as useful radiopharmaceuticals for the estimation of myocardial fatty acid metabolism. We have reported that Tc-99m-labeled *N*-[[[(2-mercaptoethyl)amino]carbonyl]methyl]-*N*-(2-mercaptoethyl)-6-aminohexanoic acid ([^{99m}Tc]-MAMA-HA), a medium chain fatty acid derivative, is metabolized by β-oxidation in the liver and that the MAMA ligand is useful for attaching to the omega-position of fatty acid derivatives as a chelating group for Tc-99m. On the basis of these findings, we focused on developing a Tc-99m-labeled long chain fatty acid derivative that reflected fatty acid metabolism in the myocardium. In this study, we synthesized a dodecanoic acid derivative, MAMA-DA, and a hexadecanoic acid derivative, MAMA-HDA, and performed radiolabeling and biodistribution studies. [^{99m}Tc]MAMA-DA and [^{99m}Tc]MAMA-HDA were prepared using a ligand-exchange reaction. Biodistribution studies were carried out in normal mice and rats. Then, a high initial uptake of Tc-99m was observed, followed by a rapid clearance from the heart. The maximum heart/blood ratio was 3.6 at 2 min postinjection of [^{99m}Tc]MAMA-HDA. These kinetics were similar to those with postinjection of *p*-[^{125}I]iodophenylpentadecanoic acid. Metabolite analysis showed [^{99m}Tc]MAMA-HDA was metabolized by β-oxidation in the body. In conclusion, [^{99m}Tc]MAMA-HDA is a promising compound as a long chain fatty acid analogue for estimating β-oxidation of fatty acid in the heart.

INTRODUCTION

Radiopharmaceuticals of long chain fatty acid analogues have important roles in the diagnosis of heart disease. C-11- and I-123-labeled long chain fatty acid derivatives have been reported as useful radiopharmaceuticals for the estimation of myocardial fatty acid metabolism (*1*−*4*), especially in the differential diagnosis of unstable angina or severe heart ischemia (*5*). However, an on-site cyclotron is needed to produce positron nuclides such as C-11, and radioiodinated compounds must be obtained from radiopharmaceutical companies. Since heart disease generally requires an urgent examination, it would be useful if an on-site radiopharmceutical could be used for clinical diagnosis. A Tc-99m-labeled radiopharmaceutical is most desirable because this nuclide can be supplied from a generator system whenever needed. Although many Tc-99m-labeled long chain fatty acid derivatives have been reported (*6*−*10*), no compound has been put to practical use.

We have reported that [^{99m}Tc]MAMA-HA, a medium chain fatty acid derivative, is metabolized by β-oxidation in the liver and the MAMA ligand is useful for attaching to the omega-position of fatty acid derivatives as a chelating group with Tc-99m (*11*). Based on these findings, we focused on developing a Tc-99m-labeled long chain fatty acid derivative that reflected fatty acid metabolism in the myocardium.

An appropriate chelating group is needed in the chemical structure to label it with Tc-99m, as mentioned above. The effect of the chelating group on the biodistribution of long chain fatty acid analogues has not been clarified. In this study, some Tc-99m-labeled fatty acid analogues, varying in carbon chain length, were synthesized and the heart uptake of these compounds was compared in vivo.

MATERIALS AND METHODS

Materials. Proton nuclear resonance (^{1}H NMR) spectra were recorded on a Bruker AC-200 spectrometer, and the chemical shifts reported in parts per million (ppm) downfield from an internal tetramethylsilane standard. Fast atom bombardment mass spectra (FABMS) were obtained with a JMS−HX/HX 110 A (JEOL Ltd. Tokyo). [^{99m}Tc]Pertechnetate ($^{99m}TcO_4^-$) was eluted in saline solution on a daily basis from Daiichi Radioisotopes Labs generator (Chiba, Japan). Reversed-phase high performance liquid chromatography (RP-HPLC) was performed

* To whom correspondence should be addressed. Tel: +81-53-435-2398. Fax: +81−53−435−2398. e-mail: magata@hama-med.ac.jp.

‡ Hamamatsu University School of Medicine.

† Department of Patho-Functional Bioanalysis, Kyoto University.

|| Chiba University.

§ Department of Nuclear Medicine and Diagnostic Imaging, Kyoto University.

10.1021/bc034190p CCC: $27.50 © 2004 American Chemical Society
Published on Web 02/28/2004

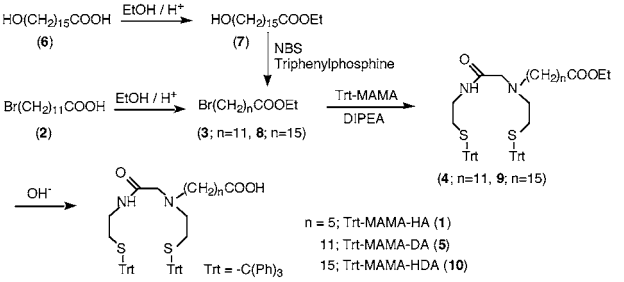


Figure 1. Synthesis of fatty acid analogues with the Trt-MAMA group at the omega position.

using a Cosmosil 5C_{18}-AR 300 column (150 × 4.6 mm; Nacalai Tesque Co., Ltd., Kyoto) eluted with a gradient solvent system (from 10% methanol/5 mM phosphate buffer pH 7.0 to 100% methanol in 60 min) at 1.0 mL/min. TLC analysis was performed with silica plates (Merck Art 5553) using 100% acetone or chloroform/methanol/water = 50/10/1 as developing solvent systems. All chemicals were of reagent grade and were used as received.

Synthesis of Fatty Acid Derivatives. Each fatty acid derivative was synthesized according to the method shown in Figure 1. In brief, the amino group of trityl-MAMA was alkylated with a ω-bromo-fatty acid analogue and hydrolyzed.

*N-[[[[2-[(Triphenylmethyl)thio]ethyl]amino]carbonyl]-methyl]-N-[2-[(triphenylmethyl)thio]ethyl]-6-aminohexanoic Acid (Trt-MAMA-HA)(**1**, n = 5).* Trt-MAMA-HA was synthesized according to a previous report (*11*).

*N-[[[[2-[(Triphenylmethyl)thio]ethyl]amino]carbonyl]-methyl]-N-[2-[(triphenylmethyl)thio]ethyl]-12-aminododecanoic Acid Ethyl Ester (**4**, n = 11, R = Et).* 12-Bromodecanoic acid (**2**) was esterified in ethanol bubbled with HCl gas. *N*-[[[2-[(Triphenylmethyl)thio]ethyl]amino]-acetyl]-*S*-(triphenylmethyl)-2-aminoethanethiol (Trt-MAMA, 250 mg, 0.37 mmol) and diisopropylethylamine (100 μL) were dissolved in 6 mL of DMF. To this mixture was added ethyl 12-bromodecanoate (**3**, $n = 11$, R = Et) (110 mg, 0.38 mmol) in DMF under stirring. After being heated at 140 °C for 12 h, the mixture was subjected to silica gel column chromatography with ethyl acetate/hexane = 4/7 as an eluting solvent. Yield: 150 mg (yellow oil, 43.8%). ^{1}H NMR ($CDCl_3$): δ 7.45−7.15 (overlapped m, 30H), 4.08 (q, 2H), 2.97 (td, 2H), 2.82 (s, 2H), 2.40−2.23 (overlapped m, 10H), 1.58−1.22 (overlapped, 21H). FABMS calcd for $C_{58}H_{68}N_2O_3S_2$ (M + H^+): *m/z* 905. Found: 905.

*N-[[[[2-[(Triphenylmethyl)thio]ethyl]amino]carbonyl]-methyl]-N-[2-[(triphenylmethyl)thio]ethyl]-12-aminododecanoic Acid (Trt-MAMA-DA) (**5**, n = 11).* Compound **4** was hydrolyzed by sodium hydroxide in methanol. Yield: 99.9%. ^{1}H NMR (CD_3OD): δ 7.42−7.16 (overlapped m, 30H), 3.02(t, H), 2.82−2.69 (overlapped m, 8H), 2.33 (t, 2H), 2.23 (t, 2H), 1.60−1.25 (overlapped m, 18H). FABMS calcd for $C_{56}H_{64}N_2O_3S_2$ (M+ H^+): *m/z* 876. Found: 876. Elemental analysis agreed with the calculated value for $C_{56}H_{64}N_2O_3S_2$: C; 76.66%, H; 7.37%, N; 3.19%. Found: C; 76.51%, H; 7.41%, N; 2.92%.

*N-[[[[2-[(Triphenylmethyl)thio]ethyl]amino]carbonyl]-methyl]-N-[2-[(triphenylmethyl)thio]ethyl]-16-aminohexadecanoic Acid Ethyl Ester (**9**, n = 15, R = Et).* 16-Hydroxyhexadecanoic acid (**6**) (1.0 g, 3.67 mmol) was added to 50 mL of dry ethanol followed by concentrated sulfonic acid (0.5 mL). The reaction mixture was stirred for 5 h at room temperature. After evaporation of the solvent, 1.1 g of ethyl 16-hydroxyhexadecanoate as white crystals (**7**) (yield > 99%) was obtained. A mixture of 1.0 g of ethyl 16-hydroxyhexadecanoate (**7**) (3.49 mmol), *N*-bromosuccinimide (0.62 g, 3.49 mmol), and triphenylphophine (0.92 g, 3.49 mmol) was dissolved in 30 mL of dry chloroform. After being heated for 1 h at 50 °C, the solvent was evaporated in vacuo. The residue was purified by column chromatography with ethyl acetate/hexane = 1/3, and ethyl 16-bromohexadecanoate (**8**) was obtained as a pale yellow oil in a yield of 400 mg (32.8%). The bromo compound (400 mg, 1.10 mmol) was dissolved in 5 mL of DMF, and the DMF solution was added to a mixture of Trt-MAMA (900 mg, 1.32 mmol) and diisopropylethylamine (400 μL) dissolved in 6 mL of DMF. After being heated at 140 °C for 12 h, the mixture was subjected to silica gel column chromatography with ethyl acetate/hexane = 4/7 as an eluting solvent. Yield: 170 mg (yellow oil, 16.1%). ^{1}H NMR ($CDCl_3$): δ 7.45−7.15 (overlapped m, 30H), 4.08 (q, 2H), 2.97 (td, 2H), 2.82 (s, 2H), 2.40−2.23 (overlapped m, 10H), 1.58−1.22 (overlapped, 29H). FABMS calcd for $C_{62}H_{76}N_2O_3S_2$ (M+ H^+): *m/z* 961. Found: 961.

*N-[[[[2-[(Triphenylmethyl)thio]ethyl]amino]carbonyl]-methyl]-N-[2-[(triphenylmethyl)thio]ethyl]-16-aminohexadecanoic Acid (Trt-MAMA-HDA) (**10**, n = 15).* Compound **9** was hydrolyzed by sodium hydroxide in methanol. Yield: 99.9%. ^{1}H NMR ($CDCl_3$): δ 7.40−7.15 (overlapped m, 30H), 3.30(t, 2H), 2.90 (t, 2H), 2.84 (s, 2H), 2.47−2.22 (overlapped m, 12H), 1.59−1.23 (overlapped m, 26H). FABMS calcd for $C_{62}H_{76}N_2O_3S_2$ (M + H^+): *m/z* 933. Found: 933. The result of the elemental analysis agreed with the calculated value for $C_{62}H_{76}N_2O_3S_2$: C; 77.20%, H; 7.79%, N; 3.00%. Found: C; 77.00%, H; 7.76%, N; 2.83%.

Tc-99m-Labeling of Fatty Acid Derivatives. Each compound was labeled with Tc-99m by a ligand exchange reaction according to a previously reported method with a slight modification (*11*). In brief, a bistritylated fatty acid analogue (1 mg) was treated with TFA under cation-trapping conditions (5% triethylsilane) (*12*). After removal of the solvent under a stream of N_2, the residue was solved in 0.5 mL of a 40% methanol/phosphate buffer (0.1 M, pH 8.0). [^{99m}Tc]GH (0.5 mL) was added to a solution of a bisthiol compound, and the reaction mixture was heated for 1 h at 90 °C. The labeled compound was extracted with a mixture of ethyl acetate/hexane = 1/4, and the organic layer was evaporated in vacuo.

The radiochemical yield and purity of Tc-99m-labeled fatty acid analogues were determined by RP-HPLC, and the TLC was developed with acetone.

Radiolabeling of *p*-Iodophenylpentadecanoic Acid (IPPA). *p*-Iodophenylpentadecanoic acid (IPPA) (0.5 mg) was solved in a mixture of acetonitrile 950 μL and water 50 μL. Copper sulfate (4 mM, 20 μL), ammonium chloride (0.15 M, 10 μL), and [^{125}I]NaI were added to the IPPA solution, and the reaction mixture was heated in a closed system for 3 h at 120 °C. [^{125}I]IPPA was purified by RP-HPLC eluted with a gradient mobile phase starting from 100% water to 100% methanol for 20 min at a flow rate of 1 mL/min. The retention volumes of IPPA and NaI were 26 mL and 2.5 mL, respectively. The radiochemical yield was 84.7%.

Stability of [^{99m}Tc]MAMA-Fatty Acids. To evaluate the stability of [^{99m}Tc]MAMA-fatty acids, [^{99m}Tc]MAMA-HA, [^{99m}Tc]MAMA-DA, and [^{99m}Tc]MAMA-HDA were each incubated in a 40% ethanol/0.1 M phosphate buffer (pH 7.4) at 37 °C. After incubation for 3, 6, and 12 h, the radiochemical purity was analyzed by TLC developed with chloroform/methanol/water = 50/10/1. Moreover, the stability of these fatty acid compounds in rat plasma was

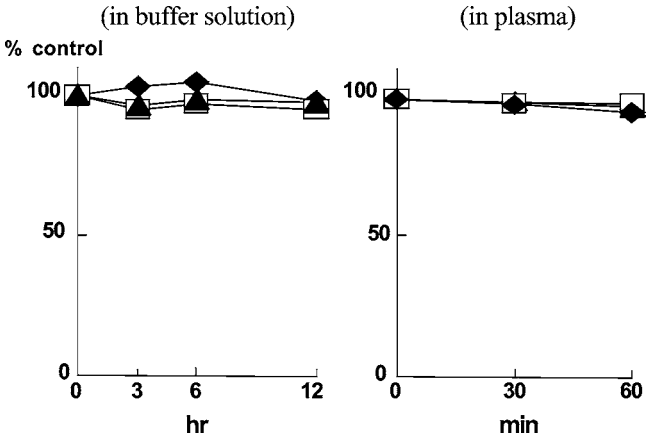


Figure 2. Stability of Tc-99m-MAMA-fatty acid analogues. Closed diamonds, [^{99m}Tc]MAMA-HA; open squares, [^{99m}Tc]-MAMA-D; closed triangles, [^{99m}Tc]MAMA-HDA.

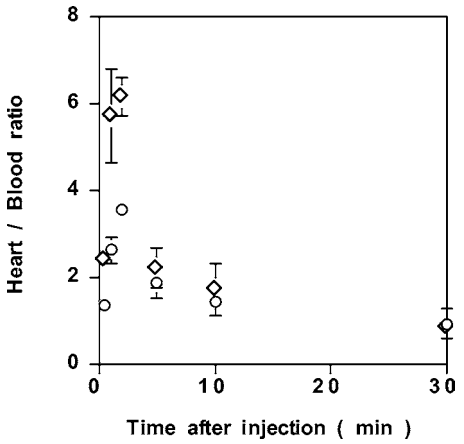


Figure 3. Comparison of heart/blood ratio of Tc-99m-MAMA-HDA and I-125-IPPA in normal rats. Open diamonds, [^{125}I]IPPA; open circles, [^{99m}Tc]MAMA-HDA.

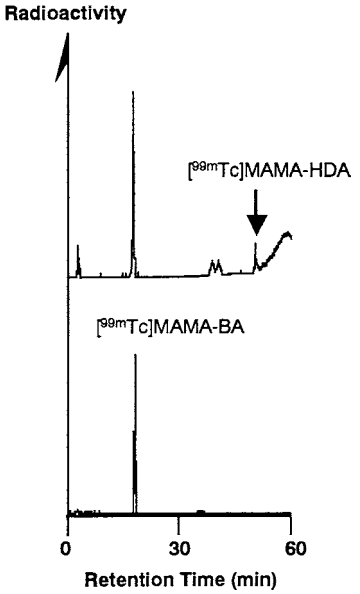


Figure 4. Metabolite analysis in urine postinjection of Tc-99m-MAMA-HDA in normal rats. Upper chart: radiochromatogram in urine at 30 min postinjection of [^{99m}Tc]MAMA-HDA; lower chart: radiochromatogram of authentic labeled compound of [^{99m}Tc]MAMA-BA.

evaluated. Then, 10 μL of labeled compound was added to 1 mL of rat plasma and the mixture was incubated at 37 °C. After incubation for 30 and 60 min, 100 μL of the mixture was sampled and 200 μL of ethanol was added. The mixture was filtered with a 0.45 μm Millipore filter, and the radiochemical purity was analyzed by RP-HPLC.

Biodistribution Studies. Male ddY mice (25−30 g) and male Wistar rats (150−200 g) were housed for 1 week under a 12-h light/12-h dark cycle with free access to food and water for subsequent biodistribution studies and metabolic analyses. Animals were fasted before experiments for 12 h.

For biodistribution studies, [^{99m}Tc]MAMA-HA was solved in saline. [^{99m}Tc]MAMA-DA and [^{99m}Tc]MAMA-HDA were solved in a 40% ethanol solution after being radiolabeled and 100 μL of the solution was added to 1 mL of saline, containing 1% human serum albumin. After passing through a 0.22 μm Millipore filter, the solution (37 kBq in 0.1 mL) was administered to normal mice via the tail vein. At appropriate time points after the administration, mice were sacrificed by decapitation. Samples of blood and organs of interest were excised and weighed, and radioactivity was quantified using a NaI-(Tl) gamma scintillation counter (Packard Auto-Gamma 500, Packard Inst. Co., Albertville, MI). The results are expressed as the percent injected dose/gram of blood or organs after decay correction.

A mixture of [^{99m}Tc]MAMA-HDA and [^{125}I]IPPA was injected into normal rats via the tail vein. At appropriate time points after the administration, rats were sacrificed by decapitation and calculations made as mentioned above.

Metabolic Analysis. At 30 min postinjection of [^{99m}Tc]-MAMA-HDA in normal rats, urine samples were obtained from the bladder. After filtration of the urine samples through a 0.22 μm Millipore filter, the filtrate was analyzed by RP-HPLC eluted with a gradient mobile phase starting from 10% methanol in a 0.05 M phosphate buffer (pH 7.0) to 100% methanol for 60 min at a flow rate of 1 mL/min.

RESULTS

Synthesis of Fatty Acid Derivatives. Each fatty acid derivative was synthesized according to the method shown in Figure 1. In brief, the amino group of trt-MAMA was alkylated with a ω-bromo-fatty acid analogue. After hydrolysis of the ester group, trt-MAMA-DA and trt-MAMA-HDA were obtained as a yellow oil with overall yields of 43.8% and 5.3%, respectively (calculated from the starting compound of fatty acid derivative).

Tc-99m-Labeling of Fatty Acid Derivatives. Each compound was labeled in a ligand exchange reaction with [^{99m}Tc]pertechnetate reduced by Sn(II) glucoheptonate in diluted ethanol solution and purified by HPLC. The retention times of [^{99m}Tc]MAMA-DA and [^{99m}Tc]MAMA-HDA were 43 and 49 min, respectively. The retention time of [^{99m}Tc]MAMA-HA was 23 min (*11*). The radiochemical yields of [^{99m}Tc]MAMA-DA and [^{99m}Tc]MAMA-HDA were 70% and 75%, respectively. The radiochemical purity of both labeled compounds was >99%.

Stability of [^{99m}Tc]MAMA-Fatty Acids in Vitro. Figure 2 shows the stability of three [^{99m}Tc]MAMA-fatty acids, [^{99m}Tc]MAMA-HA, [^{99m}Tc]MAMA-DA, and [^{99m}Tc]-MAMA-HDA, in a phosphate-buffered solution and rat plasma in vitro. High stability was observed for all radiochemical compounds in these solutions.

Biodistribution Studies. Table 1 shows the biodistribution of Tc-99m-labeled fatty acids in normal mice. A rapid clearance of radioactivity from the blood was observed for all compounds. [^{99m}Tc]MAMA-HDA showed

Table 1. Biodistribution of [^{99m}Tc]MAMA-Fatty Acids in Normal Mice[a]

	time after injection (min)				
	0.5	2	5	20	60
			MAMA-HDA		
heart	11.22 (0.25)	5.46 (1.15)	2.40 (0.22)	0.60 (0.03)	0.32(0.09)
blood	9.84 (1.11)	3.61 (0.30)	2.91 (0.29)	0.78 (0.07)	0.37 (0.01)
lung	7.51 (0.32)	3.53 (2.15)	2.27 (0.51)	0.72 (0.30)	0.35 (0.05)
liver	21.07 (1.35)	25.79 (4.72)	25.88 (4.71)	18.14 (2.96)	13.21 (3.49)
			MAMA-DA		
heart	5.68 (0.61)	2.83 (0.30)	1.50 (0.09)	0.82 (0.10)	0.40 (0.09)
blood	12.35 (0.10)	4.48 (2.72)	3.64 (1.30)	1.54 (0.14)	0.96 (0.14)
lung	9.26 (1.26)	4.24 (0.41)	2.72 (0.13)	1.39 (0.22)	0.79 (0.14)
liver	15.74 (1.70)	24.63 (2.51)	18.13 (10.18)	18.20 (3.60)	14.51 (1.74)
			MAMA-HA		
heart	4.04 (0.72)	1.46 (0.22)	0.70 (0.15)	0.29 (0.03)	0.19 (0.08)
blood	8.28 (1.24)	2.66 (0.45)	1.17 (0.13)	0.47 (0.07)	0.29 (0.02)
lung	5.42 (1.05)	1.92 (0.27)	0.98 (0.18)	0.38 (0.07)	0.23 (0.03)
liver	11.57 (2.81)	26.86 (2.39)	31.83 (0.83)	35.00 (6.59)	30.95 (4.56)

[a] Each value shows the mean (SD) of % dose/g ($n = 5$).

the highest uptake in the mouse heart among the three Tc-99m-labeled fatty acids. Only [^{99m}Tc]MAMA-HDA had a heart-to-blood ratio greater than one through to 2 min postinjection of the compound.

[^{99m}Tc]MAMA-HDA and [^{125}I]IPPA were simultaneously injected into normal rats. The heart-to-blood ratio was 3.6 at 2 min postinjection of [^{99m}Tc]MAMA-HDA in normal rats, while it was 6.2 at 2 min postinjection of [^{125}I]IPPA. The kinetics of the clearance of radioactivity from the heart were very similar between [^{99m}Tc]MAMA-HDA and [^{125}I]IPPA (Figure 3).

Metabolic Analysis. Rat urine samples were collected at 30 min postinjection of [^{99m}Tc]MAMA-HDA and the metabolites in them were analyzed by RP-HPLC. The lower chart of Figure 4 shows a typical chromatogram of [^{99m}Tc]MAMA-BA (*11*). The retention time of [^{99m}Tc]-MAMA-BA was 17 min. The major peak in the urine samples was observed at retention time of 17 min on RP-HPLC (Figure 4, upper).

DISCUSSION

External imaging of energy production levels of living cells with Tc-99m-labeled compounds is a challenging task for the development of Tc-99m-radiopharmaceuticals. Indeed, efforts have been made to develop Tc-99m-labeled long chain fatty acid analogues for myocardial imaging studies. However, their application has been hampered by poor accumulation in the heart, and it appeared that these Tc-99m-labeled fatty acid analogues were not recognized as substrates for β-oxidation (*8*, *9*).

In this study, two long chain fatty acid derivatives, including the MAMA group as a chelating group with Tc-99m, were synthesized according to the method shown in Figure 1. Their chemical structures were assigned based on instrumental analyses. Tc-99m labeling reactions were carried out according to a previously reported method (*11*) with a slight modification. MAMA-HA, which is a medium chain fatty acid derivative reported previously, was radiolabeled with Tc-99m in solution because of its hydrophilicity. However, the long chain fatty acid derivatives MAMA-HDA and MAMA-DA were radiolabeled in a 40% ethanol solution because their solubility in solution was poor compared with that of the medium chain fatty acid analogues. Tc-99m-labeled compounds were obtained at a good yield by this method, despite the ethanol-containing condition. This exchange labeling method is useful for Tc-99m labeling of MAMA chelating groups. Moreover, the high stability of each labeled compound is shown in Figure 2.

The myocardium uses long chain fatty acids as its energy source under normal conditions, although it is affected by the blood sugar or nonesterified fatty acid concentration in the serum (*13*). Biodistribution studies in mice showed that the longer the carbon chain, the higher the heart uptake. Only [^{99m}Tc]MAMA-HDA showed a heart-to-blood ratio of radioactivity uptake greater than one in the early phase postinjection of the compound (Table 1).

Then, a mixture of [^{99m}Tc]MAMA-HDA and [^{125}I]IPPA was injected into normal rats, and the heart uptake of both was compared. Although the uptake of the radioactivity of Tc-99m was almost half the value of that of I-125, the heart-to-blood ratio (%dose/g) of both Tc-99m and I-125 showed similar curves (Figure 3). The heart-to-blood ratio of Tc-99m was about 3.6 at 2 min postinjection. Metabolites in urine were evaluated (Figure 4). In this figure, [^{99m}Tc]MAMA-BA was observed at 30 min postinjection of [^{99m}Tc]MAMA-HDA. This [^{99m}Tc]MAMA-BA was observed after six rounds of β-oxidation. The result indicated that [^{99m}Tc]MAMA-HDA was recognized as a fatty acid in the body. The metabolite [^{99m}Tc]MAMA-BA has been observed postinjection of the medium chain fatty acid derivative, [^{99m}Tc]MAMA-HA (*11*). Since long chain fatty acids are metabolized by β-oxidation in the liver as well as in the heart, β-oxidation of the compound in the heart should be evaluated. Although the metabolism of [^{99m}Tc]MAMA-HDA is now being evaluated, this compound has been recognized as a long chain fatty acid in vivo.

In conclusion, [^{99m}Tc]MAMA-HDA is a promising compound as a long chain fatty acid analogue for estimation of the β-oxidation of fatty acids in the heart. Further investigation with metabolites is now under way.

ACKNOWLEDGMENT

A part of this study was supported by Grant in Aide for the Center of Excellence (COE) from the Ministry of Education, Culture, Sports, Science and Technology, Japan.

LITERATURE CITED

(1) Fujino, T., Ishii, Y., Takeuchi, T., Hirasawa, K., Tateda, K., Kikuchi, K., and Hasebe, N. (2003) Recovery of BMIPP Uptake and Regional Wall Motion in Insulin Resistant Patients Following Angioplasty for Acute Myocardial Infarction. *Circ. J. 67*, 757−762.

(2) Hoshina, M., Shiraishi, H., Igarashi, H., Kikuchi, Y., Ichihashi, K., and Momoi, M. Y. (2003) Efficacy of iodine-123-

15-(*p*-iodophenyl)-3-R, S-methylpentadecanoic acid single photon emission computed tomography imaging in detecting myocardial ischemia in children with Kawasaki disease. *Circ. J. 67*, 663−666.

(3) Kates, A. M., Herrero, P., Dence, C., Soto, P., Srinivasan, M., Delano, D. G., Ehsani, A., and Gropler, R. J. (2003) Impact of aging on substrate metabolism by the human heart. *J. Am. Coll. Cardiol. 41*, 293−299.

(4) Schelbert, H. R. (2000) PET contributions to understanding normal and abnormal cardiac perfusion and metabolism. *Ann. Biomed. Eng. 28*, 922−929.

(5) Nishimura, S., and Ohta, Y. (1999) BMIPP in angina pectoris. *Int. J. Card. Imaging 15*, 35−39.

(6) Karesh, S. M., Eckelman, W. C., and Reba, R. C. (1977) Biological distribution of chemical analogues of fatty acids and long chain hydrocarbons containing a strong chelating agent New compounds: fatty acid and long chain hydrocarbon derivatives containing a strong chelating agent. *J. Pharm. Sci. 66*, 225−228.

(7) Astheimer, L., Linse, K. H., Ramamoorthy, N., and Schwochau, K. (1987) Synthesis, characterization and evaluation of 99Tc/99mTc DIARS and DMPE complexes containing pentadecanoic acid. *Int. J. Rad. Appl. Instrum. B 14*, 545−553.

(8) Mach, R. H., Kung, H. F., Jungwiwattanaporn, P., and Guo, Y. Z. (1991) Synthesis and biodistribution of a new class of 99mTc-labeled fatty acid analogues for myocardial imaging. *Int. J. Rad. Appl. Instrum. B 18*, 215−226.

(9) Jones, G. S., Jr., Elmaleh, D. R., Strauss, H. W., and Fischman, A. J. (1994) Synthesis and biodistribution of a new 99mtechnetium fatty acid. *Nucl. Med. Biol. 21*, 117−123.

(10) Jones, G. S., Jr., Elmaleh, D. R., Strauss, H. W., and Fischman, A. J. (1996) 7,10-Bis(2-mercapto-2-methyl)propyl-7, 10-diazapalmitic acid: A novel, N2S2 ligand for technetium-99m. *Bioorg. Med. Chem. Lett. 6*, 2399−2404.

(11) Yamamura, N., Magata, Y., Arano, Y., Kawaguchi, T., Ogawa, K., Konishi, J., and Saji, H. (1999) Technetium-99m-labeled medium-chain fatty acid analogues metabolized by β-oxidation: radiopharmaceutical for assessing liver function. *Bioconjug. Chem. 10*, 489−495.

(12) Meltzer, P. C., Blundell, P., Jones, A. G., Mahmood, A., Garada, B., Zimmerman, R. E., Davison, A., Holman, B. L., and Madras, B. K. (1997) A technetium-99m SPECT imaging agent which targets the dopamine transporter in primate brain. *J. Med. Chem. 40*, 1835−1844.

(13) Corbett, J. R. (1999) Fatty acids for myocardial imaging. *Semin. Nucl. Med. 29*, 237−258.

BC034190P

Synthesis of Ultrasmall Superparamagnetic Iron Oxides Using Reduced Polysaccharides

Kenneth G. Paul,[§] Timothy B. Frigo,* Jesse Y. Groman,[†] and Ernest V. Groman[§]

Advanced Magnetics, Inc., 61 Mooney Street, Cambridge, Massachusetts 02138-1038. Received October 22, 2003; Revised Manuscript Received January 6, 2004

Investigation into the effect of the reducing sugar of dextran on formation and stability of dextran-coated ultrasmall superparamagnetic iron oxides (USPIO) has demonstrated that reduction of the terminal reducing sugar can have a significant effect on particle size, coating stability, and magnetic properties. Four aspects of polysaccharide-coated USPIO particle synthesis were investigated: (i) the effect reduction of the terminal polysaccharide sugar has upon polysaccharide usage, particle size, stability, and magnetic susceptibility; (ii) the effect an exogenous reducing sugar can have upon particle synthesis; (iii) the effect the molecular weight of the reduced polysaccharide has on particle synthesis; and (iv) the effectiveness of reduced and native dextrans in stabilizing a preformed magnetic sol. For low molecular weight dextrans (MW ≤10 kDa), reduction resulted in a 10 fold or greater decrease in the carbohydrate-to-iron ratio necessary during particle formation to produce the desired particle size (<20 nm). Particles prepared at the equivalent dextran-to-iron ratio using the equivalent native dextrans yielded larger particles except for a 70 kDa dextran where reduced and native dextran yielded identical particles with respect to size and magnetic properties. The stability of particle size and coating was studied using 10 kDa native and reduced dextran. Particles prepared with reduced dextran yielded a more stable coating as evidenced by stability on autoclaving. For native dextrans (MW < 70 kDa), small (≤30 nm) particles could be obtained at much higher dextran-to-iron ratios, but only the 10 kDa dextran gave a particle with comparable magnetic properties (susceptibility > 20 000 × 10^{-6} cgs). Similar results were obtained with a 12 kDa pullulan. The effect of polysaccharide molecular weight on particle size was studied, wherein higher molecular weight reduced dextrans produced larger particles. The effectiveness of the reduced and native dextrans in stabilizing a preformed magnetic sol was compared. Reduced dextrans were found to be superior for stabilizing the magnetic sol. The observed effects of reduction of the terminal sugar in dextran compared with the native dextran were modeled using the Langmuir adsorption isotherm. A good fit of experimental data with this model was found.

INTRODUCTION

Ultrasmall superparamagnetic iron oxides (USPIO) have been investigated in many biological applications, both in vitro and in vivo. As a result of their small size (diameter < 30 nm), these particles are not immediately removed from the circulation by the reticuloendothelial system. This results in a longer blood half-life and a wider biodistribution for the particle and allows potential targeting with appropriate bioconjugates to specific tissues both normal and tumorous. For example, MION (*1*), prepared by chromatography of ferumoxides (*2*), and similar materials (*3*) that may be prepared without chromatographic separation have been proposed for use as contrast agents in magnetic resonance angiography (*4*) and lymph node imaging (*5*). Several of these particles are now in late-phase clinical trials (*6*). In addition, attachment of small, bioactive peptides (*7*) or antibodies (*8*) to the particle coating has been reported to allow site-specific directability. Other applications being actively pursued include cell sorting, magnetically directed drug transport, localized therapeutic hyperthermia, immunoassays, and related applications (*9*−*12*).

In the majority of these potential uses, attachment of a drug or bioconjugate to USPIO for targeting is a prerequisite or greatly improves efficacy. Bioconjugation must attach to the organic coating surrounding the magnetic core. The preponderance of USPIO described in the literature has been prepared with a polysaccharide coating, most often dextran. For the purpose of bioconjugation, the dextran may be activated for attachment, for example by periodate oxidation (*13*). Alternatively, the dextran may be activated or the bioconjugate prepared prior to particle formation. Since the coating process is highly inefficient (most of the coating is lost after particle formation through purification by ultrafiltration) and the conditions of particle formation (high pH and heat) will inactivate most biologically derived conjugates, this second approach is unattractive. Any change in particle synthesis that addresses these problems would be desirable for making the second approach viable.

Considering the wide use of dextran-coated particles, it is surprising that even the most elementary aspects of particle synthesis, the effect of polymer molecular weight

* To whom correspondence should be addressed. Phone: 617-497-2070. Fax: 617-547-2445. E-mail: tfrigo@advanced-magnetics.com.

[§] Current address: BioPhysics Assay Laboratory, Inc., 80 Webster St., Worcester, MA, 01603.

[†] Current address: Safeco Life & Investments, 5069 154th Place NE, Redmond, WA 98052.

[1] Abbreviations: kDa, kilodalton; MVD, mean volume diameters; MW, molecular weight; nm, nanometer, ND, native dextran; RD, reduced dextran; MS, magnetic susceptibility; USPIO, ultrasmall superparamagnetic iron oxides.

10.1021/bc034194u CCC: $27.50 © 2004 American Chemical Society
Published on Web 02/26/2004

and the effect of polymer modification on particle size, stability, and coating efficiency, have not been reported in the literature. In this initial report, we describe the effect of reduction of the terminal reducing sugar in the coating polysaccharide on the particle size and magnetic properties of USPIO. This effect was investigated for a series of dextrans of varying molecular weight as well as a nondextran polysaccharide. Finally, we modeled these effects using a Langmuir isotherm and obtained a reasonable fit of experimental data with this model.

EXPERIMENTAL SECTION

Analytical Methods. Particle sizes were determined by dynamic light scattering in a Microtrac UPA instrument (Honeywell IAC Microtrac, Fort Washington, PA) and are reported as the mean volume diameter (MVD). Magnetic susceptibility was determined with a Mathey Johnson magnetic susceptibility balance. Iron concentrations were determined utilizing a bipyridyl assay (*14*). Size exclusion chromatography was used to determine retention times of reduced and native polysaccharides using a Waters Ultrahydrogel 250 column with RI detection. The elution buffer and flow rate were 20 mM phosphate containing 0.25% sodium chloride and 0.1% sodium azide (pH 7.3) and 0.4 mL/min. Residual aldehyde concentrations was determined using a modified tetrazolium blue assay (*15*). Dextran was determined by a phenol/sulfuric acid assay. (*16*)

Materials. Dextrans T1, T10, and T70 were obtained from Pharmacia (Upsala, Sweden) and dextran T5 was obtained from Carbomer (Westborough, MA). Pullulan was obtained from Waters (Milford, MA). All other chemicals were obtained from common commercial sources and used without purification.

Modified Dextrans. Reduced polysaccharides were prepared by treatment with excess sodium borohydride and generally purified using five cycles of ultrafiltration. In the case of pullulan, the reduction mixture was used without further purification. In all cases the products showed less than 5% residual aldehyde content. In cases where ultrafiltration was omitted, it was demonstrated that, except for the dextran T1, the residual borate salts did not affect particle formation. When ultrafiltration was used to purify the modified dextrans, a small decrease in retention times for the reduced dextrans relative to the starting native dextrans was sometimes observed.

Reduced Dextran T1. Dextran T1 (10 g) was dissolved in 100 mL of deionized water at 25 °C, 1 g of sodium borohydride was added, and the mixture was stirred 12 h. The pH was brought to 5.0 using 6 M HCl, and 200 mL of ethanol (absolute) was added. The ethanol/water layer was decanted, and the residue was dissolved in 100 mL of deionized water. Adding 200 mL of absolute ethanol made a second precipitation, and the ethanol/water was again decanted. The product was dissolved in water and lyophilized to produce a white solid in 60% yield. HPLC retention times (min): reduced dextran = 24.4; native dextran = 24.4.

Reduced Dextran T5. Dextran T5 (4 g) was dissolved in 25 mL of deionized water at 25 °C, 83 mg of sodium borohydride was added, and the mixture was stirred 12 h. The pH was brought to 5.0 using 6 M HCl. The mixture was ultrafiltered against a 1 kDa membrane. The product was lyophilized to produce a white solid in 70% yield. HPLC retention times (min): reduced dextran = 22.9; native dextran = 21.9.

Reduced Dextran T10. Dextran T10 (10 g) was dissolved in 100 mL of deionized water at 25 °C, 1 g of sodium borohydride was added, and the mixture was stirred 12 h. The pH was brought to 5.0 using 6 M HCl. The mixture was ultrafiltered against a 3 kDa membrane. The product was lyophilized to produce a white solid in 63% yield. HPLC retention times (min): reduced dextran = 21.6; native dextran = 21.1.

Reduced Dextran T70. Dextran T70 (10 g) was dissolved in 100 mL of deionized water at 25 °C, 0.2 g of sodium borohydride was added, and the mixture was stirred 12 h. The pH was brought to 5.0 using 6 M HCl. The mixture was ultrafiltered against a 10 kDa membrane. The product was lyophilized to produce a white solid in 68% yield. HPLC retention times (min): reduced dextran = 18.4; native dextran = 18.4.

Reduced Pullulan. Pullulan (90 mg) was dissolved in 0.8 mL of deionized water at 25 °C, 1 mg of sodium borohydride was added, and the mixture was stirred 12 h. This material was used directly in the preparation of pullulan-coated iron oxide particles.

Preparation of Polysaccharide-Coated Particles. Identical procedures were utilized for the preparation of polysaccharide-coated iron oxide particles with each pair of native and reduced polysaccharide having the same molecular weight. In particular, polysaccharide-to-iron ratios and iron concentrations were chosen for the reduced polysaccharide-coated particles to yield a 0.2 μm filterable particle with a diameter of less than 30 nm and a magnetic susceptibility of greater than 20 000 $\times$ 10^{-6} cgs. The same conditions were then used in the particle synthesis for the native polysaccharide of the same molecular weight. The general procedure involves addition of excess ammonium hydroxide to a solution of iron salts (Fe^{3+}/Fe^{2+}) and dextran, followed by heating and six cycles of ultrafiltration against deionized water using a 100 kDa membrane. After ultrafiltration, the reduced dextran particles were 0.2 μm filtered and stored at 4 °C. In the preparations with the native dextran, only the native dextran T10- and T70-coated particles could be 0.2 μm filtered. The size and magnetic susceptibility were then measured except for those samples containing particulate materials.

Preparation of Native and Reduced Dextran T1-Coated Particles. Native or reduced dextran T1 (1.7 g) was dissolved in 20 mL of deionized water. A mixture of 3 g of ferric chloride hexahydrate and 1.5 g of ferrous chloride tetrahydrate dissolved in 32 g of deionized water was added. The mixture was purged with nitrogen for 30 min and cooled to 5 °C, and 12.7 g of ammonium hydroxide (28%) added with stirring over 2 min. The mixture was heated to 60 °C over 40 min, at 80 °C for 2 h, and purified as indicated above.

Preparation of Native and Reduced Dextran T5-Coated Particles. Native or reduced dextran T5 (0.45 g) was dissolved in 13 mL of deionized water. A mixture of 0.5 g of ferric chloride hexahydrate and 0.25 g of ferrous chloride tetrahydrate dissolved in 4.5 g of deionized water was added. The mixture was purged with nitrogen for 30 min and cooled to 5 °C, and 1.42 g ammonium hydroxide (28%) added with stirring over 2 min. The mixture was heated at 80 °C for 2 h and purified as indicated above.

Preparation of Native and Reduced Dextran T10-Coated Particles. Native or reduced dextran T10 (2.7 g) was dissolved in 70 mL of deionized water. A mixture of 2.0 g of ferric chloride hexahydrate and 1.0 g of ferrous chloride tetrahydrate dissolved in 27 g of deionized water was added. The mixture was purged with nitrogen for 30 min and cooled to 5 °C, and 8.5 g of ammonium hydroxide (28%) added with stirring over 2 min. The

Table 1. Conditions Used in the Formation of Reduced and Native Dextran-Coated Magnetic Sol

dextran	sol[a] mg Fe	polysaccharide/Fe g/g	[Fe] mg/mL
T1	24	1.6	12
T5	24	2.9	12
T10	13	4.6	6.5
T70	3	8.7	1.5

[a] An amount of magnetic sol was added to a solution of dextran or reduced dextran as shown.

mixture was heated at 80 °C for 2 h and purified as indicated above.

Preparation of Native and Reduced Dextran T70-Coated Particles. Native or reduced dextran T70 (0.2 g) was dissolved in 10 mL of deionized water. A mixture of 0.06 g of ferric chloride hexahydrate and 0.03 g of ferrous chloride tetrahydrate dissolved in 15 g of deionized water was added. The mixture was purged with nitrogen for 30 min and cooled to 5 °C, and 1.0 g of ammonium hydroxide (28%) added with stirring over 2 min. The mixture was heated at 80 °C for 1 h and purified as indicated above.

Preparation of Native and Reduced Pullulan-Coated Particles. Native or reduced pullulan (0.045 g) was dissolved in 0.4 mL of deionized water. A mixture of 0.106 g of ferric chloride hexahydrate and 0.05 g of ferrous chloride tetrahydrate dissolved in 1.3 g of deionized water was added. The mixture was purged with nitrogen for 30 min and cooled to 5 °C, and 0.044 g of ammonium hydroxide (28%) added with stirring over 2 min. The mixture was heated at 80 °C for 0.67 h and purified as indicated above.

Effect of Molecular Weight of Reduced Dextrans on Particle Size Using Constant Polysaccharide/Fe Ratios and Constant [Fe]. Reduced dextran (T1, T5, T10, or T70) (0.26 g) was dissolved in 6.8 g of deionized water, and a mixture of 0.193 g of ferric chloride hexahydrate and 0.096 g of ferrous chloride tetrahydrate dissolved in 2.4 g of deionized water was added. The mixture was purged with nitrogen for 30 min and cooled to 5 °C, and 0.82 g of ammonium hydroxide (28%) added with stirring over 2 min. The mixture was heated at 80 °C for 1 h. The mixture was diluted to 25 mL with deionized water, 0.2 μm filtered when possible, and analyzed for size and magnetic susceptibility without further purification.

Preparation of Magnetic Sol. At 25 °C, 60 g of ammonia hydroxide (28%) was added to 30.0 g of ferric chloride hexahydrate and 15.1 g of ferrous chloride tetrahydrate dissolved in 321 g of deionized water. After 5 min of mixing, concentrated HCl was added to reach pH 1.6. The sol was ultrafiltered against a 100 kDa membrane to achieve pH 3.25. Deionized water was the diluent. The magnetic sol was 0.2μ filtered, concentrated to 50 mg Fe/g, and stored at 5 °C. Yield of iron: 55%. MVD = 16 nm.

Reaction of Reduced Dextrans with Magnetic Sol. An amount of magnetic sol was added to a solution of dextran or reduced dextran as shown in Table 1. The dextran/iron ratios and iron concentrations were identical to those that yielded magnetic particles with the reduced dextrans during in situ formation. The mixture was incubated for 15 min, and the pH was adjusted to 7.4 ± 0.4. The size was determined without purification.

RESULTS

Effect of Reduction of the Terminal Sugar on Particle Size, Magnetic Susceptibility, and Stability. The treatment of a polysaccharide such as dextran with sodium borohydride results in the conversion of the terminal reducing sugar to a linear polyol. This very minor change of the polysaccharide structure is shown in Scheme 1.

Further illustrating the small magnitude of the change produced by reduction, we note that in a dextran of molecular weight 10 kDa only one of its 63 glucose residues is altered by reduction. This residue represents 1.6% of the total mass of the polymer. Additionally, there are 191 hydroxyl groups in the hemiacetal and aldehyde forms of the native polysaccharide and 192 hydroxyls in the reduced polysaccharide. The one additional hydroxyl is introduced by the formation of the linear polyol. The gross structure of the reduced and native dextran is identical as indicated by hydrodynamic measurements. The mol percent that the terminal sugar represents in each of the polysaccharides studied is listed in Table 2.

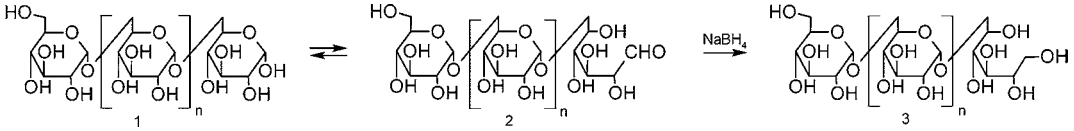
The profound effect that reduction of the terminal sugar in polysaccharides can have in the synthesis of USPIO is illustrated in Table 2 which presents the mean volume diameters (MVD) determined for particles formed with native and reduced polysaccharide pairs. The polysaccharide/Fe ratio and dilution of these reagents were optimized to yield particles with diameters of ≤30 nm with the reduced polysaccharide; the same ratio was used with native polysaccharides. For the lower molecular weight polysaccharides, the native dextran gave a consistently larger particle. As the size of the polysaccharide increased the effect became less pronounced and disappeared when the molecular weight reached 70 kDa. In all cases, particles synthesized with reduced polysaccharides yielded higher susceptibility values than the corresponding particles synthesized with native polysaccharide.

Ultrasmall iron oxide particles were prepared with the low molecular weight native dextrans but this required about a 10 to 34-fold increase in the polysaccharide-to-iron ratio relative to that used for USPIO prepared with reduced dextrans of corresponding molecular weight (Table 3). For particles prepared with native dextran T1 and T5 the magnetic properties of the particles were markedly inferior to corresponding particles prepared with their reduced counterpart. Particles prepared with native and reduced dextrans T70 used identical polysaccharide/Fe ratios and each yielded nearly identical particles with respect to size and magnetic susceptibility.

Besides providing a more efficient use of the polysaccharide in USPIO synthesis than the corresponding native dextran, the reduced dextran-coated USPIO is more stable. When USPIO prepared with reduced dextran T10 was autoclaved for 30 min at 121 °C, its size did not change (Table 4); however, when USPIO prepared with native dextran T10 is similarly treated its size increases dramatically. Another indicator of stability is provided by the bound dextran/Fe ratio. A higher ratio suggests more stability and tighter binding. Both before and after autoclaving particles prepared with reduced dextran had higher ratios than the corresponding particles prepared with native dextran.

Effect of Addition of Glucose to Reduced Dextrans on Particle Size and Magnetic Susceptibility. To determine whether the effect of reduced polysaccharide on particle size resulted from removal of the reducing sugar from the reaction mixture, reduced dextran T10 colloidal USPIO were prepared as described in Experimental except that increasing amounts of glucose were added to the dextran/iron-solution before addition of ammonium hydroxide. The effect on particle size and

Scheme 1. Illustration of the Chemical Change in a Polysaccharide Such as Dextran upon Treatment with Sodium Borohydride[a]



[a] The hemiacetal form of the polysaccharide (structure **1**) is in equilibrium with the aldehyde form of the polysaccharide (structure **2**). Structure **2** represents less than 0.01% of the equilibrium mixture (*17*). Treatment of structure **2** with sodium borohydride results in its irreversible conversion to the linear polyol form of the polysaccharide (structure **3**). The dynamic equilibrium between structures **1** and **2** allows complete conversion, when treated with sodium borohydride, to the linear polyol (structure **3**).

Table 2. Comparison of Reduced Polysaccharides with Their Respective Native Dextrans in the Synthesis of USPIO

					particle			
	synthesis conditions				native coating		reduced coating	
coating agent	MW kDa	polyol[a]	[M][b]m/L	coating/Fe[c] g/g	MVD[d]	MS[e]	MVD[d]	MS[e]
dextran T1	1000	16.2	0.12	1.6	2764	1953	18	13323
dextran T5	5000	3.24	0.22	2.9	1916	*f*	16	33943
dextran T10	10000	1.62	0.19	4.6	757	31252	21	31743
dextran T70	70000	0.23	0.08	8.7	21	25085	20	30905
pullulan	12000	1.35	0.13	3.9	1184	*f*	20	27066

[a] Percentage of monosaccharide units present as polyol in the reduced polysaccharides assuming a nonbranched polysaccharide. [b] Concentration of monomeric glucose units (wt. polysaccharide/162/vol). [c] The polysaccharide/Fe ratio was fixed for each pair of reduced/native polysaccharide at a ratio optimized to give reduced polysaccharide particles with MVD < 30 nm. [d] Mean volume diameter (nanometers). [e] Magnetic susceptibility ($\times 10^{-6}$ cgs/g Fe). [f] The sample was particulate, could not be 0.2 μm filtered, and was not analyzed for magnetic susceptibility.

Table 3. Comparison of Reduced Polysaccharides with Their Respective Native Dextrans in the Synthesis of USPIO

	native polysaccharide				reduced polysaccharide			
	[R][a]/[Fe]	dextran[b]/Fe g/g	MVD nm	MS[c]	[R][a]/ [Fe]	dextran[b]/Fe g/g	MVD nm	MS[c]
dextran T1	3.08	55	27	2325	<0.01	1.6	18	13323
dextran T5	0.49	44	20	1285	<0.01	2.9	16	33943
dextran T10	0.25	44	21	32712	<0.01	4.6	12	31743
dextran T70	0.007	8.7	21	25085	<0.01	8.7	20	30905

[a] R stands for the terminal reducing sugar. The R/Fe ratio is expressed as a mol/mol ratio. [b] The polysaccharide/Fe ratio was varied for each dextran to yield a particle with a MVD less than ≤30 nm. [c] Magnetic susceptibility ($\times 10^{-6}$ cgs/g Fe).

Table 4. Effect of Autoclaving on USPIO Prepared with Native or Reduced Dextran T10

USPIO	untreated		autoclaved[a]	
dextran T10 coating	bound dextran g/g Fe	MVD nm	bound dextran g/g Fe	MVD nm
native	0.79	21	0.56	587
reduced	1.26	18	0.96	23

[a] Particle was autoclaved at a concentration of 20 mg Fe/g for 30 min at 121 °C. [b] Bound dextran was determined from total and free dextran determined with a phenol/sulfuric acid assay. Free dextran was separated from the colloid by ultrafiltration.

Table 5. Effect of Added Glucose on Particle Size and Magnetic Susceptibility for USPIO Prepared with Reduced Dextran T10

% glucose[a]	[glucose]/[Fe]	MVD[b] nm	MS[c]
0	0	26	33027
2.5	0.06	24	30456
10	0.24	24	23090
25	0.60	28	9884
50	1.20	32	2773
native dextran	0.026[d]	>700	31252

[a] The amount of glucose added in each experiment is expressed as a percent of the weight of reduced dextran. [b] Colloids were not purified by ultrafiltration resulting in slightly larger particle size measurements. [c] Magnetic susceptibility ($\times 10^{-6}$ cgs/g Fe). [d] [Reducing glucose]/[Fe] of native dextran T10 for the conditions as shown in Table 2.

magnetic susceptibility was determined (Table 5). Even the addition of 50 wt % glucose to the reduced dextran T10 had only minimal effect on particle size, resulting in an increase of only 10 nm compared with particles prepared in the absence of glucose. This last addition of glucose represents a greater than 40-fold increase in reducing sugar concentration over that present in the native dextran T10 preparation in Table 1. For comparison, particles prepared with native dextran T10 had a particle size of greater than 700 nm. Evidently, simple elimination of reducing sugar from the reaction solution is not a controlling factor in particle size. The decrease in particle size, improvement in polysaccharide usage, and increased colloid stability must all, therefore, result from introduction of the linear polyol. When present in sufficient concentration; added glucose lowers the magnetic susceptibility of the particles by 1 order of magnitude.

Effect of the Molecular Weight of Reduced Dextrans on Size of USPIO. Because the iron and polysaccharide concentrations varied for the different molecular weight dextrans in obtaining the data shown in Table 2, no conclusion regarding the effect of polymer molecular weight alone on particle formation could be derived from these results. Therefore, the data shown in Table 6 were obtained at a constant concentration by weight of both dextran and iron. The constant concentration by weight for each reduced dextran represents a constant molar concentration of glucose monomeric units but a decreasing concentration of terminal polyol with increase in polymer molecular weight. The results demonstrate an increase in USPIO particle size with an increase in dextran molecular weight. Because these particles were not purified by ultrafiltration somewhat larger sizes are observed than for comparable data in Table 2.

Coating of Magnetic Sol. The preparations of USPIO described thus far have involved formation of the mag-

Table 6. Effect of Molecular Weight of Reduced Dextrans on USPIO Particle Size at a Constant Concentration of Glucose Monomer (0.16 M)

reduced dextran	MW, kDa	MVD,[a] nm	relative particle size	MS[b]
T1	1000	20	1	2903
T5	5000	25	1.25	33058
T10	10000	28	1.40	35377
T70	70000	41	2.05	35768

[a] Colloids were not purified by ultrafiltration resulting in slightly larger particle size measurements. [b] Magnetic susceptibility ($\times 10^{-6}$ cgs/g Fe).

Table 7. Stabilization of Magnetic Sol with Reduced and Native Dextran

dextran	MVD, nm	MID,[a] nm
dextran T1	2590	2903
reduced dextran T1	3791	3791
dextran T5	3174	3173
reduced dextran T5	2953	3073
dextran T10	1973	2018
reduced dextran T10	85.4	135
dextran T70	52.9	255.9
reduced dextran T70	47.9	69.8

[a] MID (mean intensity diameter) has been included because it is weighted toward larger particles and better shows the small but real increase in size on going from reduced dextran T70 to dextran T70.

netic particle by precipitation of the iron salts in the presence of polysaccharide. In this complex system the coating polysaccharide can participate both in the synthesis of the particle and in its ultimate stabilization by acting as a steric repulsion-coating agent. To separate these two functions and allow study of the stabilizing function of the coating polysaccharide alone, USPIO were prepared without a coating agent by precipitation of the iron salts with base (*18*). These magnetic sols are unstable and aggregate at pH greater than 3. Measurement of particle size, after addition of native or reduced dextrans to the magnetic sol and neutralization of the mixture, was used to assess the effectiveness of these polysaccharides to bind to the iron oxide surface (Table 7). Colloidal material could not be obtained with either native or reduced dextran T1, dextran T5, or with native dextran T10. Reduced dextran T10 yielded a colloidal product. For colloidal USPIO prepared with dextran T70, the reduced dextran was slightly more effective at coating the iron oxide surface than native dextran T70.

From consideration of the results presented in Tables 2 and 7, we see that reduced dextrans coat USPIO particles more effectively while present during iron oxide crystal formation compared with coating preexisting iron oxide particles. Whether iron oxide particles are coated with polysaccharide during particle growth or post particle synthesis, the reduced dextran is a more effective coating and steric stabilizing agent than the corresponding native dextran.

DISCUSSION

General Observations. While we are not the first to suggest using reduced polysaccharides for coating USPIO particles (*19*), no reports detail the profound effect this seemingly small change within the polysaccharide polymer (Scheme 1) can have upon resulting particle properties. Four aspects of polysaccharide-coated USPIO particle synthesis were investigated: (i) the effect reduction of the terminal polysaccharide sugar has upon polysaccharide usage, particle size, stability, and magnetic susceptibility; (ii) the effect an exogenous reducing sugar can have upon particle synthesis; (iii) the effect the molecular weight of the reduced polysaccharide has on particle synthesis; and (iv) the effectiveness of reduced and native dextrans in stabilizing a preformed magnetic sol. In this study, we investigated four characterizing aspects of particle formation: particle size, coating efficiency, coating stability, and magnetic properties.

We discovered that a significant decrease in dextran-to-iron ratio could be employed with low molecular weight reduced dextrans to obtain the same particle size with equal or improved magnetic properties relative to the native polymer. Moreover, using reduced polysaccharides increases coating stability as evidenced by the stability of particles to autoclaving. The effect of exogenous reducing sugar on particle size is minimal as shown by addition of high concentrations of glucose to the reaction mixture used in the synthesis of reduced dextran T10-coated USPIO. An inverse relationship between polysaccharide molecular weight and particle size was observed. Finally, reduced dextrans proved to be more effective in coating preformed iron oxide crystals than their corresponding native dextrans.

Our results suggest that the coating polysaccharides are involved in the earliest stages of USPIO formation affecting particle composition and magnetic properties. With low molecular weight reduced dextrans small magnetite crystals are obtained with high magnetic susceptibility. In contrast with low molecular weight native dextrans small particle size can be achieved only at the expense of magnetic properties. This suggests that in these cases the presence or absence of reducing sugar affect crystal growth. In the presence of reducing sugar the transformation of the initially formed ferric and ferrous hydroxides into superparamagnetic magnetite crystals is inhibited. (The identity of these oxides has not been determined.) Further support for the early involvement of the polysaccharide in particle synthesis is the relative inability of the native and reduced dextrans to coat and stabilize preformed magnetite crystals. This decreased effectiveness of polymer to coat oxide demonstrates that polymer is involved early in particle formation and is not limited to determining particle size alone, i.e., to coating completed particles.

Modeling of our data using equations derived from the Langmuir isotherm (see Appendix and Figure 1) indicate that binding of dextran to the iron oxide surface requires two binding events. Data from Table 2 suggests that polyol binding is rate limiting, and modeling suggests that a second internal glucose residue must contact the iron oxide surface to achieve tight and relatively irreversible binding. These conclusions are consistent with previously published observations that multiple sites of attachment are necessary for the noncovalent adsorption of polymer to surfaces (*20*). Modeling further predicts that particle size will increase with increasing molecular weight of the coating polymer. A good fit of the experimental data was found after making corrections for diffusional effects of the polymer.

We are surprised to discover that a seemingly simple change in the terminal sugar of a coating polysaccharide used during USPIO particle formation can have a large effect on polysaccharide usage and particle stability. This result suggests that other modifications of both the terminal and backbone sugars in polysaccharides such as introduction of charged species (e.g., amino and carboxyl groups) will have a profound effect on USPIO particle formation. We have also observed that oxidation of dextran with sodium periodate followed by reduction

by sodium borohydride to introduce open chain alcohols into the polymer chain also increases coating efficiency (*21*). The results observed with reduced polysaccharides as coating agents of USPIO particles may be expected to apply to other metal oxides and minerals and may very well be found to generalize to other surfaces (*22*).

APPENDIX

Langmuir Isotherm Modeling. Our results, particularly the decrease in size of particles obtained in the presence of reduced dextrans of low molecular weight, suggest that polysaccharide exerts a kinetic control over particle synthesis where the terminal, open chain reduced sugar (linear polyol) is more effective than either the reducing or chain sugars in complexing with the iron oxide surface. Two conclusions follow from this suggestion. First, if adsorbed polymer blocks crystal growth and aggregation, then use of polymers that adsorb to the iron oxide surface faster and with greater tenacity should result in smaller particles. Second, as the molecular weight of the dextran increases, the decreasing concentration of linear polyol relative to the chain sugars will minimize the effect the linear polyol has on particle synthesis.

The observations for the reduced and native dextrans described in Tables 3 and 6 can be modeled to fit the Langmuir isotherm for competitive adsorption onto a surface by treating the backbone sugars and terminal open chain polyol as competitive inhibitors to crystal growth. The Langmuir isotherm for competitive gas adsorption onto a surface is expressed in eq 1 (*23*),

$$\nu_x = \frac{k_x p_x}{1 + K_x p_x + \sum K_i p_i} \tag{1}$$

where ν_x is the velocity of adsorption of gas x, k_x is the rate constant for adsorption of x, K_x is the equilibrium constant for adsorption of x, K_i is the equilibrium constant for competitive inhibitor i, p_x is the partial pressure of x, and p_i is the partial pressure for inhibitor i.

Assuming crystal growth is inhibited by the adsorption of backbone glucose monomeric units (G) and either the terminal reducing sugar (R) for the native dextran or the terminal linear polyol (P) of the reduced dextran and ν_x = rate of adsorption of an iron species X (crystal growth); then the expressions for the crystal growth in the presence of native dextran (ν_{ND}) or reduced dextran (ν_{RD}) are given by eqs 2 and 3 by expansion of eq 1 to two terms with appropriate substitutions of X and the growth controlling factors G, R, and P and substituting concentrations for partial pressures,

$$\nu_{ND} = \frac{k_X[X]}{1 + K_X[X] + K_G[G] + K_R[R]} \tag{2}$$

$$\nu_{RD} = \frac{k_x[X]}{1 + K_X[X] + K_G[G] + K_P[P]} \tag{3}$$

where k_x is the rate constant for iron adsorption, K_X is the equilibrium constant for iron adsorption, K_G is the equilibrium constant for glucose adsorption, K_R is the equilibrium constant for terminal reducing sugar adsorption, and K_P is the equilibrium constant for polyol adsorption. In eqs 2 and 3 the glucose monomeric units, terminal reducing sugar and polyol are treated as independent binding species and their concentrations are related by eqs 4−7

$$[M] = \frac{\text{dextran mass/volume}}{MW_G} \tag{4}$$

$$[P] = [R] = \frac{\text{dextran mass/volume}}{MW_D} \tag{5}$$

$$[P] = [R] = [M]\frac{MW_G}{MW_D} \tag{6}$$

$$[G] = [M]\left(1 - \frac{MW_G}{MW_D}\right) \approx [M] \tag{7}$$

where M is the total number of monomeric units as shown in Table 2 including terminal reducing sugar or polyol, MW_G is the molecular weight of a glucose monomeric unit (162), and MW_D is the molecular weight of the dextran. For simplicity the small MW_G/MW_D term in the expression for [G] will be neglected; when included it has no significant effect on the fit to experimental data.

Dividing eq 2 by eq 3 and expressing the inhibitor concentrations in terms of [M] yields eq 8 which defines the relative rates of crystal growth for native and reduced dextrans of identical molecular weights,

$$\frac{\nu_{ND}}{\nu_{RD}} = \frac{1 + K_X[X] + K_G[M] + K_p[M]\frac{MW_G}{MW_D}}{1 + K_X[X] + K_G[M] + K_R[M]\frac{MW_G}{MW_D}} = \frac{\alpha + K_p[M]\frac{MW_G}{MW_D}}{\alpha + K_R[M]\frac{MW_G}{MW_D}} \tag{8}$$

where $\alpha = 1 + K_X[X] + K_G[M]$.

Qualitative analysis of eq 8 shows that as the molecular weight of dextran increases, the ratio of crystal growth rates for the reduced versus native dextran pair decreases and tend to approach a value of 1. As a consequence of increasing polymer molecular weight, the linear polyol concentration becomes so small that its contribution becomes negligible as was observed with the particles prepared with native or reduced dextran T70.

A more quantitative approach may be taken by making the following two assumptions. First, the ratio of the rate of crystal growth ν_x is proportional to the final particle diameter. Second, because the ratio of rates (diameters) for the particles is mathematically very dependent on the MVDs obtained for the small reduced dextran particles where the analytical method has a larger percentage error, we assume a constant small size for the reduced dextran particles. As a result, the particle diameters for the native dextrans (MVD_{ND}) are proportional to the ratio of the rates of crystal growth for native and reduced dextran for a particular polymer molecular weight (eq 9).

$$MVD_{ND} \approx \frac{\nu_{ND}}{\nu_{RD}} \tag{9}$$

Applying these assumptions, a theoretical fit to the experimental data can be calculated by setting α to a constant value. Since any value of α will give the same solution, we set α equal to 1, insert the values for [M] as shown in Table 2, and calculate K_p by an iterative process minimizing the difference between the data and theoretical points. As can be seen in Figure 1, the fit with experimental data is poor. However, as shown in Figure

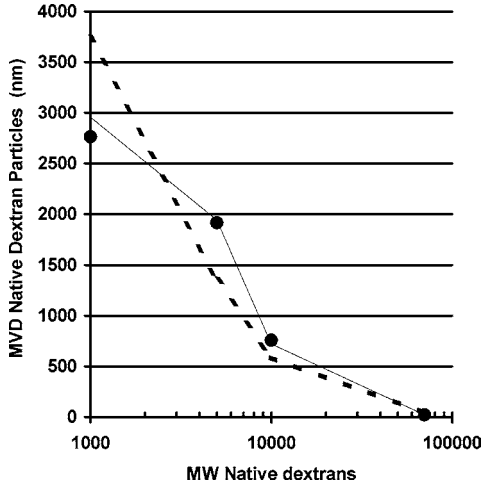


Figure 1. Plot of particle size versus dextran molecular weight; observed data, ● and model data calculated from eq 8 assuming a dependence on [M], - - - -; and $[M]^2$, ——.

1, an excellent fit is obtained if the same iterative process is employed using the values of $[M]^2$ in place of [M]. This can best be explained if it is assumed that simple adsorption of polyol or the reducing sugar is insufficient to form a thermodynamically stable attachment and further adsorption of a second sugar is necessary. Then ν_{RD} is more properly defined as in eq 10 than eq 2 (ν_{ND} is treated the same way). Substituting [P] (or [R] for native dextran) from eq 6 gives eq 11, and eq 8 becomes eq 12, in agreement with experimental data. Since the experimental data gives no information on the number of sugars necessary for stable attachment without involvement of polyol a $[M]^n$ term has been introduced in eq 10. From the values of K_P and K_G determined by fitting the plot a value of K_P/K_G of 1.3×10^9 was determined. The actual values of K_P and K_G are dependent on the true value of α; however, their ratio is independent of α. This large value may be the result of two factors: first, the inherent increased binding strength of the polyol, and second, that in the case of the reducing sugar, two or more additional sugars in the chain must bind to obtain a thermodynamically stable attachment; i.e., the reaction order shown in eq 13 is greater than 2 and K_G as shown includes additional concentration terms [M]

$$\nu_{RD} = \frac{k_X[X]}{1 + K_X[X] + K_G[G]^n + K_P[P][G]} \quad (10)$$

$$[P][G] = [M]^2\frac{MW_G}{MW_D}\left(1 - \frac{MW_G}{MW_D}\right) \approx [M]^2\frac{MW_G}{MW_D} \quad (11)$$

$$\frac{\nu_{ND}}{\nu_{RD}} = \frac{1 + K_X[X] + K_G[M]^n + K_P[M]^2\frac{MW_G}{MW_D}}{1 + K_X[X] + K_G[M]^n + K_R[M]^2\frac{MW_G}{MW_D}} = \frac{\alpha + K_P[M]\frac{MW_G}{MW_D}}{\alpha + K_R[M]\frac{MW_G}{MW_D}} \quad (12)$$

where $\alpha = 1 + K_X[X] + K_G[M]^n$.

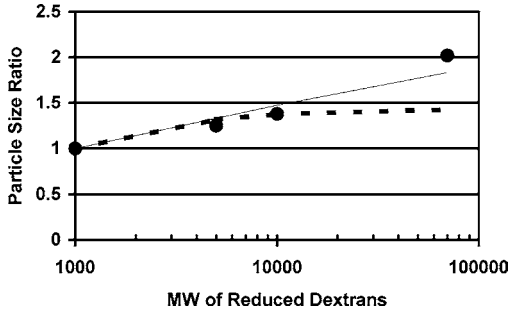


Figure 2. Plot of relative particle size versus reduced dextran molecular weight; observed data, ●, and model data calculated from eq 12, - - - -, or eq 13,——. Particle size ratio is particle size relative to the reduced T1-coated particle from Table 6.

Our model can also be used to predict the observed effect of polymer molecular weight for a series of reduced dextrans on particle size as shown in Table 6. In this case, we are comparing the formation of two particles prepared with reduced dextrans of different molecular weight at identical concentrations of glucose monomer, [M]. Equation 13 is obtained by dividing eq(s) 8 (expanded for multiple attachments as in eq 13) for reduced dextrans of different molecular weights ($\nu_{RD1} = MW_{D1}$, $\nu_{RD2} = MW_{D2}$). In this case, the concentration related terms for each molecular weight dextran are equal resulting in an expression dependent only on MW

$$\frac{\nu_{RD2}}{\nu_{RD1}} = \frac{1 + K_X[X] + K_G[M]^n + K_P[M]^2\frac{MW_G}{MW_{D1}}}{1 + K_X[X] + K_G[M]^n + K_P[M]^2\frac{MW_G}{MW_{D2}}} = \frac{\alpha + K_P[M]\frac{MW_G}{MW_{D1}}}{\alpha + K_P[M]\frac{MW_G}{MW_{D2}}} \quad (13)$$

where

$$\alpha = \frac{1 + K_X[X] + K_G[M]^n}{K_P[M]^2}$$

As with eq 7 a value for α can be determined to give a best fit to experimental data. The comparison of the theoretical plot versus the experimental results is shown in Figure 2. Qualitatively, the results agree with the experimental data showing an increase in particle size associated with an increase in polymer molecular weight. The theoretical plot predicts that as the particle size increases a maximum will be reached as the polyol concentration becomes negligible. The unexpectedly large size obtained for the particle prepared with dextran T70 compared to the predicted value is probably the result of a diffusion term in K_G and K_P making these values molecular weight dependent. Since the rate of diffusion is proportional to $MW^{-1/3}$, an approximation for this effect can be introduced as shown in eq 14. The improved correlation with the experimental data is also shown in Figure 2.

$$\frac{\nu_{RD2}}{\nu_{RD1}} = \frac{1 + K_X[X] + K_G\frac{[M]^n}{MW_{D1}^{1/3}} + K_P[M]^2\frac{MW_G}{MW_{D1}^{4/3}}}{1 + K_X[X] + K_G\frac{[M]^n}{MW_{D2}^{1/3}} + K_P[M]^2\frac{MW_G}{MW_{D2}^{4/3}}} = \frac{\alpha + \frac{\beta}{MW_{D1}^{1/3}} + \frac{1}{MW_{D1}^{4/3}}}{\alpha + \frac{\beta}{MW_{D2}^{1/3}} + \frac{1}{MW_{D2}^{4/3}}} \quad (14)$$

where

$$\alpha = \frac{1 + K_X[X]}{K_P[M]^2 \times MW_G}, \beta = \frac{K_G[M]^{n-2}}{K_P \times MW_G}$$

LITERATURE CITED

(1) Weissleder, R., Elizondo, G., Wittenberg, J., Rabito, C. A., Bengele, H. H., and Josephson, L. (1990) Ultrasmall superparamagnetic iron oxide: characterization of a new class of contrast agents for MR imaging. *Radiology 175*, 489−493

(2) Jung, C. W., and Jacobs, P. (1995) Physical and chemical properties of superparamagnetic iron oxide MR constrast agents: ferumoxides, ferumoxtran, ferumoxsil. *Magn. Reson. Imag. 13* (5), 661−674.

(3) Hasegawa, M., Hanaichi, T., Shoji, H., Kawaguchi, T., and Maruno, S. (1998) Biological behavior of dextran-iron oxide magnetic fluid injected intravenously in rats. *Jpn. J. App. Phys., Part 1 37* (3A), 1029−1032.

(4) Anzai, Y., Prince, M. R., Chenervert, T. L., Maki, J. H., Londy, F., London, M., and McLachlan, S. J. (1997) MR angiography with an ultrasmall superparamagnetic iron oxide blood pool agent. *J Magn. Reson. Imag. 7* (1), 209−214.

(5) Mühler, A., Zhang, X., Wang, H., Lawaczeck, R., and Weinmann, H−J. (1995) Investigation of mechanisms influencing the accumulation of ultrasmall superparamagnetic iron oxide particles in lymph nodes. *Invest. Radiol. 30*, 98−103.

(6) Bellin, M. F., Roy, C., Kinkel, K., Thoumas, D., Zaim, S., Vanel, D., Tuchmann, C., Richard, F., Jacqmin, D., Delcourt, A., Challier, E., Lebret, T., and Cluzel, P. (1998) Lymph node metastases: safety and effectiveness of MR imaging with ultrasmall superparamagnetic iron oxide particles—initial clinical experience. *Radiology 207* (3), 799−808.

(7) Shen, T. T., Bogdanov, A., Jr., Bogdanova, A., Poss, K., Brady, T. J., and Weissleder, R. (1996) Magnetically labeled secretin retains receptor affinity to pancreas acinar cells. *Bioconjugate Chem. 7* (3), 311−316.

(8) Weissleder, R., Lee, A. S., Fischman, A. J., Reimer, P., Shen, T., Wilkenson, R., Callahan, R. J., and Brady, T. J. (1991) Polyclonal human immunoglobulin G Labeled with Polymeric Iron Oxide: antibody MR imaging. *Radiology 181* (1), 245−249.

(9) Devineni, D., Blanton, C. D., and Gallo, J. M. Preparation and in vivo evaluation of magnetic microsphere-methotrexate conjugate drug delivery systems. (1995) *Bioconjugate Chem. 6*, 203−210

(10) Jordan, A., Scoltz, R., Fähling, H., Krause, J., Konstanczak, P., Woldarzyk, W., Sander, B., Vogl, T., and Felix, R. (1996) Effects of magnetic fluid hyperthemia (MFH) on C3H mammary carcinoma in vivo. *Int. J. Hyperthemia 6*, 1−20.

(11) Autenshlysus, A. I., Bruesentov, N. A., and Lockshin, A. (1993) *J. Magn. Mater. 122*, 360−363.

(12) Schütt, W., Grüttner, C., Häfeli, U., Zborowski, M., Teller, J., Putzar, H., and Schümichen, C. (1997) Applications of Magnetic Targeting in Diagnosis and Therapy—Possibilities and Limitations: A Mini-Review. *Hybridoma 16*, 109−117.

(13) Kresse, M., Wagner, S., Pfefferer, D., Lawaczeck, R., Elste, V., and Semmler, W. (1998) Targeting of ultrasmall superparamagnetic iron oxide particles to tumor cells in vivo by using transferrin receptor pathways. *Magn. Reson. Med. 40*, 236−242.

(14) Kumar, K. (1997) Iron assay and size exclusion high performance liquid chromatography of ferritin and magnetoferritin. *J. Liq. Chromatogr. Relat. Technol. 20*, 3351−3364.

(15) Jue, C. K., and Lipke, P. N. (1985) Determination of reducing sugars in the nanomole range with tetrazolium blue. *J. Biochem. Biophys. Methods 11*, 109−115.

(16) Kitchen, R. (1983), Total polysaccharide test and quantitative method for dextran analysis. *Proc. Sugar Process. Res. Conf.* 232−247.

(17) Gyozo, B. (1974) *Organic Chemistry. Amino Acids, Peptides and Carbohydrates*, p 991, Tankonykiado Press, Budapest.

(18) Hasagawa, M. et al. (1995) U.S. Patent 5,424,419.

(19) Herb, J. R. (1977) U.S. Patent 4,180,567.

(20) Hlady, V., Lykelema, J., and Fleer, G. J. (1982) Effect of polydispersity on the adsorption of dextran on silver iodide. *J. Colloid Interace Sci. 87*, 395−406.

(21) Gulyas, G., unpublished results from Advanced Magnetics, Inc.

(22) Tadros, Th. F. (1982) *Polymer Adsorption and Dispersion Stability. The Effect of Polymers on Dispersion Properties* (Th. F. Tadros, Ed.) pp 1−38, Academic Press, New York.

(23) Laidler, K. (1965) *Chemical Kinetics*, pp 267−269, McGraw-Hill Book Company, New York.

BC034194U

O^6-3-[^{131}I]iodobenzylguanine: Improved Synthesis and Further Evaluation of a Potential Agent for Imaging of Alkylguanine-DNA Alkyltransferase

Ganesan Vaidyanathan,*,† Donna J. Affleck,† Joseph Norman,† Phil Welsh,† Wenge Liu,‡ Stewart P. Johnson,§ Henry S. Friedman,|| and Michael R. Zalutsky†

Departments of Radiology, Biomedical Engineering, Pediatrics, Surgery, and Medicine, Duke University Medical Center, Durham, North Carolina 27710. Received October 27, 2003; Revised Manuscript Received January 28, 2004

O^6-Benzylguanine derivatives with suitable radionuclides attached to the benzyl ring are potentially useful in the noninvasive imaging of the DNA repair protein, alkylguanine-DNA alkyltransferase (AGT). Previously, O^6-3-[^{131}I]iodobenzylguanine ([^{131}I]IBG) was prepared using a two-step approach; we now report its synthesis in a single step by the radioiododestannylation of O^6-3-(trimethylstannyl)-benzylguanine in 85−95% radiochemical yield. The in vitro specific uptake of [^{131}I]IBG in DAOY human medulloblastoma cells, in TE-671 human rhabdomyosarcoma cells and a CHO cell line transfected to express AGT was linear (r^2 = 0.9−1.0) as a function of cell density. After intravenous injection of [^{131}I]IBG in athymic mice bearing TE-671 xenografts, tumor uptake was 1.38 ± 0.34% ID/g at 0.5 h and declined at 2 and 4 h. Preadministration of O^6-(3-iodobenzyl)guanine (IBG) at 0.5 h increased uptake not only in tumor but also in several normal tissues. Notable exceptions were thyroid (p < 0.05), lung (p <0.05) and stomach. After intratumoral injection of [^{131}I]IBG in the same xenograft model, the uptake in tumors that were depleted of AGT by BG treatment (165.8 ± 27.5% ID/g) was about 60% of that in control mice (272.4 ± 48.2% ID/g; p < 0.05).

INTRODUCTION

The cytotoxicity of alkylating chemotherapeutic agents stems primarily from their ability to alkylate DNA guanine residues at their O^6-position, which in turn triggers a cascade of events ultimately resulting in DNA strand breaks (*1*). Although a number of other factors are involved, drug resistance in alkylator chemotherapy is often mediated by the role played by the DNA repair protein, alkylguanine-DNA alkyltransferase (AGT) (*2*, *3*). This protein transfers alkyl groups such as methyl, ethyl, benzyl, or pyridyloxybutyl from the O^6-position of the guanine residues in DNA to the Cys-145 residue in its active site in a suicidal manner. The alkylated protein is ubiquitinated and undergoes degradation, and its recovery is entirely from de novo synthesis (*4*). The ability of tumor cells to be resistant to the toxic effects of alkylating agents is thus dependent on cellular AGT levels; the higher the AGT content, the less effective will be the cytotoxicity by alkylator therapy. It is highly imperative, therefore, to determine the cellular AGT content in tumor cells in order to compensate for the AGT-mediated repair process, or select alternative therapies that will not be compromised by elevated AGT levels.

Methods currently exist for quantifying AGT (*5*−*7*); however, these techniques are performed in vitro or ex vivo and therefore necessitate that tumor samples be obtained by invasive procedures. A method to assay AGT by a noninvasive means in individual patients would greatly enhance proper therapy planning. Because O^6-benzylguanine (BG) is a substrate of AGT (*8*), it might be possible to radiolabel AGT in vivo by administering a suitable BG analogue substituted with radionuclides such as ^{18}F or $^{124/123}$I on its benzyl moiety.

With regard to currently available potential radiolabeled AGT probes, the preparation of ^{125}I-labeled guanosine derivatives has been reported but their usefulness as an AGT labeling agents was not evaluated (*9*). A ^{14}C-labeled guanosine derivative (*10*) and a BG derivative labeled with ^{3}H (*11*) also have been described; however, it is not practical to perform external imaging of these radionuclides. More recently, the synthesis of several BG derivatives labeled with ^{11}C and ^{18}F have been reported but the in vivo behavior of these tracers has largely been unexplored (*12*−*17*).

The efforts of our group in developing a radioligand for monitoring AGT have involved the synthesis and preliminary evaluation of O^6-4-[^{18}F]fluorobenzylguanine ([^{18}F]FBG) and O^6-3-[^{131}I]iodobenzylguanine ([^{131}I]IBG) (*18*). The ability of unlabeled IBG and FBG to deplete AGT in CHO cells transfected with AGT was similar to that of BG and the labeled compounds bound specifically to pure AGT. The labeled IBG was prepared, by first radioiodinating O^6-3-(trimethylstannyl)benzyl-N^9-(trimethylsilyl)ethoxymethylguanine (SEM-TMSBG) and subsequently removing the SEM group of the intermediate product. In this paper, we describe the synthesis of O^6-3-(trimethylstannyl)benzylguanine and its conversion to [^{131}I]IBG in a single step. Moreover, we have evaluated further the potential of this compound for imaging by performing additional in vitro assays and by determining its biodistribution in a murine xenograft model.

* To whom correspondence should be addressed. Ganesan Vaidyanathan, Ph.D., Box 3808, Department of Radiology, Duke University Medical Center, Durham, NC 27710. Tel: (919) 684-7811. Fax: (919) 684-7122. E-mail: ganesan.v@duke.edu.

† Department of Radiology.

‡ Department of Biomedical Engineering.

§ Department of Pediatrics.

|| Department of Medicine.

⊥ Department of Surgery.

10.1021/bc0341977 CCC: $27.50 © 2004 American Chemical Society
Published on Web 02/20/2004

EXPERIMENTAL SECTION

General. All chemicals were purchased from Aldrich Chemical Co. except as noted. O^6-(3-Iodobenzyl)guanine was prepared as reported before (*18*). Sodium [^{131}I]iodide in 0.1 N NaOH was supplied by Perkin-Elmer Life Sciences (North Billerica, MA).

High-pressure liquid chromatography (HPLC) was performed using one of two systems: (1) a Beckman System Gold HPLC equipped with a Model 126 programmable solvent module, a Model 168 diode array detector, a Model 170 radioisotope detector, and a Model 406 analog interface module; or (2) a Beckman System Gold HPLC equipped with a Model 126 programmable solvent module, a Model 166 NM variable wavelength detector, a Model 170 radioisotope detector, and a Beckman System Gold remote interface module SS420X; the data was acquired using a 32 karat software. Normal-phase HPLC was performed using a 4.6 × 250 mm Partisil (10 μm) column (Alltech, Deerfield, IL). Analytical TLC was performed on aluminum-backed sheets (Silica gel 60 F_{254}), and normal-phase column chromatography was performed using Silica gel 60, both obtained from EM Science (Gibbstown, NJ). Column chromatography fractions were collected using a ISCO Foxy 200 fraction collector (Lincoln, NE) with an ISCO UA-6 UV−Vis detector placed between the column outlet and the fraction collector to identify fractions. The homogeneity of fraction composition was verified by TLC. Preparative thick layer chromatography was performed using 20 × 20 cm, 1000 μm plates (Whatman, Clifton, NJ). Before applying the sample, the plates were run in ethyl acetate to clean the plates of any adsorbed impurities. Radio-TLC was initially analyzed using a System 200 Imaging Scanner (BioScan, Washington, D.C.) and then cut into strips and counted using an automatic gamma counter (LKB 1282, Wallac, Finland). NMR spectra (^{1}H-300 MHz) were obtained on a Varian Mercury 300 spectrometer. Chemical shifts are reported in δ units; solvent peaks were referenced appropriately. Mass spectra were obtained on a JEOL SX-102 high-resolution mass spectrometer.

***O*^{6}-3-(Trimethylstannyl)benzylguanine (TMS-BG).** Dichlorobis(triphenylphosphine)palladium (50 mg, 0.07 mmol) was added to a mixture of IBG (84 mg, 0.23 mmol), hexamethylditin (820 mg, 2.5 mmol), and 5 mL of anhydrous dioxane in a dry, argon-purged flask. The flask was heated in an oil bath at 100 °C for 1−2 h. Dioxane was evaporated, and the residue was applied to a bed of silica gel containing fluorescent indicator in a frit funnel with a quartz body. The most nonpolar components were eluted out using hexane, and the required product and other polar impurities were eluted from the bed with 5% (v/v) methanol in ethyl acetate. A UV lamp was used to visualize the bands. The latter fractions were concentrated and the required product was isolated from this crude mixture as an oil (80 mg; 86%) by silica gel chromatography using 0−5% methanol in ethyl acetate. ^{1}H NMR (CD_3OD) 0.27 (s, 9H [^{119}Sn−H, d]), 5.53 (s, 2H), 7.33 (t, 1H), 7.44 (m, 2H), 7.61 (s, 1H), 7.83 (s, 1H). MS (FAB$^+$) *m/z*: cluster peaks around 406 (MH^+), 390. HRMS (FAB$^+$) calcd for $C_{15}H_{20}N_5O^{116}Sn$ (MH^+) 406.0690. Found 406.0693 ± 0.0012.

***O*^{6}-3-[^{131}I]Iodobenzylguanine.** A solution of TMS-BG in methanol (0.2 mg in 50 μL) was taken in a half-dram vial and the methanol evaporated with argon. To this was added ^{131}I (1−2 mCi in 1−3 μL 0.1 N NaOH) followed by 10 μL of 3:1 (v/v) mixture of acetic acid and 30% (w/v) hydrogen peroxide. The mixture was sonicated for 1 min and injected into a normal phase HPLC column eluted isocratically with 2% MeOH in EtOAc at 1 mL per min. The product (t_R = 13 min) was isolated in 85−95% radiochemical yield. Quality control HPLC has shown a single radioactive peak with no UV peaks, suggesting more than 99% chemical and radiochemical purity. In the preparative runs, a small coeluting peak has been observed. From comparison with HPLC of IBG standards, a specific activity of 200 Ci/mmol has been achieved to date. For biological assays, the solvents were evaporated from the HPLC fractions and resolubilizing the residual activity in PBS or tissue culture medium. While this process takes only 5−10 min with about 5% loss of radioactivity, the tracer is not very soluble in aqueous buffers. However, sufficient quantities can be solubilized in PBS for using it in biological assays.

In Vitro Uptake of [^{131}I]IBG as a Function of Cell Concentration. (*A) TE−671 and DAOY Cells*. The uptake of [^{131}I]IBG in TE-671 human rhabdomyosarcoma and DAOY human medulloblastoma cell lines (*19*) was measured at three different cell concentrations. About 100 nCi of nca [^{131}I]IBG was incubated in quadruplicate for 30 min at 37 °C with these two cell lines in a 96-well plate having filters at densities of (1.25, 2.5, and 5) × 10^5 cells per well in 0.3 mL of zinc option media. To determine nonspecific binding, the cells were preincubated with 25 μM BG for 10 min. At the end of incubation, the plate was placed on a vacuum manifold to remove media. Each well was washed twice with 0.25 mL of ice-cold buffer and dried overnight. The filters were removed using a punch apparatus and counted for ^{131}I activity.

(B) B4 CHO Cells Transfected To Express AGT. CHO-K1 cells were grown in α-MEM supplemented with 10% fetal bovine serum. Cells were transfected with pCMV-Neo-Bam or pCMV-AGT (*20*; obtained from Professor A. E. Pegg, Hershey Medical Center, Pennsylvania State University) using the FuGene 6 transfection reagent (Roche Applied Science). After 2 days of culture, transfectants were selected by the addition of 0.5 mg/mL Geneticin (Invitrogen). Clones were isolated by picking resistant foci.

B4 CHO cells were plated at densities of (6.25, 12.5, 25, and 50) × 10^4 per 3 mL medium/well in six-well plates. After 24 h at 37 °C, the medium was removed and supplemented with 1 mL of fresh medium (α-MEM with L-glutamine and without ribonucleosides, deoxynucleosides, and FBS), with or without 25 μM BG, and the cells were incubated for 4 h at 37 °C. Subsequently, 25 nCi of [^{131}I]IBG was added to all wells in 5−10 μL of the medium and the cells were allowed to take up the tracer for 2 h at 37 °C. After removing unbound radioactivity, the cells were solubilized by incubation with 0.5 N NaOH overnight at 37 °C and harvested with cotton swabs. The cell-associated radioactivity was counted using a gamma counter.

Biodistribution of [^{131}I]IBG in Mice Bearing TE−671 Rhabdomyosarcoma Xenografts. Animal studies were performed under the guidelines established by the Duke University Institutional Animal Care and Use Committee. Athymic mice were obtained from a closed breeding colony maintained at the Duke University Cancer Center Isolation Facility. Age- and sex-matched BALB/c *nu/nu* mice weighing 25−30 g were utilized in these studies. TE-671 human rhabdomyosarcoma xenografts were established as reported (*21*). Briefly, (1−4) × 10^8 TE-671 cells in 1−4 mL of zinc option minimal essential medium were inoculated subcutaneously in the right flank of mice. Tumors were allowed to grow and

then removed from animals after killing them by cervical dislocation. Tumor homogenate was prepared by first passing tumor fragments through a bilayered 20-mesh screen in a tissue press and then passing them consecutively through smaller gauge needles. Thirty microliters of the tumor homogenate was inoculated with a 19-gauge needle into the right flank of recipient mice. Subcutaneous tumors were measured periodically until they reached a volume of 250−500 mm^3.

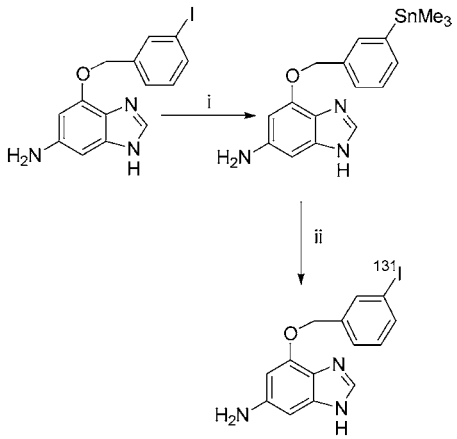
(A) Intravenous Administration. Three groups of five mice were administered nca [^{131}I]IBG (2 μCi/100 μL PBS/mouse) via the tail vein. Mice were killed by an overdose of halothane at 0.5, 2, and 4 h after injection of the tracer. Tissues of interest were isolated, blot-dried, weighed, and counted for radioactivity, along with injection standards, using an automated gamma counter. The uptake in each tissue was expressed as percent of injected dose per gram of tissue (%ID/g). To determine the effect of unlabeled IBG on tissue distribution, another group was pretreated with the unlabeled compound (0.22 mg/100 μL/mouse; 8 mg/kg; iv) 30 min before injecting the tracer and then killed 30 min thereafter. Preliminary studies with ^{18}F-labeled BG showed maximum tumor uptake at 30 min postinjection (unpublished results). It was expected that AGT will be depleted to a maximum extent 30 min after iv administration of unlabeled IBG. The dose of IBG for this experiment was prepared by dissolving it in a 3:1 (v/v) mixture of Cremophor-EL (Sigma) and DMSO (22.2 mg/mL) and diluting it 10 times with PBS. The statistical significance of differences of uptake in various tissues between the two 0.5 h groups was calculated using an unpaired Student's *t* test. A *p* value of less than 0.05 was considered to be statistically significant.

(B) Intratumoral Administration. Using the same xenografts model, a group of five mice were administered BG (1.5 mg BG in 300 μL of 40% PEG 400/PBS; 60−75 mg/kg) ip 1 h prior to injection of [^{131}I]IBG in order to deplete tumor AGT content. A second group of five mice received just the vehicle. One hour later, all mice were injected with about 1 μCi of no-carrier-added [^{131}I]IBG in 5 μL of PBS by the intratumoral route. The 1 h duration was chosen based on the fact that in mice bearing D456 intracranial glioma tumor or A549 lung tumor, tumor AGT levels were reduced to 50% and 20%, respectively 1 h after intraperitoneal injection of BG in PEG/saline vehicle (*22*). Mice were killed 30 min later, and the uptake of radioactivity in tumor and normal tissues was determined.

RESULTS AND DISCUSSION

With the goal of developing a tracer that could be used for the noninvasive mapping of AGT levels, several laboratories including our own have undertaken the synthesis of radiolabeled derivatives of BG based on the fact that BG is the prototypical AGT depleting agent. Earlier, we described a method for the synthesis of [^{131}I]-IBG involving two radiochemical steps (*18*). Our attempts to synthesize a tin derivative of 4-bromobenzylguanine, from which radioiodinated 4-IBG could have been generated in a single step, were not successful. It was reasoned that this might be due to the poor solubility of the bromobenzylguanine in dioxane, the solvent used for the stannylation reaction. We assumed that the same problem would be encountered with the 3-iodo derivative; therefore, we introduced a protecting group at the N^9-position to increase the solubility of 3-IBG and to make the synthetic manipulations more facile. This necessitated the use of an additional step in removing this protecting group after radioiodination. It is highly desirable that the synthesis of radiolabeled compounds be performed via a single, fast and high yielding step. To achieve this goal for [^{131}I]IBG preparation, we now have succeeded in synthesizing O^6-3-(trimethylstannyl)benzylguanine from IBG via a modified Stille coupling (*23*). It was possible to convert this tin derivative to [^{131}I]IBG in about 90% radiochemical yield in a reaction time of only 1 min (Scheme 1).

Scheme 1 [a]



[a] Reagents and conditions: (i) Hexamethyl ditin, $(Ph_3P)_2PdCl_2$, dioxane. (ii) ^{131}I, H_2O_2, HOAc, sonicate.

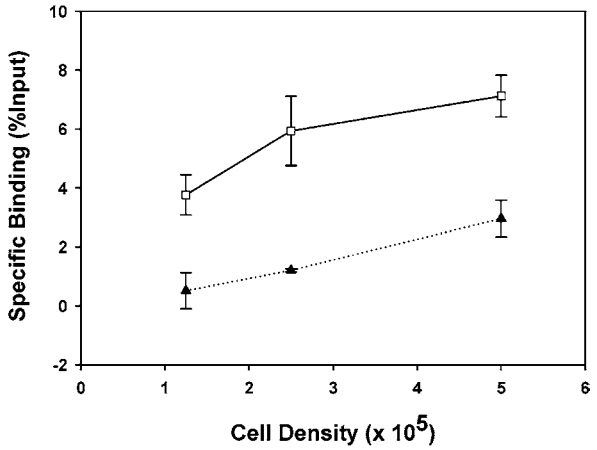


Figure 1. Cell density-dependent binding of [^{131}I]IBG to DAOY (□) and to TE-671 (▲) cells: Cells at various densities were incubated with [^{131}I]IBG in the absence or presence of 25 μM BG. Results expressed are specific binding values (difference between total and that in the presence of BG).

Our ultimate objective is to quantify AGT in tumor cells, and therefore it is imperative to demonstrate that labeled BG analogues bind to tumor cells proportionate to their AGT content. To investigate this, the specific binding of [^{131}I]IBG to two cell lines that are known to contain AGT was determined as a function of cell density. As shown in Figure 1, the specific binding of [^{131}I]IBG increased as a function of cell density in both cases, and although only three cell densities were studied in this preliminary experiment, no saturation of binding was observed. A good correlation was seen between the tracer uptake and cell density with each cell line; the r^2 values were 0.88 and 1.00 for DAOY and TE-671 cells, respectively. The percent specific binding for DAOY was higher than that for TE-671. Although we did not estimate the AGT content of these cells, typical literature values for DAOY and TE-671 cells are about 350 (*24*) and 100 fmol/mg protein (*25*), respectively. The relative uptake of [^{131}I]-

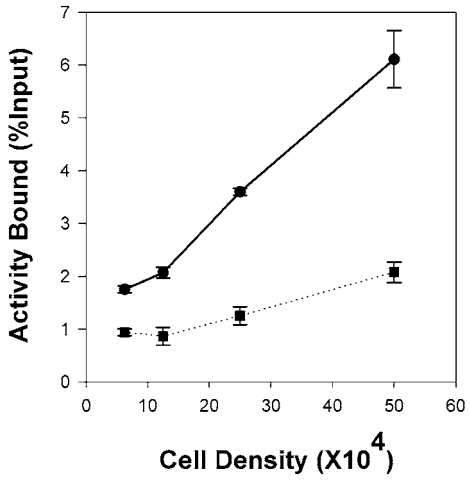


Figure 2. Total (●) and nonspecific binding (■) of [^{131}I]IBG to B4 CHO cells transfected with AGT. Cells were pretreated with 25 μM BG 4 h before adding the tracer to determine the nonspecific binding.

IBG uptake in these two cell lines was reasonably consistent with these values. It should be pointed out that a considerable amount of nonspecific binding (up to 67% of total binding values) was seen with both cell lines at all cell densities.

We also studied the cell-density-dependent uptake of [^{131}I]IBG using a CHO cell line transfected to express AGT. As shown in Figure 2, the cell line B4 demonstrated a linear increase ($r^2 = 1.0$) in cell-bound radioactivity with increasing cell density, and the total-to-nonspecific binding ratios were higher than that seen for DAOY and TE-671 cells.

The nonspecific binding seen in the above assays was rather high. A possible reason for this in the case of DAOY and TE-671 cells may be that the cells were preincubated with 25 μM BG only for 10 min before the addition of the tracer. We chose this time based on the fact that the AGT levels of HT 29 human colon carcinoma cells were reduced to 10% of the original level when incubated for 10 min with 2.5 μM BG (*26*). However, in the case of CHO cells, we did pretreat the cells for 4 h. This was done because a number of studies in the literature have used a 4 h incubation time when determining the potency of newer BG analogues. Even with the 4 h pretreatment, 34−54% of nonspecific binding was observed. Besides the above methodological considerations, the high nonspecific binding also may be due to factors including lipophilicity and metabolic degradation (loss of radionuclide-carrying benzyl group) of [^{131}I]IBG, or binding of [^{131}I]IBG to other proteins. AGT is located in the nuclei of the cells (*27*, *28*) and it is necessary that the labeled BG analogues reach the nuclei intact before it can react with the AGT. Thus, cellular transport may be another factor. Cellular transport of oligodeoxynucleotides has been shown to be a major obstacle for their inhibition of telomerase activity (*29*). Also, 8-[^{3}H]-O^6-benzylguanine was more rapidly distributed to the tumor in vivo when administered in a poly(ethylene glycol) vehicle than in Cremophor-EL (*30*). It has been suggested that the ability of BG analogues to react with AGT in cells may be influenced by their ability to pass through cell membranes and on their metabolism (*31*). If this process plays the primary role in determining cell uptake and retention of IBG analogues, then it may be difficult to use these molecules for measuring AGT in tumor cells. On the other hand, it may be possible to achieve higher specific binding by modifying the structure of labeled BG analogues in such a way that they will be less lipophilic and less susceptible to metabolism. The N^9-position of BG is a potentially valuable site for such modifications (*31*, *32*).

Table 1. Tissue Distribution of ^{131}I in Nude Mice Hosting TE-671 Human Rhabdomyosarcoma Xenografts after Administration of nca [^{131}I]IBG

	%ID/g (mean ± SD; $n = 5$)			
tissue	0.5 h (−IBG)	0.5 h (+IBG)	2 h	4 h
liver	5.80 ± 2.48	9.54 ± 1.67[b]	2.17 ± 0.73	2.37 ± 0.87
spleen	1.86 ± 0.42	2.46 ± 0.90	1.02 ± 0.31	0.85 ± 0.21
lungs	4.44 ± 0.88	2.76 ± 1.37[b]	2.17 ± 1.09	2.34 ± 0.35
heart	1.42 ± 0.23	4.04 ± 1.40[b]	0.56 ± 0.17	0.66 ± 0.25
kidneys	2.24 ± 0.34	5.90 ± 1.53[b]	0.87 ± 0.20	0.82 ± 0.25
stomach	18.29 ± 5.36	12.78 ± 4.36	6.65 ± 2.76	16.23 ± 4.23
sm. int.	18.67 ± 3.05	20.48 ± 1.39	3.19 ± 0.90	2.56 ± 1.11
lg. int.	1.51 ± 0.23	3.16 ± 0.60[b]	26.03 ± 2.18	18.96 ± 2.59
thyroid[a]	0.60 ± 0.12	0.18 ± 0.03[b]	1.66 ± 0.45	2.16 ± 0.77
muscle	0.65 ± 0.14	1.35 ± 0.43	0.26 ± 0.08	0.29 ± 0.08
blood	2.72 ± 0.40	2.81 ± 0.59	1.13 ± 0.45	1.20 ± 0.35
tumor	**1.38 ± 0.34**	**1.94 ± 0.39**[b]	**0.47 ± 0.14**	**0.73 ± 0.57**

[a] %ID/organ. [b] Difference between the values at 0.5 h for pretreated and nonpretreated groups are statistically significant ($p < 0.05$).

Yet another reason for the observed higher nonspecific binding in the case of CHO cells might be the incomplete inhibition of AGT as a result of faster cell growth especially because an incubation time of 4 h was used. A doubling time of 19 h has been reported for a CHO line transfected with pSV2dhfr plasmid (*33*). We obtained a doubling time of 14 h for the B4-CHO cells used in our study following a protocol similar to that utilized by the above authors. Thus, it is unlikely that the cells must have multiplied to a considerable degree during this incubation period. On the other hand, the cells may not divide normally when AGT is inhibited. At a concentration of 100 μM, BG is known to arrest 70% of CHO cells in G_1 phase of the cell cycle (*34*). In our laboratories, various cells were routinely maintained at 10 μM BG, and no such effect was seen (unpublished results). A study using P19 embryonic carcinoma cells has shown that their growth and differentiation is not affected by BG at concentrations of 5 and 10 μM whereas slight effects were seen (decrease of <5% of control) at concentrations of 25 μM; significant effects were seen only at 100 μM of BG (*35*).

Then again, the higher nonspecific binding may be simply due to the fact that the concentration of BG (25 μM) that was used to deplete AGT was insufficient, especially at the higher cell densities. While IC_{50} values to deplete AGT from CHO cells were 50 nM and 15 nM for FBG and IBG, respectively, the concentration of IBG and FBG necessary to reduce the binding of their respective labeled derivatives to pure AGT to 50% of control values was in the micromolar range (*18*). Although the IC_{50} values for depleting AGT by BG decreases in the order of pure AGT, cell-free extracts, and intact cells (*31*), it is necessary to establish the concentration of BG needed to reduce the binding of labeled BG derivatives to AGT present in intact cells to a nonspecific level for each individual cell line. This work is currently in progress.

The biodistribution of [^{131}I]IBG was first measured after iv administration in athymic mice bearing subcutaneous TE-671 rhabdomyosarcoma xenografts, and the results are summarized in the Table 1. The distribution pattern in tumor and normal tissues was somewhat similar to that reported for 8-[^{3}H]-O^6-benzylguanine (8-[^{3}H]BG) in athymic mice bearing D456 MG human

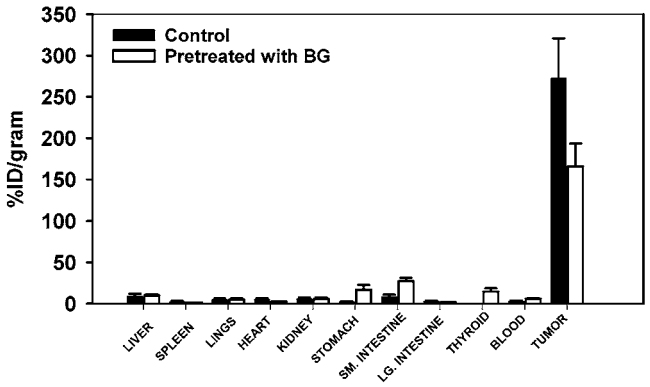


Figure 3. Radioiodine uptake in tumor and selected tissues 0.5 h after intratumoral injection of [^{131}I]IBG in athymic mice hosting TE-671 rhabdomyosarcoma xenografts ($n = 5$).

glioblastoma multiforme xenografts and that for [^{14}C]-O^6-benzyl-*N*-acetylguanosine ([^{14}C]BNAG; label at the benzylic carbon) in nude mice bearing M4Beu human melanoma xenografts (*30*, *36*). A majority of the activity was cleared rapidly via urine. Tumor uptake was 1.38 ± 0.34% ID/g at 0.5 h and decreased at 2 and 4 h. Preadministration of unlabeled IBG 30 min prior to the labeled molecule increased the uptake of radioiodine at 0.5 h postinjection not only in tumor but also in a number of other normal tissues. Notable exceptions were thyroid ($p < 0.05$), lung ($p < 0.05$), and stomach. We speculate that the increase in the uptake in some tissues when unlabeled IBG was preadministered may be due to two processes. First, a higher concentration of IBG may enhance transfer of label to AGT, as the transfer of alkyl groups to AGT follows a second-order kinetics (*37*, *38*). Substantially higher concentrations of unlabeled IBG may be needed to have saturation effects. Second, the presence of unlabeled IBG decreased the rate of dehalogenation of the labeled IBG as reflected in the lower uptake of radioactivity in thyroid and stomach. High uptake of activity in normal tissues, especially liver and intestine, is not surprising due to the fact that a number of human, rat, and mouse tissues including liver and intestines contain a significant amount of AGT (*39*). Other labeled BG derivatives whose biodistribution has been studied also have exhibited relatively high uptake in normal tissues such as the liver and intestines. For example, in mice bearing D456 MG tumors, the hepatic and intestinal uptake of 8-[^{3}H]-BG at 1 h postinjection was about 8% ID/g compared to about 2% ID/g in tumor (*30*). Relatively high uptake in the gastrointestinal tract for [^{14}C]BNAG also has been reported (*36*). Caution should be exercised, however, in comparing our data with these because the label was in the guanine skeleton in 8-[^{3}H]BG and, unlike BG, BNAG is not a free base.

Although the tumor uptake of [^{131}I]IBG was lower than that observed in several normal tissues (particularly those that contain significant levels of AGT), this may not interfere with the intended application of this tracer if a correlation can be obtained between the tumor AGT content and the magnitude of tumor uptake. Our goal is not to develop an imaging agent for tumor identification but rather to quantify AGT levels present in tumors whose anatomic location is known by other means. For comparison, it should be noted that the tumor uptake reported in rats and mice for agents used in the functional imaging of P-glycoprotein (P-gp), a transmembrane pump responsible for multidrug resistance, is generally less than 1% ID/g. For example, the uptake of [^{99m}Tc]-sestamibi in P-gp-lacking MDA 435 and the drug-resistant MDA/T03 human breast carcinoma xeografts in mice was 0.80 ± 0.21% ID/g and 0.30 ± 0.07% ID/g, respectively, at 15 min postinjection of the tracer (*40*). Similarly, the tumor uptake in the Mat B rat breast carcinoma xenograft and in its drug resistant Adr^R xenograft implanted in the same rat was 0.40 ± 0.08% ID/g and 0.28 ± 0.01% ID/g, respectively (*41*). Thus, the modest tumor uptake of [^{131}I]IBG after intravenous injection, while not ideal, may not prohibit its use for its intended purpose.

Another biodistribution study was performed after administration of [^{131}I]IBG via intratumoral injection. Intratumoral administration was performed in order to minimize potential problems related to tumor blood flow, transmembrane transport, and tumor morphology in the delivery and retention of labeled BG analogues. Although a tracer that requires delivery to the tumor, via i.t. administration, is not useful for clinical applications, the purpose of the i.t. experiment was to investigate the effect of BG under conditions where tracer delivery issues were excluded. Figure 3 shows the %ID/g values for tumor and a number of normal tissues in both control and BG-treated mice 0.5 h after injecting the tracer. The tumor uptake of [^{131}I]IBG in BG-treated mice (165.8 ± 27.5% ID/g; 60% of control) was significantly lower than that of the control mice (272.4 ± 48.2% ID/g; $p < 0.05$). SDS PAGE was performed on tumor removed from these animals. A band corresponding to AGT was seen in the mice not receiving the blocking dose of BG, while this band was absent in sample obtained from BG-treated

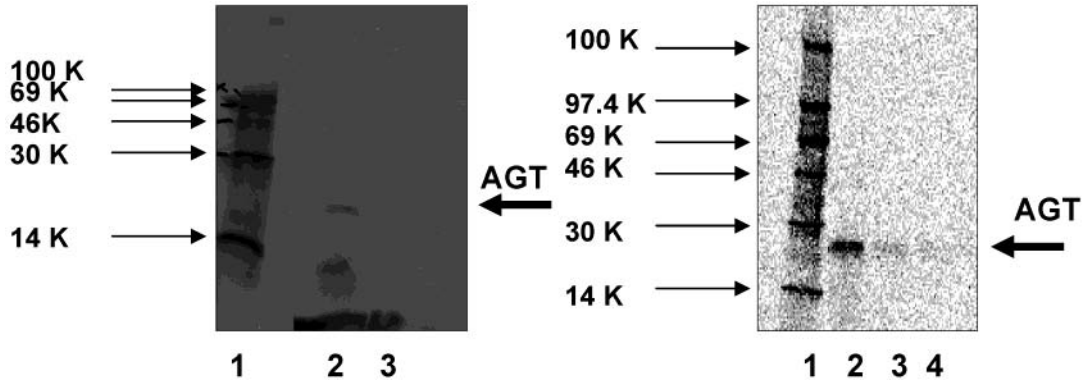


Figure 4. Left panel: Gel electrophoresis of tumor samples obtained from mice 0.5 h after receiving [^{131}I]IBG via intratumoral injection. Lane 1: C-14 protein standards; Lane 2: Sample obtained from control mice; Lane 3: Sample from mice pretreated with BG. Right panel: Lane 1: C-14 protein standards; Lane 2−4: pure AGT labeled with [^{125}I]IBG and serially diluted. Note that electrophoresis conditions (gel gradient) are different from those used to obtain data in the left panel; also, phosphor imaging (versus regular film for the data in left panel) was used to visualize the bands.

mice (Figure 4). Although this was a very preliminary experiment, the results suggest that it may be possible to differentiate between tumors with high and low AGT content in vivo. Unlike the iv injection experiment, BG treatment increased the uptake in thyroid and stomach in addition to lowering tumor uptake. The higher uptake in stomach and thyroid could be due to greater leakage of the tracer into the remainder of the body. In the iv injection experiment, like the tracer, the unlabled IBG also was injected intravenously and at a much lower dose than the dose of BG used in i.t. experiment. That IBG dose was chosen roughly based on its IC_{50} value determined from the binding of [^{131}I]IBG to pure AGT (*18*). As discussed before, it appears that substantially higher doses are needed to deplete AGT completely. In the intratumoral injection experiment, BG was administered i.p. at 60−75 mg/kg dose. This was based on the fact that BG at this dose depletes AGT in HT29 xenografts to less than 2% of untreated controls (*42*).

In summary, a method has been developed by which [^{131}I]IBG could be prepared in a single step rapidly (<1 min) and in excellent radiochemical yields. Although the uptake in tumor cells in vitro and in xenografts in vivo after intratumoral administration suggests that [^{131}I]IBG may be potentially useful in quantitating AGT, a tracer with more optimal properties is desired. Efforts are under way to develop other analogues of BG that may be less lipophilic, more metabolically stable, and that can be translocated to the nucleus.

ACKNOWLEDGMENT

This study was funded by Grants CA93371, CA86186, and NS20023 from the National Institutes of Health. The authors want to thank Susan Slade for her excellent technical assistance.

LITERATURE CITED

(1) Spiro, T. P., Gerson, S. L., Liu, L., Majka, S., Haaga, J., Hoppel, C. L., Ingalls, S. T., Pluda, J. M., and Wilson, J. K. V. (1999) O^6-Benzylguanine: a clinical trial establishing the biochemical modulatory dose in tumor tissue for alkyltransferase-directed DNA repair. *Cancer Res. 59*, 2402−2410.

(2) Pegg, A. E., Dolan, M. E., and Moschel, R. C. (1995) Structure, function, and inhibition of O^6-alkylguanine-DNA alkyltransferase. *Prog. Nucl. Acid Res. Mol. Biol. 51*, 167−223.

(3) Margison, G. P., and Santibanez-Koref, M. F. (2002) O^6-alkylguanine-DNA alkyltransferase: role in carcinogenesis and chemotherapy. *Bioessays 24*, 255−266.

(4) Srivenugopal, K. S., Yuan, X.-H., Friedman, H. S., and Ali-Osman, F. (1996) Ubiquitination-dependent proteolysis of O^6-methylguanine-DNA methyltransferase in human and murine tumor cells following inactivation with O^6-benzylguanine or 1,3-bis(2-chloroethyl)-1-nitrosourea. *Biochemistry 35*, 1328−1334.

(5) Belanich, M., Ayi, T. C., Li, B. F., Kibitel, J. T., Grob, D. W., Randall, T., White, A. B., Citron, M. L. and Yarosh, D. B. (1994) Analysis of O^6-methylguanine-DNA methyltransferase in individual human cells by quantitative immunofluorescence microscopy. *Oncol. Res. 6*, 129−137.

(6) Lee, S. M., Reid, H., Elder, R. H., Thatcher, N. and Margison, G. P. (1996) Inter- and intracellular heterogeneity of O^6-alkylguanine-DNA alkyltransferase expression in human brain tumors: possible significance in nitrosourea therapy. *Carcinogenesis 17*, 637−641.

(7) Li, B. F. (1999) Methods of assaying DNA-repairing enzymes and their alkylated derivatives. US Patent 5,879,899.

(8) Dolan, M. E. and Pegg, A. E. (1997) O^6-Benzylguanine and its role in chemotherapy. *Clin. Cancer Res. 3*, 837−847.

(9) Mounetou, E., Cussac, C., Mathieu, F., Maurizis, J.-C., Labarre, P., Moreau, M.-F., Veyre, A., and Madelmont, J.-C. (1995) Synthesis of three no-carrier-added O^6-4-[^{125}I] iodobenzylguanine derivatives, new reagents for the assay of O^6-alkylguanine-DNA alkyltransferase activity. *J. Labeled. Compd. Radiopharm. 36*, 1215−1225.

(10) Madelmont, J. C., Cussa, C., Dupuy, J. M., Rapp, M., Labarre, P., Chabard, J. L., Maurizis, J. C., Sauzieres, J., Baudry, J. P., Godeneche, D., and Veyre, A. (1992) Marquage par ^{14}C et ^{13}C de la N acetyl O^6 benzyl guanosine. *J. Labeled Compd. Radiopharm. 31*, 793−800.

(11) Ciocco, G. M., Moschel, R. C., Chae, M.-Y., McLaughlin, P. J., Zagon, I. S., and Pegg, A. E. (1995) Specific labeling of O^6-alkylguanine-DNA alkyltransferase by reaction with O^6-(*p*-hydroxy[^{3}H]methylbenzyl)guanine. *Cancer Res. 55*, 4085−4091.

(12) Schirrmacher, R., Nesseler, E., Hamkens, W., Eichhorn, U., Schreckenberger, M., Kaina, B., and Rosch, F. (2002) An approach to the evaluation of the activity of the DNA repair enzyme O6-methylguanine-DNA-methyl-transferase in tumor tissue in vivo: syntheses of 6-benzyloxy-9-(2-[^{18}F]fluoroethyl)-9H-purin-2-yl-amine and 6-benzyloxy-7-(2-[^{18}F]fluoroethyl)-7H-purin-2-yl-amine. *Appl. Radiat. Isot. 56*, 511−517.

(13) Schirrmacher, R., Muhlhausen, U., Wangler, B., Schirrmacher, E., Reihard, J., Nagel, G., M., Kaina, B., Piel, M., Weisler, M., and Rosch, F. (2002) Synthesis of 2-amino-6-(2-[^{18}F]fluoro-pyridine-4-ylmethoxy)-9-(octyl-β-D-glucosyl)-purine: a novel radioligand for positron emission tomography studies of the O^6-methylguanine-DNA methyltransferase (MGMT) status of tumor tissue. *Tetrahedron Lett. 43*, 6301−6304.

(14) Zheng, Q.-H., Liu, X., Fei, X., Wang, J.-Q., Ohannesian, D. W., Erickson, L., Stone, K. L. Martinez, T. D., Miller, K. D., and Hutchins, G. D. (2002) *J. Labeled Compd. Radiopharm. 45*, 1239−1252.

(15) Liu, X., Zheng, Q.-H., Fei, X., Wang, J.-Q., Ohannesian, D. W., Erickson, L. C., Stone, K. L., and Hutchins, G. D. (2003) Synthesis and preliminary biological evaluation of 6-*O*-[^{11}C]-[(methoxymethyl)]benzylguanines, new potential PET breast cancer imaging agents for the DNA repair protein AGT. *Bioorg. Med. Chem. Lett. 13*, 641−644.

(16) Liu, X., Zheng, Q.-H., Hutchins, G. D., Fei, X., Erickson, L. C., Miller, K. D., Mock, B. H., Glick-Wilson, B. E., Winkle, W. L., Stone, K. L. and Carlson, K. A. (2003) A convenient procedure for the synthesis of O6-benzylguanine derivatives by phase transfer catalysis. *Synth. Commun. 33*, 941−952.

(17) Zheng, Q.-H., Liu, X., Fei, X., Wang, J.-Q., Ohannesian, D. W., Erickson, L. C., Stone, K. L., and Hutchins, G. D. (2003) Synthesis and preliminary biological evaluation of radiolabeled O6-benzylguanine derivatives, new potential PET imaging agents for the DNA repair protein O6-alkylguanine-DNA alkyltransferase in breast cancer. *Nucl. Med. Biol. 30*, 405−415.

(18) Vaidyanathan, G., Affleck, D. J., Cavazos, C. M., Johnson, S. P., Shankar, S., Friedman, H. S., Colvin, M. O. and Zaltuksy, M. R. (2000) Radiolabeled guanine derivatives for the in vivo mapping of O^6-alkylguanine-DNA alkyltransferase: 6-(4-[^{18}F]Fluoro-benzyloxy)-9*H*-purin-2-ylamine and 6-(3-[^{131}I]iodo-benzyloxy)-9*H*-purin-2-ylamine. *Bioconjugate Chem. 6*, 868−875.

(19) Friedman, H. S., Colvin, O. M., Skapek, S. X., Ludeman, S. M., Elion, G. B., Schold, S. C., Jr., Jacobsen, P. F., Muhlbaier, L. H., and Bigner, D. D. (1988) Experimental chemotherapy of human medulloblastoma cell lines and transplantable xenografts with bifunctional alkylating agents. *Cancer Res. 48*, 4189−4195.

(20) Loktionova, N. A. and Pegg, A. E. (1996) Point mutations in human O^6-alkylguanine-DNA alkyltransferase prevent the sensitization by O^6-benzylguanine to killing by *N*, *N*′-bis(2-chloroethyl)-*N*-nitrosourea. *Cancer Res. 56*, 1578−1583.

(21) Friedman, H. S., Schold, S. C., Jr., Bigner, D. D. (1986) Chemotherapy of subcutaneous and intracranial human medulloblastoma xenografts in athymic nude mice. *Cancer Res. 46*, 224−228.

(22) Ewesuedo, R. B., Wilson, L. R., Friedman, H. S., Moschel, R. C. and Dolan, M. E. (2001) Inactivation of O^6-alkylguanine-

DNA alkyltransferase by 8-substituted O^6-benzylguanine analogues in mice. *Cancer Chemother. Pharmacol. 47*, 63−69.

(23) Wigerinck, P., Kerremans, L., Claes, P., Snoeck, R., Maudgal, P., De Clercq, E., and Herdewijn, P. (1993) Synthesis and antiviral activity of 5-thien-2-yl-2′-deoxyuridine analogues. *J. Med. Chem. 36*, 538−543.

(24) Kokkinakis, D. M., von Wronski, M. A., Vuong, T. H., Brent, T. P., and Schold, S. C., Jr. (1997) Regulation of O^6-methylguanine-DNA methyltransferase by methionine in human tumor cells. *Br. J. Cancer 75*, 779−788.

(25) Friedman, H. S., Dolan, M. E., Kaufmann, S. H., Colvin, O. M., Griffith, O. W., Moschel, R. C., Schold, S. C., Bigner, D. D., and Ali-Osman, F. (1994) Elevated DNA polymerase, and DNA topoiosomerase II in a melphalan-resistant rhabdomyosarcoma xenografts that is cross-resistant to nitrosoureas and topotecan. *Cancer Res. 54*, 3487−3493.

(26) Dolan, M. E., Moschel, R. C., and Pegg, A. E. (1990) Depletion of mammalian O^6-alkylguanine-DNA-alkytransferase activity by O^6-benzylguanine provides a means to evaluate the role of this protein in protection against carcinogenic and therapeutic alkylating agents. *Proc. Natl. Acad. Sci. U.S.A. 87*, 5368−5372.

(27) Lim, A. and Li, B. F. L. (1996) The nuclear targeting and nuclear retention properties of a human DNA repair protein O^6-methylguanine-DNA methyltransferase are both required for its nuclear localization: the possible implications. *EMBO J. 15*, 4050−4060.

(28) Ali, R. B., Teo, A. K.-C., Oh, H.-K., Chuang, L. S.-H, Ayi, T.-C., and Li, B. F. L. (1998) Implication localization of human DNA repair enzyme O^6-methylguanine-DNA methyltransferase at active transcription sites in transcription-repair coupling of the mutagenic O^6-methylguanine lesion. *Mol. Cell. Biol. 18*, 1660−1669.

(29) Duncan, V. E., Ajmani, P. S., and Hughes, J. A. (1998) Cellular delivery is a major obstacle for oligodeoxynucleotide inhibition of telomerase activity. *AntiCancer Res. 18*, 4105−4108.

(30) Dolan, M. E., Pegg, A. E., Moschel, R. C., Vishnuvajjala, B. R., Flora, K. P., Grever, M. R., and Friedman, H. S. (1994) Biodistribution of O^6-benzylguanine and its effectiveness against human brain tumor xenografts when given in poly(ethylene glycol) or cremophor-EL. *Cancer Chemother. Pharmacol. 35*, 121−126.

(31) Pegg, A. E., Chung, L., and Moshel, R. C. (1997) Effect of DNA on the inactivation of O^6-alkylguanine-DNA alkyltransferase by 9-substituted O^6-benzylguanine derivatives. *Biochem. Pharmacol. 53*, 1559−1564.

(32) Dolan, M. E., Roy, S. K., Garbiras, B. J., Helft, P., Paras, P., Chae, M.-Y., Moschel, R. C., and Pegg, A. E. (1998) O^6-Alkylguanine-DNA alkyltransferase inactivation by ester prodrugs of O^6-benzylguanine derivatives and their rate of hydrolysis by cellular esterases. *Biochem. Pharamacol. 55*, 1701−1709.

(33) Mellgren, R. L., Lu, Q., Zhang, W., Lakkis, M., Shaw, E. and Mericle, M. T. (1996) Isolation of a Chinese Hamster Ovary cell clone possessing decreased μ-Calpain content and a reduced proliferative growth rate. *J. Biol. Chem. 271*, 15568−15574.

(34) Cai, Y., Ludeman, S. M., Wilson, L. R., Chung, A. B. and Dolan, M. E. (2001) Effect of O^6-benzylguanine on nitrogen mustard-induced toxicity, apoptosis, and mutagenicity in Chinese Hamster Ovary Cells. *Mol. Cancer Ther. 1*, 21−28.

(35) Seeley, M. R. and Faustman, E. M. (1998) Effects of O^6-benzylguanine on growth and differentiation of P19 embryonic carcinoma cells treated with alkylating agents. *Teratogenesis, Carcinogenesis, and Mutagenesis 18*, 111−122.

(36) Cussac, C., Mounetou, E., Rapp, M., Madelmont, J. C., Maurizis, J. C., Labarre, P., Chollet, P., Chabard, J. L., Godeneche, D., Baudry, J. P., and Veyre, A. (1994) Disposition and metabolism of O^6-alkylguanine-DNA alkyltransferase inhibitor in nude mice bearing human melanoma. *Drug Metab. Disp. 22*, 637−642.

(37) Spratt, T. E., and de los Santos, H. (1992) Reaction of O^6-alkylguanin-DNA alkyltransferase with O^6-methylguanine analogues: evidence that oxygen of O^6-methylguanine is protonated by the protein to effect methyl transfer. *Biochemistry 31*, 3688−3694.

(38) Spratt, T. E., and Campbell, C. R. (1994) Synthesis of oligodeoxynucleotides containing analogues of O^6-alkylguanine DNA alkyltransferase. *Biochemistry 33*, 11364−11371.

(39) Gerson, S. L., Trey, J. E., Miller, K., and Berger, N. A. (1986) A comparison of O^6-alkylguanine-DNA -alkyltransferase activity based on cellular DNA content in human, rat and mouse tissues. *Carcinogenesis 7*, 745−749.

(40) Ballinger, J. R., Hua, H. A., Berry, B. W., Firby, B. P., and Boxen, I. (1995) ^{99m}Tc-sestamibi as an agent for imaging P-glycoprotein-mediated multi-drug resistance: in vitro and in vivo studies in a rat breast tumor cell line and its doxorubicin-resistant variant. *Nucl. Med. Commun. 16*, 253−257.

(41) Barbarics, E., Kronauge, J. F., Cohen, D., Davison, A., Jones, A. G., and Croup, J. M. (1998) Characterization of P-glycoprotein transport and inhibition in vivo. *Cancer Res. 58*, 276−282.

(42) Michell, R. B., Moschel, R. C., and Dolan, M. E. (1992) Effect of O^6-benzylguanine on the sensitivity of human tumor xenografts to 1,3-bis(2-chloroethyl)-1-nirosourea and on DNA interstand cross-link. *Cancer Res. 52*, 1171−1175.

BC0341977

Silicon Nanoparticles as a Luminescent Label to DNA

L. Wang,* V. Reipa, and J. Blasic

Biotechnology Division, National Institute of Standards and Technology, Gaithersburg, Maryland 20899-8312.
Received October 28, 2003; Revised Manuscript Received December 26, 2003

We successfully conjugated 1−2 nm diameter silicon nanoparticles to a 5′-amino-modified oligonucleotide (60mer) that contains a C6 linker between amide and phosphate groups. The conjugation was implemented via two photoinduced reactions followed by a DNA labeling step through formation of a carboxamide bond. Photoluminescence of the conjugates is dominated by two blue bands (400 and 450 nm maximal) under 340 nm excitation. The quantum yield of oligonucleotide-conjugated nanoparticles was determined to be 0.08 as measured against quinine sulfate in 0.1 M $HClO_4$ as a reference standard. We report a conjugation process that allows labeling of Si nanoparticles to an oligonucleotide in aqueous solutions. Ways to further optimize the procedure in order to achieve narrower and brighter photoluminescence are discussed.

INTRODUCTION

The rapid development of pharmacogenomic research and drug discovery, diagnostics of infectious and genetic disease, and methodologies for forensic and genetic identification has stimulated the search for novel fluorophores. Recently, binary semiconductor quantum dots have been demonstrated to possess certain advantages over organic fluorophores (*1*). However, their inherent toxicity and chemical instability require polymer encapsulation before the bioconjugation step (*2*). Si nanoparticles (*3*) have been shown to have similar room-temperature photoluminescence quantum yields, but higher chemical stability, thus making them attractive for bioconjugation.

The surface chemistry of silicon is still a very active field despite the ubiquitous presence of silicon in microelectronics since the 1960s (*4*). The growing interest is partly attributed to novel applications of silicon chips, which require fine controls over the interfacial characteristics. Recently, silicon nanoparticles with discrete sizes and distinct emission in the blue, green, and red were produced by using anodic etching in hydrofluoric acid (*3*). Similar to binary semiconductor nanocrystals (*5*), Si nanoparticles display a relatively narrow emission and high quantum efficiency.

Several studies have been published, aiming at functionalizing bulk Si surfaces for biomolecule attachment (*6*−*9*). Wagner and co-workers (*6*) produced bioreactive self-assembled monolayers on hydrogen-passivated Si(111) as atomically flat substrates for biological scanning probe microscopy. Wojtyk et al. (*9*) also reported the formation of activated ester monolayers on porous silicon surfaces that could be readily attached to biomolecules. The present study is intended for conjugating individual Si nanoparticles suspended in an organic medium to an oligonucleotide in water through chemical derivatization of the nanoparticle outer layer. We have characterized the nanoparticle-labeled nucleotide in terms of the overall size, absorbance, and luminescence quantum yield.

* Corresponding author. Phone: (301) 975-2447; e-mail: lili.wang@nist.gov.

MATERIALS AND METHODS

Si nanoparticles were produced using lateral electrochemical anodization (*10*). (100) Si wafer (p-type, B doped, resistance $R = 2$ to 10 Ω, Virginia Semiconductor, VA)[1] was cut into 5 cm × 5 cm pieces and etched in (vol) 20% HF, 60% H_2O_2, 20% ethanol bath at room temperature. A constant current of 50 mA was maintained by a galvanostat while the etching solution was slowly pumped into the cell. Electrical contact to the substrate was provided by InGa eutectic, and Pt mesh served as a cathode. A 100 W halogen lamp illuminated both wafer sides in the procedure. Total etching time per wafer was 30 min. Following etching, wafers were flushed with ethanol and dried in the Ar stream. They were immediately placed in Ar purged 1-octene (or 1-hexene) and sonicated for 1 h in an ultrasound bath (model SC507H, Sonicor Inc., Copiaque, NY). After centrifugation to remove aggregates, the nanoparticles in supernatant were illuminated by 236 nm light (Spectroline, ENF-240C) in a 10 mL quartz cell for 2 h while maintaining a vigorous Ar purge. The residual solvent was evaporated under the Ar flow, resulting in dry 1-octene (or 1-hexene) monolayer-coated Si particles.

Activation was carried out by adding 0.2 mL of a 15 mM solution of 4′-[3-(trifluoromethyl-3*H*-diazirin-3-yl)]-benzoic acid, *N*-hydroxysuccinimide ester (TDBA-OSu) [Photoprobes, Industrie Nord, Switzerland] in anhydrous carbon tetrachloride to dried silicon particles and immediately illuminating with a 365 nm lamp (Spectroline, ENF-240C) for 15 min under vigorous magnetic stirring to ensure uniform illumination. After the reaction, carbon tetrachloride was evaporated using an Ar stream. The dried, activated silicon nanoparticles were dissolved in 15 μL of anhydrous DMSO and slowly added to 0.5 mL of the 5′-amino-modified oligonucleotide solution (2 μg/mL) in water. The 5′ amino-modified oligonucleotide (60mer) was obtained from Qiagen (Valencia, CA, se-

[1] Certain commercial equipment, instruments, and materials are identified in this paper to adequately specify the experimental procedure. In no case does such identification imply recommendation or endorsement by the National Institute of Standards and Technology, nor does it imply that the materials or equipment are necessarily the best available for the purpose.

10.1021/bc030047k Not subject to U.S. Copyright. Published 2004 by American Chemical Society
Published on Web 02/28/2004

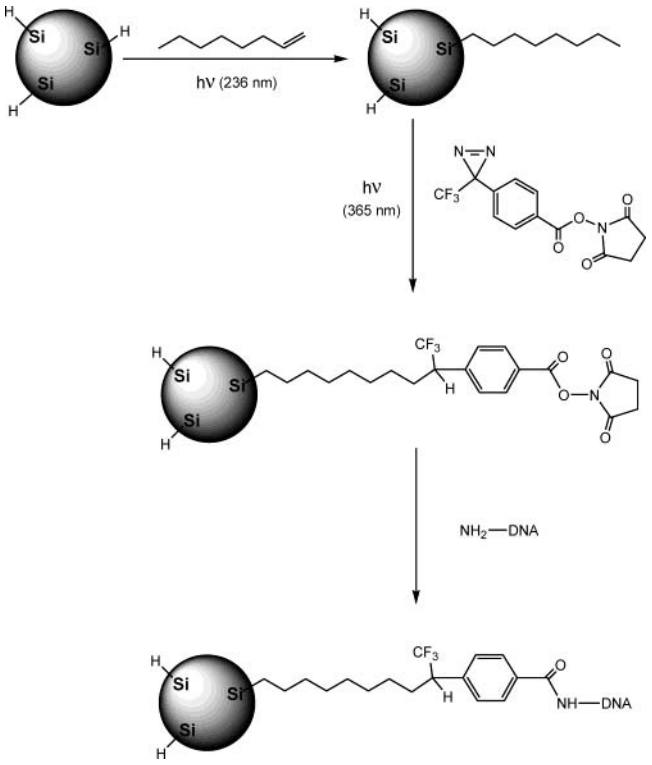


Figure 1. A reaction diagram displaying the three steps used to produce oligonucleotide-conjugated Si nanoparticles by using single-surface Si−H bond and 1-octene as an example. In this case, carbene addition at the terminal methyl group is the main outcome of the reaction between the 1-octene-coated nanoparticle and the cross-linker, TDBA-OSu.

quence: 5′-TTAAAAGAGAACTCCAGCTTGGACTTCT-TTCCGTAGTCGACAGAGAGCCTCTCCATCAGC-3′) and contained a C6 linker between amide and phosphate groups at the 5′ end. This sequence is part of the rat tubulin gene. The reaction was carried out in the dark for 1 h with magnetic stirring. The total volume was then decreased to ∼20 μL by vacuum centrifugation before purification by electrophoresis in 18% polyacrylamide gel with TBE (90 mM Tris, 90 mM boric acid, 2 mM EDTA) as the running buffer and the voltage set at 115 V for 40 min. A 10 bp DNA ladder from Invitrogen Corporation (Carlsbad, CA) was used to examine the equivalence in the size of Si nanoparticle-labeled oligonucleotide relative to double-stranded DNA. The labeled nucleotide was recovered from polyacrylamide gel using Ultrafree-MC centrifugal filter devices (Durapore 0.22 μm, Millipore Corporation Bedford, MA). The hybridization between the gel-purified nanoparticle-labeled nucleotide and the complementary strand was performed in 100 mM Tris-HCl, 1 mM EDTA, pH 7.5, using the following protocol: 95 °C for 30 s, then decreasing the temperature to 60 °C at the rate of 0.2 °C/s, incubation for 30 s at 60 °C and then lowering the temperature to 4 °C. The complementary strand was also obtained from Qiagen with the sequence, 5′-GCTGATGGAGAGGCTCTCTGTCGACTA-CGGAAAGAAGTCCAAGCTGGAGTTCTCTTTTAA-3′.

RESULTS AND DISCUSSION

The multiple chemical steps for obtaining oligonucleotide-conjugated Si nanoparticles are illustrated in Figure 1. Under 236 nm illumination in 1-octene (or 1-hexene), hydrogen-passivated silicon particles attained from electrochemical etching are coated with a layer of 1-octene (or 1-hexene). The reaction is driven by formation of free radicals that interact with 1-octene to generate Si−C bonds (*11*−*13*). In the following step, TDBA-OSu, a photoactivatable aryldiazirine cross-linker, is inserted into the C−H bonds of the CH_2 groups within the hydrocarbon chain through a highly reactive carbene intermediate under 365 nm illumination in dry carbon tetrachloride (*14*, *15*). The report by Nassal (*14*) has demonstrated that under the radiation of high pressure mercury lamp the singlet carbene can react even with cyclohexane that is considered as an inert solvent. The author carefully characterized the photolysis products with cyclohexane in the presence and absence of oxygen. While purging argon prior to photolysis, the relative yield of carbene addition product is as high as 73% in addition to byproducts from the reaction of triplet carbene with residual oxygen. On the other hand, Cicero and co-

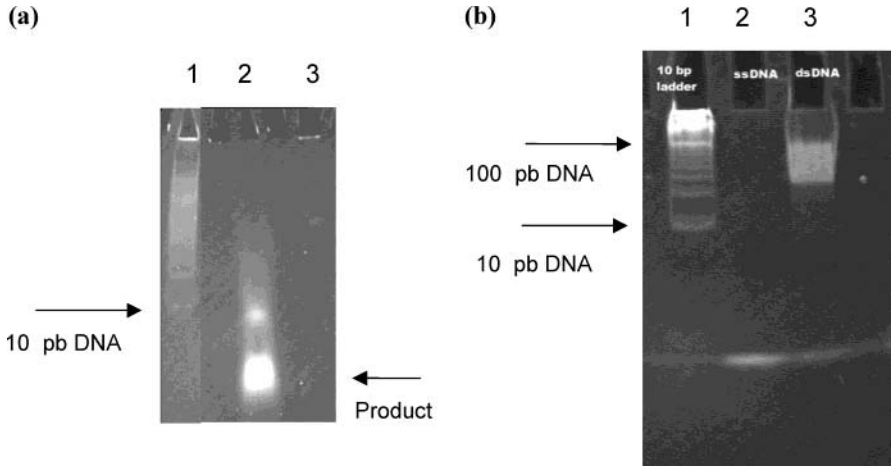


Figure 2. (a) Polyacrylamide gel electrophoresis of the products of the labeling reaction (Figure 1) in the presence (lane 2) and absence (lane 3) of TDBA-OSu as well as the 10 bp DNA ladder (lane 1). The gel portion with the DNA ladder was stained with ethidium bromide (5 μg/mL in TBE). The brightly luminescent band (the first band) in lane 2 is from nanoparticle-labeled oligonucleotide (the main product), which was cut and extracted for the spectral characterization and hybridization with the complementary strand. No luminescent product was detected for the labeling reaction in the absence of TDBA-OSu. (b) Polyacrylamide gel electrophoresis of gel-purified silicon nanoparticle-labeled oligonucleotide (lane 2) and its hybridization product with the complementary strand (lane 3) as well as the 10 bp DNA ladder (lane 1). The gel was stained with ethidium bromide in order to examine the positions of Si nanoparticle-labeled oligonucleotide and the hybridization product relative to double-stranded DNA. The band of the labeled nucleotide is below that of 10 bp DNA, and the band of the hybridization product is located near the 60mer, double-stranded DNA.

workers (*13*) demonstrated that in the absence of oxygen, 1-octene could form a compact monolayer on the surface of hydrogen-terminated silicon(111) just alike 1-octadecene. In our case, since C6 hydrocarbon chains surrounding the nanoparticles might not form an ordered monolayer like C8 hydrocarbon chains the carbene addition could take place at multiple CH_2 sites within the C6 carbon chain. However, we anticipate the insertion yields at sites closer to the surface of the particle are much lower than those at sites away from the surface of the particle because of the spatial hindrance of the sites near particle surface. As suggested by Nassal (*14*), the reactions by triplet carbene will not involve the silicon particles. The CH insertion at the terminal methyl group will likely be the main product, particularly in the case of C8 hydrocarbon chain-coated particles shown in Figure 1 as an example of the outcomes by the reactive singlet carbene. Additional control experiments were carried out to compare the results in the presence and absence of the photoactivatable aryldiazirine cross-linker, TDBA-OSu. Figure 2a shows the products of the labeling reactions with TDBA-OSu (lane 2) and without the reagent (lane 3) as well as a 10 bp DNA ladder (lane 1). The bright, intrinsic luminescent band in lane 2 (the first band) is from silicon nanoparticle-labeled oligonucleotide. In the absence of the cross-linker, the labeling reaction was not successful (lane 3). Only the gel piece with DNA ladder was stained with ethidium bromide (EtBr). The control experiment clearly shows the importance of the photoactivatable cross-linker. The photoinduced reaction generates amino-reactive *N*-succinimidyl groups on the outer layer of the particles, which are used to immobilize the amino-modified oligonucleotide in the final step. Note that it is critically important to dissolve TDBA-OSu-activated particles in dry DMSO prior to the immobilization of the nucleotide. Without such step we were unable to produce nucleotide-conjugated nanoparticles.

Figure 2b shows polyacrylamide gel electrophoresis of purified silicon nanoparticle-labeled 60mer oligonucleotides (lane 2) and their hybridization products with the complementary strand (lane 3) as well as the 10 bp DNA ladder (lane 1). The band of the labeled nucleotides and the hybridization products can be visualized under a UV lamp. The gel was stained with ethidium bromide (EtBr), and a transilluminator equipped with a UV lamp centered at 302 nm and a band-pass filter for EtBr detection was used to image the gel. This allows visualizing the DNA ladder and more importantly, confirming the existence of the hybridization products. The single-stranded 60mer oligonucleotide as a control runs out the gel in the time setting for the electrophoresis (40 min). Considering the diameter of B-form double-stranded DNA is about 2 nm, it is reasonable to estimate the diameter of Si nanoparticle conjugated to the 60mer oligonucleotide to be smaller than 2 nm. The diameter and mass of Si-nanoparticle resulted in the running location of labeled nucleotide in the polyacrylamide gel. The band of the hybridization products is somewhat spread out. This observation clearly shows that Si nanoparticles are conjugated to the 60mer oligonucleotide. The band at the same running position (lane 3) as that of Si nanoparticles (lane 2) is mostly due to the unhybridized particles. An additional experimental control in the absence of the 5′-amino-modified oligonucleotide in the final immobilization step (Figure 1) did not produce a detectable band at this position.

The absorption spectrum of the purified nucleotide is shown in Figure 3a. Absorbance above 300 nm is due to Si nanoparticles, while below 290 nm it can be attributed

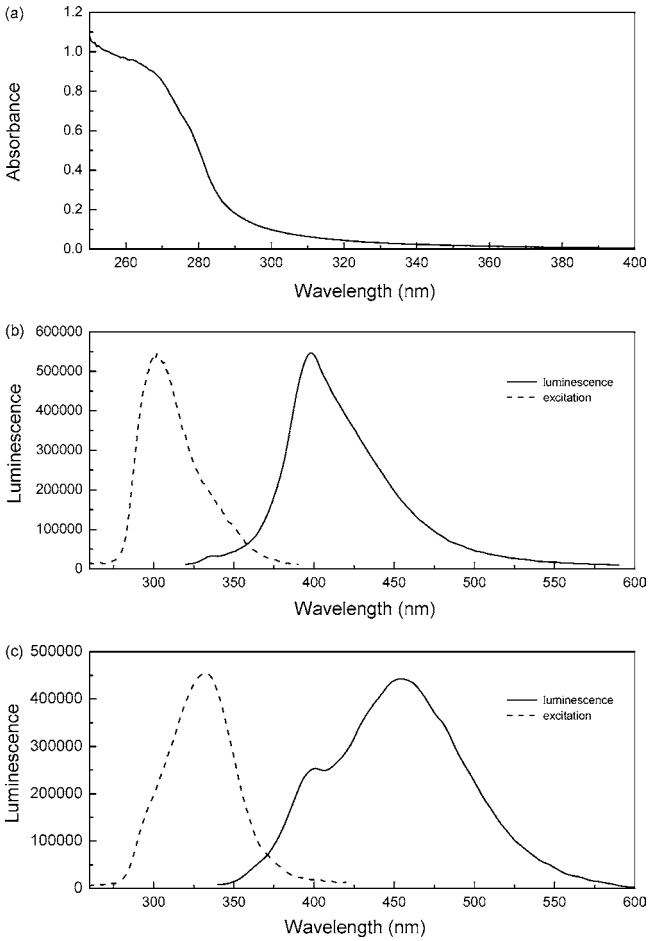


Figure 3. Spectroscopic characterization of purified oligonucleotide-conjugated Si nanoparticles: (a) absorbance; (b) excitation spectrum with luminescence monitored at 400 nm (dash line) and emission spectrum under 300 nm excitation (solid line), 1-hexene used in the first step; (c) excitation spectrum with luminescence monitored at 450 nm (dash line) and emission spectrum under 330 nm excitation (solid line), 1-octene used in the first step (see text).

to both DNA and nanoparticles. Figure 3b shows the excitation and photoluminescence spectra of the labeled nucleotides coated with a layer of 1-hexene. The excitation profile was recorded with photoluminescence fixed at 400 nm, and the emission spectrum was obtained with the excitation wavelength set at 300 nm. The excitation spectrum is peaked at 300 nm and luminescence spectrum contains a peak at 400 nm with a shoulder above 440 nm. When 1-octene is used instead of 1-hexene, both excitation and luminescence peaks shift to 332 and 450 nm, respectively (Figure 3c). Interestingly, the 400 nm emission peak is clearly resolved from the dominant peak at 450 nm. It may be that Si nanoparticles with two discrete sizes are present. According to Belomoin and coworkers (*16*), the emission at 400 and 450 nm is characteristic to ∼1 nm and ∼1.2 nm Si particles based on high-resolution transmission electron microscopy measurements. It is worthy to mention that the diluted nucleotide-conjugated Si nanoparticles are stable in aqueous solutions at least a week without deterioration in the luminescence.

We determined the photoluminescence quantum yield of nucleotide-conjugated Si nanoparticles, using quinine sulfate in 0.1 M $HClO_4$ as a reference standard (*17*). The quantum yields are 0.08 ± 0.002 (standard deviation) and 0.05 ± 0.003 for 1-octene- and 1-hexene-coated nanoparticles, respectively. Since a homogeneous nanoparticle

preparation would be expected to have about 20 nm to 30 nm photoluminescence bandwidth (*5*), our conjugates suggest moderate size inhomogeneity; therefore, size exclusion chromatography separation would be justified in addition to ultracentrifugation prior to 1-alkene monolayer binding. Moreover, the use of a longer carbon chain would be expected to provide a better-ordered self-assembled monolayer (SAM), thus lowering nonradiative recombination channel concentration and increasing photoluminescence quantum yield.

CONCLUSIONS

A key requirement for the effective use of Si nanoparticles in biological applications is aqueous solubility. In the present study, we successfully conjugated 1−2 nm diameter silicon nanoparticles to a 5′-amino-modified oligonucleotide through a three-step procedure. Under UV excitation, photoluminescence of the conjugates is dominated by two blue bands (400 and 450 nm maximal). The quantum yield of oligonucleotide-conjugated nanoparticles that were coated with a layer of 1-octene was determined to be 0.08 as measured against quinine sulfate in 0.1 M $HClO_4$ as a reference standard. We have demonstrated the feasibility of the present coupling chemistry to obtain Si nanoparticle-labeled nucleotides. Ways to reduce size inhomogeneity and surface defects of Si nanoparticles in order to achieve narrower and brighter photoluminescence will be addressed in further studies.

LITERATURE CITED

(1) Ouellete, J. (2003) Quantum Dots for Sale. *Ind. Phys. Feb/March*, 14−17.

(2) Ding, Z., Quinn, M. B., Haram, A. K., Pell, L. E., Korgel, B. A., and Bard, A. J. (2002) Electrochemistry and Electrogenerated Chemiluminescence from Silicon Nanocrystal Quantum Dots. *Science 296*, 1293−1297.

(3) Belomoin, G., Therrien, J., Smith, A., Rao, S., Twesten, R., Chaieb, S., Nayfeh, M. H., Wagner, L., and Mitas, L. (2002) Observation of a Magic Discrete family of Ultrabright Si Nanoparticles. *Appl. Phys. Lett. 80*, 841−843.

(4) Buriak, J. M. (2002) Organometallic Chemistry on Silicon and Germanium Surfaces. *Chem. Rev. 102*, 1271−1308.

(5) Alivisatos, A. P. (1996) Perspectives on the Physical Chemistry of Semiconductor Nanoparticles. *J. Phys. Chem. B 100*, 13226−13239.

(6) Wagner, P., Nock, S., Spudich, J. A., Volkmuth, W. D., Chu, S., Cicero, R. L., Wade, C. P., Linford, M. R., and Chidsey, C. E. D. (1997) Bioreactive Self-Assembled Monolayers on Hydrogen-Passivated Si(111) as a New Class of Atomically Flat Substrates for Biological Scanning Probe Microscopy. *J. Struct. Biol. 119*, 189−201.

(7) Cicero, R. L., Wagner, P., Linford, M. R., Hawker, C. J., Waymouth, R. M., and Chidsey, C. E. D. (1997) Functionalization of Alkyl Monolayers on Surfaces with Diverse Amines: Photochemical Chlorosulfonation Followed by Sulfonamide Formation. *Polym. Prepr. 38*, 904−905.

(8) Boukherroub, R., and Wayner, D. D. M. (1999) Controlled Functionalization and Multistep Chemical Manipulation of Covalently Modified Si(111) Surfaces. *J. Am. Chem. Soc. 121*, 11513−11515.

(9) Wojtyk, J. T. C., Morin, K. A., Boukherroub, R., and Wayner, D. D. M. (2002) Modification of Porous Silicon Surfaces with Activated Ester Monolayers. *Langmuir 18*, 6081−6087.

(10) Jung, K. H., Shih, S., Hsieh, T. Y., Kwong, D. L., and Lin, T. L. (1991) Intense Photoluminescence from Laterally Anodized Porous Si. *Appl. Phys. Lett. 59*, 3264−3266.

(11) Linford, M. R., Fenter, P., Eisenberger, P. M., and Chidsey, C. E. D. (1995) Alkyl Monolayers on Silicon Prepared from 1-Alkenes and Hydrogen-Terminated Silicon. *J. Am. Chem. Soc. 117*, 3145−3155.

(12) Boukherroub, R., Morin, S., Bensebaa, F., and Wayner, D. D. M. (1999) New Synthetic Routes to Alkyl Monolayers on the Si(111) Surface. *Langmuir 15*, 3831−3835.

(13) Cicero, R. L., Linford, M. R., and Chidsey, C. E. D. (2000) Photoreactivity of Unsaturated Compounds with Hydrogen-Terminated Silicon(111). *Langmuir 16*, 5688−5695.

(14) Nassal, M. (1984) 4′-(1-Azi-2,2,2-trifluoroethyl)phenylalanine, a Photolabile Carbene-generating Analogue of Phenylalanine. *J. Am. Chem. Soc. 106*, 7540−7545.

(15) Brunner, J. (1993) New Photolabeling and Cross-linking Methods. *Annu. Rev. Biochem. 62*, 483−514.

(16) Belomoin, G., Therrien, J., and Nayfeh, M. (2000) Oxide and Hydrogen Capped Ultrasmall Blue Luminescent Si Nanoparticles. *Appl. Phys. Lett. 77*, 779−781.

(17) Velapoldi, R. A., and Mielenz, K. D. (1980) Standard Reference Materials: A Fluorescence SRM: Quinine Sulfate Dihydrate (SRM 936). *NBS Spec. Publ.* 260−264.

BC030047K

AMD3100 Conjugates as Components of Targeted Nonviral Gene Delivery Systems: Synthesis and in Vitro Transfection Efficiency of CXCR4-Expressing Cells

Bertrand Le Bon,[†] Nathalie Van Craynest,[†] Jean-Michel Daoudi,[†] Christophe Di Giorgio,[†] Abraham J. Domb,[‡] and Pierre Vierling*[,†]

Laboratoire de Chimie Bioorganique, UMR 6001 CNRS, Faculté des Sciences, Université de Nice-Sophia Antipolis, 06108 Nice Cédex 2, France, and Department of Medicinal Chemistry and Natural Products, School of Pharmacy, Faculty of Medicine, The Hebrew University, Jerusalem 91120, Israel. Received December 5, 2003

We describe the synthesis of a series of AMD3100−lipid and AMD3100−polycationic conjugates which were used as components of targeted lipoplexes (in conjunction with (poly)cationic lipids) and polyplexes, respectively, for mediating specific gene transfer into cells expressing CXCR4 which displays a high affinity for AMD3100. Transfection studies were investigated with suspension CXCR4(+) human lymphoma Jurkat cells and with adherent CXCR4(−) human glioblastoma T98G and human lung carcinoma A549 cells lines in order to demonstrate a receptor-mediated endocytosis pathway and to minimize nonspecific transfection pathways. Altogether, our results show that polyplexes formulated with AMD-labeled polymers constitute, under certain conditions, specific gene transfer systems into suspension CXCR4(+) Jurkat cells. This is more particularly the case when the nonspecific transfection pathways are minimized (i.e. for $N/P \leq 2.5$ AMD-labeled polyplexes) and in the presence of phorbol myristate acetate which triggers CXCR4 receptor endocytosis of the AMD-labeled polyplexes to a larger extent than that of their respective nonlabeled ones. Although encouraging, the transfection specificities and efficiencies obtained with these compounds should however be improved. This study also illustrates the difficulties to demonstrate and to obtain a specific and efficient gene transfer system with cationized ligand-labeled DNA particles which also provide receptor-independent nonspecific gene transfer to cells, and more particularly to adherent cells.

INTRODUCTION

The specific and efficient delivery of therapeutic genes into targeted cells such as cancer or virus-infected cells is one of the important goals in gene therapy. To increase DNA uptake by cells, viral and nonviral vehicles have been developed. To trigger receptor-mediated gene delivery and to increase cell and tissue DNA uptake specificity, various cell targeting ligands (for a recent review see ref 1)), including RGD peptides (*2*), folate (*3*, *4*), transferrin (*5*), saccharides (*6*, *7*), or antibodies (*7*), were conjugated to the DNA vectors. As part of our contribution into this field, we elaborated novel AMD3100-lipid and polycationic conjugates as targeting components of nonviral DNA vectors (lipoplexes or polyplexes) for specific gene transfer into CXCR4(+) cells. AMD3100 (Figure 1) is one of the rare nonpeptidic and small synthetic molecules that binds with a high affinity and selectivity to CXCR4 thus blocking HIV entry into T-lymphocytes (*8*−*12*). The CXCR4 chemokine receptor is indeed the coreceptor used by HIV-1 X4 strains for infecting T-lymphocytes which are one of the predominant cell HIV reservoirs (*13*−*15*). CXCR4 plays an important role not only in HIV progression but also in chemotactic T-cell responses and in T-lymphocyte recruitment at sites of inflammation (*16*). CXCR4 has been recently described as one of the overexpressed receptors on glioblastoma tumors (*17*−*23*). CXCR4 appears also to play a central role in breast carcinoma metastasis (*24*).

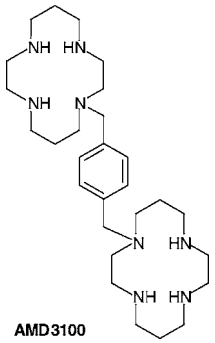
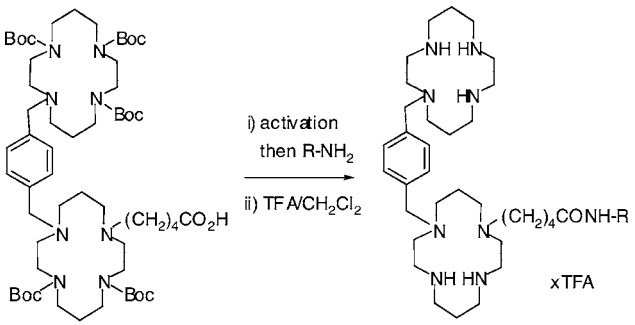


Figure 1. Chemical structure of AMD3100 (*8*).

In an effort to address a specific gene delivery toward CXCR4-expressing tumors and T-lymphocytes, we report herein on (i) the synthesis of the AMD3100-lipid and AMD3100-polycationic conjugates (derivatives DC18-[NH]-[AMD], PEI-[AMD]*p*, or ^{i}Bu[NH_2]-80-[AMD]4 in Figure 2, respectively), and (ii) our in vitro attempts to transfect Jurkat cells, a CXCR4(+) human cell line grown in suspension, via a receptor-mediated endocytosis pathway with AMD3100-labeled DNA complexes. However, cationized DNA particles can also provide receptor-independent gene transfer to cells, owing to electrostatic interactions with anionic proteins which might be expressed on their cell surface (*25*, *26*). Therefore, we also report on the ability of AMD3100-labeled lipoplexes and polyplexes to mediate, in vitro, a nonspecific gene transfer into adherent CXCR4(−) A549 and T98G cells. Indeed,

* To whom correspondence should be addressed. E-mail: vierling@unice.fr.
[†] Université de Nice-Sophia Antipolis.
[‡] The Hebrew University.

10.1021/bc034220o CCC: $27.50 © 2004 American Chemical Society
Published on Web 02/17/2004



R-NH_2 =

$[H(CH_2)]_{18}]_2NC(O)CH_2CH_2SCH_2CH_2C(O)NHCH_2CH_2NH_2$: DC18-[$NH_2$]

$[Me_2CHCH_2]_2NC(O)CH_2CH_2S[CH_2CH[C(O)NHCH_2CH_2NH_2]]_{95}$-H: iBu-[$NH_2$]$_{95}$

PEI (branched, 25 kDa)

Figure 2. Synthetic pathway to the lipid and polycationic AMD3100 conjugates. For R-NH_2 = DC18-[NH_2]: (i) BOP/NEt_3/CH_2Cl_2; for R-NH_2 = ^{i}Bu[NH_2]95: (i) BOP/NEt_3/CH_3CN; for R-NH_2 = PEI: (i) EDC/HOBt or DCC/NHS in CH_3CN.

adherent cells are easier to transfect nonspecifically than cells grown in suspension. This is likely due to overexpression of anionic proteoglycans on the surface of adherent cells (*25*, *26*) and to sedimentation of the DNA complexes onto the adherent cell monolayer recovering the well bottom. This study was aimed at optimizing the conditions under which a specific gene transfer into suspension CXCR4(+) Jurkat cells could more likely be evidenced by minimizing the nonspecific transfection pathways. The AMD3100-labeled lipoplexes and polyplexes were formulated with the DC18-[NH]-[AMD] conjugate and well-documented (poly)cationic lipids (i.e. DOTAP (*27*), DOGS (*28*), or DC18-[NH_2]20 (*29*)), and with the AMD3100-labeled polycationic polymers shown in Figure 2, respectively. With the aim at demonstrating a specific receptor-mediated transfection process, all these assays were performed in the absence or presence of an excess of "free" AMD3100 as CXCR4 antagonist. These additional control experiments were also intended to highlight the effects of AMD3100 (i) on the nonspecific transfection of control CXCR4(−) cells with AMD3100-labeled DNA complexes, and (ii) on the specific transfection of CXCR4(+) cells with control nonlabeled DNA complexes. Indeed, AMD3100 is an octaamine that might coat onto the DNA complexes and/or adsorp onto the cells and, consequently, it can then take part in both these transfection processes. In the case of the CXCR4(+) Jurkat cells, transfection experiments were also performed in the absence or presence of phorbol myristate acetate (PMA) which was shown to enhance the transfection of these suspension cells (*30*) and to trigger CXCR4 receptor endocytosis (*31*), even in the presence of AMD3100 (*32*).

MATERIALS AND METHODS

General Experimental and Analytical Conditions. All the reactions were performed in anhydrous solvents under dry and oxygen-free nitrogen. The purifications by column chromatography were carried out using silica gel 60 (Merck, 70−230 mesh) and chloroform ($CHCl_3$), dichloromethane (CH_2Cl_2), methanol (MeOH), or mixtures thereof as indicated. Purifications by exclusion gel chromatography were performed on Sephadex LH-20 or LH-60 (Fluka, Amersham) in methanol. Advancement of the reactions was followed by thin-layer chromatography (TLC) on silica plates (SDS 60F254, 60/15 μm). The following development systems were used: UV light (254 nm); Draggendorff reagents (Sigma), ninhydrin (Sigma), H_2SO_4, and $KMnO_4$.

DOGS (dioctadecylamidoglycylspermin tetrafluoroacetate) (*28*), DC18-[NH_2], DC18-[NH_2]20 (*29*), ^{i}Bu-[NH_2]-95 (*33*), AMD3100, and Boc-AMD-$(CH_2)_4$COOH (see structure in Figure 2) (*34*) were prepared according to the literature. DOTAP (1,2-dioleoyloxy-3-(trimethylammonio)propane iodide), DOPE (dioleylphosphatidylethanolamine), DCC (dicyclohexylcarbodiimide), NHS (*N*-hydroxysuccinimide, Sigma), HOBt (hydroxybenzotriazole), EDC (*N*-(3-dimethylaminopropyl)-*N*′-ethylcarbodiimide), NEt_3 (triethylamine), and TFA (trifluoroacetic acid) were purchased from Sigma. BOP (benzotriazol-1-yloxytris-(dimethylamino)phosphonium hexafluorophosphate) came from Calbiochem. These chemicals were used without further purifications.

^{1}H, ^{13}C, and ^{19}F NMR spectra were recorded on a Bruker AC-200 at 200, 50.3, and 188.3 MHz, respectively. Chemical shifts (δ) were measured relative to $CHCl_3$ (δ 7.27 ppm) or CH_3OD (δ 3.35 ppm) for ^{1}H, to $CDCl_3$ (δ 76.9 ppm) for ^{13}C and expressed indirectly in relation to TMS, and to CCl_3F as internal reference for ^{19}F. The following abbreviations are used to describe the signal multiplicities: s (singlet), d (doublet), t (triplet), q (quadruplet), and m (multiplet). The signals are listed as follows: δ in ppm (multiplicity, integration, coupling, and attribution). Melting points were measured on a Electrothermal Digital Series 9100 and were not corrected. Mass spectra (MS) were recorded on a Finnigan MAT TSQ 7000 equipped with an atmospheric pressure ionization (API) source. Electrospray ionization mass spectrometry (ESI-MS) was used. This method used in positive mode can give either a $(M + H)^+$ or a $(M + Na)^+$ signal.

Chemistry. *General Boc-Deprotection Procedure.* The *N*-Boc-protected derivatives in 4 mL of anhydrous TFA:CH_2Cl_2 (1:1 v:v) were stirred for 1−5 h at 0 °C and then for a further 4 h period at room temperature until disappearance of the starting material (TLC and/or ^{1}H NMR monitoring). The reaction mixture was then evaporated under reduced pressure, followed by several coevaporations with a CH_2Cl_2:cyclohexane mixture (1:1 v:v), and the crude residue was purified by alumina column chromatography, size exclusion gel column chromatography, or directly lyophilized giving the desired derivatives as TFA salts.

Synthesis of DC18-[NH]-AMD. To a solution of 28 mg (0.03 mmol) of DC18-[NH_2], 36 mg (0.03 mmol) of Boc-AMD-$(CH_2)_4$COOH, and 10 μL (0.07 mmol) of NEt_3 in 2 mL of CH_2Cl_2 at 0 °C was added 16 mg (0.03 mmol) of BOP. The solution was stirred during 4 h at room temperature. After completion of the reaction followed by TLC, the organic phase was washed successively with $NaHCO_3$ (5%), $KHSO_4$ (5%), and water and dried over Na_2SO_4. The solution was then filtered and concentrated under vacuum. The residue was further purified by silica gel column (CH_2Cl_2:MeOH, from 100:0 to 9:1: v/v as eluent) and LH-20 gel permeation chromatography (CH_2Cl_2) to give 44 mg (0.02 mmol 74%) of DC18-[NH]-AMD-(Boc) as a white solid [TLC (CH_2Cl_2:MeOH, 9:1 v:v, ninhydrin): R_f = 0.6; ^{1}H NMR ($CDCl_3$): 0.85 (t, 6H, $^3J_{HH}$ = 6.5 Hz, CH_3); 1.10−1.30 (m, 60H, $(CH_2)_{15}$); 1.30−2.00 (m, 61H, CH_3(Boc), CH_2CH$_2$N and CH_2CH$_2$CO); 2.00−2.70 (m, 20H, CH_2CO and CH_2N); 2.70−2.90 (m, 4H, CH_2S); 3.10−3.60 (m, 28H, CH_2NBoc and CH_2Ph); 6.70−

7.10 (m, 2H, NHCO); 7.15 (s, 4H, Ph); ^{13}C NMR $CDCl_3$): 14.2 (s, CH_3); 22.7 (s, CH_2CH_3); 27.1 and 28.1 (s, CH_2S); 28.4 and 28.5 (s, CH_3(Boc)); 26.9, 27.1,27.8, 29.1, 29.4, 29.5 and 29.7 (s, $(CH_2)_{14}$); 31.9 (s, $CH_2CH_2CH_3$); 33.3 and 36.5 (s, CH_2CO); 39.8 and 40.0 (s, CH_2NH); 46.3 and 48.0 (s, CH_2NCO); 45.0−49.0 and 51.0−56.0 (m, CH_2N et CH_2-NBoc); 59.4 (sl, CH_2Ph); 79.5 and 79.7 (s, C(Boc)); 128.9 (sl, CH_2Ph); 137.2 (sl, C(Ph)); 155.6 (s, CO(Boc)); 170.6 (s, CON); 172.3 and 174.1 (s, CONH); resonances for $CH_2CH_2CH_2CO$ and $CH_2CH_2CH_2N$ could not be detected]. The Boc-deprotection procedure, when applied to 44 mg (0.02 mmol) DC18-[NH]-AMD(Boc), afforded, after purification by alumina column chromatography (eluent CH_2-Cl_2:MeOH from 100:0 to 50:50 v:v) and lyophilization, 21 mg (0.01 mmol, 39%) of DC18-[NH]-AMD as its octa-TFA salt (white solid). ^{1}H NMR ($CDCl_3$): 0.85 (t, 6 H, $^3J_{HH}$ = 6.5 Hz, CH_3); 1.10−1.40 (m, 60H, $(CH_2)_{15}$); 1.40−2.10 (m, 16H, $CH_2CH_2CH_2N$ and $CH_2CH_2CH_2CO$); 2.10−3.10 (m, 44H, CH_2CO, CH_2N and CH_2S); 3.10−3.80 (m, 12H, CH_2-NHCO, CH_2NCO and CH_2Ph); 4.20−4.90 (m, 8H, NH); 7.31 (s, 4H, Ph); 7.65−8.10 (m, 2H, NHCO). ^{13}C NMR ($CDCl_3$): 14.2 (s, CH_3); 22.7 (s, CH_2CH_3); 23.9, 24.7, 24.9, 25.8, 26.6 and 27.3 (s, CH_2CH_2N and $CH_2CH_2CH_2CO$); 27.1 and 28.1 (s, CH_2S); 26.9, 27.4, 27.8, 29.1, 29.4, 29.5 and 29.7 (s, $(CH_2)_{14}$); 31.9 (s, $CH_2CH_2CH_3$); 33.5 (s, CH_2-CO); 36.5 (sl, CH_2CO); 39.4 and 39.8 (s, CH_2NHCO); 46.2 and 48.0 (s, CH_2NCO); 45.5, 46.5, 46.6, 47.6, 48.4, 49.1, 49.5, 49.7, 50.4, 51.5, 51.9 and 52.5 (s, CH_2N); 57.5 and 58.2 (s, CH_2Ph); 129.6 (sl, CH(Ph)); 130.0 (s, CH(Ph)); 136.4, 136.5, 136.7 and 138.3 (s, C(Ph)); 170.7 (s, CON); 171.9 and 172.1 (s, CONH); 174.1 and 174.5 (s, CONH). The CF_3CO_2 resonances could not be located. The doubling of some signals is due to the restricted rotation of the amide bond. ^{19}F NMR (CD_3OD): −76.7 ($CF_3CO_2^-$). ESI-MS: $m/2z$ = 655.5 and m/z =1309.2 in agreement with the mass calculated for $[C_{77}H_{149}N_{11}O_3S + 2H^+]/2$ and $[C_{77}H_{149}N_{11}O_3S + H^+]$, respectively.

Synthesis of ^{i}Bu-[NH_2]80-[AMD]4. A 10 mg (9.0 μmol) amount of Boc-AMD-$(CH_2)_4$COOH, 4.0 mg (9.0 μmol) of BOP, 12.6 μL (90 μmol) of NEt_3, and 10 mg (0.47 μmol) of ^{i}Bu-[NH_2]95 were dissolved in 4 mL of CH_3CN at 0 °C. The solution was stirred overnight at room temperature. The solution was concentrated under vacuum. The resulting residue was washed with Et_2O and purified by gel permeation chromatography using a LH-20 column (MeOH) to give 6.0 mg (0.24 μmol) of compound ^{i}Bu-[NH_2]-*n*-[AMD(Boc)]*p* with n = 80 and p = 4, as a white amorphous solid [^{1}H NMR (CD_3OD):0.74−0.90 (m, 12H, CH_3, ^{i}Bu); 1.00−2.80 [m, 539 (= 3*n* + 73*p* + 7)H, CH_2-CH, CH_2S, CH_2CO, $C(CH_3)_3$, $N(CH_2)_4CO$, NCH_2CH_2-CH_2N, NCH_2CH_2N,]; 2.90−3.70 [m, 420 (= 4*n* + 24*p* + 4)H, CH_2NH]; 7.26 (sl, 16 (= 4*p*)H, Ph) in agreement with n = 80 and p = 4]. The Boc-deprotection procedure, when applied to 6.0 mg (0.24 μmol) of ^{i}Bu-[NH_2]80-[AMD-(Boc)]4, led after purification by LH-20 gel permeation chromatography (MeOH) and lyophilization to 5.9 mg (0.24 μmol) of ^{i}Bu-[NH_2]80-[AMD]4 as a white solid. ^{1}H NMR (CD_3OD): 0.70−0.90 (m, 12H, CH_3 ^{i}Bu); 1.10−2.80 [m, 359 (= 3*n* + 28*p* + 7)H, CH_2CH, CH_2S, CH_2CO, $NCH_2CH_2CH_2N$, $N(CH_2)_4CO$, NCH_2CH_2N]; 2.85−3.70 [m, 420 (= 4*n* + 24*p* + 4)H, CH_2NH_2, CH_2Ph]; 7.34 (m, 16 (= 4*p*)H, CH−Ph) in agreement with n = 80 and p = 4. ^{19}F NMR (CD_3OD): −76.7 ($CF_3CO_2^-$).

Synthesis of PEI-[AMD]p (p = 17, 28) Conjugates. A 21 mg (1.9 μmol) amount of Boc-AMD-$(CH_2)_4$COOH, 7.3 mg (38 μmol) of EDC, and 7.7 mg (57 μmol) of HOBt were dissolved at 0 °C in 4 mL of CH_3CN. The solution was stirred overnight at room temperature and then cooled to 0 °C before 16.4 mg (0.65 μmol) of PEI (25 kDa) (respectively 7.8 mg, 0.31 μmol) in 4 mL of H_2O (respectively 2 mL) was added. After disappearance of the activated acid (TLC monitoring), the solution was concentrated under vacuum. The residue was then purified by several LH-20 and LH-60 gel permeation chromatographies (MeOH) to give 18.2 mg of PEI-[AMD(Boc)]17 (respectively 9.3 mg of PEI-[AMD(Boc)]28) as a resin [^{1}H NMR (CD_3OD): 1.00−2.00 [m, 57pH, $C(CH_3)_3$, CH_2CH_2-CH_2N, $NCH_2(CH_2)_2CH_2CON$]; 2.00−3.70 [m, (40*p* + 2320)H, CH_2-PEI, CH_2CO, CH_2N, CH_2Ph]; 7.24−7.29 (m, 4pH, CH−Ph), in agreement with p = 17 (respectively p = 28)]. The general BOC-deprotection procedure, when applied to 18.2 mg of PEI-[AMD(Boc)]17 (respectively 9.3 mg of PEI-[AMD(Boc)]28), gave 33 mg of PEI-[AMD]17 (respectively 13 mg of PEI-[AMD]28) as a white powder. ^{1}H NMR (D_2O): 0.70−2.70 [m, 12pH, $NCH_2CH_2CH_2$, $NCH_2(CH_2)_2CH_2CON$]; 2.75−4.20 (m, (40*p* + 2320)H, CH_2-PEI, CH_2N, CH_2CO, CH_2Ph]; 7.30−7.40 (m, 4pH, CH−Ph) in agreement with p = 17 (respectively p = 28). ^{19}F NMR (CD_3OD): −76.7 ($CF_3CO_2^-$).

Preparation of the DNA Complexes. The lipoplexes and polyplexes were formulated with the luciferase-encoding plasmid pTG11033 (pCMV-intronHMG-luciferase-SV40pA; 9572 bp) and pTG11236 (pCMV−SV40pA, 5739 bp), respectively. These plasmids were produced by Transgène SA (Strasbourg, France). The endotoxin content of the plasmid preparation was checked using a Limulus Amebocyte Lysat kit (Biogenic, Maurin, France). This value was below 1 endotoxin unit/mg of plasmid, hence below the 5 e.u./mg of DNA recommended for in vivo protocols.

The lipoplexes were formulated from (poly)cationic lipids, CL (CL = DOGS, DOTAP or DC18-[NH_2]20), with and/or without DOPE or DC18-[NH]-AMD. These lipids were dissolved in an appropriate solvent ($CHCl_3$ and/or MeOH or EtOH) at a concentration of 10 mg/mL. Adequate volumes of each of the desired lipid solution were mixed in order to obtain DOGS:DOPE:DC18-[NH]-AMD and DOTAP:DOPE:DC18-[NH]-AMD 1:1:*x* (*x* = 0 and 0.1) mol, and DC18-[NH_2]20:DC18-[NH]-AMD 1:*x* (*x* = 0, 0.1 and 0.2) mol solutions. Each solution was concentrated under vacuum and dispersed in a glucose solution (5%) in order to obtain a final concentration of 1 mg/mL with respect to CL. The preparations were stirred during 14 h and finally homogenized in an ultrasound bath (Branson B-30) for 5 min in order to obtain liposomal dispersions. The volumes of liposomal dispersion used to form lipoplexes were calculated according to the desired DNA concentration of 0.1 mg/mL, the *N*/*P* ratio, the molar weight, and the number of potential positive charges in the selected CL (*N* represents the number of cationic amine equivalents brought by CL only; *P* represents the number of phosphate equivalents in DNA). The DNA complexes were formulated by adding a desired volume of liposomal preparation at a CL concentration of 1 mg/mL (in 5% glucose) to the desired volume of DNA solution to reach the desired DNA concentration of 0.1 mg/mL, as described in the literature (*35*, *36*). This preparation was vortexed for 10 s and was used within 24 h for the particle size measurements and the in vitro transfection experiments.

A similar procedure was used for the ^{i}Bu-[NH_2]95, ^{i}Bu-[NH_2]80-[AMD]4, PEI, or PEI-[AMD]*p* (*p* = 17 or 28) polyplexes (final DNA concentration of 0.1 mg/mL), except that they were formulated from solutions of the respective polymer in 5% glucose at a concentration of 10 mg/mL, as described in the literature (*36*, *37*). In the *N*/*P* ratio of the AMD-labeled polyplexes, *N* represents the number of amine equivalents of the labeled polymer which was calculated by dividing the amount of polymer

used by the molecular weight of the monomer unit (as the number of AMD equivalents in the labeled polymers is low with respect to the number of monomer units, this number can be neglected).

Measurement of the Sizes of the DNA Complexes. The average sizes were measured by photon correlation spectroscopy using a Coulter N4Plus particle size analyzer. The analyses were performed at 25 °C, after equilibrating the sample at 25 °C for 20 min. The sample was diluted with 5% glucose in the measurement tube and homogenized. These analyses were carried out on naked plasmids and on complexes having a 10 μg/mL concentration of DNA. Formulations and analyses were reproduced twice.

Agarose Gel Electrophoresis. Each sample (0.5 μg of plasmid) was analyzed by electrophoresis for about 30 min under 75 V/cm, through a 0.8% agarose gel in TAE 1 x (Tris−acetate−EDTA) buffer. The DNA was visualized in 400 mL of TAE buffer containing 40 μL of ethidium bromide (10 mg/mL, Sigma, Saint Quentin Fallavier, France). The plasmid integrity in each sample (0.25 μg) was confirmed by electrophoresis after decomplexing the lipoplexes or polyplexes (10 μL of a plasmid 0.05 mg/mL) with sodium dodecyl sulfate, SDS (10 μL, 80 g/L).

In Vitro Transfection. Twenty-four hours before transfection, adherent A549 (epithelial cells derived from human pulmonary carcinoma) or T98G cells (neural cells derived from human glioblastoma, gift from Laboratoire de Neurobiologie Fondamentale et Clinique, Université de Nice-Sophia Antipolis, France) were grown in Dulbecco's-Modified Eagle culture Medium (DMEM) (Invitrogen, Life Technologies, Cergy Pontoise, France) with 10% fetal calf serum, FCS (Sigma) in 96-well plates (2×10^4 cells per well), in a wet (37 °C) and 5% CO_2/95% air atmosphere. The medium also contained 1% glutamine (200 mM, Sigma), 0.4% gentamicine (10 μg/mL, Sigma) for A549 cells, and 1% glutamine (200 mM, Sigma), 100 μg/mL penicillin and 100 μg/mL streptomycin (Sigma) for T98G cells. Volumes of 10 μL and 5 μL of the above-described lipoplex dispersion were diluted to 100 μL in DMEM supplemented with 10% FCS in order to obtain 1 and 0.5 μg of DNA per well, respectively. The resulting solutions were then added to the cells after the culture medium had been removed. After 4 and 24 h, 50 μL and 100 μL of DMEM supplemented with 30 and 10% FCS were added, respectively. Forty-eight hours after transfection, the culture medium was discarded, and the cells were washed with 100 μL of PBS and then lysed with 50 μL of lysis buffer (Promega, Charbonnières, France). The lysates were frozen at −32 °C awaiting analysis of luciferase activity.

A similar procedure was applied for the transfection of Jurkat cells (T lymphocytes from human leukemia, gift from Dr N. Taylor, UMR−CNRS 5535, IGMM, Montpellier, France). Twenty-four hours before transfection, Jurkat cells were grown in suspension in RPMI-1640 Glutamax II (Invitrogen, Life Technologies, Cergy Pontoise, France) containing 100 μg/mL penicillin and 100 μg/mL streptomycin with 10% FCS in 96-well plates (1×10^5 cells per well). The 96-well plates were centrifuged (5 min, 500 rcf), and the medium was removed and replaced by 100 μL of RPMI-1640 supplemented with 10% FCS containing the desired amount of complexed DNA. After 4 and 24 h, 50 μL and 100 μL of RPMI-1640 supplemented with 30 and 10% FCS, respectively, were added. Forty-eight hours after transfection, the plates were centrifuged (5 min, 500 rcf), the culture medium was removed, and the cells were then lysed with 50 μL of lysis buffer (Promega, Charbonnières, France). The lysates were frozen at −32 °C awaiting analysis of luciferase activity.

For the transfection experiments of the A549 or T98G cells (respectively Jurkat cells) performed in the presence of AMD3100, 30 min before addition of the DNA complexes, the medium was removed (respectively after centrifugation of the 96-well plates for 5 min at 500 rcf) and replaced by 50 μL of AMD3100 solution (0.6 mg/mL; respectively 2 mg/mL) in DMEM (respectively RPMI-1640) containing 10% FCS. A 50 μL volume of a solution containing the DNA complexes at a DNA concentration of 20 or 10 μg/mL was then added to the medium to reach a final volume of 100 μL and a DNA concentration of 1 or 0.5 μg per well. These solutions were obtained by diluting 20 or 10 μL of the above-described stock DNA complexes at DNA concentration of 0.1 mg/mL with DMEM (respectively RPMI-1640) containing 10% FCS to 100 μL.

For the transfection experiments of the Jurkat cells performed in the presence of PMA (Phorbol-Myristate-Acetate, Sigma) which were also run at 37 °C, 3 h after addition of the above-described DNA complexes to the cells, 1 μL of PMA solution (10 μg/mL in DMSO) was added to the medium in order to reach a final concentration of 100 ng/mL per well.

Determination of Luciferase Expression. The measurement was done for 10 s on 10 μL of the lysis mixture in a Berthold LB96P luminometer in dynamic mode, using the "Luciferase" determination system (Promega) in 96-well plates. The total protein concentration per well was determined using conventional techniques (BCA test, Pierce, Montluçon, France). For cells grown in the absence of DNA complexes, a well contains 30−50 μg of proteins for the T98G and A549 cells, and 90−110 μg of proteins for the Jurkat cells. Each DNA formulation was prepared twice, and each preparation was tested at least in triplicate.

Statistical Analyses. Statistical tests were performed with STATGRAPHICS Plus5.0 software. Analysis of variance (Anova) was run on the logarithmic transformation of luciferase expression levels (Log10(fg luciferase/mg protein)) or on cell viability percentages to fit normal distributions of the data. Up to five factors, i.e., component(s) of the lipoplex or polyplex formulation, DNA amount per well (0.5 and 1 μg per well), *N*/*P* ratio, presence or not of AMD3100, and presence or not of PMA, were analyzed as sources of the variation of logarithmic transformation of the transfection levels, using a multiple comparison procedure. Tukey's honestly significant difference (HSD) method was used to discriminate among the means of the logarithmic transformation of luciferase expression levels.

RESULTS AND DISCUSSION

Synthesis. Conjugation of AMD3100 to the aminolipid DC18-[NH_2] (*29*), telomer ^{i}Bu-[NH_2]95 (*33*), or branched 25 kDa PEI was performed from the *N*-pentanoic *N*-Boc-protected AMD3100 derivative, Boc-AMD-$(CH_2)_4$COOH (*34*), using a conventional two-step procedure (Figure 2). This procedure consisted of (i) the coupling of Boc-AMD-$(CH_2)_4$COOH with the amino derivative via BOP/NEt_3, EDC/NHS, or HOBt activation, followed by (ii) the Boc-deprotection of the AMD moiety with an excess of TFA: CH_2Cl_2 (1:1).

For the reactions involving the ^{i}Bu-[NH_2]95 and PEI polyamines which contain a mean of 95 and 145 primary amino functions, respectively, the conjugation was per-

formed with 1 equiv of Boc-AMD-$(CH_2)_4$COOH for 10 amino equivalents of ^{i}Bu-[NH_2]95 or PEI and for 30 amino equivalents of PEI. The resulting Boc-AMD conjugates were purified by exclusion gel chromatography (LH-20 or LH-60). The average numbers of grafted Boc-AMD residues and of unsubstituted NH_2 groups in (i) ^{i}Bu-[NH_2]80-[AMD(Boc)]4 and (ii) PEI-[AMD]*p* ($p = 17$ and 28) were determined by ^{1}H NMR by comparing the integration of the aromatic and Boc protons with the integration (i) of the methyl (isobutyl) and all the other remaining protons, and (ii) of the methylene protons of PEI, respectively. The quantitative Boc-deprotection was confirmed by ^{1}H NMR (absence of the resonances corresponding to the Boc protons).

Formation and Characterization of Targeted DNA Complexes. The nontargeted (control) and targeted lipoplexes were formulated from the cationic DOGS: DOPE (1:1 mol), DOTAP:DOPE (1:1 mol), or DC18-[NH_2]20 formulations without and with 10 or 20 mol % of the DC18-[NH]-AMD conjugate, respectively. The control and targeted polyplexes were prepared from ^{i}Bu-[NH_2]95 or PEI and from the telomer ^{i}Bu-[NH_2]80-[AMD]4 or PEI-[AMD]*p* ($p = 17$, 28) conjugates, respectively. In addition, DNA complexes were also formulated with AMD3100 alone. All these targeted and control DNA complexes were further prepared using various *N*/*P* ratios (10, 5, 2.5, 1.25, and 0.8) where *N* is the number of amine equivalents of the DNA-condensing (poly)cationic lipid or polymer, and *P* the number of DNA phosphate equivalents. Thus, for a given *N*/*P* ratio and a given CL, the various CL:DOPE:DC18-[NH]-AMD (1:*x*:*y* mol with $x = 0$ or 1 and $y = 0$, 0.1, or 0.2) lipoplexes listed in Table 1 contain the same molar amount of CL. However, their exact N_{total}/P ratios are equal to 1.4 × *N*/*P* or 1.8 × *N*/*P* when 10 or 20 mol % of DC18-[NH]-AMD was included in the formulation, respectively. Indeed, one AMD unit is equivalent, at physiological pH, to four protonated amines, considering the fact that the pK_a values of the cyclam moiety are of 11.5, 10.3, 1.6, 0.9 (*38*). These studies were performed with luciferase-encoding plasmids, also used for the in vitro transfection screening assays (see below). The procedure applied for the formulation of the DNA complexes relied on the dilution from CL:DOPE:DC18-[NH]-AMD (1:*x*:*y* mol with $x = 0$ or 1 and $y = 0$, 0.1, or 0.2) liposomal dispersions, or from ^{i}Bu-[NH_2]80-[AMD]4, PEI-[AMD]*p* ($p = 17$, 28), ^{i}Bu-[NH_2]95, or PEI solutions in 5% glucose. Their mean average sizes and those of the naked plasmids were measured by light scattering spectroscopy and are collected in Table 1. All the formulations were also analyzed by gel electrophoresis (data not shown) which indicated the presence of fully complexed (not accessible to ethidium bromide) plasmids for $N/P \geq 2.5$ whereas accessible DNA was observed for *N*/*P* 1.25 and 0.8. It is noticeable that all the targeted and control lipid formulations and polymers as well as the octaamine AMD3100 alone were able to condense DNA into often small-sized particles (Table 1). Furthermore, gel electrophoresis assays performed in the presence of excess SDS showed that, with respect to dissociation, the DNA/AMD3100 complexes displayed a stability that is comparable and higher to that of the polyplexes and lipoplexes, respectively: indeed for $N/P \geq 2.5$, the plasmid remained still partially complexed to AMD3100 or to any of the targeted and control polymers, while fully decomplexed plasmid was detected for any of the lipoplexes investigated here (data not shown).

It is worth noting that formulation of labeled lipoplexes with 10 or 20% mol of DC18-[NH]-AMD conjugate had no effect on their mean particle sizes (Table 1). Indeed, for a given cationic lipid and *N*/*P* ratio, polydispersed preparations of particles in the 90−250 nm range or precipitates for a *N*/*P* ratio of 1.25 were measured, whether DC18-[NH]-AMD was added or not. Similar results were obtained with the nontargeted and targeted polyplexes which display a mean size in the 115−300 and 90−250 nm range, respectively (Table 1).

It should be further emphasized that several *N*/*P* 2.5, 1.25 and even 0.8 formulations do not precipitate while most often precipitates were formed with (poly)cationic lipids for *N*/*P* 2.5 or 1.25 (*35*, *39*, *40*). These results are indeed worth being noted if in vivo uses of such formulations are contemplated.

Table 1. Mean Sizes Determined by Light Scattering Spectroscopy of the Lipoplexes and Polyplexes Formed between Plasmid PTG11033 and Lipids, and between Plasmid PTG11236 and Polycationic Polymers, Respectively. The Sizes of the Naked Plasmids Ranged from 1.0 to 1.1 μm

formulation	molar ratio	*N*/*P* ratio[a]	mean diameter in nm (SD)
DOGS:DOPE:DC18-[NH]-AMD	1:1:0	5	115 (40)
	1:1:0.1	5	nd[b]
	1:1:0.2	5	120 (45)
DOTAP:DOPE:DC18-[NH]-AMD	1:1:0	2.5	150 (50)
	1:1:0.1	2.5	130 (50)
	1:1:0.2	2.5	140 (50)
	1:1:0	0.8	170 (50)
	1:1:0.1	0.8	250 (75)
	1:1:0.2	0.8	170 (50)
DC18-[NH_2]20:DC18-[NH]-AMD	1:0	10	nr[c]
	1:0.1	10	nr[c]
	1:0.2	10	nr[c]
	1:0	5	100 (35)
	1:0.1	5	110 (40)
	1:0.2	5	110 (45)
	1:0	2.5	100 (35)
	1:0.1	2.5	90 (30)
	1:0.2	2.5	95 (35)
	1:0	1.25	p[d]
	1:0.1	1.25	p[d]
	1:0.2	1.25	p[d]
	1:0	0.8	100 (35)
	1:0.1	0.8	100 (30)
	1:0.2	0.8	100 (35)
AMD3100[f]		10	nr[c]
		5	95 (30)
		2.5	140 (45)
		2.5	*p*[d]
		1.25	130 (45)
		1.25	*165 (l*[e]*)*
		0.8	140 (50)
		0.8	*425 (l*[e]*)*
^{i}Bu[NH_2]95		2.5	115 (40)
		1.25	p[d]
		0.8	120 (45)
^{i}Bu[NH_2]80-[AMD]4		2.5	p[d]
		1.25	180 (70)
		0.8	150 (l[e])
PEI (25 kDa)		2.5	p[d]
		1.25	270 (70)
		0.8	290 (l[e])
PEI-[AMD]28		2.5	140 (l[e])
		1.25	90 (l[e])
		0.8	175 (25)
PEI-[AMD]17		2.5	160 (10)
		1.25	232 (l[e])
		0.8	245 (20)

[a] *N* = amine equivalents of the cationic lipid or polymer: *P* = plasmid phosphate equivalents. For the formulations containing 10 or 20 mol % of DC18-[NH]-AMD, the exact N_{total}/P ratio is equal to 1.4 × *N*/*P* or 1.8 × *N*/*P*, respectively. [b] nd = not determined. [c] nr = not reproducible. [d] p = precipitate. [e] l = large. [f] With plasmid pTG11033 and in italics with plasmid pTG11236.

In Vitro Transfection. Our main objective was to demonstrate that targeted lipoplexes or polyplexes formulated with AMD3100 conjugates (used as targeting component in the lipoplexes or as condensing and targeting components in the polyplexes), were able to specifically deliver genes to cells expressing CXCR4 chemokine receptors. However, cationic DNA complexes also provide receptor-independent gene transfer to cells (and more particularly to adherent cells) which involves electrostatic interactions between the cationized-DNA particles and the anionic cell proteoglycans expressed on the cell surface (*25*, *26*). It was therefore necessary to determine the conditions under which a nonspecific gene transfer process into CXCR4(−) or CXCR4(+) cells can occur with the AMD-labeled lipoplexes and polyplexes. To evaluate the "nonspecific" transfection potential of the targeted formulations into CXCR4(−) cells and to further minimize the nonspecific transfection pathway into CXCR4-(+) cells, we selected adherent cells (i.e. human lung carcinoma A549 and human glioblastoma T98G cells) and suspension cells (i.e. lymphoma Jurkat cells), respectively. Indeed, adherent cells, which overexpress anionic proteoglycans on their cell surface, are much easier to transfect non specifically than suspension cells.

Aiming at these goals, the potential of the various above-described CL:DOPE:DC18-[NH]-AMD (1:*x*:*y* mol with $x = 0$ or 1 and $y = 0.1$ or 0.2) lipoplexes and ^{i}Bu-[NH_2]80-[AMD]4, PEI-[AMD]*p* polyplexes for mediating a nonspecific and a specific transfection was screened in vitro on control adherent CXCR4(−) A549 and T98G cells, and on suspension CXCR4(+)Jurkat cells, respectively. The (non)expression of CXCR4 on these three cell lines was attested by FACS analysis. Though literature has reported CXCR4-expression on various human primary and cultured glioblastoma cells (*17*−*23*) as well as on A549 cells (*41*), we found that CXCR4 was neither expressed on the glioblastoma T98G cells nor on the A549 cells we used for our in vitro transfection assays. Control experiments were also realized with nontargeted CL:DOPE (1:*x* mol with $x = 0$ or 1) lipoplexes, ^{i}Bu-[NH_2]95 and PEI polyplexes, AMD3100/DNA complexes, and naked DNA. The transfection efficiency of these DNA complexes (expressed in femtograms (fg) of luciferase/mg of protein) was evaluated (i) in the absence or presence of AMD3100 (1 mg/well) for the reasons stated in the Introduction, (ii) for a *N*/*P* ratio of 0.8, 1.25, 2.5, 5, and/or 10, (iii) for a DNA dose of 0.5 and 1 μg/well, and (iv) in the presence of 10% serum. The cell viability of the DNA complexes was also checked by determining the total protein amount per well of the transfected cells relative to that measured for untreated cells. It should also be emphasized that two different plasmids were used for transfecting the adherent and suspension cells, respectively. Importantly, we selected pTG11236 for transfecting the latter ones. Indeed, it was found in our laboratory that higher luciferase expression levels (up to 2 orders of magnitude) were obtained upon transfection of adherent A549 cells with pTG11236-based lipoplexes rather than with pTG11033-based ones (*29*, *33*). This was more particularly of concern with the suspension cells that are more difficult to transfect than the adherent ones. The higher efficiency of pTG11236 is to some extent related to its shorter size (5739 bps vs 9572 bps for pTG11033), owing to the shorter size of its 16S/19S SV40 intron as compared to that of the HMG intron of pTG11033. Thus, for a given DNA amount, a larger number of DNA copies can be delivered with pTG11236 than with pTG11033.

Transfection of CXCR4(−) A549 and T98G Cells. The results concerning the transfection and cell viability of the control CXCR4(−) A549 and T98G cells with the lipoplexes and their statistical analyses are illustrated in Figures 3 and 4, respectively. As comparable levels of luciferase were obtained in most cases with a DNA dose of 0.5 and 1 μg/well (analysis not shown), only the data for a DNA dose of 1 μg/well are presented in Figure 3. However, the data obtained for both DNA doses were taken for the statistical analyses.

Both cell lines gave very similar results. Indeed, the highest levels of luciferase were obtained with the DOTAP:DOPE lipoplexes and the *N*/*P* 10 PEI polyplexes (Figure 4A and 4B). More importantly, the statistical analysis of the transfection data indicated that labeled lipoplexes, whether formulated with DOGS:DOPE, DOTAP:DOPE, or DC18-[NH_2]20, and 10 or 20 mol % of DC18-[NH]-AMD, do allow DNA transfection with an efficiency comparable with that of their respective nonlabeled formulation (see abscissas b, d, and g(h) as compared to abscissas a, c, and f, respectively in Figure 4A and 4B, and curves g, h as compared to curve f, in Figure 4C and 4D). Furthermore, transfection of the labeled lipoplexes increased with increasing their *N*/*P* ratio, as illustrated in Figure 4C and 4D. It should be noted that lipoplexes formulated with DC18-[NH]-AMD alone, but for a *N*/*P* ratio of 10 only, were able to transfect significantly T98G cells (curve e in Figure 4C). All these observations together led us to foresee a nonspecific endocytosis mechanism proceeding by electrostatic interactions between the cationic (un)labeled lipoplexes and the proteoglycans expressed at the cell membrane of these adherent cells. It is also noticeable that no significant in(de)crease of cell viability could be detected when DC18-[NH]-AMD conjugate was used as lipoplex component (see abscissas b, d, and g(h) as compared to abscissas a, c, and f, respectively, in Figure 4G and 4H).

It should further be emphasized that the various DNA complexes obtained from AMD3100 alone, whatever their *N*/*P* ratio, were unable to transfect the A549 or T98G cells. For these formulations, the levels of luciferase expression were indeed close to those measured for naked DNA (Figure 3). The absence of transfection activity of AMD3100, despite its strong interactions with DNA, are likely related to its pK_a values (11.5, 10.3, 1.6, and 0.9 (*38*)) which are out of the pH range found in the endosomes. As a consequence, AMD3100 is unable to prevent endosome acidification and, consequently, to facilitate the escape of the DNA complexes from the endosomes before their lysosomal destruction.

To highlight the effects of AMD3100 on nonspecific-mediated transfection with the labeled and nonlabeled lipoplexes (Figure 4E and 4F), control experiments were performed in the presence of 30 μg of AMD3100 per well. This dose corresponds to a 30-fold (respectively 2000-fold) molar excess over DC18-[NH]-AMD conjugate for the formulations that contain the highest (respectively lowest) number of AMD equivalents tested, i.e., *N*/*P* 10 lipoplexes containing 20 mol % of DC18-[NH]-AMD and for a DNA dose of 1 μg per well (respectively *N*/*P* 0.8 formulations containing 10% mol of DC18-[NH]-AMD and for a DNA dose of 0.5 μg per well). The statistical analysis of our results showed that AMD3100 likely does not interfere with the nonspecific transfection process of these cells with any type of lipoplexes, except for the transfection of the A549 cells with DOTAP:DOPE:DC18-[NH]-AMD lipoplexes (abscissa d in Figure 4F). In this latter case, the presence of AMD3100 enhanced luciferase expression, and more particularly that with the *N*/*P* 0.8

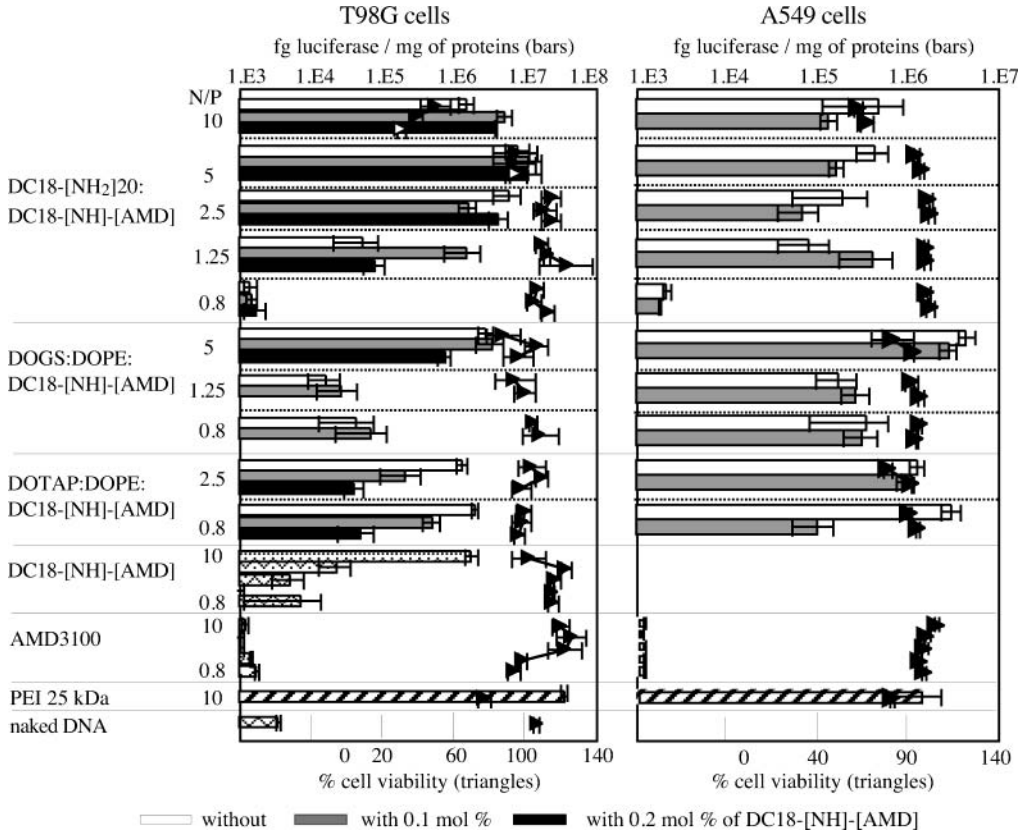


Figure 3. Luciferase expression (bars) and cell viability (triangles) of the pTG11033 complexes made with various lipid formulations [DOGS:DOPE:DC18-[NH]-AMD, DOTAP:DOPE:DC18-[NH]-AMD 1:1:*x* (*x* = 0 and 0.1) mol, and DC18-[NH_2]20:DC18-[NH]-AMD 1:*x* (*x* = 0, 0.1, and 0.2) mol], PEI or AMD3100 in T98G and A549 cells, and for a DNA dose of 1 μg per well. Transfection was performed in the presence of 10% fetal calf serum. Data represent the means ± SEM from two independent experiments, each performed in triplicate (for more details, see Materials and Methods). For more details concerning the *N*/*P* ratio, see footnote of Table 1.

ones (analysis not shown). These results are likely attributable to the electrostatic coating of these "negatively charged" lipoplexes by polycationic AMD3100 and/or to the strong DNA complexing properties of AMD3100 which is accessible in these lipoplexes, as mentioned in the preceding section. The DNA complexing properties of AMD3100 have, in turn, more incidence on lipoplexes that are formulated with monocationic lipids (i.e. DOTAP) than with polycationic lipids (i.e. DOGS).

Transfection of CXCR4(+) Jurkat Cells. The transfection and cell viability results obtained with the CXCR4(+) Jurkat cells and their statistical analyses are illustrated in Figures 5 and 6, respectively. To minimize nonspecific-mediated transfection pathways, mostly formulations of *N*/*P* ratio ≤ 2.5 were investigated. With the aim at demonstrating a specific receptor-mediated transfection process, these experiments were run without and with an excess of "free" AMD3100 as CXCR4 antagonist (100 μg per well, which corresponds to 500 to 1000 equivalents for one AMD-ligand equivalent in the labeled DNA complexes). Therefore, transfection experiments were performed only with polyplexes. Indeed, agarose gel electrophoresis with and without SDS highlighted the much lower stability of the AMD-labeled lipoplexes as compared with that of the AMD3100/DNA, PEI/DNA, or ^{i}Bu-[NH_2]95/DNA complexes (data not shown). The strong interactions between polycationic AMD3100 and DNA were thus expected to modify the integrity of the lipoplexes more drastically than that of the polyplexes. Moreover, AMD3100 was found in some cases to increase the nonspecific transfection pathway (see preceding section). It was thus feared that an unambiguous analysis of the assays run with the labeled lipoplexes and in the presence of AMD3100 could not be performed. The transfection experiments were also run without and with PMA (100 ng per well). Although PMA is a protein kinase C (PKC) activator and a tumor promoter, we selected PMA for this in vitro model study because PMA is known to induce phorbol ester-receptor endocytosis of DNA complexes and to increase transgene expression in Jurkat cells (*30*). As comparable luciferase levels were obtained for a DNA dose of 0.5 and 1 μg per well, only the data corresponding to a DNA dose of 1 μg per well are shown in Figure 5. However, the statistical analyses were performed with the data obtained for both DNA doses.

The control nonlabeled *N*/*P* ≤ 2.5 PEI and ^{i}Bu-[NH_2]-95 polyplexes displayed a transfection efficiency that is comparable to naked DNA (Figure 5), indicating that an enhancement of transfection of the CXCR4(+) Jurkat cells through a CXCR4-receptor-mediated endocytosis process could likely be detected for *N*/*P* ≤ 2.5 polyplexes. These results also confirmed the difficulty of transfecting cells in suspension through a nonspecific pathway (*30*, *43*). Indeed, the Jurkat cells could be transfected only with the *N*/*P* 10 PEI formulation, although moderate levels of luciferase expression (10^4 fg per mg of protein) were obtained (Figures 5 and 7).

When the transfection of the Jurkat cells with the nonlabeled *N*/*P* ≤ 2.5 PEI or ^{i}Bu-[NH_2]95 polyplexes was performed in the presence of AMD3100, neither a decrease nor an increase of luciferase expression was detected (Figure 6). This was also the case for the *N*/*P* 10 polyplexes (Figure 7). These data indicate that polycationic AMD3100 is not able to trigger transfection of the CXCR4(+) Jurkat cells with the nonlabeled PEI or ^{i}Bu-[NH_2]95 polyplexes neither (i) nonspecifically by

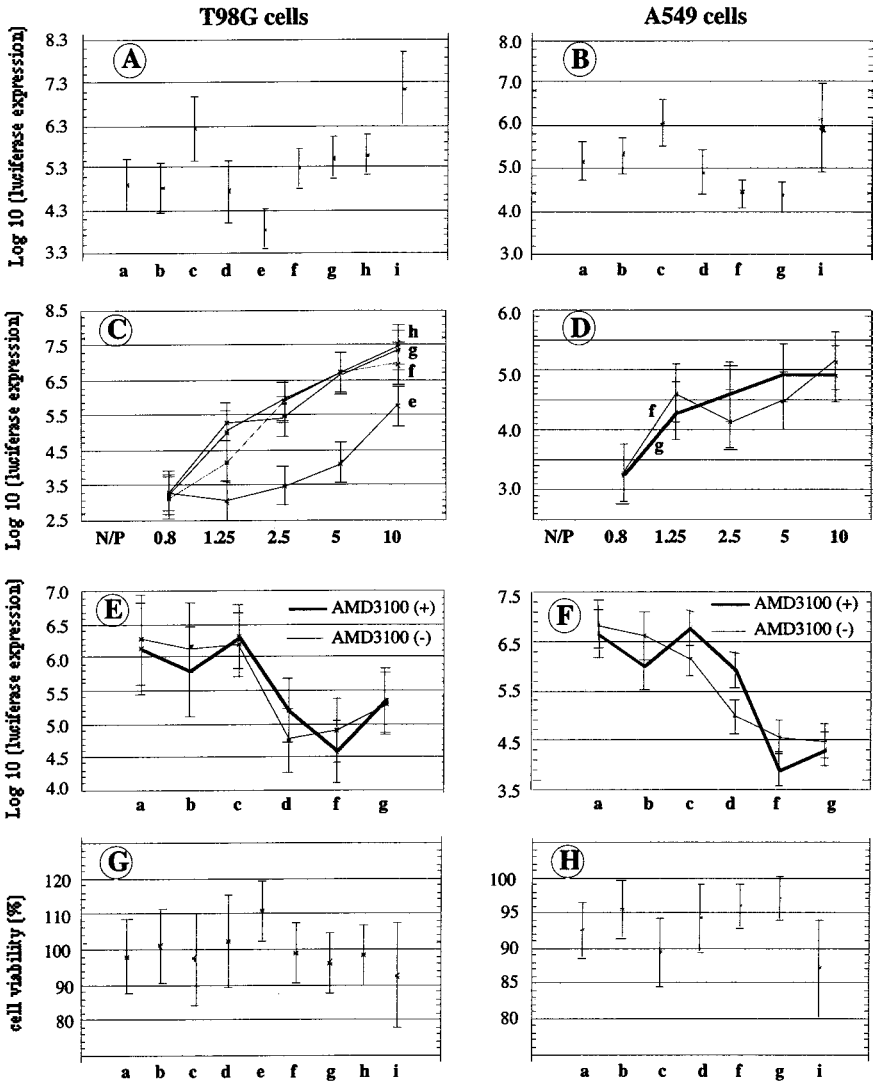


Figure 4. Means and 95.0% Tukey HSD intervals of the logarithmic transformation of luciferase expression levels (log_{10} (fg luciferase/mg protein)) (Panels A to F) and of cell viability percentages (Panels G and H) for the pTG11033 formulations of Figure 3 in T98G cells (left panels) and A549 cells (right panels). Panels A, B, G, and H: irrespective of the DNA dose (1 and 0.5 μg/well) and of the *N*/*P* ratio (0.8, 1.25, and 5 for a and b; 0.8 and 2.5 for c and d; 0.8, 1.25, 2.5, 5, and 10 for e, f, and g; 10 for PEI). Panels C and D: irrespective of the DNA dose (1 and 0.5 μg/well) and as a function of the *N*/*P* ratio for the indicated formulations. Panels E and F: irrespective of the DNA dose (1 and 0.5 μg/well) and of the *N*/*P* ratio (5 for a and b; 0.8 and 2.5 for c and d; 1.25 and 2.5 for f and g), and as a function of the presence of AMD3100 (30 μg per well) or not. Statistical tests were performed with STATGRAPHICS Plus5.0 software. This comparison was performed using the multiple sample comparison procedure, and the method used to discriminate among the means of the logarithmic transformation of luciferase expression levels or of the cell viability percentages was the Tukey's honestly significant difference (HSD) procedure. a: DOGS:DOPE (1:1); b: DOGS:DOPE:DC18-[NH]-[AMD] (1:1:0.1); c: DOTAP:DOPE (1:1); d: DOTAP:DOPE:DC18-[NH]-[AMD] (1:1:0.1); e: DC18-[NH]-[AMD]; f: DC18-[NH_2]20; g: DC18-[NH_2]20:DC18-[NH]-[AMD] (1:0.1); h: DC18-[NH_2]20:DC18-[NH]-[AMD] (1:0.2); i: PEI. For more details concerning the *N*/*P* ratio, see footnote of Table 1.

increasing the cationic charge of the polyplexes and consequently their nonspecific binding through electrostatic interactions to anionic proteins expressed on the cell membrane surface, nor (ii) specifically by increasing their binding to CXCR4 leading to a receptor-mediated endocytosis pathway.

Where transfection of the Jurkat cells with the $N/P \leq 2.5$ AMD-labeled polyplexes is concerned, no improvement of luciferase expression was obtained with any of the labeled polyplexes investigated as compared with that of their respective controls (abscissas c, and e(f) versus abscissas b and d, respectively, in Figure 6). That no substantial increase of transfection through specific AMD-CXCR4 interactions was detected with any of these targeted formulations could likely be attributed to the AMD inhibition of CXCR4-mediated endocytosis pathway. Indeed, recent research has demonstrated that the binding of AMD3100 to CXCR-4 receptor in human astroglioma U87 cells inhibited the endocytosis process of this receptor (*32*). To evaluate this hypothesis, we performed a series of transfection experiments in the presence of PMA which is known to trigger lipoplex and polyplex endocytosis of the Jurkat cells grown in suspension (*30*) and also to mediate CXCR4 receptor endocytosis (*31*), even in the presence of AMD3100 (*32*).

Concerning the PMA-triggered transfection assays with the nonlabeled $N/P \leq 2.5$ PEI or ^{i}Bu-[NH_2]95 polyplexes, one observed a statistically significant 2- and 4-fold increase of luciferase expression, respectively (Figure 6A, curve PMA(+)/AMD(−)). Very interestingly, a significantly larger increase (6- to 12-fold) was obtained with the AMD-targeted polyplexes and even with AMD3100/DNA complexes (9-fold). The larger transfection improvements obtained with the AMD-labeled poly-

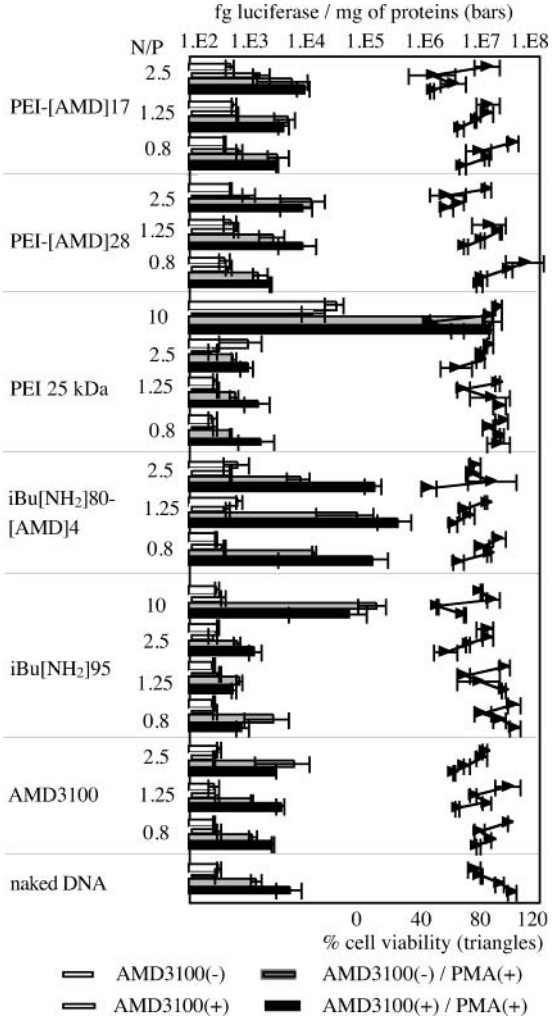


Figure 5. Luciferase expression (bars) and cell viability (triangles) in suspension CXCR4(+) Jurkat cells of the pTG11236 complexes made with various AMD-labeled polycationic polymers [PEI-[AMD]*p* (p = 17, 28), ^{i}Bu[NH_2]80-[AMD]4], PEI, ^{i}Bu[NH_2]95, or AMD3100 and for a DNA dose of 1 μg per well. Transfection was performed in the presence of 10% fetal calf serum, without and with AMD3100 or PMA. Data represent the means ± SEM from two independent experiments, each performed in triplicate (for more details, see Materials and Methods).

plexes as compared with their respective nonlabeled polyplexes in the presence PMA are likely attributable to a specific adsorption of the labeled AMD-polyplexes onto the CXCR4(+) cells, as a result of AMD-CXCR4 interactions and, consequently, to a higher receptor-mediated cellular uptake of the DNA complexes triggered by PMA. Surprisingly, when these transfection experiments were further run in the presence of AMD3100 (curve PMA(+)/AMD(+) in Figure 6A), a statistically significant additional 5-fold increase of luciferase expression was measured for the ^{i}Bu-[NH_2]80-[AMD]4 polyplexes. This represents an overall 60-fold increase with respect to the luciferase level obtained without AMD3100 and PMA. That transfection with these AMD-labeled polyplexes in the presence of PMA was increased by AMD3100 indicates that AMD3100 could serve as a template between the polyplexes and CXCR4. However, the lack of transfection inhibitory effects of AMD3100 indicates likely that nonspecific PMA-induced endocytotic pathways of the polyplexes involving other cellular receptors than CXCR4 take place. This is strongly supported, as illustrated in Figure 7A, by the nearly

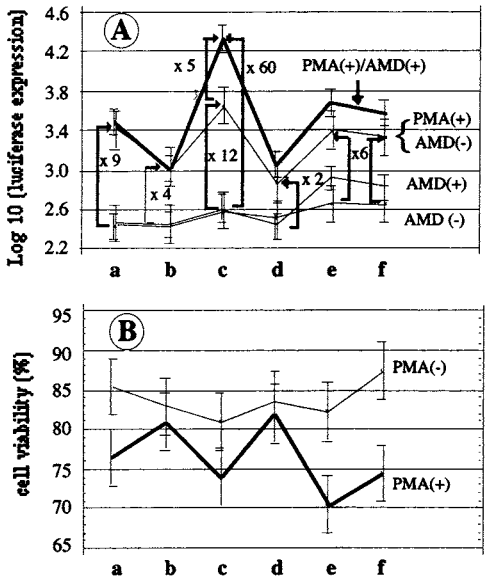


Figure 6. Means and 95.0% Tukey HSD intervals of the logarithmic transformation of luciferase expression levels ($\log_{10}$ (fg luciferase/mg protein)) (Panel A) and of cell viability percentages (Panel B) for the pTG11236 formulations of Figure 4 in Jurkat cells. Panels A and B: irrespective of the DNA dose (1 and 0.5 μg/well) and of the *N*/*P* ratio (0.8, 1.25, and 2.5 for a to f). Panel A, curve AMD(−): without AMD3100; curve AMD(+): with AMD3100 (100 μg per well); curve PMA(+)/AMD(−): with PMA (100 ng per well) and without AMD3100; curve PMA(+)/AMD(+): with PMA (100 ng per well) and AMD3100 (100 μg per well). Panel B: curves PMA(−) and PMA(+): without and with PMA, irrespective of the presence or absence of AMD3100. a: AMD3100; b: ^{i}Bu[NH_2]95; c: ^{i}Bu[NH_2]80-[AMD]4; d: PEI; e: PEI-[AMD]17; f: PEI-[AMD]28. For more details concerning the statistical analyses, see caption of Figure 3.

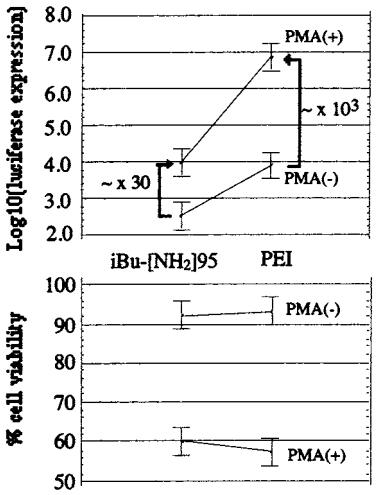


Figure 7. Means and 95.0% Tukey HSD intervals of the logarithmic transformation of luciferase expression levels ($\log_{10}$ (fg luciferase/mg protein)) (Panel A) and of cell viability percentages (Panel B) for the *N*/*P* 10 ^{i}Bu[NH_2]95 or PEI polyplexes made with plasmid pTG11236 in Jurkat cells with respect to the presence or absence of PMA (curves PMA(+) and PMA(−), respectively). Panels A and B: irrespective of the DNA dose (1 and 0.5 μg/well) and of the presence or absence of AMD3100. For more details concerning the statistical analyses, see caption of Figure 3.

1000- and 30-fold increase of luciferase expression obtained with the highly cationic *N*/*P* 10 PEI or ^{i}Bu-[NH_2]-95 polyplexes, respectively, when the assays were run in the presence of PMA.

It is, however, worth noting that the transfection enhancements in the presence of PMA were accompanied

by a significant cell viability decrease (Figure 6B and 7B). Furthermore, the higher the transfection enhancement, the lower the cell viability. These observations are in agreement with a higher cellular uptake of the DNA complexes.

Altogether, our results show that polyplexes formulated with AMD-labeled polymers constitute, under certain conditions, specific gene transfer systems into suspension CXCR4(+) Jurkat cells. This is more particularly the case when the nonspecific transfection pathways are minimized (i.e. for $N/P \leq 2.5$ AMD-labeled polyplexes) and in the presence of phorbol myristate acetate (PMA) which triggers CXCR4 receptor endocytosis of the AMD-labeled polyplexes to a larger extent than of their respective nonlabeled ones. These targeted AMD-polymers appear thus as promising synthetic vectors for specific in vivo gene delivery to CXCR4-expressing tumors, providing however that CXCR4-mediated endocytosis can be induced by nontumor promoters (e.g. prostratin (*43*, *44*)) by contrast to PMA which is a tumor promoter. The effect of the chemokine SDF-1, the natural ligand of CXCR4 (*13*, *15*), on the CXCR4-mediated transfection should also be investigated. These assays are further of interest as SDF-1 does not inhibit CXCR4 endocytosis by contrats to AMD3100 (*32*). Although encouraging, the transfection efficiencies and specificities obtained with these compounds should, however, be improved. This study also illustrates the difficulties to demonstrate and obtain a specific and efficient gene transfer system with cationized ligand-labeled DNA particles which also provide receptor-independent nonspecific gene transfer to cells and more particularly to adherent cells.

ACKNOWLEDGMENT

B. Le Bon is grateful to the Région Provence-Alpes-Côte d'Azur and Transgène SA (Strasbourg, France) for a grant. We wish to thank Transgène, Drs. S. Braun, O. Meyer, and B. Cavallini (from Transgène) for their interest in this project and for supplying plasmids. Many thanks to Dr. N. Taylor (UMR-CNRS 5535, IGMM, Montpellier, France) for performing the FACS analyses on the A549, T98G, and Jurkat cells. We are also grateful to the AFIRST, French-Israeli Cooperation on Gene Therapy, for financial support.

LITERATURE CITED

(1) Merdan, T., Kopecek, J., and Kissel, T. (2002) Prospects for cationic polymers in gene and oligonucleotide therapy against cancer. *Adv. Drug Delivery Rev. 54*, 715−718.

(2) Kunath, K., Merdan, T., Hegener, O., Haberlein, H., and Kissel, T. (2003) Integrin targeting using RGD-PEI conjugates for in vitro gene transfer. *J. Gene Med. 5*, 588−599.

(3) Zuber, G., Zammut-Italiano, L., Dauty, E., and Behr, J. P. (2003) Targeted Gene Delivery to Cancer Cells: Directed Assembly of Nanometric DNA Particles Coated with Folic Acid. *Angew. Chem., Int. Ed 42*, 2666−2669 and references therein.

(4) Hofland, H. E., Masson, C., Iginla, S., Osetinsky, I., Reddy, J. A., Leamon, C. P., Scherman, D., Bessodes, M., and Wils, P. (2002) Folate-targeted gene transfer in vivo. *Mol. Ther. 5*, 739−744 and references therein.

(5) Ogris, M., and Wagner, E. Targeting tumors with nonviral gene delivery systems. (2002) *Drug Discovery Today 7*, 479−485 and references therein.

(6) Fabio, K., Gaucheron, J., Di Giorgio, C., and Vierling, P. (2003) Novel galactosylated polyamine bolaamphiphiles for gene delivery. *Bioconjugate Chem. 14*, 358−367, and references therein.

(7) Erbacher, P., Bettinger, T., Belguise-Valladier, P., Zou, S., Coll, J. L., Behr, J. P., and Remy, J. S. (1999) Transfection and physical properties of various saccharide, poly(ethylene glycol), and antibody-derivatized polyethylenimines (PEI). *J. Gene Med. 1*, 210−222.

(8) De Clercq, E., Yamamoto, N., Pauwels, R., Balzarini, J., Witvrouw, M., De Vreese, K., Debyser, Z., Rosenwirth, B., Peichl, P., and Datema, R. (1994) Highly potent and selective inhibition of human immunodeficiency virus by the bicyclam derivative JM3100. *Antimicrob. Agents Chemother. 38*, 668−674.

(9) Donzella, G. A., Schols, D., Lin, S. W., Este, J. A., Nagashima, K. A., Maddon, P. J., Allaway, G. P., Sakmar, T. P., Henson, G., De Clercq, E., and Moore, J. P. (1998) AMD3100, a small molecule inhibitor of HIV-1 entry via the CXCR4 co-receptor. *Nat. Med. 4*, 72−77.

(10) Este, J. A., Cabrera, C., De Clercq, E., Struyf, S., Van Damme, J., Bridger, G., Skerlj, R. T., Abrams, M. J., Henson, G., Gutierrez, A., Clotet, B., and Schols, D. (1999) Activity of different bicyclam derivatives against human immunodeficiency virus depends on their interaction with the CXCR4 chemokine receptor. *Mol. Pharmacol. 55*, 67−73.

(11) Labrosse, B., Treboute, C., Brelot, A., and Alizon, M. (2001) Cooperation of the V1/V2 and V3 domains of human immunodeficiency virus type 1 gp120 for interaction with the CXCR4 receptor. *J. Virol. 75*, 5457−5464.

(12) Schols, D., Este, J. A., Henson, G., and De Clercq, E. (1997) Bicyclams, a class of potent anti-HIV agents, are targeted at the HIV coreceptor fusin/CXCR-4. *Antiviral Res. 35*, 147−156.

(13) Bleul, C. C., Farzan, M., Choe, H., Parolin, C., Clark-Lewis, I., Sodroski, J., and Springer, T. A. (1996) The lymphocyte chemoattractant SDF-1 is a ligand for LESTR/fusin and blocks HIV-1 entry. *Nature 382*, 829−833.

(14) Hendrix, C. W., Flexner, C., MacFarland, R. T., Giandomenico, C., Fuchs, E. J., Redpath, E., Bridger, G., and Henson, G. W. (2000) Pharmacokinetics and safety of AMD-3100, a novel antagonist of the CXCR-4 chemokine receptor, in human volunteers. *Antimicrob. Agents Chemother. 44*, 1667−1673.

(15) Oberlin, E., Amara, A., Bachelerie, F., Bessia, C., Virelizier, J. L., Arenzana-Seisdedos, F., Schwartz, O., Heard, J. M., Clark-Lewis, I., Legler, D. F., Loetscher, M., Baggiolini, M., and Moser, B. (1996) The CXC chemokine SDF-1 is the ligand for LESTR/fusin and prevents infection by T-cell-line-adapted HIV-1. *Nature 382*, 833−835.

(16) Murdoch, C. (2000) CXCR4: chemokine receptor extraordinaire. *Immunol. Rev. 177*, 175−184.

(17) Sehgal, A., Keener, C., Boynton, A. L., Warrick, J., and Murphy, G. P. (1998) CXCR-4, a chemokine receptor, is overexpressed in and required for proliferation of glioblastoma tumor cells. *J. Surg. Oncol. 69*, 99−104.

(18) Sehgal, A., Ricks, S., Boynton, A. L., Warrick, J., and Murphy, G. P. (1998) Molecular characterization of CXCR-4: a potential brain tumor-associated gene. *J. Surg. Oncol. 69*, 239−248.

(19) Oh, J. W., Drabik, K., Kutsch, O., Choi, C., Tousson, A., and Benveniste, E. N. (2001) CXC chemokine receptor 4 expression and function in human astroglioma cells. *J. Imunol. 166*, 2695−2704.

(20) Zhou, Y., Larsen, P. H., Hao, C., and Yong, V. W. (2002) CXCR4 is a major chemokine recptor on glioma cells and mediates their survival. *J. Biol. Chem. 277*, 49481−49487.

(21) Rempel, S. A., Dudas, S., Ge, S., and Gutierrez, J. A. (2000) Identification and localization of the cytokine SDF1 and its receptor, CXC chemokine receptor 4, to regions of necrosis and angiogenesis in human glioblastoma. *Clin. Cancer Res. 6*, 102−111.

(22) Bajetto, A., Bonavia, R., Barbero, S., Florio, T., and Schettini, G. (2001) Chemokines and their receptors in the central nervous system. *Front. Neuroendocrinol. 22*, 147−184.

(23) Bonavia, R., Bajetto, A., Barbero, S., Pirani, P., Florio, T., and Schettini, G. (2003) Chemokines and receptors in the CNS: expression of CXCL12/SDF-1 and CXCR4 and their role in astrocyte proliferation. *Toxicol. Lett. 139*, 181−189.

(24) Muller, A., Homey, B., Soto, H., Ge, N., Catron, D., Buchanan, M. E., McClanahan, T., Murphy, E., Yuan, W., Wagner, S. N., Barrera, J. L., Mohar, A., Verastegui, E., and Zlotnik, A. (2001) Involvement of chemokine receptors in breast cancer metastasis. *Nature* 410, 50−56.

(25) Wiethoff, C. M., Smith, J. G., Koe, G. S., and Middaugh, C. R. (2001) The potential role of proteoglycans in cationic lipid DNA complexes with model glycosaminoglycans. *J. Biol. Chem. 276*, 32806−32813.

(26) Belting, M. (2003) Heparan sulfate proteoglycan as a plasma membrane carrier. *Trends Biochem. Sci. 28*, 145−151.

(27) Leventis, R., and Silvius, J. R. (1990) Interactions of mammalian cells with lipid dispersions containing novel metabolizable cationic amphiphiles. *Biochim. Biophys. Acta* 1023, 124−132.

(28) Behr, J. P., Demeinex, B., Loeffler, J. P., and Perez-Mutul, J. (1989) Efficient gene transfer into mammalian primary endocrine cells with lipopolyamine-coated DNA. *Proc. Natl. Acad. Sci. U.S.A. 86*, 6982−6986.

(29) Verderone, G., Van Craynest, N., Boussif, O., Santaella, C., Bischoff, R., Kolbe, H. V., and Vierling, P. (2000) Lipopolycationic telomers for gene transfer: synthesis and evaluation of their in vitro transfection efficiency. *J. Med. Chem. 43*, 1367−1379.

(30) Schifferli, K. P., and Ciccarone, V. (1996) Optimization of Cationic Lipid Reagent-Mediated Transfection for Suspension Cell Lines. *Focus 18*, 45−47.

(31) Signoret, N., Oldridge, J., Pelchen-Matthews, A., Klasse, P. J., Tran, T., Brass, L. F., Rosenkilde, M. M., Schwartz, T. W., Holmes, W., Dallas, W., Luther, M. A., Wells, T. N., Hoxie, J. A., and Marsh, M. (1997) Phorbol esters and SDF-1 induce rapid endocytosis and down modulation of the chemokine receptor CXCR4. *J. Cell Biol. 139*, 651−664.

(32) Hatse, S., Princen, K., Bridger, G., De Clercq, E., and Schols, D. (2002) Chemokine receptor inhibition by AMD3100 is strictly confined to CXCR4. *FEBS Lett. 527*, 255−262.

(33) Le Bon, B., Van Craynest, N., Boussif, O., and Vierling, P. (2002) Polycationic Diblock and Random Polyethylene Glycol- or Tris(hydroxymethyl)methyl-Grafted (Co)telomers for Gene Transfer: Synthesis and Evaluation of Their in Vitro Transfection Efficiency. *Bioconjugate Chem. 13*, 1292−1301.

(34) Dessolin, J., Galea, P., Vlieghe, P., Chermann, J. C., and Kraus, J. L. (1999) New bicyclam-AZT conjugates: design, synthesis, anti-HIV evaluation, and their interaction with CXCR-4 coreceptor. *J. Med. Chem. 42*, 229−241.

(35) Gaucheron, J., Santaella, C., and Vierling, P. (2001) Highly fluorinated lipospermines for gene transfer: synthesis and evaluation of their in vitro transfection efficiency. *Bioconjugate Chem. 12*, 114−128.

(36) Van Craynest, N., Santaella, C., Boussif, O., and Vierling, P. (2002) Polycationic telomers and cotelomers for gene transfer: synthesis and evaluation of their an vitro transfection efficiency. *Bioconjugate Chem. 13*, 59−75.

(37) Boussif, O., Lezoualc'h, F., Zanta, M. A., Mergny, M. D., Scherman, D., Demeinex, B., and Behr, J. (1995) A Versatile Vector for Gene and Oligonucleotide Transfer into Cells in Culture and in vivo: Polyethyleneimine. *Proc. Natl. Acad. Sci. U.S.A. 92*, 7297−7301.

(38) Bridger, G. .J., Skerlj, R. T., Padmanabhan, S., Martellucci, S.A., Henson, G. W., Abrams, M. J., Joao, H. C., Witvrouw, M., De Vreese, K., Pauwels, R., and De Clercq, E. (1996) Synthesis and structure−activity relationships of phenylenebis(methylene)-linked bis-tetraazamacrocycles that inhibit human immunodeficiency virus replication. 2. Effect of heteroaromatic linkers on the activity of bicyclams. *J. Med. Chem. 39*, 109−19.

(39) Byk, G., Dubertret, C., Escriou, V., Frederic, M., Jaslin, G., Rangara, R., Pitard, B., Crouzet, J., Wils, P., Schwartz, B., and Scherman, D. (1998) Synthesis, activity, and structure−activity relationship studies of novel cationic lipids for DNA transfer. *J. Med. Chem. 41*, 229−235.

(40) Pitard, B., Aguerre, O., Airiau, M., Lachages, A. M., Boukhnikachvili, T., Byk, G., Dubertret, C., Herviou, C., Scherman, D., Mayaux, J. F., and Crouzet, J. (1997) Virus-sized self-assembling lamellar complexes between plasmid DNA and cationic micellles promote gene transfer. *Proc. Natl. Acad. Sci. U.S.A. 94*, 14412−14417.

(41) Murdoch, C., Monk, P. N., and Finn, A. (1999) Functional expression of chemokine receptor CXCR4 on human epithelial cells. *Immunology 98*, 36−41.

(42) Simoes, S., Slepushkin, V., Gaspar, R., Pedroso de Lima, M. C., and Duzgunes, N. (1999) Successful transfection of lymphocytes by ternary lipoplexes. *Biosci. Rep. 19*, 601−609.

(43) Gustafson, K. R., Cardellina, J. H., 2nd, McMahon, J. B., Gulakowski, R. J., Ishitoya, J., Szallasi, Z., Lewin, N. E., Blumberg, P. M., Weislow, O. S., Beutler, J. A., et al. (1992) A nonpromoting phorbol from the samoan medicinal plant Homalanthus nutans inhibits cell killing by HIV-1. *J. Med. Chem. 35*, 1978−86.

(44) Kulkosky, J., Culnan, D. M., Roman, J., Dornadula, G., Schnell, M., Boyd, M. R., and Pomerantz, R. J. (2001) Prostratin: activation of latent HIV-1 expression suggests a potential inductive adjuvant therapy for HAART. *Blood 98*, 3006−15.

BC034220O

TECHNICAL NOTES

Synthesis of Heterotelechelic Poly(ethylene glycol) Derivatives Having α-Benzaldehyde and ω-Pyridyl Disulfide Groups by Ring Opening Polymerization of Ethylene Oxide Using 4-(Diethoxymethyl)benzyl Alkoxide as a Novel Initiator

Yoshitsugu Akiyama,[†] Yukio Nagasaki,[‡] and Kazunori Kataoka*,[†]

Department of Materials Science, Graduate School of Engineering, The University of Tokyo, 7−3−1 Hongo, Bunkyo-ku, Tokyo 113-8656, Japan, and Department of Material Science & Technology, Tokyo University of Science, 2641 Yamazaki, Noda-shi, Chiba 278-8510, Japan. Received September 30, 2003; Revised Manuscript Received January 15, 2004

New heterotelechelic PEG-containing benzaldehyde and 2-pyridyldithio endgroup (CHO-Bz-PEG-SSpyl) was synthesized with high efficiency and high selectivity. An α-benzylacetal-ω-methansulfonyl PEG was prepared as the first step to CHO-Bz-PEG-SSpyl through the ring-opening polymerization of ethylene oxide (EO) initiated by potassium 4-(diethoxymethyl)benzyl alkoxide (PDA), followed by the successive conversion of the end-alkoxide group to a methanesulfonyl group and then to dithiocarbonate derivative. Further, deprotection of the dithiocarbonate derivative and subsequent conversion to the 2-pyridyldithio group at the ω-end was successfully performed through a one-step reaction to form α-benzylacetal-ω-2-pyridyldithio PEG (aceBz-PEG-SSpyl). The aceBz-PEG-SSpyl was then treated with an aqueous HCl solution (pH 5.0) to generate the benzaldehyde group at the α-end. Molecular functionalities of the benzaldehyde and the 2-pyridyldithio end group of the heterotelechelic PEG (CHO-Bz-PEG-SSpyl) thus prepared were characterized by ^{1}H and ^{13}C NMR, showing that the reaction proceeded almost quantitatively. The benzaldehyde end group is available to conjugate various ligands having a primary amino group by forming the pH-sensitive imine linkage (−N═CHC$_6$H$_4$−).

Heterotelechelic poly(ethylene glycol) (PEG) derivatives possessing different functional groups at the α- and ω-chain ends have received increasing interest as PEGylation reagents (*1*−*4*) in such areas as drug delivery systems (DDS) (*5*−*7*) and diagnostics (*8*−*11*). For example, protein conjugates with heterotelechelic PEG are expected not only to have a propensity of decreased immunogenicity due to steric repulsion effects, but also to possess the availability of further conjugation of the ligand moiety to the distal end of PEG. Although several types of heterotelechelic PEGs have already been prepared based on the derivatization of α,ω-dihydroxy-PEG (*12*−*15*), there are still many obstacles such as complicated reaction steps with low yield and limited selectivities. These obstacles in the heterotelechelic PEG synthesis may be resolved by taking the alternative approach of the direct ring opening polymerization of ethylene oxide (EO) using a metal alkoxide initiator with a protected functional group (*16*−*20*).

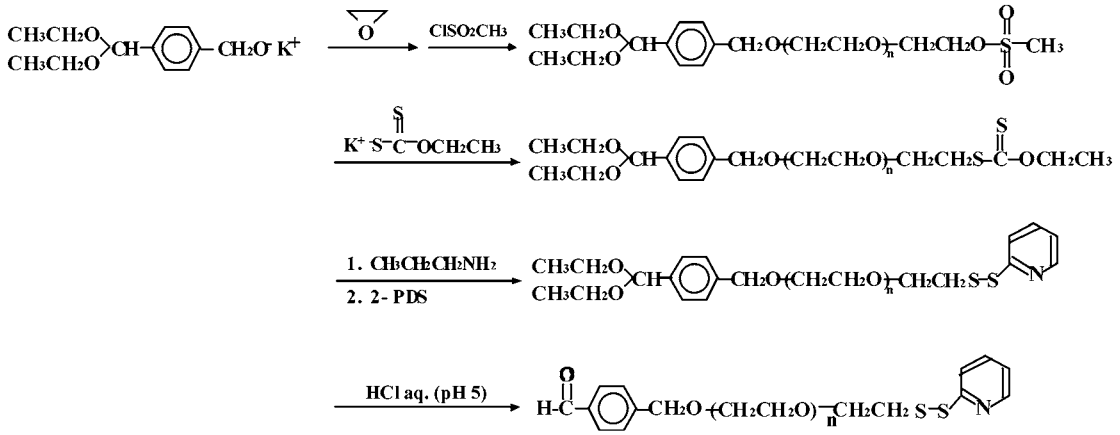
As a novel heterotelechelic PEG with high potential utility in bioconjugation field, we focused on the one with α-benzaldehyde and ω-2-pyridyldithio groups. The benzaldehyde group is able to react with the primary amino group under physiological condition (pH 7.4), generating a stable imine linkage (−N═CHC$_6$H$_4$−) which needs no further reductive amination. The imine linkage is also known to be hydrolyzed at acidic condition (*21*, *22*). Furthermore, self-condensation of PEG due to an aldol reaction, which is a major side reaction in the utilization of aldehyde-functionalized PEG derivatives, does not occur in the benzaldehyde-functionalized PEG due to a lack of α-proton. The 2-pyridyldithio group at the ω-end can be utilized for the selective PEGylation at the cysteine residue of natural as well as recombinant protein molecules (*23*, *24*). Note that the α-benzaldehyde-ω-2-pyridyldithio PEG is also useful for the functional PEGylation of gold and silver substrates used in bioassay systems, including surface plasmon resonance and colloidal colorimetry (*25*). In this study, a novel synthetic route was established for α-benzaldehyde-2-pyridyldithio-PEG (CHO−Bz-PEG-SSpyl) through the ring opening polymerization of EO initiated with potassium 4-(diethoxymethyl)benzylalkoxide (PDA) as summarized in Scheme 1.

4-(Diethoxymethyl)benzyl alcohol was prepared by the reduction of 4-(diethoxymethyl)benzaldehyde with sodium borohydride ($NaBH_4$) in dry methanol according to the literature with a slight modification (*26*). Conversion to the 4-(diethoxymethyl)benzyl alcohol was confirmed by ^{1}H and ^{13}C NMR (JEOL EX 300 spectrometer) analysis (S-1,2; Supporting Information). Potassium 4-(diethoxy-

* To whom correspondence should be addressed. Professor Kazunori Kataoka: Tel: +81-3-5841-7138, Fax: +81-3-5841-7139, e-mail: kataoka@bmw.t.u-tokyo.ac.jp.
[†] The University of Tokyo.
[‡] Tokyo University of Science.

10.1021/bc0341775 CCC: $27.50 © 2004 American Chemical Society
Published on Web 02/26/2004

Scheme 1



methyl)benzylalkoxide (PDA) as an initiator for EO polymerization was then prepared by metalation of 4-(diethoxymethyl)benzyl alcohol with potassium naphthalene. The synthesis of the heterotelechelic PEG possessing benzylacetal and methansulfonyl endgroups (aceBz-PEG-OSO_2CH_3) was done as the first step to CHO-Bz-PEG-SSpyl as follows: THF solutions of 4-(diethoxymethyl)benzyl alcohol (0.19 g, 0.90 mmol) and potassium naphthalene (0.90 mmol) were mixed into dry THF (30 mL) under an argon atmosphere to form PDA. After the mixture was stirred for 10 min, 4.5 g (102 mmol) of liquid EO, cooled below 0 °C, was added to the solution via a cooled syringe. After the mixture was allowed to react for 2 days at room temperature, potassium naphthalene (0.4 mmol) and triethylamine (0.82 g, 8.1 mmol) were added to the stirring polymer solution. Then, the solution was slowly added dropwise into methanesulfonyl chloride (0.72 g, 6.3 mmol) in dry THF (10 mL), to introduce methanesulfonyl groups at one of the PEG ends without any side reactions, and then added to the chloroform followed by washing with saturated $NaCl_{aq}$ for purification. The organic layer was dried with anhydrous $MgSO_4$. After evaporation of excess solvent, samples were reprecipitated into diethyl ether to obtain the polymer as a white precipitate. The recovered polymer was dried in vacuo and then freeze-dried from benzene. The yield of the obtained polymer after purification was 82% (3.69 g).

From the GPC diagram (TOSOH HLC-8220: a TSKgel column ($G4000H_{HR}$ and $G3000H_{HR}$)), the number-average molecular weight (M_n) and the molecular weight distribution (MWD) were determined to be 5410 and 1.03, respectively (S-3, Supporting Information). The polymer has a very narrow MWD, and its M_n is close to the calculated value derived from the monomer/initiator ratio, indicating that the polymerization of EO from PDA as an initiator proceeds without any remarkable side reactions. The end-group analysis was then done by ^{1}H NMR spectroscopy according to the assignments of PEG and 4-(diethoxymethyl)benzyl alcohol (S-4, Supporting Information). The molecular weight determined from the intensity ratio of the oxymethylene peak of the PEG signals (OCH_2CH_2) with the methyl proton peaks of benzylacetal ($(CH_3CH_2O)_2CH$) was 5820, which is in a good agreement with the M_n determined by GPC analysis (M_n 5410).

To convert a methanesulfonyl group to a *O*-ethyldithiocarbonate group, the aceBz-PEG-OSO_2CH_3 was reacted with potassium *O*-ethyldithiocarbonate in the mixture of THF and DMF under an argon atmosphere for 4 h. The ω-end conversion from methanesulfonate to the ethyldithiocarbonate moiety was confirmed to be quantitative based on the ^{1}H NMR data (S-5, Supporting Information). The ω-end conversion to the 2-pyridyldithio group was then performed by the deprotection of the dithiocarbonate moiety in THF as follows: AceBz-PEG-S(C=S)OCH_2CH_3 (100 mg, 0.0186 mmol) and 2-pyridyl 2-disulfide (410 mg, 1.86 mmol) were dissolved in dry THF (15 mL), and *n*-propylamine (1.75 mL) was slowly added. The mixture was stirred for 3 h at room temperature and then dialyzed against MeOH followed by the complete evaporation of the solvent under vacuum. The polymer was purified by ether reprecipitation from $CHCl_3$ solution. Finally, the obtained polymer was freeze-dried from benzene (yield: 89 mg (89%)). Figure 1 shows the ^{1}H NMR spectrum of the obtained aceBz-PEG-SSpyl. The signals of the methyl (1.4 ppm) and methylene (4.6 ppm) protons of the *O*-ethyldithiocarbonate moiety had completely disappeared, while new peaks appeared at 7.1, 7.7, 7.8, and 8.5 ppm assignable to the pyridyl moiety. The ω-end conversion of *O*-ethyldithiocarbonate to the 2-pyridyldithio group was confirmed to be 99% based on the peak ratio of pyridyl to benzylacetal in the ^{1}H NMR spectrum. The aceBz-PEG-SSpyl was then treated with an aqueous HCl solution (pH 5.0) to generate the benzaldehyde group at the α-end through the deprotection of the benzylacetal moiety under the following conditions:

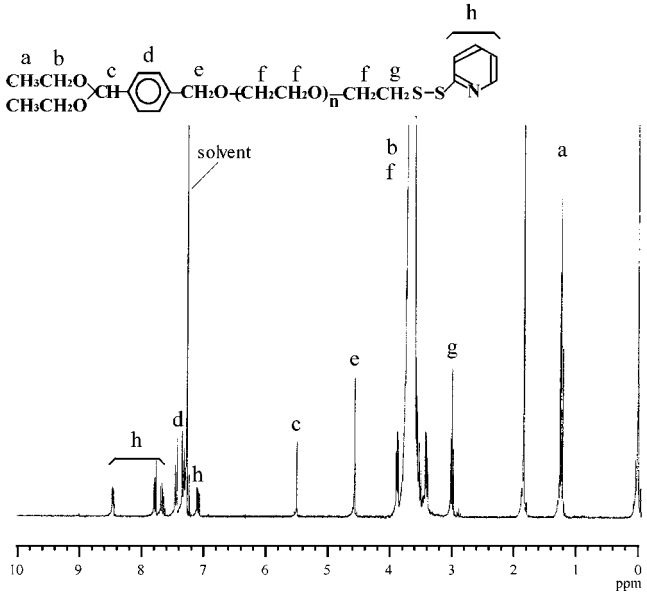


Figure 1. ^{1}H NMR spectrum of aceBz-PEG-SSpyl in $CDCl_3$ at room temperature.

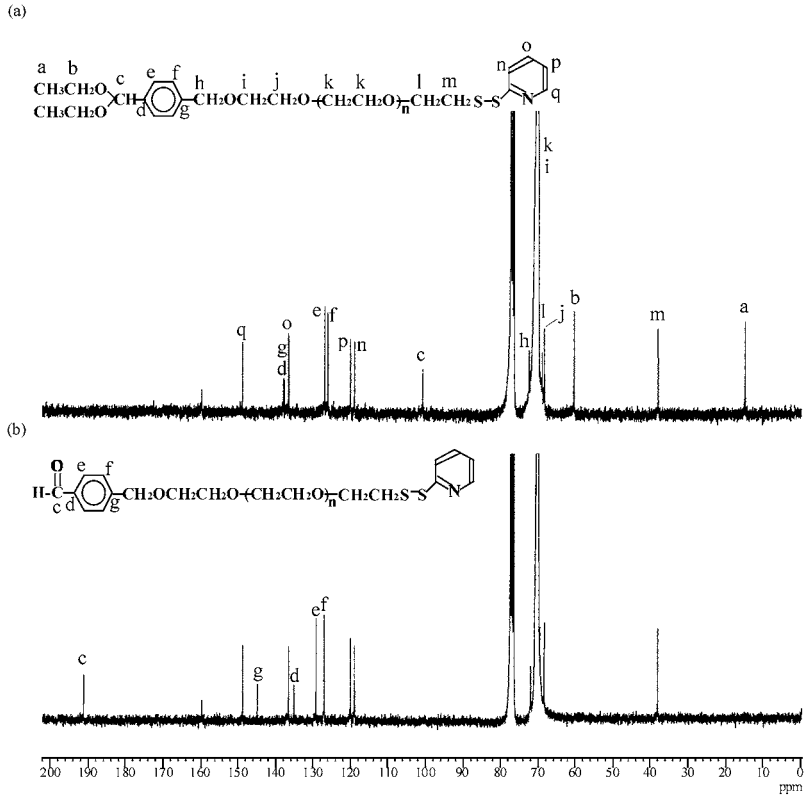


Figure 2. ^{13}C NMR spectra in $CDCl_3$ at room temperature of (a) aceBz-PEG-SSpyl and (b) CHO−Bz-PEG-SSpyl.

aceBz-PEG-SSpyl (70 mg, 0.013 mmol) was dissolved in an aqueous HCl solution (pH 5.0; 10 mL) and allowed to react for 6 h at room temperature. Dialysis against distilled water was then carried out followed by freeze-drying. Figure 2 shows ^{13}C NMR spectra of the polymer sample before and after the deprotection of the benzylacetal group. Carbon signals of the benzylacetal group, such as CH_3CH_2O and CH_3CH_2O appearing at 15.0 and 60.8 ppm, respectively, completely disappeared after the treatment with the aqueous HCl solution (pH 5.0) (Figure 2b). On the other hand, the deprotected sample has a new peak in the ^{13}C NMR spectrum appearing at 191.8 ppm, assignable to the aldehyde of the benzaldehyde group. These results clearly indicate the successful conversion of the α-benzylacetal group to the benzaldehyde group, which was further confirmed by ^1H NMR analysis as shown in Figure 3. Signals of the methyl and methylene groups of the benzylacetal group completely disappeared, while a new peak appeared at 10.06 ppm (s, 1H), which was attributable to the benzaldehyde proton at the end of the polymer chain. The α-end conversion from the benzylacetal to benzaldehyde moiety was again confirmed to be almost quantitative (90%) based on the peak intensity ratio of the aldehyde proton of the benzaldehyde group (10.06 ppm) and the methylene protons next to the 2-pyridyl disulfide group (3.0 ppm) in the ^1H NMR, indicating an almost quantitative conversion of the α-end to the benzaldehyde group. It should be noted that the intensity of the signals derived from the pyridyl end groups did not change throughout the deprotection process under the acidic conditions, indicating that the obtained PEG contains benzaldehyde (α-end) and 2-pyridyldithio (*ω*-end) groups. Worth mentioning is the fact that the benzaldehyde group has no active proton on the α-carbon to undergo aldol condensation. Indeed, the peak for dimerization products was not detected (data not shown). Consequently, the obtained heterotelechelic

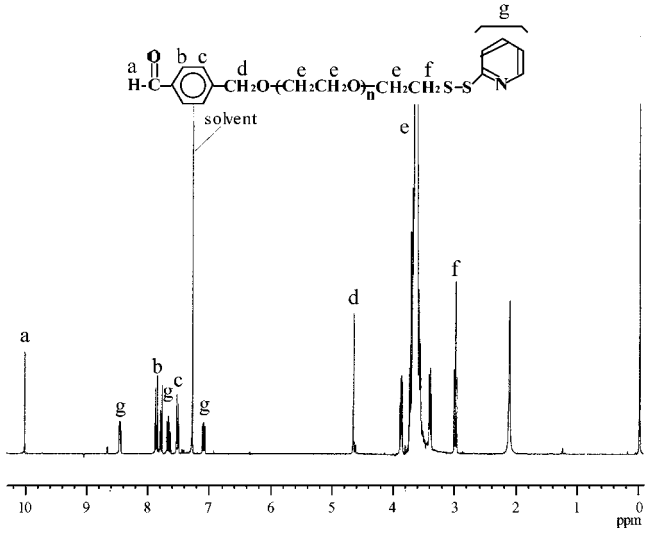


Figure 3. ^1H NMR spectrum of CHO-Bz-PEG-SSpyl in $CDCl_3$ at room temperature.

CHO-Bz-PEG-SSpyl and its precursor, aceBz-PEG-SSpyl, have a wide potential utility as selective heterolinkers in various bioconjugation reactions as well as surface modifiers of gold and silver substrates to construct reactive PEG-brush layers useful for biosensing, such as surface plasmon resonance (SPR) sensor technology. Research in this direction is now underway in our laboratory, and the results will be reported elsewhere.

ACKNOWLEDGMENT

This work was financially supported by Special Coordination Funds for Promoting Science and Technology from the Ministry of Education, Culture, Sports, Science

and Technology of Japan (MEXT) as well as by the Core Research Program for Evolutional Science and Technology (CREST) from the Japan Science and Technology Corporation (JST).

Supporting Information Available: Experimental procedures for the synthesis of 4-(diethoxymethyl)benzyl alcohol, aceBz-PEG-OSO_2CH_3, and aceBz-PEG-S(C═S)-OCH_2CH_3, as well as GPC and ^{1}H NMR of new polymers. This material is available free of charge via the Internet at http://pubs.acs.org.

LITERATURE CITED

(1) Harris, J. M., Ed. (1992) *Poly(ethylene glycol) Chemistry, Biotechnical and Biomedical Applications*, Plenum Press, New York.

(2) Harris, J. M., and Zalipsky, S., Ed. (1998) *Poly(ethylene glycol): Chemistry and Biological Applications*, ACS Symposium Series 680, American Chemical Society, Washington, DC.

(3) Anne, A., Demaille, C., and Mirous, J. (1999) Elastic bounded diffusion, dynamics of ferrocene-fabeled poly(ethylene glycol) chains terminally attached to the outermost monolayer of successively self-assembled monolayers of immunoglobulins. *J. Am. Chem. Soc. 121*, 10379−10388.

(4) Wen, X., Wu, Q.-P., Lu, Y., Fan, Z., Charnsangave, C., Wallace, S., Chow, D., and Li, C. (2001) Poly(ethylene glycol)-conjugated anti-EGF receptor antibody C225 with radiometal chelator attached to the termini of polymer chains. *Bioconjugate Chem. 12*, 545−553.

(5) Kataoka, K., Harada, A., and Nagasaki, Y. (2001) Block copolymer micelles for drug delivery: design, characterization and biological significance. *Adv. Drug Deliv. Rev. 47*, 113−131.

(6) Deguchi, Y., Kurihara, A., and Pardridge, W. M. (1999) Retention of biologic activity of human epidermal growth factor following conjugation to a blood-brain barrier drug delivery vector via an extended poly(ethylene glycol) linker. *Bioconjugate Chem. 10*, 32−37.

(7) Greenwald, R. B., Yang, K., Zhao, H., Conover, C. D., Lee, S., and Filpula, D. (2003) Controlled release of proteins from their poly(ethylene glycol) conjugates: drug delivery systems employing 1,6-elimination. *Bioconjugate Chem. 14*, 395−403.

(8) Otsuka, H., Nagasaki, Y., and Kataoka, K. (2001) Self-assembly of poly(ethylene glycol)-based block copolymers for biomedical applications. *Curr. Opin. Colloid Interface Sci. 6*, 3−10.

(9) Kurihara, A., and Pardridge, W. M. (2000) $A^{\beta 1-40}$ reptide radiopharmaceuticals for brain amyloid imaging: $^{[1]}$In chelation, conjugation to poly(ethylene glycol)-biotin linkers, and autoradiography with alzheimer's disease brain sections. *Bioconjugate Chem. 11*, 380−386.

(10) Unger, E. C., Shen, D., Wu, G., Stewart, L., Matsunaga, T. O., and Trouard, T. P. (1999) Gadolinium-containing copolymeric chelates-a new potential MR contarast agent. *Magn. Reson. Mater. Phys., Biol. Med. 8*, 154−162.

(11) Torchilin, V. P. (1999) Polymeric micelles in diagnostic imaging. *Colloids Surf. B. 16*, 305−319.

(12) Roberts, M. J., Bentley, M. D., and Harris, J. M. (2002) Chemistry for peptide and protein PEGylation. *Adv. Drug Delivery Rev. 54*, 459−476.

(13) Zalipsky, S. (1995) Functionalized poly(ethylene glycols) for preparation of biologically relevant conjugates. *Bioconjugate Chem. 6*, 150−165.

(14) Kaiser, K., Marek, M., Haselgrubler, T., Schindler, H., and and Gruber, H. J. (1997) Basic studies on heterobifunctional biotin-PEG conjugates with a 3-(4-pyridyldithio)propionyl marker on the second terminus. *Bioconjugate Chem. 8*, 545−551.

(15) Bettinger, T., Remy, J. S., Erbacher, P., and and Behr, J. P. (1998) Convenient polymer-supported synthetic route to heterobifunctional poly(ethylene glycol)s. *Bioconjugate Chem. 9*, 842−846.

(16) Nagasaki, Y., Kutsuna, T., Iijima, M., Kato, M., and Kataoka, K. (1995) Formyl-ended heterobifunctional poly(ethylene oxide): synthesis of poly(ethylene oxide) with a formyl group at one end and a hydroxyl group at the other end. *Bioconjugate Chem. 6*, 231−233.

(17) Nagasaki, Y., Iijima, M., Kato, M., and Kataoka, K. (1995) Primary amino-terminal heterobifunctional poly(ethylene oxide), facile synthesis of poly(ethylene oxide) with a primary amino group at one end and a hydroxyl group at the other end. *Bioconjugate Chem. 6*, 702−704.

(18) Nakamura, T., Nagasaki, Y., and Kataoka, K. (1998) Synthesis of heterobifunctional poly(ethylene glycol) with a reducing monosaccharide residue at one end. *Bioconjugate Chem. 9*, 300−303.

(19) Yokoyama, M., Okano, T., Sakurai, Y., Kikuchi, A., Osako, N., Nagasaki, Y., and Kataoka, K. (1992) Synthesis of poly(ethylene oxide) with heterobifuntional reactive groups at its terminals by an anionic initiator. *Bioconjugate Chem. 3*, 275−276.

(20) Akiyama, Y., Otsuka, H., Nagasaki, Y., Kato, M., and Kataoka, K. (2000) Selective synthesis of heterobifunctional poly(ethylene glycol) derivatives containing both mercapto and acetal terminals. *Bioconjugate Chem. 11*, 947−950.

(21) Chafi, N., Kolli, M., Vergnaud, J. M., and Montheard, J. P. (1991) Amine release from schiff bases polymers and diffusion from dosage forms with eudragit RL in acidic medium. *J. App. Polym. Sci. 43*, 1837−1847.

(22) Kamogawa, H., Sakai, T., and Sohma, H. (1988) Chemical release control: Schiff bases of vinylbenzaldehyde and functional amines. *J. Polym. Sci. Part A: Polym. Chem. 26*, 1335−1341.

(23) Stayton, P. S., Shimoboji, T., Long, C., Chilkoti, A., Chen, G., Harris, J. M., and Hoffman, A. S. (1995) Control of protein−ligand recognition using a stimuli-responsive polymer, *Nature 378*, 472−474.

(24) Manjula, B. N., Tsai, A., Upadhya, R., Perumalsamy, K., Smith, P, K., Malavalli, A., Vandegriff, K., Winslow, R. M., Intaglietta, M., Prabhakaran, M., Friedman, J. M., and Acharya, A. S. (2003) Site-specific PEGylation of hemoglobin at Cys-93(β): Correlation between the Colligative Properties of the PEGylated Protein and the Length of the Conjugated PEG Chain. *Biochonjugate Chem. 14*, 464−472.

(25) Otsuka, H., Akiyama, Y., Nagasaki, Y., and Kataoka, K. (2001) Quantitative and reversible lectin-induced association of gold nanoparticles modified with α-lactosyl-ω-mercapto-poly(ethylene glycol). *J. Am. Chem. Soc. 123*, 8226−8230.

(26) Paolesse, R., Macagnano, A., Monti, D., Tagliatesta, P., and Boschi, T. (1998) Synthesis and characterization of meso-tetraphenylporphyrin-corrole unsymmetrical dyads. *J. Porphyrins Phthal. 2*, 501−510.

BC0341775

Incorporation of Chemoselective Functionalities into Peptoids via Solid-Phase Submonomer Synthesis

Thomas Horn,*,† Byoung-Chul Lee,‡ Ken A. Dill,§ and Ronald N. Zuckermann*,†

Chiron Corporation, 4560 Horton Street, Emeryville, California 94608 and Graduate Group in Biophysics and Department of Pharmaceutical Chemistry, University of California, San Francisco, California 94143 .
Received October 3, 2003; Revised Manuscript Received December 12, 2003

A simple route to the introduction of a number of chemoselective functional groups into peptoids (oligo(N-substituted glycines)) by an extension of the standard solid-phase submonomer method is reported. The following groups were introduced: aminooxyacetamide, *N*-(carbamoylmethyl)acetohydrazide, mercaptoacetamide, 2-pyridinesulfenylmercaptoacetamide, and aldehyde-terminated peptoids. The method uses commercially available reagents, is fully compatible with standard peptoid submonomer synthesis conditions, is easily automated, and generates the desired functionalized peptoid in high yield and purity. Peptoids with suitable pairs of chemoselective ligation groups were joined in high yield.

INTRODUCTION

Biomolecules conjugated to particles, surfaces, or reporter groups are widely used to measure molecular interactions in rapid screening procedures (*1*−*5*) and in diagnostics and therapeutics (*6*). These bioconjugates are expensive to prepare and are often of limited stability. With the advent of combinatorial libraries, scientists now want to attach synthetic compounds to surfaces, biomolecules, and reporter groups to perform similar analyses.

Advances in combinatorial chemistry have made huge numbers of synthetic molecules available; and small organic molecules, shorter peptide oligomers (*7*), and nucleic acids (*8*, *9*), as well as nonnatural oligomers (peptoids (*10*) and other peptomimetics), have found numerous practical applications. The ability to attach synthetic ligands to surfaces has led to discoveries in chemical genomics (*11*), proteomics (*12*, *13*), and drug discovery (*7*).

Screening procedures that require the synthetic molecules to be attached to a solid phase, such as a bead, or a planar surface, can be prepared by chemical synthesis of the synthetic compound library directly onto the surface, or by synthesis, cleavage, and reattachment of the compound. Some methods involve synthesis of peptides and DNA oligomers directly on glass (*9*), cellulose membranes (*14*), and hydrophilic beads (*15*). The main disadvantage of these approaches, however, is that it is not possible to analyze or purify the immobilized compounds prior to screening.

We were interested in approaches where individual compounds of a library are assembled by chemical synthesis on a solid support in a form suitable for subsequent specific conjugation to a surface or a reporter group. This route facilitates compound analysis and purification, as well as conjugation of the compound library to the type of surface that is best suited for the actual screening procedures. Alternatively, synthetic soluble ligands with appropriate functional groups can be conjugated to another molecule to add useful properties (such as a drug, toxin, fluorophore, photoprobe, inhibitor, enzyme, hapten, reporter group, and (poly(ethylene glycol)) spacer). Synthetic proteins have been assembled from short functionalized peptides using conjugation techniques that rely on unique chemical moieties (native protein ligation (*16*), protein analogues (*17*), cyclic peptides (*18*), template-assembled synthetic proteins (*19*)).

Many chemoselective groups are conveniently introduced into peptides and other ligands by direct chemical solid-phase synthesis, but the necessary reagents are seldom commercially available and have in the past required the elaborate synthesis of protected amino acid compounds (*20*, *21*). It is therefore highly desirable to simplify the introduction of chemoselective groups into molecules, especially in the parallel synthesis of large numbers of potential ligands.

Peptoids (N-substituted glycines) are an important class of biomimetic oligomers that in recent years have made a significant impact in the areas of combinatorial drug discovery (*22*), gene therapy (*23*), drug delivery (*24*), and biopolymer folding (*25*, *26*). Sequence-specific peptoid oligomers are easily assembled from primary amines by a solid-phase submonomer method (*27*, *28*).

Here we describe a simple direct chemical route to the introduction of a number of chemoselective groups into peptoids by an extension of the standard solid-phase submonomer method: aminooxyacetamide, *N*-(carbamoylmethyl)acetohydrazide, mercaptoacetamide, *S*-acetylmercaptoacetamide, 2-pyridinesulfenylmercaptoacetamide, and aldehyde-terminated peptoids. The method uses commercially available reagents, is fully compatible with standard peptoid submonomer synthesis conditions, is easily automated, and generates the desired functionalized peptoid in high yield and purity. We also demonstrate the conjugation of these functionalized peptoids with themselves to generate peptoid dimers, a necessary step toward the synthesis of artificial proteins (*26*). These methods should also be applicable to the synthesis of

* To whom correspondence should be addressed. E-mail: thomas_horn@chiron.com, ron_zuckermann@chiron.com.
† Chiron Corporation.
‡ Graduate Group in Biophysics.
§ Department of Pharmaceutical Chemistry.

10.1021/bc0341831 CCC: $27.50 © 2004 American Chemical Society
Published on Web 02/21/2004

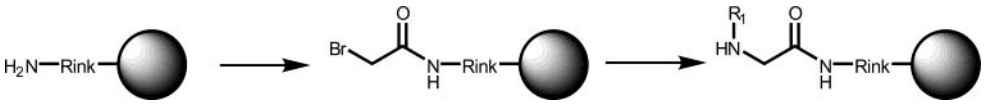


Figure 1.

Table 1. Chemoselective Pairs Commonly Used in Bioconjugation

reactant 1	reactant 2	type of bond formed
aldehyde/ketone	hydrazide	hydrazone
aldehyde/ketone	aminooxy	oxime
thiol	maleimide	thioether
thiol	iodoacetyl	thioether
thiol	activated disulfide	disulfide

many other molecules (heterocycles, peptides, β-peptides, and others (*29*)) assembled on a solid support. These features should greatly expand the utility of synthetic combinatorial libraries, since a diverse set of compounds can be simultaneously functionalized and conjugated to another molecule or surface of interest.

RESULTS AND DISCUSSION

Formation of chemically defined conjugates requires the introduction of uniquely reactive chemical moieties into each ligation partner, preferably at a specific location that does not interfere with the desired activities. These conjugation methods rely on chemoselective pairs of functionalities that are orthogonal to other groups in the molecules to be conjugated. Additionally, the conjugation reaction conditions should be conducted under mild conditions and be compatible with physiological conditions to preserve biological activity. A number of electrophile−nucleophile pairs, that fulfill these requirements, are listed in Table 1.

Peptoids can be efficiently prepared by submonomer solid-phase synthesis (Figure 1). Each monomer addition cycle consists of two steps: (1) acylation of an N-terminal amino group with bromoacetic acid in the presence of a condensing agent, and (2) nucleophilic displacement of the bromide with excess primary amine (*27*). These two steps are repeated with the appropriate amines to build the desired N-substituted glycine sequence.

Chemoselective ligation groups are introduced at the N-terminus with one additional submonomer cycle. The N-terminus, typically a secondary amine, is bromoacetylated and the desired ligation group is then introduced by displacement of the bromide by an excess of a nucleophilic reagent. In a final step, any protecting group on the newly introduced functionality is removed with an appropriate reagent, or further treatment converts it into the desired ligation group prior to cleavage of the product peptoid from the solid support. In some cases the protecting group comes off during trifluoroacetic acid (TFA[1]) cleavage. If desired, a spacer can be added prior to introduction of the ligation group to increase the distance between the conjugated molecules.

To demonstrate the utility of this method, a simple model peptoid (Figure 2) was synthesized and functionalized with several useful ligation groups. The product peptoids were characterized by reverse-phase HPLC and electrospray mass spectrometry (Table 2).

[1]Abbreviations: FMOC, 9-fluorenylmethoxycarbonyl; Boc, *tert*-butoxycarbonyl; Tr = trityl, triphenylmethyl; TFA, trifluoroacetic acid; DBU, diazabicyclo[5.4.0]undecane; DTT, dithiothreitol; DTNB, 5, 5′-dithio-bis(2-nitrobenzoic acid) (Ellman's reagent); TCEP, tris(2-carboxyethyl)phosphine; DCE, 1,2-dichloroethane.

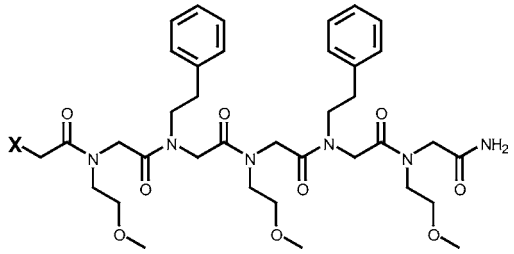


Figure 2. 2. Model peptoid pentamer. X denotes chemoselective functionality.

Table 2. Analytical Data

compound	synthesis yield, %	purity, %	mass spec (calcd/exp)
1	70	95	757.9/758.4
2	60	95	798.9/799.4
3	65	85	852.8/853.3
4	55	85	826.0/827.3
5	95	95	801.0/801.3
7a[a]	79	95	868.1/868.3
7b[a]	77	90	956.1/956.3
7c[a]	75	85	913.1/913.3
6[b]	80	85	758.9/759.3
7d[b]	90	95	912.1/912.3
8[b]	60	95	1515.9/1516.6

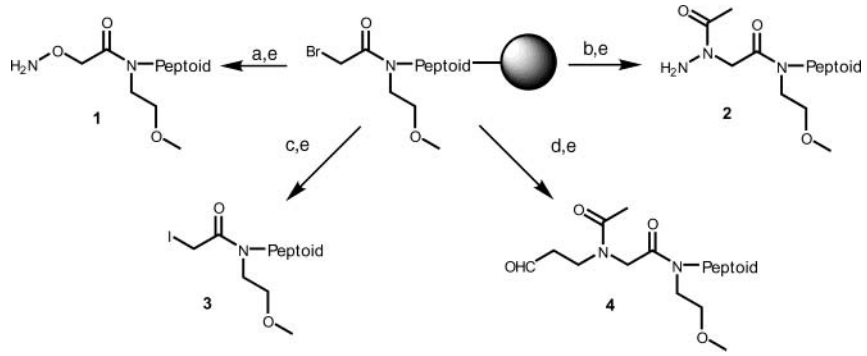
[a] Derived from *S*-acetyl intermediate, **5**. [b] Derived from *S*-trityl intermediate, **10**.

Aminooxyacetamide (aldehyde-specific). Oxime bond formation has been utilized extensively for the introduction of aminooxyacetamide-containing ligands into biomolecules. An aminooxy linker was added to a DNA oligomer during solid-phase synthesis, and conjugation with an aldehyde-containing reporter group was efficient and rapid (*30*). Site-specific modification of peptides and proteins with aminooxy groups was used to prepare well-defined biosensors and probes assembled via oxime linkages (*31*). A new strategy for the assembly of triple-function branched peptides through stepwise chemoselective ligations via oxime bonds has been reported (*32*). Oxime linkages have also been used in the assembly of peptide-based conjugates, such as peptide vaccine candidates (*33*) and in protein conjugates of defined structure (*34*). In those reports an N-Boc-protected aminooxyacetic acid was coupled to the N-terminus of peptides during solid-phase synthesis in the presence of a condensing agent (*34*−*37*). The N-protected aminooxyacetic acid reagent is, however, a rather expensive intermediate.

We introduced the same conjugation moiety by a much simpler submonomer route. The aminooxyacetamide functionality was generated in high yield using *N*-hydroxysuccinimide in the displacement of a solid supported N-terminal bromoacetamide−peptoid (Scheme 1A). Removal of the *N*-succinimide protection with hydrazine hydrate gave the free aminooxyacetamide−peptoid, **1**. *N*-Aminooxyacetamide−peptoid reacted rapidly with benzaldehyde in dilute aqueous solution at pH 4.5 to give the oxime in nearly quantitative yield (data not shown). An aminooxyacetamide−peptoid was ligated to an aldehyde−peptoid (see Peptoid-to-Peptoid Ligation).

Carboxyhydrazide (aldehyde-specific). Carboxyhydrazides form hydrazones with aldehydes and ketones that in general are fairly stable (*38*). They have been used

Scheme 1. Ligation Groups from Bromoacetylated Peptoids[a]



[a] Reagents: (a) (i) *N*-hydroxysuccinimide/DBU, (ii) hydrazine; (b) (i) Boc-$NHNH_2$, (ii) Ac_2O/pyridine; (c) KI; (d) (i) $(CH_3O)_2CHCH_2CH_2NH_2$, (ii) Ac_2O/pyridine; (e) 95% aq TFA.

extensively for conjugation of ligands with biomolecules that contain saccharides (glycoproteins such as antibodies, glycoconjugates, and enzymes (like horseradish peroxidase)) because aldehyde groups are readily introduced into such molecules by enzymatic or chemical (periodate) oxidation (*39*).

Many reporter groups, such as hydrazide derivatives of biotin and fluorescein dyes, are commercially available. Peptides containing a C-terminal hydrazide have been prepared by using an ester linkage to the solid support and cleaving the completed peptide chain by hydrazinolysis (*40*). Reagents have also been developed for converting lysine residues in peptides and proteins into hydrazide functionalities in aqueous solution (*41*), and in a scheme for the chemoselective acylation of 2-hydrazinylacetamide peptides a tris-Boc derivative of 2-hydrazinylacetic acid had to be prepared in order to avoid polymerization of 2-(2-*tert*-butoxycarbonylhydrazinyl)-acetic acid during coupling (*21*).

Using the new modified submonomer procedure, a hydrazide group is readily introduced at N-terminal and internal positions of a peptoid oligomer. Displacement of the bromoacetamide with N-Boc-protected hydrazine (Boc-$NHNH_2$), followed by acetylation with acetic anhydride (Ac_2O) in pyridine produced the N-terminal *N*-(carbamoylmethyl)acetohydrazide−peptoid, **2**. Displacement with N-Boc protected hydrazine (Boc-$NHNH_2$) and continuation of peptoid synthesis produced a peptoid with an internal hydrazide function. Cleavage of the product peptoid with TFA simultaneously removed the Boc group. The resulting hydrazide−peptoid undergoes rapid hydrazone formation with benzaldehyde in dilute aqueous solution at pH 4.5 (data not shown). The N-terminal 2-hydrazinylacetamide peptoid is the product if the acetylation step is omitted. A hydrazide group, incorporated at internal position of a peptoid, reacted with an intramolecular aldehyde to generate a cyclic peptoid (E. Beausoleil, personal communication). A *N*-(carbamoylmethyl)acetohydrazide peptoid was ligated to an aldehyde−peptoid (see Peptoid-to-Peptoid Ligation).

Iodoacetyl (thiol-specific). The iodoacetyl and maleimido groups are thiol-specific ligation groups that generate a stable thioether linkage. Numerous iodoacetyl reagents are commercially available (such as fluorescent derivatives from Molecular Probes). We have also routinely coupled iodoacetic acid and 3-maleimidopropionic acid (*42*) to the N-terminus of peptides and peptoids during solid-phase synthesis, and they have been used successfully for ligations.

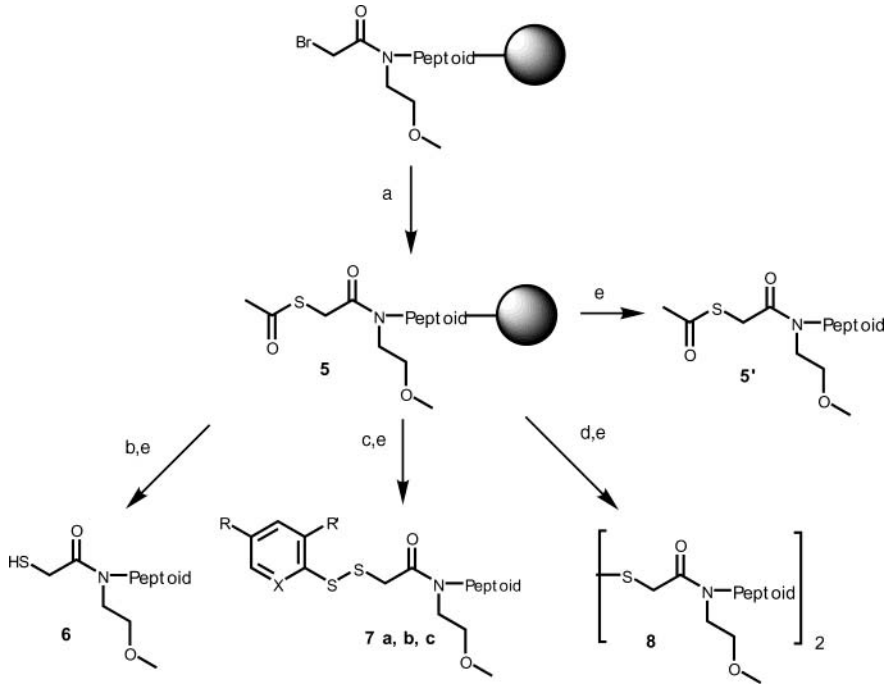
To simplify the synthesis of a thiol-specific group, we first investigated the N-terminal bromoacetamide−peptoid but found that the bromoacetamide group is not completely stable to the acid cleavage and deprotection conditions (using 95% aqueous TFA), resulting in the formation of 5−10% 2-hydroxyacetamide−peptoid byproduct. Instead, we used a displacement reaction on-resin (as an alternative to direct coupling of iodoacetic acid to the peptoid) to generate the more stable iodoacetamide−peptoid, **3**, by a Finkelstein reaction with potassium iodide in DMF (*43*), a reaction that proceeded in quantitative yield. The iodoacetamide−peptoid reacts readily with a thiol compound in aqueous solution at pH 8 to form a thioether (data not shown).

Aldehyde Groups. Peptides with aldehyde moieties have often been synthesized by incorporation of an N-terminal serine. After synthesis, the serine is oxidized to a terminal aldehyde with aqueous sodium periodate. Others have synthesized peptides as the C-terminal ester on a PAM support and released the C-terminal masked aldehyde by aminolysis with aminoacetaldehyde dimethyl acetal followed by TFA treatment to give the unprotected peptide aldehyde. This could then be coupled to aminooxyacetamide peptide derivatives by chemoselective ligation in aqueous solution (*44*). Recently, DNA probes that incorporate a modified nucleoside containing a ketone functionality allowed postsynthetic introduction of several aminooxyacetyl ligands under physiological conditions (*45*). The synthesis of oxime-linked mucin mimics was accomplished via the incorporation of multiple ketone residues into a peptide followed by reaction with aminooxy sugars corresponding to the tumor-related TN and sialyl TN (STN) antigens (*46*).

Peptoids containing aldehyde groups are readily synthesized. An aldehyde is incorporated at any position of the peptoid using commercially available amino aldehydes where the aldehyde function is protected (1-amino-2,2-dimethoxyethane and 1-amino-3,3-diethoxypropane were used in this study) as a submonomer. The CHO−peptoid, **9**, was synthesized in high yield. It reacted with aminooxyacetic acid in aqueous solution at pH 4 to give the oxime in high yield (data not shown). An aldehyde−peptoid was ligated to aminooxyacetamide− and hydrazide−peptoids (see Peptoid-to-Peptoid Ligation).

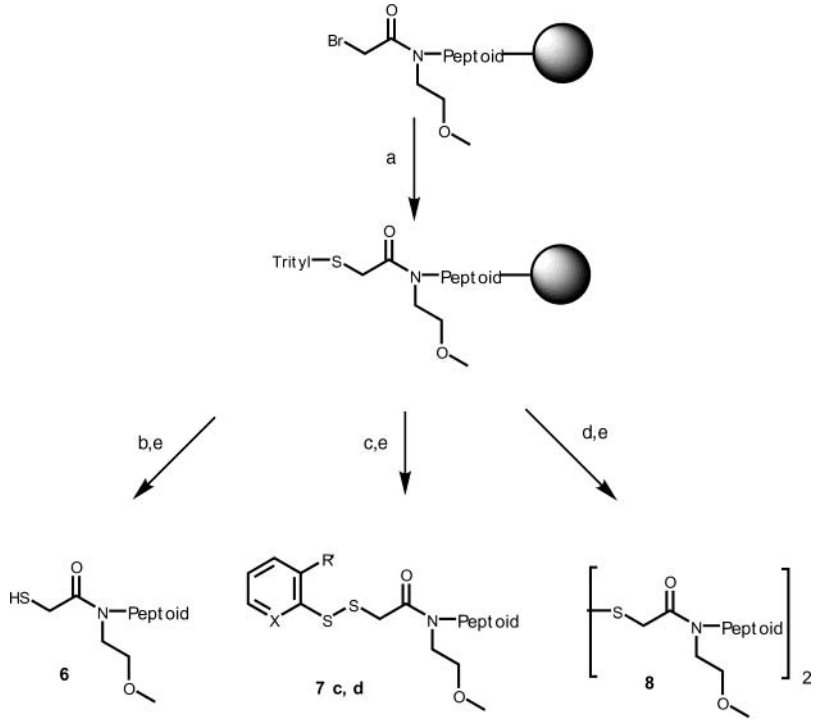
Thiol/Activated Disulfide/Homodisulfide Peptoids. Properly protected cysteine (Cys) residues incorporated during peptide synthesis have been used extensively to modify peptides for conjugation with proteins, labels, surfaces, etc., and typically results in a cleavable disulfide or thioether linkage (*47*) in the conjugate. To introduce a thiol functionality by a simple submonomer protocol we used potassium thioacetate (1 M in DMF/water (95:5 v/v)) and triphenylmethylmercaptan (0.25 M in DMF containing 1 equiv of DBU) to displace the bromide in the bromoacetamide−peptoid to generate key

Scheme 2. Thiol Peptoids via 2-(*S*-Acetylthio)acetamide Intermediate[a]



[a] Reagents: (a) Ac-S$^-$K$^+$; (b) NH_2OH/pyridine; (c) (i) NH_2OH/pyridine, (ii) 2,2′-dithiodipyridine (for **7a**), 5,5′-dithiobis(2-nitrobenzoic acid) (for **7b**), or 2,2′-dithiobis(5-nitropyridine) (for **7c**); (d) (i) NH_2OH/pyridine, (ii) iodine; (e) 95% aq TFA.

Scheme 3. Thiol Peptoids via 2-(*S*-Tritylthio)acetamide−Peptoid Intermediate[a]



[a] Reagents: (a) triphenylmethylmercaptan/DBU; (b) TFA/Et_3SiH; (c) 3-nitro-2-pyridinesulfenyl chloride (for **7c**) or 2-nitrophenylsulfenyl chloride (for **7d**); (d) iodine; (e) 95% aq TFA.

intermediate S-protected mercaptoacetamide−peptoids, 2-(S-acetylthio)acetamide−peptoid, **5** (Scheme 2), and 2-(S-tritylthio)acetamide−peptoid, **10** (Scheme 3). Both can be directly converted into the free thiol or into a number of useful thiol derivatives as described below.

Free Thiol. The free mercaptoacetamide peptoid, **6**, can be obtained in high yield from the *S*-acetyl derivative, **5**, by treatment with hydroxylamine (1 M hydroxylamine hydrochloride in pyridine) (*48*) followed by cleavage with TFA. The 2-mercaptoacetamide peptoid can also be obtained from the *S*-trityl derivative by a modified TFA cleavage mixture that contains a scavenger (TFA/H_2O/triethylsilane (Et_3SiH) (92.5:5:2.5 v/v)) (*49*). A mercaptoacetamide−peptoid forms the mixed disulfide with 5,5′-dithio-bis(2-nitrobenzoic acid) (Ellman's reagent; DTNB) in sodium phosphate buffer at pH 8 (data not shown).

We have successfully reacted the solid-supported mercaptoacetamide−peptoid, derived from the *S*-acetylmercaptoacetamide derivative, **5**, by treatment with hydroxylamine, with maleimide compounds, and reaction with

fluorescein-5-malemide (25 mM in pyridine for 1 h) resulted in the formation of the acid-stable thioether-linked chromophore adduct in 90% yield (data not shown).

A thiol is readily incorporated into peptoids at internal positions using the standard 2-(*S*-tritylthio)ethanamine monomer unit (*50*). The intermediate 2-(*S*-tritylthio)-ethyl−peptoid can be manipulated on the support as described for the terminal 2-(*S*-tritylthio)acetamide−peptoid. A mercaptoacetamide−peptoid was ligated to disulfide-activated peptoids (see Peptoid-to-Peptoid Ligation).

Activated Disulfides. The resin-bound *N*-mercaptoacetamide peptoid, **6**, is readily converted into activated disulfides. Treatment with 2,2′-dipyridyl disulfide (1 M in DMF/acetic acid (95:5 v/v)) resulted in the formation of 2-pyridinesulfenylmercaptoacetamide−peptoid, **7a**, in high yield. Other activated disulfides are also readily prepared by disulfide exchange: 4-nitro-3-carboxybenzenesulfenylmercaptoacetamide, **7b**, by treatment with 5,5′-dithiobis(2-nitrobenzoic acid) (1 M in pyridine), and 3-nitro-2-pyridinesulfenylmercaptoacetamide, **7c**, with 2,2′-dithiobis(5-nitropyridine) (1 M in DMF/acetic acid (95:5 v/v)). The activated disulfides are stable to TFA deprotection and underwent complete exchange with excess thiol compounds under mildly acidic conditions at pH 6 (for **7a** and **7c**) (*47*) and mildly basic conditions at pH 8 (for **7b**) (data not shown).

Treatment of resin-bound 2-(*S*-tritylthio)acetamide−peptoid, **10**, with 2-nitrophenylsulfenyl chloride (0.25 M in dichloroethane/acetic acid (95:5 v/v)) converts it directly into 2-nitrophenylsulfenylmercaptoacetamide−peptoid, **7d**. (*47*, *51*) This activated disulfide is completely stable to TFA deprotection, and it underwent complete exchange with excess thiol compounds under mildly basic conditions at pH 8 (*47*) (data not shown). 3-Nitro-2-pyridinesulfenyl chloride can also be used, and the resulting 3-nitro-2-pyridinesulfenylmercaptoacetamide−peptoid, **7b**, is stable to acid deprotection. It underwent complete exchange with excess thiol compounds under mildly acidic conditions at pH 6 (*47*) (data not shown). Treatment on the support or in solution with tris(2-carboxyethyl)phosphine (TCEP) (*52*) or dithiothreitol (DTT) (*53*) completely reduced the activated disulfides to the mercaptoacetamide−peptoid. Disulfide activated peptoids were ligated to a mercaptoacetamide−peptoid (see Peptoid-to-Peptoid Ligation).

Peptoid Disulfides. Exposure of resin-bound mercaptoacetamide peptoid, **6**, or 2-(*S*-tritylthio)acetamide−peptoid, **10**, to dilute iodine in DCE resulted in complete conversion to the homo-peptoid disulfide which was cleaved from the support and deprotected with TFA to give free homo-peptoid disulfide, $(SAc\text{-}N\text{−}peptoid\text{-}NH_2)_2$, **8**, in high yield. We have successfully used this route to dimerize the model pentamer peptoid at the N-terminus, and a hexamer peptoid that contains a 2-(*S*-tritylthio)-ethyl side group near the C-terminus. Mercaptoacetamide−peptoids were also readily oxidized with iodine in aqueous solution to the corresponding homo-peptoid disulfides, $(SAc\text{-}N\text{−}peptoid\text{-}NH_2)_2$ and $(Ac\text{-}N\text{−}peptoid\text{-}N\text{-}(ethyl\text{-}S\text{-})CH_2CONH_2)_2$, respectively, in high yield (data not shown).

The acid-stable 2-(*S*-acetylthio)acetamide−peptoid, **9**, was also cleaved from the support with TFA. The *S*-acetyl protection group could conveniently be removed in situ with hydroxylamine (0.05 M) in aqueous solution (phosphate buffer at pH 7.5), and the liberated mercaptoacetamide reacted completely with 3-maleimidopropionic acid or Ellman's reagent in a reaction sequence similar to bioconjugations using *N*-succinimidyl *S*-acetylthioacetate (SATA) (*48*).

Peptoid-to-Peptoid Ligations. To demonstrate the utility of some of the ligation groups, we chose to synthesize peptoid dimers. We joined peptoids using several of the most common ligation pairs (Table 1, entries a−c). Reactions were performed with the two types of peptoids in 1:1 stoichometry in dilute solution (0.1 and 0.5 mM of each component) for 30 min. Higher yields could be expected if higher concentrations and longer reaction times were used. Hydrazone formation by reaction of an aldehyde and a hydrazide peptoid proceeded in 45% yield (a result that is comparable to yields recorded in the literature (*38*)). Oxime formation between aldehyde and aminooxyacetamide peptoids resulted in dimer formation in 83% yield (Rose et al. (*36*) observed near-quantitative yields after 20 h). Disulfide formation between mercaptoacetamide peptoid and 2-nitrophenylsulfenylmercaptoacetamide and 2-pyridylsulfenylmercaptoacetamide peptoids proceeded in 88% and 92% yield, respectively. HPLC chromatograms of peptoid-to peptoid ligations are available in the Supporting Information.

CONCLUSION

We have shown that several chemoselective functionalities can readily be introduced into peptoids (and presumably into peptides and many other solid-phase organic chemistries) using a simple extension of the standard solid-phase peptoid submonomer method. The method was implemented primarily for N-terminal modification. Several of the functionalities can also be incorporated into peptoids at internal positions using standard monomers: thiol, aldehyde, and hydrazide functions are added using 2-(*S*-tritylthio)ethanamine (*50*), 1-amino-3,3-diethoxypropane, and $Boc\text{−}NHNH_2$, respectively. Alternatively, this method can be adapted so the desired functional group can be placed at other positions by using orthogonal protection of a lysine residue (for peptides) or an alkyl diamine monomer (for peptoids and peptides (*54*)). Some of the steps in this method may not be fully compatible with all functionalities in peptides, or non-standard protection schemes may be required.

The method uses commercially available reagents, is fully compatible with standard peptoid submonomer synthesis conditions, is easily automated, and generates the desired peptoid in high yield and purity. The method should simplify the introduction of chemoselective functionalities into molecules assembled by a solid-phase synthesis strategy (combinatorial libraries of ligands) for further screening for compounds with useful properties.

EXPERIMENTAL PROCEDURES

All chemicals were purchased from Aldrich, except for fluorescein-5-malemide (Molecular Probes, Eugene, OR), hydroxylamine hydrochloride, and tris(2-carboxyethyl)-phosphine (TCEP) (Pierce). The 2-(S-tritylthio)ethanamine monomer unit was prepared as described (*50*).

General Procedures. *Peptoid Synthesis.* Peptoid oligomer syntheses were performed on a robotic synthesizer (*55*). The syntheses were conducted with Rink amide polystyrene resin (50 μmol; 65 mg; substitution level 0.75 mmol/g). Acylation reactions were performed by the addition of bromoacetic acid (0.83 mL of 1.2 M in DMF; 1 mmol), followed by *N*,*N*′-diisopropylcarbodiimide (200 μL, 1.25 mmol). Reaction mixtures were agitated at 35 °C for 20 min. Displacement reactions were performed by addition of primary amine as 1 M solutions in DMF (1.0 mL; 1.0 mmol), followed by agitation for 20 min at

35 °C. These two steps are repeated with the appropriate amines to build the desired N-substituted glycine sequence.

Chemoselective Ligation Group Synthesis. The chemoselective ligation group was next introduced at the N-terminus with one additional submonomer cycle. The N-terminus, typically a secondary amine, was bromoacetylated, as described above, and the desired ligation group was introduced by displacement of the bromide by an excess of a nucleophilic reagent. In each reaction 1.25 mL of reagent was used, and the reaction mixture was agitated at 35 °C for 20 min. A common wash cycle consisting of 5 × 2 mL of DMF was used after each reagent addition with agitation at 35 °C for 1 min. All nucleophilic displacement reagents and auxiliary solutions were prepared immediately before use.

Aminooxyacetamide, 1. Bromoacetylated peptoid was treated with (a) *N*-hydroxysuccinimide/DBU (1.25 mL; 1 M/1 M in DMF) for 20 min, followed by (b) hydrazine hydrate (1.25 mL; 1 M in DMF) for 20 min.

***N*-(Carbamoylmethyl)acetohydrazide, 2.** Bromoacetylated peptoid was treated with Boc-$NHNH_2$ (1.25 mL; 1 M in DMF) for 20 min, followed by acetic anhydride (1.25 mL; 1 M in pyridine) for 20 min.

Iodoacetamide, 3. Bromoacetylated peptoid was treated with KI (1.25 mL; 1 M in DMF) for 20 min.

Aldehyde, 4. Bromoacetylated peptoid was treated with (a) 1-amino-3,3-diethoxypropane or 1-amino-2,2-dimethoxyethane (1.25 mL; 1 M in DMF) for 20 min, followed by (b) acetic anhydride (1.25 mL; 1 M in pyridine) for 20 min.

2-(*S*-Acetylthio)acetamide, 5. Bromoacetylated peptoid was treated with potassium thioacetate (1.25 mL; 1 M in DMF/water (95:5 v/v)) for 20 min.

2-Mercaptoacetamide, 6. *S*-Acetylmercaptoacetamide, **5**, was treated with hydroxylamine-HCl (1.25 mL; 1 M in pyridine) for 20 min.

2-Pyridinesulfenylmercaptoacetamide, 7a. *S*-Acetylmercaptoacetamide, **5**, was treated with a) hydroxylamine·HCl (1.25 mL; 1 M in pyridine) for 20 min, followed by b) 2,2′-dithiodipyridine (1.25 mL; 0.25M in DMF/acetic acid (95:5 v/v)) for 20 min.

4-Nitro-3-carboxyphenylsulfenylmercaptoacetamide, 7b. Acetylmercaptoacetamide, **5**, was treated with (a) hydroxylamine·HCl (1.25 mL; 1 M in pyridine) for 20 min, followed by (b) 5,5′-dithiobis(2-nitrobenzoic acid) (1.25 mL; 0.25 M in pyridine) for 20 min.

3-Nitro-2-pyridinesulfenylmercaptoacetamide, 7c. Acetylmercaptoacetamide, **5**, was treated with (a) hydroxylamine-HCl (1.25 mL; 1 M in pyridine) for 20 min, followed by (b) 2,2′-dithiobis(5-nitropyridine) (1.25 mL; 0.25M in DMF/acetic acid (95:5 v/v)) for 20 min.

Homo-disulfide-acetamide (SAc-N−peptoid-NH_2)$_2$, 8. Acetylmercaptoacetamide, **5**, was treated with (a) hydroxylamine-HCl (1.25 mL; 1 M in pyridine) for 20 min, followed by (b) iodine (1.25 mL; 0.05 M in DCE) for 20 min.

2-(*S*-Tritylthio)acetamide, 10. Bromoacetylated peptoid was treated with triphenylmethanethiol/DBU (1.25 mL; 0.25 M/0.25 M in DMF) for 40 min. The triphenylmethanethiol/DBU reagent is prepared by first dissolving triphenylmethanethiol in DMF followed by addition of the equimolar amount of DBU.

2-Mercaptoacetamide, 6. 2-(*S*-Tritylthio)acetamide, **10**, was treated with TFA/H_2O/triethylsilane (92.5:5:2.5 v/v; 2.5 mL) for 60 min.

3-Nitro-2-pyridinesulfenylmercaptoacetamide, 7c. 2-(*S*-Tritylthio)acetamide, **10**, was treated with 3-nitro-2-pyridinesulfenyl chloride (1.25 mL; 0.25 M in DCE/acetic acid (95:5 v/v)) for 20 min.

2-Nitrophenylsulfenylmercaptoacetamide, 7d. 2-(*S*-Tritylthio)acetamide, **10**, was treated with 2-nitrophenylsulfenyl chloride (1.25 mL; 0.25 M in DCE/acetic acid (95:5 v/v)) for 20 min.

Homo-disulfide-acetamide (SAc-N−peptoid-NH_2)$_2$, 8. 2-(*S*-Tritylthio)acetamide, **10**, was treated with iodine (1.25 mL; 0.05 M in DCE) for 20 min.

After conclusion of the synthesis, side-chain protecting groups were removed, and the oligomer was released from the resin support by treatment of the oligomer-resin with 95% trifluoroacetic acid in water (2.5 mL) for 60 min at room temperature, followed by filtration, dilution, and lyophilization. The crude products were analyzed by reversed-phase HPLC using the following conditions: Duragel G C18 (5 mμ; 50 × 2 mm) column; 5−95% gradient at 1 mL/min over 10 min at 60 °C; solvent A: water + 0.1% (v/v) TFA, solvent B: acetonitrile + 0.095% (v/v) TFA.

Ligation of Peptoids. The crude functionalized peptoids were purified by reversed-phase HPLC prior to ligation using the following conditions: Duragel G C4 HS (5 mμ; 50 × 20 mm) column; 20−65% gradient at either 20 or 40 mL/minute over 30 min at 60 °C; solvent A: water + 0.1% (v/v) TFA, solvent B: acetonitrile + 0.1% (v/v) TFA, using a Rainin dynamics SD-200 solvent delivery system.

Aldehyde/Aminooxyacetamide and Aldehyde/Hydrazide Ligations. Aminooxyacetamide−peptoid, **1**, or *N*-(carbamoylmethyl)acetohydrazide−peptoid, **2** (2 μL of a 5 mM stock solution in water containing 20% acetonitrile) and aldehyde−peptoid **4** (88 μL of a 100 μM stock solution in water containing 30% acetonitrile and 0.1% TFA) were added to 10 μL of a 1 M sodium acetate (pH 4.7) buffer. The reaction mixture was incubated at 20 °C for 30 min prior to HPLC analysis.

Mercaptan and Activated Disulfide Ligations. Mercaptoacetamide−peptoid, **6** (5 μL of a 5 mM stock solution in water containing 20% acetonitrile) and activated disulfide−peptoid, **7a** or **7d** (5 μL of a 5 mM stock solution in water containing 45% acetonitrile), were added to 40 μL 20mM tris-HCl buffer (pH 8.0) containing 0.4 mM EDTA/acetonitrile (1:1 v/v). The reaction mixtures were incubated at 20 °C for 30 min prior to hplc analysis.

Ligation mixtures were analyzed by reversed-phase HPLC using the following conditions: Duragel G C4 (5 micron; 50 × 2 mm) column; 5−95% gradient at 0.8 mL/minute over 10 min at 60 °C; solvent A: water + 0.1% (v/v) TFA, solvent B: acetonitrile + 0.095% (v/v) TFA. HPLC chromatograms of peptoid-to peptoid ligations are available in the Supporting Information.

ACKNOWLEDGMENT

The authors wish to thank Dr. Deborah H. Charych and Dr. Eric Beausoleil for suggestions and advice during this investigation.

Supporting Information Available: HPLC chromatograms of functionalized peptoids and of peptoid dimer ligations. This material is available free of charge via the Internet at http://pubs.acs.org.

LITERATURE CITED

(1) Berkum, N. L. v., and Holstege, F. C. (2001) DNA microarrays: raising the profile. *Curr. Opin. Biotechnol. 12*, 48−52.
(2) Tillib, S. V., and Mirzabekov, A. D. (2001) Advances in the analysis of DNA sequence variations using oligonucleotide microchip technology. *Curr. Opin. Biotechnol. 12*, 53−58.
(3) Tyers, M., and Mann, M. (2003) From genomics to proteomics. *Nature 422*, 193−197.

(4) Haab, B. B., Dunham, M. J., and Brown, P. O. (2001) Protein microarrays for highly parallel detection and quantitation of specific proteins and antibodies in complex solutions. *Genome Biol. 2* (2), research 4.1−4.13.

(5) Rich, R. L., and Myszka, D. G. (2000) Advances in surface plasmon resonance biosensor analysis. *Curr. Opin. Biotechnol. 11*, 54−61.

(6) Hermanson, G. T. (1996) *Bioconjugate Techniques*, 1st ed., Academic Press, Inc., San Diego.

(7) Zhang, Z., Zhu, W., and Kodadek, T. (2000) Selection and application of peptide-binding peptides. *Nat. Biotechnol. 18*, 71−74.

(8) Southern, E., Mir, K., and Shchepinov, M. (1999) Molecular interactions on microarrays. *Nat. Genet. 21*, 5−9.

(9) Fodor, S., Read, J., Pirrung, M., Stryer, L., Liu, A., and Solas, D. (1991) Lightdirected, spatially addressable parallel chemical synthesis. *Science 251*, 767−773.

(10) Alluri, P. G., Reddy, M. M., Bachhawat-Sikder, K., Olivos, H. J., and Kodadek, T. (2003) Isolation of Protein Ligands from Large Peptoid Libraries. *J. Am. Chem. Soc. 125*, 13995−14004.

(11) Schreiber, S. L. (2000) Target-oriented and diversity-oriented organic synthesis in drug discovery. *Science 287*, 1964−1969.

(12) Kodadek, T. (2002) Development of protein-detecting microarrays and related devices. *Trends Biochem. Sci. 27*, 295−300.

(13) Reimer, U., Reineke, U., and Schneider-Mergener, J. (2002) Peptide arrays: from macro to micro. *Curr. Opin. Biotechnol. 13*, 315−320.

(14) Reineke, U., Volkmer-Engert, R., and Schneider-Mergener, J. (2001) Applications of peptide arrays prepared by the SPOT-technology. *Curr. Opin. Biotechnol. 12*, 59−64.

(15) Rademann, J., Grøtli, M., Meldal, M., and Bock, K. (1999) SPOCC: A resin for solid-phase organic chemistry and enzymatic reactions on solid phase. *J. Am. Chem. Soc. 121*, 5459−5466.

(16) Dawson, P. E., Muir, T. W., Clark-Lewis, I., and Kent, S. B. H. (1994) Synthesis of proteins by native chemical ligation. *Science 266*, 776−779.

(17) Zhang, L., Torgerson, T. R., Liu, X.-Y., Timmons, S., Colosia, A. D., Hawiger, J., and Tam, J. P. (1998) Preparation of functionally active cell-permeable peptides by single-step ligation of two peptide modules. *Proc. Natl. Acad. Sci. U.S.A. 95*, 9184−9189.

(18) Botti, P., Pallin, T. D., and Tam, J. P. (1996) Cyclic peptides from linear unprotected peptide precursors through thiazolidine formation. *J. Am. Chem. Soc. 118*, 10018−10024.

(19) Rau, H. K., DeJonge, N., and Haehnel, W. (2000) Combinatorial synthesis of four-helix bundle hemoproteins for tuning of cofactor properties. *Angew. Chem., Int. Ed. 39*, 250−253.

(20) Bark, S. J., Schmid, S., and Hahn, K. M. (2000) A highly efficient method for site-specific modification of unprotected peptides after chemical synthesis. *J. Am. Chem. Soc. 122*, 3567−3573.

(21) Bonnet, D., Rommens, C., Gras-Masse, H., and Melnyk, O. (2000) Chemoselective acylation of hydrazinopeptides: a novel and mild method for the derivatization of peptides with sensitive fatty acids. *Tetrahedron Lett. 41*, 45−48.

(22) Zuckermann, R. N., Martin, E. J., Spellmeyer, D. C., Stauber, G. B., Shoemaker, K. R., Kerr, J. M., Figliozzi, G. M., Goff, D. A., Siani, M. A., Simon, R. J., Banville, S. C., Brown, E. G., Wang, L., Richter, L. S., and Moos, W. H. (1994) Discovery of nanomolar ligands for 7-transmembrane G-protein coupled receptors from a diverse (N-substituted)-glycine peptoid library. *J. Med. Chem. 37*, 2678−2685.

(23) Murphy, J. E., Uno, T., Hamer, J. D., Cohen, F. E., Dwarki, V., and Zuckermann, R. N. (1998) A combinatorial approach to the discovery of efficient cationic peptoid reagents for gene delivery. *Proc. Natl. Acad. Sci. U.S.A. 95*, 1517−1522.

(24) Wender, P. A., Mitchell, D. J., Pattabiraman, K., Pelkey, E. T., Steinman, L., and Rothbard, J. B. (2000) The design, synthesis, and evaluation of molecules that enable or enhance cellular uptake: Peptoid molecular transporters. *Proc. Natl. Acad. Sci. U.S.A. 97*, 13003−11300.

(25) Kirshenbaum, K., Barron, A. E., Goldsmith, R. A., Armand, P., Bradley, E. K., Truong, K. T. V., Dill, K. A., Cohen, F. E., and Zuckermann, R. N. (1998) Sequence-specific polypeptoids: A diverse family of heteropolymers with stable secondary structure. *Proc. Natl. Acad. Sci. U.S.A. 95*, 4303−4308.

(26) Burkoth, T. S., Beausoleil, E., Kaur, S., Tang, D., Cohen, F. E., and Zuckermann, R. N. (2002) Amphiphilic helical peptoid assembly. *Chem. Biol. 9*, 647−654.

(27) Zuckermann, R. N., Kerr, J. M., Kent, S. B. H., and Moos, W. H. (1992) Efficient method for the preparation of peptoids [oligo(N-substituted glycines)] by submonomer solid-phase synthesis. *J. Am. Chem. Soc. 114*, 10646−10647.

(28) Burkoth, T. S., Fafarman, A. T., Charych, D. H., Connolly, M. D., and Zuckermann, R. N. (2003) Incorporation of Unprotected Heterocyclic Side Chains into Peptoid Oligomers via Solid-Phase Submonomer Synthesis. *J. Am. Chem. Soc. 125*, 8841−8845.

(29) Barron, A. E., and Zuckermann, R. N. (1999) Bioinspired polymeric materials: between proteins and plastics. *Curr. Opin. Chem. Biol. 3*, 681−687.

(30) Defrancq, E., and Lhomme, J. (2001) Use of an aminooxy linker for the functionalization of oligodeoxyribonucleotides. *Bioorg. Med. Chem. Lett. 11*, 931−933.

(31) Adamczyk, M., Gebler, J. C., Reddy, R. E., and Yu, Z. (2001) A chemoselective method for site-specific immobilization of peptides via aminooxy group. *Bioconjugate Chem. 12*, 139−142.

(32) Lelievre, D., Bure, C., Laot, F., and Delmas, A. (2001) Synthesis of peptide di-aldehyde precursor for stepwise chemoselective ligations via oxime bonds. *Tetrahedron Lett. 42*, 235−238.

(33) Zeng, W., Jackson, D. C., and Rose, K. (1996) Synthesis of a new template with a built-in adjuvant and its use in constructing peptide vaccine candidates through polyoxime chemistry. *J. Pept. Sci. 2*, 66−72.

(34) Vilaseca, L. A., Rose, K., Werlen, R., Meunier, A., Offord, R. E., Nichols, C. L., and Scott, W. L. (1993) Protein conjugates of defined structure: Synthesis and use of a new carrier molecule. *Bioconjugate Chem. 4*, 515−520.

(35) Rose, K. (1994) Facile synthesis of homogeneous artificial proteins. *J. Am. Chem. Soc. 116*, 30−33.

(36) Rose, K., Zeng, W., Regamey, P.-O., Chernushevich, I. V., Standing, K. G., and Gaertner, H. F. (1996) Natural peptides as building blocks for the synthesis of large protein-like molecules with hydrazone and oxime linkages. *Bioconjugate Chem. 7*, 552−556.

(37) Tuchscherer, G. (1993) Template assembled synthetic proteins: condensation of a multifunctional peptide to a topological template via chemoselective ligation. *Tetrahedron Lett. 34*, 8419−8422.

(38) King, T. P., Zhao, S. W., and Lam, T. (1986) Preparation of protein conjugates via intermolecular hydrazone linkage. *Biochemistry 25*, 5774−5779.

(39) Wilchek, M., and Bayer, E. A. (1987) Labeling glycoconjugates with hydrazide reagents. *Methods Enzymol. 138*, 429−442.

(40) Kessler, W., and Iselin, B. (1966) Selective cleavage of substituted phenylsulfenyl protecting groups in peptide synthesis. *Helv. Chim. Acta 149*, 1330.

(41) Scott, W. L., and Cwi, C. (1996) Synthesis of reagents for the one step incorporation of hydrazide functionality onto the lysine residues of proteins, and their use as linkers for carbonyl containing molecules. *Bioorg. Med. Chem. Lett. 6*, 1491−1496.

(42) Marburg, S., Neckers, A. C., and Griffin, P. R. (1996) Introduction of the maleimide function onto resin-bound peptides: A simple, high-yield process useful for discriminating among several lysines. *Bioconjugate Chem. 7*, 612−616.

(43) Finkelstein, H. (1910) Preparation of organic iodides from the corresponding bromide and chloride compounds. *Berichte 43*, 1528−1532.

(44) Lelievre, D., Chabane, H., and Delmas, A. (1998) Simple and efficient solid-phase synthesis of unprotected peptide aldehyde for peptide segment ligation. *Tetrahedron Lett. 39*, 9675−9678.

(45) Dey, S., and Sheppard, T. L. (2001) Ketone-DNA: A versatile postsynthetic DNA decoration platform. *Org. Lett. 3*, 3983−3986.

(46) Marcaurelle, L. A., Shin, Y., Goon, S., and Bertozzi, C. R. (2001) Synthesis of oxime-linked mucin mimics containing the tumor-related TN and sialyl TN antigens. *Org. Lett. 3*, 3691−3694.

(47) Brocklehurst, K. (1979) Specific covalent modification of thiols: applications in the study of enzymes and other biomolecules. *Int. J. Biochem. 10*, 259−274.

(48) Duncan, R. J. S., Weston, P. D., and Wrigglesworth, R. (1983) A new reagent which may be used to introduce sulfhydryl groups into proteins, and its use in the preparation of conjugates for immunoassay. *Anal. Biochem. 132*, 68−73.

(49) Pearson, D. A., Blanchette, M., Baker, M. L., and Guindon, C. A. (1989) Trialkylsilanes as scavengers for the trifluoroacetic acid deblocking of protecting groups in peptide synthesis. *Tetrahedron Lett. 30*, 2739−2742.

(50) Gazal, S., Glukhov, E., Gilon, C., and Gellerman, G. (2001) Synthesis of novel protected N-alpha(omega-thioalkyl) amino acid building units and their incorporation in backbone cyclic disulfide and thioetheric bridged peptides. *J. Pept. Res. 58*, 527−539.

(51) Fontana, A. (1975) Selective removal of sulphur protecting groups of cysteine residues by sulfenyl halides. *J. Chem. Soc., Chem. Commun.*, 976−977.

(52) Burns, J. A., Butler, J. C., Moran, J., and Whitesides, G. M. (1991) Selective reduction of disulfides by tris(2-carboxyethyl)phosphine. *J. Org. Chem. 56*, 2648−2650.

(53) Cleland, W. W. (1964) Dithiothreitol, a new protective reagent for SH groups. *Biochemistry 4*, 480−482.

(54) Kumar, V., and Aldrich, J. V. (2003) A solid-phase synthetic strategy for labeled peptides: Synthesis of a biotinylated derivative of the ∂ opioid receptor antagonist TIPP (Tyr-Tic-Phe-Phe-OH). *Org. Lett. 5*, 613−616.

(55) Zuckermann, R. N., Siani, M. A., and Banville, S. C. (1992) Design, construction and application of a fully automated equimolar peptide mixture synthesizer. *Int. J. Pept. Protein Res. 40*, 498−507.

BC0341831

MAY/JUNE 2004
Volume 15, Number 3

© Copyright 2004 by the American Chemical Society

Bioconjugate Chemistry

COMMUNICATIONS

Native Chemical Ligation of Hydrophobic Peptides in Lipid Bilayer Systems

Christie L. Hunter[†] and Gerd G. Kochendoerfer*

Gryphon Therapeutics, 600 Gateway Boulevard,
South San Francisco, California 94080. Received February 19, 2004; Revised Manuscript Received March 9, 2004

The covalent modification of water-insoluble membrane polypeptides incorporated into lipid bilayers by native chemical ligation is described. The key feature of this strategy is the use of cubic lipidic phase (CLP) matrixes as reaction media. The CLP-matrix consists of a lipid bilayer into which hydrophobic polypeptides and folded membrane proteins can be inserted and two unbounded aqueous channels that give the aqueous phase access to both sides of an infinite lipid bilayer and thus ensure that modification of solvent-exposed sites is independent of the topology of membrane incorporation. The enzymatic removal of an N-terminal proteolytic cleavage sequence from the membrane polypeptide exposes an N-terminal cysteine residue. Subsequently, a C-terminal thioester peptide is joined to the N-terminus of the polypeptide by a native chemical ligation reaction. By use of this approach, incorporation of a variety of molecular tools, such as spectroscopic probes, unnatural amino acids, and molecular markers into membrane proteins that cannot be easily solubilized in detergent or denaturant solutions, may be achieved.

Chemical synthesis and modification of membrane proteins (*1*−*3*) employing chemoselective ligation strategies (*4*−*7*) such as native chemical ligation (NCL)[1] (*5*) is a powerful strategy to introduce noncoded amino acids and reporter groups into members of this important class of proteins. Semisynthetic approaches such as expressed protein ligation apply NCL (*5*) to the linkage of polypeptides in which one or both reaction partners have been produced by recombinant means (*8*−*11*). A truncated version of the ion channel protein Kcsa of *Streptomyces lividans* has been synthesized and subsequently folded by the addition of a synthetic peptide to the C-terminus of a recombinantly produced thioester peptide (*12*). Typically, such reactions are performed in mixed aqueous−organic solvents, or in the presence of detergents (*1*−*3,12*). By contrast, it would be desirable to modify synthetic or recombinant hydrophobic polypeptides in their native lipid environment and thus take advantage of the lipid as the reaction medium or "solvent". This would be applicable to peptide and bioconjugate chemistry, both for the enzymatic modification of polypeptides

* To whom correspondence should be addressed. Tel: (650) 360 1418; Fax: (650) 952 3055. E-mail: Gkochendoerfer@gryphonRX.com.

[†] Current address: Applied Biosystems, 850 Lincoln Centre Dr., Foster City, CA 94404.

[1] Abbreviations: bR bacteriorhodopsin; CLP, cubic lipidic phase; ESI-MS, electrospray ionization mass spectrometry; FTIR, Fourier transfer infrared; MALDI-TOF, matrix-assisted laser desorption ionization time-of-flight spectrometry; NCL, native chemical ligation; RP-HPLC, reversed-phase high-performance liquid chromatography.

10.1021/bc049959s CCC: $27.50 © 2004 American Chemical Society
Published on Web 04/24/2004

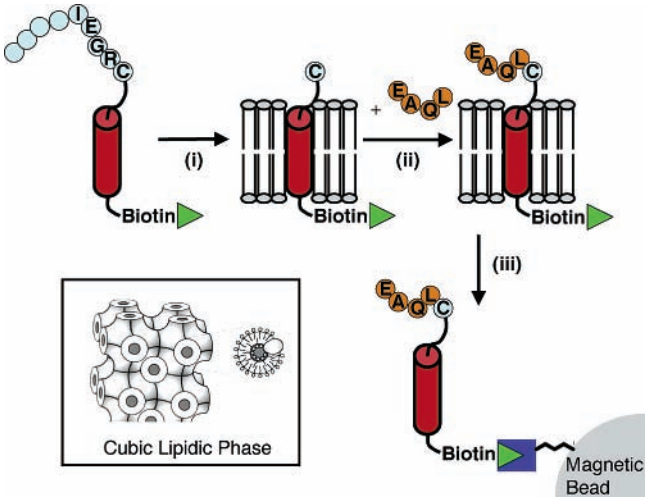


Figure 1. Schematic of the experimental design demonstrating native chemical ligation in cubic lipidic phases. After incorporation of a peptide corresponding to the first membrane-spanning helix of bacteriorhodopsin (bR) into the lipid bilayer, a peptide containing the protease recognition site was removed by Factor Xa cleavage (i). A peptide tetramer corresponding to the N-terminus of bR was then ligated to the transmembrane peptide to obtain the full bacteriorhodopsin N-terminus (ii). The extent of cleavage and the progress of the ligation inside the CLP was followed by MALDI-TOF mass spectrometry of the respective peptides after extraction with β-D-octylglucopyranoside and affinity capture on streptavidin beads through an *N*-imino-biotin label (iii). The inset shows a schematic of a cubic lipidic phase (reprinted from plate 9, ref 14, with kind permission from Elsevier).

and for native chemical ligation reactions. Here, we describe a strategy for the introduction of wild-type or labeled peptides to the N-terminus of a synthetic membrane polypeptide in a lipid bilayer environment. As outlined in Figure 1, the enzymatic removal of a proteolytic cleavage sequence from the N-terminus (*10, 11*) of a membrane polypeptide incorporated into a lipid bilayer generates a free N-terminal cysteine residue. Subsequently, a C-terminal thioester peptide is added to the N-terminus of the protein by a NCL reaction, yielding the desired construct. If desired, ligated polypeptides can be isolated from the lipidic phase after completion of the reaction.

A key feature of the approach is the cleavage and ligation reaction of a membrane polypeptide reconstituted into a cubic lipidic phase (CLP). The CLP-matrix consists of a lipid bilayer into which hydrophobic polypeptides and folded membrane proteins can be inserted and two aqueous channels that are both topologically unbounded, giving the aqueous phase access to both sides of an infinite lipid bilayer (*13, 14*). This feature ensures that all modifications are independent of the topology of membrane incorporation. By contrast, if a more traditional lipid system such as a standard liposome preparation were used for the reaction, the population of peptides that are incorporated with the N-terminus protruding to the inside of the vesicle would not be able to react with extraneously added reactants and vice versa. Since CLPs do not exhibit "inside" or "outside" regions, both the N-terminus and C-terminus of a polypeptide will be amenable for reaction with water-soluble reactants.

Since lipid and water diffusion rates inside the CLP-matrix are comparable or slightly slower than those in lamellar lipid phases and bulk water, respectively, sufficient reaction and modification rates can be achieved as also demonstrated in this study (*14*−*16*). Incorporation into a CLP also may overcome the difficulty in refolding membrane proteins after ligation reactions under denaturing conditions (*1*−*3, 12, 17*), since the reaction can be performed on a membrane polypeptide in the folded state under mild conditions. Finally, a possible shielding effect of detergent molecules that has been observed previously to prevent the ligation reactions of hydrophobic peptides (our own unpublished observation) can be avoided.

To demonstrate this approach, we performed an NCL reaction between a synthetic, membrane-incorporated polypeptide (named bRhel)[2] derived from the first transmembrane helix of bacteriorhodopsin (bR) of *Halobacterium salinarium*, and a four-amino acid residue oligopeptide corresponding to the N-terminus of bR (Figure 1). Dissolution of this peptide into typical denaturant buffers was not successful, and ligation thus could not be performed using traditional chemoselective reaction conditions (*4*−*7*). By contrast, incorporation into the CLP overcame this solubility problem. To facilitate ligation, Thr^5 of bR was replaced with Cys^5 to serve as ligation site. This Cys residue was capped with the N-terminal Factor Xa protease recognition site, IEGR (*10, 11*), to avoid the presence of a free N-terminal cysteine residue during the bilayer reconstitution process and to extend applicability of this approach to recombinant membrane proteins. Alternatively, intein-based expression approaches could be employed to generate proteins with N-terminal cysteines (*18*).

To form the CLP, the bRhel peptide in powder form was mixed with 1-monooleoyl-*rac*-glycerol (C18:1,[*cis*]-9) (MO) and 200 mM Tris-HCl buffer (pH 8), forming a cloudy suspension. The suspension was spun in a tabletop centrifuge for 3 h (see Supporting Information for more details). The formation of CLPs was indicated by the formation of optically clear, gellike phases, suggesting that the water-insoluble peptide was incorporated into the lipid phase. The phases remained optically clear at room temperature for at least two months, suggesting high thermodynamic stability. CD and polarized FTIR spectroscopy and proteolysis protection experiments on a bRhel analogue lead to the prediction that this peptide inserts into lipid bilayers in an α-helical structure (*19*). bRhel proved to be insoluble in aqueous buffers, even in the presence of strong denaturants such as 6 M guanidinium chloride, leading to turbid solutions of aggregated peptide. By contrast, no visible aggregation of hydrophobic peptide was observed after incorporation of bRhel peptide into a CLP at a lipid:peptide ratio of 100:1 and prolonged centrifugation of the CLPs. Taken together, these observations suggest that bRhel is associated with the cubic lipidic phase bilayer, possibly in a helical conformation.

Rapid monitoring of the progress of the ligation reaction within the CLP was essential for method development; therefore, an assay was developed that employs affinity capture and subsequent MALDI-TOF mass spectrometry to qualitatively follow the extent of ligation (Figure 2). An *N*-imino-biotin label was introduced at position Lys^{41} to facilitate purification and to allow for subsequent affinity capture. MALDI-TOF analysis was performed directly from the affinity beads in order to monitor the ligation reaction immediately without any chromatographic purification step and to avoid errors due to differential ease of release from the affinity beads of

[2] The sequence of bRhel is GKGYI EGR ^{5}CG ^{7}RPEWI ^{12}WLALG ^{17}TALMG ^{22}LGTLY ^{27}FLVKG ^{32}MGVSD ^{37}PDAKK. The residues are numbered according to their position in the sequence of wild-type bacteriorhodopsin.

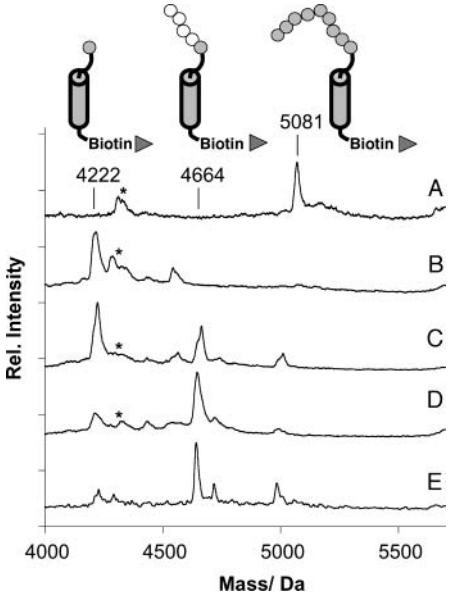


Figure 2. MALDI-TOF analysis of the progress of native chemical ligation in cubic lipidic phases. (A) MALDI-TOF spectra of bRhel prior to protease cleavage. (B) MALDI-TOF spectra of this peptide after protease cleavage. (C−E) MALDI-TOF spectra of this peptide after ligation with peptide EAQL after 25 min (C), 75 min (D), and overnight (E). The peaks of varying intensity marked with an asterisk are due to impurities associated with the purification and analysis process. Spectra were obtained directly from the affinity beads plated on MALDI slides.

the various constructs. The uneven surface of the matrix spot due to the presence of the beads on the plate is the cause of the low resolution and mass accuracy observed in the mass spectra shown.

Spectrum A presents a MALDI-TOF spectrum of bRhel after incorporation into a CLP, followed by dissolution of the CLP in a buffer containing 20 mM Bis-Tris Propane buffer (1,3-bis[tris(hydroxymethyl)methylamino]propane) (pH = 9.5), 27% β-D-octylglucopyranoside, and 20% β-mercaptoethanol, and affinity capture onto streptavidin-coated beads. The reducing agent was added to keep all peptide components and ligation products in the reduced, disulfide-free state during analysis and workup. The spectrum displays one major peak at m/z = 5081, corresponding to the mass of uncleaved bRhel. Smaller peaks (labeled with an asterisk) represent impurities from the lipid matrix, extraction process, and/or the affinity beads and were also present in the mass spectra in the absence of protein (data not shown). Whereas these impurities vary in intensity between individual time-points due to variations in the number of beads spotted on the plate, they do not interfere with the peaks of most interest and therefore the monitoring of the progress of the reaction. Spectrum B presents a mass spectrum of the same peptide after cleavage with Factor Xa inside the CLP overnight. The disappearance of the major peak at m/z = 5081 concomitant with the appearance of a major peak at m/z = 4222 is consistent with efficient removal of the Cys-capping sequence GKGYIEGR by the Factor Xa protease.

Spectra C, D, and E show the appearance of ligation product after addition of a 2-fold excess of N-terminal peptide EAQL thioester with 0.5% thiophenol to the CLP after 25 and 75 min and overnight incubation, respectively. The gradual disappearance of the peak at m/z = 4222 Da with a concomitant increase of a peak at m/z = 4664 Da demonstrates the progress of the formation of a native amide bond between the bR transmembrane peptide and the bR N-terminus.

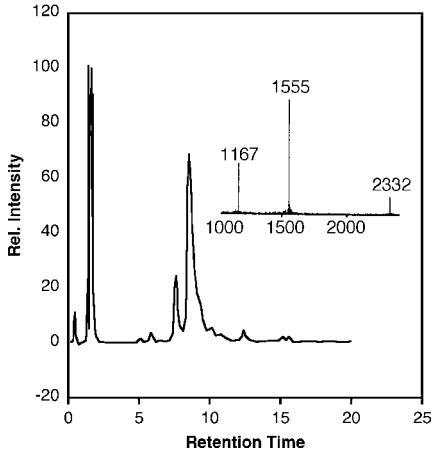


Figure 3. RP-HPLC chromatogram (detected at 280 nm) after dissolution of the CLP in 60% 2-propanol, 30% acetonitrile, and 10% water containing 0.1% trifluoroacetic acid. The major peak at 9 min correlates with the desired reaction product (observed MW = 4663 ± 1 Da (theoretical MW = 4663, average isotope composition).

After the reaction was complete, the reaction mixture was further analyzed and purified by RP-HPLC and subsequent electrospray mass spectrometry. For this analysis, the CLP was dissolved in 60% 2-propanol, 30% acetonitrile, and 10% water containing 0.1% trifluoroacetic acid. The analytical RP-HPLC chromatogram of an aliquot of the resultant solution is presented in Figure 3. The chromatogram exhibits a dominant peak at ∼ 9 min retention time. ESI-MS analysis of this peak indicates this component has the same mass as the desired reaction product (4663 ± 1 Da, see Figure 3 inset) and that it can be isolated with high purity. Reactions were typically performed at a 600 μg scale starting material (see Supporting Information), and the overall yield of pure product purified by RP-HPLC was typically ∼33% (200 μg). Preparation of CLPs is scalable and is expected to be amenable to multi-milligram scale modification of hydrophobic polypeptides.

The synthetic strategy described in this communication has several applications in the synthesis and modification of hydrophobic polypeptides. The limited solubility of hydrophobic membrane polypeptides in aqueous solvents has been a challenge to their modification (*1*−*3*, *12*). Application of lipid bilayer systems, in particular CLPs, may make chemoselective ligation techniques more applicable to this important class of peptides. Our approach may allow researchers to modularly assemble such membrane proteins from separately synthesized (or recombinantly expressed) subunits. In particular, multiple-membrane spanning proteins can be assembled from individual membrane-spanning domains without possible worries of incorporation of the peptides in incompatible relative orientation due to the unique topological features of the CLP system.

Incorporation of a variety of molecular tools, such as spectroscopic probes, unnatural amino acids, and molecular markers into membrane proteins at yields that significantly exceed those accessible with currently available techniques, may thus be achieved.

NOTE ADDED AFTER PRINT PUBLICATION

In the manuscript title, the word “Hydrophobic” was misspelled in the version of this paper published 4/24/2004 (ASAP) and in the May/June 2004 issue

(Vol. 15, No. 3, pp 437−440). The correct electronic version was published on the Web 6/4/2004, and a Correction appears in the July/August 2004 issue (Vol. 15, No. 4).

ACKNOWLEDGMENT

We thank Stephen B.H. Kent (University of Chicago) for advice and encouragement.

Supporting Information Available: Detailed descriptions of experimental procedures. This material is available free of charge via the Internet at http://pubs.acs.org.

LITERATURE CITED

(1) Kochendoerfer, G. G., Salom, D., Lear, J. D., Wilk-Orescan, R., Kent, S. B. H., and DeGrado, W. F. (1999) Total Chemical Synthesis of the Integral Membrane Protein Influenza A Virus M2: Role of Its C−Terminal Domain in Tetramer Assembly. *Biochemistry 38*, 11905−11913.

(2) Clayton, D., Shapovalov, G., Maurer, J. H., Dougherty, D. A., Lester, H. A., and Kochendoerfer, G. G. (2004) Total chemical synthesis and electrophysiological characterization of mechanosensitive channels from Escherichia coli and Mycobacterium tuberculosis. *Proc. Natl. Acad. Sci. 101*, 4764−4769.

(3) Kochendoerfer, G., Jones, D., Lee, S., Oblatt-Montal, M., Opella, S., and Montal, M. (2004) Functional characterization and NMR spectroscopy on full-length Vpu from HIV-1 prepared by total chemical synthesis. *J. Am. Chem. Soc. 137*, 2439−2446.

(4) Schnölzer, M., and Kent, S. B. H. (1992) Constructing Proteins by Dovetailing Unprotected Synthetic Peptides: Backbone-Engineered HIV Protease. *Science 256*, 221−225.

(5) Dawson, P. E., Muir, T. W., Clark-Lewis, I., and Kent, S. B. (1994) Synthesis of proteins by native chemical ligation. *Science 266*, 776−779.

(6) Dawson, P. E., and Kent, S. B. H. (2000) Synthesis of native proteins by chemical ligation. *Annu. Rev. Biochem 69*, 923−962.

(7) Kochendoerfer, G. G. (2001) Chemical protein synthesis methods in drug discovery. *Curr. Opin. Drug. Discovery Dev. 4*, 205−214.

(8) Muir, T. W. (2003) Semisynthesis of proteins by expressed protein ligation. *Annu. Rev. Biochem. 72*, 249−289.

(9) Muir, T. W., Sondhi, D., and Cole, P. A. (1998) Expressed protein ligation: a general method for protein engineering. *Proc. Natl. Acad. Sci. U.S.A. 95*, 6705−6710.

(10) Xu, R., Ayers, B., Cowburn, D., and Muir, T. W. (1999) Chemical ligation of folded recombinant proteins: segmental isotopic labeling of domains for NMR studies. *Proc. Natl. Acad. Sci. U.S.A. 96*, 388−393.

(11) Erlanson, D. A., Chytil, M., and Verdine, G. L. (1996) The leucine zipper domain controls the orientation of AP-1 in the NFAT.AP-1.DNA complex. *Chem. Biol. 3*, 981−991.

(12) Valiyaveetil, F. I., MacKinnon, R., and Muir, T. W. (2002) Semisynthesis and folding of the potassium channel KcsA. *J. Am. Chem. Soc. 124*, 9113−9120.

(13) Luzzatti, V., Gulik-Krzywicki, T., and Tardieu, A. (1968) Polymorphism of lecithins. *Nature 218*, 1031−1034.

(14) Lindblom, G., and Rilfors, L. (1989) Cubic phases and isotropic structures formed by membrane lipids- possible biological relevance. *Biochim. Biophys. Acta 988*, 221−256.

(15) Rowinski, P., Korytkowska, A., and Bilewicz, R. (2003) Diffusion of hydrophilic probes in bicontinuous lipidic cubic phase. *Chem. Phys. Lip. 124*, 147−156.

(16) Portmann, M., Landau, E. M., and Luisi, P. L. (1991) Spectroscopic and Rheological Studies of Enzymes in Rigid Lipidic Matrixes: The Case of α-Chymotrypsin in a Lysolecithin/Water cubic Phase. *J. Phys. Chem. 95*, 8437−8440.

(17) Valiyaveetil, F., Zhou, Y., and MacKinnon, R. (2002) Lipids in the structure, folding, and function of the KcsA K^+ channel. *Biochemistry 41*, 10771−10777.

(18) Perler, F. B., Xu, M. Q., and Paulus, H. (1997) Protein splicing and autoproteolysis mechanisms. *Curr. Opin. Chem. Biol. 1*, 292−299.

(19) Hunt, J. F., Bousche, O., Meyers, K. M., Rothschild, K. J., and Engelman, D. M. (1991) Biophysical studies of the integral membrane protein folding pathway. *Biophys. J. 59*, 400a.

BC049959S

ARTICLES

Core-Cross-Linked Polymeric Micelles as Paclitaxel Carriers

Xintao Shuai,[†] Thomas Merdan,[†] Andreas K. Schaper,[‡] Fu Xi,[§] and Thomas Kissel*[,†]

Department of Pharmaceutics and Biopharmacy, and Department of Geosciences & Materials Science Center, Philipps-University of Marburg, Ketzerbach 63, D-35032 Marburg, Germany, and Institute of Chemistry, The Chinese Academy of Sciences, Beijing 100080, China. Received July 8, 2003; Revised Manuscript Received November 11, 2003

Cross-linkable di- and triblock copolymers of poly(ϵ-caprolactone) (PCL) and monomethoxyl poly(ethylene glycol) (MPEG) were synthesized. These amphiphilic copolymers self-assembled into nanoscale micelles capable of encapsulating hydrophobic paclitaxel in their hydrophobic cores in aqueous solutions. To further enhance their thermodynamic stability, the micelles were cross-linked by radical polymerization of the double bonds introduced into the PCL blocks. Reaction conditions were found to significantly affect both the cross-linking efficiency and the micelle size. The encapsulation of paclitaxel into the micelles was confirmed by the proton nuclear magnetic resonance (^{1}H NMR) spectroscopy. Encouragingly, paclitaxel-loading efficiency of micelles was enhanced significantly upon micelle core-cross-linking. Both the micelle size and the drug loading efficiency increased markedly with increasing the PCL block lengths, no matter if the micelles were core-cross-linked or not. However, paclitaxel-loading did not obviously affect the micelle size or size distribution. The cross-linked micelles exhibited a significantly enhanced thermodynamic stability against dilution with aqueous solvents. The efficient cellular uptake of paclitaxel loaded in the nanomicelles was demonstrated by confocal laser scanning microscopy (CLSM) imaging. This new biodegradable nanoscale carrier system merits further investigations for parenteral drug delivery.

INTRODUCTION

Paclitaxel (Taxol), an anticancer agent isolated from the bark of the pacific yew tree (*Taxus brevifolia*) (*1*), is active against a wide range of solid tumors such as advanced ovarian and breast cancer (*2*). Major problems encountered in paclitaxel chemotherapy are the low aqueous solubility of paclitaxel and the severe side effects (*3*−*5*). Currently, a Cremophor EL−ethanol vehicle (50:50 mixture) is clinically used for paclitaxel chemotherapy. However, serious side effects (*6*−*8*), such as hypersensitivity and neurotoxicity, were induced by Cremophor EL. To overcome these problems, liposomes (*9*−*10*) and polymeric micelles (*11*−*12*) are two promising alternatives for the Cremophor EL−ethanol vehicle. The distinct characteristics of polymeric micelles formed from amphiphilic block copolymers (*13, 14*) include nanoscale size, thermodynamic stability in aqueous solution compared to small molecular micelles, and a unique core−shell-type architecture, which can mimic naturally occurring transport systems such as lipoproteins and viruses (*15*). The hydrophobic core of the micelles offers a carrier compartment that accommodates predominately hydrophobic drugs, and the shell consists of a brushlike protective corona that stabilizes the nanoparticles in aqueous solution (*15*−*17*). Using encapsulation within the micelles, one obtains systems in which solubility limits for hydrophobic drugs can be exceeded. In addition to their nanoscale dimension, which is favorable for intravenous administration and cellular uptake, polymeric micelles for drug delivery offer other advantages, e.g. their high and controllable drug loading and release capacities, their biocompatibility, and the diversity of drugs they can accommodate (*16*−*18*). Therefore, polymeric micelles are particularly promising carriers of many hydrophobic anticancer agents including paclitaxel.

Another advantage of polymeric micelles is a passive targeting effect due to an increased permeability of tumor endothelia in connection with a lack of normal lymphatic drainage and hypervasculature of the tissue (*19*). This effect is known as enhanced permeability and retention effect (EPR) and leads to capture of macromolecular structures within the tumor interstitium. The EPR effect has been demonstrated for a variety of macromolecules (*20*) and liposomes (*21*). Through this passive targeting mechanism, highly selective delivery of anticancer agent to specific tumor sites using polymeric micelles as carriers can be achieved (*22*).

Several reports have demonstrated controllable encapsulation efficacy, high antitumor activity, and desirable biodistribution of paclitaxel-loaded micelles based on biodegradable block copolymers such as poly(ethylene glycol)-b-poly(D,L-lactide) (*23*), poly(ϵ-caprolactone)-b-poly(ethylene glycol) (*24*), and poly(ϵ-caprolactone)-b-poly(2-ethyl-2-oxazoline) (*25*). These micelles are formed through interactions of intermolecular hydrophobic blocks

* To whom correspondence should be addressed: Tel +49-6421-282-5881; fax +49-6421-282-7016; e-mail: kissel@mailer.uni-marburg.de.

[†] Department of Pharmaceutics and Biopharmacy, Philipps-University of Marburg.

[‡] Department of Geosciences & Materials Science Center, Philipps-University of Marburg.

[§] Chinese Academy of Sciences.

10.1021/bc034113u CCC: $27.50 © 2004 American Chemical Society
Published on Web 05/01/2004

of linear amphiphilic block copolymers. Although thermodynamically more stable in aqueous media than micelles formed with small molecular surfactants, they are still subject to in vivo disintegration upon dilution that occurs in biological fluids. Kataoka et al. have proven micelle core cross-linking to be an effective way to avoid the micellar disintegration upon dilution. They demonstrated that core-cross-linked micelles of poly(ethylene glycol)-b-poly(D,L-lactide) possess high stability against dilution, temperature change, and even dissolution of surfactants (*26*).

In the present work, we aimed at developing novel core-cross-linked micelles for efficient paclitaxel encapsulation and delivery. To this end, we synthesized di- and triblock copolymers of MPEG and PCL, with cross-linkable double bonds located in the PCL block. Core-cross-linked micelles (<200 nm in diameter) were prepared, using the cross-linked polymers synthesized under optimized reaction conditions. Paclitaxel loading and in vitro release was investigated. The efficient cellular internalization of paclitaxel-loaded micelles was demonstrated using confocal laser scanning microscopy.

EXPERIMENTAL SECTION

Materials. ϵ-Caprolactone (Sigma-Aldrich, Taufkirchen, Germany) was purified by vacuum distillation over calcium hydride (CaH_2). Toluene (Sigma-Aldrich, Taufkirchen, Germany) for azeotropic distillation was dried by refluxing over sodium (Sigma-Aldrich, Taufkirchen, Germany) and distilled under dry argon. Monomethoxyl poly(ethylene glycol)s (Sigma-Aldrich, Taufkirchen, Germany) were first purified by precipitation from tetrahydrofuran (THF, Sigma-Aldrich, Taufkirchen, Germany) into hexane (Sigma-Aldrich, Taufkirchen, Germany), and then the vacuum-dried precipitates were further dried by azeotropic distillation with dry toluene. Stannous(II) octoate (SnOct), maleic anhydride, thionyl chloride, α,α'-azoisobutyronitrile, and potassium persulfate ($K_2S_2O_8$) were all from Sigma-Aldrich, Taufkirchen, Germany, and used as received. Paclitaxel (Genexol) is a kind gift from Sam Yang Genex, Korea. The fluorescent-labeled paclitaxel, Oregon Green 488, was purchased from Molecular Probes (USA). Bovine serum albumin (BSA) was purchased from Sigma. Phosphate-buffered saline (PBS) was prepared in our laboratory. All organic solvents are of analytic grade.

NIH/3T3 (Swiss mouse embryo) cell line was purchased from the German Collection of Microorganisms and Cell Cultures (DSMZ, Braunschweig, Germany). Cells were cultured according to the protocols suggested by the supplier.

Synthesis of Monohydroxy-Terminated and Maleic-Capped Diblock Copolymers of PCL and MPEG. Detailed synthetic methods for these two types of block copolymers have been described in our recent publication (*27*). Briefly, the monohydroxy-terminated diblock copolymers were synthesized by ring-opening polymerization of ϵ-caprolactone at 115 °C using MPEG as a macroinitiator and SnOct as a catalyst, with yields >95%. The maleic-capped diblock copolymers were then synthesized by esterification of the monohydroxy-terminated diblock copolymers and maleic anhydride, with yields >92%.

Synthesis of Cross-Linkable Triblock Copolymers. To activate the diblock copolymer, maleic-capped diblock copolymer (1 g) and thionyl chloride (3 times the molar amount of polymer) were dissolved in dry toluene (10 mL) and then refluxed under argon for 2 h at 50 °C. Toluene and the excessive thionyl chloride were then removed by distillation under reduced pressure. The hydroxyl-terminated and the carbonyl-chloride-activated diblock copolymers (1:1 in molar ratio) were mixed in the reaction vial. Under high vacuum, the mixture was magnetically stirred for 2∼8 h at 80 °C.

The crude product was dissolved in toluene and then precipitated in hexane. The triblock copolymer, monomethoxylpoly(ethylene glycol)-b-poly(ϵ-caprolactone)-b-monomethoxylpoly(ethylene glycol) (MPEG-PCL-MPEG), was then recovered by filtration, and dried under vacuum, with yields >95%.

Controlled Cross-Linking of Di- and Triblock Copolymers. To obtain core-cross-linked micelles smaller than 200 nm in diameter, the control of polymer cross-linking conditions was crucial. Reaction was conducted under various reaction conditions, i.e., reaction temperature and time, solvent, and catalyst, etc. In an optimized cross-linking reaction, cross-linkable di- or triblock copolymer (300 mg) was dissolved in acetone (20 mL) in a reaction vial equipped with refluxing condenser, magnetic stirring bar, and argon inlet protection pipe. Distilled water (40 mL) was then added. After the solution was bubbled for 30 min with argon, $K_2S_2O_8$ (1 wt % polymer) was added to the mixture and subsequently the reaction temperature was raised to 50 °C. The solution under argon protection was stirred at 50 °C for 24 h. After the reaction, solvents (acetone and water) were removed by rotary evaporation. The product was redissolved in acetone, filtered to remove insoluble inorganic initiator residues, dialyzed against acetone to eliminate the non-crosslinked polymer, and precipitated into hexane. The cross-linked polymer recovered by filtration was finally dried under vacuum, with yields >87%.

Preparation of Paclitaxel-Loaded Micelles. Polymeric micelles containing paclitaxel were prepared as follows: polymer (20 mg) and paclitaxel (2 mg) were added to acetone (4 mL) in a glass beaker. The solution was heated to 40 °C to codissolve the polymer and paclitaxel and then was cooled to room temperature. Afterward, the solution was dropwise added to pure water (20 mL) under vigorous agitation. The beaker was then opened to air overnight, allowing slow evaporation of acetone and formation of micelles. The residual acetone was completely removed by vacuum distillation with a rotary evaporator, and then the micelle solution was filtered with a microfilter (pore size: 0.4 μm) to eliminate the uncomplexed paclitaxel and aggregated particles. The micelles thus obtained were directly characterized with ^{1}H NMR, dynamic light scattering (DLS), and ultraviolet (UV) measurements. To obtain the powder samples, the micelle solutions were frozen and lyophilized.

The paclitaxel-loading content (PLC) and efficiency (PLE) was calculated from the following equations:

$$\mathrm{PLC} = \frac{\text{amount of paclitaxel in micelle}}{\text{amount of paclitaxel-loaded micelle}} \times 100$$

$$\mathrm{PLE} = \frac{\text{paclitaxel amount in micelle}}{\text{paclitaxel amount used for micelle preparation}} \times 100$$

Characterization of Polymers. Fourier transform infrared (FTIR) spectral studies were carried out with a Nicolet 510P FTIR spectrometer in the range between 4000 and 400 cm^{-1}, with a resolution of 2 cm^{-1}. All powder samples were compressed into KBr pellets for the FTIR measurements. ^{1}H NMR spectra were recorded on a JEOL GX 400 D spectrometer in deuterated chloroform ($CDCl_3$) or water (D_2O) at room temperature.

Gel permeation chromatography (GPC) was employed to determine the molecular weight and the molecular weight distribution. GPC analysis was carried out using a SDV Linear M 5μ 8 × 300 mm column (Polymer Standard Service, Mainz, Germany) with dichloromethane (DCM) as an eluent (1 mL/min) and polystyrene standards for column calibration. 20 μL samples were injected with a Merck Hitachi autosampler AS-2000A. The eluent was analyzed with a differential refractive index (RI) detector RI-71 from Merck and 18 angle laser light scattering detector from Wyatt Technologies (DAWN EOS, GaAs laser 690 nm, 30 mW, K5 cell).

Determination of Paclitaxel-Loading Content (PLC). PLC was determined by UV measurements. The freeze-dried micelle particles were dissolved in a mixture of methanol and *N*,*N*-dimethylacetamide (1:2, v/v). The absorbance at 265 nm was detected with a Shimadzu UV-160 UV−visible recording spectrophotometer. Paclitaxel solutions of various concentrations were prepared, and the absorbance at 265 nm was measured to generate a calibration curve for calculating the PLC of various micelles.

Photon Correlation Spectroscopy. The size and size distribution of the polymeric micelles were determined by photon correlation spectroscopy. Measurements were performed on a Zetasizer 3000 HS from Malvern Instruments, Herrenberg, Germany (10 mW HeNe laser, 633 nm). Scattered light was detected at 90° angle through a 400 micron pinhole at a temperature of 25 °C. For each sample, data obtained in three measurements were averaged to get the final size and size distribution.

Electron Microscopy. Paclitaxel-loaded micelle based on a cross-linked diblock copolymer, MPEG5k-b-PCL18k, was chosen for the transmission electron microscopy study (TEM). The paclitaxel-loading content in these micelles is 5.1%. A drop of the micelle solution was deposited on the carbon hole-coated grid and then allowed to dry overnight at room temperature. The grid was exposed to the vapor of a 2% solution of osmium tetroxide for 2 h. TEM observations were made with a JEOL 3010 transmission electron microscope supplemented with a 2k × 2k CCD camera at 300 kV.

Confocal Laser Scanning Microscopy. For confocal microscopy experiments, a Zeiss Axiovert 100M microscope coupled to a Zeiss LSM 510 scan module was used. NIH/3T3 cells were seeded at a density of 50 000 cells per well in eight-well chamber slides (LabTek, Nunc, Wiesbaden, Germany). After 24 h, medium was removed and micelles containing Oregon Green 488 labeled paclitaxel (Sigma-Aldrich, Taufkirchen, Germany) were added in fresh media. After 4 h, the medium was removed again and cells were washed four times with phosphate-buffered saline (PBS). Fixation of cells was done by incubation with 400 μL paraformaldehyde solution 3% in PBS for 20 min. Cells were regarded in FluorSave Reagent (Calbiochem, San Diego, CA). Excitation of Oregon Green was performed using an argon laser with a wavelength of 488 nm and a long-pass filter of 505 nm. Paclitaxel-loaded micelle based on a cross-linked triblock copolymer (MPEG5k-(PCL3.8k)$_2$-MPEG5k) was used in the CLSM study. The paclitaxel-loading content in this micelle is 2.7%.

RESULTS AND DISCUSSION

Polymer Synthesis. Synthesis of block copolymer of PCL and PEG, using hydroxyl-terminated PEG as an initiator and stannous(II) octoate as a catalyst, has been reported earlier (*27*). The ring-opening polymerization was conducted in bulk at an elevated temperature (115 °C). In this way, we synthesized the monohydroxyl-terminated diblock copolymers of MPEG and PCL (MPEG-b-PCL-OH), which were then reacted with maleic anhydride to introduce a reactive maleic moiety to the PCL block end. Activation of a carboxyl-terminated diblock copolymer with thionyl chloride resulted in the maleic chloride-capped diblock copolymer, which was esterified with MPEG-b-PCL-OH to yield a triblock copolymer (MPEG-PCL-MPEG) bearing a reactive maleic ester moiety in the middle of the PCL block, as shown in Scheme 1. Properties of cross-linkable di- and triblock copolymers thus synthesized are summarized in Table 1.

Scheme 1. Synthetic Approach to Cross-Linkable Di-and Triblock Copolymers

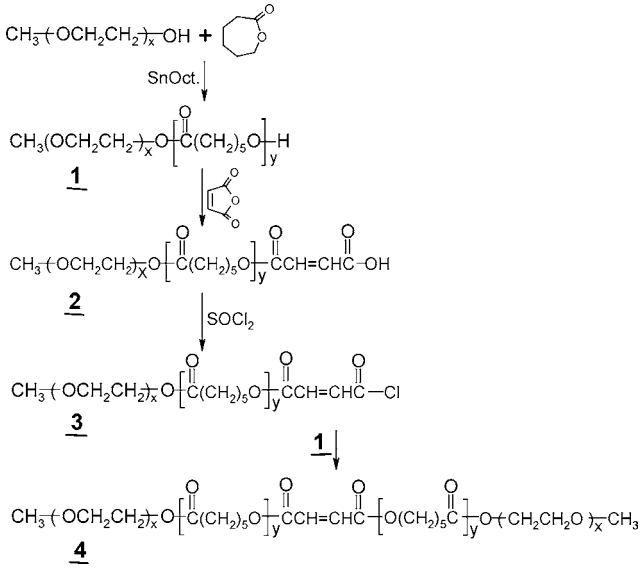


Table 1. Molecular Weights of Di- and Triblock Copolymers

entry	M_{n-MPEG}	diblock copolymer: $M_{n-copolymer}$[a]	triblock copolymer: $M_{n-copolymer}$[b]
1	550	1100	not measured
2	2000	3200	6920
3	2000	3980	7640
4	2000	4700	10300
5	5000	8800	19500
6	5000	23500	41760

[a] ^{1}H NMR results. [b] GPC results.

FTIR, ^{1}H NMR, and GPC measurements were employed to demonstrate the successful synthesis of the block copolymers. Figure 1 shows the FTIR spectra of a hydroxyl-terminated diblock copolymer and the cross-linkable di- and triblock copolymers. PCL and PEG blocks were characterized by prominent absorptions at 1726 cm^{-1} (s, $\nu_{C=O}$) and 1105 cm^{-1} (s, ν_{C-O}), respectively. Obviously, both PCL and PEG blocks are present in all block copolymers. A strong absorption of the incorporated maleic segment at 1635 cm^{-1} (s, $\nu_{C=C}$), which is absent in the spectrum of the hydroxyl-terminated prepolymer, was observed for both cross-linkable di- and triblock copolymers. In addition, the maleic-capped cross-linkable diblock copolymer showed very strong and broad absorption around 3450 cm^{-1}, which results from the stretching vibration of carboxylic end group (s, ν_{O-H}). In comparison, other two copolymers showed only very weak absorption in this region, likely due to residual humidity in the samples.

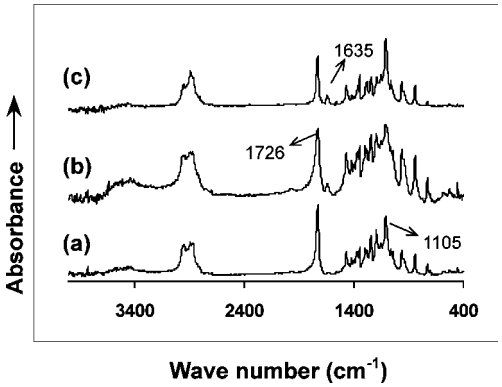


Figure 1. FTIR spectra of HO-terminated diblock copolymer MPEG2k-b-PCL1.2k (a), carboxyl-terminated MPEG2k-b-PCL1.2k (b), and triblock copolymer MPEG2k-(PCL1.2k)$_2$-MPEG2k (c).

In the ^{1}H NMR spectra of all block copolymers, the characteristic resonances of both PCL (1.376 ppm, 1.65 ppm, 2.306 ppm, and 4.057 ppm) and MPEG (3.385 ppm and 3.643 ppm) were observed, suggesting the coexistence of two blocks (*27*). For the diblock copolymers, the lengths of PCL blocks were estimated from the integrals of characteristic peaks of PEG (e.g. CH_3O at ~3.38 ppm) and PCL (e.g. C(=O)CH_2 at ~2.3 ppm), using the known molecular weights of MPEGs (*27*). The expansion of ^{1}H NMR spectra, as shown in Figure 2, provides evidence for the expected structures of block copolymers. Cross-linkable di- and triblock copolymers exhibited distinct resonance signals of maleic moieties at ~6.4 ppm (two *doublets*, C(=O)C*H*=C*H*C(=O)OH) and at ~6.83 ppm (*singlet*, C(=O)C*H*=C*H*C(=O)) respectively, which are not present in the spectrum of MPEG-b-PCL-OH containing no maleic moiety. ^{1}H NMR absorptions around ~4.2 ppm, i.e., triplet peaks a and b, strongly demonstrated the exact local linkage structures between PCL and PEG blocks, and between PCL blocks and maleic moieties, as expected from Scheme 1. Molecular weights characterized by GPC measurements also demonstrated the successful synthesis of block copolymers. For all block copolymers, unimodal distributions were observed in the GPC elugrams (not shown). It is noteworthy that, for the diblock copolymers, molecular weights detected by GPC are in reasonable agreement with those calculated from ^{1}H NMR data. Unfortunately, it is impossible to calculate the molecular weights of the triblock copolymers based on the ^{1}H NMR data, unless the samples are completely free of the diblock copolymers. Therefore, the molecular weights of the triblock copolymers were all estimated from the GPC measurements.

Micelle Preparation and Core Cross-Linking. Micelles were prepared by a solvent-evaporation method (*28*, *19*). Acetone was selected as the organic solvent because it dissolves both copolymer and paclitaxel, evaporates easily at room temperature, and is miscible with water. Most of the micelles possess sizes < 100 nm in mean diameter independent of paclitaxel loading (Table 2).

We investigated various approaches to achieve the core-cross-linked micelles and to control the micelle size < 200 nm. In all cases, radical polymerization was conducted under argon as described in the Experimental Section. Direct core cross-linking of micelles of poly(ethylene glycol)-b-poly(D,L-lactide) was achieved successfully in aqueous micellar solution by Kataoka et al., using either inorganic (*30*) or organic (*26*) initiators for radical polymerization. In light of their discovery, we attempted to directly cross-link the core of micelles in the aqueous micelle solutions. Micelles were first prepared with the cross-linkable di- and triblock copolymers. Then the radical polymerization was initiated at elevated temperatures (e.g. 50 °C) using α,α′-azoisobutyronitrile or $K_2S_2O_8$. α,α′-Azoisobutyronitrile was dissolved in DCM (2 mg/mL) and then added to the micelle solution (*26*). After stirring for 2 h at room temperature to distribute the initiator to the micelle cores, DCM was removed by rotary evaporation before the core radical polymerization at elevated temperatures. When $K_2S_2O_8$ was used as an initiator, it was added directly to the micelle solution. The radical polymerization progress was followed by ^{1}H NMR spectroscopy, monitoring the decrease of maleic protons (C*H*=C*H*). In contrast to poly(ethylene glycol)-b-poly(D,L-lactide) micelles, we found that the direct polymerization of MPEG-b-PCL micelles in solution at 40 °C, 50 °C, and 60 °C did not proceed effectively, independent of the initiator used. We believe that differences in both double bond densities and intrinsic reactivities of the double bonds have contributed to these results. Steric hindrances as well as different electron

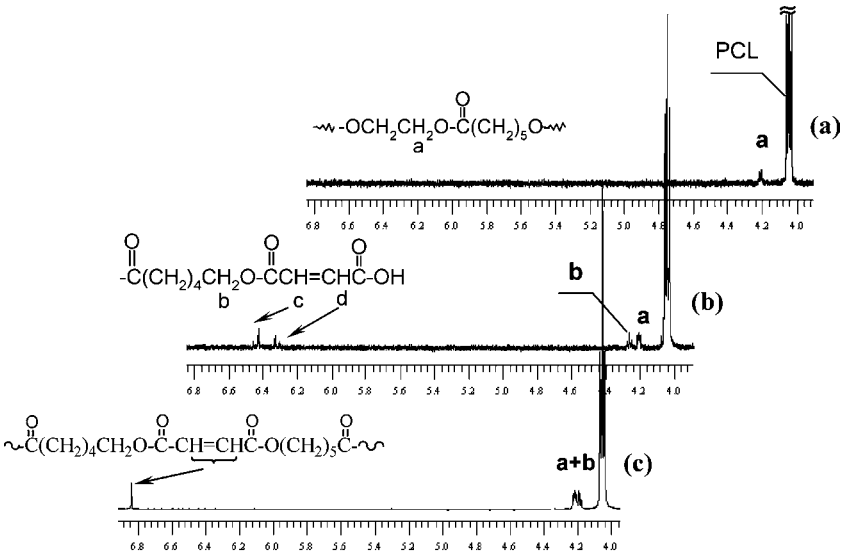


Figure 2. ^{1}H NMR spectra of HO-terminated diblock copolymer MPEG2k-b-PCL1.2k (a), carboxyl-terminated MPEG2k-b-PCL1.2k (b), and triblock copolymer MPEG2k-(PCL1.2k)$_2$-MPEG2k (c).

Table 2. Influence of Core-Cross-Linking on the Micelle Size Detected by DLS Measurements[a]

	mean diameters of micelles before core-cross-linking (nm)		mean diameters of core-cross-linked micelles (nm)	
copolymer	drug free	drug loaded	drug free	drug loaded
PCL1.2k-b-MPEG2k	29.4 ± 0.7	31.3 ± 0.4	53.3 ± 1.2	72.3 ± 6.2
$(PCL1.2k\text{-}b\text{-}MPEG2k)_2$[b]	31.8 ± 0.5	29.9 ± 1.2	46.2 ± 1.8	44.3 ± 2.6
PCL2.7k-b-MPEG2k	37.3 ± 5.2	42.6 ± 1.6	56.6 ± 0.5	65.3 ± 2.2
$(PCL2.7k\text{-}b\text{-}MPEG2k)_2$[b]	48.1 ± 1.5	46.6 ± 2.5	55.4 ± 6.7	57.9 ± 3.8
PCL3.8k-b-MPEG5k	71.8 ± 6.4	65.3 ± 2.2	81.7 ± 1.9	78.0 ± 2.7
$(PCL3.8k\text{-}b\text{-}MPEG5k)_2$[b]	67.7 ± 0.9	80.4 ± 1.6	99.2 ± 1.2	98.5 ± 9.1
PCL18k-b-MPEG5k	97.7 ± 0.9	91.9 ± 0.7	151.5 ± 1.4	161.1 ± 1.2
$(PCL18k\text{-}b\text{-}MPEG5k)_2$[b]	146.7 ± 1.2	123.4 ± 1.7	173.7 ± 9.8	201.7 ± 2.9

[a] Core-cross-linked micelles were prepared by solvent-evaporation method with copolymers cross-linked in solution of acetone and water (1:2 v/v) for 24 h at 50 °C. [b] Triblock copolymers.

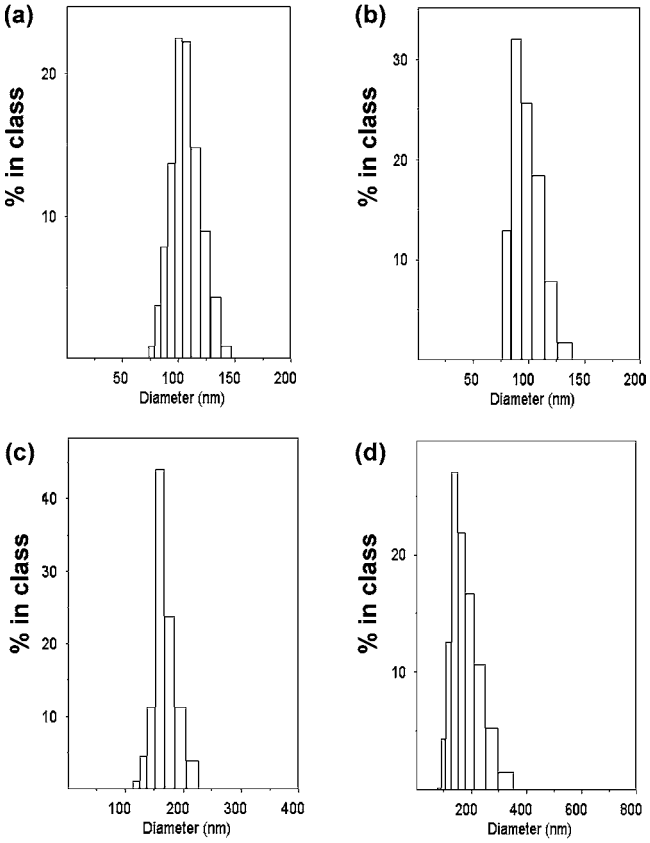


Figure 3. Size distributions of paclitaxel-free non-cross-linked micelle (a), paclitaxel-loaded non-cross-linked micelle (b), paclitaxel-free cross-linked micelle (c), and paclitaxel-loaded cross-linked micelle (d), based on the cross-linkable diblock copolymer MPEG5k-b-PCL18k.

densities of the maleic moieties in cross-linkable MPEG-b-PCL, compared to methacrylate, are likely reasons for inefficient cross-linking of our micellar structures.

Furthermore, it is known that once a crystalline polymer phase is formed, it can no longer accommodate foreign substances such as initiator molecules. Therefore, the direct core polymerization of MPEG-b-PCL micelles was not possible at temperatures < 60 °C, due to the tendency of PCL to form a crystalline phase. As expected, slow polymerizations were indeed detected at temperatures > 80 °C. However, DLS measurements demonstrate that polymerization > 3 days, at 80 °C or above generally resulted in significant size increase (up to 800 nm) and broad size distribution (up to ~20) of micelles.

As an alternative we studied the radical polymerization of cross-linkable polymers in toluene solution at a reaction temperature of 60 °C or in a mixture (50 °C) of acetone and water (1:2 in v/v). Using α,α′-azoisobutyronitrile as an initiator, micelles in toluene solutions underwent fast cross-linking reaction. High degrees of cross-linking were achieved within 8 h. However, micelles prepared with these cross-linked copolymers also showed significant size increase and broad size distributions (data not shown).

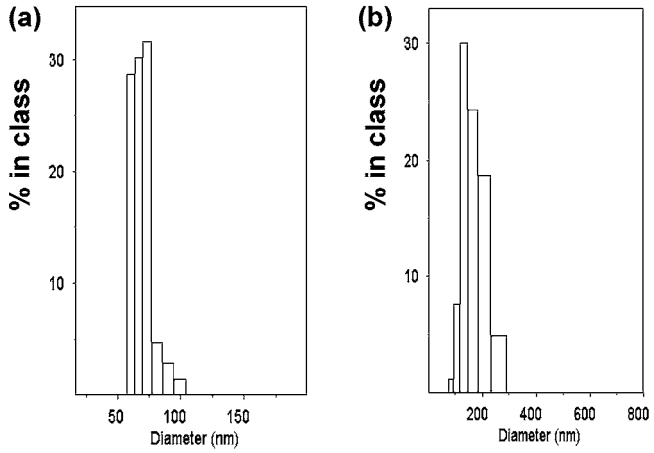


Figure 4. Size distributions of non-cross-linked MPEG2k-$(PCL2.7k)_2$-MPEG2k micelle in water (a), and a 1:2 mixture (v/v) of acetone and water (b).

Polymerization in solvent mixtures of acetone and water (1:2 in v/v), using $K_2S_2O_8$ as an initiator, proceeded smoothly. When reaction time reached 72 h, precipitates were generally observed. This phenomenon can be explained by high molecular weight polymers, which are insoluble in the solvent. However, polymerization for 24 h at 50 °C in the mixed solution was found to be suitable for a sufficient and controlled cross-linking of cross-linkable di- and triblock polymers.

As shown in Table 2, the micelle size increased upon cross-linking, both for drug-free and drug-loaded cross-linked micelles, but they were smaller than 200 nm in diameter. DLS measurements further demonstrated that cross-linked micelles have similar narrow size distributions compared to their non-cross-linked counterparts (Figure 3). From these results, we speculate that a "pseudomicellar" structure is achieved, in which the micelle cores were no longer compact and highly crystalline because the PCL solubility was increased upon adding acetone. DLS measurements demonstrated that the particle size increased in acetone/water mixtures. Consequently, the initiator molecules may diffuse into the PCL phase, and the chance for reactive double bonds to react was increased due to the enhanced chain mobility resulting from the swelling of PCL cores. For instance, as exemplified in Figure 4, the size of the non-cross-linked MPEG2k-$(PCL2.7k)_2$-MPEG2k micelle in an ac-

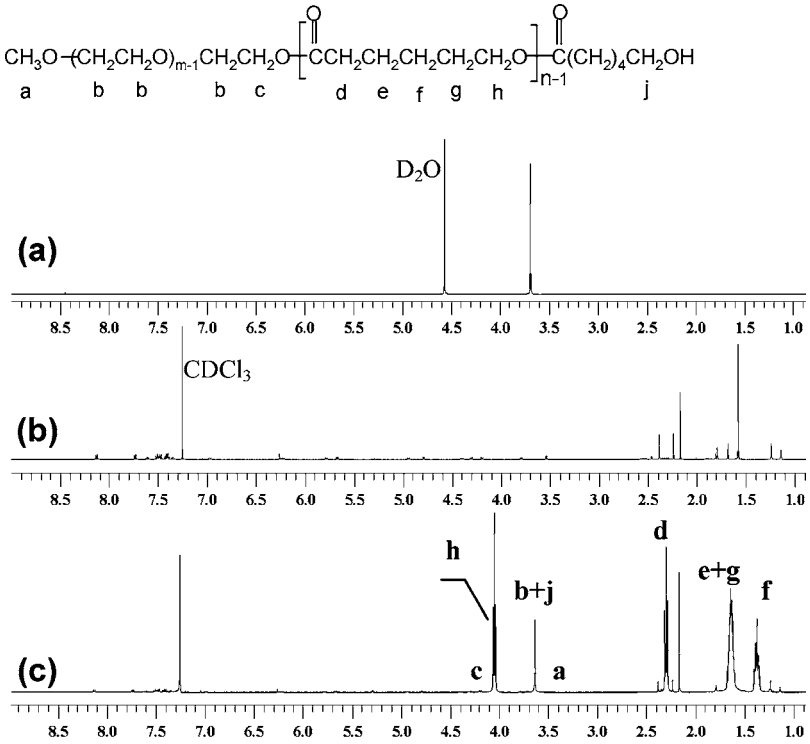


Figure 5. ^{1}H NMR spectra of the paclitaxel-loaded micelle in D_2O (a), paclitaxel in $CDCl_3$ (b), and the paclitaxel-loaded micelle in $CDCl_3$ (c). The micelle was formed with the hydroxyl-terminated MPEG5k-b-PCL18k.

etone/water mixed solution (1:2 in v/v) increased to ~140 nm from ~50 nm, the size of micelle in water. Hence, by controlling the reaction time and solvent composition, a predominantly intra-pseudomicellar radical polymerization leads to controlled micellar sizes.

As shown in Table 2, micelle size also depends on the copolymer composition. In general, copolymers with longer PCL blocks formed larger micelle particles. Despite the micelle size increase, the cross-linked micelles are small enough for the intravenous administration. Interestingly, paclitaxel-loading did not affect the sizes of micelles. In addition, as reported also by Lee et al. (*24*), paclitaxel-loading did not change the narrow size distributions of micelles (Figure 3).

Encapsulation of paclitaxel inside the micelle cores was demonstrated by ^{1}H NMR measurements of the freeze-dried micelle particles. Figure 5 shows the ^{1}H NMR spectra of a paclitaxel-loaded MPEG-b-PCL-OH micelle in D_2O (a), and $CDCl_3$ (c), in comparison with the spectrum of paclitaxel in $CDCl_3$ (b). PCL, MPEG, and paclitaxel resonance peaks were observed in $CDCl_3$ indicating that the micelle contains paclitaxel. In contrast, only MPEG resonance was detected, and both the PCL and the paclitaxel resonance peaks were not detected in D_2O. These results strongly demonstrated the core−shell structure of micelles. The micelle shells consisting of PEG blocks were well dissolved in D_2O and therefore showed clear ^{1}H NMR resonance signals. By contrast, paclitaxel was included inside the micelle cores consisting of the PCL solid phase. Consequently, resonances of PCL blocks and paclitaxel were not observed in D_2O because of their insufficient mobility in solid phase.

From the results summarized in Table 3, two major factors were found to affect paclitaxel content and loading efficiency. Micelles studied in this work encapsulated paclitaxel at a level of 0.2−5.1%, depending on the PCL length and cross-linking. Long PCL blocks apparently favor paclitaxel-loading into the micelles. For instance,

Table 3. Influence of Core-Cross-Linking on Paclitaxel Loading[a]

	before crosslinking		after cross-linking	
copolymer	PLC (%)	PLE (%)	PLC (%)	PLE (%)
PCL1.2k-b-MPEG2k	0.2	3.3	0.2	3.3
$(PCL1.2k\text{-}b\text{-}MPEG2k)_2$[b]	0.2	3.3	0.3	5
PCL2.7k-b-MPEG2k	0.8	13	2.2	37
$(PCL2.7k\text{-}b\text{-}MPEG2k)_2$[b]	1.1	18	1.8	30
PCL3.8k-b-MPEG5k	1.4	23	3.1	52
$(PCL3.8k\text{-}b\text{-}MPEG5k)_2$[b]	1.7	28	2.7	45
PCL18k-b-MPEG5k	2.3	38	5.1	85
$(PCL18k\text{-}b\text{-}MPEG5k)_2$[b]	2.7	45	4.3	72

[a,b] See the footnotes to Table 2.

in comparison with the MPEG2k-b-PCL1.2k micelle, the MPEG5k-b-PCL18k micelle showed 10× higher loading and loading efficiency (PLC: 2.3% vs 0.2%, PLE: 38% vs 3.3%). Paclitaxel loading into micelles was enhanced significantly through the micelle core-cross-linking, especially for micelles bearing long PCL blocks.

We have noted that long PCL block and core-cross-linking led to increase in micelle size. The micelle size is critical for a drug delivery via intravenous injection and for efficient targeting and cell uptake. Particles < 100 nm seem to cross endothelial and epithelial barriers more efficiently. Therefore, micelle size, cross-linking and paclitaxel loading capacity need to be carefully adjusted. In this sense, cross-linked micelles based on the di- and triblock copolymers of PCL3.8k and MPEG5k showed an excellent combination in micelle size and paclitaxel-loading efficiency.

The spherical morphology and nanoscale dimension of micelle particles were demonstrated using the TEM micrographs of paclitaxel-loaded micelles prepared with the cross-linked MPEG5k-b-PCL18k, as shown in Figure 6. Micelle spheres are less than 200 nm in mean diameter. In excellent agreement with the DLS measurement results, the TEM images also indicate that the

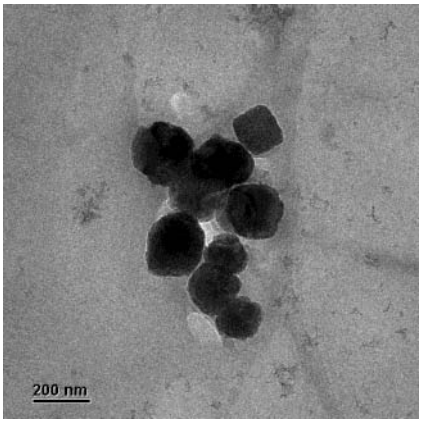


Figure 6. TEM image of a cross-linked micelle loaded with paclitaxel. The micelle was prepared with the cross-linked diblock copolymer MPEG5k-b-PCL18k. The paclitaxel-loading content in this micelle is 5.1%.

micelle particles possess quite narrow distribution of sizes.

The stability of the micelles under various conditions was investigated. For all cross-linked micelles, particle sizes increased when the micelle particles were redissolved in acetone (data not shown). Acetone is a good solvent for both PCL and PEG, indicating the swelling of micelle cores rather than the dissociation of particles. Similar results were observed by Kataoka et al. when they dissolved the core-cross-linked poly(ethylene glycol)-b-poly(D,L-lactide) micelles in dimethyl formamide (DMF) (*24*).

Further, the core-cross-linked micelles were stable against dilution in water. No micelle collapse was detected by DLS and GPC measurements when the micelle solutions were diluted by a factor of 1000×. Micelle stability against storage at 4 °C depended on the polymer composition but showed no correlation with the micelle cross-linking and drug loading. No size change was detected within two weeks for all micellar systems. However, large aggregates or even precipitates were observed when the micelles containing PCL3.8k or PCL18k were stored for three months, independent of cross-linking and paclitaxel loading.

Micelle stability in the presence of serum albumin (BSA, 2.5 wt %) and/or relatively high ionic strength (10 mM PBS) was again dependent on the PCL block length. With longer PCL blocks, large aggregates were formed faster. For examples, when BSA solution (2.5 wt %) or 10 mM PBS solution was mixed (1:1 in v/v) with the 0.5% cross-linked MPEG5k-b-$(PCL18k)_2$-b-MPEG5k micellar solution, precipitates formed immediately. However, under the same conditions, MPEG2k-b-$(PCL1.2k)_2$-b-MPEG2k micelle solutions did not show any aggregates upon storage for two weeks at 4 °C. This unsatisfactory stability of the micelle solutions in the presence of serum protein (BSA, 2.5 wt %) and/or relatively high ionic strength is obviously a drawback for the in vivo application, especially for the micelles containing long PCL blocks and needs further optimization.

The inhibition of tumor cell proliferation by the paclitaxel-loaded micelles has been reported (*25*). However, only limited information is available on the interaction between micelles and cells. Very recently, Maysinger et al. demonstrated the cellular internalization of a fluorescent-labeled MPEG-b-PCL micelle into 3T3 mouse fibroblasts (*18*, *31*). This type of micelle can encapsulate DAF (a membrane selective dye) and transport it into cytoplasm. In the present work using confocal laser scanning microscopy technique, we investigated the uptake of a micelle loaded with the fluorescent-labeled paclitaxel into 3T3 fibroblasts. As shown in Figure 7, paclitaxel loaded in the cross-linked micelle was transported efficiently into the cytoplasm.

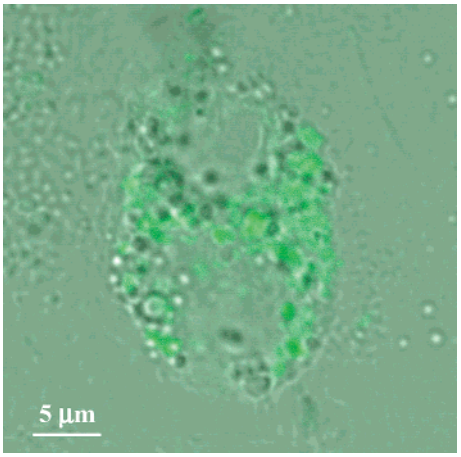


Figure 7. CLSM-imaged 3T3 cellular internalization of fluorescent-labeled paclitaxel encapsulated inside the cross-linked MPEG5k-$(PCL3.8k)_2$-MPEG5k nano particles. The paclitaxel-loading content in this micelle is 2.7%. The incubation time was 4 h.

The investigation of the controlled release behavior of different paclitaxel-loaded micelles is now under way in our lab. Our preliminary results indicate that the cross-linking of micelle cores does not markedly change the paclitaxel-releasing profile of the non-cross-linked micelles, i.e., both micelles showed rather fast paclitaxel release in the initial stage, and then a sustained slow release was detected.

ACKNOWLEDGMENT

We thank the Deutsche Forschungsgemeinschaft (DFG) for financial support. X.S. is grateful to the Alexander von Humboldt Foundation (Germany) for a research fellowship. A grant to X. S. and F. Xi from the National Natural Science Foundation of China (No. 50073026) is acknowledged.

LITERATURE CITED

(1) Wani, M. C., Taylor, H. L., Wall, M. E., Coggon, P., and McPhail, A. T. (1971) Plant antitumor agents. VI. The isolation and structure of Taxol, a novel antileukemic and antitumor agent from Taxus Brevifolia. *J. Am. Chem. Soc. 93*, 2325−2327.

(2) McGuire, W. P., Rowinsky, E. K., Rosenshein, N. B., Grumbine, F. C., Ettinger, D. S., Armstrong, D. K., and Donehower, R. C. (1989) Taxol: A unique antineoplastic agent with significant activity in advanced ovarian epithelial neoplasms. *Ann. Intern. Med. 111*, 273−279.

(3) Liggins, R. T., Hunter, W. L., and Burt, H. M. (1997) Solid-state characterization of paclitaxel. *J. Pharm. Sci. 86*, 1458−1463.

(4) Suffness, M. (1993) Taxol: From discovery to therapeutic use. *Annu. Rep. Med. Chem. 28*, 305−314.

(5) Straubinger, R. M. (1995) Biopharmaceutics of paclitaxel (taxol): Formulation, activity, and pharmacokinetics. *Taxol Science and Applications* (Suffness, M., Ed.) pp 237−258, Boca Raton, CRC Press.

(6) Panchagnula, R. (1998) Pharmaceutical aspects of paxlitaxel. *Int. J. Pharm. 172*, 1−15.

(7) Onetto, N., Canett, R., Winograd, B., Catane, R., Dougan, M., Grechko J. et al. (1993) Overview of taxol safety, *J. Natl. Cancer Inst. Monogr. 15*, 131−139.

(8) Mazzo, D., Nguyen Huu, J. J., Pagniez, S., and Denis, P. (1997) Compatibility of docetaxel and paclitaxel in intravenous solutions with poly(vinyl chloride) infusion materials. *Am. J. Health Syst. Pharm. 54*, 566−69.

(9) Campbell, R. B., Balasubramanian, S. V., and Straubinger, R. M. (2001) Influence of cationic lipids on the stability and membrane properties of paclitaxel-containing liposomes. *J. Pharm. Sci. 90*, 1091−1105.

(10) Sharma, A., Mayhew, E., Bolcsak, L., Cavanaugh, C., Harmon, P., Janoff, A., and Bernacki, R. J. (1997) Activity of paclitaxel liposome formulations against human ovarian tumor xenografts. *Int. J. Cancer 71*, 103−107.

(11) Zhang, X., Jackson, J. K., and Burt, H. M. (1996) Development of amphiphilic diblock copolymers as micellar carriers of Taxol. *Int. J. Pharm. 132*, 195−206.

(12) Leung, S. Y. L., Jackson, J., Miyake, H., Burt, H., and Gleave, M. E. (2000) Polymeric micellar paclitaxel phosphorylates Bcl-2 and induces apoptotic regression of androgen-independent LNCaP prostate tumors. *The Prostate 44*, 156−163.

(13) Gao, Z., and Eisenberg, A. (1993) A model of micellization for block copolymers in solutions. *Macromolecules 26*, 7353−7360.

(14) Malmsten, M., and Lindman, B. (1992) Self-assembly in aqueous block copolymer solutions. *Macromolecules 25*, 5440−5445.

(15) Kataoka, K., Kwon, G. S., Yokoyama, M., Okano, T., and Sakurai, Y. (1993) Block copolymer micelles as vehicles for drug delivery. *J. Controlled Release 24*, 119−132.

(16) Kataoka, K., Harada, A., Nagasaki, Y. (2001) Block copolymer micelles for drug delivery: design, characterization and biological significance. *Adv. Drug Delivery Rev. 47*, 113−131.

(17) Jeong, B., Bae, Y. H., Lee, D. S., and Kim, S. W. (1997) Biodegradable block copolymers as injectable drug-delivery systems. *Nature 388*, 860.

(18) Savic, R., Luo, L., Eisenberg, A., and Maysinger, D. (2003) Micellar nanocontainers distributed to defined cytoplasmic organelles. *Science 300*, 615−618.

(19) Matsumura, Y., and Maeda, H. (1986) A new concept for macromolecular therapeutics in cancer chemotherapy: mechanism of tumoritropic accumulation of proteins and the antitumor agent smancs. *Cancer Res. 46*, 6387−6392.

(20) Shiah, J. J., Sun, Y., Peterson, C. M., and Kopecek, J. (1999) Biodistribution of free and N−(2-hydroxypropyl)-methacrylamide copolymer-bound mesochlorin e(6) and adriamycin in nude mice bearing human ovarian carcinoma OVCAR-3 xenografts. *J. Controlled Release 61*, 145−157.

(21) Yuan, F., Leunig, M., Huang, S. K., Berk, D. A., Papahadjopoulos, D., and Jain, R. K. (1994) Microvascular permeability and interstitial penetration of sterically stabilized (stealth) liposomes in a human tumor xenograft, *Cancer Res 54*, 3352−3356.

(22) Yokoyama, M., Okano, T., Sakurai, Y., Fukushima, S., Okamoto, K., and Kataoka, K. (1999) Selective delivery of adriamycin to a solid tumor using a polymeric micelle carrier system. *J. Drug Target. 7*, 171−186.

(23) Zhang, X., Burt, H. M., von Hoff, D., Dexter, D., Mangold, G., Degen, D., Oktaba, A. M., and Hunter, W. L. (1997) An investigation of the antitumor activity and biodistribution of polymeric micellar paclitaxel. *Cancer Chemother. Pharm. 40*, 81−86.

(24) Kim, S. Y., and Lee, Y. M. (2001) Taxol-loaded block copolymer nanospheres composed of methoxy poly(ethylene glycol) and poly(ϵ-caprolactone) as novel anticancer drug carriers. *Biomaterials 22*, 1697−1704.

(25) Lee, S. C., Kim, C., Kwon, I. C., Chung, H., and Jeong, S. Y. (2003) Polymeric micelles of poly(2-ethyl-2-oxazoline)-*block*-poly(ϵ-caprolactone) copolymer as a carrier for paclitaxel. *J. Controlled Release 89*, 437−446.

(26) Iijima, M., Nagasaki, Y., Okada, T., Kato, M., and Kataoka, K. (1999) Core-polymerized reactive micelles from heterotelechelic amphiphilic block copolymers. *Macromolecules 32*, 1140−1146.

(27) Shuai, X., Merdan, T., Unger, F., Wittmar, M., and Kissel, T. (2003) Novel biodegradable ternary copolymers *hy*-PEI-*g*-PCL-b-PEG: synthesis, characterization and potential as efficient nonviral gene delivery vectors, *Macromolecules 36*, 5751−5759.

(28) Kim, C., Lee, S. C., Kwon, I. C., Chung, H., and Jeong, S. Y. (2002) Complexation of poly(2-ethyl-2-oxazoline)-*block*-poly(ϵ-caprolactone) micelles with multifunctional carboxylic acids. *Macromolecules 35*, 193−200.

(29) Ge, H., Hu, Y., Jiang, X., Chen, D., Yuan, Y., Bi, H., and Yang, C. (2002) Preparation, characterization, and drug release behaviors of drug nimodipine-loaded poly(ϵ-caprolactone)-poly(ethylene oxide)-poly(ϵ-caprolactone) amphiphilic triblock copolymer micelles. *J. Pharm. Sci. 91*, 1463−1473.

(30) Emoto, K., Nagasaki, Y., and Kataoka, K. (1999) Coating of surfaces with stabilized reactive micelles from poly(ethylene glycol)-poly(DL-lactic acid) block copolymer. *Langmuir 15*, 5212−5218.

(31) Luo, L., Tam, J., Maysinger, D., and Eisenberg, A. (2002) Cellular internalization of poly(ethylene oxide)-b-poly(ϵ-caprolactone) diblock copolymer micelles. *Bioconjugate Chem. 13*, 1259−1265.

BC034113U

NMR Studies of Fully Modified Locked Nucleic Acid (LNA) Hybrids: Solution Structure of an LNA:RNA Hybrid and Characterization of an LNA:DNA Hybrid

Katrine E. Nielsen, Jill Rasmussen, Ravindra Kumar, Jesper Wengel, Jens Peter Jacobsen, and Michael Petersen*

Nucleic Acid Center, Department of Chemistry, University of Southern Denmark, 5230 Odense M, Denmark.
Received August 22, 2003; Revised Manuscript Received December 17, 2003

LNA is a bicyclic nucleic acid analogue that contains one or more 2′-*O*,4′-*C* methylene linkage(s), which effectively locks the furanose ring in a C3′-endo conformation. We report here the NMR solution structure of a nonamer LNA:RNA hybrid and a structural characterization of a nonamer LNA:DNA hybrid, where the LNA strands are composed entirely of LNA nucleotides. This is the first structural characterization of fully modified LNA oligonucleotides. The high-resolution structure reveals that the LNA:RNA hybrid adopts an almost canonical A-type duplex morphology. The helix axis is almost straight and the duplex geometry is regular. This shows that fully modified LNA oligomers can hybridize with complementary RNA and form duplexes within the Watson−Crick framework. The LNA:DNA hybrid structurally resembles an RNA:DNA hybrid as shown by determination of deoxyribose sugar puckers and analysis of NOESY NMR spectra.

INTRODUCTION

High-affinity binding to complementary nucleic acids has a number of applications, for example in oligonucleotide-based therapeutics and in the general area of biotechnology. From the vast number of chemically modified nucleotide analogues synthesized, it appears that a sugar engineered into an N-type (RNA-like) pucker usually conveys an increase in helical thermostability when hybridized with complementary RNA (*1*). Prominent examples of such N-type nucleic acid analogues are 2′-*O*-alkylated RNA (*2*), 2′F-RNA (*3*), phosphoramidates (*4*), HNA (*5*), and LNA (*6*−*9*).

In LNA (see Figure 1), the furanose conformation is chemically locked in an N-type (C3′-endo) conformation by the introduction of a 2′-*O*,4′-*C* methylene linkage. LNAs[1] have shown hitherto unprecedented thermal affinities when hybridized with either DNA ($\Delta T_m = 1-8$ °C per modification) (*6*−*11*), RNA ($\Delta T_m = 2-10$ °C per modification) (*6*−*9*, *11*−*13*) or LNA ($\Delta T_m > 5$ °C per modification) (*14*). The high thermal stability of LNA modified nucleic acids is achieved with sequence specificity comparable to or slightly better than native nucleic acids (*6*). Thus, short, fully modified LNA oligonucleotides combine high-affinity binding toward DNA and RNA with minimal oligonucleotide length.

LNA is emerging as a useful tool in therapeutics and diagnostics with an increasing number of reports appearing. In the context of antisense therapeutics, LNA/DNA gapmers are recognized and cleaved by RNase H (*13*). Thus, the high-affinity binding properties of LNA can be employed to access mRNA targets with highly ordered tertiary structures. In a broader therapeutical view, LNAs have been employed as aptamers for transcription factor κB (NF-κB) (*15*) and have been successfully incorporated into DNAzymes (*16*). For use in diagnostics, LNA probes are employed for the detection of single nucleotide polymorphisms (*17*, *18*). Reference 9 is a recent review on applications of LNA oligonucleotides.

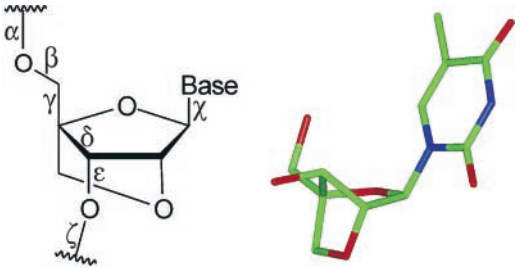


Figure 1. Structure of LNA with torsion angles labeled (left) and stick plot showing the C3′-endo furanose conformation (right).

In this study, we have characterized an LNA:DNA hybrid and determined the solution structure of an LNA:RNA hybrid. In both of these hybrids the LNA strand is composed entirely of LNA monomers. This is the first structural study of fully modified LNA oligonucleotides. The base composition and numbering of the two hybrids is shown in Scheme 1.

As for the LNA:RNA hybrid, we have previously studied the corresponding, isosequential unmodified DNA:RNA hybrid and the two partly modified hybrids with LNA modifications at position 5 and positions 2, 5, and 7, respectively (these hybrids are labeled LNA1:RNA and LNA3:RNA henceforth) (*12*, *19*). These studies showed that with an increasing number of LNA nucleotides incorporated into the hybrids, an increasing A-like character of the duplex structure ensued. This is due to the LNA nucleotides being locked in a C3′-endo confor-

* To whom correspondence should be addressed. E-mail: mip@chem.sdu.dk.
† Odense University.
‡ University of Copenhagen.
[1] We have defined LNA as an oligonucleotide containing one or more 2′-*O*,4′-*C*-methylene-β-D-ribofuranosyl nucleotide monomer(s).

10.1021/bc034145h CCC: $27.50 © 2004 American Chemical Society
Published on Web 05/04/2004

Scheme 1. Numbering Scheme and Base Composition of the Two Hybrids Studied[a]

		1	*2*	*3*	*4*	*5*	*6*	*7*	*8*	*9*	
LNA:RNA	5′-	(^{me}**C**	**T**	**G**	**A**	**T**	**A**	**T**	**G**	^{me}**C**)^{L}	-3′
	3′-	r(G	A	C	U	A	U	A	C	G	)-5′
		18	*17*	*16*	*15*	*14*	*13*	*12*	*11*	*10*	
LNA:DNA	5′-	(^{me}**C**	**T**	**G**	**A**	**T**	**A**	**T**	**G**	^{me}**C**)^{L}	-3′
	3′-	d(G	A	C	T	A	T	A	C	G	)-5′

[a] LNA nucleotides are shown in bold.

mation and because LNA nucleotides, in addition, steer the sugar conformations of neighboring nucleotides, predominantly in the 3′-direction, into N-type (C3′-endo) sugar conformations. Indeed, in the LNA3:RNA hybrid, all nonterminal deoxyriboses were found with N-type sugar puckers, even though deoxyriboses possess an inherent preference for S-type sugar puckers, and hence this hybrid adopts an A-like duplex geometry. We now extend the studies of this nonamer LNA:RNA series with the high-resolution structure of the fully modified hybrid. The structure was determined employing NOE-derived distance restraints in a simulated annealing scheme.

With respect to the LNA:DNA hybrid, we have hitherto studied a number of LNA:DNA hybrids with varying numbers of LNA monomers incorporated in one of the strands. As for LNA:RNA hybrids, a conformational tuning of neighboring deoxyriboses is observed, albeit in a less pronounced manner, as it requires two flanking LNA monomers to shift the deoxyribose pucker into a pure N-type conformation. For LNA:DNA hybrids, we also observe a slight increase in N-type conformation of the deoxyriboses on the base-paired strand. We extend here our studies of LNA:DNA hybrids, with the characterization of a fully modified hybrid by analysis of 2D NMR spectra. In addition, we have determined the sugar puckers of the deoxyribose strand by analysis of COSY-type spectra.

MATERIALS AND METHODS

Sample Preparation. The modified oligonucleotide was synthesized as described elsewhere (*6*, *20*). The DNA oligonucleotide was purchased from DNA Technology, Århus, Denmark, and the RNA oligonucleotide was synthesized at University of Copenhagen. All oligonucleotides were purified by site-exclusion on a Sephadex G15 column. The samples were obtained by dissolving equimolar amounts of the two single strands in 0.5 mL of 10 mM sodium phosphate buffer (pH 7.0), 100 mM NaCl, and 0.05 mM NaEDTA. For experiments carried out in D_2O, the duplex solutions were lyophilized three times from D_2O and redissolved in 99.96% D_2O (Cambridge Isotope Laboratories). Mixtures of 90% H_2O and 10% D_2O (0.5 mL) were used for experiments examining exchangeable protons. The final concentration of the hybrids were 0.8 mM (LNA:RNA) and 2.0 mM (LNA:DNA).

NMR Experiments. NMR experiments were performed on either a Varian INOVA 500 spectrometer or a Varian INOVA 800 spectrometer at 25 °C. For the LNA:RNA hybrid the following spectra were obtained: NOESY spectra (mixing times: 80 and 250 ms) were acquired at 800 MHz in D_2O using 1110 t_1-experiments with 24 scans, 2048 complex points in t_2, a pulse repetition time of 2.5 s, and spectral widths of 8000 Hz. The States phase cycling scheme was used, and the residual signal from HOD was removed by low-power presaturation. An inversion recovery experiment to extract the T_1 relaxation rates was also obtained at 800 MHz. The remaining spectra were all obtained at 500 MHz. A NOESY spectrum in H_2O (mixing time: 200 ms) using the WATERGATE NOESY pulse sequence with 2048 complex points in t_2, 900 t_1-experiments with 112 scans, and a spectral width of 10000 Hz. TOCSY spectra (mixing times: 60 and 90 ms) using 1024 complex points in t_2 and 600 t_1-experiments with 42 scans. A DQF−COSY spectrum using 4096 complex points in t_2, 1024 t_1-experiments with 64 scans, and a gradient $^1H-^{13}C$ HSQC spectrum using 2048 complex points in t_2, 750 t_1-experiments with 80 scans, and spectral widths of 5000 and 10000 Hz for the ^1H and ^{13}C dimensions, respectively.

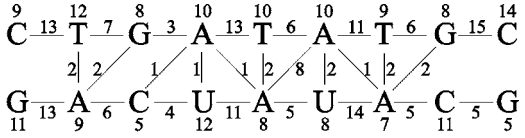


Figure 2. The distribution of the NOE restraints. The numbers of intranucleotide, sequential and cross-strand restraints are indicated. In addition to the restraints shown, six further restraints were also obtained (C1-G3, T7-C9, A6-U15, T7-A14 (two), C9-A12).

For the LNA:DNA hybrid, the following spectra were obtained at 500 MHz: A NOESY spectrum (mixing time: 200 ms) in D_2O using 640 t_1-experiments with 96 scans, 2048 complex points in t_2, a pulse repetition time of 2.4 s, and spectral widths of 5000 Hz. The States phase cycling scheme was used, and the residual signal from HOD was removed by low-power presaturation. A NOESY spectrum in H_2O (mixing time: 200 ms) using the WATERGATE NOESY pulse sequence with 2048 complex points in t_2, 512 t_1-experiments with 128 scans, and a spectral width of 10000 Hz. A TOCSY spectrum (mixing time: 90 ms) using 1024 complex points in t_2 and 512 t_1-experiments with 64 scans. In addition, selective DQF−COSY and E-COSY spectra were acquired using a pulse sequence where the first pulse was replaced with an E-BURP type selective pulse (*21*) in order to enhance the digital resolution in F1. These spectra were acquired with spectral widths of 5000 Hz in F2 and 1200 Hz in F1, respectively. For the DQF−COSY spectrum, a total of 1472 t_1-experiments were recorded, each with 64 scans, with 4096 complex points in t_2. For the E-COSY spectrum, a total of 700 t_1-experiments were recorded, each with 96 scans, with 2048 complex points in t_2.

The acquired data were processed at optimal conditions using FELIX (version 98.0, MSI, San Diego, CA). Particularly, the NOESY spectra recorded in the build-up of the LNA:RNA hybrid were linear predicted from 555 points to 750 points in t_1 and baseline-corrected in F2 using the FLATT algorithm (*22*).

Distance Restraints. A total of 333 distance restraints were obtained from 2D NOE cross-peak intensities using the method of Wijmenga et al. (*23*); in this variation of the isolated spin pair approximation, spin diffusion is accounted for in an average manner. NOESY cross-peak intensities from the 80 and 250 ms spectra were corrected for saturation effects using T_1 relaxation times obtained from an inversion recovery experiment and were subsequently transformed to distance restraints by calibrating against all known distances. Upper and lower distance bounds were set to the calculated distances ±15%. The distribution of NOE restraints for the LNA:RNA hybrid is shown in Figure 2. In total we had 166 intranucleotide, 139 internucleotide and 28 cross-strand restraints. The average width of the distance restraints was 1.50 Å, and the average restraint length 4.66 Å.

Normal Watson−Crick base pairing was inferred from the NOESY spectrum acquired in H_2O, and consequently 22 hydrogen bond distance restraints were included in the calculations. Target values for these restraints were taken from crystallographic data (*24*).

All distance restraints were incorporated into the AMBER potential energy by a flat-well pseudopotential with the form:

$$E_{NOE} = \begin{cases} -K_{NOE}r + (r_1 - 0.25\ \text{Å})K_{NOE}, & \text{if } r \le r_1 - 0.5\ \text{Å} \\ K_{NOE}(r - r_1)^2, & \text{if } r_1 - 0.5\ \text{Å} < r < r_1 \\ 0, & \text{if } r_1 \le r \le r_2 \\ K_{NOE}(r - r_2)^2, & \text{if } r_2 < r < r_2 + 0.5\ \text{Å} \\ K_{NOE}r + (r_2 + 0.25\ \text{Å})K_{NOE}, & \text{if } r \ge r_2 + 0.5\ \text{Å} \end{cases}$$

where the force constants, K_{NOE}, are in units of kcal/(mol Å) or kcal/(mol Å^2), and r_1 and r_2 are the lower and upper distance bounds, respectively.

Structure Calculations. All calculations were performed with the AMBER6 suite of programs (*25*) on SGI/O2 workstations. A simulated annealing (SA) protocol was utilized to obtain the structure of the hybrid. The starting structure (A-form duplex) was obtained with the *nucgen* module of AMBER6. The appropriate nucleotides were modified to LNA nucleotides, and atomic charges for the modified nucleotides were calculated using the RESP procedure (*26*). A table with atomic charges for the four LNA nucleotides is included in Supporting Information.

Initially the starting structure was restrained energy minimized before being subjected to 28 ps of molecular dynamics in time-steps of 1 fs: 4 ps at 600 K followed by cooling to 250 K over 24 ps. Finally, a further restrained energy minimization was carried out. In the SA scheme, the force constant, K_{NOE}, was ramped from 50 kcal/(mol Å^2) to 250 kcal/(mol Å^2) over the initial 2 ps, kept constant at 250 kcal/(mol Å^2) from 2 to 8 ps, decreased to 50 kcal/(mol Å^2) from 8 to 12 ps, and afterward kept constant at 50 kcal/(mol Å^2). A distance dependent dielectric constant, $\epsilon = 4r$, was used and the nonbonded cutoff was 30 Å.

Deoxyribose Ring Conformations. The H1′ to H2′ and H2″ region of the selective DQF−COSY and E-COSY spectra, respectively, was used as input to CHEOPS (*27*) to obtain the values of the *J* coupling constants for the H1′, H2′, H2″, and H3′ deoxyribose ring protons. The deoxyribose ring conformations were analyzed assuming a fast two-state equilibrium between N- and S-type conformations with a modified version of the program PSEUROT (*28*). The standard version of PSEUROT obtains the best fit of the parameters P_N, P_S, $\Phi_{max,N}$, $\Phi_{max,S}$, and %N to the experimental coupling constants. $P_{N,S}$ and $\Phi_{N,S}$ are the pseudorotation angle and puckering amplitude, respectively, of the N- and S-type conformation and %N is the mole fraction of N-type conformation. In our randomized version of PSEUROT, we include the effect of uncertainties in the determined set of coupling constants by generating 1000 sets of coupling constants according to a normal distribution in which the dispersion is set according to the uncertainty of each determined coupling constant. Uncertainties of the coupling constants were carefully assessed by how well the back-calculated spectra correlated with the experimental spectra and by the difference in the coupling constants obtained by analysis of the two types of COSY spectra. Subsequently, PSEUROT calculations were performed for all the generated sets of coupling constants and the mean values and standard deviations of the parameters returned by PSEUROT were calculated.

Table 1. Melting Temperatures of LNA:RNA and LNA:DNA Hybrids. Unmodified Duplexes of Identical Base Sequence Are Included for Comparison[a]

duplex	T_m, °C	ΔT_m per modification, °C	duplex	T_m, °C	ΔT_m per modification, °C
LNA:RNA	74	5.2	LNA:DNA	62	3.8
LNA3:RNA	52	8.3	LNA3:DNA	44	5.3
LNA1:RNA	37	10.0	DNA:DNA[b]	28	–
DNA:RNA	27	–	RNA:DNA[b]	27	–
RNA:RNA[b]	38	–			

[a] T_m is the duplex melting temperature and ΔT_m the increase in melting temperature per LNA monomer compared with that of the corresponding unmodified duplex. [b] In these duplexes, one of the terminal base pairs is switched, i.e. C−G to G−C, relative to the duplexes in this work. These data are from S. K. Singh and J. Wengel (1998) *Chem. Commun.*, 1247−1248.

Thermal Stability Studies. The thermal stability of the hybrids was determined spectrophotometrically with a spectrophotometer equipped with a thermoregulated Peltier element. The hybridization mixtures were prepared by dissolving equimolar amounts (ca. 2.5 μM) of the oligonucleotides in 10 mM sodium phosphate buffer (pH 7.0), 100 mM NaCl, and 0.05 mM EDTA. The absorbance at 260 nm was monitored while the temperature was raised linearly from 10 to 80 °C (1 °C/min). The melting temperatures (T_m values) were obtained as the maxima of the first derivative of the melting curves.

Circular Dichroism Spectra. A CD spectrum of the LNA:RNA hybrid from 350 to 200 nm was measured on a JASCO 710/720 spectropolarimeter. The sample was prepared by dissolving equimolar (65 μM) amounts of the oligonucleotides in 10 mM sodium phosphate buffer (pH 7.0) and 0.05 mM EDTA. The spectrum of the buffer solution was subtracted from the spectrum. The molar CD of the duplex was calculated from eq 1 (*29*, *30*), where θ is the measured ellipticity in degrees, L is the path length in centimeters, and C is the concentration of the duplex. An absorbance spectrum was measured on a Lambda 17 spectrophotometer. The concentration of the duplex was determined from the absorbance at 260 nm using an extinction coefficient $\epsilon = 161.800\ M^{-1}\ cm^{-1}$.

$$\Delta\epsilon = \frac{\theta}{32.98CL} \quad (1)$$

Protein Data Bank Accession Codes. Coordinates and restraints employed in calculations have been deposited in the Protein Data Bank (accession code: 1h0q).

RESULTS

Thermal Stabilities. The thermal stabilities of the two hybrids studied were determined and compared with those of hybrids with isosequential base composition (Table 1). Sharp monophasic transitions were obtained with hyperchromicities of 1.2−1.3. No indications of biphasic transitions were detected. For the fully modified LNA:RNA and LNA:DNA hybrids, we observe increases in the melting temperatures of 5.2 °C and 3.8 °C per modification relative to the unmodified DNA:RNA and dsDNA reference duplexes, respectively. These results emphasize the substantial increases in thermal stability displayed by LNA modified oligonucleotides when hybridized with complementary RNA or DNA.

Spectral Analysis. The 1D ^{1}H NMR spectra of the two hybrids both show exclusively lines from the expected LNA:RNA and LNA:DNA hybrids at 25 °C. No signs of

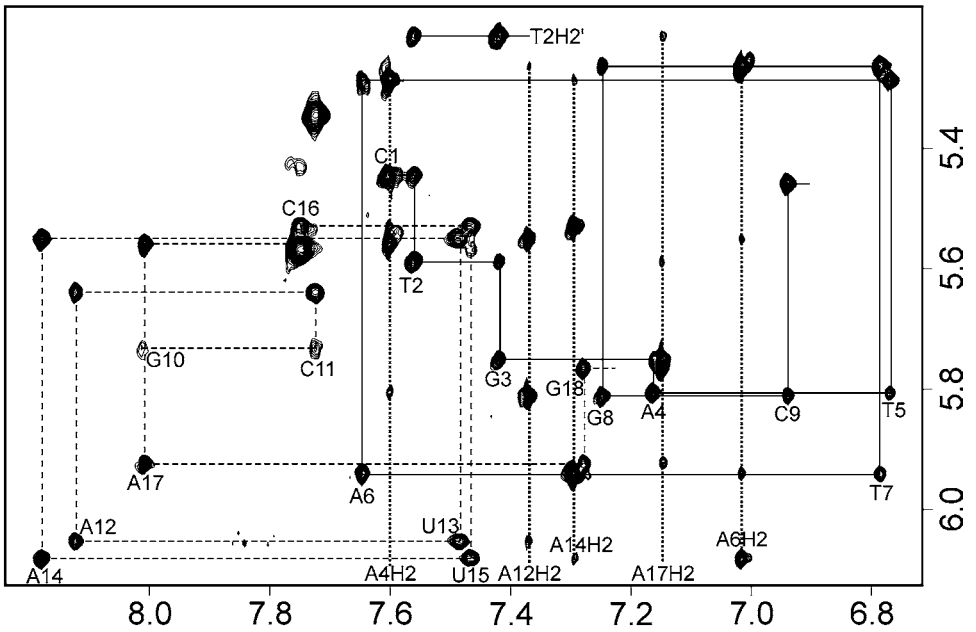


Figure 3. The aromatic to H1′ region of the NOESY spectrum with a mixing time of 250 ms of the LNA:RNA hybrid. The sequential H1′(n-1)−H6/8(n)−H1′(n) connectivity pathways are indicated; unbroken line for the LNA strand and broken line for the RNA strand. Adenine H2 resonances are shown with dotted lines.

alternative hybridization were observed. The NOESY spectra of both hybrids display the characteristic connectivities of right-handed nucleic acid duplexes with an overall A-type geometry, as gauged from cross-peaks involving adenine H2 protons, and with all the nucleobases in the anti conformation. The assignment of the nonexchangeable protons was performed using standard methods (*31*−*34*). The NOESY spectra with short mixing times allowed unambiguous assignments of the H2′ and H2″ resonances. The H6′ and H6″ resonances in the 2′-*O*,4′-*C*-methylene bridge of the LNA nucleotides were assigned by their strong intranucleotide cross-peaks to H1′ of the modified nucleotides. The aromatic to H1′ region of the 200 ms NOESY spectrum of the LNA:RNA hybrid is shown in Figure 3. The NOESY spectra acquired in H_2O exhibited normal Watson−Crick connectivities and were employed in the assignment of the exchangeable protons. Selections of chemical shift values for the hybrids are included in Supporting Information.

Furanose Ring Conformations in the LNA:DNA Hybrid. All nucleotides in the LNA strand are found in N-type conformations as shown by the absence of COSY cross-peaks between the H1′ and H2′ protons due to cancelation of anti-phase lines ($J_{H1'H2'} < \sim 2$ Hz). The favorable spectral dispersion of the H1′, H2′, and H2″ resonances of the deoxyriboses allowed simulation of all cross-peaks and consequently determination of sugar puckers for the entire DNA strand. In Figure 4, a comparison between the experimental DQF−COSY spectrum and the spectrum obtained by spectral simulations with CHEOPS is shown. Very good agreement between the simulated and the experimental spectrum is observed. The simulated E-COSY spectrum of the hybrid agreed equally well with the experimental one. The coupling constants returned by CHEOPS were used as input for our randomized version of PSEUROT. The uncertainties of the coupling constants were gauged by monitoring the dependence of the simulation procedure on alterations in the input parameters and the difference in the coupling constants obtained from each of the two types of spectra. The coupling constants obtained, molar fractions of S-type sugar conformations, and pseudorotation angles calculated for the LNA:DNA hybrid are given in Table 2.

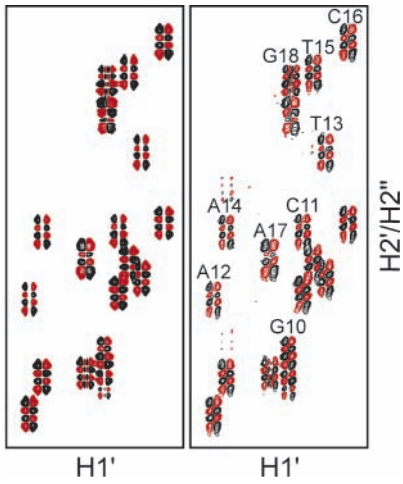


Figure 4. Comparison of the H1′ to H2′/H2″ regions of the calculated (left) and the experimental (right) DQF−COSY spectra for the LNA:DNA hybrid.

We tried to fit the experimental coupling constants to a one-state model; however, the RMSD between calculated and experimental coupling constants was on average 1.9 Hz, which is more than the uncertainty on the experimental coupling constants. When fitting with a two-state model, the average RMSD was 0.5 Hz. In the two-state model, we allowed three parameters (the two pseudorotation angles and the molar fraction of N-type conformation) to be fitted, while in the one-state fit only two parameters (the pseudorotation angle and the puckering amplitude) were free. Obviously, the larger number of degrees of freedom in the two-state fit dictates a lower RMSD than in the one-state fit; however, we think that the decrease observed in RMSD is significant although we did not perform any statistical analysis.

All deoxyribose sugars in the LNA:DNA hybrid possess sugar puckers in equilibria between N- and S-type conformations. The population of S-type conformation ranges from 57% (A12) to 80% (A17) with the populations

Table 2. Coupling Constants for the Deoxyribose Sugar Protons in the LNA:DNA Hybrid and the Sugar Conformations Derived[a]

	$J_{1'2'}$/Hz	$J_{1'2''}$/Hz	$J_{2'3'}$/Hz	$J_{2''3'}$/Hz	%S[b]	P_S, deg[c]	P_N, deg[d]
G10	6.1	4.7	4.7	3.8	62 (7)	165 (12)	−28 (16)
C11	5.7	6.4	4.3	4.0	62 (9)	185 (15)	−11 (17)
A12	5.2	6.2	4.5	4.3	57 (8)	183 (16)	−16 (17)
T13	6.1	6.4	5.5	4.0	60 (9)	172 (25)	−9 (33)
A14	5.7	6.4	4.7	4.0	62 (9)	183 (18)	−14 (21)
T15	6.5	6.5	4.9	3.8	65 (9)	178 (18)	−5 (32)
C16	7.0	6.3	4.7	3.8	68 (8)	175 (16)	−5 (26)
A17	8.7	5.4	4.6	3.0	80 (7)	164 (12)	
G18	8.4	6.4	5.7	2.4	76 (13)	160 (28)	

[a] The coupling constants were derived from the H1′−H2′ and H1′−H2″ cross-peaks in the selective DQF−COSY and E-COSY spectra using CHEOPS. The $J_{2'2''}$ coupling constants returned were between −14.2 and −15.0 Hz, values typical for deoxyribose. The sugar conformations were calculated using a randomized version of the PSEUROT program. In PSEUROT calculations, the puckering amplitudes were fixed at 36°. The standard deviations are given in brackets. [b] Percent S-type sugar conformation calculated using PSEUROT. [c] Pseudorotation angle calculated for the S-type sugar conformation. [d] Pseudorotation angle calculated for the N-type sugar conformation. If the mole fraction of the N-type conformer was calculated to be below 25%, the *P* value was not considered to be determined with sufficient accuracy.

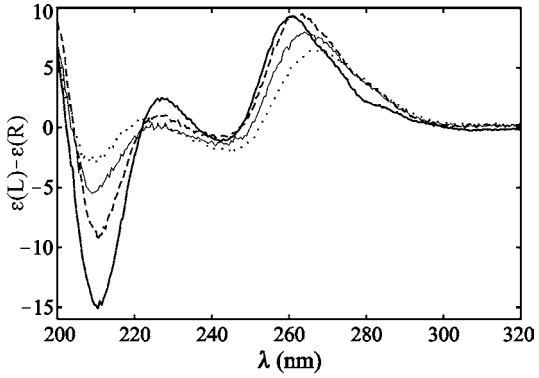


Figure 5. The CD spectra of various DNA:RNA and LNA:RNA hybrids of identical base sequence; DNA:RNA (dotted line), LNA1:RNA (thin line), LNA3:RNA (dashed line), and the fully modified hybrid (thick line).

being fairly uniform (at 60−65%) except for the two 3′-terminal nucleotides, A17 and G18, which possess slightly higher populations of S-type puckers than the remaining nucleotides in the DNA strand. This is also shown by the slightly larger $J_{H1'H2'}$ coupling constants for these nucleotides (see Table 2).

CD Spectra. The CD spectrum of the fully modified LNA:RNA hybrid is shown in Figure 5 along with the spectra of the unmodified reference hybrid and the LNA1:RNA and LNA3:RNA hybrids. All of the hybrids adopt an overall A-type duplex geometry as evidenced by the negative bands at ∼210 nm and the positive bands at ∼260 nm. These bands become progressively more intense upon introduction of either one or three LNA modifications in accordance with our previous structural studies showing an increase in the A-like character of these duplexes (*12*, *19*). For the fully modified LNA:RNA hybrid, the band at ∼260 nm has approximately the same intensity as for the hybrid with three modifications. This band is progressively blue-shifted with an increasing number of LNA monomers. The band at ∼210 nm is even more intense for the fully modified hybrid than for any of the other hybrids. Altogether, the CD spectrum of the fully modified LNA:RNA hybrid points to a regular A-like duplex structure.

Table 3. Structural Parameters for the LNA:RNA Structure[a]

structure	E_{AMBER} (kcal/mol)	E_{NOE} (kcal/mol)	Δd_{av} (Å)	RMSD (Å)
A-type	208.8	412.6	0.058	1.06
NMR	98.4	8.2	0.023	0.64[b]

[a] Force field (E_{AMBER}) and restraint (E_{NOE}) energies, average restraint violations (Δd_{av}), and atomic RMSD for the A-type starting structure and the NMR structure. All-atomic RMSDs were calculated for all atoms of the seven internal base pairs. [b] Average pair-wise atomic RMSD for the 20 structures calculated.

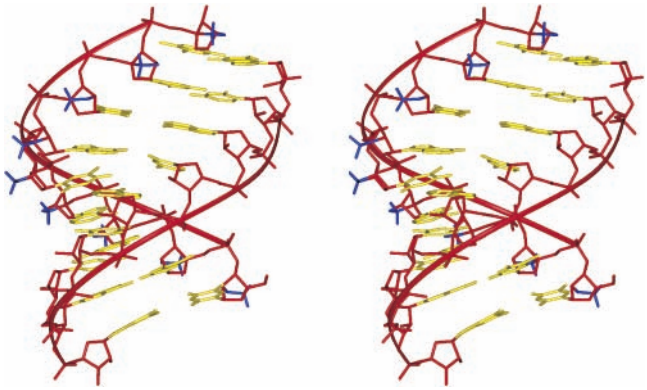


Figure 6. Stereoview of the LNA:RNA structure viewed into the minor groove. For clarity, only hydrogens on the 2′-*O*,4′-*C* LNA methylene bridge are shown. The coloring scheme: nucleobases, yellow; sugar−phosphate backbone, red; 2′-*O*,4′-*C* methylene bridges, blue.

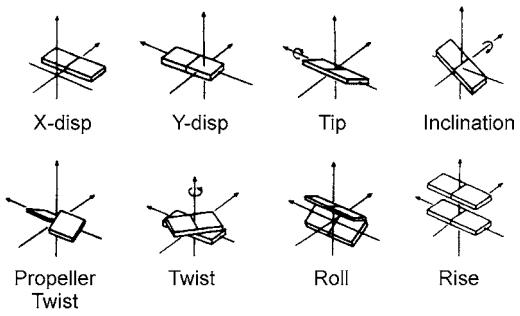
Structure of the Fully Modified LNA:RNA Hybrid. The high-resolution structure was generated starting from a canonical A-type duplex geometry (see Materials and Methods). The use of an A-type structure as starting structure is justified as the N-type conformation of both the LNA and RNA nucleotides is demonstrated by the absence of H1′−H2′ cross-peaks in COSY spectra. A total of 20 final structures were calculated using the protocol described by randomly varying the initial atomic velocities. These structures all converged to one family of structures with an average pair-wise all-atomic RMSD of 0.85 Å (0.64 Å for nonterminal base pairs). Only one distance violation in excess of 0.2 Å was observed, and in addition the hybrid features a low distance restraint energy (see Table 3) and low distance violations as compared to the starting structure.

General Description of the Structure. As suggested by the CD spectrum and by inspection of the NOESY spectra, the fully modified LNA:RNA hybrid has the overall appearance of an A-type duplex; for example, the minor groove is very wide and shallow, and the base pairs are displaced relative to the long axis of the helix. The RMSD between the calculated NMR structure and the energy-minimized A-type starting structure is 1.1 Å. The 2′-*O*,4′-*C* methylene bridges of the LNA nucleotides are located at the brim of the minor groove where they pose no steric hindrance for duplex formation (see Figure 6). All glycosidic angles are in anti conformations and Watson−Crick base pairing is maintained for all base pairs. The hybrid is regular as shown by the nearly straight helix axis as calculated by CURVES 5.2 (*35*, *36*). Thus, the structure shows that a nucleic acid strand composed entirely of LNA monomers can be hybridized with an RNA strand and still retain a normal Watson−

Table 4. A Selection of Helix Parameters for the LNA:RNA Hybrid. Values for Standard A- and B-Type Duplexes Are Included for Comparison

	X-disp (Å)	Y-disp (Å)	tip, deg	inclination, deg	prop. twist, deg		twist, deg	roll, deg	rise (Å)
C1	−5.8	0.0	−5.7	13.0	−11.2	C1-T2	28.1	−0.1	2.43
T2	−6.0	−0.1	−6.0	12.2	−10.9	T2-G3	30.0	5.6	2.24
G3	−5.7	−0.2	−4.9	12.9	−15.7	G3-A4	30.1	−1.5	2.56
A4	−5.8	−0.3	−5.0	11.8	−13.7	A4-T5	30.8	−3.3	2.84
T5	−5.9	−0.4	−6.0	13.5	−16.6	T5-A6	33.9	10.4	1.84
A6	−5.9	−0.4	−5.2	13.4	−18.2	A6-T7	29.9	−4.5	3.01
T7	−5.8	−0.3	−6.5	8.8	−11.2	T7-G8	29.0	4.2	2.70
G8	−5.7	−0.3	−5.2	5.6	−10.2	G8-C9	25.0	0.9	2.80
C9	−6.0	−0.6	−4.6	2.1	−10.0				
A-type	−5.4	0.0	0.0	19.1	−13.7		32.7	0.0	2.56
B-type	−0.7	0.0	0.0	−5.9	−3.7		36.0	0.0	3.38

Scheme 2. Graphical Representations of Helix Parameters Discussed in the Text



Crick duplex framework. A stereoview of the structure is presented in Figure 6.

Interstrand purine−purine stacking is observed between G3/A17, A6/A14, and G8/A12. This stacking arrangement stabilizes the inherently weaker pyrimidine−purine base pair steps in which little/no intrastrand stacking is taking place. An identical stacking pattern was observed for the previously studied LNA:RNA hybrids and for the unmodified hybrid as well, and is, as such, not a property specific for LNA modified hybrids but rather a sequence-specific property (*19*). The minor groove width of the hybrid is uniform along the helix ranging from 9.7 to 10.3 Å, with the average being 10.0 Å.

Helix Parameters. The global helix axis and helical parameters were calculated with CURVES 5.2. The global helix axis is rather straight with a slight bend at the T5pA6 base pair step. In general the helix parameters are uniform along the duplex, with slight variations toward the 3′-end of the LNA strand for some parameters and some minor variations in the T5pA6 base pair step as a consequence of the slight bend in the helix axis. A selection of the helical parameters is given in Table 4, and graphic representations of the helical parameters discussed are shown in Scheme 2. X-displacement, Y-displacement, inclination, and tip are the helix parameters with which the global helix axis is determined. X-displacement, with an average value of −5.8 Å, and inclination, with an average of 10.4°, are both close to the values expected for an A-type duplex. The Y-displacement and tip parameters both show that the duplex is regular in its geometry. Other parameters indicative of the A-type geometry are the average propeller twist of −13.1° and the average rise of 2.55 Å. Rise shows some variations in the A4pT5, T5pA6, and A6pT7 steps, which is caused by the curvature of the helix axis at this point. This decreases rise for the T5pA6 step which, in turn, is balanced by increases in the two juxtaposed base pair steps. The kink in the helix axis is shown by a roll of 10° in the T5pA6 step, and a negative value of opening for A6 shows that the axis is bending toward the major groove. The average base pair twist is 29.6°, and this corresponds to a slight unwinding of the helix (for a canonical A-type duplex geometry, the base pair twist is 33°). In the corresponding unmodified DNA:RNA hybrid and the LNA3:RNA hybrid, we found average twists of 32.8° and 33.4°, respectively (*19*). As such, a slight unwinding of the helix might be a consequence of the fully modified LNA strand.

Table 5. Average Backbone Torsion Angles and Sugar Puckers (in degrees) in the Two Strands of the LNA:RNA Hybrid[a]

	α	β	γ	δ	ϵ	ζ	χ	*P*	Φ_{max}
LNA	−72	179	59	66	−165	−61	−164	13	60
RNA	−78	181	61	79	−161	−68	−162	15	39

[a] A complete table with torsion angles for individual nucleotides is included in Supporting Information.

Sugar Conformations. All nucleotides in the hybrid adopt N-type sugar puckers, the average pseudorotation angles being 13° and 15° for LNA and RNA strands, respectively. The corresponding puckering amplitudes are 60° and 39°, respectively. The sugar puckers are experimentally corroborated by vanishing H1′−H2′ cross-peaks ($J_{H1'H2'} < \sim 2$ Hz) in DQF−COSY spectra. The very large puckering amplitude for the LNA sugars is a consequence of the locked bicyclic ring system. The large puckering amplitude shifts the δ backbone angle to 66° (see below).

Backbone Geometry. The regularity of the duplex is accentuated by analysis of the backbone torsion angles as these all lie in the standard genus for an A-type duplex geometry, that is (α to ζ) gauche−, trans, gauche+, gauche+, trans, gauche−, with only very slight variations along each of the strands (see Table 5). In the LNA strand, the average δ angle is 66° (as compared to 79° in the RNA strand) owing to the large puckering amplitude of the LNA furanoses (see above). This alteration of 13° is absorbed by slight changes in the ϵ and ζ angles and appears not to translate into any global perturbation of the duplex geometry.

For the ribose nucleotides C11, A12, and U13, we observe that in some of the 20 structures calculated for the hybrid, the α and γ torsion angles adopt α,γ:trans,-trans conformations. This is a consequence of the dynamic nature of the nucleic acid sugar−phosphate backbone and because both the α,γ:gauche−,gauche+ and α,γ:trans,trans backbone conformations are allowed by the NOE restraints employed in the structure calculations.

The glycosidic angles, χ, are found in anti conformations for all nucleotides as expected from the NOESY spectra. Again there are only minute variations along the duplex, and between the strands, with the average value being −163°.

DISCUSSION

The LNA:DNA Hybrid. The LNA:DNA hybrid exhibits NMR spectral features typical of an A-like right-handed nucleic acid duplex with normal Watson−Crick base pairs and all nucleobases in anti conformations.

The chemical shifts of the hybrid are somewhat altered in the LNA strand relative to the corresponding hybrid with three LNA nucleotides incorporated (*37*). This is a consequence of changes in the geometry owing to the added LNA nucleotides. As for the DNA strand, the chemical shift values are fairly unchanged, which shows that the overall geometry of the strand is unaltered even though the sugar equilibria of the deoxyriboses are changed (see below).

Our analysis of the deoxyribose conformations in the LNA:DNA hybrid show that they all exist in equilibria between N- and S-type puckers, with the population of S-type ranging from 57 to 80% (Table 2). In the corresponding unmodified dsDNA duplex, all deoxyriboses possessed in excess of 80% S-type conformation and in a partly modified isosequential LNA:DNA hybrid (LNA monomers at positions 2, 5 and 7), the deoxyriboses of the DNA strand possessed between 71 and 93% S-type conformation (*38*). Obviously, the inclusion of LNA monomers in one of the strands gradually tunes the base paired strand into larger populations of N-type sugar puckers. If analyzed with a two-state model, deoxyriboses in RNA:DNA hybrids usually possess approximately 60−70% S-type sugar conformation (*19*, *39*−*42*). As such, the pucker pattern of the deoxyriboses in the LNA:DNA hybrid resembles that of an RNA:DNA hybrid.

Although we have not determined the structure of the fully modified LNA:DNA hybrid, it appears reasonable from the evidence presented above to assume that such a hybrid structurally resembles an RNA:DNA hybrid. That is, repuckering deoxyribose sugars, a geometry intermediate of A- and B-type (albeit closer to A-type than B-type), with, for example, a minor groove width intermediate of that of A- and B-type geometries (∼8−9 Å).

There is some debate as to whether the deoxyriboses in RNA:DNA hybrids are best described by an O4′-endo sugar pucker, (*43*, *44*) a two-state model (*39*, *41*, *45*), or a model including more than two states (*46*). We have in this and previous work (*19*) experienced that *J* coupling constants can generally be fitted better with a two-state N/S model than with a single-state O4′-endo model. However, a two-state N/S model does not exclude that intermediate conformations are transiently occupied. If one assumes an S-type population of 67%, the energy difference between the two low-energy conformations would be ∼0.4 kcal/mol (based on a Boltzmann distribution), which is in good agreement with gas-phase ab initio calculations on a deoxyribose model system (*47*). In these calculations, the O4′-endo energy barrier to pseudorotation is ∼1.5 kcal/mol. Doing a statistical weighting with these energies, Brameld and Goddard calculates that the population of the "eastern" quadrant of the pseudorotation circle is 18%. This is actually in very good agreement with the 20% O4′-endo conformation proposed by Damha and co-workers based on NOE distances in a study of an RNA:DNA hybrid (*46*). Summarizing, we propose that it is apt to apply a two-state model to describe the sugar pucker of deoxyriboses in RNA:DNA hybrids; however, one should interpret the two sugar puckers determined as the two low-energy conformations and keep in mind that a continuum of conformations will be populated according to a Boltzmann distribution.

The LNA:RNA Hybrid. The chemical shifts of this hybrid show only the expected changes owing to the LNA nucleotides relative to the unmodified, LNA1:RNA and LNA3:RNA hybrids. In particular the chemical shifts of the RNA strand are almost unaltered between the four hybrids, and this shows that the conformation of the RNA strand is rather unperturbed by the increasing number of LNA nucleotides incorporated in the cognate strand.

The structure of the fully modified LNA:RNA hybrid has the general appearance of an A-type duplex as indicated by the large displacement of base pairs relative to the helix axis, by a number of helical parameters, and by sugar conformations in the N-range of the pseudorotation cycle. In addition, we find a minor groove width of 10.0 Å which is typical for an A-type duplex. This is in perfect agreement with the CD spectrum of the hybrid, which displayed all the characteristics of an A-type duplex geometry. Analysis of helical parameters and backbone torsion angles show that the duplex is regular; particularly the distributions of the backbone torsion angles are very uniform along the duplex with only very small variations between the LNA and RNA strands. The slight alteration of the δ angle, as imposed by the very large puckering amplitude of the LNA nucleotides, is absorbed by the neighboring torsion angles.

Altogether, we have shown that a fully modified LNA strand can be hybridized with its complementary RNA strand in the usual Watson−Crick manner; moreover, the resulting hybrid adopts an almost canonical A-type duplex geometry. Thus, LNA acts as an RNA mimic, and LNA fits seamlessly into an A-type Watson−Crick duplex framework.

Fully modified LNA:RNA hybrids do not elicit RNase H cleavage of the RNA strand (*48*). The predominant hypothesis is that RNase H recognizes a minor groove width intermediate of A- and B-type duplexes (∼8−9 Å), and the A-like structure, with a broad minor groove, of the fully modified LNA:RNA hybrid explains the RNase H inamenability of these hybrids.

We have determined the structure of the corresponding partly modified LNA:RNA hybrid with three LNA modifications (at positions 2, 5, and 7; LNA3:RNA) (*19*). This hybrid also adopts an almost canonical A-type duplex geometry. As such, the structural alteration introduced by the increased number of LNA monomers is small, yet the increase in helical thermostability is substantial (ΔT_m = 22 °C; although the inclusion of the two 5-methylcytosines may account for approximately 2 °C).

The NMR structure does not give any clues as to the origin of this thermostability. It is very likely that the 2′-oxygen of the LNA nucleotides partake in the solvation of the minor groove. Water bridges between the O2′ of the LNA bridge and O4′ of the 3′-flanking sugar are possible, thus enhancing the minor groove hydration. Such a hydration pattern would be less pronounced in the hybrid with just three LNA nucleotides. In addition, the T1 relaxation times measured for the fully modified LNA:RNA hybrid are very long (data not shown). For example, H1′ and aromatic protons have T1 relaxation times of ∼7 s and the adenine H2 proton a T1 relaxation time of ∼8 s. T1 relaxation times are influenced by a number of experimental parameters and thus can be difficult to compare between different samples. However, the values observed for the fully modified hybrid are distinctly longer than those for the LNA3:RNA and unmodified hybrids. This, qualitatively, points to a very rigid molecule with little internal motion. This would be favorable for establishing a well ordered shell of hydration.

CONCLUSION

We have studied two fully modified LNA hybrids, an LNA:RNA, and an LNA:DNA hybrid. In both contexts, the LNA nucleotides appear as RNA mimics. As such, LNA:RNA or dsLNA duplexes might be employed as aptamers for proteins recognizing dsRNA duplexes, and LNA:DNA hybrids as RNA:DNA aptamers, for example to probe the importance of the 2′-OH of RNA in enzymatic reactions. In addition, with their high affinity toward RNA, LNAs might be utilized to target highly structured regions of tertiary RNA structure.

ACKNOWLEDGMENT

We thank The Instrument Centre for NMR Spectroscopy of Biological Macromolecules at The Carlsberg Laboratory, Copenhagen, granted by The Danish Natural Science Research Council for providing spectrometer time at the 800 MHz spectrometer. The Danish National Research Foundation is thanked for financial support and Britta M. Dahl (Department of Chemistry, University of Copenhagen) is thanked for oligonucleotide synthesis. The Nucleic Acid Center is funded by the Danish National Research Foundation for studies on the chemical biology of nucleic acids.

Supporting Information Available: Tables giving RESP atomic charges for the four different LNA nucleotides, chemical shifts for the two hybrids, and minor groove widths, and a comprehensive table giving backbone torsion angles. This material is available free of charge via the Internet at http://pubs.acs.org.

LITERATURE CITED

(1) Freier, S. M., and Altmann, K.-H. (1997). The ups and downs of nucleic acid duplex stability: structure−stability studies on chemically modified DNA:RNA duplexes. *Nucleic Acids Res. 25*, 4429−4443.

(2) Manoharan, M. (1999). 2′-Carbohydrate modifications in antisense oligonucleotide therapy: importance of conformation, configuration and conjugation. *Biochim. Biophys. Acta 1489*, 117−130.

(3) Kawasaki, A. M., Casper, M. D., Freier, S. M., Lesnik, E. A., Zounes, M. C., Cummins, L. L., Gonzalez, C., and Cook, P. D. (1993). Uniformly modified 2′-deoxy-2′-fluoro phosphorothioate oligonucleotides as nuclease-resistant antisense compounds with high affinity and specificity for RNA targets. *J. Med. Chem. 36*, 831−841.

(4) Gryaznov, S. M. (1999). Oligonucleotide N3′−P5′ phosphoramidates as potential therapeutic agents. *Biochim. Biophys. Acta 1489*, 131−140.

(5) Hendrix, C., Rosemeyer, H., De Bouvere, B., Van Aerschot, A., Seela, F., and Herdewijn, P. (1997). 1′,5′-Anhydrohexitol oligonucleotides: hybridisation and strand displacement with oligoribonucleotides, interaction with RNase H and HIV reverse transcriptase. *Chem. Eur. J. 3*, 1513−1520.

(6) Koshkin, A. A., Singh, S. K., Nielsen, P., Rajwanshi, V. K., Kumar, R., Meldgaard, M., Olsen, C. E., and Wengel, J. (1998). LNA (locked nucleic acids): synthesis of the adenine, cytosine, guanine, 5-methylcytosine, thymine and uracil bicyclonucleoside monomers, oligomerisation, and unprecedented nucleic acid recognition. *Tetrahedron 54*, 3607−3630.

(7) Obika, S., Nanbu, D., Hari, Y., Andoh, J., Morio, K., Doi, T., and Imanishi, T. (1998). Stability and structural features of the duplexes containing nucleoside analogues with a fixed N-type conformation, 2′-*O*, 4′-*C*-methyleneribonucleosides. *Tetrahedron Lett. 39*, 5401−5404.

(8) Wengel, J. (1999). Synthesis of 3′-*C*- and 4′-*C*-branched oligonucleotides and the development of locked nucleic acid (LNA). *Acc. Chem. Res. 32*, 301−310.

(9) Petersen, M., and Wengel, J. (2003). LNA: a versatile tool for therapeutics and genomics. *Trends Biotechnol. 21*, 74−81.

(10) Kværnø, L., Kumar, R., Dahl, B. M., Olsen, C. E., and Wengel, J. (2000). Synthesis of abasic locked nucleic acid and two *seco*-LNA derivatives and evaluation of their hybridization properties compared with their more flexible DNA counterparts. *J. Org. Chem. 65*, 5167−5176.

(11) Braasch, D. A., and Corey, D. R. (2001). Locked nucleic acid (LNA): fine-tuning the recognition of DNA and RNA. *Chem. Biol. 8*, 1−7.

(12) Bondensgaard, K., Petersen, M., Singh, S. K., Rajwanshi, V. K., Wengel, J., and Jacobsen, J. P. (2000). Structural studies of LNA:RNA duplexes by NMR: conformations and implications for RNase H activity. *Chem. Eur. J. 6*, 2687−2695.

(13) Kurreck, J., Wyszko, E., Gillen, C., and Erdmann, V. A. (2002). Design of antisense oligonucleotides stabilized by locked nucleic acids. *Nucleic Acids Res. 30*, 1911−1918.

(14) Koshkin, A. A., Nielsen, P., Meldgaard, M., Rajwanshi, V. K., Singh, S. K., and Wengel, J. (1998). LNA (locked nucleic acid): an RNA mimic forming exceedingly stable LNA:LNA duplexes. *J. Am. Chem. Soc. 120*, 13252−13253.

(15) Crinelli, R., Bianchi, M., Gentilini, L., and Magnani, M. (2002). Design and characterization of decoy oligonucleotides containing locked nucleic acids. *Nucleic Acids Res. 30*, 2435−2443.

(16) Vester, B., Lundberg, L. B., Sørensen, M. D., Babu, B. R., Douthwaite, S., and Wengel, J. (2002). LNAzymes: incorporation of LNA-type monomers into DNAzymes markedly increases RNA cleavage. *J. Am. Chem. Soc 124*, 13682−13683.

(17) Ørum, H., Jakobsen, M. H., Koch, T., Vuust, J., and Borre, M. (1999). Detection of the factor V Leiden mutation by direct allele-specific hybridization of PCR amplicons to photoimmobilized locked nucleic acids. *Clin. Chem. 45*, 1898−1905.

(18) Simeonov, A., and Nikiforov, T. T. (2002). Single nucleotide polymorphism genotyping using short, fluorescently labeled locked nucleic acid (LNA) probes and fluorescence polarization detection. *Nucleic Acids Res. 30*, e91.

(19) Petersen, M., Bondensgaard, K., Wengel, J., and Jacobsen, J. P. (2002). Locked nucleic acid (LNA) recognition of RNA: NMR solution structures of LNA:RNA hybrids. *J. Am. Chem. Soc. 124*, 5974−5982.

(20) Singh, S. K., Nielsen, P., Koshkin, A. A., and Wengel, J. (1998). LNA (locked nucleic acids): synthesis and high-affinity nucleic acid recognition. *Chem. Commun.* 455−456.

(21) Geen, H., and Freeman, R. (1991). Band-selective radiofrequency pulses. *J. Magn. Reson. 93*, 93−141.

(22) Güntert, P., and Wüthrich, K. (1992). FLATT − a new procedure for high-quality baseline correction of multidimensional NMR spectra. *J. Magn. Reson. 96*, 403−407.

(23) Wijmenga, S. S., and van Buuren, B. N. M. (1998). The use of NMR methods for conformational studies of nucleic acids. *Prog. Nucl. Magn. Reson. Spectrosc. 32*, 287−387.

(24) Saenger, W. (1984) *Principles of Nucleic Acid Structure*, Springer-Verlag, New York.

(25) Case, D. A., Pearlman, D. A., Caldwell, J. W., Cheatham, T. E., III., Ross, W. S., Simmerling, C. L., Darden, T. A., Merz, K. M., Stanton, R. V., Cheng, A. L., Vincent, J. J., Crowley, M., Tsui, V., Radmer, R. J., Duan, Y., Pitera, J., Massura, I., Seibel, G. L., Singh, U. C., Weiner, P., and Kollman, P. A. (2000) *AMBER 6* University of California, San Francisco.

(26) Bayly, C. I., Cieplak, P., Cornell, W. D., and Kollman, P. A. (1993). A well-behaved electrostatic potential based method using charge restraints for deriving atomic charges: the RESP model. *J. Phys. Chem. 97*, 10269−10280.

(27) Macaya, R. F., Schultze, P., and Feigon, J. (1992). Sugar conformation in intramolecular DNA triplexes determined by coupling constants obtained by automated simulation of P.COSY cross-peaks. *J. Am. Chem. Soc. 114*, 781−783.

(28) de Leeuw, F. A. A. M., and Altona, C. (1983). Computer-assisted pseudorotation analysis of five-membered rings by means of proton spin−spin coupling constants: program PSEUROT. *J. Comput. Chem. 4*, 428−437.

(29) Woody, R. W. (1995). Circular dichroism. *Methods Enzymol.* 34−71.
(30) Baase, W. A., and Johnson, W. C. (1979). Circular dichroism and DNA secondary structure. *Nucleic Acids Res. 6*, 797−814.
(31) Hare, D. R., Wemmer, D. E., Chou, S.-H., Drobny, G., and Reid, B. R. (1983). Assignment of the nonexchangeable proton resonances of d(C-G-C-G-A-A-T-T-C-G-C-G) using two-dimensional nuclear magnetic resonance methods. *J. Mol. Biol. 171*, 319−336.
(32) Feigon, J., Leupin, W., Denny, W. A., and Kearns, D. R. (1983). Two-dimensional proton nuclear magnetic resonance investigation of the synthetic deoxyribonucleic acid decamer $d(ATATCGATAT)_2$. *Biochemistry 22*, 5943−5951.
(33) Scheek, R. M., Russo, N., Boelens, R., Kaptein, R., and van Boom, J. H. (1983). Sequential resonance assignments in DNA ^{1}H NMR spectra by two-dimensional NOE spectroscopy. *J. Am. Chem. Soc. 105*, 2914−2916.
(34) Wüthrich, K. (1986) *NMR of Proteins and Nucleic Acids*, John Wiley & Sons, New York.
(35) Lavery, R., and Sklenar, H. (1988). The definition of generalized helicoidal parameters and of axis curvature of irregular nucleic acids. *J. Biomol. Struct. Dyn. 6*, 63−91.
(36) Lavery, R., and Sklenar, H. (1989). Defining the structure of irregular nucleic acids: conventions and principles. *J. Biomol. Struct. Dyn. 7*, 655−667.
(37) Jensen, G. A., Singh, S. K., Kumar, R., Wengel, J., and Jacobsen, J. P. (2001). A comparison of the solution structures of an LNA:DNA duplex and the unmodified DNA:DNA duplex. *J. Chem. Soc., Perkin Trans. 2* 1224−1232.
(38) Petersen, M., Nielsen, C. B., Nielsen, K. E., Jensen, G. A., Bondensgaard, K., Singh, S. K., Rajwanshi, V. K., Koshkin, A. A., Dahl, B. M., Wengel, J., and Jacobsen, J. P. (2000). The conformations of locked nucleic acids (LNA). *J. Mol. Recognit. 13*, 44−53.
(39) Gonzáles, C., Stec, W., Reynolds, M., and James, T. L. (1995). Structure and dynamics of a DNA. RNA hybrid duplex with a chiral phosphorothioate moiety: NMR and molecular dynamics with conventional and time-averaged restraints. *Biochemistry 34*, 4969−4982.
(40) Bachelin, M., Hessler, G., Kurz, G., Hacia, J. G., Dervan, P. B., and Kessler, H. (1998). Structure of a stereoselective phosphorothioate DNA/RNA duplex. *Nat. Struct. Biol. 5*, 271−276.
(41) Gyi, J. I., Lane, A. N., Conn, G. L., and Brown, T. (1998). Solution structures of DNA:RNA hybrids with purine-rich and pyrimidine-rich strands: comparison with the homologues DNA and RNA duplexes. *Biochemistry 37*, 73−80.
(42) Aramini, J. M., and Germann, M. W. (1999). Solution structure of a DNA·RNA hybrid containing an α-anomeric thymidine and polarity reversals: d(ATGG-3′-3′-αT-5′-5′-GCTC)·r(gagcaccau). *Biochemistry 38*, 15448−15458.
(43) Fedoroff, O. Y., Salazar, M., and Reid, B. R. (1993). Structure of a DNA: RNA hybrid duplex. Why RNase H does not cleave pure DNA. *J. Mol. Biol. 233*, 509−523.
(44) Fedoroff, O. Y., Ge, Y., and Reid, B. R. (1997). Solution structure of r(gaggacug):d(CAGTCCTC) hybrid: implications for the initiation of HIV-1 (+)-strand synthesis. *J. Mol. Biol. 269*, 225−239.
(45) Cheatham, T. E., III., and Kollman, P. A. (1997). Molecular dynamics simulations highlight the structural differences among DNA:DNA, RNA:RNA, and DNA:RNA hybrid duplexes. *J. Am. Chem. Soc. 119*, 4805−4825.
(46) Denisov, A. Y., Noronha, A. M., Wilds, C. J., Trempe, J.-F., Pon, R. T., Gehring, K., and Damha, M. J. (2001). Solution structure of an arabinonucleic acid (ANA)/RNA duplex in a chimeric hairpin: comparison with 2′-fluor-ANA/RNA and DNA/RNA hybrids. *Nucleic Acids Res. 29*, 4284−4293.
(47) Brameld, K. A., and Goddard, W. A., III. (1999). Ab initio quantum mechanical study of the structure and energies for the pseudorotation of 5′-dehydroxy analogues of 2′-deoxyribose and ribose sugars. *J. Am. Chem. Soc. 121*, 985−993.
(48) Sørensen, M. D., Kværnø, L., Bryld, T., Håkansson, A. E., Verbeure, B., Gaubert, G., Herdewijn, P., and Wengel, J. (2002). α-L-*ribo*-Configured locked nucleic acid (α-L-LNA): synthesis and properties. *J. Am. Chem. Soc. 124*, 2164−2176.

BC034145H

Supporting Information

Table S1. Atomic charges for LNA modified nucleotides calculated using the RESP methodology

A^L		G^L		T^L		$^{me}C^L$	
HO5'(end)	0.422147	HO5'(end)	0.422147	HO5'(end)	0.422147	HO5'(end)	0.422147
O5'(end)	−0.598876	O5'(end)	−0.598876	O5'(end)	−0.598876	O5'(end)	−0.598876
O5'(phos)	−0.487971	O5'(phos)	−0.487971	O5'(phos)	−0.487971	O5'(phos)	−0.487971
C5'	0.044409	C5'	0.044409	C5'	0.044409	C5'	0.044409
H5'	0.086419	H5'	0.086419	H5'	0.086419	H5'	0.086419
H5"	0.086419	H5"	0.086419	H5"	0.086419	H5"	0.086419
C4'	0.134159	C4'	0.134159	C4'	0.134159	C4'	0.134159
O4'	−0.358264	O4'	−0.358264	O4'	−0.358264	O4'	−0.358264
C3'	0.176766	C3'	0.176766	C3'	0.176766	C3'	0.176766
H3'	0.087216	H3'	0.087216	H3'	0.087216	H3'	0.087216
C2'	−0.001598	C2'	−0.001598	C2'	−0.001598	C2'	−0.001598
H2'	0.172345	H2'	0.172345	H2'	0.172345	H2'	0.172345
O2'	−0.408527	O2'	−0.408527	O2'	−0.408527	O2'	−0.408527
C6'	0.031728	C6'	0.031728	C6'	0.031728	C6'	0.031728
H6'	0.101307	H6'	0.101307	H6'	0.101307	H6'	0.101307
H6"	0.101307	H6"	0.101307	H6"	0.101307	H6"	0.101307
C1'	0.061466	C1'	0.042926	C1'	0.116683	C1'	−0.036224
H1'	0.192859	H1'	0.196431	H1'	0.164982	H1'	0.205448
N9	−0.056145	N9	−0.008209	N1	−0.010932	N1	−0.013980
C8	0.239929	C8	0.184193	C6	−0.244030	C6	−0.091445
H8	0.133321	H8	0.148513	H6	0.234347	H6	0.197296
N7	−0.613469	N7	−0.579078	C5	0.009683	C5	−0.110394
C5	0.062103	C5	0.160686	C5M	−0.231073	C5M	−0.189527
C6	0.693767	C6	0.506796	H5MA	0.079861	H5MA	0.064901
N6	−0.909935	O6	−0.543120	H5MB	0.079861	H5MB	0.064901
HN6A	0.413210	N1	−0.562456	H5MC	0.079861	H5MC	0.064901
HN6B	0.413210	H1	0.355198	C4	0.538615	C4	0.623580
N1	−0.786430	C2	0.860981	O4	−0.549159	N4	−0.841687
C2	0.641843	N2	−1.012507	N3	−0.412963	HN4A	0.392515
H2	0.047139	HN2A	0.442144	H3	0.332614	HN4B	0.392515
N3	−0.767107	HN2B	0.442144	C2	0.498251	N3	−0.720029
C4	0.345916	N3	−0.707355	O2	−0.574924	C2	0.732490
O3'(end)	−0.602327	C4	0.184391	O3'(end)	−0.602327	O2	−0.623582
HO3'(end)	0.413692	O3'(end)	−0.602327	HO3'(end)	0.413692	O3'(end)	−0.602327
O3'(phos)	−0.500143	HO3'(end)	0.413692	O3'(phos)	−0.500143	HO3'(end)	0.413692
P	1.203092	O3'(phos)	−0.500143	P	1.203092	O3'(phos)	−0.500143
O1P	−0.790172	P	1.203092	O1P	−0.790172	P	1.203092
O2P	−0.790172	O1P	−0.790172	O2P	−0.790172	O1P	−0.790172
		O2P	−0.790172			O2P	−0.790172

Table S2. A selection of chemical shifts (in ppm) for the (^{me}**CTGATATG** ^{me}**C**)^{L}: r(GCAUAUCAG) hybrid. Values are given at 25 °C relative to DSS.

	H6/H8	H1'	H2'	H3'	H4'	H5'	H5"
^{me}**C**^{L}**1**	7.61	5.44	5.12	4.47		3.93	3.93
T^{L}**2**	7.56	5.59	5.21	4.77		4.26	4.26
G^{L}**3**	7.42	5.75	4.97	4.79		4.25	4.25
A^{L}**4**	7.17	5.80	4.92	4.51		4.19	4.19
T^{L}**5**	6.77	5.29	4.96	4.51		4.14	4.14
A^{L}**6**	7.65	5.94	4.98	4.62		4.21	4.21
T^{L}**7**	6.79	5.26	4.96	4.53		4.16	4.16
G^{L}**8**	7.25	5.81	4.89	4.62		4.16	4.19
^{me}**C**^{L}**9**	6.94	5.46	4.31	4.02		4.08	4.11
G10	8.01	5.73	4.81	4.47	4.30	3.87	3.99
C11	7.73	5.64	4.68	4.61	4.50	4.15	
A12	8.12	6.05	4.63	4.65	4.58	4.19	4.50
U13	7.49	5.55	4.46	4.55	4.50	4.13	
A14	8.18	6.08	4.57	4.65	4.56	4.19	4.50
U15	7.47	5.53	4.35	4.40	4.46	4.09	4.56
C16	7.75	5.56	4.38	4.56	4.45	4.10	4.41
A17	8.01	5.92	4.49	4.74	4.47	4.15	4.57
G18	7.28	5.76	4.00	4.19	4.24	4.03	4.45

	H6'	H6"	H5/H2/CH_3	H1/H3	H4/<u>H4</u>
^{me}**C**^{L}**1**	4.09	4.09	1.95		6.82/8.50
T^{L}**2**	4.14	4.01	1.67	13.16	
G^{L}**3**	4.15	4.10		11.72	
A^{L}**4**	4.14	4.09	7.60		
T^{L}**5**	4.07	4.01	1.37	13.33	
A^{L}**6**	4.16	4.11	7.02		
T^{L}**7**	4.07	4.01	1.33	13.40	
G^{L}**8**	4.11	4.07		12.71	
^{me}**C**^{L}**9**	3.96	3.91	1.45		6.60/8.79
G10				–	
C11			5.34		6.86/8.53
A12			7.37		
U13			5.02	13.25	
A14			7.30		
U15			4.85	13.75	
C16			5.57		6.82/8.06
A17			7.15		
G18				–	

Table S3. A selection of chemical shifts (in ppm) for the (^{me}**CTGATATG**^{me}**C**)^{L}: d(GCATATCAG) hybrid. Values are given at 25 °C relative to DSS.

	H6/H8	H1'	H2'	H2"	H3'	H4'	H5'
^{me}**C**^{L}**1**	7.53	5.36	5.17		4.41		4.07
T^{L}**2**	7.55	5.52	5.30		4.72		4.25
G^{L}**3**	7.43	5.75	5.07		4.75		4.26
A^{L}**4**	7.24	5.77	5.00		4.50		4.19
T^{L}**5**	6.78	5.20	5.08		4.49		4.14
A^{L}**6**	7.68	5.92	5.04		4.62		4.21
T^{L}**7**	6.80	5.19	5.05		4.50		4.15
G^{L}**8**	7.28	5.79	4.92		4.63		4.17
^{me}**C**^{L}**9**	6.99	5.43	4.29		4.04		4.12
G10	8.06	6.12	2.86	2.83	4.73	4.26	3.88
C11	7.59	6.08	2.58	2.69	4.86	4.35	4.22
A12	8.14	6.34	2.71	2.94	4.87	4.45	4.29
T13	7.35	6.01	2.42	2.67	4.90	4.30	4.23
A14	8.03	6.31	2.58	2.86	4.85	4.44	4.28
T15	7.29	6.05	2.27	2.64	4.84	4.28	4.18
C16	7.48	5.95	2.20	2.56	4.84	4.22	4.16
A17	8.09	6.18	2.63	2.86	5.01	4.42	4.22
G18	7.50	6.11	2.28	2.34	4.61	4.22	4.16
	H5"	H6'	H6"	H5/H2/CH_3	H1/H3	H4/<u>H4</u>	
^{me}**C**^{L}**1**	4.05	3.91	3.91	1.89		–	
T^{L}**2**	4.25	3.99	4.11	1.64	13.52		
G^{L}**3**	4.26	4.09	4.14		11.82		
A^{L}**4**	4.19	4.10	4.14	7.68			
T^{L}**5**	4.14	4.01	4.05	1.42	13.40		
A^{L}**6**	4.21	4.14	4.14	7.01			
T^{L}**7**	4.15	4.01	4.05	1.36	13.50		
G^{L}**8**	4.17	4.07	4.09		12.82		
^{me}**C**^{L}**9**	4.12	3.92	3.92	1.47		–	
G10	3.93				–		
C11	4.30			5.39		7.03/8.60	
A12	4.29			7.48			
T13	4.34			1.21	13.27		
A14	4.25			7.36			
T15	4.21			1.02	13.56		
C16	4.29			5.44		6.80/8.11	
A17	4.14			7.29			
G18	4.22				–		

Table S4. Minor groove width (in Å) in the LNA:RNA hybrid. For comparison, the minor groove widths of the unmodified DNA:RNA and the LNA3:RNA hybrids are included [a]

	LNA:RNA	DNA:RNA	LNA3:RNA
$P_4 - P_{18}$	10.0	8.9	9.8
$P_5 - P_{17}$	9.7	9.7	10.0
$P_6 - P_{16}$	9.8	7.8	9.9
$P_7 - P_{15}$	10.2	7.6	9.5
$P_8 - P_{14}$	10.3	7.9	9.3
$P_9 - P_{13}$	10.0	10.5	9.2
average	10.0	8.7	9.6

[a] The minor groove width is defined as the shortest interstrand phosphorous distance minus 5.8 Å which is the van der Waals radius for a phosphate group.

Table S5. Backbone torsion angles and sugar puckers (in degrees) in the LNA:RNA hybrid

	α	β	γ	δ	ϵ	ζ	χ	P	ϕ_{max}
$^{me}C^{L}$1			55/184	62	−172	−66	−164	20	60
T^{L}2	−72	178	58	68	−163	−59	−163	10	59
G^{L}3	−73	178	60	66	−166	−62	−165	13	61
A^{L}4	−70	177	64	66	−164	−60	−166	16	59
T^{L}5	−73	179	59	66	−162	−60	−160	11	59
A^{L}6	−73	181	59	66	−159	−61	−164	14	60
T^{L}7	−72	175	62	68	−164	−60	−162	10	60
G^{L}8	−73	178	61	66	−168	−61	−167	14	60
$^{me}C^{L}$9	−72	183	56	66			−164	10	61
G10			54	83	−157	−64	−164	7	43
C11	−68/141[a]	184	64/188[a]	77	−163	−73	−161	11	41
A12	−74/156[a]	179	64/183[a]	83	−162	−69	−164	10	36
U13	−87/122[a]	177	69/197[a]	81	−165	−69	−157	14	37
A14	−82	183	60	78	−156	−64	−165	16	39
U15	−81	184	65	76	−164	−68	−164	18	41
C16	−77	179	61	77	−164	−69	−158	14	40
A17	−78	181	59	76	−156	−65	−165	20	39
G18	−76	180	51	76			−156	27	39

[a] These torsion angles values are correlated. For C11, A12 and U13, 8, 17 and 19 structures, respectively, were found in gauche, gauche− conformations.

Antigenicity of Recombinant Proteins after Regioselective Immobilization onto Polyanhydride-Based Copolymers

Laure Allard,[†] Valérie Cheynet,[†] Guy Oriol,[†] Gaspard Gervasi,[§] Emmanuelle Imbert-Laurenceau,[†] Bernard Mandrand,[†] Thierry Delair,[†] and François Mallet*[,†]

Unité Mixte de Recherche 2714, CNRS−bioMérieux, IFR128 Biosciences Lyon-Gerland, ENS-Lyon, 46, allée d'Italie, 69364 Lyon, France, and bioMérieux, Chemin de l'Orme, 69280 Marcy l'Etoile, France. Received August 22, 2003; Revised Manuscript Received February 13, 2004

We previously demonstrated that the introduction of a tag consisting of several contiguous lysines at the N- or C-terminus of a recombinant protein greatly improved the covalent grafting of the protein onto negatively charged maleic anhydride-*alt*-methyl vinyl ether (MAMVE) copolymer, under many different experimental conditions (Ladavière, C., et al. (1998) *Bioconjugate Chem. 9*, 655; Allard, L., et al. (2002) *Biotechnol. Bioeng. 80*, 341). The grafting efficiency was dependent on the charge and amine density of the tag, characteristics which were determined by the tag composition. The six lysine tag (Lys6) was found to be the most efficient (Allard, L., et al. (2001) *Bioconjugate Chem. 12*, 972). In the present work, the biological activity of Lys6-proteins covalently bound to polymer was investigated. N- or C-terminal Lys6-tagged HIV-1 p24 recombinant proteins (RK24H and RH24K) were grafted onto MAMVE, and the antigenicity each of the bioconjugates was evaluated using six monoclonal antibodies that recognized different epitopes distributed along the protein. We demonstrate that the position of the tag and the hydrolysis rate of the anhydride moieties of the polymer are the two main parameters involved in the conservation of the biological activity of the immobilized protein. We thus present a process which allows an efficient oriented immobilization of proteins onto copolymers with optimal biological activity that is suitable for the controlled production of active bioconjugates.

INTRODUCTION

Covalent immobilization of proteins onto polymers has found numerous applications in several fields, such as in chemotherapy to reduce proteolytic degradation (*1*) in gene therapy for targeted gene delivery (*2*) and in diagnostics to increase the stability of ELISA capture phase (*3*). However, immobilization may occur via a random attachment of the proteins to the support through several amino acid residues, leading to a partial loss of biological properties (*1*). Since protein covalent immobilization is a chemical alteration of the biomolecule, it is of great interest to make this reaction occur at a specific site of the protein that is not involved in the biorecognition process (*4*).

The approach we developed consisted in introducing an oligoamino acid sequence (tag) at a defined position on the protein. The rationale for this was that an increase in the density of reactive groups at a particular position of the protein would direct the grafting and should enhance the efficiency of the immobilization reaction. The advantage in using amide bond formation to tether biomolecules to carriers is that the chemistry is simple, reproducible, and can sustain a diversity of experimental conditions which are prerequisites for the development of a generic grafting method. We have previously shown that addition of a hexalysine tag (Lys6) at the N- or C-terminal region of a p24 recombinant protein led to a dramatic increase in the yield of the tagged protein (more than 90% versus 30% for the nontagged p24 protein) coupled to maleic anhydride-*alt*-methyl vinyl ether copolymer (MAMVE) (*5*, *6*). The presence of the Lys6 peptide allowed the immobilization of up to 50 protein molecules per polymer chain. In addition, we have shown that the efficiency of the regioselective immobilization of the tagged protein onto the copolymer depended directly on the composition of the tag. The reactivity of the tag was determined by both the density of positive charges and by the number of reactive amino groups. The most efficient tag was found to be the Lys6 tag which contained both cationic groups and primary amine groups (*7*).

Although such a tag allows quantitative efficient grafting, the localization of the tag should be carefully chosen to maintain the biological activity of the protein. We thus designed two recombinant proteins characterized by the N- or C-terminal position of the Lys6 tag, respectively termed RH24K and RK24H. The protein model used was the capsid p24 protein from HIV-1, which is well expressed in *Escherichia coli*, soluble, efficiently purified by immobilized metal affinity chromatography (IMAC) (*8*), and structurally characterized (*9*). The structure of the p24 allowed us to accurately locate domains involved in molecular recognition processes (such as epitopes and protease cleavage sites) and to evaluate the accessibility of internal lysines.

The RH24K and RK24H recombinant proteins were grafted onto MAMVE, and the antigenicity of the bioconjugates was evaluated using monoclonal antibodies (mAbs). These mAbs were selected because they recognized different epitopes distributed along the protein, in the N-terminal domain, in the flexible interdomain peptide and in the C-terminal domain. The accessibility of the different epitopes on the bound proteins was

* To whom correspondence should be addressed. E-mail: francois.mallet@ens-lyon.fr.

[†] Unité Mixte de Recherche 2714, CNRS−bioMérieux.

[§] bioMérieux, Chemin de l'Orme.

10.1021/bc034146+ CCC: $27.50 © 2004 American Chemical Society
Published on Web 05/04/2004

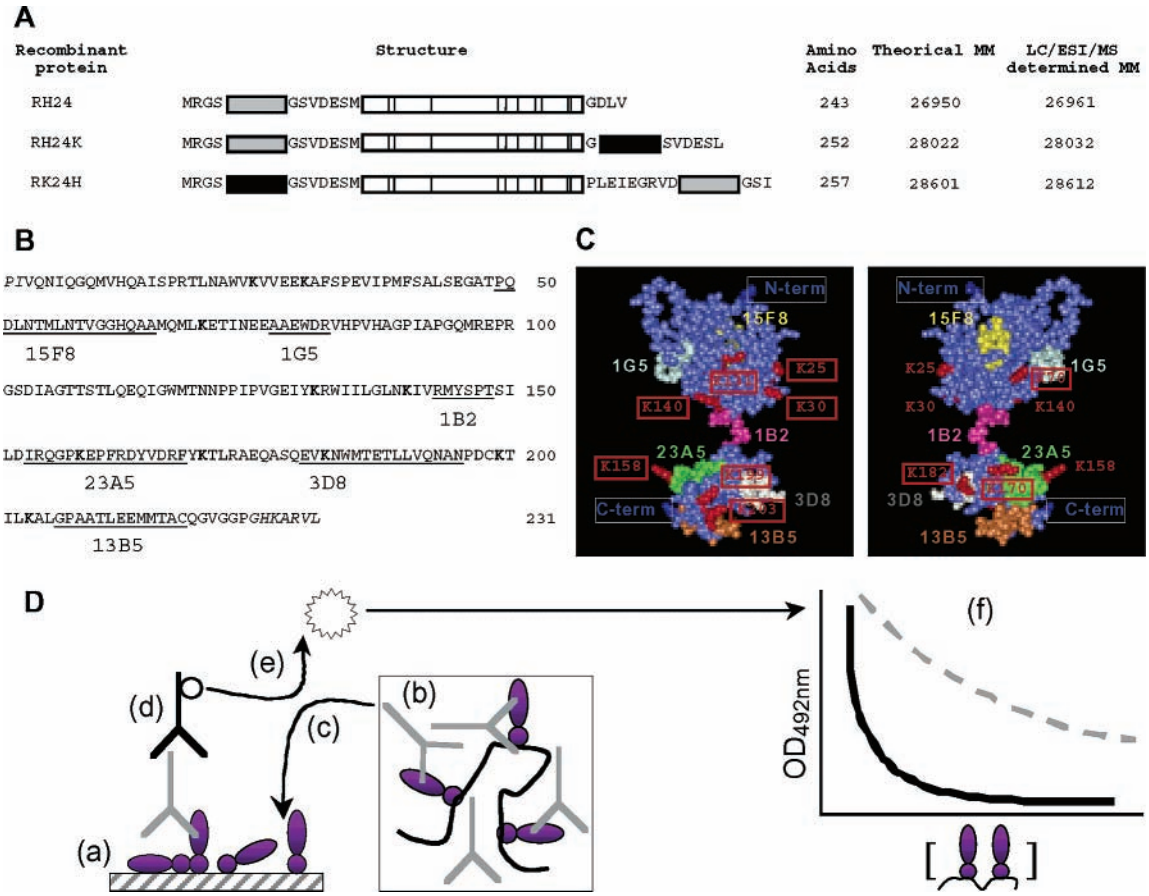


Figure 1. Chemical and antigenic features of the recombinant proteins derived from the HIV-1 p24 capsid protein. (A) Features of the three recombinant proteins, including the Lys6 (■) and His6 (■) tags, the main conserved domain (□), and specific AA residues. For each recombinant protein are indicated the length in AA and the theoretical and experimental molecular masses (MM) obtained using Mac Vector Version 6.5.3 and mass spectrometry (LC/ESI/MS), respectively. (B) Amino acid (AA) sequence of the native p24 protein from isolate HXB2. AA 3 (valine) to 224 (proline) represent the sequence conserved in all recombinant proteins. Lysine residues (K) are indicated in bold letters and epitopes recognized by 15F8, 1G5, 1B2, 23A5, 3D8, and 13B5 monoclonal antibodies (mAb) underlined. (C) In the context of a front and back RH24 3D structure, location of the N- and C-terminal ends of the protein and of the six epitopes and the 10 conserved lysines (red-squared). (D) Principle of the competitive ELISA test: (a) the RH24 protein was adsorbed on the microtiter plate, (b) various amounts of protein−polymer bioconjugate were incubated with the relevant mAb and then (c) loaded onto the RH24 capture phase; after a washing step which eliminated the bioconjugate−mAb complex, (d) the RH24 bound mAb was detected by adding an anti-mouse IgG peroxidase conjugate and (e) incubated with a colorimetric substrate; (f) curves representing the OD as a function of the bioconjugate concentrations were plotted, a rapid decrease indicating an efficient competition (black), a slow (dotted gray) or no decrease indicating an inefficient competition, which reflected an optimal or poor accessibility of the epitope, respectively.

evaluated using a competition ELISA test. The assay showed the recognition pattern of the bioconjugate epitopes was altered according to the N- or C-position of the tag. This was due to the involvement in the grafting reaction (in addition to the tag-driven grafting) of an internal lysine with spatial location close to the tag. We demonstrated that the reaction of internal lysine with the copolymer was avoided by modulating the reactivity of the latter, via controlled hydrolysis of some anhydride moieties. The location of the lysines involved in the covalent grafting of the protein onto the copolymer was determined by proteolytic digestion of the bioconjugates followed by MALDI-TOF mass spectrometry analysis. Thus, in addition to the previously demonstrated importance of the tag composition in the grafting reaction efficiency (*7*), all these results showed that the two main parameters involved in the conservation of the biological activity of the immobilized protein were the tag position and the number of reactive groups of the copolymer.

EXPERIMENTAL PROCEDURES

Isolation and Characterization of Tagged Recombinant Proteins. The p24 gene was cloned in pMR (*10*) and pMK81 and pMK83 expression vectors (*6*). Three HIV-1 p24 recombinant proteins were then obtained from *E. coli* using a procedure derived from Cheynet et al. (*8*). Each of the proteins present a His6 tag (H) at their N- or C-terminal end, allowing a one-step purification using IMAC, and two of the proteins display an additional N- or C-terminal Lys6 tag which allows efficient coupling of the protein to the copolymer (*6*, *7*). The proteins were termed RH24, RH24K, and RK24H for recombinant protein with respectively no Lys6 tag, a C-terminal tag, and a N-terminal Lys6 tag (Figure 1A). Briefly, *E. coli* strain XL1 was transformed with the expression plasmids. The extracts of soluble proteins were purified by IMAC on FPLC (Äkta explorer; Amersham Pharmacia Biotech) using a Zn−NTA-activated gel. Collected fractions were analyzed by SDS−PAGE, and the most concentrated fraction was dialyzed against phosphate buffer 50 mM, pH 7.8.

Mass spectrometry (LC-ESI-MS) analysis was performed on a single quadrupole API 100 mass spectrometer, 140B pumps, and a 785A detector (Perkin-Elmer). Reversed-phase liquid chromatography was performed on a C4 column (Vydac ref 214PT5115, 5 μm particle size).

Solvent A was 0.1% (v/v) formic acid in water, and solvent B was 0.1% (v/v) formic acid in water/acetonitrile mixture (5:95 v/v). A gradient of 40 to 60% B was used. Theoretical molar masses were determined with the Mac Vector software (version 6.5.3) and compared with the experimental values obtained by mass spectrometry.

p24 Epitope Mapping. To identify epitopes distributed along the p24 protein, we created a library of bacterial clones expressing peptide sequences of p24 (NovaTope System, Novagen). Briefly, the p24 gene was randomly cleaved in 50−150 bp fragments using DNase, and all fragments have been cloned in a plasmid designed for the inducible expression of small peptides as part of larger fusion proteins, i.e., p24 epitopes fused to phage T7 protein 10. Sixteen antibodies obtained by immunizing mice with whole HIV-1 virus extract (15F8, 1G5, 14D4, 1B2, 23A5, 3D10, 11D11, 9A4, 13H4, 11C10, 9B5) or RH24 recombinant protein (9A9, 7A1, 3D8, 4H3, 13B5) were used to screen the p24 epitope library by standard colony lift method. For each antibody, positive clones were analyzed by DNA sequencing and the epitope determined by aligning the overlapping sequences.

Isolation and Characterization of Bioconjugates. The MAMVE alternated copolymer (molar mass = 67 000 g/mol) was supplied by Polysciences Inc (Warrington, PA). The copolymer was dissolved to a final concentration of 1 g/L in either anhydrous dimethyl sulfoxide (DMSO from Aldrich) at 37 °C (named nonhydrolyzed polymer) or DMSO containing 10% (v/v) H_2O and incubated for 48 h at 37 °C (named hydrolyzed polymer). A standard reaction consisted of 36 μg of protein (12.4 μM final concentration) and 5 μg of polymer (0.71 μM final concentration) in 100 μL of 50 mM phosphate buffer, pH 7.8. The reaction mixture was stirred for 3 h at 37 °C, and then the bioconjugates were stored at 4 °C.

Bioconjugates were analyzed by size exclusion chromatography (SEC) using a Shodex Protein KW-803 (Waters), a Kontron HPLC 422 pump, a Kontron HPLC autosampler 465, and a Kontron UV diode array detector. Analyses were run in 0.1 M phosphate buffer, pH 6.8, containing 0.5% (w/v) sodium dodecyl sulfate (SDS) with a flow rate of 0.5 mL/min. Detection was achieved by measuring the absorbance at 280 nm (at the concentration used, the polymer had no absorption at 280 nm). The ratio of the peak area corresponding to the polymer-bound proteins versus the sum of the two peaks corresponding to the unbound and bound proteins (i.e. the total amount of protein involved in the reaction) gave the coupling yield.

Epitope Accessibility. The capacity of each antibody to recognize its cognate epitope was evaluated by ELISA competition. ELISA 96-well plates (Nunc Immuno Plate MaxiSorp surface) were coated overnight at room temperature with a 0.25 μg/mL solution of RH24 proteins in PBS buffer. After being coated, plates were saturated for 2 h at 37 °C with phosphate buffer saline (PBS) containing 1% dry milk. mAb and various amounts of protein−polymer bioconjugate (ranging from 0.01 to 15 μg/mL) in PBS−0.2% dry milk were incubated for 2 h at 37 °C and then added to the RH24-coated microtiter-plates. After 2 h incubation at 37 °C, plates were washed three times with PBS-0.05% Tween 20. The mAb bound to the adsorbed antigen was detected by adding 100 μL of goat anti-mouse IgG (H+L) peroxidase conjugate (Jackson ImmunoResearch) (2×10^3 fold diluted in PBS dry milk) and incubating for 1 h at 37 °C. Plates were then washed and incubated for 10 min with *O*-phenylenediamine (OPD 30 mg) (Sanofi Pasteur) diluted in 10 mL substrate buffer 0.03% H_2O_2 (Sanofi Pasteur) for 10 min in the dark at room temperature. OD values were measured at 492 nm.

Amine Titration. Protein modification rate was evaluated using fluorescamine (Acros ref 19167-5000, FW 278,26) (11), a compound which reacts with primary amines leading to the formation of fluorescent products. A standard reaction consisted of 30 μL of fluorescamine solution (0.4 g/L in anhydrous DMSO) and 90 μL of recombinant protein solution (0.34 g/L in phosphate buffer 50 mM. pH 7.8). The reaction was allowed to proceed for 20 min in the dark, at room temperature, and the fluorescence emission intensity was measured at 477 nm for an excitation wavelength of 416 nm (Perkin-Elmer LS50 fluorimeter). The modification rate of the immobilized protein was determined as follows: 100 − [fluorescence of the bound protein (assay) × 100/ fluorescence of the unbound protein].

Enzymatic Digestion of the RH24K−MAMVE67 Bioconjugates and Mass Spectrometry Analysis of the Fragments. RH24K immobilized onto nonhydrolyzed and hydrolyzed MAMVE67 copolymer was digested using Endoproteinase LysC (Roche ref 1 420 429) and protease V8 from *Staphyloccocus aureus* (Glu-C) (Roche ref 1 420 399) with an enzyme/protein ratio of 25/1 (w/w). Prior to digestion, the bioconjugates were reduced in a solution of 3 M guanidine and 20 mM DTT for 1 h at 37 °C and alkylated in 45 mM iodoacetamide for 1 h at 37 °C. Bioconjugates were then dialyzed overnight at 4 °C against 50 mM ammonium bicarbonate (Sigma lot 10K0261). Free RH24 and RH24K proteins were digested under the same conditions. Digested bioconjugates were stored at 4 °C before molecular-mass analysis on a MALDI-TOF Biflex III (Bruker, Wissembourg, France) mass spectrometer.

RESULTS AND DISCUSSION

Characterization of the p24 Recombinant Proteins. The three recombinant proteins, containing a His6 tag for IMAC purification, differed by the absence (RH24) or the presence at their N-terminal (RK24H) or C-terminal (RH24K) end of a Lys6 reactive tag for coupling onto copolymer (Figure 1A). All three recombinant proteins exhibited a high expression level representing up to 30% of the total amount of protein production by *E. coli*. Following purification by IMAC on a Zn−NTA-activated gel, the purity of the proteins was greater than 95% as determined on a Coomassie Blue stained SDS polyacrylamide gel, as described for other batches used in previous studies (*5*−*8*). Experimental determination of the molar masses was in accordance with the expected theoretical value for all recombinant proteins (Figure 1A). The amino acid sequence shared by all proteins is reported in Figure 1B. Ten lysine groups are almost evenly spaced along the nontagged RH24 protein macromolecule (residues 25, 30, 70, 131, and 140 in the N-terminal domain, residues 158, 170, 182, 199, 203 in the C-terminal domain. Residue numbering corresponds to the wild-type HIV-1 p24 HXB2 strain), and these lysine groups are conserved within all three recombinant proteins. NMR (*12*) and crystal structure data (*9*, *13*−*14*) demonstrated that, in the 3D structure, the 10 lysine groups were accessible for grafting (Figure 1C) although they displayed different reactivities (*15*).

Characterization of the p24 Recombinant-P(MAMVE) Bioconjugates. The RH24K and RK24H proteins were bound to MAMVE, and the coupling yields were determined by HPLC analysis. The coupling yields were close to 100%, irrespective of the N- or C-terminal

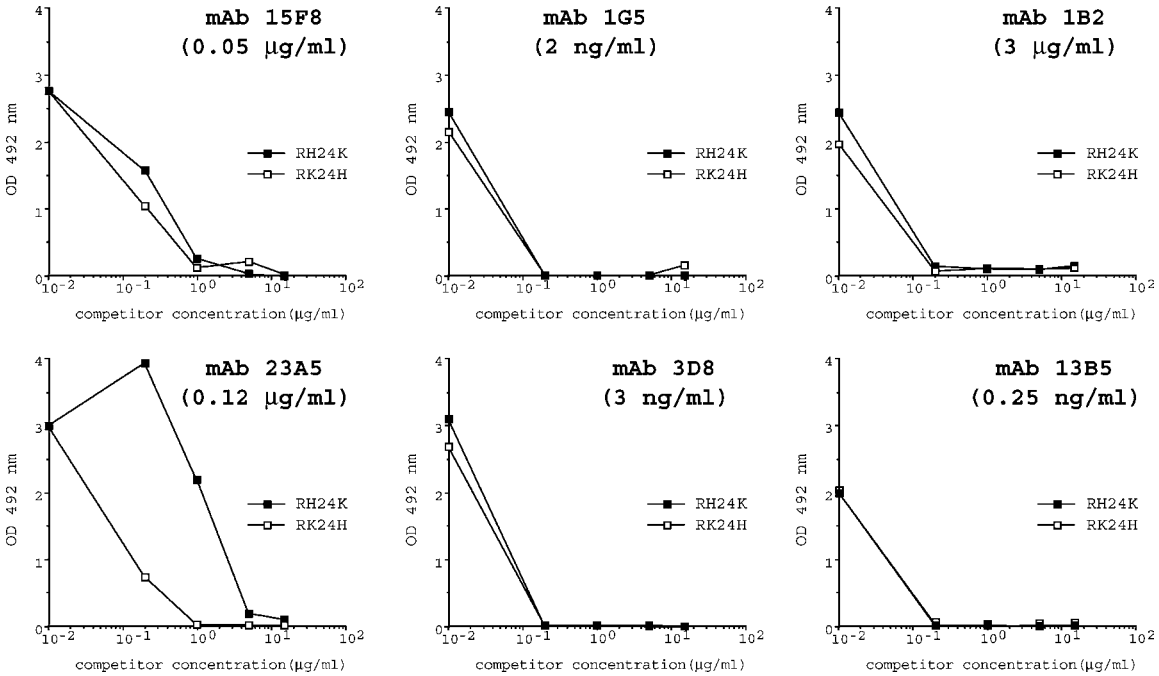


Figure 2. Influence of the Lys6 tag position on epitope accessibility on the bioconjugate. Competitive ELISA curves representing OD as a function of the bioconjugate concentration were obtained for the six mAbs used at an optimal concentration (see text) as indicated (in brackets). The two bioconjugates consisted of N- or C-terminal Lys6-tagged recombinant proteins, RK24H (□) and RH24K (■), respectively, grafted onto MAMVE copolymer. 15F8 and 1G5 mAbs targeted the N-terminal domain of p24, 1B2 the interdomain, and 23A5, 3D8, and 13B5 mAbs the C-terminal domain.

position of the Lys6 tag, as previously described (*6*), highlighting the robustness of the process. RK24H and RH24K proteins were bound to partially hydrolyzed MAMVE (48 h in DMSO, 10% H_2O; see below), and the coupling yields were 100% and 94.4% and 90%, respectively. The 0% to 10% coupling yield reductions observed with these Lys6-tagged proteins grafted onto partially hydrolyzed versus nonhydrolyzed polymers were much lower than the 82% decrease previously observed with the RH24 nontagged counterpart in similar conditions (*7*), illustrating the high grafting efficiency of the Lys6 tag which compete efficiently with the water-induced hydrolysis during the coupling reaction (*5*, *7*). Thus, the high coupling yields allowed use of the bioconjugates without subsequent purification. Although the tag position did not affect the yields, it could potentially be detrimental to the biological reactivity of the bioconjugate. We decided to use antigen (p24 epitopes)−antibody (monoclonal antibodies paratopes) recognition as a tool to analyze the biological reactivity of the immobilized proteins.

P24 Epitope Mapping. All p24-derived proteins contained a principal conserved domain which was used to construct an epitope library in order to make an epitope map of the p24 protein. The epitope library was used to screen 16 anti-p24 monoclonal antibodies (mAb). These 16 antibodies covered seven epitope regions including six nonoverlapping epitopes. Six monoclonal antibodies were retained, 15F8, 1G5, 1B2, 23A5, 3D8, 13B5 (Figure 1B). Four out of the six identified epitopes, recognized by 15F8, 1G5, 1B2, and 23A5 mAb, were in agreement with previous identifications using peptide technologies (*16*, *17*). One out of the six identified epitopes, recognized by 13B5 mAb, was in agreement with previous structural characterization determined during cocrystallization of RH24 and 13B5 Fab (*9*, *18*). More precisely, 15F8 (residues 49−65) and 1G5 (77−82) mAb recognize epitopes located in the N-terminal domain, 1B2 (143−148) in the flexible interdomain peptide, and the three remaining 23A5 (153−168), 3D8 (179−195), and 13B5 (206−218) mAb in the C-terminal domain (Figure 1B,C). As those epitopes were evenly dispersed along the p24 protein, they were flanked or contained potentially reactive lysine groups (Figure 1B,C).

Antigenicity of the Bioconjugates. Due to the homogeneous distribution and the close vicinity of epitopes and internal lysines (not belonging to the Lys6 tag), one can assume that, in the context of a protein coupled to a copolymer, any alteration of epitope−paratope interaction may reflect the involvement in the grafting reaction of residues other than those contained within the tag, leading to end-on (tag dependent) or side-on (tag unrelated) orientations as previously suggested (*5*). The bioreactivity of recombinant proteins immobilized onto copolymer was investigated in an ELISA competition test (Figure 1D), as the random adsorption of the bioconjugate onto a solid phase might have randomly hidden and/or damaged some of the recognition sites. We first determined the optimal concentration for each monoclonal antibody, using a classical ELISA test with RH24 as a coated antigen. Using a serial dilution of mAbs, we obtained OD as a function of mAb concentration curves and thus calculated the mAb concentration at the center of the linear part of the curve. This mAb concentration should be the most informative in competition assay as small variations in recognition efficiency should induce large signal variations. Determined optimal concentrations were 0.05 μg/mL, 2 ng/mL, 3 μg/mL, 0.12 μg/mL, 3 ng/mL and 0.25 ng/mL, for 15F8, 1G5, 1B2, 23A5, 3D8, 13B5 mAbs, respectively.

The bioreactivity of RH24K and RK24H proteins immobilized onto MAMVE was investigated in an ELISA competition test with the six monoclonal antibodies. No influence of the position of the tag was observed for five out of the six mAbs. This was indicated by the exponential decrease of the OD signal as a function of the bioconjugate concentration (Figure 2). Conversely, the competition curves for 23A5 mAb showed that RH24K−

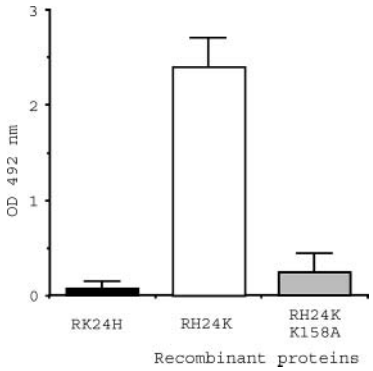


Figure 3. Influence of an internal lysine on epitope accessibility on the bioconjugate. Three bioconjugates were analyzed by competitive ELISA with the 23A5 mAb. Antibody and bioconjugate concentrations were 0.12 μg/mL and 1 μg/mL, respectively. The bioconjugates consisted of N-terminal, RK24H (black bar), or C-terminal, RH24K (empty bar), Lys6-tagged recombinant proteins, or a Lys 158 mutated form RH24K−K158A (grey bar), grafted onto MAMVE copolymer. Experiments were performed in triplicate. The indicated OD is the mean value ± two standard deviations.

MAMVE bioconjugate competes much less efficiently than the RK24H−MAMVE counterpart. This may suggest that in the context of a C-terminal Lys tag grafted protein, the 23A5 corresponding epitope is poorly recognized or not accessible. This epitope is located in the C-terminal domain of the p24 protein, as were the 3D8 and 13B5 epitopes which remained unaltered during the grafting reaction. The 23A5 epitope contained a very accessible primary amine on lysine 158, as determined by analysis of the 3D structure (SwissPdbViewer v3.6) and previously experimentally described (*15*). Another lysine (K170) was present within the 3D8 epitope but exhibited a lower accessibility than lysine 158, as determined from the 3D structure and previously observed experimentally (*15*). Overall, this suggested that the position of the tag might favor the reactivity (coupling) of the K158 intrinsic lysine, which was detrimental to the epitope accessibility.

To demonstrate the involvement of this lysine in the covalent reaction, we designed a new p24 recombinant protein, derived from the C-terminal Lys6 tag protein RH24K, where the K158 lysine was replaced with alanine, a neutral amino acid that is unable to react covalently with the anhydride moieties of the polymer. The binding of this protein, termed RH24K−K158A, onto the 23A5 mAb was not affected by the single amino acid mutation within the epitope, in a direct ELISA test (data not shown). RH24K−K158A was coupled onto MAMVE (coupling yield 100%, 90% after partial hydrolysis), and the reactivity of the 23A5 mAb toward RK24H−MAMVE, RH24K−MAMVE, and RH24K−K158A−MAMVE bioconjugates was evaluated in the ELISA competition assay. The competition effect obtained with the RH24K−K158A−MAMVE bioconjugate was approximately 10 times higher than the one produced by the original RH24K−MAMVE and was indeed similar to the inhibition produced by the N-terminal Lys6-tagged protein−polymer bioconjugate, RK24H−MAMVE (Figure 3). This result clearly demonstrated that, in the context of a C-terminal Lys6 p24, lysine 158 was involved in the coupling reaction with the polymer.

A simple way to avoid internal lysine reactivity would be to decrease the density of reactive groups on the polymer. Such a modulation of reactivity could be achieved by partial hydrolysis of the anhydride moieties of the MAMVE copolymer in DMSO containing 10% water for 48 h at 37 °C (*7*). The RH24K protein was therefore grafted onto nonhydrolyzed and partially hydrolyzed (MAMVE.hy) polymers, and the antigenic determinants reactivity of the two bioconjugates was investigated in the ELISA competition test with the six monoclonal antibodies. First, the competition curves for 23A5 mAb showed that the RH24K−MAMVE.hy bioconjugate competed much more efficiently than the RH24K−MAMVE counterpart (Figure 4A). This indicated that, in the context of a less reactive polymer, the 23A5 corresponding epitope was efficiently recognized and accessible onto the bioconjugate, in a similar way to that obtained for the RH24K−K158A−MAMVE and RK24H−MAMVE bioconjugates. These three different situations are likely to avoid the involvement of lysine 158 in the coupling reaction. It was also found that 1G5, 1B2, 3D8, and 13B5 mAbs behaved similarly, independently of the hydrolysis or nonhydrolysis status of the copolymer, as illustrated by 3D8 mAb in Figure 4A. Finally, the 15F8 mAb presented an opposing situation to the 23A5 mAb, the less competitive bioconjugate being the RH24K−MAMVE.hy, from 1 μg/mL bioconjugate concentrations (Figure 4A). In addition, independently of the C-terminal or N-terminal position of the Lys6 tag on the protein, the 15F8 corresponding epitope was less efficiently recognized following immobilization of the protein onto the partially hydrolyzed copolymer than on the nonhydrolyzed form, again from 1 μg/mL bioconjugate concentrations (data not shown). To understand why the epitope accessibility of the 15F8 mAb was lowered after grafting onto partially hydrolyzed copolymer, we compared the reactivity of 23A5, 3D8, and 15F8 mAbs in an ELISA competition assay using the unbound RH24 protein as a competitor. Classical competition curves were obtained for 23A5 and 3D8 mAbs, although they illustrated different efficiencies, probably due to different affinities, 4.1×10^8 M^{-1} and 3.6×10^9 M^{-1}, respectively (Figure 4B). Conversely, an inverted bell shape curve was obtained with 15F8 antibody which had an affinity similar to the 23A5 antibody (2.9×10^8 M^{-1}). Antigen concentrations from 1 μg/mL induced, intriguingly, a signal increase (Figure 4B). Overall, this strongly suggested that the 15F8 mAb recognized an epitope which was more efficiently displayed on the RH24K−MAMVE bioconjugate, probably as a result from several points of attachment of the protein on to the nonhydrolyzed polymer. This is in agreement with previous observations showing that a modification of the lysine residues of a recombinant p24 protein by a maleic anhydride monomer increased the affinity of a murine mAb (*15*) that recognized an epitope sharing eight residues with 15F8 mAb related epitope. Conversely, this epitope would be partially hidden either on bioconjugate defined by a tag-restricted attachment (hydrolyzed polymers) or at high concentration of noncoupled protein. These features correspond to a cryptic epitope. Indeed, (i) the 15F8 mAb was obtained by immunization with viral lysate, (ii) it recognized an epitope located within a pocket formed by the dimerization of two p24 N-terminal domains (*19*), (iii) the N-terminal composition of all p24 recombinant proteins is altered in comparison with the native p24 form, which may affect both N-terminal domain structure and self-association properties (*12*, *19*, *20*), and finally (iv) the p24 surface plasticity allows N−N and N−C intermolecular interfaces (*9*, *13*, *14*, *19*).

Identification of the Lysines Involved in the Coupling Reaction. The main results from the antigenic analysis were (i) that depending on the position of the polylysine tag, intrinsic lysines could react with

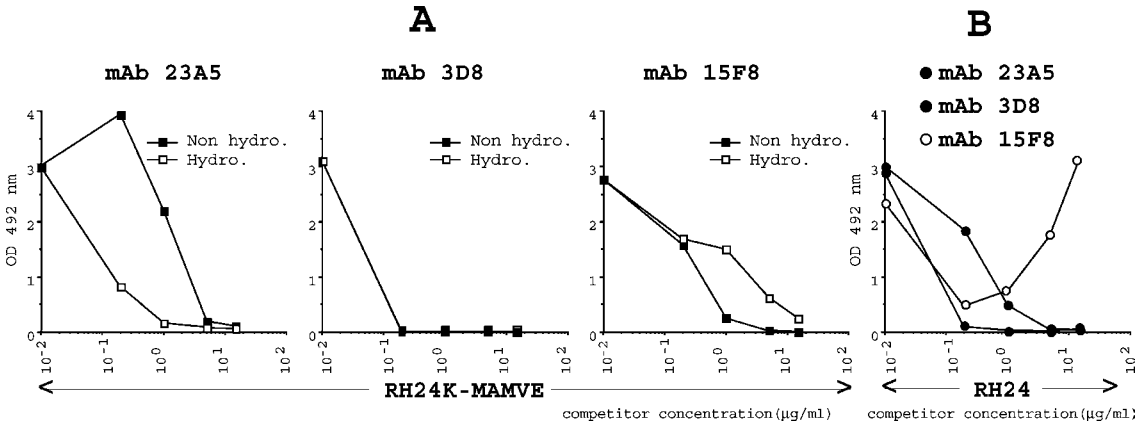


Figure 4. Influence of the hydrolysis of the polymer on epitope accessibility on the bioconjugate. (A) Competitive ELISA curves representing OD as a function of the bioconjugate concentration were obtained for the mAbs used at an optimal concentration. The two bioconjugates consisted of C-terminal Lys6-tagged recombinant protein RH24K, grafted onto nonhydrolyzed (■) or hydrolyzed (□) MAMVE copolymer. Hydrolysis of the polymer improved inhibition efficiency for the 23A5 mAb, had no effect for the 3D8 mAb (and 1G5, 1B2, and 13B5 mAbs, see text), and reduced inhibition efficiency for the 15F8 mAb. (B) Competitive ELISA curves representing OD as a function of the RH24 concentration were obtained for all mAbs. Classical inhibition curves were observed for 23A5 (●), 3D8 (●) (and 1G5, 1B2, and 13B5 mAbs), and an inverted bell shape curve was obtained for 15F8 (○) mAb.

Table 1. Quantitation of Free Amino Groups of the Unbound and Polymer-Bound Recombinant Proteins[a]

	RH24K		RH24-K158A		RK24H	
tested product[b]	$OD_{477\,nm}$	modification[c]	OD_{477nm}	modification[c]	OD_{477nm}	modification[c]
unbound proteins	747		806		863	
proteins grafted onto MAMVE	369	50.6	475	41.1	609	29.5
proteins grafted onto hydrolyzed MAMVE	593	20.6	713	11.5	750	13

[a] The presence of free amino groups was measured by detecting fluorescent products generated by the chemical reaction of fluorescamine with primary amines of the tested product (OD_{477nm}). [b] Tested product consisted of unbound proteins (RH24K, RH24K-K158A, RK24H) or proteins grafted onto nonhydrolyzed or partially hydrolyzed MAMVE copolymers. [c] The percentage of modification of the bound protein is defined as 100 − (fluorescence of bound protein × 100/fluorescence of unbound protein).

anhydride groups of MAMVE and (ii) that this involvement of internal lysines could be impeached by a decrease in the density of reactive groups of MAMVE via a controlled hydrolysis. To strengthen these conclusions, two additional methods were used to perform both quantitative and qualitative analyses.

A rough estimate of the number of lysines participating in the reaction was indirectly evaluated using fluorescamine, a compound which reacts specifically with primary amines to produce fluorescent products. Amine titers of three free p24-derived recombinant proteins and of their corresponding polymer bioconjugates were compared, and the percentages of protein modification were calculated (Table 1). The mean modification ratio of nonhydrolyzed polymer-based bioconjugates (40.4 ± 10.6) was 2.3 to 3.6 times higher than that obtained with the partially hydrolyzed ones (15.0 ± 4.9). Thus, irrespective of the recombinant protein tested, these results confirmed that the reduction of the amount of reactive groups onto the polymer reduced alterations of the grafted protein, as a consequence of a lowered involvement of intrinsic lysines in the grafting process. Nevertheless, the higher modification ratio in RH24K−MAMVE conjugates as compared to RK24H−MAMVE ones suggested that the C-terminal position of the tag might favor the involvement of intrinsic lysines, as confirmed by the RH24K−K158A mutant (Table 1).

To identify lysine residues which were involved in the coupling reaction and the direct incidence of the polymer partial hydrolysis on avoiding internal lysine reaction, we performed a comparative enzymatic digestion of the unbound C-terminally tagged RH24K protein and of the nonhydrolyzed and hydrolyzed polymer-based bioconjugates. Two different proteolytic enzymes were used, and the generated fragments were analyzed by MALDI-TOF mass spectrometry.

The three substrates were digested by *Staphylococcus aureus* protease V8, which cleaved on the C-terminal side of glutamic and aspartic acids residues in order to produce fragments containing lysines, and endoproteinase Lys-C which cleaved on the C-terminal side of lysines in order to directly check the involvement of an intrinsic lysine in the coupling reaction. Mass spectrometry analysis of peptides from protease V8 digestion of RH24K, RH24K−MAMVE, and RH24K−MAMVE-hydrolyzed allowed identification of three out of eight fragments with specific features (Table 2). First, the isolation of a 2363.2 kDa fragment, obtained exclusively after digestion of the free RH24K protein and identified as the tag-containing C-terminal portion of the protein, confirmed the direct involvement of the hexalysine tag in the grafting reaction. Second, the 1758.8 kDa fragment, absent exclusively from the RH24K−MAMVE bioconjugate and identified as the N-terminal part of the protein, suggested that the N-terminal amino group was involved in the coupling reaction onto a nonhydrolyzed polymer, but that such an involvement was avoided by partial hydrolysis of the polymer. Third, the detection of a 3291.7 kDa fragment, obtained after digestion of RH24K and RH24K−MAMVE-hydrolyzed but not RH24K−MAMVE and corresponding to the S1-E29 region, showed that the primary amino group of internal lysine 25 was involved in the grafting reaction onto the nonhydrolyzed polymer. This parasitic coupling could be avoided by partial hydrolysis of the polymer, as described above.

Mass spectrometry analysis of peptides from endoproteinase Lys-C digestion of all three substrates was indeed more informative concerning the involvement of

Table 2. Identification of Proteolysis Fragments of RH24K-Derived Bioconjugates by MALDI-TOF Analysis

protease	MM[a]	deduced sequences	amino acids position	RH24K bioconjugates[b]		
				cont	MAMVE	MAMVE.hy
V8	604.3	TINEEc	72−76	X	X	X
	677.3	KAFSPE	30−35	X	X	X
	1758.8	MRGSHHHHHHGSVDE	N-term(H_6)	X	○	X
	2363.2	MMTACQGVGGPG**KKKKKK**SVDE	(K_6)C-term	X	○	○
	2755.3	GATPQDLNTMLNTVGGHQAAMQML**K**E	46−71	X	X	X
	2779.5	TLLVQNANPDC**K**TIL**K**ALGPAATLEE[c]	188−213	X	X	X
	3291.7	SMVQNIQGQMVHQAISPRTLNAWV**K**VVEE[c]	1−29	X	○	X
	3665.8	WDRVHPVHAGPIAPGQMREPRGSDIAGTTSTLQE	80−113	X	X	X
Lys-C	111.7	RWIILGLN**K**	132−140	X	○	X
	1358.7	TLRAEQASQEV**K**	171−182	X	X	X
	1633.8	EPFRDYVDRFY**K**	159−170	X	○	X
	2032.9	NWMTETLLVQNANPDC**K**	183−199	X	○	X
	2073.1	IVRMYSPTSILDIRQGP**K**	141−158	X	○	X
	4232.0	AFSPEVIPMFSALSEGATPQDLNTMLNTVGGHQAAMQML**K**	30−70	X	○	X

[a] Molar mass (Da) of fragments observed in MALDI-TOF analysis and resulting from the digestion of the bioconjugates by *Staphylococcus aureus* V8 protease and endoproteinase Lys-C. [b] Bioconjugates consisted of free RH24K protein as a control (cont) or RH24K protein grafted onto nonhydrolyzed MAMVE (MAMVE) or hydrolyzed MAMVE (MAMVE.hy) copolymers; X and O indicated that the fragment was detected or not detected, respectively. [c] Partial proteolysis.

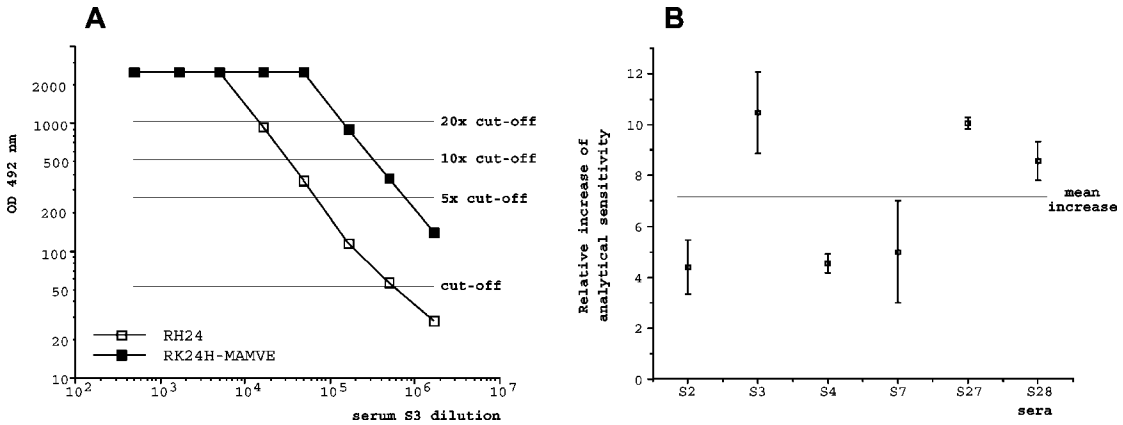


Figure 5. Relative analytical sensitivity of protein−polymer bioconjugate. (A) RH24 (□) or RK24H−MAMVE (■) antigens were coated onto microtiter plates (1 μg/mL), and anti-p24 antibodies were detected in direct ELISA, using serial dilutions of serum from one HIV-1 seropositive patient ranging from 1/500 to 1/1 665 000. OD as a function of the serum dilution is plotted. The cutoff value (mean + three standard deviations) was determined with pooled OD obtained from three control sera, from HIV-1 seronegative individuals, tested in the same conditions as in the HIV-1 assay. OD values corresponding to 5×, 10×, and 20× the cutoff value are indicated. (B) The relative increase in sensitivity was calculated for six HIV-1 positive sera tested as indicated above. For each serum, the indicated data corresponded to the mean ± two standard deviations of the increase calculated at 5×, 10×, and 20× the cutoff value. The overall mean increase is indicated by a horizontal lane.

several internal lysine residues in the coupling reaction onto nonhydrolyzed polymer (Table 2). Six clearly identified peptide fragments were generated after digestion of the RH24K protein. Five peptides were not detected after digestion of the bioconjugate based on a nonhydrolyzed polymer. This suggested an involvement of lysines 70 (N-terminal domain), 140 (flexible inter domain peptide), 158, 170, and 199 (C-terminal domain) in the formation of amide bonds with the copolymer. These results were in agreement with the antibody binding analysis showing the involvement of lysine158 (23A5 mAb analyses) and suggested the multipoint attachment process (15F8 mAb analyses) in grafting conditions with nonhydrolyzed polymer. Conversely, peptide T171-K182 was also observed after digestion of the bioconjugate based on a nonhydrolyzed polymer. It contained lysine K182 which according to the 3D structure (SwissPdbViewer v3.6) was poorly accessible and hence did not contribute to the grafting reaction. Finally, the six peptides obtained with the unbound protein were all identified after digestion of the RH24K−MAMVE-hydrolyzed bioconjugate, confirming the partial hydrolysis as a powerfull process to avoid the side-on grafting by intrinsic lysines.

CONCLUSION

We had previously demonstrated that the introduction of a six-lysine tag into a recombinant protein drastically improved the immobilization of the protein onto a copolymer, with the nature of the buffer and the nature, size, and reactivity of the polymer being minor parameters with respect to the control of the covalent immobilization (*5*, *7*). The present work demonstrated that the two main parameters involved in the conservation of the biological activity of the immobilized protein were the tag position and the number of reactive groups on the copolymer. This demonstration was achieved using bioconjugates derived from coupling of RK24H or RH24K, two recombinant proteins containing a N- or C-terminal six-lysine tag characterized by positive charges and primary amines, onto MAMVE, a copolymer bearing negative charges and anhydride moieties.

The alteration of the recognition by a specific monoclonal antibody of a bioconjugate consisting of a C-terminal Lys6-tagged p24 protein grafted onto MAMVE reflected a loss of accessibility of the corresponding epitope. The local protein conformational alteration was due to the involvement, in the grafting reaction, of an internal lysine with a spatial location close to the tag.

Such an alteration could be avoided by reducing the reactivity of the polymer, a parameter controlled by the partial hydrolysis of the anhydride moieties. These observations were confirmed by another molecular recognition process, i.e., the site specific digestion of the bioconjugates by protease V8 and endoproteinase Lys-C followed by mass spectrometry analysis. This technique highlighted the close relationships between the tag position, the position and accessibility of internal lysines, and the density of reactive anhydride groups of the copolymer.

So we have developed a process to engineer bioconjugates by using judiciously tagged recombinant proteins and polymers with a modulated reactivity. The interest of this methodology was illustrated by the using of RK24H grafted onto hydrolyzed MAMVE as a capture antigen in an ELISA test format. Serial dilutions (up to 2×10^6) of sera from six HIV-1 seropositive patients were used as sources of antibodies to compare the immunoreactivity of RK24H−MAMVE with the RH24 antigen classically used in immunoassay (*21*). A significant signal increase was observed with the bioconjugate as compared to the standard assay using RH24 (Figure 5). More precisely, the mean increase of analytical sensitivity was 7.2 ± 2.7, the minimal and maximal increase being 3.9 and 11.4, respectively. The evaluation of this bioconjugate with a panel of sera from 107 HIV-1 seropositive individuals at various stages of HIV infection, including two seroconversion panels, confirmed that such a protein−copolymer bioconjugate allowed the detection of antibody titers lower than the adsorbed protein (*6*).

Thus, based on this antigen(s)/antibody(s) model illustrating the local modifications due to the immobilization process and how to control/avoid them, we propose a versatile technology of oriented covalent immobilization of biologically active recombinant protein onto MAMVE polymer. The isolation of biologically active bioconjugates would be based on three main parameters consisting of introducing a tag of a defined composition (six lysines), in a predefined position (N- or C-terminal) with respect to the predicted or determined protein active site(s) and/or the intrinsic lysine content and/or accessibility, and using hydrolysis to control the density of reactive groups onto the polymer if the protein functional requirements imposed the tag position. To validate this concept with other proteins such as antigens, enzymes, or cell-binding ligands, a set of expression vectors was developed (*6*). More generally, it will be of interest to evaluate if the physicochemical parameters identified as critical in this protein−polymer system (refs 5−7, this study) would lead to a generic process of immobilization onto other negatively charged supports compatible with amide bond formation.

ACKNOWLEDGMENT

The authors are grateful to François Penin and Christophe Geourjon for helpful discussions, and Jennifer Burgess et Saint John Skilton for critical reading of the manuscript. We would like to thank Marcelle Sauzon for mass spectrometry analysis. L.A. is thankful to Fondation Mérieux for financial support.

LITERATURE CITED

(1) Monfardini, A., and Veronese, F. M. (1998) Stabilization of substances in circulation. *Bioconjugate Chem 9*, 418−450.

(2) Varga, C. M., Wickham, T. J., and Lauffenburger, D. A. (2000) Receptor-mediated targeting of gene delivery vectors: insights from molecular mechanisms for improved vehicle design. *Biotechnol. Bioeng. 70*, 593−605.

(3) Isosaki, K., Seno, N., Matsumoto, I., Koyama, T., and Moriguchi, S. (1992) Immobilization of protein ligands with Methyl Vinyl Ether-Maleic Anhydride copolymer. *J. Chromatogr. 597*, 123−128.

(4) Rao, S. V., Anderson, K. W., and Bachas, L. G. (1998) Oriented immobilization of proteins. *Mikrochim. Acta 128*, 127−143.

(5) Ladavière, C., Delair, T., Domard, A., Novelli-Rousseau, A., Mandrand, B., and Mallet, F. (1998) Covalent immobilization of proteins onto (maleic anhydride-*alt*-methyl vinyl ether) copolymers: enhanced immobilization of recombinant protein. *Bioconjugate Chem 9*, 655−661.

(6) Allard, L., Cheynet, V., Oriol, G., Mandrand, B., Delair, T., and Mallet, F. (2002) Versatile method for production and controlled polymer-immobilization of biologically active recombinant proteins. *Biotechnol. Bioeng. 80* (3), 341−348.

(7) Allard, L., Cheynet, V., Oriol, G., Veron, L., Merlier, F., Scémin, G., Mandrand, B., Delair, T., and Mallet, F. (2001) Mechanisms Leading to an Oriented Immobilization of Recombinant Proteins Derived from the p24 Capsid of HIV-1 onto Copolymers. *Bioconjugate Chem 12* (6), 972−979.

(8) Cheynet, V., Verrier, B., and Mallet, F. (1993) Overexpression of HIV-1 proteins in *Escherichia coli* by a modified expression vector and their one-step purification. *Protein Expression Purif. 4*, 367−372.

(9) Berthet-Colominas, C., Monaco, S., Novelli, A., Sibaï, G., Mallet, F., and Cusack, S. (1999) Head-to-tail dimers and interdomain flexibility revealed by the crystal structure of HIV-1 capsid protein (p24) complexed with a monoclonal antibody Fab. *EMBO J. 18*, 1124−1136.

(10) Arnaud, N., Cheynet, V., Oriol, G., Mandrand, B., and Mallet, F. (1997) Construction and expression of a modular gene encoding bacteriophage T7 RNA polymerase. *Gene 199*, 149−156.

(11) Ganachaud, F., Mouterde, G., Delair, T., Elaïssari, A., and Pichot, C. (1995) Preparation and characterization of cationic polystyrene latex particles of different aminated surface charges. *Polym. Adv. Technol. 6*, 480−488.

(12) Gitti, R. K., Lee, B. M., Walker, J., Summers, M. F., Yoo, S., and Sundquist, W. I. (1996) Structure of the amino-terminal core domain of the HIV-1 capsid protein. *Science 273*, 231−235.

(13) Gamble, T. R., Vajdos, F. F., Yoo, S., Worthylake, D. K., Houseweart, M., Sundquist, W. I., and Hill, C. P. (1996) Crystal structure of human cyclophilin A bound to the amino-terminal domain of HIV-1 capsid. *Cell 87*, 1285−1294.

(14) Gamble, T. R., Yoo, S., Vajdos, F. F., von Schwedler, U. K., Worthylake, D. K., Wang, H., McCutcheon, J. P., Sundquist, W. I., and Hill, C. P. (1997) Structure of the carboxy-terminal dimerization domain of the HIV-1 capsid protein. *Science 278*, 849−853.

(15) Ehrhard, B., Misselwitz, R., Welfle, K., Hausdorf, G., Glaser, R. W., Schneider-Mergener, J., and Welfle, H. (1996) Chemical modification of recombinant HIV-1 capsid protein p24 leads to the release of a hidden epitope prior to changes of the overall folding of the protein. *Biochemistry 35*, 9097−9105.

(16) Robert-Hebmann, V., Emiliani, S., Jean, F., Resnicoff, M., Traincard, F., and Devaux, C. (1992) Clonal analysis of murine B cell response to the human immunodeficiency virus type I (HIV1)-*gag* p17 and p25 antigens. *Mol. Immunol. 29*, 729−738.

(17) Janvier, B., Archinard, P., Mandrand, B., Goudeau, A., and Barin, F. (1990) Linear B-cell epitope of the major core protein of human immunodeficiency virus type 1 and 2. *J. Virol. 64*, 4258−4263.

(18) Monaco-Malbet, S., Berthet-Colominas, C., Novelli, A., Battaï, N., Piga, N., Cheynet, V., Mallet, F., and Cusack, S. (2000) Mutual conformational adaptations in antigen and antibody upon complex formation between an Fab and HIV-1 capsid protein p24. *Structure 8*, 1069−1077.

(19) Momany, C., Kovari, L. C., Prongay, A. J., Keller, W., Gitti, R. K., Lee, B. M., Gorbalenya, A. E., Tong, L., McClure, J., Ehrlich, L. S., Summers, M. F., Carter, C., and

Rossmann, M. G. (1996) Crystal structure of dimeric HIV-1 capsid protein. *Nat. Struct. Biol. 3*, 763−770.
(20) von Schwedler, U. K., Stemmler, T. L., Klishko, V. Y., Li, S., Albertine, K. H., Davis, D. R., and Sundquist, W. I. (1998) Proteolitic refolding of the HIV-1 capsid protein amino-terminus facilitates viral core assembly. *EMBO J. 17*, 1555−1568.
(21) Janvier, B., Mallet, F., Cheynet, V., Dalbon, P., Vernet, G., Besnier, J. M., Choutet, P., Goudeau, A., Mandrand, B., and Barin, F. (1993) Prevalence and persistance of antibody titers to recombinant HIV-1 core and matrix proteins in HIV-1 infection. *J. Acquir. Immune Defic. Syndr. 6*, 898−903.

BC034146+

Cross-Linked Microparticles as Carriers for the Delivery of Plasmid DNA for Vaccine Development

Sarah L. Goh, Niren Murthy, Mingcheng Xu, and Jean M. J. Fréchet*

Center for New Directions in Organic Synthesis, University of California, Department of Chemistry, Berkeley, California 94720-1460, and E. O. Lawrence Berkeley National Laboratory, Division of Materials Science, Berkeley, California 94720. Received September 8, 2003; Revised Manuscript Received February 26, 2004

Plasmid DNA was directly encapsulated into biocompatible polymer microparticles via radical polymerization in an inverse emulsion system. Acrylamide-based microspheres 0.2−1 μm in diameter were prepared using an acid-cleavable difunctional monomer. Retention of the DNA payload at physiological pH with complete release under acidic conditions at lysosomal pH was demonstrated. By trapping the plasmid DNA within the cross-linked microparticle, enzymatic degradation was prevented when exposed to serum nucleases. For vaccine development, these delivery vehicles were also investigated for their ability to generate immune responses when delivered to phagocytic cells of the immune system. Encapsulated plasmid DNA demonstrated immunostimulatory activity in macrophages, leading to cytokine secretion of IL-6 with a response ~40-fold higher than that achieved with DNA alone.

INTRODUCTION

Recent advances in polymeric drug delivery have focused on the encapsulation of biomolecules, such as protein, peptide, and DNA antigens, in microgel and hydrogel systems (*1*−*3*). DNA is a promising therapeutic for use in gene therapy applications (*4*) but may also be applicable as a coadjuvant for protein-based vaccines to stimulate the immune system (*5*, *6*). It is well-known that bacterial DNA is recognized by vertebrate immune systems as foreign and elicits a response, such as the release of cytokines or antimicrobial agents (*7*−*10*). Characteristics of bacterial DNA responsible for this activity are the higher frequency of CpG dinucleotides within the sequence as compared to vertebrate DNA, as well as the presence of unmethylated cytosine bases (*11*, *12*). Both plasmid DNA and short oligonucleotides have been shown to elicit an immune response in vertebrate systems (*12*−*15*); the incorporation of unmethylated bases is accomplished for oligonucleotides using the standard cytosine monomer during solid-phase chemistry, and for plasmid DNA through bacterial transformation. The sequence of these antigens can be selected to either provoke or prevent an immune response as desired (*14*−*17*). Delivery of immunostimulatory DNA results in the release of inflammatory triggers such as IL-6, IL-12, TNF-α, and IFN-γ. These cytokines are crucial in the maturation and activation of T cells and dendritic cells (*18*).

Encapsulation of plasmid DNA provides protection from nuclease degradation in the serum and can aid in directing its delivery to target cells, phagocytes. Current delivery vehicles for DNA-based therapeutics include cationic liposomes, lipoplexes, and polymer complexes (*19*−*31*). Many of these systems require the use of cationic polymers to entrap plasmid DNA via an electrostatic interaction with the negatively charged backbone, in addition to a neutral component to mitigate the toxicity effects. However, by using a cross-linked microparticle, we are able to encapsulate plasmids physically, rather than electrostatically, and without the use of polycations, which also allows this delivery system to be compatible with biomolecules of other charged states such as proteins. Previously, much attention has been focused on biodegradable systems, such as poly(lactic-*co*-glycolic acid), which release DNA via hydrolysis of the polymer chains (*32*−*37*). The ester backbone of these microparticles readily degrades under basic conditions and much more slowly under physiological pH. As the particles circulate throughout the body, a slow release of the encapsulated payload is observed. In contrast, we chose to design a polymer-based system that would exhibit minimal degradation in the serum at pH 7.4 until the particles encounter an acidic environment. Once internalized in lysosomal compartments of the desired cell type, the particles would rapidly degrade and deliver the encapsulated antigen.

Taking advantage of the pH differential between serum (pH 7.4) and the lysosome (pH 5.0), we have recently developed a new strategy for the delivery of protein-based vaccines using an acid-degradable microbead (*38*, *39*). Given their size of roughly 500 nm in diameter, the cross-linked microparticles should not be readily taken up by most cells. Instead, phagocytic cells such as macrophages and dendritic cells, which play a key role in the activation and maturation of the immune system, selectively ingest the microparticles, delivering the particle and its encapsulated payload to a lysosomal compartment within the cell. Cross-linked with a pH sensitive linker, the polymer microbead degrades in the acidic environment, resulting in an increase in osmotic pressure within the compartment and leading to lysosomal disruption, thus providing cytoplasmic delivery of the encapsulated biomolecule intact. Protein delivery using this microbead system has been successful at demonstrating class I antigen presentation with macrophages through the activation of cytotoxic T cells, a necessary step in vaccine development.

* To whom correspondence should be addressed. Tel (510) 643-3077. Fax (510) 643-3079. E-mail frechet@cchem.berkeley.edu.

10.1021/bc034159n CCC: $27.50 © 2004 American Chemical Society
Published on Web 04/28/2004

Therefore, it would be beneficial to combine the T cell activation ability of immunostimulatory DNA with these protein microparticles to further enhance the effectiveness of protein vaccines. Here, we extend the versatility of our acid-sensitive polymer microparticle by investigating the encapsulation and release of plasmid DNA in macrophages and examining the immunostimulatory effects as a next step in microparticle vaccine strategies.

MATERIALS AND METHODS

Reagents and Materials. β-Galactosidase reporter plasmid (*p*SV-β-gal vector, Promega, Madison, WI) was amplified by bacterial transformation with DH5α (Invitrogen, Carlsbad, CA) competent cells in Luria broth (Sigma, St. Louis, MO) and purified using a Qiagen Mega kit (Qiagen, Valencia, CA). Double-stranded DNA quantification assays were performed using PicoGreen (Molecular Probes, Eugene, OR). Absorbance and fluorescence readings were taken on a SPECTRAmax 190 and a SPECTRAmax Gemini XS, respectively, microplate reader (Molecular Devices, Sunnyvale, CA). Macrophage cell lines RAW 309.1CR and RAW 264.7 and 293T kidney cells (ATCC, Manassas, VA) were prepared by the University of California Tissue Culture/Media Facility by plating at the density indicated and then incubating overnight at 37 °C and 5% CO_2 before use.

Polyacrylamide Microparticle Synthesis. Microparticles were prepared by inverse microemulsion polymerization using a modification of a previously published procedure (*38*). β-Galactosidase reporter plasmid was dissolved in 400 μL of 300 mM sodium phosphate buffer pH 7.4 along with acrylamide (100 mg, 1.4 mmol), an acid labile cross-linker *N*,*N*′-bisacryloylbis(2-aminoethoxy)-[4-(1,4,7,10-tetraoxaundecyl)phenyl]methane (*38*) (**2**) (25 mg, 0.052 mmol, 3.6 mol %), and potassium persulfate (6 mg, 0.022 mmol) as the initiator. The organic phase consisted of 4 mL of hexane containing 120 mg of a 3:1 weight ratio of Span 80 (sorbitan monooleate) and Tween 80 (poly(ethylene glycol)−sorbitan monooleate). The emulsion was prepared by sonicating the two phases for 30 s using a Branson Sonifier 450 with an output setting of 2 and a duty cycle of 40%. Polymerization initiated by the addition of 25 μL of *N*,*N*,*N*′,*N*′-tetramethylethylenediamine (TMEDA) to the stirred mixture was continued for 10 min at room temperature before recovering the microparticles by centrifugation. The particles were washed twice with hexane to remove residual surfactant and then with acetone and finally dried under vacuum overnight. The particles were analyzed by scanning electron microscopy using a WDX ISI-ds130C instrument (Microspec Corporation, Inc.) at 15 kV.

Nondegradable beads encapsulating plasmid DNA were prepared in similar fashion, using the same wt % of cross-linker. For this set of microparticles, the aqueous phase consisted of acrylamide (100 mg, 1.4 mmol), *N*,*N*′-methylenebisacrylamide (25 mg, 0.162 mmol), and 0.50 mg of the β-galactosidase reporter plasmid in 400 μL of 300 mM sodium phosphate buffer pH 7.4 along with initiating species.

Determination of Plasmid DNA Loading. The plasmid DNA-loaded particles were washed by dispersing the particles in 300 mM sodium phosphate buffer at pH 7.4 at a concentration of 5 mg/mL using a series of sonication and vortex steps. The particles were collected as a pellet by centrifuging for 10 min. The wash supernatant was removed by pipet, and an equivalent volume of acidic buffer (pH 5.0, 300 mM acetic acid) was added to maintain the concentration. The sample was then heated overnight at 37 °C, and the hydrolyzed solution was analyzed for the concentration of double-stranded DNA using PicoGreen. All loadings were determined in triplicate.

pH Dependent Release. Plasmid-loaded microparticles were washed with 300 mM sodium phosphate pH 7.4, as described above, at a concentration of 5 mg/mL. The wash supernatant was removed, and either sodium phosphate buffer, pH 7.4, or acetic acid buffer, pH 5.0, was added, and the particle solutions were incubated at 37 °C. After the desired time point, the beads were collected by centrifugation and the supernatant removed. Any remaining particles were hydrolyzed at 37 °C overnight in acidic buffer, and both the supernatants and the hydrolyzed solutions were analyzed for the concentration of double-stranded DNA. All samples were performed in triplicate. The percent release was defined as the ratio of the concentration of DNA in the hydrolyzed solution compared to that found in both the hydrolyzed and supernatant solutions.

Microparticle Toxicity. RAW 309.1CR macrophages were plated at a cell density of 5×10^4/well in a 96-well format. Microparticles with DNA loadings of 0 (empty beads), 0.88, 2.14, and 4.29 μg plasmid DNA/mg bead were suspended in Dubelcco's Modified Eagle Medium (DMEM) at a concentration of 10 mg/mL. An aliquot of the bead solution was added to the cells, along with DMEM containing 10% fetal bovine serum (FBS) to give a final volume of 100 μL with an overall concentration of 5% FBS and 0.5 to 5 mg of beads/mL. After being incubated overnight at 37 °C and 5% CO_2, the supernatant was aspirated, and the cells were washed three times with DMEM to removed any remaining beads from the wells. To each well, 100 μL of DMEM + 10% FBS was added, and the cells were incubated for an additional 24 h. Toxicity was measured using the MTT assay (*40*); briefly, the supernatant was aspirated, and 100 μL of DMEM + 10% FBS along with 20 μL of a 5 mg/mL solution of MTT (3-(4,5-dimethylthiazol-2-yl)-2,5-diphenyl-2*H*-tetrazolium bromide) in medium were added to each well. The cells were incubated for 4 h at 37 °C and 5% CO_2, after which time the supernatant was removed, and the MTT crystals were dissolved in 200 μL of dimethyl sulfoxide (DMSO). The purple solutions (10 μL) were further diluted with 190 μL of DMSO and 25 μL of a glycine buffer (0.1 M glycine, 0.1 M NaCl, pH 10.5). The concentration of MTT was determined by measuring the UV absorbance at 570 nm.

Nuclease Stability of Encapsulated Plasmid. Microparticles with a loading of 2.14 μg DNA/mg bead were suspended in DMEM + 10% FBS to give a final concentration of 5 mg of beads/mL. The solutions were incubated at 37 °C for the desired time (0, 0.5, 1, and 2 h), and then the microparticles were collected by centrifugation. The supernatant was decanted, and the pelleted beads were washed with 300 mM sodium phosphate buffer pH 7.4 to remove the color from residual medium, as well as any fragmented DNA. Finally, the microparticles were incubated overnight at 37 °C in 300 mM acetic acid buffer pH 5.0 to fully release any remaining plasmid DNA. The stability for a given time point was calculated as the concentration of double-stranded DNA in the hydrolyzed beads compared to the concentration determined at 0 h. DNA released from the exposed beads was analyzed by agarose gel electrophoresis.

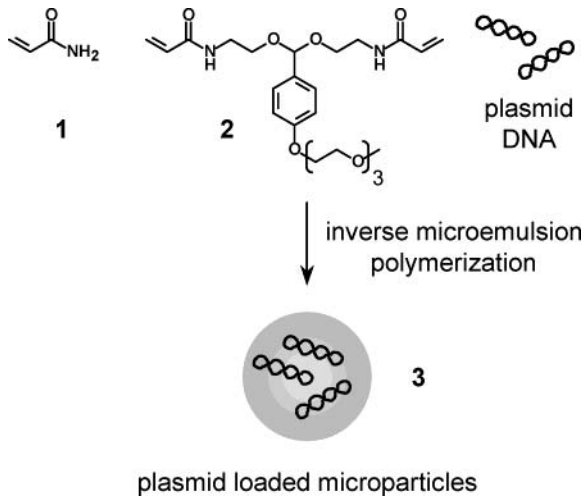
Fluorescence Microscopy. Microscopy studies were performed with both degradable and nondegradable, dextran-encapsulated microparticles. For degradable

beads, fluorescein-labeled dextran (5 mg, FITC-dextran, MW 70 kDa, Molecular Probes) was encapsulated using the inverse emulsion polymerization procedure described above using the acid sensitive cross-linker, *N*,*N*′-bisacryloylbis(2-aminoethoxy)-[4-(1,4,7,10-tetraoxaundecyl)phenyl]-methane (*38*). FITC-dextran microparticles were also prepared using 25 mg of *N*,*N*′-methylenebisacrylamide, a nondegradable cross-linker. Scanning electron micrographs of both samples showed spherical beads of similar size to the DNA-loaded microparticles. RAW 264.7 cells were prepared in a 24 well plate with cover slips at a density of 3×10^5 cells/well. The beads were suspended in DMEM + 10% FBS (5 mg/mL), and the solution delivered to the cells with additional medium to give a final volume of 1 mL and a final concentration of 0.25 mg beads/mL. After incubation overnight, the supernatant was aspirated, and the cells were washed five times with DMEM. DMEM + 10% FBS (1 mL) was then added to the cells, and they were allowed to grow for another 24 h. The cells were washed five times with phosphate-buffered saline (PBS, Gibco) and fixed to the cover slips by the addition of 1 mL per well of a paraformaldehyde solution. The cells were incubated for 10 min at room temperature and then washed twice with PBS. To prepare the paraformaldehyde solution, 1.5 g of paraformaldehyde was dissolved in 20 mL of H_2O and 20 μL of 10 M NaOH that was previously equilibrated to 56 °C. The solution was cooled to room temperature, and 25 mL of H_2O and 5 mL of 3 M sodium phosphate were added. The resulting solution was brought up to pH 10.5 using 10 M NaOH, sterilized by passing it through a 0.22 μm filter, and stored at 4 °C until needed. Micrographs were taken with a Nikon Eclipse TE300 inverted microscope, equipped with a Nikon Plan Fluor 40×/0.60 objective and the appropriate excitation/emission filters (494 nm/519 nm).

Transfection Studies. Plasmid-encapsulated beads (60 mg) were hydrolyzed by incubating them overnight in 3 mL of 300 mM acetic acid pH 5.0. The resulting plasmid was recovered by first passing the hydrolyzed solution through a Nap-25 column (Amersham, Piscataway, NJ) that had been equilibrated with water. Fractions displaying a UV absorbance at 260 nm were reduced in volume and then isolated again using a Qiagen Tip-20. 293T kidney cells were plated at a density of 6×10^4 cells/well in a 24-well plate. To each well, 500 μL of DMEM + 10% FBS was delivered along with 100 μL of a solution containing either original or isolated plasmid DNA (0.25 or 0.5 μg total) in OPTI-MEM (Gibco), in which the DNA had been complexed with 5 μg of Lipofectamine 2000 (Invitrogen) for 15 min. Control wells contained either medium alone or DNA without transfection agent. The cells were incubated overnight at 37 °C and 5% CO_2. The cells were aspirated, and 400 μL of Z buffer (*41*) was delivered to each well and incubated for an additional 6 h. The supernatant was transferred to a 96-well plate, and β-galactosidase activity was determined by monitoring the UV absorbance of the hydrolyzed phenolate at 570 nm. The Z buffer was made according to literature (*41*): 100 μM 2-mercaptoethanol, 9 mM $MgCl_2$, 0.125% NP-40 (Sigma), and 0.15 mM sodium chlorophenol red β-galactopyrandoside (CPRG, CalBioChem, San Diego, CA) in PBS.

IL-6 ELISA. A 96-well plate of RAW 264.7 macrophages at a density of 2×10^4 cells/well was incubated overnight with 100 μL of a 5 mg/mL solution of microparticles in DMEM + 10% FBS. Microparticles with DNA loadings of 0 (empty beads), 0.88, 2.14, 4.29 μg plasmid DNA/mg bead made with degradable and nondegradable cross-linkers were analyzed. Control wells consisted of untreated cells and cells with plasmid DNA alone. The media was diluted 5-fold and analyzed using an IL-6 ELISA kit (Pierce, Rockford, IL). Absorbance values were measured at $\lambda = 450$ nm and corrected using $\lambda = 550$ nm as a background reference. IL-6 concentrations were calculated using a standard curve.

Scheme 1. Synthesis of Plasmid-Loaded Microparticles



RESULTS AND DISCUSSION

Synthesis of Polyacrylamide Microparticles. Microparticles prepared using inverse microemulsion polymerization (*42*, *43*) were successfully loaded with plasmid DNA. The β-galactosidase reporter plasmid (pSV-β-gal, Promega, 6820 bp) was dissolved in aqueous buffer along with acrylamide **1** and 3.6 mol % of a bisacrylamide acetal cross-linker **2** (Scheme 1). This cross-linker was previously shown to be readily incorporated with acrylamide under free radical polymerization conditions to produce protein-loaded microparticles (*38*). The aqueous phase was dispersed in hexane containing 3% (w/v) surfactants (Span 80/Tween 80) using sonication. These neutral surfactants do not coordinate the phosphate backbone of DNA, as would ionic surfactants, thus resulting in disruption of the inverse emulsion. The radical polymerization was initiated using potassium persulfate and TMEDA, effectively trapping the plasmid inside the cross-linked beads, **3**. Following the synthesis, plasmid-loaded particles **3** were washed with excess solvent and dried under vacuum, with yields ranging from 50 to 85%. While these polymerization conditions were mild enough for protein encapsulation as shown previously, further analyses were performed to validate the stability and integrity of the encapsulated plasmid DNA.

The isolated microbeads were analyzed in the dry state using scanning electron microscopy (Figure 1). Ranging from 0.2 to 1 μm in diameter, plasmid-loaded microparticles displayed similar surface characteristics to beads that contained no DNA. This size is appropriate for targeting delivery to macrophages, which readily ingest particles of 0.5−1 μm (*44*).

Microparticle Loadings and DNA Integrity. The concentration of plasmid DNA in the microparticles was determined by first washing the microparticles in 300 mM sodium phosphate at pH 7.4. A small amount of plasmid DNA is detected in this washing step, corresponding to the removal of DNA that is physisorbed to the surface of the microparticle. The sample was then heated overnight at 37 °C in an acidic buffer to fully

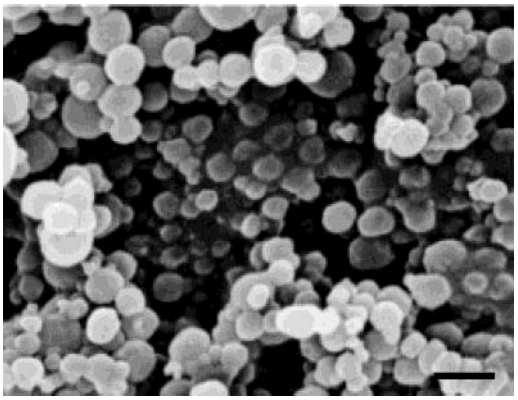


Figure 1. Scanning electron micrograph of plasmid-loaded microparticles. 15 kV, 20 000 ×. Scale bar represents 500 nm.

Table 1. Plasmid DNA Loading in Microparticles

initial DNA loading (μg/mg polymer)	observed loading (μg/mg polymer)	encapsulation efficiency, %
2.0	0.88 ± 0.15	44
4.0	2.14 ± 0.15	53
8.0	4.29 ± 0.17	54

hydrolyze the acetal cross-links, releasing linear polyacrylamide chains, a tri(ethylene glycol)-functionalized benzaldehyde, and plasmid. The concentration of double-stranded DNA in the acidic buffer was determined using PicoGreen (Table 1).

An initial loading of 2.0 μg/mg of plasmid DNA on a 125 mg scale was used in the synthesis of the acid-degradable microparticles. After the beads were washed and isolated, a loading of 0.88 μg of DNA/mg of polymer was determined, giving an encapsulation efficiency of 44%. Increasing the concentration of plasmid in the polymerization mixture to 4.0 and 8.0 μg/mg produced higher DNA loadings within the resulting microparticles. While the encapsulation efficiency remained fairly constant, the amount of DNA found encapsulated in the particles roughly doubled for each 2-fold increase in the initial concentration, with the largest loading being slightly higher than those reported with PLGA particles of comparable size (*36*, *37*).

Having successfully encapsulated plasmid DNA in microparticles, we next sought to verify that the structure of the released DNA remained intact. Should the DNA be degraded into smaller fragments during the course of the polymerization procedure, the fragments could diffuse out of the microparticle prior to phagocytosis and hydrolysis. Also of interest is preserving the tertiary structure of the plasmid. Possible detrimental conditions prevailing during the microparticle polymerization and subsequent acidic degradation include sonication to form the emulsion, reactions involving free radicals, and the use of a treatment at pH 5.0, 37 °C, for 18 h. In other microparticle formulations, plasmid DNA has been shown to be sheared during sonication in addition to being susceptible to cleavage and degradation during homogenization or drying steps (*37*, *45*, *46*). Therefore, DNA recovered from our polyacrylamide microparticles after acidic cleavage of the acetal cross-linkers was analyzed by agarose gel electrophoresis to investigate its integrity (Figure 2). The original plasmid DNA, prepared by bacterial transformation, is shown in lane 2; the upper band corresponds to the open circular form of isolated plasmid DNA and the lower to the supercoiled structure, as it is more compact and therefore migrates faster through the agarose gel. After the polymerization and hydrolysis steps, the plasmid DNA is composed mostly

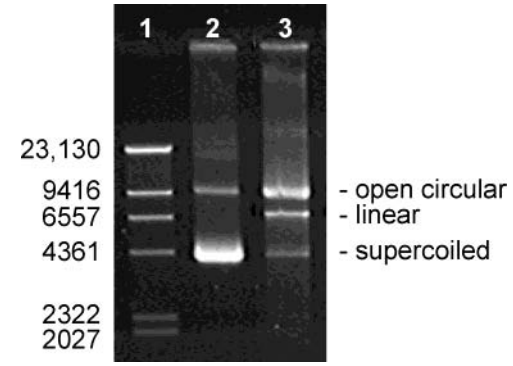


Figure 2. Analysis of released DNA by agarose gel electrophoresis. Lane 1: Lambda Hind III ladder, fragment size (bp) given to the left. Lane 2: original plasmid DNA. Lane 3: DNA recovered from microbeads after acid hydrolysis. Conditions: 1% agarose, 75 V for 1 h, stained with ethidium bromide.

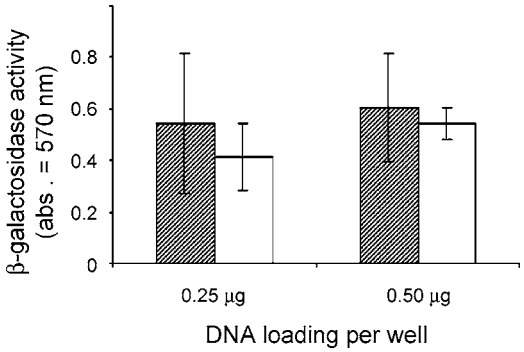


Figure 3. Transfection of 293T Cells. β-Galactosidase activity was measured as the absorbance of hydrolyzed CPRG for control (shaded) and recovered DNA (open), complexed with Lipofectamine 2000.

of the open circular form, with some linear and supercoiled structures as also seen in lane 3. A double restriction digest of each of these samples yielded identical linear fragments, another indication that the double-stranded DNA remained unchanged during the polymerization procedure and that only the tertiary structure is affected by the processing conditions. While the tertiary structure of plasmid DNA has not been studied with respect to its immunostimulatory efficiency, it has been shown that open circular and supercoiled DNA have roughly equivalent transfection capabilities (*47*, *48*).

To verify the activity of the plasmid DNA, the transfection ability of the recovered plasmid was evaluated using 293T kidney cells. Control DNA, as well as plasmid recovered from hydrolyzed microparticles, was complexed with Lipofectamine 2000, a commercially available transfection agent. From the agarose gel analysis described above, the isolated plasmid is mostly in the open circular form, whereas the original sample of DNA is mostly supercoiled (Figure 2). Both of these structures are capable of undergoing transcription in cells, but not, however, the linear species that are present in the recovered plasmid (*47*, *48*). Figure 3 depicts the transfection results of the DNA complexes with 293T kidney cells. Untreated cells or wells with DNA alone showed no β-galactosidase activity. For DNA−Lipofectamine assemblies, there is a minor decrease in the transfection ability of the isolated plasmid compared to the original DNA vector, most likely due to the presence of a small amount of linear plasmid in the isolated DNA sample. Encapsulated DNA is capable of transfection, as only the tertiary structure of the plasmid is altered by the polymerization and hydrolysis procedures. The inverse

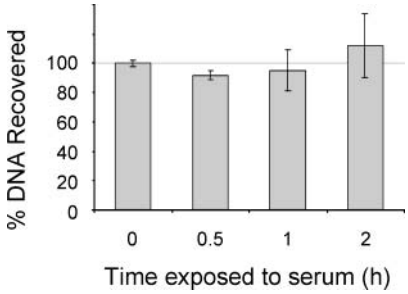


Figure 4. Nuclease stability of plasmid-encapsulated microparticles.

microemulsion polymerization technique described herein is compatible with both DNA and proteins (*38*), making possible future studies in vaccine delivery involving the encapsulation of biomolecules that vary by function (specific T cell activation, immunostimulation, or antisense) and classification (protein, DNA, or RNA).

Nuclease Stability of Encapsulated Plasmid. Stability of the microparticles at pH 7.4 is also important as the polymer scaffold functions to protect the encapsulated plasmid. Within 5 min of exposure to serum nucleases, plasmid DNA begins to break down rapidly and is completely degraded within 1 h (*49*); at pH 7.4, however, the DNA does not diffuse out of the microparticle as demonstrated in the release experiments. The pores of the microparticle are small enough to keep the plasmid DNA encapsulated until the delivery vehicle reaches the acidic environment of the phagolysosome. The serum stability of the plasmid microparticles was investigated to determine whether nucleases could enter the microparticle and degrade the DNA. To demonstrate that the microparticles actually protect the encapsulated DNA, the beads were exposed to serum nucleases by combining them with Dubelcco's modified Eagle medium containing 10% fetal bovine serum at 37 °C (Figure 4). The amount of DNA remaining in the beads was analyzed. Any degradation of the plasmid by the nucleases present in this medium would result in small, linear fragments. Since short DNA sequences cannot be retained, they would readily diffuse out of the particles. However, no appreciable decrease in the concentration of double-stranded DNA was observed with the plasmid-encapsulated particles and thus, no degradation of the DNA was observed over a period of 2 h. Additionally, when analyzed by agarose gel electrophoresis, no change was detected for the DNA recovered from microparticles that had been exposed to serum nucleases.

The toxicity of the beads was tested in RAW 309 macrophages. The cells were >65% viable for all samples tested, even at concentrations as high as 5 mg of beads/mL. There were minimal toxicity differences between polymer microparticles and plasmid-loaded particles. While polyacrylamide itself is nontoxic, the effects of the aldehyde byproducts of the degradation have yet to be examined (*50*).

pH Dependent Release of Plasmid Encapsulated Microparticles. The pH dependence of DNA release from the microparticles was evaluated by incubating the microbeads at 37 °C in pH 7.4 sodium phosphate buffer or pH 5.0 acetic acid buffer. After the desired time point, the beads were collected by centrifugation and the supernatant analyzed for DNA (Figure 5). At physiological pH, there was an initial burst release of 10%, indicating that some of the DNA is not fully encapsulated within the beads. Additional incubation at neutral pH showed no further release of DNA since the pores of the

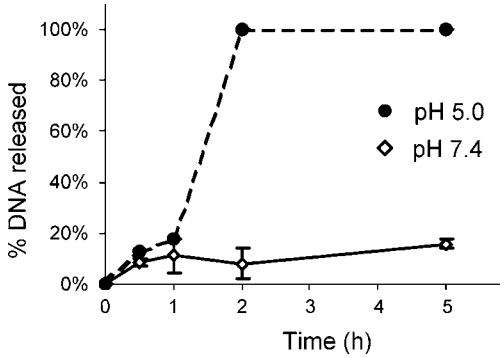


Figure 5. pH dependent release of plasmid DNA from microparticles at 37 °C.

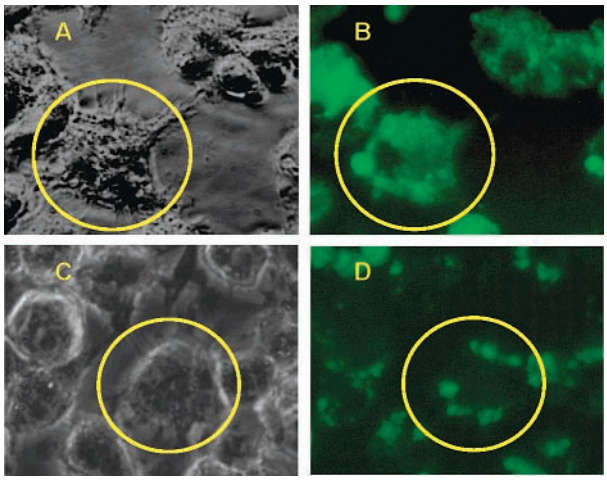


Figure 6. Fluorescence microscopy of macrophages. Phase contrast and fluorescence images of dextran-loaded microparticles with a degradable (A, B, respectively) and a nondegradable (C, D) cross-linker.

cross-linked microparticles are too small to allow for diffusion of the plasmid out of the beads. Presumably then, the microparticles would not release the DNA payload until the microparticle hydrolyzed in an acidic environment.

Under acidic conditions, however, full release of the DNA is achieved within 2 h at pH 5. The hydrolysis kinetics of acetal cross-linkers similar to **2** have been measured previously with a half-life of 24 h at pH 7.4 and only 5 min at pH 5.0 (*39*). The release of plasmid from the microbeads is slower, as would be expected given their incorporation in a cross-linked network.

Fluorescence Microscopy Studies. A key issue with DNA delivery is its distribution within the cellular environment. To examine where the payload is delivered in a macrophage, polyacrylamide microparticles were prepared encapsulating fluorescently (FITC) labeled dextran, MW 70 kDa. Dextran was labeled instead of DNA because fluorescent tags for DNA may dissociate and intercalate into cellular DNA, giving misleading results as to the location of the encapsulated biomolecule. Particles with degradable and nondegradable cross-linkers were prepared and added to RAW 264.7 macrophages. After incubation overnight, the cells were examined by phase contrast mode and with fluorescein excitation (Figure 6). Cells alone showed no autofluorescence. In contrast, cells treated with beads containing the acid sensitive cross-linker showed a diffuse fluorescence in the cytoplasm, (B), indicating that the acid labile linkage degraded in the lysosome and released the fluorescently labeled payload into the cytoplasm with no

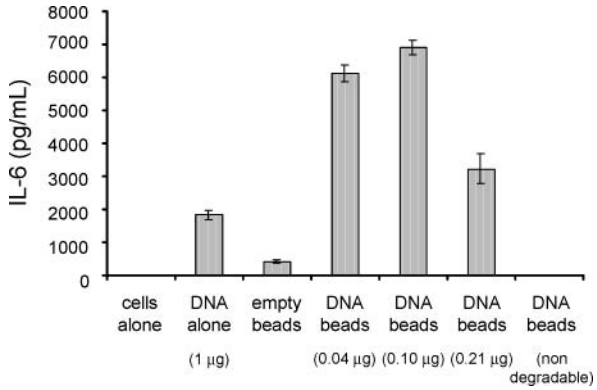


Figure 7. Interleukin-6 ELISA. Below each bar in the graph is the total mount of plasmid DNA added per well.

migration of the FITC-dextran to the nucleus. Nondegradable beads made with *N*,*N*′-methylenebisacrylamide as the cross-linker showed a much more punctate fluorescence (D), indicating that the FITC-dextran remained localized in the lysosome of the cell. The nondegradable beads are readily phagocytosed by the macrophages, but are sequestered in the lysosome as the particles possess no synthetic switch to initiate lysosomal escape.

IL-6 ELISA. Differences between bacterial and vertebrate DNA are recognized by vertebrate immune systems such that bacterial DNA will invoke a general immune response that can be characterized by the secretion of interleukins, radicals, and prostraglandins. The cytosine residues of bacterial DNA are not methylated as they are in vertebrates. In addition, there is a 6-fold increase in the percentage of CG motifs in bacterial DNA, typically ∼1.2% in vertebrate and 6−7% in bacterial plasmids (*15*). The β-galactosidase plasmid sequence used in these studies contains 6.7% of the CpG dinucleotide and therefore should be capable of inducing an immune response in macrophages.

This response is mediated by a Toll-like receptor, TLR9, which is thought to be located within the lysosome or on the cell surface (*51*−*53*). Receptor binding of TLR9 on the cell surface can only be accomplished by DNA that is located on the outside of the particle, as there is negligible release observed at neutral pH in the extracellular environment. However, if the TLR9 is recruited to the lysosome, then an immunostimulatory response should be observed when plasmid encapsulated microparticles are delivered to cells, as it has been discussed above that the DNA will be released when it encounters the acidic environment of the phagolysosome. Upon interaction of the encapsulated plasmid with TLR9, macrophages secrete IL-6 to mediate the growth and differentiation of T cells, a vital component of vaccine treatment.

To examine the immunostimulatory properties of the plasmid-loaded microparticles, RAW 264.7 macrophages were incubated overnight with 1 μg of naked plasmid or 50 μg of plasmid microbeads of various loadings. Nondegradable beads with an initial loading of 2.0 μg/mg of plasmid DNA were also tested. It was not possible to determine the true loading of these microparticles, as they are not capable of acidic degradation so the DNA cannot be recovered. Assuming a similar encapsulation efficiency as with the degradable system, the final loading of these beads should correspond to the medium-loaded beads in which 0.10 μg of plasmid were delivered per well. The supernatant was analyzed for interleukin-6 (IL-6) production using an ELISA kit (Figure 7). Beads encapsulating plasmid DNA successfully induced the secretion of IL-6, with a general trend of higher loaded plasmid beads producing larger amounts of IL-6. The maximum response is observed when just 0.1 μg of encapsulated DNA is delivered per well using beads with a loading of 2.14 μg/mg and resulted in an IL-6 response of 6890 pg/mL, which is 3.75 times that when 1 μg of DNA alone was added. Treatment with more highly loaded particles, 0.2 μg of DNA per well, did not produce an increased cytokine response, indicating that a response to DNA loading had reached a maximum. Untreated cells secreted a minimal amount of IL-6. Furthermore, negligible IL-6 concentrations were measured when unloaded beads were delivered to the cells, indicating that the polymeric microparticles themselves do not induce IL-6 production. With nondegradable particles, there was minimal immunostimulation as indicated by the ELISA results. Because the plasmid DNA is trapped inside the beads, it is not available to be recognized by Toll-like receptors either on the cell surface or within the lysosomal compartment. Only when the microparticles are capable of releasing the encapsulated DNA inside the lysosome is an enhanced response observed.

CONCLUSION

The flexibility of the inverse microemulsion polymerization allows for the encapsulation of both plasmid and protein to produce microparticles for vaccine development. The polymer scaffold serves to protect the DNA from nuclease degradation and prevents unwanted release at physiological pH. The particles are readily phagocytosed by macrophages and induce an immune response, resulting in IL-6 secretion. Knowing that the plasmid DNA released from the microparticles is capable of undergoing transfection and that, according to fluorescent microscopy studies using dextran-encapsulated microparticles, a bioactive payload is directed to the cytoplasm of macrophages, further improvements in the polymeric carrier are required to affect nuclear delivery, which would allow gene therapy applications to be accessible with this degradable microparticle system. In addition, further experiments are underway to develop multicomponent microparticles containing both protein for antigen-specific T cell activation and immunostimulatory DNA for general T cell stimulation for enhanced vaccine capabilities.

ACKNOWLEDGMENT

Financial support of this research by the United States Department of Energy, Basic Energy Sciences, Biomolecular Program at Lawrence Berkeley National Laboratory is acknowledged with thanks (Grant No. DE-AC03-76SF00098), and partial support of the biological studies by the National Institutes of Health (Grant RO1EB00-2047) is acknowledged with thanks. The Center for New Directions in Organic Synthesis is supported by Bristol-Myers Squibb as a Sponsoring Member and Novartis as a Supporting Member. We thank Tom Barber for his assistance with the fluorescent microscopy studies, and Ann Fischer at the University of California Tissue Culture/Media Facility and Kelly Flook for assistance with cell studies.

LITERATURE CITED

(1) Prokop, A., Kozlov, E., Carlesso, G., and Davidson, J. M. (2002) Hydrogel-Based Colloidal Polymeric System for Protein and Drug Delivery: Physical and Chemical Characterization, Permeability Control and Applications. *Adv. Polym. Sci. 160*, 119−173.

(2) Galaev, I. Y., and Mattiasson, B. (1999) "Smart" Polymers and What They Could Do in Biotechnology and Medicine. *Trends Biotechnol. 17*, 335−340.

(3) Park, H., and Park, K. (1996) Hydrogels in Bioapplications. *ACS Symp. Ser. 627*, 2−10.

(4) Amara, R. R., Villinger, F., Altman, J. D., Lydy, S. L., O'Neil, S. P., Staprans, S. I., Montefiori, D. C., Xu, Y., Herndon, J. G., Wyatt, L. S., Candido, M. A., Kozyr, N. L., Earl, P. L., Smith, J. M., Ma, J.-L., Grimm, B. D., Hulsey, M. L., Miller, J., McClure, H. M., McNicholl, J. M., Moss, B., and Robinson, H. L. (2001) Control of a Mucosal Challenge and Prevention of AIDS by a Multi Protein DNA/MVA Vaccine. *Science 292*, 69−74.

(5) Merad, M., Sugie, T., Engleman, E. G., and Fong, L. (2002) in Vivo Manipulation of Dendritic Cells to Induce Therapeutic Immunity. *Blood 99*, 1676−1682.

(6) Davila, E., and Celis, E. (2000) Repeated Administration of CpG ODN with Peptide/Protein Immunization Results in Enhanced CTL Response. *J. Immunol. 165*, 539−547.

(7) Lipford, G. B., Heeg, K., and Wagner, H. (1998) Bacterial DNA as Immune Cell Activator. *Trends Microbiol. 6*, 496−500.

(8) Klinman, D. M., Yi, A.-K., Beaucage, S. L., Conover, J., and Krieg, A. M. (1996) CpG Motifs Present in Bacterial DNA Rapidly Induce Lyphocytes to Secrete Interleukin 6, Interleukin 12, and Interferon Gamma. *Proc. Natl. Acad. Sci. 93*, 2879−2883.

(9) Messina, J. P., Gilkeson, G. S., and Pisetsky, D. S. (1991) Stimulation of in Vitro Murine Lymphocyte Proliferation by Bacterial DNA. *J. Immunol. 147*, 1759−1764.

(10) Gilkeson, G. S., Grudier, J. P., Karounos, D. G., and Pisetsky, D. S. (1989) Induction of Anti-Double Stranded DNA Antibodies in Normal Mice by Immunization with Bacterial DNA. *J. Immunol. 142*, 1482−1486.

(11) Weiner, G. J. (2000) The Immunobiology and Clinical Potential of Immunostimulatory CpG Oligonucleotides. *J. Leukocyte Biol. 68*, 455−463.

(12) Sparwasser, T., Koch, E.-S., Vabulas, R. M., Heeg, K., Lipford, G. B., Ellwart, J. W., and Wagner, H. (1998) Bacterial DNA and Immunostimulatory CpG Oligonucleotides Trigger Maturation and Activation of Murine Dendritic Cells. *Eur. J. Immunol. 28*, 2045−2054.

(13) Yasuda, K., Ogawa, Y., Kishimoto, M., Takagi, T., Hashida, M., and Takakura, Y. (2002) Plasmid DNA Activates Murine Macrophages to Induce Inflammatory Cytokines in a CpG Motif-Independent Manner by Complex Formation With Cationic Liposomes. *Biochem. Biophys. Res. Commun. 293*, 344−348.

(14) Cho, H. J., Takabayashi, K., Cheng, P.-M., Nguyen, M.-D., Corr, M., Tuck, S., and Raz, E. (2000) Immunostimulatory DNA-Based Vaccines Induce CTL Activity by a T-Helper Cell-Independent Mechanism. *Nat. Biotechnol. 18*, 509−514.

(15) Krieg, A. M., Yi, A.-K., Matson, S., Waldschmidt, T. J., Bishop, G. A., Teasdale, R., Koretzky, G. A., and Klinman, D. M. (1995) CpG Motifs in Bacterial DNA Trigger Direct B−Cell Activation. *Nature 374*, 546−549.

(16) Shen, W., Waldschmidt, M., Zhao, X., Ratliff, T., and Krieg, A. M. (2002) Antitumor Mechanisms of Oligodeoxynucleotides with CpG and PolyG Motifs in Murine Prostate Cancer Cells: Decrease of NF−KB and AP-1 Binding Activities and Induction of Apoptosis. *Antisense Nucleic Acid Drug Dev. 12*, 155−164.

(17) Krieg, A. M., Wu, T., Weeratna, R., Efler, S. M., Love-Homan, L., Yang, L., Yi, A.-K., Short, D., and Davis, H. L. (1998) Sequence Motifs in Adenoviral DNA Block Immune Activation by Stimulatory CpG Motifs. *Proc. Natl. Acad. Sci. 95*, 12631−12636.

(18) Hirano, T. Interleukin-6 (1998) *The Cytokine Handbook* (Thomson, A., Ed.) 3rd ed., Chapter 8, Academic Press, San Diego.

(19) Akinc, A., Lynn, D. M., Anderson, D. G., and Langer, R. (2003) Parallel Synthesis and Biophysical Characterization of a Degradable Polymer Library for Gene Delivery. *J. Am. Chem. Soc. 125*, 5316−5323.

(20) Choi, J. S., MacKay, J. A., and Szoka, F. C., Jr. (2003) Low pH Sensitive PEG Stabilized Plasmid Lipid Nanoparticles: Preparation and Characterization. *Bioconjugate Chem. 14*, 420−429.

(21) Kihara, F., Arima, H., Tsutsumi, T., Hirayama, F., and Uekama, K. (2003) in Vitro and in Vivo Gene Transfer by an Optimized α-Cyclodextrin Conjugate with Polyamidoamine Dendrimer. *Bioconjugate Chem. 14*, 342−350.

(22) Kunath, K., van Harpe, A., Fischer, D., and Kissel, T. (2003) Galactose-PEI-DNA Compelxes for Targeted Gene Delivery. *J. Controlled Release 88*, 159−172.

(23) Arbós, P., Wirth, M., Arangoa, M. A., Gabor, F., and Irache, J. M. (2002) Gantrez AN as a New Polymer for the Preparation of Ligand-Nanoparticle Conjugates. *J. Controlled Release 83*, 321−330.

(24) Erni, C., Suard, C., Freitas, S., Dreher, D., Merkle, H. P., and Walter, E. (2002) Evaluation of Cationic Solid Lipid Microparticles as Synthetic Carriers for the Target Delivery of Macromolecules to Phagocytic Antigen-Presentation Cells. *Biomaterials 23*, 4667−4676.

(25) Gregoriadis, G., Bacon, A., Caparros-Wanderley, W., and McCormack, B. (2002) A Role for Liposomes in Genetic Vaccination. *Vaccine 20*, B1−B9.

(26) McAllister, K., Sanzani, P., Adam, M., Cho, M. J., Rubinstein, M., Samulski, R. J., and DeSimone, J. M. (2002) Polymeric Nanogels Produced Via Inverse Microemulsion Polymerization as Potential Gene and Antisense Delivery Agents. *J. Am. Chem. Soc. 124*, 15198−15207.

(27) Lee, M., Nah, J.-W., Kwon, Y., Koh, J. J., Ko, K. S., and Kim, S. W. (2001) Water-Soluble and Low Molecular Weight Chitosan-Based Plasmid DNA Delivery. *Pharm. Res. 18*, 427−431.

(28) Sakurai, F., Inoue, R., Nishino, Y., Okuda, A., Matsumoto, O., Taga, T., Yamashita, F., Takakura, Y., and Hashida, M. (2000) Effect of DNA/Liposome on the Physicochemical Characteristics, Cellular Uptake, and Intracellular Trafficking of Plasmid DNA. *J. Controlled Release 66*, 255−269.

(29) Uherek, C., and Wels, W. (2000) DNA-Carrier Proteins for Targeted Gene Delivery. *Adv. Drug Delivery Rev. 44*, 153−166.

(30) (1999) *Nonviral Vectors for Gene Therapy* (Huang, L., Hung, M.-C., Wagner, E., Eds.) Academic Press, San Diego.

(31) O'Hagan, D. T., Palin, K., Davis, S. S., Artursson, P., and Sjöholm, I. (1989) Microparticles as Potentially Orally Active Immunological Adjuvants. *Vaccine 7*, 421−424.

(32) Jang, J.-H., and Shea, L. D. (2003) Controllable Delivery of Non-Viral DNA from Porous Scaffolds. *J. Controlled Release 86*, 157−168.

(33) De Rosa, G., Quaglia, F., Bochot, A., Ungaro, F., and Fattal, E. (2003) Long-Term Release and Improved Intracellular Penetration of Oligonucleotide-Polyethylenimine Compelxes Entrapped in Biodegradable Microspeheres. *Biomacromolecules 4*, 529−536.

(34) Zhou, S., Liao, X., Li, X., Deng, X., and Li, H. (2003) Poly-D, L-Lactide-*co*-Poly(Ethylene Glycol) Microspheres as Potential Vaccine Delivery Systems. *J. Controlled Release 86*, 195−205.

(35) Perez, C., Sanchez, A., Putnam, D., Ting, D., Langer, R., and Alonso, M. J. (2001) Poly(Lactic Acid)-Poly(Ethylene Glycol) Nanoparticles as New Carriers for the Delivery of Plasmid DNA. *J. Controlled Release 75*, 211−224.

(36) Tinsley-Brown, A. M., Fretwell, R., Dowsett, A. B., Davis, S. L., and Farrar, G. H. (2000) Formulation of Poly(DL-Lactic-Co-Glycolic Acid) Microparticles for Rapid Plasmid DNA Delivery. *J. Controlled Release 66*, 229−241.

(37) Walter, E., Moelling, K., Pavlovic, J., and Merkle, H. P. (1999) Microencapsulation of DNA Using Poly(DL-Lactide-*co*-Glycolide): Stability Issues and Release Characteristics. *J. Controlled Release 61*, 361−374.

(38) Murthy, N., Xu, M. C., Schuck, S., Kunisawa, J., Shastri, N., and Fréchet, J. M. J. (2003) A Macromolecular Delivery Vehicle for Protein Based Vaccines: Acid Degradable Protein Loaded Microgels. *Proc. Natl. Acad. Sci. 100*, 4995−5000.

(39) Murthy, N., Thng, Y. X., Schuck, S., Xu, M. C., and Fréchet, J. M. J. (2002) A Novel Strategy for Encapsulation and

Release of Proteins: Hydrogels and Microgels With Acid-Labile Acetal Cross-Linkers. *J. Am. Chem. Soc. 124*, 12398−12399.
(40) Freshney, R. I. (1994) *Culture of Animal Cells: A Manual of Basic Technique*, 3rd ed., Wiley-Liss, New York.
(41) Higgins, D. E., Shastri, N., and Portney, D. A. (1999) Delivery of Protein to the Cytosol of Macrophage Using Escherichia Coli K-12. *Mol. Microbiol. 31*, 1631−1641.
(42) Barton, J. (1996) Free-Radical Polymerization in Inverse Microemulsions. *Prog. Polym. Sci. 21*, 399−348.
(43) Candau, F., Leong, Y. S., and Fitch, R. M. (1985) Kinetic Study of the Polymerization of Acrylamide in Inverse Microemulsion. *J. Polym. Sci. A: Polym. Chem. 23*, 193−214.
(44) Harding, C. V., and Song, R. (1994) Phagocytic Processing of Exogenous Particulate Antigens by Macrophages for Presentation by Class I MHC Molecules. *J. Immunol. 153*, 4925−4933.
(45) Ando, S., Putnam, D., Pack, D. W., and Langer, R. (1999) PLGA Microspheres Containing Plasmid DNA: Preservation of Supercoiled DNA Via Cryopreparation and Carbohydrate Stabilization. *J. Pharm. Sci. 88*, 126−130.
(46) Wang, D., Robinson, D. R., Kwon, G. S., and Samuel, J. (1999) *J. Controlled Release 57*, 9−18.
(47) Piña, B., Haché, R. J. G., Arnemann, J., Chalepakis, G., Slater, E. P., and Beato, M. (1990) Hormonal Induction of Tranfected Genes Depends on DNA Topology. *Mol. Cell. Biol. 10*, 625−633.
(48) Harland, R. M., Weintraub, H., and McKnight, S. L. (1983) Transcription of DNA Injected in Xenopus Oocytes is Influenced by Template Topology. *Nature 302*, 38−43.
(49) Kawabata, K., Takakura, Y., and Hashida, M. (1995) The Fate of Plasmid DNA After Intravenous Injection in Mice: Involvement of Scavenger Receptors in Its Hepatic Uptake. *Pharm. Res. 12*, 825−830.
(50) Caulfield, M. J., Qiao, G. G., and Solomon, D. H. (2002) Some Aspects of the Properties and Degradation of Polyacrylamides. *Chem. Rev. 102*, 3067−3083.
(51) Hemmi, H.; Takeuchi, O.; Kawai, T.; Kaisho, T.; Sato, S.; Sanjo, H.; Matsumoto, M.; Hoshino, K.; Wagner, H.; Takeda, K.; Akira, S. (2000) A Toll-like Receptor Recognizes Bacterial DNA. *Nature 408*, 740−745.
(52) Wagner, H. (2002) Interactions Between Bacterial CpG-DNA and TLR9 Bridge Innate and Adaptive Immunity. *Curr. Top. Microbiol. Immunol. 5*, 62−69.
(53) Ahmad-Nejad, P., Häcker, H., Rutz, M., Bauer, S., Vabulas, R. M., and Wagner, H. (2002) Bacterial CpG-DNA and LPS Activate Toll-Like Receptors at Distinct Cellular Compartments. *Eur. J. Immunol. 32*, 1958−1968.

BC034159N

Arginine Carrier Peptide Bearing Ni(II) Chelator to Promote Cellular Uptake of Histidine-Tagged Proteins

Shiroh Futaki,*[,†,‡] Miki Niwa,[†] Ikuhiko Nakase,[†] Akiko Tadokoro,[†] Youjun Zhang,[†] Makoto Nagaoka,[†] Naoya Wakako,[†] and Yukio Sugiura[†]

Institute for Chemical Research, Kyoto University, Uji, Kyoto 611-0011, Japan, and PRESTO, Japan Science and Technology Agency, Kawaguchi, Saitama 332-0012, Japan. Received October 1, 2003; Revised Manuscript Received February 7, 2004

Arginine-rich peptide-mediated protein delivery into living cells is a novel technology for controlling cell functions with therapeutic potential. In this report, a novel approach for the intracellular delivery of histidine-tagged proteins was introduced where a Ni(II) chelate of octaarginine peptide bearing nitrilotriacetic acid [R8-NTA-Ni(II)] was used as a membrane-permeable carrier molecule. Significant internalization of histidine-tagged enhanced green fluorescent protein (EGFP) into HeLa cells was observed by confocal microscopic observation in the presence of R8-NTA-Ni(II). Nuclear condensation characteristic in apoptotic cell death was also induced in the cells treated with a histidine-tagged apoptosis-inducing peptide [pro-apoptotic domain peptide (PAD)], indicating that the cargo molecules really went through the membrane to reach the cytosol. The apoptosis-inducing activity of the peptide thus delivered was compared with that of the PAD peptide covalently connected with the octaarginine peptide.

INTRODUCTION

Peptide-mediated protein delivery into living cells has become recognized as a powerful tool for controlling cellular function and as a novel methodology in pharmaceutical research (*1*−*3*). The cellular introduction of the cargo molecules is easily conducted by simply conjugating cargo proteins with a peptide having a carrier function and adding these chimera molecules to the culture media. The internalization can be accomplished in a few minutes to substantially all cells. Proteins of molecular weight as high as ∼120 kDa were introduced by this methodology (*4*). One of the typical peptides to have this function is that derived from HIV-1 Tat protein [HIV-1 Tat (48-60): GRKKRRQRRRPPQ] (*5*). The peptide is highly basic and rich in arginines and lysines. We and others have shown that arginine or its guanidino moiety play a crucial role in exerting the carrier function (*6*−*10*). Using this methodology, various cellular functions such as the cell cycle and signal transduction have been successfully regulated (*2*). This methodology is thus regarded as an effective tool for understanding and controlling cellular functions.

On the other hand, the histidine-tag method is known to be one of the most efficacious means for the purification of in vivo produced proteins (*11*). The trick in this method is to prepare proteins of interest so as to have an extra tag peptide segment comprising a continuous array of histidines of about six residues. By elution of the cell extracts containing the histidine-tagged proteins of interest through a column with immobilized Ni(II), the proteins are retained in the columns by chelating with Ni(II), whereas other molecules that lack histidine tags are not. Washout of nonspecifically adsorbed materials from the column followed by the elution with an imidazole-containing buffer will yield the desired purified proteins. This method is especially useful for the purification of a small amount of products from other cellular components, and various plasmids and kits are now available for the efficient production and purification of these histidine-tagged proteins (*12*). This method would be applicable not only for the purification of proteins but also for the detachable cross-link formation between proteins.

In this report, we have developed a novel Ni(II) chelate carrier peptide and exemplified that histidine-tagged proteins were successfully delivered into the cells together with the Ni(II) chelate of octaarginine bearing nitrilotriacetic acid (NTA).

EXPERIMENTAL PROCEDURES

Preparation of Octaarginine-Bearing Nitrilotriacetic Acid (R8-NTA). Preparation of the above compound was conducted as shown in Figure 1. The peptide chain was constructed by Fmoc-solid-phase peptide synthesis (Fmoc = 9-fluorenylmethyloxycarbonyl) (*13*) on a 2-chlorotrityl chloride resin (*14*) using the standard protocol of a Shimadzu PSSM-8 peptide synthesizer. A combination of benzotriazole-1-yloxytrispyrrolidinophosphonium hexafluorophosphate (PyBOP) (*15*), 1-hydroxybenzotriazole (HOBt), and 4-methylmorpholine (NMM) was employed for a coupling system. The N-terminal was acetylated using acetic anhydride in the presence of NMM. Treatment of the peptide resin with acetic acid (AcOH)−trifluoroethanol (TFE)−dichloromethane (DCM) (1:1:8) at 20 °C for 1 h gave a protected peptide segment Ac-[Arg(Pbf)]$_8$-Gly-OH [Ac = acetyl; Pbf = N^G-2,2,4,6,7-pentamethyldihydrobenzofuran-5-sulfonyl (*16*)]. After Ac-[Arg(Pbf)]$_8$-Gly-OH was treated with diisopropylcarbodiimide (DICDI) and *N*-hydroxysuccinimide (HOSu) (2 equiv each) in DMF at 25 °C for 2 h to form the corresponding succinimidyl ester, 5 equiv of *N*-(5-amino-

* Corresponding author. Fax: +81-774-32-3038, phone: +81-774-38-3211; e-mail: futaki@scl.kyoto-u.ac.jp.
† Kyoto University.
‡ PRESTO, Japan Science and Technology Agency.

10.1021/bc034181g CCC: $27.50 © 2004 American Chemical Society
Published on Web 05/04/2004

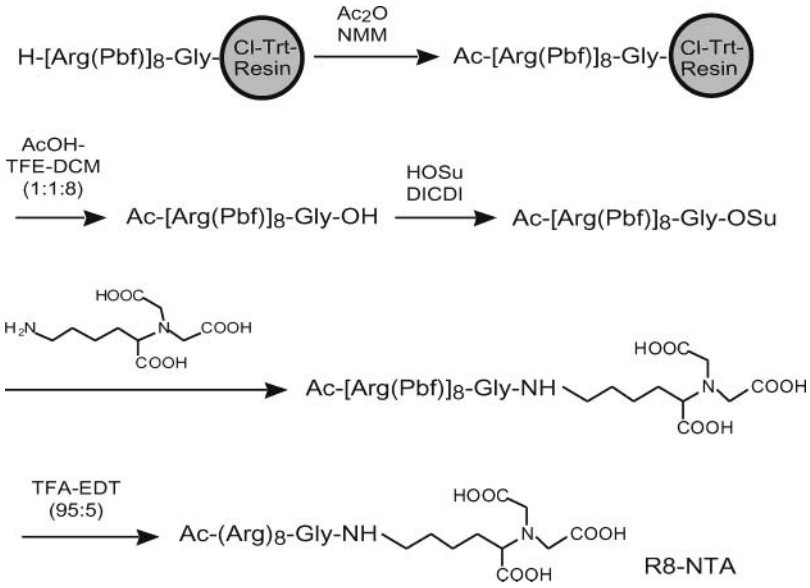


Figure 1. Design and synthesis of octaarginine bearing nitrilotriacetic acid (R8-NTA).

1-carboxypentyl)iminodiacetic acid (Dojin, Japan) in H_2O−DMF (1:3) was added to the mixture and allowed to react overnight. After evaporation of the solvent, the mixture was directly treated with trifluoroacetic acid (TFA)−ethanedithiol (EDT) (95:5) at 25 °C for 2 h. HPLC purification of the sample gave the desired compound. Yield from the starting resin, 31%. MALDI-TOFMS: 1611.7 [calcd for $(M + H)^+$: 1611.8]. Retention time in HPLC, 16.2 min [Column, Cosmosil 5C18-AR−II (10 × 250 mm); eluate, A = H_2O containing 0.1% CF_3COOH, B = CH_3CN containing 0.1% CF_3COOH; gradient, 5−65% B in A over 40 min; flow, 2 mL/min; detection, 220 nm].

Rhodamine-Labeled Octaarginine Bearing Nitrilotriacetic Acid (Rho-R8-NTA). The title compound was similarly prepared as described above, except that the N-terminus of the protected octaarginine was labeled with tetramethylrhodamine using 5(6)-carboxytetramethylrhodamine *N*-hydroxysuccinimide ester (Sigma). The peptide corresponding to the main peak on HPLC was fractionated. Yield from the starting resin, 31%. MALDI-TOFMS: 2040.8 [calcd for $(M + H)^+$: 2040.3]. Retention time in HPLC, 17.5 min [column, Symmetry 300 C18 (4.6 × 150 mm); eluate, A = H_2O containing 0.1% CF_3COOH, B = CH_3CN containing 0.1% CF_3COOH; gradient, 10−50% B in A over 40 min; flow, 1 mL/min; detection, 215 nm].

Preparation of Histidine-Tagged Enhanced Green Fluorescent Protein [H6-EGFP] and R8-Bearing EGFP (R8-EGFP). The EGFP protein bearing a $(His)_6$ segment and a thrombin cleaving site on its N-terminus was prepared as follows. The gene of the EGFP derivative was created by PCR. The 720 bp fragment (679−1398) of pEGFP-N1 (Clontech) containing the EGFP domain was amplified by primers possessing the sequences for *Bam*H I followed by $(His)_6$ and thrombin sites and for the *Eco*R I site. The amplified fragment was cleaved by *Bam*H I and *Eco*R I and cloned into pEV29b, which is a derivative of pET29b (Novagen) and has cloning sites identical to that of pEV3b (*17*). The sequence of the plasmid for H6-EGFP thus obtained was confirmed by a GeneRapid DNA sequencer (Amersham Biosciences). The H6-EGFP protein was overexpressed in the *E. coli* strain BL21(DE3)pLysS in soluble form and purified by a His·Bind Quick Column (Novagen) to give a single band in SDS−PAGE. R8-EGFP was similarly prepared using a PCR primer where the synthetic $(Arg)_8$ gene was also included between the thrombin site and the EGFP domain in the PCR primers.

H-(His)$_6$-(Gly)$_2$-D(KLAKLAK)$_2$-NH$_2$ [histidine-tagged pro-apoptotic domain peptide, H6−PAD]. The peptide chain was constructed by Fmoc-solid-phase peptide synthesis on a Rink amide resin (*18*) by a Shimadzu PSSM-8 synthesizer using a PyBOP/HOBt/NMM coupling system. Fmoc-His(Trt), Fmoc-Gly, Fmoc-D-Lys(Boc), Fmoc-D-Leu, and Fmoc-D-Ala were employed as amino acid derivatives (Trt = trityl, Boc = *tert*-butyloxycarbonyl). Treatment of the peptide resin with TFA-EDT (95:5) and HPLC purification of the deprotected sample gave a pure peptide. Yield from the starting resin, 73%. MALDI-TOFMS: 2460.3 [calcd for $(M + H)^+$: 2461.0]. Retention time in HPLC, 20.9 min [column, Cosmosil 5C18-AR−II (10 × 250 mm); eluate, A = H_2O containing 0.1% CF_3COOH, B = CH_3CN containing 0.1% CF_3COOH; gradient, 5−95% B in A over 45 min; flow, 2 mL/min; detection, 215 nm].

H-(Arg)$_8$-(Gly)$_2$-D(KLAKLAK)$_2$-NH$_2$ [R8−PAD]. The title peptide was prepared similarly to H6-PAD. Yield from the starting resin, 35%. MALDI-TOFMS: 2886.5 [calcd for $(M + H)^+$: 2886.6]. Retention time in HPLC, 20.8 min [column, Cosmosil 5C18-AR−II (10 × 250 mm); eluate, A = H_2O containing 0.1% CF_3COOH, B = CH_3CN containing 0.1% CF_3COOH; gradient, 5−95% B in A over 45 min; flow, 2 mL/min; detection, 215 nm].

H-D(KLAKLAK)$_2$-NH$_2$ (PAD). The title peptide was prepared similarly to H6-PAD. Yield from the starting resin, 39%. MALDI-TOFMS: 1524.0 [calcd for $(M + H)^+$: 1524.0]. Retention time in HPLC, 16.9 min [column, Cosmosil 5C4-AR-300 (4.6 × 150 mm); eluate, A = H_2O containing 0.1% CF_3COOH, B = CH_3CN containing 0.1% CF_3COOH; gradient, 5−95% B in A over 40 min; flow, 1 mL/min; detection, 215 nm].

Cell Culture. Human cervical cancer-derived HeLa cells (obtained from Riken BRC Cell Bank) were maintained in alpha-minimum essential medium (α-MEM) (Invitrogen) with 10% heat-inactivated calf serum (Invitrogen). Cells were grown on 60-mm dishes and incubated at 37 °C under 5% CO_2 to approximately 70% confluence. A subculture was performed every 3−4 days.

Protein Internalization and Microscopic Observation. For each assay, 5×10^4/mL cells were plated on a 35-mm glass-bottom dish (Iwaki) (2 mL/dish) and cultured for 48 h to attain complete adhesion. A typical

experiment employing 50 μM of R8-NTA-Ni(II) and 10 μM of H6-EGFP was conducted as follows. Prior to incubating with cells, R8-NTA in phosphate-buffered saline (PBS) (500 μM, 20 μL), $NiCl_2$ in H_2O (500 μM, 20 μL), and α-MEM containing 10% heat-inactivated calf serum (140 μL) were mixed together and allowed to stand for 15 min. H6-EGFP in PBS (100 μM, 20 μL) was then added to the above mixture and allowed to stand for another 1 h. The cells were incubated with the above mixture (total volume, 200 μL) at 37 °C for 3 h. The cells were washed three times with PBS. Distribution of the EGFP was analyzed using a confocal scanning laser microscope LSM 510 (Zeiss) equipped with an ×40 lens without fixing the cells. When the cells were treated with Rho-R8-NTA-Ni(II)/H6-EGFP complex, the complex was similarly prepared as stated above and applied to a Microcon YM-10 centrifugal filter (normal molecular weight limit 10 000) (Millipore) to remove excess Rho-R8-NTA-Ni(II) before addition to the cells. When the cells were treated with a complex of R8-NTA-Ni(II) with H6-EGFP at 4 °C, the cells and the medium containing R8-NTA-Ni(II)/H6-EGFP were stored at 4 °C for 1 h prior to mixing with each other. After treatment for 1 h, the cells were washed with ice-cold PBS and subjected to the microscopic observation.

In the case of observing nuclear condensation, the cells were incubated with the PAD peptides in α-MEM with 10% heat-inactivated calf serum at 37 °C for 24 h under 5% CO_2, and the medium was changed to a fresh one. Hoechst 33258 was then added to the medium (final concentration, 50 μM), and the cells were incubated for another 30 min at 37 °C under 5% CO_2. Cells were washed twice with PBS, soaked in a fresh α-MEM, and analyzed on an Olympus IX-70 fluorescence microscope using an × 20 lens.

Flow Cytometry. To analyze the internalization of EGFP proteins by FACS, 1.5×10^5 HeLa cells in fresh culture medium (1.5 mL) were plated on a 12-well microplate (Iwaki) and cultured for 48 h in α-MEM containing 10% heat-inactivated calf serum. After complete adhesion the cells were incubated at 37 °C for 1 h with fresh medium (400 μL) containing R8-NTA-Ni(II)/H6-EGFP prior to washing with PBS. The cells were then treated with 0.01% trypsin (Invitrogen) (400 μL) at 37 °C for 10 min prior to adding 600 μL of PBS. The cells were centrifuged at 2000 rpm for 5 min, and after removing the supernatant, they were washed with 1 mL of PBS and centrifuged at 2000 rpm for 5 min. After this washing cycle was repeated, the cells were suspended in PBS (1 mL) and subjected to fluorescence analysis on a FACScalibur (BD Biosciences) flow cytometer using 488-nm laser excitation and an 515−545 nm emission filter.

DNA Fragmentation Assay. HeLa cells were treated with a mixture of R8-NTA-Ni(II) (50 μM) and H6-PAD (10 μM) as described above for 24 h. DNA ladder formation was then examined by isolating oligonucleosomal DNA from cellar extracts and analyzing DNA by ethidium bromide staining after electrophoresis through 2% agarose gels, using Quick Apoptotic DNA Ladder Detection Kit (BioVision).

Evaluation of Apoptotic Cells by FITC-Annexin-V. Cells were stained with FITC-Annexin-V according to the manufacturer's specification using Vybrant Apoptosis Assay kit #3 (Molecular Probes). For analysis, 1.5×10^5 cells were plated on a 12-well plate as described above and incubated for 48 h. Cells were then incubated with fresh medium containing R8-NTA-Ni(II)/H6-PAD complex for 2 h, harvested by trypsinization and then washed with PBS. Cells were suspended in Annexin-V binding buffer (10 mM HEPES, 140 mM NaCl, and 2.5 mM $CaCl_2$, pH 7.4) (200 μL), and then incubated with FITC-Annexin-V (FITC = fluorescein isothiocyanate) (10 μL) and the propidium iodide (PI) working solution (100 μg/mL, 2 μL) at room temperature for 15 min. After the incubation period, the cells were diluted with Annexin-V binding buffer (800 μL). Apoptotic cells, which were positive for FITC-Annexin-V and negative for PI staining, were analyzed by FACS.

MTT Assay. The MTT [= 3-(4,5-dimethylthiazol-2-yl)-2,5-diphenyl-2*H*-tetrazolium bromide] assay was conducted basically in the same manner as already reported (*6*). Cells (1.5×10^3/well) were cultured on 96-microtiter plates in α-MEM with 10% heat-inactivated calf serum in the presence of peptides. Prior to incubation with the cells, R8-NTA in α-MEM (500 μM, 5 μL), $NiCl_2$ in α-MEM (500 μM, 5 μL), and fresh α-MEM containing 10% heat-inactivated calf serum (35 μL) were mixed together and allowed to stand for 15 min. H6-PAD in α-MEM (100 μM, 5 μL) was then added to the above mixture, and allowed to stand for another 1 h. The cells were incubated with the above mixture (total volume, 50 μL) at 37 °C under 5% CO_2 for 24 h. MTT (Sigma) in PBS (0.05 mg/10 μL) was added to the above medium, and the cells were further incubated for 4 h. The precipitated MTT formazan was dissolved overnight in 0.04 N HCl in 2-propanol (100 μL). The absorbance at 570 nm was then measured. Cell viability was expressed as the ratio of the A_{570} of cells treated with peptide to the control samples.

RESULTS

Design and Synthesis of Octaarginine Bearing Nitrilotriacetic Acid (NTA). Intracellular protein delivery using the Tat and other arginine-rich membrane-permeable peptides has become recognized as a novel and promising technology for the modulation of cell functions (*1*−*3*). However, it has been regarded that covalent cross-linking between the cargo proteins and the carrier peptides is necessary for the cellular introduction. Because various histidine-tagged proteins have been prepared up to now, it would be beneficial if we could develop a means of bringing these proteins into cells for the study and modulation of cellular functions without reconstruction of plasmids or systems for expression and purification. Protein purification using the histidine-tags employs immobilized Ni(II) on a chelating adsorbent bearing a nitrilotriacetic acid (NTA) derivative, which occupies four positions in the metal coordination sphere of Ni(II). The remaining two ligand positions in the octahedral coordination sphere are available for selective protein interactions. We developed a novel carrier peptide bearing NTA (Figure 1). As a membrane-permeable carrier peptide, octaarginine was selected as a representative, which was connected to the *N*-(5-amino-1-carboxypentyl)iminodiacetic acid via a glycine residue as a spacer. In the presence of Ni(II), the carrier peptide R8-NTA, and the histidine-tagged protein should form a noncovalent complex which is expected to penetrate into cells.

The synthetic scheme of the carrier peptide is shown in Figure 1, which is based on the condensation of the carrier peptide segment Ac-$[Arg(Pbf)]_8$-Gly-OH with *N*-(5-amino-1-carboxypentyl)iminodiacetic acid. Ac-$[Arg(Pbf)]_8$-Gly-OH was prepared by Fmoc-solid-phase peptide synthesis on a 2-chlorotrityl chloride resin followed by N-terminal acetylation using acetic anhydride and detachment from the resin by a treatment with AcOH-TFE-DCM (1:1:8). After the C-terminus of Ac-$[Arg(Pbf)]_8$-Gly-OH was activated as a succinimidyl ester, excess *N*-(5-

amino-1-carboxypentyl)iminodiacetic acid was added. Treatment of the sample with TFA-EDT (95:5) followed by HPLC purification yielded R8-NTA. The structure of the compound was ascertained by MALDI-TOFMS.

Intracellular Delivery of Histidine-Tagged EGFP (H6-EGFP) by R8-NTA-Ni(II). To assess the ability of the Ni(II) chelate of R8-NTA [R8-NTA-Ni(II)] for intracellular delivery of histidine-tagged proteins, we prepared an N-terminus histidine-tagged enhanced green fluorescent protein (H6-EGFP), which was expressed in *E. coli* and purified using a Ni(II) chelate affinity column to be sufficiently pure. The apparent dissociation constant (K_D) between NTA and H6-EGFP was reported to be 4.2×10^{-7} M (*19*).

Internalization of the histidine-tagged EGFP was monitored by laser confocal microscopic observation after a 3-h incubation of the protein with HeLa cells at 37 °C. Prior to incubation with the cells, R8-NTA was mixed with $NiCl_2$ and allowed to stand for 15 min, and H6-EGFP was added to the above solution and allowed to stand for another 1 h (Figure 2A). The mixture was then added to the cells and incubated for 3 h. Significant internalization of H6-EGFP was observed when the cells were treated with H6-EGFP (10 μM) in the presence of R8-NTA-Ni(II) (50 μM), showing a very similar manner of cellular localization with that of R8-EGFP (a fusion protein of an octaarginine segment and EGFP) (Figure 2B, (i) and (ii)) Particulate signals from EGFP were observed which accumulated around the perinuclear area, suggesting that significant parts of these proteins were trapped in the cellular vesicles or formed aggregates in the cell. When the cells were treated with R8-NTA-Ni(II)/H6-EGFP at 4 °C, no significant internalization of H6-EGFP was observed (data not shown). This fact suggested that an endocytic pathway predominantly contributed to the cellular uptake of H6-EGFP, as reported for the HIV-1 Tat peptide (*20*). Equimolar amounts of H6-EGFP and R8-NTA-Ni(II) (10 μM each) gave somewhat less efficient internalization of the protein (data not shown). On the other hand, little internalization of H6-EGFP was observed in the absence of R8-NTA-Ni(II) (Figure 2B, (iii)). No significant improvement in the cellular uptake of H6-EGFP was observed with the addition of R8 peptide [$(Arg)_8$-amide] (50 μM) that lacked the NTA moiety (data not shown). FACS analysis of the cells treated with H6-EGFP (10 μM) in the presence of R8-NTA-Ni(II) (50 μM) for 3 h showed that the amount of the internalized protein was almost half of that of the cells treated with R8-EGFP (10 μM) (Figure 2C). When the cells were treated with the double amount of H6-EGFP (20 μM) in the presence of R8-NTA-Ni(II) (100 μM), the amount of the internalized protein became almost comparable to that for R8-EGFP (10 μM). The above studies indicated that histidine-tagged proteins were successfully brought into the cells with the aid of R8-NTA-Ni(II), although the efficiency in the delivery of cargo proteins was not comparable to that using a covalently attached arginine peptide segment.

Interestingly, R8-NTA retained carrier ability even when R8-NTA was not treated with $NiCl_2$ (Figure 2B, (iv)); though considerably less compared with the case when R8-NTA was complexed with $NiCl_2$, some amount of H6-EGFP was still brought into the cells. Presumably, some divalent cations present in the cells or culture medium formed a complex with R8-NTA to help the internalization of H6-EGFP.

Less efficiency in the delivery using the R8-NTA-Ni(II)/H6-EGFP system in comparison with that using R8-EGFP suggested that H6-EGFP partially dissociated from R8-NTA-Ni(II) in the cells, presumably due to the presence of other cations and nucleophiles in the cells and the culture medium to compete for the coordination site of Ni(II). Acidification of the endosomic particles may also reduce the binding of H6-EGFP to R8-NTA-Ni(II). To obtain information on this matter, we prepared rhodamine-labeled R8-NTA (Rho-R8-NTA) and examined the cellular localization in comparison with that of H6-EGFP. Figure 2D shows a picture of the cells when treated with a mixture of Rho-R8-NTA-Ni(II) and H6-EGFP. The fluorescent signals from these molecules showed particulate distribution in the cells. Superimposition of these pictures yielded yellow signals. This fact suggested that a considerable part of H6-EGFP retained the complex structure with Rho-R8-NTA-Ni(II). On the other hand, signals of the respective colors were simultaneously observed, suggesting that some part of these components dissociated from each other and formed vesicles or aggregates abundant with one of these components. To confirm that proteins delivered into the cells can actually modulate biological functions and to estimate the efficiency of the delivery system of histidine-tagged proteins using R8-NTA-Ni(II), we conducted other experiments to introduce an apoptosis-inducing peptide into the cells.

Delivery of Apoptosis-Inducing Peptide. Ellerby et al. reported that an amphiphilic basic antibacterial peptide showed apoptosis-inducing activity when delivered in mammalian cells [pro-apoptotic domain peptide (PAD): $_D$(KLAKLAK)$_2$-amide] (*21*). The mechanism of apoptosis caused by this peptide is attributed to interaction with the mitochondrial membranes to disturb the mitochondrial structure. They selectively targeted this peptide to cancer cells by attaching a cyclic RGD segment to it. We have prepared a PAD peptide bearing a H6 segment (H6-PAD, Figure 3A) and assessed the internalization efficiency through its apoptosis-inducing activity in comparison with PAD covalently linked with membrane-permeable octaarginine (R8-PAD).

Condensation of the nucleus is one of the typical phenomena of apoptotic cells. We first confirmed that the intracellular delivery of the PAD peptide caused apoptosis. When the cells were treated with R8-NTA-Ni(II)/H6-PAD for 24 h, significant condensation of the nucleus was observed (Figure 3B). Similarly, condensation of the nucleus was induced by R8-PAD. On the other hand, little change was observed in the size of the nucleus after treatment of the cells with the PAD peptide (10 μM) (data not shown). Even when the peptide concentration was raised to 50 μM, only a slight extent of apoptosis was observed. The above result indicated that intracellular delivery of the PAD peptide using arginine peptides effectively promoted the induction of apoptosis for the target cells.

Induction of apoptosis by the PAD peptide was further confirmed by DNA fragmentation assay (Figure 3C). Typical ladder formation of nuclear DNA isolated from the cells treated with H6-PAD (20 μM) in the presence of 5 equiv of R8-NTA-Ni(II) was observed in the gel-electrophoresis (Figure 3C, lane 4).

Apoptosis inducing activity of the PAD peptides was assessed by a FACS analysis using FITC-conjugated Annexin-V (FITC-Annexin-V) (*22*). Annexin-V is a human anticoagulant that has high affinity for binding to phosphatidylserine (PS). In normal healthy cells, PS in the plasma membrane is oriented toward the cytoplasm. As an early event of apoptosis, the translocation of PS to the extracellular environment is observed, which can be evaluated with Annexin-V staining followed by FACS

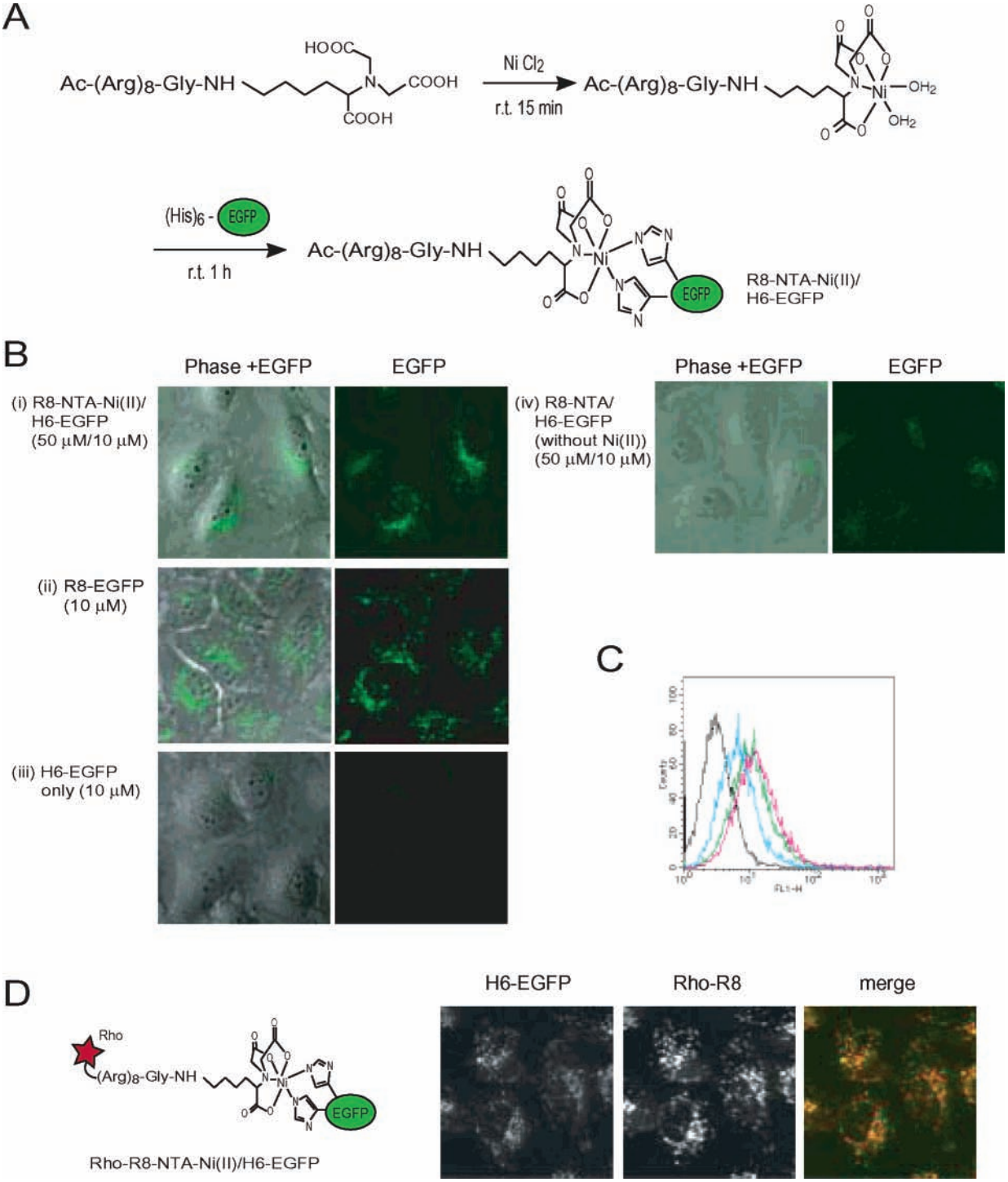


Figure 2. (A) Complex formation of H6-EGFP with the Ni(II) chelate of R8-NTA [R8-NTA-Ni(II)] and (B) confocal microscopic observation of the HeLa cells treated with R8-NTA-Ni(II)/H6-EGFP for 3 h. The R8-NTA-Ni(II)/H6-EGFP complex was formed as described in the Experimental Section. (C) FACS analysis of the internalized EGFP proteins. HeLa cells were treated with H6-EGFP (10 μM (blue) or 20 μM (red)) in the presence of 5 equiv of R8-NTA-Ni(II). Green line represents the cells treated with R8-EGFP (10 μM) and black line control cells (untreated). (D) Confocal microscopic observation of the cells treated with rhodamine-labeled R8-NTA-Ni(II) [Rho-R8-NTA-Ni(II)] and H6-EGFP. Rho-R8-NTA-Ni(II) and H6-EGFP were mixed together at a molar ratio of 5:1 to facilitate the complex formation and then applied to a Microcon YM-10 centrifugal filter (normal molecular weight limit 10 000) (Millipore) to remove excess Rho-R8-NTA-Ni(II) before addition to the cells (final concentration of H6-EGFP, 10 μM).

analysis. In combination with the cell impermeable nucleic acid stain propidium iodide (PI), apoptotic cells (Annexin-V positive/PI negative) can be differentiated from necrotic (Annexin-V positive/PI positive) and normal (Annexin-V negative/PI negative) cells. HeLa cells were treated with R8-NTA-Ni(II)/H6-PAD or R8-PAD for 2 h. FACS analysis showed that the treatment with H6-PAD (10 μM) in the presence of 5 equiv of R8-NTA-Ni(II) induced apoptosis in cells to the same extent to those treated with a typical apoptosis-inducing agent, staurosporine (400 nM). H6-PAD (20 μM) in the presence of R8-NTA-Ni(II) (100 μM) gave comparable effect with R8-PAD (10 μM) to induce apoptosis in >40% of cells, four times higher than those treated with staurosporine (400 nM).

The apoptosis-inducing activity of the peptides was also assessed in terms of the cell viability determined by the

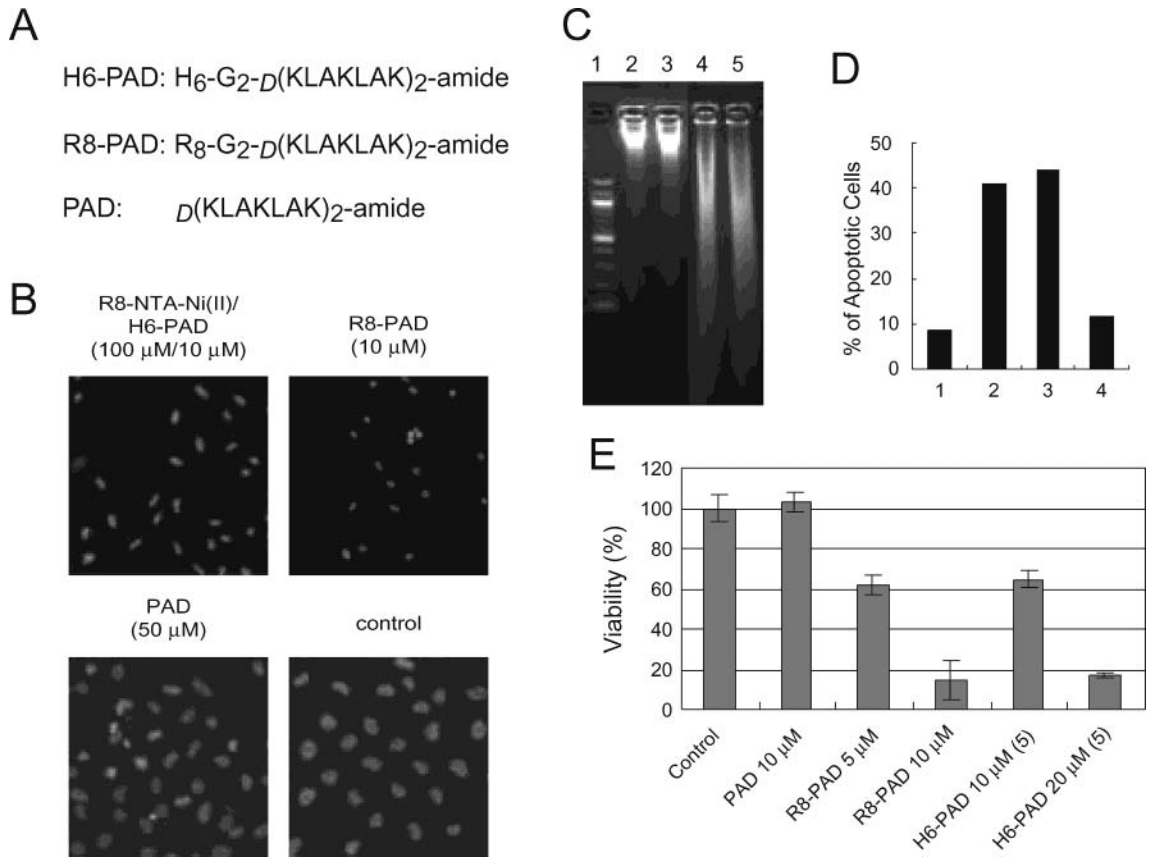


Figure 3. (A) Primary structure of histidine-tagged pro-apoptotic domain peptide (H6-PAD) and its related peptides. Amino acids are expressed by a one-letter abbreviations (H, histidine; G, glycine; R, arginine; K, lysine; L, leucine; A, alanine). (B) Nuclear condensation in apoptotic cells treated with PAD peptides for 24 h. (C) Fragmentation of the chromosomal DNA by the PAD peptides. Lane 1 contains a size marker, lane 2 contains DNA isolated from control cells (untreated), and lane 3−5 contain DNA from cells treated with PAD peptide (10 μM), H6-PAD (20 μM) in the presence of R8-NTA-Ni(II) (100 μM), and staurosporine (400 nM) for 24 h, respectively. (D) Apoptosis analysis by Annexin-V staining. Cells untreated and treated with H6-PAD (10 μM (1) and 20 μM (2)) in the presence of 5 equiv of R8-NTA-Ni(II), R8-PAD (10 μM) (3), and staurosporine (400 nM) (4) were stained with FITC-Annexin-V in the presence of PI and analyzed by flow cytometry. The percentages of cells positive for Annexin-V and negative for PI were shown. (E) Apoptotic cell death induced by the PAD peptides. The viability of the cells was determined by the MTT [3-(4,5-dimethylthiazol-2-yl)-2,5-diphenyl-2*H*-tetrazolium bromide] assay. HeLa cells were incubated in the medium containing a peptide at the indicated concentration for 24 h. Treatment of the cells with the PAD peptide at the concentration of 10 μM did not cause significant cytotoxicity to the cells. H6-PAD 10 μM (5) and H6-PAD 20 μM (5) represent the results of the cells treated with H6-PAD (10 and 20 μM) in the presence of 5 equiv of R8-NTA-Ni(II), respectively. Error bars represent the mean ± standard deviation of three to four samples.

MTT assay (Figure 3E). The peptide-induced apoptotic cell death caused a decrease in the population of live cells among the total cells. The HeLa cells were treated with H6-PAD (10 and 20 μM) in the presence of 5 equiv of R8-NTA-Ni(II) for 24 h. In such cases, viability of the cells ranged around 65% and 17%, respectively, compared with untreated cells. These values were comparable to those for R8-PAD (5 μM) (62%) and R8-PAD (10 μM) (15%). On the other hand, PAD (10 μM) showed no significant cytotoxicity under the given condition. Viability of the R8 peptide (octaarginine amide) (10 μM) was judged to be 88% (data not shown). Thus, although the internalization efficiency of the PAD peptide was a slightly less effective in the case of using the R8-NTA-Ni(II)/H6-PAD system as compared with R8-PAD, it was judged that the H6-PAD peptide was actually delivered into the cytosol to interact with the mitochondrial membranes. These facts were suggestive of the effectiveness of the R8-NTA-Ni(II) system for the intracellular delivery of histidine-tagged proteins.

DISCUSSION

In this paper, we have shown that histidine-tagged peptides and proteins were efficiently brought into the cells using a membrane-permeable octaarginine peptide bearing nitrilotriacetic acid (R8-NTA). The histidine-tagged method is one of the most popular methods for the efficient purification of proteins, and numerous proteins bearing the tag have been prepared. Using this approach, these histidine-tagged proteins are expected to be delivered into cells without modifying the plasmids and expression systems. The results obtained here also raised the possibility of bringing other chelating molecules and noncovalently assembled supramolecular complexes into cells. Other tagged systems can be applicable to the arginine-peptide mediated protein delivery into cells. Although application of the Tat peptide chelated with ^{99m}Tc was reported for in vivo imaging and radiotherapy (*23*), this is, to the best of our knowledge, the first report on the delivery achieved while retaining a chelating complex structure as a 'coupler' between carrier peptides and cargo proteins.

As shown in Figure 2D, a certain population of the carrier peptide (R8-NTA) and cargo H6-EGFP were observed without significant colocalization. This is presumably because of the nonspecific competition of intracellular nucleophilic compounds with the coordination center of Ni(II) to H6-EGFP. Protonation of histidine in

H6-EGFP by acidification of endocytic particles may also explain this fact. Although the apparent internalization efficiency of the proteins is hampered by partial dissociation of the complexes, the cargo molecules can be unequivocally delivered into cytosol to control cellular function as shown in the delivery of the PAD peptide. This characteristic may be useful when the covalent attachment of carrier peptides is undesirable for the exertion of their function or cellular localization of the cargo proteins.

Particulate cellular distribution of the cargo EGFP suggested the involvement of endocytosis in the internalization. It is also suggested that the cargo proteins diffuse into cytosol to give considerably less intense signals than when retained in endosomes. Thinking about this methodology having been successfully applied in modulating various cellular functions, the modulation may be achieved even when only a small portion of the cargo proteins trapped in endosome are released into cytosol. Thus, assessment of the internalization efficiency of proteins not only by microscopic observation or FACS analysis (corresponding to the total cellular uptake of proteins) but also by activities induced by the cargo proteins (reflecting the amount of the cytosol-released proteins) becomes crucial.

It would be implausible that the chelating molecules with dissociation constants of micromolar range can internalize into cells bearing their complex structure by direct penetration through the membranes with an unfolding process. This fact will be a criterion for discussing the mechanism of membrane permeation of the arginine-rich carrier systems.

ACKNOWLEDGMENT

This work was partly supported in part by Grants-in-Aid for Scientific Research from the Ministry of Education, Culture, Sports, Science and Technology of Japan.

LITERATURE CITED

(1) Futaki, S., Goto, S., Suzuki, T., Nakase, I., and Sugiura, Y. (2003) Structural variety of membrane permeable peptides. *Curr. Protein Pept. Sci. 4*, 87−96.

(2) Wadia, J. S., and Dowdy S. F. (2003) Modulation of cellular function by TAT mediated transduction of full length proteins. *Curr. Protein Pept. Sci. 4*, 97−104.

(3) Wright, L. R., Rothbard, J. B., and Wender, P. A. (2003) Guanidinium rich peptide transporters and drug delivery. *Curr. Protein Pept. Sci. 4*, 105−124.

(4) Schwarze, S. R., Ho, A., Vocero-Akbani, A., and Dowdy, S. F. (1999) In vivo protein transduction: delivery of a biologically active protein into the mouse. *Science 285*, 1569−1572.

(5) Vivès, E., Brodin, P., and Lebleu, B. (1997) A truncated HIV-1 Tat protein basic domain rapidly translocates through the plasma membrane and accumulates in the cell nucleus. *J. Biol. Chem. 272*, 16010−16017.

(6) Futaki, S., Suzuki, T., Ohashi, W., Yagami, T., Tanaka, S., Ueda, K., and Sugiura, Y. (2001) Arginine-rich peptides: An abundant source of membrane-permeable peptides having potential as carriers for intracellular protein delivery. *J. Biol. Chem. 276*, 5836−5840.

(7) Suzuki, T., Futaki, S., Niwa, M., Tanaka, S., Ueda, K., and Sugiura, Y. (2002) Possible existence of common internalization mechanisms among arginine-rich peptides. *J. Biol. Chem. 277*, 2437−2443.

(8) Futaki, S., Nakase, I., Suzuki, T., Zhang, Y., and Sugiura, Y. (2002) Translocation of branched-chain arginine peptides through cell membranes: flexibility in the spatial disposition of positive charges in membrane-permeable peptides. *Biochemistry 41*, 7925−7930.

(9) Wender, P. A., Mitchell, D. J., Pattabiraman, K., Pelkey, E. T., Steinman, L., and Rothbard, J. B. (2000) The design, synthesis, and evaluation of molecules that enable or enhance cellular uptake: peptoid molecular transporters. *Proc. Natl. Acad. Sci. U.S.A. 97*, 13003−13008.

(10) Umezawa, N., Gelman, M. A., Haigis, M. C., Raines, R. T., and Gellman, S. H. (2002) Translocation of a β-peptide across cell membranes. *J. Am. Chem. Soc. 124*, 368−369.

(11) Hochuli, E., Dobeli, H., and Schacher, A. (1987) New metal chelate adsorbent selective for proteins and peptides containing neighbouring histidine residues. *J. Chromatogr. 411*, 177−184.

(12) Terpe, K. (2003) Overview of tag protein fusions: from molecular and biochemical fundamentals to commercial systems. *Appl. Microbiol. Biotechnol. 60*, 523−533.

(13) Atherton, E., and Sheppard, R. C. (1989) *Solid-Phase Peptide Synthesis, A Practical Approach*, IRL Press, Oxford.

(14) Barlos, K., Chatzi, O., Gatos, D., and Stavropoulos, G. (1991) 2-Chlorotrityl chloride resin. Studies on anchoring of Fmoc-amino acids and peptide cleavage. *Int. J. Pept. Protein Res. 37*, 513−520.

(15) Coste, J., Le-Nguyen, D., and Castro, B. (1990) PyBOP: A new peptide coupling reagent devoid of toxic byproduct. *Tetrahedron Lett. 31*, 205−208.

(16) Carpino, L. A., Shroff, H., Triolo, S. A., Mansour, E. M. E., Wenschuh H., and Albericio F. (1993) The 2,2,4,6,7-pentamethyldihydrobenzofuran-5-sulfonyl group (Pbf) as arginine side chain protectant. *Tetrahedron Lett. 34*, 7829−7832.

(17) Nagaoka, M., and Sugiura, Y. (1996) Distinct phosphate backbone contacts revealed by some mutant peptides of zinc finger protein Spl: effect of protein-induced bending on DNA recognition. *Biochemistry 35*, 8761−8768.

(18) Rink, H. (1987) Solid-phase synthesis of protected peptide fragments using a trialkoxy-diphenyl-methylester resin. *Tetrahedron Lett. 28*, 3787−3790.

(19) Schmid, E. L., Keller, T. A., Dienes, Z., and Vogel, H. (1997) Reversible oriented surface immobilization of functional proteins on oxide surfaces. *Anal. Chem. 69*, 1979−1985.

(20) Richard, J. P., Melikov, K., Vivès, E., Ramos, C., Verbeure, B, Gait, M. J., Chernomordik, L. V., and Lebleu, B. (2003) Cell-penetrating peptides. A reevaluation of the mechanism of cellular uptake. *J. Biol. Chem. 278*, 585−590.

(21) Ellerby, H. M., Arap, W., Ellerby, L. M., Kain, R., Andrusiak, R., Rio, G. D., Krajewski, S., Lombardo, C. R., Rao, R., Ruoslahti, E., Bredesen, D. E., and Pasqualini R. (1999) Anticancer activity of targeted pro-apoptotic peptides. *Nat. Med. 5*, 1032−1038.

(22) Danielson, S. R., Wong, A., Carelli, V., Martinuzzi, A., Schapira, A. H., and Cortopassi, G. A. (2002) Cells bearing mutations causing Leber's hereditary optic neuropathy are sensitized to Fas-induced apoptosis. *J. Biol. Chem. 277*, 5810−5815.

(23) Polyakov, V., Sharma, V., Dahlheimer, J. L., Pica, C. M., Luker, G. D., and Piwnica-Worms, D. (2000) Novel Tat-peptide chelates for direct transduction of technetium-99m and rhenium into human cells for imaging and radiotherapy. *Bioconjugate Chem. 11*, 762−771.

BC034181G

Cellular Trajectories of Peptide-Modified Gold Particle Complexes: Comparison of Nuclear Localization Signals and Peptide Transduction Domains

Alexander G. Tkachenko, Huan Xie, Yanli Liu, Donna Coleman, Joseph Ryan, Wilhelm R. Glomm, Mathew K. Shipton, Stefan Franzen,* and Daniel L. Feldheim*

Department of Chemistry, North Carolina State University, Raleigh, North Carolina 27695. Received October 14, 2003; Revised Manuscript Received February 28, 2004

Gold nanoparticles modified with nuclear localization peptides were synthesized and evaluated for their subcellular distribution in HeLa human cervical epithelium cells, 3T3/NIH murine fibroblastoma cells, and HepG2 human hepatocarcinoma cells. Video-enhanced color differential interference contrast microscopy and transmission electron microscopy indicated that transport of nanoparticles into the cytoplasm and nucleus depends on peptide sequence and cell line. Recently, the ability of certain peptides, called protein transduction domains (PTDs), to transclocate cell and nuclear membranes in a receptor- and temperature-independent manner has been questioned (see for example, Lundberg, M.; Wikstrom, S.; Johansson, M. (2003) *Mol. Ther. 8,* 143−150). We have evaluated the cellular trajectory of gold nanoparticles carrying the PTD from HIV Tat protein. Our observations were that (1) the conjugates did not enter the nucleus of 3T3/NIH or HepG2 cells, and (2) cellular uptake of Tat PTD peptide−gold nanoparticle conjugates was temperature dependent, suggesting an endosomal pathway of uptake. Gold nanoparticles modified with the adenovirus nuclear localization signal and the integrin binding domain also entered cells via an energy-dependent mechanism, but in contrast to the Tat PTD, these signals triggered nuclear uptake of nanoparticles in HeLa and HepG2 cell lines.

INTRODUCTION

The diagnosis and treatment of disease at the cellular level would be greatly enhanced by the ability to deliver analyte probes and therapeutic agents into specific cells and cellular compartments. The nucleus is the desired target for cancer therapies that involve DNA−drug interactions, genes, short interfering RNA, and antisense strategies that target RNA splicing. These therapeutic agents are often prevented from reaching the cell nucleus because of size, charge, or, in the case of small molecules, because P-glycoproteins pump them out of the cell. Vectors that cross cell and nuclear membrane barriers efficiently and are unaffected by cellular pumping mechanisms could aid in the implementation of many novel disease treatments.

Targeted nuclear delivery is a challenging task, however, as any cell-specific nuclear probe must satisfy the following requirements: it must (i) be small enough to enter cells and cross the nuclear membrane (<100 nm for uptake by receptor-mediated endocytosis (RME) and <30 nm for import through nuclear pores), (ii) penetrate cellular membranes or bind to cell-specific plasma membrane receptors, (iii) bypass or escape endosomal/lysosomal pathways, (iv) penetrate nuclear membranes or access importins to pass through the nuclear pore complex, and (v) have low toxicity. Although viruses have evolved to deliver genes to cell nuclei, the design of synthetic systems (nonviral vectors) capable of performing all of these functions remains a challenge. Nonviral vectors such as dendrimers and liposomes currently appear to be safer and more cost-effective than viral vectors, but they are relatively less efficient at nuclear delivery (*1*). By combining membrane-translocation peptides from viruses with noninfectious materials, a potential route to safe *and* efficient nuclear targeting vectors may be afforded.

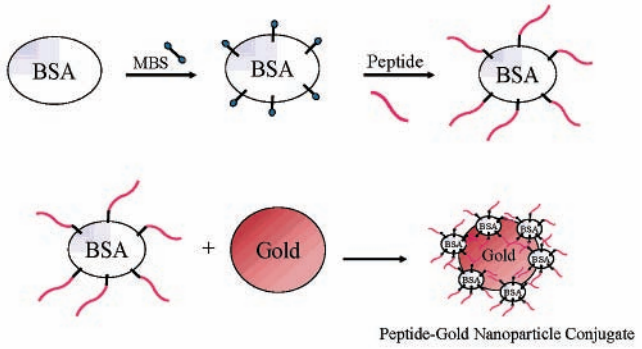


Figure 1. Illustration of the synthesis of peptide-modified gold nanoparticle conjugates for cellular targeting. A surface lysine residue of BSA is labeled using MBS (3-maleimidobenzoic acid *N*-hydroxysuccinimide ester) (*22*). The desired peptide containing a terminal cysteine is cross-conjugated by reaction with a succinimide group on the MBS reagent.

The present study demonstrates nuclear targeting by synthetic cellular targeting peptides complexed to a nanometer-sized gold particle scaffold (Figure 1). Gold makes an excellent intracellular targeting vector for three reasons. First, gold can be synthesized routinely in sizes varying continuously from 0.8 to 200 nm with <10% size dispersity. Second, gold can be modified with a large collection of small molecules, peptides, proteins, DNA, and polymers. Moreover, all of these functional elements can be combined on a single particle simultaneously, often via simple one-pot procedures. Finally, gold par-

* Address correspondence to stefan_franzen@ncsu.edu and dan_feldheim@ncsu.edu.

10.1021/bc034189q CCC: $27.50 © 2004 American Chemical Society
Published on Web 04/28/2004

Table 1. Peptide Sequences Used in Nanoparticle−BSA−Peptide Complexes[a]

no.	peptide sequence	origin of peptide	nuclear localization prediction, %	cytoplasm localization prediction, %
M1	CGGGPKKKRKVGG	SV40 large T NLS	82.6	13
M2	CGGRKKRRQRRRAP	HIV-1 Tat protein NLS	73.9	21.7
M3	CGGFSTSLRARKA	adenoviral NLS	47.8	47.8
M4	CKKKKKKGGRGDMFG	integrin binding domain and oligolysine	73.9	17.4

[a] PSORT software was used for analysis and prediction of protein sorting signals found in amino acid sequences. Results of k-NN prediction are shown (*21*).

ticles have enormous visible light extinction characteristics, ($\epsilon > 10^8$ M^{-1} cm^{-1} at ∼520 nm) (*2*), a behavior we have exploited in a modified form of video enhanced differential interference contrast light microscopy for tracking nanoparticle trajectories inside cells.

Gold particles modified with the nuclear localization signal (NLS) from SV-40 virus have been used extensively for investigating nuclear transport in the pioneering work of Feldherr and co-workers (*3*−*8*). The KKKRK sequence from the SV-40 virus has been shown to bind to importin-α, a nuclear transport protein that binds importin-*β* and enters the nucleus through the nuclear pore complex. However, in those studies the nanoparticle−peptide complex was injected directly into the cytoplasm near the nucleus, thus bypassing cellular membrane entry and endosomal/lysosomal pathways. The studies described here build on this established procedure to examine the ability of a number of viral targeting peptides to target the nucleus from outside intact cells.

The peptide sequence RKKRRQRRR from the Tat protein has been widely studied because of its role in initiation of transcription of the HIV genome. This sequence has also been found to promote uptake into cells across the plasma membrane (*9*, *10*). For example, peptides containing this sequence have been used to shuttle nanoparticles (45 nm) into progenitor cells, allowing their detection by magnetic resonance imaging (*11*). Herein we describe experiments designed to assess the ability of peptide−gold nanoparticle complexes to cross the barriers of intact cells and reach the nucleus. It is shown that particle uptake and nuclear translocation depend strongly on the surface-bound peptide sequence and on the cell type for three cell lines studied, HeLa, 3T3/NIH, and HepG2. Although a single targeting peptide can traverse multiple cellular barriers (endosomal uptake, endosomal escape, and nuclear transport), as shown in HeLa cells, this is not a general feature. On the basis of this study, we conclude that combinations of peptides may be an effective strategy for targeting the nucleus of intact cells. Indeed, in previous work, we have shown that nanoparticles carrying both NLS and RME peptides are capable nuclear targeting vectors in HepG2 cells (*12*).

MATERIALS AND METHODS

Materials. Gold nanoparticles (20 nm diameter) were purchased from Ted Pella. Bovine serum albumin (BSA) was purchased from Roche (MW: 67000). 3-Maleimidobenzonic acid *N*-hydroxysuccinimide ester (MBS) and dithiothreitol (DTT) were obtained from Pierce Chem, Co., Rockford, IL. Sephadex G10, G25, and G50 (for size exclusive liquid chromatograph) were purchased from Sigma. Centricon YM-30 and Microcon YM-100 were purchased from Millipore. 7.5% Tris-HCl prepacked gels (SDS−PAGE) (for electrophoresis) and protein assay kit (for protein concentration estimation) were purchased from Bio-Rad. Peptides were custom-made at UNC Microprotein Sequencing & Peptide Synthesis Facility (Chapel Hill, NC).

Peptides. A list of the four peptides that have been complexed to gold particles and incubated with the three cell lines is shown in Table 1. In this study, we focus on the peptide nuclear localization signal (NLS) derived from the Large T antigen of the SV40 virus (M1 in Table 1), a peptide derived from the HIV Tat protein (M2), and adenovirus fiber protein (M3), as well as a modified integrin binding domain peptide (M4). M1 is considered a classic NLS peptide and has been used as a targeting agent in cytochemical studies (*6*, *7*). The CGGRKKRRQRRRAP sequence in peptide M2 is an HIV NLS that is believed to employ an alternative nuclear transport pathway that involves only importin-*β* (*13*−*18*). The CGGFSTSLRARKA sequence in peptide M3 is derived from the adenoviral fiber protein and is also a known NLS (*19*). While the NLS sequences of peptides M1, M2, and M3 are derived from viruses, peptide M4 is largely synthetic in nature, containing only the integrin binding domain and a segment of basic lysine residues. The integrins are a family of transmembrane glycoproteins exploited by a number of viruses (adenovirus, echovirus, and foot-and-mouth-disease virus), as well as bacterial intracellular pathogens, for cell entry (*20*). We expect that vectors carrying the integrin binding domain will have high affinity for integrins that will facilitate cell binding and internalization. The short stretch of positively charged lysine residues was added to mimic the cationic nature of many nuclear localizations signals. Peptides M3 and M4 have not been used previously for intracellular nanoparticle delivery. Each peptide was prepared with a terminal cysteine to permit conjugation to the lysine residues on the surface of BSA (see below) and tested with PSORT software package, which predicts relative probability of subcellular localization of proteins based on their amino acid sequences using AAindex Analysis (*21*). Predictions for nuclear localization are shown in Table 1. The design criteria thus included both the targeting sequence and a structural component required for nanoparticle attachment and signal flexibility for proper signal−receptor interaction. Addition of six lysine residues to peptide M4 increased the calculated prediction for nuclear delivery from ∼21% to ∼74%.

Preparation of Gold Nanoparticle Vectors. Peptide−gold particle complexes were assembled by conjugating peptides to bovine serum albumin (BSA) and then attaching BSA−peptide conjugates to gold nanoparticles (Figure 1). To prepare BSA−peptide conjugates, BSA was mixed with 3-maleimidobenzoic acid *N*-hydroxysuccinimide ester (MBS) in a 1:50 ratio (*22*). The number of MBS ligands bound to BSA was determined experimentally by a fluorescent assay using fluorescamine (*22*).

The succinimide ester group of MBS subsequently was reacted with a cysteine-terminated peptide using a BSA: peptide ratio of 1:20. After purification by gel filtration on Sephadex G50, the efficiency of peptide conjugation was estimated by mobility shift assay on SDS−PAGE (7.5%).

Cell Culture and Particle Delivery. HeLa, HepG2, and 3T3/NIH cell lines were obtained from the American Type Culture Collection (Rockville, MD) and maintained in Minimum Essential Medium Eagle (EMEM) or Dulbecco's Modified Eagles Medium (DMEM) growth media (BioWhittaker, Walkersville, MD) without addition of antibiotics at 37 °C in controlled CO_2 atmosphere. For investigating the cellular localization of peptides, cells were plated on glass coverslips and grown to 75% confluency in 12-well plates and then incubated with nanoparticle conjugates (150 pM) for various times. It has been shown that the presence of serum in the culture medium inhibits cellular binding/uptake of cationic lipids and reduces their efficiency as nucleic acid carriers (*23*); therefore, most cellular delivery agents available today require serum-free media during delivery. The presence of BSA contributed greatly to the stability of nanoparticle conjugates in serum-containing media. All studies shown herein were conducted using media which contain 10% FBS. At indicated time points the coverslips were rinsed extensively with phosphate-buffered saline (PBS), and the cells were fixed with 4% paraformaldehyde in PBS for 15 min at room temperature and then rehydrated in PBS. Following fixation, the cover slip with cells were mounted onto glass slides with FluorSave (Calbiochem, San Diego, CA) mounting media and allowed to dry overnight prior to microscopy analysis.

The stability of protein−gold nanoparticle conjugates vs flocculation or protein exchange in EMEM growth media with 10% FBS was determined as follows. An aqueous suspension of gold nanoparticles (450 μL of 1.16 nM) was adjusted to pH 9 by adding 50 μL of 10 mM sodium carbonate buffer. Fluorescein isothiocyanate (FITC)-terminated M3 peptide was conjugated to BSA, and the BSA conjugate was slowly added to the gold sol. The final concentration of gold nanoparticles and M3−BSA conjugate was 0.98 nM and 1.78 μM, respectively. The mixture was incubated at room temperature for 15 min, and native BSA (20 μL of 2 mg/mL) was added to prevent flocculation. Six identical solutions were prepared using this protocol. In three of the solutions, any unbound FITC-labeled M3−BSA conjugates were removed by centrifugation. The fluorescence of the supernatant was measured to determine the concentration of unbound M3−BSA conjugate. The number of bound M3−BSA conjugates per gold nanoparticle was calculated by subtracting the number of unbound conjugates from the total number of conjugates added initially. The remaining three solutions were diluted 1:5 in EMEM growth medium without phenol-red (Cambrex Bio Science, Walkersville, MD). Visible absorption spectra of the solutions were acquired after 4 h, and no change of the gold nanoparticle plasmon absorption band was observed. The solutions were centrifuged, and the M3−BSA gold nanoparticle conjugates were then resuspended in 450 μL of sodium phosphate buffer (10 mM, pH 7). Dithiothreotol (DTT) (94 μL of 480 mM) was added and incubated for 24 h to exchange the bound M3−BSA conjugates on the gold nanoparticles. The solutions were centrifuged and the supernatants analyzed by fluorescence spectroscopy to determine the amount of bound M3−BSA conjugate on gold nanoparticles after exposure to growth medium. Since DTT may not remove all surface-bound proteins, this experiment yields an upper limit to the number of M3−BSA conjugates that are displaced in the growth medium.

Characterization of Particle Trajectories. The unique optical properties of colloidal gold enable their identification by relatively simple light microscopy techniques. Particles as small as 10 nm can be observed with video-enhanced microscopy techniques (albeit as an inflated diffraction image) (*24*, *25*). However, high contrast microscopy techniques available currently rely on time-consuming postacquisition processing. In addition, high-density cellular granules can easily be mistaken for gold nanoparticles (*26*).

To improve the visibility of gold nanoparticles in cells, we combined the high resolution afforded by color video-enhanced microscopy with the high contrast and pseudo three-dimensional imaging capabilities of differential interference contrast microscopy (DIC). This hybrid technique (video-enhanced color differential interference contrast microscopy, VECDIC) easily distinguishes gold nanoparticles from cellular granules and organelles under polarized light conditions of DIC. Since DIC allows optical sectioning of the sample, the approximate location of nanoparticles inside cells was determined by varying the focal plane of the image. VECDIC allows cells and nanoparticles as small as 20 nm to be observed simultaneously without image overlays, albeit image resolution remains at the limits of optical microscopy $\sim$ 200 nm (*27*). Thus, high throughput data analysis at the rate of several hundred slides per day is possible. VECDIC data were confirmed by TEM analysis. The colorimetric lactose dehydrogenase assay (LDH) was used to evaluate the cytotoxicity of peptide−BSA−gold nanoparticle conjugates (Cytotox 96, Promega).

Microscopy. Video-enhanced color DIC microscopy was performed on an upright Leica DMLB microscope equipped with a 0.9 numerical aperture (NA) condenser, differential interference contrast (DIC) optics, and 100× plan (NA 1.3) oil objective. The video system comprises a Nikon DMX-1200 color CCD digital camera, with software-based manual control of color balance and contrast enhancement on live and captured images.

TEM analysis was performed on a Philips CM-12 TEM (accelerating voltage was 100 kV) at the University of North Carolina Dental School Research Electron Microscopy Center. Cells were prepared for TEM by staining in 1% OsO_4, dehydrating in ethanol gradient, immersing in LR white embedding resin, and curing under UV light. Microtomed sections were then placed on Formvar grids and poststained with uranyl acetate and lead acetate. A Malvern Zetasizer 1000HS was used to determine the hydrodynamic diameter of gold nanoparticle−BSA complexes.

RESULTS

Preparation of Gold Nanoparticle Vectors. Peptide−gold particle complexes were assembled by conjugating peptides to bovine serum albumin (BSA) and then attaching BSA−peptide conjugates to gold nanoparticles (Figure 1). Since the purity of BSA varies, it is important to determine the binding efficiency of the MBS and peptides to each batch of BSA. An initial ratio MBS:BSA of 50:1 resulted in 28 ± 3 MBS linkers per BSA molecule as measured by a fluorescamine assay (*22*). The reaction of cysteine-terminated peptides with MBS−BSA conjugates was measured by gel shift assays and was found to be peptide dependent (Table 2).

BSA−peptide conjugates were complexed to 20 nm diameter gold particles in 25 mM pH 11 carbonate buffer to prevent colloidal gold aggregation caused by positively charged peptides. Dynamic light scattering and transmission electron microscopy revealed that BSA−peptide conjugates add $\sim$4 nm to the hydrodynamic diameter of a 22 nm gold particle. Prior to complexation, gold particles and BSA had average hydrodynamic diameters

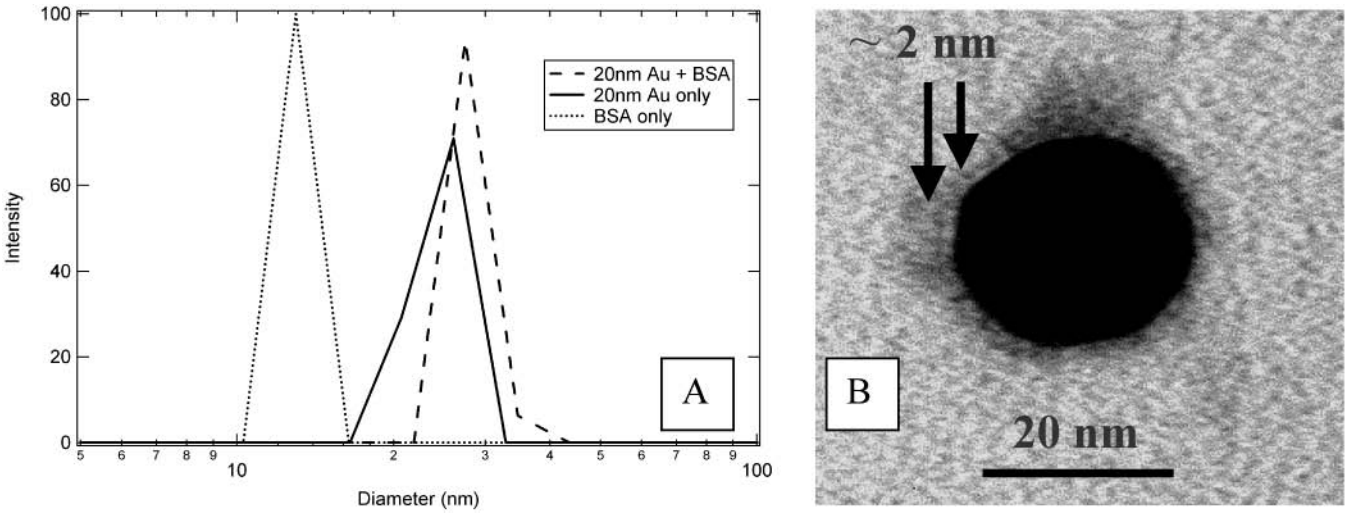


Figure 2. DLS (A) and TEM (B) data showing complex formation between 20 nm colloidal gold and BSA.

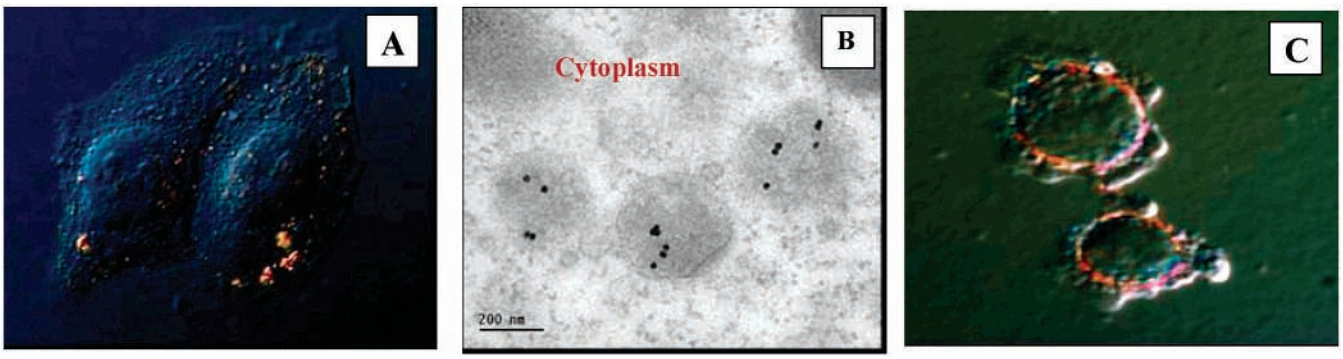


Figure 3. M1 nanoparticles incubated with HeLa cells. After 1 h nanoparticles were observed by video-enhanced color differential interference contrast microscopy (A) and transmission electron microscopy (B) clustered in compartments inside the cytoplasm. After 2 h, nanoparticles were found accumulated around the nuclear membrane (C).

Table 2. Number of Peptides Bound to BSA As Determined by 7.5% SDS−PAGE

no.	peptide sequence	peptide/BSA
M1	CGGGPKKKRKVGG	7 ± 2
M2	CGGRKKRRQRRRAP	3 ± 1
M3	CGGFSTSLRARKA	8 ± 2
M4	CKKKKKKGGRGDMFG	5 ± 2

of 22 and 12 nm, respectively (Figure 2). The average hydrodynamic diameter of the BSA−gold-nanoparticle complex increased to 26 nm. BSA is an oblong molecule that can be approximated by a cylinder 3 nm in radius and 10 in length. Since the data show that BSA adds much less than 10 nm to the diameter of gold nanoparticles, it seems likely that BSA binds to the nanoparticle along its length. The fact that BSA does not add greatly to the size of the gold particle is important in its use in constructing intracellular targeting vectors because only particles with diameters below ca. 30 nm are capable of entering cell nuclei.

A surface coverage of 160 ± 8 BSA per 20 nm gold nanoparticle was determined previously by time-resolved fluorescence spectroscopy (*22*). This amount is difficult to rationalize if BSA adsorbs along its long axis; thus, we cannot rule out that some multilayer adsorption occurs on gold nanoparticles. Quantitative exchange studies performed in the presence of EMEM/10% FBS revealed that no more than 30% of M3−BSA conjugates were displaced from the gold nanoparticle surface in 4 h. This may represent exchange of more loosely bound multilayers. Irrespective of the location of the exchangeable protein (surface or multilayer), within the time scale of a typical delivery experiment (<3 h), the data suggest that >300 peptides are bound to each nanoparticle.

Cellular trajectories of peptide−gold particle complexes were characterized in the following three cell lines: HeLa, 3T3/NIH, and HepG2. These cell lines were chosen to illustrate cell-specific differences in nuclear targeting for each peptide investigated.

Nanoparticle Delivery to HeLa Cells. The fate of nanoparticles inside HeLa cells depended upon the targeting peptide complexed to the gold surface. In general, nanoparticle uptake followed one of three pathways: (i) cell entry followed by exocytosis; (ii) cell entry and transport up to the nuclear membrane; (iii) cell entry and nuclear translocation.

Nanoparticles modified with each of the peptides listed in Table 1 were observed inside HeLa cells by video-enhanced color differential image contrast microscopy. Cellular localization was corroborated by co-analysis of samples by transmission electron microscopy (TEM) (Figure 3).

After 1 h of incubation with HeLa cells, all four peptide−nanoparticle conjugates were found clustered together in cellular compartments that appear to be endosomes as observed by TEM (see M1 conjugates in Figures 3A and B). The behaviors of the peptide−nanoparticle complexes differed once they escaped the endosomal pathway.

After 1 h, nanoparticles carrying peptide M1 were able to escape the endosomal pathway and reach the nuclear membrane. At longer times (2−3 h), M1 nanoparticles were found clustered around the cytoplasmic side of the

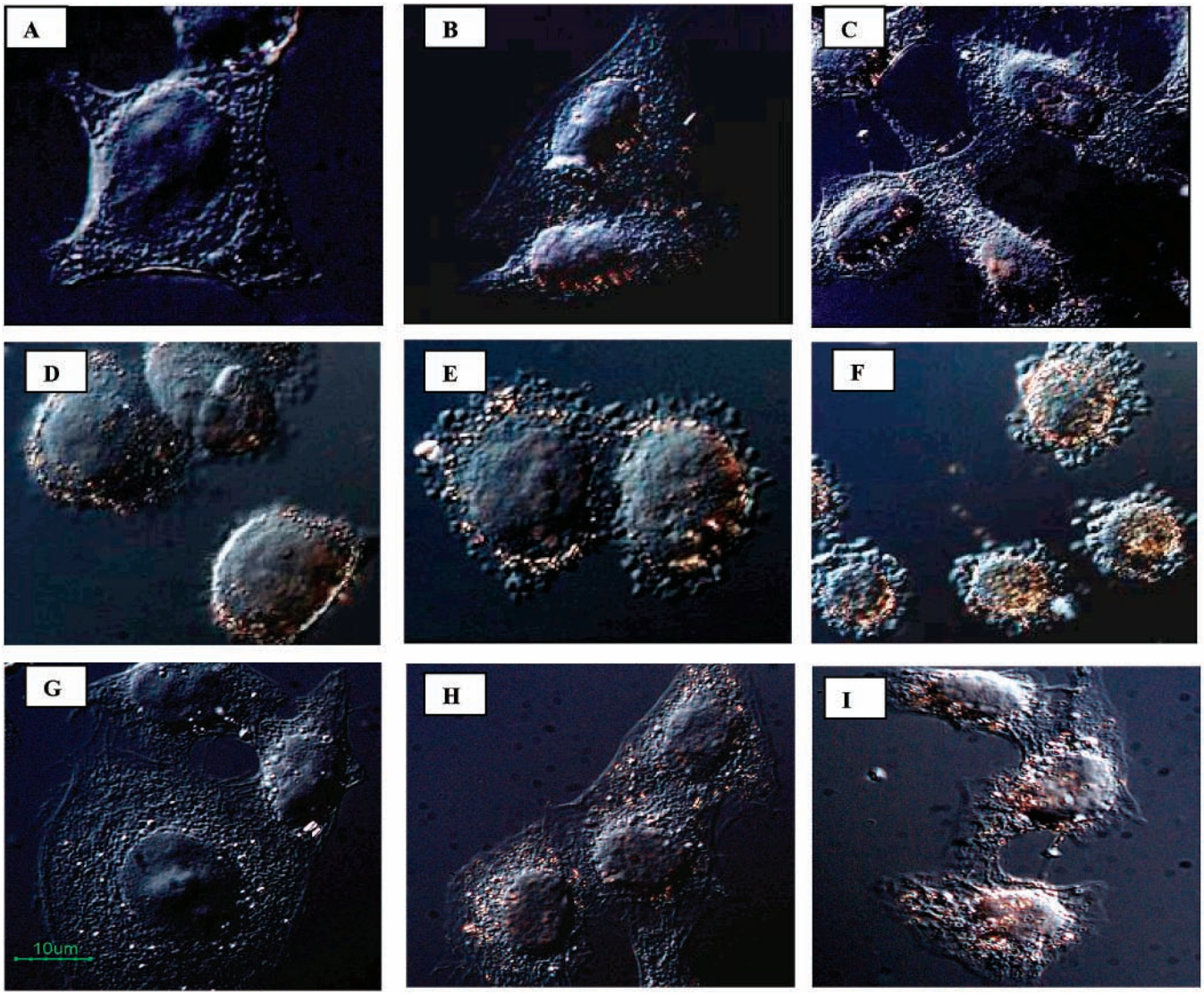


Figure 4. Incubation of HeLa cells with 20 nm diameter gold nanoparticles observed by VECDIC. Figure 4 (A−C) 0.5, 1.5, and 3 h incubation with nanoparticles carrying peptide M2; (D−F) 0.5, 1.5, and 3 h incubation with nanoparticles carrying peptide M3; (G−I) 0.5, 1.5, and 3 h incubation with nanoparticles carrying peptide M4.

nuclear membrane with relatively few located inside the nucleus (Figure 3C). Apparently, M1 nanoparticle complexes were able to enter HeLa cells and escape the endosomal pathway, but were unable to interact properly with the nuclear pore complex.

Nanoparticles carrying peptide M2 were found in the cytoplasm of HeLa cells after 1 h, and in 3 h only minimal nuclear localization was observed (Figure 4A−C). The peptide sequence from HIV Tat protein has been observed previously to bypass endosomal pathways. This occurred on a time scale of minutes, via mechanisms that are not yet well understood (*16*). In contrast to those reports, we observed slow uptake and primarily cytoplasmic uptake of M2 nanoparticles.

Nanoparticles carrying peptide M3 accumulated around the nuclear membrane after 2 h of incubation with HeLa cells; after 3 h M3 nanoparticles were also found inside the nucleus of over 70% of the observed cells (Figures 4D−F). Nuclear targeting was also observed during the delivery of nanoparticles carrying peptide M4 (Figure 4G−I). In contrast to the other peptides studied, M4 peptides do not have any previously known NLS function, carrying only the integrin binding domain plus six lysine residues.

Nanoparticle Delivery to 3T3/NIH Cells. 3T3/NIH cells appear to be more selective than HeLa cells. While M1, M3, and M4 nanoparticles were able to enter the cytoplasm after 30 min of incubation with 3T3/NIH, none of them were able to translocate the nuclear membrane within 6 h (Figure 5). M2 nanoparticles were not found inside the cytoplasm of 3T3/NIH cells by VECDIC microscopy.

Nanoparticle Delivery to HepG2 Cells. Entry into the cytoplasm of HepG2 cells was strongly dependent on the peptide sequence attached to nanoparticles. M1 and M2 nanoparticles were able to enter the cytoplasm of HepG2 cells but were not found near the nuclear membrane or inside the nucleus, which suggests that these nanoparticles were unable to escape from endosomes. While M3 nanoparticles were observed in the nucleus of HeLa cells and the cytoplasm of 3T3/NIH cells, no cellular uptake was observed when they were introduced to HepG2 cells (Figure 6D−F). The most surprising results were observed with M4 nanoparticles (Figure 6G−I). M4 nanoparticles not only entered the cytoplasm of HepG2 cells, but also accumulated inside the nucleus after 2 h of incubation time (Figure 6H,I).

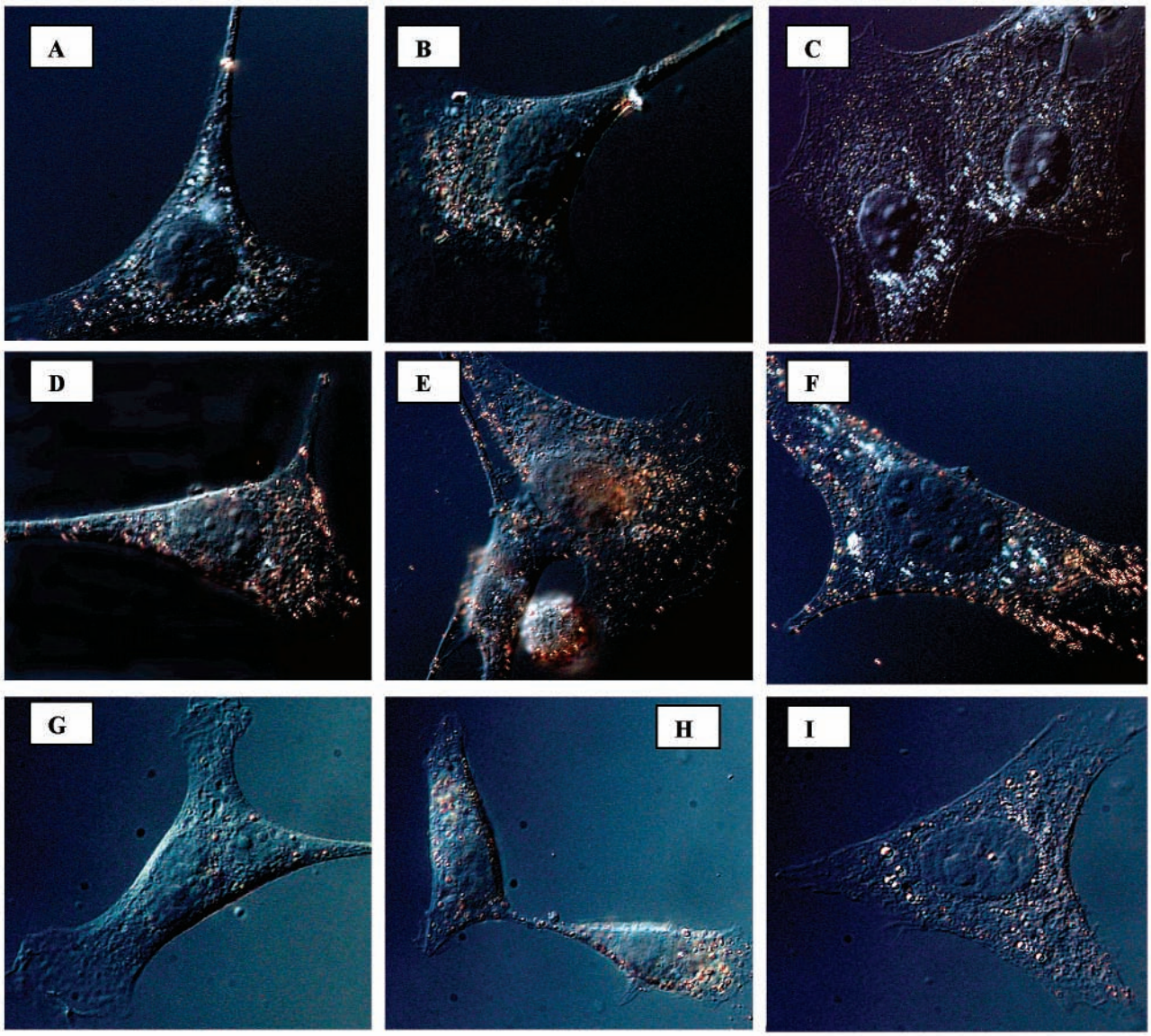


Figure 5. Incubation of NIH/3T3 cells with 20 nm diameter gold nanoparticles observed by VECDIC. (A−C) 0.5, 1.5, and 3 h incubation with nanoparticles carrying peptide M1; (D−F) 0.5, 1.5, and 3 h incubation with nanoparticles carrying peptide M3; (G−I) 0.5, 1.5, and 3 h incubation with nanoparticles carrying peptide M4.

Temperature Studies. BSA−peptide conjugates are polycationic proteins with pI values above 7.0 as determined by isoelectric focusing gel electrophoresis (not shown), and the cell membrane is a negatively charged complex aggregate of proteins, lipids, and carbohydrates. While xenobiotics are normally taken up by passive diffusion, considering the size of peptide−BSA−gold conjugates, passive diffusion is an unlikely translocation mechanism here. Pinocytosis and receptor-mediated endocytosis (RME) are the prime mechanisms for the uptake of large molecular structures (*28*). Cellular uptake of nanoparticles coated with peptide−BSA conjugates could occur by RME, or for the Tat RKKRRQRRR sequence, via the less understood peptide transduction domain mechanism (PTD). Endocytosis occurs within minutes to several hours and is energy dependent. Cell uptake by PTDs is reported to occur within minutes and is energy independent. The peptide−nanoparticle constructs reported here did not enter cells in the first 30 min of delivery, suggesting either that the PTD mechanism is slowed by the nanoparticle or that it is not the mechanism of cell entry. To test the energy dependence of uptake, experiments were performed at 4 °C. At 4 °C sufficient energy is not available to support RME pathways (*29*). Internalization of all peptide−nanoparticle complexes was inhibited at low temperature suggesting an energy-dependent transport process. These results support the involvement of endocytosis as the major route for the internalization of all peptide-nanoparticle complexes studied here, including the M2 peptide.

DISCUSSION

Cellular trajectories of the NLS peptides studied here are summarized in Table 3. Notably, the data reveal a strong dependence of cellular targeting on the cell line and peptide studied. M1 nanoparticles were able to enter all cell lines studied, but there was little or no nuclear transport of these particles although M1 is a well-known NLS. Prior results have shown that when M1 nanoparticles are injected into the cytoplasm, thus bypassing the endosomal pathway, they will translocate the nuclear membrane (*3*−*9*). If M1 can trigger RME, and is capable of nuclear translocation once in the cytoplasm, why then can it not reach the nucleus from outside an intact cell? Two possible answers are that the M1 construct is trapped in endosomes or is somehow altered inside the

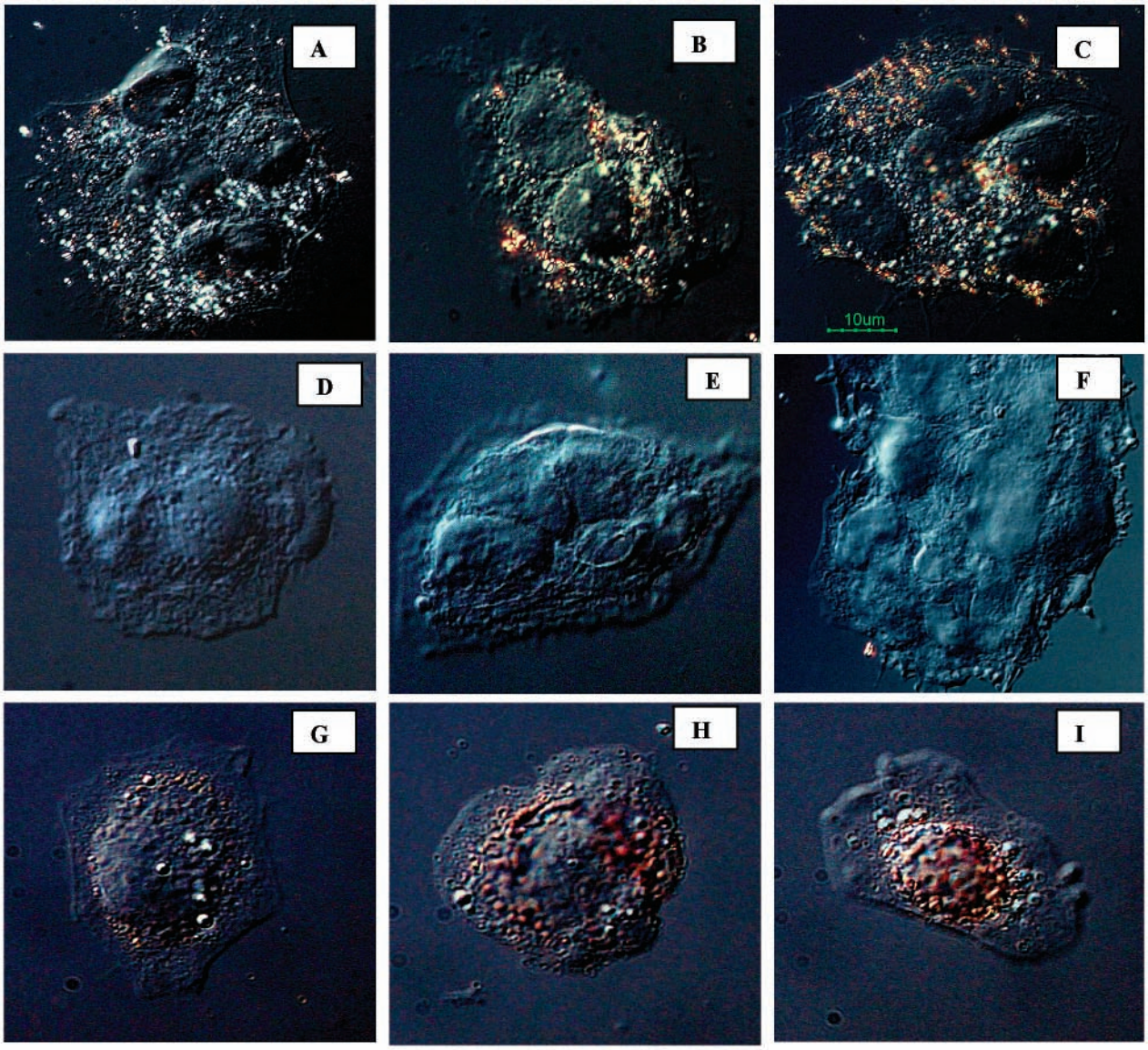


Figure 6. Incubation of HepG2 cells with 20 nm diameter gold nanoparticles observed by VECDIC. (A−C) 0.5, 1.5, and 3 h incubation with nanoparticles carrying peptide M1; (D−F) 0.5, 1.5, and 3 h incubation with nanoparticles carrying peptide M3; (G−I) 0.5, 1.5, and 3 h incubation with nanoparticles carrying peptide M4. Peptide M4 was observed in the nucleus in over 70% of cells imaged.

Table 3. Location of Peptide-Coated Nanoparticles after 3-h Incubation Times with Various Cell Lines

no.	peptide sequence	HeLa	3T3/NIH	HepG2
M1	CGGGPKKKRKVGG	cytoplasm	cytoplasm	cytoplasm
M2	CGGRKKRRQRRRAP	cytoplasm	no uptake	cytoplasm
M3	CGGFSTSLRARKA	nucleus	cytoplasm	no uptake
M4	CKKKKKKGGRGDMFG	nucleus	cytoplasm	nucleus

endosome in a way that renders it incapable of interacting with importin-α. TEM and VECDIC show that M1 nanoparticles are evenly distributed throughout the cytoplasm, rather than clustered together. It is therefore likely that the physicochemical properties of M1 are altered during endosomal transport. Whether this involves a structural or chemical change is currently unknown.

In contrast, M3 nanoparticles were seemingly unaffected by endosomal transport of HeLa cell lines. This peptide was able to enter HeLa cells, escape endosomes, and pass through the nuclear pore complex. In 3T3/NIH cells, however, M3 nanoparticles were found clustered together in endosomes, apparently unable to escape and reach the nuclear membrane. Finally, there was no observed uptake of M3 nanoparticles in HepG2 cells. These differences were also reflected in the LDH cytotoxicity assay. M3−BSA−gold nanoparticle conjugates caused 20% cell death in HeLa cells after 3 h, a result that was traced solely to the M3−BSA construct. After 3 h incubation with the same construct, 3T3/NIH cells were 95% viable. Such large differences in cell viability are likely attributable to the strong nuclear delivery of the M3 conjugate in HeLa cells. We speculate that the highly cationic M3 peptide can interact strongly with DNA inside the HeLa nucleus.

The synthetic peptide M4, composed of the integrin binding domain (RGD) and a stretch of six lysine residues, was unable to reach the nucleus 3T3/NIH cells but was the only peptide capable of targeting the nucleus of HepG2 cells. Integrin binding domains are known to induce cellular uptake by both RME and phagocytosis. However, they typically do not interact with the nuclear pore complex. Thus, it is likely that M4 nanoparticles enter the cell via the integrin binding domain and escape endosomes due to the presence of positively charged lysines, which are known to induce leakage of negatively charged vesicles and cells (*30*). The fragment of M4

consisting of six lysine residues could also be involved in nuclear transport, as it resembles the classic NLS sequences rich in lysines (e.g., large T NLS).

Perhaps the most surprising result of this study is the failure of M2 to target the nucleus of any cell line studied. M2 contains the arginine-rich sequence of the Tfr24 peptide from the HIV Tat protein. This sequence is known to bind the TAR RNA hairpin and is also one of a class of peptides known commonly as peptide transduction domains (PTDs). The observation of a PTD led to further refinement of the sequence to determine the region that was most active for transport through cell membranes. The minimal sequence for PTD activity has been determined to be the nine amino acids (RKKRRQRRR) (*18*). Most peptides that contain this sequence of nine amino acids appears to function as a PTD. PTDs have been reported to target nuclei of all cell lines using an energy-independent mechanism (*10*−*12*). Several recent studies have attributed the efficient nuclear targeting of PTDs to an artifact of cell fixation (*31*−*33*). According to these studies the positively charged peptides that contain the arginine-rich sequence bind tightly to the cell membrane. Once the cells are fixed, the membrane is disrupted and the peptides can diffuse into the cell. Once inside the cell there is a strong electrostatic attraction to DNA in the nucleus. Although similar protocols were used here for cell fixation, nuclear targeting was not observed for the M2 conjugated to gold nanoparticles. On the basis of these observations, we speculate that nanoparticle size may minimize the reported artifacts of cell fixation. This is logical since diffusion in the medium is greatly reduced for a particle of molar mass 50 MDa compared to a single small peptide.

CONCLUSIONS

Targeted nuclear delivery of diagnostic probes and therapeutics could improve disease detection and treatment. Accessing the nucleus from outside an intact cell is difficult, however, because of three membrane barriers: (1) outer cell membrane, (2) endosomal membrane, and (3) nuclear membrane. This paper highlighted the challenges associated with crossing these barriers. For example, the SV40 NLS is capable of entering HeLa cells via receptor-mediated endocytosis (this work). It is also able to cross the nuclear membrane if it is directly injected into the cytoplasm (*3*−*9*). Despite this, the SV40 NLS is not translocated from outside an intact HeLa cell to the nucleus because it cannot break free of endosomal compartments or is somehow altered as it travels through the endosomal pathway. These observations suggest that the most efficient nuclear targeting may result from a combination of targeting peptides attached to a single vector. This can be accomplished in many ways, e.g., using liposomes, dendrimers, or cyclodextrans. Our goals are to study further the ability of multipeptide gold nanoparticle conjugates to target cell nuclei.

ACKNOWLEDGMENT

The authors wish to thank The David and Lucile Packard Foundation, NSF-DMR (9900073), and NIH NCI 98194-01 for support of this work. We also thank Dr. Wallace Ambrose at the University of North Carolina—Chapel Hill for help acquiring the TEM images.

LITERATURE CITED

(1) Nagasaki, T., et al. (2003) Can Nuclear Localization Signals Enhance Nuclear Localization of Plasmid DNA? *Bioconjugate Chem. 14,* 282−286.

(2) Baudhuin, P. V. d. S., P., Beauvois, S., and Courtoy, P. J. (1989) *Colloidal Gold: Principles, Methods, and Applications* (Hayat, M. A., Ed.) Vol. 2, Academic Press, New York.

(3) Feldherr, C., and Akin, D. (1993) Regulation of Nuclear Transport in Proliferating and Quiescent Cells. *Exp. Cell Res. 205,* 179−186.

(4) Feldherr, C., and Akin, D. (1994) Variations in Signal-Mediated Nuclear Transport during the Cell Cycle in BALB/c 3T3 Cells. *Exp. Cell Res. 215,* 206−210.

(5) Feldherr, C., and Akin, D. (1999) Signal-Mediated Nuclear Transport in the Amoeba. *J. Cell Sci. 112,* 2043−2048.

(6) Feldherr, C., Lanford, R., and Akin, D. (1992) Signal-Mediated Nuclear Transport in Simian Virus 40-transformed Cells is Regulated by Large Tumor Antigen. *Proc. Natl. Acad. Sci. U.S.A. 89,* 11002−11005.

(7) Feldherr, C. M., and Akin, D. (1990) The permeability of the Nuclear Envelope in Dividing and Nondividing Cell Cultures. *J. Cell Biol. 111,* 1−8.

(8) Feldherr, C. M., Lanford, R. E., and Akin, D. (1992) Signal-Mediated Nuclear Transport in Simian-Virus 40- Transformed Cells Is Regulated by Large Tumor-Antigen. *Proc. Natl. Acad. Sci. U.S.A. 89* (22), 11002−11005.

(9) Vives, E., Brodin, P., and Lebleu, B. (1997) A truncated HIV-1 Tat protein basic domain rapidly translocates through the plasma membrane and accumulates in the cell nucleus. *J. Biol. Chem. 272,* 16010−16017.

(10) Schwarze, S., Hruska, K., and Dowdy, S. (2000) Protein Transduction: Unrestricted delivery into all cells? *Trends Cell Biol. 10,* 290−295.

(11) Lewin, M., et al. (2000) Tat Peptide-Derivatized Magnetic Nanoparticles Allow inVivo Tracking and Recovery of Progenitor Cells. *Nat. Biotechnol. 18,* 410−414.

(12) Tkachenko, A. G., Coleman, D., Glomm, W., Ryan, J., Anderson, M. F., Franzen, S., and Feldheim, D. L. (2003) Multifunctional Gold Nanoparticle-Peptide Complexes for Nuclear Targeting. *J. Am. Chem. Soc. 125,* 4700−4701.

(13) Efthymiadis, A., Briggs, L., and Jans, D. (1998) The HIV-1 Tat Nuclear Localization Sequence Confers Novel Nuclear Import Properties. *J. Biol. Chem. 273,* 1623−1628.

(14) Caron, N., et al. (2001) Intracellular Delivery of a Tat-eGFP Fusion Protein into Muscle cells. *Mol. Ther. 3* (3), 310−318.

(15) Nori, A., et al. (2003) Tat-Conjugated Synthetic Macromolecules Facilitate Cytoplasmic Drug Delivery to Human Ovarian Carcinoma Cells. *Bioconjugate Chem. 14,* 44−50.

(16) Torchillin, V., et al. (2001) TAT Peptide on the Surface of Loposomes affords their Efficient Intracellular Delivery even at Low Temperature and in the Presence of Metabolic Inhibitors. *Proc. Natl. Acad. Sci. U.S.A. 98* (15), 8786−8791.

(17) Truant, R., and Cullen, B. (1999) The Arginine Rich Domains Present in Human Immunodeficiency Virus Type 1 Tat and Rev Function as Direct Importin b-Dependent Nuclear Localization Signals. *Mol. Cell. Biol. 19* (2), 1210−1217.

(18) Silhol, M., et al. (2002) Different Mechanisms for Cellular Internalization of the HIV-1 Tat-derived Cell Penetrating Peptide and Recombinant Proteins Fused to Tat. *Eur. J Biochem. 269* (2), 494−501.

(19) Zhang, F., et al. (1999) A Transfecting Peptide Derived from Adenovirus Fiber Protein. *Gene Ther. 6,* 171−181.

(20) Hart, S., Harbottle, R., and Coutelle, C. (1995) *Integrin-Mediated Gene Delivery*, in *Targeting of Drugs 5: Strategies for Oligonucleotide and Gene Delivery in Therapy* (Gregoriadis, G., and McCormack, B., Eds.) pp 101−106, Plenum Press, New York London.

(21) Nakai, K. (2000) Protein Sorting Signals and Prediction of Subcellular Localization. *Adv. Protein Chem. 54,* 277−344.

(22) Xie, H., et al. (2003) Characterization of Peptide-modified Gold Nanoparticles by Fluorescence Spectroscopy and Time-correlated Single Photon Counting. *Anal. Chem. 75,* 5797−6001.

(23) Kang, S., Zirbes, E., and Kole, R. (1999) Delivery of Antisense Oligonucleotides and Plasmid DNA with Various Carrier Agents. *Antisense Nucleic A 9,* 497−505.

(24) Hoefsmit, E., et al. (1986) Light Microscopical Detection of Single 5 and 20 nm Particles Used for Immunolabeling of

Plasma Membrane Antigens with Silver Enhancement and Reflection Contrast. *J. Microsc. 143,* 161−169.
(25) Inoue, S. (1981) Video Image Processing Greatly Enhances Contrast, Quality and Speed in Polarization-Based Microscopy. *J. Cell Biol. 89,* 346−356.
(26) Inoue, S., and Spring, K. (1997) *Video Microscopy, The Fundamentals,* 2nd ed, p 741, Plenum Press, New York and London.
(27) Goodman, S., Park, K., and Albrecht, R. (1989) A Correlative Approach to Colloidal Gold Labeling with Video-Enhanced Light Microscopy, Low-Voltage Scanning Electron Microscopy, and High-Voltage Electron Microscopy. In *Colloidal Gold: Principles, Methods, and Applications*, pp 369−409, Academic Press, Inc., New York.
(28) Saison-Behmoaras, E., et al. (1995) Oligonucleotides: Molecular Versions for Optimal Use in Vivo. in *Targeting of Drugs 5: Strategies for Oligonucleotide and Gene Delivery in Therapy* (Gregoriadis, G., and McCormack, B., Eds.) pp 31−44, Plenum Press, New York, London.
(29) Duncan, R., and Lloyd, J. (1978) Pinocytosis in the rat visceral yolk sac. Effects of temperature, metabolic inhibitors and some other modifiers. *Biochim. Biophys. Acta 544,* 647−655.
(30) Zauner, W., et al. (1997) Glycerol and Polylysine Synergize in their Ability to Rupture Vesicular Membranes: A Mechanism for Increased Transferrin-Polylysine-Mediated Gene Transfer. *Exp. Cell Res. 232,* 137−145.
(31) Richard, J., et al. (2003) Cell-penetrating Peptides. A reevaluation of the mechanism of cellular uptake. *J. Biol. Chem. 278* (3), 585−590.
(32) Lundberg, M., Wikstrom, S., and Johansson, M. (2003) Cell Surface Adherence and Endocytosis of Protein Transduction Domains. *Mol. Ther. 8* (1), 143−150.
(33) Lundberg, M., and Johansson, M. (2002) Positively charged DNA-binding proteins can cause apparent cell membrane translocation. *Biochem. Biophys. Res. Commun. 22,* 367−371.

BC034189Q

Peptidyl Linkers for Protein Heterodimerization Catalyzed by Microbial Transglutaminase

Tsutomu Tanaka,[†] Noriho Kamiya,[§] and Teruyuki Nagamune*[,†]

Department of Chemistry and Biotechnology, School of Engineering, The University of Tokyo, 7-3-1 Hongo, Bunkyo-ku, Tokyo 113-8656, Japan, and Department of Applied Chemistry, Graduate School of Engineering, Kyushu University, 6-10-1 Hakozaki, Fukuoka 812-8581, Japan Received November 11, 2003; Revised Manuscript Received February 21, 2004

Specific peptidyl linkers that result in the heterodimerization of functional proteins, which is catalyzed by microbial transglutaminase from *Streptomyces mobaraensis* (MTG), were generated based on a ribonuclease S-peptide using site-directed mutagenesis. The peptidyl linkers designated as Lys-tag and Gln-tag were designed to possess sole reactive Lys or Gln residue that was amenable for selective Lys-Gln cross-linkage of different proteins. Green fluorescent protein variants, ECFP and EYFP, were employed as model proteins, and those Lys- and Gln-tags were fused to the N-termini of ECFP and EYFP, respectively. As a result, we succeeded in solely obtaining the ECFP-EYFP heterodimer without forming multiply cross-linked byproducts. It was found that the reactivity of peptidyl linkers varied according to the type of amino acid to be replaced. Peptidyl linkers with a basic amino acid (Arg) exhibited the highest reactivity in the cross-linking reaction, suggesting the cationic residue substrate preference of MTG. Kinetic analysis utilizing fluorescent resonance energy transfer (FRET), that is only observed upon the heterodimeric ECFP-EYFP conjugation, revealed that the amino acid replacement contributed to the acceleration of cross-linking reactions by increasing catalytic turnover (k_{cat}), rather than substrate binding affinity (K_m). Finally, using a ribonuclease S-protein, the manipulation of enzymatic protein cross-linking based on specific S-peptide:S-protein interactions was explored. Since newly designed Lys- and Gln-tags retained binding affinities to the S-protein, the heterodimerization was perfectly restrained by wrapping them with the S-protein. The results suggest the possibility of limited protein conjugation by tuning steric hindrance against the MTG. Tailoring enzymatic posttranslational modifications with either engineering peptidyl substrates or by taking specific peptide−protein interactions into consideration may facilitate the development of a new sequential protein conjugation method for the preparation of multifunctional protein.

INTRODUCTION

Site-specifically modified proteins have become a powerful research tool in many fields of biology. The introduction of probes into the desired position of target proteins is of importance when studying protein function and protein−protein interactions. In fact, the conjugation of biologically active molecules has brought about drastic developments in biotechnology. Simple combinations of distinct protein functions can generate practical advantages. For instance, bifunctional protein conjugates such as the antibody−enzyme complex in enzyme immunoassays depict the potential of such protein conjugates. Therefore, a variety of strategies for protein conjugation have been investigated. Chemical conjugation has been utilized to prepare functional protein conjugates (*1*). In this approach, functional groups on the protein surface, such as the ϵ-amino group of Lys residue and the sulfhydryl group of Cys residue, were routinely exploited. One disadvantage of this chemical approach is the heterogeneity of products caused by random modification, resulting in partial or crucial inactivation of target proteins. This is because functional groups of a protein molecule often play an important role in recognition, interaction, and enzymatic activities. To obviate such obstacles, a fully bioactive Lys-deficient protein was prepared for the site-specific conjugation at the N-terminal amino group (*2*); however, major reconstruction of a target protein seems challenging and somewhat time-consuming. Thiol-specific reagents can be utilized in site-specific coupling between a variety of functional compounds and recombinant proteins to which the Cys residue is genetically introduced at a suitable position (*3*−*6*). The combination of a Cys-specific biotinylation of proteins and a specific biotin−streptavidin interaction should be a choice in assembling proteins into designed networks (*7*). The potential of native chemical ligation and expressed protein ligation, which also utilizes thiol chemistry, has been acknowledged in protein engineering research (*8*, *9*). However, these approaches require Cys residues at desired positions, which is often not the case with natural proteins, and even in the case of recombinant proteins, the introduction of Cys residues is sometimes difficult to conduct, especially by bacterial secretion−expression system.

For comparison, genetic manipulation has enabled the preparation of chimeric fusion proteins. In addition to the direct linkage of two DNA fragments encoding the target proteins to be fused, specific protein−protein interactions have recently been employed in obtaining multifunctional fusion proteins (*10*−*12*). However, in general, the larger the size of the chimeric protein is, the

* Corresponding author. Tel: +81-3-5841-7328. Fax: +81-3-5841-8657. E-mail: nagamune@bio.t.u-tokyo.ac.jp.
[†] The University of Tokyo.
[§] Kyushu University.

10.1021/bc034209o CCC: $27.50 © 2004 American Chemical Society
Published on Web 05/01/2004

lower the yield of the active proteins. This is mainly due to misfolding and the formation of inclusion bodies, which could be accelerated by the incorporation of additional protein fragments (*10*, *12*). In addition, genetic engineering has one technical limitation: it is only applicable to the preparation of a fusion protein that is in tandem from the N-terminus to the C-terminus, such as the scFv (single chain antibody variable fragment region). An alternative strategy for covalent, site-specific protein conjugation is thus requisite for a designed arrangement of functional proteins.

Transglutaminase, which can catalyze acyl transfer reactions between Gln and Lys residues (*13*), provides a unique opportunity to assemble protein molecules as opposed to conventional techniques. The capability to posttranslationally modify target proteins allows the engineering of wide range of proteins that are expressed from appropriate hosts (*14*−*17*). The enzymatic approach to the preparation of protein conjugates can be highly selective and mild compared with conventional methods. In addition, potential advantages of the enzymatic approach are as follows: (1) The utilization of short peptidyl linkers is compatible to the current protein expression systems in which a number of peptidyl tags are employed (for protein purification and detection). (2) It is possible to create protein conjugates in which N-termini or C-termini were covalently connected because peptidyl linkers can be genetically tethered to N- and/or C-termini of target proteins.

In our previous work, it was discovered that ribonuclease S-peptide works as a specific peptidyl linker for tunable site-specific protein cross-linking (*18*). However, since this S-peptide possesses both Gln and Lys residues in its sequence, multiply cross-linked byproducts were obtained in addition to the target cross-linked dimers. More sophisticated peptidyl linkers may facilitate the limited conjugation of the two separate proteins in a stoichiometric 1:1 molar ratio, which will lead us to utilize this enzymatic method in reliable, predictable organization of different protein functions. In this study, we thus focused on MTG-mediated protein heterodimerization through designed peptidyl linkers. New peptidyl linkers were prepared, of which sole Lys or Gln residue was amenable for the selective Lys-Gln cross-linkage of different proteins. To rationally control protein cross-linking, the MTG-mediated cross-linking was investigated from both a kinetic and a structural point of view, and several conclusions were thus derived. It is suggested that the strategy proposed here will increase the versatility of enzymatic protein engineering with transglutaminase.

MATERIALS AND METHODS

Materials. Semipurified MTG was provided by Ajinomoto Co. Inc. (Japan). S-protein was purchased from Sigma-Aldrich. All other reagents used in this study were of the highest purity commercially available.

Sample Preparation. Purification of MTG was conducted using a Blue Sepharose CL-6B affinity column (Amersham Pharmacia Biotech Co.) as reported previously (*19*). The catalytic activity of purified MTG was measured using a colorimetric procedure described elsewhere (*20*). S-Peptide-based peptidyl linkers with sole glutamine or lysine residue (abbreviated as Gln- or Lys-tags)[1] were prepared as follows: A polymerase chain reaction (PCR) with Pyrobest DNA polymerase (Takara, Japan) was performed using pET32b(+) (Novagen) as a template, and the amplified gene product encoding the S-peptide was subcloned into pBluescriptSKII(+) with *Eco*RV/*Bam*HI double digestion. Site-directed mutagenesis was performed using a QuikChange site-directed mutagenesis kit (Stratagene). The primer sequences were 5′-GGT ATG AAA GAA ACC GCT GCT GCT AGA TTC GAA CGC (K11R), 5′-GGT ATG AAA GAA ACC GCT GCT GCT GAA TTC GAA CGC (K11E), 5′-GGT ATG AAA GAA ACC GCT GCT GCT AGC TTC GAA CGC (K11S), 5′-GGT ATG AAA GAA ACC GCT GCT GCT GGA TTC GAA CGC (K11G), 5′-TTC GAA CGC GCG CAC ATG GAC AGC (Q15A), and 5′- TTC GAA CGC AAC CAC ATG GAC AGC (Q15N), and complementary strands (sites of mutation are underlined). DNA fragments encoding enhanced cyan fluorescent proteins (ECFP) and enhanced yellow fluorescent proteins (EYFP) were prepared from pECFP and pEYFP plasmids (Clontech), respectively, and subcloned into Gln- or Lys-tag/pBluescript SKII with *Nco*I/*Not*I double digestion. The fragments encoding Gln- or Lys-tag-EC(Y)FP were cloned into pET32b(+) with *Msc*I/*Not*I double digestion.

All proteins were successfully expressed and purified as described before (*18*). The resultant proteins were designated as K11X/Q15A-ECFP (X = R, E, S, G: Lys-tag-ECFPs) and K5A/K11A-EYFP (Gln-tag-EYFP), respectively. In the case of Lys-tag-ECFPs, K11X/Q15N-ECFPs were also prepared. The N-terminal additional peptide sequence of Lys-tag ECFPs was thus GSG-M**K**ETAAA-X_1-EFR-X_2-HMDSGS (X_1 = R, E, G, S; X_2 = A, N) and that of Gln-tag-EYFP was GSGMAETAA-AAFER**Q**HMDSGS (the reactive residues in the cross-linking reaction are shown in bold letters, and the sequences corresponding to the original S-peptide are underlined). The homogeneity of the purified proteins was verified by sodium dodecyl sulfate−polyacrylamide gel electrophoresis (SDS−PAGE). The concentration of MTG was determined using a BCA assay kit (Pierce). The protein concentrations of Lys-tag-ECFPs and Gln-tag-EYFP were measured with a V550 UV/vis spectrophotometer (JASCO, Japan) and calculated assuming molar extinction coefficients of 83 mM^{-1} cm^{-1} (for EYFP at 515 nm) and 32 mM^{-1} cm^{-1} (for ECFP at 434 nm) (*20*).

Protein Cross-Linking Reactions. A Lys-tag-ECFP and a Gln-tag-EYFP (1.2 μM each) were dissolved in 10 mM sodium phosphate buffer (pH 7.5). The cross-linking reaction was initiated by the addition of MTG (0.25 U/mL). After incubation for 2 h at 4 °C, the reaction was terminated immediately by mixing with SDS−PAGE sample buffer (50 mM Tris, 2% SDS, 6% 2-mercaptoethanol) and boiling, and then the products were analyzed with SDS−PAGE.

Evaluation of the Reactivity of Lys-tag-ECFPs with Gln-tag-EYFP by Kinetic Analysis Using FRET. An aqueous solution of Lys-tag-ECFP and Gln-tag-EYFP were prepared in 10 mM sodium phosphate buffer (pH 7.5). After initiation of the cross-linking reaction by the addition of MTG, changes in the fluorescence spectra

[1] Abbreviations: ECFP, enhanced cyan fluorescent protein; EYFP, enhanced yellow fluorescent protein; MTG, microbial transglutaminase; FRET, fluorescence resonance energy transfer; Lys-tag, a peptidyl linker containing the sole reactive Lys residue for MTG; Lys-tag-ECFP, ECFP whose N-terminus is fused to a Lys-tag; Gln-tag, a peptidyl linker containing the sole reactive Gln residue for MTG; Gln-tag-EYFP, EYFP whose N-terminus is fused to a Gln-tag.

(excited at 434 nm) were recorded every 4 to 20 min depending on the reaction rate of each Lys-tag-ECFP using an F-2000 fluorescence spectrophotometer (Hitachi, Japan). The ratio of fluorescence emission intensity at 527 nm (EYFP) to that at 475 nm (ECFP) was normalized by the ratio at time zero (the value without MTG) and used as the FRET signal. The FRET signal increase was successfully followed as a function of time. Steady-state kinetic analysis of the cross-linking reaction was conducted. To determine the kinetic parameters of Lys-tag-ECFPs, the concentration of Gln-tag-EYFP was kept constant at 11 μM while Lys-tag-ECFP concentrations were varied from 0.01 to 3.75 μM. Initial reaction rates were evaluated by increases in FRET signal (I_{527}/I_{475}) as a function of time and fitted to the Michaelis−Menten equation using the nonlinear least-squares method with KaleidaGraph software (Synergy Software). V_{max} values were normalized by the V_{max} of K11R/Q15A-ECFP.

Inhibition of Cross-Linking Reactions. S-Protein (5 μM) and Lys-tag-ECFP (1.2 μM) as the starting material were mixed in 10 mM of sodiunm phosphate buffer (pH 7.5). After incubation for 1 h on ice, Gln-tag-EYFP (1.2 μM) was added to the mixture, and MTG treatment was conducted as described above. The same inhibition experiment by S-protein was performed using Gln-tag-EYFP as the starting material.

Measurements of Dissociation Constants. Dissociation constants between Lys-tag-ECFP, Gln-tag-EYFP, or S-tag-EYFP, and the S-protein were determined using a surface plasmon resonance (SPR) sensor, BIAcore 2000 instrument (BIAcore Inc.). The S-protein (50 μg/mL in 10 mM sodium acetate buffer, pH 4.5) was covalently attached to a CM5 carboxylated dextran sensor chip according to the manufacturer's protocol. Interaction analyses were carried out at 25 °C by injecting different amounts of the protein (10 nM ∼ 1 μM), Lys-tag-ECFP, Gln-tag-EYFP, or S-tag-EYFP (10 nM ∼ 1 μM) into 10 mM HEPES, 150 mM NaCl, 3 mM EDTA, and 0.005% Surfactant P20 (HBS-EP buffer, BIAcore Inc.) at a flow rate of 75 μL/min, signal responses (in RUs) were measured. Association and dissociation rate constants were determined using BIA evaluation software (BIAcore Inc.), in which binding curves for each set of concentrations were fit simultaneously to a 1:1 (Langmuir) binding model. The standard deviation for each parameter was calculated from the results of four independent experiments.

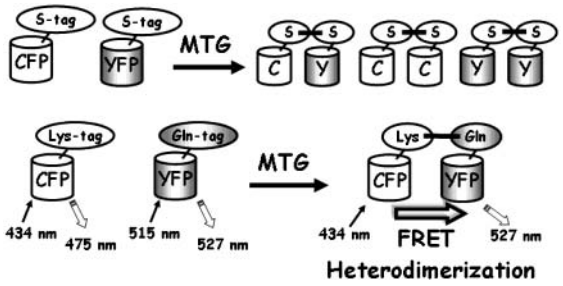
Molecular Modeling. Energy minimization of the S-protein and S-peptide or S-protein and other peptidyl tag complexes was carried out on the basis of X-ray structure of RNase S (pdb code: 1RNU) with Discovery Studio Modeling (Accelrys) following the manufacturer's procedure.

RESULTS AND DISCUSSION

Design of Peptidyl Linkers for Heterodimerization. Efficient preparation of bifunctional proteins from different proteins is the first step in preparing multifunctional proteins. The aim of this study was thus to prepare a peptidyl linker for the controlled heterodimerization of target proteins. Ribonuclease S-peptide was found to be a good candidate (*18*). However, this is not a sufficient peptidyl linker, since homodimerization, heterodimerization, and oligomerization were observed due to both reactive Gln and Lys residues located in its sequence. For instance, when S-peptide-fused ECFP and S-peptide-fused EYFP are cross-linked by MTG, the homodimeric forms, ECFP-ECFP and EYFP-EYFP, and the heterodimeric form, ECFP-EYFP, are simultaneously produced (Scheme 1). To evaluate a preferred substrate's reactivity of the cross-linking reaction for heterodimerization, and since little information is available on peptidyl tags that work as acyl acceptors in MTG-catalyzed protein cross-linking (*21*, *22*), this study focused on obtaining a Lys-tag (i.e. a peptidyl tag containing a reactive Lys residue for selective heterodimerization). Lys-tags were prepared by replacing one of the S-peptide's identified acyl acceptors, Lys11 (*18*), with Arg (cationic), Glu (anionic), Ser (nonionic), and Gly (Figure 1). The acyl donor in the Lys-tags, Gln15 (*18*), was substituted with Ala or Asn (the latter is thought to have similar chemical properties as Gln). In the case of the Gln-tag, both the acyl acceptors, Lys5 and Lys11, were substituted with Ala (Figure 1).

It was confirmed that independently, both ECFP and EYFP are not susceptible to MTG-catalyzed cross-linking, suggesting that intrinsic cross-linkable sites are not presented in those model proteins. Lys-tag-ECFP alone and Gln-tag-EYFP alone are also not susceptible to MTG-catalyzed cross-linking, suggesting the homodimeric form is not produced (data not shown). As shown in Figure 2A, Lys-tag-ECFPs and Gln-tag-EYFPs are distinctly cross-linked, yielding corresponding heterodimers based on the molecular mass of the target proteins (ca. 58 kDa). Because intrinsic cross-linkable sites are unavailable in both ECFP and EYFP, it is possible that the heterodimer was formed through Lys5-Gln15 cross-linkage. The residual fraction of the monomeric form can be produced with competitive hydrolysis of Gln to Glu (deamidation) using MTG. The upward shift of the protein band could

Scheme 1. Schematic Illustration of MTG-Mediated Protein Heterodimerization between Lys-tag-ECFP and Gln-tag-EYFP



[a] The upper half shows the cross-linking of S-peptide-fused ECFP/EYFP, yielding homo- and hetero-dimeric forms (S-peptide is denoted as S-tag). The lower half shows the selective heterodimerization of a designed peptidy tag-fused ECFP/EYFP. FRET occurs only when ECFP/EYFP heterodimer is formed.



Figure 1. Extra N-terminal peptide sequences of linkers tethered to ECFP (in the case of Lys-tag) and EYFP (in the case of Gln-tag). All peptidyl linkers were prepared by site-directed mutagenesis of the S-peptide (original sequence is shown as an S-tag).

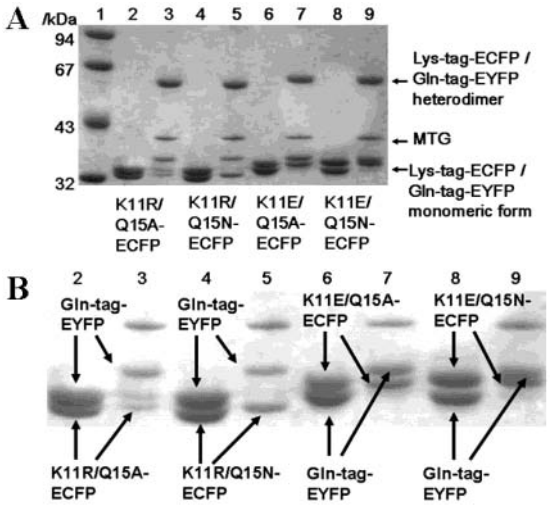


Figure 2. (A) SDS−PAGE analysis of the reaction products following MTG-catalyzed cross-linking of Lys-tag-ECFPs and Gln-tag-EYFP (lane 1, low molecular weight markers; lane 2, K11R/Q15A-tag-ECFP; lane 3 K11R/Q15A-tag-ECFP with MTG; lane 4, K11R/Q15N-tag-ECFP; lane 5, K11R/Q15N-tag-ECFP with MTG; lane 6, K11E/Q15A-tag-ECFP; lane 7 K11E/Q15A-tag-ECFP and Gln-tag-EYFP with MTG; lane 8, K11E/Q15N-tag-ECFP; lane 9, K11E/Q15N-tag-ECFP with MTG. All samples (lanes 2 to 9) contain the same amounts of Gln-tag-EYFP). (B) Magnification of the lower portion of Figure 2 (A).

be ascribed to an increase in negative charge of the Gln-tag-EYFP. This was confirmed by observations that the K11E/Q15A(N)-tag-ECFP fraction shifted slightly upward compared with the K11R/Q15A(N)-tag-ECFP fraction (compare lanes 2 and 6, or lanes 4 and 8 in Figure 2B). SDS−PAGE analysis of cross-linking reactions with all Lys-tags (results with K11S(G)/Q15A(N)-tag-ECFPs are not shown) revealed that when employing K11R/Q15A(N)-tag-ECFP, the amount of residual monomeric fraction was at its lowest among the peptidyl tags prepared, indicating that K11R substitution might enhance the reactivity in cross-linking.

Quantitative Evaluation of the Reactivity of Lys-tags in the Heterodimerization with FRET-Based Kinetic Analysis. The direct monitoring of cross-linking reactions were previously conducted with FRET analysis between the S-peptide tagged EBFP and EGFP (*18*). This analytical technique is suitable for investigating heterodimerization because FRET is only observed when a ECFP/EYFP heterodimer, not a homodimeric form (Scheme 1), is produced. In this study, the fluorescent proteins were changed from EBFP/EGFP to ECFP/EYFP to obtain more stable FRET signals. This did not affect the fluorometric monitoring of the cross-linking reaction and encouraged the application of this system in kinetic analysis of the reactivity of the peptidyl linkers in cross-linking. It is well-known that the distance between two chromophores (in this case, ECFP and EYFP) has a dominant effect on FRET efficiency. Hence, the cross-linking Lys-tag-ECFP and Gln-tag-EYFP sites were fixed at Lys5 and Gln15, respectively. This allows the assumption that the distance between the chromophores in the heterodimers with different peptidyl linkers is constant, and that an increase in FRET signal is related to the amount of heterodimer produced. To investigate the effect of Q15 substitutions, a series of Q15A and Q15N mutants were prepared.

As shown in Figure 3, K11R replacement appears to have a dominant effect on cross-linking efficiency among the peptidyl tags whereas K11E replacement has a negative effect (black bars). These results correlated well

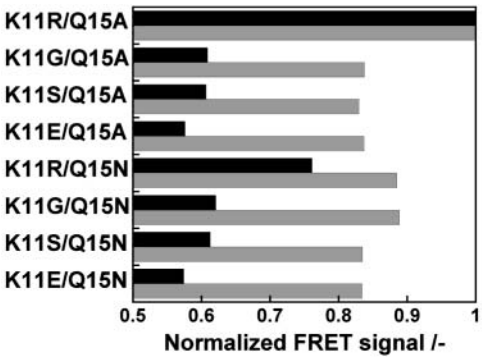


Figure 3. Comparison of FRET signals in the cross-linking reactions of Lys-tag-ECFPs and Gln-tag-EYFP. The cross-linking reaction was conducted with an equimolar mixture of a Lys-tag-ECFP and Gln-tag-EYFP (black bar) at a molar ratio of Lys-tag-ECFP to Gln-tag-EYFP of 10/1 (gray bar). All FRET signals were normalized using the value obtained with K11R/Q15A-tag-ECFP.

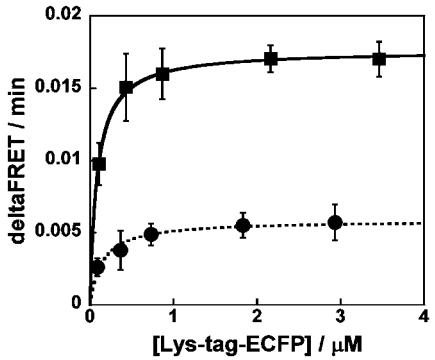


Figure 4. Kinetic analysis of the cross-linking reactions of K11R/Q15A- or K11E/Q15A-tag-ECFP and Gln-tag-EYFP (s−v plot). The reactions were conducted with excess amounts of Gln-tag-EYFP (11 μM) compared with Lys-tag-ECFPs. All FRET signals were normalized using the value obtained without MTG [closed circles with the results of curve fitting (dotted line), K11E/Q15A-tag-ECFP; closed squares and bold line, K11R/Q15A-tag-ECFP].

to those observed in Figure 2; however, it is worth noting that differences of the reactivity in cross-linking among tags is more clearly visualized with FRET-based analysis. It has been suggested that many negatively charged amino acids are located around the acyl acceptor (Lys) binding site of MTG, and therefore cationic substrates might be favorable (*23*). The results of this study seem to fit this assumption: the substitution of amino acid Lys 11 adjacent to the reactive Lys 5 to positively charged Arg (K11R) might enhance cross-linking ability more so than the negatively charged Glu (K11E). One simple strategy to increase heterodimer yield is to increase concentrations of a nucleophilic substrate (Lys-tag-ECFP). When 10-fold higher amounts of Lys-tag-ECFP were applied, the difference in FRET signal between the Lys-tag-ECFPs decreased (gray bars in Figure 3), suggesting that the cross-linking reaction surpasses competitive hydrolysis (deamidation).

Further quantitative analysis was conducted by investigating cross-linking reactions. In kinetic analysis, the initial rate of FRET signal increase was assumed to be the initial rate of heterodimerization. Figure 4 shows a typical s−v plot (with K11R/Q15A- or K11E/Q15A-ECFP and Gln-tag-EYFP) with the data fitting well to the Michaelis−Menten equation. Kinetic parameters obtained with the Lys-tag-ECFPs are listed in Table 1. K11R replacement was the most efficient in conducting successful cross-linking with respect to the specific

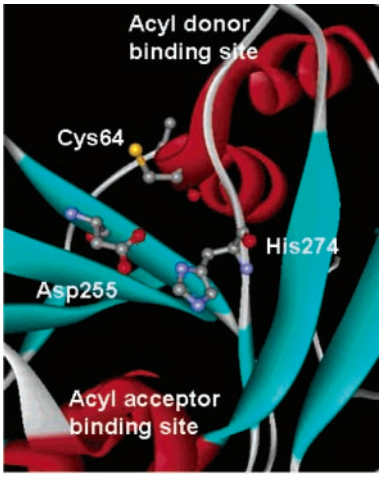


Figure 5. X-ray structure of the area around the active site of MTG (pdb code: 1IU4). The catalytic triad (Cys64, Asp255, and His274) is represented with the ball-and-stick model. The illustrations were drawn using the Weblab viewer Lite program (Molecular Simulation Inc.) Proposed acyl donor and acceptor binding sites (*23*) are also presented.

Table 1. Kinetic Parameters Obtained in Cross-Linking with Various Lys-tag-ECFPs and Gln-tag-EYFPs

amino acid substitution	normalized V_{max} (−)	K_m (μM)	normalized V_{max}/K_m (−)
K11R/Q15A	1.00 ± 0.03	0.14 ± 0.02	1.00
K11G/Q15A	0.42 ± 0.03	0.44 ± 0.01	0.13
K11S/Q15A	0.56 ± 0.06	0.62 ± 0.20	0.13
K11E/Q15A	0.33 ± 0.01	0.19 ± 0.30	0.24
K11R/Q15N	0.70 ± 0.03	0.29 ± 0.06	0.34
K11G/Q15N	0.33 ± 0.02	0.41 ± 0.04	0.11
K11S/Q15N	0.49 ± 0.04	0.36 ± 0.10	0.19
K11E/Q15N	0.36 ± 0.01	0.26 ± 0.03	0.19

constant (V_{max}/K_m) in both K11X/Q15A or K11X/Q15N series (Figures 3 and 4).

The K_m values of K11R- and K11E-substituted tags are comparable, suggesting that these oppositely charged peptidyl tags bind to the active site of MTG with a similar affinity. These results seem contradictory to the assumption that cationic K11R-tags might have a higher affinity to the negatively charged acyl acceptor-binding site of MTG than anionic K11E-tags. However, all experimental data supports distinct reactivity of K11R-tags in the cross-linking reaction among these tags: K11R substitution significantly promotes cross-linking reactions. The difference of the reactivity in cross-linking between K11R and K11E substitutions is largely due to the discrepancy of the V_{max} values, implying that retaining positive charge at position 11 contributes to an accelerated nucleophilic attack of the ϵ-amino group of reactive Lys (K5) in the formation of a ϵ-(γ-glutamyl)lysine bridge rather than substrate binding. Based on the proposed structure−function relationship and the X-ray structure of MTG (Figure 5, pdb code: 1IU4), it can be assumed that the acyl acceptors (the Lys-tags) most likely bind to the active site cleft, which covers the catalytic triad, Cys64-Asp255-His274 (*23*). The distance between Cys64 and His274 is estimated as approximately 0.7 nm, which roughly corresponds to the distance between position 5 and 11 of the Lys-tags when fully extended. Hence, an amino acid at position 11 of Lys-tags might affect the charge state of the catalytic triad especially around Asp255 and His274. It has been proposed that in an MTG-catalyzed reaction, the negatively charged Asp255 nucleophilically attacks a proton of the acyl acceptor (*23*). A possible explanation for the variation in catalytic activity is that the positive charge at position 11 (K11R) might stabilize aninonic Asp255 in the catalytic cycle and accelerate the nucleophilic reaction, while the negative charge (K11E) might lower the reaction rates (Table 1).

With respect to position 15, the replacement of Q15A to Q15N in both K11R and K11E resulted in an approximately 2-fold increase in K_m values, suggesting a decrease in affinity of the acyl acceptors. On the other hand, the substitution of Q15A to Q15N resulted in decreased V_{max} values in all Lys-tags except K11E. There is currently no clear way to interpret these phenomena.

Scheme 2. Schematic Illustration of the Suppression of Heterodimerization with the Coexistence of S-Protein



Table 2. Dissociation Constants between the S-Protein and Peptidyl Linker-Tagged Target Proteins Determined by SPR Analysis Using BIAcore 2000

target proteins	S-tag-EYFP	K11R/Q15A-tag-ECFP	Gln-tag-EYFP
K_d ($\times 10^{-7}$ M)	5.25 ± 0.60	2.85 ± 1.23	15.8 ± 0.60

Suppression of the Cross-Linking Reaction Using S-Protein as a Protecting Group. Controlling protein cross-linking reactions is important in the application of transglutaminase in protein engineering, especially when the target protein possesses multiple cross-linkable sites. If one of the cross-linkable sites of a target protein is temporally blocked and the blocking reagent is removed before the subsequent cross-linking reaction, it becomes possible to conduct sequential protein conjugation. Since ribonuclease S-protein has a high affinity with S-peptide, by wrapping around it (*24*), S-protein could be employed as the blocking reagent in protein conjugation using the S-peptide-based peptidyl linkers designed here. In this section, controllable heterodimerization is evaluated by observing specific peptide−protein interactions using Lys(K11R/Q15A)-tag, Gln-tag, and S-protein (Scheme 2).

To rationally carry out protection and deprotection during the cross-linking reaction, the affinity of peptidyl tags fused to the fluorescent proteins to the S-protein should be examined and compared with that of a S-tag-fused EYFP (possessing the intact S-peptide sequence as shown in Figure 1). Dissociation constants were determined with SPR analysis and are listed in Table 2. The K_d value obtained for S-tag-EYFP was lower than the reported value of free S-peptide (15mer), $K_d = 10^{-9}$ M (*25*−*27*), but the S-protein proved to be accessible to the S-peptide tethered to the N-terminus of the model protein. K11R/Q15A-tag-ECFP appeared to have slightly higher affinity, while Gln-tag-EYFP showed a lower affinity with the S-protein than the S-tag-EYFP. To evaluate the difference in affinity, energy minimization was conducted using DS modeling on the basis of X-ray structure of RNase S, the S-peptide:S-protein complex. With a K5A/K11A substitution for the Gln-tag, no significant difference of RNase S in solvent accessibility was observed. On the other hand, with a K11R/Q15A substitution for a Lys-tag, solvent accessibility of Phe12 (Phe8 in the original S-peptide) decreased (from 8% to 0%) and the distance from Phe12 to Val88 of the S-protein significantly shortened. Hence, the hydrophobic interaction between Phe12 (S-peptide) and Val88

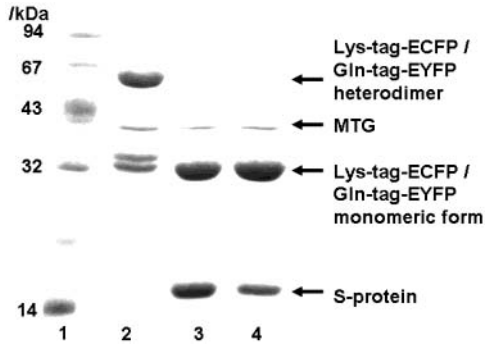


Figure 6. SDS−PAGE analyses of inhibitions of the cross-linking reactions with S-protein. Lane 1, low molecular weight markers; lane 2, K11R/Q15A-tag-ECFP and Gln-tag-EYFP treated with MTG; lane 3, after incubation of K11R/Q15A-tag-ECFP with the S-protein, Gln-tag-EYFP was added and the mixture was treated with MTG; lane 4, the protocol was the same as that outlined above for lane 3 except that Gln-tag-EYFP was used as the starting material in place of K11R/Q15A-tag-ECFP.

(S-protein) might be responsible for generating the higher affinity of the K11R/Q15A-tag with the S-protein.

The results in Table 2 indicate that the S-protein can be employed as a blocking reagent, and this was experimentally confirmed according to Scheme 2. As shown in Figure 6, when Gln-tag-EYFP or Lys-tag-ECFP was capped with an S-protein, the cross-linking reaction with MTG was restrained in both cases (lanes 3 and 4), indicating that the S-protein can be used as a protective reagent for the peptidyl tags designed in this study. It seems that differences in K_d values do not affect the capability of protection under experimental conditions (approximately 99% of engineered peptide tags were protected). Given that an engineered peptide tag is bound to the S-protein in the same manner as an S-peptide, Q15 of a Gln-tag (corresponding to Q11 in an intact S-peptide) is buried within the interior protein structure and has less solvent accessibility, suggesting that the S-protein: Gln-tag-EYFP complex is not susceptible to the cross-linking reaction. On the other hand, K5 of the Lys-tag-ECFP (corresponding to Lys1 in the intact S-peptide) seems to be exposed to the solvent, regardless to the binding of the S-protein. Furthermore, Glu6 and Thr7 of the Lys-tags should have little interaction with the S-protein (*25*, *28*), and so MTG might be accessible to the polypeptide from the Gly1 to Thr7 of K11R/Q15A-tag. However, the S-protein:K11R/Q15A-tag-ECFP complex was not recognized by the MTG, implying that the steric hindrance between MTG and the S-protein has a dominant effect on the inhibition of the cross-linking reaction. This is supported by the following experimental results: first, Ribonuclease S, which exposes the Lys1 of the S-peptide to the solvent (*28*), was not cross-linked with casein, which is MTG's preferred Gln and Lys substrate. Second, the S-protein:K11R/Q15A-tag-ECFP complex was not cross-linked with casein (data not shown). If the S-protein cannot work as a protecting group and the cross-linking reaction occurs, a heterodimer should be observed. No appearance of a heterodimer indicates that the S-protein is working as an effective protecting group (lanes 3 and 4 in Figure 6).

In closing, in the present study we validated the potential of MTG-mediated protein cross-linking in controlled protein conjugation (i.e. heterodimerization) with designed specific peptidyl linkers. The strategy proposed here addresses highly selective protein cross-linking when intrinsic cross-linkable sites targeted by MTG are unavailable in the proteins of interest. Although this limitation would narrow the application of MTG in protein conjugation, in our experience, most globular proteins would not be subjected to MTG-catalyzed protein cross-linking. The enzymatic protein cross-linking directed to recombinantly incorporated peptidyl tags into target proteins can be tuned by substrate preference of MTG and by taking specific peptide−protein interaction (e.g., S-tag:S-protein, peptidyl tag:anti peptidyl tag antibody) into consideration. Our concept was clearly illustrated by site-specific heterodimerization of the model proteins. The fact that a number of peptidyl tags are utilized in current biotechnological applications indicates the potential applicability of this enzymatic method in functional protein engineering. Our research interest has now directed to establish sequential protein conjugation coupled with reversible protection of peptidyl linkers, which will offer one way to prepare multifunctional protein conjugates.

ACKNOWLEDGMENT

We are grateful to Ajinomoto Co. Inc., for providing samples of MTG. The present work was supported mainly by a Grant-in-Aid for Exploratory Research (13875156) and partly by a Grant-in-Aid for the 21st Century COE Program, entitled "Human-Friendly Materials Based on Chemistry" from the Ministry of Education, Culture, Science, Sports and Technology, Japan.

LITERATURE CITED

(1) Hermanson, G. T. (1996) Functional targets. *Bioconjugate Techniques*, pp 3−23, Academic Press, San Diego.

(2) Yamamoto, Y., Tsutsumi, Y., Yoshioka, Y., Nishibata, T., Kobayashi, K., Okamoto, T., Mukai, Y., and Shimizu, T. (2003) Site-specific PEGylation of a lysine-deficient TNF-alpha with full bioactivity. *Nat. Biotechnol. 21.* 546−552.

(3) Velonia, K., Rowan, A. E., and Nolte, J. M. (2002) Lipase polystylene giant amphiphiles. *J. Am. Chem. Soc. 124*, 4224−4225.

(4) Lesaicherre, M.-L., Lue, R. Y. P., Chen, G. Y. J., Zhu, Q., and Yao, S. Q. (2002) Intein-mediated biotinylation of proteins and its application in a protein microarray. *J. Am. Chem. Soc. 124*, 8768−8769.

(5) Saghaterian, A., Gukian, K. M., Thayer, D. A., and Ghadiri, M. R. (2003) DNA detection and signal amplification via an engineered allosteric enzyme. *J. Am. Chem. Soc. 125*, 344−345.

(6) Shimoboji, T., Larenas, E., Fowler, T., Hoffman, A. S., and Stayton, P. S. (2003) Temprature-induced switching of enzyme activity with smart polymer-enzyme conjugates. *Bioconjugate Chem. 14*, 517−525.

(7) Ringer, E., and Schulz, G. E. (2003) Self-assembly of proteins into designed networks. *Science 302.* 106−109.

(8) Dawson, P. E., Muir, T. W., Clarklewis, I., and Kent S. B. H. (1994) Synthesis of proteins by native chemical ligation. *Science 266.* 776−779.

(9) Muir, T. W., Sondhi, D., and Cole, P. A. (1998) Expressed protein ligation: A general method for protein enginerring. *Proc. Natl. Acad. Sci. U.S.A. 95*, 6705−6710.

(10) Deyev, S. M., Waibel, R., Lebedenko, E. N., Schubiger, A. P., and Pluckthun, A. (2003) Design of multivalent complexes using the barnase-barstar module. *Nat. Biotechnol. 21*, 1486−1492.

(11) Gaidamakova, E. K., Backer, M. V., and Backer, J. M. (2001) Molecular vehicle for target-mediated delivery of therapeutics and diagnostics. *J. Contolled Release. 74*, 341−347.

(12) Sano, T., and Cantor, C. R. (2000) Streptavidin-containing chimeric proteins: Design and production. *Methods Enzymol. 326*, 305−311.

(13) Folk, E. J. (1983) Mechanism and basis for substrate specificity of transglutaminase-catalyzed ϵ-(γ-glutamyl)lysine bond formation. *Adv. Enzymol. Relat. Areas Mol. Biol. 54*, 1−56.
(14) Sato, H., Ikeda, M., Suzuki, K., and Hirayama, K. (1996) Site-specific modification of interleukin-2 by the combined use of genetic engineering technique and transglutaminase. *Biochemistry 35*, 13072−13080.
(15) Sato, H. (2002) Enzymatic procedure for site-specific pegylation of proteins. *Adv. Drug. Delivery Rev. 54*, 487−504.
(16) Bechtold, U., Otterbach, J. T., Pasternack, R., and Fuchsbauer, H.-L. (2000) Enzymic preparation of protein G-peroxidase conjugates catalysed by transglutaminase. *J. Biochem. 127*, 239−245.
(17) Kamiya, N., Takazawa, T., Tanaka, T., Ueda, H., and Nagamune, T. (2003) Site-specific cross-linking of functional proteins by transglutamination. *Enzyme Microb. Technol. 33*, 492−496.
(18) Kamiya, N., Tanaka, T., Suzuki, T., Takazawa, T., Takeda, T., Watanabe, K., and Nagamune, T. (2003) S-peptide as a potent peptidyl linker for protein cross-linking by microbial transglutaminase from *Streptomyces mobaraensis*. *Bioconjugate Chem. 14*, 351−357.
(19) Ando H., Adachi M., Umeda K., Matsuura A., Nonaka M., Uchio R., Tanaka H., and Motoki M. (1989) Purification and characteristics of novel transglutaminase derived from microorganisms. *Agric. Biol. Chem. 53*, 2613−2617.
(20) Folk, J. E., and Cole, P. W. (1966) Mechanism of action of guinea pig liver transglutaminase. I. Purification and properties of the enzyme: identification of a functional cyctein essential for activity. *J. Biol. Chem. 241*, 5518−5525.
(21) Tsien, R. Y. (1998) The green fluorescent protein. *Annu. Rev. Biochem. 67*, 509−544.
(22) Nonaka, M., Matsuura, Y., and Motoki, M. (1996) Incorporation of lysine- and lysine-dipeptides into as1-casein by Ca^{2+}-independent microbial transglutaminase. *Biosci. Biotechnol. Biochem. 60*, 131−133.
(23) Taguchi, S., Nishiyama, K., Igi, K., Ito, K., Taira, H., Motoki, M., and Momose, H. (2000) Substrate specificity analysis of microbial transglutaminase using proteinaceous protease inhibitors as natural model substrates. *J. Biochem. 128*, 415−425.
(24) Kashiwagi, T., Yokoyama, K., Ishikawa, K., Ono, K., Ejima, D., Matsi, H., and Suzuki, E. (2002) Crystal structure of microbial transglutaminase from *Streptoverticillium mobaraense*. *J. Biol. Chem. 277*, 44252−44260.
(25) Richards, F. M., and Vithayathil, P. J. (1959) The preparation of subtilisin-modified ribonuclease and the separation of the peptide and protein components. *J. Biol. Chem. 234*, 1459−1465.
(26) Shimon, L. and Arieh, B. (1976) Ribonuclease S-peptide. *J. Biol. Chem. 251*, 1333−1339.
(27) Julian, M. S., Ruby, P. H., Frederic, M. R., and Gerald, D. W. (1971) Thermodynamics of the binding of S-peptide to S-protein to form ribonuclease S′. *Biochemistry 10*, 806−817.
(28) Alan, A. S., and Robert, L. B. (1977) Mechanism of dissociation of S-peptide from ribonuclease S. *Biochemistry 16*, 4203−4209.
(29) Kim, E., E., Varadarajan, R., Wyckoff, H. W., and Richards, F. M. (1992) Refinement of the crystal structure of ribonuclease S. Comparison with and between the various ribonuclease A structures. *Biochemistry 31*, 12304−12314.

BC034209O

3′-Methylphosphonate-Modified Oligo-2′-*O*-methylribonucleotides and Their Tat Peptide Conjugates: Uptake and Stability in Mouse Fibroblasts in Culture

Chrissy E. Prater and Paul S. Miller*

Department of Biochemistry and Molecular Biology, Bloomberg School of Public Health, Johns Hopkins University, 615 North Wolfe Street, Baltimore, Maryland 21205. Received January 8, 2004; Revised Manuscript Received February 18, 2004

Antisense oligo-2′-*O*-methylribonucleotides and their methylphosphonate derivatives show high binding affinities for their complementary targets under essentially physiological conditions. Additionally, the methylphosphonate linkage is resistant to nuclease hydrolysis. Here we show that a single methylphosphonate internucleotide linkage at the 3′-end of an oligo-2′-*O*-methylribonucleotide is sufficient to prevent degradation by the 3′-exonuclease activity found in mammalian serum. Complexes formed between a cationic lipid, Oligofectamine, and 5′-[^{32}P]-labeled methylphosphonate modified oligo-2′-*O*-methylribonucleotides are taken up by mouse L_{929} fibroblasts in culture. The extent of uptake appears to be dependent upon the sequence of the oligonucleotide. Examination of lysates of oligonucleotide treated cells by polyacrylamide gel electrophoresis showed that no degradation of the oligonucleotide occurred, even after incubation for 24 h. A fluorescein-derivatized oligomer was shown to localize mainly in the cell nucleus as monitored by fluorescence microscopy. Covalent conjugates of fluorescein-derivatized 3′-methylphosphonate modified oligo-2′-*O*-methylribonucleotides with Tat peptide, a cell permeating peptide, were also prepared. The Tat peptide was coupled to the 5′-end of the oligonucleotide using either disulfide coupling chemistry or conjugation of a keto derivative of the Tat peptide via a 4-(2-aminooxyethoxy-2-(ethylureido)quinoline group at the 5′-end of the oligonucleotide. Although formation of the Tat peptide conjugates was confirmed by mass spectrometry, the propensity of these oligonucleotides to form aggregates and their apparent high affinity for plastic and glass made the conjugates unsuitable for studies of uptake by cells in culture.

INTRODUCTION

Antisense research has evolved to include many modifications that render chemically synthesized oligonucleotides resistant to hydrolysis by nucleases, while enhancing the binding affinity of these oligonucleotides for their targets. We have recently described the syntheses and binding properties of antisense oligo-2′-*O*-methylribonucleotides that contain nuclease resistant methylphosphonate internucleotide linkages (*1*−*6*). These studies demonstrated that methylphosphonate-modified oligonucleotides have high affinities for their complementary RNA targets under essentially physiological conditions. To further characterize these oligonucleotide analogues, we have studied their uptake by, and stability in, mammalian cells in culture. Here we describe the cationic lipid-mediated uptake of methylphosphonate containing oligo-2′-*O*-methylribonucleotides by mouse L_{929} fibroblasts and show they are delivered intact to the cell's nucleus. We also describe efforts to prepare covalent conjugates of fluorescein-derivatized oligomers with Tat peptide, a peptide derived from the "protein transduction domain" of HIV-1 Tat protein, which has been reported to facilitate cellular uptake of macromolecules including oligonucleotides.

EXPERIMENTAL PROCEDURES

Materials. Protected 2′-*O*-methylribonucleoside-3′-*O*-(β-cyanoethyl-*N*,*N*-diisopropyl) phosphoramidites, 5′-fluorescein phosphoramidite (6-FAM), 5′ nucleoside-derivatized controlled pore glass supports, 4,5-dicyanoimidazole, 1*H*-tetrazole, Cap Mix A, Cap Mix B, and oxidizing solution were purchased from Glen Research Inc., Sterling, VA. The exocylclic amino groups of the 2′-*O*-methylribonucleoside phosphoramidites mr-C and mr-G were protected with acetyl and isobutryl protecting groups, respectively. Protected 2′-*O*-methylribonucleoside-3′-*O*-(*N*,*N*-diisopropyl) methylphosphonamidites were purchased from ChemGenes Corp., Ashland, MA. The exocyclic amino groups of the mr-C and mr-G methylphosphonamidites were protected with isobutryl groups. The phosphoramidite and phosphonamidite solutions were prepared using synthesis grade acetonitrile (Fisher) that was dried and stored over calcium hydride. Tat peptide, residues 48−60, with the addition of a C-terminal cysteine (GRKKRRQRRRPPQC), was synthesized by the Johns Hopkins University School of Medicine Protein/Peptide Sequencing Core Facility. MALDI analysis was performed in the AB Mass Spectrometry/Proteomics Facility at Johns Hopkins School of Medicine (www.hopkinsmedicine.org/msf/) with support from a National Center for Research Resources shared instrumentation grant 1S10−RR14702. Mouse L_{929} fibroblasts were obtained from American Type Culture Collection (ATCC), Manassas, VA.

General Methods. Strong anion exchange (SAX) HPLC was carried out using Dionex DNAPac PA-100 analytical (4 × 250 mm) or semiprep (9 × 250 mm) columns purchased from Dionex Corp., Sunnyvale, CA. The columns were eluted with a 20 min (analytical) or

* To whom correspondence should be addressed. Phone: 410-955-3489. Fax: 410-955-2926. E-mail: pmiller@jhsph.edu.

10.1021/bc049977+ CCC: $27.50 © 2004 American Chemical Society
Published on Web 04/21/2004

30 min (semiprep) linear gradient of 0.0 M to 0.5 M sodium chloride in a buffer containing 100 mM Tris−hydrochloric acid, pH 7.8, and 10% acetonitrile at a flow rate of 1.0 mL/min (analytical) or 1.5 mL/min (semiprep). The columns were monitored at 260 nm for analytical runs, and 290 nm for preparative runs. C-18 reversed-phase HPLC was carried out using a Microsorb C-18 column (0.46 × 15 cm) purchased from Varian Analytical, Sunnyvale, CA. Unless otherwise noted, the column was eluted with a 20 mL linear gradient of 2−30% acetonitrile in 50 mM sodium phosphate, pH 7.8, at a flow rate of 1.0 mL/min. Denaturing polyacrylamide gel electrophoresis (PAGE) was carried out on 20 × 20 × 0.75 cm gels containing 20% acrylamide and 7 M urea. The running buffer (TBE) contained 90 mM Tris, 90 mM boric acid, and 0.2 mM ethylenediaminetetraacetate buffered at pH 8. The gel loading buffer contained 90% formamide, 0.05% xylene cyanol, and 0.05% bromophenol blue.

Syntheses of Anti-TAR and Anti-RRE Oligonucleotides. The sequences of the oligonucleotides are shown in Table 1. The 5′-phosphate derivative of oligonucleotide **1** (2) was a gift from Dr. Tomoko Hamma; it was dephosphorylated by incubating 0.03 A_{260} unit of the oligonucleotide with 1 unit of arctic shrimp alkaline phosphatase in 10 μL of buffer containing 10 mM Tris, pH 8.0, and 10 mM magnesium chloride for 60 min at 37 °C. The solution was then heated at 65 °C for 15 min to deactivate the enzyme. The other oligonucleotides were synthesized on an ABI Model 392 DNA/RNA synthesizer. The protected nucleoside methylphosphonamidites and nucleoside β-cyanoethylphosphoramidites were dissolved in anhydrous acetonitrile at a concentration of 0.15 M. The nucleoside methylphosphonamidite solutions were stored over 3 Å molecular sieves 1 h prior to use. The coupling time for nucleoside methylphosphonamidites was 120 s using a 0.25 M solution of 4,5-dicyanoimidazole (DCI) as the activating agent. A "low-water" oxidizing agent consisting of 1.27 g of iodine, 37.5 mL of tetrahydrofuran, 12.5 mL of 2,6-lutidine, and 100 μL of water was used. The capping solutions consisted of Cap A (10% acetic anhydride, 10% pyridine in tetrahydrofuran (v/v)) and Cap B (1.25 g 4-(dimethylamino)pyridine in 50 mL of anhydrous pyridine). The coupling time for nucleoside β-cyanoethylphosphoramidites was 360 s using the synthesis reagents listed above for the methylphosphonamidites, or 120 s using a solution of 1*H*-tetrazole as the activating agent and standard synthesis reagents purchased from Glen Research Inc. Fluorescein phosphoramidite coupling times were 10 min using standard synthesis reagents. Derivatization of oligonucleotide **4** with the 4-(2-aminooxyethoxy)-2-(ethylureido)quinoline (AOQ) group was performed by Dr. Tomoko Hamma using methods reported previously (*5*).

Deoxyribo and 2′-*O*-methylribo diester oligonucleotides were deprotected in 0.4 mL of concentrated ammonium hydroxide for 5 h at 65 °C in a 4.5 mL autosampler vial. After cooling, the supernatant was removed, and the support was washed twice with 0.2 mL aliquots of 50% aqueous acetonitrile. The combined supernatant and washings were evaporated to dryness. The methylphosphonate containing oligo-2′-*O*-methylribonucleotides were removed from the support by incubation in 0.4 mL of concentrated ammonium hydroxide for 2 h at room temperature in a 4.5 mL autosampler vial. The support was washed as above, and the combined supernatant and washings were evaporated to dryness under vacuum at room temperature. The residue was then deprotected with a solution containing 10 μL of water, 22.5 μL of acetonitrile, 22.5 μL of 95% ethanol, and 50 μL of ethylenediamine for 6 h at room temperature. The solution was cooled on ice and neutralized by addition of 600 μL of ice-cold 2 N hydrochloric acid. After neutralization, the solution was diluted into 10 mL of 2% acetonitrile in 50 mM sodium phosphate buffer at pH 5.8 (C-18 buffer A). This solution was loaded onto a C-18 SEP PAK cartridge (Waters Inc.) that had been preequilibrated with 10 mL of acetonitrile, 10 mL of 50% aqueous acetonitrile, and 10 mL of C-18 buffer A. The SEP PAK was washed with 10 mL of water, and the oligomer was eluted with 3 mL of 50% aqueous acetonitrile.

The AOQ-derivatized oligonucleotide was deprotected in a solution containing 5 μL of water, 11.25 μL of 95% ethanol, 11.25 of μL acetonitrile, and 25 μL of ethylenediamine for 1.5 h at room temperature and was immediately purified by C-18 HPLC as previously described (*5*).

The remaining oligonucleotides were purified by SAX HPLC. 10−40 A_{260} units of the crude oligomer was evaporated to dryness then dissolved in 500 μL of SAX buffer A (0.1 M Tris, 10% aqueous acetonitrile). These samples were then injected onto the SAX column, and the column was eluted with a linear gradient of 0−0.5 M sodium chloride for oligomers **1-2mp** and **2**, 0−0.75 M sodium chloride for oligomer **3**, 0−0.6 M sodium chloride for oligomer **2-1mp**, 0−0.65 M sodium chloride for oligomer **3-1mp**, and 0−1.0 M sodium chloride for fluoresceinated oligomer **3-1mp-F**. Oligonucleotide **3-2mp** was purified by PAGE on a 20% gel run under denaturing conditions. The oligomer was located by UV shadowing and was isolated by incubating the gel slice in 1 mL of a solution containing 0.1 M ammonium acetate and 20% aqueous acetonitrile overnight at 37 °C. The supernatant was evaporated to dryness and the residue was desalted on a C-18 SEP PAK cartridge as described above.

Oligonucleotides (with the exception of oligomer **1**) were analyzed by MALDI-TOF mass spectrometry: dT_{10} (*m*/*z*: calcd 2967.5, found 2968.5); **1-2mp** (*m*/*z*: calcd 4931.9, found 4931.4); **2** (*m*/*z*: calcd 5279.0, found 5279.1); **2-1mp** (*m*/*z*: calcd 5277.0, found 5277.1); **3** (*m*/*z*: calcd 4935.9, found 4936.4); **3-1mp** (*m*/*z*: calcd 4933.9, found 4934.8); **3-1mp-F** (*m*/*z*: calcd 5471.0, found 5474.1); **3-2mp** (*m*/*z*: calcd 4931.9, found 4931.8); **3-2-mp-F** (*m*/*z*: calcd 5748.1, found 5750.8); **4** (*m*/*z*: calcd 1598.0, found 1598.5); **AOQ-4-F** (*m*/*z*: calcd 2531.5, found 2534.6).

Oligonucleotide Stability in Serum. Oligonucleotides were phosphorylated by incubation of 2 × 10^{-7} mmol oligomer with 5 units of T_4 polynucleotide kinase in 10 μL of buffer that contained 60 μM γ-^{32}P-ATP, (specific activity, 100 Ci/mmol), 50 mM Tris, pH 7.6, 10 mM magnesium chloride, and 10 mM mercaptoethanol for 60 min at 37 °C. A 14 μL aliquot of the reaction mixture was diluted with 140 μL of 0.1 M imidazole buffer, pH 6.0, and 16 μL of 1 M 1-ethyl-3-[3-(dimethylamino)propyl]carbodiimide (Sigma). The solution was incubated at room temperature for 4 h after which 6.4 μL of ethylenediamine and 13 μL of 12 N hydrochloric acid were added. The pH of the solution was adjusted to 7.4 by further addition of hydrochloric acid, and the solution was incubated overnight at room temperature. The reaction mixture was diluted into 10 mL of C-18 buffer A, and the solution was loaded onto a preequilibrated C-18 SEP PAK cartridge and desalted as described above. The 5′-aminoethylphosphoramidate-derivatized oligomers were purified by electrophoresis on a 20% denaturing polyacrylamide gel. The oligomers were extracted from the gel by incubation of the gel slice with 1 mL of 0.1 M ammonium acetate, 20% aqueous acetoni-

trile overnight at 37 °C. The oligomers were then desalted on C-18 SEP PAK cartridges.

The 5′-aminoethylphosphoramidate derivatized oligomers (1.1×10^5 cpm) were each dissolved in 10 μL of RPMI medium supplemented with 10% fetal calf serum and incubated at 37 °C. One microliter aliquots were removed at various times, diluted into 4 μL of gel loading buffer, and analyzed on a 20% denaturing polyacrylamide gel. Products were visualized by phosphorimaging the wet gel. Percent intact oligonucleotide for each timepoint was quantitated using Image Quant 5.2 (Molecular Dynamics).

Oligofectamine Uptake of Fluorescent Oligonucleotides in L_{929} Fibroblasts. Mouse L_{929} fibroblast cells were plated at a density of 55 000 cells per 1.9 cm diameter slide chamber 24 h prior to the experiment. For each experiment, 1 μL of Oligofectamine (Invitrogen) was preincubated with 9 μL of serum-free Eagle's minimum essential media (EMEM) for 10 min at room temperature. For oligonucleotide **3-1mp-F**, 0.1 nmol was resuspended in 90 μL of serum-free EMEM, then mixed with 10 μL of preincubated Oligofectamine/EMEM and incubated at room temperature for 20 min. The cells were washed twice with 500 μL of serum-free EMEM and incubated with a solution that contained 400 μL of serum-free EMEM and 100 μL of the preincubated oligonucleotide/Oligofectamine mixture for 4 h in a 37 °C humidified CO_2 incubator. Prior to viewing, the live cells were washed twice with 1 mL of Hanks Balanced Salt Solution (HBSS), and coverslips were mounted with HBSS. The live cells were viewed on an inverted Ziess fluorescence microscope. Phase contrast and green fluorescence images of the cells treated with fluorescent oligonucleotide with or without Oligofectamine were taken at both 40× and 100× magnification.

Oligonucleotide Stability in Mouse L_{929} Fibroblasts. Oligonucleotides were phosphorylated by incubating 2.5×10^{-6} mmol oligonucleotide with 15 units T_4 polynucleotide kinase in 15 μL of buffer that contained 250 μM γ-^{32}P-ATP, (specific activity, 10 Ci/mmol), 50 mM Tris, pH 7.6, 10 mM magnesium chloride, and 10 mM mercaptoethanol overnight at 37 °C. The labeled oligomers were purified by electrophoresis on a 20% denaturing polyacrylamide gel and desalted as described above. The L_{929} cells were plated at a density of 70 000 cells/well in 12-well tissue culture plates 24 h prior to the experiment. For each timepoint, 4 μL of Oligofectamine was incubated with 6 μL of serum-free EMEM for 10 min at room temperature. For each timepoint, 0.25 nmol of oligonucleotide was resuspended in 90 μL of serum-free EMEM and mixed with 10 μL of preincubated Oligofectamine/EMEM and incubated for 20 min at room temperature. The cells were washed twice with 500 μL of serum-free EMEM and incubated with a solution containing 400 μL of serum-free EMEM and 100 μL of the preincubated oligonucleotide/Oligofectamine mixture for 4 h in a 37 °C humidified CO_2 incubator. After 4 h of incubation, all cells were washed twice with 500 μL of serum-free EMEM. At 4 h and beyond, the cells for the 8 and 24 h timepoints were incubated in 1 mL of EMEM containing 10% fetal calf serum. The cells were again washed twice with 500 μL of serum-free EMEM, then harvested by brief incubation with 500 μL of 50% aqueous acetonitrile, collected by scraping with a pipet tip, and stored at −20 °C until all timepoints were taken. The harvested cells in 50% acetonitrile were then incubated at −80 °C for 1 h to improve lysis. The majority of the cell debris was pelleted by centrifugation in a tabletop microcentrifuge at maximum speed for 3 s. The supernatants were removed and quantitated by scintillation counting. Equivalent counts (about 550 cpm/lane) of each oligonucleotide timepoint were run on a 20% denaturing polyacrylamide gel. Gel-purified, ^{32}P-labeled oligonucleotide stocks (4500 cpm/lane) were run as T_0 controls. Products were visualized by phosphorimaging the dried gels overnight.

Oligonucleotide Conjugation to Tat Peptide via 2, 2′-Dithiodipyridine. Cystamine dihydrochloride was exchanged on Amberlite quaternary amine resin (Fisher). Amberlite resin (5 g) was prepared in 20 mL of 0.5 N sodium hydroxide, poured into a 1.25 cm diameter glass column, and then equilibrated with 30 mL of 0.5 N sodium hydroxide, 50 mL of 0.1 N sodium hydroxide, and 200 mL of water. Cystamine dihydrochloride (3 mmol, 675 mg) was dissolved in deionized water and passed over the equilibrated Amberlite resin. Free cystamine was collected, evaporated, and stored at 4 °C.

Controlled-pore glass (CPG) support-bound dT_{10} (Scheme 1, **1.1**) was reacted with 81.7 mg (0.5 mmol) of carbonyldiimidazole in 1 mL of anhydrous acetonitrile for 2 h at room temperature in an ABI synthesis column. The support was washed with 10 mL of anhydrous acetonitrile and reacted with 3.4 mg of free cystamine in 200 μL of anhydrous acetonitrile at room-temperature overnight in a small Reactivial. The support was transferred back to the synthesis column and washed with 10 mL of anhydrous acetonitrile and dried on a vacuum line. The disulfide bond of the cystamine derivative was reduced by passing 1 mL of 100 mM dithiothreitol (DTT) in 50% aqueous acetonitrile through the column for 2 h at room temperature. The support was washed with 10 mL of 50% aqueous acetonitrile, followed by 10 mL of acetonitrile and dried. The support was transferred to a small Reactivial and incubated at 37 °C for 3 days in 100 μL of 0.05 M sodium phosphate buffer containing 50% acetonitrile and saturated with 6 mg of 2,2′-dithiodipyridine (Fluka). The support was then washed with 10 mL of 50% aqueous acetonitrile followed by 10 mL of acetonitrile and dried. The pyridyl disulfide-derivatized dT_{10} (Scheme 1, **1.5**) was cleaved from the support by treatment with 0.4 mL of concentrated ammonium hydroxide for 2 h at room temperature. Full-length **1.6** was purified by C-18 HPLC. Each step of the derivatization was monitored by deprotecting a small amount of the support in 100 μL of concentrated ammonium hydroxide for 1 h. The oligonucleotide derivatizations were confirmed by C-18 HPLC and by MALDI-TOF mass spectrometry: **1.3** (*m*/*z*: calcd 3147.5, found 3146.8); **1.4** (*m*/*z*: calcd 3072.4, found 3072.2); **1.6** (*m*/*z*: calcd 3181.4, found 3182.6). Purified **1.6** (0.2 A_{260} units) was reacted with a 2-fold molar excess of Tat peptide in 5 μL of 50% aqueous acetonitrile overnight at room temperature. Conjugation of the oligonucleotide with Tat resulted in a substantial change in the mobility of the oligonucleotide when the reaction mixture was analyzed on a 20% denaturing polyacrylamide gel as detected by UV shadowing. The presence of the Tat−oligonucleotide conjugate in the reaction mixture was further confirmed by MALDI-TOF mass spectrometry: **1.7** (*m*/*z*:calcd 4891.5, found 4890.1).

The above protocol was used for the conjugation of oligonucleotide **3-2mp-F** with the Tat peptide except the reaction time in DTT was decreased to 30 min. Also, the majority of the pyridyl disulfide oligonucleotide **3-2mp-F** was released from the CPG support during the pyridyl disulfide reaction and was recovered from solution. The pyridyl disulfide derivatized oligonucleotide, **3-2mp-F**, was deprotected with ethylenediamine as described above for 2′-*O*-methyl methylphosphonate-containing oligonu-

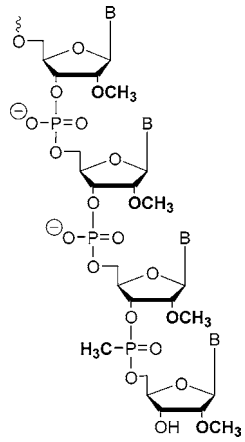


Figure 1. General structure of an oligo- 2′-*O*-methylribonucleotide containing a single methylphosphonate linkage at the 3′ end.

Table 1. Oligonucleotide Sequences[a]

oligomer	sequence
1	5′ **mr-**CpUpCpCpCpApGpGpCpUpCpApGpApU 3′
1-2mp	5′ **mr-**CpUpCpCpCpApGpGpCpUpCpA**p**GpA**p**U 3′
2	5′ **mr-**CpCpGpUpCpApGpCpGpUpCpApUpUpGpA 3′
2-1mp	5′ **mr-**CpCpGpUpCpApGpCpGpUpCpApUpUpG**p**A 3′
3	5′ **mr-**UpCpApUpUpGpApCpGpCpUpGpCpGpC 3′
3-1mp	5′ **mr-**UpCpApUpUpGpApCpGpCpUpGpCpG**p**C 3′
3-1mp-F	5′ **mr-Fp**UpCpApUpUpGpApCpGpCpUpGpCpG**p**C 3′
3-2mp	5′ **mr-**UpCpApUpUpGpApCpGpCpUpG**p**CpG**p**C 3′
3-2mp-F	5′ **mr-T*p**UpCpApUpUpGpApCpGpCpUpG**p**CpG**p**C 3′
4	5′ **mr-**CpGpUpCpA 3′
4-F	5′ **mr-Fp**CpGpUpCpA 3′

[a] The notations "**mr-**" and "**d-**" denote 2′-*O*-methyl and deoxy sugars, respectively. Methylphosphonate linkages are denoted by "**p**" within the sequence, and the "**#mp**" suffix on the oligo name. **T*p** is 5-fluorescein derivative of deoxythymidine, whose structure is shown in Scheme 1, and **Fp** is a derivative of 6-carboxyfluorescein, whose structure is shown in Scheme 2.

cleotides, purified by C-18 HPLC, and reacted with the Tat peptide as above. The presence of Tat-conjugated **3-2mp-F** was confirmed by MALDI-TOF mass spectrometry: (*m*/*z*: calcd 7670.2, found 7674.6).

Oligonucleotide Conjugation to Tat Peptide via 4-(2-Aminooxyethoxy)-2-(ethylureido)quinoline. Tat peptide (0.5 mg) was reacted with 0.2 M bromoacetone in 50 μL of acetonitrile overnight at room temperature. The keto-Tat peptide product (Scheme 2, **2.4**) was purified by C-18 HPLC using a 20 mL linear gradient of 2−35% acetonitrile in 0.1% TFA at a flow-rate of 1.0 mL/min and analyzed by MALDI-TOF mass spectrometry: (*m*/*z*: calcd 1879.0, found 1878.3). The peptide was stored dry at −20 °C.

Approximately 9.4 μg of keto-Tat peptide was reacted with 0.1 A_{260} unit of oligonucleotide **AOQ-4-F** (Scheme 2, **2.1**) in the presence of 0.09 A_{260} unit of a dT_{21} in a total volume of 10 μL of 50% aqueous acetonitrile for 1 h at room temperature. Analysis of the reaction mixture by MALDI-TOF mass spectrometry confirmed the formation of the conjugate, **Tat−4-F** (*m*/*z*: calcd 4390.6, found 4392.0).

RESULTS AND DISCUSSION

Oligonucleotides containing 2′-*O*-methylribonucleotides have been shown to have high binding affinity for RNA targets (*2*, *3*, *7*−*11*). Further modification with alternating methylphosphonate linkages has been shown to impart nuclease resistance to oligo 2′-*O*-methylribonucleotides while maintaining high binding affinity for complementary RNA (*1*, *2*). Recent reports suggest that oligo-2′-*O*-methylribonucleotides have some level of nuclease resistance (*12*−*14*) compared to oligodeoxyribonucleotides. Consequently incorporation of one or few methylphosphonate linkages into an oligo- 2′-*O*-methylribonucleotide already possessing partial nuclease resistance may be sufficient to impart nuclease resistance in vitro and in the cell. To test this possibility, we prepared oligo-2′-*O*-methylribonucleotides that contain one (Figure 1) or two methylphosphonate linkages at the 3′-end of the molecule and studied their uptake by and stability within cells in culture.

Oligo-2′-*O*-methylribonucleotides and Their Methylphosphonate Derivatives. The sequences of the three antisense oligo-2′-*O*-methylribonucleotides used in this study are shown in Table 1. Oligomer **1**, a 15-mer that is complementary to nucleotides 21−35 (GenBank accession number NC_001802) of the TAR element of HIV-1 RNA, binds with high affinity to this site (*1*, *2*). Oligomers **2**, a 16-mer, and **3**, a 15-mer, are complementary to nucleotides 7370−7385 and 7362−7385, respectively, of the Rev Response Element (RRE) of HIV-1 RNA (GenBank accession number NC_001802). Like the anti-TAR oligomer, oligomers 2 and 3 bind with high affinity to their target RNA in vitro under essentially physiological conditions, that is at 37 °C in pH 7.0 buffer containing 0.1 M sodium chloride (unpublished data).

The sequences of the methylphosphonate derivatives of these oligonucleotides are also shown in Table 1. Oligomers **1-2mp** and **3-2mp** contain two methylphosphonate linkages separated by a phosphodiester linkage at their 3′-end. Oligomers **2-1mp** and **3-1mp** contain a single 3′-terminal methylphosphonate linkage.

Oligomers **1**, **2** and **3** were synthesized using commercially available, protected 2′-*O*-methylribonucleoside-3′-*O*-β-cyanoethyl-(*N*,*N*-diisopropyl)phosphoramidites. These oligomers were deprotected by treatment with concentrated ammonium hydroxide at 55 °C and were purified by strong anion exchange (SAX) HPLC. The methylphosphonate-derivatized oligomers were prepared using commercially available 2′-*O*-methylribonucleoside-3′-*O*-methylphosphonamidites. To avoid cleavage of the methylphosphonate linkages during deprotection, the oligomers were treated briefly with concentrated ammonium hydroxide at room temperature followed by treatment with ethylenediamine at room temperature (*2*). These oligonucleotides were purified either by SAX HPLC or by preparative polyacrylamide gel electrophoresis.

Stability of Oligo-2′-*O*-methylribonucleotides in Serum. The stabilities of the 5′-[^{32}P]-labeled oligonucleotides in RPMI culture medium containing 10% fetal calf serum (FCS) was determined. To prevent possible loss of label due to serum phosphatase activity, the 5′-terminal phosphate group was converted to its 2-aminoethyl phosphoramidate derivative by reaction with ethylenediamine in the presence of 1-ethyl-3-[3(dimethylamino)propyl]carbodiimide (*2*). The labeled oligonucleotides were incubated in RPMI medium containing 10% FCS for up to 24 h at 37 °C. The reaction mixtures were then analyzed by polyacrylamide gel electrophoresis, and the gels were visualized by phosphorimaging.

Figure 2, panel A, compares the stability of all-phosphodiester oligonucleotide **1** with that of oligomer **1-2mp**, which contains two alternating methylphosphonate linkages at it's 3′ end. As shown in panel E, which shows the percentage of intact oligomer versus time, essentially all of **1-2mp** remains intact after a 2 h incubation, whereas only 18% of intact oligomer **1** is

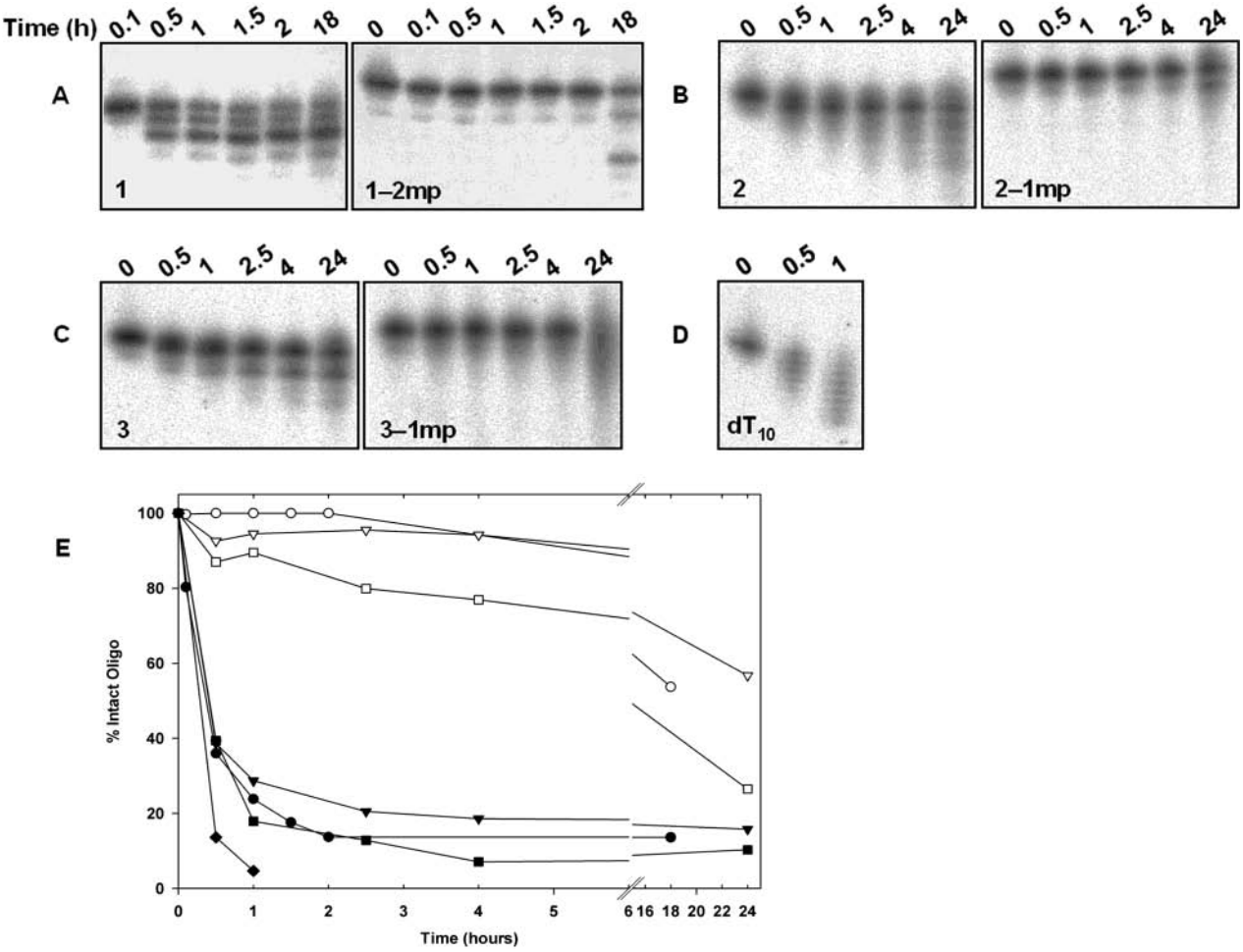


Figure 2. Stabilities of oligonucleotides in 10% fetal calf serum. ^{32}P-labeled oligonucleotides were incubated in medium containing 10% serum for the indicated lengths of time, and the reaction mixtures were analyzed by polyacrylamide gel electrophoresis. The gels (A) **1** vs **1-2mp**; (B) **2** vs **2-1mp**; (C) **3** vs **3-1mp**; (D) dT_{10} were visualized by phosphorimaging. (E) Quantitation of percent intact oligonucleotide at each timepoint: oligonucleotide **1** (●), **1-2mp** (○), **2** (▼), **2-1mp** (▽), **3** (■), **3-1mp** (□), **d−T$_{10}$** (◆).

observed. Even after an 18 h incubation, approximately 55% of **1-2mp** remains intact.

Oligomers **2-1mp** and **3-1mp**, each of which contains a single 3′-methylphosphonate linkage, display stabilities similar to that of **1-2mp** (Figure 2B and C). Thus after a 2 or 4 h incubation, between 80% to 95% of these oligomers remain intact. Even after a 24 h incubation, between 30% and 60% of each oligomer is observed intact. As was the case for oligomer **1**, the all-phosphodiester oligomers **2** and **3** were degraded approximately 80% after 2 h of incubation. However, consistent with previous findings, the rates of degradation of these all-phosphodiester oligo-2′-*O*-methylribonucleotides were significantly less than that of dT_{10}, an all-phosphodiester oligodeoxyribonucleotide that was 80% degraded after 0.5 h of incubation (Figure 2D and E).

These data are consistent with our previous results for the serum stability of a methylphosphonate-derivatized hairpin oligo-2′-*O*-methylribonucleotide (*4*) and with oligodeoxyribonucleotides having a 3′-terminal methylphosphonate linkage (*15*). The combined results show that methylphosphonate linkages located in the 3′-terminal portion of the oligomer can impart considerable protection against degradation by 3′-exonuclease activity found in mammalian sera. Furthermore, addition of a single methylphosphonate linkage at the 3′ end of oligonucleotides **2** and **3** is sufficient to significantly enhance the serum exonuclease resistance of the 2′-*O*-methyl sequences (Figure 2E) and addition of a second (alternating) methylphosphonate linkage to oligo **3-1mp** did not further enhance the nuclease resistance of the oligomer (data not shown). In separate studies, we have found that the single methylphosphonate linkage in either oligomer **2-1mp** or **3-1mp** does not perturb binding of the oligomer with its RRE RNA target (unpublished data)

Stability of Oligo-2′-*O*-methylribonucleotides in Mouse L$_{929}$ Fibroblasts. We next examined the stability of the oligo-2′-*O*-methylribonucleotides and their methylphosphonate derivatives in mouse L_{929} fibroblasts. Cationic lipids are commonly used to transfect oligonucleotides into cells in culture (*16*, *17*). Complexes of Oligofectamine, a cationic lipid, and ^{32}P-labeled oligonucleotides **2**, **2-1mp**, **3**, **3-1mp**, or dT_{15} were prepared in serum-free medium. Mouse L_{929} cells were incubated with the complexes for 4 h at 37 °C after which the cells were washed with serum-free EMEM and incubated an additional 0, 4, or 20 h with fresh oligonucleotide-free medium. No morphological changes in the cells indicative of toxicity were observed even after 24 h of incubation. The cells were then washed and lysed, cell debris were removed by centrifugation, and the amounts of radioactivity from the oligonucleotides were measured by scintillation counting. The results are shown in Table 2.

Introduction of a single methylphosphonate linkage reduces the net charge of the oligonucleotide by one, which might be expected to affect the uptake of oligonucleotides in the presence of cationic lipids. This appears to be the case for oligonucleotides **2** versus **2-1mp**, as

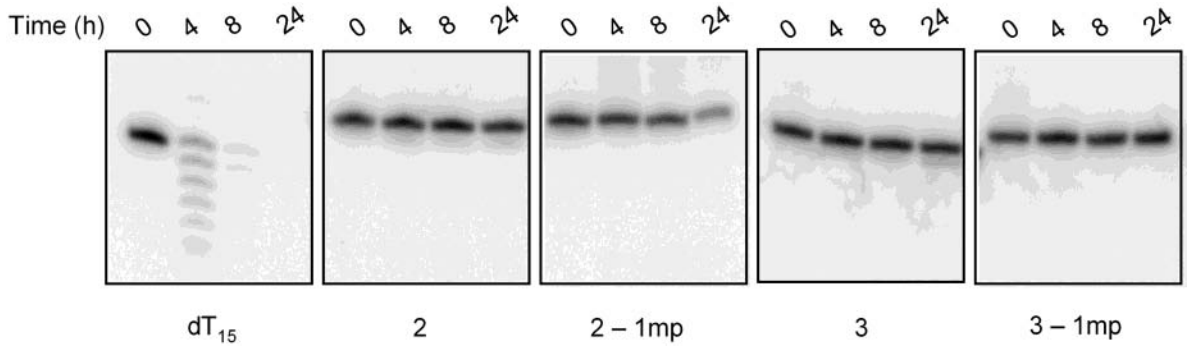


Figure 3. Stabilities of oligonucleotides in mouse L_{929} cells in culture. Mouse L_{929} fibroblasts were incubated with Oligofectamine complexes of the ^{32}P-labeled oligonucleotides for the indicated lengths of time. Lysates from the washed cells were analyzed by polyacrylamide gel electrophoresis, and the gels were visualized by phosphorimaging.

Table 2. Oligonucleotide Recovery from L_{929} Cell Lysates[a]

	oligonucleotide				
	2	**2-1mp**	**3**	**3-1mp**	dT_{15}
pmols recovered	4.61	1.14	11.8	11.8	0.335

[a] pmol of oligonucleotide recovered after Oligofectamine delivery into L_{929} cells. Quantitation based on scintillation counts of cell lysates after 4 h of incubation.

introduction of a single methylphosphonate linkage results in a significant decrease in the uptake of the oligonucleotide/Oligofectamine complex as determined by oligonucleotide recovery after 4 h (Table 2). However, essentially no difference in uptake is seen for oligonucleotides **3** versus **3-1mp**, which also differ by a single negative charge. These observations would suggest that in addition to overall charge, oligonucleotide sequence and chain length also contribute to cationic lipid-mediated uptake. Consistent with this idea is the observation that oligonucleotides **2-1mp** and **3**, which both have a net negative charge of −14 but differ in their size and sequence, show significantly different uptake when complexed with Oligofectamine.

To determine the extent of degradation of each oligonucleotide, radioactivity from the cell lysates was analyzed by denaturing polyacrylamide gel electrophoresis. The phosphorimages of these gels are shown in Figure 3. Similar to the behavior of dT_{10} in the in vitro serum stability assay (Figure 2), the oligodeoxyribonucleotide dT_{15} was degraded rapidly to give a "ladder" of oligonucleotides each differing by one nucleotide unit. The decreasing intensities of the shorter oligonucleotides in this ladder suggest that degradation occurs in a stepwise manner starting at the 3′-end of the dT_{15}. Such behavior would be consistent with the activity of a 3′-exonuclease. Only 40% of recovered dT_{15} oligonucleotide remains intact after 4 h incubation in L_{929} cells. Unlike the oligodeoxyribonucleotide, both the oligo-2′-*O*-methylribonucleotides **2** and **3**, as well as their methylphosphonate derivatives **2-1mp** and **3-1mp**, were remarkably resistant to cellular nuclease degradation. Due to low oligonucleotide recovery of sequence **2-1mp** after 24 h cell incubation, the corresponding lane in Figure 3 is underloaded with respect to adjacent lanes. As expected, the methylphosphonate-containing oligonucleotides **2-1mp** and **3-1mp** were recovered intact, with no evidence of degradation throughout the 24-h experiment Surprisingly however, similar results were seen with the all-phosphodiester oligomers **2** and **3**. Despite the appearance of a minor n-1 band in the later timepoints of panels **2** and **3** in Figure 3, 99% of the recovered oligo-2′-*O*-methylribonucleotide is full-length even after 24 h of incubation with L_{929} cells. This behavior, which is in contrast to that seen in the in vitro serum stability assay (Figure 2), suggests that the oligonucleotides may be protected from degradation by the cationic lipids and/or their exposure to exonuclease activity is limited within this particular intracellular environment.

Cationic lipids generally deliver oligodeoxyribonucleotides and oligodeoxyribonucleotide phosphorothioates to the nucleus. The localization of the fluorescein derivative of methylphosphonate oligo-2′-*O*-methylribonucleotide **3-1mp** was determined using fluorescence microscopy. The fluorescein derivative of **3-1mp** was synthesized using a commercially available fluorescein phosphoramidite and after deprotection was purified by SAX HPLC. The resulting fluorescein-derivatized oligomer, **3-1mp-F**, was complexed with Oligofectamine and incubated with mouse L_{929} fibroblasts for 4 h at 37 °C. To avoid potential artifacts due to fixing (*18*), the live cells were then washed and viewed by fluorescence microscopy as previously described (*19*). Panels A and B of Figure 4 show a representative field of cells at 40× magnification, with approximately 70% (19/26) of the live cells exhibiting fluorescence, and 40% (11/26) of the cells exhibiting nuclear fluorescence. As shown in Figure 4C, the most intense fluorescence was observed in the nucleus, with the exception of several punctate regions that may represent endosomal entrapment of the oligonucleotide/Oligofectamine complex. Additionally, weak fluorescence was observed in the cytoplasm. These results are similar to those seen for cationic lipid complexes of fluorescently derivatized all phosphodiester oligo-2′-*O*-methylribonucleotide **4-F** (data not shown). Primary localization of the oligo-2′-*O*-methylribonucleotide/Oligofectamine complexes in the nuclear compartment may explain their impressive stability in L_{929} cells versus the in vitro serum assay.

Tat Peptide−Oligonucleotide Conjugates. The experiments described above show that Oligofectamine can be used to deliver oligo-2′-*O*-methylribonucleotides and their methylphosphonate derivatives to the nuclei of mouse fibroblasts. Recent research with "protein transduction domains" (PTDs) has led to the discovery of several peptides that are reported to translocate conjugated molecules, including oligonucleotides, through the plasma membrane. This group of so-called cell-penetrating peptides contains highly basic regions from some well-known proteins including Antennapedia, VP22 herpes virus protein, and HIV−Tat (*20*). Although the mechanism by which cell-penetrating peptides deliver their cargo to the nucleus is not well understood and is the subject of some debate (*18*, *21*−*25*), a number of studies have reported enhanced antisense activity of

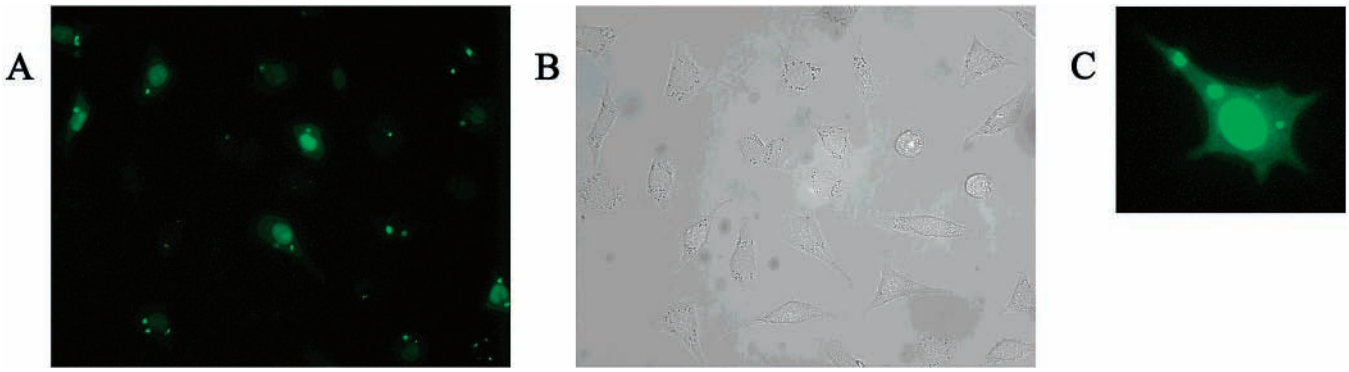
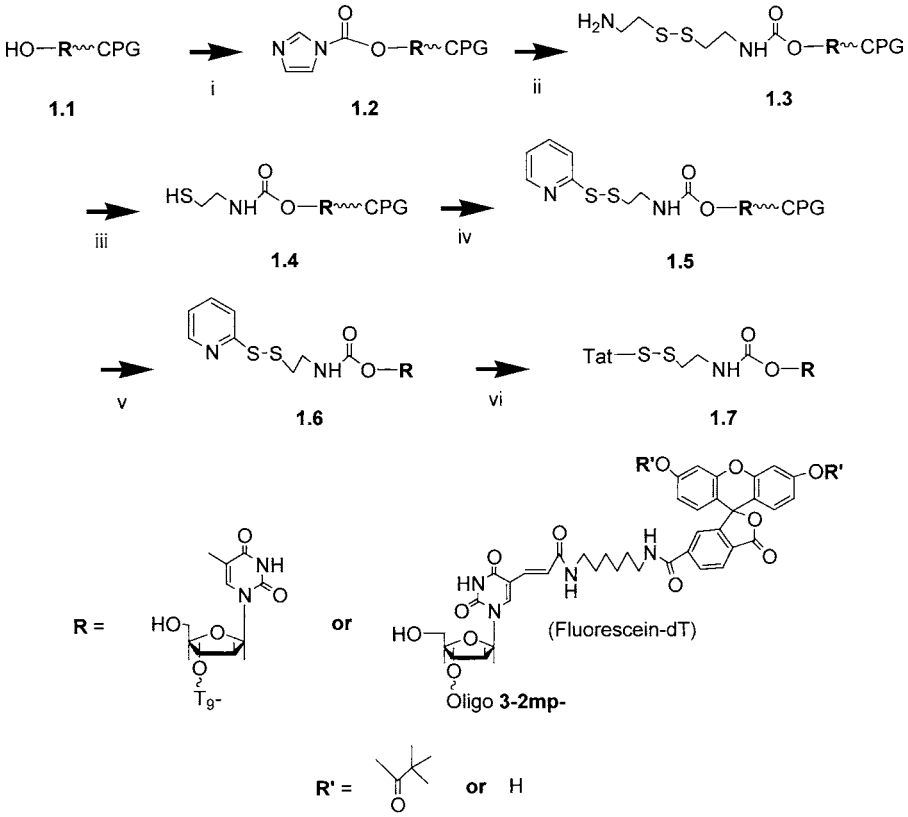


Figure 4. Fluorescence photomicrograph of mouse L_{929} fibroblasts treated with a complex of Oligofectamine and oligonucleotide **3-1mp-F**. Panels A and B show a representative field of cells at 40× magnification in fluorescence and phase-contrast modes, respectively. Panel C, single cell, 100× magnification.

Scheme 1. Tat-Oligonucleotide Conjugate Formation via Dithiodipyridine[a]



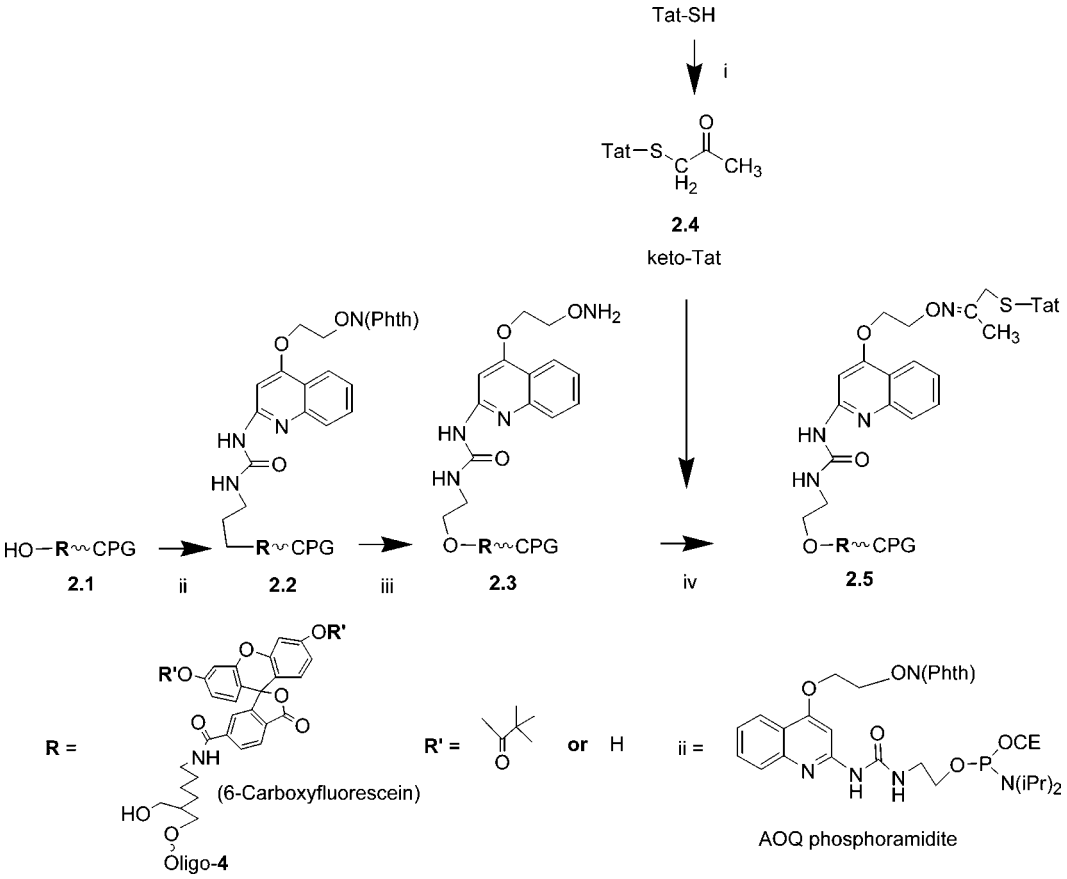
[a] Reagents: (i) carbonyldiimidazole; (ii) cystamine; (iii) dithiothreitol; (iv) dithiodipyridine; (v) deprotection and purification (see methods); (vi) Tat-SH.

oligonucleotides (*26*−*29*) and peptide nucleic acids (*30*−*32*) when covalently conjugated to cell-penetrating peptides. To explore the potential of this alternative delivery strategy, we attempted to prepare Tat derivatives of fluorescently labeled oligo-2′-*O*-methylribonucleotides and study their uptake by mouse L_{929} fibroblasts in culture.

Two approaches were used to synthesize Tat-conjugated oligonucleotides. The first, which is outlined in Scheme 1, employed disulfide-coupling chemistry to attach Tat to the oligonucleotide. We first attempted to carry out the derivatization and coupling chemistry on CPG-bound dT_{10}. The potential advantage of this approach is the oligonucleotide would remain bound to the CPG throughout the entire conjugation process, allowing excess reagents to be washed away and thus requiring minimal purification steps. Support-bound dT_{10} (Scheme 1, **1.1**) was reacted with carbonyldiimidazole to give the 5-imidazole carbamate intermediate, **1.2**, which was then converted to the 5′-cystaminyl derivative, **1.3**. The disulfide bond of **1.3** was reduced with dithiothreitol, and the resulting free sulfhydryl group was reacted with 2,2′-dithiodipyridine to give 5′-pyridyl disulfide derivatized oligonucleotide **1.5**. The progress of each derivatization step was monitored by deprotecting a small portion of the support and analyzing the reaction mixture by C-18 reversed phase HPLC. The compositions of the intermediates were also confirmed by MALDI-TOF mass spectrometry.

We encountered problems when we attempted to couple the C-terminal cysteine sulfhydryl group of Tat peptide (GRKKRRQRRRPPQC), to the oligonucleotide by exchange with the pyridylsulfide group. It appeared that the resulting conjugate strongly adhered to the CPG after ammonium hydroxide cleavage because no oligonucleotide could be recovered from the support. To circumvent this problem, we removed the 5′-pyridyl disulfide-deriva-

Scheme 2. Tat−Oligonucleotide Conjugate Formation via 4-(2-Aminooxyethoxy-2-(ethylureido)quinoline[a]



[a] Reagents: (i) bromoacetone; (ii) AOQ phosphoramidite; (iii) deprotection and purification (see methods); (iv) keto-Tat (**2.4**).

tized dT_{10}, **1.5**, from the support and purified it by C-18 reversed phase HPLC. The purified oligonucleotide, **1.6**, was then reacted with an excess of Tat peptide. Examination of the reaction mixture by polyacrylamide gel electrophoresis showed the presence of a new compound whose reduced electrophoretic mobility was consistent with formation the conjugate. Analysis of the reaction mixture by MALDI-TOF mass spectrometry confirmed the presence of the Tat−dT_{10} conjugate, **1.7**, and suggested that all of the dT_{10} had been converted to conjugate.

The same reaction protocol was applied to the fluorescein conjugate of oligomer **3-2mp**, **3-2mp-F**. This oligonucleotide was prepared using a commercially available fluorescein-dT phosphoramidite. The support-bound oligomer, **1.1**, was converted to its 5′-pyridyl disulfide derivative, **1.6**, as described above for the preparation of the dT_{10} derivative. Reaction of purified oligonucleotide with the Tat peptide resulted in almost immediate formation of a sticky orange precipitate. Similar behavior has been reported for the reaction of Tat peptide with the pyridyl disulfide derivatives of rhodamine- and fluorescein-conjugated oligonucleotides (*33*, *34*). Analysis of the reaction mixture by MALDI-TOF mass spectrometry confirmed the presence of the **Tat-3-2mp-F** conjugate. Precipitation did not occur when Tat peptide was added to fluorescein derivatized oligomer that lacked a 5′-pyridyl disulfide group, suggesting that precipitation was a property of the covalent Tat-oligonucleotide conjugate. This aggregation phenomenon proved to be an insurmountable problem in our hands and essentially prevented the purification of the conjugate in any useful amounts by C-4, C-8, or C18 reversed phase HPLC, strong anion exchange HPLC, gel filtration, diethylaminoethyl (DEAE), or carboxymethyl (CM) Sephadex. When the fluorescinated Tat−oligonucleotide conjugate was applied to DEAE or CM Sephadex loaded in a glass column, most of the conjugate appeared as a visible orange band, which could not be eluted from the column. In addition to this aggregation problem, we found that the **Tat−3-2mp-F** conjugate adhered to plastic and glass tubes, behavior that has also been observed with Tat conjugates of peptides (*35*).

In a second approach, we used oxime formation to conjugate Tat to a fluorescein derivative of penta-2′-*O*-methylribonucleotide **4**. Oligomer **4** was synthesized on controlled pore glass and derivatized with 6-carboxyfluorescein phosphoramidite to give support-bound oligomer **2.1** as shown in Scheme 2. The hydroxyl group of **2.1** was reacted with 4-(2-aminooxyethoxy-2-(ethylureido)quinoline phosphoramidite (*5*) to give 4-(2-aminooxyethoxy-2-(ethylureido)quinoline (AOQ) derivative **2.2**. The AOQ-derivatized oligomer was deprotected and purified by C-18 reversed phase HPLC to give oligomer **2.3**. Conjugation of **2.3** with keto-Tat derivative **2.4**, formed by reaction of Tat peptide with bromoacetone (*5*), gave Tat conjugate **2.5**, which precipitated from the reaction mixture. We found that this precipitation could be prevented by running the reaction in the presence of an excess of dT_{21}. Under these conditions, the reaction solution remained clear. The extent of the reaction could be determined by following the disappearance of AOQ-oligomer **2.3** on C-18 reversed phase HPLC. Based on this criterion, the reaction appeared to go to completion. However, we were unable to observe Tat conjugate **2.5** on the HPLC column, although we could detect the presence of the conjugate in the reaction mixture by MALDI-TOF mass spectrometry.

It is unclear why the Tat conjugates of the fluorescein-derivatized oligomers are insoluble. As described above, simply mixing Tat peptide with the oligonucleotide does not result in precipitation. Rather it appears that Tat must be linked covalently with the oligonucleotide for precipitation to occur. Possibly formation of a covalent conjugate between the negatively charged oligomer and the positively charged Tat peptide promotes intramolecular electrostatic interactions between the oligomer and Tat peptide that lead to a decreased solubility of the conjugate (*36*). Consistent with this idea is the observation that addition of dT_{21} prevented precipitation of the Tat-4-F during the conjugation reaction. Under these conditions, the negatively charged dT_{21} could interact with the positively charged Tat peptide to help prevent precipitation of the conjugate. However, even in the presence dT_{21} we found that **Tat−4-F** was strongly absorbed to glass surfaces (data not shown), and this absorption served as an impediment to further studying the uptake of these oligonucleotides in cell culture.

CONCLUSIONS

Our studies show that 3′-methylphosphonate-modified oligo-2′-*O*-methylribonucleotides are stable to the 3′-exonuclease activity found in mammalian serum. These oligonucleotides may be transfected into cells in culture by complex formation with cationic lipids, which deliver the oligonucleotides to the cell nucleus. Oligonucleotides delivered in this manner can be recovered intact from the cells suggesting that they are stable in the intracellular environment. These properties, along with their ability to bind with high affinity to complementary RNA targets, suggest that 3′-methylphosphonate-modified oligo-2′-*O*-methylribonucleotides may be suitable for use as antisense agents in cell culture. Our experience with the Tat-conjugated oligonucleotides suggests that they are prone to aggregation, which makes purification difficult, and that they have high affinity for glass and plastic surfaces. These properties and the recent reports questioning the mode of uptake of Tat-conjugated molecules (*18*, *21*−*25*) suggests that caution should be used when designing Tat−oligonucleotides for uptake studies.

ACKNOWLEDGMENT

The authors thank Dr. Michael Matunis for the use of his fluorescence microscope, and members of the Matunis laboratory for their valuable assistance. We thank Dr. Tomoko Hamma for providing us with oligonucleotide **1**, and for her assistance in the preparation of the AOQ phosphoramidite. This research was supported by a grant from the National Institutes of Health, GM057140.

LITERATURE CITED

(1) Miller, P. S., and Hamma, T. (1999) Studies on anti-HIV oligonucleotides that contain alternating methylphosphonate/phosphodiester linkages. *Antisense Nucleic Acid Drug Dev. 9*, 367−370.

(2) Hamma, T., and Miller, P. S. (1999) Syntheses of alternating oligo-2′-*O*-methylribonucleoside methylphosphonates and their interactions with HIV TAR RNA. *Biochemistry 38*, 15333−15342.

(3) Miller, P. S., Cassidy, R. A., Hamma, T., and Kondo, N. S. (2000) Studies on anti-human immunodeficiency virus oligonucleotides that have alternating methylphosphonate/phosphodiester linkages. *Pharmacol. Ther. 85*, 159−163.

(4) Hamma, T., and Miller, P. S. (2003) Interactions of hairpin oligo-2′-*O*-methylribonucleotides containing methylphosphonate linkages with HIV TAR RNA. *Antisense Nucleic Acid Drug Dev. 13*, 19−30.

(5) Hamma, T., and Miller, P. S. (2003) 4-(2-Aminooxyethoxy)-2-(ethylureido)quinoline-oligonucleotide conjugates: Synthesis, binding interactions, and derivatization with peptides. *Bioconjugate Chem. 14*, 320−330.

(6) Hamma, T., Saleh, A., Huq, I., Rana, T. M., and Miller, P. S. (2003) Inhibition of HIV Tat-TAR interactions by an antisense oligo-2′-*O*-methylribonucleoside methylphosphonate. *Bioorg. Med. Chem. Lett. 13*, 1845−1848.

(7) Ecker, D. J., Vickers, T. A., Bruice, T. W., Freier, S. M., Jenison, R. D., Manoharan, M., and Zounes, M. (1992) Pseudo-half -knot formation with RNA. *Science 257*, 958−961.

(8) Boulmé, F., Freund, F., Moreau, S., Nielsen, P. E., Gryaznov, S., Toulmé, J. J., and Litvak, S. (1998) Modified (PNA, 2′-*O*-methyl and phosphoramidate) anti-TAR antisense oligonucleotides as strong and specific inhibitors of in vitro HIV-1 reverse transcription. *Nucleic Acids Res. 26*, 5492−5500.

(9) Mestre, B., Arzumanov, A., Singh, M., Boulme, F., Litvak, S., and Gait, M. (1999) Oligonucleotide inhibition of the interaction of HIV-1 tat protein with the trans-activation responsive region (TAR) of HIV RNA. *Biochim. Biophys. Acta 1445*, 86−98.

(10) Arzumanov, A. A., Walsh, A. P., Liu, X., Rajwanshi, V. K., Wengel, J., and Gait, M. J. (2001) Oligonucleotide analogue interference with the HIV-1 Tat protein-TAR RNA interaction. *Nucleosides, Nucleotides Nucleic Acids 20*, 471−480.

(11) Arzumanov, A., Walsh, A. P., Rajwanshi, V. K., Kumar, R., Wengel, J., and Gait, M. J. (2001) Inhibition of HIV-1 Tat-dependent trans activation by steric block chimeric 2′-*O*-methyl/LNA oligoribonucleotides. *Biochemistry 40*, 14645−14654.

(12) Cummins, L., Owens, S., Risen, L., Lesnik, E., Freier, S., McGee, D., Guinossso, C., and Cook, P. (1995) Characterization of fully 2′-modified oligoribonucleotide hetero- and homoduplex hybridization and nuclease sensitivity. *Nucleic Acids Res. 23*, 2019−2024.

(13) Czauderna, F., Fechtner, M., Dames, S., Aygun, H., Klippel, A., Pronk, G., Giese, K., and Kaufmann, J. (2003) Structural variations and stabilizing modifications of synthetic siRNAs in mammalian cells. *Nucleic Acids Res. 31*, 2705−2716.

(14) Monia, B., Johnston, J., Sasmor, H., and Cummins, L. (1996) Nuclease resistance and antisense activity of modified oligonucleotides targeted to Ha-ras. *J. Biol. Chem. 271*, 14533−14540.

(15) Cassidy, R. A., Puri, N., and Miller, P. S. (2003) Effect of DNA target structure on triplex formation by oligo-2′-deoxy- and 2′-*O*-methylribonucleotides. *Nucleic Acids Res. 31*, 4099−4108.

(16) Gewirtz, A., Stein, C., and Glazer, P. (1996) Facilitating oligonucleotide delivery: helping antisense deliver on its promise. *Proc. Natl. Acad. Sci. U.S.A. 93*, 3161−3163.

(17) Hughes, M. D., Hussain, M., Nawaz, Q., Sayyed, P., and Akhtar, S. (2001) The cellular delivery of antisense oligonucleotides and ribozymes. *Drug Discovery Today 6*, 303−315.

(18) Richard, J. P., Melikov, K., Vivés, E., Ramos, C., Verbeure, B., Gait, M. J., Chernomordik, L. V., and Lebleu, B. (2003) Cell-penetrating peptides. A reevaluation of the mechanism of cellular uptake. *J. Biol. Chem. 278*, 585−590.

(19) Thaden, J., and Miller, P. (1993) Photoaffinity behavior of a conjugate of oligonucleoside methylphosphonate, rhodamine, and psoralen in the presence of complementary oligonucleotides. *Bioconjugate Chem. 4*, 386−394.

(20) Schwarze, S., and Dowdy, S. (2000) In Vivo Protein Transduction: Intracellular delivery of biologically active proteins, compounds and DNA. *Trends Pharmacol. Sci. 21*, 45−48.

(21) Gait, M. J. (2003) Peptide-mediated cellular delivery of antisense oligonucleotides and their analogues. *Cell. Mol. Life Sci. 60*, 844−853.

(22) Moulton, H. M., and Moulton, J. D. (2003) Peptide-assisted delivery of steric-blocking antisense oligomers. *Curr. Opin. Mol. Ther. 5*, 123−132.

(23) Vivés, E., Richard, J. P., Rispal, C., and Lebleu, B. (2003) TAT peptide internalization: seeking the mechanism of entry. *Curr. Protein Pept. Sci. 4*, 125−132.

(24) Thoren, P. E., Persson, D., Isakson, P., Goksor, M., Onfelt, A., and Norden, B. (2003) Uptake of analogues of penetratin, Tat(48−60) and oligoarginine in live cells. *Biochem Biophys Res Commun. 307*, 100−107.

(25) Vivés, E. (2003) Cellular uptake of the Tat peptide: an endocytosis mechanism following ionic interactions. *J. Mol. Recognition 16*, 265−271.

(26) Allinquant, B., Hantraye, P., Mailleux, P., Moya, K., Bouillot, C., and Prochiantz, A. (1995) Downregulation of amyloid precursor protein inhibits neurite outgrowth in vitro. *J. Cell Biol. 128*, 919−927.

(27) Troy, C. M., Derossi, D., Prochiantz, A., Greene, L. A., and Shelanski, M. L. (1996) Downregulation of Cu/Zn superoxide dismutase leads to cell death via the nitric oxide-peroxynitrite pathway. *J. Neurosci. 16*, 253−261.

(28) Astriab-Fisher, A., Sergueev, D. S., Fisher, M., Shaw, B. R., and Juliano, R. L. (2000) Antisense inhibition of P-glycoprotein expression using peptide−oligonucleotide conjugates. *Biochem. Pharmacol. 60*, 83−90.

(29) Astriab-Fisher, A., Sergueev, D. S., Fisher, M., Shaw, B. R., and Juliano, R. L. (2002) Conjugates of antisense oligonucleotides with the Tat and Antennapedia cell-penetrating peptides: Effects on cellular uptake, binding to target sequences, and biologic actions. *Pharm. Res. 19*, 744−754.

(30) Pooga, M., Soomets, U., Hallbrink, M., Valkna, A., Saar, K., Rezaei, K., Kahl, U., Hao, J. X., Xu, X. J., Wiesenfeld-Hallin, Z., Hokfelt, T., Bartfai, T., and Langel, U. (1998) Cell penetrating PNA constructs regulate galanin receptor levels and modify pain transmission in vivo. *Nature Biotechnol. 16*, 857−861.

(31) Eriksson, M., Nielsen, P. E., and Good, L. (2002) Cell permeabilization and uptake of antisense peptide-peptide nucleic acid (PNA) into *Escherichia coli*. *J. Biol. Chem. 277*, 7144−7147.

(32) Kaushik, N., Basu, A., Palumbo, P., Myers, R. L., and Pandey, V. N. (2002) Anti-TAR polyamide nucleotide analogue conjugated with a membrane-permeating peptide inhibits human immunodeficiency virus type 1 production. *J. Virol. 76*, 3881−3891.

(33) Vivés, E., and Lebleu, B. (1997) Selective coupling of a highly basic peptide to an oligonucleotide. *Tetrahedron Lett. 38*, 1183−1186.

(34) Oehlke, J., Birth, P., Klauschenz, E., Wiesner, B., Beyermann, M., Oksche, A., and Bienert, M. (2002) Cellular uptake of antisense oligonucleotides after complexing or conjugation with cell-penetrating model peptides. *Eur. J. Biochem. 269*, 4025−4032.

(35) Chico, D. E., Given, R. L., and Miller, B. T. (2003) Binding of cationic cell-permeable peptides to plastic and glass. *Peptides 24*, 3−9.

(36) Tung, C. H., and Stein, S. (2000) Preparation and applications of peptide−oligonucleotide conjugates. *Bioconjugate Chem. 11*, 605−618.

BC049977+

Cationic Oxyethylene Lipids. Synthesis, Aggregation, and Transfection Properties

Santanu Bhattacharya* and Padinjarae Vangasseri Dileep

Department of Organic Chemistry, Indian Institute of Science, Bangalore, India - 560 012. Received February 13, 2003; Revised Manuscript Received December 30, 2003

Four cationic lipids (**1**−**4**) with oligo-oxyethylene units at the linkage region between the pseudoglyceryl backbone and the hydrocarbon chains have been synthesized. Two of these lipids (**1** and **2**) have an equal number of $(CH_2CH_2O)_n$ units attached to both C-1 and C-2 positions of the pseudoglyceryl backbone, making their linkage regions similar, while the other two (**3** and **4**) are unsymmetrical in terms of the number of oxyethylene units in the linkage. Synthesis of lipids **1** and **2** involved the coupling of benzyl glycerol with the corresponding tosylates as a key step. Each of these lipids formed membranous aggregates when dispersed in water and exhibited clear thermotropic phase transitions typical of vesicular assemblies. The lipids **1**−**4** exhibited enhanced biological activities as gene transfer agents compared to their non-oxyethylene diether analogue, DHTMA. Transfection experiments using aqueous suspensions of these lipids and also their mixtures with cholesterol or dioleoyl phosphatidyl ethanolamine (DOPE) were performed on HeLa cells. The best transfection activity was demonstrated by unsymmetrical lipid **3**, which had two oxyethylene units only at the C-1 position of the pseudoglycerylbackbone.

INTRODUCTION

The recent concept of "the genetic material itself as the drug" identifies the need for efficient DNA delivery vectors (*1*, *2*). This has led to the development of many synthetic gene transfer vectors; among them are the formulations based on cationic lipids (*3*−*8*). Due to the ease of preparation and low levels of toxicity and immunogenic responses, cationic lipid-mediated transfection offers wide scope, especially in in vivo experiments (*9*) and clinical trials (*10*). However, the transfection efficiency of cationic lipid formulations has not yet been optimized to its maximum level (*11*) Due to this, the design and synthesis of novel cationic lipid molecules capable of efficient gene delivery is attracting much attention (*12*−*14*).

We have been investigating the role of various molecular level modifications in different synthetic lipids on their membrane properties and further influence on gene delivery events. We have observed that the linkage functionality between the hydrocarbon chain and the polar headgroup of a lipid molecule has significant influence on its aggregation behavior in water (*15*). Since this linkage is in a dynamic interfacial region in an aqueous suspension, even small changes at the linkage modulate the aggregation properties significantly. Such small modulations at the linkage regions of a cationic lipid is also known to have pronounced effects on its transfection efficiencies (*4*, *16*, *17*).

Along this direction, recently we have designed four cationic lipids **1**−**4** (Figure 1) having hydrophilic oxyethylene ($(CH_2CH_2O)_n$) groups at the linkage region (*18*). We envisaged the design of two types of oxyethylene-bearing cationic lipids. In one case we introduced an equal number of $(CH_2CH_2O)_n$ units to both C-1 and C-2 positions of the pseudoglyceryl backbone. In the other case, only one $(CH_2CH_2O)_2$ unit was introduced either at the C-1 or C-2 positions of the backbone, to result in an unsymmetrical system. Though synthetically more demanding, an ether linkage functionality was chosen between the pseudoglycerol backbone and the hydrophobic chains mainly due to the enhanced biological activities of cationic lipids having ether linkages compared to their ester analogues in gene delivery events (*16*, *17*), and also due to the enhanced chemical stability of ether bonds.

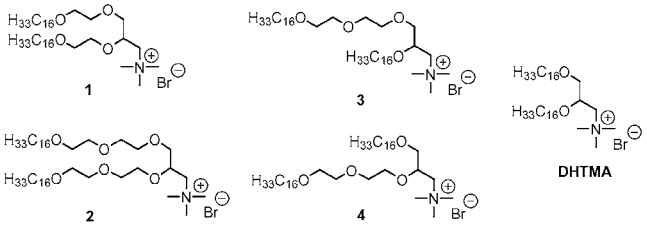


Figure 1. Molecular structures of the cationic lipids mentioned in the present study.

Though unnatural, such synthetic lipid molecules form an important class. The incorporation of $(CH_2CH_2O)_n$ groups at the linkage regions is expected to widen the membrane-bound water layer in such aggregates. Such variations at the interfacial region should in turn influence the association of such assemblies with various biomolecules. Ethyleneoxy units were chosen to be the appropriate hydrophilic linkage functionality in these lipid molecules by considering its literature precedence (*19*, *20*). Incorporation of oxyethylene units in lipid molecules have been attempted before, also for achieving some specific biological functions (*21*, *22*). We observed a pronounced enhancement in the gene delivery capabilities of cationic lipids upon incorporation of oxyethylene units at the linkage region (*23*). In this paper, we describe the detailed, optimized synthetic procedures of these biologically important compounds. We also present their aggregation properties and biological activities. To put

* To whom correspondence should be addressed. E-mail: sb@orgchem.iisc.ernet.in; also at Chemical Biology Unit, JNCASR, Bangalore.

10.1021/bc0340215 CCC: $27.50 © 2004 American Chemical Society
Published on Web 03/12/2004

our results in appropriate perspective, we compare the physicochemical and biological properties of the new lipids **1**−**4** with that of DHTMA. The molecular structure of DHTMA closely resembles that of *N*-(1-[2,3-dioleyloxy]-propyl)-*N*,*N*,*N*-trimethylammonium chloride (DOTMA), an ingredient which has been used in several commercially available formulations for gene transfection.

MATERIALS AND METHODS

General. All the reagents and chemicals used in this study were of the highest purity available. Cationic lipids were synthesized and characterized fully by their IR, ^{1}H NMR, mass spectra, and elemental analysis. 1,2-Dioleoyl-*sn*-glycero-3-phosphatidylethanolamine (DOPE) was purchased from Avanti Polar Lipids. ^{1}H NMR was recorded on JEOL JNM λ-300 (300 MHz for ^{1}H) or Bruker DRX-500 (500 MHz for ^{1}H) spectrometers. Chemical shifts (δ) are reported in ppm downfield from the internal standard; TMS, in the case of proton NMR. IR spectra were recorded on a Perkin-Elmer-781 spectrometer or on a Jasco FT-IR 410 spectrometer. Mass spectra were recorded on a Kratos PCKompact SEQ V1.2.2 MALDI-TOF spectrometer. Eluents for column chromatography, MeOH, EtOAc, $CHCl_3$ and petroleum ether (60−80 fraction), were distilled before use. Solvents used for reactions were dried before use. DMF, CH_2Cl_2, CH_3CN, and Et_3N were dried over P_2O_5. Et_3N and pyridine were stored over KOH. THF, benzene, and toluene were dried over sodium benzophenone ketyl prior to use. DMSO was dried over CaH_2, vacuum distilled, and was stored over molecular sieves. The purity of all the final lipids was checked by thin-layer chromatography (TLC) on silica gel G-60 plates (Merck) prior to vesicle preparation. TLC employed chloroform/methanol mixture as the eluent as indicated in the synthesis, and spots were visualized by staining the plates with iodine vapor. All the lipids used in this study exhibited single spots on TLC plates.

***O*-Hexadecyl Monoethylene Glycol Tosylate (6a) and *O*-Hexadecyl Diethylene Glycol Tosylate (6a).** Either of the alcohols (ethylene glycol monohexadecyl ether or diethylene glycol monohexadecyl ether) was dissolved in CH_2Cl_2 and cooled in an ice−water bath. To this was added dry pyridine (5 equiv), and the mixture was stirred for 10 min. *p*-TsCl (2.5 equiv) was added, and the mixture was stirred at 0 °C for 15 min and then for 25−50 h at rt. At the end of the reaction, the reaction mixture was dissolved in $CHCl_3$ and washed with aq 1.2 N HCl followed by 25% $NaHCO_3$, water, and brine solution. The organic layer was dried over anhyd Na_2SO_4. The desired product was isolated by silica gel column chromatography using an EtOAc−hexane solvent mixture. The isolated yields were 82% for **6a** ($R_f \sim 0.5$ in EtOAc−hexane (8:92) solvent mixture) and 68% for **6b** ($R_f \sim 0.5$ at EtOAc−hexane (10:90) solvent mixture). ^{1}H NMR ($CDCl_3$, 300 MHz): δ: (**6a**) 0.88 (t, terminal CH_3, 3H), 1.25 (br. m, CH_2 × 13, 26H), 1.54 (p, $C_{14}H_{29}CH_2$-CH_2O, 2H), 2.45 (s, CH_3Ar, 3H), 3.39 (t, $C_{15}H_{31}CH_2O$, 2H), 3.46−3.5 (m, $C_{15}H_{31}CH_2OCH_2$, 2H), 3.54−3.57 (m,$C_{15}H_{31}$-$CH_2OCH_2CH_2O$, 2H), 3.69 (t, CH_2CH_2OTs, 2H), 4.14 (t, CH_2CH_2OTs, 2H), 7.33 (d, meta H, 2H), 7.79 (d, ortho H, 2H); MS (MALDI-TOF): Calcd for $C_{25}H_{44}O_4S$: 440.7 Found: 463.9 (M + Na^+); Anal. Calcd for $C_{25}H_{44}O_4S\cdot 0.5H_2O$: C 66.77, H 10.09 Found: C 66.73, H 9.54. (**6b**) 0.88 (t, terminal CH_3, 3H), 1.26 (br. m, CH_2 × 13, 26H), 1.48 (p, $C_{14}H_{29}CH_2CH_2O$, 2H), 2.45 (s, CH_3Ar, 3H), 3.36 (t, $C_{15}H_{31}CH_2O$, 2H), 3.59 (t, CH_2CH_2OTs, 2H), 4.13 (t, CH_2CH_2OTs, 7.32 (d, meta H, 2H), 7.79 (d, ortho H, 2H); IR (cm^{-1}): 1590 (w), 1100−1150 (br. s, O−C−O str.); MS (MALDI-TOF): Calcd for $C_{27}H_{48}O_5S$: 484.7. Found: 507.9 (M + Na^+), 523.9 (M + K^+); Anal. Calcd for $C_{27}H_{48}O_5S\cdot 0.7H_2O$: C 65.21, H 10.01. Found: C 65.18, H 9.44.

***O*-Benzyl Glycerol (8).** 1,2-*O*-Isopropylidene glycerol (10 g, 75.6 mmol) was mixed with 8.8 g (156.6 mmol, 2 equiv) of powdered KOH in 45 mL of dry benzene. The solution turned yellow and then rose red within 5 min. To that was added 18 mL (19.8 g, 156.6 mmol, 2 equiv) of benzyl chloride. The mixture was refluxed at 100 °C for 23 h. The water formed during the reaction was removed by means of a phase-separating head (Deans−Stark apparatus). Then the cooled mixture was diluted with benzene (100 mL) and washed successively with water (50 mL), 0.1 N aq HCl (50 mL), 2.5% aq $NaHCO_3$ (50 mL), and again with water. The benzene phase was dried over anhyd Na_2SO_4, and the solvent was removed under reduced pressure. The crude product, 1,2-*O*-isopropylidene glycerol benzyl ether was homogenized in 100 mL of MeOH−H_2O (2:1) and to that was added 5.75 g (30.3 mmol) of *p*-TsOH. The mixture was stirred at room temperature for 1 h. The reaction mixture was neutralized with $NaHCO_3$ powder. The mixture was filtered and washed with $CHCl_3$, and then the organic layer was evaporated under reduced pressure. Traces of the remaining acid were removed by a subsequent base workup. The concentrated organic layer was diluted with $CHCl_3$ and washed with saturated aq $NaHCO_3$ (100 mL), water (50 mL), and saturated brine (50 mL). The organic layer was dried over anhyd Na_2SO_4. A 53% yield (7.3 g) of the pure compound was obtained by column chromatography on silica gel (*24*). Compound was eluted in 5% MeOH−$CHCl_3$ ($R_f \sim 0.8$ at MeOH−$CHCl_3$ (2:98)). ^{1}H NMR ($CDCl_3$, 300 MHz): δ: 2.65 (br. s, OH, 2H), 3.45−3.7 (m, 2 × CH_2O, 4H), 3.75−4 (q, OCH_2CHOCH_2O), 4.05 (s, OCH_2Ar, 2H), 7.35 (s, Ar, 5H); IR (cm^{-1}): 3100−3650 (br., OH).

1,2-Bis(2′-hexadecyloxyethoxy)-3-benzyloxypropane (9a). *O*-Benzyl glycerol (300 mg, 1.65 mmol) in 5 mL of dry DMSO was added to a precooled DMSO suspension (5 mL) of NaH (55% in oil) (237 mg, 3.3 equiv; prewashed with dry hexane) in a two-necked flask equipped with a septum and a guard tube. The mixture was stirred for 2 h at room temperature. To that were added 1.6 g of O-hexadecyl monoethylene glycol tosylate (**11a**) (3.6 mmol, 2.2 equiv) and 150 mg of $Bu_4N^+I^-$ (0.4 mmol, 0.25 equiv) in 2 mL of DMSO through a syringe. The reaction mixture was further stirred at room temperature for 24−30 h (till the alkyl tosylate was consumed, as indicated by TLC). Once the reaction was over, the reaction mixture was diluted with EtOAc and washed with 1 N aq HCl followed by 2.5% aq $NaHCO_3$, water, and brine. The aqueous layer was extracted again with EtOAc. The organic phase was dried over anhyd Na_2SO_4. Pure compound was isolated as a pale yellowish liquid by column chromatography over silica gel using 5% EtOAc−hexane as the solvent system. The isolated yield was 880 mg (74%) ($R_f \sim 0.4$ at EtOAc−hexane (5:95)). ^{1}H NMR ($CDCl_3$, 300 MHz): δ: 0.88 (t, 2 × terminal CH_3, 6H), 1.25 (br. m, 26 × CH_2, 52H), 1.55 (p, 2 × $C_{14}H_{29}CH_2$-CH_2O, 4H), 3.41 (t, 2 × $C_{15}H_{31}CH_2O$, 4H), 3.49−3.75 (m, [2 × OCH_2CH_2O] + [2 × OCH_2CHO] + OCH_2CHOCH_2O, 13H), 4.53 (s, OCH_2Ar, 2H), 7.23−7.37 (m, Ar, 5H); IR (cm^{-1}): 1100 (br. strong, C−O−C str.); MS (MALDI-TOF): Calcd for $C_{46}H_{86}O_5$: 719.2. Found: 742.5 (M + Na^+).

1,2-Bis(2′-[2″-hexadecyloxyethoxy]ethoxy)-3-benzyloxypropane (9b). 9b was synthesized following the same procedure for that of **9a**. Pure compound was isolated in 67% yield as a colorless liquid (which forms a wax on standing) by column chromatography over silica

gel using EtOAc−hexane (15:85) as the solvent system ($R_f \sim 0.4$ at EtOAc−hexane (15:85)). ^{1}H NMR ($CDCl_3$, 300 MHz): δ: 0.88 (t, 2 × terminal CH_3, 6H), 1.20 (br. m, 26 × CH_2, 52H), 1.5 (p, 2 × $C_{14}H_{29}CH_2CH_2O$, 4H), 3.6 (t, 2 × $C_{15}H_{31}CH_2O$, 4H), 3.44−3.71 (m, [4 × OCH_2CH_2O] + [2 × OCH_2CHO] + OCH_2CHOCH_2O, 21H), 4.47 (s, OCH_2Ar, 2H), 7.17−7.28 (m, Ar, 5H); IR (cm^{-1}): 1110 (br. strong, C−O−C str.); MS (MALDI-TOF): Calcd for $C_{50}H_{94}O_7$: 806.7. Found: 829.7 ($M + Na^+$).

2,3-Bis(2′-hexadecyloxyethoxy)-1-propanol (10a). **9a** (500 mg) was dissolved in 10 mL of EtOAc-MeOH mixture in a hydrogenation setup, and to that was added 240 mg of 10% Pd−charcoal. Hydrogenation was performed for 12 h at atmospheric pressure. Then Pd−charcoal was filtered off from the reaction mixture with a sintered funnel and was washed with $CHCl_3$ and EtOAc. Solvent was evaporated under reduced pressure, and the pure compound was isolated as a slight yellow gummy solid by column chromatography over silica gel with EtOAc−hexane (1:4) as the eluting solvent ($R_f \sim 0.7$ at EtOAc−hexane (1:4) solvent mixture). The isolated yield was 380 mg (87%). ^{1}H NMR ($CDCl_3$, 300 MHz): δ: 0.88 (t, 2 × terminal CH_3, 6H), 1.25 (br. m, 26 × CH_2, 52H), 1.55 (p, 2 × $C_{14}H_{29}CH_2CH_2O$, 4H), 3.4−3.71 (m, [2 × $C_{15}H_{31}CH_2O$] + [2 × OCH_2CH_2O] + [2 × OCH_2CHO], 16H), 3.82−3.88 (m, OCH_2CHOCH_2O, 1H); MS (MALDI-TOF): Calcd for $C_{39}H_{80}O_5$: 628. Found: 651 ($M + Na^+$), 667 ($M + K^+$); Anal. Calcd for $C_{39}H_{80}O_5$: C 74.46, H 12.82. Found: C 74.46, H 12.61.

2,3-Bis(2′-[2″-hexadecyloxyethoxy]ethoxy)-1-propanol (10b). **9b** (400 mg) was dissolved in 8 mL of EtOAc-MeOH mixture in a hydrogenation setup, and to that was added 135 mg of 10% Pd−charcoal. Hydrogenation was performed for 12 h at atmospheric pressure. Then Pd−charcoal was filtered off from the reaction mixture with a sintered funnel and was washed with $CHCl_3$ and EtOAc. Solvent was evaporated under reduced pressure and the pure compound was isolated as a yellow wax by column chromatography over silica with EtOAc−hexane (1:1) as the eluting solvent ($R_f \sim 0.7$ at EtOAc−hexane solvent (1:1) mixture). The isolated yield was 350 mg (80%). ^{1}H NMR ($CDCl_3$, 300 MHz): δ: 0.88 (t, 2 × terminal CH_3, 6H), 1.25 (br. m, 26 × CH_2, 52H), 1.56 (p, 2 × $C_{14}H_{29}CH_2CH_2O$, 4H), 3.42 (t, 2 × $C_{15}H_{31}CH_2O$, 4H), 3.47−3.73 (m, [4 × OCH_2CH_2O] + [2 × OCH_2CHO], 20H), 3.8−3.87 (m, OCH_2CHOCH_2O, 1H); IR (cm^{-1}): 1110 (br. strong, C−O−C str.), 3400−3480 (br., OH); Anal. Calcd for $C_{43}H_{88}O_7 \cdot 0.6H_2O$: C 70.95, H 12.35. Found: C 71.04, H 12.25.

2,3-Bis(2′-hexadecyloxyethoxy)-1-propyl Tosylate (11a). 2,3-Bis(2′-[2″-hexadecyloxyethoxy]ethoxy)-1-propanol (**10a**) (130 mg, 0.2 mmol) was dissolved in 1 mL of dry CH_2Cl_2 and was cooled in an ice−water bath. To that were added 2 mL of dry pyridine and 78.8 mg of freshly recrystallized *p*-TsCl (2 equiv). The reaction mixture was stirred at 0 °C for 30 min and then for 24 h (till the starting alcohol disappeared as indicated from TLC) at room temperature. The reaction mixture was then diluted with $CHCl_3$ and was washed with water followed by 2 N aq HCl and again with water. The organic phase was washed with brine and dried over anhyd Na_2SO_4. Solvent was evaporated under reduced pressure, and pure compound was isolated (140 mg, 85%) as a white wax by column chromatography over silica gel using EtOAc−hexane solvent mixture ($R_f \sim 0.5$ at EtOAc−hexane (15:85) solvent mixture). ^{1}H NMR ($CDCl_3$, 300 MHz): δ: 0.88 (t, 2 × terminal CH_3, 6H), 1.26 (br. m, 26 × CH_2, 52H), 1.54 (p, 2 × $C_{14}H_{29}CH_2CH_2O$, 4H), 2.45 (s, CH_3Ar, 3H), 3.38−3.67 (m, [2 × $C_{15}H_{31}CH_2O$] + [2 × OCH_2CH_2O] + [2 × OCH_2CHO], 14H), 3.72 (q, OCH_2CHOCH_2O, 1H), 4.06 (dd [J = 9 Hz, 6 Hz], HCHOTs, 1H), 4.17 (dd, [J = 9 Hz, 3 Hz], HCHOTs, 1H), 7.34 (d, meta H, 2H), 7.79 (d, ortho H, 2H); IR (cm^{-1}): 1110 (br. strong, C−O−C str.)

2,3-Bis(2′-[2″-hexadecyloxyethoxy]ethoxy)-1-Propyl Tosylate (11b). 2,3-Bis(2′-[2″-hexadecyloxyethoxy]-ethoxy)-1-propanol (**10b**) (150 mg, 0.2 mmol) was dissolved in 5 mL of dry CH_2Cl_2 and was cooled in an ice−water bath. To that were added 0.09 mL (1 mmol, 5 equiv) of dry pyridine and 79.7 mg of recrystallized *p*-TsCl (2 equiv). The reaction mixture was stirred for 27 h (till the starting alcohol disappeared as indicated from TLC) at room temperature. The reaction mixture was then diluted with $CHCl_3$ and washed with water followed by 2 N aq HCl and again with water. The organic phase was washed with brine and dried over anhyd Na_2SO_4. Solvent was evaporated under reduced pressure, and pure compound was isolated as a yellow liquid by column chromatography over silica gel. Yield was practically quantitative ($R_f \sim 0.5$ at EtOAc−hexane (30:70) solvent mixture). ^{1}H NMR ($CDCl_3$, 300 MHz): δ: 0.88 (t, 2 × terminal CH_3, 6H), 1.25 (br. m, 26 × CH_2, 52H), 1.57 (p, 2 × $C_{14}H_{29}CH_2CH_2O$, 4H), 2.45 (s, CH_3Ar, 3H), 3.43 (t, 2 × $C_{15}H_{31}CH_2O$, 4H), 3.48−3.76 (m, [4 × OCH_2CH_2O] + [2 × OCH_2CHO] + [OCH_2CHOCH_2O], 19H), 4.06 (dd [J = 9 Hz, 6 Hz], HCHOTs, 1H), 4.17 (dd, [J = 9 Hz, 3 Hz], HCHOTs, 1H), 7.34 (d, meta H, 2H), 7.80 (d, ortho H, 2H).

1-Bromo-2,3-bis(2′-hexadecyloxyethoxy)propane (12a). 2,3-Bis(2′-hexadecyloxy ethoxy)-1-propyl tosylate (**11a**) (140 mg, 0.17 mmol) and LiBr (46.56 mg, 0.53 mmol, 3 equiv) were dissolved in 2 mL of dry DMF and refluxed at 70 °C for 24 h. Then the reaction mixture was diluted with 125 mL of EtOAc and was washed with 100 mL of water followed by brine. The organic phase was dried over anhyd Na_2SO_4. Pure compound was isolated in 81% yield (100 mg) by column chromatography over silica gel ($R_f \sim 0.8$ at EtOAc−hexane (15:85)). ^{1}H NMR ($CDCl_3$, 300 MHz): δ: 0.88 (t, 2 × terminal CH_3, 6H), 1.25 (br. m, 26 × CH_2, 52H), 1.56 (p, 2 × $C_{14}H_{29}CH_2CH_2O$, 4H), 3.4−3.74 (m, [7 × CH_2O] + CH_2Br + OCH_2CHOCH_2O, 17H); IR (cm^{-1}): 1100−1130 (broad, C−O−C str.)

1-Bromo-2,3-bis(2′-[2″-hexadecyloxyethoxy]ethoxy)propane (12b). 2,3-Bis(2′-[2″-hexadecyloxy ethoxy]-ethoxy)-1-propyl tosylate (**11b**) (200 mg, 0.23 mmol) and LiBr (59.80 mg, 0.7 mmol, 3 equiv) were dissolved in 3 mL of dry DMF and refluxed at 70 °C for 8 h. Then the reaction mixture was dissolved in 100 mL of EtOAc and washed twice with water (2 × 20 mL) followed by brine. The organic phase was dried over anhyd Na_2SO_4. EtOAc was evaporated under reduced pressure, and pure compound was isolated in 84% yield (150 mg) by column chromatography over silica gel ($R_f \sim 0.7$ at EtOAc−hexane (3:7)). ^{1}H NMR ($CDCl_3$, 300 MHz): δ: 0.88 (t, 2 × terminal CH_3, 6H), 1.25 (br. m, 26 × CH_2, 52H), 1.56 (p, 2 × $C_{14}H_{29}CH_2CH_2O$, 4H), 3.42 (t, 2 × $C_{15}H_{31}CH_2O$, 4H), 3.46−3.75 (m, [9 × CH_2O] + CH_2Br + OCH_2CHOCH_2O, 21H); IR (cm^{-1}): 1140, 1200−1240 (broad, C−O−C str.)

***N*-(2,3-Bis[2′-hexadecyloxyethoxy]propyl)*N*,*N*,*N*-trimethylammonium Bromide (1).** Trimethylamine was introduced into dry CH_3CN (1 mL) in a pressure tube in an ice−acetone bath. This resulted in a 3-fold expansion of the initial volume of acetonitrile. 1-Bromo-2,3-bis(2′-hexadecyloxyethoxy)propane (**12a**) (100 mg, 0.15 mmol) was dissolved in CH_3CN−toluene mixture by slight warming and was transferred to the pressure tube.

The reaction mixture was heated at 80 °C for 24 h. The reaction mixture was cooled, and the excess trimethylamine was evaporated by warming in a water bath. Solvent was then removed under reduced pressure. Pure compound was isolated as a white solid by column chromatography over silica using MeOH−$CHCl_3$ as the solvent mixture. Yield of the reaction was 74% (80 mg). ^{1}H NMR (500 MHz, $CDCl_3$): δ: 0.88 (t, 2 × terminal CH_3, 6H), 1.26 (br. m, 26 × CH_2, 52H), 1.52−1.57 (m, 2 × $C_{14}H_{29}CH_2CH_2O$, 4H), 3.41 (s, 3 × N^+CH_3, 9H), 3.43−3.71 (m, 7 × CH_2O, 14H), 3.90−3.92 (m, OCH_2−CHO−CH_2N^+, 1H), 4.11−4.18 (m, CH_2N^+, 2H); IR (cm^{-1}): 1060−1150 (broad, C−O−C str.); MS (MALDI-TOF): Calcd for $C_{42}H_{88}O_4N$: 671.2. Found: 672.2 (M + H^+); Anal. Calcd for $C_{42}H_{88}O_4NBr{\cdot}1.5H_2O$: C 64.83, H 11.79, N 1.8. Found: C 64.93, H 12.03, N 1.65.

***N*-(2,3-Bis[2′-{2″-hexadecyloxyethoxy}ethoxy]-propyl)-*N*,*N*,*N*-trimethylammonium Bromide (2).** Trimethylamine was introduced into dry CH_3CN (1 mL) in a pressure tube in an ice-acetone bath which nearly resulted in a 3-fold expansion of the volume of CH_3CN from its initial value. 1-Bromo-2,3-bis(2′-[2″-hexadecyloxyethoxy]ethoxy)propane (**12b**) (150 mg, 0.19 mmol) was dissolved in CH_3CN−toluene mixture by light heating and was transferred to the pressure tube. The reaction mixture was heated at 80 °C for 24 h. The reaction mixture was cooled, and the excess Me_3N was evaporated by warming. Solvent was then removed under reduced pressure. Pure compound was isolated as a white wax (110 mg, 68%) by column chromatography over silica gel (100−200 mesh) using MeOH−$CHCl_3$ (1:9) as the solvent mixture. After the chromatography separation, the compound was dissolved in chloroform and was passed through a sintered funnel to remove any silica gel impurity in the eluant ($R_f \sim 0.5$ at MeOH−$CHCl_3$ (1:9) solvent mixture). ^{1}H NMR (500 MHz, $CDCl_3$): δ: 0.88 (t, 2 × terminal CH_3, 6H), 1.26 (br. m, 26 × CH_2, 52H); 1.55 (p, 2 × $C_{14}H_{29}CH_2CH_2O$, 4H), 3.38 (s, 3 × N^+CH_3, 9H), 3.39−3.67 (m, 11 × C H_2O, 22H), 3.89−3.91 (m, OCH_2−CHO−CH_2N^+, 1H), 4.04 (d, HCH−N^+, 1H), 4.16 (m, HC H-N^+, 1H); IR (cm^{-1}): 1100 (broad, C−O−C str.); MS (MALDI-TOF): Calcd for $C_{46}H_{96}O_6N$: 759.3. Found: 760.1 (M + H^+); Anal. Calcd for $C_{46}H_{96}O_6NBr{\cdot}1.9H_2O$: C 63.26, H 11.52, N 1.6. Found: C 63.25, H 11.77, N 1.43.

2-(2′-Chloroethoxy)ethyl-2″-tetrahydropyranyl Ether (13). To 2 g of 2-(2′-chloroethoxy)ethanol (16.1 mmol) were added 2.03 g of dihydropyran (24.1 mmol, 1.5 equiv) and 1 drop of concentrated HCl. It was stirred at rt for 2.5 h. The reaction mixture was initially neutralized by the addition of solid $NaHCO_3$. The reaction mixture was then diluted with EtOAc and washed with saturated aq $NaHCO_3$ solution followed by brine. The organic phase was dried over anhyd Na_2SO_4. Pure compound was isolated as a colorless liquid (quantitative conversion) chromatographically by passing through a short column of silica gel and eluting with EtOAc−hexane solvent (2:98) mixture (*25*). ^{1}H NMR (90 MHz, $CDCl_3$): δ: 1.4−2 (m, 3 × CH_2, 6H), 3.3−4 (m, [4 × C H_2O] + CH_2Cl, 10H), 4.65 (t, O−CH_2C HCH_2−O, 1H); IR (cm^{-1}): 1120 (broad, C−O−C str.)

3-Benzyloxy-2-hydroxy-1-(2′-[2″-hydroxyethoxy]-ethoxy)propane (14). To a solution containing *O*-benzyl glycerol (**8**) (0.5 g, 2.75 mmol) were added 2-(2′-chloroethoxy)ethyl 2″-tetrahydropyranyl ether (**13**) (1.72 g, 8.24 mmol, 3 equiv) and 82.1 mg of $Bu_4N^+HSO_4^-$ (0.242 mmol, 0.09 equiv) dropwise in 2 mL of 50% aq NaOH (2 g, 55 mmol, 20 equiv). The mixture was stirred and heated at 65 °C for 5 h. Then the reaction mixture was diluted with CH_2Cl_2 and washed with water followed by brine. The organic phase was dried over anhyd Na_2SO_4. However, mono- and diether derivatives could not be isolated upon column chromatography. The mixture was isolated by silica gel column chromatography using EtOAc−hexane (1:1) as the solvent system (R_f of the mixture being 0.5 at this solvent mixture). This mixture was then subjected to the acid-catalyzed deprotection of THP by stirring the compound with 10 drops of concentrated HCl in 10 mL of 1:1 MeOH−CH_2Cl_2 solvent mixture for 2 h at room temperature. The reaction mixture was then carefully neutralized with solid $NaHCO_3$ and was extracted in EtOAc and finally with $CHCl_3$. The organic solvent from the organic extracts was evaporated under reduced pressure and the required mono derivative was isolated in the pure form, as a yellow liquid, by column chromatography over silica using MeOH-EtOAc solvent system (R_f of the required mono derivative ∼ 0.6 at EtOAc). The isolated yield was 250 mg (34% overall). ^{1}H NMR (300 MHz, $CDCl_3$): δ: 3.41−3.83 (m, 6 × CH_2, 12H), 3.94 (q, $OCH_2CHOHCH_2O$, 1H), 4.48 (s, OCH_2Ar, 2H), 7.19−7.31 (m, Ar, 5H); LRMS: Calcd for $C_{14}H_{22}O_5$: 270. Found: 271 (MH^+)

1-(2′-[2″-Hexadecyloxyethoxy]ethoxy)-2-hexadecyloxy-3-benzyloxypropane (15). To a mixture containing 3-benzyloxy-2-hydroxy-1-(2′-[2″-hydroxyethoxy]-ethoxy)propane (**14**) (320 mg, 1.2 mmol), $Bu_4N^+HSO_4^-$ (26.7 mg, 0.79 mmol, 0.09 equiv), and hexadecyl chloride (699 mg, 2.68 mmol, 2.2 equiv) was added dropwise 1.4 mL of 50% NaOH. The mixture was then stirred vigorously at 65 °C for 5 days. After the reaction, CH_2Cl_2 was added to it and the organic layer was washed with water followed by brine. The organic phase was dried over anhyd Na_2SO_4, and the solvent was evaporated under reduced pressure. Pure compound was isolated as a slight yellow liquid at 53% yield (450 mg) by silica gel column chromatography using EtOAc−hexane (15:85) as the solvent system ($R_f \sim 0.8$ at this solvent system). ^{1}H NMR (300 MHz, $CDCl_3$): δ: 0.86 (t, 2 × terminal CH_3, 6H), 1.23 (br. m, 26 × CH_2, 52H), 1.54 (p, 2 × $C_{14}H_{29}CH_2CH_2O$, 4H), 3.42 (t, 2 × $C_{15}H_{31}CH_2O$, 4H), 3.48−3.67 (m, 6 × CH_2O, 12H), 3.76 (q, OCH_2CHOCH_2O, 1H), 4.53 (s, OCH_2Ar, 2H), 7.26−7.32 (m, Ar, 5H); IR (cm^{-1}): 1100 (broad, C−O−C str.)

2-Hexadecyloxy-3-(2′-[2″-hexadecyloxyethoxy]-ethoxy)-1-propanol (16). 1-(2′-[2″-Hexadecyloxyethoxy]-ethoxy)-2-hexadecyloxy-3-benzyloxypropane (**15**) (450 mg, 0.6 mmol) was dissolved in EtOAc−MeOH solvent mixture. To that was added activated 10% Pd-charcoal (100 mg). Hydrogen gas was introduced into the flask, and hydrogenation was carried out under atmospheric pressure, at room temperature for 12 h. Pd−charcoal was filtered off from the reaction mixture, and the pure compound was isolated as a low melting white solid (340 mg, 85% yield) by column chromatography over silica gel ($R_f \sim 0.4$ at EtOAc−hexane (1:4) solvent mixture). ^{1}H NMR (300 MHz, $CDCl_3$): δ: 0.86 (t, 2 × terminal CH_3, 6H), 1.23 (br. m, 26 × CH_2, 52H), 1.55 (m, 2 × $C_{14}H_{29}CH_2$-CH_2O, 4H), 3.42 (t, 2 × $C_{15}H_{31}CH_2O$, 4H), 3.47−3.7 (m, 6 × CH_2O, 12H), 3.83 (m, OCH_2CHOCH_2O, 1H); IR (cm^{-1}): 1100−1130 (broad, C−O−C str.), 3400 (br., OH); LRMS Calcd for $C_{39}H_{80}O_5$: 628. Found: 629 (MH^+); Anal. Calcd for $C_{39}H_{80}O_5{\cdot}0.4H_2O$: C 73.62, H 12.8. Found: C 73.67, H 12.84.

2-Hexadecyloxy-3-(2′-[2″-hexadecyloxyethoxy]-ethoxy)-1-propyl Tosylate (17). 2-Hexadecyloxy-3-(2′-[2″-hexadecyloxyethoxy]ethoxy)-1-propanol (**16**) (140 mg, 0.2 mmol) was dissolved in 1 mL of dry CH_2Cl_2 and cooled in an ice−water bath. To that were added 2 mL of dry pyridine and 106 mg of freshly recrystallized *p*-TsCl (0.5

mmol, 2.5 equiv). The reaction mixture was stirred at 0 °C for 15 min and then at room temperature for 24 h (till the starting alcohol disappeared as indicated from TLC). The reaction mixture was then diluted with CH_2Cl_2 and was washed with water followed by 2 N aq HCl and again with water. The organic phase was washed with brine and dried over anhyd Na_2SO_4. Solvent was evaporated under reduced pressure, and pure compound was isolated as a colorless liquid (140 mg, 80% yield) by column chromatography over silica ($R_f \sim 0.3$ at EtOAc−hexane (15:85) solvent mixture). The isolated product was found to be very hygroscopic. ^{1}H NMR ($CDCl_3$, 300 MHz): δ: 0.88 (t, 2 × terminal CH_3, 6H), 1.25 (br. m, 26 × CH_2, 52H), 1.46 (m, $C_{14}H_{29}CH_2CH_2O$, 2H), 1.55 (m, $C_{14}H_{29}CH_2CH_2O$, 2H), 2.46 (s, C H_3Ar, 3H), 3.32−3.7 (m, [7 × CH_2O] + [OCH_2CHOCH_2O], 15H), 3.96−4.01 (m, HC*H*OTs, 1H), 4.13 (dd [9 Hz, 3 Hz], HC*H*OTs, 1H), 7.32 (d, meta H, 2H), 7.78 (d, ortho H, 2H); IR (cm^{-1}): 1080−1120 (br., C−O−C str.)

1-Bromo-2-hexadecyloxy-3-(2′-[2″-hexadecyloxyethoxy]ethoxy)propane. 2-Hexadecyloxy-3-(2′-[2″-hexadecyloxyethoxy] ethoxy)-1-propyl tosylate (140 mg, 0.2 mmol) and LiBr (46.6 mg, 0.5 mmol, 3 equiv) were dissolved in 2 mL of dry DMF, and the mixture was refluxed at 70 °C for 8 h. Then the reaction mixture was diluted with 100 mL of EtOAc and was washed twice with 30 mL portions of water. The water layer was extracted with EtOAc. The organic phase was then washed with brine and was dried over anhyd Na_2SO_4. EtOAc was evaporated under reduced pressure, and the pure compound was isolated in 73% yield (90 mg) by column chromatography over silica gel ($R_f \sim 0.8$ at EtOAc−hexane (1:9)). The bromo compound was used for the next step immediately without further characterization.

***N*-(2-Hexadecyloxy-3-[2′-{2″-hexadecyloxyethoxy}-ethoxy] propyl)-*N*,*N*,*N*-trimethylammonium Bromide (3).** Dry NMe_3 gas was passed into dry CH_3CN (1 mL) in a pressure tube which was precooled cooled using an ice−acetone bath. 1-Bromo-2-hexadecyloxy-3-(2′-[2″-hexadecyloxyethoxy]ethoxy)propane (90 mg, 0.13 mmol) was dissolved in a mixture of CH_3CN (2 mL)−toluene (0.5 mL) by slight warming and was transferred to the pressure tube. (It may be mentioned herein that the bromide was not soluble in CH_3CN while it was very soluble in toluene. Thus, good yields were obtained when a minimum amount of toluene was used for the reaction.) The reaction mixture was then heated at 80 °C for 24 h. The resulting material was then cooled, and the excess trimethylamine was evaporated. This was then dissolved in $CHCl_3$, and the solvent was removed under reduced pressure. Pure compound was isolated as a colorless waxy solid (100 mg, quantitative conversion) by column chromatography over silica gel (100−200 mesh) using 10% MeOH−$CHCl_3$ as the eluting solvent. ^{1}H NMR (500 MHz, $CDCl_3$): δ: 0.90 (t, 2 × terminal CH_3, 6H), 1.27 (br. m, 26 × CH_2, 52H), 1.55 (br. m, 2 × $C_{14}H_{29}CH_2CH_2O$, 4H), 3.41−3.72 (m + s, singlet at 3.49, [7 × CH_2O] + [3 × CH_3N^+], 14H + 9H), 3.97−4.14 (m, [$OCH_2CHOCH_2N^+$] + [CH_2N^+], 1H + 2H); IR (cm^{-1}): 1100 (broad, C−O−C str.); MS (MALDI-TOF): Calcd for $C_{42}H_{88}O_4N$: 671.2. Found: 672.0 (M + H$^+$); Anal. Calcd for $C_{42}H_{88}O_4NBr\cdot 0.3H_2O$: C 66.69, H 11.81, N 1.85. Found: C 66.73, H 12.1, N 1.56.

3-Benzyloxy-2-hydroxy-1-hexadecyloxypropane (18). *O*-Benzyl glycerol (**8**) (299 mg, 1.6 mmol) was dissolved in dry THF and was cooled in an ice−water bath. NaH (55% in oil) (144 mg, 3.2 mmol), washed with dry hexane (to remove oil), was added to it and stirred at 0 °C for 15 min. To this was added 0.5 g (1.3 mmol) of hexadecyl tosylate, and the reaction mixture was refluxed for 24 h. CH_2Cl_2 was added to the reaction mixture, and the resulting mass was acidified with 1.2 N aq HCl. The organic phase was then washed with water, followed by brine. The organic layer was isolated and dried over anhyd Na_2SO_4. Solvent was evaporated under reduced pressure and the pure compound was separated (200 mg, 40%) as a colorless liquid by column chromatography over silica gel ($R_f \sim 0.5$ at EtOAc−hexane(1:4)). The spectroscopic properties match those of the reported compound. ^{1}H NMR ($CDCl_3$, 300 MHz): δ: 0.88 (t, terminal CH_3, 3H), 1.25 (br. m, 13 × CH_2, 26H), 1.55 (p, $C_{14}H_{29}C$ H_2-CH_2O, 2H), 3.4−3.71 (m, 3 × CH_2O, 6H), 3.93 (q, OCH_2CHOCH_2O, 1H), 4.54 (s, OC H_2Ar, 2H), 7.25−7.34 (m, Ar, 5H); IR (cm^{-1}): 1120 (br., C−O−C str.), 3400 (br., OH).

1-Hexadecyloxy-2-(2′-[2″-hexadecyloxyethoxy]-ethoxy)-3-benzyloxypropane (19). The alcohol **18** was taken (200 mg) in dry THF and was cooled in an ice−water bath. NaH (55% in oil) (1.5 equiv) was washed with dry hexane to remove oil and was added to the solution of alcohol in THF. The mixture was stirred at room temperature for 15 min. A white precipitate was formed in the reaction mixture. To that was added 1.5 equiv of *O*-hexadecyl diethylene glycol tosylate, and the mixture was refluxed at 89 °C. After the reaction, THF was removed by evaporation under reduced pressure. Crude mixture was then dissolved in CH_2Cl_2 and washed with 1 N aq HCl, followed by water and brine. The organic phase was dried over anhyd Na_2SO_4. The required compound was isolated in 74% isolated yielding pure form as a slight yellow colored liquid by silica gel column chromatography using 20 EtOAc−hexane ($R_f \sim 0.4$) as the elution mixture. ^{1}H NMR ($CDCl_3$, 300 MHz): δ: 0.88 (t, 2 × terminal CH_3, 6H), 1.25 (br. m, 26 × CH_2, 52H), 1.55 (p, 2 × $C_{14}H_{29}CH_2CH_2O$, 4H), 3.38−3.76 (m, [8 × CH_2O] + [OCH_2CHOCH_2O], 17H), 4.53 (s, OCH_2Ar, 2H), 7.25−7.31 (m, Ar, 5H); IR (cm^{-1}): 1110 (br., C−O−C str.).

3-Hexadecyloxy-2-(2′-[2″-hexadecyloxyethoxy]-ethoxy)-1-propanol (20). 1-Hexadecyloxy-2-(2′-[2″-hexadecyloxyethoxy]ethoxy)-3-benzyloxypropane (**19**) (260 mg, 0.36 mmol) was dissolved in 5 mL of a mixture of dry EtOAc−MeOH (1:1). To that was added activated 10% Pd−charcoal (340 mg). Hydrogen gas was introduced to the flask. Hydrogenation was allowed to continue at atmospheric pressure, at room temperature for 15 h. Pd−charcoal was filtered off from the reaction mixture, and the pure compound was isolated as a low melting white solid (180 mg, 79% yield) by column chromatography over silica gel ($R_f \sim 0.5$ at EtOAc−hexane (1:1)). ^{1}H NMR ($CDCl_3$, 300 MHz): δ: 0.88 (t, 2 × terminal CH_3, 6H), 1.25 (br. m, 26 × CH_2, 52H), 1.54−1.56 (m, 2 × $C_{14}H_{29}CH_2$-CH_2O, 4H), 3.36−3.72 (m, 8 × CH_2O, 16H), 3.83−3.87 (m, OCH_2CHOCH_2O, 1H); IR (cm^{-1}): 1100 (br., C−O−C str.), 3400 (br., OH).

3-Hexadecyloxy-2-(2′-[2″-hexadecyloxyethoxy]-ethoxy)-1-propyl Tosylate (21). 3-Hexadecyloxy-2-(2′-[2″-hexadecyloxyethoxy]ethoxy)-1-propanol (180 mg, 0.29 mmol) was dissolved in 5 mL of dry CH_2Cl_2 and was cooled in an ice−water bath. To that were added 0.2 mL of dry pyridine and 138 mg of freshly recrystallized *p*-TsCl (0.725 mmol, 2.5 equiv). The reaction mixture was stirred at 0 °C for 15 min and then at room temperature for 24 h (till the starting alcohol disappeared as indicated from TLC). The reaction mixture was then diluted with CH_2Cl_2 and was washed with 2 N aq HCl followed by water and brine. The organic layer was separated and dried over anhyd Na_2SO_4. Solvent was evaporated under reduced pressure, and the pure compound was isolated

as a colorless liquid in 85% yield by column chromatography (silica) ($R_f \sim 0.4$ at EtOAc−hexane (1:9) solvent mixture). ^{1}H NMR ($CDCl_3$, 300 MHz): δ: 0.88 (t, 2 × terminal CH_3, 6H), 1.25 (br. m, 26 × CH_2, 52H), 1.47−1.55 (m, 2 × $C_{14}H_{29}CH_2CH_2O$, 4H), 2.45 (s, CH_3Ar, 3H), 3.32−3.71 (m, [7 × CH_2O] + [OCH_2CHOCH_2O], 15H), 3.98−4.15 (m, C H_2OTs, 2H), 7.32 (d, meta H, 2H), 7.79 (d, ortho H, 2H); IR (cm^{-1}): 1080−1110 (br., C−O−C str.)

1-Bromo-2-(2′-[2″-hexadecyloxyethoxy]ethoxy)-3-hexadecyloxypropane. 3-Hexadecyloxy-2-(2′-[2″-hexadecyloxyethoxy]ethoxy)-1-propyl tosylate (190 mg, 0.24 mmol) and LiBr (63.2 mg, 0.7 mmol, 3 equiv) were dissolved in 3 mL of dry DMF and refluxed at 70 °C for 8 h. The reaction mixture was then diluted with 150 mL of EtOAc and washed twice with 30 mL portions of water. The water layer was extracted with EtOAc. The organic layers were collected together, washed with brine, and dried over anhyd Na_2SO_4. EtOAc was evaporated under reduced pressure, and pure compound was isolated in 59% yield (90 mg) by column chromatography over silica gel ($R_f \sim 0.5$ at EtOAc−hexane(5:95)). ^{1}H NMR ($CDCl_3$, 300 MHz): δ: 0.88 (t, 2 × terminal CH_3, 6H), 1.25 (br. m, 26 × CH_2, 52H), 1.54−1.56 (m, 2 × $C_{14}H_{29}CH_2CH_2O$, 4H), 3.42 (t, 2 × $C_{15}H_{31}CH_2O$, 4H), 3.46−3.75 (m, [5 × CH_2O] + [OCH_2CHOCH_2Br] + [CH_2Br], 13H); IR (cm^{-1}): 1100−1120 (br., C−O−C str.)

***N*-(3-Hexadecyloxy-2-[2′-{2″-hexadecyloxyethoxy}-ethoxy]propyl)-*N*,*N*,*N*-trimethylammonium Bromide (4).** Dry trimethylamine gas was passed into dry CH_3CN (1 mL) in a pressure tube. 1-Bromo-2-hexadecyloxy-3-(2′-[2″-hexadecyloxyethoxy]ethoxy)propane (90 mg) was dissolved in CH_3CN−toluene (1:1) mixture by warming and was transferred to the pressure tube. The reaction mixture was heated at 80 °C for 24 h. The reaction mixture was then cooled, and the excess trimethylamine was evaporated by warming the mixture on a water bath. The crude mixture was then diluted with $CHCl_3$, and the solvent was removed under reduced pressure. Pure compound was isolated as a colorless waxy solid (70 mg, 72%) by column chromatography over silica gel (100−200 mesh) using MeOH−$CHCl_3$ (1:9) as eluent. ^{1}H NMR (500 MHz, $CDCl_3$): 0.88 (t, 2 × terminal CH_3, 6H), 1.25 (br. m, 26 × CH_2, 52H), 1.54 (p, 2 × $C_{14}H_{29}CH_2$-CH_2O, 4H), 3.35 (s, 3 × CH_3N^+, 9H), 3.39−3.66 (m, 7 × CH_2O, 14H), 3.89−3.91, 4.13 (m, [CH_2N^+] + [OCH_2CHO-CH_2N^+], 2H + 1H); IR (cm^{-1}): 1070−1150 (broad, C−O−C str.); MS (MALDI-TOF): Calcd for $C_{42}H_{88}O_4N$: 671.2. Found: 671.6; Anal. Calcd for $C_{42}H_{88}O_4NBr\cdot 0.2H_2O$: C 66.84, H 11.81, N 1.86. Found: C 66.8, H 11.93, N 1.51.

Vesicle Preparation. Thin lipid films from individual lipids **1**−**4** were made in Wheaton glass vials by dissolving individual lipids in chloroform and evaporating the organic solvent under a steady stream of dry nitrogen. Last traces of organic solvent were removed by keeping these films under vacuum overnight. Water was added to each individual film and kept for hydration at 4 °C for 6−10 h. Then these samples were repeatedly freeze−thawed (ice-cold water to 50 °C) with intermittent vortexing to afford multilamellar vesicular aggregates (MLVs). Small unilamellar vesicles (SUV) were prepared by sonicating these MLVs in a bath sonicator above the phase transition temperature of the individual lipids for 10−15 min.

Transmission Electron Microscopy. Lipid suspensions were examined under transmission electron microscopy by negative staining with 1% uranyl acetate. Vesicular suspensions were made in 1% uranyl acetate solution at a concentration of 1 mM. Sonicated suspensions were spreaded onto carbon-Formvar coated copper grids (400 mesh), and the vesicles were allowed to settle onto the grid. Excess solution was wicked off using a filter paper, and the grid was air-dried for 30 min before examining under TEM. TEM was performed on a JEOL-200 CX electron microscope typically with an accelerating voltage of 100 keV. Micrographs were recorded at a magnification of 80 000.

Differential Scanning Calorimetry. Multilamellar vesicles were prepared in degassed water as mentioned above (concentration = 1 mM), and their thermotropic behavior was investigated by differential scanning calorimetry using a CSC-4100 model multicell Differential Scanning Calorimeter (Calorimetric Sciences Corporation, Utah). Baseline thermogram was obtained by using degassed water in all the ampules including the reference cell to normalize cell to cell differences. Water (0.5 mL) was used for the baseline thermogram. The measurements were carried out in the temperature range of 25 °C to 65 °C at a scan rate of 20 °C/h. Prior to the experimental thermogram, samples were subjected to repeated heating and cooling scans in DSC. The thermograms for the vesicular suspensions were obtained by subtracting the respective baseline thermogram from the sample thermogram using the software 'CpCalc' supplied by the manufacturer. Peak position in the plot of excess heat capacity vs temperature was taken as the gel to liquid crystalline phase transition temperature for each vesicular suspension. The molar heat capacities, calorimetric enthalpies (ΔH_c) and entropies (ΔS) were also computed using the same software. The size of the cooperativity unit (CU) for the phase transition of each lipid was determined using the formula

$$\mathrm{CU} = \frac{\Delta H_{\mathrm{VH}}}{\Delta H_{\mathrm{c}}}$$

where ΔH_{VH} is the vant Hoff enthalpy and ΔH_{c} is the calorimetric enthalpy. vant Hoff enthalpy was calculated from the equation

$$\Delta H_{\mathrm{VH}} = \frac{6.9 T_{\mathrm{m}}^2}{\Delta T_{1/2}}$$

where T_{m} is the phase transition temperature (in Kelvin) and $\Delta T_{1/2}$ is the full width at half-maximum of the thermogram (*26*−*28*).

Cell Culture, Plasmid DNA. HeLa cells were cultured in DMEM (Gibco BRL) supplemented with 10 fetal bovine serum (FBS) in T-25 culture flasks (Nunc, Denmark) and were incubated at 37 °C in a humidified atmosphere containing 5% CO_2. Cells were regularly passaged by trypsinization using 0.1 trypsin (EDTA 0.02%, dextrose 0.05%, and trypsin 0.1%) in PBS (pH 7.2).

Plasmid *p*EGFP−N1 (Clontech), which encodes for an enhanced green fluorescence protein (GFP) under a CMV promoter, was amplified in *Escherichia coli* (DH5α) and purified using Qiagen Maxi Prep Plasmid Purification protocol (Qiagen, Germany). Purity of the plasmid was checked by electrophoresis on 0.8% agarose gel and was found to be more than 80% supercoiled. Concentration of the DNA was estimated spectroscopically by measuring the absorption at 260 nm.

Cytotoxicity. Toxicity of each cationic lipid formulation toward HeLa cells in the presence of 10% FBS was determined using 3-(4,5-dimethyl thiazol-2-yl)-2,5-diphenyltetrazolium bromide (MTT) reduction assay following literature procedures (*29*, *30*). MTT gets converted

to an insoluble blue dye, formazan, in actively respiring cells. The assay estimates the concentration of the formazan formed, which, in turn, gives a measure of the population of cells that are metabolically active.

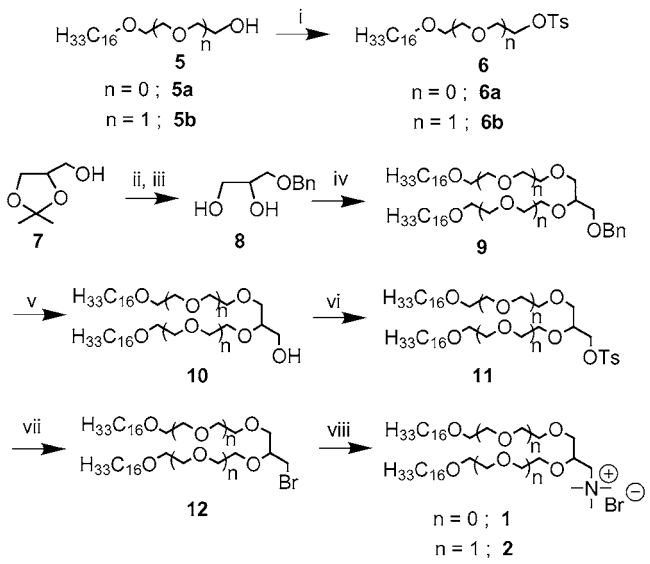
A range of liposomal concentrations between 200 nM to 500 μM were investigated for toxicity studies. Cytotoxicity of the lipid formulations optimal for transfection experiments were found out under conditions exactly similar to transfection experiments. The lipid formulations (lipid + DOPE) were complexed with DNA (0.1 μg) at various charge ratios in a range that was found to be optimal for transfections (lipid to DNA charge ratio 1−4). DNA−lipid complexes were added to the cells in the absence of serum. After 5 h of incubation, enough serum containing medium was added so as to have a final serum concentration of 10%. After 44 h, 20 μL media was replaced with 20 μL of MTT solution and was incubated further for 5 h. Following 5 h of incubation, blue formazan microcrystals were seen at the wells when checked under the microscope. One hundred microliters of 10% SDS in 0.01 N HCl was then added to each well and incubated at 37 °C for 10 h for the lysis of the cells and the solubilzation of the formazan formed. The absorbance was measured using a microtiter plate reader. The % viability was then calculated as $(OD_{570} - OD_{690})_{sample}/(OD_{570} - OD_{690})_{control} \times 100$, where the untreated cells (where no lipid suspension was added) were used as control. The assay was carried out in triplicates.

Transfection. All transfection experiments were carried out in antibiotic-free media. In a typical experiment, 96-well plates were seeded with 9000 cells/well in antibiotic-free DMEM 24 h before transfection such that they were ~70% confluent at the time of transfection. Lipid formulation and DNA were serially diluted separately in DMEM containing no serum to have the required working stocks. DNA was used at a concentration of 0.1 μg/well. The lipid and DNA were complexed in a volume of 20 μL by incubating them together at room temperature for about 30 min. The lipid concentrations were varied so as to obtain the required lipid/DNA charge ratios of 0.6, 0.8, 1.0, 1.2, 1.4, 1.6, 1.8, and 2.0. Charge ratios here represent the ratio of charge on cationic lipid (in moles) to nucleotide base molarity and were calculated by considering the average nucleotide mass of 330. After 30 min of complexation, 50 μL of medium was added to the complexes (final DNA concentration = 4.33 μM). Old medium was removed from the wells, and lipid−DNA complexes in 70 μL media were added to the cells. The plates were then incubated for 5 h at 37 °C in a humidified atmosphere containing 5% CO_2. At the end of the incubation period, 130 μL of DMEM containing 15.4% FBS was added per well such that final serum concentration in the medium is 10%. Plates were further incubated for a period of 43 h before checking for the reporter gene expression. GFP expression was estimated by fluorescent microscopy and was quantified by flow cytometry analysis. All the experiments were performed in duplicate, and the results presented are the average of at least four such independent experiments.

RESULTS AND DISCUSSION

Synthesis. The synthesis of the symmetric cationic lipids (**1** and **2**), which contain an equal number of oxyethylene units in both the chains at the C-1 and C-2 positions of the pseudoglyceryl backbone, is outlined in Scheme 1. The main step employed the coupling of the tosylates **6a** and **6b** with benzyl glycerol. The ether bond formation between benzyl glycerol and hexadecyl tosylate

Scheme 1[a]

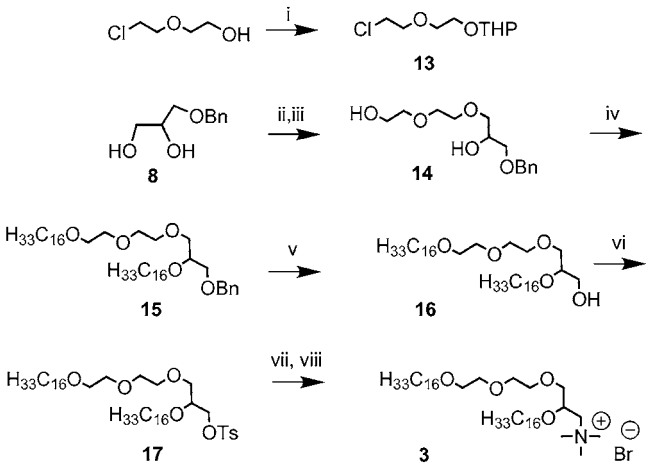


[a] Reagents and conditions: (i) *p*TsCl, Py, CH_2Cl_2, rt, 25−50 h (82% for **a** and 68% for **6b**); (ii) KOH, $PhCH_2Cl$, benzene, reflux, 23 h; (iii) *p*-TsOH, MeOH,CH_2Cl_2, rt, 5 h (overall 53% for the steps ii and iii); (iv) **6**, NaH, DMSO, $Bu_4N^+I^-$, rt, 24−30 h (74 for $n = 0$ and 67% for $n = 1$); (v) H_2, Pd/C, MeOH, EtOAc, 10 h (88% and 80%); (vi) *p*-TsCl, Py, CH_2Cl_2, rt, 27h (87% and 98%); (vii) LiBr, DMF, 70 °C, 8 h (81% and 84%); (viii) NMe_3, MeCN−toluene, 80 °C, pressure tube, 24 h (74% (68%).

works reasonably well under classical etherification conditions involving KOH/benzene (*24*) or NaH/benzene under reflux. But, we observed that, in case of tosylates containing hydrophilic oxyethylene groups **6a** and **6b**, although such conditions (NaH/benzene, reflux, 24 h) yielded the required products **9a** and **9b**, the yields were only moderate (48% and 45%, respectively) (*18*). The reaction of benzyl glycerol with the corresponding chlorides under phase-transfer conditions (50% aq NaOH, $Bu_4N^+HSO_4^-$) (*31*) also yielded the required compounds, but again the yields were substantially lower. Moreover, in this case, isolation of the pure compounds from the reaction mixture was also cumbersome. The coupling under NaH/DMF (*21*) and KOH/DMSO reflux conditions were also not satisfactory. Interestingly, good yields were obtained when benzyl glycerol was treated with the corresponding tosylates **6a** and **6b** under NaH/DMSO in the presence of a phase-transfer catalyst, $Bu_4N^+I^-$. The reaction could be carried out at room temperature, and the yields were much better (74% for **9a** and 67% for **9b**). More importantly, isolation of the pure products by column chromatography was comparatively easier under this condition. We found this method to be the most suitable one for etherification involving such hydrophilic tosylates.

In general, the synthesis of lipids **1** and **2** was achieved as follows (Scheme 1). Ethylene glycol monohexadecyl ether **5a** and diethylene glycol monohexadecyl ether **5b** on reaction with tosyl chloride in the presence of pyridine in CH_2Cl_2 afforded the corresponding tosylates **6a** and **6b**. Benzyl glycerol **8** was synthesized by slight modification of a literature procedure from (±)-1,2-*O*-isopropylidene glycerol (*24*). Benzyl glycerol **8** on reaction with either tosylate, **6a**, or **6b** in the presence of NaH/DMSO/$Bu_4N^+I^-$ at room temperature afforded **9a** or **9b**, respectively, in good yields. Debenzylation of **9** to the glycerol derivatives **10** were achieved conveniently by hydrogenolysis. The direct bromination of **10** to the primary bromide **12** under Appel conditions (CBr_4/PPh_3 in CH_2Cl_2) was a very low-yielding reaction. So the alcohols were

Scheme 2[a]



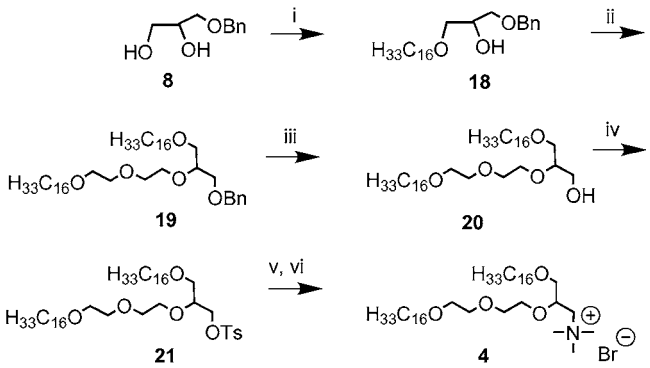
[a] Reagents and conditions: (i) DHP, concentrated HCl, rt, 1 h (98%); (ii) **13**, aq NaOH (50%), $Bu_4N^+HSO_4^-$, 65 °C, 5 h; (iii) MeOH−CH_2Cl_2, concentrated HCl, rt, 2 h (overall 34% for the steps ii and iii); (iv) $C_{16}H_{33}Cl$, aq NaOH (50%), $Bu_4N^+HSO_4^-$, 65 °C, 5 days (53%); (v) H_2, Pd/C, MeOH, EtOAc, 12 h (85%); (vi) *p*-TsCl, Py, CH_2Cl_2, rt, 24 h (80%); (vii) LiBr, DMF, 70 °C, 6 h (73%); (viii) NMe_3, MeCN−toluene, 80 °C, pressure tube, 24 h (95%).

first converted to the corresponding tosylates **11a** or **11b** which on further reaction with LiBr in DMF under refluxing conditions yielded the corresponding bromides in good yields. The substitution of the tosylate residue in **11** with NaBr in acetone was, in contrast, very sluggish. The bromides **12a** and **12b** were finally converted in good yields to the corresponding cationic lipids **1** and **2**, respectively, by reaction with trimethylamine in acetonitrile−toluene mixture in a screw-top pressure tube.

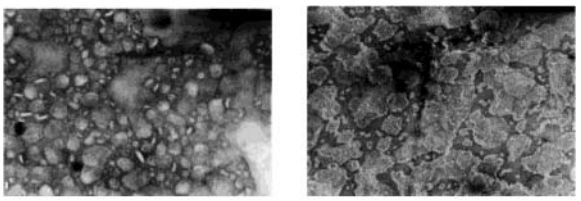
Scheme 2 depicts the synthesis of the mixed-chain lipid, **3**, in which one hydrophilic $(CH_2CH_2O)_2$ linkage has been introduced only at the C-1 position of the pseudoglyceryl backbone. The alcohol **14** was synthesized by modification of a literature procedure (*31*). Briefly, chloroethoxyethanol was protected as a tetrahydropyranyl (THP) ether, **13** (*25*, *32*). Benzyl glycerol **8** was alkylated at the primary position using **13** at the primary OH residue via a phase-transfer-catalyzed reaction, followed by the subsequent removal of the THP protecting group to yield the diol **14**. The yield of this reaction was found to be strongly dependent upon the reaction time since the corresponding dialkylated derivative (*31*) was also formed if the reaction was allowed to continue beyond 4−5 h. The separation of the individual diol derivatives resulting from mono- and dialkylation of **8** was possible although difficult. The positional identity of the diol derivative **14**, obtained by the monoalkylation, was established by converting the isolated diol **14** to a diester with palmitic acid. The downfield chemical shift of the methine proton (OCH_2CHOCH_2O) upon esterification was clearly observable. The diol **14** upon reaction with hexadecyl chloride under a similar phase-transfer etherification condition gave **15** in moderate yields. From **15**, the cationic lipid **3** was then prepared via removal of the benzyl protecting group under hydrogenolytic conditions, conversion of the alcohol to bromide via tosylate, and quaternization with trimethylamine in a manner similar to the one described in Scheme 1.

The synthesis of cationic lipid **4**, in which the $(CH_2CH_2O)_2$ unit remains at C-2 of the pseudoglyceryl backbone, has been achieved as summarized in the Scheme 3. Benzyl glycerol **8** was refluxed with 1 equiv of hexadecyl tosylate in the presence of NaH in THF to yield the monoalkylated derivative **18**. It was then treated with **6b** in the presence of NaH in dry THF to afford **19**. This upon hydrogenolysis yielded the corresponding alcohol, which was finally converted to the desired lipid **4** following the same route as described in the previous cases. All the final compounds and those intermediates that are stable upon isolation were appropriately characterized by TLC, FT-IR, ^{1}H NMR, mass spectrometry, and elemental analysis (cf. Experiment Section).

Scheme 3[a]



[a] Reagents and conditions: (i) $C_{16}H_{33}OTs$, NaH, THF, reflux, 24 h (40%); (ii) **6b**, NaH, THF, reflux, 48 h (74%); (iii) H_2, Pd/C, MeOH, EtOAc, 12 h (79%); (iv) *p*-TsCl, Py, CH_2Cl_2, rt, 24 h (85%); (v) LiBr, DMF, 70 °C, 20 h (59%); (vi) NMe_3, MeCN−toluene, 80 °C, pressure tube, 24 h (72%).



(a) lipid **1**. (b) lipid **3**.

Figure 2. Negatively stained transmission electron micrographs of aqueous suspensions of lipids **1** and **3** (scale: 90 nm for 1 cm).

Aggregation Properties. All the lipid molecules mentioned here formed stable suspensions in water. No precipitation was observed even after one month when these suspensions were stored at 4 °C. Upon hydration, the lipids having oxyethylene units at the linkage regions (**1**−**4**) were found to get dispersed in water with greater ease when compared to the lipid having just an ether linkage (DHTMA). Moreover, the suspensions formed from the lipids **1**−**4** were optically clear in contrast to DHTMA which yielded translucent suspension.

Transmission Electron Microscopy. TEM examination of air-dried aqueous suspensions revealed the existence of membranous structures for all the four lipids **1**−**4**. The suspensions formed from the lipids **1** and **2** having symmetrical chains appeared as distinct spherical aggregates in the micrographs. In contrast, the lipid **3** that has a di(oxyethylene) linkage only at the C-1 chain formed aggregates of irregular morphologies (See Figure 2). Lipid **4** formed vesicular aggregates which were considerably larger in comparison with the aggregates observed with the other lipids (not shown). The diameters of the aggregates formed from the symmetrical lipids **1** and **2** were in the range of 40−100 nm. Lipid **3** formed vesicles of diameters 90−150 nm whereas relatively larger aggregates (∼220 nm) were observed in the aqueous suspensions of lipid **4** (Table 1).

Table 1. Characteristics of the Aggregates Formed by the Lipids 1−4

lipid	T_m°[a]	ΔH (kcal mol^{-1})	ΔS[b] (cal mol^{-1} K^{-1})	CU[c]	avg diam[d] (nm)	ID_{50}[e] (μM)	% viability[f] alone	% viability[f] with 50 mol % chol
1	46.3	11.3	35.4	115	40−80	190	37	75
2	45.6	9.7	30.4	92	55−100	75	5	81
3	41.2	12.3	39.1	61	90−150	175	26	78
4	45.1	6.7	21.0	−[g]	220	195	34	76
DHTMA	45.8	16.7	52.4	42	−	>500	95	84

[a] The maximum deviation was ±0.1 °C. [b] Enthalpy and entropy for the heating scan. The ΔH and ΔS values are average of three successive runs and the values are within ±5%, [c] Size of cooperativity unit. [d] Average diameter as indicated from TEM. [e] Concentration that caused 50% cell death. [f] At [cationic lipid] = 250 μM. [g] Could not be measured reliably due to baseline drifts.

Differential Scanning Calorimetry. With all the lipid suspensions examined, clear thermotropic solid gel to fluid liquid crystalline-like phase transitions typical of membranous aggregates were observed. The phase transitions of all the individual liposomal suspensions were found to be reversible with subsequent heating and cooling scans showing essentially the same histograms. The experimentally obtained phase transition temperature (T_m) values obtained are presented in Table 1. The phase-transition temperatures of lipids **1**, **2,** and **4** were comparable to that of DHTMA (45−46 °C). In contrast, the phase transition temperature of **3** was relatively lower (41 °C). These cationic lipids **1**−**4** and DHTMA have identical headgroup and hydrocarbon chain lengths. However, they differ at the linkage region in terms of the number of oxyethylene units. Clearly the DSC results suggest that insertion of oxyethylenes at the linkage region do not affect the phase-transition temperature of the resulting membranes. In a given series of lipids, the lengthening of the chain length is expected to enhance the phase-transition temperature (*15*). However, since the T_m values do not increase relative to that of DHTMA, it is clear that incorporated oxyethylene units do not significantly contribute to chain melting transition. It may be further noted that even the unsymmetrical lipid, **4** exhibited comparable T_m as that of DHTMA. Only the lipid **3** showed a lower T_m value. Therefore the effect on the thermal properties of these membranes are manifested only when the oxyethylenes are incorporated in the C-1 position alone.

In general, there was a decrease in the enthalpy of phase transition upon incorporation of oxyethylene units at the linkage region of cationic lipids. Incorporation of oxyethylene units at the interfaces most likely enhances the hydration of the lipid assemblies. The effect of such interfacial hydration will be more predominant in the melted, disordered phase of the lipid assemblies. This may be responsible for lower phase-transition enthalpies observed with lipids **1**−**4**.

The nature of the thermal transitions of these oxyethylene-bearing cationic lipids were found to be more cooperative compared to their diether analogue DHTMA (see Table 1). Again enhanced hydration could be responsible for more cohesive interactions among such lipids leading to the manifestation of higher cooperativity.

Biological Activity: Cytotoxicity and Gene Delivery. Having investigated the aggregation properties of these lipids **1**−**4** by electron microscopy and calorimetry, we were interested in examining their biological usefulness. Toward this end, we first systematically examined the cytotoxicity manifested by these lipids and then investigated their gene transfer activity in HeLa cells.

The cytotoxic effects of the cationic lipids **1**−**4** and their diether counterpart DHTMA toward HeLa cells are shown in Figure 3 and are summarized in Table 1 along with their ID_{50} values. Incorporation of the oxyethylene units at the linkage region of a lipid molecule is found to increase its cytotoxicity. Among the lipids investigated, the lipid **2**, containing two oxyethylene units in both of the chains, is found to be the most cytotoxic formulation. The morphology of dying cells in the case of these oxyethylene lipids were considerably different from that of DHTMA. The lipid DHTMA, which has just an ether functionality at the linkage region, was least cytotoxic. Its ID_{50} value was above the range of concentrations studied (>500 μM). Notably, all the ID_{50} values were much higher than the range of concentration at which a typical transfection experiment was performed (i.e., ∼5 μM).

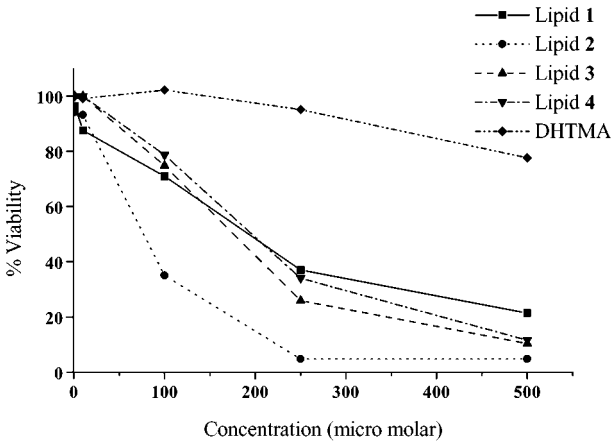


Figure 3. Cytotoxicity exhibited by the cationic lipids **1**−**4** toward HeLa cells. Toxicity exhibited by the diether lipid DHTMA is also shown. Shown are the data from one representative experiment. Standard deviations were within 5%.

The transfection efficiencies (% of fluorescent cells due to the expressed green fluorescence protein (GFP)) of various cationic lipid formulations are shown in Figure 4. The untransfected control cells and the cells exposed only to the plasmid DNA did not show any fluorescent cells 48 h posttransfection. The cationic lipid, DHTMA which possess single ether links between the pseudoglyceryl skeleton and the hydrocarbon chains, showed only basal level transfection activity. A clear enhancement in transfection efficiencies were observed with the cationic lipids bearing oxyethylene linkage functionalities. The unsymmetrical lipids **3** and **4** were more efficient than the symmetrical ones **1** and **2**. Lipid **3**, bearing two oxyethylene units only at the C-1 position of the pseudoglyceryl backbone, was found to be the best cytofectin among the lipids studied.

Effect of Helper Lipids. Incorporation of helper lipids such as cholesterol (*33, 34*) and dioleyoyl phosphatidyl ethanolamine (DOPE) (*3, 4*) is known to enhance the transfection efficiencies of many of the cationic lipid-based formulations. So, we decided to investigate how these helper lipids modify the activities of presently described oxyethylene bearing cationic lipids.

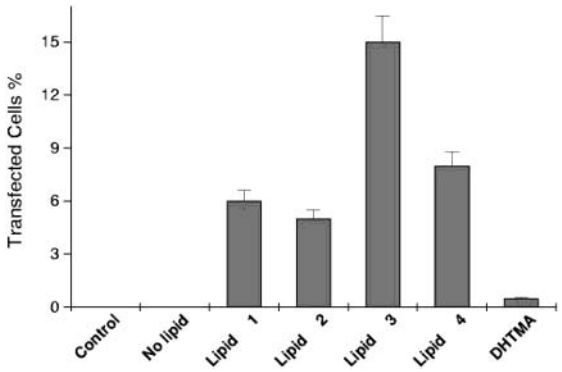


Figure 4. Potentiation of transfection abilities of cationic lipids toward HeLa cells upon incorporation of oxyethylene units at the linkage region. (control: untransfected cells; no lipid: cells exposed to DNA alone). Shown are the optimal transfection efficiencies of each liposomal formulation. Lipid to DNA charge ratio was 1−1.4. Cell viability was >80% for all the lipid formulations.

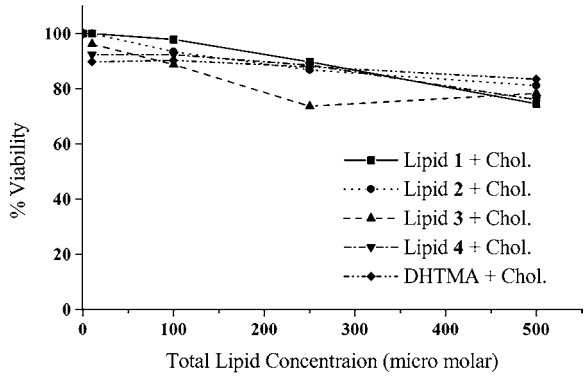


Figure 5. Cytotoxicity exhibited by the cationic liposomes containing 50 mol of cholesterol toward HeLa cells. Shown are the data from one representative experiment. Standard deviations were within 5%.

Cholesterol-Containing Cationic Liposomes. The cytotoxicities of all the oxyethylene-bearing cationic lipids were significantly reduced when cholesterol was incorporated in their liposomal formulations (Figure 5). When cholesterol was present at a 1:1 molar ratio, the ID_{50} values of all the lipid formulations were much above the range of concentrations studied. This reduction in toxicity was as high as 94% in case of lipid **2** at a cationic lipid concentration of 250 μM (Table 1). For lipids **1**, **3**, and **4**, the cell viability was increased by 50%, 66%, and 55%, respectively, upon incorporation of cholesterol under similar conditions. It is not clear whether the reduction in cytotoxicity upon inclusion of cholesterol in these liposomes is just due to the cholesterol inhibiting the cellular liposomal uptake in some fashion.

The liposomal formulations containing cholesterol at molar ratios 20 or 50 was investigated for their transfection efficiencies. The formulations in the mol-to-mol ratios of cholesterol/cationic lipid (1:4) and (1:1) were prepared by freeze−thaw followed by sonication. The transfection efficiencies of both multilamellar and unilamellar aggregates against HeLa cell line for plasmid *p* EGFP−N1 were investigated. No significant improvement in the transfection efficiencies was observed upon incorporation of cholesterol at either of these molar ratios. The observed trasnsfection efficiencies of cholesterol containing formulations were comparable to that of neat lipid formulations.

Effect of Inclusion of Dioleyoyl Phosphatidyl Ethanolamine. Though cholesterol did not influence gene transfection of cationic lipids **1**−**4**, DOPE, when used as a helper lipid, increased their transfection efficiencies significantly. There was ∼3−4 times enhancement in transfection efficiency when the liposomal formulations contained 50 mol of DOPE (see Figure 7). The lipid formulation involving the unsymmetrical lipid **3** (lipid 3/DOPE at molar ratio 1:1) was the most efficient formulation under this condition also. The addition of DOPE to DHTMA also improves the transfection efficiency, but the efficiency of formulation, 1:1 DHTMA/DOPE, is orders of magnitude lower than the highly active formulations, e.g. **3**/DOPE. It is known that lipoFECTACE (a recipe composed of 1:1 DOPE and cationic lipid) is better than the cationic lipid alone (*35*). The modulation of transfection efficiencies were only moderate when DOPE was present at 25 and 75 mol % in the lipid formulations. The transfection efficiencies showed a bell-shaped dependency on cationic lipid concentration, reaching an optimal value near lipid/DNA charge ratio 1.2 (see Figure 8). The active formulations (formulations containing 50 mol % of DOPE) exhibited very little cytotoxicity during transfection experiments. The % viability of HeLa cells under exact transfection conditions is presented in Figure 9. The toxicities of all the lipid formulations were <20% at concentrations that was optimal for maximum transfection efficiency.

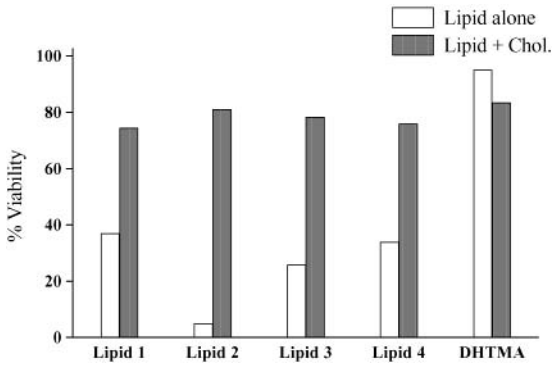


Figure 6. Reduction of cytotoxicity of cationic lipids **1**−**4** on incorporation of 50 mol % of cholesterol. Cationic lipid concentraion was 250 μM in all the formulations.

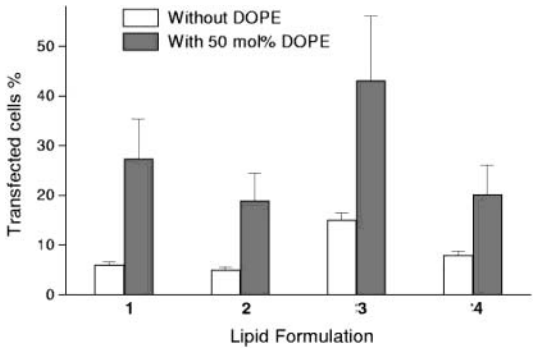


Figure 7. Enhancement in transfection efficiencies of cationic lipids **1**−**4** upon incorporation of 50 mol % of DOPE. Shown are the optimal transfection efficiencies of each lipid formulations.

CONCLUSION

Synthesis of four cationic lipids **1**−**4** with varying number of oxyethylene units at the linkage region has been achieved. These lipids formed optically clear suspensions in water with greater ease when compared to their diether analogue, DHTMA. Electron microscopy revealed the presence of closed membranous aggregates. The aqueous suspensions of all the lipids exhibited clear,

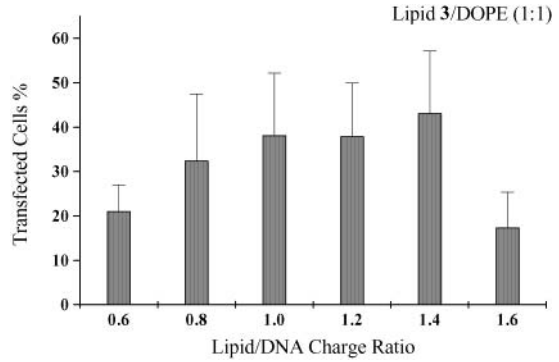


Figure 8. Optimization of lipid/DNA charge ratio for lipid **3**/DOPE (1:1) formulation. [DNA] = 0.1 μg.

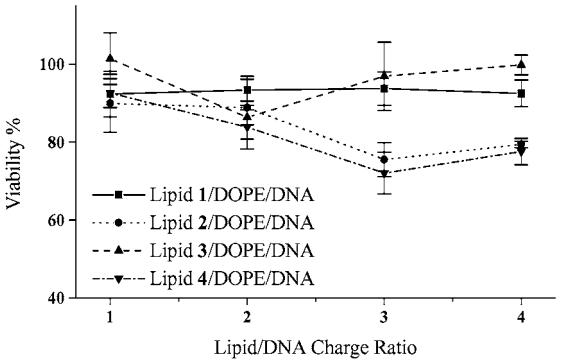


Figure 9. Viability of HeLa cells under transfection conditions. Toxicity is <20% for all the lipid formulations under optimal transfection conditions (i.e., at lipid/DNA charge ratios < 1.5).

thermotropic solidlike gel to liquid-crystalline phase transitions that are typical of lamellar aggregates. The cytotoxicities of these lipid formulations were relatively higher when compared with their diether analogue, DHTMA. The incorporation of oxyethylene units at linkages brought about a significant enhancement in the in vitro gene delivery efficiencies of the cationic lipids in mammalian cell lines. Inclusion of cholesterol in these liposomes did not modify the transfection capabilities, but it reduced their cytotoxicity. However, when DOPE was included in the cationic liposomes of **1**−**4**, a significant enhancement in transfection efficiency was observed. Optimal transfection efficiencies were observed with slightly positively charged (charge ratio ∼1.2) lipoplexes. Cytotoxicity exhibited by the lipid formulations optimized for maximal transfections were negligibly small. Thus, it has been demonstrated that the incorporation of hydrophilic oxyethylene units at the linkage region of a glyceryl-based cationic lipid in a regiospecific manner could be a useful strategy to improve its potential as promising gene delivery agents.

Although the DNA delivery to eukaryotic cells involves several steps and the mechanism of many of these steps is not very clear at the molecular level, it would be important to note some correlation between the membrane level properties and the transfection efficiencies of the present set of cationic lipids. The membrane characteristics of these oxyethylene cationic lipids were found to be very much different from that of conventional lipid, DHTMA. Oxyethylene units at the linkage region bring about significant disorder in the hydrocarbon chain packing of the lipid aggregates. It has been previously shown that the membrane perturbations due to the vector lipids are an important factor in cationic lipid-mediated DNA delivery (*36*). An oxyethylene unit in the linkage region might also affect the hydration of lipoplexes, and the hydration of lipoplexes is known to influence gene transfer events (*37*).

The unsymmetrical lipids **3** and **4** exhibited higher transfection efficiencies compared to the symmetrical ones **1** and **2**. The mismatch in the linkage region disturbs the lipid packing of such aggregates, making them more susceptible to complex with negatively charged DNA. Lipid **3** possesses the lowest gel-to-liquid crystalline phase-transition temperature among the lipids studied and it is quite close to the physiological temperature, at which transfection studies were performed. The zeta potential value of the aggregates of lipid **3** was notably higher compared to all the other lipid formulations (*38*). These factors might be responsible for the enhanced transfection efficiency of lipid formulations based on **3**. Whatever may be the actual mechanism for transfection mediated by this class of lipid formulations, the interesting and meaningful results obtained with these novel lipids should be of interest to researchers working in the field of nonviral vectors.

ACKNOWLEDGMENT

This work was supported by the Swarnajayanti Fellowship grant of the Department of Science & Technology to S.B. We thank CSIR, New Delhi, for the award of Senior Research Fellowship to Dileep P.V., Prof. A. Antony, MCBL, IISc for giving access to his laboratory.

LITERATURE CITED

(1) Miller, A. D. (1998) Cationic liposomes for gene therapy. *Angew. Chem., Int. Ed. Engl. 37*, 1768−1785.

(2) Behr, J. P. (1993) Synthetic gene-transfer vectors. *Acc. Chem. Res. 26*, 274−278.

(3) Felgner, P. L., Gadek, T. R., Holm, M., Roman, R., Chan, H. W., Wenz, M., Northrop, J. P., Ringold, G. M., and Danielsen, M. (1987) Lipofetion a highly efficient, lipid-mediated dna-transfection procedure. *Proc. Natl. Acad. Sci. U.S.A. 84*, 7413−7417.

(4) Felgner, J. H., Rajkumar, Sridhar, C. N., Wheeler, C. J., Tsai, Y. J., Border, R., Ramsey, P., Martin, M., and Felgner, P. L. (1994) Enhanced gene delivery and mechanism studies with a novel series of cationic lipid formulations. *J. Biol. Chem. 269*, 2550−2561.

(5) Felgner, P. L. and Ringold, G. M. (1989) Cationic liposome-mediated transfection. *Nature 337*, 387−388.

(6) Takahashi, T, Kono, K., Itoh, I., Emi, N., and Takagishi, T. (2003) Synthesis of novel cationic lipids having polyamidoamine dendrons and their transfection activity. *Bioconjugate Chem. 14*, 764−773.

(7) Kumar, V. V., Pichon, C., Refregiers, M., Guerin, B., Midoux, P., and Chaudhri, A. (2003) Single histidine residue in the head-group region is sufficient to impart remarkable gene transfection properties to cationic lipids: evidence for histidine-mediated membrane fusion at acidic ph. *Gene Ther. 10*, 1026−1215.

(8) Weithoff, C. M., Koe, J. G., Koe, G. S., and Middaugh, C. R. (2004) Compositional effects of cationic lipid/dna delivery systems on transgene expression in cell culture. *J. Pharm. Sci. 93*, 108−123.

(9) Elizabeth, G. N., Gordon, D., Yang, Z., Xu, L., San, H., Gregory, E. P., Wu, B., Gao, X., Huang, L., and Gary, J. N. (1992) Gene transfer in vivo with dna-liposome complexes: Lack of autoimmunity and gonadal localization. *Hum. Gene Ther. 3*, 649−656.

(10) Caplen, N. J., Alton, E. W., Middleton, P. G., Dorin, J. R., Stevenson, B. J., Gao, X., Durham, S. R., Jeffery, P. K., Hodson, M. E., Coutelle, C., Huang, L., Porteous, D. J., Williamson, R., and Geddes, D. M. (1995) Liposome-mediated cftr gene transfer to the nasal epithelium of patients with cystic fibrosis. *Nat. Med. 1*, 39−46.

(11) Zabner, J., Fasbender, A. J., Moninger, T., Poellinger, K. A., and Walsh, M. J. (1995) Cellular and molecular barriers to gene transfer by a cationic lipid. *J. Biol. Chem. 270*, 18997−19007.

(12) Zhang, G., Gurtu, V., Thomas, H. S., Nelson, P., and Steven, R. K. (1997) A cationic lipid for rapid and efficient delivery of plasmid DNA into mammalian cells. *Biochem. Biophys. Res. Commun. 236*, 126−129.

(13) Wang, J., Guo, X., Barron, L., and Francis, C. S. (1998) Synthesis and characterization of long chain alkyl acyl carnitine esters, potentially biodegradable cationic lipids for use in gene delivery. *J. Med. Chem. 41*, 2207−2215.

(14) Tang, F., and Jeffrey, A. H. (1998) Introduction of a disulfide bond into a cationic lipid enhances transgene expression of plasmid DNA. *Biochem. Biophys. Res. Commun. 242*, 141−145.

(15) Bhattacharya, S., and Haldar, S. (1995) Synthesis, thermotropic behavior, and permeability properties of vesicular membranes composed of cationic mixed-chain surfactants. *Langmuir 11*, 4748−4757.

(16) Ghosh, Y. K., Visweswariah, S. S., and Bhattacharya, S. (2000) Nature of linkage between the cationic headgroup and cholesteryl skeleton controls gene transfection efficiency. *FEBS Lett. 473*, 341−344.

(17) Song, Y. K., Liu, F., Chu, S., and Liu, D. (1997) Characterization of cationic liposome-mediated gene transfer in vivo by intravenous administration. *Hum. Gene Ther. 8*, 1585−1594.

(18) Bhattacharya, S., and Dileep, P. V. (1999) Synthesis of novel cationic lipids with oxyethylene spacers at the linkages between hydrocarbin chains and pseudoglyceryl backbone. *Tetrahedron Lett. 40*, 8167−8170.

(19) Woodle, M. C. and Lasic, D. (1992) Sterically stabilized liposomes. *Biochim. Biophys. Acta 1113*, 171−199.

(20) Heimam, U. and Vögtle, F. (1980) Hydrophile fette. *Liebigs Ann. Chem.*, 858−862.

(21) Wissner, A., Kohler, C. A., and Goldstein, B. M. (1986) Analogues of platelet activating factor. multiple oxygen substitution of the alkoxy chain. *J. Med. Chem. 29*, 1315−1319.

(22) Schule, U., Schmidt, H.-W., and Safinya, C. (1999) Synthesis of novel cationic poly(ethylene glycol) containing lipids. *Bioconjugate Chem. 10*, 548−552.

(23) Dileep, P. V., Antony, A., and Bhattacharya, S. (2001) Incorporation of oxyethylene units between hydrocarbon chain and pseudoglyceryl backbone in cationic lipid potentiates gene transfection efficiency in the presence of serum. *FEBS Lett. 509*, 327−331.

(24) Kates, M., Chan, T. H., and Stanacev, N. Z. (1963) Aliphatic diether analogues of glyceride-derived lipids. i. synthesis of d-α,*β*-dialkyl glyceryl ethers. *Biochemistry 2*, 394−396.

(25) Kyba, E. P., Helgeson, R. C., Madan, K., Gokel, G. W., Tarnowski, T. L., Moore, S. S., and Cram, D. J. (1977) Host−guest complexation. 1. concept and illustration. *J. Am. Chem. Soc. 99: 8*, 2564−2571.

(26) Hinz, H., and Sturtevant, J. M. (1972) Calorimetric studies of dilute aqueous suspensions of bilayers formed from synthetic 1-α-lecithins. *J. Biol. Chem. 247*, 6071−6075.

(27) Sturtevant, J. M. (1982) A scanning calorimetric study of small molecule-lipid bilayer mixtures. *Proc. Natl. Acad. Sci. U.S.A. 79*, 3963-3967.

(28) Ştefan Hoabi (2002) An approximate cooperativity analysis by DSC of phase transitions of DPPC-DOCNA dispersions. *Cell Mol. Biol. Lett. 7*, 230−236.

(29) Mosmann, T. (1983) Rapid colorimetric assay for cellular growth and survival: Application to proliferation and cytotoxicity assays. *J. Immunol. Methods 65*, 55−63.

(30) Hansen, M. B., Nielsen, S. E., and Berg, K. (1989) Reexamination and further development of a precise and rapid dye method for measuring cell growth/cell kill. *J. Immunol. Methods 119*, 203-210.

(31) Bartsch, R. A., Victor Cason, C., and Czech, B. P. (1989) Phase-transfer-catalysed synthesis of oligoethylene glycols and derivatives. *J. Org. Chem. 54*, 857−860.

(32) Czech, B., Czech, A., and Bartsch, R. A. (1984) Application of the okahara cyclization to the preparation of crown-ethers with aromatic units. *J. Heterocycl. Chem. 21*, 341−343.

(33) Banerjee, R., Das, P. K., Srilakshmi, G. V., and Chaudhuri, A. (1999) Novel series of nonglycerol-based cationic transfection lipids for use in liposomal gene delivery. *J. Med. Chem. 42*, 4292−4299.

(34) Crook, K., Stevenson, B., Dubouchet, M., and Porteous, D. (1998) Inclusion of cholesterol in DOTAP transfection complexes increases the delivery of DNA to cells in vitro in the presence of serum. *Gene Ther. 5*, 137−143.

(35) Okomoto, S., W., Y., Takakura, Y., and Hashida, M. (1998) Cationic lipid-mediated efficient induction of type-1 interferons by a low dose of polyG:polyC in mouse cell lines. *J. Biochem. 124*, 697−701.

(36) Mui, B., Ahkong, Q. F., Chow, L., and Hope, M. (2000) Membrane perturbation and the mechanism of lipid-mediated transfer of DNA into cells. *Biochim. Biophys. Acta 1467*, 281−292.

(37) Hirsch-Lerner, D., and Barenholz, Y. (1999) Hydration of lipoplexes commonly used in gene delivery: follow-up by laurdan fluorescence changes and quantification by differential scanning calorimetry. *Biochim. Biophys. Acta 1461*, 47−57.

(38) Bhattacharya, S., and Padinjarae, V. D. (2003) Membrane-Forming Properties of Cationic Lipids Bearing Oxyethylene-Based Linkages. *J. Phys. Chem. B 107*, 3719−3725.

BC0340215

Efficient Conjugation and Characterization of Distamycin-Based Peptides with Selected Oligonucleotide Stretches

Sumana Ghosh,[†] Eric Defrancq,[‡] Jean H. Lhomme,[†] Pascal Dumy,[‡] and Santanu Bhattacharya*[,†]

Department of Organic Chemistry, Indian Institute of Science, Bangalore 560 012, India and LEDSS, UMR CNRS 5616, Université Joseph Fourier, BP 53, 38041 Grenoble Cedex 9, France. Received September 21, 2003; Revised Manuscript Received December 10, 2003

Selected sequences of oligodeoxyribonucleotides (ODNs) have been conjugated efficiently with distamycin-based peptides containing reactive cysteine and oxyamine functionalities at the C-terminus. The conjugation was performed easily within 30−60 min, using individual modified oligonucleotide stretches having sequences of 5′-d(GCTTTTTTCG)-3′, 5′-d(GCTATATACG)-3′, and 5′-AGCGCGCGCA-3′. Two types of linkages were used for making the covalent connection: (i) a five-membered thiazolidine ring and (ii) an oxime. These distamycin-like polyamide−ODN conjugates were then converted to the corresponding DNA duplexes using complementary oligonucleotide sequences. To elucidate the binding specificity of the distamycin−oligonucleotide conjugates, UV−melting temperature measurements were performed. These studies indicated that the distamycin−ODN conjugate favored binding with the duplex with sequence 5′-d(GCTTTTTTCG)-3′ rather than 5′-d(GCTATATACG)-3′. On the other hand, no stabilization of the duplex with sequence 5′-d(AGCGCGCGCA)-3′ was observed. UV results also suggest that the thiazolidine and oxime linkages do not significantly influence the process of distamycin binding to the minor groove surface of the DNA duplex. The results obtained from duplex UV−melting studies were further corroborated by a temperature-dependent study of the circular dichroism spectra of the conjugates and a fluorescence displacement titration assay using Hoechst 33258 fluorophore as a competitive binder for the minor groove. All these studies reinforce the fact that the specific stabilization of A/T rich DNA−DNA duplexes by distamycin was preserved upon conjugation with oligonucleotide stretches.

INTRODUCTION

The complete sequencing of the human genome has a tremendous impact on biological and biomedical research (*1*). The intricate and precise regulation of the expression of various genes encoded in the DNA nucleotide sequence was achieved by influencing transcription (using groove binder, intercalator, or antigene strategy), translation (antisense strategy), or inhibiting the function of proteins (aptamer strategy) (*2*−*6*). Among all of these, the crucial factor involves reading and recognition of specific nucleotide bases on DNA. This specificity is important for the synthesis of any drug or inhibitor that can mimic the function of DNA binding proteins or enzymes.

Among the naturally occurring drugs with low molecular mass, distamycin and netropsin are well-known. They bind selectively to A/T rich sequences of the B-DNA minor groove (*7*−*11*). Hydrogen donor groups located on the concave side of these molecules establish contacts with the hydrogen bond acceptor atoms such as N-3 nitrogen of adenine and C-2 carbonyl oxygen of thymine bases in the minor groove of DNA (*12*). Such oligopeptides, by virtue of their crescent shape, adopt nearly isohelical orientation with the B-form of the duplex. Functional groups that protrude into the minor groove, such as the 2-amino group of dG-dC base pairs, (*13*, *14*) interfere with optimal binding and give rise to the noted sequence preferences. Tight binding within the minor groove by these ligands typically results in increased duplex stability (*15*).

By combining the minor groove-based selectivity with the Hoogsteen binding of an ODN in the major groove, a variety of groove-binding agents have been tethered to DNA sequences to further improve the anti-sense and anti-gene activities and to achieve greater stabilization of the duplex and triplex structures (*16*−*25*). It has been found that the affinity of some of these conjugates for the target site is enhanced by over 100-fold than that of the unlinked subunits (*26*). In an early communication (*24*), the stabilization of certain DNA/DNA duplexes by *N*-methylpyrrolecarboxamide peptide-tethered ODN has been reported. These derivatives were required to possess a spacer at the C-terminal tagged with a 2-[[4-(phenylazo)benzyl]thio]ethyl dye to facilitate the monitoring of the covalent coupling between the peptide and ODN. It was not ascertained how the presence of such an interfering spacer affected the DNA recognition event. Moreover, the synthesis of these molecules was never described. Unfortunately, however, the methods of such tethering are often not available and sometimes not reproducible. Therefore, there is a necessity to develop efficient procedures for conjugation.

In recent years, new strategies for the conjugation of oligonucleotide with a reporter group have focused on the utility of the oxime linkage. This linkage has been used efficiently for the chemical ligation of peptides (*27*, *28*), conjugation of peptides with carbohydrates (*29*−*31*), and oligonucleotides (*32*−*34*).

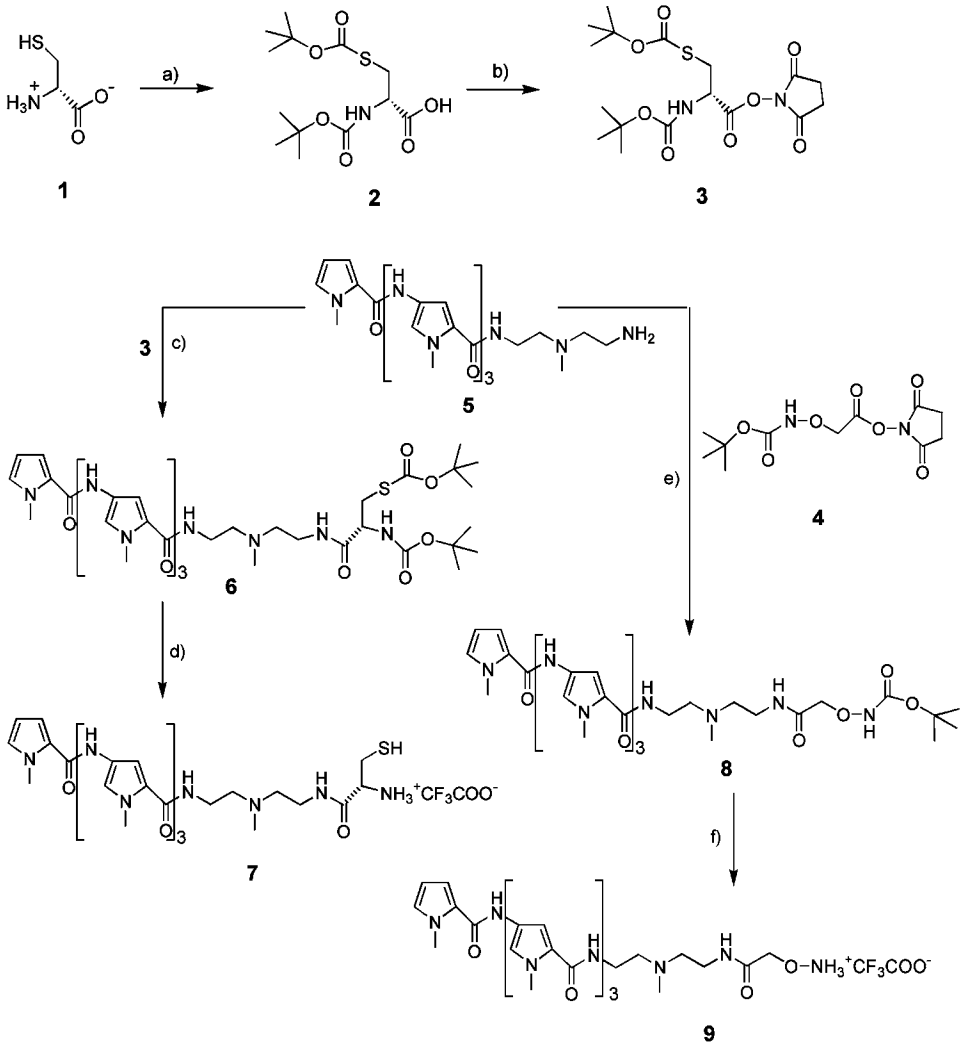
* Corresponding author and Swarnajayanti Fellow (DST, Government of India). E-mail: sb@orgchem.iisc.ernet.in. Also at the Chemical Biology Unit, JNCASR, Bangalore 560 012, India. Fax: +91-080-3600529.

[†] Indian Institute of Science.

[‡] LEDSS.

10.1021/bc0341730 CCC: $27.50 © 2004 American Chemical Society
Published on Web 03/12/2004

Scheme 1. Synthesis of Distamycin Analogues 7 and 9[a]



[a] Reagents: (a) $(Boc)_2O$, K_2CO_3, H_2O/dioxane (1:1, v:v), rt, 48 h, 60%; (b) HOSu, DCC, DMF, 0 °C for 1 h, then rt for 6 h, 80%; (c) **3**, $CHCl_3$, rt., 2 h, 50%; (d) CH_2Cl_2, TFA, EDT (1:1:0.2, v:v:v), rt, 2 h, 80%; (e) **4**, $CHCl_3$, rt., 2 h, 50%; (f) CH_2Cl_2:TFA (1:1, v:v), rt, 2 h, 80%.

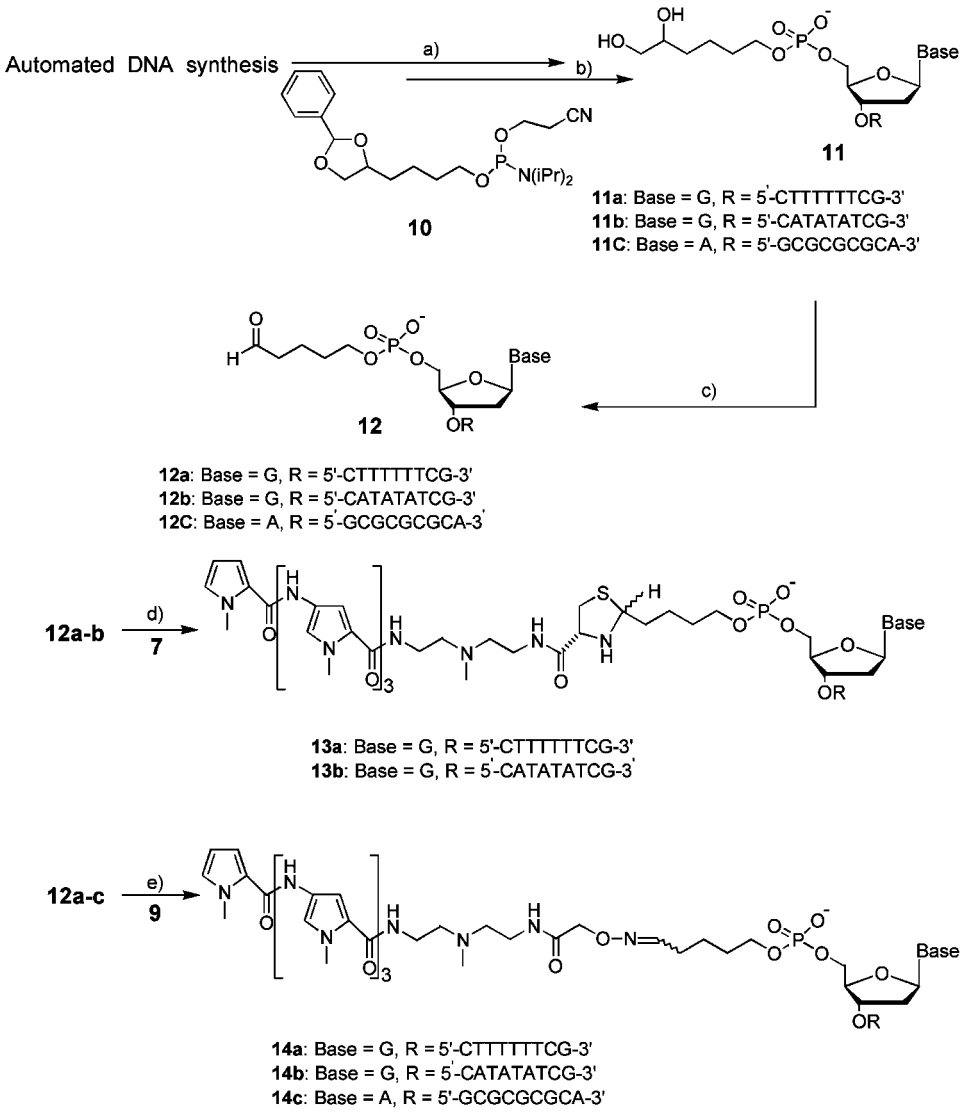
The major advantage of this ligation technique is that it requires neither a coupling reagent nor chemical manipulations except mixing of the two components, namely the oxyamine and the aldehyde moieties. Adopting this highly chemoselective ligation procedure, we have now accomplished a convenient and efficient synthesis of five novel distamycin−ODN conjugates. In these conjugates, the C-terminus of a distamycin derivative (lacking the *N*-methylformamide unit) has been covalently attached to the 5′-end of selected ODN stretches. We describe herein the method of conjugation in detail. We also discuss the results of investigation on the specificity of distamycin binding and the duplex stabilizing properties resulting from the hybridization of these ODN−distamycin conjugates to sequences of appropriate ODN stretches by UV−melting temperature measurements, temperature-dependent circular dichroism studies, and a fluorescence displacement assay using Hoechst 33258 as a minor groove competitor.

RESULTS AND DISCUSSION

Synthesis of Distamycin−Oligopeptide Derivatives 7 and 9 (Scheme 1). The *N*-methylpyrrole-based tetrapeptide **5** containing a free amine at the C-terminus represents the key intermediate for the introduction of the 1,2-aminothiol and the oxyamine moieties. The tetrapeptide **5** was synthesized in solution phase as described previously (*35*, *36*). Covalent attachment of the 1,2-aminothiol moiety to **5** was achieved upon coupling with the *N*-hydroxysuccinimide-activated ester of the cysteine derivative **3**, in which the amino terminus and the thiol residue were protected with a *t*-Boc group. Deprotection of the *t*-Boc group was carried out by treating **6** with TFA/CH_2Cl_2 solution (1:1, v/v) at room temperature for 1 h. To prevent the oxidation of thiol to the corresponding disulfide, 2% dithiotheritol (DTT) was also included in the solution. Introduction of the oxyamino group to the oligopeptide was performed via the coupling of the activated ester of *N*-*t*-Boc-*O*-(carboxymethyl)-hydroxylamine **4** with the tetrapeptide **5**. Subsequent acidic treatment with TFA/CH_2Cl_2 solution (1:1, v/v) for 1 h at room temperature of the protected intermediate **8** led to distamycin analogue **9**. The distamycin analogues **7** and **9** containing cysteine and oxyamine functionalities, respectively, were then used for conjugation with ODN stretches without further purification.

Oligonucleotides Synthesis. *Aldehyde-Containing Oligonucleotides.* The preparation of the oligonucleotides containing an aldehyde linker at the 5′-extremity was

Scheme 2. Synthesis of Different Oligonucleotides 13a,b and 14a−c[a]



[a] Reagents: (a) Incorporation of phosphoramidite **10** at the last stage of the oligonucleotide synthesis and then NH_4OH, 50 °C for 16 h; (b) aq 80% AcOH; (c) polymer-supported $NaIO_4$, rt., 1 h; (d) **7**, CH_3COONa buffer (0.2 M, pH 5.4), CH_3CN, 1 h, rt.; (e) **9**, CH_3COONa buffer (0.2 M, pH 5.4), CH_3CN, 30 min, rt.

accomplished upon minor modification of a previously reported procedure (*32*). Briefly, the strategy included the preparation of the oligonucleotides **11a**−**c** containing the 1,2-diol moiety using the corresponding phosphoramidite **10** (Scheme 2). Peroxidation of the diol upon reaction with 10-fold excess of polymer-supported $NaIO_4$ for 1 h gave the corresponding aldehydes **12a**−**c**. Subsequent conjugations were carried out without further purification of the aldehyde in the case of the preparation of the oxime conjugate. However, for the synthesis of the thiazolidine conjugate, it was necessary to purify the aldehyde from excess of periodate by reverse phase chromatography to avoid thiol oxidation (*33*).

Conjugation via Thiazolidine and Oxime Linkage. The ligation involved the reaction between aldehyde-containing ODN at the 5′-terminus with a 1,2-aminothiol for thiazolidine formation and with an oxyamino moiety for oxime bond formation as depicted in Figure 1. For both type of linkers, the conjugates were obtained in good yields under mild conditions within 1 h and without the need for a protection/deprotection step.

Thiazolidine conjugation was carried out by reacting the peptide **7** with either of the oligonucleotides **12a** or

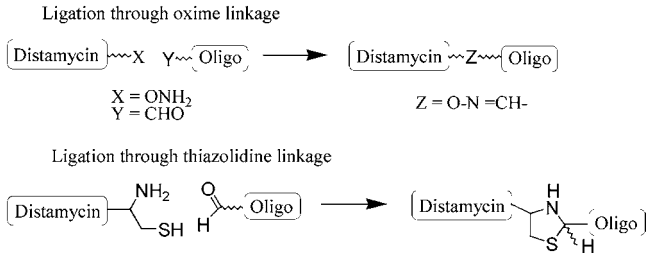


Figure 1. Strategy of efficient and facile synthesis of distamycin−ODN conjugates by using oxime and thiazolidine linkages.

12b at room temperature in sodium acetate buffer (0.2 M, pH = 5.4). The progress of the reaction was followed by C18 reverse-phase HPLC. The reaction was completed in 1 h when 4 equiv of distamycin derivative **7** were used. Figure 2A shows the evidence of clear separation of the conjugate from the crude mixture containing **12a** and **7**. After purification by RP-HPLC, the conjugates **13a**,**b** were obtained in ∼20−30% isolated yields. Formations of **13a**,**b** were confirmed by ESI-MS analysis (Table 1).

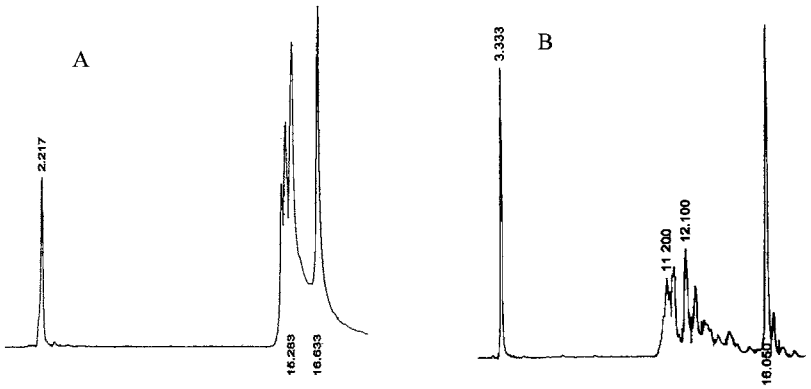


Figure 2. HPLC profiles (detection at 260 nm) of the crude reaction mixture, after 30 min of reaction of the peptide **7** (thiazolidine conjugation) (A) and **9** (oxime conjugation) (B) with the corresponding aldehyde-containing ODN **12a**. (A) Retention times 2.2, 15.3, and 16.6 min correspond to **7**, modified ODN **12a**, and the thiazolidine-conjugated distamycin−ODN **13a** respectively. (B) Retention times 3.3, 16.1 min correspond to **9** and the *N*-oxime-conjugated distamycin−ODN **14a,** respectively. Modified ODN **12a** has already been consumed within 30 min of the reaction with the peptide **9**.

Table 1. Analytical Data for Peptides 7 and 9, Oligonucleotides 11a−c and 15a−c, and Conjugates 13a,b and 14a−c

compound[a]	t_R[b] (min)	mass[c] (calcd)	mass[c] (found)
7	2.1	694.8	694.2
9	3.5	663.7	664.3
5′-XGCTTTTTTCG- 3′ **11a**	10.3	3196.02	3195.4
5′-XGCATATATCG-3′ **11b**	13.4	3222.06	3222.1
5′-XAGCGCGCGCA-3′ **11c**	11.4	3234.05	3232.9
5′-dis-th-GCTTTTTTCG-3′ **13a**	16.0	3840.02	3838.9
5′-dis-th-GCATATATCG-3′ **13b**	16.3	3866.06	3866.6
5′-dis-ox-GCTTTTTTCG-3′ **14a**	16.9	3809.02	3811.1
5′-dis-ox-GCATATATCG-3′ **14b**	17.1	3835.06	3835.8
5′-dis-ox-AGCGCGCGCA-3′ **14c**	16.5	3848.05	3847.7
3′-CGAAAAAAGC-5′ **15a**	11.8	3054.1	3054.0
3′-CGTATATAGC-5′ **15b**	10.2	3027.06	3026.6
3′-TCGCGCGCGT-5′ **15c**	14.8	3020.02	3019.3

[a] X = 5′-diol linker, dis = distamycin analogue, 'th' = thiazolidine linkage, 'ox' = oxime linkage. [b] Retention time (t_R) by analytical C18 reverse-phase HPLC using a gradient of 0 to 30% of acetonitrile over 20 min, at a flow rate of 1 mL min^{-1}. [c] Electrospray ionization MS.

Table 2. Melting Temperatures[a] Determined at Different Concentrations of Sodium Chloride

duplex sequences	T_m (°C), 0.04 M[b]	T_m (°C), 0.1 M[b]	T_m (°C), 0.5 M[b]	ΔT_m (°C), 0.04 M[b]	ΔT_m (°C), 0.1 M[b]	ΔT_m (°C), 0.5 M[b]
11a/15a	35.7	40.0	46.5	---	---	---
13a/15a	47.2	51.1	54.6	11.5	11.1	8.1
11a/15a + 7	41.6	46.5	50.3	5.9	6.5	3.8
11b/15b	34.8	38.3	44.1	---	---	---
13b/15b	39.2	43.8	47.7	4.4	5.5	3.6
11b/15b + 7	37.8	41.3	44.8	3.0	3.0	0.7
14a/15a	46.6	51.4	59.4	10.9	11.4	12.9
14b/15b	40.1	43.0	48.2	5.3	4.7	4.1
14c/15c[c]	63.9	---	---	0.3	---	---
11c/15c	64.3	---	---	---	---	---

[a] Optical melts were generated in 0.01 M sodium phosphate buffer/0.001 M EDTA containing the relevant concentrations of NaCl, pH 7.4, with [duplex] = [**7**] = 9.31×10^{-6} M. ΔT_m correspond to the difference in T_m between the modified and unmodified duplex. [b] NaCl concentrations (40, 100, 500 mM). [c] Duplex melting was measured only at 0.04 M NaCl concentration.

Oxime conjugation reaction was similarly performed by reacting the oligonucleotides **12a−c** with the peptide **9** at room temperature in sodium acetate buffer (0.2 M, pH = 5.4). This reaction was found to be quite rapid and was completed within ∼30 min when 4 equiv of peptide **9** was used. Figure 2B shows the HPLC profile of the crude reaction mixture with oligonucleotide **12a**. The yields after purification by RP-HPLC ranged from 38 to 48% and each of the conjugates **14a−c** were characterized by ESI-MS. In all cases, the experimentally determined molecular weights were in excellent agreement with the calculated values (Table 1).

Although in principle, both thiazolidine- and oxime-based oligopeptide-linked ODN should have two diastereomeric forms, but they could not be identified as two separate peaks during RP-HPLC purification process. The conjugated products (**13a**,**b**, **14a−c**) exhibited UV−vis spectra having characteristics of both DNA (λ_{max} = 260 nm) and the distamycin (λ_{max} = 316 nm) band.

Duplex-Stabilizing Properties. *Melting Temperature Analysis of Hybridization with a Target Oligonucleotide Stretch (Table 2).* The hybridization properties of the conjugates **13a**,**b** and **14a−c** were investigated by UV−melting (thermal denaturation) temperature measurements (T_m). The study was carried out with the following objectives. First, to evaluate the influence of covalent coupling of distamycin-like polyamide with the oligonucleotides and second, to examine the effects of the two kinds of linkages used to tether distamycin with ODN stretches and also their impact on the stability of the corresponding duplex oligonucleotides.

The thiazolidine conjugates **13a**,**b** and the oxime conjugates **14a−c** were individually hybridized with the corresponding complementary oligonucleotide sequences, **15a−c** 3′-d(CGAAAAAAGC)-5′, 3′-d(CGATATATGC)-5′, and 3′-d(TCGCGCGCGT)-5′, respectively. The melting temperatures of the resulting duplexes were determined by following changes in absorbance at 260 nm as a function of temperature from 20 to 80 °C. There was no hysteresis observed during heating and cooling processes of the duplex melting, suggesting a reversible binding process of tethered distamycin to the minor groove surface of duplex. The ODNs, **11a−c**, containing the diol linker at the 5′-ends were also compared. Furthermore, the effect of free distamycin analogue was verified with the corresponding unconjugated duplex. It was found that distamycin-conjugated oligonucleotides with A/T rich sequences (**13a**,**b** and **14a**,**b**) were significantly stabilized in their duplex forms. In contrast, the distamycin-linked ODNs possessing alternating G/C base pairs (**14c**) did not enhance the duplex melting temperature. This suggests that the hybridization of the DNA−distamycin conjugates with the target sequences generates a DNA minor groove surface and facilitates the binding event by the tethered distamycin unit. Besides, continuous

stretches of A/T (**13a** and **14a**) were stabilized to a greater extent than their counterparts with alternating AT base pairs (**13b** and **14b**).

Earlier studies based on NMR and chemical nuclease-mediated footprinting experiments suggest that distamycin induces a 'collapse' of a normal minor groove into a narrower groove (*37*, *38*). This should enhance the hydrogen bonding and van der Waals interactions. Such deep penetration of the drug to the walls of the minor groove in turn should favor enthalpic contribution for the binding. The ATAT sequence in the decamer d(5′-GCTATATACG-3′)$_2$ has a low intrinsic propeller twist angle, which may not facilitate the formation of a narrower minor groove for favorable binding of the distamycin (*37*). Thus the readjustment of the backbone in case of alternating A/T stretches would be difficult. This may account for the low affinity of ODN-conjugated distamycin to the alternating A/T sequence in comparison to that of a contiguous A or T sequence.

The enhancement of melting temperature (ΔT_m) was almost comparable for both thiazolidine- and *N*-oxime-linked distamycin conjugates. This suggests that the nature of linker (five-membered thiazolidine ring vs linear oxime bond) does not significantly influence and contribute to the duplex stabilization. The stabilization upon duplex formation between a complementary oligonucleotide sequence with the oligonucleotide-conjugated distamycin was also compared with respect to free distamycin binding to the corresponding DNA duplex. In each case, the stabilization was found to be more pronounced for the covalently conjugated distamycin than that of the free duplex.

Effect of Salt on Hybridization to the Target Oligonucleotides. Most of the ligands including distamycin or netropsin that bind to DNA are cationic. Therefore, experiments at varying salt concentrations provide useful information pertaining to the relative importance of nonspecific (electrostatic) and specific (hydrogen bonding, van der Waals interactions) factors on the DNA recognition process. Salt-induced ligand−DNA complex dissociation experiments are often useful for comparing the relative affinities and mode of ligand binding toward DNA (*39*). Generally for compounds with similar binding modes, the higher the binding affinity, the lower should be the dissociation of the ligand−DNA complex with increasing salt concentration. Additionally, DNA is known to undergo structural transition in the presence of high salt concentration (*40*, *41*). Strong precomplexation of a ligand with DNA should also resist such structural transition.

Duplex melting was examined at various NaCl concentrations (40, 100, 500 mM) to analyze the electrostatic effect of distamycin binding on T_m enhancement. It was observed that on increase in salt concentration, the T_m value for a given duplex was increased (Table 2). This is in agreement with known salt effects on polyelectrolyte solutions, explained on the basis of the counterion condensation theory (*42*−*45*). According to this concept, an increase in bulk salt concentration should lead to the stabilization of the duplex state of DNA as having a higher charge density as compared with the single-stranded form. This would result in an increase in T_m for the helix-to-coil transition. However, at high salt concentration such as in 500 mM, although the T_m increased to the highest extent, the ΔT_m value was found to be less compared to the ΔT_m in low salt conditions (40, 100 mM) in case of both free and covalently conjugated distamycin except for **14a**/**15a** duplex. This fact is correlated with the energetic contribution (large negative enthalpy and positive entropy value) in the distamycin−DNA binding process described earlier (*46*, *47*). The favorable entropic gain arises because of the release of ordered water molecules from the hydration shell of the DNA backbone during any ligand binding. At high salt concentration, the release of water molecules is expected to be less. This in turn would reduce the entropy gain as well as the binding energy. This may result in low ΔT_m value at higher salt concentration. Thus, for the peptide−ODN conjugates, there may be two opposite influences on the T_m of duplex formation as the concentration of salt increases, namely increased stability of the double-stranded DNA region and decreased association of the peptide portion with the oligonucleotide target.

CD Spectral Analysis of the Distamycin−ODN Conjugates. Considerable information on the binding of distamycin to nucleic acid duplex has been obtained from circular dichroism measurements (*48*, *49*). Since free distamycin does not exhibit optical activity and is therefore CD-silent. However, its binding to double-stranded nucleic acid induces a CD signal that can be used to monitor the binding process. In the present case, the conjugates **13a**,**b** and **14a**−**c** alone exhibited two positive peaks at 280 nm (DNA-CD) and 334 nm (distamycin-CD) that were characteristics of the single-stranded ODN and conjugated distamycin moiety, respectively. Efficient intraduplex binding of the covalently attached distamycin to the minor groove of the duplexes (**13a**/**15a**, **13b**/**15b**) intensifies the magnitude of molar ellipticity at 334 nm compared to their corresponding unmodified duplexes (**11a**/**15a**, **11b**/**15b**) bound with free distamycin. Between these two duplexes (**13a**/**15a**, **13b**/**15b**), the former one (with continuous A/T stretch) showed a more intense CD band than the latter (with alternating A/T stretch). These results are consistent with the data obtained from the UV−melting temperature study, suggesting that covalently conjugated distamycin stabilizes the duplex ODN more than the ODN bound noncovalently with distamycin, and it has greater sequence selectivity toward the continuous stretch of A/T rich tract than the one with alternating A/T stretch.

The nature and specificity of distamycin binding to the minor groove surface of different A/T stretch DNA duplex was further examined by duplex melting at 334 nm (distamycin-CD) as a function of temperature from 20 to 80 °C (Figure 3). The sequence specificity and mode of distamycin binding to the different ODN stretches were analyzed from the peak height and the magnitude of the peak minima of such derivative plot of d(CD)/dT vs T at 334 nm. The CD intensity (peak height) at 334 nm was higher in both ODN−distamycin conjugates (e.g. **14a**/**15a**) than the one with unmodified duplex (e.g. **11a**/**15a)** containing free distamycin. This might be due to a favorable binding of the covalently attached distamycin to an ODN stretch, owing to its higher effective concentration at the DNA minor groove. Moreover, the peak height was higher in case of continuous A/T stretch than alternating A/T sequence. Magnitude of peak minima was almost same for continuous A/T stretch duplexes (**14a**/**15a** and **11a**/**15a** + **9**). In this case, it is possible that more efficient binding of distamycin to a continuous A/T tract (as in **11a**/**15a**) probably does not allow any further conformational change of distamycin in ODN irrespective of whether it is covalently conjugated with the distamycin or not. This is in contrast to what was observed with the ODN bearing alternating A/T tract, where peak magnitude was differed by ca. 4 °C between (**14b**/**15b** and **11b**/**15b** + **9**). It may be that covalent attachment of distamycin induced a conformational change of ODN that

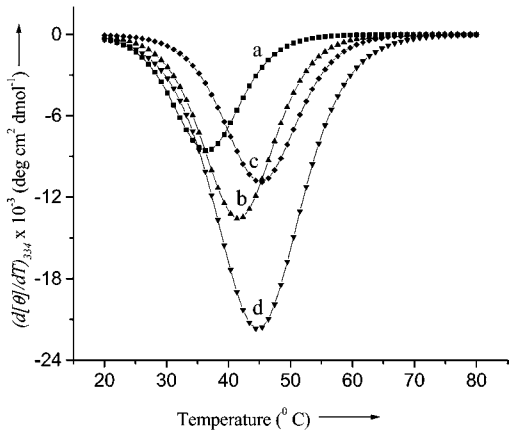


Figure 3. First derivative plot of molar ellipticity vs temperature during duplex melting at 334 nm. CD melting curves of the duplexes, 5′-dis-ox-GCATATATCG-3′ **14b**/3′-CGTATATAGC-5′ **15b** (a, ■), 5′-XGCATATATCG-3′ **11b**/3′-CGTATATAGC-5′ **15b** + **9** (b, ▲) 5′-XGCTTTTTTCG-3′ **11a**/3′-CGAAAAAAGC-5′ **15a** + **9** (c, ◆), 5′-dis-ox-GCTTTTTTCG-3′ **14a**/3′-CGAAAAAAGC-5′ **15a** (d, ▼) with change in temperature at the rate of 1 °C/min from 20 to 80 °C at 334 nm. In each case CD spectra were recorded in 0.01 M Na_2HPO_4 buffer, 0.04 M NaCl, 0.001 M EDTA, pH 7.4, with [duplex] = [**9**] = 1.3×10^{-5} M. (X = diol-modified oligonucleotide, dis = distamycin, and 'ox' corresponds to oxime-conjugated ODN−distamycin hybrid).

enhanced hydrogen-bonding interaction at its minor groove surface compared to the unmodified ODN where distamycin was not covalently attached.

It had been observed that the equilibrium between free distamycin and DNA in the binding process was affected by addition of salt to the preformed noncovalent distamycin−DNA complex. This complex dissociation process as a function of salt concentration can be followed by examining the changes in magnitude and the nature of the CD band at 334 nm. A gradual decrease in the CD band at 334 nm with a minute change at 280 nm was observed for **5**, noncovalently bound to duplex with increasing salt concentration up to ca. 1 M (*50*). But no significant change in the corresponding bands at 280 and 334 nm was observed for **14a**/**15a** and **14b**/**15b** duplexes. In both cases, addition of salt (NaCl, up to ca. 1 M) to the preformed distamycin−DNA complex and also the formation of such complexes under different salt concentrations did not lead to any significant change in the 334 nm CD band. Therefore, high salt concentration could not dissociate the tightly bound, covalently attached distamycin arm from the DNA surface, preserving the structural integrity of both the DNA and the distamycin moiety.

Competition with Hoechst 33258 Binding. In this study Hoechst 33258 fluorophore was used as a minor groove competitor, which has the same sequence selectivity but a higher DNA binding constant (ca. 10^8 mol^{-1}) (*51*) than that of distamycin (ca. 10^5 to 10^6 mol^{-1}). To determine the accessibility of strong groove binding ligands such as Hoechst 33258 to the minor groove of the distamycin−ODN conjugates, we performed fluorescence titration using the above probe. For this purpose, we compared the binding of Hoechst 33258 with unmodified ODN in the presence and absence of distamycin and also with the corresponding distamycin−ODN conjugates having two different A/T stretches.

The fluorescence intensity of Hoechst 33258 is very low in its free state in solution. However, the emission due to Hoechst 33258 increases dramatically upon binding to duplex DNA (*52*). Fluorescence titrations were performed at a fixed concentration of ODNs while varying the Hoechst 33258 concentration till saturation, as indicated from emission spectroscopy. In all the cases, the enhanced fluorescence intensity was measured after each addition (Figure 4) and the binding efficiency was compared from Hoechst 33258 concentration required to saturate its fluorescence intensity. A significantly higher concentration of Hoechst 33258 was required to saturate its fluorescence intensity in either free or covalently bound distamycin, in comparison to the duplex itself. Duplexes **11a**/**15a** and **11b**/**15b** containing noncovalently bound distamycin-like polyamide at its minor groove surface required 1 and 0.7 μM greater Hoechst 33258, respectively, to saturate its binding with respect to the duplex ODN without distamycin. In the case of duplex ODN bearing covalently tethered distamycin derivatives such as **14a**/**15a** and **14b**/**15b**, respectively, a greater Hoechst 33258 concentration was required (0.3−0.4 μM) with respect to the unconjugated duplex ODN. In both cases it was found that more Hoechst 33258 was required to saturate its fluorescence intensity in duplexes containing a continuous A/T stretch (**14a**/**15a**, **11a**/**15a** + **9**) rather than an alternating A/T stretch (**14b**/**15b**, **11b**/**15b** + **9**).

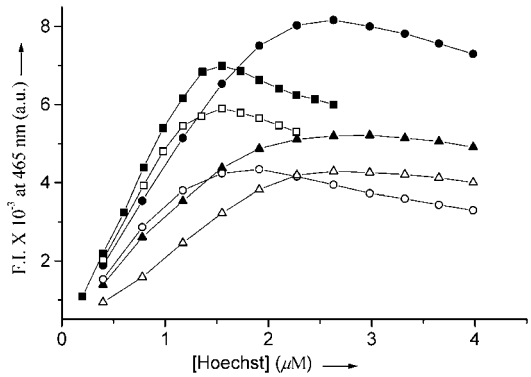


Figure 4. Fluorescence titration of corresponding duplexes with minor groove competitor Hoechst 33258, 5′-XGCTTTTTTCG-3′ **11a**/3′-CGAAAAAAGC-5′ **15a** (■), 5′-XGCTTTTTTCG-3′ **11a**/3′-CGAAAAAAGC-5′ **15a** + **9** (●), 5′-dis-ox-GCTTTTTTCG-3′ **14a**/3′-CGAAAAAAGC-5′ **15a** (▲), and 5′- XGCATATATCG-3′ **11b**/3′-CGTATATAGC-5′ **15b** (□), 5′- XGCATATATCG-3′ **11b**/3′-CGTATATAGC-5′ **15b** + **9** (○), 5′-dis-ox- GCATATATCG-3′ **14b**/ 3′-CGTATATAGC-5′ **15b** (△) in 0.01 M Na_2HPO_4 buffer, 0.04 M NaCl, 0.001 M EDTA, pH 7.4 with [duplex] = [**9**] = 3×10^{-6} M. Spectra were recorded at λ_{ex} = 350 nm, λ_{em} = 465 nm, slit width Ex/Em = 10 nm/10 nm. (X= 5′-diol modified oligonucleotide, dis = distamycin and 'ox' corresponds to oxime-conjugated ODN−distamycin hybrid).

It is known that fluorescence intensity of the Hoechst-like fluorophore is quenched after it saturates its binding to the DNA minor groove surface (*52*). This was due to the nonspecific binding of excess Hoechst 33258 molecules to the phosphate backbone of DNA. In our displacement assay, there was less quenching observed for duplexes containing free distamycin, and no such quenching was observed for the covalently bound distamycin analogue (Figure 4). When distamycin is noncovalently complexed with the duplex ODN, addition of Hoechst 33258 releases distamycin molecules from its minor groove. Such released distamycin molecules then compete for the nonspecific binding with the phosphate backbone, impeding further approach of Hoechst molecule to these sites. Interestingly, when distamycin is covalently conjugated, nonspecific binding to the phosphate sites by Hoechst was completely inhibited. Importantly, this study reinforces the fact that the duplex formation is facilitated by a covalently attached distamycin analogue

and also supports its sequence preference for a continuous A/T stretch rather than an alternating A/T sequence.

CONCLUSIONS

In summary we have reported two chemical methods for the conjugation of oligonucleotides to a minor groove-binding (MGB) polyamide. Although conjugates of MGB polyamides have been prepared in the past, the utility of the present approach is that it would be possible to prepare a selection of appropriately derivatized polyamides and oligonucleotides and ligate together in a modular fashion. Thus, if the goal is to prepare a library of compounds, then this would be a time-saving approach. The chemistry employed here for the conjugation of an ODN to a distamycin-like polyamide is an extension of existing techniques based on the reaction of an aldehyde to form an oxime linkage or a thiazolidine ring. After HPLC purification and characterization of these conjugates, we investigated the influence of tethered distamycin on duplex formation and assessed the stability with the complementary strand through interactions mediated by an A/T stretch. Hybridization by the conjugate to a target sequence converts a single-stranded species to a double-stranded complex and generates a secondary structure with both major and minor grooves. The hybridization event triggers a binding event by the 5′-end ODN-tethered distamycin within the generated minor groove structure. This was proved by the enhanced thermal denaturation temperature (ΔT_m) at 260 nm, increased CD intensity at 334 nm, and a requirement of more Hoechst 33258 molecules during the fluorescence displacement assay. Taken together, it is evident that the distamycin conjugates are more selective in binding to ODNs containing a continuous stretch of A/T base pairs rather than the one having alternating A/T tract. CD studies at different salt concentrations reinforce the specific interaction of distamycin conjugates to the corresponding duplexes. No significant binding preference was observed for the five-membered thiazolidine linker over the linear *N*-oxime-conjugated distamycin to the duplex. This could be due to long linker length between the ODN and the peptide, allowing the linker part to loop during the distamycin−DNA binding process. The combination of such hybridization-triggered binding events should provide the basis for the development of DNA-based diagnostic properties of antigens or therapeutic ODNs by enhancing its target-binding properties, cellular uptake, or exonuclease stability or can be used as an in situ hybridization probe. Since distamycin is known to form a stacked, antiparallel dimer upon binding to AT tracts of DNA (*53*, *54*), it is possible to employ distamycin−ODN conjugates for pseudo-cyclized duplex DNA and triple helix formation. Work is currently underway in this direction.

EXPERIMENTAL SECTION

Materials and Methods. All chemical reagents were of the highest purity available and were used without purification. Solid-supported $NaIO_4$ (polystyrylmethyl)-trimethylammonium metaperiodate, loading 2.5 mmol/g, was purchased from Novabiochem and 2-cyanoethyl diisopropylchlorophosphoramidite from Aldrich. The phosphoramidite **10** was prepared by analogy with the previously described protocol (*29*). The activated ester **4** of *N*-Boc-*O*-(carboxymethyl)hydroxylamine was prepared as described earlier (*55*). Thin-layer chromatography (TLC) was performed using silica gel-G, and preparative column chromatography was performed on silica gel (60−120 mesh size). DMF, CH_2Cl_2, and $CHCl_3$ were dried over P_2O_5, Et_3N was dried over KOH, and THF was dried using sodium and benzophenone ketyl. HPLC purification as well as HPLC analysis of oligonucleotides and conjugates was performed on a water system equipped with two M510 pumps, a M490E detector, and an M680-system controller. The oligonucleotides and the conjugates were purified on a μ-bondapak C-18 column (Macherey-Nagel Nucleosil: 10 × 250 mm, 7 μm) using the following system of solvent: solvent A, 20 mM ammonium acetate/CH_3CN, 95:5 (v:v); solvent B (CH_3CN); flow rate, 4 mL/min; a linear gradient from 0 to 30% B in 20 min was applied. ^{1}H NMR and ^{13}C NMR spectra were recorded on JEOL JNM λ-300 or using a Bruker AMX 400 (400 MHz for ^{1}H and 100.6 MHz for ^{13}C) NMR spectrometer. Chemical shifts (δ) are reported in ppm downfield from the internal standard (TMS). Electrospray ionization (ESI) mass spectra were measured on an Esquire spectrometer (Bruker). Analysis was performed in the negative mode for both the oligonucleotides and conjugates and in the positive mode for the peptides. The oligonucleotides and the conjugates were dissolved in 50% aqueous acetonitrile, and 1% of NEt_3 was added. The peptides were dissolved in 50% aqueous acetonitrile containing 1% of TFA.

2-*tert*-Butoxycarbonylamino-3-*tert*-butoxycarbonylsulfanylpropionic Acid 2. To a cooled aqueous/dioxane solution (1:1, v/v, 1.2 mL) of L-cysteine, **1** (0.4 g, 3.3 mmol), were added potassium carbonate (2.4 g, 18.3 mmol) and di(*tert*-butyl) dicarbonate (2.8 g, 13.2 mmol), and the mixture was stirred for 48 h at room temperature. The resulting mixture was then washed with ether to remove excess of di(*tert*-butyl) dicarbonate and acidified with 0.2 N aq HCl. The aqueous layer was then extracted with EtOAc. The organic layer was washed with brine solution, dried over anhydrous Na_2SO_4, and evaporated in a vacuum. Purification by column chromatography over silica gel (MeOH/$CHCl_3$ 1:49) afforded a white solid compound. Yield: 0.28 g, 60%; ^{1}H NMR (300 MHz, $CDCl_3$): δ 1.43 (s, 9H, C(CH_3)$_3$), 1.47 (s, 9H; C(CH_3)$_3$), 3.16−3.23 (dd, ^1J (H, H) = 14.4 Hz, ^2J (H, H) = 7.8 Hz, ^2J(H, H) = 6.6 Hz, 1H; CH_2S(Boc)), 3.3−3.4 (dd, ^1J(H, H) = 14.1 Hz, ^2J(H, H), = 4.5 Hz, ^2J(H, H) = 3.3 Hz, 1H; CH_2S(Boc)), 4.5 (m, 1H; C*H*-CH_2), 5.4 (m, 1H; N*H*); ^{13}C NMR (100.6 MHz,$CDCl_3$): δ 28.1, 28.3, 32.6, 54.4, 80.5, 85.7, 155.6, 168.7, 174.5 ppm; Elemental analysis: calcd (%) for $C_{13}H_{23}O_6NS$ (321.4): C 48.58, H 7.21, N 4.36; found: C 49.0, H 7.3, N 4.3.

2-*tert*-Butoxycarbonylamino-3-*tert*-butoxycarbonylsulfanylpropyl 2,5-Dioxopyrrolidin-1-yl Ester, 3. 2-*tert*-Butoxycarbonylamino-3-*tert*-butoxycarbonylsulfanylpropionic acid **2** (0.1 g, 0.3 mmol) was dissolved in DMF (1 mL) and cooled in an ice bath. *N*-Hydroxysuccinimide (HOSu, 0.04 g, 0.4 mmol) was added to the above solution, followed by dicyclohexylcarbodiimide (0.08 g, 0.4 mmol). The resulting solution was stirred for 1 h at 0 °C and then at room temperature for another 6 h. The precipitated dicyclohexylurea was filtered off, and the filtrate was diluted with EtOAc. The EtOAc layer was washed successively with $NaHCO_3$ and brine, dried over anhydrous Na_2SO_4, and evaporated to obtain the succinimide ester **3** as practically pure solid. Yield: 0.16 g, 80%. This was directly used for the next step without further purification; ^{1}H NMR (300 MHz, $CDCl_3$): δ 1.41 (s, 9H; C(CH_3)$_3$), 1.46 (s, 9H; C(CH_3)$_3$), 2.8 (s, 4H; CO(CH_2CH_2)-CO), 3.17−3.25 (dd, ^1J(H, H) = 14.1 Hz, ^2J(H, H) = 8.1 Hz, 1H; CH_2S(Boc), 3.4−3.45 (dd, ^1J = 14.1 Hz, ^2J = 4.6 Hz, 1H; CH_2S(Boc)), 4.82 (m, 1H; C*H*(CO)NH), 5.4 (m, 1H; N*H*).

***N*2-2-[[2-(2-*tert*-Butoxycarbonylamino-3-*tert*-butoxycarbonylsulfanylpropylamino)ethyl](methyl)amino]ethyl-1-methyl-4-[(1-methyl-4-[(1-methyl-4[(1-methyl-1*H*-pyrrol-2-yl)carbonyl]amino-1*H*-pyrrol-2-yl)carbonyl]amino-1*H*-pyrrol-2-yl)carbonyl]amino-1*H*-2-pyrrolecarboxamide, 6.** To a solution of N2-2-[(2-aminoethyl)(methyl)amino[(1-methyl-4-[(1-methyl-4-[(1-methyl-4[(1-methyl-1*H*-pyrrol-2-yl)carbonyl]amino-1*H*-pyrrol-2-yl)carbonyl]amino-1*H*-pyrrol-2-yl)carbonyl]-amino-1*H*-2-pyrrolecarboxamide **5** (0.2 g, 0.3 mmol) in $CHCl_3$ (5 mL) was added activated *N*-hydroxysuccinimide ester **3** (0.15 g, 0.4 mmol), and the resulting solution was stirred at room temperature for 2 h. At the end of this period, the reaction mixture was filtered off and the filtrate evaporated under vacuum. The resulting mixture was purified by column chromatography over silica gel using MeOH/$CHCl_3$ (3/47) as eluent. This furnished **6** as a yellow powder. Yield: 0.14 g, 50%, ^{1}H NMR (300 MHz, $CDCl_3$): δ 1.34 (s, 9H; C(CH_3)$_3$), 1.42 (s, 9H; C(CH_3)$_3$), 2.23 (s, 3H; N(CH_3)), 2.56 (s, 4H; CH_2N(Me)CH_2), 2.88−2.97 (m, 4H; 2CH_2NH(CO)), 3.12−3.47 (m, 2H; CH_2S-(Boc)), 3.79, 3.85, 3.89, 3.97 (s, 12H; 4 Py-N(CH_3)), 4.26 (m, 1H; C*H*NH(Boc)), 5.69 (m, 1H; N*H*Boc), 6.1 (dd, J(H, H) = 1.8 Hz, ^2J(H, H) = 3.8 Hz, 1H; Ar*H*), 6.5 (d, J(H, H) = 1.8 Hz, 1H; Ar*H*), 6.69 (d, J = 1.8 Hz, 1H; Ar*H*), 6.74 (s, 1H; Ar*H*), 6.83 (s, 1H; Ar*H*), 6.9 (s, 1H; Ar*H*), 7.22 (s, 2H; Ar*H*), 7.4(s, 1H; Ar*H*), 7.73, 8.41, 8.89, 9.03 (br *s*, 4H; N*H*); ^{13}C NMR (100.6 MHz, $CDCl_3$): δ 28.3, 28.1, 35.8, 36.6, 36.9, 41.3, 56.1, 56.8, 80.3, 85.8, 103.5, 103.9, 104.02, 107.4, 112.5, 119.3, 119.6, 119.8, 121.8, 122.1, 122.4, 122.7, 122.8, 125.6, 128.3, 159.0, 159.2, 159.5, 162.2, 171.3, 175.4 ppm; MS (ESI): *m*/*z* (%): 894.6 (100) [M + H]$^+$; elemental analysis calcd (%) for $C_{42}H_{59}O_9N_{11}S$. $CHCl_3$: C 50.96, H 5.97, N 15.2; found: C 50.8, H 6.1, N 15.6.

***N*2-2-[[2-(2-*tert*-Butoxycarbonylaminooxyacetylamino)ethyl](methyl)amino]ethyl-1-methyl-4-[(1-methyl-4-[(1-methyl-4[(1-methyl-1*H*-pyrrol-2-yl)carbonyl]amino-1*H*-pyrrol-2-yl)carbonyl]amino-1*H*-pyrrol-2-yl)carbonyl]amino-1*H*-2-pyrrolecarboxamide, 8.** To a solution of **4** (15 mg, 56 μmol) in chloroform was added tetrapeptide **5** (30 mg, 51 μmol) under argon. The reaction mixture was stirred at room temperature for 2 h. On completion, the reaction mixture was filtered off and the filtrate evaporated under vacuum. The resulting mixture was adsorbed in silica, and it was purified by column chromatography using MeOH/$CHCl_3$ (5/45) as eluent. The product, **8**, was obtained as a yellow powder. Yield: 20 mg, 50%; ^{1}H NMR: (300 MHz, $CDCl_3$): δ 1.4 (s, 9H; C(CH_3)$_3$), 2.4 (br s, 3H; N(CH_3)), 2.7 (br s, 4H; CH_2N(Me)CH_2), 3.4 (br s, 4H; 2CH_2NH(CO)), 3.82, 3.87, 3.89, 3.96 (s, 12H; 4 Py-N(CH_3)), 4.28 (br s, 2H; CH_2-(ONH)(Boc)), 6.1 (dd, J(H,H) = 1.8 Hz, ^2J(H,H) = 3.8 Hz, 1H; Ar*H*), 6.6 (d, J(H,H) = 1.8 Hz, 1H; Ar*H*), 6.7 (d, J = 1.8 Hz, 1H; Ar*H*), 6.8 (s, 1H; Ar*H*), 6.9 (s, 1H; Ar*H*), 7.0 (s, 1H; Ar*H*), 7.2 (s, 2H; Ar*H*), 7.3 (s,1H; Ar*H*), 7.7, 8.4, 8.9, 9.03 (br s, 4H; N*H*s); ^{13}C NMR (100.6 MHz, $CDCl_3$): δ 28.2, 36.56, 36.6, 36.7, 36.9, 40.5, 56.1, 57.1, 65.9, 82.5, 103.7, 104.0, 104.5 107.4, 112.6, 119.5, 119.7, 119.9, 121.9, 121.96, 122.0, 122.3, 122.8, 125.6, 128.4, 159.1, 159.2, 159.6, 162.6, 170.7, 174.2 ppm; MS (ESI): *m*/*z* (%) = 764.3 (100) [M + H]$^+$.

***N*2-2-[[2-(2-Amino-3-sulfanylpropylamino)ethyl]-(methyl)amino]ethyl-1-methyl-4-[(1-methyl-4-[(1-methyl-4[(1-methyl-1*H*-pyrrol-2-yl)carbonyl]amino-1*H*-pyrrol-2-yl)carbonyl]amino-1*H*-pyrrol-2yl)carbonyl]amino-1*H*-2-pyrrolecarboxamide, 7.** To a solution of **6** (10 mg, 0.011 mmol) in dichloromethane (0.2 mL) was added ethane dithiothreitol (EDT, 8 μL, 2%) first to prevent thiol oxidation. An equal volume of TFA (0.2 mL, 2.6 mmol) was added into it under cold conditions, and the reaction was continued for 2 h at room temperature under an argon atmosphere. After completion of the reaction, the excess TFA and solvent were removed in vacuo. To the residue were added $CHCl_3$ and H_2O (500 μL:500 μL) and the biphasic solution was mixed thoroughly. The excess ethane dithiothreitol (EDT) was removed in organic phase, and the aqueous phase was lyophilized to obtain **7**. It was directly used without further purification due to its instability and high reactivity. Yield: 6.1 mg, 80%; MS (ESI): *m*/*z* (%) = 694.22 (50) [M + H]$^+$, 347.76 (100) [(M + H)/2]$^+$

***N*2-2-[[2-(2-Aminooxyacetylamino)ethyl](methyl)amino]ethyl-1-methyl-4-[(1-methyl-4-[(1-methyl-4[(1-methyl-1*H*-pyrrol-2yl)carbonyl]amino-1*H*-pyrrol-2-yl)carbonyl]amino-1*H*-pyrrol-2yl)carbonyl]amino-1*H*-2-pyrrolecarboxamide, 9.** To a solution of **8** (10 mg, 0.013 mmol) in dichloromethane (0.2 mL) was added an equal volume of TFA (0.2 mL, 2.6 mmol), and the reaction mixture was stirred at room temperature for 2 h. The solvent and excess TFA was removed under vacuum, and the residue was directly used for the conjugation reaction without further purification due to its high reactivity. Yield: 6.9 mg, 80%; MS (ESI): *m*/*z* (%) = 664.22 (100) [M + H]$^+$.

Oligonucleotide Synthesis. Automated DNA synthesis was performed on a Perkin-Elmer model Expedite DNA synthesizer using standard cyanoethyl nucleoside phosphoramidite chemistry on a 1 μM scale. After cleavage from the solid support and deprotection by treatment with concentrated ammonia (28%) for 16 h at 55 °C, the oligonucleotides were purified by RP-HPLC.

Diol-Containing Oligonucleotides 11a−c. The 5′-protected oligonucleotides were treated with 80% aq AcOH for 1 h. The residue obtained after lyophilization was dissolved in water, and the aqueous layer was extensively washed with Et_2O to remove the benzylidene byproduct. Subsequent lyophilization afforded the oligonucleotides **11a**−**c**, which were characterized by ESI-MS (Table 1).

Aldehyde-Containing Oligonucleotides 12a−c. To a solution of the oligonucleotide **11a** (1 mg, 0.3 μmol) in water (1 mL) was added solid-supported $NaIO_4$ (0.67 mg, 3 μmol), and the mixture was shaken gently for ∼1 h. The solution was then decanted, and the polymer was washed twice with H_2O. Washings were added to the solution, and the resulting solution was evaporated under vacuum to remove volatiles. The product was then directly used for oxime conjugation without further purification. For thiazolidine-containing oligonucleotides, it was purified by RP-HPLC to remove excess periodate. The decamers **12b**,**c** were prepared in the same manner.

Conjugation through Thiazolidine and Oxime Linkages. *Preparation of Oligonucleotides **13a**,**b** and **14a**−**c**.* The cysteine-tethered peptide **7** (0.4 mg, 0.64 μmol) was dissolved in 0.2 M NaOAc buffer (pH = 5.4, 30 μL) and was added into 0.2 M NaOAc buffer solution (130 μL) containing the aldehyde-containing oligonucleotide **12a** (500 μg, 0.16 μmol). The mixture was stirred at room temperature, and the progress of the reaction was followed by RP-HPLC. Disappearance of the starting material **12a** was achieved in 1 h (Figure 2A). In Figure 2A, **12a** showed three peaks in HPLC profile, which correspond to the imine formation of some part of the aldehyde-containing ODN with ammonium acetate buffer used as a solvent during the HPLC elution period. Purification by HPLC afforded the conjugate **13a** in 30%

yield. The conjugate **13b** was obtained in the same manner from the oligonucleotide **12b**.

The oligonucleotides **14a**−**c** were prepared in the same manner by adding 0.2 M NaOAc buffer (pH = 5.4, 30 μL) containing oxyamine-containing peptide **9** into 0.2 M NaOAc buffer solution (130 μL) containing the reactive oligonucleotide **12a**−**c**. Disappearance of the starting material **12a**−**c** was achieved within ∼30 min, and purification by HPLC afforded the conjugate **14a**−**c** in 40% yield (Figure 2B). Subsequent lyophilization afforded the distamycin−ODN conjugates **13a**,**b** and **14a**−**c**, which were characterized by ESI-MS (Table 1).

Hybridization Experiments. Duplex formation and the melting T_m experiments were carried out by mixing equimolar amounts of the two decamer oligonucleotide strands in 10 mM Na_2HPO_4 buffer, 1 mM EDTA, and varying concentrations of NaCl (40, 100, 500 mM) at pH 7.4. All measurements were performed at 9.31 μM concentration of each strand, and the mixtures were heated at 90 °C for 6 min and then cooled slowly to room temperature to allow the formation of duplex. The melting curves (absorbance at 260 nm vs temperature) were generated using a Lambda 5 UV−vis spectrophotometer equipped with a Perkin-Elmer C570−070 temperature controller using a scan rate of 0.5 °C/min (from 20 to 70 °C) and 1 °C/min (from 70 to 80 °C). The data were recorded at each 0.1 °C interval. In all cases the buffer-corrected absorbance vs temperature curves were converted to relative absorbance, $\theta = (A_t - A_{20})/(A_{80} - A_{20})$ vs temperature (A_t correspond to the absorbance at any temperature t) to obtain the value of T_m.

Circular Dichroism Measurements. CD spectra were recorded on a JASCO (J-715) model spectropolarimeter equipped with a Perkin-Elmer temperature controller. CD melting experiments were performed using a scan rate of 1 °C/min from 20 to 80 °C, and the data were recorded at each 0.2 °C interval. All CD spectra were averaged over two acquisitions, and the scan rate was maintained at 100 nm/min with optical cells of path length 1 cm in the CD melting study and 0.2 cm for recording other CD spectra. The CD values, expressed as molar ellipticity (θ), has been calculated from the equation, $(\theta) = (100 \times \phi/l \times c)$ deg cm^2 dmol^{-1} where ϕ is the observed ellipticity in degrees, l is the path length of the cell in centimeters, and c is the concentration of DNA in base molarity. All the experiments including CD melting study were carried out in 0.01 M Na_2HPO_4 buffer and 0.04 M NaCl, pH 7.4, with 1.31×10^{-5} M duplex concentration.

Fluorescence Measurements. Fluorescence spectra were recorded on a Hitachi model F-4500 spectrofluorimeter at 25 °C with excitation and emission bandwidths fixed at 10 nm (λ_{ex} = 350 nm, λ_{em} = 464.8 nm). In each case duplex concentration was taken as 3×10^{-6} M and each time an aliquot (10 μL) of Hoechst 33258 (4.2×10^{-5} M) was added into the duplex solution in 0.01 M Na_2HPO_4 buffer, 0.04 M NaCl, pH 7.4. In the case of the duplex containing free distamycin, 3×10^{-6} M distamycin was added to the duplex and the solution was incubated for 10 min prior to the addition of Hoechst 33258. The same concentration was also maintained for the duplex ODN covalently conjugated with distamycin. The enhanced fluorescence intensity was measured at each point after 5 min of equilibration of added Hoechst 33258 into individual duplex solutions.

ACKNOWLEDGMENT

The Ministère des Affaires Etrangères and the Région Rhone-Alpes are gratefully acknowledged for a grant for S.G.

LITERATURE CITED

(1) Yager, T. D., Nickerson, D. A., and Hood, L. E. (1991) The human genome project: creating an infrastructure for biology and medicine. *Trends Biochem. Sci. 16*, 454.

(2) Praseuth, D., Guieyse, A. L., and Helene, C. (1999) Triple helix formation and the antigene strategy for sequence specific control of gene expression. *Biochim. Biophys. Acta. 1489*, 181−206.

(3) Hermann, T., and Patel, D. J. (2000) Adaptive recognition by nucleic acid aptamers. *Science 287*, 820−825.

(4) Mapp, A. K., Ansari, A. Z., Ptashne, M., and Dervan, P. B. (2000) Activation of gene expression by small molecule transcription factors. *Proc. Natl. Acad. Sci. U.S.A. 95*, 3930−3935.

(5) Trauger, J. W., Baird, E. E., and Dervan, P. B. (1998) Recognition of 16 base pairs in the minor groove of DNA by a pyrrole-imidazole polyamide. *J. Am. Chem. Soc. 120*, 3534−3535.

(6) Gottesfeld, J. M., Neely, L., Trauger, J. W., Baird, E. E., and Dervan, P. B. (1997) Regulation of gene expression by small molecules. *Nature 387*, 202−205.

(7) Bailly, C., and Charies, J. B. (1998) Sequence-specific DNA minor groove binders. Design and synthesis of netropsin and distamycin analogues. *Bioconjugate Chem. 9*, 513−538.

(8) Iida, H., Jia, G., and Lown, J. W. (1999) Rational recognition of nucleic acid sequences. *Curr. Opin. Biotechnol. 10*, 29−33.

(9) Neidle, S. (1997) Crystallographic insights into DNA minor groove recognition by drugs. *Biopolymers 44*, 105−121.

(10) Patel, D. J. (1982) Antibiotic − DNA interactions: intermolecular nuclear Overhauser effects in the netropsin − d(CGCGAATTCGCG) complex in solution. *Proc. Natl. Acad. Sci. U.S.A. 79*, 6424−6428.

(11) Schultz, P. G., and Dervan, P. B. (1984) Distamycin and penta-*N*-methylpyrrolecarboxamide binding sites on native DNA. A comparison of methidiumpropyl-EDTA-Fe(II) foot printing and DNA affinity cleaving. *J. Biomol. Struct. Dyn. 1*, 1133−1147.

(12) Lee, M., Hartley, J. A., Pon, R. T., Krowicki, K., and Lown, J. W. (1988). Sequence specific molecular recognition by a monocationic lexitropsin of the decadeoxyribonucleotide d-[CATGGCCATG]$_2$: Structural and dynamic aspects deduced from high field ^{1}H NMR studies. *Nucleic Acids Res. 16*, 665−685.

(13) Kielkopf, C. L., White, S., Szewczyk, J. W., Turner, M. T., Baird, E. E., Dervan, P. B., and Ress, D. C. (1998) A structural basis for recognition of A−T and T−A base pairs in the minor groove of B-DNA. *Science 282*, 111−117.

(14) White, S., Baird, E. E., and Dervan, P. B. (1997) Orientation preferences of pyrrole-imidazole polyamides in the minor groove of DNA. *J. Am. Chem. Soc. 119*, 8756−8765.

(15) Bhattacharya, S., and Thomas, M. (2000) DNA binding properties of novel distamycin analogues that lack the leading amide unit at the N-terminus. *Biochem. Biophys. Res. Commun. 267*, 139−144.

(16) Wiederholt, K., Rajur, S. B., Giuliano, J., Jr., O' Donnell, M. J., and Mclaughlin, L. W. (1996) DNA-tethered Hoechst groove-binding agents: Duplex stabilization and fluorescence characteristics. *J. Am. Chem. Soc. 118*, 7055−7062.

(17) Wiederholt, K., Rajur, S. B., O'Donnell, M. J., and Mclaughlin, L. W. (1997) Oligonucleotides tethering Hoechst 33258 derivatives: Effect of the conjugation site on duplex stabilization and fluorescence properties. *Bioconjugate Chem. 8*, 119−126.

(18) O'Donnell, M. J., Rajur, S. B., McLaughlin, L. W., Afonina, I., Kutyavin, I., Lukhtanov, E., Meyer, R. B., and Gamper, H. (1995) Synthesis and properties of a Hoechst-like minor-groove binding agent tethered to an oligodeoxynucleotide. *Bioorg. Med. Chem. 3*, 743−750.

(19) Kumar, S., Reed, M. W., Gamper Jr, H. B., Gorn, V. V., Lukhtanov, E. A., Foti, M., West, J., and Meyer, R. B., Jr. Schweitzer, B. I. (1998) Solution structure of a highly stable DNA duplex conjugated to a minor groove binder. *Nucleic Acids Res. 26*, 831−838.
(20) Lukhtanov, E. A., Podyminogin, M. A., Kutyavin, I. V., Meyer, R. B., and Gamper, H. (1996) Rapid and efficient hybridization-triggered cross-linking within a DNA duplex by an oligodeoxyribonucleotide bearing a conjugated cyclopropapyrroloindole. *Nucleic Acids Res. 24*, 683−687.
(21) Afonina, I., Kutyavin, I., Lukhtanov, E., Meyer, R. B., and Gamper, H. (1996) Sequence-specific arrest of primer extension on single-stranded DNA by an oligonucleotide-minor groove binder conjugate. *Proc. Natl. Acad. Sci. U.S.A. 93*, 3199−3204.
(22) Robles, J., and McLaughlin, L. W. (1997) DNA triplex stabilization using a tethered minor groove binding Hoechst 33258 analogue. *J. Am. Chem. Soc. 119*, 6014−6021.
(23) Rajur, S. B., Robles, J., Wiederholt, K., Kuimelis, R. G., and McLaughlin, L. W. (1997) Hoechst 33258 tethered by a hexa(ethylene glycol) linker to the 5′-termini of oligodeoxynucleotide 15-mers: duplex stabilization and fluorescence properties. *J. Org. Chem. 62*, 523−529.
(24) Sinyakov, A. N., Lokhov, S. G., Kutyavin, I. V., Gamper, H. B., and Meyer, R. B. (1995) Exceptional and selective stabilization of A−T rich DNA. DNA Duplexes by *N*-methylpyrrole carboxamide peptides Conjugated to oligodeoxynucleotides. *J. Am. Chem. Soc. 117*, 4995−4996.
(25) Szewczyk, J. W., Baird, E. E., and Dervan, P. B. (1996) Cooperative triple-helix formation via a minor groove dimerization domain. *J. Am. Chem. Soc. 118*, 6778−6779.
(26) Szewczyk, J. W., Baird, E. E., and Dervan, P. B. (1996) Sequence-specific recognition of DNA by a major and minor groove binding ligand. *Angew. Chem., Int. Ed. Engl. 35*, 1487−1489.
(27) Tam, J. P., Xu, J., and Eom, K. D. (2001) Methods and strategies of peptide ligation. *Biopolymers 60*, 194−205.
(28) Liu, C. F., and Tam, J. P. (1994) Peptide segment ligation strategy without use of protecting groups. *Proc. Natl. Acad. Sci. U.S.A. 91*, 6584−6588.
(29) Zhao, Y., Kent, S. B., and Chait, B. T. (1997) Rapid, sensitive structure analysis of oligosaccharides. *Proc. Natl. Acad. Sci. U.S.A. 94*, 1629−1633.
(30) Cervigny, S. E., Dumy, P., and Mutter, M. (1996) Synthesis of glycopeptides and lipopeptides by chemoselective ligation. *Angew. Chem., Int. Ed. Engl. 35*, 1230−1232.
(31) Peri, F., Dumy, P., and Mutter, M. (1998) Chemo- and stereoselective glycosylation of hydroxylamino derivatives: A versatile approach to glycoconjugates. *Tetrahedron 54*, 12269−12278.
(32) Forget, D., Boturyn, D., Defrancq, E., Lhomme, J., and Dumy, P. (2001) Highly Efficient Synthesis of Peptide−Oligonucleotide Conjugates: Chemoselective Oxime and Thiazolidine Formation. *Chem. Eur. J. 7*, 3976−3983.
(33) Zatsepin, T. S., Stetsenko, D. A., Arzumanov, A. A., Romanova, E. A., Gait, M. J., and Oretskaya, T. S. (2002) Synthesis of Peptide−Oligonucleotide Conjugates with Single and Multiple Peptides Attached to 2′-Aldehydes through Thiazolidine, Oxime, and Hydrazine Linkages. *Bioconjugate Chem. 13*, 822-830.
(34) Neuner, P., Gallo, P., Orsatti, L., Fontana, L., and Monaci, P. (2003) An Efficient and Versatile Synthesis of BisPNA-Peptide Conjugates Based on Chemoselective Oxime Formation. *Bioconjugate Chem. 14*, 276−281.
(35) Thomas, M., Vashney, U., and Bhattacharya, S. (2002) Distamycin analogues without leading amide at their N-termini-comparative binding properties to AT- and GC-rich DNA sequences. *Eur. J. Org. Chem*. 3604−3615.
(36) Bhattacharya, S., and Thomas, M. (2000) Facile synthesis of oligopeptide distamycin analogues devoid of hydrogen bond donors or acceptors at the N-terminus: sequence-specific duplex DNA binding as a function of peptide chain length. *Tetrahedron Lett. 41*, 5571−5575.
(37) Zimmer, C., Wahnert. (1986) Nonintercalating DNA-binding ligands: specificity of the interaction and their use as tools in biophysical, biochemical and biological investigations of the genetic material. *Prog. Biophys. Mol. Biol. 47*, 31−112.
(38) Wemmer, D. E., Fagan, P., and Pelton, J. G. (1990) Molecular Basis of specificity in nucleic acid−drug interaction, in *Proceedings of the 23rd Jerusalem Symposium on Quantum Chemistry and Biochemistry* (Pullman, B., and Jortner, J., Eds.) pp 95−101, Kluwer Academic Publishers, New York.
(39) Burckhardt, G., Zimmer, Ch., and Baguley, B. (1987) Binding of nonintercalative antitumor drugs to DNA-polymers: structural effects of bisquaternary ammonium heterocycles. *J. Biomol. Struct. Dyn. 4*, 815−820.
(40) Saenger. W. (1984) *Principles of Nucleic Acid Structure* (Canter, C. R., Ed.) Springer-Verlag, New York.
(41) Ivanov, V. I., Minchenkova, L. E., Schyolkina, A. K., Poletayer, A. I. (1973) Different conformation of double stranded nucleic acid in solution as revealed by circular dichroism. *Biopolymers 12*, 89−110.
(42) Record, M. T., Jr. (1975) Effects of Na^+ and Mg^{2+} ions on the helix-coil transition of DNA. *Biopolymers 14*, 2137−2158.
(43) Manning, G. S. (1978) The molecular theory of polyelectrolyte solutions with applications to the electrostatic properties of polynucleotides. *Q. Rev. Biophys. 11*, 179−246.
(44) Record, M. T., Jr., Anderson, C. F., and Lohman, T. M. (1978) Thermodynamic analysis of ion effects on the binding and conformational equilibria of proteins and nucleic acids: the roles of ion association or release, screening, and ion effects on water activity. *Q. Rev. Biophys. 11*, 103−178.
(45) Friedman, A. G., and Richard, Manning Gerald. (1984) Polyelectrolyte effects on site-binding equilibria with application to the intercalation of drugs into DNA. *Biopolymers 23*, 2671−2674.
(46) Misra, V. K., Sharp, K. A., Friedman, R. A., and Honig, B. (1995) Salt Dependence of Calicheamicin-DNA site-specific interactions. *Biochemistry 34*, 1001−1010.
(47) Krishnamurthy, G., Brenowitz, M. D., and Ellestad, G. A. (1994) Salt effects on ligand-DNA binding. minor groove binding antibiotics. *J. Mol. Biol. 238*, 245−263.
(48) Zimmer, C., and Luck, G. (1972) Stability and dissociation of the DNA complexes with distamycin A and netropsin in the presence of organic solvents, urea and high salt concentration. *Biochim. Biophys. Acta 287*, 376−385.
(49) Luck, G., Zimmer, C., Reinert, K. E., and Arcamone, F. (1977) Specific interaction of distamycin A and its analogues with (A.T) rich and (G.C) rich duplex regions of DNA and deoxypolynucleotide. *Nucleic Acids Res. 4*, 2655−2670.
(50) Thomas, M., Rao, A. R., Vashney, U., and Bhattacharya, S. (2001) Unusual DNA binding exhibited by synthetic distamycin analogues lacking the *N*-terminal amide unit under high salt conditions. *J. Biomol. Struct. Dyn. 18*, 858−871.
(51) Loontiens, F. G., Regenfuss, P., Zechel, A., Dumortier, L., and Clegg, R. M. (1990) Binding characteristics of Hoechst 33258 with calf thymus DNA, poly[d(A−T)] and d(CCGGAATTCCGG): multiple stoichiometries and determination of tight binding with a wide spectrum of site affinities. *Biochemistry 29*, 9029−9039.
(52) Gaugain, B., Barbet, J., Capelle, N., Roques, B. P., and Le Pecq, J. B. (1978) DNA bifunctional intercalators. 2. Fluorescence properties and DNA binding interaction of an ethidium homodimer and an acridine ethidium heterodimer. *Biochemistry 17*, 5078−5088.
(53) Chen, Y. H., and Lown, J. W. (1994) A New DNA Minor Groove Binding Motif: Cross-Linked Lexitropsins. *J. Am. Chem. Soc. 116*, 6995−7005.
(54) Pelton, J. G., andWemmer D. E. (1989) Structural characterization of a 2:1 distamycin A.d(CGCAAATTGGC) complex by two-dimensional NMR. *Proc. Natl. Acad. Sci. U.S.A. 86*, 5723−5727.
(55) Boturyn, D., Boudali, A., Constant, J. F., Defrancq, Eric., and Lhomme, J. (1997) Synthesis of fluorescent probes for the detection of abasic sites in DNA. *Tetrahedron 53*, 5485−5492.

BC0341730

Promotion of Peptide Antimicrobial Activity by Fatty Acid Conjugation

Alexander F. Chu-Kung,[†] Kristen N. Bozzelli,[†] Nathan A. Lockwood,[‡] Judith R. Haseman,[§] Kevin H. Mayo,[§] and Matthew V. Tirrell*[,†]

Department of Chemical Engineering, University of California, Santa Barbara, Santa Barbara, California 93106, Department of Chemical Engineering and Materials Science, University of Minnesota, Minneapolis, Minnesota 55455, and Department of Biochemistry, Molecular Biology and Biophysics, University of Minnesota, Minneapolis, Minnesota 55455. Received September 3, 2003; Revised Manuscript Received February 3, 2004

Three peptides, YGAA[KKAAKAA]$_2$ (AKK), KLFKRHLKWKII (SC4), and YG[AKAKAAKA]$_2$ (KAK), were conjugated with lauric acid and tested for the effect on their structure, antibacterial activity, and eukaryotic cell toxicity. The conjugated AKK and SC4 peptides showed increased antimicrobial activity relative to unconjugated peptides, but the conjugated KAK peptide did not. The circular dichroism spectrum of AKK showed a significantly larger increase in its α-helical content in the conjugated form than peptide KAK in a solution containing phosphatidylethanolamine/phosphotidylglycerol vesicles, which mimics bacterial membranes. The KAK and AKK peptides and their corresponding fatty acid conjugates showed little change in their structure in the presence of phosphatidylcholine vesicles, which mimic the cell membrane of eukaryotic cells. The hemolytic activity of the KAK and AKK peptides and conjugates was low. However, the SC4 fatty acid conjugate showed a large increase in hemolytic activity and a corresponding increase in helical content in the presence of phosphatidylcholine vesicles. These results support the model of antimicrobial peptide hemolytic and antimicrobial activity being linked to changes in secondary structure as the peptides interact with lipid membranes. Fatty acid conjugation may improve the usefulness of peptides as antimicrobial agents by enhancing their ability to form secondary structures upon interacting with the bacterial membranes.

INTRODUCTION

Multicellular organisms produce a wide variety of antimicrobial peptides, suggesting that they play a crucial role in innate immunity (*1*). Antimicrobial peptides are secreted constantly at low levels to prevent infection, but local production can be increased in response to an infection (*1*). The peptides are cationic, which allows them to preferentially target the negatively charged cell membranes of prokaryotes such as bacteria. Eukaryotic cells have a different lipid composition in the outer leaflet of their cell membranes, resulting in a zwitterionic surface that is less attractive to the peptides. This difference between eukaryotic and prokaryotic membranes can be utilized effectively to target many pathogens, since major changes to their membrane composition would be necessary to develop resistance (*1*). As a result, efforts are being made to develop antimicrobial peptides into drugs that will retain their effectiveness against pathogens, especially against those strains of bacteria that have already become multiple drug-resistant.

* Corresponding author: Matthew Tirrell, Department of Chemical Engineering, University of California Santa Barbara, Santa Barbara, CA 93105. Phone: (805) 893-3141. E-mail: tirrell@engineering.ucsb.edu.

[†] University of California.

[‡] Department of Chemical Engineering and Materials Science, University of Minnesota.

[§] Department of Biochemistry, Molecular Biology and Biophysics, University of Minnesota.

Antimicrobial peptides share two common features: an overall positive charge and the ability to assume a three-dimensional structure with distinct hydrophobic and hydrophilic faces, called an amphipathic structure (*2*). Despite these common features there is very little sequence conservation between antimicrobial peptides. One of the most common classes of antimicrobial peptides are linear peptides that adopt an α-helical amphipathic structure (*2*). The mode of action of this class of peptides, which includes magainins (*3*, *4*), cecropins (*5*, *6*), and mellitins (*4*, *7*) have been extensively studied. The currently accepted model for the mechanism of action of helical antimicrobial peptides involves peptides that are typically unfolded in solution but fold in the presence of membranes to form an amphipathic structure (*8*, *9*). The formation of an amphipathic structure seems to be required for membrane binding and lytic activity (*2*, *10*). When the concentration of peptide bound to the membrane reaches a critical concentration, the peptides either insert into the membrane to form pores, or destabilize the membrane by disrupting the membrane curvature (*11*).

Although they are effective antimicrobial agents in vitro, antimicrobial peptides require high doses to be effective when administered systemically, so much so that toxicity to the host becomes an issue (*12*). Clinical use of antimicrobial peptides requires improving efficacy without also increasing their toxicity to eukaryotic cells.

Some natural antimicrobial peptides, such as the polymyxin (*13*) and lipopetaibols (*14*) are coupled to fatty acid tails. Removal of the fatty acid tail decreases the

10.1021/bc0341573 CCC: $27.50 © 2004 American Chemical Society
Published on Web 05/04/2004

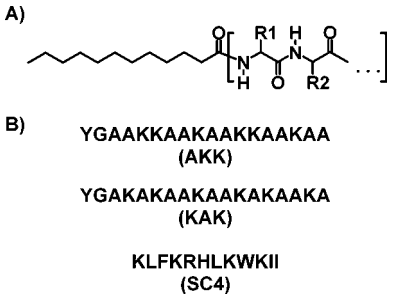


Figure 1. (A) Chemical structure of a fatty acid-conjugated peptide. The portion within the square brackets represents the two N-terminal amino acids of the peptide. (B) Sequence of the AKK, KAK, and SC4 peptides starting with the N-terminus. SC4 has an amidated C-terminus.

antimicrobial activity of polymyxin (*15*), demonstrating that it was intimately linked to the peptide activity. This has inspired attempts to increase antimicrobial activity by conjugating naturally occurring antimicrobial peptides with fatty acid tails (*16*−*18*). The effect of fatty acid tails on antifungal activity (*19*) and antiprotozoal activity (*20*) has also been studied. Work in our group (*21*−*23*), and in a group of our collaborators (*24*), has shown that addition of hydrocarbon tails to short peptides, to form peptide amphiphiles, can promote the formation of secondary structure. Since formation of secondary structure appears to be requisite for activity in antimicrobial peptides, we conjecture that fatty acid conjugation will increase activity by facilitating the formation of secondary structure.

We have conjugated three peptides to lauric acid to study the effect of fatty acid tail addition on peptide secondary structure as well as the correlation between structure and antimicrobial activity (Figure 1). Peptide AKK is based on the sequence of a previously studied synthetic leucine-lysine antimicrobial peptide (*25*). This peptide segregates its hydrophobic and hydrophilic amino acids into distinct regions on the helical wheel diagram (Figure 2). Peptide KAK is a reordering of the peptide AKK with the same amino acid composition and is based on a sequence shown to form nonamphipathic helices (*26*). Peptide SC4 is a naturally derived, α-helical antimicrobial peptide that has antimicrobial activity in the micromolar range (*27*). The helical wheel diagram of SC4 suggests a distinct hydrophilic face and a strongly hydrophobic face. All three peptides were coupled with lauric acid to form peptide amphiphiles, C12-AKK, C12-KAK, and C12-SC4. The structure of these peptides and peptide amphiphiles was studied in aqueous buffer, in the presence of vesicles composed of phosphatidylcholine (zwitterionic) or in the presence of vesicles composed of phosphatidylethanolamine mixed with phosphatidylglycerol (anionic). The peptide and peptide amphiphiles were further tested for their ability to kill bacteria, destabilize the inner membrane of Gram-negative bacteria, and lyse human red blood cells. We also observed the aggregation state of peptide amphiphiles in solution.

MATERIALS AND METHODS

Materials. Peptides AKK and KAK were synthesized by Synpep Corporation. Peptide SC4 was prepared by the Microchemical Facility at the University of Minnesota. *N*-Hydrobenzotriazole (HOBt) and 2-(1*H*-benzotriazole-1yl)1,1,3,3-tetramethyluronium hexafluorophosphate (HBTU) were purchased from Nova Biochemem. 1,2-Dilauroyl-*sn*-glycero-3-phosphocholine (DLPC), 1,2-dilauroyl-*sn*-glycero-3-phospoethanolamine (DLPE), and 1,2-dilauroyl-*sn*-glycero-3-phospoglycerol (DLPG) were purchased from Avanti Polar Lipids. All other chemical reagents were purchased through Sigma-Aldrich. Bacteria strains used to determine antimicrobial activity are *Escherichia coli* DH5α and ML-35 and *Staphylococcus epidermidis* (ATCC#12228). *E. coli* ML-35 was also used to determine cell membrane permeability.

Peptide Amphiphile Synthesis. Resin-bound peptide was received from either the Microchemical Facility at University of Minnesota or Synpep Corporation. Resin-bound peptide was deprotected with 20 vol % piperidine in dimethyl formaldehyde (DMF) for 2 h. Following deprotection, the resin-bound peptide was washed three times with DMF and then coupled to lauric acid using a 4-fold molar excess of HTBU, HOBt, *N*,*N*′-diisopropylethylamine, and lauric acid. The peptide amphiphile was then cleaved, purified, and characterized according to the method below.

Peptide Cleavage and Purification. AKK, KAK, C12-AKK, and C12-KAK were cleaved using a mixture of 95/5 vol % trifloroacetic acid (TFA)/water solution and precipitated in cold methyl *tert*-butyl ether. SC4 and C12-SC4 were cleaved a mixture of 82.5 vol % TFA, 5 vol % thioanisole, 5 vol % phenol, 5 vol % water, and 2.5 vol % ethanedithiol and then precipitated in cold methyl-*tert*-butyl-ether. Peptides were purified by reverse phase HPLC on a Vydac C4 column using 99.9/0.1 vol % water/TFA and 99.9/0.1 vol % acetonitrile/TFA as the mobile phases. The samples were lyophilized and then analyzed for molecular mass using a Thermo Bioanalysis MALDI-TOF system.

Minimum Bactericidal Concentration (MBC) Determination. Overnight cultures of test bacteria, either Gram-negative *E. coli* (strains DH5α or ML-35) or Gram-positive *S. epidermidis* (ATCC#12228), were grown at 37 °C in tryptic soy broth (TSB) for at least 18 h. The following day, subcultures were prepared by diluting the overnight cultures 1:100 in TSB. The subcultures were grown to log phase (OD_{600} of 0.5) and then diluted to a concentration of 1×10^5 to 1×10^6 colony forming units (CFU)/mL. A stock solution of test peptide was prepared at a concentration of 1 mg/mL in Millipore water to avoid aggregation. The stock peptide concentration was verified by amino acid analysis performed at the molecular structure facility at University of California—Davis. Test

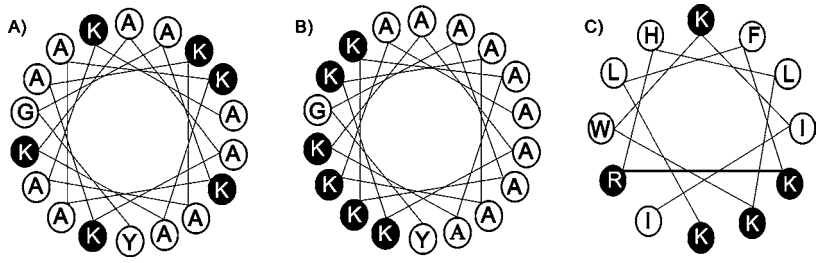


Figure 2. Helical wheel diagram of peptides (A) KAK (B) AKK and (C) SC4. The black filled circles are charged amino acids.

peptide solutions were added to polypropylene tubes and diluted with TSB to the desired concentration. The sample tubes were then inoculated with a bacterial stock solution to a final bacteria concentration of 1×10^4 to 1×10^5 CFU/mL. After incubation for 18 h at 37 °C, 50 μL aliquots were plated out and grown overnight. The MBC was taken as the lowest concentration where no colonies grew.

Hemolysis. Fresh human red blood cells were centrifuged and washed three times with phosphate-buffered saline (PBS). The red blood cells were diluted to a concentration of 0.4 vol % in PBS and placed in Eppendorf tubes. Peptide or peptide amphiphile was added at various concentrations, and the samples were incubated for 1 h at 37 °C. The samples were then centrifuged to sediment the intact red blood cells. Hemolytic activity was determined by measuring the UV absorbance at 414 nm. One hundred percent hemolysis was determined by addition of 1 vol % Triton-X100. The percentage of hemolysis was calculated as follows:

$$\% \text{ hemolysis} = 100(A_{414} \text{ with peptide} - A_{414} \text{ in plain PBS})/(A_{414} \text{ in Triton-X100} - A_{414} \text{ in plain PBS})$$

Vesicle Preparation. A chloroform solution of lipids, either 70/30 wt % DLPE/DLPG or DLPC, was dried under nitrogen until a thin film was formed. The film was then further dried under vacuum for at least 12 h. The lipids were dispersed in 10 mM sodium phosphate buffer, pH 7.4, to a concentration of 2.4 mM. The solution was then extruded through a 100 nm Millipore polycarbonate filter five times. Vesicle size was confirmed to be approximately 100 nm using dynamic light scattering. Henceforth, vesicles prepared with phosphatidylcholine are referred to as PC, and vesicles prepared with phosphatidylethanolamine and phosphatidylglycerol mixture are referred to as PE/PG.

Circular Dichroism. Circular dichroism spectra were recorded on an Olis-RSM CD with a 5 mm quartz cell. Data reported are an average of three scans. Spectra were recorded at 37 °C in 10 mM sodium phosphate buffer, pH 7.4, with a peptide concentration of 0.02 mM. Spectra were also recorded in the presence of either PE/PG or PC vesicles at a vesicle concentration of 0.3 mM. To estimate secondary structure contribution, a least-squares fit was performed using a linear combination of standard α-helix and random coil spectra (*28*).

Membrane Permeability. *E. coli* inner membrane permeability was determined by the ability of the peptide or peptide amphiphile to unmask β-galactosidase activity using ONPG (*o*-nitrophenyl-β-D-galactopyraniside) as a substrate (*29*). *E. coli* ML-35 produces the enzyme β-galactosidase, which hydrolyzes the colorless substrate ONPG to yellow *o*-nitrophenol. ONPG cannot cross an intact bacterial membrane, so the rate of hydrolysis of ONPG can be related to the rate of permeabilization of the bacterial inner membrane. Logarithmic phase *E. coli* ML-35 was centrifuged, and the resulting pellet was washed three times in 10 mM sodium phosphate buffer, pH 7.4, containing 100 mM NaCl and resuspended to a concentration of 1×10^8 CFU/mL in the same buffer. Solutions of peptide and ONPG were prepared in the same buffer, and bacteria solution was added to a final concentration of 0.02 mM peptide, 1.5 mM ONPG, and 1×10^7 CFU/mL *E. coli*. The production of *o*-nitrophenol was measured over time by UV absorbance at 420 nm.

Aggregation Assay. The aggregation state of the peptide amphiphiles was determined according to the pyrene solubilization method presented by Kim and coworkers (*30*). Pyrene is a polycyclic aromatic hydrocarbon with low solubility in aqueous solutions. Pyrene can be solubilized within the hydrophobic core of micelles providing a method to test for the presence of micelles. A test peptide dissolved in 10 mM sodium phosphate buffer, pH 7.4, containing 100 mM NaCl was added to an excess of pyrene at various concentrations. The suspension was sonicated for at least 8 h and then centrifuged. The supernatant was added to a 50 mM solution of sodium dodecyl sulfate, and the absorbance at 336 nm was recorded.

Table 1. Bactericidal Activities of AKK, KAK, SC4, C12-AKK, C12-KAK, and C12-SC4. All MBC Values Are ± 2 μM

	MBC (μM)		
	E. coli DH5α	*E. coli* ML-35	*S. epidermidis* ATCC 12228
AKK	>65	>65	>65
KAK	>65	>65	>65
SC4	17	34	48
C12-AKK	11	11	30
C12-KAK	>65	>65	>65
C12−SC4	1	4	2

RESULTS

Bactericidal activities of peptides AKK, KAK, SC4 and the peptide amphiphiles C12-AKK, C12-KAK, and C12-SC4 were measured against two strains of the Gram-negative bacteria *E. coli* (ML-35 and DH5α) and one strain of the Gram-positive bacteria S. epidermidis (ATCC#12228) (Table 1). Among the unmodified peptides only SC4 had an MBC below 65 μM, which was the highest concentration studied. The MBC of C12-SC4 was between 9- and 20-fold lower than that of SC4, indicating that fatty acid conjugation increased antimicrobial activity. C12-AKK was moderately antimicrobial. Neither KAK nor C12-KAK showed bactericidal activity in this assay.

The ability of the peptides and peptide amphiphiles to permeabilize the cytoplasmic membranes of *E. coli* ML-35 was assessed. As expected, both C12-SC4 and C12-AKK rapidly destabilized the target membrane (Figure 3A). SC4, which had moderate antimicrobial activity as measured by MBC tests, showed low membrane permeabilization activity. This result implies that SC4 may kill bacteria by another mechanism in addition to destabilization of bacterial membranes. AKK and C12-KAK showed moderate rates of ONPG hydrolysis, whereas KAK showed the lowest rate.

The toxicities of the peptides and peptide amphiphiles to eukaryotic cells were tested by their ability to lyse human red blood cells (Figure 3B). C12-KAK had no detectable hemolytic activity within the concentrations studied. AKK, KAK, and C12-AKK showed no hemolytic activity up to concentrations of 500 μM, and only exhibited mild (<15%) hemolysis at 500 μM. SC4 showed mild (<15%) hemolytic activity at 3 μM that increased slightly over the range of concentrations tested. The hemolytic activity of C12-SC4 was low at 0.3 μM but rapidly increased to over 90% hemolysis at concentrations of 18 μM. However, when tested against endothelial cells neither SC4 nor C12-SC4 demonstrate lytic activity up to 1 mM concentrations (data not shown).

Circular dichroism was used to assess the structure of the peptide and peptide amphiphiles in various environments (Figure 4). The resulting spectra were fit to evaluate the helical content in each environment (Table

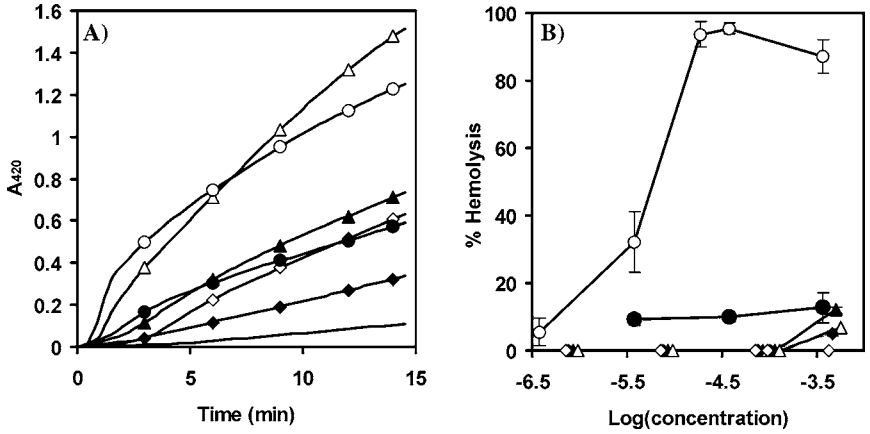


Figure 3. (A) Rate of ONPG hydrolysis of peptides SC4 (●), AKK (▲), and KAK (◆) as well as peptide amphiphiles C12-SC4 (○), C12-AKK (△), and C12-KAK (◇). The unmarked line is the baseline (no peptide added). (B) Hemolytic activity as a function of concentration for the same peptide and peptide amphiphiles (the same symbols are used).

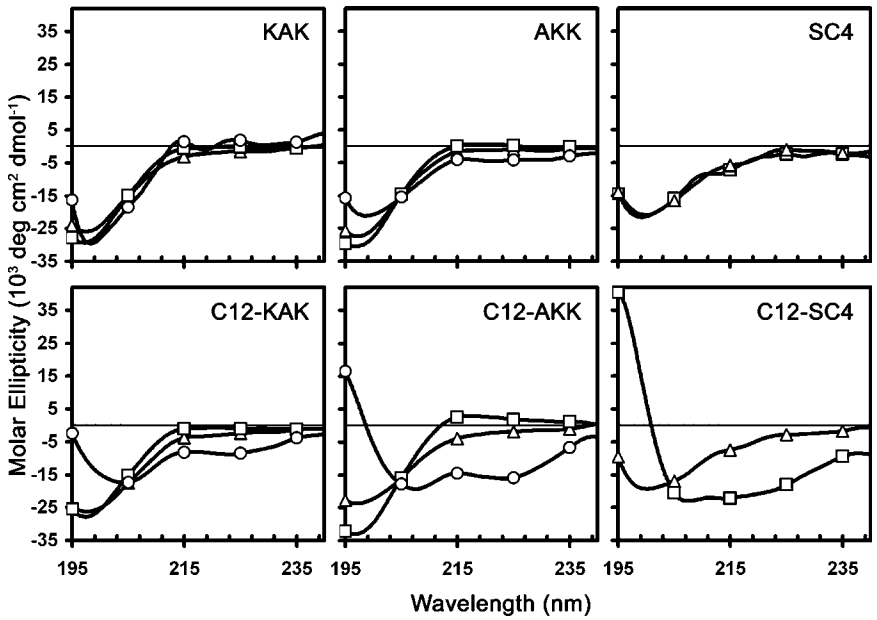


Figure 4. CD traces of peptides KAK, AKK, SC4, and peptide amphiphiles C12-KAK, C12-AKK, and C12-SC4. Experiments are conducted in sodium phosphate buffer (△) with the addition of DLPC vesicles (□) or DLPE/DLPG vesicles (○) (symbols are not data points but are solely to differentiate curves).

Table 2. Degree of Helix Formation in Sodium Phosphate Buffer Alone, with the Addition of PC Vesicles or PE/PG Vesicles

	buffer: % α-helix	PC: % α-helix	PE/PG: % α-helix
AKK	12	5	26
KAK	15	8	17
SC4	26	27	–
C12-AKK	17	0	73
C12-KAK	18	11	44
C12-SC4	32	100	–

2). AKK and C12-AKK had little α-helical character in benign sodium phosphate buffer solution or PC environments. In the presence of PE/PG vesicles, α-helical structure developed. The increase in structure with the addition of PE/PG vesicles was four times greater for C12-AKK than AKK. KAK and C12-KAK showed a similar relationship; neither had α-helical structure in sodium phosphate buffer or PC, but both showed an increase in structure in PE/PG. Again, the change in structure between the environments was greater in the peptide amphiphile than the unmodified peptide, but by less than 3-fold. KAK formed a precipitate with PE/PG vesicles, although we were still able to obtain a spectrum. Both SC4 and C12-SC4 formed precipitate in the presence of PE/PG, which prevented the collection of useable data. C12-SC4 did, however, show a significant increase in structure in PC, when compared to SC4 in PC or either sample in $NaPO_4$.

Aggregation of C12-AKK, C12-AKA, and C12-SC4 was probed by their ability to solublize the hydrophobic molecule pyrene. All the peptide amphiphiles were tested at concentrations from 1 μM to 250 μM in 10 μM sodium phosphate, 100 μM sodium chloride solutions. None of the molecules showed the ability to solubilize pyrene, implying the molecules are not aggregated below 250 μM (data not shown).

DISCUSSION

Membrane binding and membrane insertion, processes involved in the initial steps of cell lysis, are influenced by both hydrophobic and electrostatic interactions of antimicrobial peptides. Conjugation of lauric acid to antimicrobial peptides shifts the balance of electrostatic and hydrophobic forces. Increasing the hydrophobicity of the peptide can stabilize the membrane-bound secondary

structures requisite for antimicrobial activity. One potential drawback to fatty acid conjugation is that it may promote peptide folding in solution, which was previously shown to inhibit membrane binding (*31*). A second potential drawback is peptide self-assembly in solution which was previously shown to increase the potency of peptides toward zwitterionic membranes (*32*).

Fatty acid conjugation affects the structure and activity of peptides in an environment-specific manner. The high positive charge density on peptides and peptide amphiphiles tends to destabilize helical secondary structures. All the studied peptides are unstructured in solution; addition of a fatty acid tail is insufficient to overcome charge repulsion in that environment. Previous studies on peptide amphiphiles have shown stabilization of helical secondary structures in solution at concentrations above the critical micelle concentration, implying that conjugation of peptides to hydrocarbon tails facilitates cooperative folding in solution (*23*, *24*). Although all three peptide amphiphiles clearly show greater ability to fold, adhere, and destabilize bacterial membranes than their parent peptides, our pyrene solution tests indicate that the peptide amphiphiles have not formed micelles at these concentrations. These results are consistent with the low α-helical content of the samples in solution; one would expect to see more α-helical structure if the peptide amphiphiles were micellized. It is possible that some sort of peptide amphiphile self-organization takes place on the target membranes, where the local concentration of peptide amphiphile will be greater than in free solution. It is also believed that the insertion of peptides into a membrane is a cooperative process (*9*). The peptide−peptide interaction of peptide amphiphiles may be higher in the membrane-bound state, which would help the cooperative insertion into the membrane.

Activity, hemolytic or bactericidal, appears to be correlated with the degree of structure induced in the peptide by the presence of the appropriate lipids. Results of circular dichroism, MBC assays, and ONPG hydrolysis assays indicate that the interaction between the peptide and PE/PG membranes is enhanced through the addition of hydrocarbon tails. Thus, the hydrophobic attraction between lipid membranes and the antimicrobial peptides serves to promote folding of the peptide and binding to membranes independent of membrane charge. In fact, increasing the hydrophobicity of the antimicrobial peptides decreases their selectivity for bacterial membranes (*33*). Our findings are consistent with these trends. Peptide amphiphiles are more hydrophobic than their parent peptides and thus have increased interaction with membranes. This may account for the observed improved bactericidal activity for all the peptide amphiphiles compared to their simple peptide counterparts.

KAK is neither very hydrophobic, nor does it have a strong amphipathic character; thus, it is expected to be the least bactericidal of all three peptides. The addition of a lipid tail increases the hydrophobicity sufficiently that C12-KAK forms a partial helix in the presence of a bacterial membrane. Although the antimicrobial activity of C12-KAK was not detectable by MBC test, fatty acid conjugation improved the ability of KAK to permeablize *E. coli* membrane. While it is generally believed that amphipathic structure is required for wide-spectrum antimicrobial activity, studies show that some nonamphipathic peptides have mild bactericidal activity against Gram-negative bacteria (*34*). It is possible that such peptides fold into structures other than α-helices in order to maximize their amphipathicity and allow them to be mildly antimicrobial (*35*). This may also be the case with C12-KAK; we speculate that it may form a helical structure with either greater or fewer amino acids per turn than an α-helix.

AKK also lacks strongly hydrophobic amino acids, which accounts for its low antimicrobial activity. However, the hydrophobic residues create a wide hydrophobic face when the peptide is folded into an α-helix, giving AKK a greater potential for activity than KAK. We conjecture that the lipid tail of C12-AKK increases both its ability to fold and its attraction to membranes. The strong antimicrobial activity of the C12-AKK peptide amphiphile supports this conclusion. It is interesting that even the addition of the hydrophobic fatty acid tail does not cause this peptide to have significant hemolytic activity.

SC4 is the most hydrophobic of the peptides tested here and is the only peptide with measurable hemolytic activity. It has been observed that highly hydrophobic peptides tend to be more hemolytic (*36*). C12-SC4 shows a much higher degree of hemolytic activity than the SC4 peptide, which can be attributed to its even higher hydrophobicity.

In conclusion, our results indicate that peptide amphiphiles have increased formation of secondary structures in the presence of vesicles that mimic bacterial membranes. The increase in bactericidal activity accompanying coupling of the fatty acid tail clearly establishes a structure−activity relationship. Thus, the addition of fatty acid tails to form peptide amphiphiles may be a viable strategy to improve the antimicrobial activity of certain peptides. It is interesting that the improvement of bactericidal activity for C12-AKK is not accompanied by a concomitant increase in hemolytic activity as with C12-SC4. It is important to further explore the underlying reasons for the differences in the selectivity of these two antimicrobial peptides. It may elucidate other features that are important to the design of effective antimicrobial peptides with minimal toxicity to eukaryotes.

ACKNOWLEDGMENT

We would like to thank the group of Robert Hancock at the University of British Columbia for kindly providing us with *E. coli* ML-35. This work made use of MRL Central Facilities supported by the MRSEC Program of the National Science Foundation under award No. DMR00-80034. This work was supported by the National Institute of Health (award #HL62427).

LITERATURE CITED

(1) Zasloff, M. (2002) Antimicrobial peptides of multicellular organisms. *Nature 415*, 389−395.
(2) Giangaspero, A., Sandri, L., and Tossi, A. (2001) Amphipathic alpha helical antimicrobial peptides − A systematic study of the effects of structural and physical properties on biological activity. *Eur. J. Biochem. 268*, 5589−5600.
(3) Bevins, C. L., and Zasloff, M. (1990) Peptides from Frog-Skin. *Annu. Rev. Biochem. 59*, 395−414.
(4) Sansom, M. S. P. (1991) The Biophysics of Peptide Models of Ion Channels. *Prog. Biophys. Mol. Biol. 55*, 139−235.
(5) Fink, J., Boman, A., Boman, H. G., and Merrifield, R. B. (1989) Design, Synthesis and Antibacterial Activity of Cecropin-Like Model Peptides. *Int. J. Pept. Protein. Res. 33*, 412−421.
(6) Hultmark, D., Steiner, H., Rasmuson, T., and Boman, H. G. (1980) Insect Immunity − Purification and Properties of 3 Inducible Bactericidal Proteins from Hemolymph of Immunized Pupae of Hyalophora-Cecropia. *Eur. J. Biochem. 106*, 7−16.
(7) Haberman, E. (1972) Bee Wasp Venoms. *Science 177*, 314−&.

(8) Zhang, L. J., Rozek, A., and Hancock, R. E. W. (2001) Interaction of cationic antimicrobial peptides with model membranes. *J. Biol. Chem. 276*, 35714−35722.
(9) Hancock, R. E. W., and Rozek, A. (2002) Role of membranes in the activities of antimicrobial cationic peptides. *FEMS Microbiol. Lett. 206*, 143−149.
(10) Blondelle, S. E., and Houghten, R. A. (1992) Design of Model Amphipathic Peptides Having Potent Antimicrobial Activities. *Biochemistry 31*, 12688−12694.
(11) Shai, Y. (2002) Mode of action of membrane active antimicrobial peptides. *Biopolymers 66*, 236−248.
(12) Darveau, R. P., Cunningham, M. D., Seachord, C. L., Cassianoclough, L., Cosand, W. L., Blake, J., and Watkins, C. S. (1991) Beta-Lactam Antibiotics Potentiate Magainin-2 Antimicrobial Activity Invitro and Invivo. *Antimicrob. Agents Chemother. 35*, 1153−1159.
(13) Benedict, R. G., and Langlykke, A. F. (1947) Antibiotic Activity of Bacillus-Polymyxa. *J. Bacteriol. 54*, 24−25.
(14) Toniolo, C., Crisma, M., Formaggio, F., Peggion, C., Epand, R. F., and Epand, R. M. (2001) Lipopeptaibols, a novel family of membrane active, antimicrobial peptides. *Cell. Mol. Life Sci. 58*, 1179−1188.
(15) Tsubery, H., Ofek, I., Cohen, S., and Fridkin, M. (2001) *N*-terminal modifications of Polymyxin B nonapeptide and their effect on antibacterial activity. *Peptides 22*, 1675−1681.
(16) Mak, P., Pohl, J., Dubin, A., Reed, M. S., Bowers, S. E., Fallon, M. T., and Shafer, W. M. (2003) The increased bactericidal activity of a fatty acid-modified synthetic antimicrobial peptide of human cathepsin G correlates with its enhanced capacity to interact with model membranes. *Int. J. Antimicrob. Agents 21*, 13−19.
(17) Wakabayashi, H., Matsumoto, H., Hashimoto, K., Teraguchi, S., Takase, M., and Hayasawa, H. (1999) *N*-acylated and D enantiomer derivatives of a nonamer core peptide of lactoferricin B showing improved antimicrobial activity. *Antimicrob. Agents Chemother. 43*, 1267−1269.
(18) Majerle, A., Kidric, J., and Jerala, R. (2003) Enhancement of antibacterial and lipopolysaccharide binding activities of a human lactoferrin peptide fragment by the addition of acyl chain. *J. Antimicrob. Chemother. 51*, 1159−1165.
(19) Avrahami, D., and Shai, Y. (2002) Conjugation of a magainin analogue with lipophilic acids controls hydrophobicity, solution assembly, and cell selectivity. *Biochemistry 41*, 2254−2263.
(20) Chicharro, C., Granata, C., Lozano, R., Andreu, D., and Rivas, L. (2001) *N*-terminal fatty acid substitution increases the leishmanicidal activity of CA(1−7)M(2−9), a cecropin-melittin hybrid peptide. *Antimicrob. Agents Chemother. 45*, 2441−2449.
(21) Yu, Y. C., Tirrell, M., and Fields, G. B. (1998) Minimal lipidation stabilizes protein-like molecular architecture. *J. Am. Chem. Soc. 120*, 9979−9987.
(22) Yu, Y. C., Berndt, P., Tirrell, M., and Fields, G. B. (1996) Self-assembling amphiphiles for construction of protein molecular architecture. *J. Am. Chem. Soc. 118*, 12515−12520.
(23) Forns, P., Lauer-Fields, J. L., Gao, S., and Fields, G. B. (2000) Induction of protein-like molecular architecture by monoalkyl hydrocarbon chains. *Biopolymers 54*, 531−546.
(24) Fields, G. B., Lauer, J. L., Dori, Y., Forns, P., Yu, Y. C., and Tirrell, M. (1998) Proteinlike molecular architecture: Biomaterial applications for inducing cellular receptor binding and signal transduction. *Biopolymers 47*, 143−151.
(25) Haynie, S. L., Crum, G. A., and Doele, B. A. (1995) Antimicrobial Activities of Amphiphilic Peptides Covalently Bonded to a Water-Insoluble Resin. *Antimicrob. Agents Chemother. 39*, 301−307.
(26) Marqusee, S., Robbins, V. H., and Baldwin, R. L. (1989) Unusually Stable Helix Formation in Short Alanine-Based Peptides. *Proc. Natl. Acad. Sci. U.S.A. 86*, 5286−5290.
(27) Mayo, K. H., Haseman, J., Young, H. C., and Mayo, J. W. (2000) Structure−function relationships in novel peptide dodecamers with broad-spectrum bactericidal and endotoxin-neutralizing activities. *Biochem. J. 349*, 717−728.
(28) Reed, J., and Reed, T. A. (1997) A set of constructed type spectra for the practical estimation of peptide secondary structure from circular dichroism. *Anal. Biochem. 254*, 36−40.
(29) Lehrer, R. I., Barton, A., Daher, K. A., Harwig, S. S. L., Ganz, T., and Selsted, M. E. (1989) Interaction of Human Defensins with Escherichia-Coli − Mechanism of Bactericidal Activity. *J. Clin. Investig. 84*, 553−561.
(30) Kim, J. H., Domach, M. M., and Tilton, R. D. (1999) Pyrene micropartitioning and solubilization by sodium dodecyl sulfate complexes with poly(ethylene glycol). *J. Phys. Chem. B 103*, 10582−10590.
(31) Houston, M. E., Kondejewski, L. H., Karunaratne, D. N., Gough, M., Fidai, S., Hodges, R. S., and Hancock, R. E. W. (1998) Influence of preformed alpha-helix and alpha-helix induction on the activity of cationic antimicrobial peptides. *J. Pept. Res. 52*, 81−88.
(32) Sal-Man, N., Oren, Z., and Shai, Y. (2002) Preassembly of membrane-active peptides is an important factor in their selectivity toward target cells. *Biochemistry 41*, 11921−11930.
(33) Wieprecht, T., Dathe, M., Beyermann, M., Krause, E., Maloy, W. L., MacDonald, D. L., and Bienert, M. (1997) Peptide hydrophobicity controls the activity and selectivity of magainin 2 amide in interaction with membranes. *Biochemistry 36*, 6124−6132.
(34) Tossi, A., Sandri, L., and Giangaspero, A. (2000) Amphipathic, alpha-helical antimicrobial peptides. *Biopolymers 55*, 4−30.
(35) Oren, Z., Lerman, J. C., Gudmundsson, G. H., Agerberth, B., and Shai, Y. (1999) Structure and organization of the human antimicrobial peptide LL-37 in phospholipid membranes: relevance to the molecular basis for its noncell-selective activity. *Biochem. J. 341*, 501−513.
(36) Dathe, M., and Wieprecht, T. (1999) Structural features of helical antimicrobial peptides: their potential to modulate activity on model membranes and biological cells. *Biochim. Biophys. Acta 1462*, 71−87.

BC0341573

Design, Synthesis, and Evaluation of 5′-*S*-Aminoethyl-N^6-azidobenzyl-5′-thioadenosine Biotin Conjugate: A Bifunctional Photoaffinity Probe for the *es* Nucleoside Transporter

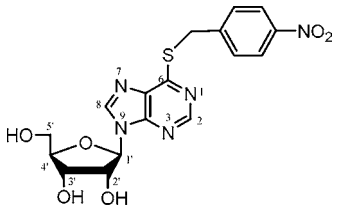
James K. Addo and John K. Buolamwini*

Department of Pharmaceutical Sciences, College of Pharmacy, University of Tennessee, Memphis, Tennessee 38163. Received September 11, 2003; Revised Manuscript Received March 12, 2004

A bifunctional biotinylated photoaffinity label for the nitrobenzylmercaptopurine riboside (NBMPR)-sensitive (*es*) nucleoside transporter (ENT1) has been synthesized and evaluated. This new probe, 5′-*S*-aminoethyladenosine-N^6-azidobenzyl-5′-thioadenosine biotin conjugate (SAEATA-14-biotin), exhibited high-affinity binding to the *es* transporter in K562 cells as determined by flow cytometry, with a K_i of 2.69 nM in competition against 5-(SAENTA)-x8-fluorescein. It also exhibited covalent linking to the *es* transporter in BeWo cell membranes upon UV irradiation. This new bifunctional probe is a potential tool for determining the amino acid residues involved in ligand binding at the NBMPR-binding site of the ENT1 nucleoside transporter, as well as for the purification of the transporter.

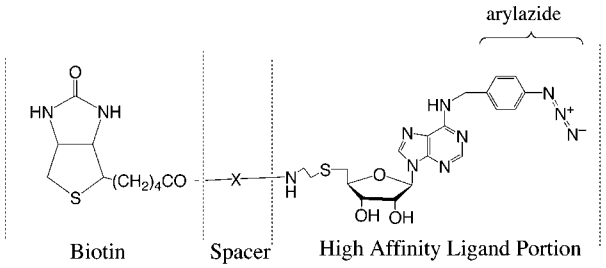
INTRODUCTION

Nucleoside transporters are integral membrane glycoproteins required for the cellular uptake of physiological nucleosides such as adenosine and their synthetic analogues. Two families of nucleoside transporters have been identified: (i) equilibrative (facilitated diffusion) transporters, ENTs, and (ii) concentrative (sodium ion-coupled) transporters, CNTs (*1*−*5*). The equilibrative transporters are found in most mammalian cells and tissues studied, whereas the concentrative transporters are limited to specialized epithelial tissues and some cultured cell lines. The ENT1 transporter also known as the *es* transporter is by far the predominant nucleoside transporter of most mammalian cells examined and can be distinguished from the other equilibrative transporter, ENT2, also known as *ei* transporter, by its high sensitivity to inhibition by S^6-(4-nitrobenzyl)mercaptopurine riboside (NBMPR, **1**). Inhibition of the *es* transporter by NBMPR arises from high-affinity binding (K_d 0.1−1.0 nM) (*6*). The *ei* transporter is at least 1000-fold resistant to inhibition by NBMPR (*4*, *7*).



1, NBMPR

Interest in nucleoside transporters has been on the increase because of their involvement in the efficacy of anticancer and antiviral nucleoside drugs, as well as their regulation of tissue adenosine levels and thereby modulation of its signal transduction functions in cardioprotection and neuroprotection. Thus, nucleoside transport inhibitors (NTIs) have potential therapeutic uses in several therapeutic areas including ischemic heart disease and stroke, cancer and viral chemotherapy, and the preservation of donor organs for transplantation (*8*). The known inhibitors are mostly unsuitable for clinical applications, and therefore novel inhibitors are needed. Several nucleoside transporters have been cloned (*9*), but structural biology studies of these transporters have been hampered by the lack of the appropriate chemical probes. Devising appropriate molecular probes for elucidation of the amino acid residues involved in inhibitor-binding will go a long way to promote these studies. In the absence of a 3D structure of the *es* transporter or its complex with an inhibitor, photoaffinity labeling offers a useful approach to identifying the amino acid residues involved in ligand binding. In this regard, NBMPR and its analogues, which bind with high affinity and high specificity to the ENT1 transporter, are excellent templates for designing affinity labels of this transporter. In this paper, we describe the design, synthesis, and evaluation of such an ENT1 transporter probe, a biotinylated azido analogue of NBMPR, termed SAEATA-x14-biotin (compound **2**).



2 (SAEATA-x14-biotin), bifunctional ENT1 photoaffinity label
Spacer X = $(NH(CH_2)_5CO)_2$

* Address correspondence to this author at Department of Pharmaceutical Sciences, College of Pharmacy, University of Tennessee Health Sciences Center, 847 Monroe Ave., Suite 327, Memphis, TN 38163. Phone (901) 448-7533. Fax (901) 448-6828. E-mail: jbuolamwini@utmem.edu.

10.1021/bc034165j CCC: $27.50 © 2004 American Chemical Society
Published on Web 05/04/2004

EXPERIMENTAL SECTION

Synthesis. Thin-layer chromatography (TLC) was conducted on silica gel F_{254} plates (Analtech). Compounds were visualized by UV light or 5% H_2SO_4 in EtOH spraying reagent. ^1H and ^{13}C spectra were recorded on Bruker ARX (500 MHz) instrument, using $CDCl_3$, CD_3OD, $(CD_3)_2SO$, or CD_3COCD_3 as solvents and tetramethylsilane (TMS) as internal standard. Flash column chromatography was performed on Fisher silica gel (170−400 mesh). Melting points were determined using a Fisher-Johns melting point apparatus and are reported uncorrected. Mass spectra were obtained on a Bruker-HP Esquire-LC mass spectrometer, and IR spectra with a Perkin-Elmer System 2000 FT-IR spectrometer. All solvents and reagents were bought from Sigma-Aldrich Chemical Co. and used without further purification, unless where specified. HPLC was performed on a GILSON Instrument with UV detection. Biotinylated SAENTA (SAENTA-x14-biotin, **3**) was prepared by reacting Biotin-xx SE (Molecular Probes, Eugene, OR) with SAENTA phthalhydrazide salt (*10*) in dimethylformamide (Buolamwini and Paterson, unpublished results). [^{3}H]NBMPR (23 Ci/mmol, 1 Ci = 37 GBq) was purchased from Moravek Biochemicals (Brea, CA). 5-(SAENTA)-x8-fluorescein was prepared as previously reported (*11*).

5′-*S*-(2-(6-(6-Biotinamidohexanoyl)aminohexanoyl)-aminoethyl)-*N*^{6}-(4-aminobenzyl)-5′-thioadenosine (4). A mixture of SAENTA-x14-biotin (**3**, 100 mg, 0.109 mmol), activated carbon (20.0 mg, G-60, 100 mesh), ferric chloride hexahydrate (10.00 mg, 0.036 mmol), and methanol (5 mL) was refluxed for 10 min with stirring. To this boiling mixture was added hydrazine hydrate (40 mg, 1.25 mmol, 99.1%) dropwise, and the mixture was stirred under reflux for an additional 12 h, cooled, and filtered, and the residue was washed with methanol (3 × 5 mL). The filtrate was evaporated to give a solid residue. The residue was recrystallized from EtOAc to give compound **4** as colorless crystals: 88 mg, 91% yield, mp 184−185 °C. ^1H NMR (500 MHz, $CDCl_3$) δ 1.166−2.022 (m), 2.484−2.571 (m), 2.782−3.316 (m), 3.98−4.01 (m), 4.08−4.14 (m), 4.26−4.31 (m), 4.511 (bs), 4.712 (bs), 5.33 (d, J = 6.0, 1H), 5.49 (d, J = 5.56 5.56, 1H), 5.88 (d, J = 5.56 Hz, 1H), 6.350 (s), 6.41 (s), 6.49 (d, J = 8.29 Hz, 1H), 7.01 (d, J = 8.29 Hz, 1H), 7.70−7.74 (m), 7.88−7.89 (m), 8.14−8.19 (m), 8.34 (bs), 9.39 (bs); IR (neat) ν_{max} (3255, 2933, 2340, 1623, 1541, 1245, 1036, 920 cm^{-1}. MS (ESI) m/z 915 $(M + H)^+$.

5′-*S*-(2-(6-(6-Biotinamidohexanoyl)aminohexanoyl)-aminoethyl)-*N*^{6}-(4-azidobenzyl)-5′-thioadenosine (2, SAEATA-x14-biotin). A solution of sodium nitrite (5.64 mg, 0.082 mmol) in cold water (0.20 mL) at 0 °C was made and added with stirring to a cold (0 °C to −5 °C) solution of compound **4** (65 mg, 0.074 mmol) in glacial acetic acid (0.5 mL). The mixture was then stirred at 0 °C for another 20 min. To the resulting solution of diazonium salt, at 0 °C, was added a solution of NaN_3 (5.33 mg, 0.082 mmol) in cold water (0.20 mL). The mixture was then allowed to stir at 0 °C for an additional 1.5 h in the dark. The reaction mixture was then evaporated to give a solid residue. H_2O (1 mL) was then added, and the reaction mixture was extracted with EtOAc (3 × 5 mL). The combined organic extracts were dried (anhydrous Na_2SO_4) and filtered. The solvent was evaporated in vacuo to give a crude solid residue. This residue was washed three times with H_2O (3 × 5 mL) and the solid obtained dried in vacuo and recrystallized in MeOH/EtOAc (1:1) to give the target compound **2** (57 mg, 85.20% yield): mp 115−116 °C. ^1H NMR (500 MHz, $CDCl_3$) δ 1.22− 2.11 (m), 1.18−2.02 (m), 2.54−3.17 (m), 3.92−4.11 (m), 4.15 (bs), 4.22−4.28 (m), 4.66−4.70 (m), 4.79−4.80 (m), 5.88 (d, J = 5.857, 1H), 7.036 (d, J = 8.785, 1H), 7.36 (d, J = 8.785 Hz, 1H) 8.19 (bs), 8.37 (s); IR (neat) ν_{max} 3303, 2925, 2854, 2363, *2110*, 1763, 1631, 1541, 1507, 1466, 1294, 1211, 1120, 1053 cm^{-1}. MS (ESI) m/z 910 $(M + H)^+$. The purity was checked by reversed phase HPLC using a C_{18} column and two different solvent systems: (1) methanol/acetonitrile (1:1 v/v) and (2) solvent methanol/water (4:1 v/v) (Fisher HPLC grade).

Cell Culture. K562 chronic myelogenous leukemia and BeWo choriocarcinoma cells were purchased from American Type Culture Collection (Rockville, MD). Stock cultures were grown in antibiotic-free growth media consisting of RPMI 1640 supplemented with 10% fetal bovine serum for K562 cells, or RPMI 1640 supplemented with 5% fetal bovine serum plus 5% Nuserum type IV for BeWo cells. Cultures were incubated at 37 °C in a humidified atmosphere containing 5% CO_2 in air.

Flow Cytometry. K562 suspension cells maintained in exponential growth (0.5×10^5 to 5×10^5 cells/mL) were used in flow cytometric evaluation of probe binding to the ENT1 (es) nucleoside transporter as previously described (*11*). Briefly, cells were washed once and suspended at 4×10^5 cells/mL in phosphate-buffered saline at pH 7.4 and incubated with 5-(SAENTA)-x8-fluorescein (25 nM) in the presence or absence of varying concentrations of test compounds at room temperature for 45 min. Flow cytometric measurements for cell-associated fluorescence were performed at the end of the incubation period with a FACSCalibur (Becton Dickinson, San Jose, CA) equipped with a 15 mW argon laser (Molecular Resources Flow Cytometry Facility, University of Tennessee Health Sciences Center). In each assay, 5000 cells were analyzed. The units of fluorescence were arbitrary mean channel numbers. Percentage (%) of control (*es* transporter-specific fluorescence in the presence of SAENTA-fluorescein without test compounds) was calculated for each sample by eq 1.

$$\% \text{ control} = \frac{(SF_s)}{(SF_f)} \times 100 \qquad (1)$$

where SF_s is the *es* transporter-specific fluorescence of test samples, and SF_f is the *es* transporter-specific fluorescence of the SAENTA-fluorescein ligand. The inhibition constant (K_i) values were calculated from the IC_{50} value obtained by nonlinear regression fitting of the concentration-effect curves using eq 2.

$$K_i = IC_{50}/(1 + [L]/K_L) \qquad (2)$$

where [L] and K_L are the concentration and the K_d value of the SAENTA-fluorescein ligand, respectively. The IC_{50} value was obtained by regression fitting to the data in Figure 1 using the Prism program (GraphPad, San Diego, CA).

BeWo Cell Membrane Preparation. BeWo cell membranes were prepared according to the protocol described in Boumah et al. (*12*). Cells were harvested by trypsinization and disrupted by sonication in the presence of a protease inhibitor (2 mM AEBSF, a water soluble analogue of the protease inhibitor PMSF). The lysates were fractionated in a 20% Percoll gradient and washed twice by centrifugation at 40000*g*, for 15 min at 4 °C in 50 mM Tris/HCl buffer (pH 7.4). Protein concentration was determined by the Lowry method (*13*).

Photolabeling. Membranes with 10−50 μg of protein were incubated with 100 nM of compound **2** in the

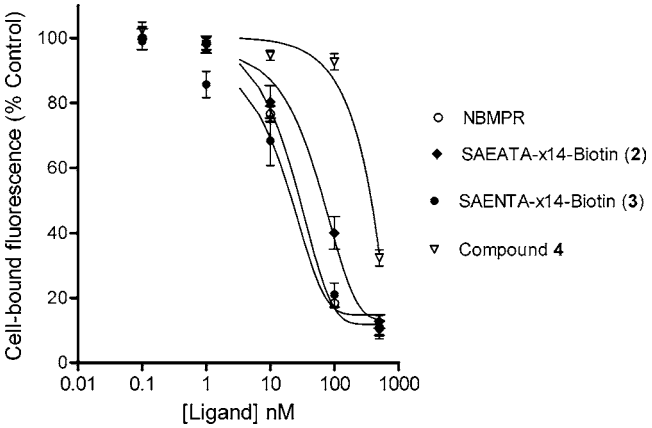


Figure 1. Flow cytometric analysis of the binding of nbmpr and biotinylated analogues to the *es* transporter of k562 leukemia cells. Cells were incubated with graded concentrations of test compounds in the presence of 25 nM 5-(SAENTA)-x8-flourescein at 22 °C for 45 min. Each data point represents the mean ± SEM for three different experiments.

presence or absence of 10 μM NBMPR in Tris/HCl buffer in the presence of AEBSF for 30 min at 22 °C, cooled to 4 °C, and then irradiated with shortwavelength UV light for 3−5 min at a distance of 3 cm. The reaction was stopped by addition of an equal volume of Tris buffer containing 12% trichloroacetic acid (TCA). The membranes were pelleted and washed twice with Tris/HCl containing TCA. For indirect determination of photo-cross-linking by compound **2**, the membranes were washed and used in [^{3}H]NBMPR binding as described below.

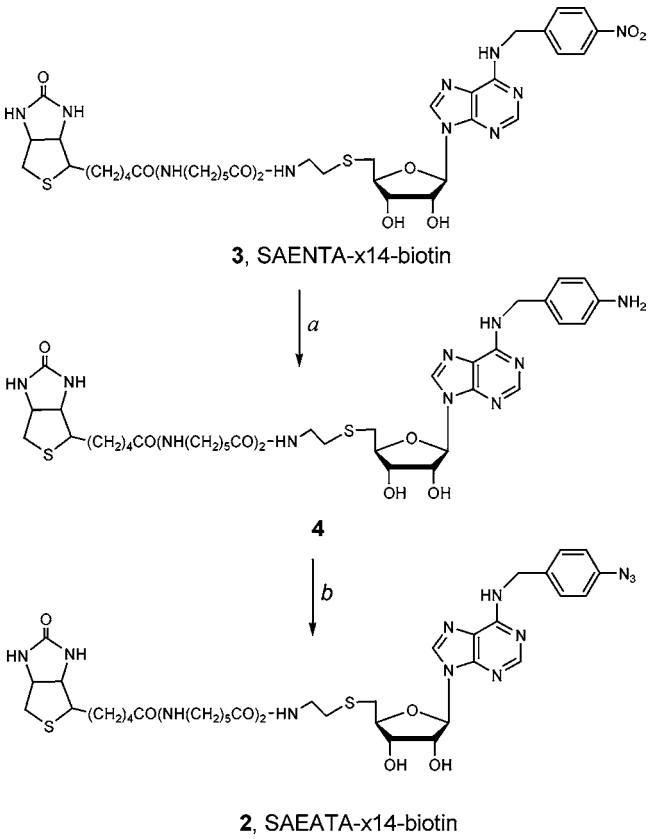
[^{3}H]NBMPR Binding to Membranes. Membrane samples containing 10 μg of protein each were incubated with [^{3}H]NBMPR (1.0 nM; 15 Ci/mmol) in binding medium (50 mM Tris/HCl, pH 7.4, 20 mM dithiothreitol) in the presence or absence of 10 μM nonradioactive NBMPR for 30 min at 22 °C. Bound and free [^{3}H]NBMPR were then separated from each other by rapid filtration with Whatman GF/B filters. The radioactivity that was retained on the filters, i.e., bound [^{3}H]NBMPR was measured by liquid scintillation counting.

Streptavidin Detection of Photo-Cross-Linked Compound 2. To detect photo-cross-linking of protein by SAEATA-x14-biotin (**2**), BeWo cell membranes (50 μg) photolabed with the probe were subjected to SDS−PAGE electrophoresis, after which the protein was electroblotted onto polyvinylidine fluoride membranes (Immobilon-P; Millipore, Bedford, MA). Membranes were blocked in BLOTTO (5% nonfat dried milk) in TBS-T: (20mM Tris-HCl, pH 7.6, 137mM NaCl, and 0.1% Tween-20) at 4 °C overnight. This was followed by incubation with horseradish peroxidase-conjugated streptavidin diluted in BLOTTO (0.5μg/mL) for 1 h. After three washes in TBS-T, the blot was treated with Enhanced ChemiLuminescence (ECL, Amersham) detection reagents as described by the manufacturer. Biotinylated proteins were visualized by exposure to X-ray film and development.

RESULTS AND DISCUSSION

Our bifunctional probe design took into consideration the following: (1) Experimental evidence shows that nucleoside analog *es* transporter inhibitors such as NBMPR do not require a free 5′-OH group on the ribose ring, and that with an appropriate spacer, the 5′-position of inhibitors is very tolerant of bulky substituents (*10*, *11*, *14*). For example, bulky fluorescein derivatives can be tethered to the 5′-position and still retain high affinity

Scheme 1. Synthetic Route to Compound 2[a]



[a] Reagents and conditions: (a) $NH_2NH_2.\cdot H_2O/FeCl_3\cdot 6H_2O$/activated carbon/MeOH/reflux; (b) (i) $NaNO_2$/aq AcOH, 0 °C, (ii) NaN_3, 0 °C.

binding with K_d values as low as 2 nM (*11*). Therefore, we decided to tether a biotin moiety via an appropriate spacer chain to the 5′-position of the nucleoside portion of the probe for avidin or streptavidin affinity purification and detection purposes. (2) The NO_2 group in NBMPR was replaced by an azido photoreactive group to use for photo-cross-linking to the transporter. The azidobenzyl moiety, like the nitrobenzyl moiety of NBMPR, affords high-affinity binding at the *es* transporter (*15*). Furthermore, *p*-azidobenzyladenosine (ABA) has been used successfully to photolabel the *es* transporter of human erythrocytes (*16*). Although NBMPR itself is a photolabeling agent, the radical species for covalent linking to the protein is produced by cleavage of the sulfur−benzyl bond (*17*), which means that before covalent linking, the high-affinity conferring nitrobenzyl group is lost. This is disadvantageous for specific labeling, because the loss of the nitrobenzyl moiety could cause a dissociation of the bound inhibitor (*18*) from the binding site prior to cross-linking with the protein, which increases the likelihood of labeling residues not involved in binding. Replacing the sulfur by NH prevents the loss of the benzyl portion upon irradiation and increases the likelihood of binding-site specific photo-cross-linking.

The synthesis of the probe followed Scheme 1 and began with the derivatizable high-affinity *es* transporter ligand 5′-*S*-(2-aminoethyl)-N^6-(4-nitrobenzyl)-5′-thioadenosine (SAENTA). In SAENTA, a 2-aminoethylthio ($H_2NCH_2CH_2S$-) has replaced the 5′-OH group to provide a handle for tethering a reporter or other group (*10*). Compound **3**, SAENTA-x14-biotin, was obtained by a procedure involving the reaction of the phthalhydrazide salt of SAENTA with (6-((6-((biotinoyl)amino)hexanoyl)-amino)hexanoic acid succinimydyl ester (biotin-xx, SE)

Table 1. K_i Values for Inhibition of SAENTA-fluor Binding to the *es* Transporter (ENT1) in K562 Cells

compound	K_i (nM)[a]
SAEATA-x14-biotin (**2**)	2.69 ± 0.36
SAENTA-biotin (**3**)	1.03 ± 0.40
4	14.99 ± 0.53
NBMPR	1.2 ± 0.22

[a] Data points are the mean ± standard deviation from three separate experiments.

in the presence of Et_3N to give this biotinylated derivative (Buolamwini and Paterson, unpublished, results). Scheme 1 was then followed for the rest of the synthesis. Reduction of the nitro group of compound **3** was effected by treatment with $FeCl_3/H_2N-NH_2 \cdot xH_2O$ in the presence of activated carbon in methanol to obtain the amino compound, **4**. Diazotization of compound **4** using aqueous $NaNO_2$ in acetic acid and subsequent displacement of the diazonium group with the azido group by treatment with NaN_3 yielded the target bifunctional photaffinity label, compound **2**.

Biological Evaluation. *Binding at the es Transporter.* The ability of this new bifunctional *es* transporter label to bind to the transporter was determined by a flow cytometric ligand-binding assay using a SAENTA-fluorescein conjugate, 5-(SAENTA)-x8-fluorecein (*11*) as the fluorescent *es* transporter competitive ligand. The results of the flow cytometric evaluation are presented in Figure 1, which shows potent concentration-dependent displacement of the competitive ligand by all the compounds but the amino compound (**4**), which is consistent with the known structure−activity relationship (*15*). The K_i values used to compare how tightly the ligands bound to the ENT1 transporter are presented in Table 1. These results indicate that the novel bifunctional photoaffinity label, compound **2**, has a high affinity for the ENT1 transporter (K_i 2.69 nM), which makes it suitable for photolabeling and probing the transporter.

Photolabeling. For the purpose of determining if compound **2** will cross-link at the NBMPR-binding site of the ENT1 transporter, cell membranes prepared from BeWo cells, known to express large numbers of ENT1 (*12*), were incubated with compound **2** in the absence or presence of the potent ENT1 inhibitor NBMPR, and the samples were irradiated with shortwave UV light. The membranes were then washed to get rid of noncovalently bound ligands and then used for [^{3}H]NBMPR specific binding analysis. The [^{3}H]NBMPR binding results for the irradiated and washed membranes are shown in Figure 2. They indicate that in the absence of the ENT1 competitive ligand NBMPR, compound **2** covalently bound to (cross-linked) the membranes and could not be completely washed off. In the samples that contained the NBMPR, cross-linking and covalent blocking of the NBMPR-binding site on ENT1 by compound **2** was inhibited. This demonstrates that the new photoaffinity probe can photo-cross-link ENT1 at the NBMPR binding site and will be a useful tool in identify amino acid residues at the NBMPR-binding site of the ENT1 (*es*) nucleoside transporter.

*Streptavidin Detection of Cross-Linked Compound **2**.* To demonstrate that the pendant biotin group of compound **2** can be detected and used as a handle in streptavidin affinity purification as well as probe detection, BeWo cell membranes were photolabeled with compound **2**, subjected to SDS−PAGE, blotted unto PVDF membranes, and probed with streptavidin horseradish peroxidase conjugate. The results shown in Figure 3 show that not only can compound **2** be used to photolabel amino acids at the NBMPR-binding site on the ENT1 transporter (Figure 2), but it can also be detected by binding it to streptavidin. Figure 3 confirms that the probe cross-links protein and suggests that compound **2** can be used as a bifunctional probe to cross-link the ENT1 transporter and be used for affinity isolation of ENT1 polypeptides. Efforts are underway to use this novel probe for photolabeling and identification of the amino acid residues of the ENT1 transporter involved in ligand binding, by mass spectrometric means similar to a recent characterization of the dexniguldipine binding site of P-glycoprotein (*19*).

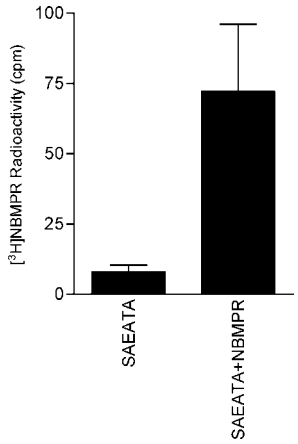


Figure 2. [^{3}H]NBMPR binding to BeWo membranes that were washed after incubation with test compounds followed by irradiation with UV light. Membranes were from samples incubated with 100 nM SAEATA-x14-biotin, samples incubated with 100 nM SAEATA-x14-biotin in the presence of 10 μM NBMPR. The data represent the mean and minimum and maximum values from two separate experiments.

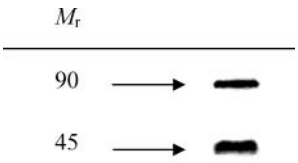


Figure 3. Streptavidin detection of compound **2** photocross-linked to BeWo cell membranes. BeWo cell membrane preparation (50 μg protein) irradiated with UV light was loaded onto 12% SDS-polyacrylamide gel and electrophoresis carried out. Protein was electroblotted unto polyvinylidine fluoride membranes (Immobilon-P; Millipore, Bedford, MA), blocked with 5% nonfat dried milk in TBS-T: (20 mM Tris-HCl, pH 7.6, 137 mM NaCl, and 0.1% Tween-20) at 4 °C overnight, followed by incubation with a horseradish peroxidase-conjugated streptavidin (0.5 μg/mL) in BLOTTO for 1 h. The membrane was washed in TBS-T, and treated with Enhanced ChemiLuminescence (ECL, Amersham) detection reagents as described by the manufacturer. Biotinylated proteins were visualized by exposure to X-ray film and development.

ACKNOWLEDGMENT

Financial support of this work came from the National Heart, Lung and Blood Institute, NIH, Grant No. HL 67479. Yaqin Zhang, Bing Chen, and Ja'Wanda Grant are credited for technical support.

LITERATURE CITED

(1) Plagemann, P. G. W., Wohlhueter, R. M., and Woffendin, C. (1988) Nucleoside and nucleobase transport in animal cells. *Biochim. Biophys. Acta 947*, 405−443.

(2) Gati, W. P., and Paterson, A. R. P. (1989) Nucleoside transport. In *The Red Cell Membrane: Structure, Function,*

and Clinical Implications (Agre, P., Parker, J. C., Eds.) pp 635−661, Marcel Dekker, New York.
(3) Belt, J. A., Marina, N. M., Phelps, D. A., and Crawford, C. R. (1993) Nucleoside transport in normal and neoplastic cells. *Adv. Enzyme Regul. 33*, 235−252.
(4) Cass, C. E. (1995) Nucleoside transport. In *Drug Transport in Antimicrobial and Anticancer Chemotherapy* (Georgopapadakou, N. H., Ed.) pp 403−451, Marcel Dekker, New York.
(5) Young, J. D., Cheeseman, C. I., Mackey, J. R., Cass, C. E., and Baldwin, S. A. (2000) Molecular mechanisms of nucleoside and nucleoside drug transport. In *Current Topics in Membranes* (Barrett, K. E., Donowitz, M., Eds.) pp 329−378, Vol. 50, Academic Press, San Diego, CA.
(6) Paterson, A. R. P., Jacobs, E. S., Harley, E. R., Fu, N.-W., Robins, M. J., and Cass, C. E. (1983) Inhibition of nucleoside transport. In *Regulatory Functions of Adenosine* (Berne, R. M., Rall, T. W., Rubio, R., Eds.) pp 203−220, Martinus, Nijhoff, The Hague,
(7) Thorn, J. A., and Jarvis, S. M. (1996) Adenosine transporters. *Gen. Pharmacol. 27*, 613−620.
(8) Buolamwini, J. K. (1997) Nucleoside transport inhibitors: structure−activity relationships, and potential therapeutic applications. *Curr. Med. Chem. 4*, 35−66.
(9) Cass, C. E., Young, J. D., and Baldwin, S. A. (1998) Recent advances in the molecular biology of nucleoside transporters of mammalian cells. *Biochem. Cell. Biol. 76*, 761−770.
(10) Agbanyo, F. R., Vijayalakshmi, D., Craik, J. D., Gati, W. P., McAdam, D. P., Asakura, J.-I., Robins, M. J., Paterson, A. R. P., and Cass, C. E. (1990) 5′-*S*-(2-Aminoethyl)-N^6-(4-nitrobenzyl)-5′-thioadenosine (SAENTA), a novel ligand with high affinity for polypeptides associated with nucleoside transport: partial purification of the nitrobenzylthioinosine-binding protein of pig erythrocytes by affinity chromatography. *Biochem. J. 270*, 605−614.
(11) Buolamwini, J. K., Wiley, J. S., Robins, M. J., Craik, J. D., Cass, C. E., Gati, W. P., Paterson, A. R. P. (1994) Conjugates of fluorescein and SAENTA (5′-*S*-(2-aminoethyl)-N^6-(4-nitrobenzyl)-5′-thioadenosine): flow cytometry probes for the *es* transporter elements of the plasma membrane. *Nucleosides Nucleotides 13*, 737−751.
(12) Boumah, C. E., Hogue, D. L, and Cass, C. E. (1992) Expression of high levels of nitrobenzylthioinosine-sensitive nucleoside transport in cultured human choriocarcinoma (BeWo) Cells. *Biochem. J. 288*, 987−996.
(13) Lowry, O. H.; Rosebrough, N. J.; Farr, A. L.; Randall, R. J. (1951) *J. Biol. Chem. 193*, 265−275.
(14) Ziemnicka-Merchant, B., Aran, J. M., Plagemann, P. G. W., Krafft, G. A. (1992) Effects of chemical modification of nitrobenzylthioinosine on its binding to high-affinity membrane binding sites and inhibition of nucleoside transport. *Biochem. Pharmacol. 44*, 1577−1583.
(15) Robins, M. J., Asakura, J.-I., Kaneku, M., Shibuya, S., Jacobs, E. S., Agbanyo, F. R., Cass, C. E., and Paterson, A. R. P. (1994) Synthesis of substituted-benzyl and sugar-modified analogues of 6-*N*-(4-nitrobenzyl)adenosine and their interactions with "*ES*" nucleoside transport systems. *Nucleosides and Nucleotides 13*, 1627−1646.
(16) Young, J. D., Jarvis, S. M., Robins, M. J., and Paterson, A. R. P. (1983) Photoaffinity labeling of the human erythrocyte nucleoside transporter by N^6-(*P*-azidobenzyl)adenosine and nitrobenzylthioinosine. Evidence that the transporter is a Band 4.5 polypeptide**.** *J. Biol. Chem. 258*, 2202−2208.
(17) Fleming, S. A., and Jensen, A. W.(1993) Photocleavage of benzyl−sulfide bonds. *J. Org. Chem. 58*, 7135−7137.
(18) Paul, B., Chen, M. F., and Paterson, A. R. P. (1975) Inhibitors of nucleoside transport: structure−activity relationships. *J. Med. Chem. 18*, 968−973.
(19) Borchers, C., Boer, R., Klemm, K., Figala, V., Denzinger, T., Ulrich, W.-R., Haas, S., Ise, W., Gekeler, V., and Przybylski, M. (2002) Characterization of the dexniguldipine binding site in the multidrug resistance-related transport protein P-glycoprotein by photoaffinity labeling and mass spectrometry. *Mol. Pharmacol. 61*, 1366−1376.

BC034165J

Synthesis of Thiol-Reactive Lipopeptide Adjuvants. Incorporation into Liposomes and Study of Their Mitogenic Effect on Mouse Splenocytes

Audrey Roth,[†] Socorro Espuelas,[†,‡] Christine Thumann,[§] Benoît Frisch,[†] and Francis Schuber*[,†]

Laboratoire de Chimie Bioorganique, Faculté de Pharmacie, UMR 7514 CNRS−Université Louis Pasteur, 74 route du Rhin, 67400 Strasbourg-Illkirch, France, Centro Galénico, Facultad de Farmacia, Universidad de Navarra, Pamplona, Spain, and Unité INSERM U544, Institut de Virologie, Université Louis Pasteur, 3 Rue Koeberlé, 67000 Strasbourg, France. Received October 6, 2003; Revised Manuscript Received January 26, 2004

Synthetic analogues of triacylated and diacylated lipopeptides derived from the N-terminal domain of respectively bacterial and mycoplasmal lipoproteins are highly potent immunoadjuvants when administered either in combination with protein antigens or covalently linked to small peptide epitopes. Because of their amphipathic properties, lipopeptides, such as *S*-[2,3-bis(palmitoyloxy)-(2*RS*)-propyl]-*N*-palmitoyl-(*R*)-cysteinyl-alanyl-glycine (Pam_3CAG), can be conveniently incorporated into liposomes and serve as anchors for antigens that are linked to them. To design vaccination constructs based on synthetic peptides and liposomes as vectors. we have accordingly synthesized a series of lipopeptides that differ by the number (Pam_3C vs Pam_2C) and nature of the acyl chains (palmitoyl vs oleoyl) and by the presence at their C-terminus of thiol-reactive functions, such as maleimide or bromoacetyl. When incorporated into liposomes, these latter functionalized lipopeptides allow, in aqueous media, a well controlled chemoselective conjugation of HS-peptides to the surface of the vesicles. Using a BALB/c mice splenocyte proliferation assay ([^{3}H]thymidine incorporation), we have measured the lymphocyte activation potency of the different lipopeptides. We found that, compared to their free (emulsified) forms, the liposomal lipopeptides were endowed with enhanced mitogenic activities; i.e., up to 2 orders of magnitude for Pam_3CAG which was more potent than Pam_2CAG. The impact of functionalization on the cellular activity of Pam_3CAG was dependent on the thiol-reactive group introduced: whereas the bromoacetyl derivative retained its full activity, the presence of a maleimide group virtually abolished the lymphocyte activation of the lipopeptide. Finally, the substitution of saturated palmitoyl chains by unsaturated oleoyl chains was inhibitory. Thus, thiol-reactive Ol_3CAG derivatives were the least active mitogens in our assay. Taken together, our findings are of importance for the further optimization of antigen-specific liposomal-based synthetic vaccines; the bromoacetyl derivative of Pam_3CAG should be a promising lipopeptide derivative serving as an anchor for peptide epitopes while retaining its lymphocyte activation activity.

INTRODUCTION

Synthetic peptide or epitope-based vaccines present a particularly attractive potential for infectious diseases or cancer (*1*−*5*). However, a major limitation in the use of short peptides resides in their poor immunogenicity which can be circumvented, to a certain extent, by their coupling to a variety of carriers such as proteins or synthetic/multimeric polymers (*6, 7*). During this past decade our understanding of the cellular and molecular aspects of the immune response has increased dramatically, and this includes also a much better knowledge of the role and mode of action of immunoadjuvants (*8*−*10*). We have now a much clearer view of what are the indispensable elements of a "designer" vaccination construct and the function(s) they are supposed to carry out at cellular levels. In the field of peptide-based vaccines, lipopeptides such as *S*-[2,3-bis(palmitoyloxy)-(2*RS*)-propyl]-*N*-palmitoyl-(*R*)-cysteinyl-alanyl-glycine (Pam_3CAG) or Pam_3CSS have a prominent position (*11*−*13*). These amphipathic synthetic analogues of the N-terminus of *Escherichia coli* lipoprotein are highly potent and nontoxic adjuvants; they are able to induce cell-mediated (*14*) as well as humoral immune responses, depending on the nature of the epitope, against low molecular weight peptides that are covalently coupled to them (*15, 16*). Among their many properties, they have been shown to be polyclonal activators of B-lymphocytes (*17*) and to trigger the synthesis of, for example, cytokines in macrophages (*18*). At molecular and cellular levels, the mode of action of these lipopeptides is far from being unraveled. A major advance came nevertheless with the realization that such structures, which constitute pathogen-associated molecular patterns (PAMPs), participate to the innate immune response by interacting with Toll-like receptor 2 (TLR2) (*19*) and to the adaptive response by triggering the maturation of dendritic cells (DC) and eliciting T-cell activation and cytokine production (*20, 21*). In addition, lipopeptides have also been shown to readily diffuse from the plasma membrane of cells, via poorly understood mechanisms, to most subcellular compartments (*22, 23*); this property presumably allows the lipopeptides to deliver their peptide cargo to the MHC class I/II molecules. At this point it should be noted that

* To whom correspondence should be addressed. Phone: + 33 390 24 41 72. Fax: +33 390 24 43 06. E-mail: schuber@pharma.u-strasbg.fr.

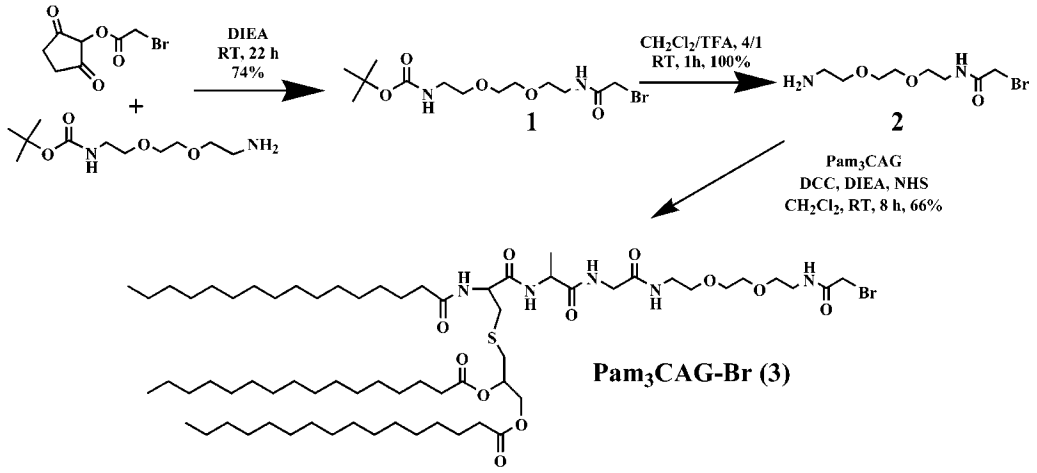
[†] UMR 7514 CNRS−Université Louis Pasteur.

[‡] Universidad de Navarra.

[§] Institut de Virologie, Université Louis Pasteur.

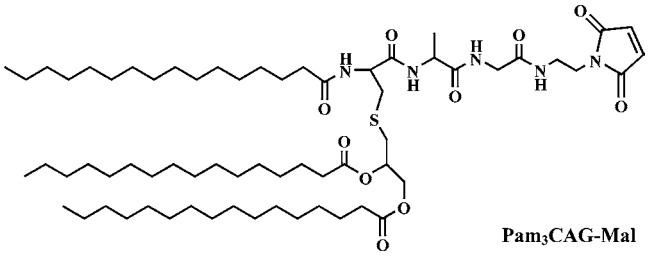
10.1021/bc034184t CCC: $27.50 © 2004 American Chemical Society
Published on Web 05/01/2004

Scheme 1. Synthesis of Pam_3CAG-Br



subcellular delivery and peptide processing were studied more thoroughly with the simpler types of lipopeptides (see below) in, for example, dendritic cells (*24, 25*). Because of these highly attractive features, lipopeptide conjugates, which are well suited for the design of novel synthetic vaccines, have been tested in a variety of applications (*11*−*13*). However, because of their physicochemical properties and relative insolubility, these molecules can prove difficult to develop even though more soluble analogues have been made (*26, 27*). The same holds true, despite their proven efficacy in producing, for example, strong cytotoxic $CD8^+$ T-cell responses against many pathogens, for less complex lipopeptides obtained by lipidation, such as palmitoylation, of terminal lysine residues of peptide epitopes (*28*−*30*).

To design epitope-driven vaccines our group has developed a somewhat different strategy based on liposomes that are used as multivalent carriers (*31*−*35*). Synthetic lipopeptide derivatives such as Pam_3CAG-Mal, which



contain a thiol-reactive maleimide function (*36*), were first incorporated into the bilayers of small unilamellar vesicles, masking the hydrophobic nature of the adjuvant. In the following steps, peptide epitopes that carry a free thiol function, either at their N- or C-terminus, are conjugated to the surface of these preformed and functionalized liposomes (*35*). An a posteriori coupling of peptide epitopes to lipopeptides, that play also the role of anchors, is thus achieved under mild conditions in aqueous media, via a well controlled, quasistoichiometric, and high yield chemoselective ligation (*37*). Because of its versatility, this strategy can be extended to the preparation of multiepitope constructs to which several different types of HS-peptides can be conjugated (*35, 37*). This approach has been used successfully for the design of highly immunogenic biepitope liposomal constructs that combine for example structurally independent B- and T-cell peptide epitopes (*35*) and also recently to antitumor vaccines (A. Roth et al., to be published).

Up to now, however, we ignore whether the C-terminal modification of lipopeptides by thiol-reactive functions is detrimental to the adjuvanticity of these molecules. Therefore, we could not answer the question whether the highly intense and long lasting immune responses, induced for example by our liposomal biepitope constructs, could be attributed to the adjuvanticity of the lipopeptides (e.g. cell activation) and/or (only) to their capacity to deliver intracellularly the linked epitopes to the MHC-I/II molecules. Therefore, to better grasp the functions of the lipopeptides and their thiol-reactive derivatives in our constructs, we have now undertaken the synthesis of several analogues and studied their comparative cellular properties. These new lipopeptides include the thiol-reactive bromoacetyl derivative of Pam_3CAG (i.e., Pam_3-CAG-Br; Scheme 1) which is chemically more stable than the Pam_3CAG-Mal (*36*) we have used previously. To increase the epitope density at the surface of the liposomal constructs we have also prepared analogues in which the palmitoyl chains have been replaced by unsaturated oleoyl chains, i.e., Ol_3CAG-Mal and Ol_3CAG-Br. These compounds are expected to be more miscible with the phospholipids used to fabricate the liposomes and less prone to engage into lateral phase separation. Finally, during the recent years it was found that MALP-2 (Pam_2-CGNNDESNISFKEK), a lipopeptide derived from a mycoplasma lipoprotein is a highly potent adjuvant when coadministered with antigens, e.g. via the mucosal route (*38*), or when conjugated to B/T peptide epitopes (*39*). This molecule which, compared to the "classical" lipopeptides, lacks the *N*-acyl chain was shown to interact with TLR2 and TLR6 (*40*−*42*), to serve as potent cytokine inducer for monocytes/macrophages and to induce the maturation of dendritic cells (*43*). For that reason we have also included in our present study the synthesis of Pam_2CAG and Pam_2CAG-Mal, i.e., analogues of the immunologically active *R*-stereoisomer (*44*) of MALP-2. We have demonstrated previously that Pam_3CAG and Pam_3CSS when incorporated into liposomes kept their ability to induce, in vitro, the proliferation of BALB/c mice splenocytes (*34*) which has been often correlated with the adjuvanticity of these compounds (*15, 17*). A similar approach was performed here which yielded a very valuable insight into the biological activity of these lipopeptide derivatives and also guidelines for the design of more efficient liposomal vaccination constructs.

EXPERIMENTAL PROCEDURES

General. Reagent-grade solvents were used without further purification. The phospholipids egg yolk L-α-

phosphatidylcholine (PC) and L-α-phosphatidyl-DL-glycerol (PG) transesterified from egg yolk PC were purchased from Sigma-Aldrich (Saint-Quentin-Fallavier, France), and their purity (over 99%) was assessed by TLC. Silica gel 60 F 254 plates for thin-layer chromatography (TLC) were purchased from Merck (Darmstadt, Germany). Column chromatographic separations were carried out as flash chromatography using silica gel (Merck) with a particle size of 0.040−0.063 mm. 2-Mercaptoethanol was obtained from Sigma-Aldrich (L'Isle d'Abeau Chesnes, France), fluorescamine (Fluram) from Fluka (L'Isle d'Abeau Chesnes, France), and Boc-Ala-Gly-OSu from Bachem (Voisins-le-Bretonneux, France). The peptide HA 307-319-C (PKYVKQNTLKLAT-C) was obtained from Neosystem (Strasbourg, France). The cysteine residue added to the C-terminus allows a facile coupling of the peptide on the lipopeptide maleimide or bromoacetyl functions. The purity of the peptide, as assessed by HPLC, was at least 80%. Pam_3CAG, prepared as previously described (*34*, *45*), was converted into the maleimide derivative Pam_3CAG-Mal by reaction with 1-(2-aminoethyl)pyrrole-2,5-dione according to Boeckler et al. (*36*). The lipopeptide Fmoc-Pam_2C was synthesized as described in the literature (*46*). Free lipopeptides used for cellular assays were suspended in PBS (pH 7.4) and emulsified by sonication for 1 h. *N*-(*tert*-butyloxycarbonyl)aminoethoxyethoxyethylamine was prepared by a simple monoprotection with a Boc moiety (*47*). ^{1}H and ^{13}C NMR were recorded on Bruker DPX-200 (200 MHz) and DPX 300 (300 MHz) spectrometers. Chemical shifts are expressed as parts per million using $CHCl_3$ ($\delta = 7.27$ ppm for ^{1}H and 77.7 ppm for ^{13}C) or CH_3OH ($\delta = 3.35$ ppm for ^{1}H and 49.0 ppm for ^{13}C) as the internal standard ($\delta = 0.0$ ppm). Mass spectra (ES-MS) were recorded on a ESI/TOF Mariner mass spectrometer by electrospray. [^{3}H]Thymidine was obtained from Amersham Biosciences (Buckinghamshire, England) with a specific activity of 25.0 Ci/mmol.

***N*-(*tert*-Butyloxycarbonyl)aminoethoxyethoxyethyl-2-bromoacetamide (1).** To a solution of *N*-(*tert*-butyloxycarbonyl)aminoethoxyethoxyethylamine (1 g, 3.25 mmol) in CH_2Cl_2 (40 mL) were added bromoacetic acid succinimidyl ester (1.15 g, 4.87 mmol) and DIEA (850 μL, 4.87 mmol). After being stirred for 22 h at room temperature, the organic phase was washed with 3 × 40 mL of a citric acid solution (5%, w/v) followed by 3 × 40 mL of water. After passage over $MgSO_4$, the solvent was evaporated to dryness. The reaction product **1** (887 mg; yield 74%) was obtained after purification by chromatography on silica gel eluted with AcOEt:hexane 2:1 to 3:1. R_f 0.63 (CH_2Cl_2:MeOH 9:1). ^{1}H NMR (300 MHz, $CDCl_3$): δ 3.84 (s, 2H, CH_2Br), 3.57−3.26 (m, 12H, (CH_2)$_2$O(CH_2)$_2$O(CH_2)$_2$), 1.40 (s, 9H, C(CH_3)$_3$). ^{13}C NMR (75 MHz, $CDCl_3$:MeOD 1:1): δ 165.59 (*C*(O)CH_2Br), 155.81 (*C*(O)OC(CH$_3$)$_3$), 79.07 (*C*(CH$_3$)$_3$), 69.16, 69.99, 70.17 (4 × *C*H$_2$O(*C*H$_2$)$_2$O*C*H$_2$), 40.16 (O(CO)NH*C*H$_2$), 39.71 (CH_2(CO)NH*C*H$_2$), 28.86 (*C*H$_2$Br), 28.23 (3 × C(*C*H$_3$)$_3$). ES-MS *m*/*z*: 392.1047 ([M + Na]$^+$), calcd: 369.1147 for $C_{13}H_{25}BrN_2O_5$.

Aminoethoxyethoxyethyl-2-bromoacetamide (2). Compound **1** (100 mg, 0.27 mmol) was dissolved in 9 mL of TFA/CH_2Cl_2 (1/4, v/v). The deprotection reaction was conducted at room temperature and under stirring. After 1 h, the solvents were evaporated under vacuum and compound **2** was obtained, with trifluoroacetate as counterion, as an oil (103 mg; yield 100%). R_f 0.12 (CH_2Cl_2 :MeOH 9:1). ^{1}H NMR (300 MHz, $CDCl_3$:MeOD 1:1): δ 3.81 (s, 2H, CH_2Br), 3.70−3,39 (m, 10H, (CH_2)$_2$O(CH_2)$_2$-OCH_2), 3.11−3.07 (m, 2H, CH_2(CO)NHCH_2).

***N*-{[2,3-Bis(palmitoyloxy)-(2*RS*)-propyl]-*N*-palmitoyl-(*R*)-cysteinyl-(*S*)-alanyl-glycyl}aminoethoxyethoxyethyl-2-bromoacetamide (3).** DCC (9.5 mg, 46.2 μmol), DIEA (10 μL, 57.8 μmol), and NHS (1.0 mg, 7.7 μmol) were added to a solution of Pam_3CAG (40 mg, 38.5 μmol) in CH_2Cl_2 (1.2 mL). The amine **2** (22 mg, 57.8 μmol) was then added to the mixture, and the reaction was left at room temperature. After 8 h, the formed precipitate was removed by filtration and the organic phase was then washed with 3 × 6 mL of 5% (w/v) citric acid in water followed by 3 × 6 mL of water. After being dried over $MgSO_4$, the solvent was evaporated to dryness. Compound **3** was finally recrystallized from $CHCl_3$:MeOH 1:4 at −20 °C, and it afforded a white powder after lyophilization from *tert*-butyl alcohol (33 mg; yield 66%). R_f 0.42 (CH_2Cl_2:MeOH 13:1). ^{1}H NMR (200 MHz, $CDCl_3$:MeOD 1:1): δ 5.21 (m, 1H, SCH$_2$C*H*(O)), 4.69 (m, 1H, SCH$_2$C*H*(NH)), 4.68−4.56 (m, 1H, NHC*H*(CH$_3$)), 4.43−4.13 (m, 2H, SCH$_2$CH(O)C*H*$_2$(O)), 4.06 (m, 2H, NHC*H*$_2$C(O)), 3.86 (s, 2H, C*H*$_2$Br), 3.65−3.43 (m, 12H, (C*H*$_2$)$_2$O(C*H*$_2$)$_2$O(C*H*$_2$)$_2$), 3.04−2.87 (m, 2H, SC*H*$_2$CH(N)), 2.81 (m, 2H, SC*H*$_2$CH(O)), 2.42−2.26 (m, 6H, CH$_3$-(CH$_2$)$_{13}$C*H*$_2$C(O)), 1.63 (m, 6H, CH$_3$(CH$_2$)$_{12}$C*H*$_2$-CH$_2$C(O)), 1.44−1.41 (d, $J = 7.3$ Hz, 3H, NHCH(C*H*$_3$)C(O)), 1.40−1.25 (m, 72H, CH$_3$(C*H*$_2$)$_{12}$(CH$_2$)$_2$C(O)), 0.90 (t, $J = 6.6$ Hz, 9H, C*H*$_3$(CH$_2$)$_{14}$C(O)). ^{13}C NMR (50 MHz, $CDCl_3$): δ 174.82 (CH$_3$(CH$_2$)$_{14}$*C*(O)N), 173.60, 173.89 (2 × CH$_3$-(CH$_2$)$_{14}$*C*(O)O), 173.50 (NHCH(CH$_3$)*C*(O)), 172.04 (SCH$_2$-CH(NH)*C*(O)), 169.34 (NHCH$_2$*C*(O)), 166.32 (NH*C*(O)-CH$_2$Br), 69.42, 70.26 (SCH$_2$*C*H(O), 4 × *C*H$_2$O(*C*H$_2$)$_2$O*C*H$_2$), 63.76 (SCH$_2$CH(O)*C*H$_2$(O)), 51.94 (SCH$_2$*C*H(NH)), 50.02 (NH*C*H(CH$_3$)), 42.93 (NH*C*H$_2$C(O)), 39.59, 39,94 (2 × NH*C*H$_2$CH$_2$O), 36.28 (S*C*H$_2$CH(NH)), 34.33 (2 × CH$_3$-(CH$_2$)$_{13}$*C*H$_2$C(O)O), 34.07 (CH$_3$(CH$_2$)$_{13}$*C*H$_2$C(O)N), 29.30, 29.33, 29.67, 31.90 (30 × CH$_3$CH$_2$(*C*H$_2$)$_{10}$(CH$_2$)$_3$C(O), *C*H$_2$-Br), 24.85, 25.53 (6 × CH$_3$(CH$_2$)$_{11}$(*C*H$_2$)$_2$CH$_2$C(O)), 22.66 (3 × CH$_3$*C*H$_2$(CH$_2$)$_{13}$C(O)), 17.14 (NHCH(*C*H$_3$)C(O)), 14.07 (3 × *C*H$_3$(CH$_2$)$_{14}$C(O)). ES-MS *m*/*z*: 1312.8418 ([M + Na]$^+$), calcd: 1289.8518 for $C_{67}H_{126}BrN_5O_{11}S$.

***N*-[*N*-(*tert*-Butyloxycarbonyl)-(*S*)-alanylglycyl]aminoethoxyethoxyethyl-2-bromoacetamide (4).** *N*-α-Boc-L-alanylglycine *N*-hydroxysuccinimide ester (282 mg, 0.822 μmol) was dissolved in CH_2Cl_2 (3 mL). The amine **2** (282 mg, 738 μmol) and DIEA (100 μL, 578 μmol) were then added, and the reaction was left at room temperature. After 12 h, the organic phase was washed with 10 mL of saturated NaCl followed by 3 × 10 mL of water. It was then dried over $MgSO_4$, and the solvent was evaporated to dryness. The reaction product was purified by column chromatography on silica gel by elution with CH_2Cl_2:MeOH 95:5 to obtain compound **4** as an oily form (250 mg; yield 68%). R_f 0.71 (CH_2Cl_2:MeOH 6:1). ^{1}H NMR (200 MHz, $CDCl_3$): δ 4.18−4.11 (m, 1H, NHC*H*-(CH$_3$)), 4.05 (m, 2H, NHC*H*$_2$C(O)), 3.87 (s, 2H, C*H*$_2$Br), 3.75−3.30 (m, 12H, (C*H*$_2$)$_2$O(C*H*$_2$)$_2$O(C*H*$_2$)$_2$), 1.41 (s, 9H, C(C*H*$_3$)$_3$), 1.37−1.34 (d, $J = 7.1$ Hz, 3H, NHCH(C*H*$_3$)-C(O)). ^{13}C NMR (50 MHz, $CDCl_3$): δ 173.72 (NHCH(CH$_3$)-*C*(O)), 169.34 (NHCH$_2$*C*(O)), 166.47 (NH*C*(O)CH$_2$Br), 155.64 (*C*(O)OC(CH$_3$)$_3$), 79.96 (*C*(CH$_3$)$_3$), 69.16, 70.00 (4 × *C*H$_2$O(*C*H$_2$)$_2$O*C*H$_2$), 50.37 (NH*C*H(CH$_3$)), 42.77 (NH*C*H$_2$-C(O)), 39.08, 39.72 (2 × NH*C*H$_2$CH$_2$O), 28.69 (*C*H$_2$Br), 28.10 (3 × C(*C*H$_3$)$_3$), 17.91 (NHCH(*C*H$_3$)C(O)). ES-MS *m*/*z*: 520.1280 ([M + Na]$^+$), calcd: 497.1380 for $C_{18}H_{33}$-BrN_4O_7.

***N*-[(*S*)-Alanylglycyl]aminoethoxyethoxyethyl-2-bromoacetamide (5).** Compound **4** was transformed into **5**, according to the procedure used for **2**, and was obtained as a yellow oil (82 mg; yield 100%). R_f 0.13 (CH_2Cl_2:MeOH 6:1). ^{1}H NMR (300 MHz, $CDCl_3$:MeOD

1:1): δ 3.54−3.50 (m, 1H, NHC*H*(CH_3)), 3.48 (m, 2H, NHCH_2C(O)), 3.35 (s, 2H, CH_2Br), 3.13−2.92 (m, 12H, (CH_2)$_2$O(CH_2)$_2$O(CH_2)$_2$), 1.04−1.02 (d, J = 7.2 Hz, 3H, NHCH(CH_3)C(O)).

***N*-[*N′*-(*tert*-Butyloxycarbonyl)-(*S*)-alanylglycyl]aminoethylmaleimide (6).** *N*-α-Boc-L-alanylglycine *N*-hydroxysuccinimide ester (500 mg, 1.46 mmol) was dissolved in CH_2Cl_2 (30 mL). A DMF solution (10 mL) of the TFA salt of 1-(2-aminoethyl)pyrrole-2,5-dione (*36*) (370 mg, 1.46 mmol) was then added followed by DIEA (254 μL, 1.46 mmol). The reaction was left, under stirring, at room temperature for 7 h. The organic phase was then washed with 3 × 30 mL of saturated NaCl, dried over $MgSO_4$, and evaporated under vacuum. The product was purified by column chromatography on silica gel by elution with CH_2Cl_2:MeOH 30:1 to 25:1 to obtain compound **6** in an oily form (412 mg; yield 77%). R_f 0.53 (CH_2Cl_2:MeOH 15:1). ^{1}H NMR (200 MHz, $CDCl_3$): δ 6.66 (s, 2H, C*H*=C*H*), 4.11−3.95 (m, 1H, NHC*H*(CH_3)), 3.87−3.75 (m, 2H, NHCH_2C(O)), 3.58−3.55 (m, 2H, C(O)NHCH_2CH_2N), 3.49−3.20 (m, 2H, C(O)NHCH_2CH_2N), 1.33 (s, 9H, C(CH_3)$_3$), 1.31−1.27 (d, J = 7.3 Hz, 3H, NHCH(CH_3)C(O)). ^{13}C NMR (50 MHz, $CDCl_3$): δ 173.44 (NHCH(CH_3)*C*(O)), 170.76 (NHCH_2*C*(O)), 169.55 (2 × CH=CH*C*(O)), 155.76 (*C*(O)OC(CH_3)$_3$), 134.02 (2 × *C*H=*C*H), 80.01 (*C*(CH_3)$_3$), 50.61 (NH*C*H(CH_3)), 42.88 (NH*C*H_2C(O)), 38.04 (C(O)NHCH_2*C*H_2N), 37.15 (C(O)NH*C*H_2CH_2N), 28.15 (3 × C(*C*H_3)$_3$), 17.79 (NHCH(*C*H_3)C(O)). ES-MS *m*/*z*: 369.1390 ([M + H]$^+$), calcd: 368.1311 for $C_{16}H_{24}N_4O_6$.

***N*-[(*S*)-Alanylglycyl]aminoethylmaleimide (7).** Compound **7** was prepared from **6** according to the procedure used to obtain **2**. Colorless oil (52 mg; yield 100%). R_f 0.11 (CH_2Cl_2:MeOH 7:1). ^{1}H NMR (300 MHz, MeOD): δ 6.81 (s, 2H, C*H*=C*H*), 4.01−3.94 (m, 1H, NHC*H*(CH_3)), 3.90−3.72 (m, 2H, NHCH_2C(O)), 3.64−3.61 (m, 2H, C(O)NHCH_2CH_2N), 3.41−3.38 (m, 2H, C(O)NHCH_2CH_2N), 1.52−1.51 (d, J = 5.3 Hz, 3H, NHCH(CH_3)C(O)). ^{13}C NMR (75 MHz, MeOD): δ 172.60 (NHCH(CH_3)*C*(O)), 171.43 (NHCH_2*C*(O)), 161.61 (2 × CH=CH*C*(O)), 135.43 (2 × *C*H=*C*H), 49.84 (NH*C*H(CH_3)), 43.19 (NH*C*H_2C(O)), 39.02 (C(O)NHCH_2*C*H_2N), 38.14 (C(O)NH*C*H_2CH_2N), 17.51 (NHCH(*C*H_3)C(O)).

***N*,*N′*-Dioleoylcystine Di-*tert*-butyl Ester (8).** DCC (2.5 g, 1.2 mmol) and DMAP (1.2 g, 1.1 mmol) were added to a solution of oleic acid (3.3 g, 1.1 mmol) in anhydrous CH_2Cl_2 (50 mL). After addition of cystine di-*tert*-butyl ester, the reaction mixture was stirred at room temperature for 3 h. The precipitate formed during the reaction was eliminated by filtration. The filtrate was then washed successively with 5 × 50 mL of a citric acid solution 5% (w/v), 3 × 50 mL of a $NaHCO_3$ solution 5% (w/v), and finally with 3 × 50 mL of water. After being dried over $MgSO_4$, the organic phase was evaporated in vacuo and the obtained residue was purified by chromatography on silica gel, eluted by hexane:AcOEt 10:1 to obtain compound **8** in an oily form (2.9 g; yield 73%). R_f 0.85 (hexane:AcOEt 3:2). ^{1}H NMR (300 MHz, $CDCl_3$): δ 5.41−5.28 (m, 4H, C*H*=C*H*), 4.78−4.72 (m, 2H, SCH$_2$C*H*(NH)), 3.21−3.19 (d, J = 5.2 Hz, 4H, SCH_2CH(NH)), 2.24 (m, 4H, CH_3(CH_2)$_7$CH=CH(CH_2)$_6$CH_2C(O)), 2.08−1.87 (m, 8H, CH_3(CH_2)$_6$CH_2CH=CHCH_2(CH_2)$_6$C(O)), 1.76−1.55 (m, 4H, CH_3(CH_2)$_7$CH=CH−(CH_2)$_5$CH_2CH_2C(O)), 1.48 (s, 18H, C(CH_3)$_3$), 1.40−1.13 (m, 40H, CH_3(CH_2)$_6$-CH_2CH=CHCH_2(CH_2)$_4$(CH_2)$_2$C(O)), 0.89 (t, J = 6.8 Hz, 6H, CH_3(CH_2)$_7$CH=CH(CH_2)$_7$C(O)). ^{13}C NMR (50 MHz, $CDCl_3$:MeOD 1:1): δ 174.07 (2 × CH_3(CH_2)$_7$CH=CH-(CH_2)$_7$*C*(O)N), 169.39 (SCH$_2$CH(NH)*C*(O)), 129.17, 129.36 (4 × *C*H=*C*H), 82.26 (*C*(CH_3)$_3$), 52.03 (2 × SCH$_2$*C*H(NH)), 39.88 (2 × S*C*H$_2$CH(NH)), 35.52 (2 × CH_3(CH_2)$_7$CH=CH-(CH_2)$_6$*C*H$_2$C(O)), 31.37 (2 × CH_3CH_2*C*H$_2$(CH_2)$_5$CH=CH-(CH_2)$_7$C(O)), 28.63, 28.74, 28.96, 29,20 (16 × CH_3(CH_2)$_2$-(*C*H$_2$)$_4$CH$_2$CH=CHCH$_2$(*C*H$_2$)$_4$(CH_2)$_2$C(O)), 27.17 (6 × C(*C*H_3)$_3$), 26.62 (4 × CH_3(CH_2)$_6$*C*H$_2$CH=CH*C*H$_2$(CH_2)$_6$-C(O)), 25.18 (2 × CH_3(CH_2)$_7$CH=CH(CH_2)$_5$*C*H$_2$CH$_2$C(O)), 22.11 (2 × CH_3*C*H$_2$(CH_2)$_6$CH=CH(CH_2)$_7$C(O)), 13.29 (2 × *C*H_3(CH_2)$_7$CH=CH(CH_2)$_7$C(O)). ES-MS *m*/*z*: 903.7101 ([M + Na]$^+$), calcd: 880.7201 for $C_{50}H_{92}N_2O_6S_2$.

***N*-Oleoylcysteine *tert*-Butyl Ester (9).** Compound **8** (2.9 g, 3.3 mmol) was dissolved in anhydrous CH_2Cl_2 (50 mL) and then reduced by dithioerythritol (780 mg, 5.1 mmol) in the presence of triethylamine (1.0 g, 10 mmol). After 4 h of reaction at room temperature, the reaction mixture was washed with 3 × 50 mL of a citric acid solution 5% (w/v), then with 50 mL of water, the two phases being saturated with nitrogen. The organic phase was then dried over $MgSO_4$ and the solvent evaporated under low pressure. The reaction product **9** was purified by chromatography on silica gel, and the elution was performed with hexane:AcOEt 6:1 to obtain a yellow oil (2.7 g; yield 70%). R_f 0.63 (hexane:AcOEt 5:1). ^{1}H NMR (300 MHz, $CDCl_3$:MeOD 1:1): δ 5.38−5.27 (m, 2H, C*H*=C*H*), 4.74 (m, 1H, SCH$_2$C*H*(NH)), 3.01−2.95 (m, 2H, SCH_2CH(NH)), 2.29 (m, 2H, CH_3(CH_2)$_7$CH=CH-(CH_2)$_6$CH_2C(O)), 2.05−1.95 (m, 4H, CH_3(CH_2)$_6$CH_2CH=CHCH_2(CH_2)$_6$C(O)), 1.67−1.57 (m,2H, CH_3(CH_2)$_7$CH=CH(CH_2)$_5$CH_2CH_2C(O)), 1.42 (s, 9H, C(CH_3)$_3$), 1.39−1.19 (m, 20H, CH_3(CH_2)$_6$CH_2CH=CHCH_2(CH_2)$_4$(CH_2)$_2$C(O)), 0.88 (t, J = 6.6 Hz, 3H, CH_3(CH_2)$_7$CH=CH(CH_2)$_7$C(O)). ^{13}C NMR (50 MHz, $CDCl_3$:MeOD 1:1): δ 174.03 (CH_3-(CH_2)$_7$CH=CH(CH_2)$_7$*C*(O)N), 168.95 (SCH$_2$CH(NH)*C*(O)), 129.11, 129.31 (2 × *C*H=*C*H), 82.19 (*C*(CH_3)$_3$), 54.06 (SCH$_2$*C*H(NH)), 35.46 (S*C*H$_2$CH(NH)), 31.96 (CH_3(CH_2)$_7$-CH=CH(CH_2)$_6$*C*H$_2$C(O)), 31.30 (CH_3CH_2*C*H$_2$(CH_2)$_5$-CH=CH(CH_2)$_7$C(O)), 27.10, 28.67, 28.89, 29,12 (8 × CH_3-(CH_2)$_2$-(*C*H$_2$)$_4$CH$_2$CH=CHCH$_2$(*C*H$_2$)$_4$(CH_2)$_2$C(O)), 26.55 (3 × C(*C*H_3)$_3$), 25.65 (2 × CH_3(CH_2)$_6$CH$_2$CH=CHCH_2(CH_2)$_6$-C(O)), 25.18 (CH_3(CH_2)$_7$CH=CH(CH_2)$_5$CH_2CH_2C(O)), 22.04 (CH_3*C*H$_2$-(CH_2)$_6$CH=CH(CH_2)$_7$C(O)), 13.21 (*C*H_3(CH_2)$_7$-CH=CH(CH_2)$_7$C(O)). ES-MS *m*/*z*: 464.3701 ([M + Na]$^+$), calcd: 441.3801 for $C_{25}H_{47}NO_3S$.

[2,3-Dihydroxy-(2*RS*)-propyl]-*N*-oleoyl-(*R*)-cysteine *tert*-Butyl Ester (10). 3-Bromo-1,2-propanediol (6.7 g, 43.5 mmol) and triethylamine (4.5 g, 44.5 mmol) were added to **9** (2.6 g, 5.9 mmol) in anhydrous DMF (50 mL). After 20 min of reaction at 80 °C, followed by 2 h at room temperature, the solvent was evaporated in vacuo. The residue was dissolved in $CHCl_3$ saturated with nitrogen (25 mL) and then washed successively with 3 × 25 mL of a citric acid solution 5% (w/v) and with 3 × 25 mL of water. After being dried over $MgSO_4$, the solvent was evaporated under low pressure. The product thus obtained was purified by chromatography on silica gel and eluted with AcOEt:hexane 9:1 to yield compound **10** in a yellow oily form (1.6 g; yield 55%). R_f 0.40 (hexane:AcOEt 1:9). ^{1}H NMR (300 MHz, $CDCl_3$:MeOD 1:1): δ 5.39−5.27 (m, 2H, C*H*=C*H*), 4.64−4.59 (m, 1H, SCH$_2$C*H*-(NH)), 3.78−3.72 (m, 1H, SCH$_2$C*H*(O)), 3.66−3.48 (m, 2H, SCH$_2$CH(O)CH_2(O)), 2.98−2.93 (m, 2H, SCH_2CH(NH)), 2.77−2.58 (m, 2H, SCH_2CH(O)), 2.24 (m, 2H CH_3(CH_2)$_7$-CH=CH(CH_2)$_6$CH_2C(O)), 2.08−1.95 (m, 4H, CH_3(CH_2)$_6$-CH_2CH=CHCH_2(CH_2)$_6$C(O)), 1.70−1.56 (m, 2H, CH_3-(CH_2)$_7$CH=CH(CH_2)$_5$CH_2–CH$_2$C(O)), 1.48 (s, 9H, C(CH_3)$_3$), 1.39−1.17 (m, 20H, CH_3(CH_2)$_6$CH$_2$CH=CHCH$_2$(CH_2)$_4$-(CH_2)$_2$C(O)), 0.87 (t, J = 6.7 Hz, 3H, CH_3(CH_2)$_7$CH=CH-(CH_2)$_7$C(O)). ^{13}C NMR (50 MHz, $CDCl_3$): δ 174.02 (CH_3(CH_2)$_7$CH=CH(CH_2)$_7$*C*(O)N), 168.55 (SCH$_2$CH-(NH)*C*(O)), 130.43, 130.69 (2 × *C*H=*C*H), 83.10 (*C*(CH_3)$_3$),

70.60 ($SCH_2CH(O)$), 66.40 ($SCH_2CH(O)CH_2(O)$), 53.64 ($SCH_2CH(NH)$), 36.60 ($SCH_2CH(NH)$), 35.74 ($CH_3(CH_2)_7$-$CH{=}CH(CH_2)_6CH_2C(O)$), 32.34 ($SCH_2CH(O)$), 31.88 (CH_3-$CH_2CH_2(CH_2)_5CH{=}CH(CH_2)_7C(O)$), 29.22, 29.29, 29.49, 29,67 (8 × $CH_3(CH_2)_2(CH_2)_4CH_2CH{=}CHCH_2(CH_2)_4(CH_2)_2$-$C(O)$), 27.97 (3 × $C(CH_3)_3$), 27.17 (2 × $CH_3(CH_2)_6CH_2CH{=}$ $CHCH_2(CH_2)_6C(O)$), 25.53 ($CH_3(CH_2)_7CH{=}CH(CH_2)_5CH_2$-$CH_2C(O)$), 22.66 ($CH_3CH_2$-$(CH_2)_6CH{=}CH(CH_2)_7C(O)$), 14.09 ($CH_3(CH_2)_7CH{=}CH(CH_2)_7C(O)$). ES-MS *m/z*: 538.4117 ($[M + Na]^+$), calcd: 515.4217 for $C_{28}H_{53}NO_5S$.

[2,3-Bis(oleoyloxy)-(2*RS*)-propyl]-*N*-oleoyl-(*R*)-cysteine *tert*-Butyl Ester (11). Oleic acid (2.3 g, 7.9 mmol), DCC (1.6 g, 7.7 mmol), and DMAP (100 mg, 0.7 mmol) were added to a solution of the compound **10** (1.6 g, 3.1 mmol) in $CHCl_3$ (50 mL). The reacting mixture was stirred for 12 h at room temperature, and then the formed precipitate was removed by filtration. The filtrate was washed successively with 3 × 50 mL of a citric acid solution 5% (w/v), with 3 × 50 mL of a $NaHCO_3$ solution 5% (w/v), and finally with 3 × 50 mL of water. After the solvent was dried over $MgSO_4$ and evaporated under reduced pressure, the residue was purified by chromatography on silica gel. The elution was performed with hexane:AcOEt 4:1 to obtain compound **11** as a colorless oil (1.1 g; yield 45%). R_f 0.40 (hexane:AcOEt 4:1). ^{1}H NMR (200 MHz, $CDCl_3$:MeOD 1:1): δ 5.37−5.31 (m, 6H, $CH{=}CH$), 4.77−4.70 (m, 1H, $SCH_2CH(O)$), 4.21−4.07 (m, 1H, $SCH_2CH(NH)$), 4.05−3.87 (m, 2H, $SCH_2CH(O)CH_2(O)$), 3.29−2.89 (m, 2H, $SCH_2CH(NH)$), 2.85−2.58 (m, 2H, $SCH_2CH(O)$), 2.55−2.24 (m, 6H, $CH_3(CH_2)_7CH{=}CH$-$(CH_2)_6CH_2C(O)$), 2.15−1.84 (m, 12H, $CH_3(CH_2)_6CH_2CH{=}$ $CHCH_2(CH_2)_6C(O)$), 1.74−1.53 (m, 6H, $CH_3(CH_2)_7CH{=}$ $CH(CH_2)_5CH_2CH_2C(O)$), 1.49 (s, 9H, $C(CH_3)_3$), 1.43−1.12 (m, 60H, $CH_3(CH_2)_6CH_2CH{=}CHCH_2(CH_2)_4(CH_2)_2C(O)$), 0.88 (t, J = 6.6 Hz, 9H, $CH_3(CH_2)_7CH{=}CH(CH_2)_7C(O)$). ^{13}C NMR (75 MHz, $CDCl_3$): δ 175.57 (3 × $CH_3(CH_2)_7CH{=}$ $CH(CH_2)_7C(O)$), 170.91 ($SCH_2CH(NH)C(O)$), 130.36, 130.49 (6 × $CH{=}CH$), 83.06 ($C(CH_3)_3$), 72.17 ($SCH_2CH(O)$), 65.,-46 ($SCH_2CH(O)CH_2(O)$), 53.91 ($SCH_2CH(NH)$), 36.58 ($SCH_2CH(NH)$), 35.14 (3 × $CH_3(CH_2)_7CH{=}CH(CH_2)_6$-$CH_2C(O)$), 32.57 ($SCH_2CH(O)$), 30.38 (3 × $CH_3CH_2CH_2$-$(CH_2)_5CH{=}CH(CH_2)_7C(O)$), 29.80, 29.86, 29.94, 30.15 (24 × $CH_3(CH_2)_2(CH_2)_4CH_2CH{=}CHCH_2(CH_2)_4(CH_2)_2C(O)$), 28.20 (3 × $C(CH_3)_3$), 27.78 (6 × $CH_3(CH_2)_6CH_2CH{=}CH$-$CH_2(CH_2)_6C(O)$), 26.45 (3 × $CH_3(CH_2)_7CH{=}CH(CH_2)_5CH_2$-$CH_2C(O)$), 23.29 (3 × $CH_3CH_2(CH_2)_6CH{=}CH(CH_2)_7C(O)$), 14.38 (3 × $CH_3(CH_2)_7CH{=}CH(CH_2)_7C(O)$). ES-MS *m/z*: 1066.8931 ($[M + Na]^+$), calcd: 1043.9031 for $C_{64}H_{117}NO_7S$.

[2,3-Bis(oleoyloxy)-(2*RS*)-propyl]-*N*-oleoyl-(*R*)-cysteine (12). Compound **12** was prepared from **11** according to the procedure used to obtain the amine **2.** Yellow oil (1 g; yield 97%). Rf 0.25 ($CHCl_3$:MeOH 20:1). ^{1}H NMR (200 MHz, $CDCl_3$:MeOD 1:1): δ 5.42−5.18 (m, 6H, $CH{=}CH$), 4.65 (m, 1H, $SCH_2CH(O)$), 4.14−4.08 (m, 1H, $SCH_2CH(NH)$), 3.95−3.63 (m, 2H, $SCH_2CH(O)CH_2(O)$), 3.13−2.87 (m, 2H, $SCH_2CH(NH)$), 2.82−2.65 (m, 2H, $SCH_2CH(O)$), 2.38−2.21 (m, 6H, $CH_3(CH_2)_7CH{=}CH$-$(CH_2)_6CH_2C(O)$), 2.15−1.78 (m, 12H, $CH_3(CH_2)_6CH_2CH{=}$ $CHCH_2(CH_2)_6C(O)$), 1.77−1.49 (m, 6H, $CH_3(CH_2)_7CH{=}$ $CH(CH_2)_5CH_2CH_2C(O)$), 1.47−1.01 (m, 60H, $CH_3(CH_2)_6$-$CH_2CH{=}CHCH_2(CH_2)_4(CH_2)_2C(O)$), 0.87 (t, J = 6.8 Hz, 9H, $CH_3(CH_2)_7CH{=}CH(CH_2)_7C(O)$). ^{13}C NMR (75 MHz, $CDCl_3$): δ 175.48 ($CH_3(CH_2)_7CH{=}CH(CH_2)_7C(O)N$), 174.81, 174.91 (2 × $CH_3(CH_2)_7CH{=}CH(CH_2)_7C(O)O$), 173.12 ($SCH_2CH(NH)C(O)$), 130.28, 130.47 (6 × $CH{=}CH$), 69.42 ($SCH_2CH(O)$), 67.25 ($SCH_2CH(O)CH_2(O)$), 52.91 (SCH_2CH-(NH)), 36.59 ($SCH_2CH(NH)$), 34.27, 34.61 (3 × $CH_3(CH_2)_7$-$CH{=}CH(CH_2)_6CH_2C(O)$), 32.51 ($SCH_2CH(O)$), 30.34 (3 × $CH_3CH_2CH_2(CH_2)_5CH{=}CH(CH_2)_7C(O)$), 27.74, 29.82, 29,92, 30.11 (24 × $CH_3(CH_2)_2(CH_2)_4CH_2CH{=}CHCH_2$-$(CH_2)_4(CH_2)_2C(O)$), 26.32 (6 × $CH_3(CH_2)_6CH_2CH{=}CHCH_2$-$(CH_2)_6C(O)$), 25.46 (3 × $CH_3(CH_2)_7CH{=}CH(CH_2)_5CH_2$-$CH_2C(O)$), 23.23 (3 × $CH_3CH_2(CH_2)_6CH{=}CH(CH_2)_7C(O)$), 14.37 (3 × $CH_3(CH_2)_7CH{=}CH(CH_2)_7C(O)$). ES-MS *m/z*: 1010.7934 ($[M + Na]^+$), calcd: 987.8034 for $C_{60}H_{109}NO_7S$.

***N*-{[2,3-Bis(oleoyloxy)-(2*RS*)-propyl]-*N*-oleoyl-(*R*)-cysteinyl-(*S*)-seryl-(*S*)-seryl}aminoethyl-maleimide (Ol_3CAG-Mal) (13).** Compound **12** (69 mg, 70 μmol) was dissolved in CH_2Cl_2 (1.5 mL). After addition of BOP (37 mg, 84 μmol) and DIEA (12 μL, 70 μmol), the reaction was continued for 30 min at 0 °C under stirring. The amine **7** (30 mg, 70 μmol) in solution in DMF (300 μL) was then added. After being stirred at room temperature for 22 h, the reaction mixture was washed with 3 × 2 mL of a citric acid solution 5% (w/v) and then with 3 × 2 mL of saturated NaCl solution and finally extracted with 2 × 6 mL CH_2Cl_2. The organic phase was dried over $MgSO_4$, and the solvents were evaporated to dryness. The residue was purified by chromatography on silica gel by elution with CH_2Cl_2:MeOH 40:1 allowing the isolation of **13** as a white powder (34 mg; yield 39%). R_f 0.40 (CH_2-Cl_2 :MeOH 13:1). ^{1}H NMR (200 MHz, $CDCl_3$:MeOD 1:1): δ 6.75 (s, 2H, $CH{=}CHC(O)$), 5.33−5.29 (m, 6H, $CH_2CH{=}$ $CHCH_2$), 4.54 (m, 1H, $SCH_2CH(O)$), 4.25−4.21 (m, 1H, $SCH_2CH(NH)$), 4.14−3.87 (m, 2H, $SCH_2CH(O)CH_2(O)$), 3.82−3.73 (m, 1H, $NHCH(CH_3)$), 3.70−3.64 (m, 2H, $NHCH_2C(O)$), 3.45−3.33 (m, 2H, $C(O)NHCH_2CH_2N$), 2.65−2.63 (m, 2H, $C(O)NHCH_2CH_2N$), 3.19−3.15 (m, 2H, $SCH_2CH(NH)$), 2.76−2.62 (m, 2H, $SCH_2CH(O)$), 2.38−2.26 (m, 6H, $CH_3(CH_2)_7CH{=}CH(CH_2)_6CH_2C(O)$), 2.09−1.88 (m, 12H, $CH_3(CH_2)_6CH_2CH{=}CHCH_2$–$(CH_2)_6C(O)$), 1.60 (m, 6H, $CH_3(CH_2)_7CH{=}CH(CH_2)_5CH_2CH_2C(O)$), 1.46−1.32 (m, 60H, $CH_3(CH_2)_6CH_2CH{=}CHCH_2(CH_2)_4(CH_2)_2C$-$(O)$), 1.30−1.26 (d, J = 5.8 Hz, 3H, $NHCH(CH_3)C(O)$), 0.85 (t, J = 3.9 Hz, 9H, $CH_3(CH_2)_7CH{=}CH(CH_2)_7C(O)$). ^{13}C NMR (75 MHz, $CDCl_3$): δ 175.53 ($CH_3(CH_2)_7CH{=}CH$-$(CH_2)_7C(O)N$), 174.14, 174.80 (2 × $CH_3(CH_2)_7CH{=}CH$-$(CH_2)_7C(O)O$), 172.18 ($SCH_2CH(NH)C(O)$), 171.10 ($NHCH$-$(CH_3)C(O)$), 169.92 ($NHCH_2C(O)$), 161.31 (2 × $CH{=}$ $CHC(O)$), 135.00 (2 × $CH{=}CHC(O)$), 130.64 (6 × $CH_2CH{=}$ $CHCH_2$), 55.90 (2 × $SCH_2CH(O)CH_2(O)$), 54.11 (SCH_2CH-(NH)), 50.84 ($NHCH(CH_3)$), 43.92 ($NHCH_2C(O)$), 38.92 ($C(O)NHCH_2CH_2N$), 37.76 ($C(O)NHCH_2CH_2N$), 37.40 ($SCH_2CH(NH)$), 36.89 (2 × $CH_3(CH_2)_7CH{=}CH(CH_2)_6$-$CH_2C(O)O$), 34.78 ($CH_3(CH_2)_7CH{=}CH(CH_2)_6CH_2C(O)N$), 32.58 ($SCH_2CH(O)$), 30.45 (3 × $CH_3CH_2CH_2(CH_2)_5CH{=}$ $CH(CH_2)_7C(O)$), 27.90, 29.83, 29,99, 30.21 (24 × CH_3-$(CH_2)_2(CH_2)_4CH_2CH{=}CHCH_2(CH_2)_4(CH_2)_2C(O)$), 26.26 (6 × $CH_3(CH_2)_6CH_2CH{=}CHCH_2(CH_2)_6C(O)$), 25.53 (3 × $CH_3(CH_2)_7CH{=}CH(CH_2)_5CH_2CH_2C(O)$), 23.35 (3 × CH_3-$CH_2(CH_2)_6CH{=}CH(CH_2)_7C(O)$), 19.17 ($NHCH(CH_3)C(O)$), 14.79 (3 × $CH_3(CH_2)_7CH{=}CH(CH_2)_7C(O)$).

***N*-{[2,3-Bis(oleoyloxy)-(2*RS*)-propyl]-*N*-oleoyl-(*R*)-cysteinyl-(*S*)-seryl-(*S*)-seryl}aminoethoxy-ethoxyethyl-2-bromoacetamide (Ol_3CAG-Br) (14).** Compound **12** (70 mg, 70.8 μmol) was dissolved in CH_2Cl_2 (1.5 mL). After addition of BOP (37 mg, 85 μmol) and DIEA (19 μL, 106.2 μmol), the reaction was continued for 30 min at 0 °C under stirring. The amine **5** (43.4 mg, 85.0 μmol) in DMF (100 μL) was then added. After 20 h at room temperature, the mixture was washed with 3 × 2 mL of a citric acid solution 5% (w/v) followed by 3 × 2 mL of water. The organic phase was dried over $MgSO_4$, and the solvent was evaporated under reduced pressure. The residue was chromatographed on silica gel, and after elution with CH_2Cl_2:MeOH 40:1 to 20:1, the compound **14**, after lyophilization from *tert*-butyl alcohol, was obtained as a white solid (11 mg; yield 11%). R_f =

0.35 (CH_2Cl_2:MeOH 12:1). ^{1}H NMR (300 MHz, $CDCl_3$:MeOD 1:1): δ 5.35−5.28 (m, 6H, C*H*=C*H*), 4.55−4.51 (m, 1H, SCH_2CH(O)), 4.31−4.24 (m, 1H, SCH_2CH(NH)), 4.11−4.08 (m, 2H, $SCH_2CH(O)CH_2$(O)), 4.02−3.92 (m, 1H, $NHCH(CH_3)$), 3.87−3.84 (m, 2H, $NHCH_2C$(O)), 3.82 (s, 2H, CH_2Br), 3.61−3.38 (m, 12H, $(CH_2)_2O(CH_2)_2O(CH_2)_2$), 3.02−2.81 (m, 2H, SCH_2CH(NH)), 2.77−2.64 (m, 2H, SCH_2CH(O)), 2.33−2.23 (m, 6H, $CH_3(CH_2)_7CH$=$CH(CH_2)_6CH_2C$(O)), 2.08−1.89 (m, 12H, $CH_3(CH_2)_6CH_2$-CH=$CHCH_2(CH_2)_6C$(O)), 1.69−1.50 (m, 6H, $CH_3(CH_2)_7CH$=$CH(CH_2)_5CH_2CH_2C$(O)), 1.40−1.38 (d, J = 6.8 Hz, 3H, $NHCH(CH_3)C$(O)), 1.36−1.13 (m, 60H, $CH_3(CH_2)_6CH_2$-CH=$CHCH_2(CH_2)_4(CH_2)_2C$(O)), 0.86 (t, J = 6.5 Hz, 9H, $CH_3(CH_2)_7CH$=$CH(CH_2)_7C$(O)). ^{13}C NMR (75 MHz, $CDCl_3$): δ 175.23 ($CH_3(CH_2)_7CH$=$CH(CH_2)_7C$(O)N), 174.45, 174.83 (2 × $CH_3(CH_2)_7CH$=$CH(CH_2)_7C$(O)O), 173.47 (SCH_2CH(NH)C(O)), 171.53 ($NHCH(CH_3)C$(O)), 170.02 ($NHCH_2$-C(O)), 165.21 ($NHC(O)CH_2$Br), 129.86, 130.18 (6 × CH=CH), 69.59, 70.28 (4 × $CH_2O(CH_2)_2OCH_2$), 55.80 (2 × $SCH_2CH(O)CH_2$(O)), 52.62 (SCH_2CH(NH)), 49.86 ($NHCH(CH_3)$), 42.71 ($NHCH_2C$(O)), 39.96, 40.10 (2 × $NHCH_2$-CH_2O), 36.32 (SCH_2CH(NH)), 36.03 (2 × $CH_3(CH_2)_7CH$=$CH(CH_2)_6CH_2C(O)O$), 34.79 ($CH_3(CH_2)_7CH$=$CH(CH_2)_6$-$CH_2C(O)N$), 32.06 (SCH_2CH(O)), 31.74 (3 × CH_3CH_2-$CH_2(CH_2)_5CH$=$CH(CH_2)_7C$(O)), 29.91 (CH_2Br), 27.35, 29.30, 29.46, 29,66 (24 × $CH_3(CH_2)_2(CH_2)_4CH_2CH$=$CHCH_2(CH_2)_4(CH_2)_2C$(O)), 25.76 (6 × $CH_3(CH_2)_6CH_2CH$=$CHCH_2(CH_2)_6C$(O)), 25.02 (3 × $CH_3(CH_2)_7CH$=$CH(CH_2)_5$-CH_2CH_2C(O)), 22.81 (3 × $CH_3CH_2(CH_2)_6CH$=$CH(CH_2)_7$-C(O)), 18.81 ($NHCH(CH_3)C$(O)), 14.15 (3 × $CH_3(CH_2)_7$-CH=$CH(CH_2)_7C$(O)).

***N*-(*tert*-Butyloxycarbonyl)-(*S*)-[2,3-bis(palmitoyloxy)propyl]-(*R*)-cysteine (16).** Potassium fluoride (182 mg, 3.13 mmol) and triethylamine (135 μL, 0.96 mmol) were added to compound **15** (*48)* (400 mg, 0.45 mmol) in DMF (4 mL). Di-*tert*-butyloxycarbonyl (127 mg, 0.58 mmol) was then added to the mixture, and the reaction was performed at room temperature. After 24 h, AcOEt (5 mL) was added to the reaction mixture, and the organic phase was then washed successively with 5 mL each of water, HCl solution 5% (w/v), $NaHCO_3$ solution 5% (w/v), and finally with a saturated NaCl solution. After being dried over $MgSO_4$, the solvent was evaporated under vacuum. The obtained residue was chromatographed on silica gel and compound **16**, eluted with CH_2Cl_2:MeOH 20:1, was obtained in a colorless oil (174 mg; yield 51%). R_f 0.61 (CH_2Cl_2:MeOH 6:1). ^{1}H NMR (200 MHz, $CDCl_3$:MeOD 1:1): δ 5.17−5.13 (m, 1H, SCH_2CH(O)), 4.42−4.34 (m, 1H, SCH_2CH(NH)), 4.27−4.09 (m, 2H, $SCH_2CH(O)CH_2$(O)), 3.06−2.98 (m, 2H, SCH_2CH(NH)), 2.86−2.73 (m, 2H, SCH_2CH(O)), 2.33−2.26 (m, 4H, CH_3-$(CH_2)_{13}CH_2C$(O)), 1.71−1.52 (m, 4H, $CH_3(CH_2)_{12}CH_2$-CH_2C(O)), 1.43 (s, 9H, $C(CH_3)_3$), 1.37−1.18 (m, 48H, $CH_3(CH_2)_{12}(CH_2)_2C$(O)), 0.86 (t, J = 6.8 Hz, 6H, CH_3-$(CH_2)_{14}C$(O)). ^{13}C NMR (50 MHz, $CDCl_3$): δ 175.24 (SCH_2-CH(NH)C(O)), 174.09, 174.47 (2 × $CH_3(CH_2)_{14}C$(O)), 156.64 (C(O)OC(CH_3)$_3$), 80.18 ($C(CH_3)_3$), 71.32 (SCH_2CH-(O)), 64.38 (SCH_2CH(NH)), 55.19 ($SCH_2CH(O)CH_2$(O)), 35.99 (SCH_2CH(NH)), 34.66, 34.86 (2 × $CH_3(CH_2)_{13}CH_2C$-(O)), 33.38 (SCH_2CH(O)), 32.56 (2 × $CH_3CH_2CH_2(CH_2)_{12}C$-(O)), 29.73, 29.98, 30.15, 30.31 (20 × $CH_3CH_2CH_2(CH_2)_{10}$-$(CH_2)_2C$(O)), 28.69 (3 × $C(CH_3)_3$), 25.55 (2 × $CH_3(CH_2)_{12}$-CH_2CH_2C(O)), 23.28 (2 × $CH_3CH_2(CH_2)_{13}C$(O)), 14.40 (2 × $CH_3(CH_2)_{14}C$(O)).

***N*-(*tert*-Butyloxycarbonyl)-(*S*)-[2,3-bis(palmitoyloxy)propyl]-(*R*)-cysteinyl-(*S*)-alanyl-glycine Benzyl Ester (17).** BOP (42 mg, 95.2 μmoles) was added to a solution of **16** (60.0 mg, 79.3 μmol) in CH_2Cl_2 (500 μL), and the mixture was stirred at 0 °C for 30 min. The amine H_2N-Ala-Gly-OBz (33.4 mg, 95.2 μmol) in 1 mL of CH_2Cl_2:DMF 9:1 was then added to the reaction mixture followed by DIEA (21 μL, 119.0 μmol). The reaction was continued at room temperature for 20 h. The organic phase was then washed with 3 × 2 mL of a citric acid solution 5% (w/v) followed by 2 mL of water. After being dried over $MgSO_4$, the solvent was evaporated in vacuo and the product was purified on silica gel, eluted with CH_2Cl_2:MeOH 80:1. Compound **17** was obtained in a solid form (53 mg; yield 67%). R_f 0.45 (CH_2Cl_2:MeOH 30:1). ^{1}H NMR (300 MHz, $CDCl_3$:MeOD 1:1): δ 7.32 (m, 5H, Ph), 5.14 (s, 2H OCH_2Ph), 5.13 (m, 1H, SCH_2CH(O)), 4.45−4.39 (m, 1H, SCH_2CH(NH)), 4.35−4.21 (m, 2H, SCH_2CH-$(O)CH_2$(O)), 4.17−4.11 (m, 1H, $NHCH(CH_3)$), 3.98 (m, 2H, $NHCH_2C$(O)), 3.01−2.79 (m, 2H, SCH_2CH(NH)), 2.76−2.74 (m, 2H, SCH_2CH(O)), 2.38−2.24 (m, 4H, CH_3-$(CH_2)_{13}CH_2C$(O)), 1.68−1.51 (m, 4H, $CH_3(CH_2)_{12}CH_2$-CH_2C(O)), 1.42 (s, 9H, $C(CH_3)_3$), 1.38−1.36 (d, J = 7.2 Hz, 3H, $NHCH(CH_3)C$(O)), 1.34−1.18 (m, 48H, CH_3-$(CH_2)_{12}(CH_2)_2C$(O)), 0.86 (t, J = 6.8 Hz, 6H, $CH_3(CH_2)_{14}C$-(O)). ^{13}C NMR (75 MHz, $CDCl_3$): δ 174.51 (SCH_2CH(NH)-C(O)), 174.02, 174.30 (2 × $CH_3(CH_2)_{14}C$(O)), 171.95 ($NHCH(CH_3)C$(O)), 171.30 ($NHCH_2C$(O)), 128.21, 128.69, 128.98, 135.37 (6 × Ph), 156.20 (C(O)OC(CH_3)$_3$), 80.84 ($C(CH_3)_3$), 71.03 (SCH_2CH(O)), 67.64 (SCH_2CH(NH), OCH_2Ph), 53.99 ($SCH_2CH(O)CH_2$(O)), 49.84 ($NHCH$-(CH_3)), 41.65 ($NHCH_2C$(O)), 35.98 (SCH_2CH(NH)), 34.62, 34.82 (2 × $CH_3(CH_2)_{13}CH_2C$(O)), 32.60 (SCH_2CH(O)), 32.49 (2 × $CH_3CH_2CH_2(CH_2)_{12}C$(O)), 29.65, 29.89, 30.07, 30.23 (20 × $CH_3CH_2CH_2(CH_2)_{10}(CH_2)_2C$(O)), 28.51 (3 × $C(CH_3)_3$), 25.46 (2 × $CH_3(CH_2)_{12}CH_2CH_2C$(O)), 23.21 (2 × $CH_3CH_2(CH_2)_{13}C$(O)), 17.72 ($NHCH(CH_3)C$(O)), 14.33 (2 × $CH_3(CH_2)_{14}C$(O)). ES-MS *m/z*: 1012.6295 ([M + Na]$^+$), calcd: 989.6395 for $C_{55}H_{95}N_3O_{10}S$.

***N*-(*tert*-Butyloxycarbonyl)-(*S*)-[2,3-bis(palmitoyloxy)propyl]-(*R*)-cysteinyl-(*S*)-alanyl-glycine (18).** Compound **17** (50 mg, 50.5 μmol) was dissolved in methanol (16 mL). After addition of anhydrous ammonium formate (9.6 mg, 151.5 μmol) and Pd/C 10% (50 mg), the reaction mixture was put under H_2. The hydrogenation reaction was performed at room temperature under stirring for 4 h. Pd/C was then removed by filtration over Celite, and the solvent was evaporated in vacuo. After purification on silica gel and elution with CH_2Cl_2:MeOH 60:1 to 10:1, compound **18** was obtained (26 mg; yield 51%). R_f 0.20 (CH_2Cl_2:MeOH 9:1). ^{1}H NMR (300 MHz, $CDCl_3$:MeOD 1:1): δ 5.15−5.12 (m, 1H, SCH_2CH(O)), 4.40−4.36 (m, 1H, SCH_2CH(NH)), 4.30−4.13 (m, 2H, $SCH_2CH(O)CH_2$(O)), 3.87−3.80 (m, 1H, $NHCH(CH_3)$), 3.67−3.62 (m, 2H, $NHCH_2C$(O)), 3.05−2.86 (m, 2H, SCH_2CH(NH)), 2.84−2.67 (m, 2H, SCH_2CH(O)), 2.34−2.27 (m, 4H, $CH_3(CH_2)_{13}CH_2C$(O)), 1.67−1.51 (m, 4H, $CH_3(CH_2)_{12}CH_2CH_2C$(O)), 1.43 (s, 9H, $C(CH_3)_3$), 1.40−1.37 (d, J = 7.1 Hz, 3H, $NHCH(CH_3)C$(O)), 1.35−1.12 (m, 48H, $CH_3(CH_2)_{12}(CH_2)_2C$(O)), 0.85 (t, J = 7.1 Hz, 6H, $CH_3(CH_2)_{14}C$(O)).

***(S)*-[2,3-Bis(palmitoyloxy)propyl]-(*R*)-cysteinyl-(*S*)-alanylglycine (Pam_2CAG) (19).** Compound **18** was prepared from **17** according to the procedure used to obtain the amine **2**. White solid (20 mg; yield 86%). R_f 0.24 (CH_2Cl_2:MeOH 4:1). ^{1}H NMR (200 MHz, $CDCl_3$:MeOD 1:1): δ 5.26−5.11 (m, 1H, SCH_2CH(O)), 4.44−4.39 (m, 1H, SCH_2CH(NH)), 4.29−4.11 (m, 2H, $SCH_2CH(O)$-CH_2(O)), 3.95−3.86 (m, 1H, $NHCH(CH_3)$), 3.73−3.58 (m, 2H, $NHCH_2C$(O)), 3.15−2.95 (m, 2H, SCH_2CH(NH)), 2.86−2.71 (m, 2H, SCH_2CH(O)), 2.37−2.27 (m, 4H, CH_3-$(CH_2)_{13}CH_2C$(O)), 1.72−1.51 (m, 4H, $CH_3(CH_2)_{12}CH_2$-CH_2C(O)), 1.38−1.35 (d, J = 6.6 Hz, 3H, $NHCH(CH_3)C$-(O)), 1.33−1.13 (m, 48H, $CH_3(CH_2)_{12}(CH_2)_2C$(O)), 0.86 (t,

J = 6.6 Hz, 6H, $CH_3(CH_2)_{14}C(O)$). ^{13}C NMR (75 MHz, $CDCl_3$): δ 174.69 ($SCH_2CH(NH)C(O)$), 174.09, 174.19 (2 × $CH_3(CH_2)_{14}C(O)$), 171.95 ($NHCH(CH_3)C(O)$), 170.60 ($NHCH_2C(O)$), 71.19 ($SCH_2CH(O)$), 67.34 ($SCH_2CH(NH)$), 53.89 ($SCH_2CH(O)CH_2(O)$), 50.28 ($NHCH(CH_3)$), 41.65 ($NHCH_2C(O)$), 35.88 ($SCH_2CH(NH)$), 34.70, 34.82 (2 × $CH_3(CH_2)_{13}CH_2C(O)$), 32.60 ($SCH_2CH(O)$), 32.56 (2 × $CH_3CH_2CH_2(CH_2)_{12}C(O)$), 29.65, 29.78, 30.00, 30.33 (20 × $CH_3CH_2CH_2(CH_2)_{10}(CH_2)_2C(O)$), 25.58 (2 × $CH_3(CH_2)_{12}CH_2CH_2C(O)$), 23.30 (2 × $CH_3CH_2(CH_2)_{13}C(O)$), 17.20 ($NHCH(CH_3)C(O)$), 14.37 (2 × $CH_3(CH_2)_{14}C(O)$). ES-MS m/z: 800.5198 ($[M]^+$), calcd: 800.5198 for $C_{43}H_{81}N_3O_8S$.

***N*-{*N*-(*tert*-Butyloxycarbonyl)-(*S*)-[2,3-bis(palmitoyloxy)propyl]-(*R*)-cysteinyl-(*S*)-alanyl-glycyl}-aminoethylmaleimide (20).** Compound **20** was prepared by the same procedure as above for **13**, using the compound **16** and the amine **7**. It was obtained in a pure form (12 mg; yield 17%) after purification on silica gel and elution with CH_2Cl_2:MeOH 60:1 to 30:1. R_f 0.38 (CH_2Cl_2:MeOH 12:1). ^1H NMR (200 MHz, $CDCl_3$:MeOD 1:1): δ 6.74 (s, 2H, $CH{=}CH$), 5.17−5.14 (m, 1H, $SCH_2CH(O)$), 4.42−4.41 (m, 1H, $SCH_2CH(NH)$), 4.37 (m, 1H, $NHCH(CH_3)$), 4.27−4.16 (m, 2H, $SCH_2CH(O)CH_2(O)$), 3.82−3.70 (m, 2H, $NHCH_2C(O)$), 3.63−3.61 (m, 2H, $C(O)NHCH_2CH_2N$), 3.41−3.38 (m, 2H, $C(O)NHCH_2CH_2N$), 3.04−2.95 (m, 2H, $SCH_2CH(NH)$), 2.84−2.75 (m, 2H, $SCH_2CH(O)$), 2.34−2.28 (m, 4H, $CH_3(CH_2)_{13}CH_2C(O)$), 1.68−1.49 (m, 4H, $CH_3(CH_2)_{12}CH_2CH_2C(O)$), 1.44 (s, 9H, $C(CH_3)_3$), 1.39−1.36 (d, J = 7.3 Hz, 3H, $NHCH(CH_3)C(O)$), 1.34−1.13 (m, 48H, $CH_3(CH_2)_{12}(CH_2)_2C(O)$), 0.86 (t, J = 6.4 Hz, 6H, $CH_3(CH_2)_{14}C(O)$). ^{13}C NMR (75 MHz, $CDCl_3$): δ 174.44 ($SCH_2CH(NH)C(O)$), 172.81, 174.18 (2 × $CH_3(CH_2)_{14}C(O)$), 172.09 ($NHCH(CH_3)C(O)$), 171.72 ($NHCH_2C(O)$), 169.92 (2 × $CH{=}CHC(O)$), 156.60 ($C(O)OC(CH_3)_3$), 134.88 (2 × $CH{=}CH$), 81.50 ($C(CH_3)_3$), 71.05 ($SCH_2CH(O)$), 64.06 ($SCH_2CH(NH)$), 53.99 ($SCH_2CH(O)CH_2(O)$), 50.71 ($NHCH(CH_3)$), 43.88 ($NHCH_2C(O)$), 39.14 ($C(O)NHCH_2CH_2N$), 38.21 ($C(O)NHCH_2CH_2N$), 35.99 ($SCH_2CH(NH)$), 34.77, 34.99 (2 × $CH_3(CH_2)_{13}CH_2C(O)$), 32.60 ($SCH_2CH(O)$), 32.35 (2 × $CH_3CH_2CH_2(CH_2)_{12}C(O)$), 29.78, 29.98, 30.18, 30.38 (20 × $CH_3CH_2CH_2(CH_2)_{10}(CH_2)_2C(O)$), 28.96 (3 × $C(CH_3)_3$), 25.55 (2 × $CH_3(CH_2)_{12}CH_2CH_2C(O)$), 23.36 (2 × $CH_3CH_2(CH_2)_{13}C(O)$), 17.71 ($NHCH(CH_3)C(O)$), 14.79 (2 × $CH_3(CH_2)_{14}C(O)$).

***N*-{(*S*)-(2,3-Bis(palmitoyloxy)propyl)-(*R*)-cysteinyl-(*S*)-alanylglycyl}aminoethylmaleimide (Pam_2CAG-Mal) (21).** Compound **21** was prepared from **20** according to the procedure used to obtain the amine **2**. After lyophilization, it gave a white powder (10 mg; yield 97%). R_f 0.46 (CH_2Cl_2:MeOH 8:1). ^1H NMR (300 MHz, $CDCl_3$:MeOD 1:1): δ 6.75 (s, 2H, $CH{=}CH$), 5.19−5.17 (m, 1H, $SCH_2CH(O)$), 4.42−4.38 (m, 1H, $SCH_2CH(NH)$), 4.31−4.29 (m, 1H, $NHCH(CH_3)$), 4.18−4.04 (m, 2H, $SCH_2CH(O)CH_2(O)$), 3.90−3.84 (m, 2H, $NHCH_2C(O)$), 3.64−3.61 (m, 2H, $C(O)NHCH_2CH_2N$), 3.42−3.34 (m, 2H, $C(O)NHCH_2CH_2N$), 3.24−2.90 (m, 2H, $SCH_2CH(NH)$), 2.80−2.78 (m, 2H, $SCH_2CH(O)$), 2.36−2.28 (m, 4H, $CH_3(CH_2)_{13}CH_2C(O)$), 1.60−1.58 (m, 4H, $CH_3(CH_2)_{12}CH_2CH_2C(O)$), 1.41−1.39 (d, J = 6.8 Hz, 3H, $NHCH(CH_3)C(O)$), 1.37−1.12 (m, 48H, $CH_3(CH_2)_{12}(CH_2)_2C(O)$), 0.85 (t, J = 6.8 Hz, 6H, $CH_3(CH_2)_{14}C(O)$). ES-MS m/z: 922.5060 ($[M]^+$), calcd: 922.5060 for $C_{49}H_{87}N_5O_9S$.

Liposome Preparation. Liposomes were prepared by mixing, in a round-bottom flask, phospholipids (PC, PG) and cholesterol (75/20/50 molar ratio), in chloroform with the appropriate thiol-reactive functionalized or nonfunctionalized lipopeptides at 5 mol %. After solvent evaporation under high vacuum, the dried lipid film was hydrated by vortex mixing after addition of 1 mL buffer (for 10 μmol lipids) containing 5% (w/v) sorbitol as follows: 10 mM HEPES buffer (pH 6.5) for the maleimide derivatives, 10 mM CHES buffer (pH 9.0) for the bromoacetyl derivatives, and HEPES buffer (pH 7.4) for the nonfunctionalized lipopeptides. The resulting suspensions were sonicated at 25 °C for 1 h (5 s cycles interrupted for 1.25 s) under a continuous flow of nitrogen, using a 3 mm diameter probe sonicator (Vibra Cell, Sonics and Material Inc, Danbury, CT) at 300 W. The SUV preparations were finally centrifuged for 10 min at 10 000*g* to remove the titanium dust originating from the probe. All the liposomal formulations were freshly prepared and sterilized before use with the cells.

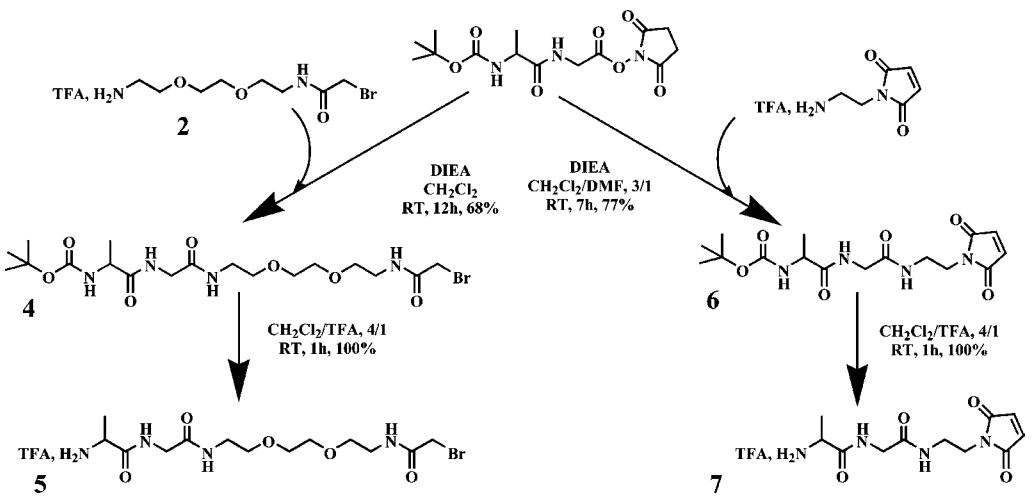
Peptide Conjugation to Liposomes Containing Thiol-Reactive Lipopeptide Derivatives. HA307-319-C, pretreated with TCEP (0.7 equiv vs peptide) to reduce the disulfide bond of any oxidized form of the peptide, was added to freshly prepared liposomes containing thiol-reactive functionalized lipopeptides (2 molar excess of peptide vs surface accessible thiol-reactive functions). The coupling of the peptide was performed at room temperature, under argon, in 10 mM HEPES (pH 6.5) or CHES (pH 9.0) buffers containing 5% (w/v) sorbitol (see above). After 2 h, a 10-fold excess of 2-mercaptoethanol was added to the preparation to derivatize all the unreacted maleimide or bromoacetyl groups. This step was performed for 1 h under argon after which the liposomal preparation was dialyzed extensively against 10 mM HEPES buffer (pH 7.4) containing 5% (w/v) sorbitol, to eliminate unconjugated peptides and excess reagents.

Analytical Techniques. Phosphorus content of the liposomes preparations was analyzed by a previously described method (*49*). The quantification of peptide associated to the vesicles was achieved by acid hydrolysis of the liposomal formulations (*35*). The amino acids that were generated were then quantitated using a fluorimetric assay with fluorescamine (*50*) as follows: 50 μL of the hydrolysis solution (containing 10 to 50 nmol of amines) were added to 1.5 mL of 50 mM sodium borate buffer (pH 9.0), followed by the addition of 500 μL of a fluorescamine solution in dioxane (300 μg/mL). After rapid mixing, the fluorescence was read immediately at λ_{em} = 475 nm (λ_{exc} = 390 nm). The contribution of the liposomes alone was evaluated using the same conditions and subtracted from the total fluorescence. Hydrolysis of known quantities of free peptides was used as standard. Liposomes were immediately used for the in vitro assays.

Light-Scattering Measurements. The size of the liposomes was determined by dynamic light scattering using a Zeta-master 3000 (Malvern Instruments, Paris, France) with the following specifications: sampling time, 30 s; medium viscosity, 1.014 cP; refractive index, 1.34; scattering angle, 90°; temperature, 25 °C. Data were collected using the multimodal number distribution software included in the instrument. All the formed vesicles were uniformly distributed in size and exhibited average diameters of 50 to 80 nm (±30 nm). No significant vesicles size changes (less than 5%) was measurable after the conjugation of the peptides.

Spleen Cell Proliferation Assay. Approximately 8−12 weeks old BALB/c female mice were sacrificed by cervical dislocation. Their spleens were excised and placed in sterile Petri dishes containing RPMI-1640 medium. Splenocyte suspensions were prepared by passing the minced spleens through a 40 μm cell strainer and were hemolyzed with Gey's buffer (HBSS, 650 mM NH_4Cl, 27 mM glucose). Cells were washed twice and resuspended in culture medium (RPMI-1640 medium

Scheme 2. Synthesis of the Functionalized Spacer-Arms 5 and 7



supplemented with 10% (v/v) fetal bovine serum (FBS), penicillin G and streptomycin, 1% nonessential amino acids, and 50 μM 2-mercaptoethanol). One hundred microliters of the splenocyte suspension at 1.5×10^6 cells/mL was plated in round-bottomed 96-well plates containing 100 μL of different lipopeptide formulations. The splenocytes were incubated for 48 h. [^{3}H]Thymidine (0.7 μCi/well) was then added, and after 18 h, the cells were collected on glass-fiber filters (Wallac, Filtermat A) with an automatic cell harvester (Micro96 Harvester, Skatron). The incorporated radioactivity, expressed as cpm, was determined by liquid scintillation counting (1205 Betaplate, Wallac).

RESULTS

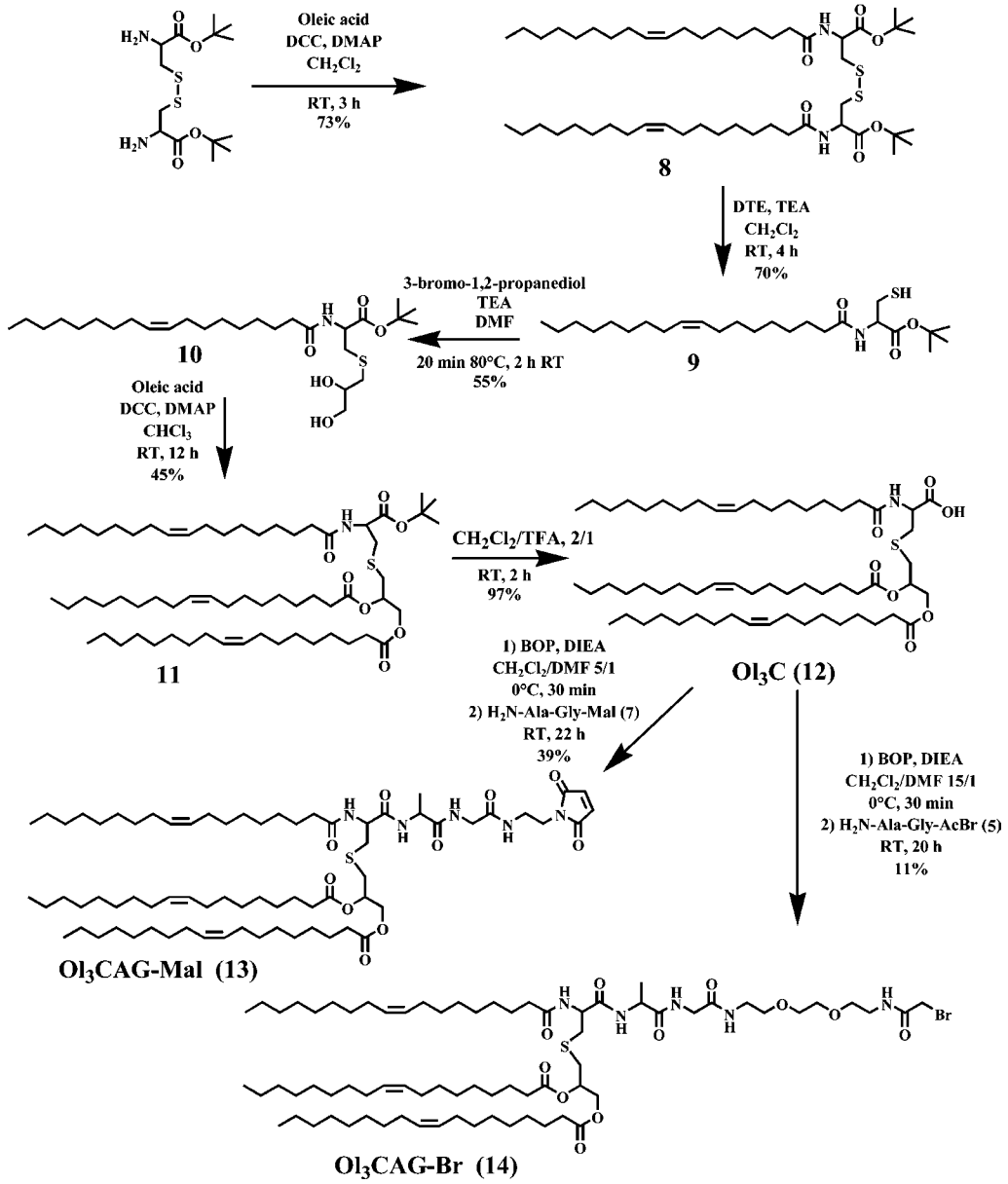
Synthesis. The synthesis of lipopeptides functionalized with the maleimide and bromoacetyl thiol-reactive groups was performed according to the procedures outlined in Schemes 1−4. The preparation of Pam_3CAG-Br (**3**) (Scheme 1) involves the reaction of monoprotected 1,8-diamino-3,6-dioxaoctane with bromoacetic acid succinimidyl ester to afford **1**. After cleavage of the Boc group, the resulting functionalized spacer arm **2** was conjugated to the racemic form of the lipopeptide Pam_3CAG, previously prepared according to refs 45 and 34, to yield **3**.

The synthesis of the two oleoyl chain-containing functionalized lipopeptides **13** and **14** (Scheme 3) first required the production of *S*-[2,3-bis(oleoyloxy)-(2*RS*)-propyl]-*N*-oleoyl-(*R*)-cysteine (Ol_3C; **12**). This was achieved in five steps, essentially following the procedure described by Wiesmuller et al. for the synthesis of Pam_3C (*45)* in which oleic acid was used instead of palmitic acid. The last step consisted of the coupling, in liquid phase, of **12** to the functionalized alanyl-glycine peptides **5** and **7**. The preparation of these two molecules is shown in Scheme 2. Compound **2** or 1-(2-aminoethyl)pyrrole-2,5-dione (*36*) were reacted with the commercially available Boc-AlaGly-OSu in the presence of DIEA to give respectively **4** and **6**. In the latter case, DMF was necessary to dissolve the TFA salt of the maleimide derivative. The final products **5** and **7** were obtained after deprotection of the Boc groups with 20% (v/v) TFA in CH_2Cl_2.

The preparations of Pam_2CAG (**19**) and its maleimide derivative (**21**) are represented in Scheme 4. These syntheses begin with the Fmoc-protected compound **15** prepared as described previously by Metzger et al. (*48)*. However, in contrast to the racemic Pam_3C and Ol_3C series of lipopeptides described above, in the present case we have synthesized the (2*R*)-stereoisomer by using (*S*)-(−)-glycidol as chiral precursor. This was justified because the *R*-isomer has been reported to be a much more potent adjuvant than the opposite isomer (*44*). The Fmoc-protecting group was first converted into a Boc derivative in a single step, by deprotection of the Fmoc with a base, potassium fluoride in the presence of triethylamine, and replacement in situ with a Boc group by reaction with Boc_2O in DMF. This change of protecting group was required by the sensitivity of the malemide moiety (step **20** → **21**) to the basic conditions generally used in Fmoc group removal. The resulting compound **16** was used for the parallel syntheses of **19** and **21**. The preparation of the lipopeptide **19** was performed in three steps. The first one consisted in the conjugation of the Ala-Gly moiety (protected with a benzyl group) by reaction with H_2N-Ala-Gly-OBz after activation of the carboxylic acid of **16** with BOP. Two different conditions were necessary to remove the Boc and benzyl protecting groups. This latter one was classically removed by catalytic hydrogenation with 10% Pd/C in methanol; however, addition of ammonium formate was needed to accelerate the process. The Boc group of the resulting compound **18** was finally cleaved by TFA in CH_2Cl_2 yielding the lipopeptide (*R*-stereoisomer) Pam_2CAG (**19**). The same lipopeptide, but functionalized with a maleimide group (**21**), was synthesized from **16** activated with BOP at 0 °C. The amine **7** (Scheme 2) and DIEA were added to achieve the coupling of the Ala-Gly-Mal moiety and yield compound **20**. A final deprotection gave in quantitative yield the functionalized lipopeptide Pam_2CAG-Mal (2*R*-stereoisomer) (**21**).

Liposome Preparation. Liposomes (small unilamellar vesicles, 50−80 nm diameter) were prepared from egg phosphatidylcholine, phosphatidylglycerol, and cholesterol (molar ratio 75/20/50) to which the different synthesized lipopeptides were added at a 5 mol % ratio. The thiol-reactive group-derivatized lipopeptides incorporated into liposomes were treated with a large excess of the permeant 2-mercaptoethanol before in vitro experiments to inactivate all the reactive functions. The conjugation of a C-terminus thiol functionalized Th peptide (HA 307−319) to the surface of preformed liposomes, containing the lipopeptide derivatives (lipopeptides were quantitatively incorporated into liposomes (*36*)), was also performed under well-defined conditions as described in the Experimental Procedures section. This coupling, which was nearly quantitative, was done to verify whether the covalent linkage of a peptide to our synthetic lipopeptides

Scheme 3. Synthesis of the Functionalized Lipopeptides Ol_3CAG-Mal (13) and Ol_3CAG-Br (14)

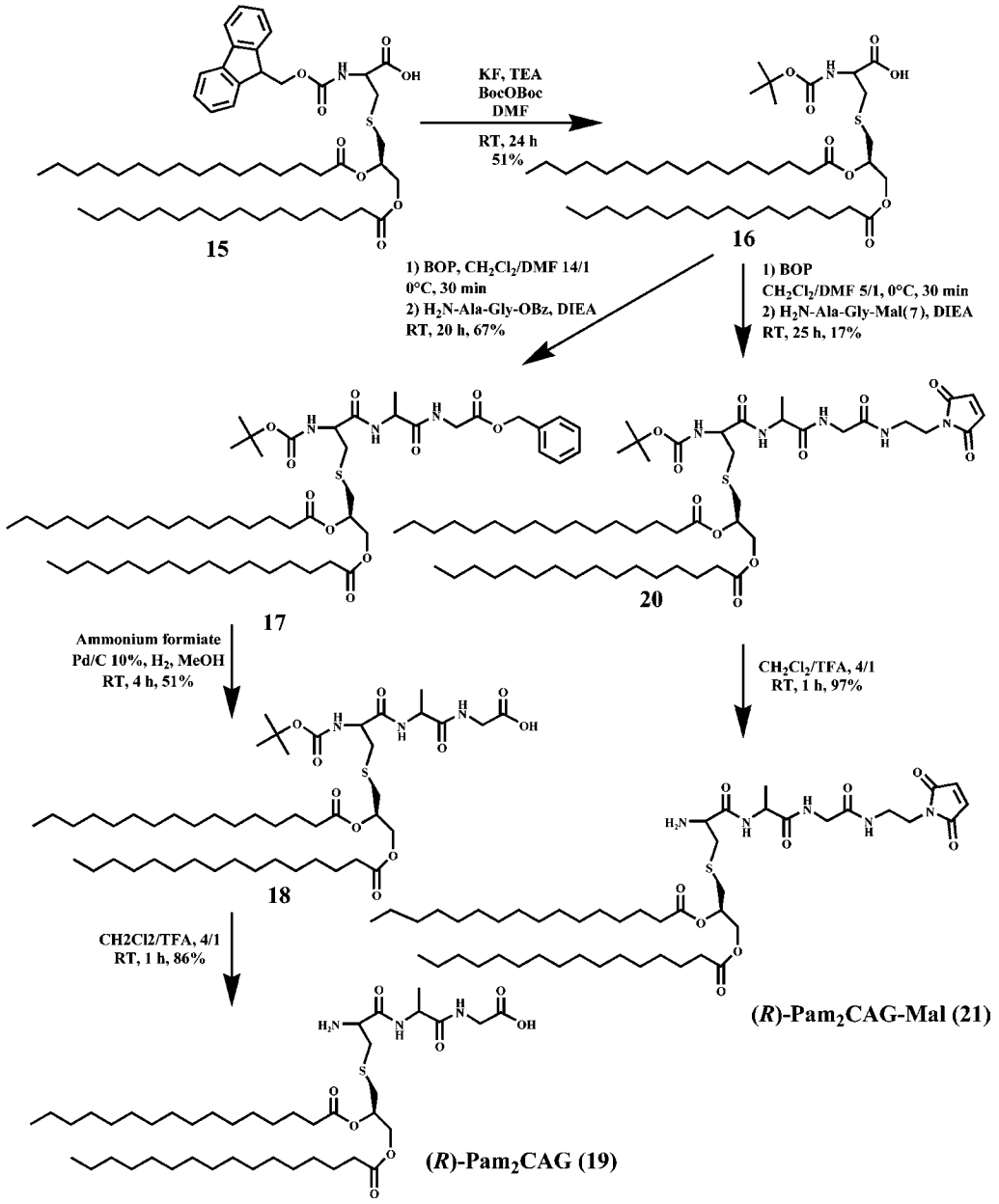


results in a modification of their cellular activities (e.g. mitogenicity).

In Vitro Mouse Splenocyte Proliferation Effect of Free and Liposomal Lipopeptides. In agreement with previous reports (*34*), free (emulsified) synthetic lipopeptide Pam_3CAG induced a dose-dependent BALB/c mouse spleen cell proliferation that was measured by [^{3}H]-thymidine incorporation (Figure 1). After 2 days of culture, cell proliferation was detected with 0.5 nmol of the lipopeptide/mL (Figure 1A). In contrast, the free diacyl lipopeptide Pam_2CAG (**19**) was about 2 times less active, and its mitogenic activity became only measurable at concentrations above 1 nmol/mL (Figure 1B). The incorporation of tripalmitoyl or dipalmitoyl lipopeptides into liposomes (SUV) was not detrimental to their cellular effect; on the contrary, it increased their mitogenic activity, and this effect was more pronounced for Pam_3CAG. Thus, the mitogenicity of Pam_3CAG and Pam_2CAG (**19**) were already measurable at concentrations of about 0.001 (see Figure 1A) and 0.1 nmol/mL (Figure 1B) of liposomal incorporated lipopeptide respectively, i.e., corresponding to about 2 and 1 orders of magnitude increase in potency, respectively.

We next examined the mitogenic activity of the liposomal thiol-reactive lipopeptides that were synthesized in order to conjugate peptide epitopes to the surface of the vesicles. We found that Pam_3CAG-Mal (*36*) lost most of its activity (Figure 1A). In sharp contrast, Pam_3CAG which has been functionalized with a bromoacetyl group (i.e., lipopeptide **3**) remained fully active (Figure 1A). In the dipalmitoyl lipopeptide series, functionalization of Pam_2CAG (**19**) by a maleimide group (lipopeptide **21**) also did not result in a change of its mitogenic activity (Figure 1B). Furthermore, conjugation of a peptide epitope to such a structure did not alter its property (Figures 1A). Finally, lipopeptides containing three oleoyl moieties and functionalized either by a maleimide (**13**) or a bromoacetyl (**14**) group induced, respectively, only a very weak or no proliferative response in splenocytes (Figure 1B). These results underline the major influence of the lipid moiety on the mitogenic properties of these lipopeptide derivatives. Mitogenic activity of the lipopeptides used in this study are also summarized in Table 1. In this table the minimal concentrations necessary to observe a doubling, over control, of [^{3}H]thymidine incorporation in murine splenocytes are compared.

Scheme 4. Synthesis of the Lipopeptides (*R*)-Pam$_2$CAG (19) and (*R*)-Pam$_2$CAG-Mal (21)



DISCUSSION

The aim of this work was the synthesis of analogues of the Pam$_3$C series of immunoadjuvants (*11*−*13*) functionalized with thiol-reactive groups which can be readily incorporated into liposomes and conjugated, under chemically well controlled conditions (*37*), to HS-peptide epitopes to realize self-adjuvanting and molecularly defined vaccination constructs (*35*). To test a representative biological activity of these new lipopeptides we have selected, among the many in vivo and in vitro activities of the "classical" lipopeptides, a prominent characteristic of these molecules such as the in vitro mitogenicity of mouse splenocytes which was shown to result more specifically from a polyclonal activation of B-lymphocytes (*17*, *51*) and to be correlated with their adjuvanticity. Although the molecular mechanisms of splenocytes/B-cell activation remain unknown they most probably involve the mediation of TLRs as was found for LPS (*52*) and some lipopeptides (*53*).

Before studying the thiol-reactive lipopeptide derivatives we have first checked whether incorporation of their nonfunctionalized precursors into liposomes had any incidence on their cellular activity. Compared to its free form, incorporation of the lipopeptide Pam$_3$CAG into phospholipid vesicles resulted in a large (2 orders of magnitude) increase in its mitogenic potency (Table 1). This improvement in activity could be due to a better solubilization of the adjuvant compared to its emulsified form. It also indicates that Pam$_3$CAG is not "buried" within the bilayer of the liposomes but remains fully accessible for example to receptor binding, either at the cell surface (e.g. TLR2), or after internalization. A similar observation, but of lesser amplitude (1 order of magnitude), was found when comparing free and liposomal (2*R*)-Pam$_2$CAG (**19**). Because free diacylated lipopeptides are more soluble per se, their insertion into vesicles might afford a lesser advantage in their stimulating activity. This hypothesis is in agreement with previous reports about the benefits of improved solubility of lipopeptides on increased in vitro stimulation of macrophages (*54*). Similarly, the in vivo immunogenicity of different lipopeptide constructs has been correlated with increased

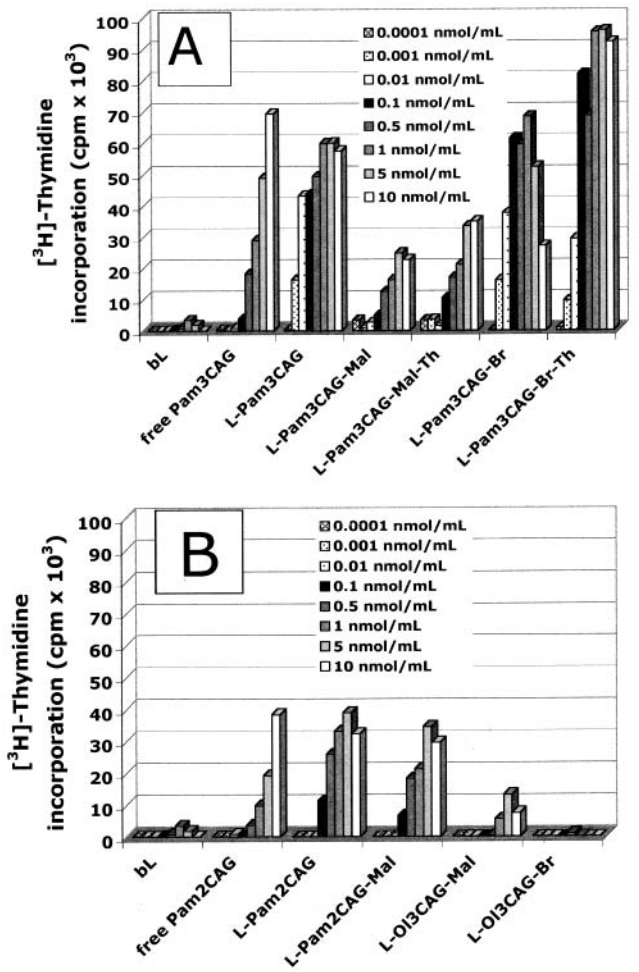


Figure 1. Dose−response relationship for the incorporation of [^{3}H]thymidine in BALB/c mice splenocytes treated with (1A) Pam_3CAG and (1B) Ol_3CAG or (2*R*)-Pam_2CAG, either nonmodified or functionalized by a maleimide or a bromoacetyl group, incorporated in liposomes. Nonmodified lipopeptides were also tested in a free (emulsified) form. Suspensions of 1.5×10^5 splenocytes per well in 200 μL of RPMI 1640 were given lipopeptides (0.0001−10 nmol/mL). After 48 h, 0.7 μCi of [^{3}H]-thymidine was added per well, and the cells were incubated for an additional period of 24 h. The values given as cpm/well and represent means ($n = 3$) for a representative experiment (SD < 6%). Similar results were obtained in four independent experiments. bL, blank liposomes; L, liposomal lipopeptide; maleimide or bromoacetyl functions have been reacted with 2-mercaptoethanol or with the T-helper (Th) peptide PKYVKQNTLKLAT-C (see Experimental Procedures).

solubility (*39*). Finally, these data are also in agreement with those published recently by Dieters and Mühlradt, who showed that MALP-2 in liposomes remains an active macrophage stimulator, both in vitro and in vivo (*55*). At this point, it should also be underlined that free (2*R*)-Pam_2CAG, which we have synthesized because of the particularly powerful activation of immunocompetent cells by MALP-2 (see Introduction), is a less potent activator of murine splenocytes proliferation than Pam_3-CAG (Figure 1 and Table 1) and the previously described Pam_2CFEPPPATTT, i.e., the only other MALP-2 analogue studied on such a cellular model (*56*). This observation indicates that in the MALP-2 series the peptide moiety might be of importance in the solubility and cellular activity of these lipopeptides.

When Pam_3CAG was transformed into Pam_3CAG-Br (**3**) and incorporated into liposomes no change in mitogenic activity could be observed; in comparison liposomal

Table 1. Comparative Mitogenic Activity of the Lipopeptides Used in This Study

	mitogenic activity		
lipopeptides	nmol/mL[a]	stimulation index[b]	maximal incorp.[c] (fold)
Pam_3CAG (free)	0.8	1	4
Pam_2CAG (free)	2	0.4	4
L-Pam_3CAG[d]	0.002	400	3.5
L-Pam_3CAG-Mal	5	0.16	2
L-Pam_3CAG-Mal-Th	2	0.4	2.5
L-Pam_3CAG-Br	0.003	300	4
L-Pam_3CAG-Br−Th	0.008	100	6
L-Pam_2CAG	0.1	8	4
L-Pam_2CAG-Mal	0.3	3	4
L-Ol_3CAG-Mal	5	0.16	2
L-Ol_3CAG-Br	no effect	no effect	1

[a] Minimal lipopeptide concentration necessary to observe a 100% increase of [^{3}H]thymidine incorporation in murine splenocytes compared to control (i.e., incorporation observed with blank liposomes; see Figure 1). [b] Mitogenic efficacy of the lipopeptides and their formulations compared to free Pam_3CAG taken as the test compound. The values were deduced from the first column. [c] Maximal [^{3}H]thymidine incorporation over background (blank liposomes) observed in the concentration range of the lipopeptides, and their formulations, given in Figure 1. [d] L, liposomal lipopeptide; Th, maleimide or bromoacetyl functions have been reacted with the T-helper peptide PKYVKQNTLKLAT-C instead of 2-mercaptoethanol (see Experimental Procedures).

Pam_3CAG-Mal was about 4 orders of magnitude less active. With regard to our vaccination strategy this is a unexpected and important result. It indicates that the C-terminus derivatization of Pam_3CAG with a maleimide or a bromoacetyl group, followed by reaction with a thiol such as 2-mercaptoethanol (or a HS-peptide), can result in dramatic differences in mitogenic potency and probably also in adjuvanticity of the functionalized lipopeptides. This underlines the sensitivity of these molecules to structural changes, e.g. thioether linkages connected to acyclic or cyclic spacers, but at the moment we have no explanation for such a wide difference in cellular activity. It should be stressed, however, that despite the large decrease of mitogenicity of the maleimide derivative, we have previously shown that liposomal constructs in which the T-helper epitopes were conjugated to Pam_3CAG-Mal afforded highly intense and long lasting T-dependent humoral immune responses (*35*). This observation indicates that in these experiments the immunization outcome was largely independent of the lipopeptide-induced B-lymphocyte mitogenicity. Taken together, the results of the present study seem to show that in our previous constructs, the lipopeptide Pam_3CAG-Mal, in the absence of its "normal" adjuvanticity (e.g. via interaction with TLR2), played another prominent role. We propose that it consists of the conveying of the Th epitope cargo within the antigen presenting cells (APCs) and its delivery to the right intracellular compartments containing the MHC-II molecule (see Introduction). Thus, in our future constructs, it would be interesting to use Pam_3CAG-Br to harness the full cellular potential of the "classical" lipopeptide adjuvants in addition to their cellular delivery properties.

A different picture has emerged with lipopeptide analogues in which the number or the nature of the acyl chains have been altered. In contrast to the Pam_3C series, derivatization of (*R*)-Pam_2CAG with a maleimide group did not result in much changes of the mitogenic potency. Thus, liposomal **21** was still active, i.e., about 1 order of magnitude more than Pam_3CAG-Mal. Such a result could originate from the differences in receptor types of the di- and triacyl lipopeptides. Whereas Pam_3CAG is a ligand

of TLR2, the MALP-2 lipopeptides interact preferentially with TLR6 which could be more lenient toward the structural modifications introduced by a maleimide moiety. Finally, the unsaturated acyl chains containing analogues Ol_3CAG-Mal (**13**) and Ol_3CAG-Br (**14**), which were synthesized to be incorporated at higher concentrations in the bilayers of liposomes and thus increase the epitope density at the surface of these vesicles, were the least mitogenic compounds of the series studied here. In analogy to Pam_3CAG-Mal, these analogues should not be expected to be very potent activators of immunocompetent cells in an immune response based, for example, on lymphocytes activation. A similar observation was made recently in a study by v.d. Esche et al. (*27*)., which showed by screening of a fatty acid lipopeptide library, that the Ol_3CSK_4 was much less active in, for example, the induction of NO release by macrophages, than Pam_3CSK_4, which is one of the most powerful lipopeptide adjuvants known. This result, which underlines the paramount importance of the nature of the lipopeptides fatty acid chains on the adjuvanticity of these compounds, does not, however, a priori, exclude the use of these analogues when the subcellular delivery of peptide epitopes is the sole aim.

In conclusion, our studies indicate that within the Pam_3C series of lipopeptides, C-terminus derivatization of the tripeptide moiety with a bromoacetyl group, to conjugate a HS-peptide epitope, bears no significant incidence on mouse splenocyte proliferation which is a hallmark of these adjuvants. It follows that liposomal Pam_3CAG-Br, which is a potent mitogen, represents a very attractive adjuvant for the design of synthetic epitope-driven vaccines. Pam_2C and Ol_3C, the other series studied here, are less mitogenic and consequently will benefit less, as immunoadjuvants, from some of the cellular activities of the "classical" lipopeptides; however, their liposomal forms could still be of great interest for the subcellular delivery of epitopes in APCs.

ACKNOWLEDGMENT

A.R. thanks the CNRS and the Région Alsace for a fellowship (BDI). S.E. had a postdoctoral grant (EX125-2002) from the Ministerio de Ciencia y Tecnología (Spain). This work was supported by the Ligue Nationale Contre le Cancer-Comité du Haut-Rhin.

LITERATURE CITED

(1) Arnon, R., and Horwitz, R. J. (1992) Synthetic peptides as vaccines. *Curr. Opin. Immunol. 4*, 449−453.

(2) Brown, F. (1994) Synthetic peptides and purified antigens as vaccines. *Int. J. Technol. Assess Health Care 10*, 161−166.

(3) BenYedidia, T., and Arnon, R. (1997) Design of peptide and polypeptide vaccines. *Curr. Opin. Biotechnol. 8*, 442−448.

(4) Arnon, R., and Ben-Yedidia, T. (2003) Old and new vaccine approaches. *Int. Immunopharmacol. 3*, 1195−1204.

(5) Purcell, A. W., Zeng, W. G., Mifsud, N. A., Ely, L. K., MacDonald, W. A., and Jackson, D. C. (2003) Dissecting the role of peptides in the immune response: Theory, practice and the application to vaccine design. *J. Pept. Sci. 9*, 255−281.

(6) Tam, J. P. (1996) Recent advances in multiple antigen peptides. *J. Immunol. Methods 196*, 17−32.

(7) Jackson, D. C., O'Brien-Simpson, N., Ede, N. J., and Brown, L. E. (1997) Free radical induced polymerization of synthetic peptides into polymeric immunogens. *Vaccine, 15*, 1697−1705.

(8) Schijns, V. (2001) Induction and direction of immune responses by vaccine adjuvants. *Crit. Rev. Immunol. 21*, 75−85.

(9) Singh, M., and O'Hagan, D. T. (2002) Recent advances in vaccine adjuvants. *Pharmaceut. Res. 19*, 715−728.

(10) Hunter, R. L. (2002) Overview of vaccine adjuvants: present and future. *Vaccine 20*, S7−S12.

(11) Bessler, W. G., and Jung, G. (1992) Synthetic lipopeptides as novel adjuvants. *Res. Immunol. 143*, 548−553.

(12) Bessler, W. G., Baier, W., van den Esche, U., Hoffmann, P., Heinevetter, L., Wiesmüller, K.-H., and Jung, G. (1997) Bacterial lipopeptides constitute efficient novel immunogens and adjuvants in parenteral and oral immunization. *Behring Inst. Mitt. 98*, 390−399.

(13) Wiesmuller, K. H., Fleckenstein, B., and Jung, G. (2001) Peptide vaccines and peptide libraries. *Biol. Chem. 382*, 571−579.

(14) Deres, K., Schild, H., Wiesmüller, K. H., Jung, G., and Rammensee, H. G. (1989) In vivo priming of virus-specific cytotoxic T lymphocytes with synthetic lipopeptide vaccine. *Nature 342*, 561−564.

(15) Reitermann, A., Metzger, J., Wiesmüller, K.-H., Jung, G., and Bessler, W. G. (1989) Lipopeptide derivatives of bacterial lipoprotein constitute potent immune adjuvants combined with or covalently coupled to antigen or hapten. *Biol. Chem. 370*, 343−352.

(16) Wiesmuller, K. H., Bessler, W. G., and Jung, G. (1992) Solid-phase peptide synthesis of lipopeptide vaccines eliciting epitope-specific B-helper, T-helper and T-killer cell response. *Int. J. Pept. Protein Res. 40*, 255−260.

(17) Bessler, W. G., Cox, M., Lex, A., Suhr, B., Wiesmüller, K. H., and Jung, G. (1985) Synthetic lipopeptide analogues of bacterial lipoprotein are potent polyclonal activators for murine B-lymphocytes. *J. Immunol. 135*, 1900−1905.

(18) Hoffmann, P., Heinle, S., Schade, U. F., Loppnow, H., Ulmer, A. J., Flad, H. D., Jung, G., and Bessler, W. G. (1988) Stimulation of human and murine adherent cells by bacterial lipoprotein and synthetic lipopeptide analogues. *Immunobiology 177*, 158−170.

(19) Takeda, K., Kaisho, T., and Akira, S. (2003) Toll-like receptors. *Annu. Rev. Immunol. 21*, 335−376.

(20) Takeuchi, O., Sato, S., Horiuchi, T., Hoshino, K., Takeda, K., Dong, Z. Y., Modlin, R. L., and Akira, S. (2002) Role of Toll-like receptor 1 in mediating immune response to microbial lipoproteins. *J. Immunol. 169*, 10−14.

(21) Hertz, C. J., Kiertscher, S. M., Godowski, P. J., Bouis, D. A., Norgard, M. V., Roth, M. D., and Modlin, R. L. (2001) Microbial lipopeptides stimulate dendritic cell maturation via toll-like receptor 2. *J. Immunol. 166*, 2444−2450.

(22) Wolf, B., Uhl, B., Hauschildt, S., Metzger, J., Jung, G., and Bessler, W. G. (1989) Interaction of the lymphoid cell line BCL1 with lipopeptide analogues of bacterial lipoprotein: electron energy loss spectroscopy (EELS) as a novel method to detect the distribution of the activator within the cells. *Immunobiology 180*, 93−100.

(23) Uhl, B., Wolf, B., Schwinde, A., Metzger, J., Jung, G., Bessler, W. G., and Hauschildt, S. (1991) Intracellular localization of a lipopeptide macrophage activator: Immunocytochemical investigations and EELS analysis on ultrathin cryosections of bone marrow-derived macrophages. *J. Leukocyte Biol. 50*, 10−18.

(24) Stittelaar, K. J., Hoogerhout, P., Ovaa, W., vanBinnendijk, R. R. S., Poelen, M. C. M., Roholl, P., vanEls, C., Osterhaus, A., and Wiertz, E. (2001) In vitro processing and presentation of a lipidated cytotoxic T-cell epitope derived from measles virus fusion protein. *Vaccine 20*, 249−261.

(25) Andrieu, M., Desoutter, J. F., Loing, E., Gaston, J., Hanau, D., Guillet, J. G., and Hosmalin, A. (2003) Two human immunodeficiency virus vaccinal lipopeptides follow different cross-presentation pathways in human dendritic cells. *J. Virol. 77*, 1564−1570.

(26) Kleine, B., Rapp, W., Wiesmuller, K. H., Edinger, M., Beck, W., Metzger, J., Ataulakhanov, R., Jung, G., and Bessler, W. G. (1994) Lipopeptide-polyoxyethylene conjugates as mitogens and adjuvants. *Immunobiology 190*, 53−66.

(27) v.d. Esche, U., Ayoub, M., Pfannes, S. D., Muller, M. R., Huber, M., Wiesmuller, K. H., Loop, T., Humar, M., Fischbach, K. F., Strunkelnberg, M., Hoffmann, P., Bessler, W. G., and Mittenbuhler, K. (2000) Immunostimulation by bacterial components: I. Activation of macrophages and enhancement

of genetic immunization by the lipopeptide P3CSK4. *Int. J. Immunopharmacol. 22*, 1093−1102.
(28) Bourel-Bonnet, L., Bonnet, D., Malingue, F., Gras-Masse, H., and Melnyk, O. (2003) Simultaneous lipidation of a characterized peptide mixture by chemoselective Ligation. *Bioconjugate Chem. 14*, 494−499.
(29) Gras-Masse, H. (2001) Chemoselective ligation and antigen vectorization. *Biologicals 29*, 183−188.
(30) BenMohamed, L., Wechsler, S. L., and Nesburn, A. B. (2002) Lipopeptide vaccines—yesterday, today, and tomorrow. *Lancet Infect. Dis. 2*, 425−431.
(31) Frisch, B., Muller, S., Briand, J. P., Van Regenmortel, M. H., and Schuber, F. (1991) Parameters affecting the immunogenicity of a liposome-associated synthetic hexapeptide antigen. *Eur. J. Immunol. 21*, 185−193.
(32) Friede, M., Muller, S., Briand, J. P., Van Regenmortel, M. H., and Schuber, F. (1993) Induction of immune response against a short synthetic peptide antigen coupled to small neutral liposomes containing monophosphoryl lipid A. *Mol. Immunol. 30*, 539−547.
(33) Friede, M., Muller, S., Briand, J. P., Plaue, S., Fernandes, I., Frisch, B., Schuber, F., and Van Regenmortel, M. H. (1994) Selective induction of protection against influenza virus infection in mice by a lipid-peptide conjugate delivered in liposomes. *Vaccine 12*, 791−797.
(34) Fernandes, I., Frisch, B., Muller, S., and Schuber, F. (1997) Synthetic lipopeptides incorporated in liposomes: In vitro stimulation of the proliferation of murine splenocytes and in vivo induction of an immune response against a peptide antigen. *Mol. Immunol. 34*, 569−576.
(35) Boeckler, C., Dautel, D., Schelté, P., Frisch, B., Wachsmann, D., Klein, J. P., and Schuber, F. (1999) Design of highly immunogenic liposomal constructs combining structurally independent B cell and T helper cell peptide epitopes. *Eur. J. Immunol. 29*, 2297−2308.
(36) Boeckler, C., Frisch, B., and Schuber, F. (1998) Design and synthesis of thiol-reactive lipopeptides. *Bioorg. Med. Chem. Lett. 8*, 2055−2058.
(37) Schelté, P., Boeckler, C., Frisch, B., and Schuber, F. (2000) Differential reactivity of maleimide and bromoacetyl functions with thiols: application to the preparation of liposomal diepitope constructs. *Bioconjugate Chem. 11*, 118−128.
(38) Rharbaoui, F., Drabner, B., Borsutzky, S., Winckler, U., Morr, M., Ensoli, B., Mühlradt, P. F., and Guzman, C. A. (2002) The Mycoplasma-derived lipopeptide MALP-2 is a potent mucosal adjuvant. *Eur. J. Immunol. 32*, 2857−2865.
(39) Zeng, W. G., Ghosh, S., Lau, Y. F., Brown, L. E., and Jackson, D. C. (2002) Highly immunogenic and totally synthetic lipopeptides as self-adjuvanting immuno-contraceptive vaccines. *J. Immunol. 169*, 4905−4912.
(40) Mühlradt, P. F., Kiess, M., Meyer, H., Sussmuth, R., and Jung, G. (1997) Isolation, structure elucidation, and synthesis of a macrophage stimulatory lipopeptide from Mycoplasma fermentans acting at picomolar concentration. *J. Exp. Med. 185*, 1951−1958.
(41) Takeda, K., Takeuchi, O., and Akira, S. (2002) Recognition of lipopeptides by Toll-like receptors. *J. Endotoxin Res. 8*, 459−463.
(42) Morr, M., Takeuchi, O., Akira, S., Simon, M. M., and Mühlradt, P. F. (2002) Differential recognition of structural details of bacterial lipopeptides by toll-like receptors. *Eur. J. Immunol. 32*, 3337−3347.
(43) Weigt, H., Mühlradt, P. F., Emmendorffer, A., Krug, N., and Braun, A. (2003) Synthetic mycoplasma-derived lipopeptide MALP-2 induces maturation and function of dendritic cells. *Immunobiology 207*, 223−233.
(44) Takeuchi, O., Kaufmann, A., Grote, K., Kawai, T., Hoshino, K., Morr, M., Mühlradt, P. F., and Akira, S. (2000) Preferentially the R-stereoisomer of the mycoplasmal lipopeptide macrophage-activating lipopeptide-2 activates immune cells through a toll-like receptor 2-and MyD88-dependent signaling pathway. *J. Immunol. 164*, 554−557.
(45) Wiesmüller, K. H., Jung, G., and Hess, G. (1983) Synthesis of the mitogenic *S*-[2,3-bis(palmitoyloxy)propyl]-*N*-palmytoylpentapeptide from *Escherichia Coli* lipopeptide. *Hoppe-Seyler's Z. Physiol. Chem. 364*, 593−606.
(46) Metzger, J., Jung, G., Bessler, W. G., Hoffmann, P., Strecker, M., Lieberknecht, A., and Schmidt, U. (1991) Lipopeptides containing 2-(palmitoylamino)-6,7-bis(palmitoyloxy)-heptanoic acid: Synthesis, stereospecific stimulation of B-lymphocytes and macrophages, and adjuvanticity in vivo and in vitro. *J. Med. Chem. 34*, 1969−1974.
(47) Trester-Zedlitz, M., Kamada, K., Burley, S. K., Fenyo, D., Chait, B. T., and Muir, T. W. (2003) A modular cross-linking approach for exploring protein interactions. *J. Am. Chem. Soc. 125*, 2416−2425.
(48) Metzger, J. W., Wiesmuller, K. H., and Jung, G. (1991) Synthesis of N alpha-Fmoc protected derivatives of S−(2,3-dihydroxypropyl)-cysteine and their application in peptide synthesis. *Int. J. Pept. Protein Res. 38*, 545−554.
(49) Rouser, G., Fleischer, J., and Yamamoto, A. (1970) Two-dimensional thin layer chromatographic separation of plant lipids and determination of phospholipids by phosphorus analysis of spots. *Lipids 5*, 494−496.
(50) Böhlen, P., Stein, S., Dairman, W., and Udenfriend, S. (1973) Fluometric assay of proteins in the nanogram range. *Arch. Biochem. Biophys. 155*, 213−220.
(51) Feng, S. H., and Lo, S. C. (1994) Induced mouse spleen B-cell proliferation and secretion of immunoglobulin by lipid-associated membrane proteins of Mycoplasma fermentans incognitus and Mycoplasma penetrans. *Infect. Immun. 62*, 3916−3921.
(52) Yamamoto, M., Sato, S., Hemmi, H., Sanjo, H., Uematsu, S., Kaisho, T., Hoshino, K., Takeuchi, O., Kobayashi, M., Fujita, T., Takeda, K., and Akira, S. (2002) Essential role for TIRAP in activation of the signalling cascade shared by TLR2 and TLR4. *Nature 420*, 324−329.
(53) Horng, T., Barton, G. M., Flavell, R. A., and Medzhitov, R. (2002) The adaptor molecule TIRAP provides signalling specificity for Toll-like receptors. *Nature 420*, 329−333.
(54) Mühlradt, P. F., Kiess, M., Meyer, H., Sussmuth, R., and Jung, G. (1998) Structure and specific activity of macrophage-stimulating lipopeptides from Mycoplasma hyorhinis. *Infect. Immun. 66*, 4804−4810.
(55) Deiters, U., and Mühlradt, P. F. (1999) Mycoplasmal lipopeptide MALP-2 induces the chemoattractant proteins macrophage inflammatory protein 1alpha (MIP-1alpha), monocyte chemoattractant protein 1, and MIP-2 and promotes leukocyte infiltration in mice. *Infect. Immun. 67*, 3390−3398.
(56) Metzger, J. W., Beck-Sickinger, A. G., Loleit, M., Eckert, M., Bessler, W. G., and Jung, G. (1995) Synthetic S−(2,3-dihydroxypropyl)-cysteinyl peptides derived from the N-terminus of the cytochrome subunit of the photoreaction centre of Rhodopseudomonas viridis enhance murine splenocyte proliferation. *J. Pept. Sci. 1*, 184−190.

BC034184T

Microwave-Supported Preparation of ^{68}Ga Bioconjugates with High Specific Radioactivity

I. Velikyan,[†,‡] G. J. Beyer,[§] and B. Långström*[,†,‡]

Department of Organic Chemistry, Institute of Chemistry, BMC, Uppsala University, Box 599, SE-751 24 Uppsala, Sweden, Uppsala Imanet AB, PO Box 967, SE-751 09 Uppsala, Sweden, and Cyclotron Unit, Geneva University Hospital, 1211 Geneva, Switzerland. Received November 7, 2003; Revised Manuscript Received March 15, 2004

The generator-produced positron-emitting ^{68}Ga ($T_{1/2}$ = 68 min) is of potential interest for clinical PET. ^{68}Ga as a metallic cation is suitable for complexation reactions with chelators, naked or conjugated, with peptides or other macromolecules. Large ^{68}Ga generator eluate volumes, metal traces from the generator column material, or reaction reagents, however, disturb a fast, reliable, and quantitative labeling procedure. In this paper we describe a simple technique, based on anion exchange, aiming first, to increase the ^{68}Ga concentration, second to purify it from competing impurities, and third to obtain a fast and quantitative ^{68}Ga-labeled peptide conjugate that can be applied in humans without further purification. Within 5 min one can obtain from the original 6 mL generator eluate a 200 μL ^{68}Ga preparation (volume reduction by a factor 30) that is suitable for direct and quantitative labeling of peptide conjugates. DOTATOC (DOTA-D-Phe^1-Tyr^3-octreotide, DOTA = 1,4,7,10-tetraazacyclododecane-1,4,7,10-tetraacetic acid) was used as a test tracer for comparing the labeling properties of the different ^{68}Ga preparations. In combination with microwave heating, peptide conjugates of 0.5−1 nmol quantities could be labeled within 10 min with the full ^{68}Ga activity of a generator. Further purification of the ^{68}Ga-labeled peptide conjugate was no longer required since the nuclide incorporation was quantitative. The specific radioactivity (with respect to the peptide) was improved by a factor ∼100 compared to the previously applied techniques using the original generator eluate. The commercial ^{68}Ge/^{68}Ga generator from Obninsk in combination with this system for purification and concentration with an integrated microwave-supported labeling technology resulted in a kitlike technology for ^{68}Ga-tracer production. The first automated prototype using this technology is being tested.

INTRODUCTION

The positron-emitting ^{68}Ga ($T_{1/2}$ = 68 min) radionuclide is of great practical interest for clinical PET. Especially the new approaches in radionuclide therapy based on radiolabeled peptides call for an individual dosimetric PET imaging protocol. The ^{68}Ga is a generator-produced nuclide and does not require cyclotron on site. The long half-life of the parent nuclide ^{68}Ge (270.8 d) provides in principle a long life-span generator. The ^{68}Ga decays by 89% through positron emission of 1.92 MeV max energy, without additional gamma contribution. The short half-life of ^{68}Ga ($T_{1/2}$ = 68 min) permits application of suitable ^{68}Ga activities while maintaining an acceptable radiation dose to the patient. The only stable chemical form in solution is the ^{68}Ga^{3+} cation, which forms stable complexes with many ligands containing oxygen and nitrogen as donor atoms. Thus, ^{68}Ga is suitable for complexation with chelators, naked or conjugated with peptides, or other macromolecules.

Many ^{68}Ga radiopharmaceuticals have been used so far for imaging of brain, renal, bone, blood pool, lung, vascular pool, and tumor (*1*). Some of the restrictions for wider use of ^{68}Ga are the chemical form in which it is obtained from the generator and contamination of the generator eluate with traces of the generator column material. Column materials proposed so far for ^{68}Ge/^{68}Ga generators are inorganic oxides such as aluminum dioxide, titanium dioxide, or tin dioxide or selective organic resins comprising phenolic hydroxyl groups or pyrogallol (*2*−*5*). Elution of the ^{68}Ga is performed using EDTA solution (*5*), relatively high concentrated HCl (*3*), or 0.1 M HCl (Cyclotron Co., Ltd, Obninsk, Russia). There are advantages with the latter generator: the ^{68}Ge is loaded onto a titanium dioxide column that is a nontoxic material, and, more importantly, ^{68}Ga is eluted in the cationic form with 0.1 M HCl, allowing universal application for radiopharmaceutical preparations. A general disadvantage related to all generators is the large primary ^{68}Ga eluate volume leading consequently to a low ^{68}Ga concentration. Contamination with the long-lived parent nuclide ^{68}Ge (breakthrough) is generally a critical value, and cationic metal ions (mainly from the column material) disturb the labeling procedure because of competition in the complexation reaction. A method based on anion exchange to purify the eluate and to reduce the volume and HCl concentration of a generator eluate has been proposed previously (*3*). Nevertheless, the final volume obtained was still large (∼4 mL). Evaporation to dryness causes activity loss due to the time factor as well as uncontrolled release losses since

* To whom correspondence should be addressed. Bengt Långström, Uppsala Imanet, P.O. Box 967, SE-751 09 Uppsala. Phone: +46 18 666 900, fax: +46 18 666 919, e-mail: Bengt.Langstrom@Uppsala.Imanet.se.

† Uppsala University.

‡ Uppsala Imanet AB.

§ Geneva University Hospital.

10.1021/bc030078f CCC: $27.50 © 2004 American Chemical Society
Published on Web 04/23/2004

the $GaCl_3$ is relatively volatile. The anion-exchange approach, however, seems to be a promising way to solve both concentration and purification problems of ^{68}Ge/^{68}Ga generator eluate more generally.

The adsorption behavior of the elements from HCl solutions on the anion-exchanger DOWEX AG1-X8 is well-known (*6*). In HCl solution, gallium forms strong anionic complexes with Cl^-, and the corresponding $[GaCl_6]^{3-}$ and $[GaCl_4]^-$ complexes are strongly adsorbed on the mentioned anion-exchange resin from HCl concentrations > 3 M. In contrast, germanium is practically not adsorbed from <5 M HCl solution; only from HCl > 6 M is it found that Ge follows Ga.

The factor that is most crucial for radiolabeling procedures with short-lived radionuclides is the time needed for a certain process. Microwave heating providing the acceleration is an attractive tool. This technique has been used for labeling different organic molecules with [^{131}I], [^{11}C], [^{15}O], [^{18}F], and [^{13}N] (*7*). Microwave heating not only shortens the chemical reaction time, but also reduces side reactions, increases the yield, and improves reproducibility (*7*). Microwave heating is especially useful for microscale organic chemistry such as radiolabeling where the size of the sample is comparable to the penetration depth of the microwave field (*7*, *8*). Microwave heating has already shown its potential in speeding up ^{68}Ga complexation with DOTA[1] bifunctional chelator coupled to oligonucleotides (*9*).

In the present paper we wish to describe a simple technological procedure based on anion-exchange reaction that allows purification of ^{68}Ga obtained from a commercial generator and reduction of the volume of the preparation in one step, thus meeting the requirement for direct highly efficient labeling of modern bioconjugates under microwave heating conditions. Special attention has been paid to reasonable high speed, reliability and simplicity, quantitative product yield, and purity. DOTA-D-Phe^1-Tyr^3-octreotide (DOTATOC,[1] where DOTA is the chelator 1,4,7,10-tetraazacyclododecane-1,4,7,10-tetraacetic acid) was used as a test molecule to study and optimize the labeling procedure.

MATERIALS AND METHODS

^{68}Ga and ^{68}Ge/^{68}Ga Generator Characterization. ^{68}Ga ($T_{1/2}$ = 68 min, β^+ = 89% and EC = 11%) was available from a ^{68}Ge/^{68}Ga generator system (Cyclotron Co., Ltd, Obninsk, Russia) where ^{68}Ge ($T_{1/2}$ = 270.8 d) was attached to a column of an inorganic matrix based on titanium dioxide. The nominal ^{68}Ge activity loaded onto the generator column was 1850 MBq (50 mCi). The specified shelf live of the generator was 2−3 years. The ^{68}Ga was eluted with 6 mL of 0.1 M hydrochloric acid. The elution profile was determined by fractionating and measuring the ^{68}Ga activity in each successive fraction of the eluate. The ^{68}Ga elution yield was expressed as the ratio between the obtained ^{68}Ga and the ^{68}Ge activity (in equilibrium with the ^{68}Ga daughter nuclide) on the generator column at the time of elution. Aliquots of the generator eluates were counted using an ionization chamber and a NaI(Tl) scintillation detector immediately and after 24−48 h in order to determine the ^{68}Ge breakthrough in the eluate. The ^{68}Ge contamination was expressed as % ^{68}Ge in the ^{68}Ga eluate in each sample. The ^{68}Ga generator eluates were analyzed for the content of trace metals by inductively coupled plasma atomic emission spectrometry (ICP-AES) using a Spectroflame P instrument (Spectro, Germany). The instrument was calibrated toward standards from Spectrascan (Reference material AB, Ulricehamn, Sweden). The detection limit of the applied inductively coupled plasma atomic emission spectroscopy (ICP-AES) analysis was approximately 0.0001%.

Table 1. Characterization of the Anion-Exchange Resins and Cartridges Used in the ^{68}Ga Purification and Preconcentration Study[a]

no.	sorbent	counter-ion	retention, %	recovery, %
1	AG 1-X8 (100−200 mesh)	HO^-	81 ± 4	69 ± 3
2	AG 1-X8 (200−400 mesh)	HO^-	98 ± 2	85 ± 5
3	AG 1-X4 (100−200 mesh)	HO^-	65 ± 5	80 ± 3
4	AG 1-X2 (200−400 mesh)	HO^-	45 ± 4	68 ± 2
5	SAX SPEC, Isolute, 50 mg	Cl^-	<4	–
6	SAX SPEC, NTK kemi, 15 mg	Cl^-	<4	–
7	SAX SPEC, Isolute, 50 mg	OH^-	9	–
8	SAX SPEC, NTK kemi, 15 mg	OH^-	7	–
9	SAX SPEC, Chromafix, 45 mg	HCO_3^-	99 ± 1	93 ± 2

[a] With retention of over 98% and a recovery yield of better than 90%, the commercial anion cartridge SAX SPEC Chromavix showed the most promising results.

Purification and Concentration of the ^{68}Ga Eluate Using Anion-Exchange Resins. Several strong basic anion-exchange resins were investigated for optimization [Dowex AG 1-X8 (100−200 mesh), AG 1-X8 (200−400 mesh), AG 1-X4 (100−200 mesh), and AG 1-X2 (200−400 mesh), see Table 1]. Three commercially available strong anion-exchange cartridges were tested as well: Isolute (50 mg, 1 mL, Cl^- form); NTK kemi, (15 mg, 3 mL, Cl^- form,), and Chromafix 30-PS−HCO_3, Macharey-Nagel. The resins were suspended in 1 M HCl for 1 h, washed several times with deionized water, suspended in 1 M NH_3 for 10 min, washed with water, and resuspended in 1 M HCl. After this procedure, the resins were centrifuged and kept under 5 M HCl for the further use. Small plastic tubes of different sizes were used as small columns. They were plugged with glass wool or polyethylene filter elements and packed with the wet resin. Just before use, the packed columns were conditioned and activated washing successively with 5 M HCl, 1 M HCl, H_2O, and again 5 M HCl. The commercial cartridges were preconditioned in the same way.

The ^{68}Ge/^{68}Ga-generator was eluted according to the manufacturer protocol with 6 mL 0.1 M solution. Five microliters of 30% HCl was added to the 6 mL of the generator eluate giving a final HCl concentration of 4.0 M. The resulting 11 mL solution in total was passed through a pretreated anion-exchange column at a flow rate of 4 mL/min (linear flow speed 25 cm/min) at room temperature. The columns were washed with 2 mL of 4 M HCl and then dried by sucking filtered air through the column, to eliminate excess 4 M HCl. The ^{68}Ga was then eluted with small fractions of deionized water (50−200 μL) at a flow rate of 0.5 mL/min. The elution profile of the small purification columns and the elution yield of ^{68}Ga were determined by measuring the ^{68}Ga activity in the 50 μL fractions of the eluate and normalizing to the end of the elution. The elution yield is expressed as % of eluted ^{68}Ga from the total ^{68}Ga activity present at

[1] Abbreviations: DOTA, 1,4,7,10-Tetraazacyclododecane-1,4,7,10-tetraacetic acid; DOTATOC, 4,7,10-Tricarboxymethyl-1,4,7,10-tetraazacyclododecan-1-yl-acetyl-D-Phe-Cys-Tyr-D-Trp-Lys-Thr-Cys-L-threoninol (DOTA-D-Phe^1-Tyr^3-octreotide); DOTA-RGD, Cys2−6; c[CH_2CO-Lys(DOTA)-Cys-Arg-Gly-Asp-Cys-Phe-Cys]-CCX_6-NH_2); ESI, electrospray ionization; NOTA, 1,4,7-triazacyclononane-1,4,7-triacetic acid; NODAGATATE, 1,4,7-tricarboxymethyl-1,4,7-triazacyclononan-1-ylacetyl-D-Phe-Cys-Tyr-D-Trp-Lys-Thr-Cys-L-Thr (NODAGA− Tyr^3−octreotate).

the generator column at the beginning of elution. The ^{68}Ge contamination was determined by recounting the fractions 48 h after collection.

Distribution Coefficients. The distribution coefficients D of ^{68}Ga between the stationary and mobile phase were determined by the column method as weight distribution coefficients, D.

$$D = \frac{A_{res}}{A_{liq}} \times \frac{m_{liq}}{m_{res}}$$

with A_{res} = ^{68}Ga activity of the dry resin (Bq), A_{liq} = ^{68}Ga activity of the solution passed through the column (Bq), m_{res} = amount of dry resin (g), m_{liq} = amount of the solution (g).

The HCl concentration of the ^{68}Ga solution was altered in the range between 0.1 and 4.3 M by addition of corresponding amounts of 30% HCl for this systematic study. Aliquot samples of the ^{68}Ga solutions (starting and eluate) were measured with a well-type scintillation counter under standardized geometry conditions. D rises from 10^5 to 2×10^6 for [HCl] = 3.5−4.3 M. ^{68}Ga retention on the cartridge of ∼99% is assured under these conditions.

Microwave Heating. Microwave heating was performed with a SmithCreator oven (Personal Chemistry AB, Uppsala, Sweden) with monomodal radiation.

Labeling of DOTATOC with the Original ^{68}Ga Generator Eluate. The pH of the original ^{68}Ge/^{68}Ga-generator eluate (6 mL, containing full ^{68}Ga activity or the 1 mL peak fraction that contained 60−65% of the available ^{68}Ga activity) was adjusted to pH ∼ 4.6 by adding sodium acetate (Aldrich, in solid form) to give finally a 0.4 M solution with regard to acetate or to pH ∼ 4.2 by adding HEPES (4-(2-hydroxyethyl)piperazine-1-ethanesulfonic acid, Sigma) to give finally a 1.0 M solution with regard to HEPES. Then 0.1−20 nmol in 1−20 μL of 1 mM and 1−5 μL of 0.1 mM DOTATOC solution (in water) were added. The reaction mixture was transferred into a Pyrex glass vial for microwave heating and exposed for 1 min to 90 ± 5 °C. Alternatively, the mixture was heated to 95 °C in a conventional heating block for up to 20 min.

Quality Control. Analytical liquid chromatography (LC) was performed using a HPLC system from Beckman (Fullerton, CA) consisting of a 126 pump, a 166 UV detector, and a radiation detector coupled in series. Data acquisition and handling was performed using the Beckman System Gold Nouveau Chromatography Software Package. The column used was a Vydac RP 300 Å HPLC column (Vydac, USA) with the dimensions 150 mm × 4.6 mm, 5 μm particle size. We applied gradient elution with the following parameters: A = 10 mM TFA; B = 70% acetonitrile (MeCN), 30% H_2O, 10mM TFA with UV-detection at 220 nm; flow was 1.2 mL/min; 0−2 min isocratic 20% B, 20−90% B linear gradient 8 min, 90−20% B linear gradient 2 min. Retention time (t_R) for the radio-HPLC signals was 6.56 ± 0.02, 5.66 ± 0.03, and 6.66 ± 0.02 min for DOTATOC, DOTA-RGD,[1] and NODAGATATE,[1] respectively.

In addition, electrospray ionization mass spectrometry (ESI-MS)[1] was performed using a Fisons Platform (Micromass, Manchester, UK) with positive mode scanning and detecting $[M + 2H]^{2+}$ and $[M + 3H]^{3+}$ species. DOTATOC was detected at m/z = 711.26, ^{69,71}Ga-DOTATOC at m/z = 746.0, DOTA-RGD at m/z = 823.44 for $[M + 2H]^{2+}$ and 549.1 for $[M + 3H]^{3+}$, ^{69,71}Ga-DOTA-RGD at m/z = 857 for $[M + 2H]^{2+}$ and 571 for $[M + 3H]^{3+}$, NODAGATATE at m/z = 704 for $[M + 2H]^{2+}$ and 470 for $[M + 3H]^{3+}$, ^{69,71}Ga-NODAGATATE at m/z = 738 for $[M + 2H]^{2+}$. The ^{69,71}Ga conjugates synthesized under identical to labeling conditions were used for the identification of the radio-HPLC chromatogram signals.

Labeling of the DOTA Conjugates with the Preconcentrated and Purified ^{68}Ga Eluate: 1. Using Sodium Acetate Buffer. Five microliters of 10 M NaOH solution were added to the 200 μL of the ^{68}Ga preconcentrated eluate containing 92 ± 4% of the initially available activity. Then the mixture was added to 16 mg of solid sodium acetate, buffering the solution to pH ∼ 4.2. Then 0.1−10 nmol of an aqueous solution of DOTATOC were added (1−10 μL of a 1 mM solution for the range of 1−10 nmol or 1−5 μL of 0.1 mM solution for the range of 0.1−0.5 nmol of the peptide conjugate, respectively). The reaction mixture was transferred to a Pyrex glass vial with an insert to accommodate the small volume (200 ± 20 μL) for microwave heating. The heating time in a conventional heating block at 95 °C was up to 20 min and in the microwave furnace 1 min at 90 ± 5 °C. The obtained product was analyzed applying the identical protocol as described above.

2. Using HEPES Buffer. The procedure was identical to the sodium acetate protocol; however, instead of 16 mg of solid sodium acetate, we used 72 mg of powdered HEPES to obtain similar pH conditions. The labeling was performed for DOTATOC and DOTA-RGD (RGD is Cys2−6; c[CH_2CO-Lys(DOTA)-Cys-Arg-Gly-Asp-Cys-Phe-Cys]-CCX_6-NH_2) conjugates.

Labeling of NOTA[1] Conjugate with Preconcentrated and Purified ^{68}Ga Eluate. NODAGATATE (NODAGA-Tyr^3-octreotate), where the bifunctional chelator is 1,4,7-triazacyclononane-1,4,7-triacetic acid, was labeled with the preconcentrated and purified ^{68}Ga eluate according to the following standardized protocol: 3 μL of 10 M NaOH solution was added to the 200 μL of the ^{68}Ga preconcentrated eluate containing 92 ± 4% of the initially available ^{68}Ga activity. Then the mixture was transferred to a vial containing 72 mg HEPES powder buffering the solution to 3 < pH < 3.5. Then 0.2−5 nmol of the NODAGATATE were added in 1−5 μL of 1 mM aqueous solution or 2−5 μL of 0.1 mM aqueous solution of the conjugate. The resulting 200 ± 20 μL reaction mixture was then transferred to a Pyrex glass vial with an insert to accommodate the small volume for microwave heating. The heating time in the microwave furnace was 1 min at 95 ± 5 °C. The obtained product was analyzed applying the protocol described above.

RESULTS AND DISCUSSION

Elution Characteristics. The generator elution yield over time revealed reproducible performance of the generators (Figure 1). In the first month the elution yield was 78 ± 2% of the theoretical amount and then it decreased slowly and continuously down to 41% after 29 month use. The ^{68}Ge elution profile and the ^{68}Ge breakthrough are presented in Figure 2. By fractionating the ^{68}Ga eluate, one can obtain approximately 65% of the available activity with only 1 mL (the third fraction, Figure 2). The ^{68}Ge breakthrough with respect to the eluted ^{68}Ga activity was found to be 0.001−0.007%, and the ^{68}Ga/^{68}Ge ratio did not change during the investigation period. It should be mentioned that ^{68}Ge breakthrough losses of 0.001% per elution are insignificant compared with ^{68}Ge decay loss, assuming two elutions per day.

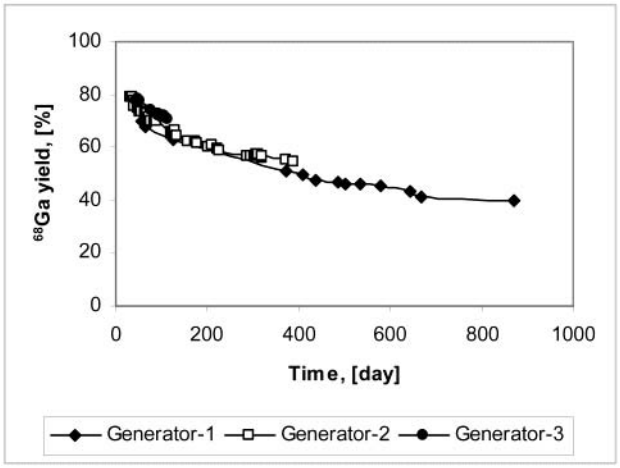


Figure 1. ^{68}Ga elution efficiency for generator-1 during 29 months, generator-2 during 14 months, and generator-3 during 3 months.

Metal Content. The metal ion content of the ^{68}Ge/^{68}Ga generator eluate depending upon elution frequency is shown in Figure 3. The concentration of the metal ions, except for Pb, was constant for a given elution frequency. The generator requires daily elution in order to keep the concentration of the contaminant metal ions as low as possible. A preventive elution 4 h prior to the synthesis is recommended since the interfering metal ion concentration can be kept at its minimum value. The generator matrix material (TiO_2) may cause relatively high nontoxic Ti concentration (close to 1000 ppm) in the eluate if the generator is not eluted regularly. The metals act as pseudocarriers requiring, consequently, higher macromolecule conjugate concentrations. The consequence is lower ^{68}Ga incorporation (low labeling yield) or a drop in the specific radioactivity of the final ^{68}Ga-labeled peptide conjugate. The proposed concentration and purification step will reduce the metal content as shown below and increase the specific radioactivity of the final product.

Labeling Reaction. The complexation reaction of ^{68}Ga with a macrocyclic chelator conjugated to the peptide already starts at room temperature, but the analytical radiochemical yield (RCY) did not exceed 24% and 30% for sodium acetate and HEPES buffers, respectively (Figure 4A). Conventional heating improved the situation but the yield and reaction time were still unsatisfactory. In the case of the HEPES buffer, the ^{68}Ga incorporation time was shorter. Microwave heating of the reaction mixture considerably shortened the reaction time and improved reproducibility. Nevertheless, a final purification step was still required for obtaining a high quality labeled peptide conjugate (Figure 4A). It was expected that a smaller volume of the reaction mixture would improve both, RCY and reaction time. In the first phase, the reduction of the reaction mixture volume was achieved by fractionation of the generator eluate (Figure 2). The third fraction of the eluate (1 mL) contained over 60% of the total available ^{68}Ga activity. Using this ^{68}Ga peak fraction the RCY for the reaction at room temperature, conventional heating as well as for microwave heating was improved (Figure 4B). Under conventional heating conditions, quantitative ^{68}Ga incorporation was achieved within 5 min for 5 nmol of DOTATOC using the HEPES buffer system. For the sodium acetate buffer system, a 3-fold amount of peptide (15 nmols) and 20 min heating were required. With microwave heating the labeling reaction was complete within 1 min, the incorporation of the activity was quantitative and the reproducibility of the reaction was improved. No further purification of the labeled peptide conjugate was required. From this study we learned that the amount of peptide needed for

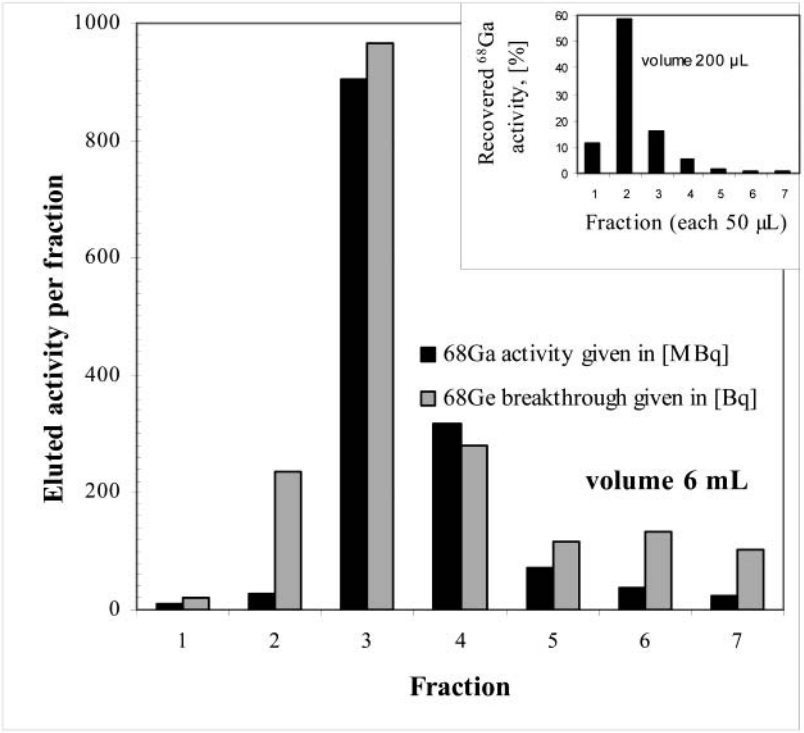


Figure 2. Elution profile of the ^{68}Ge/^{68}Ga generator where one fraction was 1 mL (fraction 1 = 0.3 mL, fraction 7 = 0.7 mL), giving a total eluted volume of 6 mL. The profiles for the ^{68}Ga elution and the ^{68}Ge breakthrough are identical; the ^{68}Ge breakthrough is $\sim 10^{-3}$%. Fraction 3 (1 mL) contains over 60% of the available ^{68}Ga activity. The insert shows the elution profile of ^{68}Ga eluted from the small SAX SPE Chromafix cartridge with small volumes of deionized water. More than 90% of the initial ^{68}Ga activity was obtained in 200 μL of solution.

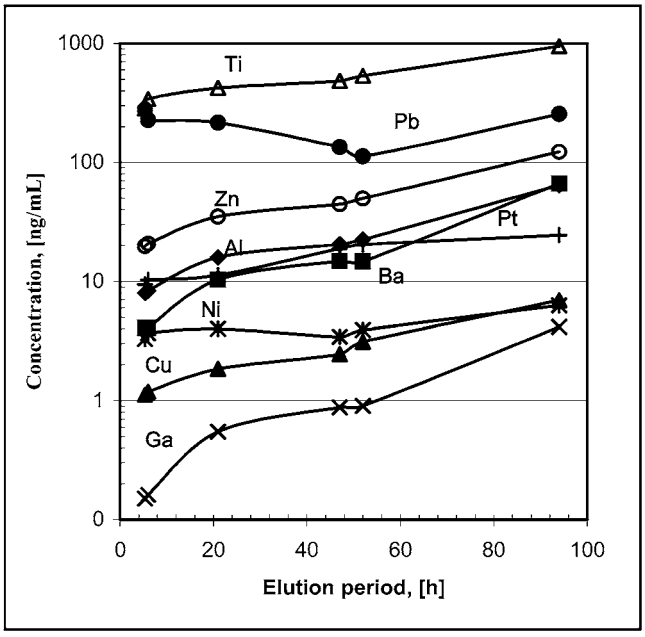


Figure 3. Metal ion content in 6 mL of the generator eluate as a function of the elution time period.

quantitative ^{68}Ga incorporation was 15 nmol at least when using sodium acetate buffer and 5 nmol in the case of HEPES (Figure 5). It is worth noting that the difference in the buffer influence is more pronounced at lower peptide quantities, indicating the sensitivity of the reaction to potential metal impurities present in the buffers as well as complexing ability of sodium acetate itself competing with DOTA when used at high concentration.

Although the ^{68}Ga incorporation was quantitative using only 5 nmol of DOTATOC, there were still drawbacks in this approach. First, about 40% of the ^{68}Ga activity is wasted and the second, even smaller peptide amounts may be required due to cost and biological properties. Thus a fast technique for the ^{68}Ge/^{68}Ga generator eluate purification and concentration was introduced.

Concentration and Purification of ^{68}Ga. Our preconcentration protocol utilized $[^{68}GaCl_4]^-$ complex formation in 4 M HCl medium. This anionic complex can be efficiently adsorbed on anion-exchange resins from HCl solutions and is efficiently eluted with a very small volume of water.

The results of the optimization studies concerning the capabilities of different anion-exchange resins are presented in Table 1. The adsorption of ^{68}Ga from HCl solution on anion-exchange cartridges increased rapidly from 0.8% at 0.1 M HCl to almost 100% at 3.8 M HCl under our conditions (4 mL/min, 4 mm column diameter) in agreement with literature data on distribution coefficients ($D > 10^5$) (*6*). The best ^{68}Ga recovery was obtained using a column diameter of 4 mm. The linear flow rate of the deionized water was 25 cm/min. Among the class of AG1-resins, Bio-Rad AG 1-X8 with fine mesh (200−400 mesh) showed the best retention and recovery characterstics and a sharp elution profile. The best agent for eluting the ^{68}Ga from the small anionic cartridges was deionized water: the HCl content at the resin was more than sufficient to avoid hydrolysis. To use sodium acetate solution directly as eluting agent is not recommended since the recovery yield of ^{68}Ga is very poor (>30% losses) as most likely the anionic Ga-acetate complex is adsorbed to the resin. Fifty percent EtOH as eluting agent could be an alternative and shows nearly the same recovery properties as pure water alone. Since the parent nuclide ^{68}Ge is not retained on the anion resin, the concentration step can also be seen as a purification of ^{68}Ga from ^{68}Ge breakthrough. In the same way the original generator eluate was purified from Ti by 90% as shown by the ICP-AES analysis data.

As seen in Table 1, among the tested commercial anionic cartridges only the SAX SPEC Chromafix cartridge showed very satisfactory results. This cartridge contains 45 mg of a strong basic anion-exchange resin based on polystyrene−divinylbenzene with HCO_3^- as the counterion and quaternary amine functional groups. Using this cartridge, we obtained 99.1% retention at a flow rate of 2 mL/min and still 98% at a flow rate of 5 mL/min. Although the lower flow rate assured higher and stable retention values, the decay losses due to time were important. Thus, it is generally more beneficial to apply a higher flow rate and accept 1−3% worse retention. Elution with deionized water resulted finally in 90 ± 2% of ^{68}Ga recovery in a total volume of 200 μL only. Another 150 μl water volume would provide only 3% increase of the ^{68}Ga recovery (Figure 2, insert). AG 1-X8 (200−400 mesh) resin and Chromafix SAX SPEC cartridges showed comparable results with respect to retention, recovery, and elution profile (Table 1). However, the Chromafix SAX SPEC cartridge as a standardized commercial product is much more suited for further standardization and automation. In total the preconcentration procedure

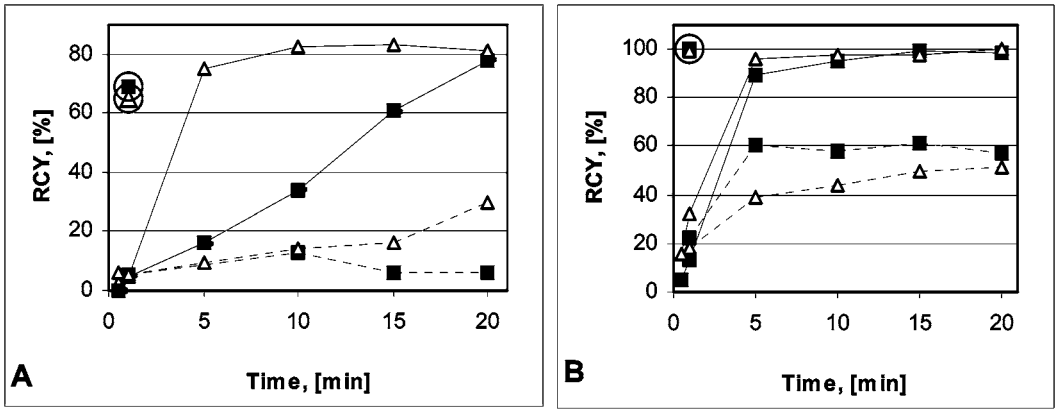


Figure 4. Time course of ^{68}Ga complexation reaction conducted using the full original ^{68}Ga eluate (6 mL) (A) or using only the 1 mL peak fraction of the generator eluate (B) at room temperature (dashed line), conventional heating at 95 °C in a heating block (solid line), and with microwave heating at 90 ± 5 °C for 1 min (circled) for two different buffer systems: ■ sodium acetate buffer, pH = 4.6, 20 nmol of DOTATOC; △ HEPES buffer, pH = 4.2, 20 nmol of DOTATOC (A), and 5 nmol of DOTATOC (B).

Table 2. Labeling Conditions and Practical Quality Parameters of the ^{68}Ga-Labeled Peptide Conjugates Obtained from Preconcentrated and Purified ^{68}Ga Preparations under Microwave Heating[a]

generator age, month	peptide conjugate	peptide amount, nmol	activity incorporation (%)	starting full ^{68}Ga activity from generator (MBq)	specific activity after synthesis (MBq/nmol)
1	DOTATOC	1	99.0	1289.0	997.7
1	DOTATOC	0.5	99.9	1286.7	2003.0
1	DOTATOC	0.3	98.8	1251.3	3307.0
14	DOTATOC	1	99.9	357.0	308.7
14	DOTATOC	0.5	99.9	337.2	537.2
14	DOTATOC	0.3	99.9	329.4	843.7
29	DOTATOC	1	99.9	78.8	61.0
1	NODAGATATE	1	99.9	1275.9	1011.1
1	NODAGATATE	0.5	99.9	1110.9	1758.4
14	NODAGATATE	1	98.7	357.4	281.3
14	NODAGATATE	0.5	96.8	323.2	493.8
29	NODAGATATE	2	98.0	77,6	30.5
1	DOTA-RGD	1	99.9	1253.0	976.0
1	DOTA-RGD	0.5	99.1	1213.9	1869.9
1	DOTA-RGD	0.25	96.5	1256.7	3756.4
14	DOTA-RGD	0.5	99.9	362.4	570.4
14	DOTA-RGD	0.25	96.2	369.8	953.0
29	DOTA-RGD	1	98.4	72.2	56.1

[a] Due to quantitative radionuclide incorporation, no further purification of the labeled product is needed.

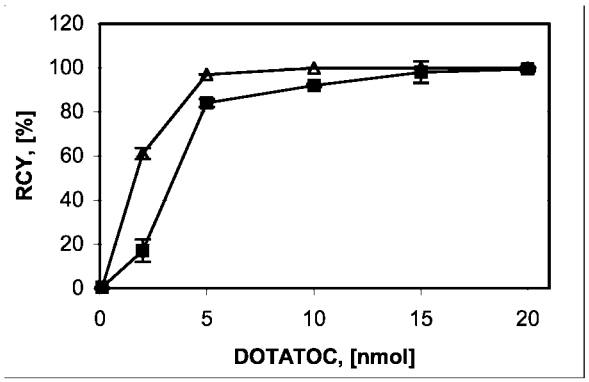


Figure 5. Influence of the buffering system (■ sodium acetate, Δ HEPES) on the radiochemical yield of ^{68}Ga complexation reaction for different DOTATOC quantities under 1 min microwave heating at 90 ± 5 °C. The reaction was conducted using the 1 mL peak fraction of the original generator eluate (see Figure 2).

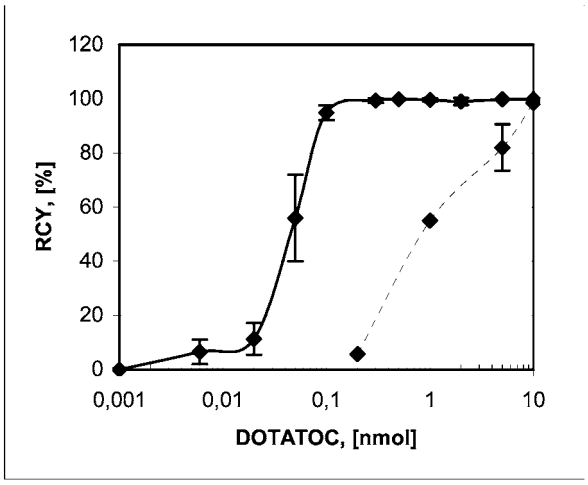


Figure 6. Influence of the DOTATOC amount on the radiochemical yield of the ^{68}Ga complexation reaction using the full available ^{68}Ga activity in 200 μL volume after the preconcentration and purification step in HEPES buffer system. solid line: 1 min microwave heating at 90± 5 °C, dashed line: 5 min conventional heating at 95 °C.

required 4 to 6 min, including filtration of the original ^{68}Ga eluate in 4 M HCl through the cartridge, the drying procedure, and the elution of the ^{68}Ga in 200 μL of pure water.

Combined Protocol: Preconcentration of ^{68}Ga and Microwave-Supported Labeling. The influence of the preconcentration step of the ^{68}Ga eluate in combination with microwave heating is demonstrated in Figure 6 and Table 2. Figure 6 illustrates that one can incorporate the full ^{68}Ga radioactivity eluted from the generator into less than 1 nmol of a peptide conjugate. In this combination the original full ^{68}Ga eluate is purified and concentrated as described, and the labeling is performed during 1 min microwave heating. Table 2 contains more details concerning the age of the generator, variation of the amount of peptide conjugate, and variation of the ligand itself. Labeling tests with equimolar quantities (^{68}Ga: bioconjugate = 1:1) using 6 pmol of DOTATOC resulted in a maximum activity incorporation of 11% and the specific radioactivity of the labeled bioconjugate only a factor 10 less than the theoretical value. Independent of the age of the generator and over a period of 2.5 years, we obtained stable and reproducible ^{68}Ga incorporation of >99% into 0.3−1 nmols of the peptide conjugate. It should be stressed that even with the lower ^{68}Ga amount and concentration with time (2.5 years) it is still possible to obtain quantitative incorporation with 1 nmol of the bioconjugate.

Quality Control. The HPLC conditions were selected so that the QC of the radiopharmaceutical prior injection could be completed within 10 min. The retention time (t_R) was 6.56 ± 0.02, 5.66 ±0.03, and 6.66 ±0.02 min for DOTATOC, DOTA-RGD, and NODAGATATE, respectively (Figure 7).

CONCLUSIONS

The introduction of the purification and concentration step in combination with the microwave heating may have very positive impact on the further utilization of ^{68}Ga in nuclear medicine, generally. The proposed technique allows elimination of an additional purification step in the preparation of ^{68}Ga labeled peptide conjugates and improves the specific radioactivity of the product by a factor 100. The over-all process can be performed in 10−12 min starting from the end of the original generator elution. The HPLC quality control (another 10 min) can be performed prior to injection in humans. Because of the excellent ^{68}Ga activity economy, one can expect to use

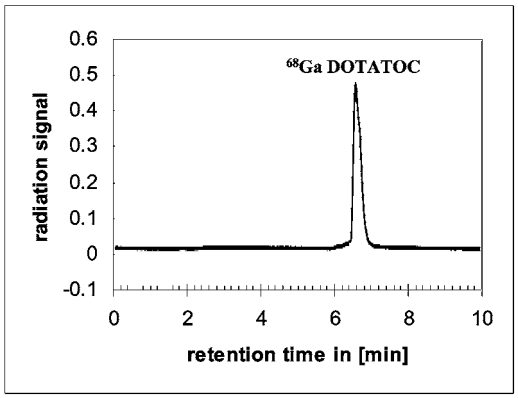


Figure 7. HPLC radiochromatogram of a ^{68}Ga-DOTATOC preparation (0.5 nmol of DOTATOC, 1 min microwave heating at 90 ± 5 °C, total reaction volume 220 μL). The ^{68}Ga incorporation is over 99.9% and the specific activity of the labeled peptide conjugate was 2 GBq/nmol.

the commercial 1850 MBq generator over a period of more than 2 years for patient studies. The proposed technique is suited for automation, and the development of a corresponding kitlike technology is in progress.

ACKNOWLEDGMENT

The authors sincerely thank Prof. Helmut Maecke (Institute of Nuclear Medicine, Division of Radiological Chemistry, University Hospital Base, Basel, Switzerland) for providing us with DOTATOC and NODAGATATE and Dr. Hege Karlsen (Department of Synthetic Chemistry, Amersham Health, Olso, Norway) for the provision of DOTA-RGD. Jean Pettersson, Department of Analytical Chemistry, Uppsala University, is gratefully acknowledged for performing the ICP analysis. The Swedish Council is acknowledged for its support by grant K3464. European Union COST Action B12 is acknowledged for its support.

LITERATURE CITED

(1) Green, M. A., and Welch, M. J. (1989) Gallium radiopharmaceutical chemistry. *Nucl. Med. Biol. 16*, 435−448.
(2) Neirinckx, R. D., and Davis, M. A. (1981) Generator for gallium-68 and compositions obtained therefrom. United States Patent US A-4264468.
(3) Schuhmacher, J., and Maier-Borst, W. (1981) A new ^{68}Ge/^{68}Ga radioisotope generator system for production of ^{68}Ga in dilute HCl. *Int. J. Appl. Radiat. Isot. 32*, 31−36.
(4) Nakayama, M., Haratake, M., Koiso, T., Ishibashi, O., Harada, K., Nakayama, H., Sugii, A., Yahara, S., and Arano, Y. (2002) Separation of Ga-68 from Ge-68 using a macroporous organic polymer containing *N*-methylglucamine groups. *Anal. Chim. Acta 453*, 135−141.
(5) Rösch, F., and Knapp, F. F. (2002) Radionuclide generators. *Handbook of nuclear and radiochemistry* (Vertes, A., Ed.) pp 1−36, Kluwer Publishers, New York.
(6) Kraus, K. A., and Nelson, F. (1956) Anion exchange studies of the fission products. *Conference on peaceful uses of atomic energy*, pp 113−125, United Nations, New York.
(7) Elander, N., Jones, J. R., Lu, S. Y., and Stone-Elander, S. (2000) Microwave-enhanced radiochemistry. *Chem. Soc. Rev. 29*, 239−249.
(8) Ohlsson, T., Vengtsson, N. E., and Risman, P. O. (1974) The frequency and temperature dependence of dielectric food data as determined by a cavity pertubation technique. *J. Microwave Power 9*, 129.
(9) Velikyan, I., Lendvai, G., Välilä, M., Roivainen, A., Yngve, U., Bergström, M., and Långström, B. (2004) Microwave accelerated ^{68}Ga-labeling of oligonucleotides. *J. Labelled Compd. Radiopharm. 47*, 79−89.

BC030078F

Two Technetium-99m-Labeled Cholecystokinin-8 (CCK8) Peptides for Scintigraphic Imaging of CCK Receptors

Peter Laverman,[†,*] Martin Béhé,[‡] Wim J. G. Oyen,[†] Peter H. G. M. Willems,[§] Frans H. M. Corstens,[†] Thomas M. Behr,[‡] and Otto C. Boerman[†]

Department of Nuclear Medicine, University Medical Center Nijmegen, Nijmegen, The Netherlands, Department of Nuclear Medicine, Phillips University, Marburg, Germany, and Department of Biochemistry, Nijmegen Center for Molecular Life Sciences, University Medical Center Nijmegen, Nijmegen, The Netherlands
Received November 10, 2003; Revised Manuscript Received February 2, 2004

A broad spectrum of radiolabeled peptides with high affinity for receptors expressed on tumor cells is currently under preclinical and clinical investigation for scintigraphic imaging and radionuclide therapy. The present paper evaluates two ^{99m}Tc-labeled forms of the C-terminal octapeptide of cholecystokinin (CCK8): sulfated (s)CCK8, with high affinity for CCK1 and CCK2 receptors, and nonsulfated (ns)CCK8, with high affinity for CCK2 receptors but low affinity for CCK1 receptors. Peptides were conjugated with the bifunctional chelator *N*-hydroxysuccinimidyl hydrazino niconitate (s-HYNIC). ^{99m}Tc-labeling, performed in the presence of nicotinic acid and tricine, was highly efficient (∼95%) and yielded products with a high specific activity (∼700 Ci/mmol) and good stability (∼5% release of radiolabel during 16 h incubation in phosphate buffered saline at 37 °C). Chinese hamster ovary cells stably expressing the CCK1 receptor (CHO-CCK1 cells) internalized ∼3% of added ^{99m}Tc-sCCK8 per confluent well during 2 h at 37 °C. Internalization was effectively blocked by excess unlabeled sCCK8. CHO-CCK1 cells did not internalize ^{99m}Tc-nsCCK8. Displacement of ^{99m}Tc-sCCK8 and -nsCCK8 by unlabeled CCK-8 (performed at 0 °C to prevent internalization) revealed 50% inhibitory concentrations (IC_{50}) of 8 nM and >1 μM, respectively. CHO-CCK2 cells internalized ∼25% and ∼5% of added ^{99m}Tc-sCCK8 and -nsCCK8, respectively. In both cases internalization was blocked by excess unlabeled peptide. IC_{50} values for the displacement of ^{99m}Tc-sCCK8 and -nsCCK8 were 3 nM and 10 nM, respectively. CHO-CCK1 cell-derived tumors present in one flank of athymic mice accumulated 2.0% of injected ^{99m}Tc-sCCK8 per gram tissue at 1 h postinjection. This value decreased to 0.6% following coinjection with excess unlabeled peptide. Uptake of ^{99m}Tc-nsCCK8 was low (0.2%) and not did change by excess unlabeled peptide (0.3%). Accumulation of ^{99m}Tc-sCCK8 and -nsCCK8 by CHO-CCK2 cell-derived tumors (present in the other flank) amounted to 4.2% and 0.6%, respectively. In both cases uptake was significantly reduced by excess unlabeled peptide to 1.0% and 0.4% for sCCK8 and nsCCK8, respectively. Accumulation of ^{99m}Tc-sCCK8 was also high in pancreas (11.7%), stomach (2.0%), and kidney (2.1%), whereas uptake of ^{99m}Tc-nsCCK8 was high in stomach (0.7%) and kidney (1.4%). Both radiolabeled peptides showed a rapid blood clearance. In conclusion, these data show that CCK8 analogues can be efficiently labeled with ^{99m}Tc using s-HYNIC as chelator and nicotinic acid/tricine as coligand system without compromising receptor binding. Furthermore, the present study demonstrates that CCK1 tumors hardly accumulate ^{99m}Tc-nsCCK8, CCK2 tumors accumulate 2 times more ^{99m}Tc-sCCK8 than CCK1 tumors, and CCK2 tumors accumulate 15 times more ^{99m}Tc-sCCK8 than ^{99m}Tc-nsCCK8. Although accumulation in some nontarget organs was also higher with ^{99m}Tc-sCCK8, this may not reflect the human situation due to a different receptor expression pattern in humans as compared to mice. Therefore, further studies are warranted to investigate the possible use of ^{99m}Tc-sCCK8 for scintigraphic imaging of CCK receptor-positive tumors in humans.

INTRODUCTION

Radiolabeled peptides with high affinity for receptors on tumor cells can be used for scintigraphic imaging and for radionuclide therapy. A broad spectrum of peptides, ranging from somatostatin analogues, RGD[1] peptides, neurotensin analogues to gastrin analogues is currently under (pre)clinical evaluation (*1*). The gastrin analogues gained interest since the discovery of the presence of cholecystokinin (CCK)/gastrin receptors on a variety of tumors (*2*). Several studies described the radiolabeling of gastrin analogues with indium-111 (^{111}In) or iodine-131 (^{131}I) for imaging and/or therapy (*3*−*6*). However,

* To whom correspondence should be addressed. Phone: +31-24-3615054. Fax: +31-24-3618942. E-mail: p.laverman@nucmed.umcn.nl.

† Department of Nuclear Medicine, University Medical Center Nijmegen.

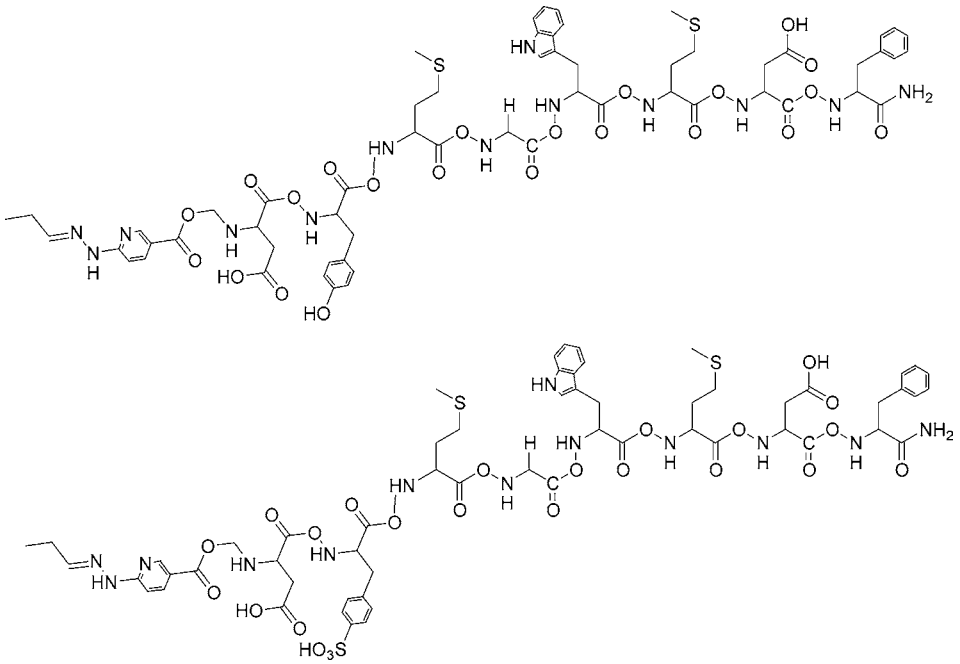
‡ Phillips University.

§ Department of Biochemistry, University Medical Center Nijmegen.

[1] Abbreviations: CCK8, cholecystokinin-8; sCCK8, sulfated cholecystokinin-8; nsCCK8, nonsulfated cholecystokinin-8; CHO, chinese hamster ovary; DMF, dimethylformamide; DMSO, dimethyl sulfoxide; DTPA, diethylenetriamine pentaacetic acid; EDDA, ethylenediaminediacetic acid; HYNIC, hydrazino nicotinamide; IC_{50}, 50% of the inhibitory concentration; keV, kilo electronvolt; PBS, phosphate buffered saline; RCP, radiochemical purity; RGD, arginine-glycine-aspartic acid; RP-HPLC, reversed phase HPLC; SPE, solid-phase extraction.

10.1021/bc034208w CCC: $27.50 © 2004 American Chemical Society
Published on Web 04/10/2004

Chart 1. Structural Formulas of HYNIC-Conjugated Nonsulfated CCK8 (upper panel) and Sulfated CCK8 (lower panel)



both radionuclides have less favorable imaging characteristics due to their high γ energies (171 and 245 keV for ^{111}In and 364 keV for ^{131}I). Technetium-99m with a γ energy of 141 keV has the ideal characteristics for imaging, combined with a relatively short half-life of 6 h. In the present paper, we report on the ^{99m}Tc labeling of two CCK8 analogues which are known to bind to CCK receptors with high affinity.

CCK receptors can be distinguished pharmacologically by their affinity for gastrin, a 33 amino acid peptide hormone involved in gastric motility (*7*). The CCK1 receptor (formerly known as CCK-A) has a low affinity for gastrin, whereas the CCK2 receptor (formerly known as CCK-B) has a high affinity for gastrin. Both receptors belong to a superfamily of G-protein-coupled receptors. The peptides of the gastrin and CCK family are characterized by an amidated C-terminal receptor binding sequence Trp-Met-Asp-Phe-NH_2. Both groups of peptides differ by the location of their tyrosyl residue in relation to the receptor binding sequence. Peptides of the gastrin family have one amino acid (usually Gly), and peptides of the CCK-family have two amino acids (Met-Gly or Thr-Gly), between this Tyr moiety and the receptor binding sequence. This Tyr residue plays a role in the receptor specificity. When this Tyr residue is sulfated, the peptides display high affinity for both the CCK1 and the CCK2 receptor. In contrast, the nonsulfated peptides show a 1000-fold lower affinity for the CCK1 receptor than for the CCK2 receptor (*8*). The CCK2 receptor is abundantly expressed in most small cell lung cancers, medullary thyroid carcinomas and in some stromal ovarian cancers and astrocytomas (*2*).

For preclinical evaluation, the rat pancreatic AR42J tumor and the human medullar thyroid carcinoma cell line TT, both expressing the gastrin/CCK2 receptor are generally used (*3*,*4*). To investigate CCK1 and CCK2 receptor binding affinity of the peptides separately we used chinese hamster ovary (CHO) cells stably transfected with cDNA encoding for either the CCK1 or CCK2 receptor. These cells are well defined with regard to their receptor expression and allow a more detailed study of the receptor specificity of the radiolabeled CCK8 peptides (*8*).

Several methods are described to radiolabel peptides with ^{99m}Tc, mostly based on the use of a bifunctional chelator. *N*-Hydroxysuccinimidyl hydrazino nicotinate (s-HYNIC) is a well-known bifunctional chelator which has proven to yield ^{99m}Tc-labeled conjugates with excellent stability, high specific activity, and high radiochemical purity (*9*). HYNIC has been used for ^{99m}Tc-labeling of proteins, peptides, and lipids (*9*−*11*). HYNIC can be conjugated to primary amino groups by using *N*-hydroxysuccinimidyl-HYNIC. The succinimidyl group facilitates conjugation of HYNIC with primary amino groups, either N-terminal or Lys residues.

The ^{99m}Tc is bound to the hydrazino moiety by forming a Tc═N bond. This binding requires coligands for proper coordination of the Tc(V) species (*12*). The nature of the coligand determines the labeling efficiency, stability, and specific activity of the ^{99m}Tc-labeled compound. Moreover, it has been reported that these coligands can affect the in vivo behavior of the ^{99m}Tc-labeled peptide or protein (*13*−*16*).

In the present study we investigated the HYNIC conjugation of both sulfated and nonsulfated CCK8 (Chart 1) (sCCK8 and nsCCK8, respectively). Furthermore, the effect of different coligand systems—tricine, ethylenediaminediacetic acid (EDDA), and tricine/nicotinic acid—on the labeling efficiency, radiochemical stability, and purity was investigated. Receptor binding and internalization studies were performed with both ^{99m}Tc-nsCCK8 and ^{99m}Tc-sCCK8 on the CCK receptor-transfected CHO cells. In addition, the in vivo receptor targeting was studied in athymic mice with CCK1 or CCK2 receptor expressing tumors on each flank.

EXPERIMENTAL PROCEDURES

Chemicals. Sulfated and nonsulfated cholecystokinin fragment 26−33 (sCCK8 and nsCCK8, respectively) were obtained from Sigma-Aldrich Chemical Co. (St. Louis,

MO). Amino acid sequences were as follows. Sulfated CCK8: Asp-Tyr(SO_3H)-Met-Gly-Trp-Met-Asp-Phe-NH_2. Nonsulfated CCK8: Asp-Tyr-Met-Gly-Trp-Met-Asp-Phe-NH_2. Tricine (*N*-[tris(hydroxymethyl)methyl]glycine) was purchased from Fluka (Buchs, Switzerland). Ethylenediaminediacetic acid (EDDA) and nicotinic acid were from Sigma-Aldrich. The propylaldehyde hydrazone of succinimidyl hydrazinonicotinate (s-HYNIC) was synthesized essentially as described by Abrams et al. (*17*) and Schwartz et al. (*18*). $Na^{99m}TcO_4$ was eluted from a commercial $^{99}Mo/^{99m}TcO_4^-$ generator (Tyco Mallinckrodt, Inc., Petten, The Netherlands). $^{111}InCl_3$ was also obtained from Tyco Mallinckrodt.

Cell Lines. Chinese hamster ovary (CHO) cells stably transfected with cDNA encoding for either the CCK1 or CCK2 receptor were used. Generation and characterization of the cell lines is described elsewhere (*8*). Cells were cultured in Dulbecco's modified Eagle's medium (DMEM, Gibco Life Technologies, Gaithersburg, MD), supplemented with 2 mmol/L glutamine, 10% (v/v) fetal calf serum, penicillin (100 U/mL), streptomycin (100 μg/mL), and gentamicin (50 μg/mL). The cells were cultured in humidified atmosphere with 5% CO_2 at 37 °C.

RP-HPLC. An Agilent 1100 series LC system (Agilent Technologies, Palo Alto, CA) equipped with an in-line Radiomatic A-500 series radiodetector (Canberra-Packard, Meriden, CT) was used for analytical and preparative reversed phase HPLC. A Zorbax R_x C18 column (5 μm, 4.6 × 250 mm) was used at a flow rate of 1 mL/min and the following solvent system. Gradient: 0−10 min 100% TFA in water (0.1% v/v), 10−20 min 0% to 100% acetonitrile. Retention times for the nonsulafted peptide were as follows: nsCCK8: 17.5 min, HYNIC-nsCCK8: 17.7 min and ^{99m}Tc-HYNIC-nsCCK8 (nicotinic acid/tricine as coligands): 18.1 min. Retention times of the sulfated peptide were: sCCK8: 17.4 min, HYNIC-sCCK8: 17.6 min, and ^{99m}Tc-HYNIC-sCCK8 (nicotinic acid/tricine as coligands): 17.9 min. Unbound pertechnetate eluted with the void volume (3.4 min).

SPE Purification. Solid-phase extraction (SPE) was used for purification of the radiolabeled peptides in the stability studies. A C_{18} SepPak-cartridge (Waters, Inc., Milford, MA) was activated with ethanol and rinsed with 5 mL of water. The radiolabeled peptide was loaded onto the cartridge. The cartridge was washed with 5 mL of water, the radiolabeled peptide was eluted with 1 mL of acetonitrile and subsequently the solvent was evaporated under vacuum. The eluted fraction was reconstituted in phosphate buffered saline (PBS), pH 7.4.

HYNIC Conjugation of CCK8. The CCK8 peptides were conjugated with s-HYNIC essentially as described previously (*10*). Briefly, 10 μL of $NaHCO_3$ (1.0 M, pH 8.2) was added to 200 μL of peptide (0.1 μmol). Subsequently, a 10-fold molar excess of s-HYNIC in 10 μL of dry DMSO was added dropwise to the mixture. The conjugation mixture was incubated for 30 min at room temperature. To remove unreacted s-HYNIC, the mixture was passed through an activated C_{18} SepPak cartridge as described above. The dried fraction was reconstituted in water, and the HYNIC-conjugated peptide was separated from underivatized peptide by preparative RP-HPLC. The fraction containing the HYNIC-CCK8 was collected and the solvent was evaporated under a stream of nitrogen.

HYNIC-nsCCK8: MALDI-TOF-MS: analysis ($C_{58}H_{71}N_{13}O_{14}S_2$) calculated 1238.4 $(M + H)^+$, found 1238.7 $(M + H)^+$. HYNIC-sCCK8: MALDI-TOF-MS: analysis ($C_{58}H_{71}N_{13}O_{17}S_3$) calculated 1318.5 $(M + H)^+$, found 1318.6 $(M + H)^+$.

^{99m}Tc-Labeling of HYNIC-CCK8. *(i) Tricine as Coligand.* Tricine (150 μL, 100 mg/mL in PBS) was added to 5 μL of HYNIC-CCK8 (1 mg/mL). Fifteen microliters of a freshly prepared solution of $SnSO_4$ (1 mg/mL in nitrogen purged 0.1 N HCl) and 100−370 MBq of $Na^{99m}TcO_4$ were added. The solution was incubated at room temperature for 30 min.

(ii) EDDA as Coligand. EDDA (500 μL, 10 mg/mL in PBS) was added to 5 μL of HYNIC-CCK8 (1 mg/mL). Five microliters of a freshly prepared solution of $SnSO_4$ (1 mg/mL in nitrogen purged 0.1 N HCl) and 100−370 MBq of $Na^{99m}TcO_4$ were added. The mixture was incubated at 75 °C for 30 min.

(iii) Nicotinic Acid/Tricine as Coligands. Tricine (400 μL, 100 mg/mL in PBS) and nicotinic acid (100 μL, 20 mg/mL in 25 mM benzoate buffer, pH 5.0) were added to 5 μL of HYNIC-CCK8 (1 mg/mL). Twenty five microliters of a freshly prepared solution of $SnSO_4$ (1 mg/mL in nitrogen purged 0.1 N HCl) and 100−370 MBq of $Na^{99m}TcO_4$ were added. The mixture was incubated at 75 °C for 30 min.

(iv) Stability Tests. The in vitro stability of both the sulfated and the nonsulfated ^{99m}Tc-labeled CCK8 peptides was investigated. Peptides were radiolabeled and purified by SPE as described above. After evaporation of the solvent, the dried ^{99m}Tc-labeled peptide was reconstituted in 200 μL of PBS. The mixture was incubated at 37 °C for 16 h. Samples of the incubation mixture were taken at 5 min and 16 h and radiochemical purity (RCP) was assessed by RP-HPLC analysis according to the method described above.

^{111}In-Labeling of sCCK8. As a control, sCCK8 was conjugated with dicyclic anhydride of diethylenetriamine pentaacetic acid (DTPA) to allow labeling with ^{111}In (*6*). Conjugation was performed at a 1:10 molar ratio, and the DTPA-conjugated peptide was purified by SPE and RP-HPLC as described above. DTPA-sCCK8 was radiolabeled with ^{111}In by incubation with $^{111}InCl_3$ in 0.15 M ammonium acetate buffer, pH 5.0, for 30 min at room temperature.

In Vitro Characterization of ^{99m}Tc-Labeled HYNIC-CCK8. *IC_{50} Determination.* The 50% inhibitory concentration (IC_{50}) for binding the CCK1 and CCK2 receptor of both peptides was determined on CCK-receptor expressing CHO cells. CHO-CCK1 and CHO-CCK2 cells were grown to confluency in 24-well plates. Cells were washed twice with binding buffer (HEPES-buffered DMEM with 1% (w/v) bovine serum albumine). After 10 min incubation at 37 °C with binding buffer, unlabeled peptide was added in a range from 0.1 to 1000 nM in combination with a trace amount of radiolabeled peptide. To prevent internalization, cells were incubated for 2 h at 0 °C. Medium was removed, and cells were washed twice with ice-cold binding buffer. Cells were scraped, and cell-associated radioactivity was counted in 3" well-type γ counter (Perkin-Elmer, Boston, MA).

Internalization Assay. Internalization of the radiolabeled peptide was assessed as follows. Cells were cultured and pretreated as described above. Radiolabeled peptides were added at a concentration of 0.1 nM (~10 000 cpm/well). Cells were incubated at 37 °C for 2 h, medium was removed, and cells were washed with ice-cold binding buffer. To remove receptor bound radiolabeled peptide, cells were incubated with acid buffer (0.1 M acetic acid, 154 mM NaCl, pH 2.0) for 10 min at 4 °C. After washing the cells twice with ice-cold binding buffer, the internalized fraction was determined by counting the cells in a γ counter.

Table 1. Labeling Efficiency (%) and Specific Activity (Ci/mmol) of Sulfated and Nonsulfated HYNIC-CCK8 Peptides, Labeled with ^{99m}Tc in the Presence of Different Coligands (n = 3/coligand)[a]

	tricine		EDDA		NA/tricine	
	labeling efficiency (%)	S.A. (Ci/mmol)	labeling efficiency (%)	S.A. (Ci/mmol)	labeling efficiency (%)	S.A. (Ci/mmol)
^{99m}Tc-HYNIC-nsCCK8	93 ± 2	400	9 ± 1	88	93 ± 3	678
^{99m}Tc-HYNIC-sCCK8	98 ± 1	445	19 ± 1	200	96 ± 3	764

[a] Labeling conditions are described in the Methods section. Tricine: *N*-[tris(hydroxymethyl)methyl]glycine; EDDA: ethylenediaminediacetic Acid; NA: nicotinic acid. S.A.: specific activity.

Release of radiolabel from the cells was studied in a separate experiment; ^{99m}Tc-sCCK8 or ^{111}In-sCCK8 (each 0.1 nM) were added to CHO-CCK-2 cells and incubated at 37 °C for 2 h. Cells were washed with acid-buffer as described above and subsequently incubated for 2 h at 37 °C with fresh medium (without peptide). Subsequently, the medium was removed and eluted over an activated C_{18} SepPak-cartridge to determine whether the radioactivity released by the cells was pertechnetate or another metabolite.

Receptor Targeting of ^{99m}Tc-Labeled HYNIC-CCK8 in Vivo. Tumor-targeting of the radiolabeled peptides was studied in female athymic BALB/c mice bearing subcutaneous tumors of CCK-receptor transfected CHO-cells. Mice were inoculated with 4×10^6 CHO-CCK1 cells in the right flank and with 4×10^6 CHO-CCK2 cells in the left flank. When tumors had reached a weight of approximately 0.2 g, mice were randomly divided into four groups of six mice each. Mice were injected intravenously with 100 μCi (17 ng) ^{99m}Tc-labeled sulfated CCK8 or nonsulfated CCK8 (tricine/nicotinic acid as coligands) with or without a 1000 molar excess of unlabeled sulfated or nonsulfated CCK8, respectively. Mice were killed by CO_2 asphyxiation 1 h after injection. Organs of interest, including the tumors, were dissected, weighed, and counted in a gamma-counter. The animal experiments were approved by the local animal welfare committee and performed according to national regulations.

RESULTS

HYNIC Conjugation and ^{99m}Tc Labeling. The efficiency of the conjugation reaction was 28 ± 3% (n = 3) for the sulfated and 34 ± 2% (n = 3) for the nonsulfated CCK8 peptide, as based on the HPLC chromatograms of the conjugation mixtures. Performing the reaction with a 50:1 or 2:1 molar excess of s-HYNIC instead of 10:1 or when using dimethylformamide (DMF) rather than PBS as the solvent, the conjugation efficiency did not improve (data not shown). The conjugated peptides were obtained carrier-free, i.e., without nonderivatized CCK8. After 6 months of storage in PBS at −20 °C, the peptides could still be labeled with high labeling efficiency, comparable to the freshly conjugated peptides (data not shown).

Technetium-99m labeling of both peptides was studied using three coligand systems: (i) tricine, (ii) EDDA and (iii) a combination of nicotinic acid and tricine. The labeling efficiency was determined by RP-HPLC. Results of the labeling efficiency are summarized in Table 1. Labeling efficiency after labeling with tricine or the combination of tricine and nicotinic acid was always higher than 90%, whereas labeling efficiency with EDDA as coligand was lower than 20%. Varying the amount of tin (from 5 to 50 μg), used for the reduction during the ^{99m}Tc-labeling, did not improve the labeling efficiency (data not shown).

Since serum proteins are known to stabilize ^{99m}Tc-HYNIC labeled peptides and proteins (*19*), the stability of the ^{99m}Tc-labeled HYNIC-peptides was studied in PBS. Moreover, the excess of coligand was removed from the labeling mixture by SPE, to prevent possible stabilization by excess unbound coligand. As summarized in Table 2, the ^{99m}Tc-peptides labeled in the presence of tricine are highly unstable. Immediately after the SPE purification, the RCP dropped to 81 ± 3% and 88 ± 2%, for ^{99m}Tc-HYNIC-nsCCK8 and ^{99m}Tc-HYNIC-sCCK8, respectively (n = 3) and were as low as 27 ± 4% and 42 ± 3% (n = 3) after overnight incubation at 37 °C. Although the labeling efficiency was low when EDDA was used as coligand, after SPE purification the peptides released less than 5% radiolabel during 16 h in PBS. Although less stable than the EDDA-labeled peptides, the combination of nicotinic acid and tricine also showed good stability, with only 4−6% of radiolabel released from the peptides during 16 h at 37 °C in PBS. Liu et al. (*20*) recently suggested that acetonitrile could also act as coligand and could lead to the formation of mixed coligand systems. Therefore, in additional experiments we used methanol instead of acetonitrile to elute peptides during SPE and found similar results, indicating no exchange of coligands with acetonitrile (data not shown).

Table 2. Stability of ^{99m}Tc-Labeled HYNIC-nsCCK8 and HYNIC-sCCK8 after SPE, during Overnight Incubation in PBS at 37 °C[a]

		tricine (%)	EDDA (%)	NA/tricine (%)
^{99m}Tc-HYNIC-nsCCK8	5 min	81 ± 3	97 ± 1	91 ± 2
	16 h	27 ± 4	92 ± 3	87 ± 4
^{99m}Tc-HYNIC-sCCK8	5 min	88 ± 2	99 ± 1	83 ± 3
	16 h	42 ± 3	92 ± 2	77 ± 2

[a] Aliquots of the incubation mixture were taken at times indicated, and RCP was assessed by RP-HPLC. Values are expressed as percentage RCP ± SD (n = 3).

In Vitro Characterization of ^{99m}Tc-Labeled HYNIC-CCK8. The 50% inhibitory concentration (IC_{50}) of the peptides was determined on the CCK-receptor expressing CHO cells. On the basis of the results obtained in the stability test, peptides were labeled with ^{99m}Tc using nicotinic acid and tricine as coligands. The IC_{50} value of nsCCK8 was 10 nM for the CCK2 receptor, and >1 μM for the CCK1 receptor. IC_{50} values for sCCK8 were 8 nM and 3 nM, for the CCK1 and CCK2 receptor, respectively.

Both ^{99m}Tc-labeled CCK8-analogues showed rapid binding to the respective receptors and a time-dependent internalization (Figure 1) in both CCK receptor-positive cell lines. Since the nsCCK8 has virtually no affinity for the CCK1 receptor no binding and internalization was observed. After 2 h incubation at 37 °C, 2.7% of the added ^{99m}Tc-sCCK8 was internalized by the CHO-CCK1 cells and 27% in the CHO-CCK2 cells. After 2 h, 4.6% of nsCCK8 was internalized in CHO-CCK2 cells, while no binding and internalization was observed in the CHO-CCK1 cells. Addition of excess unlabeled peptide blocked the binding and internalization of the radiolabeled peptides, indicating their receptor-specific binding and internalization (data not shown).

Table 3. Biodistribution of ^{99m}Tc-Labeled SCCK8 and NsCCK8 in Athymic Mice Bearing CHO-CCK1 and CHO-CCK2 Receptor Expressing Tumors in Each Flank[a]

	^{99m}Tc-sCCK8	^{99m}Tc-sCCK8 excess unlabeled	^{99m}Tc-nsCCK8	^{99m}Tc-nsCCK8 excess unlabeled
blood	0.31 ± 0.13	0.38 ± 0.08	0.21 ± 0.05	0.23 ± 0.08
muscle	0.08 ± 0.04	0.09 ± 0.02	0.05 ± 0.01	0.09 ± 0.03
CCK1 tumor	2.04 ± 0.65	0.57 ± 0.13	0.20 ± 0.08	0.33 ± 0.15
CCK2 tumor	4.15 ± 0.28	1.02 ± 0.12	0.59 ± 0.06	0.40 ± 0.07
lung	0.34 ± 0.25	0.37 ± 0.09	0.23 ± 0.05	0.38 ± 0.16
pancreas	11.7 ± 0.93	0.56 ± 0.09	0.13 ± 0.02	0.24 ± 0.11
spleen	0.09 ± 0.03	0.12 ± 0.03	0.10 ± 0.02	0.18 ± 0.04
kidney	2.14 ± 0.23	2.87 ± 0.57	1.36 ± 0.25	1.68 ± 0.14
stomach	2.01 ± 0.46	0.86 ± 0.13	0.68 ± 0.13	0.58 ± 0.14
liver	0.29 ± 0.06	0.39 ± 0.10	0.39 ± 0.07	0.68 ± 0.12
intestine	0.38 ± 0.08	0.46 ± 0.25	0.24 ± 0.04	0.31 ± 0.09
tumor 1-to-blood	7.1 ± 2.6	1.5 ± 0.2	0.9 ± 0.2	1.5 ± 0.8
tumor 2-to-blood	14.7 ± 4.3	2.8 ± 0.6	4.0 ± 2.6	1.9 ± 0.7
tumor 2/tumor 1	2.2 ± 0.8	1.8 ± 0.4	4.3 ± 2.9	1.4 ± 0.5

[a] Mice were injected with 17 ng of Tc-99m-labeled peptide (100 μCi) and were killed at 1 h postinjection. Values are expressed as percentage of the injected dose per gram tissue (% ID/g) ± SD (n = 5 mice/group).

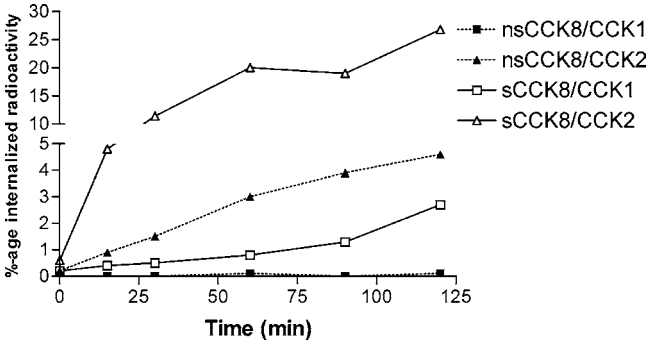


Figure 1. Internalization curve of ^{99m}Tc-nsCCK8 (dotted lines) and ^{99m}Tc-sCCK8 incubated with CHO-CCK1 (square symbols) or CHO-CCK2 (triangle symbols) cells at 37 °C. Values are expresssed as percentage of the added radioactivity present in the cells after acid wash.

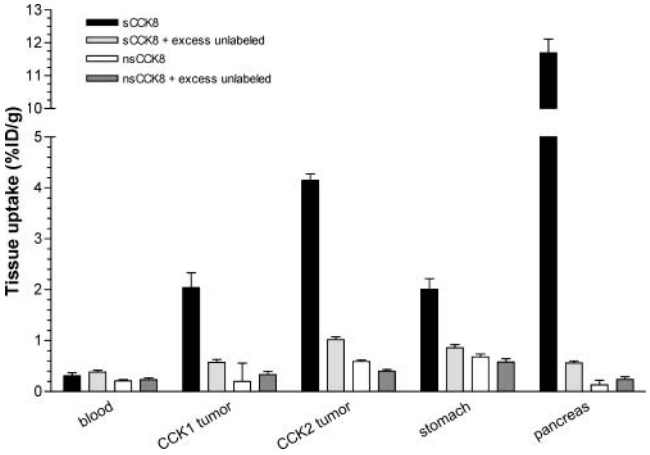


Figure 2. Biodistribution of ^{99m}Tc-nsCCK8 and ^{99m}Tc-sCCK8 in athymic mice bearing CCK1 and CCK2 receptor expressing tumors in each flank. Values are expressed as percentage of the injected dose per gram tissue (n = 5 mice/group). Blocking was performed by coinjection of a 20 000 molar excess of unlabeled minigastrin. Mice were dissected at 1 h postinjection.

In a separate in vitro experiment it was shown that the internalized radioactivity (i.e., after adding ^{99m}Tc-sCCK8) was rapidly excreted by the CHO-CCK-2 cells. After 2 h incubation in fresh medium without peptide, 36% of the internalized radiolabel was excreted into the medium, indicating that the ^{99m}Tc was not residualized in the cell. As a control, the internalization and residualization of sCCK8 labeled with the residualizing radionuclide^{111}In was investigated. In this case, no release of radioactivity from the cell was measured over a 2-h period, indicating residualization of the ^{111}In label. An additional experiment using SPE showed that 14 ± 4% (n = 3) of the excreted ^{99m}Tc activity was pertechnetate.

Receptor Targeting of ^{99m}Tc-Labeled HYNIC-CCK8 in Vivo. Both ^{99m}Tc-labeled CCK8 analogues showed a rapid blood clearance. At 1 h pi, the blood level of ^{99m}Tc-nsCCK8 was 0.21 ± 0.05% ID/g and that of ^{99m}Tc-sCCK8 was 0.31 ± 0.13% ID/g. Uptake of ^{99m}Tc-sCCK8 in CCK1 receptor-positive pancreas was 90-fold higher than that of ^{99m}Tc-nsCCK8. The biodistribution data are summarized in Table 3 and Figure 2.

Marked differences between the sulfated and nonsulfated peptides were observed in the tumor uptake in CCK2 receptor-positive tumors. Uptake of ^{99m}Tc-sCCK8 was 4.15 ± 0.28% ID/g at 1 h pi, whereas the tumor uptake of ^{99m}Tc-nsCCK8 was 7-fold lower (0.59 ± 0.06% ID/g). Blocking with an excess of unlabeled peptide resulted in a significantly lower uptake in the tumor. Uptake of ^{99m}Tc-sCCK8 dropped to only 1.02 ± 0.12% ID/g and uptake of ^{99m}Tc-nsCCK8 was reduced to 0.40 ± 0.07% ID/g, indicating CCK receptor-mediated binding of the radiolabeled peptides in the tumor. Blood levels of the radiolabeled peptides were unaffected by the excess of unlabeled peptide. Therefore, the tumor-to-blood ratios decreased from 14.7 ± 4.3 to 2.8 ± 0.6 and from 4.0 ± 2.6 to 1.9 ± 0.7 for ^{99m}Tc-sCCK8 and ^{99m}Tc-nsCCK8, respectively.

Uptake of the ^{99m}Tc-sCCK8 in the CHO-CCK1 tumor was 2.04 ± 0.65% ID/g, whereas uptake of the ^{99m}Tc-nsCCK8 was only 0.20 ± 0.08% ID/g. Tumor-to-blood ratios were 7.1 ± 2.9 and 0.9 ± 0.2 for ^{99m}Tc-sCCK8 and ^{99m}Tc-nsCCK8, respectively. ^{99m}Tc-sCCK8 uptake in the CCK1 receptor positive tumor could be specifically blocked by an excess of unlabeled sCCK8 (0.57 ± 0.13% ID/g). An excess of unlabeled nsCCK8 did not affect the tumor uptake of ^{99m}Tc-nsCCK8, indicating that this nonsulafted peptide did not localize specifically in the CCK1 receptor positive tumor. The tumor uptake remained in the same low range at 0.33 ± 0.15% ID/g.

DISCUSSION

The present study describes the characterization of the CCK8 peptide both in its sulfated and nonsulfated form and labeled with ^{99m}Tc via the bifunctional chelator hydrazino nicotinamide. Both peptides were conjugated with an efficiency of approximately 30%. This efficiency is in the same range as has been reported previously for the HYNIC conjugation of other peptides (*10*). The HYNIC-conjugated peptides showed a good shelf life

stability over a 6-month period. Although it is well-recognized that HYNIC has good stability in lyophilized products, its stability in aqueous solutions is reduced (*21*). Therefore, in the present study we used the propylaldehyde hydrazone protected HYNIC, which previously has shown improved stability in aqueous solutions (*15*). The propylaldehyde protecting group can be easily removed under mild conditions (*12*).

To obtain ^{99m}Tc-labeled peptides with maximal stability and specific activity, three different coligand systems were tested. Although tricine is the most commonly used coligand, mainly due to the high labeling efficiency obtained at room temperature, we showed that the combination of tricine and nicotinic acid yielded ^{99m}Tc-labeled peptides with the highest specific activity and improved stability in PBS. The labeling efficiency with the tricine coligand system was high, while the stability of these ^{99m}Tc-labeled peptides was poor. After 16 h incubation in PBS at 37 °C, only 27% of the ^{99m}Tc activity was still peptide associated. This is in line with other studies in which it was found that the ^{99m}Tc-tricine-HYNIC complex is stable in serum, but unstable when diluted in PBS (*22*). Most likely, the ^{99m}Tc-tricine-HYNIC complex is stabilized by the serum proteins. Ono et al. hypothesized that one of the two tricine molecules in the complex is replaced by plasma proteins which might greatly affect the circulatory half-life, especially of smaller molecules such as peptides (*19*). The EDDA coligand system showed excellent in vitro stability. However, the specific activity which could be obtained with EDDA was only 12%−25% of that obtained with the other coligand systems. Since the sulfated form of CCK8 is extremely biologically active, its possible clinical application will markedly improve when the peptide can be labeled with high specific activity preventing pharmacological side effects. Therefore, EDDA is less favorable as coligand for the CCK8 peptides.

Receptor binding and internalization studies were performed on CHO cells stably transfected with cDNA encoding for either the CCK1 or CCK2 receptor. This enabled us to investigate the receptor specifity and binding to each receptor in more detail than when using tumor cells. We found a high affinity of ^{99m}Tc-sCCK8 for both the CCK1 and CCK2 receptor and high affinity of ^{99m}Tc-nsCCK8 for the CCK2 receptor. These results are in line with those of Smeets et al., using the same cell lines but underivatized peptides (*8*). Moreover, these low IC_{50} values are in the same range as those reported for indium-111-labeled DTPA-nsCCK8 (*5*).

Both CCK receptors belong to the superfamily of G-protein-coupled receptors (GPCR) and are known to be internalized when gastrin or CCK8 binds to the receptor. Once internalized, the receptor can be recycled and re-expressed on the cell surface or be metabolized. Recycling of the receptor takes approximately 1 h (*23*). It has also been demonstrated that after internalization the peptides can end up in lysosomes and are rapidly degraded by proteolytic enzymes (*23*). In our studies we found a steady release of the ^{99m}Tc label after internalization. This released radioactivity could not be bound by the cells again, confirming processing of the radiolabeled peptide. Studies with ^{111}In-labeled nsCCK8 described internalization and subsequent retention of the radiolabel (*4*). Duncan et al. showed that ^{111}In-DTPA-labeled peptides are degraded in the lysosomes to yield ^{111}In-DTPA-amino acids, which are retained by the lysosomes (*24*). Shankar and colleagues stated that trapping in lysozomes requires the complex to be protonated at lysozomal pH ∼ 5 (*25*). Ono et al. confirmed that ^{99m}Tc-HYNIC-labeled peptides are degraded in a similar way as ^{111}In-DTPA-labeled peptides (*26*). Here we show that the ^{99m}Tc-coligand-HYNIC-amino acid complex is apparently not positively charged at lysozomal pH and is excreted by the lysosomes, because radioactivity was released by the tumor cells. Although the residualizing property of ^{111}In is beneficial for therapy purposes, residualization may not be required for receptor-mediated peptide scintigraphy, due to the shorter time frame (1−3 h postinjection) necessary for imaging with ^{99m}Tc.

The in vivo characteristics of both ^{99m}Tc-labeled peptides were investigated in athymic mice bearing subcutaneous tumors expressing either the CCK1 or CCK2 receptor. This allowed us to investigate the specificity of receptor binding in vivo. Because ^{99m}Tc-nsCCK8 had no affinity for the CCK1 receptor it did not localize specifically in the CHO-CCK1 tumor. The same holds for the pancreas, in which the CCK1 receptor is abundantly expressed in mice (*27*). The biodistribution of ^{99m}Tc-sCCK8 was markedly different from that of the ^{99m}Tc-labeled nonsulfated peptide. In general, uptake of ^{99m}Tc-sCCK8 was higher in all CCK-receptor (either CCK1 or CCK2) expressing tissues, including both tumors. Uptake in the CCK2 tumor could be blocked by an excess of unlabeled (non)sulfated CCK8, indicating receptor-mediated uptake of the ^{99m}Tc-labeled peptide in this tumor. The ^{99m}Tc-nsCCK8 uptake in the CCK1 tumor could not be blocked, indicating that the low uptake of the ^{99m}Tc-nsCCK8 was not receptor-mediated.

We showed that both CCK1 and CCK2 tumor uptake of ^{99m}Tc-sCCK8 was approximately 15-fold higher than that of ^{99m}Tc-nsCCK8. Several studies reported on the use of radiolabeled nonsulfated CCK8 for the scintigraphic imaging and/or therapy of CCK2/gastrin receptor positive tumors. The rationale for the use of nsCCK8 is its CCK2 receptor specificity, resulting in low background accumulation in CCK1 receptor-positive tissues (*3*, *4*). However, the results of the present study suggest that ^{99m}Tc-labeled sulfated CCK8 might be much more favorable for imaging and/or therapy, based on its significantly higher uptake in both the CCK1 and the CCK2 receptor positive tumors. This higher uptake may be due to the higher affinity for the CCK2 receptor (*2*). We showed in mice that uptake of the ^{99m}Tc-labeled sulfated peptide in nontarget tissue such as pancreas and stomach is also higher as compared to the accumulation of the ^{99m}Tc-labeled nonsulfated peptide, but this may be different in humans. Weinberg et al. (*28*) analyzed the CCK-receptor expression in a wide range of human tissues and in several human tumors. They showed that the CCK1 receptor is expressed mainly in gall bladder, small intestine, colon, and spleen. The CCK2 receptor is expressed in a much broader range of tissues, including pancreas, small intestine, liver, colon, stomach, spleen, and lung. Interestingly, the CCK1 receptor is expressed in pancreatic adenocarcinomas but not in normal pancreas (*28*). In contrast, in mice and rats the CCK1 receptor is abundantly expressed in the pancreas (*27*, *29*). Therefore, it is tempting to speculate that the biodistribution of both peptides in humans will be different from that observed in mice and that ^{99m}Tc-labeled sulfated CCK8 might be a good candidate for clinical testing.

CONCLUSION

CCK8 peptides can be rapidly and efficiently labeled with ^{99m}Tc using HYNIC as chelator and tricine/nicotinic acid as coligand system, without compromising the receptor binding affinity of the peptides. Both ^{99m}Tc-

labeled sulfated and nonsulfated CCK8 bind with high affinity to the CCK2 receptor, whereas ^{99m}Tc-sCCK8 also showed high affinity toward the CCK1 receptor. Studies in athymic mice revealed that uptake of ^{99m}Tc-sCCK8 in CCK1 or CCK2 receptor-positive tumors was fifteen-fold higher than that of ^{99m}Tc-nsCCK8. Although accumulation in some nontarget organs was also higher with ^{99m}Tc-sCCK8, this may not reflect the human situation, due to a different receptor expression pattern in human tisssues as compared to that in mice. Therefore, further studies are warranted to investigate the possible use of ^{99m}Tc-sCCK8 for the scintigraphic imaging of CCK receptor-positive tumors in humans.

ACKNOWLEDGMENT

We thank Mr. Gerrie Grutters and Mrs. Bianca Lemmers-de Weem (Central Animal Laboratory, University of Nijmegen, Nijmegen, The Netherlands) for skilled assistance in the animal experiments. We thank Mr. Matthias Broekema (Department of Medicinal Chemistry, Utrecht University, Utrecht, The Netherlands) for performing the MALDI-TOF-MS analysis.

Supporting Information Available: RP-HPLC, MALDI-TOF-MS data. This material is available free of charge via the Internet at http://pubs.acs.org/BC.

LITERATURE CITED

(1) Boerman, O. C., Oyen, W. J., and Corstens, F. H. (2000) Radio-labeled receptor-binding peptides: a new class of radiopharmaceuticals. *Semin. Nucl. Med. 30*, 195−208.

(2) Reubi, J. C., Schaer, J. C., and Waser, B. (1997) Cholecystokinin(CCK)-A and CCK−B/gastrin receptors in human tumors. *Cancer Res. 57*, 1377−1386.

(3) Behr, T. M., Jenner, N., Behe, M., Angerstein, C., Gratz, S., Raue, F., and Becker, W. (1999) Radiolabeled peptides for targeting cholecystokinin-B/gastrin receptor-expressing tumors. *J. Nucl. Med. 40*, 1029−1044.

(4) de Jong, M., Bakker, W. H., Bernard, B. F., Valkema, R., Kwekkeboom, D. J., Reubi, J. C., Srinivasan, A., Schmidt, M., and Krenning, E. P. (1999) Preclinical and initial clinical evaluation of ^{111}In-labeled nonsulfated CCK8 analog: a peptide for CCK−B receptor-targeted scintigraphy and radionuclide therapy. *J. Nucl. Med. 40*, 2081−2087.

(5) Reubi, J. C., Waser, B., Schaer, J. C., Laederach, U., Erion, J., Srinivasan, A., Schmidt, M. A., and Bugaj, J. E. (1998) Unsulfated DTPA- and DOTA-CCK analogues as specific high-affinity ligands for CCK−B receptor-expressing human and rat tissues in vitro and in vivo. *Eur. J. Nucl. Med. 25*, 481−490.

(6) Behe, M., Becker, W., Gotthardt, M., Angerstein, C., and Behr, T. M. (2003) Improved kinetic stability of DTPA-dGlu as compared with conventional monofunctional DTPA in chelating indium and yttrium: preclinical and initial clinical evaluation of radiometal labeled minigastrin derivatives. *Eur. J. Nucl. Med. Mol. Imag. 30*, 1140−1146.

(7) Wank, S. A., Pisegna, J. R., and de Weerth, A. (1994) Cholecystokinin receptor family. Molecular cloning, structure, and functional expression in rat, guinea pig, and human. *Ann. N. Y. Acad. Sci. 713*, 49−66.

(8) Smeets, R. L., Fouraux, M. A., van Emst-de Vries S. E., De Pont, J. J., and Willems, P. H. (1998) Protein kinase C-mediated inhibition of transmembrane signaling through CCK(A) and CCK(B) receptors. *Br. J. Pharmacol. 123*, 1189−1197.

(9) Liu, S., and Edwards, D. S. (1999) 99mTc-Labeled Small Peptides as Diagnostic Radiopharmaceuticals. *Chem. Rev. 99*, 2235−2268.

(10) Rennen, H. J., Boerman, O. C., Koenders, E. B., Oyen, W. J., and Corstens, F. H. (2000) Labeling proteins with Tc-99m via hydrazinonicotinamide (HYNIC): optimization of the conjugation reaction. *Nucl. Med. Biol. 27*, 599−604.

(11) Laverman, P., Dams, E. T., Oyen, W. J., Storm, G., Koenders, E. B., Prevost, R., van der Meer, J. W., Corstens, F. H., and Boerman, O. C. (1999) A novel method to label liposomes with ^{99m}Tc by the hydrazino nicotinyl derivative. *J. Nucl. Med. 40*, 192−197.

(12) Harris, T. D., Sworin, M., Williams, N., Rajopadhye, M., Damphousse, P. R., Glowacka, D., Poirier, M. J., and Yu, K. (1999) Synthesis of stable hydrazones of a hydrazinonicotinyl-modified peptide for the preparation of 99mTc-labeled radiopharmaceuticals. *Bioconjugate Chem. 10*, 808−814.

(13) Decristoforo, C., and Mather, S. J. (1999) Technetium-99m somatostatin analogues: effect of labeling methods and peptide sequence. *Eur. J. Nucl. Med. 26*, 869−876.

(14) Decristoforo, C., and Mather, S. J. (1999) 99m-Technetium-labeled peptide-HYNIC conjugates: effects of lipophilicity and stability on biodistribution. *Nucl. Med. Biol. 26*, 389−396.

(15) Rennen, H. J., van Eerd, J. E., Oyen, W. J., Corstens, F. H., Edwards, D. S., and Boerman, O. C. (2002) Effects of coligand variation on the in vivo characteristics of Tc-99m-labeled interleukin-8 in detection of infection. *Bioconjugate Chem. 13*, 370−377.

(16) Bangard, M., Behe, M., Guhlke, S., Otte, R., Bender, H., Maecke, H. R., and Biersack, H. J. (2000) Detection of somatostatin receptor-positive tumours using the new 99mTc-tricine-HYNIC-D-Phe1-Tyr3-octreotide: first results in patients and comparison with 111In-DTPA-D-Phe1-octreotide. *Eur. J. Nucl. Med. 27*, 628−637.

(17) Abrams, M. J., Juweid, M., tenKate, C. I., Schwartz, D. A., Hauser, M. M., Gaul, F. E., Fuccello, A. J., Rubin, R. H., Strauss, H. W., and Fischman, A. J. (1990) Technetium-99m-human polyclonal IgG radiolabeled via the hydrazino nicotinamide derivative for imaging focal sites of infection in rats. *J. Nucl. Med. 31*, 2022−2028.

(18) Schwartz, D. A., Abrams, M. J., Gladomenico, C. M., and Zubieta, J. A. (1993) Certain pyridyl hydrazines and hydrazides useful for protein labeling. US Patent 5,206,370.

(19) Ono, M., Arano, Y., Mukai, T., Uehara, T., Fujioka, Y., Ogawa, K., Namba, S., Nakayama, M., Saga, T., Konishi, J., Horiuchi, K., Yokoyama, A., and Saji, H. (2001) Plasma protein binding of (99m)Tc-labeled hydrazino nicotinamide derivatized polypeptides and peptides. *Nucl. Med. Biol. 28*, 155−164.

(20) Liu, G., Wescott, C., Sato, A., Wang, Y., Liu, N., Zhang, Y. M., Rusckowski, M., and Hnatowich, D. J. (2002) Nitriles form mixed-coligand complexes with (99m)Tc-HYNIC-peptide. *Nucl. Med. Biol. 29*, 107−113.

(21) Laverman, P., Van Bloois, L., Boerman, O. C., Oyen, W. J., Corstens, F. H., and Storm, G. (2000) Lyophilization of Tc-99m-HYNIC labeled PEG-liposomes. *J. Liposome Res. 10*, 117−129.

(22) Liu, S., Edwards, D. S., Looby, R. J., Harris, A. R., Poirier, M. J., Barrett, J. A., Heminway, S. J., and Carroll, T. R. (1996) Labeling a hydrazino nicotinamide-modified cyclic IIb/IIIa receptor antagonist with 99mTc using aminocarboxylates as coligands. *Bioconjugate Chem. 7*, 63−71.

(23) Tarasova, N. I., Wank, S. A., Hudson, E. A., Romanov, V. I., Czerwinski, G., Resau, J. H., and Michejda, C. J. (1997) Endocytosis of gastrin in cancer cells expressing gastrin/CCK−B receptor. *Cell Tissue Res. 287*, 325−333.

(24) Duncan, J. R., and Welch, M. J. (1993) Intracellular metabolism of indium-111-DTPA-labeled receptor targeted proteins. *J. Nucl. Med. 34*, 1728−1738.

(25) Shankar, S., Vaidyanathan, G., Affleck, D., Welsh, P. C., and Zalutsky, M. R. (2003) N−Succinimidyl 3-[(131)I]Iodo-4-phosphonomethylbenzoate ([(131)I]SIPMB), a Negatively Charged Substituent-Bearing Acylation Agent for the Radioiodination of Peptides and mAbs. *Bioconjugate Chem. 14*, 331−341.

(26) Ono, M., Arano, Y., Uehara, T., Fujioka, Y., Ogawa, K., Namba, S., Mukai, T., Nakayama, M., and Saji, H. (1999) Intracellular metabolic fate of radioactivity after injection of technetium-99m-labeled hydrazino nicotinamide derivatized proteins. *Bioconjugate Chem. 10*, 386−394.

(27) Bourassa, J., Laine, J., Kruse, M. L., Gagnon, M. C., Calvo, E., and Morisset, J. (1999) Ontogeny and species differences

in the pancreatic expression and localization of the CCK(A) receptors. *Biochem. Biophys. Res. Commun. 260*, 820−828.
(28) Weinberg, D. S., Ruggeri, B., Barber, M. T., Biswas, S., Miknyocki, S., and Waldman, S. A. (1997) Cholecystokinin A and B receptors are differentially expressed in normal pancreas and pancreatic adenocarcinoma. *J. Clin. Invest, 100*, 597−603.
(29) Reubi, J. C., Waser, B., Gugger, M., Friess, H., Kleeff, J., Kayed, H., Buchler, M. W., and Laissue, J. A. (2003) Distribution of CCK1 and CCK2 receptors in normal and diseased human pancreatic tissue. *Gastroenterology 125*, 98−106.

BC034208W

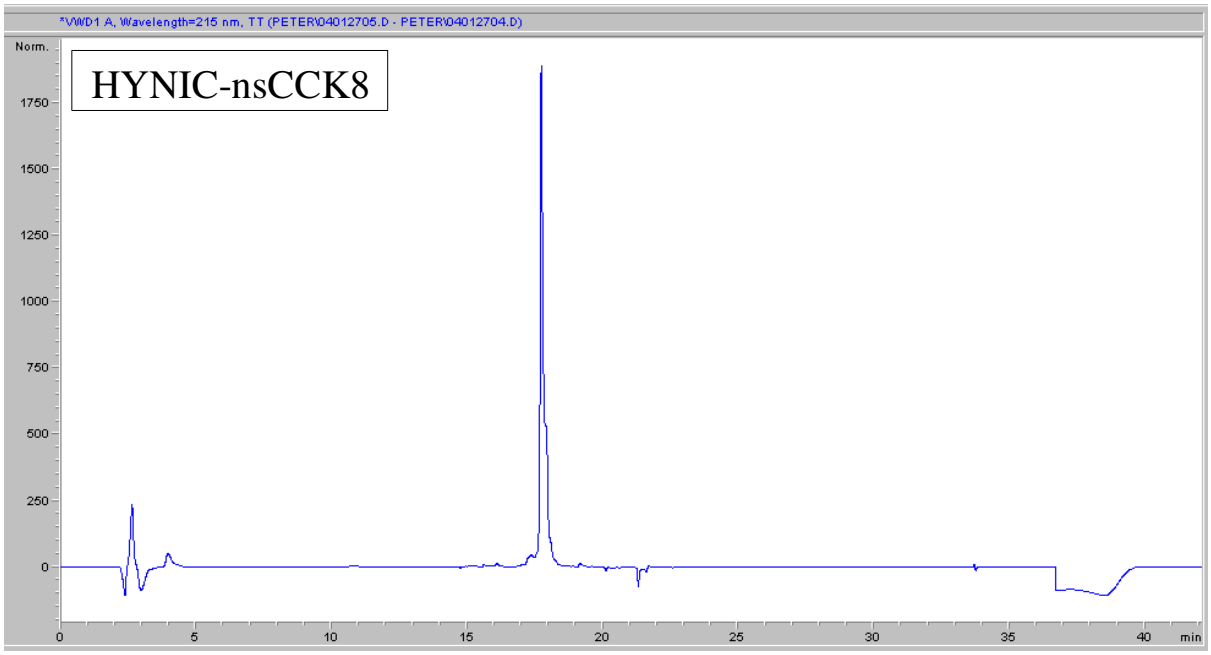
Manuscript: BC034208W

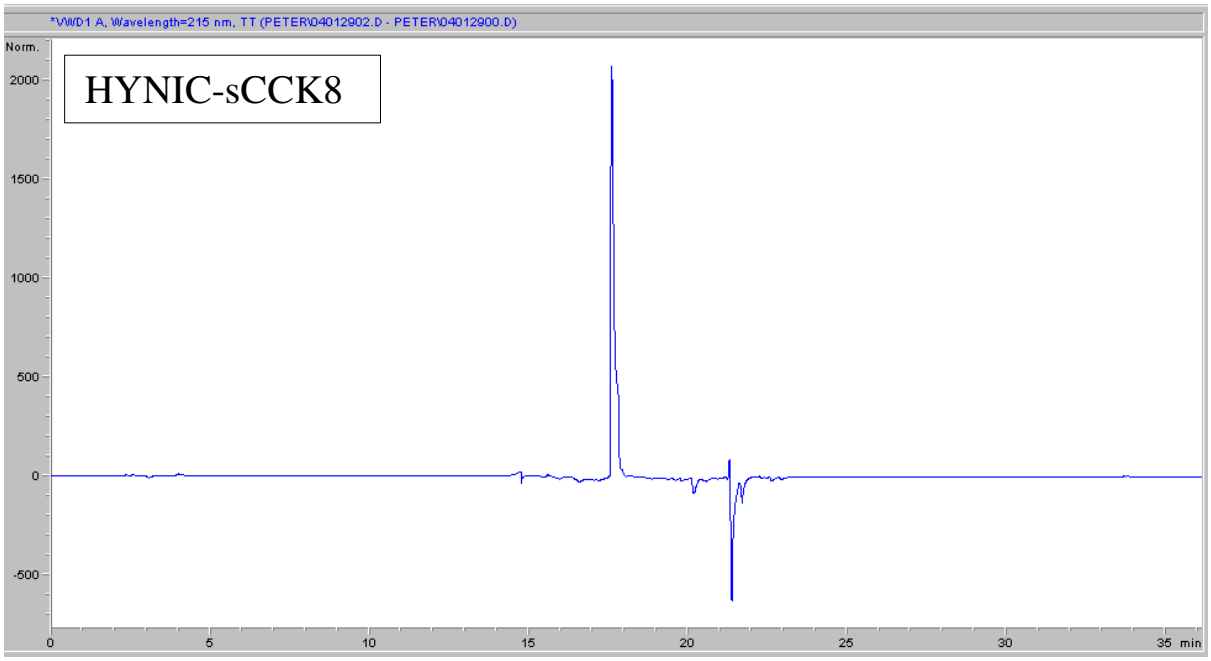
Title: TWO TECHNETIUM-99M LABELED CHOLECYSTOKININ-8 (CCK8) PEPTIDES FOR SCINTIGRAPHIC IMAGING OF CCK-RECEPTORS

Authors: P. Laverman *et al.*

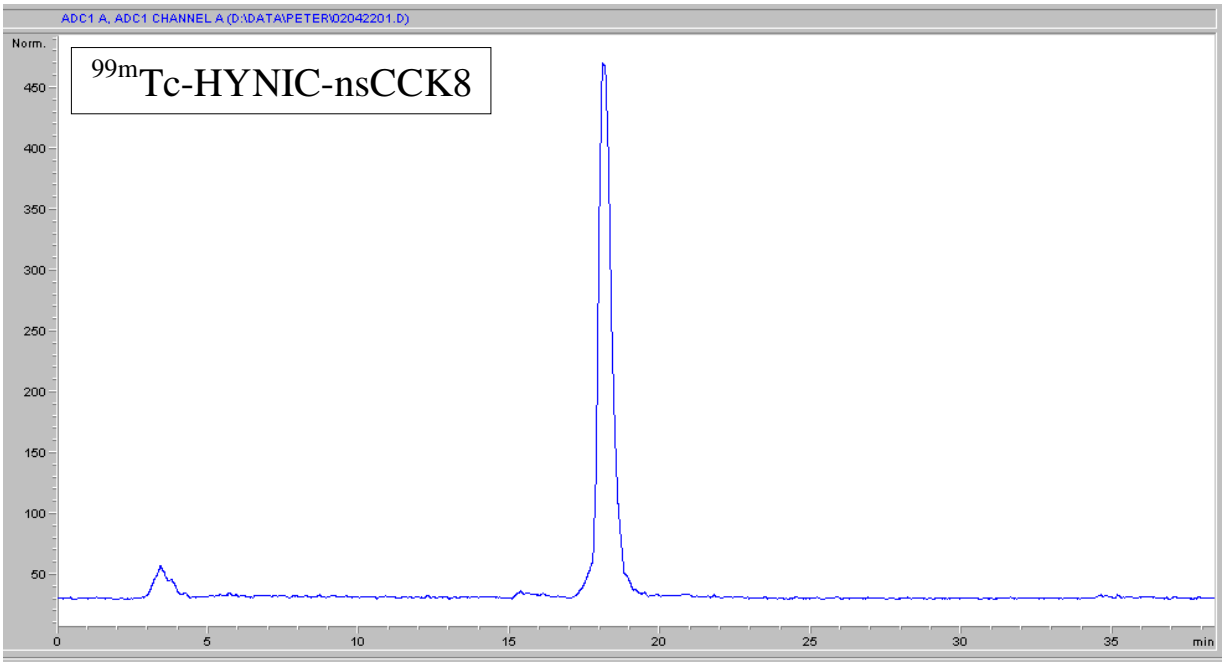
Supplement data

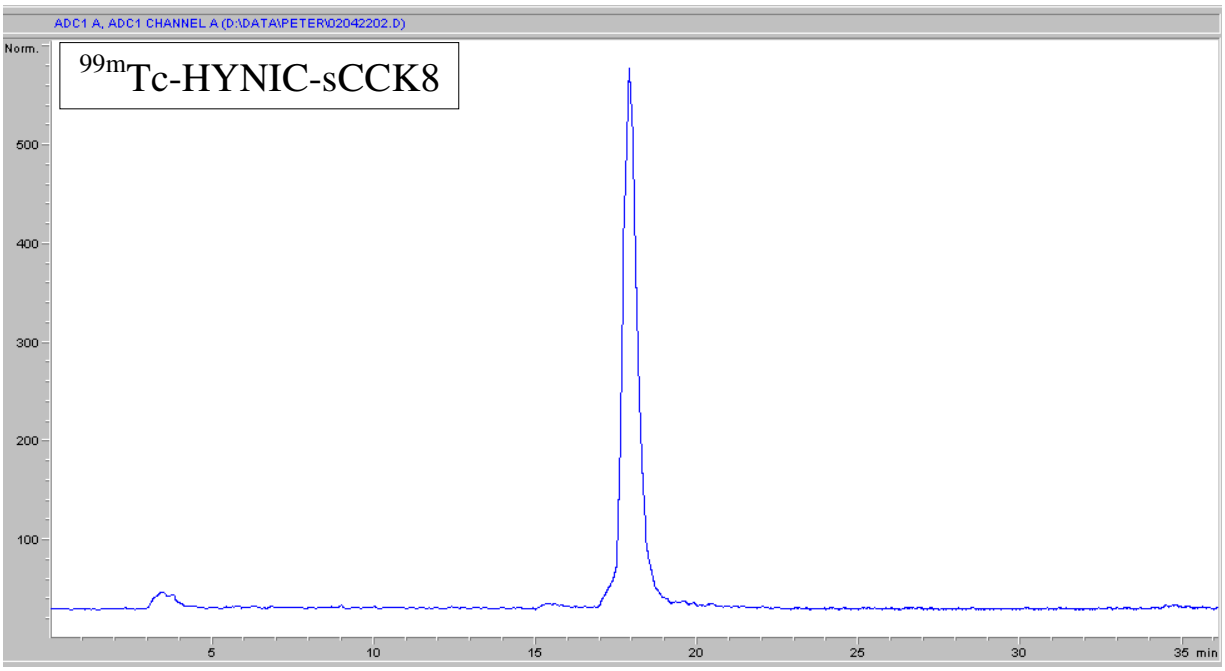
HPLC chromatograms of HYNIC-conjugated peptides.



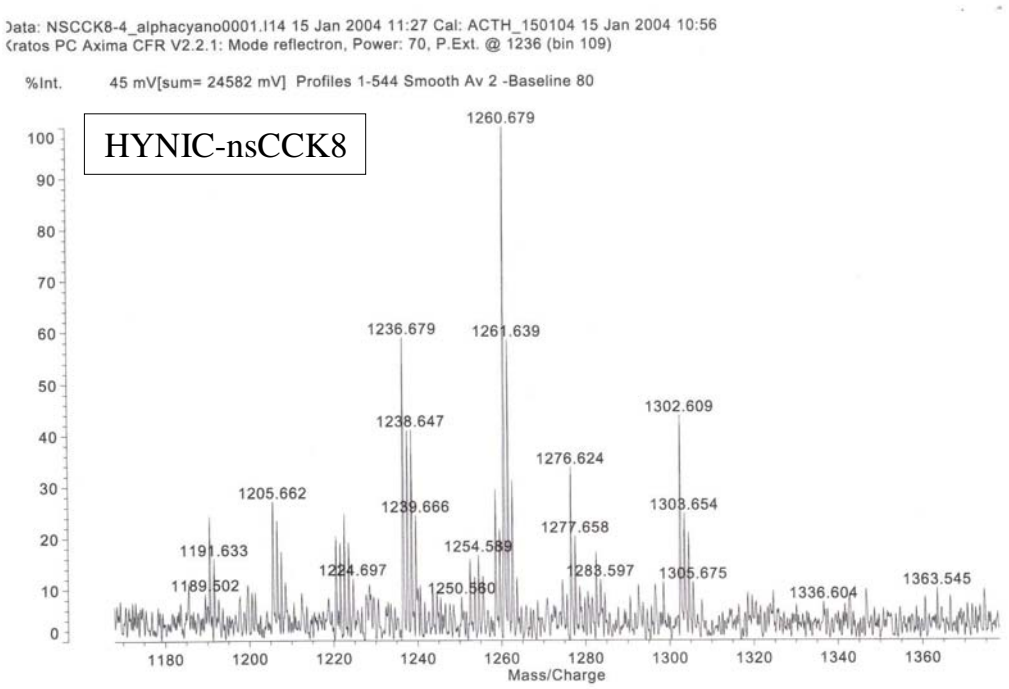


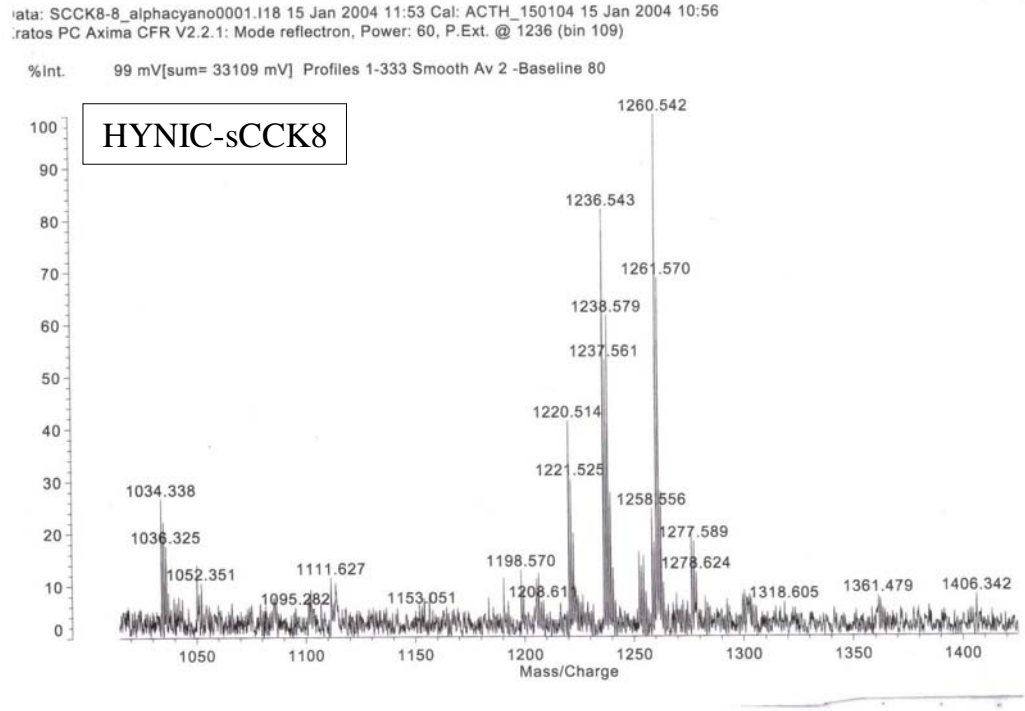
HPLC chromatograms of ^{99m}Tc-labeled, HYNIC-conjugated peptides, using tricine/nicotinc acid as coligands





MALDI-TOF-MS spectra





Methoxyoxalamido Chemistry in the Synthesis of Novel Amino Linker and Spacer Phosphoramidites: A Robust Means for Stability, Structural Versatility, and Optimal Tether Length

A. Michael Morocho, Valeri N. Karamyshev, and Nikolai N. Polushin*

Fidelity Systems, Inc., 7961 Cessna Avenue, Gaithersburg, Maryland 20879. Received December 2, 2003; Revised Manuscript Received March 4, 2004

We have developed a general route to the synthesis of novel amino linker and spacer phosphoramidites utilizing methoxyoxalamido (MOX) chemistry. The synthesis makes use of readily available and inexpensive primary aliphatic amino alcohols and diamines to produce a rich and diverse variety of phosphoramidites. Among these are monomers with exceptionally long (up to 56 atoms in length) amphipathic tethering arms. The chemistry bestows exceptional control over the physical characteristics within the tethers through the selection of appropriate building blocks. Furthermore, MOX chemistry enables fairly rapid assembly of these discrete-length tethers in a modular fashion. All novel phosphoramidites were successfully used in automated syntheses of 5′-modified oligonucleotides.

INTRODUCTION

Amino linker phosphoramidites are used to introduce an amino group onto the 5′-end of a synthetic oligonucleotide. Such 5′-amino-modified oligonucleotides are routinely utilized in DNA microarray production and as intermediates to functionally labeled oligonucleotides (*1*, *2*). Spacer phosphoramidites are commonly used to substitute for bases in a sequence, to incorporate hairpin loops and to position labels at a desired distance from the oligonucleotide (*3*, *4*).

Some amino linkers and spacers are commercially available (*5*), but they generally possess at least three limitations. First, these phosphoramidites are mainly derived from aliphatic primary alcohols and thus are not very stable even at low temperatures due to susceptibility to undergo Arbuzov rearrangement (*6*). This instability presents preparation and storage complications and also necessitates fairly rapid phosphoramidite consumption on automated DNA synthesizers, making the commercially available amino linkers and spacers less than ideal for reliable large-scale oligonucleotide production. Second, the available amino linker and spacer phosphoramidites are quite limited in variety. They are primarily flexible in nature, since they contain methylene or oxyethylene units within the tether chain and are rather short not exceeding 19 atoms in length. Third, the production chemistry for these phosphoramidites is not amenable to constructing a vast number of distinctly different monomers, each possessing varying degrees of flexibility, hydrophobicity, and length.

To overcome the aforementioned limitations, we report here on a general synthetic route toward amino linker and spacer phosphoramidites. The method is based on robust methoxyoxalamido (MOX)[1] chemistry (*6*) and offers great control over tether composition, rigidity, and length. All synthesized β-cyanoethyl phosphoramidites are derived from secondary alcohols and can be used on the synthesizer for at least two weeks without any loss in coupling efficiency.

EXPERIMENTAL PROCEDURES

MOX precursors **1** and **2** were prepared as previously described (*6*). Dimethyl oxalate, triethylamine, tetrazole, 4,7,10-trioxa-1,13-tridecanediamine (TTDD), 2,4,8,10-tetraoxaspiro[5.5]undecane-3,9-dipropanamine (TUDA), hexamethylenediamine (HMDA), 1,10-diaminodecane (DAD), 1,12-dodecanediamine (DDD), cystamine (CA), ethylenediamine (EDA), ethanolamine (EA), 2-(2-aminoethoxy)ethanol (AEE), 6-amino-1-hexanol (AH), monomethoxytrityl chloride (MMT-Cl), dimethoxytrityl chloride (DMT-Cl), and all solvents were purchased from Aldrich (Milwaukee, WI) and used without further purification. 2-Cyanoethyl-*N*,*N*,*N*′*N*′-tetraisopropylphosphorodiamidite was purchased from ChemGenes (Ashland, MA). Protected nucleoside cyanoethyl phosphoramidites were purchased from Transgenomic (Aston, PA). Tetrazole (0.45 M in acetonitrile), 5-ethylthio-1*H*-tetrazole (ETT, 0.25 M in acetonitrile), and all ancillary DNA synthesis reagents were purchased from Glen Research (Sterling, VA). Synthesis columns were purchased from Biosset (Novosibirsk, Russia). NMR and MS data for all novel compounds are presented in Supporting Information.

Thin-layer chromatography (TLC) was performed on Kieselgel 60 F_{254} plates (EM Science, Gibbstown, NJ). TLC plates were visualized under shortwave UV light, I_2-silica chamber, or by heating. Flash chromatography was performed with 200−400 mesh, 60 silica gel (EM Science). Electrophoretic gels were 1 mm thick 15−20% acrylamide−7 M urea and were run at 400−600 V using

* To whom correspondence should be addressed. E-mail: npolouchine@fidelitysystems.com.

[1] Abbreviations: AEE, 2-(2-aminoethoxy)-ethanol; AH, 6-amino-1-hexanol; CA, cystamine; DAD, 1,10-diaminodecane; DDD, 1,-12-dodecanediamine; EA, ethanolamine; EDA, ethylenediamine; ETT, 5-ethylthio-1*H*-tetrazole; HEG, hexaethylene glycol; HMDA, hexamethylenediamine; DMT-Cl, dimethoxytrityl chloride; MOX, methoxyoxalamido; MMT-Cl, monomethoxytrityl chloride; TTDD, 4,7,10-trioxa-1,13-tridecanediamine; TUDA, 2,4,8,10-tetraoxaspiro[5.5]undecane-3,9-dipropanamine.

10.1021/bc034218x CCC: $27.50 © 2004 American Chemical Society
Published on Web 04/23/2004

TBE buffer. Crude oligonucleotides were loaded as 7 M aqueous urea solutions (1 A_{260}/10 μL) at 1−2 A_{260} units/well (12 mm long). The gels were visualized by UV shadowing over a fluorescent TLC plate or by staining with Stains-all dye (Aldrich). Purified oligonucleotides were prepared by cutting out the corresponding bands, extraction with 0.25 M triethylaminobicarbonate (TEAB) for 3−5 h at room temperature, and desalting the oligonucleotide solutions on Sephadex G-25 NAP-10 columns (Pharmacia, Uppsala, Sweden).

Oligodeoxyribonucleotides were synthesized on Biosset ASM 800 DNA/RNA synthesizers (Novosibirsk, Russia). To allow ethanolamine deprotection N^4-acetyl protected deoxycytidine phosphoramidite was used (*6* and references therein). For the 5′-end derivatization the following conditions were used: 0.1 M solutions of spacer and amino linker phosphoramidites in CH_3CN or in 1:1 mixture of CH_3CN and CH_2Cl_2, a 3−5 min coupling time, and 0.25 M ETT in CH_3CN as a catalyst. Oligonucleotides were deprotected by treatment the CPG supports with ethanolamine (30 μL per 0.1−1 μmol scale) at 70 °C for 15−20 min. The reaction mixtures were diluted with water (up to 1 mL) and desalted on Sephadex G-25 NAP-10 columns (Pharmacia, Uppsala, Sweden).

Matrix-assisted laser desorption ionization mass spectra of oligonucleotides were recorded on a Voyager-DE mass spectrometer (PerSeptive Biosystems, Framingham, MA). Oligonucleotide samples were first ethanol precipitated from 5 M aqueous ammonium acetate. 3-Hydroxypicolinic acid was used as a matrix.

Procedure A. *Derivatization of a MOX Precursor/Intermediate with an Aliphatic Primary Amino Alcohol.* To a stirring solution of an aliphatic primary amino alcohol (12 mmol) in methanol (50 mL) a 10 mmol solution of MOX precursor (**1** or **2**) or MOX intermediate (**12b**, **14b**, or **16b**) in methanol/dichloromethane (1:1, v/v, 25 mL) was added. The reaction mixture was stirred for 2 h, during which time a partial precipitation of the product was typically observed. The precipitation was completed by addition of diethyl ether (300 mL). The reaction mixture was cooled to +4 °C and incubated at this temperature for 2 h. The precipitate was filtered, washed with diethyl ether (2 × 30 mL), and dried. The synthesized diol was used without further purification.

Following Procedure A, **3a** was prepared from **1** and AEE (77%), **4a** from **1** and AH (60%), **5a** from **14b** and AEE (89%), **6a** from **12b** and AEE (90%). **7a** was prepared from **16b** and AEE (91%) following Procedure A, except dichloromethane was used as solvent. All prepared diols were white solids.

Procedure B. *Derivatization of a MOX Precursor/Intermediate with an Aliphatic Primary Diamine.* The reaction was carried out analogously to Procedure A except that, instead of an amino alcohol, an aliphatic primary diamine (40 mmol, 4 times excess over MOX component) was used and the solution of MOX precursor was added portionwise over a 30-min period. The synthesized amino alcohol was used without further purification.

Following Procedure B, **8a** was prepared from **1** and EDA (95%), **9a** from **1** and HMDA (93%), **12a** from **1** and TTDD (85%), **13a** from **1** and TUDA (77%), **14a** from **2** and TTDD (82%), **15a** from **14b** and TTDD (83%), **16a** from **12b** and TTDD (85%), **17a** from **16b** and TTDD (87%). **10a** was prepared from **1** and DAD (79%), and **11a** from **1** and DDD (77%)**,** following Procedure B, except that diamines were dissolved in 100 mL of MeOH, and the products were filtered without ether addition. All prepared amino alcohols were white solids.

Procedure C. *Protection of a Primary Hydroxyl Group with DMT-Cl.* To a stirring solution or a slurry of a diol (10 mmol, prepared as described in Procedure A) in anhydrous DMF/pyridine (1:1, v/v, 100 mL) was added DMT-Cl (11 mmol). The reaction mixture was stirred overnight at room temperature. If after this time the reaction was not completed (as monitored by TLC), another portion of DMT-Cl (2 mmol) was added and the reaction mixture was stirred for an additional 5 h. The reaction was diluted with chloroform (400 mL) and extracted with a saline solution (400 mL). The organic layer was dried over anhydrous Na_2SO_4 and concentrated to ∼50 mL. To this were added diethyl ether (300 mL) and then pentane (200 mL) with stirring. The slurry was cooled to +4 °C and incubated at this temperature for 2 h. The precipitate was filtered, washed with diethyl ether/pentane (1:1, v/v, 2 × 30 mL), and dried. The synthesized DMT-protected diols were phosphitylated without further purification.

Following Procedure C, **3b** was prepared from **3a** (78%), **4b** from **4a** (85%), **5b** from **5a** (81%), **6b** from **6a** (75%), and **7b** from **7a** (86%). Compounds **3b**, **4b**, and **6b** were yellowish solids. Compounds **5b** and **7b** were white solids.

Procedure D. *Protection of a Primary Amino Group with MMT-Cl.* Protection of the primary amino group of amino alcohols (prepared as described in Procedure B) with MMT-Cl was executed analogously to Procedure C except that, due to generally poorer solubility of the amino alcohols, the reaction time was extended to 2−3 days and the chloroform solution was filtered through a thin layer of silica gel before the extraction. The synthesized MMT-protected amino alcohols were phosphitylated without further purification.

Following Procedure D **8c** was prepared from **8a** (56%), **9c** from **9a** (51%), **12c** from **12a** (65%), **13c** from **13a** (67%), **14c** from **14a** (83%), **15c** from **15a** (72%), **16c** from **16a** (61%) and **17c** from **17a** (66%). Compounds **8c**, **9c** and **12c**−**14c** were yellowish solids. Compounds **15c**−**17c** were white solids.

MMT-Protected Amino Alcohol 10c. 10a (1.68 g, 4.91 mmol) was dissolved in hot dioxane (100 mL, 70−80 °C). To this were added DBU (2.94 mL, 19.6 mmol) and MMT-Cl (0.91 g, 2.95 mmol) with stirring. The reaction mixture was stirred at 70−80 °C for 30 min. A second portion of MMT-Cl (0.91 g, 2.95 mmol) was added, and the reaction mixture was stirred for an additional 1 h. The reaction was quenched with water (400 mL) and stirred for 2 h at room temperature. The precipitate was filtered, washed with water, (2 × 100 mL) and recrystallized from ethanol to give **10c** as a white solid (1.66 g, 55%).

MMT-Protected Amino Alcohol 11c. 11c was prepared from **11a** exactly as **10c** to give a white solid (58%).

Procedure E. *Derivatization of a Primary Amino Group with Dimethyl Oxalate.* To a stirring solution of dimethyl oxalate (40 mmol) and triethylamine (20 mmol) in methanol (50 mL) was added the amino alcohol (10 mmol, prepared as described in Procedure B) portionwise over a 2-h period. The reaction mixture was stirred for an additional 1 h and concentrated to dryness. The excessive dimethyl oxalate was sublimed out at ∼3 Torr and 70 °C. The residue was dissolved chloroform, and the MOX derivative was separated by flash chromatography on silica gel (gradient of methanol in chloroform).

Following Procedure E, **12b** was prepared from **12a** (87%), and **16b** from **16a** (71%). **14b** was prepared from **14a** (90%) following procedure E, except that pyridine

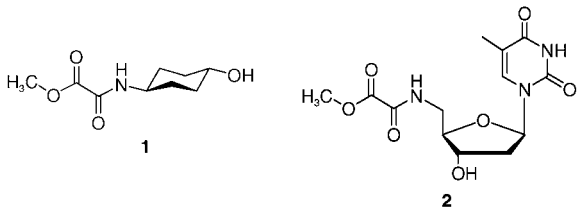


Figure 1. MOX precursors.

was used as solvent. Compounds **12b, 14b**, and **16b** were white solids.

Procedure F. *Phosphitylation of a Secondary Hydroxyl Group.* To the mixture of a dry secondary alcohol (5 mmol, prepared as described in Procedure C or D) and tetrazole (4.75 mmol) were consecutively added anhydrous dichloromethane (50 mL) and 2-cyanoethyl-*N*,*N*,-*N*′,*N*′-tetraisopropylphosphoramidite (6.5 mmol). The reaction mixture was stirred for at least 1 h or until complete disappearance of the initial solids. During the course of the reaction crystals of diisopropylamine tetrazolide were typically formed. The reaction was diluted with dichloromethane (200 mL) and extracted with a 10% aqueous $NaHCO_3$ solution (200 mL). The organic layer was dried over anhydrous Na_2SO_4 and concentrated to ~20 mL. The residue was precipitated into diethyl ether/pentane mixture (1:1, v/v, 500 mL) and allowed to settle down, at which point the supernatant was decanted. The residue was purified by flash chromatography (gradient of ethyl acetate in pentane or gradient of pyridine in ethyl acetate, where ethyl acetate contained 4% of triethylamine).

Following Procedure F, **3c** was prepared from **3b** (85%), **4c** from **4b** (84%), **5c** from **5b** (68%), **6c** from **6b** (65%), **7c** from **7b** (69%), **8d** from **8c** (85%), **9d** from **9c** (62%), **10d** from **10c** (65%), **11d** from **11c** (80%), **12d** from **12c** (91%), **13d** from **13c** (87%), **14d** from **14c** (72%), **15d** from **15c** (80%), **16d** from **16c** (83%), and **17d** from **17c** (70%). All prepared spacer phosphoramidites (compounds **3c**−**7c**) were white amorphous solids. Amino linker phosphoramidite **8d, 9d**, and **13d**−**17d** were white amorphous solids. Amino linker phosphoramidite **10d**−**12d** were clear oils.

RESULTS AND DISCUSSION

For the synthesis of novel amino linker and spacer phosphoramidites, we have engaged methoxyoxalamido chemistry that proved to be very reliable in our previous work (*6*, *7*). As starting materials, we have used *trans*-4-methoxyoxalamido-1-cyclohexanol **1** and 5′-methoxyoxalamido-5′-deoxythymidine **2** (Figure 1) based on the reasoning that both compounds could easily be synthesized from commercially available *trans*-4-amino-1-cyclohexanol and 5′-amino-5′-deoxythymidine, respectively, and both have secondary hydroxyls that endow stability to the corresponding phosphoramidites. The use of carbon skeletons with a secondary hydroxyl group also greatly facilitates the protection at the primary hydroxyl during spacer phosphoramidite preparations.

Phosphoramidite Synthetic Routes. The general synthetic routes toward novel amino linker and spacer phosphoramidites are outlined in Scheme 1. Phosphoramidite preparations proceeded by either a single synthon addition (Scheme 1A) or by means of a serial addition of tether synthons (Scheme 1B). The first route is, naturally, easier to execute. In the case of spacer phosphoramidite syntheses the MOX precursor was first reacted with a slight excess of an aliphatic amino alcohol, the amino and hydroxyl groups both being primary. The introduced primary hydroxyl was then selectively protected with DMT group, and the resultant intermediate was phosphitylated on the secondary hydroxyl to give a final product. When an amino linker had to be synthesized the MOX precursor was treated with a 4-fold excess of an aliphatic primary diamine. The excess amount of diamine was necessary to suppress dimer formation. However, due to substantial differences in solubility between the diamine and the formed amino alcohol, the former could easily be separated and recycled, if needed. The amino group of the intermediate amino alcohol was protected with MMT group, and the secondary hydroxyl of the protected amino alcohol was phosphitylated to furnish the amino linker phosphoramidite. In both spacer and amino linker preparations the reactions proceeded in a straightforward manner, and the synthesis proved to be robust. The stepwise yields were high, and crystallization or precipitation effectively cleaned up the majority of the reactions leading up to the phosphoramidite. Thus, column chromatography was only used at the final phosphitylation step. DMT/MMT-protected alcohol intermediates were generally synthesized in 50−80% isolated yields based on their MOX precursors and then converted into phosphoramidites in 60−90% isolated yields. Simple spacer phosphoramidites **3c** and **4c** and preceding intermediates **3a**,**b** and **4a**,**b** are shown in Figure 2. Simple amino linker phosphoramidites **8d**−**14d** and their intermediates **8a**,**c**−**14a**,**c** are displayed in Figure 3.

The route to compound spacer and amino linker phosphoramidites is depicted in Scheme 1B. The MOX precursors **1** and **2** were treated with appropriate diamine, and the amino group of the formed amino alcohols was reacted with a 4-fold excess of dimethyl oxalate, thus generating new two-component MOX intermediates. The excessive amount of dimethyl oxalate was necessary to suppress dimer formation, but, if needed, the excess reagent could easily be recovered from the reaction mixture by sublimation. Further treatment of these MOX intermediates with amino alcohols or diamines, followed by protection and phosphitylation, led to three-component compound spacer phosphoramidites **5c** and **6c** (Figure 2) and amino linker phosphoramidites **15d** and **16d** (Figure 3). Again, all the reactions proceeded in high or good yields, and column purification was applied only to the MOX intermediates and the final phosphoramidites. Obviously, diamine/dimethyl oxalate treatments could be applied repeatedly to the initial MOX precursor leading to multicomponent MOX precursors and, accordingly, to multicomponent phosphoramidites. To prove this concept four-component spacer phosphoramidites **7c** (Figure 2) and amino linker phosphoramidite **17d** (Figure 3) were successfully synthesized from the three-component MOX precursor **16b**.

Phosphoramidite Stability. Many of the currently available amino linker and spacer phosphoramidites are derived from primary alcohols and are generally less stable than monomers derived from secondary alcohols. The phosphoramidites in this paper have been synthesized from cyclic carbon scaffolds with a secondary hydroxyl and are as stable in solution as standard phosphoramidites. ^{31}P NMR time course experiments showed that phosphoramidite **8d**, based on a cyclohexanol skeleton, has substantially greater stability compared to commercially available C6 amino linker that has the phosphoramidite moiety attached through a primary hydroxyl (Figure 4). As one can see from Figure 4, after 20 days, phosphoramidite **8d** was still more than 90% intact while more than 40% of C6 amino linker were

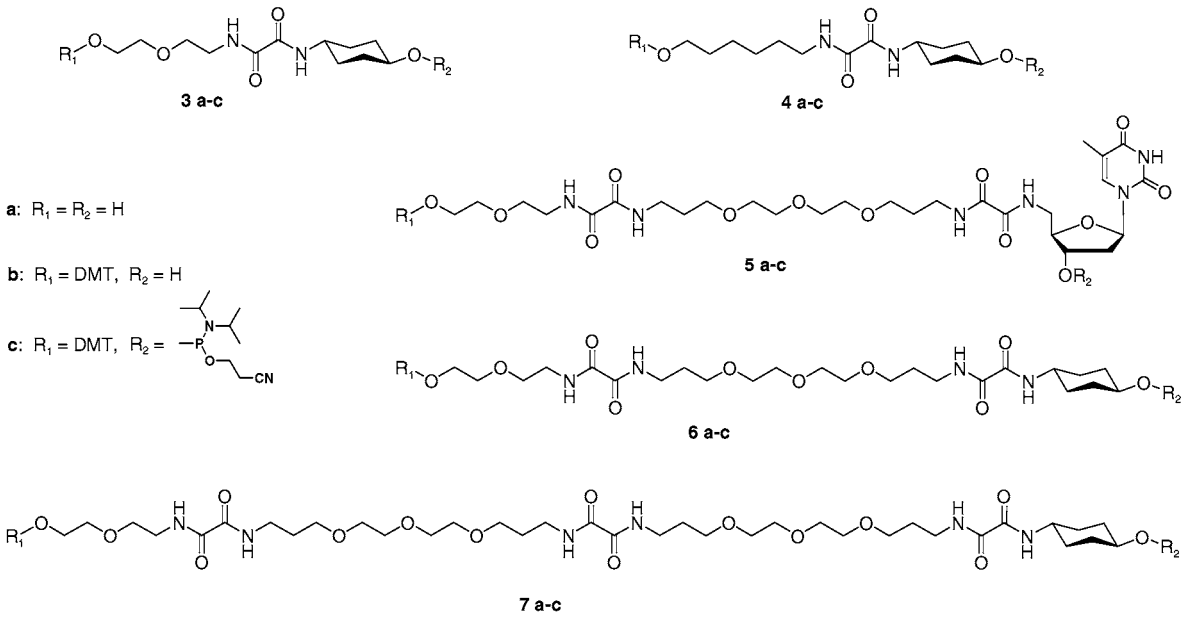
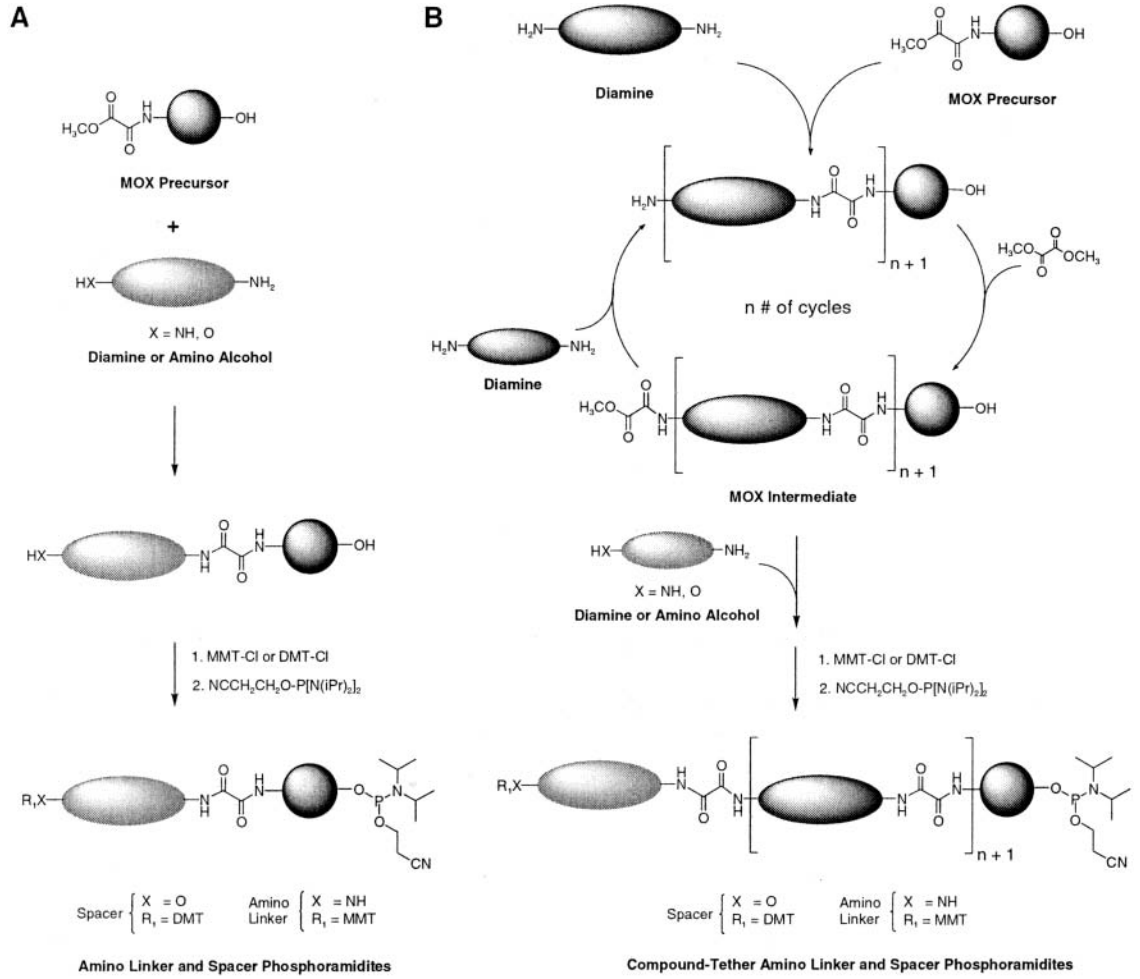


Figure 2. Spacer intermediates and phosphoramidites.

Scheme 1. Synthetic Pathways to Spacer and Amino Linker Phosphoramidites Possessing Simple (A) and Compound (B) Tethers



decomposed. We have repeated these experiments with phosphoramidite **16d**, which has a longer tether, and obtained the stability curve practically identical to the one of **8d**.

The coupling yields of the present phosphoramidites did not deteriorate within at least 2−3 weeks after phosphoramidite installation on the synthesizer. In an extreme case, PAGE analysis of amino-modified oligonucleotides using phosphoramidite **12d** showed acceptable coupling even after a 30-day sitting on the synthesizer (gel data can be viewed at http://www.fidelitysystems.com/Stability.html).

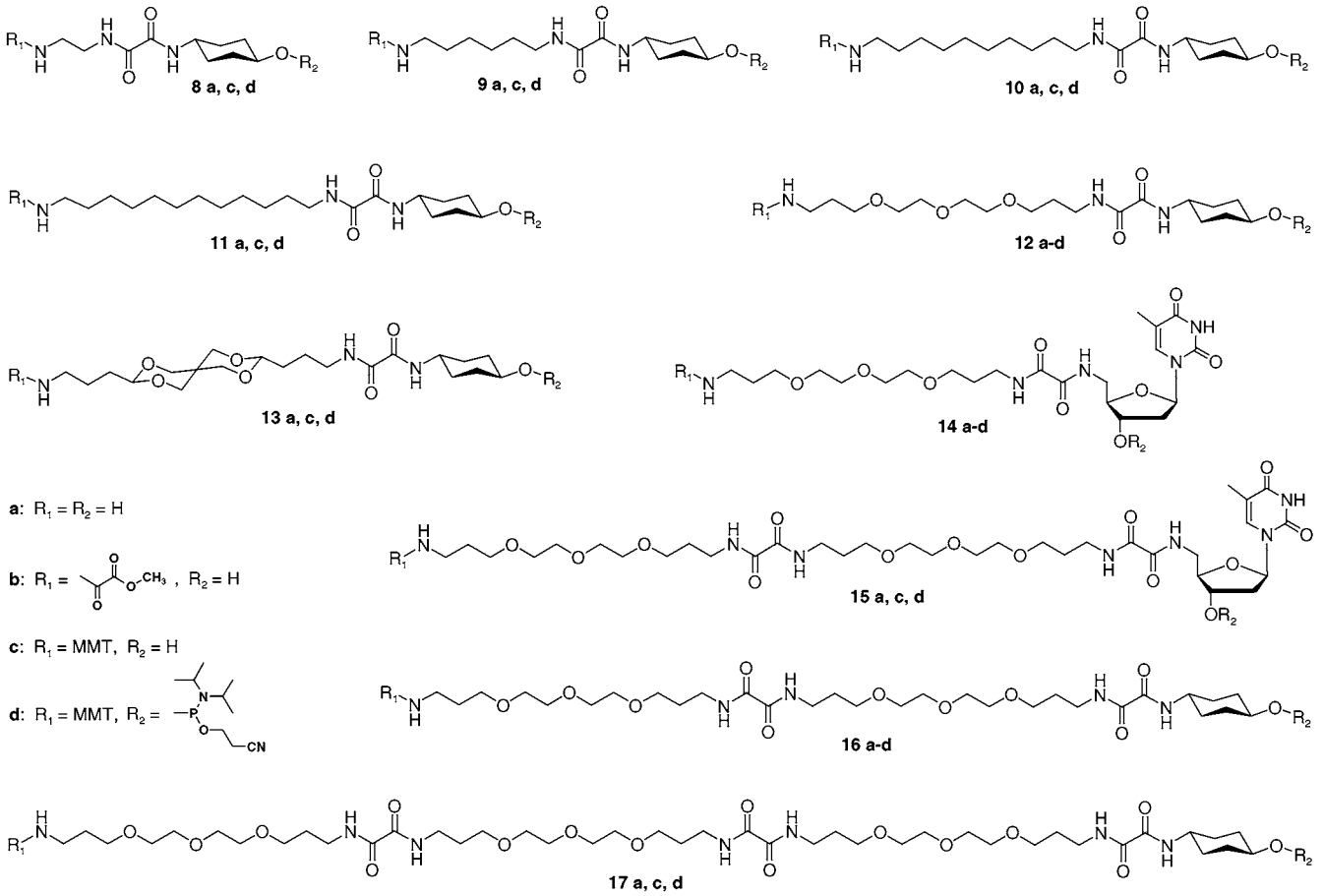


Figure 3. Amino linker intermediates and phosphoramidites.

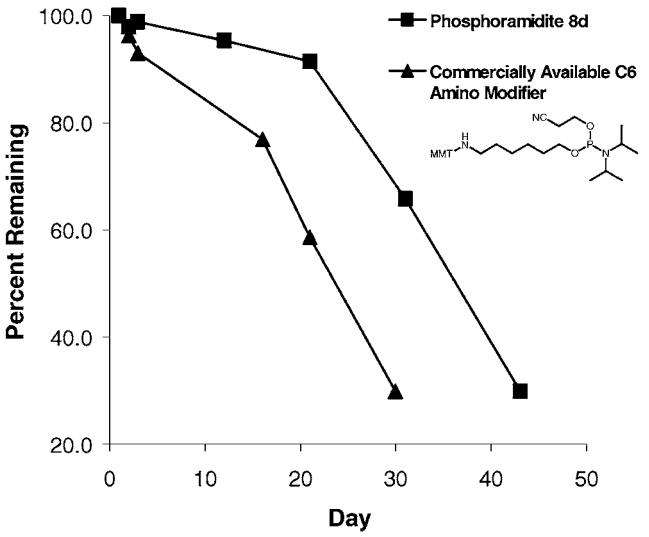


Figure 4. Comparative solution stability of an aminocyclohexanol-based phosphoramidite **8d** and one derived from a primary alcohol. Values were determined from duplicates by integration of ^{31}P NMR peaks. Conditions: 0.3 M solutions in CD_3CN under a blanket of argon at room temperature.

Structural Versatility. The practical advantage of our synthetic approach lies in its amenability to structural versatility by utilizing an arsenal of distinctly different, commercially available diamines and amino alcohols. It is possible to tailor the synthesis to suit practically any requirement in chemical or physical properties of the tethers. The present selection of tethers encompasses a short range of hydrophobicity, rigidity, and length, but the synthetic strategy can easily produce a wide variety of chain features, such as tethers possessing variable flexibility within the chain or tethers with cleavable bonds. MOX chemistry delivers great control over the physical properties of the tether because different diamines can be incorporated directly at specific regions within the chain.

Since formation of a compound tether proceeds in a modular fashion through the use of oxalamido bonds, it is easy to selectively modify the physical nature of the tether at each step. For example, if more rigidity is needed at the ends of the tether, a diamine with a constrained configuration can be used at the last step of tether construction. While the number of cycle iterations determines the overall extension of the tethering arm, it is also possible to decrease chain flexibility by repeatedly using a short diamine, which would produce a tether with fewer degrees of freedom in rotation due to shorter spacing between rigid oxalamido groups. The range in hydrophobicity can span from a highly lipophilic amino linker **11d** to the hydrophilic trioxa-tethered amino linkers **12d** and **14d**. Therefore, not only are we able to choose where to incorporate the tether building blocks, but most importantly, we are able to utilize different combinations of available diamines to make complex chains.

Optimal Tether Length. The ideal length of tethering arms on oligonucleotides is entirely application dependent (*8*−*11*). Of all the tethering arms reported in the literature, polydispersed PEG-based tethers are the longest (*8*). We have determined that amidites having

polydispersed, extremely long tethering arms based on PEG (>1500 MW) cannot be effectively used in some applications, such as Sanger fragment capture in sequencing reactions, due to track peaks smearing (unpublished results). Therefore, our approach toward long amino linkers and spacers was to synthesize the tethers embedded with discrete polyoxyethylene units. By exploiting the serial addition strategy, we have been able to synthesize a 56-atom amino linker **17d**, and a 48-atom spacer **7c**. Theoretically, there is no limit to the length that can be achieved using this strategy, and the serial addition can be increased to 5−6 repetitions to make discrete compound tethers, challenging the chain lengths achieved through the use of short (~2000 MW) polydispersed PEG tethers (*8*).

The tether length is ultimately determined by the choice of diamines or amino alcohols used in the synthesis. The simplest and shortest tether was obtained through the use of EDA for the synthesis of amino linker **8d** (Figure 3). The longest amino linker **17d** was obtained by incorporating TTDD three times to make the compound tether. On the basis of recently reported computational and crystallographic studies of oxalamide-based compounds (*12*, *13*), we presume that the most favorable configuration for the oxalamido moieties in our tethers is the trans arrangement for the carbonyl groups. This should maximize the extension of the tethering arm, and, therefore, should be beneficial for applications utilizing immobilized oligonucleotides, extending them away from an otherwise crowded solid surface (*9*, *14*).

Several reports have shown that the tether length of immobilized oligonucleotides at a solid surface is an important parameter having a significant effect on hybridization (*9*−*11*). For example, it has been shown that steric hindrance, rather than the efficiency of hybridization between the template and the immobilized oligonucleotide, is the major reason for loss in solid-phase primer extension. In one report (*11*) unfavorable interactions were minimized by increasing the tether length to 5−10 hexaethyleneglycol (HEG) units. However, by coupling HEG units sequentially to the oligonucleotide 5′-terminus two adverse events occur. The overall synthetic yield of the primer is decreased, and a net negative charge, due to phosphodiester bonds, is incorporated within the tether. This negative charge density on the tether has been shown in a previous study to decrease the yield of hybridization due possibly to electrostatic repulsion to the target (*9*). The longest amino linker **17d** with a 56-atom tether is more than 3 times the length of a HEG unit and is somewhat more rigid to ensure greater arm extension of the tether. Therefore, when used together with cyclohexanol-based long spacers (up to 48 atoms long), fewer sequential additions to the 5′-end of the oligonucleotide are necessary to attain an extended tether and, in the process, less negative charge density is incorporated.

Synthesis of Modified Oligonucleotides. Coupling and Deprotection. Most of the prepared phosphoramidites are solids, making them easy to handle, and most are freely soluble in acetonitrile. For the monomers with limited acetonitrile solubility, especially the ones possessing long aliphatic tethers, such as **10d** and **11d**, dichloromethane (50%, v/v) was used as cosolvent. The average coupling efficiency of the phosphoramidites at 0.1 M concentrations, a 3−5 min coupling time, and ETT as a catalyst was greater than 95%.

The spacers and linkers presented here have been used to synthesize a number of 5′-modified oligonucleotides. The modified oligonucleotides were observed as distinct bands on polyacrylamide gel with mobility less than that of an unmodified counterpart. As an example, Figure 5 shows a series of crude T_{10} oligonucleotides modified with amino linkers (Figure 5A) and spacers (Figure 5B). MS data for these oligomers are presented in Table 1. In the case of modification with amino linkers **9d**−**11d** (Figure 5A, lanes 3−5) some side product with mobility slightly greater than that of unmodified T_{10} (Figure 5A, lane 1) was produced. The amount of the side product depended on the solvent used for coupling and did not exceed 15% in CH_3CN/CH_2Cl_2. Leaving the MMT group on did not significantly change the extent of side product formation, ruling out susceptibility of the modified oligo to the free amine. The nature of this side product and the reason it is formed in the case of phosphoramidites **9d**−**11d**, amino linkers with aliphatic chains ranging from six to twelve carbons in length, is yet to be found. All other modifiers essentially produced a single product (Figure 5).

To determine the effect of deprotecting conditions on simple and compound tethers, we subjected several DMT/MMT-protected intermediate diols and amino alcohols to neat ethanolamine, ammonia/methylamine (30% aqueous ammonium hydroxide/2 M methanolic methylamine, 1:1, v/v), and aqueous NaOH (0.2 M NaOH in a water/

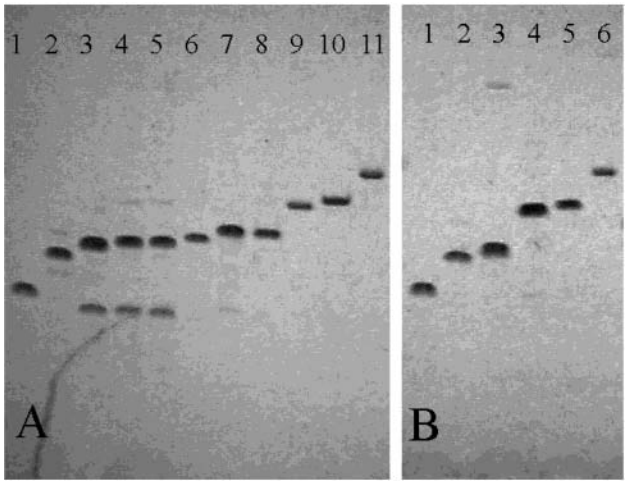


Figure 5. Amino linker (A) and spacer (B) modified crude T_{10} oligonucleotides. Lane 1 in each gel corresponds to unmodified T_{10} oligonucleotide. The other lanes are T_{10} modified by the following phosphoramidites: **8d** (A2), **9d** (A3), **10d** (A4), **11d** (A5), **12d** (A6), **13d** (A7), **14d** (A8), **16d** (A9), **15d** (A10), **17d** (A11), **3c** (B2), **4c** (B3), **6c** (B4), **5c** (B5), **7c** (B6).

Table 1. MALDI MS Data for Modified T_{10} Oligonucleotides

entry	starting oligonucleotide	modifier	lane on Figure 5	MW (calcd)	MW (exptl)
1	$(Tp)_9T$	none	A1, B1	2978	2980
2	$(Tp)_9T$	**8d**	A2	3271	3274
3	$(Tp)_9T$	**9d**	A3	3327	3329
4	$(Tp)_9T$	**10d**	A4	3383	3386
5	$(Tp)_9T$	**11d**	A5	3411	3415
6	$(Tp)_9T$	**12d**	A6	3431	3433
7	$(Tp)_9T$	**13d**	A7	3485	3488
8	$(Tp)_9T$	**14d**	A8	3557	3560
9	$(Tp)_9T$	**16d**	A9	3706	3709
10	$(Tp)_9T$	**15d**	A10	3832	3834
11	$(Tp)_9T$	**17d**	A11	3980	3983
12	$(Tp)_9T$	**3c**	B2	3316	3318
13	$(Tp)_9T$	**4c**	B3	3328	3330
14	$(Tp)_9T$	**6c**	B4	3590	3592
15	$(Tp)_9T$	**5c**	B5	3717	3719
16	$(Tp)_9T$	**7c**	B6	3865	3867

methanol mixture, 1:1, v/v). Exposure to NaOH, even for 1 h at ambient temperature, was too harsh, and some degradation of all tethers was detected under this condition. The tethers, however, did hold up to ammonia, methylamine, and ethanolamine and were stable at the temperature and duration required for complete deprotection of the modified oligonucleotides.

CONCLUSIONS

We have presented a facile, efficient, and versatile synthetic strategy for the preparation of novel phosphoramidites possessing a variety of tethers, including exceptionally long tethering arms. By utilizing the oxalamido bond as a "coupler", we can serially add appropriate diamines multiple times to make long tethers or to incorporate functionality from commercially available reagents. The only limitation of our tethering strategy lies in the requirement of using aliphatic primary diamines or amino alcohols to react with the methoxyoxalamido moieties of the starting MOX precursors and intermediates. In our experience this approach, yielding linkers and spacers with discrete lengths, has proven beneficial in minimizing steric interference for enzymatic events staged at the surface by immobilizing the oligonucleotides sufficiently away from the solid phase (unpublished results).

The synthetic method described here presents the following advantages: (i) the synthesis is robust and straightforward; (ii) the phosphoramidites are derived from secondary alcohols, making them more stable than those derived from primary alcohols; (iii) a wide range of tethers having varying degrees of hydrophobicity, flexibility, and length can be rapidly prepared; (iv) since the monomers can be coupled to the oligonucleotide 5′-terminus in high efficiency, there is no need to drastically alter standard automated DNA synthesis cycles.

We believe that the synthetic approach outlined here and the phosphoramidites derived from this methodology should find a comfortable niche in the production of microarrays and DNA chips, where unfavorable steric and electrostatic factors experienced at the surface of bound oligonucleotides may dictate the use of uncharged, selectively designed tethers. Ongoing research using this synthetic strategy includes the development of monomers with even longer tethering arms, >100 atoms in length, and the synthesis of long tethers possessing other functionalities, such as biotin. Additional phosphoramidites, that have successfully been synthesized using MOX chemistry and are beyond the scope of this paper, possess tethers with cleavable diols and disulfide linkages. It is hoped that our synthetic methodology will lead to an abundance of easily prepared monomers to supplement and offer significant advantages over currently available amino linker and spacer phosphoramidites.

Supporting Information Available: NMR and MS data for all novel compounds. This material is available free of charge via the Internet at http://pubs.acs.org.

LITERATURE CITED

(1) Schena, M., Shalon, D., Davis, R. W., and Brown, P. O. (1995) Quantitative monitoring of gene expression patterns with a complementary DNA microarray. *Science 270*, 467−470.

(2) Nelson, P. S., Kent, M., and Muthini, S. (1992) Oligonucleotide labeling methods. 3. Direct labeling of oligonucleotides employing a novel, nonnucleosidic, 2-aminobutyl-1,3-propanediol backbone. *Nucleic Acids Res. 20*, 6253−6259.

(3) Pils, W., and Micura, R. (2000) Flexible nonnucleotide linkers as loop replacements in short double helical RNAs. *Nucleic Acids Res. 28*, 1859−1863.

(4) Agrawal, S., Christodoulou, C., and Gait, M. J. (1986) Efficient methods for attaching nonradioactive labels to the 5′ ends of synthetic oligodeoxyribonucleotides. *Nucleic Acids Res. 14*, 6227−6245.

(5) Glen Research Catalog: Products for DNA Research, 2002.

(6) Polushin, N. N. (2000) The precursor strategy: terminus methoxyoxalamido modifiers for single and multiple functionalization of oligodeoxyribonucleotides. *Nucleic Acids Res. 28*, 3125−3133.

(7) Polushin, N. N. (1996) Synthesis of Functionally Modified Oligonucleotides from Methoxyoxalamido Precursors. *Tetrahedron Lett. 37*, 3231−3234.

(8) Jaschke, A., Furste, J. P., Nordhoff, E., Hillenkamp, F., Cech, D., and Erdmann, V. A. (1994) Synthesis and properties of oligodeoxyribonucleotide-poly(ethylene glycol) conjugates. *Nucleic Acids Res. 22*, 4810−4817.

(9) Shchepinov, M. S., Case-Green, S. C., and Southern, E. M. (1997) Steric factors influencing hybridisation of nucleic acids to oligonucleotide arrays. *Nucleic Acids Res. 25*, 1155−1161.

(10) Nicewarner Peña, S. R., Raina, S., Goodrich, G. P., Fedoroff, N. V., and Keating, C. D. (2002) Hybridization and enzymatic extension of Au nanoparticle-bound oligonucleotides. *J. Am. Chem. Soc. 124*, 7314−7323.

(11) Carmon, A., Vision, T. J., Mitchell, S. E., Thannhauser, T. W., Muller, U., and Kresovich, S. (2002) Solid-phase PCR in microwells: effects of linker length and composition on tethering, hybridization, and extension. *Biotechniques 32*, 410−420.

(12) Armelin, E., Aleman, C., and Puiggali, J. (2001) Structural versatility of oxalamide-based compounds: a computational study on the isomerization of the oxalamide group and the structural preferences of the polyoxalamides. *J. Org. Chem. 66*, 8076−8085.

(13) Armelin, E., Urpi, L., Solans, X., and Puiggali, J. (2001) Dimethyl N,N′-oxalamidodiethanoate. *Acta Crystallogr. C 57*, 932−933.

(14) Steel, A. B., Levicky, R. L., Herne, T. M., and Tarlov, M. J. (2000) Immobilization of nucleic acids at solid surfaces: effect of oligonucleotide length on layer assembly. *Biophys. J. 79*, 975−981.

BC034218X

Supporting Information

Analytical data for the synthesized compounds

NMR chemical shifts are reported in p.p.m. (δ units) downfield from TMS for ^{1}H-NMR and from H_3PO_4 for ^{31}P-NMR spectra. Spectra were recorded on a Varian Mercury-300 spectrometer at 300 and 121 MHz, respectively. Intermediates 10a, 10c, 11a, 11c and phosphoramidites 10d and 11d with poor solubility in DMSO-d_6 required longer acquisition times. Electrospray Ionization mass spectra (ESI MS) were recorded on a Mariner spectrometry system (PerSeptive Biosystems, Framingham, MA). Samples were dissolved in MeOH/H_2O (1:1).

Diol 3a

^{1}H NMR (DMSO-d_6) δ 8.58-8.65 (t, 1H, CH_2-N<u>H</u>-COCO), 8.45-8.52 (d, 1H, COCO-N<u>H</u>-ACH), 4.53-4.62 (m, 2H, <u>H</u>O-CH_2 + ACH-O<u>H</u>), 3.23-3.59 (m, 10H, 3 x CH_2-C<u>H</u>$_2$-O + H-4 (ACH) + C<u>H</u>$_2$-NH-COCO + H-1 (ACH)), 1.75-1.86 (br. d, 2H, 2 x CH (ACH)), 1.60-1.71 (br. d, 2H, 2 x CH (ACH)), 1.32-1.49 (m, 2H, 2 x CH (ACH)), 1.10-1.27 (m, 2H, 2 x CH (ACH)); ESI MS m/z 275.6 ($M + H^+$); calculated for $C_{12}H_{22}N_2O_5$: 274.1.

DMT-protected diol 3b

^{1}H NMR (DMSO-d_6) δ 8.58-8.66 (t, 1H, CH_2-N<u>H</u>-COCO), 8.43-8.49 (d, 1H, COCO-N<u>H</u>-ACH), 7.17-7.42 (m, 9H, DMT), 6.84-6.93 (d, 4H, DMT), 4.52-4.56 (d, 1H, ACH-O<u>H</u>), 3.69-3.77 (s, 6H, OCH_3), 3.43-3.60 (m, 5H, 2 x CH_2-C<u>H</u>$_2$-O + H-4 (ACH)), 3.25-3.39 (m, 3H, C<u>H</u>$_2$-NH-COCO + H-1 (ACH)), 2.99-3.07 (t, 2H, DMT-O-C<u>H</u>$_2$), 1.73-1.85 (br. d, 2H, 2 x CH (ACH)), 1.57-1.68 (br. d, 2H, 2 x CH (ACH)), 1.30-1.47 (m, 2H, 2 x CH (ACH)), 1.09-1.26 (m, 2H, 2 x CH (ACH)); ESI MS m/z 599.7 ($M + Na^+$); calculated for $C_{33}H_{40}N_2O_7$: 576.3.

Spacer phosphoramidite 3c

^{31}P-NMR (DMSO-d_6) δ 144.74.

Diol 4a

^{1}H NMR (DMSO-d_6) δ 8.66-8.74 (t, 1H, CH_2-N<u>H</u>-COCO), 8.39-8.47 (d, 1H, COCO-N<u>H</u>-ACH), 4.52-4.57 (d, 1H, ACH-O<u>H</u>), 4.29-4.35 (t, 1H, <u>H</u>O-CH_2), 3.43-3.59 (m, 1H, H-4 (ACH)), 3.26-3.40 (m, 3H, C<u>H</u>$_2$-OH + H-1 (ACH)), 3.04-3.14 (q, 2H, C<u>H</u>$_2$-NH-COCO), 1.74-1.85 (br. d, 2H, 2 x CH (ACH)), 1.59-1.71 (br. d, 2H, 2 x CH (ACH)), 1.09-1.50 (m, 12H, CH_2-(C<u>H</u>$_2$)$_4$-CH_2 + 4 x CH (ACH)); ESI MS m/z 287.7 ($M + H^+$); calculated for $C_{14}H_{26}N_2O_4$: 286.2.

DMT-protected diol 4b

^{1}H NMR (DMSO-d_6) δ 8.65-8.73 (t, 1H, CH_2-N<u>H</u>-COCO), 8.38-8.44 (d, 1H, COCO-N<u>H</u>-ACH), 7.17-7.39 (m, 9H, DMT), 6.84-6.92 (d, 4H, DMT), 4.52-4.57 (d, 1H, ACH-O<u>H</u>), 3.70-3.75 (s, 6H, 2 x OCH_3), 3.42-3.59 (m, 1H, H-4 (ACH)), 3.26-3.40 (m, 1H, H-1 (ACH)), 3.02-3.13 (q, 2H, C<u>H</u>$_2$-NH-COCO), 2.88-2.96 (t, 2H, DMT-O-C<u>H</u>$_2$), 1.74-1.85 (br. d, 2H, 2 x CH (ACH)), 1.60-1.70 (br. d, 2H, 2 x CH (ACH)), 1.10-1.58 (m, 12H, CH_2-(C<u>H</u>$_2$)$_4$-CH_2 + 4 x CH (ACH)); ESI MS m/z 588.7 ($M + H^+$); calculated for $C_{35}H_{44}N_2O_6$: 588.3.

Spacer phosphoramidite 4c

^{31}P NMR (DMSO-d_6) δ 145.20

Diol 5a

^{1}H NMR (DMSO-d_6) δ 11.25-11.32 (s, 1H, HN-3), 8.81-8.90 (t, 1H, $(CH_2)_3$-N<u>H</u>-COCO), 8.68-8.79 (m, 2H, COCO-N<u>H</u>-5' + N<u>H</u>-COCO), 8.56-8.65 (t, 1H, N<u>H</u>-COCO), 7.42-7.51 (s, 1H, H-6), 6.08-6.18 (t, 1H, H-1'), 5.28-5.36 (d, 1H, OH-3'), 4.55-4.64 (t, 1H, <u>H</u>O-CH_2), 4.13-4.24 (m, 1H, H-3'), 3.80-3.90 (m, 1H, H-4'), 2.97-3.58 (m, 26H, 8 x CH_2-C<u>H</u>$_2$-O + H-5',5" + O-CH_2-C<u>H</u>$_2$-NH-COCO + HO-C<u>H</u>$_2$ + 2 x O-CH_2-CH_2-C<u>H</u>$_2$-N), 1.98-2.16 (m, 2H, H-2',2"), 1.78-1.85 (s, 3H, CH_3-5), 1.62-1.76 (m, 4H, CH_2-C<u>H</u>$_2$-CH_2); ESI MS m/z 675.8 (M + H^+), 697.8 (M + Na^+); calculated for $C_{28}H_{46}N_6O_{13}$: 674.3.

DMT-protected diol 5b

^{1}H NMR (DMSO-d_6) δ 11.27-11.30 (s, 1H, HN-3), 8.82-8.89 (t, 1H, $(CH_2)_3$-N<u>H</u>-COCO), 8.71-8.78 (m, 2H, COCO-N<u>H</u>-5' + N<u>H</u>-COCO), 8.58-8.65 (t, 1H, N<u>H</u>-COCO), 7.45-7.48 (s, 1H, H-6), 7.19-7.41 (m, 9H, DMT), 6.85-6.91 (d, 4H, DMT), 6.09-6.15 (t, 1H, H-1'), 5.32-5.35 (d, 1H, OH-3'), 4.15-4.22 (m, 1H, H-3'), 3.82-3.89 (m, 1H, H-4'), 3.71-3.75 (s, 6H, OCH_3), 3.29-3.59 (m, 20H, 8 x CH_2-C<u>H</u>$_2$-O + H-5',5" + O-CH_2-C<u>H</u>$_2$-NH-COCO), 3.14-3.23 (m, 4H, 2 x $(CH_2)_2$-C<u>H</u>$_2$-NH-COCO), 3.01-3.11 (t, 2H, DMT-O-C<u>H</u>$_2$), 1.99-2.15 (m, 2H, H-2',2"), 1.78-1.82 (s, 3H, CH_3-5), 1.62-1.74 (m, 4H, CH_2-C<u>H</u>$_2$-CH_2); ESI MS m/z 697.8 (M – DMT + Na^+), 999.9 (M + Na^+); calculated for $C_{49}H_{64}N_6O_{15}$: 976.4.

Spacer phosphoramidite 5c

^{31}P NMR (DMSO-d_6) δ 147.12, 147.04.

Diol 6a

^{1}H NMR (DMSO-d_6) δ 8.67-8.79 (m, 2H, 2 x O-$(CH_2)_3$-N<u>H</u>-COCO), 8.58-8.65 (t, 1H, O-$(CH_2)_2$-N<u>H</u>-COCO), 8.40-8.48 (d, 1H, COCO-N<u>H</u>-ACH), 4.53-4.63 (m, 2H, ACH-O<u>H</u> + HO-C<u>H</u>$_2$), 3.25-3.56 (m, 20H, H-4 (ACH) + 8 x O-C<u>H</u>$_2$ + H-1 (ACH) + O-CH_2C<u>H</u>$_2$-NHCOCO), 3.13-3.23 (m, 4H, 2 x $(CH_2)_2$C<u>H</u>$_2$-NHCOCO), 3.01-3.12 (t, 2H, HO-C<u>H</u>$_2$), 1.60-1.86 (m, 8H, 4 x CH (ACH) + 2 x CH_2C<u>H</u>$_2$$CH_2$), 1.32-1.49 (m, 2H, 2 x CH (ACH)), 1.11-1.26 (m, 2H, 2 x CH (ACH)); ESI MS m/z 549.8 (M + H^+), 571.8 (M + Na^+); calculated for $C_{24}H_{44}N_4O_{10}$: 548.3.

DMT-protected diol 6b

^{1}H NMR (DMSO-d_6) δ 8.59-8.79 (m, 3H, 2 x O-$(CH_2)_3$-N<u>H</u>-COCO + O-$(CH_2)_2$-N<u>H</u>-COCO), 8.41-8.47 (d, 1H, COCO-N<u>H</u>-ACH), 7.17-7.42 (m, 9H, DMT), 6.85-6.91 (d, 4H, DMT), 4.53-4.57 (d, 1H, ACH-O<u>H</u>), 3.70-3.77 (s, 6H, 2 x OCH_3), 3.28-3.60 (m, 20H, H-4 (ACH) + 8 x O-C<u>H</u>$_2$ + H-1 (ACH) + O-CH_2C<u>H</u>$_2$-NHCOCO), 3.12-3.23 (m, 4H, 2 x $(CH_2)_2$C<u>H</u>$_2$-NHCOCO), 3.00-3.07 (t, 2H, DMT-O-C<u>H</u>$_2$), 1.75-1.87 (m, 2H, 2 x CH (ACH)), 1.61-1.74 (m, 6H, 2 x CH_2C<u>H</u>$_2$$CH_2$ + 2 x CH (ACH)), 1.32-1.49 (m, 2H, 2 x CH (ACH)), 1.10-1.27 (m, 2H, 2 x CH (ACH)); ESI MS m/z 571.6 (M - DMT + Na^+), 873.7 (M + Na^+); calculated for $C_{45}H_{62}N_4O_{12}$: 850.4.

Spacer phosphoramidite 6c

^{31}P NMR (DMSO-d_6) δ 144.74.

Diol 7a

^{1}H NMR (DMSO-d_6) δ 8.66-8.78 (m, 4H, O-$(CH_2)_3$-N<u>H</u>-COCO), 8.57-8.65 (t, 1H, O-$(CH_2)_2$-N<u>H</u>-COCO), 8.40-8.47 (d, 1H, COCO-N<u>H</u>-ACH), 4.51-4.63 (m, 2H, <u>H</u>O-CH2 + ACH-O<u>H</u>), 3.25-3.57 (m, 34H, H-4 (ACH) + 16 x C<u>H</u>$_2$ + H-1 (ACH)), 3.11-3.24 (q, 8H, 4 x $(CH_2)_2$C<u>H</u>$_2$NHCOCO), 1.60-1.86 (m, 12H, 4 x CH (ACH) + 4 x CH_2C<u>H</u>$_2$$CH_2$), 1.30-1.49 (m, 2H, 2 x CH (ACH)), 1.09-1.27 (m, 2H, 2 x CH (ACH)); ESI MS m/z 845.3 (M + Na^+); calculated for $C_{36}H_{66}N_6O_{15}$: 822.5.

DMT-protected diol 7b

^{1}H NMR (DMSO-d_6) δ 8.66-8.77 (m, 4H, 4 x O-$(CH_2)_3$-N<u>H</u>-COCO), 8.58-8.64 (t, 1H, O-$(CH_2)_2$-N<u>H</u>-COCO), 8.40-8.46 (d, 1H, COCO-N<u>H</u>-ACH), 7.17-7.42 (m, 9H, DMT), 6.85-6.92 (d, 4H, DMT), 4.52-4.56 (d, 1H, ACH-O<u>H</u>), 3.70-3.78 (s, 6H, 2 x OCH_3), 3.28-3.60 (m, 32H, H-4 (ACH) + 15 x C<u>H</u>$_2$ + H-1 (ACH)), 3.14-3.28 (q, 8H, 4 x $(CH_2)_2$C<u>H</u>$_2$NHCOCO), 3.02-3.08 (t, 2H, DMT-O-C<u>H</u>$_2$), 1.75-1.86 (m, 2H, 2 x CH (ACH)), 1.61-1.74 (m, 10H, 4 x CH_2C<u>H</u>$_2$$CH_2$ + 2 x CH (ACH)), 1.32-1.50 (m, 2H, 2 x CH (ACH)), 1.09-1.28 (m, 2H, 2 x CH (ACH)); ESI MS m/z 845.3 (M - DMT + Na^+); calculated for $C_{57}H_{84}N_6O_{17}$: 1124.6.

Spacer phosphoramidite 7c

^{31}P NMR (DMSO-d_6) δ 144.75.

Amino alcohol 8a

^{1}H NMR (DMSO-d_6) δ 8.56-8.67 (t, 1H, CH_2-N<u>H</u>-COCO), 8.37-8.48 (d, 1H, COCO-N<u>H</u>-ACH), 4.48-4.58 (d, 1H, OH), 3.43-3.58 (m, 1H, H-4 (ACH)), 3.25-3.40 (m, 1H, H-1 (ACH)), 3.04-3.13 (q, 2H, C<u>H</u>$_2$-NH-COCO), 2.55-2.63 (t, 2H, NH_2-C<u>H</u>$_2$), 1.72-1.85 (br. d, 2H, 2 x CH (ACH)), 1.58-1.70 (br. d, 2H, 2 x CH (ACH)), 1.29-1.48 (m, 2H, 2 x CH (ACH)), 1.08-1.26 (m, 2H, 2 x CH (ACH)); ESI MS m/z 230.4 ($M + H^+$); calculated for $C_{10}H_{19}N_3O_3$: 229.1.

MMT-protected amino alcohol 8c

^{1}H NMR (DMSO-d_6) δ 8.75-8.84 (t, 1H, CH_2-N<u>H</u>-COCO), 8.40-8.48 (d, 1H, COCO-N<u>H</u>-ACH), 7.11-7.41 (m, 12H, MMT), 6.78-6.86 (d, 2H, MMT), 4.52-4.58 (d, 1H, OH), 3.69-3.74 (s, 3H, OCH_3), 3.43-3.60 (m, 1H, H-4 (ACH)), 3.20-3.40 (m, 3H, C<u>H</u>$_2$-NH-COCO + H-1 (ACH)), 2.86-2.95 (m, 1H, MMT-NH), 2.03-2.15 (m, 2H, MMT-NH-C<u>H</u>$_2$), 1.74-1.86 (br. d, 2H, 2 x CH (ACH)), 1.60-1.72 (br. d, 2H, 2 x CH (ACH)), 1.32-1.50 (m, 2H, 2 x CH (ACH)), 1.10-1.28 (m, 2H, 2 x CH (ACH)); ESI MS m/z 502.6 ($M + H^+$); calculated for $C_{30}H_{35}N_3O_4$: 501.3.

Amino linker phosphoramidite 8d

^{31}P NMR (DMSO-d_6) δ 145.20.

Amino alcohol 9a

^{1}H NMR (DMSO-d_6) δ 8.75-8.64 (t, 1H, CH_2-N<u>H</u>-COCO), 8.36-8.45 (d, 1H, COCO-N<u>H</u>-ACH), 4.47-4.60 (d, 1H, OH), 3.42-3.58 (m, 1H, H-4 (ACH)), 3.24-3.40 (m, 1H, H-1

(ACH)), 3.02-3.15 (q, 2H, C<u>H</u>$_2$-NH-COCO), 2.40-2.50 (t, 2H, NH$_2$-C<u>H</u>$_2$), 1.73-1.87 (br. d, 2H, 2 x CH (ACH)), 1.58-1.71 (br. d, 2H, 2 x CH (ACH)), 1.11-1.56 (m, 12H, 4 x CH (ACH) + CH$_2$-(C<u>H</u>$_2$)$_4$-CH$_2$); ESI MS m/z 286.5 (M + H$^+$); calculated for $C_{14}H_{27}N_3O_3$: 285.2.

MMT-protected amino alcohol 9c

^{1}H NMR (DMSO-d$_6$) δ 8.62-8.73 (t, 1H, CH$_2$-N<u>H</u>-COCO), 8.35-8.43 (d, 1H, COCO-N<u>H</u>-ACH), 7.08-7.43 (m, 12H, MMT), 6.78-6.87 (d, 2H, MMT), 4.50-4.57 (d, 1H, OH), 3.67-3.74 (s, 3H, OCH$_3$), 3.42-3.59 (m, 1H, H-4 (ACH)), 3.26-3.38 (m, 1H, H-1 (ACH)), 3.00-3.12 (q, 2H, C<u>H</u>$_2$-NH-COCO), 2.34-2.45 (t, 1H, MMT-NH), 1.87-2.00 (m, 2H, MMT-NH-C<u>H</u>$_2$), 1.73-1.84 (br. d, 2H, 2 x CH (ACH)), 1.58-1.71 (br. d, 2H, 2 x CH (ACH)), 1.07-1.50 (m, 12H, 4 x CH (ACH) + CH$_2$-(C<u>H</u>$_2$)$_4$-CH$_2$); ESI MS m/z 558.8 (M + H$^+$); calculated for $C_{34}H_{43}N_3O_4$: 557.3.

Amino linker phosphoramidite 9d

^{31}P NMR (DMSO-d$_6$) δ 144.75.

Amino alcohol 10a

^{1}H NMR (DMSO-d$_6$) δ 8.76-8.63 (t, 1H, CH$_2$-N<u>H</u>-COCO), 8.36-8.45 (d, 1H, COCO-N<u>H</u>-ACH), 4.47-4.60 (d, 1H, OH), 3.42-3.58 (m, 1H, H-4 (ACH)), 3.24-3.40 (m, 1H, H-1 (ACH)), 3.02-3.15 (q, 2H, C<u>H</u>$_2$-NH-COCO), 2.41-2.50 (t, 2H, NH$_2$-C<u>H</u>$_2$), 1.73-1.87 (br. d, 2H, 2 x CH (ACH)), 1.58-1.71 (br. d, 2H, 2 x CH (ACH)), 1.11-1.56 (m, 20H, 4 x CH

(ACH) + CH_2-($C\underline{H}_2$)$_8$-CH_2); ESI MS m/z 342.6 ($M + H^+$); calculated for $C_{18}H_{35}N_3O_3$: 341.3.

MMT-protected amino alcohol 10c

^{1}H NMR (DMSO-d_6) δ 8.65-8.73 (t, 1H, CH_2-N$\underline{H}$-COCO), 8.36-8.44 (d, 1H, COCO-N$\underline{H}$-ACH), 7.11-7.45 (m, 12H, MMT), 6.80-6.89 (d, 2H, MMT), 4.50-4.57 (d, 1H, OH), 3.67-3.78 (s, 3H, OCH_3), 3.42-3.59 (m, 1H, H-4 (ACH)), 3.27-3.38 (m, 1H, H-1 (ACH)), 3.00-3.12 (q, 2H, C$\underline{H}_2$-NH-COCO), 2.36-2.45 (t, 1H, MMT-NH), 1.87-2.00 (m, 2H, MMT-NH-C$\underline{H}_2$), 1.73-1.84 (br. d, 2H, 2 x CH (ACH)), 1.58-1.71 (br. d, 2H, 2 x CH (ACH)), 1.07-1.50 (m, 20H, 4 x CH (ACH) + CH_2-($C\underline{H}_2$)$_8$-CH_2); ESI MS m/z 636.8 ($M + Na^+$), 652.9 ($M + K^+$); calculated for $C_{38}H_{51}N_3O_4$: 613.4.

Amino linker phosphoramidite 10d

^{31}P NMR (DMSO-d_6) δ 144.74.

Amino alcohol 11a

^{1}H NMR (DMSO-d_6) δ 8.75-8.63 (t, 1H, CH_2-N$\underline{H}$-COCO), 8.36-8.46 (d, 1H, COCO-N$\underline{H}$-ACH), 4.47-4.60 (d, 1H, OH), 3.42-3.58 (m, 1H, H-4 (ACH)), 3.24-3.40 (m, 1H, H-1 (ACH)), 3.02-3.15 (q, 2H, C$\underline{H}_2$-NH-COCO), 2.40-2.50 (t, 2H, NH_2-C$\underline{H}_2$), 1.73-1.87 (br. d, 2H, 2 x CH (ACH)), 1.58-1.71 (br. d, 2H, 2 x CH (ACH)), 1.11-1.56 (m, 24H, 4 x CH (ACH) + CH_2-($C\underline{H}_2$)$_{10}$-CH_2); ESI MS m/z 370.8 ($M + H^+$); calculated for $C_{20}H_{39}N_3O_3$: 369.3.

MMT-protected amino alcohol 11c

^{1}H NMR (DMSO-d_6) δ 8.72-8.62 (t, 1H, CH_2-N<u>H</u>-COCO), 8.37-8.43 (d, 1H, COCO-N<u>H</u>-ACH), 7.10-7.44 (m, 12H, MMT), 6.77-6.88 (d, 2H, MMT), 4.45-4.58 (d, 1H, OH), 3.68-3.75 (s, 3H, OCH_3), 3.43-3.60 (m, 1H, H-4 (ACH)), 3.25-3.40 (m, 1H, H-1 (ACH)), 3.02-3.15 (q, 2H, C<u>H</u>$_2$-NH-COCO), 2.35-2.45 (t, 1H, MMT-NH), 1.87-2.02 (m, 2H, MMT-NH-C<u>H</u>$_2$), 1.73-1.87 (br. d, 2H, 2 x CH (ACH)), 1.10-1.70 (m, 26H, 6 x CH (ACH) + CH_2-(C<u>H</u>$_2$)$_{10}$-CH_2); ESI MS m/z 370.8 (M - MMT + H^+); calculated for $C_{40}H_{55}N_3O_4$: 641.4.

Amino linker phosphoramidite 11d

^{31}P NMR (DMSO-d_6) δ 144.77.

Amino alcohol 12a

^{1}H NMR (DMSO-d_6) δ 8.67-8.80 (t, 1H, CH_2-N<u>H</u>-COCO), 8.40-8.55 (d, 1H, COCO-N<u>H</u>-ACH), 4.35-4.80 (br. s, 1H, OH), 3.11-3.58 (m, 16H, 6 x CH_2-C<u>H</u>$_2$-O + H-4 (ACH) + H-1 (ACH) + C<u>H</u>$_2$-NH-COCO), 2.53-2.62 (t, 2H, NH_2-C<u>H</u>$_2$), 1.32-1.87 (m, 10H, 6 x CH (ACH) + 2 x CH_2-C<u>H</u>$_2$-CH_2), 1.10-1.28 (m, 2H, 2 x CH (ACH)); ESI MS m/z 390.0 (M + H^+), 412.0 (M + Na^+); calculated for $C_{18}H_{35}N_3O_6$: 389.2.

MOX precursor 12b

^{1}H NMR (DMSO-d_6) δ 8.83-8.93 (t, 1H, COCONH, MOX), 8.65-8.73 (t, 1H, NHCOCO), 8.38-8.46 (d, 1H, COCONH, ACH), 4.53-4.58 (d, 1H, OH, ACH), 3.73-3.78 (s, 3H, OCH_3, MOX), 3.43-3.57 (m, 9H, 4 x CH_2 + CH), 3.25-3.43 (m, 5H, 2 x CH_2 +

CH), 3.10-3.24 (q, 8H, 2 x CH_2), 1.58-1.84 (overlapping multiplets, 8H, + 2 x CH_2 (ACH) + 2 x CH_2 (ACH)), 1.30-1.49 (m, 2H, CH_2, ACH), 1.07-1.26 (m, 2H, CH_2, ACH); ESI MS m/z 476.3 ($M + H^+$), 498.3 ($M + Na^+$); calculated for $C_{21}H_{37}N_3O_9$: 475.5.

MMT-protected amino alcohol 12c

^{1}H NMR (DMSO-d_6) δ 8.64-8.75 (t, 1H, CH_2-N<u>H</u>-COCO), 8.41-8.48 (d, 1H, COCO-N<u>H</u>-ACH), 7.11-7.41 (m, 12H, MMT), 6.80-6.87 (d, 2H, MMT), 4.53-4.58 (d, 1H, OH), 3.69-3.73 (s, 3H, OCH_3), 3.27-3.56 (m, 14H, 6 x CH_2-C<u>H</u>$_2$-O + H-4 (ACH) + H-1 (ACH)), 3.10-3.23 (q, 2H, C<u>H</u>$_2$-NH-COCO), 2.53-2.62 (t, 1H, MMT-N<u>H</u>), 1.97-2.08 (q, 2H, MMT-NH-C<u>H</u>$_2$), 1.74-1.86 (br. d, 2H, 2 x CH (ACH)), 1.59-1.73 (m, 6H, 2 x CH_2-C<u>H</u>$_2$-CH_2 + 2 x CH (ACH)), 1.31-1.50 (m, 2H, 2 x CH (ACH)), 1.10-1.28 (m, 2H, 2 x CH (ACH)); ESI MS m/z 662.6 ($M + H^+$), 684.6 ($M + Na^+$); calculated for $C_{38}H_{51}N_3O_7$: 661.4.

Amino linker phosphoramidite 12d

^{31}P NMR (DMSO-d_6) δ 144.78.

Amino alcohol 13a

^{1}H NMR (DMSO-d_6) δ 8.69-8.79 (t, 1H, CH_2-N<u>H</u>-COCO), 8.38-8.49 (d, 1H, COCO-N<u>H</u>-ACH), 4.40-4.53 (m, 2H, 2 x CH_2-C<u>H</u>-(O-)$_2$ (spiro ring)), 4.19-4.31 (br. d, 2H, 2 x CH (spiro ring), 3.44-3.62 (m, 5H, 4 x CH (spiro ring) + H-4 (ACH)), 3.27-3.40 (m, 3H, 2 x CH (spiro ring) + H-1 (ACH)), 3.03-3.18 (q, 2H, C<u>H</u>$_2$-NH-COCO), 2.46-2.52 (m, H_2N-C<u>H</u>$_2$), 1.74-1.88 (m, 2H, 2 x CH (ACH)), 1.60-1.73 (m, 2H, 2 x CH (ACH)), 1.31-1.59

(m, 10H, 4 x CH_2 + 2 x CH (ACH)), 2H, 1.09-1.29 (m, 2H, 2 x CH (ACH)); ESI MS m/z 444.1 ($M + H^+$); calculated for $C_{21}H_{37}N_3O_7$: 443.3.

MMT-protected amino alcohol 13c

^{1}H NMR (DMSO-d_6) δ 8.70-8.79 (t, 1H, CH_2-N<u>H</u>-COCO), 8.40-8.48 (d, 1H, COCO-N<u>H</u>-ACH), 7.11-7.41 (m, 12H, MMT), 6.80-6.89 (d, 2H, MMT), 4.53-4.58 (d, 1H, OH), 4.43-4.49 (t, 1H, CH_2-C<u>H</u>-(O-)$_2$ (spiro ring)), 4.35-4.42 (t, 1H, CH_2-C<u>H</u>-(O-)$_2$ (spiro ring)), 4.19-4.28 (br. d, 2H, 2 x CH (spiro ring), 3.68-3.74 (s, 3H, OCH_3), 3.44-3.60 (m, 5H, 4 x CH (spiro ring) + H-4 (ACH)), 3.23-3.42 (m, 3H, 2 x CH (spiro ring) + H-1 (ACH)), 3.05-3.16 (q, 2H, C<u>H</u>$_2$-NH-COCO), 1.88-2.00 (m, 2H, MMT-NH-C<u>H</u>$_2$), 1.75-1.86 (br. d, 2H, 2 x CH (ACH)), 1.60-1.72 (br. d, 2H, 2 x CH (ACH)), 1.32-1.58 (m, 10H, 4 x CH_2 + 2 x CH (ACH)), 2H, 1.11-1.27 (m, 2H, 2 x CH (ACH)); ESI MS m/z 716.2 ($M + H^+$), 738.2 ($M + Na^+$); calculated for $C_{41}H_{53}N_3O_8$: 715.4.

Amino linker phosphoramidite 13d

^{31}P NMR (DMSO-d_6) δ 145.10.

Amino alcohol 14a

^{1}H NMR (DMSO-d_6) δ 8.70-8.97 (m, 2H, $(CH_2)_3$-N<u>H</u>-COCO + COCO-N<u>H</u>-5'), 7.42-7.51 (s, 1H, H-6), 6.08-6.18 (t, 1H, H-1'), 4.15-4.23 (m, 1H, H-3'), 3.81-3.90 (m, 1H, H-4'), 3.28-3.56 (m, 14H, 6 x CH_2-C<u>H</u>$_2$-O + H-5',5"), 3.13-3.26 (m, 2H, $(CH_2)_2$-C<u>H</u>$_2$-NH-COCO), 2.52-2.62 (m, 2H, NH_2-C<u>H</u>$_2$), 1.97-2.15 (m, 2H, H-2',2"), 1.77-1.85 (s, 3H,

CH_3-5), 1.49-1.75 (m, 4H, CH_2-C<u>H</u>$_2$-CH_2); ESI MS m/z 517.0 ($M + Na^+$); calculated for $C_{22}H_{37}N_5O_9$: 515.3.

MOX precursor 14b

^{1}H NMR (DMSO-d_6) δ 11.26-11.32 (s, 1H, HN-3), 8.81-8.94 (m, 2H, 2 x $(CH_2)_3$-N<u>H</u>-COCO), 8.69-8.80 (t, 1H, COCO-N<u>H</u>-5'), 7.43-7.50 (s, 1H, H-6), 6.09-6.18 (t, 1H, H-1'), 5.27-5.38 (br. s, 1H, OH-3'), 4.14-4.23 (br. s, 1H, H-3'), 3.82-3.90 (m, 1H, H-4'), 3.73-3.79 (s, 3H, OCH_3), 3.28-3.57 (m, 14H, 6 x CH_2-C<u>H</u>$_2$-O + H-5',5"), 3.13-3.25 (m, 4H, 2 x $(CH_2)_2$-C<u>H</u>$_2$-NH-COCO), 1.98-2.18 (m, 2H, H-2',2"), 1.78-1.86 (s, 3H, CH_3-5), 1.62-1.77 (m, 4H, CH_2-C<u>H</u>$_2$-CH_2); ESI MS m/z 625.0 ($M + Na^+$); calculated for $C_{25}H_{39}N_5O_{12}$: 601.3.

MMT-protected amino alcohol 14c

^{1}H NMR (DMSO-d_6) δ 11.25-11.33 (s, 1H, HN-3), 8.71-8.98 (m, 2H, $(CH_2)_3$-N<u>H</u>-COCO + COCO-N<u>H</u>-5'), 7.46-7.51 (s, 1H, H-6), 7.11-7.43 (m, 12H, MMT), 6.79-6.88 (d, 2H, MMT), 6.09-6.19 (t, 1H, H-1'), 5.29-5.36 (d, 1H, OH-3'), 4.12-4.23 (m, 1H, H-3'), 3.82-3.91 (m, 1H, H-4'), 3.68-3.77 (s, 3H, OCH_3), 3.28-3.59 (m, 14H, 6 x CH_2-C<u>H</u>$_2$-O + H-5',5"), 3.11-3.24 (q, 2H, C<u>H</u>$_2$-NH-COCO), 2.53-2.61 (t, 2H, MMT-NH-C<u>H</u>$_2$), 1.98-2.10 (m, 2H, H-2',2"), 1.78-1.84 (s, 3H, CH_3-5), 1.61-1.76 (m, 4H, CH_2-C<u>H</u>$_2$-CH_2); ESI MS m/z 787.9 ($M + H^+$), 810.9 ($M + Na^+$); 826.9 ($M + K^+$); calculated for $C_{42}H_{53}N_5O_{10}$: 787.4.

Amino linker phosphoramidite 14d

^{31}P NMR (DMSO-d_6) δ 147.13, 147.09.

Amino alcohol 15a

^{1}H NMR (DMSO-d_6) δ 8.65-8.92 (m, 4H, 3 x N<u>H</u>-COCO + COCO-N<u>H</u>-5'), 7.44-7.50 (s, 1H, H-6), 6.07-6.17 (t, 1H, H-1'), 5.20-5.45 (br. s, 1H, OH-3'), 4.14-4.23 (m, 1H, H-3'), 3.81-3.90 (m, 1H, H-4'), 3.25-3.58 (m, 26H, 12 x CH_2-C<u>H</u>$_2$-O + H-5',5"), 3.07-3.24 (m, 8H, 3 x $(CH_2)_2$-C<u>H</u>$_2$-NH-COCO + NH_2-C<u>H</u>$_2$), 1.98-2.17 (m, 2H, H-2',2"), 1.77-1.85 (s, 3H, CH_3-5), 1.59-1.76 (m, 8H, CH_2-C<u>H</u>$_2$-CH_2); ESI MS m/z 790.7 (M + H^+); calculated for $C_{34}H_{59}N_7O_{14}$: 789.4.

MMT-protected amino alcohol 15c

^{1}H NMR (DMSO-d_6) δ 11.25-11.33 (s, 1H, HN-3), 8.82-8.91 (t, 1H, $(CH_2)_3$-N<u>H</u>-COCO), 8.62-8.80 (m, 3H, COCO-N<u>H</u>-5' + 2 x N<u>H</u>-COCO), 7.45-7.52 (s, 1H, H-6), 7.11-7.43 (m, 12H, MMT), 6.80-6.88 (d, 2H, MMT), 6.09-6.18 (t, 1H, H-1'), 5.29-5.36 (d, 1H, OH-3'), 4.13-4.23 (m, 1H, H-3'), 3.82-3.90 (m, 1H, H-4'), 3.68-3.77 (s, 3H, OCH_3), 3.28-3.59 (m, 26H, 12 x CH_2-C<u>H</u>$_2$-O + H-5',5"), 3.12-3.26 (m, 6H, 3 x $(CH_2)_2$-C<u>H</u>$_2$-NH-COCO), 2.53-2.61 (t, 2H, MMT-NH-C<u>H</u>$_2$), 1.98-2.11 (m, 2H, H-2',2"), 1.78-1.84 (s, 3H, CH_3-5), 1.61-1.76 (m, 8H, CH_2-C<u>H</u>$_2$-CH_2); ESI MS m/z 1062.8 (M + H^+); calculated for $C_{54}H_{75}N_7O_{15}$: 1061.5.

Amino linker phosphoramidite 15d

^{31}P NMR (DMSO-d_6) δ 147.12, 147.10.

Amino alcohol 16a

^{1}H NMR (DMSO-d_6) δ 8.66-8.76 (t, 3H, 3 x CH_2-N<u>H</u>-COCO), 8.40-8.47 (d, 1H, COCO-N<u>H</u>-ACH), 4.44-4.68 (br. s, 1H, OH), 3.27-3.56 (m, 26H, 12 x CH_2-C<u>H</u>$_2$-O + H-4 (ACH) + H-1 (ACH)), 3.12-3.24 (q, 6H, 3 x C<u>H</u>$_2$-NH-COCO), 2.60-2.71 (t, 2H, NH_2-C<u>H</u>$_2$), 1.75-1.86 (m, 2H, 2 x CH (ACH)), 1.55-1.74 (m, 10H, 4 x CH_2-C<u>H</u>$_2$-CH_2 + 2 x CH (ACH)), 1.32-1.49 (m, 2H, 2 x CH (ACH)), 1.10-1.27 (m, 2H, 2 x CH (ACH)); ESI MS m/z 664.3 (M + H^+); calculated for $C_{30}H_{57}N_5O_{11}$: 663.4.

MOX precursor 16b

^{1}H NMR (DMSO-d_6) δ 8.82-8.93 (t, 1H CH_3O-COCO-N<u>H</u>), 8.66-8.75 (t, 3H, 3 x CH_2-N<u>H</u>-COCO), 8.41-8.48 (d, 1H, COCO-N<u>H</u>-ACH), 4.53-4.57 (d, 1H, OH), 3.73-3.76 (s, 3H, C<u>H</u>$_3$O-COCO), 3.25-3.55 (m, 26H, 12 x CH_2-C<u>H</u>$_2$-O + H-4 (ACH) + H-1 (ACH)), 3.11-3.21 (m, 8H, 3 x C<u>H</u>$_2$-NH-COCO), 1.75-1.86 (m, 2H, 2 x CH (ACH)), 1.60-1.74 (m, 10H, 4 x CH_2-C<u>H</u>$_2$-CH_2 + 2 x CH (ACH)), 1.33-1.49 (m, 2H, 2 x CH (ACH)), 1.11-1.26 (m, 2H, 2 x CH (ACH)); ESI MS m/z 750.3 (M + H^+); calculated for $C_{33}H_{59}N_5O_{14}$: 749.4.

MMT-protected amino alcohol 16c

^{1}H NMR (DMSO-d_6) δ 8.66-8.75 (t, 3H, CH_2-N<u>H</u>-COCO), 8.41-8.48 (d, 1H, COCO-N<u>H</u>-ACH), 7.11-7.42 (m, 12H, MMT), 6.80-6.88 (d, 2H, MMT), 4.53-4.57 (d, 1H, OH), 3.69-3.74 (s, 3H, OCH_3), 3.27-3.56 (m, 26H, 12 x CH_2-C<u>H</u>$_2$-O + H-4 (ACH) + H-1 (ACH)), 3.12-3.23 (q, 6H, 3 x C<u>H</u>$_2$-NH-COCO), 2.53-2.61 (t, 1H, MMT-N<u>H</u>), 1.97-2.08 (q, 2H, MMT-NH-C<u>H</u>$_2$), 1.75-1.86 (br. d, 2H, 2 x CH (ACH)), 1.60-1.74 (m, 10H, 4 x CH_2-C<u>H</u>$_2$-

CH_2 + 2 x CH (ACH)), 1.32-1.50 (m, 2H, 2 x CH (ACH)), 1.12-1.27 (m, 2H, 2 x CH (ACH)); ESI MS m/z 936.4 ($M + H^+$); calculated for $C_{50}H_{73}N_5O_{12}$: 935.5.

Amino linker phosphoramidite 16d

^{31}P NMR (DMSO-d_6) δ 144.77.

Amino alcohol 17a

^1H NMR (DMSO-d_6) δ 8.67-8.75 (t, 5H, 5 x CH_2-N<u>H</u>-COCO), 8.40-8.47 (d, 1H, COCO-N<u>H</u>-ACH), 4.53-4.57 (d, 1H, OH), 3.25-3.55 (m, 38H, 18 x CH_2-C<u>H</u>$_2$-O + H-4 (ACH) + H-1 (ACH)), 3.12-3.23 (q, 10H, 5 x C<u>H</u>$_2$-NH-COCO), 2.55-2.62 (t, 2H, NH_2-C<u>H</u>$_2$), 1.31-1.86 (m, 18H, 6 x CH (ACH) + 6 x CH_2-C<u>H</u>$_2$-CH_2), 1.07-1.28 (m, 2H, 2 x CH (ACH)); ESI MS m/z 938.3 ($M + H^+$); calculated for $C_{42}H_{79}N_7O_{16}$: 937.6.

MMT-protected amino alcohol 17c

^1H NMR (DMSO-d_6) δ 8.67-8.75 (t, 5H, CH_2-N<u>H</u>-COCO), 8.41-8.48 (d, 1H, COCO-N<u>H</u>-ACH), 7.11-7.42 (m, 12H, MMT), 6.80-6.88 (d, 2H, MMT), 4.52-4.57 (d, 1H, OH), 3.68-3.74 (s, 3H, OCH_3), 3.25-3.56 (m, 38H, 18 x CH_2-C<u>H</u>$_2$-O + H-4 (ACH) + H-1 (ACH)), 3.11-3.23 (q, 10H, 5 x C<u>H</u>$_2$-NH-COCO), 2.53-2.60 (t, 1H, MMT-N<u>H</u>), 1.97-2.08 (q, 2H, MMT-NH-C<u>H</u>$_2$), 1.75-1.86 (br. d, 2H, 2 x CH (ACH)), 1.60-1.74 (m, 14H, 6 x CH_2-C<u>H</u>$_2$-CH_2 + 2 x CH (ACH)), 1.30-1.50 (m, 2H, 2 x CH (ACH)), 1.12-1.27 (m, 2H, 2 x CH (ACH)); ESI MS m/z 1210.3 ($M + H^+$); calculated for $C_{62}H_{95}N_7O_{17}$: 1209.7.

Amino linker phosphoramidite 17d

^{31}P NMR (DMSO-d_6) δ 144.78.

Synthesis and in Vitro Evaluation of PNA−Peptide−DETA Conjugates as Potential Cell Penetrating Artificial Ribonucleases

Lene Petersen,[†,§] Martijn C. de Koning,[†,§] Petra van Kuik-Romeijn,[‡] Jimmy Weterings,[†] Christine J. Pol,[‡] Gerard Platenburg,[‡] Mark Overhand,[†] Gijsbert A. van der Marel,[†] and Jacques H. van Boom*[,†,‡]

Leiden Institute of Chemistry and ProSensa B.V., Gorlaeus Laboratories, University of Leiden, P.O. Box 9502, 2300 RA Leiden, The Netherlands. Received December 4, 2003; Revised Manuscript Received February 24, 2004

We report the synthesis of novel artificial ribonucleases with potentially improved cellular uptake. The design of trifunctional conjugates **1a** and **1b** is based on the specific RNA-recognizing properties of PNA, the RNA-cleaving abilities of diethylenetriamine (DETA), and the peptide $(KFF)_3K$ for potential uptake into *E. coli*. The conjugates were assembled in a convergent synthetic route involving native chemical ligation of a PNA, containing an N-terminal cysteine, with the C-terminal thioester of the cell-penetrating $(KFF)_3K$ peptide to give **12a** and **12b**. These hybrids contained a free cysteine side-chain, which was further functionalized with an RNA-hydrolyzing diethylenetriamine (DETA) moiety. The trifunctional conjugates (**1a**, **1b**) were evaluated for RNA-cleaving properties in vitro and showed efficient degradation of the target RNA at two major cleavage sites. It was also established that the cleavage efficiency strongly depended on the type of spacer connecting the PNA and the peptide.

INTRODUCTION

Peptide nucleic acids (PNAs)[1] are nonionic DNA mimics composed of repeating *N*-(2-aminoethyl)glycine units, whose secondary amino atoms are anchored through methylenecarbonyl linkers to the natural nucleobases. PNAs are resistant to nuclease and protease digestion and bind exceptionally tight and with high affinity to complementary DNA and RNA (*1*−*3*). The latter features have led to the successful in vitro application of PNA as antisense agents (*4*−*8*).

A few years ago we reported the design and synthesis of an artificial ribonuclease (see Figure 1) composed of a PNA strand attached to a diethylenetriamine (DETA) moiety via a urethane bond (*9*). In vitro studies revealed that this hybrid almost completely degraded a complementary ^{32}P-labeled RNA strand within 24 h at 40 °C and pH 7.

This encouraging result was an incentive to study the potential ribonucleolytic activity of this type of artificial ribonuclease in a biological system. However, the in vivo evaluation of PNA is severely hampered by its poor membrane permeability (*10*). This obstacle can in principle be circumvented by attachment of lipophilic groups such as adamantyl (*11*, *12*) or phosphonium cation (*13*) to the PNA or by conjugation of PNA to membrane-permeable peptides (*14*−*17*). For instance, Good et al. investigated (*18*, *19*) the invasive properties of a peptide with the sequence $(KFF)_3K$—a cationic peptide that had previously been shown to permeate bacterial membranes (*20*, *21*)—attached through a spacer to the N-terminus of an antisense PNA. Markedly higher cellular uptake of the conjugate was found as judged by the dramatically increased antisense activity of the PNA−peptide conjugate compared to "naked" PNA. A recent study by Geller et al. (*22*) also demonstrated that antisense phosphorodiamidate morpholino oligomers (PMOs) showed highly improved bactericidal effects when bound covalently to the peptide $(KFF)_3KC$.

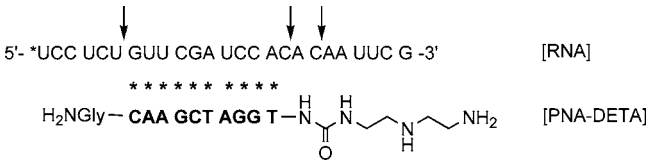


Figure 1. PNA−DETA conjugate (PNA marked in bold) synthesized by Verheijen et al. (*9*). The target RNA was cleaved at the sites indicated, the major cleavage taking place after C-17 and C-19.

It occurred to us that trifunctional constructs **1a** or **1b**, as depicted in Figure 2, containing an antisense PNA, a DETA moiety, and the $(KFF)_3K$ peptide may display enhanced cellular uptake and site-specific nuclease activity in *E. coli*.

We here report the synthesis and the in vitro nucleolytic properties of conjugates **1a** and **1b**, having different types of spacers connecting the $(KFF)_3K$ peptide to the N-terminus of the PNA.

* Corresponding author. Tel: +31 (0)71 5274274. Fax: +31 (0)71 5274307. E-mail: j.boom@chem.leidenuniv.nl.

† Leiden Institute of Chemistry.

‡ ProSensa B.V.

§ Authors contributed equally to this study.

[1] Abbreviations: ACN, acetonitrile; Boc, *tert*-butyloxycarbonyl; Bhoc, benzhydryloxycarbonyl; BOP, benzotriazol-1-yloxytris-(dimethylamino)phosphonium hexafluorophosphate; DCM, dichloromethane; DETA, diethylenetriamine; DiPEA, *N*,*N*-diisopropylethylamine; DMF, *N*,*N*-dimethylformamide; Fmoc, 9-fluorenylmethyloxycarbonyl; HATU, *O*-(7-azabenzotriazol-1-yl)-*N*,*N*,*N*′,*N*′-tetramethyluronium hexafluorophosphate; HOBT, *N*-hydroxybenzotriazole; LC-MS, liquid chromatography−mass spectrometry; MALDI TOF, matrix-assisted laser desorption ionization time-of-flight; NMP, *N*-methylpyrrolidone; PNA, peptide nucleic acid; PyBOP, benzotriazol-1-yl-oxytripyrrolidinophosphonium hexafluorophosphate. RP-HPLC, reversed phase high performance liquid chromatography; TCEP, tris(2-carboxyethyl)phosphine; TFA, trifluoroacetic acid; THF, tetrahydrofuran; TIS, triisopropylsilane; TMS, tetramethylsilane.

10.1021/bc034219p CCC: $27.50 © 2004 American Chemical Society
Published on Web 04/28/2004

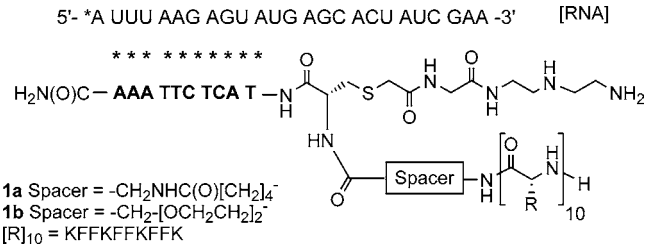


Figure 2. Structure of new trifunctional artificial ribonucleases **1a** and **1b** containing an RNA-recognizing PNA strand, a DETA moiety for RNA cleavage, and a cellular delivery peptide connected to the PNA via a spacer.

EXPERIMENTAL PROCEDURES

General Remarks. All reagents were of analytical or peptide synthesis grades and used as obtained from the suppliers. All solvents were of HPLC grade or peptide synthesis grade. Analytical LC-MS was conducted on a JASCO system using an Alltima C_{18} analytical column (5 μm particle size, flow: 1.0 mL/min). The absorbance was measured at 214 and 254 nm. The solvent system was A: 100% Water, B: 100% ACN, C: 0.5% TFA. Gradients of B in A containing 10% C were applied over 15 min. Mass spectra were recorded on a Perkin-Elmer Sciex API 165 equipped with an electrospray interface (ES). MALDI-TOF-MS spectra were recorded on a Voyager-DE PRO mass spectrometer (PerSeptive Biosystems) using a 4-hydroxy-α-cyanocinnamic acid matrix (10 mg/mL 0.2% TFA in ACN/Water, 1/1). Purifications were conducted using a BioCAD "Vision" automated HPLC system (PerSeptive Biosystems), supplied with a semi-preparative Alltima C_{18} column (5 μm particle size, running at 4.7 mL/min). Solvent system: A: 100% Water, B: 100% ACN, C: 1% TFA. Gradients of acetonitrile (B) in A containing 10% C were applied over 3 column volumes (CV). A TitroLine alpha machine or Merck Universalindikator pH 1−10 paper was used to measure the pH of buffers. The peptide and PNA fragments were prepared using an ABI 433A (Applied Biosystems) automatic peptide synthesizer. ^{1}H NMR and ^{13}C NMR spectra were recorded with a Bruker AC-200 spectrometer (200/50.1 MHz). Chemical shifts are given in ppm (δ) relative to tetramethylsilane (^{1}H NMR) as an internal standard or to the peak of the used solvent (^{13}C NMR).

Synthesis. (KFF)$_3$K−Spacer−Thioester 7a. To a suspension of 4-sulfamylbutyryl safety-catch resin **2** (1 g, loading capacity = 1.1 mmol/g, 1.1 mmol) in DMF were added DiPEA (1.92 mL, 11 mmol) and *N*-Fmoc-Gly-OH (1.64 g, 5.5 mmol). The reaction mixture was shaken for 20 min and then cooled to −40 °C, and PyBOP (2.86 g, 5.5 mmol) was added. The mixture was shaken for 1 h at −40 °C and then 5 h at −20 °C. The resin was removed by filtration and washed with DMF (3×), MeOH (3×), and DCM (3×) and then dried under a flow of air. The loading of the resin (0.4 mmol/g) was determined by standard Fmoc quantification. The peptide synthesis was carried out automatically on an ABI 433a peptide synthesizer on a 50 μmol scale using an excess (5 equiv) of the amino acid building blocks *N*-Fmoc-Phe-OH, *N*-Fmoc-Lys(Boc)-OH, and *N*-Boc-Lys(Boc)-OH, the activating agents BOP/HOBT, DiPEA as a base, and Ac_2O/DiPEA for capping. After complete synthesis, the resin was treated with trimethylsilyldiazomethane (1 M in THF/hexane, 1:1, 3 mL) and shaken for 2 h. The solvents were removed, and the resin was washed with THF (3×), DMF (3×), and THF (3×) and resubjected to trimethylsilyldiazomethane (0.66 M in THF/hexane, 2:1, 3 mL) for 45 min. The solvents were removed, and the resin was washed with THF (3×) and DMF (3×), and treated with a solution of ethyl 3-mercaptoproprionate (2 mmol, 1 M in DMF, 2 mL) containing sodium thiophenolate (2.5 mg, 0.02 mmol). The mixture was shaken for 2 days, and the resin was removed by filtration. The resin was additionally washed with DMF (3×), and the combined filtrates were evaporated under reduced pressure. The residue was treated with 95% TFA/H_2O (5 mL) and shaken for 1.5 h, and the product **7a** was precipitated from Et_2O and collected by centrifugation. LC-MS: 10−55% B, t_R = 13.4 min; ES MS: found/calcd: 1687.1/1687.1 $(M + H)^+$, 843.9/844.1 $(M + 2H)^{2+}$.

(KFF)$_3$K−Spacer−Thioester 7b. 4-Sulfamylbutyryl safety-catch resin **2** was loaded with the *N*-Fmoc-protected diethyleneglycol linker **3**, using the same method as described above, to give immobilized **4b**. After determination of the loading by standard Fmoc quantification (0.31 mmol/g), the peptide **7b** was synthesized according to similar procedures as described for thioester **7a**. LC-MS: 10−55% B, t_R = 14.2 min; ES MS: found/calcd: 1676.4/1676.1 $(M + H)^+$, 838.2/838.6 $(M + 2H)^{2+}$.

Synthesis of Cys(S*t*Bu)-PNA 11. PNA **11** was synthesized automatically on an ABI 433a peptide synthesizer on a 10 μmol scale using an excess (5 equiv) of the Fmoc/Bhoc-protected PNA monomers or Fmoc/S*t*Bu-protected cysteine (0.11 M monomer concentration) for the couplings on tentagel resin containing the Fmoc-protected Rink amide linker (loading 0.2 mmol/g). Monomers were preactivated (1 min) with HATU (4.9 equiv) and a mixture of DiPEA/lutidine as base (0.2 M DiPEA, 0.3 M lutidine in NMP). The coupling time was 30 min. Ac_2O/lutidine/NMP (5:6:89) was used for capping. After complete synthesis, the resin was treated with TFA/TIS/H_2O (90:5:5, 5 mL) for 2 h at ambient temperature, and the product **11** was precipitated from Et_2O and used without further purification. LC-MS: 5−35% B, t_R = 12.9min; ES MS: found/calcd: 1439.4/1439.5 $(M + 2H)^{2+}$, 959.8/960.0 $(M + 3H)^{3+}$, 720.2/720.3 $(M + 4H)^{4+}$.

Synthesis of PNA−Peptide Conjugates 12a, 12b. Crude PNA **11** (approximately 2 μmol) and crude peptide **7a** or **7b** (approximately 4 μmol) were dissolved in a degassed buffer solution (400 μL) containing 6 M guanidine·HCl, 0.1 M tris(2-carboxyethyl)phosphine·HCl (TCEP), and 0.1 M Na_2HPO_4. The pH was adjusted to 7.5 using 2 M NaOH. Thiophenol was added (4%, 16 μL), and the solution was shaken overnight. Complete consumption of PNA **11** was verified by LC-MS analysis. 1,4-Dithiothreitol was added, and the desired conjugate was purified by RP HPLC. PNA−peptide conjugate **12a**: LC-MS: 5−55% B, t_R = 12.4 min; ES MS: found/calcd: 2171.2/2171.3 $(M + 2H)^{2+}$, 1448.0/1447.9 $(M + 3H)^{3+}$, 1086.6/1086.2 $(M + 4H)^{4+}$, 869.4/869.1 $(M + 5H)^{5+}$, 724.6/724.4 $(M + 6H)^{6+}$. MALDI TOF MS: found/calcd: 4341/4342 $(M + H)^+$. PNA−peptide conjugate **12b**: LC-MS: 5−55% B, t_R = 12.3 min ES MS: found/calcd: 2166.2/2165.8 $(M + 2H)^{2+}$, 1444.2/1444.2 $(M + 3H)^{3+}$, 1083.6/1083.4 $(M + 4H)^{4+}$. MALDI TOF MS: found/calcd: 4329/4333 $(M + H)^+$.

({2-[*tert*-Butoxycarbonyl-(2-*tert*-butoxycarbonylaminoethyl)amino]ethylcarbamoyl}methyl)carbamic Acid 9*H*-Fluoren-9-ylmethyl Ester 14. To a solution of (2-aminoethyl)−(2-*tert*-butoxycarbonylaminoethyl)carbamic acid *tert*-butyl ester **13** (2.73 g, 9.0 mmol) in DMF (35 mL) were added *N*-Fmoc-glycine (3.48 g, 11.7 mmol), BOP (5.17 g, 11.7 mmol), HOBT (1.58 g, 11.7 mmol), and DiPEA (4.65 mL, 27 mmol). After 45 min, TLC analysis (4/1 EtOAc/PE, v/v) indicated complete consumption of the starting material. The mixture was concentrated in vacuo, and the residue was taken up in EtOAc. After being washed with 10% $KHSO_4$, 10% $NaHCO_3$, and finally with brine, the organic layer was

dried with $MgSO_4$, filtered, and evaporated under reduced pressure. The residue was applied to a silica gel column and eluted with a gradient of EtOAc in PE (50 → 100%), to yield 4.1 g (7.0 mmol, 78%) of the desired product as a white foam. ^{1}H NMR ($CDCl_3$): δ 7.43−7.25 (8H, CH arom. Fmoc), 4.40 (2H, d, CH_2 Fmoc), 4.24 (1H CH Fmoc), 3.87 (2H, bd, CH_2), 3.39 (4H, bs, 2 × CH_2), 3.28 (4H, bs, 2 × CH_2), 1.46 (9H, s, tBu Boc), 1.42 (9H, s, tBu Boc). ^{13}C{^{1}H} NMR ($CDCl_3$): δ 169.5 (C═O Fmoc), 154.2, 153.1 (C═O Boc), 127.7, 127.0, 125.0, 119.9 (CH arom Fmoc), 79.2, 80.8 (C_q, tBu), 67.1 (CH_2 Fmoc), 48.1, 44.4, 39.2 (CH_2), 47.0 (CH Fmoc), 28.3 (tBu Boc). ES MS: 583.4 $(M + H)^+$.

(2-*tert*-Butoxycarbonylaminoethyl)-{2-[2-(2-chloroacetylamino)acetylamino]ethyl}carbamic Acid *tert*-Butyl Ester 15. Compound **14** (0.5 mmol, 0.292 g) was dissolved in 20% piperidine in DMF (4 mL). After 15 min the reaction mixture was concentrated and coevaporated with toluene (3×). The residue was dissolved in dioxane (7.5 mL) to which a solution of chloroacetic acid anhydride (0.170 g, 1 mmol) in dioxane (3 mL) was added dropwise. The reaction mixture was stirred for another 1 h and then concentrated to dryness in vacuo. The residue was taken up in EtOAc and washed with 0.1 M NaOH (2×). The organic layer was dried with $MgSO_4$, filtered, and evaporated under reduced pressure. The product was purified by silica gel column chromatography (80 → 100% EtOAc in PE) to yield 0.163 g (0.37 mmol, 75%) of compound **15**. ^{1}H NMR ($CDCl_3$): δ 4.09 (2H, s, $ClCH_2$), 3.99 (2H, bs, CH_2 Gly), 3.39 (4H, bs, 2 × CH_2), 3.29 (4H, bs, 2 × CH_2), 1.46 (9H, s, tBu), 1.44 (9H, s, tBu). ^{13}C{^{1}H} NMR ($CDCl_3$): δ 168.4 (C═O amide), 166.5 (C═O amide), 158.0, 156.1 (C═O Boc), 80.4, 79.5 (C_q, tBu), 48.0, 47.3, 42.9, 42.3, 39.3, 39.2 (6 × CH_2), 28.3 (2 × tBu). ES MS: 437.2 $(M + H)^+$.

***N*-{[2-(2-Aminoethylamino)ethylcarbamoyl]methyl}-2-chloroacetamide 16.** To a solution of compound **15** (0.140 g, 0.32 mmol) was added TFA (4 mL), and the reaction mixture was stirred for 15 min. TLC analysis indicated complete disappearance of the starting compound into a baseline product. The mixture was concentrated and coevaporated with toluene under reduced pressure to yield a light yellow oil. The residue was dissolved in water and divided over 10 eppendorfer vessels (∼30 μmol/vessel) and lyophilized. ^{1}H NMR (CD_3OD): δ 4.15 (2H, s, $ClCH_2$), 3.93 (2H, s, CH_2 Gly), 3.57−3.51 (2H, m, CH_2), 3.39−3.35 (4H, m, 2 × CH_2), 3.26−3.21 (2H, m, CH_2). ^{13}C{^{1}H} NMR (CD_3OD): δ 174.8, 173.3 (C═O, amide), 50.5, 47.0, 45.4, 44.7, 38.5, 38.1 (6 × CH_2). ES MS: 236.9 $(M + H)^+$.

Synthesis of PNA−Peptide−DETA Conjugates 1a, 1b. The PNA−peptide conjugates **12a** or **12b** (approximately 0.2 μmol) were dissolved in an aqueous buffered solution (300 μL) containing 0.05 M tris(2-carboxyethyl)-phosphine (TCEP) and 0.1 M Na_2HPO_4. Compound **16** (30 μmol) was dissolved in the same buffer solution (150 μL) and added. After adjustment of the pH to 8 (2 M NaOH), the solution was shaken overnight. The progress of the reaction was monitored by LC-MS analysis. RP HPLC gave homogeneous **1a** or **1b**. PNA−peptide−DETA conjugate **1a**: LC-MS: 5−55% B, t_R = 11.9min; ES MS: found/calcd: 2272.2/2271.5 $(M + 2H)^{2+}$, 1514.4/1514.6 $(M + 3H)^{3+}$, 1136.6/1136.2 $(M + 4H)^{4+}$, 909.2/909.2 $(M + 5H)^{5+}$, 758.0/757.8 $(M + 6H)^{6+}$. MALDI TOF MS: found/calcd: 4544/4542 $(M + H)^+$, 2272/2271 $(M + 2H)^{2+}$. PNA−peptide−DETA conjugate **1b**: LC-MS: 5−50% B, t_R = 12.9 min; ES MS: found/calcd: 2266.2/2265.9 $(M + 2H)^{2+}$, 1511.0/1510.9 $(M + 3H)^{3+}$, 1133.4/1133.5 $(M + 4H)^{4+}$, 906.8/907.0 $(M + 5H)^{5+}$, 756.4/756.0 $(M + 6H)^{6+}$. MALDI TOF MS: found/calcd: 4528/4531 $(M + H)^+$.

Synthesis of PNA 17. The N-terminal Fmoc group in resin **10** (18 mg, 3.5 μmol) was cleaved with 20% piperidine/NMP followed by thorough washing of the resin with NMP and DCM. The resin was treated with Ac_2O/lutidine/NMP (5:6:89, 4 mL) for 2 min and then washed with NMP (3×) and DCM (3×). Treatment with TFA/TIS/H_2O (90:5:5, 4 mL) for 2 h at ambient temperature led to the desired product **17**, which was precipitated from Et_2O and purified by RP-HPLC. LC-MS: 5−35% B, t_R = 14.9min; ES MS: found/calcd: 1460.8/1460.5 $(M + 2H)^{2+}$, 973.8/974.0 $(M + 3H)^{3+}$. MALDI TOF MS: found/calcd: 2921/2920 $(M + H)^+$.

Synthesis of PNA−DETA 18. PNA **17** (approximately 0.5 μmol) was dissolved in a buffered solution (200 μL) containing 0.1 M tris(2-carboxyethyl)phosphine (TCEP) and 0.1 M Na_2HPO_4. The mixture was shaken for 1 h followed by addition of the DETA derivative **16** (30 μmol) dissolved in the same buffer solution (200 μL). After adjustment of the pH to 8 (2 M NaOH), the solution was shaken overnight and the product was purified by RP HPLC. LC-MS: 5−35% B, t_R = 10.6min; ES MS: found/calcd: 1517.2/1516.5 $(M + 2H)^{2+}$, 1011.4/1011.3 $(M + 3H)^{3+}$. MALDI TOF MS: found/calcd: 3032/3032 $(M + H)^+$.

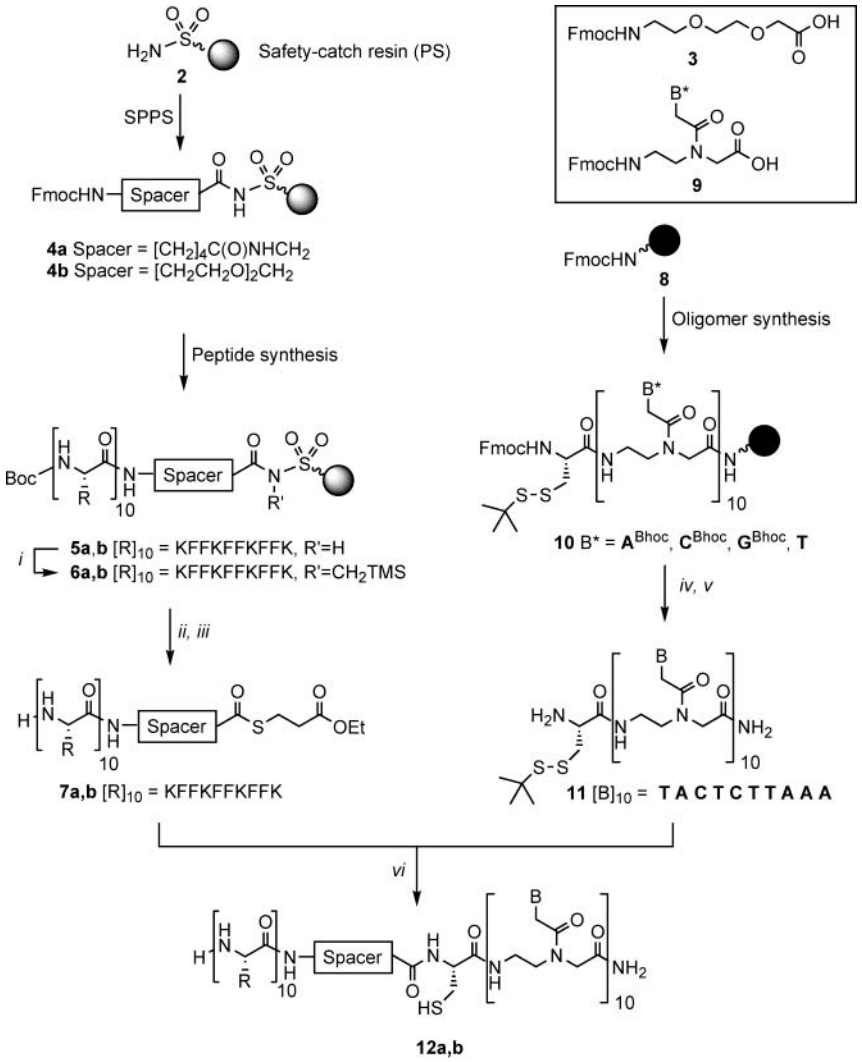
In Vitro RNA Degradation Studies. All buffers were made from highly purified Milli Q water and were sterilized before use. The radioactively labeled RNA 25-mer and the conjugate to be tested (**1a**, **1b**, **12b**, or **18**) were mixed in a Tris·HCl buffer (10 mM, pH 7) containing NaCl (100 mM) and EDTA (0.1 mM) to give the following concentrations: [RNA] = 60 nM, [conjugate] = 2 μM, as determined by A_{260} units. The samples (70 μL) were incubated at 40 °C for 16 h. After incubation, the RNA was immediately precipitated by addition of 3 M NaOAc (pH 5, 7 μL), EtOH (225 μL), and 10 μg μL^{-1} tRNA (1 μL). The precipitated RNA was recovered by centrifugation, dried, and then redissolved in 5 μL of H_2O and 5 μL of loading buffer. The solutions were heated at 80 °C for 1 min, centrifuged, and analyzed on a 20% denaturing polyacrylamide electrophoresis gel. The gel was exposed to a phosphor screen (Molecular Dynamics), and the intensity of the RNA fragments was quantified by scanning the exposed screen on the Personal Molecular Imager FX System (Bio-Rad) followed by computer analysis with Quantity One software (Bio-Rad).

RESULTS AND DISCUSSION

The synthesis of the target compound **1a** (Scheme 2) entails two distinct stages. First, PNA−peptide conjugate **12a** (Scheme 1) is prepared by native chemical ligation (*23*, *24*) of the separately prepared peptide thioester **7a** and the *S-tert*-butylthio-protected cysteine-functionalized PNA derivative **11**. The advantage of using chemical ligation is that the resulting PNA−peptide conjugate **12a** contains an exposed sulfhydryl group which can be directly used for the installation (see Scheme 2) of the DETA moiety **16** in the second step, to afford the target compound **1a**.

Peptide thioester **7a**, as depicted in Scheme 1, was prepared according to protocols developed by Pessi et al. (*25*). Thus, commercially available 4-sulfamylbutyryl safety-catch resin **2** was loaded with *N*-Fmoc-Gly-OH (5 equiv) using the coupling reagent PyBOP at temperatures ranging from −40 °C to −20 °C. Fmoc deprotection with piperidine was followed by BOP/HOBT-mediated condensation of the resulting free amine with *N*-Fmoc-5-aminopentanoic acid to give resin **4a**. Peptide elongation was executed using standard solid-phase Fmoc chemistry employing the amino acid building blocks *N*-Fmoc-Phe-OH and *N*-Fmoc-Lys(Boc)-OH. Final elon-

Scheme 1[a]



[a] Reagents and conditions: (i) TMS−CHN_2, THF/DMF, (ii) $HSCH_2CH_2CO_2Et$, NaSPh, (iii) 95% TFA/H_2O, (iv) 20% piperidine, (v) TFA/TIS/H_2O (90:5:5), (vi) 0.1 M TCEP, 6 M guanidine·HCl, 0.1 M Na_2HPO_4, pH 7.5, 4% (v/v) thiophenol.

gation with *N*-Boc-Lys(Boc)-OH led to the immobilized peptide **5a**. Cleavage of the peptide from the resin was achieved by subsequent alkylation of the sulfonamide in **5a** using trimethylsilyldiazomethane (*25*) and substitution of resulting **6a** with excess ethyl 3-mercaptopropionate in the presence of a catalytic amount of sodium thiophenolate. Cleavage of all Boc protective groups from the released peptide thioester with 95% TFA/H_2O afforded compound **7a**, which was sufficiently pure, as gauged by LC-MS analysis, for the crucial native chemical ligation step.

The decameric PNA derivative **11**, having a sequence complementary to the start codon region of the mRNA of the essential *E. coli acpP* gene and the N-terminal *S*-*tert*-butylthio protected cysteine residue, was assembled (see Scheme 1) on a solid support according to standard PNA synthesis protocols following Fmoc strategy (*26*). Thus, removal of the Fmoc group on the commercially available Rink Amide-Tentagel resin **8** with piperidine was followed by sequential elongation with Fmoc/benzhydryloxycarbonyl (Bhoc)-protected PNA building blocks **9** using the activating agent HATU (*27*) and a mixture of the bases DiPEA and lutidine (*28*). The elongation process was terminated by coupling with *N*-Fmoc-*S*-*tert*-butylthio-protected cysteine to give immobilized PNA oligomer **10**. The resin was subjected to TFA, resulting in deblocking of the Bhoc protective groups and concomitant release from the resin to afford the required major product Cys(S*t*Bu)-PNA **11** as judged by LC-MS analysis. It is worth mentioning that the cysteine *S*-*tert*-butylthio protecting group is resistant to TFA treatment, thus preventing scavenging of released benzhydryl cation by the thiol group (*26*).

At this stage, conjugate **12a** was assembled by native chemical ligation of the crude peptide thioester **7a** with the crude PNA derivative **11**. Accordingly, Cys(S*t*Bu)-PNA **11** and an excess of peptide thioester **7a** were dissolved in a denaturing phosphate buffer (0.1 M Na_2HPO_4, pH 7.5, 6 M guanidine·HCl) containing the water-soluble reducing agent tris3(2-carboxyethyl)phosphine (TCEP, 0.1 M) for the in situ unmasking of the cysteine *tert*-butylthio protective group. Additionally, an excess of thiophenol (4% (v/v)) was used as a ligation enhancer (Scheme 1).

LC-MS analysis, after 16 h incubation at ambient temperature (Figure 3), revealed complete conversion of the PNA derivative **11** and the corresponding *tert*-butylthio deprotected analogue, into the conjugate **12a**. Furthermore, we observed impurities originating from the synthesis of the PNA fragment **11** (peaks a, Figure 3) and byproducts having a mass corresponding to a possible intramolecular lactamization of the excess peptide **7a** (peaks b and c, Figure 3). RP-HPLC purification of the cude ligation product afforded homogeneous **12a**,

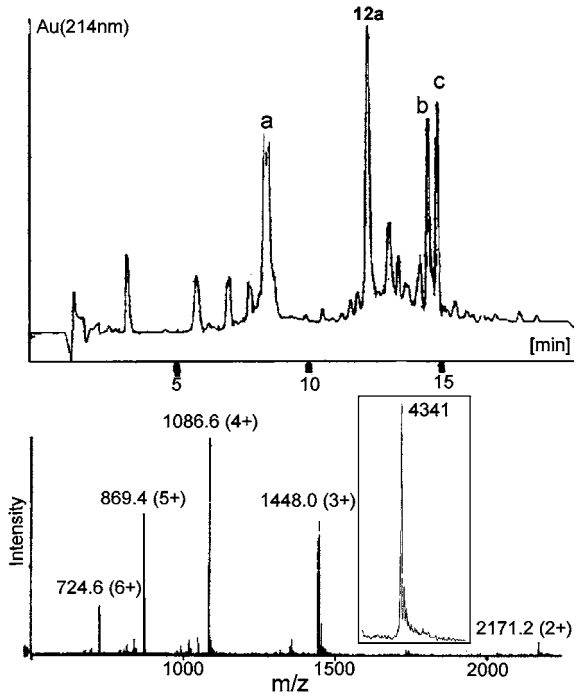


Figure 3. Top: HPLC chromatogram of the native chemical ligation mixture between thioester **7a** and Cys(S-*t*Bu)-PNA **11** after overnight incubation. The product **12a** is seen as a distinct peak together with byproducts from the PNA synthesis (peak a) and presumably lactamized peptide thioester **7a** (peaks b, c). Bottom: ES MS and MALDI-TOF MS (insert) of the purified product **12a**.

Table 1. MALDI TOF MS Values for the Conjugates

compound	spacer	MALDI (found) $(M + H)^+$	MALDI (calcd) $(M + H)^+$
18	–	3032	3032
12a	$(CH_2)_4C(O)NHCH_2$	4341	4342
12b	$(CH_2CH_2O)_2CH_2$	4329	4331
1a	$(CH_2)_4C(O)NHCH_2$	4544	4542
1b	$(CH_2CH_2O)_2CH_2$	4528	4531

the identity of which was ascertained by LC-MS analysis and MALDI-TOF mass spectrometry (Figure 3, Table 1).

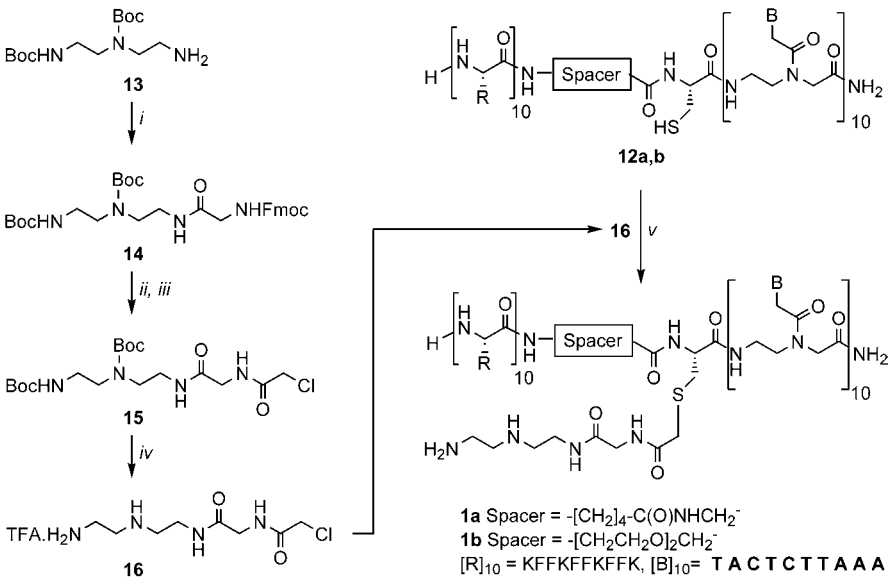
Having the PNA−peptide conjugate **12a** in hand, we focused attention on the construction of the DETA moiety **16** required for the intended condensation with the conjugate **12a** (Scheme 2). The synthesis of chloride **16** commenced with a BOP/HOBT-mediated coupling of the known di-Boc-protected diethylenetriamine **13** (9) with *N*-Fmoc-glycine to afford the Fmoc/Boc-protected compound **14** in 78% yield. Subsequent removal of the Fmoc group in **14** with piperidine and treatment of the resulting free amine with chloroacetic anhydride led to conversion of **14** into the chloride **15** in 75% yield. Removal of the Boc protective groups with TFA gave the target compound **16** as the TFA salt in a near quantitative yield.

Condensation of PNA−peptide conjugate **12a** with an excess of DETA derivative **16** (see Scheme 2) was executed under buffered conditions (0.1 M Na_2HPO_4) at pH 8. The buffer contained an additional amount of TCEP to prevent dimerization of **12a** by disulfide formation. LC-MS analysis (Figure 4), after 16 h incubation at room temperature, showed complete consumption of all starting material **12a** and formation of the product **1a**. HPLC purification afforded homogeneous **1a** as judged by LC-MS and MALDI-TOF analysis (Figure 4, Table 1).

With the objective to study the influence of the type of spacer connecting the PNA and the peptide units, compound **1b** containing an ethylene glycol linker was prepared. To this end, the safety-catch resin **2** (see Scheme 1) was loaded with the Fmoc-protected ethylene glycol spacer **3** to give immobilized **4b** which was processed further, as described for **7a**, to give peptide thioester **7b**. Compounds **12b** and **1b** were assembled starting from **7b** according to similar procedures as described earlier for the synthesis of **12a** and **1a** (Schemes 1 and 2, Table 1).

Additionally, compound **18**, lacking the $(KFF)_3K$ peptide, was synthesized to serve as a positive control (Scheme 3). Thus, the Fmoc group on immobilized PNA **10** was removed with piperidine followed by acetylation of the resulting free amine with Ac_2O. The resin was then treated with TFA/TIS/H_2O (90:5:5), leading to simultaneous cleavage of the Bhoc protection groups and release of the desired PNA derivative **17**, which was purified by RP-HPLC. Finally, **17** and chloride **16** were condensed

Scheme 2[a]



[a] Reagents and conditions: (i) Fmoc-Gly-OH, BOP, HOBT, DiPEA; 78%, (ii) 20% piperidine/DMF, (iii) $(ClCH_2CO)_2O$, 75% (two steps), (iv) 50% TFA/DCM, (v) **16**, buffer (0.05 M TCEP, 0.1 M Na_2HPO_4, pH 8).

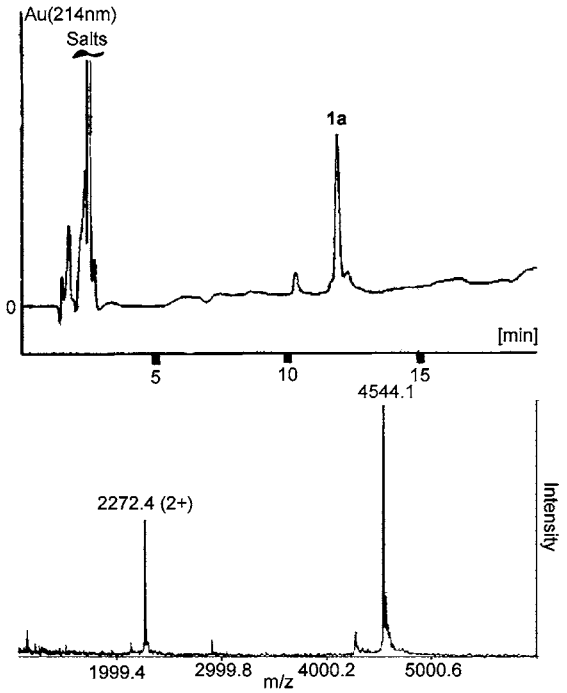


Figure 4. Top: HPLC chromatogram of the reaction mixture after overnight reaction of compounds **12a** and **16**. The product **1a** is seen as a distinct peak. Bottom: MALDI-TOF MS of the pure product **1a**.

as described earlier for the conversion of **12a** into **1a** to afford the desired product **18**, which could be readily purified by HPLC.

Having the requisite compounds in hand, we turned our attention to the in vitro degrading abilities of both PNA−peptide−DETA conjugates **1a**,**b**, the PNA−DETA **18** and the PNA−peptide conjugate **12b** as a negative control. To this end, the compounds were incubated with the 25-mer ^{32}P-labeled RNA having a sequence resembling part of the *E. coli acpP* mRNA. After 16 h at 40 °C and pH 7, the RNA fragments were precipitated, applied to a 20% denaturing polyacrylamide electrophoresis gel, and quantified.

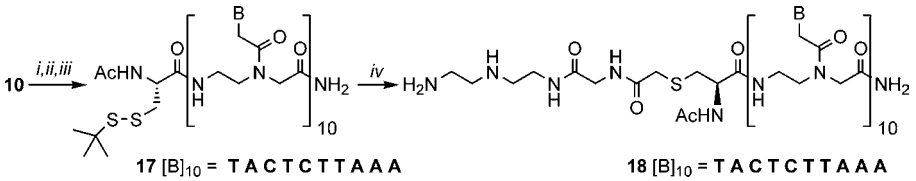
A representative gel is depicted in Figure 5 (left) whereas the quantification is shown as the average result of three separate experiments (Figure 5, right). Gratifyingly, incubation of the RNA with the conjugates **1a** and **1b** as well as the PNA−DETA **18**, lacking the $(KFF)_3K$ peptide sequence, led to the formation of two major RNA degradation products stemming from cleavage at the CA and the UA sites marked in Figure 5. The cleavage sites were determined by comparison of the mobility of the bands with those of a T1 digest of the RNA (Figure 5) and a basic hydrolysis ladder (not shown). The intensity of the fragment spots revealed that incubation of the RNA with PNA−DETA **18** resulted in significant cleavage (20%) of the RNA compared to the negative controls (i.e. PNA−peptide conjugate **12b** and RNA without any conjugate added), which only showed background cleavage of approximately 3.5%. An unexpected difference between the hydrolysis efficiency of conjugates **1a** and **1b** was observed. Conjugate **1a** showed an even improved cleavage efficiency (30%) compared to the positive control **18** (20%), whereas conjugate **1b** cleaved only 10% of the target RNA. This difference in hydrolysis ability renders conjugate **1a** three times more potent than conjugate **1b**.

CONCLUSIONS

We have reported a straightforward route to the synthesis of unprecedented, highly functionalized PNA derivatives **1a** and **1b** based on native chemical ligation between the membrane permeable peptide thioesters **7a** or **7b** and the cysteine-containing antisense PNA derivative **11**. The exposed cysteine side-chain residue in the resulting PNA−peptide conjugates was exploited for the installation through a thioether bond of a DETA-based RNA cleaving agent.

In addition, we have demonstrated that the two trifunctional conjugates **1a** and **1b**, differing only in the type of spacer connecting the PNA and the peptide, both hydrolyzed the complementary 25-mer RNA at two major cleavage sites under physiological conditions. The re-

Scheme 3[a]



[a] Reagents and conditions: (i) 20% Piperidine/NMP, (ii) Ac_2O/Lutidine/NMP (5:6:89), (iii) TFA/TIS/H_2O (90:5:5), (iv) **16**, 0.1 M Na_2HPO_4, 0.1 M TCEP, pH 8.

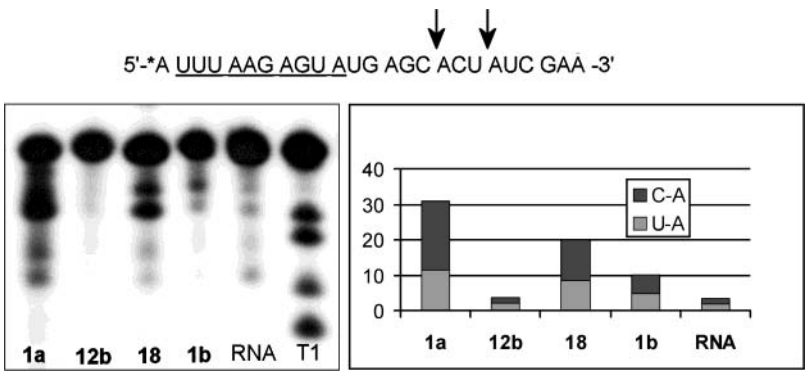


Figure 5. Top: Major cleavage sites of the target 25-mer RNA. The PNA binding region is marked underlined. Left: Autoradiograph for the cleavage of the 5′-labeled RNA 25-mer, after 16 h at pH 7 and 40 °C of compounds **1a**, **12b**, **18**, **1b**, RNA (no additives), T1 (T1 digestion); $[RNA]_0 = 60$ nM, [Conjugates] = 2 μM. Right: Average cleavage efficiency (in % degradation of mRNA) over three experiments.

markable difference in the cleaving efficiency of the two conjugates (**1a** is three times more potent than **1b**) indicate that the choice of spacer may have a great influence on the properties of the conjugate (*29*). On the other hand, the presence of the peptide does not seem to have a decisive effect on the cleavage capabilities. Although the RNA hydrolysis activity of conjugates **1a**,**b** is somewhat lower than the earlier by us reported PNA−DETA conjugate (*9*), it is still considerably improved compared to the DNA−DETA conjugate of Komiyama and co-workers (*30*). Other amine-based RNA-cleaving moieties, e.g. cyclen which efficiently hydrolyzed the HIV-1 TAR−RNA (*31*), can be easily implemented in our synthetic strategy and may further enhance the cleavage activity. Currently, the bacterial uptake of the conjugates **1a**,**b** and their effects on cell proliferation is in progress, and these results will be reported in due course.

ACKNOWLEDGMENT

L.P. acknowledges the financial support provided through the European Community's Human Potential Program under contract HPRN-CT99-00008 ENDEVAN and the Danish Research Agency.

LITERATURE CITED

(1) Nielsen, P., Egholm, M., Berg, R. H., and Buchardt, O. (1991) Sequence-selective recognition of DNA by strand displacement with a thymine-substituted polyamide. *Science 254*, 1497−1500.

(2) Hyrup, B., and Nielsen, P. E. (1996) Peptide nucleic acids (PNA): Synthesis, properties and potential applications. *Bioorg. Med. Chem. 4*, 5−23.

(3) Dueholm, K. L., and Nielsen, P. E. (1997) Chemistry, properties and applications of PNA (peptide nucleic acids). *New J. Chem. 21*, 19−31.

(4) Buchardt, O., Egholm, M., Berg, R. H., and Nielsen, P. E. (1993) Peptide nucleic acids and their potential applications in biotechnology. *Trends Biotechnol. 11*, 384−386.

(5) Nielsen, P. E., Egholm, M., Berg, R. H., and Buchardt, O. (1993) Sequence specific inhibition of DNA restriction enzyme cleavage by PNA. *Nucleic Acids Res. 21*, 197−200.

(6) Corey, D. R. (1997) Peptide nucleic acids: expanding the scope of nucleic acid recognition. *Trends Biotechnol. 15*, 224−229.

(7) Lansdorp, P. M., Verwoerd, N. P., van de Rijke, F. M., Dragowska, V., Little, M.-T., Dirks, R. W., Raap, A. L., and Tanke, H. J. (1996) Heterogeneity in telomere length of human chromosomes. *Hum. Mol. Genet. 5*, 685−691.

(8) Carlsson, C., Jonsson, M., Norden, B., Dulay, M. T., Zare, R. N., Noolandi, J., Nielsen, P. E., Tsui, L.-C., and Zielenski, J. (1996) Screening for genetic mutations. *Nature 380*, 207.

(9) Verheijen, J. C., Deiman, B. A. L. M., Yeheskiely, E., van der Marel, G. A., and van Boom, J. H. (2000) Efficient hydrolysis of RNA by a PNA-diethylenetriamine adduct. *Angew. Chem., Int. Ed. 39*, 369−372.

(10) Wittung, P., Kajanus, J., Edwards, K., Nielsen, P. E., Norden, B., and Malmstrom, B. G. (1995) Phospholipid membrane permeability of peptide nucleic acid. *FEBS Lett. 365*, 27−29.

(11) Mologni, L., Marchesi, E., Nielsen, P. E., and Gambacorti-Passerini, C. (2001) Inhibition of promyelocytic leukemia (PML)/retinoic acid receptor-α and PML expression in acute promyelocytic leukemia cells by anti-PML peptide nucleic acid. *Cancer Res. 61*, 5468−5473.

(12) Ardhammar, M., Nordèn, B., Nielsen, P. E., Malmstrom, B. G., and Wittung-Stafshede, P. (1999) In vitro membrane penetration of modified peptide nucleic acid (PNA) *J. Biomol. Struct. Dyn. 17*, 33−40.

(13) Muratovska, A., Lightowlers, R. N., Taylor, R. W., Turnbull, D. M., Smith, R. A. J., Wilce, J. A., Martin, S. W., and Murphy, M. P. (2001) Targeting peptide nucleic acid (PNA) oligomers to mitochondria within cells by conjugation to lipophilic cations: implications for mitochondrial DNA replication, expression and disease. *Nucleic Acids Res. 29*, 1852−1863.

(14) Scarfi, S., Gasparini, A., Damonte, G., and Benatti, U. (1997) Synthesis, uptake, and intracellular metabolism of a hydrophobic tetrapeptide-peptide nucleic acid (PNA)-biotin molecule. *Biochem. Biophys. Res. Commun. 236*, 323−326.

(15) Dean, D. A. (2000) Peptide nucleic acids: versatile tools for gene therapy strategies. *Adv. Drug Delivery Rev. 44*, 81−95.

(16) Tung, C., and Stein, S. (2000) Preparation and applications of peptide−oligonucleotide conjugates. *Bioconjugate Chem. 11*, 605−618.

(17) Gait, M. J. (2003) Peptide-mediated cellular delivery of antisense oligonucleotides and their analogues. *Cell. Mol. Life. Sci. 60*, 844−853.

(18) Good, L., Awasthi, S. K., Dryselius, R., Larsson, O., and Nielsen, P. E. (2001) Bactericidal antisense effects of peptide-PNA conjugates. *Nature Biotechnol. 19*, 360−364.

(19) Eriksson, M., Nielsen, P. E., and Good, L. (2002) Cell permeabilization and uptake of antisense peptide-peptide nucleic acid (PNA) into *Escherichia coli. J. Biol. Chem. 277*, 7144−7147.

(20) Rustici, A., Velucchi, M., Faggioni, R., Sironi, M., Ghezzi, P., Quataert, S., Green, B., and Porro, M. (1993) Molecular mapping and detoxification of the lipid A binding site by synthetic peptides. *Science 259*, 361−365.

(21) Vaara, M., and Porro, M. (1996) Groups of peptides that act synergistically with hydrophobic antibiotics against gram-negative enteric bacteria. *Antimicrob. Agents Chemother. 40*, 1801−1805.

(22) Geller, B. L., Deere, J. D., Stein, D. A., Kroeker, A. D., Moulton, H. M., and Iversen, P. L. (2003) Inhibition of gene expression in *Escherichia coli* by antisense phosphorodiamidate morpholino oligomers. *Antimicrob. Agents Chemother. 47*, 3233−3239.

(23) de Koning, M. C., Filippov, D. V., Meeuwenoord, N., Overhand, M., van der Marel, G. A., and van Boom, J. H. (2001) Synthesis of a PNA-peptide conjugate by chemical ligation. *Synlett 10*, 1516−1518.

(24) Dawson, P. E., Muir, T. W., Clark-Lewis, I., and Kent, S. B. H. (1994) Synthesis of proteins by native chemical ligation. *Science 266*, 776−779.

(25) Ingenito, R., Bianchi, E., Fattori, D., and Pessi, A. (1999) Solid-phase synthesis of peptide *C*-terminal thioesters by Fmoc/*t*-Bu Chemistry. *J. Am. Chem. Soc. 121*, 11369−11374.

(26) Goodwin, T. E., Holland, R. D., Lay, J. O., Jr., and Raney, K. O. (1998) A simple procedure for solid-phase synthesis of peptide nucleic acids with *N*-terminal cysteine. *Bioorg. Med. Chem. Lett. 8*, 2231−2234.

(27) Carpino, L. A. (1993) 1-Hydroxy-7-azabenzotriazole. An efficient peptide coupling additive. *J. Am. Chem. Soc. 115*, 4397−4398.

(28) Kovács, G., Timár, Z., Kupihár, Z., Kele Z., and Kovács, L. (2002) Synthesis and analysis of peptide nucleic acid oligomers using Fmoc/acyl-protected monomers. *J. Chem. Soc., Perkin Trans. 1* 1266−1270.

(29) The influence of spacer type has been recognized before in the cellular uptake of PNA−peptide conjugates (see ref 18).

(30) RNA hydrolysis efficiency of the DNA-DETA conjugate was 10 mol % after 4 h at pH 8 and 50 °C: Komiyama, M., Inokawa, T., and Yoshinari, K. (1995) Ethylenediamine-oligo DNA hybrid as sequence-selective artificial ribonuclease. *J. Chem. Soc., Chem. Commun.* 77−78.

(31) Michaelis, K., and Kalesse, M. (1999) Selective cleavage of the HIV-1 TAR−RNA with a peptide-cyclen conjugate. *Angew. Chem., Int. Ed. 38*, 2243−2245.

BC034219P

A Modular Approach to the Synthesis of New Reagents Useful in the Chemical Synthesis of Modified DNA Probes: Derivatives of 3-(*tert*-Butyldimethylsiloxy)glutaric Anhydride as Versatile Building Blocks in the Synthesis of New Phosphoramidites and Modified Solid Supports

Zbigniew Skrzypczynski* and Sarah Wayland

Third Wave Technologies, 502 South Rosa Road, Madison, Wisconsin 53719. Received December 9, 2003; Revised Manuscript Received March 17, 2004

We present a flexible and cost-efficient synthetic strategy for the preparation of a new family of phosphoramidite and solid-support reagents that can introduce a broad range of modifications into DNA probes. The key intermediate material **3** is synthesized using the inexpensive and commercially available 3-(*tert*-butyldimethylsiloxy)glutaric anhydride **1** and can be used as common starting material for the preparation of new labeling reagents.

INTRODUCTION

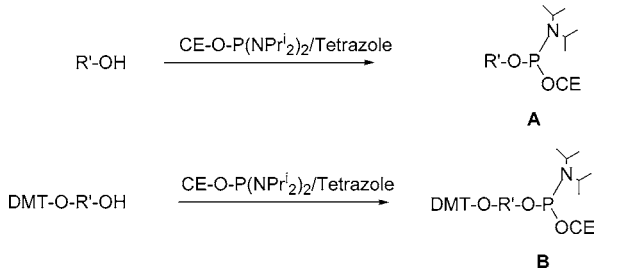
Chemically modified DNA probes and their conjugates play increasingly sophisticated roles in the disparate areas of biotechnology (*1*−*15*) medicine (*16*−*34*), and nanotechnology (*35*−*44*). Recent chemical literature reports the synthesis of a variety of reagents and modified solid supports that allow modifications to be introduced into the structure of chemically synthesized oligonucleotides (*45*−*67*). Among the many existing synthetic methods, the phosphoramidite approach is used most frequently in the synthesis of a wide variety of modified DNA probes (*68*−*73*). The efficiency and synthetic flexibility of the phosphoramidite method in preparing modified DNA probes continually stimulates interest in the development of new cost- and labor-efficient methods to prepare phosphoramidite reagents that expand the scope of available DNA probe modifications.

Generally, phosphoramidite reagents used in the synthesis of modified DNA probes can be divided into two groups: A and B (Scheme 1). Group A phosphoramidites introduce the modification into the 5′ loci of the synthesized oligonucleotide, and group B phosphoramidites introduce the modification into the 3′ or 5′ or internal loci of the synthesized DNA molecule.

Group A phosphoramidites can be prepared with the appropriate starting compound R′ that has a hydroxyl group available for further transformations. All other functional groups of compound R′ should be blocked with protecting groups that are compatible with the phosphoramidite method of oligonucleotide synthesis (*74*). The synthesis of group B phosphoramidites, however, requires preparation of an intermediate material that contains two hydroxyl groups, one of which must be selectively protected with a DMT protecting group, and one that is kept available for the phosphitylation reaction. In consequence, the preparation of group B reagents requires more labor and time-consuming synthetic effort.

* To whom correspondence should be addressed [telephone (608) 273-8933; fax (608) 273-8618; e-mail zskrzypczynski@twt.com].

Scheme 1. Preparation of Phosphoramidite Reagents for Terminal and Internal Oligonucleotide Labeling



Here we report a flexible and effective strategy for the synthesis of a new family of phosphoramidite reagents and specifically modified solid supports.

MATERIALS AND METHODS

Abbreviations used: DCC, 1,3-Dicyclohexylcarbodiimide; DMAP, 4-(dimethylamino)pyridine; DMF, *N*,*N*-dimethylformamide; EDAC, 1-ethyl-(3-dimethylaminopropyl)carbodiimide hydrochloride; HBTU, *O*-benzotriazol-1-yl)-*N*,*N*,*N*′,*N*′-tetramethyluronium; HOBT, 1-hydroxybenzotriazole hydrate; TBAF, tetrabutylammonium fluoride; TBDMS, *tert*-butyldimethylsilyl; TEA, triethylamine; THF, tetrahydrofuran.

Instruments and Reagents. HPLC analyses were performed with a Hitachi D-7000 Interface, L-7100 gradient pump, and L-7400 UV detector using a Varian Omnisphere 5 C18 column (250 × 4.6 mm) and 100 mM TEAA, pH 7/acetonitrile gradients. MS analysis of all DNA-containing species was performed using a PerSeptive Biosystems Voyager-DE Biospectrometry Workstation V800520. MS analysis of small molecules was performed using an Applied Biosystems/MDS Sciex API 365 LC/MS/MS triple quadrapole with an electrospray ionization source. Automated oligonucleotide synthesis was performed using a PerSeptive Biosystems Expedite Nucleic Acid Synthesis System. Silica gel was obtained from Sigma-Aldrich (Milwaukee, WI). Analytical TLC was carried out on EM Science F_{254} glass-backed fluo-

10.1021/bc0342231 CCC: $27.50 © 2004 American Chemical Society
Published on Web 04/29/2004

rescence indicator plates. Lcaa-CPG, used in the synthesis of **10c** and **10d**, was obtained from Glen Research (Sterling, VA). DNA synthesis reagents and columns were purchased from Applied Biosystems (Foster City, CA). All other reagents were purchased from Sigma-Aldrich and used without further purification. Solvents were dried over activated 3 Å molecular sieves.

Synthesis of Ethanolamine Trifluoroacetamide. In a round-bottom flask, methyl trifluoroacetate (10.5 g, 81.9 mmol) was added to neat ethanolamine (4.0 g, 66 mmol) at room temperature with continuous stirring. Reaction completion was determined by the absence of ninhydrin activity. After 2 h, the reaction was concentrated by rotary evaporation and purified by distillation (11 mmHg, bp 127 °C), yielding a colorless oil, 9.5 g, 93%.

Synthesis of *O*-Dimethoxytrityl Ethanolamine Trifluoroacetamide. Ethanolamine trifluoroacetamide (4.5 g, 29 mmol) was dissolved in 100 mL pyridine in a round-bottom flask. With stirring, 4,4′-dimethoxytrityl chloride (9.7 g, 29 mmol) was added to the solution as a solid. After being stirred 2 h, the slurry was filtered, and the filtrate was concentrated by rotary evaporation. The residue was purified by silica column chromatography (25% ethyl acetate/75% hexane). The product was obtained as a yellow oil (12 g, 91%). $R_f = 0.56$ (25% ethyl acetate/75% hexane).

Synthesis of *O*-Dimethoxytrityl Ethanolamine. *O*-Dimethoxytrityl ethanolamine trifluoroacetamide (12 g, 26 mmol) was dissolved in 400 mL methanol. Subsequently, 400 mL of concentrated ammonium hydroxide was added to the flask with continuous stirring. The reaction mixture was stirred for 16 h at room temperature. The mixture was concentrated by rotary evaporation, and the crude product was purified by silica column chromatography (2% methanol/5% TEA/methylene chloride), yielding a yellow oil, 9.2 g, 97%. $R_f = 0.41$ (5% methanol/5% TEA/methylene chloride). ^{1}H NMR, CD_3CN, 400 MHz, δ 7.45 (m, 2H), 7.31 (m, 6H), 7.22 (t, 1H), 6.86 (m, 4H), 3.76 (s, 6H), 3.02 (t, 2H), 2.78 (t, 2H), 2.07 (s, 2H) ppm. ESI-MS: calculated for $C_{23}H_{24}NO_3$ $(M + K)^+$ 402, found 402.

Synthesis of 2, R′ = CH_2CH_2. A 250 mL round-bottom flask was charged with *O*-dimethoxytrityl ethanolamine (4.0 g, 11 mmol), *N*,*N*-diisopropylethylamine (2.1 g, 16 mmol), and 50 mL of acetonitrile. 3-(*tert*-Butyldimethylsilyloxy)glutaric anhydride **1** (3.0 g, 12 mmol) was added as a solid with stirring. After 2h, the reaction was concentrated and the crude material was purified by silica column chromatography (2% methanol/5% TEA/methylene chloride), yielding a white solid, 6.4 g, 96%. $R_f = 0.35$ (2% methanol/5% TEA/methylene chloride). ^{1}H NMR, CD_3CN, 400 MHz, δ 7.43 (m, 2H), 7.30 (m, 6H), 7.22 (m, 1H), 6.85 (m, 5H), 4.96 (s, 1H), 4.42 (m, 1H), 3.76 (s, 6H), 3.35 (m, 2H), 3.04 (m, 2H), 2.40 (m, 4H), 0.82 (s, 9H), 0.05 (s, 3H), 0.01 (s, 3H) ppm. ESI-MS: calculated for $C_{34}H_{45}NO_7Si$ $(M + K)^+$ 646, found 646.

Synthesis of 3, R′ = CH_2CH_2. Combined material **2** (4.8 g, 7.9 mmol) and 100 mL 1,4-dioxane. *N*-hydroxysuccinimide (1.16 g, 10.1 mmol) and DCC (2.66 g, 12.9 mmol) were added as solids and the reaction was stirred for 1h. The slurry was filtered and the filtrate was evaporated to a residue that was purified by silica column chromatography (ethyl acetate). Compound **3,** R′ = CH_2CH_2, was obtained as an off-white solid (5.2, 93%). $R_f = 0.62$ (ethyl acetate). ^{1}H NMR, CD_3CN, 400 MHz, δ 7.43 (m, 2H), 7.31 (m, 6H), 7.23 (m, 1H), 6.86 (m, 4H), 6.61 (t, 1H), 4.52 (m, 1H), 3.76 (s, 6H), 3.35 (m, 2H), 3.05 (m, 2H), 2.85 (m, 2H), 2.75 (s, 4H), 2.43 (d, 2H), 0.83 (s, 9H), 0.06 (s, 3H), 0.02 (s, 3H) ppm. ESI-MS: calculated for $C_{38}H_{48}N_2O_9Si$ $(M + K)^+$ 743, found 743.

One-Pot Synthesis of 3, R′ = CH_2CH_2. Added *O*-dimethoxytrityl ethanolamine (2.7 g, 7.4 mmol) to a solution of 3-(*tert*-butyldimethylsilyloxy)glutaric anhydride **1** (2.0 g, 8.2 mmol) in THF (100 mL) with stirring. The *O*-dimethoxytrityl ethanolamine starting material was consumed after 1 h (TLC 5% methanol/5% TEA/methylene chloride), and *N*-hydroxysuccinimide (0.94 g, 8.2 mmol) and DCC (2.3 g, 11 mmol) were added to the reaction mixture. After 4 h, the reaction slurry was filtered, and the filtrate was concentrated. The crude residue was purified by silica column chromatography (50% ethyl acetate/50% hexane), and the product was isolated as an off-white solid (3.8 g, 73%). $R_f = 0.62$ (ethyl acetate). ESI-MS: calculated for $C_{38}H_{48}N_2O_9Si$ $(M + K)^+$ 743, found 743.

Synthesis of 4a. Combined compound **3**, R′ = CH_2-CH_2 (0.55 g, 0.78 mmol), with 1.5 mL of THF and dried overnight over activated sieves. 2-(Aminoethyl)-18-crown-6 (0.25 g, 0.85 mmol) was dissolved in 20 mL of THF and combined with the THF solution of **3**. The reaction mixture was stirred for 1 h, concentrated by rotary evaporation, and purified by silica column chromatography (5% methanol/5% TEA/methylene chloride), yielding a pale yellow solid 0.68 g, 99%. $R_f = 0.32$ (5% methanol/5% TEA/methylene chloride). ESI-MS: calculated for $C_{47}H_{70}N_2O_{12}Si$ $(M + K)^+$ 922, found 922.

Synthesis of 11. *N*-Hydroxysuccinimide (0.27 g, 2.3 mmol) and DCC (0.48 g, 2.3 mmol) were added to a solution of 1-pyrenebutyric acid (0.58 g, 2.0 mmol) in 1,4-dioxane (20 mL). The solution was stirred for 20 h at room temperature. Ethyl acetate (30 mL) was added, and the slurry was filtered. The filtrate was concentrated, and the resulting brown oil was used in the next step without further purification, 0.77 g. $R_f = 0.38$ (50% ethyl acetate/50% hexane). A solution of the prepared NHS ester of 1-pyrenebutyric acid (0.77 g, 2.0 mmol) in 1,4-dioxane (20 mL) was added to a solution of 4,7,10-trioxa-1,13-tridecanediamine (2.6 g, 12 mmol) in 1,4-dioxane (20 mL). The resulting solution was stirred for 1 h, concentrated by rotary evaporation, and purified by silica column chromatography (10% methanol/5% TEA/methylene chloride). Compound **11** was obtained as an oil (0.89 g, 90%). $R_f = 0.33$ (10% methanol/5% TEA/methylene chloride). ESI-MS: calculated for $C_{30}H_{38}N_2O_4$ $(M + H)^+$ 491, found 491.

Synthesis of 4b. A solution of **11** (0.89 g, 1.8 mmol) in acetonitrile (5 mL), THF (5 mL), and diisopropylethylamine (0.26 g, 2.0 mmol) was combined with a solution of **3**, R′ = CH_2CH_2 (1.2 g, 1.7 mmol), in THF (30 mL). The reaction mixture was concentrated after 1 h by rotary evaporation. The crude residue was purified by silica chromatography (5% methanol/5% TEA/methylene chloride), resulting in a pale yellow solid with a yield of 1.2 g, 68%. $R_f = 0.52$ (5% methanol/5% TEA/methylene chloride). ESI-MS: calculated for $C_{64}H_{81}N_3O_{10}Si$ $(M + Na)^+$ 1103, found 1103.

Synthesis of 4c. A solution of **3**, R′ = CH_2CH_2 (3.1 g, 4.4 mmol), in 1,4-dioxane (5 mL) and acetonitrile (30 mL) was added to a solution of 4,7,10-trioxa-1,13-tridecanediamine (3.8 g, 17 mmol) in acetonitrile (20 mL). The resulting slurry was stirred for 30 min, concentrated by rotary evaporation, and purified by silica column chromatography (10% methanol/5%TEA/methylene chloride) with a yield of 1.4 g, 40%. The product was confirmed by a positive ninhydrin test. $R_f = 0.34$ (10% methanol/5% TEA/methylene chloride). ESI-MS: calculated for $C_{44}H_{67}N_3O_9Si$ $(M + H)^+$ 811, found 811.

Synthesis of 12c. Biotin (0.86 g, 3.5 mmol), DMF (5 mL) diisopropylethylamine (1.4 g, 11 mmol), and HOBT (0.96 g, 7.2 mmol) were added to a round-bottom flask with stirring. A solution of **4c** (1.4 g, 1.8 mmol) in methylene chloride (5 mL) was added to the flask, and HBTU (1.2 g, 3.7 mmol) was added to the resulting mixture. After 2 h, the reaction mixture was concentrated and purified by silica column chromatography (10% methanol/5% TEA/methylene chloride). The product was obtained as an oil (1.5 g, 80%). $R_f = 0.44$ (10% methanol/5% TEA/methylene chloride). ESI-MS: calculated for $C_{54}H_{81}N_5O_{11}SSi$ $(M + Na)^+$ 1059, found 1059.

Synthesis of 4d. Compound **3**, $R' = CH_2CH_2$ (0.62 g, 0.88 mmol), was dissolved in 1,4-dioxane (10 mL) and added to a solution of polytetrahydrofuran-bis(3-aminopropyl) terminated, average M_n ca.. 1100 (3.9 g, 3.5 mmol) in 1,4-dioxane (20 mL). After stirring for 2 h, the solvent was evaporated and the residue was purified by silica column chromatography (7.5% methanol/5% TEA/methylene chloride), yielding an oil, 0.85 g, 57%. $R_f = 0.44$ (7.5% methanol/5% TEA/methylene chloride). MALDI-TOF MS: The mass dispersion of the starting bis-amine was centered at 580. The mass dispersion of the products (separated by 72 amu) was centered at 1190.

Synthesis of 12d. To a solution of **4d** (0.85 g, 0.71 mmol) in acetonitrile (10 mL) and THF (5 mL) were added diisopropylethylamine (0.26 g, 2.0 mmol) and *S*-ethyl trifluorothioacetate (0.32 g, 0.20 mmol) with stirring. The absence of ninhydrin activity after 3.5 h confirmed the complete protection of the amine group. The reaction mixture was concentrated and purified by silica column chromatography (7.5% methanol/5% TEA/methylene chloride). Desired product was isolated as an oil, 0.78 g, 85%. $R_f = 0.46$ (7.5% methanol/5% TEA/methylene chloride). ESI-MS: The mass dispersion of the products (separated by 72 amu) was centered at 1290.

Synthesis of 5a. Dissolved **4a** (0.68 g, 0.77 mmol) in 10 mL of TBAF (1.0 M in THF) and incubated for 20 min at room temperature. The solvent was evaporated, and the residue was purified by silica column chromatography (5% methanol/5% TEA/methylene chloride), yielding a pale yellow oil, 0.38 g, 64%. $R_f = 0.29$ (5% methanol/5% TEA/methylene chloride). ESI-MS: calculated for $C_{41}H_{56}N_2O_{12}$ $(M + K)^+$ 808, found 808.

Synthesis of 5b. Compound **4b** (1.2 g, 1.1 mmol) was dissolved in THF (5 mL), and TBAF (5 mL of 1.0 M in THF) was added to the resulting solution. The reaction mixture was incubated for 30 min and concentrated, and the residue was purified by silica column chromatography (2% methanol/5% TEA/methylene chloride). Material **5b** was obtained as an off-white solid (0.66 g, 60%). $R_f = 0.58$ (5% methanol/5% TEA/methylene chloride). ESI-MS: calculated for $C_{58}H_{67}N_3O_{10}$ $(M + H)^+$ 967, found 967.

Synthesis of 5c. Compound **12c** (1.5 g, 1.4 mmol) was dissolved in THF (5 mL), and TBAF (5 mL of 1.0 M in THF) was added to the resulting mixture. The reaction mixture was incubated for 1 h and concentrated, and the residue was purified by silica column chromatography (10% methanol/5% TEA/methylene chloride), yielding an oil, 1.3 g, 94%. $R_f = 0.32$ (10% methanol/5% TEA/methylene chloride). ESI-MS: calculated for $C_{48}H_{67}N_5O_{11}S$ $(M + K)^+$ 961, found 961.

Synthesis of 5d. Dissolved **12d** (0.50 g, 0.43 mmol) in 10 mL of TBAF (1.0 M in THF) and incubated for 15 min at room temperature. The solvent was evaporated, and the residue was purified by silica column chromatography (5% methanol/5% TEA/methylene chloride). Material **5d** was obtained as a pale brown solid (0.44 g, 98%). $R_f = 0.49$ (5% TEA/1,4-dioxane). MALDI-TOF MS: The mass dispersion of the products (separated by 72 amu) was centered at 1170.

Synthesis of 18. *N*-Hydroxysuccinimide (0.50 g, 4.3 mmol) and DCC (1.5 g, 7.3 mmol) were added to a vigorously stirred suspension of *p*-(*p*-dimethylaminophenylazo)benzoic acid, sodium salt (1.0 g, 3.4 mmol) in anhydrous 1,4-dioxane (30 mL). The resulting reaction mixture was stirred overnight at room temperature and subsequently diluted with 100 mL of dry ethyl acetate. The slurry was filtered, and the filtrate was concentrated yielding the dabcyl-NHS ester (1.1 g, 87%) as a dark red powder. TLC analysis confirmed the purity of the material. $R_f = 0.54$ (ethyl acetate). The isolated NHS active ester was dissolved in THF (50 mL) and immediately added to a vigorously stirred solution of 4,7,10-trioxa-1,13-tridecanediamine (10 g, 0.045mol) in THF (250 mL). The resulting reaction mixture was stirred at room temperature for 2 h and concentrated by rotary evaporation. Compound **18** was isolated by silica column chromatography (20% methanol/5% TEA/methylene chloride) as an orange solid (0.33 g, 26%). $R_f = 0.30$ (20% methanol/5% TEA/methylene chloride). ESI-MS: calculated for $C_{25}H_{37}N_5O_4$ $(M + H)^+$ 472, found 472.

One-Pot Synthesis of 21. 3-(*tert*-Butyldimethylsilyloxy)glutaric anhydride (0.20 g, 8.2 mmol) was added to a rapidly stirred solution of compound **18** (0.33 g, 7.1 mmol) and *N*,*N*-diisopropylethylamine (0.10 g, 7.8 mmol) in 10 mL of 1,4-dioxane. After 15 min, TLC analysis indicated the disappearance of the starting material and the formation of a new product, $R_f = 0.48$ (10% methanol/5% TEA/methylene chloride). In the subsequent step, *N*-hydroxysuccinimide (0.12 g, 1.0 mmol) and DCC (0.42 g, 2.0 mmol) were added to the reaction mixture. The DCC was added in two aliquots, 0.22 g initially and 0.20 g after 1 h. The resulting reaction mixture was stirred at room temperature for an additional 15 h. TLC analysis of the reaction mixture indicated the formation of a new, less polar material, $R_f = 0.58$ (1,4-dioxane). In the final step, 2-(2-aminoethoxyethyl)ethanol (0.73 g, 7.0 mmol) was dissolved in 4 mL of dry THF and added to the rapidly stirred reaction mixture described above. Stirring was continued for 1 h at room temperature. TLC analysis indicated the formation of a new product, $R_f = 0.38$ (1,4-dioxane). The reaction product was isolated by silica column chromatography (1,4-dioxane), yielding compound **21** as an orange solid (0.48 g, 85%). ESI-MS: calculated for $C_{40}H_{66}N_6O_9Si$ $(M + H)^+$ 804, found 804.

Synthesis of 22. Compound **21** (0.44 g, 0.55 mmol) was dissolved in 100 mL of pyridine in a round-bottom flask. With stirring, 4,4′-dimethoxytrityl chloride (0.30 g, 0.90 mmol) was added to the solution as a solid. After stirring 2 h, the solution was concentrated by rotary evaporation. The residue was purified by silica column chromatography (ethyl acetate followed by 2% methanol/5%TEA/methylene chloride). The product was obtained as an orange solid (0.40 g, 66%). $R_f = 0.20$ (5% methanol/5% TEA/methylene chloride). ESI-MS: calculated for $C_{61}H_{84}N_6O_{11}Si$ $(M + K)^+$ 1144, found 1144.

Synthesis of 5e. Compound **22** (0.40 g, 0.36 mmol) was dissolved in THF (5 mL), and tetrabutylammonium fluoride (7 mL of 1.0 M in THF) was added to the resulting solution. The reaction mixture was incubated for 30 min and concentrated, and the residue was purified by silica column chromatography (2% methanol/5% TEA/methylene chloride followed by 5% methanol/5% TEA/methylene chloride and finally 10% methanol/5% TEA/methylene chloride to elute the product), yielding an orange solid, 0.33 g, 92%. $R_f = 0.67$ (5% TEA/1,4-dioxane).

ESI-MS: calculated for $C_{55}H_{70}N_6O_{11}$ $(M + K)^+$ 1030, found 1030.

Synthesis of 8a. 5a (0.38 g, 0.50 mmol) was dissolved in methylene chloride (8 mL), and to the resulting solution were added 2-cyanoethyl-*N*,*N*,*N*′,*N*′-tetraisopropyl phosphorodiamidite (0.18 g, 0.59 mmol) and tetrazole (0.83 mL of 0.45 M in acetonitrile) with vigorous swirling. The reaction mixture was vortexed at room temperature, and after 1 h, additional 2-cyanoethyl-*N*,*N*,*N*′,*N*′-tetraisopropyl phosphorodiamidite (0.18 g, 0.59 mmol) was added. After 1.5 h, methylene chloride (30 mL) was added to the reaction to increase the volume, and the crude solution was washed with 5% sodium bicarbonate/0.5% TEA (50 mL). The organic layer was dried over magnesium sulfate for 10 min, filtered, concentrated, and coevaporated twice with acetonitrile (10 mL). The residue was dissolved in acetonitrile (6 mL) and dried over several granules of calcium hydride. The product solution was aliquoted (3 aliquots of 2 mL, 155 μmol) into amber Expedite bottles, concentrated by aspiration vacuum, and then dried overnight under vacuum in a desiccator over phosphorus pentoxide (0.45 g, 94%). $R_f = 0.63$ (5% TEA/1,4-dioxane).

Synthesis of 8b. Compound **5b** (0.66 g, 0.68 mmol) was dissolved in methylene chloride (5 mL). 2-Cyanoethyl *N*,*N*,*N*′,*N*′-tetraisopropylphosphorodiamidite (0.25 g, 0.82 mmol) was added, followed by the addition of tetrazole (1.2 mL of 0.45 M in acetonitrile) with vigorous swirling. The reaction was vortexed at room temperature for 3 h. Methylene chloride (50 mL) was added to the reaction to increase the volume, and the crude solution was washed with 5% sodium bicarbonate/0.5% TEA (75 mL). The organic layer was dried over magnesium sulfate, filtered, concentrated, and coevaporated twice with acetonitrile (10 mL). The residue was dissolved in acetonitrile (6 mL) and dried over several granules of calcium hydride. The product solution was aliquoted (3 aliquots of 2 mL, 200 μmol) into amber Expedite bottles, concentrated by aspiration vacuum, and then dried overnight under vacuum in a desiccator over phosphorus pentoxide (0.76 g, 96%). $R_f = 0.52$ (5% TEA/1,4-dioxane).

Synthesis of 8e. 5e (0.33 g, 0.33 mmol) was dissoved in methylene chloride (10 mL), and to the resulting solution were added 2-cyanoethyl *N*,*N*,*N*′,*N*′-tetraisopropylphosphorodiamidite (0.15 g, 0.50 mmol) and tetrazole (0.58 mL of 0.45 M in acetonitrile) with vigorous swirling. The reaction mixture was vortexed at room temperature, and after 1 h, additional 2-cyanoethyl *N*,*N*,*N*′,*N*′-tetraisopropylphosphorodiamidite (0.15 g, 0.50 mmol) was added. After 2 h, methylene chloride (50 mL) was added to the reaction to increase the volume, and the crude solution was washed with 5% sodium bicarbonate/0.5% TEA (75 mL). The organic layer was dried over magnesium sulfate for 10 min, filtered, concentrated, and coevaporated twice with acetonitrile (10 mL). The residue was dissolved in acetonitrile (3 mL) and dried over several granules of calcium hydride. The product solution was transferred to an amber Expedite bottles and concentrated by aspiration vacuum then dried for 1 h under vacuum in a desiccator over phosphorus pentoxide (0.37 g, 92%). $R_f = 0.83$ (5% TEA/1,4-dioxane).

Synthesis of 9c. Combined **5c** (0.24 g, 0.26 mmol), TEA (0.03 g, 0.3 mmol), and DMAP (16 mg, 0.13 mmol) in acetonitrile (20 mL). Succinic anhydride (0.04 g, 0.4 mmol) was added, and the resulting mixture was stirred for 17 h under a drying tube. The solvent was evaporated, and the crude residue was purified by silica column chromatography (10% methanol/5% TEA/methylene chloride). Compound **9c** was obtained as a white solid (0.28 g, 95%). $R_f = 0.1$ (10% methanol/5% TEA/methylene chloride). ESI-MS: calculated for $C_{52}H_{71}N_5O_{14}S$ $(M + H)^+$ 1123, found 1123.

Synthesis of 9d. Combined **5d** (0.44 g, 0.42 mmol), TEA (0.05 g, 0.5 mmol), and DMAP (26 mg, 0.21 mmol) in acetonitrile (30 mL). Succinic anhydride (0.06 g, 0.6 mmol) was added, and the resulting mixture was stirred for 3.5 h under a drying tube. The solvent was evaporated and the crude residue was purified by silica column chromatography (2% methanol/5% TEA/methylene chloride). Compound **9d** was obtained as an off-white solid (0.5 g, 96%). $R_f = 0.32$ (5% methanol/5% TEA/methylene chloride). MALDI-TOF MS: The mass dispersion of the product was centered at 1270.

Synthesis of 10c and 10d. One gram of lcaa-CPG (Glen Research, #20−0001, 1000A, 69 μmol/g) was added to a 50 mL round-bottom flask. Compound **9c** (0.14 g, 0.13 mmol) or compound **9d** (0.2 g, 0.16 mmol), respectively, was dissolved in 10 mL of pyridine and added to the CPG. DMAP (4 mg, 0.03 mmol), TEA (0.02 g, 0.02 mmol), and EDAC (0.12 g, 0.64 mmol) were added, and the reaction mixtures were vortexed at room temperature for 16 h. For the preparation of **10c**, additional aliquots of EDAC (total of 0.1 g, 0.5 mmol) and **9c** (total of 0.14 g, 0.13 mmol) were added to the reaction slurry to achieve a final loading of at least 10 μmol/g CPG. For the preparation of **10d**, additional aliquots of EDAC (total of 0.40 g, 2.1 mmol) and **9d** (total of 0.33 g, 0.26 mmol) were required. The support was filtered, washed with pyridine, methanol, and methylene chloride, and dried with argon flow. The material was capped with an equal mixture of 6% DMAP in acetonitrile and 2/3/5 (acetic anhydride/2,4,6-collidine/acetonitrile) (100 mL total volume) for 2 h and dried overnight under vacuum. The loading was calculated by combining a known mass of CPG and 3% dichloroacetic acid/methylene chloride and measuring A_{504} of the solution to determine the released trityl. The loading of the final products was calculated to be 18 μmol/g CPG and 10 μmol/g CPG for **10c** and **10d**, respectively.

Synthesis of 13a, 13b, 14c, 14d, 15, 16, 17, and 23. Oligonucleotide synthesis was carried out using standard phosphoramidite chemistry. Solutions of phosphoramidites **8a**, **8b**, and **8e** were prepared at 100 mM in acetonitrile and dried over calcium hydride granules prior to use. The coupling efficiency of the phosphoramidite **8e** was strongly dependent on the drying time over calcium hydride. In the case of **8e**, we applied extended coupling times (3 × 10 min).

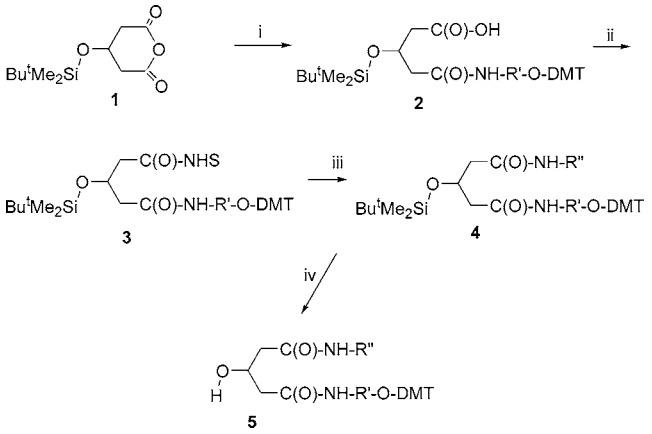
Modified CPGs **10c** and **10d** were used in Expedite columns at 1.0 μmol. Following synthesis, the support was incubated for 17 h at 55 °C in concentrated ammonium hydroxide. Volatile components were evaporated under vacuum, and the crude material was purified by C18 RP-HPLC. The purified product was confirmed by MS analysis.

RESULTS AND DISCUSSION

Our synthetic strategy is outlined in Scheme 2. This method uses commercially available and relatively inexpensive 3-(*tert*-butyldimethylsiloxy)glutaric anhydride **1** as the starting material that reacts easily with the primary amine H_2N-R′-OH containing a DMT-protected hydroxyl group, leading to the formation of **2**. Compound **2** can be converted into its NHS active ester **3** representing a key intermediate material used in the subsequent transformations

The group R′ in the structure of active ester **3** can be selected from a wide variety of hydroxy amines, depend-

Scheme 2. Synthesis of Compounds 2−5[a]



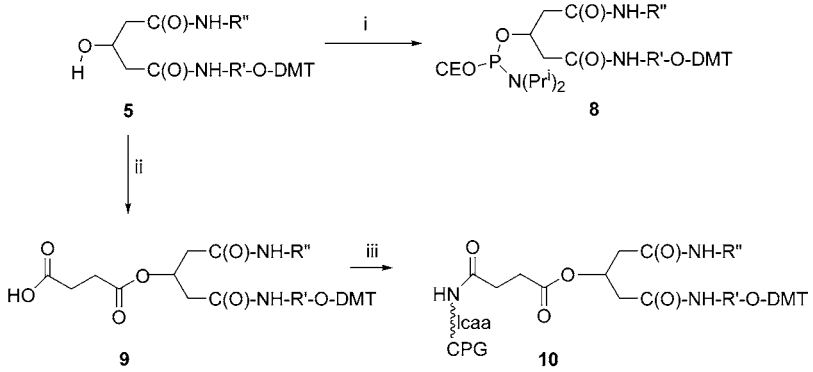
[a] Reagents and conditions: (i) H_2N-R′-O-DMT/base; (ii) NHS/DCC; (iii) H_2N-R″/base; (iv) TBAF/THF.

ing on the specific purpose of the intended modification (i.e. linker length, physicochemical or spectral properties). In the subsequent step, compound **3** can be easily converted into compound **4** by reacting with the amine H_2N-R″. Removal of the TBDMS group from material **4** leads to the formation of the compound **5** possessing a deprotected secondary hydroxyl group. In the next step of the described procedure, synthesized compound **5** is transformed into phosphoramidite **8** or modified solid support **10** as illustrated in Scheme 3. Both Schemes 2 and 3 represent general overviews which outline both the structures of the materials available from the 3-(*tert*-butyldimethylsiloxy)glutaric anhydride **1** and the reaction sequences leading to the preparation of new phosphoramidites **8** and solid supports **10**. Detailed structures of the prepared materials are presented in subsequent sections of this paper.

For our experiments, we selected R′ = CH_2CH_2 due to the relative ease of preparing *O*-DMT-protected ethanolamine. The reaction between the anhydride **1** and the *O*-DMT-protected ethanolamine was efficient and straightforward and led to the formation of an intermediate material **2**, R′= CH_2CH_2, which was isolated easily by silica gel column chromatography. However, the preparation of compound **2**, R′= CH_2CH_2, was associated with the formation of a trace amount of material that had a higher polarity than the desired reaction product. The mass spectral analysis and TLC mobility (R_f) of the isolated impurity were identical to those of the material formed when compound **2**, R′= CH_2CH_2, was treated with TBAF solution (*75*). No detailed study addressing the conditions promoting the formation of a trace amount of the desilylated material was conducted. To overcome this minor inconvenience and to simplify the synthetic protocol, we demonstrated that the active ester **3**, R′= CH_2-CH_2, could be synthesized in a one-pot procedure without isolating the corresponding intermediate material **2**.

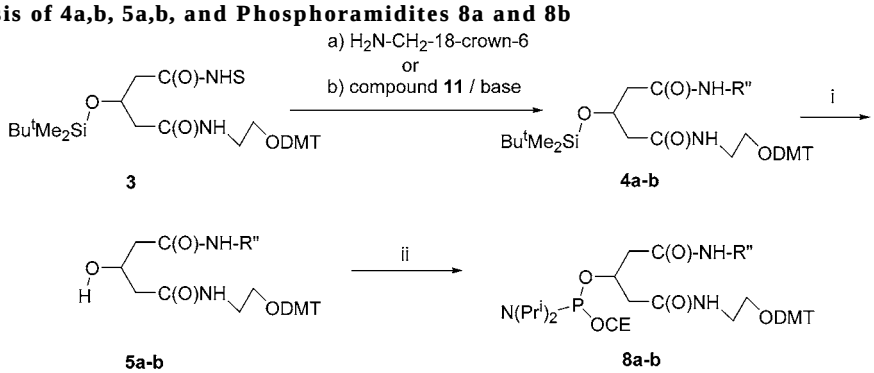
The relatively low polarity of material **3**, R′= CH_2CH_2, enabled fast and efficient purification by silica gel flash chromatography using ethyl acetate or ethyl acetate/hexane as a mobile phase. We have found that compound **3**, R′= CH_2CH_2, was stable when stored in its crystalline form at 4 °C for six months. In addition, its preparation was easily scaled up. Synthesized NHS ester **3**, R′= CH_2-CH_2, represents the key intermediate material. Schemes 4 and 5 illustrate the synthesis of four different com-

Scheme 3. General Scheme for the Preparation of the Phosphoramidite 8 and Modified Solid Support 10 from Compound 5

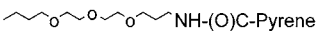


[a] Reagents and conditions: (i) CEO-P(NPr$^i_2$)$_2$/tetrazole; (ii) succinic anhydride/DMAP/base; (iii) lcaa-CPG/NHS/DCC/DMAP.

Scheme 4. Synthesis of 4a,b, 5a,b, and Phosphoramidites 8a and 8b

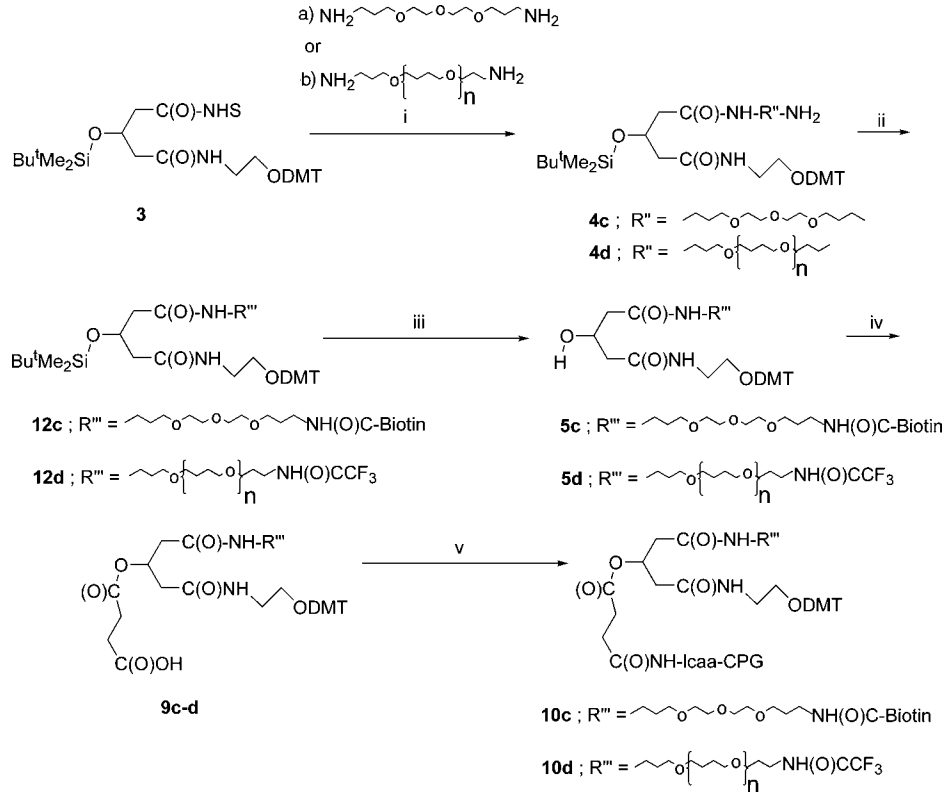


a ; R " = CH_2-18-crown-6

b ; R" = 

[a] Reagents and conditions: (i) TBAF/THF; (ii) CEO-P(NPr$^i_2$)$_2$/tetrazole.

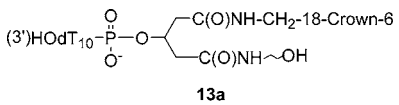
Scheme 5. Synthesis of 5c and 5d and Modified Solid Supports 10c and 10d



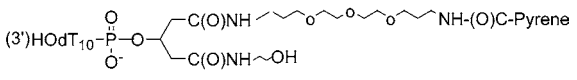
[a] Reagents and conditions: (i) (a) 4,7,10-Trioxa-1,13-tridecanediamine/base or (b) polytetrahydrofuran bis(3-aminopropyl) terminated/base; (ii) (a) biotin/HBTU/HOBT/base or (b) *S*-ethyl trifluoroacetate/base; (iii) TBAF/THF; (iv) succinic anhydride/DMAP/base; (v) lcaa-CPG/NHS/DCC/DMAP.

pounds **5a**−**d** from the same starting material **3**, (R′ = CH_2CH_2).

Compounds **4a** and **4b** (Scheme 4) were synthesized correspondingly by the direct reaction of NHS ester **3**, R′= CH_2CH_2, with commercially available 2-(aminomethyl)-18-crown-6 (*76*, *77*) or with the amino derivative of the pyrene butyric acid **11** (*78*−*82*)**.** Removal of the TBDMS from synthesized compounds **4a** and **4b** with the THF solution of TBAF under standard reaction conditions (*75*) yielded compounds **5a** and **5b** with deprotected secondary hydroxyl groups. In the subsequent step, synthesized compounds **5a** and **5b** were converted into phosphoramidites **8a** and **8b**, as illustrated in Scheme 4. When used in the synthesis of 5′-modified probes **13a** and **13b**, these phosphoramidites demonstrated full



13a



13b

compatibility with the standard phosphoramidite protocol for automated oligonucleotide synthesis.

The synthesis of compounds **5c** and **5d** (Scheme 5) required additional steps. In the first step, the active NHS ester **3**, R′= CH_2CH_2, was reacted with an excess of the appropriate bis-amine (4,7,10-trioxa-1,13-tridecanediamine or polytetrahydrofuran-bis(3-aminopropyl) terminated. The resulting intermediate compounds **4c** and **4d**, containing free primary amino groups, were isolated by silica gel chromatography.

In the next step the primary amino groups present in the isolated intermediate compounds **4c** and **4d** were reacted with either biotin NHS active ester producing compound **12c** or *S*-ethyl trifluorothioacetate (*75*) producing compound **12d**. As with the synthesis of compounds **5a** and **5b**, treatment of the amino-protected intermediate materials **12c** and **12d** with TBAF caused the removal of the TBDMS protecting group and resulted in compounds **5c** and **5d**. In all cases, standard reaction conditions for the described chemical transformations were applied. Detailed experimental procedures for the preparation of compounds **4a**−**d**, **12c**,**d**, and **5a**−**d** are in the Experimental Section.

In all described synthetic steps, the presence of the TBDMS and/or DMT protecting group significantly facilitated the chromatographic purification of their respective reaction products, particularly those with high molecular weight polymeric linkers, UV-inactive organic moieties, or moieties introducing increased polarity into the synthesized material. The advantage of using the active ester **3**, R′ = CH_2CH_2, as starting material was particularly pronounced in the synthesis of the amino derivatives **5c** and **5d**. The synthesis of those compounds required prior synthesis of derivatives **4c** and **4d**, in which the primary amino group is linked to the rest of the molecule through long polar linkers that usually contribute to difficulties in the purification process. In our experiments, however, it was found that both compounds were easily separated from the excess of the bis-amine used in the reaction through purification by silica gel chromatography.

Compounds **5c** and **5d** were used to prepare the respective solid supports, **10c** and **10d** (Scheme 5), which were used in the synthesis of 3′-modified DNA probes **14c** and **14d**.

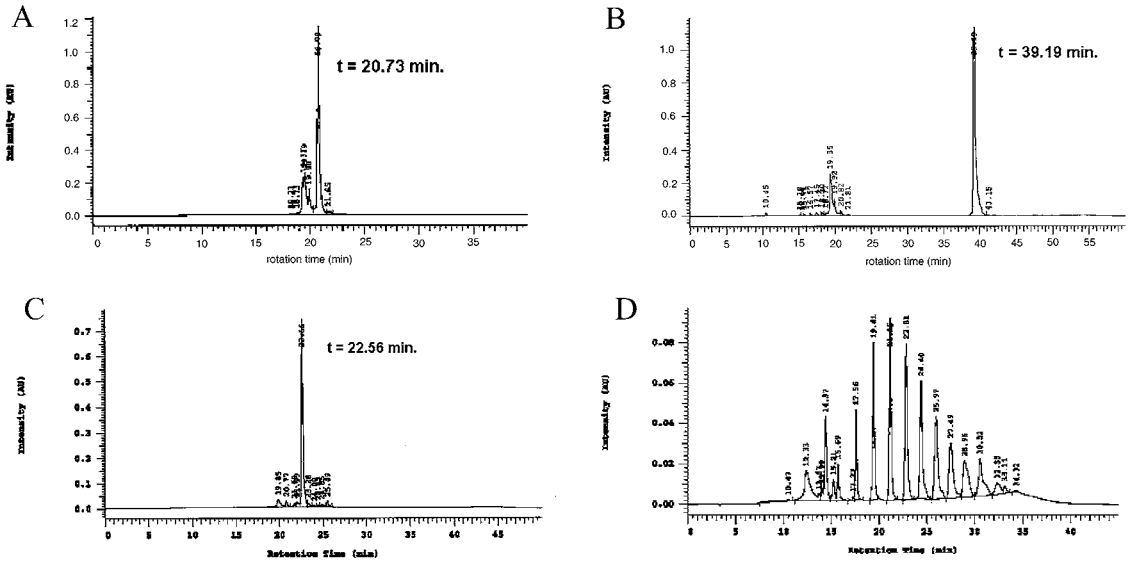


Figure 1. C18 RP HPLC analysis of the labeled probes (A) probe **13a**, 1%/min acetonitrile gradient; (B) probe **13b**, 1%/min acetonitrile gradient; (C) probe **14c**, 1%/min acetonitrile gradient; (D) probe **14d**, 2%/min acetonitrile gradient.

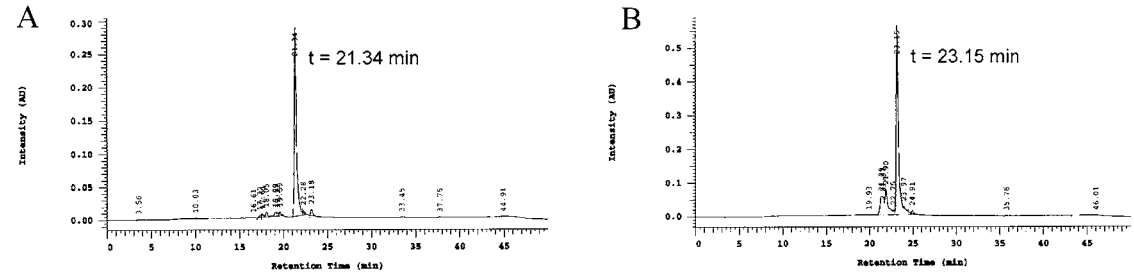


Figure 2. C18 RP HPLC analysis for the labeled probes (A) probe **15**, 1%/min acetonitrile gradient; (B) probe **16**, 1%/min acetonitrile gradient.

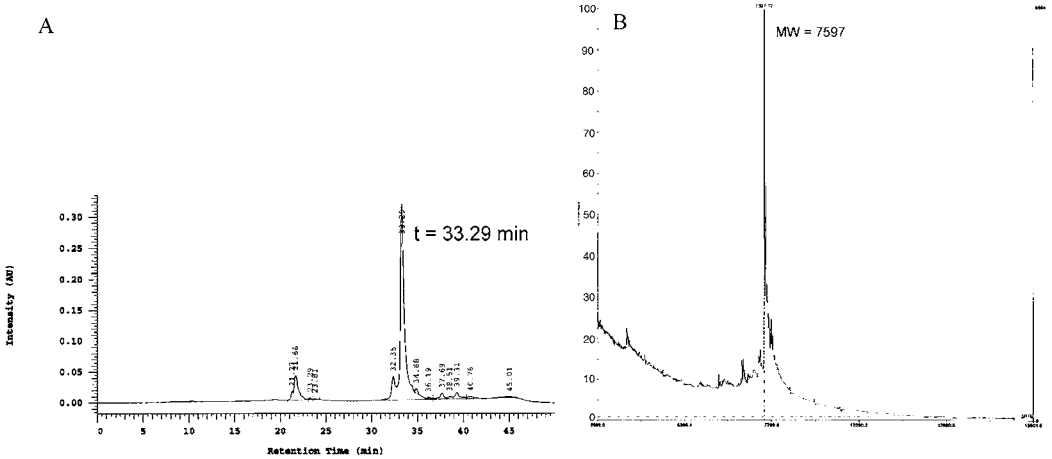
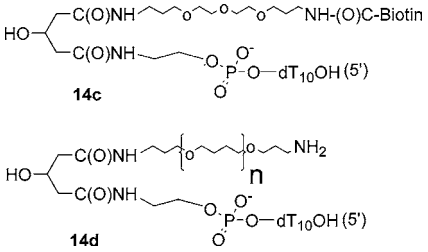


Figure 3. (A) C18 RP HPLC analysis of labeled probe **17**, 1%/min acetonitrile gradient; (B) MALDI TOF analysis of labeled probe **17**, calculated MW 7600.



Successful preparation of the 3′-amino-modified probe **14d** (R″ = poly-THF-NHC(O)CF_3, average M_n ca. 1100), in which the amino group is separated from the DNA moiety by a long polymeric linker, deserves special attention. Despite strong interest in methods that introduce polymeric linkers into DNA probes or conjugates, few procedures exist for the preparation of such materials (*83*−*92*), probably due to difficulties associated with the synthesis and purification of selectively protected derivatives of polymeric hydroxylamines or monoprotected polymeric bis-amines. The efficiency of the synthesis of modified oligonucleotide probes using phosphoramidites **8a**,**b** and modified supports **10c**,**d** is illustrated in Figure 1, where the reverse phase HPLC profiles of crude materials **13a**,**b** and **14c**,**d** are demonstrated. Synthe-

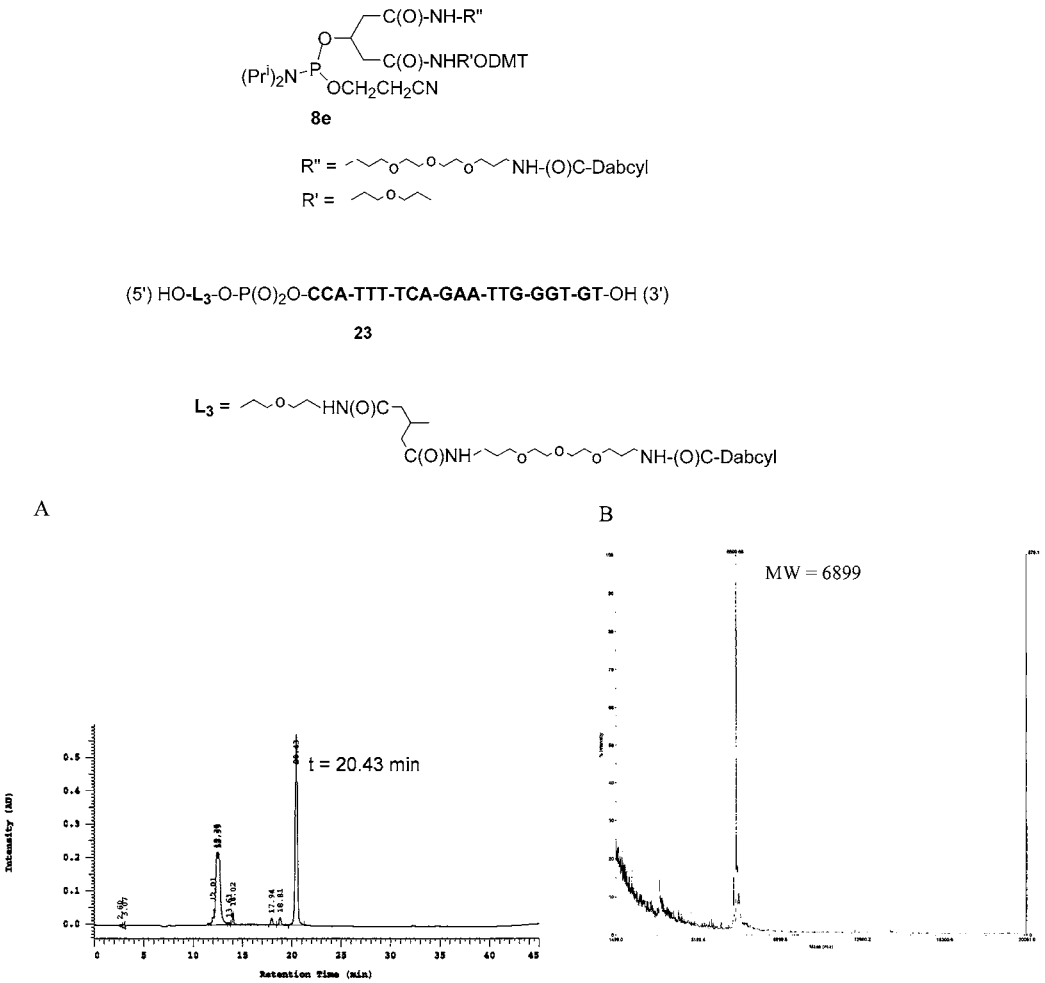
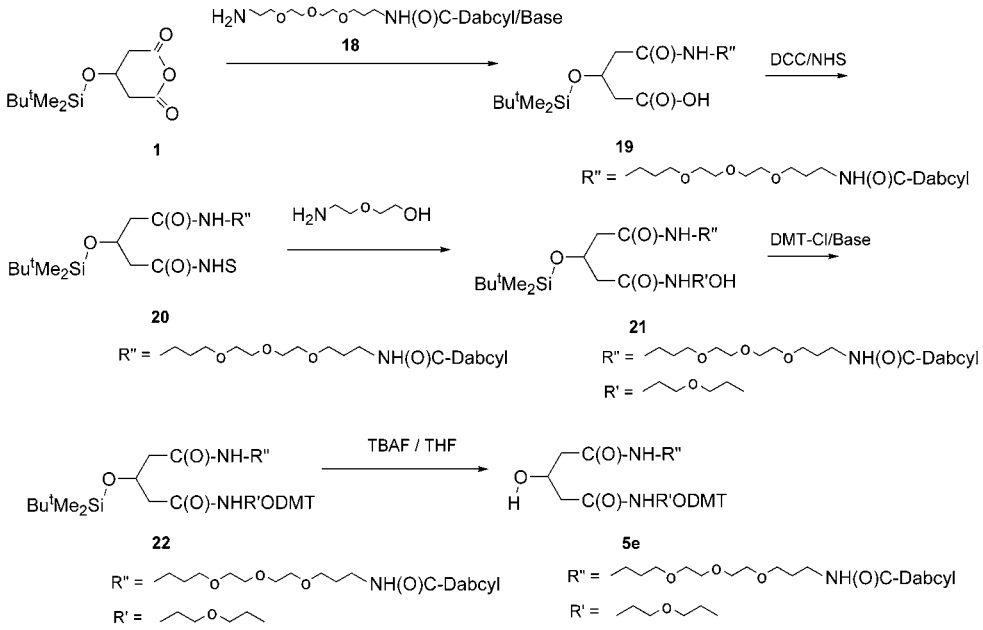


Figure 4. The structure of the phosphoramidite **8e** and the 5′-modifed DNA probe **23**. (A) C18 RP HPLC analysis of labeled probe **23**, 2%/min acetonitrile gradient. (B) MALDI TOF analysis of purified labeled probe **23**. calculated MW 6889.

Scheme 6. Alternate Route of the Synthesis of Compound 5e

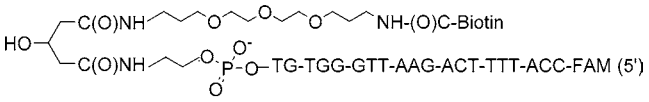


sized 5′-modified probes **13a**,**b** and 3′-modified probes **14c**,**d** were isolated by RP HPLC, and their structure was confirmed by MALDI TOF analysis.

In further attempt to test the compatibility of the synthesized reagents with the automated solid-phase synthesis of chemically modified DNA probes, we performed the synthesis of the 5′-FAM-modified, mixed base DNA probe **15** utilizing only commercial reagents and the 3′-biotin- and 5′-FAM-modified mixed base DNA probe **16** utilizing solid support **10c.**

(3') HO – TG-TGG-GTT-AAG-ACT-TTT-ACC-FAM (5')

15



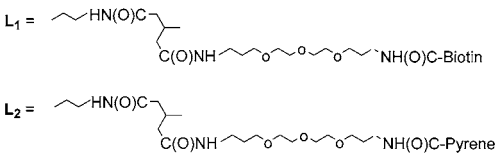
16

Comparison of the analytical RP HPLC profiles of the synthesized crude material **15** and the crude material **16** supports the conclusion that the synthetic performance of the biotin-modified solid support **10c** is similar to that of the commercially available dT-CPG solid support, Figure 2.

The applicability of the phosphoramidites **8** to the synthesis of internally modified DNA probes was additionally demonstrated by the successful synthesis of the 3′-modified and internally modified DNA probe **17**, which was performed using the solid support **10c** and the phosphoramidite **8b**.

(5') HO-**CCA-TTT-TCA-G**-O-P(O)$_2$O-**L$_2$**-O-P(O)$_2$O-**AAT-TGG-GTG-T**-O-P(O$_2$)O-**L$_1$**-OH (3')

17



The analytical RP HPLC profile of the crude material **17** along with the MALDI TOF analysis of the HPLC-purified reaction product are presented in Figure 3.

In the course of our experiments, we have also found that the synthetic strategy utilizing 3-(*tert*-butyldimethylsiloxy)glutaric anhydride **1** as a starting material can be successfully applied to the alternate approach of the synthesis of the compound **5** presented in Scheme 6. For example, the reaction of the anhydride **1** with the desired amino derivative **18** leads to the formation of compound **19**. The conversion of **19** into the NHS ester **20** and its subsequent reaction with an excess of unprotected 2-(2-aminoethoxyethyl)ethanol, leads to the formation compound **21** in a convenient one-pot reaction without isolation of the intermediate materials **19** and **20**.

After separation by column chromatography from other components present in the reaction mixture, compound **21** was easily converted into the DMT-protected derivative **22** and finally, after the removal of the TBDMS protecting group, into compound **5e**. In some cases this alternate synthetic approach may offer significant synthetic advantages, particularly when the preparation of a specific *O*-DMT-protected hydroxyloamine is synthetically difficult. Similarly, as it was observed in the synthesis of phosphoramidites **8a**,**b**, compound **5e** was easily converted into the phosphoramidite **8e** under standard reaction conditions. The reactivity of the phosphoramidite **8e** was documented by the synthesis of the 5′-modified DNA probe **23**. The structure of the phosphoramidite **8e** and compound **23** are illustrated in Figure 4. Figure 4 includes the analytical RP HPLC profile of the crude material **23** and the MALDI TOF analysis of purified **23**.

In conclusion, the presented modular approach for the synthesis of new phosphoramidites or new modified solid supports offers significant preparative advantages. The described procedure uses common starting material **3** and efficiently synthesizes new reagents that can introduce diverse modifications into DNA probes, including those which are difficult to prepare due to their physical or spectral properties (e.g. high molecular weight or lack of UV absorbency). We believe the presented approach will contribute to the cost-efficient preparation of a broader range of modified oligonuclotide probes and DNA conjugates, which can be applied in different areas of technology and biotechnology.

ACKNOWLEDGMENT

We wish to thank Andrea Mast for her assistance in preparing this manuscript and Annie Weber for her assistance in mass spectral analysis of the synthesized materials.

LITERATURE CITED

(1) Barrett, J. C., and Kawasaki, E. S. (2003) Microarrays: the use of oligonucleotides and cDNA for the analysis of gene expression. *Drug Discovery Today 8*, 134−141.

(2) Taira, S., Morita, Y., Tamiya, E., and Yokoyama, K. (2003) Self-assembled DNA-conjugated polymer for novel DNA chip. *Anal. Sci. 19*, 177−179.

(3) Patolsky, F., Weizmann, Y., Katz, E., and Willner, I. (2003) Magnetically amplified DNA assays (MADA): sensing of viral DNA and single base mismatches using nucleic acid-modified magnetic particles. *Angew Chem., Int. Ed. Engl. 42*, 2372−2376.

(4) Vercoutere, W., and Akeson, M. (2002) Biosensors for DNA sequence detection. *Curr. Opin. Chem. Biol. 6*, 816−822.

(5) Stenger, D. A., Andreadis, J. D., Vora, G. J., and Pancrazio, J. J. (2002) Potential applications of DNA microarrays in biodefense-related diagnostics. *Curr. Opin. Biotechnol. 13*, 208−212.

(6) Shoemaker, D. D., and Linsley, P. S. (2002) Recent developments in DNA microarrays. *Curr. Opin. Microbiol. 5*, 334−337.

(7) Willner, I., Willner, B., and Katz, E. (2002) Functional biosensor systems via surface-nanoengineering of electronic elements. *J. Biotechnol. 82*, 325−355.

(8) Leumann, C. J. (2002) DNA analogues: from supramolecular principles to biological properties. *Bioorg. Med. Chem. 10*, 841−854.

(9) Sohail, M., and Southern, E. M. (2002) Oligonucleotide scanning arrays: application to high-throughput screening for effective reagents and the study of nucleic acid interactions. *Adv. Biochem. Eng. Biotechnol. 77*, 43−56.

(10) Nam, J. M., Park, S. J., and Mirkin, C. A. (2002) Bio-barcodes based on oligonucleotide-modified nanoparticles. *J. Am. Chem. Soc. 124*, 3820−3821.

(11) Maxwell, D. J., Taylor, J. R., and Nie, S. (2002) Self-assembled nanoparticle probes for recognition and detection of biomolecules. *J. Am. Chem. Soc. 124*, 9606−9612.

(12) Beaucage, S. L. (2001) Strategies in the preparation of DNA oligonucleotide arrays for diagnostic applications. *Curr. Med. Chem. 8*, 1213−1244.

(13) Roth, C. M., and Yarmush, M. L. (1999) Nucleic acid biotechnology. *Annu. Rev. Biomed. Eng. 1*, 265−297.

(14) Ziegler, C., and Gopel, W. (1998) Biosensor development. *Curr. Opin. Chem. Biol. 2*, 585−591.

(15) Soukup, G. A., and Breaker, R. R. (1999) Nucleic acid molecular switches. *Trends Biotechnol. 17*, 469−476.

(16) Dias, N., and Stein, C. (2002) Potential roles of antisense oligonucleotides in cancer therapy. The example of Bcl-2 antisense oligonucleotides. *Eur. J. Pharm. Biopharm. 54*, 263−269.

(17) Manoharan, M. (2002) Oligonucleotide conjugates as potential antisense drugs with improved uptake, biodistribution, targeted delivery, and mechanism of action. *Antisense Nucleic Acid Drug Dev. 12*, 103−128.

(18) Lyngstadaas, A. (2002) Status and potential of gene therapy in clinical medicine. Assessment of an emerging health technology through systematic survey of clinical gene

therapy protocols and published results. *Int. J. Technol. Assess. Health Care 18*, 645−674.
(19) Opalinska, J. B., and Gewirtz, A. M. (2002) Nucleic-acid therapeutics: basic principles and recent applications. *Nat. Rev. Drug Discovery 1*, 503−514.
(20) Ramaswamy, S., and Golub, T. R. (2002) DNA microarrays in clinical oncology. *J. Clin. Oncol. 20*, 1932−1941.
(21) Kong, C. F., and Bowtell, D. (2002) Genomewide gene expression analysis using cDNA microarrays. *Methods Mol. Med. 68*, 195−204.
(22) Tomita, N., Morishita, R., Tomita, T., and Ogihara, T. (2002) Potential therapeutic applications of decoy oligonucleotides. *Curr. Opin. Mol. Ther. 4*, 166−170.
(23) Younes, C. K., Boisgard, R., and Tavitian, B. (2002) Labelled oligonucleotides as radiopharmaceuticals: pitfalls, problems and perspectives. *Curr. Pharm. Des. 8*, 1451−1466.
(24) Sendera, T. J., Dorris, D., Ramakrishnan, R., Nguyen, A., Trakas, D., and Mazumder, A. (2002) Expression profiling with oligonucleotide arrays: technologies and applications for neurobiology. *Neurochem. Res. 27*, 1005−1026.
(25) Braasch, D. A., and Corey, D. R. (2002) Novel antisense and peptide nucleic acid strategies for controlling gene expression. *Biochemistry 41*, 4503−4510.
(26) Anthony, R. M., Brown, T. J., and French, G. L. (2001) DNA array technology and diagnostic microbiology. *Expert Rev. Mol. Diagn. 1*, 30−38.
(27) Wang, H., Prasad, G., Buolamwini, J. K., and Zhang, R. (2001) Antisense anticancer oligonucleotide therapeutics. *Curr. Cancer Drug Targets 1*, 177−196.
(28) Lebedeva, I., and Stein, C. A. (2001) Antisense oligonucleotides: promise and reality. *Annu. Rev. Pharmacol. Toxicol. 41*, 403−419.
(29) Nees, M., and Woodworth, C. D. (2001) Microarrays: spotlight on gene function and pharmacogenomics. *Curr. Cancer Drug Targets 1*, 155−175.
(30) Micklefield, J. (2001) Backbone modification of nucleic acids: synthesis, structure and therapeutic applications. *Curr. Med. Chem. 8*, 1157−1179.
(31) Crooke, S. T. (2000) Potential roles of antisense technology in cancer chemotherapy. *Oncogene 19*, 6651−6659.
(32) Monteith, D. K., and Levin, A. A. (1999) Synthetic oligonucleotides: the development of antisense therapeutics. *Toxicol. Pathol. 27*, 8−13.
(33) Bennett, C. F., and Cowsert, L. M. (1999) Antisense oligonucleotides as a tool for gene functionalization and target validation. *Biochim. Biophys. Acta 1489*, 19−30.
(34) Agrawal, S., and Iyer, R. P. (1995) Modified oligonucleotides as therapeutic and diagnostic agents. *Curr. Opin. Biotechnol. 6*, 12−19.
(35) Zhao, X., Tapec-Dytioco, R., and Tan, W. (2003) Ultrasensitive DNA detection using highly fluorescent bioconjugated nanoparticles. *J. Am. Chem. Soc. 125*, 11474−11475.
(36) Benenson, Y., Adar, R., Paz-Elizur, T., Livneh, Z., and Shapiro, E. (2003) DNA molecule provides a computing machine with both data and fuel. *Proc. Natl. Acad. Sci. U.S.A. 100*, 2191−2196.
(37) Heller, M. J. (2002) DNA microarray technology: devices, systems, and applications. *Annu. Rev. Biomed. Eng. 4*, 129−153.
(38) Demers, L. M., Ginger, D. S., Park, S. J., Li, Z., Chung, S. W., and Mirkin, C. A. (2002) Direct patterning of modified oligonucleotides on metals and insulators by dip-pen nanolithography. *Science 296*, 1836−1838.
(39) Gerion, D., Parak, W. J., Williams, S. C., Zanchet, D., Micheel, C. M., and Alivisatos, A. P. (2002) Sorting fluorescent nanocrystals with DNA. *J. Am. Chem. Soc. 124*, 7070−7074.
(40) Yun, C. S., Khitrov, G. A., Vergona, D. E., Reich, N. O., and Strouse, G. F. (2002) Enzymatic manipulation of DNA-nanomaterial constructs. *J. Am. Chem. Soc. 124*, 7644−7645.
(41) Phadke, R. S. (2001) Biomolecular electronics in the twenty-first century. *Appl. Biochem. Biotechnol. 96*, 269−276.
(42) Willner, I., and Willner, B. (2001) Biomaterials integrated with electronic elements: en route to bioelectronics. *Trends Biotechnol. 19*, 222−230.
(43) Liu, Q., Wang, L., Frutos, A. G., Condon, A. E., Corn, R. M., and Smith, L. M. (2000) DNA computing on surfaces. *Nature 403*, 175−179.
(44) Laval, J. M., Mazeran, P. E., and Thomas, D. (2000) Nanobiotechnology and its role in the development of new analytical devices. *Analyst 125*, 29−33.
(45) Virta, P., Katajisto, J., Niittymaki, T., and Lonnberg, H. (2003) Solid-supported synthesis of oligomeric bioconjugates. *Tetrahedron 59*, 5137−5174.
(46) Zatsepin, T. S., Andreev, S., Yu, T., Hianik, I., and Oretskaya, T. O. (2003) Ferrocene-containing nucleic acids. Synthesis and electrochemical properties. *Russ. Chem. Rev. 72*, 537−554.
(47) Kachalova, A. V., Zubin, E. M., and Oretskaya, T. S. (2002) Methods for the synthesis of oligonucleotides containing reactive electrophilic groups. *Russ. Chem. Rev. 71*, 1041−1059.
(48) Walton, T. A., Lyttle, M. H., Dick, D. J., and Cook, R. M. (2002) Evaluation of new linkers and synthetic methods for internal modified oligonucleotides. *Bioconjugate Chem. 13*, 1155−1158.
(49) Niemeyer, C. M. (2002) The developments of semisynthetic DNA-protein conjugates. *Trends Biotechnol. 20*, 395−401.
(50) Ghosh, P. K., Kumar, P., and Gupta, K. C. (2000) Recent advances in synthesis of modified oligonucleotides. *J. Ind. Chem. Soc. 77*, 109−132.
(51) Tung, C. H., and Stein, S. (2000) Preparation and applications of peptide−oligonucleotide conjugates. *Bioconjugate Chem. 11*, 605−618.
(52) Nanthakumar, A., Pon, R. T., Mazumder, A., Yu, S., and Watson, A. (2000) Solid-phase oligonucleotide synthesis and flow cytometric analysis with microspheres encoded with covalently attached fluorophores. *Bioconjugate Chem. 11*, 282−288.
(53) De Napoli, L., Messere, A., Montesarchio, D., Piccialli, G., Benedetti, E., Bucci, E., and Rossi, F. (1999) A new solid-phase synthesis of oligonucleotides 3′-conjugated with peptides. *Bioorg. Med. Chem. 7*, 395−400.
(54) Devivar, R. V., Koontz, S. L., Peltier, W. J., Pearson, J. E., Guillory, T. A., and Fabricant, J. D. (1999) A new solid-phase support for oligonucleotide synthesis. *Bioorg. Med. Chem. 9*, 1239−1242.
(55) Azhayev, A. V. (1999) A new universal solid support for oligonucleotide synthesis. *Tetrahedron 55*, 787−800.
(56) Antopolsky, M., and Azhayev, A. (1999) Stepwise solid-phase synthesis of peptide−oligonucleotide conjugates on new solid supports. *Helv Chim. Acta 82*, 2130−2140.
(57) Behrens, C., and Dahl, O. (1999) Synthesis of achiral linker reagents for direct labeling of oligonucleotides on solid supports. *Nucleotides Nucleosides 18*, 291−305.
(58) Guzaev, A., and Lonnberg, H. (1999) Solid support synthesis of ester linked hydrophobic conjugates of oligonucleotides. *Tetrahedron 55*, 9101−9116.
(59) Andrus, A., Cox, S., Beavers, S., Parker, A., Anuskiewicz, J., and Mullah, B. (1999) High-throughput synthesis of functionalized oligonucleotides. *Innovation and Perspectives in Solid-Phase Synthesis & Computational Libraries* (Epton, R., Ed.) pp 67−70, Mayflower Scientific Limited, Birmingham.
(60) Verna, S., and Eckstein, F. (1998) Modified oligonucleotides: synthesis and strategy for users. *Annu. Rev. Biochem. 62*, 99−134.
(61) Lyttle, M. H., Adams, H., Hudson, D., and Cook, R. M. (1997) Versatile linker chemistry for synthesis of 3′-modified DNA. *Bioconjugate Chem. 8*, 193−198.
(62) Shchepinov, M. S., and Stetsenko, D. A. (1997) A facile route to 3′-modified oligonucleotides. *Bioorg. Med. Chem. Lett. 7*, 1181−1184.
(63) Weiler, J., and Hoheisel, J. D. (1996) Combining the preparation of oligonucleotide arrays and synthesis of high-quality primers. *Anal. Biochem. 243*, 218−227.
(64) Harrison, J. G., and Balasubramanian, S. (1997) A convenient synthetic route to oligonucleotide conjugates. *Bioorg. Med. Chem. Lett. 7*, 1041−1046.

(65) Agrawal, S. (1994) Protocols for oligonucleotide conjugates: synthesis and analytical techniques. *Methods in Molecular Biology* (Agrawal, S., Ed.) Vol. 26, Humana Press, Totowa, NJ.
(66) Wright, P., Lloyd, D., Rapp, W., and Andrus, A. (1993) Large scale synthesis of oligonucleotides via phosphoramidite nucleosides and a high-loaded polystyrene support. *Tetrahedron Lett. 34*, 3373−3376.
(67) Goodchild, J. (1990) Conjugates of oligonucleotides and modified oligonucleotides: a review of their synthesis and properties. *Bioconjugate Chem. 1*, 165−187.
(68) Sojka, B., Piunno, P. A. E., Wust, C. C., and Krull, U. J. (2000) A novel phosphoramidite method for automated synthesis of oligonucleotides on glass supports for biosensor development. *Appl. Biochem. Biotechnol. 89*, 85−103.
(69) Matsuura, K., Hibino, M., Kataoka, M., Hayakawa, Y., and Kobayashi, K. (2000) Phosphoramidite solid-phase synthesis of site-specifically glycosylated oligodeoxynucleotides. *Tetrahedron Lett. 41*, 7529−7533.
(70) Hovinen, J., Guzaev, A., Azhayev, A., and Lonnberg, H. (1994) Novel nonnucleosidic phosphoramidite building blocks for versatile functionalization of oligonucleotides at primary hydroxy groups. *J. Chem. Soc. Perkin Trans. 1* 2745−2749.
(71) Beaucage, S. L., and Iyer, R. P. (1993) Functionalization of oligonucleotides via phosphoramidite derivatives. *Tetrahedron 49*, 1925−1963.
(72) Agrawal, S. (1993) Protocols for oligonucleotides and analogues: synthesis and properties. *Methods in Molecular Biology* (Agrawal, S., Ed.) Vol. 20, Humana Press, Totowa, NJ.
(73) Beaucage, S. L., and Iyer, R. P. (1992) Advances in the synthesis of oligonucleotides by the phosphoramidite approach. *Tetrahedron 48*, 2223−2311.
(74) Sonveaux, E. (1994) Protecting groups in oligonucleotide synthesis. *Methods Mol. Biol. 26*, 1−71.
(75) Greene, T. W., and Wuts, P. G. M. (1999) *Protective groups in organic synthesis*, Wiley, New York.
(76) Vogel, S., Rohr, K., Dahl, O., and Wengel, J. (2003) A substituted triaza crown ether as a binding site in DNA conjugates. *Chem. Commun.* 1006−1007.
(77) Wu, X., and Pitsch, S. (1998) Synthesis and pairing properties of oligoribonucleotide analogues containing a metal-binding site attached to beta-D-allofuranosyl cytosine. *Nucleic Acids Res. 26*, 4315−4323.
(78) Yamana, K., Iwai, T., Ohtani, Y., Sato, S., Nakamura, M., and Nakano, H. (2002) Bis-pyrene-labeled oligonucleotides: sequence specificity of excimer and monomer fluorescence changes upon hybridization with DNA. *Bioconjugate Chem. 13*, 1266−1273.
(79) Kostenko, E., Dobrikov, M., Komarova, N., Pyshnyi, D., Vlassov, V., and Zenkova, M. (2001) 5′-bis-pyrenylated oligonucleotides display enhanced excimer fluorescence upon hybridization with DNA and RNA. *Nucleosides Nucleotides Nucleic Acids 20*, 1859−1870.
(80) Kostenko, E., Dobrikov, M., Pyshnyi, D., Petyuk, V., Komarova, N., Vlassov, V., and Zenkova, M. (2001) 5′-bis-pyrenylated oligonucleotides displaying excimer fluorescence provide sensitive probes of RNA sequence and structure. *Nucleic Acids Res. 29*, 3611−3620.
(81) Wojczewski, C., Stolze, K., and Engels, J. W. (1999) Fluorescent oligonucleotides − versatile tools as probes and primers for DNA and RNA analysis. *Synlett 10*, 1667−1678.
(82) Asseline, U., and Thuong, N. T. (1997) Synthesis and properties of oligonucleotides covalently linked to intercalating agents. *New J. Chem. 21*, 5−17.
(83) Skrzypczynski, Z., and Wayland, S. (2003) New reagents for the introduction of reactive functional groups into chemically synthesized DNA probes. *Bioconjugate Chem. 14*, 642−652.
(84) Vorobjev, P. E., Pyshnaya, I. A., Pyshnyi, D. V., Venyaminova, A. G., Ivanova, E. M., Zarytova, V. F., Bonora, G. M., Scalfi-Happ, C., and Selinger, H. (2001) Nuclease resistance and RNase H sensitivity of oligonucleotides bridged by oligomethylenediol and oligoethylene glycol linkers. *Antisense Nucleic Acid Drug Dev. 11*, 77−85.
(85) Lee, S. E., Sidorov, A., Gourlain, T., Mignet, N., Thorpe, S. J., Brazier, J. A., Dickman, M. J., Hornby, D. P., Grasby, J. A., and Williams, D. M. (2001) Enhancing the catalytic repertoire of nucleic acids: a systematic study of linker length and rigidity. *Nucleic Acids Res. 29*, 1565−1573.
(86) Pils, W., and Micura, R. (2000) Flexible nonnucleotide linkers as loop replacements in short double helical RNAs. *Nucleic Acids Res. 28*, 1859−1863.
(87) Fotin, A. V., Drobyshev, A. L., Proudnikov, D. Y., Perov, A. N., and Mirzabekov, A. D. (1998) Parallel thermodynamic analysis of duplexes on oligodeoxynucleotide microchips. *Nucleic Acids Res. 26*, 1515−1521.
(88) Bonora, G. M., Ivanova, E., Zarytova, V., Burcovich, B., and Veronese, F. M. (1997) Synthesis and characterization of high-molecular mass poly(ethylene glycol)-conjugated oligonucleotides. *Bioconjugate Chem. 8*, 793−797.
(89) Shchepinov, M. S., Case-Green, S. C., and Southern, E. M. (1997) Steric factors influencing hybridisation of nucleic acids to oligonucleotide arrays. *Nucleic Acids Res. 25*, 1155−1161.
(90) Jaschke, A., Bald, R., Nordhoff, E., Hillenkamp, F., Cech, D., Erdmann, V. A., and Furste, J. P. (1996) Synthesis and analytical characterization of RNA-poly(ethylene glycol) conjugates. *Nucleosides Nucleotides 115*, 1519−1529.
(91) Orson, F. M., Kinsey, B. M., and McShan, W. M. (1994) Linkage structures strongly influence the binding cooperativity of DNA intercalators conjugated to triplex forming oligonucleotides. *Nucleic Acids Res. 22*, 479−484.
(92) Kessler, D. J., Pettitt, B. M., Cheng, Y. K., Smith, S. R., Jayaraman, K., Vu, H. M., and Hogan, M. E. (1993) Triple helix formation at distant sites: hybrid oligonucleotides containing a polymeric linker. *Nucleic Acids Res. 21*, 4810−4815.

BC0342231

Synthesis of Marimastat and a Marimastat Conjugate for Affinity Chromatography and Surface Plasmon Resonance Studies

Kai Jenssen, Katherina Sewald, and Norbert Sewald*

Department of Chemistry, University of Bielefeld, Universitätsstrasse 25, D-33615 Bielefeld, Germany. Received December 10, 2003; Revised Manuscript Received March 22, 2004

Immobilized small-molecule inhibitors are suited for enrichment of biomolecules by affinity chromatography, as it is shown for metalloproteinases and an immobilizable derivative of the hydroxamate-type inhibitor marimastat. A new asymmetric synthesis of marimastat is presented that allows for site-specific attachment to a solid surface, e.g., a chromatography matrix or a surface plasmon resonance sensor chip. The latter technique is shown to be a valuable tool for the optimization of binding and elution conditons of biomolecules in affinity chromatography.

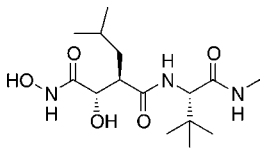
INTRODUCTION

Affinity chromatography is one of the most favored techniques for the isolation of biological macromolecules. It relies on covalent attachment of a specific ligand, which interacts with the desired macromolecule, to an insoluble solid and inert support. Then a solution containing the compound to be enriched is passed through the column, and all compounds which, under the given experimental conditions, have no affinity to the ligand will not be retarded. Compounds that display affinity will be bound by the immobilized ligand (*1*). A difficulty lies in the development of an affinity chromatography process for a certain macromolecule or a family of related macromolecules, because of the diversity of parameters that have to be taken into account. Even the optimization of appropriate elution conditions often relies on a trial and error approach. Nowadays surface plasmon resonance (SPR) provides a tool for real-time monitoring of biomolecular interactions (*2*). It also allows for optimization of the binding and elution conditions in affinity chromatography, especially because of the small sample amounts required. In a typical SPR analysis, three phases can be distinguished. Association occurs when the soluble analyte is passed through the flow cell where the binding partner is immobilized. The complex dissociates when the analyte is not present in the solution anymore. Finally, the sensor chip can be regenerated using appropriate buffer systems. The curve shape and the response difference allow for the evaluation of thermodynamic and kinetic binding parameters.

Here we describe our approach toward the development of specific, mechanism-based affinity chromatography materials that relies on a small synthetic inhibitor. With such an immobilizable inhibitor construct in hands, not only affinity purifications of proteins can be performed, but also applications in functional proteomics are feasible. This includes, in general, enrichment of overall subsets of cellular proteins, which can subsequently be resolved by one- or two-dimensional SDS−PAGE prior to indentification by mass spectrometry. This proteomics approach enables the identification of novel members of a protein family (*3*). It provides an efficient tool to identify cellular targets of the inhibitor used. Moreover, even interaction partners of the target protein can be enriched. The general process outlined has been optimized for the enrichment of metalloproteinases, especially matrix metalloproteinases.

Matrix metalloproteinases (MMPs) are a family of zinc-containing metalloendopeptidases which includes collagenases, gelatinases, and stromelysins. They are capable of degrading extracellular matrix (ECM) components, e.g., collagen, gelatin, fibronectin, and elastin (*4*, *5*). MMPs are necessary for tissue restructuring and remodeling. Therefore, they play an important role, for example, in growth and wound healing processes. However, overexpression of MMP leads to pathophysiological effects which are responsible for a variety of diseases such as arthritis, cancer, multiple sclerosis, and Alzheimer's disease (*6*).

Hydroxamic acids are known to be potent inhibitors of MMPs. Marimastat **1** was developed as a drug by British Biotech (*7*). It is an inhibitor with a good potency and shows activity toward a wide range of MMPs. The main advantage of **1** is the oral bioavailability, and clinical studies were performed. Indeed, inhibition of primary and secondary tumor growth and metastasis could be verified, but the development was finally discontinued because of severe side effects mainly caused by the lack of selectivity (*8*).



1

However, the lack of selectivity of **1** among the MMPs renders it an ideal candidate for diagnostic purposes. It can be derivatized in a way that allows for either immobilization on a chromatography matrix (affinity purification) or on a surface plasmon resonance sensor chip for binding studies. This requires the molecule to be attached covalently to a solid support with a functional group that does not interfere with binding to MMPs. Comparison of X-ray crystallographic data of MMPs, which were cocrystallized with hydroxamic acid based

* To whom correspondence should be addressed. Fax: int+ 49-521-106-8094. e-mail: norbert.sewald@uni-bielefeld.de.

10.1021/bc034225l CCC: $27.50 © 2004 American Chemical Society
Published on Web 05/01/2004

inhibitors, indicates significant structure homology between these complexes. The essentials are that the hydroxamic acid moiety binds to the zinc ion whereas the *N*-methyl carboxamide terminus of **1** is exposed to the protein surface and freely accessible. This should make a derivatization and linker attachment of **1** feasible.

EXPERIMENTAL PROCEDURES

General. Unless otherwise mentioned, materials were obtained from commercial suppliers and were used without further purification. DMF was distilled at 55 mbar over ninhydrin, and dichloromethane was distilled first over calcium chloride and then dried over calcium hydride. Diethyl ether was dried over sodium benzophenone ketyl. Melting points were recorded on a Büchi melting B-540 apparatus and are uncorrected. For thin-layer chromatography (TLC), silica gel plates Merck 60 F_{254} were used. Flash chromatography was performed using silica gel Merck 60 (size 0.040−0.063 mm).

Preparative RP-HPLC was carried out using a Thermo Separation Products system consisting of a UV1000 detector and a P4000 pump equipped with a Vydac C18 (protein and peptide, 22 × 250 mm) column. Eluents: A = water/acetonitrile/trifluoroacetic acid (95/5/0.1), B = water/acetonitrile/trifluoroacetic acid (5/95/0.1). Method: flow rate 10 mL/min, gradient (A:B) 0−5 min: 100:0, 5−30 min: 100:0−70:30, 30−40 min: 70:30−0:100, 40−50 min: 0:100−100:0. Analytical RP-HPLC was carried out using a Thermo Separation Products system consisting of a UV6000 detector and a P4000 pump equipped with a Vydac C18 (protein and peptide, 4.6 × 250 mm) column. Method: flow rate 1 mL/min, same gradient as for preparative RP-HPLC.

^{1}H NMR, ^{13}C NMR, and ^{19}F NMR spectra were recorded at room temperature on a Bruker DRX500 instrument. ^{1}H NMR and ^{13}C NMR chemical shifts are given in ppm relative to TMS as the internal standard. Infrared spectra (IR) were recorded on a Jasco FT/IR-410 spectrometer; peaks are reported in wavenumbers (cm^{-1}). Optical rotation indices were measured on a Jasco DIP-360. MALDI-ToF mass spectra were obtained on a PerSeptive Biosystems Voyager-DE and were calibrated with a PEG standard as external reference. The synthetic steps during the synthesis on solid support were monitored by MALDI-ToF MS after cleavage of small amounts from the resin. Electrospray ionization (ESI) mass spectrometry experiments were performed on a Bruker Esquire 3000. ESI- and MALDI-FT-ICR mass spectrometry experiments were performed on a Bruker Apex III spectrometer with internal calibration. Electron impact ionization (EI) and chemical ionization (CI) mass spectrometry were performed on a Micromass VG Autospec X. For the surface plasmon resonance measurements a BIAcore 3000 instrument was used. The sensor chips and coupling kits were purchased from BIAcore. The following buffer compositions were used: buffer A: 0.05 M Tris/HCl pH 7.5, 0.2 M NaCl, 5 mM $CaCl_2$, 0.02% Brij35, 0.02% NaN_3; HBS-EP buffer: 0.01 M HEPES pH 7.4, 0.15 M NaCl, 3 mM EDTA, 0.005 Surfactant P20; both buffers were sterile filtered and degassed.

Diethyl (2*S*,3*R*)-3-Isobutylmalate 4. Isobutylmagnesium bromide was prepared by dropwise addition of isobutyl bromide (6.85 g, 50.0 mmol) in diethyl ether (30 mL) to a suspension of magnesium turnings (1.21 g, 50.0 mmol) in ether (20 mL). After the addition was complete, the reaction mixture was heated for 1 h under reflux and was then allowed to settle overnight. The supernatant was withdrawn using a syringe, and the solution was kept under nitrogen atmosphere. CuCN (4.78 g, 53.3 mmol) was suspended under nitrogen atmosphere in dry diethyl ether (30 mL) and cooled to −30 °C. The Grignard solution was added quickly with mechanical stirring. After 20 min, the suspension turned yellow and then a solution of diethyl (2*S*,3*S*)-epoxysuccinate **3** (*11*) (5.00 g, 26.6 mmol) in ether (20 mL) was added dropwise. After being stirred for 1 h at −25 °C, the reaction was quenched by the addition of satd ammonium chloride solution and was then filtered through a pad of silica gel. The phases were separated, and the aqueous phase was extracted three times with ether. The combined organic layers were washed with brine and dried over Na_2SO_4. After the solvent was removed by rotary evaporation, the crude product was purified by flash chromatography (petroleum ether/ethyl acetate 7:1) (*12*). Yield: 3.02 g (12.3 mmol, 46%), colorless oil. TLC: $R_f = 0.68$ (petroleum ether/ethyl acetate (2:1)); ^{1}H NMR (500 MHz, $CDCl_3$, TMS): δ 0.92 (d, 3H, $^3J = 6.4$ Hz), 0.95 (d, 3H, $^3J = 6.4$ Hz), 1.25 (t, 3H, $^3J = 7.1$ Hz), 1.31 (t, 3H, $^3J = 7.2$ Hz), 1.50 (m, 1H), 1.59−1.84 (m, 2H), 2.93 (m, 1H), 3.66 (br. s, 1H), 4.14 (m, 1H), 4.22−4.32 (m, 4H); ^{13}C NMR (125.7 MHz, $CDCl_3$, TMS): δ 14.1 (CH_3), 14.2 (CH_3), 22.5 (CH_3), 22.6 (CH_3), 25.8 (CH), 36.9 (CH_2), 46.6 (CH), 60.8 (CH_2), 61.8 (CH_2), 71.3 (CH), 173.1 (C), 173.5 (C); MS (EI, 70 eV): *m*/*z* (%) = 247 (1, $M^{+\bullet}$ + H), 231 (0.5), 201 (5), 173 (100), 143 (10), 127 (70), 117 (26), 101 (14); $[\alpha]^{21}_D = +8.8 \pm 0.1$ (*c* = 2; ethyl acetate); IR (NaCl, cm^{-1}): $\tilde{\nu}$ = 3504, 2960, 2360, 1741, 1468, 1371, 1246, 1198, 1097, 1029, 900, 858; elemental analysis calcd for $C_{12}H_{22}O_5$ [230.30] (%) C 58.52, H 9.00, N 0.00, found C 57.85, H 8.89, N 0.00.

(2*S*,3*R*)-2-Hydroxy-3-isobutylsuccinic Acid 5. A solution of diester **4** (7.62 g, 31.0 mmol) and NaOH (5.00 g, 124 mmol) in water/1,4-dioxane (120 mL/80 mL) was stirred for 16 h at rt. Then the reaction mixture was extracted twice with diethyl ether (50 mL). The organic layer was discarded, and the aqueous phase was acidified to pH 1.5 and extracted five times with ether (200 mL). The combined organic phases were then washed with a small amount of brine and dried over Na_2SO_4, and the solvent was removed in vacuo. If necessary, the product could be purified by flash chromatography (petroleum ether/ethyl acetate/acetic acid 7:3:1). Yield: 5.24 g (27.9 mmol, 90%), slightly yellow, very viscous oil. TLC: R_f = 0.11 (petroleum ether/ethyl acetate/acetic acid (7:3:1)); ^{1}H NMR (500 MHz, $CDCl_3$, TMS): $\delta = 0.95$ (d, 3H, $^3J = 6.9$ Hz), 0.96 (d, 3H, $^3J = 6.3$ Hz), 1.60 (m, 1H), 1.68−1.79 (m, 2H), 3.10 (ddd, $^3J = 3.4$ Hz, $^3J = 7.4$ Hz, $^3J = 7.4$ Hz, 1H), 4.31 (d, 1H, $^3J = 3.1$ Hz), 8.30−9.20 (br. s, 2H); ^{13}C NMR (125.7 MHz, $CDCl_3$, TMS): δ = 22.1 (CH_3), 22.5 (CH_3), 25.6 (CH), 36.7 (CH_2), 46.2 (CH), 70.5 (CH), 177.9 (C), 178.9 (C); MS (EI, 70 eV): *m*/*z* (%) = 189 (0.1; $M^{\bullet+}$ − H), 145 (45, $M^{\bullet+}$ − ^{i}Pr), 134 (10), 126 (100, $M^{\bullet+}$ − ^{i}Pr − H_2O), 115 (20, ^{i}Bu$CH_2COO^{+\bullet}$); $[\alpha]^{21}_D = +18.7 \pm 0.2$ (*c* = 0.5; ethyl acetate); IR (NaCl, cm^{-1}): $\tilde{\nu}$ = 3500−3000, 2959, 1717, 1388, 1208, 1145, 1097, 901, 812; elemental analysis calcd for $C_8H_{14}O_5$ [190.19] (%) C 50.52, H 7.42, N 0.00, found C 50.35, H 7.39, N 0.00.

(2*R*)-4-Methyl-2-((4*S*)-5-oxo-2,2-bis(trifluoromethyl)-1,3-dioxolan-4-yl)pentanoic Acid 6. A stream of gaseous hexafluoroacetone was directed onto the surface of a well stirred solution of **5** (4.26 g, 22.4 mmol) in DMSO (15 mL). The reaction vessel was equipped with a methanol/dry ice condenser. After 3 h, completion of the reaction was indicated by a reflux of hexafluoroacetone. The solution was poured into a mixture of ice water/dichloromethane (DCM) (200 mL/200 mL), and the aqueous phase was extracted three times with DCM (100 mL). The combined organic layers were washed three times

with cold water (100 mL), the organic phase was dried over Na_2SO_4, and the solvent was removed in vacuo (*13*, *14*). Yield: 6.38 g (18.9 mmol, 84%), gray solid; mp 61 °C; ^{1}H NMR (500 MHz, $CDCl_3$, TMS): δ = 0.97 (d, 6H, ^3J = 6.3 Hz), 1.65 (m, 1H), 1.73 (m, 1H), 1.83 (m, 1H), 3.04 (ddd, 1H, ^3J = 5.8 Hz, ^3J = 8.9 Hz, ^3J = 8.9 Hz), 4.72 (d, 1H, ^3J = 5.7 Hz), 8.60 (br. s, 1H); ^{13}C NMR (125.7 MHz, $CDCl_3$, TMS): δ = 22.3 (CH_3), 22.5 (CH_3), 25.6 (CH), 35.7 (CH_2), 44.9 (CH), 75.0 (CH), 97.6 (sept, ^2J = 35.7 Hz) 118.6 (q, ^1J = 287.2 Hz, CF_3), 119.7 (q, ^1J = 288.0 Hz, CF_3), 166.4 (C), 175.1 (C); ^{19}F NMR (470.6 MHz, $CDCl_3$, $CFCl_3$ external): δ = −80.3 (q, ^3J = 7.5 Hz), −81.1 (q, ^3J = 7.5 Hz). IR (KBr, cm^{-1}): $\tilde{\nu}$ = 2965, 2594, 1852, 1727, 1471, 1390, 1373, 1319, 1232, 1192, 1132, 1066, 982, 950, 906, 807, 750, 725; MS (CI, NH_3): *m*/*z* (%) = 356 (100, $[M + NH_4]^{\bullet+}$), 236 (11), 190 (13), 172 (5, $M^{\bullet+} - F_3CC{=}OCF_3$), 157 (17), 144 (12), 127 (5), $C_{11}H_{12}O_5F_6$ [338.20].

(2*R*)-4-Methyl-2-((4*S*)-5-oxo-2,2-bis(trifluoromethyl)-1,3-dioxolan-4-yl)pentanoyl Chloride 7. Freshly distilled thionyl chloride (5 mL) and **6** (1.16 g, 3.45 mmol) were kept under reflux for 4 h. After removal of the excess thionyl choride, the crude product was sublimed in vacuo (bath temperature 40 °C/0.02 mbar) (*13*, *14*). Yield: 1.17 g (3.28 mmol, 95%), colorless solid; mp 38 °C; TLC: R_f = 0.11 (petroleum ether/ethyl acetate/acetic acid (7:3:1); ^{1}H NMR (500 MHz, $CDCl_3$, TMS): δ = 0.98 (d, 3H, ^3J = 6.5 Hz), 0.99 (d, 3H, ^3J = 6.6 Hz), 1.73 (m, 1H), 1.80 (m, 1H), 1.87 (m, 1H), 3.32 (ddd, 1H, ^3J = 5.0 Hz, ^3J = 9.0 Hz, ^3J = 9.0 Hz), 4.79 (d, 1H, ^3J = 8.4 Hz); ^{13}C NMR (125.7 MHz, $CDCl_3$, TMS): δ = 21.4 (CH_3), 22.9 (CH_3), 25.6 (CH), 35.7 (CH_2), 56.2 (CH), 73.9 (CH), 97.5 (sept, ^2J = 35.6 Hz), 119.7 (q, ^1J = 282.3 Hz, CF_3), 120.5 (q, ^1J = 285.4 Hz, CF_3), 165.1 (C), 171.6 (C). ^{19}F NMR (470.6 MHz, $CDCl_3$, $CFCl_3$ external): δ = −80.6 (q, ^3J = 7.5 Hz), −81.2 (q, ^3J = 7.5 Hz); IR (KBr, cm^{-1}): $\tilde{\nu}$ = 2966, 2361, 1851, 1792, 1470, 1321, 1242, 1195, 1135, 1082, 982, 913, 852, 726, 673, 620; MS (EI, 70 eV): *m*/*z* (%) = 355 (0.1; $M^{\bullet+}$ − H), 321 (70, $M^{\bullet+}$ − Cl), 303 (40), 293 (14, $M^{\bullet+}$ − COCl), 137 (13), 127 (28), 112 (10), 97 (17, $O{=}C{-}CF_3^{\bullet+}$), 69 (42, $CF_3^{\bullet+}$), 57 (43, $^iBu^{\bullet+}$), 43 (100, $^iPr^{\bullet+}$); elemental analysis calcd for $C_{11}H_{11}O_4ClF_6$ [356.65] (%) C 37.06, H 3.11, N 0.00, found C 37.26, H 3.10, N 0.00.

Boc-L-*tert*-leucine 9. Boc_2O (3.64 g, 16.68 mmol) was added to a solution of L-*tert*-leucine **8** (2.00 g, 15.25 mmol) and NaOH (0.67, 16.80 mmol) in water/*tert*-butyl alcohol (20 mL/20 mL). The reaction mixture was stirred overnight at rt and was then extracted three times with 50 mL of ethyl acetate. The combined organic layers were washed with satd $NaHCO_3$ solution, and the combined water phases were acidified to pH 1.5−2.0. The water phase was extracted four times with 50 mL of ethyl acetate, and the combined organic layers were washed with brine, dried over Na_2SO_4, and evaporated in vacuo. Yield: 3.28 g (14.17 mmol, 93%) (*16*); colorless solid; mp 122 °C; TLC: R_f = 0.39 (petroleum ether/ethyl acetate (2:1); ^{1}H NMR (500 MHz, $CDCl_3$, TMS): δ = 1.28 (s, 9H), 1.45 (s, 9H), 4.13 (d, 1H, ^3J = 9.5 Hz), 5.11 (d, 1H, ^3J = 9.5 Hz); ^{13}C NMR (125.7 MHz, $CDCl_3$, TMS): δ = 26.5 (CH_3), 28.3 (CH_3), 34.4 (CH), 61.6 (C), 80.0 (C), 155.6 (C), 176.9 (C); IR (KBr, cm^{-1}): $\tilde{\nu}$ = 3372, 3347, 1758, 1724, 1660, 1538, 1367, 1332, 1274, 1255, 1228, 1160, 978; MS (EI, 70 eV):*m*/*z* (%) = 175 (6; $M^{\bullet+}$ − C_4H_8, 130 (10), 119 (37), 101 (18), 86 (9), 75 (13), 57 (100), 43 (6); $[\alpha]^{24}_D$ = +5.8 ± 0.1 (*c* = 0.6; ethyl acetate); elemental analysis calcd for $C_{11}H_{21}O_4N$ [231.28] (%) C 57.12, H 9.15, N 6.05, found C 57.23, H 8.70, N 6.03.

Boc-L-*tert*-leucine-*N*-methylamide 10. Boc-L-*tert*-leucine **9** (1.00 g, 4.32 mmol), DIPEA (4.41 mL, 25.92 mmol), TBTU (1.51 g, 4.70 mmol), and *N*-methylammonium chloride (0.75 g, 14.1 mmol) were suspended in 16 mL of acetonitrile and stirred overnight at rt. Ethyl acetate (50 mL) was added to the reaction mixture, washed three times with 5% $KHSO_4$ solution, three times with satd $NaHCO_3$ solution, and two times with brine, and dried over Na_4SO_4. The solvent was then removed in vacuo, and the residue was purified by chromatography (petroleum ether/ethyl acetate 2:1). Yield: 0.74 g (3.05 mmol, 71%) (*15*); colorless solid; mp 129 °C; TLC: R_f = 0.60 (petroleum ether/ethyl acetate (1:1); ^{1}H NMR (500 MHz, $CDCl_3$, TMS): δ = 0.99 (s, 9H), 1.43 (s, 9H), 2.78 (d, 3H, ^3J = 4.8 Hz) 3.92 (d, 1H, ^3J = 9.6 Hz), 5.40 (d, 1H, ^3J = 9.6 Hz), 6.55 (d, 1H, ^3J = 3.0 Hz); ^{13}C NMR (125.7 MHz, $CDCl_3$, TMS): δ = 25.9 (CH_3), 26.5 (CH_3), 28.3 (CH_3), 34.5 (CH), 62.1 (C), 79.5 (C), 155.9 (C), 171.6 (C); IR (KBr, cm^{-1}): $\tilde{\nu}$ = 3330, 3272, 3104, 2969, 2875, 1681, 1650, 1567, 1523, 1482, 1365, 1251, 1178, 1078, 1006, 912, 863, 757; MS (ESI): *m*/*z* (%) = 266.9 (100, [M + Na]$^+$, calcd 267.2, 166.9 (28); $[\alpha]^{24}_D$ = +13.4 ± 0.2 (*c* = 1; ethyl acetate); elemental analysis calcd for $C_{11}H_{24}O_3N_2$ [244.32] (%) C 58.99, H 9.90, N 11.46, found C 58.98, H 9.88, N 11.46.

L-*tert*-Leucine-*N*-methylamide 11a. 10 (166 mg, 0.68 mmol) was dissolved in 5 mL of TFA/DCM (1:1) and reacted for 2 h at rt. After the solvent mixture was removed in vacuo, the residue was lyophilized. Yield: 174 mg (0.68 mmol, 99%), slightly yellow solid; mp 122.5 °C; MS (ESI): *m*/*z* (%) = 144.9 (100, [M + H]$^+$, calcd 145.1); $[\alpha]^{24}_D$ = +32.8 ± 0.1(*c* = 2; ethanol).

***N*$^\alpha$((2*R*)-4-Methyl-2-((4*S*)-5-oxo-2,2-bis(trifluoromethyl)-1,3-dioxolan-4-yl)pentanoyl)-L-*tert*-leucine-*N*-methylamide 13a.** A solution of 35 mg (0.13 mmol) L-*tert*-leucine-*N*-methylamide trifluoroacetate **11a** and triethylamine (36 μL, 0.26 mmol) in 10 mL of dry THF were added within 2 h at −70 °C to a solution of **7** (45 mg, 0.13 mmol) in 15 mL of dry THF with a syringe pump. The reaction mixture was allowed to warm to rt and was then filtered. After the solvent was removed in vacuo, the residue was diluted with 50 mL of cold DCM. The organic layer was then washed rapidly three times with 5 mL of ice−water and dried over Na_2SO_4. Evaporation of the solvent in vacuo yielded 55.0 mg (0.118 mmol, 91%) of **13a**, colorless solid; mp 148 °C; ^{1}H NMR (500 MHz, $CDCl_3$, TMS): δ = 0.88 (d, 3H, ^3J = 6.7 Hz), 0.89 (d, 3H, ^3J = 6.7 Hz), 0.98 (s, 9H), 1.47 (m, 1H), 1.64−1.74 (m, 2H), 2.76−2.83 (m, 4H), 4.34 (d, 1H, ^3J = 9.4 Hz), 4.73 (d, 1H, ^3J = 9.6 Hz), 6.30 (q, 1H, ^3J = 4.6 Hz), 6.82 (d, 1H, ^3J = 9.4 Hz); ^{19}F NMR (470.6 MHz, $CDCl_3$, $CFCl_3$ external): δ = −80.4 (q, ^3J = 7.5 Hz), −81.0 (q, ^3J = 7.5 Hz); IR (KBr, cm^{-1}): $\tilde{\nu}$ = 3315, 2962, 2933, 2875, 1851, 1644, 1541, 1370, 1321, 1240, 1189, 1136, 1072, 983, 722; MS (CI, NH_3): *m*/*z* (%) = 465 (100, [M + H]$^+$), 406 (14), 299 (6); MS (MALDI-FT-ICR, dihydroxybenzoic acid): *m*/*z* found 487.16360, monoisotopic mass calculated for the cation $C_{18}H_{26}F_6O_5N_2Na^+$ 487.16381.

***N*-(*N*′)-Benzyloxy-(2*R*,3*S*)-2-hydroxy-3-isobutyl-4-succinamoyl)-(*S*)-*tert*-leucine-*N*″-methylamide 15a.** A solution of *O*-benzylhydroxylamine hydrochloride (192 mg, 1.20 mmol) and triethylamine (180 μL, 1.20 mmol) in DCM (5 mL) was added at rt to a solution of **13a** (55 mg, 0.12 mmol) in DCM (2 mL). The reaction was stirred at rt for 3 h. The solvent was removed, and the residue was diluted with 20 mL of ethyl acetate/water (10:1). The phases were separated, and the organic layer was washed three times with 5% $KHSO_4$ solution, satd $NaHCO_3$ solution, and finally with brine and dried over Na_2SO_4. The solvent was removed in vacuo, and the residue was purified by flash chromatography (DCM/ethanol 30:1).

Yield: 43 mg (0.10 mmol, 85%), colorless oil; ^{1}H NMR (500 MHz, methanol-d_4): δ = 0.88 (d, 3H, ^3J = 6.5 Hz), 0.91 (d, 3H, ^3J = 6.5 Hz), 0.98 (s, 9H), 1.24 (m, 1H), 1.49−1.62 (m, 2H), 2.69 (s, 3H), 2.83 (ddd, 1H, ^3J = 5.0 Hz, ^3J = 9.5 Hz, ^3J = 9.5 Hz), 4.00 (d, 1H, ^3J = 5.8 Hz), 4.22 (s, 1H), 4.80−4.85 (m, 2H), 7.32−7.37 (m, 3H), 7.41−7.44 (m, 2H); ^{13}C NMR (125.7 MHz, methanol-d_4): δ = 22.4 (CH_3), 23.5 (CH_3), 26.0 (CH_3), 26.8 (CH), 27.2 (CH_3), 35.4 (C), 39.7 (CH_2), 61.9 (CH), 72.9 (CH), 79.0 (CH_2), 129.5 (CH), 129.7 (CH), 130.3 (CH), 136.7 (C), 171.7 (C), 173.1 (C), 175.3 (C); MS (MALDI-ToF, α-cyano-4-hydroxycinnamic acid): *m/z* (%) = 422.4 (100, $[M + H]^+$, calcd 422.2), 444.4 (76, $[M + Na]^+$, calcd 444.2), 460.4 (42, $[M + K]^+$, calcd 460.2), $C_{22}H_{35}O_5N_3$ [421.65]; IR (NaCl, cm^{-1}): $\tilde{\nu}$ = 3312, 3033, 2957, 2871, 2086, 1643, 1535, 1369, 1256, 1237, 1213, 1146, 1083, 1016, 749, 698.

***N*-((2*R*,3*S*)-3,*N*′-Dihydroxy-2-isobutyl-4-succinamoyl)-(*S*)-*tert*-leucine-*N*″-methylamide 1.** A suspension of **15a** (42 mg, 0.10 mmol) and 10% Pd/C (2.0 mg) in methanol (50 mL) was reacted under hydrogen atmosphere for 4h at rt. The catalyst was removed by filtration through a pad of silica gel. After removal of the solvent in vacuo, the crude product was further purified by RP-HPLC. Yield: 30.5 mg (0.092 mmol, 92%), colorless solid; preparative RP-HPLC: t_R = 35.5 min; analytical HPLC t_R = 30.9 min; ^{1}H NMR (500 MHz, methanol-d_4): δ = 0.88 (d, 3H, ^3J = 6.5 Hz), 0.92 (d, 3H, ^3J = 6.5 Hz), 0.98 (s, 9H), 1.26 (m, 1H), 1.54 (m, 1H), 1.64 (m, 1H), 2.71 (s, 3H), 2.84 (ddd, 1H, ^3J = 5.2 Hz, ^3J = 9.2 Hz, ^3J = 9.2 Hz), 4.02 (d, 1H, ^3J = 4.7 Hz), 4.20 (m, 1H), 7.86 (d, 1H, ^3J = 9.2 Hz); MS (MALDI-ToF, α-cyano-4-hydroxycinnamic acid): *m/z* (%) = 332.5 (40, $[M + H]^+$, calcd 332.2), 354.5 (100, $[M + Na]^+$, calcd 354.2), 370.5 (38, $[M + K]^+$, calcd 370.2), $C_{15}H_{29}O_5N_3$ [331.39].

Synthesis of 15b on Solid Support. 2-Chlorotrityl chloride resin (50 mg, Advanced ChemTech, max. capacity 1.4 mmol g^{-1}) was preswollen in DCM (100 μL). After 10 min, most of the solvent was removed and 1,8-diamino-3,6-dioxaoctane **12** (1.00 mL, 6.00 mmol) was added quickly. The reaction was stopped by the addition of methanol (2 mL) after 2 h. The resin was washed with DCM/DIPEA (19:1, 4 mL), three times with DMF (4 mL), and three times with DCM (4 mL) (*19*). Fmoc-L-*tert*-leucine (89 mg, 0.25 mmol) was dissolved together with TBTU (85 mg, 0.25 mmol) in DMF (350 μL) and added to the washed resin (two times with DMF), followed by DIPEA (90 μL). After 1 h, the resin was washed three times with DMF and three times with DCM. Estimation of the resin loading by Fmoc cleavage and UV spectroscopy gives 0.6−0.8 mmol/g. Removal of the Fmoc protecting group was accomplished by treatment with 25% piperidine/DMF (5 mL) (twice for 20 min) and by washing the resin three times with DMF and three times with DCM.

A solution of **7** (100 mg, 0.28 mmol) in THF (5 mL) was cooled to −65 °C, and then triethylamine (40 μL) and the dry, loaded resin were added portionwise. After 1 h, the resin was washed three times with triethylamine/DCM (1:2) (4 mL) and three times with DCM (4 mL). *O*-Benzylhydroxylamine hydrochloride (192 mg, 1.20 mmol) and triethylamine (180 μL, 1.20 mmol) in DCM (5 mL) were added to the resin. After 4 h, the resin was filtered and washed four times with DCM. The product **15b** was then cleaved from the resin by the addition of 1% TFA in DCM (5 mL). After 10 min, the resin was filtered and fresh cleavage solution was added. This step was repeated four more times. The volatiles were removed from the filtrate in vacuo, and the product was isolated by RP-HPLC. Overall yield: 15 mg (0.02 mmol, 28%), colorless solid; preparative RP-HPLC: t_R = 30.5 min; analytical RP-HPLC: t_R (%) = 29.3 min (94); 30.0 (5); ^{1}H NMR (500 MHz, $CDCl_3$, TMS): δ = 0.94 (d, 3H, ^3J = 6.1 Hz), 0.96 (d, 3H, ^3J = 6.5 Hz), 1.00 (s, 9H), 1.42 (m, 1H), 1.52−1.68 (m, 2H), 2.94 (m, 1H), 3.05−3.24 (m, 2H), 3.40−3.85 (m, 10H), 4.19 (m, 1H), 4.32 (m, 1H), 4.55 (br. s, 1H), 4.86−4.88 (m, 2H), 7.19 (d, 1H, ^3J = 6.8 Hz), 7.34−7.35 (m, 3H), 7.37−7.39 (m, 2H), 7.80 (s, 1H), 7.88 (br. s, 3H), 10.45 (br. s, 1H); ^{13}C NMR (125.7 MHz, $CDCl_3$, TMS): δ = 22.1 (CH_3) 22.9 (CH_3), 25.7 (CH), 26.7 (CH_3), 33.8 (C), 38.2 (CH_2), 39.3 (CH_2), 39.9 (CH_2), 47.9 (CH), 61.5 (CH), 66.5 (CH_2), 69.3 (CH_2), 69.9 (CH_2), 70.1 (CH_2), 71.8 (CH), 78.4 (CH_2), 128.6 (CH), 128.9 (CH), 129.3 (CH), 134.8 (C), 170.1 (C), 171.4 (C), 174.6 (C); MS (MALDI-ToF, α-cyano-4-hydroxycinnamic acid): *m/z* (%) = 539.5 (100, $[M + H]^+$, calcd 539.3), 561.5 (32, $[M + Na]^+$, calcd 561.3), 577.6 (9, $[M + K]^+$, calcd 577.3), $C_{29}H_{47}O_9F_3N_4$ [652.71].

***N*-((2*R*,3*S*)-*N*′,3-Dihydroxy-2-(2-isobutyl)-4-succinamoyl)−(*S*)-*tert*-leucine-*N*″-(8-amino-3,6-dioxaoct-1-yl)amide 16**. A suspension of **15b** (15 mg, 0.02 mmol) and 10% Pd/C (1.0 mg) in methanol (20 mL) was reacted in a hydrogen atmosphere for 4h at rt. The catalyst was removed by filtration through a pad of silica gel. After removal of the solvent in vacuo, the crude product is further purified by RP-HPLC. Yield: 9 mg (0.016 mmol, 80%), colorless solid; preparative RP-HPLC: t_R = 25.6 min; analytical HPLC: t_R = 20.3 min; ^{1}H NMR (500 MHz, DMSO-d_6): δ = 0.77 (d, 3H, ^3J = 6.6 Hz), 0.79 (d, 3H, ^3J = 6.6 Hz), 0.89 (s, 9H), 1.22 (m, 1H), 1.35 (m, 1H), 1.45 (m, 1H), 2.69 (m, 1H), 2.91−2.98 (m, 2H), 3.13−3.20 (m, 2H), 3.22−3.28 (m, 2H), 3.52−3.58 (m, 6H), 3.69 (d, 1H, ^3J = 8.2 Hz), 4.20 (d, 1H, ^3J = 9.4 Hz), 5.35 (br. s, 1H), 7.48 (d, 1H, ^3J = 9.7 Hz), 7.47 (br. s, 3H), 7.99 (t, 1H, ^3J = 5.6 Hz), 8.87 (s, 1H), 10.55 (s, 1H); MS (MALDI-ToF, α-cyano-4-hydroxycinnamic acid): *m/z* (%) = 449.5 (95, $[M + H]^+$, calcd 449.3), 471.5 (100, $[M + Na]^+$, calcd 471.3), 487.4 (30, $[M + K]^+$, calcd 487.2). MS (ESI-FT-ICR): *m/z* found 449.29707, monoisotopic mass calculated for the cation $C_{20}H_{41}O_7N_4^+$ 449.29698.

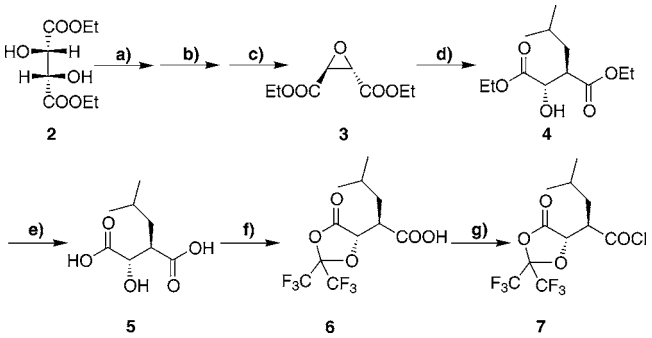
Activation of MMP-2. A freshly prepared stock solution (3 μL) of 4-aminophenyl mercuric acetate (APMA) (25 mM) in 0.1 mM NaOH was mixed with MMP-2 (30 μL, purchased from Calbiochem (Lot B41215), 40 μg mL^{-1}) and then incubated for 2 h at 37 °C.

SPR Measurements. The marimastat derivative **16** was immobilized on a CM5 sensor chip under the following conditions: flow 5 μL min^{-1}; contact time 7 min; running buffer HBS-EP buffer. The sensor chip was then activated with the EDC/NHS coupling kit on the reference and measurement flow cell. A solution of **16** in HBS-EP buffer (1.8 mM) was injected on the measurement flow cell, and the sensor chip was deactivated by the injection of ethanolamine on both flow cells. The immobilization level that could be achieved lies in the range of 40−60 RU.

Binding Studies. The system was primed with MMP-buffer A, and the flow was set to 20 μL min^{-1}; the flow path was set to both flow cells with reference subtraction. Different concentrations of MMP-2 in MMP-buffer A were injected (Figure 1). Regeneration of the surface was possible by the injection of HBS-EP buffer (two times for 10 min).

Competition in Solution Experiment. Constant concentration of MMP-2 was incubated for 30 min with varying concentrations of **16**. The samples were subsequently injected to both flow cells with reference subtrac-

Scheme 1[a]



[a] Reagents and conditions: (a) 33% HBr/AcOH, rt, 4.5 h, 66%; (b) 33% HBr/AcOH, EtOH, 70 °C, 4 h, 82%; (c) NaOEt, EtOH, 0 °C, 1 h, 79%; (d) isobutylmagnesium bromide, CuCN, Et_2O, -30 °C, 1 h, 46%; (e) NaOH, 1,4-dioxane/H_2O, rt, 16 h, 90%; (f) hexafluoroacetone, DMSO, rt, 3 h, 84%; (g) $SOCl_2$, 6 h, 80 °C, 96%.

tion. After each injection, the surface was regenerated with HBS-EP buffer (two times for 10 min).

RESULTS

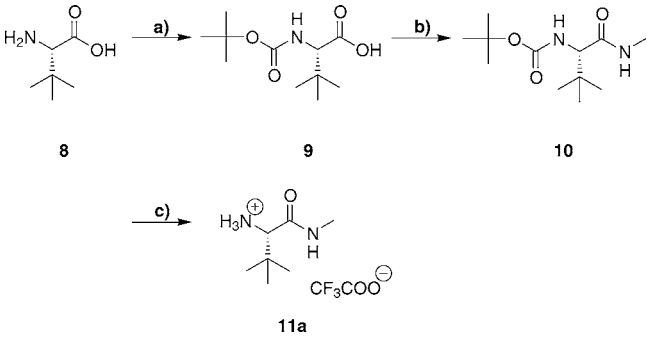
We succeeded to synthesize marimastat **1** and a new marimastat derivative **16** by a novel synthetic route. It differs from published syntheses of 2,3-disubstituted succinate derivatives, which are usually prepared by a stereoselective Ireland−Claisen rearrangement (*9*). The synthesis of marimastat analogues on solid support, where the α-hydroxy group was replaced by an α-amino group, has recently been reported (*10*).

Starting from (−)-D-diethyltartrate **2**, the C_2-symmetric epoxide **3** is obtained according to Mori et al. (Scheme 1) (*11*). According to the ^{1}H NMR integrals, an amount of 5−7% of the unwanted meso-diastereomer is obtained, which can be removed by flash chromatography. Alternatively, the undesired byproduct may be completely removed on a later stage by RP-HPLC. Compound **3** undergoes ring-opening with the Grignard-based organocuprate *i*BuCu(CN)MgBr generated in situ (*12*). Saponification of the diester **4** gives α-hydroxy acid **5**. It is known that α-hydroxy acids regioselectively form dioxolanone rings upon reaction with hexafluoroacetone (*13*). Hexafluoroacetone is especially suited as a protecting reagent for α-amino or α-hydroxy dicarboxylic acids. The lactone moiety of **6** displays high reactivity toward nucleophiles. Advantageously, ring opening and derivatization occur simultaneously in one synthetic step and usually with good yields (*14*). Moreover, conversion of the free carboxy group of **6** into the acid chloride confers the highest electrophilicity to this group and allows for the alternative regioselective derivatization. Treatment of compound **6** with thionyl chloride provides the corresponding acid chloride **7**, which serves as a common precursor for **1** and **16**.

For the synthesis of **1**, L-*tert*-leucine-*N*-methylamide **11a** is obtained as the trifluoroacetate in a three-step synthesis similar to known procedures (Scheme 2). L-*tert*-Leucine **8** is Boc-protected and then reacted with *N*-methylamine using TBTU as coupling reagent to give compound **10** (*15*, *16*). Cleavage of the Boc-protecting group by standard procedures yields compound **11a**.

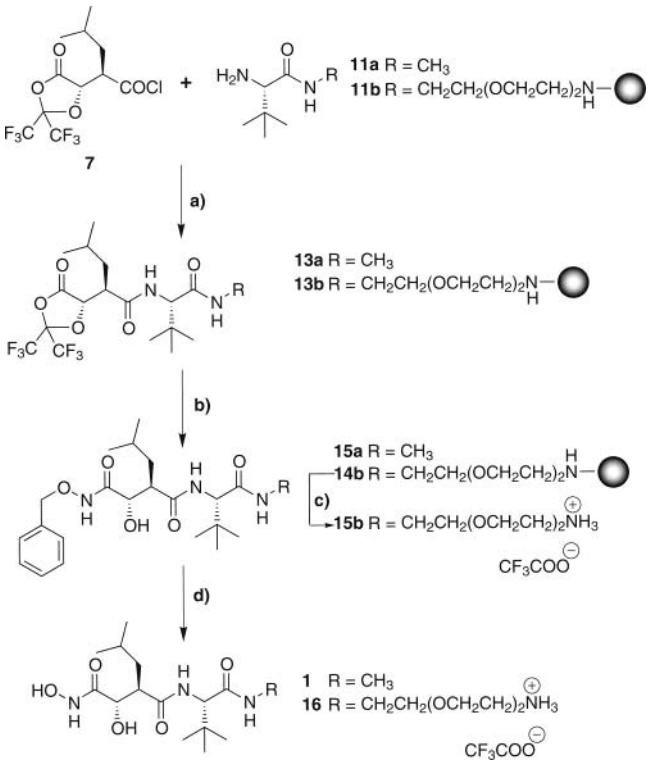
A dilute solution of **11a** and dry triethylamine in dry THF is added slowly to a solution of **7** at −65 °C (Scheme 3). Concentration, temperature, and base are very important for the success of the reaction, e.g., the amine hydrochloride formed during the reaction should be insoluble in the solvent and precipitate. Higher temperature leads to the concomitant opening of the dioxolanone ring and only to a small amount of product **13a**.

Scheme 2[a]



[a] Reagents and conditions: Boc_2O, NaOH, *tert*-butyl alcohol/H_2O, rt, 12 h, 93%; (b) *N*-methylamine, TBTU, DIPEA, acetonitrile, rt, 14 h, 71%; (c) TFA/DCM (1:1), rt, 1 h, 99%.

Scheme 3[a]



[a] Reagents and conditions: THF, NEt_3, −65 °C, 1.5 h; (b) $BnONH_2$. HCl, NEt_3, DCM, rt, 2 h; (c) 1% TFA/DCM, rt, 1 h; (d) H_2, Pd/C (5%), MeOH, rt, 4 h.

Ring-opening of the dioxolanone ring in **13a** quickly occurs upon addition of *O*-benzylhydroxylamine, an O-protected reagent suited for the synthesis of hydroxamic acids. The intermediate **15a**, obtained from **13a** has the advantage that it can be purified by column chromatography. The benzyl protecting group of **15** is easily removed by hydrogenation on Pd/C in a protic solvent like methanol or ethanol. Small amounts of catalyst prevent reductive N−O bond cleavage. Further purification of the free marimastat **1** by RP-HPLC is usually not necessary.

To permit a modular assembly of the new immobilizable marimastat derivative **16**, a linker had to be attached. The L-leucinamide derivate **11b** with a tether for immobilization attached to the amide nitrogen is obtained by solid-phase synthesis. The highly acid-labile 2-chlorotrityl chloride resin was chosen to be loaded with a large excess of the diamino triethylene glycol derivative

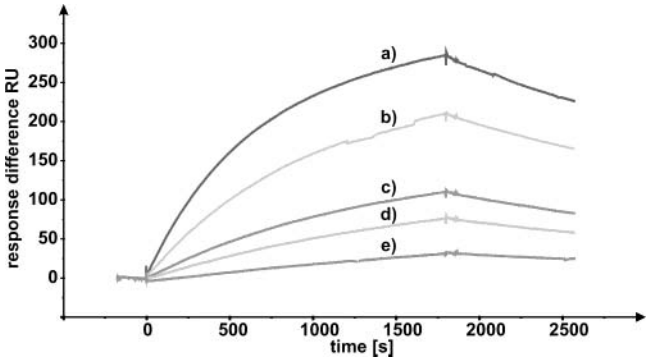
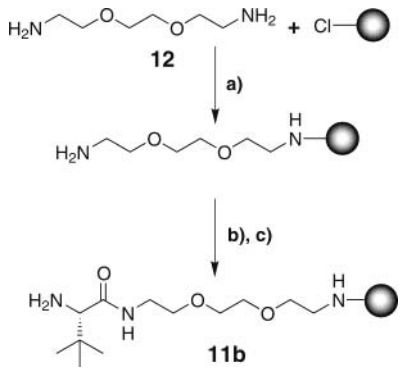


Figure 1. Binding studies with immobilized marimastat derivative on a CM5 sensorchip. Increasing concentrations of activated MMP-2 result in increasing response: (a) 55 nM, (b) 28 nM, (c) 19 nM, (d) 14 nM, (e) 3 nM.

Scheme 4[a]



[a] Reagents and conditions: DCM, rt, 2 h; (b) Fmoc-L-*tert*-leucine, DIPEA, TBTU, DMF, rt, 1 h; (c) 25% piperidine/DMF, rt, 1 h.

12 (Scheme 4), which should serve as a linker and also provide good water solubility (*17*−*19*). After the residual reactive positions are capped with methanol, Fmoc-*tert*-leucine is smoothly coupled to the free amino group using the standard TBTU coupling protocol followed by Fmoc cleavage (Scheme 4). Subsequently, coupling of the hexafluoroacetone protected acid chloride **7** to the free amino group of **11b** results in formation of resin-bound dioxolanone **13b** (Scheme 3). The dioxolanone ring is then opened with $BnONH_2$, and treatment with 1% TFA in CH_2Cl_2 cleaves the product **15b** from the resin. It is isolated in 28% overall yield after purification by RP-HPLC. After hydrogenation, product **16** is obtained in good purity, so that additional RP-HPLC is usually not necessary.

In contrast to the known synthetic routes for marimastat **1**, which start with the alkylation of (2*S*)-2-hydroxysuccinic dimethyl ester with methallyl bromide at C3 and lead to overalls yields of 5−6% (*5*), our synthesis gives overall yields which usually lie in range of 11%, although we need three more steps. Surface plasmon resonance experiments are suited to prove whether the new marimastat derivative **16** is still capable of binding MMP. The marimastat derivative **16** is successfully immobilized across the free amino group on a CM5 sensor chip using the standard EDC/NHS coupling protocol. Binding studies with activated MMP-2 show that MMP-2 binds in a concentration-dependent manner to the immobilized marimastat derivate **16**. The response levels correlate linearly with the concentration of the injected protein solution as to be expected for specific, mechanism-based binding (Figure 1). The K_D value for this complex is calculated to be 12 nM, which is in the same range of

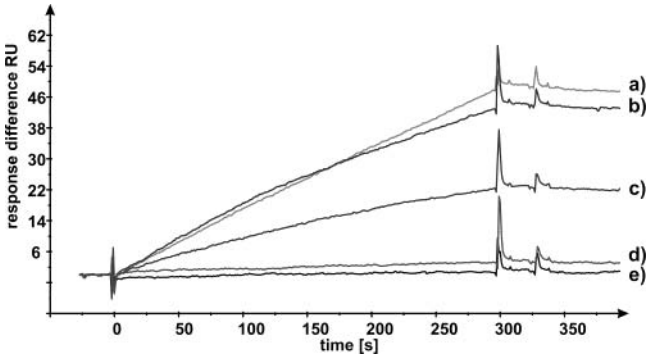


Figure 2. Competition in solution with soluble marimastat derivative **16**: 14 nM MMP-2 was incubated for 30 min with different concentrations of marimastat derivative **16** prior to the SPR experiments: (a) 0 nM, (b) 9 nM, (c) 18 nM, (d) 45 nM, (e) 180 nM.

the reported IC_{50} value for marimastat (BB-2516) against MMP-2 (6 nM) (*6*). Hence, the modified marimastat derivative **16** binds to MMP-2 with comparable affinity as the parent compound **1**. Binding specificity is clearly proven by competition in solution experiments with nonimmobilized **16** (Figure 2).

The elution conditions of bound protein are important for the application of affinity chromatography. Different approaches were tested to elute the protein from the chip surface. A shift to higher or lower pH and also a higher sodium chloride concentration do not lead to a considerable reduction of the response level. The use of a 0.5 solution of SDS causes rapid elution of MMP-2 but results in denaturation of the protein. A smooth procedure to get the bound protein released is accomplished by treatment with HBS-EP buffer (pH 7.4). Two injections over 10 min are necessary to completely release all bound MMP-2 from the surface. These conditions are supposed to be directly applicable to affinity chromatography.

DISCUSSION

Starting from D-diethyl tartrate **2**, an enantiomerically pure, selectively protected and activated marimastat precursor is obtained that permits a new route for the synthesis of both marimastat **1** and an immobilizable marimastat derivative **16**. The latter can be used for surface plasmon resonance studies with metalloproteinases. MMP-2 as the representative proteinase binds to the surface-immobilized broad-spectrum inhibitor in a concentration-dependent manner. Binding can be potentially used for affinity purification of metalloproteinases under optimized elution conditions, determined in surface plasmon resonance studies.

ACKNOWLEDGMENT

Support from Deutsche Forschungsgemeinschaft (SFB 549), University of Bielefeld and Fonds der Chemischen Industrie, Frankfurt, is gratefully acknowledged. The authors also thank Prof. Dr. Klaus Burger, University of Leipzig, for providing hexafluoroacetone trihydrate and Dr. Matthias Letzel, University of Bielefeld, for the HRMS measurements.

LITERATURE CITED

(1) Turkova, J. (1978) *Affinity Chromatography*, pp 1−11, Elsevier Scientific Publishing Company, Amsterdam-Oxford-New York.

(2) Myszka, D. G., and Rich, R. L. (2000) Implementing surface plasmon resonance biosensors in drug discovery. *Pharm. Sci. Technol. Today 3*, 310−317.

(3) Hagenstein, M. C., Mussgnug, J. H., Lotte, K., Plessow, R., Brockhinke, A., Kruse, O., and Sewald, N. (2003) Affinitätsbasierte Markierung von Proteinfamilien mit reversiblen Inhibitoren − ein Konzept für die funktionelle Proteomik. *Angew. Chem. 115*, 5793−5796; Affinity-based tagging of protein families with reversible inhibitors: a concept for functional proteomics. *Angew. Chem., Int. Ed. Engl. 42*, 5635−5638.

(4) Yamamoto, M., Tsujishita, H., Hori, N., Ohishi, Y., Inoue, S., Ikeda, S., and Okada, Y. (1998) Inhibition of membrane-type 1 matrix metalloproteinase by hydroxamate inhibitors: an examination of the subsite pocket. *J. Med. Chem. 41*, 1209−1217.

(5) Levy, D. E., Lapierre, F., Liang, W., Lange, C. W., Li, X., Grobelny, D., Casabonne, M., Tyrrel, D., Holme, K., Nadzan, A., and Galardy, R. E. (1998) Matrix metalloproteinase inhibitors: a structure−activity study. *J. Med. Chem. 41*, 199−223.

(6) Whittaker, M., Floyd, C. D., Brown, P., and Gearing, A. J. H. (1999) Design and therapeutic application of matrix metalloproteinase inhibitors. *Chem. Rev. 99*, 2735−2776.

(7) Beckett, R. P., Davidson, A. H., Drummond, A. H., Huxley, P., and Whittaker, M. (1999) Recent advances in matrix metalloproteinase inhibitor research. *Drug Discovery Today 1*, 16−26.

(8) Rasmussen, H. S., and McCann, P. P. (1997) Matrix metalloproteinase inhibition as a special novel strategy: a review with special focus on batimastat and marimastat. *Pharmacol. Ther. 75*, 69−75.

(9) Pratt, L. M., Beckett, R. P., Corkill, D. J., Cossins, J., Courtney, P. F., Davies, J. D., Davidson, A. H., Drummond, A. H., Helfrich, K., Lewis, C. N., Mangan, M., Martin, F. M., Miller, K., Nayee, P., Ricketts, M. L., Thomas, W., Todd, R. S., and Whittaker, M., (1998) The synthesis of novel metalloproteinase inhibitors employing the Ireland-Claisen rearrangement. *Bioorg. Med. Chem. Lett. 8*, 1359−1364.

(10) Barlaam, B., Koza, P., and Berriot, J. (1999) Solid-phase synthesis of hydroxamic acid based TNF-α convertase inhibitors. *Tetrahedron 55*, 7221−7232.

(11) Mori, K., Iwasawa, H. (1980) Stereoselective synthesis of optically active forms of δ-multistrain, the attractant for european populations of the smaller elm bark beetle. *Tetrahedron 36*, 87−90.

(12) Pirrung, M. C., Hang, H., Nunn, D. S., (1994) Kinetic mechanism and reaction pathway of thermus thermophilus isopropylmalate dehydrogenase. *J. Org. Chem. 59*, 2423−2429.

(13) Weygand, F., and Burger, K., (1966) 2,2-Bis-trifluormethyl-1,3-dioxolanone-(4). *Chem. Ber. 99*, 2880−2884.

(14) Burger, K., Windeisen, E., and Pires, R., (1995) New efficient strategy for the incorporation of (*S*)-isoserine into peptides. *J. Org. Chem. 60*, 7641−7645.

(15) Halab, L., and Lubell, W. D., (1999) Use of steric interactions to control peptide turn geometry. Synthesis of type VI β-turn mimics with 5-*tert*-butylproline. *J. Org. Chem. 64*, 3312−3321.

(16) Ye, T., and McKervey, M. A., (1992) Chiral N-protected α-amino-β-diketones. *Tetrahedron 48*, 8013−8014.

(17) Barlos, K., Gatos, D., Kallitsis, I., Papaioannou, D., and Sotiriu, P., (1988) Anwendung von 4-Polystyryltriphenylmethylchlorid zur Synthese von Peptiden und Aminosäuren. *Liebigs Ann. Chem*., 1079−1081.

(18) Barlos, K., Gatos, D., Kallitsis, J., Papaphotiu, G., Sotiriu, P., Wenging, Y., and Schäfer, W., (1989) Darstellung geschützter Peptid-Fragmente unter Einsatz substituierter Triphenylmethyl-Harze. *Tetrahedron Lett. 30*, 3943−3950.

(19) Nash, I. A., Bycroft, B. W., and Chan, W. C., (1996) Dde − a selective primary amine protecting group: a facile solid-phase approach to polyamine conjugates. *Tetrahedron Lett. 37*, 2625−2628.

BC034225L

Biotin Reagents in Antibody Pretargeting. 6. Synthesis and in Vivo Evaluation of Astatinated and Radioiodinated Aryl- and *nido*-Carboranyl-biotin Derivatives

D. Scott Wilbur,*,† Donald K. Hamlin,† Ming-Kuan Chyan,† Brian B. Kegley,† Janna Quinn,‡ and Robert L. Vessella‡

Departments of Radiation Oncology and Urology, University of Washington, Seattle, Washington 98195. Received December 18, 2003; Revised Manuscript Received February 21, 2004

An investigation has been conducted to prepare and evaluate several radiohalogenated biotin derivatives as part of our studies to develop reagents for carrying ^{211}At in cancer pretargeting protocols. The primary goal of the investigation was to determine the in vivo stability and distribution properties of astatinated biotin derivatives. In addition to astatination, the biotin derivatives were radioiodinated for in vitro and in vivo comparison. Biodistributions were conducted in athymic mice, with sacrifice times of 1, 4, and 24 h to correspond to 9%, 32%, and 90% of ^{211}At decay ($t_{1/2}$ = 7.21 h). In the investigation, two biotin derivatives, **1a** and **2a**, were synthesized which had structures that contain a biotin moiety, a biotinidase-blocking moiety, an ether linker moiety, and an aryl stannane moiety for radiohalogenation. Biotin derivatives **1a** and **2a** were radiolabeled with $^{125/131}$I to give [$^{125/131}$I]**1b** or [^{125}I]**2b** and with ^{211}At to give [^{211}At]**1c** or [^{211}At]**2c**. In vivo studies demonstrated that co-injected [^{125}I]**2b** and [^{131}I]**1b** had very similar tissue distributions in athymic mice. Co-injection of [^{211}At]**2c** and [^{125}I]**2b** provided data that indicated that rapid deastatination occurred in vivo. A second set of biotin derivatives, **3a**, **4a**, and **5a**, were synthesized which had structures that contain a biotin moiety, a biotinidase-blocking moiety, and an anionic *nido*-carborane moiety for radiohalogenation. The biotin derivatives **4a** and **5a** contained an aryl moiety not present in **3a**, and **5a** had a trialkylamine functionality not present in **3a** or **4a**. Biotin derivative **3a** was radioiodinated, but was not further investigated. Biotin derivatives **4a** and **5a** were radiolabeled with ^{211}At and ^{125}I to produce [^{125}I]**4b**/[^{211}At]**4c** and [^{125}I]**5b**/[^{211}At]**5c**. Comparison of [^{125}I]**4b** and (separately) [^{125}I]**5b** with [^{131}I]**1b** showed that the *nido*-carborane containing biotin derivatives were retained in blood and tissue more than the aryl iodide derivative. In vivo evaluations of [^{211}At]**4c**/[^{125}I]**4b** and (separately) [^{211}At]**5c**/[^{125}I]**5b** indicated that some deastatination occurred in these compounds, but it was much less than observed for the aryl derivative [^{211}At]**2c**. While the *nido*-carborane containing biotin derivatives provide a significant improvement in astatine stability over biotin derivatives previously studied, additional derivatives need to be prepared and studied to further improve the in vivo stability and blood/tissue clearance of these compounds.

INTRODUCTION

We are investigating the use of the α-particle-emitting radionuclide astatine-211 (^{211}At) in "targeted radionuclide therapy" [1] (TRT[2]) of metastatic cancer. α-Particle-emitting radionuclides have properties that make them favorable for use in the therapy of small groups of cancer cells (micrometastatic disease) and single cancer cells (*1*−*5*). Those favorable properties include very short path lengths (50−85 μm) of the α-particle, allowing irradiation of only a few cell diameters, and very high cellular toxicity due to a large energy deposition (e.g. 100 keV/μm) over that short path length (*6*). Among the few α-emitting radionuclides that have favorable decay properties for in vivo use (*7*), ^{211}At is particularly attractive, as it is readily prepared in quantities sufficient for clinical application (*8*). Importantly, it has a half-life that is short enough ($t_{1/2}$ = 7.2 h) for use in an outpatient approach but long enough to allow adequate targeting of cancer cells in vivo. This latter point is only true if the cancer-targeting carrier molecule used in combination with ^{211}At has appropriate pharmacokinetics.

A number of cancer-targeting intact monoclonal antibodies (mAb) and their F(ab′)$_2$ fragments have been labeled with ^{211}At (*9*). However, except in special applications, these carrier molecules do not have appropriate cancer targeting and blood clearance properties for use with ^{211}At due to its short half-life (*10*). Smaller mAb

* Address correspondence to D. Scott Wilbur, Ph.D., Department of Radiation Oncology, University of Washington, 2121 N. 35th Street, Seattle, WA 98103-9103. Phone: 206-685-3085. Fax: 206-685-9630. E-mail: dswilbur@u.washington.edu.

† Department of Radiation Oncology.

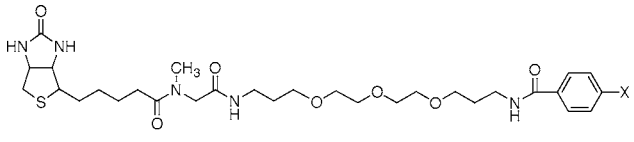
‡ Department of Urology.

[1] "Targeted radionuclide therapy", "targeted radiopharmaceutical therapy", "targeted radiotherapy", and "endoradiotherapy" are all terms used to describe an approach to radiotherapy that involves administration (injection) of a disease-targeting radiopharmaceutical that carries a therapeutic radionuclide.

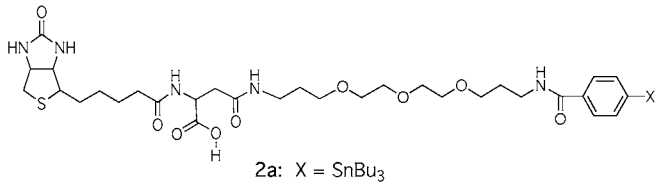
[2] Abreviations: ChT, chloramine-T.; cpm, counts per minute; DCC, 1,3-dicyclohexylcarbodiimide; DTDC.; di-*tert*-butyl dicarbonate; mAb, monoclonal antibody; NCS, *N*-chlorosuccinimide; %ID/g, percent injected dose/gram; PBS, phosphate-buffered saline; pi, postinjection; rt, room temperature, Sav, streptavidin; tBoc, *tert*-butoxycarbonyl; TFA, trifluoroacetic acid; TFP, 2,3,5,6-tetrafluorophenyl; TFP-OH, 2,3,5,6-tetrafluorophenol; TFP-OTFA, 2,3,5,6-tetrafluorophenyl trifluoroacetate; TRT, targeted radionuclide therapy.

10.1021/bc034229q CCC: $27.50 © 2004 American Chemical Society
Published on Web 04/30/2004

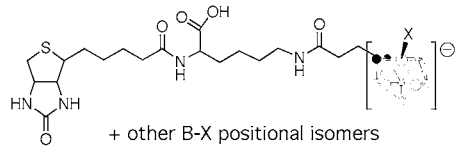
Chart 1. Biotin Derivatives Prepared in the Study



1a: X = $SnBu_3$
1b: X = I, ^{131}I
1c: X = ^{211}At

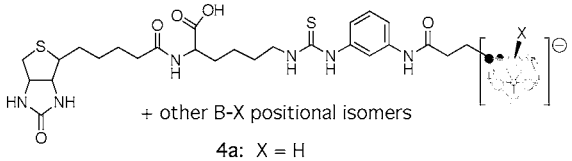


2a: X = $SnBu_3$
2b: X = I, ^{125}I
2c: X = ^{211}At



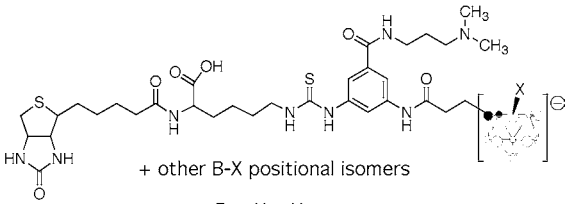
+ other B-X positional isomers

3a: X = H
3b: X = I, ^{125}I



+ other B-X positional isomers

4a: X = H
4b: X = I, ^{125}I
4c: X = ^{211}At



+ other B-X positional isomers

5a: X = H
5b: X = I, ^{125}I
5c: X = ^{211}At

fragments, such as Fab′ or single chain Fv fragments, have more appropriate pharmacokinetics, but they have a propensity to localize to kidney making their use unfavorable. To improve the pharmacokinetics of the astatine carrier molecule, we are investigating an alternative approach, termed "pretargeting" (*11*−*14*), which employs radiolabeled biotin derivatives to deliver ^{211}At to cancer cells in vivo. In the pretargeting approach, a monoclonal antibody−streptavidin conjugate (mAb−SAv) is injected and allowed to bind antigens on cancer cells. After a period of time for adequate tumor targeting (e.g. 24 h), a clearing agent is used to remove excess mAb−SAv conjugate from blood. After an appropriate time (e.g. 1−3 h), the ^{211}At-labeled biotin derivative is administered such that it can bind with the prebound (pretargeted) mAb−SAv on cancer cells. Importantly, this approach has been shown to provide very good tumor targeting, with cures for human tumor implants (xenografts) in athymic mice using other therapeutic radionuclides (*15*, *16*), and has progressed to clinical trials (*17*).

While a number of radiometal-chelated biotin derivatives have been used successfully in pretargeting protocols, there have been no reports of successful applications of radiohalogen-labeled biotin derivatives. Thus, our initial studies were focused on improving the in vivo characteristics of radiohalogenated biotin derivatives. Importantly, those studies provided information on structural requirements for blocking the serum enzyme biotinidase (*18*, *19*) while retaining the desired high binding affinity of the biotin derivatives (*20*). In some of the studies, the required structural features were combined with stannylbenzoates to prepare radioiodinated biotin derivatives for evaluation. We knew from previous studies with aryl stannanes that they could be used for astatination (*21*, *22*), leading us to believe that an astatinated biotin derivative for in vivo use could be readily obtained. However, as the studies described herein point out, astatinated aryl-biotin derivatives can be quite unstable to in vivo deastatination. Therefore, additional biotin derivatives were prepared which incorporated an alternate ^{211}At-binding moiety, a *nido*-carborane.[3]

Previous studies by Hawthorne et al. demonstrated that a *nido*-carborane conjugate could be used to radioiodinate antibodies (*23*). We also investigated *nido*-carboranes as hydrophilic pendant groups for coupling radionuclides of iodine to biomolecules (*24*, *25*). Those investigations demonstrated that *nido*-carborane-containing molecules radioiodinated rapidly (<10 s) and provided high radiochemical yields (85−99%). Importantly, the resultant radioiodinated *nido*-carboranes were stable to in vivo dehalogenation. Subsequently, we demonstrated for the first time that *nido*-carboranes could be rapidly and efficiently labeled with ^{211}At (*26*). More recently we undertook a detailed in vivo evaluation of astatinated benzamides and *nido*-carboranes, and found that some *nido*-carborane derivatives appeared to provide increased in vivo stability (*27*). On the basis of the information gained from the prior studies, we undertook the study described herein to determine if biotin derivatives containing a *nido*-carboranyl moiety were more stable to deastatination than a biotin derivative astatinated on an aryl moiety. The investigation included (a) astatination of two biotin-aryl derivatives (**1a**, **2a**), (b) in vivo evaluation of the radiohalogenated aryl-biotin derivative (**2a**), (c) syntheses and radiohalogenations of

[3] The term "*nido*-" (nestlike) signifies an icosahedral carborane cage molecule that has a boron atom removed from its apex. Borane cage molecules that have a complete (closed) icosahedron structure are referred to as "*closo*-carboranes". The borane cage molecules evaluated in this study can be referred to as dicarbaboranes, as they contain two carbon atoms. For simplicity, they are termed "carboranes" herein.

three of *nido*-carboranyl-biotin derivatives (**3a**, **4a**, **5a**), and (d) in vivo evaluations of two *nido*-carboranyl-biotin derivatives (**4a**, **5a**). In some of the studies, biotin derivatives were dual labeled (^{211}At and ^{125}I) such that a comparison of the ^{211}At and ^{125}I concentrations in tissues, particularly lung, spleen, and thyroid, of the mice could be made.

EXPERIMENTAL PROCEDURES

General. Chemicals purchased from commercial sources were analytical grade or better and were used without further purification, except where noted. 4-Pentynoic acid, **13**, was obtained from Lancaster (Windham, NC) or Farchan Laboratories (Gainesville, FL). L-Aspartic acid α-*tert*-butyl ester, **7**, and L-lysine-ϵ-*N*-*tert*-butoxycarbonyl-(Boc), **16**, were obtained from Calbiochem-Novabiochem Corp. (San Diego, CA). Chloramine-T (ChT), D-biotin, and phosphate-buffered saline (PBS) were obtained from Sigma (Sigma-Aldrich Corp., St. Louis, MO). Dimethylaminopropylamine, *N*-chlorosuccinimide, tetrafluorophenol, 1,3-phenylenediamine, **19**, 3,5-diaminobenzoic acid, **23**, and most other chemicals were obtained from Aldrich (Sigma-Aldrich Corp., Milwaukee, WI). Solvents for HPLC analysis were obtained as HPLC grade and were filtered (0.2 μm) prior to use. Tetrafluorophenyl trifluoroacetate (TFP-OTFA) was prepared as previously described (*28*). Biotin deficient/egg white enriched (avidin rich) mouse chow (#5836 test diet from basal diet #5755) was obtained from Purina Test Diets (Richmond, IN).

Radioactivity. All radioactive materials were handled according to approved protocols at the University of Washington. ^{211}At production was accomplished by α-particle irradiation (28 MeV) of natural bismuth, via ^{209}Bi(α, 2n)^{211}At reaction, on the University of Washington Scandatronix MC-50 cyclotron. The ^{211}At activity was distilled from the bismuth target at 650−700 °C into a cooled trap as previously described (*29*). The dry distillation of ^{211}At was conducted in a charcoal-filtered glovebox (Innovative Technologies, radioisotope glovebox). The ^{211}At was trapped in a cooled (−78 °C) vial and was rinsed from the vial with 0.05 N NaOH for use in the labeling experiments.

All radiohalogenation reactions ($^{125/131}$I or ^{211}At) were conducted in vials capped with Teflon-coated septa, within a radioactivity-approved fume hood. The reaction vials were vented through a 10 mL charcoal-filled syringe. Additions of reagents and radionuclides to, or removal of materials from, radiohalogenation vessels were conducted by passing a syringe needle through the septa. All radiohalogenation reactions were conducted in a charcoal-filtered Plexiglas enclosure within a radiochemical fume hood.

Na[^{125}I]I and Na[^{131}I]I were purchased from Perkin-Elmer Life and Analytical Sciences (formerly NEN/Dupont, Billerica, MA) as high concentration/high specific activity radioiodide in 0.1 N NaOH. Measurement of ^{125}I, ^{131}I, and ^{211}At was accomplished in one of two different dose calibrators. Measurements were conducted on either a Capintec CRC-15R or a Capintec CRC-6A Radioisotope Calibrator using calibration #44. Tissue samples containing these radionuclides were counted in a Wallac Wizard gamma counter with the following window settings: channels 35 to 102 (20−90 keV) and channels 165 to 185 (300−450 keV) when ^{125}I and ^{131}I were counted together. Tissue samples containing ^{211}At and ^{125}I were counted in all channels to get total radioactivity. The tissue samples were recounted in all channels after 3−5 days (0.1% of ^{211}At or less remaining) to obtain ^{125}I counts. These data were transferred to an Excel (Microsoft Corp., Redmond, WA) spreadsheet where the ^{211}At radioactivity was calculated by subtracting the ^{125}I counts from the total counts for each tissue sample. ^{211}At counts were corrected for decay during the counting process.

Spectroscopic Data. ^{1}H NMR spectra were obtained on a Bruker AC-200 (200 MHz), Bruker AF-301 (300 MHz), or Bruker AM-500 (500 MHz) instrument. The chemical shifts are expressed as ppm using tetramethylsilane as an internal standard ($\delta = 0.0$ ppm). ^{11}B NMR were obtained at 160 MHz (500 MHz for ^{1}H) and 96 MHz (300 MHz for ^{1}H). The spectra are referenced ($\delta = 0.0$ ppm) to $BF_3{\cdot}O(Et)_2$ as an external standard (insert) in the NMR tube. ^{11}B NMR included ^{1}H-coupled and -decoupled spectra for all samples examined. Only ^{1}H decoupled resonances are reported. All ^{11}B resonances were split when in the coupled spectra except in iodinated samples where one proton was not coupled. IR data were obtained on a Perkin-Elmer 1420 infrared spectrophotometer. Mass spectral data were obtained on a VG 70SEQ mass spectrometer with 11250J data system. Fast atom bombardment (FAB^+) mass spectral data were obtained at 8 kV using a matrix of 90% thioglycerol, 9% DMSO, and 1% TFA (DMIX) or propylene glycol 600 containing thioglycolate. Electrospray mass spectral data was obtained on a Micromass Quattro II Tandem Quadrupole Mass Spectrometer.

Analytical Chromatography. All reactions were monitored by HPLC. Nonradioactive samples were assessed on a system that contained a Hewlett-Packard quaternary 1050 gradient pump, a variable wavelength UV detector (254 nm), and a Varex ELSD MKIII or ELSD 2000 evaporative light-scattering detector. Analyses of the HPLC data were conducted on Hewlett-Packard HPLC ChemStation software. Reversed-phase HPLC chromatography was carried out on an Alltech Altima C-18 column (5 μm, 250 × 4.5 mm) using a gradient solvent system at a flow rate of 1 mL/min. Solvent A in the gradient was methanol. Solvent B was aqueous 0.1% HOAc. Starting from 40% A, the initial solvent mixture was held for 2 min, and then the gradient was increased linearly to 100% A over the next 10 min and 100% A was held for 8 min. Retention times (t_R) of biotin derivatives are provided with the experimental for each compound.

Radioiodinated and astatinated compounds were evaluated by reversed-phase HPLC analyses. All radioiodinated compounds were characterized by correlation with nonradioactive iodinated standards on the HPLC. Astatinated compounds generally had slightly longer retention times on reversed-phase HPLC than did the iodinated standards. The HPLC system consisted of two Beckman model 110B pumps, a Beckman 420 controller, a Beckman model 153 UV detector (254 nm), and a Beckman model 170 radioisotope detector. Analysis of the HPLC data were conducted on a PC running Hewlett-Packard HPLC ChemStation software. Reversed-phase HPLC chromatography was carried out on an Alltech Altima C-18 column (5 μm, 250 × 4.5 mm) using a gradient solvent system at a flow rate of 1 mL/min. Retention times (t_R) of biotin derivatives are provided with the experimental for each compound.

Syntheses of the following compounds were conducted as previously described in the literature: *N′*-(13-(*p*-tri-*n*-butylstannylbenzamido)-4,7,10-trioxatridecanyl)-*N*-methylglycylbiotinamide, **1a** (*18*), *N′*-(13-(*p*-iodobenzamido)-4,7,10-trioxatridecanyl)-*N*-methylglycylbiotinamide, **1b** (*18*); biotin tetrafluorophenyl ester, **6** (*30*), N-biotinyl-α-*tert*-butyl-L-aspartate TFP ester, **8** (*20*); *N*-(*tert*-butoxycarbonyl)-4,7,10-trioxa-1,13-tridecanediamine, **9** (*31*), 2-(*N*-

biotinyl)-4-(*N*′-(13′-*tert*-butoxycarbonylamino)-4′,7′,10′-trioxatridecaneamino)-L-aspartate 1-*O*-*tert*-butyl ester, **10** (*19*), 4-tri-*n*-stannylbenzoate tetrafluorophenyl ester, **12a** (*18*), 4-iodobenzoate tetrafluorophenyl ester, **12b** (*18*), pentynoic acid tetrafluorophenyl ester, **14** (*27*); 3-(*closo*-carboranyl)propionate tetrafluorophenyl ester, and **15** (*27*); *N*-(3-aminophenyl)-3-(*closo*-carboranyl)propionamide, **20** (*27*).

2-(*N*-Biotinyl)-4-(*N*′-(13′-amino-4′,7′,10′-trioxatridecaneamino)-L-aspartate, 11. A 500 mg (0.70 mmol) quantity of **10** was dissolved in 5 mL of trifluoroacetic acid (TFA). The mixture was stirred at room temperature for 30 min, and then the TFA was removed under a stream of nitrogen. The crude residue was washed with anhydrous ether (3 × 20 mL). The TFA salt of **11** was dried under vacuum and was used directly in the next step, yield ~100%. ^{1}H NMR (CD_3OD, 200 MHz) δ 1.39−1.54 (m, 4H), 1.59−1.82 (m, 6H), 1.89−2.01 (m, 2H), 2.24−2.32 (m, 2H), 2.69−2.99 (m, 4H), 3.13 (t, J = 6.3 Hz, 2H), 3.20−3.34 (m, 4H), 3.52 (t, J = 5.9 Hz, 2H), 3.57−3.77 (m, 7H), 4.33 (dd, J = 4.4, 8.1 Hz, 1H), 4.51 (dd, J = 4.4, 8.1 Hz, 1H), 4.78 (dd, J = 5.5, 7.3 Hz, 1H). HRMS (ES$^+$), calcd for $C_{24}H_{44}N_5O_8S$ (M + H)$^+$, 562.2911, found 562.2890; HPLC, t_R = 3.6 min.

2-(*N*-Biotinyl)-4-(*N*′-(13′-(4″-tri-*n*-butylstannylbenzoyl)amino)-4′,7′,10′-trioxatridecaneamino)-L-aspartate, 2a. A 150 mg (0.268 mmol) quantity of **11** and 75 μL of Et_3N were combined in 6 mL of anhydrous DMF. To that mixture was added 152 mg (0.268 mmol) of *p*-tri-*n*-butylstannylbenzoate TFP ester, **12a**, and the resultant mixture was stirred at room temperature for 30 min. The DMF was removed under vacuum on a Kugelrohr apparatus, and the crude product was placed on high vacuum overnight. The residue was placed on a silica gel column (16 g) and was eluted with 50:50 EtOAc/MeOH. The fractions containing product were concentrated and dried under vacuum to yield 180 mg (70%) of **2a**. ^{1}H NMR ($CDCl_3$, 500 MHz) δ 0.87 (t, J = 7.4 Hz, 9H), 1.06 (t, J = 8.0 Hz, 6H), 1.28−1.36 (m, 6H), 1.44−1.57 (m, 10H), 1.61−1.72 (m, 6H), 1.84−1.89 (m, 2H), 2.13−2.31 (m, 2H), 2.60−2.87 (m, 4H), 3.02−3.27 (m, 6H), 3.39−3.63 (m, 9H), 4.22−4.64 (m, 3H), 6.57 (bs, 1H), 7.50 (d, J = 8.0 Hz, 2H), 7.73 (d, J = 8.0 Hz, 2H). HRMS (ES$^+$) calcd for $C_{43}H_{73}N_5NaO_9SSn$ (M + Na)$^+$ 978.4049, found: 978.4079; HPLC, t_R = 16.5 min.

2-(*N*-Biotinyl)-4-(*N*′-(13′-(4″-iodobenzoyl)amino)-4′,7′,10′-trioxatridecaneamino)-L-aspartate, 2b. A 142 mg (0.253 mmol) quantity of **11** and 70 μL (0.505 mmol) of Et_3N were combined in 6 mL of anhydrous DMF. To that mixture was added 100 mg (0.253 mmol) of *p*-iodobenzoate TFP ester, **12b**, and the resultant mixture was stirred at room temperature for 1 h. The DMF was removed on a Kugelrohr apparatus, and the residue was placed on a silica gel column. The column was eluted with 50:50 EtOAc/MeOH. The fractions containing product were combined and dried under high vacuum to yield 159 mg (80%) of the iodobenzamidyl biotin derivative **2b** (*32*).

1-*N*-(Biotinyl)-5-*N*-(*tert*-butyloxycarbonyl)-L-lysine, 17a. Biotin tetrafluorophenyl ester **6** (1.64 g, 4.18 mmol) was added to a solution of *N*-ϵ-*tert*-Boc-L-lysine **16** (1.0 g, 4.06 mmol), $NaHCO_3$ (1.13 g, 13.40 mmol), H_2O (40 mL), and acetone (40 mL) at room temperature. The reaction mixture was stirred at room temperature for 16 h, and then volatile materials were evaporated under vacuum. The residue was washed with 60 mL of EtOAc and neutralized with 14.0 mL of 1.0 N HCl. After standing at 5 °C overnight, the product was filtered, washed with cold water, and dried under vacuum to yield 1.91 g (87%) of compound **17a** as a white solid: mp 156.8−157.5 °C. ^{1}H NMR (CD_3OD): δ 1.43 (s, 9 H), 1.48−1.90 (m, 10 H), 2.26 (t, J = 7.2 Hz, 2 H), 2.69 (d, J = 12.8 Hz, 1 H), 2.89−3.05 (m, 3 H), 3.16−3.26 (m, 1 H), 3.29−3.34 (m, 2 H), 4.26−4.34 (m, 2 H), 4.49 (dd, J = 4.8, 8.1 Hz, 1 H). HRMS (FAB$^+$) calcd for $C_{21}H_{36}N_4O_6SNa$ (M + Na)$^+$ 495.2253, found: 495.2240; HPLC: t_R = 10.3 min.

1-*N*-(Biotinyl)-L-lysine, 17b. A 1.0 g quantity (2.12 mmol) of **17a** was dissolved in 8 mL of TFA. The solution was stirred for 30 min at room temperature, and the excess TFA was removed using a gentle stream of air. The crude residue was washed 2× with 15 mL of ether. The resultant solid was dissolved in a minimum amount of MeOH, made basic with Et_3N (8 mL), and stirred for 30 min at room temperature. The MeOH and excess Et_3N were removed under a stream of air and then under vacuum to yield 772 mg (98%) of **17b** as a colorless solid. mp > 250 °C (dec); ^{1}H NMR (CD_3OD, 500 MHz) δ 1.41−1.53 (m, 4H), 1.57−1.78 (m, 6H), 1.88−1.95 (m, 1H), 2.23−2.34 (m, 2H), 2.68−2.71 (m, 1H), 2.91−2.94 (m, 3H), 3.19−3.23 (m, 1H), 3.30−3.31 (m, 1H), 4.31 (dd, J = 4.3, 8.0 Hz, 1H), 4.39 (dd, J = 4.3, 8.0 Hz, 1H), 4.50 (dd, J = 5.0, 8.0 Hz, 1H). HRMS (ES$^+$) calcd for $C_{16}H_{29}N_4O_4S$ (M + H)$^+$ 373.1910, found 373.1915; HPLC: t_R = 2.7 min.

1-*N*-(Biotinyl)-5-*N*-(3′-(*closo*-carboranyl)propionyl)-L-lysine, 18. A 750 mg quantity of **17b** (2.02 mmol) and Et_3N (285 μL, 2.02 mmol) were dissolved into 4 mL of anhydrous DMF. To the solution was added **15** (743 mg, 2.20 mmol), and the reaction mixture was stirred for 1.5 h at room temperature. The reaction solution was diluted with 10 mL of H_2O and then washed with EtOAc (2 × 25 mL). The H_2O and DMF were removed under vacuum (Kugelrohr). The residue was further dried under high vacuum to yield 966 mg (84%) of **18** as a colorless solid: mp 176−179 °C; ^{1}H NMR (CD_3OD, 200 MHz) δ 1.36−1.85 (m, 17H), 2.23−2.45 (m, 5H), 2.54−2.73 (m, 4H), 2.93 (dd, J = 5.1, 12.8 Hz, 1H), 3.12−3.26 (m, 4H), 3.29−3.32 (m, 1H), 4.27−4.38 (m, 2H), 4.49 (dd, J = 5.0, 8.0 Hz, 1H), 4.55 (bs, 1H); ^{11}B NMR (CD_3OD, decoupled, 64 MHz) δ −8.33 (4B), −10.49 (6B). HRMS (ES$^+$) calcd for $C_{21}H_{43}B_{10}N_4O_5S$ (M + H)$^+$ 573.3885, found 573.3914; HPLC: t_R= 13.2 min.

1-*N*-(Biotinyl)-5-*N*-(3′-(*nido*-carboranyl)propionyl)-L-lysine, 3a. A 50 mg quantity (0.088 mmol) of **18** was dissolved in pyrrolidine (1 mL) cooled in an ice/H_2O bath. This mixture was allowed to warm to room temperature over 30 min. H_2O (5 mL) and diethyl ether (5 mL) were added to the mixture. The ether was separated, and the H_2O layer was washed with ether (4 × 5 mL). The H_2O was removed under vacuum, and the crude residue was dissolved in a 5:4:1 mixture of H_2O:CH_3CN:MeOH (1 mL). This solution was loaded onto an ion exchange column, which was prepared as follows. The ion exchange column was prepared by connecting two Alltech IC-H ion exchange columns in series and washing them with 10 mL of 1 N NaOH. Following this, the columns were washed with H_2O until column reached neutral pH. The columns were then washed with 20 mL of 5:4:1 H_2O:CH_3CN:MeOH solution. Crude product was eluted in 1 mL fractions (20×). Fractions containing product were combined, and solvents were removed under vacuum to yield 42 mg (83%) of **3a** as a tacky solid; ^{1}H NMR (CD_3OD, 300 MHz) δ 1.33−1.91 (m, 16H), 1.98−2.02 (m, 5H), 2.25−2.31 (m, 4H), 2.69 (d, J = 12.5 Hz, 1H), 2.96 (dd, J = 5.2, 12.5 Hz, 1H), 3.15 (t, J = 6.7 Hz, 2H), 3.22−3.32 (m, 5H), 4.22 (dd, J = 4.3, 8.0 Hz, 1H), 4.33 (dd, J = 4.3, 8.0 Hz, 1H), 4.50 (dd, J = 5.0, 8.0 Hz, 1H); ^{11}B NMR (CD_3OD, decoupled, 96 MHz) δ −10.52 (2B), −13.11 (1B), −16.05 (1B), −17.82 (1B), −20.91 (1B), −32.73 (2B),

−37.04 (1B). HRMS (ES^-) calcd for $C_{21}H_{41}B_9N_4O_5S$ $(M)^-$ 560.3635, found 560.3663; HPLC: t_R= 7.9 min.

3-(3′-(*closo*-Carboranyl)propionyl)amino-1-aminobenzene, 20. A 1.0 g quantity (2.72 mmol) of **15** was dissolved in 20 mL of anhydrous DMF. In a separate flask, **19** (0.59 g, 5.43 mmol) was dissolved in 20 mL of anhydrous DMF. The solution containing **15** was added dropwise to the solution containing **19** over a 1 h period. After the addition was complete, the reaction mixture was stirred at room temperature for 2.5 h. DMF was removed under vacuum at 50 °C (Kugelrohr). The residue was dissolved in 50 mL of diethyl ether and was washed with 1% HOAc/H_2O (2 × 25 mL) and then H_2O (25 mL). The ether layer was removed under vacuum, and the colorless solid was dried under vacuum to yield 0.790 g (95%) of **20**: mp 136−137 °C; ^{1}H NMR ($CDCl_3$, 500 MHz) δ 1.57−2.51 (m, 12H), 2.57 (t, J = 7.1 Hz, 2H), 2.68 (t, J = 7.1 Hz, 2H), 3.85 (s, 1H), 6.47 (d, J = 8.0 Hz, 1H), 6.65 (d, J = 8.0 Hz, 1H), 7.06 (s, 1H), 7.09 (t, J = 8.0 Hz, 1H), 7.14 (s, 1H); ^{11}B NMR ($CDCl_3$, decoupled, 160 MHz) δ −8.66 (2B), −9.63 (2B), −10.76 (1B), −12.02 (3B), −12.98 (2B). HRMS (ES^+) calcd for $C_{11}H_{23}B_{10}N_2O$ $(M + H)^+$ 309.2741, found 309.2734; HPLC: t_R = 13.5 min.

3-(3′-(*closo*-Carboranyl)propionyl)amino-1-isothiocyanatobenzene, 21. A 81 mg quantity (0.263 mmol) of **20** was dissolved into 3 mL of DMF. To this solution was added 1,1-thiocarbonyldiimidazole (47 mg, 2.63 mmol), and the reaction mixture was stirred at room temperature for 30 min. DMF was removed under vacuum (Kugelrohr). The residue was dissolved in MeOH (0.5 mL), and 3 mL of H_2O was added. The mixture was stirred for 30 min, and the H_2O was decanted. The solid was washed with another 3 mL of H_2O and dried under vacuum to yield 50 mg (54%) of **21** as a tacky solid. ^{1}H NMR (CD_3OD, 300 MHz) δ 1.27−2.56 (m, 10H), 2.61−2.73 (m, 4H), 4.59 (bs, 1H), 6.98−7.02 (m, 1H), 7.34 (t, J = 8.0 Hz, 1H), 7.39−7.43 (m, 1H), 7.64 (t, J = 2.1 Hz, 1H); ^{11}B NMR (CD_3OD, decoupled, 96 MHz) δ −1.60 (1B), −4.89 (1B), −8.72 (2B), −10.85 (6B). HRMS (ES^+) calcd for $C_{12}H_{20}B_{10}N_2ONaS$ $(M + Na)^+$ 373.2124, found 373.2125; HPLC: t_R = 15.7 min.

3-(3′-(*closo*-Carboranyl)propionyl)amino-1-*N*-(1′-(*N*-biotinyl)-5′-lysyl-thiourea)benzene, 22. A 50 mg quantity (0.14 mmol) of **21**, **17b** (58 mg, 0.16 mmol), and Et_3N (100 μL, 0.71 mmol) were dissolved in 5 mL of DMF. The reaction mixture was stirred for 30 min, and the DMF was removed under vacuum. The residue was dissolved in minimum amount of MeOH, loaded onto a silica gel (20 g) column (1.5 cm × 26 cm), and eluted with an EtOAc/MeOH mixture (50:50). The solvents were removed from the fractions containing the product, and the colorless solid was dried under vacuum to yield 67 mg (65%) of **22**: mp 178−181 °C; ^{1}H NMR (CD_3OD, 500 MHz) δ 1.29 (s, 1H), 1.40−1.46 (m, 4H), 1.55−1.78 (m, 12H), 1.85−1.92 (m, 2H), 2.26−2.29 (m, 4H), 2.67−2.69 (m, 1H), 2.92 (dd, J = 5.0, 13.0 Hz, 1H), 3.18−3.22 (m, 2H), 3.30−3.31 (m, 5H), 3.57 (bs, 1H), 4.28−4.33 (m, 2H), 4.47 (dd, J = 5.0, 8.0 Hz, 1H), 4.61 (bs, 1H), 7.02 (d, J = 8.0 Hz, 1H), 7.29 (t, J = 8.0 Hz, 1H), 7.39 (d, J = 8.0 Hz, 1H), 7.59 (s, 1H); ^{11}B NMR (CD_3OD, decoupled, 160 MHz) δ −1.00 (2B), −8.08 (2B), −10.10 (4B), −11.40 (2B). HRMS (ES^+) calcd for $C_{28}H_{47}N_6O_5S_2B_{10}Na_2$ $(M - H + 2Na)^+$ 767.3775, found 767.3776; HPLC: t_R = 13.3 min.

3-(3′-(*nido*-Carboranyl)propionyl)amino-1-*N*-(1′-(*N*-biotinyl)-5′-lysyl-thiourea)benzene, 4a. A 44 mg quantity (0.06 mmol) of **22** was dissolved in pyrrolidine (1 mL), and the resultant mixture was stirred at room temperature for 1 h. Pyrrolidine was evaporated from the reaction mixture in a fume hood under gentle stream of air. The residue was rinsed with ether (2 × 10 mL), and the ether was decanted. The crude product was dissolved in a 5:4:1 mixture of H_2O:CH_3CN:MeOH (1 mL) and was loaded on an ion exchange column (prepared as described in the synthesis of **3a**). The column was eluted with 1 mL fractions (20×). Fractions containing **4a** were combined, and solvents were removed under vacuum to yield 28 mg (67%) of **4a** as a pale yellow solid: mp 161−163 °C; ^{1}H NMR (CD_3OD, 300 MHz) δ 1.33−1.45 (m, 3H), 1.53−1.71 (m, 6H), 1.78−1.93 (m, 11H), 2.24 (t, J = 7.3 Hz, 2H), 2.47 (t, J = 7.8 Hz, 2H), 2.64 (d, J = 12.5 Hz, 1H), 2.90 (dd, J = 5.0, 13.0 Hz, 1H), 3.06−3.11 (m, 5H), 3.24−3.29 (m, 2H), 3.49−3.57 (m, 1H), 4.20 (dd, J = 4.7, 8.3 Hz, 1H), 4.27 (dd, J = 4.3, 8.0 Hz, 1H), 4.46 (dd, J = 4.3, 8.0 Hz, 1H), 7.03 (d, J = 8.0 Hz, 1H), 7.27 (t, J = 8.0 Hz, 1H), 7.38 (d, J = 8.0 Hz, 1H), 7.57 (t, J = 2.1 Hz, 1H); ^{11}B NMR (CD_3OD, decoupled, 96 MHz) δ −10.42 (2B), −12.68 (1B), −15.92 (1B), −17.72 (1B), −32.63 (2B), −36.78 (2B). HRMS (ES^-) calcd for $C_{28}H_{47}N_6O_5S_2B_9$ $(M)^-$ 710.3887, found 710.3895; HPLC: t_R = 10.0 min.

3-(3′-(*closo*-Carboranyl)propionyl)amino-5-aminobenzoic acid, 24. 3,5-Diaminobenzoic acid dihydrochloride (**23**) (3.7 g, 16.3 mmol) and Et_3N (3.41 mL, 24.5 mmol) were dissolved in 20 mL of DMF under argon atmosphere. A 3 g quantity (8.1 mmol) of TFP ester **15** was dissolved in 20 mL of DMF and was added dropwise over 30 min. The reaction was stirred at room temperature for 1 h. the DMF was removed under vacuum. The crude product was dissolved in hexane/ethyl acetate (4:1), loaded onto a silica column (100 g), and eluted with gradient of starting with hexane/ethyl acetate (4:1). The product eluted with 100% EtOAc. Fractions containing **24** were collected, and solvent was removed under vacuum. The isolated product was dried under vacuum to yield 2.6 g (91%) of **24** as a colorless solid: mp 123−125 °C; ^{1}H NMR (CD_3OD, 500 MHz) δ 1.56−2.55 (m, 10H), 2.58−2.61 (m, 2H), 2.65−2.68 (m, 2H), 4.56 (bs, 1H), 7.11 (s, 1H), 7.24 (s, 1H), 7.41 (s, 1H); ^{11}B NMR (CD_3OD, decoupled, 160 MHz) δ −1.11 (1B), −4.32 (1B), −8.06 (2B), −10.15 (4B), −11.37 (2B). HRMS (ES^+) calcd for $C_{12}H_{22}B_{10}N_2O_3Na$ $(M + Na)^+$ 375.2459, found 375.2454; HPLC: t_R = 13.4 min.

3-(3′-(*closo*-Carboranyl)propionyl)amino-5-(*N*-*tert*-butyloxycarbonyl)aminobenzoic Acid, 25. A 1.0 g quantity (2.84 mmol) of **24** and NaOH (142 mg, 3.55 mmol) were dissolved in 20 mL of DMF/H_2O (1:1). Di-*tert*-butyl dicarbonate (776 mg, 3.55 mmol) was added to the reaction flask, and the reaction mixture was stirred for 16 h at room temperature. The solvent was removed under vacuum. Crude product was dissolved into 10 mL of water and was acidified with 4 mL of 1 N HCl. The precipitate was collected by filtration and was dried under vacuum to yield 920 mg (72%) **25** as a colorless solid: mp 185−186 °C; ^{1}H NMR (CD_3OD, 500 MHz) δ 1.52 (s, 9H), 1.58−2.54 (m, 10H), 2.61−2.64 (m, 2H), 2.66−2.70 (m, 2H), 4.58 (bs, 1H), 7.78 (s, 1H), 7.84 (s, 1H), 7.99 (s, 1H); ^{11}B NMR (CD_3OD, decoupled, 160 MHz) δ −1.11 (1B), −4.41 (1B), −8.11 (2B), −10.21 (4B), −11.41 (2B). HRMS (ES^+) calcd for $C_{17}H_{30}B_{10}N_2O_5Na$ $(M + Na)^+$ 475.2983, found 475.2995; HPLC: t_R = 14.5 min.

3-(3′-(*closo*-Carboranyl)propionyl)amino-5-(*N*-*tert*-butyloxycarbonyl)aminobenzoic Acid Tetrafluorophenyl Ester, 26. A100 mg quantity (0.22 mmol) of **25** and Et_3N (276 μL, 1.3 mmol) were dissolved into 3 mL of anhydrous DMF. The solution was cooled to 4 °C in an ice/H_2O bath. TFP-OTFA (129 μL, 0.67 mmol) was added, the reaction mixture was stirred at 4 °C for 30 min, and then 30 mL of H_2O was added. The precipitate was filtered, washed with water (4 × 10 mL), and dried

under vacuum to yield 115 mg (87%) of **26** as a colorless solid: mp 122−125 °C; ^{1}H NMR (CD_3OD, 500 MHz) δ 1.57 (s, 9H), 1.66−2.61 (m, 10H), 2.67−2.75 (m, 4H), 4.64 (bs, 1H), 7.48−7.55 (m, 1H), 8.05 (s, 1H), 8.12 (s, 1H), 8.14 (s, 1H); ^{11}B NMR (CD_3OD, decoupled, 160 MHz) δ −1.17 (1B), −4.23 (1B), −7.94 (2B), −10.04 (4B), −11.27 (2B). HRMS (ES^+) calcd for $C_{23}H_{30}B_{10}N_2O_5F_4Na$ $(M + Na)^+$ 623.2919, found 623.2929; HPLC: t_R = 15.4 min.

3-(3′-(*closo*-Carboranyl)propionyl)amino-5-(*N*-*tert*-butyloxycarbonyl)amino-1-(3′-dimethyl-aminopropyl)benzamide, 27. 3-(Dimethylamino)propylamine (49 μL, 3.84 mmol) and Et_3N (33 μL, 0.23 mmol) were dissolved in 4 mL of anhydrous DMF. To that solution was added **26** (115 mg, 0.19 mmol). The reaction mixture was stirred for 1 h at room temperature, 50 mL of water was added, and this mixture was stirred for an additional 1 h. The precipitate was filtered, washed with water (4 × 20 mL), and dried under vacuum to yield 90 mg (88%) of **27** as a colorless solid: mp 111−112 °C. ^{1}H NMR (CD_3OD, 500 MHz) δ 1.24−1.45 (m, 4H), 1.52 (s, 9H), 1.64−1.72 (m, 2H), 1.79−1.84 (m, 2H), 1.87−2.25 (m, 4H), 2.32 (s, 6H), 2.49 (t, J = 7.4 Hz, 2H), 2.61−2.64 (m, 2H), 2.66−2.70 (m, 2H), 3.39 (t, J = 7.4 Hz, 2H), 4.59 (bs, 1H), 7.54 (s, 1H), 7.62 (s, 1H), 7.81 (s, 1H); ^{11}B NMR (CD_3OD, decoupled, 160 MHz) δ −1.25 (1B), −4.09 (1B), −7.32 (1B), −8.26 (1B), −9.37 (1B), −10.45 (3B), −11.62 (2B). HRMS (ES^+) calcd for $C_{22}H_{43}B_{10}N_4O_4$ $(M + H)^+$ 537.4215, found 537.4220; HPLC: t_R = 16.4 min.

3-(3′-(*closo*-Carboranyl)propionyl)amino-5-amino-1-(3′-dimethylaminopropyl)benzamide, 28. A 73 mg quantity (0.14 mmol) of **27** was dissolved in TFA (2 mL). The solution was stirred for 30 min at room temperature, and the excess TFA was removed using a gentle stream of air in a fume hood. The crude residue was washed 2× with 3 mL of ether, and then the residue was dried under high vacuum to yield the TFA salt of **28** as a colorless tacky solid, which was used directly in the next reaction step. ^{1}H NMR (CD_3OD, 200 MHz) δ 0.74−1.47 (m, 8H), 1.61−1.76 (m, 2H), 2.17 (s, 6H), 2.28−2.35 (m, 3H), 2.45−2.61 (m, 5H), 3.27 (t, J = 7.4 Hz, 2H), 4.48 (bs, 1H), 6.71 (s, 1H), 6.98 (s, 1H), 7.08 (s, 1H); ^{11}B NMR (CD_3OD, decoupled, 96 MHz) δ −1.77 (1B), −5.30 (1B), −8.72 (2B), −10.80 (4B), −11.86 (2B). HRMS (ES^+) calcd for $C_{17}H_{35}B_{10}N_4O_2$ $(M + H)^+$ 437.3691, found 437.3698; HPLC: t_R = 12.5 min.

3-(3′-(*closo*-Carboranyl)propionyl)amino-5-(1′-(*N*-biotinyl)-5′-lysylthiourea)(3′-dimethylaminopropyl)-benzamide, 29. The crude **28** (0.14 mmol) was dissolved in a minimum amount of MeOH, made basic with Et_3N (2 mL), and stirred for 30 min at room temperature. The MeOH and excess Et_3N were removed under a stream of air and then under vacuum to yield a colorless oil. The oily residue and 1,1-thiocarbonyldiimidazole (22 mg, 0.14 mmol) were dissolved in 3 mL of anhydrous DMF. Reaction progress for formation of the phenyl isothiocyanate was followed by HPLC (1 h). Upon complete formation of the isothiocyanate, the biotin-lysine adduct **17b** (56 mg, 0.15 mmol) and Et_3N (57 μL, 0.41 mmol) were added, and then the reaction mixture was stirred for 3 h at room temperature. DMF was removed under vacuum, and the residue was dissolved in a minimum amount of MeOH. The crude reaction mixture was loaded onto a silica gel column (20 g, 2.5 cm × 35 cm) and was eluted using 1% Et_3N/MeOH. The purified product was dried under vacuum to yield 85 mg (74%) of **29** as a colorless oil: ^{1}H NMR (CD_3OD, 500 MHz) δ 1.24−1.46 (m, 4H), 1.53−1.74 (m, 6H), 1.79−1.90 (m, 4H), 2.25−2.31 (m, 3H), 2.34 (s, 6H), 2.79−2.84 (m, 4H), 2.91 (dd, J = 5.0, 13.0 Hz, 1H), 3.16−3.21 (m, 1H), 3.30−3.32 (m, 2H), 3.34−3.43 (m, 3H), 3.58 (bs, 1H), 4.25−4.30 (m, 2H), 4.45−4.49 (m, 1H), 4.62 (bs, 1H), 7.05 (s, 1H), 7.43−7.90 (m, 2H); ^{11}B NMR (CD_3OD, decoupled, 160 MHz) δ −1.08 (1B), −4.41 (1B), −8.09 (2B), −10.16 (4B), −11.40 (2B). HRMS (ES^+) calcd for $C_{34}H_{61}B_{10}N_8O_6S_2$ $(M + H)^+$ 851.5086, found 851.5083; HPLC: t_R = 12.6 min.

3-(3′-(*nido*-Carboranyl)propionyl)amino-5-(1′-(*N*-biotinyl)-5′-lysylthiourea)(3′-dimethylaminopropyl)-benzamide, 5a. A 60 mg quantity (0.07 mmol) of **29** was dissolved in pyrrolidine (1 mL) and was stirred for 30 min at room temperature. Excess pyrrolidine was removed under a gentle stream of air in a fume hood. The residue was rinsed with ether (2 × 10 mL), and the ether was decanted. The crude product was dissolved in a 5:4:1 mixture of H_2O:CH_3CN:MeOH (1 mL) and was loaded on an ion exchange column (prepared as described in the synthesis of **3a**). The column was eluted with 1 mL fractions (20×). Fractions containing **5a** were combined, and solvents were removed under vacuum to yield 40 mg (68%) of **5a** as a tacky light-yellow solid: ^{1}H NMR (CD_3OD/DMSO-d_6, 500 MHz) δ 1.11−1.27 (m, 3H), 1.51−1.60 (m, 3H), 1.65−1.74 (m, 2H), 1.80−1.84 (m, 2H), 1.87−2.01 (m, 2H), 2.08−2.22 (m, 2H), 2.25 (s, 6H), 2.26−2.32 (m, 1H), 2.53 (t, J = 7.4 Hz, 2H), 2.77 (t, J = 7.8 Hz, 2H), 2.88−2.97 (m, 2H), 3.41−3.49 (m, 2H), 3.55−3.56 (m, 2H), 3.69−3.89 (m, 4H), 4.54−4.75 (m, 4H), 7.92−8.27 (m, 3H); ^{11}B NMR (CD_3OD, decoupled, 160 MHz) δ −10.04 (2B), −12.29 (1B), −15.14 (1B), −17.13 (2B), −20.02 (1B), −31.63 (1B), −35.76 (1B). HRMS (ES^-) calcd for $C_{34}H_{59}B_9N_8O_6S_2$ $(M - H)^-$ 838.4836, found 838.4869; HPLC: t_R = 9.8 min.

General Procedure for Iodination of *nido*-Carborane Derivatives, 3a, 4a, and 5a. To a 500 μL quantity of a 2 mg/mL solution of *nido*-carborane derivative in MeOH/1% HOAc was added an appropriate microliter quantity of a 22 mg/mL solution of NaI in H_2O to introduce 0.5 mol equiv of iodide. Immediately following this, an appropriate microliter quantity of a 22 mg/mL solution of *N*-chlorosuccinimide (NCS) in MeOH was added to introduce 0.5 mol equiv. The reaction mixture generally turned light brown as the NCS was added but returned to colorless almost immediately. After 30 s, the reaction was quenched by the addition of 10 μL of a 22 mg/mL solution of sodium metabisulfite in H_2O.

Iodinated *nido*-carboranyl species were used for radio-HPLC peak identification. HPLC analysis of the reaction mixtures showed both starting material and an iodinated product. To obtain pure samples, the HPLC peak corresponding to the iodinated product was collected from HPLC effluent. Identity of the collected material was obtained from high-resolution mass spectral analysis.

1-*N*-(Biotinyl)-5-*N*-(3′-(iodo-*nido*-Carboranyl)propionyl)-L-lysine, 3b. HRMS calcd for $C_{21}H_{40}B_9N_4O_5SI$ (M^-) 686.2594, found 686.2602; HPLC: t_R = 9.8 min.

3-(3′-(Iodo-*nido*-Carboranyl)propionyl)amino-1-*N*-(1′-(*N*-biotinyl)-5′-lysylthiourea)-benzene, 4b. HRMS calcd for $C_{28}H_{46}N_6O_5S_2B_9I$ (M^-) 836.2889, found 836.2853; HPLC: t_R = 10.7 min.

3-(3′-(Iodo-*nido*-carboranyl)propionyl)amino-5-(1′-(*N*-biotinyl)-5′-lysylthiourea)(3′dimethylaminopropyl)benzamide, 5b. HRMS calcd for $C_{34}H_{58}B_9IN_8O_6S_2$ (M^-) 964.3791, found 964.3803; HPLC: t_R = 11.0 min.

General Procedure for Radiohalogenation of Arylstannanes, 1a and 2a. To a 50−100 μL aliquot of a 1 mg/mL of the aryl stannanes (**1a** or **2a**) in MeOH/5% HOAc was added 3−10 μL of Na[^{125}I]I, Na[^{131}I] in 0.1 N NaOH or Na[^{211}At] in 0.05 N NaOH. Following this, 10 μL of a 1 mg/mL solution of NCS in MeOH was added.

The reaction was allowed to proceed for 1−10 min, and then 10 μL of 1 mg/mL solution of $Na_2S_2O_5$ in H_2O was added to quench the reaction. The radiohalogenated aryl halide derivatives were isolated from reversed-phase HPLC effluent. After isolation, the MeOH and HOAc was removed under a stream of nitrogen (vented through charcoal containing syringe).

The radiohalogenation reactions can also be conducted using chloramine-T (ChT) in H_2O as described below for **2c**.

***N′*-(13-(4″-[^{131}I]iodobenzamido)-4,7,10-trioxatridecanyl)-*N*-methylglycylbiotinamide, [^{131}I]1b.** Reaction was conducted with 3 μL of Na[^{131}I] (2.14 mCi) in 0.1 N NaOH. [^{131}I]**1b** was isolated from the HPLC effluent and radio-HPLC analysis indicated that the reaction provided 95% yield, and 69% was isolated from the HPLC: t_R = 16.7 min.

***N′*-(13-(4″-[^{211}At]astatobenzamido)-4,7,10-trioxatridecanyl)-*N*-methylglycylbiotinamide, [^{211}At]1c.** Reaction was conducted with 10 μL of Na[^{211}At] (547 μCi) in 0.05 N NaOH with a 10 min reaction time. The reaction mixture containing [^{211}At]**1c** was purified by radio-HPLC to give 64% isolated yield: t_R = 12.6 min (Note: this was a different HPLC column from that used for the radioiodinated product listed above).

2-(*N*-Biotinyl)-4-(*N′*-(13′-(4″-[^{125}I]iodobenzoyl)amino)-4′,7′,10′-trioxatridecaneamino)-L-aspartate,[^{125}I]-2b. Reaction was conducted with 5 μL of Na[^{125}I] (2.76 mCi) in 0.1 N NaOH. [^{125}I]**2b** was isolated from the HPLC effluent. Radio-HPLC analysis indicated that the reaction provided 90% yield, but only 22% was isolated from the HPLC: t_R = 15.2 min. In four other experiments, 37%, 43%, 45%, and 49% (isolated) radiochemical yields were obtained.

2-(*N*-Biotinyl)-4-(*N′*-(13′-(4″-[^{211}At]astatobenzoyl)-amino)-4′,7′,10′-trioxatridecaneamino)-L-aspartate, [^{211}At]2c. Reaction was conducted with 100 μL of Na[^{211}At] (1.39 mCi) in 0.1 N NaOH. [^{211}At]**2c** was isolated from the HPLC effluent. Radio-HPLC analysis indicated that the reaction provided ∼100% yield, and 41% was isolated from the HPLC: t_R = 14.6 min.

In another experiment, 100 μL of **2a** in H_2O (1 mg/mL) and 20 μL of ChT (1 mg/mL) were reacted in Na phosphate buffer, pH 7.4 (100 μL), with 50 μL of (295 μCi) Na[^{211}At]At in 1:1 0.05 N NaOH/MeOH for 5 min at room temperature to give 23% isolated yield of [^{211}At]**2c**.

General Procedure for Radiohalogenation of *nido*-Carborane Derivatives, 3a, 4a, and 5a. To a solution containing 50−100 μL of 1 mg/mL solution of *nido*-carborane derivative (**3a**, **4a**, or **5a**) in MeOH/5%HOAc was added 1−5 μL of Na[^{125}I]I, Na[^{131}I]I, or 20−100 μL of Na[^{211}At]At in 0.05N NaOH. To the resultant solution was added 10−20 μL of a 1 mg/mL solution of NCS in MeOH or ChT in H_2O. The reaction was quenched after 30 s with 10−20 μL of a 1 mg/mL solution of $Na_2S_2O_5$ in H_2O.

Alternatively, 100 μL of a 1 mg/mL solution of *nido*-carborane derivative, **5b**, was reacted with 15−20 μg of a 1 mg/mL solution of ChT in H_2O and 5−15 μL (1.5−1.9 mCi) of Na[^{125}I]I in 0.05 N NaOH. After 1 min reaction time, the reaction was quenched with 15−20 μL of a 1 mg/mL solution of $Na_2S_2O_5$ in H_2O.

The radiohalogenated *nido*-carborane derivatives were isolated from reversed-phase HPLC effluent. After isolation, the MeOH and HOAc was removed under a stream of nitrogen (vented through charcoal containing syringe). Due to the propensity of the *nido*-carborane compounds to adhere to glass surfaces, plastic vials are routinely used. The radiohalogenated derivatives used in animal studies were diluted with a solution of 1% BSA in PBS after the MeOH/HOAc (or H_2O) was removed. This was necessary to keep the labeled material from adhering to the surfaces in the vial and syringe.

1-*N*-(Biotinyl)-5-*N*-(3′-([^{125}I]iodo-*nido*-carboranyl)-propionyl)-L-lysine, [^{125}I]3b. Reaction was conducted with 3 μL of Na[^{125}I]I (853 μCi) in 0.1 N NaOH. [^{125}I]**3b** was isolated from the HPLC effluent. Radio-HPLC indicated that the reaction provided >75% yield, and 67% was isolated from the HPLC: t_R = 14.0 min.

3-(3′-([^{125}I]Iodo-*nido*-carboranyl)propionyl)amino-1-*N*-(1′-(*N*-biotinyl)-5′-lysylthiourea)-benzene, [^{125}I]-4b. Reaction was conducted with 3 μL of Na[^{125}I]I (766 μCi) in 0.1 N NaOH. [^{125}I]**4b** was isolated from the HPLC effluent. Radio-HPLC indicated that the reaction provided 61% yield. HPLC: t_R = 16.7 min. In a separate reaction, a 59% yield was obtained.

3-(3′-([^{125}I]Iodo-*nido*-carboranyl)propionyl)amino-5-(1′-(*N*-biotinyl)-5′-lysylthiourea)(3′dimethylamino-propyl)benzamide, [^{125}I]5b. Reaction was conducted with 5 μL of Na[^{125}I]I (2.38 mCi) in 0.1 N NaOH. Radio-HPLC indicated that the reaction provided ∼61% [^{125}I]-**5b**, and 50% was isolated from the HPLC: t_R = 14.9 min. In another reaction employing NCS as the oxidant, an 83% (HPLC) yield was obtained. In two other reactions employing ChT in H_2O, 72% and 86% (HPLC) yields were obtained.

3-(3′-([^{211}At]Astato-*nido*-carboranyl)propionyl)-amino-1-*N*-(1′-(*N*-biotinyl)-5′-lysylthiourea)benzene, [^{211}At]4c. Reaction of 20 μL (160 μCi) of Na[^{211}At]-At with **4a** provided 60% radiochemical yield. The product was isolated from the HPLC effluent: t_R= 16.7 min. In a separate reaction, 40 μL (210 μCi) of Na[^{211}At]-At in a 1:1 mixture of 0.05 N NaOH/MeOH provided a 36% isolated yield.

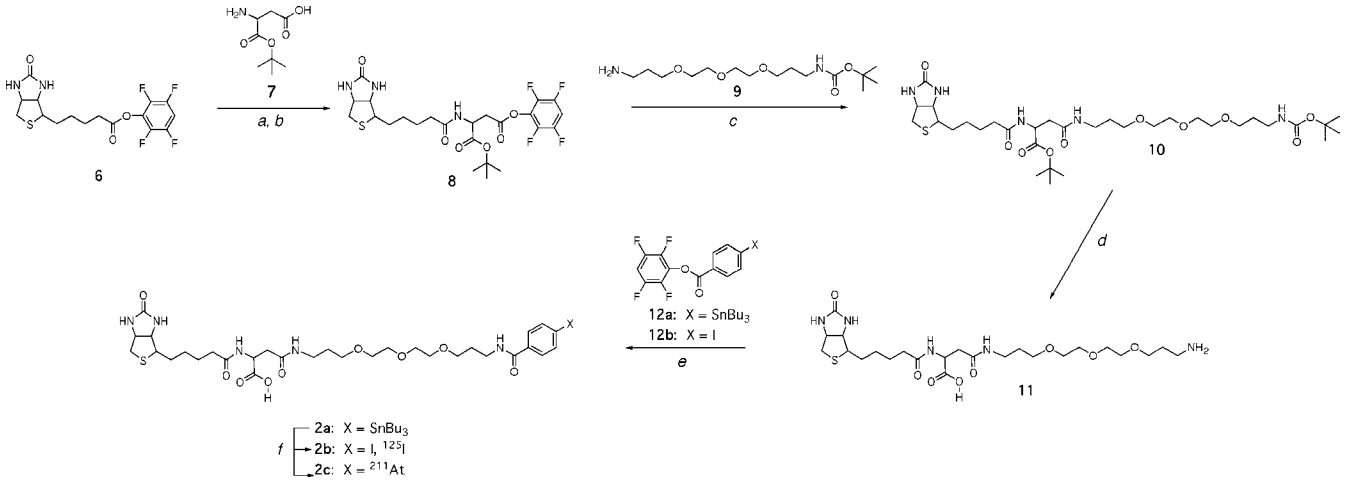
3-(3′-([^{211}At]Astato-*nido*-carboranyl)propionyl)-amino-5-(1′-(*N*-biotinyl)-5′-lysylthiourea)(3′dimethyl-aminopropyl)benzamide, [^{211}At]5c. Reaction of 3 μL of Na[^{211}At]At (853 μCi) in 0.1 N NaOH provided 23% radiochemical yield of [^{211}At]**5c**. The product was isolated from the HPLC effluent. t_R= 14.0 min. In a separate reaction, 25 μL (125 μCi) of Na[^{211}At]At in a 1:1 mixture of 0.05 N NaOH/MeOH was reacted with NCS to provide a 57% isolated yield.

Biodistribution Studies. The animal studies were approved by the University of Washington's Institutional Animal Care and Use Committee prior to being conducted. Animal care and use was conducted in accordance with the NIH guidelines.[4] Mice were placed on a biotin deficient diet for 5−7 days prior to the start of each investigation. This was done to mimic the conditions used in the pretargeting studies.

Male athymic mice (BALB/c nu/nu), 4−5 weeks of age were obtained from Simonsen Laboratories (Gilroy, CA). Mice were housed for 1 week in the animal facility prior to beginning the study. All injections of reagents were administered to mice in a total volume of approximately 100 μL (injectate weighed) via the lateral tail vein. Animals were sacrificed at 1, 4, and 24 h postinjection of the radiolabeled materials. These times correspond to 9%, 32%, and 90% decay of ^{211}At. The data for tissues excised are shown in the Tables S1−S6 in the Supporting Information, and the average animal weight in a biodistribution, and average tumor weights for groups involving mice bearing tumor xenografts are provided in the table legends. Blood samples were obtained by cardiac

[4] NIH guidelines are described in NIH Publication 86-23: "Guide for the Care and Use of Laboratory Animals".

Scheme 1. Synthesis and Radiohalogenation of 2-(*N*-Biotinyl)-4-(*N′*-(13′-*p*-(tri-*n*-butylstannyl)benzoylamino)-4′,7′,10′-trioxatridecaneamino-L-aspartate, 2a



[a] Reagents and conditions: (a) H_2O, acetone, $NaHCO_3$, rt, 6 h; (b) TFP−OTFA, Et_3N, rt, 20 min; (c) Et_3N, DMF, 4 °C−rt, 1 h; (d) TFA, rt, 30 min, ∼100%; (e) Et_3N, DMF, **12a** or **12b**, rt, 30 min to 1 h, 70% (**2a**), 80% (**2b**); (f) MeOH/5% HOAc, NaX (X = ^{125}I or ^{211}At), NCS, rt, 1−10 min.

puncture immediately before sacrifice. Urine samples were obtained by syringe bladder tap at the time the tissues were excised. Excised tissues were blotted free of blood, weighed, and counted. Calculation of the percent injected dose (%ID) and percent injected dose per gram (% ID/g) in the tissues was based on internal standards containing 1 μL of the injected dose. The standards were prepared by mixing 10 μL of the injectate with 990 μL of saline. After mixing thoroughly, four 100 μL aliquots were placed in tubes and counted as standards. Standards were counted with tissues obtained at each time point, and an average value for the four standards were used in the calculations. The ^{211}At counts were compensated for decay, and where dual radionuclide counting was required, the ^{125}I counts were compensated (13.5%) for spillover counts from the ^{131}I. Total blood volume was estimated to be 8% of body weight for the calculations (*10*). Statistical analysis of the data was conducted using the paired student's *t*-test. Differences were considered statistically significant when the $p < 0.05$.

RESULTS

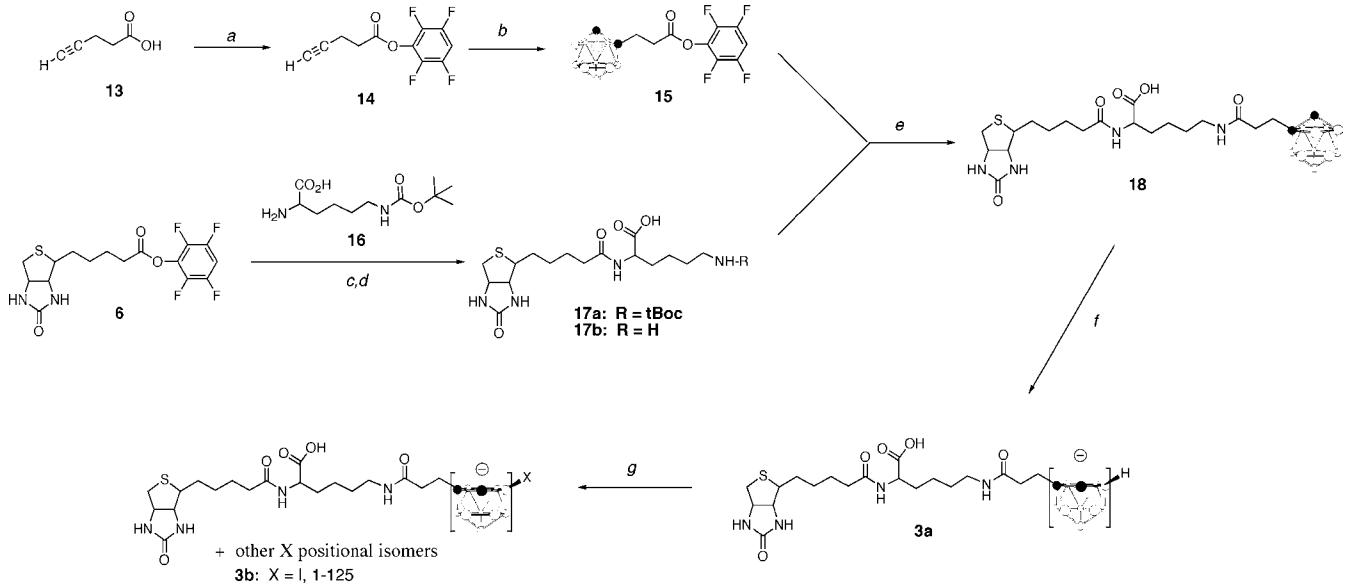
Synthesis of Biotin Compounds Containing Arylstannanes, 1a/2a, and Aryl Iodides, 1b/2b. Syntheses of **1a** and **1b** were conducted as previously described (*18*). Syntheses of **2a** and **2b** were conducted as shown in Scheme 1. Both syntheses were conducted through the common intermediate, biotin derivative **11**. The synthesis of compound **11** has been previously reported (*19*). Briefly, the synthesis started with reaction of biotin TFP ester, **6**, with aspartate α-*tert*-butyl ester, **7**, to form an adduct containing a free carboxylate. The carboxylate was subsequently esterified using TFP-OTFA to provide the TFP ester **8**. Reaction of **8** with the mono-Boc protected 4,7,10-trioxatridecane-1,13-diamine **9** gave the adduct **10**. In the previous studies, **10** was deprotected with neat trifluoroacetic acid (TFA) to provide **11**, which was then reacted with *p*-[^{125}I]iodobenzoate *N*-hydroxysuccinimide ester to form [^{125}I]**2b**. In these studies, the aryl stannanes **2a** was sought as an intermediate to prepare both [^{125}I]**2b** and [^{211}At]**2c**. To prepare **2a**, biotin derivative **11** was isolated as the TFA salt after treatment of **10** with neat TFA. Reaction of the TFA salt of **11** with *p*-(tri-*n*-butylstannyl)benzoate TFP ester **12a** and Et_3N provided **2a** in 70% yield. Similarly, reaction the TFA salt of **11** with *p*-iodobenzoate TFP ester **12b** and Et_3N provided **2b** in 80% yield.

Synthesis of Biotin Compounds 3a, 4a, and 5a, Containing *nido*-Carborane Moieties. The reactions employed to obtain the biotin-*nido*-carborane derivative **3a** are shown in Scheme 2. The synthesis of the 3-(*closo*-carboranyl)propionate TFP ester, **15**, was conducted as previously described (*27*). Briefly, the TFP ester of pentynoic acid **14** was prepared by reaction of 4-pentynoic acid with dicyclohexylcarbodiimide (DCC) and tetrafluorophenol (TFP-OH). Formation of the *closo*-carborane moiety to produce **15** was accomplished by reaction of the acetylenic group with decaborane ($B_{10}H_{14}$). It should be noted that the TFP ester was used in the reaction as free carboxylates are problematic in reactions with decaborane. Preparation of the biotin-lysine adduct **17a** was accomplished in 87% yield by reaction of biotin TFP ester **6** with ϵ-*N*-(*tert*-butoxycarbonyl)-L-lysine, **16**, and sodium bicarbonate in aqueous acetone at room temperature. Removal of the *t*-Boc protecting group from **17a** was facile in neat TFA, providing **17b** in 98% yield. Reaction of biotin-lysine adduct **17b** with **15** and Et_3N in anhydrous DMF provided the biotin derivative containing a *closo*-carborane moiety, **18**, in 84% yield. The *closo*-carborane moiety in **18** was readily converted into the *nido*-carborane by boron abstraction reaction with pyrrolidine to provide the 3-(*nido*-carboranyl)propionic acid, **3a** in 83% yield.

The synthesis employed to obtain **4a** is shown in Scheme 3. The synthesis is similar to that employed to prepare **3a**, except it incorporates 1,3-diaminobenzene, **19**, into the structure. Reaction of an excess of **19** with the 3-(*closo*-carboranyl)propionate TFP ester, **15**, in anhydrous DMF provided the *closo*-carborane adduct **20** in 95% yield. The aniline amine in **20** was converted to an isothiocyanate derivative **21** in 54% (isolated) yield by reaction with thiocarbonyldiimidazole in DMF at room temperature. The isothiocyanate **21** was reacted with the biotin-lysine adduct **17b** and Et_3N in anhydrous DMF at room temperature to provide the biotin derivative **22**, containing a *closo*-carborane moiety, in 65% yield. The targeted *nido*-carboranyl-biotin derivative **4a** was prepared in 67% yield by reaction of **22** with pyrrolidine.

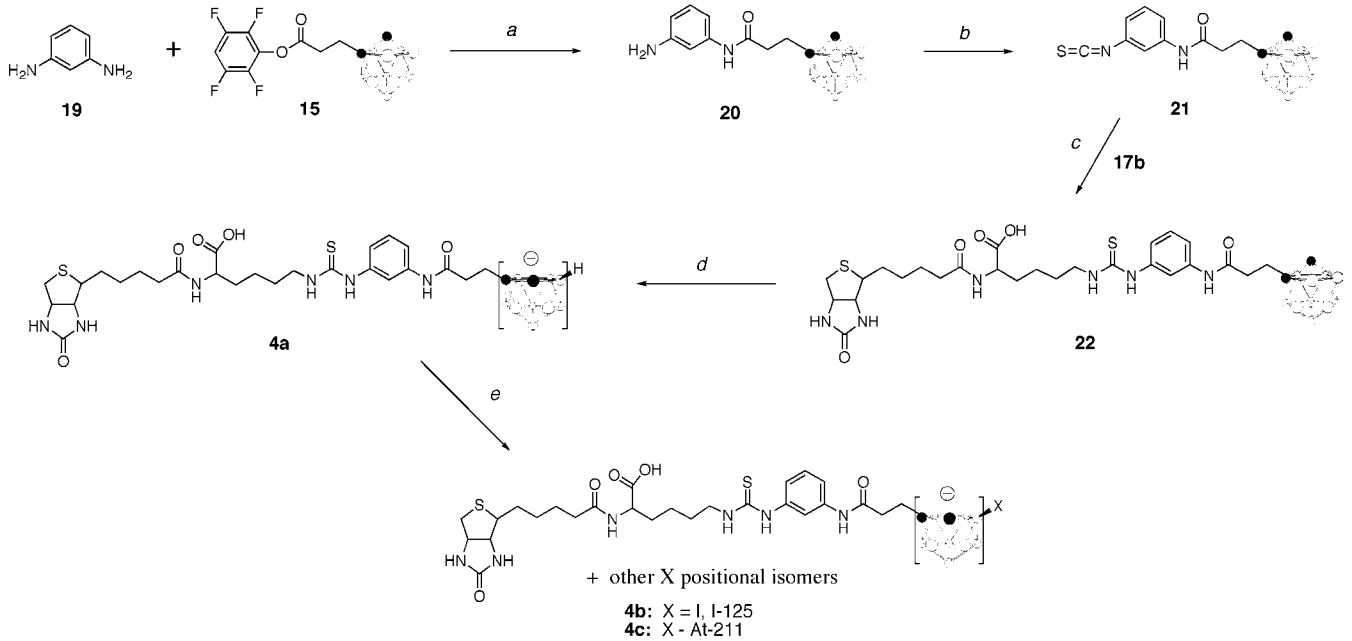
Synthesis of the biotin derivative **5a**, containing a trialkylamine moiety, is shown in Scheme 4. 3,5-Diami-

Scheme 2. Synthesis and Radioiodination of 1-*N*-(Biotinyl)-5-*N*−(3′-(*nido*-carboranyl)propionyl)-L-lysine, 3a



[a] Reagents and conditions: (In carborane structures, open circles represent boron or B−H atoms and closed circles represent carbon atoms) (a) THF, DCC, TFP−OH, rt, 16−24 h; (b) $B_{10}H_{14}$, CH_3CN, Δ, 18−24 h; (c) H_2O, acetone, $NaHCO_3$, rt, 16 h, 87%; (d) TFA, rt, 30 min, 98%; (e) DMF, Et_3N, rt, 1.5 h, 84%; (f) pyrrolidine, 0 °C − rt, 30 min, 83%; (g) MeOH/5% HOAc, NaX ($X = {}^{125}I$ or ^{211}At), NCS, rt, 1 min.

Scheme 3. Synthesis and Radiohalogenation of 3-(3′-(*nido*-Carboranyl)propionyl)amino-1-*N*-(1′-(*N*-biotinyl)-5′-lysyl-thiourea)benzene, 4a

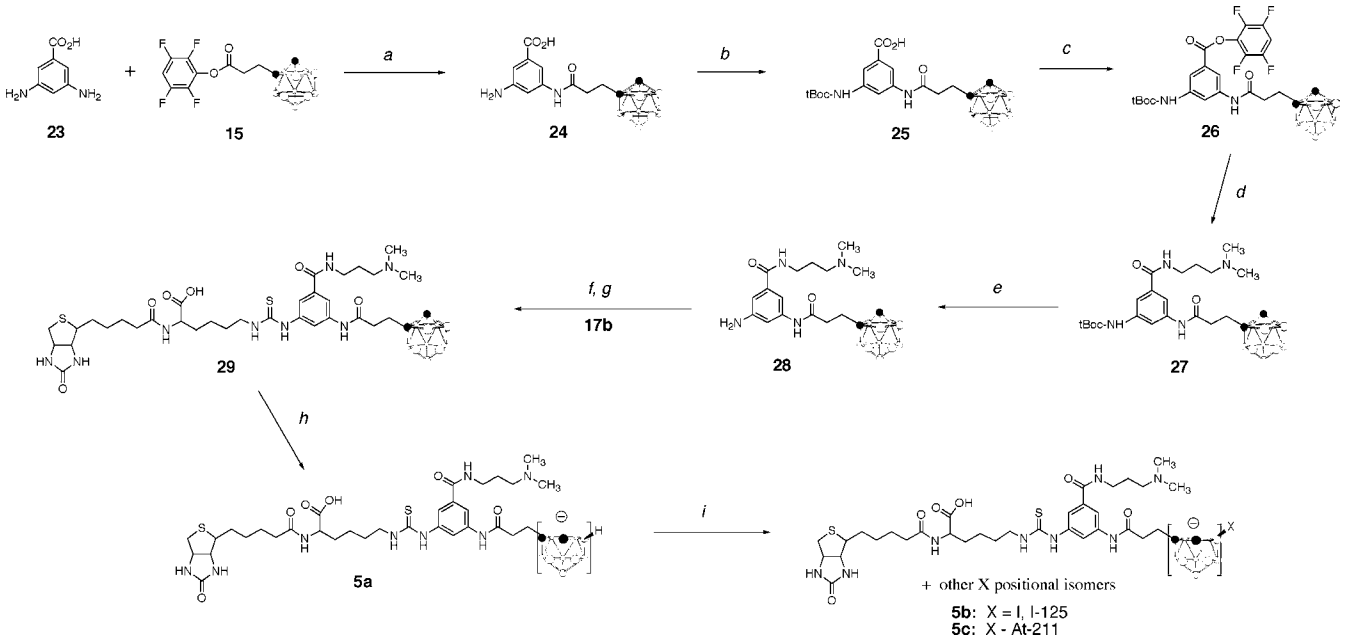


[a] Reagents and conditions: (In carborane structures, open circles represent boron or B−H atoms and closed circles represent carbon atoms) (a) DMF, rt, 3.5 h, 95%; (b) DMF, TCDI, rt, 30 min, 54%; (c) DMF, Et_3N, rt, 30 min, 65%; (d) pyrrolidine, rt, 1 h, 67%; (e) MeOH/5% HOAc, NaX (X = ^{125}I or ^{211}At), NCS, rt, 1 min.

nobenzoic acid, **23**, was used to provide a trifunctional aryl moiety for introducing a trialkylamine moiety. Reaction of an excess of **23** and Et_3N with **15** in DMF at room temperature provided the *closo*-carborane adduct **24** in 91% yield. Protection of the aniline amine of **24** to give **25** was accomplished in 72% yield by reaction with di-*tert*-butyl dicarbonate in a mixture of DMF and H_2O at room temperature. Subsequent formation of the TFP ester derivative **26** was accomplished in 87% yield by reaction of **25** with TFP-OTFA in DMF at 4 °C. Reaction of **26** with 3-(dimethylamine)propylamine and Et_3N in DMF at room temperature provided **27** in 88% yield. Removal of the *t*-Boc group from **27** with neat TFA gave the aniline **28** in nearly quantitative yield. Conversion of the aniline amine in **28** to an isothiocyanate functionality using thiocarbonyldiimidazole in anhydrous DMF was followed by reaction with the biotin-lysine adduct **17b** to provide the *closo*-carboranyl-biotin derivative **29** in 74% overall yield. Reaction of the *closo*-carborane in **29** with pyrrolidine provided the *nido*-carborane derivative **5a** in 95% yield.

Radiohalogenation Reactions of Biotin Derivatives 1a, 2a, 3a, 4a, and 5a. The product mixtures for the radiohalogenation reactions were assessed by reversed-phase HPLC using nonradioactive iodinated derivatives (**1b**, **2b**, **3b**, **4b**, **5b**) as HPLC standards. All radiolabeled

Scheme 4. Synthesis and Radiohalogenation of 3-(3′-(*nido*-Carboranyl)propionyl)amino-5-(1′-(*N*-biotinyl)-5′-lysylthiourea)−(3′dimethylaminopropyl)benzamide, 5a



[a] Reagents and conditions: (In carborane structures, open circles represent boron or B−H atoms and closed circles represent carbon atoms) (a) DMF, Et_3N, rt, 1.5 h, 91%; (b) NaOH, DMF, H_2O, DTDC, rt, 16 h, 72%; (c) DMF, Et_3N, TFP-OTFA, 4 °C, 30 min, 87%; (d) 3-(dimethylamino)propylamine, DMF, Et_3N, rt, 1 h, 88%; (e) TFA, rt, 30 min, ∼100%; (f) DMF, TCDI, 1 h (not isolated); (g) **17b**, DMF, Et_3N, rt, 3 h, 74%; (h) pyrrolidine, rt, 30 min, 95%; (i) MeOH/5% HOAc, NaX (X = ^{125}I or ^{211}At), NCS, rt, 1 min.

samples were obtained pure by collection of radioactivity from the HPLC effluent. Astatinated compounds had retention times slightly longer than that of the iodinated standard. Under the elution conditions employed, biotin derivatives containing aryl moieties had narrow HPLC peaks (sometimes as doublets), whereas, biotin derivatives containing *nido*-carboranyl moieties had much broader HPLC peaks. In most cases, radioiodination reactions were conducted multiple times. Due to the cost and quantity of ^{211}At, astatinations were (generally) conducted only at the time of the labeling for the animal study. No optimization studies of the radiohalogen labeling conditions were conducted.

Radioiodination and astatination of biotin derivatives containing aryl stannane moieties, **1a** and **2a** (50−100 μg), were conducted by reaction of *N*-chlorosuccinimide (NCS) (10 μg) and Na[^{125}I]I or Na[^{211}At]At in MeOH containing 1−5% HOAc at room temperature for 1−10 min. The reaction was then stopped by the addition of (10 μg) sodium metabisulfite. Radioiodination of **1a** has been conducted several times as the resultant compound, [$^{125/131}$I]**1b**, is used as a control in studies of biotinidase stability. As an example, isolated yields of 34%, 35%, 39%, and 69% were obtained in four radioiodination experiments. Astatination of **1a** was conducted using the same reaction conditions, giving yields of 22% after 3 min reaction time, and in a second reaction 64% after 10 min. Radioiodination of **2a** has also been conducted a number of times under the same reaction conditions. In four radioiodination experiments with **2a**, isolated yields of 37%, 43%, 45%, and 49% for [^{125}I]**2b** were obtained. Astatination of **2a** was conducted twice. One experiment was conducted using NCS as the oxidant, and the other experiment used ChT as the oxidant. The NCS reaction provided 41% isolated yield of [^{211}At]**2c**, and the ChT reaction provided 23% isolated yield.

Radioiodination was conducted on all three biotin derivatives **3a**, **4a** and **5a**, containing a *nido*-carborane moiety, whereas astatination was only conducted on **4a** and **5a**. Radioiodination of **3a**, **4a**, and **5a** were conducted by reaction of NCS and Na[^{125}I]I in MeOH containing 1−5% HOAc at room temperature for 30 s to 5 min. Following that, sodium metabisulfite was added to quench the reaction. The radiochemical yields obtained under these reaction conditions were [^{125}I]**3b**, 67%; [^{125}I]-**4b**, 82% and 59% (isolated); and [^{125}I]**5b**, 83%. Radioiodination of **5a** was also conducted by reaction of ChT and Na[^{125}I]I in H_2O at room temperature for 1 min. The radiochemical yields (HPLC) of [^{125}I]**5b** obtained in those reactions were 72% and 86%. Astatinations of **4a** and **5a** were conducted using NCS as the oxidant to give 36% and 23% isolated radiochemical yields of [^{211}At]**4c** and [^{211}At]**5c**, respectively. Astatination of **5a** was also conducted using ChT in H_2O and that reaction gave [^{211}At]-**5c** in 57% isolated yield.

Biodistributions of Radiohalogenated Biotin-lysine-*nido*-carborane Derivatives [^{125}I]1b, [^{125}I]2b, [^{211}At]2c, [^{125}I]3b, [^{125}I]4b, [^{211}At]4c, [^{125}I]5b, and [^{211}At]5c. A total of six biodistributions of radiohalogenated biotin derivatives were conducted in the investigation. Due to the propensity of the *nido*-carboranes to adhere to glass and metal surfaces, 1% BSA was added to the radiolabeled compounds when diluted from the (rotoevaporator) concentrated HPLC effluent. All studies evaluated the tissue distribution of radiolabeled compounds at 1, 4, and 24 h postinjection in athymic mice. The complete tissue distribution data are provided in the Supporting Information as Tables S1−S6.

Three biodistribution studies utilized coinjected, dual-labeled (^{125}I and ^{131}I) compounds to compare the in vivo tissue distributions of biotin derivatives that have different structures. In an initial animal study, the distribution of radioiodinated biotin derivatives [^{125}I]**2b** and [^{131}I]**1b**, containing aryl labeling moieties, were evaluated. The biodistribution data is provided as Table S1 in Supporting Information. Although the data has a fairly large spread, evaluation of concentrations of the two radionuclides in individual tissues by the Student's t-test

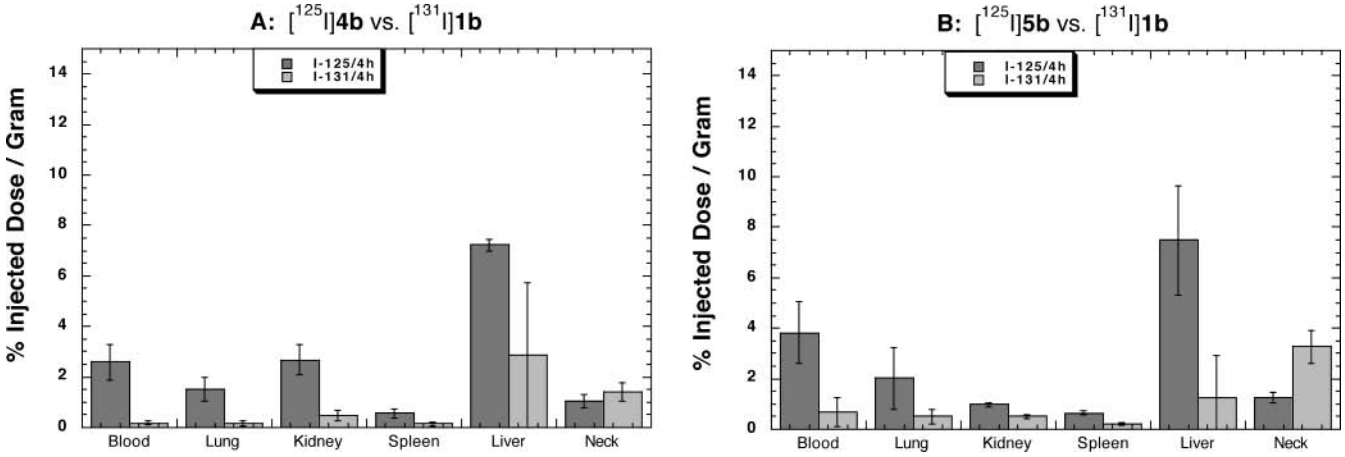


Figure 1. Concentrations of ^{125}I and ^{131}I in selected tissues at 4 h pi for the radiolabeled compounds listed (top of panels A and B). Note that the *Y*-axis range for the percent injected dose/gram has been set at 0−15 to correlate with graphs in Figure 2. Complete data sets are provided as (A) Table S3 and (B) Table S5 in the Supporting Information.

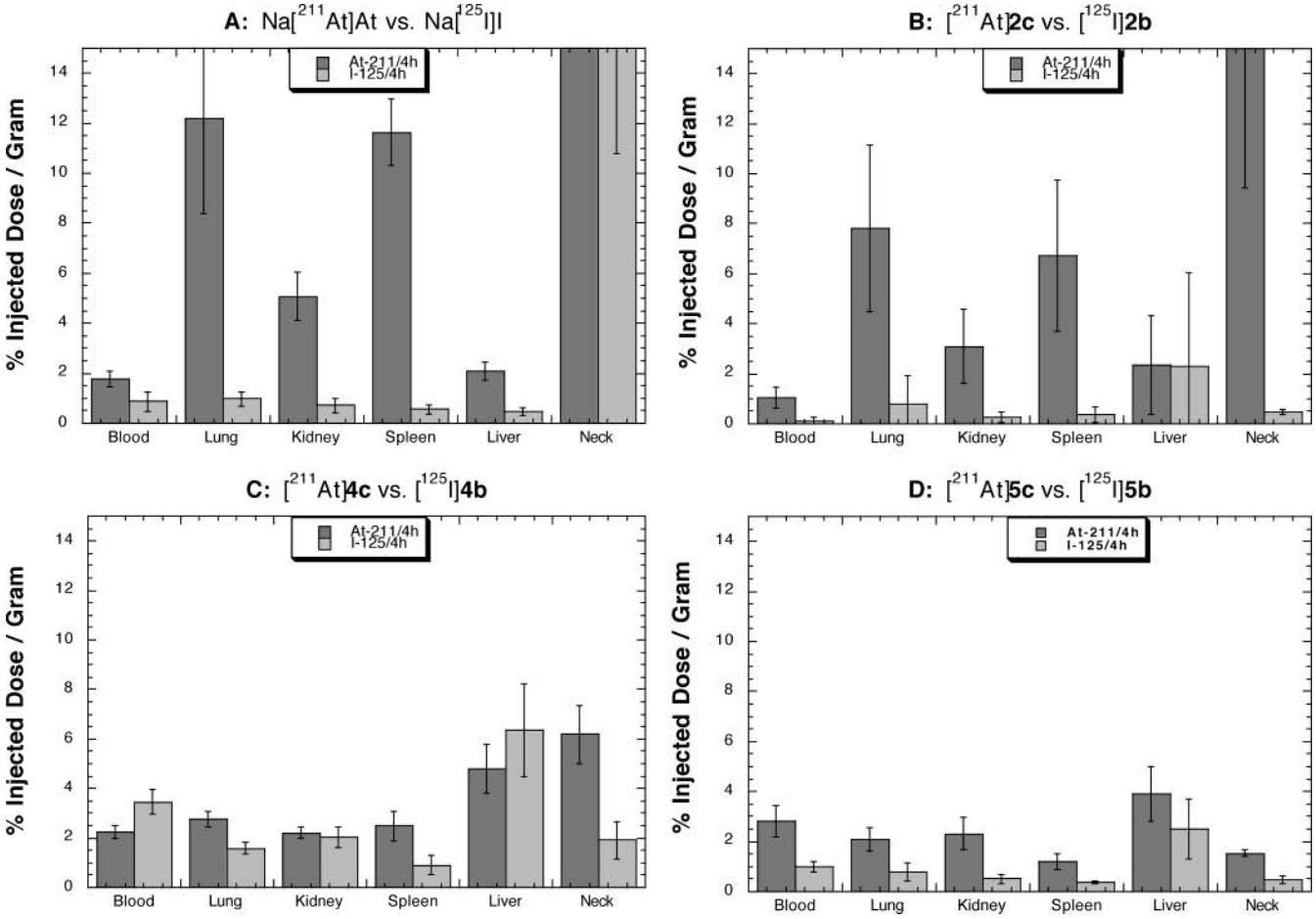


Figure 2. Concentrations of ^{211}At and ^{125}I in selected tissues at 4 h pi for the radiolabeled compounds listed (top of panels A thru D). Data for the graph in panel A was obtained from the literature (*27*) (with permission). Complete data sets are provided as (B) Table S2, (C) Table S4, and (D) Table S6 in the Supporting Information.

indicates that there is little difference between the two in vivo. The two other studies involving radioiodinated biotin derivatives compared the in vivo distribution of a biotin derivative containing an aryl moiety [^{131}I]**1b** with the biotin derivatives [^{125}I]**4b** or [^{125}I]**5b**. Both biotin derivatives **4b** and **5b** contain an aryl group and a *nido*-carborane moiety, and **5b** also contains a dimethylamine moiety. From the data obtained, it is readily apparent that the *nido*-carborane containing biotin derivative, [^{125}I]-**4b**, is cleared from blood, lung, kidney, and liver much slower than [^{131}I]**1b.** These differences are observed at all time points (Table S3, Supporting Information) and can be readily seen in the concentration of radionuclides in selected tissues at 4 h postinjection, which are plotted in Figure 1, panel A. Similar results were obtained in the comparison of [^{125}I]**5b** and [^{131}I]**1b**. The data obtained in that study are provided as Table S5 and tissue concentrations in selected tissues at 4 h postinjection are plotted in Figure 1, panel B.

Three studies were conducted to evaluate the distribution of radionuclides in mice for biotin derivatives (**2b/c**, **4b/c**, and **5b/c**), which were dual labeled with ^{211}At and

^{125}I (Figure 2, panels B−D). To use as a reference, a plot of data from a previous evaluation of free Na[^{211}At]At and Na[^{125}I]I in selected tissues of mice[27] is provided as Figure 2, panel A. The results of [^{211}At]**2c** vs [^{125}I]**2b** are provided as Table S2 in Supporting Information, and data obtained at 4 h postinjection in selected tissues are plotted in Figure 2, panel B. Unfortunately, the high concentrations of ^{211}At and large differences between ^{211}At and ^{125}I in lung, spleen, and neck indicate that [^{211}At]**2c** undergoes considerable deastatination. Indeed, comparison of the pattern of tissue concentrations in graphs provided in panels A and B of Figure 2 provides strong evidence that large amounts of free astatide are present in the animals injected with [^{211}At]**2c**.

Biodistribution data for biotin derivatives [^{211}At]**4c** and [^{125}I]**4b**, that contain a radiohalogenated *nido*-carborane moiety, are provided in Table S4 in Supporting Information, and data obtained at 4 h postinjection for selected tissues are plotted in Figure 2, panel C. Much smaller differences in the lung and spleen concentrations of the two radionuclides is observed at the three time points, indicating that the deastatination is much lower than observed for [^{211}At]**2c**. Unfortunately, while the *nido*-carborane appears to provide a more stable attachment for astatine, it also prolongs the blood residence time. The biodistribution data for the biotin derivatives [^{211}At]**5c** and [^{125}I]**5b**, containing a *nido*-carborane and a trialkylammonium moiety, are provided in Table S6 in Supporting Information, and the 4 h data for selected tissues are plotted in Figure 2, panel D. It is apparent that some deastatination also occurs with this compound because of the differences observed in the concentrations of the two radionuclides in lung, spleen, and neck.

DISCUSSION

The high cytotoxicity of radionuclides that emit α-particles makes them attractive for developing new radiopharmaceuticals for targeted radionuclide therapy (TRT) of cancer. Further, the short path length (e.g. 50−80 μm) of the emitted α-particles makes these radionuclides particularly well suited for therapy of micrometastatic disease, disease in compartmental spaces (e.g. ovarian carcinoma), and cancer cells remaining in surgical tumor resection areas. One of the most promising α-emitting radionuclides is ^{211}At. It is particularly attractive because it can be readily prepared in high radionuclidic purity and does not produce α-emitting daughter radionuclides. While its short half-life ($t_{1/2}$ = 7.21 h) is problematic for use with intact monoclonal antibodies, smaller tumor targeting agents, such as biotin derivatives or peptides, may provide good carrier molecules for this radionuclide.

There are many reagents and approaches that may be taken in TRT of cancer. One approach that utilizes the proven tumor targeting of monoclonal antibodies (mAb), is termed "pretargeting" (*13*, *14*, *33*−*35*). The pretargeting approach is particularly attractive as it employs a two- or three-step procedure to separate the pharmacokinetics of the molecule carrying the radionuclide (e.g. mAb) from the pharmacokinetics of the tumor targeting monoclonal antibody. This fact makes it attractive for use with short half-lived radionuclides such as ^{211}At. Although several different pretargeting approaches have been described, we have chosen to investigate the use of antibody-streptavidin (mAb−SAv) conjugates in combination with radiolabeled biotin derivatives. This combination of reagents using other radionuclides has been successfully applied to treatment of human tumor xenografts in athymic mice (*15*, *16*, *36*) and has undergone clinical study (*14*, *17*, *37*). The success of the approach is due, in part, to the extremely high binding affinity of biotin with streptavidin (*38*), which provides high tumor targeting efficiency and long retention at the tumor site. Further, the small size of biotin derivatives provides rapid renal clearance of radiolabeled biotin derivatives, eliminating much of the irradiation of nontarget tissues.

While a variety of biotin derivatives containing metal radionuclides have been successfully targeted to tumors in mouse models (*34*, *36*, *39*, *40*), no examples of successful cancer targeting of radiohalogenated biotin derivatives have appeared in the literature. We hypothesized that the lack of examples of pretargeting with radiohalogens was due to the structural and lipophilic differences between biotin derivatives that bind metal radionuclides and those that bind radiohalogens. On the basis of this hypothesis, we have conducted a large number of studies to optimize the structural features of biotin derivatives so the in vivo characteristics of radiohalogenated biotin derivatives are improved. Unlike radiometal-containing biotin derivatives, radiohalogenated biotin derivatives can be quite insoluble in aqueous medium, so many of the compounds that have been investigated include ether containing linkers between the biotin moiety and the radiohalogen bonding moiety. Because all biotin derivatives are subject to in vivo degradation by the enzyme biotinidase (*41*−*43*), we (*19*, *44*) and other investigators (*45*) have conducted studies to determine which structural features will block the biotinamide hydrolysis reaction of that enzyme. In addition to determining whether biotinidase cleaved biotin from radiohalogenated biotin derivatives, we also investigated the effect of structural features on biotin binding with avidin and streptavidin (*46*). We believe that it is important to retain the high binding affinity of biotin with these proteins for optimal in vivo tumor targeting. An outcome of those studies was identification of biotin derivatives which have a carboxylate functionality α to the biotinamide bond as an optimal structural feature. The α-carboxylate is optimal because it blocks biotinidase cleavage while retaining high binding affinity. Thus, all of the biotin derivatives investigated in vivo contain a carboxylate functionality α to the biotinamide bond.

The design of the biotin derivatives for carrying the radioiodine and astatine must include a moiety for radiohalogens to react with. It is very important that radiohalogenation reactions are rapid and efficient and that the radiohalogenated moiety be stable to in vivo dehalogenation. Due to the presence of deiodinase enzymes (*47*), radioiodinations of small molecules for in vivo applications are generally conducted on deactivated aryl moieties or vinyl moieties. To facilitate rapid incorporation of radiohalogens, organometallic intermediates are generally used (*48*, *49*). In these studies, stannylbenzamides and *nido*-carboranyl moieties were included in the biotin derivatives as functional moieties for reacting with radiohalogens. Aryl stannanes are very reactive toward electrophilic radiohalogens, producing site-specific incorporation. Aryl stannanes have been used extensively as intermediates for radioiodination and for astatination of molecules. Similarly, high reactivity of *nido*-carboranes with electrophilic radioiodine and astatine has been demonstrated. Pioneering work of Hawthorne and coworkers (*50*−*52*) and our previous studies (*24*, *25*, *53*) have shown radiohalogenation of *nido*-carboranes can occur in excellent radiolabeling yields under mild reaction conditions. Unlike the aryl stannanes, halogenation of *nido*-carboranes is not site-specific, with substitution potentially occurring on any boron atom of the *nido*-

carborane moiety. However, it seems most likely that when only one halogen is substituted, halogenation occurs on a boron atom in the open rim. Hawthorne et al. have reported crystal structures of two iodo-*nido*-carboranes, wherein the iodine atom substituted on the open rim α to a carbon atom (*50*, *54*). Thus, while the structures shown in Schemes 2−4 depict only one of the potential halogenated regioisomers, it is likely to be a major one. Significantly, the presence of halogenated regioisomers is not an important factor in the compounds studied, since it is very unlikely that biotin binding with streptavidin will be affected by substitution on the *nido*-carborane. Biotin binding can be affected if any of the three contiguous, all-cis, chiral centers on the thiophane ring are altered. Importantly, the all-cis (+) configuration of biotin stereocenters is retained under the reaction conditions used. A fourth chiral center is present in the aspartyl group of compound **2** and the lysine groups of compounds **3**−**5**. The presence of this chiral center does not appear to affect biotin binding (*18*−*20*). The presence of chiral centers and iodinated carboranyl regioisomers can, however, result in diasteriomeric pairs of compounds that complicate the NMR spectra and are observable as doublets in HPLC chromatograms.

In vivo stability of the ^{211}At bond to the carrier molecule is absolutely critical to its successful application in TRT. On the basis of our previous experiences, we anticipated some instability of ^{211}At in the biotin derivatives prepared. Fortunately, the release of ^{211}At from carrier molecules in vivo is easily monitored, as free ^{211}At (astatide) localizes in lung, spleen, stomach, and thyroid. Localization of ^{211}At in those tissues can be estimated by comparing its concentration against that of free radioiodine (or a radioiodinated compound). This comparison was first reported by Hamilton et al. (*55*) in an extensive study of the localization of ^{211}At (vs ^{131}I) in rats and monkeys. We have used the comparison of tissue concentrations to demonstrate that ^{211}At-labeled mAb Fab′ fragments are unstable to in vivo deastatination (*56*) and more recently to show stability of astatinated benzamides, and *nido*-carboranyl derivatives in vivo (*27*). The graphs provided as panels in Figures 1 and 2 include the ^{211}At-localizing tissues: lung, spleen, and neck (thyroid). The graphs also include concentration data from blood and the excretory tissues, kidney, and liver. Only the 4 h data for the tissues is provided in the graphs, as that data is adequate to point out the important differences between the biotin derivatives or between ^{211}At and ^{125}I. For comparison purposes, a graph of the tissue concentrations of [^{211}At]astatide and [^{125}I]iodide in the selected tissues, from data previously published, has been included as Figure 2, panel A.

The primary objective of the investigation was to determine the in vivo stability of the astatinated biotin derivatives. The biotin derivative **1a** was the first prepared for astatination and evaluation. Astatination of **1a** was fairly efficient, providing 64% isolated radiochemical yield after reaction for 10 min at room temperature. However, the astatinated compound, [^{211}At]**1c** was not evaluated in vivo, as it was subsequently shown that the biotinidase-blocking *N*-methyl group dramatically decreases binding with avidin and streptavidin (*20*). Therefore, the biotin derivative **2b**, which has a carboxylate group α to the biotinamide bond, was prepared and evaluated. In an vivo experiment, [^{125}I]**2b** and [^{131}I]**1b** were co-injected and tissue concentrations were evaluated at 1, 4, and 24 h postinjection. The results from the experiment (Table S1) indicated that there was little difference between the two compounds in vivo. Therefore, **2a** was chosen for astatination and in vivo study. In the experiment, [^{211}At]**2c** and [^{125}I]**2b** were co-injected, and their biodistribution was evaluated. The data obtained (Table S2) clearly show that [^{211}At]**2c** is unstable to in vivo deastatination based on the observed differences in ^{211}At and ^{125}I concentrations in lung, spleen, and neck (thyroid) (compare Figure 2, panels A and B). The magnitude of difference between the concentrations of ^{211}At and ^{125}I in those tissues suggests that the deastatination is very rapid.

The rationale for evaluating *nido*-carboranes as radiohalogen-binding moieties in biotin derivatives was that these moieties may provide higher in vivo stability of ^{211}At. Because boron−halogen bonds are generally stronger than aryl−halogen bonds (*57*), it seemed possible that boron−halogen bonding would be more stable in vivo. Further, our studies with structurally simple benzamide derivatives and *nido*-carboranyl derivatives appeared to indicate some in vivo stability could be gained by using astatinated *nido*-carborane derivatives (*27*). Our initial study of an astatinated biotin derivative with a *nido*-carborane moiety demonstrated that it could be rapidly astatinated; however, an in vivo evaluation was not conducted as the compound was not stable to biotinidase. The biotin derivative employed contained a methyl group α to the biotinamide moiety (*26*). In vitro studies later demonstrated that this structural feature slowed the biotinidase cleavage rate (to ∼25% of an unaltered biotinamide) but did not block it (*18*). Once it was established that an α carboxylate could be used to completely block biotinidase, a biotin-lysine adduct, **3b**, containing the *nido*-carborane moiety, was prepared and radioiodinated. However, preparation of **3b** was also premature, as other studies demonstrated that inclusion of an aryl moiety decreased the in vivo release of ^{211}At over simpler *nido*-carboranyl compounds (*27*). Therefore, a biotin derivative, **4a**, that contains a phenyl group and a *nido*-carborane, was prepared and evaluated in vivo. In an initial study, [^{125}I]**4b** was co-injected with [^{131}I]**1b** to compare the radioiodinated *nido*-carboranyl-biotin derivative with a biotin derivative containing an aryl halide. The results show that [^{125}I]**4b** is cleared much slower from blood, lung, and kidney than [^{131}I]**1b**. This was consistent with the data previously obtained with similar derivatives that did not include biotin moieties (*27*). Following that experiment, [^{211}At]**4c** and [^{125}I]**4b** were co-injected and evaluated in vivo. The differences in concentration of ^{211}At and ^{125}I in lung, spleen, and neck are much smaller, indicating that less free ^{211}At was present. This is very encouraging, but the high concentrations of astatinated and radioiodinated biotin derivatives remaining in blood and tissues makes this biotin derivative not optimal.

The cause of the longer blood residence time of the *nido*-carborane-containing compounds is not known, but it may be due to their binding with serum proteins. In our studies, it has been noted that the concentration of radiolabeled biotin derivative in aqueous solution could decrease dramatically over a short period of time, with the radioactivity being bound to the surfaces of the container. Additionally, injection or transfer of the solutions via syringes were complicated by adsorption to the metal syringe needle. We found that preparations containing *nido*-carboranes were easier to handle and quantify when a 1% BSA solution was added prior to isolation. These observations led to a conclusion that the adsorption may be due to the *nido*-carborane moiety's interaction with cationic ions on surfaces and on BSA. If this were true, it seemed that one way to potentially improve the

in vivo characteristics of biotin derivatives containing *nido*-carborane moieties would be to incorporate a trialkylamine that, when protonated, could act as an intramolecular counterion. Thus, a *nido*-carboranyl-biotin derivative which contained a trialkylamine functionality, **5a**, was prepared and tested in vivo. An initial in vivo study compared [^{125}I]**5b** with [^{131}I]**1b**. Interestingly, the tissue concentrations of [^{125}I]**5b** did not appear to be very different from that of [^{125}I]**4b**, with the exception of the kidney, which appeared to have a considerably lower concentration at the 1 and 4 h time points (compare Tables S3 and S5).

The biodistribution of [^{211}At]**5c** is very similar to that of [^{211}At]**4c** (compare Figure 2, panels C and D; Tables S4 and S6). The rationale for preparing **5a** was that this compound might have decreased blood concentration due to a lower propensity to bind with serum proteins. In the study comparing co-injected [^{211}At]**5c** and [^{125}I]**5b** (Table S6) there appeared to be a large decrease in blood concentration for [^{125}I]**5b** but not for [^{211}At]**5c**. However, the biodistribution data for [^{125}I]**5b** in the initial study (Table S5) did not show a low blood concentration. Therefore, the question of whether the intermolecular trialkylammonium counterion actually decreased the propensity to bind with serum proteins has not been answered from our data. Some differences in tissue concentrations of [^{211}At]**5c** and [^{125}I]**5b** are most likely due to having free ^{211}At present (i.e. deastatination occurred). Importantly, it appears that the deastatination is of the same magnitude as that observed for [^{211}At]**4c**, so the addition of the trialkylammonium counterion had little effect on the deastatination.

In conclusion, we have investigated the synthesis, radiohalogenation, and in vivo tissue distribution of some biotin derivatives containing aryl stannanes or *nido*-carboranes for radiohalogenation. The studies have shown that biotin derivatives containing *nido*-carboranyl moieties can be readily prepared using standard synthetic organic chemistry methods. The studies have provided data that indicate the biotin derivatives containing astatinated *nido*-carborane moieties are more stable to in vivo deastatination than aryl astatine derivatives. This is a significant improvement over the use of astatinated aryl moieties; however, the astatinated *nido*-carboranyl derivatives do undergo some deastatination. The fact that the *nido*-carboranyl biotin derivatives are not completely stable toward in vivo deastatination, along with their long retention in blood, makes these derivatives nonoptimal. Continuing studies will investigate biotin derivatives with other borane cage molecules, and different charged functionalities, in an attempt to further improve them for use in pretargeting protocols.

ACKNOWLEDGMENT

We thank Dr. Ruedi Risler for his efforts in the preparation of ^{211}At, and Kent Buhler for his participation in animal studies. We are grateful for the financial support provided by the Department of Energy, Medical Applications and Biophysical Research Division, Office of Health and Environmental Research, under grant number DE-FG06-95ER62029.

Supporting Information Available: Tables containing biodistribution data for compounds studied in vivo are included as Tables S1−S6. HPLC chromatograms, ^{1}H NMR spectra, and mass spectra are provided for new compounds (**11, 2a, 17a, 17b, 18, 3a, 20, 21, 22, 4a, 24, 25, 26, 27, 28, 29, 5a**) prepared in the research described in this manuscript. This material is available free of charge via the Internet at http://pubs.acs.org.

LITERATURE CITED

(1) Wilbur, D. S. (1991) Potential use of alpha-emitting radionuclides in the treatment of cancer. *Antibody Immunoconjugate Radiopharm. 4*, 85−97.
(2) Raju, M. R., Eisen, Y., Carpenter, S., and Inkret, W. C. (1991) Radiobiology of alpha particles. III. Cell inactivation by alpha-particle traversals of the cell nucleus. *Radiat. Res. 128*, 204−209.
(3) Humm, J. L., and Chin, L. M. (1993) A Model of Cell Inactivation by Alpha-Particle Internal Emitters. *Radiat. Res. 134*, 143−150.
(4) Allen, B. J. (1999) Targeted alpha therapy: evidence for potential efficacy of alpha-immunoconjugates in the management of micrometastatic cancer. *Australas Radiol. 43*, 480−486.
(5) Akabani, G., Kennel, S. J., and Zalutsky, M. R. (2003) Microdosimetric analysis of α-particle-emitting targeted radiotherapeutics using histological images. *J. Nucl. Med. 44*, 792−805.
(6) Hall, E. J. (1988) LET and RBE. *Radiobiology for the Radiologist*, pp 161−178, J. B. Lippincott Company, Philadelphia, PA.
(7) Feinendegen, L. E., and McClure, J. J. (1997) Alpha-Emitters for Medical Therapy − Workshop of the United States Department of Energy. *Radiat. Res. 148*, 195−201.
(8) Zalutsky, M. R., Zhao, X. G., Alston, K. L., and Bigner, D. (2001) High-level production of alpha-particle-emitting (211) At and preparation of (211)At-labeled antibodies for clinical use. *J. Nucl. Med. 42*, 1508−1515.
(9) Zalutsky, M. R., and Vaidyanathan, G. (2000) Astatine-211-labeled radiotherapeutics: an emerging approach to targeted alpha-particle radiotherapy. *Curr. Pharm. Des. 6*, 1433−1455.
(10) Fritzberg, A. R., Beaumier, P. L., Bottino, B. J., and Reno, J. M. (1994) Approaches to improved antibody- and peptide-mediated targeting for imaging and therapy of cancer. *J. Controlled Release 28*, 167−173.
(11) Goodwin, D. A., and Meares, C. F. (1997) Pretargeting: General Principles. *Cancer (Suppl.) 80*, 2675−2680.
(12) Janssen, M. L., Oyen, W. J., Dijkgraaf, I., Massuger, L. F., Frielink, C., Edwards, D. S., Rajopadhye, M., Boonstra, H., Corstens, F. H., and Boerman, O. C. (2002) Tumor targeting with radiolabeled.alpha.v.beta.3 integrin binding peptides in a nude mouse model. *Cancer Res. 62*, 6146−6151.
(13) Goodwin, D. A., and Meares, C. F. (2001) Advances in pretargeting biotechnology. *Biotechnol. Adv. 19*, 435−450.
(14) Chinol, M., Grana, C., Gennari, R., Cremonesi, M., Geraghty, J. G., and Paganelli, G. (2000) Pretargeted Radioimmunotherapy of Cancer. *Radioimmunotherapy of Cancer* (Abrams, P. G., Fritzberg, A. R., Eds.) pp 169−193, Marcel Dekker, New York.
(15) Axworthy, D. B., Reno, J. M., Hylarides, M. D., Mallett, R. W., Theodore, L. J., Gustavson, L. M., Su, F., Hobson, L. J., Beaumier, P. L., and Fritzberg, A. R. (2000) Cure of human carcinoma xenografts by a single dose of pretargeted yttrium-90 with negligible toxicity. *Proc. Natl. Acad. Sci. U.S.A. 97*, 1802−1807.
(16) Press, O. W., Corcoran, M., Subbiah, K., Hamlin, D. K., Wilbur, D. S., Johnson, T., Theodore, L., Yau, E., Mallett, R., Meyer, D. L., and Axworthy, D. (2001) A comparative evaluation of conventional and pretargeted radioimmunotherapy of CD20-expressing lymphoma xenografts. *Blood 98*, 2535−2543.
(17) Breitz, H. B., Weiden, P. L., Beaumier, P. A., Axworthy, D. B., Seiler, C., Su, F.-M., Graves, S., Bryan, K., and Reno, J. M. (2000) Clinical Optimization of Pretargeted Radioimmunotherapy with Antibody-Streptavidin Conjugate and ^{90}Y-DOTA-Biotin. *J. Nucl. Med. 41*, 131−140.
(18) Wilbur, D. S., Hamlin, D. K., Pathare, P. M., and Weerawarna, S. A. (1997) Biotin reagents for antibody pretargeting. Synthesis, radioiodination and in vitro evaluation of water soluble, biotinidase resistant biotin derivatives. *Bioconjugate Chem. 8*, 572−584.

(19) Wilbur, D. S., Hamlin, D. K., Chyan, M. K., Kegley, B. B., and Pathare, P. M. (2001) Biotin reagents for antibody pretargeting. 5. Additional studies of biotin conjugate design to provide biotinidase stability. *Bioconjugate Chem. 12*, 616−623.

(20) Wilbur, D. S., Chyan, M.-K., Pathare, P. M., Hamlin, D. K., Frownfelter, M. B., and Kegley, B. B. (2000) Biotin Reagents for Antibody Pretargeting. 4. Selection of Biotin Conjugates for in Vivo Application Based on Their Dissociation Rate from Avidin and Streptavidin. *Bioconjugate Chem. 11*, 569−583.

(21) Zalutsky, M. R., and Narula, A. S. (1988) Astatination of Proteins using an N−Succinimidyl Tri-*n*-Butylstannyl Benzoate Intermediate. *Appl. Radiat. Isot. 39*, 227−232.

(22) Wilbur, D. S., Hylarides, M. D., and Fritzberg, A. R. (1989) Reactions of organometallic compounds with astatine-211. Application to protein labeling. *Radiochim. Acta 47*, 137−142.

(23) Hawthorne, M. F., and Maderna, A. (1999) Applications of radiolabeled boron clusters to the diagnosis and treatment of cancer. *Chem. Rev. 99*, 3421−3434.

(24) Wilbur, D. S., Hamlin, D. K., and Srivastava, R. R. (1994) Radioiodinations of *nido*-Carboranes. Potential Hydrophilic Pendant Groups for Radiohalogenation of Biological Molecules. *J. Labeled Compds. Radiopharm. 35*, 199−201.

(25) Wilbur, D. S., Hamlin, D. K., Livesey, J. C., Srivastava, R. R., Laramore, G. E., and Griffin, T. W. (1994) Synthesis and radioiodination of a *nido*-1,2-carboranyl derivative of 2-nitroimidazole. *Nucl. Med. Biol. 21*, 601−611.

(26) Wilbur, D. S., Hamlin, D. K., Foulon, C. F., Zalutsky, M. R., and Pathare, P. M. (1997) Investigation of *nido*-Carboranes as Hydrophilic Pendant Groups for Astatination of Biomolecules. Application to an Astatinated Biotin Derivative. *Proceedings of the 12th International Symposium on Radiopharmaceutical Chemistry*, pp 76−78, Uppsala, Sweden.

(27) Wilbur, D. S., Chyan, M.-K., Hamlin, D. K., Kegley, B. B., Risler, R., Pathare, P. M., Quinn, J., Vessella, R. L., Foulon, C., Zalutsky, M., Wedge, T. J., and Hawthorne, M. F. (2004) Reagents for Astatination of Biomolecules. Comparison of the in Vivo Distribution and Stability of Some Radioiodinated/Astatinated Benzamidyl- and *nido*-Carboranyl Compounds. *Bioconjugate Chem. 15*, 203−223.

(28) Gamper, H. B., Reed, M. W., Cox, T., Virosco, J. S., Adams, A. D., Gall, A. A., Scholler, J. K., and Meyer, R. B. (1993) Facile Preparation of Nuclease Resistant 3′ Modified Oligodeoxynucleotides. *Nucleic Acids Res. 21*, 145−150.

(29) Wilbur, D. S., Vessella, R. L., Stray, J. E., Goffe, D. K., Blouke, K. A., and Atcher, R. W. (1993) Preparation and evaluation of *para*-[^{211}At]astatobenzoyl labeled anti-renal cell carcinoma antibody A6H F(ab′)$_2$. In vivo distribution comparison with *para*-[^{125}I]iodobenzoyl labeled A6H F(ab′)$_2$. *Nucl. Med. Biol. 20*, 917−927.

(30) Wilbur, D. S., Hamlin, D. K., Vessella, R. L., Stray, J. E., Buhler, K. R., Stayton, P. S., Klumb, L. A., Pathare, P. M., and Weerawarna, S. A. (1996) Antibody fragments in tumor pretargeting. Evaluation of biotinylated Fab′ colocalization with recombinant streptavidin and avidin. *Bioconjugate Chem. 7*, 689−702.

(31) Wilbur, D. S., Hamlin, D. K., Buhler, K. R., Pathare, P. M., Vessella, R. L., Stayton, P. S., and To, R. (1998) Streptavidin in antibody pretargeting. 2. Evaluation of methods for decreasing localization of streptavidin to kidney while retaining its tumor binding capacity. *Bioconjugate Chem. 9*, 322−330.

(32) Wilbur, D. S., Hamlin, D. K., Chyan, M.-K., Kegley, B. B., and Pathare, P. M. (2001) Biotin reagents for antibody pretargeting. 5. Additional studies of biotin conjugate design to provide biotinidase stability. *Bioconjugate Chem. 12*, 616−623.

(33) Boerman, O. C., van Schaijk, F. G., Oyen, W. J., and Corstens, F. H. (2003) Pretargeted radioimmunotherapy of cancer: progress step by step. *J. Nucl. Med. 44*, 400−411.

(34) Theodore, L. J., Fritzberg, A. R., Schultz, J. E., and Axworthy, D. B. (2000) Evolution of a Pretarget Radioimmunotherapeutic Regimen. *Radioimmunotherapy of Cancer* (Abrams, P. G., Fritzberg, A. R., Eds.) pp 195−221, Marcel Dekker, New York.

(35) Paganelli, G., Malcovati, M., and Fazio, F. (1991) Monoclonal Antibody pretargetting techniques for tumour localization: the avidin−biotin system. *Nucl. Med. Commun. 12*, 211−234.

(36) Pagel, J. M., Hedin, N., Subbiah, K., Meyer, D., Mallet, R., Axworthy, D., Theodore, L. J., Wilbur, D. S., Matthews, D. C., and Press, O. W. (2003) Comparison of anti-CD20 and anti-CD45 antibodies for conventional and pretargeted radioimmunotherapy of B-cell lymphomas. *Blood 101*, 2340−2348.

(37) Knox, S. J., Goris, M. L., Tempero, M., Weiden, P. L., Gentner, L., Breitz, H., Adams, G. P., Axworthy, D., Gaffigan, S., Bryan, K., Fisher, D. R., Colcher, D., Horak, I. D., and Weiner, L. M. (2000) Phase II trial of yttrium-90-DOTA-biotin pretargeted by NR-LU-10 antibody/streptavidin in patients with metastatic colon cancer. *Clin. Cancer Res. 6*, 406−414.

(38) Green, N. M. (1990) Avidin and Streptavidin. *Methods Enzymol. 184*, 51−67.

(39) Lewis, M. R., Wang, M., Axworthy, D. B., Theodore, L. J., Mallet, R. W., Fritzberg, A. R., Welch, M. J., and Anderson, C. J. (2003) In vivo evaluation of pretargeted ^{64}Cu for tumor imaging and therapy. *J. Nucl. Med. 44*, 1284−1292.

(40) Correa-Gonzalez, L., Arteaga de Murphy, C., Ferro-Flores, G., Pedraza-Lopez, M., Murphy-Stack, E., Mino-Leon, D., Perez-Villasenor, G., Diaz-Torres, Y., and Munoz-Olvera, R. (2003) Uptake of 153Sm-DTPA-bis-biotin and 99mTc-DTPA-bis-biotin in rat AS-30D-hepatoma cells. *Nucl. Med. Biol. 30*, 135−140.

(41) Pispa, J. (1965) Animal Biotinidase. *Ann. Med. Exptl. Bio. Fenniae 43*, 3−40.

(42) Wolf, B., Hymes, J., and Heard, G. S. (1990) Biotinidase. *Methods Enzymol. 184*, 103−111.

(43) Hymes, J., Fleischhauer, K., and Wolf, B. (1997) Biotinidase in Serum and Tissues. *Methods Enzymol. 279*, 422−434.

(44) Wilbur, D. S., Hamlin, D. K., Pathare, P. M., and Weerawarna, S. A. (1997) Biotin reagents for antibody pretargeting. Synthesis, radioiodination, and in vitro evaluation of water soluble, biotinidase resistant biotin derivatives. *Bioconjugate Chem. 8*, 572−584.

(45) Foulon, C. F., Alston, K. L., and Zalutsky, M. R. (1998) Astatine-211-Labeled Biotin Conjugates Resistant to Biotinidase for Use in Pretargeting Radioimmunotherapy. *Nucl. Med. Biol. 25*, 81−88.

(46) Wilbur, D. S., Pathare, P. M., Hamlin, D. K., Frownfelter, M. B., Kegley, B. B., Leung, W. Y., and Gee, K. R. (2000) Evaluation of biotin-Dye conjugates for use in an HPLC assay To assess relative binding of biotin derivatives with avidin and streptavidin. *Bioconjugate Chem. 11*, 584−598.

(47) Kohrle, J. (2000) The deiodinase family: selenoenzymes regulating thyroid hormone availability and action. *Cell. Mol. Life Sci. 57*, 1853−1863.

(48) Kabalka, G. W., and Varma, R. S. (1989) The Synthesis of Radiolabeled Compounds Via Organometallic Intermediates. *Tetrahedron 45*, 6601−6621.

(49) Wilbur, D. S. (1992) Radiohalogenation of proteins: an overview of radionuclides, labeling methods, and reagents for conjugate labeling. *Bioconjugate Chem. 3*, 433−470.

(50) Mizusawa, E. A., Thompson, M. R., and Hawthorne, M. F. (1985) Synthesis and Antibody-Labeling Studies with the *p*-Isothiocyanatobenzene Derivatives of 1,2-Dicarba-*closo*-dodecaborane(12) and the Dodecahydro-7,8-dicarba-*nido*-undecaborate(1-) Ion for Neutron-Capture Therapy of Human Cancer. Crystal and Molecular Stucture of Cs^+[*nido*-7-(p−C_6H_4NCS)-9-I-7,8-$C_2B_9H_{11}$]. *Inorg. Chem. 24*, 1911−1916.

(51) Varadarajan, A., Sharkey, R. M., Goldenberg, D. M., and Hawthorne, M. F. (1991) Conjugation of Phenyl Isothiocyanate Derivatives of Carborane to Antitumor antibody and in Vivo Lacalization of Conjugates in Nude Mice. *Bioconjugate Chem. 2*, 102−110.

(52) Hawthorne, M. F. (1991) Biochemical applications of boron cluster chemistry. *Pure Appl. Chem. 63*, 327−334.

(53) Wilbur, D. S., Hamlin, D. K., Pathare, P. M., and Kegley, B. B. (1999) Synthesis of a *nido*-Carborane Derivative for use as a Protein Conjugate for Direct Radioiodination. *J. Labelled Compd. Radiopharm. 42*, S288−S290.

(54) Olsen, F. P., and Hawthorne, M. F. (1965) Halodicarbaundecaborate(II) Ions. *Inorg. Chem. 4*, 1839−1840.

(55) Hamilton, J. G., Durbin, P. W., and Parrott, M. (1954) The Accumulation and Destructive Action of Astatine211 (EKA-Iodine) in the Thyroid Gland of Rats and Monkeys. *J. Clin. Endocrinol. Metab. 14*, 1161−1178.

(56) Hadley, S. W., Wilbur, D. S., Gray, M. A., and Atcher, R. W. (1991) Astatine-211 labeling of an antimelanoma antibody and its Fab fragment using N-succinimidyl *p*-[^{211}At]astatobenzoate: comparisons in vivo with the *p*-[^{125}I]iodobenzoyl conjugate. *Bioconjugate Chem. 2*, 171−179.

(57) Kerr, J. A. (1993) Strengths of Chemical Bonds. *CRC Handbook of Chemistry and Physics* (Lide, D. R., Ed.) pp 9-123−9-145, CRC Press, Boca Raton.

BC034229Q

Table S1: Distribution of Radioactivity for Co-injected [^{125}I]2b and [^{131}I]1b in BALB/c mice.[a]

Tissues	1 h[b,c]		4 h		24 h	
	I-125	I-131	I-125	I-131	I-125	I-131
blood	0.65 ± 0.87	1.17 ± 0.44	1.43 ± 1.97	0.85 ± 1.95	0.01 ± 0.00	0.01 ± 0.00
muscle	1.21 ± 0.11	0.40 ± 0.26	0.20 ± 0.18	0.13 ± 0.10	0.00 ± 0.00	0.00 ± 0.00
lung	1.61 ± 1.30	1.60 ± 0.71	1.27 ± 1.29	0.85 ± 0.86	0.01 ± 0.00	0.01 ± 0.00
kidney	0.83 ± 0.51*	5.53 ± 3.07*	0.47 ± 0.55	0.46 ± 0.22	0.01 ± 0.00	0.02 ± 0.01
spleen	0.45 ± 0.37	0.66 ± 0.24	0.31 ± 0.18	0.23 ± 0.09	0.01 ± 0.00	0.01 ± 0.00
liver	1.30 ± 1.04	2.99 ± 1.65	1.52 ± 1.26	1.34 ± 1.34	0.01 ± 0.00	0.02 ± 0.00
intestine	3.16 ± 1.56*	7.40 ± 1.31*	3.92 ± 1.88*	8.22 ± 2.12*	0.48 ± 0.27	0.27 ± 0.15
neck	0.56 ± 0.10*	3.16 ± 0.43*	0.42 ± 0.12*	1.83 ± 0.78*	0.01 ± 0.01	0.06 ± 0.04
stomach	3.31 ± 3.46	4.00 ± 2.72	0.46 ± 0.19*	1.20 ± 0.42*	0.10 ± 0.09	0.18 ± 0.14
urine[d]	6.78 ± 4.12*	84.4 ± 47.4*	3.70 ± 1.13*	27.13 ± 5.54*	0.27 ± 0.10	1.57 ± 0.84

[a]Values shown are % injected dose / gram ± standard deviation. [b]Time of sacrifice from injection of halogenated biotin derivatives. [c]Data were obtained for $n = 5$ mice at 1 h, 4 h and 24 h; average animal weight, 27.91 ± 1.97 g; Injectate for each animal had 25 μCi of [^{125}I]**2b** and 13 μCi of [^{131}I]**1b** in approximately 100 μL of 0.9% sterile saline. [b,d]Urine was collected by syringe bladder tap after sacrifice. Those tissues that had a significant difference ($p < 0.05$)in radionuclide concentrations by paired Student's t-test are marked with an asterisk (*). The data in the 24 h time point was not analyzed as the values are very small.

Table S2: Distribution of Radioactivity for Co-injected [^{211}At]2c and [^{125}I]2b in BALB/c mice.[a]

Tissues	1 h[b,c]		4 h		24 h	
	I-125	At-211	I-125	At-211	I-125	At-211
blood	0.15 ± 0.05*	1.51 ± 0.64*	0.11 ± 0.17*	1.05 ± 0.43*	0.01 ± 0.00	0.18 ± 0.08
muscle	0.06 ± 0.04	1.07 ± 0.36	0.06 ± 0.05	0.64 ± 0.32	0.01 ± 0.01	0.15 ± 0.08
lung	0.20 ± 0.06	11.8 ± 2.81	0.77 ± 1.14	7.82 ± 3.35	0.03 ± 0.02	1.54 ± 0.56
kidney	1.50 ± 0.75	7.30 ± 0.17	0.26 ± 0.23	3.09 ± 1.49	0.01 ± 0.00	0.53 ± 0.16
spleen	0.29 ± 0.34	11.47 ± 4.97	0.36 ± 0.30	6.71 ± 3.01	0.03 ± 0.03	0.56 ± 0.19
liver	16.75 ± 19.75	10.19 ± 14.94	2.32 ± 3.73*	2.36 ± 1.97*	0.01 ± 0.01	0.19 ± 0.05
intestine	28.63 ± 9.48	2.12 ± 1.72	19.01 ± 6.46	2.44 ± 2.20	2.02 ± 0.89*	1.48 ± 0.58*
neck	4.19 ± 7.25*	9.00 ± 4.70*	0.48 ± 0.12	18.62 ± 9.21	0.06 ± 0.06	3.25 ± 1.38
stomach	1.61 ± 1.49	7.43 ± 3.20	1.71 ± 0.80	10.97 ± 5.97	2.11 ± 2.36*	4.58 ± 2.37*
urine[d]	46.37 ± 31.98	11.28 ± 7.70	0.94 ± 0.53	12.93 ± 7.39	0.19 ± 0.13*	1.89 ± 3.27*

[a]Values shown are % injected dose / gram ± standard deviation. [b]Time of sacrifice from injection of halogenated *nido*-carborane derivatives. [c]Data were obtained for $n = 5$ mice at 1 h, 4 h and 24 h; average animal weight, 25.69 ± 0.93 g; Injectate for each animal had 20 μCi of [^{211}At]**2c** and 20 μCi of [^{125}I]**2b** in approximately 100 μL of 0.9% sterile saline. [b,d]Urine was collected by syringe bladder tap after sacrifice. Those tissues that have radionuclide concentrations that *are not* significantly different ($p > 0.05$) are marked with an asterisk (*).

Table S3: Distribution of Radioactivity for Co-injected [^{125}I]4b and [^{131}I]1b in BALB/c mice.[a]

Tissues	1 h[b,c]		4 h		24 h	
	I-125	I-131	I-125	I-131	I-125	I-131
blood	5.41 ± 0.71	0.70 ± 0.05	2.60 ± 0.70	0.17 ± 0.08	0.30 ± 0.10	0.01 ± 0.00
muscle	0.28 ± 0.07*	0.40 ± 0.46*	0.26 ± 0.09	0.07 ± 0.04	0.04 ± 0.01	0.00 ± 0.00
lung	1.99 ± 0.33	0.70 ± 0.16	1.49 ± 0.47	0.18 ± 0.10	0.17 ± 0.07	0.01 ± 0.00
kidney	3.74 ± 0.45*	0.30 ± 0.58*	2.68 ± 0.61	0.47 ± 0.21	0.40 ± 0.21	0.02 ± 0.01
spleen	0.88 ± 0.18*	0.50 ± 0.43*	0.57 ± 0.18	0.14 ± 0.06	0.06 ± 0.02	0.01 ± 0.00
liver	10.81 ± 1.23	2.63 ± 0.81	7.23 ± 0.23	2.85 ± 2.87	0.38 ± 0.16	0.02 ± 0.01
intestine	9.13 ± 0.92	18.66 ± 3.54	8.39 ± 5.19*	13.7 ± 8.89*	3.43 ± 3.55*	1.35 ± 1.57*
neck	1.66 ± 0.18*	1.56 ± 0.22*	1.04 ± 0.25	1.41 ± 0.34	0.15 ± 0.07	0.05 ± 0.03
stomach	0.95 ± 0.36*	1.13 ± 0.35*	3.04 ± 1.88*	1.23 ± 0.40*	2.08 ± 2.06*	0.57 ± 0.52*
urine[d]	1.99 ± 0.73	125.09 ± 39.96	4.36 ± 4.42	21.65 ± 17.42	2.48 ± 1.98*	1.93 ± 1.24*

[a]Values shown are % injected dose / gram ± standard deviation. [b]Time of sacrifice from injection of halogenated derivatives. [c]Data were obtained for $n = 5$ mice at 1, 4 and 24 h; average animal weight, 27.56 ± 2.72 g; Injectate for each animal had 10 μCi of [^{125}I]**4b** and 10 μCi of [^{131}I]**1b** in approximately 100 μL of 0.9% sterile saline. [b,d]Urine was collected by syringe bladder tap after sacrifice. Those tissues that have radionuclide concentrations that *are not* significantly different ($p > 0.05$) are marked with an asterisk (*).

Table S4: Distribution of Radioactivity for Co-injected [^{211}At]4c and [^{125}I]4b in BALB/c mice.[a]

Tissues	1 h[b,c]		4 h		24 h	
	I-125	At-211	I-125	At-211	I-125	At-211
blood	7.19 ± 1.26	5.02 ± 1.00	3.46 ± 0.48	2.23 ± 0.25	0.73 ± 0.09	0.55 ± 0.11
muscle	0.30 ± 0.02	0.44 ± 0.06	0.32 ± 0.21*	0.35 ± 0.22*	0.09 ± 0.01*	0.09 ± 0.04*
lung	2.63 ± 0.50	3.95 ± 0.64	1.58 ± 0.23	2.76 ± 0.32	0.41 ± 0.07*	0.69 ± 0.32*
kidney	2.52 ± 0.37	3.40 ± 0.68	2.02 ± 0.41*	2.21 ± 0.25*	0.51 ± 0.06*	0.54 ± 0.08*
spleen	1.20 ± 0.20	2.74 ± 0.52	0.91 ± 0.40	2.48 ± 0.59	0.20 ± 0.04	0.38 ± 0.16
liver	20.90 ± 3.16	9.73 ± 1.55	6.35 ± 1.89*	4.81 ± 1.00*	0.69 ± 0.15	1.55 ± 0.37
intestine	28.58 ± 9.05*	28.29 ± 5.08*	24.53 ± 12.65*	14.10 ± 7.11*	0.72 ± 0.19*	0.61 ± 0.16*
neck	2.19 ± 0.42	3.77 ± 0.67	1.92 ± 0.75	6.18 ± 1.16	0.28 ± 0.05	1.28 ± 0.51
stomach	1.66 ± 0.56*	2.42 ± 0.58*	0.83 ± 0.25	1.16 ± 0.14	0.22 ± 0.05	0.54 ± 0.23
urine[d]	2.05 ± 0.89*	1.85 ± 0.81*	6.07 ± 8.34*	10.09 ± 9.13*	0.81 ± 0.29	2.23 ± 1.02

[a]Values shown are % injected dose / gram ± standard deviation. [b]Time of sacrifice from injection of halogenated *nido*-carborane derivatives. [c]Data were obtained for $n = 5$ mice at 1, 4 and 24 h; average animal weight, 26.36 ± 2.09 g; Injectate for each animal had 2.5 μCi of [^{211}At]**4c** and 2.5 μCi of [^{125}I]**4b** in approximately 100 μL of 0.9% sterile saline. [b,d]Urine was collected by syringe bladder tap after sacrifice. Those tissues that have radionuclide concentrations that *are not* significantly different ($p > 0.05$) by the paired Student's t-test are marked with an asterisk (*).

Table S5: Distribution of Radioactivity for Co-injected [^{125}I]5b and [^{131}I]1b in BALB/c mice.[a]

Tissues	1 h[b,c]		4 h		24 h	
	I-125	I-131	I-125	I-131	I-125	I-131
blood	4.69 ± 0.12	0.96 ± 0.26	3.83 ± 1.21	0.68 ± 0.56	1.19 ± 0.08	0.02 ± 0.02
muscle	0.32 ± 0.10*	1.04 ± 1.30*	0.22 ± 0.05*	0.14 ± 0.10*	0.13 ± 0.00	0.01 ± 0.00
lung	1.77 ± 0.13	0.94 ± 0.24	2.02 ± 1.22	0.51 ± 0.29	0.76 ± 0.33	0.02 ± 0.02
kidney	1.22 ± 0.18	4.49 ± 1.09	0.99 ± 0.08	0.51 ± 0.08	0.67 ± 0.09	0.03 ± 0.01
spleen	0.98 ± 0.13	0.59 ± 0.15	0.65 ± 0.08	0.22 ± 0.04	0.32 ± 0.05	0.01 ± 0.01
liver	7.30 ± 1.64	3.31 ± 1.33	7.49 ± 2.15	1.25 ± 1.69	2.24 ± 0.25	0.02 ± 0.01
intestine	6.38 ± 0.88	15.29 ± 2.07	6.79 ± 1.65	15.39 ± 5.74	1.81 ± 1.97*	0.70 ± 1.11*
neck	1.42 ± 0.25	2.49 ± 0.59	1.26 ± 0.19	3.27 ± 0.64	0.70 ± 0.38*	2.09 ± 2.70*
stomach	0.91 ± 0.55	1.62 ± 0.24	2.29 ± 1.59*	2.63 ± 0.72*	0.55 ± 0.21	0.27 ± 0.20
urine[d]	1.72 ± 1.52	182.45 ± 106.63	1.14 ± 0.53	35.88 ± 12.13	0.78 ± 0.52*	2.26 ± 1.92*

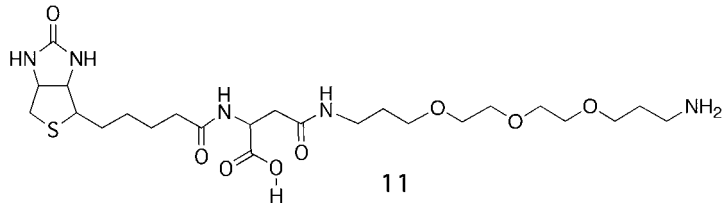
[a]Values shown are % injected dose / gram ± standard deviation. [b]Time of sacrifice from injection of halogenated *nido*-carborane derivatives. [c]Data were obtained for $n = 5$ mice at 1, 4 and 24 h; average animal weight, 27.59 ± 1.92 g; Injectate for each animal had 40 μCi of [^{125}I]**5b** and 20 μCi of [^{131}I]**1b** in approximately 100 μL of 0.9% sterile saline. [b,d]Urine was collected by syringe bladder tap after sacrifice. Those tissues that have radionuclide concentrations that *are not* significantly different ($p > 0.07$) by the paired Student's t-test are marked with an asterisk (*).

Table S6: Distribution of Radioactivity for Co-injected [^{211}At]5c and [^{125}I]5b in BALB/c mice.[a]

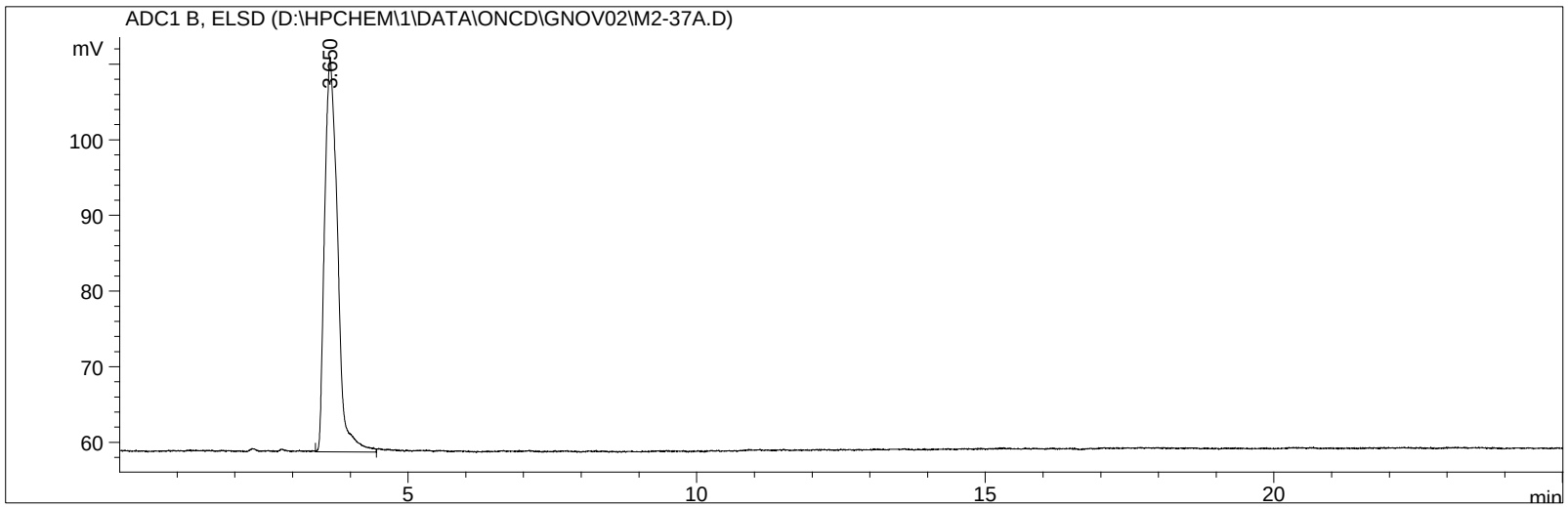
Tissues	1 h[b,c]		4 h		24 h	
	I-125	At-211	I-125	At-211	I-125	At-211
blood	1.57 ± 0.36*	4.29 ± 0.98*	0.99 ± 0.23	2.81 ± 0.63	0.30 ± 0.05	0.50 ± 0.12
muscle	0.11 ± 0.02	0.40 ± 0.07	0.13 ± 0.03	0.35 ± 0.08	0.04 ± 0.01*	0.12 ± 0.02*
lung	1.05 ± 0.91	2.47 ± 0.41	0.78 ± 0.35	2.09 ± 0.46	0.17 ± 0.05*	0.46 ± 0.04*
kidney	0.85 ± 0.10	3.22 ± 0.45	0.50 ± 0.16	2.31 ± 0.65	0.20 ± 0.06*	0.63 ± 0.10*
spleen	0.54 ± 0.45	1.23 ± 0.56	0.38 ± 0.06	1.20 ± 0.29	0.28 ± 0.19*	0.64 ± 0.25*
liver	7.22 ± 3.54*	6.37 ± 2.26*	2.50 ± 1.18	3.93 ± 1.09	0.59 ± 0.10	1.24 ± 0.24
intestine	20.60 ± 3.85*	10.31 ± 1.79*	22.70 ± 4.28	13.43 ± 2.52	2.94 ± 1.53	2.66 ± 1.27
neck	0.53 ± 0.04	1.30 ± 0.18	0.46 ± 0.15	1.53 ± 0.12	0.11 ± 0.01	0.57 ± 0.07
stomach	3.14 ± 1.91*	2.51 ± 1.10*	1.74 ± 1.97	2.14 ± 1.84	0.15 ± 0.08*	0.66 ± 0.04*
urine[d]	0.83 ± 0.69	12.43 ± 10.66	0.75 ± 0.30	12.46 ± 6.26	0.22 ± 0.06*	1.21 ± 0.58*

[a]Values shown are % injected dose / gram ± standard deviation. [b]Time of sacrifice from injection of halogenated *nido*-carborane derivatives. [c]Data were obtained for $n = 5$ mice at 1, 4 and 24 h; average animal weight, 30.19 ± 8.56 g; Injectate for each animal had 8 μCi of [^{211}At]**5c** and 8 μCi of [^{125}I]**5b** in approximately 100 μL of 0.9% sterile saline. [b,d]Urine was collected by syringe bladder tap after sacrifice. Those tissues that have radionuclide concentrations that *are not* significantly different ($p > 0.05$) by the paired Student's t-test are marked with an asterisk (*).

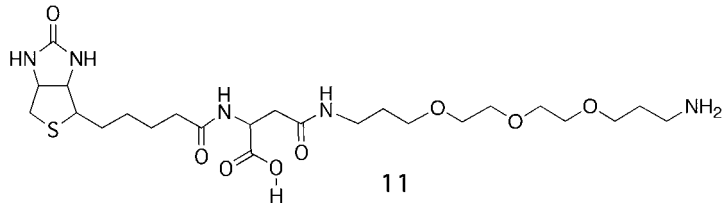
HPLC


O
HN
NH
S
H
N
O
O
O
H
N
O
O
O
NH2

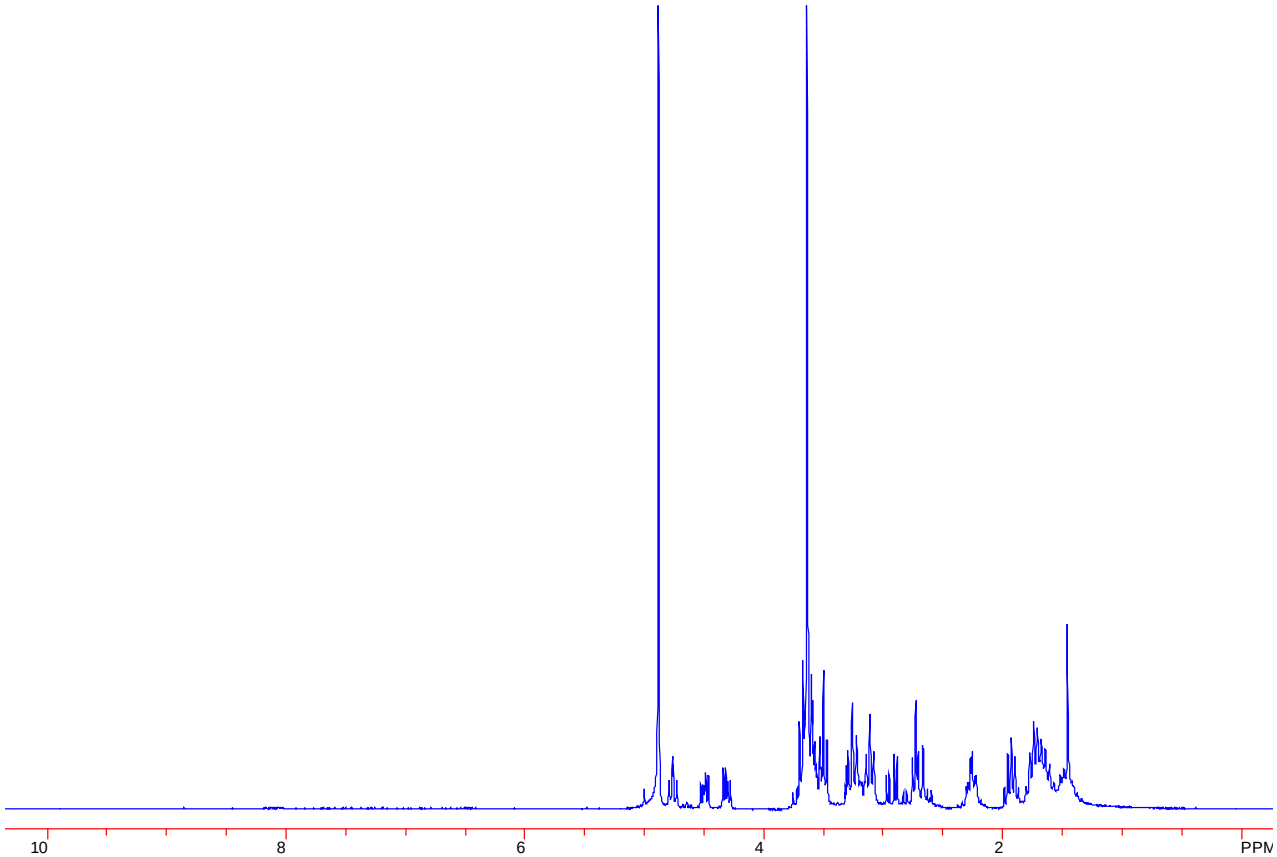
11


ADC1 B, ELSD (D:\HPCHEM\1\DATA\ONCD\GNOV02\M2-37A.D)
mV
3.650
100
90
80
70
60
5
10
15
20
min

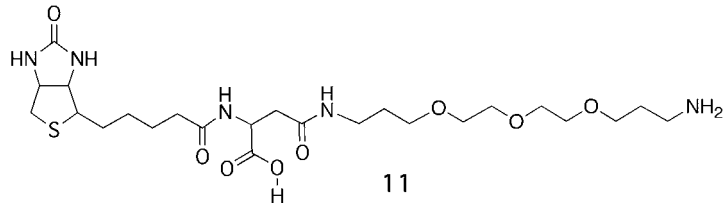
^{1}H NMR



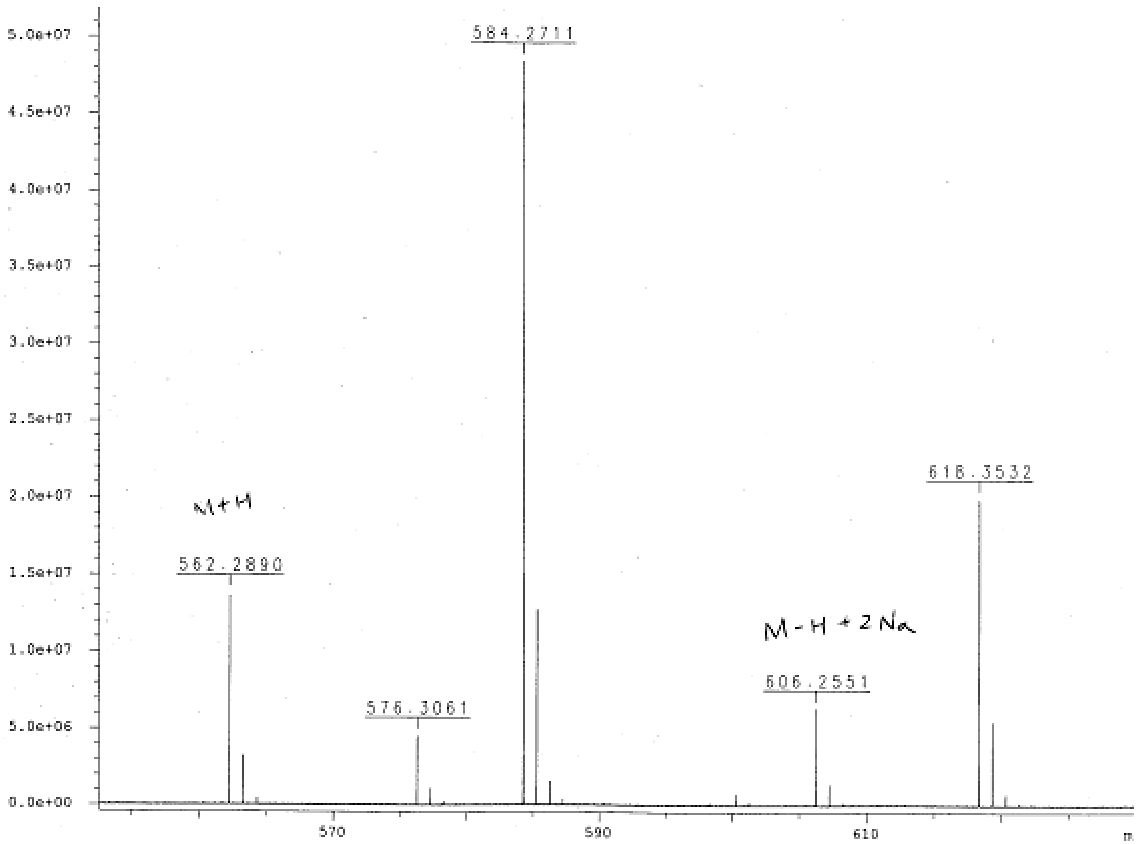
11



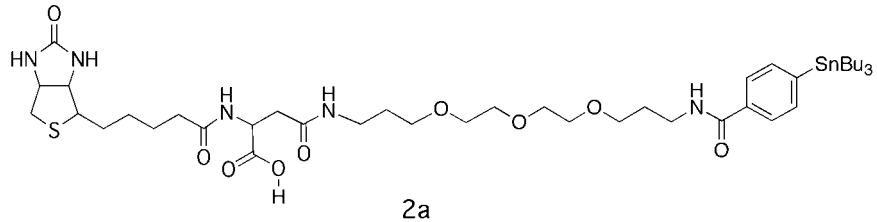
MS


O
HN
NH
S
H
N
O
O
H
N
O
O
O
NH2

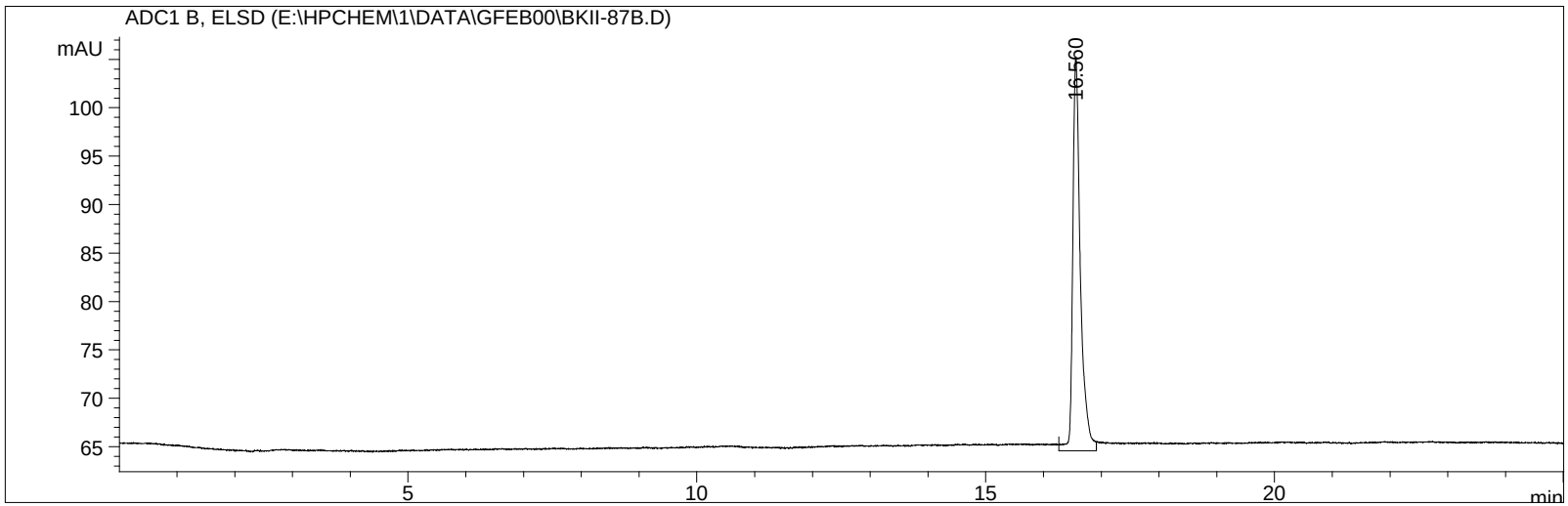
11


5.0e+07
4.5e+07
4.0e+07
3.5e+07
3.0e+07
2.5e+07
2.0e+07
1.5e+07
1.0e+07
5.0e+06
0.0e+00
584.2711
M+H
562.2890
576.3061
M-H+2Na
606.2551
616.3532
570
590
610
m

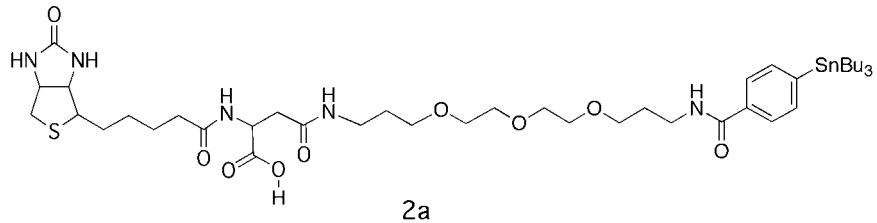
HPLC


O
HN
NH
S
H
N
O
O
O
H
N
O
O
O
O
H
N
O
SnBu3

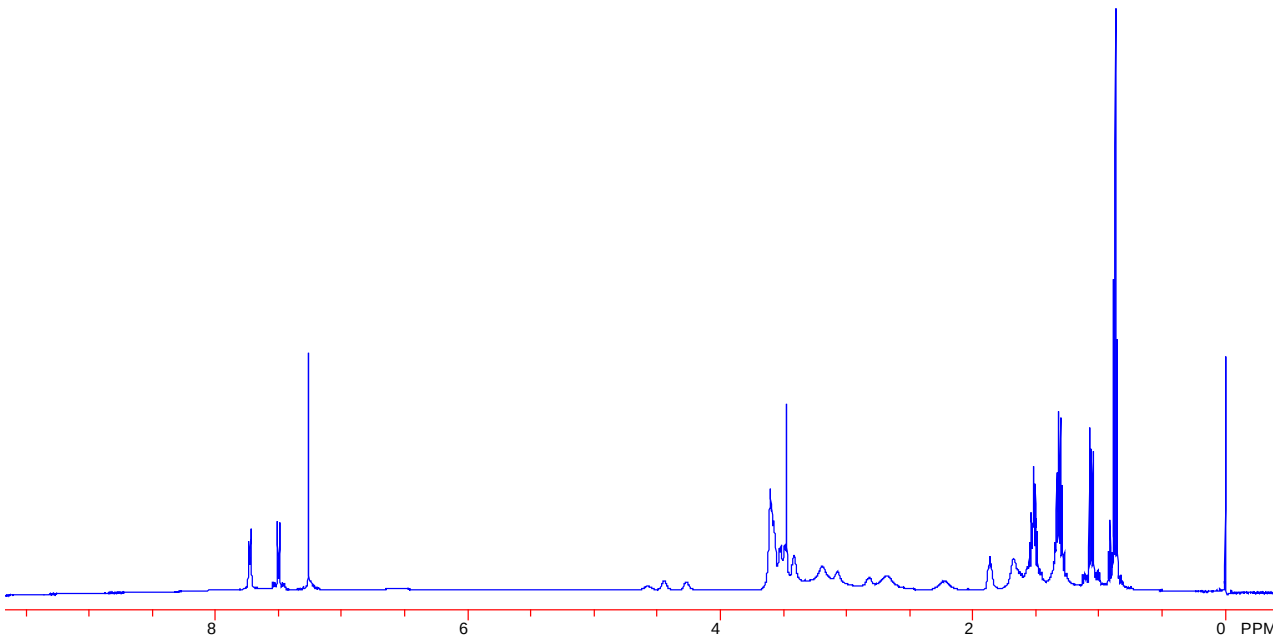
2a


ADC1 B, ELSD (E:\HPCHEM\1\DATA\GFEB00\BKII-87B.D)
mAU
100
95
90
85
80
75
70
65
16.560
5
10
15
20
min

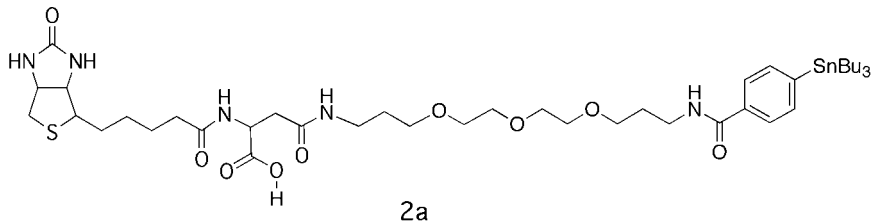
^{1}H NMR



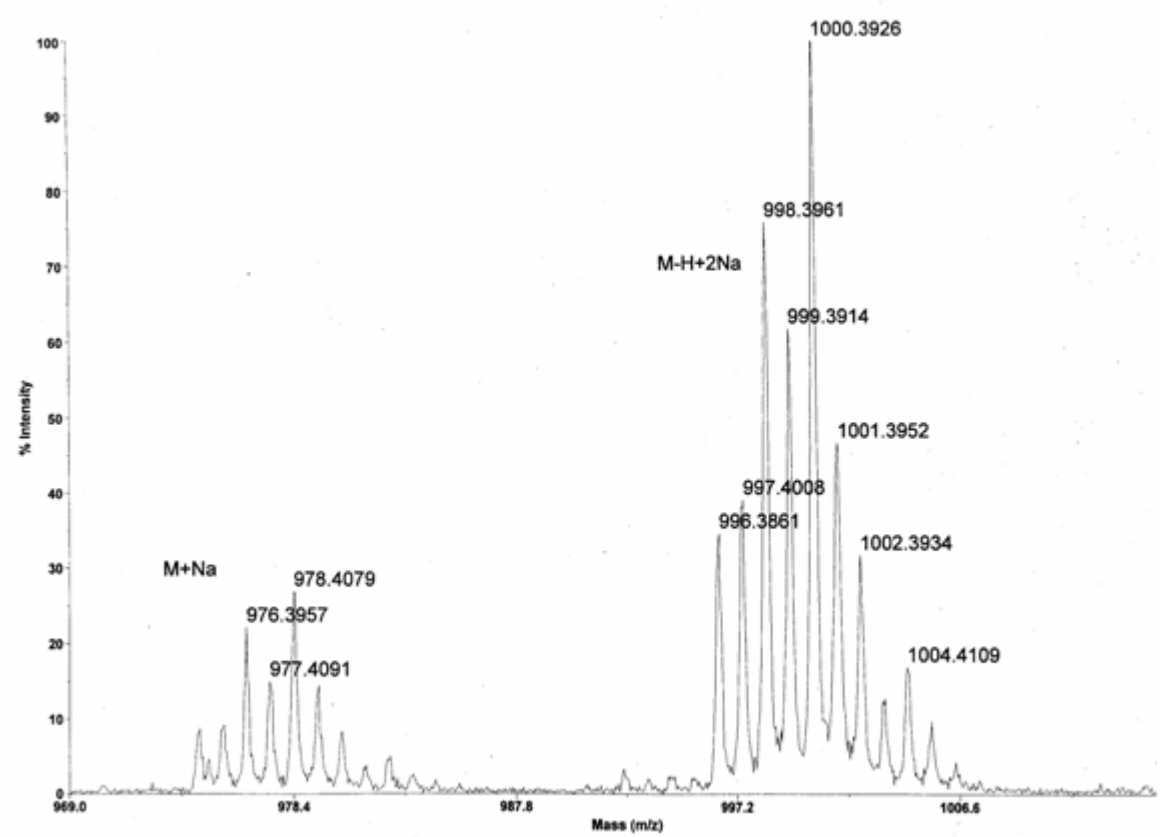
2a



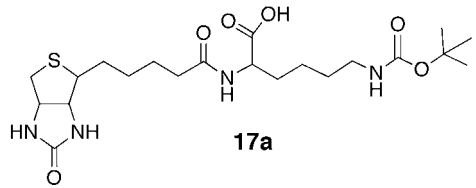
MS


O
HN
NH
S
H
N
O
O
H
N
O
H
N
O
O
O
O
H
N
O
SnBu3

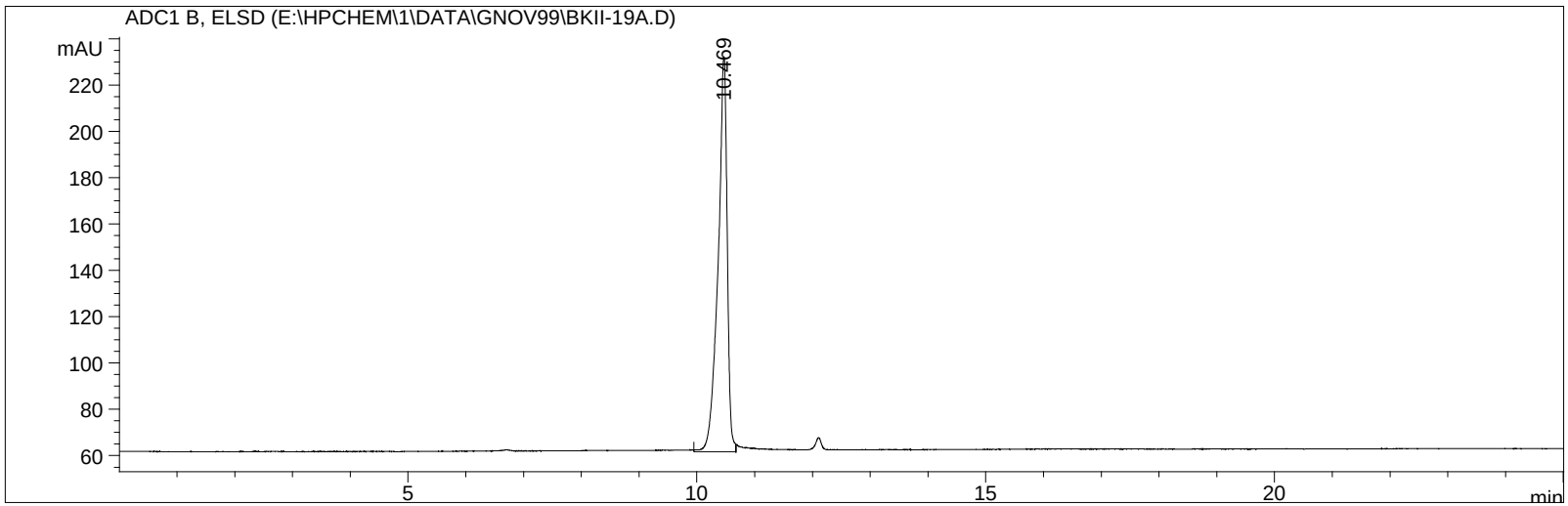
2a


1000.3926
998.3961
M-H+2Na
999.3914
1001.3952
997.4008
996.3861
1002.3934
1004.4109
M+Na
978.4079
976.3957
977.4091
% Intensity
Mass (m/z)
969.0
978.4
987.8
997.2
1006.6

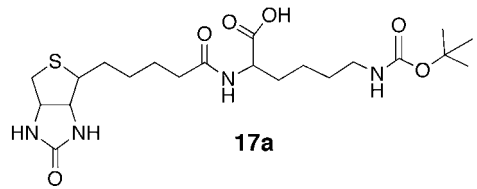
HPLC


O
OH
S
O
N
H
O
N
H
O
HN
NH
O

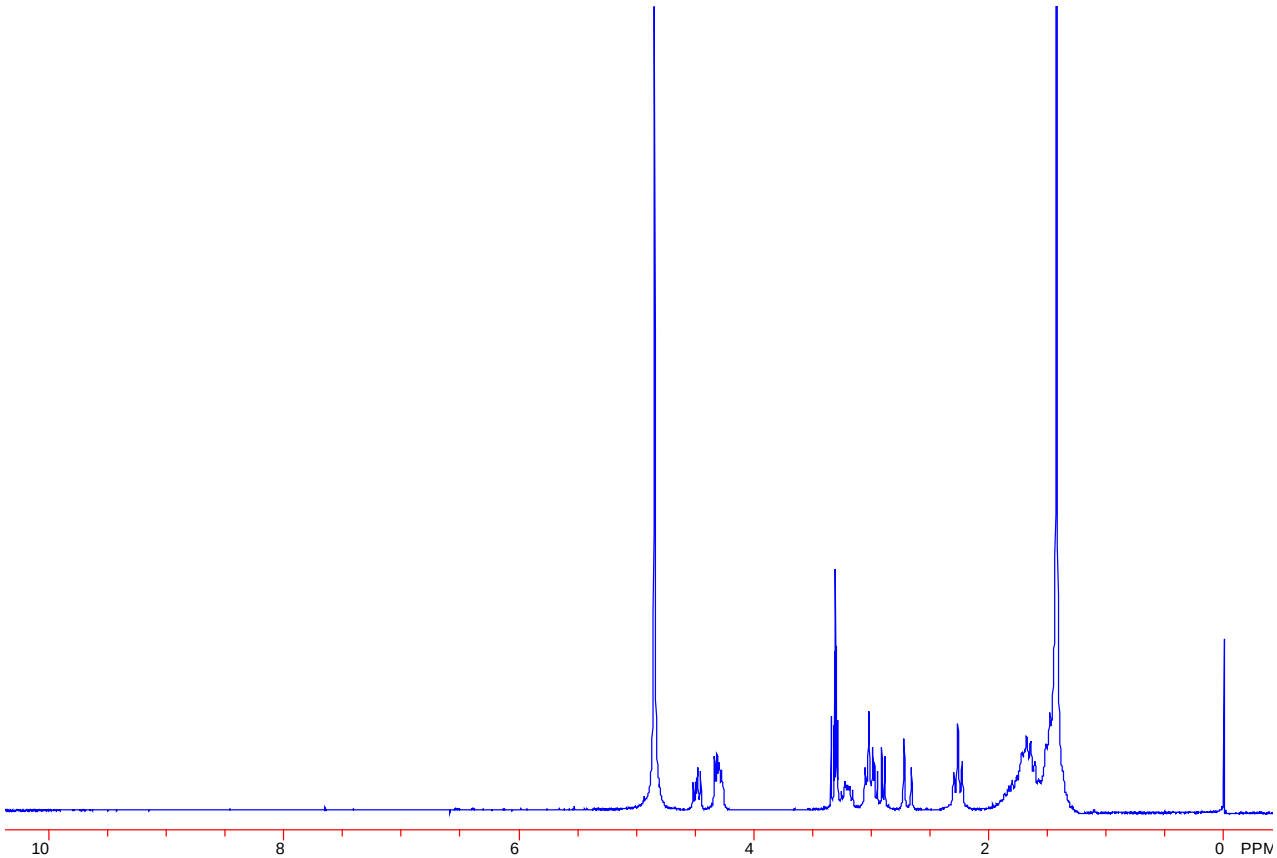
17a


ADC1 B, ELSD (E:\HPCHEM\1\DATA\GNOV99\BKII-19A.D)
mAU
220
200
180
160
140
120
100
80
60
10.469
5
10
15
20
min

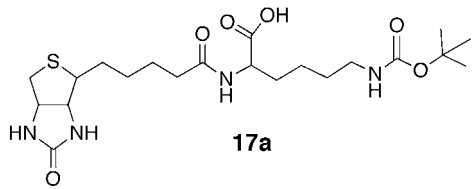
^{1}H NMR



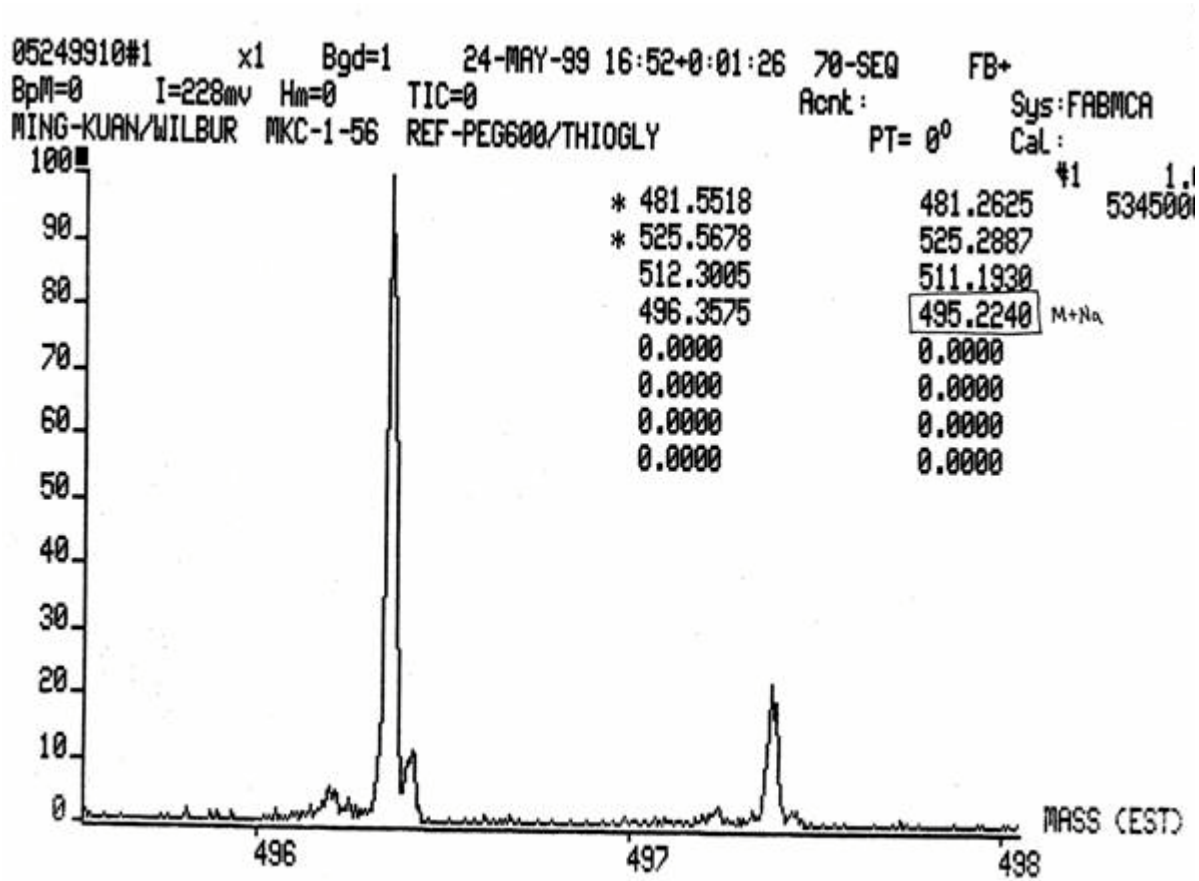
17a



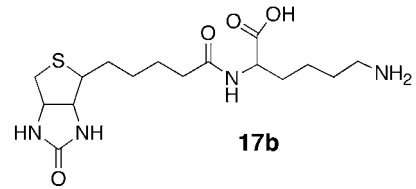
MS


O
OH
O
S
N
H
N
H
O
HN
NH
O

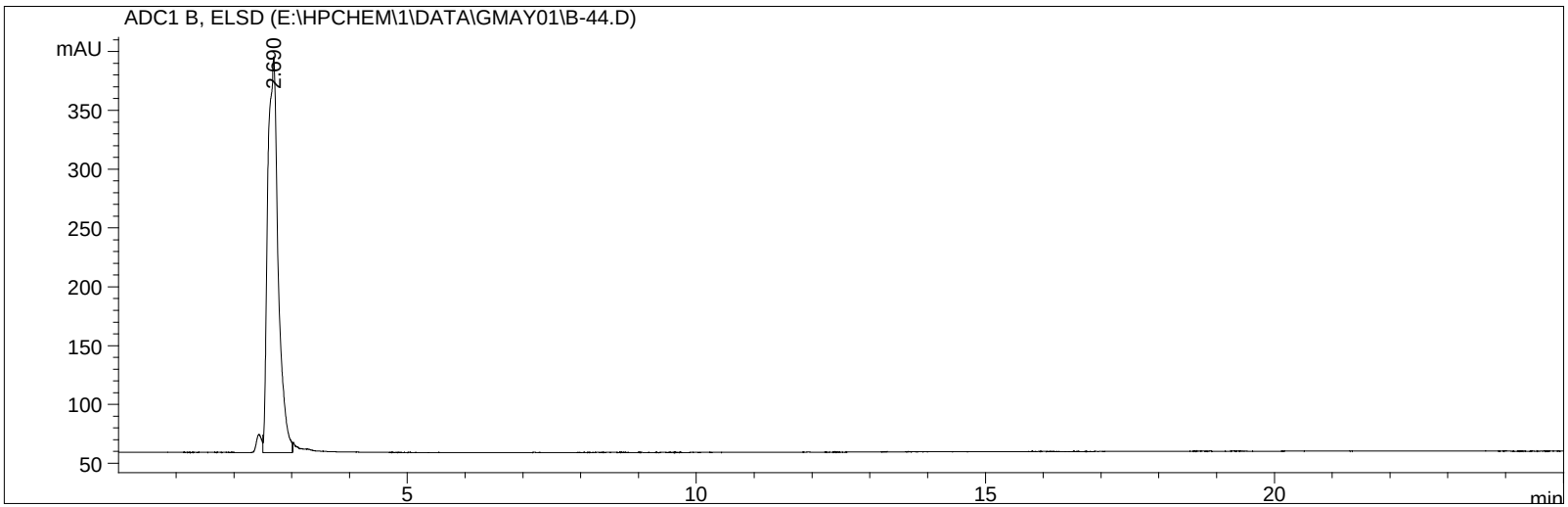
17a


05249910#1 x1 Bgd=1 24-MAY-99 16:52+0:01:26 70-SEQ FB+
BpM=0 I=228mv Hm=0 TIC=0 Acnt: Sys:FABMCA
MING-KUAN/WILBUR MKC-1-56 REF-PEG600/THIOGLY PT= 0° CaL:
#1
* 481.5518 481.2625
* 525.5678 525.2887
512.3005 511.1930
496.3575 495.2240 M+Na
0.0000 0.0000
0.0000 0.0000
0.0000 0.0000
0.0000 0.0000
100
90
80
70
60
50
40
30
20
10
0
496
497
498
MASS (EST)

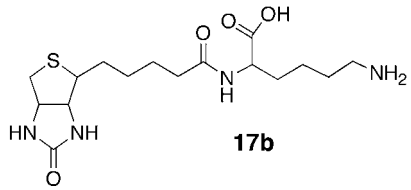
HPLC


O
OH
S
N
H
NH2
HN
NH
O

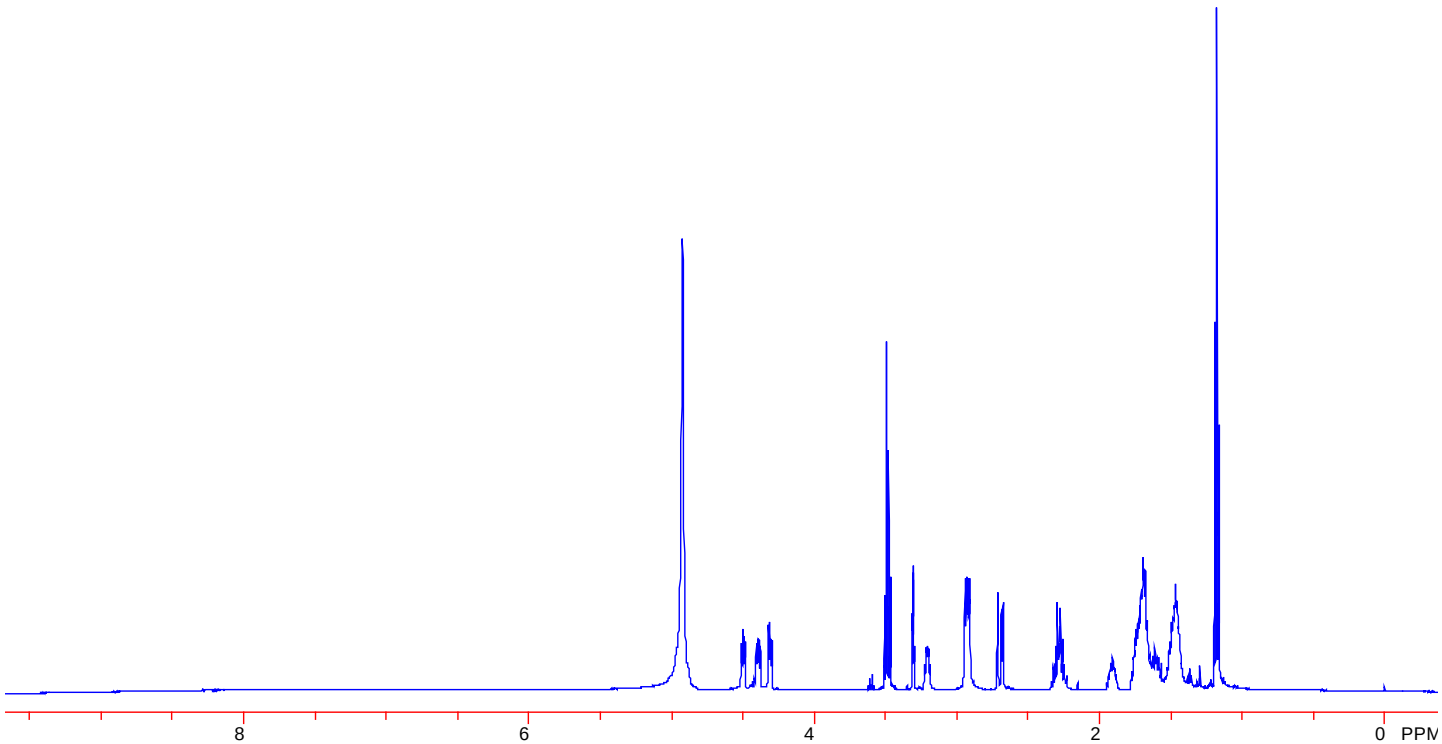
17b


ADC1 B, ELSD (E:\HPCHEM\1\DATA\GMAY01\B-44.D)
mAU
2.690
350
300
250
200
150
100
50
5
10
15
20
min

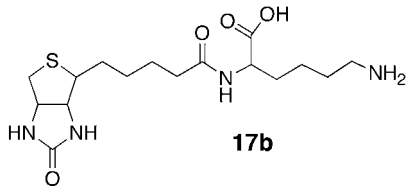
^{1}H NMR



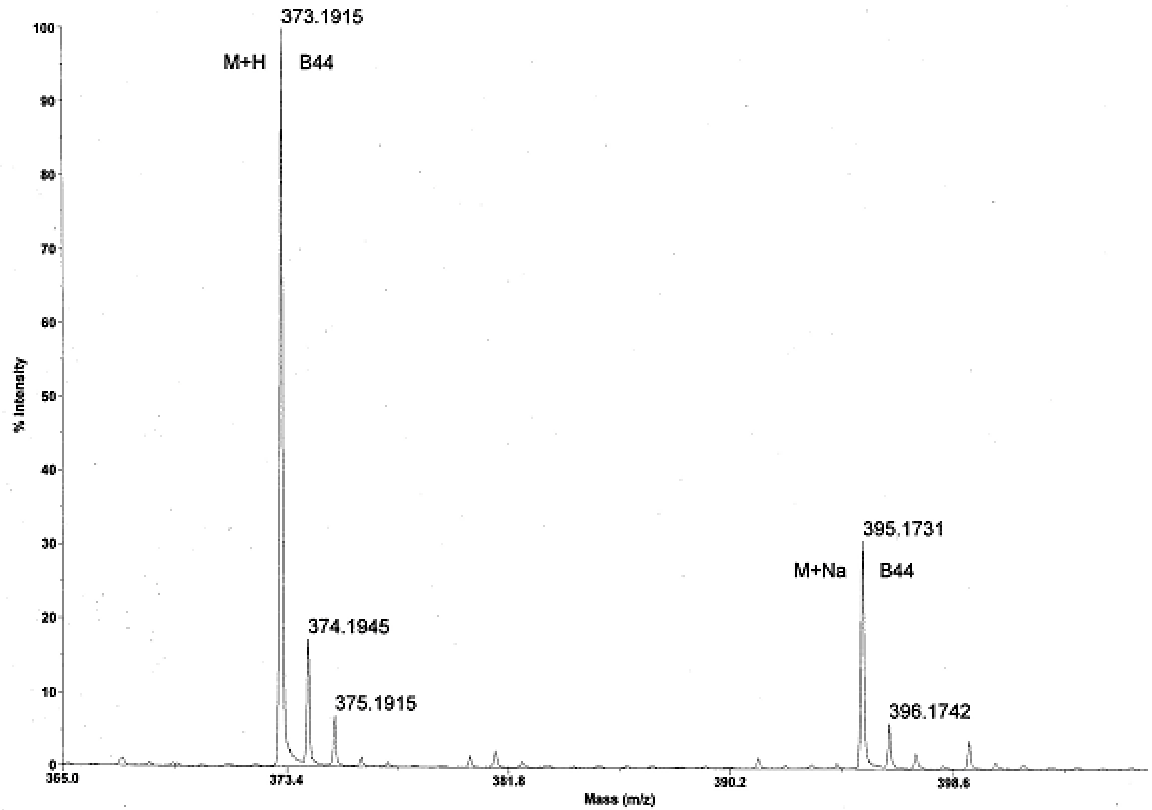
17b



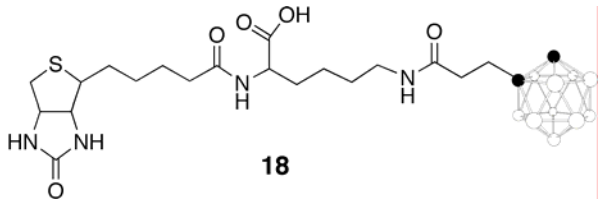
MS


O
OH
S
N
H
NH2
HN
NH
O

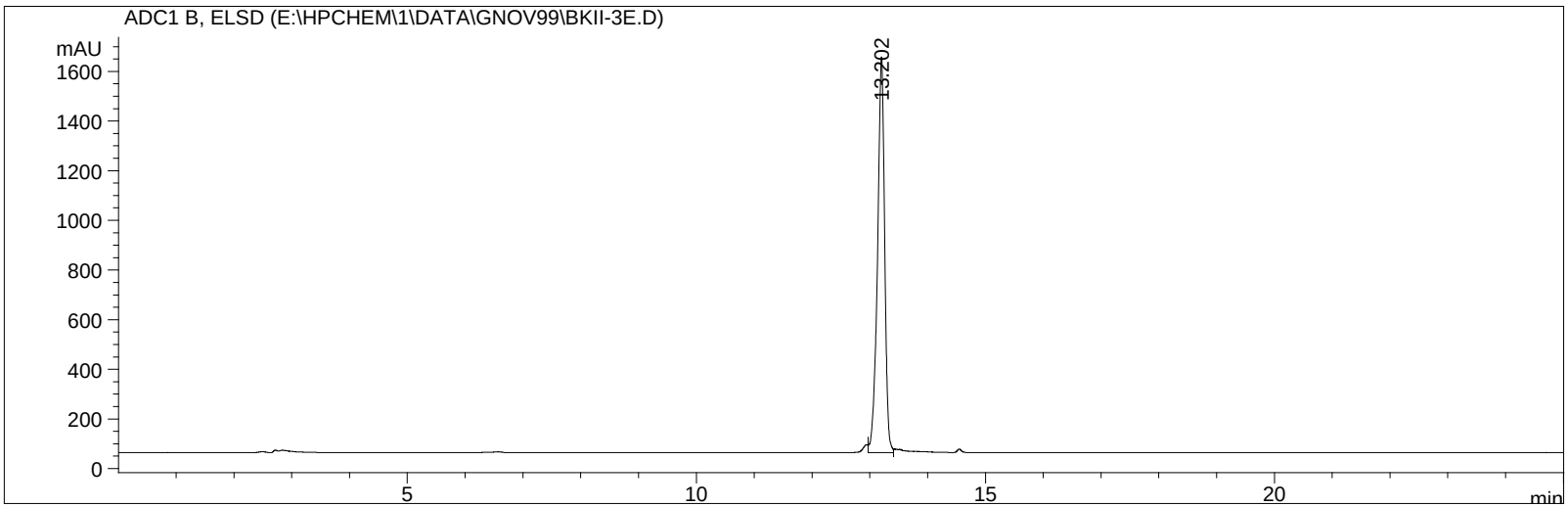
17b


373.1915
M+H
B44
374.1945
375.1915
395.1731
M+Na
B44
396.1742
% Intensity
Mass (m/z)
100
90
80
70
60
50
40
30
20
10
0
365.0
373.4
381.8
390.2
398.6

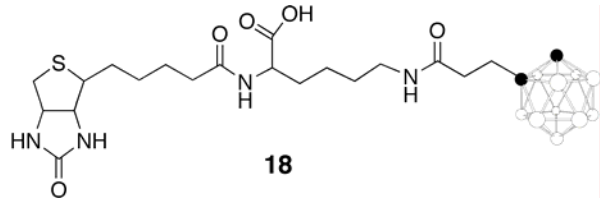
HPLC

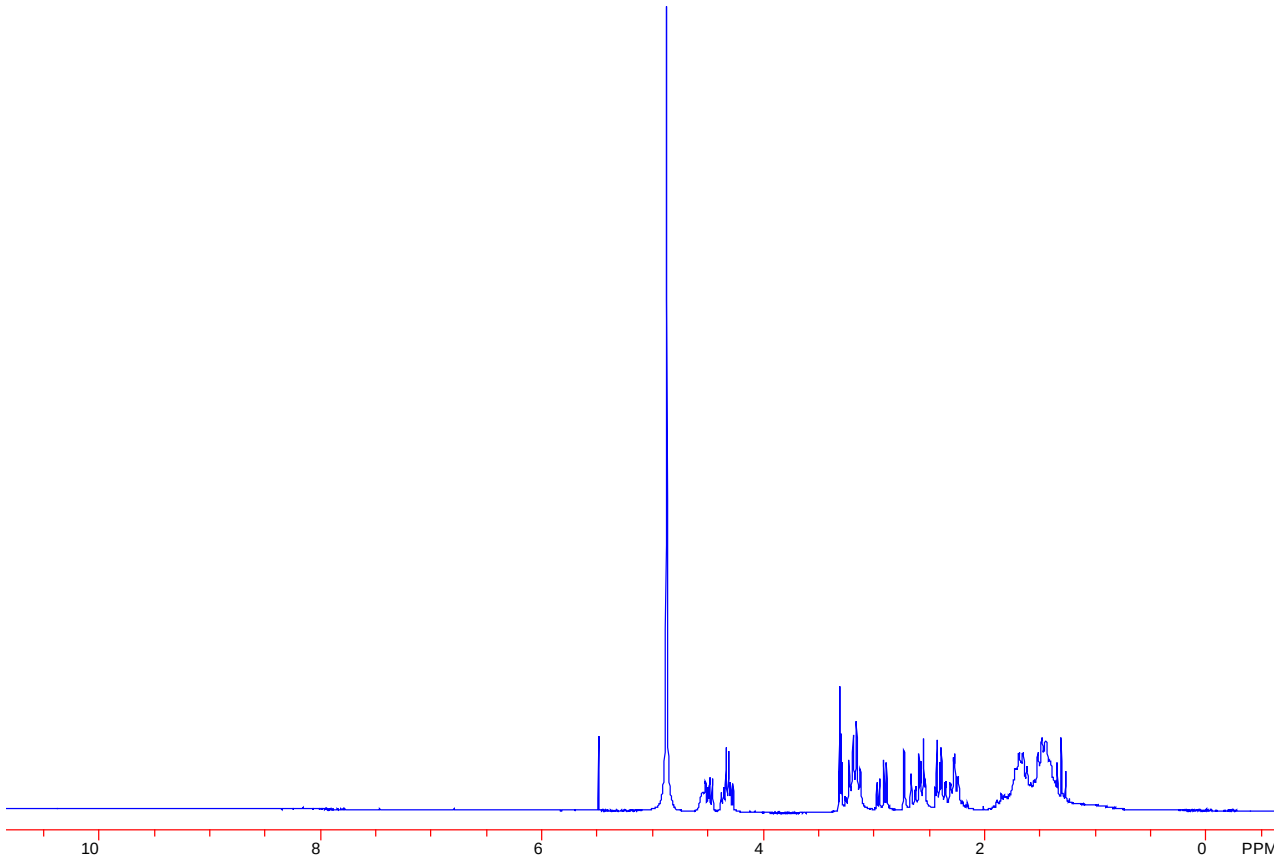

S
HN
NH
O
O
N
H
O
OH
O
N
H
O

18

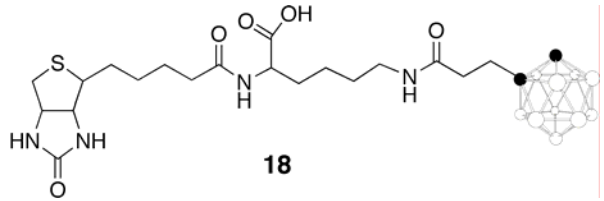

ADC1 B, ELSD (E:\HPCHEM\1\DATA\GNOV99\BKII-3E.D)
mAU
1600
1400
1200
1000
800
600
400
200
0
13.202
5
10
15
20
min

^{1}H NMR

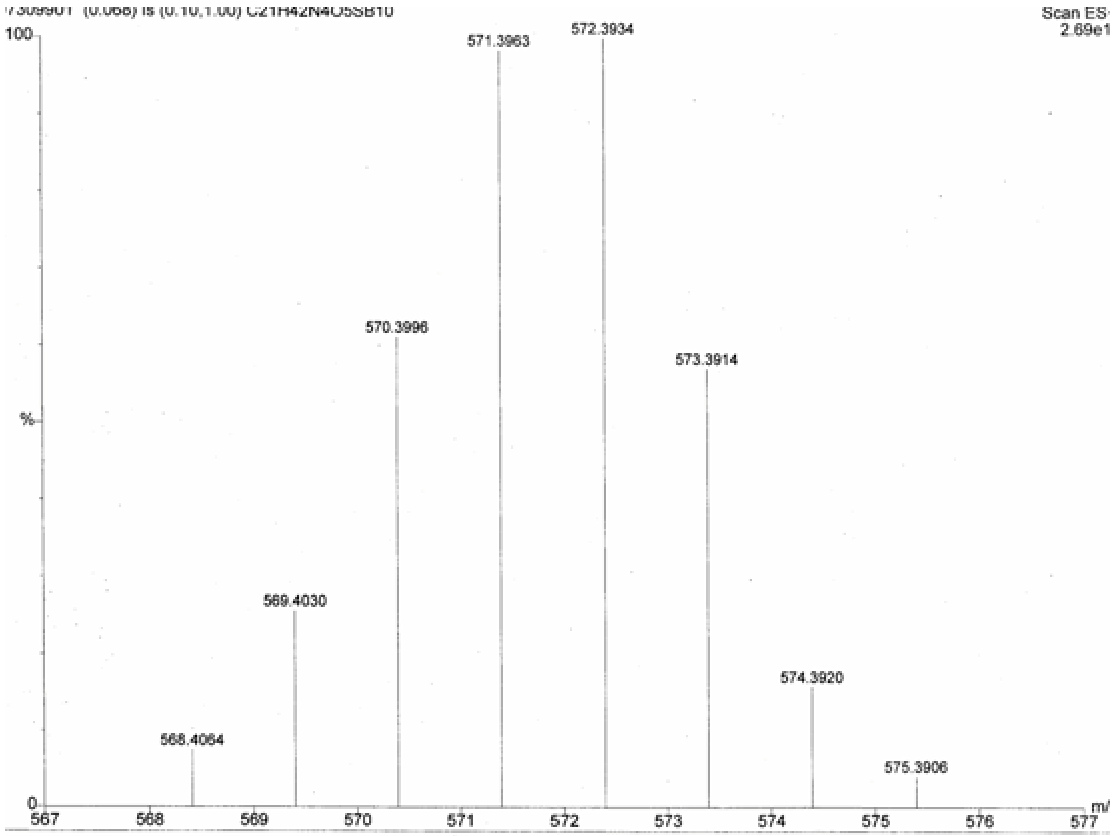




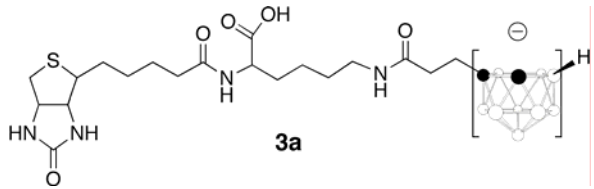
MS

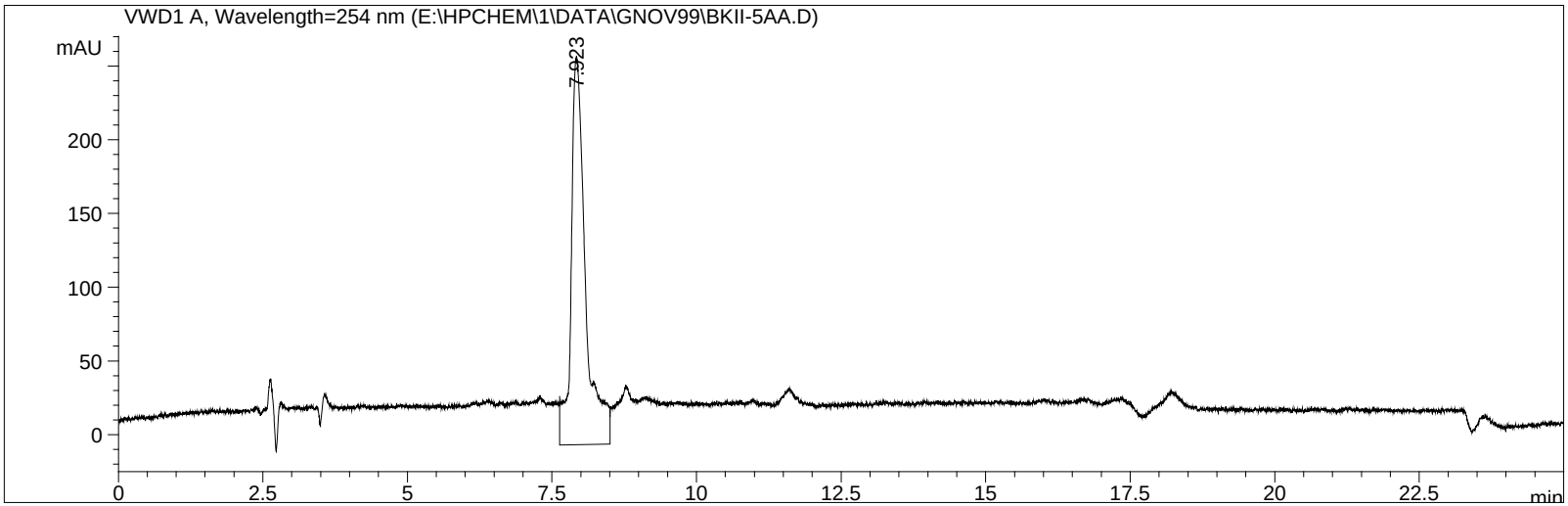

S
HN
NH
O
O
OH
N
H
O
N
H
O

18

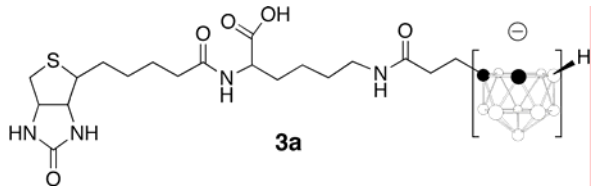

Scan ES
2.69e1
100
%
0
571.3963
572.3934
570.3996
573.3914
569.4030
574.3920
568.4064
575.3906
567
568
569
570
571
572
573
574
575
576
577
m/

HPLC

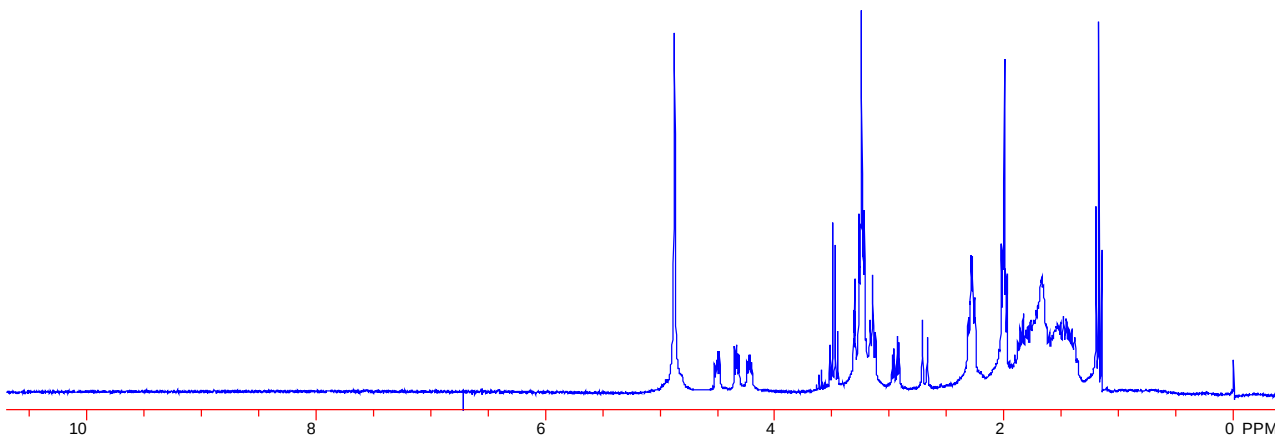

S
O
OH
N
H
O
N
H
HN
NH
O
H
3a


VWD1 A, Wavelength=254 nm (E:\HPCHEM\1\DATA\GNOV99\BKII-5AA.D)
mAU
7.923
200
150
100
50
0
0
2.5
5
7.5
10
12.5
15
17.5
20
22.5
min

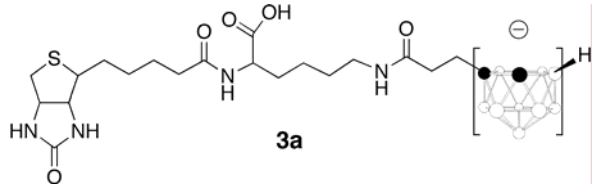
^{1}H NMR

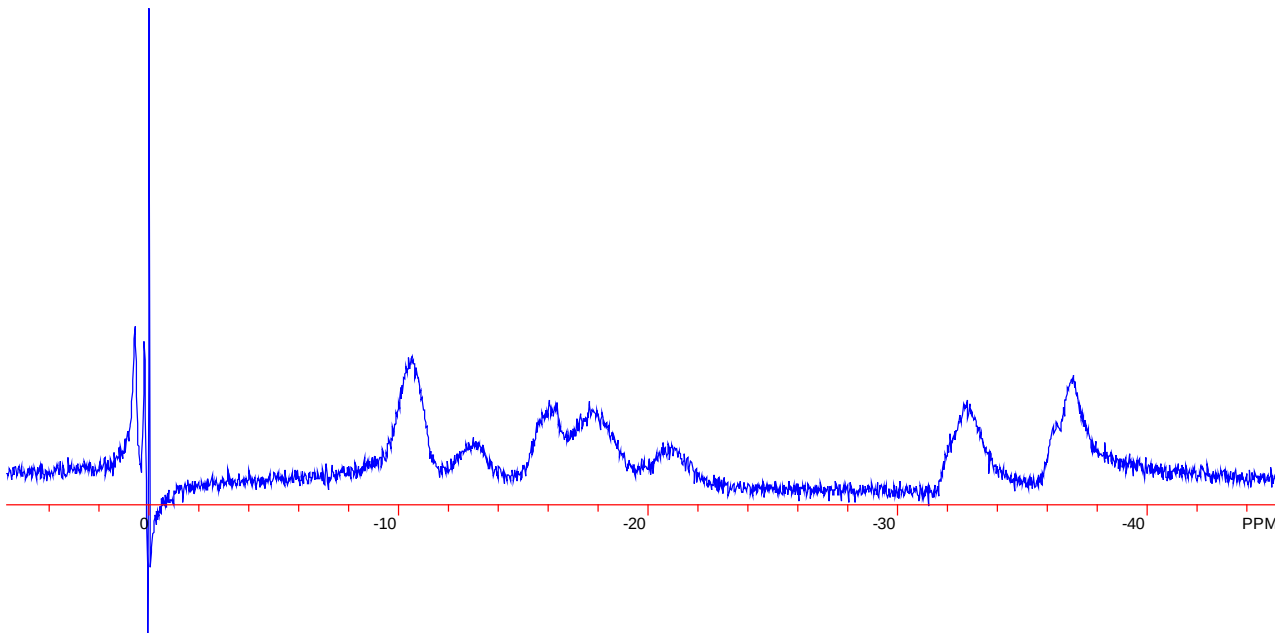


3a

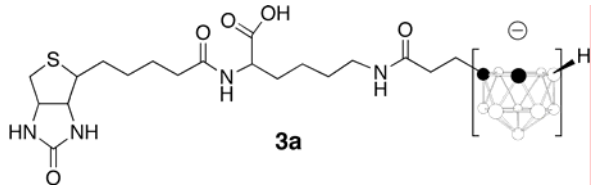


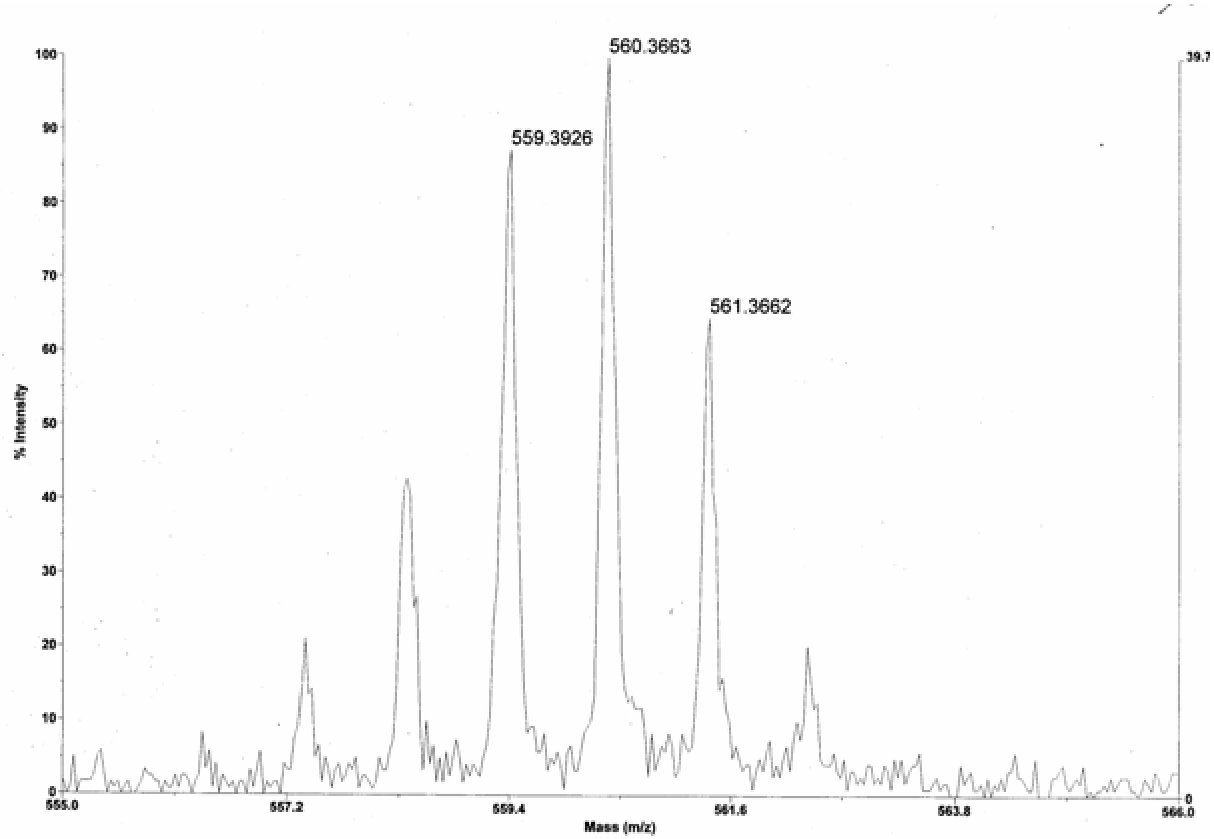
^{11}B NMR



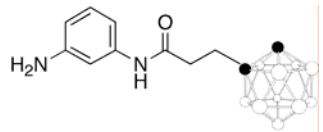


MS

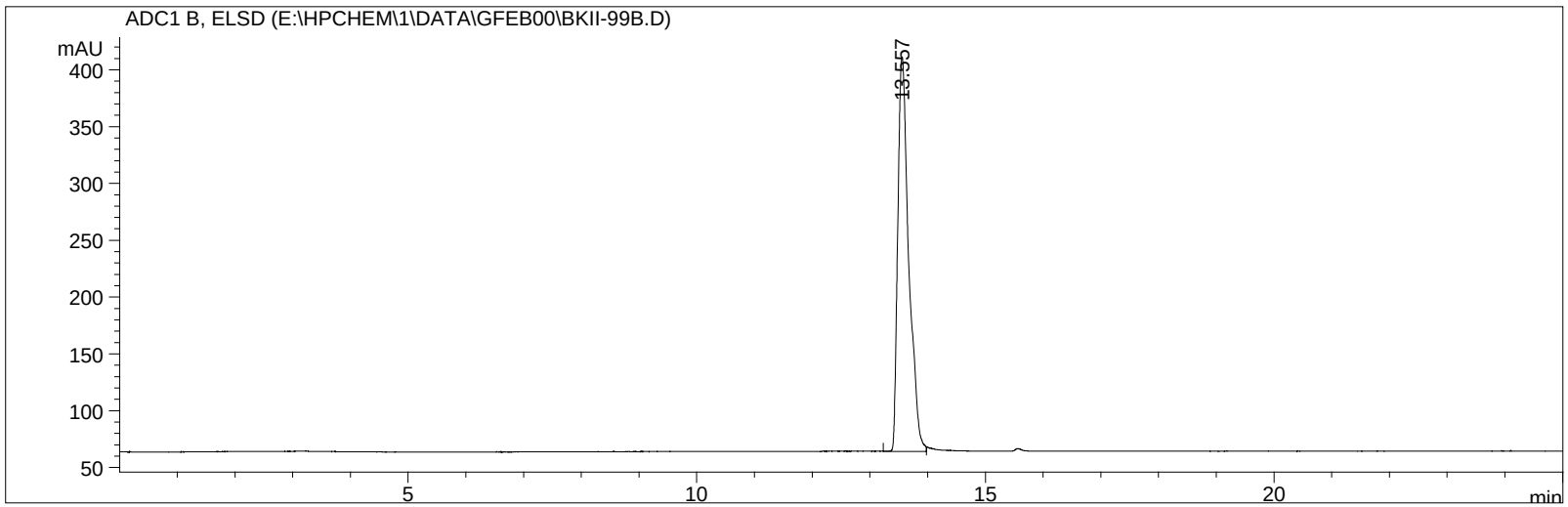

OH
O
S
HN
NH
O
N
H
O
N
H
O
H
3a


560.3663
559.3926
561.3662
% Intensity
Mass (m/z)
555.0
557.2
559.4
561.6
563.8
566.0
100
90
80
70
60
50
40
30
20
10
0

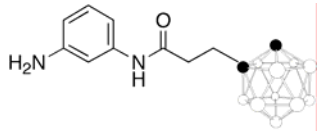
HPLC


H2N
N
H
O

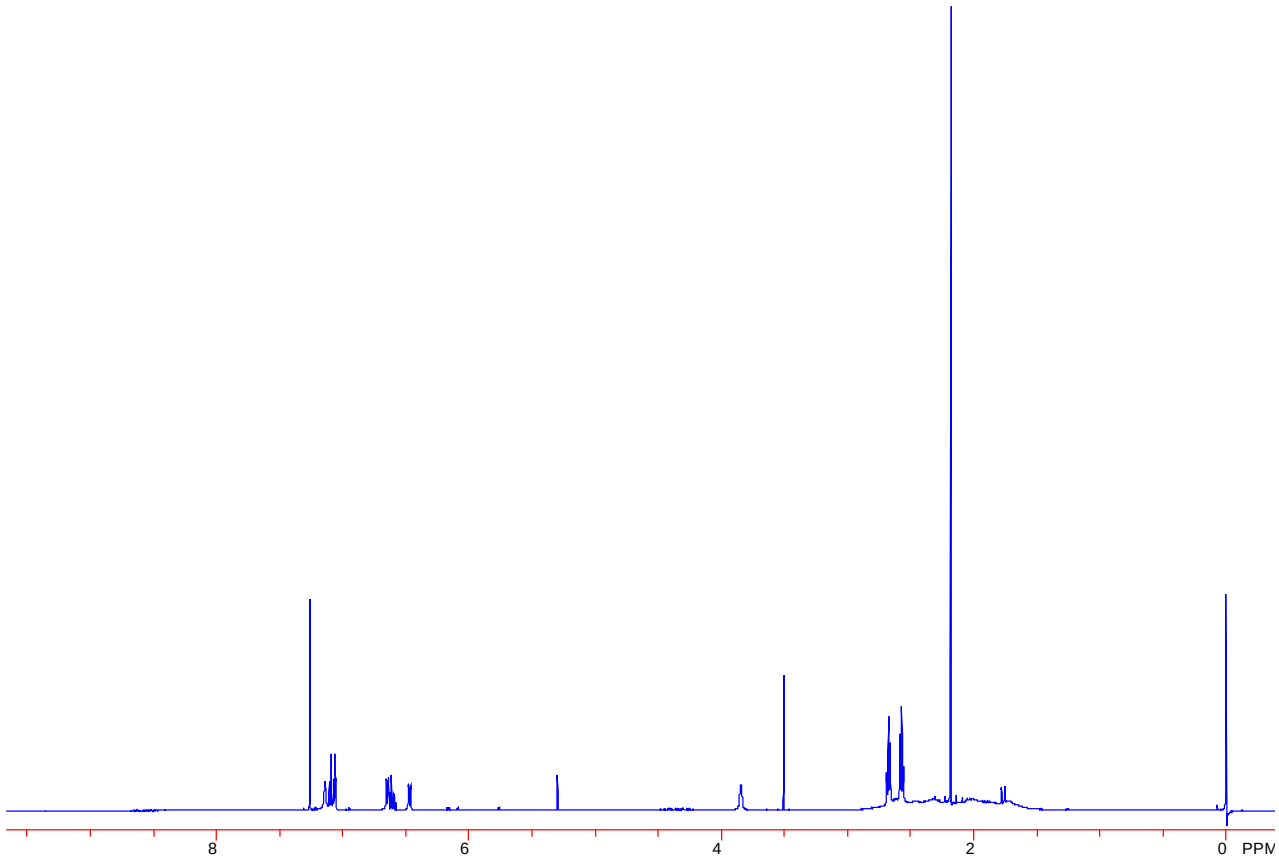
20


ADC1 B, ELSD (E:\HPCHEM\1\DATA\GFEB00\BKII-99B.D)
mAU
400
350
300
250
200
150
100
50
13.557
5
10
15
20
min

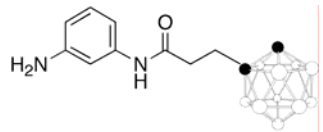
^{1}H NMR



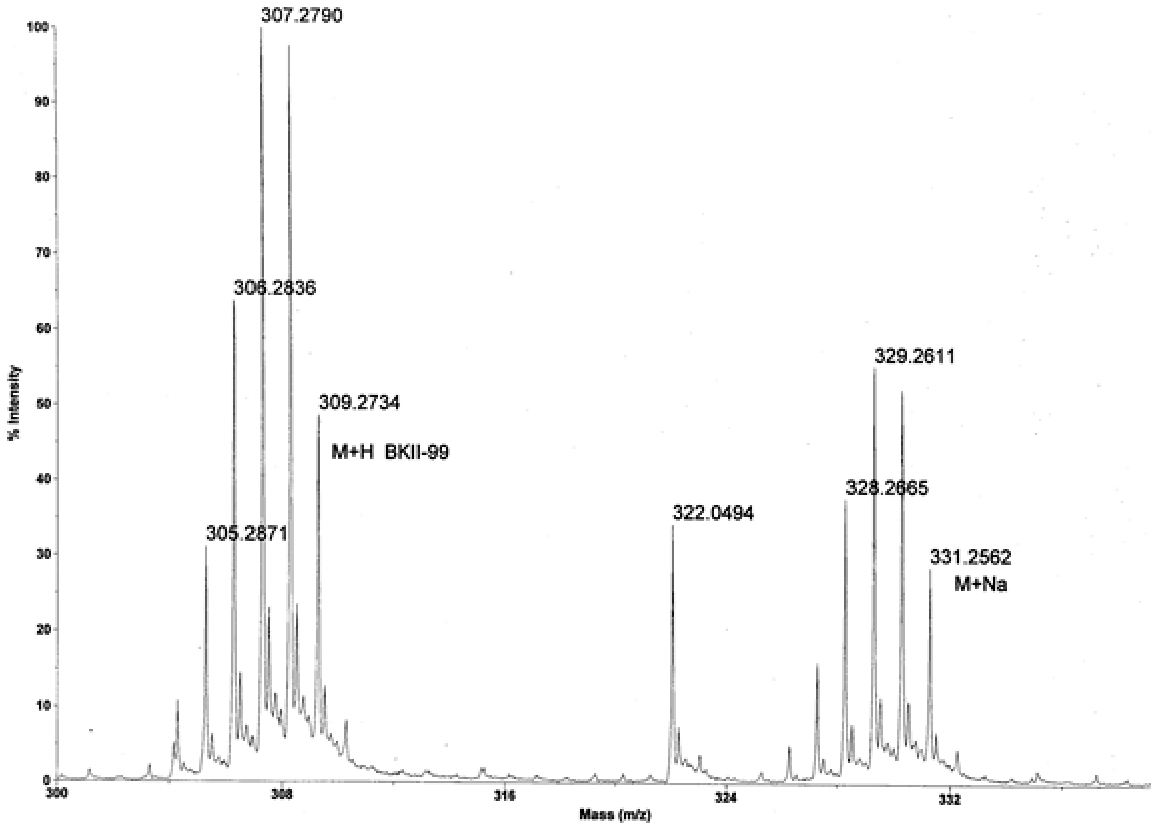
20



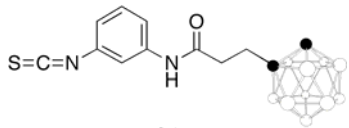
MS


H2N
N
H
O

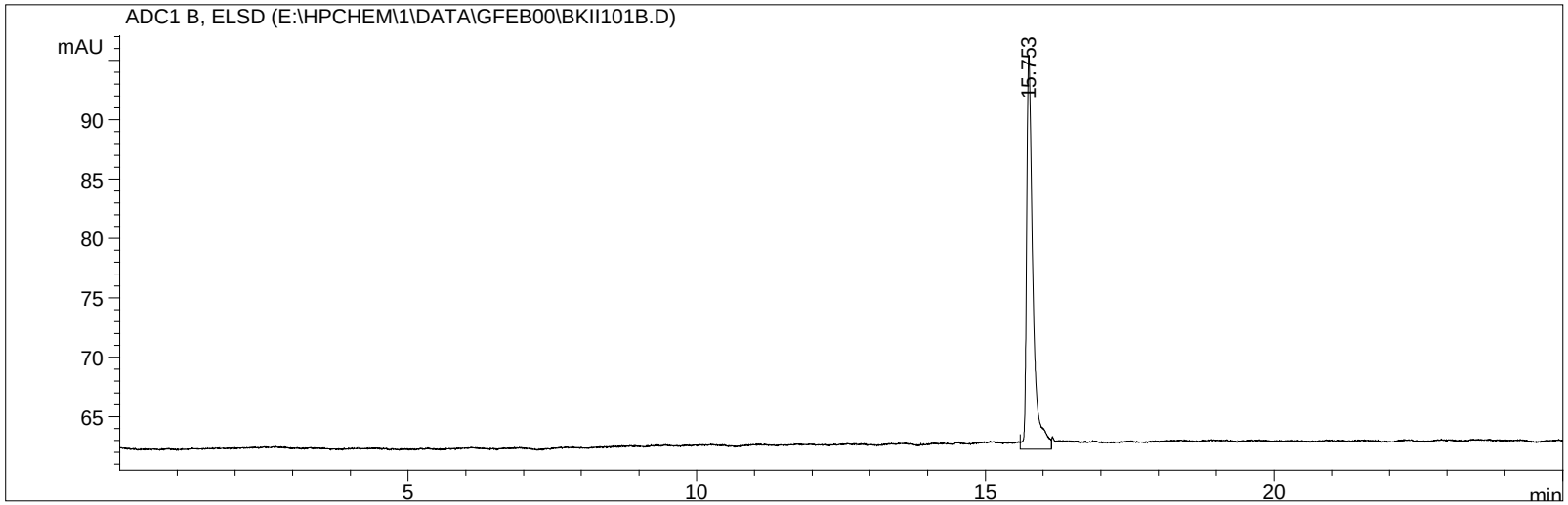
20


307.2790
306.2836
309.2734
M+H BKII-99
305.2871
322.0494
329.2611
328.2665
331.2562
M+Na
% Intensity
Mass (m/z)
100
90
80
70
60
50
40
30
20
10
0
300
308
316
324
332

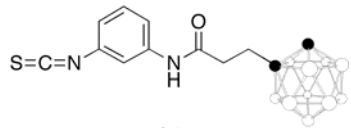
HPLC


S=C=N
N
H
O

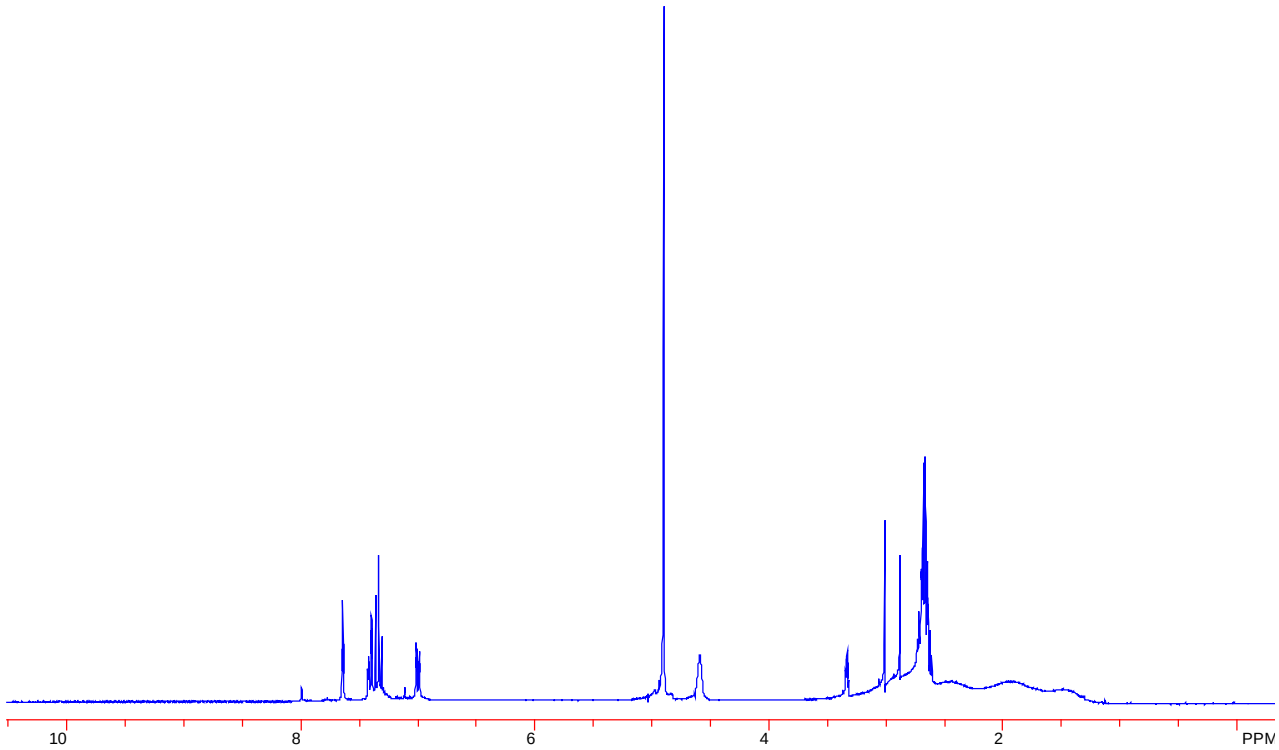
21


ADC1 B, ELSD (E:\HPCHEM\1\DATA\GFEB00\BKII101B.D)
mAU
90
85
80
75
70
65
15.753
5
10
15
20
min

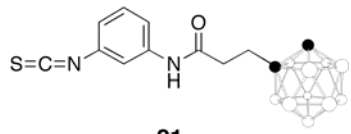
^{1}H NMR



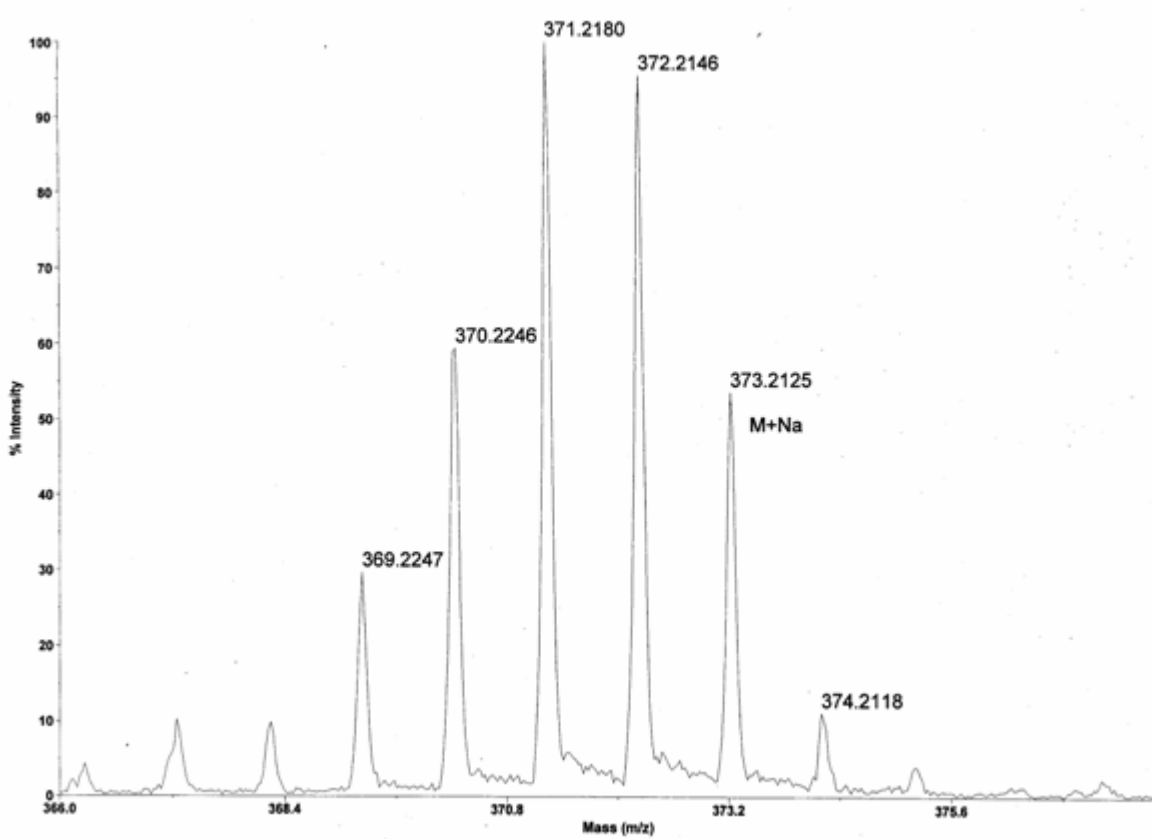
21



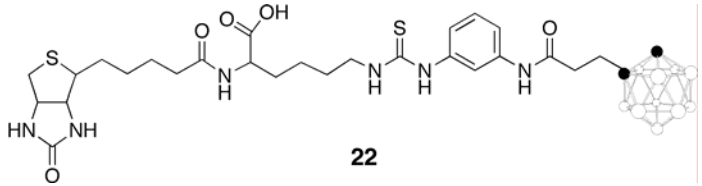
MS

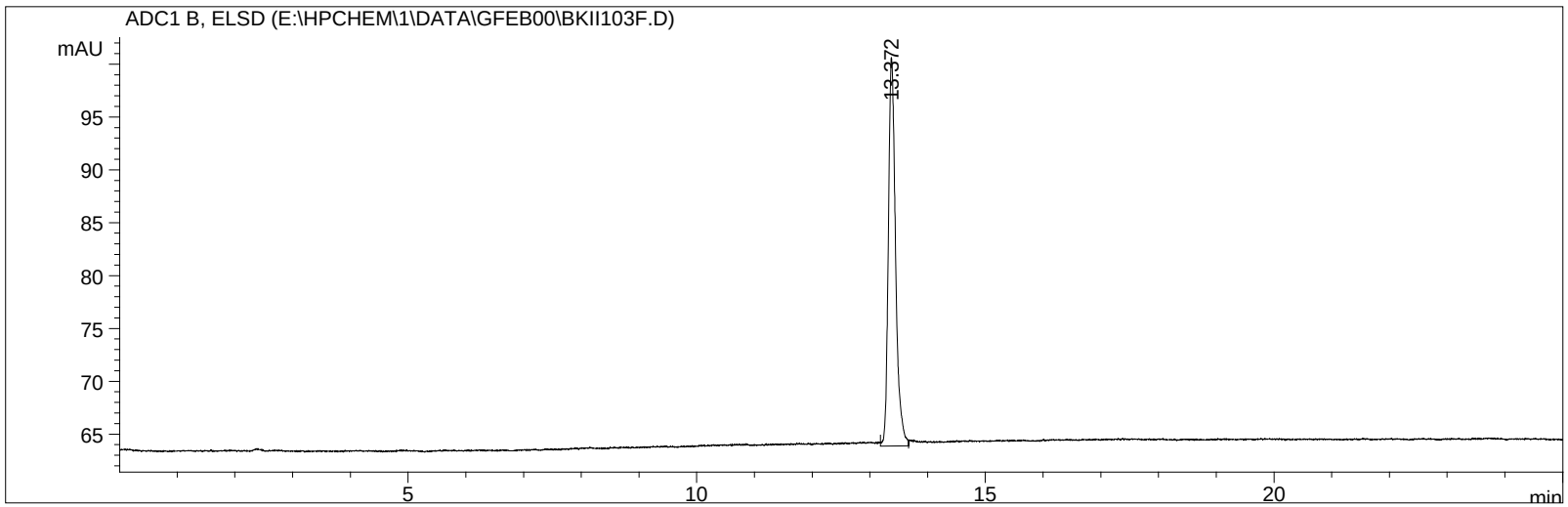

S=C=N
N
H
O

21

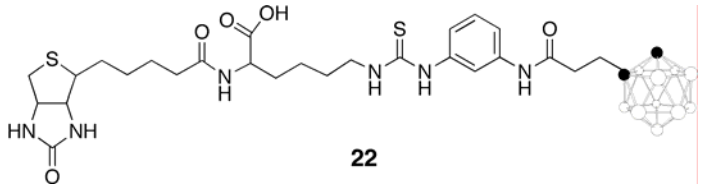

371.2180
372.2146
370.2246
373.2125
M+Na
369.2247
374.2118
% Intensity
Mass (m/z)
100
90
80
70
60
50
40
30
20
10
0
366.0
368.4
370.8
373.2
375.6

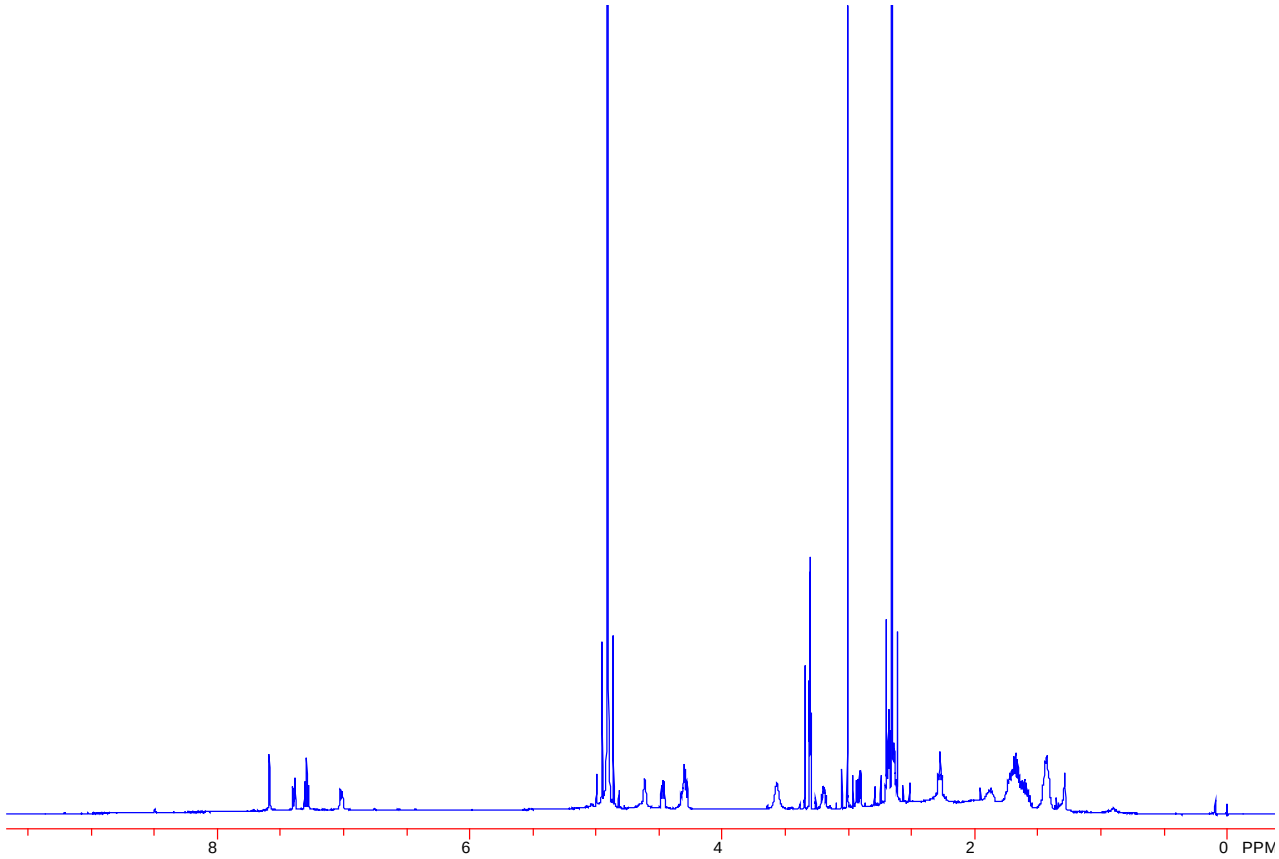
HPLC


O
OH
S
HN
NH
O
N
H
S
N
H
N
H
O
22

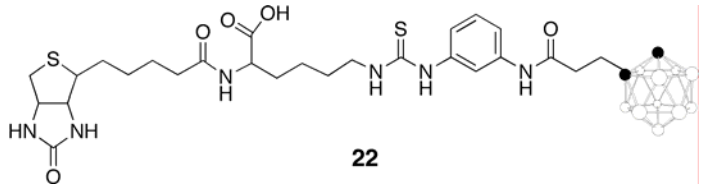

ADC1 B, ELSD (E:\HPCHEM\1\DATA\GFEB00\BKII103F.D)
mAU
95
90
85
80
75
70
65
13.372
5
10
15
20
min

^{1}H NMR

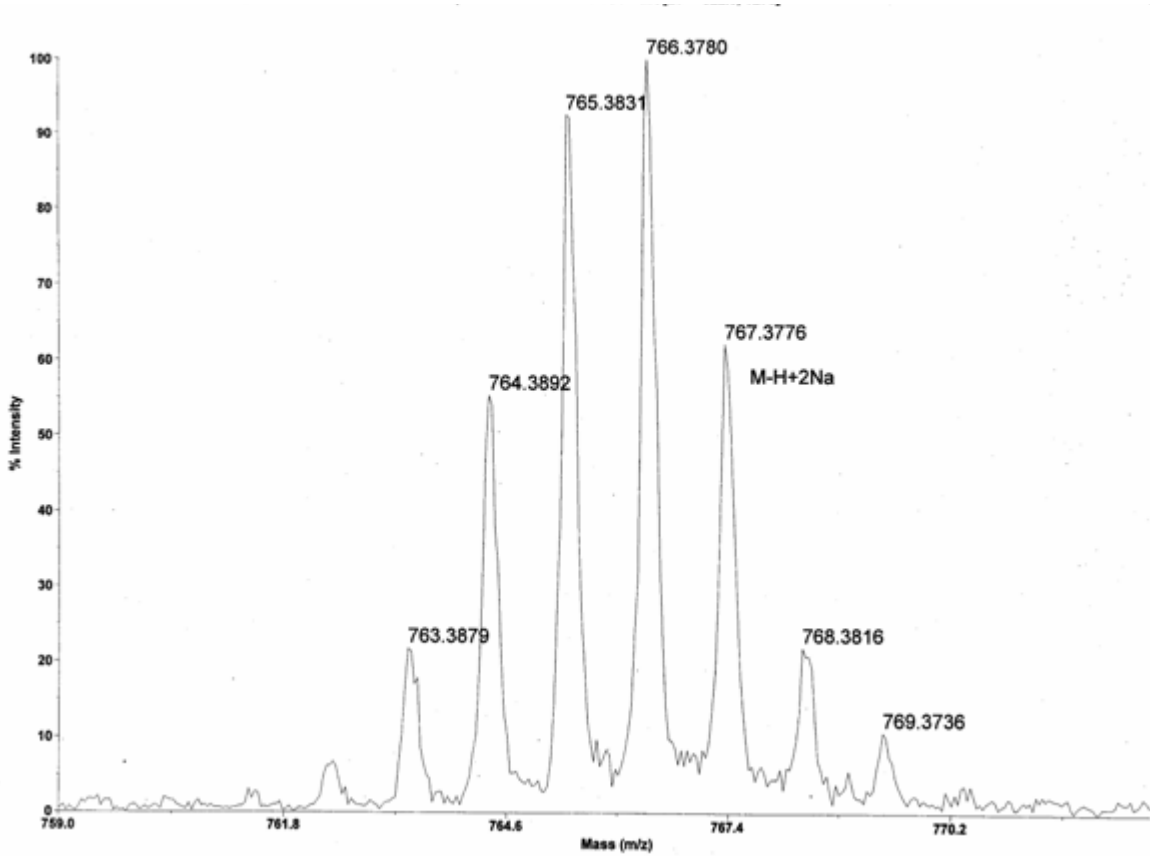




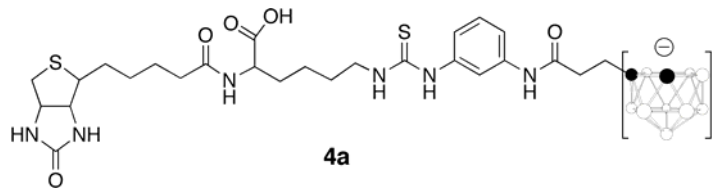
MS

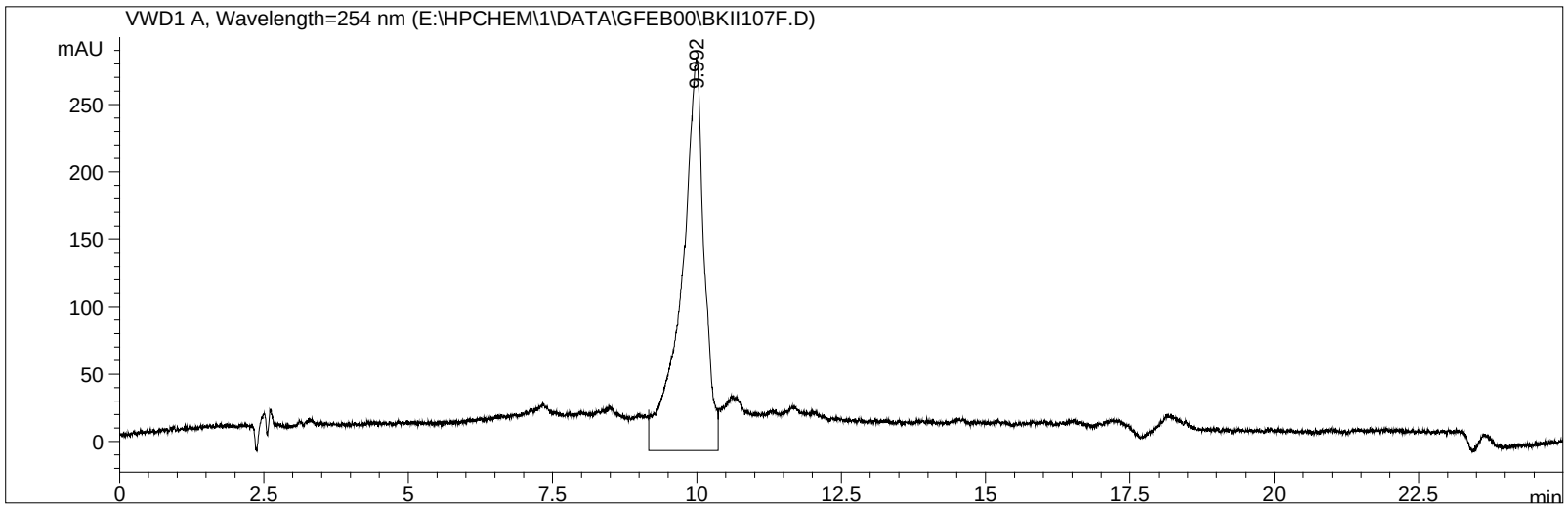

O
OH
S
HN
NH
O
N
H
S
N
H
N
H
N
H
O

22

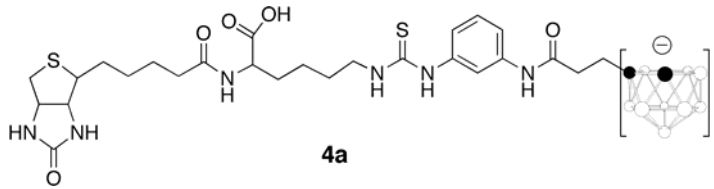

766.3780
765.3831
767.3776
M-H+2Na
764.3892
763.3879
768.3816
769.3736
% Intensity
100
90
80
70
60
50
40
30
20
10
0
759.0
761.8
764.6
767.4
770.2
Mass (m/z)

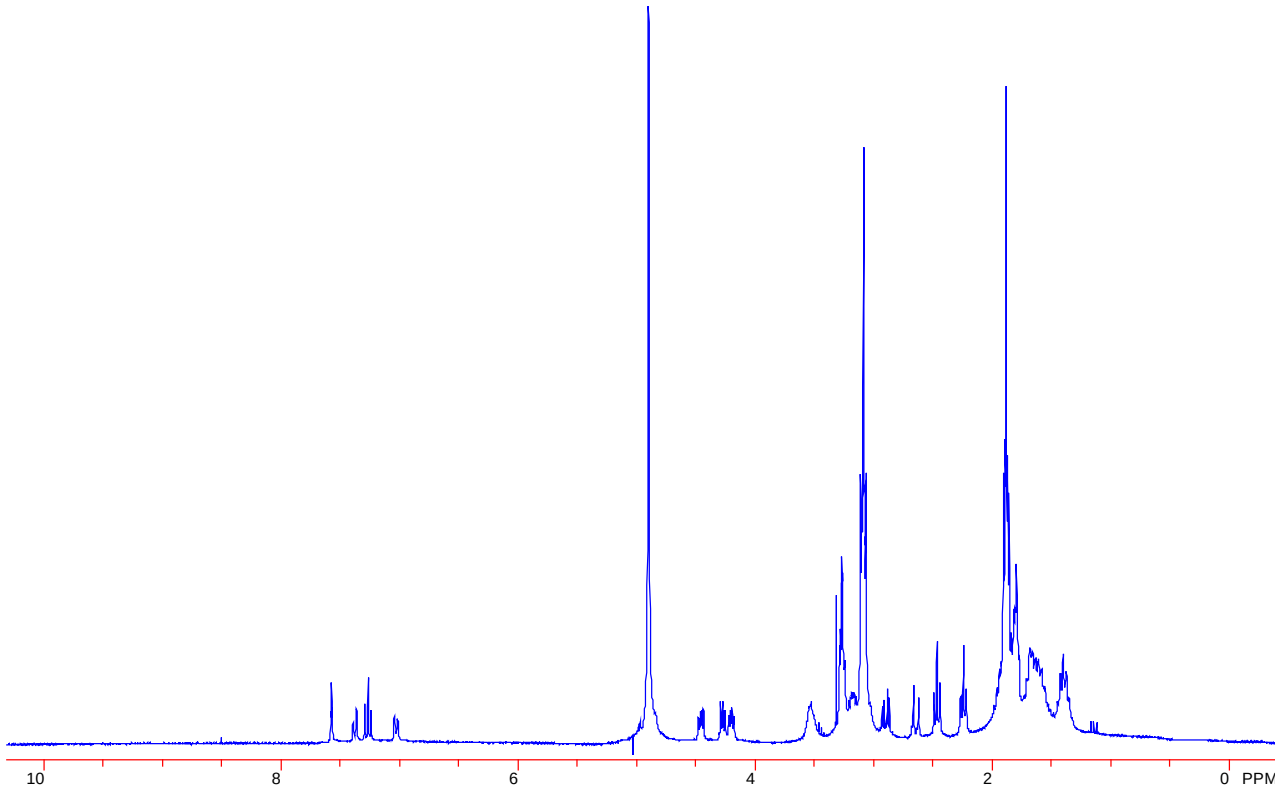
HPLC


O
OH
S
HN
NH
O
N
H
S
4a

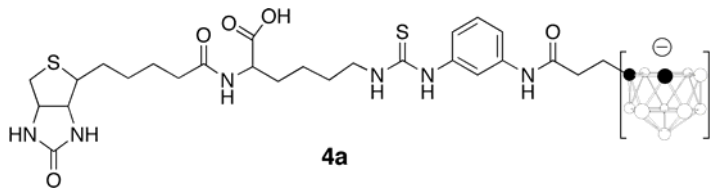

VWD1 A, Wavelength=254 nm (E:\HPCHEM\1\DATA\GFEB00\BKII107F.D)
mAU
250
200
150
100
50
0
9.992
0
2.5
5
7.5
10
12.5
15
17.5
20
22.5
min

^{1}H NMR

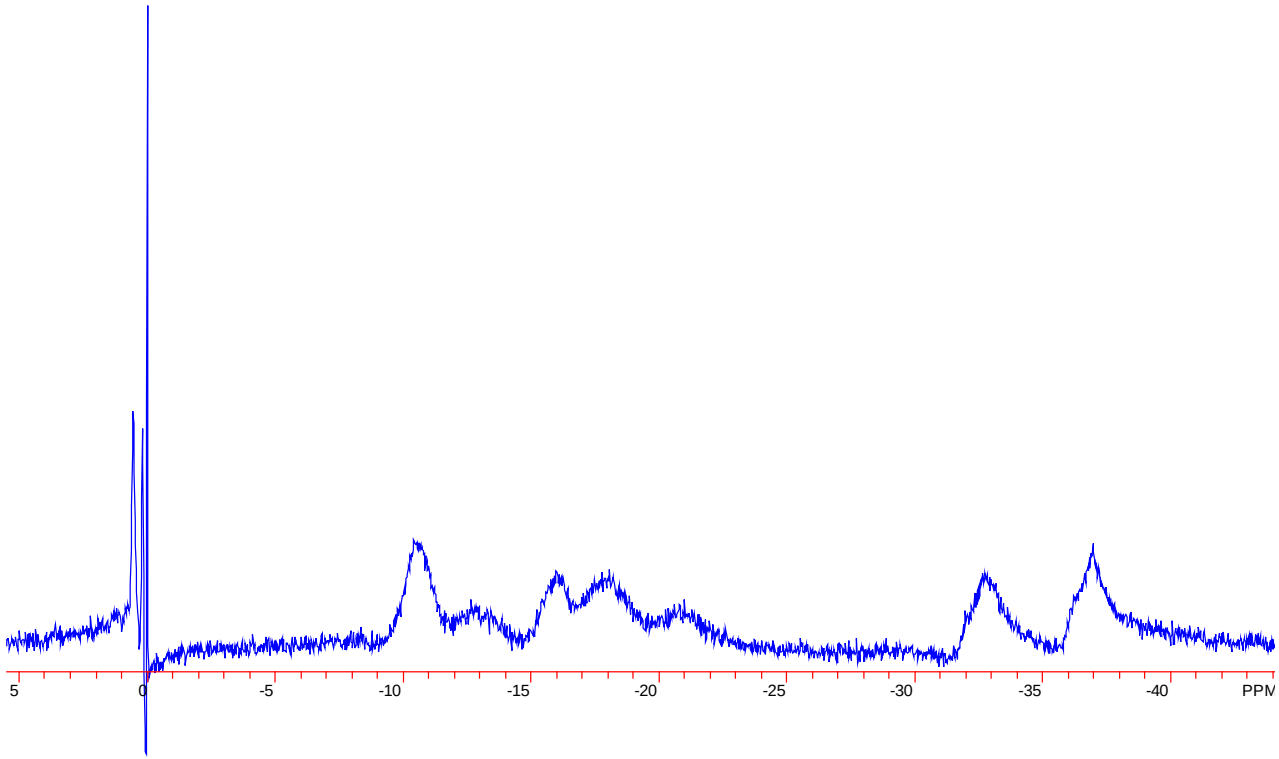




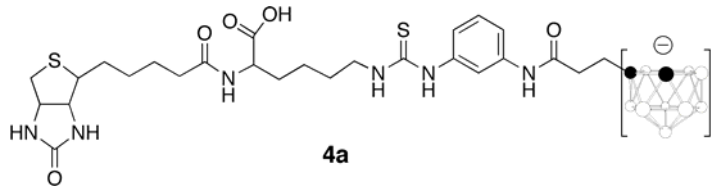
^{11}B NMR



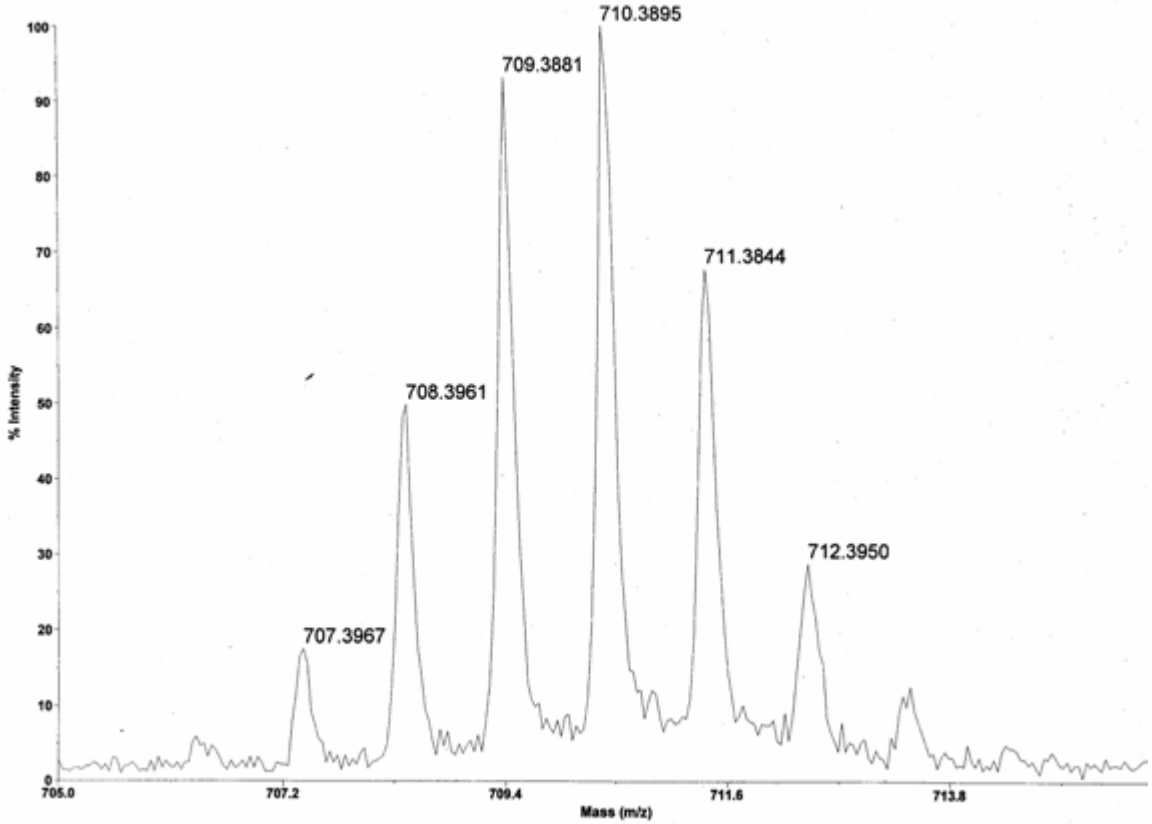
4a



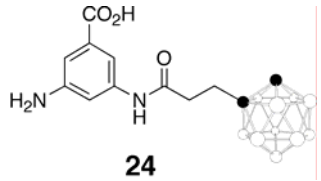
MS


OH
O
S
HN
NH
O
N
H
S
N
H
N
H
O
⊖

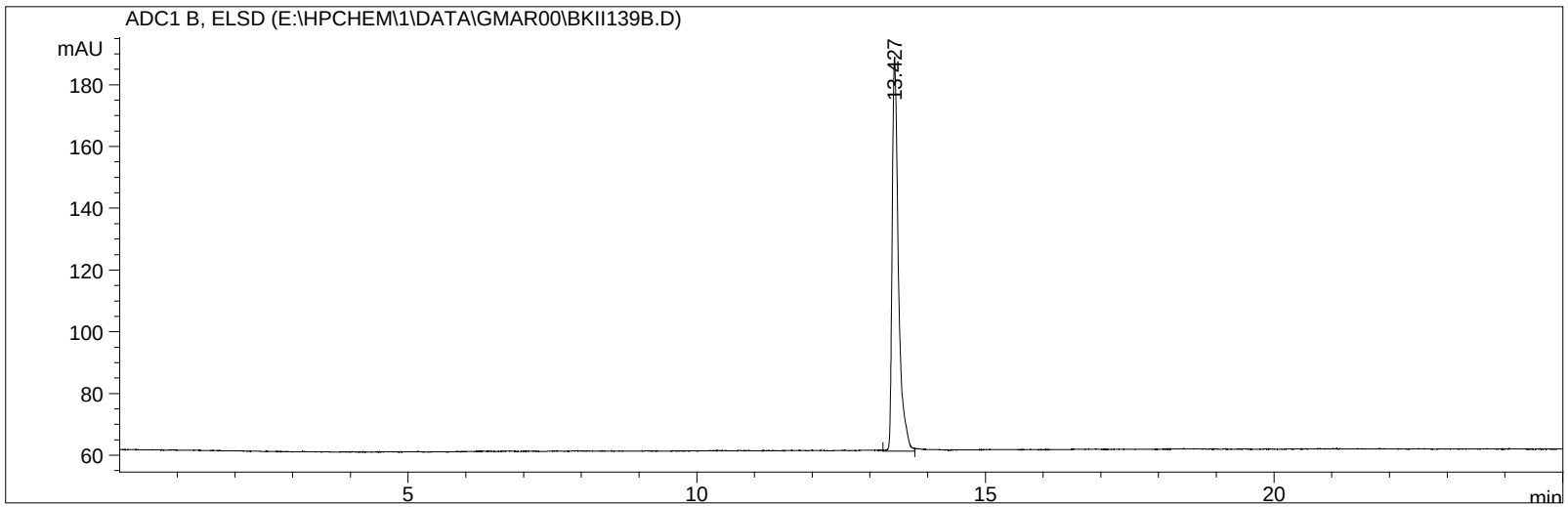
4a


710.3895
709.3881
711.3844
708.3961
712.3950
707.3967
% Intensity
100
90
80
70
60
50
40
30
20
10
0
705.0
707.2
709.4
711.6
713.8
Mass (m/z)

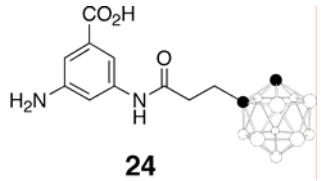
HPLC


CO2H
H2N
N
H
O

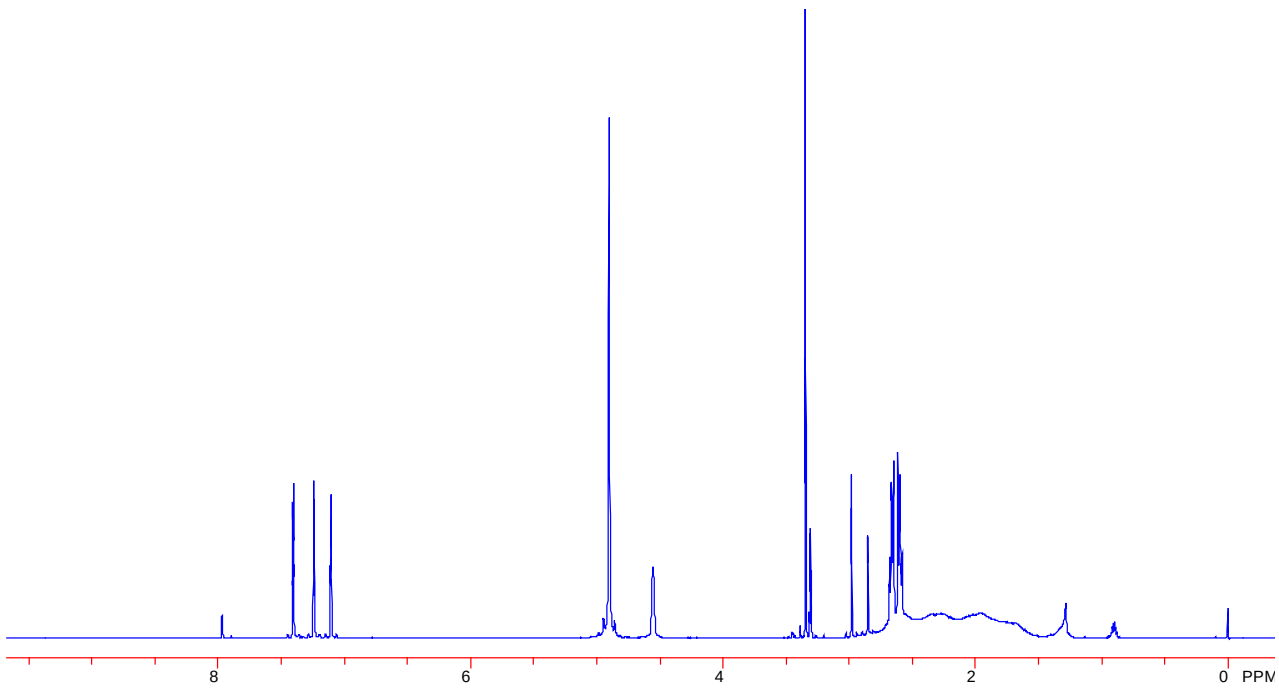
24


ADC1 B, ELSD (E:\HPCHEM\1\DATA\GMAR00\BKII139B.D)
mAU
180
160
140
120
100
80
60
13.427
5
10
15
20
min

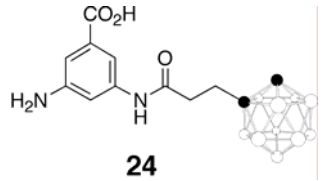
^{1}H NMR



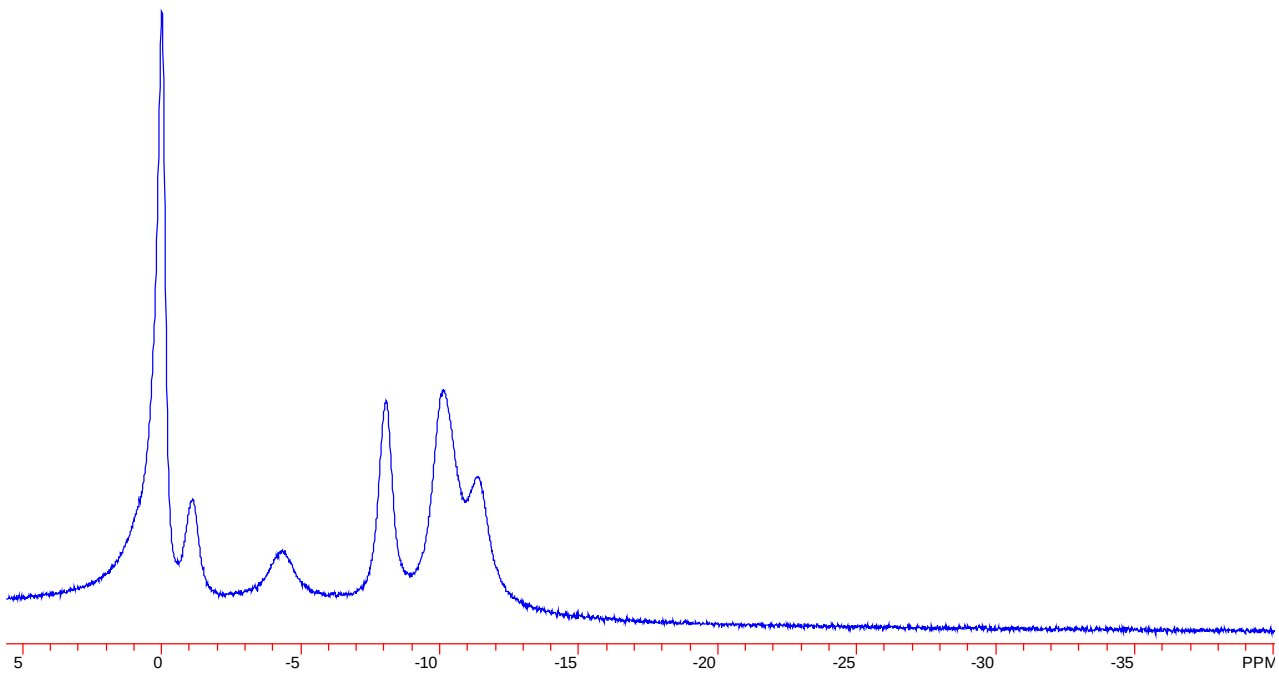
24



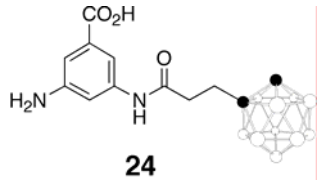
^{11}B NMR



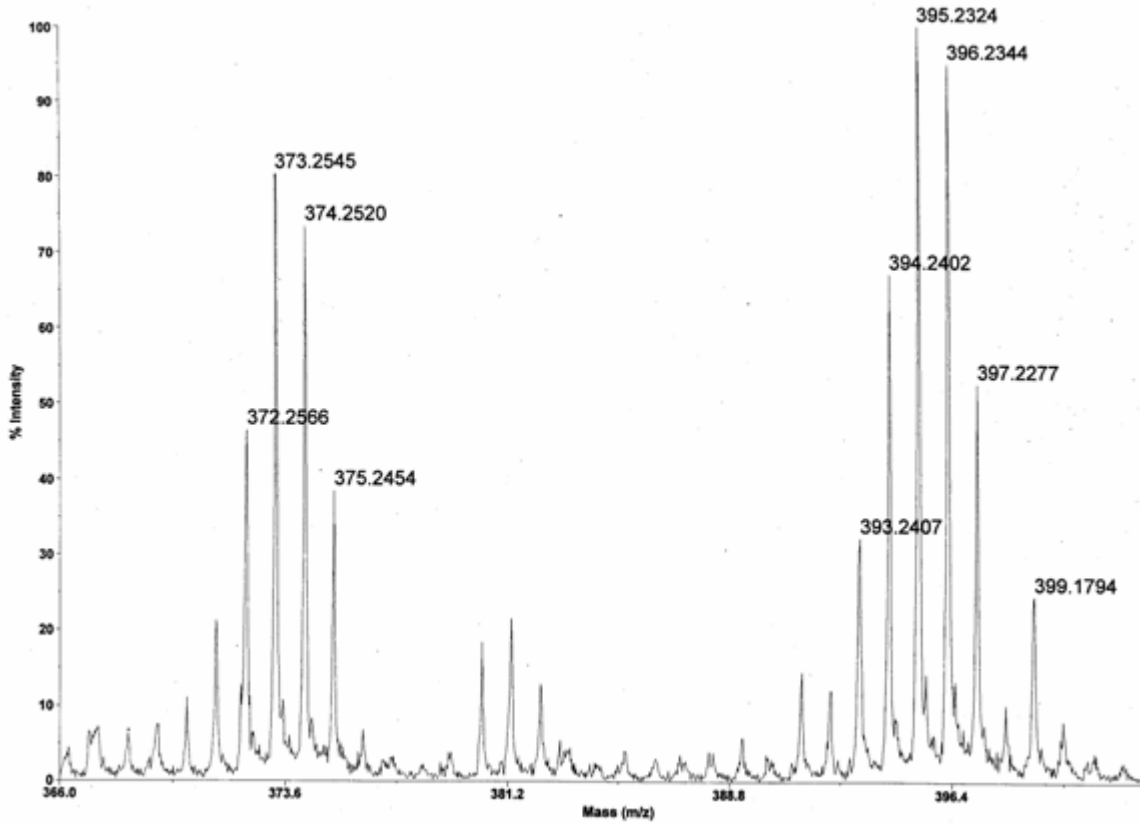
24



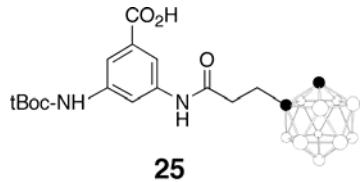
MS


CO2H
H2N
N
H
O

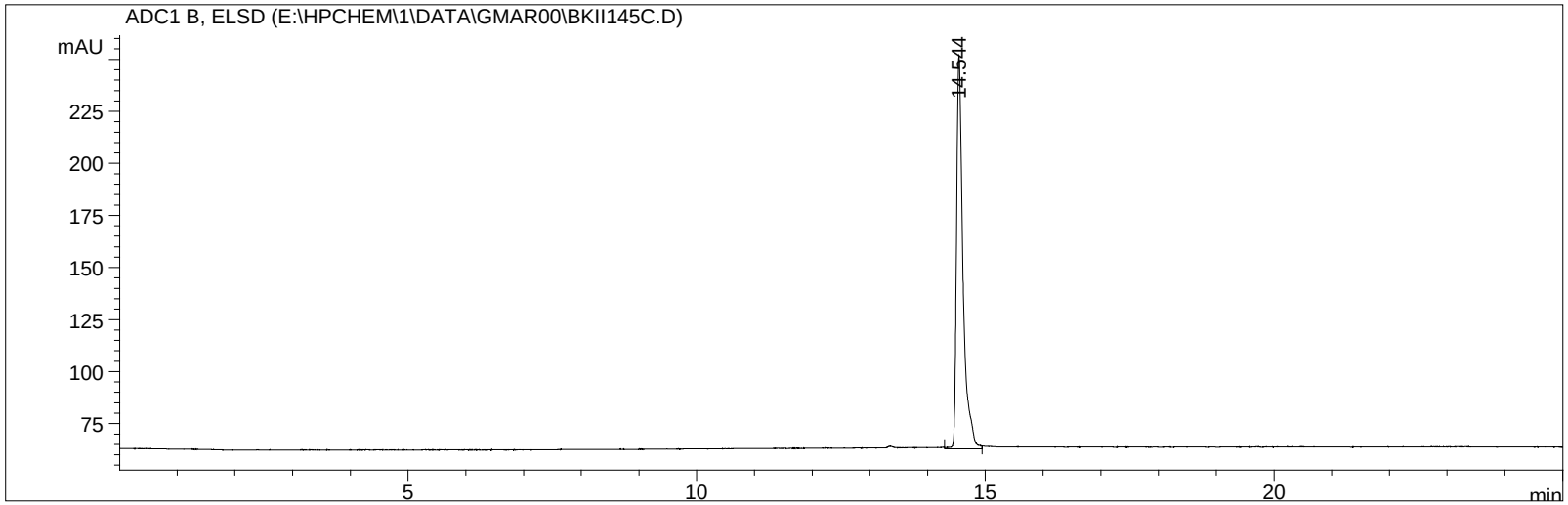
24


395.2324
396.2344
373.2545
374.2520
394.2402
397.2277
372.2566
375.2454
393.2407
399.1794
% Intensity
Mass (m/z)
366.0
373.6
381.2
388.8
396.4

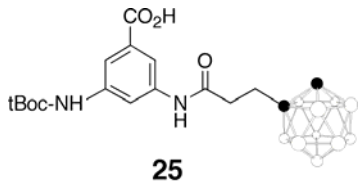
HPLC


CO2H
tBoc-NH
N
H
O

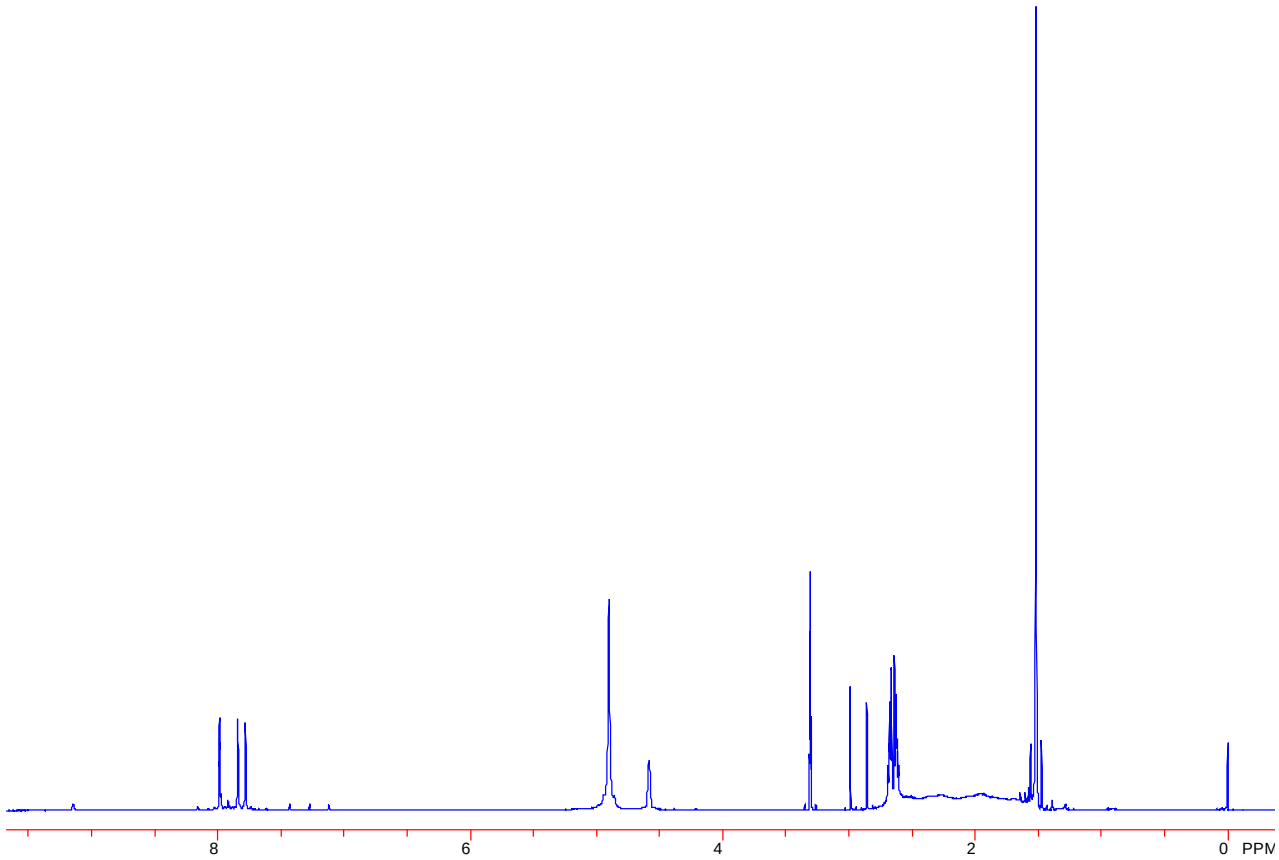
25


ADC1 B, ELSD (E:\HPCHEM\1\DATA\GMAR00\BKII145C.D)
mAU
225
200
175
150
125
100
75
14.544
5
10
15
20
min

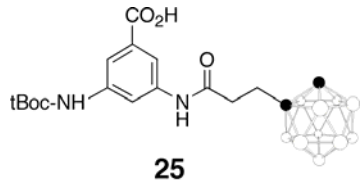
^{1}H NMR



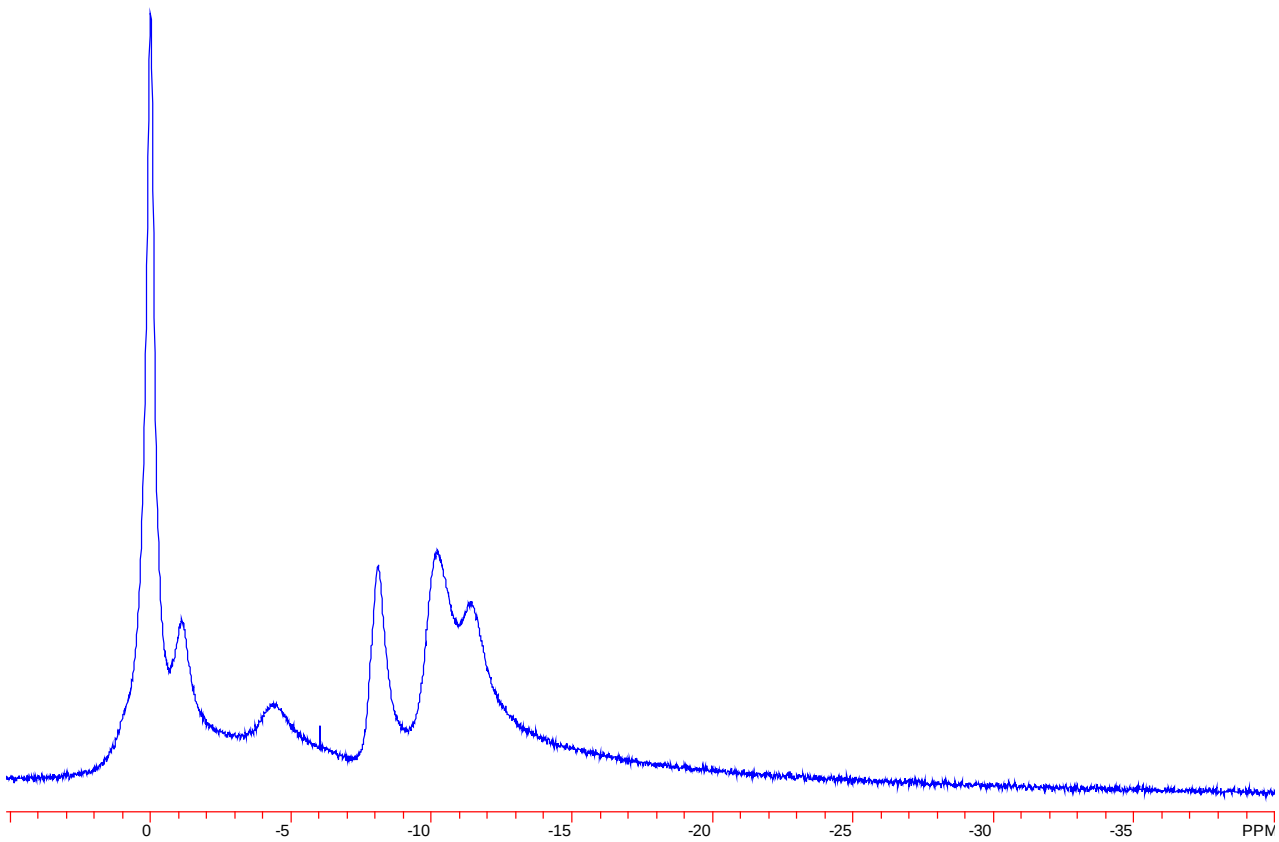
25



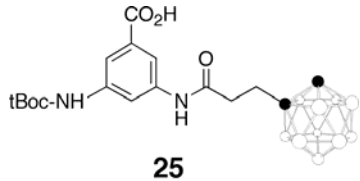
^{11}B NMR



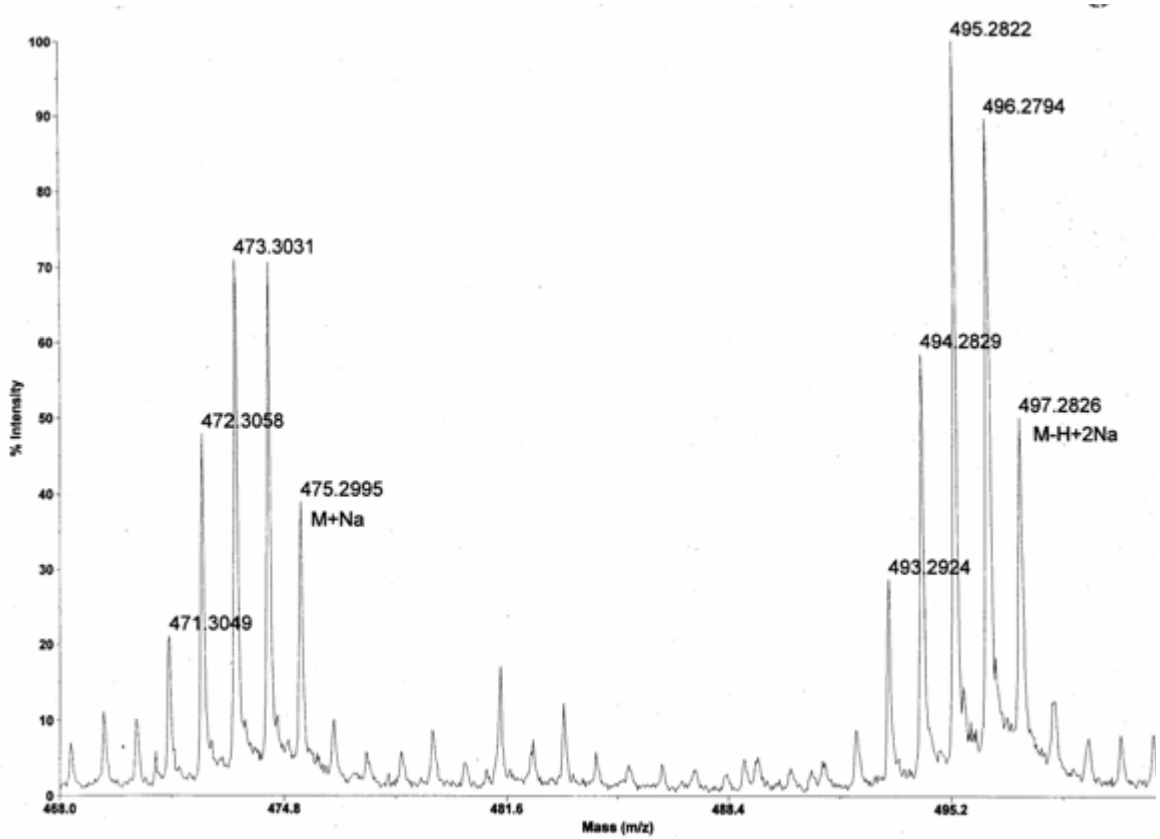
25



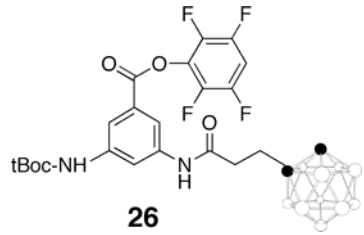
MS


CO2H
tBoc-NH
N
H
O

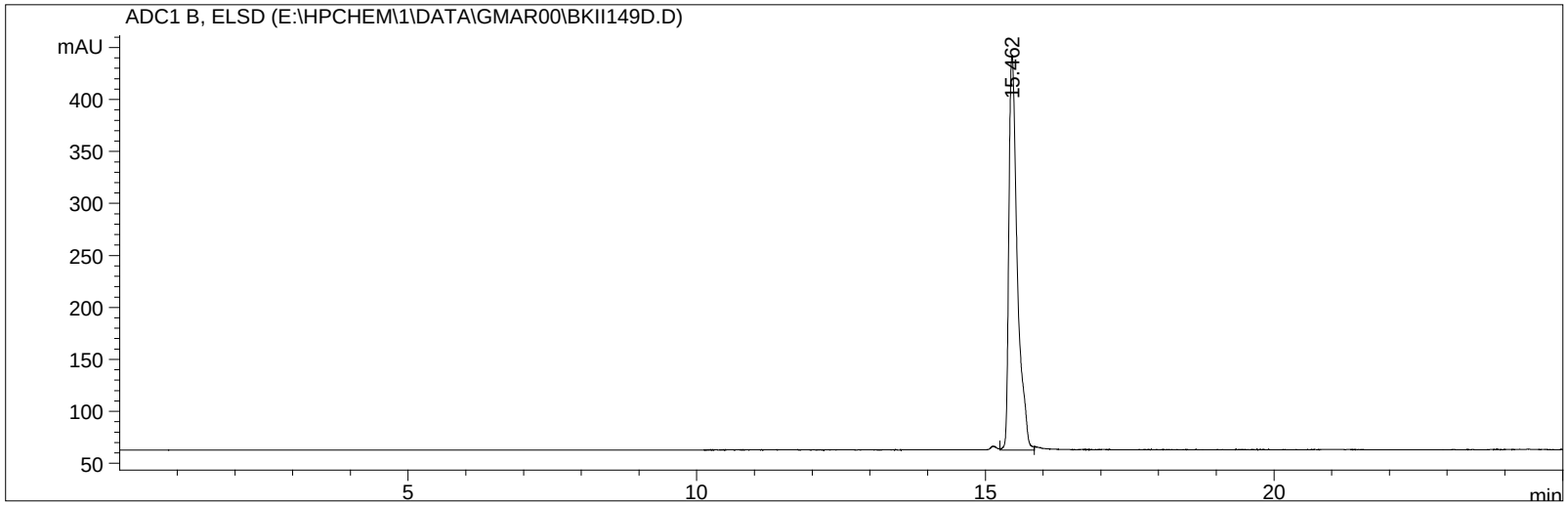
25


495.2822
496.2794
473.3031
494.2829
497.2826
M-H+2Na
472.3058
475.2995
M+Na
493.2924
471.3049
% Intensity
Mass (m/z)
100
90
80
70
60
50
40
30
20
10
0
468.0
474.8
481.6
488.4
495.2

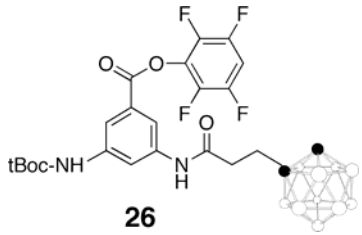
HPLC


F
F
O
O
F
F
O
tBoc-NH
N
H

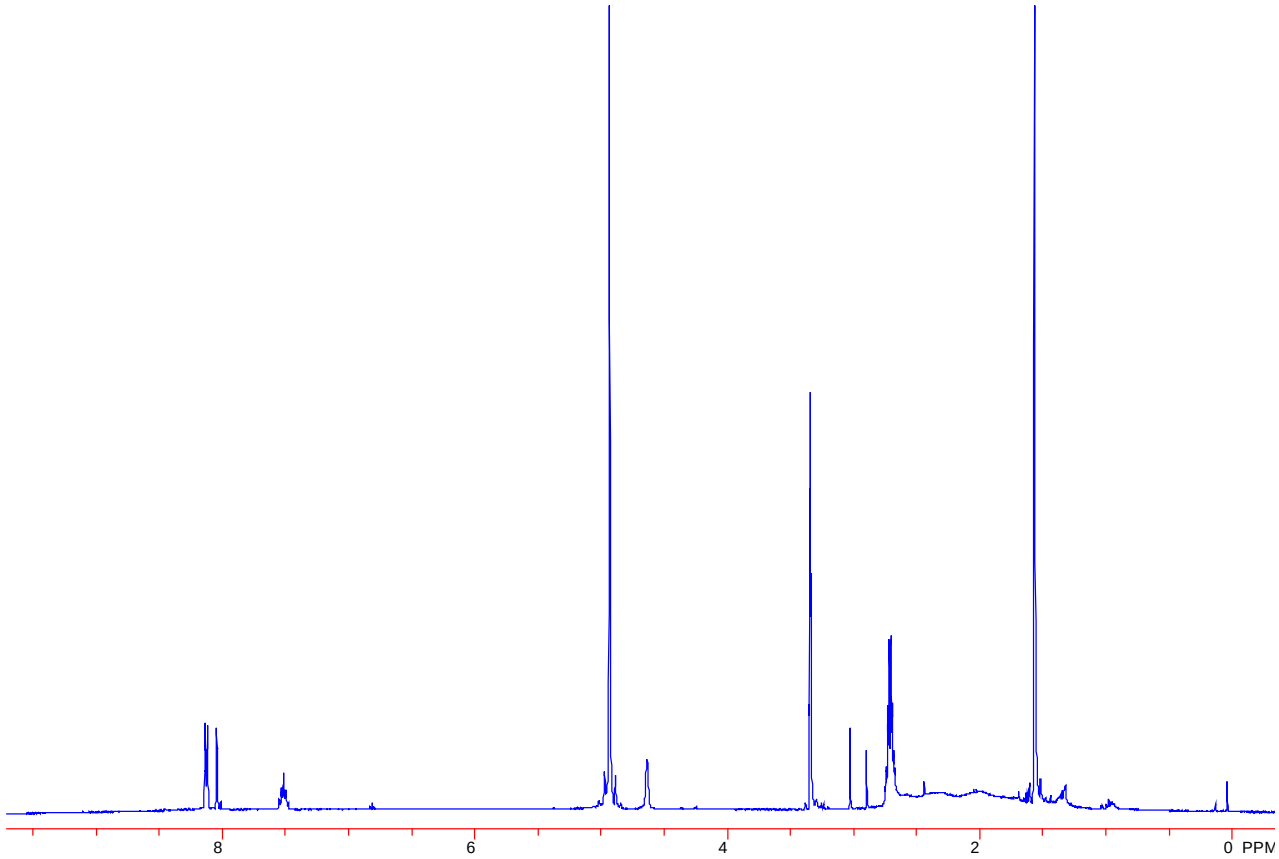
26


ADC1 B, ELSD (E:\HPCHEM\1\DATA\GMAR00\BKII149D.D)
mAU
400
350
300
250
200
150
100
50
15.462
5
10
15
20
min

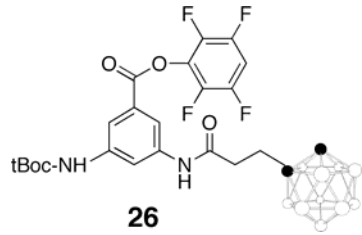
^{1}H NMR



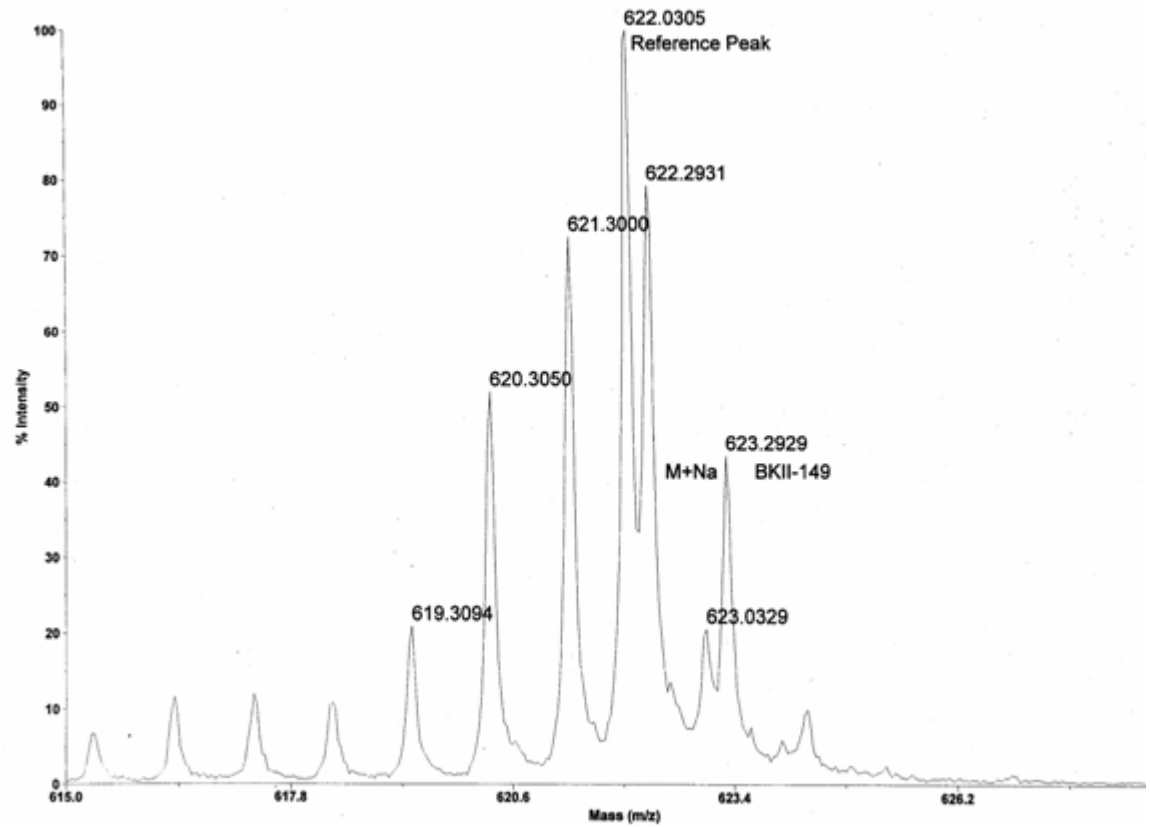
26



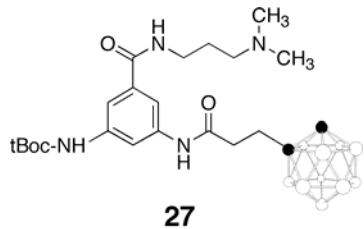
MS


F
F
O
O
F
F
O
tBoc-NH
N
H

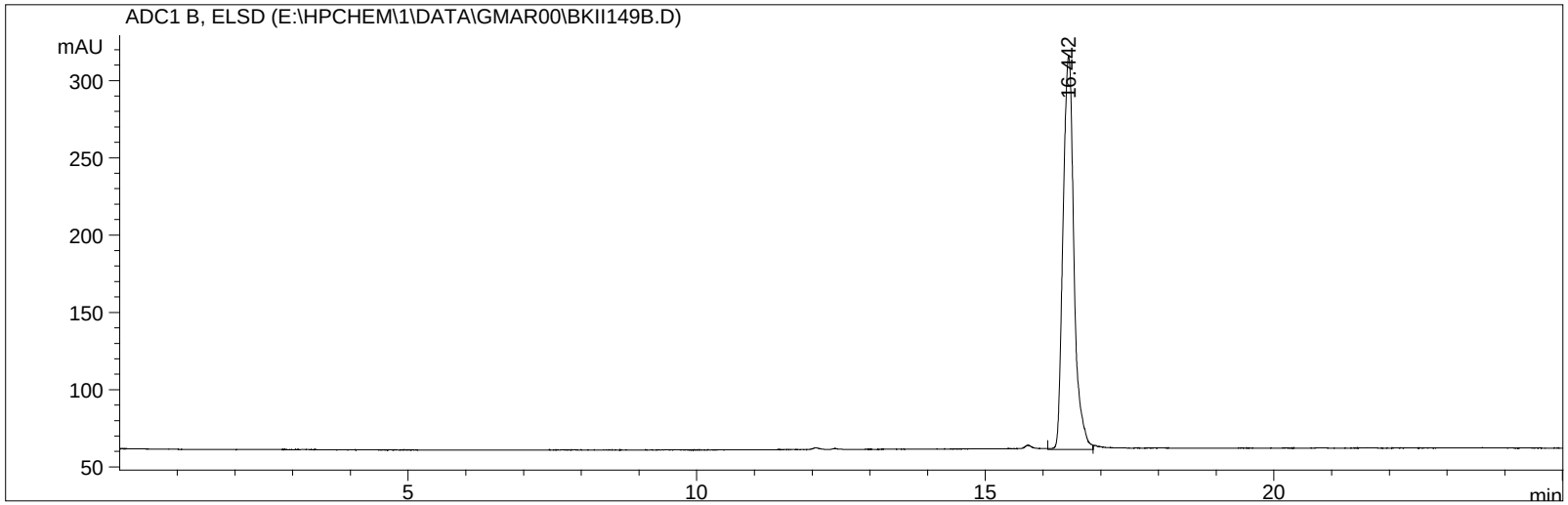
26


622.0305
Reference Peak
622.2931
621.3000
620.3050
623.2929
M+Na
BKII-149
619.3094
623.0329
% Intensity
Mass (m/z)
100
90
80
70
60
50
40
30
20
10
0
615.0
617.8
620.6
623.4
626.2

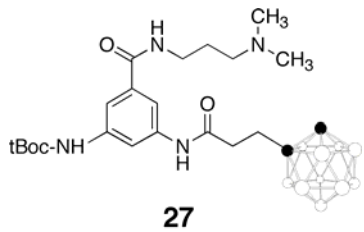
HPLC


H
N
O
CH3
N
CH3
tBoc-NH
O
N
H

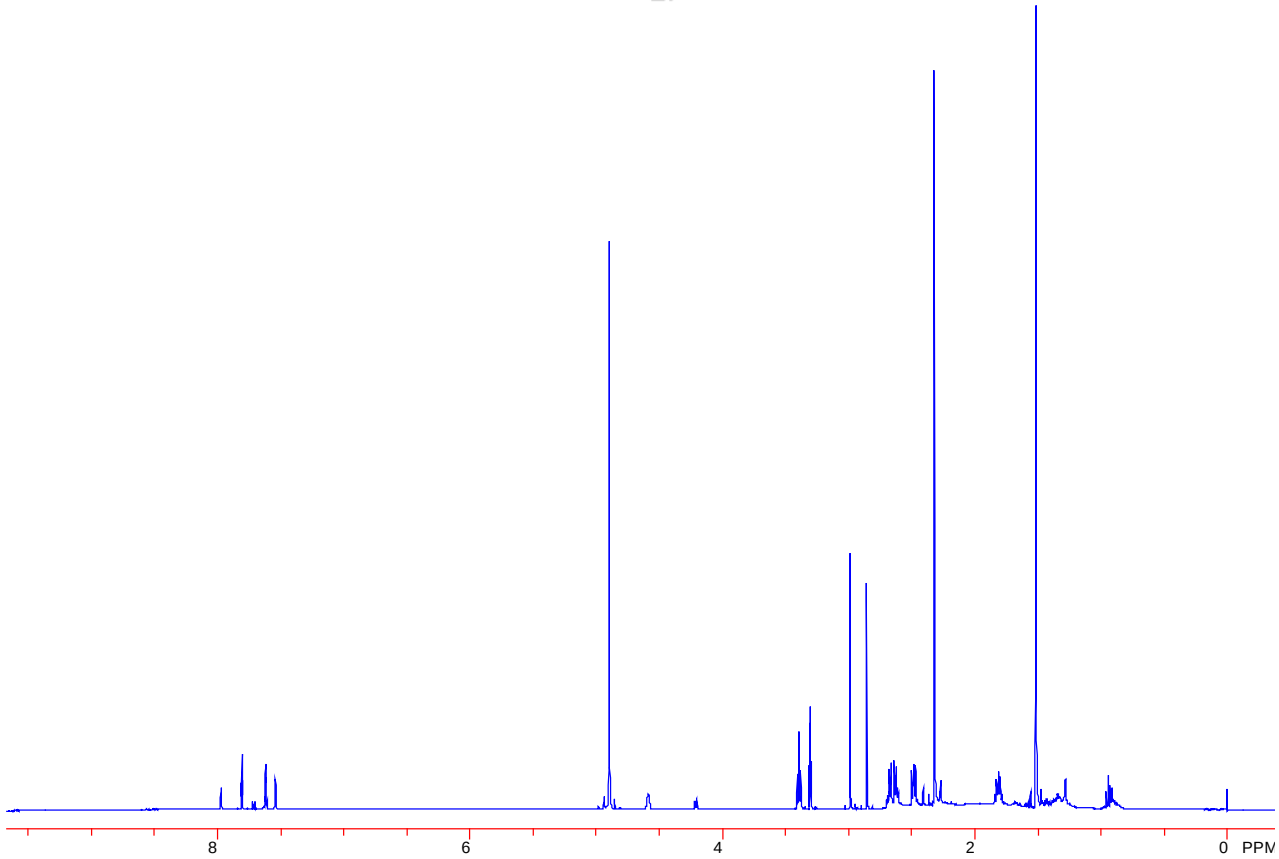
27


ADC1 B, ELSD (E:\HPCHEM\1\DATA\GMAR00\BKII149B.D)
mAU
300
250
200
150
100
50
16.442
5
10
15
20
min

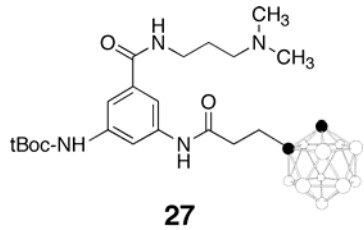
^{1}H NMR



27



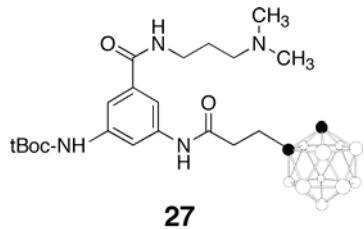
^{11}B NMR



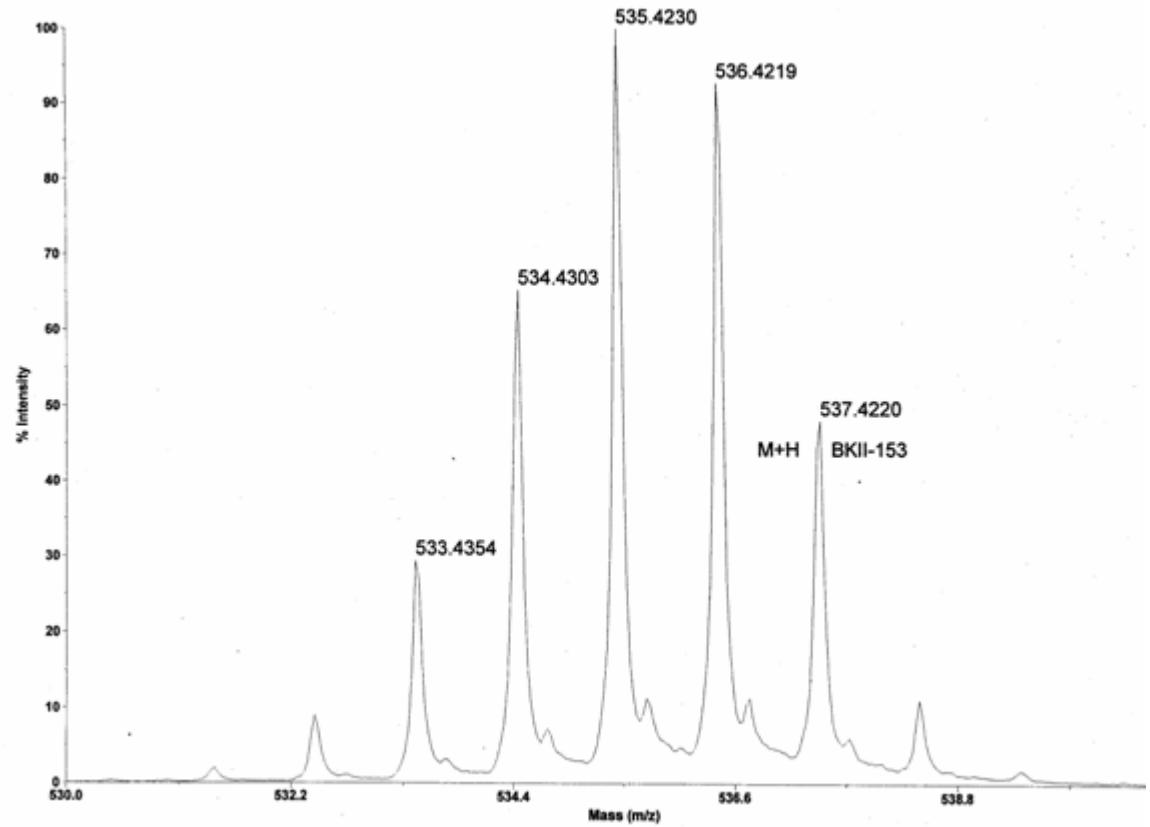
27



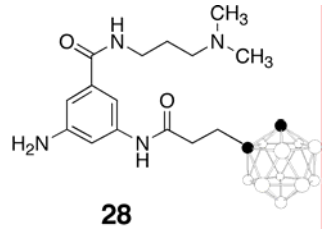
MS


H
N
O
CH3
N
CH3
tBoc-NH
O
N
H

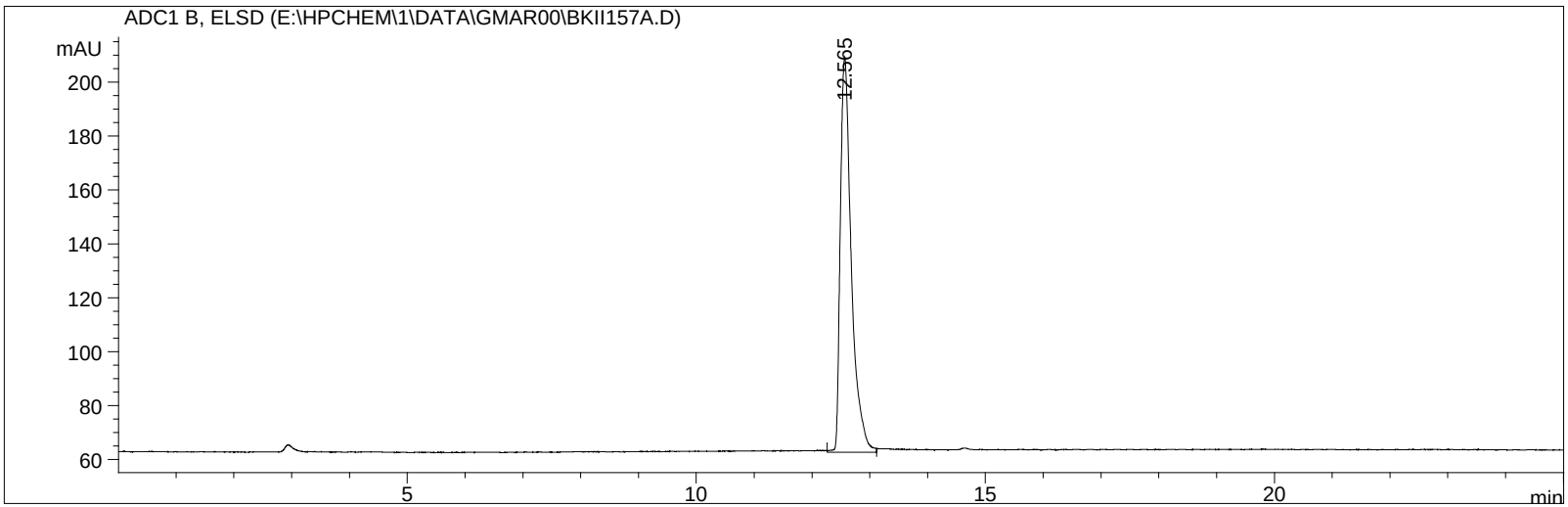
27


535.4230
536.4219
534.4303
537.4220
M+H
BKII-153
533.4354
% Intensity
Mass (m/z)
100
90
80
70
60
50
40
30
20
10
0
530.0
532.2
534.4
536.6
538.8

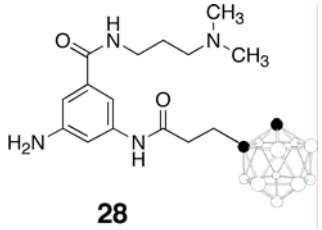
HPLC


H
N
O
CH3
N
CH3
O
H2N
N
H

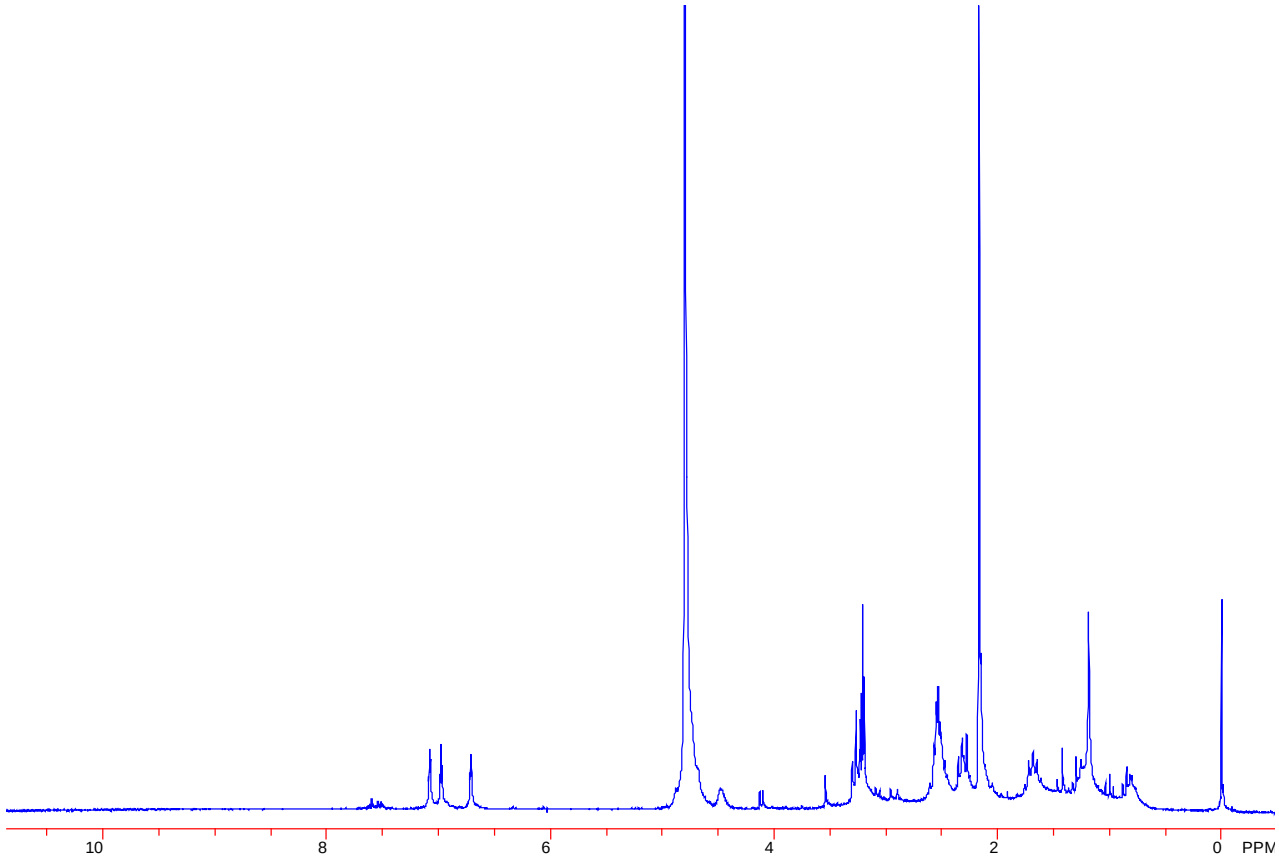
28


ADC1 B, ELSD (E:\HPCHEM\1\DATA\GMAR00\BKII157A.D)
mAU
200
180
160
140
120
100
80
60
12.565
5
10
15
20
min

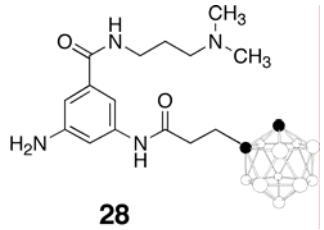
^{1}H NMR



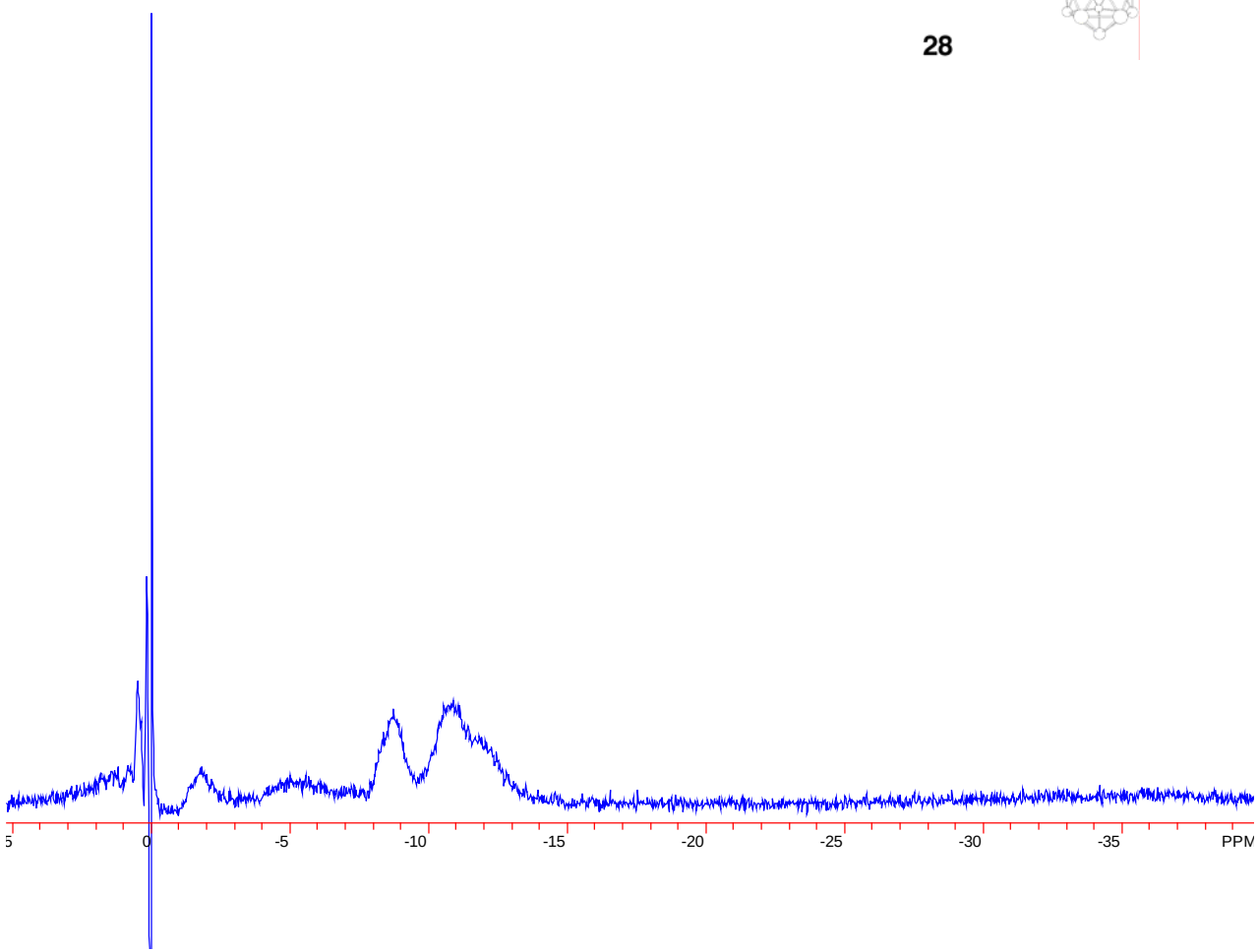
28



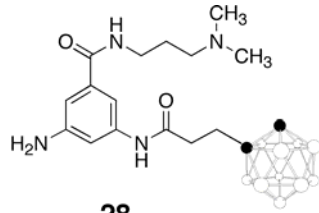
^{11}B NMR



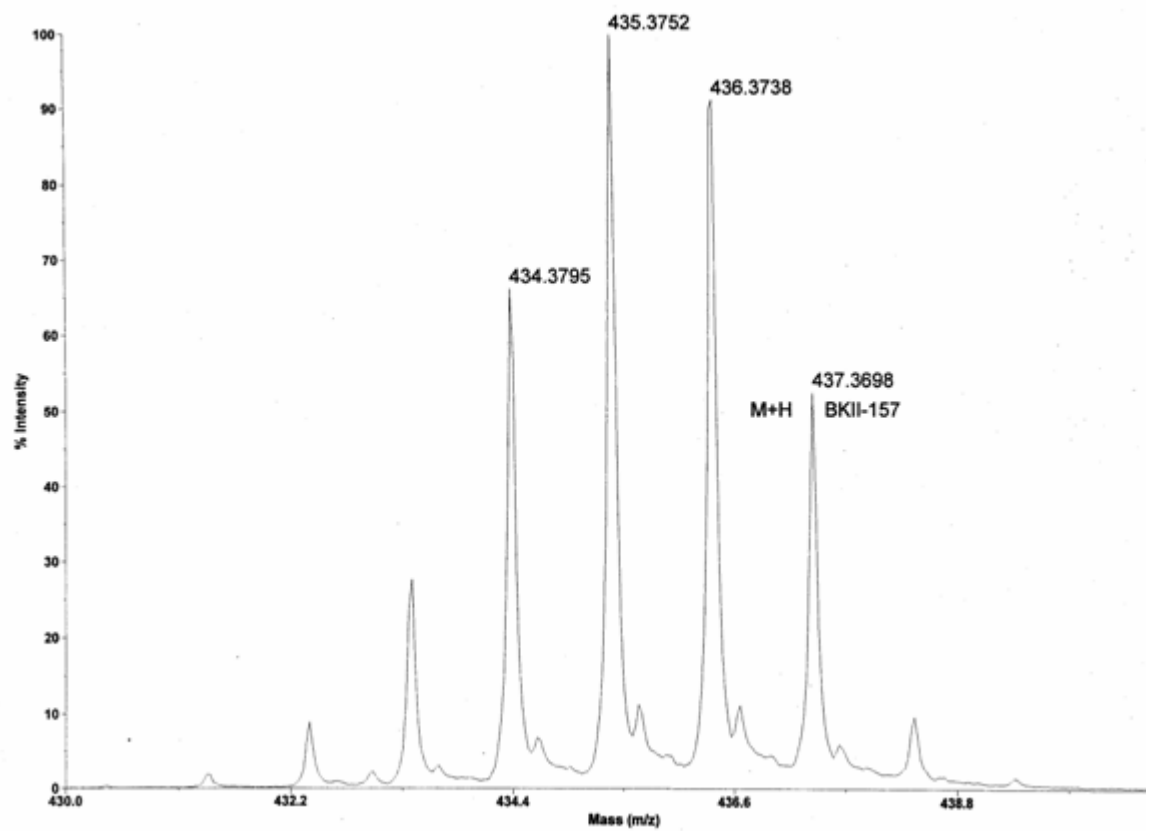
28



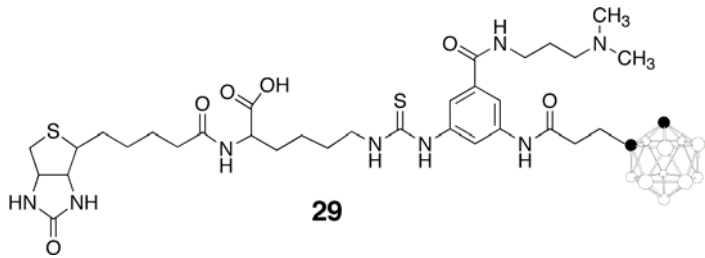
MS

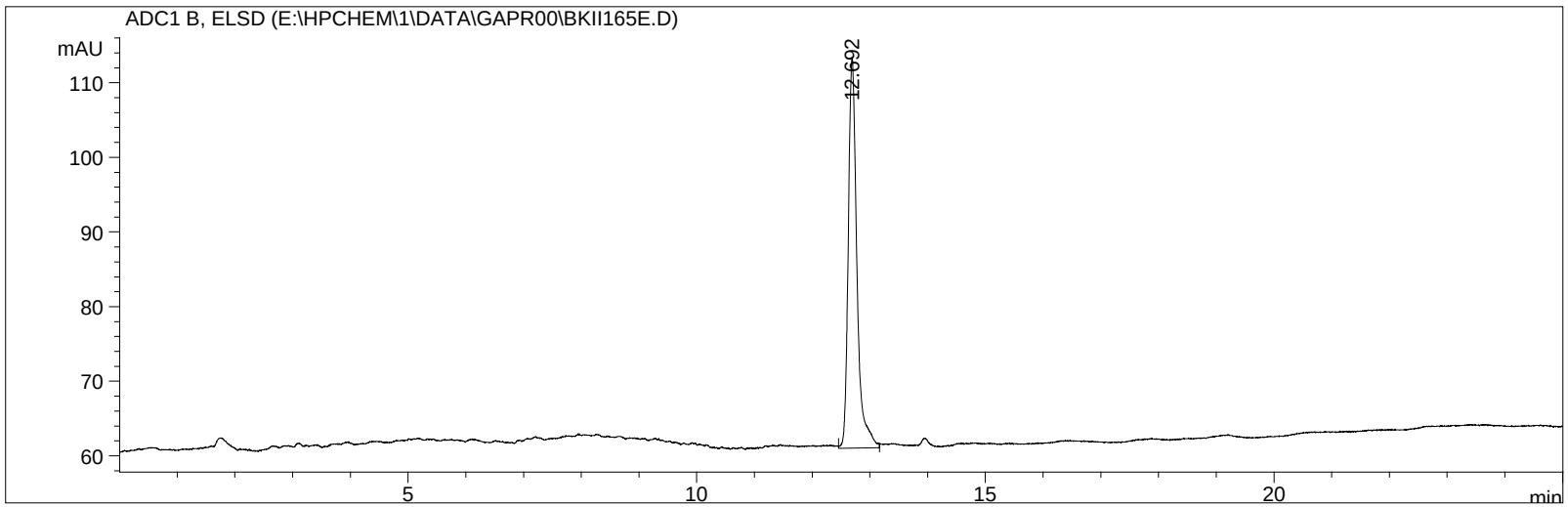


28

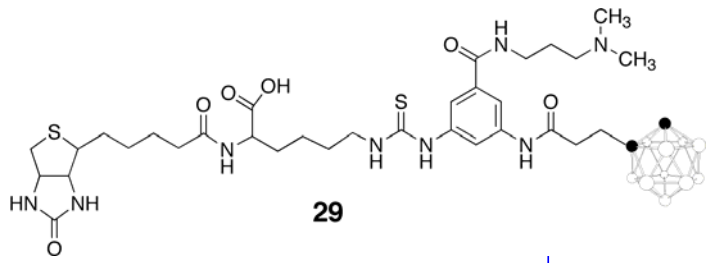

435.3752
436.3738
434.3795
437.3698
M+H
BKII-157
% Intensity
Mass (m/z)
100
90
80
70
60
50
40
30
20
10
0
430.0
432.2
434.4
436.6
438.8

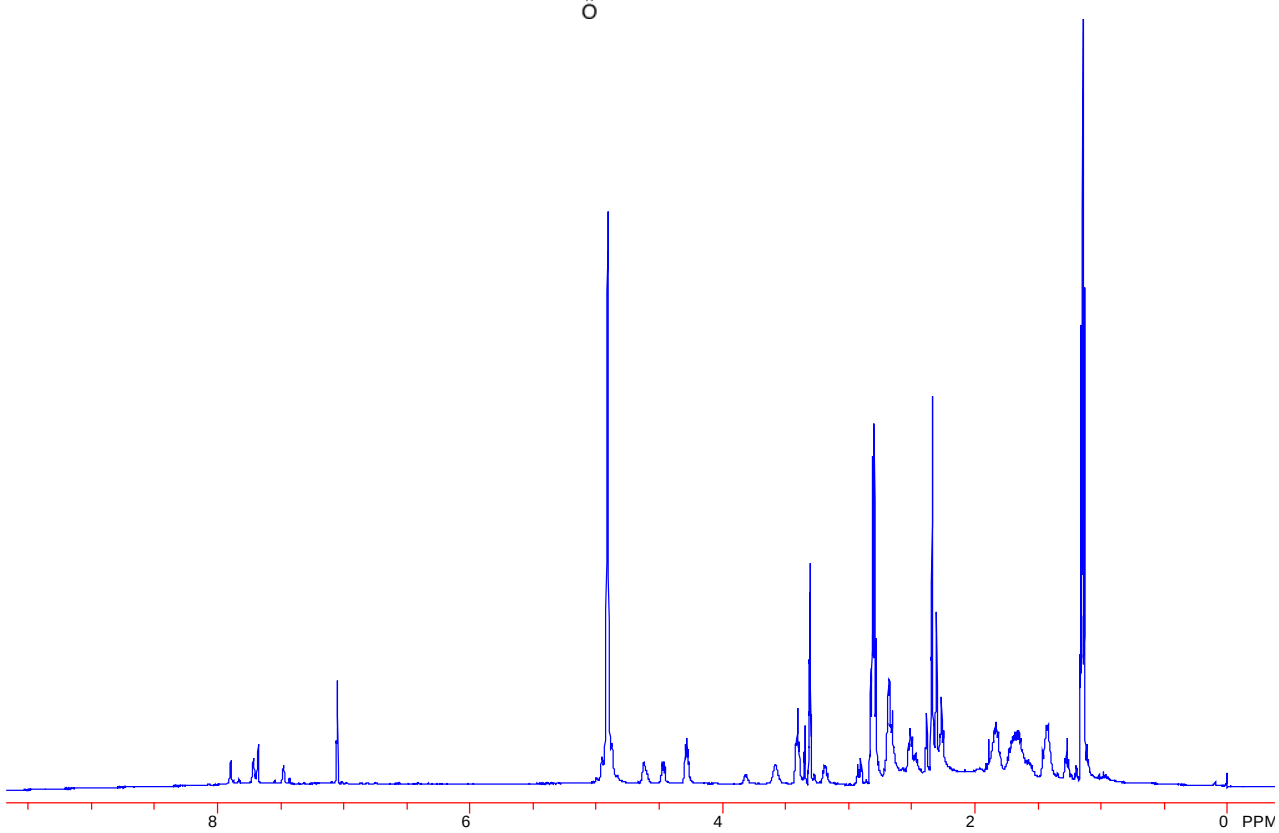
HPLC


29

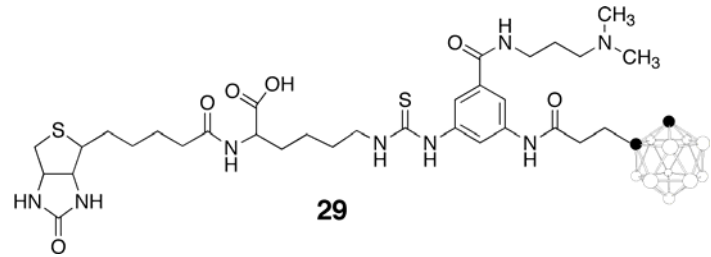

ADC1 B, ELSD (E:\HPCHEM\1\DATA\GAPR00\BKII165E.D)
mAU
110
100
90
80
70
60
12.692
5
10
15
20
min

^{1}H NMR

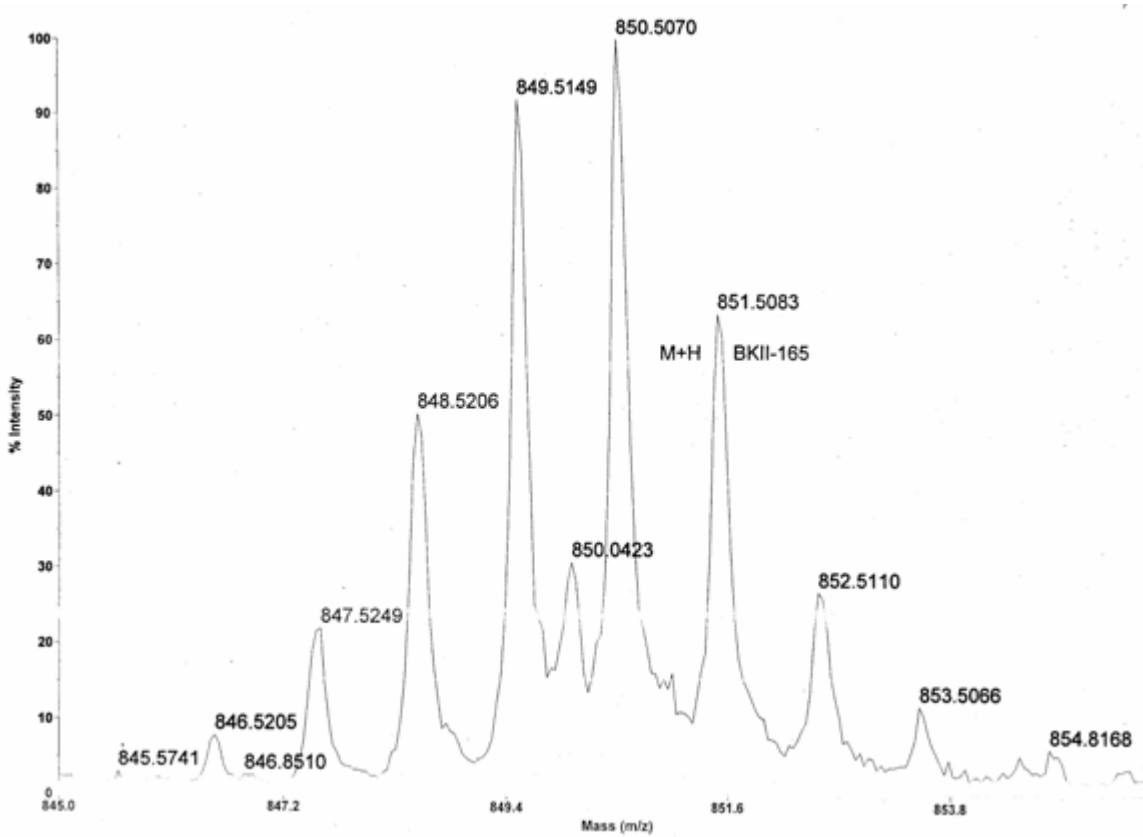




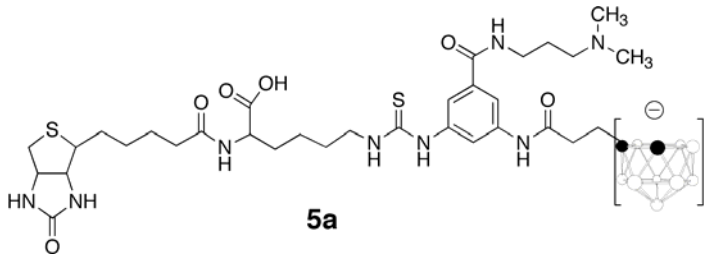
MS

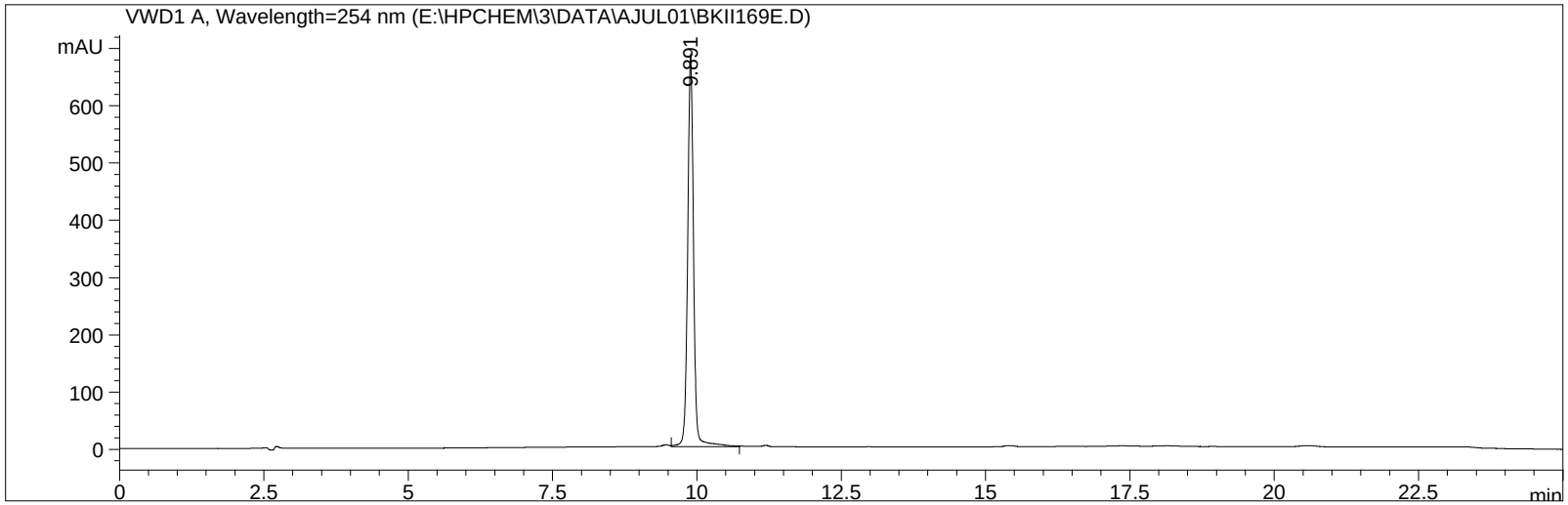


29

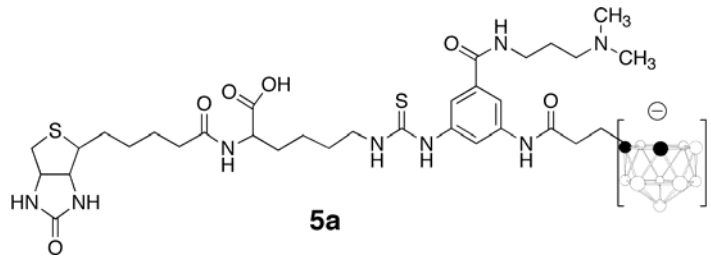

850.5070
849.5149
851.5083
M+H
BKII-165
848.5206
850.0423
852.5110
847.5249
853.5066
846.5205
854.8168
845.5741
846.8510
% Intensity
Mass (m/z)
100
90
80
70
60
50
40
30
20
10
0
845.0
847.2
849.4
851.6
853.8

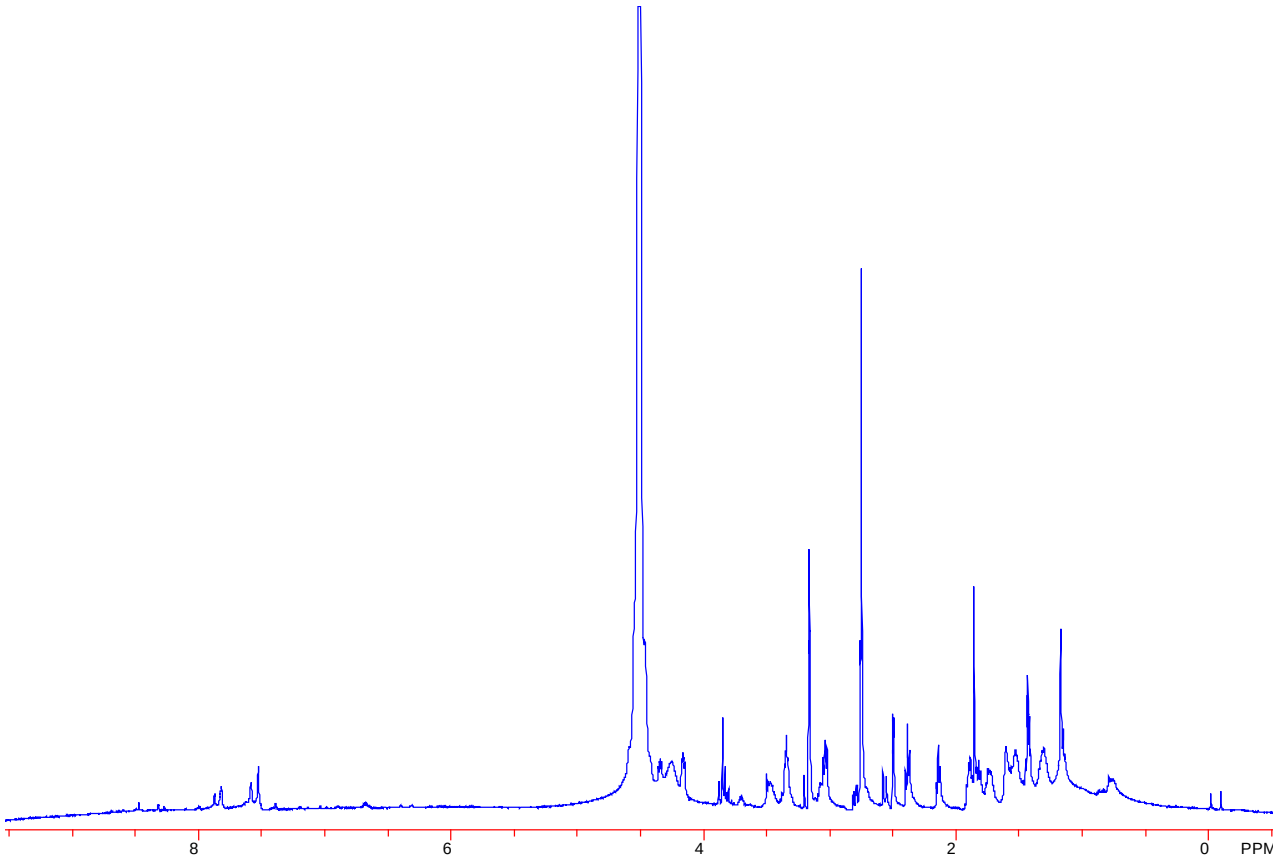
HPLC


5a

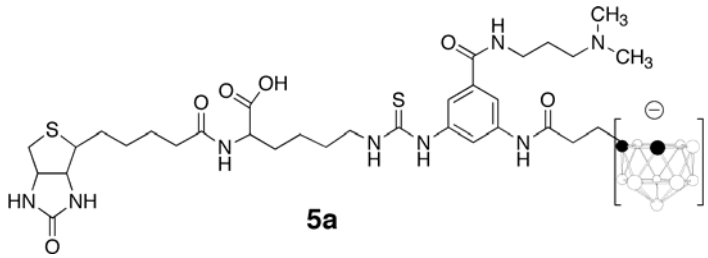

VWD1 A, Wavelength=254 nm (E:\HPCHEM\3\DATA\AJUL01\BKII169E.D)
mAU
600
500
400
300
200
100
0
9.891
0
2.5
5
7.5
10
12.5
15
17.5
20
22.5
min

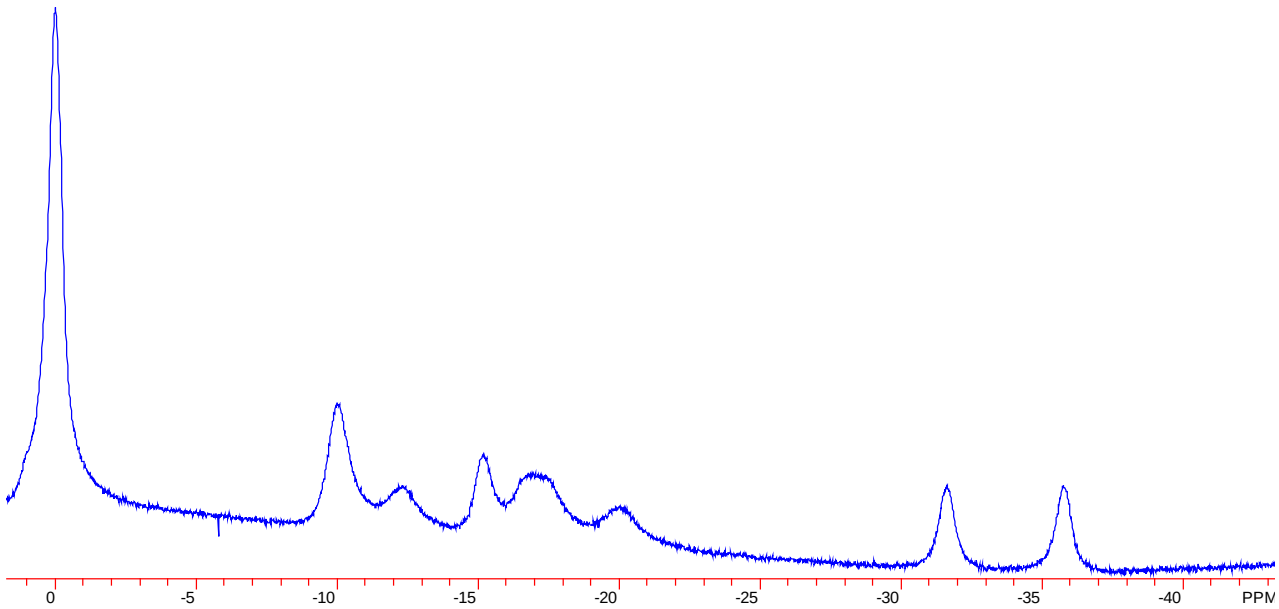
^{1}H NMR



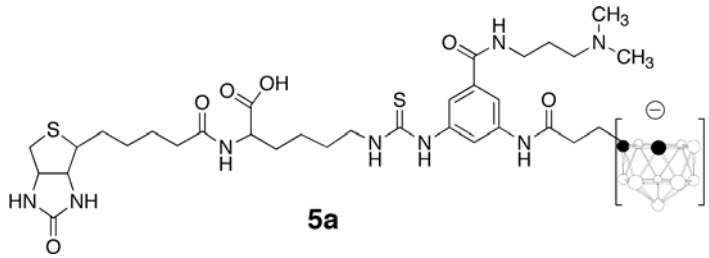


^{11}B NMR

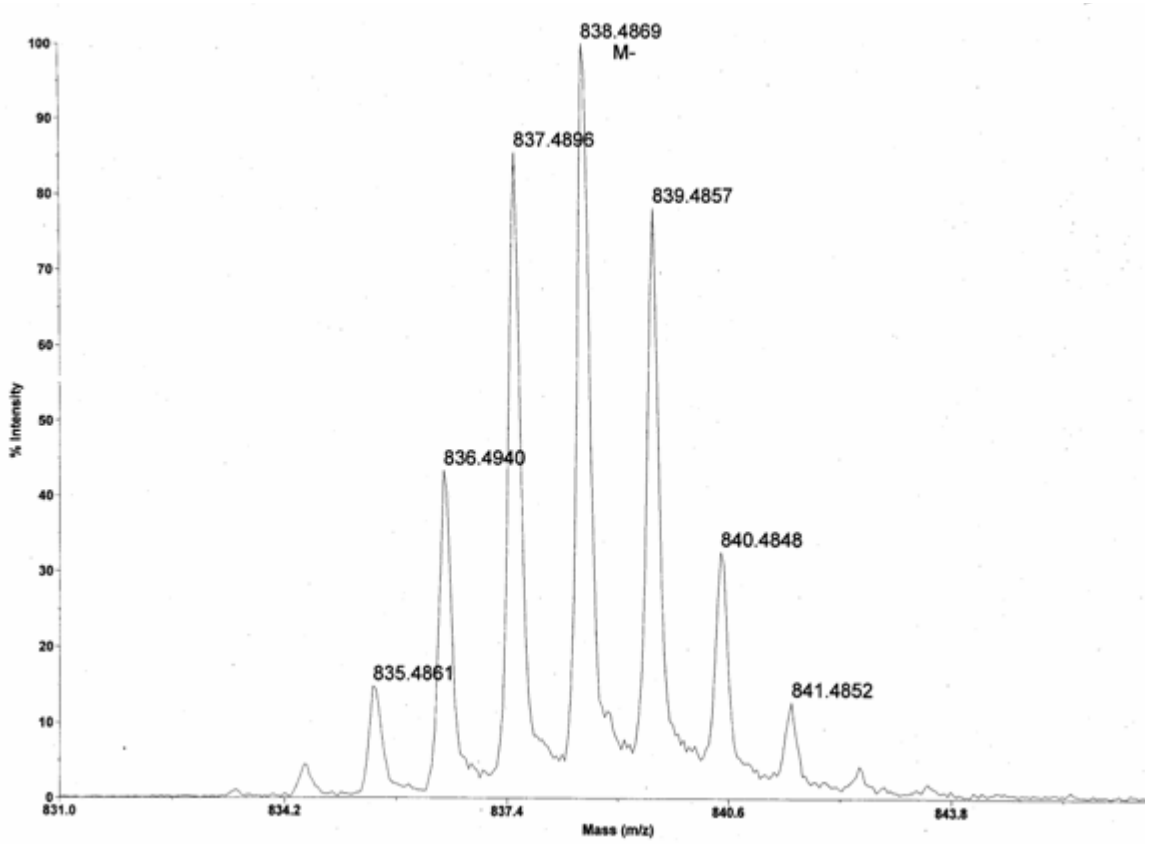




MS



5a


838.4869
M-
837.4896
839.4857
836.4940
840.4848
835.4861
841.4852
% Intensity
Mass (m/z)
831.0
834.2
837.4
840.6
843.8
100
90
80
70
60
50
40
30
20
10
0

Design and Synthesis of a New [^{18}F]Fluoropyridine-Based Haloacetamide Reagent for the Labeling of Oligonucleotides: 2-Bromo-*N*-[3-(2-[^{18}F]fluoropyridin-3-yloxy)propyl]acetamide

Bertrand Kuhnast,[†] Béatrice de Bruin,[†] Françoise Hinnen,[†] Bertrand Tavitian,[†,‡] and Frédéric Dollé*[,†]

Service Hospitalier Frédéric Joliot, Département de Recherche Médicale, CEA/DSV, 4 place du Général Leclerc, F-91401 Orsay, France, and INSERM ERM 0103, Service Hospitalier Frédéric Joliot, Département de Recherche Médicale, CEA/DSV, 4 place du Général Leclerc, F-91401 Orsay, France. Received January 7, 2004; Revised Manuscript Received February 24, 2004

Based on the recently highlighted potential of nucleophilic heteroaromatic ortho-radiofluorinations in the preparation of fluorine-18-labeled radiotracers and radiopharmaceuticals for PET, a [^{18}F]-fluoropyridine-based bromoacetamide reagent has been prepared and used in prosthetic group introduction for the labeling of oligonucleotides. [^{18}F]FPyBrA (2-bromo-*N*-[3-(2-[^{18}F]fluoropyridin-3-yloxy)propyl]acetamide) was designed as a radiochemically feasible reagent, its pyridinyl moiety both carrying the radioactive halogen (fluorine-18) and allowing its efficient incorporation via a nucleophilic heteroaromatic substitution, and its 2-bromoacetamide function, ensuring the efficient alkylation of a phosphorothioate monoester group born at the 3′- or 5′-end of single-stranded oligonucleotides. [^{18}F]-FPyBrA (HPLC-purified) was efficiently prepared in 18−20% non-decay-corrected yield (based on starting [^{18}F]fluoride) using a three-step radiochemical pathway in 80−85 min. The developed procedure involves (1) a high-yield nucleophilic heteroaromatic ortho-radiofluorination as the fluorine-18 incorporation-step (70−85% radiochemical yield) and uses [3-(3-*tert*-butoxycarbonylaminopropoxy)-pyridin-2-yl]trimethylammonium trifluoromethanesulfonate as precursor for labeling, followed by (2) rapid and quantitative TFA-removal of the *N*-Boc-protective group and (3) condensation with 2-bromoacetyl bromide (45−65% radiochemical yield). Typically, 3.3−3.7 GBq (90−100 mCi) of HPLC-purified [^{18}F]FPyBrA could be obtained in 80−85 min, starting from 18.5 GBq (500 mCi) of a cyclotron production batch of [^{18}F]fluoride. [^{18}F]FPyBrA was regioselectively conjugated with 9-mer and 18-mer single-stranded oligonucleotides, provided with a phosphorothioate monoester group at their 3′-end. Both natural phosphodiester DNAs and in vivo-stable 2′-methoxy and -fluoro-modified RNAs were used. Conjugation uses optimized, short-time reaction conditions (MeOH/0.1 M PBS pH 7.4, 15 min, 120 °C), both compatible with the chemical stability of the oligonucleotides (ONs) and the half-life of fluorine-18. Conjugated [^{18}F]ONs were finally purified by RP-HPLC and desalted using a Sephadex NAP-10 column. The whole radiosynthetic procedure, including the preparation of the fluorine-18-labeled reagent, the conjugation with the oligonucleotide, and the HPLC purification and formulation lasted 140−160 min. [^{18}F]FPyBrA represents a valuable alternative to the already reported *N*-(4-[^{18}F]fluorobenzyl)-2-bromoacetamide for the design and development of oligonucleotide-based radiopharmaceuticals for PET.

INTRODUCTION

Positron emission tomography (PET) is a high-resolution, sensitive, molecular and functional imaging technique that permits repeated, noninvasive assessment and quantification of specific biological and pharmacological processes in humans. PET is also the most advanced technology currently available for studying in vivo molecular interactions and therefore can advantageously play a key role in both drug discovery and development of pharmaceuticals, by assessing their in vivo distribution, pharmacokinetics, and dynamics, once labeled with a positron-emitter. Recent advances in positron-emitter labeling of bioconjugates now allow the design and development of complex high-molecular-weight bioactive chemical structures as radiopharmaceuticals *(1−4)*, including single-stranded oligonucleotides *(5)*.

Fluorine-18 appears often as the radionuclide of choice for the preparation of short-lived positron-emitter radiotracers and radiopharmaceuticals. In regard to its physical and nuclear characteristics, fluorine-18 displays simple decay and emission properties with a high positron abundance (97%). Compared with the other conventional short-lived positron-emitting radionuclides carbon-11, nitrogen-13, and oxygen-15, fluorine-18 has a relatively low positron emission energy (maximum 635 keV) and the shortest positron linear range in tissue (2.3 mm), resulting in the highest resolution in PET imaging. Its half-life (109.8 min) is long enough to give access to relatively extended imaging protocols compared to what is possible with carbon-11 (therefore facilitating kinetic studies and high-quality metabolite and plasma analysis) and from a chemical point of view, allows multistep synthetic approaches that can be extended over hours. This distinctive advantage, combined with its reliable multi-Curie production on widely implemented biomedical cyclotrons, has been effectively used for the labeling of various chemical structures *(1−4)*.

* To whom correspondence should be addressed. E-mail: frederic.dolle@cea.fr.

[†] Service Hospitalier Frédéric Joliot.

[‡] INSERM ERM 0103.

10.1021/bc049979u CCC: $27.50 © 2004 American Chemical Society
Published on Web 05/04/2004

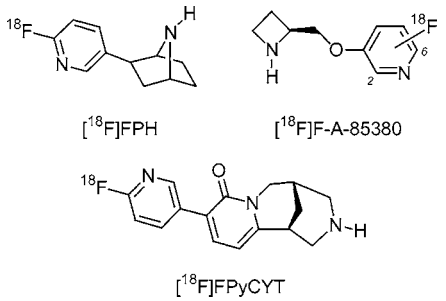


Figure 1. Chemical structures of norchloro[^{18}F]fluoroepibatidine ([^{18}F]FPH), 2- and 6-[^{18}F]fluoro-A-85380, and (−)-9-(2-[^{18}F]-fluoropyridinyl)cytisine ([^{18}F]FPyCYT).

In the macromolecule field, fluorine-18-labeling of single-stranded oligonucleotides has already been described in the literature *(6*−*16)*. It is usually performed by conjugation of a prosthetic group, carrying the radioisotope, with a reactive function of the macromolecule. This strategy has the advantage of offering a wide choice of chemical routes, including drastic chemical conditions, for the preparation of the labeled prosthetic group entity, followed by the conjugation of the latter with a macromolecule using mild conditions needed to preserve its integrity.

From a radiochemical point of view, all fluorine-18-labeled prosthetic groups described so far have been prepared using the relatively restricted labeling strategies offered by homoaromatic and aliphatic nucleophilic substitution reactions *(2, 3)*. Recently, the scope of these nucleophilic radiofluorinations has been opened to heteroaromatic substitutions, particularly in the pyridine series *(17)*. After having been evaluated and validated on the radiosynthesis of 2- and 4-[^{18}F]fluoropyridine as a model reaction *(18, 19)*, these nucleophilic heteroaromatic substitutions have since been applied successfully to the preparation of various PET radiotracers and radiopharmaceuticals, for example in the field of cholinergic $\alpha_4\beta_2$-subtype selective nicotinic radioligands, notably norchloro[^{18}F]fluoroepibatidine ([^{18}F]FPH, (±)-*exo*-2-(6-[^{18}F]fluoro-3-pyridyl)-7-azabicyclo[2.2.1]heptane) *(20*−*26)*, 2- and 6-[^{18}F]fluoro-A-85380 (2- and 6-[^{18}F]F−A-85380, 2- and 6-[^{18}F]fluoro-3-[2(*S*)-2-azetidinylmethoxy]-pyridine) *(27*−*34)*, and more recently (−)-9-(2-[^{18}F]fluoropyridinyl)cytisine ([^{18}F]FPyCYT, (−)-(1*R*,5*S*)-9-(2-[^{18}F]-fluoro-5-pyridyl)-1,2,3,4,5,6-hexahydro-1,5-methanopyrido-[1,2-*a*][1,5]diazocin-8-one) *(35)* (Figure 1).

Considering chemical structures showing a fluoropyridinyl moiety, nucleophilic heteroaromatic substitution at the ortho-position with no-carrier-added [^{18}F]fluoride appears today as the most efficient method for the radiosynthesis of radiotracers and radiopharmaceuticals of high specific radioactivity when compared to homoaromatic or aliphatic, nucleophilic radiofluorination. On the basis of these recent advances, we have designed a new [^{18}F]fluoropyridine-based haloacetamide reagent, [^{18}F]-**1** (2-bromo-*N*-[3-(2-[^{18}F]fluoropyridin-3-yloxy)propyl]-acetamide, coded [^{18}F]FPyBrA, Figure 2) as a new fluorine-18-labeled prosthetic group for the specific radioactive alkylation of (5′- or 3′-end) phosphorothioate-bearing single-stranded oligonucleotides. We herein report the synthesis of the nonlabeled fluoropyridinyl reagent (**1**, FPyBrA) as a reference, as well as the synthesis of the corresponding nitro- and trimethylammonium trifluoromethanesulfonate derivatives as precursors for labeling with fluorine-18. We also present the radiosynthesis of [^{18}F]FPyBrA ([^{18}F]-**1**) using an efficient three-step radiosynthesis, involving a nucleophilic heteroaromatic ortho-radiofluorination as the fluorine-18 incorporation-step. Finally, we describe the conjugation of this bromoacetamide reagent (FPyBrA) with various 9- and 18-mer single-stranded oligonucleotides as well as the efficient preparation of the corresponding fluorine-18-labeled oligonucleotide conjugates (Figure 2).

RESULTS AND DISCUSSION

Chemistry. The synthesis of FPyBrA (**1**, 2-bromo-*N*-[3-(2-fluoropyridin-3-yloxy)propyl]acetamide) is outlined in Schemes 1 and 2.

[3-(2-Fluoropyridin-3-yloxy)propyl]carbamic acid *tert*-butyl ester (**3a**) was prepared in 49% yield via a Mitsunobu coupling reaction *(36)* from commercially available (3-hydroxypropyl)carbamic acid *tert*-butyl ester (**2**) and 2-fluoro-3-hydroxypyridine *(27, 29)*, in THF at room temperature, using triphenylphosphine (0.8 equiv) and diisopropylazodicarboxylate (1.4 equiv) (Scheme 1). Trifluoroacetic acid (TFA) removal of the *tert*-butoxycarbonyl function of derivative **3a** was performed in dichloromethane at room temperature and gave the desired free amine **4** in 96% yield (Scheme 2). Treatment of **4** with 2-bromoacetyl bromide in the presence of *N*-methylmorpholine in dichloromethane at 0 °C gave the acetamide **1** (FPyBrA) in 24% yield (nonoptimized).

The synthesis of the *N*-Boc-protected nitro- and trimethylammonium precursors for labeling (**3c** and **3d**) is described in Schemes 1 and 3. The choice of these nitro- and trimethylammonium functions will be discussed in the radiochemistry section below.

The dimethylamino and nitro derivatives **3b** and **3c** were prepared in 43% and 40% yield, respectively, from

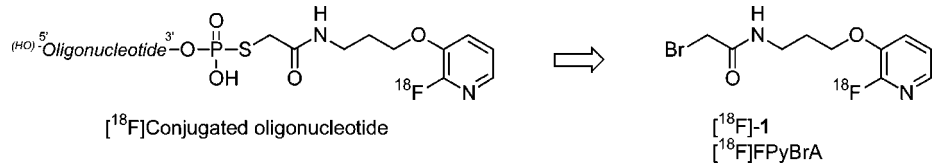


Figure 2. Fluorine-18-labeling design of phosphorothioate-bearing single-stranded oligonucleotides using 2-bromo-*N*-[3-(2-[^{18}F]-fluoropyridin-3-yloxy)propyl]acetamide ([^{18}F]FPyBrA, [^{18}F]-**1**).

Scheme 1. Preparation of 2-Fluoro-, 2-(Dimethylamino)-, and 2-Nitropyridine Derivatives 3a−**c**

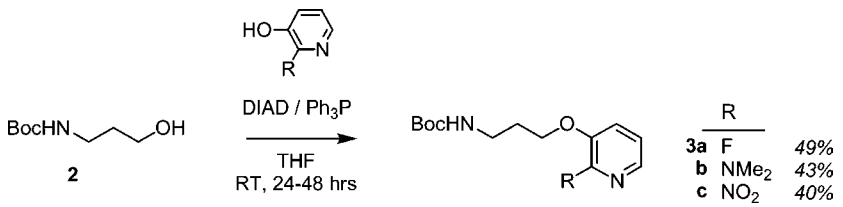


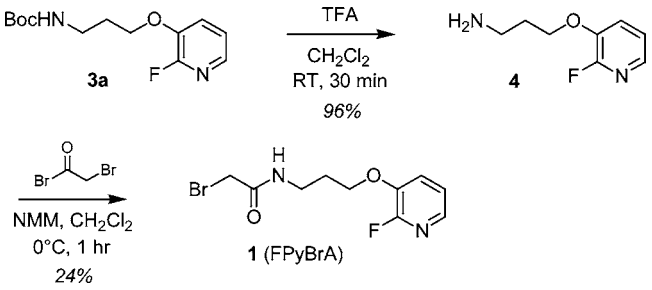
Table 1. Length, Sequence and Analytical Data for Starting- (OL1, OL2a, OL2b, and OL3) and Conjugated Oligonucleotides (C-OL1, C-OL2a, C-OL2b, and C-OL3)

Name	Length	Sequences	HPLC Rt [(a)]*	MS found (calc) [(b)]*	^{31}P NMR [(c)]*
OL1 / C-**OL1**	9 mer	A C C G A T C C G	14.0 min	2989.0 (2990.0)	δ : 14.44
OL2a / C-**OL2a**	18 mer	A G A A T A C A G G G T C C A A A T	14.1 min	5847.8 (5846.9)	δ : 14.53
OL2b / C-**OL2b**	18 mer	A G A A U A C A G G G U C C A A A U	15.4 min	6346.7 (6345.3)	δ : 13.94
OL3 / C-**OL3**	18 mer	A U U U G G A C C C U G U A U U C A	15.3 min	5989.7 (5991.0)	δ : 13.94

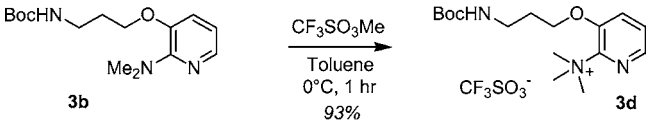
[(a)] HPLC column and conditions: C18 μBondapak® Waters (300 x 3.9 mm, porosity 10 μm); triethylammonium acetate, 50 mM, pH 7 (TEAA) and acetonitrile; gradient elution: linear 5 min from 95/5 to 90/10 (TEAA/acetonitrile) then linear 15 min from 90/10 to 60/40 and wash-out 10 min at 50/50, flow rate: 1.5 mL/min. [(b)]MALDI-TOF Spektrometer (GSG, Karlsruhe, Germany) [(c)] NMR Bruker AMX (300 MHz) apparatus; TMP as internal standard, spectra recorded in water at 298K. * Analytical data (HPLC, MS, ^{31}P NMR) belong only to the conjugated oligonucleotides.

C : Cytidine	T : Thymidine	A : Adenosine	G : Guanosine
C : 2'Methoxycytidine	U : 2'Methoxyuridine	A : 2'Methoxyadenosine	G : 2'Methoxyguanosine
C : 2'Fluorocytidine	U : 2'Fluorouridine		

Scheme 2. Preparation of 2-Bromo-*N*-[3-(2-fluoropyridin-3-yloxy)propyl]acetamide (1)



Scheme 3. Preparation of [3-(3-*tert*-Butoxycarbonylaminopropoxy)pyridin-2-yl]trimethylammonium Trifluoromethanesulfonate (3d)



the corresponding 2-(dimethylamino)-3-hydroxypyridine *(27, 29)* and 2-nitro-3-hydroxypyridine (commercially available) under Mitsunobu conditions similar to those described above for the synthesis of **3a** (Scheme 1). The trimethylammonium derivative **3d** was cleanly obtained in 93% yield by methylation of the dimethylamine **3b** using methyl trifluoromethanesulfonate (1.3 equiv) in toluene at 0 °C (Scheme 3).

The synthetic procedure of conjugation of oligonucleotides described below uses preparative-scale commercially available 3′-end phosphorothioate oligonucleotides. It is based on the efficient coupling reaction of these oligonucleotides, containing a single phosphorothioate monoester moiety, with an electrophilic reagent such as the 2-halo-*N*-substituted acetamides *(37, 38)*. Table 1 summarizes the principal characteristics of the oligonucleotides (**OL1**, **OL2a**, **OL2b**, and **OL3**) used as starting material in the present study and the corresponding conjugated oligonucleotides (C-**OL1**, C-**OL2a**, C-**OL2b**, and C-**OL3**) that we have synthesized. Sequences, lengths, chemistry (DNA, 2′-OMe-RNA, and mixed 2′-fluoropyrimidines-RNA/DNA) as well as analytical data obtained for these conjugated oligonucleotides are indicated.

The conjugation of the oligonucleotides (**OL1**, **OL2a**, **OL2b**, and **OL3**) was carried out using 10 equiv of FPyBrA (**1**) in a mixture of methanol and 0.1 M phosphate buffer saline (PBS, pH 7.4) at 80 °C for 30 min (Scheme 4). The conjugation yields were determined by HPLC (based on starting oligonucleotides) and were high: 70% to 75% for the 18-mer C-**OL2a**, C-**OL2b**, and C-**OL3** and up to 95% for the 9-mer C-**OL1**. The nonlabeled conjugated oligonucleotides (C-**OL1**, C-**OL2a**, C-**OL2b**, and C-**OL3**) were separated from the nonreacted material by semipreparative RP-HPLC and desalted using a Sephadex NAP-10 column before characterization.

The regioselectivity of the coupling was verified by ^{31}P NMR (Table 1). The chemical shift of the 3′-end phosphorus atom had moved from +42.00 ppm (single phosphorothioate monoester) to +14.44 ppm (*S*-alkyl phosphorothioate) for C-**OL1**, and analogously from +39.00 ppm to +14.53 ppm for C-**OL2a**, from +39.65 ppm to +13.94 ppm for C-**OL2b**, and from +40.97 ppm to +13.94 ppm for C-**OL3**, after alkylation (Table 1). These results are fully in agreement with published ^{31}P NMR tables *(39−43)* and previously reported data for oligonucleotides having a phosphodiester or a chemically modified backbone *(6, 11, 12, 15, 16)*. Mass spectrometry gave the expected calculated mass for all conjugated oligonucleotides (See Table 1) and higher molecular weight species could not be detected. These results clearly confirmed in all cases the monoconjugation with the 2-bromoacetamide reagent.

Radiochemistry. [18F]FPyBrA ([18F]-**1**) was synthesized in three steps from the NO_2 precursor **3c** (Scheme 5) or from the N^+Me_3 precursor **3d**. The nitro function was selected for its high potential as leaving group in comparison with the corresponding halo substituents *(18, 19)* and for its ease of preparation from commercially available starting materials. The trimethylammonium function was also chosen as leaving group for this substitution, not only for its excellent potential as leaving group *(44)* but also for the expected superior precursor separation (using HPLC or SPE-cartridge) from the reaction product (the fluoro derivative [18F]-**3a**) due to the large differences in the physicochemical properties.

The first radiochemical step in the process is the introduction of fluorine-18 into the pyridine ring, by nucleophilic heteroaromatic substitution, using the no-

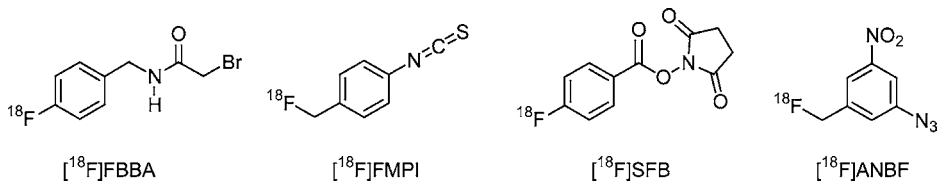
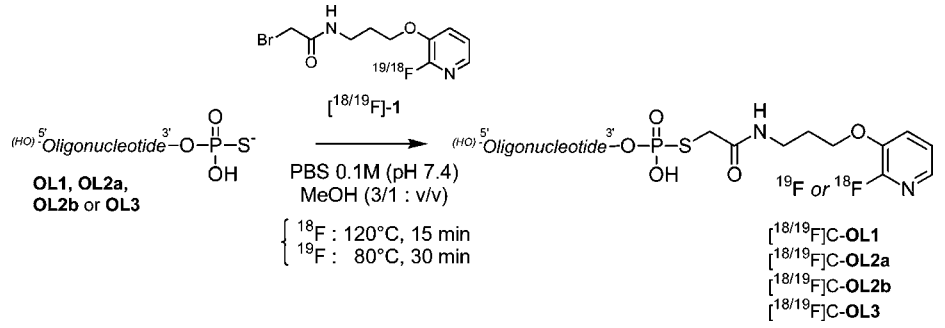
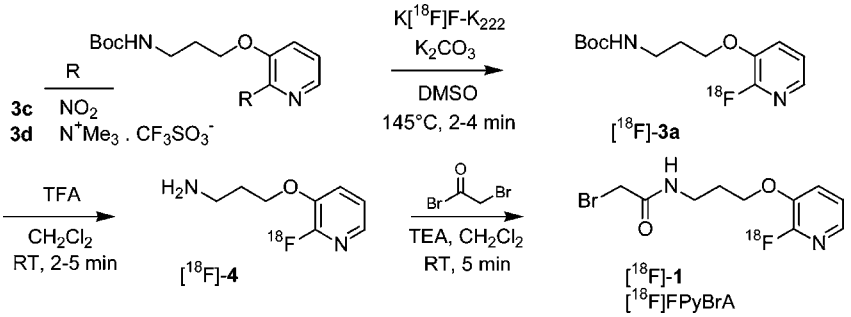


Figure 3. Chemical structures of *N*-(4-[^{18}F]fluorobenzyl)-2-bromoacetamide ([^{18}F]FBBA), 4-([^{18}F]fluoromethyl)phenyl isothiocyanate ([^{18}F]FMPI), *N*-succinimidyl 4-[^{18}F]fluorobenzoate ([^{18}F]SFB), and 3-azido-5-nitrobenzyl [^{18}F]fluoride ([^{18}F]ANBF).

Scheme 4. Synthesis of Nonlabeled and Fluorine-18-Labeled Conjugated Oligonucleotides C-OL1, C-OL2a, C-OL2b, and C-OL3



Scheme 5. Preparation of 2-Bromo-*N*-[3-(2-[^{18}F]fluoropyridin-3-yloxy)propyl]acetamide ([^{18}F]-1)



carrier-added naked [^{18}F]fluoride anion as its activated K[^{18}F]F-Kryptofix222 complex *(45)* (Kryptofix222 (K_{222}): 4,7,13,16,21,24-hexaoxa-1,10-diazabicyclo[8.8.8]hexacosane) and conventional heating in DMSO at 145 °C for 2−4 min. These nucleophilic heteroaromatic substitutions, like the aliphatic nucleophilic radiofluorinations, only require a good leaving group (a nitro in this case), and there is no need for an additional strong electron-withdrawing substituent for activation of the aromatic ring such as in the homoaromatic nucleophilic radiofluorinations. By use of the NO_2 precursor **3c**, the fluoro derivative [^{18}F]-**3a** was obtained in 45−70% radiochemical yield and purified on a C-18 cartridge. The second radiochemical step is the rapid removal of the *N*-Boc protective group (2−5 min), performed in a mixture of TFA and dichloromethane (1/50, v:v) at room temperature, quantitatively yielding the free amine [^{18}F]-**4**. The third and final step is the condensation with 2-bromoacetyl bromide, performed at room temperature for 5 min in dichloromethane containing triethylamine, giving the desired acetamide [^{18}F]-**1** in 45−65% radiochemical yield. [^{18}F]FPyBrA ([^{18}F]-**1**) was also synthesized using a similar three-step approach, but from the N^+Me_3-precursor **3d**. The nucleophilic heteroaromatic substitution with fluorine-18 was performed using again K[^{18}F]F-K_{222} and conventional heating in DMSO at 145 °C for only 2 min and gave the fluoro derivative [^{18}F]-**3a** in 70−85% radiochemical yield. Typically, 3.3−3.7 GBq (90−100 mCi) of radiochemically pure 2-bromo-*N*-[3-(2-[^{18}F]-fluoropyridin-3-yloxy)propyl]acetamide ([^{18}F]-**1**) could be obtained after semipreparative HPLC in 80−85 min starting from a 18.5 GBq (500 mCi) of a cyclotron production batch of [^{18}F]fluoride (overall radiochemical yields, based on starting [^{18}F]fluoride: 30−34% decay-corrected and 18−20% non-decay-corrected).

According to the available literature, only four fluorine-18-labeling reagents have been successfully prepared and used for prosthetic conjugation with a single-stranded oligonucleotide *(6, 7, 9, 11, 12, 14−16)* (Figure 3).

First, *N*-(4-[^{18}F]fluorobenzyl)-2-bromoacetamide ([^{18}F]-FBBA) was designed as a general and radiochemically feasible reagent, the benzyl function carrying the radioactive halogen, fluorine-18, and the 2-bromoacetamide moiety, offering the opportunity of an efficient and regioselective conjugation with an oligonucleotide provided with a phosphorothioate monoester group at its 3′- or 5′-end *(6, 11, 12, 15, 16)*. Besides natural phosphodiester DNA oligodeoxyribonucleotides, the strategy has been reliably and routinely applied to all the popular chemical modifications of oligonucleotides, such as full-length phosphorothioate diester internucleosidic-bond deoxyribonucleotides, hybrid methylphosphonate/phosphodiester internucleosidic-bond deoxyribonucleotides, and 2′-*O*-methyl-modified oligoribonucleotides *(6, 8, 10−13, 15)*. It has also been successfully applied to the labeling of Spiegelmers *(16)* (L-RNA or L-DNA *(46, 47)*) and peptide nucleic acids (PNAs) *(48, 49)*, another unique class of synthetic macromolecules (the deoxyribose phosphate backbone of DNA is replaced by a pseudo-peptide *N*-(2-aminoethyl)glycyl backbone, while retaining the nucleobases of DNA *(50, 51)*), originally designed as ligands for the recognition of double-stranded DNA. 4-([^{18}F]Fluoromethyl)phenyl isothiocyanate ([^{18}F]FMPI) is another fluorine-18-labeled reagent, which was con-

jugated with a single-stranded 18-mer oligonucleotide provided with a hexylamine linker at the 5′-end *(7)*. However, major loss of [18F]fluoride from the labeled macromolecule was observed, presumably by solvolysis *(7)*. *N*-Succinimidyl 4-[18F]fluorobenzoate ([18F]SFB), an already well-known fluorine-18-labeled reagent used in the conjugation of proteins and peptides using an amino function (α− or ϵ-NH_2-Lys) *(52*−*54)*, and 3-azido-5-nitrobenzyl [18F]fluoride ([18F]ANBF), a photosensitive fluorine-18-labeled reagent, have also been conjugated with single-stranded 18-mer oligonucleotides provided with a hexylamine linker at the 5′-end *(9, 14)*.

Even though its radiosynthesis equally uses a three-step radiochemical pathway, the yields obtained for the preparation of [18F]FPyBrA ([18F]-**1**) are higher than those described for the previously reported *N*-(4-[18F]fluorobenzyl)-2-bromoacetamide ([18F]FBBA). [18F]FBBA was obtained in only 16−25% decay-corrected overall radiochemical yield in 90 min total synthesis time (typical preparations, 2.2−2.9 GBq (60−80 mCi) of HPLC-purified [18F]FBBA starting from 20.3 to 24.0 GBq (550−650 mCi) of [18F]fluoride) *(6, 15)*. The yields obtained for the preparation of [18F]FPyBrA ([18F]-**1**) are also higher than those described for 4-([18F]fluoromethyl)phenyl isothiocyanate ([18F]FMPI) and *N*-succinimidyl 4-[18F]fluorobenzoate ([18F]SFB). 4-([18F]Fluoromethyl)phenyl isothiocyanate ([18F]FMPI) was synthesized in one radiochemical step, but obtained in only 13−15% decay-corrected overall radiochemical yield in 40 min total synthesis time *(7)*. *N*-Succinimidyl 4-[18F]fluorobenzoate ([18F]SFB) was synthesized in four radiochemical steps and obtained in 9−32% decay-corrected overall radiochemical yield in 100 min total synthesis time *(9)*. Only 3-azido-5-nitrobenzyl [18F]fluoride ([18F]ANBF), also synthesized in only one radiochemical step, was obtained in a higher overall radiochemical yield (30−50% decay-corrected) and in a shorter total synthesis time (50 min) *(14)*.

Conjugation of the 3′-phosphorothioate-oligonucleotides (**OL1**, **OL2a**, **OL2b**, and **OL3**) with the HPLC-purified [18F]FPyBrA ([18F]-**1**) (Scheme 4) was carried out in a mixture of methanol and 0.1 M phosphate buffer saline (PBS, pH 7.4) for 15 min at 120 °C. The labeled conjugated oligonucleotides [18F]C-**OL1**, [18F]C-**OL2a**, [18F]C-**OL2b**, and [18F]C-**OL3** were obtained in 50% to 75% yield (determined by HPLC and based on starting [18F]FPyBrA ([18F]-**1**)), separated from starting oligonucleotides and nonreacted [18F]-**1** by semipreparative RP-HPLC and desalted using a Sephadex NAP-10 column as mentioned above. Typically, 0.37−0.55 GBq (10−15 mCi) of pure conjugated [18F]oligonucleotides (specific activity: 37−74 GBq/μmol) could be obtained in 60−75 min starting from 1.85 GBq (50 mCi) of [18F]FPyBrA ([18F]-**1**) (20−30% non-decay-corrected isolated yield). The whole synthetic procedure has been fully automated on our Zymate robot system and lasted 140−160 min. As demonstrated by HPLC analysis, radiosynthesized, labeled, conjugated oligonucleotides ([18F]C-**OL1**, [18F]C-**OL2a**, [18F]C-**OL2b**, and [18F]C-**OL3**) coeluted with the authentic synthesized reference compounds. The fluorine-18-labeled oligonucleotides were found to be >95% chemically and radiochemically pure. The preparations were shown to be free of nonradioactive starting material and radiochemically stable for at least 120 min.

The reaction conditions and yields obtained for the conjugation of [18F]FPyBrA ([18F]-**1**) with oligonucleotides bearing a single phosphorothioate monoester at its 3′-end are comparable to those reported with *N*-(4-[18F]-fluorobenzyl)-2-bromoacetamide ([18F]FBBA) *(6, 11, 12)*. In the case of [18F]FBBA, HPLC-purified, desalted, [18F]-labeled, conjugated oligonucleotides were obtained in 90 min (reaction conditions: 120 °C, 10 min in a 1/1 mixture of methanol and 0.1 M phosphate buffer saline at pH 8) in 50% to 80% yield (determined by HPLC and based on starting [18F]FBBA). The yields obtained with [18F]-FPyBrA ([18F]-**1**) are also much higher, with shorter synthesis time, than those obtained for the conjugation of the other fluorine-18-labeled reagents mentioned above, with oligonucleotide provided with an hexylamine linker at the 5′-end. Using 3-azido-5-nitrobenzyl [18F]-fluoride ([18F]ANBF), 7−20% yield could be obtained for the photochemical-conjugation step (at 0 °C, using a 275 W Mercury lamp for 10 min, in a 10 mM potassium phosphate buffer at pH 7.4, total synthesis time 80−90 min) *(14)*. Using *N*-succinimidyl 4-[18F]fluorobenzoate ([18F]SFB), 7−23% yield could be obtained for the conjugation step (at 40 °C for 30 min, in a 1/4 mixture of DMF and 0.05 M borate buffer at pH 8.5) *(9)*. By use of 4-([18F]fluoromethyl)phenyl isothiocyanate ([18F]FMPI), only up to 8% yield could be obtained for the conjugation step (35 °C for 80 min, in a 1/2 mixture of DMF and 0.1 M NaH_2PO_4/Na_2HPO_4 buffer, pH not indicated) *(7)*. In the latter two examples, the total synthesis time was not indicated but can easily be estimated superior to 80−100 min, when only considering the 30−80 min of reaction time as well as the HPLC purification and desalting process.

Finally, five other fluorine-18-labeled reagents (chemical structures not shown) have recently been synthesized and evaluated (in comparaison with resynthesized *N*-(4-[18F]fluorobenzyl)-2-bromoacetamide [18F]FBBA) as alkylating reagents for the labeling of oligonucleotides in a model reaction using the monomer adenosine 5′-*O*-monophosphorothioate *(55)*. From this comparative study, the author concluded that 2-bromoacetamide reagents, (*N*-(4-[18F]fluorobenzyl)-2-bromoacetamide [18F]FBBA in the cited study) were the more attractive reagents for the labeling of these extremely expensive oligonucleotides, even though their preparation required a longer multistep radiosynthesis *(55)*. In this respect, [18F]FPyBrA ([18F]-**1**), both presenting the 2-bromoacetamide function for optimized conjugations to oligonucleotides and using an efficient radiosynthesis pathway for its preparation, is clearly a new valuable fluorine-18-labeled reagent.

CONCLUSION

For several years now, intense efforts have been devoted to the design and development of oligonucleotide-based radiopharmaceuticals for PET. Based on antisense strategies (specific binding of an oligonucleotide to a complementary DNA or RNA sequence via Watson−Crick base pairing), single-stranded oligonucleotides labeled with a positron-emitter could be in principle used to visualize specific gene expression, by imaging their hybridizations to target mRNAs *(5)*. In this respect, we previously demonstrated that the addition of an *N*-substituted-acetamide-based prosthetic group at the 3′-end of single-stranded oligonucleotide does not hamper the physicochemical properties of the parent oligonucleotide in vitro, including its hybridization to the complementary target *(8, 56)*. Aptamers *(57)* are another class of high-affinity oligonucleotide ligands that do not hybridize to RNA by Watson−Crick base pairing but instead are evolved and selected in vitro for their properties to recognize and bind structurally to a variety of selected molecular targets. Aptamers are an exciting approach to the creation of new contrast agents for PET imaging, and this has been claimed for Spiegelmers, a man-made, highly stable, both in vitro and in vivo, class

of single-stranded mirror-image oligonucleotides (L-RNA or L-DNA) *(46, 47)* with potential for therapeutic and diagnostic applications *(58−62)*.

The objective of the present work was to develop a [^{18}F]-fluoropyridine-based new haloacetamide reagent for the prosthetic labeling with fluorine-18 of phosphorothioate-bearing single-stranded oligonucleotides. [^{18}F]FPyBrA (2-bromo-*N*-[3-(2-[^{18}F]fluoro-pyridin-3-yloxy)propyl]acetamide) was designed as a radiochemically feasible reagent, its pyridinyl moiety both carrying the radioactive halogen (fluorine-18) and allowing its efficient incorporation via a nucleophilic heteroaromatic substitution, and its 2-bromoacetamide function, ensuring the efficient alkylation of a phosphorothioate monoester group born at the 3′- or 5′-end of single-stranded oligonucleotides. [^{18}F]FPyBrA ([^{18}F]-**1**, HPLC-purified) was efficiently prepared in 18−20% non-decay-corrected yield (based on starting [^{18}F]-fluoride) in 80−85 min using a three-step radiochemical pathway. The developed procedure involves a high-yield nucleophilic heteroaromatic ortho-radiofluorination as the fluorine-18 incorporation step and uses a trimethylammonium trifluoromethane sulfonate as the most efficient precursor leaving group for labeling (when compared to the parallely tested nitro precursor). [^{18}F]-FPyBrA ([^{18}F]-**1**) was regioselectively conjugated with 9-mer and 18-mer single-stranded oligonucleotides, provided with a phosphorothioate monoester group at their 3′-end. Both natural phosphodiester DNA oligodeoxyribonucleotides and in vivo-stable 2′-methoxy- and 2′-fluoro-modified oligoribonucleotides were used in the present work. Conjugation was achieved in high yields (50−75%) and uses optimized, short-time reaction conditions, both compatible with the chemical stability of the oligonucleotides and the relatively short half-life of the radioisotope concerned (the whole radiosynthetic procedure, including the preparation of the fluorine-18-labeled reagent, the conjugation with the oligonucleotide, and the HPLC-purification lasted 140−160 min).

Given the high radiosynthetic yields obtained using nucleophilic heteroaromatic substitutions in the pyridine series, [^{18}F]FPyBrA ([^{18}F]-**1**) represents a valuable alternative to the already reported *N*-(4-[^{18}F]fluorobenzyl)-2-bromoacetamide ([^{18}F]FBBA) *(6)* for the design and development of oligonucleotide-based radiopharmaceuticals for PET.

EXPERIMENTAL SECTION

General. Chemicals. Chemicals were purchased from standard commercial sources (Aldrich, Fluka, or Sigma, France) and were used without further purification, unless stated otherwise. Oxygen-18-enriched water ([^{18}O]H_2O, >95%) was purchased from CortecNet (Paris, France). Lyophilized, HPLC-RP-purified 3′-phosphorothioate-oligonucleotides were purchased from Genset (Paris, France) or Eurogentec (Seraing, Belgium). The oligonucleotides purchased differ either in length, in sequence, or in chemistry of the sugar−phosphate backbone: (i) **OL1**, a 9mer natural phosphodiester oligodeoxyribonucleotide (oligo-9mer-PO-3′ps); (ii) **OL2a**, an 18mer natural phosphodiester oligodeoxyribonucleotide (oligo-18mer-PO-3′ps); (iii) **OL2b**, an 18mer 2′methoxy-modified oligoribonucleotide (oligo-18mer-2′OMe-3′ps) with an identical sequence as **OL2a**; (iv) **OL3**, an 18mer with 2′ fluoro-modified pyrimidines (oligo-18mer-2′F-3′ps). Sequences of all oligonucleotides (**OL1**, **OL2a**, **OL2b**, and **OL3**) are summarized in Table 1.

Analytical Methods. Thin layer chromatography (TLC) was run on precoated plates of silica gel 60F_{254} (Merck). The compounds were localized (1) when possible at 254 nm using a UV lamp and/or (2) by dipping the TLC plates in a 1% ethanolic ninhydrin solution and heating on a hot plate. Radioactive spots were detected using a Berthold TraceMaster 20 automatic TLC linear analyzer. Flash chromatography was conducted on silica gel 63−200 μm (Merck) at 0.3 bar (compressed air).

HPLCs (Equipment: Waters or Shimadzu systems). [HPLC A]: Equipment: a Waters Prep LC 3000 system, a Shimadzu SPD10-AVP UV-multiwavelength detector; column: preparative SiO_2 Lichrosorb, Merck (250 × 27.0 mm; porosity: 7 μm); solvents and conditions: isocratic elution with heptane/EtOAc; temperature: RT; absorbance detection at λ = 254 nm. [HPLC B]: Equipment: a Waters 600 Controller Gradient system, a Waters 490E UV-multiwavelength detector and a Geiger-Müller detector; column: semipreparative C18 μBondapak, Waters (300 × 7.8 mm; porosity: 10 μm); solvents and conditions: triethylammonium acetate, 50 mM, pH 7 (TEAA) and acetonitrile; gradient elution: linear 5 min from 95/5 to 90/10 (TEAA/acetonitrile, v:v) then linear 10 min from 90/10 to 70/30 (v:v) and wash-out 10 min at 50/50 (v:v); flow rate: 6 mL/min; temperature: RT; absorbance detection at λ = 254 nm. [HPLC C]: Equipment: a Waters 510 pump, a Shimadzu SPD10-AVP UV-multiwavelength detector, and a Geiger-Müller detector; column: semipreparative SiO_2 Zorbax Rx-SIL, Hewlett-Packard (250 × 9.4 mm; porosity: 5 μm); solvents and conditions: isocratic elution with CH_2Cl_2/EtOAc: 50/50 (v:v); flow rate: 5 mL/min; temperature: RT; absorbance detection at λ = 254 nm. [HPLC D]: Equipment: a Waters 600 Controller Gradient system, a Hewlett-Packard 1100 series UV-multiwavelength detector and a Packard Flow One Scintillation Analyzer equipped with a positron-dedicated cell for radioactivity monitoring; column: analytical C18 μBondapak, Waters (300 × 3.9 mm; porosity: 10 μm); solvents and conditions: triethylammonium acetate, 50 mM, pH 7 (TEAA), and acetonitrile; gradient elution: linear 5 min from 95/5 to 90/10 (TEAA/acetonitrile, v:v) then linear 15 min from 90/10 to 60/40 (v:v) and wash-out 10 min at 50/50 (v:v), flow rate: 1.5 mL/min; temperature: RT; absorbance detection at λ = 254 nm.

NMR spectra were recorded on a Bruker AMX (300 MHz) apparatus using the hydrogenated residue of the deuterated solvents (DMSO-d_6, δ = 2.50 ppm; CD_2Cl_2, δ = 5.32 ppm; CD_3OD, δ = 3.30 and 4.78 ppm) and/or TMS as internal standards for ^{1}H NMR as well as the deuterated solvents (DMSO-d_6, δ = 39.5 ppm; CD_2Cl_2, δ = 53.8 ppm; CD_3OD, δ = 49.0 ppm) and/or TMS as internal standards for ^{13}C NMR. ^{31}P NMR were recorded in nondeuterated water using TMP as internal standard. The chemical shifts are reported in ppm, downfield from TMS (^{1}H and ^{13}C) or TMP (^{31}P) (s, d, t, q, q^5, dd, td, m, b for singlet, doublet, triplet, quadruplet, quintuplet, doublet of doublet, triplet of doublet, multiplet (or multi sharp-peak system), and broad, respectively). The mass spectra were measured on a Nermag R10−10 apparatus or a MALDI-TOF spectrometer (GSG, Karlsruhe, Germany).

Miscellaneous. Radiosyntheses using fluorine-18, including the HPLC purifications, were performed in a 7.5-cm-lead shielded cell using a computer-assisted Zymate robot system (Zymark Corporation, Paris, France). Specific radioactivity was determined as follows: the area of the absorbance peak corresponding to the radiolabeled product was measured on the HPLC chromatogram and compared to a standard curve relating mass to absorbance.

Radioisotope Production. No-carrier-added aqueous [18F]fluoride ion was produced on a CGR-MeV 520 cyclotron by irradiation of a 2 mL water target using a 17 MeV proton beam on 95% enriched [18O]water by the $[^{18}O(p,n)^{18}F]$ nuclear reaction and was transferred to the appropriate hot cell. Typical production: 20.3−24.0 GBq (550−650 mCi) of $[^{18}F]F^-$ at the end of bombardment for a 20 μA, 30 min (36 000 μC) irradiation.

Chemistry. [3-(2-Fluoropyridin-3-yloxy)propyl]-carbamic Acid *tert*-Butyl Ester (3a). To a solution of (3-hydroxypropyl)carbamic acid *tert*-butyl ester (**2**, 2.00 g, 11.4 mmol) in THF (122 mL) were added 2.39 g of triphenylphosphine (MW: 262.29, 9.1 mmol, 0.8 equiv), 1.03 g of 2-fluoro-3-hydroxypyridine (MW: 113.09, 9.1 mmol, 0.8 equiv), and dropwise 3.1 mL of diisopropyl azodicarboxylate (DIAD; MW: 202.21, d: 1.027, 15.7 mmol, 1.38 equiv). After addition, the reaction mixture was stirred at room temperature for 24 h. The reaction mixture was concentrated to dryness, and the residue was purified on silica gel. Elution with heptane/EtOAc (60/40 v/v) gave 1.51 g of **3a** as a yellow oil (49%). For analytical purposes, an aliquot was further purified by HPLC. R_f (EtOAc/heptane: 50/50 v/v): 0.44. R_t (HPLC A, heptane/EtOAc: 60/40 (v/v), flow rate: 25 mL/min): 10.2 min. ^{1}H NMR (CD_2Cl_2, 298 K): δ: 7.68 (dt, J = 3.0, 1.5 Hz, 1H); 7.28 (td, J = 7.8, 1.5 Hz, 1H); 7.10 (dd, J = 8.1, 5.1 Hz, 1H); 4.07 (t, J = 6.3 Hz, 2H); 3.27 (q, J = 6.3 Hz, 1H); 1.98 (q^5, J = 6.4 Hz, 2H); 1.39 (s, 9H). ^{13}C NMR (CD_2Cl_2, 298 K): δ: 156.3 [C]; 154.1 [d, J^1_{F-C} = 237 Hz, C]; 142.5 [d, J^2_{F-C} = 27 Hz, C]; 137.5 [d, J^3_{F-C} = 15 Hz, CH]; 123.0 [CH]; 122.2 [CH]; 79.2 [C]; 67.3 [CH_2]; 38.0 [CH_2]; 29.8 [CH_2]; 28.5 [3×CH_3]. MS (DCI/NH_4^+) $C_{13}H_{19}F_1N_2O_3$: 271 [M + H^+].

[3-(2-Dimethylaminopyridin-3-yloxy)propyl]carbamic Acid *tert*-Butyl Ester (3b). To a solution of (3-hydroxypropyl)carbamic acid *tert*-butyl ester (**2**, 0.31 g, 1.8 mmol) in THF (20 mL) were added 0.47 g of triphenylphosphine (MW: 262.29, 1.8 mmol, 1.0 equiv), 0.25 g of 2-(dimethylamino)-3-hydroxypyridine (MW: 138.00, 1.81 mmol, 1.0 equiv), and dropwise 0.35 mL of diisopropyl azodicarboxylate (DIAD; MW: 202.21, d: 1.027, 1.8 mmol, 1.0 equiv). After being stirred at room temperature for 24 h, the reaction mixture was concentrated to dryness and the residue was purified by column chromatography on silica gel. Elution with heptane/EtOAc (70/30 v/v) gave 0.23 g of **3b** as a yellow oil (43%). For analytical purposes, an aliquot was further purified by HPLC. R_f (EtOAc/heptane: 50/50 v/v): 0.35. R_t (HPLC A, heptane/EtOAc: 60/40 (v/v), flow rate: 35 mL/min): 8.6 min. ^{1}H NMR (CD_2Cl_2, 298 K): δ: 7.77 (dd, J = 4.8 Hz, 1H); 7.00 (dd, J = 7.8 Hz, J < 1.5 Hz, 1H); 6.72 (dd, J = 7.8, 4.8 Hz, 1H); 4.02 (t, J = 6.0 Hz, 2H); 3.30 (q, J = 6.0 Hz, 2H); 2.93 (s, 6H); 2.00 (q^5, J = 6.0 Hz, 2H); 1.42 (s, 9H). ^{13}C NMR (CD_2Cl_2, 298 K): δ: 156.6 [C]; 153.7 [C]; 146.2 [C]; 139.0 [CH]; 118.8 [CH]; 115.9 [CH]; 79.1 [C]; 67.4 [CH_2]; 41.1 [2×CH_3]; 38.8 [CH_2]; 32.3 [CH_2]; 28.5 [3×CH_3]. MS (DCI/NH_4^+) $C_{15}H_{25}N_3O_3$: 296 [M + H^+].

[3-(2-Nitropyridin-3-yloxy)propyl]carbamic Acid *tert*-Butyl Ester (3c). To a solution of (3-hydroxypropyl)-carbamic acid *tert*-butyl ester (**2**, 2.00 g, 11.4 mmol) in THF (122 mL) were added 2.27 g of triphenylphosphine (MW: 262.29, 8.65 mmol, 0.8 equiv), 1.23 g of 2-nitro-3-hydroxypyridine (MW: 139.01, 8.85 mmol, 0.8 equiv), and dropwise 3.1 mL of diisopropyl azodicarboxylate (DIAD; MW: 202.21, d: 1.027, 15.7 mmol, 1.38 equiv). After addition, the reaction mixture was stirred at room temperature for 24 h. The reaction mixture was concentrated to dryness and the residue was purified on silica gel. Elution with heptane/EtOAc (60/40 v/v) gave 1.37 g of **3c** as a yellow oil (40%). For analytical purposes, an aliquot was further purified by HPLC. R_f (EtOAc/heptane: 50/50 v/v): 0.19. R_t (HPLC A, heptane/EtOAc: 50/50 (v/v), flow rate: 25 mL/min): 11.5 min. ^{1}H NMR (CD_2Cl_2, 298 K): δ: 8.06 (t, J = 3.3 Hz, 1H); 7.55 (d, J = 3.0 Hz, 2H); 4.20 (t, J = 5.7 Hz, 2H); 3.28 (q, J = 6.3 Hz, 2H); 2.03 (q^5, J = 6.3 Hz, 2H); 1.41 (s, 9H). ^{13}C NMR (CD_2Cl_2, 298 K): δ: 156.3 [C]; 149.2 [C]; 147.3 [C]; 139.5 [CH]; 129.2 [CH]; 124.0 [CH]; 79.2 [C]; 68.3 [CH_2]; 37.9 [CH_2]; 29.5 [CH_2]; 28.4 [3×CH_3]. MS (DCI/NH_4^+) $C_{13}H_{19}N_3O_5$: 298 [M + H^+].

[3-(3-*tert*-Butoxycarbonylaminopropoxy)pyridin-2-yl]trimethylammonium Trifluoromethanesulfonate (3d). To a 0−3 °C solution of [3-(2-(dimethylamino)-pyridin-3-yloxy)propyl]carbamic acid *tert*-butyl ester (**3b**, 0.4 g, 1.35 mmol) in toluene was added 0.2 mL of methyl trifluoromethanesulfonate (MW: 164.10, d: 1.45, 1.77 mmol, 1.3 equiv). After 3 min, a precipitate was obtained and the reaction mixture was stirred at room temperature for 1 h. The precipitate was filtered and washed with Et_2O to give 0.58 g of **3d** as a white powder (93%). ^{1}H NMR (CD_2Cl_2, 298 K): δ: 8.10 (bd, J = 3.3 Hz, 1H); 7.66 (d, J = 8.1 Hz, 1H); 7.60 (dd, J = 6.1, 4.2 Hz, 1H); 4.31 (t, J = 6.3 Hz, 2H); 3.71 (s, 9H); 3.31 (q, J = 6.3 Hz, 2H); 2.12 (q^5, J = 6.3 Hz, 2H); 1.38 (s, 9H).^{13}C NMR (CD_2Cl_2, 298 K): δ: 156.6 [C]; 147.7 [C]; 142.6 [C]; 139.0 [CH]; 129.0 [CH]; 124.6 [CH]; 121.2 [q, J = 319 Hz, CF_3]; 79.3 [C]; 68.1 [CH_2]; 37.5 [CH_2]; 30.0 [CH_2]; 28.4 [3×CH_3].

[3-(2-Fluoropyridin-3-yloxy)]propylamine (4). To a 0−3 °C solution of [3-(2-fluoropyridin-3-yloxy)propyl]-carbamic acid *tert*-butyl ester (**3a**, 0.04 g, 0.15 mmol) in CH_2Cl_2 (1 mL) was added TFA (100 μL). After being stirred at room temperature for 1 h, the reaction mixture was concentrated to dryness to give 0.05 g of **3** as its TFA salt (quantitative). ^{1}H NMR (CD_3OD, 298 K): δ: 7.51 (bs, $w_{1/2}$ = 5.0 Hz, 1H); 7.36 (bt, $w_{1/2}$ = 25.0 Hz, 1H); 7.04 (bd, $w_{1/2}$ = 15.0 Hz, 1H); 4.03 (bt, $w_{1/2}$ = 15.0 Hz, 2H); 2.99 (bt, $w_{1/2}$ = 15.0 Hz, 2H); 2.01 (bq, $w_{1/2}$ = 15.0 Hz, 2H). ^{13}C NMR (CD_3OD, 298 K): δ: 155.3 [d, J^1_{F-C} = 237 Hz, C]; 144.3 [d, J^2_{F-C} = 24 Hz, C]; 138.5 [d, J^3_{F-C} = 13 Hz, CH]; 125.1 [CH]; 123.8 [CH]; 67.9 [CH_2]; 38.6 [CH_2]; 28.4 [CH_2]. MS (DCI/NH_4^+) $C_8H_{11}F_1N_2O_1$: 171 [M + H^+].

2-Bromo-*N*-[3-(2-fluoropyridin-3-yloxy)propyl]-acetamide (1). To a 0−3 °C solution of 3-(2-fluoropyridin-3-yloxy)propylamine (**4**, 2.90 g, 17.05 mmol) in CH_2Cl_2 (20 mL) were added 5 mL of *N*-methylmorpholine (54.5 mmol, 3.2 equiv) and 5 mL of bromoacetylbromide (MW: 201.86, d: 2.317, 57.4 mmol, 3.4 equiv). After stirring at room temperature for 1 h, H_2O was added to the reaction mixture. The solution was then transferred into a separatory funnel and extracted with CH_2Cl_2. The organic layer was dried with Na_2SO_4 and the reaction mixture was concentrated to dryness to give a residue which was purified on silica gel. Elution with CH_2Cl_2/EtOAc (80/20 to 60/40 v/v) gave 1.00 g of **1** as a yellow powder (24%). R_f (heptane/EtOAc: 70/30 v/v): 0.29. ^{1}H NMR (CD_2Cl_2, 298 K): δ: 7.73 (dd, J = 3.3, 1.8 Hz, 1H); 7.32 (td, J = 7.8 Hz, J < 1.5 Hz, 1H); 7.14 (dd, J = 7.8, 4.8 Hz, 1H); 4.12 (t, J = 6.0 Hz, 2H); 3.85 (s, 2H); 3.49 (q, J = 6.3 Hz, 2H); 2.05 (q^5, J = 6.3 Hz, 2H). ^{13}C NMR (CD_2Cl_2, 298 K): δ: 166.2 [C]; 153.8 [d, J^1_{F-C} = 235 Hz, C]; 142.3 [d, J^2_{F-C} = 25 Hz, C]; 137.5 [d, J^3_{F-C} = 13 Hz, CH]; 123.0 [CH]; 122.3 [CH]; 67.7 [CH_2]; 37.8 [CH_2]; 29.5 [CH_2]; 28.9 [CH_2]. MS (DCI/NH_4^+) $C_{10}H_{12}Br_1F_1N_2O_2$: 292 [M + H^+]; 290 [M + H^+].

Conjugation of Oligonucleotides with 2-Bromo-*N*-[3-(2-fluoropyridin-3-yloxy)propyl]acetamide (1). General Procedure for Preparation of Nonlabeled

Conjugated Oligonucleotides (C-OL1, C-OL2a, C-OL2b, and C-OL3). 50 OD of oligonucleotide (**OL1**, **OL2a**, **OL2b**, or **OL3**) (1 OD is the UV absorbance of 38 μg of an oligonucleotide regardless of the sequence of bases) dissolved in 300 μL of PBS (phosphate-buffered saline) (100 mM, pH 7.4) was mixed with an excess (10 equiv) of 2-bromo-*N*-[3-(2-fluoropyridin-3-yloxy)propyl]-acetamide (**1**), dissolved in 100 μL of MeOH, and reacted for 30 min at 80 °C. Yields of conjugation were determined by HPLC (ratio between conjugated and nonconjugated oligonucleotides). The solvents were evaporated and nonlabeled conjugated oligonucleotides (C-**OL1**, C-**OL2a**, C-**OL2b**, and C-**OL3**) were purified by semipreparative RP-HPLC (HPLC B). Conjugated oligonucleotides were desalted using a NAP-10 G25 Sephadex column (Amersham Pharmacia Biotech) before characterization. Yields of isolated conjugated oligonucleotides were determined by UV measurements and are based on starting oligonucleotides. Chemical purity of the conjugated oligonucleotides was determined using analytical RP-HPLC (HPLC D).

***N*-[3-(2-Fluoropyridin-3-yloxy)propyl]-2-(oligo-9mer-PO-3′ps)acetamide (C-OL1)**. Conjugation yield: 95% (determined by HPLC). Isolated yield: 90% (determined by UV). R_t(C-**OL1**): 10.0−10.5 min and R_t(**OL1**): 8.5−9.0 min (HPLC B). R_t(C-**OL1**): 14.0 min (>99%) (HPLC D). MS (electrospray): 2990.0 (theor), 2989.0 (exp). ^{31}P NMR (D_2O, 298 K): δ: +14.44 (OP(O)(OH)(S-acetamide)).

***N*-[3-(2-Fluoropyridin-3-yloxy)propyl]-2-(oligo-18mer-PO-3′ps)acetamide (C-OL2a)**. Conjugation yield: 70% (determined by HPLC). Isolated yield: 66% (determined by UV). R_t(C-**OL2a**): 10.0−10.5 min and R_t-(**OL2a**): 9.0−9.5 min (HPLC B). R_t(C-**OL2a**): 14.1 min (>95%) (HPLC D). MS (electrospray): 5846.9 (theor), 5847.8 (exp). ^{31}P NMR (D_2O, 298 K): δ: +14.53 (OP(O)-(OH)(S-acetamide)).

***N*-[3-(2-Fluoropyridin-3-yloxy)propyl]-2-(oligo-18mer-2′OMe-3′ps)acetamide (C-OL2b)**. Conjugation yield: 75% (determined by HPLC). Isolated yield: 62% (determined by UV). R_t(C-**OL2b**): 11.5−12.0 min and R_t-(**OL2b**): 10.5−11.0 min (HPLC B). R_t(C-**OL2b**): 15.4 min (>99%) (HPLC D). MS (electrospray): 6345.3 (theor), 6346.7 (exp). ^{31}P NMR (D_2O, 298 K): δ: +13.94 (OP(O)-(OH)(S-acetamide)).

***N*-[3-(2-Fluoropyridin-3-yloxy)propyl]-2-(oligo-18mer-2′F-3′ps)acetamide (C-OL3)**. Conjugation yield: 70% (determined by HPLC). Isolated yield: 53% (determined by UV). R_t(C-**OL3**): 11.5−12.0 min and R_t(**OL3**): 10.0−10.5 min (HPLC B). R_t(C-**OL3**): 15.3 min (>95%) (HPLC D). MS (electrospray): 5991.0 (theor), 5989.7 (exp.). ^{31}P NMR (D_2O, 298 K): δ: +13.94 (OP(O)(OH)-(S-acetamide)).

Radiochemistry. Preparation of the K[^{18}F]F−K_{222} Complex. To recover and recycle the target [^{18}O]water, the 2 mL of aqueous [^{18}F]fluoride from the target holder were passed through an anion-exchange resin (Sep-Pak Light Waters Accell Plus QMA Cartridge in the chloride form, washed with 5 mL of 1 M aq $NaHCO_3$, and then rinsed with 50 mL of water) by He pressure (1.5−2.0 bar). Helium is blown through the column to maximally extract the [^{18}O]water. The [^{18}F]fluoride ion is then eluted from the resin using 1.0 mL of a 4.5 mg/mL aqueous K_2CO_3 solution into a Vacutainer tube containing 12.0 to 15.0 mg of Kryptofix222 (K_{222}: 4,7,13,16,21,24-hexaoxa-1,10-diazabicyclo[8.8.8]hexacosane). The resulting solution was then gently concentrated to dryness at 145−150 °C under a nitrogen stream for 10 min to give no-carrier-added K[^{18}F]F−K_{222} complex as a white semisolid residue.

Preparation of 2-Bromo-*N*-[3-(2-[^{18}F]fluoropyridin-3-yloxy)propyl]acetamide ([^{18}F]-1). Procedure Using [3-(2-nitropyridin-3-yloxy)propyl]carbamic Acid *tert*-Butyl Ester (3c) as Precursor for Labeling. Freshly distilled DMSO (600 μL) containing 5.0 mg of the precursor for labeling ([3-(2-nitropyridin-3-yloxy)-propyl]carbamic acid *tert*-butyl ester, **3c**) was directly added into the Vacutainer tube containing the dried K[^{18}F]F−K_{222} complex. The tube (not sealed) was then thoroughly vortexed (15 s) and then placed in a heating block at 145 °C for 4 min without stirring the contents. The reaction vessel was then cooled using an ice−water bath, and the remaining radioactivity was measured. Initial radioactivity (90−95%) placed in the vessel was still present. The resulting dark-colored reaction mixture was then analyzed by radiochromatography. The reaction yield was calculated from the TLC radiochromatogram and defined as the radioactivity area of [3-(2-[^{18}F]fluoropyridin-3-yloxy)propyl]carbamic acid *tert*-butyl ester ([^{18}F]-**3a**) over total fluorine-18 radioactivity area ratio. (SiO_2 TLC, eluent: EtOAc, R_f: [^{18}F]-**3a**: 0.75 and R_f: [^{18}F]fluoride ion: 0.0). Radiosynthesized [^{18}F]-**3a** comigrated with an authentic sample of fluorine-19-synthesized **3a**. The reaction mixture was diluted with 1 mL of water and transferred on the top of a C18 cartridge (PrepSep R-C18, Fisher Scientific, beforehand activated with 2 mL of EtOH and then rinsed with 10 mL of water). The tube was rinsed twice with 1 mL of water which was also transferred and added to the diluted reaction mixture on top of the cartridge. After addition of another 2 mL of water, the whole was passed through the cartridge. The cartridge was washed with 1 mL of water and partially dried for 0.5 min by applying a nitrogen stream. The [3-(2-[^{18}F]fluoropyridin-3-yloxy)propyl]carbamic acid *tert*-butyl ester ([^{18}F]-**3a**) was eluted from the cartridge with 3 mL of dichloromethane into a 5 mL reaction vial containing 0.1 mL of TFA. Twice 1 mL of dichloromethane was used to wash the cartridge and to completely transfer [^{18}F]-**3a** (5% of the total radioactivity amount engaged in the fluorination process was left on the cartridge). The fluorine-18 incorporation yield was also confirmed after the C18 cartridge elution by the CH_2Cl_2-eluted radioactivity over total eluted radioactivity ($DMSO/H_2O + CH_2Cl_2$) counting ratio. The resulting CH_2Cl_2/TFA solution (50/1, v/v) was concentrated to dryness (at 65−75 °C under a gentle nitrogen stream for 4−6 min). The yield of deprotection was quantitative, and no Boc-protected [^{18}F]-**3a** could be detected by radiochromatography (SiO_2 TLC, eluent: EtOAc, R_f: [^{18}F]-**3a**: 0.75). The above residue, containing 3-(2-[^{18}F]fluoropyridin-3-yloxy)propylamine ([^{18}F]-**4**, SiO_2 TLC, eluent: EtOAc, R_f: [^{18}F]-**4**: 0.0) was redissolved in 2 mL of CH_2Cl_2 and concentrated again to dryness to minimize TFA presence (at 65−75 °C under a gentle nitrogen stream for another 2−3 min). The residue, containing [^{18}F]-**4**, was then redissolved in 600 μL of a solution of TEA in CH_2Cl_2 (40 μL/mL or 170 μmol of TEA). After addition of 400 μL of a solution of bromoacetyl bromide in CH_2Cl_2 (50 μL/mL or 230 μmol of $BrCOCH_2Br$), the reaction mixture was allowed to react for 5 min at room temperature with a smooth air-bubbling agitation. Finally, the clear solution was diluted with 200−500 μL of the HPLC solvent used for the purification, and the crude was injected onto a semipreparative HPLC. Isocratic elution (HPLC C) gave pure labeled 2-bromo-*N*-[3-(2-[^{18}F]fluoropyridin-3-yloxy)propyl]acetamide ([^{18}F]-**1**), R_t: 7.0−8.0 min.

Procedure Using [3-(3-*tert*-Butoxycarbonylaminopropoxy)pyridin-2-yl]trimethylammonium Trifluoromethanesulfonate (3d) as Precursor for Labeling. Freshly distilled DMSO (600 μL) containing 4.0 mg of the precursor for labeling ([3-(3-*tert*-butoxycarbonylaminopropoxy)-pyridin-2-yl]-trimethylammonium trifluoromethanesulfonate, **3d**) was directly added into the Vacutainer tube containing the dried K[18F]F−K_{222} complex. The tube (not sealed) was then thoroughly vortexed (15 s) and then placed in a heating block at 145 °C for 2 min without stirring the contents. The remainder of the preparation used the same procedure as described above.

Conjugation of Oligonucleotides with 2-Bromo-*N*-[3-(2-[18F]fluoropyridin-3-yloxy)propyl]acetamide ([18F]-1). General Procedure for Preparation of Labeled Conjugated Oligonucleotides ([18F]C-OL1, [18F]C-OL2a, [18F]C-OL2b, and [18F]C-OL3). 25 OD of oligonucleotides **OL1**, **OL2a**, **OL2b**, or **OL3** dissolved in 300 μL of PBS (100 mM, pH 7.4) were mixed with the HPLC-purified 2-bromo-*N*-[3-(2-[18F]fluoropyridin-3-yloxy)propyl]acetamide ([18F]-**1**), dissolved in 100 μL of MeOH, and reacted for 15 min at 120 °C in a sealed vial. The yields of conjugation of the oligonucleotides with [18F]-**1** reached 50−75% (calculated from the HPLC chromatogram). The solvents were evaporated, and the labeled conjugated oligonucleotides [18F]C-**OL1**, [18F]C-**OL2a**, [18F]C-**OL2b**, and [18F]C-**OL3** were separated from starting oligonucleotides and nonreacted [18F]-**1** by semipreparative HPLC (HPLC B). The HPLC fraction containing the labeled conjugated oligonucleotides ([18F]C-**OL1**, [18F]C-**OL2a**, [18F]C-**OL2b**, and [18F]C-**OL3**) was concentrated under reduced pressure and transferred in a volume of 1 mL onto a NAP10 G25 Sephadex column and eluted in 1.5 mL of water or buffer according to manufacturer's instructions. Typically, 0.37−0.55 GBq (10−15 mCi) of pure conjugated [18F]oligonucleotides could be obtained in 60−75 min starting from 1.85 GBq (50 mCi) of 2-bromo-*N*-[3-(2-[18F]fluoropyridin-3-yloxy)propyl]acetamide ([18F]-**1**) (20−30% non-decay-corrected yield). The whole synthetic procedure has been fully automated on our Zymate robot system and lasted 140−160 min. Quality control (radiochemical and chemical purity) was performed by HPLC (HPLC D).

***N*-[3-(2-[18F]Fluoropyridin-3-yloxy)propyl]-2-(oligo-9mer-PO-3′ps)acetamide ([18F]C-OL1).** R_t([18F]C-**OL1**): 10.0−10.5 min (HPLC B); R_t([18F]C-**OL1**): 14.0 min (>99%) (HPLC D).

***N*-[3-(2-[18F]Fluoropyridin-3-yloxy)propyl]-2-(oligo-18mer-PO-3′ps)acetamide ([18F]C-OL2a).** R_t([18F]C-**OL2a**): 10.0−10.5 min (HPLC B); R_t([18F]C-**OL2a**): 14.1 min (>99%) (HPLC D).

***N*-[3-(2-[18F]Fluoropyridin-3-yloxy)propyl]-2-(oligo-18mer-2′OMe-3′ps)acetamide ([18F]C-OL2b).** R_t([18F]C-**OL2b**): 11.5−12.0 min (HPLC B); R_t([18F]C-**OL2b**): 15.4 min (>99%) (HPLC D).

***N*-[3-(2-[18F]Fluoropyridin-3-yloxy)propyl]-2-(oligo-18mer-2′F-3′ps)acetamide ([18F]C-OL3).** R_t([18F]C-**OL3**): 11.5−12.0 min (HPLC B); R_t([18F]C-**OL3**): 15.3 min (>99%) (HPLC D).

ACKNOWLEDGMENT

The authors wish to thank the cyclotron operators Mr. Daniel Gouel, Mr. Christophe Peronne, and Mr. Christophe Lechêne for performing the irradiations, as well as Ms Badia Amekraz (Laboratoire de Spéciation des Radionucléides et des Molécules, CEA-Saclay, Gif-sur-Yvette, France) and Dr Stefan Vonhoff and Mr Kai Gottsche (Noxxon Pharma AG, Berlin, Germany) for recording the MS spectra. The authors also wish to thank Dr Dirk Roeda for proofreading the manuscript and suggesting linguistic corrections. This work was supported in part by EU contract No QLG1-CT-2000-00562.

LITERATURE CITED

(1) Kilbourn, M. R., and Welch, M. J. (1986) Fluorine-18 labeled receptor based radiopharmaceuticals. *Appl. Radiat. Isot. 37*, 677−683.

(2) Kilbourn, M. R. (1990) Fluorine-18 labeling of radiopharmaceuticals − Nuclear Science Series (Kilbourn, M. R., Ed.) pp 1−149, National Academy Press, Washington.

(3) Lasne, M. C., Perrio, C., Rouden, J., Barré, L., Roeda, D., Dollé, F., and Crouzel, C. (2002) Chemistry of β^+-emitting compounds based on fluorine-18. *Topics in current chemistry* (Krause, E., Ed.) pp 201−211, Springer Verlag, Berlin.

(4) Welch, M. J., and Redvanly, C. S. (2003) Radiochemistry and applications. *Handbook of radiopharmaceuticals* (Welch, M. J., Redvanly, C. S., Eds.) pp 1−848, Wiley-Interscience Publishers, New York.

(5) Younes, C. K., Boisgard, R., and Tavitian, B. (2002) Labeled oligonucleotides as radiopharmaceuticals: Pitfalls, problems and perspectives. *Curr. Pharm. Des. 8*, 1451−1466.

(6) Dollé, F., Hinnen, F., Vaufrey, F., Tavitian, B., and Crouzel, C. (1997) A general method for labeling oligodeoxynucleotides with 18F for in vivo PET imaging. *J. Labelled Compd. Radiopharm. 39*, 319−330.

(7) Hedberg, E., and Långström, B. (1997) Synthesis of 4-([18F]-fluoromethyl)phenyl isothiocyanate and its use in labeling oligonucleotides. *Acta Chem. Scand. 51*, 1236−1240.

(8) Tavitian, B., Terrazzino, S., Kuhnast, B., Marzabal, S., Stettler, O., Dollé, F., Deverre, J. R., Jobert, A., Hinnen, F., Bendriem, B., Crouzel, C., and DiGiamberardino, L. (1998) *In vivo* imaging of oligonucleotides with positron emission tomography. *Nat. Med. 4*, 467−471.

(9) Hedberg, E., and Långström, B. (1998) 18F-Labeling of oligonucleotides using succinimido 4-[18F]fluorobenzoate. *Acta Chem. Scand. 52*, 1034−1039.

(10) Marzabal, S., Terrazzino, S., Kuhnast, B., Dollé, F., Deverre, J. R., Jobert, A., Crouzel, C., DiGiamberardino, L., and Tavitian, B. (1999) In vivo imaging and pharmacokinetics of oligonucleotides. *Nucleosides Nucleotides 18*, 1731−1733.

(11) Kuhnast, B., Dollé, F., Vaufrey, F., Hinnen, F., Crouzel, C., and Tavitian, B. (2000) Fluorine-18 labeling of oligonucleotides bearing chemically modified ribose-phosphate backbones. *J. Labelled Compd. Radiopharm. 43*, 837−848.

(12) Kuhnast, B., Dollé, F., Terrazzino, S., Rousseau, B., Loc'h, C., Vaufrey, F., Hinnen, F., Doignon, I., Pillon, F., David, C., Crouzel, C., and Tavitian, B. (2000) A general method to label antisense oligonucleotides with radioactive halogens for pharmacological and imaging studies. *Bioconjugate Chem. 11*, 627−636.

(13) Tavitian, B., Marzabal, S., Boutet, V., Kuhnast, B., Terrazzino, S., Moynier, M., Dollé, F., Deverre, J. R., and Thierry, A. R. (2002) Characterization of a synthetic anionic vector for oligonucleotide delivery using in vivo whole body dynamic imaging. *Pharm. Res. 19*, 367−376.

(14) Lange, C. W., VanBrocklin, H. F., and Taylor, S. E. (2002) Photoconjugation of 3-azido-5-nitrobenzyl [18F]fluoride to an oligonucleotide aptamer. *J. Labelled Compd. Radiopharm. 45*, 257−268.

(15) Kuhnast, B., Hinnen, F., Boisgard, R., Tavitian, B., and Dollé, F. (2003) Fluorine-18 labeling of oligonucleotides: Prosthetic labeling at the 5′-end using the *N*-(4-[18F]fluorobenzyl)-2-bromoacetamide reagent. *J. Labelled Compd. Radiopharm. 46*, 1093−1103.

(16) Kuhnast, B., Klussmann, S., Hinnen, F., Boisgard, R., Rousseau, B., Fürste, J. P., Tavitian, B., and Dollé, F. (2003) Fluorine-18- and iodine-125 labeling of spiegelmers. *J. Labelled Compd. Radiopharm. 46*, 1205−1219.

(17) Dollé, F. (2004) Fluorine-18-labeled fluoropyridines: Advances in radiopharmaceutical design. *Curr. Pharm. Des.*, in press.

(18) Dolci, L., Dollé, F., Jubeau, S., Vaufrey, F., and Crouzel, C. (1999) 2-[18F]Fluoropyridines by no-carrier-added nucleo-

philic aromatic substitution with K[^{18}F]F−K_{222} − A comparative study. *J. Labelled Compd. Radiopharm. 42*, 975−985.

(19) Karramkam, M., Hinnen, F., Vaufrey, F., and Dollé, F. (2003) 2-, 3- and 4-[^{18}F]Fluoropyridines by no-carrier-added nucleophilic aromatic substitution with K[^{18}F]F−K_{222} − A comparative study. *J. Labelled Compd. Radiopharm. 46*, 979−992.

(20) Horti, A. G., Ravert, H. T., London, E. D., and Dannals, R. F. (1996) Synthesis of a radiotracer for studying nicotinic acetylcholine receptors: (±)-exo-2-(2-[^{18}F]fluoro-5-pyridyl)-7-azabicyclo[2.2.1]heptane. *J. Labelled Compd. Radiopharm. 28*, 355−365.

(21) Horti, A. G., Scheffel, U., Stathis, M., Finley, P., Ravert, H. T., London, E. D., and Dannals, R. F. (1997) Fluorine-18-FPH for PET imaging of nicotinic acetylcholine receptors. *J. Nucl. Med. 38*, 1260−1265.

(22) Villemagne, V. L., Horti, A. G., Scheffel, U., Ravert, H. T., Finley, P., Clough, D. J., London, E. D., Wagner, H. N., and Dannals, R. F. (1997) Imaging nicotinic acetylcholine receptors with fluorine-18-FPH, an epibatidine analogue. *J. Nucl. Med. 38*, 1737−1741.

(23) Ding, Y. S., Gatley, J., Fowler, J. S., Volkow, N. D., Aggarwal, D., Logan, J., Dewey, S. L., Liang, F., Carroll, F. I., and Kuhar, M. J. (1996) Mapping nicotinic acetylcholine receptors with PET. *Synapse 24*, 403−407.

(24) Ding, Y. S., Liang, F., Fowler, J. S., Kuhar, M. J., and Carroll, F. I. (1997) Synthesis of [^{18}F]Norchlorofluoroepibatidine and its *N*-methyl derivative: new PET ligands for mapping nicotinic acetylcholine receptors. *J. Labelled Compd. Radiopharm. 39*, 828−832.

(25) Liang, F., Navarro, H. A., Abraham, P., Kotian, P., Ding, Y. S., Fowler, J. S., Volkow, N. D., Kuhar, M. J., and Carroll, F. I. (1997) Synthesis and nicotinic acetylcholine receptor binding properties of exo-2-(2′-fluoro-5′-pyridinyl)-7-azabicyclo-[2.2.1]heptane: A new positron emission tomography ligand for nicotinic receptors. *J. Med. Chem. 40*, 2293−2295.

(26) Dolci, L., Dollé, F., Valette, H., Vaufrey, F., Fuseau, C., Bottlaender, M., and Crouzel, C. (1999) Synthesis of a fluorine-18 labeled derivative of epibatidine for in vivo nicotinic acetylcholine receptor PET imaging. *Bioorg. Med. Chem. 7*, 467−479.

(27) Dollé, F., Valette, H., Bottlaender, M., Hinnen, F., Vaufrey, F., Guenther, I., and Crouzel, C. (1998) Synthesis of 2-[^{18}F]-fluoro-3-[2(*S*)-2-azetidinylmethoxy]pyridine, a highly potent radioligand for *in vivo* imaging central nicotinic acetylcholine receptors. *J. Labelled Compd. Radiopharm. 41*, 451−463.

(28) Horti, A., Koren, A. O., Ravert, H. T., Musachio, J. L., Mathews, W. B., London, E. D., and Dannals, R. F. (1998) Synthesis of a radiotracer for studying nicotinic acetylcholine receptors: 2-[^{18}F]fluoro-3-(2(*S*)-azetidinylmethoxy)pyridine (2-[^{18}F]A-85380). *J. Labelled Compd. Radiopharm. 41*, 309−318.

(29) Dollé, F., Dolci, L., Valette, H., Hinnen, F., Vaufrey, F., Guenther, I., Fuseau, C., Coulon, C., Bottlaender, M., and Crouzel, C. (1999) Synthesis and nicotinic acetylcholine receptor in vivo binding properties of 2-fluoro-3-[2(*S*)-2-azetidinylmethoxy]pyridine: a new positron emission tomography ligand for nicotinic receptors. *J. Med. Chem. 42*, 2251−2259.

(30) Horti, A. G., Chefer, S. I., Mukhin, A. G., Koren, A. O., Gundisch, D., Links, J. M., Kurian, V., Dannals. R. F., and London, E. D. (2000) 6-[^{18}F]fluoro-A-85380, a novel radioligand for *in vivo* imaging of central nicotinic acetylcholine receptors. *Life Sci. 67*, 463−469.

(31) Scheffel, U., Horti, A. G., Koren, A. O., Ravert, H. T., Banta, J. P., Finley, P. A., London, E. D., and Dannals R. F. (2000) 6-[^{18}F]Fluoro-A-85380: an in vivo tracer for the nicotinic acetylcholine receptor. *Nucl. Med. Biol. 27*, 51−56.

(32) Koren, A. O., Horti, A. G., Mukhin, A. G., Gundisch, D., Dannals, R. F., and London, E. D. (2000) Synthesis and initial in vitro characterization of 6-[^{18}F]fluoro-3-(2(*S*)-azetidinylmethoxy)pyridine, a high-affinity radioligand for central nicotinic acetylcholine receptors. *J. Labelled Compd. Radiopharm. 43*, 413−423.

(33) Ding, Y. S., Liu, N., Wang, T., Marecek, J., Garza, V., Ojima, I., Fowler, J. S. (2000) Synthesis and evaluation of 6-[^{18}F]fluoro-3-(2(*S*)-azetidinylmethoxy)pyridine as a PET tracer for nicotinic acetylcholine receptors. *Nucl. Med. Biol. 27*, 381−389.

(34) Liu, N., Ding, Y. S., Wang, T., Garza, V., and Fowler, J. S. (2002) Synthesis of 2-[^{18}F]fluoro-3-[2(S)-2-azetidinylmethoxy]-pyridine as a radioligand for imaging nicotinic acetylcholine receptors. *Nucl. Sci. Technol. 12*, 92−97.

(35) Roger, G., Lagnel, B., Rouden, J., Besret, L., Valette, H., Demphel, S., Gopisetti, J., Coulon, C., Ottaviani, M., Wrenn, L. A., Letchworth, S. R., Bohme, G. A., Benavides, J., Lasne, M. C., Bottlaender, M., and Dollé, F. (2003) Synthesis of a [2-pyridinyl-^{18}F]-labeled fluoro derivative of (−)-cytisine as a candidate radioligand for brain nicotinic $\alpha_4\beta_2$ receptor imaging with PET. *Bioorg. Med. Chem. 11*, 5333−5343.

(36) Mitsunobu, O. (1981) The use of diethyl azodicarboxylate and triphenylphosphine in synthesis and transformation of natural products. *Synthesis* 1−28.

(37) Thuong, N. T., and Asseline, U. (1991) Oligonucleotides attached to intercalators, photoreactive and cleavage agents. *Oligonucleotides and analogues, a practical approach*, pp 283−306, IRL Press, Oxford.

(38) Fidanza, J. A., Ozaki, H., and McLaughlin, L. W. (1994) Protocols for oligonucleotides conjugates: Functionalization by incorporation of thio-specific reporter groups. *Methods in molecular biology* (Agrawal, S., Ed.) pp 121−143, Humana Press, Inc, Totawa, NJ.

(39) Emsley, J., and Hall, D. (1976) ^{31}P nuclear magnetic resonance. *The chemistry of phosphorous*, pp 78−91, Harper and Row Publishers, London.

(40) Gorenstein, D. G. (1984) Appendixes: selected compilation of ^{31}P NMR data. *Phosphorus-31 NMR: principles and applications* (Gorenstein, D. G., Ed.) pp 550−591, Academic Press, New York.

(41) Gorenstein, D. G. (1984) Chemical shifts: Principles and empirical observations. *Phosphorus-31 NMR: principles and applications*. (Gorenstein, D. G., Ed.) pp 7−33, Academic Press, New York.

(42) Gorenstein, D. G. (1992) Advances in phosphorus-31 NMR. *Handbook of organophosphorus chemistry* (Engel, R., Ed.) pp 435−469, Marcel Dekker, Inc, New York.

(43) Hirschbein, B. L., and Fearon, K. L. (1997) ^{31}P NMR spectroscopy in oligonucleotide research and development. *Antisense Nucleic Acid Drug Dev. 7*, 55−61.

(44) Haka, M. S., Kilbourn, M. R., Watkins, L., and Toorongian, S. A. (1989) Aryltrimethylammonium trifluoromethanesulfonates as precursors to aryl [^{18}F]fluorides: improved synthesis of [^{18}F]GBR-13119. *J. Labelled Compd. Radiopharm. 27*, 823−833.

(45) Hamacher, K., Coenen, H. H., and Stöcklin, G. (1986) Efficient stereospecific synthesis of no-carrier-added 2-[^{18}F]-fluoro-2-deoxy-D-glucose using aminopolyether supported nucleophilic substitution. *J. Nucl. Med. Biol. 27*, 235−238.

(46) Nolte, A., Klussmann, S., Bald, R., Erdmann, V., and Fürste, J. P. (1996) Mirror-design of L-oligonucleotide ligands binding to L-arginine. *Nat. Biotechnol. 14*, 1116−1119.

(47) Wlotzka, B., Leva, S., Eschgfäller, B., Burmeister, J., Kleinjung, F., Kaduk, C., Muhn, P., Hess-Stumpp, H., and Klussmann, S. (2002) In vivo properties of an anti-GnRH Spiegelmer: an example of an oligonucleotide-based therapeutic substance class. *Proc. Nat. Acad. Sci. U.S.A. 99*, 8898−8902.

(48) Kuhnast, B., Dollé, F., and Tavitian, B. (2001) Fluorine-18 labeling of peptide nucleic acids. *J. Labelled Compd. Radiopharm. 45*, 1−11.

(49) Hamzavi, R., Dollé, F., Tavitian, B., Dahl, O., and Nielsen, P. (2003) Modulation of the pharmacokinetic properties of PNA: preparation of galactosyl, mannosyl, fucosyl, *N*-acetylgalactosaminyl, and *N*-acetylglucosaminyl derivatives of aminoethylglycine peptide nucleic acid monomers and their incorporation into PNA oligomers. *Bioconjugate Chem. 14*, 941−954.

(50) Nielsen, P. E., Egholm, M., Berg, R. H., and Buchardt, O. (1991) Sequence-selective recognition of DNA by strand

displacement with a thymine-substituted polyamide. *Science 254*, 1497−1500.
(51) Nielsen, P. E., and Egholm, M. (1999) *Peptide Nucleic Acids: Protocols and Applications*, Horizon Scientific Press, Wymondham, England.
(52) Kilbourn, M. R., Dence, C. S., Welch, M. J., and Mathias, C. J. (1987) Fluorine-18 labeling of proteins. *J. Nucl. Med. 28*, 462−470.
(53) Wilbur, D. S. (1992) Radiohalogenation of proteins: An overview of radionuclides, labeling methods and reagents for conjugate labeling. *Bioconjugate Chem. 3*, 433−470.
(54) Okarvi, S. M. (2001) Recent progress in fluorine-18 labeled peptide radiopharmaceuticals. *Eur. J. Nucl. Med. 28*, 929−938.
(55) de Vries, E. F. J., Vroegh, J., Elsinga, P. H., and Vaalburg, W. (2003) Evaluation of fluorine-18-labeled alkylating agents as potential synthons for the labeling of oligonucleotides. *Appl. Radiat. Isot. 58*, 469−476.
(56) Deverre, J. R., Boutet, V., Boquet, D., Ezan, E., Grassi, J., and Grognet, J. M. (1997) A competitive enzyme hybridization assay for plasma determination of phosphodiester and phosphorothioate antisense oligonucleotides. *Nucleic Acids Res. 25*, 3584−3589.
(57) Gold, L., Polisky, B., Uhlenbeck, O., and Yarus, M. (1995) Diversity of oligonucleotide functions. *Annu. Rev. Biochem. 64*, 763−797.
(58) Klussmann, S., Nolte, A., Bald, R., Erdmann, V., and Fürste, J. P. (1996) Mirror-image RNA that binds D-adenosine. *Nat. Biotechnol. 14*, 1112−1115.
(59) Vater, A., and Klussmann, S. (2003) Toward third-generation aptamers: Spiegelmers and their therapeutic prospects. *Curr. Opin. Drug Discovery Dev. 6*, 253−261.
(60) Dougan, H., Weitz, J. I., Stafftord, A. R., Gillespie, K. D., Klement, P., Hobbs, J. B., and Lyster, D. M. (2003) Evaluation of DNA aptamers directed to thrombin as potential thrombus imaging agents. *Nucl. Med. Biol. 9*, 61−72.
(61) Williams, K. P., Liu, X. H., Schumacher, T. N., Lin, H. Y., Ausiello, D. A., Kim, P. S., and Bartel, D. P. (1997) Bioactive and nuclease-resistant L-DNA ligand of vasopressin. *Proc. Nat. Acad. Sc. U.S.A. 94*, 11285−11290.
(62) Purschke, G., Radtke, F., Kleinjung, F., and Klussmann, S. (2003) A DNA Spiegelmer to staphylococcal enterotoxin B. *Nucleic Acids Res. 31*, 3027−3032.

BC049979U

Synthesis, Characterization, and Biological Evaluation of Neutral Nitrido Technetium(V) Mixed Ligand Complexes Containing Dithiolates and Aminodiphosphines. A Novel System for Linking Technetium to Biomolecules

Cristina Bolzati,*[,‡] Elisa Benini,[†] Emiliano Cazzola,[†] Christian Jung,[§] Francesco Tisato,*[,‡] Fiorenzo Refosco,[‡] Hans-Jürgen Pietzsch,[§] Hartmut Spies,[§] Licia Uccelli,[†] and Adriano Duatti[†]

ICIS - CNR, Corso Stati Uniti 4, 35127 Padova, Italy, Laboratory of Nuclear Medicine, Department of Clinical & Experimental Medicine, University of Ferrara, Via Borsari 46, 44100 Ferrara, Italy, and Forschungszentrum Rossendorf, Institut für Bioanorganische und Radiopharmazeutische Chemie, PF 510 119, D-01314 Dresden, Germany. Received January 8, 2004; Revised Manuscript Received February 16, 2004

A new biomolecule labeling method that utilizes the $[^{99m}Tc(N)(PNP)]^{2+}$ metal fragment is presented. Thus, a series of nitrido mixed-ligand M(V) complexes (M = ^{99m}Tc, ^{99g}Tc, Re), [M(N)(Ln)(PNP)], where Ln is the dianionic form of a dithiolate or substituted-dithiolate ligand and PNP is an aminodiphosphine, is described. ^{99m}Tc complexes can be prepared using either a two-step or a three-step procedure starting from generator-eluted pertechnetate through a prereduced mixture of [^{99m}Tc(N)]-containing species, followed by sequential or contemporary addition of the relevant dithiolate and aminodiphosphine. The reactions of 2,3-dimercaptopropionic acid (H_2L1) with $[Tc(N)(PNP)]^{2+}$ were investigated in detail. It was found that this bidentate ligand coordinated the metal fragment through the [S^-,S^-] donor atom pair, to yield neutral mixed-ligand complexes [^{99m}Tc(N)(L1)(PNP)] in high specific activity. The additional carboxylic functional group was not involved in metal coordination, thus remaining available for conjugation to target-specific molecules. Dithiolates incorporating pendant functional group(s) gave rise to a 1:1 diastereoisomeric mixture of *syn*-[M(N)(Ln)(PNP)] and *anti*-[M(N)(Ln)-(PNP)] derivatives, depending on the relative orientation of the dithiolate substituent(s) with respect to the terminal nitrido group, and no isomeric conversion was detected. ^{99m}Tc species had been proven to be identical with the ^{99g}Tc complexes prepared at the macroscopic level by comparison of the corresponding radiometric and UV/vis HPLC profiles. Challenge experiments with cysteine or glutathione indicated that these physiological agents had no effect on the stability of this class of mixed-ligand ^{99m}Tc-complexes. Biodistribution studies in rats of selected ^{99m}Tc-complexes showed a rapid clearance from the blood and tissues after 60 min pi.

INTRODUCTION

In the past few years, the design of technetium and rhenium model compounds potentially useful for the development of new radiopharmaceuticals has taken advantage of the introduction of efficient methods for the production of ^{99m}Tc-species (*1*) and ^{188}Re-species (*2*) containing a terminal $[M(N)]^{2+}$ group at the non carrier added (NCA) level. Nitrido-containing complexes offer the advantage to be virtually red-ox inert and stable over a wide range of pH values (*3*), thereby constituting a class of interesting candidates for nuclear medicine applications.

Pioneering investigation on nitrido technetium chemistry performed by Baldas and co-workers in the 1980s (*4*) have been sharply tuned into nuclear medicine applications with the synthesis of the *neutral* myocardial imaging agent [^{99m}Tc−N−NOET] (*5*), an unexpected mimic of the $^{201}Tl^+$ agent (*6*). The [^{99m}Tc−N−NOET] is a simple bis-substituted dithiocarbamate nitrido technetium complex adopting a distorted square pyramidal configuration with the terminal nitride group at the apex and the four (*N*-ethoxy-*N*-ethyl)dithiocarbamate sulfurs at the base of the pyramid. Despite the high stability of the [Tc(N)] group and the variety of nitrido complexes reported (*7*), little effort has been made in the past to use the [Tc(N)] core for the labeling of biomolecules.

Looking for additional stable configurations including the terminal $[M(N)]^{2+}$ group, we have recently developed a synthetic strategy aiming at the incorporation of a bioactive molecule into a stable nitrido containing Tc complex (*8*). This strategy is based on the application of the so-called 'metal fragment' approach (*9*) and requires the synthesis of an asymmetrical nitrido compound characterized by the presence of two different polydentate ligands bound to the same $[Tc(N)]^{2+}$ core. It utilizes the coordination ability of π-acceptor PNP type heterodiphosphines (diphosphine including a tertiary amine nitrogen in a five-member spacer, see Figure 1) to produce the $[M(N)(PNP)]^{2+}$ metal-fragment. This strongly electrophilic synthon selectively reacts with electron rich, π-donor chelating ligands to yield monocationic or neutral asymmetrical compounds of the type $[M(N)(X-Y)(PNP)]^{+/0}$. X−Y ligands are bidentate homoatomic or heteroatomic

* Corresponding author. Fax ++39 049 8702911. E-mail bolzati@icis.cnr.it.
‡ ICIS - CNR.
† University of Ferrara.
§ Institut für Bioanorganische und Radiopharmazeutische Chemie.

10.1021/bc0499782 CCC: $27.50 © 2004 American Chemical Society
Published on Web 03/26/2004

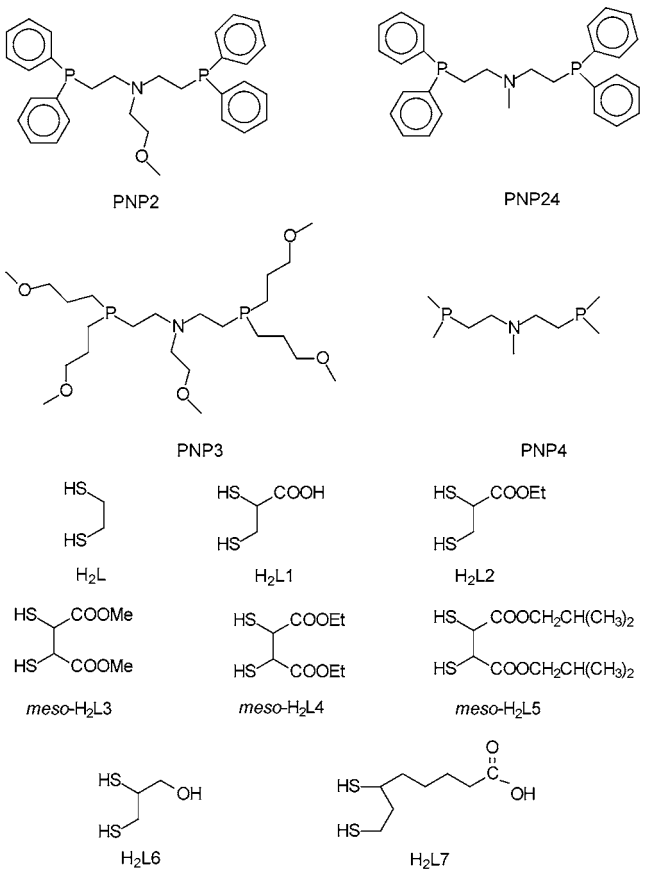


Figure 1. Aminodiphosphines (PNP) and dithiols (H_2Ln) ligands utilized in this study.

chelates having the property to become a bifunctional chelating agent (BFCA) by insertion of an additional functional group for conjugation with bioactive fragments.

Examples of mixed nitrido heterocomplexes already synthesized and thoroughly characterized include monocationic $[M(N)(DTC)(PNP)]^+$ (DTC = various dithiocarbamates) (*10*), $[M(N)(DTCZ)(PNP)]^+$ (DTCZ = S-methyl 2-methyldithiocarbazate), $[M(N)(N,S\text{-cys})(PNP)]^+$ (N,S-cys = L-cysteine ethyl ester) (*11*), and neutral [M(N)(O,S-cys)(PNP)] (O,S-cys = *N*-acetyl-L-cysteine) and [M(N)-(O,S-ma)(PNP)] (O,S-ma = mercaptoacetate) complexes (*11*). It is worth noting that the $[M(N)(PNP)]^{2+}$ moieties are stabilized by a variety of donor atom combinations (i.e. S,S^-, S,NH^-, O^-,S^-), all giving heterocomplexes in which the original, substitution-inert *fac*-$[M(N)(PNP)]^{2+}$ building-block is retained, and the incoming bidentate ligand is accommodated on the equatorial plane, cis-positioned with respect to the terminal nitride group.

A reasonable extension of the above series of ligands able to stabilize the $[M(N)(PNP)]^{2+}$ moieties comprise homoatomic dithiolate ligands for the double reason that thiolate sulfur is among the best donor for group 7 metals (*7*) and dithiolate backbones are prone to derivatization with appropriate functional groups. A wide number of thiolato mono-oxo Tc(V) model compounds including tetradentate diamine-dithiolate in $[Tc(O)(DADT)]^-$ complexes (*12*), tridentate amine-dithiolate and monodentate thiolate in [Tc(O)(SNS)(SR)] '3 + 1' complexes (*13*), and bidentate dimercaptosuccinic acid in bis-substituted [Tc-$(O)(DMSA)_2$] compounds (*14*) have been already produced. DADT, SNS, and SR frameworks have also been in turn conjugated with bioactive molecules (*15*), indicating that thiol-containing BFCAs are suitable substrates for the production of ^{99m}Tc-based receptor-specific agents under mild conditions (*15*). By using the BFCA strategy, Kung and co-workers developed the first ^{99m}Tc dopamine transporter imaging agent by conjugation of a tropane analogue onto one nitrogen of a DADT framework (*16*), and, more recently, the P829 somatostatin analogue conjugate to a N_3S-momoamine diamidethiol chelating unit formed by the (B-Dap)-Lys-Cys tripeptide sequence (*17*) has been approved by FDA as a new radiopharmaceutical for tumor imaging.

For the reasons outlined above, we thought to combine in a unique molecular system the substitution-inert property of $[M(N)(PNP)]^{2+}$ moieties with the well recognized coordination ability toward Tc and Re of dithiolates, to form neutral mixed nitrido heterocomplexes of the type [M(N)(S−S)(PNP)], aiming eventually at the design of a new system useful for the development of receptor-based radiopharmaceuticals. Hence, in this study we report on the preparation and biological evaluation of several mixed nitrido ^{99m}Tc heterocomplexes of the type [^{99m}Tc-(N)(S−S)(PNP)], along with the synthesis and physicochemical characterization of some Re and ^{99g}Tc analogues.

EXPERIMENTAL PROCEDURES

Caution! ^{99g}Tc is a weak β-emitter ($E_{\beta^-} = 0.292$ MeV, $t_{1/2} = 2.13 \times 10^5$ years). All manipulations were carried out in laboratories approved for low-level radioactivity using monitored hoods and gloveboxes. When handled in milligram amounts, ^{99g}Tc does not present a serious health hazard since common laboratory glassware provides adequate shielding. Bremsstrahlung is not a significant problem due to the low energy of the β^- particles. However, normal radiation safety procedure must be used at all times, especially with a solid samples, to prevent contamination and inhalation.

General. All common chemicals were purchased from Aldrich Chemicals. Common solvents were reagent grade and used without further purification. The aminodiphosphine ligands PNP24, PNP3, and PNP4 utilized in this study and sketched in Figure 1, were prepared according to the literature methods (*18*) or purchased from Argus Chemicals (Prato, Italy). Due to the high tendency of the alkyl bis-phosphine ligands to oxidize, all the solvent involved in the reactions with PNP3 and PNP4 were previously degassed. The dithiol ligands H_2L, H_2L1, H_2-L6, and H_2L7 were purchased from Sigma Aldrich Chemicals while the remaining dithiol ligands were synthesized as previously reported (*19*). ^{99m}Tc as Na-[$^{99m}TcO_4$] was eluted from a ^{99}Mo/^{99m}Tc generator provided by Nycomed Amersham-Sorin (Saluggia, Italy). Commercially available $NH_4[^{99g}TcO_4]$ (Oak Ridge National Lab) was purified from a black contaminant ($^{99g}TcO_2 \times nH_2O$) by addition of H_2O_2 and NH_4OH solutions followed by recrystallization from hot water. [^{99g}Tc(N)$Cl_2(PPh_3)_2$] was prepared according to the literature (*20*). [Re(N)Cl_2(PNP2)] and [Re(N)Cl_2(PNP24)] intermediate complexes were prepared as reported previously (*9*).

Elemental analyses (C, H, N, S) were performed on a Carlo Erba 1106 elemental analyzer. FT IR spectra were recorded on a Nicolet 510P Fourier transform spectrometer, in the range 4000−400 cm^{-1} and in KBr mixture using a Spectra-Tec diffuse-reflectance collector accessory. ^{1}H, ^{13}C, and ^{31}P NMR spectra were collected on a Bruker 300 instrument, using $SiMe_4$ as internal reference (^{1}H and ^{13}C) and 85% aqueous H_3PO_4 as external reference (^{31}P).

Thin-layer chromatography (TLC) and/or high performance liquid chromatography (HPLC) analyses were

Table 1.

complex	R_f Re	R_f ^{99g}Tc	R_f ^{99m}Tc	HPLC, t_R Re	HPLC, t_R ^{99g}Tc	HPLC, t_R ^{99m}Tc	yield, % ^{99m}Tc
[M(N)(L)(PNP2)]	0.60[e]			41.36[B]			
[M(N)(L)(PNP4)]			0.8[a]; 0.6[b]			19.86[A]	93.0
[M(N)(L1)(PNP3)] **a**		0.4[c]	0.4[c]		23.95[A]	24.25[A]	51.4
[M(N)(L1)(PNP3)] **b**		0.5[c]	0.5[c]		25.23[A]	25.55[A]	44.9
syn-[M(N)(L1)(PNP4)]			0.6[d]		20.12[A]	20.33[A]	49.3
anti-[M(N)(L1)(PNP4)]			0.7[d]		18.59[A]	18.90[A]	49.7
[M(N)(L2)(PNP24)] **a**	0.65[e]		0.65[e]	42.01[B]		42.32[B]	46.6
[M(N)(L2)(PNP24)] **b**	0.57[e]		0.57[e]	43.68[B]		43.96[B]	47.1
[M(N)(L3)(PNP4)] **a**		0.4[f]	0.4[f]		20.20[A]	20.61[A]	42.3
[M(N)(L3)(PNP4)] **b**		0.3 [f]	0.3[f]		21.22[A]	21.43[A]	40.8
[M(N)(L4)(PNP4)] **a**			0.36[f]			24.48[C]	45.8
[M(N)(L4)(PNP4)] **b**			0.28[f]			25.54[C]	42.3
[M(N)(L5)(PNP4)] **a**			0.3;[f] 0.37[b]			39.61[C]	46.2
[M(N)(L5)(PNP4)] **b**			0.25;[f] 0.28[b]			44.92[C]	42.6
[M(N)(L6)(PNP3)] **a**		0.3[f]			23.03[A]	23.32[A]	46.2
[M(N)(L6)(PNP3)] **b**		0.25[f]			23.66[A]	23.95[A]	42.6
[M(N)(L7)(PNP24)] **a**	0.58[e]		0.58[e]	38.83[B]		39.12[B]	94.3
[M(N)(L7)(PNP24)] **b**	0.58[e]		0.58[e]	39.98[B]		40.15[B]	94.3
[M(N)(L7)(PNP3)] **a**		0.25[f]	0.25[f]		38.22[D]	38.63[D]	42.7
[M(N)(L7)(PNP3)] **b**		0.25[f]	0.25[f]		39.32[D]	39.51D	49.1

TLC: [a]SiO_2, ETOH/$CHCl_3$/C_6H_6 (1.5/2/1.5). [b]C18 CH_3CN/NH_4Ac 0.5 M pH 5.5 (70/30). [c]C18, CH_3CN/Et_3N 0.1 M pH 3 (60/40). [d]C18, saline/CH_3OH/THF/$Hac_{(g)}$ (60/40/10/10). [e]SiO_2, CH_3Cl/CH_3OH(25/1). [f]SiO_2, ETOH/$CHCl_3$/C_6H_6 (0.3/2/1.5). HPLC: reverse-phase C_{18} column; A = Et_3N (0.1 M in 1.0 M H_3PO_4, pH 3), B = CH_3CN. [A]Gradient: 0−5 min, B, 0%, 5−15 min, B, 30%, 15−20 min, B, 50%, 20−30 min, B, 50%, 30−35 min, B 0%. [B]Gradient: 0−5 min, B, 0%, 5−15 min, B, 30%, 15−30 min, B, 60%, 30−50 min, B, 60%, 50−55 min, B 0%. [C]Gradient: 0−5 min, B, 0%, 5−15 min, B, 30%, 15−25 min, B, 50%, 25−45 min, B, 50%, 45−50 min, B 0%. [D]Gradient 0−5 min, B, 30%, 5−15 min, B, 40%, 15−50 min, B, 40%, 50−55 min, B, 0%.

used to evaluate radiochemical yield (RCY), radiochemical purity (RCP), and stability of the compounds. TLC analyses were performed using silica gel F_{254S} or C18 F_{254S} plates (Merck). The activity on the plates were located and measured using a Cyclone Instrument equipped with a phosphorus imaging screen and an OptiQuant image analysis software (Packard, Meridian, CT). HPLC was performed on a Beckman System Gold instrument equipped with a programmable solvent Model 126, a sample injection valve 210A, a scanning detector Module 166, and a radioisotope detector Model 170. HPLC analysis was carried out using a reversed-phase Beckman ODS precolumn (45 × 4.6 mm) and a reversed-phase Beckman ODS column (250 × 16 mm) at the flow rate of 1 mL/min. Chromatographic data are reported in Table 1.

Preparation of [^{99m}Tc(N)(Ln)(PNP)]: *Method 1*. Na-[$^{99m}TcO_4$] (0.250 mL, 50.0 MBq − 2.2 GBq) was added to a vial containing 5.0 mg of SDH (SDH = succinic dihydrazide), 0.1 mg of $SnCl_2$ suspended in 0.1 mL of saline, and 1.0 mL of ethanol. The vial was kept at room temperature for 15 min giving a mixture of ^{99m}Tc-nitrido precursors, $[Tc{\equiv}N]_{mix}^{2+}$. Then, 1.0 mg of the appropriate diphosphine ligand (PNP3 or PNP4 or PNP24) dissolved in 0.1 mL of ethanol was added, and the solution was left standing for 30 min at room temperature. The resulting $[^{99m}Tc(N)(PNP)]^{2+}$ intermediate complex was converted into the final product by addition of 0.1 mL of an ethanol solution containing 0.5 mg of the relevant dithiol (H_2L1, H_2L3−7) at 50 °C for 1 h (in the PNP24/H_2L2 case, 0.2 mL of an ethanol solution containing 1.0 mg of H_2L2 were added at 100 °C for 30 min, followed by 0.25 mL of phosphate buffer (1 M, pH 7.4); in the PNP4/H_2L case, 0.1 mL of an ethanol solution containing 2.5 mg of H_2L were added at 50 °C for 1 h, followed by 0.25 mL of carbonate buffer (0.5 M, pH 9.0)). In all preparations, TLC characterization showed the presence of two separate radioactive spots (1:1 ratio), which resulted from the formation of two distinct isomers (**a** and **b**) of the complexes [^{99m}Tc(N)(Ln)(PNP)] (vide infra). The total radiochemical yield (RCY) determined by TLC chromatography for the two isomers was >93%.

*Method 2***.** To a mixture of $[Tc{\equiv}N]_{mix}^{2+}$ prepared as above were simultaneously added 1.0 mg of the appropriate diphosphine ligand (PNP) dissolved in 0.1 mL of ethanol and 0.5 mg of the proper dithiol ligand dissolved in 0.1 mL of ethanol to the reaction vial and heated at 50 °C for 1 h (in the PNP24/H_2L2 case, 1.0 mg of H_2L2 was added at 100 °C for 30 min followed by 0.25 mL of phosphate buffer (1M, pH 7.4)). In all cases, total RCY determined by TLC and HPLC chromatography was 90%.

Purification of [^{99m}Tc(N)(Ln)(PNP)] Compounds. [^{99m}Tc(N)(L1)(PNP3)] and [^{99m}Tc(N)(L1)(PNP4)] were purified by HPLC, concentrated on a Sep pack C18 cartridge previously activated with 95% ethanol (5 mL) and water (5 mL), rinsed with H_2O (10 mL), and eluted using EtOH (3 × 0.5 mL). The second fraction containing all the activity was diluted with saline (1/10 EtOH/saline) and utilized for in vitro and in vivo studies. For remaining ^{99m}Tc-derivatives, the reaction mixture was diluted with 25 mL of water (50 mL for PNP4/L) and loaded onto a Sep pack C18 cartridge previously activated with 95% ethanol (5 mL) and water (5 mL). The cartridge was rinsed with water (20 mL) followed by 10% ethanol (5 mL) and 20% ethanol (0.4 mL) for [^{99m}Tc(N)(L)(PNP4)], 10% ethanol (3 mL) for [^{99m}Tc(N)(L3/L4)(PNP4)], and 30% ethanol (3 mL) for [^{99m}Tc(N)(L5)(PNP4)]. Finally, [^{99m}Tc-(N)(L)(PNP4)] was eluted with 30% ethanol (2 × 1 mL), [^{99m}Tc(N)(L3/L4)(PNP4)] was eluted with 30% ethanol (0.250 mL) followed by 60% ethanol (1 mL), and [^{99m}Tc-(N)(L5)(PNP4)] was eluted with 80% ethanol (1 × 0.4 mL; 3 × 1 mL). The second fractions eluted were utilized, after 1/10 EtOH/saline dilution, for stability studies and in vivo biodistribution studies. After purification, the radiochemical purity (RCP), evaluated by TLC chromatography, was >95%.

Preparation of [^{99g}Tc(N)(Ln)(PNP)] Complexes. To an orange-pink suspension containing 0.05 mmol of [$^{99g}TcNCl_2(PPh_3)_2$] in 5 mL of CH_2Cl_2 was added a slight excess of the relevant PNP ligand (0.060 mmol) dissolved

in 5 mL of EtOH. The reaction mixture was stirred to reflux under dinitrogen atmosphere for 30 min. Rapidly the solution became clear and the color turned to yellow. Then, an excess of Et_3N (10 drops) was added followed by 0.11 mmol of H_2Ln dissolved in 2 mL of EtOH. The mixture was heated to reflux for an additional 1 h. After cooling, the solvents were evaporated and the crude material was washed with Et_2O and *n*-hexane. Except for [^{99g}Tc(N)(L1)(PNP4)], all the derivatives were redissolved in CH_2Cl_2 (5 mL) and treated with an equal volume of water (3 × 5 mL) to remove the hydrophilic species. The organic layer was dried over anhydrous $MgSO_4$, the solvent eliminated, and the resulting residue triturated with Et_2O. A yellow solid was recovered for [^{99g}Tc(N)(L1)(PNP3)] and [^{99g}Tc(N)(L3)(PNP4)], which was dried under gentle dinitrogen stream. A yellow oil was instead collected for [^{99g}Tc(N)(L6/L7)(PNP3)]. TLC analyses, carried out on C18 or in silica, revealed the formation of two species (**a**, **b**) in an approximately 1:1 ratio.

Crude [^{99g}Tc(N)(L1)(PNP4)] was instead dissolved in the minimum amount of $CHCl_3$ (0.5 mL) and loaded onto a silica column (Ø 1 cm, l 10 cm) conditioned with $CHCl_3$. The column was eluted with $CHCl_3$ (50 mL) followed by mixtures of $CHCl_3$/MeOH 98/2 (50 mL) and $CHCl_3$/MeOH 95/5 (100 mL). Two yellow bands were separated and isolated, as yellow oily residues for [^{99g}Tc(N)(L1)(PNP4)]. The first fraction was identified as the syn isomer (**a**) and the second fraction as the anti isomer (**b**). All of the compounds are soluble in chlorinated solvents and in alcohols, insoluble in diethyl ether and *n*-hexane.

[^{99g}Tc(N)(L1)(PNP3)] (a + b). Yield: 65%. Anal. ($C_{26}H_{55}N_2O_7P_2S_2Tc$ Mw = 732.79): calcd C, 42.61; H 7.56; N 3.84; S 8.75. Found C, 42.02; H 7.4; N 3.81; S 8.32. ^{1}H NMR ($CDCl_3$, ppm): 1.69−3.75 (24H, P−CH_2CH_2CH_2-OCH_3), 1.81−2.46 (16H, P−CH_2−CH_2−N), 3.19 (3H, s; N−CH_2CH$_2$−OCH_3), 3.21 and 4.02 (4H; N−CH_2CH_2−OCH$_3$), 3.36 and 3.38 (12H; P−CH$_2$CH$_2$CH$_2$OCH_3), 4.19, 3.50 and 2.59 (3H; SCH_2C*H*(COOH)). ^{31}P NMR ($CDCl_3$, ppm): 21.9 (bs).

[^{99g}Tc(N)(L6)(PNP3)] (a + b). Yield: 75%. Anal. ($C_{26}H_{57}N_2O_6P_2S_2Tc$ Mw = 718.81): calcd C, 43.44; H 7.99; N 3.90; S 8.92. Found C, 43.15; H 7.80; N 3.78; S 8.99. ^{31}P NMR ($CDCl_3$, ppm): 22.6 (bs).

[^{99g}Tc(N)(L7)(PNP3)] (a + b). Yield: 80%. Anal. ($C_{31}H_{65}N_2O_7P_2S_2Tc$ Mw = 802.94): calcd C, 46.37; H 8.16; N 3.50; S 7.79. Found C, 46.03; H 8.10; N 3.28; S 7.32. ^{31}P NMR ($CDCl_3$, ppm): 19.4 (bs).

[^{99g}Tc(N)(L1)(PNP4)] (a + b). Yield 75%. Anal. ($C_{12}H_{27}N_2O_2P_2S_2Tc$ Mw = 456.46): calcd C, 31.58; H 5.96; N 6.16; S 14.02. Found C, 31.15; H 5.8; N 6.10; S 13.92.

syn-[^{99g}Tc(N)(L1)(PNP4)] (**a**). ^{1}H NMR ($CDCl_3$/CD_3OD 9/1, ppm): 1.76−1.90 (12H, PCH_3 + 3H, NCH_3), 1.82−2.43 (16H, CH_2 groups), 3.01, 3.19 and 3.60 (3H, dd; SCH_2C*H*(COOH)). ^{13}C NMR ($CDCl_3$/CD_3OD 9/1, ppm): 15.7 and 18.5 (d, PCH$_{3exo}$ + PCH$_{3endo}$), 29.3 (d, PCH$_2$), 39.5 (s, SCH$_2$), 45.3 (s, NCH$_3$), 51.6 and 51.7 (s + s, NCH$_2$ + SCH(COOH)), 178.1 (s, COOH). ^{31}P NMR ($CDCl_3$/CD_3-OD 9/1, ppm): ^{31}P NMR ($CDCl_3$, ppm): 10.5 (bs).

anti-[^{99g}Tc(N)(L1)(PNP4)] (**b**). ^{1}H NMR ($CDCl_3$/CD_3OD 9/1, ppm): 1.77−1.89 (12H, PCH_3 + 3H, NCH_3), 1.81−2.49 (16H, CH_2 groups), 2.66, 3.27, and 3.74 (3H, dd; SCH_2C*H*(COOH)). ^{13}C NMR ($CDCl_3$/CD_3OD 9/1, ppm): 14.8 and 18.4 (d, PCH$_{3exo}$ + PCH$_{3endo}$), 29.5 (d, PCH$_2$), 37.4 (s, SCH$_2$), 45.5 (s, NCH$_3$), 51.6 and 51.9 (s + s, NCH$_2$ + SCH(COOH)), 178.4 (s, COOH). ^{31}P NMR ($CDCl_3$/CD_3-OD 9/1, ppm): ^{31}P NMR ($CDCl_3$, ppm): 9.9 (bs).

[^{99g}Tc(N)(L3)(PNP4)] (a + b). Yield 60%. Anal. ($C_{15}H_{31}N_2O_4P_2S_2Tc$ Mw = 532.51): calcd C, 33.83; H 5.86; N 6.01; S 12.04. Found C, 33.85; H 5.93; N 6.12; S 12.32.^{1}H NMR ($CDCl_3$, ppm): 1.76−1.96 (12H, PCH_3 + 3H, NCH_3), 1.80−2.46 (16H, CH_2 groups), 3.66 and 3.74 (6H, s, s; SCH(COOCH_3)$_{exo/endo}$), 4.15 and 4.51 (2H, s, s; SC*H*(COOCH$_3$)$_{exo/endo}$). ^{31}P NMR ($CDCl_3$, ppm): 9.3 (bs).

Preparation of [Re(N)(Ln)(PNP)] Complexes. To a yellow solution containing the [Re(N)Cl$_2$(PNP)] precursor (0.1 mmol) dissolved in $CHCl_3$/EtOH (1.1) (20 mL), a slight excess of the appropriate H_2Ln dithiol (0.11 mmol) and an excess of Et_3N (10 drops) were added. The reaction mixture was refluxed for 2 h. After cooling, the solvents were evaporated under a gentle dinitrogen stream and the residue was dissolved in water (10 mL) and neutralized with 2 M citric acid. The aqueous phase was extracted three times with $CHCl_3$. The combined organic phases were washed with saline (3 × 10 mL) and dried over $MgSO_4$, and the solvent was stripped in vacuo. The oily residue was triturated with Et_2O giving a yellow powder. For [Re(N)(L7)(PNP24)], the oily residue was redissolved in $CHCl_3$ and purified by column chromatography on silica. Elution with a $CHCl_3$/MeOH mixture (10:1) gave a large yellow band. This fraction was collected and reloaded onto a silica column which was eluted with a $CHCl_3$/MeOH/acetone mixture (10:1:1). The first yellow band was collected and, after solvent removal, triturated with Et_2O giving a yellow powder as above.

[Re(N)(L)(PNP2)]. Yield 52%. Anal. ($C_{33}H_{39}N_2OP_2S_2$-Re Mw = 791.92): calcd C, 50.04; H 4.96; N 3.53; S 8.09. Found C, 49.85; H 5.01; N 3.65; S 7.86. IR (KBr, cm^{-1}): 1433 (s), 1097 (s, Re−P), 1052 (m) [ν(Re(N)], 697 (s). ^{1}H NMR ($CDCl_3$, ppm): 2.65−3.46 (16H, CH_2 groups), 3.21 (s, 3H, OCH_3), 6.86−7.99 (20H, H$_{arom}$); ^{13}C NMR ($CDCl_3$, ppm): 25.7 (d, PCH_2), 39.3 (s, dithiolate CH_2), 48.1, 52.1, 58.5, 68.7, 128.1−134.8 (C$_{arom}$); ^{31}P NMR ($CDCl_3$, ppm): 13.5 (s).

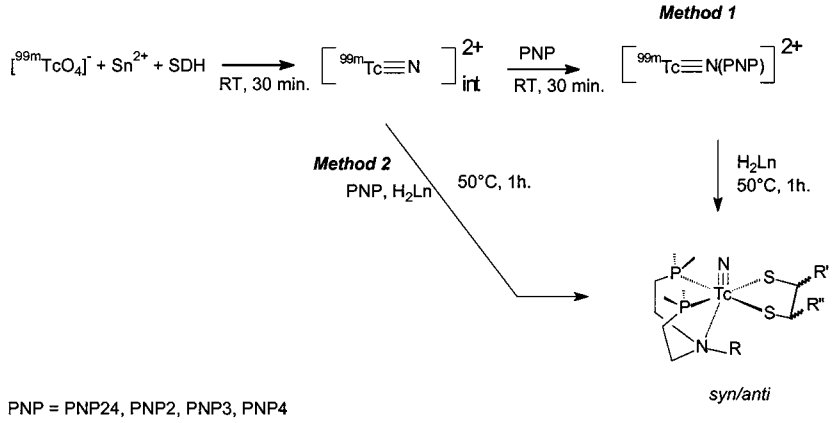
[Re(N)(L2)(PNP24)] (a + b). Yield 48%. Anal. ($C_{32}H_{35}N_2O_2P_2S_2Re$ Mw = 791.88): calcd C, 48.53; H 4.45; N 3.53; S 8.09. Found C, 48.12; H 4.60; N 3.61; S 7.72. ^{1}H NMR ($CDCl_3$, ppm): 1.23 (t, 3H; C(O)CH$_2$CH_3), 2.09 and 2.12 (s, 3H; NCH_3), 2.51−3.23 (10.5H), 3.77 (dd, 0.5H; SC*H*COEt), 4.14 (m, 2H; C(O)CH_2CH$_3$), 6.81−8.01 (20H, H$_{arom}$). ^{13}C NMR ($CDCl_3$, ppm): 14.2, 25.0, 39.2, 40.8, 46.4, 46.7, 53.5, 54.1, 59.1, 60.4, 128.0−133.0 (C$_{arom}$), 175.5 and 176.4 (*C*(O)). ^{31}P NMR ($CDCl_3$, ppm): 15.7 (d, $^2J_{PP}$ = 7.3 Hz), 16.1 (d, $^2J_{PP}$ = 7 Hz) and 15.4 (d, $^2J_{PP}$ = 7.3 Hz), 16.5 (d, $^2J_{PP}$ = 7 Hz).

[Re(N)(L7)(PNP24)] (a + b). Yield 41%. Anal. ($C_{37}H_{45}N_2O_2P_2S_2Re$ Mw = 862.01): calcd C, 51.55; H 5.26; N 3.25; S 7.44. Found C, 51.47; H 5.23; N 3.13; S 7,50. IR (KBr, cm^{-1}): 1709 (s, [νCO]), 1435 (s), 1099 (s, [νRe−P]), 1050 (m) [ν(Re(N)], 697 (s). ^{1}H NMR ($CDCl_3$, ppm): 1.64−1.24 (m, 6H), 1.90−3.11 (m, 15H), 2.35 (s, 3H; NCH_3), 6.76−8.00 (20H, H$_{arom}$). ^{13}C NMR ($CDCl_3$, ppm): 23.2, 24.3, 25.1, 27.0, 27.9, 34.0, 39.8, 42.5, 42.6, 47.0, 53.2, 53.9, 127.0−135.0 (C$_{arom}$), 177.8 (*C*(O)). ^{31}P NMR ($CDCl_3$, ppm): 15.2 (d, $^2J_{PP}$ = 7 Hz), 16.3 (d, $^2J_{PP}$ = 7 Hz).

Labeling Efficiency of H_2L1 Ligand. Ligand concentration that is required for metal complexation was determined by mixing different concentrations of H_2L1 with freshly prepared [^{99m}Tc(N)(PNP3/PNP4)]$^{2+}$ intermediate complexes following Method 1, using carrier free [Na^{99m}TcO$_4$] generator eluate containing 2.2 GBq in 0.250 mL of saline. The mixture was incubated at 50 °C or alternatively at 100 °C for 1 h. The final volume of the reaction solution was always kept within 1.5 mL by addition of ethanol. The final labeling yield was determined by HPLC and TLC analysis.

Stability Studies. Each ^{99m}Tc-complex (100 μL) was added to a propylene test tube (5 mL) containing rat

Scheme 1. Synthesis of [^{99m}Tc(Ln)(PNP)] Complexes



PNP = PNP24, PNP2, PNP3, PNP4

serum (900 μL), or alternatively saline (900 μL). The resulting mixture was incubated at 37 °C for 2 h and assayed by TLC for any changes in RCP at 15, 30, 60, and 120 min.

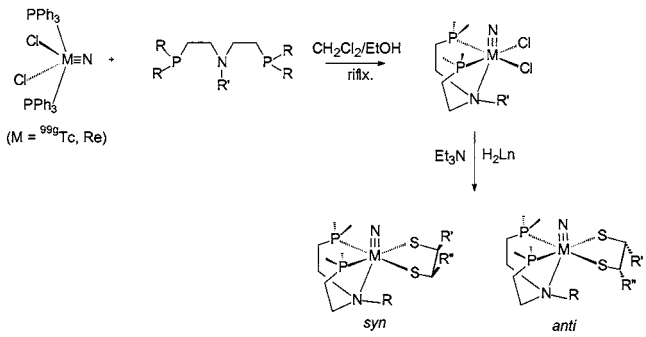
Glutathione (GSH) and Cysteine Challenge. In a propylene test tube (5 mL) containing 0.2 M phosphate buffer (250.0 μL, pH = 7.4), water (100.0 μL), and the ^{99m}Tc complex (100.0 μL), an aliquot (50.0 μL) of a 10.0 mM stock aqueous solution of GSH was added. The mixture was vortexed and incubated at 37 °C for 2 h. A blank reaction containing an equal volume of water instead of GSH was also accomplished. At 15, 30, 60, and 120 min, aliquots of the reaction mixture were withdrawn and analyzed by TLC and HPLC chromatography. All the complexes were found to be inert toward substitution by GSH. A similar procedure was applied using cysteine hydrochloride (10.0 mM and 1.0 mM) as the challenge ligand. The complexes were found to be stable toward cysteine transchelation.

Animal Studies. Biodistribution studies have been carried out in rats. After purification, the recovered activity was diluted with phosphate buffer (0.1 M, pH 7.4) to ensure that the final solution was 10% in ethanol content. Female, Sprague−Dawley rats weighing 200−250 g were anesthetized with an intramuscular injection of a mixture of ketamine (80 mg kg^{-1}) and xilazine (19 mg kg^{-1}). The ^{99m}Tc complexes (100 μL; 300−370 kBq) were injected into the jugular vein. The animals (n = 3) were sacrificed at 0, 2, 10, 20, 60 min time-intervals postinjection. The blood was withdrawn from the heart through a syringe immediately after sacrifice and counted. Organs were excised, rinsed with saline, weighed, and counted in a NaI well counter. The percent injected dose per gram (%ID g^{-1}) for each organ and blood was calculated, and the results are reported in Tables 2, 3 and 4.

RESULTS

Preparation and Characterization of ^{99m}Tc Complexes. Two different procedures were employed for preparing neutral nitrido ^{99m}Tc complexes of the type [^{99m}Tc(N)(Ln)(PNP)]. The optimal labeling procedure (Method 1, three-step synthesis) entailed the preliminary formation of a mixture of nitrido Tc-99m precursors, all containing the $[Tc{\equiv}N]^{2+}$ core, through the reduction of ^{99m}Tc pertechnetate with tin(II) chloride in the presence of SDH as donor of nitrido nitrogen. In the second step, the mixture was converted into the intermediate monosubstituted species [^{99m}Tc(N)X$_2$(PNP)] (11) (X = monodentate groups such as halides or hydroxyl) by reaction with the aminodiphosphine ligand (PNP) at room temperature. In the last step the preparation was completed by addition of the appropriate bidentate dithiol ligand (H_2Ln) to afford the final mixed nitrido complex in high RCY. Alternatively, a two-step procedure (Method 2), which required the simultaneous addition of the two polydentate ligands to the reaction vial containing the mixture of nitrido ^{99m}Tc precursors, was applied. A schematic drawing of the two synthetic methods and the hypothetical structure of the resulting complexes are illustrated in Scheme 1.

Scheme 2. Synthesis of [M(Ln)(PNP)] Complexes (M = ^{99g}Tc, Re)



The chemical identity of the ^{99m}Tc complexes was assessed by comparing their HPLC chromatograms with those of the corresponding ^{99g}Tc or Re compounds. Except for H_2L containing complexes, both TLC and HPLC techniques (Table 1) revealed the existence of two different compounds in 1:1 ratio, identified as the syn/anti isomeric forms of the mixed asymmetrical complexes (vide infra), irrespective of the aminodiphosphine or dithiol used, and of the experimental condition employed.

Preparation and Characterization of ^{99g}Tc and Re Mixed Complexes. Nitrido ^{99g}Tc and Re mixed complexes were prepared by ligand exchange reactions according to the pathway outlined in Scheme 2. Reactions of labile [M(N)Cl$_2$(PPh$_3$)$_2$] precursors with a slight excess of the appropriate aminodiphosphine ligand in dichloromethane/ethanol solutions led to the formation of the monosubstituted intermediate complexes [M(N)Cl$_2$(PNP)]. Subsequent addition of the relevant dithiol ligand in basic media by Et$_3$N produced the final neutral mixed compounds [M(N)(Ln)(PNP)]. Isolation of the [Re(N)Cl$_2$-(PNP)] intermediate complexes (*9*) was necessary to avoid formation of intractable byproducts.

Elemental analyses of all of the mixed complexes [M(N)(Ln)(PNP)], as shown in the Experimental Section, were in good agreement with the proposed formulation. Multinuclear NMR characterization (^{1}H, ^{13}C and ^{31}P)

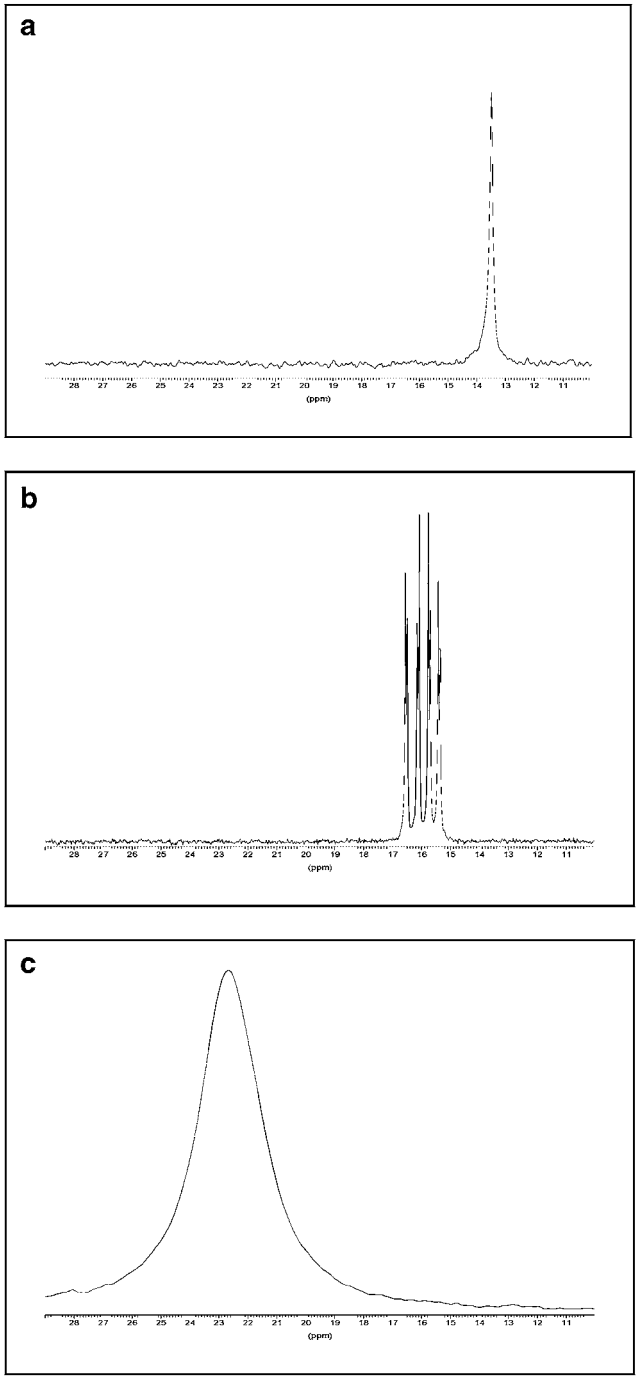


Figure 2. ^{31}P NMR spectra of selected Re and ^{99g}Tc complexes: (A) a singlet for [Re(N)(L)(pnp2)], (B) two doublets of doublets for [Re(N)(L2)(pnp24)], (C) a broad singlet for [^{99g}Tc-(N)(L6)(pnp4)].

allowed the identification of this class of dithiolate-containing species in the solution state. In particular, the ^{31}P NMR signal was diagnostic of diphosphine coordination, the associated signal being deshielded from negative ppm values in uncoordinated ligands (in the range from − 21.5 [pnp2 and pnp24] to − 52.8 ppm [pnp4]) to positive ones in coordinated compounds (in the range from 22.6 [Tc(N)(L6)(pnp3)] to 9.3 ppm [Tc(N)(L3)(pnp4)]). The ^{31}P signal is relatively sharp for rhenium complexes (half line width ($\nu_{1/2}$) of ca. 25 Hz) and broadens to $\nu_{1/2}$ = ca. 300 Hz for technetium species (Figure 2c). Such broadening was observed previously by other authors in similar diamagnetic Tc(V) compounds and attributed to the coupling of the ^{31}P nuclei with the quadrupolar ^{99}Tc center (*20*). In the complex [Re(N)(L)(PNP2)], the diphosphine phosphorus were found to be magnetically equivalent, facing the simplest symmetric dithiolato ligand of the series, thereby showing a singlet at δ = 13.5 ppm (Figure 2a). The magnetic equivalence of coordinated Ps was removed in other rhenium complexes due to the introduction of a pendant substituent onto the dithiolate framework that caused the split of the signal into two doublets of doublets. In addition, the orientation of such substituent (syn or anti positioned with respect to the terminal nitride group) induced a further split of the ^{31}P signal into two equally populated doublets of doublets (Figure 2b).

For technetium complexes, formation of the isomer pairs was detected by chromatographic methods. Both TLC and HPLC showed two distinct peaks of equal intensity in their chromatographic profiles, corroborating the view that reaction of monosubstituted dithiolate ligands onto [M(N)(PNP)] moieties is not regiospecific. For the identification of the two isomers, separation of the diastereoisomeric mixture was accomplished by column chromatography on silica on the representative [Tc(N)(L1)(pnp4)] complex. Proton NMR spectra of the two isolated fractions displayed similar patterns except for the dithiolate networks. The more lipophilic isomer (T_R = 20.12 min) identified via two-dimensional ^{1}H−^{1}H COSY-45 maps by the methyne proton at 3.60 ppm coupled with the diastereotopic methylene ones at 3.19 and 3.01 ppm, was assigned as the syn isomer by analogy with previously reported pairs of mixed nitrido heterocomplexes containing N-substituted cysteine (*21*). The less lipophilic isomer (T_R = 18.59 min.), displaying the dithiolate network spread over a wider ppm region (δ = 3.74, 3.27 and 2.66 ppm for methyne and methylene protons, respectively) was assigned as the anti isomer. The presence of diastereotopic methylene protons in the dithiolato backbone of both isomers supports the view that coordination of the dithiolate ligand occurs via the [S$^-$,S$^-$] donor set, leaving the carboxylic group out of the coordination sphere available for coupling with biomolecules. Hence, as depicted in Scheme 2, these complexes are composed by a Tc≡N group coordinated to a facially arranged aminodiphosphine ligand, the phosphorus donors of which face the dithiolato sulfurs on the equatorial plane.

Finally, a close matching of HPLC retention times of corresponding pairs of ^{99m}Tc and ^{99g}Tc complexes (see the chromatographic profiles of the diastereisomeric mixture of [Tc(N)(L1)(pnp4)] reported in Figure 3) attested the chemical identity of the species produced at nca and macroscopic levels.

Labeling Efficiency of H_2L1 ligand. The design of new ^{99m}Tc receptor-based radiopharmaceuticals requires the choice of an efficient BFCA. The main factor influencing the ^{99m}Tc-labeling kinetics is the nature of the donor atoms and the radiolabeling conditions. In addition, the use of large amount of BFCA conjugate may result in receptor site saturation, blocking the docking of the ^{99m}Tc-labeled BFCA conjugate, as well as in unwanted side effects. Consequently, the concentration of the BFCA conjugate in each kit has to be very low, usually in the 10^{-5} to 10^{-6} M range (*22*).

For these reasons, we investigated the influence of the aminodiphosphine (PNP3 or PNP4)/dithiol molar ratio on the radiochemical yield (RCY) of the resulting heterocomplexes. In detail, bidentate H_2L1 was labeled at different concentrations under standardized conditions, by adding the dithiol solution to freshly prepared [^{99m}Tc-(N)(PNP3/4)]$^{2+}$ intermediate species synthesized using different amounts of aminodiphosphine. The dependence

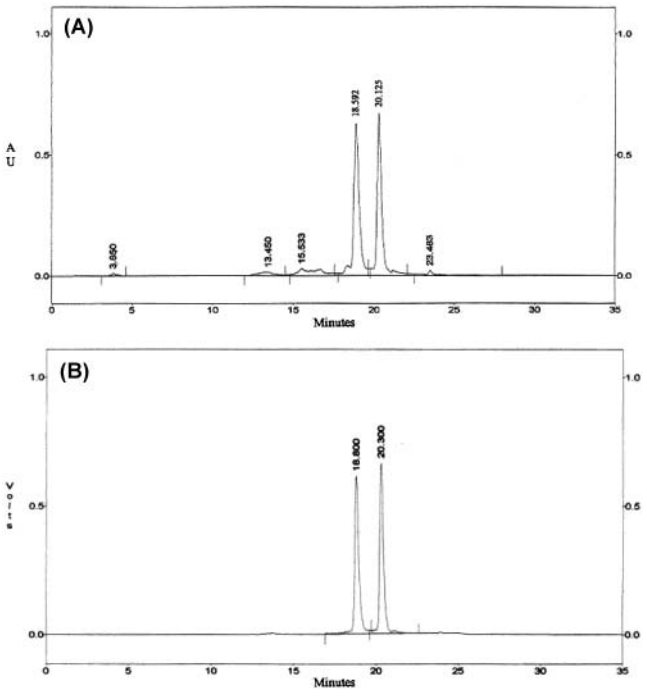


Figure 3. HPLC chromatographic profiles of the diastereomeric mixture of *syn*/*anti*-[Tc(N)(L1)(pnp4)] complexes: (A) UV−vis trace, (B) radiometric trace.

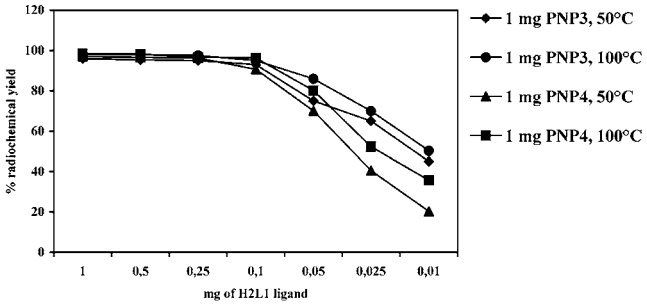


Figure 4. Radiochemical yields of [^{99m}Tc(N)(L1)(PNP)] complexes as a function of H_2L1 concentration at 50 °C and 100 °C.

of RCY of heterocomplex formation, as a function of H_2L1 concentration (1 mg − 15μg) at different temperature (50° or 100 °C), is illustrated in Figure 4. The analysis of the diagram revealed that highest RCY was achieved with a PNP/H_2L1 ratio of approximately 3.5:1, irrespective of the PNP and of the temperature used. A strictly similar behavior was detected in a related mixed system including PNP3 and substituted cysteine ligands (N,S-cys, O,S-cys), demonstrating that the ^{99m}Tc labeling efficiency of [S^-,S^-] coordinating pair was comparable with [N,S^-]-cys and/or [O^-,S^-]-cys ones (*11*). Moreover, by fixing a 3.5:1 PNP/H_2L1 molar ratio, and progressively reducing the amount (in terms of mg) of the two ligands, quantitative formation of the final complex was obtained after 1 h heating at 50 °C using 0.5 mg of PNP4 and 0.125 mg of H_2L1. The time-activity curves are reported in Figure 5a. As expected, higher RCY (>95%) was obtained at 100 °C at earlier times (30 min), using a lower amount of the two chelating ligands (PNP4 = 0.125 mg; H_2L1 = 0.03 mg) (see Figure 5b). An identical behavior was observed at 50 °C with PNP3 (data not shown), while highest labeling efficiency was detected at 100 °C reducing the amount of PNP3 at 0.062 mg and H_2L1 at 0.006 mg (3 μM) (Figure 5c).

These studies evidenced that the radio-labeling efficiency of the bidentate ligand H_2L1 is function of several

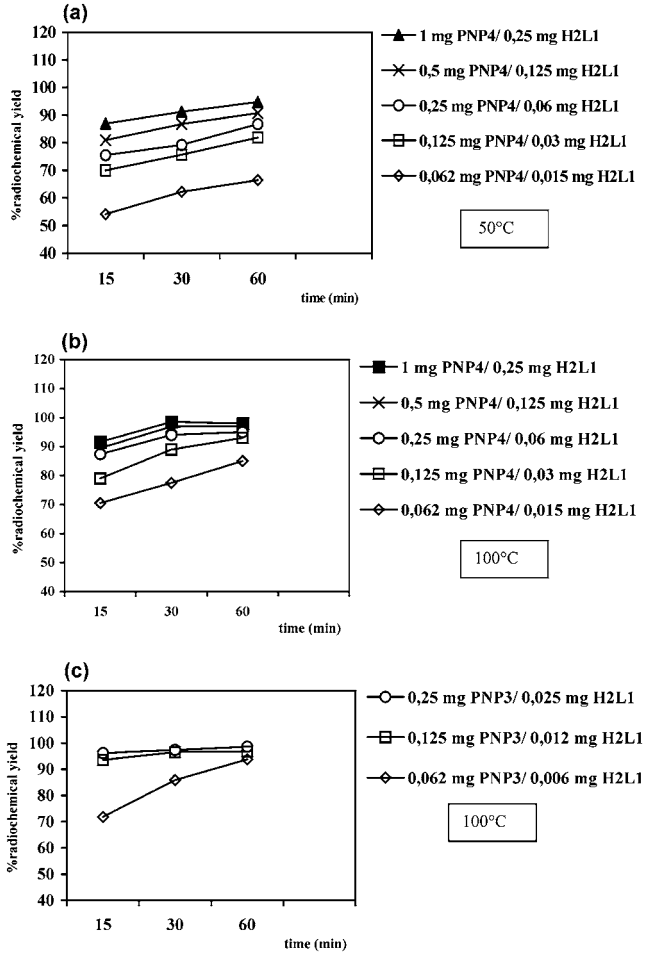


Figure 5. Time−activity curves of [^{99m}Tc(N)(L1)(PNP)] complexes.

factors, including the identity of the [^{99m}TcN(PNP)]$^{2+}$ metal fragment. In fact, by increasing the bulkiness at the aminodiphosphine substituents (PNP4 → PNP3), the radiolabeling efficiency improves by a factor of 5. Studies aiming at the comprehension of the role of different substituents, especially those at the tertiary amine nitrogen, on the overall stability of the resulting intermediate and final mixed compounds are under investigation.

Stability. Serum stability and the stability toward transchelation with GSH and cysteine of ^{99m}Tc-complexes were investigated. No significant change of radiochemical purity (RCP) was observed after 2 h of incubation at 37 °C with excess GSH or cysteine, indicating that all of these compounds are inert toward substitution. On the contrary, slight difference in serum stability was observed. Those complexes containing ester group(s) in the dithiolate backbone were rapidly transformed into more hydrophilic species, due to hydrolysis to the corresponding ionizable acid forms, a well-recognized phenomenon occurring in-vivo catalyzed by serum enzymes, and extensively reported by Seifert and co-workers (*23*). Hydrolysis proceeded with different rates, depending on the steric hindrance of the ester group(s), but, in all cases, it was completed after 60 min of incubation. On the contrary, ^{99m}Tc complexes not incorporating ester group-(s) in the dithiolate framework were found to be stable after 2 h of incubation in rat serum.

Biodistribution. The tissue distribution data of [^{99m}Tc(N)(L)(PNP4)], [^{99m}Tc(N)(L1)(PNP4)], and [^{99m}Tc-(N)(L1)(PNP3)] complexes are summarized in Tables 2,

Table 2. Biodistribution in Rats of the Complex [^{99m}Tc(N)(L)(PNP4)] (%dose/g)

organ	0 min	2 min	10 min	20 min	60 min
blood	2.41 ± 0.45	0.90 ± 0.16	0.65 ± 0.03	0.48 ± 0.02	0.32 ± 0.05
brain	0.35 ± 0.20	0.09 ± 0.01	0.05 ± 0.01	0.04 ± 0.00	0.03 ± 0.00
heart	2.49 ± 0.48	1.15 ± 0.06	0.61 ± 0.01	0.49 ± 0.04	0.32 ± 0.03
lungs	1.80 ± 0.17	1.04 ± 0.10	0.65 ± 0.05	0.54 ± 0.00	0.33 ± 0.01
liver	1.82 ± 0.44	2.09 ± 0.06	1.08 ± 0.02	0.97 ± 0.02	0.62 ± 0.04
spleen	1.20 ± 0.08	0.19 ± 0.04	0.68 ± 0.04	0.52 ± 0.03	0.36 ± 0.06
kidneys	2.66 ± 0.40	3.65 ± 0.00	1.83 ± 0.13	1.49 ± 0.34	0.89 ± 0.05
intestine	1.54 ± 0.06	2.06 ± 0.21	1.62 ± 0.24	2.22 ± 0.20	2.52 ± 0.75
muscle	0.21± 0.10	0.46 ± 0.08	0.42 ± 0.01	0.42 ± 0.01	0.32 ± 0.02

Table 3. Biodistribution in Rats of the Complex [^{99m}Tc(N)(L1)(PNP4)] (%dose/g)

organ	0 min	2 min	10 min	20 min	60 min
blood	2.89 ± 0.03	1.20 ± 0.06	0.51 ± 0.01	0.32 ± 0.05	0.15 ± 0.00
brain	0.23 ± 0.03	0.08 ± 0.00	0.03 ± 0.01	0.02 ± 0.00	0.02 ± 0.00
heart	0.80 ± 0.02	0.37 ± 0.00	0.21 ± 0.03	0.12 ± 0.01	0.07 ± 0.01
lungs	1.23 ± 0.04	0.69 ± 0.08	0.34 ± 0.03	0.22 ± 0.01	0.12 ± 0.01
liver	2.66 ± 0.02	2.95 ± 0.33	2.09 ± 0.11	1.85 ± 0.25	0.56 ± 0.07
spleen	0.49 ± 0.13	0.36 ± 0.02	0.11 ± 0.01	0.12 ± 0.01	0.05 ± 0.01
kidneys	2.52 ± 0.17	6.55 ± 1.77	2.98 ± 0.82	2.36 ± 0.09	1.28 ± 0.12
intestine	0.71 ± 0.02	1.68 ± 0.02	5.66 ± 0.90	7.20 ± 0.48	9.40 ± 2.56
muscle	0.21 ± 0.03	0.20 ± 0.01	0.15 ± 0.04	0.09 ± 0.00	0.06 ± 0.01

Table 4. Biodistribution in Rats of the Complex [^{99m}Tc(N)(L1)(PNP3)] (%dose/g)

organ	0 min	2 min	10 min	20 min	60 min
blood	4.33 ± 0.83	0.44 ± 0.11	0.20 ± 0.04	0.07 ± 0.00	0.02 ± 0.00
brain	0.25 ± 0.09	0.06 ± 0.02	0.01 ± 0.00	0.01 ± 0.00	0.01 ± 0.00
heart	0.93 ± 0.25	0.17 ± 0.04	0.07 ± 0.00	0.03 ± 0.00	0.01 ± 0.00
lungs	1.38 ± 0.48	1.34 ± 0.10	0.14 ± 0.01	0.06 ± 0.00	0.33 ± 0.00
liver	2.62 ± 0.85	3.30 ± 0.15	1.70 ± 0.57	0.34 ± 0.01	0.11 ± 0.02
spleen	0.50 ± 0.09	0.17 ± 0.02	0.05 ± 0.00	0.04 ± 0.01	0.03 ± 0.00
kidneys	1.86 ± 0.43	4.24 ± 0.35	1.01 ± 0.13	0.39 ± 0.09	0.21 ± 0.02
intestine	3.07 ± 0.65	14.62 ± 2.95	18.57 ± 2.27	15.71 ± 1.53	12.10 ± 0.90
muscle	0.15 ± 0.01	0.13 ± 0.01	0.09 ± 0.05	0.23 ± 0.03	0.05 ± 0.00

3, and 4. Before injection, the complexes were purified using the procedures outlined in the Experimental Section. RCP and stability of the purified complexes were verified before in vivo administration. PNP4 containing complexes showed an efficient clearance from the blood and target and nontarget tissues within 1h postinjection. The excretion of the radioactivity from the body occurred via both the renal and the hepatobillary (liver and intestines) systems. Even faster blood and tissues clearances were observed for the PNP3 containing complex, except for a high intestinal uptake (14.62%dose/g) at 2 min postinjection.

DISCUSSION

Dithiols and substituted dithiols ligands (H_2Ln) have been proven to be efficient chelating systems for [M(N)(PNP)] moieties (M = ^{99m}Tc, ^{99g}Tc and Re) giving neutral asymmetrical heterocomplexes of the type [M(N)(Ln)(PNP)] in high yield. According to the general synthetic pathways presented in Schemes 1 and 2, these heterocomplexes can be prepared using either a two-step or a three-step procedure involving the preliminary formation of prereduced species containing the terminal [M(N)] group, followed by contemporary or sequential addition of the relevant aminodiphosphine (PNP) and dithiol. Under the synthetic conditions utilized in this study, no detectable formation of the corresponding symmetrical nitrido compounds comprising two identical polydentate ligands (i.e. [Tc(N)$(PNP)_2$] and/or [Tc(N)$(Ln)_2$]) was observed.

The molecular structure of these mixed complexes contains the [M(N)(PNP)] metal fragment composed by the multiply bonded nitrido group and a facially arranged aminodiphosphine, to which the two sulfur of the dithiolate ligand are coordinated on the remaining equatorial sites (see Scheme 2). When pendant group(s) are introduced in the dithiolate framework, an equimolar mixture of *syn*-[M(N)(Ln)(PNP)] and *anti*-[M(N)(Ln)(PNP)] isomers was always collected. The formation of the isomer pairs depends on the orientation of the pendant dithiolate group(s) relative to the terminal [M(N)] core.

Dithiol ligands such as H_2L1 and H_2L7, which incorporate an additional potentially coordinative carboxylic function, behave as described above, giving a diastereoisomeric mixture of syn and antispecies. Also in this case, spectroscopic data (for example, the presence of diastereotopic methylene protons in the L1 backbone of the ^{1}H NMR spectrum of [^{99g}Tc(N)(L1)(PNP4)]) suggest that coordination of the substituted dithiolate occurred via the [S^-,S^-] coordinating atoms, leaving the carboxylic function outside from the metal coordination sphere, thereby offering a convenient site on which to append other molecule designed to target specific tissue or receptor.

Dithiolate-containing [^{99m}Tc(N)(Ln)(PNP)] species were found to be stable toward transchelation reactions with excess of physiologically relevant cysteine and glutathione, and incubation in rat serum revealed hydrolysis of the outer ester functions in those complexes containing ester-substituted dithiolate only, without affecting the inner coordination sphere. These data suggest high stability of the mixed [M(N)(Ln)(PNP)] configuration. Moreover, no isomeric conversion between syn and anti forms was observed under a wide range of experimental conditions (room temperature and 100 °C, pH from 5 to 9) indicating a superior chelating power of the S,S-dithiolate pairs compared to the S,O-cysteine one included in similar [M(N)(O,S-cys)(PNP)] complexes, in which conversion of the syn into the anti form was found to occur through a dissociative mechanism implying

release of the carboxylate oxygen of the O,S-cys ligand from the metal (*21*).

Dithiolates showed a radiolabeling efficiency toward the [^{99m}Tc(N)(PNP)] synthons in the micromolar range, values comparable to those exhibited by different bidentate donors such as O,S-cys and N,S-cys. This behavior is likely attributed to the peculiar electronic and steric properties of the [Tc(N)(PNP)] metal fragment. Its strong electrophilic character induces selective reactions with π-donor atoms to achieve mixed ligand arrangements, which are well tailored for the [Tc(N)] core. In addition, the facial arrangement of the PNP ligand grants the best steric configuration for the substitution of labile halides with incoming bidentate ligands. Hence, substituted dithiolates carrying further functional groups (i.e. H_2L1 and H_2L7) constitute alternative chelating systems for incorporating bioactive molecule into nitrido-containing ^{99m}Tc compounds.

Biodistribution studies in rats performed using the three representative [^{99m}Tc(N)(L)(PNP4)], [^{99m}Tc(N)(L1)-(PNP4)], and [^{99m}Tc(N)(L1)(PNP3)] showed that they were efficiently cleared from the blood, and no specific uptake or long-term retention was observed in other organs to reduce the background activity, except for a gastrointestinal tract accumulation of the PNP3 derivative. The latter behavior was already observed in a series of related nitrido ^{99m}Tc-complexes containing terminal methoxy and/or ethoxy pendant groups in the aminodiphosphine framework (*24*). This could be associated with a faster hepatobillary excretory pathway and/or with an aspecific intestinal uptake. Studies focused on the comprehension of the biological mechanism underlying this process are in progress.

The chemical flexibility of the [Tc(N)(Ln)(PNP)] system, which allows subtle tuning of the lipophilicity by insertion of variable groups onto the PNP framework of the [Tc(N)(PNP)] synthon on one side, and the possibility to conjugate biologically active fragments onto the dithiolate backbone make this class of compounds interesting candidates for the design of new receptor-based ^{99m}Tc agents.

CONCLUSION

Micromolar concentrations of dithiolate and substituted dithiolate ligands have successfully chelated [^{99m}Tc-(N)(PNP)] moieties giving neutral, mixed-ligand complexes of the type [^{99m}Tc(N)(Ln)(PNP)]. Comparison of their chromatographic profiles with those of the corresponding [M(N)(Ln)(PNP)] compounds (M = ^{99g}Tc, Re) indicated an identical molecular structure at nca and macroscopic levels. The substituent(s) incorporated in the dithiolate backbone promoted the formation of equally populated syn and anti isomers, depending on the relative orientation of the substituent(s) with respect to the terminal nitrido group. Mixture of the two isomers of each ^{99m}Tc-compound was found to be substitution-inert toward transchelation reaction when incubated with excess of cysteine or glutathione. In vivo studies in rats showed that they were efficiently cleared from the blood, and no specific uptake or long-term retention was observed in the kidneys and in other organs. The combination of the biological properties exhibited by this class of nitrido mixed-ligand compounds, along with the possibility to conjugate biologically active fragments onto the dithiolate carboxylic or hydroxylic pendant groups, make this novel molecules interesting candidates for the development of receptor-specific ^{99m}Tc-radiopharmaceuticals.

ACKNOWLEDGMENT

This work was supported by Nihon Medi-Physics Co., Ltd., Tokio, Japan. The authors wish to thank Anna Rosa Moresco for her work on the elemental analysis.

LITERATURE CITED

(1) Pasqualini, R., Comazzi, V., Bellande, E., Duatti, A., and Marchi, A. (1992) A New Efficient Method for the Preparation of ^{99m}Tc-radiopharmaceuticals Containing the Tc≡N Multiple Bond. *Int. J. Appl. Radiat. Isot. 43*, 1329−1333.

(2) Boschi, A., Bolzati, C., Uccelli, L., and Duatti, A. (2003) High-yield Synthesis of the Terminal ^{188}Re≡N Multiple Bond from Generator-produced [^{188}ReO$_4$]$^-$. *Nucl. Med. Biol. 30*, 381−387.

(3) Pasqualini, R., and Duatti, A. (1992) Synthesis and Characterization of the New Neutral Myocardial Imaging Agent [^{99m}TcN(noet)$_2$] (noet = *N*-ethy-*N*-ethoxydithiocarbamato). *J. Chem. Soc., Chem. Commun.* 1354−1355.

(4) Baldas, J., Bonnyman, J., and Williams, G. A. (1986) Studies of Technetium Complexes. 9. Use of the Tetrachloronitridotechnetate(VI) Anion for the Preparation of Nitrido Complexes of Technetium. *Inorg. Chem. 25*, 150−153.

(5) Pasqualini, R., Duatti, A., Bellande, E., Comazzi, V., Brucato, V., Hoffschir, D., Fagret, D., and Comet, M. (1994) Bis-(dithiocarbamate) Nitrido Technetium-99m Radiopharmaceuticals: A Class of Neutral Myocardial Imaging Agents. *J. Nucl. Med. 35*, 334−341.

(6) Kailasnath, P., and Sinusas, A. J. (2001) Comparison of Tl-201 with Tc-99m-labeled Myocardial Perfusion Agents: Technical, Physiologic, and Clinical Issues. *J. Nucl. Cardiol. 8*, 482−498.

(7) Bandoli, G., Dolmella, A., Porchia, M., Refosco, F., and Tisato, F. (2001) Structural Overview of Technetium Compounds (1993−1999). *Coord. Chem. Rev. 214*, 43−90.

(8) Bolzati, C., Boschi, A., Duatti, A., Prakash, S., Uccelli, L., Refosco, F., Tisato, F., and Bandoli, G. (2000) Geometrically Controlled Selective Formation of Nitrido Technetium(V) Asymmetrical Heterocomplexes with Bidentate Ligands. *J. Am. Chem. Soc. 122*, 4510−4511.

(9) Bolzati, C., Boschi, A., Uccelli, L., Tisato, F., Refosco, F., Cagnolini, A., Duatti, A., Prakash, S., Bandoli, G., and Vittadini, A. (2002) Chemistry of the Strong Electrophilic Metal Fragment [^{99}Tc(N)(PXP)]$^{2+}$ (PXP = Diphosphine Ligand). A Novel Tool for the Selective Labeling of Small Molecules. *J. Am. Chem. Soc. 124*, 11468−11479.

(10) Bolzati, C., Refosco, F., Cagnolini, A., Tisato, F., Boschi, A., Duatti, A., Uccelli, L., Dolmella, A., Marotta, E., and Tubaro M. (2004) Synthesis, Solution-State and Solid-State Structural Characterization of Monocationic Heterocomplexes [M(N)(DTC)(PNP)]$^+$ (M = ^{99}Tc, Re; DTC = Dithiocarbamate; PNP = Heterodiphosphine). *Eur. J. Inorg. Chem*, in press.

(11) Boschi, A., Bolzati, C., Benini, E., Malagò, E., Uccelli, L., Duatti, A., Piffanelli, A., Refosco, F., Tisato, F. (2001) A Novel Approach to the High-specificic-activity Labeling of Small Peptides with the Technetium-99m Fragment [^{99m}Tc(N)-(PXP)]$^{2+}$ (PXP = Diphosphine Ligand). *Bioconjugate Chem. 12*, 1035−1042.

(12) Jurisson, S. S., and Lydon, J. D. (1999) Potential Technetium Small Molecules Radiopharmaceuticals. *Chem. Rev. 99*, 2205−2218 and references therein.

(13) Pietzsch, H. J., Spies, H., and Hoffmann, S. (1989) Lipophilic Technetium Complexes. VI. Neutral Tc(V) Complexes with tridentate dithiols/monothiole ligand coordination. *Inorg. Chim. Acta 165*, 163−166.

(14) Spies, H., and Scheller, D. (1986) Chemical and 1H NMR Spectroscopic Investigations od Stereoisomeric Tc(V) DMSA Complexes. *Inorg. Chim. Acta 116*, 1−4.

(15) Liu, S., and Edwards, D. S. (1999) ^{99m}Tc Small Peptides as Diagnostic Radiopharmaceuticals. *Chem. Rev. 99*, 2235−2268 and references therein.

(16) Meegalla, S. K., Plossl, K., Kung, M. P., Stevenson, D. A., Mu, M., Liable-Sands, L. M., Rheingold, A. L., and Kung, H.

F. (1998) Specificity of Diasteromers of [^{99m}Tc]TRODAT-1 as Dopamine Transporter Imaging Agents. *J. Med. Chem. 41*, 428−436.

(17) Thakur, M. L., John, E., Li, J., Reddy, H. R., Halmos, G., and Schally A. V. (1995) Tc-99m-RC-160: A Somatostatin Analogue for Imaging Prostate Cancer: Comparison with I-125-RC-160 and In-111 Ostreotide. *J. Nucl. Med. 36*, 92P.

(18) Bianchini, C., Casares, J. A., Peruzzini, M., Romerosa, A., and Zanobini, F. (1996) The Mechanism of the Ru-assisted C−C Bond Cleavage of Terminal Alkynes by Water. *J. Am. Chem. Soc. 118*, 4585−4595.

(19) Hoepping, A., Spies, H. (1995) Preparation of 2,3-Dimercaptopropionic Acid Ethyl Ester. *Annual Report Forschungszentrum Rossendorf, FZR-122*, 89−90.

(20) Abram U., Lorenz B., Kaden L., and Scheller D. (1988) Nitrido Complexes of Technetium with Tertiary Phosphines and Arsines *Polyhedron 7*, 285−289.

(21) Bolzati, C., Mahmood, A., Malagò, E., Uccelli, L., Boschi, A., Jones, A. G., Refosco, F., Duatti, A., and Tisato, F. (2003) The [^{99m}Tc(N)(PXP)]$^{2+}$ Metal Fragment: A Technetium-Nitrido Synthon for Use with Biologically Active Molecules. The N−(2-Methoxyphenyl)piperazyl-cysteine Analogues as Examples. *Bioconjugate Chem. 14*, 1231−1242.

(22) Liu, S., Edwards, D. S., and Barrett, J. A. (1997) 99mTc Labeling of Highly Potent Small Peptides. *Bioconjugate Chem. 8*, 621−636.

(23) Seifert, S., Syhre R., Spies H., Johannsen B. (1997) Enzymatic Hydrolysis of Ester Group of Mixed-ligand Oxorhenium(V) and Oxotechnetium(V) Complexes. *Appl. Radiat. Isot. 48*, 1051−1057.

(24) Boschi, A., Uccelli, L., Bolzati, C., Duatti, A., Sabba, N., Moretti, E., Di Domenico, G., Zavattini, G., Refosco, F., Giganti, M. (2003) Synthesis and Biological Evaluation of Monocationic Asymmetric ^{99m}Tc−Nitride Heterocomplexes Showing High Heart Uptake and Improved Imaging Properties. *J. Nucl. Med. 44*, 806−814.

BC0499782

Synthesis and Fluorescence Studies of Multiple Labeled Oligonucleotides Containing Dansyl Fluorophore Covalently Attached at 2′-Terminus of Cytidine via Carbamate Linkage

Arvind Misra,† Satyendra Mishra, and Krishna Misra*

Nucleic Acids Research Laboratory, Department of Chemistry, University of Allahabad, Allahabad- 211 002, India Received January 11, 2004; Revised Manuscript Received March 2, 2004

Synthesis of modified oligonucleotides in which the specific cytidine nucleoside analogues linked at 2′-OH position via a carbamate bond with an amino ethyl derivative of dansyl fluorophore is reported. For the multiple labeling of oligonucleotides, a strategy involving prelabeling at the monomeric level followed by solid phase assembly of oligonucleotides to obtain regiospecifically labeled probes has been described. The labeled monomer was phosphitylated using 2-cyanoethyl- *N*,*N*,*N*′,*N*′-tetraisopropyl-phosphoramidite (Bis-reagent) and pyridiniumtrifluoro acetate (Py·TFA) as an activator. To ascertain the minimal number of labeled monomers required for a specific length of oligonucleotide for detection and also to assess the effect of carbamate linkage on hybridization, hexamer and 20-mer sequences were selected. Both were labeled with 1, 2, and 3 monomers at the 5′-end and hybridized with normal (unmodified) complementary sequences. As compared to midsequence or 3′-terminal labeling reported earlier, the 5′-terminal labeling has been found to have minimal contact-mediated quenching on duplex formation. This may be due to complementary deoxyguanosine (dG) rich oligonucleotide sequences or CG base pairs at a terminus that is known to yield stronger binding. This is one reason for selecting cytidine for labeling. The results may aid rational design of multiple fluorescent DNA probes for nonradioactive detection of nucleic acids.

INTRODUCTION

Fluorescent labeling of oligonucleotides has been attracting current interest in connection with the development of new methods for distinguishing and detecting nucleic acids sequences for diagnostics and homogeneous hybridization assays. Being dependent on the local environment fluorescence has proved an indispensable tool for the study of molecular interactions and several cellular functions. Fluorescently labeled oligonucleotide probes are nowadays in much regular use for nucleic acid sequencing (*1*), sequencing by hybridization (SBH) (*2*), fluorescence in situ hybridization (FISH) (*3*), fluorescence resonance energy transfer (FRET) (*4*−*6*), molecular beacons (*7*−*8*), taqman probes (*9*), and chip-based DNA arrays (*10*−*11*). This has made fluorescent probes an important tool for clinical diagnostics and made possible real-time monitoring of oligonucleotide hybridization. Furthermore, fluorescent-based diagnostics avoids the problem of storage, stability, and disposal of radioactive labels (*12*).

Application of techniques mentioned above requires appropriately labeled nucleic acids and/or oligonucleotides. Labeling techniques for the incorporation of different fluorophores at different functional positions has been very well established. The multiple functionalization may be another alternative approach for the enhancement of sensitivity of detection. Most of the synthetic strategies involving synthesis of nucleic acids incorporated with modified bases carrying nucleophilic handles such as alkylamines, hydroxyl, and sulfydryls followed by labeling reactions has been extensively reviewed (*13*). However, in the case of ribonucleotides, 2′-OH function of the ribose ring can be utilized for the covalent attachment of ligands such as fluorophores. Attachment of ligands at this position may not cause any steric hindrance and thereby any destabilization in the stable duplex formation. Few approaches to link fluorophores at the 2′-end have been addressed for particular analytical needs (*14*−*19*).

It has been reported that nucleobases in ribozyme core regions are often in a different kind of noncovalent interaction which is important for maintaining structure and function (*20*−*21*). 2′-End ligand functionalization has already proved valuable in applications such as fluorescence monitoring of tertiary folding of oligoribonucleotides (*22*). An alternative opportunity for 2′-OH functionalization is via a carbamate function which can be easily generated by reaction with *N*,*N*′-carbonyldiimidazole (CDI). This chemistry has been used successfully for 5′-modification of oligoribonucleotides (*23*), 3′-modifications (*24*), and 2′-modifications (*25*−*27*).

The present report describes the preparation of cytidine-2′-yl carbamate and its subsequent attachment with 5-*N*,*N*-dimethylaminonaphthalene sulfonyl (dansyl) ethylamine derivative to get a fluorescent analogue for its further incorporation into the oligonucleotides for multiple labeling and their hybridization with complementary sequences. The oligonucleotides were synthesized using a standard phosphoramidite protocol, and the modified fluorescent cytidine analogue was placed in the last coupling step to get terminally 5′-O-mono, di, and tridansylated oligonucleotides. The modified oligonucle-

* Corresponding author. E- mail: Krishnamisra@hotmail.com. Phone:(91)-0532-2465462/2467154/2460816/2461377- 80. Fax: (91)-0532-2461376/2608469.

† Present Address: Institute of Genomics and Integrative Biology (Formerly Centre for Biochemical Technology). Delhi University Campus, Mall Road, Delhi − 110 007 arvindmisra12@yahoo.co.in.

10.1021/bc049976h CCC: $27.50 © 2004 American Chemical Society
Published on Web 04/23/2004

otide probes have shown remarkable enhancement in the fluorescence intensity vis-à-vis the dansyl fluorophore. It is reported that placement of dansyl fluorophore in the hydrophobic environment causes a significant increase in the fluorescence intensity, quantum yield, and blue shift in the emission (*28*−*30*). Therefore, it is proposed that such labeled probes may be exploited for the characterization of the nucleobases present in ribozymes core regions because such nucleobases are important for maintaining structure and function of ribozymes. These can also be used similarly in other cases in which a hydrophobic environment exists. However, upon duplex formation with the complementary deoxyguanosine (dG) base present at the terminal 5′-position, a minimal quenching termed "contact mediated quenching" has been observed. This quenching is relatively insignificant as compared to the already reported cases in which labeling is at 3′-termini or in the middle of the sequence. The binding affinity with complementary strands has been assessed by taking UV-melting profiles. The results not only demonstrated the feasibility of covalent attachment of the fluorophore via carbamate linkage but also defines necessary requirements for achieving optimum enhancement of fluorescence intensity.

EXPERIMENTAL PROCEDURES

General. 1,3-Dichloro-1,1,3,3-tetraisopropyldisiloxane (TIPDSCl) was from Merck-Schchdart, Germany; dansyl chloride, 4,4′-dimethoxytrityl chloride (DMTr-Cl), (dimethylamino)pyridine (DMAP), and carbonydiimidazole (CDI) were from Aldrich; tetrabutylammonium fluoride (TBAF)/THF, 2-cyanoethyl *N*,*N*,*N*′,*N*′-tetraisopropylphosphoramidite (Bis-reagent), Py·TFA, LCAA-CPG loaded nucleosides of Perseptive Biosystem Gmbh (LCAA-CPG, 500 Å, 39 mmol/g), and different amidites were obtained as a generous gift from ISIS Pharmaceutical, USA. Oligonucleotide synthesis grade acetonitrile, 1*H*-tetrazole were purchased from Applied Biosystem, Perkin-Elmer, Switzerland. UV−visible spectra was recorded on Hitachi 220S UV−visible spectrophotometer. Thermal denaturation experiments with oligonucleotides were performed on a Perkin-Elmer Lambda Bio 20 UV−visible spectrometer with PTP 1 (Peltier Temperature programmer). Fluorescence spectra were recorded on Kontron SFM 25 spectrofluorometer. Purification of oligonucleotides was carried on a Shimadzu HPLC using an RP C18 Lichrosphere column employing a UV−visible detector. Synthetic grade solvents used were from Qualigens and were purified and dried prior to use. ^{1}HNMR and ^{31}P NMR were recorded on a DRX300 instrument. All the oligomers were synthesized on a ABI 392 DNA/RNA synthesizer.

***N*^{4}-Benzoyl Cytidine 2.** To the solution of cytidine (10 mmol, 2.43 g) in dry pyridine (25 mL) and DMF (10 mL) benzoic anhydride (15 mmol, 3.39 g) was added, and the reaction mixture was stirred overnight at room temperature in the presence of nitrogen. Reaction mixture was poured in water with stirring. The solvents were evaporated with anhydrous toluene to remove excess pyridine in a vacuum to leave a white solid which was extracted with diethyl ether (4 × 40 mL) to remove BzOH. Yield 92% (3.2 g). R_f 0.55 ($CHCl_3$/MeOH: 8:2 v/v) mp 218 °C. UV λ_{max} (MeOH): 305, 260 nm. IR (cm^{-1}) 1730. ^{1}HNMR (DMSO) δ ppm: 1.9−2.4 (m, 2H), 3.6 (m, 2H, H5′), 3.83 (m,1H, H4′), 4.1 (m, 1H, H3′), 4.8−5.4 (m, 2H), 6.1 (t, 1H, H1′), 7.1−7.4 (m, 4H, *J* 7.5 Hz, Ar+H-5), 8.1 (m,2H,Ar-H′ ortho to carbonyl), 8.2 (1H, *J* 7.5, H-6). Anal. Calc. $C_{16}H_{17}O_6N_3$: C 55.04%, H 4.89%, N 12.3%. Found: C 55.09%, H 4.97, N 12.37.

***N*^{4}-nCbz Cytidine 2a.** To the well-stirred solution of cytidine (10 mmol, 2.43 g) in dry THF, reagent *o*-nitrobenzyl-*p*-nitrophenyl carbonate (15 mmol, 4.8 g) in THF (15 mL) and 2 N NaOH (3 mL) was added. The reaction mixture was stirred for 3 h at r.t. TLC showed the completion of the reaction by the consumption of starting substrate into the single predominant product. Solvents were evaporated under reduced pressure. Residue obtained was dissolved in diethyl ether and washed with 1 M aqueous solution of $NaHCO_3$. The pH of the aqueous phase was made to 5.8 with 1 N HCl and extracted with diethyl ether. The combined organic layer was washed with water (3 × 15 mL), saturated brine solution, and water, and kept over anhydrous sodium sulfate, filtered, and evaporated in a vacuum to yield a white crystalline compound. Yield 70% (2.83 g). R_f 0.53 (dichloromethane/methanol: 9:1, v/v). UV λ_{max} (MeOH); 235, 255, 262, 307, 390 nm. Anal. Calc. $C_{17}H_{18}O_9N_4$: C 48.34, H 4.25, N 13.3. Found: C 48.24, H 4.35, N 13.75%. ^{1}HNMR ($CDCl_3$) δ ppm; 8.74 (br s, 1H, NH), 8.32 (d, 1H, H-6, $J_{6,5}$ 7.8 Hz), 8.71 (d, 2H, Bz, J 8.5 Hz), 5.65−5.85 (m, 1H, H1′), 3.75−3.91 (m, 1H, H4′), 4.35−4.44 (m, 1H, H2′), 3.72−3.85 (m, 3H, H3′,5′).

3′,5′-*O*-(Tetraisopropyldisiloxane-1,3-diyl)-*N*^{4}-Benzoyl Cytidine 3. To an ice-cold solution of **2** (5.8 mmol, 2.0 g) in anhydrous pyridine (10 mL) 1,1,3,3-tetraisopropyldisiloxane-1,3-dichloride (6.67 mmol, 2.1 g), dissolved in 1,2-dichloroethane (3 mL) was added dropwise with constant stirring for 30 min. After complete addition the reaction mixture was allowed to stir for another 2 h at room temperature. TLC showed the completion of the reaction in EtOH/$CHCl_3$ (1:9, v/v). Dry methanol (2 mL) was added to quench the reaction, and solvents were evaporated in a vacuum. The residue was dissolved in dichloromethane (20 mL) and washed with 1 M aq. $NaHCO_3$ (5 × 5 mL). The organic phase was dried over anhydrous $NaSO_4$, filtered, and evaporated in vacuum to afford the title compound as a white solid foam. Yield 90% (3.6 g). R_f 0.48. Anal. Calc. $C_{28}H_{43}O_7N_3Si_2$: C 57.03, H 7.29, N 7.12%. Found: C 57.15, H 7.33, N 7.23%. MALDI-TOF (2,4,6-THAP+citrate) $[M+Na]^+$, calc. 612, found 612.1, $[M+K]^+$ calc. 628.0 found 628.1. ^{1}HNMR (δ ppm) 7.4−7.7 (m, 4H), 8.1 (m, 2H), 8.2 (1H, *J* 7.6, H-6), 8.9 (s,1H, NH), 5.74 (s,1H, H1′), 5.67 (d,1H, H2′), 5.55 (d,1H, H-5), 4.71 (m,1H, H-5′), 4.38−3.96 (m, 3H, H4′, H5′), 1.2−0.9 (m, 28H, ^{i}Pr′).

3′,5′-*O*-(Tetraisopropyldisiloxane-1,3-diyl)-*N*^{4}-nCbz Cytidine 3. Compound **3a** was synthesized following the above same procedure. Yield 92% (3.48 g). R_f 0.45. Anal. Calc. $C_{28}H_{42}O_{10}N_4Si_2$: C 51.7, H 6.46, N 8.61%. Found: C 51.91, H 6.83, N 9.13%. MALDI-TOF (2,4,6-THAP+citrate) $[M+Na]^+$, Calc. 673.5 found 673.6, $[M+K]^+$ calc. 689.6 found 689.7 ^{1}HNMR ($CDCl_3$; δ ppm); 10.1 (b s, 1H, NH), 8.71 (d, 2H, J 8.75 Hz, Bz), 8.24 (d, 1H, *J* 7.3 Hz, H-6), 8.2 (d, 2H, *J* 8.79, Bz), 7.12 (1H, J 7.5 Hz, C-5) 5.74 (s, 1H, H1′), 4.87 (m, 1H, H2′), 4.38 (m, 1H, H3′), 4.15−4.59 (m, 3H, H4′, H5′), 0.9−1.2 (m, 28H, ^{i}Pr′).

2′-*O*-(Imidazol 1-yl carbonyl)-3′,5′-*O*-(Tetraisopropyldisiloxane-1,3-diyl)-*N*^{4}-benzoyl Cytidine 4. Compound **3** (3.4 mmol, 2.0 g) was taken in dry dichloromethane (30 mL), and *N*,*N*′-carbonyldiimidazole (CDI) (3.7 mmol, 0.6 g) was added. The reaction mixture was stirred for 1.5−2 h and monitored on TLC. The completion of the reaction was observed by the conversion of starting substrate into the product of lower mobility. The solution was washed with water (3 × 25 mL). The organic layer was kept over Na_2SO_4, filtered, and evaporated in a vacuum to get imidazolyl derivative in the crystalline

form. Yield 85% (2.2 g) R_f 0.4 (EtOAc). MALDI-TOF (2,4,6 THAP+citrate): $[M+Na]^+$ 706.7 expected 706.6, $[M+K]^+$ 722.8 expected 722.7.

2′-*O*-(Imidazol 1-yl carbonyl)-3′,5′-*O*-(Tetraisopropyldisiloxane-1,3-diyl)-*N*⁴-nCbz Cytidine 4a. Yield 80% (2.74 g) R_f 0.37 (EtOAc). MALDI-TOF (2,4,6 THAP+citrate): $[M+Na]^+$ 769.1 expected 768.5, $[M+K]^+$ 784.7, expected 784.6.

5-Dimethylamino-*N*-ethylamine-1-naphthalene Sulfonamide 5. To the ice-cold solution of freshly distilled ethylenediamine (25 mmol, 1.5 g) in 10% sodium bicarbonate (20 mL), dansyl chloride (5 mmol, 1.35 g) in THF (25 mL) was added dropwise in 1 h. The reaction mixture was stirred for 2 h and monitored on TLC. The solvents were evaporated in a vacuum. The residue was poured in water extracted with ethyl acetate (3 × 25 mL). The organic layer was concentrated and chromatographed using EtOAc/hexane (2:8) as eluent to afford an ethylamine derivative of dansyl as a fluorescent green oil which was solidified at −20 °C. Yield 78% (2.33 g). R_f 0.34 (8:2: EDC(1,2 dichloroethane)/MeOH). IR (cm^{-1}) 3300, 3052, 1586, 1574, 1464. UV λ_{max} (MeOH): 220, 251, 334, 385 nm. ^{1}HNMR (δ ppm); 1.38 (m, J 7.5 Hz, CH_2-CH_2NH_2), 2.89 (s, 6H, $(CH_3)_2N$), 4.62 (bt, 1H, J 5.2 Hz, SO_2NH), 8.21 (d, 1H, J 8.1 Hz, 2H). Fluorescence (MeOH, λ_{ex} 335 nm, λ_{em} 510 nm).

2′-*O*-(Dansyl-2-sulfonamido-ethylamino-carbonyl)-3′,5′-*O*-(tetraisopropyldisiloxane-1,3-diyl)-*N*⁴-benzoyl Cytidine 6. To the imidazole derivative of cytidine **4** dissolved in dry DCM (30 mL), compound **5** (3.4 mmol, 1.0 g) in dry DCM was added dropwise with constant stirring for a period of 1 h under argon. After complete addition the reaction was allowed to stir overnight. TLC showed the formation of single predominant product. The reaction mixture was washed sequentially with water, 3% citric acid, and again with water. The organic layer was kept over Na_2SO_4 and concentrated. The residue was chromatographed on a silica gel column using an increasing gradient of ethyl acetate in chloroform. Fractions containing products pooled and evaporated to dryness in a vacuum to afford the title compound as a foamy mass. Yield 73.5% (2.22 g) R_f 0.45 (DCM/MeOH: 7:3 v/v). MALDI-TOF (2,5 DHBA); [M+Na and M+K]$^+$ calc. 931.7, and 947.8, found; 932.2 and 947.9, respectively. Anal. Calc. $C_{43}H_{60}N_6O_{10}Si_2S$; C 56.83, H 6.61, N 9.25%. Found C 56.21, H 7.16, N 10.21%. ^{1}HNMR ($CDCl_3$ δ ppm); 11.2 (b s, 1H, NH), 7.40−7.48 (m, 4H, Bz, H-5), 8.29−8.36 (m, 4H, benzoyl, naphthoyl, H-6), 8.01 (t, 1H, naphthoyl), 8.42−7.67 (m, 3H, naphthoyl, *J* 9.1 Hz), 7.13 (t, 1H, NHCOO, J 5.9 Hz), 6.44−6.50 (m, 2H, H1′, naphthoyl), 5.12−5.15 (m, 1H, H2′), 4.17−4.21 (m, 1H, H3′), 3.91−3.94 (m, 2H, H4′, H5′), 3.28−3.34 (m, 4H, -$NHCH_2CH_2$-NH-), 2.85 (s, 6H, -NCH_3), 0.92−1.35 (m, 28H, ^{i}Pr′).

2′-*O*-(Dansyl-2-sulfonamido ethylamino carbonyl)-3′,5′-*O*-(tetraisopropyldisiloxane-1,3-diyl)-*N*⁴-nCbz Cytidine 6a. Yield 70% (2.17 g) R_f 0.42 (DCM/MeOH: 7:3 v/v). MALDI-TOF (2,5 DHBA); [M+Na and M+K]$^+$ calc. 931.8 and 947.9, found; 932.2 and 948.1, respectively. Anal. Calc. $C_{43}H_{60}N_6O_{10}Si_2S$; C 56.83, H 6.61, N 9.25%. Found C 56.21, H 7.16, N 10.21%. ^{1}HNMR ($CDCl_3$ δ ppm); 11.2 (b s, 1H, NH), 8.68 (d, 1H, J 8.8 Hz, Bz), 8.72 (d, 1H, J 8.9, ortho to NO_2), 7.40−7.48 (m, 3H, Bz, H-5), 8.29−8.36 (m, 3H, benzoyl, naphthoyl, H-6), 8.01 (t, 1H, naphthoyl), 8.42−7.67 (m, 3H, naphthoyl, *J* 9.1 Hz), 7.13 (t, 1H, NHCOO, J 5.9 Hz), 5.83−5.93 (m, 2H, H1′, naphthoyl), 4.98−5.12 (m, 1H, H2′), 4.15−4.17 (m, 1H, H3′), 3.89−3.92 (m, 2H, H4′, H5′), 3.29−3.36 (m, 4H, -$NHCH_2CH_2$NH-), 2.75 (s, 6H, -NCH_3), 0.9−1.25 (m, 28H, ^{i}Pr′).

2′-*O*-(Dansyl-2-sulfonamido-ethylamino-carbonyl)-*N*⁴-benzoyl Cytidine 7. Compound **6** (2.23 mmol, 2 g) was dissolved in THF (10 mL) and a 1 M solution of terabutylammonium fluoride in THF (8.8 equiv 6.0 mL) was added to it. The reaction was stirred for 15 min at room temperature and monitored on TLC (CH_3OH/$CHCl_3$: 1:4 v/v), then diluted with EtOAc (30 mL) and washed with 5% aq. $NaHCO_3$ (30 mL) solution. The aqueous layer was back triturated with EtOAc (3 × 30 mL). The organic phase was combined concentrated and again washed with brine solution (2 × 30 mL) and dried over anhydrous $MgSO_4$. The crude oily product was purified with column chromatography. The column was first eluted with EtOAc/petroleum ether (4:1 v/v) and then with 40% methanol in EtOAc. The product which was eluted with a second solvent system was pooled and evaporated in a vacuum to afford the title compound as reddish yellow gum. Yield 95% (1.43 g). R_f 0.43 ($CHCl_3$/MeOH: 8:2 v/v). UV λ_{max}(MeOH): 220, 236, 256, 336 nm. MALDI-TOF (2,5 DHBA); [M+Na and M+K]$^+$ calc. 689.4, and 705.5, found; 690.2 and 705.9, respectively. Anal. Calc. $C_{31}H_{34}N_6O_9S$; C 55.87, H 5.11, N 12.61%. Found C 55.55, H 5.51, N 13.05%. ^{1}HNMR ($CDCl_3$ δ ppm); 10.34 (s, 1H, NH), 8.27 (d, 1H, J 7.5 Hz, H-6), 8.01 (d, 2H, J 8.2 Hz, Ar), 7.37−7.43 (m, 4H, Bz, C-5), 7.53 (t, 1H, NHCOO, J 5.9 Hz), 6.24 (m, 1H, H1′), 5.02−5.06 (m, 1H, H2′), 4.16−4.19 (m, 1H, H3′), 3.87−3.92 (m, 1H, H4′), 3.64−3.68 (m, 2H, H5′), 5.31 (t, 1H, 5′-OH, J 4.7 Hz), 8.05 (t, 1H, naphthoyl), 8.52−7.87 (m, 3H, naphthoyl, *J* 9.2 Hz), 6.34−6.40 (m, 2H, H1′, naphthoyl), 3.38−3.44 (m, 4H, -$NHCH_2CH_2NH$-), 2.95 (s, 6H, -NCH_3).

2′-*O*-(Dansyl-2-sulfonamido-ethylamino-carbonyl)-*N*⁴-nCbz Cytidine 7a. Yield 95% (1.21 g). R_f 0.38 ($CHCl_3$/MeOH: 8:2 v/v). UV λ_{max}(MeOH): 220, 236, 256, 307, 336, 390 nm. MALDI-TOF (2,5 DHBA); [M+Na and M+K]$^+$ calc. 750.5, and 766.6, found; 750.9 and 707.5, respectively. Anal. Calc. $C_{31}H_{33}N_7O_{12}S$; C 51.2, H 4.54, N 13.5%. Found C 51.35, H 5.15, N 14.2%.

***N*⁴-Benzoyl-5-*O*-(4,4′-dimethoytrityl)-2′-*O*-{(2-dansyl Sulfonamido) Ethyl Carbamoyl} Cytidine 8.** Cytidin-2′-yl carbamate **7** (1.8 mmol, 1.15 g) was dried by addition and evaporation of tolune and pyridine (3 × 20 mL). To residue anhydrous pyridine (20 mL), triethylamine (2 mL), DMAP (0.02 eq 0.024 g), and 4,4′-dimethoxytrityl chloride (3.55 mmol, 1.2 g) were added under argon. The reaction mixture was stirred for 2.5 h at room temperature. TLC showed the completion of the reaction (CH_3OH/$CHCl_3$/TEA; 1:8.5:0.5); the excess of DMTr was quenched with methanol (2 mL), and solvents were evaporated in a vacuum. Syrupy mass was dissolved in chloroform (100 mL) and washed with water, 5% $NaHCO_3$, and again with water. Organic layer was pooled, kept over anhydrous Na_2SO_4, filtered, and co-evaporated with toluene to remove residual pyridine. The crude product was purified by a silica gel column using a 10% stepwise gradient of methanol in chloroform, containing 1% triethylamine as eluent. Fractions containing products were pooled and evaporated in a vacuum to get the title compound as amorphous solids. Yield 77% (1.32 g). R_f 0.57 (MeOH/$CHCl_3$/TEA). UV λ_{max}(MeOH): 220, 238, 256, 335 nm. MALDI-TOF (2,4,6 THAP) $[M+Na]^+$; calc. 976.6, found 976.6 $[M+K]^+$; calc. 995.7, found 995.9. ^{1}HNMR (DMSO) δ; 11.42 (s, 1H, NH), 8.39 (d, 1H, J 9.1 naphthoyl), 8.22−8.27 (m, 4H, 2H Bz + 1H naphthoyl+ 1H, H-6), 7.59−7.96 (d, 2H J 9.0 Hz, naphthoyl), 7.28−7.37 (m, 10H, 3H Bz + 1H naphthoyl,1H, C-5, 5H, Ar), 7.08−7.78 (d, 8H, J 8.5, DMTr), 7.53 (t, 1H, NHCOO, J 5.9 Hz), 6.65 (d, 1H, J 9.0 Hz, naphthoyl), 6.39−6.43 (m, 1H, H1′), 5.03 (m, 1H, H2′), 4.14−4.17 (m,

Table 1. Oligonucleotides Synthesized[a]

ON1	5′-CCC GAT-3′
ON2	5′-C^{fl}CC GAT-3′
ON3	5′-C^{fl}C^{fl}C GAT-3′
ON4	5′-C^{fl}C^{fl}C^{fl} GAT-3′
ON5	5′-ATC GGG-3′
ON6	5′-CCT CTG ACC CAC CCA CCA TT-3′
ON7	5′-C^{fl}CT CTG ACC CAC CCA CCA TT-3′
ON8	5′-C^{fl}C^{fl}T CTG ACC CAC CCA CCA TT-3′
ON9	5′-AAT GGT GGG TGG GTC AGA GG-3′
ON10	5′-CCC TCT GAC CCA CCC ACC AT-3′
ON11	5′-C^{fl}C^{fl}C^{fl} TCT GAC CCA CCC ACC AT-3′
ON12	5′-ATG GTG GGT GGG TCA GAG GG-3′

[a] fl = labeled with dansyl fluorophore.

2H, H3′,H4′), 4.01−4.03 (m, 2H, H5′), 3.87 (s, 6H, -OCH_3), 2.93 (s, -NCH_3), 3.23−3.35 (m, 4H, -$NHCH_2CH_2NH$).

***N*^{4}-Benzoyl-5′-*O*-(4,4′-dimethoxytrityl)-2′-*O*-{(2-dansylsulfonamido) Ethyl Carbamoyl} Cytidine-3′-*O*-(2-cyanoethyl)-*N*,*N*-diisopropylphosphoramidite 9.** To the well-stirred solution of **8** (1.1 mmol, 1.05 g) in anhydrous dichloromethane (10 mL), 2-cyanoethyl-*N*,*N*,*N*′,*N*′-tetraisopropylphosphoramidite (Bis-reagent) (3.0 mmol, 0.95 mL) was added at ambient temperature. Pyridinium trifluoroacetate (Py·TFA) (3.0 mmol, 0.7 g) was added to the reaction mixture and stirred for 3 h. After complete consumption of starting material (TLC), methanol (2 mL) was added, and the resulting solution was washed with 10% $NaHCO_3$ (3 × 10 mL). Organic layer was dried over sodium sulfate and directly applied to a silica gel column. Compound was eluted with dichloromethane/ethyl acetate/Et_3N (4.5:4.5:1, v/v). The desired fractions were pooled and dried under reduced pressure to afford title compound as amorphous yellow powder. Yield 80% (1.0 g). R_f 0.63 (CH_2Cl_2/EtOAc/Et_3A: 4.5:4.5:1, v/v), λmax 260, 333 nm, ^{31}PNMR (CH_3CN) 150.3, 149.9 ppm (diastereoisomers).

Synthesis of Oligonucleotides. All the oligomers were synthesized at 0.2 μmol scale on an ABI 392 model DNA/RNA synthesizer using nucleoside analogues (**9**) with only benzoyl group on exocyclic amino function. The last coupling cycle was increased by 10 min. All the oligomers were mixed type. Three 6-mers and three 20-mer sequences were synthesized in which the number of fluorophore was successively increased as one, two, and three by coupling modified analogues (**9**) (Table 1). All the oligomers were treated with 30% aqueous ammonia for 15 h at 65 °C to remove protecting groups from the bases and internucleotide phosphates and also to cleave oligomer from the solid support. The ammoniacal solution was concentrated under a vacuum in a speed vac, and the residue was subjected to desalting on a reverse phase silica gel column. The oligomers were purified on anion exchange FPLC and then analyzed on reverse phase HPLC with a Merck lichrosphere RP-18 column using 0.1 M ammonium acetate buffer at pH 7.1 and acetonitrile solvent. In the case of the dansyl derivative, it was very hard to separate the desired peaks. However, the desired collected portion was reinjected in 25 μL to get the 90−95% purified oligonucleotides. HPLC graph and retention time of the fluorescently labeled 20-mer oligomers have been shown in Figure 1. In the case of 2′-*O*-carbamate modified oligonucleotides, the carbamate and sulfonamide bonds were found completely stable to the condition of oligonucleotide synthesis as well as under deprotection conditions at the desired temperature. The λ max for monolabeled, dilabeled, and trilabeled 20-mers (ON7, ON8, and ON11) was 260, 295, 333 nm with the intensity of the peaks increasing, respectively.

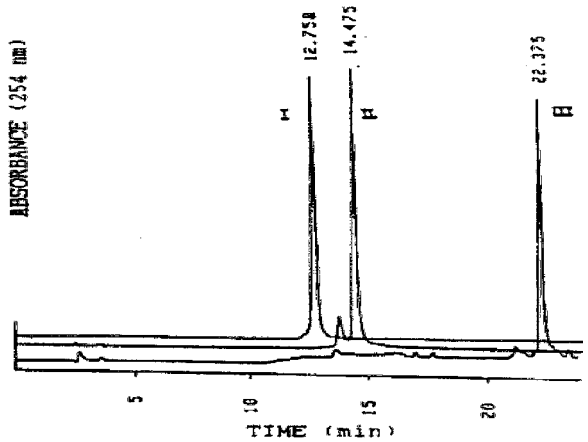
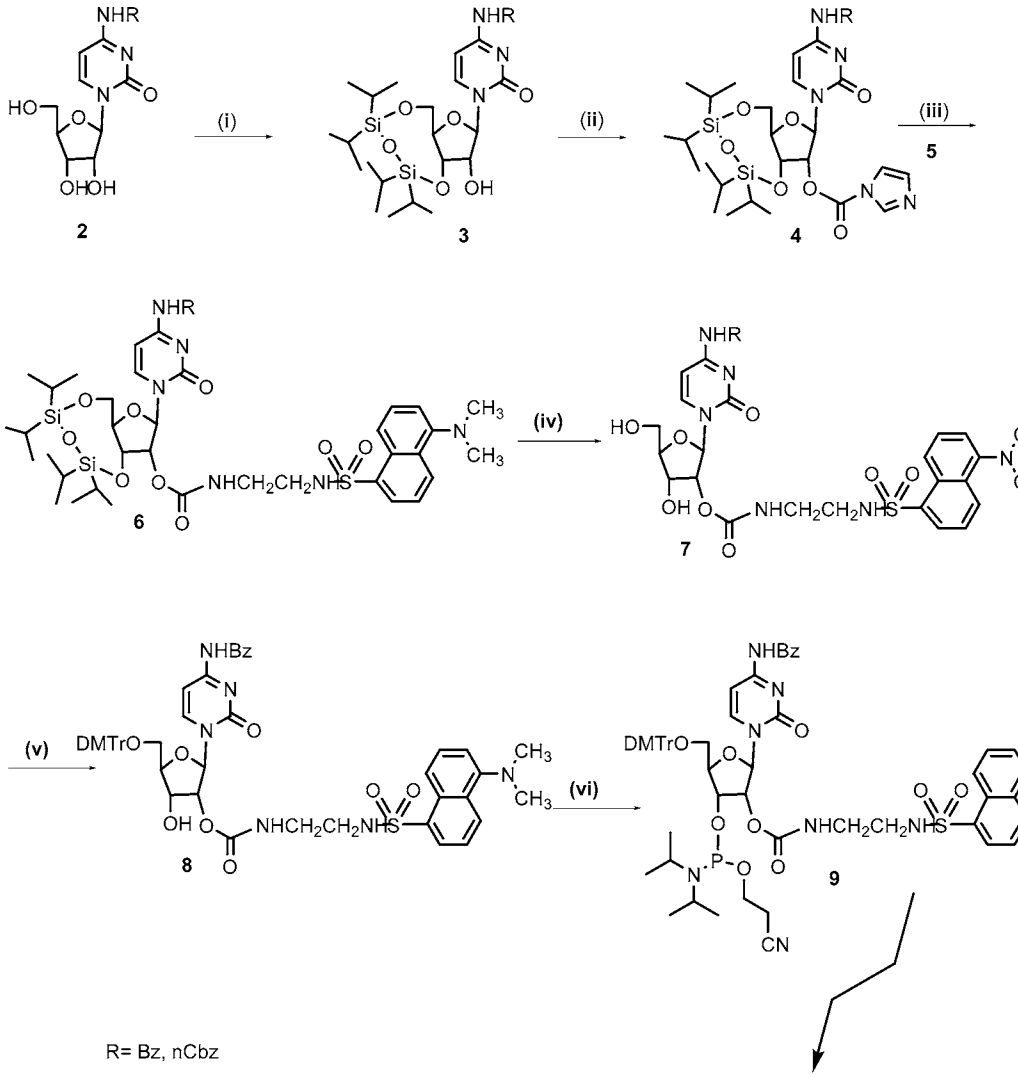


Figure 1. RP-HPLC elution profile of AEX-FPLC purified fluorescent labeled oligomers 5′-C^{fl}CT CTG ACC CAC CCA CCA TT-3′ (ON7), 5′-C^{fl}C^{fl}T CTG ACC CAC CCA CCA TT-3′ (ON8), and 5′-C^{fl}C^{fl}C^{fl} TCT GAC CCA CCC ACC AT-3′ (ON11). Conditions: column, Lichrosphere RP-18 (Merc, Germany); buffer A, 0.1 M NH_4OAc, pH 7.1; solvent B, acetonotrile; flow rate, 1.0 mL/min; gradient, 0−50% B in 30 min; aufs, 0.05.

RESULTS AND DISCUSSION

To assess (i) the minimum number of dansyl labeled nucleosides required for a specific length of oligonucleotide to act as probe, (ii) the appropriate linkage for covalent linking of fluorophore to oligonucleotide, and (iii) the specific site in the oligonucleotide for incorporation of fluorophore for stability of duplex, cytidine has been used as the 2′-O-labeled monomer. A general method for the preparation of cytidin-2′-yl-carbamate and its corresponding phosphoramidite is outlined in Scheme 1. Phosphoramidite of 2′-O-labeled cytidine (**9**) has been synthesized from N-acyl cytidine (**2**) by first protecting 3′,5′-OH with 1,3-dichloro-1,1,3,3-tetraisopropyl disiloxane as reported earlier (*31*). The crude product was purified by column chromatography in silica gel using EtOH−$CHCl_3$ to afford **3** as a white solid foam. This was then treated with CDI in dry dichloromethane (DCM) to get in situ carbamate derivative, *N*-acyl-2′-*O*-(imidazol-1-ylcarbonyl)-3′,5′-*O*-tetraisopropyldisiloxane1,3-diyl) cytidine (**4**) in quantitative yield. The imidazolide derivative **4** was not isolated and was subsequently reacted with an excess of aminoethyl dansyl derivative **5** in dry DCM to get compound **6** after stirring the reaction mixture for 2 h at r.t. which was finally purified by column chromatography. Compound **5** was synthesized by treating ethylenediamine in 10% $NaHCO_3$ with dansyl chloride in THF, in an ice bath. Monitoring on TLC showed the total conversion of starting material into the product (**5**) in 3 h. On illuminating the fluorescent plate with a UV torch at 354 nm wavelength, bright fluorescence of the dansyl derivative was observed, which was further confirmed by ninhydrin spray. Markiewicz 3′,5′-O-silyl group was removed by treating compound **6** with tetrabutylammoniumfluoride (TBAF) in THF for 15 min. The crude product was purified by column chromatography. Compound **7** was obtained as a reddish yellow gum with needlelike crystals, which was tritylated with 4,4′-dimethoxytrityl chloride in dry pyridine in the presence of DMAP and TEA to get derivative **8** in 77% yield. Phophitylation at the 3′-OH position was done using 2-cyanoethyl-*N*,*N*,*N*′,*N*′-tetraisopropyl phosphoramidite (Bis-reagent) and activator pyridinium trifluoroacetate (Py·TFA) in dry 1,2-dichloroethane. Py·TFA was used, in place of more conventional 1H-tetrazole or 4,5-dicyano imidazole (DCI) because it is an excellent activator,

Scheme 1 [a]



[a] (i) TIPDS-Cl/1,2-dichloroethane, (ii) *N*,*N*-carbonyldiimidazole/DCM, (iii) aminoethyl dansyl sulfonamide 5/DCM, (iv) TBAF/THF, (v) DMTr-Cl/DMAP/TEA, and (vi) Bis-reagent/Py·TFA.

cheaper, stable at r.t., less acidic, less toxic, and has a higher pK_a (5.23) than those (4.4−5.1) of other activating reagents (*32*). After the completion of the reaction, the crude product was immediately transferred onto a short silica column and eluted with ethyl acetate and dichloromethane (1% triethylamine) to furnish the 2′-O-carbamate amidite of cytosine (**9**), the protected monomer to be used for further synthesis of oligonucleotides.

All the cytidine derivatives from **2**−**9** were prepared with either benzoyl or *o*-nitrobenzyloxycarbonyl (nCbz), a photolabile group on the exocyclic amino function of the nucleoside. All the derivatives were properly characterized by their elemental analysis, UV, NMR, and MALDI−TOF. This photolabile group viz. (nCbz) was used by synthesizing the reagent *o*-nitrobenzyl-*p*-nitrophenyl carbonate which releases the nCbz group in the presence of NaOH, and it is then employed for the N-acylation as reported previously (*33*) by our laboratory. The advantage of the group lies in that it can be cleaved by photoirradiation at 354 nm wavelength of UV light. However, in the present case, use of the nCBz group for custom synthesis of oligonucleotide probes failed, because on photoirradiation to deprotect the photolabile group (*34*) the dansyl fluorophore was also cleaved.

Synthesis of Oligonucleotides. Three labeled hexamers and three labeled 20-mers were synthesized on an ABI 392 DNA synthesizer using CPG as support and the phosphoramidite approach, using labeled cytidine analogue (**9**) in the last coupling step to incorporate one, two, or three labeled monomers at the 5′-prime. Out of the three labeled 20-mers, two were identical sequences having one and two labeled monomers, while one had a different sequence. This was invariably done to ascertain the effect of variation in the sequence on the resulting

Table 2. Melting Temperatures of Oligonucleotide Duplexes

	oligonucleotide duplexes	T_m (°C)
ON1	5′-CCC GAT-3′ 3′-GGG CTA-5′	31.13
ON2	5′-C^{fl}CC GAT-3′ 3′-GGG CTA-5′	29.44
ON3	5′-C^{fl}C^{fl}C GAT-3′ 3′-GGG CTA-5′	29.33
ON4	5′-C^{fl}C^{fl}C^{fl} GAT-3′ 3′-GGGCTA-5′	29.12
ON6	5′-CCT CTG ACC CAC CCA CCA TT-3′ 3′-GGAGAC TGG GTG GGT GGT AA-5′	47.0
ON7	5′-C^{fl}CT CTG ACC CAC CCA CCA TT-3′ 3′-GGAGACTGGGTGGGTGGTAA-5′	45.5
ON8	5′-C^{fl}C^{fl}T CTG ACC CAC CCA CCA TT-3′ 3′-GGAGACTGGGTGGGTGGTAA-5′	45.24
ON9	5′-CCC TCT GAC CCA CCC ACC AT-3′ 3′-GGG AGA CTG GGT GGG TGG TA-5′	48.3
ON10	5′-C^{fl}C^{fl}C^{fl} TCT GAC CCA CCC ACC AT-3′ 3′-GGG AGA CTG GGT GGG TGG TA-5′	46.7

[a] fl = labeled with dansyl fluorophore.

fluorescence quantum, if any. However, it was found that one-labeled monomer is sufficient for diagnostic requirement for any 20-mer sequence. The corresponding unmodified hexamer and 20-mers having similar sequence as the labeled ones and their complementary sequences were also synthesized to study the effect of hybridization on the resulting fluorescence quantum. In the case of labeled oligonucleotides, the carbamate and sulfonamide bonds were found stable to the condition of oligonucleotide synthesis as well as the deprotection conditions. UV-spectra have shown the retention of the fluorophore in the labeled oligomers. The absorbance at ∼333−340 nm and at 260 nm due to fluorophore and DNA respectively and fluorescence emission spectra at ∼500−520 nm wavelength clearly confirmed the retention of the chromophore in the oligonucleotides. The relative enhancement in the intensity of peak due to the fluorophore was observed in the mono, di, and trilabeled oligonucleotides.

Thermal Denaturation Studies. The thermal denaturation studies of labeled oligonucleotides, i.e., three hexamers and three 20-mers with the complementary normal oligomer strands, were carried out in phosphate buffer of 0.1 M concentration having 1 M NaCl by adjusting the pH at 7.0. There was a little difference in the T_m value (in the range of ∼1.79−2.01 °C) of the normal hexamer duplex (T_m 31.13 °C) and of labeled duplexes (T_m 29.44, 29.33, 29.12 °C of monodansyl, didansyl, tridansyl labeled hexamer strands, respectively) (Table 2). The difference in the T_m value clearly showed the little bit of destablization in the duplex formation. In the case of 20-mer oligonucleotides, there was a decrease in the T_m value of about 1.5−1.7 °C as compared to the normal unmodified oligomers, thus further confirming the pattern of destabilization of the oligonucleotides (Table 2). The decrease in the T_m values may be attributed to the use of linker arm (ethylenediamine) and type of bond formations between the labeled fluorophore (sulfonamide) and the nucleoside (carbamate) at the 2′-OH end. It has been reported by Gait et al. (*25*) that most of the carbamate modifications at the 2′-end position when introduced at the terminal fraying or near the terminal end fraying or the middle of the oligomers result in a considerable decrease in the T_m values of the duplexes. The negative effect of a 2′-O-carbamate modification on the thermal stability in the case of an DNA·RNA duplex was also reported (*35*). Since we have introduced modifications at the 5′-terminal position of the oligonucleotides, destabilizations were comparatively less than placing the modifications at the middle or 3′-end terminal of the oligonucleotides. However, as the number of 2′-O-modified carbamate nucleotides increase to make oligonucleotides multiple labeled the destabilization effect seems to be functionally positive as was evident by a further decrease in the T_m values of the respective duplexes chosen in the present case. However, it would show further destabilization if such a modification was introduced in the internal positions in accordance with the earlier reported works.

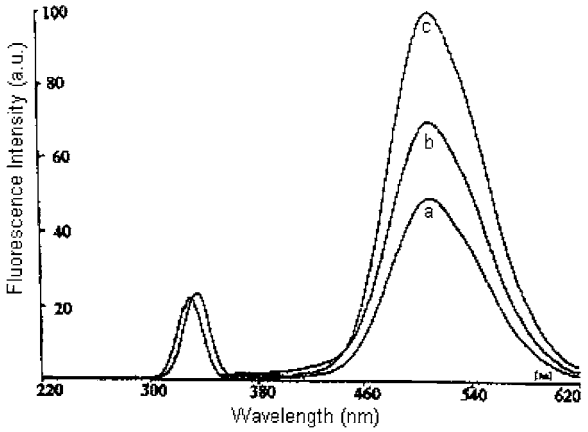


Figure 2. Fluorescence spectra of 6-mers in 0.1 M phosphate buffer containing 1.0 M NaCl by exciting at 333 nm, (a) ON2, (b) ON3, (c) ON4.

Fluorescence Studies. In the present study, dansyl fluorophore has been selected because it has a large Stokes shift and its fluorescent intensity depends much on the neighboring environment such as hydrophobicity and hydrophilicity, ligand binding, etc. Such alteration in the spectral property of the dansyl fluorophore has been used to detect the substrate binding to protein (*36*) and to study the interaction of DNA with Klenow fragment of DNA polymerase I (*37*). 4-Dansylamino-1,8-naphthalimido-*N*-pentanol has also been developed for the covalent labeling of oilgonucleotides (*38*).

Furthermore, covalent attachment of dansyl group with oligonucleotides with a relatively shorter linker arm at pyrimidine C-5 position exhibits little or no change in the fluorescence intensity on duplex formation with the complementary DNA segment (*39*−*42*). However, placing nucleoside analogues at the internal or middle position by attaching a dansyl group at C-8 position of a purine nucleobase results enhancement in the fluorescence intensity as well as the quantum yield (*43*).

UV-spectra have shown the retention of the fluorophore in the modified oligomers. The 20-mer oligonucleotide-bound dansyl conjugate was spectrally distinct from the labeled monomer. The absorbance at ∼333−340 nm and at 260 nm due to fluorophore and DNA respectively and fluorescence emission spectra at ∼500−520 nm wavelength clearly confirmed the retention of the chromophore in the oligonucleotides. The relative enhancement in the intensity of peak due to the fluorophore was observed in the mono, di, and trilabeled oligonucleotides.

All the fluorescence spectra were recorded in 0.1 M phosphate buffer containing 1.0 M NaCl by exciting the molecules at 333 nm and scanning the emission spectra in the range of 220−650 nm wavelength (Figures 2and 3). The fluorescence spectra of dansyl attached modified single-stranded oligonucleotides were recorded at 2.0 OD concentration and for homogeneous hybridization studies

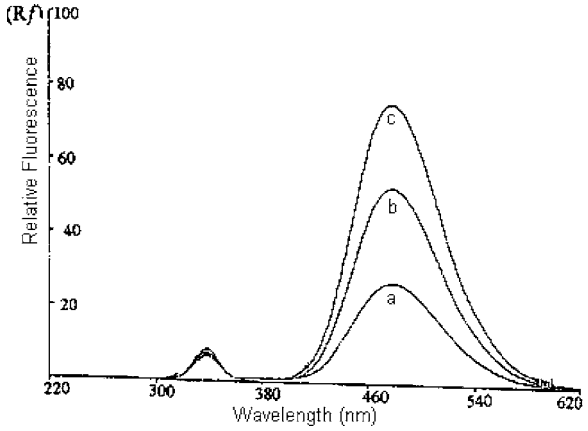


Figure 3. Fluorescence spectra of 20-mers in 0.1 M phosphate buffer containing 1.0 M NaCl by exciting at 333 nm, (a) ON7, (b) ON8, (c) ON11.

an sample containing an equimolar concentration of complementary strands was vortexed and heated at 90 °C for 15 min and was then gradually cooled at 5 °C. The process was repeated 2−3 times to ensure complete hybridization of the duplexes, and then the fluorescence spectra were recorded at 25 °C. It was observed that as the number of 2′-O-modified dansyl labeled monomer increased there was relative enhancement in the fluorescence intensity of oligonucleotides.

To observe the fluorescence pattern of duplexes of modified labeled probe with its complementary strand a model experiment was done by taking target complementary oligonucleotide of 5×10^{-5} M concentration (~1.50 OD) in phosphate buffer and the single-labeled modified 20-mer oligonucleotide of different molar concentrations was added sequentially stepwise in the order 5×10^{-6} M (0.15 OD); 1×10^{-5} M (0.3 OD); 2×10^{-5} M (0.6 OD); 3×10^{-5} M (0.9 OD); 4×10^{-5} M (1.2 OD); and 5×10^{-5} M (1.5 OD). On increasing the concentration of labeled oligonucleotide to the target DNA strand stepwise, there was relative enhancement in the relative fluorescence intensity and after reaching the equimolar concentration there was no further increase in the relative fluorescence intensity (Figure 4). The observation clearly indicated that on complete duplex formation, the dansyl fluorophore gets transferred into a less polar environment henceforth resulting in enhancement in the fluorescence intensity.

However, quenching was also observed while comparing the fluorescence intensity of individual labeled oligomers with their duplexes (Figure 5). This is may be due to the nature of interaction leading to partial compensation of carbamate and sulfonamide (electron sinker) linkages and also a stacking effect between two adjacent base pairs, i.e., intercalation and/or minor groove binding affinity may be feasible for 2′-O-modified substituents. The decrease in fluorescence intensity may also be attributed to the dansyl group, which may not remain entirely passive in duplex formation when present on the terminal nucleosides because of stacking effects at the ends of the duplex. Although the ligand intercalation and stacking effects stabilize the duplex, they may not be advantageous when the ligand is employed as a fluorophore probe. However, there is no such report about the intercalating characteristic of the dansyl fluorophore. Because dansyl is a nonplanar bulky substituent, it should be incorporated into the sugar moiety at the terminal fraying end of the oligonucleotides rather than at internal positions to retain the normal binding affinity

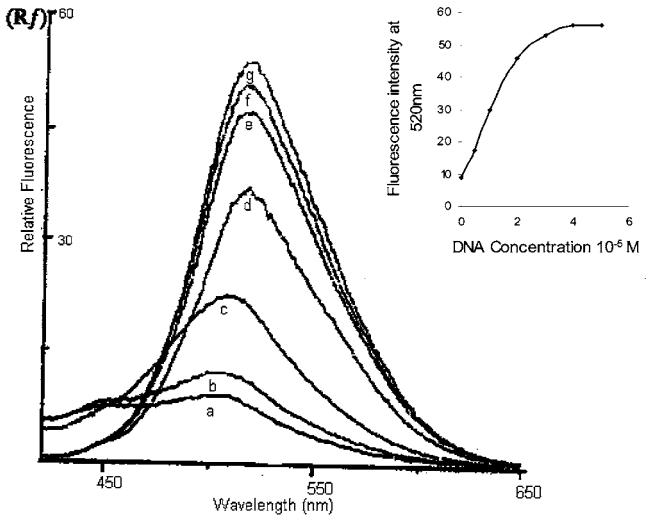


Figure 4. Fluorescence spectra with complementary sequence at 5×10^{-5} M concentration (1.5 OD) by addition of single-labeled 20-mer oligonucleotide ON7 at different concentrations. (b) 5×10^{-6} M (0.15 OD); (c) 1×10^{-5} M (0.3 OD); (d) 2×10^{-5} M (0.6 OD); (e) 3×10^{-5} M (0.9 OD); (f) 4×10^{-5} M (1.2 OD); and (g) 5×10^{-5} M (1.5 OD); (a) ON7. Inset: manual fluorescence spectra showing the trend of an increase in the relative fluorescence intensity on addition different concentrations of ON7.

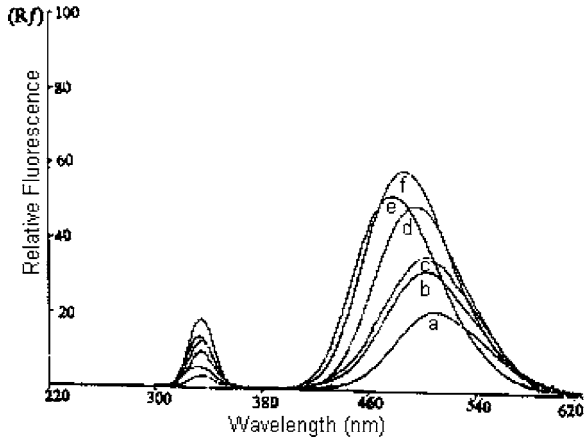


Figure 5. Fluorescence spectra of monolabeled 20-mer (ON7); (a−c) before duplex formation and (d−f) after duplex formation with complementary sequences at 25 °C.

of the complementary DNA strand and consequently enhancement in the fluorescence intensity.

Further quenching may also be due to presence of guanosine nucleotides in the complementary strand. It has been reported very well that nucleotides, especially guanosine, have the ability to quench the fluorescence intensity of the fluorophores (*44*−*46*). However, the quenching efficiency of nucleotides is not as high as with the use of standard quencher molecules. The quenching efficiency of nucleotides are in the order guanosine > adenosine > cytidine > thymidine. The same effect of guanosine nucleotides was observed in the present case, which was just complementary to the labeled modified cytidine base of the oligonucleotide strand. The quenching efficiency in the present case was found to be in the range of 30−40%. Thus, the result also demonstrated a very good example of resonance energy transfer. The results also clearly showed that nucleosides such as guanosine have the ability to quench the fluorescence intensity of the fluorophore significantly.

CONCLUSION

In this paper, a viable strategy for multiple labeling of oligonucleotide via premodified monomers has been described. Most interesting properties were demonstrated by the 2′-*O*-(dansyl ethylcarbamoyl)-cytidine containing DNA oligomers. The dansyl modification was able to stabilize selectively a duplex with a deoxyguanosine directly opposite to the carbamate-modified nucleoside. It is applicable for homogeneous hybridization assays. To avoid adverse effects of the label or the modified base on the desired hybridization characteristics, fluorophore has been incorporated regiospecifically at 2′-end of a pyrimidine base residue. This particular region of the pyrimidine base, which does not take part in base pairing, is expected to be buried in the more hydrophobic interior of the duplex on binding to the complementary DNA fragment, thereby resulting in the enhancement of the fluorescence intensity. The 5′-prime of an oligonucleotide appears to be the most suitable site for linking of a fluorophore vis-à-vis 3′-prime or midsequence.

Moreover, the fluorophore showed characteristically a considerable enhancement in the fluorescence intensity upon hybridization with complementary "G" rich DNA sequence. The 2′-*O*-carbamate modification affords a convenient way to place various ligands in the minor groove of a DNA·DNA duplex. Other possible applications include the specific minor groove delivery of reactive functions such as directed cross-linking on conjugation with peptides, modifications of a flexible part of structured RNA molecules, possible detection of point mutation in DNA, and access of the FRET phenomenon.

ACKNOWLEDGMENT

Arvind Misra is indebted to the Department of Biotechnology, New Delhi, for financial support. We are grateful to Dr. Yogesh S. Sanghvi, ISIS Pharmaceuticals, USA, for providing Bis-reagent, Py·TFA, and phosphoramidites for oligonucleotide synthesis. Thanks are due to RSIC, Lucknow, for providing all spectral data and IGIB, Delhi, for MALDI-TOF spectral analysis.

LITERATURE CITED

(1) Erlich, H. A., Gelfond, D., and Srinsky, J. J. (1991) Recent advances in polymerase chain reaction. *Science 252*, 1643−1651.

(2) Mirzabekov, A. D. (1994) DNA sequencing by hybridisation-a mega sequencing method and a diagnostic tool? *TIBTECH 12*, 27−32.

(3) Speel, E. J. M., Hopman, A. H. N., and Komminoth, P. (1999) Application Methods to increase the sensitivity of In situ hybridisation: Play CARD (S). *J. Histochem. Cytochem. 47*, 281−288.

(4) Lakowicz, J. R. *Principles of Fluorescence Spectroscopy*, Kluwer Academic/Plenum Press, New York, 1999.

(5) Selvein, P. R. (2000) The renaissance of fluorescence energy transfer. *Nat. Struct. Biol. 7*, 730−734.

(6) Singh, Y., Pandey, A., Dubey, K. K., Watal, G., and Misra, K. (2000) Fluorescence resonance energy transfer: A diagnostic tool in oligonucleotide therapy. *Curr. Sci. 78*, 487−492.

(7) Broude, N. E. (2002) Stem Loop oligonucleotides: a robust tool for molecular biology and biotechnology. *TIBTECH 20*, 249−256.

(8) http://www.molecular-beacons.org.

(9) Wittwer, C. T., Herrmann, M. G., Moss, A. A., and Rasmussen, R. P. (1997) Continuous fluorescence monitoring of rapid cycle DNA amplification. *Biotechniques 22*, 130−1, 134−8.

(10) Schena, M. (2000) Microarray Biochip Technology, Eaten Publishing Natick, MA.

(11) Drobyshov, A. N., Malogina, N., Shick, V., Pobedimskaya, D., Yershov, G., and Mirzabekov, A. D. (1997) Sequence analysis by hybridisation with oligonucleotide chip: identification of β-thalassemia mutation. *Gene 188*, 45−52.

(12) Mansfield, E. S., Worley, J. M., Mckenzie, S. E., Surry, S., Rappoport, E., and Fortina, P. (1995) Nucleic acids detection using non-radioactive labeling methods. *Mol. Cell. Probes 9*, 145−156.

(13) Davis, M. J., Shah, A., and Bruce, I. J. (2000) Synthesis of fluorescently labelled oligonucleotides and nucleic acids. *Chem. Soc. Rev. 29*, 97−107.

(14) Yamana, K., Gokota, T., Ozaki, H., Nakano, H., Sangen, O., and Shimadzu, T. (1992) Enhanced fluorescence the binding with pyrene group in the sugar fragment to complementary poly nucleotides. *Nucleosides Nucleotides 11*, 383.

(15) Yamana, K., Iwase, R., Furutani, S., Tsuchida, H., Zako, H., Yamaoko, T., and Murakami, A. (1999) 2′-Pyrene modified oligonucleotide provides a highly sensitive fluorescent probe of RNA. *Nucleic Acids Res. 27*, 2387−2392.

(16) Yamana, K., Zako, H., Asazuma, K., Iwase, H., Nakano, H., and Murakami, A. (2001) Fluorescence detection of specific RNA sequences using 2′-pyrene-modified oilgonucleotides. *Angew. Chem., Int. Ed. 40*, 1104−1106.

(17) Yamana, K., Ohashi, Y., Nunota, K., and Nakano, H. (1997) Synthesis, binding and fluorescent properties of oligonucleotide derivatives having a dansyl fluorescence label; attached to the 2′-position of a ribonucleoside. *Tetrahedron 53*, 4265−4270.

(18) Misra, A., Tripathi, S., and Misra, K. (2001) Synthesis of Terminally labeled RNA sequences: Fluorescence and Hybridisation Study of RNA-DNA Duplexes. *Nucleic Acids Symp Ser. 1*, 95−96.

(19) Misra, A., Tripathi, S., and Misra, K. (2000) Fluorescent Labeling of ribonucleosides at 2′-terminus and its Fluorescent studies. *Nucleic Acids Symp. Ser. 44*, 215−216.

(20) Lilley, D. M. J. (1999) Structure, folding and catalysis of the small nucleolytic ribozymes. *Curr. Opin. Struct. Biol. 9*, 330−338.

(21) Rupert, P. B., and Ferre-d'Amare, A. R. (2001) Crystal structure of hairpin ribozyme-inhibitor complex with implications for catalysis. *Nature 410*, 780−786.

(22) Silverman, S. K., and Cech, T. R. (1999) RNA Tertiary Folding Monitored by Fluorescence of Covalently Attached Pyrene. *Biochemistry 38*, 14224−14237.

(23) Wachter, A., Jablonski, J. A., and Ramachandran, K. L. (1986) A simple and efficient procedure for the synthesis of 5′-aminoalkyl oligodeoxynucleotides. *Nucleic Acids Res. 14*, 7985.

(24) Stirchak, P. E., Summerton, J. E., and Weller, D. D. (1987) Uncharged stereoregular Nucleic Acid analogues1. Synthesis of a cytosine containing oligomer carbamate internucleoside linkages. *J. Org. Chem. 52*, 4202−4206.

(25) Korshun, V. A., Stetsenko, D. A., and Gait, M. J. (2002) Novel uridin-2-yl Carbamates: synthesis, incorporation into oligodeoxyribonucleotides and remarkable, fluorescence properties of 2′-pyren-1-yl methylcarbamate. *J. Chem. Soc., Perkin Trans 1*, 1092−1104.

(26) Dubey, I., Pratviel, G., and Meunier, B. (2000) Synthesis and DNA cleavage of 2′-*O*-amino-linked metalloporphyrin-oligonucleotide conjugates. *J. Chem. Soc., Perkin Trans 1*, 3088−3095.

(27) Prhavc, M., Lesnik, E. A., Mohan, V., and Manoharan, M. (2001) 2′-O-Carbamate-containing oligonucleotides: synthesis and properties. *Tetrahedron Lett. 42*, 8777−8780.

(28) Chen, R. F., and Kernohan, J. K. (1967) Combination of Bovine carbonic Anhydrase with a fluorescent sulphonamide. *J. Biol. Chem. 242*, 5813−5823.

(29) Li, Y.-H., Chan, L.-M., Tyer, L., Moody, R. T., Himel, C. M., and Hercules, D. M. (1975) Solvent effects on the fluorescence of 1-(dimethylamino)-5-naphthalenesulfonic acid and related compounds. *J. Am. Chem. Soc. 97*, 3118−3126.

(30) Hoenes, G., Houser, M., and Pfleiderer, G. (1986) Dynamic total fluorescence and anisotropy decay study of the dansyl Fluorophore in model compounds and enzymes. *Photochem. Photobiol. 43*, 133−137.

(31) Sproat, B. S., and Lamond, A. I. (1991) *Oligonucleotides and Analogues: a Practical Approach, the Practical Approach*

Series, Eckstein, F., Ed., pp 49−86, Oxford University Press, Oxford, New York, Tokyo.
(32) Sanghvi, Y. S., Guo, Z., Pfundheller, H. M., and Converso, A. (2000) Improved Process for the Preparation of Nucleosidic Phosphoramidites Using a Safer and Cheaper Activator. *Org. Proc. Res. Dev. 4*, 175−181.
(33) Misra, A., Tripathi, S., and Misra, K. (2002) Photolabile groups for exocyclic amino and O6/N-1 lactam protection in oligonucleotide synthesis. *Ind. J. Chem. 41B*, 1454−1459.
(34) Epling, G. A., and Walker, M. E. (1982) A new Photochemically removable protecting groups for amines. *Tetrahedron Lett. 23*, 3843−3846.
(35) Freier, S. M., and Altman, K. H. (1997) The ups and downs of nucleic acid duplex stability: structure−stability studies on chemically modified DNA: RNA duplexes. *Nucleic Acids Res. 25*, 4429−43.
(36) Ondera, M., Shiokawa, H., and Takagi, T. (1976) Fluorescent probes for antibody active sites. I. Production of antibodies specific to the *N*-methyl-2-anilinonaphthalene-6-sulfonyl group in rabbits and some fluorescent properties of the hapten bound to the antibodies. *J. Biochem. 79*, 195−201.
(37) Guest, C. R., Hochstrasser, R. A., Dupuy, C. G., Allen, D. J., Benkovic, S. J., and Millar, D. P. (1991) Interaction of DNA with the Klenow fragment of DNA polymerase I studied by time-resolved fluorescence spectroscopy. *Biochemistry 30*, 8759−8770.
(38) Singh, Y., Misra, A., and Misra, K. (2002) Synthesis and characterisation and fluorescence study of some novel naphthalimide derivatives. *Ind. J. Chem. 41B*, 1238−1245.
(39) Allen, D. J., Darke, P. L., and Benkovick, S. J. (1989) Fluorescent oligonucleotides and deoxynucleotide triphosphates: preparation and their interaction with the large (Klenow) fragment of *Escherichia coli* DNA polymerase I. *Biochemistry 28*, 4601−4607.
(40) Allen, D. J., and Benkovick, S. J. (1989) Resonance energy transfer measurements between substrate binding sites within the large (Klenow) fragment of *Escherichia coli* DNA polymerase I. *Biochemistry 28*, 9586−9593.
(41) Guest, C. R., Hochatrasser, R. A., Dupuy, C. G., Allen, D. J., Benkovic, S. J., and Millar, D. P. (1991) Interaction of DNA with the Klenow fragment of DNA polymerase I studied by time-resolved fluorescence spectroscopy. *Biochemistry 30*, 8759−8770.
(42) Barawkar, D. A., and Ganesh, K. N. (1995) Fluorescent d (CGCGAATTCGCG): characterization of major groove polarity and study of minor groove interactions through a major grooves semantophore conjugate. *Nucleic Acids Res. 23*, 159−164.
(43) Singh, D., Kumar, V., and Ganesh, K. N. (1990) Oligonucleotides, part 5+; Synthesis and fluorescence studies of DNA oligomers d $(AT)_5$ containing adenines covalently linked to C-8 with dansyl fluorophore. *Nucleic Acids Res. 18*, 3339−3345.
(44) Crokett, A. O., and Wittwer, C. T. (2001) Fluorescein labeled oligonucleotides for real-time PCR: using the inherent quenching of deoxyguanosine nucleotide. *Anal. Biochem. 290*, 89−97.
(45) Marras, S. A. E., Kramer, F. R., and Tyagi, S. (2002) Efficiency of fluorescence resonance energy transfer and contact-mediated quenching in oligonucleotide probes. *Nucleic Acids Res. 30*, e122.
(46) Seidel, C. A. M., Schultz, A., and Sauer, M. M. H (1996) Nucleobase-specific quenching of fluorescent dyes. 1. Nucleobase one-electron redox potentials and their corelation with static and dynamic quenching efficiencies. *J. Phys. Chem. 100*, 5541−5553.

BC049976H

Evaluation of Cleavable (Tyr^3)-octreotate Derivatives for Longer Intracellular Probe Residence

Paul A. Whetstone,[‡] Hiromichi Akizawa,[‡,§] and Claude F. Meares*

Department of Chemistry, University of California, One Shields Avenue, Davis, California 95616. Received January 18, 2004; Revised Manuscript Received April 7, 2004

Radioligand targeting of somatostatin receptor subtype 2 (sstr2)-positive tumors with synthetic somatostatin analogues such as octreotide is subject to improvement in tumor to nontumor biodistribution, in part because internalization of such somatostatin analogues is limited by sstr2 recycling to the cell surface. We reasoned that it might be possible to prepare probe-carrying somatostatin analogues that would escape recycling, efficiently depositing probe molecules inside cells and ultimately increasing their intracellular concentration. We have incorporated cathepsin-B-cleavable linkers into (Tyr^3)-octreotate chelate conjugates and examined these constructs as to cellular uptake, externalization, subcellular localization, and cleavage in the rat pancreatic tumor cell line AR42J in culture. Comparison of the cleavable radioligands with a noncleavable control indicates that scission of the constituent cathepsin B substrate occurs at a rate faster than ligand externalization, depositing virtually all internalized cleaved radiochelates within lysosomal compartments.

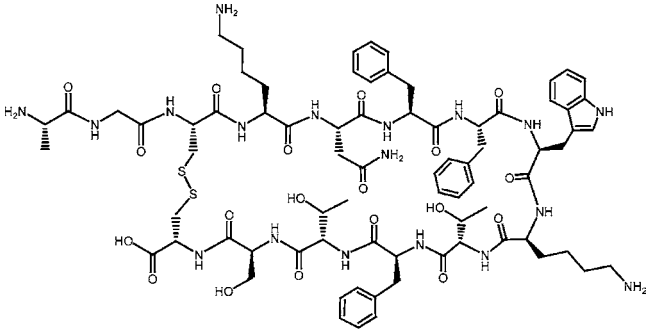
INTRODUCTION

Long-lived synthetic somatostatin analogues such as octreotide (Chart 1) are useful in targeting radiolabels to type 2 somatostatin receptor-positive tumors, for medical imaging and therapy (*1*−*3*). Their effectiveness, particularly in therapeutic applications, is limited by the balance between radiation delivered to the target and to the kidney. This situation might be improved either by facilitating kidney clearance or by enhancing tumor retention of the radiolabels. A variety of methods designed to reduce kidney accumulation of radioactivity have been examined with some success (*4*−*18*); however, we have been unable to find any reports focused on increasing the residence time of radioactivity in tumors.

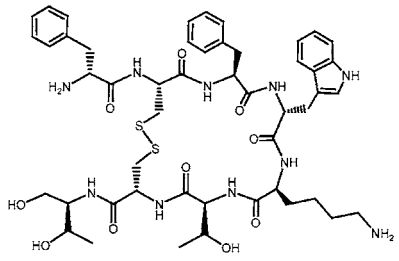
For the octreotide/sstr2 interaction, tumor retention of radioactivity is limited by receptor recycling mechanisms that involve vesicular packaging of receptor−ligand complexes and ultimately lead to radioligand externalization (*19*−*22*). It has been reported that the uptake of receptor ligands (^{111}In-DTPA-D-Phe^1)-octreotide and (^{111}In-DTPA)-sst-14 (Chart 1) in sstr-positive organs is determined predominantly by sstr2 (*23*), which efficiently internalizes these ligands. Since affinity profiling of several octreotate and octreotide derivatives demonstrated (DOTA-Tyr^3)-octreotate[1] to have the highest affinity for sstr2 of those examined (*24*), we chose this ligand as our model to study the effect of intracellular cleavage.

Experiments with conjugated antibodies have indicated that cleavably linked radiochelates do not clear subcellular compartments efficiently (*25*); however, noncleavable radiochelates conjugated to synthetic somatostatin analogues do (*19*, *20*). We reasoned that synthesis of a (DOTA-Tyr^3)-octreotate analogue with a cleavable peptide linker between chelate and (Tyr^3)-octreotate could allow vesicular proteases to separate the two during

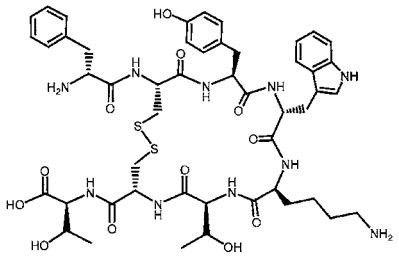
Chart 1. Chemical Structures of the Somatostatin-14 Peptide and Synthetic Analogues Octreotide and (Tyr^3)-octreotate



Somatostatin 14 (sst-14)



Octreotide



(Tyr^3)-octreotate

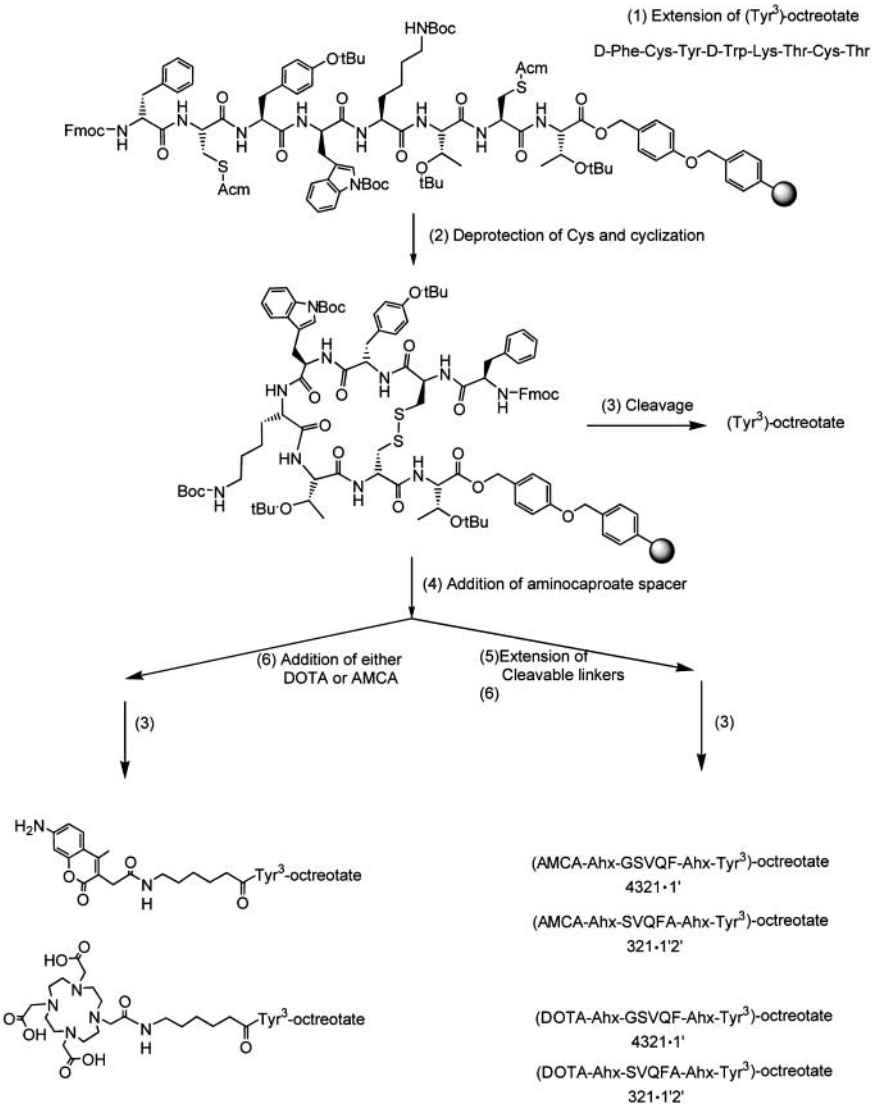
* Address correspondence to this author. Telephone: 530-752-0936. Fax: 530-752-8938. E-mail: cfmeares@ucdavis.edu.

‡ These authors contributed equally to the work.

§ Present address: Department of Molecular Imaging and Radiotherapy, Graduate School of Pharmaceutical Sciences, Chiba University, 1-8-1 Inohana, Chuo-ku, Chiba 260-8675, Japan. E-mail: aki@p.chiba-u.ac.jp.

10.1021/bc049972c CCC: $27.50 © 2004 American Chemical Society
Published on Web 04/29/2004

Scheme 1. Synthesis of Peptide Conjugates. Numbering System for Cathepsin B Cleavage Is Shown below Linker Sequences: Cleavage Occurs between Q and F Residues



internalization of the receptor-bound radiolabeled peptide. This separation could cause the radiolabel to remain inside the cell, enhancing tumor retention.

Peterson and Meares previously prepared a peptide combinatorial library and screened it to identify several excellent substrates for the intracellular proteases cathepsins B and D (*26*, *27*). Here, we have designed (Tyr^3)-octreotate derivatives that incorporate labile peptide sequences based on the decapeptide GFGSVQFAGF, which has the highest cathepsin B cleavability of those reported (*26*). To reduce the hydrophobicity of the conjugates, we investigated the pentapeptide fragments GSVQF (P_4-P_1') and SVQFA (P_3-P_2') of the GFGSVQFAGF 10-mer (Scheme 1). DOTA, a chelator that forms stable complexes with many metals useful for medicine (*6*, *28*−*37*), was used in conjunction with (Tyr^3)-octreotate, whose derivatives often show good biodistribution (*14*, *34*−*41*). In this study we synthetically incorporated the two cathepsin-B-labile peptide sequences into (Tyr^3)-octreotate conjugates and evaluated their behavior in cultured rat pancreatic tumor AR42J cells.

MATERIALS AND METHODS

Wang (*p*-benzyloxybenzyl alcohol) resin, Fmoc-amino acids, amino acid derivatives, and analogues were purchased from Novabiochem (San Diego, CA). DOTA-tris(*tert*-butyl ester) was purchased from Macrocyclics (Dallas, TX). Human liver cathepsin B was purchased from Sigma (St Louis, MO). Analytical HPLC was performed on an Alltech (Deerfield, IL) Alltima C18 column (5 μm, 250 × 4.6 mm), eluted with a linear gradient of 0.075% CF_3COOH/CH_3CN (Solvent B) in 0.1% CF_3COOH/H_2O (Solvent A) at a flow rate of 1 mL/min. Semipreparative HPLC was performed on an Alltech Alltima C18 column (5 μm, 250 × 22 mm), eluted with a linear gradient of

[1] Abbreviations: Acm, acetamidomethyl; Ahx, ϵ-aminohexanoic acid; AMC, 7-amino-4-methylcoumarin; AMCA, 7-amino-4-methyl-3-coumarinylacetic acid; CBZ, benzyloxycarbonyl; CPM, counts per minute; DIEA, *N*,*N*-diisopropylethylamine; DIPCDI, *N*,*N*′-diisopropylcarbodiimide; DMAP, 4-(dimethylamino)pyridine; DMF, *N*,*N*-dimethylformamide; DMSO, dimethyl sulfoxide; DOTA, 1,4,7,10-tetraazacyclododecane-*N*,*N*′,*N*″,*N*‴-tetraacetic acid; DTPA, diethylenetriaminepentaacetic acid; DTT, dithiothreitol; EDTA, *N*,*N*′-ethylenediaminetetraacetic acid; ESI-MS, electrospray ionization mass spectrometry; FBS, fetal bovine serum; Fmoc, 9-fluorenylmethoxycarbonyl; HEPES, 2-[4-(2-hydroxyethyl)-1-piperazinyl]-ethanesulfonic acid; HOBt, *N*-hydroxybenzotriazole; PyBOP, benzotriazole-1-yloxytrispyrrolidinophosphonium hexafluorophosphate; sst, somatostatin; sstr2, somatostatin receptor subtype II; TIS, triisopropylsilane; Tris, tris(hydroxymethyl)-aminomethane.

Solvent B in Solvent A at a flow rate of 6 mL/min. All solvent gradient programs are provided in Supporting Information. Effluent was monitored by detection of its optical absorption at 350 nm for AMCA-conjugated peptide or 280 nm for non-AMCA-conjugated peptides; the absorption at 214 nm was also measured for all effluents. ESI-MS was performed on a Thermo Finnigan (San Jose, CA) LCQ Deca instrument. Thin-layer chromatography was performed with EM Science (Gibbstown, NJ) silica gel 60 F_{254} plastic backed plates (cat. no. 5735), or with the nonfluorescent equivalent (cat. no. 5748).

Peptide Synthesis. All DOTA- and AMCA-conjugated peptides were synthesized on Wang resin (loading capacity 1.2 mmol/g) by Fmoc solid-phase peptide synthetic techniques according to Scheme 1.

Initial loading of the Fmoc-Thr(tBu)-OH amino acid onto the resin was accomplished via symmetric anhydride activation. Fmoc-Thr(tBu)-OH (5 equiv to resin, 2.385 g) was dissolved in anhydrous CH_2Cl_2 (10 mL), DIPCDI (2.5 equiv, 470 μL) was added, and the mixture was stirred for 20 min at 0 °C on ice. The CH_2Cl_2 was removed by evaporation under reduced pressure, and the residue resuspended in DMF (4.5 mL) and added along with 0.1 M DMAP in DMF solution (0.05 equiv, 0.6 mL) to preswollen resin. The mixture was then agitated by bubbling Ar gas through the resin slurry at room temperature for 2 h. After the resin was washed and dried, the loading yield was estimated by measuring the amount of Fmoc released from the resin upon piperidine treatment. Two aliquots of resin (about 1−2 mg each) were weighed into test tubes, and 20% piperidine in DMF (3 mL) was added to each. After agitation for 3 min, the absorbance at 290 nm of each solution was compared to the 20% piperidine reference solution and loading yield was estimated at 0.269 mmol/g from the equation: $\text{mmol/g} = (\text{Abs}_{\text{sample}} - \text{Abs}_{\text{ref}})/(1.65 \times \text{mg of resin})$. The remaining hydroxyl functionality on the resin was blocked by reaction with acetic anhydride (2.5 equiv, 566 μL) and 0.1 M DMAP/DMF solution (0.05 equiv, 0.6 mL) in DMF.

After the initial loading, peptides were extended in a batch-wise manner: Fmoc was removed from resin-bound N-terminal amines with 20% piperidine in DMF, and amide couplings were performed by addition of a solution containing 3 mol equiv of protected amino acid, HOBt, PyBOP, and DIEA in DMF (10 mL/g resin). Removal of the Fmoc group and completion of the conjugation reaction were monitored by the quantitative ninhydrin test (*42*).

Upon completion of the (Tyr³)-octreotate sequence (Fmoc-D-Phe-Cys(Acm)-Tyr(Boc)-D-Trp(Boc)-Lys(Boc)-Thr-($\psi^{\text{Me,Me}}$pro)-Cys(Acm)-Thr(tBu)-Wang resin), peptide cyclization was performed on the resin by concurrent oxidative removal of cysteine Acm protection and formation of the cystine bond. A solution of $Tl^{3+}(CF_3COO^-)_3$ in DMF (0.1 M, 2.5 equiv to peptide) was added and the slurry mixed by bubbling through Ar gas for 2 h (*40*, *43*−*45*). An Fmoc-aminohexanoic acid spacer was appended to the N-terminus of the (Tyr³)-octreotate peptide, after which either the cleavable linker, DOTA(tBu)$_3$, or AMCA was conjugated to the N-terminus using PyBOP and HOBt activation.

The peptide-resin was washed thoroughly and dried under reduced pressure overnight. Cleavage and deprotection of the peptide was afforded by treatment of the resin with a mixture of 95% CF_3COOH, 2.5% H_2O, and 2.5% TIS (10 mL/g peptide-resin) in a stoppered flask left to stand at room temperature for 2.5 h with occasional swirling. The resin was removed by filtration and rinsed twice with cleavage mixture, the filtrates were combined, and CF_3COOH was evaporated under reduced pressure. Cold Et_2O was added to the residue, and the resultant precipitate was extracted into water. Crude peptides were >85% pure by analytical HPLC. Following purification by semipreparative HPLC, peptides of >97% purity were lyophilized and stored at −80 °C. Peptide identities were confirmed by ESI-MS: (Tyr³)-octreotate ($C_{49}H_{65}N_{10}O_{12}S_2$), calcd $(M + H)^+$ m/z 1049.421, found 1049.7; (DOTA-Ahx-Tyr³)-octreotate ($C_{71}H_{102}N_{15}O_{20}S_2$), calcd $(M + H)^+$ m/z 1548.684, found 1548.8; (DOTA-Ahx-P_3−P_2'-Ahx-Tyr³)-octreotate ($C_{102}H_{149}N_{22}O_{28}S_2$), calcd $(M + H)^+$ m/z 2194.032, $(M + 2H)^{++}$, 1097.5, found $(M + 2H)^{++}$, 1098.3; (DOTA-Ahx-P_4−P_1'-Ahx-Tyr³)-octreotate ($C_{101}H_{147}N_{22}O_{28}S_2$), calcd $(M + H)^+$ m/z 2180.016, $(M + 2H)^{++}$, 1090.5, found $(M + 2H)^{++}$, 1091.1; (AMCA-Ahx-Tyr³)-octreotate ($C_{67}H_{85}N_{12}O_{16}S_2$), calcd $(M + H)^+$ m/z 1377.563, found 1377.6; (AMCA-Ahx-P_3−P_2'-Ahx-Tyr³)-octreotate ($C_{98}H_{132}N_{19}O_{24}S_2$), calcd $(M + H)^+$ m/z 2022.91, $(M + 2H)^{++}$, 1012.0, found $(M + 2H)^{++}$, 1012.6; (AMCA-Ahx-P_4−P_1'-Ahx-Tyr³)-octreotate ($C_{97}H_{130}N_{19}O_{24}S_2$), calcd $(M + H)^+$ m/z 2008.895, $(M + 2H)^{++}$, 1005.0, found $(M + 2H)^{++}$, 1005.4.

Radiolabeling of DOTA-Conjugated Peptides. Peptides were dissolved into 10% DMSO in 0.1 M NH_4OAc (pH 6.0) at approximate concentrations of 5 mM by mass. The true concentration of each peptide−chelate solution was then measured by radiometric assay with a standardized solution of ^{57}Co(II) (*46*, *47*).

For all cell culture experiments, the chelates and peptide chelates were radiolabeled with either ^{111}In or ^{90}Y. Indium-111 metalations were performed in 5% DMSO, 0.1 M NH_4OAc buffer (pH 5.5) with radiometal and DOTA-peptides at final concentrations of 3.3 mCi/mL and 25 μM, respectively; yields were >95%. Yttrium-90 metalations were performed in 5% DMSO, 0.4 M NH_4OAc buffer (pH 6.0) at identical concentrations; yields were >80%. Radiometal was added to the peptide−chelate solution, and the mixture vortexed and incubated at 70 °C for 45 min. To ensure that each treatment contained a single peptide species, each metalation reaction was chased with 1 equiv of cold metal ($InCl_3$ or YCl_3) to fully metalate the peptide−chelate conjugate. To then allay the toxic effects that free metal may have had upon cell culture, DTPA (10 mM, final) was added, and to then prevent free chelate from removing other minerals from the medium, $CaCl_2$ (10 mM, final) was added. After each addition, the mixture was incubated at 37 °C for 1 h. Radiochemical purity was examined by TLC (EM Science 5735), which was developed in 0.1% CF_3COOH/H_2O: 0.1% of CF_3COOH/CH_3CN (1:1). After TLC development, plates were visualized with X-ray film and cut and counted in a Beckman γ-counter. In instances where the radiolabeling of the peptide−chelate was not quantitative, final concentration of the radiopeptide was normalized to the TLC count data. Since control experiments demonstrated that the uptake of ^{111}In-DTPA and ^{90}Y-DTPA by cells was negligible, radiolabeled peptide solutions were used without further purification in all cell experiments.

Cathepsin B Cleavage in Vitro (*27*). For all peptides, experiments were performed in triplicate. To human liver cathepsin B (50 μL, about 123 units/mL in 50 mM NaOAc, 1 mM EDTA) was added 4 μL of 1 M DTT, and the mixture was preactivated at 37 °C for 30 min. A 2 μL aliquot of this preactivated solution was added to each AMCA-peptide solution (25 μL, 50 μM) in 10% DMSO, 0.1 M Me_4NOAc buffer (pH 4.8), and the mixture was incubated at 37 °C. Aliquots of this solution were removed at 15, 30, 60, 80 min, and AMCA-conjugated peptides were applied to nonfluorescent silica

gel TLC plates (EM Science 5748). The TLC was developed in 10% aqueous NH_4OAc:methanol (2:1). At the same time, cathepsin B activity was measured using the commercial substrate CBZ-Arg-Arg-AMC. To 100 μL of a 5 μM CBZ-Arg-Arg-AMC solution in 10% DMSO, 0.1 M Me_4NOAc buffer (pH 4.8) was added 8 μL of the same preactivated cathepsin B solution, and fluorescence of released AMC was measured every 30 s for 30 min (λ_{ex}= 348 nm; λ_{em}= 440−480 nm). The amount of released AMC was calculated using the calibration curve found from the fluorescence of standard AMC solutions.

Similar experiments were performed using ^{111}In-labeled DOTA-peptides. After developing TLC plates (EM Science 5735) in 0.1% CF_3COOH/H_2O: 0.1% CF_3COOH/CH_3CN (1:1), the plates were imaged by exposure to film, and then cut and counted for quantitation.

Cell Culture. AR42J (ATCC, Manassas, VA) rat pancreatic tumor cells were cultured in high glucose Dulbecco's modified Eagle's medium with 2 mM glutamine and 1.5 g/L $NaHCO_3$ (DMEM, GibcoBRL), supplemented by 10% (v/v) FBS, 100 U/mL penicillin, and 100 μg/mL streptomycin. Cultures were maintained in a humidified incubator at 37 °C, 5% CO_2. Subculturing was performed employing a 0.25% trypsin−0.1% EDTA solution.

Internalization and Externalization Experiments in Cultured AR42J Cells. Internalization experiments were performed in triplicate. AR42J cells (5×10^5/well) were distributed in 12-well plates and incubated at 37 °C for 2 days in cell culture medium (DMEM containing 10% FBS). Medium was removed, and cells were washed with Dulbecco's phosphate-buffered saline (1 mL × 1) and incubated at 37 °C in 1 mL internalization medium (DMEM containing 0.1% FBS). After 2 h, 0.5 mL of a dual-labeled radiopeptide mixture, containing equimolar amounts of (^{90}Y-DOTA-Ahx-Tyr^3)-octreotate and either (^{111}In-DOTA-Ahx-P_3−P_2′-Ahx-Tyr^3)-octreotate or (^{111}In-DOTA-Ahx-P_4−P_1′-Ahx-Tyr^3)-octreotate, were added (final total concentration: 1 nM), and the incubation was continued. At 0.5, 1, 2, and 4 h, incubation medium was removed and cells were washed and harvested. After removal of the radiolabel-containing medium, cells were washed consecutively with 1 mL of DMEM containing 10% FBS and 1 mL of Dulbecco's phosphate-buffered saline to remove free radioligand and protein. Cells were solubilized in 1 mL of 0.1% Triton X-100/0.3 M NaOH, and 0.5 mL of each cell lysate was transferred to a scintillation vial for counting both β- and γ-emissions. For each cell lysate sample, protein concentration was determined by microBCA assay (Pierce) using bovine serum albumin as a protein standard.

Competitive inhibition of radiolabel uptake was examined by repeating the internalization experiment in the presence of unmodified (Tyr^3)-octreotate at concentrations ranging from 100 pM to 10 μM. Data were numerically fit and IC_{50} values calculated with a sigmoidal dose−response regression analysis using GraphPad Prism version 3.00 for Windows (www.graphpad.com).

Externalization experiments were performed with eight replicates per sample. After 4 h internalization incubation with dual (^{90}Y and ^{111}In)-labeled peptides, cells were washed with 1 mL of DMEM containing 10% FBS. The internalization medium was replaced with DMEM containing 10% FBS and 1 μM (Tyr^3)-octreotate, added to prevent reinternalization of externalized radiolabels, and again incubated at 37 °C. At 0, 6, and 24 h, cells were washed and solubilized, and lysates assayed for radioactivity and protein concentration by the same methods used for internalization experiments.

For both internalization and externalization experiments, cell viability was assayed before and after treatment with the radiolabeled peptides using trypan blue stain. A single replicate from each treatment was treated with a 0.4% (w/v) solution of trypan blue in Dulbecco's phosphate-buffered saline and examined at 10× magnification with a microscope fitted with a 10 mm × 10 mm (0.5 mm × 0.5 mm squares) eyepiece grid reticle. Stained cells were deemed nonviable, while refractile cells were considered viable. Tallies of each species within the four central grid squares were taken, and the percentage of viable cells was calculated.

Analysis of Radiopeptide Cleavage in Cultured AR42J Cells. After internalization incubation of cultured AR42J cells with ^{90}Y-labeled peptides, cell lysates were analyzed by TLC (EM Science 5735) to evaluate whether the inserted linkers had been cleaved. For each radiopeptide at each time point, the lysates of three replicate wells of a 12-well plate were combined and used in the analysis (combination was necessary in order to obtain sufficient radioactivity for TLC visualization). Similarly to internalization experiments, 1 nM (final concentration) radiopeptide was incubated with cells. At 0.5, 1, 2, and 4 h, incubation medium (supernatant) was removed and set aside. Cells were washed with 1 mL of DMEM containing 10% FBS and 1 mL of Dulbecco's phosphate-buffered saline. Cells in one replicate well were solubilized in 200 μL of 0.1% Triton X-100/0.3 M NaOH; after complete solubilization of cells, the lysate was consecutively transferred to the next replicate well and solubilization repeated until three replicates were combined. Proteins in the cell lysates were precipitated by the addition of 200 μL of CH_3CN, and soluble portions were retained (all radioactivity remained in the soluble portion). Samples of each radiolabel in medium, cell supernatant, and cell lysate were spotted onto a silica gel TLC plate. The activity (CPM/mL) of the three solutions—medium, supernatant, and lysate—were estimated using a handheld Geiger counter and adjusted so that the amounts spotted on the TLC would yield approximately the same number of counts per sample. Four microliters (2 μL × 2) of each sample was applied to the TLC plate. Plates were developed using 0.1% CF_3COOH/H_2O: 0.1% CF_3COOH/CH_3CN (1:1) and visualized using a phosphorimaging device (Molecular Dynamics Typhoon 8600), and the spots were quantified using ImageQuant software (Molecular Dynamics, ver 5.1).

Subcellular Localization of Radioactivity in Cultured AR42J Cells. Through the application of Percoll-sucrose density gradient centrifugation (*48*, *49*), the subcellular localization of radioactivity in cultured AR42J cells immediately following radiolabel uptake, as well as in cells following 24 h of externalization, was determined. Cells were seeded at a density of 1.25×10^7 cells per dish in tissue culture Petri dishes (5 cm radius) and incubated at 37 °C for 2 days in cell culture medium (DMEM containing 10% FBS). Similarly to internalization and externalization experiments, after 2 h preincubation with DMEM containing 0.1% FBS, cells were incubated with a dual-labeled radiopeptide mixture, containing (^{90}Y-DOTA-Tyr^3)-octreotate and either (^{111}In-DOTA-Ahx-P_3−P_2′-Ahx-Tyr^3)-octreotate or (^{111}In-DOTA-Ahx-P_4−P_1′-Ahx-Tyr^3)-octreotate (final total concentration: 1 nM).

The application of dual-labeling, i.e., having both cleavable and noncleavable radiopeptides present in the same batch of cells, eliminated the necessity of normalizing the data to protein content, since the amount of each radiolabel within each fraction was directly comparable to the other.

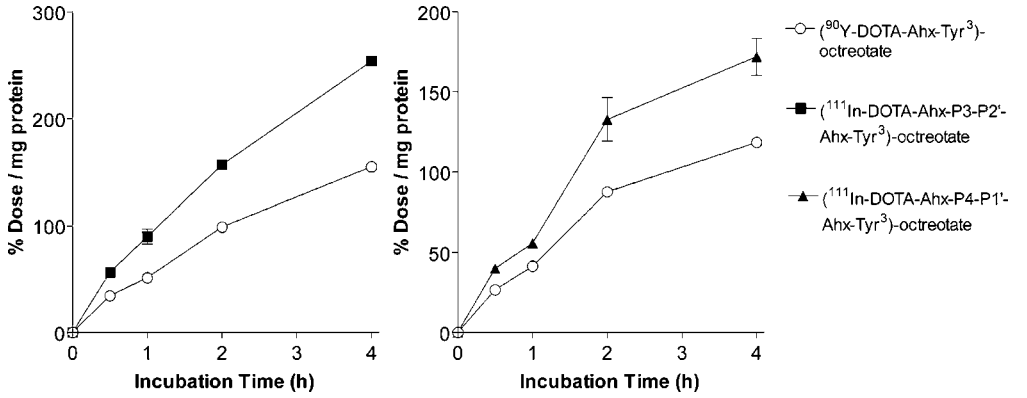


Figure 1. Internalization of mixture of (^{90}Y-DOTA-Ahx-Tyr^3)-octreotate (circle) and (^{111}In-DOTA-Ahx-P_3-P_2'-Ahx-Tyr^3)-octreotate (square) or (^{111}In-DOTA-Ahx-P_4-P_1'-Ahx-Tyr^3)-octreotate (triangle) into AR42J. SEM values indicated for all data points.

After 4 h internalization incubation, cells were washed with DMEM containing 10% FBS and Dulbecco's phosphate-buffered saline. Cells were incubated in and washed first with ice-cold glycine buffer (pH 2.8) to remove cell-surface-bound peptides (*50*) and then with Dulbecco's phosphate-buffered saline. The procedures for Percoll density gradient fractionation were performed on ice or at 4 °C (*48*, *49*). Cells were scraped off the Petri dish with a rubber policeman into 1 mL of 0.25 M sucrose/10 mM HEPES, pH 7.4, and transferred to a Dounce homogenizer (15 mL, Type A, Wheaton) with an additional 1 mL of 0.25 M sucrose/10 mM HEPES, pH 7.4. After cells were homogenized with 30 strokes, the homogenate was transferred to a falcon centrifuge tube (15 mL), diluted with an additional 1 mL of 0.25 M sucrose/10 mM HEPES, pH 7.4, and centrifuged at 500 × *g* for 5 min to pellet unbroken cells and nuclei. Postnuclear supernatant was transferred to another falcon centrifuge tube (15 mL). After the pellet was resuspended with 2 mL of 0.25 M sucrose/10 mM HEPES, pH 7.4, the suspension was centrifuged at 500 × *g* for 5 min and added to the first postnuclear supernatant fraction. The combined supernatant fractions were diluted to 10 mL with 0.25 M sucrose/10 mM HEPES, pH 7.4, and adjusted to a final concentration of 27% Percoll in 0.25 M sucrose using a 90% Percoll solution (9 parts Percoll and 1 part 2.5 M sucrose/100 mM HEPES, pH 7.4). This solution was layered over a 1 mL sucrose cushion consisting of 10 × homogenization buffer (2.5 M sucrose, 100 mM HEPES, pH 7.4) in a 16-mL round-bottom centrifuge tube (polycarbonate, 18 × 101 mm, Nalge Nunc International). Samples were centrifuged without braking at 20 000 × *g* for 120 min in a Sorvall SS-34 fixed-angle rotor (Sorvall Instruments, Newtown, CT) equipped with adaptors (Kendro) to fit the centrifuge tubes. Twenty fractions were collected starting from the top of the gradient, and the radioactivity in each dual-labeled fraction was measured by γ- and β- counters for ^{111}In and ^{90}Y, respectively.

The late endosome and lysosome marker enzyme, β-hexosaminidase, and the plasma membrane marker enzyme, alkaline phosphodiesterase I, were also assayed for each fraction (*51*). In this study, alkaline phosphodiesterase I serves as a marker of the early endosome fraction, since with this centrifugation protocol the early endosome fraction sediments with the plasma membrane fraction, and the plasma membrane has been stripped of radioligand. Enzyme assays were performed in 96-well plates, and absorbances were measured by an EL 311 microplate reader (Bio-Tek instruments) connected to Macintosh computer equipped with Deltasoft 3 (2.22 Biotek PlateReader). β-Hexosaminidase activity was measured by adding 100 μL of 10 mM *p*-nitrophenyl-*N*-acetyl-β-D-glucosaminide in 0.1 M NaOAc buffer, 0.1% Triton X-100, pH 4.1, to wells containing 10 μL of the sample. After incubation at 37 °C for 90 min, 100 μL of 1 M Na_2CO_3(aq) was added to stop the reaction. Precipitated Percoll was removed by centrifugation at 3000 × *g* for 10 min, and 150 μL of the supernatant was transferred to another 96-well plate and its absorbance read at 405 nm. Alkaline phosphodiesterase I activity was measured by adding 100 μL of 2 mM thymidine 5′-monophosphate *p*-nitrophenyl ester in 0.1 M Tris-HCl buffer, 0.1% Triton X-100, pH 8.9, to wells containing 10 μL of the sample. After incubation at 37 °C for 60 min, 100 μL of 0.1 M NaOH was added to stop the reaction, and the absorbance at 405 nm was measured.

Subcellular Localization after 24 h Externalization of the Radiolabel. After identical treatment for radiolabel internalization, cells were washed with DMEM containing 10% FBS (10 mL) and Dulbecco's phosphate-buffered saline (10 mL) and then incubated with DMEM containing 10% FBS and 1 μM (Tyr^3)-octreotate for 24 h, after which the assay for subcellular localization was performed as above.

RESULTS

In Vitro Cleavage. To verify the cathepsin B cleavage of (Tyr^3)-octreotate conjugates incorporating the P_3-P_2' and P_4-P_1' sequences, AMCA-conjugates were incubated with human liver cathepsin B in vitro. At 15 min, the CBZ-Arg-Arg-AMC control was cleaved 95±2%, the AMCA-conjugate containing P_3-P_2' 27 ± 3%, the conjugate containing P_4-P_1' 18 ± 3%, while the noncleavable AMCA-conjugate showed no cleavage. In the case of ^{111}In-labeled DOTA-peptides, similar results were observed: 24 ± 3% and 16 ± 5% cleavage, respectively, for the P_3-P_2' and P_4-P_1' containing peptides, with no cleavage of the DOTA-(Tyr^3)-octreotate peptide.

Internalization/Externalization. The uptake of radiolabeled DOTA-peptides by somatostatin receptor-positive AR42J cells was measured using dual-radiolabeling methods. Mixtures containing not only the ^{90}Y-labeled noncleavable peptide but also one of the ^{111}In-labeled cleavable peptides were incubated with cells. Although all peptides showed time-dependent uptake, cleavable linker-peptides displayed higher uptake rates than the noncleavable peptide by 64 ± 3% and 45 ± 17% for P_3-P_2' and P_4-P_1' sequences, respectively (Figure 1). Control experiments showed that switching the metal labels so that the noncleavable peptide contained ^{111}In and the cleavable contained ^{90}Y did not affect the outcome.

Uptake inhibition was also examined. Each ^{111}In-radiolabeled DOTA-(Tyr^3)-octreotate peptide (1 nM) was

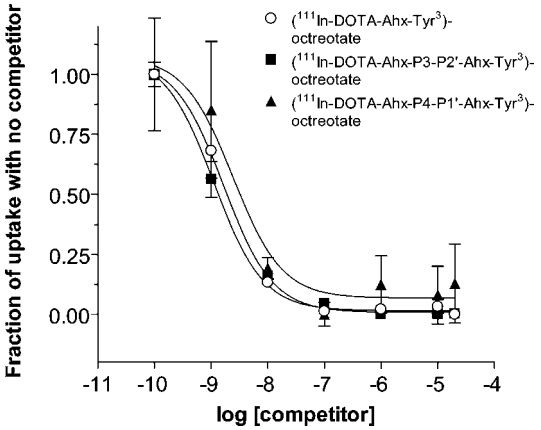


Figure 2. Internalization of (^{111}In-DOTA-Ahx-Tyr^3)-octreotate (circle), (^{111}In-DOTA-Ahx-P_3-P_2'-Ahx-Tyr^3)-octreotate (square), and (^{111}In-DOTA-Ahx-P_4-P_1'-Ahx-Tyr^3)-octreotate (triangle) in the presence of (Tyr^3)-octreotate as a competitor. Values are expressed as % of maximal uptake (i.e. uptake without inhibitor) ± SEM.

Table 1. IC_{50} Values for Rat Sstr2 of Somatostatin Analogues[a]

peptide	IC_{50} ± SEM (nM)
(DOTA-Ahx-Tyr^3)-octreotate	1.6 ± 0.4
(DOTA-Ahx-P_3-P_2'-Ahx-Tyr^3)-octreotate	1.1 ± 0.4
(DOTA-Ahx-P_4-P_1'-Ahx-Tyr^3)-octreotate	2.4 ± 0.8

[a] Determined by competitive binding with (Tyr^3)-octreotate, IC_{50} = 1.5 ± 0.4 nM (*24*).

challenged with varying concentrations of unlabeled (Tyr^3)-octreotate during incubation with AR42J. In each case, 50% inhibition of uptake was observed at approximately equimolar concentrations of (Tyr^3)-octreotate inhibitor and ^{111}In-peptide (Figure 2). At (Tyr^3)-octreotate concentrations greater than or equal to 100 nM, radiolabel uptake was almost completely inhibited. Numerical curve fitting yielded IC_{50} values (Table 1) in agreement with published values for (^{90}Y-DOTA-Tyr^3)-octreotate (*24*).

Externalization experiments were performed to examine the degree to which the internalized radioactivity was retained within AR42J cells over time. After allowing radiolabels to internalize within cells over 4 h, cells were washed and incubated with culture medium containing 1 μM unlabeled (Tyr^3)-octreotate (to prevent re-uptake of externalized peptides), and cell cultures were monitored over 24 h for loss of radioactivity. After the 24 h incubation, the noncleavable peptide showed about 40% secretion of its initial uptake, while both cleavable peptides maintained near 100% of their initial uptake (Figure 3). Ratios of cleavable to noncleavable for each of the dual-radiolabeled experiments are shown in Figure 4.

In both internalization and externalization studies, cells were assayed for viability both before and after radioligand treatment; in all cases cell viability exceeded 95%.

Intracellular Radioligand Proteolysis. The extent of peptide cleavage in cell culture was examined by TLC after incubation with ^{90}Y-labeled peptides (Figure 5). Intact peptides were compared with peptides in cell-treatment supernatant and with peptides contained in cell lysates. No cleavage of any of the peptides was apparent in culture medium either before or after incubation with cells, while both cleavable and noncleavable peptides were degraded within cells, as evidenced by changes in their R_f-values. After 4 h of incubation, the cell lysates showed less than 3% of the radioactivity from cleavable peptides migrating at the R_f of the parent peptide, while more than 80% of the noncleavable peptide remained intact.

Subcellular Localization of Radioactivity. We examined the subcellular distribution of radioactivity after cellular internalization of a mixture of ^{90}Y-labeled noncleavable and ^{111}In-labeled cleavable peptides (Figure 6). Fractionation of cell homogenate immediately following the 4 h internalization of the radiolabels showed a marked difference in subcellular localization between the cleavable and noncleavable peptide−chelates. At 4 h, lysosomal fractions contained a significantly larger percentage of the radioactivity derived from cleavable peptides than from the noncleavable peptides, which appeared in early endosomes. A two-tailed unpaired *t*-test comparison of the values observed within fractions 4 and 17 of the 4 h treatments (Figure 6, panels A and C) indicates that the observed differences between the cleavable and noncleavable peptides are significant with *P*-values of less than 0.0001. However, after 4 h of internalization followed by an additional 24 h incubation, the radioactivity from either cleavable or noncleavable peptide−chelates was located predominantly within lysosomes, with no statistical difference between the two radiolabels.

DISCUSSION

Our aim in this study was to increase the amount of radiolabeled somatostatin derivatives within tumor cells by increasing the intracellular residence time of the radiolabel. We designed and synthesized DOTA-conjugated (Tyr^3)-octreotate, that incorporated cathepsin-B-

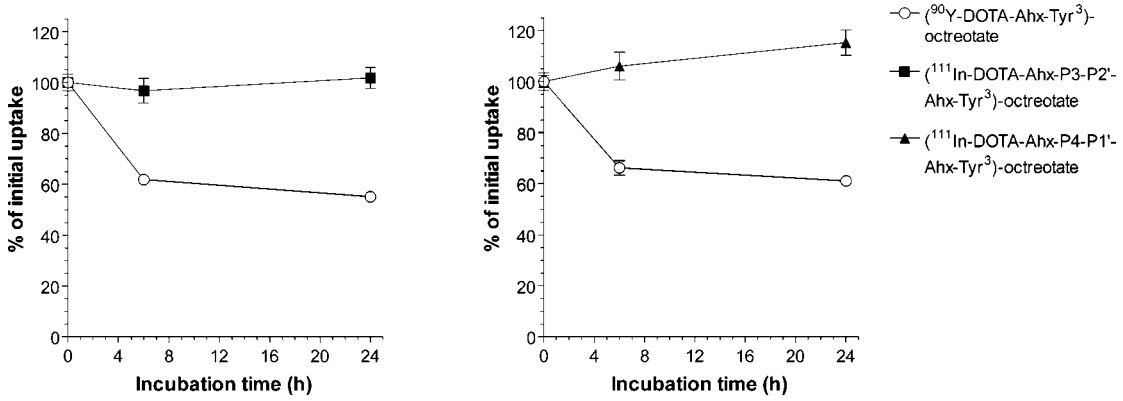


Figure 3. Externalization of mixture of (^{90}Y-DOTA-Ahx-Tyr^3)-octreotate (circle) and (^{111}In-DOTA-Ahx-P_3-P_2'-Ahx-Tyr^3)-octreotate (square) or (^{111}In-DOTA-Ahx-P_4-P_1'-Ahx-Tyr^3)-octreotate (triangle) from AR42J. *Y*-axes are expressed as % of initial content ± SEM.

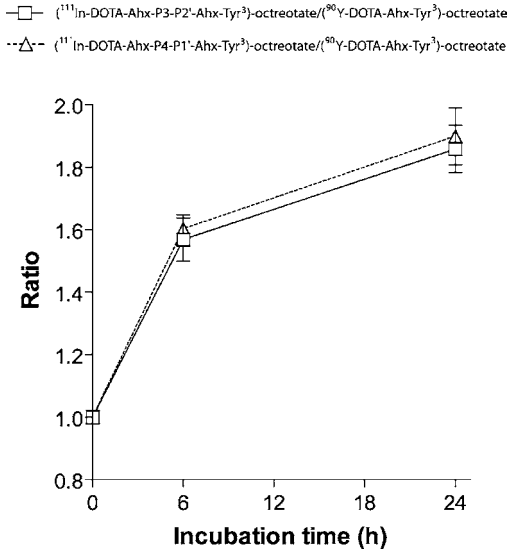


Figure 4. Externalization of mixture of (^{90}Y-DOTA-Ahx-Tyr^3)-octreotate and (^{111}In-DOTA-Ahx-P_3-P_2'-Ahx-Tyr^3)-octreotate (square) or (^{111}In-DOTA-Ahx-P_4-P_1'-Ahx-Tyr^3)-octreotate (triangle) from AR42J. *Y*-axes are expressed as the ratio of ^{111}In CPM to ^{90}Y CPM, without protein normalization. Errors indicated are SEM.

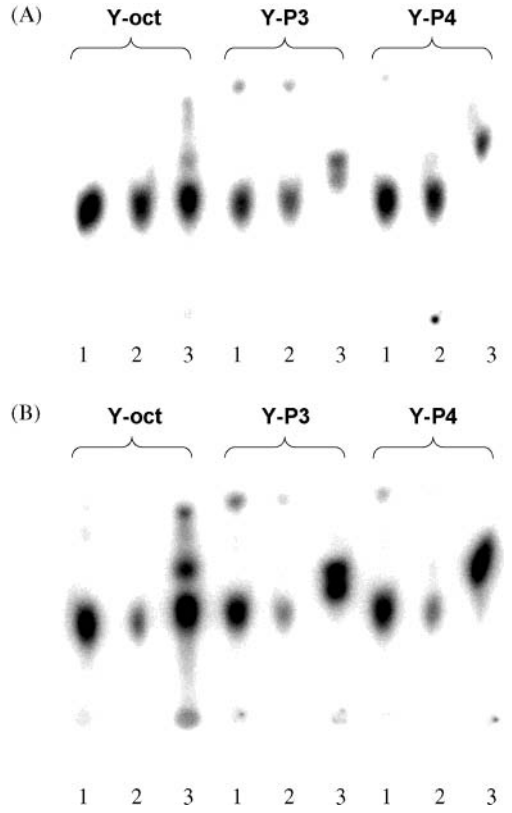


Figure 5. TLC analyses of radioactivity in AR42J cells after 2 (A) and 4 h (B) incubation with ^{90}Y-labeled peptides. Lane 1: loaded sample before incubation; lane 2: loaded sample after incubation; lane 3: CH_3CN-soluble portion of cell lysate. Y-oct: (^{90}Y-DOTA-Ahx-Tyr^3)-octreotate; Y-P3: (^{90}Y-DOTA-Ahx-P_3-P_2'-Ahx-Tyr^3)-octreotate; Y-P4: (^{90}Y-DOTA-Ahx-P_4-P_1'-Ahx-Tyr^3)-octreotate.

labile peptides (Scheme 1), and examined their behavior in vitro and in cell culture.

After receptor-mediated endocytosis, stable synthetic somatostatin analogues are externalized by receptor recycling mechanisms in which receptor−ligand complexes are packaged in endosomal vesicles within the recycling pathway and shunted back to the cell surface (*19*, *20*). We hypothesized that since internalized metal chelates tend to remain within cells, intravesicular cleavage of the radiochelate moiety from the receptor-binding somatostatin analogue might increase radiochelate retention within the cell. Assuming that low levels of proteolytic enzyme activity would be present in early endosomes or other vesicles involved in recycling somatostatin analogues, we incorporated excellent cathepsin B substrates between the chelate and (Tyr^3)-octreotate, using a previously identified peptide substrate as our model (*26*, *27*). Truncating that substrate's decapeptide sequence to the five internal residues P_3-P_2' or P_4-P_1' afforded final constructs that were significantly more water-soluble than the GFGSVQFAGF parent decapeptide. Insertion of ϵ-aminohexanoic acid spacers between the chelate and the linker, and between the linker and (Tyr^3)-octreotate, was done to maximize accessibility of the cathepsin B substrate to the enzyme and to maintain optimal affinity of the resultant peptide for the somatostatin receptor (*44*).

Linker cleavage by cathepsin B was confirmed in vitro. Both AMCA- and ^{111}In-DOTA-labeled peptides containing the P_3-P_2' or P_4-P_1' sequence (Scheme 1) were incubated in vitro with human liver cathepsin B along with positive and negative controls; examination by TLC indicated that both linkers cleaved with rates approximately 20% that of the commercial substrate CBZ-Arg-Arg-AMC. The (Tyr^3)-octreotate peptides without linker were not cleaved under these conditions. The P_3-P_2' linker cleaved slightly faster than P_4-P_1', a result consistent with the report by Portaro et al., indicating that the P_3-P_2' residues are those primarily responsible for enzyme recognition (*52*).

Cleavage in AR42J cell culture was also confirmed and was shown only to occur intracellularly. Peptide cleavage was not observed in the cell culture medium—either before or after incubation in cell culture—but was only seen in cell lysate. While all peptides, including the nonlinker control, were cleaved intracellularly, the peptide without the cleavable linker was still >80% intact after 4 h of incubation, at which time <3% of the cleavable peptides remained intact (Figure 5). Indeed, cleavage appears to be rapid compared to the recycling process, since even at 30 min of incubation in cell culture, the scissile peptides were mostly cleaved. The small difference in cleavage rate between the two cleavable substrates observed in vitro does not affect their behavior in cell culture, corroborating the hypothesis that the rate of intracellular cleavage is more rapid than the externalization process.

Figure 1 shows internalization curves. After 4 h of internalization incubation, compared to the noncleavable peptide, the P_3-P_2'- and P_4-P_1'-containing peptides displayed significantly higher uptake. Meir et al. demonstrated that N-terminal extension of the ligand peptidyl chain should not significantly change the receptor-affinity of the compound (*44*). Since the IC_{50} values for all three peptides were in the low nM range (Table 1), demonstrating that the incorporated cleavable linkers do not increase affinity, the most likely cause for the increased uptake of radioactivity is the rapid cleavage of the linkers upon internalization.

Externalization studies confirmed the net increase in internalization seen for the cleavable ligands. Cleavage not only prevents recycling of the ligand by detaching the chelate from the ligand−receptor complex, but also produces a radiolabeled product that is not membrane-permeable. While the noncleavable peptide showed a gradual decrease of intracellular radioactivity to about

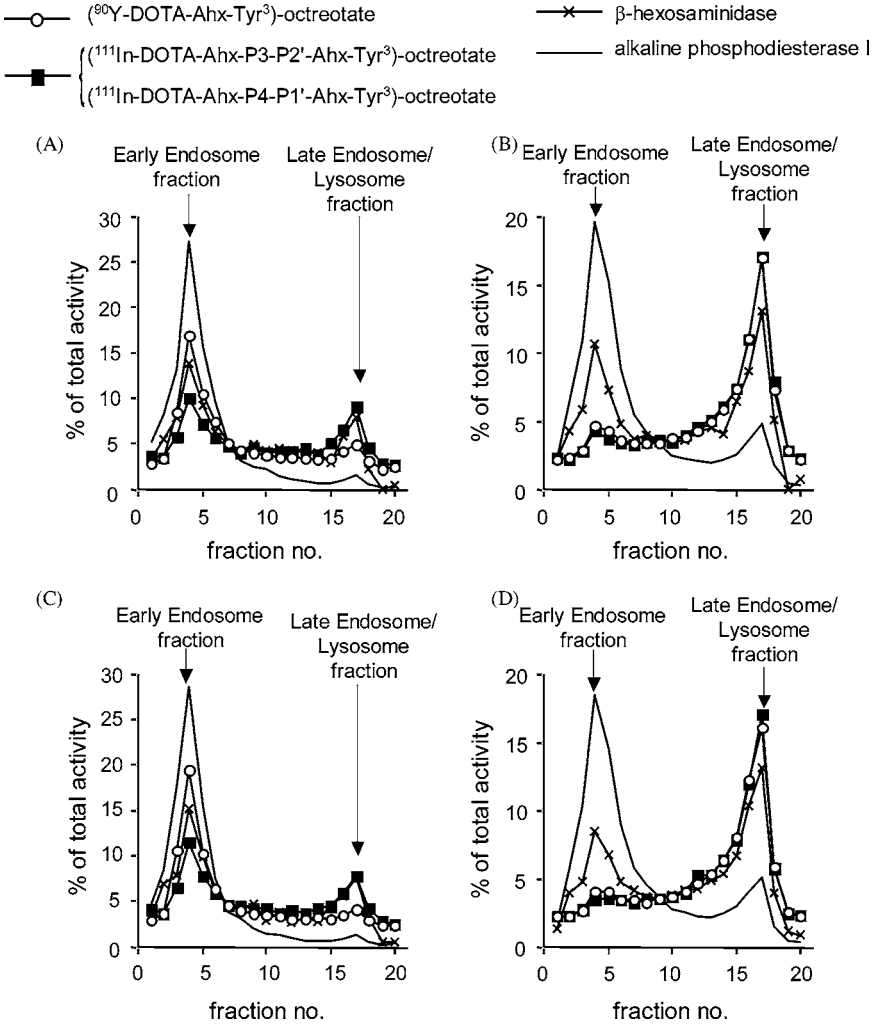


Figure 6. Subcellular localization of radioactivity after 4 h internalization (A) and 24 h externalization incubation (B) with mixture of (^{90}Y-DOTA-Ahx-Tyr^3)-octreotate (circle) and (^{111}In-DOTA-Ahx-P_3-P_2'-Ahx-Tyr^3)-octreotate (square) and after 4 h internalization (C) and 24 h externalization incubation (D) with mixture of (^{90}Y-DOTA-Ahx-Tyr^3)-octreotate (circle) and (^{111}In-DOTA-Ahx-P_4-P_1'-Ahx-Tyr^3)-octreotate (square). x: β-hexosaminidase (lysosome marker enzyme); solid line: alkaline phosphodiesterase I (plasma membrane marker enzyme). Error bars indicating ± 2 standard deviations, in all instances, are smaller than the datapoints on the graph and thus do not appear.

60% of the initial value after 24 h, the cleavable peptides maintained near 100% of initial uptake over this period (Figure 3). The P_4-P_1'-(Tyr^3)-octreotate data showed over 100% residence, but this can be attributed to an error in normalization to protein content; if the ratio of cleavable peptide to noncleavable in these double-label experiments is plotted versus time, the error resultant from normalization is removed and it becomes evident that the cleavable linker increases resident radioactivity about 2-fold over the noncleavable ligand after 24 h. Plots of the CPM ratios of each P_3-P_2' and P_4-P_1' peptide against the (DOTA-Ahx-Tyr^3)-octreotate control show identical response (Figure 4).

Investigation of the subcellular localization of radioactivity also distinguished the behavior of the cleavable peptides from the control. After 4 h internalization, the radioactivity from the noncleavable peptide remained primarily in early endosomes, while that resulting from either of the cleavable peptides was seen significantly in lysosomes. Twenty-four hours after cell loading, all intracellular radioactivity was localized in lysosomes (Figure 6), consistent with previous reports (*51*, *53*, *54*). The presence of the lysosomal marker enzyme β-hexosaminidase within both early and late fractions has been noted by others (*51*). We believe that its presence in the light fractions of the Percoll gradient is due to the enzyme's presence within early endosomes in this cell line, and thus the enzyme is acting as a marker for both early and late endosomes; as such it does not present a problem in interpreting the data. While β-hexosaminidase is seen consistently in both the early and late endosome fractions in all four panels of Figure 6 (i.e. at both 4 and 24 h, and in both experimental treatments with each cleavable peptide), the distribution of radioactivity clearly differs for the noncleavable peptide at 4 and 24 h.

We interpret the difference in localization between the two radioligands at 4 h as attributable to the difference in longevity of each ligand−receptor complex. The relatively rapid proteolytic release of the cleavable radiochelate from the ligand−receptor complex prevents its externalization and increases its rate of accumulation within lysosomes. The noncleavable radiochelate, on the other hand, remains in early endosomes as the ligand−receptor complex and is largely externalized. Thus the fast cleavage of the cathepsin-B substrate linker leads to the observed differences in subcellular localization as well as to the increase in cell resident radioactivity of the two species.

While a 2-fold increase in tumor resident radioactivity for the cleavable radioligands presents a significant improvement, the clearance of nontumor resident radioactivity is still of concern. Radiometal-labeled DOTA- or DTPA-conjugated octreotate derivatives typically show nonspecific accumulation of radioactivity within the kidneys. High intralysosomal cathepsin B activity within the kidney (*55*, *56*), should efficiently process the cleavable radiolabels to produce chelate-appended tetra- or tripeptides with a single negative charge. As in tumor cells, this cleavage might be expected to increase the radiochelate residence within the kidney. However, since renal uptake is based on adsorptive endocytosis rather than receptor-mediated endocytosis, ligand re-externalization is not significant and we expect that both cleavable and noncleavable ligands should exhibit similar retention.

This strategy to enhance radioactivity within tumor tissue could lead to improved diagnosis and therapy using radiometal-labeled somatostatin derivatives and may have application to therapy with Auger emitters such as ^{111}In, which are effective when internalized (*57*, *58*).

ACKNOWLEDGMENT

This work was supported by Research Grant CA16861 to C.F.M. from the National Institutes of Health. We thank Nathaniel G. Butlin and Todd M. Corneillie for helpful discussions, and Yayoi Whetstone for assistance in cell culturing.

Supporting Information Available: Solvent gradients for HPLC. This material is available free of charge via the Internet at http://pubs.acs.org.

LITERATURE CITED

(1) Krenning, E. P., Kooij, P. P. M., Bakker, W. H., Breeman, W. A. P., Postema, P. T. E., Kwekkeboom, D. J., Oei, H. Y., De Jong, M., Visser, T. J., Reijs, A. E. M., and Lamberts, S. W. J. (1994) Radiotherapy with a radiolabeled somatostatin analogue, [111In-DTPA-D-Phe1]-octreotide. A case history. *Ann. N.Y. Acad. Sci. 733*, 496−506.

(2) Krenning, E. P., Kwekkeboom, D. J., Bakker, W. H., Breeman, W. A. P., Kooij, P. P. M., Oei, H. Y., Vanhagen, M., Postema, P. T. E., Dejong, M., Reubi, J. C., Visser, T. J., Reijs, A. E. M., Hofland, L. J., Koper, J. W., and Lamberts, S. W. J. (1993) Somatostatin Receptor Scintigraphy With [In-111-DTPA-D-PHE(1)]- and [I-123-TYR(3)]-octreotide − The Rotterdam experience with more than 1000 patients [Review]. *Eur. J. Nuclear Med. 20* (8), 716−731.

(3) Raderer, M., Kurtaran, A., Leimer, M., Angelberger, P., Niederle, B., Vierhapper, H., Vorbeck, F., Hejna, M. H. L., Scheithauer, W., Pidlich, J., and Virgolini, I. (2000) Value of peptide receptor scintigraphy using I-123-vasoactive intestinal peptide and In-111-DTPA-D-Phe(1)-octreotide in 194 carcinoid patients: Vienna university experience, 1993 to 1998. *J. Clin. Oncol. 18* (6), 1331−1336.

(4) Jamar, F., Barone, R., Mathieu, I., Walrand, S., Labar, D., Carlier, P., De Camps, J., Schran, H., Chen, T., Smith, M. C., Bouterfa, H., Valkema, R., Krenning, E. P., Kvols, L. K., and Pauwels, S. (2003) Y-86-DOTA(0)-D-Phe(1)-Tyr(3)-octreotide (SMT487) − a phase 1 clinical study: pharmacokinetics, biodistribution and renal protective effect of different regimens of amino acid co-infusion. *Eur. J. Nuclear Med. Mol. Imag. 30* (4), 510−518.

(5) Rolleman, E. J., Valkema, R., De Jong, M., Kooij, P. P. M., and Krenning, E. R. (2003) Safe and effective inhibition of renal uptake of radiolabeled octreotide by a combination of lysine and arginine. *Eur. J. Nuclear Med. Mol. Imag. 30* (1), 9−15.

(6) De Jong, M., Breeman, W. A. P., Bernard, B. F., Bakker, W. H., Schaar, M., Van Gameren, A., Bugaj, J. E., Erion, J., Schmidt, M., Srinivasan, A., and Krenning, E. P. (2001) [Lu-177-DOTA(0), Tyr(3)]octreotate for somatostatin receptor-targeted radionuclide therapy. *Int. J. Cancer 92* (5), 628−633.

(7) Rosch, F., Herzog, H., Stolz, B., Brockmann, J., Kohle, M., Muhlensiepen, H., Marbach, P., and Muller-Gartner, H. W. (1999) Uptak.e kinetics of the somatostatin receptor ligand [Y-86]DOTA-DPhe(1)-Tyr(3)-octreotide ([Y-86]SMT487) using positron emission tomography in nonhuman primates and calculation of radiation doses of the Y-90-labeled analogue. *Eur. J. Nuclear Med. 26* (4), 358−366.

(8) De Jong, M., Bakker, W. H., Breeman, W. A. P., Bernard, B. F., Hofland, L. J., Visser, T. J., Srinivasan, A., Schmidt, M., Behe, M., Macke, H. R., and Krenning, E. P. (1998) Pre-Clinical Comparison of [Dtpa(0)] Octreotide, [Dtpa(0), Tyr-(3)] Octreotide and [Dota(0), Tyr(3)] Octreotide as Carriers for Somatostatin Receptor-Targeted Scintigraphy and Radionuclide Therapy. *Int. J. Cancer 75* (3), 406−411.

(9) Bernard, B. F., Krenning, E. P., Breeman, W. A. P., Rolleman, E. J., Bakker, W. H., Visser, T. J., Macke, H., and Dejong, M. (1997) D-Lysine Reduction of Indium-111 Octreotide and Yttrium-90 Octreotide Renal Uptake. *J. Nuclear Med. 38* (12), 1929−1933.

(10) De Jong, M., Breeman, W. A. P., Bernard, B. F., Rolleman, E. J., Hofland, L. J., Visser, T. J., Setyonohan, B., Bakker, W. H., Vanderpluijm, M. E., and Krenning, E. P. (1995) Evaluation in Vitro and in Rats of Tb-161-Dtpa-Octreotide, a Somatostatin Analogue with Potential for Intraoperative Scanning and Radiotherapy. *Eur. J. Nuclear Med. 22* (7), 608−616.

(11) Smith-Jones, P. M., Stolz, B., Albert, R., Knecht, H., and Bruns, C. (1997) Synthesis, biodistribution and renal handling of various chelate-somatostatin conjugates with metabolizable linking groups. *Nuclear Med. Biol. 24* (8), 761−9.

(12) Froidevaux, S., Eberle, A. N., Christe, M., Sumanovski, L., Heppeler, A., Schmitt, J. S., Eisenwiener, K., Beglinger, C., and Macke, H. R. (2002) Neuroendocrine tumor targeting: Study of novel gallium-labeled somatostatin radiopeptides in a rat pancreatic tumor model. *Int. J. Cancer 98* (6), 930−937.

(13) Akizawa, H., Arano, Y., Mifune, M., Iwado, A., Saito, Y., Mukai, T., Uehara, T., Ono, M., Fujioka, Y., Ogawa, K., Kiso, Y., and Saji, H. (2001) Effect of molecular charges on renal uptake of In-111-DTPA-conjugated peptides. *Nuclear Med. Biol. 28* (7), 761−768.

(14) Vaidyanathan, G., Friedman, H. S., Affleck, D. J., Schottelius, M., Wester, H. J., and Zalutsky, M. R. (2003) Specific and high-level targeting of radiolabeled octreotide analogues to human medulloblastoma xenografts. *Clin. Cancer Res. 9* (5), 1868−1876.

(15) Wester, H. J., Schottelius, M., Scheidhauer, K., Meisetschlager, G., Herz, M., Rau, F. C., Reubi, J. C., and Schwaiger, M. (2003) PET imaging of somatostatin receptors: design, synthesis and preclinical evaluation of a novel F-18-labeled, carbohydrated analogue of octreotide. *Eur. J. Nuclear Med. Mol. Imag. 30* (1), 117−122.

(16) Schottelius, M., Wester, H. J., Reubi, J. C., Senekowitsch-Schmidtke, R., and Schwaiger, M. (2002) Improvement of pharmacokinetics of radioiodinated Tyr(3)-octreotide by conjugation with carbohydrates. *Bioconjugate Chem. 13* (5), 1021−1030.

(17) Wester, H. J., Schottelius, M., Scheidhauer, K., Reubi, J. C., Wolf, I., and Schwaiger, M. (2002) Comparison of radioiodinated TOC, TOCA and Mtr-TOCA: the effect of carbohydration on the pharmacokinetics. *Eur. J. Nuclear Med. 29* (1), 28−38.

(18) De Jong, M., Rolleman, E. J., Bernard, B. F., Visser, T. J., Bakker, W. H., Breeman, W. A. P., and Krenning, E. P. (1996) Inhibition of renal uptake of indium-111-DTPA-octreotide in vivo. *J. Nuclear Med. 37* (8), 1388−1392.

(19) Koenig, J. A., Kaur, R., Dodgeon, I., Edwardson, J. M., and Humphrey, P. P. A. (1998) Fates of endocytosed somatostatin sst(2) receptors and associated agonists. *Biochem. J. 336* (Part 2), 291−298.

(20) Koenig, J. A., Edwardson, J. M., and Humphrey, P. P. A. (1997) Somatostatin Receptors in Neuro2a Neuroblastoma Cells − Ligand Internalization. *Br. J. Pharmacol. 120* (1), 52−59.

(21) Roosterman, D., Roth, A., Kreienkamp, H. J., Richter, D., and Meyerhof, W. (1997) Distinct Agonist-Mediated Endocytosis of Cloned Rat Somatostatin Receptor Subtypes Expressed in Insulinoma Cells. *J. Neuroendocrinol. 9* (10), 741−751.

(22) Nouel, D., Gaudriault, G., Houle, M., Reisine, T., Vincent, J. P., Mazella, J., and Beaudet, A. (1997) Differential Internalization of Somatostatin in Cos-7 Cells Transfected with Sst1 and Sst2 Receptor Subtypes − a Confocal Microscopic Study Using Novel Fluorescent Somatostatin Derivatives. *Endocrinology 138* (1), 296−306.

(23) Hofland, L. J., Lamberts, S. W., Van Hagen, P. M., Reubi, J. C., Schaeffer, J., Waaijers, M., Van Koetsveld, P. M., Srinivasan, A., Krenning, E. P., and Breeman, W. A. (2003) Crucial role for somatostatin receptor subtype 2 in determining the uptake of [111In-DTPA-D-Phe1]octreotide in somatostatin receptor-positive organs. *J. Nuclear Med. 44* (8), 1315−21.

(24) Reubi, J. C., Schar, J. C., Waser, B., Wenger, S., Heppeler, A., Schmitt, J. S., and Macke, H. R. (2000) Affinity profiles for human somatostatin receptor subtypes SST1-SST5 of somatostatin radiotracers selected for scintigraphic and radiotherapeutic use. *Eur. J. Nuclear Med. 27* (3), 273−82.

(25) Denardo, G. L., Kroger, L. A., Meares, C. F., Richman, C. M., Salako, Q., Shen, S., Lamborn, K. R., Peterson, J. J., Miers, L. A., Zhong, G. R., and Denardo, S. J. (1998) Comparison of 1,4,7,10-tetraazacyclododecane-N,N′,N″,N‴-tetraacetic acid (DOTA)-peptide-ChL6, a novel immunoconjugate with catabolizable linker, to 2-iminothiolane-2-[p-(bromoacetamido)benzyl]-DOTA-ChL6 in breast cancer xenografts. *Clin. Cancer Res. 4* (10), 2483−90.

(26) Peterson, J. J., and Meares, C. F. (1998) Cathepsin Substrates as Cleavable Peptide Linkers in Bioconjugates, Selected from a Fluorescence Quench Combinatorial Library. *Bioconjugate Chem. 9* (5), 618−626.

(27) Peterson, J. J., and Meares, C. F. (1999) Enzymatic cleavage of peptide-linked radiolabels from immunoconjugates. *Bioconjugate Chem. 10* (4), 553−557.

(28) Li, W. P., Smith, C. J., Cutler, C. S., Hoffman, T. J., Ketring, A. R., and Jurisson, S. S. (2003) Aminocarboxylate complexes and octreotide complexes with no carrier added Lu-177, Ho-166 and Pm-149. *Nuclear Med. Biol. 30* (3), 241−251.

(29) Breeman, W. A. P., De Jong, M., Visser, T. J., Erion, J. L., and Krenning, E. P. (2003) Optimising conditions for radiolabeling of DOTA-peptides with Y-90, In-111 and Lu-177 at high specific activities. *Eur. J. Nuclear Med. Mol. Imag. 30* (6), 917−920.

(30) Deshpande, S. V., Denardo, S. J., Kukis, D. L., Moi, M. K., McCall, M. J., Denardo, G. L., and Meares, C. F. (1990) Yttrium-90-labeled monoclonal antibody for therapy: labeling by a new macrocyclic bifunctional chelating agent. *J. Nuclear Med. 31* (4), 473−479.

(31) Hu, F., Cutler, C. S., Hoffman, T., Sieckman, G., Volkert, W. A., and Jurisson, S. S. (2002) Pm-149 DOTA bombesin analogues for potential radiotherapy − In vivo comparison with Sm-153 and Lu-177 labeled DO3A-amide-beta Ala-BBN-(7−14)NH2. *Nuclear Med. Biol. 29* (4), 423−430.

(32) Meares, C. F., Moi, M. K., Diril, H., Kukis, D. L., Mccall, M. J., Deshpande, S. V., Denardo, S. J., Snook, D., and Epenetos, A. A. (1990) Macrocyclic chelates of radiometals for diagnosis and therapy. *Br. J. Cancer 62* (Supplement 10), 21−26.

(33) Li, W. P., Lewis, J. S., Kim, J., Bugaj, J. E., Johnson, M. A., Erion, J. L., and Anderson, C. J. (2002) DOTA-D-Tyr(1)-octreotate: A somatostatin analogue for labeling with metal and halogen radionuclides for cancer imaging and therapy. *Bioconjugate Chem. 13* (4), 721−728.

(34) Kwekkeboom, D. J., Bakker, W. H., Kam, B. L., Teunissen, J. J. M., Kooij, P. P. M., Herder, W. W., Feelders, R. A., Eijck, C. H. J., Jong, M., Srinivasan, A., Erion, J. L., and Krenning, E. P. (2003) Treatment of patients with gastro-entero-pancreatic (GEP) tumours with the novel radiolabeled somatostatin analogue [Lu-177-DOTA(0), Tyr(3)]octreotate. *Eur. J. Nuclear Med. Mol. Imag. 30* (3), 417−422.

(35) Lewis, J. S., Wang, M., Laforest, R., Wang, F., Erion, J. L., Bugaj, J. E., Srinivasan, A., and Anderson, C. J. (2001) Toxicity and dosimetry of Lu-177-DOTA-Y3-octreotate in a rat model. *Int. J. Cancer 94* (6), 873−877.

(36) Breeman, W. A. P., Mearadji, A., Capello, A., Bernard, B. F., Van Eijck, C. H. J., Krenning, E. P., and De Jong, M. (2003) Antitumor effect and increased survival after treatment with [Lu-177-DOTA(0), Tyr(3)]octreotate in a rat liver micrometastases model. *Int. J. Cancer 104* (3), 376−379.

(37) Breeman, W. A. P., Van Der Wansem, K., Bernard, B. F., Van Gameren, A., Erion, J. L., Visser, T. J., Krenning, E. P., and De Jong, M. (2003) The addition of DTPA to [Lu-177-DOTA(0), Tyr(3)]octreotate prior to administration reduces rat skeleton uptake of radioactivity. *Eur. J. Nuclear Med. Mol. Imag. 30* (2), 312−315.

(38) Decristoforo, C., Maina, T., Nock, B., Gabriel, M., Cordopatis, P., and Moncayo, R. (2003) Tc-99m-Demotate 1: first data in tumour patients—results of a pilot/phase I study. *Eur. J. Nuclear Med. Mol. Imag. 30* (9), 1211−1219.

(39) Maina, T., Nock, B., Nikolopoulou, A., Sotiriou, P., Loudos, G., Maintas, D., Cordopatis, P., and Chiotellis, E. (2002) [^{99m}Tc]Demotate, a new ^{99m}Tc-based [Tyr^3]octreotate analogue for the detection of somatostatin receptor-positive tumours: synthesis and preclinical results. *Eur. J. Nuclear Med. Mol. Imag. 29* (6), 742−753.

(40) Bugaj, J. E., Erion, J. L., Johnson, M. A., Schmidt, M. A., and Srinivasan, A. (2001) Radiotherapeutic efficacy of Sm-153-CMDTPA-Tyr(3)-octreotate in tumor-bearing rats. *Nuclear Med. Biol. 28* (3), 327−334.

(41) Mier, W., Eritja, R., Mohammed, A., Haberkorn, U., and Eisenhut, M. (2000) Preparation and evaluation of tumor-targeting peptide−oligonucleotide conjugates. *Bioconjugate Chem. 11* (6), 855−860.

(42) Kaiser, E., Colescott, R. L., Bossinger, C. D., and Cook, P. I. (1970) Color test for detection of free terminal amino groups in the solid-phase synthesis of peptides. *Anal. Biochem. 34*, 595−598.

(43) Graham, K. A. N., Wang, Q., Eisenhut, M., Haberkorn, U., and Mier, W. (2002) A general method for functionalising both the C- and N-terminals of Tyr(3)-octreotate. *Tetrahedron Lett. 43* (29), 5021−5024.

(44) Mier, W., Beijer, B., Graham, K., and Hull, W. E. (2002) Fluorescent somatostatin receptor probes for the intraoperative detection of tumor tissue with long-wavelength visible light. *Bioorg. Med. Chem. 10* (8), 2543−2552.

(45) Edwards, W. B., Fields, C. G., Anderson, C. J., Pajeau, T. S., Welch, M. J., and Fields, G. B. (1994) Generally Applicable, Convenient Solid-Phase Synthesis and Receptor Affinities of Octreotide Analogues. *J. Med. Chem. 37* (22), 3749−3757.

(46) Goodwin, D. A., Meares, C. F., Watanabe, N., McTigue, M., Chaovapong, W., Ransone, C. M., Renn, O., Greiner, D. P., Kukis, D. L., and Kronenberger, S. I. (1994) Pharmacokinetics of Pretargeted Monoclonal Antibody 2D12.5 and ^{88}Y-Janus-2-(*p*-Nitrobenzyl)-1, 4, 7, 10-tetraazacyclododecanetetraacetic Acid (DOTA) in BALB/c Mice with KHJJ Mouse Adenocarcinoma: A Model for ^{90}Y Radioimmunotherapy. *Cancer Res. 54*, 5937−5946.

(47) Meares, C. F., Mccall, M. J., Reardan, D. T., Goodwin, D. A., Diamanti, C. I., and Mctigue, M. (1984) Conjugation of Antibodies with Bifunctional Chelating Agents: Isothiocyanate and Bromoacetamide Reagents, Methods of Analysis, and Subsequent Addition of Metal Ions. *Anal. Biochem. 142*, 68−78.

(48) Kornilova, E., Sorkina, T., Beguinot, L., and Sorkin, A. (1996) Lysosomal Targeting of Epidermal Growth Factor Receptors Via a Kinase-Dependent Pathway Is Mediated by the Receptor Carboxyl-Terminal Residues 1022−1123. *J. Biol. Chem. 271* (48), 30340−30346.

(49) Juuti-Uusitalo, K., Airenne, K. J., Laukkanen, A., Punnonen, E. L., Olkkonen, V. M., Gruenberg, J., Kulomaa, M., and Marjomaki, V. (2000) Selective targeting of avidin/mannose 6-phosphate receptor chimeras to early or late endosomes. *Eur. J. Cell Biol. 79* (7), 458−468.

(50) Eisenwiener, K. P., Prata, M. I. M., Buschmann, I., Zhang, H. W., Santos, A. C., Wenger, S., Reubi, J. C., and Macke, H. R. (2002) NODAGATOC, a new chelator-coupled somatostatin analogue labeled with [Ga-67/68] and [In-111] for SPECT, PET, and targeted therapeutic applications of somatostatin receptor (hsst2) expressing tumors. *Bioconjugate Chem*. *13* (3), 530−541.

(51) Duncan, J. R., Stephenson, M. T., Wu, H. P., and Anderson, C. J. (1997) Indium-111-Diethylenetriaminepentaacetic Acid Octreotide Is Delivered in Vivo to Pancreatic, Tumor Cell, Renal, and Hepatocyte Lysosomes. *Cancer Res*. *57* (4), 659−671.

(52) Portaro, F. C. V., Santos, A. B. F., Cezari, M. H. S., Juliano, M. A., Juliano, L., and Carmona, E. (2000) Probing the specificity of cysteine proteinases at subsites remote from the active site: analysis of P-4, P-3, P-2′ and P-3′ variations in extended substrates. *Biochem*. *J*. *347* (Part 1), 123−129.

(53) Arano, Y., Mukai, T., Uezono, T., Wakisaka, K., Motonari, H., Akizawa, H., Taoka, Y., and Yokoyama, A. (1994) A Biological Method to Evaluate Bifunctional Chelating Agents to Label Antibodies with Metallic Radionuclides. *J*. *Nuclear Med*. *35* (5), 890−898.

(54) Duncan, J. R., and Welch, M. J. (1993) Intracellular Metabolism of Indium-111-Dtpa-Labeled Receptor Targeted Proteins. *J*. *Nuclear Med*. *34* (10), 1728−1738.

(55) Shuja, S., Sheahan, K., Murnane, M. J. (1991) Cysteine endopeptidase activity levels in normal human tissues, colorectal adenomas and carcinomas. *Int. J*. *Cancer 49* (3), 341−346.

(56) Olbricht, J. (1992) Distribution of cathepsin B and L in the kidneyh and their role in tubuler protein absorption. *Eur*. *J*. *Clin*. *Chem*. *Clin*. *Biochem*.. *30* (10), 675−681

(57) Capello A, Krenning EP, Breeman WA, Bernard BF, de Jong M. (2003) Peptide receptor radionuclide therapy in vitro using [^{111}In-DTPA0]octreotide. *J*. *Nuclear Med*. *44* (1), 98−104.

(58) Wang M, Caruano AL, Lewis MR, Meyer LA, VanderWaal RP, Anderson CJ. (2003) Subcellular localization of radiolabeled somatostatin analogues: implications for targeted radiotherapy of cancer. *Cancer Res*. *63* (20), 6864−9.

BC049972C

Supporting Information for

Evaluation of cleavable (Tyr^3)-octreotate derivatives for longer intracellular probe residence.

Paul A. Whetstone[‡], Hiromichi Akizawa[‡,#], and Claude F. Meares*

Table S1. HPLC gradient systems

(Tyr^3)-octreotate (analysis)	time (min)	0	5	45	50
	B (%)	5	5	60	100
(Tyr^3)-octreotate (semipreparative)	time (min)	0	5	80	90
	B (%)	5	5	60	100
(DOTA-Ahx-Tyr^3)-octreotate (analysis)	time (min)	0	5	45	50
	B (%)	5	5	60	100
(DOTA-Ahx-Tyr^3)-octreotate (semipreparative)	time (min)	0	5	80	90
	B (%)	5	5	60	100
(DOTA-Ahx-P_3-P_2'-Ahx-Tyr^3)-octreotate (analysis)	time (min)	0	5	45	50
	B (%)	5	5	60	100
(DOTA-Ahx-P_3-P_2'-Ahx-Tyr^3)-octreotate (semipreparative)	time (min)	0	5	80	90
	B (%)	5	5	60	100
(DOTA-Ahx-P_4-P_1'-Ahx-Tyr^3)-octreotate (analysis)	time (min)	0	5	45	50
	B (%)	5	5	60	100
(DOTA-Ahx-P_4-P_1'-Ahx-Tyr^3)-octreotate (semipreparative)	time (min)	0	5	80	90
	B (%)	5	5	60	100
(AMCA-Ahx-Tyr^3)-octreotate (analysis)	time (min)	0	5	45	50
	B (%)	5	5	80	100
(AMCA-Ahx-Tyr^3)-octreotate (semipreparative)	time (min)	0	5	80	90
	B (%)	5	5	80	100
(AMCA-Ahx-P_3-P_2'-Ahx-Tyr^3)-octreotate (analysis)	time (min)	0	5	45	50
	B (%)	5	5	80	100
(AMCA-Ahx-P_3-P_2'-Ahx-Tyr^3)-octreotate (semipreparative)	time (min)	0	5	80	90
	B (%)	5	5	80	100
(AMCA-Ahx-P_4-P_1'-Ahx-Tyr^3)-octreotate (analysis)	time (min)	0	5	45	50
	B (%)	5	5	80	100
(AMCA-Ahx-P_4-P_1'-Ahx-Tyr^3)-octreotate (semipreparative)	time (min)	0	5	80	90
	B (%)	5	5	80	100

Direct Production of Proteins with N-Terminal Cysteine for Site-Specific Conjugation

Ian E. Gentle, David P. De Souza, and Manuel Baca*

The Walter and Eliza Hall Institute of Medical Research, 1G Royal Parade, Parkville, Victoria, 3050, Australia.
Received February 3, 2004

Proteins with N-terminal cysteine can undergo native chemical ligation and are useful for site-specific N-terminal labeling or protein semisynthesis. Recombinant production of these has usually been by site-specific cleavage of a precursor fusion protein at an internal cysteine residue. Here we describe a simpler route to producing these proteins. Overexpression in *E. coli* of several proteins containing cysteine as the second amino acid residue yielded products in which the intiating methionine residue had been completely cleaved by endogenous methionine aminopeptidase. While secondary modification of the terminal cysteine was a complicating factor, conditions were identified to eliminate or minimize this problem. Recombinant proteins produced in this way were suitable for site-specific modification of the amino terminus via native chemical ligation technology, as demonstrated by conjugation of a thioester-containing derivative of fluorescein to one such protein. The ability to directly produce proteins with N-terminal cysteine should simplify the application of native chemical ligation technology to recombinant proteins and make the technique more amenable to researchers with limited expertise in protein chemistry.

INTRODUCTION

Over the past decade, a number of new chemical methods have been devised which can be used to site-specifically modify the N-terminus of recombinant proteins (*1*−*3*). The most elegant of these, native chemical ligation (*2*), requires that the recombinant protein contain an N-terminal cysteine residue, which can then react in a specific manner with thioester-containing reagents. This method has been used to site-specifically label proteins with small molecules (*4*, *5*), to generate semisynthetic proteins via ligation of synthetic peptides (*6*) or to link together recombinantly produced protein fragments (*7*). While native chemical ligation has been extensively applied to chemically synthesized peptides (*8*), its application to recombinant proteins has been more limited. Current methods for producing N-terminal cysteine proteins usually involves cleavage of a precursor fusion protein with a site-specific protease in order to expose an internal cysteine residue as the new N-terminus (*4*, *9*). The drawbacks of this approach include possible cleavage at other sites within the protein and the need to repurify the cleaved product. Furthermore, the activity of site-specific proteases are not compatible with high levels of chaotropic agents which might otherwise be used to extract proteins from inclusion bodies and, if necessary, maintain them in solution.

A preferable approach to the production of N-terminal cysteine proteins would be to take advantage of endogenous methionine aminopeptidase (*10*) to cleave the initiating methionine from recombinantly expressed proteins containing cysteine as the second residue. As methionine excision is believed to occur cotranslationally (*11*−*13*), that is, before the completion of synthesis or folding of polypeptide chains, the expressed protein would be isolated with cysteine as the N-terminal residue. The specificity of methionine aminopeptidase is dependent upon the identity of the amino acid residue adjacent to the amino terminus. Methionine is efficiently removed from proteins when the second residue is a small side chain amino acid, even when these proteins are overexpressed (*14*−*16*). However, methionine is not cleaved when a large side chain amino acid is the adjacent residue. Variable degrees of cleavage have been reported to occur when the second residue is an intermediate sized amino acid such as cysteine (*14*, *15*). This appears to have limited attempts to produce N-terminal cysteine proteins by this route, due to a widely held belief that methionine excision will be incomplete (e.g. reference (*4*)), although at least one report has made use of this strategy (*17*).

Given the usefulness of proteins with N-terminal cysteine for site-specific modification or protein semisynthesis, we have investigated the direct production of such proteins in *E. coli* by expression of constructs containing Met-Cys- amino terminii. We report conditions for optimizing the yield of the processed product and demonstrate its utility for site-specific modification of the N-terminus.

EXPERIMENTAL PROCEDURES

Construction of Protein Expression Vectors. For expression of proteins containing an N-terminal polyhistidine tag, a modified pET15b vector (Novagen) was used. Proteins produced corresponded to fragments from suppressor of cytokine signaling (SOCS)-7 (amino acids 378−512) and SHP2 (amino acids 1−105 or 109−220). Each of the pET15b-based constructs encoded polypeptide products with either a MCSHHHHHHGARQ or MCRHHHHHHGARQ N-terminal sequence, followed by the fragments defined above. For expression of proteins containing a C-terminal polyhistidine tag, a pET22b vector (Novagen) was used. Proteins produced with this construct corresponded to fragments from SOCS7 (amino

* Corresponding author: AMRAD Corporation, 576 Swan St., Richmond, Victoria 3121, Australia; Telephone: +613 9208 4371; fax: +613 9208 4100; e-mail: mbaca@amrad.com.au.

10.1021/bc049965o CCC: $27.50 © 2004 American Chemical Society
Published on Web 05/01/2004

acids 378−512) and SHP2 (amino acids 3−105 or 110−220). Each of the pET22b constructs encoded protein products that contained a common MC N-terminal sequence, followed by the fragments defined above.

Expression, Purification, and Characterization of Protein Products. BL21 DE3 pLysS *E. coli* harboring the expression construct of interest were grown overnight in media containing ampicillin and chloramphenicol antibiotics. The overnight culture (20 mL) was used to inoculate 400 mL of super broth containing ampicillin, with or without 2% v/v glucose. Cultures were incubated with shaking at 37 °C until the optical density at 600 nm reached approximately 0.8 (typically 1.5−2 h). Protein expression was then induced by addition of isopropyl β-D-thiogalactopyranoside (IPTG)[1] to a final concentration of 200 μM, and cultures were incubated a further 2−4 h. For cultures grown in media supplemented with cysteine, 4 mL of a freshly prepared 1 M cysteine stock (pH 7.0) was added approximately 45 min prior to IPTG induction, and another 2 mL at the time of IPTG induction. Cell pellets were stored at −20 °C prior to lysis.

The frozen cell pellets were resuspended in 10 mL of lysis buffer (100 mM sodium phosphate, 10 mM Tris-HCl, pH 8.1, containing 7 M guanidine·HCl) to which methyl methanethiosulfonate had been added (10 mM final). After being stirred on ice for 30 min, the cell lysate was clarified by centrifugation and filtration, applied to a Hi-Trap Chelating HP column (Amersham-Pharmacia) precharged with nickel, and preequilibrated in lysis buffer. Following washing with lysis buffer adjusted to pH 6.3, the protein was eluted with the same buffer at pH 4.5. Samples were adjusted to pH 8.0 and reduced with DTT prior to analysis by HPLC. Reduced samples were also analyzed by matrix-assisted laser desorption/ionization time-of-flight mass spectrometry (MALDI-TOF MS) after desalting of samples with a C4 ZipTip pipet tip (Millipore).

Chemical Reversal of N-Terminal Cysteine Modification. Lyophilized protein was solubilized in 400 mM unbuffered *O*-methylhydroxylamine hydrochloride (∼pH 3), and 0.1 volumes of 200 mM aqueous tris(2-carboxyethyl)phosphine was added. Samples were incubated at room temperature and then removed at various time points for analysis by HPLC and/or MALDI-TOF MS (after desalting with a C4 ZipTip).

Preparation of Fluorescein 2-Mercaptoethanesulfonate Thioester (fluorescein-2MES). 5- (and 6-)-Carboxyfluorescein succinimidyl ester (96 mg) was combined with sodium 2-mercaptoethanesulfonate (375 mg) and solubilized in 10 mL of 0.1 M sodium borate buffer, pH 8.7. After being stirred at room temperature for 2 h, the thioester product was purified by reverse phase HPLC and lyophilized to yield 69 mg of fluorescein-2MES.

Site-Specific Ligation. Lyophilized protein was solubilized in unbuffered water at 5 mg/mL. To 13 μL of this sample were added 2.5 μL of 2 mg/mL fluorescein-2MES (in water), 1 μL of 200 mM sodium 2-mercaptoethanesulfonate (in water), and 4 μL of 500 mM sodium phosphate (pH 7.5). After 4.5 h incubation at room temperature, an equal volume of 100 mM DTT in water was added and the sample was incubated for a further 30 min. An aliquot of the reaction was then analyzed by HPLC and MALDI-TOF MS (after desalting).

RESULTS

Production of an N-Terminal Cysteine Protein. To determine whether the initiating methionine residue would be cleaved from a protein expressed in *E. coli* containing cysteine as the adjacent amino acid, we expressed the C-terminal Src homology 2 (SH2) domain from SHP2 (amino acids 109−220), a dual SH2 domain-containing protein phosphatase that we have previously studied in our laboratory (*18*). The expressed protein (SHP2C) contained the N-terminal tag sequence MCSH-HHHHHGARQ, thereby allowing purification of the recombinant product by nickel affinity chromatography. To protect the terminal and internal cysteine side chains from unwanted reactions during purification, the protein was extracted from *E. coli* by denaturing lysis buffer containing methyl methanethiosulfonate, a reagent which oxidizes sulfhydryl groups into the methyl disulfide derivative (*4*). The yield of purified protein obtained after affinity chromatography was 19 mg from a 400 mL *E. coli* culture.

To determine whether the N-terminal methionine residue had been cleaved, a sample of the protein was reduced with DTT and desalted prior to analysis by MALDI-TOF MS. The parent molecular ion observed by MALDI-TOF MS was broad, suggesting product heterogeneity, but was centered on 14 056 Da which is 110 Da lower than that of the full length methionine-containing product, but 21 Da higher than the methionine-cleaved product (Figure 1A). The MALDI-TOF MS data was not consistent with a mixture of processed and methionine-containing proteins because of an absence of defined molecular species with masses 14 035 and 14 166 Da. Rather, it suggested that the initiating methionine residue had been cleaved, but that low molecular weight modifications of the protein had also taken place. One defined species, present at a low level, was of mass 13 932 Da which is within 1 Da of that expected for a protein lacking both the N-terminal methionine and adjacent cysteine residues.

To better analyze the source of heterogeneity, a sample of the nonreduced protein was digested with trypsin, and the peptide fragments were analyzed by HPLC and MALDI-TOF MS (Figure 1B, 1C). On the basis of a comparison of the experimental versus predicted tryptic peptide masses, three peptide fragments appeared to be derived from the N-terminus of the protein. The masses of these peptides (1212, 1361, 1385 Da) were consistent with N-terminal peptide fragments SHHHHHHGAR, the methyl disulfide derivative of CSHHHHHHGAR (as expected from treatment of the protein with methyl methanethiosulfonate), and a +70 Da adduct of CSHH-HHHHGAR. The mass spectrum for the 1385 Da peptide also showed fragment ions at M − 46, M − 58, and M − 70 Da (Figure 1C). There was no tryptic fragment detected corresponding to an N-terminal methionine-containing peptide. The presence of three N-terminal tryptic peptides, in addition to the tendency for one of these to fragment in the mass spectrometer, explained why the MALDI-TOF MS data for the undigested protein showed a broad molecular ion (Figure 1A). Treatment of the tryptic mixture with the reducing agent tris(2-carboxyethyl)phosphine only affected the 1361 Da peptide, suggesting that the cysteine residue in the 1385 Da peptide was not modified by a disulfide adduct. We did not perform further characterization of the 1385 Da

[1] Abbreviations used: DTT, dithiothreitol; fluorescein-2MES, fluorescein 2-mercaptoethanesulfonate thioester; IPTG, isopropyl β-D-thiogalactopyranoside; MALDI-TOF MS, matrix-assisted laser desorption/ionization time-of-flight mass spectrometry; SH2, Src homology 2.

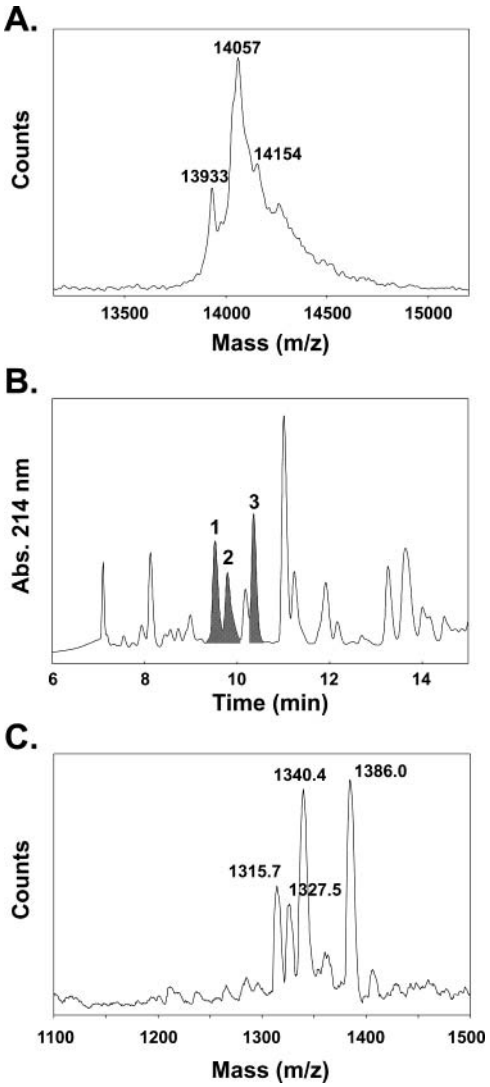


Figure 1. Analysis of modifications to N-terminal cysteine protein. Recombinantly produced SHP2C, containing the N-terminal tag sequence MCSHHHHHHGARQ, was analyzed for cleavage of the terminal methionine residue and other N-terminal modifications. (A) MALDI-TOF MS analysis of affinity-purified protein, after reduction with DTT and desalting. Labeled peaks correspond to singly charged $[M + H]^+$ ions. The expected masses for full length, des-Met[1], and des-Met[1]-Cys[2] protein products are 14 166, 14 035, and 13 392 Da, respectively (average masses, unprotonated state). (B) HPLC analysis of tryptic digest of SHP2C. The sample analyzed in (A) was digested with trypsin (without DTT reduction), and the products were separated by reverse phase HPLC. Each HPLC peak was collected and analyzed by MALDI-TOF MS. Peaks labeled 1, 2, 3 were of masses 1212, 1385, and 1361 Da, respectively. (C) MALDI-TOF analysis of N-terminal tryptic peptide 2, showing the tendency for the $[M + H]^+$ parent ion to fragment into various daughter ions.

peptide; however, this mass is consistent with the formation of a thiazolidine product by condensation of the N-terminal cysteine residue with pyruvic acid, an abundant *E. coli* metabolite.

Optimization of Culture Conditions for Producing N-Terminal Cysteine Proteins. In an attempt to minimize the formation of secondary products following cleavage of the terminal methionine residue, several modifications were made to the expression protocol. The culture time after IPTG induction was reduced from 4 to 2 h, and cysteine was added to the media to act as a scavenger of potentially reactive metabolites. We also omitted glucose from the medium to remove this as a source of pyruvic acid formation. In addition, acting on the suspicion that methionine aminopeptidase was causing some secondary cleavage of N-terminal cysteine, we replaced the small side chain amino acid at position 3 in the sequence (serine) with a large side chain amino acid (arginine).

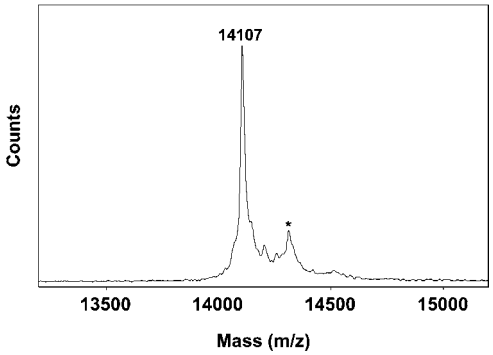


Figure 2. MALDI-TOF analysis of an N-terminal cysteine protein produced under optimized conditions. Recombinantly produced His6-SHP2C, containing the N-terminal tag sequence MCRHHHHHHGARQ, was expressed using the optimized conditions described in the text. Following affinity purification, reduction with DTT and desalting, a sample was analyzed by MALDI-TOF MS. The expected masses for full length and des-Met[1] protein products are 14235 and 14104 Da, respectively (average masses, unprotonated state). The peak marked with an asterisk (14 316 Da) is a matrix adduct of the 14 107 Da species.

Table 1. N-Terminal Cysteine Proteins Produced with a Common N-Terminal Tag[a]

protein expressed	calculated mass (Da)	observed mass (Da)
His6-SHP2C	14 235 (14 104)	14 106
His6-SHP2N	13 501 (13 370)	13 370
His6-SOCS7	17 461 (17 330)	17 328

[a] Each expressed protein encoded the common N-terminal sequence MCRHHHHHHGARQ. Calculated average masses are shown for protein products with the N-terminal methionine residue and without (in parentheses).

The alternate culture conditions were used to express an SHP2C construct containing the modified N-terminal tag sequence MCRHHHHHHGARQ (hereafter referred to as His6-SHP2C to distinguish it from the earlier sample). Following affinity purification of the protein, analysis of the product by MALDI-TOF MS showed that the terminal methionine residue had been completely removed (Figure 2). Moreover, the optimized expression protocol and modified N-terminal sequence led to a dramatic improvement in the homogeneity of the purified product. Although the yield of purified protein was lower than previously attained (7 mg from a 400 mL culture), most likely due to the shorter culture time and absence of glucose supplement, there was no detectable evidence of chemical modification to the N-terminal cysteine, nor of its cleavage from the protein.

To determine whether methionine would be cleaved from other proteins produced in the same way, we expressed two additional SH2 domain-containing protein fragments with the same N-terminal tag sequence (Table 1). Each protein was affinity purified from bacterial lysates and analyzed by HPLC and MALDI-TOF MS following reduction with DTT (Table 1). Methionine was completely excised for each of these proteins, and there was no detectable modification or cleavage of the N-terminal cysteine residue. Thus, the N-terminal methionine residue was cleaved for three different proteins produced in *E. coli* with cysteine as the second amino acid.

Table 2. Production of N-Terminal Cysteine Native Sequence Proteins

protein expressed	N-terminal sequence	calculated mass (Da)[a]	observed masses (Da)
SHP2C-His6	MCERWFHG	13 879 (13 747)	13 746, 13 777,[b] 13 819
SHP2N-His6	MCSRRWFH	13 057 (12 925)	12 829, 12 931, 12 960,[b] 13 002
SOCS7-His6	MCLYRPDS	17 249 (17 118)	17 129

[a] Calculated average masses are shown for protein products with the N-terminal methionine residue and without (in parentheses). [b] Observed ion was broad, centered on the mass indicated.

Production of N-Terminal Cysteine Native Sequence Proteins. While proteins containing N-terminal cysteine and polyhistidine tag sequences would be suitable for many applications requiring site-specific labeling, they would not be suitable for protein semisynthesis. For this application, proteins or protein fragments with native sequence downstream of an N-terminal cysteine residue are required. To determine whether methionine cleavage would occur for proteins containing native sequence downstream of methionine and cysteine as the first two amino acids, we recloned the proteins from Table 1 into a vector lacking the N-terminal polyhistidine tag. The new constructs encoded protein products with native sequences beginning at codon 3, that is, downstream of Met-Cys- in the first two positions (Table 2). These expression constructs contained a C-terminal hexahistidine tag to aid in purification of the recombinant products.

Following expression in *E. coli* using the optimized conditions previously described, proteins were affinity purified and analyzed by MALDI-TOF MS after DTT reduction (Table 2). We did not detect any retention of methionine for each of the three proteins. However, in additional to the N-terminal cysteine products, there was evidence of significant low molecular weight modification for two of the proteins, similar to that observed in our initial studies. Analysis of these two samples by reverse phase HPLC, which partially resolved modified from unmodified proteins, indicated that 40−60% of each protein was modified. Mass analysis of the modified species showed a similar profile to that seen earlier, that is, a prominent broad molecular ion centered on a mass approximately 30 Da higher than that of the N-terminal cysteine product. In addition to this modification, we detected minor secondary cleavage of the N-terminal cysteine residue in the case of the SHP2N-His6 protein, but not of the other two proteins. This was again consistent with the substrate specificity of methionine aminopeptidase. While the third amino acid was small in the case of SHP2N-His6 (Ser), the other two proteins contained bulkier amino acids at this position (Glu and Leu).

Reversal of N-Terminal Cysteine Modification. Chemical modification of the amino terminus appeared to be a recurring problem limiting the direct production of N-terminal cysteine proteins. While careful optimization of the culture conditions could be used to limit or eliminate this side reaction, we investigated whether the cysteine modification could be chemically reversed.

Formation of thiazolidines by condensation of ketones or aldehydes with the 1,2-amino thiol group of N-terminal cysteine is a reversible reaction, and the free cysteine moiety can be regenerated by covalent trapping of the ketone/aldehyde compound. Thus, if the modification observed in these studies was due to reaction with a metabolite such as pyruvic acid, then treatment with a trapping reagent should regenerate the terminal cysteine residue. To test this, an HPLC-enriched fraction of the modified SHP2N-His6 protein was treated with *O*-methylhydroxylamine, an aminoxy-containing reagent that reacts with ketones and aldehydes to form oximes. Incubation at room temperature for several hours resulted in significant conversion of the modified protein into the free cysteine-containing product (Figure 3). This result demonstrated two important points. First, that the chemical modification was most likely due to reaction of the N-terminal cysteine residue with a ketone (or aldehyde)-containing metabolite. Second, the modification can be reversed to regenerate the N-terminal cysteine. Treatment with *O*-methylhydroxylamine therefore provides a facile way of reversing the amino terminal modification and increasing the yield of N-terminal cysteine protein.

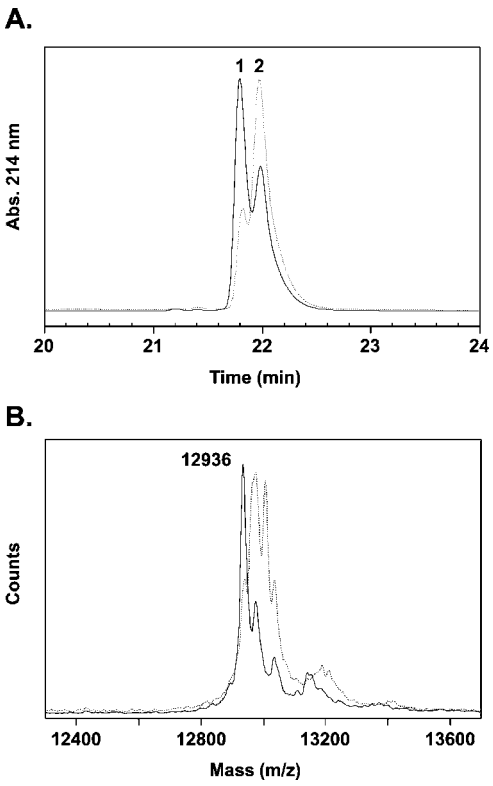


Figure 3. Chemical reversal of N-terminal cysteine modification. A sample of modified SHP2N-His6 protein was partially purified by HPLC and treated with *O*-methylhydroxylamine for 5 h to reverse the modification to the N-terminal cysteine residue. (A) Analytical HPLC traces of untreated (dashed trace) and treated (unbroken trace) protein samples. Peak 1 corresponds to the N-terminal cysteine protein, while peak 2 is the modified species. (B) MALDI-TOF MS analysis of untreated (dashed trace) and treated (unbroken trace) samples. The *O*-methylhydroxylamine-treated sample was analyzed after desalting a small aliquot of the crude reaction mixture with a C4 ZipTip pipet tip.

Site-Specific N-Terminal Labeling with Fluorescein. To confirm that N-terminal cysteine proteins generated in this way are able to react with thioester-containing compounds via native chemical ligation, we prepared a water soluble thioester derivative of fluorescein, a fluorescent agent commonly used to label proteins. Commercially available carboxyfluorescein succinimidyl ester was converted to the ethylsulfonate thioester (fluorescein-2MES) by treatment with sodium 2-mercaptoethanesulfonate. Treatment of the N-terminal cysteine-containing protein His6-SHP2C (Table 1) with fluorescein-

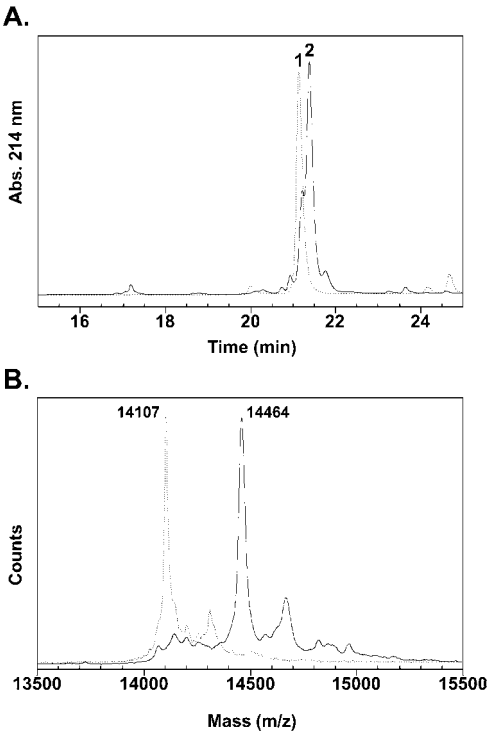


Figure 4. Native chemical ligation of a thioester-containing fluorescein derivative. Fluorescein-2MES, a thioester containing derivative of fluorescein, was ligated onto the amino terminus of the N-terminal cysteine protein His6-SHP2C. (A) Analytical HPLC trace of the ligation mixture after 5 h reaction (unbroken trace). For comparison, the HPLC trace of an unligated protein sample is also shown (dashed line). Peak 1 corresponds to the starting N-terminal cysteine protein, while peak 2 is the ligation product. (B) MALDI-TOF MS analysis of fluorescein-ligated His6-SHP2C. A sample of the crude ligation mixture was desalted with a C4 ZipTip pipet tip after 5 h reaction time and analyzed by MALDI-TOF MS. The observed mass of the major product (14464 Da, $[M + H]^+$ ion), corresponds to the addition of a single carboxyfluorescein molecule. The MALDI-TOF MS spectrum of the unligated protein is shown by dashed trace.

2MES resulted in rapid and specific labeling with a single molecule of fluorescein (Figure 4). Interestingly, we did not find it necessary to add thiol cofactors such a thiophenol or benzylmercaptan to this reaction mixture (*2*), suggesting that the ethylsulfonate thioester was sufficiently activated to achieve an adequate ligation rate, at least for this small molecule reactant. We did detect some side reactions which we attributed to formation of unwanted disulfides and/or thioester adducts; however, these were easily reversed upon addition of DTT (data not shown). Digestion of the ligated product with trypsin, followed by mass spectrometric analysis, confirmed that the modifying fluorescein group was located on the amino terminal Cys-Arg dipeptide tryptic fragment as expected (data not shown).

DISCUSSION

In this study, we found that heterologous expression in *E. coli* of proteins containing cysteine as the penultimate amino acid yielded mature products devoid of the initiating methionine residue. The side chain of cysteine is intermediate in size among the 20 amino acids found in proteins, and there have been conflicting reports as to the degree of methionine cleavage for proteins containing an adjacent cysteine residue. While one study claimed that processing efficiency was 100% (*14*), another claimed that cleavage was only partial (*15*). While these differences may have been specific to the proteins and/or expression systems under investigation, it is important to note that the latter study used Edman sequencing to quantitate the extent of methionine excision. Given we observed partial chemical modification of the N-terminal residue cysteine, it is possible that Edman sequencing would underestimate the amount of methionine excision.

Although we observed complete cleavage of N-terminal methionine for the proteins studied here, two side reactions initially limited the yield of target N-terminal cysteine protein. The first of these was a low level of additional N-terminal processing when the third amino acid residue was a serine. While there are no reports of methionine aminopeptidase having this activity, we suspect this enzyme was responsible for N-terminal cysteine cleavage, as excision only occurred for expressed proteins containing serine as the third encoded amino acid, but not the larger amino acids arginine, leucine, or glutamic acid. This may be a general problem when the third residue is a small side chain amino acid. Indeed Iwai et al. (*17*) noted partial cleavage of N-terminal cysteine for a protein containing an adjacent alanine residue. The second side reaction appeared to result from modification of the N-terminal cysteine residue by a low molecular weight metabolite. While it may be difficult to completely eliminate this side reaction, we found that optimization of the media and culture conditions suppressed the degree of modification. In addition, treatment of the recombinant product with *O*-methylhydroxylamine was shown to reverse the modification. While some degree of N-terminal heterogeneity may be acceptable depending on the application, the purity of the N-terminal cysteine product can be improved by use of optimized culture conditions, selection of protein sequences containing a large side chain amino acid at the third position, and/or treatment with a ketone trapping agent such as *O*-methylhydroxylamine. In addition, covalent capture chromatography using aldehyde-derivatized resin could also be used to selectively purify the N-terminal cysteine protein if highly pure preparations are required (*19*).

We did not investigate whether the expressed proteins were being produced in a soluble or insoluble form in *E. coli*; thus, we cannot comment on the dependence of methionine excision on the solubility of the protein. However, methionine processing has been reported to occur cotranslationally, that is, before synthesis of the protein chain is complete (*11*−*13*). Thus, the solubility of the final protein product is unlikely to have an effect on methionine excision. This fact may be of considerable advantage in using native chemical ligation for the semisynthesis of proteins. Subdomain protein fragments, which may have low intrinsic solubility, could be directly produced with the requisite N-terminal cysteine residue following extraction from inclusion bodies and purification under denaturing conditions. This product could then be ligated to a synthetic peptide fragment under denaturing conditions. By contrast, production of the same fragment by proteolytic cleavage of a fusion protein precursor may be difficult if this molecule has poor solubility in buffers compatible with the site-specific protease.

In conclusion, we have demonstrated the feasibility of directly producing N-terminal cysteine proteins in *E. coli*. This represents a significant advantage over methods which involve cleavage of fusion proteins and will hopefully make chemical ligation methods more amenable to recombinantly produced proteins.

ACKNOWLEDGMENT

M.B. is the recipient of an Australian Research Fellowship from the Australian Research Council.

LITERATURE CITED

(1) Gaertner, H. F., Rose, K., Cotton, R., Timms, D., Camble, R., and Offord, R. E. (1992) Construction of protein analogues by site-specific condensation of unprotected fragments. *Bioconjugate Chem. 3*, 262−268.

(2) Dawson, P. E., Muir, T. W., Clark-Lewis, I., and Kent, S. B. H. (1994) Synthesis of proteins by native chemical ligation. *Science 266*, 776−779.

(3) Liu, C. F., and Tam, J. P. (1994) Peptide segment ligation strategy without use of protecting groups. *Proc. Natl. Acad. Sci. U.S.A. 91*, 6584−6588.

(4) Erlanson, D. A., Chytil, M., and Verdine, G. L. (1996) The leucine zipper domain controls the orientation of AP-1 in the NFAT. AP-1.DNA complex. *Chem. Biol. 3*, 981−991.

(5) Kapanidis, A. N., and Weiss, S. (2002) Fluorescent probes and bioconjugation chemistries for single-molecule fluorescence analysis of biomolecules *J. Chem. Phys. 117*, 10953−10964.

(6) Pal, G., Santamaria, F., Kossiakoff, A. A., and Lu, W. Y. (2003) The first semi-synthetic serine protease made by native chemical ligation. *Protein Expr. Purif. 29*, 185−192.

(7) Xu, R., Ayers, B., Cowburn, D., and Muir, T. W. (1999) Chemical ligation of folded recombinant proteins: segmental isotopic labeling of domains for NMR studies. *Proc. Natl. Acad. Sci. U.S.A. 96*, 388−393.

(8) Dawson, P. E., and Kent, S. B. H. (2000) Synthesis of native proteins by chemical ligation. *Annu. Rev. Biochem. 69*, 923−960.

(9) Tolbert, T. J., and Wong, C. H. (2002) New methods for proteomic research: preparation of proteins with N-terminal cysteines for labeling and conjugation. *Angew. Chem., Int. Ed. 41*, 2171−2174.

(10) Sherman, F., Stewart, J. W., and Tsunasawa, S. (1985) Methionine or not methionine at the beginning of a protein. *Bioessays 3*, 27−31.

(11) Wilson, D. B., and Dintzis, H. M. (1970) Protein chain initiation in rabbit reticulocytes. *Proc. Natl. Acad. Sci. U.S.A. 66*, 1282−1289.

(12) Yoshida, A., Watanabe, S., and Morris, J. (1970) Initiation of rabbit hemoglobin synthesis: methionine and formylmethionine at the N-terminal. *Proc. Natl. Acad. Sci. U.S.A. 67*, 1600−1607.

(13) Jackson, R., and Hunter, T. (1970) Role of methionine in the initiation of haemoglobin synthesis. *Nature 227*, 672−675.

(14) Boissel, J. P., T. J., K., and Bunn, H. F. (1988) Cotranslational amino-terminal processing of cytosolic proteins. Cell-free expression of site-directed mutants of human hemoglobin. *J. Biol. Chem. 263*, 8443−8449.

(15) Hirel, P. H., Schmitter, M. J., Dessen, P., Fayat, G., and Blanquet, S. (1989) Extent of N-terminal methionine excision from Escherichia coli proteins is governed by the side-chain length of the penultimate amino acid. *Proc. Natl. Acad. Sci. U.S.A. 86*, 8247−8251.

(16) Huang, S., Elliott R. C., Liu P. S., Koduri R. K., Weickmann J. L., Lee J. H., Blair L. C., Ghosh-Dastidar P., Bradshaw R. A., Bryan K. M., Einarson, B., Kendall, R. L., Kolacs, K. H., and Saito, K. (1987) Specificity of cotranslational amino-terminal processing of proteins in yeast. *Biochemistry 26*, 8242−8246.

(17) Iwai, H., and Pluckthun, A. (1999) Circular beta-lactamase: stability enhancement by cyclizing the backbone. *FEBS Lett. 459*, 166−172.

(18) De Souza, D., Fabri, L. J., Nash, A., Hilton, D. J., Nicola, N. A., and Baca, M. (2002) SH2 domains from suppressor of cytokine signaling-3 and protein tyrosine phosphatase SHP-2 have similar binding specificities. *Biochemistry 41*, 9229−9236.

(19) Villain, M., Vizzavona, J., and Rose, K. (2001) Covalent capture: a new tool for the purification of synthetic and recombinant polypeptides. *Chem. Biol. 8*, 673−679.

BC049965O

An S-Layer Heavy Chain Camel Antibody Fusion Protein for Generation of a Nanopatterned Sensing Layer To Detect the Prostate-Specific Antigen by Surface Plasmon Resonance Technology

Magdalena Pleschberger,[†,‡] Dirk Saerens,[§] Stefan Weigert,[‡] Uwe B. Sleytr,[†,‡] Serge Muyldermans,[§] Margit Sára,[†,‡] and Eva M. Egelseer*[,†,‡]

BMT-Biomolecular Therapeutics GmbH, Brunnerstrasse 59, A-1235 Vienna, Austria, Center for Ultrastructure Research and Ludwig Boltzmann-Institute for Molecular Nanotechnology, University of Natural Resources and Applied Life Sciences, A-1180 Vienna, Austria, and Vrije Universiteit Brussel, Vlaams Interuniversitair Instituut voor Biotechnologie, Pleinlaan 2, B-1050 Brussel, Belgium. Received February 13, 2004

The bacterial cell surface layer (S-layer) protein of *Bacillus sphaericus* CCM 2177 assembles into a square lattice structure and recognizes a distinct type of secondary cell wall polymer (SCWP) as the proper anchoring structure in the rigid cell wall layer. For generating a nanopatterend sensing layer with high density and well defined distance of the ligand on the outermost surface, an S-layer fusion protein incorporating the sequence of a variable domain of a heavy chain camel antibody directed against prostate-specific antigen (PSA) was constructed, produced, and recrystallized on gold chips precoated with thiolated SCWP. The S-layer protein moiety consisted of the N-terminal part which specifically recognized the SCWP as binding site and the self-assembly domain. The PSA-specific variable domain of the camel heavy chain antibody was selected by several rounds of panning from a phage display library of an immunized dromedary, and was produced by heterologous expression in *Escherichia coli*. For construction of the S-layer fusion protein, the 3′-end of the sequence encoding the C-terminally truncated form $rSbpA_{31-1068}$ was fused via a short linker to the 5′-end of the sequence encoding cAb-PSA-N7. The S-layer fusion protein had retained the ability to self-assemble into the square lattice structure. According to the selected fusion site in the SbpA sequence, the cAb-PSA-N7 moiety remained located on the outer surface of the protein lattice. After recrystallization of the S-layer fusion protein on gold chips precoated with thiolated SCWP, the monomolecular protein lattice was exploited as sensing layer in surface plasmon resonance biochips to detect PSA.

INTRODUCTION

Crystalline bacterial cell surface layers (S-layers) can be considered one of the most common surface structures in prokaryotic cells (*1*−*5*). S-Layers of bacteria and archaea are composed of identical protein or glycoprotein subunits, which completely cover the cell surface during all stages of bacterial growth and division. The S-layer subunits can be aligned in lattices with oblique, square, or hexagonal symmetry with a center-to-center spacing of the morphological units of approximately 3 to 35 nm. In bacteria, the S-layer subunits are linked to each other and to the underlying cell envelope layer by noncovalent interactions. In the case of *Bacillaceae*, the N-terminal part is involved in anchoring the S-layer subunits to the rigid cell wall layer via a distinct type of secondary cell wall polymer (SCWP) (*5*−*10*). The polymer chains are covalently linked to the peptidoglycan backbone. Because many S-layer subunits self-assemble in suspension or recrystallize into regularly structured monolayers on solid supports, such as noble metals, plastics, or silicon wafers, as well as on Langmuir lipid films, on liposomes, and at the air−water interphase, they can be considered as unique biomaterials with properties most relevant for applications in molecular nanotechnology, nanobiotechnology, and biomimetics (*1*−*3*).

The S-layer protein of *Bacillus sphaericus* CCM 2177 assembles into a square lattice with a center-to-center spacing of the morphological units of 13.1 nm. On SDS-gels, this S-layer protein migrates as a single band with an apparent relative molecular mass of 127 000. The gene encoding SbpA has been sequenced, cloned in plasmid pET28a, and expressed in *Escherichia coli* HMS174(DE3) (*11*). The protein precursor includes a 30 amino acid long typical Gram-positive signal peptide and consists of total of 1268 amino acids. Since the N-terminal part of SbpA carries an S-layer homologous (SLH)-domain which is required for binding of the S-layer subunits to the SCWP, the surface accessibility of selected amino acid positions in the C-terminal part was investigated after fusion of the short affinity peptide *Strep*-tag I (STI) for binding of streptavidin. In comparison to the entire SbpA ($rSbpA_{31-1268}$), the C-terminally truncated form $rSbpA_{31-1068}$ showed a significantly increased accessibility of the C-terminal end. Despite the deletion of 200 C-terminal amino acids, $rSbpA_{31-1068}$/STI was still capable of self-assembling into the square lattice structure. Since the fused *Strep*-tag I remained located on the outer surface

* To whom correspondence should be addressed: Center for Ultrastructure Research, University of Natural Resources and Applied Life Sciences, Gregor Mendelstrasse 33, A-1180 Vienna, Austria. Tel: +43-1-47 654 2208; Fax: +43-1-47 89 112; e-mail: eva-maria.egelseer@boku.ac.at.

† BMT-Biomolecular Therapeutics GmbH.

‡ University of Natural Resources and Applied Life Sciences.

§ Vrije Universiteit Brussel.

10.1021/bc049964w CCC: $27.50 © 2004 American Chemical Society
Published on Web 04/20/2004

of the protein lattice, $rSbpA_{31-1068}$ was used as base form for the construction of various S-layer fusion proteins.

The S-layer protein SbpA recognizes a distinct type of SCWP consisting of eight to nine disaccharide repeating units as the proper anchoring structure in the rigid cell wall layer. As described in a previous study, the SCWP can be exploited for an oriented binding of rSbpA-fusion proteins on solid supports to generate regularly structured functional protein lattices (*12*).

The *Camelidae* is the only taxonomic family known to possess functional heavy chain antibodies lacking light chains. These unique antibody isotypes interact with the antigen by virtue of a single variable domain, termed VHH. The variable domain of a camel heavy chain antibody is the smallest known complete antigen binding fragment from a functional immunoglobulin. The single domain nature of VHHs gives rise to several unique features as compared to antigen-binding derivatives of conventional antibodies. Besides the advantage of single gene cloning and selection from an in vivo matured library, recombinant VHHs have other technological, functional, and physicochemical advantages, such as (i) high expression yields and ease of purification, (ii) a highly soluble and stable single domain immunoglobulin fold, (iii) the generation of antigen-specific, high-affinity binders, (iv) the recognition of unique conformational epitopes with the dominant involvement of its enlarged variable region CDR3, and (v) the close homology to human VH fragments (*13, 14*). These features can be expected to lead to a number of applications in which VHHs perform better than conventional antibody fragments, e.g., as enzyme inhibitors, as modular building units for multivalent or multifunctional constructs or as immunoadsorbents and detection units in biosensors (*13, 14*).

The prostate-specific antigen (PSA) is a useful marker to screen potential prostate cancer patients. The current diagnostic test systems determine the concentration of total PSA with monoclonal antibodies that recognize free as well as PSA complexed with α-1-anti-chymotrypsin (ACT). For the employment of a VHH in a PSA biosensor, VHHs that recognize free and complexed PSA are required. Moreover, the kinetic requirements in the biosensor impose a high probe density that can probably only be obtained with single domain VHHs.

For generating a monomolecular protein lattice capable of binding PSA on the outermost surface in high density, an S-layer fusion protein incorporating the VHH domain of a heavy chain camel antibody directed against PSA was constructed and the sequence encoding the fusion protein heterologously expressed in *E. coli*. After recrystallization of the S-layer fusion protein on gold chips precoated with thiolated SCWP, the monomolecular protein lattice was exploited as sensing layer in surface plasmon resonance (SPR) biochips.

MATERIALS AND METHODS

Immunization of a Dromedary for Generating PSA Binding Antibodies and Fractionation of IgG Subclasses. One male dromedary (*Camelus dromedarius*) kept at the Central Veterinary Research Laboratories (Dubai, United Arabic Emirates) was injected seven times subcutaneously at weekly intervals with 500 μg of highly purified PSA, mixed in Gerbu adjuvans. Forty-five days after beginning of immunization, 100 mL of anticoagulated blood was collected, from which plasma and peripheral blood lymphocytes were isolated with a lymphocyte preparation kit from WAK (WAK, Chemie, Steinbach, Germany).

Separation of the different plasma immunoglobulin G (IgG) subclasses was performed by differential adsorption on Hitrap-proteinA and Hitrap-proteinG columns (Pharmacia). The IgG3 and IgG1 subclasses were eluted from the proteinG column with sodium acetate buffer (pH 3.5) and glycine-HCl buffer (pH 2.7), respectively. The flow-through was subsequently loaded onto the Hitrap-proteinA column to recover the IgG2 subclass during elution with acetate buffer (pH 3.5).

Construction of a Library and Selection of PSA Specific Antibody Fragments. The mRNA was extracted from the peripheral blood lymphocytes (*15*). In a subsequent step, the cDNA was prepared using Ready-to-Go beads (Pharmacia). The gene fragments encoding the variable domain until the CH2 domain were amplified with the specific primers CALL001 (5′-GTC CTG GCT CTC TTC TAC AAG G-3′) and CALL002 (5′-GGT ACG TGC TGT TGA ACT GTT CC-3′), which anneal at the leader sequence and at the CH2 exon of the heavy chains of all dromedary immunoglobulins, respectively. After reamplification of the VHH gene fragments with nested primers annealing at the framework1 and framework4 regions (*15*), the final PCR fragments were cloned into the phagemid vector pHEN4, using the restriction sites *Pst*I and *Not*I. The VHH library was expressed on phages after infection with M13K07 helper phages. Specific VHHs against PSA were enriched by three consecutive rounds of in vitro selection on biotinylated PSA captured on an ELISA plate coated with 10 μg of Neutravidin (PIERCE) per well. Bound phage particles were eluted with 100 mM triethylamine (TEA, pH 10.0). Solutions containing eluted particles were immediately neutralized with 1 M Tris-HCl buffer (pH 7.4) and used to infect exponentially growing *E. coli* TG1 cells. The enrichment of phage particles carrying the antigen-specific VHHs was assessed by comparing the number of eluted phages from antigen-coated versus non-antigen-coated wells. After the second and third round of panning, individual colonies were picked up and expression of genes encoding VHHs was induced by the addition of 1 mM isopropyl-β-D-thiogalactopyranoside (IPTG). The recombinant VHH extract from the periplasm was tested for antigen recognition in ELISA (*15*).

Expression and Purification of Antibody Fragments. The VHH genes of the clones that scored positive in ELISA were recloned into the expression vector pHEN6, using the restriction enzymes *Pst*I and *BstE*II. The plasmid constructs were transformed into *E. coli* WK6(su^-) cells. Production of recombinant VHHs was performed in shaking flasks by growing the bacterial culture in Terrific Broth supplemented with 0.1% glucose and ampicillin. When the optical density measured at 600 nm was between 0.6 and 0.9, expression was induced by the addition of 1 mM IPTG. Cultures were then incubated for 16 h at 28 °C. After pelleting the cells, the periplasmic proteins were extracted by osmotic shock and the extract was loaded onto a Ni-nitrilotriacetic acid (Ni−NTA) Superflow Sepharose column (Qiagen). After being washed, the bound proteins were eluted with sodium acetate buffer (pH 4.7). The eluted fraction was concentrated on Vivaspin concentrators with a molecular mass cut off of 5 kDa (Vivascience), and the purity was checked by SDS−PAGE.

Solid-Phase ELISA for the Detection of PSA-Specific Phages. Maxisorb 96-well plates (Nunc, Maxisorb) were coated with Neutravidin or the PSA-specific monoclonal antibody 3E6 (DIAMED) at a concentration of 5 μg/mL in phosphate-buffered saline (PBS) overnight at 4 °C. Residual sites were blocked for 2 h at room

temperature with 1% (wt/vol) casein in PBS. After incubation with biotinylated PSA (1 μg/mL), serial dilutions of purified IgG subclasses, phages from different rounds of panning, or soluble VHHs were added. Detection was performed with a rabbit anti-dromedary IgG antiserum, a horseradish peroxidase-anti-M13 conjugate (Pharmacia), a mouse anti-hemagglutinin decapeptide tag (BAbCO), or an anti-His tag antiserum (Serotec), respectively. The absorption at 405 nm was measured 15 min after the addition of the substrate *p*-nitrophenyl phosphate (p-NPP, Sigma).

Further Characterization of cAb-PSA-N7 by Epitope Mapping by Means of ELISA and Affinity Measurements by Surface Plasmon Resonance (SPR). Either Neutravidin (5 μg/mL) or the PSA-specific monoclonal antibody 3E6 (5 μg/mL) were coated on ELISA plates, followed by the addition of 1 μg/mL biotinylated or nonbiotinylated PSA or PSA−ACT complex. Bound VHHs were detected with an anti-His tag monoclonal antibody or Nickel Express Doctor (Killguard Laboratories), respectively.

Affinity measurements were assessed by the addition of different concentrations of PSA to purified His-tailed VHHs coated on a Ni−NTA-biochip (Biacore) according to the manufacturer's descriptions. The kinetic parameters and K_D were determined with the BIAevaluation software (Biacore).

Cloning of the Chimeric Gene Encoding the Fusion Protein rSbpA$_{31-1068}$/cAb-PSA-N7. All PCR reactions were performed as described by Jarosch et al. (*16*). The sequence encoding the C-terminally truncated form rSbpA$_{31-1068}$ was PCR amplified from chromosomal DNA of *B. sphaericus* CCM 2177 by using the oligonucleotide primers *sbpA*/*Nco*I [5'-CG GAT T**CC ATG G**CG CAA GTA AAC GAC TAT AAC AAA ATC-3'] and *sbpA*/*Nhe*I [5'-GAC CGC **GCT AGC** TTC TGA ATA TGC AGT AGT TGC TGC C-3'], which introduced the restriction sites (bold) *Nco*I or *Nhe*I. The *cAb-PSA-N7* sequence was amplified from plasmid *cAb-PSA-N7*-pHEN6 by using the oligonucleotide primers *cAb*/*Nhe*I [5'-CGG ATT **GCT AGC** GAT GTG CAG CTG CAG GAG-3'] and *cAb*/*Xho*I [5'-GAC CG**C TCG AG**T TAT GAG GAG ACG GTG ACC TGG G-3'], which introduced the restriction sites *Nhe*I or *Xho*I. To obtain plasmid pET28a−*sbpA*$_{(93-3204)}$, the gel-purified PCR product *sbpA*$_{(93-3204)}$ was ligated into the corresponding restriction sites of plasmid pET28a, which was established in *E. coli* TG1. For generating the chimeric *sbpA*$_{(93-3204)}$/*cAb-PSA-N7* gene, the gel-purified PCR product *cAb-PSA-N7,* encoding the VHH domain of the camel antibody directed against PSA, was ligated into the corresponding restriction sites of plasmid pET28a−*sbpA*$_{(93-3204)}$. This was used for transformation of *E. coli* TG1.

Expression of the Chimeric *sbpA*$_{(93-3204)}$/*cAb-PSA-N7* Gene and Isolation of the S-Layer Fusion Protein from the Host Cells. The plasmid stability test and heterologous expression of the *sbpA*$_{(93-3204)}$/*cAb-PSA-N7* gene in *E. coli* One Shot BL21 Star (DE3) (Invitrogen) were performed as described by Jarosch et al. (*16*). Samples of the *E. coli* One Shot BL21 Star cultures were taken 1 to 5 h after induction of *sbpA*$_{(93-3204)}$/*cAb-PSA-N7* gene expression by the addition of 1 mM IPTG (Gerbu). Preparation of samples for SDS−PAGE analysis was carried out as described by Laemmli (*17*). For electron microscopic investigation, whole cells of *E. coli* One Shot BL21 Star (DE3) were prepared as described (*18*).

Isolation of the S-layer fusion protein from *E. coli* One Shot BL21 Star (DE3) cells induced to express the *sbpA*$_{(93-3204)}$/*cAb-PSA-N7* gene and purification by gel permeation chromatography (GPC) was performed as described (*19*) except that DNA was degraded by DNAse treatment. For that purpose, the insoluble pellet obtained after sonification of whole cells and centrifugation of the suspension was treated with a solution of 1 mg/mL DNAseI (Roche) in 100 mM $MgCl_2 \cdot 7H_2O$ in MilliQ-water. For removal of residual DNAseI, the pellet was washed twice with 1% Triton X-100 in 50 mM Tris-HCl buffer (pH 7.2) and 50 mM Tris-HCl buffer (pH 7.2). After the pellet was resuspended in 4 mL of 5 M guanidine hydrochloride (GHCl) in 50 mM Tris-HCl buffer (pH 7.2) and centrifugation, the clear supernatant was subjected to GPC. Fractions eluting at a molecular mass of ~123 000 Da expected for rSbpA$_{31-1068}$/cAb-PSA-N7 were pooled, dialyzed against distilled water for 18 h at 4 °C, lyophilized, and stored at −20 °C. Immunoblotting using a polyclonal rabbit antiserum raised against the S-layer protein of *B. sphaericus* CCM 2177 and a polyclonal rabbit anti-camel antiserum (Sigma C7540) was performed as described (*19, 20*).

Investigation of the Self-Assembly Properties of the S-Layer Fusion Protein and Recrystallization on Peptidoglycan-Containing Sacculi. The production of self-assembly products as well as recrystallization of the S-layer fusion protein on peptidoglycan-containing sacculi was performed as described (*19*). Peptidoglycan-containing sacculi carrying a monolayer of recrystallized S-layer fusion protein are referred to as recrystallization products in all further experiments. To keep the S-layer fusion protein water-soluble, the GHCl-extract was dialyzed against 1 mM 1,4-dithio-DL-threitol (DTT) in MillQ-water.

Dot Blot Assays for Investigating the Accessibility of the Fused cAb-PSA-N7. To investigate the accessibility of the fused cAb-PSA-N7 in the water-soluble, self-assembled, or recrystallized S-layer fusion protein, 5 μL samples with an S-layer protein content of 1 mg/mL were dried onto a nitrocellulose membrane. Plain rSbpA (1 mg/mL) was taken as blank and patient serum containing PSA (diluted 1:20 in TBS) was used as positive control. Dot blot assays were carried out as described in a previous study (*19*). For binding of PSA, the membrane was incubated with 20 ng of PSA from patient serum in 20 mL of blocking solution (2% Top Block (Fluka) in TBS) for 1 h at 20 °C. To detect PSA, the monoclonal mouse antibody 3E6 raised against PSA (1.38 mg/mL; diluted 1:2000 in blocking solution) was used.

Binding of cAb-PSA-N7 and the S-Layer Fusion Protein rSbpA$_{31-1068}$/cAb-PSA-N7 to a CM5 SPR Sensor Chip with Immobilized PSA. SPR experiments were performed using a Biacore 2000 system (Biacore, Sweden). For covalent binding of PSA on a CM5 sensor chip (Biacore, Sweden), the carboxylic groups on the CM5 matrix were activated by injecting a mixture containing 0.1 M *N*-hydroxysuccinimide (NHS, Fluka) and 0.4 M 1-ethyl-3-[3-(dimethylamino)propyl]carbodiimide hydrochloride (EDC, Sigma) for 7 min at a flow rate of 5 μL/min. Subsequently, a PSA (Scipac, UK) solution was passed over the surface with an appropriate reaction time, followed by a 7 min injection of 1 M ethanolamine-HCl solution (pH 8.5) to block nonreacted activated groups. The amount of covalently bound PSA was expressed in terms of resonance units (RU; 1000 RU correspond to approximately 1 ng/mm^2). For investigation of the affinity to immobilized PSA, cAb-PSA-N7 and the S-layer fusion protein, 1 μg/mL and 100 μg/mL, respectively, in HBS buffer (10 mM Hepes, 150 mM NaCl, 3

mM EDTA, 0.005% Tween) pH 7.2, were conducted over the chip with a flow rate of 2 μL/min. Afterward, four steps of regeneration with 10 mM glycine-HCl buffer (pH 2.2) were performed to ensure the removal of noncovalently bound proteins. To generate reference surfaces, all experiments were performed as described above with the exception that no PSA was supplied.

Recrystallization of rSbpA$_{31-1068}$/cAb-PSA-N7 on Gold Chips Precoated with Thiolated SCWP and Evaluation by Atomic Force Microscopy (AFM). Coating of gold chips (silicon ⟨100⟩ , coated with 1 nm Ti and 60 nm Au) with an area of 1 cm^2 with thiolated SCWP and recrystallization of the S-layer fusion protein was done as described (*19*). A Nanoscope III AFM (Digital Instruments, Santa Barbara, CA) equipped with a liquid cell and a 120 μm scanner and oxide-sharpened Si_3N_4 tips (NanoProbes, Digital Instruments, Santa Barbara, CA) with a nominal spring constant of 0.06 N/m was used for all AFM investigations. Imaging of recrystallized rSbpA$_{31-1068}$/cAb-PSA-N7 was carried out in contact mode in liquid (100 mM NaCl). Height and deflection signals were recorded simultaneously (error signal mode). The applied force was kept at a minimum in order not to destroy the sample. The scan rate was 5.1 Hz at a scan size of 1 by 1 μm.

Investigation of the PSA Binding Capacity of the rSbpA$_{31-1068}$/cAb-PSA-N7 Monolayer Obtained by Recrystallization of this S-Layer Fusion Protein on SCWP-Coated Gold Chips by SPR. The S-layer fusion protein was recrystallized on SCWP-coated gold chips (Biacore, Sweden) at a concentration of 100 μg/mL for 25 min at a flow rate of 1 μL/min. For reference studies, rSbpA$_{31-1068}$ was used. Patients' sera containing PSA (diluted 1:5 in HBS buffer to obtain a final concentration of 20 ng/mL) were injected. To verify specific binding of PSA, a solution of female blood serum (200 μL) was injected. During the reaction time, a continuous flow of HBS buffer (10 μL/min) was maintained over the sensor surface. The contact and dissociation time for PSA was 40 min and 800 s, respectively.

RESULTS

Immunization of a Dromedary with PSA for Provoking a Humoral Response. A dromedary received seven injections with purified PSA. Forty-five days after the first injection, blood was drawn and the immunoglobulins were purified from its plasma by differential adsorption on proteinA and proteinG columns. The immune response in subclasses IgG1, IgG2, and IgG3 was assessed by ELISA. Starting from 5 μg/mL, serial dilutions of purified IgG1, IgG2, and IgG3 were used in a solid-phase ELISA with biotinylated PSA captured onto a Neutravidin coat. Bound IgG was subsequently detected with rabbit anti-dromedary IgG antiserum (Figure 1).

An antigen-specific response was observed for heavy chain antibodies (IgG2 and IgG3) and conventional antibodies (IgG1) (*21*).

Construction of a Library and Selection of PSA Specific Antibody Fragments. A library was constructed starting from 1.5 $\times$ 10^7 lymphocytes. After extraction of mRNA, cDNA was prepared and the genes coding for the variable domains of the immunoglobulins were amplified. The final *VHH* gene product was ligated into the phagemid vector pHEN4. A *VHH* library of 1.5 $\times$ 10^7 individual transformants was obtained when 3 μg of vector was transformed. As determined by PCR, 90% of the clones within the library carried a *VHH* gene insert

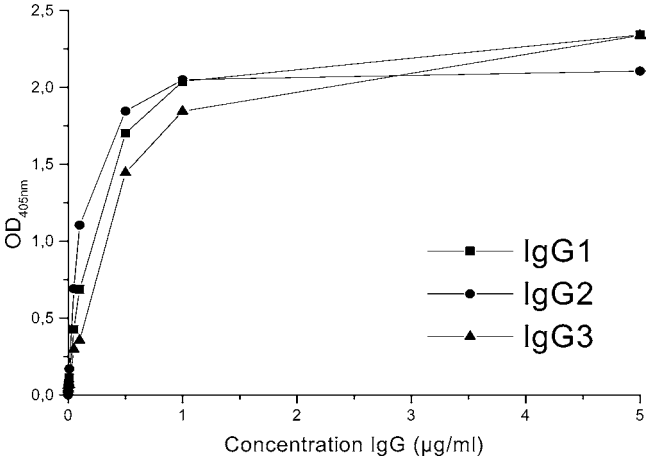


Figure 1. Analysis of antigen-specific antibodies. Solid-phase ELISA for detection of serial dilutions of fractionated IgG against PSA. Biotinylated PSA (1 μg/mL) was captured onto 5 μg/mL Neutravidin coating. Bound IgG1 (■), IgG2 (●), and IgG3 (▲) was detected with rabbit anti-dromedary IgG antiserum.

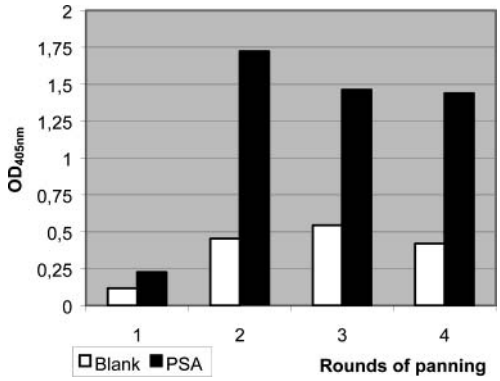


Figure 2. Enrichment of PSA-specific virons by consecutive rounds of in vitro selection. Solid-phase ELISA for detection of antigen-specific phages from different rounds of panning. Biotinylated PSA (1 μg/mL) was captured on 5 μg/mL Neutravidin coating. Virons (10^9) of the library (1), after the first (2), after the second (3) and the third round (4) of panning were loaded onto the antigen. Bound phages were detected with anti-M13 horse-radish peroxidase conjugate.

of proper size. The *VHH* repertoire from the library was expressed on phages after infection with helper phages M13K07. Three rounds of in vitro selection or panning were performed on biotinylated PSA captured by a Neutravidin coat. After being extensively washed, bound phages were eluted with TEA. The enrichment factors were calculated in two different ways. First, it was calculated as the ratio of the number of PSA specific colonies to the number of nonspecific colonies. An enrichment was observed in the second round, with the maximum enrichment after the last round of selection. Second, the enrichment was also assessed in solid-phase phage ELISA adding 10^9 virons per well (Figure 2).

From the corrected signals ($OD_{PSA} - OD_{Blank}$), the best ratio (specific to nonspecific) was found after the second round of panning. In total, 25 different VHHs binding specifically to PSA were isolated. For the present study, the specific binder cAb-PSA-N7 was selected.

Further Characterization of cAb-PSA-N7 by Epitope Mapping and Affinity Measurements. The epitope region recognized by cAb-PSA-N7 was mapped in ELISA. Binding of the VHH was tested on different forms of PSA, such as free PSA and PSA complexed with ACT. Both forms were captured onto either the 3E6

Table 1. Different Characteristics of the PSA-Specific Single Domain Antibody, cAb-PSA-N7[a]

	binding to free PSA	binding to PSA−ACT	binding to biotinylated PSA	K_D (nM)
cAb-PSA-N7	+	+	+	0.09

[a] Recognition of free PSA, PSA complexed with ACT (PSA−ACT), and biotinylated PSA by cAb-PSA-N7 was assessed by solid-phase ELISA. The dissociation constant (K_D) was calculated from the kinetic constants measurements by SPR.

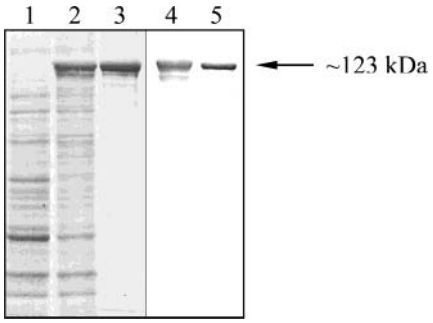


Figure 3. SDS−PAGE patterns (lanes 1−3) of SDS-extracts of whole cells of *E. coli* One Shot BL21 Star cells harboring the vector pET28a containing the *sbpA*$_{(93-3204)}$*/cAb-PSA-N7* gene construct, before (lane 1) and 5 h (lane 2) after induction of gene expression. Lane 3: SDS-extracts of GPC purified rSbpA$_{31-1068}$/cAb-PSA-N7. Immunoblot analysis (lanes 4 and 5) of SDS-extracts of GPC purified rSbpA$_{31-1068}$/cAb-PSA-N7. The presence of the SbpA-portion was detected with anti-SbpA antiserum and anti-rabbit IgG-alkaline phosphatase conjugate (lane 4). The presence of the cAb-PSA-N7 moiety was checked with anti-dromedary IgG antiserum and anti-rabbit IgG-alkaline phosphatase conjugate (lane 5).

monoclonal antibody or after biotinylation onto Neutravidin. Since binding of cAb-PSA-N7 was observed on PSA captured by 3E6 as well as on the PSA-ACT complex (Table 1), the results indicated binding onto a region of PSA different from its interaction site with ACT and from the epitope region recognized by 3E6. To further characterize its binding properties, the kinetic constants of cAb-PSA-N7 for PSA were measured by SPR on Biacore 3000 and the dissociation constant (K_D) was calculated accordingly (Table 1). Because of its high affinity, the specific binder cAb-PSA-N7 was selected out of 25 different binders (Saerens et al., unpublished data).

Cloning and Expression of the Gene Encoding rSbpA$_{31-1068}$/cAb-PSA-N7 and Isolation of the S-Layer Fusion Protein from the Host Cells. The PCR product obtained by amplification of the *sbpA* gene using the primers *sbpA*/*Nco*I and *sbpA*/*Nhe*I which encoded the truncated form of the S-layer protein SbpA (rSbpA$_{31-1068}$) was ligated into the pET28a vector. After transformation of *E. coli* TG1, amplification and isolation of the plasmid pET28a−*sbpA*$_{(93-3204)}$, the gene encoding cAb-PSA-N7 was ligated into this plasmid via the corresponding restriction sites. The resulting vector pET28a−*sbpA*$_{(93-3204)}$*/cAb-PSA-N7* was established in *E. coli* One Shot BL21 Star and expression was induced by the addition of IPTG. Biomass samples were harvested at various points of time and subjected to SDS−PAGE analysis and ultrathin sectioning. In comparison to *E. coli* cells harvested before the addition of IPTG (Figure 3; lane 1), an additional high molecular mass protein band with an apparent molecular mass of 123 000 Da was observed on SDS-gels in samples from *E. coli* cultures induced to express the chimeric *sbpA*$_{(93-3204)}$*/cAb-PSA-N7* gene (Figure 3; lane 2).

As derived from SDS−PAGE, the S-layer fusion protein had accumulated in the insoluble fraction of the lysed *E. coli* One Shot BL21 Star cells. This was in agreement with data from ultrathin-sectioned preparations of whole cells, which revealed the presence of inclusion bodies in the cytoplasm of the host cells (not shown). The insoluble fraction of the lysed *E. coli* cells was extracted with 5 M GHCl and subjected to GPC. After unifying the fractions from the second peak and removing GHCl by dialysis, only a single major protein band with an apparent molecular mass of 123 000 Da was observed on SDS-gels (Figure 3; lane 3). On immunoblots, a strong cross reaction was observed between the high molecular mass protein band and the polyclonal rabbit antiserum raised against the S-layer protein SbpA of *B. sphaericus* CCM 2177, as well as with the polyclonal rabbit antiserum raised against dromedary IgG (Figure 3; lanes 4 and 5, respectively).

Investigation of the Self-Assembly and Recrystallization Properties of the S-Layer Fusion Protein and of the Accessibility of the Fused cAb-PSA-N7 Moiety by Dot Blot Immunoassay. To investigate the self-assembly properties, purified and lyophilized rSbpA$_{31-1068}$/cAb-PSA-N7 was denatured in 5 M GHCl, and the solution was dialyzed against 10 mM $CaCl_2$ in 1 mM DTT. Negative-staining confirmed that the S-layer fusion protein had self-assembled into flat double layer sheets, which clearly exhibited the square lattice structure (not shown). The S-layer fusion protein recognized peptidoglycan-containing sacculi of *B. sphaericus* CCM 2177 as binding site and recrystallized into the square lattice type (Figure 4 A).

Dot blot assays were performed in order to investigate the accessibility of the fused cAb-PSA-N7 moiety in the water-soluble, self-assembled, and recrystallized S-layer fusion protein. Patient's serum containing PSA used as positive control (Figure 5; spot 1) led to a strong reaction with a monoclonal mouse antibody raised against PSA, whereas no reaction was observed with plain rSbpA taken as negative control (Figure 5; spot 2). As shown in Figure 5 (spots 3−5), the reaction toward PSA was independent of the state of the S-layer fusion protein and comparable for all samples.

Assuming an identical functionality of cAb-PSA-N7 in all S-layer fusion protein samples, these findings indicated that the accessibility of the fused functional sequence for the antigen was not reduced in the self-assembled or recrystallized state of the S-layer fusion protein.

Binding of cAb-PSA-N7 and the S-Layer Fusion Protein rSbpA$_{31-1068}$/cAb-PSA-N7 to a CM5 SPR Sensor Chip with Immobilized PSA. To compare the affinity of cAb-PSA-N7 and the chimeric S-layer fusion protein to PSA by SPR, PSA was covalently bound to the activated carboxylic acid groups of a CM5 sensor chip (Figure 6). This lead to an increase in 916 RU which corresponded to 3.05×10^{-5} nM/mm^2. By passing cAb-PSA-N7 over the sensor surface, an increase in 197 RU was measured which corresponded to 1.29×10^{-5} nM/mm^2, or to a molar ratio between bound cAb-PSA-N7 and PSA of 0.43. In the case of rSbpA$_{31-1068}$/cAb-PSA-N7, an increase in 570 RU was measured. This value corresponded to 4.6×10^{-6} nM/mm^2, or to a molar ratio between bound S-layer fusion protein and immobilized PSA of 0.16. The lower molar ratio as determined for the binding of the S-layer fusion protein to immobilized PSA can be explained by the 8-fold higher molecular mass of rSbpA$_{31-1068}$/cAb-PSA-N7 in comparison to cAb-PSA-N7.

Investigation of the PSA Binding Capacity of the rSbpA$_{31-1068}$/cAb-PSA-N7 Monolayer Obtained by Recrystallization of This S-Layer Fusion Protein

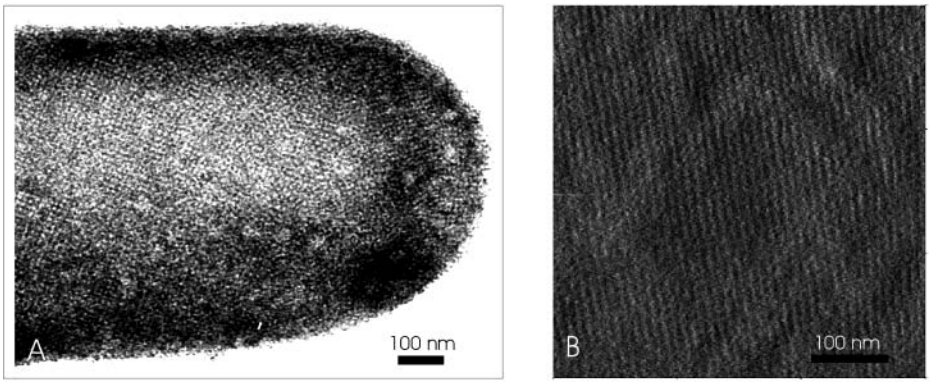


Figure 4. (A) Electron micrograph of a negatively stained preparation of recrystallization products obtained with $rSbpA_{31-1068}$/cAb-PSA-N7 exhibiting the square S-layer lattice type. (B) AFM image of the S-layer fusion protein $rSbpA_{31-1068}$/cAb-PSA-N7 recrystallized on a gold chip precoated with thiolated SCWP.

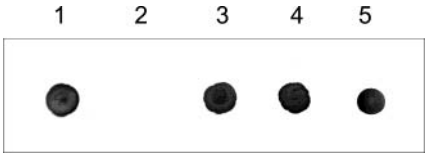


Figure 5. Dot blot assay indicating the accessibility of the cAb-PSA-N7 moiety in the water-soluble, self-assembled, and recrystallized S-layer fusion protein. Spot 1: patient serum containing PSA (diluted 1:20 in TBS) used as positive control; spot 2: rSbpA used as negative control; spot 3: water-soluble $rSbpA_{31-1068}$/cAb-PSA-N7; spot 4: self-assembly products formed by $rSbpA_{31-1068}$/cAb-PSA-N7; spot 5: recrystallization products obtained with $rSbpA_{31-1068}$/cAb-PSA-N7.

on SCWP-Coated Gold Chips by SPR. As shown by AFM analysis, the S-layer fusion protein was capable of recrystallizing into the square lattice structure on gold chips precoated with thiolated SCWP (Figure 4 B). For generating a sensing layer with well defined arrangement of the ligand on the outer surface of a monomolecular protein lattice, the S-layer fusion protein was conducted over an SPR gold chip precoated with thiolated SCWP. Recrystallization of the S-layer fusion protein led to an increase in the SPR signal to 5770 RU, which corresponded to 4.6×10^{-5} nM/mm^2, and therefore to a monolayer of the S-layer fusion protein. When a solution of PSA containing patient serum diluted 1:5 in HBS buffer was conducted over the $rSbpA_{31-1068}$/cAb-PSA-N7 monolayer, specific binding of the antigen was observed. For female blood serum, no specific binding was observed (data not shown). In Figure 7, the sensorgram of a $rSbpA_{31-1068}$ monolayer used as the reference was subtracted from that obtained with the S-layer fusion protein.

By this subtraction, a value of 1074 RU could be calculated for bound PSA, which corresponded to 3.6×10^{-5} nM/mm^2. When this value was correlated to the value of 4.6×10^{-5} nM/mm^2 calculated for the $rSbpA_{31-1068}$/cAb-PSA-N7 monolayer, a molar ratio of 0.78 PSA molecules per S-layer fusion protein was obtained. These measurements reveal that at least three PSA molecules were bound per morphological unit of the square S-layer lattice consisting of four S-layer fusion protein subunits. Since PSA showed no affinity to $rSbpA_{31-1068}$ at all, it was confirmed that binding of PSA to the S-layer fusion protein was due to specific interactions with the cAb-PSA-N7 moiety.

DISCUSSION

Studies on the structure−function−relationship of the S-layer protein SbpA revealed that the N-terminal part is required for anchoring the S-layer subunits via a distinct type of SCWP to the rigid cell wall layer and that 200 C-terminal amino acids could be deleted without interfering with the self-assembly properties (*11*, *12*). Since the SCWP could be exploited to achieve an oriented binding of the S-layer subunits via their N-terminal region to solid supports, amino acid positions in the C-terminal part of the SbpA sequence were screened in order to identify potential fusion sites that were located on the outer surface of the protein lattice. For that purpose, the sequence encoding *Strep*-Tag I was fused to the 5′-end of the sequence encoding various C-terminally truncated rSbpA forms. Since after recrystallization of $rSbpA_{31-1068}$/STI on peptidoglycan-containing sacculi the fused *Strep*-Tag I was accessible to streptavidin binding on the outer surface of the protein lattice to a significantly higher extent than in the case of the entire rSbpA (*11*), the sequence encoding $rSbpA_{31-1068}$ was exploited for the construction of various S-layer fusion proteins. Such fusion proteins comprised either the sequence of the major birch pollen allergen (*11*), the Fc-binding ZZ-domains (*22*), or the VHH of a heavy chain camel antibody directed against lysozyme (*19*). Depending on the fused functional sequence, the S-layer fusion proteins were either used for the development of an anti-allergic vaccine (*23*, *24*), or as immunoadsorbent to remove autoantibodies from patients' sera suffering from autoimmune disease (*22*). Due to the stability properties of heavy chain camel antibodies, appropriate S-layer fusion proteins were constructed for the development of novel diagnostic test systems (*19*). The S-layer fusion protein carrying the heavy chain camel antibody directed against lysozyme ($rSbpA_{31-1068}$/cAb-Lys3) was recrystallized on ELISA plates to provide a surface with a well-defined number and distance of the ligand. According to the construction principle of this S-layer fusion protein, each subunit carried one cAb-Lys3 moiety. The monolayer generated by recrystallization of the S-layer fusion protein on ELISA plates showed the same performance as the rSbpA monolayer to which cAb-Lys3 had been immobilized by chemical coupling. In this case, eight to nine cAb-Lys3 molecules were available per morphological unit of the square S-layer lattice, which was twice as much as in the case of the monolayer consisting of the S-layer fusion protein (*19*). Although several studies indicated that the S-layer fusion protein had attached with the inner surface to the ELISA plates, this orientation was guaranteed when solid supports carrying the SCWP were used for recrystallization. Besides peptidoglycan-containing sacculi of *B. sphaericus* CCM 2177, gold chips precoated with thiolated SCWP fulfilled such

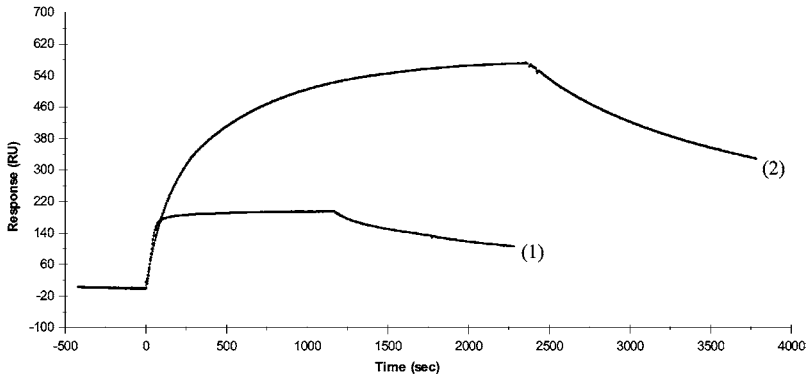


Figure 6. Sensorgrams obtained by binding of cAb-PSA-N7 (1) and the chimeric S-layer protein rSbpA$_{31-1068}$/cAb-PSA-N7 (2) to PSA covalently bound to a CM5 sensor chip. The sensorgrams were obtained by subtracting the respective blank sensorgram from flow cell 1.

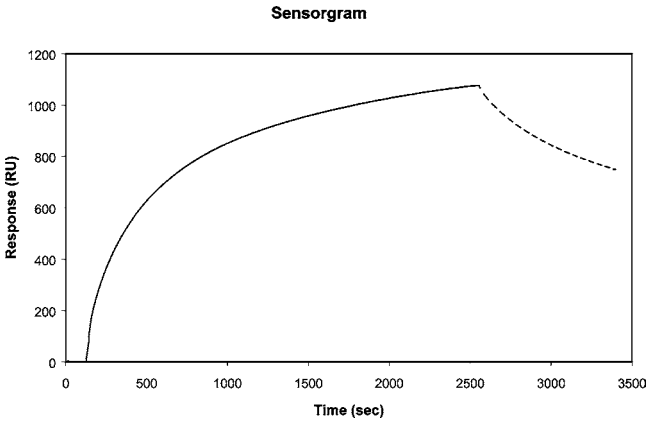


Figure 7. Sensorgram showing association (—) and dissociation (- - -) between PSA and rSbpA$_{31-1068}$/cAb-PSA-N7 recrystallized on a gold chip precoated with thiolated SCWP. The sensorgram indicated specific binding of PSA to the S-layer fusion protein.

requirements. The latter were exploited for the recrystallization of the S-layer fusion protein rSbpA$_{31-1068}$/cAb-PSA-N7 which comprised the sequence of a heavy chain camel antibody that specifically recognized PSA. For isolation of genes encoding appropriate heavy chain camel antibodies, a dromedary was immunized with purified PSA. This proved to be successful since all IgG subclasses reacted positive on PSA. The genes encoding VHHs were amplified from the purified lymphocytes and cloned into a phage vector resulting in a VHH immune library. After panning on biotinylated PSA, we identified more than 20 different binders, characterized by ELISA, and the kinetic parameters were investigated by SPR. The VHH cAb-PSA-N7 with the highest affinity to PSA (K_D 0.09 nM) was chosen for further analysis to enable highly sensitive detection of the analyte.

The S-layer fusion protein rSbpA$_{31-1068}$/cAb-PSA-N7 formed self-assembly products and recrystallized on peptidoglycan-containing sacculi of *B. sphaericus* CCM 2177. In both cases, the S-layer lattice exhibited the square structure with a center-to-center spacing of the morphological units of 13.1 nm. The accessibility of the fused cAb-PSA-N7 moiety for PSA was proved for the water-soluble, self-assembled, and recrystallized S-layer fusion protein, which independent of its state led to comparably strong reactions in dot blot immunoassays.

To generate a PSA-specific sensing layer for SPR measurements, the S-layer fusion protein rSbpA$_{31-1068}$/cAb-PSA-N7 was recrystallized on gold chips precoated with thiolated SCWP. The formation of the monomolecular protein lattice was confirmed by AFM analysis, as well as by the level of the measured SPR signal. As derived from the response levels measured for binding of PSA to the rSbpA$_{31-1068}$ /cAb-PSA-N7 monolayer, the molar ratio between bound PSA and the S-layer fusion protein was 0.78, which means that at least three PSA molecules were bound per morphological unit of the square S-layer lattice. Comparative studies with an rSbpA monolayer confirmed that the measured response levels were specific for PSA binding.

To summarize, by using the SCWP as biomimetic linker to gold chips, a sensing layer for SPR could be generated by recrystallization of an S-layer fusion protein. Due to the crystalline structure of the S-layer lattice, the fused ligand sequences show a well defined distance in the protein lattice, and according to the selected fusion site in the S-layer protein, they are located on the outermost surface, which will reduce diffusion limited reactions. A further advantage can be seen in the constant and low distance of the ligands from the optically active gold layer, which is exclusively determined by the thickness of the S-layer and lies in the range of only 10 to 15 nm. Thus, S-layer fusion proteins can be considered as key element for the development of label free detection systems such as SPR, surface acoustic wave (SAW), or quartz crystal microbalance (QCM-D), in which the binding event can be measured directly by a mass increase without the need of any labeled molecule.

ACKNOWLEDGMENT

This work was supported by the Austrian Science Foundation, project P14689-MOB, by the Competence Center “Biomolecular Therapeutics” and by the EU project PAMELA. We thank Jacqueline Friedmann for excellent technical assistance concerning the AFM studies and Prof. Dr. Georg Steiner from the AKH for providing us with PSA-containing serum samples from patients. This work was supported by a predoctoral grant from the Institute for the promotion of Innovation by Science and Technology in Flanders (IWT-Flanders) to Dirk Saerens.

LITERATURE CITED

(1) Sleytr, U. B., Egelseer, E. M., Pum, D., and Schuster, B. (2004) S−Layers. In *NanoBiotechnology* (Niemeyer, C. M., and Mirkin, C. A., Eds.) pp 77−92, Wiley-VCH, Weinheim.

(2) Sleytr, U. B., Sára, M., Pum, D., Schuster, B., Messner, P., and Schäffer, C. (2003) Self-Assembly Protein Systems: Microbial S−Layers. In *Biopolymers* (Steinbüchel, A., and Fahnestock, S., Eds.) Vol. 7, pp 285−338, Wiley-VCH, Weinheim, Germany.

(3) Sleytr, U. B., Messner, P., Pum, D., and Sára, M. (1999) Crystalline bacterial cell surface layers (S-layers): from supramolecular cell structure to biomimetics and nanotechnology. *Angew. Chem., Int. Ed. 38*, 1034−1054.
(4) Sleytr, U. B., Sara, M., and Pum, D. (2000) Crystalline bacterial cell surface layers (S-layers): a versatile self-assembly system. In *Supramolecular Polymers* (Ciferri, A., Ed.) pp 177−213, Marcel Dekker, Inc., New York, Basel.
(5) Sára, M., and Sleytr, U. B. (2000) S-Layer proteins. *J. Bacteriol. 182*, 859−868.
(6) Brechtel, E., and Bahl, H. (1999) In *Thermoanaerobacterium thermosulfurigenes* EM1 S-layer homology domains do not attach to peptidoglycan. *J. Bacteriol. 181*, 5017−5023.
(7) Chauvaux, S., Matuschek, M., and Beguin, P. (1999) Distinct affinity of binding sites for S-layer homologous domains in *Clostridium thermocellum* and *Bacillus anthracis* cell envelopes. *J. Bacteriol. 181*, 2455−2458.
(8) Lemaire, M., Miras, I., Gounon, P., and Beguin, P. (1998) Identification of a region responsible for binding to the cell wall within the S-layer protein of Clostridium thermocellum. *Microbiology 144*, 211−217.
(9) Mesnage, S., Fontaine, T., Mignot, T., Delepierre, M., Mock, M., and Fouet, A. (2000) Bacterial SLH domain proteins are noncovalently anchored to the cell surface via a conserved mechanism involving wall polysaccharide pyruvylation. *EMBO J. 19*, 4473−4484.
(10) Sára, M. (2001) Conserved anchoring mechanisms between crystalline cell surface S-layer proteins and secondary cell wall polymers in Gram-positive bacteria? *Trends Microbiol. 9*, 47−49.
(11) Ilk, N., Völlenkle, C., Egelseer, E. M., Breitwieser, A., Sleytr, U. B., and Sára, M. (2002) Molecular characterization of the S-layer gene, *sbpA*, of *Bacillus sphaericus* CCM 2177 and production of a functional S-layer fusion protein with the ability to recrystallize in a defined orientation while presenting the fused allergen. *Appl. Environ. Microbiol. 68*, 3251−3260.
(12) Ilk, N., Kosma, P., Puchberger, M., Egelseer, E. M., Mayer, H. F., Sleytr, U. B., and Sára, M. (1999) Structural and functional analyses of the secondary cell wall polymer of *Bacillus sphaericus* CCM 2177 that serves as an S-layer-specific anchor. *J. Bacteriol. 181*, 7643−7646.
(13) Muyldermans, S. (2001) Single domain camel antibodies: current status. *Mol. Biotechnol. 74*, 277−302.
(14) Nguyen, V. K., Desmyter, A., and Muyldermans, S. (2001) Functional heavy-chain antibodies in *Camelidae*. *Adv. Immunol. 79*, 261−296.
(15) Vu, K. B., Ghahroudi, M. A., Wyns, L., and Muyldermans, S. (1997) Comparison of llama VH sequences from conventional and heavy chain antibodies. *Mol. Immunol. 34*, 1121−1131.
(16) Jarosch, M., Egelseer, E. M., Mattanovich, D., Sleytr, U. B., and Sára, M. (2000) S-layer gene *sbsC* of *Bacillus stearothermophilus* ATCC 12980: molecular characterization and heterologous expression in *Escherichia coli*. *Microbiology 146*, 273−281.
(17) Laemmli, U. K. (1970) Cleavage of structural proteins during the assembly of the head of bacteriophage T4. *Nature 227*, 680−685.
(18) Messner P., Hollaus F., and Sleytr, U. B. (1984) Paracrystalline cell wall surface layers of different *Bacillus stearothermophilus* strains. *Int. J. Syst. Bacteriol. 34*, 202−210.
(19) Pleschberger, M., Neubauer, A., Egelseer, E. M., Weigert, S., Lindner, B., Sleytr, U. B., Muyldermans, S., and Sára, M. (2003) Generation of a functional monomolecular protein lattice consisting of an S-layer fusion protein comprising the variable domain of a camel heavy chain antibody. *Bioconjugate Chem. 14*, 440−448.
(20) Egelseer, E. M., Schocher, I., Sleytr, U. B., and Sára, M. (1996) Evidence that an N-terminal S-layer protein fragment triggers the release of a cell-associated high-molecular-weight amylase in *Bacillus stearothermophilus* ATCC 12980. *J. Bacteriol. 178*, 5602−5609.
(21) Lauwereys, M., Arbabi Ghahroudi, M., Desmyter, A., Kinne, J., Holzer, W., De Genst, E., Wyns, L., and Muyldermans, S. (1998) Potent enzyme inhibitors derived from dromedary heavy-chain antibodies. *EMBO J. 17*, 3512−3520.
(22) Völlenkle, C., Weigert, S., Ilk, N., Egelseer, E. M., Weber, V., Loth, F., Falkenhagen, D., B., Sleytr, U. B., and Sára, M. (2004) Construction of a functional S-layer fusion protein comprising an immunglobulin G-binding domain for development of specific adsorbents for extracorporeal blood purification. *Appl. Environ. Microbiol. 70*, 1514−1522.
(23) Breitwieser, A., Egelseer, E. M., Moll, D., Ilk, N., Hotzy, C., Bohle, B., Ebner, C., Sleytr, U. B., and Sára, M. (2002) A recombinant bacterial cell surface (S-layer)-major birch pollen allergen-fusion protein (rSbsC/Bet v1) maintains the ability to self-assemble into regularly structured monomolecular lattices and the functionality of the allergen. *Protein Eng. 15*, 243−249.
(24) Bohle, B., Breitwieser, A., Zwölfer, B., Jahn-Schmid, B., Sára, M., Sleytr, U. B., and Ebner, C. (2004) A novel approach to specific allergy treatment: The recombinant fusion protein of a bacterial surface (S-layer) protein and the major birch pollen allergen Bet v1 (rSbsC-Bet v1) combines reduced allergenicity and immunomodulating capacity. *J. Immunol.*, in press.

BC049964W

JULY/AUGUST 2004
Volume 15, Number 4

© Copyright 2004 by the American Chemical Society

Bioconjugate Chemistry

COMMUNICATIONS

Poly(ethylene glycol)-Supported Enzyme Inactivators. Efficient Identification of the Site of Covalent Attachment to α-Chymotrypsin by PEG-TPCK

Christine A. Schering, Boyu Zhong,[‡] Jonathan C. G. Woo,[†] and Richard B. Silverman*

Department of Chemistry, Department of Biochemistry, Molecular Biology, and Cell Biology, and the Drug Discovery Program, Northwestern University, 2145 Sheridan Road, Evanston, Illinois 60208-3113. Received March 9, 2004; Revised Manuscript Received May 6, 2004

A new methodology utilizing an enzyme inactivator covalently attached to poly(ethylene glycol) (PEG) is described in which the PEG affords facile and mild quantification, isolation, and identification of the site of enzyme inactivation. As proof of concept, the known affinity labeling agent for α-chymotrypsin, *N*-tosyl-L-phenylalanine chloromethyl ketone (TPCK), was linked to PEG. The synthesis of the PEG-bound inactivator PEG-TPCK was carried out in good yields using standard solution-phase chemistry. Inactivation of α-chymotrypsin with PEG-TPCK was monitored via UV−vis spectroscopy in aqueous conditions, which resulted in less than 3% remaining activity, indicating that 97% of the α-chymotrypsin was covalently modified with PEG-TPCK. The MALDI-TOF mass spectrum showed only one new peak that was distinct in shape and corresponded to the mass of PEG-TPCK−α-chymotrypsin. Following proteolytic digestion, the PEG-TPCK−peptide was easily discernible from the rest of the digest in a HPLC trace because of its characteristic prolonged retention time and broad polymer shape. MALDI-TOF MS was used to determine the mass of the PEGylated peptide. Without prior removal of the PEG, the amino acid site to which PEG-TPCK covalently bound was determined via Edman sequencing. In comparison to other methods, the PEG-supported inactivator system is significantly cheaper and safer than the synthesis of radiolabeled compounds; furthermore, isolation of the PEGylated peptide is milder and more selective than standard affinity binding columns. Edman sequencing provides an exact determination of the site of inactivator covalent attachment without extensive, tedious LC-MS analysis of a complex peptide mixture. The method described here could be applied to a variety of enzymes as an alternative to current techniques.

The assessment of enzyme inactivators is an important tool to understand the catalytic mechanism and active site topology of enzymes. The traditional method to identify the site of covalent attachment involves synthesizing a radiolabeled inactivator (*1*). Because of the high cost of radiolabeled starting materials, the difficulty in synthesis, and many federal regulations, alternative methods are desirable. Site-directed mutagenesis has been used to determine the importance of an active-site residue, but this method lacks definitive support for

* To whom correspondence should be addressed. E-mail: Agman@chem.northwestern.edu.
[†] Current address: Lilly Research Laboratories, Indianapolis, IN 46285.
[‡] Current address: Johnson & Johnson Pharmaceutical Research & Development, L.L.C., Titusville, NJ 08560.

10.1021/bc049940p CCC: $27.50 © 2004 American Chemical Society
Published on Web 06/09/2004

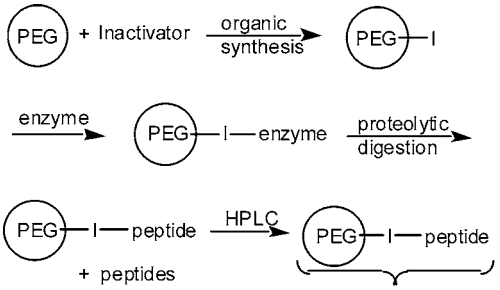


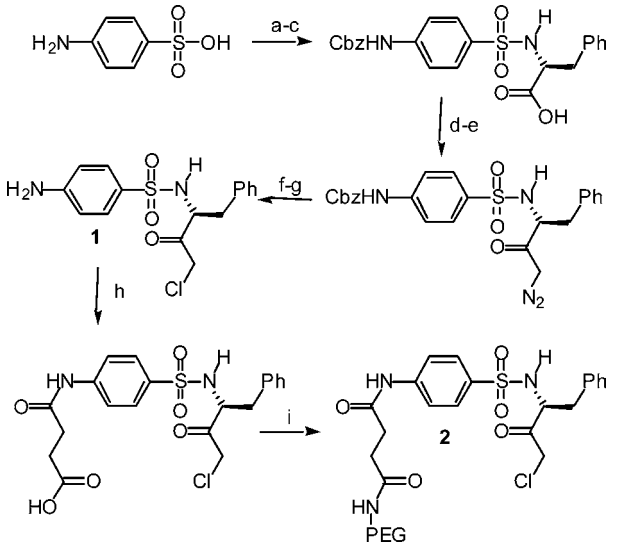
Figure 1. PEG-supported inactivator methodology.

inactivator binding (*2*). Affinity techniques, such as biotin/avidin, vary in selectivity and many times require nonaqueous incubation systems and harsh cleavage conditions (*3*). Recently, mass spectrometry has been used to analyze digested inactivated enzymes; however, the quality and complexity of the digest greatly influence the degree of difficulty and methodological approach of the subsequent MS analysis, and it does not always provide convenient identification of the site of inactivator binding (*3, 4*). An alternative method that would retain the positive features but overcome the failings of current approaches would facilitate the assessment of enzyme inactivators.

Poly(ethylene glycol) (PEG) is a water- and organic-soluble polymer utilized in chemistry because its homogeneous reaction conditions contribute to fast kinetics and high loading levels, while PEG's propensity to precipitate in ether aids in facile purification during PEG-supported synthesis of small molecules and biopolymers (*5*−*10*). PEGylation, the biological technique of covalently attaching PEG to nucleophilic amino acids of enzymes and peptides, produces new pharmaceutical agents and organic catalysts with enhanced stability and performance (*11*−*14*).

PEG's ability to impart its physiochemical properties on other molecules in both chemical and biological systems could allow it to overcome the above-mentioned failings of current approaches to identify the enzyme inactivator covalent binding site (Figure 1). Synthesis of a PEG-supported inactivator through standard solution-phase organic synthesis would be simpler and cheaper than synthesis of a radiolabeled molecule, with the added benefit that the PEG-supported inactivator could be subsequently characterized via NMR and MALDI-TOF MS (*15*). Because of the homogeneous aqueous reaction conditions and the flexible PEG framework, the PEG-bound inactivator should be capable of inactivating the enzyme similarly to that of the unmodified inactivator (*16*). The inactivation of the enzyme and the concurrent formation of the PEGylated proteins can be quantified by the same assays used on the unmodified inactivator. The inactivated PEGylated enzyme can be quickly purified by size-exclusion chromatography and identified by MALDI-TOF MS because of the drastically altered retention time, molecular weight, and broad peak shape of PEGylated peptides and proteins (*17, 18*). Furthermore, a variety of proteolytic enzymes are known to cleave PEGylated proteins (*12*). Once digested, PEG alters the properties of the PEGylated peptide from those of the unmodified peptides, aiding in HPLC purification and identification of the PEGylated peptide by MALDI-TOF MS (*19*). Finally, MALDI-TOF MS and Edman sequencing are both amenable for use with PEGylated peptides, allowing determination of the covalent attachment site

Scheme 1. Synthesis of PEG-TPCK[a]



[a] Reagents and conditions: (a) benzyl chloroformate, Na_2CO_3, 95%; (b) PCl_5, 75%; (c) L-Phe, acetone, Na_2CO_3, 84%; (d) oxalyl chloride, DMF, CH_2Cl_2; (e) diazomethane, ether, 0 °C; (f) $HCl_{(g)}$, ether, 0 °C, three steps 30%; (g) 30% HBr in acetic acid, 65%; (h) succinic anhydride, DIPEA, $CHCl_3$, 85%; (i) PEG-NH_2 (MW 5000 g/mol), HATU, DIPEA, CH_2Cl_2, DMF, 80% yield, 90% loading.

without prior cleavage of the PEG handle (*12*−*17*). A PEG-supported inactivator would behave as both a tag to identify any polymer covalently modified species as well as a handle to isolate the PEGylated moieties. Exact determination of the site of inactivator covalent attachment would be possible at low cost, in mild and standard conditions, without harsh cleavage conditions to remove the polymer or analysis of a complicated digestion mixture.

This new methodology utilizing a PEG-supported inactivator was developed using the known affinity labeling agent for α-chymotrypsin, *N*-tosyl-L-phenylalanine chloromethyl ketone (TPCK) (*20*). TPCK is known to bind covalently to His 57, part of the catalytic triad of α-chymotrypsin, with both time and concentration dependence (*20*−*22*). An analogue of TPCK, *S*-1-[1-*N*-(4-amino benzenesulfonyl)aminophenethyl] chloromethyl ketone (**1**, Scheme 1), was synthesized (*23*−*24*). Replacement of the methyl group with the isosteric amino group provided a handle to link the PEG. Monomethoxyamino PEG (MW 5000) and the TPCK analogue were linked via succinic anhydride, resulting in a stable and UV-active diamide linker (**2**, Scheme 1).

As with TPCK, the time and concentration dependent inactivation of α-chymotrypsin with PEG-TPCK (**2**) was monitored by the cleavage of L-benzyltyrosine methyl ester until less than 3% of the activity remained (24 h), implying 97% linkage of the PEG-TPCK to the α-chymotrypsin. Dialysis (MWCO 10 000 Da) was used to remove unreacted PEG-TPCK and buffer salts prior to MALDI-TOF MS analysis. Comparison of the molecular weight of the inactivated α-chymotrypsin (31 060 Da, broad) with those of the control α-chymotrypsin (25 230 Da, sharp) clearly indicated that the PEG-TPCK (approximately 5400 Da) was covalently bound to the α-chymotrypsin. The peak shapes also supported complete covalent binding of PEG-TPCK to α-chymotrypsin; the control is a sharp peak as would be expected for a single protein whereas the inactivated enzyme is a uniquely shaped broad peak caused by the polydisperse PEG covalently bound to the enzyme.(Figure 2).

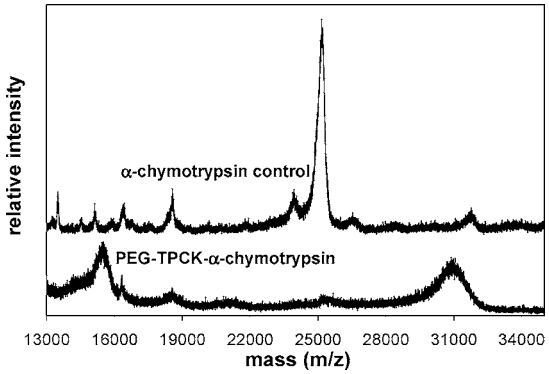


Figure 2. MALDI-TOF MS of α-chymotrypsin and PEG-TPCK−α-chymotrypsin (positive mode, CHCA matrix). The unique peak shape and large mass difference clearly indicate covalent attachment of the polydisperse PEG-TPCK (MW ∼ 5450, g/mol) to α-chymotrypsin.

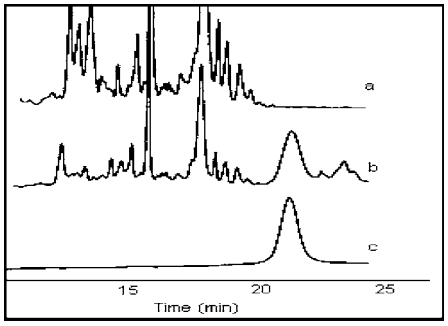


Figure 3. HPLC analysis (Vydac C8, A:H2O, 0.1% TFA, B: ACN, 0.1% TFA, 20−80% in 40 min) of digested (a) α-chymotrypsin control, (b) PEG-TPCK−α-chymotrypsin, and (c) purified PEG-TPCK−peptide. The prolonged retention time and unique peak shape aid in immediate identification of the modified peptide and facile isolation of the peak.

PEG-TPCK-α-chymotrypsin (900 μM) was denatured, reduced, alkylated, and then subsequently digested with α-chymotrypsin. The digestion was stopped by allowing the mixture to run through a PD-10 desalting column. The PEG-TPCK−peptide peak in the HPLC (Figure 3b) was easily identified because it appears as a distinct broad peak as the result of the polydispersity of the PEG not present in the digested control (Figure 3a). It is known that PEGylated peptides and proteins elute as polydisperse peaks following the nonPEGylated moieties because of an increase in size and decrease in polarity (*18, 25*). This new peak was isolated by HPLC (Figure 3c) and characterized by MALDI-TOF MS to be a PEGylated peptide because of the distinct polydispersed peak centered around 7400 g/mol (Figure 4).

Gas-phase Edman sequencing identified only two peptides, offset by three amino acids because of partial cleavage after Thr 54; the sequence of one peptide was VVTAA**X**C′GVTTSD- - -A and the sequence of the other was AA**X**C′GVTTSDVVVAGEF. Both sequences correlate to the known primary sequence of α-chymotrypsin with the indeterminable amino acid (**X**) corresponding to His 57, the known site of TPCK covalent binding to α-chymotrypsin. The expected molecular weight for each sequence through Phe 71 is 2017.98 g/mol and 1718.79 g/mol, respectively. If the molecular weights of the inactivator (MW 450.92 g/mol) and PEG (MW 5000 g/mol) are added to these, then the expected molecular weights of the PEG-TPCK−peptides would be 7468.89 and 7169.71 g/mol. These masses agree with the broad peak seen by MALDI-TOF MS (Figure 4). No other free or PEG-TPCK-bound peptide sequences were detected by Edman sequencing or mass spectrometry.

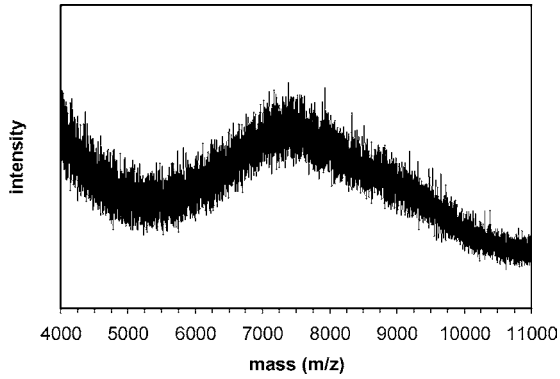


Figure 4. MALDI-TOF MS on the purified PEG-TPCK−peptide (negative mode, DHB matrix). The distinct shape is indicative of a PEGylated peptide.

This new methodology utilizing an enzyme inactivator covalently bound to PEG enabled facile, mild, and selective isolation and identification of the site of PEG-TPCK covalent attachment to α-chymotrypsin, the same residue to which unmodified TPCK binds. The polydisperse nature of the PEG aided in visualization and subsequent isolation of the PEGylated enzyme and peptide. Inexpensive starting materials were used to synthesize PEG-TPCK. The inactivation occurred in aqueous conditions and thereby could be easily monitored and purified via standard techniques. The PEGylated enzyme was fragmented into small peptides via proteolytic digestion. HPLC was used to easily identify and then purify the PEG-TPCK−peptide from the digested mixture. The peptide sequence was determined by Edman sequencing without prior cleavage of the PEG, indicating without ambiguity the site of PEG-TPCK attachment. Because of its facile and mild nature, this method could be applied to a variety of enzymes instead of currently used techniques.

ACKNOWLEDGMENT

This research was supported by NIH (GM32634). Edman sequencing was performed by the Protein Separations and Analysis Laboratory at Purdue University.

Supporting Information Available: Experimental procedures and spectrometric data. This material is available free of charge via the Internet at http://pubs.acs.org.

LITERATURE CITED

(1) Suketa, Y., and Inagai, T. (1975) Active site directed inactivators of mouse submaxillary renin. *Biochemistry 14* (14), 3188−3194.

(2) Delaire, M., Labia, R., Samama, J. P., and Masson, J. M. (1992) Site-directed mutagenesis at the active site of *Escherichia coli* TEM-1 beta-lactamase. Suicide inhibitor-resistant mutants reveal the role of arginine 244 and methionine 69 in catalysis. *J. Biol. Chem. 267* (29), 20600−20606.

(3) Hubalek, F., Pohl., and Edmondson, D. E. (2003) Structural Comparison of Human Monoamine Oxidases A and B: Mass Spectrometry Monitoring of Cysteine Reactivities. *J. Biol. Chem. 278* (31), 28612−28618.

(4) McCarter J. D., Burgoyne D. L., Miao S., Zhang S., Callahan J. W., and Withers S. G. (1997) Identification of Glu-268 as the catalytic nucleophile of human lysosomal beta-galactosidase precursor by mass spectrometry. *J. Biol. Chem. 272* (1), 396−400.

(5) Toy, P. H., and Janda, K. D. (2000) Soluble polymer bound cleavage reagents: a multipolymer strategy for the cleavage of tertiary amines from REM resin. *Org. Lett. 2* (15), 2205−2207.
(6) Mutter, M., Hagenmaier, H., and Bayer, E. (1971) New method of polypeptide synthesis. *Angew. Chem. Int. 10* (11), 811−812.
(7) Pillai, V. N. R., Mutter, M. Bayer, E., and Gatfield, I.,(1980) New, easily removable poly(ethylene glycol) supports for the liquid-phase method of peptide synthesis. *J. Org. Chem. 45* (26), 5364−5370.
(8) Tamada, K., Fujita, E., and Nishimura, S. I. (1998) High performance polymer supports for enzyme-assisted synthesis of glycoconjugates. *Carbohydr. Res. 305* (3−4), 443−461.
(9) Bonora, G. M. (1987) Use of poly(ethylene glycol) (PEG) as a soluble polymeric support in the oligonucleotide synthesis. A proposal for a new liquid-phase method. *Gazz. Chim. Ital. 117* (6), 379−80.
(10) Gravert, D. J., and Janda, K. D. (1997) Organic Synthesis on Soluble Polymer Supports: Liquid-Phase Methodologies. *Chem. Rev. 97* (2), 489−509.
(11) Roberts, M. J., Bentley, M. D., and Harris, J. M. (2002) Chemistry for peptide and protein PEGylation. *Adv. Drug Delivery Rev. 54* (4), 459−476.
(12) Veronese, F. M. (2001) Peptide and protein PEGylation. A review of problems and solutions. *Biomaterials 22* (5), 405−417.
(13) Delgado, C., Francis, G. E., and Fisher, D. (1992) The uses and properties of PEG-linked proteins. *Crit. Rev. Ther. Drug Carrier Syst. 9* (3−4), 249−304.
(14) Matsushima, A., Okada, M., and Inada, Y. (1984) Chymotrypsin modified with poly(ethylene glycol) catalyzes peptide synthesis reaction in benzene. *FEBS Lett. 178* (2), 275−277.
(15) Pillai, V. N. R., and Mutter, M. (1981) Conformational studies of poly(oxyethylene)-bound peptides and protein sequences. *Acc. Chem. Res. 14* (4), 122−130.
(16) Hooftman, G., Herman, S., and Schacht, E. J. (1996) Poly-(ethylene glycol)s with reactive end groups. II. Practical consideration for the preparation of protein-PEG conjugates. *Bioact. Compatible Polym. 11* (2), 135−159.
(17) Drioli, S., Adamo, I., Ballico, M., Morvan, F., and Bonora, G. M. (2002) Liquid-Phase synthesis and characterization of a conjugated chimeric oligonucleotide-PEG-peptide. *Eur. J. Org. Chem.* (20), 3473−3480.
(18) Suzawa, T., Nagamura, S., Saito, H., Ohta, S., Hanai, N., and Yamasaki, M. (2000) Synthesis and HPLC analysis of enzymatically cleavable linker consisting of poly(ethylene glycol) and dipeptide for the development of immunoconjugate. *J. Control. Release 6*9 (1), 27−41.
(19) Clark, R., Olson, K., Fuh, G., Marian, M., Mortensen, D., Teshima, G., Chang, S., Chu, H., Mukku, V., Canova-Davis, E., Somers, T., Cronin, M., Winkler, M., and Wells, J. A. (1996) Long-acting growth hormones produced by conjugation with poly(ethylene glycol). *J. Biol. Chem. 271* (36), 21969−21977.
(20) Schoellmann, G., and Shaw, E. (1963) Direct evidence for the presence of histidine in the active center of chymotrypsin. *Biochemistry 2*, 252−255.
(21) Ong, E. B., Shaw, E., and Schoellmann, G. (1965) The identification of the histidine residue at the active center of chymotrypsin. *J. Biol. Chem. 240* (2), 694−698.
(22) Kédzy, F. J., Thomson, A., and Bender, M. L. (1967) Reaction of chymotrypsin and L-1-chloro-3-tosylamido-4-phenyl-2-butanone. *J. Am. Chem. Soc. 89* (4), 1004−1009.
(23) Jameson, G. W., and Elmore, D. T. (1974) Affinity chromatography of bovine trypsin. A rapid separation of bovine alpha- and beta-trypsin. *Biochem. J. 141* (2), 555−565.
(24) Popenoe, E. A., and du Vigneaud, V. (1954) Synthesis of L-phenylalanyl-L-glutaminyl-L-asparagine. *J. Am. Chem. Soc. 76*, 6202−6203.
(25) Snider, J., Neville, C., Yuan, L. C., and Bullock, J. (1992) Characterization of the heterogeneity of poly(ethylene glycol)-modified superoxide dismutase by chromatographic and electrophoretic techniques. *J. Chromatogr. 599* (1−2), 141−55.

BC049940P

ARTICLES

Physicochemical and Biological Characterization of Polyethylenimine-graft-Poly(ethylene glycol) Block Copolymers as a Delivery System for Oligonucleotides and Ribozymes

Carola Brus,[†] Holger Petersen,[†] Achim Aigner,[‡] Frank Czubayko,[‡] and Thomas Kissel*[,†]

Department of Pharmaceutics and Biopharmacy, Philipps-University, Ketzerbach 63, 35037 Marburg, Germany, and Department of Pharmacology and Toxicology, School of Medicine, Philipps-University, Karl-von-Frisch-Strasse 1, 35033 Marburg, Germany. Received September 9, 2003; Revised Manuscript Received April 28, 2004

Two different series of polyethylenimine (PEI) block copolymers grafted with linear poly(ethylene glycol) (PEG) were investigated as delivery systems for oligodeoxynucleotides (ODN) and ribozymes. The resulting interpolyelectrolyte complexes were characterized with respect to their physicochemical properties, protection efficiency against enzymatic degradation, complement activation, and biological activity under in vitro conditions. The effect of PEG molecular weight and the graft density of PEG blocks on complex characteristics was studied with two different series of block copolymers. The resulting ODN complexes were characterized by photon correlation spectroscopy (PCS) and laser Doppler anemometry (LDA) to determine complex size and zeta potential. Electrophoresis was performed to study the protective effects of the different block copolymers against enzymatic degradation of ODN. Intact ODN was quantified via densitometric analysis. Ribozymes, a particularly unstable type of oligonucleotides, were used to examine the influence of block copolymer structure on biological activity. The stabilization of ribozymes was also characterized in a cell culture model. Within the first series of block copolymers, the grafted PEG chains (5 kDa) had marginal influence on the complex size. Two grafted PEG chains were sufficient to achieve a neutral zeta potential. Within the second series, size and zeta potential increased with an increasing number of PEG chains. A high number of short PEG chains resulted in a decrease in complex size to values comparable to that of the homopolymer PEI 25 kDa and a neutral zeta potential, indicating a complete shielding of the charges. Complement activation decreased with an increasing number of short PEG 550 Da chains. Ribozyme complexes with PEG-PEI block copolymers achieved a 50% down-regulation of the target mRNA. This effect demonstrated an efficient stabilization and biological activity of the ribozyme, which was comparable to that of PEI 25 kDa. PEGylated PEI block copolymers represent a promising new class of drug delivery systems for ODN and ribozymes with increased biocompatibility and physical stability.

INTRODUCTION

Oligodeoxynucleotides (ODN) and ribozymes have stimulated significant interest as tools for sequence-specific down-regulation of gene expression (*1*−*3*). To improve limited cellular uptake and poor stability of ODN, several carrier systems are currently under investigation, e.g., cationic lipids (*4*) and cationic polymers (*5*). Recently, important discoveries have led to a deeper understanding of the self-assembly processes between cationic polymers and DNA (*6*−*10*). Complexation with polycations by electrostatic interactions causes condensation of the DNA (*11*). The ratio of DNA to polymer, expressed as the N/P ratio, determines the extent of condensation (*12*). Furthermore, DNA stability against enzymatic degradation is increased by complexation with the polycations (*13*). Although, similar mechanisms have been proposed for polyplexes containing ODN (*10*, *14*), they are considered to be one of the most difficult classes of polynucleotides to be complexed by and delivered with polycations. It has been postulated that the limited number of negative charges presented by ODN may be insufficient for cooperative binding (*15*). Additionally, such interpolyelectrolyte complexes often suffer from a poor stability in solution leading to rapid aggregation (*14*, *16*, *17*). To overcome this problem, block copolymers containing a water-soluble nonionic segment, such as poly(ethylene glycol) (PEG), have been recently introduced. These include PEG-polyspermine (*14*), PEG-polylysine (PLL) (*9*, *10*), and di- or trimethylammonioethyl methacrylate (DMAEMA or TMAEMA)-based copolymers coupled to PEG or other hydrophilic polymers such as poly[*N*-(2-hydroxypropyl)methacrylamide] (pHPMA) (*18*, *19*), PLL-pHPMA (*18*), PLL-dextran (*20*), and PEG-polyethylenimine (PEI) (*7*). Promising results were reported using

* To whom correspondence should be addressed. Tel: (0049)-6421-2825881; fax: (0049)-6421-2827016; e-mail: kissel@mailer.uni-marburg.de.

[†] Department of Pharmaceutics and Biopharmacy.

[‡] Department of Pharmacology and Toxicology.

10.1021/bc034160m CCC: $27.50 © 2004 American Chemical Society
Published on Web 06/08/2004

these water-soluble block copolymers for ODN complexation, indicating an increased solubility and stability against enzymatic degradation (*7*). Cell culture and in vivo experiments have also demonstrated a decreased cytotoxicity (*14*) and high antisense activity (*21*−*23*). A possible explanation for these positive features of ODN copolymer complexes could be the arrangement of the ODN. It is hypothesized that the ODN is trapped within a polycationic core with the hydrophilic polymer chains oriented to the surrounding aqueous environment, creating a hydrophilic shell (*16*). This core shell structure possibly prevents aggregation due to steric repulsion, thus stabilizing the particles in solution. Furthermore, enzymatic attacks are prevented by the surrounding hydrophilic shell, leading to increased nuclease resistance (*7*, *10*). The degree of PEG substitution was found to influence physicochemical properties of the resulting complexes such as complex size, nuclease resistance (*9*), and even complement activation (*24*), posing restrictions for intravenous application of these delivery systems, as demonstrated by the appearance of serious side effects under in vivo conditions (*25*). Studies using plasmid DNA further revealed an influence of PEG molecular weight on condensation properties, biocompatibility, and biological activity (*26*).

The aim of this study was to establish the structure−property relationships of block copolymer ODN and ribozyme complexes. The influence of PEGylation degree and PEG molecular weight on physicochemical and biological properties was systematically investigated.

MATERIALS AND METHODS

Materials. The 20 mer DNA oligodeoxynucleotide (ODN) with the sequence 5′ TTC CAA TAC AGA AAC TCT CT- 3′ was purchased from Biospring (Frankfurt, Germany), dissolved in sterile water and stored at −20 °C until use. The 40 mer ribozyme Luc Rz 227 with the sequence 5′-ACU GCA UAC CUG AUG AGU CCG UUA GGA CGA AAC GAU UCU G-3′, directed against the luciferase mRNA, was purchased from GENSET S.A (Paris, France). PEI 25 kDa (Polymin water free, 99%) was a gift from BASF (Ludwigshafen, Germany). PEG-monomethyl ether (mPEG) 550 and mPEG 5000 were obtained from Aldrich (Taufkirchen, Germany). Block copolymers were synthesized by grafting linear PEG onto branched PEI using a diisocyanate linker as described in detail previously (*27*, *28*). Polymers were used as sterile filtered aqueous stock solutions (0.9 mg/mL) of pH 7.4. All other materials were of analytical grade.

Preparation of Polymer−ODN Complexes. Complexes were prepared as previously published by diluting the appropriate amount of ODN stock solution (100 μg/mL in sterile water), as well as polymer stock solution (0.9 mg/mL in sterile water, pH 7.4) in 50 μL of 150 mM NaCl, vortexing and incubating for 10 min (*13*). The polymer solution was added to the ODN solution, vortexed again, and incubated for a further 10 min. The polymer/DNA ratio was expressed as the nitrogen/phosphate (N/P) ratio and calculated on the basis that 1 μg of DNA corresponds to 3 nmol of phosphate, while 1 μL of PEI stock solution contains 10 nmol of nitrogen (*13*). For photon correlation spectroscopy and transfection experiments complexes were prepared in 150 mM NaCl. For atomic force microscopy, 10 mM NaCl was used to prevent salt crystal formation.

Photon Correlation Spectroscopy (PCS). The hydrodynamic diameter of freshly prepared complexes with a ODN concentration of 40 μg/mL were measured using a Zetasizer 3000 HS form Malvern Instruments (Herrenberg, Germany) equipped with a 10 mW HeNe laser at a wavelength of 633 nm at 25 °C. Scattered light was detected at 90° angle through a 400 μm pinhole, and the viscosity and refractive index of pure water at 25 °C were used for data analysis. Measurements were analyzed using the CONTIN algorithm. Values given are the means of 10 runs of 60 s ± standard deviation. The instrument was routinely calibrated with Standard Reference Latex Particles (AZ 55 Electrophoresis Standard Kit, Malvern Instruments).

Laser Doppler Anemometry (LDA). The zeta potential of freshly prepared complexes with an ODN concentration of 40 μg/mL was determined using the standard capillary electrophoresis cell of the Zetasizer 3000 HS form Malvern Instruments at position 17.0 at 25 °C. Average values were calculated with the data of 10 runs ± standard deviation.

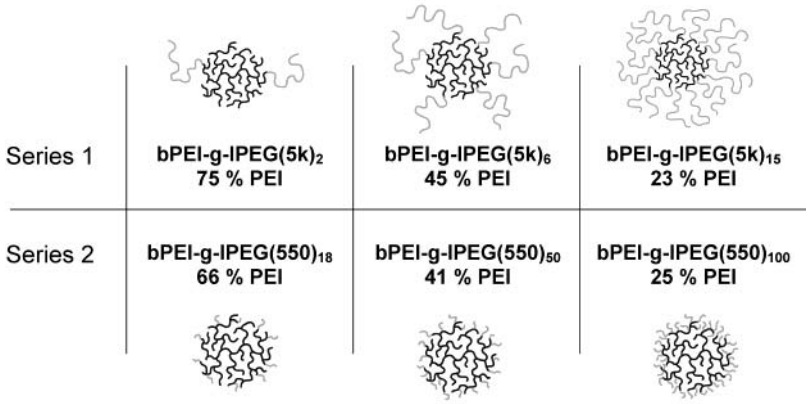
Atomic Force Microscopy (AFM). AFM images were conducted on a Dimension3000 Scanning Probe Microscope from Digital Instruments (Santa Barbara, CA) with a Nanoscope IIIa controller. All imaging was carried out in the tapping mode at a scan speed of approximately 2 Hz with 512 × 512 pixel data acquisition. V-shaped cantilevers with a pyramidal tip of silicon nitride were used (Park Scientific, CA).

Nuclease Stability. Freshly prepared complexes were incubated with 5 units DNase 1 (Roche Diagnostics GmbH, Mannheim, Germany) per μg DNA for 3 h at 37 °C. The samples were then transferred to a water bath of 70 °C for 30 min to inactivate the nuclease. The ODN was displaced from the complex by adding 8 μL 10% (w/v) sodium dodecyl sulfate (SDS) in water, vortexing, and incubating for a further 10 min. A 10 μL volume of each sample was loaded onto a 15% polyacrylamide gel containing 7 M urea, corresponding to total amount of 0.2 μg of ODN. Electrophoresis was carried out at 200 V for approximately 50 min (Consort E332 power supply, Roth, Karlsruhe, Germany). Afterward, gels were stained for 5 min in a 1:1000 dilution of SYBR Gold (MoBiTech GmbH, Göttingen, Germany) in water and digitalized using the BioDocAnalyze gel documenting system (Biometra, Göttingen, Germany) with an excitation wavelength of 312 nm.

Densitometric Analysis. Electrophoretic gels were analyzed using the software program Scion Image 4.0.2. beta (Scion Corporation, Frederick, MD). The amount of intact ODN was calculated via a four point standard curve on every single gel using three ODN dilutions of 0.2, 0.1, and 0.05 μg, respectively, plus the point of origin. Values given are the difference between the calculated ODN amount of each sample and the intact amount of the noncomplexed ODN control and are expressed as the percentage which was protected by the complex. The linear relationship between the amount of the ODN and the optical density of the bands was previously proven by a calibration curve. Five independent calibration curves using nine different dilutions were measured. Linear regression of the means exhibited a correlation coefficient of 0.9947. Differences were considered significant for $P \leq 0.05$ based on One-way ANOVA using Origin software package (Microcal Software, Inc. Northampton, MD).

Complement Activation. The principle of the hemolytic assay is based on the concentration-dependent consumption of complement components by complement-activating agents when serum is preincubated with these agents (*24*). The subsequent hemolysis of antibody-sensitized sheep erythrocytes by the so-called membrane

Table 1. Nomenclature of the Two Grafted PEI-*g*-PEG Block Copolymer Series. It Is Further Given the Average PEI Content and the Schematic Structure of the Single Copolymers. The Black Part of the Structure Represents the Branched PEI 25 KDa, and the Gray Part Represents the Nonionic Linear PEG Segments



attack complex formed by the remaining complement components is decreased as compared to that of untreated serum. Gelatin veronal buffer (GBV) and antibody-sensitized sheep erythrocytes were both purchased from Sigma-Aldrich (Taufkirchen, Germany). The required serum dilution of 1:10 in GBV, necessary for the lysis of 50% of the erythrocytes, was determined using the Krogh equation as described (*29*) and expressed as $CH50_{max}$ value. The procedure was performed according to the protocol by Plank et al. (*24*). Briefly, five different concentrations (25 mg/L; 12.5 mg/L; 6.25 mg/L; 1.56 mg/L and 0.39 mg/L) of freshly prepared bPEI-*g*-lPEG−ODN complexes at N/P ratio 20 were preincubated with serum. The resulting CH50 of the serum, after preincubation with complexes, was compared to $CH50_{max}$ and expressed as percentage of $CH50_{max}$ = (CH50 sample/$CH50_{max}$) × 100 (*24*).

Cell Culture. SKOV-3 ovarian carcinoma cells (American Type Culture Collection, Manassas, VA), stably transfected with the luciferase gene, were cultured in Iscove's modified Dulbecco's medium IMDM (PAA Laboratories, Cölbe, Germany) supplemented with 10% FCS at 37 °C and 5% CO_2 (v/v).

Ribozyme Activity Assay. SKOV-3 cells, stably transfected with the luciferase gene (Aigner and Urban-Klein, unpublished results), were seeded at a density of 34 000 (Figure 6a and b) or 70 000 (Figure 6c) cell/well in 24-well plates, respectively. After 6 h, medium was exchanged and the cells were incubated with freshly prepared complexes. Ribozyme−PEI complexes were prepared according to the standard protocol containing 0.25 μg of ribozyme directed against the luciferase mRNA and unrelated ribozyme as a control where indicated. Experiments were carried out at two different N/P ratios of 6.7 and 20 for PEI homopolymers and all PEI-*g*-PEG block copolymers. Cells incubated with 0.25 μg of non-complexed ribozyme were used as a control. Medium was exchanged after 4 h. Luciferase activity was determined after a further 44 h using the Luciferase Assay System from Promega according to the manufacturer's instructions. All experiments were performed in triplicates. The protein concentration in each sample was determined using a BCA assay (*30*).

RESULTS AND DISCUSSION

Two series of block copolymers were chosen to study the influence of PEGylation on the physicochemical properties and biological activity of the resulting interpolyelectrolyte complexes with ODN and ribozymes. In both series, branched (b) PEI 25 kDa was grafted with an increasing number of linear (l) PEG chains, with a molecular weight of 5 kDa within the first and 550 Da within the second series, respectively (Table 1). These graft (*g*) copolymers were designated using the following nomenclature: bPEI(25k)-*g*-lPEG(x)$_n$ with b and l denoting a branched or linear structure, respectively. The number in brackets (25k or x, where x = 5k or 550) represent the MW of the PEI or the PEG block, and the index n is the average number of PEG blocks per PEI molecule. This number was calculated based on ^{1}H NMR spectra as described previously (*27*).

Photon Correlation Spectroscopy (PCS). The hydrodynamic diameters of ODN−PEG-PEI complexes were determined at two different nitrogen to phosphate (N/P) ratios of 6.7 and 20 (Figure 1). All PEG-PEIs formed very small complexes in the range of 7 to 40 nm. No specific trend could be observed within the first series (Figure 1a). The complex size was only marginally influenced by the increasing degree of PEG substitution with 5 kDa PEG chains. At both N/P ratios, the average diameters were below 30 nm. bPEI(25k)-*g*-lPEG(5k)$_{15}$ formed larger complexes of 40 nm at N/P 6.7, possibly due to a decreased condensation efficiency of this highly grafted derivative. At N/P 20, small complex sizees were also observed. A decrease in complex size at higher N/P ratios using PEI 25 kDa has been previously reported for unmodified ODN and a phosphorothioate oligonucleotide previously (*31*). Petersen et al. also found smaller complex sizes when using five different PEI-*g*-PEG block copolymers with plasmid DNA at different N/P ratios (*26*). In the second series, polymer grafted with shorter 550 Da PEG chains, up to a substitution degree of 50, showed increases in complex size (Figure 1b). Complexes at an N/P ratio 6.7 exhibited in all cases larger average diameters, which suggest that the ability of these polymers to condense ODN at this N/P ratio is impaired. Interestingly, PEG-PEI copolymers with 100 PEG chains of 550 Da exhibited complex sizes, which were comparable to those of the homopolymer PEI 25 kDa. PEG-PEI complexes with ODN are generally found to yield small diameters and narrow size distributions (*15*). Vinogradov et al. described a copolymer composed of a PEI 2 kDa grafted with an average number of 1.7 PEG (8 kDa) chains, which produced complexes with a phosphorothioate (PS) ODN of 32 nm (*7*). While experimental conditions and especially chemical modifications of the ODN seem

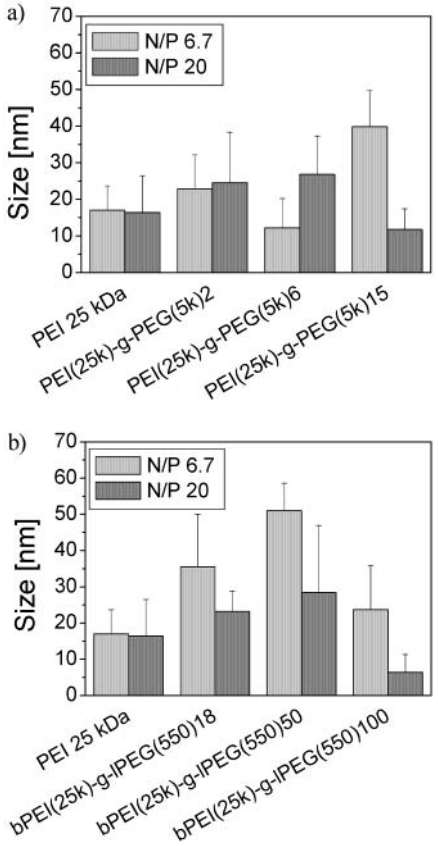


Figure 1. Hydrodynamic diameters of ODN−PEI-25 kDa and block copolymer complexes (a) of the Series 1 and (b) of Series 2 at N/P ratios 6.7 and 20. Values are presented as the mean of 10 runs ± standard deviation.

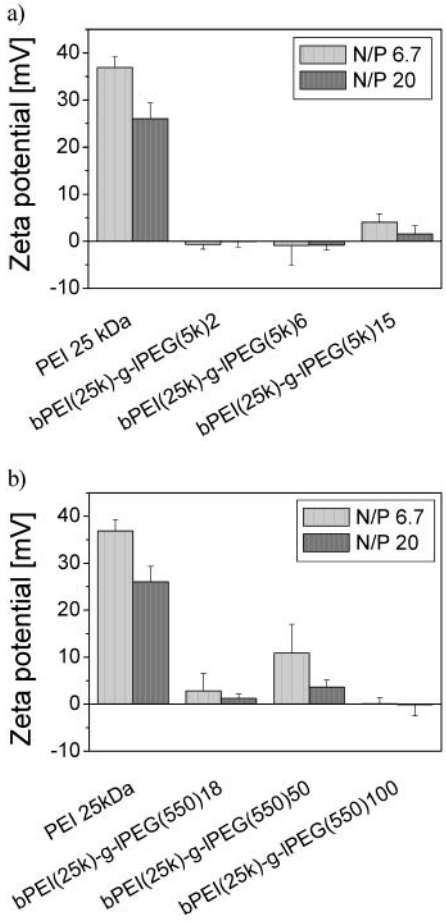


Figure 2. Zeta potentials of ODN−PEI 25 kDa and block copolymer complexes (a) of the Series 1 and (b) of Series 2 at N/P ratios 6.7 and 20. Values are presented as the mean of 10 runs ± standard deviation.

to have a great influence on complex formation of PEI 25 kDa complexes (*31*), further studies are necessary to determine the influence of chemical modification on the complexation with block copolymers.

Laser Doppler Anemometry (LDA). The surface charge of PEG-PEI complexes was determined at the two different N/P ratios, 6.7 and 20, using LDA. The results are shown in Figure 3. PEI 25 kDa complexes revealed high positive surface charges of +35 mV at N/P 6.7 and +25 mV at N/P 20. A decrease in the zeta potential with increasing N/P ratio has been previously reported for plasmid PEI complexes, as well (*26*, *32*). Zeta potentials of the block copolymer complexes were reduced to nearly neutral values as documented for both series 1 (Figure 2a) and 2 (Figure 2b). Our results are compatible with a core−shell structure, in which hydrophilic PEG chains are oriented toward the surface. Hence, the positive charge of the PEI core is shielded as previously discussed (*10*, *15*). Full shielding was already achieved at the lowest degree of PEGylation investigated in this study of PEG-$(5k)_2$ or PEG$(550)_{18}$, respectively. A further increase of the PEGylation degree had only marginal effects on the zeta potential. The net charge of plasmid DNA complexes could be fully shielded only with block copolymers containing more than six PEG (5 kDa) chains or one very long PEG chain of 20 kDa (*26*). The substantial difference in DNA size seems to be responsible for the lower degree of condensation of plasmid DNA within the polycationic core (*15*). Surprisingly, under our experimental conditions only bPEI(25k)-*g*-lPEG$(550)_{50}$ led to a clear positive surface charge possibly caused by a difference in stoichiometry of ODN to polymer which is also reflected by the increased complex size.

Atomic Force Microscopy (AFM). To visualize the shape of the PEG-PEI complexes, we performed atomic force microscopy studies with ODN−PEI 25 kDa complexes and the block copolymer, bPEI(25k)-*g*-lPEG$(550)_{100}$ (Figure 3). AFM imaging was performed directly in solution; however, a lower salt concentration of 10 mM NaCl, pH 7.4, was necessary to prevent salt crystal formation (*26*). Complexes were imaged at an N/P ratio of 6.7. PEI 25 kDa showed images of very small, compact, homogeneously distributed complexes with a nearly spherical shape (Figure 3a,b). PEGylation affected the condensation of the complexes, as is shown for the block copolymer complexes of bPEI(25k)-*g*-lPEG$(550)_{100}$ (Figure 3c,d). This has been previously reported for plasmid DNA complexes as well (*26*). The complexes lost their spherical, well-defined shape and appeared to be more "fuzzy". Wolfert et al. reported a similar phenomenon for PEGylated PLL (*8*). The reason for the decreased condensation efficiency of PEGylated derivatives is not yet clear. It might be the result of a reduced ability to collapse into small particles, due to hydrogen bonding of the PEG with water (*8*, *15*).

Nuclease Stability. It is well established that complexation with polycations leads to protection of DNA from enzymatic digestion (*6*, *13*). PEG-PEI have demonstrated a high protection efficiency for ODN (*7*, *9*). However, it remains to be investigated whether the degree of PEGylation and PEG molecular weight have an impact on the stabilization efficiency of block copolymers. Both ODN complex series were incubated with

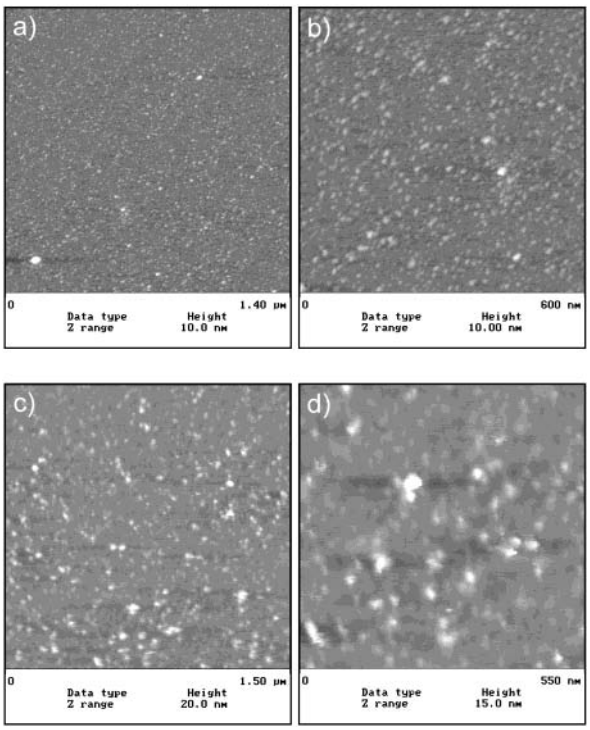


Figure 3. AFM images of ODN complexes of PEI 25 kDa (a and b) in two different resolutions and bPEI(25k)-*g*-lPEG(550)$_{100}$ (c and d) in two different resolutions at N/P ratio 6.

DNase 1 for 3 h. Afterward the nuclease was denatured and the ODN displaced from the complex. DNase 1 is a double-strand-specific endonuclease, which also cleaves single stranded ODN, albeit more slowly. Accordingly, nearly 75% of the noncomplexed control was degraded after 3 h in contrast to plasmid DNA which is totally degraded within this period. The percentage of nondegraded control was subtracted from the intact amount of the single samples in order to obtain the real protected fraction, as shown in Figure 4. All block copolymers revealed a protection equal to that of PEI 25 kDa. In contrast, Dash et al. achieved a higher protection of plasmid DNA by a PEGylated PLL in comparison to the non-PEGylated derivative (*33*). This effect could be explained by steric hindrance of the nucleolytic attack by the PEG shell (*7, 9*). Under our experimental conditions, however, no specific trend could be distinguished within both series 1 (Figure 4a) and 2 (Figure 4b), suggesting a more complete protection of the ODN by entrapment within the polycationic core. Similarly, Harada et al. reported that an increased degree of polymerization of PEG-PLL block copolymers positively influenced the protection efficiency, which likewise provided evidence for protection via the polycationic segment (*9*).

Complement Activation. The interaction of interpolyelectrolyte complexes with blood and blood components seems to be a major obstacle for their intravenous administration (*17, 34*). Components of the complement system, as part of the nonadaptive immune system of vertebrate species, have been demonstrated to interact with non viral vectors (*24*). The binding of complement proteins to DNA complexes leads inevitable to complement-dependent phagocytosis as demonstrated for liposomes (*25*). Clearance by the reticuloendothelial system reduces the complex half-life within the blood stream. Plank et al. studied the complement activation of commonly used nonviral vectors (*24*). They reported that a high degree of PEGylation decreased complement activation. In this study, the influence of the PEGylation degree, as well as that of PEG molecular weight, on complement activation was systematically investigated. Dilutions of the two series of ODN block copolymer complexes were examined according to the protocol of Plank et al. (*24*). The appropriate initial serum dilution required for 50% hemolysis was determined and expressed as $CH50_{max}$. In theory, binding of complement components to the PEG-PEI/ODN complexes during incubation with serum results in a consumption of these complement factors. Thus, they are no longer available for the following hemolysis, leading to a concentration dependent decrease of $CH50_{max}$. The PEG-PEI complexes of the first series consumed complements component to the same extent as PEI 25 kDa (Figure 5a). Thus, it may be concluded that the shielding obtained by PEGylation with 5 kDa PEG does not necessarily result in decreased complement activation. Increasing PEGylation up to 77% PEG content did not show any positive effects. This is in line with the results of Plank et al. who did not observe a decrease in complement activation of PEGylated PLL when investigating copolymers with up to 20 PEG chains and molecular weights ranging from 1 to 12 kDa. Only larger PEGylation degrees finally led to decreased complement activation (*24*). On the other hand, PEGylation with 550 Da PEG (Series 2) achieved decreased complement activation (Figure 5b). A correlation between the increase in $CH50_{max}$ and the PEGylation degree was observed. The fact that the PEG-PEIs with 100 chains of PEG 550 Da and 15 chains of PEG 5 kDa contain approximately the same amount of PEG, suggests that not the total PEG content, but rather the PEG molecular weight and, hence, the degree of substitution influences complement activa-

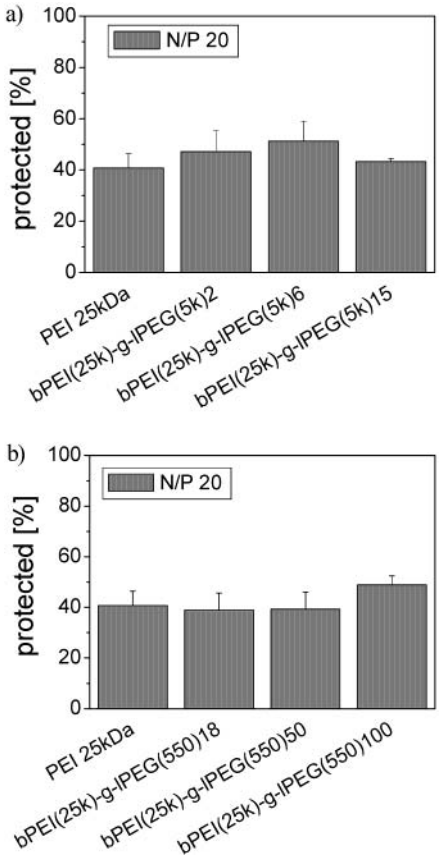


Figure 4. Nuclease stability of ODN−PEI 25 kDa and block copolymer complexes (a) of Series 1 and (b) of Series 2, at N/P ratio 20. All experiments were run in triplicate. (One-way ANOVA statistic test revealed no significant difference).

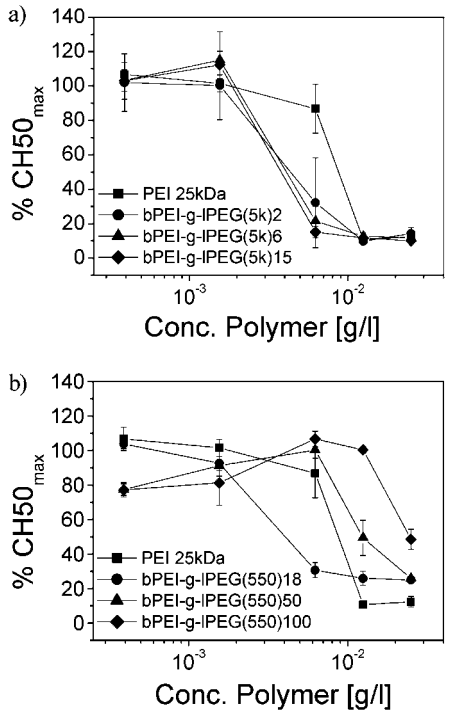


Figure 5. Complement activation of ODN−PEI 25 kDa and block copolymer complexes (a) of Series 1 and (b) of Series 2, at N/P ratio 20. All experiments were run in triplicate.

tion. We hypothesize that a high degree of substitution leads to a brushlike PEG coverage of the polycationic surface. This "crew-cut" micelle structure, achieved only when using the small 550 Da PEG chains, is better capable of preventing complement activation. Movement of the smaller number of longer PEG chains possibly enables contact with the polycationic core. The zeta potential values of all block copolymer complexes suggest that simple shielding of the surface charge is not sufficient to prevent complement activation.

Biological Activity of Ribozymes. Ribozymes are short single-stranded RNA−ODN capable of cleaving their target mRNA in a sequence-specific manner (*35*). Due to the RNA structure, these molecules are even more accessible to enzymatic degradation than the corresponding DNA-ODN (*36*). It could be previously demonstrated that PEI is able to stabilize ribozymes even under in vivo conditions (*37*). The ribozyme-based assay used in this study, therefore, was designed to investigate the influence of PEI-*g*-PEG block copolymer structure on two effects simultaneously: First, the ability to protect ribozymes under cell culture conditions and, second, the biological activity of the ribozyme, therefore, representing very drastic conditions. Ribozymes directed against the luciferase mRNA in stably transfected SKOV-3 cells cause sequence-specific cleavage of the target mRNA, resulting in a decrease of luciferase activity. When cells were incubated with noncomplexed ribozyme as a control, no ribozyme activity could be observed, due to degradation of the ribozyme by the 10% FCS supplement in the cell culture medium. Luciferase activity was comparable to untreated cells, as seen in Figure 6a. Also an unrelated ribozyme, not complementary to the luciferase mRNA, did not affect luciferase activity. In contrast, exposure of cells to ribozyme PEG-PEI complexes led to approximately a 50% down-regulation of the luciferase activity. The interpolyelectrolyte complexes of series 1 (Figure 6b) as well as of series 2 (Figure 6c), demonstrated ribozyme activity comparable to that of PEI 25

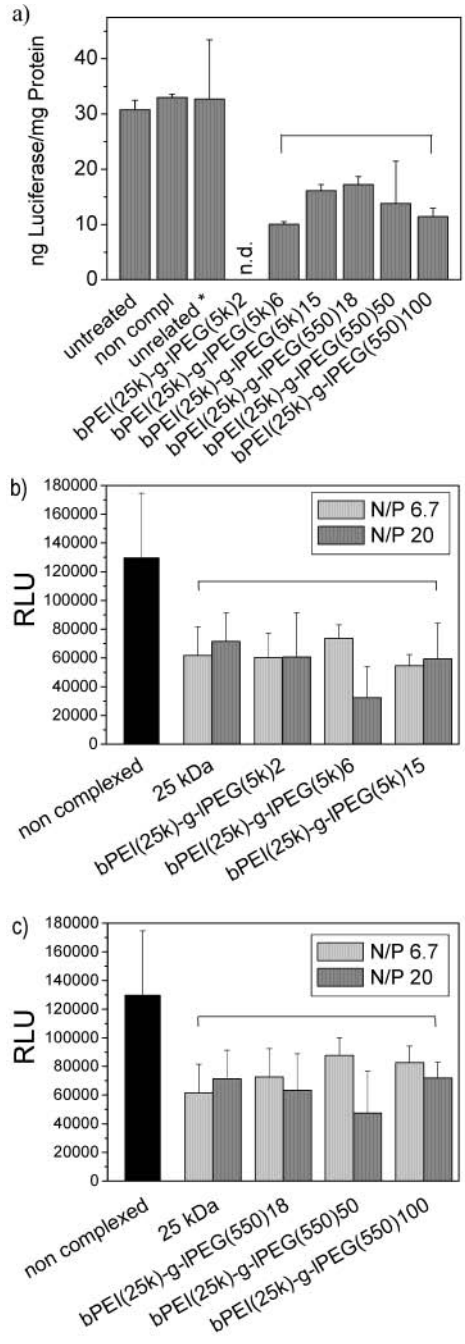


Figure 6. Biological activity (a) as ng luciferase/mg protein of ribozyme block copolymer complexes at the N/P ratio of 20 in comparison to unrelated ribozyme (* complexed to bPEI(25k)-*g*-lPEG(5k)6) and noncomplexed ribozyme and as relative light units (RLU) of ribozyme block copolymer complexes (b) of Series 1 and (c) of Series 2, at the N/P ratios 6.7 and 20 in comparison to PEI 25 kDa. All experiments were run in triplicate. One-way ANOVA statistic test revealed no significant difference between biological activity of PEI 25 kDa complexes and block copolymer complexes.

kDa. Furthermore, no influence of increasing PEGylation on the activity could be distinguished. Surprisingly, the N/P ratio of 6 and 20, respectively, had only a marginal effect on ribozyme activity. In contrast to our observations with ribozyme, it has been reported that the delivery of plasmid DNA using PEG modified PEI often caused a dramatic decrease of transfection efficiency (*38*, *39*). Recently, the transfection activity of five different PEI-*g*-PEG block copolymers used for plasmid delivery was studied systematically (*26*). It was found that trans-

fection was negatively influenced by an increasing degree of PEGylation. This was explained by the differences in cytotoxicity and zeta potential of the various complexes. Under our experimental conditions, only marginal differences in the zeta potentials of the different PEI-*g*-PEG block copolymer complexes could be observed, which correlates well with the similar biological activity observed. It was speculated that the small ribozyme could be condensed more effectively and the shielding of the positive surface charges could be achieved with lower degrees of PEGylation. It has been reported that the transfection efficiency of PEG-PEI complexes with pSV-β-gal plasmid was slightly decreased with an increase in PEG content. However, PEGylation did not affect the transfection efficiency of the complex for 48 h transfection in the presence of serum (*40*), analogous to the observation period in this study. Only limited results are available reporting successful ODN transfection using block copolymers (*14*, *21*, *22*). An antisense effect directed against amphiphysin was achieved at a very low ODN concentration using a PEGylated polyspermin (*22*). However, this provides evidence that PEG-PEI copolymers do have potential for an efficient ODN delivery. Under our experimental conditions, ODN transfer was as effective as with PEI 25 kDa. This trend might be further increased using even higher N/P ratios, as demonstrated for plasmid DNA. bPEI(25k)-*g*-lPEG(550)35 at N/P 50 achieved transfection rates 1 order of magnitude higher than that of PEI 25 kDa at N/P 20, possibly due to the decreased toxicity of PEGylated PEI derivatives (*26*). Whether this trend in transfection efficiency of plasmid DNA and ODN are comparable remains to be resolved.

CONCLUSIONS

The results of this study demonstrate that PEI-*g*-PEG block copolymers formed very small, homogeneously distributed nucleic acid complexes with high nuclease protection and transfection efficiency. Block copolymers with a high number of short PEG chains (550 Da) achieved a decreased activation of the complement system without losses in biological activity. Therefore, the favorable characteristics of highly grafted copolymers with low molecular weighted PEG are suitable for the delivery of ODN and ribozymes. These new insights into the structure−property relationships of ODN copolymer complexes are valuable for the optimization of hydrophilic nonviral carriers for an efficient ODN delivery.

ACKNOWLEDGMENT

The authors thank Beata Urban-Klein for expert assistance with SKOV-3 cell culture.

LITERATURE CITED

(1) Crooke, S. T. (1998) An overview of progress in antisense therapeutics. *Antisense Nucleic Acid Drug Dev. 8*, 115−122.
(2) Dass, C. R. (2002) Vehicles for oligonucleotide delivery to tumors. *J. Pharm. Pharmacol. 54*, 3−27.
(3) Haseloff, J., and Gerlach, W. L. (1988) Simple RNA enzymes with new and highly specific endo ribonuclease activities. *Nature 334*, 585−591.
(4) Zelphati, O., and Szoka, F. C., Jr. (1996) Intracellular distribution and mechanism of delivery of oligonucleotides mediated by cationic lipids. *Pharm. Res. 13*, 1367−1372.
(5) Merdan, T., Kopecek, J., and Kissel, T. (2002) Prospects for cationic polymers in gene and oligonucleotide therapy against cancer. *Adv. Drug Delivery Rev. 54*, 715−758.
(6) Kabanov, A. V., and Kabanov, V. A. (1995) DNA complexes with polycations for the delivery of genetic material into cells. *Bioconjugate. Chem. 6*, 7−20.
(7) Vinogradov, S. V., Bronich, T. K., and Kabanov, A. V. (1998) Self-assembly of polyamine-poly(ethylene glycol) copolymers with phosphorothioate oligonucleotides. *Bioconjugate. Chem. 9*, 805−812.
(8) Wolfert, M. A., Schacht, E. H., Toncheva, V., Ulbrich, K., Nazarova, O., and Seymour, L. W. (1996) Characterization of vectors for gene therapy formed by self-assembly of DNA with synthetic block copolymers. *Hum. Gene Ther. 7*, 2123-2133.
(9) Harada, A., Togawa, H., and Kataoka, K. (2001) Physicochemical properties and nuclease resistance of antisense-oligodeoxynucleotides entrapped in the core of polyion complex micelles composed of poly(ethylene glycol)-poly(L-lysine) block copolymers. *Eur. J. Pharm. Sci. 13*, 35−42.
(10) Kataoka, K., Togawa, H., Harada, A., Yasugi, K., Matsumoto, T., and Katayose, S. (1996) Spontaneous Formation of Polyion Complexes Micelles with Narrow Distribution from Antisense Oligonucleotides and Cationic Block Copolymer in Physiological Saline. *Macromolecules 29*, 8556−8557.
(11) Bloomfield, V. A. (1996) DNA condensation. *Curr. Opin. Struct. Biol. 6*, 334−341.
(12) Dunlap, D. D., Maggi, A., Soria, M. R., and Monaco, L. (1997) Nanoscopic structure of DNA condensed for gene delivery. *Nucleic Acids Res. 25*, 3095−3101.
(13) Boussif, O., Lezoualc'h, F., Zanta, M. A., Mergny, M. D., Scherman, D., Demeneix, B., and Behr, J. P. (1995) A versatile vector for gene and oligonucleotide transfer into cells in culture and in vivo: polyethylenimine. *Proc. Natl. Acad. Sci. U.S.A. 92*, 7297−7301.
(14) Kabanov, A. V., Vinogradov, S. V., Suzdaltseva, Y. G., and Alakhov, V. (1995) Water-soluble block polycations as carriers for oligonucleotide delivery. *Bioconjugate Chem. 6*, 639−643.
(15) Seymour, L. W., Kataoka, K., and Kabanov, A. V. (1998) Cationic block copolymers as self-assembling vectors for gene delivery. *Self-assembling Complexes for Gene Delivery. From Laboratory to Clinical Trial.* (Kabanov, A. V., Felgner, P. L., Seymour, L. W., Eds.) pp 219−239, John Wiley & Sons, New York.
(16) Kabanov, V. A., and Kabanov, A. V. (1998) Interpolyelectrolyte and block ionomer complexes for gene delivery: physicochemical aspects. *Adv. Drug Delivery Rev. 30*, 49−60.
(17) Wiethoff, C. M., and Middaugh, C. R. (2003) Barriers to nonviral gene delivery. *J. Pharm. Sci. 92*, 203-217.
(18) Read, M. L., Dash, P. R., Clark, A., Howard, K. A., Oupicky, D., Toncheva, V., Alpar, H. O., Schacht, E. H., Ulbrich, K., and Seymour, L. W. (2000) Physicochemical and biological characterisation of an antisense oligonucleotide targeted against the bcl-2 mRNA complexed with cationic-hydrophilic copolymers. *Eur. J. Pharm. Sci. 10*, 169−177.
(19) Deshpande, M. C., Garnett, M. C., Vamvakaki, M., Bailey, L., Armes, S. P., and Stolnik, S. (2002) Influence of polymer architecture on the structure of complexes formed by PEG-tertiary amine methacrylate copolymers and phosphorothioate oligonucleotide. *J. Controlled Release 81*, 185−199.
(20) Maruyama, A., Katoh, M., Ishihara, T., and Akaike, T. (1997) Comb-type polycations effectively stabilize DNA triplex. *Bioconjugate Chem. 8*, 3−6.
(21) Roy, S., Zhang, K., Roth, T., Vinogradov, S., Kao, R. S., and Kabanov, A. (1999) Reduction of fibronectin expression by intravitreal administration of antisense oligonucleotides. *Nat. Biotechnol. 17*, 476−479.
(22) Mundigl, O., Ochoa, G. C., David, C., Slepnev, V. I., Kabanov, A., and De Camilli, P. (1998) Amphiphysin I antisense oligonucleotides inhibit neurite outgrowth in cultured hippocampal neurons. *J. Neurosci. 18*, 93−103.
(23) Vinogradov, S., Batrakova, E., Li, S., and Kabanov, A. (1999) Polyion complex micelles with protein-modified corona for receptor-mediated delivery of oligonucleotides into cells. *Bioconjugate. Chem. 10*, 851−860.
(24) Plank, C., Mechtler, K., Szoka, F. C., Jr., and Wagner, E. (1996) Activation of the complement system by synthetic DNA complexes: a potential barrier for intravenous gene delivery. *Hum. Gene Ther. 7*, 1437−1446.
(25) Wassef, N. M., and Alving, C. R. (1993) Complement-dependent phagocytosis of liposomes. *Chem. Phys. Lipids 64*, 239−248.

(26) Petersen, H., Fechner, P. M., Martin, A. L., Kunath, K., Stolnik, S., Roberts, C. J., Fischer, D., Davies, M. C., and Kissel, T. (2002) Polyethylenimine-graft-poly(ethylene glycol) copolymers: influence of copolymer block structure on DNA complexation and biological activities as gene delivery system. *Bioconjugate Chem. 13*, 845−854.

(27) Petersen, H., Fechner, P., Fischer, D., and Kissel, T. (2002) Synthesis, Characterization, and Biocompatibility of Polyethylenimine-graft-poly(ethylene glycol) Block Copolymers. *Macromolecules 35*, 6867−6874.

(28) Kissel, T., Petersen, H., Fischer, D., Kunath, K., and von Harpe, A. (1999) Kationische Blockcopolymere. DE19933024A1 (EP00/06214/WO01/05875A1), Germany.

(29) Whaley, K., and North, J. (1997) Hemolytic assays for whole complement activity and individual components. *Complement. A practical approach* (Dodds, A. W., and Sim, R. B., Eds.) pp 19−47, Oxford University Press, New York.

(30) Hill, H. D., and Straka, J. G. (1988) Protein determination using bicinchoninic acid in the presence of sulfhydryl reagents. *Anal. Biochem. 170*, 203−208.

(31) Dheur, S., Dias, N., van Aerschot, A., Herdewijn, P., Bettinger, T., Remy, J. S., Helene, C., and Saison-Behmoaras, E. T. (1999) Polyethylenimine but not cationic lipid improves antisense activity of 3′-capped phosphodiester oligonucleotides. *Antisense Nucleic Acid Drug Dev. 9*, 515−525.

(32) Kunath, K., Harpe von, A., Petersen, H., Fischer, D., Voigt, K., Kissel, T., and Bickel, U. (2002) The Structure of PEG-Modified Poly(ethylen imines) Influences Biodistribution and Pharmacokinetics of their Complexes with NF-kB Decoy in Mice. *Pharm. Res. 19*, 810−817.

(33) Dash, P. R., Toncheva, V., Schacht, E., and Seymour, L. W. (1997) Synthetic polymers for vectorial delivery of DNA: characterisation of polymer-DNA complexes by photon correlation spectroscopy and stability to nuclease degradation and disruption by polyanions in vitro. *J. Controlled Release 48*, 269−276.

(34) Kircheis, R., Wightman, L., and Wagner, E. (2001) Design and gene delivery activity of modified polyethylenimines. *Adv. Drug Delivery Rev. 53*, 341−358.

(35) Birikh, K. R., Heaton, P. A., and Eckstein, F. (1997) The structure, function and application of the hammerhead ribozyme. *Eur. J. Biochem. 245*, 1−16.

(36) Scherr, M., Grez, M., Ganser, A., and Engels, J. W. (1997) Specific hammerhead ribozyme-mediated cleavage of mutant N-ras mRNA in vitro and ex vivo. Oligoribonucleotides as therapeutic agents. *J. Biol. Chem. 272*, 14304−14313.

(37) Aigner, A., Fischer, D., Merdan, T., Brus, C., Kissel, T., and Czubayko, F. (2002) Delivery of unmodified bioactive ribozymes by an RNA-stabilizing polyethylenimine (LMW−PEI) efficiently down-regulates gene expression. *Gene Ther. 9*, 1700−1707.

(38) Nguyen, H. K., Lemieux, P., Vinogradov, S. V., Gebhart, C. L., Guerin, N., Paradis, G., Bronich, T. K., Alakhov, V. Y., and Kabanov, A. V. (2000) Evaluation of polyether-polyethyleneimine graft copolymers as gene transfer agents. *Gene Ther. 7*, 126−138.

(39) Erbacher, P., Bettinger, T., Belguise-Valladier, P., Zou, S., Coll, J. L., Behr, J. P., and Remy, J. S. (1999) Transfection and physical properties of various saccharide, poly(ethylene glycol), and antibody-derivatized polyethylenimines (PEI). *J. Gene Med. 1*, 210−222.

(40) Choi, J. H., Choi, J. S., Suh, H., and Park, J. S. (2001) Effect of Poly(ethylene glycol) Grafting on Polyethylenimine as a Gene Transfer Vector in vitro. *Bull. Korean Chem. Soc. 22*, 46−52.

BC034160M

Synthesis and Characterization of Bioconjugates of S-Layer Proteins

Parthasarathy Sampathkumar and M. Lane Gilchrist, Jr.*

Departments of Chemical and Biomedical Engineering, The City College of the City University of New York, New York, New York 10031. Received November 6, 2003; Revised Manuscript Received February 11, 2004

The self-assembling proteins that form crystalline surface layers (S-layers) on many microbial species have found numerous applications due to their nanostructured nature. To devise a new method to construct surface displays that exploit S-layer self-assembly activity and nanostructural properties, we have constructed polymer bioconjugates of S-layer proteins. The conjugates formed are similar in function to the monomer alkanethiols that form self-assembled monolayers (SAMs) on gold surfaces. However, the self-assembly is driven by the protein "headgroup" that positions polymer-tethered endgroups on a surface. This paper examines the integration of protein purification, conjugation, and surface assembly that has led to the development of this new method for the formation of nanostructured surfaces. Purified S-layer proteins from *Lactobacillus brevis* were conjugated with small molecule probes and polymers using amine-based reactions. To keep multiple labeling of protein amine groups to acceptable levels, the conjugations were performed at pH 6.5, allowing for limited yields (24−39%) as determined by mass spectrometry and SDS-polyacrylamide gel electrophoresis. As the presence of high levels of unlabeled S-layer proteins is undesired, we have developed a protocol for further purification that employs monomeric avidin affinity chromatography. The surface self-assembly of the polymer bioconjugates onto amine-terminated microspheres was studied using epi-fluorescence, confocal, and scanning electron microscopy. The surfaces obtained exhibited homogeneous distributions of tethered molecules. Also, in cases where the modular assembly of two distinct types of tethered endgroups was accomplished, there was no evidence for phase separation in the surfaces. The modular assembly method will provide a potential route to controlling surface display density as the starting assembly conditions guide displayed endgroup concentrations in mixed molecular monolayers.

INTRODUCTION

Microorganisms often employ crystalline surface monolayers of self-assembling proteins for molecular display, exozyme binding, and other extracellular functions (*1*). These protein monolayers, collectively known as the crystalline surface layer or S-layer, contain subunits with molecular weights ranging from 40 to 200 kDa, depending on the species (*1*−*8*). In the assembled form, the S-layer proteins form porous crystalline molecular monolayers with unit cell dimensions on the order of 4−15 nm (*5*). The regular nanostructure and high degree of long-range order provides favorable attributes for potential uses of the assembled S-layer in nanostructured materials (*1*, *2*, *7*, *9*). This study concerns the development of a new method to be used for building nanostructured, self-assembled monolayers based on S-layer bioconjugates.

Various subtypes of S-layer proteins have been used in wide ranging applications such as ultrafiltration membranes (*2*), solid supports for lipid bilayer membranes (*10*), and nanoparticle arrays (*11*). S-Layer proteins that associate with the peptidoglycan layer of the microbial cell wall, can in general, be disassembled, but not denatured, by treatment with chaotropic agents such as LiCl or guanidine HCl. These proteins can be separated from cells and media by centrifugation and then reassembled in vitro by dialyzing out the chaotrope or salt. Thus, successive steps of disassembly and reassembly can be used to obtain gram quantities of highly purified S-layer proteins. The reassembly of these proteins onto interfaces can be controlled via surface charge or hydrophobicity. This process has been studied extensively by Sleytr and co-workers (*1*, *2*, *9*). These advances in purification and reassembly have facilitated the ultrastructural analysis of the assembled layers and paved the way for nano- and biotechnological applications (*2*, *5*).

The crystalline nanostructure of the S-layer gives rise to protein surface sites that repeat regularly in two dimensions over the structure assembled onto an interface. The arrays of protein reactive sites provided by surfaces of assembled S-layer proteins have been used for the conjugation of antibodies, vaccine adjuvants, and other molecules. Thus, the proteins produce a very high-density array of displayed molecules that retain the underlying regular spacing of the S-layer (*2*, *9*). A recent major advance involved the successful construction of S-layer fusion proteins containing antibody fragments and streptavidin monomers that have been assembled onto surfaces (*12*, *13*). In previous studies involving surface chemical modification, the conjugation was carried out by first assembling the S-layer and then conjugating a single moiety (*9*).

In contrast, the aim of the research described here is to first build individual bioconjugates of various functionalities tethered by highly hydrophilic poly(ethylene glycol) (PEG) linkers and then assemble them in a modular fashion onto surfaces. The driving force for self-assembly is provided by the S-layer protein, and, in essence, the S-layer proteins serve as headgroups in molecules designed to form self-assembled monolayers (SAMs). The PEG tethers are included so as to provide

10.1021/bc034204r CCC: $27.50 © 2004 American Chemical Society
Published on Web 07/03/2004

passivation from nonspecific protein adsorption (*14*−*17*). The important aspect of SAM formation by this method is that a new route to form surfaces of controlled surface density that contain mixtures of displayed functional groups is envisioned. As this system is built upon the nanometer spacing of the S-layer, larger molecules such as polymers are displayed in adjacent lattice sites with imposed separation. This spacing imparts two major favorable characteristics to such self-assembled monolayers. First, phase separation during assembly of mixed monolayers would be suppressed, leading to uniform surface distributions of displayed molecules of disparate sizes or functionalities (*18*−*20*). Second, the intrinsic separation between neighboring endgroups would curb steric hindrance of molecular recognition and block interendgroup interactions that could result in aggregation and loss of functional activity. The overall consequence would be the placement of more active and accessible endgroup molecules per unit area, leading to optimized molecular recognition at interfaces and increased miniaturization and complexity of the resulting molecular array.

This paper provides a detailed description of the synthesis and characterization of S-layer protein bioconjugates, spanning from small molecule probes to biotinylated polymers. Reversed-phase high performance chromatography/mass spectrometry (RP-HPLC-MS) and polyacrylamide gel electrophoresis (SDS−PAGE) were used to obtain bioconjugation reaction yields. Gel filtration and monomeric avidin affinity chromatography was used to purify the bioconjugates. S-Layer bioconjugates were assembled onto amine-terminated polystyrene beads, and ligand display and surface distribution were studied using epi-fluorescence, confocal, and electron microscopy.

MATERIALS AND METHODS

Materials. S-Layer proteins (SLP) were extracted from the surface of the bacteria *Lactobacillus brevis* ATCC 8287 that were purchased from ATCC, Manassas, VA. Biotin-PEG_{3400}-*N*-hydroxysuccinimide (Bio-PEG-NHS), fluorescein-PEG_{2000}-*N*-hydroxysuccinimide (Fl-PEG-NHS), and vinyl sulfone-PEG_{3400}-*N*-hydroxysuccinimide (VS-PEG-NHS) were purchased from Shearwater Polymers (Huntsville, AL). Fluoroscein isothiocyanate (FITC) was obtained from Sigma, St. Louis, MO. BODIPY 558/568-*N*-hydroxysuccinimide (Bodipy558), D(+)-biotin, and NeutrAvidin-coated TransFluoSpheres fluorescent nanospheres (100 nm nominal size; 488 nm excitation/605 nm emission) were obtained from Molecular Probes, Eugene, OR. Monomeric avidin affinity column gels and Sephadex G-50 and G-25 gel supports were purchased from Sigma, St. Louis, MO. Biotin-*N*-hydroxysuccinimide (Bio-NHS) and BS^3 (bis(sulfosuccinimidyl) suberate) were obtained from Pierce Chemical, Rockford, IL. All other chemicals used to make buffers were purchased from Sigma except for glycine (BioRad Laboratories, Hercules, CA). The regenerated cellulose dialysis tubing used during purification was purchased from Fisher Scientific (nominal molecular weight cut off between 12 000 and 14 000).

S-Layer Protein Purification. The bacteria (*L. brevis* ATCC 8287) were grown unstirred in MRS broth (Difco Laboratories, Sparks, MD) at 37 °C for 2 days after inoculation with 3% (v/v) 2 day culture. The extraction and purification steps are similar to that performed by Lortal and co-workers (*21*). Exponential-phase cells were recovered by centrifugation at 14 000*g* for 20 min. The cell pellets were resuspended in distilled water to wash the remaining broth and centrifuged again at 14 000 g for 20 min. After two such wash cycles, 10−15 mg of moist pellet was suspended per milliliter of 5 M lithium chloride (LiCl) (Sigma) and incubated for 30 min at 4 °C to extract the S-layer protein. The extract was then centrifuged at 14 000*g* for 20 min, and the supernatant was designated as crude extract.

The crude extract was purified using a gel filtration chromatography column, 2.5 × 50 cm, with a uniform packing of Sephacryl S200 HR (Sigma) gel, equilibrated with 5 M LiCl. The protein was eluted at 30 mL/h, and 1.5 mL fractions were collected. In some runs, the crude extract was concentrated prior to injection into the column. They were concentrated 10-fold using Millipore Ultrafree-15 centrifugal filter device (Sigma) having a 30 kDa cut off. The device was first washed for 10 min with deionized water, and then the protein was added (in 5 M LiCl solution) and spin-filtered at 4000*g* until the final concentration was reached. In some other runs, the protein was first dialyzed against water overnight, and the assembled protein was resuspended in 5 M LiCl before injection.

Construction of Bioconjugate Modules. Purified protein suspended in 5 M LiCl was dialyzed overnight against water. The assembled proteins were dissolved separately in 50 mM sodium phosphate buffers at pH 6.5 to obtain a final protein concentration of 5−10 mg/mL. The probes were then dissolved in deionized water and immediately added to the protein solution for conjugation. All reactions were carried out at 4 °C in darkness, in a flask shaker. Twenty-fold molar excess of small molecule probes (FITC, Bodipy558, and Bio-NHS) and 10 molar fold excess of Fl-PEG-NHS, Bio-PEG-NHS, and VS-PEG-NHS were used for conjugation, with 24 and 12 h reaction times, respectively. The reactions were terminated with 150 mM hydroxylamine (Sigma) at pH 7. Unreacted probes were removed by gel filtration either through Sephadex G-25 (Sigma) (small molecule probes) or Sephadex G-50 (PEG-tethered probes) gravity columns that have been equilibrated with 50 mM, pH 6.5 sodium phosphate buffer. The gels were hydrated for 1 h and 3 h, respectively, and decanted for any floating particles prior to loading. The S-layer protein small molecule probe conjugates were analyzed with HPLC in tandem with mass spectrometry (HPLC-MS) to identify their respective yields. PEGylated S-layer protein yields were obtained from gel desitomograms of 4−15% Tris SDS−PAGE (Bio-Rad Laboratories, Hercules CA) runs carried out in a minigel apparatus with Coomassie protein staining. Gel densitomograms were obtained using a 16 bit Umax flatbed scanner, with image processing carried out using Igor Pro 4.0.

Monomeric Avidin Affinity Column Purification. To separate the biotinylated conjugates from the unlabeled S-layer protein, we used affinity columns containing monomeric avidin. These columns selectively retain the biotinylated proteins during disassembly process or 5 M LiCl wash. The required biotinylated and fluorescently labeled protein monomers were eluted with free biotin buffer (50 mM sodium phosphate, 150 mM sodium chloride containing 1 mg/mL D(+)-biotin).

The affinity gels after packing were washed with four column volumes of 50 mM sodium phosphate with 1 mg/mL of D-biotin, pH 7. Subsequently, the columns were washed with 8 to 10 volumes of 100 mM glycine·HCl, pH 2, to displace biotin from exchangeable sites. The resins were then reequilibrated with 50 mM sodium phosphate, 150 mM sodium chloride, pH 7, prior to sample injection. Samples of volume approximately 10% the column volume were injected to saturate the resin. The resins were

mildly agitated once to ensure proper mixing of the contents and incubated in dark for 30 min. The buffer was then replaced with 5 M LiCl, and the resin was again incubated in dark for 1 h to facilitate complete disassembly of the S-layer protein multimers. Following the incubation, there was 5 M LiCl wash to remove unlabeled S-layer proteins, followed by a neutral buffer wash and free biotin elution of the conjugates at 15 mL/h flow rate with all the fractions being collected. The affinity-purified biotinylated conjugate is recovered during the free biotin buffer elution (50 mM sodium phosphate with 1 mg/mL of D-biotin, pH 7). All the peak fractions were pooled and collected for further analysis.

Microsphere Surface Assembly Experiments. Purified S-layer bioconjugates were assembled onto amine-terminated polystyrene microspheres (6 μm nominal size; Polysciences, Inc, Warrington, PA) using the following procedure. Purified S-layer bioconjugates at 2 mg/mL concentration were centrifuged at 14 000*g* to remove assembled fragments. The resulting supernatant containing disassembled S-layer conjugates and unlabeled S-layer protein was used in surface assembly. To conduct modular self-assembly, desired proportions of individual conjugates were mixed and added to amine-terminated S-layers in large excess to total surface area. The self-assembly was conducted at pH 8 in phosphate buffer for 24 h at 4 °C. Subsequently, the assembly solution was removed by 50*g* centrifugation-induced settling of the microspheres. The microspheres were then gently washed with pH 8 buffer to remove any remaining unassembled protein, and then the amine-reactive homobifunctional cross-linker BS^3 was added at a concentration of 10 mM for a 30-min reaction in 50 mM sodium phosphate buffer, pH 8 at 4 °C. The cross-linking reaction was quenched with hydroxylamine (150 mM), followed by a washing step with pH 8 buffer to remove any remaining deactivated BS^3. At this stage the microspheres assembled with biotin-PEG_{3400}−S-layer conjugates were incubated overnight with and excess of NeutrAvidin-coated TransFluoSpheres fluorescent nanospheres at 4 °C, followed by washing with pH 8 buffer to remove any excess unbound nanospheres.

Mass Spectrometry. S-Layer protein samples and their small fluorophore bioconjugates were analyzed using reversed-phase HPLC (C-18 column) in line with an electrospray ionization mass spectrometer. The studies were carried out using an HPLC-ESI-MS Agilent Chem Station at the Hunter College of the City University of New York Mass Spectrometry facility. The samples were prepared to give an average protein content of 10−15 μg in a 10% acetic acid solution. The samples injected into the C18 column of the HPLC-MS were eluted at the rate of 0.5 mL/min with a gradient flow of acetonitrile.

Confocal, Epi-Fluorescence, and Electron Microscopy. Samples were imaged using a Leica TCS-SP four channel confocal microscope at the Mt. Sinai School of Medicine, using 488 nm excitation for fluorescein and 568 nm for the TransFluoSpheres fluorescent nanospheres. The transmitted light channel was used to position the imaging plane at the center of the microspheres. Epi-fluorescence microscopy was conducted using a Nikon TE300 inverted microscope with B-2A and G-2E/C filter cubes for fluorescein and TransFluoSpheres fluorescent nanospheres, respectively. Samples for scanning electron microscopy were dried, sputter-coated with gold, and observed with a JEOL 35 scanning electron microscope at the Mt. Sinai School of Medicine. Image analysis, including fluorescence emission intensity profiling, was accomplished with IgorPro 4.0 and NIH Image 1.63.

RESULTS AND DISCUSSION

Purification of *Lactobacillus brevis* S-Layer Protein. Surface layer proteins range in size from 40 to 200 kDa, depending on the species of origin. Our rationale for the choice of the smaller *Lactobacillus* variant S-layer protein for these studies was based on suitability for facile characterization by both mass spectrometry and eventually high-resolution solid-state NMR. The *Lactobacillus brevis* S-layer protein was obtained at yield of greater than 100 mg/L of microaerobic culture in MRS broth. At these high yields a 10 g pellet of the bacterial cells will conservatively yield ∼0.5 g of S-layer protein. The protein purification was monitored using SDS−PAGE, shown in Figure 1A. The S-layer protein crude extract is run through two cycles of (1) dialysis (assembly: 30 kDa Mw cutoff), (2) 5 M LiCl disassembly, and (3) dialysis once again to bring the purity up to >50%, shown in Figure 1, Lane 2. Three main impurities remain with estimated molecular weights of 23, 27, and 35 kDa. Gel permeation chromatography was used to isolate the *L. brevis* S layer protein with a final purity of >95%, shown in Lane 3. The target protein for the bioconjugation studies was first cloned and sequenced by Vidgren and Palva (*22*). Their nucleic acid sequence analysis revealed a 465 residue open reading frame with a capacity to encode a 48 159 Da protein. This sequence contains a 30 residue signal peptide common to Gram-positive species. Analysis of the purified protein with reversed-phase HPLC electrospray mass spectrometry (RP-HPLC-MS) gave a molecular weight of 45 238 Da. The molecular mass of the *L. brevis* S-layer protein corresponds to the 465 residue open reading frame with the 30 residue signal peptide removed, resulting in a 435 residue protein. This purified S-layer protein is the starting material for the bioconjugation studies outlined below.

Construction of *Lactobacillus brevis* S-Layer Protein Bioconjugates. The goal of this work was to produce functional S-layer bioconjugates by tethering molecules of various sizes while retaining the self-assembly "activity" of the S-layer protein. As this protein contains no cysteines and many (over 30 each) primary amines, carboxylates, and hydroxyls, when using standard coupling strategies, the challenge is to limit multiple labeling. To achieve this outcome, we have used amine-based coupling chemistry, targeting the α-amino group of the amine terminus by running the coupling reaction at below neutral pH to suppress ϵ-amino lysine reactivity. An additional, S-layer specific consideration in the conjugation is the multimeric state of the protein. In these studies the S-layer protein is undergoing the bioconjugation reaction in the assembled form. Thus, the majority of the protein is assembled into multimeric sheet structures with up to micron length scales (as evidenced by visual light scattering and fluorescence microscopy; data not shown). In this state, the larger multimers in the solid state are in dynamic equilibrum with a soluble form of the protein, likely composed of monomers or smaller multimers. Conjugation in the assembled form is dictated by the fact that the fully disassembled or soluble form of the protein is obtained only at high concentrations of LiCl or guanidine hydrochloride, solution conditions incompatible with bioconjugation reactions. An inherent advantage is that reactive sites left exposed when the protein is in the assembled form will most likely lead to conjugates that retain the ability to self-assemble.

To initiate the studies and probe the reactivity of the S-layer protein amines at lower pH, we have employed number of amine-reactive labels for bioconjugation, rang-

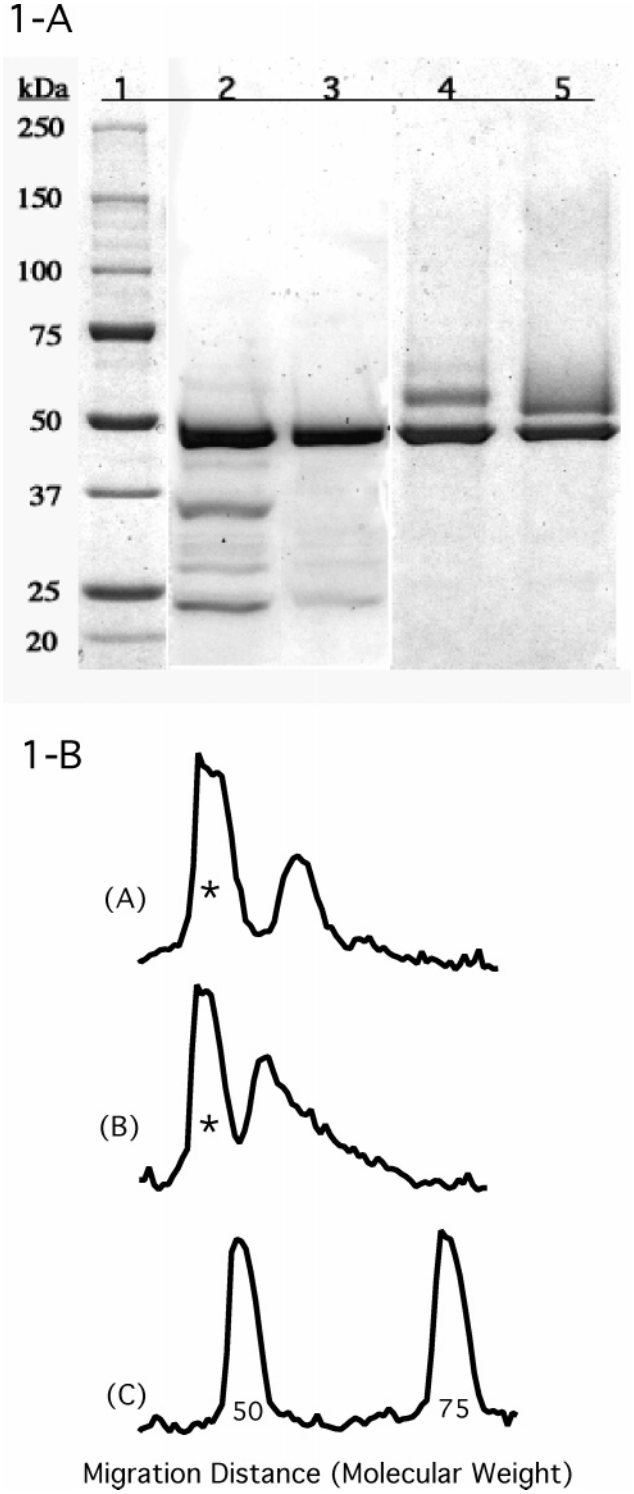


Figure 1. Gel electrophoresis results for the purification of *L. Brevis* S-layer protein and synthesis of poly(ethylene glycol)-based bioconjugates (SDS−PAGE 4−15% Gel). Lane 1 is from the molecular weight markers. Lane 2 is from proteins extracted from the surface of the cells after two cycles of: (1) dialysis (30 kDa Mw cutoff), (2) washing, (3) 5 M LiCl disassembly followed by concentration to give 10 mg/mL. Lane 3 is after prep-scale gel permeation chromatography using sephacryl SH-200 as the support. Lanes 4 and 5 were obtained after conjugation of vinyl sulfone-PEG_{3400} and fluorescein-PEG_{2000}, respectively. The bottom figure shows gel densitomograms of lanes 4 and 5 in traces A and B, respectively, zoomed into the relevant molecular weight range.

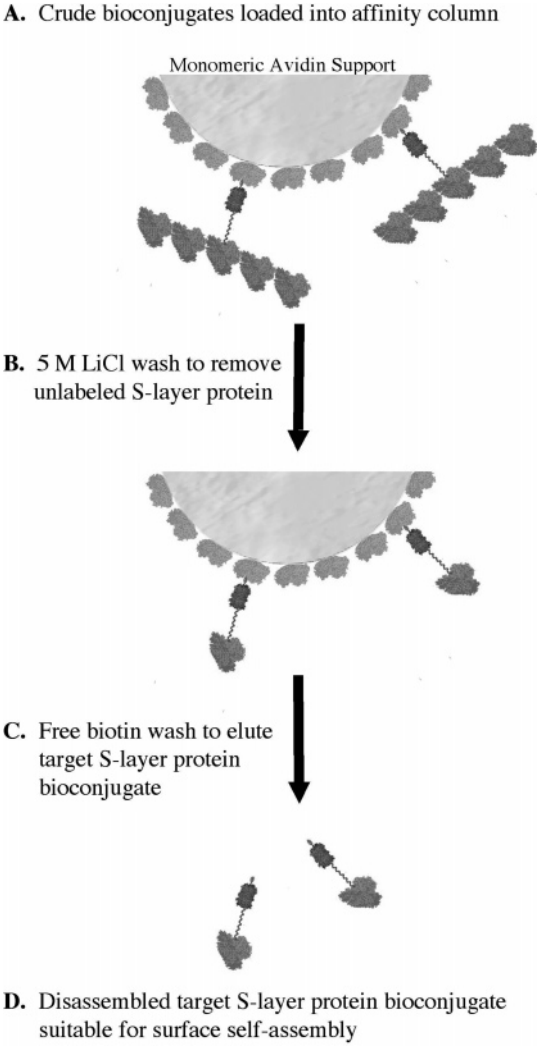
ing from fluorescent probes to polymers. RP-HPLC-MS was used to calculate the yields for the fluorescent probes; for the polymer conjugates, SDS−PAGE densitometry was employed. After exploring a range of conditions in preliminary bioconjugation studies, we converged upon two sets of conditions for low molecular weight probes and polymers. The results of bioconjugation at these two sets of conditions are tabulated in Table 1. In general, the reactions were conducted at S-layer protein concentrations of greater than 5 mg/mL with 20-fold and 10-fold molar excess of reactant for low molecular weight probes and polymers, respectively. However, presumably only low levels of reactive *N*-hydroxysucccinimate and isothiocyanate moieties remained at these 12−24 h long reaction times. For all cases, the yields of singly labeled bioconjugates ranged 24−39%. In all cases except for the FITC coupling, doubly labeled species were obtained, with yields ranging from 4 to 16%. While formed in substantial amounts, these multiply labeled bioconjugates are not expected to limit the applicability of the method as long as self-assembly activity is maintained. For the polymer bioconjugates, the yield of the reactions was estimated from gel densitomograms, shown in Figure 1B. Trace A, obtained from the vinyl sulfone-PEG_{3400}−SLP bioconjugates, contains the unlabeled protein (denoted with an asterisk) and two peaks of successively smaller areas from the bioconjugates. The peaks are Gaussian in line shape, leading to straightforward peak fitting to calculate the yields. For the case of the fluorescein-PEG_{2000}−SLP bioconjugate, the peak resulting from the conjugates is more complex and complicated by the fact that the migration in the gel is less for the smaller polymer bioconjugate (2000 vs 3400 Da for the vinyl sulfone-PEG) (*23*).

To limit the yield of multiply labeled species, we have conducted the conjugation at pH 6.5 in order to protonate the ϵ-amino groups of surface lysines and thus lower their reactivity. One consequence of this reaction condition is that the majority of the protein remains unlabeled and thus must be separated from the conjugates. In the more common conjugation scenario where multiple labeling is desired, repeated cycles of labeling are carried out to increase the yield. However, in this case this strategy is expected to give unwanted higher levels of multiple site labeling that could potentially affect self-assembly. Since the conjugation is conducted while the S-layer protein is in the multimeric assembled form, this provides an added purification obstacle. The conjugated proteins are likely to be present in multimeric structures and surrounded by unreacted protein monomers. The logical separation strategy would be to disassemble and purify; however, the conditions for disassembly are expected to have deleterious effects on the conjugated target protein or group. For the case of the poly(ethylene glycol) conjugates, our observation is that precipitation or "salting out" occurs at levels of LiCl necessary for disassembly. To explore a means for obtaining high purity S-layer protein bioconjugates, we have employed avidin affinity chromatography, in which the specific binding of biotin ligands to the protein avidin is used to bind the target biotinylated bioconjugate to the column via the formation of an high-affinity ligand−protein complex ($K_D \approx 10^{-15}$ M). The monomeric avidin support was selected over tetrameric avidin as the conditions for retrieving the final product are milder and higher yields can be obtained. The method we have employed is shown schematically in Scheme 1. In the first step, crude S-layer bioconjugates are loaded onto the support. As shown in panel A, the conjugates bind to the column via biotins on the surface of target protein (or polymer). This is followed by a washing step to remove the unlabeled S-layer protein

Table 1. Types and Yields of S-Layer Protein Bioconjugates Constructed

reactant	characteristics	probe to target molar ratio	reaction time, h	% yield (pH 6.5) single label	% yield (pH 6.5) double label
fluorophores/probes (<1 kDa)					
fluorescein isothiocyanate	emission 518 nm (green)	20:1	12	29	ND
BODIPY 558/568-*N*-hydroxysuccinimide	emission 568 nm (red)	20:1	12	30	16
biotin-*N*-hydroxysuccinimide	ligand	20:1	12	37	8
polymers (<5 kDa)					
fluorescein-PEG2000-NHS	surface passivation em. 518 nm	10:1	24	39	16
biotin-PEG3400-NHS	surface passivation/ligand	10:1	24	24	8
vinyl sulfone-PEG3400-NHS	surface passivation/R−SH coupling	10:1	24	34	4

Scheme 1. Affinity Purification of S-Layer Protein Bioconjugates[a]



[a] To remove the unlabeled S-layer proteins, monomeric avidin supports were used to bind the biotinylated conjugates, followed by elution of the unlabeled proteins in 5 M LiCl disassembly solution. For fragile tethered functionalities, an extended buffer wash is used to remove the unlabeled S-layer protein. To obtain the purified conjugates, a free biotin (1 mg/mL) elution step is employed

(panel B). In the case where the conjugated group is robust under conditions of high salt, a 5 M LiCl wash is used to disassemble and remove the unlabeled S-layer protein. In other cases an extended washing with pH 7 phosphate buffer is employed. As the assembled, unlabeled proteins are in exchange with the soluble form, over longer elution times the unlabeled proteins will be removed, leaving behind the biotinylated conjugates. In addition, conjugates formed from the PEG labels without biotin, ~20% of the activated PEG reactant, are also

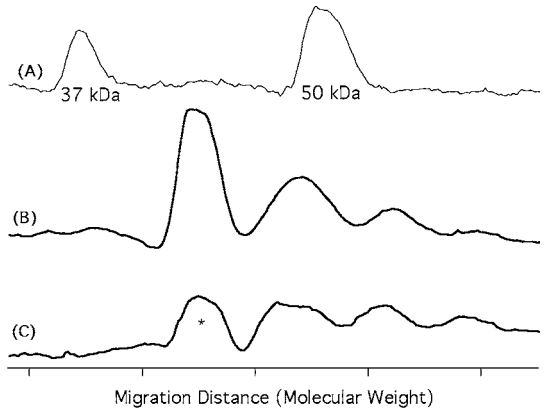


Figure 2. Gel densitometry results for biotin PEG_{2000} S-layer protein bioconjugate purified via monomeric avidin affinity chromatography. Trace A is the molecular weight marker. Trace B is from the unpurified biotin-PEG_{2000}−S-layer protein bioconjugate. Trace C was obtained after monomeric affinity purification (Scheme 2) of the biotin-PEG_{2000}−S-layer protein bioconjugate (trace B was the starting material for the purification).

removed during this step. In the final step the purified bioconjugates are eluted from the support with a free biotin wash. The amount of protein eluted can be adjusted by varying the amount of loaded affinity support bead volume. This protocol provides a precise means of controlling the concentration of S-layer bioconjugates used for assembling surfaces in a modular fashion.

Figure 2 displays the results of the monomeric avidin affinity chromatography conducted on the biotin PEG_{3400} S-layer protein bioconjugate, displayed as SDS−PAGE densitomograms. Trace A was obtained from the molecular weight marker, trace B is from the biotin-PEG_{3400}−S-layer protein bioconjugate, the starting material. The affinity purified conjugate is shown in trace C, eluted from the column with a free biotin wash. Comparison of traces B and C shows a dramatic decrease in the unlabeled S-layer protein, labeled with an asterisk (*); peak analysis gives an approximate 50% decrease in unlabeled S-layer protein. We also obtain higher yields of the multiply biotinylated S-layer proteins since they bind to the monomeric avidin support with higher efficiency.

Surface Assembly of S-Layer Protein Bioconjugates. Thus far we have produced sets of S-layer bioconjugates with PEG tethers for modular assembly onto surfaces; the following section details surface self-assembly. It has been previously established that S-layers from Gram-positive microorganisms assemble in vitro onto surfaces that are positively charged (*2*, *6*, *21*, *24*). Thus, we have conducted assembly experiments using 6 μm amine-terminated polystyrene beads as the assembly substrate. Figure 3, panel 3-A, displays a confocal image of the S-layer−PEG_{2000}−fluorescein bioconjugate assembled onto a 6 μm amine-terminated polystyrene bead, taken as 2D XY slice through the center of the bead. The

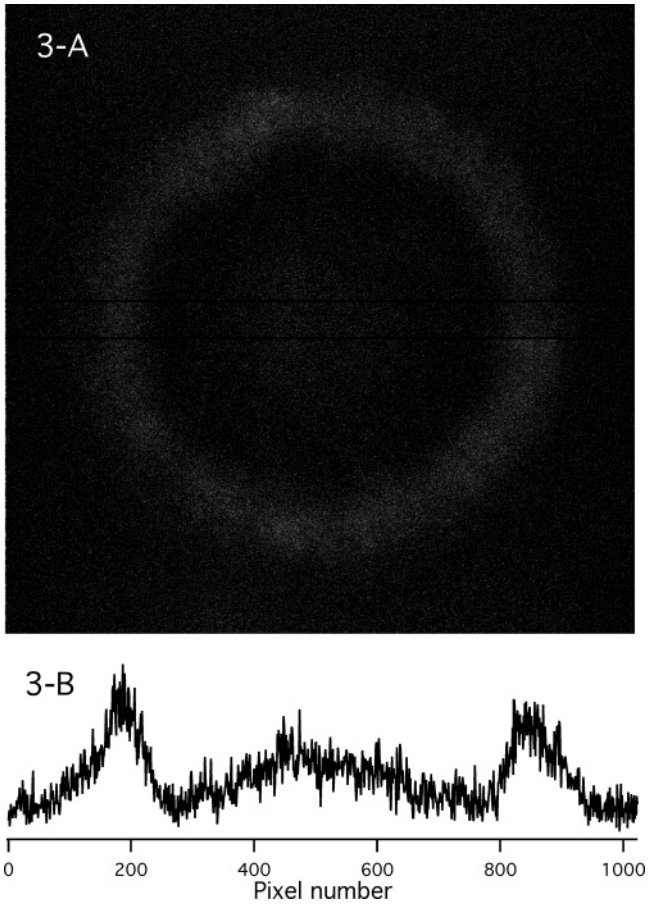


Figure 3. Confocal micrograph of S-layer−PEG_{2000}−fluorescein bioconjugate assembled onto a 6 μm amine-terminated polystyrene microsphere. The top panel (3-A) was obtained from the XY plane that intersects center of the bead. The fluorescence emission intensity profile shown in panel 3-B was obtained from image analysis inside the area bounded by the horizontal lines in 3-A.

light area exhibited symmetrically around the particle is the emission of green (515 nm) fluorescence that has been converted to gray scale in the image. The bottom panel 3-B shows the fluorescence emission intensity profile taken through the center of the image, highlighting the annular distribution of fluorescence intensity arising from the conjugate assembled at the membrane surface. As can be seen from inspection of this image, fluorescence intensity profiles obtained from other angles relative to horizontal gave similar results. This image provides direct evidence that the fluorescence is emitted evenly over this microsphere within the resolution of this image. In other microspheres in the sample a similar even surface distribution was seen (data not shown). This confocal data is consistent with complete coverage of the microspheres with a surface layer of S-layer proteins and S-layer−PEG_{2000}-fluorescein bioconjugates. We note that before the microsphere self-assembly stage the NHS-PEG_{2000}-fluorescein reactant has been carefully removed via gel filtration to preclude nonspecific adsorption artifacts. Furthermore, the highly hydrophilic nature of the polymer retards adsorption of any residual reactant.

As a test system for the assessment of the display capabilities of our S-layer bioconjugates, we have used biotin, in this case, specifically biotin tethered to the S-layer proteins via PEG_{3400} linkages. To detect the surface display of tethered biotin positioned on the surface resulting from modular self-assembly of the S-layer protein conjugates, 100 nm sized avidin-coated,

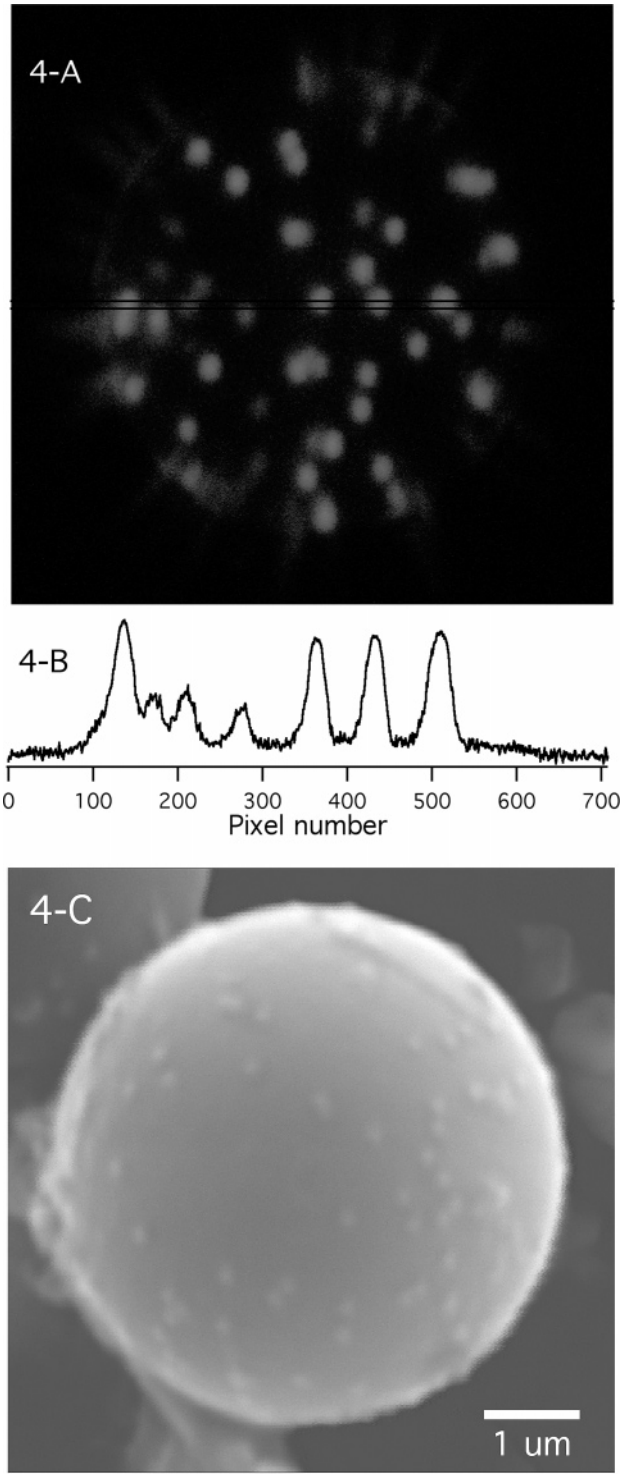


Figure 4. Confocal micrograph of monomeric avidin affinity purified S-layer−PEG_{3400}-biotin bioconjugate assembled onto a 6 μm amine-terminated polystyrene microsphere, followed by biotin−avidin complex formation with 100 nm avidin-coated nanospheres. The top panel, 4-A, was obtained from averaging over 20 XY sections. The fluorescence emission intensity profile shown in panel 4-B was obtained from image analysis inside the area bounded by the horizontal lines in 4-A. The relative intensities of the nanospheres were affected somewhat by photobleaching and scattering artifacts; however, this did not preclude accurate measurements of nanosphere binding. Panel 4-C is a scanning electron micrograph taken of a microsphere from the same sample that was sputter-coated with gold.

fluorescent nanospheres (nanospheres) were used. Figure 4 shows the results obtained from the self-assembly of avidin-affinity purified S-layer−PEG_{3400}-biotin conjugates

onto 6 μm amine-terminated polystyrene beads. Panel 4-A was obtained from the average of confocal images taken as 2D slices in the XY plane, detecting the red fluorescence emission of the nanospheres (here shown in gray scale as dots). This image gives the localization of nanospheres over the entire surface of the larger microsphere. The nanospheres appear to be evenly distributed, thus the PEGylated and unlabeled S-layer proteins are not assembled onto the surface in separate domains (i.e. phase separation in SAM research). The middle graph (Panel 4-B) shows the image line profile taken through a section of the image as indicated, highlighting, in this case, the nanospheres. As expected, at the edges of the microsphere no peak in fluorescence emission intensity is evidenced; even intensity that potentially originates from the scattering of emitted light of the highly fluorescent nanospheres is absent (as is often seen in epi-fluorescence images). To further assess the surface features of the biotin-PEG_{3400}−S-layer bioconjugates assembled on the microspheres, scanning electron micrographs (SEM) were obtained from the same samples (Panels 4-A, 4-B) that were sputter-coated with a thin layer of gold atoms. An SEM image of a microsphere with avidin-affinity purified S-layer−PEG_{3400}-biotin conjugates assembled on the surface is shown in Panel 4-C (prepared from the same sample from Panel 4-A). Over the predominantly smooth surface of the microsphere (at >50 nm resolution) faint yet evident bump-like features are seen from the avidin nanospheres bound to surface-displayed biotin. At this resolution level it appears that the microspheres are completely covered with an even monolayer of assembled S-layer bioconjugates. Furthermore, there is no evidence for multiple layers or for uneven coverage over the surface. Thus far we have produced sets of S-layer bioconjugates with PEG tethers for modular self-assembly onto surfaces.

Our work provides a new route for the formation of surfaces that contain homogeneous displays of mixtures of molecular functionalities. To first demonstrate the concept, we have performed modular self-assembly of S-layer−PEG_{3400}-biotin and S-layer−PEG_{2000}−fluorescein onto 6 μm amine-terminated polystyrene beads. Figure 5, panel A, shows a confocal microscopy image in which both the green (fluorescein) and red (nanosphere) fluorescence emission from multiple 2D confocal XY planes were averaged into a single image and converted to gray scale. The nanospheres are seen as prominent gray dots, and the fluorescein conjugate emission is seen as the background microsphere fluorescence with a peak in emission intensity distributed around the rim of the microsphere. This is emphasized by the emission intensity profile in which the features from the nanosphere are seen as sharp peaks bounded on each side by smaller peaks at the edge of the microsphere. In this image, in contrast to Figure 3, panel 3-B, the fluorescein emission intensity is also substantial in the middle of the image line profile of the microsphere as this is an average over multiple 2D confocal slices over the whole microsphere. Upon inspection of the Figure 5 confocal image, it is apparent that the modular self-assembly resulted in a relatively sparse yet homogeneous surface, as no evidence of phase separation was seen. This is to be expected, as the tether differences in the two conjugates are slight (77 vs 45); studies involving more disparate endgroups are in progress.

It is evident from comparison of the avidin nanosphere coverage in Figures 4A and 5A that differences in the assembly conditions in terms of the starting concentration of S-layer−PEG_{3400}-biotin conjugates led to markedly disparate surface displays of biotin. To further examine

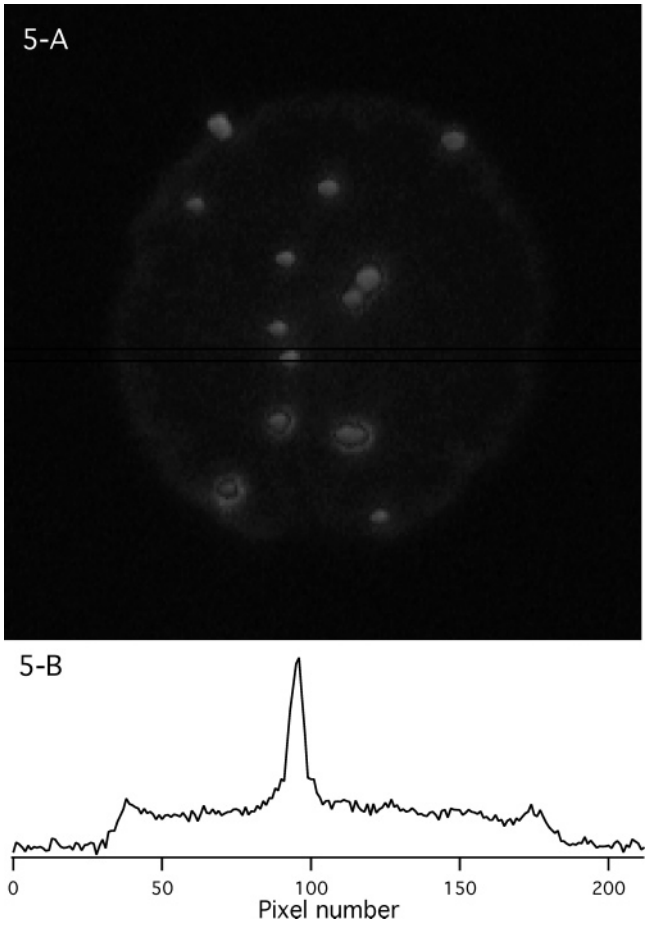


Figure 5. Confocal micrograph of S-layer−PEG_{2000}−fluorescein and S-layer−PEG_{3400}-biotin bioconjugates coassembled onto a 6 μm amine-terminated polystyrene microsphere from a 1:1 mixture, followed by biotin−avidin complex formation with 100 nm avidin-coated nanospheres. The top panel, 4-A, was obtained from averaging over 20 XY sections. The fluorescence emission intensity profile shown in panel 5-B was obtained from image analysis inside the area bounded by the horizontal lines in 5-A.

this difference, the average number of nanospheres bound per microsphere was determined using epi-fluorescence microscopy. Figure 6 shows comparative results of average surface coverage obtained from four samples (20 microspheres averaged): (A) control amine-terminated polystyrene microspheres, (B) microspheres formed from S-layer−PEG_{2000}−fluorescein conjugates, (C) microspheres formed from the modular assembly of S-layer−PEG_{2000}−fluorescein and S-layer−PEG_{3400}-biotin conjugates and (D) microspheres formed from affinity-purified S-layer−PEG_{3400}-biotin conjugates. In the control samples that did not contain biotin, nonspecific adsorption of nanospheres was observed at low levels (A and B). Specifically for the S-layer−PEG_{2000}−fluorescein sample (B), the presence of polymer endgroups gave rise to significant suppression of this nonspecific adsorption of avidin-coated nanospheres. Studies to further examine this suggested inhibition of nonspecific protein adsorption by displayed polymer endgroups are underway.

When biotin-PEG_{3400}−S-Layer conjugates are assembled onto microsphere surfaces, greater numbers of nanospheres bind to the microspheres due to the formation of avidin-biotin complexes. This is shown in the average surface coverage results for C and D of Figure 6, acquired from the samples that were used to obtain the confocal images in Figures 5A and 4A, respectively. As these samples were prepared at different times, only

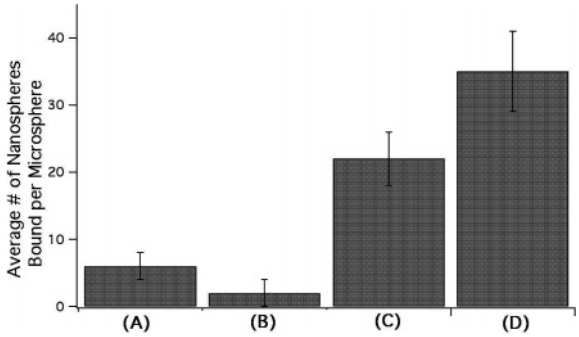


Figure 6. Average number of nanospheres bound per microsphere obtained from epi-fluorescence microscopy. Each data point was derived from the average of 20 microspheres, with error bars set from approximately the full width half-maximum of histograms from the data. Data from experimental controls (without biotin) are shown in sample A, amine-terminated microspheres, and sample B, from assembly of S-layer−PEG_{2000}−fluorescein conjugates onto 6 μm amine-terminated polystyrene microspheres. Sample C was obtained from a 1:1 mixture of S-layer−PEG_{2000}−fluorescein and S-layer−PEG_{3400}-biotin bioconjugates coassembled onto 6 μm amine-terminated polystyrene microspheres. Sample D was obtained from monomeric avidin affinity purified S-layer−PEG_{3400}-biotin bioconjugates assembled onto 6 μm amine-terminated polystyrene microspheres.

qualitative comparison of the nanosphere binding is intended here. However, an important trend is apparent in that the surface density of displayed biotin can be manipulated by increasing the starting concentration of biotin-PEG_{3400}−S-layer conjugates in the surface assembly. In these samples the levels of nanosphere coverage obtained from biotin-PEG_{3400}−S-layer conjugates are far below that of complete coverage based on surface geometry arguments, approximately <1−5% of total coverage. We are currently conducting the assembly using high purity S-layer bioconjugates to fully exploit the methodology. At the purity levels used in these studies, the surface assembly and coverage is dominated by unlabeled S-layer protein monomers. These were present at higher concentrations and in addition are likely to have faster assembly kinetics than the polymer conjugates. We are currently investigating these effects in detailed studies of S-layer bioconjugate assembly kinetics.

CONCLUSIONS

The construction of assembly competent S-layer bioconjugates was described, based on the conjugation of small molecule and poly(ethylene glycol)-based probes to the S-layer protein from *L. brevis*. The purification of the S-layer protein was accomplished using successive cycles of assembly/disassembly followed by gel permeation chromatography, allowing for the production of copious amounts of starting material for the conjugation. Limited conjugation yields were obtained via pH 6.5 reaction conditions; however SDS−PAGE gel densitometry results provided evidence for predominantly single site labeling as was desired. To provide a route to obtain high purity conjugates free of unlabeled protein, avidin affinity chromatography was employed, leading to a method to control surface assembly conditions and a means for potential scale-up.

The S-layer bioconjugates were assembled onto amine-terminated polystyrene beads to probe surface self-assembly. The surface coverage of polymer conjugates was found to be homogeneous in nature, with no evidence of phase separation of polymer-conjugated S-layer with unlabeled S-layer on the surfaces as assessed using fluorescence and electron microscopy. A reduction in nonspecific binding of avidin-coated nanospheres was obtained with polymer endgroups displayed via S-layer−PEG_{2000}−fluorescein bioconjugates assembled on the microspheres. Modular surface assembly was achieved using S-layer−PEG_{2000}−fluorescein and S-layer−PEG_{3400}-biotin conjugates, also resulting in homogeneous coverage and no detectable phase separation. With this approach, we have also shown that the surface densities of mixed displays can be controlled by changing the relative bulk concentrations of S-layer bioconjugate self-assembly suspensions.

A significant feature of this method is that the mixed monolayers formed would retain the underlying natural nanostructure of the S-layer array. Thus, the spacing of the functional endgroups will be dictated by the underlying S-layer protein matrix. Another potential significant feature of our method is that self-assembled monolayers could be formed using monomer units with larger functional endgroups than is possible with current technologies, such as for example, proteins, polymers, or nanoparticles. This potential benefit stems from the fact that the headgroup protein size is substantially larger than most functional endgroups and the highly stable S-layer structure is energetically favored due to protein−protein and protein−substrate interactions. This could significantly advance self-assembled monolayer technology, providing a new route for the display of intact proteins and other large molecules at an interface.

ACKNOWLEDGMENT

Financial support for this project from the Army Research Office is gratefully acknowledged (45349-LS-HSI), through the Department of Defense Hispanic Serving Institutions Research and Instrumentation Program. Cliff Soll of the Hunter College Chemistry Department contributed crucial guidance and mass spectrometry expertise. We acknowledge Norman Katz and Ron Gordon for their patience and electron microscopy expertise. Confocal and electron microscopy were performed at the Mt. Sinai Medical School−Microscopy Shared Research Facility, supported, in part, with funding from NIH-NCI shared resources grant (1 R24 CA095823-01).

LITERATURE CITED

(1) Sara, M., and Sleytr, U. B. (2000) S.-Layer proteins. *J. Bacteriol. 182* (4), 859−868.
(2) Sleytr, U. B., Sara, M., Pum, D., and Schuster, B. (2001) Characterization and Use of Crystalline Bacterial Cell Surface Layers. *Progress in Surface Science 68*, 231−278.
(3) Kalmokoff, M. L., Austin, J. W., Whitford, M. F., and Teather, R. M. (2000) Characterization of a major envelope protein from the rumen anaerobe Selenomonas ruminantium OB268 [In Process Citation]. *Can. J. Microbiol. 46* (4), 295−303.
(4) Sleytr, U. B., and Beveridge, T. J. (1999) Bacterial S-layers. *Trends Microbiol. 7* (6), 253−260.
(5) Engelhardt, H., and Peters, J. (1998) Structural research on surface layers: a focus on stability, surface layer homology domains, and surface layer-cell wall interactions. *J. Struct. Biol. 124* (2−3), 276−302.
(6) Sleytr, U. B., and Sara, M. (1997) Bacterial and archaeal S-layer proteins: structure−function relationships and their biotechnological applications. *Trends Biotechnol. 15* (1), 20−26.
(7) Sleytr, U. B., Pum, D., and Sara, M. (1997) Advances in S-layer nanotechnology and biomimetics. *Adv. Biophys. 34*, 71−79.

(8) Sleytr, U. B., Bayley, H., Sara, M., Breitwieser, A., Kupcu, S., Mader, C., Weigert, S., Unger, F. M., Messner, P., Jahn-Schmid, B., Schuster, B., Pum, D., Douglas, K., Clark, N. A., Moore, J. T., Winningham, T. A., Levy, S., Frithsen, I., Pankovc, J., Beale, P., Gillis, H. P., Choutov, D. A., andMartin, K. P. (1997) Applications of S-layers. *FEMS Microbiol. Rev. 20* (1−2), 151−175.

(9) Mader, C., Kupcu, S., Sleytr, U. B., and Sara, M. (2000), S-layer-coated liposomes as a versatile system for entrapping and binding target molecules. *Biochim. Biophys. Acta. 1463* (1), 142−150.

(10) Wetzer, B., Pum, D., and Sleytr, U. B. (1997) S-layer stabilized solid support lipid bilayers. *J. Struct. Biol. 119* (2), 123−128.

(11) Shenton, W., Pum, D., and Sleytr, U. B. (1997) Synthesis of cadmium sulphide superlattices using self-assembled bacterial S-layers. *Nature 389*, 585−587.

(12) Pleschberger, M., Neubauer, A., Egelseer, E. M., Weigert, S., Lindner, B., Sleytr, U. B., Muyldermans, S., and Sara, M. (2003) Generation of a functional monomolecular protein lattice consisting of an s-layer fusion protein comprising the variable domain of a camel heavy chain antibody. *Bioconjugate Chem. 14* (2), 440−448.

(13) Moll, D., Huber, C., Schlegel, B., Pum, D., Sleytr, U. B., and Sara, M. (2002) S-layer-streptavidin fusion proteins as template for nanopatterned molecular arrays. *Proc. Natl. Acad. Sci. U.S.A. 99* (23), 14646−14651.

(14) Jeon, S. I., and Andrade, J. D. (1991) Protein Surface Interactions in the Presence of Poly(ethylene oxide) 0.2. Effect of Protein Size. *J. Colloid Interface Sci. 142* (1), 159−166.

(15) Jeon, S. I., and Andrade, J. D. (1992) The Steric Repulsion Properties of Poly(ethylene oxide). *Bull. Kor. Chem. Soc. 13* (3), 245−248.

(16) Jeon, S. I., Lee, J. H., Andrade, J. D., and Degennes, P. G. (1991) Protein Surface Interactions in the Presence of Poly-(ethylene oxide) 0.1. Simplified Theory. *J. Colloid Interface Sci. 142* (1), 149−158.

(17) Andrade, J. D., Hlady, V., and Jeon, S. I. (1996) Poly-(ethylene oxide) and protein resistance − Principles, problems, and possibilities. *Hydrophilic Polymers*, pp 51−59, Vol. 248.

(18) Folkers, J. P., Laibinis, P. E., Whitesides, G. M., and Deutch, J. (1994) Phase-Behavior of 2-Component Self-Assembled Monolayers of Alkanethiolates On Gold. *J. Phys. Chem. 98* (2), 563−571.

(19) Laibinis, P. E., Nuzzo, R. G., and Whitesides, G. M. (1992) Structure of Monolayers Formed By Coadsorption of 2 Normal- Alkanethiols of Different Chain Lengths On Gold and Its Relation to Wetting. *J. Phys. Chem. 96* (12), 5097−5105.

(20) Shevade, A. V., Zhou, J., Zin, M. T., and Jiang, S. Y. (2001) Phase behavior of mixed self-assembled monolayers of alkanethiols on Au(111): A configurational-bias Monte Carlo simulation study. *Langmuir 17* (24), 7566−7572.

(21) Lortal, S., van Heijenoort, J. V., Gruber, K., and Sleytr, U. B. (1992) S-layer of Lactobacillus helveticus ATCC 12046: isolation, characterization and re-formation after extraction with lithium chloride. *J. Gen. Microbiol. 138*, 611−618.

(22) Vidgren, G., Palva, I., Pakkanen, R., Lounatmaa, K., and Palva, A. (1992) S-layer protein gene of Lactobacillus brevis: cloning by polymerase chain reaction and determination of the nucleotide sequence. *J. Bacteriol. 174* (22), 7419−27.

(23) Dhara, D., and Chatterji, P. R. (1999) Electrophoretic Transport of PEG Chains Thru Polyacrylamide Gel. *J. Phys. Chem. B 103*, 8458−8461.

(24) Masuda, K., and Kawata, T. (1979) Ultrastructure and partial characterization of a regular array in the cell wall of Lactobacillus brevis. *Microbiol Immunol 23* (10), 941−53.

BC034204R

De Novo Design of Peptides with L-α-Nucleobase Amino Acids and Their Binding Properties to the P22 boxB RNA and Its Mutants

Hideo Miyanishi, Tsuyoshi Takahashi,* and Hisakazu Mihara

Department of Bioengineering, Graduate School of Bioscience and Biotechnology, Tokyo Institute of Technology, 4259 Nagatsuta, Yokohama 226-8501, Japan. Received November 12, 2003;
Revised Manuscript Received April 26, 2004

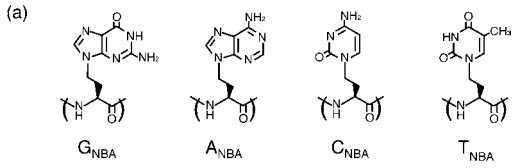
A method to design novel molecules that specifically recognize a structured RNA would be a promising tool for the development of drugs or probes targeting RNA. In this study, the de novo design of the α-helical peptides having L-α-amino acids with nucleobases (nucleobase amino acids, NBAs) was carried out. Binding affinities of the peptides for a hairpin RNA derived from P22 phage were dependent on the types and positions of the NBA units they have. Some NBA peptides bound to the wild-type RNA or its mutant with high affinity and high specificity compared with the native P22 N peptide. These results indicate that the NBA units on the peptides interact with the RNA bases in a specific manner. It is demonstrated that the de novo design of peptides with the NBA units is an effective way to construct novel RNA-binding molecules.

INTRODUCTION

RNA−protein interactions play important roles in organisms. The specific interaction between proteins and RNA regulates many biological functions, including transcription, RNA splicing, translation and so on (*1*). In many cases, RNA-binding proteins recognize a specific site of RNA such as hairpin loops, internal loops, and bulges (*1*). Therefore, construction of the novel molecules that specifically recognize a structured RNA could lead to the development of drug design and specific probes against RNA. However, construction of RNA-binding molecules is difficult compared to that of DNA-binding molecules because of the structural diversity of RNA (*2*).

On the other hand, we utilized artificial amino acids having nucleobases in their side chain (nucleobase amino acids, NBAs) (Figure 1a) for constructing novel functional peptides and proteins (*3*−*5*). It has been reported that the NBA units were incorporated into the designed α-helix peptides and the nucleobase interaction on the peptides can regulate the peptide−peptide recognition effectively (*3*). In the design of RNA-binding molecules, NBAs were studied as building blocks capable of interacting with RNA bases specifically (*4*, *5*). For instance, NBA units were incorporated into the HIV-1 nucleocapsid protein NCp7, and their binding affinities for the HIV-1 Ψ-RNA SL3 region were evaluated (*5*). An NCp7 protein containing two NBA units at the specific sites showed a higher binding affinity and specificity than the wild-type NCp7. The study demonstrated the applicability of the NBA units as building blocks for constructing RNA-binding molecules. The peptide and protein engineering studies derived from native proteins showed an advantage for designing more specific molecules than the natural counterparts.

However, this protein-engineering strategy has the limitation that a lot of proteins with NBAs are difficult to be prepared easily with chemical methods. Furthermore, it is hard to design RNA-binding molecules targeting a variety of RNAs by using natural proteins. On this standpoint, we have attempted to start the de novo design of artificial NBA peptides with simple amino acid sequences in short length. A variety of peptides with various sequences are more easily synthesized than the larger protein. Four kinds of NBA units (adenine, guanine, thymine, and cytosine) could be placed on various positions of peptides capable of forming secondary structures, such as an α-helix and a *β*-structure. A strategy using de novo design has a high probability of constructing the molecules targeting a variety of structures and sequences of RNA. To approach this goal, in this study, we have performed de novo design of the NBA peptides



(b) Ac-AA**X**AR**Y**AARR**Z**RA-NH_2 (3, 6, 11)

Peptide	X	Y	Z
GCG	G_{NBA}	C_{NBA}	G_{NBA}
GTG	G_{NBA}	T_{NBA}	G_{NBA}
GAG	G_{NBA}	A_{NBA}	G_{NBA}
GGG	G_{NBA}	G_{NBA}	G_{NBA}
CGG	C_{NBA}	G_{NBA}	G_{NBA}
TGG	T_{NBA}	G_{NBA}	G_{NBA}
AGG	A_{NBA}	G_{NBA}	G_{NBA}
GGA	G_{NBA}	G_{NBA}	A_{NBA}
AlaGG	Ala	G_{NBA}	G_{NBA}
GAlaG	G_{NBA}	Ala	G_{NBA}
GGAla	G_{NBA}	G_{NBA}	Ala
A9R4	Ala	Ala	Ala

Figure 1. (a) Structures of the NBA units. (b) Amino acid sequences of the de novo designed peptides.

* To whom correspondence should be addressed. Fax: +45-924-5833. E-mail; ttakahas@bio.titech.ac.jp.

10.1021/bc034210n CCC: $27.50 © 2004 American Chemical Society
Published on Web 07/02/2004

that have high binding affinities and specificities for a hairpin RNA. The findings in this study lead to a way for constructing novel molecules working against RNAs.

MATERIALS AND METHODS

Chemicals and Reagents. All chemicals and solvents were of reagent or HPLC grade. Amino acid derivatives and reagents for peptide synthesis were purchased from Watanabe Chemical (Hiroshima, Japan). MALDI-TOF MS was measured on a Shimadzu MALDI III mass spectrometer by using 3,5-dimethoxy-4-hydroxycinnamic acid as a matrix. HPLC was carried out on a YMC ODS A-302 5C18 column (4.6 mm × 150 mm; YMC, Tokyo, Japan) or a YMC ODS A-323 5C18 column (10 mm × 250 mm) by employing a Hitachi L-7000 HPLC system. Amino acid analyses were performed by using the phenyl isothiocyanate (PTC) method on a Wakopak WS-PTC column (Wako Chemical; Osaka, Japan). Synthetic DNA templates were purchased from Sigma Genosys (Ishikari, Japan). Fluorescein-labeled DNA was purchased from Espec Oligo Service (Tsukuba, Japan). A RiboMAX large-scale RNA production system T7 was purchased from Promega (Tokyo, Japan). T4 RNA ligase was purchased from Takara Bio (Osaka, Japan).

Peptide Synthesis. Fmoc-protected NBA monomers (Fmoc-G_{NBA}-OH, Fmoc-C_{NBA}(Z)-OH, Fmoc-A_{NBA}(Z)-OH, Fmoc-T_{NBA}-OH) were synthesized according to the reported methods (*4b*). The peptides were synthesized by the solid-phase method using the Fmoc strategy with *O*-(7-azabezotriazole-1-yl)-1,1,3,3-tetramethyluronium hexafluorophosphate (HATU) or 2-(1*H*-benzotriazole-1-yl)-1,1,3,3-tetramethyluronium hexafluorophosphate (HBTU) and 1-hydroxybenzotriazole hydrate (HOBt·H_2O) as the coupling reagents (*6*). To synthesize the acetylated-peptide resin, the Fmoc-deprotected peptide resin was reacted with acetic anhydride (10 equiv) in *N*-methylpyrrolidone (NMP) for 20 min. To remove the resin and the protecting groups, the peptide resin was treated with trifluoroacetic acid (TFA) containing *m*-cresol, triethylsilane, and thioanisole as scavengers for 1 h at room temperature. For the peptide resin with the Z groups on A_{NBA} and C_{NBA}, the reaction was carried out for 2.5 h. The product was solidified with diethyl ether in an ice bath. All crude peptides were purified with RP-HPLC on a YMC ODS A-323 column using a linear gradient of 8−38% acetonitrile/0.1% TFA (30 min) to give the purified peptides. Peptides were identified by their molecular ion peak $(M + H)^+$ on MALDI-TOF MS: *m*/*z* found (calcd) P22N, 2234.0 (2232.6); A9R4, 1324.7 (1324.7); GCG, 1774.8 (1774.0); GTG, 1788.0 (1788.0); GAG, 1797.8 (1798.0); GGG, 1812.9 (1814.0); CGG, 1774.3 (1774.0); TGG, 1789.0 (1788.0); AGG, 1796.7 (1798.0); GGA, 1796.9 (1798.0); AlaGG, 1649.9 (1650.9); GAlaG, 1652.1 (1650.9); GGAla, 1652.7 (1650.9).

Preparation of Fluorescein-Labeled P22 boxB RNA and Mutants. The P22 boxB RNA was prepared by transcription of a synthetic DNA template (5′-AATTTAATACGACTCACTATAGGTGCGCTGACAAAGCGCGCC-3′ and 5′-GGCGCGCTTTGTCAGCGCACCTATAGTGAGTCGTATTAAATT-3′) by using the RiboMAX large-scale RNA production system T7 (Promega). The template DNA was degraded by RNase-free DNase I, and then the RNA was purified by polyacrylamide gel electrophoresis (PAGE) (15% acrylamide). The fluorescein-labeled DNA oligomer was incorporated into the product RNA using T4 RNA ligase in Tris-HCl buffer (50 mM, pH 7.5) that contained $MgCl_2$ (10 mM), 1,4-dithiothreitol (DTT, 10 mM), adenosine triphosphate (ATP, 1 mM), bovine serum albumin (BSA, 0.05%), and dimethyl sulfoxide (DMSO, 10%). The solution was incubated at 15 °C for 16 h. The fluorescein-labeled boxB RNA was purified by ethanol precipitation and PAGE. The mutant RNAs were also prepared using the same method. Concentrations of RNAs were determined by the absorbance at 260 nm.

CD Measurements. CD spectra of the peptides were measured on a Jasco J-720WI spectropolarimeter using a quartz cell with 1.0 mm path length in the region of 195−250 nm. Peptides were dissolved in 10 mM Tris-HCl buffer (pH 7.5) containing 100 mM KCl and 1 mM $MgCl_2$ or trifluoroethanol (TFE) solution (peptide concentration of 10 μM).

Fluorescence Anisotropy Measurements. Fluorescence anisotropy measurements were carried on a Shimadzu RF-5300PC spectrofluorophotometer using a quartz cell with a 1.0 cm path length at 10 °C in *N*-(2-hydroxylethyl)piperazine-*N*-(2-ethanesulfonic acid) (HEPES)−KOH buffer (10 mM, pH 7.5) containing KCl (100 mM), $MgCl_2$ (1 mM), and EDTA (0.5 mM). Fluorescence anisotropy was calculated by the intensities at 520 nm excited at 480 nm.

Determination of Dissociation Constants between Peptides and RNAs. The binding affinities of the peptides for the RNA were determined by fluorescence anisotropy measurements. The fluorescein-labeled RNA (5.0 nM) in the buffer solution was titrated with a peptide solution. After each addition of a peptide, samples were stirred for 30 s and equilibrated for 4.5 min at 10°C, and then fluorescence anisotropy was measured. The dissociation constants of the peptides and RNAs were calculated using eq 1 and Kaleida Graph (Synergy Software), assuming a 1:1 stoichiometry:

$$A = \frac{(A_b - A_f)\{[F]_0 + [P]_0 + K_d - (([F]_0 + [P]_0 + K_d)^2 - 4([F]_0[P]_0)^{1/2})\}}{2[F]_0} \quad (1)$$

$[F]_0$ and $[P]_0$ represent the initial concentrations of the fluorescent RNA and a peptide, respectively. A, A_b, and A_f are the anisotropy values of each solution, the bound fluorescent RNA, and the free fluorescent RNA, respectively. K_d is the dissociation constant between the peptide and RNA.

RESULTS AND DISCUSSION

Design and Synthesis of the Peptides. To achieve the de novo design of NBA peptides that interact with a hairpin RNA, four kinds of NBA units, alanine, and arginine residues were used. A hairpin RNA was selected as a target molecule because of its important functions in nature such as that in some viral RNAs (HIV-1 TAR, λ phage boxB) and ribosomal RNAs (*7*). A hairpin RNA studied here is derived from the boxB region of phage P22 RNA that contains a stable GNRA-like (G, guanine; N, any bases; R, guanine and adenine; A, adenine) tetraloop structure (Figure 2a) (*8*, *9*). For the design of the NBA peptides targeting the P22 RNA, NBA units were incorporated into positions 3, 6, and 11 of the peptides (Figure 1b). It was expected that the NBA at position 3 could interact with the stem region of the RNA (Figure 2a). In addition, the NBA units at positions 6 and 11 were expected to interact with the bases of the loop region of the RNA. These expectations were based on the structure of the complex between the boxB RNA and P22 N peptide (*8*), the N-terminal region of P22 phage N protein (*10*). In this peptide−RNA complex, the peptide forms an α-helical conformation, the amino acid residue

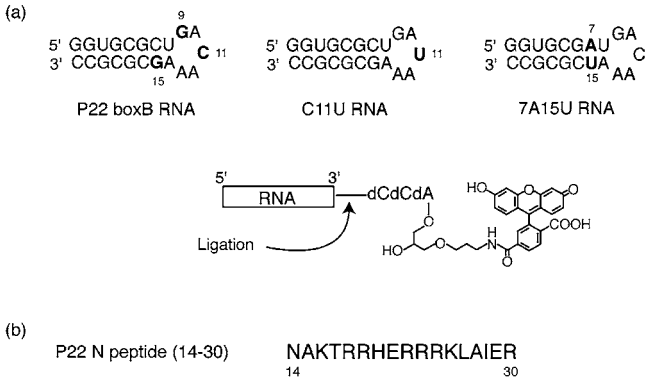


Figure 2. (a) Secondary structures of the P22 boxB RNA and its mutants (C11U and 7A15U). The fluorescein group was incorporated into each RNA by using T4 RNA ligase. (b) Amino acid sequence of the P22 N peptide (14−30).

Table 1. α-Helix Content of the Peptides in TFE Solution

peptide	α-helicity (%)	peptide	α-helicity (%)
GCG	58	TGG	50
GTG	67	AGG	58
GAG	58	GGA	72
GGG	71	P22N	62
CGG	57	A9R4	55

at position 3 is located in the major groove region, and the residues at positions 6 and 11 are located near the bases of the loop region of the boxB RNA. According to the findings, a variety of NBA peptides (13AA) with three NBA units at positions 3, 6, and 11 were designed. Each peptide has six alanine and four arginine residues in addition to the NBA units (Figure 1b). Alanine was selected to generate a high ability to form an α-helical structure (*11*). Arginine residues were incorporated into the positions expected to interact with phosphate groups electrostatically. In addition to these NBA peptides, the peptides with two guanine NBA units and one alanine residue at these positions were designed. These peptides were expected to clarify the contribution of the NBA unit at each position to the RNA-binding. The A9R4 peptide having three alanine residues at positions 3, 6, and 11 was also designed as a reference molecule for evaluating the NBA function.

Peptides were synthesized using the Fmoc solid-phase method (*6*) and purified by reversed-phase HPLC with high purity. The P22 N peptide was also synthesized as a reference molecule (Figure 2b). All peptides were identified by matrix-assisted laser desorption ionization time-of-flight mass spectrometry (MALDI-TOF MS), and peptide concentrations were determined by amino acid analyses.

Circular Dichroism Study. The designed peptides were expected to form an α-helical conformation when the peptide bound to the RNA. Circular dichroism (CD) spectra of the peptides were measured in 10 mM Tris-HCl buffer (pH 7.5) containing 100 mM KCl and 1 mM $MgCl_2$ or trifluoroethanol (TFE). In the buffer solution, both the peptides with three NBA units and the P22 N peptide did not form an α-helical structure sufficiently. These results should be due to the repulsions between positively charged residues in the peptides. In contrast, all the peptides with three NBA units showed a typical α-helix CD pattern as well as the P22 N peptide in TFE solution. The α-helicities of the peptides were estimated from the molecular ellipticity at 222 nm (*12*). As shown in Table 1, the α-helix content of the NBA peptides was estimated as around 50−70%. These results indicate that the NBA peptides have potential to form an α-helical structure. The previous study demonstrated that the incorporation of one or two NBA units does not disturb the conformational properties of the peptides and proteins (*3, 5*). Considering that the α-helix content of the A9R4 peptide was estimated as 55%, in this study, incorporations of three NBA units also do not disturb the abilities of the peptides to form an α-helical structure.

Table 2. Dissociation Constants (K_d) of the Peptides with the P22 boxB RNA

peptide	K_d (μM)	relative affinity[a]
GCG	1.2 ± 0.1	100
GTG	1.9 ± 0.1	63
GAG	0.86 ± 0.03	140
GGG	0.27 ± 0.02	444
CGG	0.85 ± 0.04	141
TGG	0.79 ± 0.04	152
AGG	0.93 ± 0.03	129
GGA	0.32 ± 0.01	375
AlaGG	0.53 ± 0.02	226
GAlaG	3.0 ± 0.3	40
GGAla	0.57 ± 0.02	211
P22N	0.88 ± 0.03	129
A9R4	120 ± 10	1.00

[a] The relative affinity represents the ratio of dissociation constants between the A9R4 peptide and other peptides to the P22 boxB RNA.

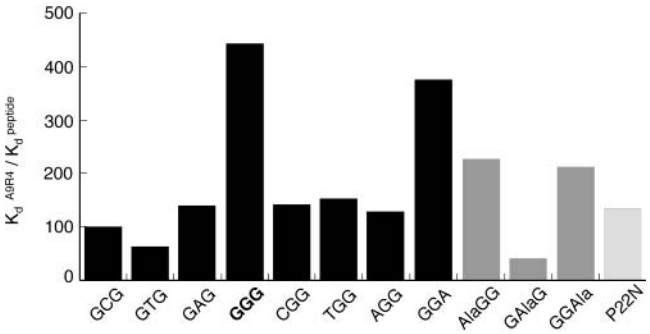


Figure 3. Relative binding affinities between the peptides and the A9R4 peptide with the P22 boxB RNA. $K_d^{A9R4}/K_d^{peptide}$ represents the ratio of the dissociation constants between the A9R4 peptide and each peptide to the P22 boxB RNA.

Binding Analyses of the NBA Peptides with the P22 boxB RNA. To evaluate the binding affinities of the NBA peptides for the boxB RNA, the fluorescein moiety was incorporated into the RNA using T4 RNA ligase (Figure 2b) (*13*). Dissociation constants (K_d) of the peptides with the RNA were determined by fluorescent anisotropy measurements. In this method, the binding affinity of the A9R4 peptide for the RNA was estimated as the K_d value of 120 μM. Binding affinity of each peptide was compared with that of A9R4 (Table 2 and Figure 3).

At first, the binding affinities of the NBA peptides with G_{NBA} at positions 3 and 11 and the several types of the NBA units at position 6 were compared. The GGG peptide having three G_{NBA} units showed a binding affinity with $K_d = 0.27$ μM, a value that indicates affinity ca. 450-fold higher than that of the A9R4 peptide. Furthermore, the GGG peptide showed a higher affinity (3.5-fold) than the natural counterpart P22 N peptide, which is known to bind to the P22 boxB RNA. In contrast, the peptides having other types of NBA units at position 6 (A, T, and C bases) bound to the target RNA at a similar or lower level of the P22 N peptide. These results strongly suggested that $G_{NBA}6$ could work more effectively in the interaction with the boxB RNA than the other types of nucleobases.

Next, the binding affinities of the peptides with the various NBA units at position 3 for the boxB RNA were also compared. In this case, the GGG peptide bound to the target RNA more strongly than the other peptides having adenine, thymine, and cytosine NBA units at position 3. These results indicated that $G_{NBA}3$ could interact with the RNA base more effectively than the other types of NBA units at its position. $G_{NBA}11$ was also evaluated to interact with the RNA effectively by a comparison of the binding affinities between the GGG and GGA peptides for the RNA. Therefore, the GGG peptide showed the highest affinity for the P22 boxB RNA in the series of de novo peptides. These results indicated that three guanine bases of the GGG peptide could work effectively for the RNA binding. Generally in RNA, guanine base can interact with not only cytosine base by making the Watson−Crick type base pairing but also guanine by making the Hoogsteen type pairing. Therefore, it seems that three guanines of the GGG peptide are able to interact with a G−C base pair on the stem region of the P22 boxB RNA and guanine and cytosine bases on the loop region. The specific interaction may include not only hydrogen bonding but also hydrophobic interaction. The NMR analysis of the P22 N peptide−boxB RNA complex revealed that the amino acid residues of the peptide at positions 3, 6, and 11 are located near the C7-G15, G9, and C11 bases of the boxB RNA, respectively (*7*). Along with these data, it was estimated that the de novo designed NBA peptides might be located at a position similar to that of the P22 N peptide in the peptide−RNA complex when the NBA peptides could take the α-helical conformation by binding to the RNA. In addition, the other peptides with two guanine bases also showed higher binding affinities than the A9R4. This finding indicates that the two guanine moieties interact with the RNA bases in a manner similar to the case of GGG, and another base (A, T, or C) might interact weakly with RNA by a nonspecific manner.

To investigate the contribution of each G_{NBA} unit to the RNA-binding, one of the G_{NBA} units of the GGG peptide was replaced by an alanine residue (Figure 1). As a result, the AlaGG and GGAla peptides showed the binding affinities with $K_d = 0.53$ and 0.57 μM, respectively, which is ca. 2-fold lower than the GGG peptide. In contrast, the GAlaG peptide that has the alanine residue at position 6 showed significantly lower binding affinity ($K_d = 3.0$ μM) than the other peptides. It was implied that $G_{NBA}6$ contributed to the RNA-binding to a larger extent than the G_{NBA} units at the other positions. These results do not contradict the facts that the GGG peptide with G at position 6 shows significantly higher affinity for the RNA than the peptides with the A, T, and C bases at the position. Moreover, considering that the binding affinities of the AlaGG and the GGAla peptides were decreased compared with the GGG peptide, $G_{NBA}3$ and $G_{NBA}11$ are also important for the RNA-binding. Consequently, since three guanine moieties of the GGG peptide interacted with RNA bases effectively, the GGG peptide showed the higher binding affinity for the P22 boxB RNA than the other peptides including P22 N.

Binding Analyses of the NBA Peptides with the Mutant RNAs. By using the NBA units and the de novo designed α-helical peptides, we have successfully demonstrated the construction of the novel RNA-binding molecules. For the evaluation of the specificity of the NBA peptides with the P22 boxB RNA, two types of the mutant RNAs (7A15U and C11U) were prepared (Figure 2a). It was expected that the peptide with the NBA units corresponding to the bases of the mutant RNA showed a higher affinity for the mutants than for the wild-type boxB RNA.

Table 3. Dissociation Constants of the Peptides with the C11U Mutant RNA

peptide	K_d (μM)	K_d^{P22}/K_d^{C11U} [a]
GGG	0.41 ± 0.02	0.66
GGA	0.18 ± 0.02	1.78
P22N	0.92 ± 0.03	0.96

[a] K_d^{P22}/K_d^{C11U} represents the ratio of the dissociation constants of each peptide to P22 boxB RNA and the C11U mutant RNA.

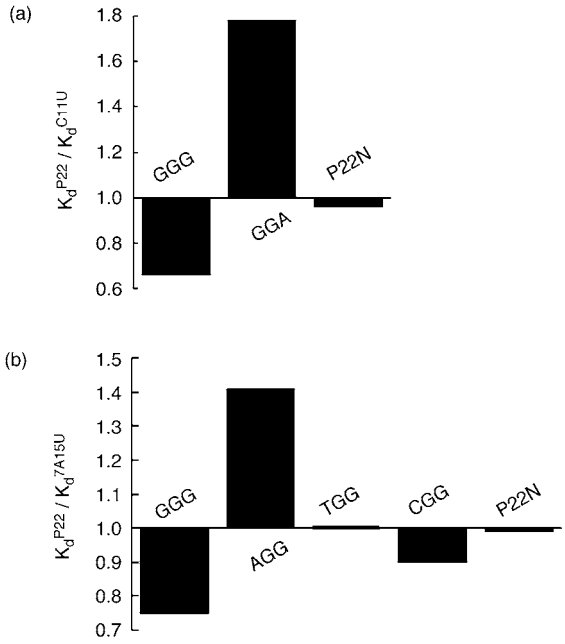


Figure 4. (a) Relative binding affinities of the peptides for the P22 boxB RNA and the C11A mutant RNA. K_d^{P22}/K_d^{C11U} represents the ratio of the dissociation constants of each peptide to P22 boxB RNA and the C11U mutant RNA. (b) Relative binding affinities of the peptides for the P22 boxB RNA and the 7A15U mutant RNA. K_d^{P22}/K_d^{7A15U} represents the ratio of the dissociation constants of each peptide to P22 boxB RNA and the 7A15U mutant RNA.

Binding affinities of the GGA and GGG peptides for the C11U RNA were determined using the same strategy in the case of the boxB RNA (Table 3). Figure 4a shows the relative binding affinities of the peptides for the P22 boxB RNA and the C11U mutant RNA. The GGA peptide bound to the mutant RNA ($K_d = 0.18$ μM) more strongly than to the boxB RNA ($K_d = 0.32$ μM). In contrast, the GGG peptide showed the binding affinity for the C11U RNA as the K_d value of 0.41 μM; this value is inferior to that for the boxB RNA ($K_d = 0.27$ μM). Noticeably, the GGA peptide bound to the C11U mutant RNA more strongly than the GGG peptide did, although the opposite result was obtained in the case of the wild-type RNA. Thus, the GGG and GGA peptides showed a selectivity to the wild-type RNA and the mutant RNA, respectively (Figure 4a). These findings suggested that $A_{NBA}11$ of the GGA peptide could interact more specifically with the U11 base of the RNA than $G_{NBA}11$ of GGG did, and its specific interaction enhanced the binding affinity for the mutant RNA. On the other hand, the binding affinity of the wild-type P22N peptide for the C11U RNA ($K_d = 0.92$ μM) was almost the same as that for the P22 boxB RNA ($K_d = 0.88$ μM). That is, the GGG and GGA peptides could recognize the difference between the cytosine base of the wild-type P22 boxB RNA and the uracil of the C11U mutant more efficiently than the P22 N peptide did. In

Table 4. Dissociation Constants of the Peptides with the 7A15U Mutant RNA

peptide	K_d (μM)	K_d^{P22}/K_d^{7A15U} [a]
GGG	0.36 ± 0.01	0.75
AGG	0.66 ± 0.04	1.41
TGG	0.79 ± 0.05	1.00
CGG	0.94 ± 0.05	0.90
P22N	0.89 ± 0.03	0.99

[a] K_d^{P22}/K_d^{7A15U} represents the ratio of the dissociation constants of each peptide to P22 boxB RNA and the 7A15U mutant RNA.

the NMR structural analyses, Arg11 of P22 N peptide interacts with the phosphate group and the sugar at C11 of the wild-type RNA in an electrostatic manner and as a van der Waals contact, respectively. These interactions, however, are not specific for the C11 base of the wild-type RNA. By use of the de novo designed NBA peptide GGG or GGA, cytosine 11 or uracil 11 of the wild-type or the C11U mutant RNA, respectively, can be recognized more specifically by the nucleobase moiety at position 11 of these peptides than the arginine residue of native P22 N.

The binding affinities of the peptides for the 7A15U mutant RNA were also evaluated (Table 4 and Figure 4b). In this mutant assay, the AGG peptide showed a selectivity for the 7A15U mutant RNA, and the GGG peptide was selective for the wild-type RNA, while TGG, CGG, and P22N did not show the selective binding for the RNA. The AGG peptide showed a higher binding affinity for the 7A15U RNA ($K_d = 0.66$ μM) than for the wild-type boxB RNA ($K_d = 0.93$ μM). In contrast, the binding affinity of the GGG peptide for the 7A15U RNA ($K_d = 0.36$ μM) was slightly lower than that for the wild-type boxB RNA ($K_d = 0.27$ μM). The TGG and CGG peptides showed almost the same affinity as a lower level for both the boxB and the 7A15U RNA. These results indicated that $G_{NBA}3$ could recognize the C7-G15 base pair of the wild-type RNA more effectively than the A7-U15 pair of the 7A15U mutant. In contrast, $A_{NBA}3$ could recognize the A7-U15 pair more effectively than the C7-G15. Incorporation of the NBA units corresponding to the RNA bases into the peptides increases the binding affinities and specificities with the RNA. On the other hand, the dissociation constant of the P22 N peptide for the 7A15U mutant was estimated as $K_d = 0.89$ μM, a value that is similar to that for the wild-type RNA ($K_d = 0.88$ μM). These results of the native P22 were similar to the case of the C11U mutant. That is, the P22 N peptide could not recognize the differences between the C7-G15 and A7-U15 base pairs nor between the C11 and U11 bases. By use of three NBA peptides (GGG, GGA, and AGG), the mutation of the C7-G15 base pair or the C11U of the P22 boxB RNA can be clarified by the difference of their binding affinities.

CONCLUSION

To construct the novel molecules that specifically recognize a hairpin RNA, a series of artificial α-helical peptides with three NBA units were synthesized. These peptides were de novo designed to have simple amino acid sequences. These synthetic peptides showed sufficient potential for forming an α-helical structure. Binding analyses revealed that the NBA units on the peptides could recognize the RNA bases in a specific manner, and some NBA peptides showed selectivity for recognizing the differences between the wild-type and the mutant RNAs. The combined strategy using the NBA units and peptide scaffolds will be developed to design RNA-binding molecules targeting desired sequences and structures of the RNA.

LITERATURE CITED

(1) Caprara, M. G., and Nilsen, T. W. (2000) RNA: Versatility in form and function. *Nat. Struct. Biol. 7*, 831−833.
(2) Moore, P. B. (1999) Structural motifs in RNA. *Annu. Rev. Biochem. 68*, 287−300.
(3) (a) Matsumura, S., Takahashi, T., Ueno A., and Mihara, H. (2003) Complementary nucleobase interaction enhances peptide−peptide recognition and self-replicating catalysis. *Chem.−Eur. J. 9*, 4829−4837. (b) Matsumura, S., Ueno, A., Mihara, H. (2000) Peptides with nucleobase moieties as a stabilizing factor for a two-stranded α-helix. *Chem. Commun.* 1615−1616.
(4) (a) Takahashi, T., Hamasaki, K., Kumagai, I., Ueno, A., and Mihara, H. (2000) Design of a nucleobase-conjugated peptide that recognizes HIV-1 RRE IIB RNA with high affinity and specificity. *Chem. Commun.* 349−350. (b) Takahashi, T., Hamasaki, K., Ueno, A., and Mihara, H. (2001) Construction of peptides with nucleobase amino acids: design and synthesis of the nucleobase-conjugated peptides derived from HIV-1 Rev and their binding properties to HIV-1 RRE RNA. *Bioorg. Med. Chem. 9*, 991−1000.
(5) Takahashi, T., Ueno, A., and Mihara, H. (2002) Nucleobase amino acids incorporated into HIV-1 nucleocapsid protein increased the binding affinity and specificity to a hairpin RNA. *ChemBioChem 3*, 543−549.
(6) Chan, W. C., and White, P. D. (2000) *Fmoc Solid Phase Peptide Synthesis: A Practical Approach* (Chan, W. C., and White, P. D., Eds.) pp 41−76, Oxford University Press, Inc., New York.
(7) Draper, D. E. (1999) Themes in RNA−protein recognition. *J. Mol. Biol 293*, 255−270.
(8) Cai, Z., Gorin, A., Frederick, R., Ye, X., Hu, W., Majumdar, A., Kettani, A., and Patel, D. J. (1998) Solution structure of P22 transcriptional antitermination N peptide−box B RNA complex. *Nat. Struct. Biol 5*, 203−212.
(9) Legault, P., Li, J., Mogridge, J., Kay, L. E., and Greenblatt, J. (1998) NMR structure of the bacteriophage λ N peptide/boxB RNA complex: recognition of a GNRA fold by an arginine-rich motif. *Cell 93*, 289−299.
(10) Lazinski, D., Grzadzielska, E., and Das, A. (1989) Sequence-specific recognition of RNA hairpins by bacteriophage antiterminatiors requires a conserved arginine-rich motif. *Cell 59*, 207−218.
(11) Marqusee, S., Robbins, V. H., and Baldwin, R. L. (1989) Unusually stable helix formation in short alanine-based peptides. *Proc. Natl. Acad. Sci. U.S.A. 86*, 5286−5290.
(12) Scholtz, J. M., Qian, H., York, E. J., Stewart, J. M., and Baldwin, R. L. (1991) Parameters of helix−coil transition theory for alanine-based peptides of varying chain length in water. *Biopolymers 31*, 1463−1470.
(13) Romaniuk, P. J., and Uhlenbeck, O. C. (1983) Joining of RNA molecules with RNA ligase. *Methods Enzymol. 100*, 52−59.

BC034210N

Peptide-Derivatized Shell-Cross-Linked Nanoparticles. 1. Synthesis and Characterization

Matthew L. Becker,[†] Edward E. Remsen,[‡] Dipanjan Pan, and Karen L. Wooley*

Center for Materials Innovation and Department of Chemistry, Washington University, One Brookings Drive, Saint Louis, Missouri 63130. Received March 4, 2004; Revised Manuscript Received April 26, 2004

The conjugation of the protein transduction domain (PTD) from the HIV-1 Tat protein to shell-cross-linked (SCK) nanoparticles is reported as a method to facilitate cell surface binding and transduction of SCK nanoparticles. Attaching increasing numbers of peptide sequences to SCK nanoparticles in a global solution-state functionalization strategy has been devised as a method for increasing the efficiency of the cell-penetrating process. The numbers of peptides per SCK were controlled through stoichiometric balance and measured experimentally by two independent methods, UV−visible spectroscopy and phenylglyoxal analysis. PTD was conjugated in (0.005, 0.01, and 0.02) molar ratios, relative to the acrylic acid residues in the shell, to the SCK nanoparticles resulting in SCK populations possessing nominally 52, 104, and 210 (41, 83, and 202 as measured by phenylglyoxal analysis) PTD peptides per particle, respectively. The methodologies for the block copolymer and nanoparticle syntheses, peptide derivatization, and characterization of peptide-functionalized SCK nanoparticles are reported and the feasibility and efficiency of intracellular internalization of the respective SCKs were quantified.

INTRODUCTION

The interactions of biological species with synthetic constructs are dominated by surface-mediated interactions (*1*). Transduction (*2*) of peptides, proteins, and synthetic constructs, not normally able to access intracellular components, across the cellular plasma membrane is an area of promising research directed toward applications such as disease-state detection and diagnosis, and the delivery of therapeutics. Several proteins (*3*, *4*) and synthetic peptide sequences (*5*−*7*) have been identified as ligands that facilitate transduction, and the sequence and structural effects on the efficiency of uptake are being elucidated (*8*). These sequences are being exploited as facilitators for the cellular membrane transduction of proteins (*9*), antibodies (*10*), block copolymers (*11*, *12*), inorganic nanoparticles (*13*, *14*), and liposomes (*15*), which are, otherwise, ineffective for intracellular and nuclear targeting and delivery strategies.

Advances in the design and preparation of synthetic constructs have enabled rapid progress in their use as transduction media. For example, the self-assembly of block copolymers has emerged as a popular route for the production of complex nanostructured materials (*16*), and recent synthetic advancements in living free radical polymerization (*17*, *18*) have allowed for the preparation of large macromolecular assemblies consisting of well-defined block copolymer precursors. Shell-cross-linked (SCK) nanoparticles (*19*−*21*) are core−shell nanoparticles inspired from biological constructs and are optimized for guest packaging (*22*). SCKs are constructed from polymer micelles assembled in aqueous solution from amphiphilic block copolymer precursors and stabilized through the incorporation of covalent cross-links in the shell layer (*23*). The easily controlled structural and chemical features (*24*) play significant synergistic roles in the resulting binding and sequestration (*25*, *26*) properties of the nanoparticles. Previously, the conjugation of the protein transduction domain (PTD) of the HIV-1 Tat protein to the surface of shell-cross-linked nanocages (*23*) (core-excavated SCKs) using a solid-support resin was demonstrated. The derivatization, which limited (to approximately one) the number of peptides that were presented from the nanocage surface, provided bioactive nanostructures with demonstrated cell surface binding and preliminary evidence of transduction (*27*). Attaching increasing numbers of peptide sequences to the SCK in a global solution-state functionalization strategy was, therefore, devised as a methodology for increasing the efficiency of the cell-penetrating process. SCK assembly, peptide derivatization, and detailed characterization of peptide-functionalized SCK nanoparticles with enhanced transduction capability are reported.

EXPERIMENTAL SECTION

Materials. Unless otherwise listed, all solvents and reagents were purchased from Sigma Aldrich Chemical Co. (St. Louis, MO) and used as received. Monomers were purchased from Sigma Aldrich and distilled over calcium hydride. FMOC-protected amino acids and preloaded solid-phase Wang resins were purchased from NovaBiochem-CalBiochem Corp (San Diego, CA). Spectra/Por dialysis membranes (Spectrum Laboratories, Inc., Rancho Dominguez, CA) were purchased from Fisher Scientific Company (Pittsburgh, PA). Prolong antifade mounting medium was purchased from Molecular Probes Inc. (Eugene, OR).

Measurements. ^{1}H NMR (300 MHz) and ^{13}C NMR (75 MHz) spectra were recorded as solutions on a Varian

* To whom correspondence should be addressed. Tel. (314) 935-7136. Fax (314) 935-9844. E-mail: klwooley@artsci.wustl.edu.

[†] Current address: National Institute of Standards and Technology, Polymer Division, Biomaterials Group, Gaithersburg, MD 20899-8543.

[‡] Current address: Cabot Microelectronics Corporation, Core Technology Group, 870 North Commons Dr., Aurora, IL 60504-7963.

10.1021/bc049946e CCC: $27.50 © 2004 American Chemical Society
Published on Web 06/16/2004

Mercury 300 MHz spectrometer with the solvent signal as standard. IR spectra were obtained on a Perkin-Elmer Spectrum BX FT-IR system using diffuse reflectance sampling accessories. Mass spectra were obtained from a Voyager DE-RP MALDI-TOF mass spectrometer (PE Biosystem). HPLC was performed using a Hewlett-Packard Series 1100 with reversed phase C18 column (Dynamax, 300 Å, Rainin) equipped with quaternary pump, solvent degasser, and diode array detector.

Size Exclusion Chromatography (SEC). Size exclusion chromatography was conducted on a Model 150-CV (Waters Chromatography Inc., Medford, MA). The instrument was equipped with a Model 410 differential refractometer, a Model PD2040 dual-angle (15° and 90°) light scattering detector (Precision Detectors Inc., Bellingham, MA), and a three-column set of gel-mixed-bed styrene−divinylbenzene columns (Polymer Laboratories Inc., Amherst, MA). The SEC system was equilibrated at 35 °C in anhydrous THF, which served as the polymer solvent and eluent (flow rate set to 1.00 mL/min then determined gravimetrically). An injection volume of 400 μL was used, and the polymer concentrations ranged from 5 to 10 mg/mL. Data collection was performed with program Precision Acquire (Precision Detectors Inc., Bellingham, MA). Data analysis was performed with program Discovery32 (Precision Detectors Inc., Bellingham, MA). Interdetector delay volume and the light scattering detector calibration constant were determined from a nearly monodisperse polystyrene calibrant (M_p = 90 000 g/mol, M_w/M_n < 1.04; Pressure Chemical Co., Pittsburgh, PA). The differential refractometer was calibrated with standard polystyrene reference material (SRM 706; NIST, Gaithersburg, MD), of known specific refractive index increment, dn/dc (0.184 mL/g). The dn/dc of the analyzed polymers was then determined from the differential refractometer response.

Differential Scanning Calorimetry (DSC). The glass transition temperature (T_g) was measured by differential scanning calorimetry on a Perkin-Elmer DSC-4 differential scanning calorimeter. Heating rates were 10 °C/min and reported values of T_g were measured at the midpoint of the inflection tangent, upon the third heating scan.

Sedimentation Equilibrium (SE). A Beckman Instruments Co. Model Optima XL-I analytical ultracentrifuge operated with a Model An60-Ti, four-hole rotor was used to centrifuge 50 mM NaH_2PO_4, 50 mM NaCl, (PBS) pH 7.1 solutions of the SCK to sedimentation equilibrium. All measurements were made at 20 ± 0.1 °C. Rotor speeds of 2000, 3000, 5000, and 8000 rpm were used. Sedimentation equilibrium data were obtained for three SCK solution concentrations. Resulting sedimentation equilibrium profiles were recorded with the instrument's Rayleigh interferometric (refractive index) detection optics. The ultracentrifuge sample cell was assembled from an Epon charcoal-filled, six-channel centerpiece and matched sapphire windows. The solution volume and the cell's optical path length were 110 μL and 12 mm, respectively. The solution volume and optical path length employed corresponded to a "short" column sedimentation equilibrium experiment with a column height of approximately 2.5 mm. A centrifugation time of 3 to 5 days was used to reach sedimentation equilibrium. Partial specific volume (ν) values for the SCKs were determined via sedimentation equilibrium analysis for protonated and deuterated buffer solutions of SCKs as described previously (*24*). Solutions of the SCK in deuterated buffer were prepared by exhaustive dialysis of protonated buffer stock solutions of SCKs against 50 mM PBS, pD 7.1, in 99.9 atom % D_2O. Calculation of molecular weight employed a built-in data analysis program that employed standard multicomponent least-squares fitting routines. Density at 20.0 ± 0.1 °C for protonated and deuterated buffers was determined with a Mettler-Parr digital density meter. Measurements of ν were reproducible to within ±1% of the mean value given by three determinations. The values of ν obtained by SE were also used for the determination of the weight concentrations of SCK nanoparticle solutions. The digital density meter was employed to measure the solution density at 20.0 ± 0.1 °C for the SCK solutions and their corresponding PBS buffers to an accuracy of ±0.0001 g/mL. These values were used in conjunction with the SE-measured value of ν to determine the weight concentration, C_{SCK}, of the SCK solution in PBS buffer:

$$C_{SCK} = (\rho_{SCK} - \rho_b)/(1 - \nu\rho_b)$$

where ρ_b is the density of the buffer and ρ_{SCK} is the density of the SCK solution.

UV−Visible Spectroscopy. Absorption measurements were made using a Molecular Devices Corp (Sunnyvale, CA) UV−visible spectrophotometer. A Thermomax multiplate reader using SOFTmax PRO software was employed. The concentrations of PTD and SCK in aqueous solutions of functionalized SCK nanoparticles were simultaneously determined using the UV absorbance measured at 230 and 276 nm. Measurements obtained at 230 and 276 nm corresponded to the turbidity of the SCK nanoparticle and the tyrosine (TYR) absorbance of the PTD at these wavelengths. The total absorbance for a functionalized SCK at a given wavelength, A^{λ}, was given by the sum of the absorbances of the nanoparticle's SCK component, $A_{SCK}{}^{\lambda}$, and its PTD component, $A_{TYR}{}^{\lambda}$:

$$A^{230} = A_{SCK}{}^{230} + A_{TYR}{}^{230} \quad (1)$$

$$A^{276} = A_{SCK}{}^{276} + A_{TYR}{}^{276} \quad (2)$$

The individual concentrations of the SCK and PTD (C_{SCK} and C_{TYR}, respectively) components constituting a functionalized nanoparticle were obtained by simultaneously solving eqs 1 and 2 after calibration of the UV spectrum at 230 and 276 nm with PTD and SCK standards of known concentration. The calibration yielded a set of calibration coefficients, K, for the components at 230 and 276 nm:

$$A^{230} = K_{SCK}{}^{230}C_{SCK} + K_{TYR}{}^{230}C_{TYR} \quad (3)$$

$$A^{276} = K_{SCK}{}^{276}C_{SCK} + K_{TYR}{}^{276}C_{TYR} \quad (4)$$

Measured values A^{230} and A^{276} were substituted into eqs 3 and 4 which were expressed in matrix form (eq 5) and then solved by inversion of the matrix of calibration coefficients, **K**:

$$\mathbf{A} = \mathbf{KC} \quad (5)$$

$$\mathbf{K^{-1}A} = \mathbf{K^{-1}KC} \quad (6)$$

$$\mathbf{C} = \mathbf{K^{-1}A} \quad (7)$$

Substitution of computed values of $\mathbf{K^{-1}}$ in eq 7 provided the expressions used to calculate the weight concentrations of SCK and PTD in solution:

$$C_{SCK} = 8.6405A^{230} - 41.5418A^{276} \quad (8)$$

$$C_{TYR} = 9.5652A^{230} - 1.5869A^{276} \quad (9)$$

Experimentally determined weight concentrations were converted to molar concentrations using the known molecular weight of the PTD and the measured molecular weight of the SCK. Molar concentrations of each component provided the requisite information to evaluate the number of peptides (PTD) per SCK nanoparticle (no. peptides per SCK = C_{PTD} (M)/C_{SCK} (M)).

Phenylglyoxal Analysis Measurements. The number of arginine residues (and PTD) was determined experimentally using phenylglyoxal analysis (*28*, *29*). The assay was calibrated by adding aliquots (100 μL) of a PTD solution (100 μL in PBS with 10% methanol, volume fraction) in row 1 of a quartz 96-well plate and diluting serially through column 11. SCK solutions (100 μL) (0.0, 0.5, 1.0, and 2.0%) of known concentrations (1.20, 2.00, 1.20, and 0.60 mg/mL, respectively) were added to each well in the first column and diluted serially as described above. An aliquot (100 μL) of a phenylglyoxal solution (600 μM), in identical buffer, was then added to each well of the plate, and the reaction was allowed to incubate at 4 °C overnight. The 96-well plate was read for absorbance at λ = 310 nm in each well. The control phenylglyoxal absorbance spectrum was subtracted from the PTD absorbance spectra, and by plotting the residual absorbance numbers vs the known concentration of PTD in each well, a calibration curve was generated from which the amount of PTD in unknown solutions could be determined. Measurement of the SCK concentrations by other methods and converting molar ratios provided quantitative information on the number of peptides per particle in each of the four samples.

Dynamic Light Scattering (DLS). Hydrodynamic diameter distribution and distribution averages for the SCKs in PBS solution were determined by dynamic light scattering. A Brookhaven Instruments Co. (Holtsville, NY) DLS system equipped with a Model BI-9000AT digital correlator, a Model EMI-9865 photomultiplier, and a Model 95-2 Ar ion laser (Lexel Corporation, Fremont, CA), operated at 514.5 nm, was used. Measurements were made at 20 ± 0.1 °C. Nanoparticles were dialyzed into 50 mM PBS, pH 7.1, prior to analysis. Buffered nanoparticle solutions were either centrifuged in a model 5414 microfuge (Brinkman Instrument Company, Westbury, NY) for 4 min or filtered through 0.22 μm poly(vinylidene fluoride) and 0.1 μm ceramic filters (Whatman, Maidstone, UK) to remove dust particles. Scattered light was collected at a fixed angle of 90°. The digital correlator was operated with 522 ratio spaced channels, an initial delay of 1.6 μs, a final delay of 10 ms, and a duration time of 15 min. A photomultiplier aperture of 400 μm was used, and the incident laser power was adjusted to obtain a photon counting rate between 200 and 300 Kcps. Only measurements for which the measured and calculated baselines of the intensity autocorrelation function agreed to within ±0.1% were used to calculate nanoparticle hydrodynamic diameter values. All determinations were made in triplicate. The calculations of the nanoparticle diameter distributions and distribution averages were performed with the ISDA software package (Brookhaven Instruments Co.), which employed single-exponential fitting, cumulants analysis, and nonnegatively constrained least-squares particle size distribution analysis routines.

Zeta Potential. Zeta potential (ζ) values for the SCKs were determined with a Brookhaven Instrument Co. (Holtsville, NY) Model ZetaPlus zeta potential analyzer. Measurements were made following dialysis (MWCO 12−14k dialysis tubing, Spectrum Laboratories, Rancho Dominguez, CA) of SCK solutions into 1 mM KH_2PO_4, 1 mM KCl, pH 7.1 buffer. Data were acquired in the phase analysis light scattering (PALS) mode (*30*), following solution equilibration at 25 °C. Calculation of ζ from the measured nanoparticle electrophoretic mobility (μ) employed the Smoluchowski equation:

$$\mu = \epsilon\, \zeta/\eta$$

where ϵ and η are the dielectric constant and the absolute viscosity of the medium, respectively. Measurements of ζ were reproducible to within ±2 mV of the mean value given by 16 determinations of 10 data accumulations.

Transmission Electron Microscopy (TEM). Transmission electron microscopy carbon grids were prepared by oxygen plasma treatment to make the surface hydrophilic. Particle samples were diluted 9:1 in water and further diluted 1:1 with a 1% (mass fraction) phosphotungstinic acid (PTA) stain. Micrographs were collected at 100 000 magnification and calibrated using a 41 nm polyacrylamide bead from NIST. Histograms of particle diameters were generated from the analyses of a minimum of 150 particles from at least three different micrographs.

Atomic Force Microscopy (AFM). Tapping-mode atomic force microscopy measurements were conducted in air with a Nanoscope III Bioscope system (Digital Instruments, Santa Barbara, CA) operated under ambient conditions with standard silicon tips (OTESPA-70; L, 160 μm; normal spring constant, 50 N/m; resonance frequency, 246−282 kHz). The samples were prepared for AFM analysis by depositing a 2-μL drop of the solution onto freshly cleaved mica and allowing it to dry freely in air. Histograms of particle heights were generated from the section analysis of a minimum of 150 particles from at least five different analyses regions.

Cell Lines. Chinese hamster ovary (CHO) cells (ATCC) were obtained as a gift from Professor Jacob Schaefer. (Washington University, Saint Louis, MO). CHO cells were maintained in Roswell Park Memorial Institute (RPMI, Life Technologies, Rockville, MD) 1640 supplemented with 10% (volume fraction) heat-inactivated fetal bovine serum (FBS, Life Technologies, Rockville, MD), in 5% CO_2:95% air (volume fractions) at 37 °C.

Transduction Experiments. CHO cells were cultured, counted, and resuspended to a final concentration of 100 000 cells/mL. An aliquot of the cell suspension (3.00 mL) was deposited into each well of a tissue culture treated six-well plate (Falcon, 3043), which contained a No. 1.5 glass cover slip (Corning). After 48 h, the cells (50−60% confluence) in each six-well plate were washed with PBS (2 × 5.00 mL). An aliquot of serum free RPMI 1640 media (3.00 mL) was added to each well followed by the respective SCK solutions (1.00 mL each). The plates were then returned to the incubator to incubate at 37 °C. After 1 h, the nanoparticles were removed, and each well was washed with PBS (3 × 5.00 mL). The cells were then fixed using a 4% (mass fraction) paraformaldehyde solution (2.00 mL) in each well and allowing ambient temperature incubation for 1 h. After fixation, the cells were mounted in Prolong antifade mounting medium (Molecular Probes, Eugene, OR) and viewed under bright field and fluorescent conditions using an Olympus IX-70 inverted microscope. The transduction

experiments were repeated using RPMI 1640 media supplemented with 0.1% (mass fraction) sodium azide, and at 4 and 37 °C. For quantification by flow cytometry, the transduction experiments were repeated except that the cells were grown directly on the tissue cultured plates instead of glass cover slips. The cells were trypsinized to remove most of the surface bound particles and release the cells from the plate, centrifuged at 4 °C, and resuspended in PBS and stored on ice briefly. Less than 5 min prior to flow cytometry analysis, propidilium iodide (5.0 μL) was added to each centrifuge tube. Analysis was done on a FACS Calibur (BD Biosciences, Franklin Lakes, NJ) instrument using CellQuest software.

Fluorescence and Confocal Microscopy. Confocal microscopy was accomplished using a Leica TCS SP2 scanning confocal microscopy system equipped with Ar^+, Kr^+, and HeNe laser systems. The excitation wavelength was 488 nm, and the emission was collected over the range of 510−530 nm. Optical slices were taken on 0.5 μm centers with the Leica software compiling the collections of images into the 3-D reconstructions. The incubation and fixation experimental parameters outlined previously were strictly adhered to in the confocal microscopy experiments with the following exceptions. The cover slips from the 37 °C experiments were mounted on slides fitted with a small spacer and PBS was added as the medium. These experiments were repeated with cells being incubated at 4 °C for 1 h and washed and mounted with cold buffer. The cells were viewed for a maximum of 20 min as live whole, unfixed specimens.

FMOC-Solid-Phase Synthesis of PTD on Wang's Resin (1). The protein transduction domain sequence (GGGGYGRKKRRQRRR) was synthesized by standard solid-phase synthesis using Fmoc chemistry. A small amount of beads were removed and washed with NMP, DMF, CH_2Cl_2, and methanol three times each. Peptide cleavage was achieved through treatment of the resin with a 95% TFA:2.5% TIS:2.5% (volume fractions) water solution (10 mL) for a minimum of 4 h. The solution was filtered, and the beads were rinsed with TFA. The solution was concentrated in vacuo, and the concentrate was precipitated into cold ether. The precipitates were centrifuged at 3500 rpm for 10 min. The supernatant was decanted, the pellet was resuspended in cold ether, and the centrifugation process was repeated. The pellet was purified by reversed phase HPLC. MS (MALDI): 1789.5022 $[M + H]^+$ (calcd: 1788.03 MW).

Poly(*tert*-butyl acrylate) (2). A 100 mL Schlenk flask that had been oven-dried overnight, flame-dried under vacuum, and back-filled with argon was charged with copper(I) bromide (891.6 mg, 6.2×10^{-3} mol). *tert*-Butyl acrylate (38.00 mL, 2.6×10^{-1} mol), PMDETA (1.30 mL, 6.2×10^{-3} mol), and ethyl-2-bromopropionate (403 μL, 3.1×10^{-3} mol) were added via argon-washed syringes. The solution was degassed by three cycles of freeze−pump−thaw, and following the final thaw cycle, the mixture was stirred for 10 min before being immersed in an oil bath at 50 °C. After 80 min, the polymerization was quenched by immersion in liquid nitrogen. The reaction mixture was dissolved in THF and passed through an alumina plug to remove the metal/ligand catalyst system. The polymer solution was concentrated and then precipitated into cold methanol. $M_n = 7400$ from SEC, based on multiangle light scattering (MALS). $M_w/M_n = 1.12$. The isolated yield was 28.83 g (85%). $(T_g)_{tBA} = 33$ °C. IR: 3440, 2980, 1750, 1450, 1380, 1265, 1150, 850, 760, 625 cm^{-1}. ^1H NMR ($CDCl_3$) δ 1.05 (d, CH_3CH end group), 1.22 (t, CH_3CH_2O end group), 1.20−1.50 (broad, $(CH_3)_3C$), 1.24−1.70 (broad, meso and racemo CH_2 of the polymer backbone), 1.74−1.94 (broad, meso CH_2 of the polymer backbone), 2.15−2.35 (broad, CH of the polymer backbone), 4.05 (br overlapping m, CH_3CH_2O and $CHBr$ end groups) ppm. ^{13}C NMR ($CDCl_3$) δ 27.9−28, 35.5−37.4, 41.5−41.4, 80.3, 173.6, 173.9 ppm.

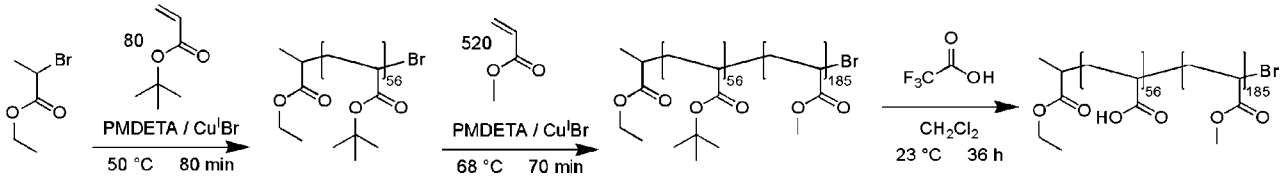
Poly(*tert*-butyl acrylate-*b*-methyl acrylate) (3). A Schlenk flask (100 mL) was oven-dried overnight, flame-dried under vacuum, back-filled with argon, and charged with copper(I) bromide (184.1 mg, 1.3×10^{-3} mol) and poly(*tert*-butyl acrylate) **2** (4.7381 g, 6.4×10^{-4} mol). PMDETA (268 μL, 1.3×10^{-3} mol) and methyl acrylate (30.00 mL, 3.3×10^{-1} mol) were added via argon-washed syringes. The solution was degassed by three cycles of freeze−pump−thaw, and following the final thaw cycle, the mixture was stirred for 10 min before being immersed in an oil bath at 68 °C. After 70 min, the polymerization was quenched by immersion in liquid nitrogen. The reaction mixture was dissolved in THF and passed through an alumina plug to remove the metal/ligand catalyst system. The polymer solution was concentrated and then precipitated into a cold methanol/water solution. $M_n = 23\,400$ from SEC, based on MALS. $M_w/M_n = 1.13$. The isolated yield was 9.18 g (16%). $(T_g)_{PtBA} = 32$ °C. $(T_g)_{PMA} = 14$ °C. IR: 3650, 3450, 2970, 1990, 1550, 1450, 1180, 1080, 850 750, 625 cm^{-1}. ^1H NMR ($CDCl_3$) δ 1.20−1.50 (broad, $(CH_3)_3C$), 1.25−1.95 (broad, CH_2 of the polymer backbone), 1.74−1.94 (broad, CH_2 of the polymer backbone), 2.15−2.40 (broad, CH of the polymer backbone), 3.55−3.65 (broad, OCH_3) ppm. ^{13}C NMR ($CDCl_3$) δ 27.9−28, 35.5−37.4, 41.5−41.4, 51.5, 80.3, 173.4, 173.6 ppm.

Poly(acrylic acid-*b*-methyl acrylate) (4). The *tert*-butyl esters along the poly(*tert*-butyl acrylate) block of **3** were cleaved selectively by adding trifluoroacetic acid (30.00 mL) to the diblock, **3** (8.5600 g, 3.66×10^{-4} mol), in dichloromethane (100 mL). After 36 h, the solvent was evaporated in vacuo, and the residue was dissolved in THF and purified by dialysis in presoaked dialysis tubing (MWCO 12−14k) against Nanopure (18.0 mΩ cm^{-1}) water for 3 days. Lyophilization yielded poly(acrylic acid-*b*-methyl acrylate) as a white powder. Yield: 7.25 g (98%); $(T_g)_{PAA} = 145$ °C. $(T_g)_{PMA} = 14$ °C. IR: 3500−2500, 1760, 1660, 1445, 1280, 1180, 1050, 850, 725, 610 cm^{-1}. ^1H NMR ($CDCl_3$) δ 1.25−2.0 (broad, CH_2 of the polymer backbone), 1.74−1.94 (broad, CH_2 of the polymer backbone), 2.20−2.45 (broad, CH of the polymer backbone), 3.55−3.65 (broad, OCH_3) ppm. ^{13}C NMR ($CDCl_3$) δ 34−36.4, 40.5−42.4, 50.5, 173, 178 ppm.

Micelle Formation (5). Polymer micelles of narrow size distribution were obtained by dissolving the block copolymer **4** (1.9968 g, 8.53×10^{-5} mol) in THF (1.000 L, 1.997 mg/mL) followed by gradual addition (20.00 mL/h) of an equal volume of nonsolvent (H_2O) for the hydrophobic poly(methyl acrylate) to induce micellization. The micelles were stirred for 12 h before being transferred to presoaked and rinsed dialysis bags (MWCO 12−14k) and dialyzed against Nanopure (18.0 MΩ cm^{-1}) water for 3 days to remove the organic solvent. The final volume was 2.250 L of aqueous micelle solution for a final concentration of 0.89 mg/mL. DLS: $D_h = 38$ nm, ZETA: $\zeta = -27 \pm 0.7$ mV, TEM: 21.3 ± 3.8 nm.

Shell-Cross-Linked (SCK) Nanoparticle Formation (6). 2,2′-(Ethylenedioxy)-bis(ethylamine) (192 μL, 1.3×10^{-3} mol) was added to 2.125 L of micelle solution (0.90 mg/mL) of poly(acrylic acid-*b*-methyl acrylate). After 30 min, an aqueous solution of 1-(3′-dimethylaminopropyl)-3-ethylcarbodiimide hydrochloride (2.0201 g, 1.05×10^{-2} mol) was added to the reaction vessel. The reaction mixture was stirred for 24 h, and it was then dialyzed

Scheme 1. Sequential ATRP of *tert*-Butyl Acrylate and Methyl Acrylate Afforded Well-Defined Poly(*tert*-butyl acrylate-*b*-methyl acrylate)[a]



[a] The *tert*-butyl esters were cleaved selectively through treatment of the diblock copolymer with TFA in CH_2Cl_2 for 36 h.

against Nanopure water for 3 days to remove residuals. The SCKs were dialyzed into 50 mM sodium phosphate, 50 mM sodium chloride, pH 7.4 buffer, and the number-average hydrodynamic diameter (D_n) of was determined by dynamic light scattering. DLS: $D_n = 37$ nm. ZETA: $\zeta = -20 \pm 0.5$ mV. TEM: 18.3 ± 3.6 nm. AFM: 3.8 ± 1.8 nm. IR: 3385, 2949, 1738, 1568, 1442, 1163, 829 cm^{-1}. DSC: $T_g = 15$ °C. ^1H NMR (D_2O:THF-d_8, 1:2) δ 1−3.0 (aliphatic protons of polymer backbone), 3.50−3.70 (OCH_3) ppm.

General Procedure for the Functionalization of (SCK) Nanoparticles with Various Molar Ratios of PTD. An SCK solution (50.00 mL, 0.895 mg/mL) was placed into a 100 mL round-bottom flask equipped with a stir bar. Sodium chloride (1.00 g) was placed into each of the flasks to minimize aggregation. A stock solution (50.00 mg/mL) of 1-(3′-dimethylaminopropyl)-3-ethylcarbodiimide hydrochloride in sodium phosphate buffer, pH 7.4, was created, and 1.00 mL aliquots (2.5×10^{-4} mol) were added to each flask to activate the acrylic acid residues. A stock solution (18.21 mg/mL) of the PTD peptide, **1**, was made in sodium phosphate buffer, pH 7.4, and aliquots of the solution were added to the respective flasks 20 min after the addition of the carbodiimide.

0.5% PTD Functionalized (7). A PTD stock solution (61 μL, 18.21 mg/mL, 6.25×10^{-7} mol) was added to the activated SCK solution, and the mixture was allowed to react overnight. Following the allocated reaction time, the solution was transferred to presoaked dialysis tubing (MWCO 12−14k) and allowed to dialyze for 3 days against 50 mM sodium phosphate, 50 mM sodium chloride, pH 7.4 buffer, prior to analysis. DLS: $D_n = 35 \pm 3$ nm. ZETA: $\zeta = -28 \pm 0.9$ mV. TEM: 20.2 ± 3.7 nm.

1.0% PTD Functionalized (8). A PTD stock solution (123 μL, 18.21 mg/mL, 1.25×10^{-6} mol) was added to the activated SCK solution, and the mixture was allowed to react overnight. Following the allocated reaction time, the solution was transferred to presoaked dialysis tubing (MWCO 12−14k) and allowed to dialyze for 3 days against 50 mM sodium phosphate, 50 mM sodium chloride, pH 7.4 buffer, prior to analysis. DLS: $D_n = 36 \pm 3$ nm. ZETA: $\zeta = -23 \pm 0.7$ mV. TEM: 21.4 ± 3.6 nm.

2.0% PTD Functionalized (9). A PTD stock solution (245 μL, 18.21 mg/mL, 2.50×10^{-6} mol) was added to the activated SCK solution, and the mixture was allowed to react overnight. Following the allocated reaction time, the solution was transferred to presoaked dialysis tubing (MWCO 12−14k) and allowed to dialyze for 3 days against 50 mM sodium phosphate, 50 mM sodium chloride, pH 7.4 buffer, prior to analysis. DLS: $D_n = 32 \pm 3$ nm. ZETA: $\zeta = -22 \pm 0.5$ mV. TEM: 21.6 ± 3.3 nm.

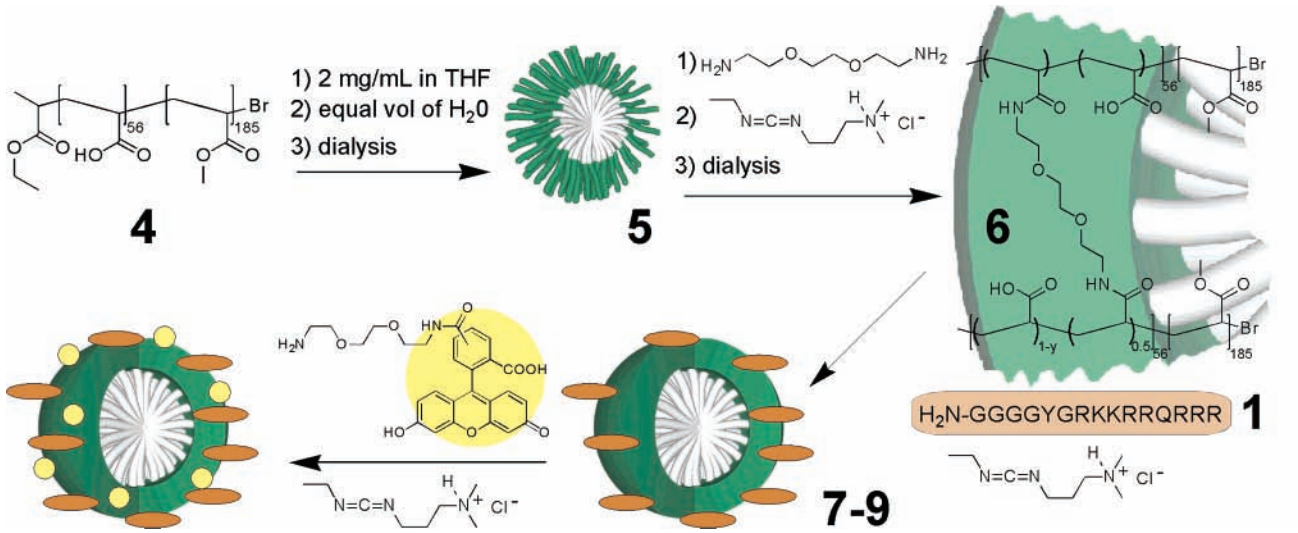
General Procedure for the Conjugation of a Fluorescent Tag to the PTD-Functionalized Nanoparticles (10−13). The respective PTD-functionalized SCK solutions (10.00 mL, 0.895 mg/mL) (2.24×10^{-9} mol) were placed into 50 mL round-bottom flasks. A 4.0 M KCl solution (1.00 mL) was added to each flask. The vessels were allowed to equilibrate for 30 min before 0.500 mL of a 50 mg/mL carbodiimide stock solution (1.25×10^{-4} mol) was added to each vessel. After 15 min, 200 μL of a 0.400 mg/mL stock solution (1.58×10^{-7} mol) of the fluorescein derivative was added to each round-bottom flask, and the reactions were stirred overnight. The solutions were then transferred to presoaked dialysis bags (MWCO 12−14K) and allowed to dialyze for 3 days against 50 mM phosphate, 50 mM NaCl buffer at pH 7.4. The reaction resulted in approximately 70 fluorophores being coupled to each nanoparticle based on calculations assuming ideal reaction efficiency.

RESULTS AND DISCUSSION

SCK Synthesis and Peptide Derivitization. The amphiphilic block copolymer precursor to the SCKs was prepared by sequential atom transfer radical polymerizations (*17*, *31*) of *tert*-butyl acrylate and methyl acrylate followed by the selective acidolysis of the *tert*-butyl esters. The poly(*tert*-butyl acrylate) macroinitiator was afforded through the polymerization of *tert*-butyl acrylate at 50 °C for 80 min using ethyl 2-bromopropionate as the initiator and the Cu^IBr/PMDETA catalytic system (*32*). The chain was further extended through the addition polymerization of methyl acrylate in bulk in the presence of Cu^IBr/PMDETA at 68 °C for 70 min as shown in Scheme 1. By allowing the reaction to proceed under conditions of high dilution (in monomer), low conversion, and by using a liquid nitrogen quench, a narrow molecular weight distribution for the block copolymer was maintained (*33*). The *tert*-butyl esters were cleaved selectively upon reaction with TFA in CH_2Cl_2, as described previously (*32*, *34*). The solvation of the purified poly(acrylic acid-*b*-methyl acrylate) block copolymer in tetrahydrofuran (1.99 mg/mL) followed by the controlled addition of Nanopure (18 MΩ cm) water (20.00 mL/h), and extensive dialysis against deionized water afforded micelles.

SCKs were formed by intramicellar conversion of approximately 50% of the 1-[3′-(dimethylamino)propyl]-3-ethylcarbodiimide hydrochloride activated acrylic acid residues in the shell layer to amides using 2,2′-(ethylenedioxy)bis(ethylamine), as shown in Scheme 2. The protein transduction domain sequence of HIV-1 Tat protein extended by four glycine residues (GGGGYGRKKRRQRRR) used in this study was chemically synthesized by Fmoc (9-fluorenylmethoxycarbonyl) solid-phase peptide methodologies. The four additional glycine residues were placed at the N-terminus to function as a spacer between the active peptide sequence and the macromolecular assembly. The peptide was cleaved from the support, purified by reverse phase HPLC, and then coupled in 0.005, 0.01, and 0.02 molar ratios, relative to the acrylic acid residues within the SCK nanoparticles. The peptide coupling to the SCKs involved amidation of the N-terminus to the carboxylic acid residues within the SCK

Scheme 2. SCK 6 Was Prepared through the Micellization of the Block Copolymer 4, Followed by the Cross-Linking of Approximately 50 % of the Acrylic Acid Residues in the Shell Layer with 2,2′-(Ethylenedioxy)-bis(ethylamine)[a]



[a] The SCKs were functionalized with various molar quantities of PTD **1** under high ionic strength conditions to minimize aggregation and interparticle cross-linking. A linker-derivatized 5(6)-carboxyfluorescein dye (approximately 70 fluorophores per particle) was coupled to each of the SCK samples **6**−**9** to facilitate observation under fluorescence conditions.

shell. The molar amounts correspond to approximately 52, 104, and 210 PTD sequences per particle, respectively, assuming complete conversion and using the aggregation number (185 ± 7) of block copolymers within each particle. Following the conjugation, the respective solutions were then purified by dialysis against buffer for 5 days to remove the noncoupled peptide sequences. Noncoupled PTD was identified by UV measurements made at sedimentation equilibrium (SE), as described below.

Molecular Weight and Aggregation Number. The absolute weight-average molecular weight, M_w, of PTD-functionalized SCK nanoparticles was evaluated by sedimentation equilibrium (SE) analysis. Representative SE data (fringe displacement versus radial position, r) are presented in Figure 1A. The partial specific volume, ν, for the SCKs was also determined by SE using a previously described methodology (*24*) that employed sedimentation equilibrium profiles collected for the SCK dispersed in both protonated and deuterated buffer. Linear SE plots were obtained by plotting the log(fringe displacement) versus $r^2/2$ from which the slopes of the plots were determined and ν was computed:

$$\nu = [k - (\sigma_D/\sigma_H)]/[(\rho_D - \rho_H(\sigma_D/\sigma_H)]$$

where ρ_D is the density of the deuterated buffer, ρ_H is the density of the protonated buffer, and k is the ratio of the molar masses for the deuterated SCK to the protonated SCK (*24*).

SE analysis of M_w employed the nonlinear, least-squares fitting of sedimentation equilibrium profiles represented by the data in Figure 1A to a single-component model with ρ_H and ν held constant as measured parameters. The initial concentration of the nanoparticle at the mensicus, c_0, of the sedimentation column, the baseline offset, N_0, and an apparent weight-average molecular weight, $M_{w,app}$, were calculated as adjustable parameters in the fitting procedure. The computed $M_{w,app}$ when expressed as $1/M_{w,app}$ and plotted against the initial loading concentration of SCK nanoparticle, c, showed a dependence on both c and the rotor speed. The observed trends are indicative of molecular weight heterogeneity and nonideal sedimentation due to interparticle interactions or cross-linking. Extrapolation of $1/M_{w,app}$ to zero concentration for the lowest rotor speed employed provided the evaluation of M_w. As summarized in Table 1, the 0% PTD-functionalized SCK nanoparticle produced a ν of 0.556 ± 0.007 mL/g, resulting in a M_w of 4 000 000 ± 151 000 g/mol. Dividing M_w by the copolymer weight-average molecular weight, corrected for the molar mass increase due to 50% cross-linking of each copolymer chain (21 664 g/mol), resulted in a weight-average degree of aggregation, $N_{w,agg}$, of 185 ± 7. The absolute weight-average molecular weights, M_w, of the PTD-functionalized SCK nanoparticles were also evaluated by SE analysis. Interestingly, M_w for the 0.5%, 1%, and 2% PTD-functionalized SCKs were 31%, 37%, and 41% higher, respectively, than M_w for 0% functionalized SCK. Functionalization of the preformed SCK (0% PTD) with the peptide was expected to produce small M_w increases through the incremental addition of molar mass from the PTD. The observed increases in M_w exceed the expected increase by at least 10-fold, suggesting that functionalization with PTD was accompanied by a small percentage of inter-nanoparticle cross-linking reactions or electrostatic aggregation events due to the zwitterionic character of the PTD- functionalized nanoparticles.

Collection of SE profiles using UV−visible detection optics allowed the analysis of the peptide content of the nanoparticles at centrifugation equilibrium. Free peptides were uniformly dispersed throughout the solution volume while the relatively massive particles were depleted from the meniscus along with the peptides bound to them. Therefore, the amount of free vs SCK-bound peptide in solution was determined by the ratio of absorbance at the meniscus to the absorbance of the unfunctionalized micelle and SCK. No absorbance for the tyrosine (λ_{276}) was detected near the meniscus in the 0.5% and 1.0% solutions relative to controls at 5000 rpm, indicating that all of the absorbance from the tyrosine residue of the PTD sequence is associated with the SCK nanoparticle as shown in Figure 1B.

A slight amount of absorbance observed for the 2.0% functionalized SCK solution suggested free peptide in solution however, increasing the rotor speed to 8000 rpm, which depleted the meniscus of nanoparticles indicated

Table 1. Summary of Physical Characterization Data Collected for the Parent SCK Nanoparticle and the PTD-Functionalized SCKs

particle	ν (mL/g)	M_w ($\times 10^6$ Da)	no. of peptides	ζ (mV)	DLS D_n (nm)	TEM D_{av} (nm)
micelle	n.d.	n.d.	0	-27 ± 0.7	38 ± 3	21.3 ± 3.8
SCK	0.556 ± 0.007	4.004 ± 0.151	0	-20 ± 0.5	37 ± 2	18.3 ± 3.6
0.5%	0.587 ± 0.009[a]	5.900 ± 0.241	52 ± 2	-28 ± 0.9	35 ± 3	20.2 ± 3.7
1.0%	0.622 ± 0.009	7.017 ± 0.304	104 ± 4	-23 ± 0.7	36 ± 3	21.4 ± 3.6
2.0%	0.661 ± 0.007	7.818 ± 0.248	210 ± 10	-22 ± 0.5	32 ± 4	21.6 ± 3.3

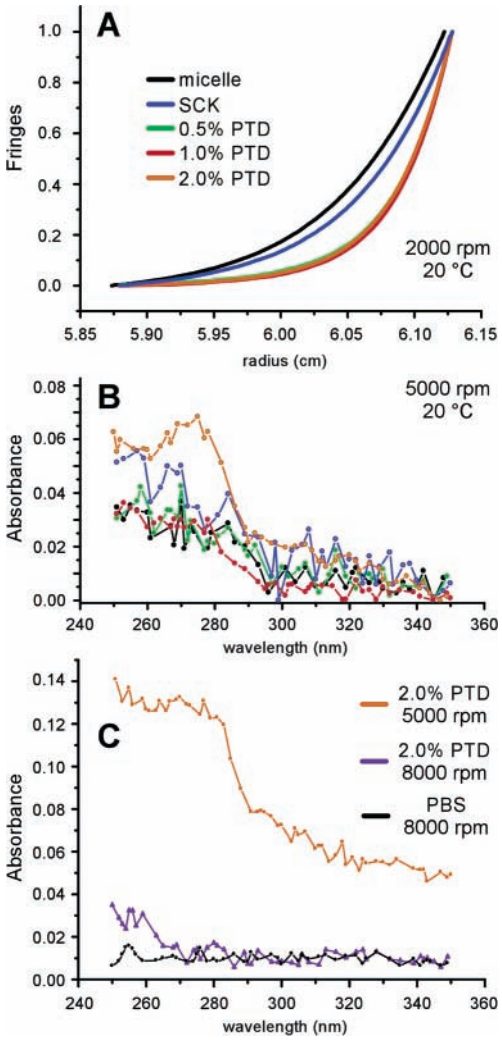


Figure 1. (A) Sedimentation equilibrium profiles collected using an interferometry detector for the micelles, SCKs, and peptide-functionalized nanoparticles. The dramatic increase in weight average molecular weight (M_w) was due to a small percentage of interparticle cross-linking (covalent or electrostatic), which contributed significantly to the molecular weight calculations. (B) UV spectra, recorded near the meniscus of solutions at sedimentation equilibrium, showed negligible absorbance due to free tyrosine residues within the PTD, relative to controls. (C) Repeating the experiment at 8000 rpm indicated that the meniscus was fully depleted of SCK at 8000 rpm, but not at 5000 rpm, and also confirmed that all the PTD was attached to the SCK.

that no free peptide was present in the solution (Figure 1C). This measurement is of particular importance for two reasons: (1) the presence of free peptide can compete with and inhibit the binding of the bioconjugate (*35*), and (2) the PTD sequence has measurable effects on in vitro cell viability and inflammatory response both of which are discussed in detail in the following article of this journal.

Particle Analysis. The SCK nanoparticles were characterized extensively to probe for the differences in size, surface charge, and morphology as a result of post-cross-linking functionalization with the arginine-rich PTD sequence. Dynamic light scattering (DLS) measurements were collected in sodium PBS buffer, pH 7.4. This precaution was used to minimize dilute solution aggregation of the nanoparticles. The polymeric micelle precursor to the SCK was shown to have a number-average diameter, D_n, of 38 ± 3 nm. The corresponding SCK, prepared with 50% cross-linking of its shell, was found to have a D_n of 37 ± 2 nm. A comparison of D_n values calculated using the nonnegatively constrained least squares (NNLS) model for the diameter distributions of the 0.5% (**7**), 1.0% (**8**), and 2.0% (**9**), PTD-functionalized nanoparticles resulted in values of 35 ± 3, 36 ± 3, and 32 ± 4 nm, respectively. When the volume-average diameter, D_v, and the intensity-average diameter, D_z, distributions for the nanoparticles were calculated, the presence of small amounts of aggregated species, representing a maximum of 5 vol %, was apparent in the D_v and D_z diameter distributions. The likely source of these larger diameter fractions is interparticle cross-linking due to the presence of the PTD sequence; however, it is unknown whether the nature of the aggregation arises from covalent cross-linking or electrostatic attraction. These findings are consistent with the large increases noted in M_w for the PTD-functionalized SCKs relative to M_w obtained for preformed SCK, **6**. Since these aggregated species were less than 100 nm in diameter, filtration and/or dialysis were not effective in their removal from the majority population of smaller nanoparticles. However, because these species represent less than 1% of the nanoparticle population by number, the contribution of these aggregates to data sets collected using imaging methods, such as atomic force microscopy (AFM), transmission electron microscopy (TEM), and confocal fluorescence microscopy, was negligible. Analysis of the SCKs by TEM depicted circular shapes that possessed narrow size distributions. The observed TEM nanoparticle diameters were smaller than those measured as D_n in buffer solution, due to drying and the effects of the phosphotunstic acid staining process employed during the TEM sample preparation. Zeta potential measurements also showed a diminishment in the negative surface charge density with increasing functionalization. The zeta potential (ζ) data for the functionalized SCKs are included in Table 1.

Quantification of PTD Functionalization. The number of peptides per particle in each sample was quantified using UV−visible spectroscopy and reaction of phenylglyoxal with the guanidine functionality of arginine as two independent methods of analysis. The number of peptides per particle was measured from UV spectroscopy by solving simultaneously for the peptide and SCK concentration using absorbance measurements recorded at two different wavelengths, λ_{230} and λ_{276}. Analysis of SCK samples **7**, **8**, and **9** resulted in values of 38, 86, and ~500 peptides per particle, respectively. The large number of peptides measured in sample **9** is a result of a slight amount of turbidity arising from aggregation, which dominates the absorbance measure-

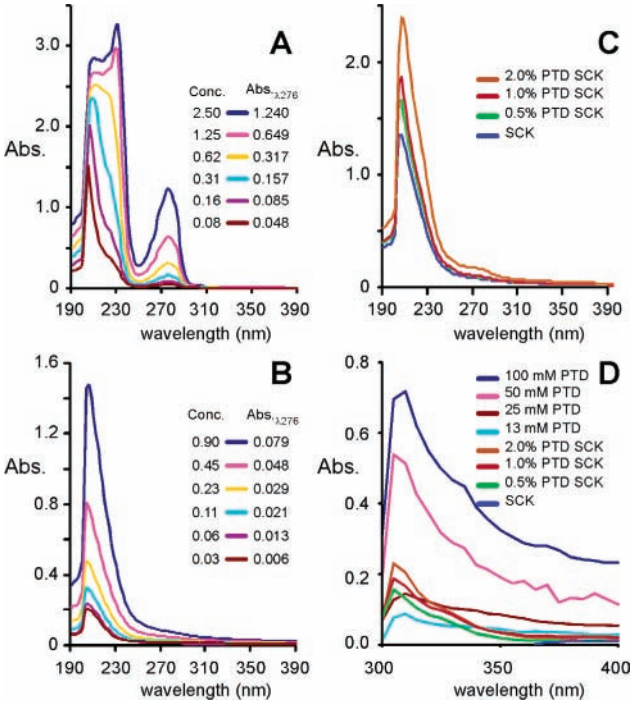


Figure 2. UV−visible spectroscopy afforded the quantitative calculation of the number of peptides per particle by two different methods. The first method involved the simultaneous solving of two unknowns as determined from PTD (A) and SCK (B) concentration calibration plots at λ_{230} and λ_{276}. From the calibration curve generated from A and B, the concentration of PTD in the respective SCK solutions (C) were calculated. The large number of peptides calculated to be in the 2.0% sample is a result of the slight amount of turbidity present in that sample due to aggregation, which is reflected in the absorbance measurement of that sample (orange). The second method involves the measurement of phenylglyoxal derivative formation (D). Phenylglyoxal reacts specifically with the guanidine groups on the side chains of arginine residues yielding a derivative with an absorbance red-shifted (λ_{310}) from that of the parent compound. From a calibration curve generated from known amounts of PTD, the molar concentration of the peptide in unknown solutions was determined. Molar ratios were then applied to quantify the number of peptides per particle.

ment at 230 nm as shown in Figure 2C. The coupling efficiency was approximately 80% and correlated well with the expected peptide numbers.

The second assay performed to quantify the number of peptides per particle employed absorbance measurements at 310 nm, which exhibited a negligible contribution from solution turbidity. Phenylglyoxal reacts specifically with the guanidine group of arginine residues under mild conditions (*29*). The PTD sequence contains six arginine residues which react with one phenylglyoxal moiety each in a mechanism outlined previously (*28*).

Measurements made using this method, again comparing molar ratios, resulted in degrees of functionalization of 41, 83, and 202 peptides for **7**, **8**, and **9**, respectively. These values are in good agreement with the dual wavelength, simultaneous UV spectroscopic determinations for the degree of functionalization in **7** and **8**. The value 202 determined by the phenylglyoxal method for **9** was in better agreement with expected values based on the measured M_w for the SCK (Table 1). The validity of the phenylglyoxal method as a specific assay for the PTD moieties attached to a SCK was also confirmed by performing the same experimental conditions for the nonfunctionalized SCK, as a negative control experiment, which showed no absorbance due to the phenylglyoxal

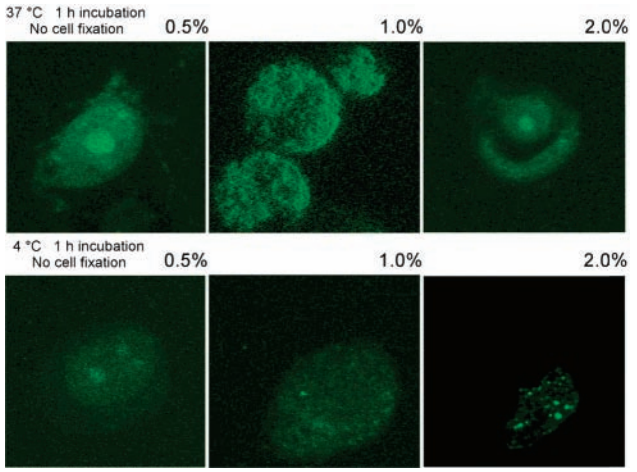


Figure 3. Live cell confocal fluorescence microscopy showing internalization of the 0.5, 1.0, and 2.0% PTD-functionalized nanoparticles at both 37 °C and 4 °C in CHO cells. No uptake or internalization was seen for the unfunctionalized, parent SCK under live cell conditions.

Table 2. the Quantification of PTD Functionalization in Each of the Respective SCK Samples Using Two Different Methods Afforded Similar Numbers of Peptides Per Particle

particle	no. of peptides nominal	no. of peptides UV−vis	no. of peptides phenylglyoxal
SCK	0	0	0
0.5%	52 ± 2	38	41
1.0%	104 ± 4	87	83
2.0%	210 ± 10	∼500	202

derivatization and thus no reaction of phenylygloxal with the unfunctionalized SCK, **6**.

Transduction Experiments. A mixed 5(6)-carboxyfluorescein derivatized with a 2,2′-(ethylenedioxy)bis(ethylamine) linker was conjugated to the PTD-functionalized nanoparticles to visually image binding interactions of the conjugates with mammalian cells using fluorescence microscopy. This type of fluorophore derivatization does not contribute to enhanced cellular uptake (*14*). The conjugation was performed on a molar equivalence basis and resulted in approximately 70 dye molecules per particle, assuming complete conversion. Free dye did not contribute to the analysis, as it was removed via dialysis against sodium PBS buffer. The cell uptake of PTD-functionalized SCKs was investigated by the in vitro transduction of CHO cells. Numerous examples exist describing the sequence specificity (*8*), mechanism (*7*, *35*), cofactor, and cell-type dependence (*36*) on the efficiency of cellular uptake. The mechanism, efficiency, and energy dependence of the particle translocation was investigated in this instance by varying the metabolic conditions of the experiments. Conditions included 1 h incubation times at 37 °C and 4 °C in serum free media, and in the presence of 0.1% sodium azide. Bright field, fluorescence, and confocal microscopies were performed on live cells as well as specimens that were fixed through 1 h incubations at ambient temperature in a 4% paraformaldehyde solution. Confocal microscopy of fixed cells clearly showed an accumulation of the fluorescent PTD functionalized nanoparticles inside the cells in all cases. Although the nonfunctionalized nanoparticles are also internalized, the apparent fluorescence intensities are qualitatively less than those of the PTD functionalized particles. Since fixation of cells involves the inherent perturbation of the cellular membrane, live cells were viewed without fixation to see whether rapid internaliza-

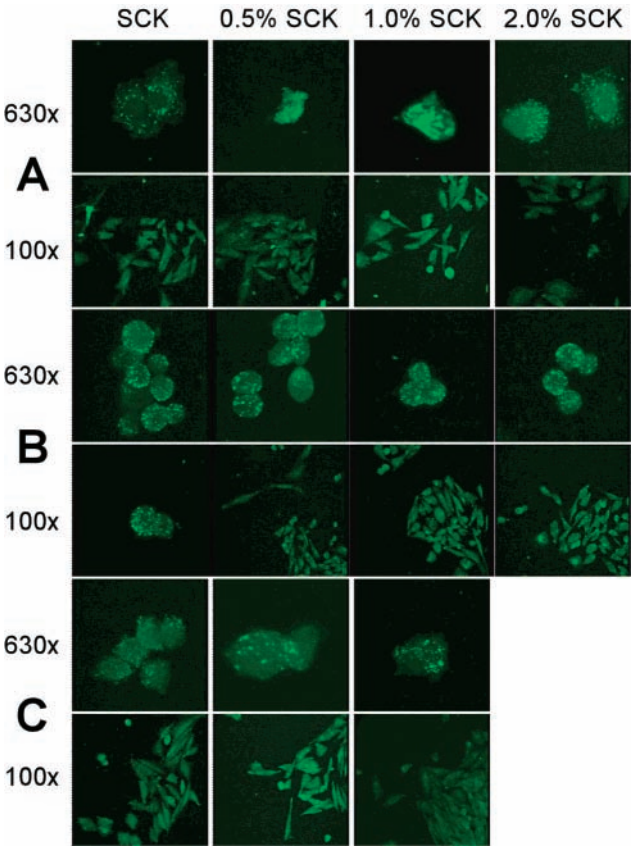


Figure 4. Confocal fluorescence microscopy of PTD-functionalized SCKs using CHO cells fixed with a 4% paraformaldehyde solution commonly used in the literature, shows nonspecific uptake of the nonfunctionalized SCKs, which was not observed in the live cell experiments, in addition to the qualitatively enhanced uptake in each of the PTD functionalized samples. A and B show the confocal reconstructions of the respective SCK samples at 37 °C and 4 °C, respectively, following 1 h incubations and cell fixation. C shows CHO cells that were incubated for 1 h in 0.1% sodium azide with the SCK samples.

tion occurred without the benefit of fixation. In the cases where the cellswere not fixed with the 4% paraformaldehyde solution, the non-PTD-functionalized SCKs were not observed in the intracellular space under fluorescence conditions when incubated at 37 °C or 4 °C, and therefore it was determined that they were either not internalized nonspecifically or not at a level that was readily measurable using optical or fluorescence microscopies. However, the 0.5%, 1.0%, and 2.0% PTD-functionalized SCK nanoparticles were readily internalized at 37 °C, 4 °C, and in the presence of 0.1% sodium azide, regardless of disruptive fixative processes that may or may not contribute to an enhanced nonspecific effect.

Flow Cytometry Analysis. The efficiency of PTD-functionalized SCK cell transduction was quantified by fluorescence activated cell sorting (FACS). Data in Table 2, which indicate the percentage of cells that are fluorescent for the respective samples, depict a trend of increasing cell transduction efficiency with increasing PTD/SCK stoichiometry. The slight decrease in the efficiency of uptake at 4 °C and in the presence of sodium azide, which depletes cellular ATP, relative to measured values at physiological temperatures suggest that endocytotic processes are also contributing to the SCK internalization. However, it is evident that nonendocytotic pathways contribute significantly to cell entry. While FACS analysis of the PTD-functionalized SCKs suggests multiple mechanisms of uptake, the intracellular internalization as visualized by live cell confocal microscopy cannot be disputed. It is important to note however that FACS analysis does not discriminate between internalized and surface bound particles, and efforts to further quantify the efficiency of uptake and exchange of the respective samples by radiolabeling methods are ongoing. The involvement of a single cellular process governing the internalization process has been shown to be increasing unlikely (*37*). While the ionic interactions between the Tat-derivatized species and the cell membrane are generally thought to be the initial step in the internalization process (*38*), the overall negative surface charge density, as measured by zeta potential, of the PTD-functionalized SCK nanoparticles suggest that further evidence is required to bolster that assessment. Recently, Dowdy et al. have shown that Tat-fusion proteins were internalized in a multistep process starting with a receptor-independent association of the fusion protein with the cell surface followed by a lipid raft-dependent macropinocytosis, which was demonstrated to be independent of interleukin-2 receptor/raft-, caveolar- and clathrin-mediated endocytosis (*39*). While these findings shed critical new and thorough insights on the mechanism of internalization, additional research on the nature of the initial construct−cell surface association step is needed.

Table 3. Percentage of Fluorescent CHO Cells Following the Transduction of Fluorescein-Labeled SCKs and PTD-Functionalized SCKs Quantified by Fluorescence-Activated Cell Sorting

particle	37 °C	4 °C	37 °C w/NaN_3	4 °C w/NaN_3
SCK	5.6	7.3	5.2	7.1
0.5%	33.9	10.3	16.3	8.5
1.0%	42.9	32.6	25.7	12.3
2.0%	47.0	36.4	51.8	13.8

CONCLUSIONS

The assembly of well-defined polymeric nanoparticles has been described, and subsequent functionalization of the SCK nanoparticles with PTD has been shown to facilitate their transduction across cellular membranes. The numbers of peptides per SCK were controlled through stoichiometric balance and measured experimentally by two independent methods. The feasibility and efficiency of intracellular internalization were quantified. In the next manuscript of this issue, the biocompatibility of these peptide-deriviatized SCK nanoparticles is measured by enzymatic and apoptosis assays, which measure the effects of SCK exposure on cellular viability, by real-time polymerase chain reaction (RT-PCR) measurements, which quantitatively assess the acute inflammatory response caused by the peptide-functionalized nanoparticles, and by a three-month mouse immunization protocol involving the measurement of IgG levels in the serum in response to nanoparticle immunizations. The biocompatibility evaluation of peptide-functionalized SCK nanoparticles and the identification of potentially detrimental interactions between biological species and SCK nanoparticles is crucial to further efforts to develop in vivo applications.

ACKNOWLEDGMENT

The authors gratefully acknowledge the National Cancer Institute (N01-CO-27103), and a Training Fellowship (M.L.B.) for the Chemistry-Biology Interface Program at Washington University funded by the NIH-NRSA (5-T32-GM08785-02) for supporting this research. Mouse myeloma B and CHO cells were kindly provided

by Professor Jacob Schaefer. TEM and confocal microscopy technical support from senior microscopist G. Michael Veith of the Washington University Department of Biology is gratefully acknowledged. Information related to the use of the phenylglyoxal assay for arginine residue analysis was generously provided by Dr. David C. Wood (Pfizer Inc.).

LITERATURE CITED

(1) Mammen, M., Choi, S. K., and Whitesides, G. M. (1998) Polyvalent Interactions in Biological Systems. *Angew. Chem., Int. Ed. 37*, 2754−2794.

(2) Wadia, J. S., and Dowdy, S. F. (2002) Protein Transduction Technology. *Curr. Opin. Biotechnol. 13*, 52.

(3) Green, M., and Loewenstein, P. (1988) Autonomous Functional Domains of Chemically Synthesized Human Immunodeficiency Virus tat Trans-activator Protein. *Cell 55*, 1179−1188.

(4) Frankel, A., and Pabo, C. (1988) Cellular Uptake of the tat Protein from Human Immunodeficiency Virus. *Cell 55*, 1189−1193.

(5) Schwarze, S. R., Ho, A., Vorcero-Akbani, A., and Dowdy, S. F. (1999) In vivo Protein Transduction: Delivery of a Biologically Active Protein into the Mouse. *Science 285*, 1569−72.

(6) Wender, P. A., Mitchell, D. J., Pattabiraman, K., Pelkey, E. T., Steinman, L., and Rothbard, J. B. (2000). The Design, Synthesis, and Evaluation of Molecules that Enable or Enhance Cellular Uptake: Peptoid Molecular Transporters. *Proc. Natl. Acad. Sci. U.S.A. 97*, 13003.

(7) Futaki, S., Nakase, I., Suzuki, T., Youjun, Z., and Sugiura, Y. (2002) Translocation of Branched Chain Arginine Peptides through Cell Membranes: Flexibility in the Spatial Disposition of Positive Charges in the Membrane-Permeable Peptides. *Biochemistry 41*, 7925.

(8) Gammon, S. T., Villalobos, V. M., Prior, J. L., Sharma, V., and Piwnica-Worms, D. (2003) Quantitative Analysis of Permeatation Peptide Complexes Labeled with Technetium-99m: Chiral and Sequence-Specific Effects on Net Cell Uptake. *Bioconjugate Chem. 14*, 368−376.

(9) Nagahara, H., Vocero-Akbani, H. M., Snyder, E. L., Ho, A., Latham, D. G., Lissy, N. A., Becker-Hapak, M., Ezhevsky, S. A., and Dowdy, S. F. (1998) Transduction of Full length TAT Fusion Proteins into Mammalian Cells: TAT-p27 induces Cell Migration. *Nat. Med. 4*, 1449.

(10) Niesner, U., Halin, C., Lozzi, L., Gunthert, M., Neri, P., Wunderli-Allenspach, H., Zardi, L., and Neri, D. (2002) Quantitation of the Tumor-Targeting Properties of Antibody Fragments Conjugated to Cell-Permeating HIV-1 Tat Peptides. *Bioconjugate Chem. 13*, 729.

(11) Jensen, K. D., Nori, A., Tijerina, M., Kopeckova, P., and Kopecek, J. (2003) Cytoplasmic Delivery and Nuclear Targeting of Synthetic Macromolecules. *J. Controlled Release 87*, 89−105.

(12) Nori, A., Jensen, K. D., Tijerina, M., Kopeckova, P., and Kopecek, J. (2003) Tat-Conjugated Synthetic Macromolecules Facilitate Cytoplasmic Drug Delivery To Human Ovarian Carcinoma Cells. *Bioconjugate Chem. 14*, 44−50.

(13) Sandhu, K. K., McIntosh, C. M., Simard, J. M., Smith, S. W., and Rotello, V. M. (2002) Gold Nanoparticle-Mediated Transfection of Mammalian Cells. *Bioconjugate Chem. 13*, 3.

(14) Zhao, M., Kircher, M. F., Josephson, L., and Weissleder, R. (2002) Differntial Conjugation of Tat Peptide to Superparamagnetic Nanoparticles and its Effects on Cellular Uptake. *Bioconjugate Chem. 13*, 840−844.

(15) Torchilin, V., Rammohan, R., Weissig, V., and Levchenko, T. S. (2001) Tat Peptide on the Surface of Liposomes Affords their Efficient Intracellular Delivery Even at Low Temperature and in the Presence of Metabolic Inhibitors. *Proc. Natl. Acad. Sci. U.S.A. 98*, 8786.

(16) Klok, H.-A., and Lecommandoux, S. (2001) Supramolecular Materials via Block Copolymer Self-Assemble. *Adv. Mater. 34*, 1217−1229.

(17) Matyjaszewski, K., and Xia, J. (2001) Atom Transfer Radical Polymerization. *Chem. Rev. 101*, 2921−2990.

(18) Hawker, C. J., Bosman, A. W., and Harth, E. (2001) New Polymer Synthesis by Nitroxide Mediated Living Radical Polymerizations. *Chem. Rev. 101*, 3661−3688.

(19) Thurmond, K. B., II, Kowalewski, T., and Wooley, K. L. (1996) Water-Soluble Knedel-like Structures: The Preparation of Shell-Cross-Linked Small Particles. *J. Am. Chem. Soc. 118*, 7239−7240.

(20) Liu, S., Weaver, J. V. M., Save, M., and Armes, S. P. (2002) Synthesis of pH-Responsive Shell Cross-Linked Micelles and Their Use as Nanoreactors for the Preparation of Gold Nanoparticles. *Langmuir 18*, 8350−8357.

(21) Buetuen, V., Lowe, A. B., Billingham, N. C., and Armes, S. P. (1999) Synthesis of Zwitterionic Shell Cross-Linked Micelles. *J. Am. Chem. Soc. 121*, 4288−4289.

(22) Wooley, K. L. (2000) Shell Cross-linked Polymer Assemblies: Nanoscale Constructs Inspired from Biological Systems. *J. Polym. Sci., Part A: Polym. Chem. 38*, 1397−1407.

(23) Huang, H., Kowalewski, T., Remsen, E. E., Gertzmann, R., and Wooley, K. L. (1997) Hydrogel-Coated Glassy Nanospheres: A Novel Method for the Synthesis of Shell Cross-Linked Knedels. *J. Am. Chem. Soc. 119*, 11653−11659.

(24) Remsen, E. E., Thurmond, K. B., II, and Wooley, K. L. (1999) Solution and Surface Charge Properties of Shell Cross-Linked Knedel Nanoparticles. *Macromolecules 32*, 3685−3689.

(25) Huang, H., Wooley, K. L., and Schaefer, J. (2001) REDOR Determination of the Composition of Shell Cross-Linked Amphiphilic Core−Shell Nanoparticles and the partitioning of Sequestered Fluorinated Guests. *Macromolecules 34*, 547−551.

(26) Kao, H.-M., O'Connor, R. D., Mehta, A. K., Huang, H., Poliks, B., Wooley, K. L., and Schaefer, J. (2001) Location of Cholic Acid Sequestered by Core−Shell Nanoparticles Using REDOR NMR. *Macromolecules 34*, 544−546.

(27) Liu, J., Zhang, Q., Remsen, E. E., and Wooley, K. L. (2001) Bioconjugates of Protein Transduction Domain(PTD) and Shell Cross-Linked Nanoparticles: Nanostructured Materials Designed for Delivery into Cells. *Biomacromolecules 2*, 362−368.

(28) Jairajpuri, M. A., Azam, N., Baburaj, K., Bulliraju, E., and Durani, S. (1998) Charge and Solvation Effects in Anion Reactive Centers: an Inquiry Exploiting Reactive Arginines. *Biochemistry 37*, 10780−10791.

(29) Takahashi, K. (1968) The Reaction of Phenylglyoxal with Arginine Residues in Proteins. *J. Biol. Chem. 243*, 6171−6179.

(30) Miller, J. F., Schatzel, F., and Vincent, B. (1991). The Determination of very Small Electrophoretic Mobilities in Polar and Nonpolar Colloidal Dispersions Using Phase-Analysis Light-Scattering *J. Colloid Interface Sci. 143*, 532.

(31) Wang, J.-S., and Matyjaszewski, K. (1995) Controlled/Living Radical Polymerization. Atom Transfer Radical Polymerization in the Presence of Transition Metal Complexes. *J. Am. Chem. Soc. 117*, 5614−15.

(32) Ma, Q., and Wooley, K. L. (2000) The Preparation of tert-Butyl Acrylate, Methyl Acrylate, and Styrene Block Copolymers by Atom Transfer Radical Polymerization: Precursors to Amphiphilic and Hydrophilic Block Copolymers and Conversion to Complex Nanostructured Materials. *J. Polym. Sci., Part A: Polym. Chem. 38*, 4805−4820.

(33) Becker, M. L., Remsen, E. E., and Wooley, K. L. (2001) Diblock Copolymers, Micelles, and Shell Cross-linked Nanoparticles Containing Poly(4-fluorostyrene): Tools for Detailed Analysis of Nanostructured Materials. *J. Polym. Sci.: Polym. Chem. 39*, 4215.

(34) Murthy, K. S., Ma, Q., Clark, C. G., Jr., Remsen, E. E., and Wooley, K. L. (2001) Fundamental Design Aspects of Amphiphilic Shell-Cross-linked Nanoparticles for Controlled Release Applications. *Chem. Commun.*, 773−774.

(35) Suzuki, T., Futaki, S., Niwa, M., Tanaka, S., Ueda, K., and Sugiura, Y. (2002) Possible Existence of Common Internaliza-

tion Mechanisms among Arginine Rich Peptides. *J. Biol. Chem. 277*, 2437−43.
(36) Mai, J., C., Shen, H., Watkins, S., C., Cheng, T., and Robbins, P. D. (2002) Efficiency of Protein Transduction is Cell Type Dependent and is Enhanced by Dextran Sulfate. *J. Biol. Chem. 277*, 30208−30218.
(37) Vives, E., Richard J. P., Rispal, C., Lebleu, B. (2003) TAT Peptide Internalization: Seeking the Mechanism of Entry. *Curr. Protein Pept. Sci. 4*, 125−132.
(38) Vives, E. (2003) Cellular Uptake of the Tat Peptide: An Endocytosis Mechanism Following Ionic Interactions. *J. Mol. Recognit. 16*, 265−272.
(39) Wadia, J. S., Stan, R. V., Dowdy, S. F. (2004) Transducible TAT-HA Fusogenic Peptide Enhances Escape of TAT-fusion Proteins After Lipid Raft Macropinocytosis. *Nat. Med. 10* (3), 310−315.

BC049946E

Peptide-Derivatized Shell-Cross-Linked Nanoparticles. 2. Biocompatibility Evaluation

Matthew L. Becker,*[,†,‡] LeeAnn O. Bailey,[‡] and Karen L. Wooley*[,†]

Center for Materials Innovation and Department of Chemistry, Washington University, One Brookings Drive, St. Louis, Missouri 63130, and National Institute of Standards and Technology, Polymers Division, Biomaterials Group, Gaithersburg, Maryland 20899-8543. Received March 4, 2004; Revised Manuscript Received April 26, 2004

The conjugation of the protein transduction domain (PTD) from the HIV-1 Tat protein to shell cross-linked (SCK) nanoparticles is a method to facilitate cell surface binding and transduction. In the previous report, the preparation, derivatization, and characterization of peptide-functionalized SCK nanoparticles were reported in detail. Following assembly, the constructs were evaluated in vitro and in vivo to obtain a preliminary biocompatibility assessment. The effects of SCK exposure on cell viability were evaluated using a metabolic 3-(4,5-dimethylthiazol-2-yl)-2,5-diphenyl-2*H*-tetrazolium bromide (MTT) and a fluorescent apoptosis assay. Furthermore, stages of apoptosis were quantified by flow cytometry. Although higher levels of peptide functionalization resulted in decreased metabolic function as measured by MTT assay, significant apoptosis was not observed below 500 mg/L for all the samples. To evaluate the potential immunogenic response of the peptide-derivatized constructs, a real-time polymerase chain reaction (RT-PCR) system that allows for the in vitro analysis and quantification of the cellular inflammatory responses tumor necrosis factor alpha (TNF-α) and interleukin-1 beta (IL1-*β*) was utilized. The inflammatory response to the peptide-functionalized SCK nanoparticles as measured by RT-PCR show statistically significant increases in the levels of both TNF-α and IL1-*β* relative to tissue culture polystyrene (TCPS). However, the measured cytokine levels did not preclude the further testing of SCKs in an in vivo mouse immunization protocol. In this limited assay, measured increases in immunoglobulin G (IgG) concentration in the sera were minimal with no specific interactions being isolated, and more importantly, none of the mice (>50) subjected to the three 100 *μ*g immunization protocol have died. Additionally, no gross morphological changes were observed in postmortem organ histology examinations.

INTRODUCTION

New synthetic methodologies (*1*−*3*) are enabling remarkable advances in the rational design of polymeric materials that actively control cellular and physiologic responses. These methods produce well-defined materials that are incorporated into scaffolds capable of performing specific functions while being minimally detrimental to normal cellular processes and surrounding tissues for use in therapeutic (*4*−*6*), drug delivery (*7*−*10*), and tissue engineering applications (*11, 12*). One of the critical challenges in clinical medicine currently under intense investigation is the efficient delivery of macromolecules into cells for the purposes of drug, gene, and cancer therapies (*13, 14*). In the previous article of this issue, the preparation, characterization, and biological evaluation of peptide-functionalized shell-cross-linked (SCK) nanoparticles are reported. SCK nanoparticles (*15, 16*) are micellar assemblies of amphiphilic copolymers that have been stabilized through the incorporation of covalent cross-links in the shell layer (*17*). Syntheses of complex block copolymer precursors have afforded control over the physicochemical properties of the respective nanoparticle domains (*6*, *18*, *19*). Surface charge (*20*) and functionality are controlled easily and can be tailored for specific applications (*21*). The protein transduction domain (PTD) of HIV-1 Tat (*22, 23*) has been shown to shuttle much larger molecules into cells independent of classical endocytosis (*24*) which affords intracellular access to living cells for nuclear targeting strategies (*25*), gene (*14, 26*), radiotherapies (*27*−*29*) and other purposes. The attachment of increasing numbers of protein transduction domain (PTD) motifs to SCK nanoparticles is being investigated as a method to increase the efficiency of cell-penetrating transduction. Further extension of the peptide-derivatized conjugates into biological applications requires the elucidation of how increasing peptide functionality affects the biocompatibility of the derivatized nanostructures, including the cellular apoptosis and inflammatory responses. The effects on cell viability are evaluated by metabolic and flow cytometry assays. Measuring the effects of foreign substances on in vitro cell viabilities is typically accomplished by the exposure of a cell population to the conjugate and then monitoring the enzymatic reduction of MTT to formazan in the mitochondria of living cells (*30*). The viability is then expressed as a percentage of

* To whom correspondence should be addressed. K.L.W.: Tel. (314) 935-7136, fax (314) 935-9844, e-mail: klwooley@artsci.wustl.edu. M.L.B.: Tel. (301) 975-6842, e-mail: mlbecker@nist.gov.

† Washington University.

‡ National Institute of Standards and Technology.

[1] Abbreviations: ATCC, American Type Culture Collection; CHO, chinese hamster ovary; ELISA, enzyme-linked immunosorbent assay; FMOC, 9-fluorenylmethyloxycarbonyl; HBSS, Hanks buffered salt solution; IgG, immunoglobulin G; IL, interleukin; MTT, 3-(4,5-dimethylthiazol-2-yl)-2,5-diphenyl-2*H*-tetrazolium bromide; PBS, phosphate-buffered saline; PS, phospholipid phosphatidylserine; PTD, protein transduction domain; RPMI, Roswell Park Memorial Institute; RT-PCR, real-time polymerase chain reaction; SCK, shell-cross-linked nanoparticle; SDS, sodium dodecyl sulfate; TNF, tumor necrosis factor.

10.1021/bc049945m CCC: $27.50 © 2004 American Chemical Society
Published on Web 06/16/2004

cells that are dead as a function of the nanoparticle concentration. Another method to measure cell viability is an apoptosis assay, which is a technique that monitors cell membrane translocation events and the accessibility of nuclear material in response to extracellular perturbations, and the various stages of apoptosis are then quantified by flow cytometry. The ability to monitor the emission wavelengths of the respective fluorophores affords flow cytometry the ability to discriminate and quantify distinct populations of cells (*31*). It is anticipated that the two techniques will provide a complementary and accurate assessment of the effects of SCK exposure on cell viability.

Measurement of the acute inflammatory reaction in response to peptide-derivatized SCK nanoparticle exposure is another critical component in the assessment of the biocompatibility. Inflammation is characterized by the regulation of cytokines, which are responsible for the initiation, mediation, and propagation of the inflammatory response including lymphocyte activation, proliferation, differentiation, angiogenesis, and apoptosis (*32*). Quantifying the regulatory profile of cytokines at the protein level is difficult due to small sample sizes, which has created a need for alternative measurement methods. The measurement of mRNA levels is used widely to investigate the cytokine profiles at sites of inflammation (*32*). There are several techniques, aside from PCR-based methodologies, used commonly to quantify mRNA expression including Northern blotting, in situ hybridization, RNase protection assays, and cDNA arrays, each of which is limited by low measures of sensitivity (*33, 34*). Real-time polymerase chain reaction (RT-PCR) is a method for enzymatically amplifying defined sequences of mRNA, and it is the most sensitive, accurate, and adaptable of the mRNA quantitative techniques (*33, 35*). Quantitative RT-PCR has the advantage of being extremely sensitive over a large range of quantification, requires no post-PCR sample handling (*36, 37*), and has previously afforded measurement of the genetic regulatory profiles for inflammatory cytokines in response to synthetic materials (*38, 39*). Herein, a preliminary biocompatibility assessment of peptide-derivatized SCK nanoparticles is described in detail including enzymatic and apoptosis assays, which measure the effects of SCK exposure on cellular viability. In addition, RT-PCR measurements were used to quantitatively assess the inflammatory response caused by the peptide-functionalized nanoparticles. Following in vitro testing methodologies, a three-month mouse immunization protocol involving multiple booster immunizations found minimal increases in IgG levels in the serum and furthermore elucidated no specific immunogenic response. The initial biocompatibility evaluation of peptide-functionalized SCK nanoparticles described in this article, while limited in scope, is a critical first step toward the identification of potentially detrimental interactions between biological species and SCK nanoparticles. Furthermore, these in vitro assays and limited in vivo studies provide justification for additional animal studies, including biodistribution and liver function assays, which are crucial to efforts to develop in vivo therapeutic applications.

EXPERIMENTAL PROCEDURES

Materials. FMOC-protected amino acids and preloaded solid-phase Wang resins were purchased from NovaBiochem-CalBiochem Corp (San Diego, CA). Sodium dodecyl sulfate (SDS), 3-(4,5-dimethylthiazol-2-yl)-2,5-diphenyl-2*H*-tetrazolium bromide (98%) (MTT), Tween20, mouse IgG (Fc, Sigma I-8765), and goat anti-mouse IgG alkaline phosphatase conjugate (Fc specific, Sigma A-1418) were purchased from Sigma (St. Louis, MO). Alkaline phosphate substrate solution was purchased from BioRad (Hercules, CA). Spectra/Por dialysis membranes (Spectrum Laboratories, Inc., Rancho Dominguez, CA), 96-well polystyrene plates (Falcon), and ELISA plates (Nunc-Immuno, Maxisorp) were purchased from Fisher Scientific Company (Pittsburgh, PA). QuantiTect SYBR Green RT-PCR Kit and Rneasy Kit were obtained from Qiagen (Valencia, CA). Primer identification, isolation, and probe development were nearly identical to methods described previously (*38, 39*).

Certain commercial materials and equipment are identified in this paper in order to specify adequately the experimental procedure. In no case does such identification imply recommendation by the National Institute of Standards and Technology nor does it imply that the material or equipment identified is necessarily the best available for this purpose.

The Animal Facility at the Washington University Department of Biology handled immunizations, sera collections, and organ histology. Animal studies were conducted under Protocol 20010343 approved by the Animal Studies Committee of Washington University.

Cell Lines. Mouse myeloma B cells (ATCC, Manassas, VA) CRL-1581.1 and CHO cells (ATCC) were obtained as gifts from Professor Jacob Schaefer (Washington University, St. Louis, MO). Mouse myeloma B cells were cultured in RPMI (Life Technologies, Rockville, MD) 1640 media using TCM serum replacement (10%, volume fraction) obtained from Celox Laboratories (St. Paul, MN). RAW 264.7 cells were purchased from ATCC. RAW 264.7 and CHO cells were maintained in RPMI supplemented with 10% (volume fraction) heat-inactivated fetal bovine serum (FBS, Life Technologies, Rockville, MD), in 5% CO_2:95% air (volume fractions) at 37 °C. To harvest, RAW 264.7 cells were washed with calcium- and magnesium-free phosphate-buffered saline and subsequently incubated with HBSS to promote release from the flask.

Determining Cell Viability via MTT Assay. Mouse myeloma B cells were counted and diluted into fresh media at concentrations of 50 000 cells/mL and an aliquot (100 μL) was seeded to each well in a 96-well plate. After deposition of the cell suspension, the plates were placed in an incubator (37 °C, 5% CO_2, volume fraction) and allowed to grow for 24 h. Fresh 96-well plates were loaded with sterile buffer (40 μL), and the first column of each row was loaded with polymer or SCK stock solutions of known concentration. The first columns in each plate were then diluted serially from columns 2 to 11. The last columns were held as controls with no polymer or SCK added. Fresh media (50 μL) was then added to every well in the plates. The original plates were removed from the incubator, and the premixed sample solutions were added to the corresponding wells in each plate. After 24 h incubation, the inoculated plates were removed from the incubator, and an aliquot of MTT (Sigma) (20 μL, 5.00 mg/mL) in PBS (0.05 mol/L phosphate, 0.05 mol/L sodium chloride, pH 7.4) was added to each well. The plates were returned to the incubator and allowed to equilibrate for 2 h. After 2 h, extraction buffer (80 μL, 20% (mass fraction) SDS (Sigma) in 50:50 DMF:H_2O, volume fraction, pH 4.7) was added to each well to extract the aqueous insoluble formazan product. The plates were then returned to the incubator for 18 h to allow for the extraction after which the absorbance of each solution was measured at 560 nm. Concentrations were determined by the weight of lyophilized polymer sample dissolved in PBS and then adjusted for the dilution of

the media. Results are an average of four values, and the standard deviation is reported for each concentration.

Apoptosis Assay. Apoptotic analysis of RAW 264.7 cells was assessed using the Guava Nexin Kit (Guava Technologies, Hayward, CA). RAW 264.7 cells were plated in 12-well plates at 50 000 to 100 000 cells per well and allowed to adhere for 24 h, after which the cells were inoculated with 100 μL aliquots of the respective samples. The initial quantity of SCK was suspended in 0.500 of PBS. The respective samples were subsequently added to RAW 264.7 cultures (100 μL). After 24 h, the media was removed from the cells, and the cultures were washed with PBS. To promote release from the plate, the cells were incubated with 1 mL of HBSS for 30 min. The cells were then gently removed from the plate, and the volume was adjusted to 300 μL. The cell suspension was incubated with 5 μL of Nexin 7-AAD and 5 μL of Annexin V−PE for 5 min in a light-protected environment and subsequently analyzed.

Flow Cytometry. Apoptotic analysis of RAW 264.7 cells incubated on the thin films or in the presence of the nanoparticles was assessed using the Guava Nexin Kit (Guava Technologies, Hayward, CA). RAW 264.7 cells were plated in 24-well plates (50 000 to 100 000) cells per well and allowed to adhere on tyrosine-derived polycarbonate thin films or tissue culture polystyrene for 24 h prior to analysis by flow cytommetry. Full experimental details were described previously (*38, 39*).

mRNA Extraction. Cells were plated in sterile 150 mm × 25 mm nonpyrogenic polystyrene dishes (Daigger, Vernon Hills, IL). SCK nanoparticles were added to plated cells 24 h following seeding. The mRNA extraction was carried out using the materials and protocol provided in the Rneasy Kit from Qiagen (Valencia, CA). The mRNA extraction protocol was followed according to the manufacturer's specification, except a 21-gauge needle was used to homogenize the sample. The RNA was treated with RNA Secure immediately following elution and stored at −20 °C. Standard spectrophotometric measurements were taken, and a 2% (mass fraction) agarose gel stained with 10 μg/mL ethidium bromide (Sigma, St. Louis, MO) was used to image the RNA. Densitometry was performed using the Versa Doc imaging system (Bio-Rad, Hercules, CA).

Standards. The plasmids containing the cDNA inserts for TNF-α, IL-1β, and the18 S ribosomal subunit were purchased from ATCC. The plasmids were grown in *luria-bertani* (LB) medium (ATCC, medium 1065) with 100 μg/mL of ampicillin for selection purposes. Plasmid DNA was isolated using the Plasmid Giga Kit (Qiagen, Valencia, CA) following the manufacturer's protocol. Spectrophotometric measurements were made at 260 nm, and a 1% (mass fraction) agarose gel stained with 10 μg/mL ethidium bromide (Sigma, St. Louis, MO) was used to image the DNA. Densitometry was performed using the Versa Doc imaging system (Bio-Rad, Hercules, CA).

Primer Design. Primers were designed using Primerfinder (Whitehead Institute for Biomedical Research) for the RT-PCR experiments. The primers generated were used in both PCR and RT-PCR experiments. They are as follows:

18S: 5′ agcgaccaaaggaaccataa 3′ and 3′ ctcctcctcctcctctctcg 5′

TNF-α: 5′ tttcctcccaataccccttc 3′ and 3′ agtgcaaaggctccaaagaa 5′

IL-1β: 5' tgtgaaatgccacctttga 3' and 3' gtagctgccacagcttctcc 5'

The amplicons generated from these primers are 204 base pairs, 202 base pairs, and 205 base pairs, respectively. DNA sequencing was performed using the Big Dye Terminator Kit (ABI, Foster City, CA) on a 310 DNA Genetic Analyzer (ABI, Foster City, CA).

RT-PCR. RT-PCR was carried out using the Quanti-Tect SYBR Green RT-PCR Kit and protocol (Qiagen, Valencia, CA). All RT-PCR experiments were performed using the iCycler (Bio-Rad, Hercules, CA). The protocol utilizes the following thermal parameters: Reverse Transcription: 30 min at 50 °C. Activation step: 15 min at 95 °C. Three-step cycling: denaturation for 30 s at 95 °C, annealing for 2 min at 57 °C, extension for 2 min at 72 °C for 45 cycles. A melt curve was subsequently performed to analyze the products generated, which began at 50 °C and increased to 95 °C in 1 °C increments.

Immunization of Mice. For each sample, five mice (female, balb c, 7 weeks old) were inoculated with 100 μL of polymer or SCK solution (1 mg/mL in PBS) at (0, 4, and 8) weeks. The mice were bled for preimmunoserum screening prior to the primary injection. Blood samples were then collected 14 d after (4 and 8)-week booster immunizations, respectively. Serum was obtained after clotting at 4 °C, for 24 h, and centrifugation. Serum samples were stored at −20 °C in small aliquots for later use.

Determining Antibody Titer by ELISA Assay. Samples for ELISA for the five mice were first prepared by dilution in five 96-well plates. PBS buffer (100 μL) was added to each well in the plates. The serum vials were thawed, and each serum sample (5 μL) was diluted 1:100 in PBS and was transferred, in quadruplicate, in aliquots (100 μL) to the first four wells in the top row of each corresponding plate. The serum obtained following the first booster immunization was added to the next four wells, and the serum obtained following the second booster immunization was added to the final four wells, columns 9 to 12. The serum was then serially diluted 2-fold in rows 2−7 in each plate. Following dilution, 100 μL from each well was transferred to a corresponding ELISA (Nunc-Immuno, Maxisorp) plate and incubated overnight at 4 °C. The wells were washed three times with PBS buffer (300 μL) containing 0.05% (mass fraction) Tween 20 (Sigma), and the remaining binding sites on the plates were blocked with sodium caseinate (100 μL, 2.5%, mass fraction, in PBS) followed by overnight incubation at 4 °C. The wells were again washed three times, and a 1:40 000 dilution of goat anti-mouse IgG alkaline phosphatase conjugate (100 μL, Sigma) was added to each well and allowed to incubate for 1 h at room temperature before being washed five times. Alkaline phosphatase substrate solution (100 μL, BioRad) was added to each well. Color development was allowed to take place for 30 min and then was quenched with 4 mol/L H_2SO_4 (50 μL per well). Absorption measurements were made at 405 nm. To determine the absolute antibody concentrations, mouse IgG standards were run in parallel with each ELISA plate. Serial dilutions of mouse IgG (from 5.00 to 0.08 μg/mL) were used to generate the linear calibration plot of absorbance vs concentration. The value corresponding to 0 μg/mL was the background reading and was subtracted from all samples.

RESULTS AND DISCUSSION

The assessment of material biocompatibility is a complicated process, which includes both in vitro and in vivo measurement methods, each of which depend on the physical and chemical nature of the material and the nature of the biological interaction. Surface characteristics such as hydrophobicity, morphology, surface charge, and chemical functionality are all known to play key roles

Table 1. PTD-Derivatized SCK Characterization Data

no.	sample composition	no. of peptides nominal	no. of peptides UV−vis	no. of peptides phenylglyoxal	zeta (mV)	DLS D_n (nm)
5	micelle	0	0	0	−27 ± 0.7	38 ± 3
6	SCK	0	0	0	−20 ± 0.5	37 ± 2
7	0.5% PTD SCK	52 ± 2	38	41	−28 ± 0.9	35 ± 3
8	1.0% PTD SCK	104 ± 4	87	83	−23 ± 0.7	36 ± 3
9	2.0% PTD SCK	210 ± 10	~500	202	−22 ± 0.5	32 ± 4

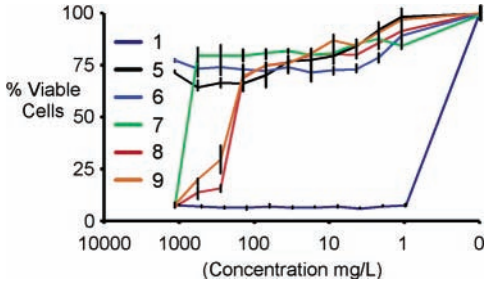


Figure 1. The conjugation of the PTD sequence to the SCKs has dramatic effects on the resulting cell viability. The 2.0% PTD-functionalized SCK **9** is toxic to the cells between 7 mol/L to 13 mol/L in PTD. The 0.5% and 1.0% PTD-functionalized SCKs (**7** and **8**) are toxic between 14 mol/L to 28 and 7 mol/L to 15 mol/L in PTD, respectively. The parent micelles and SCKs (**5** and **6**) did not affect the viability of the cells at any measured concentration. Error bars are representative of one standard deviation from the mean of quadruplicate samples harvested from four separate wells of mouse myeloma B cells and are the estimates of the standard uncertainties.

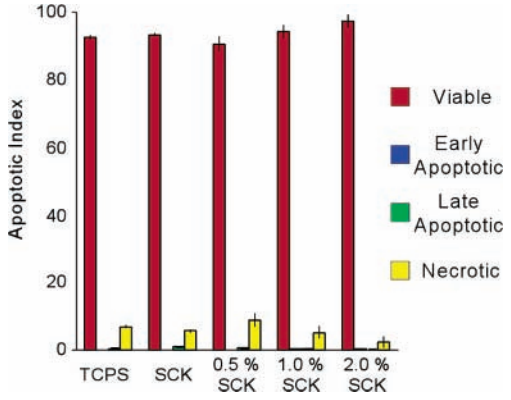


Figure 2. Four distinct populations of cells can be identified with flow cytometry. Viable cells: Annexin V (−) and 7-AAD (−); early apoptotic cells: Annexin V (+) and 7-AAD (−); late stage apoptotic: Annexin V (+) and 7-AAD (+); necrotic: Annexin V (−) and 7-AAD (+). Error bars are representative of one standard deviation from the mean of triplicate samples, each harvested from three separate populations of RAW 264.7 cells, and are the estimates of the standard uncertainties.

in governing cell adhesion and proliferation (*40*). Several physicochemical parameters for the PTD-derivatized SCK nanoparticles whose syntheses and characterization are described in the previous article of this issue are outlined in Table 1. However, a clear framework outlining the critical physiochemical and surface-mediated interactions within which to facilitate the development of materials minimally detrimental to cells does not exist. For applications concerning the delivery of macromolecules into cells, the enhanced efficiency of conjugate transduction must be weighed against any detrimental biological interactions including effects on both cell viability and immune response. The cell viabilities in the presence of the peptide-derivatized polymeric constructs were evaluated by MTT assay (*30*), which monitors enzymatic activity of a cell organelle (in this case mitochondria), and flow cytometry. Previously, the protein transduction sequence has been used at concentrations of up to 100 μmol/L without affecting the viability of certain cell lines (*41*).

As illustrated by the data of Figure 1, the PTD sequence, with four additional glycine residues, was found to decrease the enzymatic reduction of MTT in the mitochondria of mouse myeloma B cells at approximately 110 μmol/L concentrations. In contrast, the viabilities of the cells upon exposure to buffered solutions of micelles or SCKs remain (70 to 90) % at concentrations above 100 mg/L. The small drop in viability is due primarily to the dilution of the media as shown by control experiments in which buffer and no buffer were added to different cell populations. Exposure of the cells to the parent PAA_{56}-*b*-PMA_{185} micelles, **5**, and the corresponding unfunctionalized SCK, **6**, did not affect cell viability up to 1125 mg/L concentrations. However, the derivatization of the nanoparticle with increasing numbers of the PTD sequence has a significant effect on the viability of the cell populations as measured by the enzymatic function. The 2.0% PTD-functionalized SCK **9** is toxic to the cells between (140 and 280) mg/L (7 μmol/L to 13 μmol/L in PTD). The 0.5% and 1.0% PTD-functionalized SCKs (**7** and **8**) are toxic between (560 and 1125) mg/L (14 μmol/L to 28 μmol/L and 7 μmol/L to 15 μmol/L in PTD, respectively). The mechanism of toxicity has not been determined.

In addition to the MTT enzymatic assay, the peptide-derivatized nanoparticles have been evaluated by a fluorescent flow cytometry experiment to determine the effects of incubation with SCKs upon the induction of apoptosis. Apoptosis is characterized by numerous morphological changes, the first of which involves the translocation of phosphatidylserine (PS) from the inner to the outer surface of the cellular plasma membrane. Once exposed to the extracellular environment, PS sites are accessible to Annexin V, a phospholipid binding protein with a high affinity for PS. For measurement purposes, Annexin V is conjugated to FITC and used for the identification of cells in the early stages of apoptosis via flow cytometry. Because PS binding sites are also accessible when the cells are in a necrotic state, Annexin V is not an absolute marker of apoptosis. Therefore, it is often used in conjunction with 7-aminoactinomysin, (7-AAD) which binds to exposed nucleic acids, when the cell membrane integrity is compromised. Cells that are negative (unstained) for both Annexin V and 7-AAD have no indications of apoptosis: PS translocation has not occurred, and the plasma membrane remains intact. Cells that are Annexin V (+) and 7-AAD (−), however, are in early apoptosis, as PS binding sites are exposed, but the plasma membrane is still intact. Cells that are (+) for both Annexin V and 7-AAD are either in the late apoptosis (irreversible) stage or are not viable. The flow cytometry data shown in Figure 2 indicate that the SCKs do not induce apoptosis at the concentrations tested. The total inoculated concentration was 0.5 mg/mL (500 mg/L) for each SCK sample. In addition, a visual assessment of the effects of exposure to PTD-derivatized SCKs at the 5 day time point indicated that the nanoparticles did not affect the continued growth of the cells nor did they

induce significant morphological changes (data not shown). These results are comparable to the MTT assay results. Although the MTT assay depicts a shutdown in mitochondrial function at certain concentrations, exposure of each of the samples to the cells at concentrations of 500 mg/L did not lead to cellular apoptosis.

Immunogenicity Results. The extent of PTD functionality is of significant importance as it may affect the immune response. The nature of the response has significant clinical implications, as severe inflammatory responses may prevent in vivo applications. Recent literature has reported that the addition of HIV Tat PTD enhances minigene epitope presentation in tissue culture, but the attachment of PTD to full-length proteins does not enhance the immune response of the construct (*42*). The reported data were for a 1:1 stoichiometry of PTD: protein, and it is unclear whether the presentation of multiple copies of the sequence on the surface of an SCK would have a synergistic or negligible effect on the cellular immune response. The initiation and propagation of an immune response is ultimately regulated by cytokines. Cytokines are the primary mediators of a host immune response and are able to both induce apoptosis and modulate survival through the activation of genes in response to bacterial toxins, inflammatory products, and other invasive stimuli (*43*). Two of the most important cytokines in the acute inflammatory response are tumor necrosis factor alpha (TNF-α) and interleukin-1 beta (IL1-*β*) (*44*). TNF-α is synthesized and secreted by macrophages. TNF-α is part of a complex network of cytokines and is capable of initiating cascades, which control the synthesis and expression of signaling molecules, hormones, and their receptors (*45*−*47*). Knowledge of the cellular cytokine profile is key to identifying the processes involved in the immune response (*48*) and crucial to the further elucidation on the physicochemical properties of the bioconjugate that are inducing the response. Another prominent cytokine involved in the inflammatory responses is interleukin-1 (IL-1). Although IL-1 protects the organism by enhancing the response to pathogens and initiating healing process, its overproduction can induce numerous pathological consequences including septic shock and leukemia (*21*). The measurement of mRNA levels has been used widely to measure cytokine proliferation, which is responsible for the initiation, mediation, and propagation of cellular inflammatory responses (*32*). The genetic expression profiles of IL-1*β* and TNF-α have been measured by real-time polymerase chain reaction (RT-PCR) (*49*). In this study, the mRNA profiles of TNF-α and IL-1*β* in response to PTD, SCKs, and SCKs derivatized with increasing amounts of PTD sequences were investigated using RT-PCR. In the previous manuscript of this issue, PTD was conjugated in (0.005, 0.01, and 0.02) molar ratios, relative to the acrylic acid residues in the shell, to the SCK nanoparticles resulting in SCK populations nominally possessing 52, 104, and 210 (41, 83, and 202 as measured by phenylglyoxal) PTD peptides per particle, respectively. RAW 264.7 cells were used because they retain the characteristics of primary cultured macrophages in vitro, including the ability to release cytokines (*50*−*53*). Cells were exposed to the respective SCK nanoparticle samples by adding the conjugates to the murine macrophages 24 h following seeding. After a 24 h incubation period, the mRNA was extracted from the cell populations. Using a reverse transcriptase enzyme, mRNA is converted to the cDNA template necessary for amplification. Once cDNA is generated, gene specific primers, a DNA polymerase, and a fluorescent moiety are utilized to amplify and label

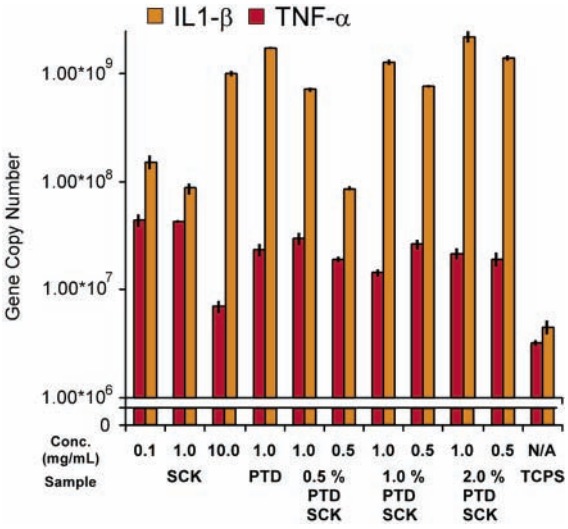


Figure 3. Genetic cellular inflammatory responses exhibited 24 h after incubation with different concentrations of peptide-functionalized SCK nanoparticles were quantified by RT-PCR. The data depict minimal increases in the production of TNF− and an elevation in the levels of IL-1 relative to tissue culture polystyrene. Error bars are representative of one standard deviation from the mean of triplicate samples, each harvested from three separate populations of RAW 264.7 cells, and are the estimates of the standard uncertainties.

the amplicon generated. The gene product accumulation was then measured during the exponential phase of the amplification reaction (*36*). The copy number from each of the samples was obtained by extrapolating to a standard gene curve of known concentration and copy number to yield quantitative data. The assay also includes the analysis of mRNA that does not change in relative abundance (18S) during the course of treatment to serve as an internal control (*54*). The genetic profiles of the inflammatory response to SCKs (**1**−**3**), PTD (**4**), PTD-functionalized SCK nanoparticles (**5**−**10**), and tissue culture polystyrene (TCPS, **11**) are shown in Figure 3.

TNF-α mRNA synthesis was up-regulated 2-fold to 14-fold (depending on concentration) in response to exposure of the parent SCK nanoparticle, **6**, over TCPS. It is interesting to note that the highest concentration, 10.0 mg/L, of the parent SCK **6** actually caused less of an increase, 2.2-fold, than lower concentrations, 0.1 and 1.0 mg/L, of SCK **6**, 13.5-fold and 13.2-fold, respectively. When looking at the effects of parent SCK concentration on TNF-α production, the difference between (0.1 and 1.0) mg/mL are statistically insignificant, while the 10.0 mg/mL sample measures 6.1-fold less than at the 1.0 mg/mL level. Interestingly, the down-regulation of TNF-α has been demonstrated previously in liposome vectors formulated with cationic lipids (*55*). The measured TNF-α levels for the PTD-functionalized SCKs are less than the levels of the parent SCK in all cases (1.5-fold to 3.0-fold) and show no concentration or functionality dependence. The levels of TNF-α measured in response to the peptide-functionalized nanoparticles, regardless of the extent of derivatization and concentration tested, are statistically insignificant when compared to the levels induced by the PTD domain itself. The copy numbers, fold increases, and the p values ($p < 0.05$ significant at 95% confidence, derived from the students t-test) indicating statistical significance are listed in Table 2.

The measured increases of IL1-*β* production in response to PTD-, SCK-, and PTD-functionalized SCKs are much more pronounced than the copy number levels of TNF-α as compared to TCPS. The measured levels range

Table 2. Nanoparticle Concentration, Copy Number Identification, and Evaluation of Statistical Significance[a]

			gene copy number		increase over TCPS		increase over PTD		increase over SCK (**2**)	
no.	sample composition	concentration mg/mL	TNF-α	IL1-β	TNF-α p(95%)	IL1-β p(95%)	TNF-α p(95%)	IL1-β p(95%)	TNF-α p(95%)	IL1-β p(95%)
1	SCK	0.1	4.33×10^7	1.52×10^8	13.5	33.4	1.9	(11.2)	1	1.8
					0.0067	0.0076	0.0136	0.0003	*0.8499*	0.0177
2	SCK	1.0	4.25×10^7	8.65×10^7	13.2	18.8	1.8	(19.8)	1	1
					0.0007	0.0054	0.0027	0.0001		
3	SCK	10.0	7.01×10^6	1.01×10^9	2.2	221.9	(3.3)	(1.7)	(6.1)	11.7
					0.0241	0.0011	0.0170	0.0003	0.0001	0.0014
4	PTD	0.1	2.30×10^7	1.71×10^9	8.6	375.8	1	1	(1.8)	19.8
					0.0089	0.0001			0.0027	0.0001
5	0.5% PTD SCK	1.0	2.93×10^7	7.06×10^8	9.1	155.2	1.3	(2.4)	(1.5)	8.2
					0.0067	0.0005	*0.25*	0.0011	0.0103	0.0010
6	0.5% PTD SCK	0.5	1.88×10^7	8.59×10^7	5.8	18.9	(1.2)	(19.9)	(2.3)	1
					0.0018	0.0008	*0.19*	0.001	0.0041	*0.9404*
7	1.0% PTD SCK	1.0	1.42×10^7	1.27×10^9	4.4	279.1	(1.6)	(1.3)	(3.0)	14.7
					0.0045	0.0015	*0.0598*	0.0164	0.0033	0.0018
8	1.0% PTD SCK	0.5	2.60×10^7	7.57×10^8	8.0	166.4	1.1	(2.3)	(1.6)	8.8
					0.0053	0.0002	*0.4806*	0.0007	0.0214	0.0005
9	2.0% PTD SCK	1.0	2.15×10^7	2.20×10^9	6.7	483.5	(0.9)	1.3	(2.0)	25.4
					0.0067	0.0049	*0.6930*	0.0890	0.0123	0.0053
10	2.0% PTD SCK	0.5	1.91×10^7	1.38×10^9	5.9	303.3	(0.8)	(1.2)	(2.2)	16.0
					0.0090	0.0007	*0.3600*	0.0206	0.0100	0.0009
11	TCPS	N/A	3.22×10^6	4.55×10^6	1	1	-	-	-	-

[a] Parentheses indicate decreases in copy number, and italic numbers denote comparisons that are statistically insignificant.

from 18.8-fold to 483.5-fold increases over TCPS and 1-fold to 25.4-fold increase over SCKs of similar concentration and show statistical dependence with regard to both concentration and PTD functionalization. The differences in TNF-α and IL1-β expression measured in this series reflect different pathways of signal transduction (*56*) with regard to both the time frame and the severity of the response (*31, 38, 57, 58*) to the respective inflammatory stimuli.

Following the in vitro measurements on cell viability and inflammatory response, the SCKs and PTD-derivatized SCKs were then tested in vivo to gauge their immunogenic response in balb c mice. Enzyme-linked immunosorbent assays (ELISA) were used to quantify the increases in IgG production in response to immunization with the test compounds. Efforts to isolate specific responses by plating the SCKs on the ELISA plate prior to serum incubation were not successful due to an insignificant specific antibody response. This result can be attributed to two possible factors: (1) the nanoparticles could induce a nonspecific immune response, and (2) the sera used for the ELISA measurements were collected 14 d following the respective immunization, a sufficiently long time that any acute inflammatory response may have passed. We therefore decided to look at the increases in IgG concentration on an individual mouse basis to look for relatively large increases. Figure 4 shows the three antibody titers determined for each mouse in the study. The PTD peptide by itself is not immunogenic after two booster immunizations, and the parent SCKs possessing poly(acrylic acid-*co*-acrylamide) shells display negligible values of titer increases over the control PBS injections. Those SCKs possessing various amounts of PTD functionality, 0.5%, 1.0%, and 2.0% (**7**, **8**, and **9**), qualitatively showed a general trend of increasing antibody titer in the serum with increasing degrees of nanoparticle functionalization. The relative increases in antibody titer relative to the initial value are listed in Table 2. Qualitatively, the only significant immunogenic response depicted arose from the 2.0% functionalized SCK, **9**. The 0.5%, 1.0%, and 2.0% SCKs (**7**, **8**, and **9**) exhibited increases of 100% or more in 20% (1 of 5), 60% (3 of 5), and 100% (5 of 5) of the mice, respectively, following two booster injections.

While limited in scope, the immunogenicity results for the SCKs functionalized to a lesser degree are consistent

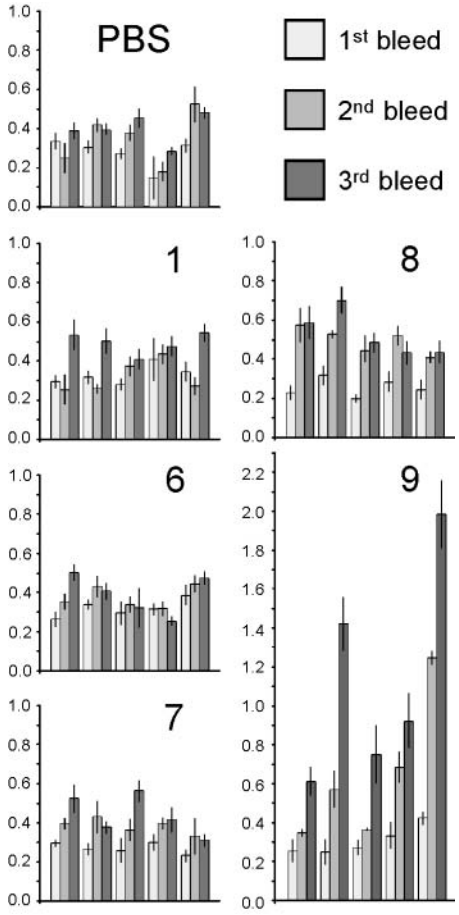


Figure 4. Each group of three bars within a data set corresponds to a titer measurement from an individual mouse. The red bars correspond to the prebleed, the orange bars represent the bleed two weeks after the 1st booster immunization, and the yellow bars represent the bleed two weeks following the 2nd booster immunization. Detrimental immunogenic effects, relative to controls, are negligible in all samples except for the 2.0% (**9**) sample, which suggests that the quantity of PTD and the manner in which it is presented on the surface have a synergistic effect that is able to produce an immune response significantly greater that the response elicited by the peptide itself. Error bars are representative of one standard deviation from the mean of triplicate samples harvested from two separate serum vials and are the estimates of the standard uncertainties.

Table 3. Relative Percent Increase in Antibody Titers Quantified by ELISA Following Two Booster Injections over Preimmunization Baseline Levels

	% increase after one booster over baseline levels mouse					% increase after two boosters over baseline levels mouse				
sample	**1**	**2**	**3**	**4**	**5**	**1**	**2**	**3**	**4**	**5**
1	6	34	-19	-14	-21	16	47	58	82	57
6	33	27	15	1	16	88	21	9	-19	23
7	34	63	41	32	43	78	43	118	39	33
8	153	66	124	84	68	158	121	147	53	80
9	36	130	34	106	194	140	475	177	178	368
PBS	-26	37	38	22	67	16	29	67	93	53

with the literature (*42*), but when large numbers of PTD are presented, the particles do elicit an increase in IgG concentration within the serum. While no specific responses could be detected for the any of the SCK nanoparticles, it is perhaps more important that no deaths resulted from the mice (>50) being subjected to the immunization protocol (three × 100 μg) and no gross morphological changes were observed in postmortem organ histology examinations.

CONCLUSIONS

SCK nanoparticles derivatized with various stoichiometric derivatizations with PTD have been evaluated in vitro and in vivo for biocompatibility. Although these data are somewhat limited in scope, the initial evaluation and early identification of detrimental interactions between biological species and SCK nanoparticles are crucial to further efforts to develop in vivo applications. Apoptosis assays measured by flow cytometry have complemented enzymatic (MTT) toxicity results demonstrating a lack of detrimental effects on cell viability below 500 mg/L for all the samples. Although higher levels of peptide functionalization resulted in decreased metabolic function, loss of cell viability was observed at a sufficiently high concentration, suggesting the use of even 2% PTD-functionalized SCKs would not be prohibited in vivo. In addition, RT-PCR data have provided quantitative information regarding the lack of immunogenicity elicited by SCKs and peptide-derivatized SCK nanoparticles. The inflammatory response to the peptide-functionalized SCK nanoparticles as measured by RT-PCR show increases in the levels of both TNF-α and IL1-β relative to TCPS. Although these levels are statistically significant and show large increases of IL1-β with increasing peptide functionalization, the levels did not preclude the preliminary testing of SCKs in vivo. An in vivo mouse immunization model found measured increases in IgG concentration were minimal with no specific interactions being identified, and more importantly, none of the mice (>50) subjected to the three 100 μg immunization protocol died. Additionally, no gross morphological changes were observed in postmortem organ histology examinations. While these in vitro assessments and preliminary in vivo tests show promising results, additional in vivo animal studies, which are currently in progress including biodistribution and nanoparticle clearance, are needed to compliment these initial findings and to extend the potential therapeutic applications of functionalized SCKs. However, up-regulation of IL1-β and larger than expected IgG increases for the 2.0% PTD-functionalized SCKs suggest that nanoparticles functionalized in polyvalent strategies may be interesting scaffolds for the attachment of known antigens for use in vaccination applications.

ACKNOWLEDGMENT

The authors gratefully acknowledge the National Cancer Institute (N01-CO-27103), and a Postdoctoral Fellowship (M.L.B.) from the National Research Council for supporting this research. Immunization, sera collections, and suggestions from Dan Piatchek and Jack Diani of the Washington University Department of Biology are gratefully acknowledged.

LITERATURE CITED

(1) Matyjaszewski, K., and Xia, J. (2001) Atom Transfer Radical Polymerization. *Chem. Rev. 101*, 2921−2990.
(2) Hawker, C. J., Bosman, A. W., and Harth, E. (2001) New Polymer Synthesis by Nitroxide Mediated Living Radical Polymerizations. *Chem. Rev. 101*, 3661−3688.
(3) Frechet, J. M. J. (2003) Dendrimers and Other Dendritic Macromolecules: From Building Blocks to Functional Assemblies in Nanoscience and Nanotechnology. *J. Polym. Sci., Part A: Polym. Chem. 41*, 3713−3725.
(4) Duncan, R. (2003) The Dawning Era of Polymer Therapeutics. *Nat. Rev. Drug Discovery 2*, 347−360.
(5) Nishiyama, N., Okazaki, S., Cabral, H., Miyamoto, M., Kato, Y., Sugiyama, Y., Nishio, K., Matsumura, Y., and Kataoka, K. (2003) Novel Cisplatin-incorporated Polymeric Micelles can Eradicate Solid Tumors in Mice. *Cancer Res. 63*, 8977−8983.
(6) Pan, D., Turner, J., and Wooley, K. L. (2003) Folic Acid-conjugated Nanostructured Materials Designed for Cancer Cell Targeting. *Chem. Commun*. 2400−2401.
(7) Haag, R. (2004) Supramolecular Drug-Delivery Systems Based on Polymeric Core−Shell Architectures. *Angew. Chem., Int. Ed. 43*, 278−282.
(8) Hubbell, J. A. (2003) Enhancing Drug Function. *Science 300*, 595−596.
(9) Moses, M. A., Brem, H., and Langer, R. (2003) Advancing the Field of Drug Delivery: Taking Aim at Cancer. *Cancer Cell 4*, 337−341.
(10) Kataoka, K., Harada, A., and Nagasaki, Y. (2001) Block Copolymer Micelles for Drug Delivery: Design, Characterization and Biological Significance. *Ad. Drug Delivery Rev. 47*, 113−131.
(11) Hubbell, J. A. (2003) Materials as Morphogenetic Guides in Tissue Engineering. *Curr. Opin. Biotechnol. 14*, 551−558.
(12) Bourke, S. L., and Kohn, J. (2003) Polymers Derived from the Amino Acid L-tyrosine: Polycarbonates, Polyarylates and Copolymers with Poly(ethylene glycol). *Adv. Drug Delivery Rev. 55*, 447−466.
(13) Wadia, J. S., and Dowdy, S. F. (2003) Modulation of Cellular Function by TAT Mediated Transduction of Full Length Proteins. *Curr. Protein Pept. Sci. 4*, 97−104.
(14) Beerens, A. M. J., Al Hadithy, A. F. Y., Rots, M. G., and Haisma, H. J. (2003) Protein Transduction Domains and the Utility in Gene Therapy. *Curr. Gene Ther. 3*, 486-494.
(15) Thurmond, K. B., II, Kowalewski, T., and Wooley, K. L. (1996) Water-Soluble Knedel-like Structures: The Preparation of Shell-Cross-Linked Small Particles. *J. Am. Chem. Soc. 118*, 7239−7240.
(16) Wooley, K. L. (2000) Shell Cross-linked Polymer Assemblies: Nanoscale Constructs Inspired from Biological Systems. *J. Polym. Sci., Part A: Polym. Chem. 38*, 1397−1407.
(17) Huang, H., Remsen, E. E., and Wooley, K. L. (1998) Amphiphilic Core−shell Nanospheres Obtained by Intramicellar Shell Cross-linking of Polymer Micelles with Poly(ethylene oxide) Linkers. *Chem. Commun. 13*, 1415−1416.
(18) Joralemon, M. J., Murthy, K. S., Remsen, E. E., Becker, M. L., and Wooley, K. L. (2004) Synthesis, Characterization, and Bioavailability of Mannosylated Shell Cross-linked Nanoparticles. *Biomacromolecules 5*, 903−913.
(19) Murthy, K. S., Ma, Q., Remsen, E. E., Kowalewski, T., and Wooley, K. L. (2003) Thermal Shaping of Shell-Cross-linked (SCK) Nanoparticles, Facilitated by Nanoconfinement of Fluidlike Cores. *J. Mater. Chem. 13*, 2785−2795.
(20) Remsen, E. E., Thurmond, K. B., II, and Wooley, K. L. (1999) Solution and Surface Charge Properties of Shell Cross-Linked Knedel Nanoparticles. *Macromolecules 32*, 3685−3689.
(21) Liu, J., Zhang, Q., Remsen, E. E., and Wooley, K. L. (2001) Bioconjugates of Protein Transduction Domain(PTD) and

Shell Cross-linked Nanoparticles: Nanostructured Materials Designed for Delivery into Cells. *Biomacromolecules 2*, 362−368.

(22) Green, M., and Loewenstein, P. (1988) Autonomous Functional Domains of Chemically Synthesized Human Immunodeficiency Virus TAT Trans-activator Protein. *Cell 55*, 1179−1188.

(23) Frankel, A., and Pabo, C. (1988) Cellular Uptake of the TAT Protein from Human Immunodeficiency Virus. *Cell 55*, 1189−1193.

(24) Wadia, J. S., and Dowdy, S. F. (2002) Protein Transduction Technology. *Curr. Opin. Biotechnol. 13*, 52.

(25) Nagahara, H., Vocero-Akbani, H. M., Snyder, E. L., Ho, A., Latham, D. G., Lissy, N. A., Becker-Hapak, M., Ezhevsky, S. A., and Dowdy, S. F. (1998) Transduction of Full-length TAT Fusion Proteins into Mammalian Cells: TAT-p27 Induces Cell Migration. *Nat. Med. 4*, 1449.

(26) Torchilin, V. P., Levchenko, T. S., Rammohan, R., Volodina, N., Papahadjopoulos-Sternberg, B., and D'Sousa, G. G. M. (2003) Cell Transfection in vitro and in vivo with Nontoxic TAT Peptide Liposome-DNA Complexes. *Proc. Natl. Acad. Sci. 100*, 1972−1977.

(27) Polyakov, V., Sharma, V., Dahlheimer, J. L., Pica, C. M., Luker, G. D., and Piwnica-Worms, D. (2000) Novel Tat-Peptide Chelates for Direct Transduction of Technetium-99m and Rhenium into Human Cells for Imaging and Radiotherapy. *Bioconjugate Chem. 11*, 762−771.

(28) Gammon, S. T., Villalobos, V. M., Prior, J. L., Sharma, V., and Piwnica-Worms, D. (2003) Quantitative Analysis of Permeatation Peptide Complexes Labeled with Technetium-99m: Chiral and Sequence-Specific Effects on Net Cell Uptake. *Bioconjugate Chem. 14*, 368−376.

(29) Bullok, K. E., Dyszlewski, M., Prior, J. L., Pica, C. M., Sharma, V., and Piwnica-Worms, D. (2002) Characterization of Novel Histidine-Tagged Tat-Peptide Complexes Dual-Labeled with 99mTc-Tricarbonyl and Fluorescein for Scintigraphy and Fluorescence Microscopy. *Bioconjugate Chem. 13*, 1226−1237.

(30) Hansen, M. B., E., N. S., and Berg, K. J. (1989). *J. Immunol. Methods 119*, 203−210.

(31) Catelas, I., Huk, O. L., Petit, A., Zukor, D. J., Marchand, R., and Yahida, L. H. (1998) Flow Cytometric Analysis of Macrophage Response to Ceramic and Polyethylene Particles: Effects of Size, Concentration, and Composition. *J. Biomed. Mater. Res. 41*, 600−607.

(32) Oppenheim, J. J. (2001) Cytokines: Past, Present, and Future. *Int. J. Hematol. 74*, 3−8.

(33) Wang, T., and Brown, M. J. (1999) mRNA Quantification by Real-time TaqMan Polymerase Chain Reaction: Validation and Comparison with RNase Protection. *Anal. Biochem. 269*, 198−201.

(34) Melton, D. A., Krieg, P. A., Rebagliati, M. R., Maniatis, T., Zinn, K., and Green, M. R. (1984) Efficient in vitro Synthesis of Biologically Active RNA and RNA Hybridization Probes from Plasmids Containing a Bacteriophage SP6 Promoter. *Nucleic Acids Res. 12*, 7035−7056.

(35) Morrison, T. B., Weis, J. J., and Wittwer, C. T. (1998) Quantification of Low-copy Transcripts by Continuous SYBR Green I Monitoring During Amplification. *Biotechniques 24*, 954−958.

(36) Bustin, S. A. (2000) Absolute Quantification of mRNA Using Real-time Reverse Transcription Polymerase Chain Reaction Assays. *J. Mol. Endocrinol. 25*, 169−193.

(37) Guatelli, J. C., Gingeras, T. R., and Richman, D. D. (1989) Nucleic Acid Amplification in vitro: Detection of Sequences with Low Copy Numbers and Application to Diagnosis of Human Immuno Deficiency Type 1 Infection. *Clin. Mirobiol. Rev. 2*, 217−226.

(38) Bailey, L., Washburn, N., Simon, C. G., Chan, E., and Wang, F. W. (2004) The Quantification of Inflammatory Cellular Responses Using Real-Time Polymerase Chain Reaction (RT-PCR). *J. Biomed. Mater. Res. 69*, 305−313.

(39) Bailey, L., Weir, M., and Washburn, N. (2004) The Quantification of Cellular Viability and Inflammatory Response to Dental Bonding Resins. *J. Dental Res.*, submitted.

(40) Brodbeck, W. G., Voskerician, G., Ziats, N. P., Nakayama, Y., Matsuda, T., and Anderson, J. M. (2003) In Vivo Leukocyte Cytokine mRNA Responses to Biomaterials are Dependent on Surface Chemistry. *J. Biomed. Mater. Res. 64*, 320−329.

(41) Suzuki, T., Futaki, S., Niwa, M., Tanaka, S., Ueda, K., and Sugiura, Y. (2002) Possible Existence of Common Internalization Mechanisms among Arginine Rich Peptides. *J. Biol. Chem. 277*, 2437−2443.

(42) Liefert, J. A., Harkins, S., and Whitton, J. L. (2002) Full-length Proteins Attached to the HIV tat Protein Transduction Domain are Neither Transduced between Cells, nor Exhibit Enhanced Immunogenicity. *Gene Ther. 9*, 1422−1428.

(43) Vassalli, P. (1992) The Pathophysiology of Tumor Necrosis Factors. *Annu. Rev. Immunol. 10*, 411−452.

(44) Kumar, V., Cotran, R. S., and Robbins, S. L. (1997) *Basic Pathology*, Saunders, New York.

(45) Beutler, B., and Cerami, A. (1988) Tumor Necrosis, Cachexia, Shock and Inflammation: A Common Mediator. *Annu. Rev. Biochem. 57*, 505−518.

(46) Cannon, J. G., and St. Pierre, B. A. (1998) Cytokines in Exertion Induced Skeletal Muscle Injury. *Mol. Cell Biochem. 179*, 159−167.

(47) Illei, G. G., and Lipsky, P. E. (2000) Novel, Antigen-specific Therapeutic Approaches to Autoimmune/ inflammatory Diseases. *Curr. Opin. Immunol. 12*, 712−718.

(48) Dai, Z., and Lakkis, F. G. (1999). *Curr. Opin. Immunol. 11*, 504−508.

(49) Giulietti, A., Overbergh, L., Valckx, D., Decallonne, B., Bouillon, R., and Mathieu, C. (2001) An Overview of Real-time Quantitative PCR: Applications to Quantify Cytokine Gene Expression. *Methods Enzymol. 25*, 386−401.

(50) Chapekar, M. S., Zaremba, T. G., Kuester, R. K., and Hitchins, V. M. (1996) Synergistic Induction of Tumor Necrosis Factor alpha by Bacterial Lipopolysaccharide and Lipoteichoic Acid in Combination with Polytetrafluoroethylene Particles in a Murine Macrophage Cell Line RAW 264.7. *J. Biomed. Mater. Res. 31*, 251−256.

(51) Funatogawa, K., Matsuura, M., Nakano, M., Kiso, M., and Hasegawa, A. (1998) Relationship of Structure and Biological Activity of Monosaccharide Lipid A Analogues to Induction of Nitric Oxide Production by Murine Macrophage RAW264.7 Cells. *Infect. Immun. 66*, 5792−5798.

(52) Jue, D. M., Sherry, B., Luedke, C., Manogue, K. R., and Cerami, A. (1990) Processing of Newly Synthesized Cachectin/ tumor Necrosis Factor in Endotoxin-stimulated Macrophages. *Biochemistry 29*, 8371−8377.

(53) Tiffany, C. W., and Burch, R. M. (1989) Bradykinin Stimulates Tumor Necrosis Factor and Interleukin-1 Release from Macrophages. *FEBS Lett 247*, 189−192.

(54) Suzuki, T., Higgins, P. J., and Crawford, D. R. (2000) Control Selection for RNA Quantitation. *Biotechniques 29*, 332−337.

(55) Filion, M. C., and Phillips, N. C. (1997) Toxicity and Immunomodulatory Activity of Liposomal Vectors Formulated with Cationic Lipids Toward Immune Effector Cells. *Biochim. Biophys. Acta 1329*, 345−356.

(56) Raabe, T., Bukrinsky, M., and Currie, R. A. (1998) Relative Contribution of Transcription and Translation to the Induction of Tumor Necrosis Factor-alpha by Lipopolysaccharide. *J. Biol. Chem. 273*, 974−980.

(57) Baer, M., Dillner, A., Schwartz, R. C., Sedon, C., Nedospasov, S., and Johnson, P. F. (1998) Tumor Necrosis Factor alpha Transcription in Macrophages is Attenuated by an Autocrine Factor that Preferentially Induces NF-kappaB p 50. *Mol. Cell Biol. 18*, 5678−5689.

(58) Tang, L., and Eaton, J. W. (1995) Inflammatory Responses to Biomaterials. *Am. J. Clin. Pathol. 103*, 466−471.

(59) "Official contribution of the National Institute of Standards and Technology; not subject to copyright in the United States."

BC049945M

Combinatorial Chemical Reengineering of the Alpha Class Glutathione Transferases

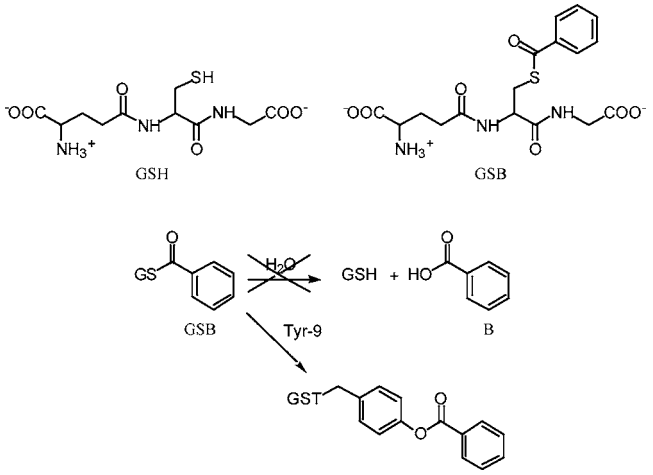
Johan Viljanen, Lotta Tegler, and Kerstin S. Broo*

IFM, Department of Organic Chemistry, Linköping University,
S-581 83 Linköping, Sweden. Received October 21, 2003; Revised Manuscript Received March 16, 2004

Previously, we discovered that human glutathione transferases (hGSTs) from the alpha class can be rapidly and quantitatively modified on a single tyrosine residue (Y9) using thioesters of glutathione (GS-thioesters) as acylating reagents. The current work was aimed at exploring the potential of this site-directed acylation using a combinatorial approach, and for this purpose a panel of 17 GS-thioesters were synthesized in parallel and used in screening experiments with the isoforms hGSTs A1-1, A2-2, A3-3, and A4-4. Through analytical HPLC and MALDI-MS experiments, we found that between 70 and 80% of the reagents are accepted and this is thus a very versatile reaction. The range of ligands that can be used to covalently reprogram these proteins is now expanded to include functionalities such as fluorescent groups, a photochemical probe, and an aldehyde as a handle for further chemical derivatization. This site-specific modification reaction thus allows us to create novel functional proteins with a great variety of artificial chemical groups in order to, for example, specifically tag GSTs in biological samples or create novel enzymatic function using appropriate GS-thioesters.

Creating new function in an existing protein scaffold is a challenging task, even though progress has been made lately through rational design (*1*−*3*) and combinatorial approaches (*4*, *5*). A less explored route to novel functional proteins is that of chemical modification of a protein scaffold to introduce an artificial group (*6*−*9*). Picking a versatile scaffold is of course crucial in any protein reengineering project, and we have focused on the glutathione transferases (GSTs, EC 2.5.1.18),[1,2] a large family of phase II detoxication enzymes that catalyze the nucleophilic addition of glutathione (GSH, Scheme 1) to a broad range of hydrophobic electrophilic molcules (*10*−*13*). The proteins exist as homo- or heterodimers (*12*, *14*), and the mode of binding of GSH in the N-terminal domain is essentially conserved throughout the classes (*10*, *15*). The differences between the isoenzymes are generally located in the promiscuous hydrophobic electrophile binding sites (H-sites) to provide a broad substrate specificity (*16*). The catalytic function is highly dependent on a conserved tyrosine, serine or cysteine residue in the glutathione-binding site (G-site) that aids in the ionization of GSH to form the more reactive thiolate ion (*10*). The modular features of these proteins with a stringent G-site and an adjacent, promiscuous H-site, in combination with their stability and ease of purification (*17*) and the vast knowledge of structure−activity relationships (*18*), are all factors that point to the GSTs as ideal candidates in protein engineering experiments (*19*−*26*) with the goal of obtaining novel function.

Scheme 1



Previously, we found that a thioester of glutathione (GS-thioester) termed GSB (Scheme 1) was able to rapidly modify Y9 (Figure 1) of the human GSTs from the alpha class (*27*). The reaction is highly specific and, for example, targets one out of 51 nucleophiles in hGST A1-1. Out of the three GS-thioesters we investigated, two were able to acylate the alpha class GSTs (*27*). The covalent modification reaction presents us with the

* To whom correspondence should be addressed. Fax +46-13-12 25 87, e-mail: kerbr@ifm.liu.se.

[1] Abbreviations: ACN, acetonitrile; C18, octadecyl; DCM, dichloromethane; DIPCDI, *N*,*N*′-diisopropylcarbodiimide; DIPEA, diisopropylethylamine; DMF, dimethylformamide; DTNB, 5, 5′-dithiobisnitrobenzoic acid; Fmoc, 9-fluorenylmethyloxycarbonyl; GSH, glutathione, γ-Glu-Cys-Gly; GST, glutathione transferase; hGST A1-1, GST A1-1 isoform from human; G-site, glutathione-binding site; GS-thioester, thioester of glutathione; HOBt, 1-hydroxybenzotriazole; HPLC, high performance liquid chromatography; H-site, hydrophobic electrophile binding site; NMR, nuclear magnetic resonance; MALDI-MS, matrix assisted laser desorption mass spectrometry; Mmt, 4-methoxytrityl; NaP_i, sodium phosphate; TFA, trifluoroacetic acid; TNB, thionitrobenzoic acid; TOF, time-of-flight; UV, ultraviolet.

[2] This nomenclature is derived from that recommended by Mannervik, B. et al. (1992) *Biochem J 282 (Pt 1)*, 305−6.

10.1021/bc034192+ CCC: $27.50 © 2004 American Chemical Society
Published on Web 05/21/2004

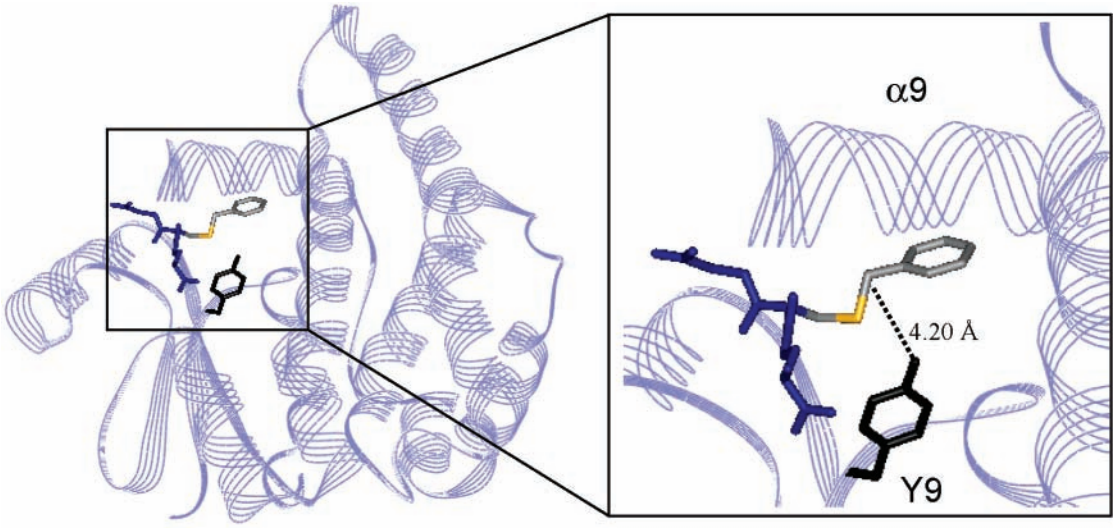
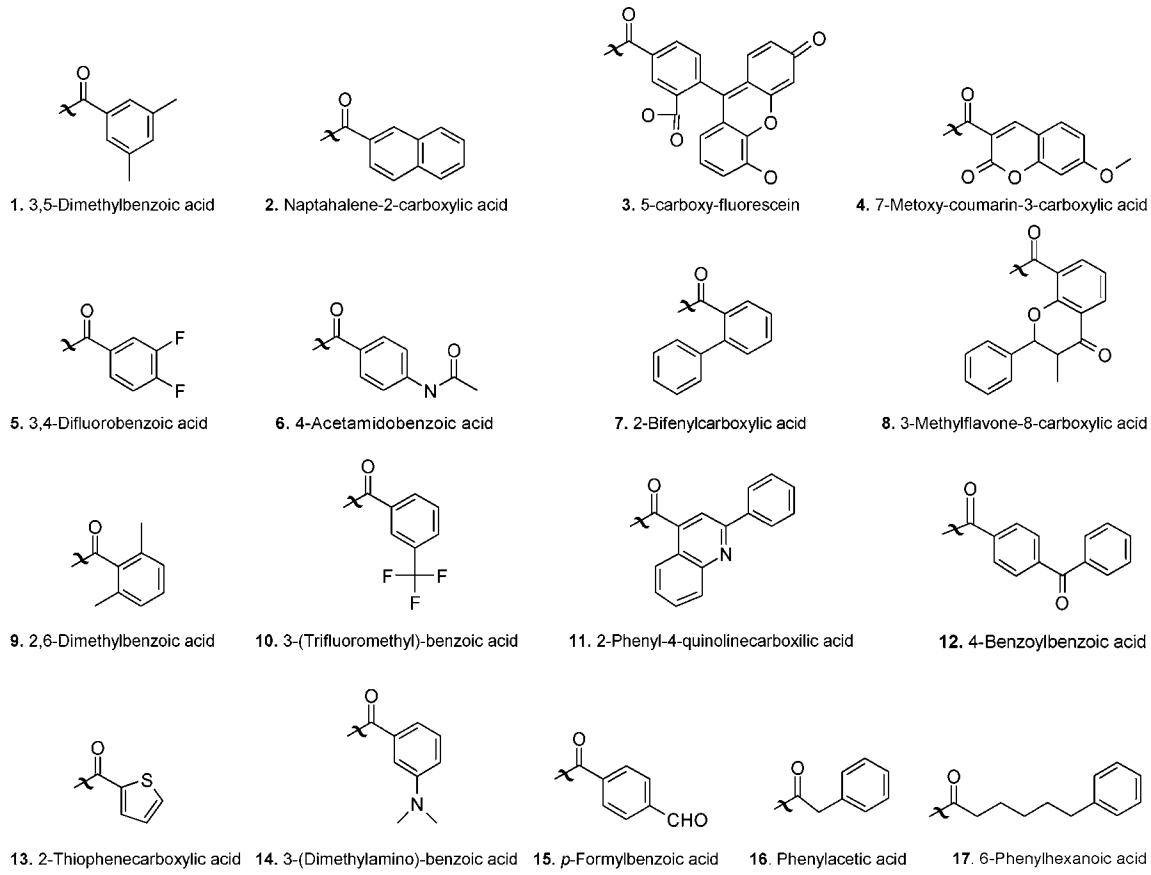


Figure 1. A close-up of the crystal structure (1GUH) of hGST A1-1 in a complex with *S*-benzyl-glutathione (*15*). The distance between the hydroxyl oxygen of Y9 and the ligand benzyl CH_2 is 4.2 Å. The distinguishing feature of the alpha class GSTs helix 9 (α9) is also indicated in the figure. The protein is dimeric but shown here as a monomer for reasons of clarity of presentation.

Chart 1



opportunity to create novel functional proteins through the design and synthesis of GS-thioesters with appropriate chemical groups. Thioesters could be synthesized to introduce, for example, a fluorescent group that could bind in the nearby H-site to form the basis for a biosensor system, or an artificial catalytic group that could result in a new type of enzymatic activity (*28*, *29*). It is thus important to understand the potential and limitations of the reaction. To do so, we synthesized 17 different GS-thioesters (Chart 1) in parallel and screened this collection against hGSTs A1-1, A2-2, A3-3, and A4-4. The combined screening of both reagents and proteins was done in order to investigate if any of the alpha class isoenzymes is better suited as a scaffold for protein reengineering experiments and also to try to obtain general information about reagent requirements. The GS-thioesters therefore span a wide range of reactivities, hydrophobicities, shapes, and sizes. Some of the reagents have functionalities that can be used in downstream experiments, for example fluorescent groups (GS-3, GS-4) and a handle for further chemical derivatization (GS-15).

MATERIALS AND METHODS

Protected amino acids and acids (DiversiChem kit) were purchased from Novabiochem (Läufelfingen, Switzerland). Preactivated acids (5-carboxyfluorescein succinimidyl ester, *p*-formylbenzoic acid succinimidyl ester, 4-benzoylbenzoic acid succinimidyl ester) were purchased from Molcular Probes. All chemicals and reagents used were of the highest purity available. The glutathione transferases were kind gifts from the group of Professor Bengt Mannervik at the Department of Biochemistry, Uppsala University, Sweden. All solid-phase syntheses were carried out in a VacMaster (International Sorbent Technology). The HPLC experiments were carried out using a Kromasil C_8-column (4.6 mm × 250 mm, Supelco inc.) attached to a Varian system with a ProStar 230 Delivery System, a ProStar 330 Photodiode Array Detector, controlled by the Varian LC Software. All mass spectra were recorded with a MALDI/TOF-MS (Voyager System 4212, Applied Biosystems) with detection in the positive mode. The UV measurements were performed using a Varian Cay 100 Scan UV−visible spectrophotometer and analyzed with the CaryWin UV software.

Synthesis of Fully Protected, Polymer-Bound, γ-Glu-Cys-Gly. The tripeptide γ-Glu-Cys-Gly (0.71 mmol scale) was synthesized using standard Fmoc protocols starting from Fmoc-Gly-Wang resin. The thiol was orthogonally protected with the Mmt group to enable selective deprotection with 1% TFA in DCM. Each deprotection and coupling step was monitored by a Kaiser test (*30*), to estimate the amount of free amino groups. After completed synthesis, the polymer was washed thoroughly with DMF and DCM and dried under vacuum.

Synthesis of Thioester Reagents. The GS-thioesters were synthesized in parallel using 0.03 mmol polymer for each ligand. In each case, the Mmt-group was removed with DCM:TFA:TIS (97:1:2). After deprotection of the thiol the polymer was washed with DMF, and the subsequent coupling of the acid was performed in DMF using acid: HOBt:DIPCDI:DIPEA (2:3:3:6) with addition of a catalytic amount of 4-pyrrolidinopyridine. The couplings were allowed to proceed overnight following an additional boosting of the same amount of coupling-cocktail after 1 h. Preactivated acids (5-carboxyfluorescein succinimidyl ester, *p*-formylbenzoic acid succinimidyl ester, 4-benzoylbenzoic acid succinimidyl ester) were coupled using a mixture of ester:DIPEA (2:6) in DMF during the first hour, after which DIPCIDI:HOBt:DIPEA (2:3:3:6) was added and the coupling was allowed to proceed overnight. Global deprotection and simultaneous cleavage from the solid support was achieved with TFA: H_2O (97.5:2.5). Following precipitation with ice-cold diethyl ether and lyophilization, each GS-thioester was dissolved in 5 mL of Milli-Q water as a stock solution used for all further experiments. The concentrations of the stock solutions were calculated from the weights of the products assuming 100% purity. The yields of the syntheses, according to weighing, range from 11% to 48%, with most of them around 30%. The peptides were analyzed with reversed-phase HPLC using a C8 column and a shallow H_2O:ACN (both 0.1% TFA) gradient. The identities of the products were confirmed with MALDI-TOF MS using an α-cyano-4-hydroxycinnamic acid matrix with detection in the positive mode. The measured masses of the GS-thioesters were in good agreement with the calculated masses.

Amount of GSH in the GS-Thioester Stock Solutions. The Ellmans test (*31*) was carried out to analyze the amount of unreacted GSH in the GS-thioester solutions. The samples were prepared by adding 10 μL of GS-thioester stock solution to 90 μL of 10 mM DTNB in 0.1 M NaPi, pH 8. Thiol groups react with DTNB and produces equivalent amounts of TNB. The amount of produced TNB (ϵ_{412} = 13 600 M^{-1} cm^{-1}) was measured using a Fluostar Galaxy plate-reader (BMG Lab technologies) equipped with a 420 nm filter. The amount of free GSH varied from 0.5 to 3%. These calculations did not take into account the GS-thioesters intrinsic absorbances at this wavelength and correspond therefore to an upper limit.

Glutathione Transferases. The activities of the GSTs were checked with a standard assay (*32*) containing 1 mM each of 1-chloro-2,4-dinitrobenzene and GSH (pH 6.5 in 0.1 M NaP_i at 30 °C). Protein concentrations were estimated using previously published extinction coefficients for hGSTs A1-1 (*33*), A2-2 (*34*), A3-3 (*35*), A4-4 (*23*). The proteins were stored in NaP_i-buffered solutions containing NaCl and 10% glycerol at −80 °C or −20 °C until used in the experiments.

Modification Reactions. A typical modification reaction was performed with 100 μM GS-thioester and 50 μM GST in buffer (0.1 M NaP_i, pH 7). The reaction was allowed to proceed at 25 °C for 5 h. To control the temperature, the incubation was performed in an Eppendorf Master cycler gradient.

Proteolytic Digestion of Modified GSTs. The digestions were performed in the following way: 5 μL of modification mixture was diluted with 13 μL of buffer (50 mM NH_4OAc, pH 4), 2 μL of *Staphylococcus areus* V-8 Protease from Pierce Biotechnology, Inc., Rockford, IL, (stock solution 1 μg/μL) was added, and the sample was incubated at 25 °C for up to 2 h. The sample was then acidified with 20 μL of 0.1% TFA and desalted with C_{18} ZipTips (Millipore Corporation, Bedford, MA). In the case of tryptic digestion, 10 μL of modification mixture was diluted with 10 μL of buffer (0.2 M $NaHCO_3$, pH 8), and the reaction was initiated by adding 1 μL of trypsin (stock solution 0.2 μg/μL in 0.1 mM HCl) and allowed to proceed at 25 °C for up to 2 h. The sample was then analyzed directly or acidified and desalted (C_{18} ZipTips) prior to MALDI-MS analysis.

HPLC Analysis of the Modification Reactions of hGST A1-1. Each GS-thioester (100 μM) was incubated with hGST A1-1 (50 μM) at 25 °C (in 100 mM NaP_i, pH 7) in a total volume of 36 μL. After 5 h, the reaction was quenched by adding 4 μL of a mixture of TFA (final concentration 0.4% v:v) and internal standard, 2-chloro-4-nitrophenol (final concentration 200 μM). As a reference, each GS-thioester was also incubated in buffer without protein and quenched after 5 h. All samples were then analyzed with reversed-phase HPLC using a C8 column and a shallow H_2O:ACN (both 0.1% TFA) gradient. The injection volumes were 25 μL. The quenched samples from the HPLC experiments were also digested with trypsin as described before except that 2 μL of each sample mixture was diluted with 18 μL of buffer before adding the enzyme. After 2 h of incubation, the samples were analyzed with MALDI-MS. To each sample was added 0.1 M citrate to the matrix on the MALDI plate to enable analysis without desalting. In some cases, the peak of the modified protein fragment coincided with other peptides, and we then used *S. areus* V-8 protease to digest the protein mixture.

Acyl Group Exchange Experiment. hGST A1-1 (5 μM) was reacted overnight at 25 °C with 100 μM GSB. The reaction mixture was desalted with YM-30 filters (Millipore) and washed with 0.1 mM NaP_i pH 7. The sample was then diluted back to the original volume and

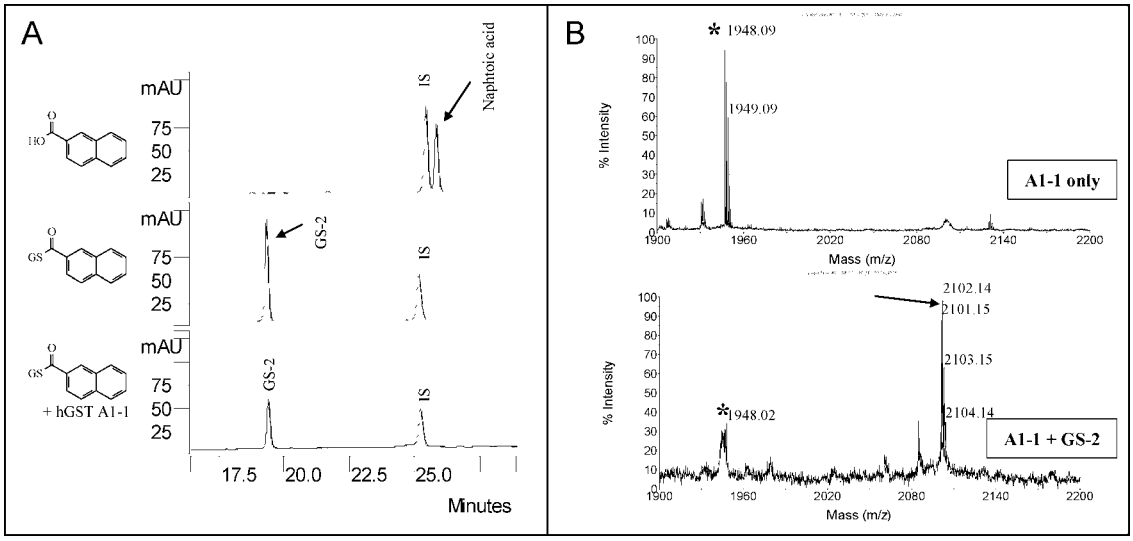


Figure 2. The reaction between GS-2 (100 μM) and hGST A1-1 (50 μM) at pH 7 monitored by (A) HPLC and (B) MALDI-MS. The chromatograms are shown at 250 nm for naphthoic acid, a reference sample of GS-2 incubated without protein, and the GS-2 sample incubated with protein for 5 h at 25 °C. The internal standard (2-chloro-4-nitrophenol) is abbreviated IS. The MALDI-MS are recorded after proteolytic (*S. aureus* V8) digestion, and both the unmodified and the modified fragment (AEKPKLHY*FNARGRME) containing Y9 are indicated in the sample incubated with GS-2.

subjected to 100 or 10 μM GS-2. Samples were withdrawn at 15 min, 1 h, 5 h, and after overnight incubation at 25 °C. The time-points were digested with trypsin and analyzed by MALDI-MS.

RESULTS

Quality and Yield of GS-thioesters. The GS-thioesters were synthesized from one batch of fully protected, polymer-bound GSH with yields ranging from 11% to 48% according to weighing. All GS-thioesters were identified with MALDI-MS. According to the Ellmans test (*31*), the amount of free thiol, i.e., free GSH, was between 0,5% and 3%. In addition to the Ellmans tests, the qualities of the products were evaluated from HPLC (for an example, see Figure 2, GS-2) and deemed satisfactory for use in the screening experiments without further purification.

Addition of the GS-thioester Panel to hGST A1-1. The outcome of adding the GS-thioesters to hGST A1-1 was investigated by analytical HPLC. Each reagent (100 μM, except GS-17, see Discussion) was incubated with protein (50 μM) at 25 °C, and the reaction was quenched after 5 h by adding a solution of TFA (0.4% final concentration) and an internal standard (2-chloro-4-nitrophenol). The thoroughly investigated GSB (*27*) was also incorporated as one of the reagents in order to include a positive control. As a reference, each GS-thioester was also incubated without protein for 5 h in buffer at 25 °C. The samples were then analyzed with reversed-phase HPLC (Figure 2). The peak area of each reagent incubated with protein was compared with the peak area of the reagent in the reference sample and also to a sample of the corresponding acid injected on the same gradient. These data were used to assess whether there was any decrease in thioester concentration and/or increase in free acid concentration (Table 1).

The quenched samples from the HPLC experiments were also analyzed by MALDI-MS following proteolytic digestion in order to ensure that decreases in peak areas corresponded to modifications of Y9 (Figure 2). If Y9 becomes covalently modified, the mass of the fragment containing Y9 increases with the mass of the corresponding acid minus the weight of water (Scheme 1). Out of the 18 GS-thioesters we investigated (GSB included), 14, or 78%, were able to covalently modify hGST-A1 as judged by both HPLC and MALDI-MS (Table 1).

Table 1. GS-thioesters after Five Hours Incubation, pH 7 and 25 °C

	HPLC[a]			
name	hGSTA1-1 sample GSX peak	acid peak	reference sample acid peak	MALDI-MS[b]
GSB	+	−	−	+
GS-1	+	−	−	+
GS-2	+	−	−	+
GS-3	+	−	−	+
GS-4	+	−	−	+
GS-5	+	−	−	+
GS-6	+	−	−	+
GS-7	−	−	−	−
GS-8	+	−	−	+
GS-9	−	−	−	−
GS-10	+	−	−	+
GS-11	−	+	+	−
GS-12	+	+	−	+
GS-13	+	−	−	+
GS-14	+	−	−	+
GS-15	+	−	−	+
GS-16	+	+	−	−
GS-17	+	−	−	+

[a] + corresponds to decrease of GSX peak (cutoff 20% decrease) and − corresponds to appearance of acid peak (cutoff 5% increase). [b] + and − corresponds to modified or not modified Y9 fragment, respectively.

MALDI-MS Screening of the GS-thioester Panel against hGSTs A2-2, A3-3, and A4-4. The acyl group preferences of hGSTs A2-2, A3-3, and A4-4 were investigated using the panel of GS-thioesters with GSB included as a positive control. For each reagent, the reaction was monitored with a GS-thioester concentration of 100 μM (except GS-17, see Discussion), and protein concentrations ranging from 5 μM to 50 μM, with an incubation time of 5 h at 25 °C. After incubation, the samples were digested with trypsin or *S. aureus* protease V-8 depending on possible overlaps from other fragments. Through MALDI-MS experiments, we then identified modified Y9-fragments for 83% of the GS-thioesters for both hGSTs A2-2 and A3-3, and for 72% of the reagents for hGST A4-4 (Table 2, Figure 3). A positive identifica-

Table 2. Modification Reactions of the Alpha Class GSTs

	hGST			
substrate	A1-1	A2-2	A3-3	A4-4
GSB	+	+	+	+
GS-1	+	+	+	+
GS-2	+	+	+	+
GS-3	+	+	+	−
GS-4	+	+	+	+
GS-5	+	+	+	+
GS-6	+	+	+	+
GS-7	−	−	+	−
GS-8	+	+	+	+
GS-9	−	−	−	−
GS-10	+	−	−	+
GS-11	−	+	−	−
GS-12	+	+	+	+
GS-13	+	+	+	+
GS-14	+	+	+	+
GS-15	+	+	+	+
GS-16	−	+	+	−
GS-17	+	+	+	+

(a) + and − corresponds to modified or not modified Y9 fragment.

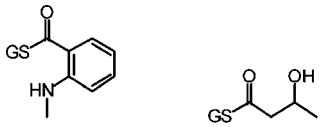
tion corresponds to more than 10% modified Y9-fragment relative to the parent fragment (unmodified Y9). This relatively low threshold was set because MALDI-MS is not a quantitative technique and also because of the relatively large error in estimating GS-thioester concentrations (Discussion).

Exchange of Acyl Groups in Already Modified hGST A1-1. The ability to exchange acyl groups in already modified hGST A1-1 was investigated by subjecting benzoic acid-modified hGST A1-1 (5 μM) to GS-2 at two different concentrations (10 and 100 μM) (Figure 4). Time points were withdrawn, and the reaction mixtures were digested and analyzed with MALD-MS to obtain semiquantitative data regarding the amount of modification for each acyl group.

DISCUSSION

The speed and selectivity of the previously described site-directed covalent modification reaction between hGSTs from the alpha class and GS-thioesters (*27*) encouraged us to investigate the potential of this reaction both with respect to protein promiscuity and also to the linked question of reagent requirements. The natural substrates of GSTs differ widely in size and hydrophobicity (*16*), and we therefore found it likely that this would be a quite general modification reaction. The previous report was based on a set of three different GS-thioesters (Scheme 1 and Chart 2); GSB, GS-ANT, and *S*-lactoylglutathione. Out of these, the only one that did not react with Y9 was the only one that was not an aromatic GS-thioester (*S*-lactoylglutathione). This, in combination with the report that rat GST A1-1, highly homologous to hGST A1-1, hydrolyses a nonaromatic GS-thioester (*36*), raised the question that this perhaps was a unique reaction only involving aromatic GS-thioesters. With the intention to study this, we therefore included GS-16 and GS-17 (Scheme 1) in the panel of GS-thioesters. The individual GS-thioesters within the set of 17 new reagents thus vary widely in size, shape, hydrophobicity, and also reactivity (pK_a of acid) in order to screen as many parameters as possible.

Chart 2



GS-ANT S-lactoylglutathione

HPLC and MALDI-MS Analysis of the Reactions between the GS-thioester Panel and hGST A1-1. The outcome of adding the panel of reagents to hGST A1-1 was analyzed using both HPLC and MALDI-MS with the objective to get detailed information about the fate of the acyl group. Previously, we did a thorough investigation and could conclude that GSB reacts with hGST A1-1 in a stoichiometric fashion to produce 1 equiv of GSH and one 1 equiv of benzoic acid-modified protein (*27*). The reagent GSB is not hydrolyzed upon incubation at pH 7, even after 9 days, but instead the acyl group migrates to the α-amino group of GSH. However, we could not assume that this was valid for all GS-thioesters. To track the acyl group, we therefore incubated the reagents with

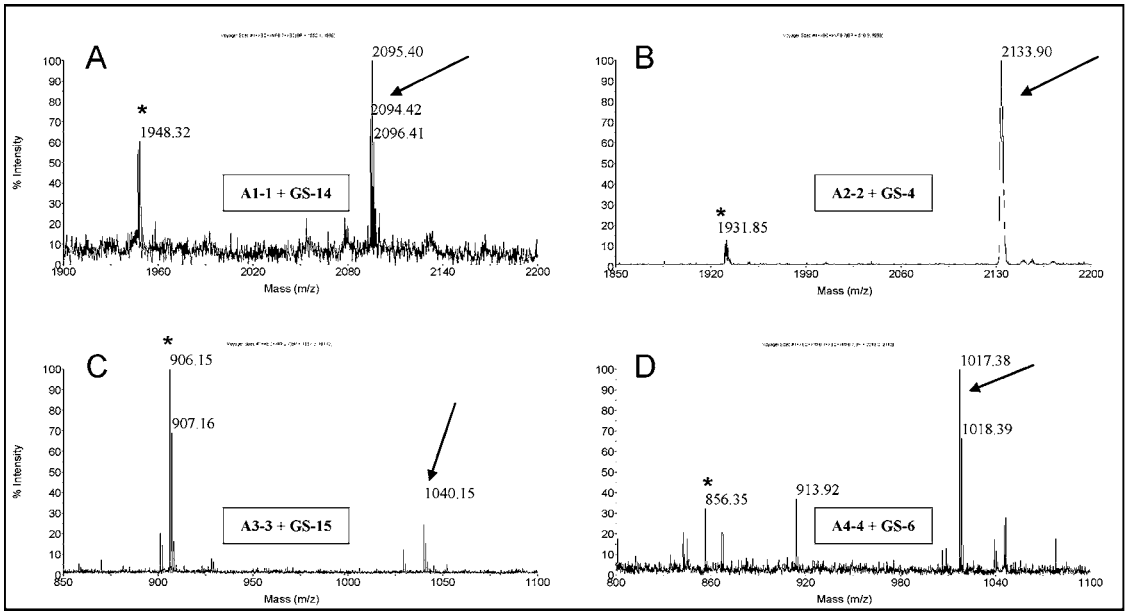


Figure 3. MALDI-MS spectra of proteolytic peptide fragments from hGSTs (A) A1-1, (B) A2-2, (C) A3-3, and (D) A4-4 following 5 h incubations with different GS-thioesters (100 μM) specified in the figure. The interval containing the Y9 fragments are shown in the figure. Parent fragments are indicated with asterisks, and modified fragments are highlighted with arrows.

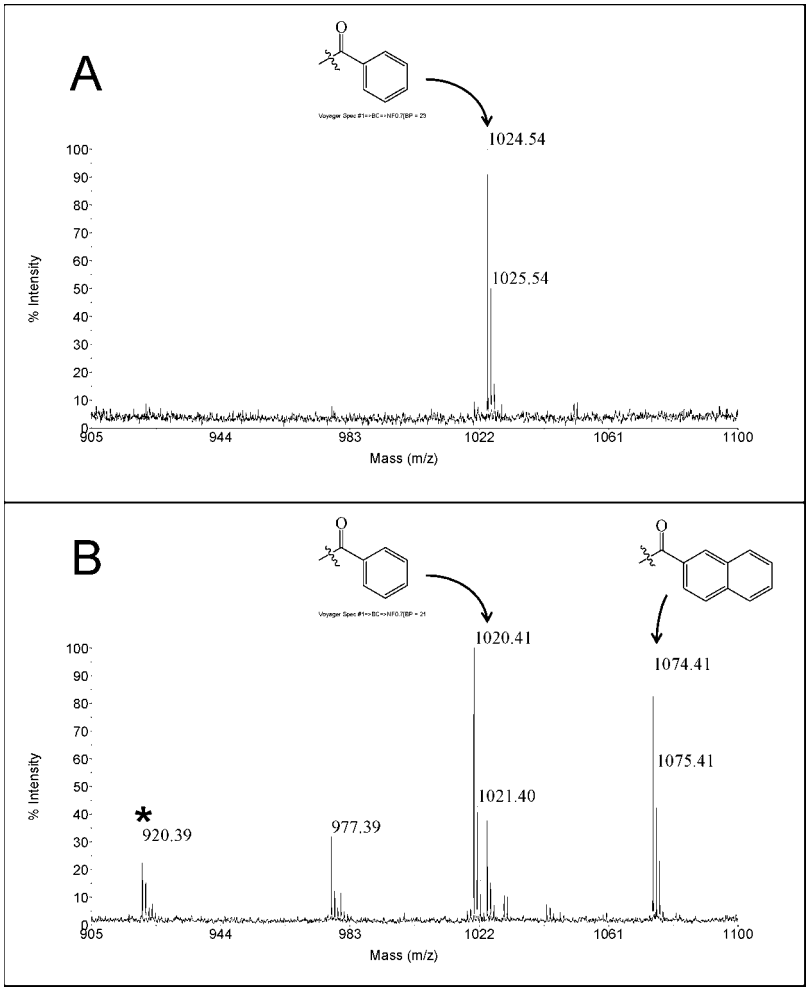


Figure 4. Benzoic acid-modified hGST A1-1 (5 μM) was subjected to GS-2, time points were withdrawn, and the reaction mixtures were digested with trypsin and analyzed with MALDI-MS. The figure shows (A) the spectrum before GS-2 was added and (B) the spectrum after 5 h incubation with 100 μM GS-2. The interval containing the Y9 fragments are shown in the figure. The parent fragment is indicated with an asterisk.

and without hGST A1-1 for 5 h, and we also injected the acids using the same gradient. A decrease in the peak area of the GS-thioester reagent that is due to hydrolysis can then be identified in the chromatogram. If a rearrangement reaction takes place, the result is not so easily interpreted since a migration event, in combination with oxidation of the produced thiol, would result in a total of up to five or even seven peaks, should hydrolysis also occur. The areas of the peaks thereby become very low and would be hard to detect at the concentration of GS-thioesters used during the experiments. Because of the relative concentration of reagent to protein (2:1), the maximum decrease of any GS-thioester peak should be 50% when hGST A1-1 is added if the event corresponds to modification of hGST A1-1. However, since the concentrations of the GS-thioester solutions are derived from weighing, the decreases could be greater than 50% even if the only event that takes place is modification of the protein in the sample. This is due to several reasons: this is a screening approach and we have not purified each substrate but used them after only ether precipitation (see above), the mixtures contain a small amount of free GSH (less than 3%), and peptides are also inherently hygroscopic. Weighing does therefore overestimate the amount of thioester reagent in the reaction mixture. The HPLC data is therefore presented in Table 1 as decrease or no decrease of thioester reagent. The exact figures can be found in the Supporting Information. The conditions we have used to analyze these reactions are not suitable for direct detection of the modified protein since it elutes as a very broad peak preceding the internal standard (Figure 2). Through these experiments we found that the great majority of the reagents are stable under the reaction conditions (5 h incubation at 25 °C). The migration event could be observed for GS-17 to some extent, and this, in combination with the poor extinction coefficient, motivated us to use a higher initial concentration of this reagent (250 μM) in the derivatization experiments. Only in one case (GS-11) was an acid peak observed in the absence of protein.

The quenched samples from the HPLC experiments were also digested and analyzed directly with MALDI-MS, and the results from the HPLC experiments could be verified (Table 1) in that we detected fragments that corresponded to modified Y9. In the presence of hGST A1-1, some of the GS-thioesters were hydrolyzed to some extent, most notably GS-11 and GS-16; however, none of these did show up as modified Y9 fragments in the MALDI-MS experiments and were thus classified accordingly.

In one case (GS-12) we could observe a small peak of the expected mass in the beginning of the ionization process, but the peak disappeared as the laser beam continued, and it did not reappear. It is perhaps likely that this is due to the acyl group itself, since it is photolabile and it might thus be destroyed in the MALDI-MS. Overall, the correlation between the HPLC and the MALDI-MS results is very good. The combined results

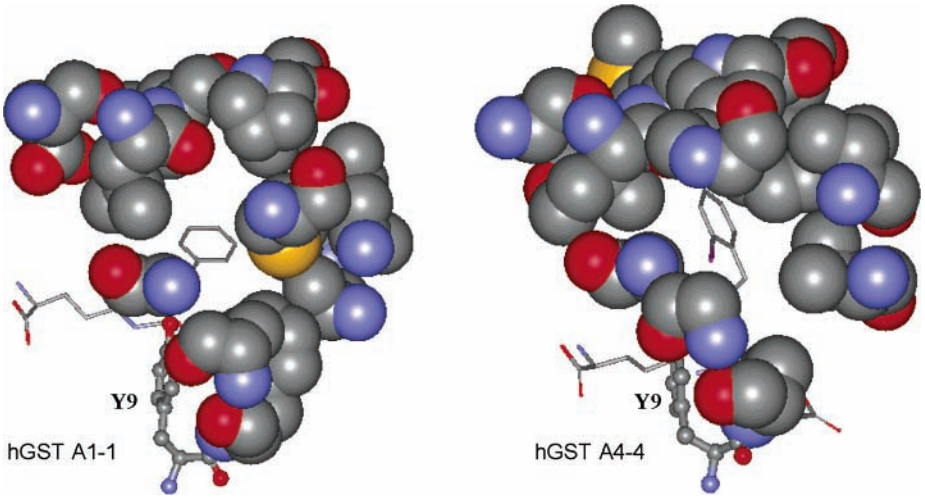


Figure 5. Close-ups of the crystal structures of hGST A1-1 (1GUH) (*15*) and hGST A4-4 (1GUL) (*41*) crystallized with glutathione conjugates showing the potential "back-door" leading out from the hydrophobic binding site. The H-site residues are shown in CPK, the G-site residues Y9 in ball-and-stick, and the glutathione-derived ligands in line representation. Both proteins are dimeric, but here are shown as monomers for reasons of clarity of presentation.

from MALDI-MS and HPLC thus showed that 14 of the GS-thioesters, or 78%, were able to modify hGST A1-1 (Table 1).

Modification of the Alpha Class hGSTs A2-2, A3-3, and A4-4. To explore the versatility of each of the alpha class proteins, we also screened hGSTs A2-2, A3-3, and A4-4 against all GS-thioesters (Table 2) using proteolytic digestion and MALDI-MS. Since the HPLC experiments had demonstrated that the GS-thioesters were stable in the absence of hGST A1-1, we chose to focus on the MALDI-MS experiments that more directly show the presence of modified protein. We found that all of the alpha class GSTs are highly promiscuous, and the percentage of accepted modification reagents range from 72 to 83%. This is perhaps not so surprising since the isoenzymes catalyze reactions where the hydrophobic substrates vary hugely in size and hydrophobicity (*16*, *21*, *34*, *37*−*40*). The relaxed hydrophobic substrate specificity of the GSTs that originates from their biological function as detoxication enzymes make them ideally suited as protein scaffolds in reprogramming experiments, and there is also room left, both in the G-site and in the H-site, even after Y9 has been modified with a new functional group. In all, the alpha class GSTs seems to be equally well suited as protein scaffolds in chemical reengineering experiments since they can all be reprogrammed with a large variety of functional groups.

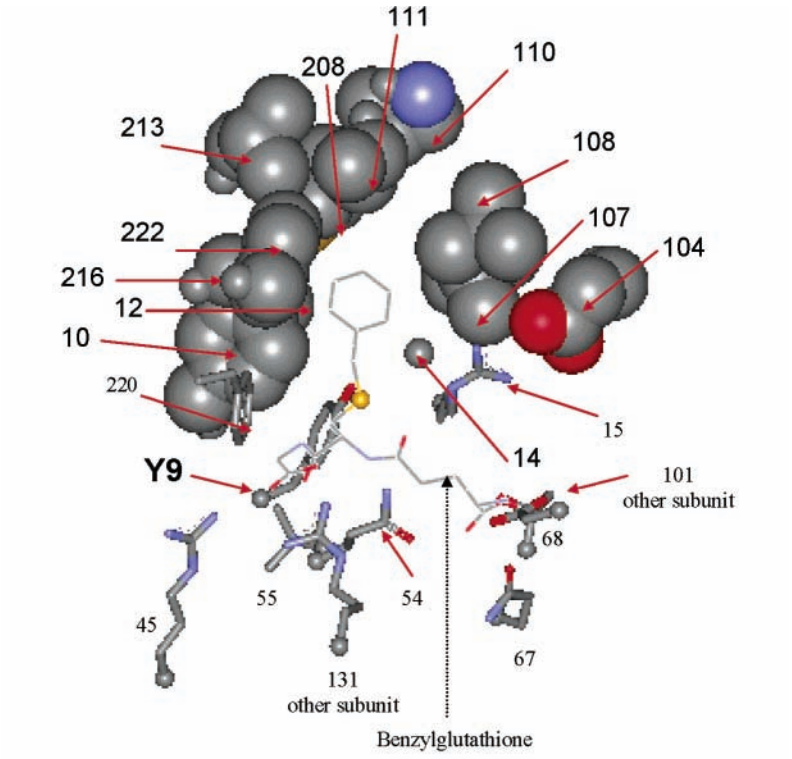
The extent of modification varies, which is not surprising, since we used standardized conditions with respect to incubation time, temperature, and reagent concentration for all reactions. In our previous paper (*27*), we could observe that the extent of modification using GSB and hGST A1-1 was a function of time and concentration of reagent. We tried to maximize the extent of modification in one case, hGST A3-3 and GS-15 (Figure 3C), but we were not able to achieve more than a slight increase of modified protein even after raising the concentration of modifying reagent and allowing 24 h of modification. It is probably due to hydrolysis of the reagent as can be seen in Table 1 already after 5 h and also perhaps due to the slow deterioration of the protein at room temperature. The rate of modification, hydrolysis, and deterioration are in this case probably incompatible.

There are crystal structures of hGSTs A1-1 (*15*) and A4-4 (*41*) (Figure 5), and the distinguishing feature of the alpha class is helix 9 (α9) that forms a lid over the active site (Figure 1). The H-sites of the alpha class proteins differ from hGSTs A1-1 in three (A2-2), four (A3-3), and nine amino acids (A4-4), respectively (Figure 6). The differences within the alpha class lead to subtle differences in substrate specificity and also in the dynamic features of the proteins. For instance, α9 can be observed in the crystal structure of hGST A4-4 without ligand (*41*), but for hGST, A1-1 α9 is only ordered in the presence of a substrate (*15*, *42*). It is thus an advantage that all of the alpha class hGSTs are amenable to this type of chemical reengineering experiment because different qualities may become useful in different types of applications. In addition, one can also potentially refine the properties of the proteins through combinatorial approaches such as gene shuffling experiments (*43*) due to the high homology between the isoenzymes, without losing the ability of chemical reengineering of the resulting protein scaffolds.

No Apparent GS-thioester Requirements. There does not seem to be a systematic reason (size, reactivity, hydrophobicity, substitution pattern, etc.) predicting the ability of a GS-thioester to modify an alpha class GST. The reaction seems to be pretty general, and we found only one unreactive GS-thioester (GS-9). This acyl group (2,6 dimethylbenzoic acid) is di-ortho-substituted, and the likely explanation is that GS-9 is too sterically hindered to function, especially since the di-meta-substituted analogue GS-1 (3,5-dimethylbenzoic acid) is an excellent derivatization reagent for all four proteins.

The size of the acyl group does not seem to be of importance since these vary from 2-thiophenecarboxylic acid (GS-13) to 5-carboxyfluorescein (GS-3). Again, this is not surprising since the natural substrates of GSTs range widely in size and shape (*16*). This tolerance could perhaps in part be explained by observing the crystal structures of hGST A1-1 and A4-4, where there seems to be something like a "back door" leading out from the H-site (Figure 5).

The relative reactivities of the GS-thioesters correlate with the leaving group, which is GSH in all cases, and also with the pK_a value of the acyl group. The reported (*44*) or calculated (*45*) pK_a values of the acyl groups in the series (Supporting Information) span a range from 3.35 (2,6-dimethylbenzoic acid) to 4.80 (6-phenylhexanoic acid), but these differences are not reflected in the ability of a GS-thioester to function as an acylating reagent. The



Position	10	12	14	104	107	108	110	111	208	213	216	222
GST A1	F	A	G	E	L	L	P	V	M	L	A	F
GST A3	:	G	:	:	:	:	:	L	A	:	:	:
GST A2	S	I	:	:	:	:	:	F	:	:	S	:
GST A4	P	G	:	:	I	M	:	F	P	V	V	P

Figure 6. The hydrophobic binding sites of hGSTs A2-2, A3-3, and A4-4 differ from that of hGST A1-1 (*15*) in up to nine positions, as indicated in the table. In this figure, the H-site residues are shown as CPK models with the α-carbons as balls. G-site residues are shown in stick model, again with the α-carbons as balls. The sulfur atom of the ligand *S*-benzylglutathione is also shown as a ball. Amino acids 101 and 131 originate from the other subunit in the dimeric protein and protrude into the G-site.

hydrophobicities of the acyl groups also differ quite substantially with log *P* values (the partitition coefficient between water and *n*-octanol) from 1.3 (4-acetamidobenzoic acid) to 3.8 (2-phenyl-4-quinolinecarboxylic acid) (Supporting Information). This trend is again not reflected in the success of modification.

In our previous work we commented on the fact that there might be a need for an aromatic GS-thioester for this reaction to work (*27*). This was based on the observation that in our small set of three reagents, the two aromatic ones were able to acylate Y9 whereas the naturally occurring, alkyl thioester *S*-lactoylglutathione was not (Scheme 1 and Chart 2). In addition, rat GST A1-1 has been shown to function as a thioester hydrolase for the alkyl thioester GS-ethacrynic acid (*36*). To illuminate this, we included two acyl groups: phenylacetic acid (GS-16) and 6-phenylhexanoic acid (GS-17) that are closely related to benzoic acid (GSB). Even though the hydrophobicity would increase, we chose to use 6-phenylhexanoic acid instead of merely hexanoic acid since the phenyl ring is valuable as a UV marker in HPLC experiments. The reactivities of these GS-thioesters are very similar since the pK_a values are 4.2, 4.3, and 4.8 for benzoic acid, phenyl acetic acid, and 6-phenylhexanoic acid, respectively (Supporting Information). This range is included within the span of aromatic GS-thioesters that work as acylating reagents. The hydrophobicities are also within the span of the other reagents (Supporting Information) since the log *P* values are 1.9, 1.4, and 3.3 for benzoic acid, phenylacetic acid, and 6-phenylhexanoic acid, respectively. It does appear as if adding hGST A1-1 to GS-16 increases the rate of hydrolysis of the reagent (Table 1). However, the results suggest that even though the phenylacetic acid-derived GS-16 did not acylate hGSTs A1-1 and A4-4, the reagent with the longer spacer, GS-17, did function as an acylating reagent for all of the GSTs (Tables 1 and 2). On the basis of theses screening experiments, we can now conclude that there does not appear to be an absolute need for an aromatic GS-thioester for the acylation reaction to work, something that significantly expands the versatility of the chemical reengineering approach.

Besides the possible bias against di-ortho-substituted acyl groups, we cannot state any specific reagent requirements, in part because of the high success rate (>70%) in this set of GS-thioesters. Not all reagents work for all alpha class GSTs, and the reasons behind a successful modification probably depends on the combination of

protein and reagent that in turn leads to an optimal positioning of the reactive Y9 residue for the reaction to occur.

Benzoic Acid-Modified hGST A1-1 Can Be Morphed into Naphthoic Acid-Modified A1-1. We found through exchange experiments that benzoic acid-modified hGST A1-1 can be altered by adding another thioester reagent (GS-2) to instead form the naphthoic acid-modified protein (Figure 4). Intriguingly, part of the premodified protein becomes deacylated during the incubation, which is odd since the benzoic acid-modified protein is completely stable during identical reaction conditions without GS-2 (*27*). Also, in the reaction between GS-2 and hGST A1-1, we observe naphthoic acid-modified protein but no free naphthoic acid (Table 1) as would be expected should the deacylation reaction proceed through a naphthoic acid intermediate. This finding is thus quite interesting and needs to be further studied.

CONCLUSIONS

Through a combinatorial screening approach we have substantially expanded the range of GS-thioesters that are able to covalently modify the alpha class hGSTs. The set now includes fluorescent probes and a handle for chemical derivatization. The covalent modification reaction is very versatile in that a large number of GS-thioesters are accepted by the alpha class GSTs, and the reaction is fast and site-directed toward one residue in the protein with minimal side reactions. This precision allows for chemical reengineering of protein scaffolds with the goal of obtaining new function through the design and synthesis of appropriate GS-thioesters.

ACKNOWLEDGMENT

Kerstin S. Broo thanks the Wenner-Gren Foundation for a postdoctoral fellowship. The authors are indebted to Professor Bengt Mannervik and co-workers for contributing recombinant GSTs. This work was financially supported by The Wenner-Gren Foundation, The Carl-Trygger Foundation, the Knut and Alice Wallenberg Foundation, and the Swedish Research Council.

Supporting Information Available: Table 1 but with the exact figures obtained in the HPLC experiments. A table containing the experimental (*44*) or calculated (*45*) pK_a and log *P* values of acyl groups in the panel of GS-thioesters. This material is available free of charge via the Internet at http://pubs.acs.org.

LITERATURE CITED

(1) Bolon, D. N., Voigt, C. A., and Mayo, S. L. (2002) De novo design of biocatalysts. *Curr. Opin. Chem. Biol. 6*, 125−129.
(2) Penning, T. M., and Jez, J. M. (2001) Enzyme redesign. *Chem. Rev. 101*, 3027−3046.
(3) Rowan, S. J., and Sanders, J. K. (1997) Enzyme models: design and selection. *Curr. Opin. Chem. Biol. 1*, 483−490.
(4) Hilvert, D. (2000) Critical analysis of antibody catalysis. *Annu. Rev. Biochem. 69*, 751−793.
(5) Farinas, E. T., Bulter, T., and Arnold, F. H. (2001) Directed enzyme evolution. *Curr. Opin. Biotechnol. 12*, 545−551.
(6) Qi, D., Tann, C. M., Haring, D., and Distefano, M. D. (2001) Generation of new enzymes via covalent modification of existing proteins. *Chem. Rev. 101*, 3081−3111.
(7) Ren, X., Jemth, P., Board, P. G., Luo, G., Mannervik, B., Liu, J., Zhang, K., and Shen, J. (2002) A semisynthetic glutathione peroxidase with high catalytic efficiency. Selenoglutathione transferase. *Chem. Biol. 9*, 789−794.
(8) DeSantis, G., and Jones, J. B. (1999) Chemical modification of enzymes for enhanced functionality. *Curr. Opin. Biotechnol. 10*, 324−330.
(9) Hamachi, I., Nagase, T., Tajiri, Y., and Shinkai, S. (1997) Incorporation of an artificial receptor into a native protein: new strategy for the design of semisynthetic enzymes with allosteric properties. *Bioconjugate Chem. 8*, 862−868.
(10) Sheehan, D., Meade, G., Foley, V. M., and Dowd, C. A. (2001) Structure, function and evolution of glutathione transferases: implications for classification of nonmammalian members of an ancient enzyme superfamily. *Biochem. J. 360*, 1−16.
(11) Strange, R. C., Spiteri, M. A., Ramachandran, S., and Fryer, A. A. (2001) Glutathione-S-transferase family of enzymes. *Mutat. Res. 482*, 21−26.
(12) Armstrong, R. N. (1997) Structure, catalytic mechanism, and evolution of the glutathione transferases. *Chem. Res. Toxicol. 10*, 2−18.
(13) Mannervik, B. (1996) Evolution of glutathione transferases and related enzymes for the protection of cells against electrophiles. *Biochem. Soc. Trans. 24*, 878−880.
(14) Pettigrew, N. E., and Colman, R. F. (2001) Heterodimers of glutathione S-transferase can form between isoenzyme classes pi and mu. *Arch. Biochem. Biophys. 396*, 225−230.
(15) Sinning, I., Kleywegt, G. J., Cowan, S. W., Reinemer, P., Dirr, H. W., Huber, R., Gilliland, G. L., Armstrong, R. N., Ji, X., Board, P. G., and et al. (1993) Structure determination and refinement of human alpha class glutathione transferase A1−1, and a comparison with the Mu and Pi class enzymes. *J. Mol. Biol. 232*, 192−212.
(16) Hayes, J. D., and Pulford, D. J. (1995) The glutathione S-transferase supergene family: regulation of GST and the contribution of the isoenzymes to cancer chemoprotection and drug resistance. *Crit. Rev. Biochem. Mol. Biol. 30*, 445−600.
(17) Lim, K., Ho, J. X., Keeling, K., Gilliland, G. L., Ji, X., Ruker, F., and Carter, D. C. (1994) Three-dimensional structure of *Schistosoma japonicum* glutathione S-transferase fused with a six-amino acid conserved neutralizing epitope of gp41 from HIV. *Protein Sci. 3*, 2233−2244.
(18) Ketterer, B. (2001) A bird's eye view of the glutathione transferase field. *Chem. Biol. Interact. 138*, 27−42.
(19) Micaloni, C., Kong, G. K., Mazzetti, A. P., Nuccetelli, M., Antonini, G., Stella, L., McKinstry, W. J., Polekhina, G., Rossjohn, J., Federici, G., Ricci, G., Parker, M. W., and Lo Bello, M. (2003) Engineering a new C-terminal tail in the H-site of human glutathione transferase P1−1: structural and functional consequences. *J. Mol. Biol. 325*, 111−122.
(20) Nuccetelli, M., Mazzetti, A. P., Rossjohn, J., Parker, M. W., Board, P., Caccuri, A. M., Federici, G., Ricci, G., and Lo Bello, M. (1998) Shifting substrate specificity of human glutathione transferase (from class Pi to class alpha) by a single point mutation. *Biochem. Biophys. Res. Commun. 252*, 184−189.
(21) Pettersson, P. L., Johansson, A. S., and Mannervik, B. (2002) Transmutation of human glutathione transferase A2−2 with peroxidase activity into an efficient steroid isomerase. *J. Biol. Chem. 277*, 30019−30022.
(22) Widersten, M., Hansson, L. O., Tronstad, L., and Mannervik, B. (2000) Use of phage display and transition-state analogues to select enzyme variants with altered catalytic properties: glutathione transferase as an example. *Methods Enzymol. 328*, 389−404.
(23) Nilsson, L. O., Gustafsson, A., and Mannervik, B. (2000) Redesign of substrate-selectivity determining modules of glutathione transferase A1−1 installs high catalytic efficiency with toxic alkenal products of lipid peroxidation. *Proc. Natl. Acad. Sci. U.S.A. 97*, 9408−9412.
(24) Hansson, L. O., and Mannervik, B. (2000) Use of chimeras generated by DNA shuffling: probing structure−function relationships among glutathione transferases. *Methods Enzymol. 328*, 463−477.
(25) Hansson, L. O., Widersten, M., and Mannervik, B. (1999) An approach to optimizing the active site in a glutathione transferase by evolution in vitro. *Biochem. J. 344 Pt 1*, 93−100.
(26) Mannervik, B., Cameron, A. D., Fernandez, E., Gustafsson, A., Hansson, L. O., Jemth, P., Jiang, F., Jones, T. A., Larsson,

A. K., Nilsson, L. O., Olin, B., Pettersson, P. L., Ridderstrom, M., Stenberg, G., and Widersten, M. (1998) An evolutionary approach to the design of glutathione-linked enzymes. *Chem. Biol. Interact. 111*−*112*, 15−21.
(27) Håkansson, S., Viljanen, J., Broo, K. S. (2003) Programmed delivery of novel functional groups to the alpha class glutathione transferases. *Biochemistry 42*, 10260−10268.
(28) Davies, R. R., and Distefano, M. D. (1997) A semisynthetic metalloenzyme based on a protein cavity that catalyzes the enantioselective hydrolysis of ester and amide substrates. *J. Am. Chem. Soc. 119*, 11643−11652.
(29) Haring, D., and Distefano, M. D. (2001) Enzymes by design: chemogenetic assembly of transamination active sites containing lysine residues for covalent catalysis. *Bioconjug. Chem. 12*, 385−390.
(30) Kaiser, E., Colescott, R. L., Bossinger, C. D., and Cook, P. I. (1970) Color test for detection of free terminal amino groups in the solid-phase synthesis of peptides. *Anal. Biochem. 34*, 595−598.
(31) Ellman, G. L. (1959) Tissue sulfhydryl groups. *Arch. Biochem. Biophys. 82*, 70−77.
(32) Habig, W. H., and Jakoby, W. B. (1981) Assays for differentiation of glutathione S-transferases. *Methods Enzymol. 77*, 398−405.
(33) Gustafsson, A., and Mannervik, B. (1999) Benzoic acid derivatives induce recovery of catalytic activity in the partially inactive Met208Lys mutant of human glutathione transferase A1−1. *J. Mol. Biol. 288*, 787−800.
(34) Pettersson, P. L., and Mannervik, B. (2001) The role of glutathione in the isomerization of delta 5-androstene-3, 17-dione catalyzed by human glutathione transferase A1−1. *J. Biol. Chem. 276*, 11698−704.
(35) Johansson, A. S., and Mannervik, B. (2001) Human glutathione transferase A3−3, a highly efficient catalyst of double-bond isomerization in the biosynthetic pathway of steroid hormones. *J. Biol. Chem. 276*, 33061−5.
(36) Dietze, E. C., Grillo, M. P., Kalhorn, T., Nieslanik, B. S., Jochheim, C. M., and Atkins, W. M. (1998) Thiol ester hydrolysis catalyzed by glutathione S-transferase A1−1. *Biochemistry 37*, 14948−57.
(37) Johansson, A. S., and Mannervik, B. (2002) Active-site Residues Governing High Steroid Isomerase Activity in Human Glutathione Transferase A3−3. *J. Biol. Chem. 277*, 16648−54.
(38) Dreij, K., Sundberg, K., Johansson, A. S., Nordling, E., Seidel, A., Persson, B., Mannervik, B., and Jernstrom, B. (2002) Catalytic activities of human alpha class glutathione transferases toward carcinogenic dibenzo[a, l]pyrene diol epoxides. *Chem. Res. Toxicol. 15*, 825−31.
(39) Hubatsch, I., Ridderstrom, M., and Mannervik, B. (1998) Human glutathione transferase A4-4: an alpha class enzyme with high catalytic efficiency in the conjugation of 4-hydroxynonenal and other genotoxic products of lipid peroxidation. *Biochem. J. 330 (Pt 1)*, 175−9.
(40) Wang, J., Bauman, S., and Colman, R. F. (2000) Probing subunit interactions in alpha class rat liver glutathione S-transferase with the photoaffinity label glutathionyl S-[4-(succinimidyl)benzophenone]. *J. Biol. Chem. 275*, 5493−503.
(41) Bruns, C. M., Hubatsch, I., Ridderstrom, M., Mannervik, B., and Tainer, J. A. (1999) Human glutathione transferase A4−4 crystal structures and mutagenesis reveal the basis of high catalytic efficiency with toxic lipid peroxidation products. *J. Mol. Biol. 288*, 427−39.
(42) Cameron, A. D., Sinning, I., L'Hermite, G., Olin, B., Board, P. G., Mannervik, B., and Jones, T. A. (1995) Structural analysis of human alpha-class glutathione transferase A1−1 in the apo-form and in complexes with ethacrynic acid and its glutathione conjugate. *Structure 3*, 717−27.
(43) Kolkman, J. A., and Stemmer, W. P. (2001) Directed evolution of proteins by exon shuffling. *Nat. Biotechnol. 19*, 423−8.
(44) http://chemfinder.cambridgesoft.com/result.asp.
(45) CompuDrug, I., Inc. (1995), 705, Grandview Drive, South San Francisco, CA 94080.

BC034192+

Pyridine-Containing 6-Hydrazinonicotinamide Derivatives as Potential Bifunctional Chelators for ^{99m}Tc-Labeling of Small Biomolecules

Ajay Purohit, Shuang Liu,* Charlie E. Ellars, Dave Casebier, Stephen B. Haber, and D. Scott Edwards

Discovery Chemistry, Bristol-Myers Squibb Medical Imaging, 331 Treble Cove Road, North Billerica, Massachusetts 01862. Received August 14, 2003; Revised Manuscript Received April 30, 2004

As a continuation of our interest in novel ^{99m}Tc chelating systems, several pyridine-containing HYNIC (6-hydrazinonicotinamide) derivatives (L1−L5) have been synthesized and characterized by NMR (^{1}H and ^{13}C) and LC−MS. ^{99m}Tc complexes of L1−L5 were prepared by the reaction of the HYNIC derivative with $^{99m}TcO_4^-$ in the presence of excess tricine and stannous chloride. Results from this study show that the attachment site of the linker is critical for the formation of macrocyclic ^{99m}Tc complexes. For example, the pyridine-N in L3 is not able to bond to the Tc, because the lysine linker is attached to the 4-position. When the linker is at the 2-position, L1 forms the macrocyclic complex [^{99m}Tc(L1)-(tricine)], but the radiochemical purity is relatively low. If the linker is attached to the 3-position of the pyridine ring, the HYNIC derivatives form macrocyclic complexes [^{99m}Tc(L)(tricine)] (L2, L4, and L5) in high yield (>95%). The HPLC data suggest that the macrocyclic complex [^{99m}Tc(L2)(tricine)] exists in solution as four isomers: two diastereomers and two conformational isomers. Diastereomers are due to a combination of the chirality of the lysine linker and of the Tc chelate. Replacing lysine with a pentamethylenediamine linker results in the macrocyclic complex [^{99m}Tc(L4)(tricine)] with two conformational isomers, which interconvert rapidly at room temperature. Changing the linker from pentamethylenediamine to hexamethylenediamine did not eliminate the minor isomer; but the percentage of the minor isomer was reduced from ∼10% for [^{99m}Tc(L4)(tricine)] to only 6% for [^{99m}Tc-(L5)(tricine)]. The linker length is an important parameter to minimize the minor isomer. LC−MS data of complexes [^{99m}Tc(L)(tricine)] (L2, L4, and L5) are completely consistent with their proposed compositions. On the basis of these data, it is concluded that pyridine-containing HYNIC derivatives have the potential as bifunctional chelators for ^{99m}Tc-labeling of small biomolecules if the linker is attached to the 3-position of the pyridine ring.

INTRODUCTION

For the last several years, we have been successful in using a ternary ligand system (HYNIC, tricine, and TPPTS) (HYNIC = 6-hydrazinonicotinamide, TPPTS = trisodium triphenylphosphine-3,3′,3″-trisulfonate) for ^{99m}Tc-labeling of small biomolecules (BM), including chemotactic peptides (*1*) and LTB_4 receptor antagonists (*2, 3*) for imaging infection and inflammation, integrin $\alpha_v\beta_3$ receptor antagonists for tumor imaging (*4*), and a GPIIb/IIIa receptor antagonist for imaging thrombus (*5*−*10*). The combination of HYNIC−BM, tricine, and TPPTS results in a unique and versatile ternary ligand system that forms ^{99m}Tc complexes [^{99m}Tc(HYNIC−BM)(tricine)-(TPPTS)] (BM = peptide or nonpeptide receptor ligands) with extremely high specific activity. These ternary ligand−^{99m}Tc complexes are stable in solution for at least 6 h and are formed as equal mixtures of two diastereomers, if the biomolecule has a chiral center. The composition of ternary ligand−^{99m}Tc complexes has been determined to be 1:1:1:1 for Tc:HYNIC−BM:tricine:TPPTS, through a series of mixed ligand experiments, and confirmed by LC−MS at both the tracer (^{99m}Tc) and macroscopic (^{99}Tc) levels (*11, 12*). The use of HYNIC for ^{99m}Tc-labeling of small biomolecules has recently been reviewed (*13*−*16*).

Previously, we reported two prototype phosphine-containing HYNIC chelators (Figure 1), HYNIC−Kp-DPPB and HYNIC−Ko-DPPB (K = lysine, DPPB = diphenylphosphinobenzoic acid), and their macrocyclic ^{99m}Tc complexes (*17*). We found that both HYNIC−Kp-DPPB and HYNIC−Ko-DPPB form highly stable ^{99m}Tc complexes, [^{99m}Tc(HYNIC−Ko-DPPB)(tricine)] and [^{99m}Tc-(HYNIC−Kp-DPPB)(tricine)]. We also found that [^{99m}Tc-(HYNIC−Kp-DPPB)(tricine)] exists as only one *detectable* isomer in solution while [^{99m}Tc(HYNIC−Ko-DPPB)(tricine)] has three isomers, which interconvert at elevated temperatures. Unfortunately, HYNIC−Kp-DPPB is very prone to oxidation during radiolabeling. This presents a significant challenge, since the oxidized phosphine-containing HYNIC chelator (HYNIC−Kp-ODPPB) will form a binary ligand complex, [^{99m}Tc(HYNIC−Kp-ODP-PB)$(tricine)_2$], as a radioimpurity.

Like phosphines, pyridine analogues have also been used as coligands for ^{99m}Tc-labeling of small biomolecules (*10*). Compared to phosphines, pyridine analogues are air-stable and are more amendable for further derivatization. Therefore, as a continuation of our interest in new ^{99m}Tc chelating systems, we now present the synthesis of several pyridine-containing HYNIC derivatives (Figure

* To whom correspondence should be addressed at the Department of Industrial and Physical Pharmacy, School of Pharmacy, Purdue University, 575 Stadium Mall Drive, West Lafayette, IN 47907-2051. Phone: 765-494-0236. Fax 765-496-3367. E-mail: lius@pharmacy.purdue.edu.

10.1021/bc034141c CCC: $27.50 © 2004 American Chemical Society
Published on Web 07/01/2004

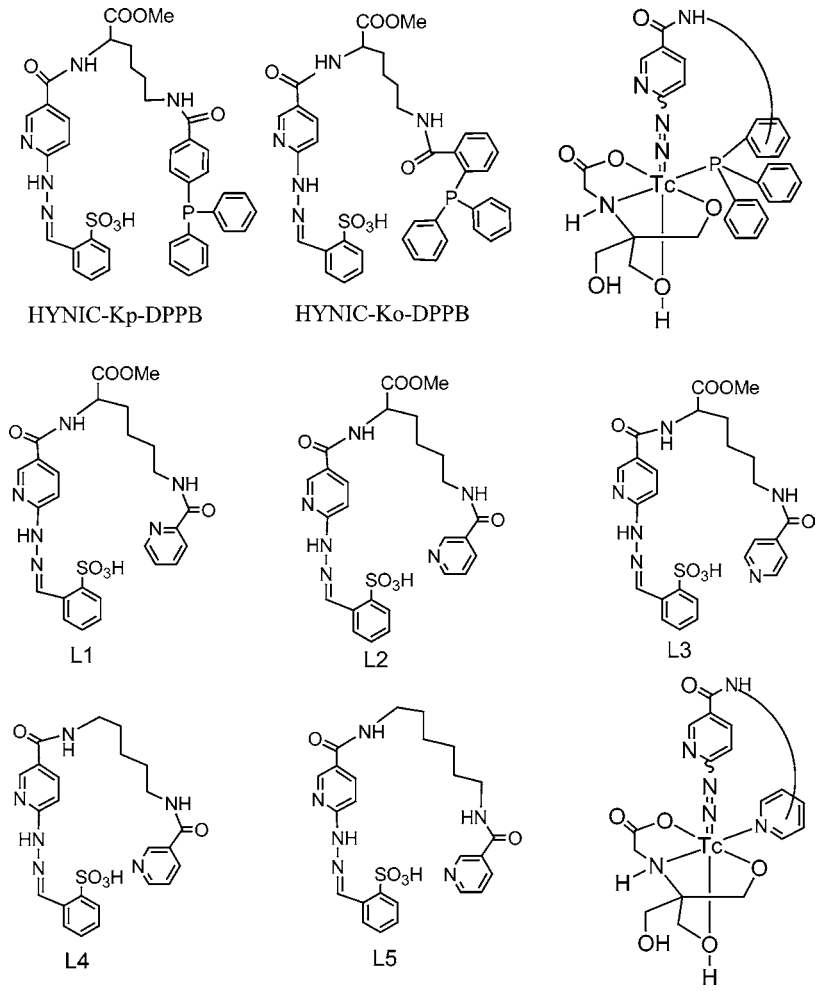


Figure 1. Phosphine- and pyridine-containing HYNIC derivatives and their macrocyclic Tc complexes.

1, L1−L5). [1] The main objective of this study is to explore the potential of L1−L5 as bifunctional chelators (BFCs) for ^{99m}Tc-labeling of small biomolecules.

EXPERIMENTAL SECTION

N-ϵ-(*tert*-Butoxycarbonyl)lysine methyl ester hydrochloride was purchased from Calbiochem Inc. 1,6-Diaminohexane, 1,5-diaminopentane, 1-hydroxyazabenzotriazole, 4 M HCl in dioxane, isonicotinic acid, nicotinic acid, picolinic acid, 1-*O*-(*N*,*N*′,*N*″,*N*‴-tetramethyluronium)-azabenzotriazoloxy hexafluorophosphate, and tricine were purchased from Sigma-Aldrich (St. Louis, MO). $Na^{99m}TcO_4$ was obtained from a Technelite $^{99}Mo/^{99m}Tc$ generator at Bristol-Myers Squibb Medical Imaging Inc., N. Billerica, MA. Sodium succinimidyl 6-(2-(2-sulfonatobenzaldehyde)-hydrazono)nicotinate (HYNIC−NHS) was prepared according to a literature procedure (*18*). Synthesis of *N*-α-(6-(2-(2-sulfonatobenzaldehyde)hydrazono)nicotinyl)-lysine methyl ester was described in our previous communication (*17*).

[1] [1]Abbreviations: L1 = *N*-ϵ-(isonicotinyl)-*N*-α-(6-(2-(2-sulfonatobenzaldehyde)hydrazono)nicotinyl)lysine methyl ester; L2 = *N*-ϵ-(nicotinyl)-*N*-α-(6-(2-(2-sulfonatobenzaldehyde)hydrazono)-nicotinyl)lysine methyl ester; L3 = *N*-ϵ-(picolinyl)-*N*-α-(6-(2-(2-sulfonatobenzaldehyde)hydrazono)nicotinyl)lysine methyl ester; L4 = 1-(*N*-(6-(2-(2-sulfonatobenzaldehyde)hydrazono)nicotinyl))-6-(nicotinoyl)pentanediamine; and L5 = 1-(*N*-(6-(2-(2-sulfonatobenzaldehyde)hydrazono)nicotinyl))-6-(nicotinoyl)hexanediamine.

Instruments. NMR spectral data (^{1}H and ^{13}C) were recorded on a 600 MHz Bruker DRX FT NMR spectrometer and are reported as δ (ppm) relative to TMS. Electrospray MS analyses were performed using an IonSpec Ultima FT mass spectrometer in the positive ion mode. LC−MS spectral data were collected using a HP1100 LC/MSD system with an API-electrospray interface. The LC−MS method used a Zorbax C_{18} column (4.6 mm × 150 mm, 3.5 μm particle size). The flow rate was 1 mL/min with a gradient mobile phase starting at 80% solvent A (25 mM ammonium acetate buffer, pH 6.8) and 20% solvent B (acetonitrile) and going to 75% A and 25% solvent B at 20 min.

The preparative HPLC method used a Varian Prep Star system equipped with an UV/visible detector (λ = 220 nm) and a Jupiter C_{18} prep column (15 μm, 300Å, 21.2 × 250 mm). The flow rate was 80 mL/min with the mobile phase starting with 100% solvent A (0.1%TFA in water) and going to 80% solvent B (0.1%TFA in 90% acetonitrile) and 20% solvent A at 40 min. The radio-HPLC methods used a HP-1100 system with an IN-US radio-detector and a Zorbax C_{18} column (4.6 mm × 250 mm, 300 Å). The flow rate was 1 mL/min with a gradient mobile phase starting at 80% solvent A (25 mM ammonium acetate buffer, pH 6.8) and 20% solvent B (acetonitrile) and going to 75% A and 25% solvent B at 20 min. The ITLC method used GelmanSciences silica gel paper strips and a 1:1 mixture of acetone and saline as eluant. By this method, ^{99m}Tc complexes migrate to

the solvent front while $^{99m}TcO_4^-$ and [^{99m}Tc]colloid remain at the origin.

Synthesis of *N*-ε-(Isonicotinyl)-*N*-α-(6-(2-(2-sulfonatobenzaldehyde)hydrazono)nicotinyl)lysine Methyl Ester (L1). To a 25 mL round-bottom flask was added isonicotinoyl chloride hydrochloride (16.0 mg, 0.90 mmol) and 3 mL of DMF. To the solution above was added *N*-α-(6-(2-(2-sulfonatobenzaldehyde)hydrazono)-nicotinyl)lysine methyl ester hydrochloride (50 mg, 0.10 mmol), followed by addition of DIEA (0.0695 mL, 51.62 mg) in DMF (1 mL). The reaction mixture was stirred for 20 min. DMF was removed in vacuo and the crude oil subjected to HPLC purification. The collected fractions were combined and lyophilized to give a white powder. The yield was 35.5 mg (~70%). MS (ESI, +ve): m/z = 463.15 for $C_{20}H_{25}N_5O_6S$ ([M + H]$^+$). ^{1}H NMR (DMSO-d_6 + D_2O): 9.38 (s, 1H), 9.06 (d, 2H, J = 6.6 Hz), 8.632 (s, 1H), 8.49−8.36 (m, 4H), 7.81 (dd, 1H, J = 8.4, 7 Hz), 7.4 (m, 2H), 7.22 (br, 1H), 4.4 (m, 1H), 3.65 (s, 3H), 3.3 (m, 2H), 1.86 (m, 2H), 1.59−1.43 (m, 4H).

Synthesis of *N*-ε-(Nicotinyl)-*N*-α-(6-(2-(2-sulfonatobenzaldehyde)hydrazono)nicotinyl)lysine Methyl Ester (L2). To a 25 mL round-bottom flask was added nicotinic acid hydrochloride (14.32 mg, 0.09 mmol), followed by 5 mL of DMF and 1-*O*-(*N*,*N*′,*N*″,*N*‴-tetramethyluronium)azabenzotriazoloxy hexafluorophosphate (41 mg, 0.1 mmol), 1-hydroxyazabenzotriazole (14.6 mg, 0.1 mmol) and DIEA (0.104 mL, 0.774 g). After stirring for 5 min, *N*-α-(6-(2-(2-sulfonatobenzaldehyde)hydrazono)nicotinyl)lysine methyl ester hydrochloride (50 mg, 0.10 mmol) was added. The resulting solution was stirred for 30 min. DMF was removed under vacuum and the crude oil subjected to HPLC purification. The collected fractions were combined and lyophilized to give a fluffy white solid. The yield was 42 mg (82%). MS (ESI, +ve): m/z = 569.1815 for $C_{26}H_{28}N_6O_7S$ ([M + H]$^+$). ^{1}H NMR (DMSO-d_6 + DCl): 9.3 (d, 2H, J = 16.2 Hz), 9.0 (d, 1H, J = 4.8 Hz), 8.9 (d, 1H, J = 8.4 Hz), 8.6 (s, 1H), 8.49 (d of d, 1H, J = 2.4, 7.2 Hz), 8.43 (d, 1H), 8.1 (m, 1H), 7.8 (dd, 1H, J = 2.4, 1.2 Hz), 7.4(m, 2H). 7.28(d, 1H), 4.4 (m, 1H), 3.65 (s, 3H), 3.29 (m, 2H), 1.8 (m, 2H), 1.59−1.44 (m, 4H).

Synthesis of *N*-ε-(Picolinyl)-*N*-α-(6-(2-(2-sulfonatobenzaldehyde)hydrazono)-nicotinyl)lysine Methyl Ester (L3). To a round-bottom flask were added picolinic acid (10 mg, 0.08 mmol), 5 mL of DMF, 1-*O*-(*N*,*N*′,*N*″,*N*‴-tetramethyluronium)azabenzotriazoloxy hexafluorophosphate (38 mg, 0.1 mmol), 1-hydroxyazabenzotriazole (14.6 mg, 0.1 mmol), and DIEA (0.104 mL, 0.077 gm). After the solution was stirred for 7 min, *N*-α-(6-(2-(2-sulfonatobenzaldehyde)hydrazono)nicotinyl)lysine methyl ester hydrochloride (50 mg, 0.10 mmol) was added. The reaction mixture was stirred for another 30 min. DMF was removed under vacuum and the crude oil subjected to HPLC purification. The collected fractions were combined and lyophilized to give a fluffy white solid. The yield was 34 mg (73%). MS (ESI, +ve): m/z = 569.1815 for $C_{26}H_{28}N_6O_7S$ ([M + H]$^+$). ^{1}H NMR (DMSO-d_6 + DCl): 9.32 (br s, 1H), 8.62 (m, 1H), 8.52 (s, 1H), 8.3 and 8.24 (bs, 2H), 8.0−7.9 (m, 2H), 7.8 (dd, 1H, J = 1.2 Hz, J = 6 Hz), 7.5 (m, 1H), 7.4 (m, 2H), 7.19 (d, 1H, 9.6 Hz), 4.4 (m, 1H), 3.64 (s, 3H), 3.3 (m, 2H), 1.9−1.8 (m, 2H), 1.6−1.54 (m, 2H), 1.45−1.25 (m, 2H).

Synthesis of 1-(*N*-(6-(2-(2-Sulfonatobenzaldehyde)hydrazono)nicotinyl))-6-(nicotinoyl)pentanediamine (L4). To a 15 mL round-bottom flask was added sodium succinimidyl 6-(2-(2-sulfonatobenzaldehyde)hydrazono)nicotinate (50 mg, 0.113 mmol) followed by DMF (3 mL) and by pentamethylenediamine (13.8 mg, 0.135 mmol). The mixture was stirred for 30 min. A precipitate begins to form a few minutes into the reaction. The precipitate was filtered and was confirmed as the intermediate product according to LC−MS. The intermediate was used directly without any further purification for the next step.

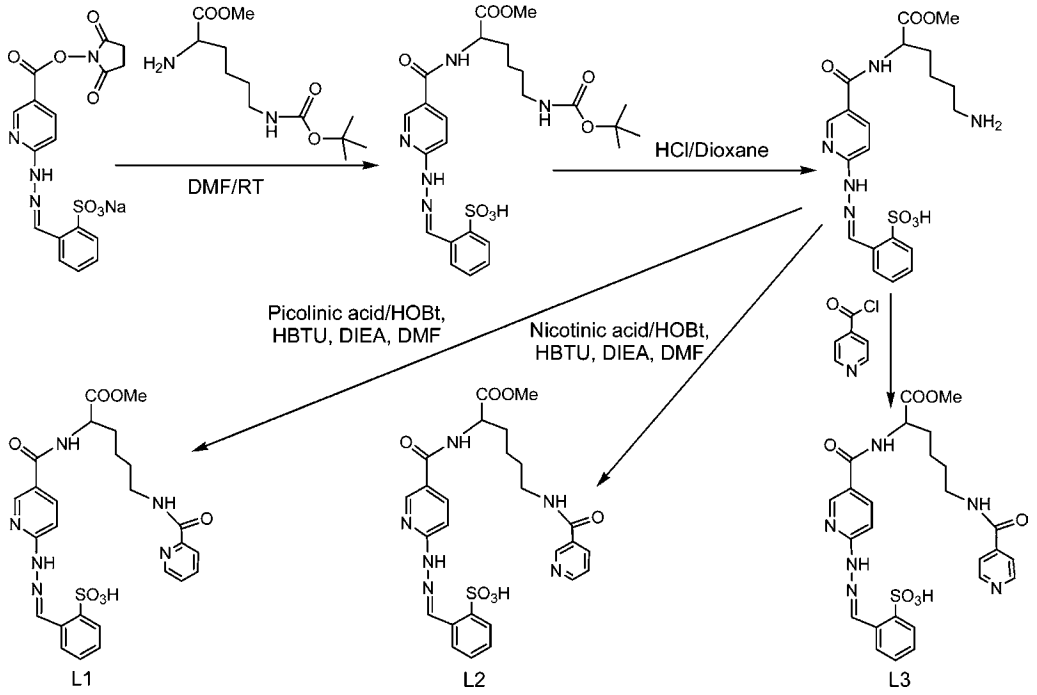
1-(*N*-(6-(2-(2-Sulfonatobenzaldehyde)hydrazono)nicotinyl))pentanediamine (23 mg, 0.056 mmol) was added to a flask containing nicotinic acid (7.5 mg, 0.061 mmol), 1-*O*-(*N*,*N*′,*N*″,*N*‴-tetramethyluronium)azabenzotriazoloxy hexafluorophosphate (24 mg, 0.063 mmol), and diisopropylethylamine (58 mg, 0.45 mmol) in DMF (3 mL). The reaction mixture stirred at room temperature for 4 h. DMF was removed in vacuo and the crude product was purified by HPLC. The collected fractions were combined and lyophilized to give a fluffy white solid. The yield was 15 mg (52%). MS (ESI, +ve; m/z = 511.1754 for $C_{24}H_{26}N_6O_5S$ ([M + H]$^+$). ^{1}H NMR (600 MHz, DMSO-d_6 + DCl): 9.35 (s, 1H), 9.33 (s, 1H), 9.0 (m, 2H), 8.58 (s, 1H), 8.4 (d of d, 1H, J = 2.0, 7.2 Hz), 8.1 (m, 1 H), 7.8 (m, 1H), 7.4 (m, 2H), 7.23 (br, 1H), 3.3 (t, 2H), 3.2 (t, 2H), 1.5 (m, 4H), 1.3 (m, 2H).

Synthesis of 1-(*N*-(6-(2-(2-Sulfonatobenzaldehyde)hydrazono)nicotinyl))hexanediamine. To a 15 mL round-bottom flask was added sodium succinimidyl 6-(2-(2-sulfonatobenzaldehyde)hydrazono)nicotinate (100 mg, 0.226 mmol) followed by DMF (3 mL) followed by hexamethylenediamine (26.3 mg, 0.226 mmol). The mixture was stirred for 10 min. DMF was removed in vacuo and the crude mixture subjected to purification by HPLC. The collected fractions were combined and lyophilized to give a white solid. The yield was 46 mg (~49%). MS (ESI, +ve): m/z = 406.15 for $C_{18}H_{24}N_5O_4S$ ([M + H]$^+$). ^{1}H NMR (DMSO-d_6 + DCl): 9.34 (s, 1H), 8.59 (s, 1H), 8.50 (dd, 2H, J = 2.0, 7.2 Hz), 8.09 (t, 1 H), 7.8 (m, 1H), 7.4 (m, 2H), 7.23 (br, 1H), 3.25 (t, 2H), 2.73 (m, 2H), 1.5 (m, 4H), 1.31 (m, 4H).

Synthesis of 1-(*N*-(6-(2-(2-Sulfonatobenzaldehyde)hydrazono)nicotinyl))-6-(nicotinoyl)hexanediamine (L5). To a 15 mL round-bottom flask was added nicotinic acid (5.34 mg, 0.043 mmol) and 1-*O*-(*N*,*N*′,*N*″,*N*‴-tetramethyluronium)azabenzotriazoloxy hexafluorophosphate(18.14 mg, 0.047 mmol). To the above mixture were added DMF (3 mL) and diisopropylethylamine (16.78 mg, 0.130 mmol, 0.022 mL). The solution was stirred for 5 min, after which 1-(*N*-(6-(2-(2-sulfonatobenzaldehyde)hydrazono)nicotinyl))hexanediamine (20 mg, 0.047 mmol) was added in one lot. The reaction mixture was stirred for another 30 min at room temperature. After removal of DMF, the crude oil was subjected to HPLC purification. The collected fractions were combined and lyophilized to give a white solid. The yield was 18 mg (80%). MS (ESI, +ve): m/z = 525.1915 for $C_{25}H_{28}N_6O_5S$ ([M + H]$^+$). ^{1}H NMR (600 MHz, DMSO-d_6 +DCl): 9.3 (d, 2H, J = 7.2 Hz), 9.04 (d, 1H, J = 5.4 Hz), 9.02 (d, 1H, J = 8.4 Hz), 8.58 (s, 1H), 8.48 (dd, 2H, J = 1.8, 7.8 Hz), 8.17 (m, 1H), 7.79 (m, 1H), 7.4 (m, 2H), 7.23 (br, 1H), 3.3 (t, 2H, J = 7.2 Hz), 3.2 (t, 2H, J = 7.2 Hz), 1.54 (m, 4H), 1.35 (m, 4H).

General Procedure for Preparation of ^{99m}Tc Complexes. To a 5.0 mL vial were added the HYNIC chelator (1.0−40 μg), 0.4 mL of 0.25 M succinate buffer (pH = 5.0), and 0.4 mL of tricine solution (25−100 mg/mL in 0.25 M succinate buffer, pH = 5.0). After addition of 0.5 mL of $^{99m}TcO_4^-$ solution (40−80 mCi/mL in saline) and 25 μL of $SnCl_2 \cdot 2H_2O$ solution (1.0 mg/mL in 0.1 N HCl), the mixture was heated in a water bath at 95−100 °C for 10−15 min. After cooling to room temperature, a sample

Scheme 1. Synthesis of L1−L3



of the resulting solution was analyzed by radio-HPLC and ITLC. In all cases, formation of [^{99m}Tc]colloid was minimal.

Solution Stability Studies. For solution stability in the kit matrix, the macrocyclic complex [^{99m}Tc(L2)-(tricine)] was prepared, and samples of the resulting reaction were analyzed by radio-HPLC at t = 0, 1, 2, 3, and 4 h postlabeling. For solution stability of HPLC-purified [^{99m}Tc(L2)(tricine)], peaks A and C were collected into a 25 mL round-bottom flask. Solvents were removed using a rotary evaporator. The residue was dissolved in saline, and samples of the resulting solution were analyzed by radio-HPLC over 4 h postpurification. For TPPTS and cysteine challenge experiments, the complex [^{99m}Tc(L2)(tricine)] was prepared first and diluted with an equal volume of saline containing TPPTS (1 mg/mL) or cysteine (1 mg/mL). Samples of the resulting solution were analyzed by radio-HPLC over 6 h.

Radiolabeling Efficiency Experiment. To a 5.0 mL vial were added 0.05−0.5 mL of the L2 solution (20 μg/mL) in 0.25 M succinate buffer (pH = 5.0) and 0.2 mL of tricine solution (100 mg/mL in 0.25 M succinate buffer, pH = 5.0). The total volume in each vial was adjusted to ∼1.2 mL using 0.25 M succinate buffer, pH = 5.0). After addition of 0.3 mL of $^{99m}TcO_4^-$ solution (∼30 mCi) and 25 μL of $SnCl_2 \cdot 2H_2O$ solution (1.0 mg/mL in 0.1 N HCl), the mixture was heated at 100 °C for 10 min. After cooling to room temperature, the resulting solution was analyzed by radio-HPLC. Each condition was carried out in duplicate and the radiolabeling yield was calculated as the average of the two vials.

General Procedure for Preparation of Macrocyclic ^{99}Tc Complexes. To a 5.0 mL vial were added the pyridine-containing HYNIC chelator (500−1000 μg), 0.5 mL of 0.25 M succinate buffer (pH = 5.0), and 0.5 mL of tricine solution (100 mg/ mL in 0.25 M succinate buffer, pH = 5.0). After addition of 0.5 mL of $^{99}TcO_4^-$ solution (1 mg/mL in water) and 25 μL of $SnCl_2 \cdot 2H_2O$ solution (10 mg/mL in 0.1 N HCl), the mixture was heated at 100 °C for ∼15 min. After cooling to room temperature, a sample of the resulting solution was analyzed by LC−MS.

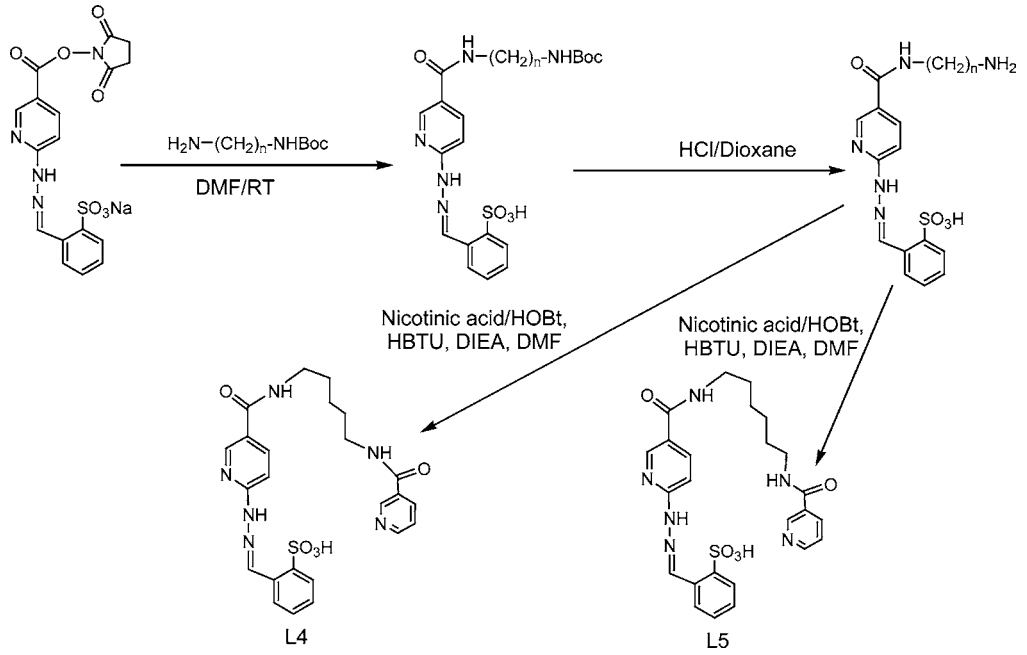
RESULTS AND DISCUSSION

Synthesis of Pyridine-Containing HYNIC Derivatives. L1−L5 were prepared according to Schemes 1 and 2. For L1−L3, HYNIC−NHS was allowed to react with ω-Boc-lysine methyl ester at room temperature in DMF to give the intermediate HYNIC−(ω-Boc)K as its methyl ester. The Boc-protecting group was readily removed in a 4 M HCl dioxane solution to afford HYNIC−K(OMe) as the hydrochloride salt. Conjugation of HYNIC−K(OMe) with picolinic acid, nicotinic acid, and isonicotinyl chloride produced L1−L3, respectively, as their methyl esters. For L4 and L5, the synthetic procedure was similar to that for the synthesis of L1−L3, except that pentamethylenediamine and hexamethylenediamine were used as the linker instead of lysine methyl ester. L1−L5 were purified by HPLC with the purity being >98% before radiolabeling. NMR (^{1}H and ^{13}C) and mass spectral data are completely consistent with the proposed structures.

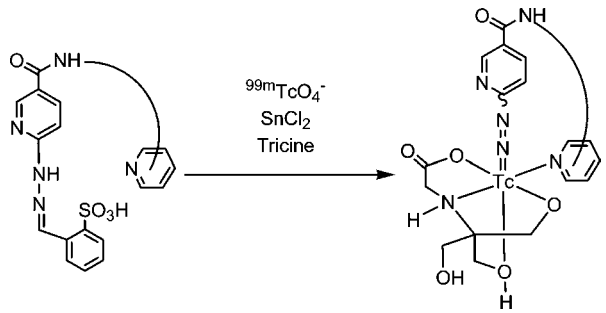
Synthesis of ^{99m}Tc Complexes. ^{99m}Tc complexes of L1−L5 were prepared (Scheme 3) using conditions similar to those described in our previous communication (*17*). The HYNIC derivative was allowed to react directly with $^{99m}TcO_4^-$ in the presence of stannous chloride and excess tricine. Radiolabeling was achieved by heating the reaction mixture at 100 °C for 10−15 min. Since the pyridine-containing HYNIC derivatives are air-stable, there was no need for exclusion of air before addition of $^{99m}TcO_4^-$. After radiolabeling, a sample of the resulting solution was analyzed by radio-HPLC and TLC. The ^{99m}Tc-labeling efficiency is extremely high for L2, L4, and L5. The minimum amount of L2 to achieve high-yield ^{99m}Tc-labeling (>95%) was about 1 μg for 30 mCi of $^{99m}TcO_4^-$, corresponding to a molar ratio of ∼8:1 for L2:Tc.

We also tried to use other polydentate aminocarboxylates, such as nitrilotriacetic acid (NTA), *N*-(2-hydroxyethyl)iminodiacetic acid (HIDA), *N*-(2-hydroxyethyl)-glycine (monocine), ethylenediamine-*N*,*N*′-diacetic acid (EDDA), and *N*-(hydroxyethyl)ethylenediamine triacetic acid (HEDTA), as coligands to replace tricine. The yields for these ^{99m}Tc complexes were always low (<30%).

Scheme 2. Synthesis of L4 and L5



Scheme 3. Synthesis of ^{99m}Tc Complexes: [^{99m}Tc(L)(tricine)] (L = L1−L5)



Among various polydentate aminocarboxylates, tricine remains the best coligand with respect to the radiolabeling yield, radiochemical purity, and the number of isomers formed. The concentration of the tricine coligand ranges from 10 to 100 mg/mL. If the tricine concentration is <10 mg/mL, the formation of [^{99m}Tc]colloid may become significant. If the tricine concentration is >100 mg/mL, the radiolabeling yields for the ^{99m}Tc complexes decreases.

Attachment Site and Macrocyclic Chelate Formation. L1−L3 were specifically designed to study the impact of the attachment site on the formation of macrocyclic Tc chelates. To determine if pyridine-N atoms in L1−L3 are able to bond to the Tc, we also used HYNIC−(ω-Boc)K to prepare the binary ligand ^{99m}Tc complex [^{99m}Tc(HYNIC−(ω-Boc)K)(tricine)$_2$]. A reverse-phase HPLC method (20−25% acetonitrile over 20 min) was used to analyze the synthesized ^{99m}Tc complexes. Figure 3 shows radio-HPLC chromatograms of ^{99m}Tc complexes [^{99m}Tc(L1)(tricine)] (top) and [^{99m}Tc(L2)(tricine)] (bottom). Figure 4 shows radio-HPLC chromatograms of [^{99m}Tc(L3)(tricine)$_2$] (top) and [^{99m}Tc(HYNIC−(ω-Boc)K)-(tricine)$_2$] (bottom). In the absence of the pyridine-N donor, the radio-HPLC chromatogram of the binary ligand ^{99m}Tc complex [^{99m}Tc(HYNIC−(ω-Boc)K)(tricine)$_2$] always shows multiple peaks between 3 and 25 min. The radio-HPLC chromatogram of [^{99m}Tc(L3)(tricine)$_2$] is very similar to that of [^{99m}Tc(HYNIC−(ω-Boc)K)(tricine)$_2$] (Figure 4). It is quite clear that the 4-substituted analogue is not able to bond to the Tc. Thus, L3 is not a suitable BFC for the ^{99m}Tc-labeling of small biomolecules, at least when lysine is used as the linker.

The complex [^{99m}Tc(L1)(tricine)] shows two major radiometric peaks at ~3.7 and 10 min. Obviously, the pyridine-N in L1 is able to bond to the Tc. Many attempts have been made to minimize the peak at 3.7 min by changing component levels in the formulation matrix, but these were not successful. Thus, the peak at 3.7 min is treated as a radioimpurity, instead of part of [^{99m}Tc(L1)-(tricine)]. Since the radiolabeling yield for [^{99m}Tc(L1)-(tricine)] is low (65−70%), L1 is not an ideal BFC for the ^{99m}Tc-labeling of small biomolecules either.

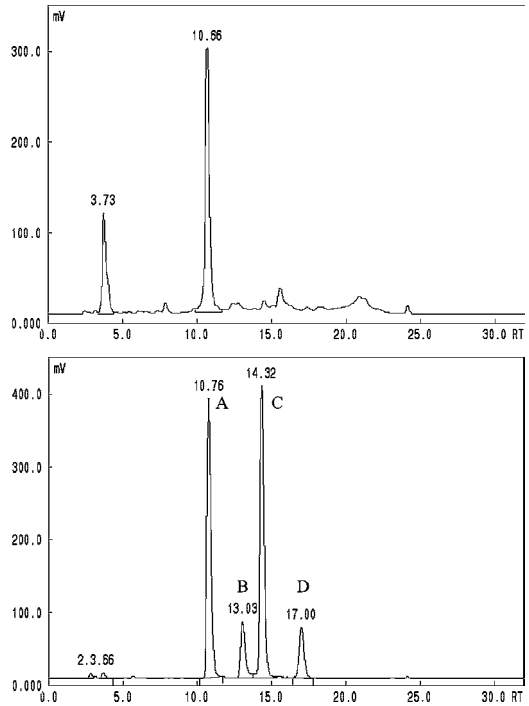


Figure 2. Typical radio-HPLC chromatograms of macrocyclic complexes [^{99m}Tc(L1)(tricine)] (top) and [^{99m}Tc(L2)(tricine)] (bottom).

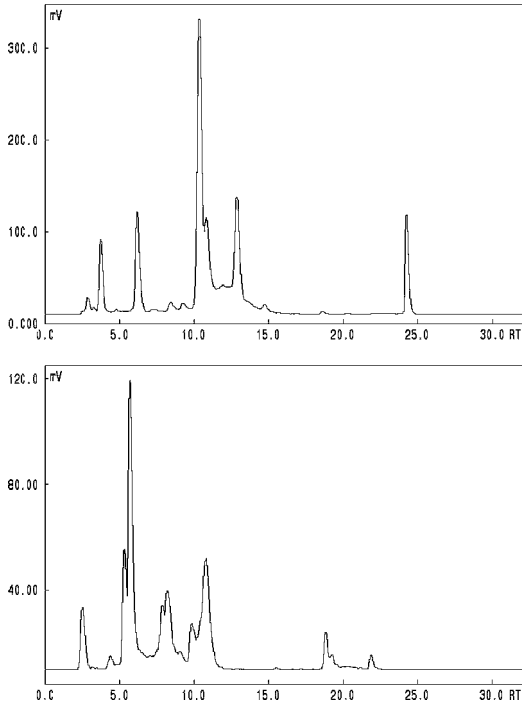


Figure 3. Radio-HPLC chromatograms of ^{99m}Tc complexes [^{99m}Tc(L3)(tricine)$_2$] (top) and [^{99m}Tc(HYNIC−(ω-Boc)K)-(tricine)$_2$] (bottom).

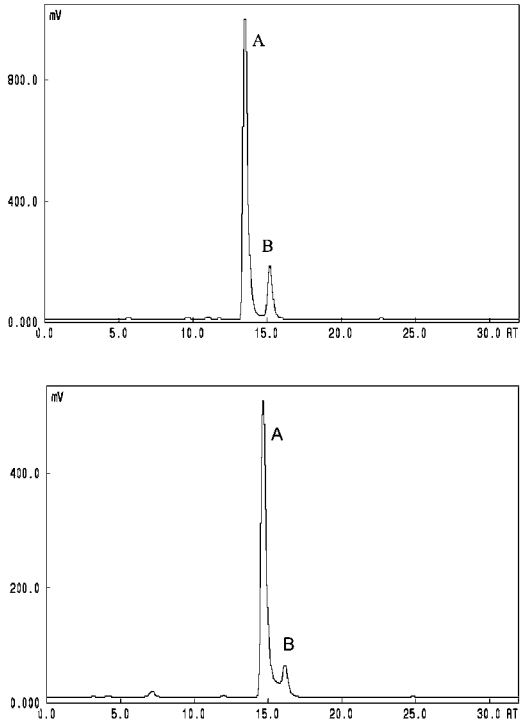


Figure 4. Typical radio-HPLC chromatograms for macrocyclic complexes [^{99m}Tc(L4)(tricine)] (top) and [^{99m}Tc(L5)(tricine)] (bottom).

The radio-HPLC chromatogram of [^{99m}Tc(L2)(tricine)] (Figure 2) shows two pairs of radiometric peaks. The peak ratio of (A + D) over (B + C) is always close to 50%:50%. The relative peak ratios remain constant over 6 h postlabeling. Apparently, the pyridine-N in L2 is bonded to the Tc and forms a macrocyclic Tc chelate ring, and the position for attachment of the linker is critical for both the formation of macrocyclic Tc chelate and the number of isomeric forms of the resulting ^{99m}Tc complex

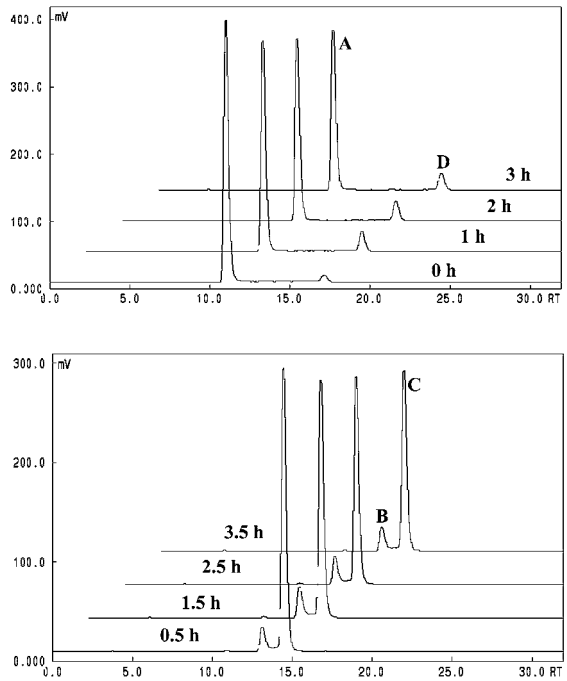


Figure 5. Conversion from A to D (top) and C to B (bottom) for the macrocyclic complex [^{99m}Tc(L2)(tricine)] at room temperature.

in solution. The 3-position seems to be the best for attachment of the lysine linker.

Isomerism in Macrocyclic ^{99m}Tc Complexes. In ternary ligand ^{99m}Tc complexes [^{99m}Tc(HYNIC−BM)-(tricine)(L)] (BM = biomolecules; L = phosphines and pyridine analogues), there are always two diastereomers due to the asymmetric bonding of the tricine coligand, if the targeting biomolecule contains one or more chiral centers. That often leads to the observation of two radiometric peaks in their radio-HPLC chromatograms (*5*−*10*). There are two pairs of radiometric peaks in the HPLC chromatogram of [^{99m}Tc(L2)(tricine)]. Apparently, the chiral center in the lysine linker plays a significant role for the presence of these two pairs of isomers.

To prove this assumption, we prepared L4 and L5, which contain no chiral centers on the linker. Macrocyclic complexes [^{99m}Tc(L4)(tricine)] and [^{99m}Tc(L5)(tricine)] were prepared in the same fashion as [^{99m}Tc(L2)(tricine)]. Figure 5 shows radio-HPLC chromatograms of [^{99m}Tc(L4)-(tricine)] and [^{99m}Tc(L5)(tricine)]. Only two isomers are detectable if the linker contains no chiral centers. This experiment clearly demonstrates that [^{99m}Tc(L2)(tricine)] exists in solution as a pair of diastereomers (A and C or B and D) and a pair of conformational isomers (A and D or B and C).

How do we know that A and D or B and C are conformational isomers in the complex [^{99m}Tc(L2)(tricine)]? To answer that question, we isolated A and C and studied their relationship with the other two peaks. Peaks A and C were separated by HPLC into two separate flasks. After removal of volatiles, the residue in each flask was redissolved in saline to give a concentration of 2 mCi/mL. The resulting solutions were analyzed by HPLC every 30 min over 4 h. Figure 5 shows "staggered" HPLC chromatograms for A and C. At room temperature, part of A was rapidly converted to D while part of C was converted to B. There is no conversion from A to C or C to A. The conversion from A to D or B to C suggests that A and D or C and B are most likely conformational isomers due to restricted rotations of the macrocycle.

Table 1. LC−MS Data for Macrocyclic ^{99m}Tc Complexes

macrocyclic ^{99m}Tc complex	formula ($[M + H]^+$)	formula weight	found ($[M + H]^+$)
[^{99m}Tc(L2)(tricine)], A	$C_{25}H_{33}N_7O_9Tc$	674.48	674.1
[^{99m}Tc(L2)(tricine)], C	$C_{25}H_{33}N_7O_9Tc$	674.48	674.2
[^{99m}Tc(L4)(tricine)], A	$C_{23}H_{31}N_7O_7Tc$	616.44	616.1
[^{99m}Tc(L5)(tricine)], A	$C_{24}H_{33}N_7O_7Tc$	630.47	630.2

Table 2. LC−MS Data for Macrocyclic ^{99}Tc Complexes

macrocyclic ^{99}Tc complex	formula ($[M + H]^+$)	formula weight	found ($[M + H]^+$)
[^{99}Tc(L2)(tricine)], A	$C_{25}H_{33}N_7O_9Tc$	674.48	674.1
[^{99}Tc(L2)(tricine)], B	$C_{25}H_{33}N_7O_9Tc$	674.48	674.3
[^{99}Tc(L2)(tricine)], C	$C_{25}H_{33}N_7O_9Tc$	674.48	674.2
[^{99}Tc(L2)(tricine)], D	$C_{25}H_{33}N_7O_9Tc$	674.48	674.1
[^{99}Tc(L4)(tricine)], A	$C_{23}H_{31}N_7O_7Tc$	616.44	616.1
[^{99}Tc(L4)(tricine)], B	$C_{23}H_{31}N_7O_7Tc$	616.44	616.1
[^{99}Tc(L5)(tricine)], A	$C_{24}H_{33}N_7O_7Tc$	630.47	630.2
[^{99}Tc(L5)(tricine)], B	$C_{24}H_{33}N_7O_7Tc$	630.47	630.2

The fast rate of conversion from A to D and from C to B is significant. In our previous communication (*17*), we found that the major isomer of [^{99m}Tc(HYNIC−Ko-TPPB)-(tricine)] remained relatively unchanged at room temperature and was converted to the other two isomers only at elevated temperatures (>50 °C). Compared to the triphenylphosphine moiety, the pyridine group is much smaller. The energy barrier between different conformational isomers is much lower than that in [^{99m}Tc(HYNIC−Ko-TPPB)(tricine)]. It is not surprising that A is able to convert to D (or C to B) and to reach equilibrium within 3 h even at room temperature.

To further support these hypothesis, we used LC−MS to determine the composition of each isomer of complexes [^{99m}Tc(L)(tricine)] (L = L2, L4, and L5) at the tracer level. The LC−MS data are listed in Table 1. Due to the extremely low concentration, determination of the composition for the smaller peaks {B and D of [^{99m}Tc(L2)-(tricine)] and B of [^{99m}Tc(L4)(tricine)] and [^{99m}Tc(L5)-(tricine)]} was not possible at the tracer level. Therefore, we prepared ^{99}Tc complexes [^{99}Tc(L)(tricine)] (L = L2, L4, and L5) at the milligram level. The composition of all the isomers in the macrocyclic complexes [^{99}Tc(L)(tricine)] (L2, L4, and L5) has been determined. The LC−MS data for macrocyclic ^{99}Tc complexes are listed in Table 2 and are completely consistent with the proposed composition for macrocyclic ^{99m}Tc complexes [^{99m}Tc(L)(tricine)]. All four isomers of [^{99}Tc(L2)(tricine)] have the same molecular weight at $m/z = 674$ for $[M + H]^+$. Both isomers of [^{99}Tc(L)(tricine)] (L = L4 and L5) also have the same molecular weight at $m/z = 616$ for [^{99}Tc(L4)(tricine)] and $m/z = 630$ for [^{99}Tc(L5)(tricine)]. These results clearly show that the presence of four peaks in the radio-HPLC chromatogram of [^{99m}Tc(L2)(tricine)] is indeed due to resolution of four different isomers. The formation of these four isomers is in part due to the presence of chirality in the lysine linker and in part due to the restricted rotation of the macrocyclic Tc chelate ring.

Linker Length and Isomerism in Macrocyclic ^{99m}Tc Complexes. In ternary ligand ^{99m}Tc complexes, [^{99m}Tc(HYNIC−BM)(tricine)(L)] (L = pyridine analogues), HYNIC is most likely monodentate due to the presence of the tricine and monodentate pyridine coligands (*10*). However, the HYNIC group in [Tc(L)(tricine)] (L = L2, L4, and L5) may be forced to become bidentate (Figure 6) due to the bonding of pyridine-N. The tridentate tricine may result in formation of many different coordination isomers due to its asymmetric nature in bonding to the Tc. If that were true, the coordinated tricine would have been much more fluxional and there would have been a rapid exchange among all four isomers (A, B, C, and D). The fact that there is no conversion from A to C or C to A is not consistent with this explanation. Therefore, HYNIC is most likely to be monodentate in [Tc(L)-(tricine)] (L = L2, L4, and L5).

There are several ways to minimize the number of conformational isomers. These include (1) increasing the linker length so that the macrocycle can rotate freely and (2) reducing the linker length in such a way that only one conformational isomer is possible. We prepared HYNIC−en-NIC to see if the use of the 1,2-ethylenediamine linker would result in the reduction of isomerism. Unfortunately, the ethylenediamine linker is too short for the pyridine-N of the nicotinyl group to bond to the Tc (unpublished data). The minimum linker length seems to be C4−C5 or an equivalent. In this study, we prepared L5 using a hexamethylenediamine linker. In doing so, we were able to reduce the percentage of the minor isomer B from ~10% for [^{99m}Tc(L4)(tricine)] to only ~6% for [Tc(L5)(tricine)]. However, we were not able to totally eliminate the minor conformational isomer at ~16 min (Figure 4).

Solution Stability of Macrocyclic ^{99m}Tc Complexes. We examined the solution stability of the macrocyclic complex [^{99m}Tc(L2)(tricine)] in the kit matrix. The stability was assessed by radio-HPLC by performing six injections over 6 h. Figure 7 shows the plot of RCP versus time for [^{99m}Tc(L2)(tricine)]. There is no significant RCP change over 6 h, suggesting that [^{99m}Tc(L2)(tricine)] is stable in the kit matrix for at least 6 h. We also examined the solution stability of the HPLC-purified [^{99m}Tc(L2)-(tricine)]. Peaks A and C were collected into separate flasks. After removal of volatiles under vacuum, the residue was dissolved in saline. The solution was then monitored by radio-HPLC. It was found that [^{99m}Tc(L2)-(tricine)] remains stable for at least 4 h at room temperature after HPLC purification (Figure 5). There is no indication of any significant decomposition during this period of time, suggesting that [^{99m}Tc(L2)(tricine)] is

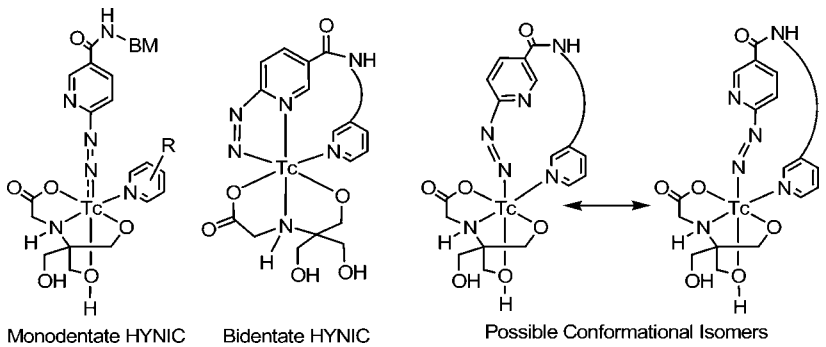


Figure 6. Possible structures for macrocyclic complexes [^{99m}Tc(L)(tricine)] (L = L2, L4 and L5).

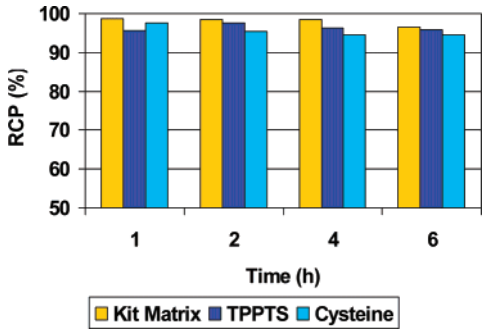


Figure 7. Solution stability of the complex [^{99m}Tc(L2)(tricine)] in the matrix and in the presence of TPPTS (1 mg/mL) or cysteine (1 mg/mL).

Table 3. Radiolabeling Yield for the Macrocyclic Complex [^{99m}Tc(L2)(tricine)]

L2 level (μg)	amount of $^{99m}TcO_4^-$ (mCi)	average % yield
1	30	94.8
2	30	95.6
4	30	96.8
5	30	98.8
10	30	98.8

highly stable, since the decomposition of the ^{99m}Tc complex often leads to formation of $^{99m}TcO_4^-$.

For the TPPTS and cysteine challenge experiments, we added TPPTS and cysteine (1 mg/mL: $2-5 \times 10^{-3}$ M) into solutions containing [^{99m}Tc(L2)(tricine)]. It was found that the addition of TPPTS or cysteine caused minimal changes in the radiochemical purity over 6 h at room temperature (Figure 7). The fact that [^{99m}Tc(L2)-(tricine)] remains intact in the presence of a large excess (10^7-fold) of TPPTS is significant, because TPPTS is a much stronger ligand than pyridine analogues (*10*). This suggests that the ligand exchange reaction is not dependent on the concentration of the entering ligand, and dissociation of pyridine-N is most likely the rate-limiting step. Therefore, the high solution stability of [^{99m}Tc(L2)-(tricine)] is probably due to its kinetic inertness. Similar results were also obtained for ternary ligand ^{99m}Tc complexes [^{99m}Tc(HYNIC−BM)(tricine)(L)] (L = pyridine analogues) (*10*) and the macrocyclic ^{99m}Tc complex [^{99m}Tc-(HYNIC−Ko-DPPB)(tricine)] (*17*).

Radiolabeling Efficiency. We examined the radiolabeling efficiency of L2 by varying the L2 concentration in the formulation matrix from 1 to 10 μg/mL for 30 mCi of $^{99m}TcO_4^-$. The tricine concentration remained the same in all cases. Each condition was carried out in duplicate and the yield was reported as the average of two vials. The radiolabeling yield was calculated as the total percentage of all four peaks (A, B, C, and D), and is summarized in Table 3. It is clear that [^{99m}Tc(L2)(tricine)] could be prepared in high yield (>95%) using 1 μg of L2 for 30 mCi of $^{99m}TcO_4^-$, corresponding to the molar ratio of 8:1 for L2:^{99m}Tc.

The fact that the pyridine-N atoms in L2, L4, and L5 are able to bond to the Tc and form the macrocyclic Tc chelate is truly amazing. Traditionally, it is often believed that for the chelator to form a stable metal chelate, the number of atoms in each chelate ring is ether five or six. Chelate rings containing more than six atoms often result in less stability. The number of atoms between the β-N of HYNIC and pyridine-N of the nicotinyl group is more than 18 in macrocyclic complexes [^{99m}Tc(L)(tricine)] (L = L2, L4, and L5), but these macrocyclic complexes are formed with high stability and extremely high radiolabeling efficiency.

There are several factors contributing to the high solution stability of macrocyclic complexes [^{99m}Tc(L)-(tricine)] (L = L2, L4, and L5). The pyridine-containing HYNIC chelators (L2, L4, and L5) are designed in such a way that when HYNIC binds to the Tc center, the "effective concentration" of the attached pyridine-N donor in the vicinity of Tc will be increased dramatically. This makes it much easier for the pyridine-N donor to bond to the Tc and form a macrocyclic ^{99m}Tc chelate. Of course, the linker length and the attachment site on the pyridine ring have to be appropriate for metal binding, as demonstrated in this study. Once the pyridine-N donor binds to the Tc and completes the octahedral coordination sphere, it is hard for the pyridine-N to become dissociated, since six-coordinated Tc(III) complexes are often kinetically inert (*11*). This is supported by the fact that [^{99m}Tc(L2)(tricine)] remains intact in the presence of a large excess (10^7-fold) of TPPTS while the corresponding ^{99}Tc analogue, [^{99}Tc(L2)(tricine)], remains stable in aqueous solution for 2−3 weeks without any significant decomposition.

Since Abrams and co-workers first reported the use of organic hydrazines as BFCs for the ^{99m}Tc-labeling of polyclonal IgG (*19*, *20*), HYNIC has been used for ^{99m}Tc-labeling of a variety of biomolecules for the development of target-specific radiopharmaceuticals. These include antibodies (*19*−*22*), chemotactic peptides (*23*−*26*), somatostatin analogues (*27*−*32*), liposomes (*33*), antisense oligonucleotides (*34*, *35*), and a folate receptor ligand (*36*). It is well-documented that the ^{99m}Tc-labeled HYNIC−protein conjugates have very high solution stability (*19*−*22*), while the ^{99m}Tc-labeled small biomolecule−HYNIC conjugates are not stable and exist in solution as a mixture of multiple species if tricine or glucoheptonate is used as coligand (*1*, *5*, *14*, *27*, *31*). We are also puzzled by the high level of blood activity for ^{99m}Tc-labeled HYNIC conjugates of small biomolecules, including somatostatin analogues (*27*, *31*) and oligonucleotides (*34*, *35*). Results from this study provide a reasonable explanation of these observations.

Proteins, including antibodies and antibody fragments, contain histidine residues. When the HYNIC group bonds to the Tc, the imidazole-N from a nearby histidine residue may be able to coordinate to the Tc and form an "intramolecular" macrocycle, which is kinetically inert toward further ligand exchange with other chelators. As a result, the ^{99m}Tc-labeled HYNIC−protein conjugates often show high in vitro and in vivo stability. On the other hand, small biomolecules often contain no histidine residues and are not able to form the "intramolecular" macrocycle. When tricine is used as the coligand, the HYNIC−BM conjugates will form binary ligand complexes [^{99m}Tc(HYNIC−BM)(tricine)$_2$], which are not stable and exist as multiple species in solution. Once the binary ligand complex [^{99m}Tc(HYNIC−BM)(tricine)$_2$] is injected into the biological system, it may react with the imidazole group of the histidine residue from circulating blood proteins such as albumin. The serum protein binding capability is most likely responsible for the high blood activity levels of ^{99m}Tc-labeled HYNIC−BM conjugates.

CONCLUSIONS

In this study, we report the synthesis of several pyridine-containing derivatives (L1−L5) and their ^{99m}Tc complexes. Preliminary results have demonstrated that the attachment site of the linker on the pyridine ring is critical for the formation of macrocyclic ^{99m}Tc complexes. For example, the pyridine-N in L3 is not able to bond to

the Tc because the lysine linker is at the 4-position. If the lysine linker is at the 2-position, L1 is able to form the macrocyclic complex [^{99m}Tc(L1)(tricine)], but the radiochemical purity is low. When the lysine linker is attached to the 3-position of the pyridine-N, L2 is able to form the macrocyclic complex [^{99m}Tc(L2)(tricine)] in high yield (>95%). The radio-HPLC data suggest that [^{99m}Tc(L2)(tricine)] exists in solution as four isomers: two diastereomers and two conformational isomers. Diastereomers are formed due to the chirality of the lysine linker and the Tc chelate. Replacing lysine with a pentamethylenediamine linker results in the macrocyclic complex [^{99m}Tc(L4)(tricine)] with only two conformational isomers, which interconvert rapidly at room temperature. Changing the linker from pentamethylenediamine to hexamethylenediamine did not completely eliminate the minor isomer, but the percentage of the minor isomer was reduced from ~10% for [^{99m}Tc(L4)(tricine)] to only 6% for [^{99m}Tc(L5)(tricine)]. The LC−MS data for complexes [^{99m}Tc(L)(tricine)] (L2, L4, and L5) are completely consistent with the proposed composition.

On the basis of these results, it is concluded that pyridine-containing HYNIC chelators have the potential as bifunctional chelators for ^{99m}Tc-labeling of small biomolecules, if the linker is attached to the 3-position of the pyridine ring. Although L2 is able to form the macrocyclic ^{99m}Tc complex in high yield (>95%) and high radiolabeling efficiency, it is not ideal as a BFC for the ^{99m}Tc-labeling of small biomolecules, mainly due to the presence of two diastereomers and two conformational isomers. Our ultimate goal is to develop a chelating system that forms the macrocyclic ^{99m}Tc complex with only diastereomers or more preferably without isomerism.

LITERATURE CITED

(1) Edwards, D. S., Liu, S., Ziegler, M. C., Harris, A. R., Crocker, A. C., Heminway, S. J., Barrett, J. A., Bridger, G. J., Abrams, M. J., and Higgins, J. D. (1999) RP463: A stabilized technetium-99m complex of a hydrazino nicotinamide conjugated chemotactic peptide for infection imaging. *Bioconjuate Chem. 10*, 884−891.

(2) Brouwers, A. H., Laverman, P., Boerman, O. C., Oyen, W. J. G., Barrett, J. A., Harris, T. D., Edwards, D. S., and Corstens, F. H. M. A (2000) ^{99}Tc^{m}-labeled leukotriene B4 receptor antagonist for scintigraphic detection of infection in rabbits. *Nucl. Med. Commun. 21*, 1043−1051.

(3) Liu, S., Edwards, D. S., Ziegler, M. C., and Harris, A. R. (2002) ^{99m}Tc-labeling of a hydrazinonictotinamide-conjugated LTB_4 receptor antagonist useful for imaging infection. *Bioconjugate Chem. 13*, 881−886.

(4) Liu, S., Edwards, D. S., Ziegler, M. C., Harris, A. R., Hemingway, S. J., and Barrett, J. A. (2001) ^{99m}Tc-Labeling of a hydrazinonictotinamide-conjugated vitronectin receptor antagonist. *Bioconjugate Chem. 12*, 624−629.

(5) Liu, S., Edwards, D. S., Looby, R. J., Harris, A. R., Poirier, M. J., Barrett, J. A., Heminway, S. J., and Carroll, T. R. (1996) Labeling a hydrazinonicotinamide-modified cyclic IIb/IIIa receptor antagonist with ^{99m}Tc using aminocarboxylates as co-ligands. *Bioconjugate Chem. 7*, 63−70.

(6) Edwards, D. S., Liu, S., Barrett, J. A., Harris, A. R., Looby, R. J., Ziegler, M. C., Heminway, S. J., and Carroll, T. R. (1997) A new and versatile ternary ligand system for technetium radiopharmaceuticals: Water soluble phosphines and tricine as coligands in labeling a hydrazino nicotinamide-modified cyclic glycoprotein IIb/IIIa receptor antagonist with ^{99m}Tc. *Bioconjugate Chem. 8*, 146−154.

(7) Edwards, D. S., Liu, S., Harris, A. R., and Ewels, B. A. (1999) ^{99m}Tc-labeling hydrazones of a hydrazinonicotinamide conjugated cyclic peptide. *Bioconjuate Chem. 10*, 803−807.

(8) Liu, S., Edwards, D. S., Harris, A. R., Ziegler, M. C., Poirier, M. J., Ewels, B. A., DiLuzio, W. R., and Hui, P. (2001) Towards developing a non-$SnCl_2$ formulation for DMP444: A new radiopharmaceutical for thrombus imaging. *J. Pharm. Sci. 90*, 114−123.

(9) Edwards, D. S., Liu, S., Harris, A. R., and Ewels, B. A. (1999) ^{99m}Tc-labeling hydrazones of a hydrazinonicotinamide conjugated cyclic peptide. *Bioconjuate Chem. 10*, 803−807.

(10) Liu, S., Edwards, D. S., and Harris, A. R. (1998) A novel ternary ligand system for technetium radiopharmaceuticals: Imine-N containing heterocycles as coligands in labeling a hydrazinonicotinamide-modified cyclic platelet glycoprotein IIb/IIIa receptor antagonist with ^{99m}Tc. *Bioconjuate Chem. 9*, 583−595.

(11) Liu, S., Edwards, D. S., Harris, A. R., Heminway, S. J., and Barrett, J. A. (1999) Technetium complexes of a hydrazinonicotinamide-conjugated cyclic peptide and 2-hydrazinopyridine: Synthesis and characterization. *Inorg. Chem. 38*, 1326−1335.

(12) Liu, S., Ziegler, M. C., and Edwards, D. S. (2000) Radio-LC-MS for the characterization of ^{99m}Tc-labeled bioconjugates. *Bioconjugate Chem. 11*, 113−117.

(13) Liu, S., Edwards, D. S., and Barrett, J. A. (1997) ^{99m}Tc-labeling of highly potent small peptides. *Bioconjuate Chem. 8*, 621−636.

(14) Edwards, D. S., and Liu, S. (1997) ^{99m}Tc-labeling of hydrazinonicotinamide modified highly potent small molecules: Problems and solutions. *Transition Met. Chem. 22*, 425−426.

(15) Liu, S., and Edwards, D. S. (1999) ^{99m}Tc-labeled small peptides as diagnostic radiopharmaceuticals. *Chem. Rev. 99*, 2235−2268.

(16) Liu, S., and Edwards, D. S. (2001) New Radiopharmaceuticals for imaging infection and inflammation. *Drugs Future 26*, 375−382.

(17) Purohit, A., Liu, S., Casebier, D., and Edwards, D. S. (2003) Phosphine-containing HYNIC derivatives as potential bifunctional chelators for ^{99m}Tc-labeling of small biomolecules. *Bioconjugate Chem. 14*, 720−727.

(18) Harris, T. D., Sworin, M., Williams, N., Rajopadhye, M., Damphousse, P. R., Glowacka, D., Poirier, M. J., and Yu, K. (1998) Synthesis of stable hydrazones of a hydrazinonicotinyl-modified peptide for the preparation of ^{99m}Tc-labeled radiopharmaceuticals. *Bioconjugate Chem. 10*, 808−814.

(19) Abrams, M. J., Juweid, M., tenKate, C. I., Schwartz, D. A., Hauser, M. M., Gaul, F. E., Fuccello, A. J., Rubin, R. H., Strauss, H. W., and Fischman, A. J. (1990) Technetium-99m-human polyclonal IgG radiolabeled via the hydrazino nicotinamide derivative for imaging focal sites of infection in rats. *J. Nucl. Med. 31*, 2022−2028.

(20) Schwartz, D. A., Abrams, M. J., Hauser, M. M., Gaul, F. E., Larsen, S. K., Rauh, D., and Zubieta, J. (1991) Preparation of hydrazino-modified proteins and their use for the synthesis of ^{99m}Tc-protein conjugates. *Bioconjugate Chem. 2*, 333−336.

(21) Ultee, M. E., Bridger, G. J., Abrams, M. J., Longley, C. B., Burton, C. A., Larsen, S., Henson, G. W., Padmanabhan, S., Gaul, F. E., and Schwartz, D. A. (1997) Tumor imaging with technetium-99m-labeled hydrazinonicotinamide-Fab' conjugates. *J. Nucl. Med. 38*, 133−138.

(22) Bridger, G. J., Abrams, M. J., Padmanabhan, S., Gaul, F. E., Larsen, S., Henson, G. W., Schwartz, D. A., Burton, C. A., and Ultee, M. E. (1996) A comparison of cleavable and noncleavable hydrazinopyridine linkers for the ^{99m}Tc-labeling of Fab' monoclonal antibody fragments. *Bioconjugate Chem. 7*, 255−264.

(23) Babich, J. W., Solomon, H., Pike, M. C., Kroon, D., Graham, W., Abrams, M. J., Tompkins, R. G., Rubin, R. H., and Fischman, A. J. (1993) Technetium-99m labeled hydrazino nicotinamide derivatized chemotactic peptide analogues for imaging focal sites of bacterial infection. *J. Nucl. Med. 34*, 1967−1974.

(24) Babich, J. W., and Fischman, A. J. (1995) Effect of "coligand" on the biodistribution of ^{99m}Tc-labeled hydrazino nicotinic acid derivatized chemotactic peptides. *Nucl. Med. Biol. 22*, 25−30.

(25) Babich, J. W., Graham, W., Barrow, S. A., and Fischman, A. J. (1993) Comparison of the infection imaging properties

of a ^{99m}Tc labeled chemotactic peptide with ^{111}In IgG. *Nucl. Med. Biol. 22*, 643−648.

(26) Babich, J. W., Coco, W. G., Barrow, S. A., Fischman, A. J., Femia, F. J., and Zubieta, J. (2000) ^{99m}Tc-labeled chemotactic peptides: Influence of coligands on distribution of molecular species and infection imaging properties. Synthesis and structural characterization of model complexes with the {Re(η^2-HNNC$_5$H$_4$N)(η^1-HNNC$_5$H$_4$N)} core. *Inorg. Chim. Acta 309*, 123−136.

(27) Decristoforo, C., and Mather, S. J. (1999) ^{99m}Tc-labeled peptide-HYNIC conjugates: Effect of lipophilicity and stability on biodistribution. *Nucl. Med. Biol. 26*, 389−396.

(28) Decristoforo, C., and Mather, S. J. (1999) Preparation, ^{99m}Tc-labeling, and in vitro characterization of HYNIC and N$_3$S modified RC-160 and [Tyr^3]Octreotide. *Bioconjugate Chem. 10*, 431−438.

(29) Decristoforo, C., and Mather, S. J. (1999) Technetium-99m somatostatin analogues: Effect of labeling methods and peptide sequence. *Eur. J. Nucl. Med. 26*, 869−876.

(30) Decristoforo, C., Melendez, L., Sosabowski, J. K., and Mather, S. J. (2000) ^{99m}Tc−HYNIC-[Tyr^3]-octreotide for imaging somatostatin-receptor-positive tumors: Preclinical evaluation and comparison with ^{111}In−Octreotide. *J. Nucl. Med. 41*, 1114−119.

(31) Bangard, M., Béhé, M., Guhlke, S., Otte, R., Bender, H., Maecke, H. R., and Birsack, H. J. (2000) Detection of somatostatin receptor-positive tumours using the new ^{99m}Tc-tricine-HYNIC-D-Phe^1-Tyr^3-octreotide: First results in patients and comparison with ^{111}In-DTPA-D-Phe^1-Tyr^3-octreotide. *Eur. J. Nucl. Med. 27*, 628−637.

(32) Decristoforo, C., Mather, S. J., Cholewinski, W., Donnemiller, E., Riccabona, G., and Moncayo, R. (2000) ^{99m}Tc-EDDA/HYNIC-TOC: A new ^{99m}Tc-labeled radiopharmaceutical for imaging somatostatin receptor-positive tumors: First clinical results and intrapatient comparison with ^{111}In-labeled octreotide derivatives. *Eur. J. Nucl. Med. 27*, 1318−1325.

(33) Laverman, P., Dams, E. T. M., Oyen, W. J. G., Storm, G., Koenders, E. B., Prevost, R., van der Meer, J. W. M., Corstens, F. H. M., and Boerman, O. C. (1999) A novel method to label liposomes with ^{99m}Tc by the hydrazine nicotinyl derivative. *J. Nucl. Med. 40*, 192−197.

(34) Zhang, Y.-M., Liu, N., Zhu, Z.-H., Rusckowski, M., and Hnatowich, D. J. (2000) Influence of different chelators (HYNIC, MAG$_3$ and DTPA) on tumor cell accumulation and mouse biodistribution of technetium-99m labeled antisense DNA. *Eur. J. Nucl. Med. 27*, 1700−1707.

(35) Hnatowich, D. J., Winnard P., Jr., Virzi, F., Santo, T., Smith, C. L., Cantor, C. R., and Rusckowski, M. (1995) Technetium-99m labeling of DNA oligonucleotides. *J. Nucl. Med. 36*, 2036−2314.

(36) Guo, W., Hinkle, G. H., and Lee, R. J. (1999) ^{99m}Tc-HYNIC-folate: A novel receptor-based targeted radiopharmaceutical for tumor imaging. *J. Nucl. Med. 40*, 1563−1569.

BC034141C

Amphiphilic Corroles Bind Tightly to Human Serum Albumin

Atif Mahammed,[†] Harry B. Gray,*[,‡] Jeremy J. Weaver,[‡] Karn Sorasaenee,[‡] and Zeev Gross*[,†]

Department of Chemistry and Institute of Catalysis Science and Technology, Technion - Israel Institute of Technology, Haifa 32,000, Israel, and Department of Chemistry and Beckman Institute, California Institute of Technology, Pasadena, California 91125. Received September 30, 2003; Revised Manuscript Received May 3, 2004

Amphiphilic 2,17-bis-sulfonato-5,10,15(trispentafluorophenyl)corrole (**2**) and its Ga and Mn complexes (**2-Ga** and **2-Mn**) form tightly bound noncovalent conjugates with human serum albumin (HSA). Protein-induced changes in the electronic absorption, emission, and circular dichroism spectra of these corroles, as well as results obtained from HPLC profiles of the conjugates and selective fluorescence quenching of the single HSA tryptophan, are interpreted in terms of multiple corrole:HSA binding sites. High-affinity binding sites, close to the unique tryptophan, are fully occupied at very low concentrations. At biologically relevant HSA concentrations (2−3 orders of magnitude larger than those employed in our studies), all corroles (**2**, **2-Ga**, and **2-Mn**) may be considered as fully conjugated.

INTRODUCTION

The bioinorganic chemistry of porphyrins is a broad field, ranging from natural to completely synthetic systems. The field also includes work on a large variety of porphyrin-like molecules (porphyrinoids), such as the chlorophyll-related chlorins and bactereochlorins as well as completely synthetic phthalocyanines and expanded porphyrins (*1, 2*). A great deal of research has been devoted to the interactions of porphyrinoids with biomolecules, owing to their tendency to accumulate in cancer cells and to intercalate DNA (*3, 4*). Surprisingly, although corroles have been known for almost four decades (*5, 6*), there has been very little work on their interactions with biological molecules. This situation does not reflect a lack of interest in these tetrapyrrolic macrocycles (they are related to the cobalt-chelating corrin in vitamin B_{12} by virtue of an identical carbon skeleton and to porphyrins by being fully conjugated), but only because their syntheses heretofore have been long and tedious. This situation has recently changed in dramatic fashion: facile synthetic methodologies have been introduced during the last 5 years, allowing for the preparation of more than 100 new corroles (*7*−*17*); transition metal complexes (Cr, Mn, Fe, Rh) of the most extensively investigated derivative (tris(pentafluorophenyl)corrole, **1**) function as versatile catalysts for a variety of organic reactions (*18*−*22*); and the Ga^{III} and Al^{III} complexes of corrole **1** are highly fluorescent, with quantum yields (0.37 up to 0.76) that exceed those of all other porphyrinoids (*23, 24*). In addition, it has been discovered recently that electrophilic substitution of **1** offers a facile and highly selective synthetic method for the preparation of corroles with polar headgroups located in only one-half of the macrocycle (amphiphilic corroles) (*25, 26*). This finding is key for the utilization of corroles in biological systems, since amphiphilic porphyrinoids have been shown to be the molecules of choice for many applications (*27*−*29*).

As the most abundant protein in blood plasma, human serum albumin (HSA) plays a role in many biological processes (*30*−*32*). Available are high-resolution X-ray structures of HSA as well as information about its binding affinities to many natural and synthetic molecules (*33*). However, with the exception of one preliminary report, there are no X-ray structures of HSA conjugates with any porphyrinoid or related macrocyclic molecule (*34*). Accordingly, information about noncovalent binding of porphyrinoids to HSA comes from data acquired by spectroscopic methods (*35*). Selected results from such investigations are set out in Table 1 (*36*−*45*).

In many cases, the conclusions about the number of binding sites and the association constants are based on a limited number of spectroscopic measurements, a likely reason for the significant scattering in published results that is evident from inspection of rows 6−9. Nevertheless, it is clear that only negatively charged porphyrinoids associate with HSA, and, in most cases, the protein has one well-defined high-affinity site and several other lower-affinity sites (*42*). Another important finding is the inverse relationship between the association constants and the number of charged groups. The strongest association to HSA occurs with porphyrinoids that contain only two carboxylato or sulfonato groups located on the pyrrole, benzopyrrole, or phenyl rings. Intriguingly, these dipolar and amphiphilic molecules are also the most active derivatives in photodynamic therapy. A major drawback, however, is that porphyrins or phthalocyanines with a limited (less than four) number of polar headgroups are not readily accessible, as illustrated by the bis-sulfonated phthalocyanines that are obtained and used as a mixture of at least eight nonseparable isomers, even after separation of derivatives with a different degree of sulfonation (*46*). In sharp contrast to all other synthetic porphyrinoids, the amphiphilic 2,17-bis-sulfonato-5,10,15(trispentafluorophenyl)corrole (**2**) with its two precisely located sulfonate groups can be obtained in very simple synthetic steps from readily available starting materials (Scheme 1) (*25, 26*). Accordingly, we decided to investigate the association of **2** and its gallium(III) and manganese(III) complexes (**2-Ga**, and **2-Mn**, respectively) to HSA as a first step toward utilization of corroles in bioinorganic applications. Employing several complementary physical methods, we have found that all three corroles form noncovalent conjugates with HSA. The binding affinities of these conjugates decrease ac-

[†] Technion - Israel Institute of Technology.
[‡] California Institute of Technology.

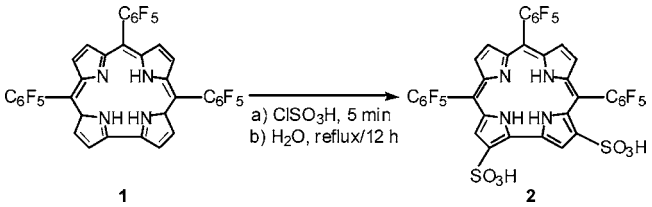
10.1021/bc034179p CCC: $27.50 © 2004 American Chemical Society
Published on Web 06/19/2004

Table 1. Association Constants of HSA:Porphyrinoid Conjugates[a]

no.	ligand	no. of binding sites	association constant, K (M^{-1})	method	ref
1	uroporphyrin I	$N = 1$	$(8.8 \pm 0.51) \times 10^4$	*b*	[36]
2	uroporphyrin I	$N = 1$	2.0×10^4	*c*	[37]
3	heptacarboxylporphyrin	$N = 1$	$(2.39 \pm 0.16) \times 10^5$	*b*	[36]
4	coproporphyrin I	$N = 1$	$(1.61 \pm 0.11) \times 10^6$	*b*	[36]
		another weak site	$(3.1 \pm 0.3) \times 10^5$	*b*	
5	coproporphyrin I	$N = 1$	$(1.3 \pm 0.11) \times 10^5$	*d*	[37]
6	protoporphyrin IX	$N = 1$	$(9.34 \pm 0.3) \times 10^6$	*b*	[36]
7	protoporphyrin IX	$N = 1$	0.5×10^6	*c*	[38]
8	protoporphyrin IX	$N = 1$	1.3×10^6	*c*	[37]
9	protoporphyrin IX	$N = 1$	2.8×10^8	*e*	[39]
10	hemin	$N_{strong} = 1$	5×10^7	*f* & *c*	[40]
		$N_{weak} \geq 4$	–		
11	mesoporphyrin IX		$(2.5 \pm 0.7) \times 10^7$	*e*	[41]
12	Mg-mesoporphyrin IX		$(1.7 \pm 0.5) \times 10^7$	*e*	[40]
13	Al (PcS1)	$N_{strong} = 1$	$(4.2 \pm 0.8) \times 10^7$	*f*	[42]
		$N_{weak} = 8$	$(3.8 \pm 0.9) \times 10^4$		
14	Al (PcS2) (opp)	$N_{strong} = 1$	$(2.8 \pm 1.1) \times 10^7$	*f*	[42]
		$N_{weak} = 8$	$(4.0 \pm 0.7) \times 10^4$		
15	Al (PcS2) (adj)	$N_{strong\ cooperative\ site} = 1$	$(5.8 \pm 0.6) \times 10^6$	*f*	[42]
		$N_{weak} = 8$	$(2.7 \pm 0.8) \times 10^4$		
16	Al (PcS3)	$N_{strong\ cooperative\ site} = 1$	$(2.5 \pm 1.2) \times 10^6$	*f*	[42]
		$N_{weak} = 8$	$(2.5 \pm 0.7) \times 10^4$		
17	Al(PcS4)	nonsaturable	–	*f*	[42]
18	Al(PcS2)		10^4	*f*	[43]
19	tpss		$(5.0 \pm 2) \times 10^6$	*f*	[44]
			$(0.2 \pm 0.1) \times 10^6$	*c*	
20	Zn(2,6-Cl, $3SO_3H$)tpp	$N = 7$	–	*f*	[45]

[a] Abbreviations: PcS1, PcS2, PcS3, PcS4: phthalocyanine with 1, 2, 3, and 4 sulfonato groups, respectively, where opp and adj stand for the relative positions of the sulfonato groups in PcS2 on opposite and adjacent benzopyrrole rings, respectively; tpss: 5,10,15,20-tetrakis(*p*-sulfonatophenyl)porphyrin; (2,6-Cl, 3-SO_3H)tpp: 5,10,15,20-tetrakis(2,6-dichloro-3-sulfonatophenyl)porphyrin. [b] Affinity capillary electrophoresis. [c] Fluorescence quenching of HSA by the porphyrinoid. [d] Equilibrium dialysis. [e] HSA-initiated changes in the fluorescence of the porphyrinoid. [f] HSA-initiated changes in the absorbance of the porphyrinoid.

Scheme 1



cording to **2** ≤ **2-Ga** < **2-Mn**. It is apparent that corrole **2** and its metal complexes will be fully bound to HSA under physiological conditions; accordingly, any biological activity observed for these molecules likely will be attributable to their protein conjugates.

EXPERIMENTAL PROCEDURES

Chemicals. Preparations of corrole **2** and its metal complexes are described in previous publications (*25*, *26*). HSA was purchased from Sigma (essentially fatty acid free, catalog no. A 1887) and used as received. Throughout these studies, 0.1 M phosphate buffer solutions of pH 7.0 were used. The extinction coefficients of the corroles under these conditions are as follows: **2**: ϵ (414 nm) = 71000 M^{-1} cm^{-1}; **2-Ga**: ϵ (424 nm) = 75000 M^{-1} cm^{-1}; **2-Mn**: ϵ (422 nm) = 21000 M^{-1} cm^{-1}; and for HSA, ϵ (280 nm) = 37400 M^{-1} cm^{-1}. Importantly, perfectly linear plots of OD vs corrole concentration were obtained in the range of 10^{-6} to 10^{-4} M, ruling out self-aggregation phenomena at the concentrations that were used in these studies. Further support for this conclusion comes from the practically identical extinction coefficients measured in aqueous and polar organic solvents (CH_3CN, MeOH).

Electronic Spectroscopy. UV/Vis absorption measurements were performed on a HP8452A diode array spectrophotometer, using 3 mL of corrole solutions at $2-10 \times 10^{-5}$ M and adding either microliter portions of HSA solution or milligram amounts of solid HSA.

Emission Spectroscopy. The fluorescence of HSA or the corroles was measured on an AB2 Luminescence Spectrometer. For titration of HSA's fluorescence, microliter portions of concentrated corrole solutions were added to 3 mL solutions of HSA wherein the absorbance at the excitation wavelength of 280 nm was less than 0.15. For titration of **2** or **2-Ga**, either microliter portions of a concentrated HSA solution or milligram amounts of solid HSA were added to 3 mL solutions of the corroles until no further changes in the emission intensity occurred.

Circular Dichroism Spectroscopy. CD spectra were recorded in the visible range on an Aviv model 62A DS Circular Dichroism Spectrometer using 3 mL of corrole solutions at $2-10 \times 10^{-5}$ M and adding either microliter portions of concentrated HSA solution or milligram amounts of solid HSA. UV−CD spectra were recorded using an HSA concentration of 1.8×10^{-6} M (in a 4-mm cuvette) and 3.7×10^{-6} M (in a 10-mm cuvette) with varying ratios of **2-Ga**.

Reversed Phase HPLC. HPLC analyses were performed on Merck Hitachi HPLC linear gradient using LiChrospher 100, a RP-18 column (5 μm, 4 × 125 mm), and a flow rate of 1 mL/min. The mobile phase was 100% water at time zero, turning to 100% acetonitrile within 15 min, continued for 5 min with acetonitrile only, turning back to 100% water within another 15 min, and continued for 10 min with water only. Eluted components were monitored spectrophotometrically at 436, 426, and 486 nm for **2**, **2-Ga**, and **2-Mn**, respectively, wavelengths at which the absorbances of free and conjugated corroles are identical. An initial concentration of [HSA] = 2.5×10^{-4} M was used for experiments at [HSA]:[corrole] ratio of 5:1 and [corrole] = 5×10^{-5} M for the [HSA]:[corrole] ratio of 1:5 experiments. The cells were made of quartz with a 10 mm path length.

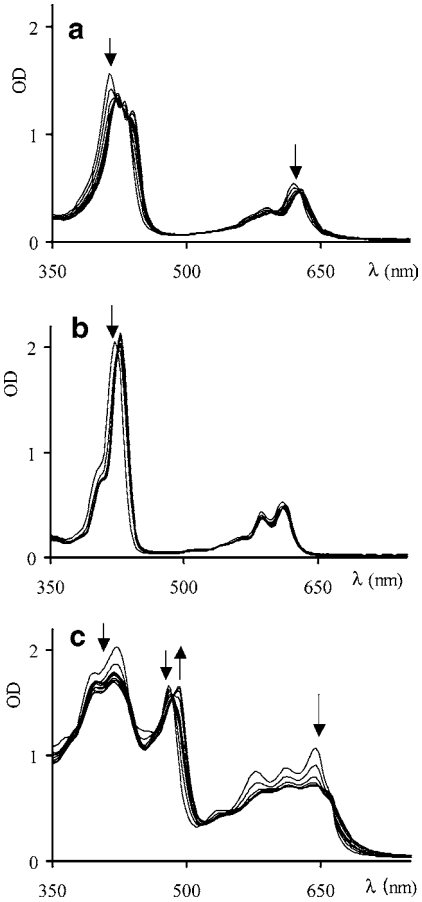


Figure 1. Changes in the UV−vis spectra of corrole **2** (a) and its metal complexes **2-Ga** (b), and **2-Mn** (c), upon titration with increasing amounts of HSA. [**2**] = 2.2 × 10^{-5} M, [**2-Ga**] = 2.7 × 10^{-5} M, [**2-Mn**] = 10^{-4} M; [HSA] = 0−10^{-4} M.

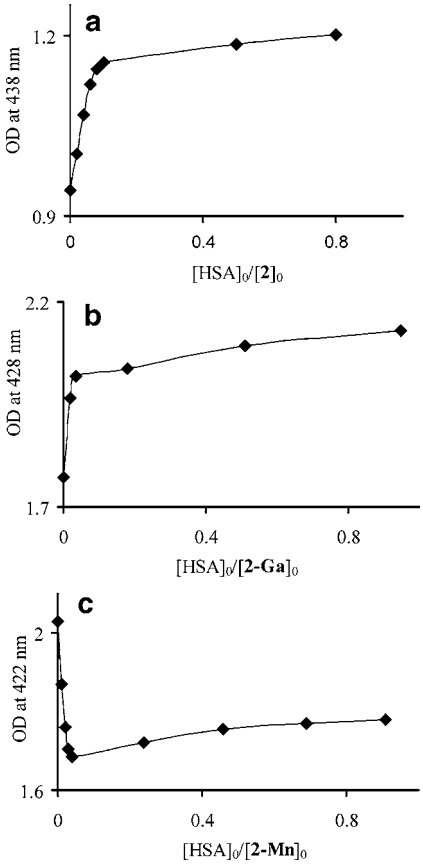


Figure 2. UV-vis spectral changes at selected wavelengths as a function of the [HSA]:[corrole] ratio for (a) **2**, (b) **2-Ga**, and (c) **2-Mn**.

RESULTS AND DISCUSSION

Binding of Corroles to HSA. Electronic spectra of corroles when treated with increasing amounts of HSA are shown in Figure 1. For **2** and **2-Ga**, respective shifts of the Soret bands from 416 to 424 nm and from 424 to 430 nm are observed. For metal-free **2**, this effect could indicate changes in the protonation state of the inner N_4 core from triply to doubly protonated. The pK_a for this process has been determined to be 5.2 in water (*47*), and it might be quite different in a more hydrophobic environment. We do not believe this explanation is correct: the changes in the Q-bands upon titration with HSA are very different from those observed upon NH-deprotonation of **2** in aqueous solutions (*47*), so the results are likely attributable to a "solvent effect" that would manifest itself in the interior of the protein. The same interpretation also accounts for the Soret shift of **2-Ga**. Spectral changes for **2-Mn** were most pronounced: most bands just decreased in intensity, but the 480 nm band was clearly replaced by a 492 nm band. It is known that this particular band (No. V in manganese(III) porphyrins) is very sensitive to axial ligation. Adding imidazole to an aqueous solution of **2-Mn** gave almost the same spectrum as addition of HSA, suggesting the participation of histidine residues in the binding of this metal complex. In all three cases, there were no more spectral changes after the addition of about 1 equiv of HSA, suggesting very strong association. More detailed information was obtained by following the intensity changes at selected wavelengths (Figure 2). The majority of the intensity increase at 438 and 428 nm for **2** and **2-Ga**, respectively, is complete much before a 1:1 ratio is achieved, suggesting that there are multiple HSA binding sites for these corroles. This phenomenon is even more pronounced for **2-Mn**: the intensity at 422 nm decreases sharply up to a [HSA]:[**2-Mn**] ratio of 0.04 and increases slightly when a 1:1 ratio is approached. Taken together, the results clearly indicate that several corrole molecules associate with one protein and that redistribution takes place at higher [HSA]:[corrole] ratios in favor of the 1:1 conjugate. As the number of binding sites in protein−chromophore conjugates and the corresponding binding constants are frequently determined from Scatchard plots (*48*), we also attempted to do so. However, this method and the underlying equations require the presence of unbound chromophore, while our later indications show that there is no free corrole at the lowest concentrations that can be measured by UV−vis (10^{-6} M). Accordingly, none of the binding constants can be determined by UV−vis titrations.

Effect of HSA on Corrole Fluorescence. Binding of corroles to HSA can be quantified by monitoring the highly intense fluorescence of **2** and **2-Ga**, allowing experiments to be performed at significantly lower corrole concentrations. Another major advantage of fluorescence monitoring is that free and bound corroles might have different emission maxima and/or intensities. The differences in emission wavelengths of both **2** and **2-Ga** in the presence and absence of HSA are only a few nm, but the fluorescence intensities are very sensitive to the [HSA]:[corrole] ratio (Figure 3). These effects are further demonstrated for selected wavelengths in Figure 4: the initial fluorescence of **2** is reduced to less than 40% at a [HSA]:[**2**] ratio of 0.1:1 and it is 60% of the initial intensity at a 1:1 ratio. The results for **2-Ga** were

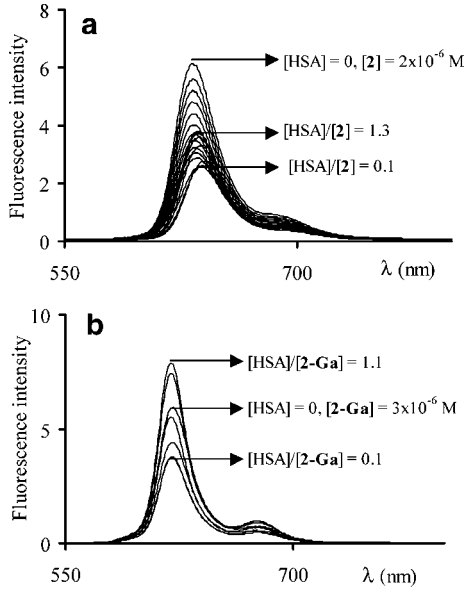


Figure 3. Emission spectra of corrole **2** (a, $\lambda_{exc} = 436$ nm) and **2-Ga** (b, $\lambda_{exc} = 426$ nm) as a function of added HSA.

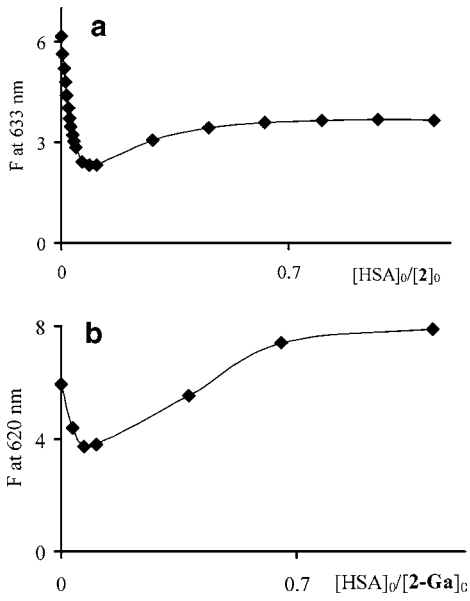


Figure 4. Fluorescence intensity at selected wavelengths of **2** (a) and **2-Ga** (b) as a function of the HSA:corrole ratio.

even more pronounced: about 40% reduction at a [HSA]:[**2-Ga**] ratio of 0.1:1 and 130% of the initial intensity at a 1.1:1 ratio. The latter phenomenon suggests that the extent of nonradiative decay of the excited state is lowered upon binding of the fluorophore to the protein (less degrees of freedom), reflected in increased fluorescence. Nevertheless, the intensity becomes lower when many corrole molecules are bound to the same protein because of self-quenching.

For quantitative elucidation of the dissociation constants (K_d) assigned to the high-affinity binding sites, the fluorescence intensities of equimolar conjugates were measured as a function of concentration, with the expectation of a nonlinear correlation if there is significant dissociation. However, a linear correlation was obtained in the range [**2-Ga**] = [HSA] = 2×10^{-6} to 4×10^{-8} M, thereby confirming that no significant dissociation takes place, even at very low (40 nM) conjugate concentrations.

Circular Dichroism (CD). CD spectra of corrole solutions as a function of HSA concentration are shown in Figure 5. Since HSA does not absorb visible light, the CD spectrum at long wavelengths ($\lambda > 360$ nm) can only be attributed to corrole interactions with the chiral environment of the folded protein. Intriguingly, the **2-Mn** CD signal (Figure 5c) is centered at around 490 nm, which is the region of the spectrum that is most sensitive to axial ligands. Moreover, the response to HSA addition is irregular, as can be seen from the shifts of λ_{max} and the inversion from negative to positive ellipticity at 482 nm. This phenomenon is amplified at 440 and 425 nm, respectively, in the spectra of **2** and **2-Ga** (Figure 5a,b). These data accord with the earlier conclusions about weak and strong binding sites, which in the present case is observed by redistribution of weakly bound corroles (under the conditions of [corrole] ≫ [HSA]) as the [corrole]:[HSA] ratio approaches 1:1. The results show that there are multiple chiral binding sites, albeit with significant differences in wavelengths and ellipticities.

CD spectra of HSA in the region 200−250 nm as a function of added **2-Ga** also were obtained to monitor possible changes of protein secondary structure in response to corrole binding (*49*). As can be seen in Figure 6, HSA gives rise to a strong CD signal at 222 nm, attributable to α-helical structures. The intensity of the signal drops as a function of the [**2-Ga**]:[HSA] ratio (0.4%, 1.1%, 1.5%, 2% at 1:1, 2:1, 3:1, and 4:1, respectively), and, at a ratio of 10:1, roughly 8% of helical structure is lost. Although there is some degree of conformational change, these corrole-induced perturbations of protein secondary structure are smaller than those observed for BSA−porphyrin conjugates (*48*).

HPLC of HSA:Corrole Conjugates. There are many precedents in which serum albumins are used to affect the retention time of ligands with which they interact strongly, including even the immobilization of BSA or HSA on HPLC stationary phases (*50*). However, we are not aware of any report about noncovalent conjugates of HSA remaining intact during HPLC separation. Apparently, under the high dilution conditions intrinsic to the experiment, most conjugates dissociate. Nevertheless, because of the aforementioned indications of extremely low dissociation constants of the noncovalent HSA/corrole conjugates, we decided to examine them by HPLC. Separate injections revealed that HSA is eluted much faster (1 min, indicative of negligible interaction with the solid phase) than any of the corroles (9−10 min) on the reversed-phase column. Next, HPLC chromatograms of premixed mixtures of HSA and the corroles were examined, setting the detector wavelength at $\lambda > 400$ nm (436, and 426, and 486 nm for **2**, **2-Ga**, and **2-Mn**, respectively) as to determine if the eluted HSA fractions contain bound corrole. The results shown in Figure 7 clearly demonstrate the following phenomena: the fastest eluting peak (at 1−2 min) corresponds to HSA-bound corrole, while the two later peaks (at ∼8 min and ∼9 min) to corrole that dissociated from HSA during chromatography (*50*). For an initial ratio of [HSA]:[corrole] of 5:1, the percentage of corrole that remained bound to HSA was 80, 70, and 40% for **2**, **2-Ga**, and **2-Mn**, respectively. (With 0.1 M phosphate buffer solutions of pH 7.0 instead of unbuffered water, the percentage of corrole that remained bound to HSA was 74, 66, and 46% for **2**, **2-Ga**, and **2-Mn**, respectively). This indicates that the relative dissociation constants (K_d) of the conjugates are in the order **2** ≤ **2-Ga** < **2-Mn**. Since an excess of HSA was used, we may safely assume that this trend reflects the K_d of particularly strong binding sites. This assumption was checked by the following experiments: injection of mixtures that contain an initial 1:5 ratio of

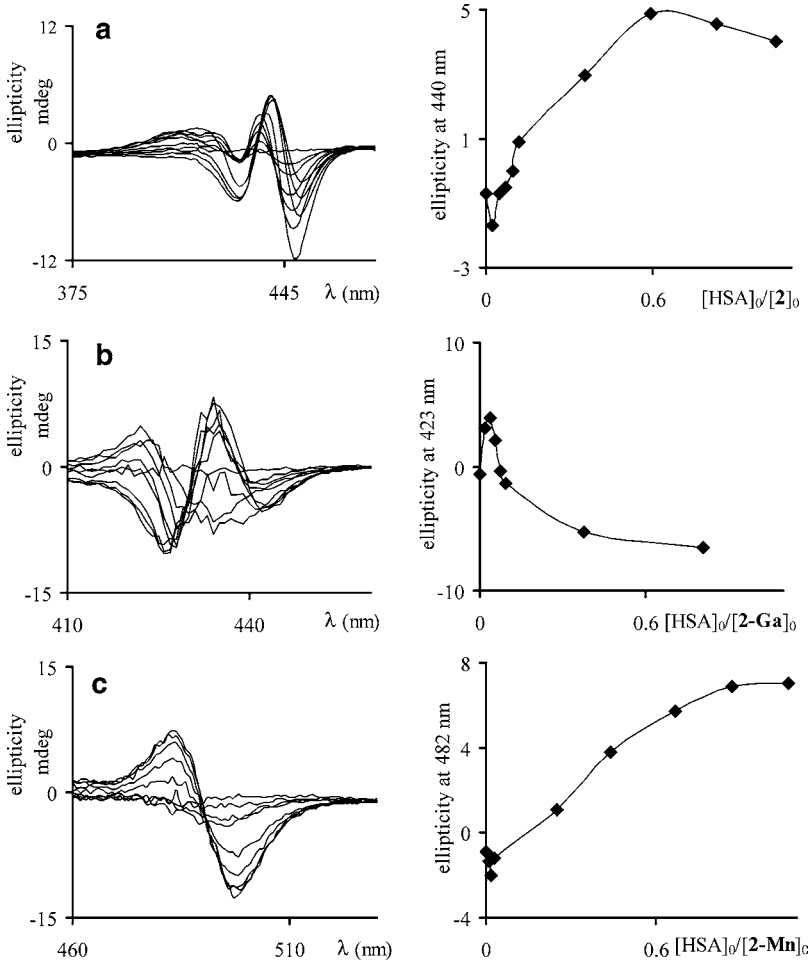


Figure 5. HSA titrations of (a) **2**, (b) **2-Ga**, and (c) **2-Mn**, followed by CD spectroscopy. [**2**] = 2.11 × 10^{-5} M, [**2-Mn**] = 10^{-4} M, [**2-Ga**] = 2.7 × 10^{-5} M; [HSA] = 0−10^{-4} M.

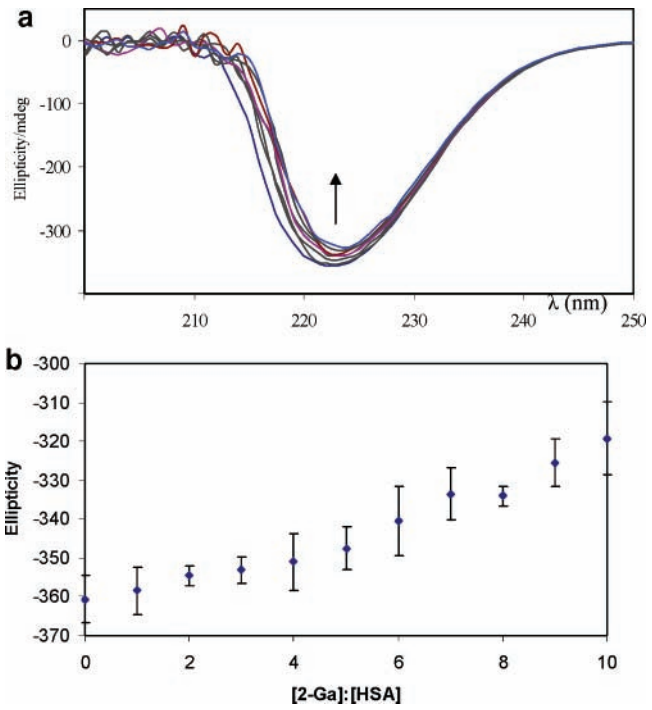


Figure 6. (a, b) CD spectra of HSA as a function of [**2-Ga**]:[HSA] (0, 1, 2...10) at constant [HSA] (3.7 × 10^{-6} M).

[HSA]:[corrole], isolation of the HSA containing fraction, and examination of the [HSA]:[corrole] therein by recording the full electronic spectrum and relying on the corresponding ϵ values. The results show that [HSA]:[corrole] ratios in the HPLC-eluted conjugates were 1:0.5, 1:0.4, and 1:0.2 for **2**, **2-Ga**, and **2-Mn**, respectively. Apparently, the final [HSA]:[corrole] ratio did not exceed 1:1 even with corrole in excess; thus, the K_d trend **2** ≤ **2-Ga** < **2-Mn** reflects only the high-affinity binding sites. Since hemin also has been reported to form a tight conjugate with HSA (K_d = 10^{-8} M), it also was analyzed by HPLC. At a [HSA]:[hemin] ratio of 5:1, 92% of hemin remained HSA-bound, and when the initial ratio of [HSA]:[hemin] was 1:5, the [HSA]:[hemin] ratio in the HPLC-eluted conjugates was 1: 0.5. All these results show that HPLC experiments provide a good tool for estimating noncovalent binding of porphyrinoids to proteins. Nevertheless, the acquired information must be considered as qualitative rather than quantitative, since other factors such as the water solubility of different porphyrinoids (hemin vs corrole in the current case) may affect the results significantly.

Quenching of Trp^{214} Emission. One of the earliest and simplest methods that was used for investigating hemin binding is fluorescence quenching of the single tryptophan residue (Trp^{214}) in HSA (*40*). The advantage of this approach is that it reports selectively on binding sites that are not too distant from the fluorophore. Results obtained by exciting HSA's Trp^{214} at 280 nm and recording its emission (λ_{max} = 340 nm) as a function of the concentration of **2-Ga** are shown in Figure 8a. Notably, full and selective quenching was achieved, as can be seen from the residual emission (λ_{max} = 310 nm) due to the many tyrosine residues that are present in

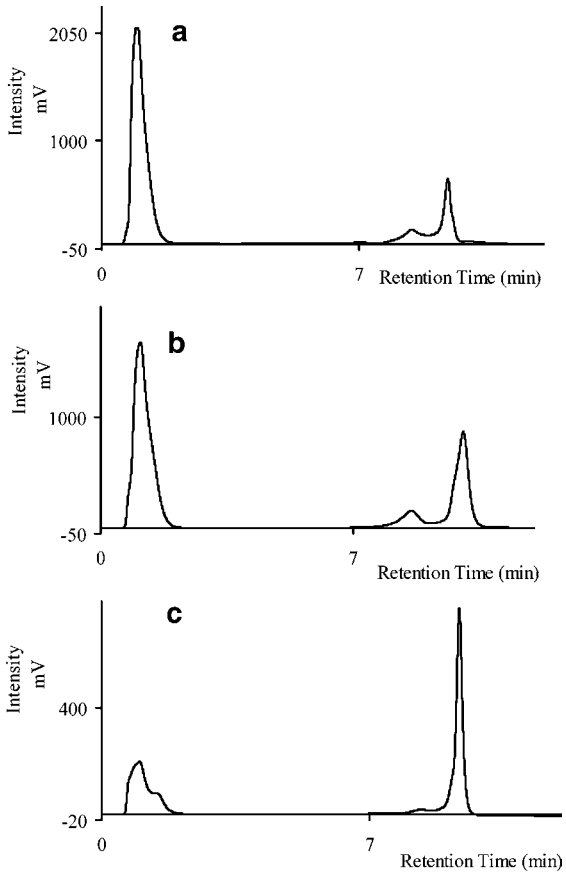


Figure 7. HPLC chromatograms of HSA conjugates (a) **2**, (b) **2-Ga**, and (c) **2-Mn**, ([HSA]$_0$ = 2.5 × 10^{-4} M, [corrole]$_0$ = 5 × 10^{-5} M) with the detector set at the wavelength where the absorbance of free and conjugated corroles are identical (436, 426, 486 nm for a, b, c).

HSA. More quantitative information was obtained from plots of fluorescence intensity as a function of the [HSA]:[corrole] ratio (Figure 8b). The responses (slopes) of **2** and **2-Ga** are practically identical, and that of **2-Mn** somewhat smaller. The up to 50% quenching at equimolar concentrations of HSA and corrole obtained in the first two cases implies that **2** and **2-Ga** occupy close to Trp^{214} binding sites with very high-affinity. If **2-Mn** also associates to similar binding sites, Figure 8b may be analyzed as reflecting an opposite relationship between the steepness of the slopes and the K_d of the HSA:corrole conjugates. This would lead to relative K_d from high-affinity sites in the order of **2** ∼ **2-Ga** < **2-Mn**, in line with the previously mentioned indications. The roughly 50% quenching at a 1:1 ratio between HSA and **2** or **2-Ga** may be interpreted either one of two limiting ways: 100% quenching efficiency by sites that are only 50% occupied (= large K_d) or 50% quenching efficiency by sites that are 100% occupied (= small K_d). Two sets of experiments were performed to distinguish between these possibilities. The first consisted of dilution experiments on 1:1 mixtures of HSA and the corroles. For all three corroles (data for **2-Ga** are shown in the inset of Figure 9) there was no deviation from linearity in the concentration vs fluorescence-intensity plots in the range 4 × 10^{-6} to 7 × 10^{-7} M (K_d < 10^{-8} M for the conjugates). Figure 9 shows the other set of experiments: measuring fluorescence intensity of HSA as a function of the relative amount of **2-Ga**, at four different absolute concentrations. The normalized plots are identical as long as the corrole is not in excess of HSA, clearly confirming the absence of any dissociation. The plots become different only after

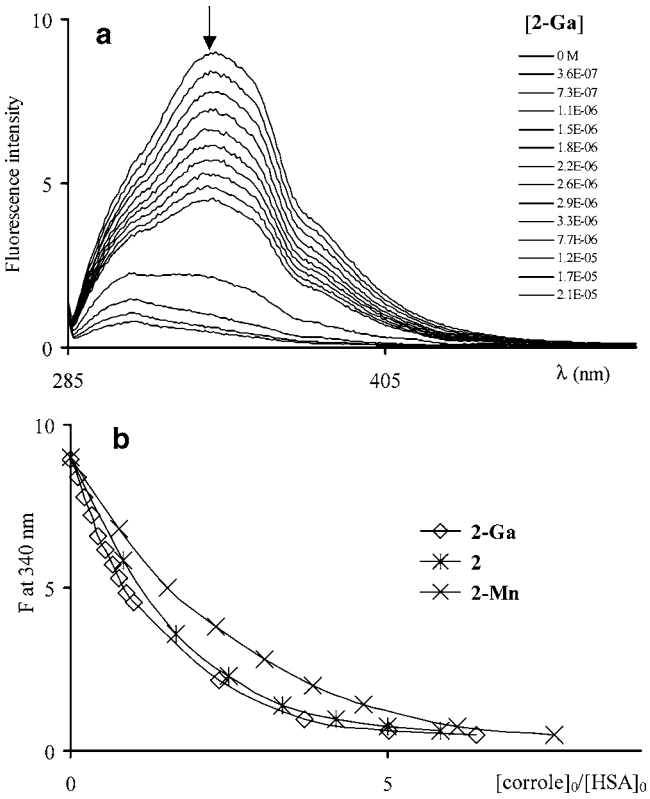


Figure 8. Quenching of the emission of HSA by (a) increasing amounts of **2-Ga** and (b) the dependence of the emission on the [corrole]/[HSA] ratio. λ_{exc} = 280 nm, [HSA] = 3.3 × 10^{-6} M.

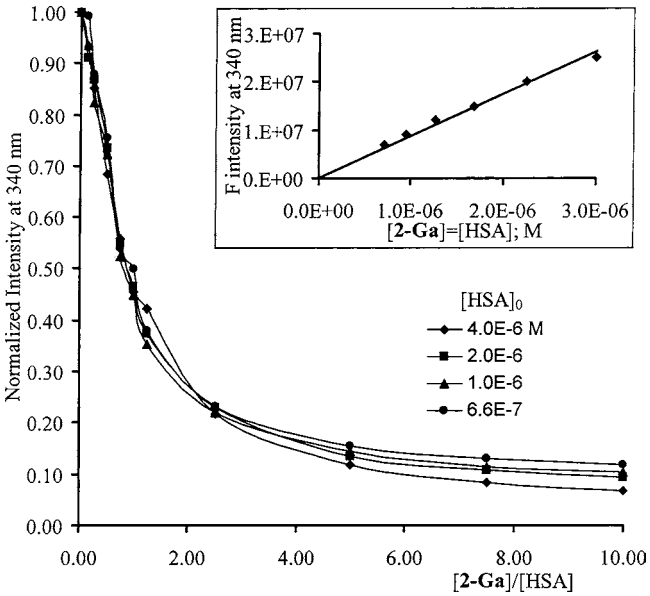


Figure 9. Normalized fluorescence intensity of HSA as a function of the [**2-Ga**]:[HSA] ratio at different initial concentrations of HSA. Inset: Fluorescence intensity at 340 nm of equimolar concentrations of **2-Ga** and HSA at different absolute concentrations.

the [**2-Ga**]:[HSA] is above 1, indicating the presence of slightly weaker secondary binding sites. Importantly, although a reliable measurement of K_d is problematic because of the large number of corrole molecules that can be accommodated by HSA, the trends of Figure 9 show that dissociation from weaker binding sites is very small as well. Therefore, the approximately 50% quenching seen at a 1:1 ratio between HSA and corrole is consistent with incomplete quenching of Trp^{214} fluorescence by corroles that occupy high affinity sites.

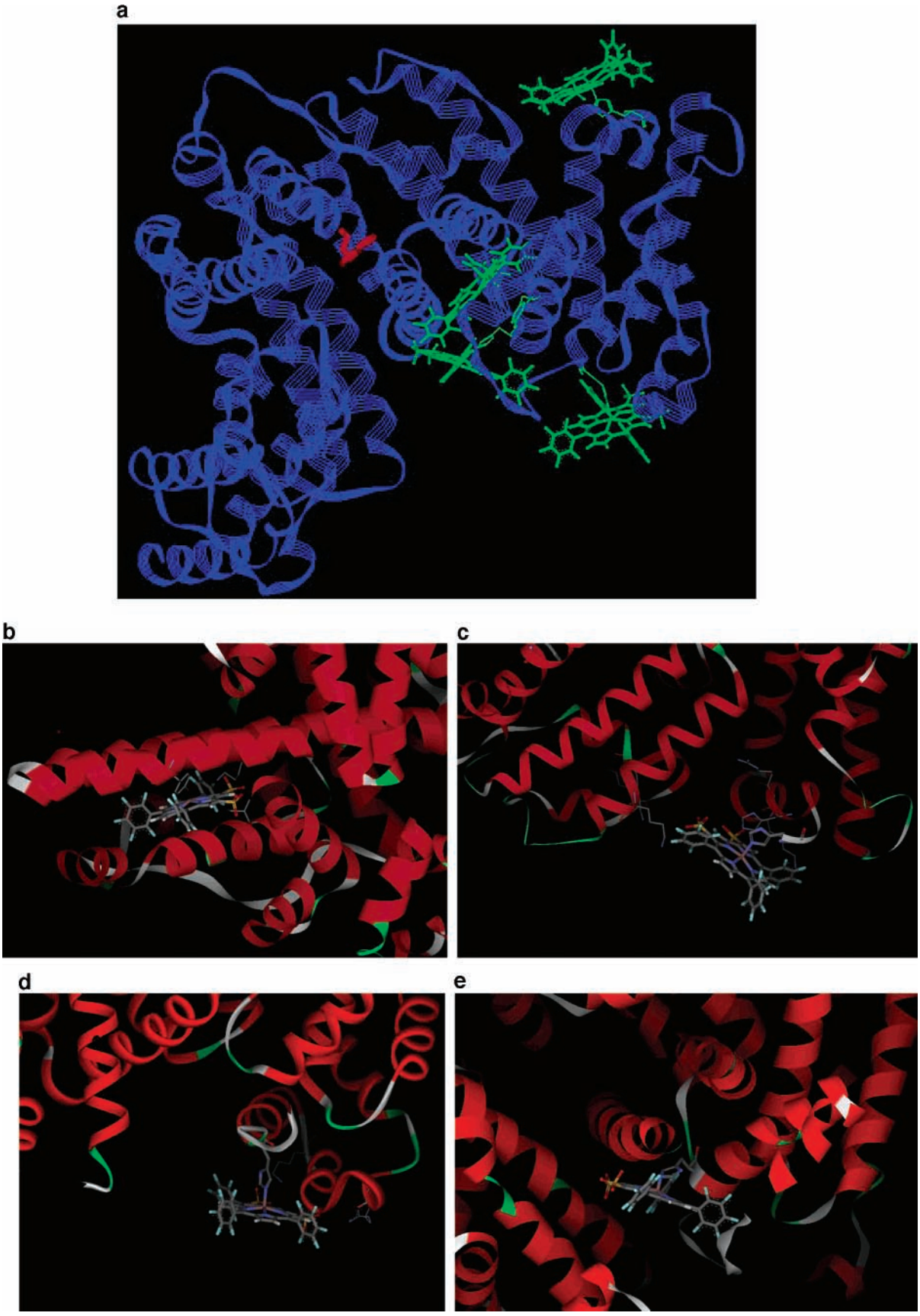


Figure 10. (a) Structural models depicting four potential binding sites for **2-Ga** to HSA. (b) **2-Ga** in place of the heme of methemalbumin. (c) **2-Ga** coordinated to His^{3}. (d) **2-Ga** coordinated to His^{105}. (e) **2-Ga** coordinated to His^{146}. The proposed locations were chosen as follows: one is the heme binding site; others are histidine binding sites whose positions are consistent with the Trp^{214} quenching experiments, except for e.

Binding Sites for 2-Ga. Since the three-dimensional structure of HSA is known, we have attempted to estimate the distance between Trp^{214} and a corrole binding site via standard Förster energy transfer equa-

tions, using the roughly 50% fluorescence quenching by **2-Ga**.

$$R_o^6 = 8.8 \times 10^{-5}(\kappa^2 n^{-4} \phi_o J) \quad (1)$$

$$J = \frac{\int_0^\infty F_o(\lambda) E_A(\lambda)\, \lambda^4 \mathrm{d}\lambda}{\int_0^\infty F_o(\lambda) \mathrm{d}\lambda} \quad (2)$$

Equations 1 and 2 were used for evaluation of the Förster distance (*51*, *52*), where J is the overlap between the luminescence spectrum of the donor and the absorption spectrum of the acceptor (weighted by λ^4), ϕ_o is the luminescence quantum yield in the absence of energy transfer, n is the refractive index, and κ is an orientation factor dependent on the alignment of the donor and acceptor dipoles ($\kappa^2 = 2/3$ for random alignment). According to the above expressions, our experimental data yielded a value for the overlap integral J between the fluorescence spectrum of the protein HSA and the absorption spectrum of the quencher **2-Ga** of 6.26×10^{14}. Based on the J value and eq 1, the Förster distance (R_o) between **2-Ga** and Trp^{214} (HSA) was calculated to be 30 Å. Moreover, models of the **2-Ga**−HSA conjugate based on crystallographic data for [Ga(tpfc)(py)] (tpfc = 5,10,15-tris(pentafluorophenyl)corrolate; py = pyridine) and HSA were constructed (*53*). In the HSA crystal structure, a heme (Fe^{III}-protoporphyrin IX) is located in a hydrophobic pocket in subdomain IB, and there are additional interactions involving Tyr^{161}, Ile^{142}, Tyr^{138}, His^{146}, and Lys^{190} with the heme. In one of our proposed structures, where noncovalent interactions are dominant (Figure 10a), **2-Ga** replaces the heme in the hydrophobic cavity; at this site, the distances between **2-Ga** and Trp^{214} are 20−24 Å (from the edge of the corrole−from the metal), in fair agreement with the estimated distance based on fluorescence quenching. Figures 10b and 10c show two **2-Ga**-HSA interactions that involve metal-coordination to His. As examples, we propose that **2-Ga** could bind to surface-exposed His^3 and His^{105} with distances between His-bound **2-Ga** and Trp^{214} of 24−30 and 30−34 Å, respectively. We also note that coordination of **2-Ga** to His^{146} located in the heme binding pocket (Figure 10d) is unlikely due to a considerable difference between the Förster distances measured in the model and that estimated from quenching experiments (16−19 Å vs 30 Å).

CONCLUDING REMARKS

We report results from an investigation of interactions between corroles and biomolecules. Corrole **2** is especially promising for biomedical research because of its structural similarity to the most active porphyrin-based drugs and because amphiphilicity is easily achieved. Our work has focused on interactions with HSA because any medical application must take into account associations with the most abundant protein in serum. Two metal complexes of **2** were investigated, with the goal of elucidating any effects due to ligation to relevant residues of the protein.

The changes in the electronic absorption spectra of **2**, **2-Ga**, and **2-Mn** as well as in the emission spectra of **2** and **2-Ga** as a function of increasing amounts of HSA revealed many protein binding sites. With corrole in excess, both absorption and emission intensities decreased, which is behavior that is frequently encountered when porphyrins form aggregates, usually because of limited solubility in water. However, the corroles of the current investigation do not aggregate in aqueous solutions, and, accordingly, we propose that the above phenomena are due to self-quenching of many corrole molecules that are aggregated/associated in binding pockets within the protein. Examination of published crystal structures of HSA reveals the presence of a large calixarene-like amphiphilic pocket that seems appropriate for accommodation of the corroles. When the [corrole]:[HSA] ratio approaches 1:1, the absorption and emission intensities increase, thereby indicating redistribution of corroles from the weaker binding pocket to high-affinity sites.

We have used many different methods to investigate the interactions of corroles with HSA. The results clearly show that all derivatives form tightly bound conjugates with the protein, with dissociation constants in the nanomolar range in the order **2** ≤ **2-Ga** < **2-Mn**. Under biologically relevant conditions (HSA concentrations 2 to 3 orders of magnitude larger than those examined here), all the derivatives will be fully bound to proteins. This information is of prime importance for any potential utilization of the corroles in bioinorganic systems such as for therapeutic applications and biomimetic catalysis, approaches that are currently under investigation in our laboratories.

ACKNOWLEDGMENT

Work at the Technion was supported by the STAR (Chicago) Foundation (Z.G.) and the Israel Science Foundation (Z.G.); work at Caltech was supported by JPL-NASA (K.S.) and the National Science Foundation (H.B.G., J.J.W.).

LITERATURE CITED

(1) Sessler, J. L., Tvermoes, N. A., Davis, J., Anzenbacher, P., Jursikova, K., Sato, W., Seidel, D., Lynch, V., Black, C. B., Try, A., Andrioletti, B., Hemmi, G., Mody, T. D., Magda, D. J., and Kral, V. (1999) Expanded porphyrins. Synthetic materials with potential medical utility. *Pure Appl. Chem. 71*, 2009−2018.

(2) MacDonald, I. J. and Dougherty, T. J. (2001) Basic principles of photodynamic therapy. *J. Porphyrins Phthalocyanines 5*, 105−129.

(3) Via, L. D., and Magno, S. M. (2001) Photochemotherapy in the treatment of cancer. *Curr. Med. Chem. 8*, 1405−1418.

(4) Dougherty, T. J., Gomer, C. J., Henderson, B. W., Jori, G., Kessel, D., Korbelik, M., Moan, J., and Peng, Q. (1998) Photodynamic therapy. *J. Natl. Cancer. Inst. 90*, 889−905.

(5) Sessler, J. L., and Weghorn, S. J. (1997) *Expanded, Contracted, & Isomeric Porphyrins*, pp 1−9, Pergamon, Oxford.

(6) Paolesse, R. (2000) Syntheses of Corroles. *The Porphyrin Handbook, Vol. II.* (Kadish, K. M., Smith, K. M., and Guilard, R., Eds.) pp 201−232, Academic Press, New York.

(7) Gross, Z., Galili, N., and Saltsman, I. (1999) The first direct synthesis of corroles from pyrrole. *Angew. Chem., Int. Ed. 38*, 1427−1429.

(8) Gross, Z., Galili, N., Simkhovich, L., Saltsman, I., Botoshansky, M., Bläser, D., Boese, R., and Goldberg, I. (1999) Solvent-free condensation of pyrrole and pentafluorobenzaldehyde: A novel synthetic pathway to corrole and oligopyrromethenes. *Org. Lett. 1*, 599−602.

(9) Paolesse, R., Jaquinod, L., Nurco, D. J., Mini, S., Sagone, F., Boschi, T., and Smith, K. M. (1999) 5,10,15-triphenylcorrole: a product from a modified rothemund reaction. *Chem. Commun.* 1307−1308.

(10) Simkhovich, L., Goldberg, I., and Gross, Z. (2000) First syntheses and X-ray structures of a *meso*-alkyl substituted corrole and its Ga(III) complex. *J. Inorg. Biochem. 80*, 235−238.

(11) Cho, W.-S., and Lee, C.-H. (2000) Customized, core-modified corroles from [2+2] condensation of dipyrromethanes. *Tetrahedron Lett. 41*, 697−701.

(12) Gryko, D. T. (2000) A simple, rational synthesis of meso-substituted A(2)B-corroles. *Chem. Commun.* 2243−2244.
(13) Briñas, R. P., and Brückner, C. (2001) Triarylcorroles by oxidative coupling of triaryltetrapyrranes. *Synlett* 442−444.
(14) Gryko, D. T., and Jadach, K. (2001) A simple and versatile one-pot synthesis of meso-substituted trans-A(2)B−corroles. *J. Org. Chem. 66*, 4267−4275.
(15) Ka, J.-W., Cho, W.-S., and Lee, C.-H. (2000) Expedient synthesis of corroles by oxidant-mediated, direct α−α′ coupling of tetrapyrromethanes. *Tetrahedron Lett. 41*, 8121−8125.
(16) Paolesse, R., Nardis, S., Sagone, F., and Khoury, R. G. (2001) Synthesis and functionalization of meso-aryl-substituted corroles. *J. Org. Chem. 66*, 550−556.
(17) Asokan, C. V., Smeets, S., and Dehaen, W. (2001) Sterically encumbered triarylcorroles from aryldipyrromethanes and aromatic aldehydes. *Tetrahedron Lett. 42*, 4483−4485.
(18) Gross, Z., Simkhovich, L., and Galili, N. (1999) First Catalysis by corrole metal complexes: epoxidation, hydroxylation, and cyclopropanation. *J. Chem. Soc., Chem. Commun.* 599−600.
(19) Gross, Z., Golubkov, G., and Simkhovich, L. (2000) Epoxidation catalysis by a manganese(III) corrole and isolation of an oxomanganese(V) corrole. *Angew. Chem., Int. Ed. 39*, 4045−4047.
(20) Simkhovich, L., Mahammed, A., Goldberg, I., and Gross, Z. (2001) Synthesis and characterization of germanium, tin, phosphorous, iron, and rhodium complexes of tris(pentafluorophenyl)corrole, and the utilization of the iron and rhodium corroles as cyclopropanation catalysts. *Chem. Eur. J. 7*, 1041−1055.
(21) Golubkov, G., Bendix, J., Gray, H. B., Mahammed, A., Goldberg, I., Di Bilio, A. J., and Gross, Z. (2001) High valent manganese corroles and the first perhalogenated corrole-based catalyst. *Angew. Chem., Int. Ed. 40*, 2132−2134.
(22) Simkhovich, L., and Gross, Z. (2001) Iron(IV) corroles are potent catalysts for aziridination of olefins by chloramine-T. *Tetrahedron Lett. 42*, 8089−8092.
(23) Bendix, J., Dmochowski, I. J., Gray, H. B., Mahammed, A., Simkhovich, L., and Gross, Z. (2000) Structural, electrochemical, and photophysical properties of gallium(III) 5,10,-15-tris(pentafluorophenyl)corrole. *Angew. Chem., Int. Ed. 39*, 4048−4051.
(24) Mahammed, A., and Gross, Z. (2002) Aluminum corrolin, a novel chlorophyll analogue. *J. Inorg. Biochem. 88*, 305−309.
(25) Mahammed, A., Goldberg, I., and Gross, Z. (2001) Highly selective chlorosulfonation of tris(pentafluorophenyl)corrole as a synthetic tool for the preparation of amphiphilic corroles and metal complexes of chiral planarity. *Org. Lett. 3*, 3443−3446.
(26) Saltsman, I., Mahammed, A., Goldberg, I., Tkachenko, E., Botoshansky, M., and Gross, Z. (2002) Selective substitution of corroles: nitration, hydroformylation, and chlorosulfonation. *J. Am. Chem. Soc. 124*, 7411−7420.
(27) Allen, C. M., Langlois, R., Sharman, W. M., La Madeleine, C., and Van Lier, J. E. (2002) Photodynamic properties of amphiphilic derivatives of aluminum tetrasulfophthalocyanine. *Photochem. Photobiol. 76*, 208−216.
(28) Boyle, R. W., and Dolphin, D. (1996) Structure and biodistribution relationships of photodynamic sensitizers. *Photochem. Photobiol. 64*, 469−485.
(29) Bonnett, R. (1999) Photodynamic therapy in historical perspective. *Rev. Contemp. Pharmacother. 10*, 1−17.
(30) Chuang, V. T. G., Kragh-Hansen, U., and Otagiri, M. (2002) Pharmaceutical strategies utilizing recombinant human serum albumin. *Pharm. Res. 19*, 569−577.
(31) Kragh-Hansen, U., Chuang, V. T. G., and Otagiri, M. (2002) Practical aspects of the ligand-binding and enzymatic properties of human serum albumin. *Biol. Pharm. Bull. 25*, 695−704.
(32) Peters, T. (1996) *All About Albumin: Biochemistry, Genetics, and Medical Applications*, Academic Press, San Diego.
(33) Sugio, S., Kashima, A., Mochizuki, S., Noda, M., and Kobayashi, K. (1999) Crystal structure of human serum albumin at 2.5 angstrom resolution. *Protein Eng. 12*, 439−446 and references therein.
(34) Wardell, M., Wang, Z., Ho, J. X., Robert, J., Ruker, F., Ruble, J., and Carter, D. C. (2002) The atomic structure of human methemalbumin at 1.9 angstrom. *Biochem. Biophys. Res. Commun. 291*, 813−819.
(35) Bertucci, C. and Domenici, E. (2002) Reversible and covalent binding of drugs to human serum albumin: Methodological approaches and physiological relevance. *Curr. Med. Chem. 9*, 1463−1481.
(36) Ding, Y. S., Lin, B. C., and Huie, C. W. (2001) Binding sudies of porphyrins to human serum albumin using affinity capillary electrophoresis. *Electrophoresis 22*, 2210−2216.
(37) Morgan, W. T., Smith, A., and Koskelo, P. (1980) The interaction of human serum albumin and hemopexin with porphyrins *Biochim. Biophys. Acta 624*, 271−285.
(38) Datta-Gupta, N., Malakar, D., and Dozier, J. (1989) Binding studies of 4 free base porphyrins and 6 Fe(III) porphyrins with human serum albumin. *Res. Commun. Chem. Pathol. Pharmacol. 63*, 289−292.
(39) Rotenberg, M., Cohen, S., and Margalit, R. (1987) Thermodynamics of porphyrin binding to serum-albumin − Effects of temperature, of porphyrin species and of albumin-carried fatty-acids. *Photochem. Photobiol. 46*, 689−693.
(40) Beaven, G. H., Chen, S. H., Dalbis, A., and Garatzer, B. W. (1974) Spectroscopic study of hemin-human serum albumin system. *Eur. J. Biochem. 41*, 539−546.
(41) Bardos-Nagy, I., Galantai, R., Kaposi, A. D., and Fidy, J. (1998) Difference in the transport of metal and free-base porphyrins: Steady-state and time-resolved fluorescence studies. *Int. J. Pharm. 175*, 255−267.
(42) Gantchev, T. G., Ouellet, R., and van Lier, J. E. (1999) Binding interactions and conformational changes induced by sulfonated aluminum phthalocyanines in human serum albumin. *Arch. Biochem. Biophys. 366*, 21−30.
(43) Ambroz, M., MacRobert, A. J., Morgan, J., Rumbles, G., Foley, M. S. C., and Phillips, D. (1994) Time-resolved fluorescence spectroscopy and intracellular imaging of disulfonated aluminum phthalocyanine. *J. Photochem. Photobiol. B22*, 105−117.
(44) Andrade, S. M., and Costa, S. M. B. (2002) Spectroscopic studies on the interaction of a water soluble porphyrin and two drug carrier proteins. *Biophys. J. 82*, 1607−1619.
(45) Davila, J., and Harriman, A. (1990) Photochemical and radiolytic oxidation of a zinc porphyrin bound to human serum albumin. *J. Am. Chem. Soc. 112*, 2680−2690.
(46) Bishop, S. M., Khoo, B. J., MacRobert, A. J., Simpson, M. S. C., and Phillips, D. (1993) Characterization of the photochemotherapeutic agent disulfonated aluminum phthalocyanine and its high-performance liquid-chromatographic separated components. *J. Chromatogr. 646*, 345−350.
(47) Mahammed, A., Gray, H. B., Weaver, J., and Gross, Z. (2003) How acidic are corroles and why? *Tetrahedron Lett. 44*, 2077−2079.
(48) Chatterjee, S., and Srivastava, T. S. (2000) Spectral investigations of the interaction of some porphyrins with bovine serum albumin. *J. Porphyrins Phthalocyanines 4*, 147−157.
(49) Cai, X. and Dass, C. (2003) Conformational analysis of proteins and peptides. *Curr. Org. Chem. 7*, 1841−1854.
(50) Fitos, I., Visy, J., and Simonyi, M. J. (2002) Species-dependency in chiral-drug recognition of serum albumin studied by chromatographic methods. *J. Biochem. Biophys. Methods 54*, 71−84 and references therein.
(51) Dunn, A. R., Dmochowski, I. J., Winkler, J. R., and Gray, H. B. (2003) Nanosecond photoreduction of cytochrome P450cam by channel-specific Ru-diimine electron tunneling wires. *J. Am. Chem. Soc. 125*, 12450−12456.
(52) Turro, N. J. (1978) *Modern Molecular Photochemistry*, Benjamin/Cummings Inc., Menlo Park.
(53) Structural models were built using the Accelrys DS ViewerPro 5.0 software package. The structure of **2-Ga** was obtained by addition of two sulfonate groups and removal of the axial pyridine from the published crystal structure (ref 23): **2-Ga** was then inserted into putative HSA binding sites (crystal structure from ref 34).

BC034179P

Reversible Meso-Scale Smart Polymer−Protein Particles of Controlled Sizes

Samarth Kulkarni,[†] Christine Schilli,[‡] Axel H. E. Müller,*[,‡] Allan S. Hoffman,*[,†] and Patrick S. Stayton*[,†]

Department of Bioengineering, University of Washington, Seattle, Washington 98195 and Makromolekulare Chemie II, Universität Bayreuth, D-95440 Bayreuth, Germany. Received November 20, 2003; Revised Manuscript Received May 4, 2004

Functionalized beads and particles in the size range of tens to hundreds of nanometers (nano- to meso-scale) are finding increased applications in the bioanalytical field. We show here that conjugates of streptavidin and the temperature-responsive polymer poly(*N*-isopropylacrylamide) (PNIPAAm), synthesized with low polydispersities by reversible addition−fragmentation chain transfer (RAFT) polymerization, rapidly formed mesoscale polymer−protein particles above the lower critical solution temperature (LCST). The average hydrodynamic diameters of these particles could be controlled between 250 nm to 900 nm by the choice of conjugate concentration and polymer molecular weight, and/or through control of the rate of temperature change. Once formed, the biohybrid particles were found to be stable for >16 h at the controlled size, unlike the free PNIPAAm which continued to aggregate and grow over time into very large and polydisperse aggregates. The reversibility between the smart polymer−protein particles and the free polymer−protein conjugates opens potential uses in traditional diagnostic formats and in microfluidic formats where the differential diffusive and physical properties might be exploited for separations, analyte concentration, and signal generation.

INTRODUCTION

There is a continuing need for better upstream processing of sample fluids, control over molecular recognition events, and better sensitivity in the bioanalytical field. Important developments in the synthesis of micro- and nanoparticles with controlled physical and chemical properties are providing new opportunities for this field (*1*−*3*). Controlled structures such as micelles, cylindrical rods, and vesicles self-assemble in aqueous phases from amphiphilic block copolymers or synthetic peptides and can be subsequently derivatized with functional biomolecules (*4, 5*). There has also been considerable progress recently in the synthesis of metal-based and inorganic nanoparticles that exhibit interesting optical properties and which can be functionalized with a variety of synthetic and biomolecular coatings (*6, 7*).

"Smart" beads are another interesting class that exhibit a reversible change in their properties in response to signals such as temperature or pH. A variety of synthetic techniques have been described to construct such beads, typically based on incorporating a stimuli-responsive polymer into a cross-linked bead or particle, or by grafting a stimuli-responsive polymer onto the cross-linked bead or particle (*8, 9*). Our own group has been developing biohybrid materials that utilize the stimuli-responsiveness of the smart polymer chain to control the molecular recognition activity of proteins or to reversibly control smart bead aggregation in microfluidic channels (*10, 11*). The polymer component serves as an antenna and a switch to reversibly control the activity and aggregation state of smart polymer−protein conjugates or smart polymer−bead conjugates. It was recently shown that one mechanism by which protein switching activity can be designed involves reversible particle formation and dissolution that is driven by the polymer phase transition (*12*). The free polymer−protein conjugates in solution were in an on-state, and the switching activity (i.e. off-state) was found to be dependent on the orientation of the protein active site relative to the polymer in the aggregated particle state. These initial findings motivated the current study of the physical properties of the smart polymer−protein particles. Better control of the size and formation kinetics of these smart meso-scale particles that form and dissolve upon exposure to specific stimuli should provide design opportunities for bioanalytical and diagnostic technologies.

EXPERIMENTAL PROCEDURES

Materials. *N*-Isopropylacrylamide (Aldrich, 97%) was recrystallized twice from benzene/hexane 3:2 (v:v) and dried under vacuum prior to use. 1,4-Dioxane (Merck) was refluxed over potassium for 3 days and then distilled. Azobis(isobutyronitrile) (AIBN, Fluka) was recrystallized from methanol and dried under vacuum prior to use. 1-Biotinamido-4-[4′-(maleimidomethyl)cyclohexanecarboxamido]butane (BMCC) was obtained from Pierce, IL. Recombinant streptavidin was expressed in *Escherichia coli* and purified as previously described (*13*).

Synthesis of PNIPAAm with Functional SH End Group. PNIPAAm with narrow molecular weight distribution was synthesized using the reversible addition−

* To whom correspondence should be addressed. P.S.S.: tel 206-685-8148, fax 206-685-8256, e-mail stayton@u.washington.edu; A.S.H.: tel 206-543-9423, fax 206-543-6124, e-mail hoffman@u.washington.edu, A.H.E.M.: tel +49-921-553399, fax +49-921-553393, e-mail axel.mueller@uni-bayreuth-.de.

[†] University of Washington.

[‡] Universität Bayreuth.

10.1021/bc034215k CCC: $27.50 © 2004 American Chemical Society
Published on Web 06/30/2004

fragmentation chain transfer (RAFT) polymerization technique as described previously (*14*). The chain transfer agent (CTA), benzyl 1-pyrrolecarbodithioate, was synthesized as described (*15*). RAFT polymerization was performed at 60 °C using the benzyl CTA, AIBN as initiator, and the monomer under a nitrogen atmosphere in 1,4-dioxane as a solvent. For the polymerization series conducted at different benzyl CTA concentrations, stock solutions were prepared with a monomer concentration of 1.8 mol/L, an initiator concentration of 6.90 mmol/L, and CTA concentrations of 3.92×10^{-2}, 1.96×10^{-2}, and 4.90×10^{-3} mol/L. CTA (0.915−0.114 g; 3.92−0.49 mmol) was dissolved in 1,4-dioxane (98 mL), and the solution was degassed by three freeze−thaw evacuation cycles. AIBN (0.115 g, 0.70 mmol) was dissolved separately in 1,4-dioxane (2 mL) and degassed by three freeze−thaw evacuation cycles. The monomer (20.37 g, 0.18 mol) was added via a Schlenk tube under nitrogen to the solution of the chain transfer agent in dioxane. After the monomer was completely dissolved and the mixture heated to 60 °C (temperature of oil bath), the initiator solution was injected with a syringe. All polymerization reactions were carried out under nitrogen atmosphere and aliquots were withdrawn at different time intervals. The aliquots were immediately immersed in liquid nitrogen and subsequently freeze-dried. Residual monomer was removed by sublimation. The dried samples were dissolved in THF containing 0.25% tetrabutylammonium bromide for GPC analysis. The dithiocarbamate end groups of the synthesized polymers were hydrolyzed under basic conditions to yield the corresponding thiol-terminated polymers. The polymer was dissolved in a mixture of MeOH/aq 28% NaOH (7:3) for 4 h. Ethylenediaminetetra(acetic acid) (EDTA) was added to the solution to prevent oxidation of the resultant thiol groups. The reaction mixture was acidified with 88% formic acid, MeOH was evaporated, and the residue was freeze-dried.

Lower Critical Solution Temperature (LCST) Measurement of PNIPAAm. The LCST was determined as the temperature at 10% of the maximum absorbance at 600 nm. PNIPAAm at a concentration of 0.25 wt. % in deionized H_2O was used. The data were collected using a UV−vis spectrophotometer with a jacketed cuvette holder to control the temperature of the sample. A heating rate of 0.5 °C/min was used, and absorbance values were measured every 30 s.

Biotinylation of PNIPAAm and Complexation with Streptavidin. The PNIPAAm-SH was biotinylated using a functionalized biotin, 1-biotinamido-4-[4′-(maleimidomethyl)cyclohexanecarboxamido]butane (BMCC). Briefly, BMCC was dissolved in DMSO at a concentration of 2.4 mg/mL. Four milligrams of PNIPAAm was dissolved in 875 μL of phosphate buffer (PB), 50 mM, pH 7.0, just prior to the reaction. BMCC solution (75 μL) was added to the PNIPAAm solution and the reaction proceeded overnight at RT. The excess BMCC was removed by desalting on a PD-10 column (Pierce) using PB, 50mM, pH 7.0, as an eluent. The efficiency of biotinylation of the PNIPAAm was determined using the neutravidin−HABA assay as described by Lackey et al (*16*). The biotinylated PNIPAAm (b-PNIPAAm) was physically mixed with streptavidin in PB, 50 mM, pH 7.4, and incubated overnight for conjugation. The b-PNIPAAm and tetrameric streptavidin were mixed stoichiometrically at a 4:1 ratio.

Dynamic Light Scattering. Sizing measurements were performed using a Brookhaven BI90Plus instrument equipped with a 535-channel correlator. A 656 nm laser source was used as the incident beam, and measurements were performed at a 90° angle. Samples were filtered through 0.2 μm cutoff mixed cellulose ester filters (Whatman), and 75 μL sample volumes were used for measurement. PB, 50 mM, pH 7.4, was used as a diluent to achieve various concentrations of the conjugate. A heater within the cuvette holder of the instrument was used to heat or cool the sample to various temperatures. The temperature of the sample was measured using a thin wire thermocouple (Cole Palmer). Measurements were performed at several temperatures below and above the LCST of the PNIPAAm. For each conjugate concentration, fresh samples were prepared on different days and measurements were performed in triplicate.

The intensity autocorrelation function (ACF), $G^{(2)}(\tau)$, was measured in the self-beating mode and can be expressed by the Siegert relationship:

$$G^{(2)}(\tau) = B(1 + f^2|g^{(1)}(\tau)|^2)$$

where τ is the decay time, B is a measured baseline, f is the coherence factor, and $g^{(1)}(\tau)$ is the normalized first-order electric field time autocorrelation function $E(\tau)$. $g^{(1)}(\tau)$ is related to the line-width distribution $G(\Gamma)$ by:

$$|g^{(1)}(\tau)| = \int_0^\infty G(\Gamma)\exp(-\Gamma\tau)d\Gamma$$

Using the cumulant analysis (*17*),

$$|g^{(1)}(\tau)| = \exp(-\Gamma\tau)[1 + (\mu_2/2!)\tau^2 - (\mu_3/3!)\tau^3 + ...]$$

the average line width $\langle\Gamma\rangle$ is obtained. This yields the apparent diffusion coefficient, $D_{app} = \langle\Gamma\rangle/q^2$, which can be extrapolated to zero scattering vector, q, to obtain the translational diffusion coefficient, D. The hydrodynamic radius, R_h, is then determined using the Stokes−Einstein relation:

$$R_h = k_B T/(6\pi\eta_o D)$$

where k_B, T, and η_o are the Boltzmann constant, the absolute temperature, and solvent viscosity, respectively. For relatively narrow decay-rate distributions, the second moment, μ_2, designated as the polydispersity index, can be used to estimate the relative distribution width. Assuming a log-normal size distribution for the particles, the full-width at half-maximum (fwhm) was calculated from R_h and μ_2 using:

$$\text{fwhm} = 2R_h\text{sqrt}(\mu_2)$$

The reliability of size measurements by the cumulant analysis was verified by applying other established models to the obtained correlation function. The models chosen were the nonnegatively constrained least squares (NNLS) (*18*, *19*) and CONTIN (*20*, *21*). Root-mean-square deviations for each of the model fits were calculated and used for preliminary comparison of model fits.

Stability of the Nanoparticles. To determine the stability of the particles, a 100 μL sample of PNIPAAm−streptavidin conjugate was heated to 42.5 °C in the cuvette as described above. An airtight lid on the cuvette was used to minimize evaporation. Size measurements were taken at different time points up to 1000 min. As a control, a b-PNIPAAm sample, without the streptavidin was used. This PNIPAAm sample had the same molar concentration as that of the polymer (both bound and unbound) in the conjugate solution.

Particle Formation and Dissolution Kinetics. Since sizing measurements cannot be performed within

small time intervals, the scattering intensity, *I*, in counts per second (CPS), was used as an index of nanoparticle formation. As the PNIPAAm−streptavidin conjugates transform from free soluble conjugates to particulate form above the LCST, the scattering intensity increases. This scattering intensity is measured to analyze the kinetics of formation of the particles. The cuvette containing the conjugate sample was cooled to 23 °C and then placed in the heated cuvette holder of the DLS instrument maintained at 42.5 °C. The intensities were measured at a sampling interval of 5 μs as the temperature increased and finally equilibrated at 42.5 °C. For particle dissolution studies, the conjugate sample incubated at 42.5 °C in a cuvette was subsequently placed in the jacketed cuvette holder maintained at 25 °C. Intensities were measured at a sampling interval of 5 μs as the sample cooled. The temperature profile for the sample was recorded using a thermocouple with a sampling interval of 15 s.

Dependence of Nanoparticle Size on Concentration and Molecular Weight of PNIPAAm. Nanoparticle hydrodynamic diameters were measured for the bioconjugates of streptavidin with PNIPAAm of molecular weights (number-averaged molecular weight, M_n) 2.9 kDa, 4.8 kDa, 14.9 kDa, and 25.9 kDa, respectively, to determine the dependence of size on molecular weight of the polymer. The concentration dependence was determined by using concentrations of 9 μM, 3 μM, 1 μM, 500 nM, and 100 nM for each bioconjugate. The Tukey−Kramer multiple comparisons statistical test was used to analyze the data.

Effect of Heating Rate. Size measurements were made at three different heating rates for the 14.9 kDa PNIPAAm−streptavidin conjugate at a 1 μM concentration. The cuvette containing the conjugate was cooled to 23 °C and then placed in the heated cuvette holder of the DLS instrument maintained at 33, 38.5, and 42.5 °C to get different heating rates. The temperature of the conjugate solution in the cuvette was measured using a thermocouple with a sampling time of 15 s. The heating rates were measured by calculating the derivative of the temperature−time curve at the respective LCST values. Heating rates of 0.04 °C/s, 0.12 °C/s, and 0.16 °C/s were obtained for the 32.5, 38.5, and 42.5 °C block temperatures, respectively.

RESULTS

Synthesis of PNIPAAm with Narrow Molecular Weight Distributions. Using the RAFT technique, PNIPAAm of different molecular weights with narrow molecular weight distributions were synthesized. A range of four molecular weights (M_n) were chosen for conjugation to streptavidin: 25.9 kDa (polydispersity = 1.08), 14.8 kDa (polydispersity = 1.09), 4.8 kDa (polydispersity = 1.16), and 2.9 kDa (polydispersity = 1.16). The dithiocarbamate end group on the polymer from the chain transfer agent was cleaved to generate a functional thiol end group that was used for end-specific biotin conjugation. The LCST values, as defined by 10% change in absorbance at 0.2 mg/mL polymer concentration, for the 25.9 kDa (31 °C) and 14.9 kDa (31.4 °C) polymers were similar, but those for the 2.9 kDa (26.8 °C) and 4.8 kDa polymers (29.0 °C) were slightly lower. A linear dependence of LCST values versus reciprocal molecular weight values was previously described for the dithiocarbamate-terminated polymers (*22*).

Biotinylation of PNIPAAm and Complexation with Streptavidin. Biotinylation efficiencies calculated by the HABA assay yielded average values of 57% for the 25.9 and 14.9 kDa polymers, 62% for the 4.8 kDa polymer, and 60% for the 2.9 kDa polymer. The biotinylation efficiency was used to calculate the amount of polymer to be added to streptavidin for complexation. We have shown previously that a maximum of two biotinylated polymers are bound per tetrameric streptavidin due to steric hindrance (*23*). In these studies, a ratio of 2.4 biotinylated PNIPAAm polymer chains to streptavidin tetramer was used.

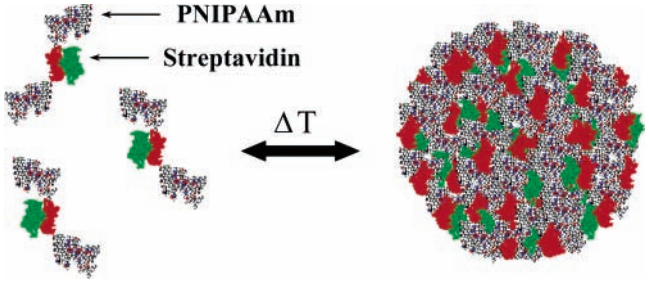


Figure 1. Schematic representation of the formation of PNIPAAm−streptavidin smart nanoparticles. Below the LCST, the PNIPAAm is hydrophilic and the bioconjugate remains in solution. Above the LCST, the hydrophobicity of the PNIPAAm directs the aggregation of the bioconjugates into nanoparticles of defined sizes. The hydrophilic streptavidin stabilizes the nanoparticles and prevents further aggregation.

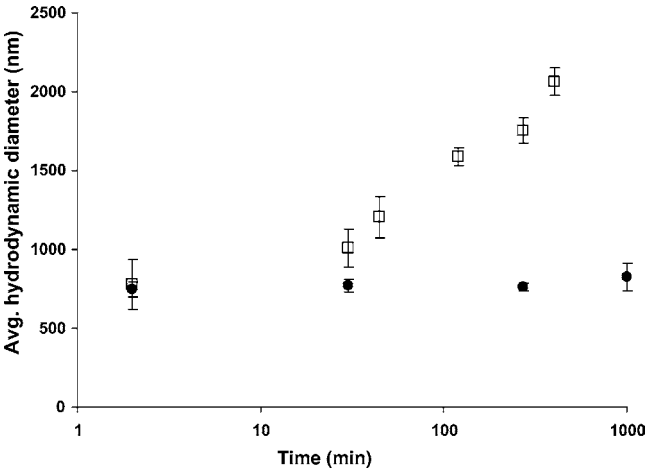


Figure 2. Stability of the nanoparticles formed from the 14.9 kDa PNIPAAm−streptavidin conjugate at 42.5 °C and a concentration of 3 μM is shown. The particles fomed by the bioconjugate (●) are stable in size for over 16 h. In contrast, aggregates of b-PNIPAAm (□) at the same concentration do not have a hydrophilic moiety to stabilize the size and aggregate over time into larger particles. Error bars represent ± 1 standard deviation over the three measurements.

Stability and Kinetic Properties of Streptavidin−PNIPAAm Particle Formation. The polymer−streptavidin conjugates are soluble at temperatures below the LCST of PNIPAAm, and no sizing measurements could be made due to the low level of scattering intensities. As the conjugate was heated to temperatures above the LCST of PNIPAAm, the polymer becomes hydrophobic and drives the aggregation of the conjugates into uniform and stable particles (Figure 1). The stability of the nanoparticle size for the 14.9 kDa conjugate at a fixed concentration of 3 μM is shown in Figure 2. Once formed, the particles did not aggregate further and had the same average size after 16 h (Tukey−Kramer test, $p < 0.05$). In contrast, PNIPAAm−biotin alone continued to aggregate into larger particles over this time period (>1 μm diameter after 1 h). Sizing measurements could not

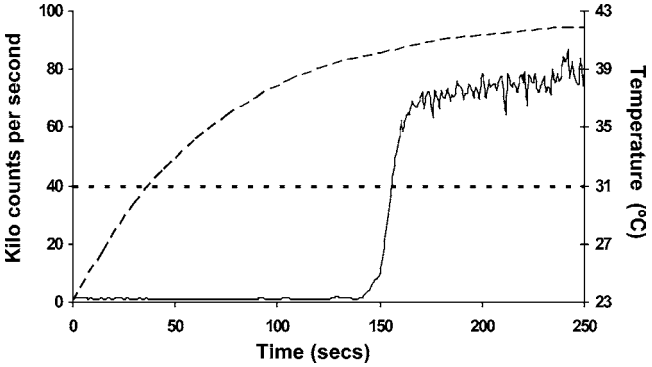


Figure 3. The kinetics of formation of particles by the 14.9 kDa PNIPAAm−streptavidin conjugate at a concentration of 1 μM as measured by light scattering intensity is shown. The scattering intensity (—) is measured as the temperature of the conjugate is ramped from 23 °C to 42.5 °C. As the particles are formed, the scattering intensity, measured in kilocounts per second (kCPS), increases in a highly cooperative manner. The increase in sample temperature (– – –) with time is overlaid onto the kinetic trace. The LCST of the PNIPAAm (- - -) is shown on the temperature axis.

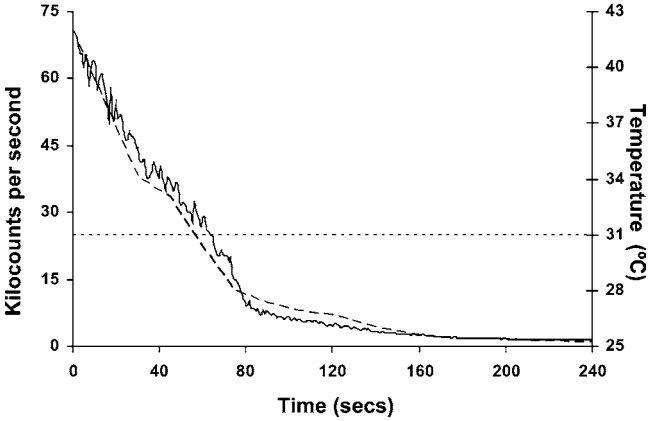


Figure 4. Dissolution kinetics for the 14.9 kDa PNIPAAm−streptavidin conjugate at a concentration of 1 μM is shown. The scattering intensity is measured as the sample is cooled from 42.5 °C to 25 °C. As the particles dissolve, the scattering intensity (—), measured in kilocounts per second (kCPS), decreases. The decrease in sample temperature (– –) with time is overlaid onto the kinetic trace. The LCST of the PNIPAAm (···) is shown on the temperature axis.

be made beyond 400 min for the PNIPAAm−biotin as the size exceeded the range of the instrument.

The particle formation kinetics, measured by the increase in scattering intensity as the conjugate was heated from 20 °C to 42.5 °C, are shown in Figure 3. The transition from soluble conjugates to particles was found to be rapid (within 20 s) and occurs in a narrow temperature range at the critical point. The time lapse of ca. 100 s observed after the temperature of the solution surpasses the LCST suggests that there is an induction period with early nucleation events that fall below the resolution of this observation technique. After reversal of the temperature stimulus, the scattering intensity decreased by more than 90% within 2 min, consistent with the dissolution of the particles in this time period (Figure 4). In Figure 4, it is seen that the dissolution of the particles commences as soon as the sample is removed from the 42.5 °C heat block and exposed to the atmosphere. This anomaly could be due to dissolution of particles exposed to the surface, where cooling is faster than in the bulk (where temperature was measured).

Particle Size Controlled by Concentration and Molecular Weight. At temperatures above the LCST, the bioconjugates assemble into stable particles whose size is dependent on the concentration and the molecular weight of the PNIPAAm (Table 1). The dependence of particle hydrodynamic diameter on conjugate concentration for the 14.9 kDa conjugate at 42.5 °C is shown in Figure 5. The particle size increases with the concentration of the bioconjugate for all the molecular weights of PNIPAAm tested (a complete concentration curve could not be obtained for the 2.9 kDa polymer due to insufficient scattering intensity at low concentrations). Furthermore, the particles were stable once formed (>16 h) and further dilution at the elevated temperatures did not significantly affect the size of the particles (data not shown).

The hydrodynamic particle sizes also depend on the molecular weight of the PNIPAAm used for conjugation. Figure 6 shows the dependence of particle diameter on PNIPAAm molecular weight for a fixed concentration of the conjugate. Particle sizes were comparable for the 25.9, 14.9, and 4.8 kDa conjugates, with no significant change in size with change in molecular weight ($p < 0.05$). The 2.9 kDa conjugate had a much smaller size, indicating that below a threshold molecular weight, the nucleation and growth mechanism changes. Table 1 shows particle sizes and full widths at half-maximum (fwhm) for the

Table 1. Particle Sizes of Streptavidin−PNIPAAm Bioconjugates[a]

M_n of PNIPAAm conjugate to streptavidin		concentration 9 μM	3 μM	1 μM	0.5 μM	0.1 μM
PNIPAAm−25.9 kDa-Stav	D_h (nm)	719	670	426	336	236
	fwhm (nm)	51	92	131	123	81
PNIPAAm−14.9 kDa-Stav	D_h (nm)	744	711	571	381	271
	fwhm (nm)	53	157	141	124	75
PNIPAAm−4.8 kDa-Stav	D_h (nm)	975	751	381	375	243
	fwhm (nm)	198	256	78	126	85
PNIPAAm−2.9 kDa-Stav	D_h (nm)	449	305			
	fwhm (nm)	124	149			

[a] Size data for the particles formed from PNIPAAm−streptavidin conjugates of different molecular weights and different concentrations is shown. The particles were formed by heating the sample to 42.5 °C. D_h represents the average hydrodymamic diameter, and fwhm represents the relative width of the size distribution. Sizing data for the 2.9 kDa PNIPAAm conjugate could not be obtained at lower concentrations due to insufficient scattering from the particles. Values represent the average of three measurements for each molecular weight and concentration.

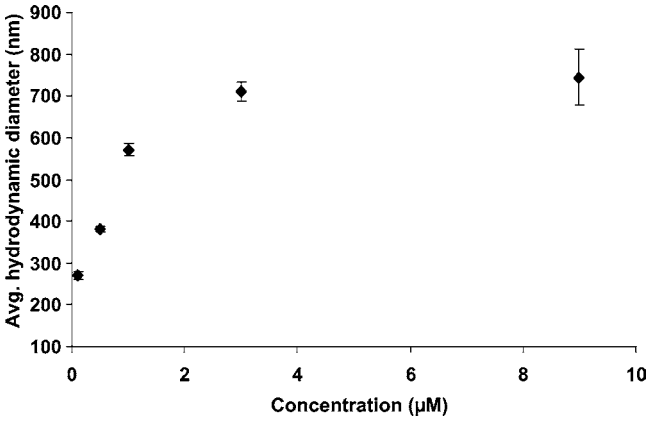


Figure 5. Dependence of the average hydrodynamic particle diameter on conjugate concentration is shown for the 14.9 kDa PNIPAAm−streptavidin conjugate at 42.5 °C. Size measurements were performed 20 min after particle formation. Error bars represent ± 1 standard deviation over three measurements with freshly prepared samples. The average hydrodynamic diameters increase with concentration.

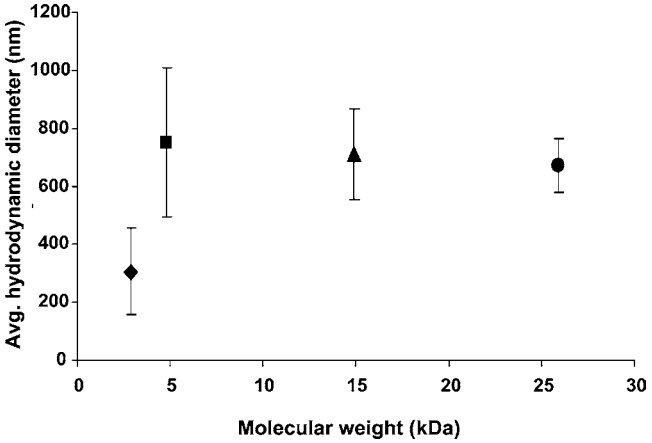


Figure 6. Dependence of the average hydrodynamic particle diameter on molecular weight (number averaged molecular weight) of the PNIPAAm used for conjugation to streptavidin is shown for the 25.9 kDa (●), 14.8 kDa (▲), 4.8 kDa (■), and 2.9 kDa (◆) conjugates at a concentration of 3 μM at 42.5 °C. Average particle hydrodynamic diameters are comparable for the 25.9 kDa, 14.8 kDa, and 4.8 kDa conjugates but significantly lower for the 2.9 kDa conjugate. Error bars represent ± 1 standard deviation from triplicate sizing measurements made for each conjugate.

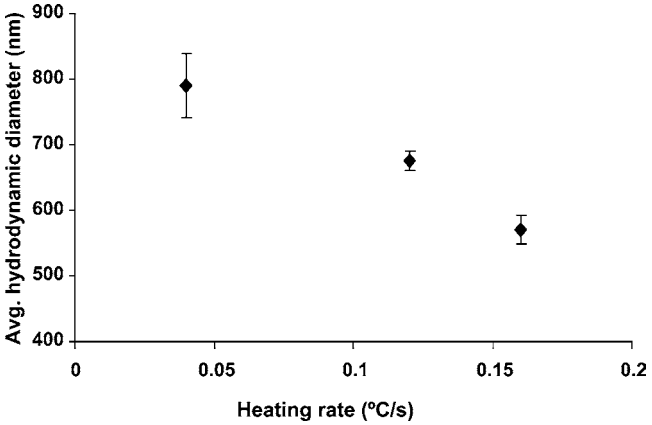


Figure 7. Effect of heating rate on the hydrodynamic particle diameter for the 14.9 kDa PNIPAAm−streptavidin conjugate at a concentration of 1 μM is shown. Different heating rates were achieved by heating the sample incubated at 23 °C to final temperatures of 33, 38, and 42.5 °C corresponding to heating rates of 0.04, 0.12, and 0.16 °C/s, respectively. The size measurements were made 5 min after reaching the final temperature. The average hydrodynamic diameter of the particles decreases with heating rate. Error bars represent ± 1 standard deviation from three measurements.

different polymer molecular weights and concentrations. The fwhm values have been calculated from the second moment μ_2 (polydispersity index) and reflect the relative distribution width of the particles. The average values of the polydispersity index ranged from 0.02 to 0.18, indicating narrow distributions of particle size. From the fwhm values, it was observed that the higher molecular weight polymers yielded particles with narrower relative (to size) distribution widths. This indicates that conjugates of higher molecular weight polymers form more uniform particles. Taken together, these data demonstrate that discrete particle sizes between the range of ca. 250 and 900 nm can be designed through appropriate choice of polymer molecular weight and concentration.

Effect of Heating Rate on Particle Size. Particle size was observed to be dependent on the heating rate of the conjugate solution (Figure 7). Smaller particles were formed at higher heating rates and nanoparticles of fixed sizes could be formed by varying the heating rate. For example, the size of the 14.9 kDa PNIPAAm−streptavidin conjugate could be tightly controlled to 675 nm (± 20 nm) at a concentration of 1 μM by choosing a heating rate of 0.12 °C/s. Additionally, it was observed that the particles had a wider distribution when formed at lower heating rates. The different heating rates were achieved by incubating the sample at 23 °C and then inserting into heating blocks maintained at different temperatures, resulting in different final temperatures for each sample. Our experimental set up did not allow the sample to be ramped to the same final temperatures at different heating rates. To address the question of relative importance of the final temperature (equilibrium effect) versus the heating rate (kinetic effect) on particle size, the temperatures were changed after formation of the particles. Particles of size 790 nm (± 50 nm) were formed on ramping the temperature to 33 °C at a heating rate of 0.04 °C/s. There was no significant change in the size of these particles by subsequently raising the temperature of this sample to 42.5 °C (data not shown). Similarly, no change in size was observed when particles that were formed by heating to 42.5 °C were cooled to 38 °C (data not shown). This demonstrates that the particle size is largely governed by the kinetics of aggregation at defined concentrations and polymer molecular weights.

DISCUSSION

The particle properties of a temperature-responsive polymer−streptavidin conjugate have been investigated in this study. The size of the particles formed above the PNIPAAm LCST could be controlled across an interesting and application relevant mesoscale of ca. 250−900 nanometers by manipulating the polymer molecular weight, the conjugate concentration, and/or the heating rate. Once formed, the particles were remarkably stable with narrow size distributions and yet could be formed or dissolved rapidly. This behavior was not seen with PNIPAAm alone, even at dilute concentrations, as the polymer aggregated into continually larger aggregates over time.

The aggregation of PNIPAAm polymers at dilute concentrations into mesoscopic globules above its LCST has also been reported by Gorelov et al. (*24*). The authors reported that the mesoglobules formed by high molecular weight PNIPAAm (M_n = 2−9 MDa), at dilute concentrations of 1−5 nM, are stable and do not aggregate further. In our experiments, however, we have observed that at concentrations typical of bioanalytical reactions, aggregates formed from lower M_n PNIPAAm alone are unstable and aggregate continuously (Figure 2). Particles formed from the biohybrid conjugates, however, are stabilized by the charged and hydrophilic streptavidin and remain stable in size even at higher concentrations. The protein thus serves as a hydrophilic capping agent to limit the bioconjugate particle size, similar to surfactants that prevent the superaggregation of similar temperature-responsive polymers (*25*). Similar observations have been made with colloidal particles of DNA−PNIPAAm conjugates where the DNA acts as the hydrophilic shell (*26*).

These experiments also indicate that the formation of the particles is largely a kinetic phenomenon dependent on the concentration and heating rate of the sample. The predominant effect of heating rate over the final equilibrium temperature on particle size demonstrates that once formed, the particles are kinetically stable and changes in equilibrium conditions over the temperature range studied do not alter the particle size. This is also

substantiated by the fact that dilution after formation of the particles does not significantly change the particle size distribution.

The properties of this meso-particle system provide interesting opportunities for the bioanalytical field. The reversibility of the bioconjugate particle formation allows molecular recognition steps to be performed with the free conjugates, while then enabling separation and concentration steps based on particle properties or vice versa. For example, the streptavidin conjugates can be used to capture biotinylated antibodies and their targets in homogeneous solution but can then be filtered as the mesoscale beads after temperature-triggered particle formation. After isolation, the bioconjugates can be released back as free molecular species with simple temperature reversal. Alternatively, the different diffusive properties of the particles might be exploited in microfluidic devices to separate particle-bound targets from freely diffusing contaminants, with the benefit again of being able to regenerate the bioconjugate species at controlled places in the channel device for capture or release (*27*, *28*).

In addition to these microfluidic device applications, many lab assays (e.g., PCR) depend on sequential processing steps that could benefit from all reagents being placed in a single complex mixture. The timing of each processing step could subsequently be controlled by sequential signals directing flocculation/aggregation and redispersal of specific biomolecular species. In this application it would be desirable to have the aggregated species turned off, which we have shown can be accomplished by controlling the orientation of the protein active site relative to the polymer (*12*). Similarly, for bioprocessing applications relying on sequential enzyme reactions, it should be possible to control sequential enzyme activities by bringing them together at specific times to amplify the sequential nature of the reactions.

ACKNOWLEDGMENT

The authors thank Dr. M. Schurr (University of Washington) and W. Bernt (Brookhaven Instruments) for useful discussions. The authors gratefully acknowledge NIH grant No. EB00252, DFG grant No. Mu896/13-1, and the NSF-funded Center for Nanotechnology, University of Washington (UIF fellowship to S.K.).

LITERATURE CITED

(1) Cao, Y. W. C., Jin, R. C., and Mirkin, C. A. (2002) Nanoparticles with Raman spectroscopic fingerprints for DNA and RNA detection. *Science 297* (5586), 1536−1540.

(2) Niemeyer, C. M. (2001) Nanoparticles, proteins, and nucleic acids: Biotechnology meets materials science. *Angew. Chem., Int. Ed. 40* (22), 4128−4158.

(3) Alivisatos, P. (2004) The use of nanocrystals in biological detection. *Nat. Biotechnol. 22* (1), 47−52.

(4) Hartgerink, J. D., Beniash, E., and Stupp, S. I. (2002) Peptide-amphiphile nanofibers: A versatile scaffold for the preparation of self-assembling materials. *Proc. Natl. Acad. Sci. U.S.A. 99* (8), 5133−5138.

(5) Discher, B. M., Won, Y. Y., Ege, D. S., Lee, J. C. M., Bates, F. S., Discher, D. E., and Hammer, D. A. (1999) Polymersomes: Tough vesicles made from diblock copolymers. *Science 284* (5417), 1143−1146.

(6) Mirkin, C. A., Letsinger, R. L., Mucic, R. C., and Storhoff, J. J. (1996) A DNA-based method for rationally assembling nanoparticles into macroscopic materials. *Nature 382* (6592), 607−609.

(7) Chan, W. C. W., and Nie, S. M. (1998) Quantum dot bioconjugates for ultrasensitive nonisotopic detection. *Science 281* (5385), 2016−2018.

(8) Sershen, S. R., Westcott, S. L., Halas, N. J., and West, J. L. (2000) Temperature-sensitive polymer-nanoshell composites for photothermally modulated drug delivery. *J. Biomed. Mater. Res. 51* (3), 293−298.

(9) Takata, S., Shibayama, M., Sasabe, R., and Kawaguchi, H. (2003) Preparation and structure characterization of hairy nanoparticles consisting of hydrophobic core and thermosensitive hairs. *Polymer 44* (2), 495−501.

(10) Malmstadt, N., Yager, P., Hoffman, A. S., and Stayton, P. S. (2003) A smart microfluidic affinity chromatography matrix composed of poly(*N*-isopropylacrylamide)-coated beads. *Anal. Chem. 75* (13), 2943−2949.

(11) Shimoboji, T., Larenas, E., Fowler, T., Kulkarni, S., Hoffman, A. S., and Stayton, P. S. (2002) Photoresponsive polymer-enzyme switches. *Proc. Natl. Acad. Sci. U.S.A. 99* (26), 16592−16596.

(12) Shimoboji, T., Larenas, E., Fowler, T., Hoffman, A. S., and Stayton, P. S. (2003) Temperature-induced switching of enzyme activity with smart polymer−enzyme conjugates. *Bioconjugate Chem. 14* (3), 517−525.

(13) Chilkoti, A., Tan, P. H., and Stayton, P. S. (1995) Site-Directed Mutagenesis Studies of the High-Affinity Streptavidin−Biotin Complex − Contributions of Tryptophan Residue-79, Residue-108, and Residue-120. *Proc. Natl. Acad. Sci. U.S.A. 92* (5), 1754−1758.

(14) Schilli, C., Lanzendörfer, M. G., and Müller, A. H. E. (2002) Benzyl and cumyl dithiocarbamates as chain transfer agent in the RAFT polymerization of *N*-isopropylacrylamide. In situ FT-NIR and MALDI-TOF MS investigation. *Macromolecules 35* (18), 6819−6827.

(15) Chiefari, J., Mayadunne, R. T. A., Moad, G., Rizzardo, E., and Thang, S. H. (1999) WO 99/31144 (inventors: DuPont Co.).

(16) Lackey, C. A., Murthy, N., Press, O. W., Tirrell, D. A., Hoffman, A. S., and Stayton, P. S. (1999) Hemolytic activity of pH-responsive polymer−streptavidin bioconjugates. *Bioconjugate Chem. 10* (3), 401−405.

(17) Koppel, D. E. (1972) Analysis of Macromolecular Polydispersity in Intensity Correlation Spectroscopy: The Method of Cumulants. *J. Chem. Phys. 57* (11), 4814−4820.

(18) Gulari, E., Gulari, E., Tsunashima, Y., and Chu, B. (1979) Photon-Correlation Spectroscopy of Particle Distributions. *J. Chem. Phys. 70* (8), 3965−3972.

(19) Chu, B., Gulari, E., and Gulari, E. (1979) Photon-Correlation Measurements of Colloidal Size Distributions. 2. Details of Histogram Approach and Comparison of Methods of Data-Analysis. *Phys. Script. 19* (4), 476−485.

(20) Provencher, S. W. (1982) A Constrained Regularization Method for Inverting Data Represented by Linear Algebraic or Integral-Equations. *Comput. Phys. Commun. 27* (3), 213−227.

(21) Provencher, S. W. (1982) Contin − a General-Purpose Constrained Regularization Program for Inverting Noisy Linear Algebraic and Integral-Equations. *Comput. Phys. Commun. 27* (3), 229−242.

(22) Schilli, C. M., Müller, A. H. E., Rizzardo, E., Thang, S. H., and Chong, Y. K. (2003) RAFT polymers: Novel precursors for polymer-protein conjugates. *Adv. Controlled/Living Radical Polymerization* (Matyjaszewski, K., Ed.) *ACS Symp. Ser. 854*, 603−618.

(23) Ding, Z. L., Fong, R. B., Long, C. J., Stayton, P. S., and Hoffman, A. S. (2001) Size-dependent control of the binding of biotinylated proteins to streptavidin using a polymer shield. *Nature 411* (6833), 59−62.

(24) Gorelov, A. V., DuChesne, A., and Dawson, K. A. (1997) Phase separation in dilute solutions of poly (*N*-isopropylacrylamide). *Physica A 240* (3−4), 443−452.

(25) Meewes, M., Ricka, J., Desilva, M., Nyffenegger, R., and Binkert, T. (1991) Coil globule transition of poly(*N*-isopropylacrylamide). A study of surfactant effects by light-scattering. *Macromolecules 24* (21), 5811−5816.

(26) Mori, T., and Maeda, M. (2002) Stability change of DNA-carrying colloidal particle induced by hybridization with target DNA. *Polym. J. 34* (8), 624−628.

(27) Hatch, A., Kamholz, A. E., Hawkins, K. R., Munson, M. S., Schilling, E. A., Weigl, B. H., and Yager, P. (2001) A rapid diffusion immunoassay in a T-sensor. *Nature Biotechnol. 19* (5), 461−465.
(28) Burns, M. A., Johnson, B. N., Brahmasandra, S. N., Handique, K., Webster, J. R., Krishnan, M., Sammarco, T. S., Man, P. M., Jones, D., Heldsinger, D., Mastrangelo, C. H., and Burke, D. T. (1998) An integrated nanoliter DNA analysis device. *Science 282* (5388), 484−487.

BC034215K

A New Triantennary Galactose-Targeted PEGylated Gene Carrier, Characterization of Its Complex with DNA, and Transfection of Hepatoma Cells

Benoît Frisch,[†] Marie Carrière,[‡] Céline Largeau,[‡] Frédéric Mathey,[†] Christophe Masson,[‡] Francis Schuber,[†] Daniel Scherman,[‡] and Virginie Escriou*[,‡]

Unité de Pharmacologie Chimique et Génétique, CNRS FRE2463, INSERM U640, Faculté des Sciences Pharmaceutiques et Biologiques de Paris, 4 av de l'Observatoire, 75270 Paris Cedex 06, France, and Laboratoire de Chimie Bioorganique, UMR 7514 CNRS/ULP, Faculté de Pharmacie, 74 rte du Rhin, BP 24, 67401 Illkirch Cedex, France. Received January 22, 2004; Revised Manuscript Received April 27, 2004

Nonviral gene vectors remain inefficient in vivo largely because of their rapid clearance from the circulation and also their nonspecific association with the extracellular matrix. To overcome such drawbacks, cationic lipoplexes are now frequently coated with hydrophilic polymers such as PEGs to reduce nonspecific interactions, and ligands are also linked to their surface to obtain cell-specific gene transfer. In view of the development of vectors for systemic gene delivery, we have designed and studied lipoplexes that carry a triantennary galactosyl ligand attached to the distal end of a $(PEG)_{45}$-conjugated lipid. We incorporated this targeted PEGylated lipid into lipoplexes using two strategies of formulation, i.e., using either preformed micelles or liposomes. We demonstrated that the incorporation of PEG chains stabilized lipoplexes and masked, but only partially, the positive charges exposed on the surface of the particles. We have also shown that incorporation into lipoplexes of a lipidated PEG chain, bearing a ligand at its distal end, yielded particles that exhibited an accessible ligand throughout the whole range of cationic lipid to DNA ratios. We obtained a targeted transfection in HepG2 cells with one of the formulations. Our results strengthen the validity of using a ligand carried by a long PEG spacer arm for targeted gene transfer.

INTRODUCTION

Clinical applications of gene therapy require the development of vectors allowing systemic administration and target tissue restricted gene delivery (*1*). Viral vectors are generally effective gene transfer agents; however, their use remains hampered by safety concerns. For that reason, vectors such as cationic polymers and cationic lipids, although less efficient, represent attractive alternatives that have been extensively explored during the past decade (*2*). However, gene transfer efficiency of polyplexes and lipoplexes (cationic polymer/DNA and cationic lipid/ DNA complexes, respectively) remains quite low in vivo, in part due to their rapid clearance from the circulation by the cells of the reticuloendothelial system (RES) and also to nonspecific association with the extracellular matrix (*3*, *4*). This situation has imposed severe limitations on the use of these nonviral vectors for therapeutic gene delivery (*5*). To overcome such drawbacks, lipoplexes or polyplexes can be coated with polymers such as poly(ethylene glycol) (PEG), which introduce a steric barrier at their surface (Figure 1). These PEGylated lipoplexes or polyplexes exhibit a reduction of interaction with opsonins and/or nonspecific interactions with RES cells (*6*). However, the PEG coating may also reduce the cationic particle−cell membrane interactions that are needed for cell uptake, the consequence of which would lead to a decrease in gene transfer. Another approach to enhance the gene transfer efficiency of nonviral vectors is to incorporate targeting elements that bind efficiently to cell-surface receptors (*7*, *8*). However, when targeted lipoplexes are used, PEG coating may interfere with the recognition between the ligand and its specific receptor on the target cell surface. Therefore, it was found preferable to conjugate the ligand at the distal end of a PEG spacer arm linked to polylysine (*9*−*11*), to PEI (*12*−*15*), or to a lipid (*16*−*21*). These targeted PEG−lipids were mostly incorporated in liposomes (*16*, *17*, *20*, *21*) or vesicles (*19*) but only rarely in lipoplexes (*18*).

In view of the development of vectors for systemic gene delivery, we have designed and studied lipoplexes that carry a triantennary galactosyl ligand attached to the distal end of a $(PEG)_{45}$-conjugated lipid (Figure 2). This ligand was used previously to target lipoplexes in vitro to human hepatoma cells (*22*). Because of the length of the spacer (PEG_{45}), we expected the ligand to protrude from lipoplexes and interact without hindrance with the Gal/GalNAc receptor expressed at the surface of the target cells. In the present work, we have explored the feasibility of forming PEG-modified lipoplexes and assessed (i) the effect of PEG on their physicochemical characteristics and (ii) their capacity to mediate targeted cell transfection.

EXPERIMENTAL PROCEDURES

General. Reagent-grade solvents were used without further purification. *N*,*N*′-Dicyclohexylcarbodiimide (DCC), *N*-hydroxysuccinimide (NHS), *N*-ethyldiisopropylamine (DIPEA), and *O*,*O*′-bis(2-aminoethyl)poly(ethylene glycol)

* To whom correspondence should be addressed. Phone: 33 1 53 73 95 75. Fax: 33 1 43 26 69 18. E-mail: virginie.escriou@univ-paris5.fr.

‡ CNRS FRE2463.

† UMR 7514 CNRS/ULP.

10.1021/bc049971k CCC: $27.50 © 2004 American Chemical Society
Published on Web 06/18/2004

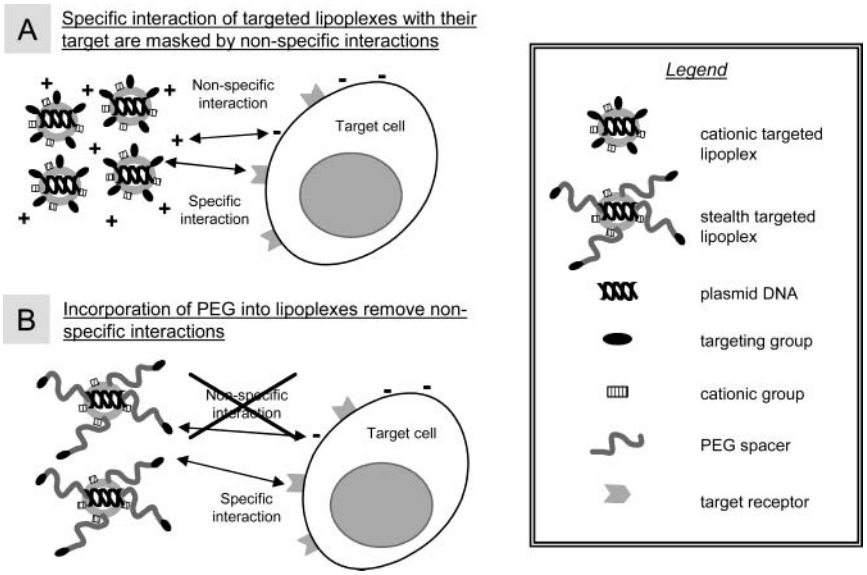


Figure 1. Schematic representation of the interaction of targeted lipoplexes with their target cells.

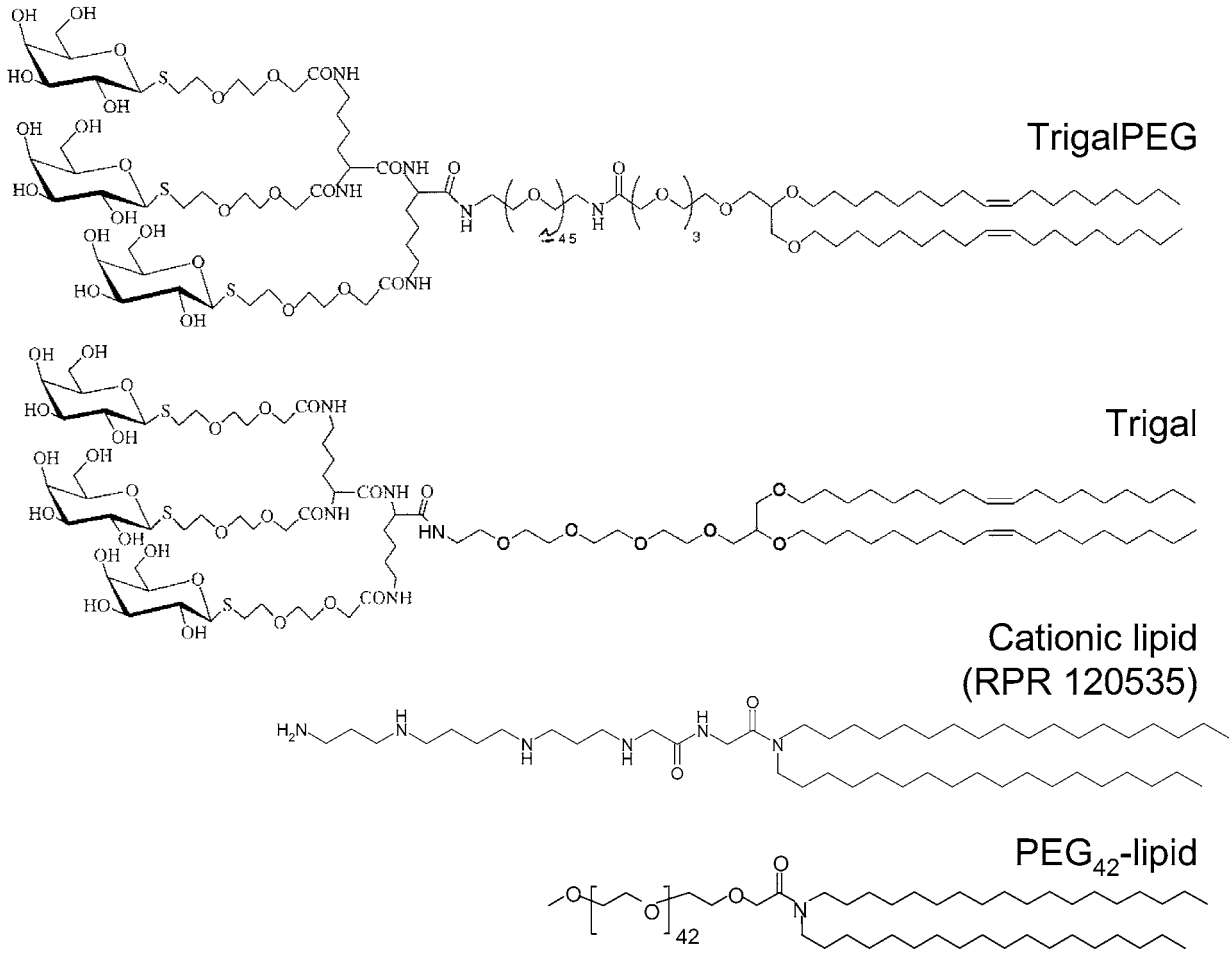


Figure 2. Molecular structure of the cationic, neogalactosylated, and PEGylated lipids used in this study. Targeted lipids consisted of a triantennary galactosyl headgroup linked to a double C18:1 lipid anchor via a $(PEG)_{45}$ spacer (TrigalPEG) or via a $(PEG)_3$ spacer (Trigal). RPR 120535 contained a spermine as cationic headgroup linked to a double C18:0 anchor via a short spacer. PEG-modified lipid contained a $(PEG)_{42}$ linked to a double C18:0 lipid chain.

(MW 2000) ($NH_2PEG_{45}NH_2$) were from Fluka (L'Isle D'Abeau Chesnes, France). Silica gel 60 F 254 plates for thin-layer chromatography were purchased from Merck (Darmstadt, Germany). ^1H NMR spectra were recorded on Bruker DPX 200 (200 MHz) and DPX 300 (300 MHz) spectrometers.

Lipids (Figure 2). DOPE (1,2-dioleoyl-*sn*-glycerol-3-phosphoethanolamine) was purchased from Avanti Polar. Cationic lipid RPR 120535 was prepared as described (*23*).

Preparation of PEG_{42}−Lipid (MeO−$(PEG)_{42}$−DODA). PEG_{42}−lipid (MeO−$(PEG)_{42}$−DODA) was pre-

pared by condensation of dioctadecylamine on previously oxidized MeO−$(PEG)_{42}$ (*24*). The one-step synthesis was carried out using Castro's reagent in alkaline medium (*25*) and the expected product was purified by preparative HPLC [C4 phase, water (+0.1% TFA)/acetonitrile (+0.08% TFA) gradient, UV detection 220 nm]. MeO−$(PEG)_{42}$−DODA was isolated as a white lyophilisate; ^{1}H NMR, MS (electrospray), and IR assessed structure and purity.

Synthesis of (2-{2-[2-(2,3-Bis(octadec-9-enyloxy)-propoxy)ethoxy]ethoxy}ethoxy)acetic Acid ($DOGP_3$-COOH). $DOGP_3OH$ (*26*) was dissolved in 40 mL of acetone. Under stirring, 1.7 mL of 2.67 M Jones reagent (26.72 g of chromium(IV) oxide in 23 mL of concentrated sulfuric acid brought to a final volume of 100 mL of water) was added dropwise over 15 min. After 2 h a few drops of 2-propanol were added followed by 50 mL of water to dissolve the precipitated chromium salts. The organic solvent was then removed under reduced pressure and the aqueous phase extracted three times with 100 mL of CH_2Cl_2. The combined organic extracts were dried on $MgSO_4$ and concentrated, and the residue was chromatographed on a silica gel column eluted with CH_2Cl_2:CH_3OH (20:1 to 20:2). The product was obtained as a colorless oil (1 g, 60% yield): R_f 0.46 (CH_2Cl_2:CH_3OH, 9:1); ^{1}H NMR ($CDCl_3$:CD_3OD, 1:1, 200 MHz) δ 5.35 (m, 4H, *CH*=*CH*), 4.00 (s, 2H, COCH_2O), 3.75−3.44 (m, 21H, OCH_2, *CHCH*$_2$O, CH_2CH_2O), 2.01 (m, 8H, CH_2CH=CHCH_2), 1.55 (m, 4H, $OCH_2CH_2CH_2$), 1.33−1.30 (m, 44H, $CH_3(CH_2)_6$, $OCH_2CH_2(CH_2)_5$, 0.91 (t, J = 6.6 Hz, 6H, CH_3).

Synthesis of $DOGP_{45}NH_2$. $DOGP_3COOH$ (1 g, 1.28 mmol) was added to a solution of 20 mL of anhydrous CH_2Cl_2 containing $NH_2PEG_{45}NH_2$ (5.2 g, 2.56 mmol), DCC (400 mg, 1.92 mmol), and *N*-hydroxysuccinimide (147 mg, 1.28 mmol). The coupling reaction was carried out overnight, under argon, at room temperature. After elimination of dicyclohexylurea by filtration, the solvents were removed under reduced pressure. The title compound was purified by chromatography on a 400 mL silica gel column eluted with CH_2Cl_2:CH_3OH (95:5 to 85:15). The organic phase was concentrated under reduced pressure. The product was obtained as a white solid (1.2 g, 34% yield): R_f 0.6 (CH_2Cl_2:CH_3OH, 85:15); ^{1}H NMR ($CDCl_3$, 200 MHz) δ 5.35 (m, 4H, *CH*=*CH*), 4.00 (s, 2H, COCH_2O), 3.75−3.38 (m, 200H, OCH_2, *CHCH*$_2$O, CH_2CH_2O, NH_2CH_2, CH_2NH), 2.01 (m, 8H, CH_2CH=CHCH_2), 1.55 (m, 4H, $OCH_2CH_2CH_2$), 1.29−1.26 (m, 44H, $CH_3(CH_2)_6$, $OCH_2CH_2(CH_2)_5$, 0.91 (t, J = 6.6 Hz, 6H, CH_3).

Synthesis of $DOGP_{45}TG(Ac)$. $DOGP_{45}NH_2$ (1 g, 0.36 mmol) and DIPEA (61 μL, 0.36 mmol) were dissolved in 10 mL of anhydrous CH_2Cl_2. The mixture was added to a solution of 15 mL of anhydrous CH_2Cl_2 containing TG(Ac) (*27*) (711 mg, 0.4 mmol), DCC (82 mg, 0.4 mmol), and *N*-hydroxysuccinimide (46 mg, 0.4 mmol). The coupling reaction was carried out overnight, under argon, at room temperature. After elimination of *N*,*N*′-dicyclohexylurea by filtration, the solvents were removed under reduced pressure. The title compound was purified by chromatography on a 400 mL silica gel column eluted with CH_2Cl_2:CH_3OH (95:5 to 80:20). The organic phase was concentrated under reduced pressure. The product was obtained as a colorless oil (1 g, 60% yield): ^{1}H NMR ($CDCl_3$, 200 MHz) δ 5.41 (d, 3H, H_4-sugar, J = 3.39 Hz), 5.35 (m, 4H, *CH*=*CH*), 5.23−5.14 (m, 3H, H_2-sugar), 5.05 (m, 3H, H_3-sugar), 4.61−4.51 (m, 3H, H_1-sugar), 4.49−4.24 (m, 2H, *CH*CONH), 4.23−3.90 (m, 17H, OCH_2CO, H_6-sugar, H_5-sugar), 3.79−3.38 (m, 220H, OCH_2, *CHCH*$_2$O, CH_2CH_2O, NHCH_2, CH_2NH), 3.32−3.22 (m, 4 H, CONHCH_2), 2.99−2.75 (m, 6H, SCH_2), 2.13; 2.05; 2.03; 1.96 (4s, 12H, CH_3COO), 2.01 (m, 8H, CH_2CH=CHCH_2), 1.95−1.47 (m, 16H, CH$CH_2CH_2CH_2$, $OCH_2CH_2CH_2$), 1.29−1.26 (m, 44H, $CH_3(CH_2)_6$, $OCH_2CH_2(CH_2)_5$, 0.91 (t, J = 6.6 Hz, 6H, CH_3).

Synthesis of TrigalPEG ($DOGP_{45}TG$). $DOGP_{45}TG$-(Ac) (1 g, 0.22 mmol) and K_2CO_3 (110 mg, 0.8 mmol) were dissolved in 10 mL of methanol. The deacetylation reaction was carried out for 3 h, under argon, at room temperature; the solvents were then removed under reduced pressure. The title compound was purified by chromatography on a 200 mL silica gel column eluted with CH_2Cl_2:CH_3OH:H_2O (60:40:0 to 60:40:5). The solvents were eliminated under reduced pressure. The product was obtained as a colorless oil (540 mg, 64% yield): ^{1}H NMR ($CDCl_3$, 200 MHz) δ 5.35 (m, 4H, *CH*=*CH*), 4.53 (d, 3H, H_1-sugar, J = 9.04 Hz), 4.42−4.33 (m, 2H, *CH*CONH), 4.23−3.90 (m, 11H, OCH_2CO, H_4-sugar), 3.84−3.38 (m, 240H, OCH_2, *CHCH*$_2$O, CH_2CH_2O, NHCH_2, CH_2NH, H_6-sugar, H_5-sugar, H_3-sugar, H_2-sugar), 3.32−3.22 (m, 4 H, CONHCH_2), 3.02−2.83 (m, 6H, SCH_2), 2.01 (m, 8H, CH_2CH=CHCH_2), 1.95−1.47 (m, 16H, CH$CH_2CH_2CH_2$, $OCH_2CH_2CH_2$), 1.29−1.26 (m, 44H, $CH_3(CH_2)_6$, $OCH_2CH_2(CH_2)_5$, 0.91 (t, J = 6.6 Hz, 6H, CH_3).

Synthesis of $DOGP_3TG(Ac)$. $DOGP_3NH_2$ (*28*) (100 mg, 0.13 mmol) was dissolved in 1 mL of anhydrous CH_2Cl_2. The mixture was added to a solution of 5 mL of anhydrous CH_2Cl_2 containing TG(Ac) (230 mg, 0.13 mmol), DCC (30 mg, 0.145 mmol), and *N*-hydroxysuccinimide (15 mg, 0.13 mmol). The coupling reaction was carried out for 2 days, under argon, at room temperature. After elimination of *N*,*N*′-dicyclohexylurea by filtration, the solvents were removed under reduced pressure. The title compound was purified by chromatography on a 120 mL silica gel column eluted with CH_2Cl_2:CH_3OH (100:0 to 95:5). The organic phase was concentrated under reduced pressure. The product was obtained as a colorless oil (130 mg, 42% yield): ^{1}H NMR ($CDCl_3$, 200 MHz) δ 5.44 (d, 3H, H_4-sugar, J = 3.2 Hz), 5.35 (m, 4H, *CH*=*CH*), 5.23−5.14 (m, 3H, H_2-sugar), 5.05 (m, 3H, H_3-sugar), 4.61−4.51 (m, 3H, H_1-sugar), 4.49−4.24 (m, 2H, *CH*-CONH), 4.23−3.90 (m, 15H, OCH_2CO, H_6-sugar, H_5-sugar), 3.80−3.20 (m, 43H, OCH_2, *CHCH*$_2$O, CH_2CH_2O, NHCH_2), 3.00−2.80 (m, 6H, SCH_2), 2.15; 2.06; 2.03; 1.98 (4s, 12H, CH_3COO), 2.20−1.98 (m, 8H, CH_2CH=CHCH_2), 1.95−1.47 (m, 16H, CH$CH_2CH_2CH_2$, $OCH_2CH_2CH_2$), 1.29−1.26 (m, 44H, $CH_3(CH_2)_6$, $OCH_2CH_2(CH_2)_5$, 0.88 (t, J = 6.58 Hz, 6H, CH_3).

Synthesis of Trigal ($DOGP_3TG$). $DOGP_3TG(Ac)$ (130 mg, 0.13 mmol) was dissolved in 10 mL of methanol:water:DIPEA (5:4:1, v:v:v). The deacetylation reaction was carried out for 72 h, under argon, at room temperature. The solvents were removed under reduced pressure. The title compound was purified by chromatography on a 120 mL silica gel column eluted with CH_2Cl_2:CH_3OH:H_2O (90:10:0 to 65:25:4). The organic phase was concentrated under reduced pressure. The product was obtained as a colorless oil (50 mg, 50% yield): ^{1}H NMR ($CDCl_3$, 200 MHz) δ 5.39 (m, 4H, *CH*=*CH*), 4.42 (d, 3H, H_1-sugar, J = 9.16 Hz), 4.35−4.22 (m, 2H, *CH*CONH), 4.22−3.90 (m, 9H, OCH_2CO, H_4-sugar), 3.84−3.38 (m, 54H, OCH_2, *CHCH*$_2$O, CH_2CH_2O, NHCH_2, H_6-sugar, H_5-sugar, H_3-sugar, H_2-sugar), 3.32−3.22 (m, 4 H, CONHCH_2), 3.02−2.83 (m, 6H, SCH_2), 2.01 (m, 8H, CH_2CH=CHCH_2), 1.95−1.47 (m, 16H, CH$CH_2CH_2CH_2$, $OCH_2CH_2CH_2$), 1.29−1.26 (m, 44H, $CH_3(CH_2)_6$, $OCH_2CH_2(CH_2)_5$, 0.91 (t, J = 6.6 Hz, 6H, CH_3).

Cationic Liposomes and Micelles Preparation. *Cationic Liposome Preparation*. The lipids were dissolved in chloroform in 10 mL round-bottom flasks, and a film

Table 1. Composition of Liposomes and Micelles

name	composition (mol)
	Liposomes
C	RPR 120535/DOPE (1/1)
PEG	RPR 120535/DOPE/PEG_{42}−lipid (1/1/0.1)
TrigalPEG	RPR 120535/DOPE/TrigalPEG (1/1/0.1)
Trigal	RPR 120535/DOPE/Trigal (1/1/0.1)
	Micelles
C	RPR 120535
PEG	RPR120535/PEG_{42}−lipid (1/0.1)
TrigalPEG	RPR 120535/TrigalPEG (1/0.1)

was obtained after evaporation of the solvent, under vacuum at 20 °C overnight, using a Heidolph rotating-desiccator. The dried film was then hydrated for 24 h with sterile MilliQ water at 4 °C to produce large multilamellar vesicles. The suspension was finally sonicated at 4 °C for 2 min (115 V, 80 W, 50−60 Hz) with a G112SP1G model sonicator (Laboratory Supplies Co. Hicksville, NY) to obtain small unilamellar liposomes. The opalescent liposome preparation was stored up to 1 month at 4 °C. Four different liposome types were prepared (see Table 1).

Micelle Preparation. MilliQ water was added to the appropriate amount of lipids. The resulting suspensions were then heated at 60 °C and sonicated as described above until the suspension became clear. Three types of micelle were prepared (see Table 1).

Preparation of Lipoplexes. Plasmid pXL3031 (pCMV−Luc+), obtained as described elsewhere (*29*) and suspended in 300 mM NaCl, was mixed with an equivalent volume of aqueous suspensions of liposomes or micelles prepared at the appropriate concentrations. Since the cationic lipid RPR120535 has three positive groups, a ratio of 6 nmol of cationic lipid/μg DNA corresponds to a charge ratio of 6. The lipoplexes were formed at room temperature for at least 30 min. For transfection assays and ζ-potential measurements, the final concentrations of plasmid DNA were 5 and 10 μg/mL, respectively.

Size Measurement by Photon Correlation Spectroscopy. Dynamic light scattering analyses of liposomes and lipoplexes were performed on a Coulter N4-Plus nanosizer. The liposome preparation was diluted to the hundredth in a final volume of 800 μL of water for injection (wfi) before the measurement. Lipoplexes were not diluted for the assay. After 3 min equilibration, sizes were measured at 90° for 10 min.

Determination of ζ-Potential. Suspensions of liposomes (100 μL in 2 mL of 20 mM NaCl) or lipoplexes (800 μL prepared as described above in 4 mL wfi) were injected into a Malvern Zetasizer 3000 HS. From three to five determinations were made at 25 °C with 10 s between each measure.

Agglutination Assays with *Ricinus communis* Agglutinin (RCA_{120}). The agglutination assay was adapted from ref 30 and performed in standard 96-microwell plates. The liposome suspensions were diluted in 200 μL of 150 mM NaCl and the aggregation of the vesicles was assessed by following the changes, at room temperature, of the turbidity at 450 nm after addition of 10 μg of RCA_{120} (*R. communis* agglutinin, Sigma). With this lectin concentration, the carbohydrate binding sites were almost equimolar to the galactose ligands present on the targeted liposomes, micelles, and lipoplexes. The absorbance at 450 nm was measured 10 times over the time course of 20 min in a Wallac Victor^2 microplate reader. The absorbance of the control (diluted liposomal preparation without addition of the RCA_{120} solution) was subtracted from the absorbance of the aggregated liposomal suspension. The reversibility of the agglutination was verified by addition of 20 μL of 1 M galactose to the aggregated suspensions. For agglutination assay of the lipoplexes, the particles were prepared as described above and RCA_{120} was directly added to the lipoplex dispersion.

Cell Culture. SK-Hep-1 (human adenocarcinoma from liver; ATCC HTB-52) and HepG2 (human hepatocellular carcinoma; ECACC 85011430) cells were grown in minimum essential medium (MEM, Gibco, Invitrogen Corp.) supplemented with 2 mM glutamine, penicillin/streptomycin (100 U/mL and 100 μg/mL, respectively), 1 mM sodium pyruvate, nonessential amino acids, and 10% (v/v) foetal bovine serum. Cultures were maintained at 37 °C in a 5% CO_2/air incubator. Both cell lines were tested for the expression of the Gal/GalNAc receptor by western blot (see Supporting Information) using a mouse monoclonal antibody anti-human Gal/GalNAc receptor (no. 183120, Calbiochem) (*31*). HepG2 cells expressed the protein, whereas, as expected (*32*), SK-Hep-1 cells did not. We verified the localization of the protein on the cell surface by immunomicroscopy with the same antibody (see Supporting Information).

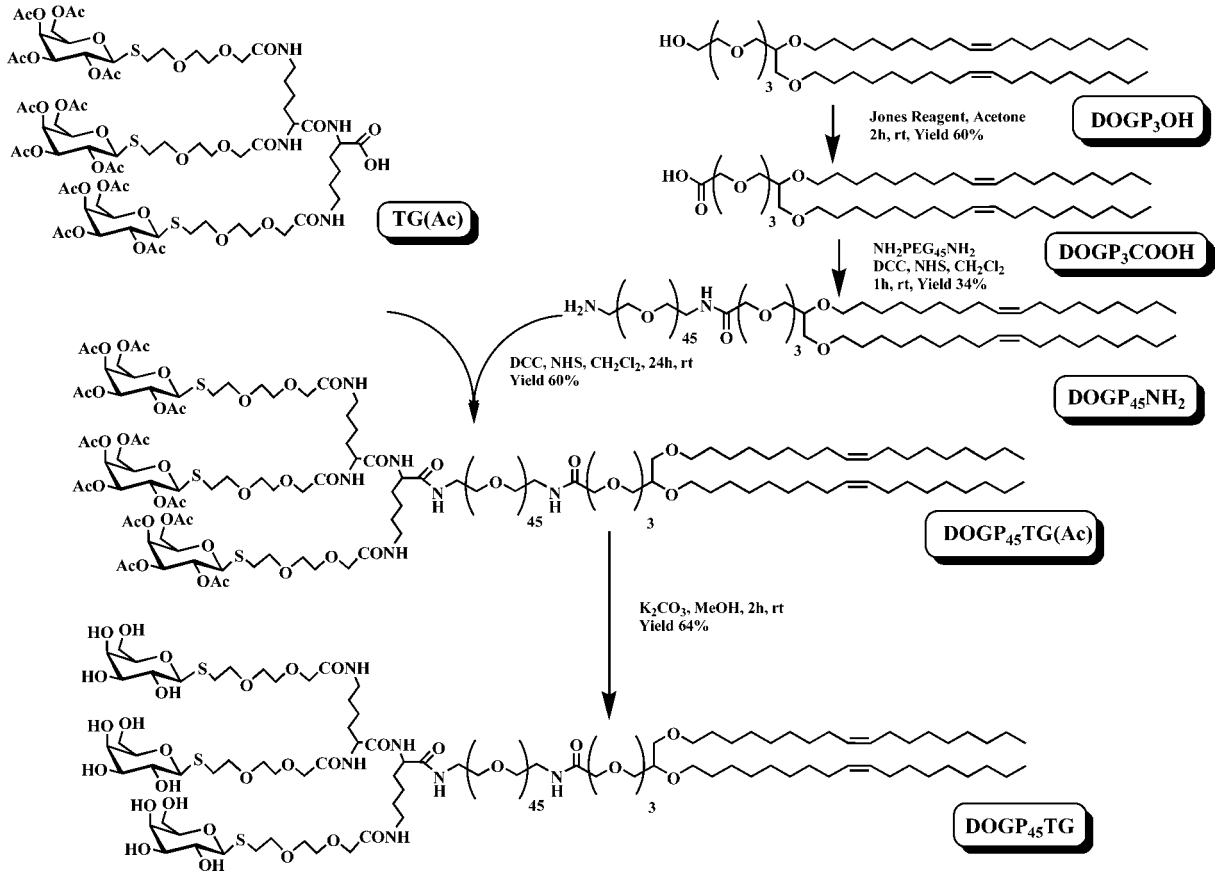
Transfection. Cells were seeded on 24-well culture plates the day before the transfection experiments (120 000 and 80 000 cells/well for HepG2 and SK Hep-1 cells, respectively). Lipoplexes prepared as described above were diluted in incomplete (without serum) cell culture medium containing 100 μM chloroquine. This transfection medium was added to the cells that were further incubated for 36 h at 37 °C in the presence of 5% CO_2. The transfected cells were then washed twice with PBS and lysed with 200 μL cell culture lysis reagent (Promega). Light emission due to luciferase was measured in white 96-microwell plates (OptiPlate TM, Packard) using a Wallac Victor^2 microplate reader equipped for luminescence. The results are expressed in cps (count per second) normalized to the protein concentration of each sample, as determined using the Pierce BCA assay (Interchim).

Cellular Uptake of Fluorescently Labeled Lipoplexes. For lipoplexes prepared from liposomes, fluorescent lipoplexes were obtained by incorporating rhodamine-labeled DOPE in liposomes (5 mol % of total lipid). For lipoplexes prepared from micelles, a fluorescent plasmid was used to form the labeled lipoplexes. Fluorescent plasmid was prepared as described previously (*33*) and contained 30 fluorophores by plasmid DNA. Fluorescent lipoplexes were made and incubated with the cells as described above, except that cells were grown on glass coverslips. At the end of the incubation time, the cells were rinsed with PBS, fixed with 3% paraformaldehyde, stained with DAPI (0.1 μg/μL in PBS), and mounted on slides in Mowiol for examination with a Zeiss Axiophot fluorescence microscope, with a 100× objective lens, coupled to a CCD camera (Hamamatsu) using a Samba imaging software (Unilog, France).

RESULTS

Synthesis of Galactosylated Targeted PEGylated Lipid. The synthesis of TrigalPEG ($DOGP_{45}TG$) (Scheme 1) first required the production of the lipid $DOGP_3OH$ which was synthesized in eight steps starting from glycerol, tetraethylene glycol, and oleyl alcohol according to a procedure described previously (*26*). The primary alcohol of $DOGP_3OH$ was then first oxidized with Jones reagent to give $DOGP_3COOH$ with a good yield. $DOGP_{45}$-NH_2 was readily obtained by reacting the carboxylic function of $DOGP_3COOH$ with an excess of commercial

Scheme 1. Synthesis of the Conjugate TrigalPEG[a]



[a] $DOGP_{45}TG$ is three galactose residues attached to a di-L-lysine scaffold that is conjugated to a dioleyl glycerol anchor via a long polyethylene glycol spacer arm.

$NH_2PEG_{45}NH_2$ in the presence of DCC and NHS. The carboxylic acid function of TG(Ac) (*27*) was activated with DCC and NHS at room temperature in the presence of diisopropylethylamine and reacted with the free amine of $DOGP_{45}NH_2$ to give $DOGP_{45}TG(Ac)$.

The final product TrigalPEG ($DOGP_{45}TG$) was obtained after deprotection of the acetyl groups of the galactose residues with potassium carbonate in methanol. Trigal ($DOGP_3TG$) (Scheme 2) was synthesized according to the same series of reactions starting this time with $DOGP_3NH_2$ (*28*). PEG_{42}−lipid was synthesized to provide a PEGylated lipid equivalent to TrigalPEG but lacking the galactosylated ligand.

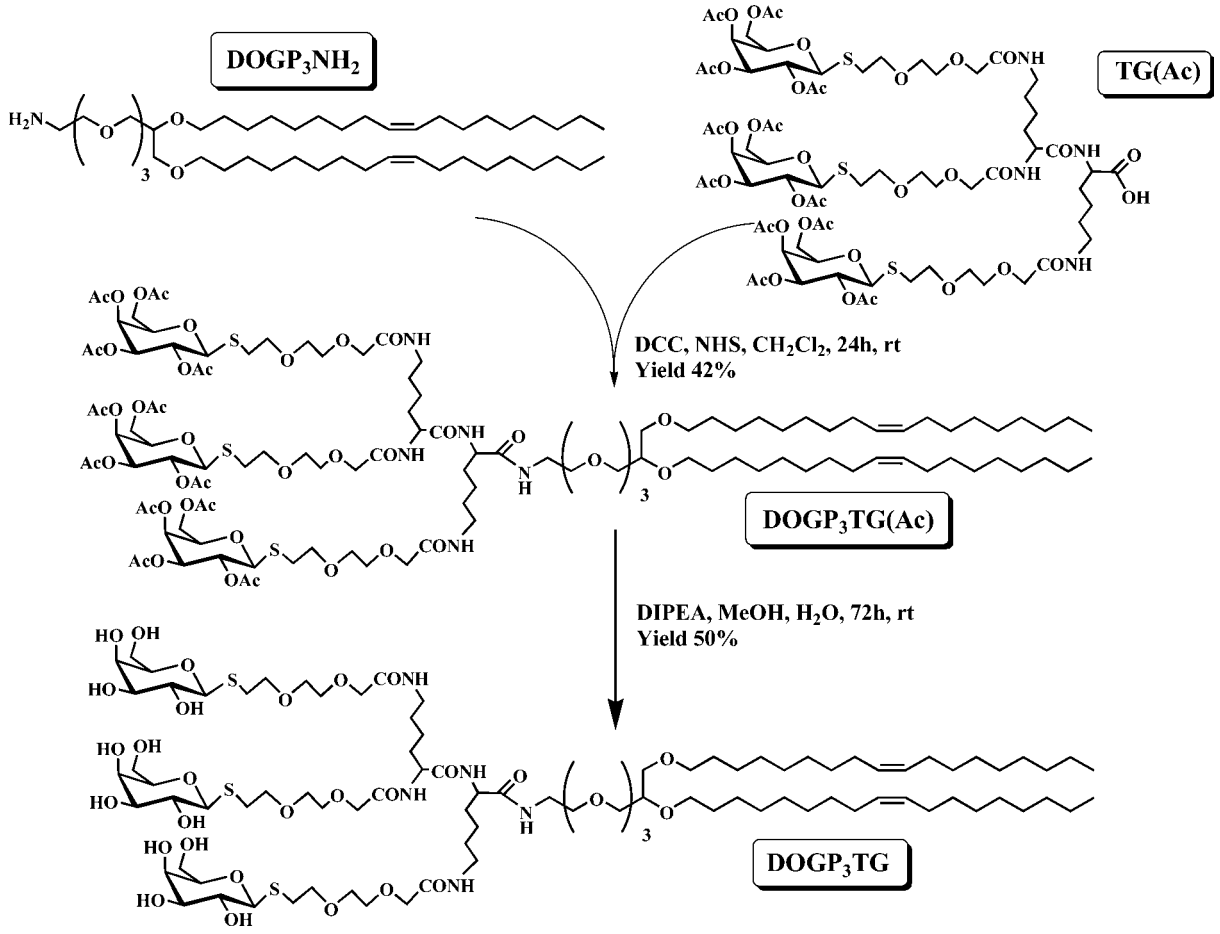
Preparation and Characterization of Targeted Stealth Lipoplexes. Two main strategies exist to prepare targeted lipoplexes; they involve the complexation/condensation of plasmid DNA with either positively charged liposomes or positively charged micelles. Targeted liposomes are formed by mixing neutral (e.g. DOPE) and cationic lipids with a lipid carrying a ligand. Targeted micelles are prepared from cationic lipids and the targeted lipid. If the targeted lipid contains a PEG spacer between the ligand and the lipid group, stealth liposomes or stealth micelles are obtained. Targeted lipoplexes are then prepared by adding plasmid DNA to targeted cationic liposomes or micelles.

We have prepared stealth targeted cationic liposomes and micelles by classical methods (see experimental procedures) with the lipids described in Figure 2. PEGylated liposomes and micelles contained 5 and 10 mol % of lipid−PEG, respectively (see Table 1 for the composition). 5 mol % was the maximal amount of TrigalPEG that could be incorporated in the lipidic film to obtain liposomes. When we tried to incorpore more than 5 mol % of TrigalPEG, we failed to obtain liposomes, probably due to the fact that TrigalPEG can adopt a micellar structure in aqueous environment and therefore it is no longer available to be incorporated into liposomes. Targeted PEGylated micelles containing up to 10 mol % TrigalPEG were more easily prepared than targeted PEGylated liposomes. Nontargeted control stealth liposomes or micelles (PEG) were prepared using PEG_{42}−lipid. Standard control liposomes or micelles (C), without PEG−lipids, were also prepared. Lipoplexes were formed by addition of the appropriate amount of liposomes or micelles to plasmid DNA (see the Experimental Procedures).

Lipoplexes prepared with the control liposomes and micelles lacking PEG exhibited an aggregation zone around 2 nmol of cationic lipid/μg of DNA (data not shown), which corresponds to globally neutral particles as previously described (*34*). PEG-containing lipoplexes had a constant size, around 150 nm, in the whole range of charge ratios examined, independent of the presence of the ligand (data not shown). In conclusion, due to the incorporation of PEG in lipoplexes, the aggregation zone of the lipoplexes disappeared. Moreover, the presence of the ligand at the distal end of the PEGylated ligand did not modify the stability of the PEGylated lipoplexes.

Is the Incorporation of PEG in Lipoplexes Efficient To Mask Completely the Surface Charge of the Lipoplexes? Incorporation of 5 mol % PEG−lipid resulted in the decrease of the positive ζ-potential of cationic liposomes from 100 to 130 mV (for liposome C) to 20−25 mV (for both PEG and TriGalPEG liposomes) (data not shown).

Scheme 2. Synthesis of the Conjugate Trigal[a]



[a] $DOGP_3TG$ is three galactose residues attached to a di-l-lysine scaffold that is conjugated to a dioleyl glycerol anchor via a short polyethylene glycol spacer arm.

In the presence of increasing amounts of cationic lipid for a given amount of plasmid DNA, lipoplexes were formed that were characterized by a gradually increase of the ζ-potential, which eventually reached a plateau (Figure 3). When PEG−lipid was incorporated into liposomes to form lipoplexes, ζ-potentials reached a plateau at about 20 mV for PEG lipoplexes and 25 mV for TrigalPEG lipoplexes, whereas the plateau was at 50 mV for lipoplexes without PEG. When micelles were used to form lipoplexes, ζ-potentials reached a plateau at about 10 mV for PEG lipoplexes and 5 mV for TrigalPEG lipoplexes, whereas the plateau was at 40 mV for lipoplexes without PEG. The decreased values of ζ-potential obtained at the plateau for lipoplexes prepared with micelles compared to lipoplexes prepared with liposomes probably reflected the decrease in the amount of lipid−PEG incorporated in liposomes (5 mol %) compared to micelles (10 mol %)

In conclusion, incorporation of PEG into lipoplexes substantially masked the positive surface charge of lipoplexes. However, even with 10 mol % of lipid−PEG, the masking of the charge was not complete.

Are the Ligands Properly Exposed on the Surface of Such Lipoplexes? Accessibility of the galactosyl ligands at the particle surface was assayed using the ricin agglutination test. Ricin agglutinin (RCA) is able to aggregate particles (liposomes, micelles, or lipoplexes) that exhibit galactose residues on their surface. This agglutination is inhibited in the presence of an excess of free galactose. All the assays were performed with the same amount of lectin and the same final concentration of galactosylated lipid, namely, 15 μM. We first tested the agglutination of liposomes or micelles without DNA. As indicated in Figure 4A, micelles or liposomes that contained TrigalPEG were agglutinated by ricin, whereas control preparations, lacking galactosyl ligands, were not affected. This agglutination was specific, since it could be reversed by addition of galactose (100 mM).

Lipoplexes formed with micelles or liposomes were then assayed at different cationic lipid to DNA ratios (Figure 4B). An increase of agglutination was observed when the cationic lipid to DNA ratio was increased, despite the fact that the concentration of the galactosylated lipid remained unchanged. For lipoplexes, at cationic lipid to DNA ratio of 6, the agglutination level was nearly the same as the one observed with particles without DNA added. This result was observed for lipoplexes formed from liposomes as well as from micelles. In conclusion, the galactose ligand is accessible to external proteins in all the particles it was inserted in, i.e., lipoplexes, liposomes, or micelles. In the case of lipoplexes, this accessibility is greatest in particles formed with an excess of cationic lipid.

Does the Incorporation of PEG in Lipoplexes Increase the Accessibility of Ligand? To address this question, we have prepared liposomes with Trigal (Figure 2), a lipid containing the same trigalactosyl ligand as TrigalPEG but lacking the $(PEG)_{45}$ spacer. In analogy to the results described above, Trigal-containing liposomes were reversibly agglutinated by ricin (Figure 4A). We also prepared lipoplexes with different cationic lipid to DNA ratios and tested them for agglutination (Figure 4B).

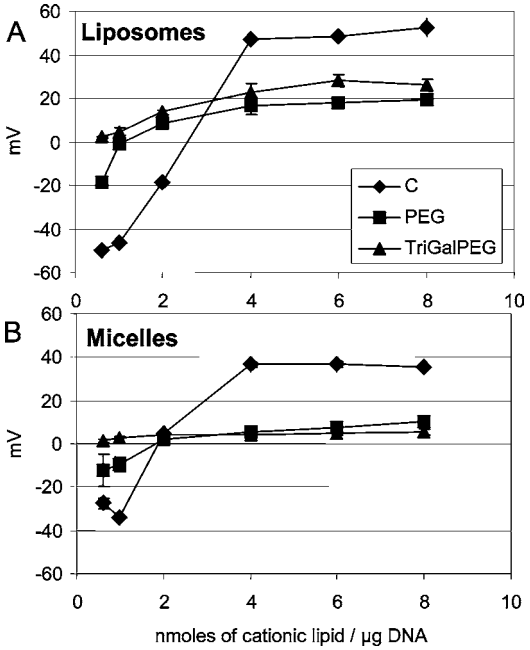
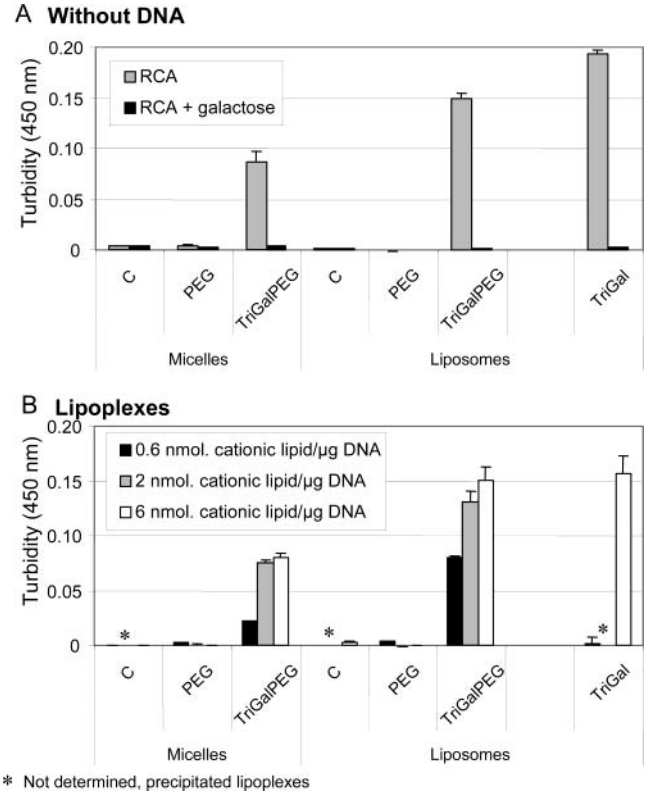


Figure 3. ζ-Potentials of PEG-modified lipoplexes at various cationic lipid to DNA ratios. ζ-Potential of lipoplexes formed with liposomes (A) or micelles (B) at various charge ratios (expressed in nanomoles of cationic lipid per micrograms of DNA) were measured in 150 mM NaCl. C: control lipoplexes with (A) RPR 120535/DOPE (1/1) or (B) RPR 120535. PEG: lipoplexes with (A) RPR 120535/DOPE/$(PEG)_{42}$−lipid (1/1/0.1) or (B) RPR 120535/$(PEG)_{42}$−lipid (1/0.1). TriGalPEG: lipoplexes with (A) RPR 120535 /DOPE/TrigalPEG (1/1/0.1) or (B) RPR 120535/TrigalPEG (1/0.1).



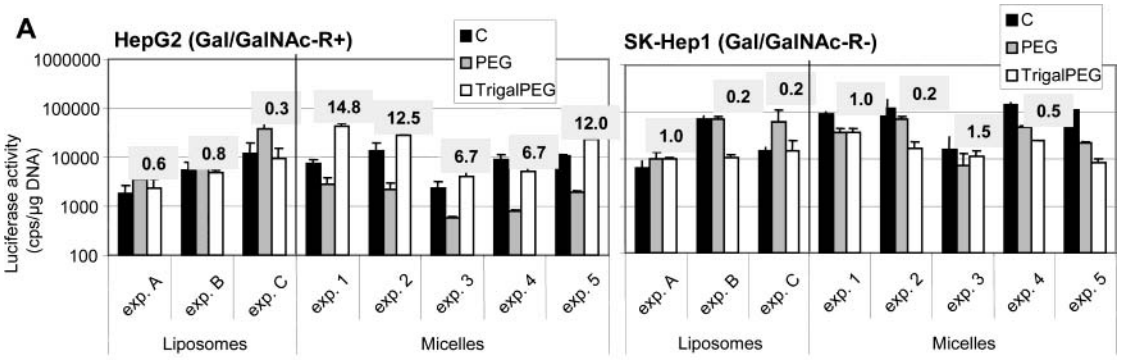
* Not determined, precipitated lipoplexes

Figure 4. Agglutination of liposomes, micelles and lipoplexes by ricin. Liposomes, micelles or lipoplexes were mixed with *R. communis* agglutinin (RCA) (50 µg/mL) at a final concentration of galactosylated lipid of 15 µM. Nontargeted particles were assayed at an equivalent concentration of cationic lipid. Agglutination was followed by measuring the increase of turbidity (at 450 nm). For all samples assayed, increased turbidity was inhibited by an excess of free galactose (100 mM). (A) Agglutination of micelles and liposomes without DNA. Micelles: C, RPR 120535; PEG, RPR 120535/$(PEG)_{42}$−lipid (1/0.1); TriGalPEG, RPR 120535/TrigalPEG (1/0.1). Liposomes: C, RPR 120535/DOPE (1/1); PEG, RPR 120535/DOPE/$(PEG)_{42}$−lipid (1/1/0.1); TriGalPEG, RPR 120535/DOPE/TrigalPEG (1/1/ 0.1); Trigal, RPR 120535/DOPE/Trigal (1/1/0.1). (B) Agglutination of lipoplexes prepared at three lipid to DNA ratios (0.6, 2, and 6 nmol of cationic lipid/µg of DNA). * indicates that the agglutination test was not performed since at this charge ratio lipoplexes lacking PEG aggregated spontaneously.

When compared to lipoplexes containing TrigalPEG, we found that for a cationic lipid to DNA ratio of 6 nmol cationic lipid/µg of DNA, the presence of PEG had no effect on the extent of agglutination. For a ratio of 2 nmol cationic lipid/µg DNA, the lipoplexes lacking PEG aggregated spontaneously and the lectin-triggered agglutination test became unapplicable; in contrast, at the same ratio, the TrigalPEG lipoplexes were stable and, in the presence of ricin, exhibited nearly the same agglutination as liposomes or lipoplexes at a ratio of 6. For the ratio of 0.6 nmol cationic lipid/µg DNA, no agglutination could be observed for lipoplexes lacking PEG, whereas PEG-containing lipoplexes exhibited an agglutination that represented half of the maximal agglutination value. In conclusion, incorporation into lipoplexes of a lipidated PEG chain, bearing a ligand at its distal end, led to particles that exhibited an accessible ligand throughout the whole range of cationic lipid to DNA ratios.

Does Incorporation of PEG Lead to Targeted Gene Transfer? Lipoplexes, prepared with liposomes or micelles, were used to transfect two cell lines, HepG2 and SK-Hep-1. Both derive from human hepatocyte carcinoma, but only HepG2 cells express the Gal/GalNAc receptor at their surface (see Supporting Information). Transfection was performed with a pCMVLuc plasmid during 36 h at 37 °C in the presence of 100 µM chloroquine and in the absence of serum. This treatment resulted in the reduction of the cell growth, as indicated by the determination of the amount of proteins (Figure 5B), but the cells kept a normal morphology upon examination by phase contrast. In addition, there was no noticeable difference of cytotoxicity between the various formulations or type of lipoplexes. Thus, despite the toxicity of the treatment, we considered that we could compare the efficiency of gene transfer of formulations tested under the same culture conditions. In the absence of chloroquine, only lipoplexes lacking PEG led to an efficient transfection (data not shown). As shown in Figure 5A, for lipoplexes prepared from liposomes, no appreciable difference in transfection yield was observed, for both cell lines, between either TrigalPEG lipoplexes or PEG lipoplexes. In addition, the transfection efficiency obtained with PEG-containing lipoplexes was rather surprising, since incorporation of PEG should have been inhibitory. For lipoplexes prepared with micelles, the presence of TriGalPEG resulted in a targeted transfection, since we observed an increased transfection efficiency with HepG2 cells (10.5-fold ± 3.3, $n = 5$) compared to PEG-containing lipoplexes or control lipoplexes; no such targeting effect was found with SK-Hep-1 cells (0.7-fold ± 0.5, $n = 5$). No targeted transfection was observed in the presence of serum (data not shown).

We next wondered whether this targeted transfection could be related to an enhanced uptake of the targeted lipoplexes in HepG2 compared to SK-Hep-1 and to nontargeted lipoplexes. We then incubated fluorescent lipoplexes under culture conditions needed to obtain a



B

	Culture condition			
	10% serum	without serum	10% serum 0.1 mM chloroquine	without serum 0.1 mM chloroquine
HepG2	100	60 ± 30	37 ± 15	20 ± 10
SK-Hep1	100	80 ± 25	40 ± 15	25 ± 10

Figure 5. Transfection efficiency of targeted lipoplexes on human hepatocyte cell lines. (A) HepG2 (Gal/GalNAc−R^+) and SK-Hep-1 (Gal/GalNAc−R^-) cells were transfected in the absence of serum, in the presence of 100 μM chloroquine with lipoplexes prepared at 6 nmol cationic lipid/μg pCMV−Luc+ plasmid (ratio = 6 nmol cationic lipid/μg of DNA) for 36 h at 37 °C (0.5 μg of DNA/well, each condition in triplicate) in 24-well culture plates. Three (for liposomes) and five (for micelles) independent experiments are shown. Composition of the lipoplexes is as indicated in the legend of Figure 4. The numbers indicated at the top of the bars are the enhancement factor between transfection with the targeted TriGalPEG lipoplexes and untargeted PEG lipoplexes. (B) Toxicity study. For each culture condition, the amount of proteins was determined at the end of the transfection. Results are given as percentage of the value obtained with 10% serum in the culture medium. For a given culture condition, there was no significant difference in the amount of proteins recovered for cells transfected with any of the different lipoplexes.

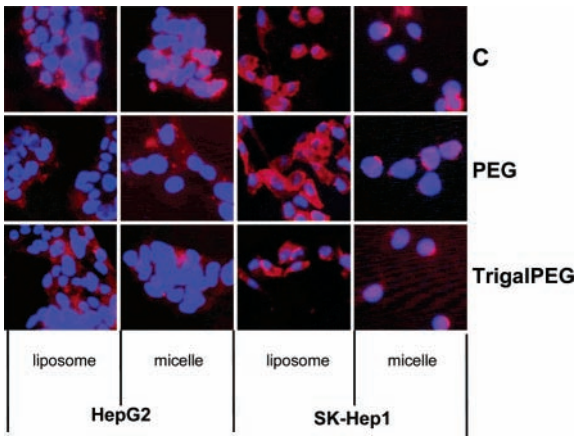


Figure 6. Uptake of fluorescent lipoplexes by human hepatocyte cell lines. HepG2 (Gal/GalNAc−R^+) and SK-Hep-1 (Gal/GalNAc−R^-) cells were incubated with fluorescent lipoplexes as described in the legend of Figure 5. After 36 h of incubation, cells were fixed and mounted for observation.

targeted transfection and examined the cells using a fluorescent microscope. As shown in Figure 6, all lipoplexes, including the PEGylated lipoplexes, were efficiently internalized by both cell lines. Although, compared to control lipoplexes, the uptake of PEGylated lipoplexes appeared less efficient, we observed no clear-cut correlation between a targeted uptake and a targeted transfection.

DISCUSSION

Shortly after the initial utilization of liposomes as drug delivery systems, it became apparent that these lipid vesicles are rapidly removed from the circulation by the cells/organs comprising the reticuloendothelial system (see review in ref 35). Early studies demonstrated that several physical and chemical properties of conventional liposomes, such as size, lipid composition, and surface charge, are able to influence their pharmacokinetic parameters (*36*). Subsequently, the ability of incorporated amphipathic PEG conjugates to prolong the circulation time of these so-called "stealth" liposomes has been demonstrated (*36*). It has also been suggested that PEG chains may provide a steric hydrophilic barrier, which results in a reduced interaction with opsonins and with the RES cells (*37*). Cationic lipoplexes and polyplexes are also cleared extremely rapidly from the circulation in mice (*3*, *4*) because of binding to serum components and nonspecific ionic interactions with cells. Due to these shortcomings, which severely limit their use in vivo, at least after systemic administration, lipoplexes and polyplexes, in analogy to stealth liposomes, have also been coated with hydrophilic polymers, such as PEG (*6*, *17*, *38*, *39*). Such a strategy should result in lipoplexes or polyplexes with a decreased ability to nonspecifically interact with the cells. However, the incorporation of a ligand is required to trigger a specific binding and internalization of the complexes into the target cells (*10*, *17*, *18*). Whereas several groups have described the synthesis of conjugated PEG−lipids bearing a ligand at the distal end of the PEG (*16*−*21*), these targeted PEG−lipids were mostly incorporated in liposomes (*16*, *17*, *20*, *21*) or vesicles (*19*) but only rarely in lipoplexes (*18*). We have chosen a ligand that has been previously used to successfully target hepatocytes (*22*) and linked it at the distal end of a PEGylated lipid. This targeted PEGylated lipid has then been inserted into lipoplexes formulated with a cationic lipid that has been extensively studied (*23*, *40*). We have first characterized the size and the charge of these targeted lipoplexes.

We have demonstrated that the incorporation of PEG into lipoplexes results in a stabilization of the complexes

and in a decrease of their charge surface. However, ζ-potential measurements indicated that the positive charges on the lipoplexes (ratio of 6 nmol cationic lipid/μg DNA) were not completely shielded through use of about 5 or 10 mol % PEG-modified lipids. Consequently, one should expect that nonspecific interactions of PEGylated positively charged lipoplexes with the negatively charged cell surfaces cannot be totally avoided. This observation could explain why PEG-containing lipoplexes lacking a ligand still exhibited a good transfection activity in the presence of chloroquine, a compound known to breach endosomal compartments. If PEG-containing lipoplexes are internalized by cells due to their residual surface charge, chloroquine can promote their escape from endosomes and lead to an efficient gene transfer. Our fluorescence microscopy data suggest an efficient uptake of PEG-containing lipoplexes (Figure 6), which tends to prove that our PEGylated complexes are indeed internalized by cells. In the absence of chloroquine, PEG-containing lipoplexes had no transfection efficiency. In that case, we suspected that lipoplexes were internalized but were unable to escape from endosomes and probably ended up in the lysosomal degradative processes. Of note, an incomplete masking of the charges in PEGylated complexes, resulting in an uptake of the complexes, has already been described (*41*−*43*).

Some authors have recently suggested that PEG-induced inhibition of cell transfection by PEGylated lipoplexes could be explained by a reduction of the insertion of perturbing lipids, such as DOPE, into the endosome/lysosome membranes rather than by inhibiting the interaction of the complexes with the cell surface (*41*, *43*−*45*). It has been shown that lipoplexes are highly ordered structures and that inverted hexagonal phases in the complexes, e.g. provided by DOPE, strongly promote transfection efficiency (*44*, *46*, *47*). In contrast, the presence of lamellar phases in the complex is correlated with stable particles that display substantially lower transfection potency (*44*, *46*). Incorporation of PEG into lipoplexes (with or without DOPE) could stabilize the lamellar phases in the complexes by preventing their transition to hexagonal phases and decrease the transfection potency of these particles. In our case, the addition of chloroquine could be sufficient to destabilize endosomes and lead to an efficient gene transfer.

We also studied the accessibility of the ligand at the surface of the complexes. In analogy to conventional liposomes (*16*, *48*) and cationic lipids (*18*), we attached the trigalactosyl ligand at the distal end of a PEG chain. According to this strategy, the ligand can extend from the lipoplex at the end of a long and flexible spacer arm. We have demonstrated that the trigalactosyl ligand was easily accessible when assayed in an agglutination test with ricin agglutinin. In addition, this accessibility was largely enhanced by incorporation of a PEG spacer. For instance, for lipoplexes lacking PEG, no aggregation with RCA could be obtained at cationic lipid to DNA ratio of 0.6. This probably resulted from the presence of noncompacted DNA that extends around the lipoplexes and prevents the association of galactosylated ligands with RCA. When the charge ratio increases, with increasing amounts of cationic lipid for a given amount of DNA, DNA becomes completely compacted and is no longer able to prevent the binding between the lectin and its ligand. For lipoplexes containing PEG, at the same ratio, a significant aggregation could be obtained. This enhanced accessibility of the ligand due to the presence of PEG was encouraging in the perspective of in vivo targeting lipoplexes.

We were nonetheless unable to obtain a targeted gene transfer with TrigalPEG-lipoplexes prepared from cationic liposomes. We suspect that these lipoplexes are still able to bind nonspecifically to cells, despite the presence of PEG, and that these nonspecific interactions, which lead to an efficient transfection, largely mask the specific, targeted transfection. We succeeded, however, in obtaining a targeted transfection with lipoplexes that were formed with micelles, i.e., particles that lack DOPE. With such lipoplexes, we obtained a 1 order of magnitude enhancement of transfection with TrigalPEG lipoplexes compared to control lipoplexes using HepG2 cells that contain the specific receptor. This was not the case with SK-Hep-1 cells that do not express the Gal/GalNAc receptor. We have also tried to perform a competition study by addition of an excess of free galactose in the transfection medium. However, we obtained poorly reproducible results. We hypothesized that a single galactose molecule was not an efficient enough competitor for a triantennary ligand, due to the binding cooperativity resulting from the presence of three galactose residues in an adequate spatial arrangement (clustering effect). It was, however, surprising that this targeted transfection was only observed with lipoplexes formulated from micelles and not with lipoplexes formulated with liposomes. In addition, in the presence of serum, we failed to observe a targeted transfection, but our lipoplexes induced an efficient transfection. In line with other reports (*12*, *49*−*51*), targeted transfection is not easy to observe and seems to appear only in a rather limited window in which specific interactions between the ligand and its receptor are prominent over nonspecific interactions. This window is determined by various factors, namely charge ratio, relative amount of ligand, size of the complexes, presence or absence of serum, and maybe in our case formulation of lipids in micelles rather than in liposomes.

In conclusion, we have proved for lipoplexes the validity of using a targeted ligand carried by a long PEG spacer arm. Indeed, the presence of PEG stabilized lipoplexes and enhanced the accessibility of the ligand throughout the lipid to DNA ratios range used. However, the presence of residual surface charges and the fact that an efficient targeted transfection was only obtain in the presence of chloroquine, in the absence of serum and with micelle formulations, suggest that other strategies than simple PEGylation should be explored in order to develop an in vivo application of targeted lipoplexes. These strategies could use the design of (i) PEGylated lipids that contain acid-sensitive linkages between PEG and lipids that would be susceptible to "depegylate" in acidic endosomes (*14*, *52*) or (ii) other polymers than PEG that would mask more completely the surface charge of the complexes and would not stabilize lipoplexes in lamellar phases. We are currently working on these options.

Supporting Information Available: Western blot of total cell lysate obtained from HepG2 and SK-Hep-1 cell lines and localization of the Gal/GalNAc receptor on the surface of HepG2 by immunofluorescence microscopy. This material is available free of charge via the Internet at http://pubs.acs.org.

LITERATURE CITED

(1) Mountain, A. (2000) Gene therapy: The first decade. *Trends Biotechnol. 18*, 119−128.

(2) Ferber, D. (2001) Gene therapy: Safer and virus-free? *Science 294*, 1638−1642.

(3) Stankovics, J., Crane, A. M., Andrews, E., Wu, C. H., Wu, G. Y., and Ledley, F. D. (1994) Overexpression of human methylmalonyl CoA mutase in mice after in vivo gene transfer with asialoglycoprotein/polylysine/DNA complexes. *Hum. Gene Ther. 5*, 1095−1104.

(4) Lew, D., Parker, S. E., Latimer, T., Abai, A. M., Kuwahara-Rundell, A., Doh, S. G., Yang, Z.-Y., Laface, D., Gromkowski, S. H., Nabel, G. J., Manthorpe, M., and Norman, J. (1995) Cancer gene therapy using plasmid DNA: Pharmacokinetic study of DNA following injection in mice. *Hum. Gene Ther. 6*, 553−564.

(5) Davis, M. E. (2002) Nonviral gene delivery systems. *Curr. Opin. Biotechnol. 13*, 128−131.

(6) Ogris, M., Brunner, S., Schüller, S., Kircheis, R., and Wagner, E. (1999) PEGylated DNA/transferrin-PEI complexes: Reduced interaction with blood components, extended circulation in blood and potential for systemic gene delivery. *Gene Ther. 6*, 595−605.

(7) Wagner, E. (1998) Receptor-mediated delivery of plasmid DNA. *Biogenic Amines 14*, 519−536.

(8) Ogris, M. and Wagner, E (2002) Targeting tumors with nonviral gene delivery systems. *Drug Delivery Today 7*, 479−485.

(9) Choi, Y. H., Liu, F., Choi, J. S., Kim, S. W., and Park, J. S. (1999) Characterization of a targeted gene carrier, lactose-poly(ethylene glycol)-grafted poly-L-lysine, and its complex with plasmid DNA. *Hum. Gene Ther. 10*, 2657−2665.

(10) Leamon C. P., Weigl D., and Hendren R. W. (1999) Folate copolymer-mediated transfection of cultured cells. *Bioconugate. Chem. 10*, 947−957.

(11) Nah, J. W., Yu, L., Han, S., Ahn, C. H., Kim, S. W. (2002) Artery wall binding peptide-poly(ethylene glycol)-grafted-poly(L-lysine)-based gene delivery to artery wall cells. *J. Controlled Release 78*, 273−284.

(12) Guo, W., and Lee, R. J. (1999) Receptor-targeted gene delivery via folate-conjugated polyethylenimine. *AAPS Pharmsci. 1*, article 19.

(13) Sagara, K., and Kim, S. W. (2002) A new synthesis of galactose-poly(ethylene glycol)-polyethylenimine for gene delivery to hepatocytes. *J. Controlled Release 79*, 271−281.

(14) Kursa, M., Walker, G. F., Roessler, V., Ogris, M., Roedl, W., Kircheis, R., and Wagner, E. (2003) Novel shielded transferring-poly(ethylene glycol)-polyethylenimine/DNA complexes for systemic tumor-targeted gene transfer. *Bioconjugate Chem. 14*, 222−231.

(15) Merdan, T., Callahan, J., Petersen, H., Kunath, K., Bakowsky, U., Kopeckova, P., Kissel, T. and Kopecek, J. (2003) Pegylated polyethylenimine-Fab′ antibody fragment conjugates for targeted gene delivery to human ovarian carcinoma cells. *Bioconjugate Chem. 14*, 989−996.

(16) Zalipsky, S., Mullah, N., Harding, J. A., Gittelman, J., Guo, L., and DeFrees, S. A. (1997) Poly(ethylene glycol)-grafted liposomes with oligopeptide or oligosaccharide ligands appended to the termini of the polymer chains. *Bioconjugate Chem. 8*, 111−118.

(17) Meyer, O., Kirpotin, D., Hong, K., Sternberg, B., Park, J. W., Woodle, M. C., and Papahadjopoulos, D. (1998) Cationic liposomes coated with poly(ethylene glycol) as carriers for oligonucleotides. *J. Biol. Chem. 273*, 15621−15627.

(18) Hofland, H. E. J., Masson, C., Iginla, S., Osetinsky, I., Reddy, J. A., Leamon, C. P., Scherman, D., Bessodes, M., and Wils, P. (2002) Folate-targeted gene transfer in vivo. *Mol. Ther. 5*, 739−744.

(19) Dauty, E., Rémy, J.-S., Zuber, G., and Behr, J.-P. (2002) Intracellular delivery of nanometric DNA particles via the folate receptor *Bioconjugate Chem. 13*, 831−839.

(20) Gosselin, M. A., Guo, W. and Lee, R. J. (2002) Incorporation of reversibly cross-linked polyplexes into LPDII vectors for gene delivery. *Bioconjugate Chem. 13*, 1044−1053.

(21) Zhou, W., Yuan, X., Wilson, A., Yang, I., Mokotoff, M., Pitt, B. and Li, S. (2002) Efficient intracellular delivery of oligonucleotides formulated in folate receptor-targeted lipid vesicles. *Bioconjugate Chem. 13*, 1220−1225.

(22) Rémy, J.-S., Kichler, A., Mordvinov, V., Schuber, F., and Behr, J.-P. (1995) Targeted gene transfer into hepatoma cells with lipopolyamine-condensed DNA particles presenting galactose ligands: A stage toward artificial viruses. *Proc. Natl. Acad. Sci. U.S.A. 92*, 1744−1748.

(23) Byk, G., Dubertret, C., Escriou, V., Frédéric, M., Jaslin, G., Rangara, R., Pitard, B., Crouzet, J., Wils, P., Schwartz, B., and Scherman, D. (1998) Synthesis, Activity, and Structure−Activity Relationship Studies of Novel Cationic Lipids for DNA Transfer. *J. Med. Chem. 41*, 224−235.

(24) Masson, C., Scherman, D., and Bessodes, M. (2001) 2,2,6,6-Tetramethyl-1-piperidinyl-oxyl/[bis(acetoxy)-iodo]benzene-mediated oxidation: A versatile and convenient route to poly(ethylene glycol) aldehyde or carboxylic acid derivatives. *J. Polym. Sci. 39*, 4022−4024.

(25) Castro, B., Dormoy, J. R., Evin, G., and Selve, C. (1975) Peptide coupling reagents. IV. N-[Oxytris(dimethyl-amino) phosphonium] benzotriazone hexafluorophosphate. *Tetrahedron Lett. 16*, 1219−1222.

(26) Pack, D. W., Chen, G., Maloney, K. M., Chen, C. T., and Arnold, F. H. (1997) A metal-chelating lipid for 2D protein crystallisation via coordination of surfaces histidines. *J. Am. Chem. Soc. 119*, 2479−2487.

(27) Kichler, A., and Schuber, F. (1995) Versatile synthesis of bi- and tri-antennary galactose ligands: Interaction with the Gal/GalNAc receptor of human hepatoma cells. *Glycoconjugate J. 12*, 275−281.

(28) Espuelas, S., Haller, P., Schuber, F., and Frisch, B. (2003) Synthesis of an amphiphilic tetraantennary mannosyl conjugate and incorporation into liposome carriers. *Bioorg. Med. Chem. Lett. 13*, 2557−2560.

(29) Soubrier, F., Cameron, B., Manse, B., Somarriba, S., Dubertret, C., Jaslin, G., Jung, G., LeCaer, C., Dang, D., Mouvault, J. M., Scherman, D., Mayaux, J. F., and Crouzet, J. (1999) pCOR: A new design of plasmid vectors for nonviral gene therapy. *Gene Ther. 6*, 1482−1488.

(30) Haensler, J., and Schuber, F. (1988) Preparation of neogalactosylated liposomes and their interaction with mouse peritoneal macrophages. *Biochim. Biophys. Acta 946*, 95−105.

(31) Kohgo, Y., Kato, J., Nakaya, R., Mogi, Y., Yago, H., Sakai, Y., Matsushita, H., and Niitsu, Y. (1993) Production and characterization of specific asialoglycoprotein receptor antibodies. *Hybridoma 12*, 591−598.

(32) Wu, G. Y., and Wu, C. H. (1987) Receptor-mediated in vitro gene transformation by a soluble DNA carrier system. *J. Biol. Chem. 262*, 4429−4432.

(33) Escriou, V., Carrière, M., Bussone, F., Wils, P., and Scherman, D. (2001) Critical assessment of the nuclear import of plasmid during cationic lipid-mediated gene transfer. *J. Gene Med. 3*, 179−187.

(34) Pitard, B., Aguerre, O., Airiau, M., Lachages, A. M., Boukhnikachvili, T., Byk, G., Dubertret, C, Herviou, C., Scherman, D., Mayaux, J. F., Crouzet, J. (1997) Virus-sized self-assembling lamellar complexes between plasmid DNA and cationic micelles promote gene transfer. *Proc. Natl. Acad. Sci. U.S.A. 94*, 14412−14417.

(35) Lasic, D. D., and Papahadjopoulos, D. (1995) Liposomes revisited. *Science 267*, 1275−1276.

(36) Papahadjopoulos, D., Allen, T. M., Gabizon, A., Mayhew, E., Matthay, K., Huang, S. K., Lee, K.-D., Woodle, M. C., Lasic, D. D., Redemann, C., and Martin, F. J. (1991) Sterically stabilized liposomes: Improvements in pharmacokinetics and antitumor therapeutic efficacy. *Proc. Natl. Acad. Sci. U.S.A. 88*, 11460−11464.

(37) Lasic, D. D., Martin, F. J., Gabison, A., Huang, S. K., and Papahadjopoulos, D. (1991) Sterically stabilized liposomes: A hypothesis on the molecular origin of the extended circulation times. *Biochim. Biophys. Acta 1070*, 187−192.

(38) Choi, Y. H., Liu, F., Park, J. S., and Kim, S. W. (1998) Lactose-poly(ethylene glycol)-grafted poly-L-lysine as hepatoma cell-targeted gene carrier. *Bioconjugate Chem. 9*, 708−718.

(39) Harada-Shiba, M., Yamauchi, K., Harada, A., Takamisawa, I., Shimokado, K., and Kataoka, K. (2002) Polyion complex micelles as vectors in gene therapy-pharmacokinetics and in vivo gene transfer. *Gene Ther. 9*, 407−414.

(40) Escriou, V., Ciolina, C., Lacroix, F., Byk, G., Scherman, D., and Wils, P. (1998) Cationic lipid-mediated gene transfer: Effect of serum on cellular uptake and intracellular fate of lipopolyamine/DNA complexes *Biochim. Biophys. Acta 1368*, 276−288.

(41) Harvie, P., Wong, F. M., and Bally, M. B. (2000) Use of poly(ethylene glycol)−lipid conjugates to regulate the surface attributes and transfection activity of lipid−DNA particles. *J. Pharm. Sci. 89*, 652−663.

(42) Nicolazzi, C., Mignet, N., De la Figuera, N., Cadet, M., Torero Ibad, R., Seguin, J., Scherman, D., and Bessodes, M. (2003) Anionic poly(ethylene glycol) lipids added to cationic lipoplexes increases their plasmatic circulation time. *J. Controlled Release 88*, 429−443.

(43) Shi, F., Wasungu, L., Nomden, A., Stuart, M. C. A., Polushkin, E., Engberts, J. B., and Hoekstra, D. (2002) Interference of poly(ethylene glycol)−lipid analogues with cationic lipid-mediated delivery of oligonucleotides; role of lipid exchangeability and nonlamellar transitions. *Biochem. J. 366*, 333−341.

(44) Holland, J. W., Cullis, P. R., and Madden, T. D. (1996) Poly(ethylene glycol)−lipid conjugates promote bilayer formation in mixtures of nonbilayer-forming lipids. *Biochemistry 35*, 2610−2617.

(45) Song, L. Y., Ahkong, Q. F., Rong, Q., Wang, Z., Ansell, S., Hope, M. J., and Mui, B. (2002) Characterization of the inhibitory effect of PEG−lipid conjugates on the intracellular delivery of plasmid and antisense DNA mediated by cationic lipid liposomes. *Biochim. Biophys. Acta 1558*, 1−13.

(46) Koltover, I., Salditt, T., Rädler, J. O., and Safinya, C. R. (1998) An inverted hexagonal phase of cationic liposome-DNA complexes related to DNA release and delivery. *Science 281*, 78−81.

(47) Smisterova, J., Wagenaar, A., Stuart, M. C. A., Polushkin, E., ten Brinke, G., Hulst, R., Engberts, J. F. B. N., and Hoekstra, D. (2001) Molecular shape of the cationic lipid controls the structure of cationic lipid/dioleylphosphatidylethanolamine−DNA complexes and the efficiency of gene delivery. *J. Biol. Chem. 276*, 47615−47622.

(48) Lee, R. J., and Low, P. S. (1994) Delivery of liposomes into cultured KB cells via folate receptor-mediated endocytosis. *J. Biol. Chem. 269*, 3198−3204.

(49) Lee, R. J., and Huang, L. (1996) Folate-targeted, anionic liposome-entrapped polylysine-condensed DNA for tumor cell-specific gene transfer. *J. Biol. Chem. 271*, 8481−8487.

(50) Kunath, K., von Harpe, A., Fischer, D., and Kissel, T. (2003) Galactose-PEI-DNA complexes for targeted gene delivery: Degree of substitution affects complex size and transfection efficiency. *J. Controlled Release 88*, 159−172.

(51) Fabio, K., Gaucheron, J., Di Giorgio, C., and Vierling, P. (2003) Novel galactosylated polyamine bolaamphiphiles for gene delivery. *Bioconjugate Chem. 14*, 358−367.

(52) Choi, J. S., MacKay, J. A., and Szoka, F. C. (2003) Low-pH-sensitive PEG- stabilized plasmid−lipid nanoparticles: Preparation and characterization. *Bioconjugate Chem. 14*, 420−429.

BC049971K

Secondary mAb−vcMMAE Conjugates Are Highly Sensitive Reporters of Antibody Internalization via the Lysosome Pathway

Kerry Klussman, Bruce J. Mixan, Charles G. Cerveny, Damon L. Meyer, Peter D. Senter, and Alan F. Wahl*

Departments of Biochemistry and Chemistry, Seattle Genetics, Inc., 21823 - 30th Drive Southeast, Bothell, Washington 98021. Received January 26, 2004; Revised Manuscript Received April 30, 2004

Monoclonal antibodies (mAb) selectively recognizing tumor surface antigens are an important and evolving approach to targeted cancer therapy. One application of therapeutic mAbs is drug targeting via mAb−drug conjugate (ADC) technology. Identification of mAbs capable of internalizing following antigen binding has been accomplished by tracking decline of surface-bound mAb or by internalization of a secondary mAb linked to a toxin. These methods may not be sufficiently sensitive for screening nor wholly predictive of the mAbs' capacity for a specific drug delivery. We have developed a highly selective and sensitive method to detect mAbs for cell internalization and drug delivery. This system uses secondary anti-human or anti-murine mAbs conjugated to the high-potency drug monomethyl auristatin E (MMAE) via a highly stable, enzymatically cleavable linker. Prior studies of this drug linker technology demonstrated internalization of a primary ADC leads to trafficking to lysosomes, drug release by lysosomal cathepsin B, and ensuing cell death. A secondary antibody−drug conjugate (2°ADC) capable of binding primary mAbs bound to the surface of antigen-positive cells has comparable drug delivery capability. The system is sufficiently sensitive to detect internalizing mAbs in nonclonal hybridoma supernatants and is predictive of the activity of subsequently produced primary ADC. Because of their high extracellular stability, the noninternalized 2°ADC are 100−1000-fold less toxic to cells over extended periods of time, permitting an assay in which components can be added without need for separate wash steps. This homogeneous screening system is amenable to medium-throughput screening applications and enables the early identification of mAbs capable of intracellular trafficking for drug delivery and release.

INTRODUCTION

Monoclonal antibodies (mAbs) that are selective for tumor cells but not efficacious in antitumor treatment are being increasingly applied as vectors for the therapeutic delivery of toxins or cytotoxic agents to the interior of tumor cells (*1*). Success in this latter application requires that the antibody−drug conjugate (ADC) remain stable in circulation, display tumor selectivity, and be internalized upon binding of surface antigen into an appropriate intracellular pathway facilitating drug release and delivery. The utility of mAbs conjugated to small, highly potent cytotoxics has increased with the advance of more potent agents and development of conditionally labile linkage systems. These linkers exhibit a high degree of stability in plasma and selective drug release within the tumor cell (*2*). Current methods to identify mAbs for drug delivery applications depend on a primary screen for selective binding to the tumor cell, and then on secondary assessment for internalization, prior to construction and evaluation of direct mAb−drug conjugates. Approaches to assessing candidate mAbs for internalization include direct labeling with indicators such as colloidal gold or fluorophores for microscopy (*3*, *4*), direct labeling of mAbs with toxins such as Pseudomonas exotoxin A (*5*), or by use of a secondary mAb, reactive with the first and linked to a toxin such as ricin A chain (*6*). The latter approach, while advancing the field of antibody−drug conjugate discovery, may be skewed by the behavior of the protein toxin compared to the trafficking and release of a high potency small molecule. Additionally, the composition of these toxin conjugates may be heterogeneous and the linkage used in such reporters is not sufficiently stable (*7*) to permit continuous cell exposure without significant background toxicity. Taken together, existing tools may demonstrate characteristics and selectivity that may not be optimal for homogeneous screening of hybridoma arrays for mAb with drug delivery capability.

To speed the discovery of tumor-selective internalizing mAbs from hybridoma screening efforts, we have constructed homogeneous assays employing secondary antibody−drug conjugates (2°ADC), composed of secondary antibodies stably linked to the potent cytotoxic agent MMAE via a valine-citrulline peptide linker (*2*). This linker was originally identified based on its high stability outside of cells and ability to be efficiently and selectively cleaved by lysosomal cathepsin B (*8*). Antigen-dependent internalization and lysosomal release was initially shown for doxorubicin (*8*, *9*), but subsequent studies with taxanes and camptothecin (*10*, *11*) and most recently auristatins (*2*) have extended the capability of this linker to other drugs. Two secondary mAbs were examined with specificities toward IgGs of either human or mouse origin and exhibited cytotoxicity dependent upon the binding, internalization, and lysosomal transit characteristics of the primary antibody. We have previously shown the drug remains stably appended to the mAb in serum or plasma and is highly attenuated when incubated with

* To whom correspondence and reprint requests should be sent: Phone: (425) 527-4610. Fax: (425) 527-4609. E-mail: awahl@seagen.com.

10.1021/bc049969t CCC: $27.50 © 2004 American Chemical Society
Published on Web 06/18/2004

antigen-negative cells (*2*, *12*). Upon ADC binding and internalization in antigen-positive cells, the drug linkage is fragmented by lysosomal proteases (*8*) releasing the cytotoxic agent MMAE into the cytosol. Internalization results in a 100−1000× increase in selectivity over noninternalizing mAb−2°ADC pairs. Thus the system is sufficiently sensitive to identify small amounts of internalizing mAbs in heterogeneous mixtures such as nonclonal hybridoma cultures.

MATERIALS AND METHODS

Cells and Reagents. Hybridomas for mAb HB43, a murine IgG1 reactive with human IgG1 gamma heavy chain (*13*), mAb 187.1, a rat IgG1 reactive with mouse kappa light chain (*14*), and OKT9, a murine IgG1 specific for human transferrin receptor (*15*), were obtained from the American Type Culture Collection (ATCC, Manassas, VA). mBR96 is a murine IgG3 reactive with an extended form of the Lewis Y (Le^y) antigen found on numerous human carcinoma cells (*16*). cBR96 is a chimeric form of mBR96 composed of a human IgG1 H and L framework (*17*). mAC10 is a murine IgG2b reactive with human CD30 (18). cAC10 is a chimeric form of mAC10 composed of a human IgG1 H and L framework (*19*). mAb hup97 is a human IgG1 directed against melanotransferrin. cL6 is a chimeric form of mL6, a monoclonal antibody recognizing a tumor-associated antigen, known as L6 antigen, present on carcinomas of the lung, breast, colon and ovary, composed of a human IgG1 H and L framework (20). H460, H358, H226, and A549 lung carcinoma and MDA-MB-453 breast carcinoma lines were obtained from ATCC. H3677 and H3396 breast carcinoma were gifts from Dr. I. Hellstrom (Pacific Northwest Research Foundation, Seattle, WA). LX-1 lung carcinoma was a gift from Dr. E. Neuwelt (Oregon Health Sciences University, Portland, OR) and was originally isolated at the Mason Research Institute, Worcester, MA. The anaplastic large cell lymphoma (ALCL) line, Karpas 299, was obtained from the DSMZ (Braunschweig, Germany). All cell lines and hybridomas were grown in RPMI-1640 media (Life Technologies Inc., Gaithersburg, MD) supplemented with 10% fetal bovine serum (Life Technologies Inc.) and were verified to be mycoplasma-free by PCR (ATCC Mycoplasma detection kit, American Type Culture Collection, Manassas, VA). Antibody was purified from culture supernatants by Gamma Bind (Amersham Pharmacia Biotech, Piscataway, NJ) chromatography. Goat anti-mouse-FITC and goat anti-human-FITC were from Jackson Immunoresearch, (West Grove, PA).

Linker Synthesis. The synthesis of the activated valcit linkage system to append drug was modified from the previously described procedure (*9*).

Drug Synthesis. The synthesis of auristatin E has been previously described (*21*). The monomethyl derivative of auristatin E (MMAE) was prepared by replacing a protected form of monomethylvaline for *N*,*N*-dimethylvaline in the synthesis of auristatin E. MMAE was then further modified with an activated derivative of maleimidocaproyl-valine-citrulline that contained a *p*-aminobenzylcarbamate spacer between the MMAE and the linker as previously described (*2*).

Conjugate Preparation. *Antibody Reduction.* To 5 mL of each mAb (10 mg/mL) was added 600 μL of 500 mM sodium borate/500 mM NaCl, pH 8.0, followed by 600 μL of 100 mM DTT in water. After incubation at 37 °C for 30 min, the buffer was exchanged by elution over G25 resin equilibrated and eluted with PBS containing 1 mM DTPA (Aldrich, Milwaukee, WI). The thiol/Ab value was checked by determining the reduced antibody concentration from the absorbance at 280 nm of the solution, and the thiol concentration by reaction with DTNB (Aldrich) and determination of the absorbance at 412 nm.

Conjugation of the Reduced Antibody. The reduced mAb was chilled on ice. The drug-linker (vcMMAE) was used as a frozen DMSO solution of known concentration, and the quantity of drug-linker added to the reaction mixture was calculated as follows:

L stock solution = $V \times$ [Ab] × fold excess/[drug-linker], where V and [Ab] are the volume and molar concentration of the reduced antibody solution, respectively. Cold PBS/DTPA (2.3 mL) was added to each of the two reduced antibody solutions. For the vcMMAE conjugate, 133.6 μL of 7.5 mM maleimidocaproyl-vcMMAE stock solution was diluted into 1.47 mL of acetonitrile. The acetonitrile drug-linker solution was chilled on ice then added to the reduced antibody solutions. The reactions were terminated after 1 h by the addition of a 20-fold molar excess of cysteine over maleimide. The reaction mixtures were concentrated by centrifugal ultrafiltration and purified by elution through desalting G25 in PBS. ADCs were then filtered through 0.2 μm filters under sterile conditions and immediately frozen at −80 °C. ADCs were analyzed for concentration, by UV absorbance; aggregation, by size exclusion chromatography; drug/Ab, by measuring unreacted thiols with DTNB; and residual free drug, by reverse phase HPLC. The procedure reproducibly yielded ADC of <3% aggregate, 8 drugs/mAb and <1% free drug.

Flow Cytometric Analysis of mAb Binding. To evaluate binding of the primary mAbs to cells, 4×10^5 cells were combined with mAb at 10 μg/mL in ice-cold staining media (PBS/2% FBS/0.02% sodium azide) for 30 min on ice and washed twice with ice cold PBS. Cells were then incubated with either goat anti-mouse-IgG FITC or goat anti-human-IgG-FITC, depending on the primary mAb at 10 μg/mL in ice-cold staining media on ice for 30 min and washed as described above. Labeled cells were resuspended in 0.3 mL of PBS and then analyzed on a FACScan (Becton Dickinson Immunocytometry Systems, Mansfield, MA) using the CellQuest software package. Data are shown in histogram format with fluorescence intensity displayed in log intervals on the *x*-axis and number of events (linear scale) on the *y*-axis.

Cytotoxicity Assays. Cell lines were plated at previously determined densities (based on proliferation rates and Alamar Blue labeling efficiency) in 100 μL of complete media and cultured overnight to adhere to the well. Primary mAb and 2°ADC were combined at a ratio of 1:2 in complete media and allowed to complex at room temperature for 15 min prior to serial dilution in complete media. Fifty microliters of these dilutions was added to the cell plate, and the plates were incubated at 37 °C for 96 h. At 92 h cells were labeled with Alamar Blue (Biosource International, Camarillo, CA), at a final concentration of 10% culture volume, and cytotoxicity was measured according to manufacturers directions on a Fusion HT fluorescent plate reader (Packard Instruments, Meriden, CT). (*22*). Raw data was analyzed in an Excel spreadsheet and cytotoxicity expressed by dose−response curves plotted for percent cell viability compared to untreated control wells (*y*-axis), versus concentration of mAb/ADC treatments (*x*-axis).

For comparison of the activity of the 2°ADC with two commercially available secondary immunotoxins (2° IT), Mab-ZAP (*23*) and Hum-ZAP (Advanced Targeting Systems, San Diego, CA), MDA-MB-453 breast carcinoma

cells (Le^{y+}) were plated at 1×10^5 cells/mL (0.1 mL/well) in RPMI 1640 + 10% FBS and allowed to incubate overnight at 37 °C. The following day the 2°ADC or 2°IT was added to cultures at 2 μg/mL (100 ng/well) in complete medium. Immunotoxins consisted of goat-anti-mouse IgG-saporin (Mab-ZAP) or a goat-anti-human-saporin (Hum-ZAP). Serial dilutions of mAb were then added to the cultures and incubated for 96 h. Cytotoxicity was measured by reduction of Alamar Blue. Secondary reagents were tested in the absence of targeting mAb in this system and had no effect on cell growth.

Evaluation of Hybridoma Supernatants and Purified mAb for Internalization by 2°ADC. Three NSCLC cell lines, H460, H358, and H226, were combined and plated at 1×10^3 cells of each line/well in complete media and allowed to adhere overnight. As released drug is distributive to bystander cells, combining multiple cell lines allows identification of internalization if only one cell line is antigen positive. Fifty microliters of neat hybridoma-conditioned culture supernantant from a NSCLC immunization/fusion was combined with 2°ADC, allowed to complex for 15 min at RT, then added to cells for a 6-day incubation at 37 °C. Master wells were frozen for subsequent reculture. Alamar Blue label was added for the last 4 h of culture and fluorescence measured to assess cell viability compared to cells in untreated control wells. Frozen master wells were recultured, and those with supernatant showing >60% cytotoxicity were recloned and the conditioned media evaluated as above. This evaluation was continued through subsequent rounds to purified antibody from isolated clonal cells.

RESULTS

Characterization of mAbs and Cell Lines. As models for evaluation, we selected mAbs and antigen expressing cell lines previously shown to have varying levels of internalization following mAb binding. Cell lines used were also demonstrated to show similar sensitivity to MMAE, with IC_{50} values of the following: 0.88 nM, A549; 0.07 nM, Karpas 299; 0.4 nM, H3396; 1.2 nM, LX-1; and 0.52 nM, H3677. mAb BR96 targets an extended form of the Le^y antigen present on numerous carcinomas and undergoes rapid internalization following antigen ligation (*16*). mAb OKT9 recognizes the transferrin receptor (CD71) expressed on most dividing cells and has also been shown to undergo efficient internalization upon antigen binding (*24*). We have recently shown that cAC10, a chimeric antibody against the CD30 antigen present on numerous hematalogic malignancies, is a highly effective internalizing mAb for intracellular drug delivery (*12*). Murine AC10 and cAC10, a chimeric version of AC10, were evaluated both as an unmodified mAb in combination with 2°ADC, and cAC10 as a direct antibody−drug conjugate. mAb L6 is reactive with L6 antigen expressed on lung, breast, and colon carcinomas (*25*). mAb L6 has been shown to mediate both complement activation (CDC) and antibody-dependent cellular cytotoxicity (ADCC) leading to the destruction of human tumor cells in vitro (*26*), yet was shown to be poorly internalizing when examined as a conjugate with ricin A chain toxin (*27*). Cytotoxicity, and presumably internalization of mAb L6-toxin conjugates, could be increased in combination with the lysosomal disrupting agent listeriolysin, suggesting that internalization of L6-toxin was not followed by release of the active toxin from the lysosome (*27*) and further suggesting that mAb L6 could not effectively deliver a drug via the lysosomal pathway. mAbs hup97 and L49 bind the human melanoma-associated antigen, melanotransferrin (p97). P97 is stably expressed on the cell surface and not detectably internalized upon mAb binding (*28*, *29*). The p97 mAb/Ag complex served as a noninternalizing control in these studies. The antigen expressing lines, reactive antibodies, and respective 2°ADC are summarized in Table 1.

Table 1. Primary and Secondary Reagents

antigen	primary mAb	secondary ADC
CD71	OKT9	187.1-vcMMAE (RAM-MMAE)
Le^Y	cBR96	HB43-vcMMAE (MAH-MMAE)
Le^Y	mBR96	187.1-vcMMAE (RAM-MMAE)
L6 Ag	cL6	HB43-vcMMAE (MAH-MMAE)
p97	huAnti-p97	HB43-vcMMAE (MAH-MMAE)
CD30	cAC10	HB43-vcMMAE (MAH-MMAE)
CD30	mAC10	187.1-vcMMAE (RAM-MMAE)

Comparison of p97- and L6-Targeted Internalization. To evaluate the 2°ADC reporter, H3677 melanoma cells and A549 and LX-1 lung carcinoma cell lines were evaluated for cytotoxicity in response to internalization and drug release by mAb/2°ADC complexes. Figure 1A shows FACS analysis of the relative levels of binding of the previously reportedly noninternalizing mAbs L6 and L49 to their respective antigens on A549, LX-1, and H3677 cells as compared to binding of the secondary FITC reporter reagent alone. FACS evaluations were done at 4 °C in the presence of NaN_3 to stabilize surface binding and to block modulation. All three cell lines were positive for both antigens, with the L6 antigen showing ~1-log greater expression as judged by mAb binding compared to p97.

The cytotoxicity of L6-positive, p97-positive cells was examined in response to mAbs, 2°ADCs, or mAb/2°ADC complexes. Figure 1B shows the sensitivity of LX-1 cells to mAb L6/2°ADC or mAb p97/2°ADC complexes or the 2°ADCs alone. mAb L6/2°ADC was significantly more potent (IC_{50} = 1 μg/mL) than either mAb p97/2°ADC complexes or the 2°ADC alone (IC_{50} indeterminate). Figures 1C and 1D show parallel studies preformed on A549 (lung) and H3677 (melanoma) lines, respectively. As with LX-1 cells, only the combination of anti-L6 and 2°ADC resulted in significant cytotoxicity (IC_{50} on A549 and H3677 = 9 ng/mL and 10 ng/mL, respectively) while nominal cytotoxicity was observed from treatment with the noninternalizing anti-p97/2°ADC complexes or the 2°ADC alone (IC_{50} > 5 μg/mL). Together these data indicate the primary mAb L6 was efficiently internalized to deliver the associated 2°ADC with cytotoxic effect and, contrary to early reports examining L6-toxin conjugates (27), suggest mAb L6 provided efficient delivery of a small, high potent drug.

Le^y-, CD30-, and CD71-Targeted Internalization. To evaluate internalization of mAbs directed to antigens Le^y, CD30 and CD71, the breast carcinoma line H3396 and the anaplastic large cell lymphoma line Karpas 299 were first analyzed for the presence of these antigens by flow cytometry. Figure 2A (upper panels) shows that H3396 cells stained strongly with cBR96 (against the Le^y antigen) moderately with OKT9 (CD71 antigen) and not with cAC10 (CD30 antigen). Karpas 299 cells displayed moderate to high levels of staining with both cAC10 and OKT9, reflecting high expression of the CD30 and CD71 antigens respectively, and nominal staining for Le^y (Figure 2A, lower panel). Together, H3396 and Karpas 299 cells provided reciprocal, nonbinding controls for these studies. As both cell lines expressed CD71, mAb OKT9 was used as a common positive control for internalization.

Using the CD30+ cell line, Karpas 299, both AC10 and cAC10 forms of the CD30 antibody were evaluated for

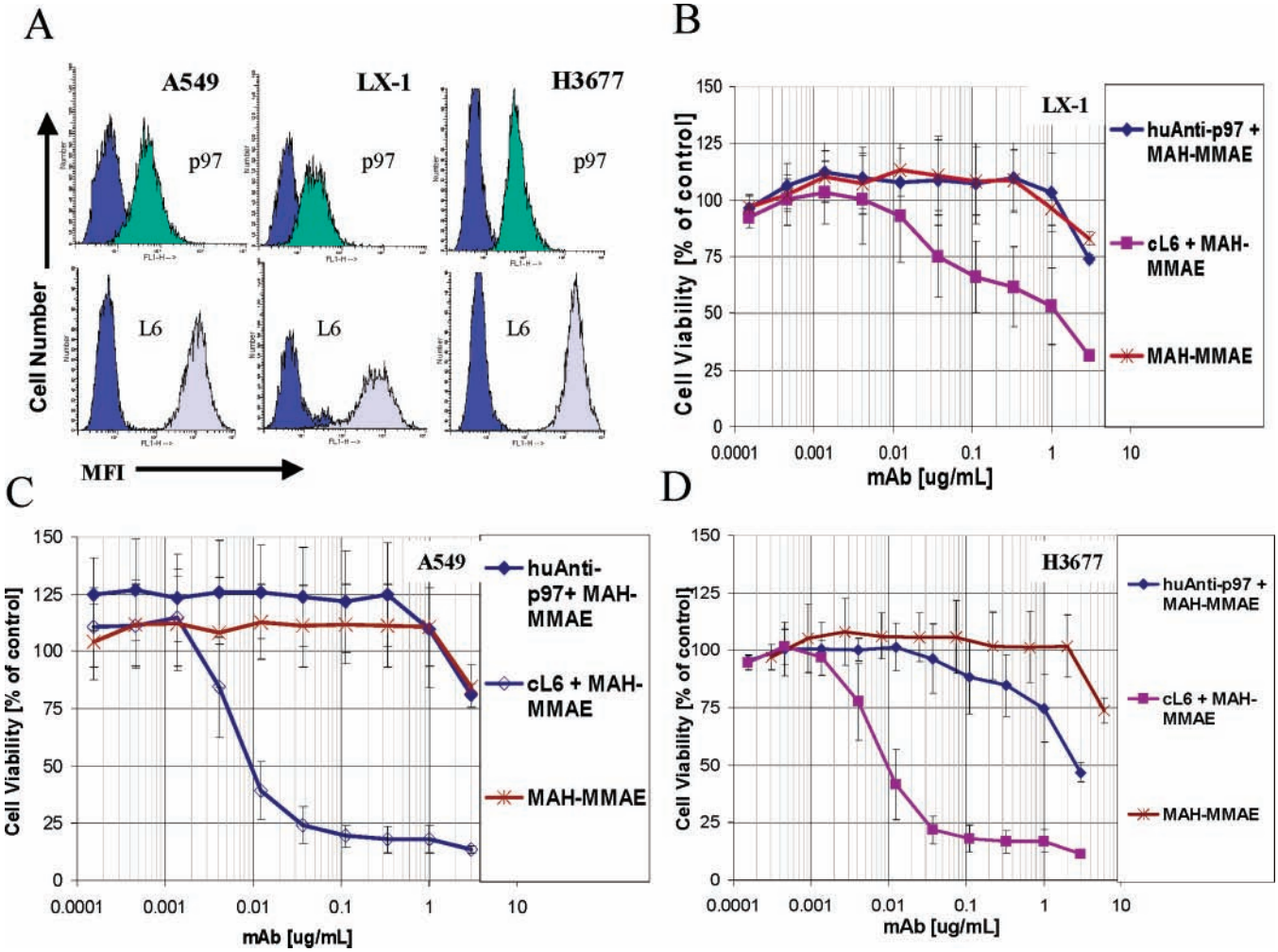


Figure 1. (A) Evaluation of p97 and L6 mAbs on tumor cells. A549, LX-1, and H3677 tumor cells (4 × 10^5 of each) were stained for 30 min on ice with 10 μg/mL of the designated primary mAbs, washed as described in Materials and Methods followed by incubation with 10 μg/mL FITC-labeled secondary Ab for 30 min on ice. After final washes, cells were resuspended in PBS and the resultant fluorescent intensity analyzed by flow cytometry. Blue histograms indicate staining with secondary anti-human FITC only. Shaded histograms, top panel huAnti-p97/secondary anti-human FITC, bottom panel cL6/secondary anti-human FITC. (B) Sensitivity of LX-1 cells to a secondary 2°ADC complexed with mAb-p97 or mAb-L6. (C) Sensitivity of A549 cells to a secondary 2°ADC complexed with mAb-p97 or mAb-L6. (D) Sensitivity of H3677 cells to a secondary ADC complexed with anti-p97 or anti-L6. Cells (2 × 10^3) were plated in microtiter wells in complete media and allowed to adhere overnight, and titrations of primary mAbs complexed with a 2°ADC were added. Mab/2°ADC complexes were preformed at RT for 15 min, and titrations were made in complete media and added to plates containing cells. Cultures were incubated for a total of 96 h at 37 °C, and Alamar Blue label was added for the last 4 h of incubation. A 96-well fluorescence plate reader measuring emission from metabolized dye was used to assess cell viability compared to control wells containing cells as described in Materials and Methods. Shown are the dose−response curves resulting from primary mAb−2°ADC complexes and 2°ADC alone. Data points are the mean of quadruplicate determinations.

CD30-targeted internalization using corresponding anti-mouse or anti-human 2°ADCs (Figure 2B). The nonbinding and binding primary mAbs mBR96 and OKT9 were included as negative and positive controls, respectively, as were the two 2°ADCs alone. Treatment with either AC10 or cAC10 in combination with their respective 2°ADCs resulted in similar IC_{50}s of 3−4 ng/mL. OKT9/2°ADC complexes gave intermediate toxicity (IC_{50} = 50 ng/mL), perhaps attributable to the lower CD71 levels compared to CD30 on the cells (Figure 2A). In contrast, neither the nonbinding control complex, BR96/2°ADC, nor the 2°ADCs alone resulted in cytotoxicity at concentrations below 3 μg/mL (Figure 2B). These results suggest that the 2°ADCs were capable of internalization and delivering drug to the cytosol only when complexed with the internalizing anti-CD30 mAbs or anti-CD71 mAbs. The ~1000-fold potency difference between relevant and irrelevant mAbs also suggest the 2°ADCs remain intact and do not release free drug outside the cell during the course of the 96 h assay.

In a reciprocal experiment, Le^y-positive/CD30-negative H3396 cells were treated with mBR96 or cBR96 (binding Le^y) and their appropriate anti-mouse or anti-human 2°ADCs. mAb OKT9, binding CD71 on these cells, and the nonbinding mAb mAC10 were also evaluated in the presence of 2°ADCs, as were the two 2°ADCs alone. Figure 2C shows moderate H3396 sensitivity to OKT9/2°ADC and high sensitivity to the two BR96 mAbs in the presence of their respective 2°ADCs. IC_{50}s were 80 ng/mL for OKT9/2°ADC and 20−25 ng/mL for the cBR96/2°ADC and mBR96/2°ADC, respectively. The difference in sensitivity may be attributable, in part, to the ~2-logs greater expression of Le^y compared to CD71 on H3396 cells. IC_{50}s for the 2°ADCs alone were indeterminate, and no toxicity was observed with the primary mAbs alone tested at up to 3 μg/mL (data not shown).

Comparison of mAb/2°ADC Complex versus Primary ADC. The results of mAb/2°ADC studies shown above suggested that a direct drug conjugate constructed from mAbs cAC10 or cL6 would efficiently kill respective

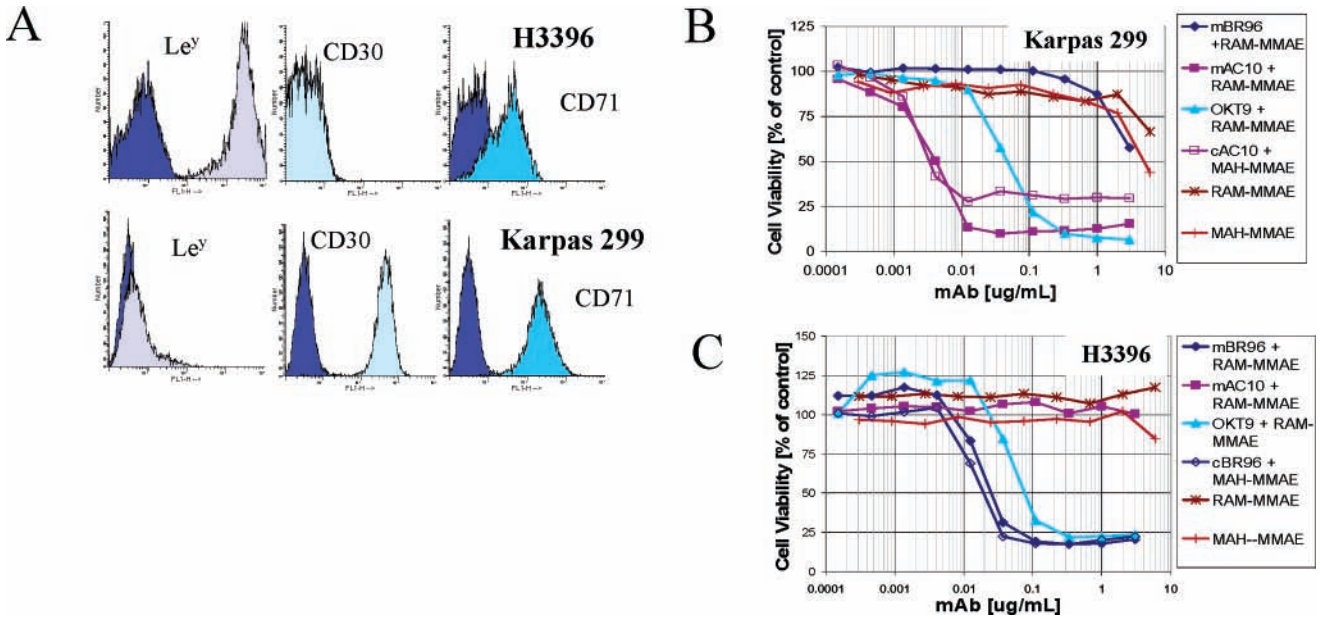


Figure 2. (A) Binding levels of mAb to Le^y, CD30, and CD71 on H3396 and Karpas 299 cells. Tumor cells (4×10^5) were pelleted and resuspended in 10 μg/mL primary mAb in ice-cold staining media and incubated on ice for 30 min, washed as described in Materails and Methods, and resuspended in 10 μg/mL FITC-labeled secondary Ab in ice-cold staining media. Following a 30-min incubation on ice, cells were washed, resuspended, and analyzed by flow cytometry as described in Materials and Methods. Blue histograms indicate FITC-labeled secondary antibody staining only, anti-human FITC (left and center panels), and anti-mouse FITC (right panel). Shaded histograms indicate staining in conjunction with primary mAbs, cBR96 (left panel), cAC10 (center panel) and OKT9 (right panel). (B). Cytotoxic effect of chimeric and murine anti-CD30 mAbs combined with respective 2°ADCs on CD30-positive Karpas 299 cells. Karpas cells were plated at 1×10^4/well in 100 μL of complete media. Precomplexed primary mAbs + 2°ADCs were titrated and added to wells containing cells. Cultures were incubated 96 h at 37 °C with addition of Alamar Blue label for the last 4 h of culture. Fluorescence from the metabolized dye was measured to assess cell viability compared to control wells containing untreated cells as described in Materials and Methods. Response curves show the effects of primary mAbs cAC10 (chimeric) and mAC10 (murine), complexed with their appropriate 2°ADC. IC_{50} values in μg/mL = 0.0034 and 0.004, respectively. Response curves for irrelevant control mAb mBR96/2°ADC complex, IC_{50} = >3 μg/mL, positive internalization control mAb OKT9/2°ADC complex, IC_{50} = 0.047 μg/mL, and the secondary ADCs alone, with IC_{50} values ≥ 5 μg/mL are also shown. C. Cytotoxic effect of chimeric and murine anti-Le^y mAb BR96 combined with anti-human or anti-mouse 2°ADCs on Le^y-positive H3396 carcinoma cells. Cells were plated at 4×10^3/well in microtiter wells in 100 μL/well complete media. Following overnight adherence, titrations of primary mAb + 2°ADC that had been allowed to precomplex for 15 min at RT were added in 50 μL/well, and the assay evaluation was carried out as in B above. Response curves indicate effects of primary mAbs mBR96 (murine) and cBR96 (chimeric), complexed with their appropriate 2°ADC. IC_{50} values in μg/mL = 0.024 and 0.02, respectively. Also shown are response curves for positive internalization control mAb OKT9/2°ADC complex, IC_{50} = 0.075 μg/mL, irrelevant control mAb mAC10/2°ADC complex, and the secondary ADCs alone, IC_{50}s indeterminate. Data points are the mean of quadruplicate determinations.

antigen-positive cells. We have previously shown that conjugation of mAbs via this method does not change binding characteristics as compared to the parent mAb (*2*, *12*). Primary ADCs were prepared from the two mAbs, and their potency and selectivity were compared with that of the primary mAb/2°ADC complex.

The L6-positive cell line A549 was used to evaluate mAb cL6 in the form of a primary ADC (cL6−vcMMAE) or L6 mAb/2°ADC complex, and the resultant dose−responses are shown in Figure 3A. The primary ADC and the primary mAb/2°ADC complexes showed comparable cytotoxicity (IC_{50} = 0.02−0.03 μg/mL for either treatment) whereas the 2°ADC alone had no significant effect.

In a parallel study, the cytotoxicity of a direct conjugate of mAb cAC10 (cAC10−vcMMAE) was compared with that of a cAC10 mAb/2°ADC complex (cAC10 + MAH−vcMMAE). Figure 3B shows CD30-positive Karpas 299 cells treated with either cAC10 + MAH−vcMMAE or cAC10−vcMMAE resulted in IC_{50}s = 8 and 4 ng/mL, respectively. These data suggest that cytotoxicity resulting from the screening with primary mAb/2°ADC complexes would be predictive of the potency of a subsequently produced primary ADC. In the absence of a target-specific primary mAb, the 2°ADC alone demonstrated limited or no cytotoxicity with an IC_{50} not reached for the 2°ADC alone on cells treated up to 6 μg/mL.

Comparison of 2°ADC with 2°IT. The Le^y-positive/CD30-negative cell line MDA-MB-453 was used to compare the potency of a secondary vcMMAE ADC with that of a commercially available 2° IT. Using either mBR96 or cBR96 in combination with their respective 2°ADC gave IC_{50}s of 0.12 and 0.3 μg/mL (Figure 4). In contrast, the IC_{50} was indeterminate using a secondary anti-human immunotoxin (Figure 4A). The potency of an anti-mouse immunotoxin to detect internalization of the mBR96 was diminished 100-fold over that detected with a secondary anti-mouse ADC (Figure 4B). No cytotoxicity was detected with either secondary reagent alone or these secondary reagents in the presence of an irrelevant (anti-CD30) primary mAb at exposures up to 2 μg/mL (data not shown). These data suggest that the route of internalization and degradation of BR96 mAbs is more amenable to delivering the vcMMAE ADC than a protein toxin, as only the 2°ADC reagents retained their antigen selectivity and drug delivery capability in the presence of primary mAb over the concentration range examined.

Screening of Hybridoma for Internalizing mAb. The characteristics of the secondary anti-mouse ADC, high stability and attenuated toxicity outside of cells and highly potent cytotoxicity upon internalization, suggested it could be used to identify internalizing mAbs at low concentration early in the hybridoma screening process. To examine this utility, a primary hybridoma fusion,

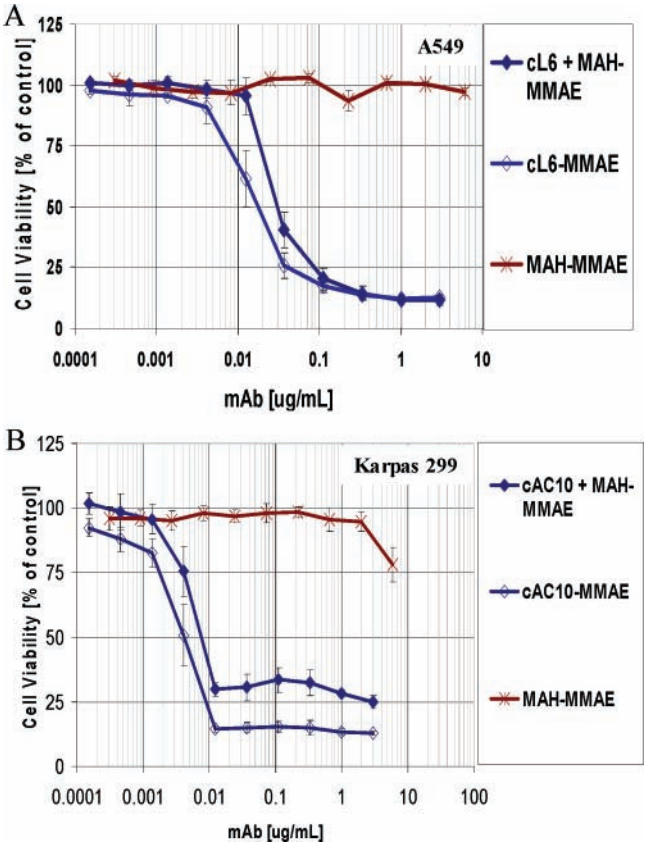


Figure 3. Comparative cytoxicity of primary ADC versus primary mAb/2°ADC complex. (A) mAb cL6 on L6 antigen-positive cells. A549 carcinoma cells were plated at 1×10^3/microtiter well in 100 μL/well complete media. Following overnight adherence, cells were exposed to a titration of either a primary antibody−drug conjugate or a primary antibody complexed with a 2°ADC. Mab/2°ADC complexes were preformed at RT for 15 min, and titrations were made in complete media and added to plates containing cells. Cultures were incubated for a total of 96 h at 37 °C, and Alamar Blue label was added for the last 4 h of incubation. A 96-well fluorescence plate reader measuring emission from metabolized dye was used to assess cell viability compared to control wells containing cells as described in Materials and Methods. Dose−responses shown are for primary mAb/2°ADC complexes, primary ADC, and 2°ADC alone. All data points are an average of quadruplicate determinations. (B) anti-CD30 on CD30-positive cells. CD30 positive Karpas 299 cells were plated at 1×10^4/well in 100 μL of complete media. Titrations of either a primary ADC or primary mAb/2°ADC complex were added to cells plated in microtiter wells and assays carried out as in A above. Data points are the mean of quadruplicate determinations (±SE).

producing mAb against an immunization of multiple NSCLC membrane antigens was arrayed in 15 96-well plates at ∼4−10 different clones/well. The hybridoma were cultured for 5 days followed by three daily media changes. Following this, hybridoma were allowed to condition the media for an additional 72 h, and an aliquot of culture supernantant was removed for screening. Hybridoma plates were frozen for subsequent reculture, and an aliquot of supernatant (50 μL) was combined with a final concentration of 2 μg/mL of secondary anti-mouse ADC and added to wells containing normal lung epithelium or the NSCLC line mixture H460, H358, and H226. Free MMAE is distributive, and ADC internalization and drug release by one antigen-positive cell will result in cytotoxicity of neighboring antigen-negative cells (data not shown). Cultures were incubated for 6 days to allow maximum opportunity of internalization and resultant toxicity evaluated as described above. This method identified multiple wells in which viability was reduced by >60% compared to untreated control (Figure 5A). Plates were thawed, positive wells were expanded, and the screening was repeated with serial dilution. Figure 5B shows the titrated cytotoxicity of supernatant from clone 5D7 and other positive cultures following secondary expansion of masterwells in combination with 2°ADC. Following reexpansion and final cloning of well 5D7, the mAb was purified and evaluated for cytotoxicity in combination with 2°ADC in parallel with known internalizing and noninternalizing controls (Figure 5C). Of note, mAb 5D7 was identified as an IgM, and its stability as a purified mAb has been problematic. This could account for the diminished activity observed with the purified antibody (Figure 5C) but points up the ability of this system to identify both IgG and IgM isotypes.

These data suggest the 2°ADC is sufficiently sensitive to identify low levels of an internalizing mAb in a small volume of nonclonal hybridoma supernatant.

DISCUSSION

The successful use of antibody−drug conjugates for targeted-tumor drug delivery requires that the ADCs be directed to the site via tumor-selective antigens, undergo internalization through antigen modulation, and release drug by intracellular processes. We have combined the elements of a highly potent cytotoxic agent, MMAE, with a highly stable valine-citrulline linker system that is selectively cleavable by lysosomal proteases (*2*, *9*). This lysosomally cleavable linker has been shown to be broadly applicable to intracellular delivery of a variety of cytotoxic agents including doxorubicin, paclitaxel, and camptothecin (*8*−*11*). The resultant ADCs are potent drug delivery systems to antigen-positive cells yet are significantly less toxic to cells lacking the antigen even under conditions of sustained exposure (*2*, *12*). These qualities also suggested this ADC system could be applied early in the screening process for the identification of mAbs that would optimally internalize and deliver drug.

In the course of discovery of internalizing mAbs it would not be practical to prepare primary drug conjugates from the thousands of mAb candidates emanating from a single hybridoma fusion. A screening strategy for internalizing antibodies using a secondary antibody coupled to a protein toxin was initially described by Till et al. (*6*). We have applied this strategy using a novel drug linker and describe here an approach to the discovery of internalizing mAbs using highly sensitive secondary anti-mouse or anti-human antibody−drug conjugate (2°ADC) reporters. These permit the screening of heterogeneous mixtures at low concentrations typically found in early, nonclonal hybridoma supernatants. In the presence of the 2°ADC, internalizing primary mAbs can be clearly identified by resultant cytotoxicity of cultured tumor cell lines using a homogeneous format. The system provides several appealing features: the high potency of the released drug, MMAE, produces significant cytotoxicity only in the presence of an internalizing primary mAb, whereas the attenuation and high stability of the 2°ADC outside the cell allows them to be combined with test cells in the absence of a internalizing mAb for extended periods of time (observed up to 6 days) without appreciable increase in cytotoxicity. This characteristic also allows for addition of the primary mAb and 2°ADC, and eventually cell viability reagent, without the need for intermediate wash steps. The necessity to wash cells at progressive steps adds significantly to the work and assay variability when assessing thousands of hybridoma

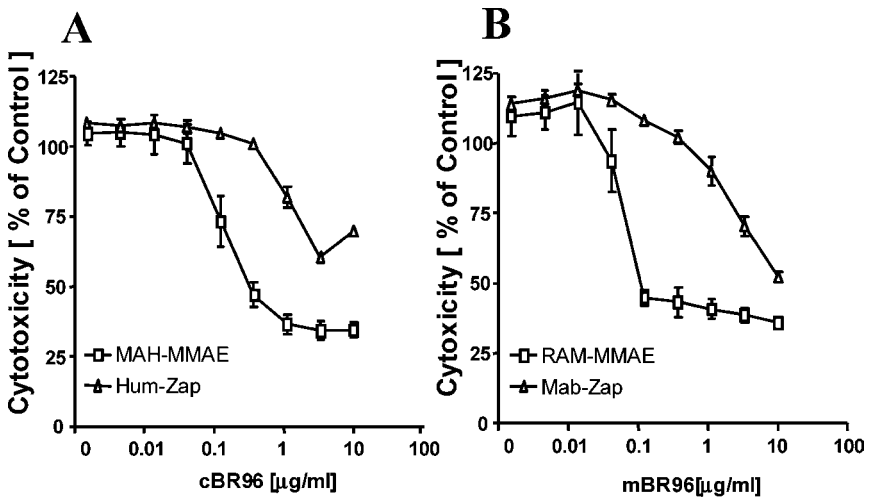


Figure 4. Comparison of 2°ADC and 2°IT reporters. The cell line MDA-MB-453 (Le^y-positive/CD30-negative) was used to compare the potency of a secondary vcMMAE ADC with that of a 2°IT. Cells were exposed to (A) human chimeric mAb BR96 combined with either MAH-MMAE or with Hum-ZAP, or (B) murine mAb BR96 combined with either RAM-MMAE or with Mab-ZAP. Viability was assessed by Alamar Blue metabolism following 96 h incubation. Data points are the mean of quadruplicate determinations (± SE).

supernatants. Additionally, the continuous cell exposure for the duration of a 6 day assay of such supernatants produces >1000-fold difference between internalizing and noninternalizing primary mAb, allowing the identification of even very weakly internalizing mAbs or those present at low (ng/mL) concentrations.

Importantly, comparison of mAb conjugated to drug and immunotoxin (Figure 4) suggests that evaluation of a mAb via a 2° IT reporter may not be predictive of the potential of this mAb to deliver a small drug from conjugate. Previous studies with immunotoxin reporters used primary mAb at 10 μg/mL in order to detect internalization (*16*). In the present study cytotoxicity is clearly detectable at 1/100 this level of primary mAb. It is unclear whether these differences are a function of drug potency or alternate routes of trafficking and release, but worth noting that under the conditions described, the 2° IT would likely not have identified mAb BR96 as internalizing. At the highest concentration of cBR96 tested, cytotoxicity appeared to decrease with the Hum-ZAP (Figure 4A), suggesting that optimal sensitivity is dependent on an optimal ratio of primary mAb and secondary indicator. This was not seen with the 2°ADC reporter suggesting it is less sensitive to the ratio of primary and secondary mAb.

We have examined the effect of 2°ADC reagents on cytotoxicity when used in combination with mAbs and antigens previously reported to rapidly internalize and recycle (*24*), internalize upon mAb ligation (*16*, *12*), or not to undergo antigenic modulation after mAb binding (*28*, *29*). In general our results with the 2°ADC confirm the previously reported behavior of the primary mAbs. Treatment of the cell lines H3396 and Karpas 299 with anti-transferrin receptor mAb, OKT9/2°ADC, resulted in comparable cytotoxicity on the antigen-positive lines. The internalizing mAb BR96, in both murine and chimeric forms, was cytotoxic on Le^y+ H3396 and diminished by >1000-fold on antigen-negative Karpas 299 cells (Figure 2A,B). Conversely, mAb AC10, tested in either its murine or chimeric form, complexed with 2°ADC, showed potent cytotoxicity on the CD30+ line Karpas 299 and diminished by >1000-fold on antigen-negative H3396. Comparison of the direct conjugate cAC10−vcMMAE and the cAC10/2°ADC complex gave similar cytotoxicity on CD30-positive cells, suggesting that results with the mAb/2°ADC complex can predict the activity of a direct ADC made from the primary mAb. Additionally, the comparable cytotoxicity resulting from murine and chimeric forms of a mAb in combination with anti-mouse or anti-human 2°ADC may be a useful indicator of how well antigen recognition and trafficking is preserved in the chimerization or huminazation process.

Studies with the noninternalizing antigen p97, when evaluated with anti-human p97 mAb/2°ADC on three antigen-positive lines, showed significant cytoxicity only at 2−3 logs higher concentration than other mAbs. These results are in agreement with the previous observation that p97 does not undergo mAb-mediated modulation.

mAb L6 has been shown to mediate both CDC and ADCC activity (26), yet L6 conjugated to ricin A chain internalized poorly upon Ag binding (27). Interestingly, treatment of all three L6 antigen-positive lines with mAb cL6/2°ADC resulted in significant cytotoxicity (Figure 1B−D), an effect paralleled by the potency of the direct cL6−vcMMAE conjugate. These data again suggest that the efficacy of mAb−toxin conjugates or secondary mAb−toxin reporters may not be predictive of the activity of the same mAb delivering a drug such as MMAE, and that the 2°ADC system is predictive of the activity of an ADC subsequently produced with the primary mAb.

The system described herein enables the identification of internalizing mAbs against tumor cell antigens based on their optimal delivery of this drug linker system. Because of the significant (3−4 log) increase in cytotoxicity upon binding and internalization, the system is amenable to the identification of internalizing mAbs in dilute and heterogeneous media from hybridoma culture. The high stability and low toxicity of the 2°ADC linker system outside the cell allow for a simple, homogeneous screening tool with significant signal-to-noise ratio when performed over 96 h of continuous exposure. To this end we have successfully used this method to screen a series of hybridoma-conditioned supernatants to identify tumor reactive, internalizing mAbs. The released MMAE is distributive, and ADC internalization and drug release by one antigen-positive cell will result in cytotoxicity of neighboring antigen-negative cells. Thus multiple carcinoma lines can be combined in screening for internalizing antibodies against unknown tumor markers. One mAb identified in this manner and conjugated to vcMMAE was shown to be a potent and selective antitumor agent (A. F. Wahl, manuscript in preparation), validating the

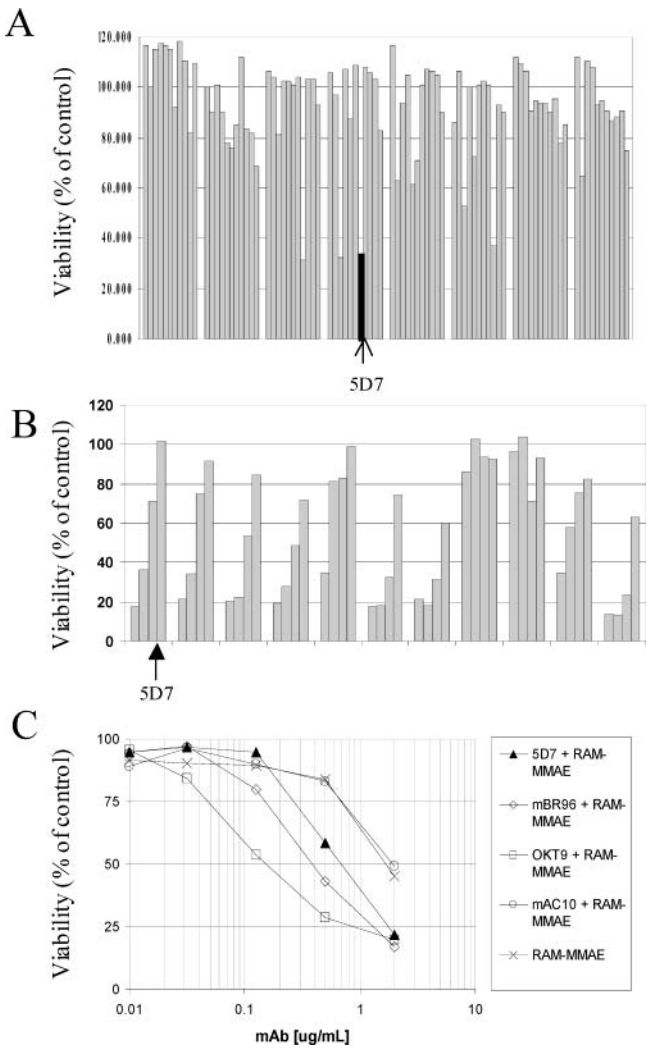


Figure 5. Evaluation of hybridoma supernatants and purified mAb for internalization by 2°ADC. (A). Three NSCLC cell lines, H460, H358, and H226, were combined and plated at 1×10^3 cells of each line/well and allowed to adhere overnight. Fifty microliters of neat hybridoma-conditioned culture supernatant from a NSCLC immunization/fusion were combined with 2°ADC, allowed to complex for 15 min at RT, and then added to cells for a 6-day incubation at 37 °C. Alamar Blue label was added for the last 4 h of culture and fluorescence measured to assess cell viability compared to cells in untreated control wells as described in Materials and Methods. Signal from cells treated with representative positive well 5D7 shown in black bar. (B) Cytotoxicity evaluation of well 5D7 supernatant and other internalization-positive cultures in serial dilution (left to right) following secondary expansion of masterwells. (C) Cytotoxicity evaluation of purified antibody from subsequently isolated clone 5D7 in combination with 2°ADC. Also shown are the 2°ADC alone, and 2°ADC in combination with internalizing mAbs OKT9 and BR96 and nonbinding control mAb AC10.

2°ADC system for discovery. Together with the results presented here this 2°ADC system is a highly useful screening tool to identify optimal antitumor mAbs for drug delivery.

LITERATURE CITED

(1) Naito, K., Takeshita, A., Shigeno, K., Nakamura, S., Fujisawa, S., Shinjo, K., Yoshida, H., Ohnishi, K., Mori, M., Terakawa, S., Ohno, R. (2000) Calicheamicin-conjugated humanized anti-CD33 monoclonal antibody (gemtuzumab zogamicin, CMA-676) shows cytocidal effect on CD33-positive leukemia cell lines, but is inactive on P-glycoprotein-expressing sublines. *Leukemia 14*, 1436−43.

(2) Doronina, S. O., Toki, B. E., Torgov, M. Y., Mendelsohn, B. A., Cerveny, C. G., Chace, D. F., DeBlanc, R. L., Gearing, R. P., Bovee, T. D., Siegall, C. B., Francisco, J. A., Wahl, A. F., Meyer, D. L., Senter, P. D. (2003) Development of potent monoclonal antibody auristatin conjugates for cancer therapy. *Nat. Biotechnol. 21*, 778−784.

(3) Raub, T. J., and Roberts, R. M. (1986) Cell surface glycoproteins of CHO cells. II. Surface distribution and pathway of internalization. *Exp. Cell Res. 165*, 92−106.

(4) Titus, J. A., Haugland, R., Sharrow, S. O., and Segal, D. M. (1982) Texas Red, a hydrophilic, red-emitting fluorophore for use with fluorescein in dual parameter flow microfluorometric and fluorescence microscopic studies. *J. Immunol. Methods 50*, 193−204.

(5) Kondo, T., FitzGerald, D. J. P., Adhya, S., and Pastan, I. (1988) Activity of immunotoxins constructed with modified Pseudomonas exotoxin A lacking the cell recognition domain. *J. Biol. Chem. 263*, 9470−9475.

(6) Till M., May R. D., Uhr, J. W., Thorpe, P. E., and Vitetta, E. S. (1988) An assay that predicts the ability of monoclonal antibodies to form potent ricin A chain-containing immunotoxins. *Cancer Res. 148*, 1119−23.

(7) Bross, P. F., Beitz, J., Chen, G., Chen, X. H., Duffy, E., Kieffer, L., Roy, S., Sridhara, R., Rahman, A., Williams, G., and Pazdur, R. (2001) Approval summary: gemtuzumab ozogamicin in relapsed acute myeloid leukemia. *Clin. Cancer Res. 7*, 1490−6.

(8) Dubowchik, G. M. and Firestone, R. A. (1998) Cathepsin B-sensitive dipeptide prodrugs. 1. A model study of structural requirements for efficient release of doxorubicin. *Bioorg. Med. Chem Lett. 8*, 3341−6.

(9) Dubowchik, G. M., Radia, S., Mastalerz, H., Walker, M. A., Firestone, R. A., King, D. H., Hofstead, S. J., Willner, D., Lasch, S. J.; Trail PA. (2002) Doxorubicin immunoconjugates containing bivalent, lysosomally cleavable dipeptide linkages. *Bioorg. Med. Chem. Lett. 12*, 1529−32.

(10) Dubowchik, G. M., Mosure, K., Knipe, J. O. and Firestone, R. A. Cathepsin B-sensitive dipeptide prodrugs. 2. Models of anticancer drugs paclitaxel (Taxol), mitomycin C and doxorubicin. (1998) *Bioorg. Med. Chem. Lett. 8*, 3347−3352.

(11) Walker, M. A., Dubowchik, G. M., Hofstead, S. J., Trail, P. A. and Firestone, R. A. (2002) Synthesis of an immunoconjugate of camptothecin. *Bioorg. Med. Chem. Lett. 12*, 217−9.

(12) Francisco, J. A., Cerveny, C. G., Meyer, D. L., Mixan, B. J., Klussman, K., Chace, D. F., Rejniak, S. X., Gordon, K. A., DeBlanc, R., Toki, B. E., Law, C. L., Doronina, S. O., Siegall, C. B., Senter, P. D., and Wahl, A. F. (2003) AC10-vcMMAE, an anti-CD30-monomethyl auristatin E conjugate with potent and selective antitumor activity. *Blood 102*, 458−1465.

(13) Mariani, E., Mariani, A. R., Monaco, M. C., Lalli, E., Vitale, M., and Facchini, A. (1991) Commercial serum-free media: hybridoma growth and monoclonal antibody production. *J. Immunol. Methods. 145*, 175−183.

(14) Yelton, D. E., Desaymard, C., and Scharff, M. D. (1981) Use of monoclonal anti-mouse immunoglobulin to detect mouse antibodies. *Hybridoma 1*, 5−11.

(15) Aisenberg, A. C., and Wilkes, B. M. (1980) Unusual human lymphoma phenotype defined by monoclonal antibody. *J. Exp. Med. 152*, 1126−1131.

(16) Hellström, I., Garrigues, H., Garrigues, U., and Hellström, K. E. (1990) Highly tumor-reactive, internalizing, mouse monoclonal antibodies to Le^y-related cell surface antigen. *Cancer Res. 50*, 2183-2190.

(17) Yarnold, S., and Fell, H. P. (1994) Chimerization of antitumor antibodies via homologous recombination conversion vectors. *Cancer Res. 54*, 506−512.

(18) Bowen, M. A., Olsen, K. J., Cheng, L., Avila, D., and Podack, E. R. (1993) Functional effects of CD30 on a large granular lymphoma cell line, YT. Inhibition of cytotoxicity, regulation of CD28 and IL-2R, and induction of homotypic aggregation. *J. Immunol. 151*, 5896−906.

(19) Wahl, A. F., Klussman, K., Thompson, J. D., Chen, J. H., Francisco, L. V., Risdon, G., Chace, D. F., Siegall, C. B., and Francisco, J. A. (2002) The Anti-CD30 Monoclonal Antibody SGN-30 Promotes Growth Arrest and DNA Fragmentation in Vitro and Affects Antitumor Activity in Models of Hodgkin's Disease. *Cancer Res. 62*, 3736−42.

(20) Fell, H. P., Margit, A. G., Yelton, D., Lipsich, L., Schieven, G. L., Marken, J. S., Aruffo, A., Hellström, K. E., Hellström, I., and Bajorath, J. (1992) Chimeric L6 antitumor antibody. *J. Biol. Chem. 267*, 15552−15558.

(21) Pettit, G. R., (1997) The dolastatins. *Fortschr. Chem. Org. Naturst. 7*, 1−79.

(22) Nakayama, G. R., Caton, M. C., Nova, M. P., and Parandoosh, Z. (1997) Assessment of the Alamar Blue assay for cellular growth and viability in vitro. *J. Immunol. Methodol. 204*, 205−208.

(23) Kohls, M. D., and Lappi, D. A. (2000) Mab-Zap: A tool for evaluating antibody efficacy for use in an immunotoxin. *Biotechniques 28*, 162−165.

(24) Hansen, S. H., Sandvig, K., and van Deurs, B. (1992) Internalization efficiency of the transferrin receptor. *Exp. Cell Res. 199*, 19−28.

(25) Hellström, I., Horn, D., Linsley, P., Brown, J. P., Brankovan, V., and Hellström, K. E. (1986) Monoclonal antibodies raised against human lung carcinoma. *Cancer Res. 46*, 3917−3923.

(26) Hellström, I., Beaumier, P. L., and Hellström, K. E. (1986) Antitumor effects of L6, an IgG2a antibody that reacts with most human carcinomas. *Proc. Natl. Acad. Sci. U.S.A. 83*, 7059−63.

(27) Kerr, D. E., Wu, G. Y., Wu, C. H. and Senter, P. D. (1997) Listeriolysin O potentiates immunotoxin and bleomycin cytotoxicity. *Bioconjugate Chem. 8*, 781−784.

(28) Hellström, I., Brown, J. P., and Hellström, K. E. (1983) Melanoma-associated antigen p97 continues to be expressed after prolonged exposure of cells to specific antibody. *Int. J. Cancer 31*, 553−555.

(29) Siemers, N. O., Kerr, D. E., Yarnold, S., Stebbins, M. R., Vrudhula, V. M., Hellström, I., Hellström, K. E., and Senter, P. D. (1997) Construction, expression, and activities of L49-sFv-beta-lactamase, a single-chain antibody fusion protein for anticancer prodrug activation. *Bioconjugate Chem. 8*, 510−519.

BC049969T

Interaction of Poly(amidoamine) Dendrimers with Supported Lipid Bilayers and Cells: Hole Formation and the Relation to Transport

Seungpyo Hong,[§,▽] Anna U. Bielinska,[||,▽] Almut Mecke,[⊥,▽] Balazs Keszler,[||,▽] James L. Beals,[||,▽] Xiangyang Shi,[||,▽] Lajos Balogh,[§,||,▽] Bradford G. Orr,[†,⊥,▽] James R. Baker, Jr.,[||,▽] and Mark M. Banaszak Holl*[,†,‡,§,⊗,▽]

Programs in Applied Physics, Biophysics, and Macromolecular Science and Engineering, Departments of Internal Medicine, Physics, and Chemistry, and Center for Biologic Nanotechnology, University of Michigan, Ann Arbor, Michigan 48109. Received February 17, 2004; Revised Manuscript Received May 4, 2004

We have investigated poly(amidoamine) (PAMAM) dendrimer interactions with supported 1,2-dimyristoyl-sn-glycero-3-phosphocholine (DMPC) lipid bilayers and KB and Rat2 cell membranes using atomic force microscopy (AFM), enzyme assays, flow cell cytometry, and fluorescence microscopy. Amine-terminated generation 7 (G7) PAMAM dendrimers (10−100 nM) were observed to form holes of 15−40 nm in diameter in aqueous, supported lipid bilayers. G5 amine-terminated dendrimers did not initiate hole formation but expanded holes at existing defects. Acetamide-terminated G5 PAMAM dendrimers did not cause hole formation in this concentration range. The interactions between PAMAM dendrimers and cell membranes were studied in vitro using KB and Rat 2 cell lines. Neither G5 amine- nor acetamide-terminated PAMAM dendrimers were cytotoxic up to a 500 nM concentration. However, the dose dependent release of the cytoplasmic proteins lactate dehydrogenase (LDH) and luciferase (Luc) indicated that the presence of the amine-terminated G5 PAMAM dendrimer decreased the integrity of the cell membrane. In contrast, the presence of acetamide-terminated G5 PAMAM dendrimer had little effect on membrane integrity up to a 500 nM concentration. The induction of permeability caused by the amine-terminated dendrimers was not permanent, and leaking of cytosolic enzymes returned to normal levels upon removal of the dendrimers. The mechanism of how PAMAM dendrimers altered cells was investigated using fluorescence microscopy, LDH and Luc assays, and flow cytometry. This study revealed that (1) a hole formation mechanism is consistent with the observations of dendrimer internalization, (2) cytosolic proteins can diffuse out of the cell via these holes, and (3) dye molecules can be detected diffusing into the cell or out of the cell through the same membrane holes. Diffusion of dendrimers through holes is sufficient to explain the uptake of G5 amine-terminated PAMAM dendrimers into cells and is consistent with the lack of uptake of G5 acetamide-terminated PAMAM dendrimers.

INTRODUCTION

Poly(amidoamine) (PAMAM) dendrimers have demonstrated great promise for a variety of biomedical applications. This class of polymers has a number of favorable properties including well-defined chemical structure, globular shape, low polydispersity index (close to 1.0), biocompatibility, and controlled terminal functional groups. Amine-terminated PAMAM dendrimers have proven to be effective as a nonviral cell transfection agent (*1*, *2*). Modification of the PAMAM dendrimer surface functional groups with targeting compounds, fluorescent groups, and drugs have produced promising imaging and therapeutic agents (*3*−*7*).

The success of PAMAM dendrimers in biomedical applications such as those mentioned above raises the question regarding how PAMAM dendrimers interact with cell membranes at the molecular level. The complex structure of cell membranes has prompted several research groups to employ phosphatidylethanolamine-containing vesicles as model systems. Efficient cross-membrane transport and membrane disruption were observed with a strong dependence on dendrimer size (generation), chemical structure of the dendrimer, and composition of the model membranes (*8*−*10*). Based upon these studies, the internalization mechanism of dendrimers into cells has been explained as a dendrimer-mediated endocytosis. Endocytosis is a complex multistep process and can be generally described in terms of cell transfection efficiency. A cationic polymer (e.g. poly(lysine) or PAMAM dendrimer) is proposed to bind with the outer cell membrane and be internalized into the cell through endocytosis. The polymer then exits from the endosome, which is a step that controls the transfection efficiency (*11*). The electrostatic interaction between the polymer and the lipid bilayer membrane and concomitant osmotic imbalance have been understood as important driving forces for polycation-mediated endocytosis (*10*, *12*). Other oligomers that may follow similar pathways include the cell-penetrating peptides (CPPs) such as Tat and oligoarginine (*13*, *14*).

The model systems studied to date show good evidence for membrane disruption by PAMAM dendrimers (*8*, *10*).

* To whom correspondence should be addressed. Phone: (734) 763-2283. Fax: (734) 763−2307. E-mail: mbanasza@umich.edu.
† Program in Applied Physics.
‡ Program in Biophysics.
§ Program in Macromolecular Science and Engineering.
|| Department of Internal Medicine.
⊥ Department of Physics.
⊗ Department of Chemistry.
▽ Center for Biologic Nanotechnology.

10.1021/bc049962b CCC: $27.50 © 2004 American Chemical Society
Published on Web 06/22/2004

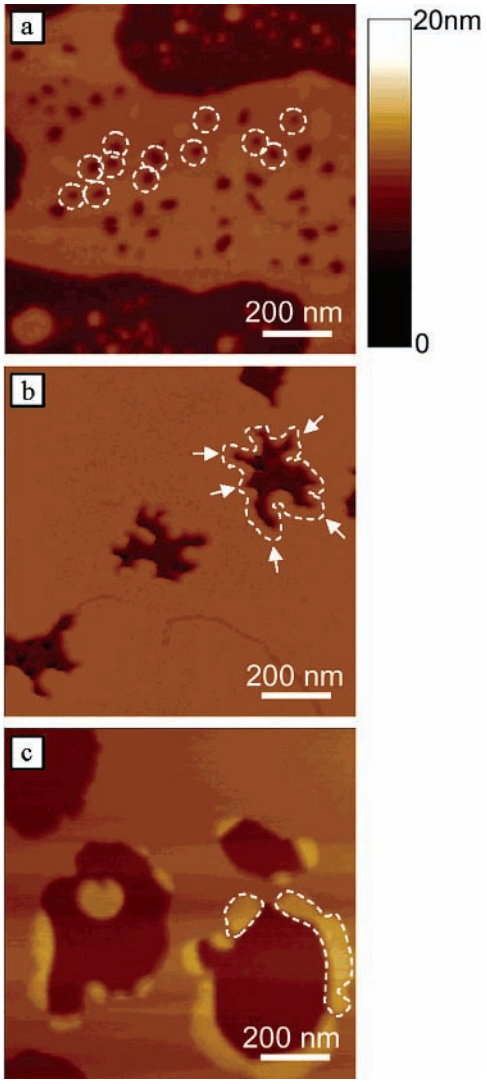


Figure 1. AFM height images of DMPC bilayer after interaction with dendrimers. White lines highlight some of the areas where dendrimers have affected the bilayer (the dendrimer themselves cannot be seen on these images). (a) G7-NH_2 cause the formation of small holes, 15−40 nm in diameter, in the previously intact parts of the bilayer (see dark spots). (b) G5-NH_2 remove lipid molecules primarily from edges of existing bilayer defects, i.e., dark areas grow in size, see arrows. (c) G5-Ac do not remove lipid molecules from the surface. Instead they adsorb to edges of existing bilayer defects.

However, they do not provide direct evidence for the nature of the membrane/dendrimer interaction or the endocytosis process. To study this interaction in greater detail, we have used atomic force microscopy (AFM) to directly image supported DMPC lipid bilayers upon exposure to PAMAM dendrimers. The results of this study are summarized in Figure 1 (*15*, *16*). G7 with amine-terminated surfaces (G7-NH_2) generated 15−40 nm-size holes in the bilayer (Figure 1a). In the case of G5-NH_2, however, few new holes were observed (Figure 1b). Instead, the dendrimer removed lipid molecules from edges of existing bilayer defects expanding the size. Amine-terminated dendrimers are protonated in neutral water (*9*, *17*) and therefore can be anticipated to have a substantial electrostatic interaction with the DMPC lipid. The G7-NH_2 has a larger number of primary amine groups (512) than the G5-NH_2 (128) at the same molar concentrations, resulting in a greater charge density. G7-NH_2 also has a larger radius of curvature. These two physical differences likely contribute to the higher level of membrane disruption for the G7 dendrimer. Varying the chemical functionality of the surface significantly changed the outcome of the interaction. Acetamide-terminated G5 PAMAM dendrimer (G5-Ac) did not result in hole formation or the expansion of existing defects. Instead, G5-Ac intercalated at edges of preexisting bilayer defects (Figure 1c). These results illustrate that holes are formed and/or expanded in DMPC-supported bilayers by the addition of G7-NH_2 or G5-NH_2 (both positively charged in neutral water). The addition of neutral G5-Ac dendrimer does not cause hole formation at 10−100 nM concentrations. This set of results is particularly striking because PAMAM dendrimers must have charge-neutralized surfaces for selective drug delivery applications (*3*, *18*). These results confirm that amine-terminated materials show undesirable nonselective uptake into tested cell types. In contrast, the amine-terminated dendrimers are highly efficient nonspecific transfection agents while the acetamide-terminated polymers do not transfect cells.

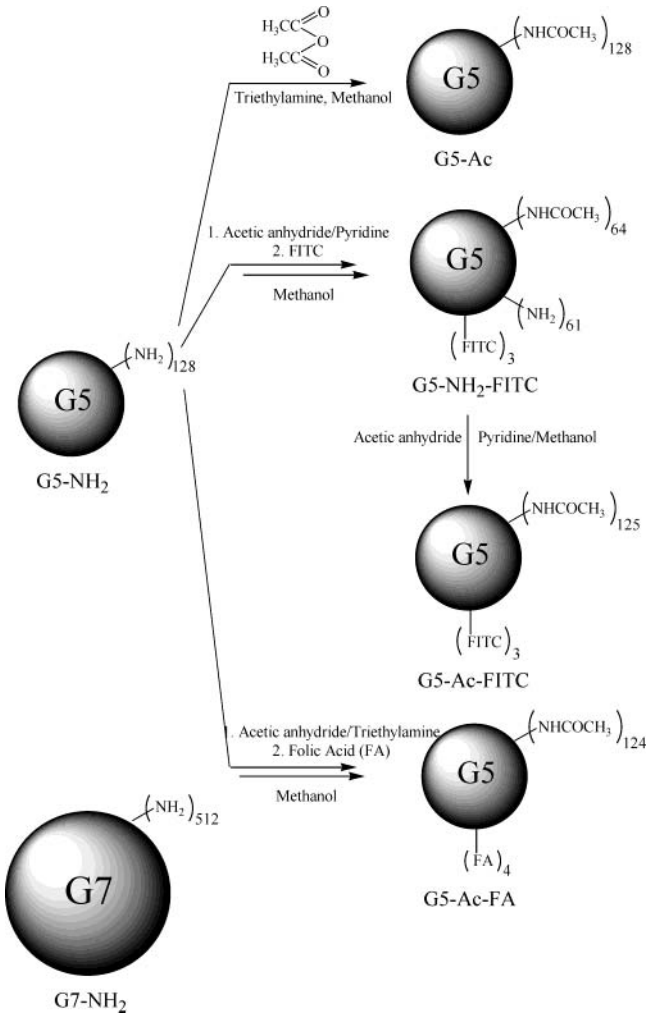
The AFM experiments on supported lipid bilayers suggest the following hypotheses: (1) amine-terminated PAMAM dendrimers can induce the formation of holes in cell membranes, (2) the holes generated in the cell membranes allow the diffusion of molecules into and out of the cell, (3) acetamide-terminated dendrimers do not enter cells because they do not interact with membrane phospholipids and generate holes.

In this paper, we test the three hypotheses by investigating the interaction of G7-NH_2, G5-NH_2, and G5-Ac PAMAM dendrimers with KB and Rat2 cell membranes. We have evaluated the release of two cytosolic enzymes, lactate dehydrogenase (LDH) and luciferase (Luc), from the cells upon exposure to dendrimers in terms of generation and the identity of surface functional group (amine or acetamide). The temperature dependence of the binding and internalization has also been studied. It was found that G7-NH_2 and G5-NH_2 PAMAM dendrimers induce significant leakage of LDH and Luc whereas G5-Ac does not. Similarly, the presence of G5-NH_2 was shown to make the cell membrane permeable to the small molecules such as propidium iodide (indicating diffusion into cells) and fluorescein (indicating diffusion out of cells) even though the cell was still viable. These results, in addition to others discussed in this paper and the AFM data illustrated in Figure 1, provide direct experimental support for hypotheses 1, 2, and 3.

EXPERIMENTAL PROCEDURES

Preparation of Materials. Generation 5 and 7 PAMAM dendrimers were synthesized at the Center for Biologic Nanotechnology, University of Michigan. All other chemicals were acquired from Aldrich and used without further purification. Water used in this work was purified by Milli-Q Plus 185 system and had a resistivity higher than 18 MΩ/cm. The PAMAM dendrimers were purified using ultrafiltration and dialysis (*2*). Purified PAMAM dendrimers were then acetamide capped using triethylamine (20% mol excess to acetic anhydride) as a proton acceptor as described in the literature (*18*). Folic acid (FA) was conjugated to G5 PAMAM dendrimers after partial acetylation, followed by full acetylation (*3*). Numbers of primary amine end groups were measured by potentiometric titration (*18*) and numbers of modified end groups were calculated based upon the titration result of the starting G5-NH_2.

Scheme 1. End Group Modification of PAMAM Dendrimers Investigated in This Study: Amine End Groups (−NH_2, Generations 5 and 7) and Acetamide End Groups (−$NHCOCH_3$, Generation 5)[a]



[a] Note that the numbers of end groups and functional groups are given as the theoretical values in this scheme.

Dendrimer−fluorescein conjugates were obtained as follows. G5-NH_2 (54.4 mg) in 5 mL of methanol was acetylated by adding 11.7 mg of acetic anhydride in an equal volume of methanol and vigorously stirring the mixture for 24 h, resulting in acetylation of half the primary amine groups (Scheme 1). Fluorescein isothiocyanate (FITC) (2.62 mg) in 10 mL of methanol was then added, and the mixture was stirred for 24 h. 10 mL of the reaction mixture was then dialyzed against 0.5 M NaCl solution followed by dialysis against water (six times, 4 L) for 3 days to remove methanol solvent and unreacted small molecules. The water was removed using a rotary evaporator, and the resulting solids were redissolved into 3−5 mL of water. Lyophilization for 3 days produced solid G5-NH_2−FITC conjugate. The remaining 10 mL of the reaction mixture including unpurified G5-NH_2−FITC conjugate and unreacted small molecules was fully acetylated and purified, resulting in G5-Ac−FITC.

Identification of Dendrimer Conjugates. The dendrimer-based conjugates (G5-Ac−FA, G5-NH_2−FITC, and G5-Ac−FITC) were analyzed by UV/vis spectroscopy. The maximum absorbance (λ_{max}) of FA was shifted from 280 to 289 nm after conjugation, indicating that FA was conjugated to the PAMAM. Absorbance peaks of free FITC appeared at wavelengths of 270 and 490 nm. After the conjugation reaction, the FITC peaks were shifted to 280 and 500 nm, respectively. Further purification of synthesized dendrimers was performed by repeated ultrafiltration, dialysis with water and methanol, and lyophilization (*3*, *19*). The dendrimer−FITC conjugates were also evaluated by gel eletrophoresis after purification using agarose gel with 2% ethidium bromide to confirm that the polymers have the desired charged groups and no impurities are present such as free FITC.

MALDI-TOF measurements were carried out using a Waters Tofspec-2E (Milford, MA) using the linear delayed extraction mode. The instrument was calibrated with a mixture of known proteins in a sinapinic acid matrix before use. Five microliters of each sample solution in ultrapure water/methanol (50/50 by vol %) was mixed with 5 μL of matrix solution, and 1 μL spots were placed on the target. The matrix solution was 2,5-dihydroxybenzoic acid (Aldrich, Milwaukee, WI), dissolved in 50/50 acetonitrile/water with 0.1% TFA, at a concentration of 10 mg/mL. Five laser shots were added per spectrum, and multiple spectra were added together. The mean smoothing algorithm was applied to the data, and the baseline was subtracted. A comparison between theoretical and experimental molar masses is provided in Table 1.

Preparation and AFM Measurement of Supported DMPC Lipid Bilayers. DMPC lipid bilayers were chosen since these phospholipids are an important part of mammalian cell membranes, and the lipid bilayers are easily accessible to high-resolution imaging by AFM under physiological conditions. DMPC was purchased from Avanti Lipids, Alabaster, AL. A 0.5−0.7 mg/mL suspension of small, unilamellar vesicles (SUVs) was prepared using literature procedures (*15*). Supported lipid bilayers were formed by depositing 80 μL of liposome suspension on a piece of freshly cleaved mica. After an incubation time of about 20 min, the sample was gently rinsed with water to remove excess lipids and placed in the AFM for imaging as described elsewhere (*15*). All AFM measurements were performed in tapping mode on a Nanoscope IIIa Multimode scanning probe microscope from Digital Instruments (DI, Veeco Metrology Group, Santa Barbara, CA). The AFM was equipped with a liquid cell (DI) and a silicone nitride cantilever (DI model NPS, spring constant 0.32 N/m, length 100 μm) operating at a drive frequency of about 6−9 kHz. After taking an initial image of the bilayer, 20−30 μL of dilute dendrimer solution was injected into the liquid cell. The resulting dendrimer concentrations were in the range of 10−100 nM. After adding the dendrimers, imaging continued to observe their effect on the bilayer.

Cell Lines. The KB and Rat2 cell lines were purchased from the American Type Tissue Collection (ATCC; Manassas, VA) and grown continuously as a monolayer at 37 °C, and 5% CO_2 in RPMI 1640 medium (Mediatech, Herndon, VA) and Dulbecco's modified Eagle's medium (DMEM, Gibco, Eggenstein, Germany), respectively. Both cell lines were transfected to permanently express the Luc gene using PAMAM dendrimer-mediated gene transfection as previously reported (*1*, *20*). The Luc expressing KB and Rat2 Cells are noted as KBpLuc and Rat2pLuc, respectively. The RPMI 1640 and DMEM media were supplemented with penicillin (100 units/mL), streptomycin (100 μg/mL), and 10% heat-inactivated fetal bovine calf serum (FBS) before use. Folic acid receptor expressing KB cell line (FAR-KB) was also used for specific binding with G5-Ac−FA. The KB cell line for specific binding was cultured in the RPMI 1640 medium without

Table 1. Molar Mass and Chemical Composition of the Dendrimers Employed in This Study

dendrimers	no. of amine terminal groups	no. of acetamide terminal groups	no. of FITC	no. of FA	theoretical molar mass[d]	experimental molar mass[e]
G5-NH_2	110[a]	-	-	-	28826	28260
G5-Ac	0	110[b]	-	-	32880	32254
G5-NH_2−FITC	51[c]	55[c]	3[c]	-	29939	29820
G5-Ac−FITC	0	106[c]	3[c]	-	32081	31186
G5-Ac−FA	13[c]	93[c]	-	4[c]	33394	32519

[a] Measured by potentiometric titration. [b] Calculated from titration result of G5-NH_2. [c] Determined by stoichiometry of the conjugation reaction based on the titration data of starting G5-NH_2. [d] Theoretical molar mass values for G5-Ac, G5-NH_2−FITC, G5-Ac−FITC, and G5-Ac−FA are calculated based upon the experimental molar mass of the G5-NH_2 starting material employed. Note that G5-Ac and G5-Ac−FA were prepared from G5-NH_2 containing 110 primary amine groups and having a molar mass of 28,260 as measured by MALDI-TOF. The G5-NH_2−FITC and G5-Ac−FITC were prepared from starting G5-NH_2 with 109 primary amine groups and molar mass of 26,462 as measured by MALDI-TOF. [e] Measured by MALDI-TOF spectroscopy.

folic acid (Mediatech, Herndon, VA) for at least 4 days, resulting in the FAR-KB cell line.

Luc and LDH Assays. To assess the release of cytosolic enzymes caused by general toxicity, the cytotoxicity of the G5 dendrimers was preassayed using a BCA protein assay (*21*). The assay results show that the both G5-NH_2 and G5-Ac are not cytotoxic up to a 500 nM concentration (>90% cell viability). Based on this information, the assays performed to investigate the cytosolic enzyme release were carried out in a dendrimer concentration range of 10−500 nM. Within this range, dendrimers are non-cytotoxic so the observed enzyme release can be ascribed to an increase in cell membrane permeability as opposed to general lysis due to cell death.

A concentration of 5×10^4 cells/well of both KBpLuc and Rat2pLuc cells were seeded on 24-well plates to prepare cell monolayers. After 24 h, cell culture media were removed and replaced by 300 μL/well of dendrimer/PBS (Ca^{2+}, Mg^{2+}) solutions at various dendrimer concentrations. Cells were incubated either at 6 or 37 °C at 5% CO_2. The supernatants were then collected at specific time points ranging from 1 h to 3 h. Cell debris were removed by centrifugation of the supernatant (at 400 × g for 2 min).

The LDH activity in the cell supernatant was analyzed using an LDH assay kit (Promega Co., Madison, WI). The supernatant (20 μL) was mixed with 50 μL of reagent solution, incubated at room temperature for 30 min, followed by adding 50 μL of stop solution (acetic acid). The change in absorbance (proportional to LDH activity) was measured at 490 nm at room temperature using Spectra Max 340 ELISA Reader (Molecular Devices, Sunnyvale, CA) spectrophotometer. Luc activity was quantified using a chemiluminescence assay. Light emission from collected supernatants (10 μL) incubated with 2.35×10^{-2} μmol of luciferin substrate (Promega Co., Madison, WI) was measured in the chemiluminometer (LB96P; EG & G/Berthold, Gaithersburg, MD). The measured LDH and Luc activities were either adjusted for the protein concentration of the sample or recalculated by percentage to the activities of cell lysates of intact cells.

Fluorescence Microscopy Observation. Rat2 cells (4×10^4) were seeded on six MatTek glass-bottom Petri dishes (35 mm) and incubated at 37 °C under 5% CO_2 for 24 h. The media was removed, and 2 mL of dendrimer−FITC conjugate/PBS (Ca^{2+}, Mg^{2+}) solution was added. Three dishes were incubated with added dendrimer solutions at 37 °C under 5% CO_2 for 1 h. The other three dishes were precooled at 6 °C for 30 min before adding the dendrimer solutions and incubated with the dendrimer solution at 6 °C for 1 h. Dendrimer solutions were removed, and the resulting cell monolayer was washed with PBS. Cells were fixed with 2% formaldehyde

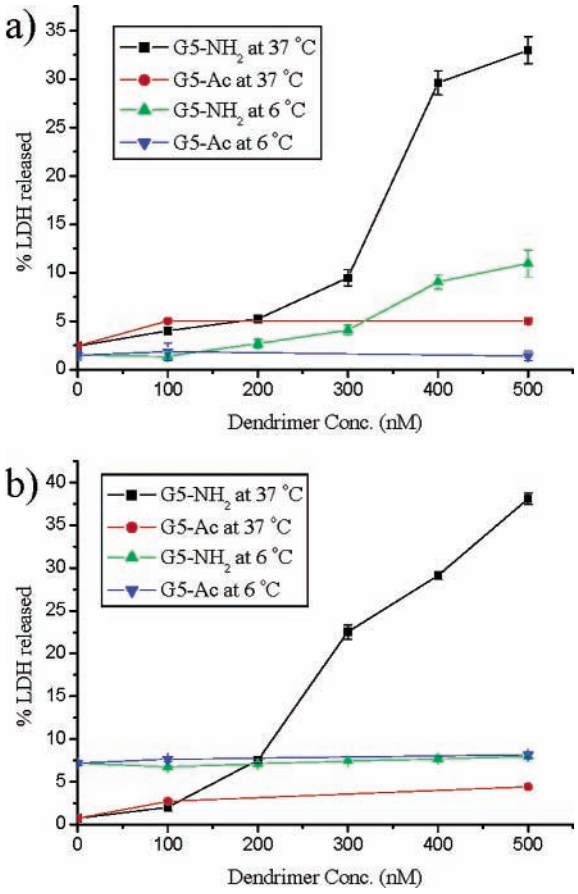


Figure 2. Dose-dependent LDH release from (a) KBpLuc and (b) Rat2pLuc cell lines at 37 °C and 6 °C by G5-NH_2 and G5-Ac PAMAM dendrimers.

in the PBS (Ca^{2+}, Mg^{2+}) at room temperature for 10 min, followed by washing with PBS twice. DNA in the cell nucleus was then stained by DAPI. The samples were imaged with a Nikon diaphot 200 inverted microscope, using appropriated filters and dichroic to image FITC (465−495 nm excitation, 505 nm dichroic, 515−555 nm emission). A mercury vapor lamp was the light source for the epiflourescense imaging. Nikon 20× plan Apo 0.9 na was used as an objective. Images were captured with an Orca-ER16 bit gray scale CCD. The light path filters were controlled with Sutter Instrument Company's Lambda N2 TTL controller, and the camera was driven with Compix software.

Assessment of Reversibility of Dendrimer-Induced Membrane Permeability. Four wells with 5×10^4 Rat2 cells were prepared for each particular dendrimer concentration resulting in 16 wells in total. The supernatants were removed from two wells out of four

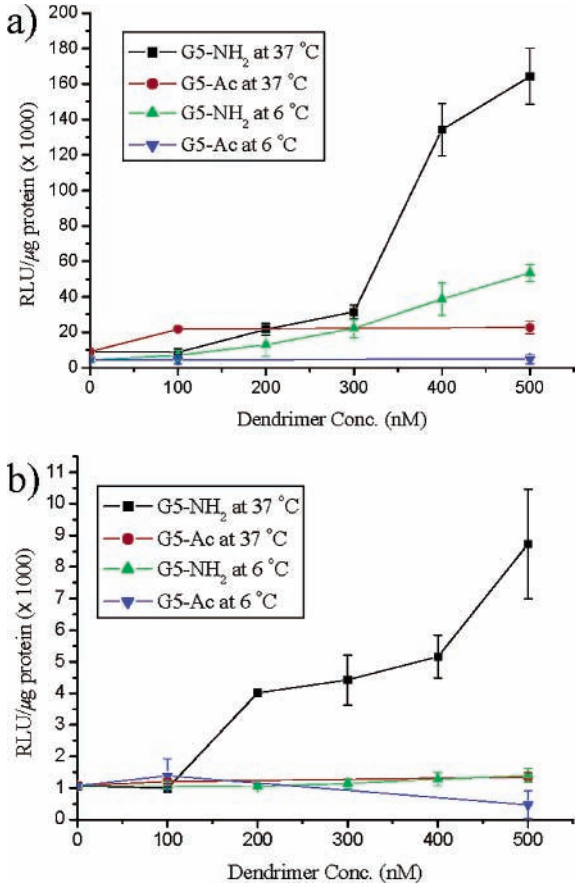


Figure 3. Dose-dependent Luc release from (a) KBpLuc and (b) Rat2pLuc cell lines at 37 °C and 6 °C by G5-NH_2 and G5-Ac PAMAM dendrimers.

wells after 1 h incubation and assayed using the techniques described above for LDH. These wells were then replaced with PBS and assayed again after an additional2 h. The other two wells were incubated with G5-NH_2 dendrimer solutions for 3 h and also assayed.

PI and FDA Staining and Flow Cytometry. The cells were stained with propidium iodide (PI; Molecular Probes, Eugene, OR) and fluorescein diacetate (FDA; Molecular Probes, Eugene, OR) by modification of a protocol described previously (*22*). One milliliter of 2.5 $\times$ 10^5 KB and Rat2 cells was seeded in 12-well plates and incubated at 37 °C under 5% CO_2 for 24 h. FDA staining was performed as follows. The media was removed, and 50 μL of 10 mg/mL FDA/H_2O solution was added. Dendrimer/PBS solution (300 μL) was then added after 30 min and incubated for another 30 min. For PI staining, 300 μL of dendrimer/PBS solution was added after removal of cell culture media followed by addition of 50 μL of 10 mg/mL PI/H_2O solution. For both PI and FDA staining, total incubation time was 1 h. After the incubation, cells were trypsinized with trypsin−EDTA and centrifuged at 1200 rpm for 5 min. Resulting cell pellets were then resuspended in PBS with 0.1% bovine serum albumin (BSA).

The fluorescence signal of individual cells was assessed with a Coulter EPICS/XL MCL Beckman-Coulter flow cytometer and data were analyzed using Expo32 software (Beckman-Coulter, Miami, FL) (*23*, *24*).

RESULTS

Dendrimer-Induced Enzyme Leakage from Cells. The effects of G7-NH_2, G5-NH_2, and G5-Ac dendrimers on the membrane permeability of KB and Rat2 cells were investigated using LDH and Luc assays. Concentration dependent dendrimer-induced LDH release at 37 and 6 °C is shown in Figure 2. As the concentration of G5-NH_2 increases, the LDH release from both KBpLuc and Rat2pLuc increases. In contrast, neither cell line releases a significant amount of LDH as a result of exposure to G5-Ac. KBpLuc and Rat2pLuc cells incubated with both G5-NH_2 and G5-Ac at 6 °C exhibited no LDH release. Luc release followed the same general trend observed for LDH release (Figure 3).

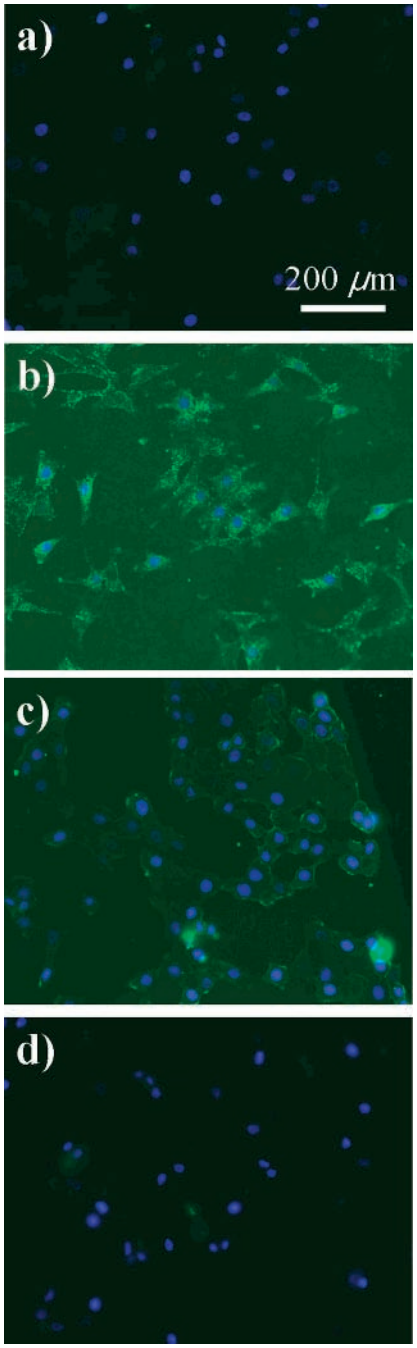


Figure 4. Fluorescence microscopy of (a) untreated Rat2 cells (control), (b) Rat2 cells incubated with 200 nM G5-NH_2−FITC at 37 °C for 1 h, (c) Rat2 cells incubated with 200 nM G5-NH_2−FITC at 6 °C for 1 h, and (d) Rat2 cells incubated with 200 nM G5-Ac−FITC at 37 °C for 1 h. Blue spots represent the cell nucleus stained by DAPI and green spots are dendrimer−FITC conjugates.

Binding and Internalizaton of Dendrimers. To investigate the binding and internalization of den-

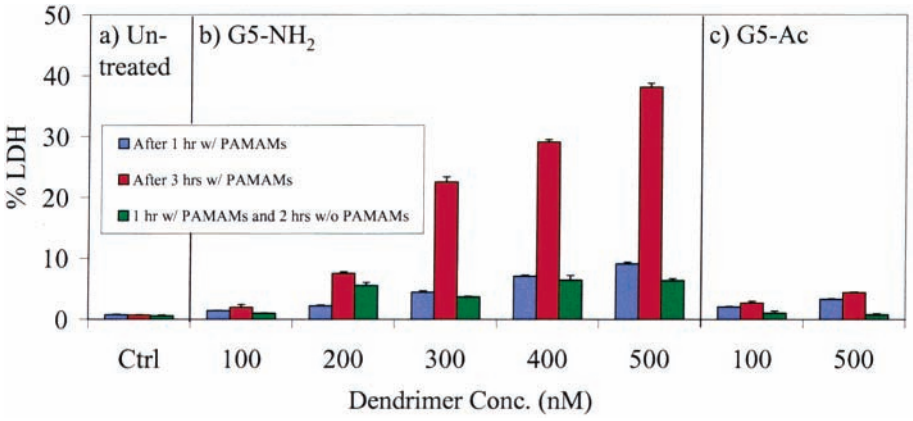


Figure 5. Enzyme release of Rat2 incubated with (a) G5-NH_2 and (b) G5-Ac. Light blue and red bars represent the release after 1 h and 3 h incubation with dendrimer solutions, respectively. Green bars represent enzyme release after 1 h incubation with dendrimers followed by washing and 2 h incubation in pure PBS buffer to allow recovery of membrane integrity.

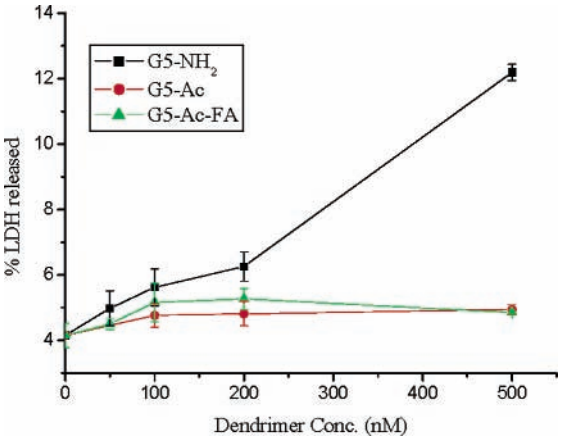


Figure 6. Comparison of interaction of G5-NH_2, G5-Ac, and G5-Ac−FA with FAR-KB cell line. Note that G5-Ac−FA is internalized by receptor-mediated endocytosis.

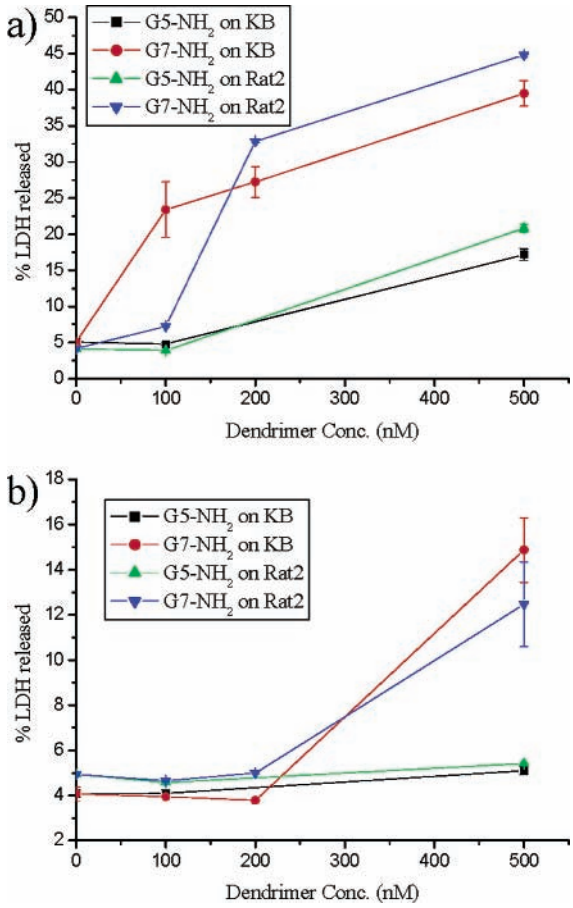


Figure 7. Comparison of different dendrimer generations: Enzyme release from KB and Rat2 cells after incubation with G5-NH_2 and G7-NH_2 at (a) 37 °C and (b) 6 °C.

drimers, fluorescence images of Rat2 cells were taken after incubation with dendrimer−FITC conjugates at different temperatures. Rat2, a fibroblast cell line, was chosen in this experiment due to its stable surface adherence. DNA in the cell nucleus was stained by DAPI. The stained nuclei can be seen as blue spots in Figure 4a−d while dendrimer−FITC conjugates emit green fluorescence. Figure 4b shows a fluorescence image of Rat2 cells incubated with 200 nM of G5-NH_2−FITC at 37 °C for 1 h. Dendrimers are apparent both inside the cells as well as associated with the membrane. This indicates that the G5-NH_2−FITC dendrimers interact with the cell membrane and enter the cell at physiological temperature (37 °C). At 6 °C, however, although the dendrimers associate with the cell membrane, no significant internalization was observed (Figure 4c). Identical experiments employing G5-Ac−FITC at 200 nM concentration indicate no association with the cell membrane nor internalization into the cell (Figure 4d).

Reversibility of Dendrimer-Induced Membrane Permeability. Testing the reversibility of the dendrimer-induced membrane permeability was performed by replacing a solution of G5-NH_2 dendrimer with a dendrimer-free PBS and monitoring the LDH release. The dendrimer-induced membrane permeability of cell lines in the presence of G5-NH_2 was not permanent and cells recovered their membrane integrity upon removal of dendrimer/PBS solutions (Figure 5), as indicated by LDH release. This "resealing" behavior is consistent with the observation that G5-NH_2 dendrimers are not cytotoxic up to 500 nM as after removal of the dendrimer solution. The cell can return the membrane permeability back to the normal level.

The Role of Dendrimer Surface Functionalization: Amine vs Acetamide. To test possible mechanisms of internalization and their implications for cytosolic enzyme release (Figure 6), comparisons between G5-NH_2, G5-Ac, and G5-Ac−FA were carried out using the LDH assay. It has been demonstrated that internalization of G5-Ac−FA occurs through receptor-mediated endocytosis, initiated by binding of folic acid (FA) to folic acid receptors (FAR) on KB cells (*3*). Under the same conditions, no uptake of G5-Ac is observed. The LDH

assay results show no significant LDH release from KB cells following a 3-h incubation with G5-Ac−FA or G5-Ac. However, incubation with G5-NH_2 induced significant LDH release, consistent with previous experiments.

Effect of Dendrimer Generation on Cell Membrane Permeability. It is well-known that high generation PAMAM dendrimers are unusually effective at disrupting cell membranes (*10, 25*). We also observed a distinct difference in the ability to form holes in supported DMPC bilayers (Figure 1). To test this effect upon LDH release, G5-NH_2 and G7-NH_2 dendrimers were analyzed at 37 and 6 °C. The results of an LDH assay comparing enzymatic leakage for both KB and Rat2 cell lines after exposure to varying concentration of G5-NH_2 and G7-NH_2 are shown in Figure 7. At 37 °C, G7-NH_2 causes a greater release of LDH than G5- NH_2 at all concentrations. In addition, whereas LDH release was not observed for G5-NH_2 at 6 °C, the G7-NH_2 was still capable of causing LDH release (Figure 7b).

Are Holes Present in the Cellular Membrane? Tests for Diffusion of Dyes. To study passive diffusion in and out of the cell, small molecular probes (PI and FDA) were used according to a modification of a previous literature method (*22*). PI is readily internalized into cells with disrupted membranes but is excluded from cells with intact membranes. On the other hand, FDA, a nonfluorescent compound, readily enters intact cells and then undergoes hydrolysis by endogenous esterase, resulting in release of fluorescein into the cytosol. The cytosolic fluorescein is not able to transverse a normal cell membrane without holes. Thus, the FDA is used as a marker for diffusion-out. Consequently, it is presumed that fluorescence intensity of PI should be increased and that of fluorescein should be decreased if the presence of G5-NH_2 makes the membrane permeable to these dyes.

Figure 8 shows flow cytometer data of Rat2 cells incubated with G5 PAMAM dendrimers and then stained with PI. As illustrated in Figure 8a−c and 8e, PI is internalized into the cells in a G5-NH_2 concentration dependent manner. In the case of G5-Ac, however, no significant difference in PI incorporation was observed as compared to the control cells (Figure 8d,e).

Fluorescence intensity of fluorescein in cells as a function of G5-NH_2 dendrimer concentration is illustrated in Figure 9. Consistent with previous results (*22*), FDA was internalized through intact cell membranes, resulting in a substantial signal for free fluorescein in Rat2 cells. As the G5-NH_2 concentration increased, however, the signal intensity of the fluorescein significantly decreased, indicating that the membrane had become permeable (Figure 9e). Rat2 cells incubated with G5-Ac did not show any noticeable difference from the control experiment (Figure 9d).

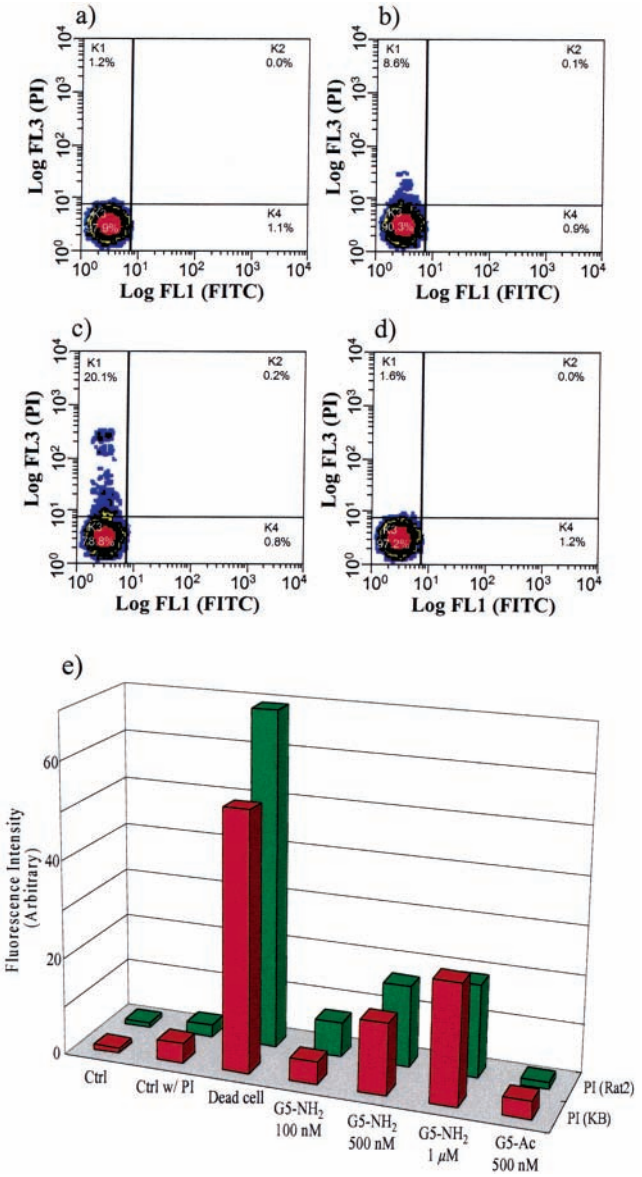


Figure 8. Flow cytometer diagrams of Rat2 cells at several representative conditions. (a) untreated, (b) incubated with PI, (c) incubated with 500 nM G5-NH_2 and PI, and (d) incubated with 500 nM G5-Ac and PI at 37 °C for 1 h. (e) Signal intensity of PI fluorescence for KB and Rat2 cells after incubation with dendrimers. Controls (first three columns): cells in pure PBS buffer, cells in the buffer with PI, and dead cells incubated with 30% ethanol solution for 30 min.

DISCUSSION

Summary of Evidence for PAMAM-Induced Hole Formation in the Cell Lipid Bilayer. AFM observation (Figure 1) of holes formed in DMPC lipid bilayers triggered our in vitro experiments to investigate the interactions between dendrimers and viable cell membranes. The release of cytosolic enzymes, LDH and Luc, demonstrates an increase in membrane permeability (Figures 2 and 3). The increased permeability is consistent with the hypothesis of PAMAM-induced hole formation in the cell lipid bilayer. The larger enzyme of the two, LDH, is a 135−140 kDa complex protein with a hydrodynamic radius of ∼4.3 nm (*26*). Thus, it is small enough to fit through the 15−40 nm holes suggested by the AFM experiment. The smaller 62 kDa enzyme, Luc composed of α- and β-subunits, should be able to diffuse through the hole. The overall dimensions of this heterodimer are reported as 7.5 nm × 4.5 nm × 4.0 nm (∼2.7 nm in radius) (*27*). Membrane permeability returns to normal following removal of the dendrimer-containing solution. In contrast to the supported lipid bilayer, where holes remain for a relatively long time, the cell has additional lipid available and the membrane can regenerate its membrane within 2 h (as assayed by permeability in Figure 5).

Although permeability to cytosolic enzymes is consistent with hole formation, the possibility that cytosolic enzymes leak out during an endocytosis process must be addressed. This is a particularly important issue since amine-terminated PAMAM dendrimers, protonated in aqueous solution, have been proposed to enter cells via an endocytosis mechanism (*11*). However, experiments

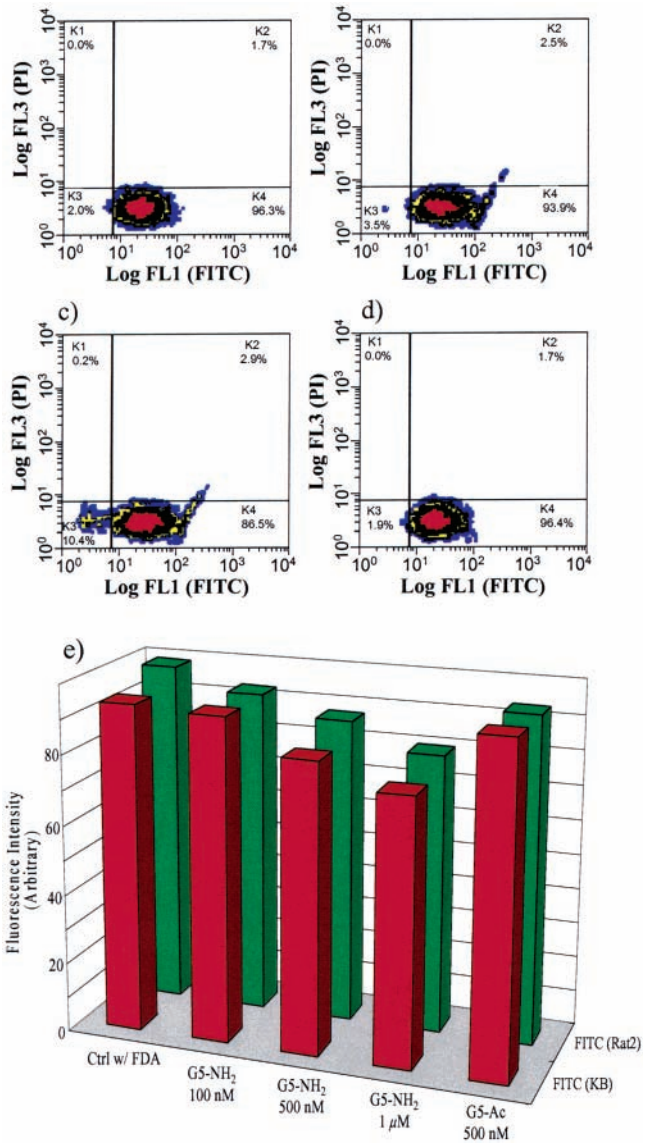


Figure 9. Flow cytometer diagrams of Rat2 cells at several representative conditions. (a) untreated, (b) incubated with FDA and 500 nM G5-NH_2, (c) incubated with FDA and 1 μM G5-NH_2, and (d) incubated with FDA and 500 nM G5-Ac at 37 °C for 1 h. (e) Signal intensity of fluorescein fluorescence for KB and Rat2 cells after incubation with dendrimers. Control (first column): cells with FDA in PBS buffer.

using G5-Ac−FA, a material known to undergo endocytosis via the folic acid receptor, did not cause leakage of LDH or Luc (Figure 6). This demonstrates that noncharged PAMAM dendrimers can enter the cell via receptor-mediated endocytosis without causing cytosolic enzyme leakage (*13*, *14*). However, we still cannot rule out the possibility that the G5-NH_2 dendrimer undergoes an endocytosis process sufficiently different in mechanism to cause leakage. To test this possibility, we examined the behavior of two common dyes in the presence of G5-NH_2 and G5-Ac dendrimers.

PI and FDA were used respectively as tests for the mechanistic process of diffusion in and out of the cells. If dendrimer-induced holes are present, the dyes would be expected to diffuse in and out of the cell, respectively. However, the positively charged PI would be repelled from the polycationic G5-NH_2 dendrimer in aqueous solution and would not be anticipated to accompany the dendrimer during endocytosis. The experimental data shows that as G5-NH_2 concentration increases, PI signal intensity is increased while FITC intensity is decreased (Figures 8 and 9). The diffusion behavior of these small molecular probes is consistent with the formation of small holes in the membrane. The PI data is inconsistent with the molecules accompanying a polycation-mediated endocytosis.

To further test the possibility of an endocytosis mechanism, we examined the temperature dependence of cytosolic enzyme leakage (Figures 2, 3, 4, and 7). At 6 °C, no enzyme leakage is observed for G5-NH_2 dendrimers at concentrations showing substantial leakage at 37 °C. This is consistent with either endocytosis or hole formation mechanisms as both would be expected to be temperature dependent. When G7-NH_2 dendrimer is employed at 6 °C, however, cytosolic enzyme leakage can again be observed. Note that endocytosis processes will be just as disfavored as for the G5-NH_2 case. However, as indicated in Figure 1, G7-NH_2 has a greater propensity to form holes. Thus, it is not surprising that G7-NH_2 can continue to cause hole formation in the cell plasma membrane.

Taken as a whole, the leakage of the cytosolic enzymes, the free diffusion of PI and FITC dye, and the direct observations made by fluorescence microscopy as shown in Figures 2, 3, 4, 7, 8, and 9 provide experimental support for hypotheses 1 and 2: (1) amine-terminated PAMAM dendrimers can induce the formation of holes in cell membranes, and (2) the holes generated in the cell membranes allow the diffusion of polymers, enzymes, and molecules into and out of the cell. In addition, these data support hypothesis 3 that acetamide terminated dendrimers do not cause holes (Figure 1) or induce enzyme release (Figures 2 and 3). These data are consistent with previous observations that acetylated PAMAM dendrimers prevent nonselective interaction between dendrimers and cell membrane (*3*, *18*).

Cell transfection (internalization) is a complicated process. It has previously been reported that dendrimer-mediated transfection occurs mainly through active uptake (e.g. in the case of dendrimer/DNA complexes or noncharged dendrimers with a cell surface targeting moiety) (*11*). Evidence of membrane disruption caused by positively charged dendrimers has been demonstrated using model membranes such as anionic vesicles (*8*) as well as synthetic membranes with a preference for nonlamellar phases (*10*). The experimental data in this paper suggests an alternative mechanism involving the formation of 15−40 nm holes in the membrane. This proposal is consistent with the previous experiments showing dendrimer-mediated transfection and dendrimer-induced membrane disruption as well as the cytosolic enzyme leakage assays, dye diffusion, fluorescence microscopy, and AFM experiments discussed in this paper. Additional experiments are planned to fully address this question and will be the subject of future reports.

Conclusions: Relationship of These Experiments to Targeted Drug Delivery. Intracellular drug delivery has advantages over simple diffusion of drug into cells. A number of candidates for drug delivery vehicles have been evaluated mostly based on charged polymeric materials (*5*, *28*). Higher drug efficiency can be achieved with therapeutic transport agents targeted to specific cells. From our results, the positively charged polymeric material causes the formation of holes or the dendroporation of the cell membrane leading to nonselective internalization into cells. Moreover, the polycation eventually causes cell death if the concentration is high enough (>500 nM in this study). Charge neutral dendrimers, however, do not cause hole formation or den-

droporation and show no nonspecific binding or internalization. They can be internalized into the cell only if the dendrimer is linked to a targeting compound such as FA as previously described (*3*).

ACKNOWLEDGMENT

This project has been funded with federal funds from the National Cancer Institute, National Institutes of Health, under Contract # NOI-CO-97111. S.H. appreciates the Dwight F. Benton Fellowship from the Program in Macromolecular Science and Engineering, College of Engineering, University of Michigan.

LITERATURE CITED

(1) Bielinska, A., Kukowska-Latallo, J. F., Johnson, J., Tomalia, D. A., and Baker, J. R. (1996) Regulation of in vitro gene expression using antisense oligonucleotides or antisense expression plasmids transfected using starburst PAMAM dendrimers. *Nucleic Acids Res. 24*, 2176−2182.

(2) Kukowska-Latallo, J. F., Raczka, E., Quintana, A., Chen, C. L., Rymaszewski, M., and Baker, J. R. (2000) Intravascular and endobronchial DNA delivery to murine lung tissue using a novel, nonviral vector. *Hum. Gene Ther. 11*, 1385−1395.

(3) Quintana, A., Raczka, E., Piehler, L., Lee, I., Myc, A., Majoros, I., Patri, A. K., Thomas, T., Mulé, J., and Baker, J. R. (2002) Design and function of a dendrimer-based therapeutic nanodevice targeted to tumor cells through the folate receptor. *Pharm. Res. 19*, 1310−1316.

(4) Esfand, R., and Tomalia, D. A. (2001) Poly(amidoamine) (PAMAM) dendrimers: from biomimicry to drug delivery and biomedical applications. *Drug Discovery Today 6*, 427−436.

(5) Gillies, E. R., and Fréchet, J. M. J. (2002) Designing macromolecules for therapeutic applications: Polyester dendrimer-poly(ethylene oxide) "bow-tie" hybrids with tunable molecular weight and architecture. *J. Am. Chem. Soc. 124*, 14137−14146.

(6) Morgan, J. R., and Cloninger, M. J. (2002) Heterogeneously functionalized dendrimers. *Curr. Opin. Drug Discovery Dev. 5*, 966−973.

(7) Langer, R. (1998) Drug delivery and targeting. *Nature 392*, 5−10.

(8) Zhang, Z. Y., and Smith, B. D. (2000) High-generation polycationic dendrimers are unusually effective at disrupting anionic vesicles: Membrane bending model. *Bioconjugate Chem. 11*, 805−814.

(9) Ottaviani, M. F., Matteini, P., Brustolon, M., Turro, N. J., Jockusch, S., and Tomalia, D. A. (1998) Characterization of starburst dendrimers and vesicle solutions and their interactions by CW- and pulsed-EPR, TEM, and dynamic light scattering. *J. Phys. Chem. B 102*, 6029−6039.

(10) Karoonuthaisiri, N., Titiyevskiy, K., and Thomas, J. L. (2003) Destabilization of fatty acid-containing liposomes by. polyamidoamine dendrimers. *Colloid Surface B 27*, 365−375.

(11) Rolland, A. P. (1998) From genes to gene medicines: Recent advances in nonviral gene delivery. *Crit. Rev. Ther. Drug 15*, 143−198.

(12) Tang, M., Redemann, C. T., and Szoka, F. C. (1995) Biophysical and Chemical Determinants of Efficient Gene Delivery By Polyamidoamine Dendrimers. *J. Cell. Biochem.* 400−400.

(13) Fischer, R., Köhler, K., Fotin-Mleczek, M., and Brock, R. (2004) A stepwise dissection of the intracellular fate of cationic cell-penetrating peptides. *J. Biol. Chem. 279*, 12625−12635.

(14) Thorén, P. E. G., Persson, D., Esbjörner, E. K., Goksor, M., Lincoln, P., and Nordén, B. (2004) Membrane binding and translocation of cell-penetrating peptides. *Biochemistry 43*, 3471−3489.

(15) Mecke, A., Uppuluri, S., Sassanella, T. M., Lee, D.-K., Ramamoorthy, A., Baker, J. R., Orr, B. G., and Banaszak Holl, M. M. (2004) Direct Observation of Lipid Bilayer Disruption by Polyamidoamine Dendrimers. *Chem. Phys. Lipids*, accepted.

(16) Mecke, A., Lee, I., Orr, B. G., Banaszak Holl, M. M., and Baker, J. R. (2004) Deformability of Poly(amidoamine) Dendrimers. *Eur. Phys. J. E 14* (1), 7−16.

(17) van Duijvenbode, R. C., Borkovec, M., and Koper, G. J. M. (1998) Acid−base properties of poly(propylene imine) dendrimers. *Polymer 39*, 2657−2664.

(18) Majoros, I. J., Keszler, B., Woehler, S., Bull, T., and Baker, J. R. (2003) Acetylation of poly(amidoamine) dendrimers. *Macromolecules 36*, 5526−5529.

(19) Wiener, E. C., Konda, S., Shadron, A., Brechbiel, M., and Gansow, O. (1997) Targeting dendrimer-chelates to tumors and tumor cells expressing the high-affinity folate receptor. *Invest. Radiol. 32*, 748−754.

(20) Bielinska, A. U., Kukowska Latallo, J. F., and Baker, J. R. (1997) The interaction of plasmid DNA with polyamidoamine dendrimers: mechanism of complex formation and analysis of alterations induced in nuclease sensitivity and transcriptional activity of the complexed DNA. *BBA-Gene Struct. Expr. 1353*, 180−190.

(21) Hong, S., Bielinska, A. U., Banaszak Holl, M. M., Orr, B. G., and Baker, J. R. (2003). Unpublished work.

(22) Umebayashi, Y., Miyamoto, Y., Wakita, M., Kobayashi, A., and Nishisaka, T. (2003) Elevation of plasma membrane permeability on laser irradiation of extracellular latex particles. *J. Biochem. 134*, 219−224.

(23) Myc, A., Kukowska-Latallo, J. F., Bielinska, A. U., Cao, P., Myc, P. P., Janczak, K., Sturm, T. R., Grabinski, M. S., Landers, J. J., Young, K. S., Chang, J., Hamouda, T., Olszewski, M. A., and Baker, J. R. (2003) Development of immune response that protects mice from viral pneumonitis after a single intranasal immunization with influenza A virus and nanoemulsion. *Vaccine 21*, 3801−3814.

(24) Myc, A., Arscott, P. L., Bretz, J. D., Thompson, N. W., and Baker, J. R. (1999) Characterization of FAP-1 expression and function in thyroid follicular cells. *Endocrinology 140*, 5431−5434.

(25) Jevprasesphant, R., Penny, J., Jalal, R., Attwood, D., McKeown, N. B., and D'Emanuele, A. (2003) The influence of surface modification on the cytotoxicity of PAMAM dendrimers. *Int. J. Pharm. 252*, 263−266.

(26) Andersson, M. M., Hatti-Kaul, R., and Brown, W. (2000) Dynamic and static light scattering and fluorescence studies of the interactions between lactate dehydrogenase and poly(ethyleneimine). *J. Phys. Chem. B 104*, 3660−3667.

(27) Baldwin, T. O., Christopher, J. A., Raushel, F. M., Sinclair, J. F., Ziegler, M. M., Fisher, A. J., and Rayment, I. (1995) Structure of bacterial luciferase. *Curr. Opin. Struct. Biol. 5*, 798−809.

(28) Fischer, D., Li, Y. X., Ahlemeyer, B., Krieglstein, J., and Kissel, T. (2003) In vitro cytotoxicity testing of polycations: influence of polymer structure on cell viability and hemolysis. *Biomaterials 24*, 1121−1131.

BC049962B

Synthetic Bivalent CD4-Mimetic Miniproteins Show Enhanced Anti-HIV Activity over the Monovalent Miniprotein

Hengguang Li, Haijing Song, Alonso Heredia, Nhut Le, Robert Redfield, George K. Lewis, and Lai-Xi Wang*

Institute of Human Virology, University of Maryland Biotechnology Institute, University of Maryland, Baltimore, Maryland 21201. Received February 18, 2004; Revised Manuscript Received May 2, 2004

HIV-1 envelope glycoprotein gp120 is displayed as a trimeric complex on the surface of virion and infected T-cells, making it a typical multivalent target. This paper describes the design and synthesis of bivalent CD4-mimetic miniproteins to target the conserved CD4-binding pockets in the trimeric gp120. Using miniprotein CD4M9 as the model inhibitor, we created bivalent inhibitors in which two CD4M9 moieties were tethered by a spacer of varied length and evaluated their anti-HIV activity using a cell culture assay. The synthetic bivalent miniproteins showed 5−21-fold enhancement in anti-HIV activity over the monovalent miniprotein. The activity enhancement is dependent on the length of the spacer. The study suggests that targeting the oligomeric gp120 complex by novel multivalent ligands offers a valuable strategy for developing highly specific and effective HIV entry inhibitors.

INTRODUCTION

In the absence of an effective vaccine, anti-HIV drugs will continue to play a key role in combating the worldwide epidemic of HIV/AIDS. Most FDA-approved anti-HIV drugs target two viral proteins: the HIV protease and reverse transcriptase (*1*). The highly active antiretroviral therapy (HAART) that combines two or more reverse transcriptase/protease inhibitors has prolonged the survival of AIDS patients and significantly reduced plasma viral loads in HIV infected patients. However, the toxicity and emergency of drug-resistant viruses associated with current drug regimen prompt development of new drugs that act with different mode of action and with improved anti-HIV potency (*2*). The initial step of HIV entry is characterized by the interaction of HIV-1 envelope glycoprotein gp120 with host receptor CD4 (*3*). The CD4 binding site on gp120 is centered on a conserved, hydrophobic pocket denoted the "Phe43 cavity" (*4*, *5*). The conserved CD4-binding site of gp120, therefore, provides an attractive target for HIV entry inhibitor design. It was demonstrated that molecules targeting the conserved CD4-binding pocket, such as soluble CD4 and HIV-neutralizing antibody b12, are potent inhibitors against HIV infection (*6*−*10*). Through rational engineering, Vita et al. generated a series of scorpion toxin-based miniproteins that reproduce the nativelike conformation and gp120-binding domain of CD4 (*11*). A 28-mer CD4-mimetic miniprotein, CD4M9, was shown to bind to the Phe43 cavity of gp120 and inhibit HIV-1 infection at μM concentration (*12*). Further engineering of CD4M9 with nonnatural amino acid substitutions led to another miniprotein CD4M33 that can inhibit the binding of CD4 to gp120 at nM concentration (*13*).

* Corresponding author. Address: Institute of Human Virology, University of Maryland Biotechnology Institute, University of Maryland, 725 W. Lombard Street, Baltimore, MD 21201. Telephone: 410-706-4982. Fax: 410-706-5068. E-mail: wangx@umbi.umd.edu.

Compelling data from recent structural and biochemical studies have demonstrated that the HIV-1 envelope glycoprotein gp120 is displayed as a gp41-associated trimer and forms envelope spikes on the surface of HIV virions (*14*−*18*). Recent electron tomography further confirmed the notion (*19*). Thus, the trimeric gp120 complex of the envelope spike constitutes a typical multivalent target, which presents three Phe43 cavities. On the other hand, enormous examples have demonstrated that multivalent interactions generated by a multivalent ligand for a multivalent target can be collectively much stronger than corresponding monovalent interactions (*20*−*25*). On the basis of these observations, we hypothesize that multivalent inhibitors capable of simultaneously occupying two or more of the CD4-binding cavities in the trimeric gp120 complex will bind to the envelope spikes much more tightly and thus will be more effective in blocking HIV-1 infection. As the first step to test the hypothesis, we describe in this paper the design, synthesis, and anti-HIV activity of CD4M9-based bivalent miniproteins. Our experimental data have shown that synthetic bivalent CD4M9 miniproteins, in which two CD4M9 moieties were spaced with a linker of varied length, demonstrate significantly enhanced anti-HIV activity over the monovalent miniprotein CD4M9.

EXPERIMENTAL PROCEDURES

General. All Fmoc-protected amino acids used for peptide synthesis were purchased from Novabiochem. HATU, DIPEA, and Fmoc-PAL-PEG-PS were purchased form Applied Biosystems. HPLC-grade acetonitrile was purchased from Fisher Scientific. DMF was purchased from B & J Biosynthesis. 1,11-Bis-maleimidotetraethyleneglycol (bi-maleimide-SS) was purchased from Pierce. All other chemicals were purchased from Pierce or Aldrich/Sigma and used as received. ^{1}H and ^{13}C NMR spectra were recorded on Inova 500 NMR machine. The ESI-MS spectra were measured on a Waters ZMD mass spectrometer. TLC was performed on glass plates coated with silica gel 60 F254 (E. Merck). Flash column chro-

10.1021/bc049960r CCC: $27.50 © 2004 American Chemical Society
Published on Web 06/16/2004

matography was performed on silica gel 60 (EM Science, 230−400 mesh). Analytical HPLC was carried out with a Waters 626 HPLC instrument on a Waters Nova-Pak C18 column (3.9 × 150 mm) at 40 °C. The column was eluted with a linear gradient of 0−70% MeCN containing 0.1% TFA at a flow rate of 1 mL/min over 20 min. Compounds were detected at 214 nm. Preparative HPLC was performed with a Waters 600 HPLC instrument of a Waters C18 column (Symmetry 300, 19 × 300 mm). The column was eluted with a suitable gradient of MeCN containing 0.1% TFA at 12 mL/min.

1,8-Bis-(6-maleimidocaproylamido)triethyleneglycol (bi-Maleimide-MS). To a solution of 2,2′-(Ethylenedioxy)bis-(ethylamine) (10 mg, 67 μmol) in THF (2 mL) containing a few drops of $NaHCO_3$ (0.1 M) was added N-(6-maleimidocaproyloxy)succinimide ester (EMCS) (42 mg, 135 μmol). After stirring for 3 h, the reaction mixture was condensed by a rotary evaporator under diminished pressure. The residue was subject to flash column chromatography using methanol/ethyl acetate (1:9, v/v) as the eluent to give bi-Maleimide-MS as a light white solid (29 mg, 81%): mp 112−114 ° C; ^{1}H NMR (500 MHz, $CDCl_3$/TMS): δ 6.69 (s, 4H, 2 CH═CH), 5.99 (br. s, 2H, 2 NH), 3.62 (s, 4H, OCH_2CH_2O), 3.56 (t, 4H, J = 5.2 Hz, 2 NCH_2CH_2O), 3.51 (t, 4H, J = 7.2 Hz, 2 $N-CH_2$), 3.46 (q, 4H, J = 5.3 Hz, 2 NCH_2CH_2O), 2.17 (t, 4H, J = 7.4 Hz, 2 CH_2CON), 1.66 (q, 4H, J = 7.5, 7.6 Hz, 2 $CH_2C\ H_2$-CON), 1.60 (q, 4H, J = 7.5, 7.4 Hz, 2 $N-CH_2CH_2$), 1.32 (q, 4H, J = 7.5, 7.9 Hz, 2 $N-CH_2CH_2\ CH_2H_2CH_2CON$); ^{13}C NMR (500 MHz, $CDCl_3$/TMS) 134.05, 70.21, 69.92, 39.12, 37.62, 28.23, 26.32, 25.04; ESI-MS calcd for $C_{26}H_{38}N_4O_8$ (M) 534.27; found 535.46 $(M + H)^+$.

1,8-Bis-[6-(4-N-maleimidomethylcyclohexane-1-carboxyl)amido]caproxyltriethyleneglycol (bi-Maleimide-LS). A mixture of 2,2′-(ethylenedioxy)bis(ethylamine) (4.1 mg, 28 μmol) and succinimidyl-4-(N-maleimidomethyl)-cyclohexane-1-carboxy-(6-amidocaproate) (LC-SMCC) (25 mg, 56 μmol) in THF (2 mL) containing $NaHCO_3$ was reacted as described for the preparation of bi-maleimide-SS. Column chromatography of the residue gave bi-maleimide-LS as a light white solid (9 mg, 76%): mp 178−180 ° C; ^{1}H NMR (500 MHz, $CDCl_3$/TMS), δ 6.69 (s, 4H, 2 CH═CH), 6.22 (br. s, 2H, 2 NH), 5.78 (br. s, 2H, 2 NH), 3.62 (s, 4H, OCH_2CH_2O), 3.57 (t, 4H, J = 5.3 Hz, 2 NCH_2CH_2O), 3.44 (m, 4H, 2 NCH_2CH_2O), 3.36 (d, 4H, 6.8 Hz, 2 $N-CH_2$), 3.21 (m, 4H, 2 $CONHCH_2$), 2.18 (t, 4H, J = 7.4 Hz, 2 $CH_2CONHCH_2CH_2O$), 1.87 (m, 4H, 2 $CH_2CONHCH_2CH_2O$), 1.73 (m, 4H, 2 $CH_2CONHCH_2$-CH_2), 1.62 (s, 8H, cyclohexane), 1.49 (t, 4H, J = 6.8 Hz, $CHCONHCH_2CH_2CH_2CH_2CH_2CONH$), 1.44 (m, 2H, 2 cyclohexane-$CHCH_2N$), 1.42 (m, 2H, 2 cyclohexane-$CHCONH$), 1.33 (m, 4H, cyclohexane), 0.99 (m, 4H, cyclohexane); ^{13}C NMR (500 MHz, $CDCl_3$/TMS) 133.96, 70.22, 69.88, 45.91, 43.64, 39.55, 38.98, 36.32, 36.30, 29.82, 29.20, 28.90, 26.31, 24.96; ESI-MS calcd for $C_{42}H_{64}N_6O_{10}$ (M) 812.47; found 813.65 $(M + H)^+$

Peptide Synthesis. Peptides were synthesized on a Pioneer automatic peptide synthesizer (Applied Biosystems) using fluorenylmethyloxycarbonyl (Fmoc)-protected amino acids as building blocks, 2-(1-H-azabenzotriazol-1-yl)-1,1,3,3-tetramethyluronium hexafluorophosphate (HATU) as the coupling reagent and poly(ethylene glycol)-polystyrene resin with a peptide amide linker (PAL-PEG-PS resin) as the solid support. Reduced peptide red-CD4M9-Cys was synthesized on a 0.2 mmol scale and cleaved from resin and deprotected as described previously (*26*). The crude peptide was precipitated in ethyl ether and purified through PR−HPLC to give red-CD4M9-Cys (320 mg, 52%). t_R =13.20 min (under the analytical HPLC condition described in the general method); ESI-MS calcd M = 3089.83; found 1030.88 $(M + 3H)^{3+}$, 773.43 $(M + 4H)^{4+}$, and 619.12 $(M + 5H)^{5+}$.

Folding of Red-CD4M9-Cys. The reduced peptide red-CD4M9-Cys (37 mg, 12 μmol) was dissolved in degassed guanidine hydrochloride (1 M, 75 mL). Reduced glutathione (9.5 mg, 31 μmol) was added into the mixture followed by addition of oxidized glutathione (19 mg, 31 μmol). To the mixture was added a $NaHCO_3$ solution (0.1 M) to adjust pH to 8.5. The mixture was shaken under N_2 overnight when HPLC indicated the formation of a major single peak that moved faster then the reduced peptide. Lyophilization of the reaction mixture and subsequent HPLC purification gave the folding product CD4M9-Cys-Glutathione (30.5 mg, 75%). t_R =11.06 min (Under the analytical HPLC condition described in the general method); ESI-MS calcd M = 3389.08; found 1695.41 $(M + 2H)^{2+}$, 1130.50 $(M + 3H)^{3+}$, 848.29 $(M + 4H)^{4+}$, 678.96 $(M + 5H)^{5+}$, and 565.79 $(M + 6H)^{6+}$.

Selective Cleavage of the Intermolecular Disulfide Bond to Give CD4M9-Cys. The folded product CD4M9-Cys-Glutathione (15 mg, 4.4 μmol) was dissolved in degassed guanidine hydrochloride (30 mL, 1 M). To the solution was added tris[2-carboxyethyl]phosphine hydrochloride (TCEP) (7.57 mg, 26.4 μmol). The mixture was gently shaken for 10 h and then lyophilized. HPLC purification gave the desired product CD4M9-Cys with a free cysteine at the C-terminus (10.6 mg, 78%). t_R =11.67 min (under the analytical HPLC condition described in the general method); ESI-MS calcd M = 3083.16; found 1542.69 $(M + 2H)^{2+}$, 1028.69 $(M + 3H)^{3+}$, 771.91 $(M + 4H)^{4+}$, and 617.75 $(M + 5H)^{5+}$.

Tagging of the Free Cysteine in CD4M9-Cys with Iodoacetamide. A solution of CD4M9-Cys (2 mg) in a phosphate buffer (1 mL, pH 8.0) was treated with iodoacetamide (50 mM) for 2 h at room temperature. RP-HPLC purification gave the acetamide-tagged miniprotein (2 mg, quantitative). t_R =11.62 min (Under the analytical HPLC condition described in the general method); ESI-MS calcd M = 3141.12; found 1047.98 $(M + 3H)^{3+}$, 786.26 $(M + 4H)^{4+}$, and 629.20 $(M + 5H)^{5+}$.

Proteolytic Digestion and Edman Degradation. The above-described acetamide-tagged miniprotein (1.5 mg, 1 mg/mL) was treated with trypsin and chymotrypsin (20 μL, 0.5 mg/mL each) at room temperature in 50 mM Tris buffer (pH 8.3) containing 0.005% Triton X-100 and 20 mM $CaCl_2$. The reaction was monitored by analytical RP-HPLC (monitored at 214 nm), and the peptide fragments were isolated and subject to ESI-MS analysis. A major fragment with a mass of 1486.2 Da (fragment c) was subject to one-step manual Edman degradation. Briefly, the peptide was suspended in pyridine/water (1:1, 300 μL), to which 20 μL phenylisothiocyanate (PITC) was added. The mixture was incubated at 50°C for 30 min, and the solvent was removed under vacuum. TFA (200 μL) was added, and the mixture was reacted at 50°C for 15 min to cleave the N-terminal residues. TFA was removed under vacuum and the residue was suspended in water (200 μL). After extraction with pentane/ethyl acetate (4:1, 200 μL), the aqueous solution was subject to HPLC, and the fragments were isolated and analyzed by ESI-MS. Again, a major fragment with a mass of 874.1 Da (fragment g) was isolated and was subject to two steps of Edman degradation following the procedures described above. The degradation products were analyzed by HPLC and ESI-MS.

General Procedures for Chemoselective Ligation of CD4M9-Cys with Bis-maleimide Scaffold. CD4M9-Cys (1.2 mol. equiv. per maleimide functionality) was

dissolved in degassed phosphate buffer (50 mM, pH 6.6) containing 50% acetonitrile. Then a solution of bis-maleimide scaffold (bi-maleimide-SS, bi-maleimide-MS, or bi-maleimide-LS) in acetonitrile was added. The mixture was gently shaken under N_2 at room temperature. The processing of ligation was monitored with analytic HPLC and the reaction was complete within 1−2 h. The ligation product was purified and characterized by ESI-MS.

Bi-CD4M9-SS (With a Shorter Spacer). 90% yield; t_R 12.20 min (under the analytical HPLC condition described in the general method); ESI-MS calcd M = 6520.50; found 1305.08 $(M + 5H)^{5+}$, 1087.74 $(M + 6H)^{6+}$, 932.54 $(M + 7H)^{7+}$, 816.12 $(M + 8H)^{8+}$, 725.54 $(M + 9H)^{9+}$.

Bi−CD4M9-MS (With a Medium Spacer). 80% yield; t_R 12.37 min (Under the analytical HPLC condition described in the general method); ESI-MS calcd M = 6703.50; found 1118.18 $(M + 6H)^{6+}$, 958.56 $(M + 7H)^{7+}$, 838.97 $(M + 8H)^{8+}$, 745.83 $(M + 9H)^{9+}$, 671.37 $(M + 10H)^{10+}$.

Bi-CD4M9-LS (With a Longer Spacer). 56% yield; t_R 12.66 min (Under the analytical HPLC condition described in the general method); ESI-MS calcd M = 6980.97; Found 1164.50 $(M + 6H)^{6+}$, 998.34 $(M + 7H)^{7+}$, 873.71 $(M + 8H)^{8+}$, 776.77 $(M + 9H)^{9+}$, 699.20 $(M + 10H)^{10+}$, 635.76 $(M + 11H)^{11+}$.

Antiviral Assays. Peripheral blood mononuclear cells (PBMCs) were separated from whole blood of HIV-seronegative donors by density centrifugation over Ficoll-Hypaque (Sigma). The culture medium consisted of RPMI supplemented with 10% fetal bovine serum (FBS), 2 mM glutamine, and penicillin/streptomycin (Gibco, Grand Island, NY). For infection studies, PBMCs were stimulated with 2.5 μg/mL phytohemagglutinin (PHA; Boehringer Mannheim, Indianapolis, IN) for 3 days. Stimulated PBMCs were infected by incubation with HIV-1_{IIIB} at a multiplicity of infection of 1000 $TCID_{50}/10^6$ PBMC for 2 h. PBMCs were then washed three times with PBS and cultured at 37 °C in RPMI/10% FBS supplemented with 100 units/ml rIL-2 (Boehringer Mannheim) and the bivalent inhibitors at varied concentrations. PBMCs were seeded in 96-well flat-bottom plates at a density of 2×10^5 PBMCs/200 μl. Following 3 days of culture, half of the medium was replaced with fresh medium containing IL-2 and the antiviral agents. After 7 days of culture, virus production in the culture supernatant was assayed by measuring HIV-1 reverse transcriptase (RT) activity as described (*27*). Cell viability in culture in the presence or absence of antiviral agents was measured by commercial MTT assay, as per the manufacturer's instructions (Boehringer, Mannheim, Germany).

RESULTS AND DISCUSSION

1. Design. Although the crystal structure of the truncated gp120 core has been solved (*4*), the atomic structure of the proposed gp120 trimer is not known. Nevertheless, Kwong et al. have modeled the orientation of gp120 in the trimer by using quantifiable criteria of carbohydrate exposure, occlusion of conserved residues, and steric considerations with regard to the binding of the neutralizing antibody 17b (*17*). It was assumed that the trimeric model of gp120 was constrained to be 3-fold symmetric (*17*). To measure the distance across the three Phe43 cavities of the CD4-binding sites in the trimeric gp120, we performed similar modeling of the trimeric gp120 using the same structural constraints (data not shown). We found that the trimeric complex of gp120 is

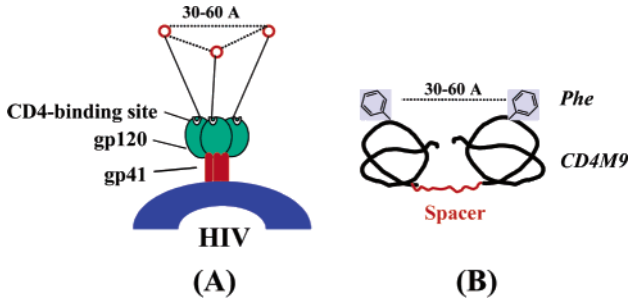
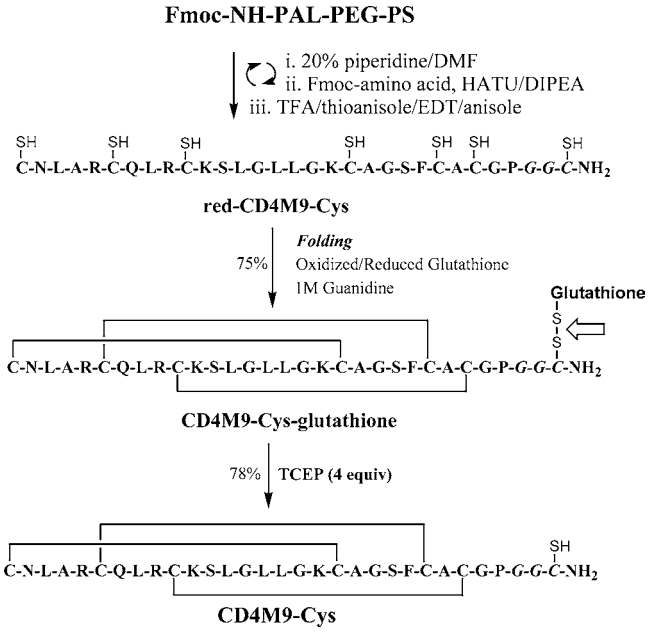


Figure 1. Schematic depiction of the trimeric gp120 complex (A) and the designed bivalent miniproteins (B). (Illustration is not to scale.)

a dynamic structure and the distance between any two of the Phe43 cavities was estimated to be in the range of 30−60 Å (Figure 1a). To match the distance between any two of the CD4-binding cavities, we designed bivalent miniproteins by tethering two CD4M9 moieties through a linker of varied length. A general structure of the designed bivalent inhibitors was shown in Figure 1b. For constructing such a covalently linked bivalent miniprotein, we decided to introduce an extra cysteine residue at the C-terminus of CD4M9 as a tag for late-stage chemoselective ligation, because the model of the interaction between CD4M9 and gp120 suggested that the C-terminus of CD4M9 did not have any contact with residues of gp120 and was pointed away from the binding sites (*12*). The length and flexibility of the linker are critical to place the two CD4M9 moieties in an appropriate spatial position to match the two binding sites in the trimeric gp120. We envision that this could be probed by varying the length of the linker.

2. Synthesis of a Modified Miniprotein CD4M9-Cys. For chemoselective conjugation, a tripeptide sequence GGC was added to the C-terminus of the CD4M9 sequence to give a 31-amino acid peptide. The reduced, 31-mer precursor was synthesized by solid-phase peptide synthesis using Fmoc-chemistry. After HPLC purification, the reduced peptide was then folded in the presence of reduced/oxidized glutathione in a 1M guanidine−HCl solution. HPLC monitoring indicated that the folding proceeded smoothly to give a major product. The expected mass of the folded miniprotein would be 3083.16 Da, whereas ESI-MS analysis of the folding product gave a molecular mass of 3389.1 Da, indicating the introduction of a glutathione moiety to the folded molecule. The glutathione moiety was most likely linked to the molecule through an intermolecular disulfide bond formation with the extra cysteine residue in the molecule. This notion was confirmed by the selective cleavage of the intermolecular disulfide linkage. Thus, treatment of the glutathione-tagged protein with tris[2-carboxyethyl]phosphine hydrochloride (TCEP) selectively removed the glutathione moiety to give the miniprotein CD4M9-Cys (Scheme 1). It should be pointed out that using other reducing agents such as DTT and β-mercaptoethanol resulted in a complicated mixture (as revealed by HPLC monitoring), probably due to simultaneous cleavage of intramolecular disulfide bonds and subsequent misfolding of the protein (thiol−disulfide shuffling). The product CD4M9-Cys was purified by HPLC and analyzed by ESI-MS spectrometry. As described in the Experimental Section, the molecular mass of the reduced miniprotein red-CD4M9-Cys was found to be 3089.6 Da, while the molecular mass of the final, folded miniprotein CD4M9-Cys was found to be 3083.38 Da. A 6 Da difference in molecular mass of the reduced and folded

Scheme 1. Synthesis of Cysteine-Tagged Miniprotein CD4M9-Cys



forms clearly indicated the formation of three pairs of disulfide bonds in the folded miniprotein CD4M9-Cys with an extra free cysteine residue.

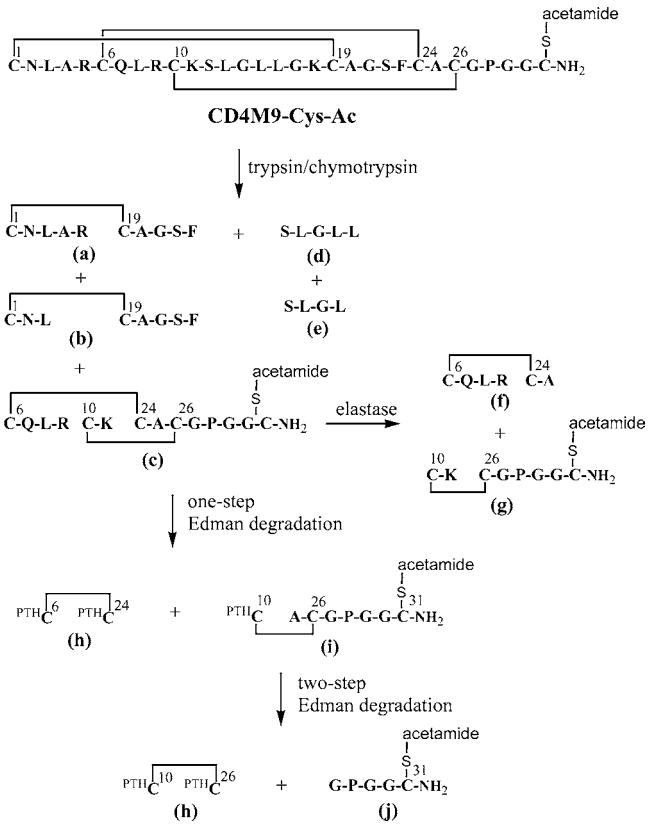
3. Validation of Correct Folding of the Modified Miniprotein. CD4M9-Cys was modified from the known miniprotein CD4M9 by introducing a three peptide sequence GGC at the C-terminus. The disulfide connectivity of CD4M9 was previously assigned as $C^{1-}C^{19}$, $C^{6-}C^{24}$, and $C^{10-}C^{26}$ (*12*). The NMR structure of CD4M9 and the molecular modeling of the complex of CD4M9 with gp120 indicated that the C-terminus was pointing away from the folding core and did not seem to be involved in direct interaction with gp120 (*12*, *13*). Therefore, we assume that introduction of a sequence GGC at the C-terminus would not interrupt the folding of the protein. However, it is still possible that the introduction of an extra cysteine in the molecule may lead to misfolding through a thiol−disulfide shuffling. To validate the disulfide connectivity in the folded CD4M9-Cys, we performed proteolytic digestion of the miniprotein and subsequent Edman degradation of key peptide fragments, following a recently published procedure (*28*). First, the free cysteine in CD4M9-Cys was tagged with an acetamide group for final identification. The tagged protein was then digested with trypsin and chymotrypsin. Trypsin is specific for amides with positively charged side-chains, e.g., Lys and Arg, while chymotrypsin is specific for amides with aromatic or other large hydrophobic side-chains such as Phe and Leu. Treatment of the acetamide-tagged CD4M9-Cys with trypsin and chymotrypsin yielded several major fragments which were separated by reverse phase HPLC. ESI-MS analysis of the peptide fragments gave the information on their molecular masses: 1057.5, 829.4, 1486.2, 501.4, and 388.3 Da, corresponding to the fragments a−e, respectively (Table 1 and Scheme 2). The isolation of fragments a and b clearly indicated a disulfide pairing between C^1 and C^{19}. To determine the next disulfide connectivity, fragment c was subject to enzymatic hydrolysis with elastase, which is specific for Ala residue. Elastase treatment resulted in formation of fragment f (708.5 Da) and fragment g (795.7 Da). The formation of fragment f indicated that C^6 was paired with C^{24} in the folded protein, because the connection of C^6

Table 1. ESI-MS Analysis of the Fragments Derived from Emzymatic Digestion and Edman Degradation of the Modified Miniprotein

	MW (Da)		
fragments (#)	calcd	found	HPLC*a* (t_R, min)
a	1057.5	1057.5	7.95(1)
b	829.9	829.4	8.56(1)
c	1486.3	1486.2	6.12(1)
d	501.6	501.4	10.11(1)
e	388.2	388.3	8.80(1)
f	708.4	708.5	7.93(1)
g	795.2	795.7	8.05(1)
h	510.3	510.9	9.62(2)
i	874.8	874.1	11.27(2)
j	447.1	447.4	12.34(2)

[a] Analytical HPLC was performed on a Waters Nova-Pak C18 column (3.9 × 150 mm) at 40 °C. The column was eluted with a linear gradient of MeCN containing 0.1% TFA at a flow rate of 1 mL/min, and fragments were detected at 214 nm: (1) the column was eluted with 0−90% MeCN in 30 min; (2) the column was eluted with 0−90% MeCN in 15 min. The peptide fragments derived from the proteolytic digestion and Edman degradation were isolated by HPLC and subject to ESI-MS analysis.

Scheme 2. Validation of the Miniprotein's Folding Pattern by Proteolytic Digestion and Edman Degradation



with any other cysteine residues would not give fragment f after elastase treatment. This was further verified by one-step Edman degradation of fragment c. Edman degradation would tag all the three N-terminal amino acid residues with a phenylthiohydantoin (PTH) derivative and simultaneously cleave the first amide bonds from the three N-termini. The identification of fragment h (510.9 Da) and fragment i (874.1 Da) confirmed the assignment of C^6-C^{24} connection. Finally, to determine whether C^{10} was connected to C^{26} or C^{31}, the fragment i was subject to two-step Edman degradation to give two fragments, h and j (447.4 Da). The identification of these two fragments unambiguously confirmed the disulfide

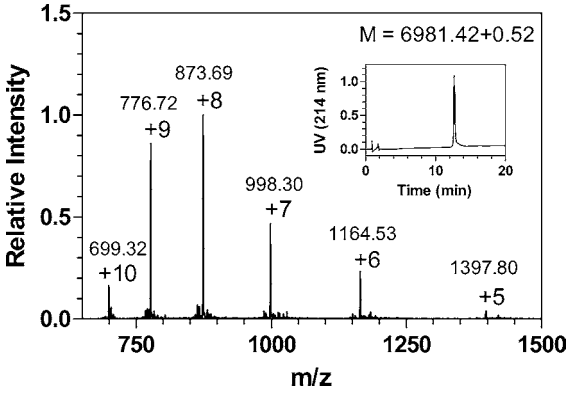


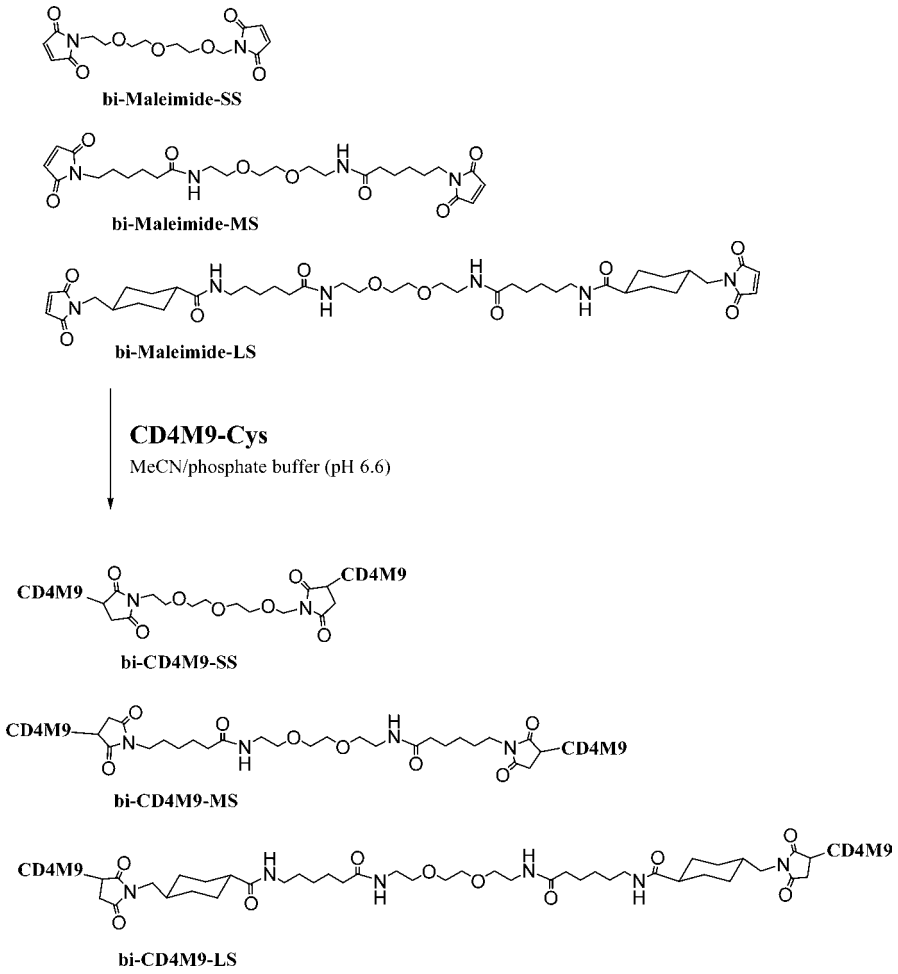
Figure 2. The ESI-MS and HPLC profiles of the bivalent minprotein bi-CD4M9-LS. Analytical HPLC was performed on a Waters Nova-Pak C18 column (3.9x150 m) at 40 °C. The column was eluted with a linear gradient of 0-70% MeCN containing 0.1% TFA at a flow rate of 1 mL/min over 20 min (detection: 214 nm).

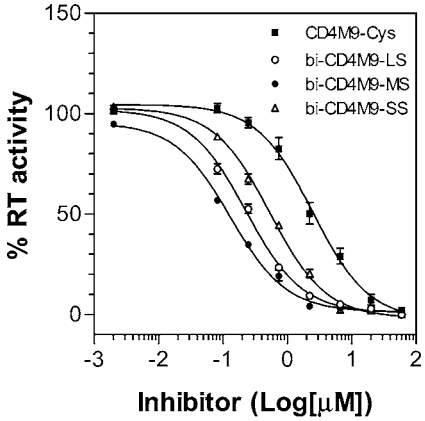
connection between C^{10} and C^{26}. The results were summarized in Table 1 and Scheme 2. It should be pointed out that the fragment j somehow appeared very hydrophobic compared to other fragments under the reverse-phase HPLC conditions (Table 1). Taken together, the enzymatic digestion coupled with Edman degradation unambiguously verified the assumed folding pattern of CD4M9-Cys, which would have a free cysteine at the C-terminus and bear the following disulfide connectivity: $C^{1-}C^{19}$, $C^{6-}C^{24}$, and $C^{10-}C^{26}$.

To confirm that the synthetic miniprotein maintains the same activity as the parent compound CD4M9, we performed anti-HIV assays of the synthetic CD4M9-Cys and compared its activity with standard CD4M9. Both miniproteins showed no difference in anti-HIV activities in our assays with peripheral blood mononuclear cells (PBMCs) as the host cells with infection by HIV-1_{IIIB}. The IC50 (concentration for 50% inhibition of HIV infection) for both CD4M9-Cys and CD4M9 was found to be 1−5 μM, depending on the donors of PBMCs. The results further suggested that the protein was properly folded and the introduction of a C-terminal tag GGC did not seem to interfere with its anti-HIV activity.

4. Synthesis of Bivalent Miniproteins. To construct bivalent CD4M9, three bivalent maleimides were chosen as the scaffolds, in which the two maleimide moieties were spaced at a maximum of 18, 32, and 44 Å in distance, respectively. The ligation of the scaffold and CD4M9-Cys was performed in a phosphate buffer (pH 7.2) containing acetonitrile to give the corresponding bivalent miniproteins bi-CD4M9-SS, bi-CD4M9-MS, and bi-CD4M9-LS with a short, medium, and a long spacer, respectively (Scheme 2). The products were purified by HPLC and characterized by ESI-MS. A typical HPLC and ESI-MS profiles for the purified bivalent minprotein bi-CD4M9-LS was shown in Figure 2, which indicates the purity and identity of the ligation product. Based on the folded structure of CD4M9 (*12*), the distance between the C-terminal Cys in CD4M9-Cys and the Phe residue, which binds to the "Phe43 cavity" of gp120, was estimated to be ca. 10 Å. Therefore, it can be deduced that

Scheme 3. Synthesis of Bivalent CD4M9 Miniproteins





Compound	IC50 (μM)	Relative activity
CD4M9-Cys	2.5	1
bi-CD4M9-LS	0.23	11
bi-CD4M9-MS	0.12	21
bi-CD4M9-SS	0.54	4.6

Figure 3. Inhibition of HIV-1 infection by bivalent CD4M9 miniproteins. PBMCs were infected by HIV-1_{IIIB} in the presence or absence of the synthetic miniproteins at various concentrations. Virus production was assessed by measuring viral reverse transcriptase (RT) activity. The IC50 was defined as the concentration that reaches 50% inhibition of viral production.

the maximal distance between the two Phe groups in the synthetic bivalent miniproteins would be 38, 52, and 64 Å for bi-CD4M9-SS, bi-CD4M9-MS, and bi-CD4M9-LS, respectively. The maximal distance of the two Phe ligands in the synthetic bivalent ligands falls into the estimate range of 30−60 Å between any two of the three "Phe43 cavities" in the modeled trimeric gp120 complex (*17*).

5. Evaluation of Anti-HIV Activity of the Synthetic Bivalent Miniproteins. The antiviral activity of the synthetic bivalent inhibitors was examined on donor peripheral blood mononuclear cells (PBMCs) infected with HIV-1_{IIIB}. All the bivalent miniproteins showed enhanced anti-HIV activity over the monovalent miniprotein CD4M9-Cys (Figure 3). In comparison, the best bivalent miniprotein bi-CD4M9-MS, in which the two Phe residues could be spaced in a maximal distance of 52 Å, showed a 21-fold increase of anti-HIV activity over the monovalent inhibitor. The bivalent inhibitors bi-CD4M9-SS (with a shorter spacer) and bi-CD4M9-LS (with a longer spacer) showed a 4.6 and 11-fold increase over the monvalent inhibitor, respectively. Although we have not yet performed direct binding studies of the synthetic bivalent inhibitors with reconstituted oligomeric gp120 (*14*, *15*), we assume that this activity enhancement could be resulted directly from the enhanced binding of the bivalent inhibitors to the multivalent CD4-binding sites of the trimeric gp120 complex. The difference in activities among the bivalent inhibitors with a linker of varied length suggests that the two binding ligands in the bivalent miniproteins should be spaced adequately to match the binding sites on the trimeric gp120, so that a simultaneous multivalent interaction can occur to achieve a high affinity binding.

In conclusion, our experiments demonstrated that creation of simple bivalent inhibitors could lead to a significant enhancement of anti-HIV activity over the corresponding monvalent inhibitor. This preliminary study provides proof-of-concept data, suggesting that attacking the multivalent target, the oligomeric gp120, by creating a multivalent ligand constitutes a valuable approach toward effective HIV inhibition. Thus, it is conceivable to think that trivalent or multivalent ligands that can occupy the three CD4-binding sites in the trimeric gp120 complex simultaneously might be super active in inhibiting HIV infection. Research along this direction is currently in progress and will be reported in due course.

ACKNOWLEDGMENT

We thank Drs. Wuyuan Lu and Zhibin Wu for valuable discussions. The work was supported in part by the Institute of Human Virology, University of Maryland Biotechnology Institute, and National Institutes of Health (NIH Grants AI51235 and AI54354 to L.X.W.).

LITERATURE CITED

(1) Richman, D. D. (2001) HIV chemotherapy. *Nature 410*, 995−1001.
(2) Wensing, A. M., and Boucher, C. A. (2003) Worldwide transmission of drug-resistant HIV. *AIDS Rev. 5*, 140−155.
(3) Chan, D. C., and Kim, P. S. (1998) HIV entry and its inhibition. *Cell 93*, 681−684.
(4) Kwong, P. D., Wyatt, R., Robinson, J., Sweet, R. W., Sodroski, J., and Hendrickson, W. A. (1998) Structure of an HIV gp120 envelope glycoprotein in complex with the CD4 receptor and a neutralizing human antibody. *Nature 393*, 648−659.
(5) Wyatt, R., Kwong, P. D., Desjardins, E., Sweet, R. W., Robinson, J., Hendrickson, W. A., and Sodroski, J. G. (1998) The antigenic structure of the HIV gp120 envelope glycoprotein. *Nature 393*, 705−711.
(6) Smith, D. H., Byrn, R. A., Marsters, S. A., Gregory, T., Groopman, J. E., and Capon, D. J. (1987) Blocking of HIV-1 infectivity by a soluble, secreted form of the CD4 antigen. *Science 238*, 1704−1707.
(7) Traunecker, A., Luke, W., and Karjalainen, K. (1988) Soluble CD4 molecules neutralize human immunodeficiency virus type 1. *Nature 331*, 84−86.
(8) Deen, K. C., McDougal, J. S., Inacker, R., Folena-Wasserman, G., Arthos, J., Rosenberg, J., Maddon, P. J., Axel, R., and Sweet, R. W. (1988) A soluble form of CD4 (T4) protein inhibits AIDS virus infection. *Nature 331*, 82−84.
(9) Burton, D. R., Pyati, J., Koduri, R., Sharp, S. J., Thornton, G. B., Parren, P. W., Sawyer, L. S., Hendry, R. M., Dunlop, N., Nara, P. L., Lamacchia, M., Garratty, E., Stiehm, E. R., Bryson, Y. T., Moore, J. P., Ho, D. D., and Barbas, C. F. (1994) Efficient neutralization of primary isolates of HIV-1 by a recombinant human monoclonal antibody. *Science 266*, 1024−1027.
(10) Saphire, E. O., Parren, P. W., Pantophlet, R., Zwick, M. B., Morris, G. M., Rudd, P. M., Dwek, R. A., Stanfield, R. L., Burton, D. R., and Wilson, I. A. (2001) Crystal structure of a neutralizing human IGG against HIV-1: a template for vaccine design. *Science 293*, 1155−1159.
(11) Martin, L., Barthe, P., Combes, O., Roumestand, C., and Vita, C. (2000) Engineering novel bioactive mini-proteins on natural scaffolds. *Tetrahedron 56*, 9451−9460.
(12) Vita, C., Drakopoulou, E., Vizzavona, J., Rochette, S., Martin, L., Menez, A., Roumestand, C., Yang, Y. S., Ylisastigui, L., Benjouad, A., and Gluckman, J. C. (1999) Rational engineering of a miniprotein that reproduces the core of the

CD4 site interacting with HIV-1 envelope glycoprotein. *Proc. Natl. Acad. Sci. U.S.A. 96*, 13091−13096.
(13) Martin, L., Stricher, F., Misse, D., Sironi, F., Pugniere, M., Barthe, P., Prado-Gotor, R., Freulon, I., Magne, X., Roumestand, C., Menez, A., Lusso, P., Veas, F., and Vita, C. (2003) Rational design of a CD4 mimic that inhibits HIV-1 entry and exposes cryptic neutralization epitopes. *Nat. Biotechnol. 21*, 71−76.
(14) Sanders, R. W., Vesanen, M., Schuelke, N., Master, A., Schiffner, L., Kalyanaraman, R., Paluch, M., Berkhout, B., Maddon, P. J., Olson, W. C., Lu, M., and Moore, J. P. (2002) Stabilization of the soluble, cleaved, trimeric form of the envelope glycoprotein complex of human immunodeficiency virus type 1. *J. Virol. 76*, 8875−8889.
(15) Schulke, N., Vesanen, M. S., Sanders, R. W., Zhu, P., Lu, M., Anselma, D. J., Villa, A. R., Parren, P. W., Binley, J. M., Roux, K. H., Maddon, P. J., Moore, J. P., and Olson, W. C. (2002) Oligomeric and conformational properties of a proteolytically mature, disulfide-stabilized human immunodeficiency virus type 1 gp140 envelope glycoprotein. *J. Virol. 76*, 7760−7776.
(16) Salzwedel, K., and Berger, E. A. (2000) Cooperative subunit interactions within the oligomeric envelope glycoprotein of HIV-1: functional complementation of specific defects in gp120 and gp41. *Proc. Natl. Acad. Sci. U.S.A. 97*, 12794−12799.
(17) Kwong, P. D., Wyatt, R., Sattentau, Q. J., Sodroski, J., and Hendrickson, W. A. (2000) Oligomeric modeling and electrostatic analysis of the gp120 envelope glycoprotein of human immunodeficiency virus. *J. Virol. 74*, 1961−1972.
(18) Staropoli, I., Chanel, C., Girard, M., and Altmeyer, R. (2000) Processing, stability, and receptor binding properties of oligomeric envelope glycoprotein from a primary HIV-1 isolate. *J. Biol. Chem. 275*, 35137−35145.
(19) Zhu, P., Chertova, E., Bess, J., Jr., Lifson, J. D., Arthur, L. O., Liu, J., Taylor, K. A., and Roux, K. H. (2003) Electron tomography analysis of envelope glycoprotein trimers on HIV and simian immunodeficiency virus virions. *Proc. Natl. Acad. Sci. U.S.A. 100*, 15812−15817.
(20) Mammen, M., Choi, S. K., and Whitesides, G. M. (1998) Polyvalent interactions in biological systems: Implications for design and use of multivalent ligands and inhibitors. *Angew. Chem., Int. Ed. Engl. 37*, 2754−2794.
(21) Kitov, P. I., Shimizu, H., Homans, S. W., and Bundle, D. R. (2003) Optimization of tether length in nonglycosidically linked bivalent ligands that target sites 2 and 1 of a Shiga-like toxin. *J. Am. Chem. Soc. 125*, 3284−3294.
(22) Dekker, F. J., de Mol, N. J., van Ameijde, J., Fischer, M. J., Ruijtenbeek, R., Redegeld, F. A., and Liskamp, R. M. (2002) Replacement of the intervening amino acid sequence of a Syk-binding diphosphopeptide by a nonpeptide spacer with preservation of high affinity. *Chembiochem 3*, 238−242.
(23) Kitov, P. I., Sadowska, J. M., Mulvey, G., Armstrong, G. D., Ling, H., Pannu, N. S., Read, R. J., and Bundle, D. R. (2000) Shiga-like toxins are neutralized by tailored multivalent carbohydrate ligands. *Nature 403*, 669−672.
(24) Fan, E., Zhang, Z., Minke, W. E., Hou, Z., Verlinde, C. L. M. J., and Hol, W. G. J. (2000) High-affinity pentavalent ligands of E. coli heat-labile enterotoxin by modular structure-based design. *J. Am. Chem. Soc. 122*, 2663−2664.
(25) Kiessling, L. L., Gestwicki, J. E., and Strong, L. E. (2000) Synthetic multivalent ligands in the exploration of cell-surface interactions. *Curr. Opin. Chem. Biol. 4*, 696−703.
(26) Wang, L. X., Ni, J., and Singh, S. (2003) Carbohydrate-centered maleimide cluster as new types of templates for multivalent peptide assembling: Synthesis of multivalent HIV-1 gp41 peptides. *Bioorg. Med. Chem. 11*, 129−136.
(27) Willey, R. L., Smith, D. H., Lasky, L. A., Theodore, T. S., Earl, P. L., Moss, B., Capon, D. J., and Martin, M. A. (1988) In vitro mutagenesis identifies a region within the envelope gene of the human immunodeficiency virus that is critical for infectivity. *J. Virol. 62*, 139−147.
(28) Wu, Z., Prahl, A., Powell, R., Ericksen, B., Lubkowski, J., and Lu, W. (2003) From pro defensins to defensins: synthesis and characterization of human neutrophil pro alpha-defensin-1 and its mature domain. *J. Pept. Res. 62*, 53−62.

BC049960R

Design and Synthesis of AX7574: A Microcystin-Derived, Fluorescent Probe for Serine/Threonine Phosphatases

Kevin R. Shreder,* Yongsheng Liu, Tyzoon Nomanhboy, Stacy R. Fuller, Melissa S. Wong, Wen Zhi Gai, Jiangyue Wu, Phillip S. Leventhal, Jennie R. Lill, and Sergio Corral

ActivX Biosciences, Inc., 11025 N. Torrey Pines Road; La Jolla, California 92037. Received February 20, 2004; Revised Manuscript Received May 1, 2004

The design and synthesis of AX7574, a microcystin-derived probe for serine/threonine phosphatases, is described. A key step in the synthesis was the conjugation under basic conditions of a tetramethylrhodamine 1,3-diketone derivative to the arginine side chain present in microcystin-LR. The resulting conjugate specifically labeled the active site of protein phosphatases 1 (PP-1) with a 1:1 stoichiometry and IC_{50} of 4.0 nM. AX7574 was used to isolate and identify PP-1, PP-2A, PP-4, and PP-6 in Jurkat cells. Finally, AX7574 was able to record changes in the phosphatase activity levels of calyculin A treated Jurkat cells versus untreated control cells.

INTRODUCTION

A major challenge that faces proteomic research is to develop methods to characterize and functionally annotate the more than 30000 protein products encoded by the human genome (*1, 2*). While two-dimensional gel electrophoresis (2DE) and mass spectrometry (MS) have been developed to determine the relative abundance of proteins in complex proteomic mixtures, these conventional methods provide only a global analysis of protein expression levels and lack the ability to detect variation in the functional state of individual proteins and protein families (*3*). To address these shortcomings, a chemical proteomic method referred to as activity-based protein profiling (ABPP) has recently been developed that utilizes active site-directed probes to directly monitor the functional state of enzyme families in complex proteomes. For example, activity-based probes (ABPs) have been successfully generated for cysteine and serine hydrolases (*4*).

The latter set, serine hydrolase probes, are based on the fluorophosphonate (FP) affinity label for this enzyme family and are perhaps the most studied example of an ABP. Such tagged chemical probes are composed of three structural elements: an enzyme reactive headgroup, a linker, and a tag that can be used for quantitation and/or capture of the covalently modified enzyme (*5*). Pioneered by Cravatt et al. (*6*), FP probes have been used, for example, to identify up- and down-regulated serine hydrolases in invasive cancer cell lines (*7*) and in the proteomic screening of enzyme inhibitors (*8*). In their tetramethylrhodamine (TAMRA) tagged form (*9*), they have been shown to have superior sensitivity and quantitative ability versus their biotinylated congeners (*10*).

Like the serine hydrolases, the phosphatase enzyme family is an attractive target for the design of ABPs. Over 100 phosphatases are known and phosphatases, many yet to be discovered, have been estimated to constitute greater than 1% of all proteins in the human genome (*11*). In addition, because of the important regulatory role that phosphatases play in a variety of disease states, the pharmaceutical industry is becoming increasingly interested in the design of phosphatase inhibitors as therapeutic agents (*12, 13*). Thus, reagents that can detect and quantify phosphatase activity will play an important role in deconvoluting phosphatase biology and could lead to the discovery of novel enzymatic targets for drug discovery.

One pharmaceutically relevant subclass of phosphatases, the phosphoprotein phosphatases (i.e. enzymes that use phosphoproteins or phosphopeptides as substrates), can be broken down into three categories: protein tyrosine phosphatases (PTPases), serine/threonine phosphatases, and dual specificity (serine/tyrosine) phosphatases. An ABP for the PTPase category has been described by Lo et al. (*14, 15*). The authors synthesized both biotin- and fluorophore-tagged versions of 4-(fluoromethyl)phenyl phosphate, a mechanism-based phosphatase inhibitor that upon dephosphorylation generates a protein-alkylating quinone methide (*16*). A dansylated version was reported to label PTB-1B but not trypsin or β-galactosidase. The biotin-tagged probe was reported to label PTB-1B selectively in the presence of five other bystander proteins. Despite the interest in understanding the role that serine/threonine phosphatases, such as PP-1 and PP-2, play in cell signaling pathways (*17*) and tumorigenesis (*18*), there are no prior reports of probes to study this important class of phosphatases.

In the present work, we present the design and synthesis of AX7574, a fluorescent probe that takes advantage of the ability of microcystin, a natural product toxin, to irreversibly bind serine/threonine phosphatases. A key step in the synthesis was the conjugation of TAMRA to the arginine side chain present in microcystin-LR. The resulting phosphatase probe specifically labeled the active site of PP-1 with a 1:1 stoichiometry and IC_{50} of 4.0 nM. Furthermore, AX7574 was used to isolate, identify, and record changes in the activity levels of serine/threonine phosphatases in Jurkat cells.

EXPERIMENTAL PROCEDURES

Materials. All solvents and reagents were obtained from the Sigma-Aldrich Co. (St. Louis, MO, and Milwaukee, WI) unless otherwise indicated. The mixed succinimidyl esters of 5-(and-6)-carboxytetramethylrhodamine

* Corresponding author. Phone: 858-526-2517. E-mail: kevins@activx.com.

10.1021/bc0499580 CCC: $27.50 © 2004 American Chemical Society
Published on Web 06/18/2004

(TAMRA-OSu) was obtained from Molecular Probes (Eugene, OR). Microcystin-LR, calyculin A, rabbit protein phosphatase inhibitor 2, and fostriecin were purchased from Calbiochem (San Diego, CA). PP-1 (rabbit) was purchased from New England BioLabs, Inc. (Beverly, MA).

Synthesis Methods. Proton nuclear magnetic resonance (^{1}H NMR) spectra were recorded on a Bruker 400 MHz NMR spectrometer using the residual solvent peak as the internal standard. LC/MS analysis was performed on an Agilent 1100 Series LC/MSD (electrospray ionization) using ChemStation software. High-resolution mass spectrometry (MALDI−FTMS) was determined by The Scripps Center for Mass Spectrometry (The Scripps Research Institute; La Jolla, CA) using 2,5-dihydroxybenzoic acid (DHB) as the matrix. Preparative HPLC was carried out on a C_{18} reverse phase column (Polaris, 5 μm column, 150 mm × 21 mm; Varian; Torrance, CA) using a binary system of water and acetonitrile with 0.1% trifluoroacetic acid as a modifier. Analytical LC/MS was carried out on a C_{18} reverse phase column (Polaris, 5 μm column, 50 × 4.6 mm; Varian; Torrance, CA) using a binary system of water and acetonitrile with 0.1% trifluoroacetic acid as a modifier. The purity of HPLC fractions was determined by analyzing the LC/MS trace at both 220 and 550 nm.

***N*-Piperidin-4-ylmethylamino-TAMRA·TFA (1).** To a solution of 4-(aminomethyl)-1-*N*-Boc-piperidine (24 mg, 0.10 mmol) in DMSO (1.0 mL) was added *N*-methylmorpholine (20 μL) followed by TAMRA-OSu (25 mg, 0.05 mmol). The reaction was stirred at ambient temperature for 6 h and then lyophilized to remove the DMSO. To the residue was added 1:1 TFA/CH_2Cl_2 (3.0 mL) and the reaction was allowed to stand for 1.5 h. The solvent was removed using rotary evaporation and the resulting solid was dissolved in a minimal amount of DMSO and purified by C_{18} reverse phase chromatography. The fractions containing the product in >95% HPLC purity were collected, and the solvent was removed using lyophilization, affording compound **2** as a dark purple solid (24 mg, 75% yield). ^{1}H NMR δ (D_2O): 8.39 (d, 0.6H), 8.10 (d, 0.4H), 8.00 (m, 1H), 7.67 (bs, 0.4H), 7.45 (d, 0.6H), 7.01 (m, 2H), 6.69 (m, 2H), 6.24 (m, 2H), 3.37 (m, 4H), 3.20 (d, 1H), 2.96 (s, 12H), 2.87 (m, 1H), 1.93 (m, 3H), 1.40 (m, 2H). ESMS: 527.0 $[M + H]^+$. MALDI−FTMS (DHB): *m*/*z* 527.2635 ($C_{31}H_{33}N_4O_4$ + H requires 527.2653).

***N*-[1-(4,6-Dioxoheptanoyl)piperidin-4-ylmethylamino]-TAMRA (2).** A solution of 4,6-dioxoheptanoic acid (36 mg, 0.23 mmol) and 1,1′-carbonyl-diimidazole (30 mg, 0.19 mmol) in anhydrous THF (0.7 mL) was stirred at ambient temperature for 1.5 h. To the stirred solution was added dropwise a solution of compound **1** (37 mg, 0.07 mmol) and TEA (49 μL, 0.36 mmol) in anhydrous DMSO (0.7 mL). The reaction was stirred for 2.5 h and then quenched with 4 drops of H_2O. This crude mixture was purified by reverse phase chromatography. The fractions containing the product in >95% purity by HPLC were collected and lyophilized overnight, affording compound **3** as a dark purple solid (31 mg, 66% yield). ^{1}H NMR δ (CD_3CN): 8.67 (d, 0.6H), 8.33 (d, 0.4H), 8.21 (dd, 0.6H), 8.09 (dd, 0.4H), 7.74 (d, 0.4H), 7.57 (t, 0.6H), 7.42 (m, 1H), 7.11 (d, 2H), 6.94 (dd, 2H), 6.84 (d, 2H), 5.65 + 5.63 (enol H's, 2 x S, 0.49H), 4.45 (m, 1H), 3.91 (m, 1H), 3.65 + 3.63 (dione CH_2's, 2 × S, 1.38H), 3.42 (m, 2H), 3.25 (s, 12H), 3.00 (m, 4H), 2.59 (m, 2H), 2.15 + 2.14 (dione-CH_3's, 2 × S, 1.77H), 2.00 + 1.99 (enol-CH_3's, 2 × S, 1.23H), 1.79 (m, 3H), 1.18 (m, 2H). ESMS: 667.0 $[M + H]^+$. MALDI−FTMS (DHB): *m*/*z* 667.3102 ($C_{38}H_{41}N_4O_7$ + H requires 667.3126).

AX7574. Microcystin-LR (578 μg, 0.58 μmol) and compound **2** (4 mg, 6.0 μmol) in 1 M $NaHCO_3$ (pH 9.0, 40 μL) and dioxane (10 μL) were heated for 2 days at 65 °C. LC/MS analysis indicated the consumption of microcystin-LR and the presence of a new TAMRA-containing peak (as evidenced by its absorption at 550 nm) with the desired product mass. This material was purified via preparative C_{18} HPLC using a flow rate of 30 mL/min and a 90 min gradient of 0.08% TFA/acetonitrile:0.1% TFA/water (2−98%) to yield the title compound as a purple solid. The quantity of the probe was determined spectroscopically in MeOH using an extinction coefficient of 95 000 M^{-1} cm^{-1} (34 μg, 4%) (*19*). MALDI−FTMS (DHB): *m*/*z* 1625.8402 ($C_{87}H_{112}N_{14}O_{17}$ + H requires 1625.8464). ES-MS: 813.4 $[M + 2H]^{2+}$. ES-MS/MS (*m*/*z* 813.4): (1099.5 ± 0.5, 55%), (527.4 ± 0.5, 100%). ES-MS/MS/MS (*m*/*z* 527.4): (430, 30%), (369, 22%), (341, 70%), (297, 35%). ES-MS/MS/MS (*m*/*z* 1099.5): (1071, 25%), (695, 100%), (842, 45%), (814, 35%), (674, 84%), (657, 51%), (592, 52%), (574, 35%), (408, 55%), and (390, 25%).

Structural Characterization Using Mass Spectrometry. The structure of AX7574 was characterized using tandem mass spectrometry (MS^n). Analyses were performed in an LCQ Deca ion trap mass spectrometer (Thermo Finnigan, San Jose, CA). AX7574 was dissolved in 1:1 methanol/deionized water and injected into the electrospray ionization source of the mass spectrometer with a syringe pump at a flow rate of 4 μL/min. The analysis was performed in the positive ion mode using the following parameters: spray voltage, 4 kV; sheath gas flow, 30 units; capillary temperature, 200 °C; capillary voltage, 46 V; relative collision energy, 40%. Two major fragment ions (*m*/*z* 1099.5 ± 0.5, 55% and *m*/*z* 527.4 ± 0.5, 100%) from AX7574 (*m*/*z* 813.4 ± 0.5, MH_2^{2+}) were further isolated individually and MS/MS/MS fragmentation was performed to obtain additional structural information. Four major fragment ions (*m*/*z* 430, 30%; *m*/*z* 369, 22%; *m*/*z* 341, 70%; and *m*/*z* 297, 35%) along with other minor fragments (relative abundance < 20%) were observed from the MS^3 on ion *m*/*z* 527. Ten major fragment ions (*m*/*z* 1071, 25%; *m*/*z* 965, 100%; *m*/*z* 842, 45%; *m*/*z* 814, 35%; *m*/*z* 674, 84%; *m*/*z* 657, 51%; *m*/*z* 592, 52%; *m*/*z* 574, 35%; *m*/*z* 408, 55%; and *m*/*z* 390, 25%) along with other minor fragments (relative abundance < 20%) were observed in the MS^3 experiment on ion *m*/*z* 1099.

Labeling of PP-1 with AX7574. To analyze the kinetics of PP-1 labeling, PP-1 (25 nM) was incubated with AX7574 (0.5 μM) in 50 mM HEPES, 5% DMSO, 0.01% Triton x-100, pH 7.4, at room temperature. At 1, 3, 6, 11, 21, 25, and 28 h, 20 μL sample aliquots were quenched with an equal volume of 2X gel sample buffer (120 mM Tris pH 6.8, 20% glycerol, 4% SDS, and 5% β mercaptoethanol), after which the samples were completely denatured by heating at 65 °C for 10 min. The denaturing protein conditions used in this analysis were presumed to break any noncovalent interaction between AX7574 and PP-1. To examine the inhibition of AX7574 labeling of PP-1 by phosphatase inhibitors, PP-1 (25 nM) was first preincubated with either calyculin A, protein phosphatase inhibitor 2, or fostriecen (100 nM each) for 10 min at room temperature. As a positive control, a reaction sample was included without any added phosphatase inhibitor. In addition, as a negative control, a reaction sample containing PP1 that was denatured by heating at 65 °C for 10 min was also included. AX7574 (0.5 μM) was then added and the labeling reaction quenched after 3 h and denatured as described above.

Determination of PP-1 IC_{50} Values for Microcystin and AX7574. PP-1 IC_{50} values for microcystin and AX7574 were determined by examining the inhibition of *p*-nitrophenyl phosphate (pNPP) hydrolysis by PP-1. PP-1 was diluted in 50 mM Tris, pH 7.0, 0.1 mM NaEDTA, 5 mM DTT, and 0.025% Tween 20. Inhibitors and substrate were diluted in 50 mM Tris, pH 8.1, 20 mM $MgCl_2$, 0.2 mM $MnCl_2$, and 0.5 mg/mL BSA. The reaction was initiated by first incubating PP-1 (10 μL) with each compound (10 μL) at various concentrations for 10 min, followed by addition of pNPP substrate (30 μL). The final concentrations of PP-1 and substrate were 5 nM and 20 mM, respectively, while the inhibitors were used at a range of concentrations between 0 and 30 nM. A control was included for background subtraction without any phosphatase or inhibitor. Samples were incubated at 37 °C for 90 min and the A_{450} of the samples was determined using a VERSAmax microplate reader (Molecular Devices, Sunnyvale, CA). SOFTmax Pro Version 3.1.2 software (Molecular Devices, Sunnyvale, CA) was used to analyze the data. For each inhibitor, A_{450} was plotted versus the inhibitor concentration, and the points were fit to the following equation to estimate the IC_{50} of the inhibitors:

$$A = A_{\min} + \frac{(A_{\max} - A_{\min})}{\left\{\left[1 + \left(\frac{IC_{50}}{[Inh]}\right)^{s}\right]\right\}}$$

where A is A_{450}, $A_{\min}$ is the A_{450} in the absence of enzyme, $A_{\max}$ is the A_{450} in the absence of inhibitor, and s is a parameter determining the slope of the curve. Curve-fitting was carried out using the Igor Wave Metrics software (Wave Metrics, Lake Oswego, OR).

Gel Electrophoreses Protocol and Data Analysis. Samples were loaded onto 8 × 10 cm, 12.5% Laemli gels and electrophoresed for 55 min at 200 V. The gels were then scanned on a flatbed scanner (FMBio II, Hitachi Genetic Systems; Alameda, CA) with excitation provided by the 532-nm line of a 50 mW neodymium-doped yttrium−aluminum-garnet laser. A 605 nm band-pass filter was used to detect TAMRA fluorescence. The scanned images were analyzed using Image Analysis 3.0 software (Hitachi Genetic Systems; Alameda, CA) and the integrated band intensities (normalized for volume) were calculated for the activity levels of the labeled proteins. The integrated fluorescence of TAMRA was correlated to probe-labeled protein concentration by use of a calibration curve generated from treatment of known quantities of fatty acid amide hydrolase with a TAMRA-FP serine hydrolase probe (*20*).

Identification of AX7574-Labeled Proteins. Isolation of AX7574-labeled proteins was achieved using anti-TAMRA antibody beads as previously described for serine hydrolase fluorophosphonate probes (*21*) After elution of the immunocaptured samples, enriched microcystin-probe-labeled proteins were separated by SDS−PAGE. 1D gels were poured using Bind Silane solution (Amersham Biosciences, Piscataway, NJ) to adhere the gel to the bottom plate. Use of this agent enabled the removal of the short plate such that a gel band could be picked directly off of the bottom plate without disturbing the integrity of the entire gel. The fluorescent gel bands of interest were excised using an Ettan spot picker (Amersham Biosciences; Piscataway, NJ). Gel plugs were picked into a 96 well polystyrene microtiter plate (Costar) in methanol (100 μL). The plate was then placed on an Ettan digestion station (Amersham Biosciences; Piscataway, NJ) for a wash series. After washing with water (3 × 50 μL), 70:30 20 mM ammonium bicarbonate/acetonitrile (3 × 50 μL), and again with water (3 × 50 μL), the gel pieces were evaporated to dryness using a steady stream of nitrogen gas at 60 °C (TurboVap 96; Fisher; Tustin, CA), after which an overnight, in-gel tryptic digestion (porcine modified trypsin, 80 ng per spot, Promega, Madison, WI) was performed in the presence of 20 mM ammonium bicarbonate, pH 8.0. This buffered solution was removed and the gel pieces washed with 0.1:40:60 TFA/water/acetonitrile (20 μL) with vortexing. The ammonium bicarbonate and the TFA/water/acetonitrile solutions were pooled, the volume was reduced to 5 μL, and 5% acetic acid (20 μL) was added to the concentrate. The resultant peptides were separated using nanocapillary reverse-phase chromatography by loading the concentrate solution at a flow rate of 10 μL/min onto a reverse phase micro-precolumn (Agilent; Palo Alto, CA) and then washing the column for 10 min at the same rate in solvent A [water + 0.1% formic acid (Sigma; St, Louis, MO)] to remove inorganic salts. The column was then back-flushed onto a nanocapillary analytical column (pulled fused silica, 100 μm inner diameter × 10 cm) packed with C_{18} reverse phase media (Zorbax C_{18}; Agilent; Palo Alto, CA) at a flow rate of 400 nL/min with a 50 min gradient from 10 to 90% 0.08% formic acid/acetonitrile in 0.08% formic acid/water. Peptides were analyzed in data-dependent mode with an ion trap mass spectrometer (LCQ Deca XP; Thermo Electron; San Jose, CA). The heated capillary was set at 180 °C with a spray voltage of 1.8 kV. Peptides were scanned between 400 and 1500 Da with three microscans collected per scan. Peptides were sequenced and the corresponding proteins identified using the Mascot search algorithm (Matrix Science; London, UK) (*22*).

Cell Culture and Cell Lysate Preparation. Jurkat cells were grown in RPMI medium 1640 containing 10% fetal calf serum (Gibco/Invitrogen Corp., San Diego, CA). Cells were harvested by centrifugation and washed twice with cold phosphate-buffered saline, pH 7.4. Cell pellets were briefly sonicated and Dounce homogenized in 50 mM HEPES, pH 7.4. Cell extracts were centrifuged at 100 000*g* to provide soluble cellular proteome fractions.

Labeling of Cell Lysates with AX7574. Soluble fractions were adjusted to a final protein concentration of 1.5 mg/mL in 50 mM HEPES (pH 7.4) and treated with AX7574 (0.5 μM) for 60 min at room temperature. Control reactions consisting of soluble fractions were preincubated with microcystin (1 μM) and calyculin A (1 μM) for 10 min prior to the addition of AX7574. Reactions were quenched with one volume of standard 2× SDS/PAGE loading buffer (reducing), separated from unreacted probe by SDS/PAGE, and visualized in-gel with a Hitachi FMBio IIe flatbed fluorescence scanner (Mirai-Bio; Alameda, CA)

Western Blot Analysis. Quenched AX7574 reactions were separated using SDS−PAGE (20 μg/lane). Proteins were then transferred by electroblotting onto nitrocellulose membranes (Protran). Western blot analysis using an anti-PP1 mouse monoclonal antibody and anti-PP2A rabbit polyclonal antibody (Santa Cruz Biotechnology; Santa Cruz, CA) were conducted as described previously (*20*).

RESULTS AND DISCUSSION

Microcystins are a class of toxic cyclic peptides produced by the cyanobacterial genera, *Microcystis*, *Oscillatora*, *Anabaena*, and *Nostoc*. Many variants have been

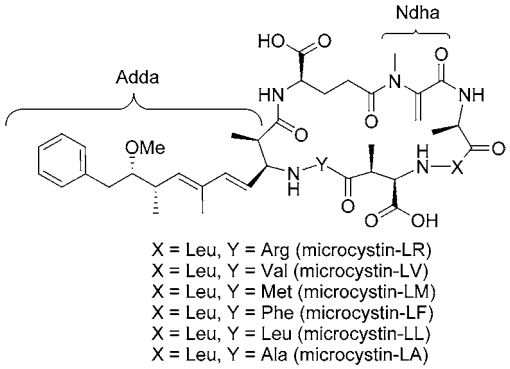


Figure 1. Structure of microcystin variants. Ndha = *N*-methyldehydroalanine; Adda = 3-amino-9-methoxy-2,6,8-trimethyl-10-phenyldeca-4(*E*),6(*E*)-dienoic acid.

identified and are differentiated by their amino acid residue composition (*23*). Accordingly, nomenclature is defined using the single amino acid letter codes of these interchangeable residues (Figure 1). In countries where freshwater is susceptible to contamination by cyanobacterial blooms, microcystins have been responsible for a variety of adverse effects on human health. For example, in China the incidence of colorectal and liver cancer has been shown to be considerably higher than average among populations drinking water contaminated with microcystins (*24*, *25*). Since their identification as the causative agent in such outbreaks, microcystins have been determined to be potent hepatotoxins (*26*) and tumor promoters (*27*).

As part of the investigation into the molecular nature of this toxicity, serine/threonine phosphatases, such as PP-1 and PP-2A, were identified as the enzymatic target of microcystins. A mechanistic study by Holmes et al. reported that these phosphatases are irreversibly inhibited by microcystin such as LR, LA, and LL via a two-step mechanism (*28*). The first step includes the rapid binding and reversible inhibition of these phosphatases. The second step involves the covalent attachment of the bound microcystin to the phosphatase, as evidenced by protein adducts observable via HPLC. While the kinetics of the first step is fast, on the order of minutes, the second step takes place on the order of hours. More specifically, after incubation of PP-1 with microcystin-LR for 16 h, 65% of the covalent adduct was formed.

The potency of microcystin-LR for PP-1 is relatively insensitive to substitution of the arginine residue. Microcystin-LR is considered a potent inhibitor of PP-1, with IC_{50} values ranging from 0.15 to 6 nM, depending on the assay used to measure inhibition (*29*). Seven other variants of the LR type, in which the arginine residue was replaced with a more hydrophobic side chain, were isolated from *Microcystis aeruginosa* and associated strains present in Canadian lakes. When the PP-1 IC_{50}s for these varieties, which included the microcystins LV, LM, LF, and LL, were determined, the values were found to range between 0.06 and 0.4 nM. By comparison, the IC_{50} value of microcystin-LR was determined in the same study to be 0.15 nM (*30*). Thus, the arginine residue of microcystin-LR can be modified without a significant impact on the potency of the microcystin scaffold.

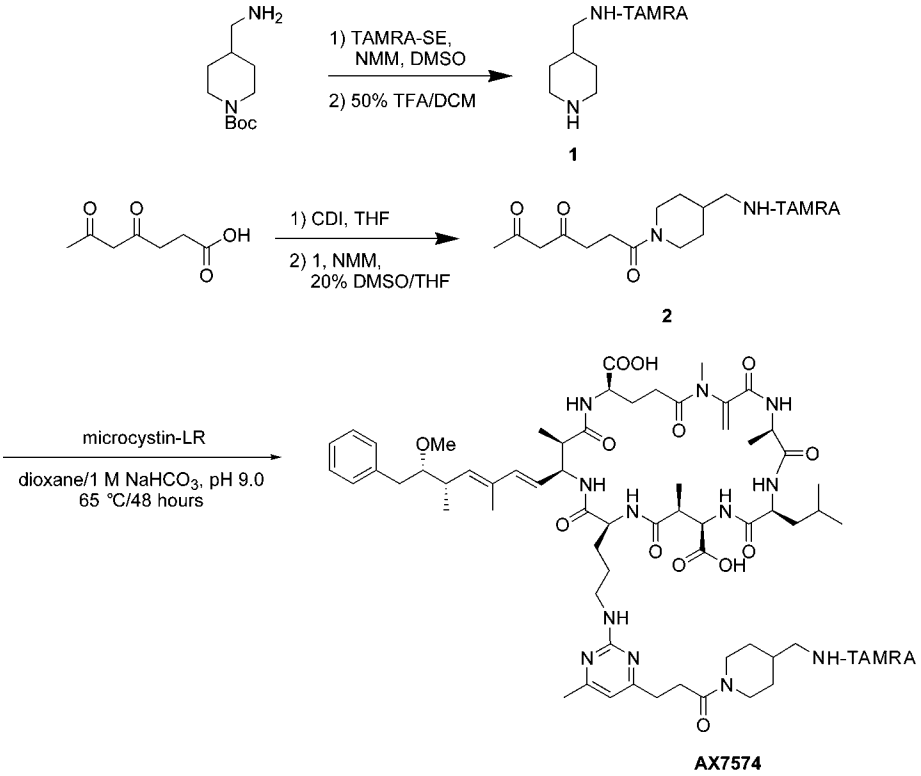
When the crystal structure of the microcysin-LR/PP-1 complex was solved, both the nature of the irreversible binding and the interchangeability of arginine were made clear (*31*). The joining between inhibitor and enzyme is the result of a Michael-type addition of the active site Sγ atom of Cys273 to the terminal carbon atom of the microcystin *N*-methyldehydroalanine (Ndha, Figure 1) side chain. Furthermore, the crystal structure explained the tolerance of the arginine residue for substitution: when the inhibitor is complexed, the arginine side chain is solvent-exposed. Consequently, changing this residue does not interrupt any critical inhibitor−protein interactions. Interestingly, a comparison of the solid state complexed microcystin-LR to the solution structure of microcystin-LR shows both to have similar conformations, a fact that likely contributes entropically to the high affinity of microcystin-LR for PP-1 (*32*).

To synthesize a functional probe for serine/threonine phosphatases based on microcystin, we wished to maintain both the high affinity associated with microcystins as well as the ability of microcystins to covalently modify their enzymatic targets. While two synthetic methodologies to create microcystin conjugates are known from the literature, neither was suitable to achieve these goals. In the first approach, a thioether bond is formed by the addition of thiol nucleophiles to the microcystin Ndha residue via a Michael-like addition. This chemistry was utilized to derivatize microcystins with redox sensitive (ferrocene) (*33*) and chemiluminescent responsive (dansyl) (*34*) tags for quantitative HPLC analysis. This same synthetic approach has also been used to create a microcystin-LR-biotin conjugate suitable for phosphatase affinity chromatography. Modification of the Ndha residue with a dithiol linker followed by treatment with iodoacetyl−LC−biotin yielded a biotinylated derivative that could be used in conjunction with an avidin column (*35*). Interestingly, detoxification of microcystin in the liver proceeds in an analogous Michael-like fashion, albeit enzymatically, with glutathione (*36*). Unfortunately for our purposes, in all of these cases the resulting thioether conjugates are rendered impotent with respect to their ability to irreversibly modify phosphatases. Because a microcystin derived probe would need to covalently tag its enzymatic target, Michael addition chemistry could not be used.

In the second known synthetic approach, Diels−Alder chemistry has been used to create a linker between microcystin and the fluorescent tag DMEQ-TAD, a reagent designed to react with diene-containing natural products (*37*). When DMEQ-TAD was reacted with microcystin-LR, modification of the diene-containing Adda residue (Figure 1) resulted in two sterochemically distinct adducts (*38*). Again, this chemistry was designed for derivatization and subsequent quantitative HPLC analysis; no information on the potency or binding properties of these conjugates for phosphatases was given. Because the Adda residue makes several hydrophobic contacts critical to the formation of the microcystin-LR/PP-1 complex, we forewent this approach as well.

To avoid any modifications to the microcystin scaffold that would adversely impact its binding properties, we chose to target the arginine side chain of microcystin-LR for linker incorporation. Because this side chain did not make any significant contacts with PP-1, a fluorophore conjugated through this residue was expected to have minimal impact on the activity of any so-derivatized microcystin probe. To effect the modification, the 1,3-diketone functionality was chosen, a group long known as an arginine-specific modifying agent (*39*, *40*). Upon condensation and subsequent dehydration, 1,3-diketones will convert an arginine residue to a hydrolytically stable N^{δ}-(2-pyrimidyl)ornithyl residue. A recent application of this condensation by Budzikiewicz and Kinzel has been used to conjugate the cyclic peptide pyoverdin to cephalexin through a 4,6-dioxoheptanoic acid linker (*41*). The authors showed pyoverdin could be modified directly with

Scheme 1. Synthesis of the Microcystin−TAMRA Probe AX7574



4,6-dioxoheptanoic acid to form a carboxylic acid bearing derivative. However, this acid was not further elaborated upon. In the end, they chose a synthetic route in which 4,6-dioxoheptanoic acid was carbodiimide coupled to cephalexin and the resulting dione conjugated to pyoverdin in 20% yield. Because microcystin modification with 4,6-dioxoheptanoic acid would yield a tricarboxylic acid, any resulting amidation with an amine bearing fluorophore derivative would be difficult to accomplish selectively. Consequently, we started our approach, analogous to the case of cephalexin, with the synthesis of a fluorophore-dione derivatization reagent. In particular, we chose to use tetramethylrhodamine (TAMRA) as the fluorophore, because of its previous success as a sensitive and quantitative tag for ABPs.

The requisite dione was prepared from the mixed succinimidyl esters of 5-(and 6)-carboxytetramethylrhodamine (TAMRA-OSu). Reaction of TAMRA-OSu with (Boc-4-aminomethyl)piperidine followed by treatment of the resulting product with 1:1 TFA/DCM produced the secondary amine **1** (Scheme 1). When this amine was treated with an excess of *N*,*N*′-carbonyldiimidazole-activated 4,6-dioxoheptanoic acid, compound **1** was quantitatively converted into the desired dione **2**. After purification via C_{18} reverse phase HPLC, the TAMRA-dione **2** was isolated in 66% yield. As expected, ^{1}H NMR analysis showed the presence of resonances for both the enol and dione form of compound **2**. Furthermore, doubling of the enol, dione, and aromatic resonances was observed from the use of the mixed TAMRA isomer starting material.

The probe AX7574 was produced from the condensation of compound **2** with microcystin-LR under basic conditions. Microcystin-LR (580 μg) was heated with a 10-fold excess of dione in a mixture of 20% dioxane/1 M $NaHCO_3$ (pH 9.0) for 2 days at 65 °C. LC/MS analysis indicated the consumption of microcystin-LR and the presence of a new TAMRA-containing peak (as evidenced by an absorption at 550 nm) with the desired product mass (MALDI−FTMS (DHB): *m*/*z* 1625.8402 − $C_{87}H_{112}N_{14}O_{17}$ + H requires 1625.8464). AX7574 was isolated from other impurities using C_{18} reverse phase chromatography in 4% yield.

AX7574 was characterized structurally using tandem mass spectrometry. Fragmentation of the parent ion (MS/MS) resulted in two major ions, 1099.5 and 527.4. These ions were assigned to the fragments that result from the N−CO cleavage of the tertiary amide bond found in the linker. Further isolation and fragmentation of these ions (MS/MS/MS) were consistent with the expected structure of AX7574 (see Figure 2). For the former ion, fragmentations corresponding to cleavage of the cyclic peptide backbone, decarbonylation, and loss of the pyrimidine moiety were seen. For the latter ion, fragments corresponding to cleavage about the amide bond of the linker−TAMRA moiety were observed.

Once the structure of AX7574 was secured, attention was turned to demonstrating its ability to label PP-1. PP-1 (25 nM) was incubated with AX7574 (0.5 μM) in 50 mM HEPES, 5% DMSO, 0.01% Triton x-100, pH 7.4, at ambient temperature. At various timepoints, sample aliquots were removed, quenched with DTT-containing sample buffer, and then heat-denatured. The resulting samples were subjected to denaturing SDS−PAGE, and labeled enzyme was visualized using a flatbed laser-induced fluorescence scanner. Importantly, the TAMRA tag provided a sensitive fluorescent handle by which the degree of labeling could be quantified (see Experimental Procedures). Consistent with the results of Holmes et al. (vide supra), the kinetics of PP-1 labeling was on the order of hours (see Figure 3) with 65% of the labeling occurring at ∼16 h. When the time course data were fit to a single exponential, maximal labeling was determined to approach a ratio of 1:1 PP-1 to AX7574.

Several additional experiments were run to determine if the observed labeling was specific for the active site of

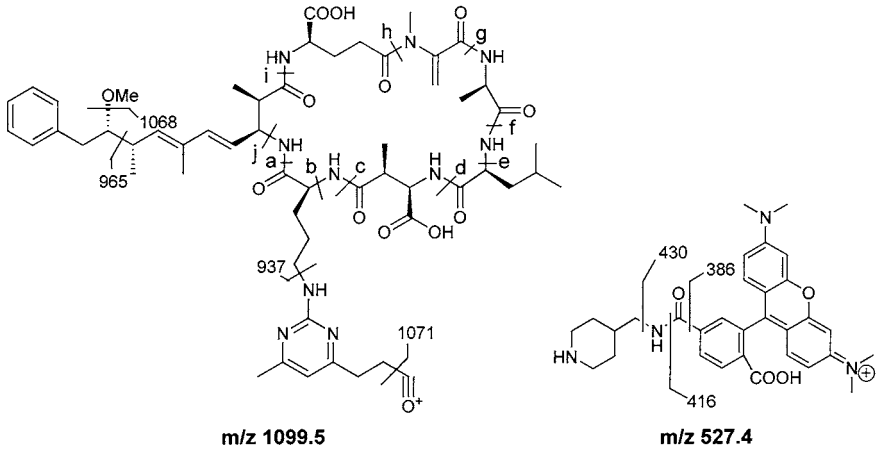


Figure 2. Mass spectrometric (MS) structural identification of AX7574. Shown are some of the observed fragmentation patterns from the two major parent ions observed during the MS/MS analysis of the doubly charged parent ion peak. Dual letter fragment masses (vide infra) are derived from a counterclockwise trace along the cyclic peptide backbone of AX7574 from the designated point of fragmentation to the next indicated point of fragmentation: ea − H_2O = 592, ga + NH_2−H_2O = 521, fb = 842, fb − CO = 814, dc = ih = 971, gc = ai = 786, hc = 703, ic = ag = 574, ad = 390, af = 503, ah = 657, jh = 674, hj − H_2O = 408.

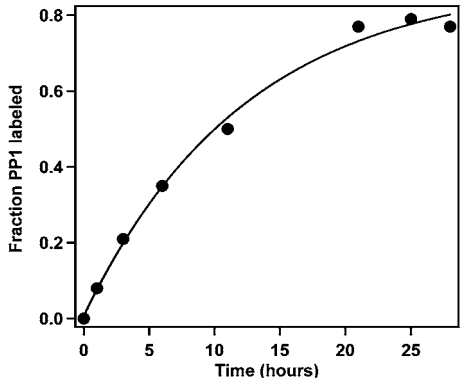


Figure 3. Kinetics of AX7574 labeling of PP-1. PP-1 (25 nM) was labeled with AX7574 (0.5 μM). At the indicated timepoints, sample aliquots were quenched. The quenched samples were electrophoresed, the gel was scanned, and the fraction of PP-1 labeled was determined as described in the Experimental Procedures. The curve drawn is the best fit of the data to a single exponential.

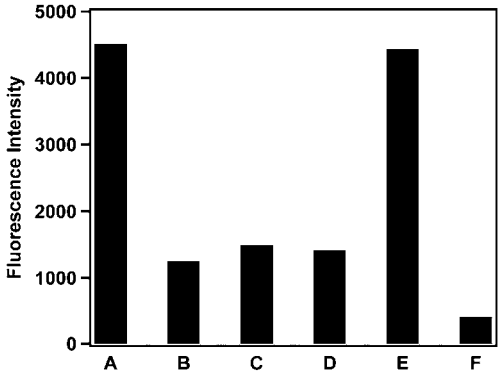


Figure 4. Inhibition of AX7574 labeling of PP-1 with phosphatase inhibitors. PP-1 (25 nM) was labeled with AX7574 (0.5 μM) (A) in the absence of phosphatase inhibitors or in the presence of (B) microcystin-LR, (C) calyculin A, (D) protein phosphatase inhibitor 2, and (E) fostriecen at 100 nM each. An additional AX7574 (0.5 μM) labeling experiment using denatured PP-1 (25 nM, F) is also shown. Labeling reactions were quenched after 3 h. The samples were electrophoresed, the gel was scanned, and the scanned image was quantified as described in the Experimental Procedures.

PP-1 (see Figure 4). In the first set of experiments, inhibition of AX7574 labeling with known inhibitors of

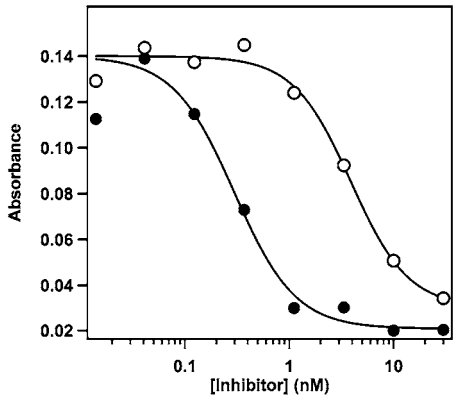


Figure 5. PP-1 IC_{50} determination for microcystin (●, IC_{50} = 0.3 nM) and AX7574 (○, IC_{50} = 4.0 nM). The curves drawn are the best fit of the data to a variation of the Hill equation (see Experimental Procedures section).

PP-1 was tested. The inhibitors selected included microcystin, calyculin A (PP-1 IC_{50} = 1.2 nM) (*29*), and protein phosphatase inhibitor 2 (PP-1 IC_{50} = 1 nM) (*42*). These particular inhibitors were selected because they interact with phosphatases through diverse mechanisms. For example, microcystin is an irreversible inhibitor, and both calyculin A and protein phosphatase inhibitor 2 are reversible ones. Furthermore, while microcystin and calyculin A are small molecules, protein phosphatase inhibitor 2 is a protein macromolecule (MW = 31 kDa). In addition, fostriecin, a weak inhibitor of PP-1 (PP-1 IC_{50} = 131 μM, PP-2A IC_{50} = 3.2 nM), was included as a negative control. PP-1 (25 nM) was preincubated for 10 min with microcystin (100 nM), calyculin A (100 nM), protein phosphatase inhibitor 2 (100 nM), or fostriecin (100 nM) or allowed to stand for 10 min in the absence of added phosphatase inhibitors. Afterward, AX7574 (0.5 μM) was added to each sample and the labeling reaction stopped after 3 h using DTT-containing sample buffer. When compared to the same labeling reaction done in the absence of phosphatase inhibitors, significantly less labeling with AX7574 was observed in the presence of microcystin, calyculin A, or protein phosphatase inhibitor 2. In the case of microcystin and calyculin A, the results indicate that AX7574 competes for the active site where these inhibitors are known to bind. As expected, the PP-2A specific inhibitor, fostriecin, did not cause a significant decrease in labeling of PP-1 by AX7574.

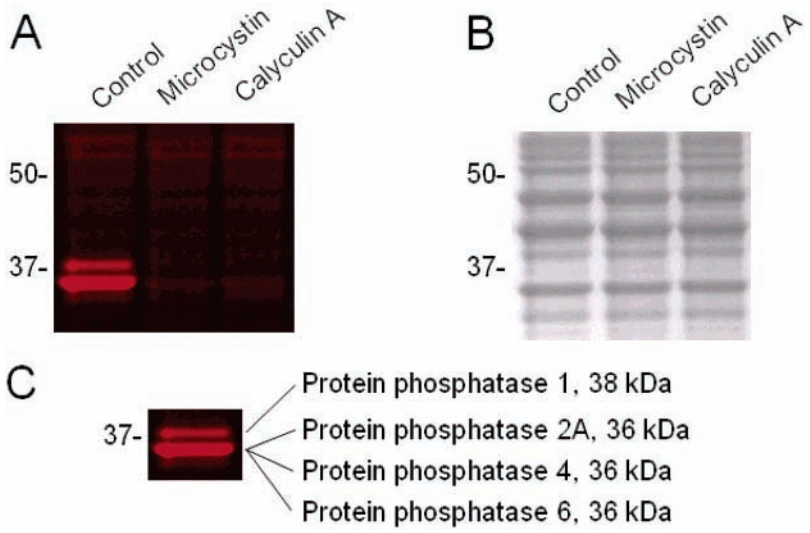


Figure 6. AX7574 can detect serine/threonine phosphatases in a proteome. (A) Soluble proteome derived from Jurkat cells preincubated with or without microcystin (1 μM) or calyculin a (1 μM) for 10 min and then treated with AX7574 (0.5 μM) for 60 min. Reactions were quenched with standard 2× SDS/PAGE loading buffer (reducing), separated from unreacted AX7574 using SDS−PAGE, and visualized in-gel using a flatbed laser-induced fluorescence scanner. (B) Coomassie blue stained gel from Figure 6A confirming that all three lanes contained approximately equal amounts of protein. (C) AX7574-labeled proteins identified using MS protein identification.

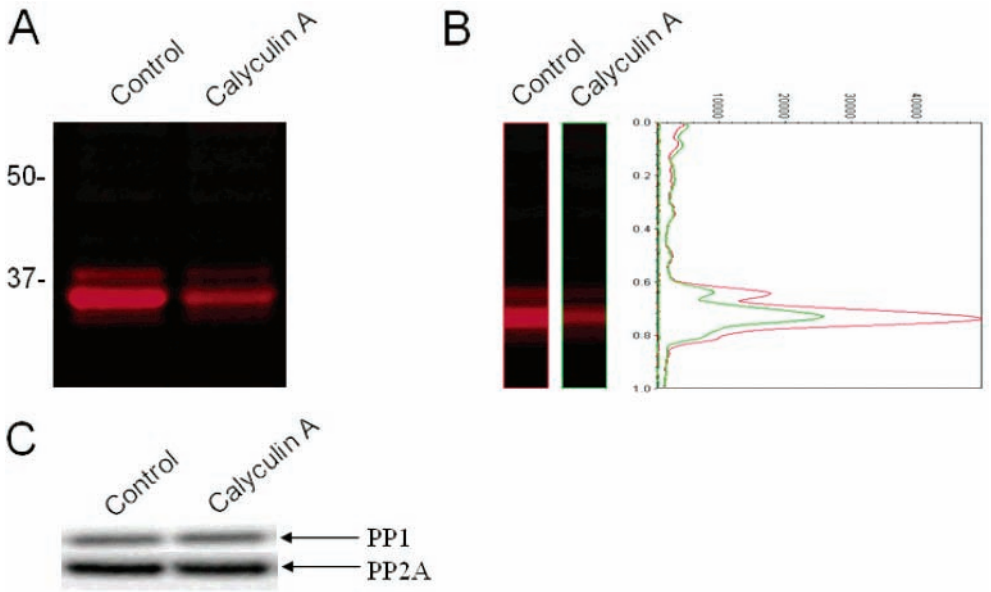


Figure 7. AX7574 can detect the decrease of serine/threonine protein phosphatase activities in calyculin A-treated Jurkat T cells. (A) Jurkat cells treated with calyculin A (25 nM) for 60 min or control DMSO, and soluble proteome derived from these cells were treated with AX7574 (0.5 μM) for 60 min. Reactions were quenched with standard 2× SDS/PAGE loading buffer (reducing), separated by SDS/PAGE, and visualized in-gel using a flatbed laser-induced fluorescence scanner. (B) Side-trace analysis of the gel data from Figure 7A. (C) The scanned gel from A was transferred to nitrocellulose and immunoblotted with anti-PP1 and anti-PP2A.

A second kind of experiment was carried out to examine whether the labeling of PP-1 by AX7574 required PP-1 to retain its native tertiary structure (see Figure 4). To address this question, PP-1 (25 nM) was first denatured by heating the protein at 65 °C for 10 min. The subsequent addition of AX7574 (0.5 μM) resulted in no significant labeling of PP-1. This result indicates that the recognition and subsequent attachment of AX7574 to PP-1 does in fact require the native structure of PP-1.

To investigate the impact of TAMRA conjugation on the affinity of the microcystin scaffold for PP-1, the IC_{50} values of both microcystin-LR and AX7574 for PP-1 were determined and compared (see Figure 5). Both compounds at various concentrations (0−30 nM) were incubated with PP-1 (5 nM) for 10 min. Postincubation, *p*-nitrophenyl phosphate (pNPP, 20 mM) was added and the degree of substrate hydrolysis measured spectroscopically at 450 nm. For each inhibitor, A_{450} was plotted versus inhibitor concentration, and the points were fit to a variation of the Hill equation (*43*) to determine IC_{50} values. Such an analysis yielded IC_{50} values of 0.3 and 4.0 nM for microcystin and AX7574, respectively. By comparison, a similar pNPP-based determination yielded a PP-1 IC_{50} value of 0.25 nM for microcystin-LR (*44*). As evidenced by these values, TAMRA conjugation had only a modest impact on binding and the resulting probe AX7574 remained a potent PP-1 inhibitor.

To test whether AX7574 would react with serine/threonine protein phosphatases in a complex proteome, we incubated soluble fractions of Jurkat cells with this probe (0.5 μM) for 60 min. Protein separation of the

sample was achieved using SDS−PAGE and visualized in-gel using a flatbed laser-induced fluorescence scanner. As seen in Figure 6A, AX7574 strongly labeled only two sets of proteins (36 and 38 kDa) and the labeling of these proteins by AX7574 was strongly inhibited by both microcystin and calyculin A. Protein staining revealed that all lanes contained approximately equal amounts of protein (Figure 6B), an indication that the labeling was specific for the proteins in those bands and not merely the result of labeling highly abundant proteins nonspecifically.

To confirm that the proteins labeled by AX7574 in Jurkat soluble fractions were serine/threonine protein phosphatases, mass spectrometric (MS) protein identification was performed (see Experimental Procedures): The two fluorescent gel bands were excised (Figure 6A), labeled proteins isolated using anti-TAMRA antibody beads, and the captured proteins digested using trypsin. Subsequent MS sequence analysis of the resulting peptides was used to identify the protein composition of each band. The 38-kDa protein band was shown to be PP-1 and the 36-kDa protein band was found to contain PP-2A, PP-4, and PP-6 (Figure 6C). Both PP-2A and PP-4, a phosphatase closely related to PP-2A (*45*), have previously been shown to be inhibited by microcystin-LR with IC_{50} values of 0.15 nM for both enzymes (*46*, *47*). In addition, PP-2A, PP-4, and PP-6 have been captured *noncovalently* using a microcystin−sepharose column as part of an effort to purify these proteins from soluble bovine testes extracts. Our data, which relies on the covalent labeling of these phosphatases, is the first account, to the best of our knowledge, of the irreversible binding of PP-4 and PP-6 by a microcystin derivative. Ultimately, and perhaps most importantly, the MS identification results demonstrate that AX7574 is able to react with and detect numerous serine/threonine phosphatases in a crude cell sample.

To test whether AX7574 could record changes in serine/threonine protein phosphatase activity levels, we treated Jurkat cells with calyculin A dissolved in a minimal amount of DMSO (2% v/v) such that the final concentration of inhibitor was 25 nM. Calyculin A was chosen not only for its cell permeability but also its potent activity against both PP1 (IC_{50} = 1.2 nM) and PP2A (IC_{50} = 7.3 nM) (*29*). As a control, Jurkat cells were treated with an equivalent volume of DMSO alone. After labeling with AX7574 (0.5 μM) for 60 min, AX7574-reactive serine/threonine protein phosphatases showed significantly lower labeling intensities in the calyculin A-treated Jurkat cells versus the control Jurkat cells (see Figure 7A and 7B). These results indicated that serine/threonine protein phosphatase activities were strongly inhibited by calyculin A. Critically, western blot analysis using anti-PP1 and anti-PP2A antibodies identified the same quantity of PP1 and PP2A in both control and calyculin A-treated Jurkat cells (see Figure 7C). These results further confirm that AX7574 labels serine/threonine protein phosphatases in an activity-dependent manner, recording variations in protein phosphatase activity rather than protein level. Without the AX7574 probe, western blot analysis and/or standard proteomics studies would have difficulties in distinguishing active from inactive protein phosphatases in these samples.

In conclusion, we describe herein the synthesis of AX7574, a microcystin derived fluorescent probe for serine/threonine phosphatases. The conjugation of a 1,3-diketone-containing fluorophore to the arginine-containing scaffold of microcystin was critical in maintaining the specific, high affinity, and irreversible-bond forming nature of the microcystin-phosphatase interaction. The ability to form a covalent bond within the phosphatase active site allowed this tagged chemical probe to capture and visualize the activity of this important class of enzymes in a complex proteome. Importantly, AX7574 expands the range of activity-based probes and provides a means to investigate the role that serine/threonine phosphatases play in physiological and/or pathological events.

ACKNOWLEDGMENT

The authors thank Drs. John Kozarich, Katrin Szardenings, and David Campbell for helpful suggestions concerning this work and/or the manuscript.

LITERATURE CITED

(1) Anderson, N. L., and Anderson, N. G. (1998) Proteome and proteomics: New technologies, new concepts, and new words. *Electrophoresis 19*, 1853−1861.
(2) Pandey, A., and Mann, M. (2000) Proteomics to study genes and genomes. *Nature 405*, 837−846.
(3) Burbaum, J., and Tobal, G. M. (2002) Proteomics in drug discovery. *Curr. Opin. Chem. Biol. 6*, 427−433.
(4) Cravatt B. F., and Sorensen E. J. (2000) Chemical strategies for the global analysis of protein function. *Curr. Opin. Chem. Biol. 4*, 663−668.
(5) Patricelli, M. P. (2002) Activity-based probes for functional proteomics. *Briefings Funct. Genomics Proteomics 1* (2), 151−158.
(6) Liu, Y., Patricelli, M. P., and Cravatt, B. F. (1999) Activity-based protein profiling: The serine hydrolases. *Proc. Natl. Acad. Sci. U.S.A. 96(26)*, 14694−14699.
(7) Jessani, N., Liu Y., Humphrey, M., and Cravatt B. F. (2002) Enzyme activity profiles of the secreted and membrane proteome that depict cancer cell invasiveness. *Proc. Natl. Acad. Sci. U.S.A. 99* (16), 10335−10340.
(8) Leung, D., Hardouin, C., Boger, D. L., and Cravatt, B. F. (2003) Discovering potent and selective reversible inhibitors of enzymes in complex proteomes. *Nat. Biotechnol. 21* (6), 687−691.
(9) Patricelli, M. P., Giang, D. K., Stamp, L. M., and Burbaum J. J. (2001) Direct visualization of serine hydrolase activities in complex proteomes using fluorescent active site-directed probes. *Proteomics 1*, 1067−1071.
(10) Kidd, D., Liu, Y., and Cravatt, B. F. (2001) Profiling serine hydrolase activity in complex proteomes. *Biochemistry 40*, 4005−4015.
(11) Taylor, W. P., and Widlanski, T. S. (1995) Charged with meaning: The structure and mechanism of phosphoprotein phosphatases. *Chem. Biol. 2(11)*, 713−718.
(12) van Huijsduijnen, R. H., Bombrun, A., and Swinnen, D. (2002) Selecting protein tyrosine phosphatases as drug targets. *Drug Discov. Today 7* (19), 1013−1019.
(13) Honkanen, R. E., and Golden, T. (2002) Regulators of serine/threonine protein phosphatases at the dawn of a clinical era? *Curr. Med. Chem. 9(22)*, 2055−2075.
(14) Lo, L.-C., Wang, H.-Y., and Wang, Z.-J. (1999) Design and synthesis of an activity probe for protein tyrosine phosphatases. *J. Chin. Chem. Soc. 46(5)*, 715−720.
(15) Lo, L.-C., Pang, T.-L., Kuo, C.-H., Chiang, Y.-L., Wang, H.-Y., and Lin, J.-J. (2002) Design and synthesis of class-selective activity probes for protein tyrosine phosphatases. *J. Proteome Res. 1* (1), 35−40.
(16) Myers, J. K., and Widlanski, T. S. (1993) Mechanism-based inactivation of prostatic acid phosphatase. *Science 262*, 1451−1453.
(17) Cohen, P. T. W. (2002) Protein phosphatase 1—Targeted in many directions. *J. Cell. Sci. 115* (2), 241−256.
(18) Parsons, R. (1998) Phosphatases and tumorigenesis. *Curr. Opin. Oncol. 10* (1), 88−91.
(19) Haugland, R. P. *Handbook of Fluorescent Probes and Research Chemicals* (2003) Molecular Probes, Inc., Eugene, Oregon.

(20) Patricelli, M. P., and Cravatt, B. F. (2000) Clarifying the catalytic roles of conserved residues in the amidase signature family. *J. Biol. Chem. 275* (25), 19177−19184.
(21) Adam G. C., Burbaum J., Kozarich J. W., Patricelli M. P., and Cravatt B. F. (2004) Mapping Enzyme Active Sites in Complex Proteomes *J. Am. Chem. Soc. 126* (5), 1363−1368.
(22) Perkins, D. N., Pappin, D. J. C., Creasy, D. M., and Cottrell, J. S. (1999) Probability-based protein identification by searching sequence databases using mass spectrometry data. *Electrophoresis 20* (18), 3551−3567.
(23) Lam, P. K., Yang, M., and Lam, M. H. (2000) Toxicology and evaluation of microcystins. *Ther. Drug. Monit. 22* (1), 69−72.
(24) Zhou, L., Yu, H., and Chen, K. (2002) Relationship between microcystin in drinking water and colorectal cancer. *Biomed. Environ. Sci. 15* (2), 166−171.
(25) Yu, S., Zhao, N., and Zi, X. (2001) The relationship between cyanotoxin (microcystin, MC) in pond-ditch water and primary liver cancer in China. *Zhonghua Zhong Liu Za Zhi. 23* (2), 96−99.
(26) Runnegar, M. T., Kong, S., and Berndt, N. (1993) Protein phosphatase inhibition and in vivo hepatoxicity of microcystins. *Am. J. Physiol. 265* (2/1), 224−230.
(27) Nishiwaki-Matsushima, R., Ohta, T., Nishiwaki, S., Suganuma, M., Kohyama, K., Ishikawa, T., Carmichael, W. W., and Fujiki, H. (1992) Liver tumor promotion by the cyanobacterial cyclic peptide toxin microcystin-LR. *J. Cancer Res. Clin. Oncol. 118* (6), 420−424.
(28) Craig, M.; Luu, H.-A.; McCready, T. L.; Williams, D.; Andersen, R. J.; and Holmes, C. F. B. (1996) Molecular mechanisms underlying he interaction of motuporin and microcystins with type-1 and type-2A protein phosphatases. *Biochem. Cell Biol. 74* (4), 569−578.
(29) Gupta, V., Ogawa, A. K., Du, X., Houk, K. N., and Armstrong, R. W. (1997) A model for binding of structurally diverse natural product inhibitors of protein phosphatases PP1 and PP2A. *J. Med. Chem. 40* (20), 3199−3206.
(30) Craig, M., McCready, T. L., Luu, H. A., Smillie, M. A., Dubord, P., and Holmes, C. F. B. *Toxicon* **1993**, *31* (12), 1541−1549.
(31) Goldberg, J.; Huang, H.; Kwon, Y.; Greengard, P.; Nairn, A. C.; and Kuriyan, J. (1995) Three-dimensional structure of the catalytic subunit of protein serine/threonine phosphatase-1. *Nature 376*, 745−753.
(32) Bagu, J. R., Sykes, B. D., Craig, M. M., and Holmes, C. F. (1997) A molecular basis for the different interactions of marine toxins with protein phosphatase-1. Molecular models for bound motuporin, microcystins, okadaic acid, and calyculin A. *J. Biol. Chem. 272* (8), 5087−5097.
(33) Lo, K. K.-W., Ng, D. C.-M., Lau, J. S.-Y., Wu, r. S.-S., and Lam, P. K.-S. (2003) Derivatisation of microcystin with a redox -active label for high performance liquid chromatography/electrochemical detection. *New J. Chem. 27*, 274−279.
(34) Murata, H., Shoji, H., Oshikata, M., Harada, K.-I., Suzuki, M., Kondo, F., and Goto H. (1995) High-performance liquid chromatography with chemiluminescence detection of derivatized microcystins. *J. Chromatograph. A 693*, 263−270.
(35) Campos, M., Fadden, P., Alms, G., Qian, Z., and Haystead, T. A. J. (1996) Identification of protein phosphatase-1-binding proteins by microcystin-biotin affinity chromatography. *J. Biol. Chem. 271* (45), 28478−28484.
(36) Pflugmacher, S., Wiegand, C., Oberemm, A., Beattie, K. A., Krause, E., Codd, G. A., and Steinberg, C. E. W. (1998) Identification of an enzymatically formed glutathione conjugate of the cyanobacterial hepatotoxin microcystin-LR: The first step of detoxification *Biochem. Biophys. Acta 1425*, 527−533.
(37) Shimizu, M., Takahashi, T., Uratsuka, S., and Yamada, S. (1990) Synthesis of highly fluorescent dienophiles for detecting conjugated dienes in biological fluid. *J. Chem. Soc. Chem. Commun.* 1416−1417.
(38) Harada, K., Oshikata, M., Shimada, T., Nagata, A., Ishikawa, N., Suzuki, M., Kondo, F., Shimizu, M., and Yamada, S. (1997) High-performance liquid chromatographic separation of microcystins derivatized with a highly fluorescent dienophile. *Natural Toxins 5*, 201−207.
(39) Yankeelov, J. A., Jr. (1972) Modification of arginine by diketones *Methods Enzymol. 25*, 566−579.
(40) Gilbert, H. F., and O'Leary, M. H. (1975) Modification of arginine and lysine in proteins with 2,4-pentanedione. *Biochemistry 14*, 5194−5199.
(41) Kinzel, O.; and Budzikiewicz, H. (1999) Synthesis and biological evaluation of a pyoverdin-beta-lactam conjugate: A new type of arginine-specific cross-linking in aqueous solution. *J. Pept. Res. 53*, 618−625.
(42) Park, I. K., Roach, P., Bondor, J., Fox, S. P., and DePaoli-Roach, A. A. (1994) Molecular mechanism of the synergistic phosphorylation of phosphatase inhibitor-2. Cloning, expression, and site-directed mutagenesis of inhibitor-2. *J. Biol. Chem 269*, 944−954.
(43) Fersht, A (1985) *Enzyme Structure and Mechanism*, pp 272−276, W. H. Freeman and Company, New York.
(44) An, J., and Carmichael, W. W. (1994) Use of a colorimetric protein phosphatase inhibition assay and enzyme linked immunosorbent assay for the study of microcystins and nodularins. *Toxicon 32(12)*, 1495−1507.
(45) Huang, X., Cheng, A., and Honkanen, R. E. (1997) Genomic organization of the human PP4 gene encoding a serine/threonine protein phosphatase (PP4) suggests a common ancestry with PP2A. *Genomics 44*, 336−343.
(46) Hastie, C. J., and Cohen, P. T. W. (1998) Purification of protein phosphatase 4 catalytic subunit: Inhibition by the antitumour drug fostriecin and other tumour suppressors and promoters. *FEBS Lett. 431*, 357−361.
(47) Craig, M., Luu, H. A., McCready, T. L., Williams, D., Anderson, R. J., and Holmes, C. F. B. (1996) Molecular mechanisms underlying the interaction of motuporin and microcystins with type-1 and type-2A protein phosphatases. *Biochem. Cell Biol. 74*, 569−578.

BC0499580

A Liposomal System for Contrast-Enhanced Magnetic Resonance Imaging of Molecular Targets

Willem J. M. Mulder,*,† Gustav J. Strijkers,† Arjan W. Griffioen,‡ Louis van Bloois,§ Grietje Molema,|| Gert Storm,§ Gerben A. Koning,§,⊥ and Klaas Nicolay†

Biomedical NMR, Department of Biomedical Engineering, Eindhoven University of Technology, P.O. Box 513, 5600 MB Eindhoven, The Netherlands. Angiogenesis Laboratory, Department of Pathology/Internal Medicine, Maastricht University & University Hospital, P.O. Box 5800, 6225 EH Maastricht, The Netherlands, Department of Pharmaceutics, Utrecht Institute for Pharmaceutical Sciences, UIPS, TB 3508, Utrecht, The Netherlands, Department of Pathology and Laboratory Medicine, Medical Biology Section, Groningen University, P.O. Box 30001, 9700 RB Groningen, The Netherlands, and Department of Radiochemistry, Interfaculty Reactor Institute, Delft University of Technology, Mekelweg 15, 2629 JB Delft, The Netherlands. Received March 3, 2004; Revised Manuscript Received April 29, 2004

Pegylated paramagnetic and fluorescent immunoliposomes were designed to enable the parallel detection of the induced expression of molecular markers on endothelial cells with magnetic resonance imaging (MRI) and fluorescence microscopy. MRI is capable of three-dimensional noninvasive imaging of opaque tissues at near cellular resolution, while fluorescence microscopy can be used to investigate processes at the subcellular level. As a model for the expression of a molecular marker, human umbilical vein endothelial cells (HUVEC) were treated with the pro-inflammatory cytokine tumor necrosis factor α (TNFα) to upregulate the expression of the adhesion molecule E-selectin/CD62E. E-selectin-expressing HUVEC were incubated with pegylated paramagnetic fluorescently labeled liposomes carrying anti-E-selectin monoclonal antibody as a targeting ligand. Both MRI and fluorescence microscopy revealed the specific association of the liposomal MR contrast agent with stimulated HUVEC. This study suggests that this newly developed system may serve as a useful diagnostic tool to investigate pathological processes in vivo with MRI.

INTRODUCTION

A challenge in diagnostics is noninvasive detection of molecular markers of disease in order to identify and visualize pathology in an early stage and to be able to follow the effect of therapy (*1*). Traditional immunohistochemical techniques can only be applied after invasive procedures, which excludes their use for in vivo detection and thus makes longitudinal studies of disease progression impossible.

In recent years, magnetic resonance imaging (MRI) has emerged as one of the leading noninvasive imaging modalities (*2*). With MRI it is possible to measure the morphology and function of healthy and diseased soft tissues in vivo by exploiting a remarkable range of physical and chemical properties of water protons, including the T_1 relaxation time. MRI, however, suffers from limited resolution and specificity, compared to optical and traditional staining techniques. In contrast to nuclear tracer methods such as PET or SPECT, MRI has a relatively low inherent sensitivity (*3*). A number of approaches can be taken to overcome these limitations. First, specific information on molecular markers can be obtained with the use of targeted contrast agents, which are directed to a molecular entity of interest, e.g. an endothelial cell surface receptor that is overexpressed as a consequence of a disease process. Second, the low inherent sensitivity of MRI requires that the targeted contrast agent is very effective in producing a local MRI signal change. This can be achieved by the use of colloidal particles that can accommodate large amounts of Gd-chelates (*4*−*6*), which are widely used for contrast-enhanced T_1-weighted MRI. Additional information can be obtained by labeling such particles with markers for other imaging modalities, such as fluorescence imaging (*7*), for multimodality characterization of (patho)physiological processes.

In this paper, we report on the development and application of targeted liposomes that carry a high payload of MRI contrast agent. Liposomes have been studied extensively during the last two decades as drug carrier vehicles (*8*−*11*). For that purpose, liposomes have previously been optimized in terms of their stability, circulation time in vivo, and membrane composition (*11*). Liposomes are biocompatible, they are composed of either natural or synthetic amphiphilic lipids, they can be sized to a defined diameter in the range of 50 to 500 nm, and they can be coated with polymers to increase stability and to prolong circulation half-life in vivo (*12*). A wide range of amphiphilic and hydrophobic molecules can be incorporated in the bilayer of the liposomes. The aqueous interior can be loaded with water soluble drugs, proteins, or DNA for therapeutic applications (*13*). Another potential application is the use of liposomes as a (targetable) contrast agent for MRI (*4*, *5*, *14*−*16*).

The goal of this study was to develop paramagnetic pegylated liposomes with a targeting ligand coupled to

* To whom correspondence should be addressed. Telephone: (+31)402474853. Fax: (+31)402432598. E-mail: w.j.m.mulder@tue.nl.
† Eindhoven University of Technology.
‡ Maastricht University & University Hospital.
§ Utrecht Institute for Pharmaceutical Sciences.
|| Groningen University.
⊥ Delft University of Technology.

10.1021/bc049949r CCC: $27.50 © 2004 American Chemical Society
Published on Web 06/15/2004

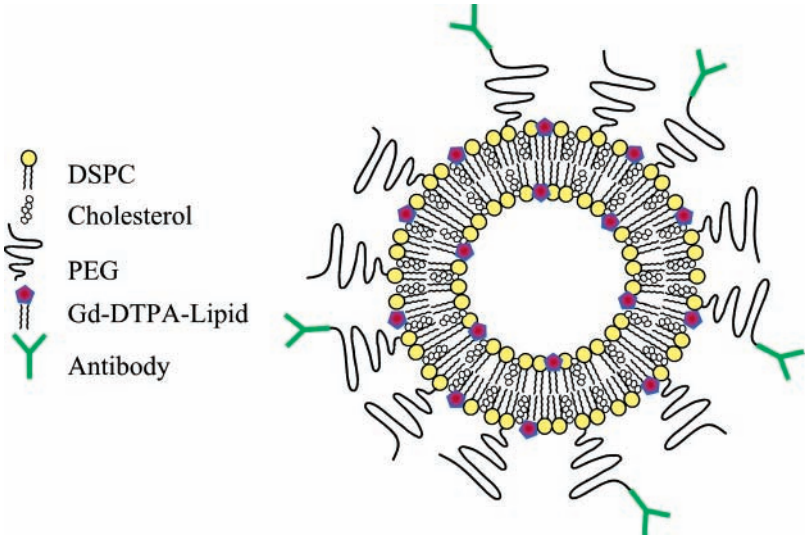


Figure 1. Schematic representation of a pegylated paramagnetic liposome that is composed of Gd-DTPA-bis(stearylamide) (Gd-BSA), 1,2-distearoyl-*sn*-glycero-3-phosphocholine (DSPC), cholesterol (Chol), and 1,2-distearoyl-*sn*-glycero-3-phosphoethanolamine-*N*-[methoxy(poly(ethylene glycol))-2000] (PEG2000-DSPE) and has antibodies coupled to the distal end of the PEG-chains.

the distal end of the PEG-chains for contrast-enhanced MR imaging of molecular markers (Figure 1). Gd-DTPA-bis(sterylamide) (Gd-BSA) was incorporated in the bilayer of the liposomes as a paramagnetic MRI contrast agent. We have used the antibody-conjugated liposomal system to detect E-selectin expression on HUVEC in vitro. This is an attractive model for receptor expression on endothelial cells, since E-selectin levels can be up-regulated approximately 10-fold by TNFα (*17*−*19*). E-selectin can be considered a model system for a variety of endothelial cell surface receptors that are of pathophysiological and therapeutic importance, including αvβ3-integrins (*20*, *21*) and vascular endothelial growth factor receptor (*22*, *23*). We show that the association to TNFα stimulated HUVEC was specific for liposomes carrying E-selectin antibodies. The antibody-dependent liposomal association was accompanied by a pronounced shortening of the T_1 relaxation time of HUVEC suspensions as evidenced by MRI.

MATERIALS AND METHODS

Materials. 1,2-Distearoyl-*sn*-glycero-3-phosphocholine (DSPC), cholesterol (Chol), 1,2-distearoyl-*sn*-glycero-3-phosphoethanolamine-*N*-[methoxy(poly(ethylene glycol))-2000] (PEG_{2000}-DSPE), 1,2-distearoyl-*sn*-glycero-3-phosphoethanolamine-*N*-[maleimide(poly(ethylene glycol))2000] (Mal-PEG_{2000}-DSPE), and 1,2-dipalmitoyl-*sn*-glycero-3-phosphoethanolamine-*N*-(lissamine rhodamine B sulfonyl) (rhodamine-PE) were obtained from Avanti Polar Lipids (Albaster, AL). Gd-DTPA-bis(stearylamide) (Gd-BSA) was purchased from Gateway Chemical Technology (St. Louis, MO). *N*-Succinimidyl *S*-acetylthioacetate (SATA) and calcein were obtained from Sigma Chemical Co. (St. Louis, MO), and HEPES was obtained from Merck (Darmstadt, Germany). All other chemicals were of analytic grade or the best grade available. Polycarbonate filters for liposome extrusion were from Costar (Cambridge, MA).

H18/7 monoclonal antibody against human E-selectin, kindly donated by Dr. M. A. Gimbrone (Boston, MA), was isolated from hybridoma culture supernatant using protein A affinity chromatography according to standard procedures.

Preparation of Paramagnetic PEG Liposomes. Liposomes were prepared by lipid film hydration. A mixture of the appropriate amounts of lipids (typically: 120 μmol of total lipid) was dissolved in chloroform/methanol 1:1 (v/v) and evaporated to dryness by rotary evaporation at 40 °C. For the paramagnetic PEG-liposomes, Gd-BSA, DSPC, cholesterol, and PEG_{2000}-DSPE were used at a molar ratio of 0.75/1.10/1/0.15. For PEG-liposomes that were used to attach antibodies to the distal end of the PEG-chains, Gd-BSA, DSPC, cholesterol, PEG_{2000}-DSPE, and Mal-PEG_{2000}-DSPE were mixed at a molar ratio of 0.75/1.10/1/0.075/0.075. For fluorescence microscopy, 0.1 mol % of rhodamine-PE was added to these preparations. The lipid film was subsequently hydrated in 3 mL of HEPES-buffered saline (HBS), containing 20 mM HEPES, 135 mM NaCl (pH 6.5). The resulting lipid dispersion was extruded sequentially six times through polycarbonate membrane filters with a pore diameter of 400 nm and subsequently 10 times through filters with a pore diameter of 100 nm using a Lipofast Extruder (Avestin, Canada). The temperature during extrusion was 60 °C.

Coupling of the Antibodies to Liposomes. The monoclonal antibody H18/7 against human E-selectin (AbEsel) was coupled to liposomes containing Mal-PEG_{2000}-DSPE by a sulfhydryl-maleimide coupling method as described previously (*18*, *24*). In short, H18/7 monoclonal antibody (1 mg/mL) was modified with *N*-succinimidyl *S*-acetylthioacetate (8:1 SATA:antibody mole:mole ratio) and incubated for 45 min at a roller-bench at room temperature. Free SATA was separated from the antibody/SATA solution by centrifugation on Vivaspin concentrator with a 50 kD MW cut-off filter followed by thorough washing four times with HBS. The SATA-derivatized antibody was deacetylated by incubation with a hydroxylamine solution for 1 h at room temperature. The activated antibody was added to the Mal-PEG_{2000}-DSPE-containing liposomes in a 50 μg/μmol protein/lipid ratio. This preparation was stored at 4 °C under N_2 overnight. Uncoupled antibody was separated from immunoliposomes by centrifugating two times at 65 000 rpm for 45 min. The supernatant was removed and an appropriate amount of buffer, typically 1.5 mL, was added to the pellet to obtain a lipid suspension with a lipid concentration of approximately 20 mM. The final liposomal suspension was stored at 4 °C under N_2 and used within 7 days.

Liposome Characterization. *Size, Lipid/Protein Ratio.* The size and size distribution of the bare liposomes and the antibody-coupled liposomes were determined by dynamic light scattering (DLS) at 25 °C with a Malvern 4700 system using an argon-ion laser (488 nm) operating at 10.4 mW (Uniphase) and PCS (photon correlation spectrometry) software for Windows version 1.34 (Malvern, U.K.). For data analysis, the viscosity and refractive index of water was used. The system was calibrated with a polystyrene dispersion containing particles of 100 nm. The phospholipid content of the liposome preparations was determined by phosphate analysis according to Rouser (*25*) after destruction with perchloric acid, and the protein content was determined according to Petterson (*26*).

Efficiency of Gd-BSA Incorporation. The efficiency of Gd-BSA incorporation in the liposomal bilayer was determined as a function of the Gd-BSA fraction in the lipid mixture. Lipid films of Gd-BSA/DSPC/Chol/Mal-PEG_{2000}-DSPE with 10, 20, 30, and 50 mol % Gd-BSA were prepared by dissolving the lipids in chloroform/methanol (1:1), followed by evaporation to dryness. The combined Gd-BSA and DSPC content was kept constant at 62 mol %, while the molar ratios of cholesterol and Mal-PEG_{2000}-DSPE were fixed at 33 and 5 mol %, respectively. The lipid film was subsequently hydrated in 3 mL of HBS and the phosphate and gadolinium content were determined. The resulting lipid dispersion was extruded as described above, after which the phosphate and gadolinium content were again determined. The extruded liposomes were centrifuged at 65 000 rpm for 45 min, and the phosphate and gadolinium content of the pellet and the supernatant were once more determined. Phosphate determinations were done according to Rouser (*25*) and gadolinium content was determined by inductively coupled plasma-atomic emission spectroscopy (ICP-AES).

Membrane Stability of the Liposomes. Calcein has been used as a fluorescent marker to investigate membrane permeability (*27*) and its release profile from the liposomal lumen reflects membrane stability. Calcein containing DSPC/Chol/Mal-PEG_{2000}-DSPE liposomes and calcein containing Gd-BSA/DSPC/Chol/Mal-PEG_{2000}-DSPE (25 mol % Gd-BSA) liposomes were prepared as described above by hydration with 50 mM calcein/150 mM sucrose/10 mM Hepes buffer (pH 7.4). The prepared liposomes were dialyzed at 4 °C for 4 days with phosphate-buffered saline (PBS, pH 7.4) to remove the untrapped calcein. The size and the lipid/calcein ratio were determined. Following dialysis both formulations were tested for the release of calcein upon incubation in 10% calf serum at 37 °C for 24 h. Calcein leakage from the aqueous interior of the liposomes was determined fluorometrically at excitation and emission wavelengths of 485 and 512 nm, respectively, using a fluorescence spectrophotometer. After incubation liposome size was determined again.

T_1 Relaxation Time Measurements. An important quality criterion for MRI contrast agents is their molar relaxivity r_1 (in units of $mM^{-1}\ s^{-1}$). A higher r_1 will lower the detection threshold of local contrast agent deposition with T_1-weighted MRI. MR spectroscopic measurements of the T_1 relaxation times of 0.5 mL of buffered liposome suspensions (leading to final concentrations of 7.1, 3.6, 1.8, and 0.9 mM gadolinium) and Gd-DTPA solutions (5.0, 2.5, 1.3, and 0.6 mM gadolinium) were performed using a 7 T MR spectrometer (Varian, Palo Alto, CA). T_1 relaxation times were obtained by the inversion recovery method, using 13 different inversion times, ranging from 10 to 3100 ms in an exponential fashion, and a repetition time of 10 s. To determine the temperature dependence of T_1, the temperature was varied between 25 and 80 °C, using steps of 5 °C and an equilibration time of 10 min. For comparison the T_1 relaxation times of 2 mL of buffered liposome suspensions (7.1, 3.6, and 0.9 mM gadolinium) were also determined at 1.5 T, a field strength frequently used in clinical MRI, using a Philips S15/ACS whole-body MR scanner. The molar relaxivity r_1 was obtained from the slope of the linear fit of the inverse of the measured T_1-values as a function of the gadolinium concentration (*28*).

In Vitro Targeting Experiments. Human umbilical vein-derived endothelial cells (HUVEC) were cultured on gelatin (0.2% in PBS)-coated tissue culture flasks (Costar, Cambridge, MA) in culture medium, RPMI-1640 (Life Technologies, Breda, The Netherlands), 20% human serum (HS; University Hospital Maastricht, The Netherlands), 2 mM glutamine (Life Technologies), and 100 U/mL penicillin and 0.1 mg/mL streptomycin (ICN Biomedicals, Aurora, OH). For all incubations, 10^6 cells of passage 2−3 were used for experiments.

Association of paramagnetic AbEsel-immunoliposomes (25 mol % Gd-BSA) to endothelial cells was assessed using fluorescence microscopy and magnetic resonance imaging. For this, HUVEC were grown to 70−80% of confluence in tissue culture flasks and stimulated for 3 h with 4 ng/mL human recombinant TNFα (rhTNFα; Boehringer, Germany). The effect of the stimulation was verified by FACS analysis of E-selectin expression (*17, 29*) and by visual verification of the change in cell shape. Control cells were left untreated. Subsequently, paramagnetic AbEsel-immunoliposomes and bare paramagnetic liposomes were added to control and TNFα-treated cells (1000 nmol lipid/mL medium). After 3.5 h of incubation with liposomes, the cultures were washed two times with PBS, and cells were harvested by incubation in EDTA and a mild trypsinization procedure. Cells and medium were collected in tubes and were washed twice in PBS. A small amount of cells (10^4) was taken to assess the association of liposomes using fluorescence microscopy. The obtained pellets, $10^6 \pm 10^5$ cells, were put in small eppendorf-cups, and 40 μL of 4% paraformaldehyde solution was added to a final volume of approximately 50 μL. Next, the samples were used for MR imaging.

Magnetic Resonance Imaging of Cell Pellets. MRI was performed on pellets of HUVEC, using a 6.3 T horizontal 9.5 cm bore magnet. A 3 cm send and receive birdcage coil was used. In all imaging experiments the samples described above were placed in a custom-made sample holder, capable of carrying four eppendorf-cups. A T_1-weighted spin−echo sequence (TR 1200 ms, TE 9 ms) was used for imaging. For absolute quantification of T_1, an inversion recovery spin−echo sequence was used with 13 different inversion times, ranging from 10 to 3100 ms in an exponential fashion. For quantification of T_2 a spin−echo sequence was used with different echo times, ranging from 9 to 64 ms. In all experiments the FOV was 3×3 cm^2, matrix size was 256×128, and the slice thickness was 1 mm. From the images, a T_1-map or a T_2-map was calculated using Mathematica (Wolfram Research, Inc.). T_1 and T_2 of the different cell pellets were determined in regions-of-interest and averaged for three independent experiments.

Statistical Analysis. Values for T_1, obtained from the pellets of HUVEC as described above were analyzed using multiple *t*-tests ($p < 0.05$) with correction for multiple comparisons (*30*).

RESULTS

Characterization of the Paramagnetic Liposomes. The mean size of a typical batch of liposomes before coupling of the AbEsel-antibody was 120 nm with a polydispersity index of 0.05. After the antibody was coupled, the mean size of the liposomes increased to 150 nm and the polydispersity index increased to 0.2. The initial coupling started with 50 μg protein/μmol lipid. The final protein-to-lipid ratio was 25 μg protein/μmol lipid, corresponding to a 50% efficiency. This corresponds to an estimated number of 30 antibody molecules per liposome.

First, we established the maximal amount of Gd-BSA that could be incorporated in the liposomal bilayer. From a standard DSPC/Chol/PEG-DSPE 1.85/1/0.15 formulation an increasing amount of DSPC was replaced by Gd-BSA. When DSPC was replaced by 10, 20, or 30 mol % Gd-BSA (percentage of the total amount of lipid), all Gd-BSA did incorporate into the bilayer, and the phosphate/Gd ratio before and after extrusion of the liposomal dispersion was identical. Higher percentages of Gd-BSA resulted in a decrease of the incorporation efficiency: at 50 mol % Gd-BSA, the Gd-to-total lipid ratio in the liposomal suspension after extrusion was decreased from an expected value of 50 mol % to a value of 40 mol %.

Incorporation of a large amount of Gd-DTPA-bis(stearylamide) (Gd-BSA) might affect the stability of the liposomes. Therefore, the stability of liposomes with a Gd-BSA/DSPC/Chol/PEG (25 mol % Gd-BSA) formulation was compared with a DSPC/Chol/PEG formulation by enclosing calcein in the aqueous lumen and monitoring the release of calcein upon incubation in serum. Both formulations did not show a measurable release of calcein upon incubation at 4 °C in buffer for 24 h. Upon incubation of the liposomes in 10% calf serum buffer at 37 °C for 24 h, both formulations showed a calcein release of 4−6%. The size of both liposome preparations remained the same after the 24 h incubation in serum, as determined from dynamic light scattering data. Based on the above data, it was decided to use a molar percentage of 25% Gd-BSA in the E-selectin targeting studies on HUVEC cells.

Since the Gd-BSA-containing liposomes are to be used in contrast-enhanced T_1-weighted MRI, it is critical to determine the efficiency with which the paramagnetic particles shorten the T_1 relaxation time of water. This efficiency is conveniently expressed as the molar relaxivity, r_1, in units $mM^{-1}\ s^{-1}$, which is determined from the dependence of the measured T_1 relaxation rate on the contrast agent concentration. The longitudinal relaxivity r_1 of a buffered liposome suspension was determined at 7 T as a function of temperature and was compared with the r_1 of free Gd-DTPA that is in clinical use (Figure 2). At 37 °C, the r_1 of Gd-BSA contained in the liposomal membrane was 1.5 times that of the solution with free Gd-DTPA. The r_1 of Gd-DTPA decreased with increasing temperature. For the liposomal Gd-BSA suspension, r_1 increased up to 55 °C, while decreasing above 55 °C. The r_1 of the liposome suspension as measured at 1.5 T was 5.5 $mM^{-1}\ s^{-1}$ at room temperature, which is similar to the r_1 at 7 T at room temperature (5.2 $mM^{-1}\ s^{-1}$).

In Vitro Targeting Experiments. Treatment of endothelial cells with TNFα leads to activation and overexpression of adhesion molecules involved in leukocyte interactions. When HUVEC were treated with 4 ng/mL TNFα, next to a morphological change, E-selectin protein expression increased 10-fold as deduced from FACS analysis (data not shown). Fluorescence microscopy showed a pronounced association of the AbEsel-immunoliposomes to TNFα-treated HUVEC (Figure 3B). The association of the AbEsel-immunoliposomes by the HUVEC was partly due to internalization of the liposomes into the cytosol (insert Figure 3B). Nontargeted liposomes did not associate with either resting (data not shown) or TNFα-activated HUVEC (Figure 3C).

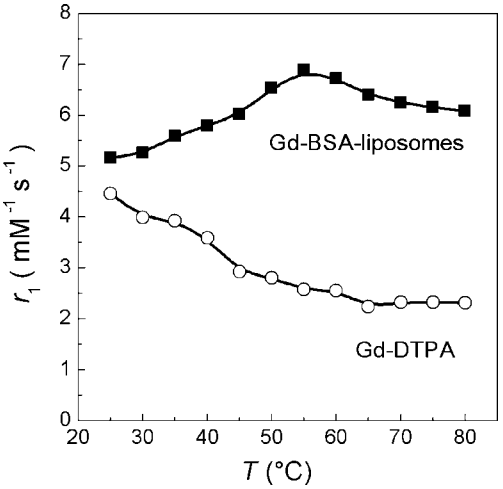


Figure 2. The molar relaxivities r_1 of free Gd-DTPA (○) and Gd-BSA containing liposomes (■) were determined as function of the temperature at a field strength of 7 T. The Gd-DTPA concentration was varied between 0.6 and 5.0 mM. The Gd-BSA content of the liposomes was fixed at 25 mol %, while the effective Gd-BSA concentration in the medium was varied from 0.9 to 7.1 mM Gd-BSA to determine r_1. The lines connecting the data points are aimed to guide the eye.

For MR imaging, HUVEC treated with TNFα and incubated with AbEsel-immunoliposomes were compared with three controls. Figure 4 shows a schematic representation of these experiments. A T_1-weighted image, a T_1-map, and a T_2-map of a typical experiment are depicted in Figure 5. The average T_1 and T_2 of different systems are listed in Table 1. In the T_1-weighted image (Figure 5A) the region corresponding with the test incubation, TNFα-treated HUVEC incubated with AbEsel-immunoliposomes, was much brighter than the three control incubations, indicating that there is a distinct difference in T_1 of the test incubation compared to the controls. This difference was quantified by generating a T_1-map of the setup (Figure 5B) with an inversion recovery experiment and averaging the T_1s found in three independent experiments (Table 1). The T_1 of the pellet of stimulated HUVEC incubated with AbEsel-immunoliposomes was 457 ± 62 ms, which is almost a factor 5 lower than the T_1 of the nonstimulated cells incubated with AbEsel-immunoliposomes (T_1 of 2156 ± 130 ms). The stimulated cells that were incubated with nontargeted liposomes had a T_1, which was comparable with the T_1 of nonstimulated cells incubated with AbEsel-immunoliposomes: both T_1s were approximately 2150 ms. The pellet of control HUVEC had a T_1 of 2412 ± 122 ms, which was significantly longer than all other three systems. The same trend was observed for the T_2 values (Figure 5D, Table 1). The association of AbEsel-immunoliposomes with TNFα-activated HUVEC led to a decrease in the T_2 relaxation time from 103 ± 12 to 16 ± 1 ms (Table 1). The other incubations of paramagnetic liposomes with HUVEC did not cause significant alterations in the T_2 of water.

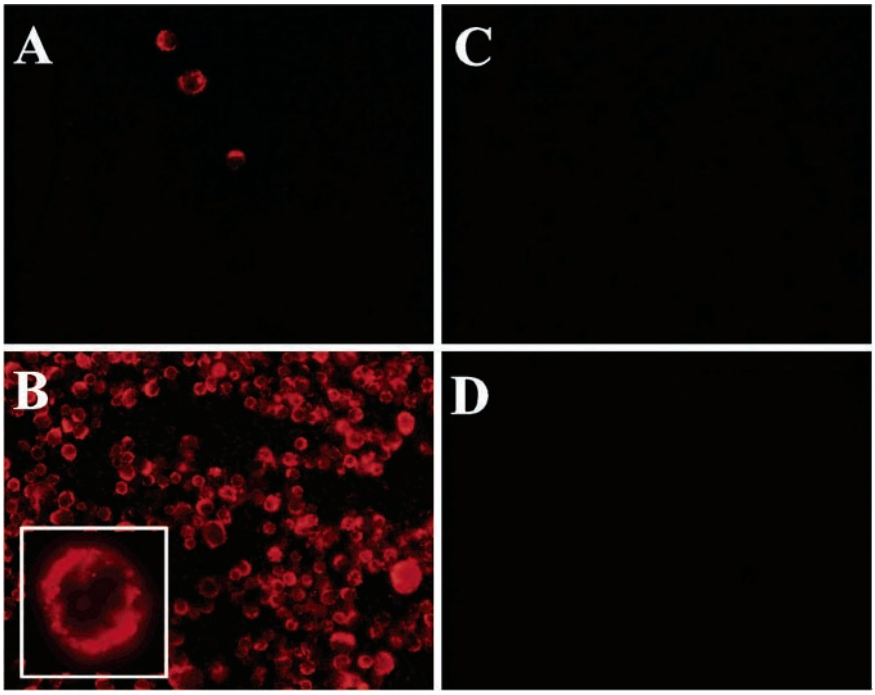


Figure 3. Fluorescence microscopy of liposomal targeting to HUVEC. (A) Fluorescence microscopy image of nonstimulated HUVEC that were incubated for 3.5 h with paramagnetic AbEsel-immunoliposomes showed very little fluorescence. (B) TNFα-treated HUVEC showed massive association of paramagnetic AbEsel-immunoliposomes. Insert in B demonstrates that the fluorescence partly originates from the cell interior (magnification 630 ×). (C) TNFα-treated HUVEC incubated with nontargeted liposomes. (D) Control HUVEC that were not incubated with liposomes.

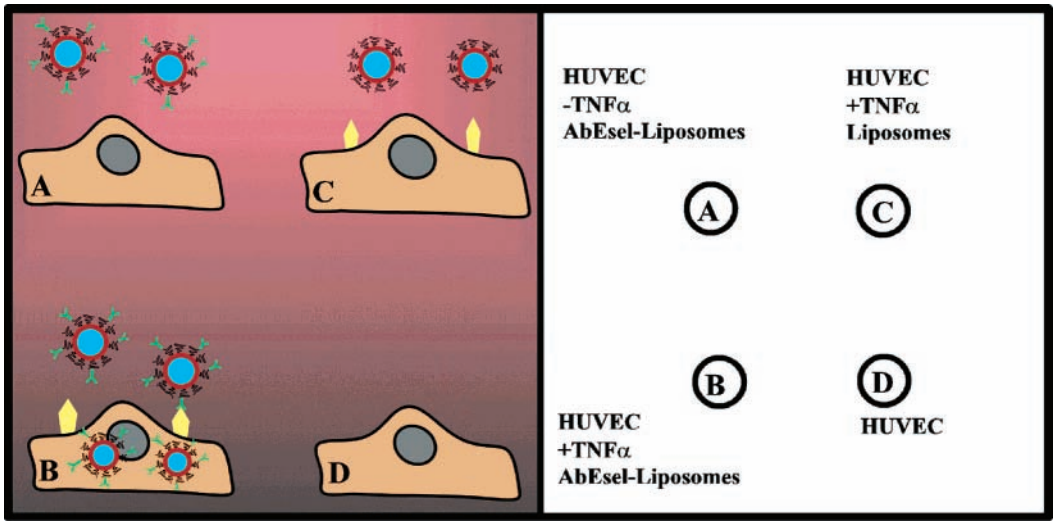


Figure 4. Schematic representation of the setup used for MRI analysis of liposomal targeting to HUVEC. The left side of the figure schematically depicts the setup of the experiment, in which B is the test incubation (TNFα-treated HUVEC incubated with AbEsel-immunoliposomes). A (non-TNFα-treated HUVEC incubated with AbEsel-immunoliposomes), C (TNFα-treated HUVEC incubated with bare liposomes), and D (HUVEC) are controls. The right side of the figure gives the setup of the pellets of HUVEC used for MR imaging.

DISCUSSION

The in vivo upregulation of receptors expressed on vascular endothelial cells at diseased sites represents an attractive target for early detection of a range of important disease processes (*31*). In inflamed or angiogenic tissues, such as tumors, atherosclerotic plaques, or rheumatic joints, blood vessels express high and upregulated levels of activation-related receptors. E-selectin, a molecule involved in leukocyte vessel wall interactions, is profoundly upregulated in tissues exposed to inflammatory cytokines (*32*). Detection of such receptors can be of prime importance in diagnosis of these diseases at an early stage. An established in vitro system for endothelial cells, which allows the induction of the typical inflammation related adhesion molecule E-selectin has been described previously (*18*, *19*, *33*, *34*). In these studies endothelial cells (HUVEC) were stimulated by cytokines such as IL-1β or TNFα, which resulted in a strong upregulation of E-selectin. Particles carrying antibodies against E-selectin are capable of specific binding to HUVEC-expressing E-selectin and can be internalized by these cells. Previous studies have shown an efficient association of AbEsel-immunoliposomes targeted to E-selectin, using the H18/7 antibody as a targeting ligand, by activated endothelial cells in vitro *(18*, *19*). The use of an H18/7 Fab-coupled iron oxide particle to target

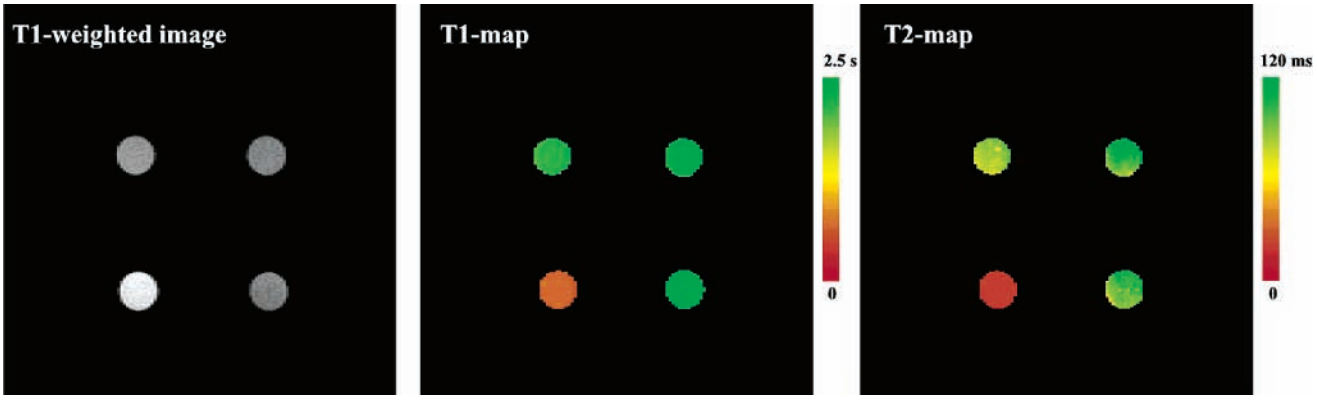


Figure 5. MR image of a typical experiment shows a slice through four pellets of HUVEC of the setup schematically depicted in Figure 4. The test incubation (B) showed enhanced signal intensity in the T_1-weighted image (TR 1200 ms, TE 9 ms). The T_1-map and T_2-map, generated as described in Materials and Methods, revealed a dramatic shortening of both T_1 and T_2 of the stimulated cells incubated with paramagnetic AbEsel-immunoliposomes, while the T_1 and T_2 of nonstimulated cells and the stimulated cells that were incubated with liposomes, that did not contain an antibody, only slightly differed from the control HUVEC.

Table 1. Quantification of T_1 and T_2 of HUVEC[a]

batch ($n = 3$)	T_1 (ms)	T_2 (ms)
A HUVEC, − TNFα, AbEsel-L	2156 ± 130	90 ± 11
B HUVEC, + TNFα, AbEsel-L	457 ± 62	16 ± 1
C HUVEC, + TNFα, Bare-L	2135 ± 84	106 ± 12
D HUVEC	2412 ± 122	103 ± 12

[a] MRI-based quantification of the water T_1 and T_2 (mean ± SD) in pellets of $10^6 \pm 10^5$ HUVEC of the different incubations ($n = 3$). A−D refer to the systems described in Figure 4. The T_1s of the different incubations have been analyzed using multiple *t*-tests ($p < 0.05$) with correction for multiple comparisons. The T_1 of incubation B is significantly different from incubations A, C, and D. The difference between the T_1 of A and C is not significant, whereas the T_1 of D is significantly higher than that of other incubations.

E-selectin on endothelial cells in vitro showed the capability of detecting E-selectin expression with MRI (*33*). The contrast generated by iron oxide particles can be ascribed to their superparamagnetic properties. This results in a dramatic shortening of T_2 and causes dark spots in T_2- and T_2*-weighted images, which is termed negative contrast (*35*, *35*, *36*).

In this study we tested the possibility to MR image the uptake of Gd-DTPA-based paramagnetic AbEsel-immunoliposomes, which is accompanied by signal enhancement (i.e., positive contrast) in T_1-weighted imaging, by activated endothelial cells. AbEsel (H18/7) antibodies were covalently coupled to the distal end of the PEG-chains of the paramagnetic liposomes, which resulted in an efficient conjugation of 25 μg protein/umol lipid without compromising the liposomal size distribution. The average diameter of the AbEsel-immunoliposomes was 150 nm diameter, with a polydispersity index of 0.2. Sipkins et al. (*4*) and Lanza et al. (*6*) have described paramagnetic particles of approximately 250 nm in size, without a PEG-coating, to which antibody was coupled via a noncovalent biotin−avidin interaction. When comparing these two paramagnetic particles, the immunoliposomal system described in this study has several advantages: it has a high flexibility in size (ranging from ca. 80 to 500 nm), it may be expected to have long circulation times because of the PEG-coating (*11*), and it has the antibody covalently coupled. The applied covalent coupling of targeting ligands is advantageous as it is more efficient (*37*) and does not involve a large protein complex like in the biotin−avidin−biotin method, which is known to be strongly immunogenic (*38*). The coupling of the antibody at the terminal end of the PEG chain is known to result in liposomes that retain their favorable pharmacokinetic behavior (*39*, *40*) and likely have prolonged circulation times compared to the existing paramagnetic systems. These properties may result in a more efficient targeting of our liposomal contrast agent in vivo. Liposomes composed of DSPC/Chol/PEG were stable upon incubation in serum containing buffer. The incorporation of 20−30 mol % of Gd-BSA did not significantly alter the stability properties of the liposomes. The stability data suggest that the Gd-BSA-containing liposomes may also be used as a drug carrier vehicle, carrying a payload of water soluble drugs in the aqueous interior or carrying hydrophobic drugs in the liposomal bilayer. The system could thus be a tool for combining molecular marker imaging with local therapy.

The relaxivity properties of the paramagnetic liposomes differed from the relaxivity properties of free Gd-DTPA. At room temperature the r_1 of the paramagnetic liposomes and Gd-DTPA were approximately the same. The longer rotational correlation time of the liposomes was expected to result in a larger relaxivity. With increasing temperature the r_1 of Gd-DTPA decreased, whereas the r_1 of the liposomes increased up to a temperature of 55 °C (Figure 2). From 55 °C the r_1 of the liposomes decreased again but remained higher than the r_1 of Gd-DTPA. The peak of the liposomal r_1 at 55 °C might be explained by the increasing water exchange across the liposome membrane at higher temperatures allowing Gd-chelates present on the inner side of the bilayer to contribute more to the overall relaxivity. The transition temperature of this liposomal formulation is ca. 55 °C (*41*), implying that the liposomal bilayer is in the gel phase below 55 °C and in the fluid phase above 55 °C. A bilayer in the fluid phase is more permeable to water (*41*). These results suggest that at room temperature only part of the gadolinium contributes to the overall relaxivity. Therefore, a liposomal formulation with a transition temperature below the physiological temperature may be more suitable as an in vivo contrast agent in terms of relaxation properties. On the other hand, the altered composition might result in impaired stability and/or decreased Gd-BSA loading capacity.

Strongly enhanced interaction of AbEsel-immunoliposomes with TNFα-treated cells was observed by fluorescence microscopy compared to control incubations. The fluorescence pattern represents a combination of cell membrane binding of fluorescent liposomes as well as intracellularly present fluorescence representing internalized liposomes, which is in agreement with previous studies (*18*, *19*). Internalization of the liposomes might

be important for in vivo detection since the low inherent sensitivity of MRI requires large amounts of Gd-DTPA to be present at the targeted site. Binding of the liposomes to the receptors expressed at the endothelium alone might not generate sufficient contrast in MR imaging to localize the liposomes with this technique.

MRI experiments on pellets of 10^6 HUVEC were in excellent agreement with fluorescence microscopy. The T_1-weighted image of the pellet containing TNFα-treated HUVEC incubated with AbEsel-immunoliposomes (Figure 5A) had a much higher signal intensity than that of the three control systems. This can be explained by the large shortening of the T_1 in the former system (Figure 5B). The much less pronounced shortening of T_1 for the nonactivated HUVEC, incubated with AbEsel-immunoliposomes, as well as the mild shortening of T_1 for the HUVEC that were stimulated and incubated with liposomes that did not contain the anti-E-Selectin antibody can be explained by a low affinity, nonspecific cellular uptake of liposomes.

In vivo, this anti-E-selectin MR contrast agent can be useful for the detection of atherosclerosis, angiogenesis, and inflammation. The described technique is also applicable for detection of other internalizing cell surface receptors as markers of the activated and/or angiogenic endothelial phenotype.

CONCLUSIONS

We described the preparation, characterization, and successful in vitro targeting of paramagnetic liposomes for use in combination with MRI. The liposomes have a PEG-coat, and they do not leak upon incubation in serum. An anti-E-selectin antibody was coupled to the distal end of the PEG-chains of the liposomes. Other targeting ligands, like peptides (*42*) can also be coupled. The system both carries a MR-marker and a fluorescent marker, and we have demonstrated the E-selectin-dependent association of the liposomes to stimulated HUVEC by MRI and fluorescence microscopy. These results imply that this novel MR contrast agent may potentially serve as a useful diagnostic tool to investigate disease processes in vivo and to follow therapeutic efficacy.

ACKNOWLEDGMENT

The authors would like to thank Prof. Dr. Ben de Kruijff, Dr. Eefjan Breukink, and Dr. Marcel van Genderen for useful discussions and Larry de Graaf for technical assistance.

LITERATURE CITED

(1) Weissleder, R., and Mahmood, U. (2001) Molecular imaging. *Radiology 219*, 316−333.

(2) Aime, S., Dastru, W., Crich, S. G., Gianolio, E., and Mainero, V. (2002) Innovative magnetic resonance imaging diagnostic agents based on paramagnetic Gd(III) complexes. *Biopolymers 66*, 419−428.

(3) Aime, S., Cabella, C., Colombatto, S., Geninatti, C. S., Gianolio, E., and Maggioni, F. (2002) Insights into the use of paramagnetic Gd(III) complexes in MR-molecular imaging investigations. *J. Magn Reson. Imaging 16*, 394−406.

(4) Sipkins, D. A., Cheresh, D. A., Kazemi, M. R., Nevin, L. M., Bednarski, M. D., and Li, K. C. (1998) Detection of tumor angiogenesis *in vivo* by alphaVbeta3-targeted magnetic resonance imaging. *Nat. Med. 4*, 623−626.

(5) Sipkins, D. A., Gijbels, K., Tropper, F. D., Bednarski, M., Li, K. C., and Steinman, L. (2000) ICAM-1 expression in autoimmune encephalitis visualized using magnetic resonance imaging. *J. Neuroimmunol. 104*, 1−9.

(6) Lanza, G. M., Yu, X., Winter, P. M., Abendschein, D. R., Karukstis, K. K., Scott, M. J., Chinen, L. K., Fuhrhop, R. W., Scherrer, D. E., and Wickline, S. A. (2002) Targeted antiproliferative drug delivery to vascular smooth muscle cells with a magnetic resonance imaging nanoparticle contrast agent: implications for rational therapy of restenosis. *Circulation 106*, 2842−2847.

(7) Huber, M. M., Staubli, A. B., Kustedjo, K., Gray, M. H., Shih, J., Fraser, S. E., Jacobs, R. E., and Meade, T. J. (1998) Fluorescently detectable magnetic resonance imaging agents. *Bioconjugate Chem. 9*, 242−249.

(8) Mastrobattista, E., Koning, G. A., and Storm, G. (1999) Immunoliposomes for the targeted delivery of antitumor drugs. *Adv. Drug Deliv. Rev. 40*, 103−127.

(9) Metselaar, J. M., Mastrobattista, E., and Storm, G. (2002) Liposomes for intravenous drug targeting: design and applications. *Mini. Rev. Med. Chem. 2*, 319−329.

(10) Allen, T. M. Liposomes. (1997) Opportunities in drug delivery. *Drugs 54 Suppl 4*, 8−14.

(11) Allen, T. M. (1994) Long-circulating (sterically stabilized) liposomes for targeted drug delivery. *Trends Pharmacol. Sci. 15*, 215−220.

(12) Allen, T. M., Hansen, C., Martin, F., Redemann, C., and Yau-Young, A. (1991) Liposomes containing synthetic lipid derivatives of poly(ethylene glycol) show prolonged circulation half-lives *in vivo*. *Biochim. Biophys. Acta 1066*, 29−36.

(13) Koning, G. A., Schiffelers, R. M., and Storm, G. (2002) Endothelial cells at inflammatory sites as target for therapeutic intervention. *Endothelium 9*, 161−171.

(14) Storrs, R. W., Tropper, F. D., Li, H. Y., Song, C. K., Sipkins, D. A., Kuniyoshi, J. K., Bednarski, M. D., Strauss, H. W., and Li, K. C. (1995) Paramagnetic polymerized liposomes as new recirculating MR contrast agents. *J. Magn Reson. Imaging 5*, 719−724.

(15) Leclercq, F., Cohen-Ohana, M., Mignet, N., Sbarbati, A., Herscovici, J., Scherman, D., and Byk, G. (2003) Design, synthesis, and evaluation of gadolinium cationic lipids as tools for biodistribution studies of gene delivery complexes. *Bioconjugate Chem. 14*, 112−119.

(16) Glogard, C., Stensrud, G., Hovland, R., Fossheim, S. L., and Klaveness, J. (2002) Liposomes as carriers of amphiphilic gadolinium chelates: the effect of membrane composition on incorporation efficacy and in vitro relaxivity. *Int. J. Pharm. 233*, 131−140.

(17) Griffioen, A. W., Damen, C. A., Blijham, G. H., and Groenewegen, G. (1996) Tumor angiogenesis is accompanied by a decreased inflammatory response of tumor-associated endothelium. *Blood 88*, 667−673.

(18) Everts, M., Koning, G. A., Kok, R. J., Asgeirsdottir, S. A., Vestweber, D., Meijer, D. K., Storm, G., and Molema, G. (2003) In vitro cellular handling and *in vivo* targeting of E-selectin-directed immunoconjugates and immunoliposomes used for drug delivery to inflamed endothelium. *Pharm. Res. 20*, 64−72.

(19) Spragg, D. D., Alford, D. R., Greferath, R., Larsen, C. E., Lee, K. D., Gurtner, G. C., Cybulsky, M. I., Tosi, P. F., Nicolau, C., and Gimbrone, M. A., Jr. (1997) Immunotargeting of liposomes to activated vascular endothelial cells: a strategy for site-selective delivery in the cardiovascular system. *Proc. Natl. Acad. Sci. U.S.A. 94*, 8795−8800.

(20) Griffioen, A. W., Coenen, M. J., Damen, C. A., Hellwig, S. M., van Weering, D. H., Vooys, W., Blijham, G. H., and Groenewegen, G. (1997) CD44 is involved in tumor angiogenesis; an activation antigen on human endothelial cells. *Blood 90*, 1150−1159.

(21) Brooks, P. C., Montgomery, A. M., Rosenfeld, M., Reisfeld, R. A., Hu, T., Klier, G., and Cheresh, D. A. (1994) Integrin alpha v beta 3 antagonists promote tumor regression by inducing apoptosis of angiogenic blood vessels. *Cell 79*, 1157−1164.

(22) Dias, S., Hattori, K., Heissig, B., Zhu, Z., Wu, Y., Witte, L., Hicklin, D. J., Tateno, M., Bohlen, P., Moore, M. A., and Rafii, S. (2001) Inhibition of both paracrine and autocrine VEGF/ VEGFR-2 signaling pathways is essential to induce long-term remission of xenotransplanted human leukemias. *Proc. Natl. Acad. Sci. U.S.A. 98*, 10857−10862.

(23) Witte, L., Hicklin, D. J., Zhu, Z., Pytowski, B., Kotanides, H., Rockwell, P., and Bohlen, P. (1998) Monoclonal antibodies

targeting the VEGF receptor-2 (Flk1/KDR) as an anti-angiogenic therapeutic strategy. *Cancer Metastasis Rev. 17*, 155−161.
(24) Koning, G. A., Morselt, H. W., Velinova, M. J., Donga, J., Gorter, A., Allen, T. M., Zalipsky, S., Kamps, J. A., and Scherphof, G. L. (1999) Selective transfer of a lipophilic prodrug of 5-fluorodeoxyuridine from immunoliposomes to colon cancer cells. *Biochim. Biophys. Acta 1420*, 153−167.
(25) Rouser, G., Fkeischer, S., and Yamamoto, A. (1970) Two-dimensional then layer chromatographic separation of polar lipids and determination of phospholipids by phosphorus analysis of spots. *Lipids 5*, 494−496.
(26) Petterson, G. L. (1977) A simplification of the protein assay method of lowry et al. which is more generally applicable. *Anal. Biochem. 83*, 346−356.
(27) Mastrobattista, E., Koning, G. A., van Bloois, L., Filipe, A. C., Jiskoot, W., and Storm, G. (2002) Functional characterization of an endosome-disruptive peptide and its application in cytosolic delivery of immunoliposome-entrapped proteins. *J. Biol. Chem. 277*, 27135−27143.
(28) Caravan, P., Ellison, J. J., McMurry, T. J., and Lauffer, R. B. (1999) Gadolinium(III) chelates as MRI contrast agents: Structure, dynamics, and applications. *Chem. Rev. 99*, 2293−2352.
(29) Griffioen, A. W., Damen, C. A., Martinotti, S., Blijham, G. H., and Groenewegen, G. (1996) Endothelial intercellular adhesion molecule-1 expression is suppressed in human malignancies: the role of angiogenic factors. *Cancer Res. 56*, 1111−1117.
(30) Tello, R. and Crewson, P. E. (2003) Hypothesis testing II: means. *Radiology 227*, 1−4.
(31) Griffioen, A. W. and Molema, G. (2000) Angiogenesis: potentials for pharmacologic intervention in the treatment of cancer, cardiovascular diseases, and chronic inflammation. *Pharmacol. Rev. 52*, 237−268.
(32) Blankenberg, S., Barbaux, S., and Tiret, L. (2003) Adhesion molecules and atherosclerosis. *Atherosclerosis 170*, 191−203.
(33) Kang, H. W., Josephson, L., Petrovsky, A., Weissleder, R., and Bogdanov, A., Jr. (2002) Magnetic resonance imaging of inducible E-selectin expression in human endothelial cell culture. *Bioconjugate Chem. 13*, 122−127.
(34) Bhatti, M., Chapman, P., Peters, M., Haskard, D., and Hodgson, H. J. (1998) Visualising E-selectin in the detection and evaluation of inflammatory bowel disease. *Gut 43*, 40−47.
(35) Wang, Y. X., Hussain, S. M., and Krestin, G. P. (2001) Superparamagnetic iron oxide contrast agents: physicochemical characteristics and applications in MR imaging. *Eur. Radiol. 11*, 2319−2331.
(36) Bonnemain, B. (1998) Superparamagnetic agents in magnetic resonance imaging: physicochemical characteristics and clinical applications. A review. *J. Drug Target. 6*, 167−174.
(37) Hansen, C. B., Kao, G. Y., Moase, E. H., Zalipsky, S., and Allen, T. M. (1995) Attachment of antibodies to sterically stabilized liposomes: evaluation, comparison and optimization of coupling procedures. *Biochim. Biophys. Acta 1239*, 133−144.
(38) Phillips, N. C., Gagne, L., Tsoukas, C., and Dahman, J. (1994) Immunoliposome targeting to murine CD4+ leucocytes is dependent on immune status. *J. Immunol. 152*, 3168−3174.
(39) Koning, G. A., Morselt, H. W., Gorter, A., Allen, T. M., Zalipsky, S., Kamps, J. A., and Scherphof, G. L. (2001) Pharmacokinetics of differently designed immunoliposome formulations in rats with or without hepatic colon cancer metastases. *Pharm. Res. 18*, 1291−1298.
(40) Allen, T. M., Brandeis, E., Hansen, C. B., Kao, G. Y., and Zalipsky, S. (1995) A new strategy for attachment of antibodies to sterically stabilized liposomes resulting in efficient targeting to cancer cells. *Biochim. Biophys. Acta 1237*, 99−108.
(41) Phospholipids Handbook. (1993) Marcel Dekker, New York.
(42) Janssen, A. P., Schiffelers, R. M., ten Hagen, T. L., Koning, G. A., Schraa, A. J., Kok, R. J., Storm, G., and Molema, G. (2003) Peptide-targeted PEG-liposomes in anti-angiogenic therapy. *Int. J. Pharm. 254*, 55−58.

BC049949R

Chemical Conjugation of Heterologous Proteins on the Surface of Cowpea Mosaic Virus

Anju Chatterji,[†] Wendy Ochoa,[†] Lara Shamieh,[‡] Shant P. Salakian,[†] Sek Man Wong,[§] Gail Clinton,[‡] Partho Ghosh,[||] Tianwei Lin,*[,†] and John E. Johnson*[,†]

Department of Molecular Biology and Center for Integrative Molecular Biosciences and The Scripps Research Institute, 10550 N. Torrey Pines Road, La Jolla, California 92037, Center for Bio/Molecular Sciences and Engineering, 4555 Overlook Avenue SW, Oregon Health Sciences University, Portland, Oregon, Department of Biological Sciences, National University of Singapore, Science Drive 4, Singapore, 117543, and Department of Chemistry and Biochemistry, University of California, San Diego, 9500, Gilman Drive, La Jolla, California 92093. Received March 13, 2004; Revised Manuscript Received May 18, 2004

Genetic economy leads to symmetric distributions of chemically identical subunits in icosaherdal and helical viruses. Modification of the subunit genes of a variety of viruses has permitted the display of polypeptides on both the infectious virions and virus particles made in expression systems. Icosahedral chimeric particles of this type often display novel properties resulting in high local concentrations of the insert. Here we report an extension of this concept in which entire proteins were chemically cross-linked to lysine and cysteine residues genetically engineered on the coat protein of icosahedral Cowpea mosaic virus particles. Three exogenous proteins, the LRR domain of internalin B, the T4 lysozyme, and the Intron 8 gene product of the of the HER2 tyrosine kinase receptor were derivatized with appropriate bifunctional cross-linkers and conjugated to the virus capsid. Characterization of these particles demonstrated that (1) virtually 100% occupancy of the 60 sites was achieved; (2) biological activity (either enzyme or binding specificity) of the attached protein was preserved; (3) in one case (LRR-internalin B) the attached protein conformed with the icosahedral symmetry to the extent that a reconstruction of the derivatized particles displayed added density with a shape consistent with the X-ray structure of the attached protein. Strategies demonstrated here allow virus particle targeting to specific cell types and the use of an icosahedral virus as a platform for structure determination of small proteins at moderate resolution.

INTRODUCTION

Several rod shaped and icosahedral viruses have been used for expression and display of foreign peptides (*1*−*10*). Cowpea mosaic virus (CPMV) offers novel advantages for presentation of foreign epitopes on its surface (*1*−*6*). The virus capsid is highly permissive to genetic alterations, accumulates to high levels in plants, and the virus is stable over a wide range of pH and temperature conditions, making it amenable for chemical modification. The structure of the virus has been resolved to 2.8 Å resolution, allowing rational designing of peptide presentation on the virus surface (*11*−*15*). The inherent nature of the viral symmetry coupled with the polyvalent display of exogenous protein opens up additional venues for structure determination of the foreign epitope being displayed (*16*−*18*).

Surface presentation of foreign polypeptides that are introduced genetically into the capsid, however, is restricted to approximately 30 amino acids (*4*, *18*−*19*). A useful extension of this technology will be to display full-length proteins and protein domains on the virus capsid. We explored the option of chemically coupling exogenous proteins to the virus capsid using a variety of readily available homo-and heterobifunctional cross-linkers and investigated the suitability of CPMV to serve as a scaffold for structure determination of the conjugated proteins by directly imaging the altered virus particle with methods that make use of the icosahedral redundancy.

The CPMV genome consists of two separately encapsidated RNA molecules of 6.0 kb (RNA 1) and 3.5 kb (RNA2) (*20*, *21*). The viral capsids contain 60 copies each of the large and small coat protein subunits arranged with icosahedral symmetry (*22*). Any attachment on the viral capsid therefore translates into the heterologous protein being presented on the virus surface 60 times, assuming 100% occupancy. To illustrate the versatility of CPMV as a polyvalent display platform, we used proteins with different biological functions as well as size range for cross-linking (8−22 kDa) to the virus surface. Some of these proteins were chosen to provide the necessary proof of principle that the structural information derived from the virus-protein-conjugated complexes is authentic while others were selected to determine the effect of enhanced local concentration from the multivalent presentation of the protein on the virus capsid.

The attachment sites for chemical derivatization of the viral capsid were engineered by site-specific mutagenesis of four of the five surface lysine residues to arginine thereby retaining only one reactive lysine on the virus (*23*). Further, wild-type CPMV does not have any surface

* To whom correspondence should be addressed. Ph: (858)-784-9705. Fax: (858)-784-8660. E-mail: jackj@scripps.edu (J.E.J.); Ph: (858)-784-9730. Fax: (858)-784-7775. E-mail: twlin@scripps.edu (T.L.).

[†] Department of Molecular Biology and Center for Integrative Molecular Biosciences and The Scripps Research Institute.

[‡] Oregon Health Sciences University.

[§] National University of Singapore.

[||] University of California.

10.1021/bc0402888 CCC: $27.50 © 2004 American Chemical Society
Published on Web 07/01/2004

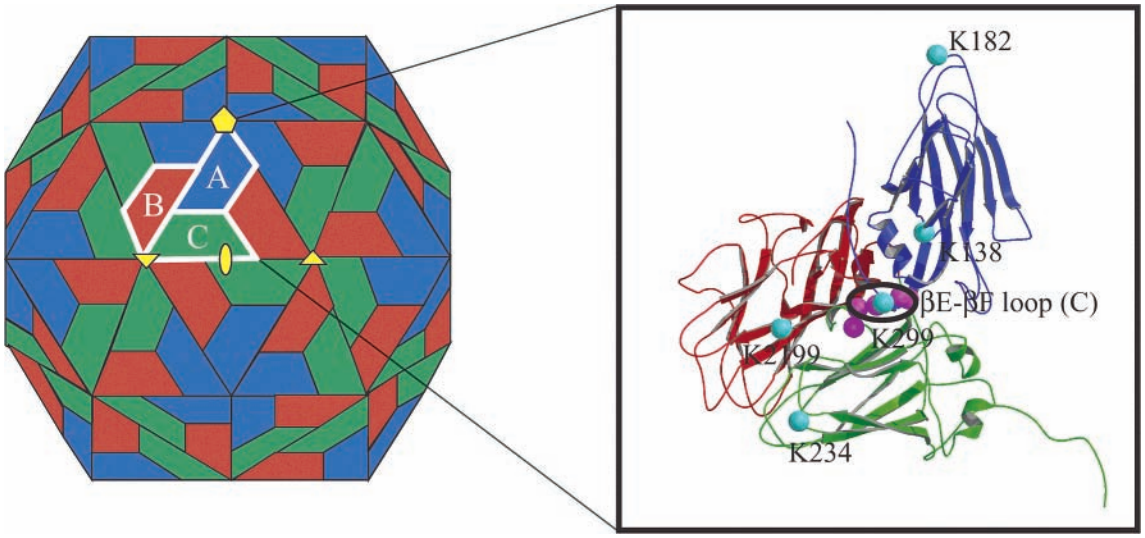


Figure 1. Left. Schematic diagram of CPMV capsid. The reference asymmetric unit is framed and the symmetry elements are labeled. Small (S) subunits labeled A are in blue, and the large (L) subunits formed by two domains are in red (B domains) and in green (C domains). The oval represents a 2-fold axis; the triangle is a 3-fold axis and the pentagon a 5-fold axis. Right. Ribbon diagram of the asymmetric unit comprised by three jellyroll β sandwiches with surface Lys residues represented as spheres in cyan. Residue numbers are preceded by a 1, if they are in the small subunit and a 2, if they are in the large subunit. K138 and K182 are in the A domain, K299 and K234 are in the C domain, while K2199 is in the B domain. Two mutants were used for the conjugation. Mutant vK299 contains the unique K299 (encircled) and mutant vEFB contains a unique cysteine engineered in the βE-βF loop of the C domain (magenta). The figure is drawn with MOLSCRIPT.

exposed cysteines on the virus capsid; hence, it was straightforward to engineer a cysteine residues at a unique location on the virus surface (*24, 25*). These CPMV mutants were used for directed modification of the virus with foreign proteins (Figure 1).

EXPERIMENTAL PROCEDURES

Propagation of the Virus in Plants. The primary leaves of cowpea seedlings were mechanically inoculated with 10 μg each of cDNA plasmids encoding RNA1 (pCP1) and RNA2 (pCP2) (*26*). The initial virus inoculum was extracted from infected cowpea leaves with 0.1 M potassium phosphate, pH 7.0 (phosphate buffer) 7 days post infection. Typically 50 plants were infected with the plant extract, and the symptomatic leaves were harvested after three weeks. For the lysine and cysteine mutants of CPMV, the respective mutant cDNA clones of RNA 2 in conjunction with pCP1 were used to initiate the infection.

Purification of LRR-internalin B, T4 Lysozyme, and Intron 8. The LRR domain of internalin B (LRR-InlB, *27)* and the Intron 8 proteins (Int 8, *28*) were cloned as plasmids in *E coli* expression vectors (pet 28 and pet 30, respectively, Novagen) and overexpressed in bacterial cells BL21 under the control of T7 promoter. Both proteins have the 6xHIS tag and therefore can be purified readily on Ni-NTA beads using the well-developed metal affinity chromatography (*29*). The cys mutant of T4 lysozyme was purified by ion exchange chromatography on a Mono S column (Amersham Pharmacia Biotech). The proteins were further purified on Superdex 200 (Amersham Pharmacia Biotech) columns by size exclusion chromatography and confirmed by immunoblots using anti HIS antibody (Clontech).

Chemical Conjugation of Heterologous Proteins on the Virus Capsid. Both LRR−InlB and the T4 lysozyme have cys residues that were used as the reactive groups to attach a homo- or a heterobifunctional cross-linker with its reactive maleimide or NHS ester group cross-linked to the unique cysteine or lysine residues on the virus, respectively. There are no unique cysteines present on the Int 8; therefore, thiolation reagent SATA was used to modify the N-terminal amine of the protein to introduce a protected thiol group (*30*). The protected thiol group is treated with hydroxylamine hydrochloride just before addition of the cross-linked virus to deprotect the introduced thiol and used for conjugation.

Briefly, the conjugation reaction was completed in two steps. In the first step, the heterobifunctional cross-linker, 50 μL of 5 mg/mL solution of sulfo SMCC (Pierce) dissolved in DMSO (Pierce), was added to the virus sample (4−5 mg) and stirred gently at room temperature for 1 h. The samples were later purified on a Sephadex G-25 column to get rid of the excess cross-linker and added to the protein samples in 50× excess molar ratios of protein to the virus. The samples were incubated at room temperature for 2 h or overnight at 4 °C. The conjugated samples were finally purified on superose6 column and the virus specific peak was collected and analyzed for the conjugated reaction products by western blots.

Biochemical Analysis of the Conjugated Samples. Typically, the retention time of wt CPMV on Superose6 column (Pharmacia) is 12 min (at flow rate 0.4 mL/min), but the conjugated samples eluted at approximately 8.7 min, indicating that the virus size was larger than the wild type. The virus conjugate peak was collected and analyzed on 4−12% Bis Tris gels (NuPAGE, Invitrogen) and probed with both CPMV and anti HIS antibodies using standard procedures for immunoblotting (*31*).

Bioassays for T4 Lysozyme and Int 8. *T4 Lysozyme.* The rate of lysis of *Micrococcus lysodeikticus* is determined as suggested by Shugar et al. (*32*). The cells were prepared by suspending 9 mg of dried *M. lysodeikticus* (Sigma) cells in 25 mL of 0.1 M potassium phosphate buffer, pH 7.0. A 100 μL aliquot of the virus-T4-conjugated sample (4 mg/mL) was mixed with 1 mL of *M. lysodeikticus* cell suspension. The samples were then analyzed on a UV−vis spectrophotometer to record the decrease in the absorbance of the samples at 450 nm as a function of time.

Intron 8. Monolayer cultures of $\approx 5 \times 10^6$ NIH-3T3 cells stably transfected with HER-2 (17−3−1) or parental

NIH-3T3 cells were plated in 10-cm tissue culture plates and incubated with the virus-Int 8 conjugate or wild-type CMPV in serum-free DMEM for 30 min at 37 °C. The cells were washed two times with phosphate buffered saline (PBS) and extracted in MTG (50 mM Tris·HCl (pH 7.0), 1.0% NP-40, 0.1% deoxycholic acid, 30 mM Na_3VO_4, 1 mM PMSF). Lysates were cleared by centrifugation and quantified using the Bradford Assay (BioRad). Equal amounts (20 μg total protein per lane) were resolved by SDS−PAGE in a 4−12% gradient polyacrylamide gel and transferred onto nitrocellulose. Ponceau stain was used to assess protein transfer and protein amounts in loaded samples. Membranes were blocked in 5% milk and then probed with α-CPMV or α Int 8 antibody, to assess virus-Int 8 binding, or with α-phosphotyrosine (Sigma) to assess receptor activation.

Electron Microscopy and Image Reconstruction of the Conjugates. Bioconjugated samples at a concentration of 1 mg/mL in 100 mM potassium phosphate, pH 7.0 (phosphate buffer), were placed on glow-discharged carbon film and stained for 1 min with 2% uranyl acetate. The grids were observed under a Philips CM120 microscope operated at 100 kV at a magnification of 45 000×. The micrographs were recorded under minimal dose conditions (<20 e/Å^2) on Kodak S0−163 film using a nominal defocus of ∼1.0 μm and scanned to a final resolution of 21 μm on a Zeiss SCAI scanner. The particles were selected manually using the program Boxer, and an initial map at 25 Å resolution of WT-CPMV was used as starting model for the classification procedure. Initial origin and orientation values were determined for 200 particles for LRR−InlB.

Multiple cycles of refinement, computed with the program SPIDER (*33*), yielded final three-dimensional maps at ∼26−28 Å resolution. The atomic models determined by X-ray crystallography were fitted into the electron density maps determined by electron microscopy with the aid of program O (*34*). The programs WEB (*33*) and Bobscript (*35*) were used for final rendering of the images.

RESULTS AND DISCUSSION

Conjugation of Heterologous Proteins on the Virus Capsid. Different conjugation schemes were investigated to cross-link foreign proteins on the virus capsid depending upon the features of the foreign protein being cross-linked.

Bioconjugation of LRR−InlB to CPMV. LRR−InlB, is a 22 kDa, leucine rich repeat (LRR) domain of internalin B protein isolated from the bacterial pathogen *Listeria monocytogenes* (*36*). The rationale for choosing LRR−InlB for attachment to the virus capsid was based upon its ability to induce specific internalization into different mammalian nonphagocytic cell types (*37*−*39*). A CPMV-LRR−InlB conjugate therefore could have potential applications as a drug delivery vehicle if LRR−InlB can confer the cell invasion property to the virus after conjugation. In addition, the crystal structure of LRR−InlB is known (*27*, *38*, *40*) and serves as a control for the structural information derived from the CPMV-LRR−InlB conjugates.

The LRR−InlB domain has a unique cysteine at its C-terminus, and this was conjugated to the Cys mutant of CPMV with the homobifunctional, bismaleimide thiol-reactive cross-linker ($BMPEO_4$). This cross-linker was selected because it has an eight-atom polyether spacer arm (17.8 Å) that separates the two reactive maleimide groups and may therefore have a reduced chance of conjugate precipitation during cross-linking. Also, the reactive cysteine on the virus surface is not fully exposed but resides in a cavity near the 5-fold axis of the virus. A long cross-linker will have a greater probability to reach the somewhat hidden cysteine on the virus capsid and form the thioether linkages.

The conjugation reaction was completed in two steps. First, LRR−InlB was mixed with the cross-linker and the excess cross-linkers and the byproducts were removed on Sephadex G-50 columns. Second, the activated protein was incubated with the virus to effect the final conjugation reaction. The conjugate was subsequently passed through a Superose6 size exclusion column to isolate the decorated virus.

The CPMV-LRR−InlB conjugate was verified in SDS PAGE gels by an increase in the molecular weight of the modified viral subunit. The purified LRR−InlB protein has a 6× His tag at its N-terminus. The large subunit of the viral capsid is 38 kDa but after cross-linking with the LRR−InlB protein (22 kDa), the size of the large subunit increased to 60 kDa (Figure 2A, lane 1) as probed by anti HIS antibodies in a western blot. The same 60 kDa band was also detected in western blots probed with anti CPMV antibody confirming that the increase in the size of the large subunit was due to the conjugation reaction with LRR−InlB (Figure 2A, lane 2). The fact that no protein band corresponding to 38 kDa was detected in blots probed with anti CPMV antibodies indicated that the modification of the large subunit was probably complete (Figure 2A).

The images obtained after 3D reconstruction revealed extra electron density around the capsid that was associated with the attached LRR−InlB molecules (Figure 2B). The docking of atomic structure into the EM map obtained was performed manually using the program O. (*34*). The Inl B protein was located on the virus surface in a manner that its unique cysteine and the viral surface cysteine were facing each other at a distance of ∼20 Å, corresponding with the size of the cross-linker used. In this position the conjugated InlB protein lays flat on the virus surface fitting the density and keeping the correct distance with the virus capsid and symmetry related neighbor proteins (Figure 2C).

The structural information for LRR−InlB derived from the image reconstruction of the conjugate demonstrated that CPMV could be used as a scaffold for structural studies of small proteins by electron microscopy.

Bioconjugation of T4 Lysozyme to CPMV. We chose the bacteriophage T4 lysozyme for attachment to CPMV surface to investigate the effects of chemical coupling on the activity of the conjugated enzyme because it can be readily assayed using UV−vis spectrophotometry. T4 lysozyme (cys mutant) was conjugated to wt CPMV with a heterobifunctional cross-linker, sulfo SMCC. This is a water-soluble cross-linker (11.6 Å in length) with a cyclohexane bridge to provide extra stability to the maleimide reactive group in aqueous solutions. The NHS ester end of the cross-linker was reacted with the primary amines on the wild-type CPMV to form stable amide bonds. There are five surface exposed lysine residues present per asymmetric unit of the virus capsid and in situations that require maximum number of molecules being conjugated for greatest efficacy rather than their icosahedral distribution, the wild-type virus capsid becomes a preferred platform as opposed to the unique lysine mutants of CPMV. Therefore, for T4 lysozyme conjugation, wt CPMV was chosen to permit maximum loading of the lysozyme molecules.

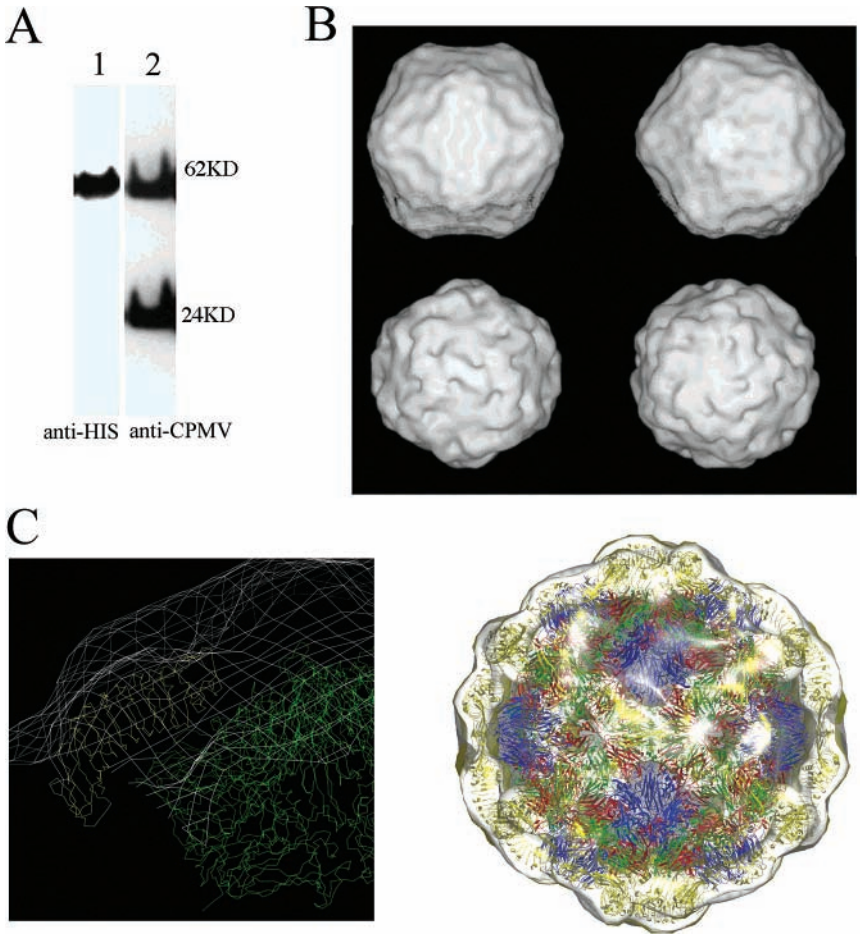


Figure 2. (A) Detection of CPMV-LRR−InlB conjugate by immunoblotting. The CPMV-LRR−InlB conjugate was made using a bis-maleimide reactive homobifunctional cross-linker and purified on a size exclusion column. The virus specific peak eluted from the Superose6 column was probed with anti HIS antibody (Lane 1) as well as anti CPMV antibody (Lane 2). The relative position of the modified large subunit of the virus is indicated by the molecular weight marker. (B) Surface morphology of the wild type, unmodified CPMV (top) and the CPMV-LRR−InlB conjugated particles (bottom) as visualized by electron microscopy and image reconstruction. The particles were stained with 2% uranyl acetate. A total of 200 particles were selected and 3D reconstruction was performed applying icosahedral symmetry using EMAN and SPIDER program packages. (C) Left. The docking of atomic structure of LRR−InlB (gold) and CPMV into the electron density map. The electron density is in chicken wire. The LRR−InlB model is drawn in yellow tracing and the C domain is in green. LRR−InlB lays on the virus surface fitting the density and keeping the correct distance with the virus capsid atoms and symmetry related neighbor proteins. Right. The ribbon diagram of CPMV/LRR−InlB conjugate and the electron density generated from electron microscopy. The electron density is transparent and depicted in pale white; LRR−InlB is shown in yellow. The capsid A domain is represented in blue, B domain is drawn in red, and the C domain is illustrated in green.

The water-soluble cross-linker was dissolved in 100 mM phosphate buffer. Since the NHS ester end of the cross-linker is more easily hydrolyzed in solution, the lysine modification of the virus was done first followed by the maleimide reaction on the lysozyme. The virus specific peak identified with size exclusion chromatography was analyzed by immunoblotting using anti CPMV antibody (Figure 3A). It is evident from the chromatogram that the conjugated virus elutes faster than the native, unconjugated virus, indicating an increase in the molecular weight of the modified virus. Immunoblotting of the conjugated virus specific peak revealed an increase in the molecular weight of capsid subunits, suggesting that both the large and the small subunits of the virus capsid were modified since the surface lysine residues are present on both subunit types (Figure 3B, lane 1, *32*). The products of cross-linking reaction prior to purification on the size exclusion column (Figure 3A) are shown in the adjacent lane (Figure 3B, lane 2). The functionality of the conjugated T4 enzyme was determined with turbidity assays. The reduction in the turbidity of the cell suspension was used as a measure of the enzymatic activity. About 6×10^6 cells of *M. lysodeikticus* were incubated with the 100 μg of T4-virus conjugate and the decrease in the absorbance at 450 nm was measured over a period of time. As depicted in the Figure 3C, the T4-CPMV conjugate efficiently lysed the bacterial cells over a period of 4 min whereas the wild-type unconjugated CPMV did not affect the turbidity of the cell suspension at all. On the basis of the coupling efficiency, the slope of the curve, and the concentration of the virus in solution (*32*) it was calculated that 0.8 mg of lysozyme was conjugated per 100 μg of virus. The activity of the conjugated lysozyme was estimated to be 22 000 units/mg that is comparable to 27 000 units/mg of the unattached enzyme. These results demonstrated that the chemical cross-linking procedure did not affect the biological activity of the conjugated enzyme adversely.

Bioconjugation of Int8 to CPMV. The above examples of protein conjugation rely on the availability of reactive functional groups (either a lysine or a cysteine) being present on the attached proteins. However, even in the absence of either of the two most nucleophilic groups on the heterologous protein, the viral scaffold can still be used for presentation of the foreign proteins by modifying the cross-linking schemes for conjugation. We accom-

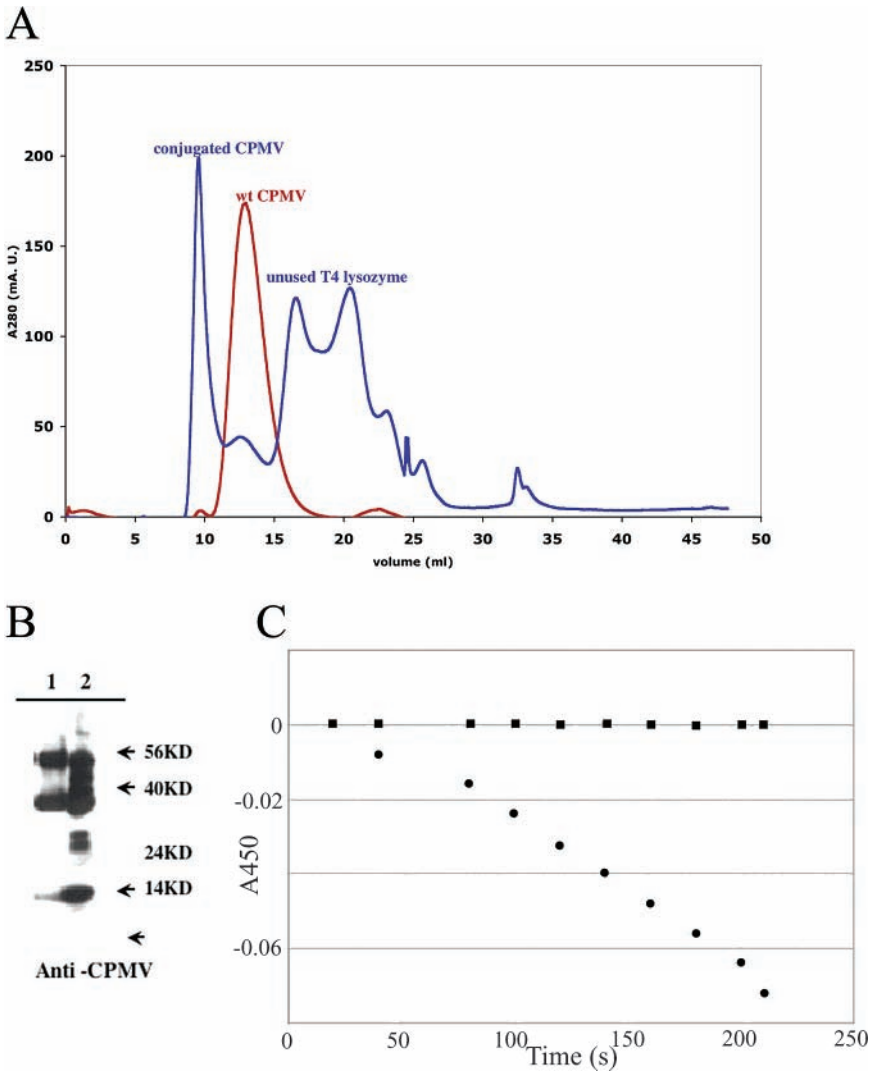


Figure 3. (A) Size exclusion chromatography profile of conjugation reaction products as resolved on a superose 6 column (blue trace). Besides the main virus peak that elutes at 8.7 mL, there are other smaller protein species that might represent either the dimerized T4 or the excess, unconjugated T4 lysozyme. The red trace indicates the retention time of the native, unconjugated virus on the same column. (B) Western blot analysis of CPMV-T4 lysozyme conjugate as probed with anti CPMV antibody. The T4 lysozyme was conjugated on wild-type CPMV using a heterobifunctional cross-linker, SMCC. The success of the conjugation reaction is supported by an increase in the molecular weight of both the small (~40 kDa) and the large (~56 kDa) subunits of the virus coat protein (Lane1). Lane 2 shows the cross-linked reaction products prior to virus conjugate purification on the Superose6 column. (C) Biological activity of conjugated T4 lysozyme−CPMV complex. The enzyme activity was assessed by the ability of the conjugated CPMV sample (circular dots) to hydrolyze a suspension of *M. lysodeikticus* cells. Unconjugated wt CPMV (shown in squares) was used as a control. The change in turbidity of cell suspension was recorded by a decrease in the absorbance at 450 nm over time. At the beginning of the experiment, the samples were blanked to 0 against the cell suspension at 450 nm.

plished this by coupling the intron 8-encoded domain (Int 8) of Herstatin on the virus surface using thiolation reagents.

Herstatin, an auto inhibitor of the ErbB family of receptor tyrosine kinases, is a product of an alternate splicing event from the Her2/neu gene. Her-2 intron 8 is retained and a translational read through results in a truncated protein consisting of subdomains I and II of the HER 2 receptor followed by a 79 amino acid C-terminal extension encoded by intron 8 (Int 8, *41*). Herstatin blocks receptor activation and modulates intracellular signaling through these receptors (*41*−*43*). The Int 8 is a receptor-binding module that binds with nanomolar affinity to epidermal growth factor receptor (EGFR) and HER-2 receptors (*41* and Shamieh et al., manuscript in preparation). The Int 8 was considered a candidate with therapeutic potential for conjugation to CPMV capsid, because of its role in binding to carcinoma cells that overexpress and are driven by HER-2 or the EGFR.

The attachment of functional Int 8 to CPMV was not straightforward because it does not have any lysine or cysteine residues in its sequence. In addition, the protein is soluble and stable only above pH 8 and forms oligomers at moderate concentrations. A strategy was developed to modify the protein with a thiolation reagent before conjugation with a heterobifunctional cross-linker. The active NHS ester end of SATA (N-succinimidyl S-acetylthioacetate) was reacted with the N-terminal amine in Int 8 at pH 8.0 to form a stable amide linkage (Figure 4A, top, i). The modified Int 8 now contained a protected thiol that could be stored without degradation and precluded oligomerization of the heterologous protein. The sulfhydral-modified Int 8 was coupled with maleimide-activated CPMV (unique lysine mutant, vK299) after deacetylation with an excess of hydroxylamine HCl (Figure 4A, top,

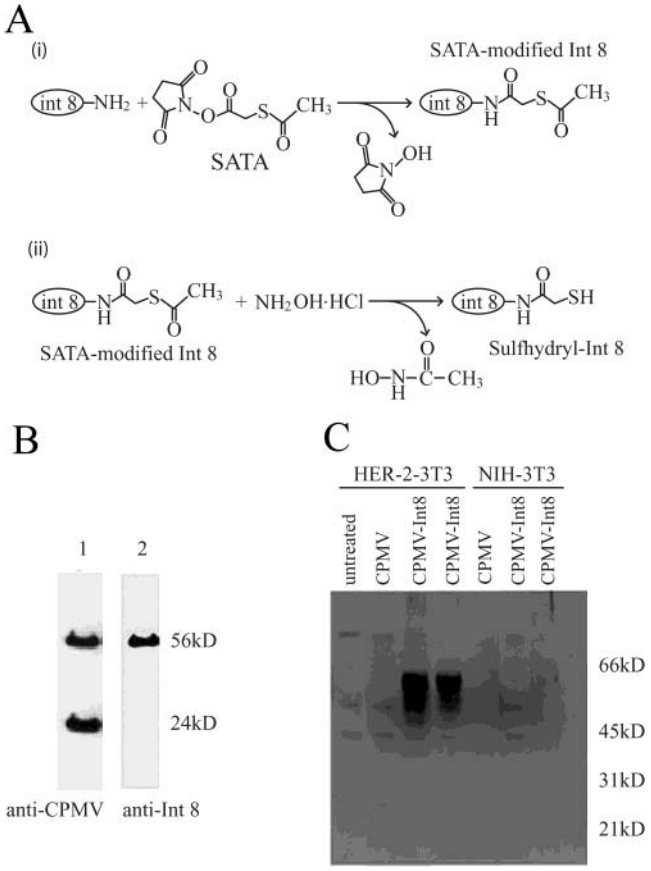


Figure 4. (A) Top: Reaction scheme for generating a thiol group on the Int 8 using the thiolation reagent SATA. (i) The active NHS ester end of SATA reacts with the N-terminal amine of Int 8 to form a protected sulfhydryl derivative and (ii) deprotection with hydroxylamine of the acetylated thiol of SATA modified Int8 yields a free sulfhydryl group that can be used for conjugation to CPMV using SMCC. (B) Detection of Int 8-CPMV conjugate by Western blotting. The Int 8 peptide was cross-linked to the virus capsid via unique lysine residue present on the large subunit using a heterobifunctional cross-linker. Virus specific peak was eluted from the Superose6 column and verified with anti CPMV (Lane 1) and anti Int 8 (Lane 2) antibodies. The retarded band at 56 kDa indicates the increase in the molecular weight of the viral large subunit as a result of conjugation. The specificity of the reaction was judged by the absence of any modification of the small subunit with Int 8. (C) Specific binding of the CPMV−Int8 conjugate to NIH-3T3 cells stably transfected with HER 2. A slow migrating band at approximately 56 kDa was observed with anti CPMV antibodies only in conjugated samples (Lanes 3 and 4). The wild-type CPMV (Lanes 2 and 5) did not show any binding to HER-2 transfected or parental 3T3 cells indicating that the intron 8-encoded domain is needed to direct binding to the HER-2 receptor. The untreated cells were used as a negative control (Lane 1). The specificity of binding was also confirmed by assessing the ability of the conjugate to bind to parental NIH 3T3 (Lanes 5−7).

ii). The reaction was mixed gently and left at 4 °C to allow a slow but specific reaction. Western blots analysis of Int 8-modified CPMV samples revealed that the viral large subunit was modified with the heterologous protein, and the increase in size of the large subunit was consistent with the corresponding size of Int 8 attached to the virus capsid (Figure 4B).

The CPMV−Int 8 conjugate was tested in vitro for specific binding to NIH-3T3 cells expressing the HER2 gene. As shown in the blots (Figure 4C), the CPMV−Int 8 conjugate was found to specifically associate with NIH-3T3 cells stably transfected with HER-2 but not with parental cells. Also, the wild type CPMV did not show binding to either of the two cell types tested, indicating that the bound Int 8 was biologically active and responsible for specific binding to the receptor overexpressing cells. The fact that the heterologous proteins displayed on the virus capsid retain their biological properties and function after conjugation suggests that cross-linking to the virus capsid may be a potential strategy to target and deliver drug molecules into the cell.

CONCLUSIONS

We have extended the chimera technology for surface display of full length, biologically active heterologous proteins by chemical cross-linking methods using CPMV as a platform. In addition, it is demonstrated that the icosahedral presentation of the foreign proteins allows CPMV to be used as a scaffold for imaging and structure determination of proteins that are too small to be analyzed by electron microscopy. It is reasonable to expect that there might be a limitation with respect to the size of the heterologous protein being conjugated to the capsid. Thus far, the largest protein that has been coupled to the virus surface with complete occupancy is the 22 kDa LRR domain of LRR−InlB. However, with larger proteins such as the 45 kDa CD48 molecule we only observed 60% modification of the virus capsid (data not shown), suggesting that additional coupling schemes or alternate cross-linkers may have to be explored to present larger proteins on the virus surface. The recently reported grafting techniques using synthetic scaffolds (*44*, *45*) also suffer from size constraints (<19 amino acid), and in this respect CPMV has surpassed the size barrier to tolerate modification of the viral capsid with much larger heterologous proteins. Finally, since the cross-linking approach reported here preserves the biological activity of the heterologous protein as well as its structure, it opens up prospects to simultaneously present ligands involved in cellular uptake, trafficking or delivery on the virus surface for generating nano delivery capsules with biomedical applications.

ACKNOWLEDGMENT

A.C. thanks Erica Strable for helpful discussions. The authors wish to acknowledge the support from NIH (R01EBB00432 02 to J.E.J., the Office of Naval Research grants # N00014-00-1-0671 to J.E.J., and N00173-01-C2012 to T.L.) G.C. would like to acknowledge funding from NIH (NIHCA83503).

LITERATURE CITED

(1) Lomonossoff, G. P., and Johnson, J. E. (1995) Viral expression system for peptides. *Semin. Virol 6*, 257−267.
(2) Lomonossoff, G. P., and Johnson, J. E. (1996) Use of macromolecular assemblies as expression systems for peptides and synthetic vaccines. *Curr. Opin. Struct. Biol. 6*, 176−82.
(3) Porta, C., Spall, V. E., Lin, T., Johnson, J. E., and Lomonossoff, G. P. (1996) The development of cowpea mosaic virus as a potential source of novel vaccines. *Intervirology 39*, 79−84.
(4) Johnson, J. E., Lin, T., and Lomonossoff, G. P. (1997) Presentation of heterologous peptides on plant viruses: Genetics, structure and function. *Annu. Rev. Phytopathol. 35*, 67−86.
(5) Porta, C., Spall, V. E., Loveland, J., Johnson, J. E, Barker, P J., and Lomonossoff, G. P. (2002) Development of cowpea mosaic virus as a high-yielding system for the presentation of foreign peptides. *Virology 202*, 949−55.
(6) Lin, T., and Johnson, J. E. (2003) Structures of picorna like plant viruses: Implications and applications. *Adv. Virus. Res. 62*, 167−239.

(7) Ernst, W. J., Spenger, A., Toellner, L., Katinger, H., and Grabherr, R. M. (2000) Expanding baculovirus surface display. Modification of the native coat protein gp64 of *Autographa californica* NPV. *Eur. J. Biochem. 267*, 4033−4039.
(8) Gupta, A., Onda, M., Pastan, I., Adhya, S., and Chaudhary, V. (2003) High-density functional display of proteins on bacteriophage lambda. *J. Mol. Biol. 334*, 241−54.
(9) Peabody, D. S. (2003) A Viral Platform for Chemical Modification and Multivalent Display. *J. Nanobiotechnol. 1*, 5−13.
(10) Woiwode, T. F., Haggerty, J. E., Katz, R., Gallop, M. A., Barrett, R. W., Dower, W. J., and Cwirla, S. E. (2003) Synthetic compound libraries displayed on the surface of encoded bacteriophage. *Chem. Biol. 10*, 847−58.
(11) Johnson, J. E., and Hollingshead, C. (1981) Crystallographic studies of cowpea mosaic virus by electron microscopy and X-ray diffraction. *J. Ultrastruct. Res. 74*, 223−231.
(12) Porta, C., Wang, G., Cheng, H., Chen, Z., Baker, T. S., and Johnson, J. E. (1994) Direct imaging of interactions between an icosahedral virus and conjugate F(ab) fragments by cryoelectron microscopy and X-ray crystallography. *Virology 204*, 777−88.
(13) Lin, T., Porta, C., Lomonossoff, G., and Johnson, J. E. (1996) Structure-based design of peptide presentation on a viral surface: the crystal structure of a plant/animal virus chimera at 2.8 A resolution. *Fold Des. 1*, 179−87.
(14) Lin, T., Chen, Z., Usha, R., Stauffacher, C. V., Dai, J. B., Schmidt, T., and Johnson, J. E. (1999) The refined crystal structure of cowpea mosaic virus at 2.8 A resolution. *Virology 265*, 20−34.
(15) Lin, T., Clark, A. J., Chen, Z., Shanks, M., Dai, J. B., Li, Y., Schmidt, T., Oxelfelt P., Lomonossoff, G. P., and Johnson, J. E. (2000) Structural fingerprinting: subgrouping of comoviruses by structural studies of red clover mottle virus to 2.4-A resolution and comparisons with other comoviruses. *J. Virol. 74*, 493−504.
(16) Taylor, K. M., Porta, C., Lin, T., Johnson, J. E., Barker, P. J., and Lomonossoff, G. P. (1999) Position-dependent processing of peptides presented on the surface of cowpea mosaic virus. *Biol. Chem. 380*, 387−92.
(17) Taylor, K. M., Lin, T., Porta, C., Mosser, A. G., Giesing, H. A., Lomonossoff, G. P., and Johnson, J. E. (2000) Influence of three-dimensional structure on the immunogenicity of a peptide expressed on the surface of a plant virus. *J. Mol. Recognit. 13*, 71−82.
(18) Chatterji A., Burns, L. L., Taylor, S. S., Lomonossoff, G. P., Johnson, J. E., Lin T., and Porta, C. (2002) Cowpea mosaic virus: from the presentation of antigenic peptides to the display of active biomaterials. *Intervirology 45*, 362−70.
(19) Porta, C., Spall, V. E., Findlay, K. C., Gergerich, R. C., Farrance, C. E., and Lomonossoff, G. P. (2003) Cowpea mosaic virus-based chimaeras. Effects of inserted peptides on the phenotype, host range, and transmissibility of the modified viruses. *Virology 310*, 50−63.
(20) van Wezenbeek, P., Verver. J., Harmsen. J., Vos. P., and van Kammen. A. (1985) Primary structure and gene organization of the middle-component RNA of cowpea mosaic virus. *EMBO J. 2*, 941−946.
(21) Lomonossoff, G. P., and Shanks, M. (1983) The nucleotide sequence of cowpea mosaic virus B RNA. *EMBO J. 2*, 2253−2258.
(22) Lomonossoff, G. P., and Johnson, J. E. (1991) The synthesis and structure of comovirus capsids. *Prog. Biophys. Mol. Biol. 55*, 107−37.
(23) Chatterji A., Ochoa W., Paine, M., Ratna, B. R., Johnson, J. E., and Lin, T. (2004) New addresses on an addressable virus nanoblock: uniquely reactive lys residues on Cowpea mosaic virus. *Chem. Biol*., in press.
(24) Wang, Q., Lin T., Johnson J. E., and Finn M. G. (2002) Natural supramolecular building blocks. Cysteine-added mutants of cowpea mosaic virus. *Chem. Biol. 9*, 813−819.
(25) Wang Q., Kaltgrad, E., Lin, T., Johnson, J. E., and Finn M. G. (2002) Natural supramolecular building blocks. Wild-type cowpea mosaic virus. *Chem. Biol. 9*, 805−11.
(26) Dessens, J. T., and Lomonossoff, G. P. (1993) Cauliflower mosaic virus 35S promoter controlled DNA copies of cowpea mosaic virus RNAs are infectious on plants. *J. Gen. Virol. 74*, 889−892.
(27) Marino, M., Braun, L., Cossart, P., and Ghosh, P. (2001) Structure of the lnlB leucine-rich repeats, a domain that triggers host cell invasion by the bacterial pathogen *L. monocytogenes. Mol. Cell. 4*, 1063−72.
(28) Doherty, J. K., Bond, C., Jardim, A., Adelman, J. P., and Clinton, G. M. (1999) The HER-2/neu receptor tyrosine kinase gene encodes a secreted autoinhibitor. *Proc. Natl. Acad. Sci. U.S.A. 14*, 10869−74.
(29) Sulkowski, E. (1985) Purification of proteins by IMAC. *Trends Biotechnol. 3*, 1−7.
(30) Hermanson, T G. (1996) *Bioconjugate techniques*, Academic Press, San Diego, California.
(31) Ausubel, F. M., Brent, R., Kingston, R. E., Moore, D. D., Seidman, J. G., Smith, J. A., and Struhl, K. (1999) *Short Protocols on Molecular Biology*, 4th ed., John Wiley and Sons, New York.
(32) Shughar, D. (1952) The measuremnt of lysozyme activity and the ultraviolet inactivation of lysozyme. *Biochem. Biophys. Acta 8*, 302−309.
(33) Frank J., Radermacher, M., Penczek, P., Zhu, J., Li, Y., Ladjadj, M., and Leith, A. (1996) SPIDER and WEB: processing and visualization of images in 3D electron microscopy and related fields. *J. Struct. Biol. 116*, 190−199.
(34) Jones, T. A., and Liljas, L. (1984) Crystallographic refinement of macromolecules having noncrystallographic symmetry. *Acta Crystallogr. A 40*, 50−57.
(35) Esnouf, R. M. (1997) An extensively modified version of MolScript that includes greatly enhanced coloring capabilities. *J. Mol. Graphics 15*, 132−134.
(36) Bierne H., and Cossart P. (2002) InlB, a surface protein of *Listeria monocytogenes* that behaves as an invasion and a growth factor. *J. Cell Sci. 115*, 3357−67.
(37) Machner, M. P., Frese, S., Schubert, W. D., Orian-Rousseau, V., Gherardi, E., Wehland, J., Niemann, H. H., and Heinz, D. W. (2003) Aromatic amino acids at the surface of InlB are essential for host cell invasion by *Listeria monocytogenes*. *Mol. Microbiol. 48*, 1525−36.
(38) Marino, M., Banerjee, M., Jonquieres, R., Cossart, P., and Ghosh, P. (2002) GW domains of the *Listeria monocytogenes* invasion protein InlB are SH3-like and mediate binding to host ligands. *EMBO J. 121*, 5623−34.
(39) Shen, Y., Naujokas, M., Park, M., and Ireton, K. (2000) InIB-dependent internalization of *Listeria* is mediated by the Met receptor tyrosine kinase. *Cell 103*, 501−10.
(40) Schubert, W. D., Gobel, G., Diepholz, M., Darji, A., Kloer, D., Hain, T., Chakraborty, T., Wehland, J., Domann, E., and Heinz, D. W. (2001) Internalins from the human pathogen *Listeria monocytogenes* combine three distinct folds into a contiguous internalin domain. *J. Mol. Biol. 312*, 783−94.
(41) Azios, N. G., Romero, F. J., Denton, M. C., Doherty, J. K., and Clinton, G. M. (2001) Expression of herstatin, an autoinhibitor of HER-2/neu, inhibits transactivation of HER-3 by HER-2 and blocks EGF activation of the EGF receptor. *Oncogene 20*, 5199−209.
(42) Molina, M. A., Saez, R., Ramsey, E. E., Garcia-Barchino, M. J., Rojo, F., Evans, A. J., Albanell, J., Keenan, E. J., Lluch, A., Garcia-Conde, J., Baselga, J., and Clinton, G. M. (2002) NH(2)-terminal truncated HER-2 protein but not full-length receptor is associated with nodal metastasis in human breast cancer. *Clin. Cancer Res. 8*, 347−53.
(43) Justman, Q. A., and Clinton, G. M. (2003) Herstatin, an autoinhibitor of the human epidermal growth factor receptor2 Tyrosine kinase, modulates epidermal growth factor signaling pathways resulting in growth arrest. *J. Biol. Chem. 277*, 20618−20624.
(44) Sia, S. K., and Kim, P. S. (2003) Protein grafting of an HIV-1-inhibiting epitope. *Proc. Natl. Acad. Sci. U.S.A. 100*, 9756−61.
(45) Ye, Y., Shealy, S., Lee, H. W., Torshin, I., Harrison, R., and Yang, J. J. (2003) A grafting approach to obtain site-specific metal-binding properties of EF-hand proteins. *Protein Eng. 16*, 429−34.

BC0402888

Nuclear Localization Signal-Targeted Poly(ethylene glycol) Conjugates as Potential Carriers and Nuclear Localizing Agents for Carboplatin Analogues

Olga Aronov,[†] Aviva T. Horowitz,[‡] Alberto Gabizon,[‡] Miguel A. Fuertes,[§] José Manuel Pérez,[§] and Dan Gibson*[,†,||]

Department of Medicinal Chemistry and Natural Products, School of Pharmacy, P.O. Box 12065, The Hebrew University of Jerusalem, Jerusalem 91120, Israel, Oncology Institute, Shaare Zedek Medical Center, Jerusalem, Israel, Departamento de Quimica Inorgánica y Centro de Biología Molecular (CSIC-UAM), Facultad de Ciencias, Universidad Autonoma de Madrid, 28049-Madrid, Spain, and The David R. Bloom Center for Pharmacy, The Hebrew University of Jerusalem, Israel. Received March 14, 2004; Revised Manuscript Received May 12, 2004

Carboplatin is a low-molecular-weight anticancer drug that acts by binding to the nuclear DNA of cells. Thus, efficient delivery of the platinum drugs to the nucleus of the cancer cells may enhance the cytotoxicity of the drug. Efficient drug delivery to the nucleus of cancer cells requires three levels of localization: targeting to the cancerous tissue, accumulation in the cancer cells, and intracellular localization in the nucleus. Nuclear localization signals (NLS) are short positively charged basic peptides that actively transport large proteins across the nuclear membrane. We have prepared conjugates in which the NLS is tethered to poly(ethyleneglycol)carboplatin conjugate (NLS−PEG−Pt) and compared their pharmacological properties to those of their untargeted analogues that do not possess the NLS (PEG−Pt). NLS−PEG−Pt conjugates are rapidly internalized into cancer cells and accumulate in the nucleus. Despite their rapid nuclear localization, they form less Pt−DNA adducts than the untargeted analogues, PEG−Pt, and are also less cytotoxic. These results support the hypothesis that carboplatin (unlike cisplatin) may require cytosolic activation prior to its binding to nuclear DNA.

INTRODUCTION

Cisplatin, carboplatin, and oxaliplatin (See Figure 1) are three FDA approved anticancer agents that are believed to owe their anticancer activity to their ability to covalently modify cellular DNA (*1*, *2*). Cisplatin and carboplatin form the identical major adducts with DNA where the *cis*-$[Pt(NH_3)_2]^{2+}$ moiety is covalently coordinated to the N7 atoms of two adjacent guanines on the same strand forming the 1,2-d(G*pG*) intrastrand cross-link (*3*). The 1,2 intrastrand cross-links bend the DNA toward the major groove, resulting in a local distortion of the double helix, and it is this distortion that is believed to trigger a series of cellular events that results in the eventual death of the cancer cell (*4*). The most common dose limiting effects for platinum based drugs are nephrotoxicity, ototoxicity, neurotoxicity, and myelosuppression. In addition, cancer cells are either inherently refractory to the platinum drugs or can acquire resistance to the drugs. There are several known resistance mechanisms to cisplatin: reduced cellular accumulation, increased production of intracellular platinophiles such as glutathione and metalothionein, enhanced DNA repair and increased tolerance to DNA platination, and decreased cellular apoptotic response (*5*−*7*). The first two mechanisms of resistance attempt to prevent the drug from reaching the nuclear DNA, its critical binding site. Higher levels of Pt−DNA adducts are expected to result in improved cytotoxicity. Thus, rapid and efficient delivery of the platinum drugs to the nucleus of the cancer cells may overcome some of the resistance pathways and could enhance the cytotoxicity of the drugs.

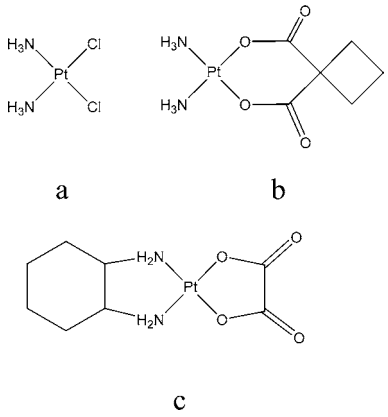


Figure 1. Platinum-based anticancer drugs: (a) cisplatin, (b) carboplatin, and (c) oxaliplatin.

Efficient drug delivery to the nucleus of cancer cells requires three levels of localization: targeting to the cancerous tissue, accumulation in the cancer cells, and intracellular localization in the nucleus (*8*, *9*). We recently described the preparation and pharmacological properties of a conjugate comprised of a poly(ethylene glycol) (PEG)[1] carrier to which folic acid (FA) was attached on one end (to exploit the folic acid receptor mediated endocytotic

* Corresponding author.
[†] School of Pharmacy, The Hebrew University of Jerusalem.
[‡] Shaare Zedek Medical Center.
[§] Universidad Autonoma de Madrid.
[||] The David R. Bloom Center for Pharmacy, The Hebrew University of Jerusalem.

10.1021/bc0499331 CCC: $27.50 © 2004 American Chemical Society
Published on Web 07/01/2004

pathway) and a carboplatin analogue to the other end (FA−PEG−Pt) (*10*). PEG was chosen as the carrier because attaching a low molecular-weight drug to a hydrophilic polymer such as PEG results in high aqueous solubility, slower clearance, reduced systemic toxicity, and efficient accumulation in tumors through enhanced permeability and retention (EPR) (*11*). PEG is a water soluble amphiphilic polymer showing excellent biocompatibility and is frequently used in biomedical applications. Several drugs such as doxorubicin, camptothecin and paclitaxel, have been conjugated to PEG carriers and these conjugates are in various stages of clinical trials (*12*). Folic acid has been used extensively to internalize covalently tethered cargos into cancer cells, via the FRME, since many cancer cell lines overexpress folic acid receptors (*13*, *14*).

When the cell uptake, cellular DNA binding and cytotoxicity of FA−PEG−Pt were compared to those of the PEG−Pt conjugate (without the FA), it was found that FA−PEG−Pt conjugates were taken into the cytosols of the cancer cells significantly more rapidly than the PEG−Pt conjugates. Yet incubation with the PEG−Pt conjugates afforded twice as many platinum cellular DNA adducts as did FA−PEG−Pt. This is not necessarily surprising since it has been reported that most endocytosed compounds end up in the lysosome or in some compartment that is separated from the cytosol by a membrane, preventing them from reaching their critical biological targets (*15*). Thus, there is a need to explore a nonendocytotic pathway for the efficient delivery of platinum complexes to the nuclei of cancer cells.

The research following discovery that the HIV-1 Tat protein can cross cellular membranes, established that positively charged peptides such as Tat(49−57) and Antp-(43−58) have membrane translocating properties that can be exploited for the delivery of oligonucleotides, proteins, imaging agents liposomes, etc. (*16*, *17*). While the exact mechanism by which the basic peptides enter the cells remains to be elucidated, it seems that they do not enter the cells by endocytosis and it is the amphipathicity of the peptides that is responsible for the cellular translocation. Nuclear localization signals (NLS) are short positively charged basic peptides that actively transport large proteins across the nuclear membrane. They have been used to localize cargo molecules (to which they have been conjugated) from the cytosol to the cell nucleus (*18*).

The cellular delivery and particularly intracellular localization of therapeutics are two of the foremost challenges facing the medicinal chemists. In this manuscript we report the design, synthesis, and preliminary pharmacological properties of novel PEG−NLS conjugates as carriers for carboplatin analogues.

EXPERIMENTAL PROCEDURES

Materials. All reagents were purchased from Sigma-Aldrich Israel, Ltd., at least reagent-grade and were used without purification. Solvents for synthesis and for HPLC were synthesis and HPLC-grade accordingly.

Compound Preparation. *NH_2-GABA-Cys-Gly-Gly-Pro-Lys-Lys-Lys-Arg-Lys-Val-Gly-Gly-CO−Resin (**1**).* GABA−FMOC. A 1 g (9.7 mmol) sample of γ-aminobutyric acid (GABA) was dissolved in 10% $NaHCO_3$. A 1.5 g (5.8 mmol) sample of FMOC−Cl was dissolved in 30 mL of acetonitrile and was added dropwise over 2 h to the GABA solution. The reaction mixture was allowed to stand for 1 additional hour, and then the acetonitrile was evaporated and the solution was acidified to pH 1 with HCl. The white precipitate was filtered, washed with two portions of water and one portion of ethyl acetate, and desiccated over P_2O_5 (yield 80%).

NH_2-Cys-Gly-Gly-Pro-Lys-Lys-Lys-Arg-Lys-Val-Gly-Gly-CO−Resin. The peptide NH_2-Cys-Gly-Gly-Pro-Lys-Lys-Lys-Arg-Lys-Val-Gly-Gly-COOH was synthesized by the solid-phase FMOC method on a Rink amide resin with the carboxy terminus still attached to the resin and the amino acid side chains protected as follows: Lys (ϵ-N-BOC), Arg(Pmc), and Cys(S-Trt).

NH_2-GABA-Cys-Gly-Gly-Pro-Lys-Lys-Lys-Arg-Lys-Val-Gly-Gly-CO−Resin. A 50 mg (0.017 mmol) sample of the peptide on the resin was put in a Merrifield vessel, and 14 mg (0.043 mmol) of GABA−FMOC, 2 mL of NMP, 19 mg (0.043 mmol) of BOP-reagent and 50 μL of DIEA were added. The reaction was agitated overnight at room temperature, after which the reaction mixture was filtered and a sample from the resin was used for a Kaiser test (for primary amines). If the test was positive, the reaction was repeated until the test came negative, indicating complete coupling. The resin was washed with 2 mL portions of DMF, and then 2 mL of a 20% piperidine in DMF was added and the deprotection was allowed to proceed for 2 h at room temperature with constant shaking and subsequently the resin was washed with four 2 mL portions of DMF.

*FITC-NH-GABA-Cys-Gly-Gly-Pro-Lys-Lys-Lys-Arg-Lys-Val-Gly-Gly-CO−Resin (**2**).* A 10 mg (0.043 mmol) sample of FITC, 2 mL of DMF, and 50 μL of TEA were shaken overnight with the resin at room temperature, the resin was filtered, and a small portion of the resin was tested for free amines using the Kaiser test. After a negative Kaiser test was obtained the resin was washed with four 2 mL portions of DMF.

*HO-NLS−Cys−GABA−FITC (**3**).* A 150 mg sample of phenol, 0.05 mL of thioanisole, 0.05 mL of water, and 0.025 mL of dithioethane in 2 mL of TFA were added to the resin, and the reaction was left for 3 h at room temperature with constant shaking. The reaction mixture was filtered, 20 mL of diethyl ether was added, and the orange precipitate that was formed was isolated by centrifugation. The precipitate was washed with three 20 mL portions of diethyl ether and then dissolved in 2 mL of water and lyophilized to yield an orange powder (yield 60%). RP18 HPLC: Rt = 10.2 min. Mass spectra (ESIMS): four peaks corresponding to four charge states of the compound were observed at *m*/*z* values of 423.4, 564.1, 845.3 and 1688.4, indicating a molecular mass of 1687.4 (calcd 1687.2)

*H_2N-PEG-NH_2 (**4**).* The compound was prepared as described by us recently (*10*).

*Cbz−PEG-NH_2 (**5**).* A 500 mg sample of Na_2CO_3 and 3 g of H_2N-PEG-NH_2 (1 mmol) were dissolved in 150 mL of water, and 50 mL of acetonitrile was then added. A 170 mg (1 mmol) sample of benzyl chloroformate was dissolved in 50 mL of acetonitrile and was added very slowly at room temperature over approximately 3 h to the reaction mixture. After the addition of the benzyl

[1] Abbreviations: CBDCA, cyclobutane-1,1-dicarboxylate; PEG,-poly-(ethylene glycol); FA, folic acid; FRME, folate receptor-mediated endocytosis; FMOC, fluorenylmethyl chloroformate; Cbz-Cl, benzyl chloroformate; FITC, fluorescein isothiocyanate; DCC, dicyclohexylcarbodiimide; DCU, dicyclohexylurea; ECI, 1-[3-(dimethylamino)propyl]-3-ethylcarbodiimide hydrochloride; DIEA diisopropylethyl-amine; AA, atomic absorption; CPG, carboxypepidase G; MALDI-TOFMS, matrix-assisted laser desorption ionization time-of-flight mass spectrometry; HiFr, high folate receptor; Icp-Ms, inductively coupled plasma mass spectrometry; FACS, fluorescence-assisted cell sorting; MB, methylene blue; PEG3000,-$(CH_2CH_2O)_{68}$-; NHS, N-hydroxysuccinimide.

chloroformate was completed, the acetonitrile was removed under reduced pressure, and the remaining aqueous solution was extracted with two 100 mL portions of dichloromethane. The organic fractions were combined, dried over $MgSO_4$, and crystallized from 100 mL of diethyl ether. The crude product contained some starting material (H_2N-PEG-NH_2), the desired product (Cbz−PEG-NH_2), and some Cbz−PEG−Cbz. The desired monocationic momoprotected PEG was purified by cation exchange chromatography on a Sephadex CM-50 resin with UV detection at 254 nm. The reaction mixture was dissolved in a minimal amount of water (5 mL) and loaded on the column, and the neutral Cbz−PEG−Cbz was removed from the column with deionized water. The desired product was eluted with 25 mM NaCl and showed a UV absorption at 254 nm and also gave a positive test for a primary amine with fluorescamine. The product was lyophilized and dissolved in 100 mL of dichloromethane, the NaCl was filtered off, the solvent was removed, and the product was crytalized from 50 mL of diethyl ether. The yield was 30%. RP18-HPLC: one peak Rt = 16.2 min. ^{1}H NMR (DMSO-d_6) δ(ppm):

7.32(m, 5H, −CH−(ph)), 7.23(t, 1H, Cbz-*NH*−), (bs, ∼280H, −PEG_{3000}−), 3.14(q, 2H, Cbz-NH-CH_2−, 2.95(t, 2H, −CH_2-NH_2).

*FA−PEG-NH_2 (**6**).* The synthesis of FA−PEG−FMOC was described in ref *10*. FA−PEG−FMOC was used as the starting material for the preparation of FA-PEG-NH_2. The FMOC protecting group was removed from FA-PEG-FMOC by piperidine treatment. FA−PEG−FMOC (400 mg) was dissolved in 50 mL of 25% aqueous piperidine. The white precipitate was removed by filtration, the solvents were evaporated to remove all traces of piperidine, and the product was dissolved in water and evaporated again. The process was repeated twice. RP18-HPLC: Rt = 14.34 min. ^{1}H NMR (D_2O) δ(ppm): 8.62(s, 1H, *folate-C(8)H*), 7.65(d, 2H, *folate*(*PABA*)H_2), 6.81(d, 2H, *folate*(*PABA*)H_2), 4.51(s, 2H, *folate*(NH-CH_2)), 3.6(bs, ∼280H, −PEG_{3000}−), 3.14(m, 2H, folate-NH−CH_2), 2.95-(t, 2H, -CH_2−NH_2), 2.21−1.95(bm, 4H, *folate*(*Glu*)β,γ-CH_2) 4.22(m, 1H, *folate*(*Glu*)α-*CH*).

*FA−PEG−Maleimide (**7**).* 300 mg (0.095 mmol) of FA−PEG-NH_2 was dissolved in a 5 mL of a saturated solution of $NaHCO_3$, and the solution was cooled in an ice bath. An 80 mg (0.52 mmol) sample of N-methoxycarbonylmaleimide was added with stirring, and the reaction mixture was left in the ice bath for 15 min and was stirred for an additional 30 min at room temperature. The product was isolated on a Sephadex 25 column and immediately lyophilized to yield a white powder. Yield, 90%. RP18-HPLC: Rt = 16.51min. ^{1}H NMR (D_2O) δ(ppm): 8.62(s, 1H, *folate-C(8)H*), 7.65(d, 2H, *folate*-(*PABA*)H_2), 7.01(2H, −*CH*=*CH*−), 6.81(d, 2H, *folate*-(*PABA*)H_2), 4.51(s, 2H, *folate*(NH-CH_2)), 4.22(m, 1H, *folate*(*Glu*)α-*CH*) 3.6(bs, ∼280H, −PEG_{3000}−), 3.14(m, 4H, maleimide-NH-CH_2-/folate-NH-CH_2), 2.21−1.95(bm, 4H, *folate*(*Glu*)β,γ-CH_2).

*NLS−FITC−PEG−FA (**8**).* A 100 mg sample of FA−PEG−maleimide (**7**) was dissolved in a 50 mM phosphate buffer (pH 5.8), and to the reaction mixture was added 70 mg of HO-NLS−Cys−GABA−FITC (**3**) (0.041 mmol) and the reaction mixture was stirred at room temperature for 45 min. The product was isolated by semipreparative RP-HPLC and was lyophylized. The yield was 50%. A 10 mg sample of (8) was dissolved in 10 mL of PBS buffer, and the concentrations of the fluorescein (ϵ_{490} = 67 000) and folate (ϵ_{363} = 6197) were determined. The ratio between the fluorescein and the folate was 1.0: 0.95, attesting to the purity of the product. RP18 HPLC: Rt = 14.17 min. MALDI-TOF-MS showed a bell distribution with the center around 5412 amu).

*Cbz−PEG−Maleimide (**9**).* A 300 mg (0.095 mmol) sample of Cbz−PEG-NH_2 was dissolved in a 5 mL saturated solution of $NaHCO_3$, and the solution was cooled in an ice bath. An 80 mg (0.52 mmol) sample of *N*-methoxycarbonylmaleimide was added with stirring, and the reaction mixture was left in the ice bath for 15 min and was stirred for an additional 30 min at room temperature. The product was isolated on a Sephadex 25 column and immediately lyophilized to yield a white powder. Yield, 90%. RP18 Rt = 17.15 min.

*NLS−PEG−FITC (**10**).* A 100 mg (0.031 mmol) sample of Cbz−PEG−maleimide was dissolved in a 50 mM phosphate buffer (pH 5.8), 70 mg (0.041 mmol) of NLS−Cys−GABA−FITC was added, and the reaction mixture was stirred for 45 min. The product was purified and isolated by semipreparative RP-HPLC and lyophilized to yield an orange powder. Yield, 60%. RP18 HPLC Rt = 15.11 min. MALDI-TOF-MS a bell distribution centered around 5200 amu (Calc. 5203 amu).

*Di-tert-butyl 2-(3-succininylaminopropyl)malonate (**11**).* The synthesis and characterization of compound **11** were detailed in ref *10*.

^{1}H NMR (DMSO-d_6) δ(ppm): 7.84(bt, 1H, C(O)-*NH*−), 3.16(t, 1H, α-*CH*−), 2.99(q, 2H, NH-CH_2−), 2.38(t, 2H, *succ.*-CH_2−), 2.29(t, 2H, *succ.*-CH_2−), 1.61(m, 2H, −CH_2-CH−), 1.41(bs, 20H, −CH_2-CH_2-CH_2-/*t-Bu*).

*Cbz−PEG−Mal−(tBu) (**12**).* The synthesis and characterization of compound **12** were detailed in ref 10.

*Maleimide−PEG−Malonic Acid, Disodium Salt (**13**).* Initially the Cbz protective group of compound **12** was removed by hydrogenation, and then the primary amine was converted to the maleimide in the same way as was done for the preparation of compound **7**. The hydrolysis of the *tert*-butyl protecting groups was performed by dissolving 500 mg of maleimide−PEG−Mal-tBu in 30 mL of 25% TFA in CH_2Cl_2; after 2 h of stirring the solvent was removed, and the product was taken up in 3 mL of 50 mM Na_2CO_3. The product was purified on a Sephadex 25 column and lyophilized yielding a white solid (yield 90%).

^{1}H NMR (D_2O) δ(ppm): 6.88(s, 2H, −*CH*=*CH*-), 3.6-(bs, ∼280H, −PEG_{3000}−), 3.36(t, 4H, PEG-CH_2-N), 3.14-(t, 2H, −NH-CH_2−), 2.92(t, 2H, α-*CH*−), 2.48(m, 4H, *succ.*-CH_2−), 1.60(m, 2H, −CH_2-CH−), 1.37(m, 2H, −CH_2-CH_2-CH_2−).

cis-Diamminediaquaplatinum(II) (**14**). The *cis*-[Pt-$(NH_3)_2(D_2O)]^{2+}$ was obtained by reacting *cis*-Pt$(NH_3)_2Cl_2$ with 1.95 equiv of $AgNO_3$ in D_2O as previously described (*10*). ^{195}Pt NMR (D_2O) δ(ppm): −1580 maleimide−PEG-Pt (**15**).

The platination, purification, and characterization of the Pt conjugate were performed by reacting a slight excess of compound 13 with compound 15, as previously described (*10*). RP18 HPLC: Rt = 16.3 min

^{1}H NMR (D_2O) δ(ppm): 6.88(s, 2H, −*CH*=*CH*−), 3.6-(bs, ∼280H, −PEG_{3000}−), 3.36(t, 4H, PEG-CH_2-NH−), 3.14(t, 2H, −NH-CH_2−), 3.08(t, 2H, α-*CH*−), 2.48(m, 4H, *succ.*-CH_2−), 2.21(m, 2H, −CH_2-CH−), 1.49 (m, 2H, −CH_2-CH_2-CH_2−). ^{195}Pt NMR (D_2O) δ(ppm): −1703.

*NLS−PEG−Pt (**16**).* Compound **15** was coupled to the commercially prepared NLS peptide (including the terminal Cys) using the procedure described for the preparation of compound **8**. The reaction was monitored by RP-HPLC Rt(product) = 14.8 min and Rt(reactant) = 16.3 min. The reaction was over in 45 min, and the product was purified by semipreparative HPLC with a yield of 50%.

RP18 HPLC: Rt = 14.8 min.

^{195}Pt NMR (D_2O) δ(ppm): −1701.

FITC−PEG−Pt(17/18). Compounds **18** and **19** were prepared using the methodologies described above.

^{195}Pt NMR (D_2O) δ(ppm): −1689(31), −1692(32).

*FITC−Pt (**19**).* Di-*tert*-butyl 2-(3-Aminopropyl)malonate was prepared as described (*10*). A 100 mg (0.37 mmol) sample of this compound was dissolved in 30 mL of pyridine and 100 mg (0.26 mmol) of FITC, and 50 μL of TEA was added with stirring. The reaction was left overnight, and subsequently the solvent was removed under reduced pressure. The residue was taken up by 50 mL of CH_2Cl_2, and the excess amine was removed by washing with two portions of 50 mL solutions of 10% acetic acid. After evaporation an orange solid is obtained. Yield 80%. Mass Spectrum, (LC ESIMS): single peak at 553.2 (calculated 552.7). The deprotection of the malonate and platination was performed as described above, and the product precipitated as an orange solid and was filtered and washed with ethanol and ether. Yield 90%. ^{195}Pt NMR (D_2O) δ(ppm): −1708 ppm.

NMR Spectroscopy. NMR data were collected on a Varian Unity Inova 500 MHz spectrometer equipped with a 5 mm switchable probe for ^{1}H, ^{13}C, ^{195}Pt NMR, and 500 MHz ^{1}H{^{13}C/X} 5 mm PFG tunable triple inverse detection probe for 2D-[^{1}H,^{15}N] HSQC.

^{195}Pt NMR. The platinum chemical shifts were measured relative to the external reference signal of K_2PtCl_4, set at −1624 ppm. A line-broadening (lb) of 300 Hz was normally applied, and data were processed using the VNMR software.

Inductively Coupled Plasma Mass Spectrometry (Icp-Ms). Icp-Ms measurements were performed on a Elan-DRC II, Perkin-Elmer Sciex spectrometer. The platinum concentration was calculated according to a known concentration of a K_2PtCl_4 standard solution (10 ng/mL Pt).

Cell Culture and Biological Studies. Medium. Cells were cultured in FA-free RPMI medium (RPMI-1640, Biological Industries, Beyt Haemek, Israel), with 10% fetal bovine serum (GIBCO, Grand Island, NY), 2 mM glutamine, 50 units/mL penicillin, and 50 μg/mL streptomycin. The concentration of FA in serum-containing FA-free medium is only 3 nM, as opposed to 2.26 μM (1 mg/L) under normal culture conditions. Cells were routinely passaged by treatment with a trypsin (0.05%)/EDTA (0.02%) solution in calcium- and magnesium-free phosphate-buffered saline (PBS).

Cell Lines. M109 is a murine lung carcinoma line of BALB/c mice (*19*). By culturing these cells in FA-free medium for several passages, we obtained a subline expressing a high amount of FA receptors, named M109 HiFR or M109FR, to emphasize the overexpression of folic acid receptors (*20*).

Fluorescent Microscopy Studies. Cells were grown on eight-well glass slides (Nunk). Forty-eight hours prior to the experiment, 0.2×10^5 cells were seeded per each well of the slide. The cells were washed with FA, serum-free RPMI medium and incubated for 4 h at 37 °C with 0.2 mL of a 0.5 μM solution of fluorescein-labeled PEG's in FA, serum-free RPMI medium. Free folate competition experiments were conducted under the same conditions, except that incubation solutions contained, in addition to fluorescein-labeled PEG, free folic acid at a concentration of 1 mM. After incubation, cells were washed three times with 0.5 mL of RPMI medium and fixed with 3% formaldehyde in PBS. The fluorescent images were obtained with an LSM410 invert Laser Scan Confocal Microscope, at the wavelength $\ddot{I}$) 488 nm.

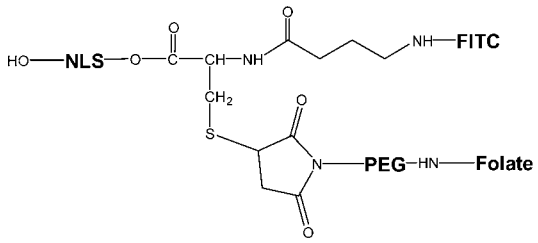
Cell Growth Inhibition Studies. The cytotoxic effect of free carboplatin and two PEG−Pt conjugates (FA−PEG−Pt and PEG−Pt) was assayed colorimetrically by the MB staining method described previously (*10*). In our assays, M109HiFR cells in 200 μL aliquots were plated onto 96-well flat-bottom microtiter plates. Following 20 h in culture, 20 μL of the tested drug was added to each well. For each 10-fold increase in drug concentration, five drug concentration points were tested. Each test was performed in triplicate wells and in two parallel plates. The cells were treated continuously for 72 h. The drug concentration which caused a 50% inhibition of the control growth rate (IC_{50}) was calculated by interpolation of the two closest values of the growth inhibition curve.

Cell Lines and Culture Conditions for the Cytotoxicity Measurement with the Human Ovarian Cancer Cell Lines. Cultures of pairs of cisplatin sensitive and resistant ovarian cancer cell lines (A2780/A2780cisR, 41M/41McisR, and CH1/CH1cisR) have been described elsewhere (*21*). These pairs of cell lines were selected on the basis of encompassing all of the known major mechanisms of resistance to cisplatin: 41McisR being resistant primarily through reduced drug transport (*22*), CH1cisR through enhanced DNA repair/tolerance (*23*), and A2780cisR through a combination of decreased uptake, enhanced DNA repair/tolerance, and elevated GSH levels (*24*).

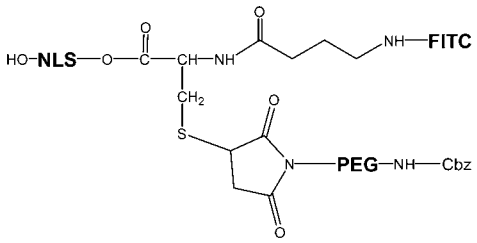
Cell survival in compound-treated cultures was evaluated by the MTT method as previously reported (*25*). Platinum compounds were added to 96 microwell plates containing the cell cultures at final concentrations between 0 and 200 μM. After 24 h, cell survival was evaluated by measuring the absorbance at 520 nm, using a Whittaker microplate reader 2001. IC_{50} values (compound concentration that produces 50% of cell killing) were calculated from curves constructed by plotting cell survival (%) versus compound concentration (μM). Experiments were carried out in quadruplicate.

Pt Accumulation Studies with Continuous Incubation. The cellular accumulation of the Pt compounds was assayed through measurement of the level of cell-associated Pt. Forty-eight hours prior to an assay, 2×10^6 cells were seeded per 60 mm dish, to obtain 5×10^6 cells/plate. At the day of the assay, plates were washed twice with RPMI medium and incubated for 4 h at 37 °C with 2 mL of FA-free RPMI medium, containing three different concentrations (100, 200, and 500 μM) of the platinum compound. Then the incubation solution was removed, and cells were washed with 2 mL of RPMI medium, released from plates with trypsin/EDTA treatment, washed three times with PBS, counted, and dried under reduced pressure. Cell-associated platinum was extracted with 0.1 mL of concentrated nitric acid for 15 min at 90 °C. Subsequently, solutions were diluted with water, and the Pt concentration was established using Icp-Ms.

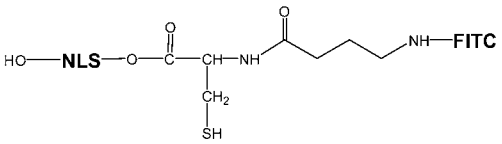
Pt Binding to Cellular DNA. Cells were centrifuged, and the DNA was extracted by the salting out procedure (*26*). Cells were re-suspended in 10 mL of Nuclear Lysis buffer (10 mM Tris at pH 8.2, 400 mM NaCl, 2 mM EDTA). The cell lysates were digested for 4 h at 37 °C with 0.5 mL of 10% SDS and 0.1 mL of protease K solution (Sigma, 20 μg/mL water solution). Then, 5.5 mL of a saturated NaCl solution was added to the lysates, and the mixture was shaken vigorously followed by centrifugation at 10 000 rpm for 15 min. The supernatant containing the DNA was transferred to another tube,



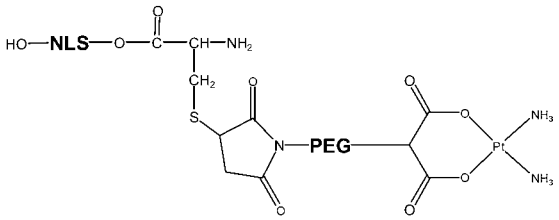
NLS-FITC-PEG-FA



NLS-FITC-PEG



NLS-FITC



NLS-PEG-Pt

Figure 2. The NLS conjugates that were prepared for this study.

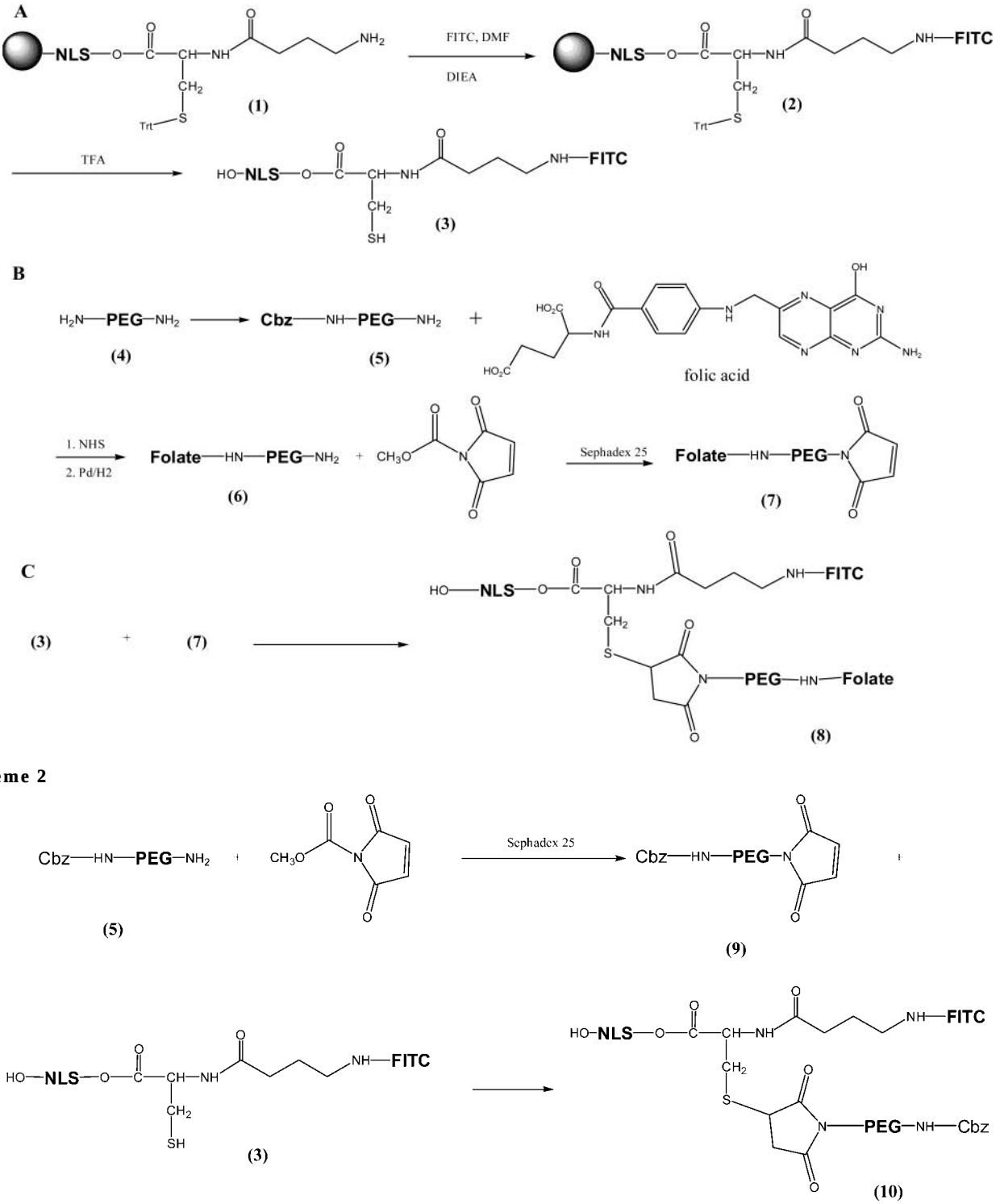
containing 20 mL of absolute ethanol and mixed gently. DNA strands were removed, washed three times in water/ethanol mixture (1:1), and dissolved in 2 mL of distilled water. DNA concentration was established according to absorbance at 260 nm, and the samples were diluted with TE buffer (10 mM Tris pH 8, 1 mM EDTA) buffer. DNA purity was determined by calculating the ratio of absorbance at 260 nm to absorbance at 280 nm. All samples showed the *A*260/*A*280 ratio of 1.7−1.9, which indicates that we obtained DNA with a high degree of purity. The platinum content in the DNA solutions was determined by Icp-Ms measurements.

RESULTS

Synthesis. The conjugates that were prepared for this study, NLS−FITC−PEG−FA, NLS−FITC−PEG, NLS−FITC, and NLS−PEG−Pt, are depicted in Figure 2. Since the NLS is the terminal moiety of all of these conjugates and since the NLS is prepared on a solid phase support, it seems like the synthesis of a NLS−PEG conjugates would best be performed by conjugating the PEG moiety to the peptide while the latter is still bound to the solid phase column. This would result in a single product that could be easily purified by size exclusion chromatography. All attempts to couple the PEG moiety to the peptide while still bound to the solid-phase resin were unsuccessful. Therefore another strategy for the synthesis of NLS−FITC−PEG−FA conjugate was devised and is shown in Scheme 1. The approach taken was to initially prepare the fluorophorated peptide (**3**), then the functionalized PEG (**7**), and in the final step to conjugate them to each other in solution to obtain the desired product (**8**). Often, conjugation of peptides is accomplished by coupling the primary amine of the peptide to a carboxylate group of the cargo thereby forming a stable amide linkage. There are two main reasons for not using the primary amine groups of the NLS peptide for coupling the peptide to the PEG: (a) since there are several primary amines on the peptide (four lysines and one terminal amine), from a chemical point of view, it will be impossible to obtain selectivity in coupling the peptide to a PEG-carboxylate and obtain only one product; (b) from a biological point of view, the lysines and arginines of the NLS are essential for attaining nuclear localization and should not be tampered with. Thus, a unique functional group that can be used for coupling to the PEG must be appended to the peptide. Thiols are known to react rapidly and selectively with maleimide groups, even in the presence of primary amine, and so we decided to add a thiol to the peptide and a maleimide to the PEG conjugate to allow selective and efficient coupling. The details of the synthetic approach are depicted in Scheme 1A. A cysteine was appended to the NLS sequence to provide a specific coupling moiety (**1**). A spacer of γ-aminobutyric acid (GABA) was added to the cysteine, and the fluorophore (FITC) was selectively coupled to the primary amine of the GABA on the solid-phase resin (while all the other amines were still protected). After deprotection and purification by RP-HPLC the peptide (**3**) was obtained and was characterized by electrospray ionization mass spectrometry and NMR spectroscopy. Thiols can be air oxidized to disulfides that are unreactive toward maleimide. High-performance liquid chromatography was used to check for the formation of intermolecular disulfide bond. Very little oxidation was observed but to be on the safe side, DTT was added to the peptide prior to coupling of the thiol to the maleimide.

The second component of the final conjugate (see Scheme 1B) was a PEG_{3000} to which a maleimide group was appended on one end. The synthetic approach was to initially prepare the monoprotected Cbz−HN-PEG-NH_2 (**5**) as the universal starting material for all subsequent syntheses of the PEG conjugates. The unprotected free primary amine was coupled to the desired carboxylate, and subsequently, the Cbz protecting group was removed by hydrogenation and the primary amine at the other side of the PEG could be coupled to another carboxylate group, yielding a nonsymmetric bifunctionally modified PEG. In this specific case, the folic acid was activated by NHS as previously described (*10*), followed by the removal of the protecting group to yield H_2N−PEG−FA (**6**). Since the hydrodynamic properties of the PEG dominate the chromatographic behavior of the conjugates, it is difficult, if not impossible, to separate

Scheme 1



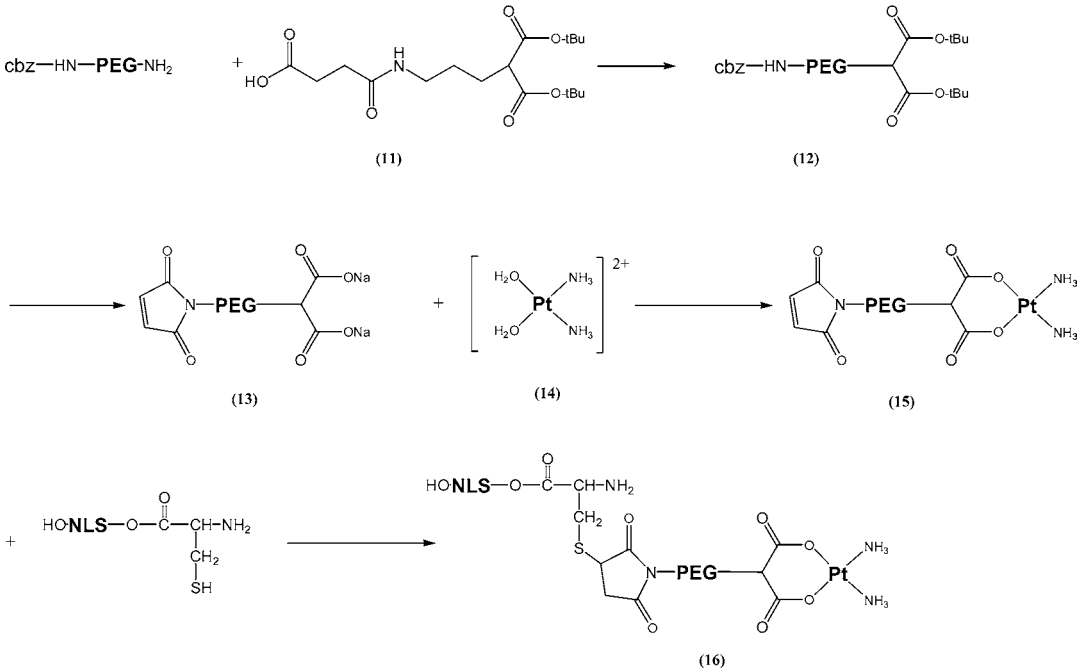
Scheme 2

the PEG conjugates from the unmodified PEGs. Therefore, a large excess of the low molecular weight moieties was used in all the conjugation reactions, to try and force the reaction to completion and to simplify the purifications.

The preparation of a PEG having a terminal maleimide is depicted in Scheme 1B. The amino terminus of the FA−PEG-NH_2 was converted to the maleimide using the *N*-methoxycarbonylmaleimide reagent, followed by purification by gel-permeation chromatography (GPC), and was characterized by ^{1}H NMR spectroscopy. The double bond of the maleimide reacts specifically and rapidly with thiols yielding stable thioether bonds (Scheme 1C). The reaction between the PEG−maleimide and the NLS−Cys−GABA−FITC was monitored by RP-HPLC and after 45 min the reaction was complete. The product, FA−FITC−PEG−FA (**8**), was purified by HPLC and characterized by mass spectrometry.

The synthesis of NLS−PEG−FITC (**10**) is depicted in Scheme 2. Initially the Cbz−PEG-NH_2 (**5**) was synthesized, and subsequently the NH_2 was converted to the maleimide with N-methoxycarbonylmaleimide (**9**). An excess of the flourophorated peptide (**3**) was reacted with the FA-PEG-maleimide, and the conjugate was purified by HPLC.

Scheme 3



The synthesis of the NLS−PEG−Pt is depicted in Scheme 3. Di-*tert*-butyl 2-(3-succininylaminopropyl)malonate (**11**) and **1**−Cbz,*ω*-aminopolyoxyethylene3000, Cbz−PEG-NH_2 (**5**), were prepared as previously described (*10*). and then were coupled using EDCI to yield compound (**12**). The Cbz was removed by hydrogenation, and the resulting primary amine was converted to a maleimide group as described to yield compound (**13**). The NLS with the appended cysteine (without the GABA and FITC) was prepared and purified as described. There are two synthetic pathways that could be taken at this point: to first couple the peptide to the PEG-di-tBu-malonate (**13a**), remove the *tert*-butyl protecting group with acid, and neutralize the resulting diacid (**13b**), converting the maloante into the disodium salt (**13c**); and finally to platinate the ligand (conjugate). The second option is to first deprotect the malonate and convert it to the disodium salt (**13c**), then platinate and purify the platinum complex and finally to conjugate the NLS−PEG to the Pt−malonate. More often than not, the approach taken by the bioinorganic chemists and by the inorganic medicinal chemists is to initially complete the ligand synthesis and leave the platination for the last step. In this instance we chose the opposit approach, as depicted in Scheme 3. The rationale behind this choice stems from the fact that the reactive *cis*-$[Pt(NH_3)_2(H_2O)]^{2+}$ (**14**) could react with the thioether that connects the PEG-maleimide with the NLS−Cys and even possibly with the lysines and arginines of the peptide.

On the other hand, the diamminemalonate coordination sphere of the platinum(II) renders the Pt(II) quite inert, and the reaction of the cysteine thiol with the maleimide is expected to be faster and more selective than its reaction with the inert Pt moiety. There are reports in the literature showing that carboplatin can react with the thioether of methionine (*27*), raising question as to the potential stability of the conjugate. We have checked the stability of the conjugate by HPLC and by preparing the ^{15}N labeled Pt complex and measuring the two-dimensional NMR [^1H,^{15}N] HSQC spectrum. The cross-peak of the diamminemalonate at −78.8/4.15 was stable for weeks in solution, and no cross-peak was observed in the ^{15}N chemical shift range around −40 ppm, which is typical for the thioether binding. The observed stability is probably due to the polymeric moiety (PEG) that separates the Pt from the sterically hindered thioether and prevents facile intramolecular reactions. At pharmacological concentrations there is probably no need to worry about intermolecular interactions between two conjugates.

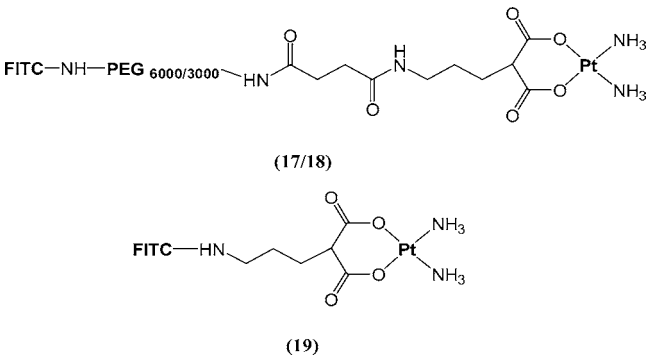


Figure 3. Pt−PEG conjugates that were prepared for this study.

To test how the Pt moiety and the properties of the PEG affect cellular uptake, three more fluorophorated platinum complexes (FITC−PEG_{6000}−Pt, FITC−PEG_{3000}−Pt, and FTIC−Pt) (**17**, **18** and **19**, respectively) were prepared as controls for the cell uptake and cytotoxicity studies of the conjugates. The molecules are depicted in Figure 3, and their synthesis was accomplished using the chemistry described above.

Cell Accumulation and Intracellular Distribution. We initially designed and prepared the FITC−PEG-NLS−FA conjugate in order to obtain: selectivity toward cancer cells, in which the FA receptors are overexpressed, uptake by FRME, and accumulation in the nucleus with the aid of the NLS. A 25 μM solution of compound (**8**) was incubated with M109FR cells for 2 h, and the results of the confocal microscopy are depicted in Figure 4A, clearly demonstrating that the conjugates have accumulated in the cell nucleus. Since this conjugate has two moieties (the NLS and the FA) capable of transferring the conjugate across the cell membrane, further

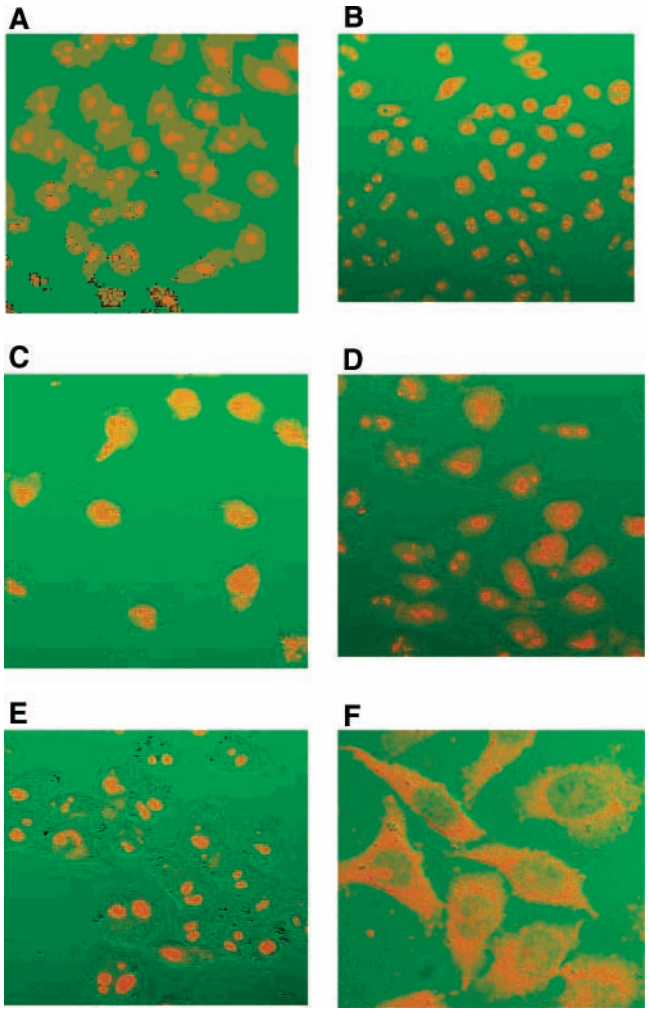


Figure 4. Confocal microscopy pictures showing the cellular localization of (a) NLS−FITC−PEG−FA with M109FR cells, (b) NLS−FITC−PEG with M109FR cells, (c) NLS−FITC with M109FR cells,(d) NLS−FITC−PEG−FA with M109FR cells in the presence of an excess of FA, (e) NLS−FITC−PEG−FA with wild-type M109 cells, and (f) FITC−PEG−FA with M109FR cells.

experiments were performed to establish the mechanism of cellular internalization. The FITC−PEG−NLS conjugate (**10**) was prepared and incubated with the M109FR cells, and again, nuclear localization was observed (Figure 4B), demonstrating that the peptide itself can translocate the conjugate across the cell membrane. Just to verify that it is indeed the NLS, and not the PEG, which is responsible for the cell internalization, the NLS was conjugated directly to the FITC (without the PEG), and again, nuclear localization was obtained (Figure 4C). To establish whether the NLS or the FA are the dominant factors in the cell internalization of compound (**8**) that contains both moieties, we studied the cell accumulation of this compound in the M109FR cell line when in competition with free FA. In the competition experiment with a large excess of free FA, the cellular accumulation was not affected (Figure 4D), indicating that the conjugate does not enter the cell via the FRME. In addition, we also studied the cellular accumulation in the native M109 cell line that is not enriched with FA receptors in order to factor out the contribution of the folic acid. The accumulation profile in M109 cells (Figure 4E) is practically identical to that observed in M109FR cells, reinforcing the results of the previous experiments. Incubation of the conjugate without the NLS (FITC−PEG−FA) with

Table 1. Pharmacological Data on the NLS−PEG−Pt Conjugate[a]

	IC_{50} μM	uptake ng Pt/10^6 cells	DNA-adducts ng Pt/mg DNA
carboplatin	33.15 ± 0.5	6.7 ± 1.2	10.75 ± 2.5
NLS−PEG−Pt	83.5 ± 2.1	19 ± 1.7	5.9 ± 1.8

[a] Based on experiments with M109 cell line.

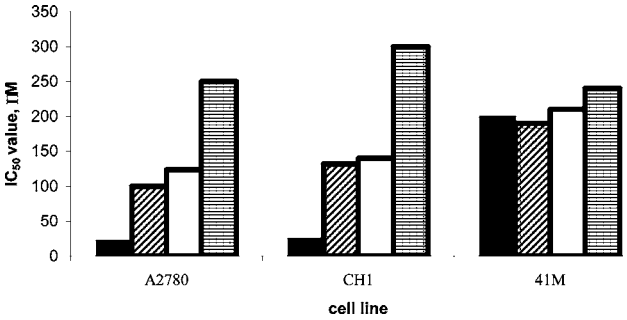


Figure 5. Cytotoxicity data for the interactions of carboplatin and compounds 17−19 (left to right) with human ovarian cancer cell lines. Each result is an average of three measurements with an average standard deviation of ±3.

the M109FR cells results in cytosolic accumulation of the conjugate (Figure 4f). Thus, both the experiments show clearly that the conjugate does not enter the cells via the FRME suggesting that it is the NLS that is responsible for both cellular accumulation and nuclear localization. Therefore, in the presence of NLS, the FA moiety does not contribute to selectivity via FR and pathway of uptake via FRME of the conjugates. NLS appears to be the prevailing moiety responsible for cell uptake of the conjugate.

We also studied the cellular accumulation of Pt−PEG complexes with an FITC reporter group. Toward this end the molecules (**17**−**19**) in Figure 3 were prepared and purified, and their cellular accumulation was studied by confocal microscopy, FACS and ICPMS. The results indicate that the PEGless Pt−FITC conjugate (**19**) is accumulated within the M109 cells approximately twice as much as the Pt−$PEG_{6000/3000}$−FITC conjugates (the FACS intensities were 71, 71, and 126 for compounds **17**, **18**, and **19**, respectively). This indicates that PEGylation of the conjugate retards cell uptake. However, PEGylation may also retard efflux of the conjugate from the cell and enable more effective activation of carboplatin in the cytosol, as shown previously (*10*).

Cytotoxicity and Intracellular DNA Adduct Levels. The pharmacological data for the studies performed in wild-type M109 cancer cells are listed in Table 1. Contrary to our expectation, the NLS−PEG−Pt conjugate was less cytotoxic than the Pt−PEG conjugate and produced less DNA−Pt adducts, despite the higher cellular accumulation and nuclear localization of the NLS conjugates observed by confocal microscopy. This indicates that NLS delivers carboplatin to the nucleus in a nonbioavailable form.

The cytotoxicity of FITC−PEG_{3000}−Pt, FITC−PEG_{6000}−Pt, and FTIC−Pt was measured in three human ovarian cell lines (A2780, CH1, and 41M), and the results are depicted in Figure 5. It is interesting to note that although FITC−Pt is accumulated within the cells twice as efficiently as the FITC−PEG−Pt conjugates, it is significantly less cytotoxic than the FITC−PEG−Pt conjugates. Also, it seems that the length of the PEG (3000 vs 6000) does not affect the cellular accumulation nor does it have an effect on the cytotoxicity.

DISCUSSION

A commonly accepted notion is that rapid nuclear localization should result in a higher level of formation of platinum−DNA adducts and hence superior cytotoxicity. Thus, over the years many attempts have been made to conjugate platinum complexes to DNA binding moieties such as intercalators (*28*−*32*) in order to increase the DNA binding affinity and specificity. The tethering of DNA binding agents to platinum complexes via stable covalent bonds yields in fact novel complexes that are bound to have properties that are quite different from those of the active moieties and thus they cannot be considered true delivery systems or prodrugs for the established drugs. One of the major concerns during the design of these systems is to ensure that the cytotoxic moiety, *cis*-$[Pt(NH_3)_2]^{2+}$ in this case, separates from the carrier at the right time and location. This rationale dictated for our choice of a carboplatin analogue since the release of the *cis*-$[Pt(NH_3)_2]^{2+}$ is expected to occur in a fashion similar to what happens with carboplatin itself. Yet, not only was the cytotoxicity of the NLS−PEG−Pt conjugate inferior to that of PEG−Pt but also the latter attained higher platination levels with cellular DNA despite its inferior cellular accumulation and intracellular localization. Clearly, the cytotoxic *cis*-$[Pt(NH_3)_2]^{2+}$ moiety is not efficiently released from the carrier in the nuclear environment.

The activation of carboplatin has been subject to a certain amount of debate since direct reaction of carboplatin with double stranded DNA results in very low levels of DNA platination (*33*). Fichtinger-Schepman observed that exposure of carboplatin to Chinese hamster ovary cells and subsequent reaction with Salmon sperm DNA resulted in much higher DNA platination levels when compared with platination levels of cell-free Salmon sperm DNA by carboplatin. In fact the platination was 10 times more efficient (*34*). This may indicate that carboplatin requires some intracellular activation by yet unknown mechanisms is order to be able to more efficiently platinate DNA. Sadler has shown that carboplatin can be chemically activated by thiols that react with the platinum complex, forcing the ring opening of the chelating malonate and rendering the Pt moiety more reactive (*35*). Sadler's work was performed in vitro and describes one possible mechanism for the activation of carboplatin though other intracellular activation processes may be involved.

When the platinum medicinal chemists design novel platinum anticancer agents, they normally tend to think of the cytosol of the cancer cell, with its wealth of platinophiles, as an obstacle that the platinum drug has to be overcome en route to the nuclear DNA. Yet it may be worthwhile to make a distinction between the more reactive diaminedichloroplatinum(II) complexes such as cisplatin, *trans*-platinum complexes with iminoether, aliphatic amines, planar amines, and nonplanar cyclic amine ligand and the inert compounds such as carboplatin, oxaliplatin, and nedaplatin, for which intracellular activation may be necessary for their activity. The results of this study suggest that the activation process, whatever it may be, probably takes place in the cytosol rather than in the nucleus. Thus, NLS based delivery is probably not suitable for carboplatin, oxaliplatin, and nedaplatin or any other platinum complex that requires cytosolic activation. We are in the process of testing the NLS−PEG conjugates as delivery systems for other anticancer drugs that bind to nuclear DNA.

The PEG itself, at the lengths tested, impedes the cellular uptake of the platinum complexes yet it enhances the cytotoxicity of the conjugates relative to those without the PEG. This may be due to the fact that while carboplatin or FITC−Pt are taken into the cell efficiently they might also be effluxed more easily than the PEGylated analogues (*10*), and since carboplatin analogues probably require relative long cytosolic residence times for activation, the PEG conjugates may just provide this necessary time frame for activation. It is noteworthy that the FITC−Pt conjugate is significantly less cytotoxic than carboplatin, indicating that the intracellular interactions of the two compounds are not identical. Since attempts to study the intracellular distribution of platinum compounds often entail functionalizing them with fluorophores that significantly alter the properties of the drug, the results reported here indicate that great care must be taken in the interpretation of such experiments.

ACKNOWLEDGMENT

This work was supported partially by the European Cooperation in the Field of Scientic and Technical Research Network (COSTD20/003/00 Action: "Biochemistry, Structural and Cellular Biology of Non-Classical Antitumor Platinum Compouds" (J.M.P. and D.G.). The work done at Dr. Gabizon's laboratory was supported in part by a grant from the Israel Cancer Association. A specific and institutional grant from Fundación Ramón Areces is also acknowledged (J.M.P.). D.G. acknowledges the support from "The Grass Center for Drug Design and Synthesis of Novel Therapeutics".

LITERATURE CITED

(1) Lokich, J. (2001) What is the "best" platinum: cisplatin, carboplatin, or oxaliplatin? *Cancer Invest. 19*, 756−760.

(2) Lokich, J., and Anderson, N. (1998) Carboplatin versus cisplatin in solid tumors: an analysis of the literature. *Ann. Oncol. 9*, 13−21.

(3) Cohen, S. M., and Lippard, S. J. (2001) Cisplatin: from DNA damage to cancer chemotherapy. *Prog. Nucleic Acid Res. Mol. Biol. 67*, 93−130.

(4) Brabec, V. (2002) DNA modifications by antitumor platinum and ruthenium compounds: their recognition and repair. *Prog. Nucleic Acid Res. Mo.l Biol. 71*, 1−68.

(5) Fuertes, M. A., Alonso, C., and Perez, J. M. (2003) Biochemical modulation of Cisplatin mechanisms of action: enhancement of antitumor activity and circumvention of drug resistance. *Chem. Rev. 103*, 645−662.

(6) Perez, R. P. (1998) Cellular and molecular determinants of cisplatin resistance. *Eur. J. Cancer 34*, 1535−1542.

(7) Kelland, L. R. (1994) The molecular basis of cisplatin sensitivity/resistance. *Eur. J. Cancer 30A*, 725−727. (*1*)

(8) Widder, K. J., Senyei, A. E., and Ranney, D. F. (1979) Magnetically responsive microspheres and other carriers for the biophysical targeting of antitumor agents. *Adv. Pharmacol. Chemother. 16*, 213−271.

(9) Langer, R. (1998) Drug delivery and targeting. *Nature 392*, 5−10.

(10) Aronov, O., Horowitz, A. T., Gabizon, A., and Gibson, D. (2003) Folate-targeted PEG as a potential carrier for carboplatin analogues. Synthesis and in vitro studies. *Bioconjugate Chem. 14*, 563−574.

(11) Takakura, Y., and Hashida, M. (1996) Macromolecular carrier systems for targeted drug delivery: pharmacokinetic considerations on biodistribution. *Pharm. Res. 13*, 820−831.

(12) Zalipsky, S. (1995) Chemistry of Polyethylene-Glycol Conjugates with Biologically-Active Molecules. *Adv. Drug Delivery Rev. 16*, 157−182.

(13) Wang, S., and Low, P. S. (1998) Folate-mediated targeting of antineoplastic drugs imaging agents, and nucleic acids to cancer cells. *J. Controlled Release 5*3, 39−48.

(14) Sudimack, J., and Lee, R. J. (2000) Targeted drug delivery via the folate receptor. *Adv. Drug Delivery Rev. 4*1, 147−162.

(15) Castino, R., Demoz, M., and Isidoro, C. (2003) Destination 'lysosome': a target organelle for tumour cell killing? *J. Mol. Recognit. 16*, 337−348.

(16) Green, M., and Loewenstein, P. M. (1988) Autonomous functional domains of chemically synthesized human immunodeficiency virus tat trans-activator protein. *Cell 55*, 1179−1188.

(17) Joliot, A., Pernelle, C., Deagostini-Bazin, H., and Prochiantz, A. (1991) Antennapedia homeobox peptide regulates neural morphogenesis. *Proc. Natl. Acad. Sci. U.S.A. 88*, 1864−1868.

(18) Pipkorn, R., Waldeck, W., and Braun, K. (2003) Synthesis and application of functional peptides as cell nucleus-directed molecules in the treatment of malignant diseases. *J. Mol. Recognit. 16*, 240−247.

(19) Marks, T. A., Woodman, R. J., Geran, R. I., Billups, L. H., and Madison, R. M. (1977) Characterization and responsiveness of the Madison 109 lung carcinoma to various antitumor agents. *Cancer Treat. Rep. 61*, 1459−1470.

(20) Gabizon, A., Horowitz, A. T., Goren, D., Tzemach, D., Mandelbaum-Shavit, F., et al. (1999) Targeting folate receptor with folate linked to extremities of poly(ethylene glycol)-grafted liposomes: in vitro studies. *Bioconjugate Chem. 10*, 289−298.

(21) Kelland, L. R., Abel, G., McKeage, M. J., Jones, M., Goddard, P. M., Valenti, M., Murrer, B. A., and Harrap, K. R. (1993) Preclinical antitumor evaluation of bis-acetato-ammine-dichloro-cyclohexy-lamine platinum(IV): an orally active platinum drug. *Cancer Res. 53*, 2581−2586.

(22) Loh, S. Y., Mistry, P., Kelland, L. R., Abel, G., and Harrap, K. R. (1992) Reduced drug accumulation as a major mechanism of acquired resistance to cisplatin in a human ovarian carcinoma cell line: circumvention studies using novel platinum (II) and (IV) am-mine/amine complexes. *Br. J. Cancer 66*, 1109−1115.

(23) Goddard, P. M., Orr, R. M., Valenti, M. R., Barnard, C. F., Murrer, B. A., Kelland L. R., and Harrap, K. R. (1996) Novel *trans*-platinum complexes: comparative in vitro and in vivo activity against platinum-sensitive and resistant murine tumors. *Anticancer Res. 1*6, 33−38.

(24) Behrens, B. C., Hamilton, T. C., Masuda, H., Grotzinger, K. R., Whang-Peng, J., Louie, K. G., Knutsen, T., McKoy, W. M., Young, R. C., and Ozols, R. F. (1987) Characterization of a *cis*-diamminedichloroplatinum(II)-resistant human ovarian cancer cell line and its use in evaluation of platinum analogues. *Cancer Res. 47*, 414−418.

(25) Alley, M. C., Scudiero, D. A., Monks, A., Hursey, M. L., Czerwinski, M. J., Fine D. L., Abbott, B. J., Mayo, J. G., Shoemaker, R. H., and Boyd, M. R. (1988) Feasibility of drug screening with panels of human tumor cell lines using a microculture tetrazolium assay. *Cancer Res. 48*, 589−601

(26) Miller, S. A., Dykes, D. D., and Polesky, H. F.(1988) A simple salting out procedure for extracting DNA from human nucleated cells. *Nucleic Acids Res. 16*, 1215.

(27) Barnham, K. J., Djuran, M. I., Murdoch, P. S., Ranford, J. D., and Sadler, P. J. (1996) Ring-Opened Adducts of the Anticancer Drug Carboplatin with Sulfur Amino Acids. *Inorg. Chem. 35*, 1065−1072.

(28) Gibson, D., Gean, K. F., Benshoshan, R., Ramu, A., Ringel, I., et al. (1991) Preparation, Characterization, and Anticancer Activity of a Series of Cis-$PtCl_2$ Complexes Linked to Anthraquinone Intercalators. *J. Med. Chem. 34*, 414−420.

(29) Gibson, D., Binyamin, I., Haj, M., Ringel, I., Ramu, A., et al. (1997) Anthraquinone intercalators as carrier molecules for second-generation platinum anticancer drugs. *Eur. J. Med. Chem. 32*, 823−831.

(30) Fisher, D. M., Fenton, R. R., and Aldrich-Wright, J. R. (2003) Platinum(II) intercalators as potential anti-cancer agents. *J. Inorg. Biochem. 96*, 131−131.

(31) Baruah, H., and Bierbach, U. (2003) Unusual intercalation of acridin-9-ylthiourea into the 5′-GA/TC DNA base step from the minor groove: implications for the covalent DNA adduct profile of a novel platinum-intercalator conjugate. *Nucleic Acids Res. 31*, 4138−4146.

(32) Palmer, B. D., Lee, H. H., Johnson, P., Baguley, B. C., Wickham, G., et al. (1990) DNA-directed alkylating agents. 2. Synthesis and biological activity of platinum complexes linked to 9-anilinoacridine. *J. Med. Chem. 33*, 3008−3014.

(33) Natarajan, G., Malathi, R., and Holler, E. (1999) Increased DNA-binding activity of *cis*-1,1-cyclobutanedicarboxylatodiammineplatinum(II) (carboplatin) in the presence of nucleophiles and human breast cancer MCF-7 cell cytoplasmic extracts: activation theory revisited. *Biochem. Pharmacol. 58*, 1625−1629.

(34) Blommaert, F. A., van Dijk-Knijnenburg, H. C., Dijt, F. J., den Engelse, L., Baan, R. A., Berends, F., and Fichtinger-Schepman, A. M. (1995) Formation of DNA adducts by the anticancer drug carboplatin: different nucleotide sequence preferences in vitro and in cells. *Biochemistry 34*, 8474−8480.

(35) Guo, Z. J., Hambley, T. W., Murdoch, P. D., Sadler, P. J., and Frey, U. (1997) Chelate-ring-opened adducts of Pt(en)(Me-Mal-O,O′) (en equals ethane-1,2-diamine, Me-Mal equals 2-methylmalonate) with methionine derivatives: Relevance to the biological activity of platinum anticancer agents. *J. Chem. Soc., Dalton Trans.* 469−478.

BC0499331

Novel Polyamine−Dialkyl Phosphate Conjugates for Gene Carriers. Facile Synthetic Route via an Unprecedented Dialkyl Phosphate

Takehisa Dewa,*[,†,‡] Yukari Ieda,[†] Kazuyuki Morita,[†] Li Wang,[§] Robert C. MacDonald,[§] Kouji Iida,[⊥] Keiji Yamashita,[†] Naoto Oku,[∥] and Mamoru Nango*[,†]

Materials Science and Engineering, Nagoya Institute of Technology, Gokiso-cho, Showa-ku, Nagoya 466-8555 Japan, PRESTO (JST), Department of Biochemistry, Molecular Biology, and Cell Biology, Northwestern University, Evanston, Illinois 60208, Nagoya Municipal Industrial Research Institute, 3-4-41 Rokuban-cho, Atsuta-ku, Nagoya 456-0058 Japan, and Department of Medical Biochemistry and COE Program in the 21st Century, University of Shizuoka School of Pharmaceutical Sciences, 52−1 Yoda, Shizuoka, Japan. Received March 25, 2004; Revised Manuscript Received April 22, 2004

To develop a novel nonviral gene carrier, three types of polyamine−dialky phosphates conjugates were synthesized via an unprecedented synthetic intermediate, dimerized dicetyl phosphate (DCP) anhydride, and the transfection efficiency and the complexation properties of the conjugate−DNA were evaluated. Condensation of DCP by 1,3,5-triisopropylbenzenesulfonyl chloride, TPSCl, gives the dimerized anhydride, which is stable enough to isolate by column chromatography in ∼90% yield. The anhydride is reactive with various amines, i.e., spermidine, spermine, and polyethylenimine (PEI-(1800)), providing corresponding polyamine−DCP conjugates via phosphoramidate linkage. The polyamine−DCP conjugates exhibited moderate transfection efficacy evaluated by β-galactosidase assay. The conjugate−DNA complex was observed by using an atomic force microscope (AFM), revealing that the PEI(1800)−DCP conjugate, which showed the most efficient transfection, enables the formation of the more compact complex with DNA.

INTRODUCTION

Development of more efficient and safer gene-transfer systems is one of the most challenging aspects of gene therapy (*1*). The two major approaches at present for gene transfer are viral and nonviral systems. The latter is safer and easier for mass production despite the higher efficiency of the former. Therefore, nonviral systems, such as cationic liposomes and polycations (*2*−*8*) as well as nonionic carriers (*9*), continue to be developed to improve their efficiency.

The mechanism of gene delivery by such cationic carriers probably involves an endosomal pathway (*10*); however, the details remain to be clarified. In this regard, the polymorphism including lamellar, multilamellar, and hexagonal structures of polycation−DNA complexes have been studied (*11*−*16*). A nucleosome-like structure in which DNA wraps around an aggregate of dioctadeyl-amidoglycylspermine (DOGS)[1] molecules has been reported by Yoshikawa et al. by using fluorescence and electron microscopy (*11*). The nucleosome-like assemblies further associate with each other to form a network, which may play a role in effective transfection. However, the relationship between polycation−DNA assembly and the efficiency of gene transfection is far from well-understood.

We have recently reported that polycation liposomes (PCL) composed of cetylated polyethylenimine (cetyl-PEI) possess high gene transfer activity (*17*−*20*). In the most recent report, we proposed a possible mechanism of PCL-mediated gene transfer wherein PCL−DNA complexes are taken up by endosomal pathway; this was based on tracking of fluorescence-labeled components, PCL lipid, cetyl-PEI, and DNA, as cetyl PEI−DNA complex is released and transferred into the nucleus via the cytosol (*20*). The key step of gene transfer mediated by cationic liposomes is thought to be entry into the nucleus (*21*). Thus, compaction of DNA should be crucial; both electrostatic and hydrophobic interactions in the cetyl PEI−DNA complex are likely to be responsible for its effective compaction.

PEI is used as a gene transfer vector by itself; however, it has inherent disadvantages, i.e., cytotoxicity and polydispersity. In this report, we synthesize a series of polyamine−dicetyl phosphate (DCP) conjugates via reaction of a novel synthetic intermediate, dimerized DCP anhydride, with various polyamines, spermidine, spermine, and PEI (Scheme 1). Since spermidine and spermine are naturally occurring polyamines, we expected low cytotoxicity. These conjugates exhibited moderate gene transfer activity. We also observed the morphology of the conjugate−DNA complex by using atomic force microscopy (AFM). We briefly discuss the relationship between the assembling structure of the conjugate−DNA and their transfection efficiency.

EXPERIMENTAL PROCEDURES

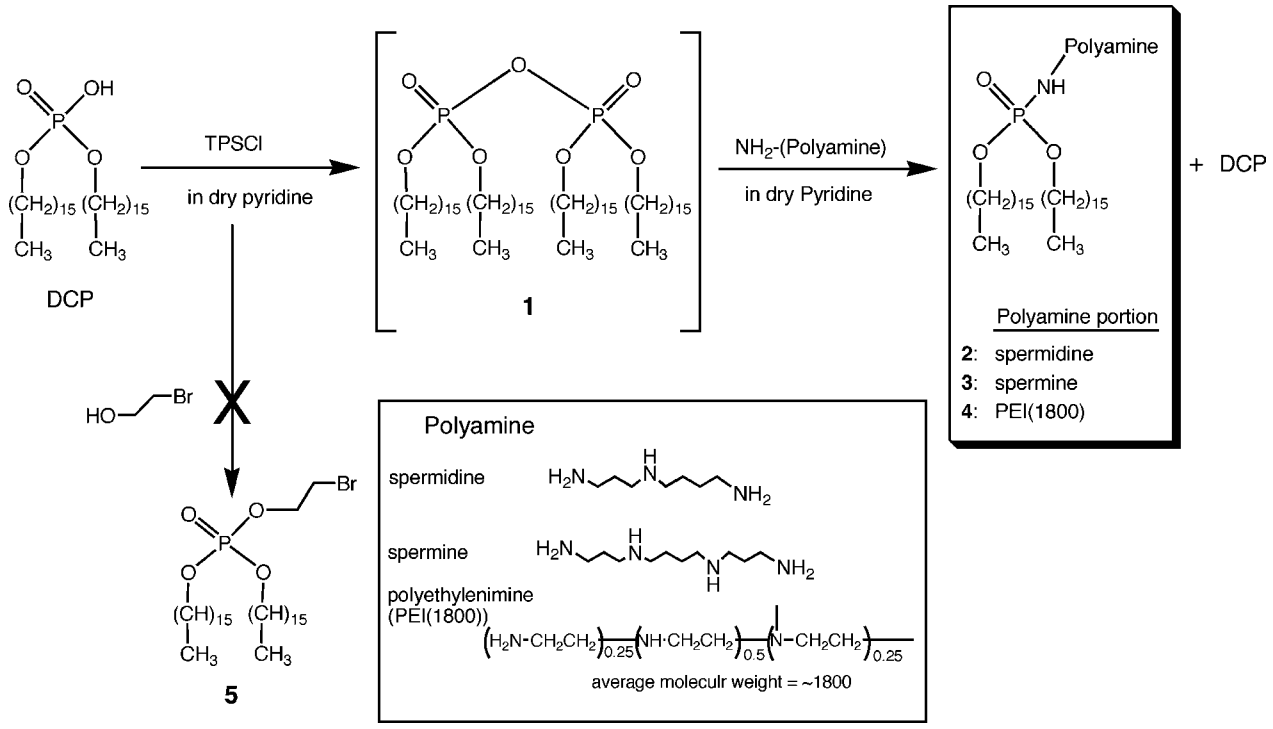
General Methods. Unless stated otherwise, all chemicals and reagents were obtained commercially and used

* To whom correspondence should be addressed. Tel/Fax: +81-52-735-5226. E-mail: nango@nitech.ac.jp.
[†] Nagoya Institute of Technology.
[‡] PRESTO (JST).
[§] Northwestern University.
[⊥] Nagoya Municipal Industrial Research Institute.
[∥] University of Shizuoka School of Pharmaceutical Sciences.

[1] Abbreviations: DOGS, dioctadeylamidoglycylspermine; PCL, polycation liposome; PEI, polyethylenimine; cetyl-PEI, cetylated polyethylenimine; DCP, dicetyl phosphate; AFM, atomic force microscopy; EtBr, ethidium bromide; DLS, dynamic light scatterig; TPSCl, 1,3,5-triisopropylbenzenesulfonyl chloride; FBS, fetal bovine serum.

10.1021/bc049925k CCC: $27.50 © 2004 American Chemical Society
Published on Web 06/05/2004

Scheme 1. Synthetic Strategy for Polyamine−DCP Conjugates via Synthetic Intermediate, 1, DCP Anhydride



without further purification. DCP was purchased from Sigma. PEI(1800) with an average molecular weight of 1800 was kindly provided by Nippon Shokubai Co., Ltd (Osaka, Japan). The PEI(1800) was purified by ultrafiltration with an ultrafilter membrane (YM-1, Amicon Corp., Danvers, MA). NMR spectra were recorded on either a Varian Gemini-2000 (300 MHz) or a Bruker AVANCE600 (600 MHz) instrument. Secondary ion mass spectra were obtained by using HITACHI M-2000S. Infrared spectroscopy was carried out on a PerkinElmer Spectrum 2000 FT-IR spectrometer. Suspensions of polyamine conjugates were prepared in Tris-HCl buffer (15 mM, pH 8.4) by ultrasonication for 3 min. To the suspension was added 5 μg of ColE1 plasmid DNA (6646 bp, Nippon Gene), followed by equilibration for 15 min at room temperature. Displacement of ethidium bromide, EtBr, intercalated into DNA was measured with a fluorescence spectrophotometer FP-777 (JASCO) at EtBr/nucleotide = 50/1 (mol/mol) with varying polyamine contents. EtBr fluorescence at 590 nm (excitation wavelength: 260 nm) was recorded to obtain the relative fluorescence intensity, I/I_0, where I and I_0 are fluorescence intensities in the presence and the absence of polyamine derivatives, respectively. Measurement of dynamic light scattering was carried out on a Nicomp Model 370 particle size analyzer. AFM images of the conjugate−DNA complexes were acquired with a JEOL JSPM-4210 equipped with a cantilever (MikroMasch, type A: 110 μm, 7.5 N/m), using the discrete contact mode (AC mode). A sample was deposited on a dry mica surface by spin coating, followed by drying at ambient pressure. For observation of a negatively charged specimen, e.g., ColE1 plasmid DNA, a mica surface was premodified with polylysine. For DLS and AFM measurements, suspensions of the polyamine conjugates were prepared in distilled and deionized water.

Synthesis of Dimerized Dicetyl Phosphate Anhydride (1). Dicetyl phosphate, DCP (50 mg, 90 μmol), was dissolved in 1 mL of anhydrous pyridine. To this solution was added 1,3,5-triisopropylbenzenesulfonyl chloride (TPSCl, 277 mg, 0.91 mmol) as a powder. After the reaction mixture was stirred for a few hours at room temperature under a nitrogen atmosphere, DCP was converted into DCP anhydride, whose molybdenum blue-active spot appeared at R_f 0.97 (SiO_2, $CHCl_3$/MeOH/H_2O, 13/6/1). The solvent was evaporated, and the crude product was purified by column chromatography (Aldrich silica gel, eluted by $CHCl_3$). After being dried in vacuo, the isolated pure product, **1**, was obtained as a white powder (44.3 mg, 41 μmol, 90% yield). ^{1}H NMR (600 MHz, $CDCl_3$) δ: 0.88 (t, 12H), 1.25 (br s, 96H), 1.37 (m, 8H), 1.70 (m, 8H), 4.0−4.2 (m, 8H); ^{31}P NMR (243 MHz, $CDCl_3$, 10% H_3PO_4 in D_2O as an external standard) δ: −12.27, −0.13; ^{13}C NMR (150 MHz, $CDCl_3$) 14.01, 22.68, 25.36, 25.45, 29.16, 29.36, 29.54, 29.60, 29.66, 29.71, 30.31, 31.92, 67.67, 69.12; FT-IR (KBr) ν (cm^{-1}): 2849, 1471, 1294, 1108, 1021, 952; SIMS for $(C_{64}H_{133}O_7P_2)^+$ calcd 1075.9, found 1075.4.

Synthesis of Dicetyl Phosphate−Spermidine Conjugate (2). To a solution of spermidine (6.74 mg, 46 μmol) in 0.5 mL of dry pyridine was added **1** (10 mg, 9.3 μmol) in 0.1 mL of anhydrous pyridine. The reaction mixture was stirred under nitrogen atmosphere for 5 h at room temperature. Removal of solvent under reduced pressure, followed by column chromatography [1 g of silica gel, eluting with $CHCl_3$/MeOH/Et_3N (10/1/0.1, v/v/v) and then $CHCl_3$/MeOH/Et_3N (1/1/0.02, v/v/v), gave 4.9 mg (78%) of **2** as a white powder. ^{1}H NMR (300 MHz, $CDCl_3$) δ: 0.88 (t, 6H), 1.26 (s, 52H), 1.56 (m, 4H), 1.70 (m, 6H), 2.61−3.12 (bm, 12H), 3.98 (bm, 4H); FT-IR (KBr) ν (cm^{-1}): 3235, 2917, 2850, 1636, 1467, 1210, 959; SIMS for $(C_{39}H_{85}N_3O_3P)^+$ calcd 674.6, found 674.8.

Synthesis of Spermine−Dicetyl Phosphate Conjugate (3). To a solution of spermine (10 mg, 49 μmol) in 0.5 mL of dry pyridine was added **1** (10 mg, 9.3 μmol) in 0.1 mL of anhydrous pyridine. The reaction mixture was stirred under a nitrogen atmosphere for 5 h at room temperature. Removal of solvent under reduced pressure was followed by column chromatography [1 g of silica gel, eluting with $CHCl_3$/MeOH/Et_3N (10/1/0.1, v/v/v)] to re-

move free DCP component. The product absorbed on the silica gel was eluted by washing with $CHCl_3$/MeOH/Et_3N (1/1/0.02, v/v/v), giving 4.5 mg (66%) of **3** as a white powder. ^{1}H NMR (300 MHz, $CDCl_3$) δ: 0.88 (t, 6H), 1.26 (s, 52H), 1.42 (bm, 8H), 1.55 (bm, 4H), 2.15 (br, 5H), 3.17 (bm, 8H), 3.63 (bm, 4H), 3.97 (m, 4H). ^{31}P NMR (243 MHz, $CDCl_3$, 10% H_3PO_4 in D_2O as external standard) δ: 9.76. FT-IR (KBr) ν (cm^{-1}): 3426, 3235, 2917, 2850, 1637, 1466, 1212, 1012; SIMS for $(C_{42}H_{92}N_4O_3P)^+$ calcd 731.7, found 731.5.

Synthesis of PEI(1800)−Dicetyl Phosphate Conjugate (4). To a solution of PEI(1800) (16.7 mg, 9.3 μmol) in 0.5 mL of dry pyridine was added **1** (10 mg, 9.3 μmol) in 0.1 mL of anhydrous pyridine. The reaction mixture was stirred under a nitrogen atmosphere for 5 h at room temperature. Removal of solvent under reduced pressure was followed by column chromatography [1 g of silica gel, eluting with $CHCl_3$/MeOH/Et_3N (10/1/0.1, v/v/v)] to remove free DCP component. The product absorbed on the silica gel was extracted by washing out with $CHCl_3$/MeOH/Et_3N (1/1/0.02, v/v/v), giving 3.5 mg (20.7%) of **4**. ^{1}H NMR (300 MHz, $CDCl_3$) δ: 0.88 (t, 6H), 1.1−1.6 (br, 83H), 1.65 (bm, 4H), 2.5−3.1 (bm, 125H), 4.1 (m, 4H); FT-IR (KBr) ν (cm^{-1}): 3253, 2915, 2846, 1637, 1466, 1214, 1033.

Cell Culture. Primary vascular smooth muscle cells were obtained by removal of the thoracoabdominal aortas of Wistar rats, which were then stripped of endothelium and adventitia (*22*). Medial VSMCs were maintained in Dulbecco's Modified Eagle's Medium (DMEM), 20% fetal bovine serum (FBS), 200 units/mL penicillin, 200 μg/mL streptomycin (all Gibco, Gaithersburg, MD) at 37 °C with 5% CO_2. At confluence, the cells were passaged using 0.25 mg/mL trypsin/EDTA (Clonetics, Walkersville, MD).

Transfection Procedure. The cells were seeded in 96-well plates at 24 h before transfection at densities to give about 80% confluence at the time of transfection. β-Galactosidase plasmid DNA (purchased from Clontech Labtories Inc. (Palo Alto, CA) and propagated and purified by Bayou Biolabs (Harahan, LA)) was diluted in serum-free cell culture medium to 20 μg/mL. The transfection reagents were suspended in D-PBS at 1 mg/mL, diluted in the same volume of serum-free cell culture medium as that of DNA (the dilution factor was varied as appropriate to give the desired ratio of the transfection reagent to DNA), and then pipetted into plasmid DNA. The resultant complexes were incubated at room temperature for 15 min and then added to the cells that were either in medium lacking serum or medium containing 20% fetal bovine serum (FBS). At 3 h after addition of complexes, the cells were washed with PBS and fresh medium containing 20% FBS was added.

Cells were assayed for β-galactosidase activity 24 h after transfection with a microplate fluorometric assay (*23*), modified by inclusion of a heating step (50 °C, 45 min) to inactivate endogenous enzyme activity. Following aspiration of the medium from each well, the cells were washed once with PBS and then lysed by addition of 100 μL of lysis buffer (0.03% Triton X-100 in 100 mM HEPES, pH 7.8, containing 1 mM $MgSO_4$, 10 mM KCl). The plates were placed at 50 °C for 45 min and then allowed to cool to room temperature. Into each well was added 10 μL of fluorescein di-β-D-galactopyranoside, FDG (100 μM). Fluorescence was measured with a microplate fluorimeter (Model 7620, Cambridge Technology Inc.) after incubation at 37 °C overnight. Under these assay conditions, 0.1 milliunit of β-galactosidase corresponded to 16 000 fluorescence units.

RESULTS AND DISCUSSION

Synthetic Strategy for Polyamine−Dialkyl Phosphate Conjugates via a Synthetic Intermediate. Our preliminary idea for the syntheses of polyamine−DCP conjugates was to use the bromoethylated compound, **5**, as a synthetic intermediate via condensation of DCP and 2-bromoethanol (Scheme 1) by using TPSCl (*24*, *25*). Instead of the expected adduct, **5**, however, we obtained another product having a high R_f value, 0.97 (R_f = 0.56 for DCP by eluting $CHCl_3$/MeOH/H_2O = 13/6/1, v/v/v). The resulting product is stable enough to be isolated by column chromatography. SIMS indicates almost double molecular mass, 1075.4 (546.9 for DCP). The observed IR absorption band at 952 cm^{-1} is assignable to the P−O−P stretching mode. The ^{31}P NMR spectrum of the product, whose signals appear at δ = −12.27 and −0.13 ppm, is clearly distinguishable from that of DCP having a signal at δ = 2.15 ppm. This evidence, taken together, leaves no doubt that the product is dimerized DCP in anhydrous form, **1** $[(C_{64}H_{133}O_7P_2)^+$ calcd 1075.9], connected via P−O−P bonding. Hydrolytic decomposition of **1** is negligible for a few days in chloroform or anhydrous pyridine at room temperature. In wet chloroform, however, the decomposition is accelerated, and under acidic and basic conditions, e.g., chloroform containing small amount of diluted HCl, sodium carbonate, ammonia, or triethylamine, the decomposition is further accelerated. There are some prior examples in the synthesis of pyrophosphate derivatives bearing small alkyl moieties, methyl, ethyl, propyl, and butyl (*26*); however, the dimerized anhydride, **1**, bearing phospholipid-like long alkyl chains is an unprecedented compound. This compound is a convenient synthetic intermediate for formimg phosphoramidate bonds, as described below.

The anhydride **1** readily react with amines, e.g., spermidine, spermine, and even polymer, PEI(1800), to form the phosphoramidate, P−N bond, providing the corresponding adducts, **2**, **3**, and **4**, respectively. The reactivity toward these nucleophiles indicates that the anhydrous compound **1** is potentially a good synthetic intermediate for making polyamine−dialkyl phosphate conjugates via the P−N bond. When reacted with spermine, for example, the adduct **3** readily forms, concomitantly with the loss of DCP. The ^{31}P NMR signal of compound **3** is shifted downfield, to 9.76 ppm compared with that of DCP at 2.15 ppm, indicating the formation of the P−N bond in the compound. The downfield-shifted signal is attributed to the lower electronegativity of the nitrogen atom in spermine relative to the oxygen atom in DCP. Although structural ambiguity of the resulting adducts, **2**, **3**, and **4**,[2] cannot be completely eliminated, anhydride **1** is a useful synthetic intermediate because it is (1) stable yet reactive with amino groups, (2) very simple and easy to prepare, and (3) produced in high yield (∼90%). In addition, it should be noted that a potential advantage of the conjugation via P−N bond is that it may cleave in endosomes, because the linkage is very unstable under acidic conditions. Such a cleavable bond would have advantages in terms of disruption of endosomes: the cleaved DCP portion could facilitate release of the polyamine−DNA complex from the endosome. In addition, it should confer biodegradability on the compound.

[2] The asymmetric molecule, spermidine, has two distinguishable primary amines. Product **2**, bearing a spermidine moiety, has two isomers, which, to date, have not been identified spectroscopically. Along the similar lines, content of primary amine of PEI(1800) in the product **4** is 25% in total amino moieties; thus, the structural uncertainty cannot be avoided.

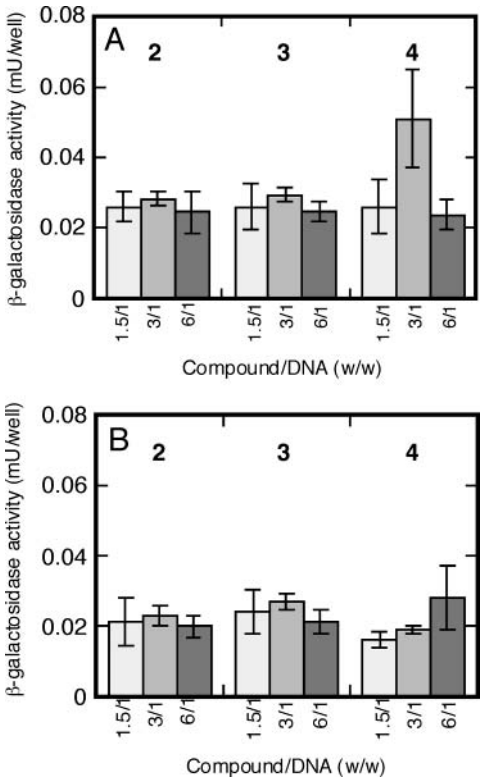


Figure 1. Transfection efficacy of polyamine−DCP conjugates **2**−**4** on VSMC, in the absence (A) and the presence of 20% of FBS (B). The ratios of compound−β-galactosidase plasmid DNA (w/w) were 1.5/1, 3/1, and 6/1, respectively.

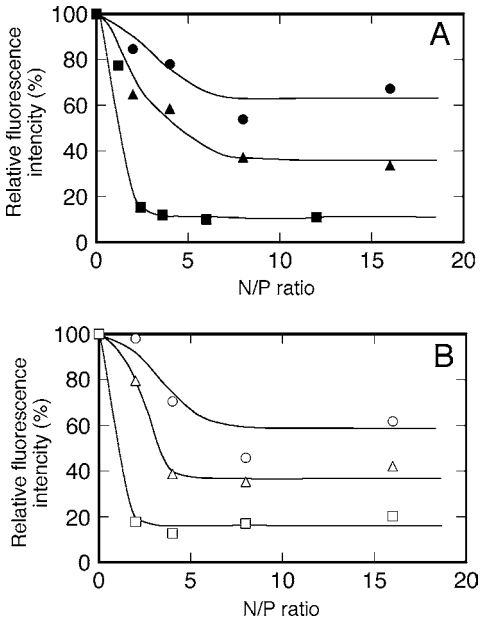


Figure 2. Changes in fluorescence intensity of ethidium bromide intercalated into Col E1 plasmid DNA−polyamine compounds: (A), spermidine (●), spermine (▲), and PEI(1800) (■); (B), spermidine−DCP (○), spermine−DCP (△), and PEI-(1800)−DCP (□).

These compounds could hence provide new category of polycationic lipids.

Transfection Efficacy. The polyamine−DCP conjugates **2**−**4** were subjected to transfection assay using the β-galactosidase expression system. Figure 1A shows the transfection efficiency of **2**, **3**, and **4** evaluated according to β-galactosidase activity (milliunit/well), in the absence of FBS. Compared with the commercially available transfection reagent, *O*-ethyl DOPC (E-DOPC) (*5*), which produced 0.1 milliunit/well transgene expression, compounds **2**−**4** exhibit moderate efficiency, ∼30 to 50% of the efficiency of E-DOPC. The transfection efficiencies of the components themselves, i.e., DCP, spermidine, spermine, and PEI(1800), were almost negligible (data not shown). Thus, the transfection activity results from the conjugation of two moieties: a hydrophilic polyamine and a hydrophobic DCP. Compound **4** shows the highest efficiency at 3/1 (w/w) of **4**−DNA, whereas the efficiency of the other compounds are comparable and insensitive to the compound−DNA ratio within the range of error. In Figure 1B is shown the transfection efficiency in the presence of 20% FBS. The efficiency of these compounds was not influenced by the presence of 20% FBS, retaining 80−100% of the activity (except compound **4** at 3/1 (w/w)). Such serum-resistant activity was also observed for the PCL gene transfection system previously reported (*19*). It is well-known that serum often inhibits transfection; such inhibition is due to binding of negatively charged serum proteins to the cationic transfection reagents resulting in forming aggregates ineffective to the transfection. Although it is not clear why the polyamine−DCP conjugates are not influenced by the presence of the serum, the polyamine part may be assumed to efficiently interact with DNA via electrostatic interactions.

Compound **4** exhibits maximum efficacy at a 3/1 of **4**−DNA ratio in this series (Figure 1A). We examine complexation of the polyamine−DCP conjugates with DNA by intercalation of EtBr, DLS, and AFM as described below.

Complexation with ColE1 Plasmid DNA. It was found that DNA (ColE1 plasmid DNA) complexes with various polyamines (A) and polyamine−DCP conjugates (B) by monitoring the decrease of fluorescence from EtBr initially intercalated into DNA (Figure 2A and 2B). With an increase in the cation (*N*)/anion (*P*) ratio, defined as *N*/*P*, the relative fluorescence intensity decreased as a result of complexation of DNA and polyamine. As shown in Figure 2A, the polymeric molecule, PEI(1800) ($N \sim 42$ per molecule) most efficiently forms a complex with DNA; the complexation was almost complete at $N/P = 3$. Spermidine ($N = 3$ per molecule) and spermine ($N = 4$ per molecule) are less effective than PEI(1800), however, with complexation being complete at around $N/P \sim 7$. For polyamine−DCP conjugates (Figure 2B), the tendency for the fluorescence intensity to decrease is due to the complexation with DNA in the same way as that of the free amines, although influence of the hydrophobic alkyl chain in the complexation is not at all pronounced.

The mean particle diameters of various polyamine−DCP conjugates in an aqueous suspension, as given by dynamic light scattering, is summarized in Table 1: 155 ± 54 nm for **2**, 173 ± 46 nm for **3**, and 128 ± 38 nm for **4**. AFM images for the suspension of these compounds exhibited spherical or ellipsoidal particles, whose sizes, defined according to diameter for the spheres and major × minor axes for the ellipsoid, were 132 nm for **2**, 156 nm for **3**, and 209 × 145 nm for **4** (Figure 3A, B, and C, respectively). The particle sizes for these compounds as observed by AFM show good agreement with those obtained by DLS. The molecular shapes of these compounds are regarded to be the "cone" type, due to the attachment of the large polyamine moiety. We have endeavored to make liposome from these compounds; however, entrapment of a fluorescence probe, calcein, was

Table 1. Estimated Size and Shape of 2−4 and Complexes with ColE1 DNA Suspended in Aqueous Solution[a]

	DLS (nm)		AFM/shape (size (nm)) and height (nm)[b]			
compound	conjugate alone	complex with DNA	conjugate alone		complex with DNA	
2	155 ± 54	409 ± 115	sphere (132)	21	aggregate (∼1000 × 437)	16
3	173 ± 46	237 ± 127	sphere (156)	24	aggregate (569 × 317)	20
4	128 ± 38	115 ± 40	ellipsoid (209 × 145)	12	sphere (120)	20

[a] The ratio of polyamine conjugate−DNA was 3/1 (w/w). Complexation of polyamine conjugate with DNA was carried out in water. [b] Sample solution was spreaded on a mica surface and dried. AFM images were obtained under dry condition. Width and height of the complexes were estimated from the AFM images in Figures 3 and 4.

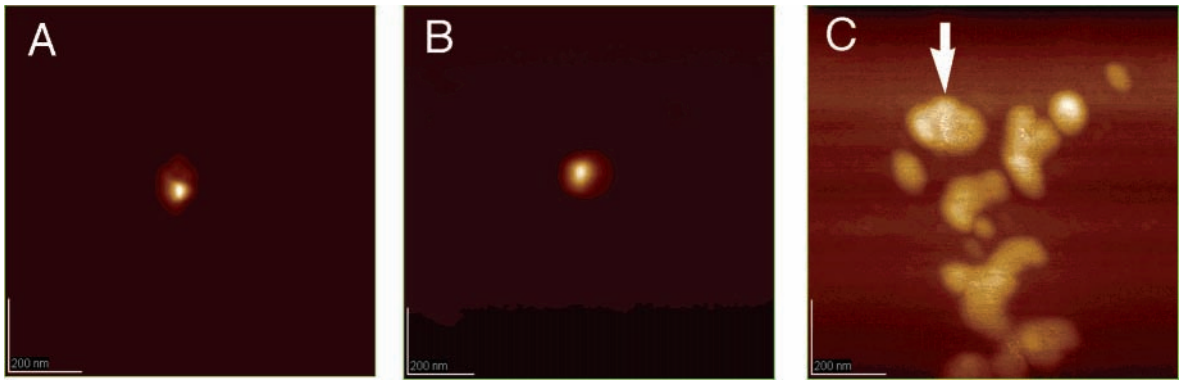


Figure 3. AFM images of arrays of compounds **2** (A), **3** (B), and **4** (C). The compound was suspended in distilled water and then dropped onto a mica surface by spin coating. All scale bars represent 200 nm. The object indicated by the arrow is discussed in the text.

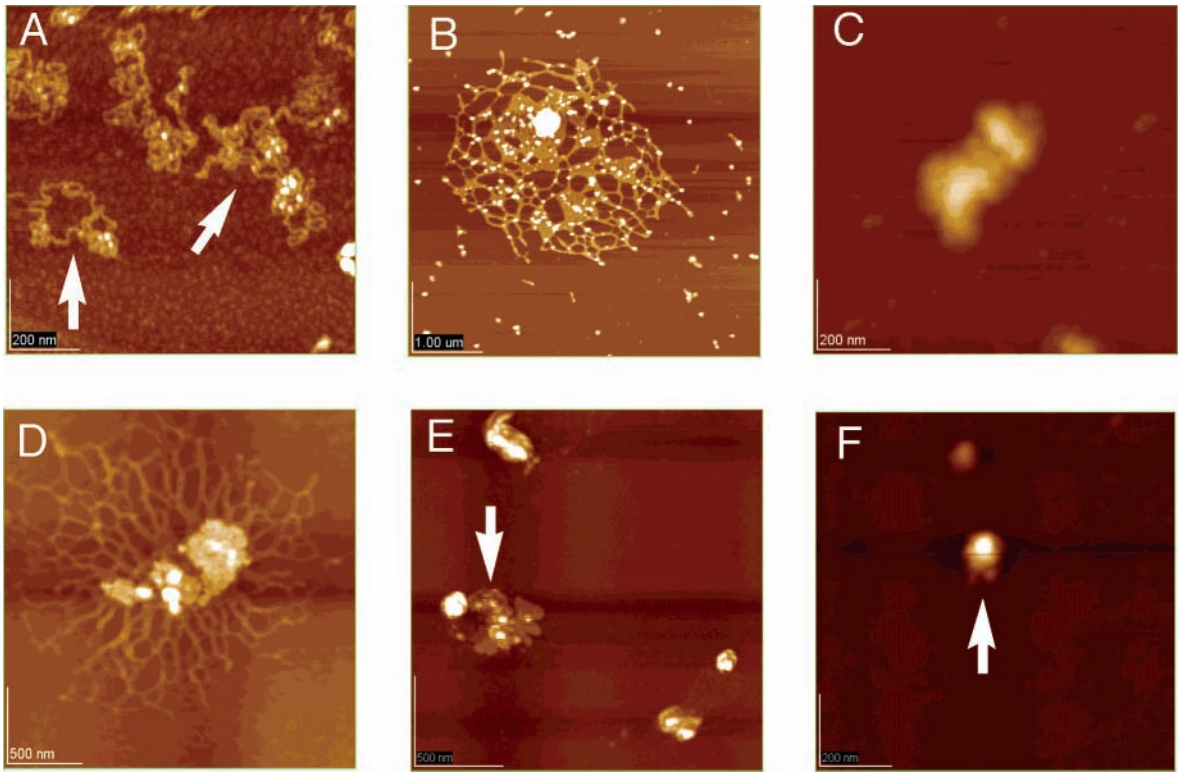


Figure 4. AFM images of polyamine-ColE1 plasmid DNA complexes: (A), ColE1 plasmid DNA alone on polylysine-treated mica; (B), spermine−DNA; (C), PEI(1800)−DNA; (D), spermidine−DCP−DNA; (E), spermine−DCP−DNA; (F), PEI(1800)−DCP−DNA. The polyamine−DNA ratio was 3/1 (w/w). Scale bars inserted in these images represent (A) 200, (B) 1000, (C) 200, (D) 500, (E) 500, and (F) 200 nm, respectively. The objects indicated by arrow(s) are discussed in the text.

impossible. Therefore, we assume that the particle consisting of polyamine−DCP conjugates is a micellelike aggregate.

Particle sizes of the conjugate−DNA (3/1: w/w) complex evaluated by DLS is 409 ± 115 nm for **2**, 237 ± 127 nm for **3**, and 115 ± 40 nm for **4**, respectively (Table 1). With increase in the size of polyamine portion, the particle size significantly decreases. AFM images support this conclusion. Figure 4 shows an AFM image of DNA (A) and of the complexes it forms with various polyamines (B−F). Figure 4A reveals a clear image of partially coiled ColE1 plasmid DNA (6646 bp), whose size is estimated to be 300−400 nm. The height is ∼2 nm, corresponding to the diameter of B-form DNA, ca. 2.4 nm. When DNA was complexed with compound **2**, a "spider nest"-like structure was observed (Figure 4D). The size of the

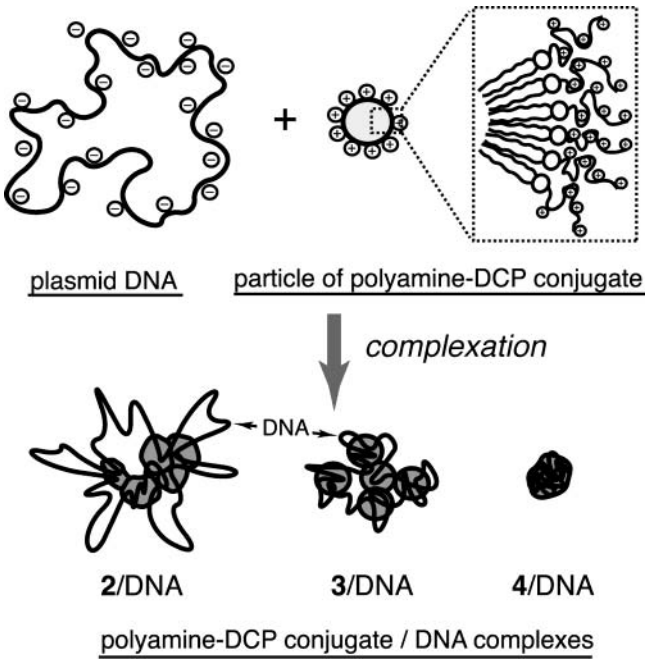


Figure 5. Hypothetical complexation of polyamine−DCP conjugates **2**−**4**, with ColE1 plasmid DNA based on the AFM images as shown in Figures 3 and 4. The bright-gray sphere represents micelle of polyamine−DCP conjugate **2**, **3**, or **4**. When the plasmid DNA complexes with the conjugate micelles via electrostatic interaction, different types of conjugate−DNA, **2**−DNA, **3**−DNA, and **4**−DNA, form depending on the conjugates. The solid lines and the dark-gray spheres depicted in the complexes represent the plasmid DNA and aggregates consisting of the conjugate and DNA, respectively.

"quasi-ellipsoidal core region" is ∼1000 × 437 nm and the height is ∼16 nm. The height of the radiating peripheral "nest" region is ∼2 nm, suggesting the nest region consists of free DNA. The height of the core region (∼16 nm) is clearly larger than that of the DNA part; therefore, the core region of the structure must consist of the **2**−DNA complex. Thus, complexation of compound **2** and DNA gives rise to a segregated array, having complex and free DNA portions. Compound **3** forms a similar but distinguishably different complex structure with DNA (Figure 4E), which resembles a "pearl necklace-like" aggregate (*11*), 569 × 317 nm in the plane of the substrate and 4−20 nm in height. The size of the pearl parts is 120−170 nm in diameter and 11−20 nm in height. These parts are connected by a region that is 4−5 nm in height. It appears from the image that the assembly consists of a tightly packed **3**−DNA complex and regions of partially compacted DNA parts. Pronounced compaction of the complex was observed for the **4**−DNA, which formed a spherical cluster (120 nm in width and ∼20 nm in height) (Figure 4F). The order of increasing compaction of DNA, **2** < **3** < **4**, is consistent with the extent of intercalation of EtBr (Figure 2B); that is, the more tightly packed was the DNA complex, the lower was the extent of intercalation of EtBr. On the basis of the AFM images of the polyamine conjugate−DNA complexes, the hypothetical shapes of the complexes are as depicted in Figure 5.

Upon comparison of the observed DNA complex with free polyamines, spermine (Figure 4B) and PEI (1800) (Figure 4C), the complex size and shape are obviously distinguishable from the corresponding conjugate forms; much larger complexes form with these free polyamines. The dimension of the spermine−DNA complex (Figure 4B) is ∼3 μm; the compaction of DNA is obviously incomplete, judging from the presence of the "nest" portion of DNA that is similar to peripheral part of the **2**−DNA complex (Figure 4D). The PEI(1800)−DNA complex is smaller (416 × 218 nm by 22 nm high) than the former complex, suggesting that the greater cationic charge makes the complex smaller. When one considers the effect of the hydrophobic portion in the polyamine compound on the size of the complex, it is clear that hydrophobic alkyl parts in the conjugates play an important role in the compaction of DNA, which is most prominently observed in conjugate **4** (Figure 4C vs 4F). From these results, the prominent transfection efficiency of **4** likely results from the more efficient compaction of DNA in the complex **4**−DNA, whereas the lower activity of **2** and **3** is likely due to their much weaker compaction.

Because high compaction is needed for transfection, **2** and **3** exhibited only moderate transfection activity. The efficiency of **2** and **3** does not depend on the dose in the range of 1.5/1 to 6/1 (w/w), whereas the efficacy of conjugate **4** decreases at 6/1 (w/w). This may be a consequence of the cytotoxicity of PEI portion. One may wonder why the morphologies of the complexes of **2** and **3** with DNA are so different despite the small structural difference in the cationic portion. It might come from the difference in delicate balance of hydrophilic/hydrophobic factor and/or molecular shapes which reflect a packing parameter. A wide variety of similar polyamine−dialkyl phosphate derivatives bearing different type of hydrophobic alkyl chain, e.g., shorter or unsaturated, is synthetically available. It should be intriguing to see the effect of hydrophilic/hydrophobic balance on not only the morphology of the complex with DNA but also transfection efficacy.

Although the precise mechanism remains to be clarified, the compaction by these polyamine compounds probably plays an important role because entry into the nucleus is thought to be a key step and a smaller complex is likely to be associated with more efficient transfection. The conjugates in this study possibly decompose into separate polyamine and DCP portions in the endosome. We assume that two critically important factors are involved in the present transfection system: compaction of DNA by the polyamine part and with the hydrophobic dialkyl portion and decomposition of the conjugate in the endosome so as to liberate the DNA−polyamine complex to be transported into nucleous. As previously reported, DNA accompanied by cetyl-PEI enters into the nucleus.

In conclusion, we described herein novel types of polyamine−dialkyl phosphate conjugates that have moderate gene transfection activity for the β-galactosidase assay. These conjugates are easy to prepare via a novel synthetic intermediate, dimerized DCP anhydride, **1**. The synthetic approaches described herein are flexible and possess potential for the rationale design of highly efficient gene carriers with single or narrow ranges of molecular weight. It is one of critical aspects for practical usage.

ACKNOWLEDGMENT

The authors thank professor Akihiro Yoshino, Nagoya Institute of Technology, for helpful discussion and comments. This study was supported by PRESTO (JST), the NITECH 21st Century COE Program "World Ceramics Center for Environmental Harmony", NEDO, and Takemoto Oil and Fat Co.

LITERATURE CITED

(1) Kay, M. A., Liu, D., and Hoogerbrugge, P. M. (1997) Gene therapy. *Proc. Natl. Acad. Sci. U.S.A. 94*, 12744−12746.

(2) Lasic, D. D. (1997) *Liposomes in Gene Delivery*, CRC Press, New York.
(3) Miller, A. D. (1998) Cationic Liposomes for Gene Therapy. *Angew. Chem., Int. Ed. 37*, 1768−1785.
(4) Meyer, O., Kirpotin, D., Hong, K., Sternberg, B., Park, J. W., Woodle, M. C., and Papahadjopoulos, D. (1998) Cationic liposomes coated with poly(ethylene glycol) as carriers for oligonucleotides. *J. Biol. Chem. 273*, 15621−15627.
(5) MacDonald, R. C., Ashley, G. W., Shida, M. M., Rakhmanova, V. A., Tarahovsky, Y. S., Pantazatos, D. P., Kennedy, M. T., Pozharski, E. V., Baker, K. A., Jones, R. D., Rosenzweig, H. S., Choi, K. L., Qiu, R., and McIntosh, T. J. (1999) Physical and biological properties of cationic triesters of phosphatidylcholine. *Biophys. J. 77*, 2612−2629.
(6) Nakanishi, M., and Noguchi, A. (2001) Confocal and probe microscopy to study gene transfection mediated by cationic liposomes with a cationic cholesterol derivative. *Adv. Drug Delivery Rev. 52*, 197−207.
(7) Behr, J.-P. (1994) Gene transfer with synthetic cationic amphiphiles: Prospects for gene therapy. *Bioconjugate Chem. 5*, 382−389.
(8) Kichler, A., Mechtler, K., Behr, J.-P. and Wagner, E. (1997) Influence of membrane-active peptides on lipospermine/DNA complex mediated gene transfer. *Bioconjugate Chem. 8*, 213−221.
(9) Nakai, T., Kanamori, T., Sando, S., and Aoyama, Y. (2003) Remarkably size-regulated Cell invasion by artificial viruses. Saccharide-dependent self-aggregation of glycoviruses and its consequences in glycoviral gene delivery. *J. Am. Chem. Soc. 125*, 8465−8475.
(10) Wrobel, I., and Collins, D. (1995) Fusion of cationic liposomes with mammalian cells occurs after endocytosis. *Biochim. Biophys. Acta 1235*, 296−304.
(11) Yoshikawa, Y., Emi, N., Kanbe, T., Yoshikawa, K., and Saito, H. (1996) Folding and aggregation of DNA chains induced by complexation with lipospermine: formation of a nucleosome-like structure and network assembly. *FEBS Lett. 396*, 71−76.
(12) Rädler, J. O., Koltover, I., Jamieson, A., Salditt, T., and Safinya, C. R. (1998) Structure and interfacial aspects of self-assembled cationic lipid−DNA gene carrier complexes. *Langmuir 14*, 4272−4283.
(13) Martin-Herranz, A., Ahmad, A., Evans, H. M., Ewert, K., Schulze, U., and Safinya, C. R. (2004) Surface functionalized cationic lipid-DNA complexes for gene delivery: PEGylated lamellar complexes exhibit distinct DNA-DNA interaction regimes. *Biophys. J. 86*, 1160−1168.
(14) Kennedy, M. T., Pozharski, E. V., Rakhmanova, V. A., and MacDonald, R. C. (2000) Factors governing the assembly of cationic phospholipid-DNA complexes. *Biophys. J. 78*, 1620−1633.
(15) Koynova, R., and MacDonald, R. C. (2003) Mixtures of cationic lipid *O*-ethylphosphatidylcholine with membrane lipids and DNA: Phase diagrams. *Biophys. J. 85*, 2449−2465.
(16) Raspaud, E., Pitard, B., Durand, D., Aguerre-Chariol, O., Pelta, J., Byk, G., Scherman, D., and Livolant, F. (2001) Polymorphism of DNA/multi-cationic lipid complexes driven by temperature and salts. *J. Phys. Chem. 105*, 5291−5297.
(17) Yamazaki, Y., Nango, M., Matsuura, M., Hasegawa, Y., Hasegawa, M., and Oku, N. (2000) Polyamine liposomes, a novel nonviral gene transfer system, constructed drom cetylated polyethyleninine. *Gene Ther. 7*, 1148−1155.
(18) Oku, N., Yamazaki, M., Matsuura, M., Sugiyama, M., Hasegawa, M., and Nango, M. (2001) A novel nonviral gene transfer system, polycation liposomes. *Adv. Drug Delivery Rev. 52*, 209−218.
(19) Matsuura, M., Yamazaki, Y., Sugiyama, M., Kondo, M., Ori, H., Nango, M., and Oku, N. (2003) Polycation liposome-mediated gene transfer in vivo. *Biochim. Biophys. Acta 1612*, 136−143.
(20) Sugiyama, M., Matsuura, M., Takeuchi, Y., Kosaka, J., Nango, M., and Oku N. (2004) Possible mechanism of polycation liposome (PCL)-mediated gene transfer. *Biochim. Biophys. Acta 1660*, 24−30.
(21) Harashima, H., Shinohara, Y., and Kiwada, H. (2001) Intracellular control of gene trafficking using liposomes as drug carriers. *Eur. J. Pham. Sci. 13*, 85−89.
(22) Crowley, S. T., Dempsey, E. C., Horwitz, K. B., and Horwitz, L. D. (1994) Platelet-induced vascular smooth muscle cell proliferation is modulated by the growth amplification factors serotonin and adenosine diphosphate. *Circulation 90*, 1908−1918.
(23) Rakhmanova, V. A., and MacDonald, R. C. (1998) A microplate fluorimetric assay for transfection of the β-galactosidase reporter gene. *Anal. Biochem. 257*, 234−237.
(24) Uragami, M., Miyake, Y., and Regen, S. L. (2000) Influence of headgroup chirality on the mixing behavior of phosphatidylglycerol mimics in fluid bilayers. *Langmuir 16*, 3491−3496.
(25) Tanaka, T., Sakata, T., Fujimoto, K., and Ikehara, M. (1987) Synthesis of oligonucleotide with aliphatic amino or phosphate group at the 5′ end by the phosphotriester method on a polystyrene support. *Nucleic Acids Res. 15*, 6209−6224.
(26) Cullis, P. M., Kaye, A. D., and Trippett, S. (1987) On the mechanism of reaction of activated phospholyl compounds with phosphoryl anions: a reassessment of the role of dioxadiphosphetanes. *J. Chem. Soc., Chem. Commun*. 1464−1466.

BC049925K

Cyclodextrin-Modified Polyethylenimine Polymers for Gene Delivery

Suzie H. Pun,[†,||] Nathalie C. Bellocq,[†] Aijie Liu,[†] Greg Jensen,[†] Todd Machemer,[‡] Erlinda Quijano,[‡] Thomas Schluep,[‡] Shufen Wen,[‡] Heidrun Engler,[‡] Jeremy Heidel,[§] and Mark E. Davis*[,§]

Insert Therapeutics Inc., 2585 Nina Street, Pasadena, California 91107, Canji, Inc., 3525 Johns Hopkins Court, San Diego, California 92121, and Chemical Engineering, California Institute of Technology, Pasadena, California 91125. Received May 3, 2004; Revised Manuscript Received June 3, 2004

Linear and branched poly(ethylenimines), lPEI and bPEI, respectively, grafted with β-cyclodextrin are prepared to give CD−lPEI and CD−bPEI, respectively, and are investigated as in vitro and in vivo nonviral gene delivery agents. The in vitro toxicity and transfection efficiency are sensitive to the level of cyclodextrin grafting. The cyclodextrin-containing polycations, when combined with adamantane−poly(ethylene glycol) (AD−PEG) conjugates, form particles that are stable at physiological salt concentrations. PEGylated CD−lPEI-based particles give in vitro gene expression equal to or greater than lPEI as measured by the percentage of EGFP expressing cells. Tail vein injections into mice of 120 μg of plasmid DNA formulated with CD−lPEI and AD−PEG do not reveal observable toxicities, and both nucleic acid accumulation and expression are observed in liver.

INTRODUCTION

Cationic polymers have received much attention for their potential use as nonviral gene delivery agents. Under certain conditions, these polymers self-assemble with poly(nucleic acids) via electrostatic interactions and condense them into submicron size particles that can be endocytosed by cells. Polymeric gene delivery vehicles have several advantages over their viral counterparts including nonimmunogenicity, adaptability, and ease of manufacture that make their development of interest for gene therapy applications. However, many polymers used for gene delivery are not suitable for systemic administration due to their toxicity and tendency to aggregate under physiological conditions (*1*).

We have previously demonstrated the use of cyclodextrins (cyclic oligomers of glucose) as building blocks for the preparation of a suite of linear, cyclodextrin-based polycations (CDPs) that have been used for gene delivery (*2*−*9*). Like other polycations, these polymers assemble with plasmid DNA via electrostatic interactions to form small spherical particles with diameters ∼100 nm. The particles are able to transfect cultured mammalian cells and show low toxicity both in vitro and in vivo (*2*−*9*). The importance of the cyclodextrin in mediating low toxicity was demonstrated by the high in vitro toxicity of poly(amidine) polymers lacking cyclodextrins. Although these polymers still transfected cells with high efficiency, their IC_{50}'s were 2−3 orders of magnitude lower than cyclodextrin-based poly(amidine) polymers (*3*, *5*, *9*).

While other polycations show reduced toxicities with sugar and/or other functional group incorporation (*10*−*12*), cyclodextrins are unique entities because they also serve as potential sites for modification via inclusion compound formation. Cyclodextrins are water-soluble, cup-shaped molecules that form inclusion complexes with small, hydrophobic compounds such as adamantane. The ability of cyclodextrins to form inclusion complexes can be utilized to modify the surface of the cyclodextrin-based, DNA-containing particles without interfering with polycation/DNA interactions and particle morphology (*4*, *8*, *9*). For example, adamantane−poly(ethylene glycol) (AD−PEG) conjugates provide salt stability to β-cyclodextrin-based particles (*4*, *9*). The adamantane in the AD−PEG conjugates form inclusion complexes with the β-cyclodextrins that are on the particle surfaces and thus anchor the PEG polymers to the surface to provide a PEG brush layer for particle stabilization. We have demonstrated the use of this inclusion formation technology to provide particle stability, tune particle surface charge, and modify particles with targeting ligands (*9*) such as galactose (*4*) and transferrin (*8*). This modification method utilizes self-assembly for the formulation, allows for great diversity in the types of surface modification, and is easily scalable.

Poly(ethylenimine) (PEI) is a cationic polymer often used in nonviral gene transfer. PEI can provide for efficient, in vitro gene transfer, and this efficiency is speculated to be at least partially due to enhanced endosomal escape via pH-buffering (*13*, *14*). PEI is one of the few polymers where transfection efficiency is not significantly increased by the presence of chloroquine, and this may be because of its mechanism of endosomal release (*15*). Nevertheless, the use of PEI as in vitro and in vivo transfection reagent is severely limited by its toxicity and difficulties in formulation. The LD_{50} of linear PEI (lPEI) is reported to be 4 mg/kg in Balb/C mice (*16*), 50-fold less than the LD_{50} of linear, cyclodextrin-based polymers (at least 200 mg/kg in Balb/C mice (*3*)). Particles formed from the condensation of PEI with poly(nucleic acids) ("PEI-based polyplexes"), like most polyplexes, also

* To whom correspondence should be addressed. E-mail: mdavis@cheme.caltech.edu.
† Insert Therapeutics Inc.
‡ Canji, Inc.
§ California Institute of Technology.
|| Current address: Department of Bioengineering, University of Washington, Seattle, WA.

10.1021/bc049891g CCC: $27.50 © 2004 American Chemical Society
Published on Web 06/29/2004

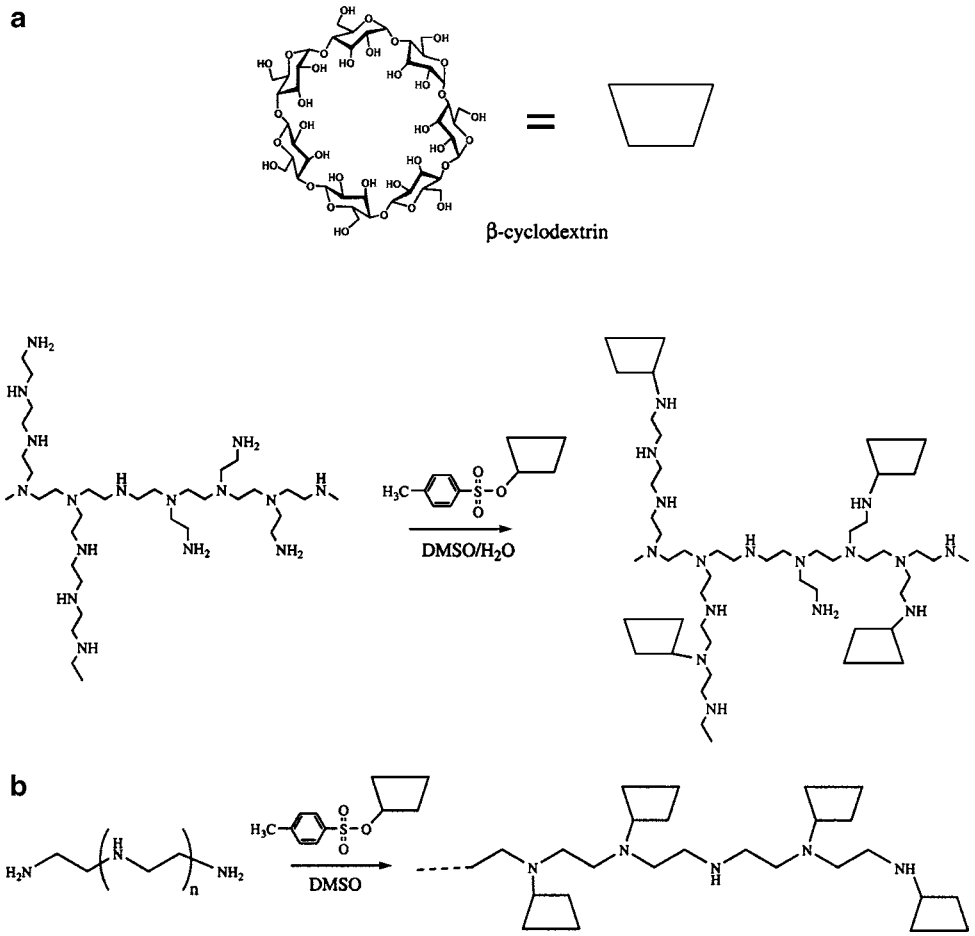


Figure 1. (a) Synthesis of β-CD−bPEI. (b) Synthesis of β-CD−lPEI.

aggregate rapidly in physiological salt conditions. Approaches for improving the stability of PEI-based polyplexes include grafting of PEI with PEG and grafting of preformed PEI-based polyplexes with amine-reactive PEG (*17*, *18*). However, PEI−PEG may not condense DNA into small spherical particles; rodlike and wormlike structures are often instead observed by transmission electron microscopy (*1*). Also, grafting of polyplexes with reactive PEG is difficult to control and scale-up.

The objective of our study is to merge the beneficial qualities of the cyclodextrin-based polymers (low toxicity and the ability to modify the polyplex via inclusion complex formation) with the desirable features of the PEI polymers (efficient transfection). In this work, we describe the synthesis of β-cyclodextrin-grafted PEI (CD−PEI) polymers and their use as in vitro and in vivo nonviral gene delivery media. It is shown here that the transfection and toxicity profiles of the β-CD−PEI polymers are sensitive to the level of cyclodextrin grafting. The resulting polyplexes can be modified and stabilized by adamantane−poly(ethylene glycol) conjugates via inclusion complex formation. This modification creates particles that are formulated at high concentrations without flocculation, are stable in physiological salt concentrations, and are applicable for in vivo, systemic administration. Systemic delivery of plasmids containing the p53 gene with cyclodextrin-containing PEI delivery vehicles show significantly reduced toxicity when compared to PEI-based delivery vehicles in mice. Additionally, p53 gene expression is observed in liver when using cyclodextrin-containing PEI's (unmodified PEI's typically reveal expression in lung).

Table 1. Effect of Reaction Solvent on β-Cyclodextrin Grafting to BPEI

H_2O/DMSO (mL/mL)	amount of water (%)	amine grafting (%)
60/40	60	5
40/60	40	6
20/80	20	7
5/95	5	8
1/99	1	10
0.1/99.9	0.1	12
0/100	0	16

EXPERIMENTAL PROCEDURES

Synthesis and Characterization of Cyclodextrin−PEI Polymers. *Preparation of Cyclodextrin-Grafted Branched PEI (CD−bPEI) (Figure 1a).* Branched $PEI_{25\,000}$ (282 mg, 11.3 μmol, Aldrich, Milwaukee, WI) and 6-monotosyl-β-cyclodextrin (2.18 g, 1.69 mmol, Cyclodextrin Technologies Development, Inc.) were dissolved in 100 mL of various H_2O/DMSO solvent mixtures (Table 1). The resulting solution was stirred at 70 °C for 72 h and then transferred to a Spectra/Por MWCO 10 000 membrane and dialyzed against water for 6 days. The dialyzed solutions were lyophilized to afford a slightly colored solid. Cyclodextrin/PEI ratio was calculated based on the proton integration of ^{1}H NMR and shown in Table 1 (Varian 300 MHz, D_2O) δ 5.08 ppm (s br., C_1H of CD), 3.3−4.1 ppm (m br. C_2HC_6H of CD), 2.5−3.2 ppm (m br. CH_2 of PEI).

Preparation of Cyclodextrin-Grafted Linear PEI (CD−lPEI) (Figure 1b). Linear $PEI_{25\,000}$ (500 mg, 20 μmol, Polysciences, Inc., Warrington, PA) and 6-monotosyl-β-cyclodextrin (3.9 g, 3 mmol, Cyclodextrin Technologies

Development, Inc.) were dissolved in 36 mL of DMSO. The resulting mixture was stirred at 70 °C for 6 days. The solution turned slightly yellow. The solution was then transferred to a Spectra/Por MWCO 10 000 membrane and dialyzed against water for 6 days. Water was then removed by lyophilization to afford a slightly colored solid. Cyclodextrin/PEI ratio was calculated based on the proton integration of ^{1}H NMR (Varian 300 MHz, D_2O) δ 5.08 ppm (s br., C_1H of CD), 3.3−4.1 ppm (m br. C_2H-C_6H of CD), 2.5−3.2 ppm (m br. CH_2 of PEI) and found to be 1 CD: 8.4 amines.

pH-Titration. Each polymer was dissolved to a concentration of 11.7 mM of amines in 150 mM NaCl and titrated with 0.1 N HCl or 0.1 N NaOH (*19*). pH measurements were carried out at 25 °C with a Beckman Coulter pH meter Φ340.

Adamantane−Poly(ethylene glycol) (AD−PEG) Synthesis. AD−PEG was synthesized as described previously (*4*). In brief, PEG_{5000}−SPA (Nektar AL, Huntsville, AL) was reacted with 5 equiv of 1-adamantanemethylamine (Aldrich) in dichloromethane. The solvent was removed in vacuo and water added to the remaining solution. The solution was centrifuged at 15 K rcf for 15 min to precipitate unreacted 1-adamantanemethylamine. The aqueous portion was then dialyzed (Slide-A-Lyzer MWCO 3500 Pierce, Rockford, IL) for 24 h against water and lyophilized to yield a white, fluffy powder in 97% yield.

Cell Culture and Plasmids. PC3 (human prostatic carcinoma) cells were purchased from the ATCC and cultured in DMEM/F12 media containing 10% (v/v) fetal bovine serum containing 100 units/mL penicillin in a 5% CO_2 humidified atmosphere at 37 °C. The pGL3-CV (containing the luciferase gene under the control of the SV40 promoter) and pEGFPLuc (containing the gene coding for an EGFP/luciferase fusion protein under the control of the CMV promoter) plasmids were purchased from Promega (Madison, WI) and Clontech (Palo Alto, CA), respectively, and amplified by Elim Biopharmaceuticals (Hayward, CA).

Formulation and Characterization of CD−PEI/DNA Complexes. *Formulation.* CD−PEI/DNA polyplexes were prepared by adding an equal volume of CD−PEI solution (CD−PEI dissolved in dH_2O) to a plasmid DNA solution (0.1 mg DNA/mL in dH_2O) at the appropriate N/P ratio. PEGylated CD−PEI/DNA polyplexes were prepared by mixing equal volumes (25% of final volume) of CD−PEI and AD−PEG solutions (both dissolved in dH_2O). The CD−PEI/AD−PEG solution was then added to an equal volume of plasmid DNA solution (0.1 mg DNA/mL in dH_2O).

Transmission Electron Microscopy. Polyplexes containing the pGL3-CV plasmid were prepared as described above. Five microliters of sample was then applied to glow-discharged, 400-mesh carbon-coated copper grids for 45 s, after which excess liquid was removed by blotting. The samples were then negatively stained with 2% uranyl acetate for 45 s before observation. Images were recorded using a Philips 201 electron microscope operated at 80 kV.

Salt Stability Study. Two micrograms of pGL3-CV plasmid was formulated with CD−PEI, CD−PEI/AD−PEG, PEI, or PEI/AD−PEG as described above. One sample was diluted by the addition of 1.2 mL of water to determine initial particle size. A second duplicate sample was then diluted by the addition of PBS (pH 7.2) to determine salt stability. Particle size was recorded every minute for 10 min using a ZetaPALS dynamic light scattering detector (DLS, Brookhaven Instruments Corporation, Holtsville, NY).

In Vitro Transfection and Toxicity Assays. *Luciferase Expression.* PC3 cells (human prostate epithelial adenocarcinoma cells from ATCC) were plated at 50 000 cells/well in 24-well plates 24 h before transfection. Immediately prior to transfection, cells in each well were rinsed once with PBS before the addition of 200 μL of Opti-MEM (Invitrogen, Carlsbad, CA) containing polyplexes (1 μg of DNA complexed with polycation at 10 N/P). After 4 h, transfection media was aspirated and replaced with 1 mL of complete media. Forty-eight hours after transfection cells were washed with PBS and lysed by the addition of 100 μL of Cell Culture Lysis Buffer (Promega, Madison, WI). Cell lysates were analyzed for luciferase activity with Promega's luciferase assay reagent. Light units were integrated over 10 s with a luminometer (Monolight 3010C, Becton Dickinson).

Toxicity. The IC_{50}'s of the various polymers to PC3 cells were determined by MTT assay as described previously (*3*). All experiments were conducted in triplicate and averaged. Average absorbance was plotted versus polymer concentration and IC_{50} values were determined by interpolation.

Plasmid Delivery. PC3 cells were plated at 1 000 000 cells/well in six-well plates. After 24 h, the cells were exposed to 5 μg of fluorescently labeled plasmid (pEGFPLuc plasmid labeled with YOYO-1 (Molecular Probes, Eugene, OR) at a density of 1 dye molecule per 100 bp DNA) complexed with polymer at 10 N/P in 1 mL of OptiMEM (Gibco, Carlsbad, CA). Fifteen minutes after initial exposure, the polyplex-containing, culture media was aspirated. Cells were washed with PBS, Cell Scrub buffer (Gene Therapy Systems, San Diego, CA), trypsinized, and analyzed by flow cytometry for the uptake of the polyplexes.

EGFP Expression. PC3 cells were plated at 250 000 cells/well in six-well plates. After 48 h, the cells were transfected with 5 μg of pEGFPLuc plasmid assembled with polymer at 10 N/P in 1 mL of OptiMEM (for some samples, OptiMEM containing 100 μM chloroquine was added). Four hours after transfection, the culture media was removed and replaced with 5 mL of complete media. Cells were washed with PBS, trypsinized, and analyzed by flow cytometry for EGFP expression 48 h after transfection.

In Vivo Experiments. Tolerability was evaluated in immune competent female Balb/c mice. Animals were injected with the various formulations into the tail vein using a 0.4 mL volume and an injection speed of approximately 0.2 mL/15 s. Animals were sacrificed at 24 h after treatment by carbon dioxide euthanasia. Blood was collected by heart-puncture into sodium citrate containing tubes (platelets and white blood cell (WBC) counts) and serum tubes (transaminases, creatinine). Platelets and WBC counts were evaluated at Biomedical Testing Services Inc., and transaminases (ALT/AST) and creatinine using a Cobas Mira (Roche) autoanalyzer. Livers and lungs were collected, formalin fixed, sections H & E (hematoxilin (stains nucleus) and eosin (stains cytoplasm)) stained, and pathologically examined.

Tolerability and transgene expression were evaluated in immune-compromised female nude mice bearing subcutaneous PC3 tumors. Tumors were established by injecting 1×10^7 PC3 cells in a volume of 0.2 mL subcutaneously in the left flank of animals. Tumors were grown to an average size of 100 mm^3 before treatment. Animals were injected with complexes intravenously into the tail vein using a 0.4 mL volume and an injection

speed of approximately 0.2 mL/15 s. Animals were sacrificed at 24 h after treatment and blood and serum collected as described above. Organs were collected into identically sized aluminum foil, weighed, and snap-frozen in liquid nitrogen for PCR/RT-PCR analysis.

Quantitative PCR and RT-PCR (QPCR, QRT-PCR) were used to quantify p53 DNA and transgene expression as previously described (*20*). Briefly, DNA and RNA were coextracted from approximately 100 mg of tissue using Tri-reagent (Molecular Research Center, Inc., Cincinnati, OH). Purified RNA was DNased and complete removal of DNA was confirmed by PCR. QPCR/QRT-PCR was performed using the ABI 7900 sequence detector (Applied Biosystems, Inc., Foster City, CA). Rodent GAPDH DNA and RNA were used as internal controls to assess the quality of purified RNA and DNA and to ensure equal amounts of sample input. Primer and probe sequence used for QPCR and QRT-PCR were as follows: p53; forward primer 5′-AACGGTACTCCGCCACC-3′, reverse primer 5′-CGTGTCACCGTCGTGGA-3′ and probe FAM-CAGCTGCTCGAGAGGTTTTCCGATCC-TAMRA. GAPDH; forward primer, 5′-ACGTGCCGCCTGGAGAA-3′, reverse primer, 5′-CATGAGGTCCACCACCCTGTT-3′ and probe FAM-ATGACATCAAGAAGGTGGTGAAGCAGGC-TAMRA.

Tissue matched p53 standards were used to quantify p53 DNA levels in tissues as described previously (*21*). To generate the standardards, briefly, liver, kidney, lung and tumor were collected from naïve animals. Tissues were minced thoroughly and aliquoted into several 100 mg samples. Six to eight 10-fold serially diluted samples of p53 plasmid, ranging from 1.0×10^3 to 1×10^9 particles, were spiked into each aliquot. p53-spiked tissue aliquots were extracted and processed for QPCR in a manner identical to the test samples, generating standard curves for each type of tissue. Standard curves were used to estimate the number of p53 DNA in test samples, which were expressed as genome equivalent fg per mg of tissue. p53 mRNA was quantified using rAd-p53 cRNA as reported previously (*20*) and was expressed as copies/mg of tissue.

RESULTS

Synthesis and Characterization of CD−bPEI and CD−lPEI Conjugates. β-Cyclodextrin-grafted poly(ethylenimines) (CD−PEI's) were synthesized by reaction of mono-tosylated cyclodextrins with the primary and secondary amines of poly(ethylenimine) using a protocol similar to that described by Suh et al. (Figure 1) (*22*). This synthesis approach resulted in cyclodextrin conjugation to both branched and linear PEI (denoted here as CD−bPEI and CD−lPEI, respectively). The degree of CD substitution was determined by integration of the appropriate ^{1}H NMR spectra and was found to depend on the amount of water in the reaction solvent. This effect was expected since the tosyl activating group is readily hydrolyzed by water. A series of CD−bPEI polymers with varying degrees of CD substitution (ranging from 5% to 16% amine substitution) were synthesized by changing the water to DMSO solvent ratio (Table 1). The transfection efficiency and toxicity of these various polymers were measured as described below to determine the synthesis conditions necessary for the best in vitro gene delivery behavior. CD−lPEI was also prepared following a similar protocol.

Effect of CD-Grafting on Transfection and Toxicity of bPEI. The CD−bPEI polymers were formulated with pGL3-CV at charge ratios ranging from 2 N/P (amine to phosphate) to 20 N/P and exposed to PC-3 cells plated in 24-well plates. The cells were lysed and analyzed for gene expression 48 h after transfection. Luciferase expression was detected at 4 N/P for all polymers and increased with charge ratio until toxicity was observed (generally around 15 N/P; results not shown). A comparison of transfection efficiency at 10 N/P as a function of CD grafting is shown in Figure 2. Luciferase activity is not normalized by total cell protein levels (RLU/mg) because this practice gives artificially high values for samples with low protein levels resulting from polymer toxicity. Instead, total luciferase activity per sample (RLU/well) is reported with polymer toxicity analyzed separately.

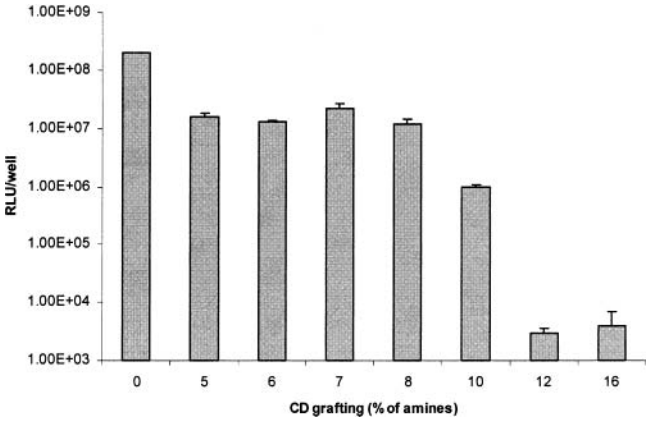


Figure 2. Effect of cyclodextrin grafting on CD−bPEI transfection efficiency to PC3 cells. CD−bPEI polymers were complexed with pGL3-CV plasmid at 10 N/P to form polyplexes for transfection. Luciferase activity was measured 48 h after transfection and reported as mean RLU/well ± SD for three replicates. Error bar on 0% CD grafting is too small to be observed.

Grafting of CD to bPEI reduces transfection efficiency. Modification of only 5% of the bPEI amines decreases luciferase activity by 1 order of magnitude (2×10^8 RLU/well for bPEI vs $(1-2) \times 10^7$ RLU/well for CD−bPEI with 5% to 8% amine grafting). CD grafting level is correlated with lower transfection; 10% amine modification results in a 2 orders of magnitude decrease in transfection to 1×10^6 RLU/well, and 16% amine modification reduces luciferase activity by over 4 orders of magnitude to 5×10^3 RLU/well.

The toxicities of bPEI and the CD−bPEI polymers were determined by comparing the IC_{50} values of the polymers with PC3 cells as measured by the MTT assay (Figure 3). PC3 cells were plated in 96-well plates and exposed to serially diluted concentrations of the polymers. The cells were then assayed for cell viability 24 h after initial polymer addition and IC_{50} values calculated by interpolation. All IC_{50} values are reported as ethylenimine monomer concentrations. The IC_{50} values of CD−bPEI polymers are proportional to the extent of cyclodextrin grafting. At lower grafting percentages, polymer IC_{50}'s are 2- to 5-fold higher (CD−bPEI IC_{50} of 0.64 mM and 1.45 mM for 5% and 8%, respectively, compared with bPEI's IC_{50} of 0.28 mM). High levels of cyclodextrin grafting increases IC_{50} values by over 20-fold (4.8 mM for 12% grafting and 6.7 mM for 16% grafting).

On the basis of the transfection and toxicity data, the CD−bPEI with 8% amine modification was chosen as the polymer with the best in vitro transfection and tolerability characteristics. This CD−bPEI polymer was used in the experiments described below. A similar synthesis procedure was used to prepare CD−lPEI (with 12% CD

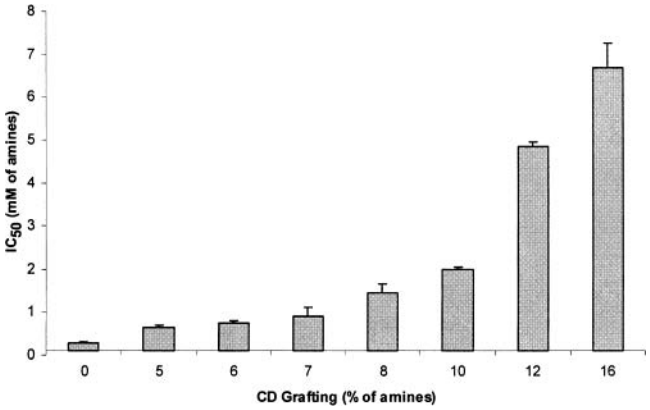


Figure 3. Effect of cyclodextrin grafting on CD−bPEI toxicity to PC3 cells. Polymers were exposed to PC3 cells in serial dilutions for 24 h. Cells were then assayed for viability by MTT assay. The IC_{50}'s, reported as ethylenimine monomer concentrations, were determined by interpolation on a best-fit line and reported mean values ± SD for three replicates.

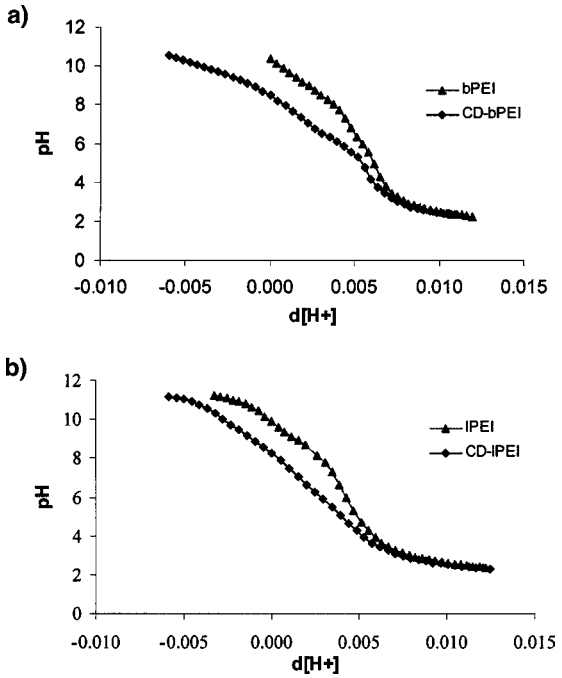


Figure 4. Acid/base titration curves for bPEI, lPEI, CD−bPEI, and CD−lPEI polymers. The value reported on the *x*-axis is the change in concentration of hydrogen ion required to achieve the pH indicated on the *y*-axis. (a) bPEI and CD−bPEI; (b) lPEI and CD−lPEI.

modification). Cyclodextrin modification of lPEI reduced polymer toxicity. The IC_{50} for lPEI was increased by severalfold by cyclodextrin grafting (0.38 mM for lPEI compared with 0.92 mM for CD−lPEI; all IC_{50}'s determined in triplicate and averaged). This CD−lPEI was also used in subsequent experiments. The titration curves of the CD−bPEI (8% amine modification), CD−lPEI (12% amine modification), and the unmodified bPEI and lPEI polymers are shown in Figure 4.

Salt Stabilization of CD-PEI Polymers by AD−PEG. CD−bPEI and CD−lPEI polymers self-assemble with and condense plasmid DNA to small spherical particles with average diameters ranging from 100 to 160 nm (not shown), as measured by dynamic light scattering (DLS). The particles can be PEGylated by the addition of AD−PEG_{5000} (poly(ethylene glycol) conjugated to adamantane). The adamantanes form inclusion complexes with the cyclodextrins on the surface of the particles, resulting in particle PEGylation (Figures 5a and 5b). PEGylation does not significantly affect particle size or particle morphology (Figures 5c and 5d). The PEGylated particles, like the unmodified particles, are predominately spherical in structure.

Table 2. Blood Chemistry Data

	nude mice		Balb/c mice	
blood parameter	D5W[a]	CD−lPEI + AD−PEG[b]	untreated	CD−lPEI + AD−PEG[b]
ALT (U/L)[c]	38	32	25	29
AST (U/L)[d]	60	53	45	75
Balb/c mice platelets (/mL)[e]	1175	1458	1335	624
WBC (/mL)[f]	12.5	9.6	7.4	6.4
CRE (mg/dL) [g]	n/a	n/a	0.8	0.9

[a] D5W: 5 wt % dextrose solution used as control. [b] Particles formulated with CD−lPEI + AD−PEG and plasmid DNA (120 μg). Average particle diameter was 117 nm. [c] Alanine aminotransferase (ALT). [d] Aspartate aminotransferase (AST). [e] Platelet count per milliliter. [f] White blood cell count per milliliter. [g] Creatinine.

Salt stability of the unmodified and PEGylated CD−PEI particles was tested by formulating the particles in a small volume of water (40 μL), adding 1.2 mL of PBS (150 mM salt concentration), and immediately monitoring average particle size by DLS with recorded measurements every minute for 10 min. All samples were run in triplicate and averaged for each time point. Figure 6 shows particle diameter versus time in salt solution for each type of formulation. All unmodified polyplexes aggregate in salt solutions. The addition of AD−PEG at 1 AD to 1 CD ratio reduces aggregation rate by forming a protective hydrophilic PEG brush layer on the particle surface. Complete particle stabilization is obtained by formulation with AD−PEG at 2 AD:1 CD (not shown). AD−PEG addition to bPEI and lPEI polyplexes does not stabilize the particles.

Plasmid Uptake with CD−PEI Polymers. CD−bPEI, CD−lPEI, bPEI, and lPEI were complexed with fluorescently labeled plasmids at 10 N/P and exposed to PC-3 (human prostatic carcinoma) cells for 15 min. The cells were then washed with PBS and Cell Scrub Buffer (to remove surface-associated polyplexes), trypsinized, and analyzed for polyplex uptake by flow cytometry. Uncomplexed plasmids were not readily taken up by cells (<1% cells YOYO-1 positive). lPEI and bPEI mediated plasmid uptake to PC3 cells (Figure 7). CD−lPEI and CD−bPEI both demonstrated higher plasmid uptake than the unmodified PEI polymers (Figure 7). The addition of AD−PEG to either CD-containing polymers did not impede plasmid uptake (Figure 7).

Comparison of Plasmid Delivery Efficiencies. The in vitro transfection efficiencies of the CD−PEI polymers were determined by delivery of the EGFP plasmid to PC3 cells with analysis by flow cytometry. Cyclodextrin grafting to the PEI's did not reduce transfection efficiencies from the parent PEI's (Figure 8). Addition of AD−PEG did not practically lower transfection with CD−lPEI but significantly lowered the number of expressing cells with CD−bPEI (Figure 8).

Chloroquine is an endosomal buffering agent often used to enhance nonviral transfection efficiency. When transfections were conducted in the presence of 100 μM chloroquine, CD−PEI-mediated transfection increased in the presence and absence of AD−PEG (Figure 8). In contrast, bPEI and lPEI did not benefit from chloroquine addition as has been reported in the literature.

In Vivo Experiments. Table 2 lists the results obtained from blood analyses. Balb/c mice tolerated the

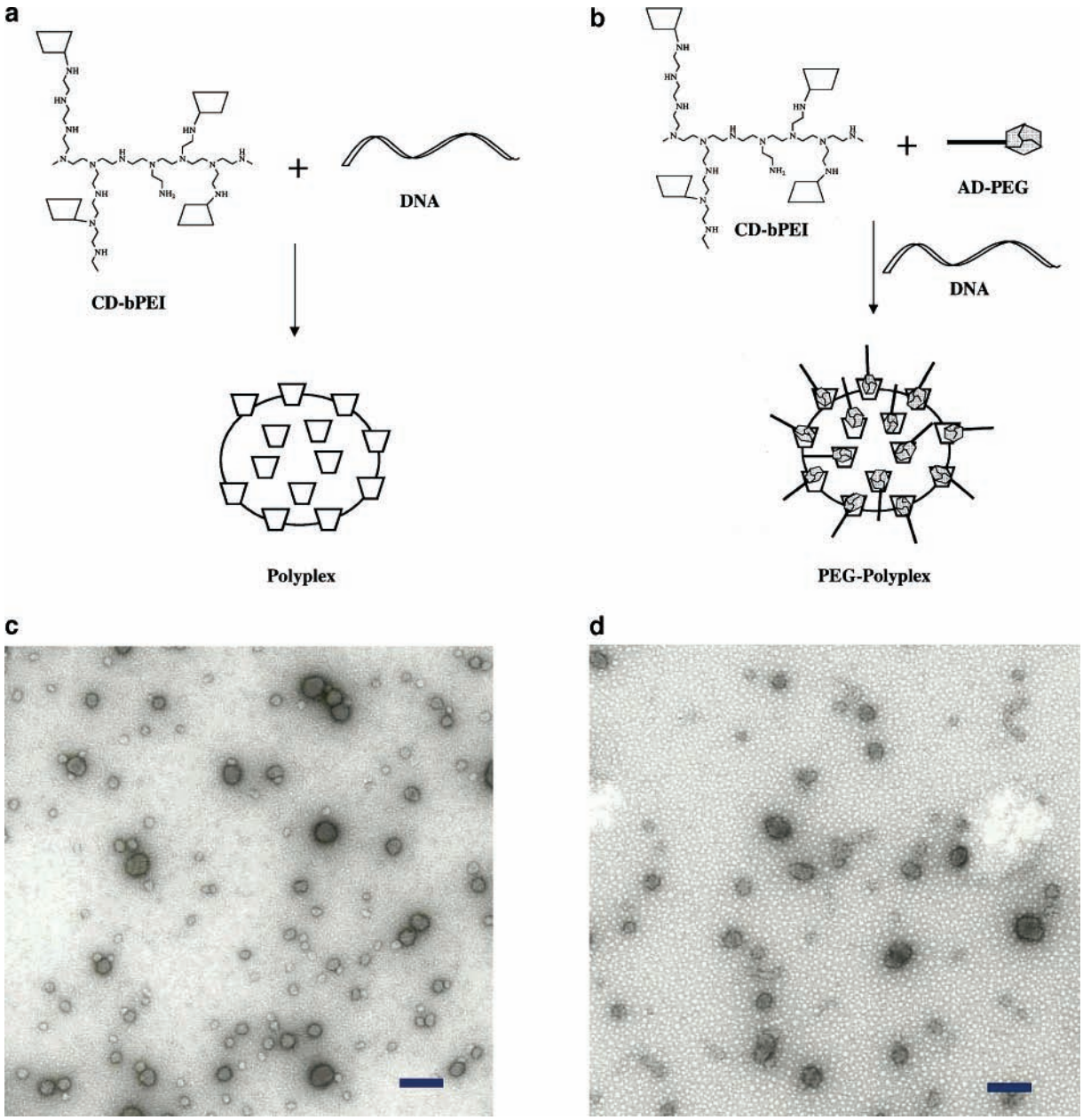


Figure 5. Schematics and electron micrographs of CD−bPEI (a and c) and PEGylated CD−bPEI polyplexes (b and d). Polyplexes were negatively stained with uranyl acetate and images recorded using a Philips 201 electron microscope. Bar represents 200 nm.

treatment well, and, with the exception of platelets, no significant difference in any blood parameter was seen between treated and untreated animals. Specifically, no liver toxicity as indicated by elevated liver enzymes (ALT/AST) or kidney toxicity as indicated by elevated creatinine levels was observed. Platelets dropped to approximately 50% of untreated animals, a phenomenon not observed in nude mice. Additionally, in a histological evaluation, liver and lung tissue sections appeared to be essentially normal, with no necrosis or excessive lymphoid infiltrates observed (Figure 9). These are common toxicities associated with intravenous delivery of lPEI−DNA complexes (*16*).

Nude mice tolerated the treatment equally well; no significant differences in any blood parameter was measured between the CD−lPEI + AD−PEG particles and a D5W control (Table 2). The biodistribution of the p53 plasmid was measured by PCR in three animals that each received a 120 μg dose of plasmid delivered in particles containing CD−lPEI + AD−PEG. At 24 h postinjection, the liver, kidney, and lung had $4.6 \pm 2.1 \times 10^7$, $1.9 \pm 1.3 \times 10^3$, and $4.2 \pm 1.4 \times 10^4$ fg p53/mg tissue, respectively (tumor of treated animals and all tissues of D5W controls were below quantitation limits). Additionally, expression of p53 (mRNA expression measured by RT-PCR) was only observed in liver ($0.9 \pm 0.4 \times 10^4$ copies of p53 mRNA/mg tissue).

DISCUSSION

β-Cyclodextrin-grafted poly(ethylenimine) polymers were synthesized by reaction of a mono-tosylated cyclodextrin with PEI amines in an effort to impart the advantageous properties associated with cyclodextrins (low toxicity, high water solubility, inclusion complex formation ability) to PEI (Figure 1). Reaction via nucleophilic substitution is preferred for several reasons. First, grafting density can be easily controlled and high grafting levels (up to 16%) are readily obtained. Second, the activated cyclodextrins react with both primary and secondary amines; therefore, CD−lPEI can also be syn-

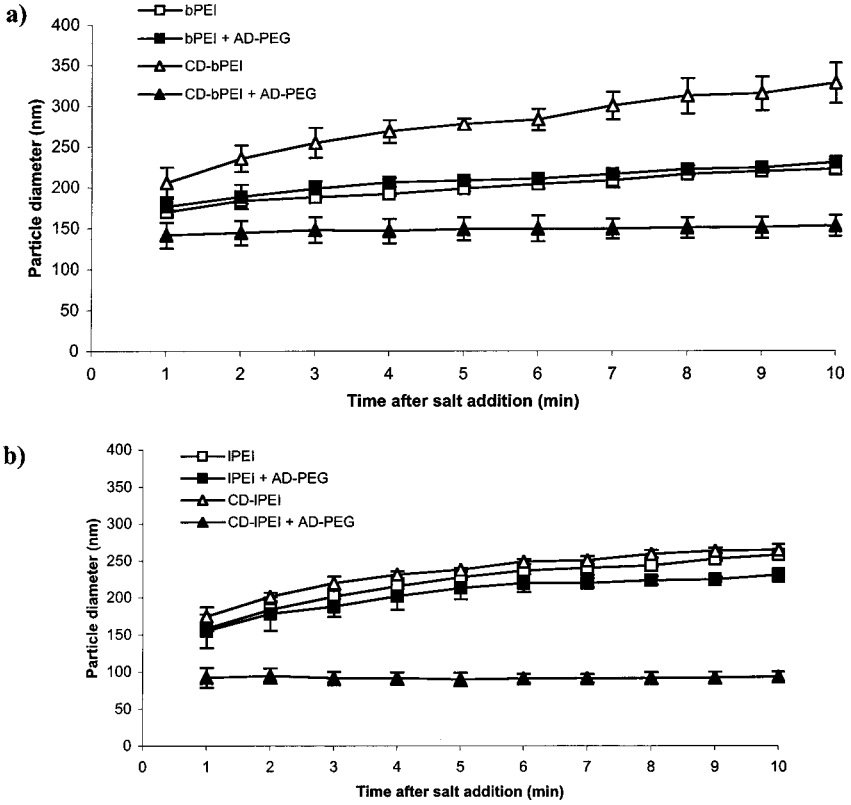


Figure 6. Salt stabilization of PEGylated CD−PEI polyplexes. Polyplexes were prepared at 10 N/P in 40 μL of water. PBS, pH 7.2. (1.2 mL), was then added and particle size monitored by dynamic light scattering for 10 min after salt addition. All measurements were conducted in triplicate and averaged for each time point. Particle diameters were measured as a function of time. (a) bPEI and CD analogues; (b) lPEI and CD analogues.

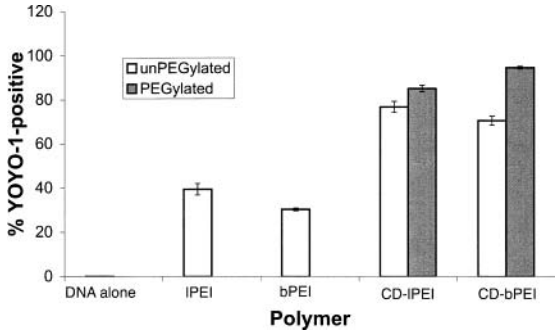


Figure 7. Comparison of plasmid uptake efficiencies of PEI and CD−PEI polymers. Polymers were complexed with YOYO-1-labeled plasmids at 10 N/P and exposed to PC3 cells for 15 min. Cells were washed with PBS and Cell Scrub buffer to remove surface-associated particles and analyzed for polyplex uptake by flow cytometry. Each value represents the mean ± SD of three experiments.

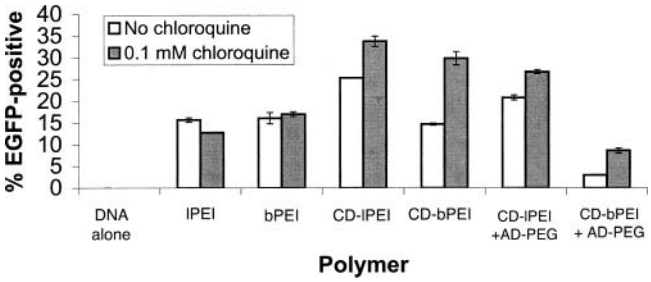


Figure 8. Comparison of transgene expression from PEI and CD−PEI polymers in the presence or absence of 0.1 mM chloroquine. Polymers were complexed with pEGFPLuc at 10 N/P and exposed to PC3 cells for 4 h in the presence and absence of 0.1 mM chloroquine. Cells were analyzed for EGFP expression by flow cytometry 48 h after initial transfection. Each value represents the mean ± SD of three experiments.

thesized. Finally, unlike reaction by reductive amination, this conjugation approach leaves the cyclodextrin intact and available for inclusion complex formation.

A series of CD−bPEI polymers with levels of CD grafting ranging from 5% to 16% of the PEI amines were synthesized (Figure 1, Table 1). The effect of CD grafting on the in vitro transfection efficiency and toxicity of CD−bPEI was determined by luciferase expression using transfection and MTT assays, respectively. Although all CD−bPEI polymers transfected PC3 cells, the efficiency was reduced as the CD grafting increased (Figure 2). At higher levels of CD grafting, dramatic reductions (up to 4 orders of magnitude) in luciferase expression were observed. Because all polymers condensed DNA to similar-sized particles (~100−160 nm), the CDs are unlikely interfering with DNA association and protection. Rather, high levels of CD conjugation may reduce endosomal release efficiencies by changing the pK_a profile of the PEI amines. Suh et al. report that the amines of CD-grafted dendrimer poly(ethylenimines) have substantially lower pK_a's than the parent polymers, requiring more acidic conditions for protonation (*23*). Cyclodextrin-modified PEI's possess substantially reduced buffering capacities from the unmodified PEI polymers (Figure 4). Because the high transfection efficiency of PEI is attributed to the buffering ability of the secondary amines in the acidic endosomes, any substantial shifts in the secondary amine pK_a is therefore likely to hinder or eliminate this endosomal release ability, thereby also reducing transfection efficiency.

Cyclodextrin grafting to bPEI also reduces polymer toxicity (Figure 3). Polymers with higher CD grafting densities have increased IC_{50}'s over the unmodified bPEI. For example, the IC_{50} of CD−bPEI with 16% grafting is

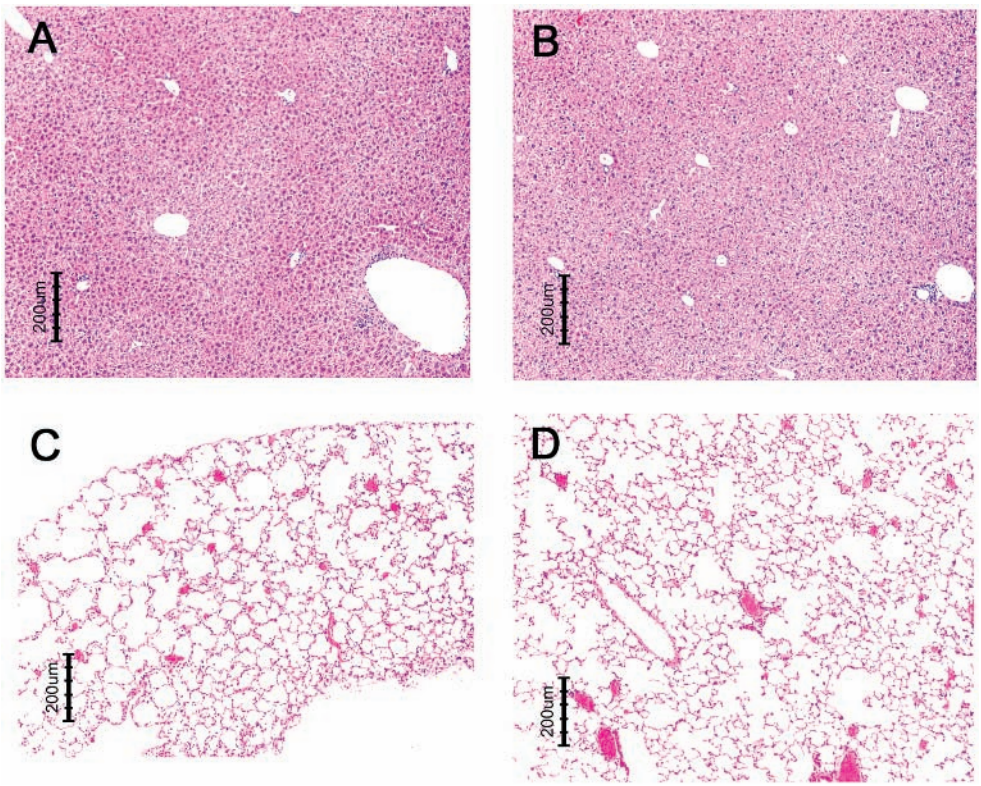


Figure 9. H&E stained tissue sections from nude mice treated with 120 μg of plasmid DNA formulated with CD−lPEI + AD−PEG. (A) Liver of treated animal; (B) liver of untreated animal; (C) lung of treated animal; (D) lung of untreated animal.

6.7 mM (concentration of amines), over 20-fold higher than bPEI (0.28 mM). The cyclodextrin grafting could reduce polycation toxicity by increasing polymer solubility, by capping primary amines, or by reducing binding affinity. Hydrophobic polymers tend to impart higher cell toxicity. Previous structure/function studies with other CD-polymers revealed reduced IC_{50}'s with less water-soluble polymers (*3*, *4*−*7*, *9*). Cyclodextrins are highly water soluble molecules, and linear, CD-containing polymers have very high water solubility. Indeed, the CD−bPEI-based polyplexes have higher critical flocculation concentrations than bPEI-based polyplexes. The CD-monotosylates also react with PEI primary amines. Lipids containing primary amines have been reported to disrupt PKC function, causing cell toxicity (*24*). One proposed mechanism of polycation toxicity has been interference with protein kinase activity after internalization. Removal of the primary amines may therefore reduce polymer toxicity if at least a portion of the toxicity is from this mechanism. PEI derivatives prepared by chemical modification of the nitrogen atoms, including galactosylated, mannosylated, and acetylated PEI synthesized by reactions with primary amines, have also demonstrated reduced toxicity over the parent polymers (*10*−*12*). CD−PEI may have decreased toxicity in a similar fashion. Cyclodextrin grafting can also mediate lower toxicity by decreasing nonspecific binding of PEI with proteins or cellular structures. In addition to converting primary amines to secondary amines, cyclodextrins are also large, bulky molecules that can sterically reduce nonspecific binding affinities.

It is interesting to note that Uekama and colleagues have noticed the opposite effect of cyclodextrin grafting on cyclodextrin-dendrimer conjugates (*25*, *26*). Their initial study demonstrated that α-, β-, and γ-cyclodextrin conjugation to polyamidoamine dendrimers increases transfection efficiency, with the proposed mechanism of enhancing endosomal release (*25*). α-Cyclodextrin-dendrimers were found to have the highest transfection efficiency and a subsequent paper focusing on these dendrimers reports increased transfection and toxicity with higher cyclodextrin substitution (*25*).

The best CD−bPEI for plasmid delivery was determined to have 8% PEI amine grafting. Similarly, the best CD−lPEI was synthesized with 12% grafting. The abilities of these polymers to complex and deliver nucleic acids were compared with bPEI and lPEI. CD−bPEI and CD−lPEI spontaneously condense plasmid DNA to small, spherical particles (Figure 5). Although polycation/DNA complexes can be reproducibly formulated with spherical morphologies in water solutions, complexes aggregate rapidly in the presence of salt. This rapid aggregation, along with serum protein or platelet interactions, can cause death in vivo by blockage of lung capillaries (*16*). For systemic administration, a vital concern is the stabilization of these polyplexes. We have demonstrated previously a particle modification approach based on inclusion complex formation between adamantane and cyclodextrin (*4*, *8*, *9*). Here, this methodology is extended to stabilize CD−PEI polyplexes against salt-induced aggregation. A solution of AD−PEG (at a 2 AD:1 CD ratio) was added to DNA to formulate stabilized particles. The adamantane assembles inside the CD cup, leaving the PEG to form a protective brush layer on the particle surface (Figure 5b). Polyplex morphology is not significantly changed by this method of PEGylation (Figures 5c and 5d). Particle stabilization by PEGylation was assessed by monitoring particle size in salt solutions as a function of time. Without PEGylation, PEI and CD−PEI polyplexes aggregate upon exposure to ionic solutions (150 mM strength), as indicated by the increase in particle diameter measured by light scattering (Figure 6). These polyplexes have high zeta potentials (∼30−40 mV, not shown). The addition of AD−PEG to PEI

particles does not prevent aggregation because the PEG remains free in solution, unable to associate with the particles. AD−PEG is able to stabilize CD−bPEI and CD−lPEI particles (zeta potentials ∼10 mV, not shown) by forming inclusion complexes with surface available cyclodextrins (Figure 6). The PEGylated particles completely form by self-assembly (electrostatic interactions between CD−PEI and DNA, guest−host hydrophobic interactions between adamantane and cyclodextrin) and can be formulated under several conditions. For example, stable particles can be prepared at a wide range of concentrations and volumes and with different formulation orders. Our preferred method involves first mixing the AD−PEG and CD−PEI polymers and then adding the solution to DNA because this procedure allows for particles to be formulated at high concentrations (if AD−PEG is added to preformed polyplexes, the concentration is limited by the critical flocculation concentration of the polyplexes).

The best CD−PEI polymers were tested for their ability to deliver plasmids to cultured cells (Figure 7). The labeled plasmids were complexed with PEI and CD−PEI polymers and exposed to PC3 cells for 15 min. Surface-associated polyplexes were removed, and DNA uptake was analyzed by flow cytometry. CD−PEI polymers deliver plasmids with higher efficiency than the parent PEI polymers (75% CD−lPEI vs 40% for lPEI and 70% for CD−bPEI vs 30% for bPEI). Additionally, PEGylation does not impede the uptake of CD−PEI delivery vehicles.

The transfection efficiencies of the CD−PEI polymers were compared to their parent PEI's by using the expression of EGFP (analysis by flow cytometry) in PC3 cells. lPEI and bPEI show approximately 15% EGFP positive cells, and this amount is not changed by the addition of chloroquine (Figure 8). These data are very consistent with literature reports. CD−bPEI reveals the same transfection results as bPEI in the absence of chloroquine, but in its presence, shows significantly enhanced transfection (Figure 8). CD−lPEI gives better expression than lPEI in both the presence and absence of chloroquine (Figure 8). It is possible that the greater than or equal to transfection of the CD−PEI's compared to the parent PEI's is due to their increased uptake (Figure 7). Of interest is the fact that chloroquine significantly enhances the transfection with the CD−PEI's while it does not with the parent PEI's, indicating that there are differences in the intracellular behaviors of the CD-containing and parent PEI's. While recent evidence does support the "proton sponge hypothesis" for enhanced transfection using polycation−DNA polyplexes containing proton buffering polyamines (*27*), it is likely that it is not the only factor contributing to the transfection efficiencies of PEI (*28*, *29*). Itaka et al. suggest that both lPEI and bPEI complexes rapidly escape endosomes but that the lPEI dissociates more readily from the plasmid DNA to enhance gene expression (*29*). The PEGylation of the CD−PEI delivery vehicles produces a reduction in the transfection, expecially for the CD−bPEI. Mishra et al. have shown that PEI-based polyplexes aggregate in culture media, enter cells as aggregates, and have high expression while PEGylated PEI-based particles enter cells as individual particles and give lower gene expression (*30*). It is most likely that the PEGylated CD−PEI particles are not aggregating prior to cell uptake as opposed to either unPEGylated CD−PEI- or PEI-containing polyplexes (Figure 6). Of significance is the observation that the PEGylated CD−lPEI particles can provide good transfection in the absence of chloroquine. This formulation has several desirable features for in vivo use: (i) reduced toxicity, (ii) stable in physiologic salt solutions, and (iii) good transfection efficiencies. This formulation was investigated in mice.

The low toxicity of the CD−PEI delivery particles compared to the PEI-based particles obtained from in vitro experiments was also observed in vivo. Tail vein injections in mice of up to 120 μg of DNA formulated with CD−lPEI + AD−PEG did not produce any acute toxicity. lPEI−DNA polyplexes at this dose are lethal to mice (*16*). Additionally, numerous blood chemistries (Table 2) suggest that this dose of CD−lPEI + AD−PEG + DNA is well tolerated. PEI−DNA complexes administered iv cause liver necrosis as well as red bood cell adhesion in the lung (*16*). Balb/c mice treated with CD−lPEI + AD−PEG did not show any of these symptoms and organs essentially looked normal (Figure 9). When lower doses of PEI−DNA are injected into the tail vein of mice, the main organ accumulating the DNA is the lung (*16*, *31*). This is likely due to aggregation of the polyplexes and their capture by the lung microvasculature. With PEGylated CD−lPEI−DNA particles, the aggregation rate is substantially reduced and they primarily accumulate in liver as opposed to lung (4 orders-of-magnitude larger amount in liver than lung). Additionally, gene expression is observed in the liver and is below detection limits in all other organs. Thus, the CD−lPEI + AD−PEG + DNA delivery vehicle provides an avenue for liver gene expression from a systemic administration.

ACKNOWLEDGMENT

J.D.H. acknowledges the Whitaker Foundation for a doctoral fellowship.

LITERATURE CITED

(1) Hwang, S., and Davis, M. E. (2001) Cationic polymers for gene delivery: Designs for overcoming barriers to systemic administration. *Curr. Opin. Mol. Ther. 3*, 183−191.

(2) Gonzalez, H., Hwang, S., and Davis, M. E. (1999) New class of polymers for the delivery of macromolecular therapeutics. *Bioconjugate Chem. 10*, 1068−1074.

(3) Hwang, S., Bellocq, N., and Davis, M. E. (2001) Effects of Structure of Beta-Cyclodextrin-Containing Polymers on Gene Delivery. *Bioconjugate Chem. 12*, 280−290.

(4) Pun, S. H., and Davis, M. E. (2002) Development of a Non-Viral Gene Delivery Vehicle for Systemic Application. *Bioconjugate Chem. 13*, 630−639.

(5) Reineke, T. M., and Davis, M. E. (2003) Structural effects of carbohydrate-containing polycations on gene delivery. 1. Carbohydrate size and its distance from charge centers. *Bioconjugate Chem. 14*, 247−254.

(6) Reineke, T. M., and Davis, M. E. (2003) Structural effects of carbohydrate-containing polycations on gene delivery. 2. Charge center type. *Bioconjugate Chem. 14*, 255−261.

(7) Popielarski, S. R., Mishra, S., and Davis, M. E. (2003) Structural effects of carbohydrate-containing polycations on gene delivery. 3. CD type and functionalization. *Bioconjugate Chem. 14*, 672−678.

(8) Bellocq, N., Pun, S., and Davis, M. E. (2003) Transferrin-containing, cyclodextrin polymer-based particles for tumor-targeted gene delivery. *Bioconjugate Chem. 14*, 1122−1132.

(9) Davis, M. E., Pun, S. H., Bellocq, N. C., Reineke, T. M., Popielarski, S. R., Mishra, S., and Heidel, J. D. (2004) Self-Assembling Nucleic Acid Delivery Vehicles via Linear, Water-Soluble, Cyclodextrin-Containing Polymers. *Curr. Med. Chem. 11*, 1241−1253.

(10) Zanta, M., Boussif, O., Adib, A., and Behr, J.-P. (1997) In Vitro Gene Delivery to Hepatocytes with Galactosylated Polyethylenimine. *Bioconjugate Chem. 8*, 839−844.

(11) Forrest, M. L., Meister, G. E., Koerber, J. T., and Pack, D. W. (2003) Partial acetylation of polyethylenimine enhances in vitro gene delivery. *Pharm. Res. 21*, 365−371.

(12) Thomas, M., and Klibanov, A. (2002) Enhancing polyethylenimine's delivery of plasmid DNA into mammalian cells. *Proc. Natl. Acad. Sci. U.S.A.* 99, 14640−14645.
(13) Boussif, O., Lezoualcl'h, F., Zanta, M., Mergny, M., Scherman, D., Demeneix, B., and Behr, J.-P. (1995) A versatile vector for gene and oligonucleotide transfer into cells in culture and in vivo: Polyethylenimine. *Proc. Natl. Acad. Sci. U.S.A. 92*, 7297−7301.
(14) Brunner, S., Sauer, T., Carotta, S., Cotten, M., Saltik, M., and Wagner, E. (2000) Cell cycle dependence of gene transfer by lipoplex, polyplex and recombinant adenovirus. *Gene Ther. 7*, 401−407.
(15) Kichler, A., Leborgne, C., Coeytaux, E., and Danos, O. (2001) Polyethylenimine-mediated gene delivery: a mechanistic study. *J. Gene Med. 3*, 135−144.
(16) Chollet, P., Favrot, M., Hurbin, A., and Coll, J.-L. (2001) Side-effects of a systemic injection of linear polyethylenimine-DNA complexes. *J. Gene Med. 4*, 84−91.
(17) Ogris, M., Brunner, S., Schüller, S., Kircheis, R., and Wagner, E. (1999) PEGylated DNA/transferrin−PEI complexes: reduced interaction with blood components, extended circulation in blood and potential for systemic gene delivery. *Gene Ther. 6*, 595−605.
(18) Erbacher, P., Bettinger, T., Belguise-Valladier, P., Zou, S., Coll, J.-L., Behr, J.-P., and Remy, J.-S. (1999) Transfection and Physical Properties of Various Saccharide, Poly(ethylene glycol), and Antibody-Derivatized Polyethylenimines (PEI). *J. Gene Med. 1*, 210−222.
(19) Tang, M. X., and Szoka, F. C. (1997) The Influence of Polymer Structure on the Interactions of Cationic Polymers with DNA and Morphology of the Resulting Complexes. *Gene Ther. 4*, 823−832.
(20) Wen, S. F., Zie, L., McDonald, M., DiGiacomo, R., Chang, A., Gurnani, M., Shi, B., Liu, S., Indelicato, S. R., Hutchins, B., and Nielsen, L. L. (2000) Development and validation of sensitive assays to quantitate gene expression after p53 gene therapy and paclitaxel chemotherapy using in vivo dosing in tumor xenograft models. *Cancer Gene Ther. 7*, 1469−1480.
(21) Wen, S. F., Chen, Z., Nery, J., and Faha, B. (2002) Characterization of adenovirus p21 gene transfer, biodistribution, and imune response after local ocular delivery in New Zealand white rabbits. *Exp. Eye Res. 77*, 355−365.
(22) Suh, J., Lee, S. H., and Zoh, K. D. (1992) A novel host containing both binding site and nucleophile prepared by attachment of β-cyclodextrin to poly(ethylenimine). *J. Am. Chem. Soc. 114*, 7916−7917.
(23) Suh, J., Hah, S. S., and Lee, S. H. (1997) Dendrimer Poly(ethylenimine)s linked to β-cyclodextrin. *Bioorg. Chem. 25*, 63−75.
(24) Bottega, R., and Epand, R. (1992) Inhibition of Protein Kinase C by Cationic Amphiphiles. *Biochemistry 31*, 9025−9030.
(25) Arima, H., Kihara, F., Hirayama, F., and Uekama, K. (2001) Enhancement of gene expression by polyamidoamine dendrimer conjugates with α-, β- and γ-cyclodextrins. *Bioconjugate Chem. 12*, 476−484.
(26) Kihara, F., Arima, H., Tsutsumi, T., Hirayama, F., and Uekama, K. (2003) In vitro and in vivo gene transfer by an optimized α-cyclodextrin conjugate with polyamidoamine dendrimer. *Bioconjugate Chem. 14*, 342−350.
(27) Sonawane, N. D., Szoka, F. C., and Verkman, A. J. (2003) Chloride Accumulation and Swelling in Endosomes enhances DNA Transfer by Polyamine-DNA Polyplexes. *J. Biol. Chem. 278*, 44826−44831.
(28) Funhoff, A. M., van Nostrum, C. F., Koning, G. A., Schuurmans-Nieuwenbroek, N. M. E., Crommelin, D. J. A., and Hennick, W. E. (2004) Endosomal Escape of Polymeric Gene Delivery Complexes is Not Always Enhanced by Polymers Buffering at Low pH. *Biomacromolecules 5*, 32−39.
(29) Itaka, K., Harada, A., Yamasaki, Y., Nakamura, K., Kawaguchi, H., and Kataoaka, K. (2004) In Situ Single Cell Observation by Fluorescence Resonance Energy Transfer Reveals Fast Intra-Cytoplasmic Delivery and Easy Release of Plasmid DNA Complexed with Linear Polyethylenimine. *J. Gene Med. 6*, 76−84.
(30) Mishra, S., Webster, P., and Davis, M. E. (2004) PEGylation Significantly Affects Cellular Uptake and Intracellular Trafficking of Nonviral Gene Delivery Particles. *Eur. J. Cell Biol. 83*, 1−15.
(31) Zou, S.-M., Erbacher, P., Remy, J.-S., and Behr, J.-P. (2000) Systemic linear polyethylenimine (L-PEI)-mediated gene delivery in the mouse. *J. Gene Med. 2*, 128−134.

BC049891G

Self-Assembling Nanocomplexes from Insulin and Water-Soluble Branched Polyesters, Poly[(vinyl-3-(diethylamino)-propylcarbamate-*co*-(vinyl acetate)-*co*-(vinyl alcohol)]-graft-poly(L-lactic acid): A Novel Carrier for Transmucosal Delivery of Peptides

M. Simon,[†] M. Wittmar,[†] U. Bakowsky,[‡] and T. Kissel*[,†]

Department of Pharmaceutics and Biopharmacy, Philipps-University, Ketzerbach 63, D-35037, Marburg, Germany, and Department of Biopharmaceutics and Pharmaceutical Technology, Saarland-University, Im Stadtwald, D-66123, Saarbrücken, Germany. Received September 9, 2003; Revised Manuscript Received May 6, 2004

The design of carriers for protein delivery that provide protection against enzymatic degradation and facilitate protein transport across epithelial surfaces, thus avoiding parenteral administration, remains a challenge. Self-assembling nanoscale protein/polymer complexes might present a promising approach. We synthesized water-soluble, amphiphilic polyesters, poly[(vinyl-3-(diethylamino)-propylcarbamate-*co*-(vinyl acetate)-*co*-(vinyl alcohol)]-graft-poly(L-lactic acid), containing a positively charged backbone, and studied the spontaneous formation of nanocomplexes (NC) with insulin. NC were characterized using dynamic light scattering, zeta-potential measurements, and atomic force microscopy (AFM). Insulin loading was determined with HPLC, and the binding constants were obtained by isothermal titration calorimetry (ITC). The NC formation was followed using nephelometric and light scattering techniques. Water-soluble, positively charged, branched polyesters with amphiphilic properties were obtained in a three-step polymer-analogous reaction. The degree of amine substitution, DS, in the PVAL backbone was varied between 0.04 and 0.5, and grafting this backbone with L-lactide increased the molecular weight from 18 kDa to 81 kDa. The polymer composition was optimized to facilitate NC formation with insulin resulting in a DS of 0.09 and a poly(L-lactide) side chain substitution of 0.5 with an average chain length of two lactic acids. Depending on polymer composition, stable NC of 200−500 nm diameter were formed with insulin, and the binding constants ranged from 4.7×10^5 to 9.5×10^6 M^{-1}. Positively charged surface charges ranging from +5 to +35mV and an insulin loading up to 98% of 33 IU/mL were obtained. The NC visualized by AFM revealed spheroidal particles with an entangled internal structure. It was demonstrated that this class of multifunctional polymers is capable of self-assembly with a peptidic substrate. The resulting nanosized complexes offer the potential for mucosal insulin/protein delivery and merit further investigations under in vivo conditions.

INTRODUCTION

Diabetes mellitus is the most common of the serious metabolic diseases and prevalence in Western societies is estimated to be about 1%. Long-term complications involving the eyes, kidneys, nerves, and blood vessels present a heavy burden for the health care system in western societies. The intensified insulin therapy for diabetic patients requires up to four subcutaneous injections per day to maintain adequate control of serum glucose levels. Compliance with such demanding dosing regimes is difficult for the patient and make the development of an alternative form of insulin administration clearly appealing.

Numerous attempts to deliver insulin by application routes avoiding injections have been reported in the literature. Peroral, pulmonary, and nasal insulin administrations fall into this category, but enzymatic lability and inefficient transport across mucosae provide formidable challenges and lead to low and variable bioavailabilities (*1*). The intranasal route is most attractive for chronic administration of peptides and proteins (*2*). However, nasal insulin absorption is low without coadministration of absorption enhancers which open the epithelial barrier and/or prolong the residence time in the nasal cavity. Promoters such as bile salts, chelating agents, or the surfactant laureth-9 have shown undesirable toxic side effects after chronic administration (*3*).

Proteins delivery systems relying on complexation and assembly of proteins with amphiphilic polymers could present an alternative to the absorption enhancers described above. These polymers form nanoscale complexes with proteins through electrostatic and van der Waals interactions, protecting them against loss of biological activity and increasing their transmucosal uptake. Several polymers such as chitosan (*4*), poly(glutamine) (*5*), poly(ethylenimine-*co*-polyester) (*6*), AB block-copolymers, e.g., PEO−poly(L-lysine) (*7*) or PEO−PLGA (*8*), polyacrylates (*9, 10*), or poly(L-lysine) derivates (*11*) have been proposed for insulin delivery.

Nanoscale delivery systems with strong bioadhesive properties seem to be a promising approach (*12*) because significant insulin uptake after nasal or oral administra-

* To whom correspondence should be addressed. Tel: +49-6421-282 5881, Fax: +49-6421-282 7016, E-mail: kissel@staff.uni-marburg.de.

[†] Philipps-University.

[‡] Saarland-University.

10.1021/bc0341627 CCC: $27.50 © 2004 American Chemical Society
Published on Web 07/01/2004

tion without use of penetration enhancers was observed. Nanoparticles (NP) of insulin and chitosan were obtained in the size range of ca. 350 nm by ionotropic gelation, leading to blood glucose reduction in rabbits after nasal administration (*4*). Oral administration of insulin containing NP (~700 nm) from a fumaric and sebacic acid copolyanhydride resulted in a significant blood glucose reduction and strong adhesive NP/mucus interactions (*13*). For intranasal drug delivery polymers with positively charged groups such as chitosan, poly-L-lysines, or protamine has been demonstrated to increase bioadhesion and membrane permeability (*3*).

Another important concern is the fabrication of NP. Nanoencapsulation techniques often rely on formation of emulsions with subsequent solvent evaporation. Usually a high energy input is necessary to obtain nanoemulsions and hence NP. Under those conditions, protein stability is often compromised through temperature, pH, and shear stress at interfacial surfaces with organic solvents (*14*).

Therefore, a self-assembling system composed of an "intelligent" polymer designed for spontaneous complexation of a target-protein under gentle aqueous conditions might provide advantages over classic nanoencapsulation strategies. Since the pioneering work of Morawetz and Hugues (*15*), it is recognized that globular proteins can form stable complexes with polyelectrolytes. The association of proteins with polyelectrolytes can result in soluble complexes, complex coacervation, precipitation, or gelation of the resulting system (*16, 17*). The two most important parameters governing polymer/protein association in water are the hydrophobicity and the electrostatic interactions of the partners. Additional phenomena, such as gelation and retardation of precipitation, are thought to result directly from the presence of hydrophobic association in polyelectrolyte complexes (PEC) (*18*).

Optimal polymer properties for self-assembly with proteins are rarely found in naturally occurring macromolecules. We report here the design and characterization of new synthetic polymers with amphiphilic properties suitable as a self-assembling protein carrier system. By grafting L-lactide onto a hydrophilic, charge-modified poly(vinyl alcohol) backbone with covalently bound diethylaminopropylamine groups, amphiphilic biodegradable comb polyesters with lipophilic side chains were obtained. We hypothesized that insulin, dissolved at a pH above its point of isocharge (PI ~ pH 5.3), carries an overall negative charge (*19*) and will form PEC with the cationic polymers by electrostatic and hydrophobic interactions. This work is an extension of our experiments using negatively charged branched polyesters, namely SB−PVA-*g*-PLGA for transmucosal delivery of tetanus toxoid (*20, 21*).

EXPERIMENTAL PROCEDURES

Materials. Diethylaminopropylamine (purum, >98%), poly(vinyl alcohol) (PVA) (15000 g/mol; degree of polymerization 300 ($P = 300$); degree of hydrolysis 86−89%), carbonyl diimidazole, (CDI), (purum, 97%), *N*-methylpyrrolidone (NMP) (purum, absolute), and 1,3-dimethyl-3,4,5,6-tetrahydro-2(1*H*)-pyrimidinone (DMPU) (puriss., absolute, over molecular sieves) were purchased from Fluka GmbH Germany and used as received. L-lactide-(S-grade) (Boehringer Ingelheim, Germany) was recrystallized twice from ethyl acetate. Tin(II) 2-ethylhexanoate (Aldrich, Germany) was used as received. Tetrahydrofuran (THF) (BASF, Germany) was dried over sodium and distilled under nitrogen before use. *N*,*N*-Dimethylacetamide (for HPLC, 99.8%) was purchased from Fluka and Lithium bromide (extra pure) was ordered from Merck. Human recombinant insulin powder (26.2 IU/mg) was a gift from Aventis Pharma AG (Germany). All other chemicals were of the highest analytical grade commercially available.

Polymer Synthesis. The synthesis was described in detail elsewhere (*22*). Poly[(vinyl-3-(diethylamino)propylcarbamate-*co*-(vinyl acetate)-*co*-(vinyl alcohol)]-graft-poly(L-lactic acid) were synthesized in a three-step synthesis. Briefly, amino functions were introduced to the PVA backbone using CDI linker chemistry followed by grafting of L-Lactic acid chains using a ring-opening polymerization in bulk. The products were purified by ultrafiltration and lyophilized.

Nomenclature. The source-based IUPAC nomenclature for these polymers is poly(vinyl 3-(diethylamino)-propylcarbamate-*co*-vinyl acetate-*co*-vinyl alcohol)-graft-poly(L-lactide). As abbreviation we used 'DEAPA' (diethylaminopropylamine) followed by the average number of amine-carrying monomer units per 'PVA' (poly(vinyl alcohol)) chain with a polymerization degree of 300. The grafting of PLLA with the average chain length, calculated from feeding, in parentheses follows (e.g., DEAPA-(26)-PVA_{300}-*g*-PLLA(2)). For simplification, the following code was selected: P for the DEA(P)A substitution, afterward the number of amine groups per PVA in parentheses, followed by number of the lactide amount from feeding and LL as index, indicating grafting with pure L-lactide side chains (e.g. $P(26)\text{-}2_{LL}$).

Polymer Characterization. ^1H and ^{13}C NMR spectroscopic data were collected using a JEOL Eclipse+ 500 and a JEOL GX 400 D at a frequency of 500 or 400 MHz for ^1H NMR and 126 or 101 MHz for ^{13}C NMR, respectively, at 50 °C in d_6-DMSO (euriso-top, <0.02% HDO+D_2O). 40 to 50 mg samples were used for each measurement. ^1H NMR was performed with 64 and ^{13}C NMR with 4096 scans.

Gel permeation chromatography (GPC) was performed using a SDV linearM column (8 × 300 mm, 5 μm, with precolumn 8 × 50 mm) from Polymer Standard Services (Mainz). The eluent was dimethylacetamide with an addition of 2.50 g LiBr/L and a flow rate of 0.5 mL/min at 60 °C. The GPC consisted of a Merck-Hitachi AS-2000A autosampler, an L-6000 pump, a Merck T-6300 Column Thermostat and Differential Refractometer Optilab DSP, a Wyatt DAWN Eos multiangle light-scattering detector (The d*n*/d*c* was calculated with total mass recovery, Dawn EOS calibrated against PMMA 200k) and a Duratec DDG-75 degasser. The molecular weights of the samples were determined (third-order fit) with the Wyatt Astra V4.73 Software.

Nanocomplex Preparation and Characterization. *Preparation of Insulin Nanocomplexes.* An insulin stock solution (2.50 mg/mL) was prepared in two steps. 1. The insulin powder was dissolved in 87% (V/V) 1.15×10^{-2} N HCl in 10.0 mL Pyrex tubes. 2. 13% (V/V) of 0.1 N tris-(hydroxymethyl)aminomethane solution was added resulting in a clear Tris-buffer with low ionic strength ($I = 0.01$) and pH 7.40. Polymer stock solutions in concentrations (Table 2) from 0.64 mg/mL for P(150) up to 7.0 mg/mL for $P(26)\text{-}3_{LL}$ were prepared in Tris-buffer. An equal volume of the stock solutions of insulin and polymer were mixed resulting in defined mass ratios (Table 2) of insulin/polymer 1: 0.26−2.8 (m/m) in the final NC-solution. The colloidal polymer−insulin complexes formed immediately after mixing by spontaneous self-assembly.

Particle Size and ζ-Potential. Average size and the size distribution of the NCs was investigated using photon

Table 1. Physicochemical Properties of the Polymers

polymer	length of side chain[a]	MW, g/mol[b]	M_n/M_w (by LS)[c] g/mol	substitution (amine)[d]/%	substitution (lactide)[d]/%	yield (w/w)[f] %
DEAPA(13)	–	16200	14640/16640	4.4	–	78
DEAPA(26)	–	17800	15410/19590	8.1	–	74
DEAPA(68)	–	23900	33590/67790	22.7	–	42
DEAPA(150)	–	38700	–	50.0	–	22
DEAPA(26)-(1)	2.1	34500	42940/81680	8.1	32.1	84
DEAPA(26)-(2)	3.1	51700	221900/385500[e]	8.1	48.7	67
DEAPA(26)-(2)	2.8	48300	–	8.5	46.8	–
DEAPA(26)-(3)	4.3	74600	71550/124500	8.1	60.9	70

[a] Average lactic acid units per chain calculated by ^{1}H NMR data. [b] Molecular weight calculated from ^{1}H NMR data. [c] Molecular weights measured by GPC-MALLS (dawn Eos + optilab). [d] Percent of hydroxyl groups carrying amine or lactid calculated on *P* (PVAL) = 300 (*P*: degree of polymerization). [e] Heavy polymer aggregation. [f] Yield calculated on used educt masses and resulting product mass.

Table 2. Characterization of NC

polymer	mass ratio: insulin/polymer[a]	PCS: NC sizes/nm	AFM: NC sizes/nm[b]	AFM: diameter/height	ζ-potential, mV	drug loading[c]	charge ratio±[d]	stoichiometry: turb./ITC[e]
DEAPA(13)	1:0.45	450 ± 89	–	–	3.0 ± 0.4	20.4 ± 0.6	1.15	–
DEAPA(26)	1:0.50	394 ± 61	274 ± 68	1.04	17.7 ± 2.7	78.9 ± 1.2	0.97	12.4/22.0
DEAPA(68)	1:0.23	195 ± 30	–	–	24.6 ± 3.2	94.0 ± 2.9	0.75	25.6/83.2
DEAPA(150)	1:0.26	430 ± 98	434 ± 43	1.27	34.6 ± 4.7	97.1 ± 2.5	0.61	45.4/164
DEAPA(26)-(1)	1:1.60	370 ± 48	418 ± 51	1.15	15.0 ± 2.4	72.4 ± 2.6	0.56	7.1/16.0
DEAPA(26)-(2)	1:1.70	250 ± 39	285 ± 65	1.07	18.8 ± 3.3	76.4 ± 13.4	0.75	9.5/16.0
DEAPA(26)-(3)	1:2.80	290 ± 120	340 ± 86	1.35	32.7 ± 2.5	98.7 ± 0.1	0.50	–

[a] Optimized mixing ratios, standard insulin concentration 1.25 mg/mL in NC solution. [b] Measured from 25 × 25 μm scale AFM images. [c] Determined by HPLC after filtration of NC with 0.22 μm. [d] Ratios at the turbidimetric/scattering extrema. [e] Molar insulin/polymer ratio: first value at extrema turbidimetry, second value at turning point ITC.

correlation spectroscopy (*21*) with a Zetasizer 4 equipped with an AZ110 cell (Malvern Instruments UK), a 4-mV laser source, a 64-channel correlator, and a multiangle photomultiplier. Each buffer solution was filtered through 0.2 μm Acrodisc filters (Gelman Laboratory), and measurements were performed in serial mode. The photon correlation spectroscopy (V.1.26 Software) was used to calculate particle mean diameter and width of the fitted Gaussian distribution. The ζ-potential of the NC suspension was determined by laser-Doppler-anemometry in distilled water (conductance 0.055 μs/cm) using the AZ 104 cell. The ζ-potential was derived from electrophoretic mobility of the NC. Each measurement was performed in triplicate.

Insulin Loading of Nanocomplexes. After centrifugation of the complex dispersions in 2.0 mL Eppendorf-Cups for 30 min at 14,000 rpm, the supernatant was filtered through 0.1 μm Millex (Millipore), and the insulin content was determined by high performance liquid chromatography (HPLC). HPLC was based on a LiChrosphere100 RP18 (5 μm), 250 × 4 mm column (Merck) with isocratic elution (65% H_2O + 0.1% TFA/35% acetonitrile 90/ H_2O 10 + 0.1%TFA (flow rate 1.0 mL/min) and detection of insulin by a fluorescence spectrophotometer (Ex 276 nm/ Em 600 nm). The HPLC system consisted of a T6300 column thermostat, a 6200A pump, a F1050 fluorescence spectrophotometer, an AS 2000A autosampler (Merck, Germany), and a vacuum degasser (Duratec). Data processing was performed with the Millenium^{32} software Version 3.05. (Waters).

Isothermal Titration Calorimetry. Microtitration calorimetry was performed using the MSC-ITC equipment from Microcal Inc. (Northampton). The cell volume was 1351 μL containing insulin, and the syringe volume was 250 μL with the respective polymer solution. All Tris buffer solutions were filtered with 0.2 μm Acrodisc filters, and the pH values in the final solutions were maintained at 7.40 to avoid pH compensation signals. The injection scheme was 14 × 15 μL every 190 s at 400 rpm at 25 °C, and data processing was performed with the software Microcal Origin 3.5. The measurements were carried out in triplicate.

NC Stoichiometry by Colloid Titration. Turbidimetric measurements were carried out according to the method of Kokufuta et al. (*23, 24*). A constant volume of 0.30 mL insulin stock solution (2.50 mg/mL) was mixed with an appropriate volume of polymer solution and filled up with Tris buffer to a constant volume of 3.30 mL to avoid dilution effects. Transmission data were recorded on a Shimadzu UV-160 spectrophotometer at 630 nm using Suprasil cuvettes with 10 mm path length. Scattering data were obtained in the same way as PCS at an angle of 90°. The extrema were read directly from curves after plotting the data points with B-spline connection using Microcal Origin 6.0 software. Determinations were carried out in triplicate.

Atomic Force Microscopy. The polymer/insulin NC were prepared as described above. After 20 min, the complexes were directly transferred onto a silicon chip by dipping into the NC solution. Atomic force microscopy was performed on a Digital Nanoscope IV Bioscope (Veeco Instruments, Santa Barbara, CA) as described elsewhere (*25*). The microscope was vibration-damped. Commercial pyramidal Si_3N_4 tips (NCH-W, Veeco Instruments, Santa Barbara, CA) on a cantilever with a length of 125 μm, a resonance frequency of about 220 kHz, and a nominal force constant of 36 N/m were used. All measurements were performed in tapping mode to avoid damage of the sample surface. The scan speed was proportional to the scan size, and the scan frequency was between 0.5 and 1.5 Hz. Images were obtained by displaying the amplitude signal of the cantilever in the trace direction, the height signal in the retrace direction, and the phase signal in retrace direction, both signals being simultaneously recorded. The results were visualized either in height, amplitude, or/and in phase modus. The phase mode permits assessment of material properties (viscoelastic properties). These are expressed as "brightness" of the AFM image.

RESULTS AND DISCUSSION

Synthesis and Structural Characterization of the Copolymers. Nanoscience is a rapidly developing area of research with considerable potential for drug delivery because cellular interaction and transport of nanoscale objects may offer new opportunities not available to larger devices. Especially NP based on hydrophilic/biodegradable polymers can be designed to provide particle characteristics, protease inhibition, and permeation enhancement for peptidic drugs.

To explore the potential of the NP approach, novel materials are necessary which allow formation of NP under mild conditions, such as self-assembly leading to nanocomplexes. We have designed amphiphilic charge-containing biodegradable copolyesters composed of a hydrophilic PVA backbone grafted with short hydrophobic lactic acid groups to complex proteins and peptides. Cationic carriers such as DEAE-dextran, chitosan, and poly(L-lysin) are suitable for complexation of a large number of negatively charged pharmacologically active agents, e.g. insulin, oligonucleotides, and DNA (*26*−*28*).

The use of CDI chemistry allows the modification of amine substitution in a broad range. We coupled amino groups to the PVA backbone and investigated the effect of different degrees of DEAPA substitution on complex formation with insulin. PVA is known as a nontoxic and biocompatible polymer which exhibits mucoadhesive properties and is therefore used in drug delivery (*29*). The degree of amino substitution was varied from moderate 13 (DS = 0.04), up to a highly substituted backbones with 150 (DS = 0.5) of the ca. 300 hydroxyl groups of PVA substituted (cf. Table 1). To introduce amphiphilicity in the PVA backbone, hydrophobic L-lactic acid side chains were grafted to the backbone in a second step to yield a brushlike and biodegradable copolyester structure. For a P(26) backbone (DS = 0.09), the highest possible lactic acid substitution while remaining water soluble was 1:3 (w/w). By combining hydrophilic backbones with hydrophobic domains, numerous benefits were reported in the literature such as increased drug loading, self-association, or complex stability (*18, 30, 31*).

The polyesters were characterized using ^{1}H NMR spectroscopy and gel permeation chromatography. A typical ^{1}H NMR spectrum (Figure 1) of these graft polymers show signals of both polymers, PVA, and poly(L-lactide). The ratio between end group and central group integrals depends on the side chain length and could be used to calculate the average chain length and the molecular weight (MW) of the sample. The reproducibility of the synthesis is demonstrated for two different batches of polymer P(26)-2_{LL} (Table 1) with similar degrees of substitution. It could be shown that the MW of the polyesters is increasing as expected. The polymer with the highest calculated side chain length, P(26)-3_{LL}, shows the highest molecular weight, and the polymer with the lowest lactic acid grafting, P(26)-1_{LL}, yields the smallest molecular weight of all polyesters. The molecular weights calculated from NMR spectra of all tested polymers are in good agreement with the number average molecular weights, M_n, obtained by GPC/MALLS. The only exception was P(26)-2_{LL}, which exhibited an apparent higher molecular weight measured by light scattering caused by a fraction of polymer aggregates. Otherwise, the elution time of P(26)-2_{LL} measured by a refractive index detector is in the range of the other polyesters (Figure 2), indicating a MW of the same order of magnitude.

Formation of NC with Insulin. Complex formation between proteins and polymers is influenced by a large

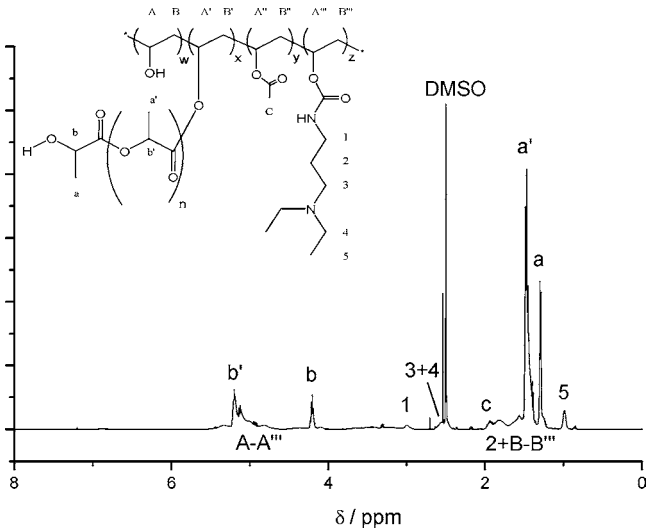


Figure 1. ^{1}H NMR of DEAPA(26)−(3) and the correlation of structure and signal. The lactide chains have four different signals. These are the multiplet of the methine central groups between 5.24 and 5.03 ppm, the multiplet of the methine end group between 4.25 and 4.15 ppm, the multiplet of the methyl central groups between 1.51 and 1.40, and the multiplet of the methyl end groups between 1.32 and 1.27.

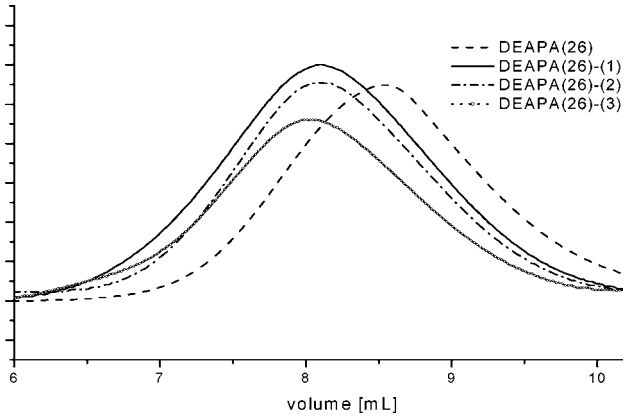


Figure 2. GPC signals of the refractive index detector of the polymers DEAPA-(26),-(26)-(1), -(2), and -(3). There is only a small difference between the three polyesters. The modified PVA shows a higher eluation volume.

number of parameters. Apart from mixing conditions (polymer concentration, rate of mixing, stirring), medium parameters (pH value, ionic strength, type of salt, polarity of solvent) and particularly the characteristics of the polyelectrolyte (molecular weight, polydispersity, branching, charge density) are known to play an important role. We investigated the complexation process in a systematic manner using turbidity as a simple and noninvasive measurement of NC formation (*32*). The formation of supramolecular structures leads to a corresponding increase in particle mass, which can be sensitively monitored by light scattering. In turbidimetric studies, the transmission of a light beam passing through a cuvette with a dispersion is given by $T = I/I_0 = \exp(-\tau l)$ where I_0 is the intensity of the light beam, I is the intensity after the cuvette of the length l, and τ is the turbidity. In nonabsorbing systems (630 nm), the transmittance is determined by the scattering of light. According to the Rayleigh theory, the scattered intensity is proportional to the square of the mass of the particles (*33, 34*). Turbidimetry monitors structural changes caused by the onset of association respectively particle formation. The characteristics of a turbidimetric curve for different

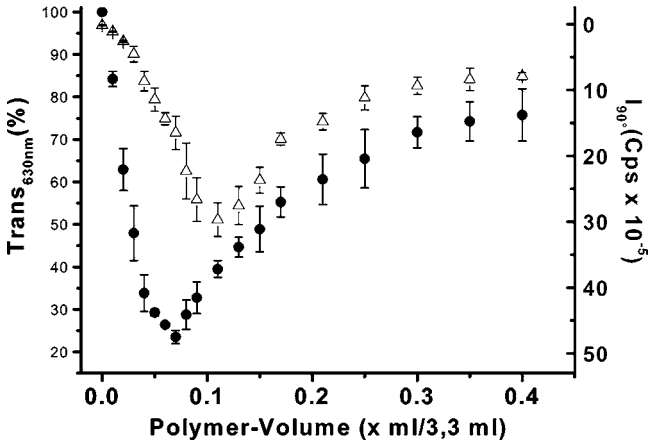


Figure 3. Turbidimetry (●) and scattering (△) of DEAPA(26) and insulin.

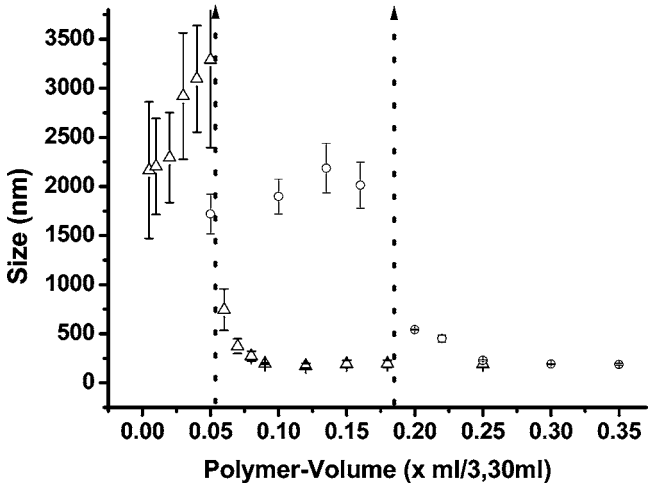


Figure 4. Size measurements for DEAPA(68) (Δ) and DEAPA-(26)-(3) (O). Dashed lines represent turbidimetric/scattering extrema: Abrupt size decrease to defined NC after exceeding critical mixing ratios.

mixing ratios of a 3.2×10^{-5} mol insulin solution with increasing concentrations of polymer are shown in Figure 3. The graph does not represent a classic colloid titration because every data point was generated from a separate experiment with a constant volume of 3.30 mL to eliminate dilution effects. All polymers exhibited the same turbidimetric profile characterized by a sharp decrease of transmission and a sharp increase of scattered light at increasing polymer concentrations resulting in distinct minima and maxima. The turbidimetric profile suggests that at initially low polymer concentration, large and incoherent complexes are formed with an excess of insulin. These complexes condense to a more defined and compact structure at increasing polymer concentration, corresponding-to-mixing ratios at the extrema and the ascending part of the turbidimetric curve. Furthermore, addition of the same type of polymer to NC dispersion leads to a redistribution of the insulin to the new binding partner resulting in a decrease of scattering intensity and absorption. The NC size measurements as a function of the mixing ratios confirm this assumption (Figure 4). A transition to small-sized NC was achieved upon exceeding the described minima/maxima.

At a physiological pH human insulin carries two negative charges per molecule (*19*). The terminal tertiary amino groups of DEAPA are predominantly protonated at neutral pH, allowing calculation of charge ratios at the extreme values of the turbidity curves. The calculations are based on the total concentrations. In Figure 5, a linear relationship between the number of DEAPA groups in the backbone and the molecular ratio of insulin/polymer is shown. With higher degrees of amino substitution, increasing from 13 to 150, higher molar ratios between DEAPA and insulin with 1:7 up to 1:45 are observed. These data suggest that at the extreme values, approximately 1:1 charge ratios are observed (Table 2) and highlight the importance of electrostatic interactions. On the other hand, with increasing amounts of lactic acid grafting, no change in the molar ratio of insulin/polymer is observed. This suggests that the stoichiometry of the complexes is primarily determined by Coulombic interactions and that hydrophobic forces play a minor role.

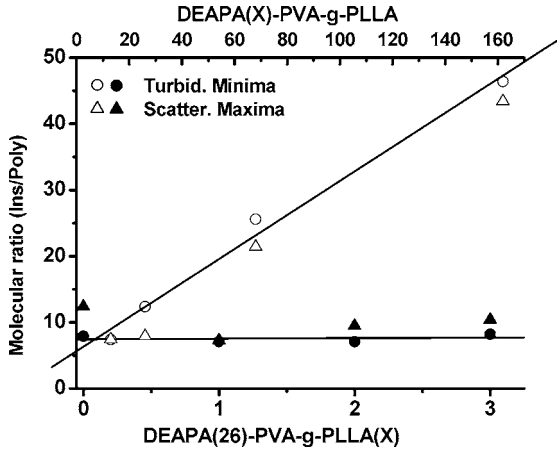


Figure 5. Turbidimetric and scattering extrema: correlation of molecular ratio and substitution degree of DEAPA (○, △) respective amount grafted lactide (●, ▲).

Under our experimental conditions, the NC demonstrated no tendencies of precipitation or macroscopic flocculation. The only exception is P(26)-3_{LL}-NC which tended to precipitate after ~1−2 h, possibly due to the high lactic acid grafting. It is very important to mention that turbidimetry does not provide information on the affinity between insulin and the different polymers. Therefore, isothermal microtitration calorimetry was performed.

Nanocomplex Characterization. Ideal nanocomplexes containing insulin should meet the following requirements: (i) particle sizes <500 nm to facilitate epithelial uptake (*35*); (ii) high positive ζ−potential to increase interaction with negatively charged cell surfaces (*36*); and (iii) high insulin loading. These parameters were determined at different points of the turbidimetric profile (Figure 4). It was found that the optimal range is located at the ascending part of the profile. This observation was made with all polymers and thus permitted a calculation and even a prediction of the optimal ratios of both binding partners (Table 2).

Using a simple mixing procedure and short incubation times, it was possible to obtain NC with an average diameter of ~200 to 500 nm. Within a homologous series of backbone composition, an increasing amount of lactic acid grafting ($0 < 1_{LL} < 2_{LL}$) led to more compact and smaller NC, pointing to the influence of hydrophobic interactions for the complex structure.

The degrees of amino substitution allowed variation of the positive surface charge of the NC. The observed ζ-potentials ranged from +3 mV at a low ('13') to + 35 mV with a higher degree of substitution ('150'). Furthermore, when the number of amino groups was kept constant at 26 and the lactic acid ratio was increased from 1_{LL} to 3_{LL}, the ζ-potential increased from +15 mV to +33 mV. This

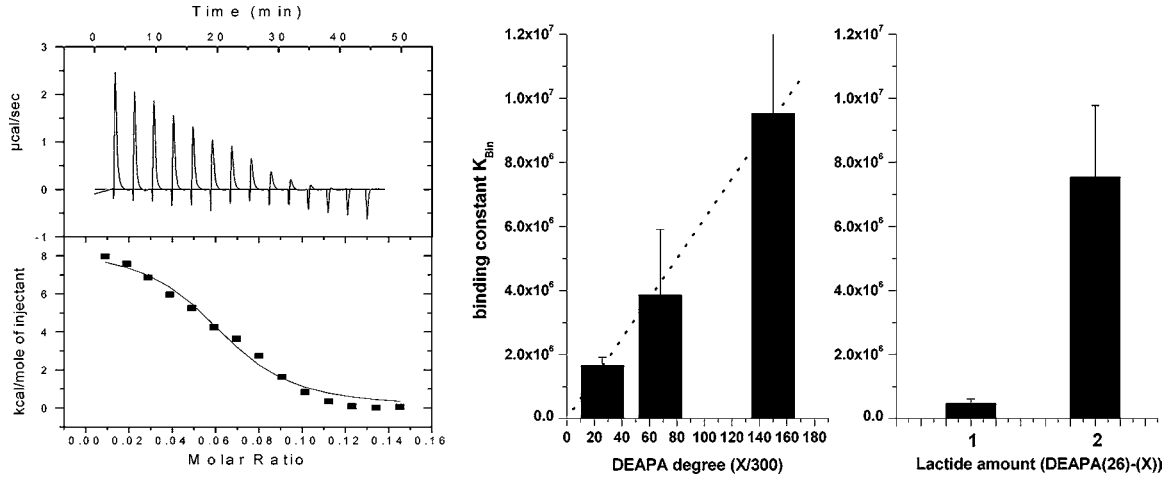


Figure 6. Left: MTC final plot of DEAPA(26)-(1)/insulin, right: correlation of binding constants for different amine substitutions (26, 68, 150) of PVAL and comparison of polyesters DEAPA(26)-(1) and-(2).

could be explained by increased internal hydrophobic interactions leading to a displacement of positive charges from the inner parts of the complex to the outer layer.

The high loading of insulin (Table 2) in NC was obtained either with high degrees of amine substitution or by a combination of medium charge density ('26') and a higher lactic acid grafting (2_{LL}, 3_{LL}). At the standard concentration of 1.25 mg/mL insulin (26.2 IU/mg), ca. 98% were bound in NC. A degree of amino substitution of 0.04 was insufficient for efficient insulin complexation.

The hydrophobic B-chain, C-terminal end plays an important role in the complexation behavior of insulin (e.g. self-association or fibrillation). The increased complexation capacity of the higher grafted polyesters possibly results from more pronounced hydrophobic interactions with these nonpolar residues of insulin. In the literature, the formation of complexes was even observed with partners of the same charge, namely serum albumin and hydrophobically modified anionic poly(acrylic acid) (*37*), pointing to the importance of hydrophobic interactions.

Microcalorimetry. Interactions between proteins and polymers and their assembly to NC, are the result of cooperative interactions of many weak inter- and intramolecular forces. Isothermal titration calorimetry (ITC) provides a tool to determine equilibrium constants and enthalpies under identical experimental conditions. From these data, entropy values and standard free energies can be derived, giving insight into the complexation reactions. The binding constant, K_{bin}, allows an assessment of the influence of polymer modifications on the affinity to a target-protein. The so-called "final plot" in Figure 6 displays the titration of insulin solution with P(26)-1_{LL} polymer. The peaks in the upper window represent the heat flow of the ongoing complexation reaction. This continues until only dilution effects of excessive polymer addition are detected within the last 3−4 peaks. The lower window represents the fit of the integrals according to the least-squares method. The binding constants ranged from 4.68×10^5 with P(26)-1_{LL} to 9.53×10^6 M^{-1} with P(150) (Figure 6 right).

An increase in the binding constant can be attained by two ways: First is with a higher degree of amine substitution, leading to a higher charge density. The binding constant increased almost linearly (correlation coefficient ~0.998) for P(26), -(68) and -(150). Second is by the introduction of short hydrophobic lactic acid side chains, which have to exceed a critical length to influence the complexation of insulin significantly. A strong increase of K_{bin} to 7.54×10^6 M^{-1} was seen when lactic acid grafting increased from (1_{LL}) to (2_{LL}), due to additional hydrophobic binding forces. It was not possible to investigate P(13) because of its weak complexation properties and P(26)-3_{LL} due to its precipitation tendency.

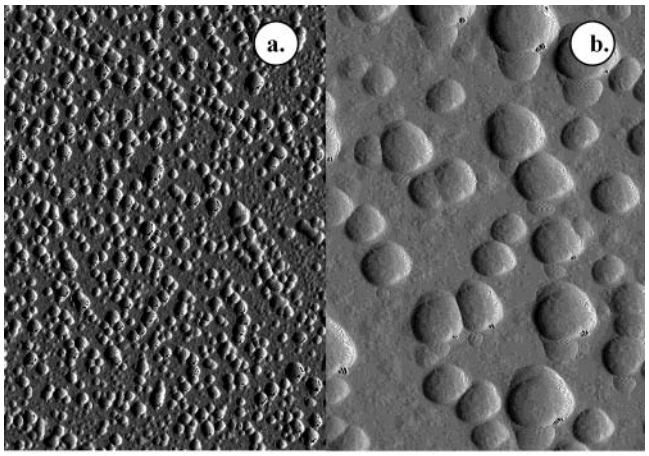


Figure 7. Tapping mode AFM images: Overview of DEAPA-(26)/insulin complexes: (a) 10.0 μm and (b) 2.0 μm scale.

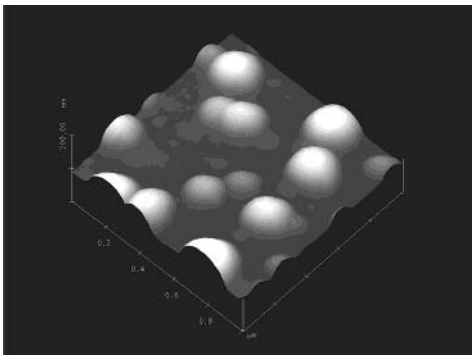


Figure 8. Three-dimensional structure of nanocomplexes.

For comparison, the binding constant for soluble insulin to crystals of cationic protamine/insulin (0.27 mg/100 IU) at pH 7.5 is (buffer dependent) $15.5-37.7 \times 10^5$ M^{-1} (*38*) and the strong binding of the two first hexacoordinated zinc atoms per insulin hexamer is in the magnitude of $1.9-4.7 \times 10^6$ M^{-1} (*39*), documenting a substantial affinity of insulin to the DEAPA polymers.

The calorimetric enthalpy change (ΔH) measured in an ITC experiment is the total change in enthalpy for the whole system. That means exothermic or endothermic

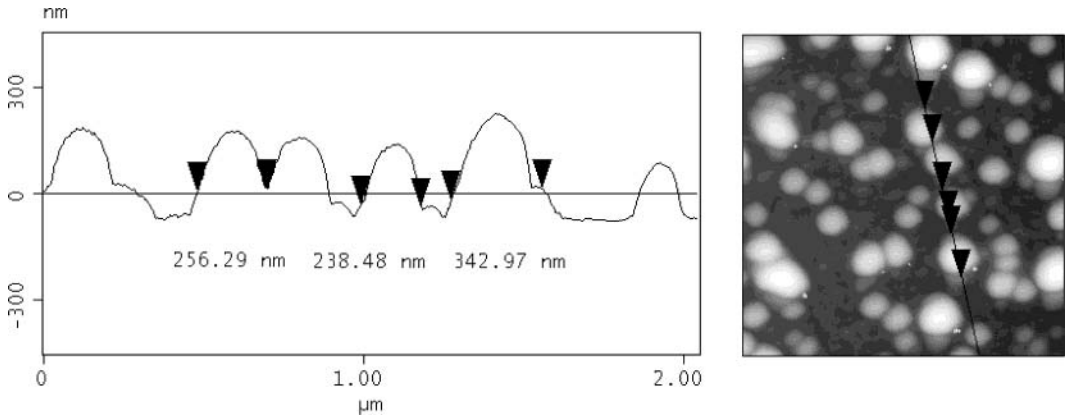


Figure 9. Cross-section for nanocomplexes from AFM line analysis.

events can be associated with conformational change of the reactants, ionization of polar groups, and interactions with the solvent. The determination of the true (intrinsic) enthalpy requires additional experiments in different solvents and should in this context not be discussed in detail. The driving force of complex formation is mainly the gain in entropy due to the liberation of the low molecular counterions. The derived entropy values for the complexation reactions ranged from 45 for P(26) to 255 kcal/mol for P(150). From a thermodynamic point of view, polyelectrolytes with stronger ionic groups and/or higher molecular masses are generally favored in complex formation (*33*).

Another parameter directly obtained by ITC is the stoichiometry of the binding partners at the turning point of the isotherm. This stoichiometry cannot be directly compared with turbidimetry due to different physicochemical principles. The thermodynamic stoichiometry of insulin/polymer was about two to three times higher than the molar ratios derived from turbidimetry (Table 2).

Visualization of NC. Atomic force microscopy (AFM) is a microscopic technique which allows the imaging of NC formulations independent of their composition under wet (physiological) conditions. Using AFM, in contrast to the electron microscopy, samples can be measured without preparation or fixation. AFM is an excellent method for imaging soft and flexible objects with high resolutions, allowing determination of particles sizes and surface morphology on a nanometer scale resolution. For size determination, all NC within a representative scan area ($25 \times 25\ \mu$m) were evaluated individually (Table 2). These data can deviate from the results of PCS measurements for several reasons. First, interaction of soft and flexible polymer NC with the surface of the silicon support can cause artifacts. The individual particle analysis allows exclusion of such artifacts.

In addition, the visualization and evaluation of NC enables us to investigate the stability of these particles. The morphology of spreaded surface films of the pure polymer solution exhibited a uniform appearance for all polymers. The polymers form globular structures with a high tendency to generate fractal structures. The size for the globuli ranged between 25 nm for P(26) (Figure 10/B) and 38 nm for P(26)-2_{LL}. The investigated polymer/insulin nanocomplexes showed average particle sizes between 274 nm (P(26)) and 434 nm (P(150)). These values are in excellent accordance with the results determined by PCS. A general overview of a NC distribution is seen in Figure 7 for P(26)/insulin. All particles were of round shape and stable; no tendency for agglomeration could be observed. Only the formulation of

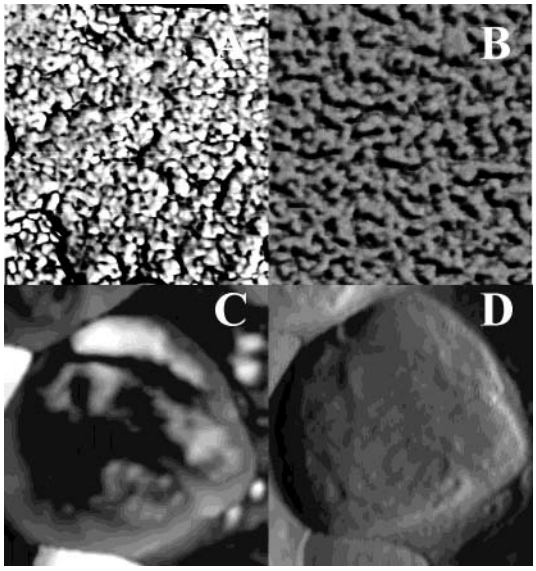


Figure 10. AFM phase mode: (A) Insulin (B) DEAPA(26)-polymer (C) NC of a/b, AFM Tapping mode: (D) surface structure of C.

P(26)-3_{LL} NC showed a very inhomogeneous particle distribution and the tendency of stack formation. In the case of P(26), two major subpopulations were observed. The smaller fraction had an average diameter of approximately 204 nm, and the larger fraction showed sizes between 300 and 400 nm. This feature also explains the differences in the size measurements between the used methods. The surface of the particle is very smooth; no breaks or cracks could be seen.

A general problem with soft objectives such as NC, even in the noncontact mode, is to obtain accurate height information. Often nanoparticles show a tendency to coalesce at the surface, leading to significant height differences and very flat structures (*40*). Under our experimental conditions, the NC exhibited a good aspect ratio between height and diameter (Figure 8) which was confirmed by a cross-section of 2 μm and additional height measurements (Figure 9).

A special technique of AFM is the so-called phase imaging mode measuring the material contrasts, depending on the stiffness or elasticity of the object (*41*). Differing material properties are presented in different color intensities in images of insulin (a) and DEAPA polymers (b) as shown in Figure 10. More rigid materials show a brighter image than softer materials. In the case of P(26), different bright areas within the particles could be observed (Figure 10/c). The areas were very small with

a size between 5 and 20 nm and can be discussed as a distribution of polymer/insulin nanostructures with different compositions. Brighter areas consist of domains with a higher content of insulin and were more rigid, while darker areas consist of regions with higher polymer content. The results of the AFM investigation are compatible with a spheroidal shape for the nanocomplexes and an entangled internal structure for insulin and DEAPA polymers.

CONCLUSION

A series of polymers was synthesized and characterized exhibiting a comblike structure. The variation of hydrophobicity by lactic acid side chain grafting and charged groups, at physiological pH, resulted in branched polyesters with a positively charged backbone offering multiple binding sites for the preparation of colloidal nanocarrier systems. It was possible to manipulate the hydrophilic−hydrophobic balance of these polyesters by factors such as molecular weight, PLLA chain lengths, and degree of amine substitution. Water solubility of these polymers allowed the self-assembling of small NC with narrow size distribution without any mechanic emulsification procedures and without the use of surfactants.

Insulin was complexed to a high extent, resulting in uniform particles with an entangled structure. The increase in binding affinity, drug loading, zeta potential, and the decrease in size could be correlated with a higher substitution degree of DEAPA groups and a higher lactic acid grafting of the backbone. The possibility of designing the polymer structure in a rational manner may provide significant advantage for generating nanocarriers for mucosal drug delivery. The potential of these NC for nasal delivery of insulin with in vivo models is currently under investigation in our laboratory.

ACKNOWLEDGMENT

Financial support of this work by the German Research Foundation (DFG) is gratefully acknowledged.

LITERATURE CITED

(1) Pillai, O., and Panchagnula, R. (2001) Insulin therapies − past, present and future. *Drug Discovery Today 6* (20), 1056−1061.

(2) Behl, C. R., Pimplaskar, H. K., Sileno A. P., Xia, W. J., Gries, J. C., and Romeo, V. D. (1998) Optimization of systemic nasal drug delivery with pharmaceutical excipients. *Adv. Drug Delivery Rev. 29*, 117−133.

(3) Hinchcliffe, M., and Illum, L. (1999) Intranasal insulin delivery and therapy. *Adv. Drug Delivery Rev. 35*, 199−234.

(4) Fernandez-Urrusuno, R., Calvo, P., Remunan-Lopez, C., Vila-Jato, J. L., and Alonso, M. J. (1999) Enhancement of Nasal Absorption of Insulin Using Chitosan Nanoparticles. *Pharm. Res. 16* (10), 1576−1581.

(5) Iuchi, S., Hoffner, G., Verbeke, P., Djian, P., and Green, H. (2003) Oligomeric and polymeric aggregates formed by proteins containing expanded polyglutamine. *Proc. Natl. Acad. Sci. U.S.A. 100* (5), 2409−2414.

(6) Nam, Y. S., Kang, H. S., Han, S. H., and Chang, I. S. (2003) Amphiphilic biodegradable block copolymers and self-assembled polymer aggregates formed from the same in aqueous milieu. U.S. Pat. Appl. US2003009004, 1−16.

(7) Xiong, X., Li, Z., Du, F., and Li, F. (2001) Synthesis of new block copolymer containing glycopolymer segment PEO-b−P(lys-ML) and their aggregation behavior in water. *Gaofenzi Xuebao 6*, 787−792.

(8) Morlock, M., Kissel, T., Li, Y. X., Koll, H., and Winter, G. (1998) Erythropoietin loaded microspheres prepared from biodegradable LPLG-PEO-LPLG triblock copolymers: protein stabilization and in-vitro release properties. *J. Controlled Release 56* (1−3), 105−115.

(9) Nath, S., Patrickios, C. S., and Hatton, T. A. (1995) Turbidimetric Titration Study of the Interaction of Proteins with Acrylic Polyampholytes. *Biotechnol. Prog. 11* (1), 99−103.

(10) Patrickios, C. S., Hertler, W. R., and Hatton, T. A. (1994) Protein complexation with acrylic polyampholytes. *Biotechnol. Bioeng. 44* (9), 1031−1039.

(11) Maruyama, A., Ishihara, T., Kim, J. S., Kim, S. W., and Akaike, T. (1997) Nanoparticle DNA carrier with poly(L-lysine) grafted polysaccharide copolymer and poly(D, L-lactic acid). *Bioconjug. Chem. 8* (5), 735−742.

(12) Takeuchi, H., Yamamoto, H., and Kawashima, Y. (2001) Mucoadhesive nanoparticulate systems for peptide drug delivery. *Adv. Drug Delivery Rev. 47*, 39−54.

(13) Mathiowitz, E., Jacob J. S., Jong Y. S., Carino, G. P., Chickering, D. E., Chaturvedi, P., Santos, C. A., Vijayaraghavan, K., Montgomery, S., Bassett, M., and Morell, C. (1997) Biologically erodable microspheres as potential oral drug delivery systems. *Nature 386* (27), 410−414.

(14) Schwendemann, S. P., Cardamone, M., Klibanov, A., and Langer, R. (1996) Stability of proteins and their delivery from biodegradable polymer microspheres. *Microparticulate Systems for the Delivery of Proteins and Vaccines* (Cohen, S., Bernstein, H., Eds.) pp 1−49, Marcel Dekker, New York.

(15) Morawetz, H., and Hugues, W. L. (1951) The interaction of proteins with synthetic polyelectrolytes. I. Complexing of bovine serum albumine. *J. Phys. Chem. 56*, 64−69.

(16) Tribet, C., Audebert, R., and Popot, J. L. (1996) Amphipols: polymers that keep membrane proteins soluble in aqueous solutions. *Proc. Natl. Acad. Sci. U.S.A. 93*, 15047−15050.

(17) Ahmed, L. S., Xia, J., and Dubin, P. L. (1994) Stoichiometry and the mechanism of complex formation in protein-polyelectrolyte coacervation. *J. M. S. Pure Appl. Chem. A31* (1), 17−29.

(18) Tribet, C. (2000) Complexation Between Amphiphilic Polyelectrolytes and Proteins: From Necklaces to Gels. *Physical Chemistry of Polyelectrolytes* (Radeva, T., Ed.) pp 687−741, Marcel Dekker, New York.

(19) Brange, J. (1987) *Galenics of Insulin: The Physio-chemical and Pharmaceutical Aspects of Insulin and Insulin Preparations*, pp 1−103, Springer-Verlag, Berlin

(20) Jung, T., Kamm, W., Breitenbach, A., Kaiserling, E., Xiao, J. X., and Kissel, T. (2000) Polymeric carriers for the oral delivery of polypeptides and peptides based on biodegradable nanoparticles from charge containing brush-like branched polyesters. *Eur. J. Pharm. Biopharm. 50*, 147−160.

(21) Jung, T., Kamm, W., Breitenbach, A., Klebe, G., and Kissel, T. (2002) Loading of Tetanus Toxoid to Biodegradable Nanoparticles from Branched Poly(Sulfobutyl-Poly(vinylalcohol))-*g*-(Lactide-Co-Glycolide) Nanoparticles by Protein Adsorption: A Mechanistic Study. *Pharm. Res. 19(8)*, 1105−1113.

(22) Wittmar, M. (2004) Charge-modified, comb-like graft-polyesters for drug delivery and DNA vaccination: Synthesis and characterization of poly(vinyl dialkylaminoalkylcarbamate-co-vinyl acetate-co-vinyl alcohol)-graft-poly(D,L-lactide-co-glycolide), Dissertation, Department of Pharmaceutical Technology and Biopharmacy, Philipps University of Marburg.

(23) Tsuboi, A., Izumi, T., Hirata, M., Xia, J., Dubin, P. L., and Kokufuta, E. (1996) Complexation of proteins with a strong polyanion in an aqueous salt-free system. *Langmuir 12* (26), 6295−6303.

(24) Kokufuta, E., Shimizu, H., and Nakamura, I. (1982) Stoichiometric complexation of human serum albumin with strongly acidic and basic polyelectrolytes. *Macromolecules 15*, 1618−1621

(25) Oberle, V., Bakowsky, U., Zuhorn, I., and Hoekstra, D. (2000) Lipoplex formation under equilibrium conditions revals a three step mechanism. *Biophys. J. 79* (3), 1447−1454.

(26) Manosroi, A., and Bauer, K. H., (1990) Interaction of human insulin with DEAE-dextran. *Drug Dev. Ind. Pharm. 16* (5), 807−819.

(27) Liu, G., Molas, M., Grossmann, G. A., Gregory, A., Pasumarthy, M., Perales, J. C., Cooper, M. J., and Hanson, R. W. (2001) Biological properties of poly-L-lysine-DNA com-

plexes generated by cooperative binding of the polycation. *J. Biol. Chem. 276* (37), 34379−34387.
(28) Zimmer, A., Zobel, H. P., Werner, D., Noe, C. R., and Kreuter, J. (1997) Cationic nanoparticles as enhancers for cellular uptake of antisense oligonucleotides. *Proc. Int. Symp. Control. Release Bioact. Mater. 24th*, 679−680.
(29) Breitenbach, A., Jung, T., Kamm, W., and Kissel, T. (2002) Biodegradable Comb Polyesters Containing Polyelectrolyte Backbones Facilitate the Preparation of Nanoparticles with Defined Surface Structure and Bioadhesive Properties. *Polym. Adv. Technol. 13*, 938−950.
(30) Ouchi, T., Hirano, T., Maruhashi, S., Nishizawa, H., Shizuno, K., and Ohya, Y. (2000) Synthesis of biomedical graft-copolymers using polysaccharides as backbone polymers. *Abstr. Pap. Am. Chem. Soc.* 220th, Poly-222.
(31) Kang, H., Jong-Duk, K., Sang-Hoon, H., Ich-Seop, C. (2002) Self-aggregates of poly(2-hydroxyethyl aspartamide) copolymers loaded with methotrexate by physical and chemical entrapments. *J. Controlled. Release 81*, 135−144.
(32) Park, J. M., Muhoberae B. B., Dubin, P. L., and Xia, J. (1992) Effects of protein charge heterogeneity in protein-polyelectrolyte complexation. *Macromolecules 25*, 290−295.
(33) Dautzenberg, H. (2000) Polyelectrolyte Complex Formation in Highly Aggregating Systems: Methodical Aspects and General Tendencies. *Physical Chemistry of Polyelectrolytes* (Radeva, T., Ed.) pp 743−792, Marcel Dekker, New York.
(34) Burgess, D. J. (1994) Complex Coacervation: Microcapsule Formation. *Macromolecular Complexes in Chemistry and Biology* Dubin, P., Bock, J., Davies, R. M., Schulz, D. N., Thies, C., Eds.) pp 285−300, Springer-Verlag, Berlin.
(35) Jani, P., Halbert, G. W., Langridge, J., and Florence, A. T. (1990) Nanoparticle Uptake by the Rat Gastrointestinal Mucosa: Quantitation and Particle Size Dependency. *J. Pharm. Pharmacol. 42*, 821−826
(36) Soane, R. J., Frier, M., Perkins, C., Jones, N. S., Davis, S. S., and Illum, L. (1999) Evaluation of the clearance characteristics of bioadhesive systems in human. *Int. J. Pharm. 178*, 55−65.
(37) Tribet, C., Porcar, I., Bonnefont, P. A., and Audebert, R. (1998) Association between hydrophobically modified polyanions and negatively charged bovine serum albumin. *J. Phys. Chem. 102*, 1327−1333.
(38) Dodd, S. W., Havel, H. A., Kovach, P. M., Lakshminarayan, C., Redmon, M. P., Sargeant, C. M., Sullivan, G. R., and Beals, J. M. (1995) Reversible Adsorption of Soluble Hexameric Insulin onto the Surface of Insulin Crystals Cocrystallized with Protamine: An Electrostatic Interaction. *Pharm. Res. 12* (1), 60−68.
(39) McGraw, S. E., Lindenbaum, S. (1990) The Use of Microcalorimetry to Measure Thermodynamic Parameters of the Binding of Ligands to Insulin. *Pharm. Res. 7* (6), 606−611.
(40) Montasser, I., Fessi, H., and Coleman, A. W. (2002) Atomic force microscopy imaging of novel type of polymeric colloidal nanostructures. *Eur. J. Pharm. Biopharm. 54*, 281−284.
(41) Yip, C. M., Brader, M. L., Frank, B. H., DeFelippis, M. R., and Ward, M. D. (2000) Structural Studies of a Crystalline Insulin Analogue Complex with Protamine by Atomic Force Microscopy. *Biophys. J. 78*, 466−473.

BC0341627

^{99m}Tc-Neolactosylated Human Serum Albumin for Imaging the Hepatic Asialoglycoprotein Receptor

Jae Min Jeong,[§,†] Mee Kyoung Hong,[§,†] Jaetae Lee,[‡] Miwon Son,[||] Young So,[§,†] Dong Soo Lee,[§] June-Key Chung,*[,§,†] and Myung Chul Lee[§]

Department of Nuclear Medicine, Seoul National University College of Medicine, Seoul, Korea, Cancer Research Institute, Seoul National University College of Medicine, Seoul, Korea, Department of Nuclear Medicine, Kyungpook National University Hospital, Daegu, Korea, and Research Laboratories, Dong-A Pharmaceutical Co. Ltd., Yongin, Kyunggi, Korea. Received November 10, 2003

^{99m}Tc-Labeled diethylenetriaminepentaacetic acid (DTPA)-coupled neogalactosyl human serum albumin (GSA) is used as an imaging agent for asialoglycoprotein receptor of the liver. However, its labeling is inconvenient because it should be incubated for 30 min at 50 °C. In addition, the conjugated DTPAs can cause decrease of pI and denaturation of protein. Therefore, we developed an improved agent ^{99m}Tc-neolactosyl human serum albumin (LSA) which contains a terminal galactose. LSA was synthesized by conjugating lactose to human serum albumin by the formation of a Schiff's base and successive reduction with sodium cyanoborohydride. The number of conjugated lactose molecules per LSA was 40.7 ± 12.3. To simplify the labeling procedure, we used a direct labeling method that adopts a high affinity ^{99m}Tc binding site concept in antibody labeling. The produced LSA was reduced by β-mercaptoethanol to generate sulfhydryl groups and purified by PD-10 size-exclusion column. The number of generated sulfhydryl groups per LSA was 21.9 ± 3.0. Medronate and stannous chloride were added to the reduced LSA and freeze-dried. Finally, ^{99m}Tc-pertechnetate (37 MBq, 1 mL) was added to the vial and incubated for 10 min at room temperature. The labeling efficiency of ^{99m}Tc-LSA was higher than 98%, and the stability in human serum at 37 °C for 24 h was over 90%. Biodistribution study using balb/c mice and imaging study using SD rats showed high initial liver uptake and slow increase in the intestine due to hepatobiliary excretion after metabolism in the hepatocytes. Negligible spleen uptake was found while ^{99m}Tc-tin colloid showed significant amount of spleen uptake due to reticuloendothelial uptake. In conclusion, an improved agent, ^{99m}Tc-LSA, for imaging asialoglycoprotein receptor of the liver was successfully developed which showed a simple labeling procedure, high labeling efficiency, high stability, and high initial liver uptake.

INTRODUCTION

Traditionally, radiocolloids, e.g. ^{99m}Tc-tin colloid, ^{99m}Tc-sulfur colloid, ^{99m}Tc-phytate colloid, etc., have been used for imaging liver function (Stern et al., 1966; Arzoumanian et al., 1977). However, the images obtained by radiocolloids do not represent the function of hepatocytes which comprise 85% of the liver cells playing a key role in liver function. Rather, the images represent the function of the reticuloendothelial system which comprises only 15% of the liver cells playing a defensive role. Although, the function of hepatocytes could be indirectly estimated by measuring serum level of liver enzymes such as ALT and AST, direct estimation of liver function using functional imaging can provide more useful information.

Asialoglycoprotein receptors are known to exist on the mammalian liver (Ashwell and Morell, 1974) and play an important role in the hepatic metabolism of serum proteins (Ashwell and Steer, 1981). It has been reported that the asialoglycoprotein receptors exist on the surface of hepatocytes (Stokert and Morell, 1983), and it has also been suggested that quantitative imaging of asialoglycoprotein receptors estimates the function of the liver (Krohn et al., 1982; Lee, 1998; Miki et al., 2001).

A novel neogalactosylalbumin has been developed and labeled with ^{99m}Tc for imaging the liver (Krohn et al., 1980). Receptor-mediated binding to hepatocytes was also investigated both in vitro and in vivo (Vera et al., 1984a,b). Later preclinical studies proved the stability and safety of ^{99m}Tc-neogalactosylalbumin (Vera et al., 1985). However, it was necessary to develop a simpler and more convenient method, because the electrolytic labeling method used could not be performed practically in most clinical fields.

To make the labeling procedure simple, diethylenetriaminepentaacetic acid (DTPA)-conjugated neogalactosylalbumin (GSA) has been developed as an instant kit (Kubota et al., 1986). The GSA kit can be labeled with ^{99m}Tc more easily and consequently they are used widely for imaging liver function especially in Japan. The development and application of ^{99m}Tc-GSA has been published in an informative review (Stadalnik and Vera, 2001).

However, it is predicted that ^{99m}Tc would make less stable complexes with hard bases such as carboxyl or tertiary amine groups of DTPA, because it is a soft acid (Huheey, 1983). In fact, it has been reported that a

* Corresponding author: Department of Nuclear Medicine, Seoul National University Hospital, 28 Yungun-dong Chongro-ku, Seoul 110-744 Korea; jkchung@plaza.snu.ac.kr; tel: +82-2-760-3376; fax: +82-2-745-7690.

[§] Department of Nuclear Medicine, Seoul National University College of Medicine.

[†] Cancer Research Institute, Seoul National University College of Medicine.

[‡] Kyungpook National University Hospital.

[||] Dong-A Pharmaceutical Co. Ltd.

10.1021/bc0342074 CCC: $27.50 © 2004 American Chemical Society
Published on Web 07/03/2004

significant amount of ^{99m}Tc nonspecifically binds to antibodies instead of the DTPA residue when attempting to label DTPA-conjugated antibodies (Childs and Hnatowich, 1985). In addition, conjugation of DTPA to human serum albumin can lead to denaturation, polymerization, and decrease of isoelectric point. Conjugation of DTPA and galactose to the same protein molecule would make them compete with each other because both bind to the amino group.

In this paper, we introduced a direct labeling concept instead of conjugation of DTPA to human serum albumin. Thiol-containing antibodies, after reduction of disulfide bonds using a reducing agent such as β-mercaptoethanol, can be labeled directly with ^{99m}Tc (Schwarz and Steinsträsser, 1987; Mather and Ellison, 1990). Similarly, human serum albumin containing 17 intramolecular disulfide bonds should also be labeled with ^{99m}Tc directly after reduction with β-mercaptoethanol.

Another important aspect of this experiment is that the conjugated sugar is not a galactose but a lactose. Lactose is a disaccharide of galactose and glucose: 4-*O*-β-D-galactopyranosyl-D-glucose. The aldehyde group of the glucose residue and the amino group of human serum albumin form a reversible Schiff's base and are subsequently reduced into an secondary amine to form an irreversible covalent bond. Thus the galactose residues of neolactosylated human serum albumin (LSA) are intact even after conjugation and act as ligands of asialoglycoprotein receptors.

EXPERIMENTAL PROCEDURES

Materials and Instruments. Human serum albumin was purchased from Green Cross Corp. (Seoul, Korea) as a 20% solution in normal saline. For purification of neolactosylated human serum albumin (LSA), ready-made Sephadex G-25 columns were purchased as PD-10 columns from Pharmacia (Uppsala, Sweden). Disposable aseptic 0.22 μm filters were purchased from Millipore Company. ^{99}Mo/^{99m}Tc-generators were purchased from Du Pont Company. ITLC plates were purchased from Gelman Company. Tin colloid kits (0.15 mg of stannous fluoride and 1 mg of sodium fluoride) and human serum albumin (HSA) kits (50 mg of HSA and 0.5 mg of stannous chloride hydrate) for ^{99m}Tc-labeling were purchased from Daiichi Co. The particle size of ^{99m}Tc-tin colloid has been reported as 0.1−0.5 μm (McClelland et al. 2003). All the other reagents and solvents, if not specified, were purchased from Aldrich, Fluka, or Sigma and were used without further purification.

Radio-TLC chromatograms were obtained using a Bio-Scan System 200 imaging scanner. A gamma scintillation counter Cobra II model from Packard Canberra Company was used for counting radioactivity of organs in the biodistribution study. A gamma camera Sigma 410 model from Ohio-Nuclear equipped with a low-energy collimator was used for imaging rats.

Preparation of LSA. LSA was prepared using minor modification of the previously reported reductive lactosamination method (Lim et al., 1996; Wilson, 1978). The overall reaction procedure is described in Figure 1. In 50 mL of 0.2 M potassium phosphate buffer (pH = 8.0), 680 mg of human serum albumin was dissolved completely and 1 g of α-lactose was dissolved successively. One gram of sodium cyanoborohydride was added, and the solution was filtered using a 0.22 μm filter. The filtered solution was incubated at 37 °C with slow stirring for 14 days. The resulting reactant was centrifuged at 3000 rpm for 5 min to remove any precipitate. The supernatant was recovered and stored at −70 °C until used.

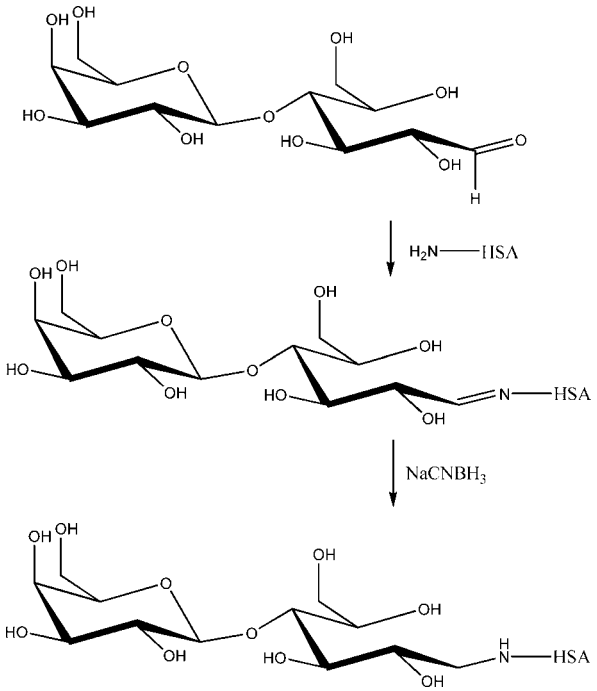


Figure 1. Conjugation of lactose to human serum albumin by reductive amination. The aldehyde group of glucose residue makes a Schiff's base with the amino group of human serum albumin, and then it is reduced to a stable amine by sodium cyanoborohydride.

Preparation of Disulfide-Reduced LSA (rLSA). Reduction of LSA was performed in a similar way with that of monoclonal antibody for labeling with ^{99m}Tc (Mather and Ellison, 1990). To 1 mL of the above prepared LSA, 40 μL of 0.3 M EDTA (pH = 8.0), 40 μL of 1 M sodium bicarbonate, and 50 μL of 1.5 M β-mercaptoethanol were added successively and incubated at 37 °C for 1 h. After purification of the rLSA using Sephadex G-25 column/phosphate-buffered saline (pH = 6.0), 0.3 mL of sodium medronate (1.25 mg/mL, pH 7.6, containing 68 μg SnF_2) was added. The solution was dispensed into vials as an aliquot containing 3 mg of protein and stored in a refrigerator after freeze-drying.

Determination of the Conjugation Number of Lactose. The conjugated number of lactose per molecule of human serum albumin was calculated by measuring galactose concentration from the absorbance at 485 nm using the phenol/sulfuric acid method (Dubios et al., 1956); since the secondary amine formed by reductive amination is acid-stable, only galactose is produced during the hydrolysis (Wilson, 1978).

Determination of the Number of Thiols. The number of thiol groups on an rLSA molecule was determined before addition of sodium medronate containing SnF_2. It was determined by measuring absorbance at 410 nm after 400 μL of sample was reacted with 2 mL of 0.1 M Ellman's reagent (5,5′-dithio-bis(2-nitrobenzoic acid). Serially diluted cysteine solution was used as a standard.

Labeling with ^{99m}Tc. To the above freeze-dried vial, 2−5 mL aliquot of generator-eluted ^{99m}Tc-pertechnetate was added and incubated at room temperature for 1−30 min. Unreduced LSA was also labeled using the same method for comparison. The labeling efficiencies were checked using ITLC/Umezawa (ethanol:10% ammonium acetate = 1:1) and 5% bovine serum albumin (BSA) impregnated paper chromatography/saline. Unbound ^{99m}Tc moved to the solvent-front, and LSA-bound ^{99m}Tc stayed at the origin on ITLC/Umezawa. All ^{99m}Tc activity

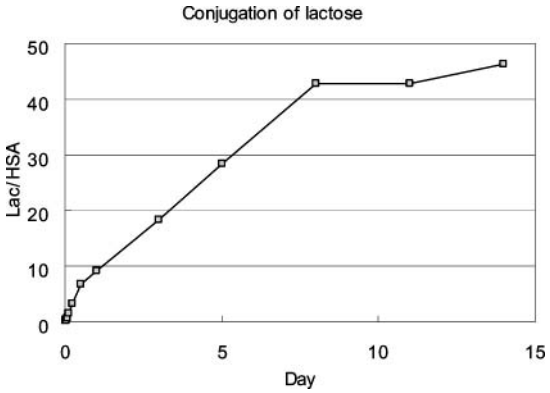


Figure 2. Number of lactose molecules conjugated to human serum albumin by incubation time. The conjugated number becomes maximized after incubation for 8 days at 37 °C.

except reduced hydrolyzed ^{99m}Tc moved to the solvent-front on 5% BSA-impregnated paper chromatography/saline.

Stability Test. Stability of the labeled LSA was checked at room temperature. Stability in human serum at 37 °C was also checked. The bound and free form of ^{99m}Tc was determined using ITLC/Umezawa and 5% BSA-impregnated paper chromatography/saline as described above. The pH of the reaction mixture during stability test was measured by pH paper.

Biodistribution Study in Mice. For biodistribution, 37 kBq of ^{99m}Tc-LSA was injected into each mouse (male, ICR, ~20 g, $n = 4$) through the tail vein. The mice were sacrificed at 10 and 60 min. The weight and radioactivity of the blood, muscle, fat tissue, heart, lung, liver, spleen, stomach, intestine, kidney, and bone from the sacrificed mice were measured using an electronic balance and gamma scintillation counter. The percentage of injected dose per gram tissue was calculated.

Imaging Study in Rats. For imaging, 7.4 MBq of ^{99m}Tc-LSA was injected into each rat (male, Sprague−Dawley, ~200 g) through the tail vein. Planar images of the rats in prone position after 15 and 30 min were obtained using a gamma camera equipped with a low-energy collimator. Imaging with ^{99m}Tc-tin colloid by the same procedure was performed for comparison.

RESULTS

Preparation and Characterization of rLSA. The entire procedure was performed in an aseptic manner to prevent bacterial growth. Excess lactose (lactose:HSA = 285:1) was added to make the reaction close to complete. The conjugated number of lactose to human serum albumin reached almost maximum after incubation at 37 °C for 8 days (Figure 2). The maximum number of conjugated lactose per human serum albumin was about 43. The average conjugated number after 11 days incubation was 40.7 ± 12.3.

For labeling with ^{99m}Tc, the LSA was reduced by β-mercaptoethanol. The remaining β-mercaptoethanol was removed by PD-10 size-exclusion column, and rLSA was obtained in phosphate-buffered saline (pH 6.0). The average number of sulfhydryl groups per rLSA measured by Ellman's reagent was 21.9 ± 3.0. For ^{99m}Tc labeling and stabilization, 0.3 mL of sodium medronate (1.25 mg/mL, pH 7.6, containing 68 μg SnF_2) was added, then dispensed into 3-mg protein aliquots and freeze-dried.

Labeling with ^{99m}Tc and Radiochemical Study. After labeling of rLSA with ^{99m}Tc, free ^{99m}Tc was determined by ITLC/Umezawa and colloid was determined by 5% BSA-impregnated Whatman No.1/saline (Figure 3).

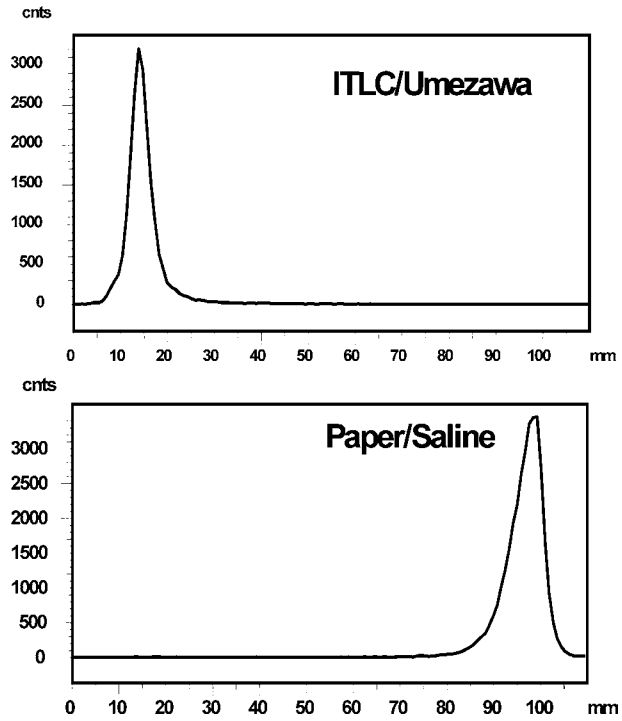


Figure 3. Determination of labeling efficiency. Labeled and colloidal ^{99m}Tc remains at the origin, and all the other activities move to the solvent-front by ITLC/Umezawa and all activities except colloidal ^{99m}Tc move to the solvent-front of the paper chromatography/saline.

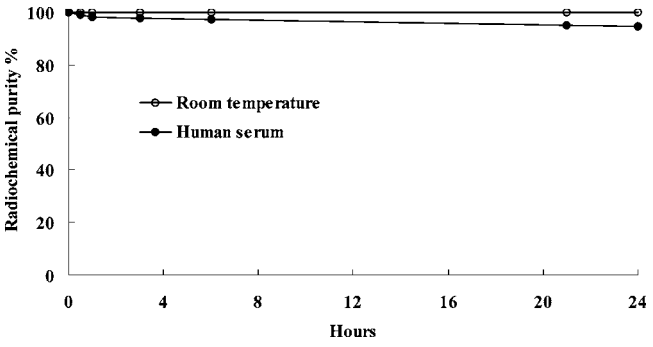


Figure 4. Stability test of ^{99m}Tc-LSA at room temperature and at 37 °C in human serum.

Table 1. Labeling Efficiency of ^{99m}Tc-LSA Determined by ITLC and Paper Chromatography

	added volume of ^{99m}Tc-pertechnetate[a]	
incubation time (min)	2 mL	5 mL
1	98.5	98.9
3	98.2	99.0
7	98.9	100
15	98.9	99.3
30	100	100

[a] The values denote labeling efficiency (%).

Labeling was finished in 1 min with >98% efficiency at room temperature (Table 1). The volume of ^{99m}Tc-pertechnetate, either 2 mL or 5 mL, did not affect the labeling efficiency.

The preparation of the ^{99m}Tc-LSA was stable for at least 24 h when stored at room temperature, and it was also stable in serum at 37 °C for 24 h (Figure 4).

Biodistribution Study in the Mice. ^{99m}Tc-HSA showed high blood pool activity. High activities in the liver, spleen, and kidney seem to be caused by high blood content in those tissues (Figure 5A). ^{99m}Tc-LSA ac-

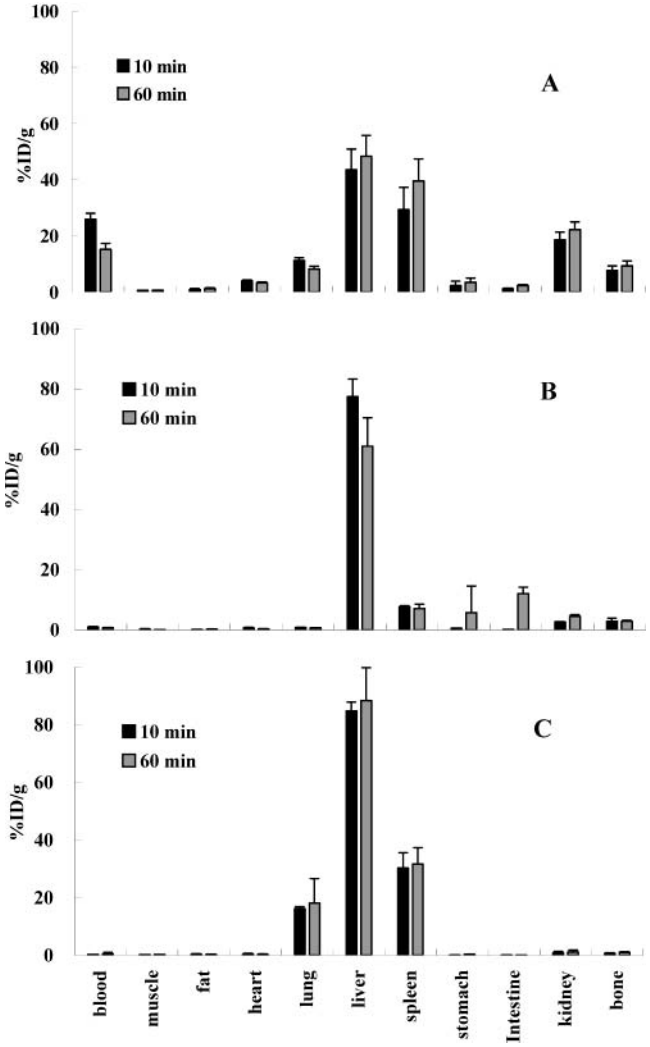


Figure 5. Biodistribution of ^{99m}Tc-HSA (A), ^{99m}Tc-LSA (B), and ^{99m}Tc-tin colloid (C) in mice (male, ICR).

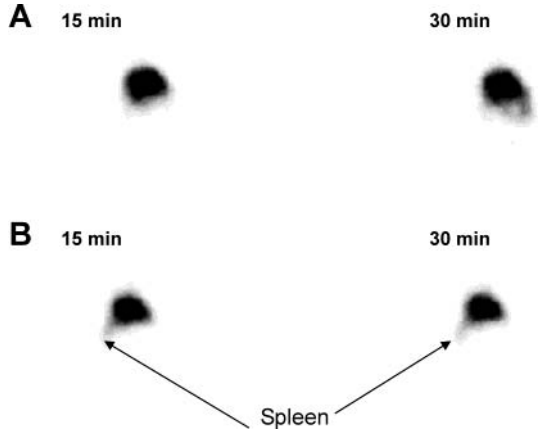


Figure 6. Imaging after injection of ^{99m}Tc-LSA (A) and ^{99m}Tc-tin colloid (B) in rats (male, Sprague−Dawley).

cumulated mainly in the liver and was excreted into the intestine slowly, which is evidence of specific uptake by the asialoglycoprotein receptor and successive metabolism (Figure 5B). ^{99m}Tc-Tin colloid, known to be taken up by the reticuloendothelial system, showed high accumulation in the liver, and the radioactivity was not excreted as expected (Figure 5C). It also showed high accumulation in the spleen. The radioactivity in the lung is due to capillary blockage by aggregated ^{99m}Tc-tin colloid. Very low radioactivity in the intestine indicates little or no metabolism in the liver (Figure 5C). Unlike ^{99m}Tc-HSA, both ^{99m}Tc-LSA and ^{99m}Tc-tin colloid showed very low blood activity due to rapid uptake by the liver.

Imaging Study in Rats. ^{99m}Tc-LSA was taken up by the liver quickly at 15 min, and some activity was excreted into the intestine at 30 min (Figure 6A). No spleen uptake was found. ^{99m}Tc-Tin colloid accumulated mainly in the liver, although some activity was found in the spleen. The activity did not change significantly with time (Figure 6B). These results were consistent with the biodistribution results in the mice.

DISCUSSION

Previously reported galactosylation method has a problem because it requires long preliminary steps for synthesis of precursor of galactosylation (Kudo et al., 1994). In addition the precursor, 2-imino-2-methoxyethyl-1-thio-β-D-galactose, is not suitable for long-term storage due to instability. So the precursor of the precursor, 2,3,4,6-tetra-*O*-acetyl-1-thio-β-D-galactose, is generally synthesized and used for synthesis of 2-imino-2-methoxyethyl-1-thio-β-D-galactose to conjugate to human serum albumin. On the other hand, lactose, the precursor of lactosylation, is commercially available at an economical price.

After reductive lactosaminylation, glucose residue of lactose is opened and reduced to a glucitol type linker which is neutral and hydrophilic. Generally, neutral and hydrophilic linkers are ideal for conjugation of haptens to proteins because they may not have much of an effect on the tertiary structure of the conjugated proteins.

Major advances in the labeling of proteins with ^{99m}Tc have been developed with monoclonal antibodies. Many bifunctional chelating agents for linking ^{99m}Tc and antibody have been used. Although DTPA was the first introduced bifunctional chelating agent for labeling antibodies with ^{99m}Tc, it was not used widely because of the problems previously discussed in the Introduction section. Another extensively studied bifunctional chelating agent was N_3S type compound (Kasina et al., 1998). Although this bifunctional chelating agent showed excellent radiochemical and biological properties, the labeling procedure was complicated because of prelabeling and postconjugating procedure. A preconjugation and postlabeling type bifunctional chelating agent, hydrazinonicotinic acid (HYNIC), has been developed to facilitate labeling (Abrams et al., 1990) and has been adapted by many researchers due to excellent labeling efficiency and simple labeling procedure (Schwartz et al., 1991; Blankenberg et al., 1999). The most up-to-date method of labeling proteins might be using tricarbonyl intermediate complex (Alberto et al., 1998; Egli et al., 1999). This method is currently widely studied by many researchers due to high labeling efficiency and high stability despite its two-step labeling procedure.

We applied a direct labeling method to label LSA with ^{99m}Tc, which has been studied for a long time. Direct labeling can be applied only to proteins containing disulfide bonds or sulfhydryl groups. Direct ^{99m}Tc-labeling method of HSA using stannous ion was first reported by Eckelman et al. in 1971. It has been found that preliminary reduction of proteins with stannous tartrate allows for labeling small amounts of proteins (Pettit et al., 1980). A specific labeling method to the high affinity sites of antibodies with ^{99m}Tc to acquire high stability after labeling has been reported (Paik et al., 1985). A practical method with higher than 90% labeling efficiency which employs preliminary reduction with β-mercaptoethanol

and using a weak chelator has also been reported (Mather and Ellison, 1990). The role of the weak chelator was the prevention of colloid formation and weak labeling to the antibodies. In this experiment, we used medronate as a weak chelator and found that colloid formation was completely suppressed, and labeled LSA was stable. Labeling efficiency was also very high (>98%) even after 1 min incubation at room temperature. It is a significant improvement compared to a commercialized GSA kit (neogalactosyl-DTPA-human serum albumin) which requires 30 min incubation at 50 °C for labeling.

Dosage of LSA was formulated as 3 mg/vial in this research. It has been reported that administration of 3 mg of ^{99m}Tc-GSA would be less extensively affected by the physiological asialoglycoprotein (Ha-Kawa et al., 1997). The number of total asialoglycoprotein receptors on the normal liver is $2.5-10 \times 10^{16}$. About 2.4×10^{16} molecules are in 3 mg of LSA. To evaluate the function of the liver, it is necessary to administer close to the saturation number of ligands. If the number of ligands is low, then the image will be normal even though the number of asialoglycoprotein receptors decreases.

Slow increase of radioactivity in the intestines after initial uptake in the liver is due to metabolism in the hepatocytes and successive hepatobiliary excretion. ^{99m}Tc-Tin colloid which is not metabolized showed constant biodistribution as expected. A blood pool imaging agent, ^{99m}Tc-HSA, showed high blood activity. Biodistribution and imaging study show well-correlated results in this experiment.

CONCLUSION

A new imaging agent for asialoglycoprotein receptors of the liver, ^{99m}Tc-LSA, was successfully developed. The new agent showed promising practicability with easy labeling, high labeling efficiency, high stability, and high liver uptake.

ACKNOWLEDGMENT

We would like to express our gratitude to Mr. Keagan H. Lee for his assistance in the English language for this manuscript.

LITERATURE CITED

(1) Abrams, M. J., Juweid, J., tenKate, C. I., Schwartz, D. A., Hauser, M. M., Gaul, F. E., Fuccello, A. J., Rubin, R. H., Strauss, H. W., and Fischman, A. J. (1990) Technetium-99m-human polyclonal IgG radiolabeled via the hydrazine nicotinamide derivative for imaging focal sites of infection in rats. *J. Nucl. Med. 31*, 2022−2026.

(2) Alberto, R., Schibli, R., Egli, A., and Schubiger, A. P. (1998) A novel organometallic aqua complex of technetium for the labeling of biomolecules: synthesis of $[^{99m}Tc(OH_2)_3(CO)_3]^+$ form $[^{99m}TcO_4]^-$ in aqueous solution and its reaction with a bifunctional ligand. *J. Am. Chem. Soc. 120*, 7987−7988.

(3) Arzoumanian, A., Rosenthall, L., and Seto, H. (1977) Clinical comparison of ^{99m}Tc-labeled preformed phytate colloid and sulfur colloid: concise communication. *J. Nucl. Med. 18*, 118.

(4) Ashwell, G., and Morell, A. G. (1974) The role of surface carbohydrates in the hepatic recognition and transport of circulating glycoproteins. *Adv. Enzymol. 41*, 99−128.

(5) Ashwell, G., and Steer, C. J. (1981) Hepatic recognition and catabolism of serum glycoprotein. *J. Am. Med. Assoc. 246*, 2358−2364.

(6) Blankenberg, F. G., Katsikis, P. D., Tait, J. F., Davis, E., Naumovski, L., Ohtsuki, K., Kopiwoda, S., Abrams, M. J., and Strauss, H. W. (1999) Imaging of apoptosis (programmed cell death) with ^{99m}Tc annexin V. *J. Nucl. Med. 40*, 184−191.

(7) Childs, R. L., and Hnatowich, D. J. (1985) Optimum conditions for labeling of DTPA-coupled antibodies with technetium-99m. *J. Nucl. Med. 26*, 293−299.

(8) Dubois, M., Gilles, K. A., Hamilton, J. K., Rebers, P. A., and Smith, F. (1956) Colorimetric method for determination of sugars and related substances. *Anal. Chem. 28*, 350−356.

(9) Eckelman, W. C., Meinken, G., and Richards, P. (1971) ^{99m}Tc-Human serum albumin. *J. Nucl. Med. 12*, 707−710.

(10) Egli, A., Alberto, R., Tannahill, L., Schibli, R., Abram, U., Schaffland, A., Waibel, R., Tourwé, D., Jeannin, L., Iterbeke, K., and Schubiger, P. A. (1999) Organometallic ^{99m}Tc-aquaion labels peptide to an unprecedented high specific activity. *J. Nucl. Med. 40*, 1913−1917.

(11) Ha-Kawa, S. K., Tanaka, Y., Hasabe, S., Kuniyasu, Y., Koizumi, K., Ishii, Y., Yamamoto, K., Kashiwagi, T., Ito, M., Kudo, M., Ikekubo, K., Tsuda, T., and Murase, K. (1997) Compartmental analysis of asialoglycoprotein receptor scintigraphy for quantitative measurement of liver function: A multicentre study. *Eur. J. Nucl. Med. 24*, 130−137.

(12) Huheey, J. E. (1983) Inorganic Chemistry: Principles of Structure and Reactivity, 3rd ed. Chapter 7. Acid−Base Chemistry. pp 286−327, Ed. Wasserman, M., Harper & Row Publishers, Inc. New York.

(13) Kasina, S., Sanderson, J. A., Fitzner, J. N., Ananthachari, S., Rao, T. N., Hobson, L. J., Reno, J. M., Axworthy, D., B., Beaumier, P. L., and Fritzberg, A. R. (1998) Simplified preformed chelate protein radiolabeling with technetium-99m mercaptoacetamidoadipoylglycylglycine (N3S-adipate). *Bioconjugate Chem. 9*, 108−117.

(14) Krohn, K. A., Vera, D. R., and Stadalnik, R. C. (1982) A complementary radiopharmaceutical and mathematical model for quantitating hepatic-binding protein receptors. *Receptor-Binding Radioreceptors*, (Eckelman, W. C., Ed.) Vol. II, pp 41−59, CRC Press, Boca Raton, FL.

(15) Krohn, K. A., Vera, D. R., and Steffen, S. M. (1980) ^{99m}Tc-Neogalactosylalbumin: a general model for some bifunctional carbohydrates. *J. Labelled Compd. Radiopharm. 18*, 91−93.

(16) Kubota, Y., Kojima, M., Hazama, H., Kawa, S., Nakazawa, M., Nishiyama, Y., Nakagawa, S., Murase, T., Okuno, H., Naitoh, H., Washno, K., Hasegawa, T., Sawamura, T., Tashiro, Y., Tanaka, Y., Shiozake, Y., and Sameshima, Y. (1986) A new liver function test using the asialoglycoprotein-receptor on the liver cell membrane. 1. Evaluation of liver imaging using the Tc-99m-neoglycoprotein. *Jpn. J. Nucl. Med. 23*, 899−905.

(17) Kudo, M., Washino, K., Yamamichi, Y., and Ikekubo, K. (1994) Synthesis and radiolabeling of galactosyl human serum albumin. *Methods Enzymol.* (Biomedical Applications) *247*, 383−395.

(18) Lee, J. (1998) Quantitative evaluation of liver function with hepatic receptor scintigraphy using Tc-99m galactosylated serum albumin (GSA). *Korean J. Nucl. Med. 32*, 305−313.

(19) Lim, C.-R., Oh, K.-H., Kim, K. M., Yuk, S.-H., Lee, H.-B., and Kim, C.-K. (1996) The enhancement of liver targetability of [^{3}H]methotrexate-galactosylated serum albumin conjugate in mice. *Int. J. Pharm. 132*, 175−182.

(20) Mather, S. J., and Ellison, E. (1990) Reduction-mediated technetium-99m labeling of monoclonal antibodies. *J. Nucl. Med. 31*, 692−697.

(21) McClelland, C. M., Onuegbulem, E., Carter N. J., Leahy, M., O'doherty, M. J., Pooley, F. D., O'doherty, T., Newsam, R. J., Ensing, G. J., and Blower, P. J. (2003) ^{99m}Tc-SnF_2 colloid 'LLK': particle size, morphology and leucocyte labeling behaviour. *Nucl. Med. Commun. 24*, 191−202.

(22) Miki, K., Kubota, K., Inoue, Y., Vera, D. R., and Makuuchi, M. (2001) Receptor measurements via Tc-GSA kinetic modeling are proportional to functional hepatocellular mass. *J. Nucl. Med. 42*, 733−737.

(23) Paik, C. H., Phan, L. N. B., Hong, J. J., Sahami, M. S., Heald, S. C., Reba, R. C., Steigman, J., and Eckelman, W. C. (1985) The labeling of high affinity sites of antibodies with ^{99m}Tc. *Int. J. Nucl. Med. Biol. 12*, 3−8.

(24) Pettit W. A., DeLand, F. H., Bennett, S. J., and Goldenberg, D. M. (1980) Improved protein labeling by stannous tartrate reduction of pertechnetate. *J. Nucl. Med. 21*, 59−62.

(25) Schwarz, D. A., Abrams, M. J., Hauser, M. M., Gaul, F. E., Larsen, S. K., Rauh, D., and Zubieta, J. A. (1991) Preparation of hydrazine-modified proteins and their use for the synthesis of ^{99m}Tc-protein conjugates. *Bioconjugate Chem. 2*, 333−336.

(26) Schwarz, A., and Steinsträsser, A. (1987) A novel approach to Tc-99m-labeled monoclonal antibodies. *J. Nucl. Med. 28*, 721.

(27) Stadalnik, R. C., and Vera, D. R. (2001) The evolution of ^{99m}Tc-NGA as a clonically useful receptor-binding radiopharmaceutical. *Nucl. Med. Biol. 28*, 499−503.

(28) Stern, H. S., McAfee, J. G., and Subramanian, G. (1966) Preparation, distribution and utilization of technetium-99m sulfur colloid. *J. Nucl. Med. 7*, 665.

(29) Stockert, R. J., and Morell, A. G. (1983) Hepatic binding protein: the galactose-specific receptor of mammalian hepatocytes. *Hepatology 3* 750−757.

(30) Vera, D. R., Krohn, K. A., Stadalnik, R. C., and Schreibe, P. O. (1984a) Tc-99m galactosyl-neoglycoalbumin: In vitro characterization of receptor-mediated binding. *J. Nucl. Med. 25*, 779−787.

(31) Vera, D. R., Krohn, K. A., Stadalnik, R. C., and Schreibe, P. O. (1984b) Tc-99m galactosyl-neoglycoalbumin: In vivo characterization of receptor-mediated binding to hepatocytes. *Radiology 151*, 191−196.

(32) Vera, D. R., Stadalnik, R. C., and Krohn, K. A. (1985) Technetium-99m galactosyl-neoglycoalbumin: preparation and preclinical studies. *J. Nucl. Med. 26*, 1157−1167.

(33) Wilson, G. (1978) Effect of reductive lactosamination on the hepatic uptake of bovine pancreatic ribonuclease A dimer. *J. Biol. Chem. 253*, 2070−2072.

BC0342074

Novel Procedures for Preparing ^{99m}Tc(III) Complexes with Tetradentate/Monodentate Coordination of Varying Lipophilicity and Adaptation to ^{188}Re Analogues

S. Seifert,* J.-U. Künstler, E. Schiller, H.-J. Pietzsch, B. Pawelke, R. Bergmann, and H. Spies

Forschungszentrum Rossendorf, Institut für Bioanorganische und Radiopharmazeutische Chemie, PF 510 119, D-01314 Dresden, Germany. Received December 5, 2003; Revised Manuscript Received March 22, 2004

Improved methods are presented for the preparation of ^{99m}Tc and ^{188}Re mixed-ligand complexes with tetradentate and monodentate ligands of the general formula $[M^{III}(L^m)(L^n)]$ (M = Tc, Re; $L^m = NS_3$ or NS_3COOH; L^n = isocyanide or phosphine). To avoid the undesired formation of reduced-hydrolyzed species of both metals, the preparation of complexes is performed in a two-step procedure. At first the Tc(III)− or Re(III)−EDTA complex is formed which reacts in a second step with the tripodal ligand 2,2′,2″-nitrilotris(ethanethiol) (NS_3) or its carboxyl derivative NS_3COOH (**a**) and the monodentate phosphine ligands (triphenylphosphine **L^1**, dimethylphenylphosphine **L^2**) or isocyanides (*tert*-butyl isonitrile **L^3**, methoxyisobutyl isonitrile **L^4**, 4-isocyanomethylbenzoic acid-L-arginine **L^5,** 4-isocyanomethylbenzoic acid-L-arginyl-L-arginine **L^6**, 4-isocyanomethylbenzoic acid-neurotensin(8−13) **L^7**) to the so-called '4+1' complex. Copper(I) isocyanide complexes are used for preparing the '4+1' complexes. That facilitates storage stability and allows kit formulations, and, moreover, enables the formation of ^{188}Re complexes in acidic solution. Only micromolar amounts of the monodentate ligand are needed, and that results in high specific activity labeling of interesting molecules. The lipophilicity of complexes can be controlled by introducing a carboxyl group into the tetradentate ligand and/or derivatization of the monodentate ligands. Furthermore, the carboxyl group enables the conjugation of biomolecules. As an example, the neurotensin derivative CN-NT(8−13) was prepared and labeled with ^{99m}Tc according to the '4+1' approach, and its behavior in vivo was studied.

INTRODUCTION

Technetium and rhenium mixed-ligand complexes represent an important approach to the development of radiotracers for diagnostic and therapeutic application because of the many possibilities to vary their biobehavior. Such complexes contain the metal ion stabilized in an appropriate oxidation state by means of a suitable ligand framework, which only partially fills the coordination sphere. Examples are the technetium and rhenium tricarbonyl moiety $[M^I(CO)_3]^+$ (*1*), the "super-nitrido" $[Tc^V(N)(PNP)]^{2+}$ (PNP = tridentate aminediphosphine ligand) fragment (*2*), the substitution-inert $[Re^V(O)(L)]^{2+}$ moiety (L = bidentate functionalized phosphine) (*3*), and the $[M^V(O)(SES)]^+$ (SES = tridentate dithiol ligand; E = S, NR, O) group of the well-known '3+1' Tc and Re complexes (*4*, *5*). In all cases the coordination sphere of the metal ion is completed by substitution of mono-, bi-, or tridentate coligands, which may balance the charge of the complexes.

However, differences were observed in connection with the stability of the final complexes in vitro and in vivo. Especially the 3+1 complexes undergo a substitution reaction in vivo with the SH-group-containing molecules such as cysteine or glutathione (*6*−*9*). To overcome this problem, the search focused on stable mixed-ligand complexes of technetium and rhenium at other oxidation states than +V and led to the development of the so-called '4+1' and '3+2' Tc(III) complexes (*10*, *11*).

This class of technetium and rhenium mixed-ligand complexes at the oxidation state III with tetradentate/monodentate NS_3/isocyanide or phosphine coordination, the so-called '4+1' complexes, was described some years ago (*12*, *13*). Recently the synthesis and structural analysis of ^{99}Tc complexes with simple isocyanides was performed and a first way of the no-carrier-added preparation was investigated (*14*). Moreover, the '4+1' approach was used for preparing receptor-affine complexes which contain isocyanides with the receptor binding region 2-methoxyphenylpiperazine, derived from the selective receptor antagonist WAY 100 635 ([*N*-(2-(1-(4-(2-methoxyphenyl)piperazinyl)ethyl))-*N*-(2-pyridinyl)cyclohexanecarboxamide]) (*15*).

The trigonal-bipyramidal '4+1' Re and Tc complexes containing NS_3[1] and isocyanides or phosphines as coligands are stable against ligand exchange with cysteine or glutathione and in vitro in incubations with plasma as well as whole blood of rats and represent therefore an alternative to the '3+1' complexes concerning the possibilities of designing biologically interesting ^{99m}Tc- or ^{188}Re-labeled compounds (*14*).

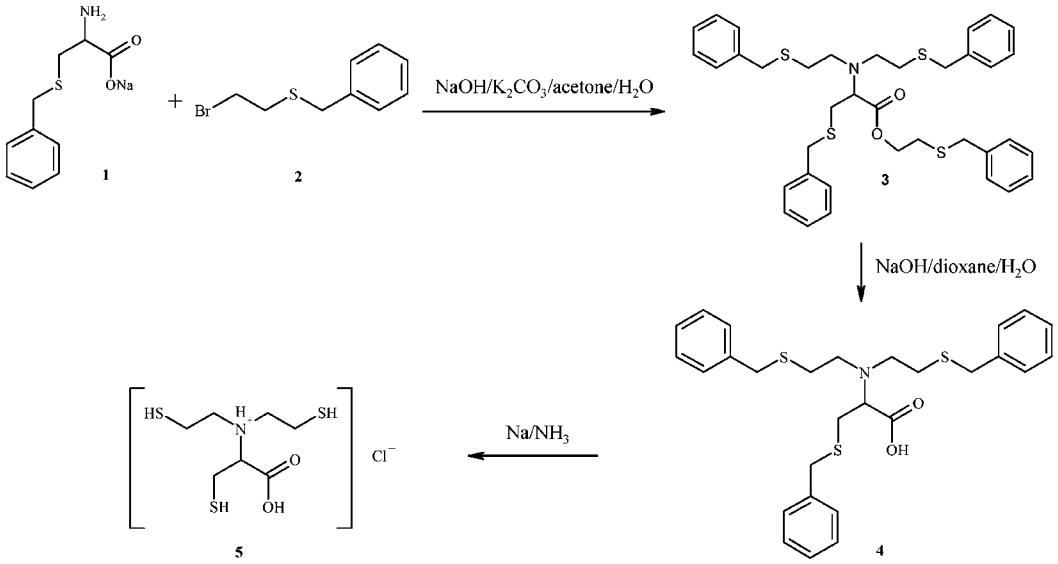
In the present paper, we report on improved preparation methods for no carrier added '4+1' ^{99m}Tc and carrier

* To whom correspondence should be addressed. Tel: (0351) 260 2442. Fax: (0351) 260 3232. s.seifert@fz-rossendorf.de.

[1] Abbreviations: NS_3, 2,2′,2″-nitrilotris(ethanethiol); NS_3-COOH, 2-[bis(2-mercaptoethyl)amino]-3-mercaptopropionic acid; TBI, *tert*-butyl isonitrile; MIBI, methoxy isobutyl isonitrile; PPh_3, triphenylphosphine; PMe_2Ph, dimethylphenylphosphine; CN-NT(8−13), 4-isocyanomethylbenzoic acid-Arg^8-Arg^9-Pro^{10}-Tyr^{11}-Ile^{12}-Leu^{13}; CN-Arg-Arg, 4-isocyanomethylbenzoic acid-L-arginyl-L-arginine; CN-Arg, 4-isocyanomethylbenzoic acid-L-arginine; BFCA, bifunctional coupling agent; CN-BFCA, 4-isocyanomethylbenzoic acid-2,3,5,6-tetrafluorophenyl ester; EHIDA, ethylene hepatobiliary iminodiacetic acid, (*N*-(2,6-diethylphenylcarbamoylmethyl)iminodiacetic acid); EIBI, ethoxy isobutyl isonitrile.

10.1021/bc0300798 CCC: $27.50 © 2004 American Chemical Society
Published on Web 06/19/2004

Scheme 1



free '4+1' ^{188}Re complexes, present a kit preparation, demonstrate possibilities of "fine-tuning" the lipophilicity and biodistribution using the simple NS_3 ligand or a carboxyl group-substituted NS_3 ligand as tripodal ligands and isocyanides as well as various phosphines as monodentate ligands, and describe the possibilities of labeling of biomolecules.

EXPERIMENTAL PROCEDURES

Materials and Methods. EDTA was purchased from Riedel-deHaen. Isocyanides were obtained from Johnson Matthey GmbH, TBI from Alfa Products, and a commercial Cardiolite kit and MIBI from Bristol-Myers-Squibb. PPh_3 and PMe_2Ph were purchased from Aldrich. All solvents and commercially available substances were of reagent grade and used without further purification. The tripodal ligand NS_3 was prepared according to standard procedures starting from tris(2-chloroethyl)-amine hydrochloride (*16*). ^{99}Tc as NH_4TcO_4 was obtained from Amersham as a 0.3 M aqueous solution. $^{99m}TcO_4^-$ was eluted from a commercial $^{99}Mo/^{99m}Tc$ generator (Mallinckrodt). $^{188}ReO_4^-$ was eluted from a $^{188}W/^{188}Re$ generator (Oak Ridge National Laboratories, Oak Ridge, TN).

Thin-layer chromatography (TLC) and high performance liquid chromatography (HPLC) analyses were performed for controlling the identity, the radiochemical purity, and the stability of the preparations. For TLC studies, silica gel strips (Kieselgel 60, Merck) or cellulose strips (Merck) were used and developed with mobile phases of acetone and water. The strips were scanned with a Raytest Rita radioanalyzer. HPLC analyses were performed on a Perkin-Elmer device consisting of a Turbo LC System with a quaternary pump (Series 200 LC Pump), a Programmable Absorbance Detector Model 785A, and a homemade γ-ray detector (Bohrloch, NaI-(Tl) crystal). HPLC analyses were carried out with a Hypersil ODS column (250 × 4 mm) using a gradient eluant of methanol/0.01 M phosphate buffer, pH 7.4, and a flow rate of 1.0 mL/min or with a Zorbax 300SB-C18 column (5 μm, 250 × 9.4 mm, Agilent) using a gradient eluant of acetonitrile (A) with 0.04% TFA/water (B) with 0.05% TFA, gradient elution: 0−12 min 5 to 70% A, 12−15 min 70−90% A, 15−18 min 90% A, and a flow rate of 2.0 mL/min. The effluent from the columns was monitored by UV absorbance at 254 nm for ^{99}Tc or Re reference complexes or γ-ray detection for the ^{99m}Tc and ^{188}Re complexes. The following three methods were used for HPLC analyses of derivatized peptides and rhenium complexes thereof.

Method 1: Jupiter C-18 (5 μm, 300 Å, 250 × 4,6 mm, Phenomenex), 1 mL/min, rt, solvent A comprised water with 0.1% trifluoroacetic acid (TFA) and solvent B comprised acetonitrile with 0.1% TFA, gradient elution: 0−20 min 20 to 80% B, 20−40 min 80% B.

Method 2: Zorbax 300SB-C18 (5 μm, 250 × 9,4 mm, Agilent), 3 mL/min, r.t., solvent A comprised water with 0.1% TFA and solvent B comprised acetonitrile with 0.1% TFA, gradient elution: 0−20 min 20 to 80% B, 20−40 min 80% B.

Method 3: Zorbax 300SB-C18 (5 μm, 250 × 9,4 mm, Agilent), 2 mL/min, 40 °C, solvent A comprised water with 0.04% TFA and solvent B comprised acetonitrile with 0.05% TFA, gradient elution: 0−12 min 5 to 70% B, 12−15 min 70−90% B, 15−18 min 90% B.

Mass spectrometric analyses were carried out on a Micromass Tandem Quadrupole Mass Spectrometer (Quattro LC) operating in the MS mode. Mass spectral data were recorded at the negative and positive ESI mode using a cone voltage of 20 or 60 V. About 0.1 mg of the sample dissolved in 1.0 mL methanol/water (50/50) and 0.05% formic acid was infused at a flow rate of 5 μL/min. Nuclear magnetic resonance spectra were recorded on a 400 MHz Varian Inova 400 spectrometer. Chemical shifts are reported as δ in ppm relative to the residual solvent signal or TMS. IR spectra were recorded on the FTIR spectrometer IR 2000 (Perkin-Elmer) using KBr pellets.

Preparation of Copper Isocyanide Complexes. Copper isocyanide complexes were prepared as described for $[Cu(TBI)_4]Cl$ (17) to stabilize the ligands against oxidation and to generate a lyophilizable form of the ligands.

Preparation of NS_3COOH. The NS_3COOH ligand (**5**) was prepared from *S*-benzylcysteine (**1**) by reaction with 1-benzylsulfanyl-2-bromoethane (**2**) to give 3-benzylsulfanyl-2-[bis(2-benzylsulfanylethyl)amino]propionic acid 2-benzylsulfanyl ethyl ester (**3**), hydrolysis of the ester, and deprotection with sodium in liquid ammonia (Scheme 1).

S-Benzylcysteine **1** is commercially available (Arcos Organics), and 1-benzylsulfanyl-2-bromoethane **2** was

synthesized according to the method described by Trujillo and co-workers (*18*).

Preparation of 3-Benzylsulfanyl-2-[bis(2-benzylsulfanylethyl)amino]propionic Acid 2-Benzylsulfanylethyl Ester 3. Acetone (50 mL) was added to an aqueous solution of 0.01 mol (2.33 g) **1**, 0.04 mol (5.52 g) K_2CO_3, and 0.04 mol (1.6 g) NaOH. Afterward 0.05 mol (11.56 g) **2** dissolved in 10 mL of acetone was added dropwise at room temperature. The reaction mixture was stirred at room temperature for 6 days, and then the volume was reduced in vacuo. The remaining solution was extracted with diethyl ether. Removal of the solvent in vacuo gave a pale yellow oil which was purified by column chromatography (silica gel, *n*-hexane/ethyl acetate/triethylamine (75:25:0.1)). Yield: 38% pale yellow oil.

Analytical Data for ***3***. ^{1}H NMR: ($CDCl_3$): δ 2.37 (t, 4H), 2.63 (m, 8H), 3.73 (t, 1H), 3.65 (s, 6H), 3.73 (s, 2H), 4.16 (t, 2H), 7.26 (m, 20$H_{arom.}$). ^{13}C NMR: ($CDCl_3$): δ 29.7, 30.5, 31.7, 36.2, 36.4, 36.8, 51.4, 62.8, 63.8, 127.0, 127.1, 127.2, 128.5, 128.6, 128.9, 137.9, 138.2, 138.4, 171.3. ESI-MS (*m*/*z*) calcd (found): 663 (663) for $[M + H]^+$.

Preparation of 3-Benzylsulfanyl-2-[bis(2-benzylsulfanylethyl)amino]propionic Acid 4. A solution of 1 mmol (0.66 g) **3** in 10 mL of 1 N NaOH and 10 mL of dioxane was heated under reflux for 3 h. After cooling, 10 mL of acetic acid were added, and the reaction mixture was stirred at room temperature for another 1 h. Afterward it was extracted three times each with 10 mL $CHCl_3$. After drying over $MgSO_4$ and filtration, the organic solvent was removed in vacuo. The remaining oil was purified by column chromatography (silica, *n*-hexane/ethyl acetate (1:1)). Yield: 78% colorless oil.

Analytical Data for ***4***. ^{1}H NMR: ($CDCl_3$): δ 2.39 (t, 4H), 2.64 (m, 5H), 3.04 (dd, 1H), 3.30 (dd, 1H), 3.65 (m, 4H), 3.69 (s, 2H), 7.27 (m, 15$H_{arom.}$). ^{13}C NMR: ($CDCl_3$): δ 29.4, 30.1, 36.3, 37.6, 50.4, 64.2, 127.2, 127.3, 128.6, 128.7, 128.9, 137.9, 173.0.

Preparation of 2-[Bis(2-mercaptoethyl)amino]-3-mercaptopropionic Acid Hydrochloride 5. A solution of 0.4 mmol (0.2 g) **4** in 2 mL of dry THF was dropped to about 5 mL of liquid ammonia. Sodium was added in small portions until the solution remained deep blue for 15 min. The solvents were removed in an argon stream. To the white residue was added 5 mL water, and the solution was acidified with 1 N HCl (pH 2−3). The solution was extracted with ethyl acetate (3 × 5 mL). The combined organic phases were extracted with 1 N HCl (4 × 5 mL). Removal of the water in vacuo yielded 0.1 g (90%) of a colorless viscous oil.

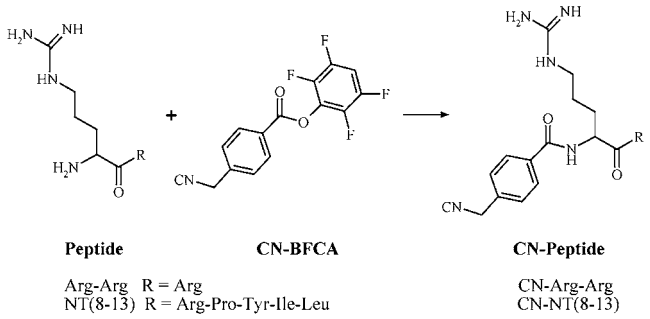
Analytical Data for ***5***. ^{1}H NMR: (D_2O): δ 2.97 (t, 4H), 3.12 (dd, 1H), 3.23 (dd, 1H), 3.56 (m, 4H), 4.22 (t, 1H). ^{13}C NMR: (D_2O): δ 18.8, 20.8, 54.4, 67.0, 169.6. ESI-MS (*m*/*z*) calcd (found): 242 (242) for $[M + H]^+$.

Preparation of CN-NT(8−13), CN-Arg-Arg, CN-Arg. As an example for the labeling of interesting biomolecules following the 4+1 principle, isocyanide-derivatized peptides were prepared in the following way (Scheme 2).

Preparation of 4-Isocyanomethyl Benzoic Acid 2,3,5,6-Tetrafluorophenyl Ester (CN-BFCA). The CN-BFCA compound **C** was prepared by formylation of 4-aminomethyl benzoic acid to give **A**, esterification with 2,3,5,6-tetrafluorophenol, and converting **B** to **C**.

Preparation of 4-Formylaminomethyl Benzoic Acid (A). 4-Aminomethyl benzoic acid (7 g, 0.046 mol) was dissolved in 80 mL of formic acid and 50 mL of acetic anhydride and heated under reflux for 3 h. After removal of the solvent, the remaining white powder was washed with diethyl ether and recrystallized from 2-propanol. Yield: 90%.

Scheme 2



Preparation of 4-Formylaminomethyl Benzoic Acid 2,3,5,6-Tetrafluorophenyl Ester (B). A (6 g, 0.033 mol) was dissolved in 30 mL of *N*,*N*-dimethylformamide (DMF), and a solution of 6.9 g (0.033 mol) *N*,*N*′-dicyclohexylcarbodiimide in 15 mL of DMF was added at 0 °C. After the mixture was stirred for 20 min, 5.7 g (0.033 mol) of 2,3,5,6-tetrafluorophenol dissolved in 5 mL of DMF was added. The mixture was stirred for 4 h at 0 °C and overnight at room temperature. The formed precipitate was separated by filtration, the supernatant was evaporated, and the remaining product was recrystallized from chloroform and *n*-hexane. Yield: 70%.

Preparation of 4-Isocyanomethyl Benzoic Acid 2,3,5,6-Tetrafluorophenyl Ester (C). B (0.5 g, 1.5 mmol) was dissolved in 12 mL of anhydrous pyridine, and 430 mg (2.25 mmol) of *p*-toluenesulfonyl chloride was added. After being stirred for 1.5 h at room temperature, the mixture was transferred in a flask filled with ice. After of the ice was slowly melted, the precipitate was filtered off and washed with water until no pyridine smell was noticed. The product was purified by column chromatography on silica gel 60 using a mixture of *tert*-butyl methyl ether and *n*-hexane (5:2) as eluent. The product fraction was evaporated and recrystallized from chloroform and *n*-hexane. Yield. 45%. ^{1}H NMR: (DMSO-d_6): δ 5.09 (s, 2H), 7.66 (d, 2H_{arom}), 7.98−8.07 (m, 1H), 8.24 (d, 2H_{arom}). IR: 1759 cm^{-1} (st, C═O), 2167 cm^{-1} (m, C≡N).

Preparation of CN-NT(8−13), CN-Arg-Arg, CN-Arg. NT(8−13) (70%) (4.7 mg, 4 μmol) was dissolved in 400 μL of DMF and 1.2 μL (8 μmol) of triethylamine, and 1.2 mg (4 μmol) of CN-BFCA dissolved in 100 μL of DMF was added. Alternatively, 7.9 mg (15 μmol) of L-arginyl-L-arginine (63%) or 5.3 mg (25 μmol) of L-arginine dihydrochloride were dissolved in a mixture of 800 μL of DMF and 150 μL of water. Triethylamine (35 μL, 0.25 mmol) and 7.7 mg (25 μmol) of CN-BFCA were added to the L-arginyl-L-arginine solution, and 20 μL (0.15 mmol) of triethylamine and 4.6 mg (15 μmol) of CN-BFCA were added to the L-arginine solution. After being stirred for 4−6 h at room temperature, the solvent was removed. The residues were dissolved in a mixture of acetonitrile and water (1:1) and then purified by semipreparative HPLC (method 2). The product fraction was neutralized with aqueous ammonia (2.5%) immediately after collecting and lyophilized. Yields: 50−60%. The substances were checked by HPLC and ESI-MS. HPLC: t_R = 10.1 min for CN-NT(8−13), t_R = 4.9 min for CN-Arg-Arg, t_R = 5.6 min for CN-Arg (method 1). ESI-MS (*m*/*z*) calcd (found): 961 (961) for $[CN\text{-}NT(8-13)]^+$, 474 (474) for [CN-Arg-Arg]$^+$, 318 (318) for $[CN\text{-}Arg + H]^+$.

Preparation of Reference Rhenium Complexes. *[Re(NS$_3$)CN-BFCA].* CN-BFCA (170 mg, 0.54 mmol) dissolved in 4 mL of chloroform were added to 206 mg

(0.4 mmol) of [Re(NS_3)PMe_2Ph] dissolved in 4 mL of chloroform. The mixture was stirred at 50 °C for 1 h and then evaporated to give an oily residue which was washed with diethyl ether to obtain an olive-brown powder. The substance was crystallized from chloroform after adding of methanol and diethyl ether at −18 °C. Yield: 95%. ^{1}H NMR: (DMSO-d_6): δ 2.8−3.2 (broad s, 12H), 6.15 (s, 2H), 7.79 (d, 2$H_{arom.}$), 7.97−8.07 (m, 1H), 8.20 (d, 2$H_{arom.}$). IR: 1752 cm^{-1} (st, C═O), 1922 cm^{-1} (st, C≡N). ESI-MS (*m*/*z*) calcd (found): 690, 692 (690, 692) for $[M + H]^+$.

[Re(NS_3)CN$CH_2C_6H_4$COOH]. A solution of 13 mg (0.3 mmol) of LiOH·H_2O in 3 mL of water was added to 54 mg (80 μmol) of [Re(NS_3)CN-BFCA] dissolved in 5 mL of tetrahydrofuran. After being stirred for 2 h at room temperature, the mixture was acidified with concentrated HCl. The olive precipitate was separated by filtration, washed with water and recrystallized from acetonitrile and methanol. Yield: 70−80%. ^{1}H NMR: (DMSO-d_6): δ 2.8−3.2 (broad s, 12H), 6.07 (s, 2H), 7.62 (d, 2H_{arom}), 7.94 (d, 2H_{arom}). IR: 1685 cm^{-1} (st, C═O), 1988 cm^{-1} (st, C≡N). HPLC: t_R = 17.9 min (method 1), t_R = 16.8 min (method 3), ESI-MS (*m*/*z*) calcd (found): 542, 544 (542, 544) for $[M + H]^+$.

[Re(NS_3)CN-NT(8−13)], [Re(NS_3)CN-Arg-Arg], [Re(NS_3)CN-Arg]. NT(8−13) (70%) (4.7 mg, 4 μmol) was dissolved in 400 μL of DMF, 1.2 μL (8 μmol) of triethylamine, and 2.8 mg (4 μmol) of [Re(NS_3)CN-BFCA] dissolved in 100 μL of DMF were added. Alternatively, 3.2 mg (15 μmol) of L-arginine dihydrochloride and 7.9 mg (15 μmol) of L-arginyl-L-arginine (63%) were dissolved separately in a mixture of 500 μL of DMF, 100 μL of water, and 20 μL (0.15 mmol) of triethylamine. [Re(NS_3)-CN-BFCA] (10.3 mg, 15 μmol) dissolved in 100 μL of DMF was added to each reaction mixture. After being stirred for 4−6 h at room temperature, the solvent was removed. The residues were dissolved in a mixture of acetonitrile and water (1:1), purified by semipreparative HPLC (method 2), and lyophilized. Yields: 50−60%. HPLC: t_R = 14.9 min (method 1), 14.5 min (method 3) for [Re(NS_3)-CN-NT(8−13)]; t_R = 12.5 min (method 1), 13.1 min (method 3) for [Re(NS_3)CN-Arg-Arg]; t_R = 13.8 min (method 1), 14.1 min (method 3) for [Re(NS_3)CN-Arg]. ESI-MS (*m*/*z*) calcd (found): 1341, 1343 (1341, 1343) for $[Re(NS_3)CN\text{-}NT(8-13)]^+$; 854, 856 (854, 856) for $[Re(NS_3)CN\text{-}Arg\text{-}Arg]^+$; 698, 700 (698, 700) for $[Re(NS_3)CN\text{-}Arg + H]^+$.

[Re(NS_3)PMe_2Ph] and Re or ^{99}Tc references for the 4 + 1 ^{99m}Tc complexes were synthesized according to (3).

Synthesis Procedure for the '4 + 1' ^{99m}Tc Complexes. *^{99m}Tc-EDTA.* To a kit formulation containing 5 mg of EDTA, 5 mg of mannitol, and 0.08 mg of $SnCl_2$ in freeze-dried form under nitrogen was added 2−5 mL of eluate of a ^{99}Mo/^{99m}Tc generator, and the solution was allowed to stand for 5 min at room temperature. Radiochemical purity: >95% (TLC).

'4+1' ^{99m}Tc Complexes. *Method 1.* NS_3 or NS_3COOH (0.3 mg) and isocyanide (0.05 mg) or phosphine (0.05−0.1 mg) were dissolved in 0.5−1.0 mL of methanol and added to the ^{99m}Tc-EDTA solution using a syringe. The reaction mixture was heated at 75 °C in a glycol bath for 30 min. Radiochemical purity: 90−97% (HPLC and TLC).

Method 2. ^{99m}Tc-EDTA solution (2.0−5.0 mL) prepared as described above was added to a kit vial containing 0.1 mg of the tetradentate ligand and 0.05 mg of [Cu(isocyanide)$_4$]Cl. The solution was allowed to stand at room temperature for 30−45 min or was heated at 50 °C for 15 min. Radiochemical purity: 90−97% (HPLC and TLC). The identity of the species obtained was confirmed by comparison with the HPLC profiles of ^{99}Tc or Re analogues. For stability and biodistribution studies, the ^{99m}Tc preparations were purified by semipreparative HPLC, the organic eluants were evaporated in vacuo, and the complexes were redissolved in saline and 20% propylene glycol.

Synthesis Procedure for the '4+1' ^{188}Re Complexes. *^{188}Re-EDTA.* Perrhenate eluate (3−5 mL) from a ^{188}W/^{188}Re generator was added together with 0.5 mL of 0.1 N HCl to a kit vial containing 5 mg of EDTA, 5 mg of mannitol, and 1.0 mg of $SnCl_2$ in freeze-dried form under nitrogen. After 20−30 min at room temperature, the complex formation is finished. Yield: >95% (TLC).

'4+1' ^{188}Re Complexes. NS_3 ligand (0.3 mg) and phosphine (0.05−0.20 mg) or [Cu(isocyanide)$_4$]Cl (0.05 mg) dissolved in 0.5 mL of water and 0.5 mL of methanol were added with a syringe to the Re-EDTA preparation, and the solution was heated at 90 °C for 30 min or at 50 °C for 1 h. Radiochemical purity: 75−85% (HPLC and TLC).

Determination of Partition Coefficients. Partition coefficients of the model ^{99m}Tc and ^{188}Re complexes were determined by shake-flask method by mixing 0.5 mL of the complex solution (0.1 M phosphate buffer pH 7.4 with 20% propylene glycol) and 0.5 mL of octanol and shaking for 5 min. After centrifugation aliquots of both phases were counted and the partition coefficient calculated.

Stability Studies. The in vivo stability of [^{99m}Tc(NS_3)-CN-NT(8−13)] was studied using rat arterial blood samples at various time points (0.5, 3, and 24 min) after injection of 50 MBq of [^{99m}Tc(NS_3)CN-NT(8−13)]. Ethanol (150 μL) was added to 100 μL of the supernatants obtained after centrifugation (11000*g*, 3 min) of the blood samples to precipitate the blood cells. Than the samples were cooled at −60 °C for 5 min. After centrifugation, the supernatant was analyzed by HPLC. For in vitro experiments, 500 μL of rat blood and plasma were incubated with the ^{99m}Tc compound (2−5 MBq) at room temperature for 120 min. The samples were treated as described above and analyzed by HPLC. To identify the degradation products, their t_R values were compared with [^{99m}Tc(NS_3)CN-NT(8−13)], [^{99m}Tc(NS_3)CN-Arg-Arg], [^{99m}Tc(NS_3)CN-Arg], [Re(NS_3)$CNCH_2C_6H_4$COOH] and $^{99m}TcO_4^-$ or coinjection experiments were performed.

Biodistribution Studies. The animal studies were carried out according to the relevant national regulations using male Wistar rats (5−6 weeks old). The ^{99m}Tc complex solution (0.5 MBq) (0.5 mL) was injected into the tail vein under slight ether anesthesia. After the injection, the rats were sacrificed by heart puncture 5 and 60 min postinjection (pi). Selected organs were isolated for weighing and counting. The activity concentration in the tissue of organs was calculated in terms of percentage of injected total activity (dose) per gram tissue (% ID/g).

RESULTS AND DISCUSSION

To find out optimum preparation conditions and to study the possibilities of "fine-tuning" of lipophilicity and their consequences on biodistribution in rats, simple isocyanides and phosphines as well as ligands containing carboxyl or ether functionalities were used (Figure 1). Moreover, as an example for labeling of biomolecules the peptides NT(8−13) as well as Arg-Arg and Arg (as reference complex) were labeled with ^{99m}Tc using the '4+1' approach and its stability in vitro and in vivo was studied.

Preparation of the '4+1' ^{99m}Tc Complexes. When the '4+1' technetium-99m complexes were prepared by

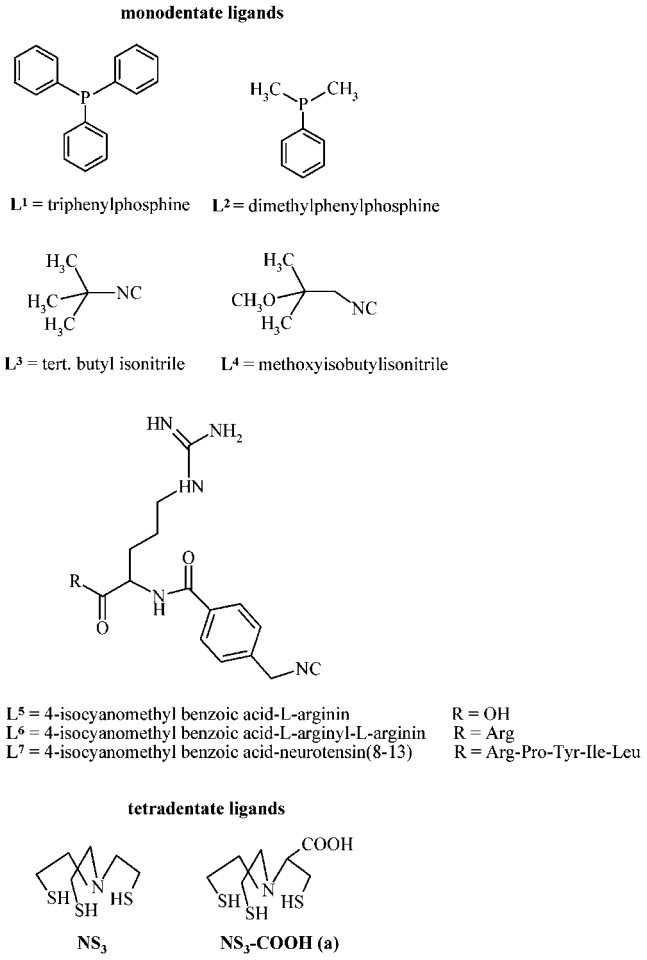


Figure 1. Structures of the ligands used for present studies.

a one-step procedure starting from pertechnetate with stannous chloride as reducing agent, more than 30% of reduced-hydrolyzed technetium was formed. These undesired large amounts of Tc hydroxide motivated us to search for a better reaction route. To avoid the formation of Tc hydroxide we prepared the '4+1' complexes in a two-step procedure. At first the ^{99m}Tc(III)-EDTA complex was formed, which in a second step reacts with both ligands to the desired '4+1' complex (Scheme 3).

To prepare the Tc-EDTA complex, a kit formulation was used. Five milligrams of EDTA, 5 mg of mannitol, and 0.08 mg of stannous chloride, which are contained in a vial in freeze-dried form and under nitrogen, are optimum amounts also for the complexation of high radioactive concentrations of technetium-99m (1−3 GBq/mL eluate). It was observed that the stability of such a Tc-EDTA preparation decreased when lower ligand concentrations were applied. Lower ^{99m}Tc activities (10−100 MBq/mL) need only 0.2 mg of EDTA and 0.01 mg of $SnCl_2$ for complete reduction of pertechnetate. The higher amounts of EDTA did not influence the ligand exchange reaction with the NS_3 ligand and the isonitrile or phosphine. We found that in order to prepare the intermediate complex it is also possible to use an EHIDA-kit (ROTOP Pharmaka GmbH) which contains 20 mg of the aminopolycarboxylic acid. In all cases >95% of the desired Tc-EDTA complex were formed and less than 1−2% of Tc hydroxide was detected by TLC.

In a second preparation step the ^{99m}Tc-EDTA complex reacts with optimized ligand amounts to the '4+1' complex. As an example, we studied the reaction of NS_3 and TBI with the Tc-EDTA complex and found that at high temperatures (30 min at 75 °C) 0.3 mg of NS_3 and 0.04 mg of TBI are sufficient ligand amounts to achieve a radiochemical purity of more than 95%. With 0.01 mg of TBI yields of about 70% were still obtained.

Table 1. Partition Coefficients Log *P* (octanol/0.1 M phosphate buffer, pH 7.4) of the '4+1' ^{99m}Tc and ^{188}Re Complexes (n = 3)

complex no.	log $P_{o/w}$ ^{99m}Tc	log $P_{o/w}$ ^{188}Re
1	1.83	1.78
1a	1.54	1.01
2	1.27	1.25
2a	1.10	0.96
3	1.28	1.14
3a	0.31	0.46
4	1.35	1.34
4a	−0.42	−0.27

A further improvement of preparation conditions was realized by using a copper(I) isocyanide complex instead of the free isonitrile ligand. That allows to prepare freeze-dried kit formulations. The complex $[Cu(TBI)_4]Cl$ was prepared and for optimum reaction conditions per vial 0.05 mg of the copper complex were lyophilized together with 0.1 mg of NS_3-oxalate. The Tc-EDTA solution was added with a syringe to the vial containing both of the ligands and the '4+1' ^{99m}Tc complex was formed with yields of >95% by incubation the reaction solution for 10 min at 50 °C. Reaction at room temperature requires a longer time of about 30 min.

Preparation of the '4+1' ^{188}Re Complexes. In principle, the preparation of the '4+1' ^{188}Re complexes followed the same two-step procedure as described for the technetium-99m complexes. At first the ^{188}Re-EDTA complex was prepared. Surprisingly, this was accomplished under relatively mild conditions with at least 1.0 mg $SnCl_2$. Lower Sn^{2+} concentrations or pH values >3 led to incomplete reduction of perrhenate. The addition of both ligands for the second step of reaction had to occur in the acidic solution. In the case of phosphines that was unproblematic. However, isocyanides are not stable under acidic conditions, but react with water to give the corresponding formamide and finally the amine. The use of copper isocyanide complexes widely prevents the degradation of isocyanides and thus allows the preparation of the corresponding '4+1' ^{188}Re complexes.

According to the optimized reaction conditions various '4+1' ^{99m}Tc and ^{188}Re complexes were prepared with the ligands listed in Figure 1, purified by HPLC, and characterized. We determined the influence of the carboxyl group of the NS_3COOH ligand on the octanol/water partition coefficient and the biodistribution of the complexes. Moreover, the biodistribution of ^{99m}Tc complexes with simple monodentate ligands (TBI, Me_2PhP) was compared with that of an ether group-containing ligand (MIBI). As examples for labeling of biomolecules two peptides and arginine were functionalized and labeled according to the '4+1' approach.

Comparison of the Log $P_{o/w}$ Values. Examination of the octanol/water partition coefficients suggests comparable high lipophilicity for ^{99m}Tc and ^{188}Re complexes with NS_3 and alkyl or aryl group-containing monodentate ligands. As shown in Table 1, the lipophilicity decreases at the introduction of a carboxyl group into the tetradentate ligand. Especially complexes with a small isonitrile (TBI) or an ether-derivatized monodentate ligand (MIBI) show increased hydrophilicity. The effect is less intensive using small phosphines as monodentate ligands.

Biodistribution of Complexes 2/2a−4/4a and 5 in Rats. Only ^{99m}Tc complexes were used to study the

Scheme 3

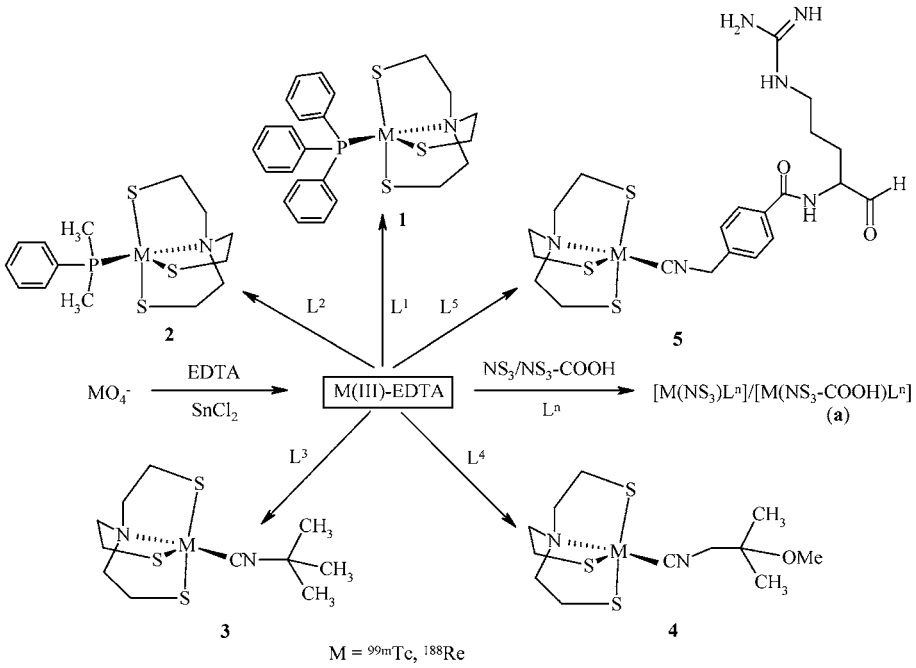


Table 2. Biodistribution (% ID/g)[a] of Some '4+1' ^{99m}Tc Complexes in Wistar Rats, 5 and 60 min after Intravenous Administration

complex	min, pi	blood	brain	heart	kidneys	lungs	liver
[^{99m}Tc]2	5	0.27 ± 0.05	0.42 ± 0.09	0.41 ± 0.07	0.72 ± 0.11	0.96 ± 0.08	5.91 ± 0.52
	60	0.17 ± 0.02	0.03 ± 0.00	0.12 ± 0.01	0.67 ± 0.06	0.71 ± 0.12	4.98 ± 0.54
[^{99m}Tc]2a	5	0.39 ± 0.07	0.02 ± 0.00	0.46 ± 0.04	5.87 ± 1.15	0.30 ± 0.02	10.0 ± 1.41
	60	0.22 ± 0.15	0.01 ± 0.00	0.13 ± 0.10	1.97 ± 0.90	0.11 ± 0.06	5.18 ± 1.55
[^{99m}Tc]3	5	0.13 ± 0.00	0.29 ± 0.03	0.25 ± 0.01	0.51 ± 0.03	0.60 ± 0.13	1.89 ± 0.18
	60	0.13 ± 0.04	0.04 ± 0.01	0.12 ± 0.03	0.66 ± 0.10	0.40 ± 0.14	2.85 ± 0.50
[^{99m}Tc]3a	5	2.78 ± 0.10	0.06 ± 0.00	1.28 ± 0.08	8.36 ± 1.12	1.31 ± 0.08	2.50 ± 0.06
	60	0.77 ± 0.35	0.03 ± 0.01	0.34 ± 0.14	2.41 ± 0.82	0.44 ± 0.23	1.13 ± 0.53
[^{99m}Tc]4	5	0.29 ± 0.06	0.35 ± 0.02	0.42 ± 0.05	1.12 ± 0.14	0.53 ± 0.06	4.89 ± 0.63
	60	0.23 ± 0.04	0.03 ± 0.00	0.12 ± 0.01	1.41 ± 0.18	0.19 ± 0.03	5.43 ± 0.46
[^{99m}Tc]4a	5	1.40 ± 0.11	0.04 ± 0.01	0.52 ± 0.05	7.29 ± 1.88	0.81 ± 0.12	5.82 ± 1.37
	60	0.23 ± 0.14	0.01± 0.00	0.08 ± 0.05	1.74 ± 0.68	0.14 ± 0.09	1.14 ± 0.52
[^{99m}Tc]5	5	0.30 ± 0.06	0.01± 0.00	0.12 ± 0.02	1.67 ± 0.22	0.32 ± 0.04	7.74 ± 0.80
	120	0.15 ± 0.06	0.01 ± 0.00	0.06 ± 0.02	0.76 ± 0.21	0.13 ± 0.04	2.28 ± 1.24

[a] Values represent the means ± SD (n = 4) of the percent injected dose/gram.

biodistribution in rats. In case of ^{188}Re complexes the risk of reoxidation of Re(III) to Re(VII) is higher than for ^{99m}Tc complexes and can lead to other results. This will be subject of another study. In general, the low accumulation of radioactivity in the stomach and the thyroid indicates the stability of the chelate unit (data not shown). The change of lipophilicity of the ^{99m}Tc complexes caused by variation of the outer sphere of the complexes is reflected by their biodistribution in rats (Table 2).

The introduction of a carboxyl group in the NS_3 ligand results in an obvious decrease of lipophilicity of complexes, especially in the case of isocyanide complexes (Table 1). That results in a high renal excretion of these complexes. The washout from the liver is also accelerated. The remarkably high primary concentration of complexes **3a** and **4a** in the blood may be caused by an unspecific binding of these complexes to plasma proteins. Such a plasma protein binding was also observed by HPLC analyses of in vivo plasma samples prepared 60 min after injection. It was not found for complex **2a**.

The increasing uptake of complexes **2**, **3**, and **4** in the liver and kidneys over time could be the result of other accumulation mechanisms of the complexes in these organs, which will be subject to further analysis. As known from the Tc(I) isocyanide complexes [^{99m}Tc-(MIBI)$_6$]$^+$ and [^{99m}Tc(EIBI^{13})$_6$]$^+$ which both contain ether groups in the ligand molecules, the clearance of such a complex through the liver is enlarged in comparison with the [^{99m}Tc(TBI)$_6$]$^+$ complex (*19*, *20*). That difference is not observed for the '4+1' complexes **3** and **4**. Despite the ether group of the MIBI complex **4**, the liver uptake is higher and increases with time in almost the same manner as observed for **3**.

Since the main catabolite of the in vivo degradation of complex **7**, the complex **5**, showed high in vivo stability over 120 min, its biodistribution in Wistar rats 5 and 120 min pi was also determined. The elimination of **5** from the blood was comparable with that of complexes **2**, **2a**, and **4**. After fast accumulation of **5** in the liver the activity decreased to about 2.3% ID/g after 60 min, which is comparable with the activity concentration in the liver of the other ^{99m}Tc complexes.

Stability Studies. Stability studies in vitro and in vivo were performed with the NT(8−13)-containing complex **[^{99m}Tc]7**. Generally, catabolites of ^{99m}Tc-labeled biomolecules can be generated by proteolytic degradation, by other elimination processes or by derivatization of the chelate unit and/or the biomolecules by various enzymatic reactions in vivo. Preliminary studies have provided an indication of in vitro and in vivo stability of the used '4+1'

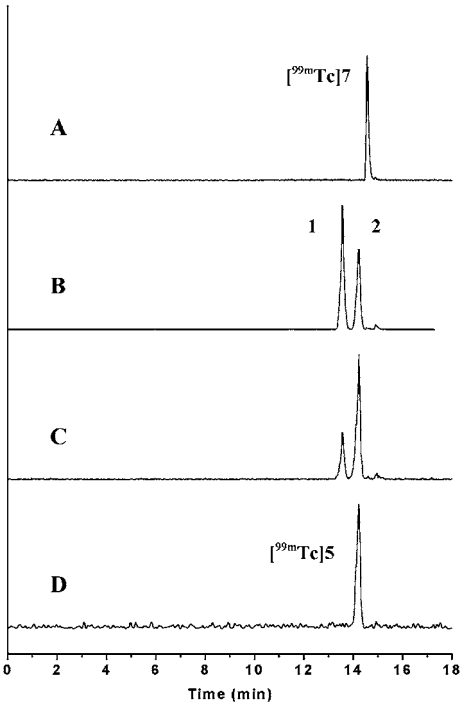


Figure 2. Catabolism of **[^{99m}Tc]7** in rats. (A) radioactive trace of complex **7**, (B) rat plasma sample, 0.5 min pi, (C) 3 min p.i., (D) 24 min pi; experiments were performed using a reversed-phase column (Zorbax 300SB-C18 (Agilent); 5 μm, 250 × 9.4 mm).

chelate unit (*3*). It is assumed that catabolites of **[^{99m}Tc]-7** are primarily formed by converting of the bound NT-(8−13). In vivo, NT(8−13) is extensively degraded by peptidases. That was also observed for the '4+1' ^{99m}Tc complex **7**. **[^{99m}Tc]7** was degraded so fast in vivo that already 0.5 min after injection the original compound was no longer detected in the plasma sample. **[^{99m}Tc]5** (catabolite 2) was identified by comparison with the Re reference complexes as the main degradation product in the plasma samples in vivo. It was the only ^{99m}Tc-labeled compound in the plasma 24 min after injection. Catabolite 1 was not identified, but it should be an intermediate product formed during the catabolism of complex **7**.

In vitro, 85−90% of **[^{99m}Tc]5** were detected after incubation with rat plasma for 120 min (Figure 2).

CONCLUSION

A novel two-step procedure allows "kitlike" preparations of '4+1' ^{99m}Tc and ^{188}Re complexes. In a first step, the metal(III)-EDTA complex is formed, which reacts in a second step with optimized ligand amounts to the desired '4+1' complex. Using oxalate salts of NS_3 ligands and copper isocyanide complexes or phosphonium salts as monodentate ligands, kit formulations can be prepared and reconstituted with pertechnetate or perrhenate in high yields. Only micromolar amounts of the monodentate ligand are needed and that results in high specific activity labeling of interesting molecules. The reduction of perrhenate has to be performed in acidic solutions and needs more quantities of EDTA and of the reducing agent stannous chloride, but not of the NS_3 ligand and the isocyanide or phosphine. Thus, high labeling yields are possible at low ligand concentration also with ^{188}Re. The lipophilicity of complexes can be controlled by introducing a carboxyl group into the tetradentate ligand and/or derivatization of the monodentate ligand. Moreover, the described approach allows the functionalization of a biomolecule with the tripodal as well as the monodentate ligand. The isocyanides and phosphines offer the possibility to vary the length and type of spacer for coupling the biomolecule. As an example, the neurotensin derivative CN-NT(8−13) was labeled with ^{99m}Tc according to the '4+1' approach and its behavior in vivo was studied. Although no stabilization effect after complexation of the peptide against peptidases was observed, the example demonstrates the usefulness of the '4+1' approach for high specific activity labeling of biomolecules under mild conditions with ^{99m}Tc and ^{188}Re.

ACKNOWLEDGMENT

We would like to thank Dr. Wunderlich (Klinik und Poliklinik für Nuklearmedizin, TU Dresden) for generously providing a ^{188}W/^{188}Re generator and Dr. S. H. Park (Division of Radioisotope Production and Application, HANARO center, Korea) for determination of partition coefficients.

LITERATURE CITED

(1) Alberto, R., Schibli, R., Angst, D., Schubiger, P. A., Abram, U., Abram, S., and Kaden, T. A. (1997) Application of technetium and rhenium carbonyl chemistry to nuclear medicine. *Trans. Met. Chem. 22*, 597−601.

(2) Bolzati, C., Boschi, A., Duatti, A., Prakash, S., Uccelli L., Refosco, F., Tisato, F., and Bandoli, G. (2000) Geometrically controlled selective formation of nitrido technetium(V) asymmetrical heterocomplexes with bidentate ligands. *J. Am. Chem. Soc. 122*, 4510−4511.

(3) Bolzati, C., Porchia, M., Bandoli, G., Boschi, A., Malagò, E., and Uccelli, L. (2001) Oxo-rhenium(V) mixed-ligand complexes with bidentate functionalized phosphines and tridentate Schiff base ligands. *Inorg. Chim. Acta 315*, 205−212.

(4) Pietzsch, H.-J., Spies, H., and Hoffmann, S. (1989) Lipophilic technetium complexes. VI. Neutral Tc(V) complexes with tridentate dithiol/monothiol ligand coordination. *Inorg. Chim. Acta 165*, 163−166.

(5) Spyriounis, D. M., Pelecanou, M., Stassinopoulou, C. I., Raptopoulou, C. P., Terzis, A., and Chiotellis, E. (1995) Synthesis and characterization of oxotechnetium(V) complexes with aza-substituted 2,6-dimethyl-4-azaheptane-2,6-dithiol ligands and benzyl mercaptan as coligand. *Inorg. Chem. 34*, 1077−1082.

(6) Syhre, R., Seifert, S., Spies, H., Gupta, A., and Johannsen, B. (1998) Stability versus reactivity of "3+1" mixed-ligand technetium-99m complexes *in vitro* and *in viv*o. *Eur. J. Nucl. Med.* 793−796.

(7) Pelecanou, M., Pirmettis, I. C., Nock, B. A., Papadopoulos, M., Chiotellis, E., and Stassinopoulou, C. I. (1998) Interaction of [ReO(SNS)(S)] and [99m Tc(SNS)(S) mixed ligand complexes with glutathione: isolation and characterization of the product. *Inorg. Chim. Acta 281*, 148−152.

(8) Nock, B. A., Maina, T., Yannoukakos, D., Ioannis, C., Papadopoulos, M., and Chiotellis, E. (1999) Glutathione-mediated metabolism of technetium-99m SNS/S mixed ligand complexes: a proposed mechanism of brain retention. *J. Med. Chem. 42*, 1066−1075.

(9) Gupta, A., Seifert, S., Syhre, R., Scheunemann, M., Brust, P., and Johannsen, B. (2001) Reactivity of ^{99m}Tc(V) "3+1" mixed-ligand complexes towards glutathione. *Radiochim. Acta 89*, 43−49.

(10) Pietzsch, H.-J., Gupta, A., Syhre, R., and Spies, H. (1999) Synthesis and characterization of trigonal-bipyramidal technetium(III) complexes with tetradentate/monodentate NS_3/isocyanide coordination: Potencies of the "4+1" Tc chelate system for the design of neutral, nonpolar and lipophilic complexes stable *in vivo. Report July − December 1999*, FZR-283, pp 84−88, Institute of Bioinorganic and Radiopharmaceutical Chemistry, Dresden.

(11) Pietzsch, H.-J., Seifert, S., Syhre, R., Tisato, F., Refosco, F., Leibnitz, P., and Spies, H. (2003) Synthesis, characterization and biological evaluation of technetium(III) complexes

with tridentate/bidentate S, E, S/P, S coordination (E = O, $N(CH_3)$, S): A novel approach to robust technetium chelates suitable for linking the metal to biomolecules. *Bioconjugate Chem. 14*, 136−143.

(12) Spies, H., Glaser, M., Pietzsch, H.-J., Hahn, F. E., Kintzel, O., and Lügger, T. (1994) Trigonal-bipyramidale Technetium- und Rhenium-Komplexe mit vierzähnigen tripodalen NS_3 Liganden. *Angew. Chem. 106*, 1416−1419.

(13) Spies, H., Glaser, M., Pietzsch, H.-J., Hahn, F. E., Kintzel, O., and Lügger, T. (1995) Synthesis and reactions of trigonal bipyramidal rhenium and technetium complexes with a tripodal NS_3 ligand. *Inorg. Chim. Acta 240*, 465−478.

(14) Pietzsch, H.-J., Gupta, A., Syhre, R., Leibnitz, P., and Spies, H. (2001) Mixed-ligand technetium(III) complexes with tetradentate/monodentate NS_3/isocyanide coordination: A new non-polar technetium chelate system for the design of neutral and lipophilic complexes stable in vivo. *Bioconjugate Chem. 12*, 538−544.

(15) Drews, A., Pietzsch, H.-J., Syhre, R., Seifert, S., Varnäs, K., Hall, H., Halldin, C., Kraus, W., Karlsson, P., Johnsson, C., Spies, H., and Johannsen, B. (2002) Synthesis and biological evaluation of technetium(III) mixed-ligand complexes with high affinity for the cerebral 5-HT_{1A} receptor and the alpha1-adrenergic receptor. *Nucl. Med. Biol. 29*, 389−398.

(16) de Vries, N., Davison, A., and Jones, A. (1989) Trigonal-bipyramidal compounds of technetium with tetradentate umbrella ligand. *Inorg. Chim. Acta, 165*, 9−10.

(17) Carpenter, A. P., Linder, K. E., Maheu, L. J., Patz, M. A., Thompson, J. S., Tulip, T. H., and Subramanyam, V. (1987) Metal-isonitrile adducts for preparing radionuclide complexes. *EP 211 424 B1*.

(18) Trujillo, D. A., McMahon, W. A., and Lyle, R. E. (1987) A convenient synthesis of haloethyl alkyl sulfides. *J. Org. Chem. 52*, 2932−2933.

(19) Kronauge, J. F., Kawamura, M., Lepisto, E., Holman, B. L., Davison, A., Jones, A. G., Costello, C. E., and Zeng, C.-H. (1990) Metabolic studies of the myocardial perfusion agent Tc-MIBI. *Technetium and Rhenium in Chemistry and Nuclear Medicine 3* (Mazzi, U., Ed.) Cortina International, Verona.

(20) Barbarics, E., Kronauge, J. F., Costello, C. E., Janoki, G. A., Holman, B. L., Davison, A., and Jones, A. G. (1994) In vivo metabolism of the technetium isonitrile complex $[Tc(2\text{-ethoxy-2-methyl-1-isocyano-propane})_6]^+$. *Nucl. Med. Biol. 21*, 583−591.

BC0300798

^{99m}Tc-Labeling and in Vitro and in Vivo Evaluation of HYNIC- and (N_α-His)Acetic Acid-Modified [D-Glu^1]-Minigastrin

E. von Guggenberg,[†] M. Behe,[‡] T. M. Behr,[‡] M. Saurer,[§] T. Seppi,[§] and C. Decristoforo[†,*]

Department of Nuclear Medicine, Leopold-Franzens-University of Innsbruck, Innsbruck, Austria, Department of Nuclear Medicine, Philipps-University of Marburg, Marburg, Germany, and Department of Radiotherapy and Radiooncology, Leopold-Franzens-University of Innsbruck, Innsbruck, Austria.
Received December 18, 2003; Revised Manuscript Received March 24, 2004

Gastrin/CCK-2 receptors are overexpressed in a number of tumors such as medullary thyroid cancer (MTC) and small cell lung cancer (SCLC). Recently [D-Glu^1]-minigastrin (MG) has been radiolabeled with ^{131}I, ^{111}In, and ^{90}Y and evaluated in patients. This study describes the labeling and evaluation of MG with technetium-99m using two different labeling approaches: HYNIC as bifunctional coupling agent and (N_α-His)Ac as tridentate ligand for ^{99m}Tc(CO_3) labeling. Labeling was perfomed at high specific activities using Tricine and EDDA as coligands for HYNIC-MG and $[^{99m}Tc(OH_2)_3(CO)_3]^+$ for (N_α-His)Ac-MG. Stability experiments were carried out by reversed phase HPLC analysis in PBS, serum, histidine, and cysteine solutions, as well as rat liver and kidney homogenates. Receptor binding and internalization experiments were performed using CCK-2 receptor positive AR42J rat pancreatic tumor cells. Biodistribution experiments were carried out in nude mice carrying AR42J tumors by injection of ^{99m}Tc-labeled peptide with or without coinjection of 50 μg of minigastrin I human (MGh). HYNIC-MG and (N_α-His)Ac-MG could be radiolabeled at high specific activities (>1 Ci/μmol). For HYNIC-MG, high labeling yields (>95%) were achieved using Tricine and EDDA as coligands. Stability experiments of all ^{99m}Tc-labeled conjugates revealed a high stability of the label in PBS and serum as well as toward challenge with histidine and cysteine. Incubation in kidney homogenates resulted in a rapid degradation of all conjugates with <10% intact peptide after 60 min at 37 °C, with no considerable differences between the radiolabeled conjugates; a somewhat lower degradation rate was seen in liver homogenates. Protein binding varied considerably with lowest levels for ^{99m}Tc-EDDA/HYNIC-MG. Competition experiments of unlabeled conjugates on AR42J membranes versus [^{125}I-Tyr^{12}]-gastrin I showed high CCK-2 receptor affinity for all conjugates under study. Internalization behavior was very rapid for all radiolabeled conjugates in the order of ^{99m}Tc-(N_α-His)Ac-MG > ^{99m}Tc-EDDA/HYNIC-MG > ^{99m}Tc-Tricine/HYNIC-MG. In tumor-bearing nude mice the highest tumor-uptake was observed with ^{99m}Tc-EDDA/HYNIC-MG (8.1%ID/g) followed by ^{99m}Tc-Tricine/HYNIC-MG (2.2%ID/g) and ^{99m}Tc-(N_α-His)Ac-MG (1.2%ID/g) which correlated with kidney uptake (101.0%ID/g, 53.8%ID/g, 1.8%ID/g respectively). In this series of compounds ^{99m}Tc-EDDA/HYNIC-MG with its very high tumor/organ ratios except for kidneys seems to be the most promising agent to target CCK-2 receptors. Despite promising properties concerning receptor binding, internalization, and in vitro stability, ^{99m}Tc-(N_α-His)Ac-MG showed low tumor uptake in vivo.

INTRODUCTION

Cholecystokinin-2 (CCK-2, formerly CCK-B)/gastrin receptors have recently found increasing interest as targets for nuclear medicine applications. A high incidence of CCK-2 receptors has been found in human samples of medullary thyroid cancer (MTC), small cell lung cancer (SCLC), stromal ovarian cancers (*1*), and also in vivo in gastrointestinal neuroendocrine tumors, especially if somatostatin receptor scintgraphy is negative (*2*). Radiolabeled analogues of both CCK (*3*) and gastrin (*4*) have been developed. [DTPA-D-Glu^1]-minigastrin (DTPA-MG) radiolabeled with ^{111}In has shown promising properties for detection of CCK-2 receptor positive tissue in patients (*5*) and has been extensively evaluated clinically, radiolabeled with ^{90}Y even for therapeutic purposes in MTC (*6*). For diagnostic applications, technetium-99m still is the label of choice for routine applications due to its availability, low costs, low radiation dose for the patient, and optimal gamma-energy profile. Labeling approaches of peptides with ^{99m}Tc have to fulfill several criteria (*7*): labeling has to be achieved at high specific activities without interfering with the amino acid sequence responsible for receptor binding, and it has to ensure reasonably hydrophilic properties of the peptide resulting in predominant renal clearance and a high in vivo stability of the ^{99m}Tc complex. These criteria limit the numbers of available labeling approaches, and only a few have so far shown applicability in patient studies. Hydrazinonicotinic acid (HYNIC) is a bifunctional coupling agent for ^{99m}Tc-labeling of peptides and has been used to radiolabel a number of peptides such as somatostatin analogues (*8*) or GPIIb/IIIa antagonists (*9*). In

* Corresponding author: Clemens Decristoforo, Department of Nuclear Medicine, Leopold-Franzens-University of Innsbruck, Anichstrasse 35, A-6020 Innsbruck, Austria. Tel: +43-512-504-2671. Fax: +43-512-504-2683. E-mail: Clemens.Decristoforo@uibk.ac.at.

[†] Department of Nuclear Medicine, Leopold-Franzens-University of Innsbruck.

[‡] Philipps-University of Marburg.

[§] Department of Radiotherapy and Radiooncology, Leopold-Franzens-University of Innsbruck.

10.1021/bc0300807 CCC: $27.50 © 2004 American Chemical Society
Published on Web 07/02/2004

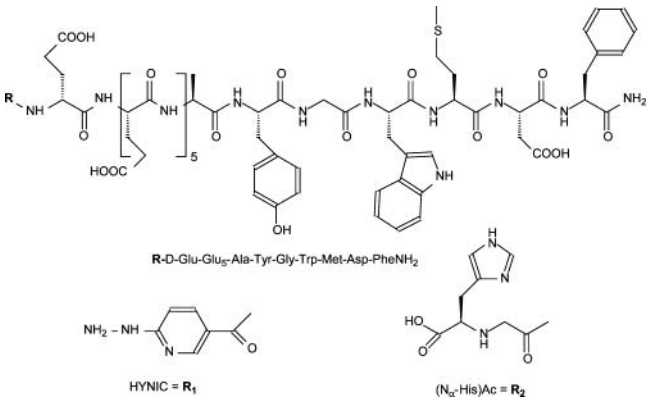


Figure 1. Molecular formulas of HYNIC and (N_α-His)acetic acid conjugated to [D-Glu]^1-minigastrin (MG).

the HYNIC labeling approach, technetium-99m is bound to the hydrazino group, and the other coordination sites are occupied by one or more coligands. A number of suitable coligands has been described, but it is also known that the choice of coligand can influence the stability and lipophilicity of the radiolabeled peptide and in the end the biodistribution (*10*). Another interesting approach to radiolabel peptides at high specific activities is the use of the technetium−carbonyl-core [$Tc(CO)_3$]. Alberto et al. described the one-step synthesis of the technetium−carbonyl aquaion [$^{99m}Tc(OH_2)_3(CO)_3]^+$ (*11*). This precursor has been shown to have a high affinity for histidine (His) and radiolabels peptides at very high specific activities (*12*). Further, the denticity of the $Tc(CO)_3$ coordinating ligand can influence the biological behavior of radiolabeled peptides, and tridentate ligands have advantages over bidentate systems (*13*). One promising tridentate derivative for peptide conjugation is (N_α-His)Ac that has shown suitable properties for ^{99m}Tc labeling after conjugation to a neurotensin derivative (*14*). We herein describe the labeling, in vitro characterization including receptor binding, and biodistribution of HYNIC and (N_α-His)acetic acid conjugated to [D-Glu]^1-minigastrin (MG, D-Glu-Glu_5-Ala-Tyr-Gly-Trp-Met-Asp-$PheNH_2$), Figure 1.

EXPERIMENTAL PROCEDURES

Materials. Reagents were purchased from Aldrich-Sigma Chemical Co. unless stated otherwise and used as they were received. [HYNIC-D-Glu^1]-minigastrin (HYNIC-MG) and [(N_α-His)Acetyl-D-Glu^1]-minigastrin ((N_α-His)Ac-MG) were synthesized by PiChem (Graz, Austria) with a purity of >95% as analyzed by reversed phase HPLC (RP-HPLC) and MS. [^{125}I -Tyr^{12}]-gastrin I was purchased from Perkin-Elmer Life Science (Boston, MA). Na $^{99m}TcO_4$ was obtained from a commercial ^{99}Mo/^{99m}Tc generator (ULTRATECHNEKOW, Mallinckrodt, The Netherlands).

Analytical Methods. *HPLC.* A Gynkotek M480 pump with a Spectra Physics Spectra Chrom 100 variable UV detector and Bioscan radiometric detection was used for RP-HPLC analysis. A Macherey & Nagl Nucleosil 120-5 C18 250 × 4.6 mm column, flow rates of 1 mL/min, and UV detection at 220 nm were employed with the following gradients:

Method 1: Acetonitrile (ACN)/0.1% trifluoroacetic acid (TFA)/H_2O: *t*: 0−3 min 0% ACN, 3−5 min 0−25% ACN, 5−20 min 25−40% ACN, 20−25 min 40−60% ACN, 25−28 min 60−0% ACN, 28−33 min 0% ACN

Method 2: 0.05 M Na acetate pH 5.4/ACN: *t*: 0−3 min: 0% ACN, 3−33 min: 0−100% ACN, 33−35 min: 100% ACN, 35−36 min: 100−0% ACN.

Purification by Solid-Phase Extraction (SPE). For purification of the radiolabeled peptide for stability studies, a SPE method was used. The radiolabeling mixture was passed through a C18-SEPPAK-mini cartridge (Waters, Milford, MA). The cartridge was washed with 5 mL of saline, and the radiolabeled peptide was eluted with 70% ethanol. This method efficiently removed all hydrophilic, nonpeptide bound impurities (mainly $^{99m}TcO_4^-$, ^{99m}Tc coligands).

^{99m}Tc-Labeling. *HYNIC-MG: Tris(hydroxymethyl)-methylglycine (Tricine) as Coligand.* In a rubber-sealed vial, 3 μg of HYNIC-MG was incubated with 0.5 mL of Tricine solution (70 mg/mL in water), 0.5 mL of $^{99m}TcO_4^-$ solution (>200 MBq), and 20 μL of tin(II) solution (10 mg of $SnCl_2 \cdot 2H_2O$ in 10 mL of nitrogen purged 0.1 N HCl) for 20 min at room temperature or 75 °C.

Ethylenediaminediacetic Acid (EDDA) as Coligand. In a rubber-sealed vial, 10 μg of HYNIC-MG was incubated with 0.5 mL of EDDA solution (20 mg/mL in pH 6−7), 0.5 mL of $^{99m}TcO_4^-$ solution (400 MBq), and 20 μL of tin-(II) solution (10 mg of $SnCl_2 \cdot 2H_2O$ in 10 mL of nitrogen purged 0.1 N HCl) for 30 min at room temperature and for 10 min in a boiling water bath.

Tricine/EDDA Exchange Labeling. In a rubber-sealed vial, 20 μg of HYNIC-MG was incubated with 1 mL of EDDA/Tricine solution (20 mg/mL Tricine, 10 mg/mL EDDA in pH 6−7), 1 mL of $^{99m}TcO_4^-$ solution (800 MBq), and 20 μL of tin(II) solution (10 mg of $SnCl_2 \cdot 2H_2O$ in 10 mL of nitrogen purged 0.1 N HCl) for 10 min in a boiling water bath.

(N_α-His)Ac-MG. Carbonyl aquaion [$^{99m}Tc(OH_2)_3(CO)_3]^+$ was prepared as described previously (*15*). Briefly, in a rubber-sealed vial 4 mg of Na_2CO_3, 5.5 mg of $NaBH_4$, and 20 mg of NaK−tartrate were CO-purged for 15 min and reacted with 2.5 mL of $^{99m}TcO_4^-$ solution (3−4 GBq) for 30 min at 75 °C. Pressure from the evolving H_2 gas was balanced with a 20 mL syringe, and 1 M NaH_2PO_4 was added for neutralization. Quality control was performed by HPLC method 1.

Peptide Labeling. In a rubber-sealed vial 20 μg of (N_α-His)Ac-MG was incubated with 0.5 mL of Carbonyl precursor (800 MBq) for 30 min at 75 °C. Radiolabeled peptides were characterized and labeling yields determined by HPLC methods 1 and 2.

In Vitro Evaluation of Radiolabeled Peptides. Stability. The stability of the radiolabeled peptides in aqueous solution was tested by incubation of the reaction mixture purified by SPE at a concentration of 200−1000 pmol peptide/mL in phosphate buffer (pH 7.4), in a solution containing 10 000-fold molar excess of cysteine or histidine (pH 7.4) over the peptide and in fresh human plasma at 37 °C up to 24 h. After incubation, plasma samples were precipitated with acetonitrile and centrifuged (1750*g*, 5 min). Degradation of the ^{99m}Tc complexes was assessed by HPLC method 1.

For protein binding assessment, the SPE-purified complexes were incubated at a concentration of 20−100 pmol peptide/mL in fresh human plasma at 37 °C and analyzed for up to 6 h by size-exclusion chromatography (MicroSpin G-50 Columns; Sephadex G-50). Protein binding of the ^{99m}Tc complex was determined by measuring column and eluate in a gamma counter.

For incubation in kidney and liver homogenates, kidneys or liver freshly excised from rat were rapidly rinsed and homogenized in 20 mM HEPES buffer pH 7.3 with an Ultra-Turrax T25 homogenator for 1 min at RT. The radiopeptides were incubated with fresh 30% homogenates at a concentration of 250−500 pmol peptide/mL at 37 °C for up to 2 h. Samples were precipitated with

acetonitrile, centrifuged (1750*g*, 5 min), and analyzed by HPLC method 1.

Receptor Binding Studies. The binding affinity of peptide conjugates was tested in a competition assay against [^{125}I-Tyr^{12}]-gastrin I. Rat pancreatic tumor (AR42J) cell membranes were used as the source for gastrin receptors. For membrane preparation, cells were homogenized three times for 10 s at 4 °C with an Ultra-Turrax T25 homogenator in 20 mM HEPES buffer pH 7.3/10 mM $MgCl_2$/10 μM bacitracin, and protein concentration was assessed to 50 μg/100 μL (Bradford assay). In a Multiscreen well plate (glass fiber filters; Whatman GF/C), 50 μL of competitor solution of increasing concentrations (0.001−1000 nM in 1% BSA/10 mM $MgCl_2$/10 μM bacitracin), 50 μL of radioligand solution (50 000 cpm in 1% BSA/10 mM $MgCl_2$/10 μM bacitracin), and 100 μL of membrane solution (50 μg protein/tube) were incubated in triplicates for 2 h at RT. Incubation was interrupted by filtration of the medium and rapid rinsing with ice-cold washing buffer (1 × 200 μL, followed by 1 × 50 μL 15 mM TRIS/139 mM saline pH 7.4), and filters were counted in a gamma-counter. IC_{50} values were calculated following nonlinear regression with Origin software (Microcal Origin 5.0, Northampton MA).

For saturation studies, similar to that described above for the competition assays on membranes, in a Multiscreen well plate, radiolabeled peptide conjugate of increasing concentrations (0.05−20 nM in 1% BSA/10 mM $MgCl_2$/10 μM Bacitracin) and AR42J membrane solution (50 μg protein/tube) were incubated in triplicate for 2 h at RT in a total volume of 200 μL. Nonspecific binding was determined in a parallel series containing 1 μM MGh. K_d values were calculated following nonlinear regression and Scatchard plot (linear regression) with Origin software (Microcal Origin 5.0, Northampton MA).

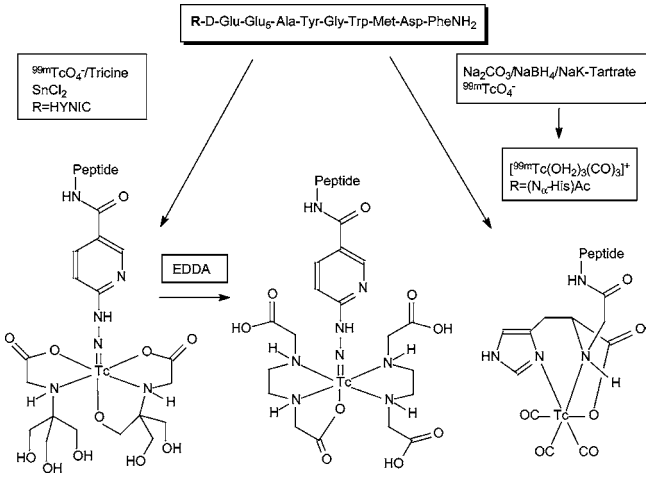
Internalization Studies. For internalization experiments, AR42J cells were seeded at a density of 1 × 10^6 cells per well in six-well plates (Greiner Labortechnik, Germany) and grown to confluency for 48 h. On the day of the experiment, cells were washed twice with ice-cold internalization medium prepared by RPMI1640 supplemented by 1% (v/v) fetal bovine serum. The cells were supplied with fresh medium (1.2 mL) and incubated with 300 000 cpm of the radiolabeled peptide (150 μL in PBS/0.5%BSA buffer, corresponding roughly to 200 fmol of total peptide) and either PBS/0.5%BSA buffer alone (150 μL, total series) or with 10 μM MGh in PBS/0.5%BSA buffer (150 μL, nonspecific series). The cells were incubated at 37 °C in triplicate for each time point of 5, 15, 30 min, 1 and 2 h incubation. Incubation was interrupted by removal of the medium and rapid rinsing with ice-cold internalization medium two times. Thereafter, the cells were incubated twice at ambient temperature in acid wash buffer (50 mM glycine buffer pH 2.8, 0.1 M NaCl) for 5 min, a period sufficient to remove over 90% of membrane-bound radioligand. The supernatant was collected, and the cells were rinsed with PBS/0.5% BSA (membrane bound radioligand fraction). Finally, cells were lyzed by treatment in 1 N NaOH and collected (internalized radioligand fraction). All fractions were counted in a gamma-counter, and mean specific values were calculated. The internalized fraction was expressed in relation to the total activity added (% of total) as well as in relation to the activity bound to the cells, i.e., internalized plus membrane bound fraction (% of bound).

In Vivo Evaluation of Radiolabeled Peptides. Biodistribution. All animal experiments were conducted in compliance with the Austrian animal protection laws and with approval of the Austrian Ministry of Science. Normal biodistribution studies were performed in Balb/c mice (Charles River, Germany). On the day of experiment, three mice received the radioactive conjugate (1 MBq/mouse, corresponding to 0.15−0.2 μg of peptide) intravenously injected into the tail vein, with or without coinjection of 50 μg of MGh. They were sacrificed by cervical dislocation 4 h postinjection. Different organs and tissues (blood, lung, heart, stomach, spleen, liver, pancreas, kidneys, muscle, intestine) were removed. The amount of radioactivity was determined with a gamma-counter. Results were expressed as percentage of injected dose per gram of tissue (%ID/g).

Tumor uptake studies were performed in nu/nu mice (Charles River, Germany). For the induction of tumor xenografts, AR42J cells were subcutaneously injected at a concentration of 10 × 10^6 cells/mouse, and tumors were allowed to grow until they had reached a size of 0.5−1 mL (10−15 days). On the day of the experiment, the animals were treated as described above. Tumors and other tissues (blood, lung, heart, stomach, spleen, liver, pancreas, kidneys, muscle, intestine) were removed. The amount of radioactivity was determined with a gamma-counter. Results were expressed as percentage of injected dose per gram of tissue (%ID/g), and tumor-to-organ, stomach-to-organ, pancreas-to-organ, and kidney-to-organ ratios were calculated.

Metabolic Stability. To evaluate the in vivo degradation of the conjugate, urinary excretion products were characterized by RP-HPLC (method 1).

Scheme 1. ^{99m}Tc-Labeling Routes of HYNIC- and (N_α-His)Ac-MG[a]



[a] Complex structures of ^{99m}Tc-Tricine/HYNIC-MG, ^{99m}Tc-EDDA/HYNIC-MG, and ^{99m}Tc(CO)$_3$-(N_α-His)Ac-MG according to refs 16, 17, and 13, respectively.

RESULTS

Radiolabeling. Radiolabeling of all peptide conjugates could be performed according to Scheme 1 at high specific activities (>70 GBq/μmol) with high yields. In the case of HYNIC-MG, only Tricine as coligand resulted in reasonable labeling yields, whereby two main peaks could be characterized by HPLC. At room temperature a shift to the more hydrophilic species over time was observed; by heating the reaction mixture at 80 °C for 15 min, only this peak was detected. Addition of monodentate ligands such as nicotinic acid to the reaction mixture did not significantly alter the HPLC profile. Therefore, ^{99m}Tc-HYNIC-MG prepared at higher temperature was chosen for further characterization. EDDA as coligand resulted in very low labeling yields even at elevated temperature;

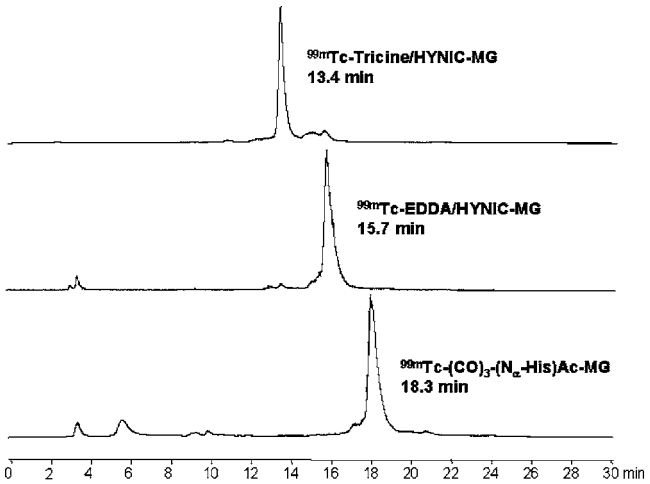


Figure 2. HPLC-radiochromatograms of the radiolabeled peptides (HPLC method 1).

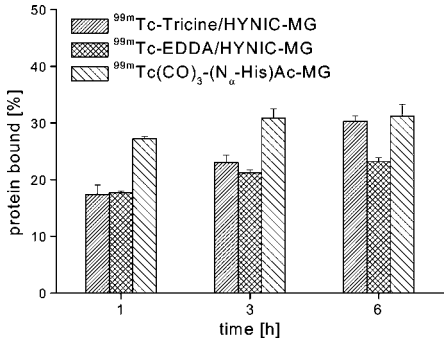


Figure 3. Protein binding over time determined by size exclusion chromatography (MicroSpinTM G-50 columns, Sephadex G-50).

Table 1. Retention Times of the Radiolabeled Peptides in Two Different HPLC Gradients

HPLC gradient	retention time (min)		
	^{99m}Tc-Tricine/HYNIC-MG	^{99m}Tc-EDDA/HYNIC-MG	^{99m}Tc(CO)$_3$-(N$_\alpha$-His)Ac-MG
method 1	13.4	15.7	18.3
method 2	14.3	14.9	15.8

however, using an exchange labeling approach from Tricine to EDDA and boiling the reaction mixture for 10 min, a single peak (^{99m}Tc-EDDA/HYNIC-MG) with distinct retention time on HPLC to the ^{99m}Tc-Tricine/HYNIC-MG complex was observed with labeling yields >90%. (N$_\alpha$-His)Ac-MG could be radiolabeled by addition of $[^{99m}Tc(OH_2)_3(CO)_3]^+$; high labeling yields >90% were achieved only when the concentration of peptide in the reaction solution was kept higher than 20 μM. In Figure 2 are shown typical HPLC-radiochromatograms of reaction mixtures of all three ^{99m}Tc-labeled MG derivatives. Retention times were different, utilizing two different HPLC gradients at different pH values (methods 1 and 2) and are summarized in Table 1. Lipophilicity as determined from the RP-HPLC retention behavior was increasing in the order ^{99m}Tc-Tricine/HYNIC-MG < ^{99m}Tc-EDDA/HYNIC-MG < ^{99m}Tc(CO)$_3$-(N$_\alpha$-His)Ac-MG.

Stability Studies. Plasma protein binding behavior at different time points is presented in Figure 3. At early time points, ^{99m}Tc(CO)$_3$-(N$_\alpha$-His)Ac-MG showed considerably higher levels compared to ^{99m}Tc-HYNIC conjugates. At later time points, ^{99m}Tc-Tricine/HYNIC-MG showed increasing values reaching levels comparable to ^{99m}Tc-(CO)$_3$-(N$_\alpha$-His)Ac-MG after 6 h incubation. Protein binding values of ^{99m}Tc-EDDA/HYNIC-MG were similar to its Tricine counterpart at 1 h with little change over time.

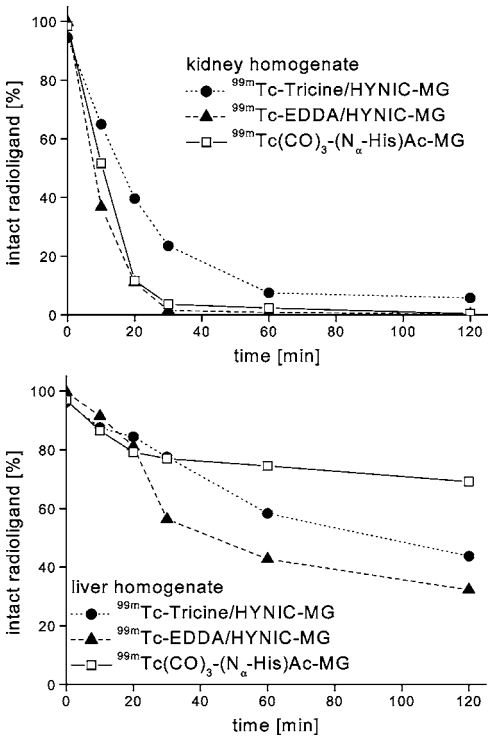


Figure 4. Stability of radiolabeld peptides in rat tissue homogenates: (a) kidney, (b) liver.

Table 2. Stability of the Radiolabeled Peptides in Aqueous Solutions

	0 h	1 h	2 h	4 h	24 h
Intact ^{99m}Tc-Tricine/HYNIC-MG (%)					
phosphate	99.6	98.2	96.3	91.1	80.8
serum	98.9	98.8	98.4	96.7	94.6
cysteine	95.5	92.6	92.5	88.4	81.4
histidine	93.4	90.1	89.3	88.4	81.4
Intact ^{99m}Tc-EDDA/HYNIC-MG (%)					
phosphate	99.9	99.4	99.1	99.4	94.8
serum	99.7	99.3	96.6	97.4	90.9
cysteine	99.0	99.2	98.7	99.1	96.4
histidine	99.5	99.2	99.1	99.4	96.1
Intact ^{99m}Tc(CO)$_3$-(N$_\alpha$-His)Ac-MG (%)					
phosphate	98.8	99.6	98.7	99.2	96.8
serum	98.6	99.6	98.2	98.9	94.4
cysteine	98.5	99.8	99.4	99.9	96.2
histidine	98.7	99.7	99.9	99.9	97.6

Results from stability studies are summarized in Table 2. Incubation in PBS, serum, cysteine, and histidine for up to 24 h of SPE-purified peptides revealed high stability of all ^{99m}Tc-labeled peptide conjugates under investigation. Only ^{99m}Tc-Tricine/HYNIC-MG showed generally somewhat lower purity levels, especially after 24 h in all incubation solutions (80.8−81.4%) except serum.

Incubation in kidney homogenates resulted in a very rapid decrease of activity related to the original peptide peak (Figure 4a). After 30 min incubation, less than 10% intact peptide could be detected for ^{99m}Tc(CO)$_3$-(N$_\alpha$-His)-Ac-MG and ^{99m}Tc-EDDA/HYNIC-MG; for ^{99m}Tc-Tricine/HYNIC-MG, this value was reached only after 60 min incubation. After incubation in liver homogenates (Figure 4b), also a low stability of all three peptide conjugates was found with differences in the rate of decrease, reaching 69% for ^{99m}Tc(CO)$_3$-(N$_\alpha$-His)Ac-MG, 32% for ^{99m}Tc-EDDA/HYNIC-MG, and 44% for ^{99m}Tc-Tricine/HYNIC-MG after 120 min incubation time.

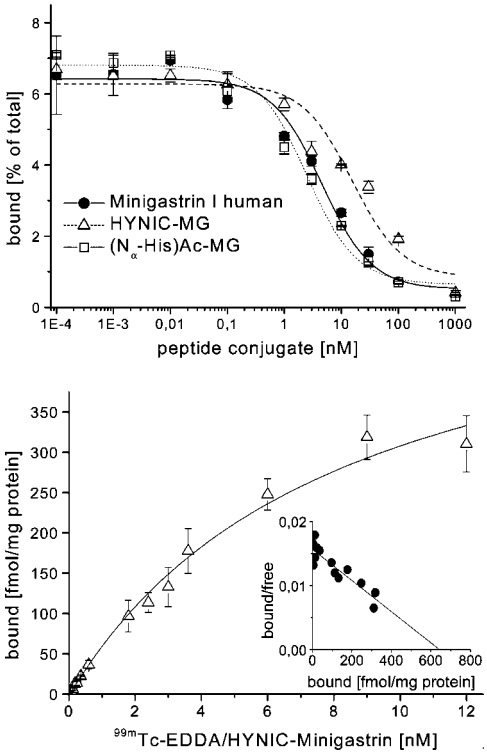


Figure 5. Receptor binding on AR42J membranes: (a) Displacement curves of [^{125}I-Tyr^{12}]-gastrin I using minigastrin I human (IC_{50} = 4.58 nM), HYNIC-MG (IC_{50} = 15.5 nM) and (N_α-His)Ac-MG (IC_{50} = 2.45 nM) as competitors (mean ± sd, n = 3). (b) Saturation curve and Scatchard plot of ^{99m}Tc-EDDA/HYNIC-MG (K_d = 10.3 nM, B_{max} = 647 fmol/mg protein).

Receptor Binding and Internalization. Both HYNIC-MG and (N_α-His)Ac-MG had a high affinity to the gastrin/CCK-2 receptor. Displacement of [^{125}I-Tyr^{12}]-gastrin I by the two peptide conjugates in comparison with unmodified MG is shown in Figure 5a. IC_{50} values for HYNIC-MG were somewhat higher (15.5 nM) compared to (N_α-His)Ac-MG (2.45 nM) and MG (4.58 nM). Saturation assay of ^{99m}Tc-EDDA/HYNIC-MG revealed high binding affinity of the ^{99m}Tc-labeled peptide with a K_d of 10.3 nM and a B_{max} of 647 fmol/mg protein (Figure 5b).

Internalization behavior on AR42J cells is summarized in Figure 6. All three ^{99m}Tc-labeled compounds showed a rapid internalization of cell-bound activity, reaching a plateau of more than 80% internalized fraction after 30 min incubation (Figure 6a). Looking at the percentage internalized activity of the total activity added, we observed differences (Figure 6b). ^{99m}Tc(CO)$_3$-(N_α-His)Ac-MG showed the highest percentage of internalized activity (reaching 13.7% after 120 min incubation), followed by ^{99m}Tc-EDDA/HYNIC-MG (10.1%) and ^{99m}Tc-Tricine/HYNIC-MG (7.0%).

Biodistribution and Tumor Uptake. Biodistribution in Balb/c mice 4 h pi revealed a rapid elimination from most organs and mainly renal excretion (Figure 7). Intestinal activity was minimal, varying from 1.18%ID/g for ^{99m}Tc-Tricine/HYNIC-MG to 0.44%ID/g for ^{99m}Tc-EDDA/HYNIC-MG, indicating low hepatobiliar excretion. However, great differences were observed in kidney uptake. ^{99m}Tc(CO)$_3$-(N_α-His)Ac-MG showed renal retention of 2.81%ID/g, whereas ^{99m}Tc-EDDA/HYNIC-MG and ^{99m}Tc-Tricine/HYNIC-MG accumulated to much higher levels in the kidneys with 127 and 73%ID/g, respectively. In animal urine only degradation products of the ^{99m}Tc-labeled peptide conjugates could be detected by RP-HPLC.

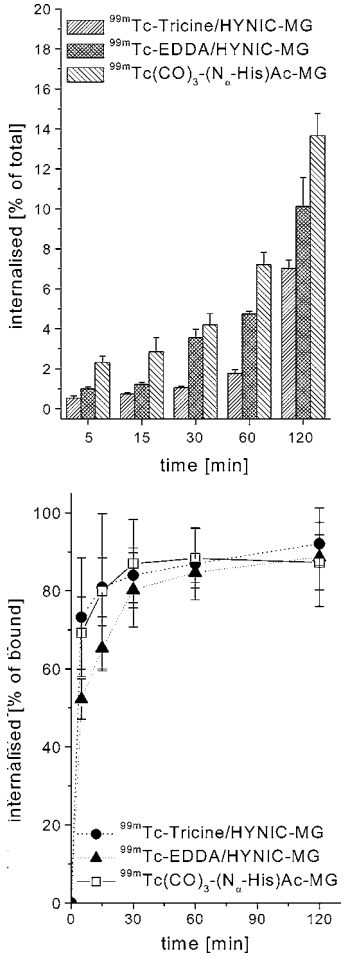


Figure 6. Time dipendent internalization of radiolabeled peptides in AR42J cells expressed as (a) % of total activity, (b) % of bound activity (mean ± sd, n = 3).

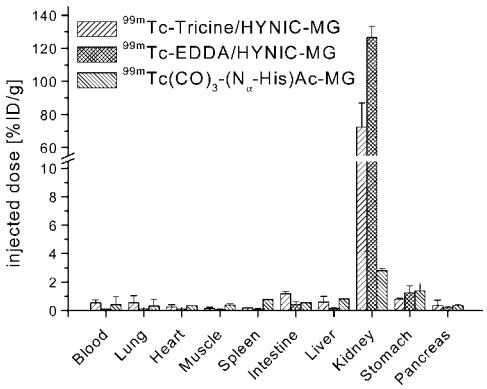


Figure 7. Normal biodistribution of the radiolabeled peptides in Balb/c mice 4 h after injection. Values are expressed as %ID/g = percentage injected dose/g tissue (means ± sd, n = 3).

Similar differences were also observed in a mouse tumor model. Results of biodistribution in nu/nu mice bearing AR42J tumor xenografts 4 h pi is summarized in Table 3. Whole body retention in this tumor model 4 h pi were 23.96 ± 4.02%ID for ^{99m}Tc-Tricine/HYNIC-MG, 38.96 ± 2.78%ID for ^{99m}Tc-EDDA/HYNIC-MG, and 2.38 ± 0.53%ID for ^{99m}Tc(CO)$_3$-(N_α-His)Ac-MG. Again, low levels of intestinal activity and accumulation in other organs were detected (<1.2%ID/g), whereas kidney uptake varied from 101%ID/g for ^{99m}Tc-EDDA/HYNIC-MG, 53.8%ID/g for ^{99m}Tc-Tricine/HYNIC-MG, down to only

Table 3. Biodistribution of the Radiolabeled Peptides in AR42J Tumor-Bearing Nu/Nu Mice 4 h after Injection. Values Are Expressed as %ID/g = Percentage Injected Dose/g Tissue (means ± sd, $n = 3$)

organ	^{99m}Tc-Tricine/ HYNIC-MG	^{99m}Tc-Tricine/ HYNIC-MG blocked[a]	^{99m}Tc-EDDA/ HYNIC-MG	^{99m}Tc-EDDA/ HYNIC-MG blocked[a]	^{99m}Tc(CO)$_3$-(N_α-His)Ac-MG	^{99m}Tc(CO)$_3$-(N_α-His)Ac-MG blocked[a]
blood	0.36 ± 0.12	0.32 ± 0.10	0.06 ± 0.002	0.05 ± 0.01	0.06 ± 0.003	0.06 ± 0.002
lung	0.59 ± 0.31	0.46 ± 0.29	0.06 ± 0.01	0.07 ± 0.01	0.13 ± 0.01	0.13 ± 0.001
heart	0.32 ± 0.14	0.23 ± 0.13	0.06 ± 0.03	0.04 ± 0.002	0.05 ± 0.001	0.06 ± 0.004
muscle	0.16 ± 0.03	0.16 ± 0.09	0.03 ± 0.004	0.04 ± 0.02	0.01 ± 0.001	0.01 ± 0.003
spleen	0.38 ± 0.17	0.28 ± 0.11	0.05 ± 0.01	0.04 ± 0.01	0.07 ± 0.01	0.08 ± 0.01
intestine	1.05 ± 0.66	1.13 ± 0.51	0.21 ± 0.07	0.32 ± 0.16	0.23 ± 0.13	0.26 ± 0.13
liver	0.73 ± 0.30	0.66 ± 0.20	0.10 ± 0.01	0.07 ± 0.03	0.34 ± 0.02	0.30 ± 0.04
kidney	53.81 ± 15.55	50.96 ± 13.40	101.00 ± 3.47[b]	79.14 ± 6.98	1.77 ± 0.33	2.85 ± 1.26
stomach	1.05 ± 0.30[b]	0.62 ± 0.03	0.73 ± 0.17[b]	0.23 ± 0.04	0.32 ± 0.10[b]	0.10 ± 0.06
pancreas	0.31 ± 0.13[b]	0.12 ± 0.03	0.07 ± 0.01[b]	0.03 ± 0.003	0.04 ± 0.003	0.03 ± 0.004
tumor	2.18 ± 0.53[b]	1.23 ± 0.24	8.09 ± 1.87[b]	2.96 ± 0.10	1.20 ± 0.44	0.73 ± 0.14

[a] Coinjection of 50 μg of minigastrin I human. [b] Significant $p = 0.05$.

Table 4. Tissue Ratios of Biodistribution in AR42J Tumor-Bearing Nu/Nu Mice

	tumor									
	blood	lung	heart	muscle	spleen	intestine	liver	kidney	stomach	pancreas
^{99m}Tc-Tricine/HYNIC-MG	6.01	3.72	6.90	13.81	5.81	2.07	2.97	0.04	2.08	7.11
^{99m}Tc-EDDA/HYNIC-MG	133.75	128.62	126.98	288.65	169.28	37.65	77.06	0.08	11.16	121.09
^{99m}Tc(CO)$_3$-(N_α-His)Ac-MG	18.61	9.24	23.11	90.13	17.42	5.29	3.58	0.68	3.76	30.05

	stomach									
	blood	lung	heart	muscle	spleen	intestine	liver	kidney	pancreas	tumor
^{99m}Tc-Tricine/HYNIC-MG	2.89	1.79	3.32	6.64	2.79	1.00	1.43	0.02	3.42	0.48
^{99m}Tc-EDDA/HYNIC-MG	11.99	11.53	11.38	25.87	15.17	3.37	6.91	0.01	10.85	0.09
^{99m}Tc(CO)$_3$-(N_α-His)Ac-MG	4.96	2.46	6.15	24.00	4.64	1.41	0.95	0.18	8.00	0.27

	pancreas									
	blood	lung	heart	muscle	spleen	intestine	liver	kidney	stomach	tumor
^{99m}Tc-Tricine/HYNIC-MG	0.84	0.52	0.97	1.94	0.82	0.29	0.42	0.01	0.29	0.14
^{99m}Tc-EDDA/HYNIC-MG	1.10	1.06	1.05	2.38	1.40	0.31	0.64	0.001	0.09	0.01
^{99m}Tc(CO)$_3$-(N_α-His)Ac-MG	0.62	0.31	0.77	3.00	0.58	0.18	0.12	0.02	0.12	0.03

1.8%ID/g for ^{99m}Tc(CO)$_3$-(N_α-His)Ac-MG. Tumor uptake also varied considerably from 8.09%ID/g for ^{99m}Tc-EDDA/HYNIC-MG, 2.18%ID/g for ^{99m}Tc-Tricine/HYNIC-MG, to only 1.2%ID/g for ^{99m}Tc(CO)$_3$-(N_α-His)Ac-MG. Tumor uptake could be blocked by coinjection of 50 μg of MGh reducing values to 2.96, 1.23, and 0.73%ID/g, respectively; this reduction was significant for ^{99m}Tc-EDDA/HYNIC-MG and ^{99m}Tc-Tricine/HYNIC-MG ($p < 0.05$). A significant reduction of tissue uptake by coinjection of MGh was also observed in stomach for all three radiolabeled compounds, in pancreas for the ^{99m}Tc-HYNIC conjugates, and in kidneys for ^{99m}Tc-EDDA/HYNIC-MG.

Table 4 shows tumor/organ, stomach/organ, and pancreas/organ ratios (receptor positive organs) calculated from the mouse tumor model studies. Highest ratios for tumor and receptor positive organs (stomach and pancreas) were found in most cases for ^{99m}Tc-EDDA/HYNIC-MG and lowest for ^{99m}Tc(CO)$_3$-(N_α-His)Ac-MG except for the kidney where this relationship was reversed.

DISCUSSION

Radiolabeling. Using both HYNIC and (N_α-His)Ac conjugated to [D-Glu^1]-MG, high labeling yields were achieved. Experiments were performed at high specific activities using small amounts of peptide conjugate (3−20 μg). In the case of HYNIC with Tricine as coligand, labeling was achieved directly. However, the presence of two major peaks dependent on the temperature and incubation time, the absence of multiple peaks as described for other peptides (*1*), and the failure to produce different complexes by addition of pyridine derivatives indicate some unique properties of this specific peptide. It could be argued that one of the carboxyl groups of the Glu-residues at the amino-terminus is involved in the complex formation resulting in a different species at higher temperature, a phenomenon that already has been described for ^{111}In-labeling of DTPA-MG (*5*). By addition of EDDA to the reaction mixture in a concentration of 5 mg/mL and heating the reaction solution, another complex formed in high yields. It could be shown for a somatostatin analogue that under these conditions Tricine as coligand is replaced by EDDA resulting in a more stable complex (*17*). Overall, radiolabeling of HYNIC-MG revealed some specific properties in the formation of technetium complexes. The characteristic feature of HYNIC-derivatized peptides, that by varying the coligand, different complexes were formed, was preserved. In contrast, radiolabeling of (N_α-His)Ac-MG resulted in a single peak independent of the reaction conditions. However, high labeling yields were dependent on a high concentration of the peptide in the reaction solution and not only on the specific activity (i.e. molar relation of peptide versus technetium). Therefore, comparably higher amounts of peptide (20 μg) were used to allow a volume (0.5 mL) potentially suitable in a clinical setting.

Complex Characterization and Stability Studies. All three complexes showed distinct retention times in different HPLC systems. In contrast to other peptides (*18*), with Tricine as coligand the lowest retention times were observed.

^{99m}Tc(N_α-His)Ac-MG showed the longest retention times, indicating the highest lipophilicity of all three complexes under study. This was underlined by its plasma protein binding behavior, showing the highest levels after a short incubation time. The observed tendency of increasing plasma protein binding over time for ^{99m}Tc-Tricine/

HYNIC-MG is a phenomenon already described for other HYNIC-peptide conjugates (*10*) and indicates a higher complex instability compared to ^{99m}Tc-EDDA/HYNIC-MG. Other experiments on the ^{99m}Tc-complex stability failed to reveal differences between the radiolabeled peptide conjugates. All complexes showed no major sign of complex degradation in different solutions; a somewhat lower stability for the Tricine-HYNIC derivative was observed. No considerable ligand exchange after challenge with amino acids could be detected. Especially the high stability of the ^{99m}Tc(CO)$_3$-(N_α-His)Ac-MG complex toward histidine indicates a high complex stability. It is known that the Tc(CO)$_3$ core has a very high affinity for His (*12*), and these findings underline the importance of a tridentate ligand coupled to the peptide for this labeling approach (*13*). In contrast to these results all ^{99m}Tc-peptide conjugates revealed a rather low stability independent of the labeling approach after incubation in kidney and liver homogenates. It can be assumed that this behavior is a result of an enzymatic cleavage of the peptide chain itself. This is underlined by the finding that on RP-HPLC various degradation products were observed with retention times different from low molecular ^{99m}Tc complexes such as ^{99m}Tc-cysteine or ^{99m}Tc-histidine (data not shown). This instability of the peptide toward enzymatic degradation is also confirmed by the observation that only degradation products could be detected in urine of mice injected with the radiolabeled conjugates. However, the high stability of the complexes in serum should be taken into account when judging the suitability of these radiolabeled MG derivatives to target receptor positive tumors in vivo.

Receptor Binding and Internalization. Derivatization of MG did not considerably impair receptor binding. Although HYNIC-MG showed lower IC_{50} values in comparison with unmodified MG, it still can be considered to have a high affinity to the gastrin/CCK-2 receptor. Of greater importance to judge the tumor targeting properties seemed to be the results from internalization studies. All compounds investigated showed very rapid internalization of surface-bound activity and very high uptake in receptor positive cells to a value up to 14%, levels comparable or even higher to high-affinity ^{99m}Tc-HYNIC−somatostatin conjugates in the same system (*8*). The highest levels of internalized activity were found for ^{99m}Tc(CO)$_3$-(N_α-His)Ac-MG, and somewhat lower levels were found for both HYNIC conjugates, possibly reflecting a lower receptor affinity.

Biodistribution and Tumor Targeting Properties. Overall, all derivatives showed a rapid elimination with predominant renal excretion and low retention in blood and most tissues. However, considerable differences in the organ uptake were observed, both in normal and tumor-bearing mice. The differences between ^{99m}Tc-Tricine/HYNIC-MG and ^{99m}Tc-EDDA/HYNIC-MG in normal organ uptake reflect the known differences in complex stability between the coligands (*16*). In accordance with previous findings (*19*) all organs except kidney showed higher levels of activity for ^{99m}Tc-Tricine/HYNIC-MG, indicating higher unspecific retention of ^{99m}Tc. An unexpected finding was the great difference in kidney retention between ^{99m}Tc labeled HYNIC and (N_α-His)Ac-MG conjugates. Uptake of radiolabeled peptides in the kidney by a tubular reabsorption mechanism is a well-known phenomenon (*20*) and ideally should be as low as possible. A very high kidney retention was found both for ^{99m}Tc-Tricine/HYNIC-MG and ^{99m}Tc-EDDA/HYNIC-MG with over 50%ID/g, in accordance with the behavior of ^{111}In-DTPA-MG reported previously (*5*). This high kidney uptake is a usual observation with radiolabeled MG derivatives and is unlikely to be related to a specific interaction with the MG receptor but a result of tubular reabsorption. On the other hand, ^{99m}Tc(CO)$_3$-(N_α-His)Ac-MG showed kidney uptake levels of less than 3%ID/g both in normal and tumor-bearing mice. An explanation of this phenomenon with a complex instability in vivo, possibly in the kidney, seems unlikely, as no correlation with the in vitro stability experiments can be found. It also seems unlikely that other tridentate ligand systems such as (N_ϵ-His)Ac coupled to peptides, as recently described (*21*), would behave differently. This in vivo behavior could, however, result from a difference in charge of the complexes, assuming a less negatively charged ^{99m}Tc(CO)$_3$-(N_α-His)Ac-MG complex. It recently has been shown that reduction of the number of Glu-residues (negatively charged) in the gastrin sequence leads to lower levels of renal retention (*22*). Another option would be a rapid washout from the kidney, which is supported by the high in vitro stability and the much lower whole body retention observed for ^{99m}Tc(CO)$_3$-(N_α-His)Ac-MG in comparison with the ^{99m}Tc-HYNIC conjugates. Unfortunately, the low kidney uptake of ^{99m}Tc-(CO)$_3$-(N_α-His)Ac-MG was also accompanied by a significantly lower specific uptake in stomach, pancreas, and especially tumor. Whereas ^{99m}Tc-EDDA/HYNIC-MG showed a promising high tumor uptake of more than 8%ID/g that could be reduced to less than 3%ID/g by coinjection of MGh, much lower levels of 1.2%ID/g were found for ^{99m}Tc(CO)$_3$-(N_α-His)Ac-MG, and although blocking with MGh reduced uptake, this reduction was not significant. Comparable results in other gastrin/CCK-2 receptor positive organs such as pancreas and stomach confirm this finding. Therefore, in this series, ^{99m}Tc-EDDA/HYNIC-MG seems to be the most promising agent for imaging gastrin/CCK-2 receptor positive tumors, showing very similar properties to ^{111}In-DTPA-MG, which already has been used successfully in patients (*23*). However, the high kidney uptake renders this compound developmental. Optimization of the peptide sequence leading to reduced kidney uptake without sacrificing tumor uptake should be attempted before patient studies are initiated.

CONCLUSION

This study describes for the first time a direct comparison of peptides radiolabeled with ^{99m}Tc via the HYNIC and the Tc(CO)$_3$ approach. Overall, MG derivatized with HYNIC and (N_α-His)acetic acid could be radiolabeled with ^{99m}Tc at high specific activities. Although only minor differences in vitro concerning stability and receptor binding were observed, the labeling approach significantly altered the biodistribution and tumor-targeting properties of the radiolabeled peptides. For these specific peptides, the HYNIC approach using a suitable coligand showed some advantages with respect to receptor specific uptake in vivo, partially outweighed by a very high kidney uptake. Further studies to improve tumor uptake and at the same time reduce kidney retention by optimizing the peptide sequence should be attempted.

ACKNOWLEDGMENT

This study in part was supported by the COST B12 Action "Radiotracers for the in vivo assessment of biological function" and by a "Gertrude Pfeiffer" scholarship of the Austrian Society of Nuclear Medicine. We specifically thank Prof. Hermann Dietrich for his help in the animal

tumor model as well as Ira Skvortsova, Gholamali Shabani Kakroodi, and Sonja Georgievska for their helping hands.

LITERATURE CITED

(1) Reubi, J. C., Schaer, J. C., and Waser, B. (1997) Cholecystokinin (CCK)-A and CCK-B/gastrin receptors in human tumors. *Cancer Res. 57*, 1377−1386.

(2) Gotthart, M., Grass, J., Schipper, M. L., Höffken, H., Schlieck, A., Schurrat, T., Pollum, H., Béhé M. P., and Behr, T. M. (2003) Scintigraphy with In-111-DTPA-D-Glu1-Minigastrin and In-111-DTPA-D-Phe1-Octreotide in Patients with Gastrointestinal Neuroendocrine Tumors: Results of the first 60 Patients. *Eur. J. Nucl. Med. Mol. Imaging 30*, S181.

(3) de Jong, M., Bakker, W. H., Bernard, B. F., Valkema, R., Kwekkeboom, D. J., Reubi, J. C., Srinivasan, A., Schmidt, M., and Krenning, E. P. (1999) Preclinical and Initial Clinical Evaluation of ^{111}In-Labeled Nonsulfated CCK$_8$ Analog: A Peptide for CCK−B Receptor-Targeted Scintigraphy and Radionuclide Therapy. *J. Nucl. Med. 40*, 2081−2087.

(4) Behr, T. M., Jenner, N., Radetzky, S., Béhe, M., Gratz, S., Yücekent, S., Raue, F., and Becker, W. (1998) Targeting of cholecystokinin-B/gastrin receptors in vivo: preclinical and initial clinical evaluation of the diagnostic and therapeutic potential of radiolabelled gastrin. *Eur. J. Nucl. Med. 25*, 424−430.

(5) Béhé, M., Becker, W., Gotthardt, M., Angerstein, C., and Behr, T. M. (2003) Improved kinetic stability of DTPA-DGlu as compared with conventional monofunctional DTPA in chelating indium and yttrium: preclinical and initial clinical evaluation of radiometal labelled minigastrin derivatives. *Eur. J. Nucl. Med. Mol. Imaging 30*, 1140−1146.

(6) Behr, T. M., and Behe, M. P. (2002) Cholecystokinin-B/Gastrin receptor-targeting peptides for staging and therapy of medullary thyroid cancer and other cholecystokinin-B receptor-expressing malignancies. *Semin. Nucl. Med. 32*, 97−109.

(7) Liu, S., and Edwards, D. S. (1999) ^{99m}Tc-Labeled Small Peptides as Diagnostic Radiopharmaceuticals. *Chem. Rev. 99*, 2235−68.

(8) Decristoforo, C., Melendez-Alafort, L., Sosabowski, J. K., and Mather, S. J. (2000)^{99m}Tc-HYNIC-[Tyr^3]-Octreotide for Imaging Somatostatin-Receptor-Positive Tumors: Preclinical Evaluation and Comparison with ^{111}In-Octreotide. *J. Nucl. Med. 41*, 1114−1119.

(9) Barrett, J. A., Crocker, A. C., Damphousse, D. J., Heminway, S. J., Liu, S., Edwards, D. S., Lazewatsky, J. L., Kagan, M., Mazaika, T. J., and Carroll, T. R. (1997) Biological Evaluation of Thrombus Imaging Agents Utilizing Water Soluble Phosphines and Tricine as Coligands When Used To Label a Hydrazinonicotinamide-Modified Cyclic Glycoprotein IIb/IIIa Receptor Antagonist with ^{99m}Tc. *Bioconjugate Chem. 8*, 155−60.

(10) Decristoforo, C., and Mather, S. J. (1999) 99m-Technetium-Labeled Peptide-HYNIC Conjugates: Effects of Lipophilicity and Stability on Biodistribution. *Nuclear Med. Biol. 26*, 389−396.

(11) Alberto, R., Schibli, R., Egli, A., and Schubiger, A. P. (1998) A Novel Organometallic Aqua Complex of Technetium for the Labeling of Biomolecules: Synthesis of $[^{99m}Tc(OH_2)_3(CO)_3]^+$ from $[^{99m}TcO_4]^-$ in Aqueous Solution and Its Reaction with a Bifunctional Ligand. *J. Am. Chem. Soc. 120*, 7987−7988.

(12) Egli, A., Alberto, R., Tannahill, L., Schibli, R., Abram, U., Schaffland, A., Waibel, R., Tourwé D., Jeannin, L., Iterbeke, K., and Schubiger, P. A. (1999) Organometallic ^{99m}Tc-Aquaion Labels Peptide to an Unprecedented High Specific Activity. *J. Nucl. Med. 40*, 1913−1917.

(13) Schibli, R., La Bella, R., Alberto, R., Garcia-Garayoa, E., Ortner, K., Abram, U., and Schubiger, P. A. (2000) Influence of the denticity of ligand systems on the in vitro and in vivo behavior of (99m)Tc(I)-tricarbonyl complexes: a hint for the future functionalization of biomolecules. *Bioconjugate Chem. 11*, 345−51.

(14) García-Garayoa, E., Bläuenstein, P., Bruehlmeier, M., Blanc, A., Iterbeke, K., Conrath, P., Tourwé, D., and Schubiger, P. A. (2002) Preclinical Evaluation of a New, Stabilized Neurotensin(8−13) Pseudopeptide Radiolabeled with ^{99m}Tc. *J. Nucl. Med. 43*, 374−83.

(15) Alberto, R., Schibli, R., Egli, A., and Schubiger, P. A. (1998) A Novel Organometallic Aqua Complex of Technetium for the Labeling of Biomolecules: Synthesis of $[^{99m}Tc(OH_2)_3(CO)_3]^+$ from $[^{99m}TcO4]^-$ in Aqueous Solution and Its Reaction with a Bifunctional Ligand. *J. Am, Chem. Soc. 120*, 7987−7988.

(16) Liu, S., Edwards, D. S., Looby, R. J., Harris, A. R., Poirier, M. J., Barrett, J. A., Heminway, S. J., and Carroll, T. R. (1996) Labeling a Hydrazino Nicotinamide-Modified Cyclic IIb/IIIa Receptor Antagonist with ^{99m}Tc Using Aminocarboxylates as Coligands. *Bioconjugate Chem. 7*, 63−71.

(17) von Guggenberg, E., Sarg, B., Lindner, H., Melendez Alafort, L., Mather, S. J., Moncayo, R., and Decristoforo, C. (2002) Preparation via coligand exchange and characterization of [^{99m}Tc-EDDA-HYNIC-D-Phe^1,Tyr^3]Octreotide (^{99m}Tc-EDDA/HYNIC-TOC). *J. Labelled Compd. Radiopharm. 46*, 307−318.

(18) Decristoforo, C., and Mather, S. J. (1999) Preparation, ^{99m}-Tc-Labeling, and in Vitro Characterization of HYNIC and N_3S Modified RC-160 and [Tyr^3]Octreotide. *Bioconjugate Chem. 10*, 431−438.

(19) Decristoforo, C., and Mather, S. J. (1999) Technetium-99m somatostatin analogues: effect of labeling methods and peptide sequence. *Eur. J. Nucl. Med. 26*, 869−876.

(20) Trejtnar, F., and Laznicek, M. (2002). Analysis of renal handling of radiopharmaceuticals. *Q. J. Nucl. Med. 46*, 181−194.

(21) Pak, J. K., Benny, P., Spingler, B., Ortner, K., and Alberto, R. (2003) N$^\epsilon$ Functionalization of Metal and Organic Protected L-Histidine for a Highly Efficient, Direct Labeling of Biomolecules with $[Tc(OH_2)_3(CO)_3]^+$. *Chemistry 9*, 2053−61.

(22) Béhé, M., de Jong, M., Reubi, J. C., Nock, B., Schmitt, J. S., Maecke, H., Breeman, W. A. P., Krenning, E., and Behr, T. M. (2003) Optimising of In-111 labeled minigastrin related to the kidney uptake. *Eur. J. Nucl. Med. Mol. Imaging 30*, S199.

(23) Béhé, M., and Behr, T. M. (2002) Cholecystokinin-B (CCK-B)/gastrin receptor targeting peptides for staging and therapy of medullary thyroid cancer and other CCK-B receptor expressing malignancies. *Biopolymers 66*, 399−418.

BC0300807

In Vitro and in Vivo Comparison of Human *Escherichia coli* Heat-Stable Peptide Analogues Incorporating the ^{111}In-DOTA Group and Distinct Linker Moieties

Michael F. Giblin,[||,†] Hariprasad Gali,[||] Gary L. Sieckman,[§] Nellie K. Owen,[||] Timothy J. Hoffman,[||,‡,§] Leonard R. Forte,[§,⊥] and Wynn A. Volkert[||,§,†,*]

Research Service, Harry S. Truman Memorial Veterans' Administration Hospital, Columbia, Missouri 65201, and Departments of Radiology, Pharmacology, Internal Medicine, and The Nuclear Sciences and Engineering Institute, University of Missouri—Columbia, Columbia, Missouri 65211. Received January 14, 2004; Revised Manuscript Received April 19, 2004

Three human *Escherichia coli* heat-stable peptide (ST_h) analogues, each containing a DOTA chelating group, were synthesized by SPPS and oxidative refolding and compared in in vitro and in vivo systems. One analogue, DOTA−F^{19}-ST_h(1−19), contains an N-terminal DOTA group attached via an amide bond linkage to an ST_h moiety which is essentially wild-type except for a Tyr to Phe alteration at position 19 of the molecule. A second analogue, DOTA−$R^{1,4}$,F^{19}-ST_h(1−19), differs from the first in that asparagine residues in positions 1 and 4 have been altered to arginine residues in order to examine the effect of positively charged groups in the linker domain. A third analogue, DOTA−11AUN−F^{19}-ST_h(1−19), differs from the first in that it incorporates an 11-aminoundecanoic acid spacer group between the DOTA group and the first asparagine residue. In vitro competitive binding assays utilizing T-84 human colon cancer cells demonstrated that significant alterations to the N-terminal region of the ST_h molecule were well tolerated and did not significantly affect binding affinity of ST_h for the guanylyl cyclase C (GC-C) receptor. Internalization and efflux studies of the indium-labeled species demonstrated that inclusion of positive charge in the linker moiety inhibits internalization of the compound within tumor cells. The characteristics of the three analogues were compared in an in vivo model utilizing T-84 human colon cancer cell xenografts in SCID mice. Clearance of all analogues was rapid, primarily via renal excretion into the urine, with >89% ID excreted into the urine at 1 h pi for all analogues. The ^{111}In-DOTA−$R^{1,4}$,F^{19}-ST_h(1−19) and ^{111}In-DOTA−11AUN−F^{19}-ST_h(1−19) analogues both had longer residence times in the blood than did the ^{111}In-DOTA−F^{19}-ST_h(1−19) analogue, probably accounting for increased %ID/g values for tumors and nontarget tissues at 1 h pi. At 4 h pi, significant differences between analogues were only seen with respect to metabolic routes of excretion, indicating that increased blood residence time did not result in increased tumor residualization. Reduction of hepatic uptake of these compounds, however, could have significance in the development of agents for the imaging of hepatic metastases. The ability to manipulate in vivo pharmacodynamics and tumor uptake of radiolabeled ST_h peptides through modification of linker moieties is under continuing investigation in order to produce optimal imaging and therapeutic radiopharmaceuticals.

INTRODUCTION

Colorectal cancer is the third most common neoplasm and the second most common cause of cancer mortality in the United States (*1*). Colorectal cancer metastases most commonly localize to the pelvis, liver, and lungs, and the majority of patients who die from colon cancer have liver metastases (*2*). Improved ability to determine the location and extent of metastatic disease could have a significant impact on treatment planning for individuals with confirmed diagnoses of primary tumors. Since the early 1990s, several radioimmunoscintigraphic agents have gained approval in the United States or Europe for the imaging of colorectal carcinomas. Each of these agents when added to diagnostic protocols was shown to increase the sensitivity and/or specificity of diagnosis relative to the use of anatomical imaging (CT) alone (*3*−*8*). Two such agents, OncoScint CR/OV (Cytogen Corp., Princeton NJ) and HumaSPECT-Tc (Intracel Corp., Rockville, MD) are monoclonal antibodies of murine and human origin, respectively (*5*, *9*). A third, CEA-Scan (Immunomedics, Inc., Morris Plains, NJ), is a murine IgG1-derived Fab′ fragment (*3*, *10*). In general, the smaller size of Fab′ fragments relative to unmodified antibodies results in greater tumor penetration and more rapid blood clearance, thus reducing accumulation in nontarget tissues (*11*).

Extending the logic of reducing the size of targeted radiopharmaceuticals in order to improve their pharmacokinetic properties and reduce their immunogenicity, interest in using radiolabeled peptides as diagnostic and

* To whom correspondence should be sent: Prof. Wynn A. Volkert, Radiopharmaceutical Sciences Institute, 143 Major Hall, DC200.0 HSC, University of Missouri—Columbia, Columbia, MO 65212; e-mail: volkertw@health.missouri.edu; phone: 573-882-6759; fax: 573-882-6129.

§ Harry S. Truman Memorial Veterans' Administration Hospital.

|| Department of Radiology, University of Missouri.

⊥ Department of Pharmacology, University of Missouri.

‡ Department of Internal Medicine, University of Missouri.

† The Nuclear Sciences and Engineering Institute, University of Missouri.

10.1021/bc049974x CCC: $27.50 © 2004 American Chemical Society
Published on Web 05/27/2004

therapeutic agents has rapidly increased over the past decade (*12*, *13*). Radiolabeled variants of somatostatin receptor targeting peptides are being used for imaging of neuroendocrine tumors and pulmonary masses (*12*). Analogues of bombesin (*38*−*41*), α-MSH (*42*−*45*), and numerous other receptor-avid peptides are under investigation for oncologic imaging of a variety of tumor types. Vasoactive intestinal peptide (VIP) and the *E. coli* heat-stable peptide (ST_h) are both under investigation as imaging agents for colorectal cancer (*14*, *18*−*24*). In a study directly comparing a ^{123}I-labeled VIP analogue with the approved agent OncoScint CR/OV, the labeled peptide was found to possess higher sensitivity in imaging intestinal carcinomas and metastatic spread (*15*). In principle, ^{123}I-labeled VIP produces an image by virtue of overexpression of its cognate receptor on the surface of colorectal cancer cells. However, VIP also targets receptors expressed in normal tissues such as the lung (*12*, *13*, *15*).

Guanylate cyclase C (GC-C) has been shown to be expressed on brush borders of intestinal epithelial cells, as well as on transformed human colon cancer cell lines such as the T-84 cell line (*16*, *17*). Importantly, GC-C is also expressed at much lower levels in normal human extraintestinal tissues (*18*, *46*−*48*). Circulation accessible when expressed on primary and metastatic colon cancer tissues, GC-C provides a uniquely specific target for receptor avid peptide radiopharmaceuticals (*18*−*24*). As normally expressed within the lumen of the gut, GC-C binds the endogenous peptides guanylin and uroguanylin, which act to regulate ion and fluid homeostasis and also may regulate epithelial cell turnover (*25*, *26*). Perhaps via gene transfer from vertebrate hosts, enteropathogenic strains of *E. coli* have evolved a homologous peptide, the human *E. coli* ST peptide (ST_h), which has the highest affinity for GC-C of any known ligand (*25*). The goal of the work presented here is to develop analogues of ST_h with N-terminal pendant DOTA chelating moieties that can deliver imaging and therapeutic radionuclides to primary and metastatic colon cancer tissues.

EXPERIMENTAL SECTION

All solvents were either ACS certified or HPLC grade solvents obtained from Fischer Scientific and used as received. The fmoc-Phe-Wang resin and fmoc-protected amino acids were purchased from Calbiochem-Novabiochem Corp (San Diego, CA) and the other peptide reagents from Applied Biosystems, Inc. (Foster City, CA). DOTA-tris (*tert*-butyl ester) was purchased from Macrocyclics (Dallas, TX) and fmoc-11-aminoundecanoic acid from Advanced ChemTech (Louisville, KY). $^{111}InCl_3$ was obtained from Mallinckrodt Medical, Inc (St. Louis, MO) as a 0.05 N HCl solution. Na^{125}I was obtained as a 10 μM NaOH solution from PerkinElmer (Boston, MA). All other reagents were purchased from Aldrich Chemical Co. Human colon carcinoma T-84 cells were obtained from American Type Culture Collection (ATCC) and maintained and grown for use in these studies in the University of Missouri Cell and Immunology Core facilities. Electrospray mass spectral analyses and amino acid analyses were performed by Synpep Corporation (Dublin, CA).

High Performance Liquid Chromatography (HPLC). High performance liquid chromatography (HPLC) analyses were performed on a Waters 600E system equipped with a Varian 2550 variable absorption detector, Packard Radiometric 150TR flow scintillation analyzer, sodium iodide crystal radiometric detector, Eppendorf TC-50 column temperature controller, and Hewlett-Packard HP3395 integrators. HPLC solvents consisted of H_2O containing 0.1% trifluoroacetic acid (Solvent A) and acetonitrile containing 0.1% trifluoroacetic acid (Solvent B). Conditions: A Phenomenex Jupiter C-18 (5 μm, 300 Å, 4.6 × 250 mm) column was used with a flow rate of 1.5 mL/min. Gradient purification of compounds is achieved during a linear 30 min ramp from 20% B to 30% B, followed by column rinse and reequilibration.

Peptide Synthesis. Synthesis of linear peptides was carried out on a Perkin-Elmer Applied Biosystems Model 432 automated peptide synthesizer employing traditional Fmoc chemistry. Fmoc-Phe-Wang resin (25 μmol), Fmoc-protected amino acids with appropriate side-chain protections (75 μmol), and DOTA-tris (*tert*-butyl ester) (75 μmol) were used for the synthesis. Final products were cleaved by a standard procedure using a cocktail containing thioanisol, water, ethanedithiol, and trifluoroacetic acid in a ratio of 2:1:1:36 and precipitated into methyl *tert*-butyl ether. Yield of the reduced, linear peptides ranged between 50 and 70%. All peptides contained a tyrosine to phenylalanine substitution in position 19. This substitution was originally made to simplify the process of generating monoiodinated ST_h tracer labeled at tyrosine 5. Previous work (*23*) has suggested that this substitution has no effect on receptor binding affinity of ST_h.

Peptide Refolding. After cleavage and deprotection of the peptides, reduced linear species were oxidatively refolded by stirring a 0.1 mg/mL peptide solution in 0.1 M ammonium formate, pH 8.0, at room temperature for periods up to 5 days. Refolded peptides were purified by C18 RP-HPLC and characterized by ESI-MS. The lack of free thiols in refolded peptides was confirmed by Ellman's test. Additionally, the DOTA−F^{19}-ST_h(1−19) analogue was produced using an orthogonal deprotection scheme in which pairs of free cysteine residues were sequentially deprotected and oxidized using Trt, Acm, and tBu thiol protecting groups. Both oxidative refolding and orthogonal deprotection produced identical products as assessed by RP-HPLC retention time, ESI-MS, and receptor binding assay.

^{125}I Labeling. F^{19}-ST_h(1−19) was iodinated by a modified lactoperoxidase method. Briefly, 2 μg of peptide was suspended in 50 μL of 100 mM sodium phosphate buffer, pH 7.5, containing 2 μg of lactoperoxidase and 300 μCi of Na^{125}I. The reaction was initiated by addition of 2 μL of a 1:10,000 dilution 30% H_2O_2. The reaction was incubated 30 min at room temperature with occasional mixing and then diluted with distilled H_2O and purified to homogeneity by RP-HPLC.

Indium Labeling. For the synthesis of ^{111}In-labeled compounds, aliquots of $^{111}InCl_3$ (0.2−0.6 mCi, 7.4−22.2 MBq, 4−12 μL) were added to solutions of DOTA−F^{19}-ST_h(1−19) (25 μg), DOTA−R^{1,4},F^{19}-ST_h(1−19) (25 μg), or DOTA−11AUN−F^{19}-ST_h(1−19) (25 μg) in 0.4 M ammonium acetate (200 μL). The pH of the reaction mixture was adjusted to 5.8. The reaction mixture was incubated for 1 h at 80 °C. After 1 h, an aliquot of 0.002 M EDTA (50 μL) was added to the reaction mixture to complex unreacted $^{111}In^{3+}$. Radiolabeling efficiencies ranged between 60 and 80%. The resulting conjugates were purified to homogeneity by RP-HPLC. The ^{111}In-metalated conjugates eluted between 0.9 and 1.8 min before the associated nonmetalated species enabling collection of high-specific activity, no carrier-added ^{111}In−ST_h conjugates. All purified ^{111}In−ST_h conjugates were then concentrated by passing through a 3M Empore C-18 HD high

performance extraction disk (7 mm/3 mL) cartridge and eluting with 50% ethanol in 0.1 M NaH_2PO_4 buffer (500 μL). The concentrated fraction was then reduced in volume under a stream of $N_{2(g)}$ and finally diluted with 0.1M NaH_2PO_4 buffer, pH 7.0, to a final activity of approximately 2 μCi/100 μL.

Macroscopic quantities of indium complexes were synthesized by an analogous synthetic protocol. 0.2 mg DOTA−F^{19}-ST_h(1−19), DOTA−$R^{1,4}$,F^{19}-ST_h(1−19), or DOTA−11AUN−F^{19}-ST_h(1−19), each in 100 μL 0.4 M ammonium acetate, pH 6.0, were added to 100 μg of indium chloride. Reactions were incubated at 80 °C for 1 h. The resulting indium complexes were purified by RP-HPLC and analyzed by ESI-MS.

In Vitro Cell Binding Studies. IC_{50}'s of DOTA−F^{19}-ST_h(1−19), DOTA−$R^{1,4}$,F^{19}-ST_h(1−19), and DOTA−11AUN−F^{19}-ST_h(1−19) and the corresponding indium complexes were determined by a competitive displacement cell binding assay using ^{125}I-F^{19}-ST_h(1−19). Briefly 3×10^6 cells suspended in DMEM/F-12 media containing 15 mM MES and 0.2% BSA, pH 5.5, were incubated at 37 °C for 1 h in the presence of approximately 20 000 cpm ^{125}I-tracer and increasing concentration of the metalated and nonmetalated DOTA−ST_h conjugates. After the incubation, the reaction medium was aspirated, and cells were washed three times with media. The radioactivity bound to the cells was counted in a Packard Riastar gamma counting system. The % ^{125}I-F^{19}-ST_h(1−19) bound to cells was plotted vs increasing concentrations of F^{19}-ST_h(1−19), DOTA−F^{19}-ST_h(1−19), DOTA−$R^{1,4}$,F^{19}-ST_h-(1−19), and DOTA−11AUN−F^{19}-ST_h(1−19) (both metalated and nonmetalated) to determine the respective IC_{50} values. An ST_h analogue lacking tertiary structure by virtue of alanine substitutions for the six cysteine residues present in the wild-type molecule evaluated using this same system does not exhibit measurable binding to GC-C receptors (i.e., $IC_{50} > 10^{-6}$ M). For statistical considerations, three separate in vitro cell binding experiments with each analogue were performed in duplicate. IC_{50} calculations were performed using the four-parameter logistic model within the program grafit (Erithacus Software, Ltd).

Internalization/Efflux Studies. In vitro studies to measure rates of internalization and efflux of labeled compounds from T-84 human colon carcinoma cells were carried out as described previously (*22*). For measurement of internalization, 3×10^6 cells suspended in DMEM/F-12 media containing 15 mM MES and 0.2% BSA, pH 5.5, were incubated for varying times at 37 °C with ∼20 000 cpm ^{125}I-F^{19}-ST_h(1−19), ^{111}In-DOTA−F^{19}-ST_h(1−19), ^{111}In-DOTA−$R^{1,4}$,F^{19}-ST_h(1−19), or ^{111}In-DOTA−11AUN−F^{19}-ST_h(1−19). At designated times, binding media was aspirated and cells were washed 3× with 4 °C binding media and then washed 2× with 4 °C acid/saline solution (0.5 M NaCl, 1.2% CH_3COOH). The activity of the acid/saline rinse and the cell pellet were determined and represent surface and internalized activity, respectively. For efflux experiments, all samples were initially incubated for 1 h under the above conditions and then washed 3× with 37 °C binding media to remove free label. The initial (t0) sample was then washed 3× with 4 °C binding media and then 2× with 4 °C acid/saline wash. Subsequent timepoints were treated identically, with surface and internalized activity determined as above.

In Vivo Pharmacokinetic Studies of ^{111}In-ST_h Analogues in SCID Mice. Four- to five-week old female ICR SCID (severe combined immunodeficiency) mice were obtained from Taconic (Germantown, NY). The mice were housed five animals per cage in sterile micro isolator cages in a temperature- and humidity-controlled room with a 12-h light/12-h dark schedule. The animals were fed sterile rodent chow (Ralston Purina Company, St. Louis, MO) and water ad libitum. Animals were housed one week prior to inoculation of tumor cells and anesthetized for injections with isoflurane (Baxter Healthcare Corp., Deerfield, IL) at a rate of 2.5% with 0.4 L oxygen through a non-rebreathing anesthesia vaporizer.

Human colon cancer T-84 cells were injected on the bilateral subcutaneous (sc) flank with $\sim 5 \times 10^6$ cells in a suspension of 100 μL of normal sterile saline per injection site. T-84 cells were allowed to grow in vivo three to four weeks postinoculation, developing tumors ranging in sizes from 0.02 to 0.95 g. The biodistribution and uptake of ^{111}In-DOTA−F^{19}-ST_h(1−19), ^{111}In-DOTA−$R^{1,4}$,F^{19}-ST_h(1−19), and ^{111}In-DOTA−11AUN−F^{19}-ST_h(1−19) in tumor-bearing SCID mice were studied. The mice (average weight, 25 g) were injected with aliquots (50−100 μL) of the radiolabeled peptide solution (55−90 kBq) in each animal via the tail vein. Tissues, organs, and tumors were excised from animals sacrificed at 1 h and 4 h pi, weighed, and counted. Radioactivity was measured in a NaI counter, and the percent-injected dose per organ (%ID) and the percent-injected dose per gram tissue (%ID/g) were calculated. %ID in urine was obtained by combining activity measured in urinary bladder with activity measured on a cage lining of absorbent paper. Animal studies were conducted in accordance with the highest standards of care as outlined in the NIH guide for Care and Use of Laboratory Animals and the Policy and Procedures for Animal Research at the Harry S. Truman Memorial Veterans' Hospital and according to approved protocols.

RESULTS

DOTA−ST_h conjugates were synthesized by SPPS and oxidatively refolded for a period of up to 5 days in dilute aqueous solution at pH 8.0. The ST_h molecule possesses three disulfide bonds, arranged in a 1−4, 2−5, 3−6 array (Figure 1). Fifteen possible conformational isomers therefore exist for this molecule, depending on disulfide connectivity (*27*). Conformational isomers in which disulfide connectivity is incorrect generally lose activity in GC-C binding assays (*27*, *28*). In each case investigated here, the major product of the refolding process lacked free thiol residues as determined by Ellman's assay (*29*), had the appropriate mass by ESI-MS, and retained activity in a competitive binding assay utilizing ^{125}I-F^{19}-ST_h(1−19) radioligand and T-84 human colon cancer cells (Table 1). Additionally, the DOTA−F^{19}-ST_h(1−19) analogue was synthesized via a different route, utilizing orthogonal protection of cysteine residues such that disulfides were formed sequentially with intervening purification of folding intermediates (*23*). DOTA−F^{19}-ST_h-(1−19) synthesized in this manner was shown to be identical to the final product obtained from simultaneous cystine formation via oxidative refolding in aqueous solution, providing further evidence that the major product of this thermodynamically controlled process is indeed the correctly folded ST_h isomer.

The binding affinities of each analogue were compared in competitive binding assays using T-84 human colon cancer cells and an iodinated ST_h radioligand (Figure 2, Table 1). IC_{50} values for the metalated and nonmetalated analogues ranged between 2.9 ± 0.3 nM for the DOTA−F^{19}-ST_h(1−19) analogue and 6.0 ± 0.7 nM for the In-DOTA−11AUN−F^{19}-ST_h(1−19) analogue. Parallel stud-

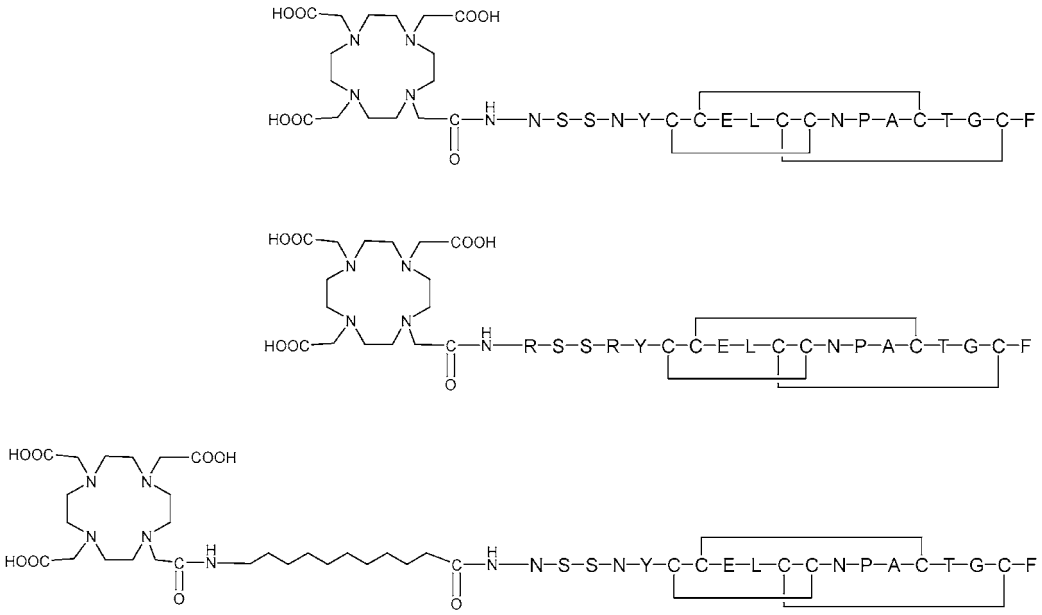


Figure 1. 1. Structures of DOTA−ST_h analogues. Top to bottom: DOTA−F^{19}-ST_h(1−19), DOTA−$R^{1,4}$,F^{19}-ST_h(1−19), DOTA−11AUN−F^{19}-ST_h(1−19).

Table 1. Calculated and Observed Molecular Weights (MW) and IC_{50} Values for ST_h Peptide Analogues

peptide	IC_{50} (nM)	MW (calcd)	MW (obsd)
DOTA−F^{19}-ST_h(1−19)	2.9 ± 0.3	2413.6	2412.6
In-DOTA−F^{19}-ST_h(1−19)	4.9 ± 2.8	2525.4	2525.1
DOTA−$R^{1,4}$,F^{19}-ST_h(1−19)	3.0 ± 0.2	2497.8	2497.0
In-DOTA−$R^{1,4}$,F^{19}-ST_h(1−19)	4.1 ± 3.3	2609.6	2609.5
DOTA−11AUN−F^{19}-ST_h(1−19)	3.8 ± 0.4	2595.9	2595.1
In-DOTA−11AUN−F^{19}-ST_h(1−19)	6.0 ± 0.7	2707.7	2707.8

ies with F^{19}-ST_h(1−19) demonstrated an IC_{50} value of 4.2 ± 0.8 nM for the species lacking the N-terminal DOTA moiety. These IC_{50} values are similar to results in the literature for the wild-type ST_h molecule (*16*, *30*), confirming that the binding affinity of the receptor targeting moiety is relatively unaffected by significant structural variations at the N-terminus of the molecule (*31*). Incorporation of In^{3+} into the DOTA moiety generally resulted in a less than 2-fold decrease in receptor binding affinity (Table 1).

DOTA−ST_h analogues were labeled with In-111 by heating a 0.2 mg/mL solution of peptide (pH 5.8) with $^{111}InCl_3$ at 80 °C for 1 h. After the labeling reaction was quenched with excess EDTA to sequester unbound $^{111}In^{3+}$, ^{111}In-DOTA−ST_h complexes were purified by C18 RP-HPLC. The impact of the different linker moieties on the relative hydrophobicities of the three molecules was clearly evident by RP-HPLC (Figure 3). Substitution of asparagine residues at positions 1 and 4 with arginine residues resulted in a decrease in hydrophobicity, while inclusion of the 11-undecanoic acid spacer greatly increased the hydrophobicity of the compound. All labeled analogues eluted earlier than their respective unlabeled congeners, allowing purification of high specific activity, no carrier added tracer.

Specific binding of all ^{111}In-labeled analogues was demonstrated in vitro using high specific activity ^{111}In-DOTA−ST_h conjugates and T-84 human colon cancer cells. In the absence of competing unlabeled ST_h, 9−15% of labeled analogue is associated with T-84 cells. In the presence of 1×10^{-6} M unlabeled ST_h, less than 3% of labeled ST_h is cell-associated. In general, specific binding of ^{111}In tracers exceeded NSB by 8−10-fold.

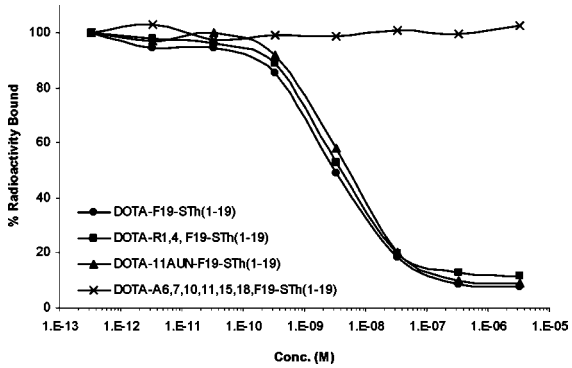


Figure 2. IC_{50} analyses using human T-84 colon carcinoma cells of DOTA−F^{19}-ST_h(1−19) (IC_{50} = 2.9 ± 0.3 nM), DOTA−$R^{1,4}$,F^{19}-ST_h(1−19) (IC_{50} = 3.0 ± 0.2 nM), and DOTA−11AUN−F^{19}-ST_h(1−19) (IC_{50} = 3.8 ± 0.4 nM). An analogue lacking tertiary structure due to alanine substitution of six cysteine residues showed no displacement in this assay.

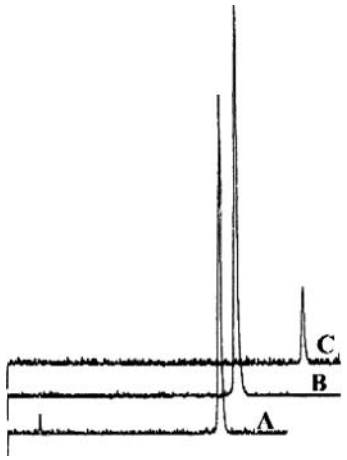


Figure 3. C18 RP-HPLC elution profiles of (A) ^{111}In-DOTA−$R^{1,4}$,F^{19}-ST_h(1−19) (t_R = 15.9 min), (B) ^{111}In-DOTA−F^{19}-ST_h(1−19)) (t_R = 17.1 min), and (C) ^{111}In-DOTA−11AUN−F^{19}-ST_h(1−19)) (t_R = 22.3 min).

An important parameter that impacts the performance of radiopharmaceutical compounds in vivo is the degree to which these compounds are residualized within tumor

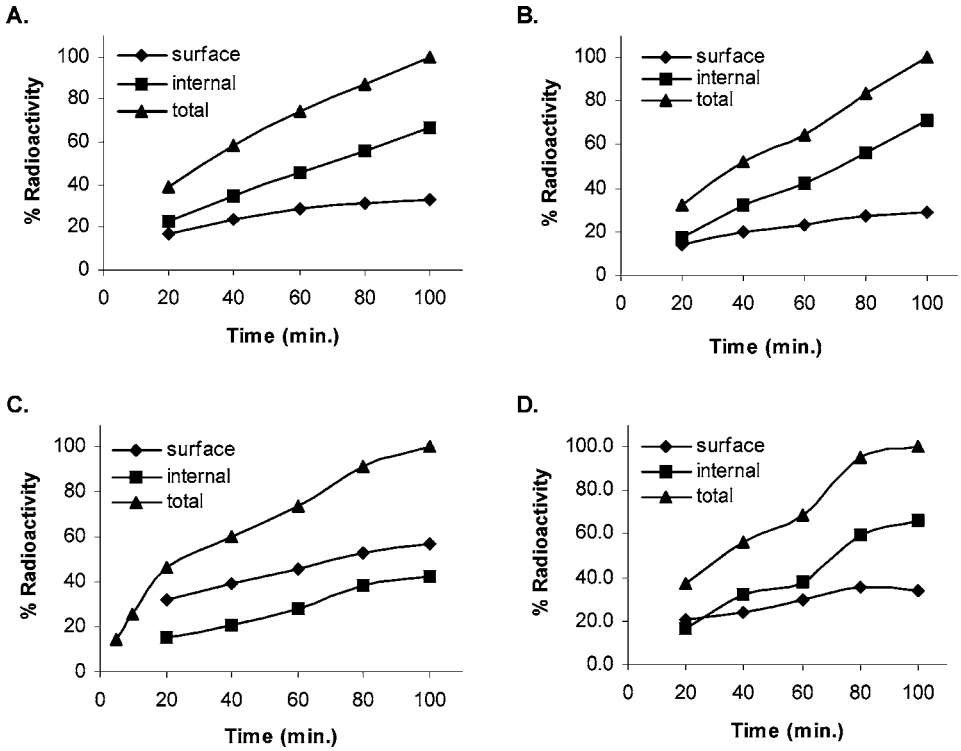


Figure 4. Determination of % internalized radioactivity in T-84 human colon carcinoma cells for (A) ^{125}I-F^{19}-ST$_h$(1−19), (B) ^{111}In-DOTA−F^{19}-ST$_h$(1−19), (C) ^{111}In-DOTA−R^{1,4},F^{19}-ST$_h$(1−19), (D) ^{111}In-DOTA−11AUN−F^{19}-ST$_h$(1−19).

cells. Residualization within tumor cells is a function of both the internalization rate and the rate of efflux of internalized peptide. Previous studies have shown that the GC-C receptor does undergo endocytosis following binding to ST$_h$ (*32*). As shown in Figure 4, both ^{111}In-DOTA−F^{19}-ST$_h$(1−19) and ^{125}I-F^{19}-ST$_h$(1−19) analogues are internalized by T-84 cells in vitro. For both, the degree of internalization of cell-associated radioactivity was similar, with approximately 60% of cell-bound radioactivity at 100 min. remaining cell-bound after incubation in pH 2.5, 0.5 M saline stripping buffer. Contrasted with this result, the ^{111}In-DOTA−R^{1,4},F^{19}-ST$_h$-(1−19) analogue, bearing a net 2+ charge in the linker moiety, shows decreased internalization, with only ∼40% of cell-associated radioactivity internalized at 100 min. Results for the positively charged analogue indicate that the majority of cell-associated radioactivity remains surface bound (Figure 4C). Comparison of rates of efflux of labeled analogues (Figure 5) demonstrates that for both the ^{111}In-DOTA−R^{1,4},F^{19}-ST$_h$(1−19) and ^{111}In-DOTA−11AUN−F^{19}-ST$_h$(1−19) species, internalized radioactivity is released from T-84 cells at approximately the same rate, with ∼90% of internalized radioactivity remaining cell-associated after a 3 h incubation at 37 °C. This indicates that once internalized, the ^{111}In-DOTA moiety is effectively trapped intracellularly. The higher amount of surface bound activity for the ^{111}In-DOTA−R^{1,4},F^{19}-ST$_h$-(1−19) analogue resulted in a lower amount of total radioactivity retained for this analogue. The efflux rate for the ^{125}I-F^{19}-ST$_h$(1−19) species (Figure 5A) is lower than would be expected if the peptide was degraded intracellularly, releasing monoiodotyrosine. This is perhaps due to the proximity of the tyrosine residue to the extremely stable disulfide-stabilized core of the molecule, which may limit generation of monoiodotyrosine.

Biodistribution analyses of the three ^{111}In-labeled analogues were carried out in T-84 xenografted SCID mice. Biodistributions at 1 h pi are shown in Tables 2 and 4. For all analogues, radioactivity cleared rapidly from the bloodstream, with 89−93% ID in the urine at 1 h pi. The primary route of excretion of all analogues is via the kidneys into the urine (Table 2). Both the ^{111}In-DOTA−R^{1,4},F^{19}-ST$_h$(1−19) and the ^{111}In-DOTA−11AUN−F^{19}-ST$_h$(1−19) analogues showed significantly decreased urinary excretion and significantly increased blood activity at 1 h pi. Most nontarget tissues, as well as tumor tissue, showed increased %ID/g values for both analogues at 1 h pi, probably reflecting blood perfusion of both target and nontarget tissues.

Specificity of tumor uptake of ST$_h$ analogues has been demonstrated previously by coinjection of 4 mg/kg unlabeled ST$_h$ (*21*, *23*). Significant reductions in tumor uptake upon blocking were seen for labeled ST$_h$ analogues at 1 h postinjection with diverse linker moieties in both LS-180 and T84 human colon cancer tumor xenografts (*21*, *23*). Tumor uptake in these studies was reduced by coinjection of unlabeled peptide from 0.94 ± 0.31%ID/g to 0.46 ± 0.22%ID/g in an LS180/SCID model (*21*) and from 2.04 ± 0.3%ID/g to 0.81 ± 0.25%ID/g in a T84/SCID model (*23*). These 50−60% reductions in tumor uptake are comparable to reductions in uptake of radiolabeled bombesin in PC-3 human pancreatic cancer tumor xenografts by coinjection of unlabeled bombesin (*38*).

At 4 h pi, ∼95% of injected activity had been excreted via the renal/urinary route for all analogues (Table 3, 5). No significant differences in tumor uptake were seen between analogues at this time. The only significant differences between analogues related to kidney uptake and hepatic excretion. Uptake in the liver for both the ^{111}In-DOTA−R^{1,4},F^{19}-ST$_h$(1−19) and the ^{111}In-DOTA−11AUN−F^{19}-ST$_h$(1−19) analogues was significantly lower than for the ^{111}In-DOTA−F^{19}-ST$_h$(1−19) analogue at 4 h pi. Intestinal uptake for both was significantly higher, however. In addition, the ^{111}In-DOTA−R^{1,4},F^{19}-ST$_h$(1−19) analogue had the highest kidney retention of the three analogues, although the difference was only significant ($p < 0.05$) with respect to ^{111}In-DOTA−11AUN−F^{19}-ST$_h$-(1−19).

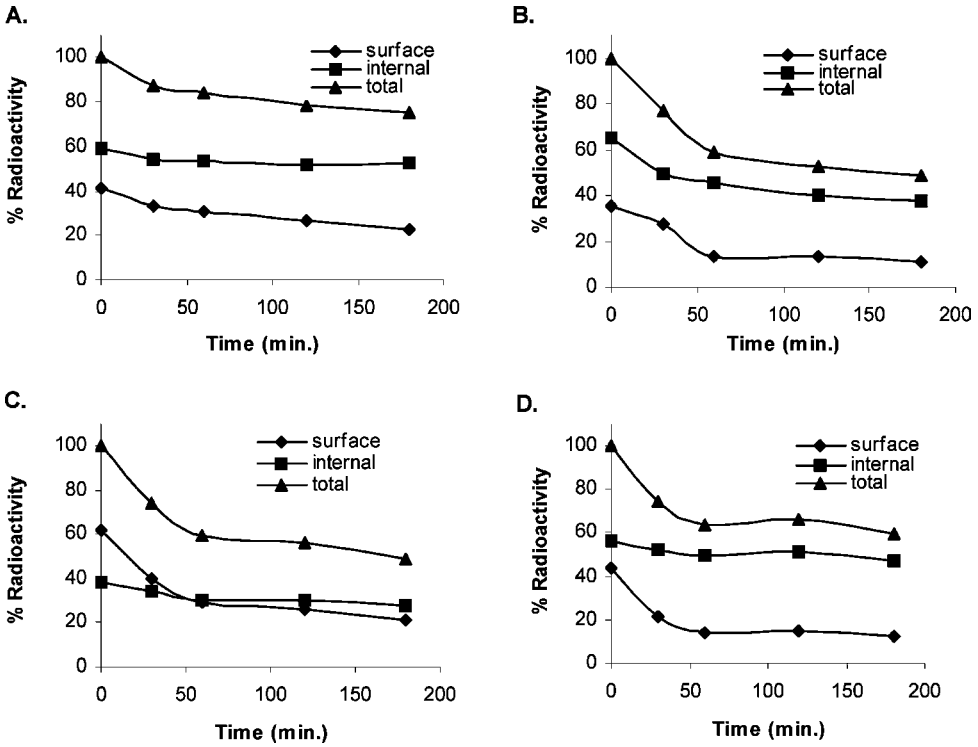


Figure 5. Determination of % efflux of radioactivity from T-84 human colon carcinoma cells for (A) ^{125}I-F^{19}-ST$_h$(1−19), (B) ^{111}In-DOTA−F^{19}-ST$_h$(1−19), (C) ^{111}In-DOTA−R^{1,4},F^{19}-ST$_h$(1−19), (D) ^{111}In-DOTA−11AUN−F^{19}-ST$_h$(1−19).

Table 2. In Vivo Biodistribution Analysis (%ID/g (SD)) of ^{111}In-DOTA−ST$_h$ Analogues in T-84 Human Colon Cancer Tumor Bearing SCID Mice at 1 h pi

tissue/organ	^{111}In-DOTA−F^{19}-ST$_h$(1−19)[a]	^{111}In-DOTA−R^{1,4}, F^{19}-ST$_h$(1−19)[b]	^{111}In-DOTA−11AUN−F^{19}-ST$_h$(1−19)[b]
blood	0.32 (0.12)[d,e]	0.76 (0.25)[c]	0.65 (0.22)[c]
heart	0.07 (0.06)[d,e]	0.30 (0.09)[c]	0.32 (0.33)[c]
lung	0.30 (0.18)[d,e]	0.93 (0.18)[c]	0.85 (0.30)[c]
liver	0.25 (0.29)[d]	0.59 (0.18)[c]	0.52 (0.11)
spleen	0.22 (0.41)	0.50 (0.69)	0.26 (0.38)
stomach	0.09 (0.04)[d,e]	0.71 (0.77)[c]	0.46 (0.22)[c]
intestine	0.56 (0.10)[d,e]	1.54 (0.93)[c]	1.32 (0.10)[c]
kidney	3.75 (1.37)[d,e]	5.93 (2.09)[c]	7.73 (1.55)[c]
urine (%ID)	93.4 (1.91)[d,e]	89.3 (2.6)[c]	90.4 (1.5)[c]
muscle	0.10 (0.14)	0.14 (0.07)	0.09 (0.17)
pancreas	0.08 (0.05)[d,e]	0.24 (0.18)[c]	0.32 (0.20)[c]
tumor	1.81 (0.63)[d,e,f]	2.83 (1.08)[c,g]	3.12 (1.12)[c,h]
tumor/blood	5.7	3.7	4.8
tumor/muscle	18.1	20.2	34.7
tumor/liver	7.2	4.8	6.0
tumor/kidney	0.48	0.48	0.40

[a] $n = 10$ [b] $n = 5$ [c] $P < 0.05$ versus ^{111}In-DOTA−F^{19}-ST$_h$(1−19) value, determined by Student's *t*-test. [d] $P < 0.05$ versus ^{111}In-DOTA−R^{1,4}, F^{19}-ST$_h$(1−19) value, determined by Student's *t*-test. [e] $P < 0.05$ versus ^{111}In-DOTA−11AUN−F^{19}-ST$_h$(1−19) value, determined by Student's *t*-test. [f] Average tumor mass = 0.27 g. [g] Average tumor mass = 0.12 g. [h] Average tumor mass = 0.11 g.

DISCUSSION

Research into the interaction between the heat-stable enterotoxin peptide and its cognate receptor GC-C has generated >100 synthetic analogues of the peptide, several of which have been investigated as imaging or therapeutic agents for colorectal cancers (*20*−*24*, *26*, *31*, *33*). In the work described here, we have appended a DOTA chelating moiety to the N-terminus of the ST$_h$ molecule via a series of hydrophilic and hydrophobic spacer groups. The DOTA chelating framework is capable of complexing a wide range of trivalent metals, including $^{90}Y^{3+}$, $^{111}In^{3+}$, $^{149}Pm^{3+}$, $^{153}Sm^{3+}$, $^{166}Ho^{3+}$, and $^{177}Lu^{3+}$. Such a broad array of radioisotopes suitable for complexation by DOTA will allow a single designed analogue to be used both for the imaging and treatment of colorectal cancers. For example, the 171 and 245 keV γ emissions of In-111 are suitable for SPECT imaging, while the particle emitting lanthanides provide a broad range of emission energies that could be appropriate for use therapeutically against either solid primary tumors or smaller distant metastases.

Our strategy for producing radiolabeled ST$_h$ analogues has been to covalently link the DOTA chelating moiety to the ST$_h$ peptide via a series of spacer groups. In the work described here, three highly dissimilar spacer groups were used. This illustrates the ability to generate a wide range of properly folded, bioactive ST$_h$ molecules with disparate physiochemical characteristics. Modulation of these characteristics can in turn significantly impact the pharmacokinetic properties of these compounds in vivo. Further, incorporation of such modifications at the N-terminus of ST$_h$ does not affect the binding affinity of modified analogues for the GC-C receptor. Three important physiochemical parameters that have

Table 3. In Vivo Biodistribution Analysis (%ID/g (SD), $n = 5$) of ^{111}In-DOTA−ST_h Analogues in T-84 Human Colon Cancer Tumor-Bearing SCID Mice at 4 h pi

tissue/organ	^{111}In-DOTA−F^{19}-ST_h(1−19)	^{111}In-DOTA−$R^{1,4}$, F^{19}-ST_h(1−19)	^{111}In-DOTA−11AUN−F^{19}-ST_h(1−19)
blood	0.14 (0.07)	0.08 (0.05)	0.09 (0.14)
heart	0.06 (0.06)	0.10 (0.14)	0.08 (0.09)
lung	0.22 (0.24)	0.22 (0.14)	0.22 (0.22)
liver	0.64 (0.11)[b,c]	0.37 (0.06)[a,c]	0.13 (0.03)[a,b]
spleen	0.72 (0.30)	0.70 (0.94)	0.35 (0.77)
stomach	0.03 (0.02)	0.17 (0.12)	1.01 (2.13)
intestine	0.35 (0.10)[b]	1.60 (1.14)[a]	1.50 (1.18)
kidney	3.43 (0.49)	4.31 (0.99)[c]	2.81 (0.67)[b]
urine (%ID)	95.3 (1.2)	94.7 (2.3)	95.4 (2.9)
muscle	0.03 (0.05)	0.03 (0.07)	0.27 (0.24)
pancreas	0.05 (0.02)	0.06 (0.05)	0.17 (0.24)
tumor	1.58 (0.65)[d]	1.64 (0.29)[e]	1.64 (0.62)[f]
tumor/blood	11.3	20.5	18.2
tumor/muscle	52.7	54.7	6.1
tumor/liver	2.5	4.4	12.6
tumor/kidney	0.46	0.38	0.58

[a] $P < 0.05$ versus ^{111}In-DOTA−F^{19}-ST_h(1−19) value, determined by Student's *t*-test. [b] $P < 0.05$ versus ^{111}In-DOTA−$R^{1,4}$, F^{19}-ST_h(1−19) value, determined by Student's *t*-test. [c] $P < 0.05$ versus ^{111}In-DOTA−11AUN−F^{19}-ST_h(1−19) value, determined by Student's *t*-test. [d] Average tumor mass = 0.49 g. [e] Average tumor mass = 0.10 g. [f] Average tumor mass = 0.11 g.

Table 4. In Vivo Biodistribution Analysis (%ID/organ (SD)) of ^{111}In-DOTA−ST_h Analogs in T-84 Human Colon Cancer Tumor-Bearing SCID Mice at 1 h pi

tissue/organ	^{111}In-DOTA−F^{19}-ST_h(1−19)[a]	^{111}In-DOTA−$R^{1,4}$, F^{19}-ST_h(1−19)[b]	^{111}In-DOTA−11AUN−F^{19}-ST_h(1−19)[b]
blood[c]	0.52 (0.19)	0.90 (0.25)	0.73 (0.20)
heart	0.01 (0.01)	0.02 (0.01)	0.03 (0.03)
lung	0.06 (0.03)	0.13 (0.02)	0.12 (0.04)
liver	0.29 (0.30)	0.46 (0.11)	0.39 (0.04)
spleen	0.01 (0.02)	0.01 (0.02)	0.01 (0.01)
stomach	0.05 (0.02)	0.28 (0.33)	0.15 (0.08)
intestine	1.26 (0.15)	3.07 (1.83)	2.27 (0.25)
kidney	1.14 (0.53)	1.21 (0.21)	1.45 (0.2)
urine (%ID)	93.4 (1.9)	89.3 (2.6)	90.4 (1.5)
muscle	0.01 (0.02)	0.03 (0.02)	0.01 (0.02)
pancreas	0.02 (0.01)	0.06 (0.03)	0.06 (0.04)
tumor	0.48 (0.43)	0.30 (0.14)	0.30 (0.29)

[a] $n = 10$. [b] $n = 5$. [c] %ID in blood was estimated assuming the whole blood volume to be 6.5% of the total body weight (*49*).

Table 5. In Vivo Biodistribution Analysis (%ID/organ (SD), $n = 5$) of ^{111}In-DOTA−ST_h Analogues in T-84 Human Colon Cancer Tumor-Bearing SCID Mice at 4 h pi

tissue/organ	^{111}In-DOTA−F^{19}-ST_h(1−19)	^{111}In-DOTA−$R^{1,4}$, F^{19}-ST_h(1−19)	^{111}In-DOTA−11AUN−F^{19}-ST_h(1−19)
blood[a]	0.20 (0.09)	0.08 (0.05)	0.09 (0.14)
heart	0.01 (0.01)	0.01 (0.01)	0.01 (0.01)
lung	0.04 (0.05)	0.03 (0.02)	0.03 (0.03)
liver	0.65 (0.14)	0.29 (0.03)	0.11 (0.02)
spleen	0.03 (0.02)	0.01 (0.01)	0.01 (0.02)
stomach	0.02 (0.02)	0.05 (0.05)	0.29 (0.59)
small intestine	0.78 (0.13)	2.80 (2.25)	2.61 (1.78)
kidney	0.69 (0.09)	0.86 (0.18)	0.54 (0.10)
urine (%ID)	95.3 (1.2)	94.7 (2.3)	95.4 (2.9)
muscle	0.00 (0.01)	0.00 (0.01)	0.03 (0.02)
pancreas	0.01 (0.01)	0.01 (0.01)	0.03 (0.05)
tumor	0.81 (0.70)	0.17 (0.14)	0.16 (0.09)

[a] %ID in blood was estimated assuming the whole blood volume to be 6.5% of the total body weight (*49*).

been altered in these experiments are the relative hydrophobicity of the molecules, their overall net charge, and the nature of the metabolites that could be formed upon intracellular degradation following internalization.

Although the ST_h molecule is extremely stable to both heat and proteolytic degradation (*23*, *34*), it is likely that the N-terminal tail of the molecule ($N^1S^2S^3N^4Y^5$-), which has a limited effect on receptor binding (*31*) and lies outside of the disulfide-stabilized core of ST_h, is vulnerable to enzymatic cleavage. Such cleavage, if occurring within the lysosome following cellular internalization, would probably result in formation of ^{111}In-DOTA−amino acid conjugates as have been shown to result from intracellular metabolism of labeled antibodies and glycoproteins (*35*−*37*). If intracellular metabolism does proceed along these lines for the analogues studied here, the ^{111}In-DOTA−$R^{1,4}$,F^{19}-ST_h(1−19) molecule would yield a zwitterionic ^{111}In-DOTA−Arg fragment, while the ^{111}In-DOTA−F^{19}-ST_h(1−19) and ^{111}In-DOTA−11AUN−F^{19}-ST_h(1−19) analogues would each yield negatively charged fragments by virtue of the DOTA linkage to the N-terminal α amine.

The direct linkage of the ^{111}In-DOTA moiety to a positively charged arginine residue in the ^{111}In-DOTA−$R^{1,4}$,F^{19}-ST_h(1−19) analogue did result in increased kidney uptake. This is probably due to trapping of a zwitterionic ^{111}In-DOTA−Arg fragment within lysosomes of proximal tubule cells following pinocytotic reabsorption of the intact molecule during glomerular filtration in the kidney (*35*). Increased retention of this analogue within

T-84 cell tumor xenografts, however, was not observed at 4 h pi. This lack of increased tumor retention could perhaps be explained by the decreased rate of GC-C receptor-mediated internalization observed for this analogue (Figure 4). However, the ^{111}In-DOTA−11AUN−F^{19}-ST$_h$(1−19) analogue also demonstrated decreased tumor retention, despite internalization and efflux rates similar to those of the ^{111}In-DOTA−F^{19}-ST$_h$(1−19) analogue. The reasons for these differences in residualization properties will therefore require further study.

The addition of the hydrophobic 11-aminoundecanoic acid spacer to the ST$_h$ molecule resulted in increased hepatic metabolism of the resulting compound. This modification also resulted in a faster rate of hepatic excretion, such that residual activity in the liver was ∼5-fold lower than for the analogue lacking the spacer at 4 h pi. The same trends were observed, albeit to a lesser degree, for the positively charged analogue, which had approximately half the liver activity of the analogue lacking spacer at 4 h pi. While radioactivity in the liver increased between 1 and 4 h pi for the ^{111}In-DOTA−F^{19}-ST$_h$(1−19) analogue, both the hydrophobic and charged analogues showed a decrease in liver activity over this period. It is important to note that for all three analogues, the total liver uptake is quite low. However, in the context of developing agents for imaging liver metastases of colorectal cancer, the ability to manipulate the timecourse of hepatic uptake and clearance could have significance.

While the increased rate of hepatic excretion of the ^{111}In-DOTA−R^{1,4},F^{19}-ST$_h$(1−19) and ^{111}In-DOTA−11AUN−F^{19}-ST$_h$(1−19) analogues did result in lower background activity in the liver at 4 h pi, increased early hepatic metabolism of these compounds resulted in a large increase in background activity in the large and small intestines at this timepoint. Due to the generally rapid rate of elimination of these compounds from the bloodstream into the urine, this effect is most clearly seen by normalizing residual activity to the total amount remaining in the body at the given timepoint. For example, at 4 h pi, an average of 33.5% of activity remaining in the body is localized in tumor tissue using the ^{111}In-DOTA−F^{19}-ST$_h$(1−19) analogue. In contrast, only 6.9% and 7.6% of remaining activity is localized in tumor tissue for the ^{111}In-DOTA−R^{1,4},F^{19}-ST$_h$(1−19) and ^{111}In-DOTA−11AUN−F^{19}-ST$_h$(1−19) analogues, respectively. Further, while only an average of 16.6% of remaining activity was localized to the intestinal tract for the ^{111}In-DOTA−F^{19}-ST$_h$(1−19) analogue at 4 h pi, 46.9% and 55.9% of remaining activity was localized there for the ^{111}In-DOTA−R^{1,4},F^{19}-ST$_h$(1−19) and ^{111}In-DOTA−11AUN−F^{19}-ST$_h$(1−19) analogues, respectively.

CONCLUSION

This work demonstrates that a broad spectrum of N-terminally modified ^{111}In-labeled ST$_h$ molecules can be successfully synthesized which retain highly specific binding affinity for the GC-C receptor. Both the incorporation of highly charged and extended hydrophobic linkers had little effect on receptor binding affinity, yet had significant effects on the pharmacokinetics of these compounds in vivo. The more rapid liver metabolism of the ^{111}In-DOTA−R^{1,4},F^{19}-ST$_h$(1−19) and ^{111}In-DOTA−11AUN−F^{19}-ST$_h$(1−19) compounds relative to ^{111}In-DOTA−F^{19}-ST$_h$(1−19) could potentially allow superior images of hepatic metastases to be obtained in vivo. The lack of significant nontarget tissue uptake of ST$_h$ relative to other receptor-targeted radiopharmaceuticals clearly shows the potential of ST$_h$ analogues for use in the imaging and treatment of colon carcinoma. Future work will focus on the design of analogues optimized for both imaging and therapeutic applications.

ACKNOWLEDGMENT

This material is the result of work supported with resources and the use of facilities at the Harry S Truman Memorial Veterans' Hospital, Columbia, MO 65201, and the University of Missouri-Columbia School of Medicine Department of Radiology, Columbia, MO 65211. This work was supported by a grant from the National Institute of Health (CA95075).

LITERATURE CITED

(1) Greenlee, R. T., Murray, T., Bolden, S., and Wingo, P. A. (2000) Cancer Statistics 2000. *CA Cancer J. Clin. 50*, 7−33.
(2) Cohen, A. M., Minsky, B. D., and Schilsky, R. L. (1997) Cancer of the colon and rectum. *Cancer: Principles and Practice of Oncology* (DeVita, V. T., Hellman, S., Rosenberg, S. A., Eds.) 5th ed., Lippincott-Raven, Philadelphia, PA.
(3) Lechner, P., Lind, P., and Goldenberg, D. M. (2000) Can Postoperative surveillance with serial CEA immunoscintigraphy detect resectable rectal cancer recurrence and potentially improve tumor-free survival? *J. Am. Coll. Surg. 191*, 511−518.
(4) Harrison, K. A., and Tempero, M. A. (1995) Diagnostic use of radiolabeled antibodies for cancer. *Oncology 9*, 625−631.
(5) Serafini, A. N., Klein, J. L., Wolff, B. G., Baum, R., Chetanneau, A., Pecking, A., Fischman, A. J., Wynant, G. E., Subramanian, R., Goroff, D. K., and Hanna, M. G., Jr. (1998) Radioimmunoscintigraphy of recurrent, metastatic, or occult colorectal cancer with technetium 99m-labeled totally human monoclonal antibody 88BV59. *J. Clin. Oncol. 16*, 1777−1787.
(6) Wolff, B. G., Bolton, J., Baum, R., Chetanneau, A., Pecking, A., Sarafini, A. N., Fischman, A. J., Hoover, H. C., Jr., Klein, J. L., Wynant, G. E., Subramanian, R., Goroff, D. K., and Hanna, M. G., Jr. (1998) Radioimmunoscintigraphy of recurrent, metastatic, or occult colorectal cancer with technetium Tc99m 88BV59H21−2V67−66 (HumaSPECT-Tc), a totally human monoclonal antibody. *Dis. Colon Rectum 41*, 953−962.
(7) Divgi, C. R. (1996) Status of radiolabeled monoclonal antibodies for diagnosis and therapy of cancer. *Oncology 10*, 939−953.
(8) Goldenberg, D. M. (1997) Perspectives on oncologic imaging with radiolabeled antibodies. *Cancer Supp. 80*, 2431−2435.
(9) Bohdiewicz, P. J. (1998) Indium-111 Satumomab Pendetide: the first FDA-approved monoclonal antibody for tumor imaging. *J. Nucl. Med. Technol. 26*, 155−163.
(10) Erb, D. A., and Nabi, H. A. (2000) Clinical and technical considerations for imaging colorectal cancers with technetium-99m-labeled AntiCEA Fab′ fragment. *J. Nucl. Med. Technol. 28*, 12−18.
(11) Moffat, F. L., Jr., Gulec, S. A., Serafini, A. N., Sfakianakis, G. N., Pop, R., Robinson, D. S., Franceschi, D., Boggs, J., and Livingstone, A. S. (1999) A thousand points of light or just dim bulbs? Radiolabeled antibodies and colorectal cancer imaging. *Cancer Invest. 17*, 322−334.
(12) Boerman, O. C., Oyen, W. J. G., and Corstens, F. H. M. (2000) Radio-labeled receptor-binding peptides: a new class of radiopharmaceuticals. *Sem. Nucl. Med. 30*, 195−208.
(13) Weiner, R. E., and Thakur, M. L. (2001) Radiolabeled peptides in diagnosis and therapy. *Semin. Nucl. Med. 31*, 296−311.
(14) Raderer, M., Kurtaran, A., Hejna M., Vorbeck, F., Angelberger, P., Scheithauer, W., and Virgolini, I. (1998) 123I-labelled vasoactive intestinal peptide receptor scintigraphy in patients with colorectal cancer. *Br. J. Cancer 78*, 1−5.
(15) Raderer, M., Becherer, A., Kurtaran, A., Angelberger, P., Li, S., Leimer, M., Weinlaender, G., Kornek, G., Kletter, K., Scheithauer, W., and Virgolini, I. (1996) Comparison of iodine-123-vasoactive intestinal peptide receptor scintigraphy and indium-111-CYT-103 immunoscintigraphy. *J. Nucl. Med. 37*, 1480−1487.
(16) Guarino, A., Cohen, M., Thompson, M., Dharmsathaphorn, K., and Giannella, R. (1987) T84 cell receptor binding and

guanyl cyclase activation by *Escherichia coli* heat-stable toxin. *Am. J. Physiol. 253*, G775−780.
(17) Vaandrager, A. B., Schulz, S., De Jonge, H. R., and Garbers, D. L. (1993) Guanylyl cyclase C is an N-linked glycoprotein receptor that accounts for multiple heat-stable enterotoxin-binding proteins in the intestine. *J. Biol. Chem. 268*, 2174−2179.
(18) Carrithers, S. L., Parkinson, S. J., Goldstein, S., Park, P., Robertson, D. C., and Waldman, S. A. (1994) Escherichia coli heat-stable toxin receptors in human colonic tumors. *Gastroenterology 107*, 1653−1661.
(19) Carrithers, S. L., Parkinson, S. J., Goldstein, S. D., Park, P., Urbanski, R. W., and Waldman, S. A. (1996) Escherichia coli heat-stable enterotoxin receptors: A novel marker for colorectal tumors. *Dis. Colon Rectum 39*, 171−181.
(20) Gali, H., Sieckman, G. L., Hoffman, T. J., Owen, N. K., Chin, D. T., Forte, L. R., and Volkert, W. A. (2001) In vitro and in vivo characterization of a new receptor specific indium-111 labeled DOTA-ST conjugate for targeting guanylin receptors in human colon cancer cells. *J. Labelled. Compd. Radiopharm. 44*, S682−S684.
(21) Gali, H., Sieckman, G. L., Hoffman, T. J., Owen, N. K., Chin, D. T., Forte, L. R., and Volkert, W. A. (2001) In vivo evaluation of an 111In-labeled ST-peptide analogue for specific targeting of human colon cancers. *Nucl. Med. Biol. 28*, 903−909.
(22) Gali, H., Sieckman, G. L., Hoffman, T. J., Kiefer, G. E., Chin, D. T., Forte, L. R., and Volkert, W. A. (2001) Synthesis and in vitro evaluation of an 111In-labeled ST-peptide enterotoxin (ST) analogue for specific targeting of guanylin receptors on human colonic cancers. *Anticancer Res. 21*, 2785−2792.
(23) Gali, H., Sieckman, G. L., Hoffman, T. J., Owen, N. K., Mazuru, D. G., Forte, L. R., and Volkert, W. A. (2002) Chemical synthesis of *Escherichia coli* STh analogues by regioselective disulfide bond formation: biological evaluation of an 111In-DOTA−Phe19-STh analogue for specific targeting of human colon cancers. *Bioconjate Chem. 13*, 224−231.
(24) Wolfe, H. R., Mendizabal, M., Lleong, E., Cuthbertson, A., Desai, V., Pullan, S., Fujii, D. K., Morrison, M., Pither, R., and Waldman, S. A. (2002) *In vivo* imaging of human colon cancer xenografts in immunodeficient mice using a guanylyl cyclase C-specific ligand. *J. Nucl. Med. 43*, 392−399.
(25) Forte, L. R., and Currie, M. G. (1995) Guanylin: a peptide regulator of epithelial transport. *Faseb J. 9*, 643−650.
(26) Pitari, G. M., Di Guglielmo, M. D., Park, J., Schulz, S., and Waldman, S. A. (2001) Guanylyl cyclase C agonists regulate progression through the cell cycle of human colon carcinoma cells. *Proc. Natl. Acad. Sci. U.S.A. 98*, 7846−7851.
(27) Shimonishi, Y., Hidaka, Y., Koizumi, M., Hane, M., Aimoto, S., Takeda, T., Miwatani, T., and Takeda, Y. (1987) Mode of disulfide bond formation of a heat-stable enterotoxin (ST_h) produced by a human strain of enterotoxigenic *Escherichia coli*. *FEBS Lett. 215*, 165−170.
(28) Gariepy, J., Judd, A. K., and Schoolnik, G. K. (1987) Importance of disulfide bridges in the structure and activity of *Escherichia coli* enterotoxin ST1b. *Proc. Natl. Acad. Sci. U.S.A. 84*, 8907−8911.
(29) Ellman, G. L. (1959) Tissue sulfhydryl groups. *Arch. Biochem. Biophys. 82*, 70−77.
(30) Hugues, M., Crane, M., Hakki, S., O'Hanley, P., and Waldman, S. A. (1991) Identification and characterization of a new family of high-affinity receptors for *Escherichia coli* heat-stable enterotoxin in rat intestinal membranes. *Biochemistry 30*, 10738−10745.
(31) Wolfe, H. R., and Waldman, S. A. (2002) A comparative molecular field analysis (COMFA) of the structural determinants of heat-stable enterotoxins mediating activation of guanylyl cyclase C. *J. Med. Chem. 45*, 1731−1734.
(32) Urbanski, R., Carrithers, S. L., and Waldman, S. A. (1995) Internalization of E. coli ST mediated by guanylyl cyclase C in T84 human colon carcinoma cells. *Biochim Biophys Acta 1245*, 29−36.
(33) Pitari, G. M., Zingman, L. V., Hodgson, D. M., Alekseev, A. E., Kazerounian, S., Bienengraeber, M., Hajnoczky, G., Terzic, A., and Waldman, S. A. (2003) Bacterial enterotoxins are associated with resistance to colon cancer. *Proc. Natl. Acad. Sci. U.S.A. 100*, 2695−2699.
(34) Dreyfus, L. A., Frantz, J. C., and Robertson, D. C. (1983) Chemical properties of heat-stable enterotoxins produced by enterotoxigenic Escherichia coli of different host origins. *Infect. Immun. 42*, 539−548.
(35) Duncan, J. R., and Welch, M. J. (1993) Intracellular metabolism of Indium-111-DTPA-labeled receptor targeted proteins. *J. Nuc. Med. 34*, 1728−1738.
(36) Franano, F. N., Edwards, W. B., Welch, M. J., and Duncan, J. R. (1994) Metabolism of receptor targeted ^{111}In-DTPA-glycoproteins: Identification of ^{111}In-DTPA-ϵ-lysine as the primary metabolic and excretory product. *Nucl. Med. Biol. 21*, 1023−1034.
(37) Rogers, B. E., Franano, F. N., Duncan, J. R., Edwards, W. B., Anderson, C. J., Connett, J. M., and Welch, M. J. (1995) Identification of metabolites of ^{111}In-diethylenetriaminepentaacetic acid-monoclonal antibodies and antibody fragments *in vivo*. *Cancer Res. (Suppl.) 55*, 5714s−5720s.
(38) Hoffman, T. J., Gali, H., Smith, C. J., Sieckman, G. L., Hayes, D. L., Owen, N. K., and Volkert, W. A. (2003) Novel series of ^{111}In-labeled bombesin analogues as potential radiopharmaceuticals for specific targeting of gastrin-releasing peptide receptors expressed on human prostate cancer cells. *J. Nucl. Med. 44*, 823−831.
(39) Nock, B., Nikolopoulou, A., Chiotellis, E., Loudos, G., Maintas, D., Reubi, J. C., and Maina, T. (2003) [99mTc]-Demobesin 1, a novel potent bombesin analogue for GRP receptor-targeted tumour imaging. *Eur. J. Nucl. Med. Mol. Imaging 30*, 247−58.
(40) Smith, C. J., Gali, H., Sieckman, G. L., Higginbotham, C., Volkert, W. A., and Hoffman, T. J. (2003) Radiochemical investigations of ^{99m}Tc−N_3S−X−BN[7−14]NH_2: an in vitro/in vivo structure−activity relationship study where X= 0-, 3-, 5-, 8-, and 11-carbon tethering moieties. *Bioconjugate Chem. 14*, 93−102.
(41) La Bella, R., Garcia-Garayoa, E., Bahler, M., Blauenstein, P., Schibli, R., Conrath, P., Tourwe, D., and Schubiger, P. A. (2002) A ^{99m}Tc(I)-postlabeled high affinity bombesin analogue as a potential tumor imaging agent. *Bioconjugate Chem. 13*, 599−604.
(42) Bard, D. R., Knight, C. G., and Page-Thomas, D. P. (1990) A chelating derivative of α-melanocyte stimulating hormone as a potential imaging agent for malignant melanoma. *Br. J. Cancer 62*, 919−922.
(43) Giblin, M. F., Wang, N. N., Hoffman, T. J., Jurisson, S. S., and Quinn, T. P. (1998). Design and characterization of α-melanotropin peptide analogues cyclized through rhenium and technetium metal coordination. *Proc. Natl. Acad. Sci. U.S.A. 95*, 12814−12818.
(44) Froidevaux, S., Calame-Christe, M., Sumanovski, L., Tanner, H., and Eberle, A. N. (2003) DOTA-α-melanocyte stimulating hormone analogues for imaging metastatic melanoma lesions. *Ann. N. Y. Acad. Sci. 994*, 378−383.
(45) Miao, Y., Whitener, D., Feng, W., Owen, N. K., Chen, J., and Quinn, T. P. (2003) Evaluation of the human melanoma targeting properties of radiolabeled α-melanocyte stimulating hormone peptide analogues. *Bioconjugate Chem. 14*, 1177−1184.
(46) Fava, T. A., Desnoyers, R., Schulz, S., Park, J., Weinberg, D., Mitchell, E., and Waldman, S. A. (2001) Ectopic expression of guanylyl cyclase C in CD34+ progenitor cells in peripheral blood. *J. Clin. Oncol. 19*, 3951−3959.
(47) Kulaksiz, H., Rehberg, E., Stremmel, W., and Cetin, Y. (2002) Guanylin and functional coupling proteins in the human salivary glands and gland tumors. *Am. J. Pathol. 161*, 655−664.
(48) Forte, L. (1999) Guanylin regulatory peptides: structures, biological activities mediated by cyclic GMP and pathobiology. *Regul. Peptides 81*, 25−39.
(49) Crispens, C. G. (1975) *Handbook on the Laboratory Mouse*, Charles C. Thomas, Springfield, IL.

BC049974X

A Gadolinium(III) Complex of a Carboxylic-Phosphorus Acid Derivative of Diethylenetriamine Covalently Bound to Inulin, a Potential Macromolecular MRI Contrast Agent

Petra Lebdušková,[†,‡] Jan Kotek,[†,‡] Petr Hermann,[‡] Luce Vander Elst,[§] Robert N. Muller,[§] Ivan Lukeš,*[,‡] and Joop A. Peters*[,†]

Laboratory of Applied Organic Chemistry and Catalysis, Delft University of Technology, Julianalaan 136, 2628 BL Delft, The Netherlands, Department of Inorganic Chemistry, Charles University, Hlavova 2030, 12840, Prague, Czech Republic, and Department of Organic Chemistry, University of Mons-Hainaut, B-7000, Mons, Belgium. Received January 30, 2004; Revised Manuscript Received April 21, 2004

A novel conjugate of a polysaccharide and a Gd(III) chelate with potential as contrast agent for magnetic resonance imaging (MRI) was synthesized. The structure of the chelate was derived from H_5DTPA by replacing the central pendant arm by a phosphinic acid functional group, which was covalently bound to the polysaccharide inulin. On the average, each monosaccharide unit of the inulin was attached to approximately one (0.9) chelate moiety. The average molecular weight is 23110 and the average number of Gd^{3+} ions per molecule is 24. The ligand binds the Gd^{3+} ion in an octadentate fashion via three nitrogen atoms, four carboxylate oxygen atoms, and one P−O oxygen atom, and its first coordination sphere is completed by a water molecule. This compound shows promising properties for application as a contrast agent for MRI thanks to a favorable residence lifetime of this water molecule (170 ns at 298 K), a relatively long rotational correlation time (866 ps at 298 K), and the presence of two water molecules in the second coordination sphere of the Gd^{3+} ion. Furthermore, its stability toward transmetalation with Zn(II) is as high as that of the clinically used $[Gd(DTPA)(H_2O)]^{2-}$.

INTRODUCTION

Paramagnetic metal complexes are widely used in clinical diagnostics as contrast agents for magnetic resonance imaging (MRI). They are used to enhance the contrast between normal and diseased tissue or to indicate blood flow and/or organ function (*1*, *2*). Nowadays, more than 30% of the examinations are performed after administration of a contrast agent. Paramagnetic contrast agents may improve the image contrast by enhancing the relaxation rate of water proton nuclei in their surroundings. The most commonly used paramagnetic metal ion in these contrast agents is Gd^{3+}, which is very efficient in enhancing relaxation rates by virtue of its seven unpaired electrons and its relatively long electronic relaxation time. The efficiency of an MRI contrast agent usually is expressed as the relaxivity, r_1, which is the enhancement of the water proton relaxation rate in s^{-1} mM^{-1} per Gd^{3+} ion. The relaxivity is governed mainly by the residence lifetime of water molecules coordinated in the first coordination sphere of the central metal ion, τ_M, by the complex reorientation time, τ_R, and by the longitudinal and transversal electronic relaxation times, τ_{s1}, τ_{s2} (*1*, *3*, *4*). Currently applied low molecular weight complexes, such as Gd^{3+} complexes of 1,1,4,7,7-diethylenetriaminepentaacetic acid (H_5DTPA) or 1,4,7,10-tetraazacyclododecane-1,4,7,10-tetraacetic acid (H_4DOTA), have their relaxivity limited by fast rotation and, therefore, a short rotational correlation time, τ_R. New generations of contrast agents with improved relaxivity and specificity are desired. There are possibilities to enhance the relaxivity by increasing the τ_R value. This can be achieved by, for example, covalent or noncovalent binding of a low molecular weight chelate to macromolecules (*3*) or by self-assembly of monomeric complexes into micelles or particulates (*5*).

The residence lifetime of the inner-sphere water molecule, τ_M, is a very important parameter in relation to the relaxivity of high molecular weight MRI contrast agents. Theory predicts that its optimal value is in the range of 20−50 ns at 298 K (*3*). The currently used contrast agents, such as the above-mentioned $[Gd(DTPA)(H_2O)]^{2-}$ and $[Gd(DOTA)(H_2O)]^{-}$, have τ_M values of 303 and 244 ns at 298 K, respectively, which is far from the optimum (*6*). Upon conjugation of these complexes to a macromolecule, the relaxivities may therefore be limited by this parameter. The water exchange rate can be enhanced by, for example, introducing negative charge (*7*) in the neighborhood of the Gd^{3+} bound water or by increasing its steric strain, which favors the dissociative mechanism of the water exchange (*8*−*12*). Previously, we reported on the low-molecular weight complex $[Gd(DT4AP^{Ph})(H_2O)]^{2-}$ (see Chart 1), which was designed on the basis of these ideas (*11*). It appeared to have a τ_M value of 92 ns, which is three times smaller than the currently used contrast agent $[Gd(DTPA)(H_2O)]^{2-}$. Furthermore, this complex has two second-sphere water molecules, which are contributing to the overall relaxivity. Here, we report on the synthesis of an analogous chelate (**8**) and its conjugate with the polysaccharide inulin (**L**, Chart 1). The relaxivity of both the parent chelate (**8**) and its conjugate and the parameters governing it are evaluated.

* Corresponding authors. J.A.P.: telephone: (+31)15 27 85892; fax: (+31)15 27 84289; e-mail: J.A.Peters@tnw.tudelft.nl. I.L.: telephone: (+420)221952357; fax: (+420)221952378; e-mail: lukes@natur.cuni.cz.

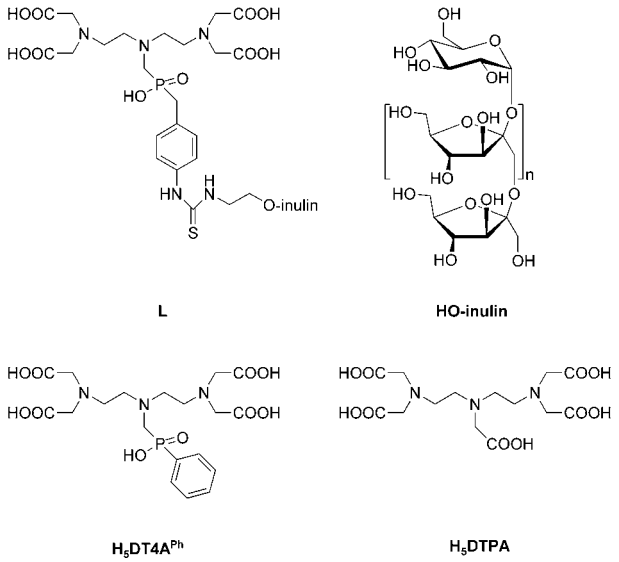
[†] Delft University of Technology.

[‡] Charles University.

[§] University of Mons-Hainaut.

10.1021/bc049966g CCC: $27.50 © 2004 American Chemical Society
Published on Web 05/27/2004

Chart 1. Molecular Structures of Ligands Discussed



EXPERIMENTAL PROCEDURES

Materials. Commercially available diethylenetriamine, phthalanhydride, ethyl chloroformate, and ethyl bromoacetate had synthetic purity and were used as received. Arsenazo III used for free-gadolinium tests was purchased from Aldrich Chemical Co. (Milwaukee, WI). The 10% Pd/C-catalyst for the hydrogenation reactions was obtained from Acros (Geel, Belgium). Inulin was obtained from Sensus Coöperatie Cosun U.A. (Roosendaal, The Netherlands) and had an average degree of polymerization (*dp*) of 25. This "long chain" fraction was obtained by recrystalization of inulin from water, thereby selectively removing the low-molecular-weight components. Paraformaldehyde was obtained by filtration of aged aqueous formaldehyde solutions and was dried in a desiccator over concentrated sulfuric acid. *p*-Nitrobenzyl phosphinic acid was prepared by alkylation of $P(CH(OEt)_2)(OSiMe_3)(OEt)$ with *p*-nitrobenzyl bromide followed by hydrolysis in aqueous HCl according to a procedure published elsewhere (*13*).

NMR Spectroscopy. ^{1}H (300 MHz), ^{13}C (75.5 MHz), ^{17}O (40.7 MHz), and ^{31}P NMR spectra (121.5 MHz) were recorded on a Varian INOVA-300 spectrometer using 5 mm sample tubes. Unless stated otherwise, NMR experiments were performed at 25 °C. Chemical shifts δ are given in ppm. For measurements in D_2O, *tert*-butyl alcohol was used as an internal standard with the methyl signal referenced to 1.2 ppm (^{1}H) or 31.2 ppm (^{13}C). Deuterium oxide (100%) was used as an external chemical shift reference for ^{17}O resonances. The ^{31}P chemical shifts were measured with respect to 1% H_3PO_4 in D_2O as an external standard (substitution method). The pH values of the samples were measured at ambient temperature using a Corning 125 pH meter with a calibrated microcombination electrode purchased from Aldrich Chemical Co. The pH values of the solutions were adjusted using dilute aqueous solutions of NaOH and HCl.

Mass Spectrometry. Mass spectra were obtained on a Q-tof 2 mass spectrometer (Micromass, Manchester, UK). Samples were dissolved in H_2O and injected at a rate of 5 μL/min. The cone voltage was 170 V (T = 80 °C); 850 spectra were accumulated. The reported mass corresponds to the most abundant isotopic peak.

Bis(phthaloyl)diethylenetriamine (1). This compound was synthesized according to a known procedure (*14*). ^{1}H NMR (DMSO-d_6), δ 2.76 and 3.59 (t, $^3J_{HH}$ = 6.3 Hz, 2 × 4H, CH_2), 7.80 (m, 8H, arom). ^{13}C NMR (DMSO-d_6), δ 37.14 and 46.10 (NCH_2CH_2N), 122.70, 131.59 and 134.07 (arom), 167.81 (*C*O).

Ethyl *p*-Nitrobenzylphosphinate (3). An excess of pyridine (3.45 g, 43.6 mmol) was slowly dropped to a suspension of *p*-nitrobenzylphosphinic acid (**2**) (*13*) (5.00 g, 24.9 mmol) and ethylchloroformate (3.47 g, 32.0 mmol) in $CHCl_3$ (200 mL) during a period of 2 h. The mixture obtained was stirred for 42 h at room temperature and then washed with water (3 × 150 mL). The organic layer was dried over Na_2SO_4 after which the solvents were evaporated off. The excess of chloroformate was removed by codistillation with toluene (2 × 50 mL) and dry ethanol (2 × 50 mL) to yield 5.25 g (92%) of **3** as a light yellow oil. ^{31}P NMR ($CDCl_3$), δ 33.39 (doublet of multiplets, $^1J_{PH}$ = 551 Hz). ^{13}C NMR ($CDCl_3$), δ 147.08 ($^5J_{CP}$ = 4.4 Hz, *C*-NO_2), 138.28 ($^2J_{CP}$ = 8.2 Hz, C_{arom}-CH_2), 130.80 ($^3J_{CP}$ = 6.0 Hz, arom), 123.83 ($^4J_{CP}$ = 2.7 Hz, arom), 63.10 ($^2J_{CP}$ = 7.1 Hz, OCH_2), 36.91 ($^1J_{CP}$ = 86.3 Hz, *C*H_2P), 16.21 ($^3J_{CP}$ = 6.0 Hz). ^{1}H NMR ($CDCl_3$) δ 8.2 (AA′BB′ system, 4H, arom), 7.20 ($^1J_{PH}$ = 554 Hz, 1H, P*H*), 4.15 (m, 2H, OCH_2), 3.42 ($^1J_{HP}$ = 19 Hz, 2H, CH_2P), 1.33 (m, 3H, CH_3).

Ethyl *N*,*N*″-Bis(phthaloyl)diethylenetriamine-*N*′-methylene(*p*-nitrobenzyl)phosphinate (4). Freshly prepared ethyl *p*-nitrobenzylphosphinate (**3**) (5.25 g, 22.9 mmol) was dissolved in a mixture of 100 mL of toluene and 30 mL of dry ethanol. Bis(phthaloyl)diethylenetriamine (**1**) (5.00 g, 13.8 mmol) was added, and the mixture was heated to reflux under a Dean−Stark trap. Paraformaldehyde (0.41 g, 13.8 mmol) was added portionwise during 1.5 h. After the addition was completed, the reaction mixture was refluxed for another 1.5 h. The solvent in the trap was removed, and a second portion of paraformaldehyde (0.41 g) was added. The mixture was then heated for 18 h at 100 °C. The excess of ethyl *p*-nitrobenzylphosphinate and the byproduct ethyl hydroxomethyl(*p*-nitrobenzyl)phosphinate were not removed, and the crude product was used in the next step without purification. ^{13}C NMR ($CDCl_3$), δ 16.98 (*C*H_3), 35.23 ($^1J_{CP}$ = 86 Hz, $O_2NC_6H_4CH_2$P), 35.80 (NCH_2CH_2-NPht), 53.05 (NCH_2P, $^1J_{CP}$ = 87); 53.63 (NCH_2CH_2NPht), 61.87 (POCH_2), 123.70, 131.19 and 134.53 (all Pht), 123.75, 132.53, 139.89, 147.27 (arom), 168.66 (*C*O).

Diethylenetriamine-*N*′-methylene(*p*-nitrobenzyl)-phosphinic-*N*,*N*,*N*″,*N*″-tetraacetic Acid (7). Hydrazine hydrate (2.00 g, 62.4 mmol) was added to a solution of crude **4** in dry ethanol (100 mL), and the mixture was refluxed for 6 h. After cooling, the precipitated phthalhydrazide was filtered off. The solvent was evaporated and water was removed by codistillation with dry ethanol. The crude product **5** was used in the next reaction step without further purification. All material obtained was dissolved in DMF (70 mL). $BrCH_2CO_2Et$ (20.04 g, 0.12 mol) and K_2CO_3 (15.12 g, 0.11 mol) were added to the solution obtained. After being stirred at room temperature for 24 h, the solids were filtered off and the mixture was diluted with a saturated solution of $NaHCO_3$ (70 mL). The product was extracted into toluene (150 mL). The organic layer was washed with a saturated solution of $NaHCO_3$ (3 × 100 mL) and with brine (100 mL). The organic phase was dried (Na_2SO_4), filtered and evaporated until dryness to give crude **6**.

All material obtained above was dissolved in 200 mL of diluted HCl (1:1). After being refluxed for 21 h, the mixture was filtered and evaporated to dryness. The residue was dissolved in water and poured onto a column of cation exchanger (Dowex 50, 200 mL, H^+-form). Nonbasic impurities were removed by elution with water

(~1 L). The crude product was eluted using a diluted ammonia (1:3) solution. The orange fraction obtained was evaporated to dryness, dissolved in water, and poured onto a column of an anion exchanger (Dowex 1, 250 mL, OH^--form). After being washed with water, some yellow-colored impurities were removed by elution with 10% acetic acid. The product was collected by elution with aqueous HCl (1:3). The fractions containing the product were evaporated to dryness. Trituration with 300 mL of acetone afforded a light yellow solid, which was filtered off, washed with acetone, and dried under vacuum. The product was recrystallized by dissolution in water with a minimal amount of ammonia and acidification with HCl to pH ~ 0. Overall yield (based on compound (**1**)): 5.61 g (70%). Elemental analysis showed that the compound contains a small amount of NaCl (calcd for **7**·$2H_2O$, $C_{20}H_{33}N_4O_{14}P$, $M = 584.47$) C 41.55 (41.10); H 5.63 (5.69); N 9.86 (9.59); Cl 1.01 (0.00). ^{31}P NMR (D_2O, pH = 0.5), δ 36.85. ^{13}C NMR (D_2O, pH = 0.5), δ 37.08 (d, $^1J_{CP} = 86$ Hz, $O_2NC_6H_4CH_2P$), 51.12 (PCH_2NCH_2), 51.65 (d, $^1J_{CP} = 80$ Hz, NCH_2P), 52.27 ($PCH_2NCH_2CH_2N$), 55.37 (NCH_2-CO), 124.05, 130.91 (d, $^3J_{CP} = 8.0$ Hz), 140.95 (d, $^2J_{CP} = 8.2$) and 146.66, (arom), 169.75 (*C*O). ^1H NMR (D_2O, pH = 0.5), δ 3.03 (d, $^2J_{HP} = 6.6$ Hz, $O_2NC_6H_4CH_2P$), 3.18 and 3.67 (m, CH_2 groups of skeleton and bearing phosphorus moiety), 4.01 (s, NCH_2CO); 7.38 and 8.08 (arom).

Diethylenetriamine-*N′*-methylene(*p*-aminobenzyl)-phosphinic-*N*,*N*,*N″*,*N″*-tetraacetic Acid (8). Compound **7** (0.5 g, 0.86 mmol) was dissolved in water (10 mL) with addition of a small amount of a solid LiOH. Hydrogenation catalyst (0.05 g of 5% Pd/C) was added, and the mixture was stirred under a H_2 atmosphere for 3 days. The reaction mixture was then filtered and purified by chromatography on a column of a strong anion exchanger (Dowex 1, AcO^--form, 25 mL). After washing with water, the product was eluted with HCl (1:3). The fractions containing the product were evaporated to dryness. The product was triturated using dry ethanol, collected by filtration, and dried under vacuum. Yield: 0.68 g (92%) Elem. anal. (calcd for (**8**)·$12H_2O$·HCl, $C_{20}H_{56}ClN_4O_{22}P$, M = 771.16) C 30.98 (31.15); H 5.26 (7.32); N 7.27 (7.27); Cl 2.08 (4.60). ^{31}P NMR (D_2O, pH = 0.5), δ 37.72. ^{13}C NMR (D_2O, pH = 0.5): 36.80 (d, $^1J_{CP} = 87$, $H_2NC_6H_4CH_2P$); 51.23 (PCH_2NCH_2); 51.65 (d, $^1J_{CP} = 90$, NCH_2P); 52.20 ($PCH_2NCH_2CH_2N$); 55.50 (NCH_2CO); 123.50, 128.73, 131.57 and 133.76 (arom); 169.96 (*C*O). ^1H NMR (D_2O, pH = 0.5), 3.05 (d, $^2J_{HP} = 6.9$ Hz, $H_2NC_6H_4CH_2P$), 3.18 and 3.39 (m, CH_2 groups of skeleton and bearing phosphorus moiety), 4.02 (s, NCH_2CO); 7.34 (arom).

Diethylenetriamine-*N′*-methylene(*p*-isothiocyanatobenzyl)phosphinic-*N*,*N*,*N″*,*N″*-tetraacetic Acid (9). Compound **8** (0.5 g, 0.65 mmol) was dissolved in water (5 mL), and the pH was adjusted to 2 by several drops of concentrated aqueous HCl. A solution of thiophosgene (80 mg in 3 mL CCl_4, 0.68 mmol, 1.05 equiv) was added in one portion, and then the mixture was stirred vigorously at room temperature for 48 h. The water phase was separated off and evaporated to dryness. Yield: 0.51 g. ^{31}P NMR (D_2O, pH = 0.5), δ 36.16. ^{13}C NMR (D_2O, pH = 0.5), δ 36.85 (d, $^1J_{CP} = 86$ Hz, $SCNC_6H_4CH_2P$), 49.38 (PCH_2NCH_2), 52.51 ($PCH_2NCH_2CH_2N$), 52.55 (d, $^1J_{CP} = 102$ Hz, NCH_2P), 57.29 (NCH_2CO), 126.00, 131.14, 134.24 and 134.99 (arom), 170.52 (*C*O); S*C*N was not observed, probably due to its very slow relaxation.

***O*-Cyanoethylinulin (11)** (*15*). Inulin (**10**) (dp 25, 5 g, 31 mmol of sugar units) was dissolved together with 0.26 g of NaOH (6.5 mmol) in water (8.9 mL, 0.49 mmol) by stirring at 45 °C. Then, acrylonitrile (3.28 g, 62 mmol) was added, and the mixture was stirred for 1 h at 45 °C. The mixture was diluted with water (20 mL) and neutralized by addition of 30% HCl (1 mL), followed by small amounts of $NaHCO_3$ (until CO_2 bubbles were observable). The reaction mixture was evaporated to dryness, and the residue was dissolved in 50% ethanol (100 mL). Salts were removed by membrane filtration (20 bar, UTC 60 membrane, Torey Industies Inc., Tokyo, Japan). The product was freeze-dried, and integration of the ^1H NMR spectrum showed the average degree of substitution to be 1.13. Yield: 5.70 g. ^1H NMR (D_2O), δ 2.6−2.9 (19% of overall intensity, CH_2CN); 3.5−4.4 (81% of overall intensity, remaining protons).

***O*-Aminopropylinulin (12)** (*16*)**.** *O*-Cyanoethylinulin (**11**) (1.00 g, 4.5 mmol) was dissolved in a mixture of liquid ammonia (100 mL) and dry ethanol (50 mL). Metallic lithium (0.53 g, 77 mmol) was added portionwise during 30 min at −50 °C. A deep blue color was visible for several seconds after each addition of the metal. The mixture was refluxed for 1 h. Then the ammonia was evaporated off over 3 h using a cold water bath, and the resulting mixture was diluted with water (50 mL). A stream of CO_2 was bubbled through the suspension to neutralize LiOH. The mixture was filtered and evaporated to dryness. The product was extracted with water (150 mL). Salts were removed by membrane filtration (UTC 60 membrane), and the filtrate was freeze-dried. The degree of substitution was determined by integration of the ^1H NMR spectrum to be 0.99. Yield: 0.88 g. ^1H NMR (D_2O, pH = 10.5), δ 1.5−2.0 (15% of overall intensity, $CH_2CH_2NH_2$), 2.6−2.9 and 2.9−3.1 (15% of overall intensity, $CH_2CH_2NH_2$); 3.4−4.3 (70% of overall intensity, remaining protons). ^1H NMR (D_2O, pH = 0), δ 1.5−2.0 1.65−1.85 (17% of overall intensity, $CH_2CH_2NH_2$); 2.8−3.0 (16% overall intensity, $CH_2CH_2NH_2$), 3.3−4.2 (67% of overall intensity, remaining protons). ESI-MS: *m*/*z*: 5676 (the mean value cossponds to dp ~ 26 with ds ~ 0.99). For MS data see Supporting Information (Figure S1).

Conjugate of Ligand 9 and *O*-Aminopropylinulin, L. *O*-Aminopropylinulin (**12**) (0.203 g, 0.93 mmol amino groups) was dissolved in water (7 mL), and the pH was adjusted to 9−10 with diluted KOH. Compound **9** (freshly prepared from 1.0 g of **8**, 1.30 mmol, 1.4 equiv) was added, and the reaction mixture was stirred at room temperature for 24 h. The reaction mixture was purified by gel chromatography (Sephadex G-25, 110 × 2 cm) using distilled water for elution. Four fractions of 100 mL were collected. The first two of them contained only inorganic salts and low molecular weight compounds and were discarded. The last two fractions containing the macromolecular material were freeze-dried. Yield: 0.91 g. ^{31}P NMR (D_2O), δ 34.18. ^1H NMR (D_2O), δ 2.0−2.2 ($CH_2CH_2NH_2$), 2.8−3.0 ($CH_2CH_2NH_2$), 3.1−3.3 (NCH_2CH_2N), 3.3−3.6 (NCH_2COOH), 3.7−4.2 (inulin *H*), 7.43 and 7.54 (arom). Comparison of the integrals of the aromatic protons and those of the sugar protons indicated that the degree of substitution was 0.86.

Gd(III) Complex of L, Gd_xL. In following text, for clarity, the abbreviation Gd_x**L** will be used for the final conjugate complex without specification of the number of metal ions per inulin molecule, the number of coordinated water molecules, and the charge. Ethylenediaminetetraacetic acid (H_4EDTA) (0.29 g, 1 mmol) was suspended in water (3 mL). Concentrated aqueous ammonia was added dropwise until all H_4EDTA was dissolved. Then, a solution of 0.22 g of $GdCl_3·6H_2O$ (0.59 mmol) in water (3 mL) was added, and the reaction mixture was stirred at room temperature. After 30 min,

all Gd(III) was complexed (as checked with Arsenazo III). A solution of **L** (0.10 g in 2 mL of water) was added, and the reaction mixture was stirred at room temperature for 36 h. The pH was not adjusted, and it had a value of 5.0.

The solution was then dialyzed (cellulose membrane, Sigma, retains mol. wt > 12 000). The water used in the dialysis was checked for the presence of Gd(III) by measuring its ^{17}O NMR shift. When the chemical shift of the water signal remained constant, the dialysis was terminated. The final solution was once again checked for the presence of free Gd(III) with Arsenazo III, and no free Gd(III) was detected. The solution of the Gd_x**L** complex was freeze-dried. Yield: 0.11 g of white hygroscopic solid. ESI-MS: *m*/*z*: 23110 (the mean value corresponds to dp ∼ 27 with ds ∼ 0.86 (number of Gd(III) complexes per sugar unit)). For the MS data see Supporting Information (Figure S1).

Variable Temperature ^{17}O NMR Study of the Gd_xL. A sample of the Gd(III) complex of **L** was prepared by dissolution of 0.0486 g of Gd_x**L** in 0.3621 g of deionized water. Then, 64 mg of ^{17}O enriched water (10% $H_2{}^{17}O$) was added, and the pH was determined to be 5.79. The exact concentration of Gd(III) was determined to be 82 mM from the bulk magnetic susceptibility shift, which was determined using the procedure described previously (*17*). All NMR spectra were acquired without frequency lock. To correct the ^{17}O NMR shift for a contribution of the BMS, the difference between chemical shifts of proton signals of *tert*-butyl alcohol in the paramagnetic sample and in pure water was applied according to the procedure described previously (*18*). Longitudinal ($1/T_1$) and transversal ($1/T_2$) relaxation rates were obtained by the inversion recovery method (*19*) and the Carr−Purcell−Meiboom−Gil pulse sequence (*20*), respectively.

Measurement of $1/T_1$ ^1H NMRD Profiles. The sample was prepared by dissolution of the freeze-dried complex Gd_x**L** in the appropriate amount of deionized water. The pH value was 7.11 and was not further adjusted. The exact concentration of Gd(III) was determined using the BMS method (*17*) and from proton relaxivity measurements at 20 MHz and 37 °C after complete hydrolysis in 25% HNO_3. The $1/T_1$ NMRD profiles were measured at 5, 25, and 37 °C at magnetic field strengths between $4.7 \cdot 10^{-4}$ T and 0.35 T using a Stelar SpinMaster FFC-2000 relaxometer. Measurements at 0.47, 1.42, and 7.05 T were performed on a Bruker Minispec PC-20 and Mq-60 and on a Bruker AMX-300 spectrometer and were included in the profiles. The experimental data were fitted simultaneously with ^{17}O NMR data employing a least-squares fitting procedure using the Micromath Scientist program version 2.0 (Salt Lake City, UT) as described previously (*21*, *22*).

Transmetalation. The stability of Gd(III) complex was determined using a transmetalation experiment with $ZnCl_2$ (*23*). This measurement was done using a buffered solution (phosphate buffer, total concentration 67 mM, pH 7) containing 2.5 mM of Gd_x**L** and 2.5 mM of $ZnCl_2$. The transmetalation was followed via the ^1H longitudinal relaxation rates of the water using the Bruker Minispec 20 MHz at 37 °C.

RESULTS AND DISCUSSION

Synthesis of the Conjugate of the Chelate and Its Gd(III) Complex. The conjugate of inulin and the carboxylic-phosphorus acid derivative of diethylenetriamine (**8**) was synthesized following the route outlined in Scheme 1. Inulin was chosen as a carrier for the chelating ligand, because its high flexibility allows the preparation of highly functionalized derivatives suitable for conjugation. In the present case the inulin was functionalized with *O*-aminopropyl groups by cyanoethylation of inulin with acrylonitrile and base, followed by reduction of the cyano groups with metallic Li in liquid ammonia/methanol at low temperature (*15*, *16*). A degree of substitution (ds, defined as the average number of substituents per monosaccharide unit; the theoretical maximum ds is three corresponding to three free hydroxy groups per sugar unit) of 1.0 was obtained. Previous studies have indicated that the cyanoethyl groups in *O*-cyanoethyl inulin are distributed uniformly along the inulin chain and that within each fructose unit, the 4-position is the most reactive toward cyanoethylation (*15*).

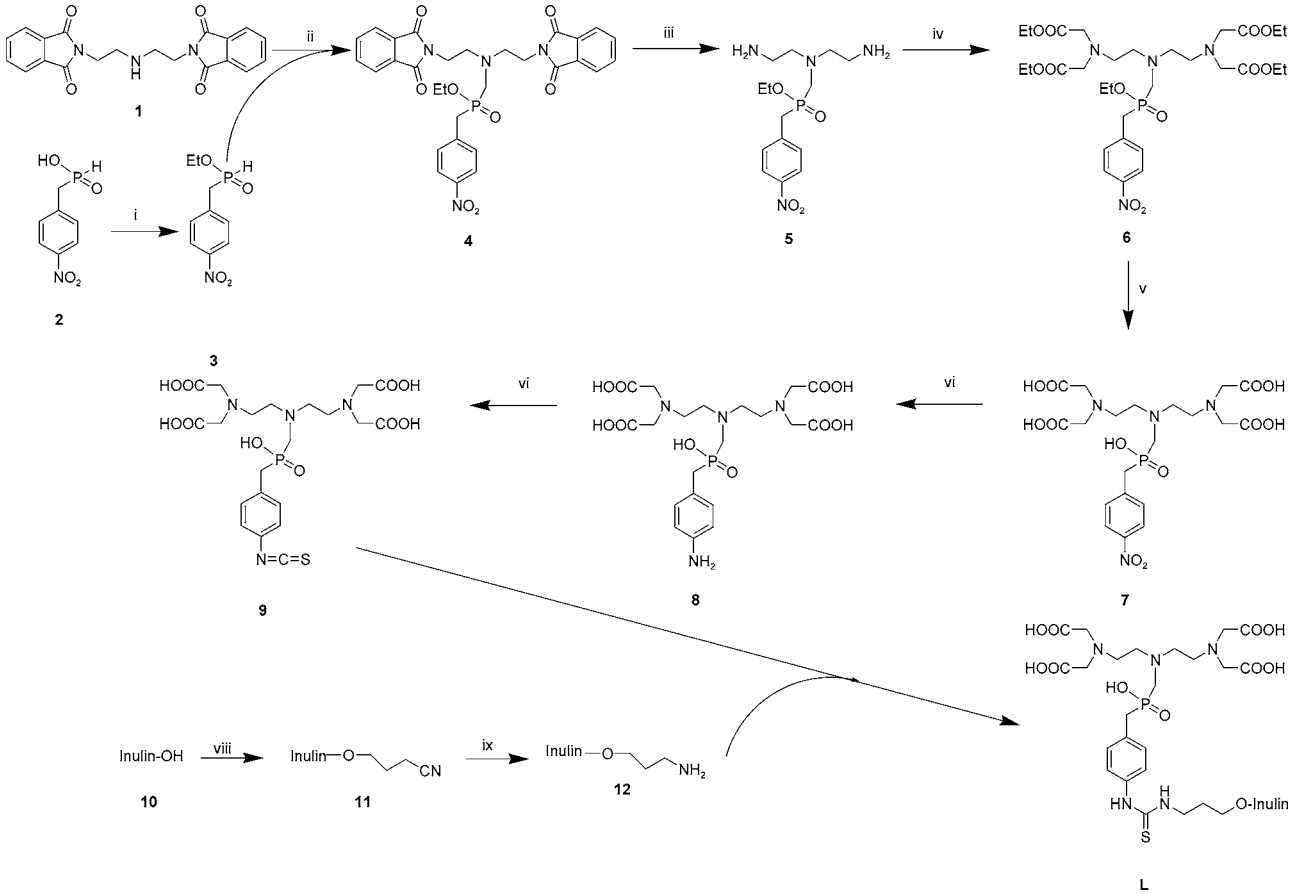
The Gd(III) chelating ligand (**8**) was prepared starting from *p*-nitrobenzylphosphinic acid (**2**). Its ethyl ester (**3**) was obtained by esterification using chloroformate and base, employing conditions published for phenylphosphinate (*24*). The phosphinic ester was attached to phthaloyl-protected diethylenetriamine by a Mannich-type reaction (*11*) to give intermediate **4**. Removal of the phthaloyl protective groups by reaction with hydrazine hydrate followed by alkylation with ethyl bromoacetate and hydrolysis of the ester groups gave nitro derivative **7**. The *p*-amino derivative **8** was obtained by hydrogenation with Pd/C as the catalyst. The latter compound was linked to *O*-aminopropylinulin (**12**) by means of a reaction with isothiocyanate to give macromolecular ligand **L**. The ds obtained was 0.86.

Attempts to prepare the Gd(III) complex by mixing aqueous solutions of the ligand and $GdCl_3$ followed by adjusting the pH failed. A precipitate was formed, which did not dissolve even after lowering the pH (4−5) and increasing the temperature to 50 °C. Therefore, the Gd(III) complex was prepared by a transmetalation reaction with NH_4[Gd(EDTA)]. Removal of the excess of this complex, free H_4EDTA, and salts by means of dialysis using a tubing with a cutoff of 12 000 Da afforded pure Gd(III) complex of **L**, Gd_x**L**. An ESI-mass spectrum showed that the average molecular weight is 23 110 Da, which means that the average dp is 27 and that on the average each molecule carries 24 Gd^{3+} ions.

Evaluation of the Relaxivity and the Parameters Governing It. To assess the efficacy of the novel macromolecular contrast agent, Gd_x**L**, we measured the longitudinal relaxation rate enhancements of water protons as a function of the Larmor frequency induced by this complex. In Figure 1, the resulting NMRD profile at 300 K is compared with that of the previously reported Gd(III) complex of the corresponding unconjugated chelate, $[Gd(DT4AP^{Ph})(H_2O)]^{2-}$ (*11*) and $[Gd(DTPA)(H_2O)]^{2-}$ (*6*).

The shape of the NMRD curve of the Gd_x**L** complex, particularly the maximum around 40 MHz, is characteristic for high-molecular-weight complexes and reflects the effect of the relatively low tumbling time of the complex (*1*, *3*). Clinically, MRI exams are performed at a magnetic field between 0.5 and 2 T (corresponding with ^1H Larmor frequencies of 20−85 MHz). The relaxivity of the novel contrast agent at these field strengths (20 s^{-1} mM^{-1} at 20 mHz and 37 °C) is considerably higher than that of the currently available contrast agents (<5 s^{-1} mM^{-1} at 20 MHz and 37 °C) and comparable or higher than the relaxivity of reported macromolecular conjugates. According to the literature data, macromolecular conjugates of a similar molecular weight, such as conjugates of H_5DTPA and poly(ethylene glycol) (*25*), H_5DTPA and polyethylene (*26*), and dendrimeric H_3DO3A derivatives

Scheme 1. Synthesis of L[a]



[a] Reagents and conditions: (i) EtO_2CCl, pyridine, $CHCl_3$, rt; (ii) $(CH_2O)_n$, toluene, reflux; (iii) hydrazine hydrate, EtOH, reflux; (iv) ethyl bromoacetate, K_2CO_3, DMF, rt; (v) aq HCl, reflux; (vi) H_2, Pd/C, water, rt; (vii) $CSCl_2$, CCl_4/water, rt; (viii) acrylonitrile, aq NaOH, 45 °C; (ix) Li, NH_3(l):EtOH, −50 °C; (x) water, rt.

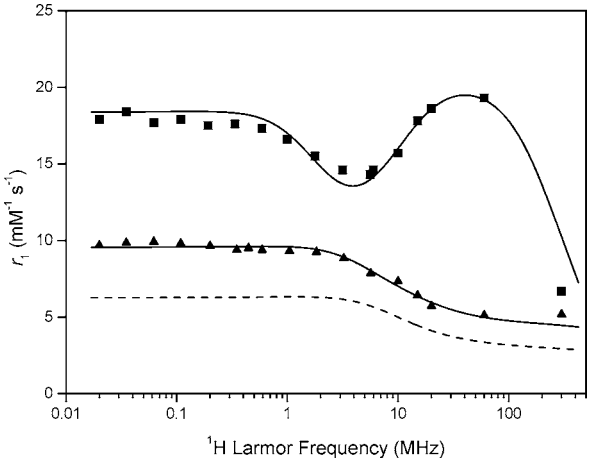


Figure 1. Comparison of the ^{1}H NMRD profiles of the Gd_x**L** (full squares), $[Gd(DT4AP^{Ph})(H_2O)]^{2-}$ (full triangles) (the lines represent the best simultaneous fits), and $[Gd(DTPA)(H_2O)]^{2-}$ (dashed line, simulated on the basis of parameters from ref 6), at 37 °C.

(*27*), have relaxivities in the range of 6 to 16 s^{-1} mM^{-1} at 20 MHz and 310 K. A comparable relaxivity was also found for the Gd^{3+} complex of another *O*-aminopropyl-inulin derivative with a very high degree of substitution (ds = 1.5), which was conjugated with H_3DO3A-squaric acid (about 20 s^{-1} mM^{-1} at 20 MHz and 310 K) (*22*). However, the relaxivities of conjugates of $Gd(DTPA)^{2-}$ to inulin have been found to be only slightly higher than that of $Gd(DTPA)^{2-}$ itself (*28*).

The overall relaxivity (r_1^{obs}) of the Gd(III) chelate can be described using a model that considers three different contributions: inner sphere (r_1^{IS}), second sphere (r_1^{SS}), and outer sphere (r_1^{OS}) (see eq 1).

$$r_1^{obsd} = r_1^{IS} + r_1^{SS} + r_1^{OS} \quad (1)$$

The inner-sphere contribution arises from the water molecule(s) coordinated directly to the Gd(III) ion, while the outer-sphere contribution involves all the solvent molecules diffusing along the complex. The term "second-sphere" concerns contributions arising from water molecules interacting via hydrogen bonds with the electronegative atoms of the ligand and therefore staying in the second coordination/hydration sphere of Gd(III). The inner-sphere contribution represents the most important term, and therefore most efforts toward improvement of new contrast agents are focusing on the optimization of this part. It is influenced by the chemical exchange of the water molecule (τ_M), the electron spin relaxation (τ_{S1} and τ_{S2}), and the reorientation of the Gd−H_w vector (τ_R) and is described by the Solomon−Bloembergen−Morgan equations (see Supporting Information) (*29*). The second-sphere contributions can be described by the same equations but with different values for some of the parameters. The outer-sphere contribution is usually described by the Freed equations (*30*).

The increase of the value of τ_R (by increasing the molecular weight of the paramagnetic complex) causes the increase of total relaxivity; however, τ_M then steps out to be the limiting factor. Therefore, the optimization

of the residence lifetime of the inner-sphere water turns out to be the crucial step. The optimum lies in the range of 20−50 ns at 298 K (*3*).

If second-sphere water molecules are present, they can also greatly influence the overall relaxivity because the structural arrangement (such as hydrogen bonds with the polar groups of the ligand) brings the second-sphere water protons close to the paramagnetic center, and therefore they are strongly relaxed.

The compound under study, $Gd_x\mathbf{L}$, is a modification of a previously published complex $[Gd(DT4AP^{Ph})(H_2O)]^{2-}$ (*11*), which is now covalently bound to the polysaccharide inulin. The structure of the Gd(III) chelate is derived from H_5DTPA where the central carboxylic group has been replaced by a phosphinate (see Chart 1). The presence of the more bulky phosphinate favors the dissociation of the inner-sphere water, causing a shorter τ_M (closer to the optimal value). The previously published parent molecule, $[Gd(DT4AP^{Ph})(H_2O)]^{2-}$, had a residence lifetime of the inner-sphere water molecule at 298 K (τ_M^{298}) of 92 ns, which is three times shorter than that of the currently used contrast agents, such as $[Gd(DTPA)(H_2O)]^{2-}$ (303 ns). Furthermore, it also has two water molecules in the second sphere. To determine the parameters influencing relaxivity, ^{1}H NMRD profiles of $Gd_x\mathbf{L}$ were recorded at 278, 298, and 310 K (see Figure 2a) and were fitted together with the results of variable temperature of ^{17}O NMR measurements (see below).

^{17}O NMR relaxation rates and angular frequencies of the solution of the Gd(III) complex and an acidified water reference at different temperatures were measured, from which the reduced relaxation rates and chemical shifts were calculated ($1/T_{1r}$, $1/T_{2r}$, and $\Delta\omega_r$), using eqs 2 and 3,

$$1/T_{ir} = 1/P_m(1/T_i - 1/T_{iw}),\ i = 1, 2 \qquad (2)$$

$$\Delta\omega_r = 1/P_m(\omega - \omega_w) \qquad (3)$$

where P_m is the mole fraction of bound water and index w stands for the variable of the acidified water reference sample (see Figure 2b,c).

The calculated reduced relaxation rates and chemical shifts are listed in the Supporting Information (Table S1). The resulting NMRD and ^{17}O NMR data were fitted simultaneously with the set of Solomon−Bloembergen−Morgan equations, the Freed equations, and the set of equations usually used to predict the variable temperature ^{17}O NMR chemicals shifts and relaxation rates (*2*) (see Supporting Information). Simultaneous fitting has the advantage of putting constraints on the parameters. In total, 18 parameters have to be taken into account (see Table 1), and some of them are common for both sets of data.

The distance between the coordinated water oxygen and the Gd^{3+} ion (r_{GdO}) was fixed at 2.5 Å (*6*) and that between the coordinated water proton and Gd(III) (r_{GdH}) at 3.1 Å. For the second-sphere water molecule, this distance (r_{GdH}^{2S}) was fixed at 3.5 Å, whereas the number of second-sphere water molecules, q_S, was treated as an adjustable parameter. The activation energy of τ_V, E_V, had to be fixed during the fitting at 1 kJ mol^{-1}, since unrealistically small numbers were obtained if it was left variable. The hyperfine coupling constant ($A/\hbar$) was at the value that was measured for the parent molecule $[Gd(DT4AP^{Ph})]^{2-}$, -3.61×10^6 rad s^{-1} (*11*). The quadrupolar coupling constant ($\chi(1+\eta^2)^{1/2}$) was taken equal to that determined for the $[Gd(DOTA)(H_2O)]^-$ complex (5.2 MHz) (*32*). Furthermore, the values of the self-diffusion

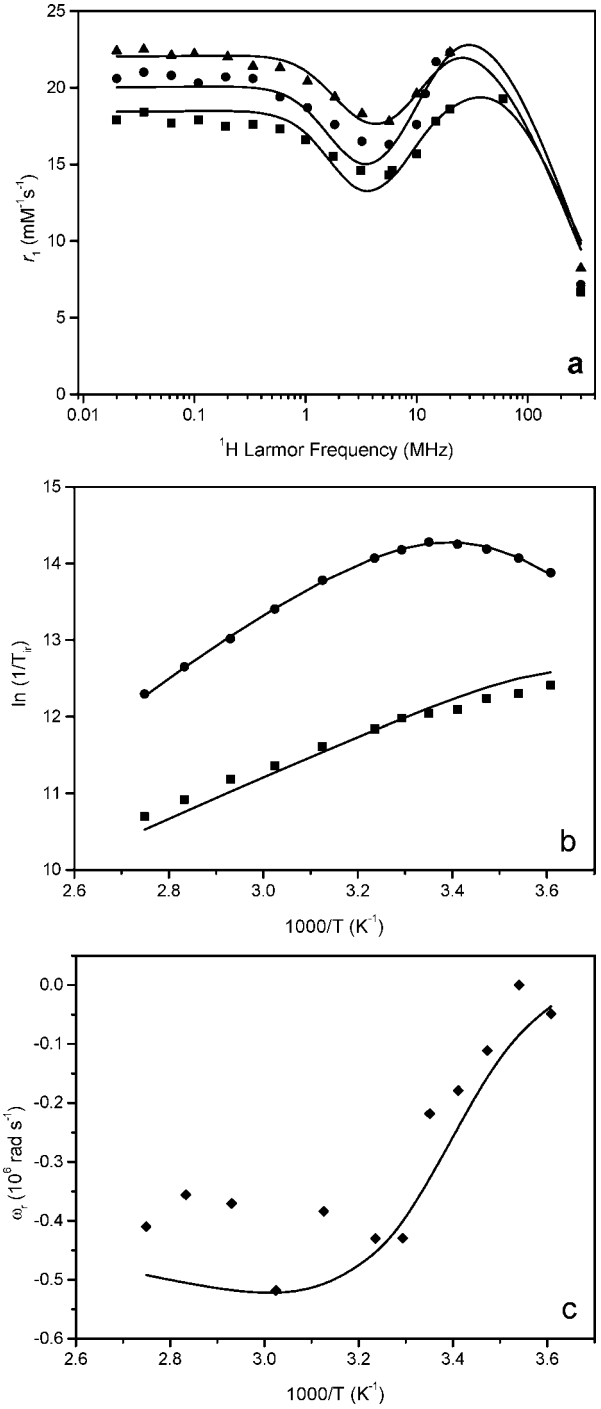


Figure 2. ^{1}H NMRD and ^{17}O NMR measurements of $Gd_x\mathbf{L}$. (a) The proton relaxivity dependence on the magnetic field at 37 °C (squares), 25 °C (circles), and 5 °C (triangles). (b) The temperature dependence of logarithms of the reduced relaxation rates (upper line (circles) corresponds to $\ln(1/T_{2r})$; lower line (squares) corresponds to $\ln(1/T_{1r})$). (c) The temperature dependence of the reduced frequency (diamonds). The curves are calculated with optimized parameters compiled in Table 1.

coefficients of water at the various temperatures were calculated with the semiemperical equation of Hindman (*33*). Since the size of the $Gd_x\mathbf{L}$ complex is much larger than that of water, the self-diffusion constant ($D_{complex}^{298}$) would be much smaller than its value for water. Therefore, this parameter was neglected in the fittings. The distance of cloasest approach of a water molecule to Gd(III) was fixed at 3.5 Å.

A model with different rotational correlation times for ^{1}H NMRD and ^{17}O NMR (τ_R(H) and τ_R(O), respectively)

Table 1. Parameters for Gd_xL Complex As Obtained from the Simultaneous Fitting of ^1H NMRD and ^{17}O NMR Data

parameter	Gd_x**L**	$[Gd(DT4AP^{Ph})(H_2O)]^{2-}$ [a]	$[Gd(DTPA)(H_2O)]^{2-}$ [b]
r_{GdH} (Å)	3.1[c]	3.1	3.1
r_{GdH}^{2s} (Å)	3.5[c]	3.5	3.5
$\Delta H^{\#}$ (kJ mol^{-1})	45.6	37.0	51.6
$\Delta H^{\#2s}$ (kJ mol^{-1})	26.6	45.8kJ	–
τ_M^{298} (ns)	170	91.6	303
τ_M^{2982s} (ps)	32.3	50.0	–
E_R (kJ mol^{-1})	21.8	19.	17.3
τ_R^{298}(H) (ps)	866	110	58
τ_R^{298}(O)/τ_R^{298}(H)	1.59	2.72	–
E_V (kJ mol^{-1})	1[c]	1	1.6
τ_V^{298} (ps)	35.6	27.0	25
Δ^2 (s^{-2})	1.4×10^{19}	3.2×10^{19}	4.6×10^{19}
$A/\hbar$ (rad s^{-1})	-3.61×10^6 [c]	-3.61×10^6	-3.8×10^6
C_{OS}	0.00[c]	0.00	0.18
δg_L^2	0.32	0.085	0.012
r_{GdO} (Å)	2.5[c]	2.5	2.2
$\chi(1+\eta^2/3)^{1/2}$ (MHz)	5.2[c]	5.2	7.58
q^{2s}	2.03	2.06	–

[a] Taken from ref 11. [b] Taken from ref 6. [c] Parameter fixed duringthe simultaneous fitting.

was used. There is a large difference in the concentrations (and, therefore, viscosities) of the samples for ^{17}O NMR (82 mM) and ^1H NMRD (1 mM) measurements (*34*), which, together with the fact that the two experiments are considering the rotations of two different vectors (Gd−O and Gd−H vectors), leads to two different values of τ_R (*32*).

A good fit for the NMRD and ^{17}O NMR data was obtained for the parameters listed in Table 1 (see Figure 2). For comparison the values of the parameters for the parent complex, $[Gd(DT4AP^{Ph})(H_2O)]^{2-}$ and for $[Gd(DTPA)(H_2O)]^{2-}$ are included in Table 1.

The simultaneous fits resulted in a value of $\tau_R^{298}(H) = 866$ ps and the ratio $\tau_R^{298}(O)/\tau_R^{298}(H) = 1.59$, which is in excellent agreement with the value reported by Dunand et al. (*32*). The rotational correlation time of Gd_x**L** ($\tau_R^{298}(H) = 866$ ps) is smaller than expected for a macromolecular compound, based solely on its molecular weight. From the Debye−Stokes−Einstein equation, it can be estimated that $\tau_R^{298} \approx 8$ ns for compounds in this molecular weight range (*35*). The relatively low τ_R-value for Gd_x**L** is probably due to some local mobility in the Gd_x**L** complex. The source of this mobility might be the aminopropyl-aminobenzyl linkage between the inulin backbone and the chelate that is probably rather flexible and allows additional motion of the chelate, which leads to a decrease in τ_R. Local mobility has been observed in many other macromolecular systems, including the Gd(III) complex of DO3A-squarate chelate linked to aminopropylinulin (*22*), which had a τ_R^{298} value of 735 ps.

The residence time of the inner-sphere water molecule (τ_M) is almost twice as high as that of $[Gd(DT4AP^{Ph})(H_2O)]^{2-}$. This can probably be ascribed to the structural differences between the two chelates. While in the low-molecular-weight molecule, $[Gd(DT4AP^{Ph})(H_2O)]^{2-}$, the phenyl group is directly attached to the phosphinate moiety, and here it is separated from it by a methylene group. Possibly, this results in somewhat less steric strain around the Gd(III)-bound water molecule and consequently an increase in the energy barrier in the dissociative mechanism and a larger τ_M. However, the τ_M^{298} value of the macromolecular complex (170 ns) is still substantially lower than that of commercially contrast agents, such as $[Gd(DTPA)(H_2O)]^{2-}$ (see Table 1) and its bisamides.

The temperature dependence of the relaxivity at constant magnetic field (20 MHz) shows a maximum at around 288 K (see Figure 3). The trend toward higher temperatures is decreasing, which means that τ_R is the limiting factor for relaxivity at temperatures above 288 K because of the increased tumbling rate at higher temperatures. At low temperatures the relaxivity increases with increasing temperature, which indicates that the influence of the increasing τ_R is competing with the limitation from τ_M. This could also explain the crossing of the NMRD curves at higher fields (see Figure 2a), where the relaxivity measured at 298 K is higher than the one measured at 278 K. At low temperature (<298 K) the relaxivity is limited by τ_M.

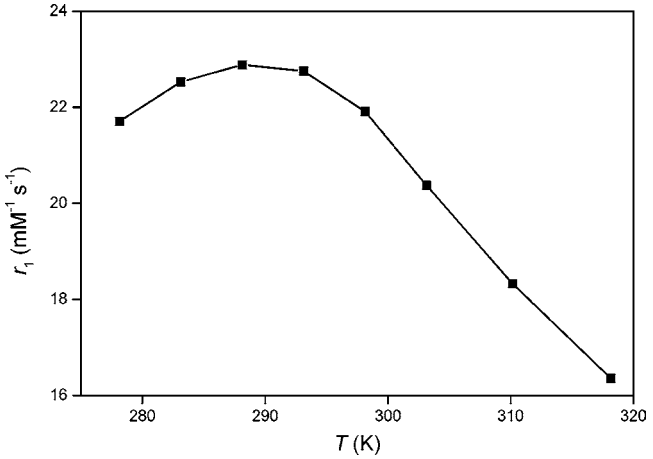


Figure 3. Proton longitudinal relaxivity at 20 MHz as a function of temperature for Gd_x**L**. The line is only a guide for the eye.

A good fit could only be obtained assuming the presence of two water molecules in the second coordination sphere of Gd(III). This is similar to what has been found previously for the low-molecular-weight analogue $[Gd(DT4AP^{Ph})(H_2O)]^{2-}$ (*11*). The residence time of the second-sphere water molecules ($\tau_M^{2s} = 32$ ps) is somewhat shorter but of the same magnitude as those for related ligands (*10*, *28*, *35*).

Transmetalation. The Gd(III) chelates can be sensitive to transmetalation by endogenous ions, such as Cu^{2+}, Ca^{2+}, and Zn^{2+} (*37*−*41*). The concentration of Cu^{2+} in blood is very small, about 1 μmol/L, whereas Ca^{2+}, on the other hand, has approximately 10 orders of magnitude lower affinity than Gd^{3+} toward organic ligands of the type of H_5DTPA (*42*). Out of the three metals mentioned, Zn^{2+} combines a rather high concentration (50 μmol/L) with a high affinity toward polyaminopoly-

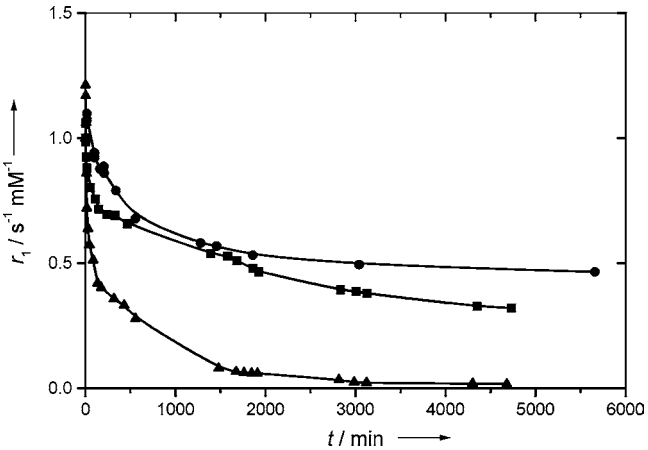


Figure 4. Evolution of the water proton paramagnetic longitudinal relaxation rate R_1^p vs time in 2.5 mM Zn^{2+} aqueous solution for Gd_x**L** (squares), $[Gd(DT4AP^{Ph})(H_2O)]^{2-}$ (triangles) and $[Gd(DTPA)(H_2O)]^{2-}$ (circles). The lines are only guides for the eye.

carboxylates. Therefore, this metal ion is able to replace a significant amount of Gd^{3+}, which may result in the release of the toxic Gd(III) aqua ion in the body (*42*). To investigate the kinetic stability of the macromolecular phosphorus containing complex, we performed a relaxometric study of its transmetalation with $ZnCl_2$. The mixture of Gd_x**L** and an equal amount of $ZnCl_2$ in phosphate buffer was monitored at 20 MHz and 310 K by measuring the proton longitudinal relaxation rate. Upon transmetalation of a paramagnetic Gd^{3+} ion by a diamagnetic Zn^{2+} ion in phosphate buffer, the released Gd^{3+} precipitates as $GdPO_4$ and does not contribute to the relaxivity anymore. Therefore, the overall relaxivity of the solution decreases upon time with a rate depending on the rate of transmetalation. This decrease in relaxivity is a good estimation of the kinetic stability of the Gd(III) complex. The result of this experiment is depicted in Figure 4, together with the curves previously measured for $[Gd(DT4AP^{Ph})(H_2O)]^{2-}$ and for $[Gd(DTPA)(H_2O)]^{2-}$ (*6*,*11*). The kinetic stability appears to decrease in the order: $[Gd(DTPA)(H_2O)]^{2-}$ > Gd_x**L** ≫ $[Gd(DT4AP^{Ph})(H_2O)]^{2-}$. The novel macromolecular complex is, therefore, comparable in terms of kinetic stability with $[Gd(DTPA)(H_2O)]^{2-}$, which is being used clinically as an MRI contrast agent.

CONCLUSIONS

Replacement of the central pendant arm of the ligand in $[Gd(DTPA)(H_2O)]^{2-}$ by a phosphinic functional group has a positive influence on the residence water lifetime, τ_M, which is much closer to the optimal value for high relaxivity than that of the currently used contrast agents. The presence of two second coordination-sphere water molecules results in an increase of the relaxivity. Upon conjugation of these complexes to the oligosaccharide inulin, these parameters do not change much, and therefore in these conjugates, the increase in relaxivity thanks to the increase of the rotational correlation time, τ_R, is almost optimal. Only at temperatures below 288 K is the relaxivity limited by τ_M. The rotational correlation time is somewhat lower than expected on the basis of the molecular weight, which can be ascribed to local mobility, probably due to the flexibility of the tether. Further improvements may be achieved by more rigid linking groups and/or by decreasing of the local mobility through an increase of the degree of substitution of the inulin (*22*). The stability of the Gd(III) complex toward transmetalation with Zn^{2+} is comparable with that of $[Gd(DTPA)(H_2O)]^{2-}$.

ACKNOWLEDGMENT

This work was performed within the framework of the EU COST action D18: "Lanthanide chemistry for diagnosis and therapy". Thanks are due to the EU for financial support via a Marie Curie training site host fellowship (QLK5-CT-2000-60062) and to Grant Agency of the Czech Republic (203/02/0493 and 203/03/0168). J.K. thanks to the Grant Agency of Charles University (250/2003/B-Ch). We are very grateful to Dr. S. Laurent (University of Mons-Hainaut, Belgium) for measuring the mass spectra.

Supporting Information Available: ESI-mass spectrum of Gd_x**L**. Tables with reduced variables from ^{17}O NMR measurements and with the NMRD data in Gd_x**L**. Description of the equation used in the simultaneos fitting of the ^{17}O NMR and NMRD data. This material is available free of charge via the Internet at http://pubs.acs.org/BC.

LITERATURE CITED

(1) Caravan, P., Ellison, J. J., McMurry, T. J., and Lauffer, R. B. (1999) Gadolinium(III) chelates as MRI contrast agents: structure, dynamics, and applications. *Chem. Rev. 99*, 2293−2352.

(2) Merbach, A. E., and Tóth, É. (Eds.) (2001) *The Chemistry of Contrast Agents in Medical Magnetic Resonance Imaging*, Wiley, Chichester, England.

(3) Lauffer, R. B. (1987) Paramagnetic metal complexes as water proton relaxation agents for NMR imaging − theory and design. *Chem. Rev. 87*, 901−927.

(4) Aime, S., Botta, M., Fasano, M., and Terreno, E. (1998) Lanthanide(III) chelates for NMR biomedical applications. *Chem. Soc. Rev. 27*, 19−29.

(5) André, J. P., Tóth, É., Fischer, H., Seelig, A., Mäcke, H. R., and Merbach, A. E. (1999) High relaxivity for monomeric Gd-(DOTA)-based MRI contrast agents, thanks to micellar self-organization. *Chem. Eur. J. 5*, 2977−2983.

(6) Powell, D. H., Dhubhghaill, O. M. N., Pubanz, D., Helm, L., Lebedev, Y. S., Schlaepfer, W., and Merbach, A. E. (1996) Structural and dynamic parameters obtained from O-17 NMR, EPR, and NMRD studies of monomeric and dimeric Gd^{3+} complexes of interest in magnetic resonance imaging: an integrated and theoretically self-consistent approach. *J. Am. Chem. Soc. 118*, 9333−9346.

(7) André, J. P., Mäcke, H. R., Tóth, É., and Merbach, A. E. (1999) Synthesis and physicochemical characterization of a novel precursor for covalently bound macromolecular MRI contrast agents. *J. Biol. Inorg. Chem. 4*, 341−347.

(8) Aime, S., Botta, M., Geninatti Crich, S., Giovenzana, G. B., Pagliarin, R., Piccinini, M., Sisti, M., and Terreno, E. (1997) Towards MRI contrast agents of improved efficacy. NMR relaxometric investigations of the binding interaction to HSA of a novel heptadentate macrocyclic triphosphonate Gd(III)-complex. *J. Biol. Inorg. Chem. 2*, 470−479.

(9) Aime, S., Botta, M., Geninatti Crich, S., Giovenzana, G., Pagliarin, R., Sisti, M., and Terreno, E. (1998) NMR relaxometric studies of Gd(III) complexes with heptadentate macrocyclic ligands. *Magn. Reson. Chem. 36*, S200−S208.

(10) Aime, S., Botta, M., Frullano, L., Geninatti Crich, S., Giovenzana, G., Pagliarin, R., Palmisano, G., Sirtori, F. R., and Sisti, M. (2000) $[GdPCP2A(H_2O)_2]^{(-)}$: A paramagnetic contrast agent designed for improved applications in magnetic resonance imaging. *J. Med. Chem. 43*, 4017−4024.

(11) Kotek, J., Lebdušková, P., Hermann, P., Vander Elst, L., Muller, R. N., Geraldes, C. F. G. C., Maschmeyer, T., Lukeš, I., and Peters J. A. (2003) Lanthanide(III) complexes of novel mixed carboxylic-phosphorus acid derivatives of diethylenetriamine. A step towards more efficient MRI contrast agents. *Chem. Eur. J. 9*, 5899−5915.

(12) Laus, S., Ruloff, R., Tóth, É., and Merbach, A. E. (2003) Gd(III) complexes with fast water exchange and high thermodynamic stability: potential building block for high-relaxivity MRI contrast agents. *Chem. Eur. J. 9*, 3555−3566.
(13) Rudovsky, J., Kotek, J., Hermann, P., Lukes, I, Mainero, V., and Aime, S. (2004) Gadolinium(III) complex of a monophosphonic DOTA analogue ligand endowed with an optimal water exchange rate for MRI applications. *Chem. Commun.*, submitted.
(14) Ng, C. Y., Motekaitis, R. J., and Martell, A. E. (1979) New multidentate ligands. 18. Synthesis of 1,4-bis(bis(2-aminoethyl)aminomethyl)benzene: binuclear chelating tendencies and mixed-ligand binuclear chelate formation. *Inorg. Chem. 18*, 2982−2986.
(15) Verraest, D. L., da Silva, L. P., Peters, J. A., and van Bekkum, H. (1996) Synthesis of cyanoethyl inulin, aminopropyl inulin and carboxyethyl inulin. *Starch-Stärke 48*, 191−195.
(16) Verraest, D. L., Zitha-Bovens, E., Peters, J. A., and van Bekkum, H. (1998) Preparation of O-(aminopropyl)inulin. *Carbohydr. Res. 310*, 109−115.
(17) Corsi, D. M., Platas-Iglesias, C., van Bekkum, H., and Peters, J. A. (2001) Determination of paramagnetic lanthanide(III) concentrations from bulk magnetic susceptibility shifts in NMR spectra. *Magn. Reson. Chem. 39*, 723−726.
(18) Zitha-Bovens, E., Vander Elst, L., Muller, R. N., van Bekkum, H., and Peters, J. A. (2001) Relaxivity studies on a gadolinium(III) complex of a macrocyclic DTPA derivative. *Eur. J. Inorg. Chem*. 3101−3105.
(19) Vold, R. L., Waugh, J. S., Klein, M. P., and Phelps, D. E. (1968) Measurement of spin relaxation in complex systems. *J. Chem. Phys. 48*, 3831−3832.
(20) Meiboom, S., and Gill, D. (1958) Modified spin−echo method for measuring nuclear relaxation times. *Rev. Sci. Instrum. 29*, 688−691.
(21) Vander Elst, L., Maton, F., Laurent, S., Seghi, F., Chapelle, F., and Muller, R. N. (1997) A multinuclear MR study of Gd-EOB-DTPA: comprehensive preclinical characterization of an organ specific MRI contrast agent. *Magn. Reson. Med. 38*, 604−614.
(22) Corsi, D. M., Vander Elst, L., Muller, R. N., van Bekkum, H., and Peters, J. A. (2001) Inulin as a carrier for contrast agents in magnetic resonance imaging. *Chem. Eur. J. 7*, 64−71.
(23) Laurent, S., Vander Elst, L., Copoix, F., and Muller, R. N. (2001) Stability of MRI paramagnetic contrast media: a proton relaxometric protocol for transmetalation assessment. *Invest. Radiol. 36*, 115−122.
(24) Hewit, D. G. (1979) Organophosphorus compounds. II. Ethyl phenylphosphinate. *Aust. J. Chem. 32*, 463−464.
(25) Tóth, É., van Uffelen, I., Helm, L., Merbach, A. E., Ladd, D., Briley-Saebo, K., and Kellar, K. E. (1998) Gadolinium-based linear polymer with temperature-independent proton relaxivities: a unique interplay between the water exchange and rotational contributions. *Magn. Reson. Chem. 36*, S125−S134.
(26) Tóth, É., Helm, L., Kellar, K. E., and Merbach, A. E. (1999) High-pressure NMR kinetics. 87. Gd(DTPA-bisamide)alkyl copolymers: a hint for the formation of MRI contrast agents with very high relaxivity. *Chem. Eur. J. 2*, 1202−1211.
(27) Tóth, É., Pubanz, D., Vauthey, S., Helm, L., and Merbach, A. E. (1996) High-pressure NMR kinetics. 72. The role of water exchange in attaining maximum relaxivities for dendrimeric MRI contrast agents. *Chem. Eur. J. 2*, 1607−1615.
(28) Armitage, F. E., Richardson, D. E., and Li, K. C. P. (1990) Polymeric contrast agents for magnetic resonance imaging: synthesis and characterization of gadolinium diethylenetriaminepentaacetic acid conjugated to polysaccharides. *Bioconjugate Chem*. 365−374.
(29) Hardcastle, K. I., Botta, M., Fasano, M., and Digilio, G. (2000) Experimental evidence for a second coordination sphere water molecule in the hydration structure of YbDTPA − insights for a re-assessment of the relaxivity data of GdDTPA. *Eur. J. Inorg. Chem*., 971−977.
(30) Freed, J. H. (1978) Dynamic effects of pair correlation functions on spin relaxation by translational diffusion in liquids. II. Finite jumps and independent T1 processes. *J. Chem. Phys. 68*, 4034−4037.
(31) Frullano, L., Rohovec, J., Peters, J. A., and Geraldes, C. F. G. C. (2002) Structures of MRI contrast agents in solution. *Top. Curr. Chem. 221*, 25−60.
(32) Dunand, F. A., Borel, A., and Merbach, A. E. (2002) How does internal motion influence the relaxation of the water protons in Ln^{III}DOTA-like complexes? *J. Am. Chem. Soc. 124*, 710−716.
(33) Hindman, J. C. (1974) Relaxation processes in water: viscosity, self-diffusion, and spin−lattice relaxation. A kinetic model. *J. Chem. Phys. 60*, 4488−4496.
(34) Vander Elst, L., Laurent, S., and Muller, R. N. (1998) Multinuclear magnetic resonance characterization of paramagnetic contrast agents − the manifold effects of concentration and counterions. *Invest. Radiol. 33*, 828−834.
(35) Bertini, I., and Luchinat, C. (1996) NMR of paramagnetic substances. *Coord. Chem. Rev. 150*, 1−292.
(36) Botta, M. (2000) Second coordination sphere water molecules and relaxivity of gadolinium(III) complexes: implications for MRI contrast agents. *Eur. J. Inorg. Chem*. 399−407.
(37) Puttagunta, N. R., Gibby, W. A., and Puttagunta, V. L. (1996) Comparative transmetalation kinetics and thermodynamic stability of gadolinium-DTPA-bis-glucosamide and other magnetic resonance imaging contrast media. *Invest. Radiol. 31*, 619−624.
(38) Puttagunta, N. R., Gibby, W. A., and Puttagunta, V. L. (1996) Human in vivo comparative study of zinc and copper transmetalation after administration of magnetic resonance contrast agents. *Invest. Radiol. 31*, 739−742.
(39) Corot, C., Idee, J. M., Hentsch, A. M., Santus, R., Mallet, C., Goulas, V., Bonnemain, B., and Meyer, D. (1998) Structure−activity relationship of macrocyclic and linear gadolinium chelates: investigation of transmetalation effect on the zinc dependent metallopeptidase angiotensin-converting enzyme. *J. Magn. Reson. Imag. 8*, 695−702.
(40) Corot, C., Hentsch, A. M., and Curtelin, L. (1994) Interaction of gadolinium complexes with metal-dependent biological systems. *Invest Radiol. 29* (Suppl. 2), S164−S167.
(41) Cacheris, W. P., Quay, S. C., and Rocklage, S. M. (1990) The relationship between thermodynamics and the toxicity of gadolinium complexes. *Magn. Reson. Imag. 8*, 467−481.
(42) Tweedle, M. F., Hagan, J. J., Kumar, K., Mantha, S., and Chang, C. A. (1991) Reaction of gadolinium chelates with endogenously available ions. *Magn. Reson. Imaging 9*, 409−415.

BC049966G

Solid-Phase Synthesis of Multiantennary Oligonucleotide Glycoconjugates Utilizing On-Support Oximation

Johanna Katajisto,* Pasi Virta, and Harri Lönnberg

Department of Chemistry, University of Turku, FIN-20014 Turku, Finland. Received February 23, 2004; Revised Manuscript Received May 14, 2004

A novel method for preparation of multivalent oligonucleotide glycoconjugates on a solid support has been described. A pentaerythritol-based phosphoramidite (**1**) bearing two masked aminooxy groups has been used as the key building block. After conventional chain assembly, the aminooxy functions have been deblocked by a hydrazinium acetate treatment and subsequently oximated with fully acetylated 4-oxobutyl α-D-mannopyranoside. The conjugates obtained have been shown to withstand standard ammonolytic deprotection and cleavage from the support. Four different oligonucleotide glycoconjugates containing two, four, or six α-D-mannopyranosyl units (**12**−**15**) have been prepared to demonstrate the applicability of the procedure. The glycosyl residues only moderately retards hybridization of the oligonucleotide moiety.

INTRODUCTION

Multivalent carbohydrate−protein interactions play a crucial role in glycobiological recognition processes of both normal and malignant cells (*1*). The affinity of a single monosaccharide ligand to proteins (*2*−*6)* is usually low and, hence, a multipoint interaction with several covalently clustered sugar units is a prerequisite for efficient binding. These cluster effects have recently received considerable interest, since they offer a potential way to target drugs tissue- or cell-type specifically. The drug molecule may either be noncovalently complexed with a carbohydrate-based carrier or it may be covalently conjugated to an appropriate oligosaccharide construct designed to recognize a given cell-type. For these purposes, a variety of multiantennary glycoclusters *(7*−*15*) glycodendrimers (*16*−*18*), glycopeptides (*19*), cyclodextrin-based glycoclusters (*20, 21*), and glycopolymers (*22*−*25)* have been synthesized.

The glycocluster approach may also be expected to find applications in cell-specific targeting of antisense oligonucleotides, a novel class of chemotherapeutic agents that allow highly selective inhibition of gene expression (*26*). Enrichment of an oligonucleotide glycoconjugate or carbohydrate complex on the surface of a certain cell-type evidently leads to enhanced internalization of the conjugate by endocytosis. However, only few noncovalent carriers or covalent conjugates have been prepared. The examples available include electrostatic complexation of an oligonucleotide with glycosylated polylysine (*27*−*29),* chemical ligation to galactosylated polylysine (*30, 31*), a cholane scaffold (*32*), or a neoglycopeptide (*33*), on-support glycosylation with glycosyl trichloroacetimidates (*34*), and use of base moiety-glycosylated nucleoside phosphoramidites (*35*−*37*), and glycoside phosphoramidites (*38, 39*) as building blocks for the chain assembly. Recently, an elegant method for the solid-phase synthesis of oligonucleotide−glycocluster conjugates containing a tetraantennary construct at the 5′-terminus has been described (*40*). Building blocks derived from pentaerythritol has been used as branching units, and glycoside phosphoramidites for insertion of the 5′-terminal glycosyl groups. We now report on an alternative procedure for preparation of multivalent oligonucleotide glycoconjugates on a solid support. The key building block is a pentaerythritol-based phosphoramidite (**1**) that bears two masked aminooxy groups and additionally allows normal chain elongation (Chart 1). Accordingly, the distance between the site of attachment of the glycosyl groups may be tuned with additional nucleosidic or nonnucleosidic phosphoramidite building blocks. After exposing the aminooxy functions by removal of the phthaloyl protections, the support-bound oligonucleotide is reacted with the desired fully acetylated glycoside bearing an anomeric aldehyde tether (**2**) (Chart 1). The final deprotection and cleavage from the support is achieved by conventional ammonolysis. Four different oligonucleotide glycoconjugates containing two, four or six α-D-mannopyranosyl units have been prepared to demonstrate the applicability of the procedure.

* To whom correspondence should be addressed. E-mail: jokrka@utu.fi.

EXPERIMENTAL SECTION

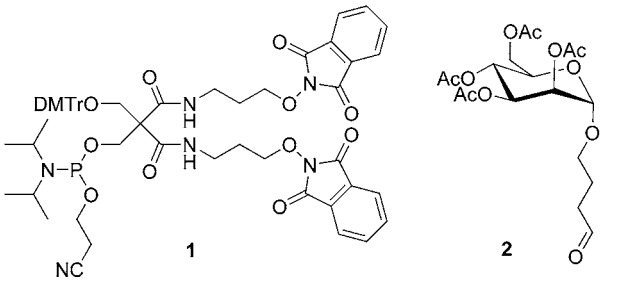
General Methods and Materials. The NMR spectra were recorded at 200, 400, or 500 MHz in deuteriochloroform. The chemical shifts are given in ppm from internal TMS and the coupling constants in hertz. The mass spectra were recorded by ESI ionization. For detailed information, see Supporting Information.

High-Performance Liquid Chromatography (HPLC). The oligonucleotide conjugates were analyzed and isolated on an analytical ThermoHypersil C-18 column (4.6 × 150 mm, 5 μm, a gradient elution from 0 to 100% B in 30 min, flow rate 1 mL min^{-1}, buffer A = 0.05 M NH_4Ac (aq), buffer B = buffer A in 65% MeCN) and finally desalted.

Diethyl 2-Methoxy-1,3-dioxane-5,5-dicarboxylate (4). A catalytic amount of *p*-toluenesulfonic acid monohydrate was added to a mixture of diethyl 2,2-bis-(hydroxymethyl)malonate (**2**, 10.0 g, 45.4 mmol) and trimethyl orthoformate (6.5 mL, 59.0 mmol) in dry THF (60 mL). The mixture was stirred overnight at room temperature and then slowly poured into magnetically

10.1021/bc049955n CCC: $27.50 © 2004 American Chemical Society
Published on Web 06/29/2004

Chart 1. The Synthesized Building Blocks 1 and 2



stirred ice-cold aqueous $NaHCO_3$ (100 mL of 5% aq soln). The mixture was extracted with diethyl ether, washed with brine, and dried with Na_2SO_4. The solvent was removed under reduced pressure, and the residue was chromatographed on a silica gel column eluting with DCM. Compound **4** was obtained as a colorless oil in 94% yield (11.2 g). ^{1}H NMR ($CDCl_3$, 200 MHz) δ 5.28 (s, 1H), 4.54 (d, 2H, J^2_{AB} = 10,5 Hz), 4.04−4.52 (m, 6H), 3.38 (s, 3H), 1.23−1.34 (m, 6H); ^{13}C NMR ($CDCl_3$, 50 MHz) δ 169.5, 167.4, 108.9, 62.8, 62.1, 52.8, 13.9; HRMS (ESI) $[M + Na]^+$ calcd 285.0945, obsd 285.0950.

***N,N*-Bis(3-hydroxypropyl)-2-methoxy-1,3-dioxane-5,5-dicarboxamide (5).** The mixture of compound **4** (7.00 g, 26.7 mmol) and 3-aminopropanol (160 mmol, 13.5 mL) was refluxed for 48 h. Compound **5** was isolated from the crude reaction mixture by silica gel chromatography (5% MeOH in DCM) in a 76% yield (6.5 g).^{1}H NMR ($CDCl_3$, 200 MHz) δ 5.29 (s, 1H), 4.50 (d, 2H, J^2_{AB} = 13.6 Hz), 4.18 (d, 2H, J^2_{AB} = 13.6 Hz), 3.61−3.73 (m, 4H), 3.38−3.55 (m, 7H), 1.73 (m, 4H); ^{13}C NMR ($CDCl_3$, 50 MHz) δ 169.6, 169.6, 109.8, 65.1, 59.6, 58.3, 53.2, 36.9, 18.3; HRMS (ESI) $[M + Na]^+$ calcd 343.1476, obsd 343.1469.

2,2-Bis(hydroxymethyl)-*N,N*-bis(3-phthalimidooxypropyl)malondiamide (6). Compound **5** (1.10 g, 3.43 mmol) was coevaporated twice with dry benzene. The residue, triphenylphosphine (1.98 g, 7.55 mmol), and *N*-hydroxyphthalimide (1.23 g, 7.55 mmol) were dissolved in dry THF (20 mL), and diethyl azodicarboxylate (DEAD) (1.17 mL, 7.55 mmol) was added dropwise. After stirring the reaction mixture overnight at room temperature, the consumption of **5** was complete according to TLC (5% MeOH in DCM). The solvent was removed under reduced pressure, and the residue was applied onto a silica gel column and eluted with a gradient from neat DCM to a 97:3 (v/v) mixture of DCM and *i*-PrOH. Purification of crude 2-methoxy-*N*,*N*-bis(3-phthalimidooxypropyl)-1,3-dioxane-5,5-dicarboxamide was seriously hampered by the presence of triphenylphosphine oxide formed during the reaction. The product still contaminated by some triphenylphosphine oxide exhibited ^{1}H NMR signals ($CDCl_3$, 200 MHz) at δ 7.45−7.84 (m, 8H), 5.27 (s, 1H), 4.56 (d, 2H, J^2_{AB} = 10.3 Hz), 4.20−4.31 (m, 6H), 3.58 (m, 4H), 3.36 (s, 3H), 2.01 (m, 4H), and ^{13}C NMR signals ($CDCl_3$, 100 MHz) at δ 169.4, 168.9, 163.7, 134.5, 132.0, 123.0, 109.7, 76.1, 64.9, 62.1, 53.1, 36.5, 27.5. The observed HRMS (ESI) $[M + Na]^+$ 633.1776 verified the identity of the compound (calcd 633.1803). To avoid further loss of the material by repeated purifications, the crude product was subjected to acid-catalyzed hydrolysis to remove the methoxymethylene protection. The crude sample was dissolved in 80% aqueous AcOH (20 mL) and left for 2 h at room temperature. The solution was evaporated to an oil and coevaporated with water. Purification by silica gel chromatography (0 to 5% MeOH in DCM) afforded **6** as a clear oil in a 15% yield (300 mg).^{1}H NMR ($CDCl_3$, 200 MHz) δ 7.72−7.91 (m, 8H), 4.26 (t, 4H, J = 5.7 Hz), 3.26 (q, 4H, J = 7.5 and 11.3 Hz), 2.01 (m, 4H); ^{13}C NMR ($CDCl_3$, 100 MHz) δ 169.5, 168.9, 163.6, 134.6, 131.8, 123.5, 65.0, 55.0, 36.4, 27.9; HRMS (ESI) $[M + H]^+$ calcd 569.1878, obsd 569.1896.

2-(4,4′-Dimethoxytrityloxymethyl)-2-(hydroxymethyl)-*N,N*-bis(3-phthalimidooxypropyl)malondiamide (7). Compound **6** (700 mg, 1.23 mmol) was dried by repeated coevaporations with dry pyridine and dissolved in dry pyridine (10 mL). 4,4′-Dimethoxytrityl chloride (417 mg, 1.23 mmol) was added, and the reaction mixture was left to stand overnight at room temperature. Pyridine was removed in vacuo, and the residue was subjected to DCM/aq 5% $NaHCO_3$ workup. The organic phase was dried with Na_2SO_4, and the oily residue was chromatographed on a silica gel (0 to 3% MeOH in DCM), giving **7** as a white solid foam in a 40% yield (440 mg). ^{1}H NMR ($CDCl_3$, 400 MHz) δ 7.78−7.83 (m, 4H), 7.71−7.76 (m, 4H), 7.66 (t, 2H, J^3 = 6.4 Hz), 7.11−7.38 (complex, 9H), 6.80 (m, 4H), 4.18 (m, 4H), 4.10 (d, 2H, J^3 = 6.4 Hz), 3.81 (t, 1H, J^3 = 6.4 Hz), 3.75 (s, 6H), 3.46−3.62 (m, 6H), 1.96 (m, 4H); ^{13}C NMR ($CDCl_3$, 100 MHz) δ 170.9, 163.5, 158.5, 144.3, 135.3, 134.5, 130.1, 128.9, 128.1, 127.9, 126.9, 123.6, 113.2, 86.5, 76.0, 65.1, 64,0, 58.7, 55.2, 36.4, 27.9; HRMS (ESI) $[M + Na]^+$ calcd 893.3004, obsd 893.3046.

2-Cyanoethyl 3-[(4,4′-Dimethoxytrityl)oxy]-2,2-bis[2-aza-1-oxo-5-(phthalimidooxy)pentyl]prop-yl *N,N*-Diisopropylphosphoramidite (1). Compound **7** (220 mg, 0.25 mmol) was predried overnight in vacuo over P_2O_5. 2-Cyanoethyl *N*,*N*-diisopropylphosphonamidic chloride (62 μL, 0.28 mmol) was added to a solution of **7** and triethylamine (175 μL, 1.26 mmol) in dry MeCN (2 mL) under nitrogen. The reaction mixture was left to stand at room temperature. The reaction was completed in 45 min, according TLC analysis (60% ethyl acetate in hexane). The reaction mixture was applied onto a short dried silica gel column, and the pure compound was isolated eluting with a mixture of ethyl acetate, hexane, and triethylamine (60:39:1, v/v/v). Phosphoramidite **1** was obtained as a white solid foam in a 85% yield (230 mg). ^{1}H NMR ($CDCl_3$, 200 MHz) δ 7.71−7.84 (m, 8H), 7.61 (t, 3H), 7.10−7.45 (complex, 9H), 6.80 (m, 4H), 4.03−4.45 (m, 4H), 3.69−3.78 (complex, 10H), 3.25−3.57 (m, 6H), 2.56 (t, 2H, J^2 = 7.2 Hz), 1.91−1.99 (m, 4H), 1.12 (t, 12H, J^2 = 7.2 Hz); ^{13}C NMR ($CDCl_3$, 50 MHz) δ 170.7, 163.3, 159.5, 144.1, 135.1, 134.3, 129.9, 128.7, 127.9, 127.7, 123.3, 113.1, 86.4, 75.9, 64.8, 64.5, 53.5, 59.4, 58.7, 58.3, 55.0, 43.0, 36.2, 27.9, 24.3, 18.7; ^{31}P NMR ($CDCl_3$, 200 MHz) δ 146.6; MS (ESI) $[M + Na]^+$ calcd 1093.4, obsd 1094.1.

4-Hydroxybutyl 2,3,4,6-tetra-*O*-acetyl-α-D-mannopyranoside (9). α-D-Mannopyranosyl pentaacetate (**8**) (5.00 g, 12.8 mmol) was dried by repeated coevaporations with dry benzene. The residue was dissolved in dry MeCN (30 mL) together with 1,4-butanediol (1.10 mL, 12.8 mmol). Boron trifluoride etherate (4.82 mL, 38.4 mmol) was added under nitrogen, and the reaction was allowed to proceed at room temperature for 2 h. DCM was added, and the mixture was washed with water, dried with Na_2SO_4, and evaporated to dryness. Purification of the crude product on a silica gel column (ethyl acetate in hexane, 2/1, v/v) gave **9** as colorless oil in a 19% yield (1.05 g). ^{1}H NMR ($CDCl_3$, 400 MHz) δ 5.33 (dd, 1H, J = 4.1 and 10.8 Hz), 5.29 (t, 1H, J = 10.8 Hz), 5.22 (dd, 1H, J = 4.3 and 1.6 Hz), 4.81 (d, 1H, J = 1.4 Hz), 4.28 (dd, 1H, J = 5.4 and 12.7 Hz), 4.10 (dd, 1H, J = 2.9 and 12.7 Hz), 3.58 (m, 1H), 3.73 (m, 1H), 3.68 (t, J = 5.4 Hz), 3.50 (m, 1H), 2,14, 2.10, 2.05 and 1.99 (each s, each 3H), 1.63−1.72 (m, 4H); ^{13}C NMR ($CDCl_3$, 100 MHz) δ

170.7, 170, 1, 169.9, 169.8, 97.6, 69.7, 69.1, 68.4, 68.3, 66.2, 62.5, 62.3, 29.4, 25.7, 20.7, 20.9, 20.8; MS (ESI) $[M + Na]^+$ calcd 443.1524, obsd 443.1516.

4-Oxobutyl 2,3,4,6-tetra-*O*-acetyl-α-D-mannopyranoside (2). DMSO (2.70 mL, 38.1 mmol) was added dropwise under vigorous stirring to a solution of oxalyl chloride (1.67 mL, 19.1 mmol) in dry DCM (5 mL) at −60 °C under argon. The mixture was stirred for 30 min at the same temperature, after which a solution of **9** (1.00 g, 2.38 mmol) in dry DCM (10 mL) was slowly added to the reaction mixture, and the stirring was continued for 40 min at −60 °C. Triethylamine was added (7.91 mL, 57.1 mmol), and the solution was allowed to warm to 0 °C. The mixture was poured into vigorously stirred ice−water, and the aqueous phase was extracted with diethyl ether. The combined organic phases were washed with ice-cold aq HCl (1 mol L^{-1}), water, saturated $NaHCO_3$ and brine, dried with Na_2SO_4, and evaporated in vacuo. The residue was purified by silica gel chromatography eluting with a mixture of ethyl acetate and hexane (2/1, v/v). Compound **2** was obtained as a clear oil in a 60% yield (595 mg). ^1H NMR ($CDCl_3$, 500 MHz) δ 9.82 (s, 1H), 5.12−5.31 (complex, 3H), 4.80 (s, 1H), 4.28 (dd, 1H, J = 5.6 and 12.9 Hz), 4.12 (m, 1H), 3.95 (m, 1H), 3.75 (m, 1H), 3.50 (m, 1H), 2.58 (m, 2H), 2.16, 2.11 and 2.05 (each s, each 3H), 1.77−2.00 (complex, 5H); ^{13}C NMR ($CDCl_3$, 125 MHz) δ 201.3, 170.6, 170.1, 169.9, 169.7, 97.5, 69.6, 68.9, 68.3, 67.9, 66.1, 62.4, 40.5, 22.3, 21.9, 20.9, 20.7, 20.4, 20.2; MS (ESI) $[M + Na]^+$ calcd 441.13673, obsd 441.13667.

Oligodeoxyribonucleotide Synthesis. The oligodeoxyribonucleotides were assembled on an Applied Biosystems 392 DNA synthesizer in 1.0 μmol scale using commercial 1000 Å CPG-succinyl-thymidine support and phosphoramidite chemistry. Phosphoramidite **1** was used as a 0.15 mol L^{-1} solution in dry MeCN, the coupling time being 600 s. After coupling of **1,** the detritylation was carried out by using two consecutive "#14 (acid solution) to column" steps (2 × 60 s) separated by a trityl flush step (5 s). Otherwise standard protocols were employed.

Synthesis of Oligonucleotide Glycoconjugates 12 and 13. Protected oligonucleotide sequences 5′-d(TTTXTTT)-3′ and 5′-d(TXTGACGATCTCAT)-3′, where X stands for the nonnucleosidic building block **1**, were synthesized as described above. The support-bound oligonucleotides were treated with 0.5 mol L^{-1} hydrazine acetate solution (0.124/4/1, $H_2NNH_2 \cdot H_2O$/pyridine/AcOH, v/v/v) for 30 min, washed with pyridine and acetonitrile, and dried. The supports were transferred to microcentrifuge tubes, a solution of the aldehyde tethered sugar ligand **2** (50 molar equiv in 200 μL of MeCN) was added, and the mixtures were shaken at ambient temperature for 4 h. The supports were filtered, washed with MeCN, dried, and treated with concentrated ammonia (33% aqueous NH_3, 7 h at 55 °C) to release and deprotect the resulting oligonucleotide glycoconjugates. Evaporation, dissolution in water, RP HPLC purification, desalting, and finally characterization by ESI-MS verified the formation of the expected conjugates **12** and **13** (Table 1).

Synthesis of Oligonucleotide Glycoconjugates 14 and 15. The conjugates **14** [sequence: 5′-d(TXTXTGACGATCTCAT)-3′] and **15** [sequence: 5′-d(TXTXTXTGACGATCTCAT)-3′] were prepared as described for **12** and **13** except for a prolonged reaction time of 16 h and larger excess of the sugar ligand (**2**) (100 or 150 molar equiv, respectively, in 200 μL of MeCN) used upon the oxymation step. The authenticity of **14** and **15** was verified by ESI-MS (Table 1).

Table 1. Properties of the Oligonucleotide Glycoconjugates

entry	oligonucleotide glycoconjugate	retention time (min)[a]	observed mass	calculated mass	purity, %[b]
1	12	13.7	2597.4	2597.9	84
2	13	15.9	4758,7	4759.3	68
3	14	15.8	5897.3	5898.4	54
4	15	16.4	7037.5	7037.3	45

[a] RP HPLC; for detailed chromatographic conditions, see Experimental Section. [b] Percentage of the conjugate in the crude reaction mixture on the basis of HPLC signal areas.

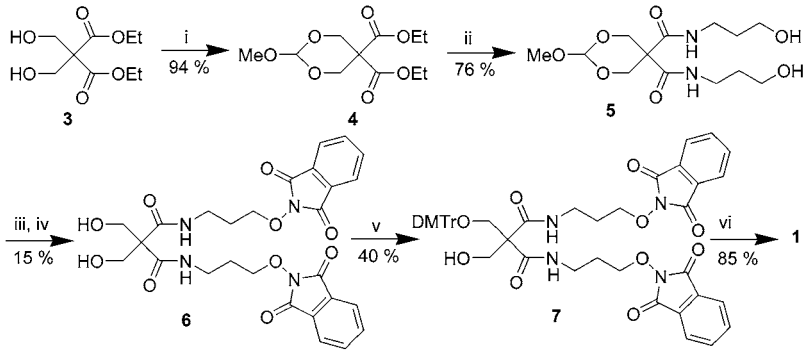
Melting Temperature Studies. The melting curves (absorbance versus temperature) were measured at 260 nm on a Perkin-Elmer Lambda 2 UV−vis spectrometer equipped with Peltier Temperature controller by using a rate of 1 °C min^{-1} (from 15 to 90 °C). The experiments were performed in 10 mmol L^{-1} potassium phosphate buffer (pH 7) containing 100 mmol L^{-1} NaCl. The concentration of the oligonucleotide conjugate and its complementary sequence was 2 μmol L^{-1}.

RESULTS AND DISCUSSION

An aminoxy group is known to be a powerful nucleophile, in particular when an attack on a carbonyl carbon is concerned. The oxime linkage formed is stable over a wide pH range, and the conjugation reaction can be conducted under physiological conditions. The oxime linkage has been efficiently used for the chemoselective conjugation of fully unprotected peptides (*41*−*43*) and carbohydrates (*44*) with oligonucleotides in solution. Thus, it is somewhat surprising that the aminoxy-functionalized oligonucleotides have not been extensively utilized in solid-supported conjugation. A 5′-terminal aminoxy group has been introduced as a 2-[(2-ureido)-4-(2-phthalimidooxyethoxy)quinoline]ethyl (*43*), 11-phthalimidoxy-3,6,9-trioxaundecyl (*45*), or *N*-trityl-6-aminooxyhexyl phosphoramidite (*46*). The phthaloyl protection has been removed with hydrazinium acetate in pyridine and the trityl protection with acid, i.e., under conditions that do not cleave the normal succinyl linker. Aldehydes react readily with the exposed aminoxy group, affording fully protected oxime conjugates that may be cleaved from the support by normal ammonolysis (*45*). The phthaloyl protection strategy has been applied in the present study to obtain glycoconjugates on a solid-support.

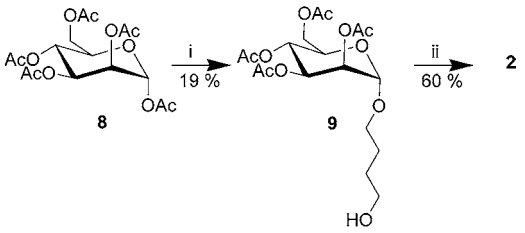
Synthesis of Phosphoramidite 1. Building block **1** was synthesized from commercially available diethyl 2,2-bis(hydroxymethyl)malonate (**3**), as outlined in Scheme 1. It has been shown previously (*47*) that compound **3** and its mono-4,4′-dimethoxytrityl (DMTr) derivative are decomposed by release of formaldehyde when treated with primary amines. Accordingly, **3** was converted to its di-*O*-methoxymethylene derivative (**4**) prior to aminolysis with 3-aminopropanol to obtain **5**. The free hydroxy functions of **5** were then subjected to a Mitsunobu reaction (*48*) using *N*-hydroxyphthalimide as a nucleophile and diethyl azodicarboxylate (DEAD) and triphenylphosphine as activators. After 24 h treatment, the starting material was entirely consumed and no side products were observed. Despite this, the purification of the desired di-*O*-phthalimido derivative turned out to be problematic. For this reason, the crude product was subjected to acid-catalyzed hydrolysis to remove the methoxymethylene protection. The resulting bis(hydroxymethyl) derivative (**6**) was then isolated by column chromatography, although in a relatively low 15% yield. One of the hydroxy groups of **6** was subsequently

Scheme 1 [a]



[a] Reagents and conditions: (i) $(MeO)_3CH$, *p*-TsOH, (ii) 3-aminopropanol, reflux, (iii) *N*-hydroxyphthalimide, PPh_3, DEAD, THF, (iv) 80% aqueous AcOH, (v) DMTrCl, pyridine, (vi) *2*-cyanoethyl *N,N*-diisopropylphosphonamidic chloride, NEt_3, dichloromethane.

Scheme 2 [a]



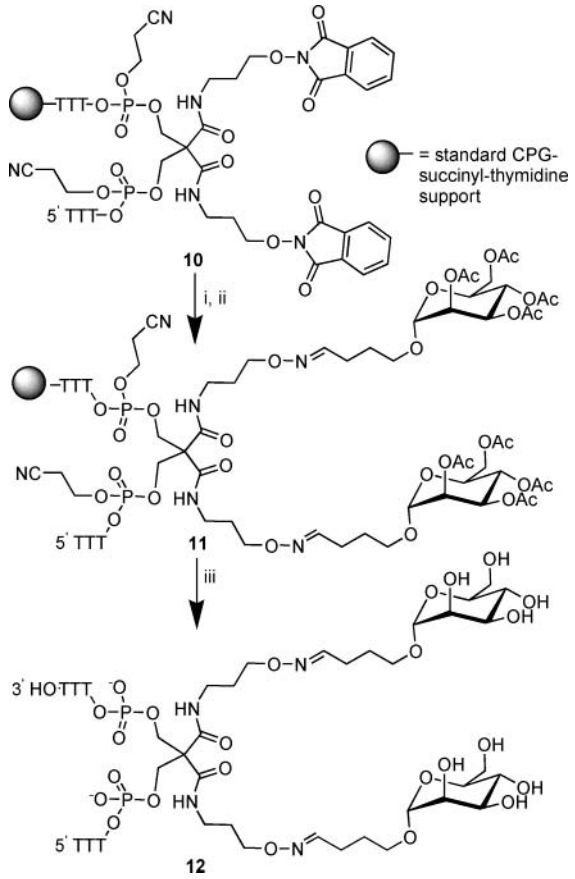
[a] Reagents and conditions: (i) 1,4-Butanediol, $BF_3{\cdot}Et_2O$, MeCN,(ii) oxalyl chloride, DMSO, NEt_3, dichloromethane.

protected as a DMTr ether (**7**). Standard phosphitylation of the remaining hydroxy function with 2-cyanoethyl *N,N*-diisopropylphosphonamidic chloride completed the synthesis of **1**.

Synthesis of the Mannosyl Ligand (2). Fully acetylated 4-oxobutyl α-D-mannopyranoside (**2**) was selected as the sugar ligand with which the solid-supported oximation was attempted. This compound was easily obtained via a two-step procedure (Scheme 2). Boron trifluoride etherate promoted glycosidation (*49*) of commercially available peracetylated α-D-mannopyranose (**8**) with 1,4-butanediol gave a 4-hydroxybutyl mannoside peracetate (**9**), which was then subjected to Swern oxidation (*50*) to obtain **2**. The synthesis was not optimized

Synthesis of the Oligonucleotide Glycoconjugates. To test the coupling efficiency of phosphoramidate **1** and the applicability of the developed protocol, a T_6 sequence containing an internally embedded **1** (**10**) was first assembled (Scheme 3). The standard phosporamidate protocol was applied, except that a prolonged coupling time (600 s) was used for the nonnucleosidic building block **1**. On the basis of the DMTr-cation assay (*51*), an acceptable 95% coupling efficiency was obtained. Next, the phthaloyl protections were removed by 30 min treatment with 0.5 mol L^{-1} hydrazinium acetate. The exposed aminoxy groups were then converted to stable oxime conjugates (**11**) by reacting them with the mannopyranosyl aldehyde building block (**2**). The conjugation reaction of the globally protected, hydrophobic species was performed in acetonitrile at room temperature. The reaction proceeded essentially to completion within 4 h to afford exclusively the support-bound oxime **11**. Standard ammonolytic treatment (33% aqueous NH_3, 7 h at 55 °C) released the crude oxime conjugate (**12**) in solution. No signs of hydrolysis or degradation products were observed consistent with previous results (*45*). RP HPLC analysis of the crude product showed the desired conjugate to be the main product (Table 1; entry 1, for the RP

Scheme 3 [a]



[a] Reagents and conditions: (i) Hydrazinium hydrate, pyridine, AcOH (0.124/4/1), (ii) **2** in MeCN, (iii) aqueous NH_3.

HPLC chromatogram of crude **12**, see the Supporting Information). After RP HPLC purification, conjugate **12** was characterized by ESI-MS (Table 1; entry 1), which definitely proved the identity of the product.

The applicability of the protocol developed for the construction of multivalent oligonucleotide glycoconjugates was demonstrated by preparing three heterosequences (**13**−**15**) containing one, two and three nonnucleosidic units (**1**), i.e., two, four and six mannopyranosyl units, respectively. Essentially the same procedure was applied for the synthesis, except for the larger excess of the aldehydic sugar ligand **2** and prolonged reaction times used in the oxyamination step upon the synthesis of the larger conjugates (**14**, **15**). In all cases, a thymidine residue was inserted between the nonnucleosidic branching units to avoid unnecessary crowding and, hence, to

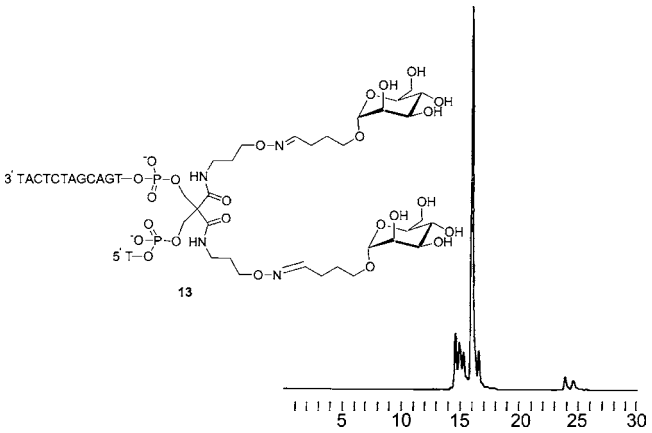


Figure 1. RP HPLC profile of crude **13** at 260 nm. For detailed chromatographic conditions, see Experimental Section.

ensure efficient coupling. RP HPLC analyses of the crude products showed that the expected conjugate was the main product in each case (Figures 1−3 and Table 1; entries 2−4). The authenticity of all products was verified by ESI-MS (Table 1; entries 2−4).

6-Aldehydo derivative of methyl α-D-mannopyranoside 2,3,4-tri-*O*-acetate was also prepared and used in the solid-supported oximation similarly to **2**. The oximation was successful, but upon the standard ammonolytic cleavage, the sugar ligand underwent dehydration to a 4,5-ene derivative, in all likehood because of conjugation of the 4,5- and 6,N-double bonds.

Melting Studies. Melting temperature (T_m) measurements showed that the oligonucleotide glycoconjugates obtained (**13**−**15**) form stable duplexes with complementary DNA oligonucleotides. Conjugates **13**−**15** were first hybridized with a complementary 12mer oligodeoxyribonucleotide in such a manner that the glycosylated 5′-terminus fell outside the duplex. The thermal stabilities of these duplexes were compared to that of a fully complementary 12mer duplex, which had a T_m value of 48.0 °C (Table 2; entry 1). Conjugate **13** showed es-

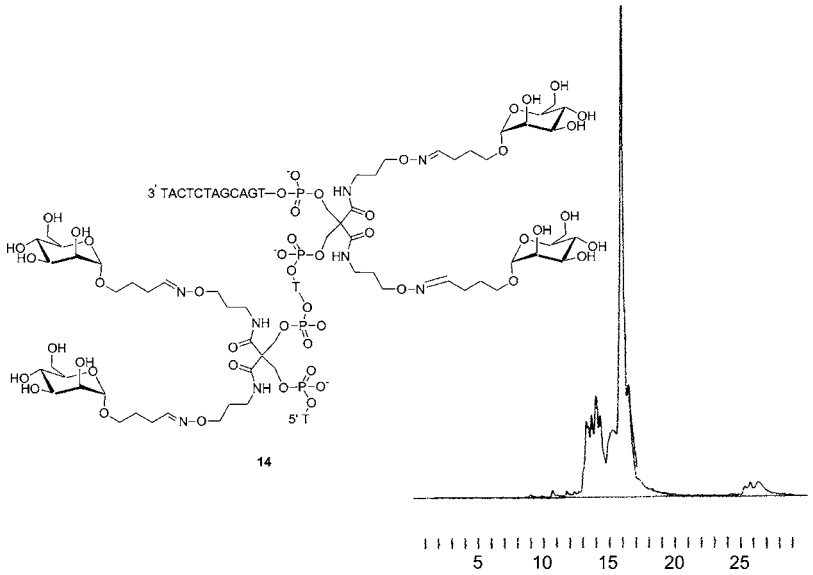


Figure 2. RP HPLC profile of crude **14** at 260 nm. For detailed chromatographic conditions, see Experimental Section.

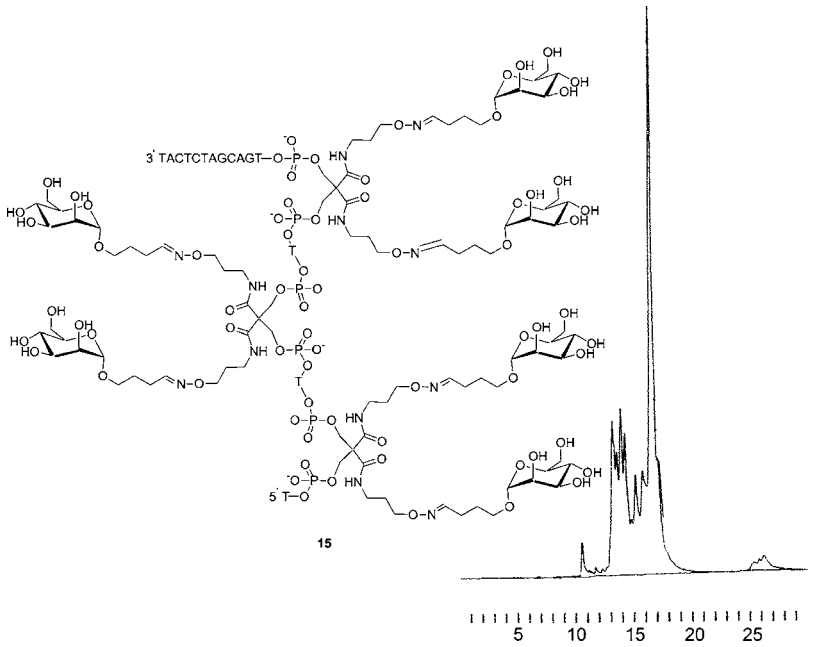


Figure 3. RP HPLC profile of crude **15** at 260 nm. For detailed chromatographic conditions, see Experimental Section.

Table 2. Melting Temperatures of the Duplexes Formed by Hybridization of the Oligonucleotide Conjugates with Complementary DNA Sequences[a]

		DNA d(ATGAGATCGTCA)	DNA d(ATGAGATCGTCAAAAAAA)
entry	oligonucleotide or conjugate	$T_m \pm 0.5$ °C	$T_m \pm 0.5$ °C
1	d(TACTCTAGCAGT)	48.0	-
2	**13**	47.5	44.8
3	**14**	44.9	41.9
4	**15**	45.0	41.3

[a] For detailed T_m measurement conditions, see Experimental Section.

sentially unaltered T_m (Table 2; entry 2), while the larger conjugates **14** and **15** slightly decrease the stability (Table 2; entries 3−4). No substantial difference was observed between **14** and **15** (T_m = 45 °C for each). Similar results were obtained when the conjugates were hybridized with a complementary 18mer DNA carrying a A_7 sequence at the 3′-terminus, i.e. opposite to the glycosylated part of **13**−**15**. A melting point of 45 °C was observed for the hybridization of **13** (Table 2; entry 2), and slightly lower melting points of 42 and 41 °C for the hybridization of **14** and **15**, respectively (Table 2; entries 3 and 4). Accordingly, the duplex structure was not significantly disrupted.

CONCLUDING REMARKS

A nonnucleosidic phosphoramidate building block has been prepared and used for solid-supported synthesis of oligonucleotide glycoconjugates containing up to six sugar ligands. As shown by the set of synthesized conjugates, the protocol developed allows the construction of high molecular weight, multivalent glycoconjugates in a site-specific manner. The methodology enables variation of the number, site, and identity of the sugar ligands and hence meets the requirements for the creation of conjugate libraries. The synthesized oxime conjugates are highly water soluble and stable at physiological pH and, hence, applicable to biological screening.

ACKNOWLEDGMENT

The authors wish to thank Dr. Petri Heinonen for performing ^{1}H and ^{13}C NMR analysis on Bruker 400 and 500 NMR spectrometers.

Supporting Information Available: Experimental details and spectral data for the compounds **1**, **2**, **4**−**7**, and **9**, and HPLC analytical data and ESI-MS spectra for the oligonucleotide glycoconjugates **12**−**15**. The material is available free of charge via the Internet at http://pubs.acs.org.

LITERATURE CITED

(1) Dwek, R. A. (1996) Glycobiology: Toward understanding the function of sugars. *Chem. Rev. 96*, 683−720.
(2) Lee, Y. C., and Lee, R. T. (1995) Carbohydrate-protein interactions: basis of glycobiology. *Acc. Chem. Res. 28*, 321 327.
(3) Mammen, M., Choi, S., and Whitesides, G. M. (1998) Polyvalent interactions in biological systems: implications for design and use of multivalent ligands and inhibitors. *Angew. Chem., Int. Ed. Engl. 37*, 2755−2794.
(4) Sharon, N., and Lis, H. (1989) Lectins as cell recognition molecules. *Science 246*, 227−234.
(5) Taylor, M. E., Bezouška, K., and Drickamer, K. (1992) Contribution to ligand binding by multiple carbohydrate-recognition domains in the macrophage mannose receptor. *J. Biol. Chem. 267*, 1719−1726.
(6) Dimick, S. M., Powell, S. C., McMahon, S. A., Moothoo, D. N., Naismith, J. H., and Toone, E. J. (1999) On the meaning of affinity: Cluster glycoside effects and concavalin A. *J. Am. Chem. Soc. 121*, 10286−10296.
(7) Sreedhara, A., and Cowan, J. A. (2001) Targeted site-spesific cleavage of HIV-1 viral Rev responsive element by copper aminoglycosides. *J. Biol. Inorg. Chem. 6*, *166−172.*
(8) Hanessian, S., Qiu, D., Prabhanjan, H., Reddy, G. V., and Lou, B. (1996) Synthesis of clustered D-GalNAc (Tn) and D-Galβ(1→3)GalNAc (T) antigenic motifs using a pentaerythritol scaffold. *Can. J. Chem. 74*, 1738−1747.
(9) Hansen, H. C., Haataja, S., Finne, J., and Magnusson, G. (1997) Di-, tri- amd tetravalent dendritic galabiosides that inhibit hemagglutination by *Streptococcus suis* at nanomolar concentration. *J. Am. Chem. Soc. 119*, 6974−6979.
(10) Hanessian, S., and Prabhanjan, H. (1994) design and synthesis of glycomimetic prototypes − A model sialyl Lewis^x ligand for E-selectin. *Synlett* 868−870.
(11) Lehmann, J., and Scheuring, M. (1995) mono-, di- and tetraantennary D-galactose ligands as competitive inhibitors and photoaffinity labels of the hexose transporting system in erythrocytes. A model for the irreversible blocking of receptors in cell membranes. *Carbohydr. Res. 276*, 57−74.
(12) Lehmann, J., and Weitzel, U. P. (1996) Synthesis and application of α-D-mannosyl clusters as photoaffinity ligands for mannose-binding proteins: Concavalin A as a model receptor. *Carbohydr. Res. 294*, 65−94.
(13) Veeneman, G. H., Van der Hulst, R. G. A., Van Boeckel, C. A. A., Philipsen, R. L. A., Ruigt, G. S. F., Tonnaer, J. A. D. M., Van Delft, T. M. L., and Konings, P. N. M. (1995) Synthesis of sialic acid-lipid conjugates and their neuritogenic effects on N1E.115 neuroblastoma cells. *Bioorg. Med. Chem. Lett. 5*, 9−14.
(14) Lindhorst, T. K., Dubber, M., Krallmann-Wenzel, U., and Ehlers, S. (2000) Cluster mannosides as inhibitors of type 1 fimbrae-mediated adhesion of Escherichia coli: Pentaerythritol derivatives as scaffolds. *Eur. J. Org. Chem*. 2027−2034.
(15) Liu, B., and Roy, R. (2001) Synthesis of clustered xenotransplantation antagonist using palladium-catalyzed cross-coupling of propynyl α-D-galactopyranoside. *J. Chem. Soc., Perkin Trans. 1. 8*, 773−779.
(16) Roy, R., Zanini, D., Meunier, S. J., and Romanowska, A. (1993) Solid-Phase synthesis of dendritic sialoside inhibitors of influenza A virus haemagglutin. *J. Chem. Soc., Chem. Commun*. 1869−1872.
(17) Pagé, D., Zanini, D., and Roy, R. (1996) Macromolecular recognition: Effect of multivalency in the inhibition of binding of yeast mannan to concavalin A and pea lectins by mannosylated dendrimers. *Bioorg. Med. Chem. 4*, 1949−1961.
(18) Ježek, J., Velek, J., Vepřek, P., Velková, V., Trnka, T., Pecka, J., Ledvina, M., Vondrášek, J., and Písačka M. (1999) Solid-phase synthesis of glycopeptide dendrimers with Tn antigenic stucture and their biological activities. Part I. *J. Pept. Sci. 5*, 46−55.
(19) Virta, P., Katajisto, J., Niittymäki, T., and Lönnberg, H. (2003) Solid-supported synthesis of oligomeric bioconjugates. *Tetrahedron 59*, 5137−5174.
(20) Fulton, D. A., and Stoddart, J. F. (2001) Synthesis of cyclodextrin-based carbohydrate cluster by photoaddition reactions. *J. Org. Chem. 66*, 8309−8319.
(21) André, S., Kaltner, H., Furuike, T., Nishimura, S., and Gabius, H. (2004) Persubstituted cyclodextrin-based glycoclusters as inhibitors of protein-carbohydrate recognition using purified plant and mammalian lectins and wild-type

and lectin-gene-transfected tumor cells as targets. *Bioconjugate Chem. 15*, 87−98.
(22) Manning, D. D., Strong, L. E., Hu, X., Beck, P. J., and Kiessling, L. L. (1997) Neoglycopolymers inhibitors of the selectins. *Tetrahedron 53*, 11937−11952.
(23) Mann, D. A., Kanai, M., Maly, D. J., and Kiessling. L. L. (1998) Probing low affinity and multivalent interactions with surface plasmon resonance: Ligands for Concavalin A. *J. Am. Chem. Soc. 120*, 10575−10582.
(24) Strong, L. E., and Kiessling, L. L. (1999) A general route to defined, biologically active multivalent arrays. *J. Am. Chem. Soc. 121*, 6193−6196.
(25) Owen, R. M., Gestwicki, J. E., Young, T., and Kiessling, L. L. (2002) Synthesis and applications of end-labeled neoglycopolymers *Org. Lett. 4*, 2293−2296.
(26) Wang, L., Prakash, R. K., Stein, C. A., Koehn, R. K., and Ruffner, D. E. (2003) Progress in the delivery of therapeutic oligonucleotides: organ/cellular distribution and targeted delivery of oligonucleotides in vivo. *Antisense Nucleic Acid Drug Dev. 13*, 169−189.
(27) Midoux, P., Mendes, C., Legrand, A., Raimond, J., Mayer, R., Monsigny, M., and Roche, A. C. (1993) Spesific gene transfer mediated by lactosylated poly-L-lysine into hepatoma cells. *Nucleic Acids Res. 21*, 871−878.
(28) Liang, W., Shi, X., Deshpande, D., Malanga, C. J., and Rojanasakul, Y. (1996) Oligonucleotide targeting to alveolar macrophages by mannose receptor-mediated endocytosis. *Biochim. Biophys. Acta 1279*, 227−234.
(29) Erbacher, P., Roche, A. C., Monsigny, M., and Midoux, P. (1997) The reduction of the positive charges of polylysine by partial gluconoylation increases the transfection efficiency of polylysine/DNA complexes. *Biochim. Biophys. Acta 1324*, 27−36.
(30) Bonfils, E., Depierreux, C., Midoux, P., Thuong, N. T., Monsigny, M., and Roche, A. C. (1992) Drug targeting: synthesis and endocytosis of oligonucleotide-neoglycoprotein conjugates. *Nucleic Acids Res. 20*, 4621−4629.
(31) Biessen, E. A. L., Vietsch, H., Rump, E. T., Fluiter, K., Kuiper, J., Bijsterbosch, M. K., and Van Berkel, T. J. C. (1999) Targeted delivery of oligodeoxynucleotides to parenchymal liver cells in vivo. *Biochem. J. 340*, 783−792.
(32) Maier, M. A., Yannopoulos, C. G., Mohamed, N., Roland, A., Fritz, H., Mohan, V., Just, G., and Manohara, M. (2003) Synthesis of antisense oligonucleotides conjugated to a multivalent carbohydrate cluster for cellular targeting. *Bioconjugate Chem. 14*, 18−29.
(33) Hangeland, J. J., Flesher, J. E., Deamond, S. F., Lee, Y. C., Ts'O, P. O. P., and Frost, J. J. (1997) Tissue distribution and metabolism of the [^{32}P]-labeled oligodeoxynucleoside methylphosphonate-neoglycopeptide conjugate, [YEE(ah-GalNAc)$_3$]-SMCC-AET-pU^{m}pT$_{7'}$ in the mouse. *Antisense Nucleic Acid Drug Dev. 7*, 141−149.
(34) Adinolfi, M., Barone, G., De Napoli, L., Guariniello, L., Iadonisi, A., and Piccialli, G. (1999) Solid-phase glycosidation of oligonucleotides. *Tetrahedron Lett. 40*, 2607−2610.
(35) Hunziker, J. (1999) Synthesis of 5-(2-amino-2-deoxy- -D-glucopyranosyloxymethyl)-2′-deoxyuridine and its incorporation into oligothymidylates. *Bioorg. Med. Chem. Lett. 9*, 201−204.
(36) Matsuura, K., Hibino, M., Yamada, Y., and Kobayashi, K. (2001) Construction of glyco-clusters by self-organization of site-specifically glycosylated oligonucleotides and their cooperative amplification of lectin-recognition. *J. Am. Chem. Soc. 123*, 357−358.
(37) De Kort, M., Ebrahimi, E., Wijsman, E. R., Van der Marel, G. A., and Van Boom, J. H. (1999) Synthesis of oligodeoxynucleotides containing 5-(β-D-glucopyranosyloxymethyl)-2′-deoxyuridine, a modified nucleoside in the DNA of *Trypanosoma Brucei. Eur. J. Chem.* 2337−2344.
(38) Akhtar, S., Routledge, A., and Patel, R. (1995) Synthesis of mono- and dimannoside phosphoramidate derivatives for the solid-phase conjugation to oligonucleotides. *Tetrahedron Lett. 36*, 7333−7336.
(39) Sheppard, T. L., Wong, C., and Joyce, G. F. (2000) Neoglycoconjugates: Design and synthesis of a new class of DNA-carbohydrate conjugates. *Angew. Chem., Int. Ed. 39*, 3660−3663.
(40) Dubber, M., and Fréchet, J. M. J. (2003) Solid-phase synthesis of multivalent glycoconjugates on a DNA synthesizer. *Bioconjugate Chem. 14*, 239−246.
(41) Forget, D., Boturyn, D., Defrancq, E., Lhomme, J., and Dumy, P. (2001) Highly efficient synthesis of peptide−oligonucleotide conjugates: chemoselective oxime and thioazolidine formation. *Chem. Eur. J. 7*, 3976−3984.
(42) Zatsepin, T. S., Stetsenko, D. A., Arzumanov, A. A., Romanova, E. A., Gait, M. J., and Oretskaya, T. S. (2002) Synthesis of peptide−oligonucleotide conjugates with single and multiple peptides attached to 2′-aldehydes through thioazolidine, oxime and hydrazine linkages. *Bioconjugate Chem. 13*, 822−830.
(43) Hamma, T., and Miller, P. S. (2003) 4-(2-Aminoxyethoxy)-2-(ethylureido)quinoline-oligonucleotide conjugates: Synthesis, binding interactions, and derivatization with peptides. *Bioconjugate Chem. 14*, 320−330.
(44) Forget, D., Renaudet, O., Defrancq, E., and Dumy, P. (2001) Efficient preparation of carbohydrate-oligonucleotide conjugates (COCs) using oxime bond formation. *Tetrahedron Lett. 42*, 7829−7832.
(45) Salo, H., Virta, P., Hakala, H., Prakash, T. P., Kawasaki, A. M., Manoharan, M., and Lönnberg, H. (1999) Aminoxy functionalized oligonucleotides: Preparation, on-support derivatization, and postsynthetic attachment to polymer support. *Bioconjugate Chem. 10*, 815−823.
(46) Defrancq, E., and Lhomme, J. (2001) Use of an aminoxy linker for the functionalization of oligodeoxyribonucleotides. *Bioorg. Med. Chem. Lett. 11*, 931−933.
(47) Guzaev, A., Salo, H., Azhayev, A., and Lönnberg, H. (1996) Novel nonnucleosidic building blocks for the preparation of multilabeled oligonucleotides. *Bioconjugate Chem. 7*, 240−248.
(48) Mitsunobu, O. (1981) the use of diethyl azodicarboxylate and triphenylphosphine in synthesis and transformation of natural products. *Synthesis* 1−28.
(49) Salvador, L. A., Elofsson, M., and Kihlberg, J. (1995) Preparation of buiding blocks for glycopeptide synthesis by glycosylation of Fmoc amino acids having unprotected carboxyl groups. *Tetrahedron 51*, 5643−5656.
(50) Mancuso, A. J., Huang, S., and Swern, D. (1978) Oxidation of long-chain and related alcohols to carbonyls dy dimethyl sulfoxide "activated" by oxalyl chloride.
(51) Atkinson, T., and Smith, M. (1984) *Oligonucleotide Synthesis: A Practical Approach* (Gait, M. J., Ed.) p 48, IRL Press, Oxford, U.K.

BC049955N

Toxicity of Gold Nanoparticles Functionalized with Cationic and Anionic Side Chains

Catherine M. Goodman, Catherine D. McCusker, Tuna Yilmaz, and Vincent M. Rotello*

Department of Chemistry, University of Massachusetts, Amherst, Massachusetts 01003. Received March 2, 2004

The structure and properties of gold nanoparticles make them useful for a wide array of biological application. Toxicity, however, has been observed at high concentrations using these systems. MTT, hemolysis, and bacterial viability assays were used to explore differential toxicity among the cell types used, using 2 nm core particles. These studies show that cationic particles are moderately toxic, whereas anionic particles are quite nontoxic. Concentration-dependent lysis mediated by initial electrostatic binding was observed in dye release studies using lipid vesicles, providing the probable mechanism for observed toxicity with the cationic MMPCs.

The development of alternate drug delivery agents and drug scaffolds is an ongoing task in medicinal chemistry (*1*−*3*). The recent burst of research involving gold nanoparticles as transfection vectors (*4*−*6*), DNA-binding agents (*7*−*9*), protein inhibitors (*10*), and spectroscopic markers (*11*−*14*) demonstrates the versatility of these systems in biological applications. Gold particles display several features that make them well suited for biomedical applications, including straightforward synthesis (*7*), stability (*15*), and the facile ability to incorporate secondary tags such as peptides targeted to specific cell types to afford selectivity (*16*−*18*). These nanoparticle systems, however, have not been well evaluated to determine their interactions with cells beyond the designated functions.

Recently, we have shown that cationically functionalized mixed monolayer protected gold clusters (MMPCs) are capable of mediating DNA translocation across the cell membrane in mammalian cells at levels much higher than polyethyleneimine (PEI), a widely used transfection vector (*4*). At higher nanoparticle concentrations, however, transfection efficiency decreases due to cytotoxicity. While many available drugs display toxicity at sufficiently elevated concentrations (*19*−*20*), the toxicity of the nanoparticles was observed in this case at concentrations only 2-fold in excess of that found to have maximal transfection activity.

To provide insight into the origins of toxicity in MMPC systems, we fabricated cationic nanoparticle **1** and anionic particle **2**. (Figure 1). The quaternary ammonium-functionalized nanoparticle (MMPC **1**) is composed of the same monolayer components as those demonstrated to cause cytotoxicity in the mammalian cell cultures (*4*). The carboxylate-substituted nanoparticle (MMPC **2**) does not bind DNA (*7*) and was therefore not tested in the previous report. The negative substituents on the surface of MMPC **2** are not anticipated to interact with the cell membrane, given the overall negative charge of the lipid bilayer (*24*). The structure of the gold core and alkane thiol components, however, is identical to that of MMPC **1** and so should provide information relevant to the toxicity due to the particle structure and charge.

We utilized cells Cos-1 cells, red blood cells, and bacterial cultures (*Escherichia coli*) to probe the effect of the nanoparticles on cell viability. Further insight into the origin of toxicity was obtained using dye release studies using lipid vesicles. Dye release from these vesicles has been strongly correlated with the ability of amphiphilic polymers to lyse bacterial cells (*25*), providing an indication of whether membrane disruption is a significant factor in the mechanism of toxicity. Taken together, these studies provide insight into the origins of the toxicity observed, allowing design of new particles with an improved toxicity profile.

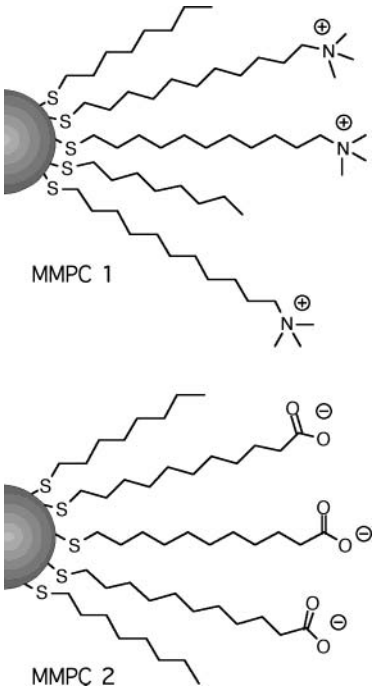


Figure 1. Schematic of the structures of MMPCs **1** and **2**. Each monolayer consists of approximately 70 charged thiols and 30 unsubstituted thiols.

MATERIALS AND METHODS

Colorimetric (MTT) kit for cell survival and proliferation was purchased from Chemicon International. Dulbecco's Modified Eagle Medium, L-glutamine, fetal bovine serum, trypsin, Trypan Blue stain (0.4%), and gentamicin

* To whom correspondence should be addressed. E-mail: rotello@chem.umass.edu.

10.1021/bc049951i CCC: $27.50 © 2004 American Chemical Society
Published on Web 06/05/2004

were purchased from Gibco. Tissue culture plates were purchased from Costar. Cos-1 cells purchased from ATCC. Acetic acid, ampicillin sodium salt, and sodium phosphate were purchased from EM. LB broth (Miller) and bacto-agar were purchased from DIFCO. Calcein, rhodamine 6G, 11-mercaptoundecanoic acid, and Triton X-100 were purchased from Sigma-Aldrich. Sodium chloride was purchased from Mallinckrodt. L-α-Stearoyl-oleoyl-phosphotidylcholine (SOPC) and L-α-stearoyl-oleoyl-phosphotidylserine (SOPS) were purchased from Avanti Polar Lipids, Inc. (Alabaster, AL). Ampicillin was dissolved in double distilled H_2O to yield stock solutions of 50 mg/mL, and aliquots were stored at −20 °C. All other materials were used as received. Gold nanoparticles were fabricated as previously described (*7*).

Cos-1 Viability Assay. Cos-1 cells were split to approximately 80% confluency in a 96-well culture plate the day preceding the assay. Cells were incubated at 37 °C in 7.5% CO_2 for 1, 2.5, 6, or 24 h with either MMPC **1** or **2** at 0.38, 0.75, 1.5, or 3 μM. Positive controls contained no nanoparticles. Following incubation periods, the media and nanoparticles were aspirated from the wells, cells were washed 2× with PBS, and fresh media was added. Following the MTT kit protocol, viability was measured by enzymatic reduction of the yellow tetrazolium MTT to a purple formazan, as measured using an EL808IU microplate reader (Biotek Instruments, Inc.) for absorbance readings (*26*). Mortality studies using Trypan Blue staining were performed using a modified procedure from the described above. In this case, the fresh media to harvest the cells was replaced by 20 μL of trypsin (0.25%), and 20 μL of Trypan Blue was added 5 min before counting cells on a hemocytometer.

Top Agar Assays. This procedure was adapted from a bacteriophage λ assay (*27*). BL21 (dE3) *E. coli* cells, transformed with a Pet16b vector encoding for ampicillin resistance and cellular retinoic acid binding protein I (*28*), were grown for 4−20 h in LB media with 0.1 mg/mL ampicillin. The OD of the cells at 600 nm was then measured and the relative concentration diluted to 0.5×10^{-4} absorbance using LB media or double distilled H_2O. A volume of 20 μL of the resultant cell solution was diluted with 0.55 mL of a LB-agar mix (25 g/L LB, 7.5 g/L agar) and 1−20 μL 833 μM MMPC solution and poured onto 3.5 cm LB-agar plates (25 g/L LB, 15 g/L agar, 0.1 mg/mL ampicillin). The plates were incubated overnight at 37 °C, and all resultant colonies were counted. The growth of the treated cells is reported relative to control plates.

Hemolysis Assay. This method was modified from a published procedure (29). In the studies, 40 μL of red blood cells from a healthy human donor were diluted with 10 mL of 10 mM Tris 150 mM NaCl buffer (pH 7) filtered with a 0.2 μm Acrodisc syringe filter (Pall Corporation, Ann Arbor, MI). The cell solution was centrifuged at 3000 rpm for 5 min, and the supernatant was poured off. Cells were washed until supernatant was clear, and the packed cells were resuspended in a final volume of 10 mL of Tris buffer. A volume of 80 μL of the resultant solution was incubated with 20 μL of MMPC solution (stocks ranging from 0.27 to 833 μM) with shaking for 30 min at 37 °C in a 96-well plate. Sample solutions were then diluted as necessary to allow quantification on an EL808IU microplate reader (Biotek Instruments, Inc.) at 405 nm with 5 s shaking prior to reading the sample. Nanoparticle absorbance was subtracted out according to the absorbance of the nanoparticles in buffer, and the resultant intensity due to detection of heme in solution was used to determine LC_{50} values.

Table 1. LC_{50} Values of MMPC 1 and 2 in Mammalian Cells and *E. coli*

	MMPC **1**, μM	MMPC **2**, μM
Cos-1	1.0 ± 0.5[a]	>7.37[b]
red blood cells	1.1 ± 0.1	72 ± 18
E. coli	3.1 ± 0.6	>28[c]

[a] LC_{50} value for MMPC **1** observed after 1 h of nanoparticle incubation. [b] Cells were 100% viable after 24 h of incubation with MMPC **2**. Higher concentrations of nanoparticles could not be completely washed from wells, and interfered with absorbance readings. [c] Higher concentrations could not be tested due to decreasing visibility of the colonies on the nanoparticle-doped agar.

Vesicle Leakage Assay. This assay was adapted from a previous report (*25*). Vesicles were prepared by evaporating the solvent from SOPC (0.55 mL 25 mg/mL solution in $CHCl_3$) or a mixture of SOPC/SOPS (0.5 mL 25 mg/mL:0.15 mL 10 mg/mL solution in $CHCl_3$, resulting in an 8.5:1 mole ratio) with a stream of N_2 (g). The dried lipids were resolubilized in 40 mM sodium phosphate buffer containing 100 mM calcein (further adjusted to pH 7 using NaOH and HCl) or 6.42 mM rhodamine. Three freeze−thaw cycles were then performed using a dry ice/acetone bath. The vesicles were then either sonicated gently two times for 10 min each using a 150T aquasonic sonicator (VWR), followed by an additional freeze−thaw cycle, or extruded using a 1 μm polycarbonate membrane (Avanti Polar Lipids, Inc) (*30*, *31*). Free fluorophore was removed by elution through a Sephadex 25 column with 90 mM sodium chloride and 10 mM sodium phosphate buffer adjusted to pH 7 or 7.4. Samples were prepared by diluting 0.2 or 0.3 mL of the collected vesicles to 2 mL using the sodium chloride buffer. The baseline fluorescence was corrected according to calibration of the nanoparticles with the fluorophore only or with Triton-lysed vesicles to control for light absorption by the particles. Components were added as aliquots of 1−10 μL of 0.005−10 mg/mL solutions, and the increasing fluorescence from vesicle lysis was monitored for 300 s at 515 nm ($\lambda_{ex} = 490$ nm) for calcein solutions and 554 nm ($\lambda_{ex} = 524$ nm) for rhodamine. The emission slit width was 1.5 or 3 nm. Complete leakage was caused by the addition of 50 μL 0.2% Triton X-100 in DMSO; the fluorescence intensity measured as a result was fixed at 100% vesicle lysis.

RESULTS AND DISCUSSION

MMPCs **1** and **2** were tested for toxicity in red blood cells, Cos-1 cells, and bacteria (*E. coli*). LC_{50} values determined in each case are shown in Table 1. Toxicity profiles for the two mammalian cells are virtually indistinguishable, while a 2- to 3-fold increase is required as a lethal concentration for the bacterial cultures. This modest increase may be due to the nature of the bacterial assay: use of a low-density cross-linked agar matrix will decrease the mobility of both the cells and nanoparticles, potentially altering slightly the manner in which the two components interact. Alternatively, the difference observed may be due to the increased protection provided by the outer membrane and cell wall surrounding the Gram-negative *E. coli* (*24*), requiring a higher nanoparticle concentration to fully rupture the bacteria.

The small variation in LC_{50} values observed suggests that the mechanism of toxicity is similar for the three cell types. This implies that the nanoparticles interact with the cells in a passive process, as the receptors and other related molecules active in energy-dependent processes are likely to be different for the separate species.

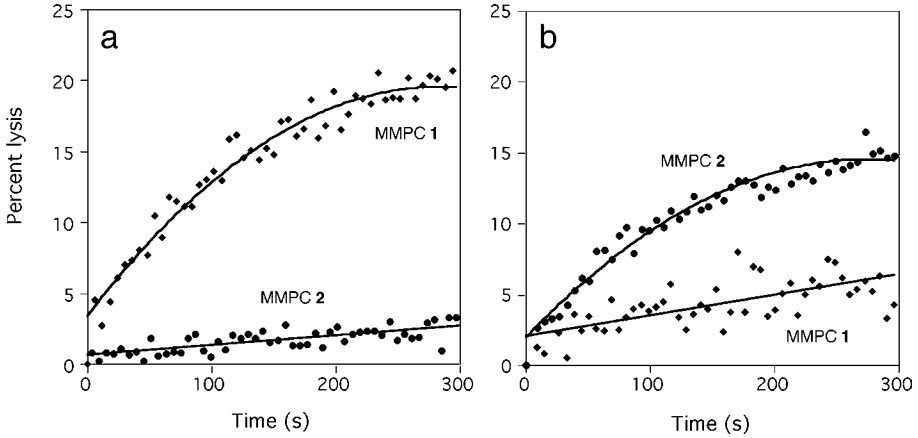


Figure 2. Comparison of MMPC **1** and **2** in disrupting vesicles with an overall negative (SOPC/SOPS; panel a) or neutral (SOPC only; panel b) charge. Nanoparticle concentration is 220 nM. Curves are meant to lead the eye.

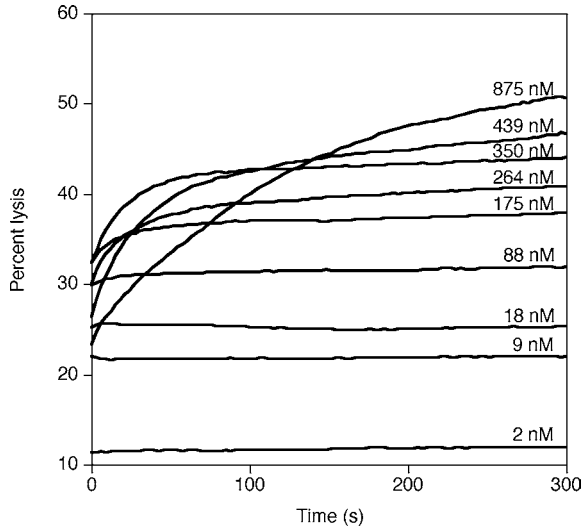


Figure 3. Concentration dependence of vesicle rupture by MMPC **1**. Higher concentrations could not be tested due to light absorption by the nanoparticles. Curves are meant to lead the eye.

Furthermore, the endocytic pathway is actively utilized by Cos-1 cells, but not erythrocytes, suggesting that toxicity is not caused by cellular uptake via endocytosis.[1] One mechanism anticipated to be similar in comparing the eukaryotic and prokaryotic samples is membrane adhesion or cell lysis by the nanoparticles. Certainly the specific lipids in the bilayer for each cell type are different in identity or percent composition, but all cell types feature an overall negative charge with both highly charged and amphiphilic substituents (*24*). MMPC **1** would be drawn to the negative membrane, whereas MMPC **2** would not be attracted as strongly. Once bound to the cell, the amphiphilicity of the mixed monolayer of MMPC **1** could induce a variety of further interactions.

To evaluate this potential mode of action, we performed a vesicle-disruption assay, in which a fluorescent dye is released from vesicles by molecules capable of interrupting the lipid bilayer. An increase in fluorescence in this assay is typically interpreted as an indication that a designed molecule may be antibacterial due to membrane leakage, as the bilayer is representative of the bacterial cell membrane (*25*). Two vesicle systems were examined, one composed of phosphotidylcholine (SOPC) and phosphotidylserine (SOPS) (net negative charge), and a second preparation of SOPC only (no net charge). MMPC **1** lysed the SOPC/SOPS vesicles more efficiently than MMPC **2** due to the electrostatic complementarity of the cationic substituents and the SOPS lipids (Figure 2a). In the case of the neutral SOPC vesicles, MMPC **2** showed higher levels of fluorophore release than MMPC **1**, although the intensity was less than that of MMPC **1** with the negatively charged vesicles (Figure 2b). This result demonstrates that the specific charge pairing of the nanoparticles and lipid bilayers mediates membrane interaction and lysis to release the fluorophore. This process is concentration dependent, as demonstrated by the increased lysis of the negative SOPC/SOPS vesicles observed with increasing concentrations of MMPC **1** (Figure 3). The reason for the decrease in lysis rate at higher MMPC concentrations is unclear and is currently under investigation.

In summary, we have demonstrated that the toxicity of the gold nanoparticles is related to their interactions with the cell membrane, a feature initially mediated by their strong electrostatic attraction to the negatively charged bilayer. We are currently designing nanoparticles with different properties to ameliorate the observed toxicity and will report our findings in due course.

[1] We cannot rule out the possibility of these more complex pathways of internalization when nanoparticles are in use as drug vectors.

ACKNOWLEDGMENT

We thank Joseph Simard for synthesis of the nanoparticles, Jennifer Habink for the generous donation of the *Escherichia coli* cell line, Renuka Sivendran for advice concerning the top-agar assay, Lachelle Arnt for assistance with the hemolysis assay, and Nandini Chari and Firat Ilker for assistance with the vesicle assay (Univeristy of Massachusetts). This research was funded by NIH (GM 62998) C.M.G. acknowledges NIH Chemistry-Biology Interface Training Grant GM 08515.

LITERATURE CITED

(1) Hruby, V. J. (2002) Designing peptide receptor agonists and antagonists. *Nat. Rev. Drug Discovery 1*, 847−858.

(2) Opalinska, J. B., and Gewirtz, A. M. (2002) Nucleic-acid therapeutics: basic principles and recent applications. *Nat. Rev. Drug Discovery 1*, 503−14.

(3) LaVan, D. A., Lynn, D. M., and Langer, R. (2002) Moving smaller in drug discovery and delivery. *Nat. Rev. Drug Discovery 1*, 77−84.

(4) Sandhu, K. K., McIntosh, C. M., Simard, J. M., Smith, S. W., and Rotello, V. M. (2002) Gold nanoparticle-mediated transfection of mammalian cells. *Bioconjugate Chem. 13*, 3−6.

(5) O'Brien, J., amd Lummis, S. C. (2002) An improved method of preparing microcarriers for biolistic transfection. *Brain Res. Protoc. 10*, 12−15.
(6) Muangmoonchai, R., Wong, S. C., Smirlis, D., Phillips, I. R., and Shephard, E. A. (2002) Transfection of liver in vivo by biolistic particle delivery: its use in the investigation of cytochrome P450 gene regulation. *Mol Biotechnol. 20*, 145−51.
(7) McIntosh, C. M., Esposito, E. A., Boal, A. K., Simard, J. M., Martin, C. T., and Rotello, V. R. (2001) Inhibition of DNA transcription using cationic mixed monolayer protected gold clusters. *J. Am. Chem. Soc. 123*, 7626−7629.
(8) Wang, G., Zhang, J., and Murray, R. W. (2002) DNA binding of an ethidium intercalator attached to a monolayer-protected gold cluster. *Anal. Chem. 74*, 4320−4327.
(9) Gearheart, L. A., Ploehn, H. J., and Murphy, C. J. (2001) Oligonucleotide adsorption to gold nanoparticles: A surface-enhanced Raman spectroscopy study of intrinsically bent DNA. *J. Phys. Chem. B 105*, 12609−12615.
(10) Fischer, N. O., McIntosh, C. M., Simard, J. M., and Rotello, V. M. (2002) Inhibition of chymotrypsin through surface binding using nanoparticle-based receptors. *Proc. Natl. Acad. Sci. 99*, 5018−5023.
(11) Park, S. J., Taton, T. A., and Mirkin, C. A. (2002) Array-based electrical detection of DNA with nanoparticle probes. *Science 295*, 1503−1506.
(12) Weizmann, Y., Patolsky, F., and Willner, I. (2001) Amplified detection of DNA and analysis of single base mismatches by the catalyzed deposition of gold on Au nanoparticles. *Analyst 126*, 1502−1504.
(13) Gole, A., Dash, C., Soman, C., Sainkar, S. R., Rao, M., and Sastry, M. (2001) On the preparation, characterization, and enzymatic activity of fungal protease-gold colloid bioconjugates. *Bioconjugate Chem. 12*, 684−690.
(14) Otsuka, H., Akiyama, Y., Nagasaki, Y., and Kataoka, K. (2001) Quantitative and reversible lectin-induced association of gold nanoparticles modified with alpha-lactosyl-omega-mercapto-poly(ethylene glycol). *J. Am. Chem. Soc. 123*, 8226−8230.
(15) Zheng, M., Davidson, F., and Huang, X. Y. (2003). Ethylene glycol monolayer protected nanoparticles for eliminating nonspecific binding with biological molecules. *J. Am. Chem. Soc. 125*, 7790−7791.
(16) Ogris, M., Carlisle, R. C., Bettinger, T., and Seymour, L. W. (2001) Melittin enables efficient vesicular escape and enhanced nuclear access of nonviral gene delivery vectors. *J. Biol. Chem. 276*, 47550−47555.
(17) Kullberg, E. B., Bergstrand, N., Carlsson, J., Edwards, K., Johnsson, M., Sjöberg, S., and Gedda, L. (2002) Development of EGF-conjugated liposomes for targeted delivery of boronated DNA-binding agents. *Bioconjugate Chem. 13*, 737−743.
(18) Leuschner, C., Enright, F. M., Melrose, P. A., and Hansel, W. (2001) Targeted destruction of androgen-sensitive and -insensitive prostate cancer cells and xenografts through luteinizing hormone receptors. *The Prostate 46*, 116−125.
(19) Georgieva, R., Tsevi, R., Kossev, K., Kusheva, R., Balgjiska, M., Petrova, R., Tenchova, V., Gitsov, I., and Troev, K. (2002) Immobilization of aminothiols on poly(oxyalkylene phosphates). Formation of poly(oxyethylene phosphates)/cysteamine complexes and their radioprotective efficiency. *J. Med. Chem. 45*, 5797−5801.
(20) Dietze, E. C., Schäfer, A., Omichinski, J. G., and Nelson, S. D. (1997) Inactivation of glyceraldehyde-3-phosphate dehydrogenase by a reactive metabolite of acetaminophen and mass spectral characterization of an arylated active site peptide. *Chem. Res. Toxicol. 10*, 1097−1103.
(21) García, M. T., Campos, E., Sánchez-Leal, J., and Ribosa, I. (1999) Effect of the alkyl chain length on the anaerobic biodegradability and toxicity of quaternary ammonium based surfactants. *Chemosphere 38*, 3473−3483.
(22) Versteeg, D. J., Stanton, D. T., Pence, M. A., and Cowan, C. (1997) Effects of surfactants on the rotifer, *Brachionus Calyciflorus*, in a chronic toxicity test and in the development of QSARS. *Environ. Tox. Chem. 16*, 1051−1058.
(23) García, M. T., Ribosa, I., Guindulain, T., Sánchez-Leal, J., and Vives-Rego, J. (2001) Fate and effect of monoalkyl quaternary ammonium surfactants in the aquatic environment. *Environ. Poll. 111*, 169−175.
(24) Voet, D., and Voet, J. G. (1995) *Biochemistry*, John Wiley and Sons, Inc., New York.
(25) Liu, D., and DeGrado, W. F. (2001) De novo design, synthesis, and characterization of antimicrobial β-peptides. *J. Am. Chem. Soc. 123*, 7553−7559.
(26) Wasserman, T. H., and Twentyman, P. (1988) Use of a colorimetric microtiter (MTT) assay in determining the radiosensitivity of cells from murine solid tumors. *Int. J. Radiat. Oncol. Biol. Phys. 3*, 699−702.
(27) Sambrook, J., Fritsch, E. F., and Maniatis, T. (1989) *Molecular cloning: A laboratory manual*, Cold Spring Harbor Laboratory Press, Cold Spring Harbor, NY.
(28) Clark, P. L., Weston, B. F., and Gierasch, L. M. (1998) Probing the folding pathway of a β-clam protein with single-tryptophan constructs. *Folding Des. 3*, 401−412.
(29) Porter, E. A., Weisblum, B., and Gellman, S. H. (2002). Mimicry of host-defense peptides by unnatural oligomers: Antimicrobial beta-peptides. *J. Am. Chem. Soc. 124*, 7324−7330.
(30) Oliger, P., Hebrant, M., Grison, C., Coutrot, P., and Tondre, C. (2001). Preparation and properties of vesicles formed from phospholipid analogues of *N*-(phosphonoacetyl)-L-aspartate (PALA) by sonication or extrusion: Transition temperature, particle size, glucose entrapment, and P-31 NMR. *Langmuir 17*, 6426−6432.
(31) Oliger, P., Schmutz, M., Hebrant, M., Grison, C., Coutrot, P., and Tondre, C. (2001). Vesicle-forming properties of new phospholipid analogues derived from *N*-phosphonoacetyl-L-aspartate (PALA): Particle features and morphology in relation with alkyl chain lengths. *Langmuir 17*, 3893−3897.

BC049951I

Transfection with Fluorinated Lipoplexes Based on New Fluorinated Cationic Lipids and in the Presence of a Bile Salt Surfactant

Caroline Boulanger, Christophe Di Giorgio, Jérôme Gaucheron, and Pierre Vierling*

Laboratoire de Chimie Bioorganique, UMR 6001 CNRS, Université de Nice Sophia-Antipolis, Faculté des Sciences, 06108 Nice Cédex 2, France. Received March 8, 2004; Revised Manuscript Received April 21, 2004

The synthesis of two fluorinated cationic lipids, which are analogues of frequently used synthetic gene carrier agents (including the cationic 2,3-dioleoyloxy-*N*-[2-(spermine-carboxamido)ethyl]-*N*,*N*-dimethyl-1-propanaminium (DOSPA) component of the commercially available liposomal Lipofectamine), and the disintegration and DNA accessibility (evaluated by the ethidium bromide (BET) intercalation assay) as well as the in vitro transfection efficacy of cationic lipoplexes formulated with these new lipids in conjunction with conventional or fluorinated helper lipids, in the absence or presence of sodium taurocholate (STC), a powerful anionic bile salt detergent, is reported. A higher stability, with respect to the STC lytic activity and DNA accessibility, of the fluorinated cationic lipoplexes as compared with their respective lipofectamine-based ones was demonstrated. Indeed, while the Lipofectamine lipoplexes were fully disintegrated at a [STC]/[lipid] molar ratio of 2000, only 40−60% of the DNA intercalation sites of the lipoplexes based on the fluorinated analogue of DOSPA were accessible to ethidium bromide. A higher transfection potential in the presence of STC was further found for the lipoplexes formulated with the fluorinated analogue of DOSPA as compared with the Lipofectamine preparation. For a STC concentration of 7.5 mM, lipofection mediated with these fluorinated lipoplexes was significantly higher (nearly 30- to 50-fold, $p < 0.05$) than with the Lipofectamine ones. These results confirm the remarkable transfection potential of fluorinated lipoplexes.

INTRODUCTION

Synthetic gene transfer systems based on (poly)cationic lipids, liposomes, or polymers (e.g. lipoplexes or polyplexes, respectively) have become very promising novel forms of molecular medicine (for recent reviews, see refs 1−8 and references therein). Although the gene expression levels obtained with these systems are transient and lower than with viral vectors, they present several advantages including low-cost and large-scale production, safety, and capacity to deliver large gene fragments. However, there is still a need for the development of gene transfer systems with improved and original properties. Progress in this field also requires systems which allow efficient gene expression in various biological fluids. In the field of gene transfer and gene therapy of cystic fibrosis and of cystic fibrosis-associated diseases for example, systems which enable efficient gene expression in the presence of various surfactants (pulmonary ones for the gene transfer to the respiratory epithelium, bile salts for the biliar epithelium) are required. Indeed, pulmonary surfactants constitute a barrier to transfection of the endobronchial airway (*9*). Such surfactants were also found to inhibit lipofection of various cell lines with cationic lipids (*9*−*12*).

In our laboratory, fluorinated cationic lipoplexes, i.e., lipoplexes resulting from the formulation of DNA with highly fluorinated cationic lipids (analogues of DOTMA, DMRIE, DPPES, and DOGS)[1] (*13*, *14*) and/or highly fluorinated helper lipids (analogues of DOPE) (*15*, *17*) (see structures in Figure 1), were shown to constitute very promising transfection systems. Such fluorinated cationic lipoplexes exhibited in vitro (*13*−*17*) and in vivo (*15*) a higher transfection potential than their conventional lipoplex counterparts and more particularly in the presence of a powerful anionic surfactant (*16*). Their remarkable transfection potency was attributed to the unique lipophobic and hydrophobic character of the fluorinated lipids used for their formulation, thus preventing DNA from interactions with lipophilic and hydrophilic biocompounds, and from degradation (*16*).

We report herein on the synthesis of F-DMAEA and F-DOSPA which are fluorinated analogues of frequently used synthetic gene carrier agents, i.e., GAP-DLRIE (*18*) and DOSPA (which is the cationic component of commercially available liposomal Lipofectamine) (*19*) (see structure in Figure 1), and on their ability to compact, transfer, and express DNA into cells in the absence or presence of a powerful anionic detergent (e.g. sodium taurocholate, STC, which is a model of bile salts). The

* Corresponding author. Phone: 33 4 92 07 61 43. Fax: 33 4 92 07 61 51. E-mail: vierling@unice.fr.

[1] Abbreviation: BET, ethidium bromide; CL, cationic lipid; DMRIE, 1,2-dimyristyloxypropyl-3-dimethylhydroxyethylammonium bromide; DPPES, 1,2-dipalmitoylphosphatidylethanolamidospermine-4 trifluoroacetate; DOGS, *N*,*N*-dioctadecylamidoglycylspermine; DOPE, 1,2-dioleoyl-sn-glycero-3-phosphoethanolamine; DOSPA, 2,3-dioleoyloxy-*N*-[2-(spermine-carboxamido)ethyl]-*N*,*N*-dimethyl-1-propanaminium trifluoroacetate; DOTMA, *N*-[1-(2,3-dioleoyloxy)propyl]-*N*,*N*,*N*-trimethylammonium chloride; F-PE: fluorinated analogue of DOPE.; GAP-DLRIE: *N*-(3-aminopropyl)-*N*,*N*-dimethyl-2,3-bis(dodecyloxy)-1-propanammonium bromide; HL: helper lipid; *N*/*P*, *N* = number of amine equivalents of the cationic lipid; *P* = number of DNA phosphate equivalents; STC, sodium taurocholate.

10.1021/bc049942+ CCC: $27.50 © 2004 American Chemical Society
Published on Web 05/25/2004

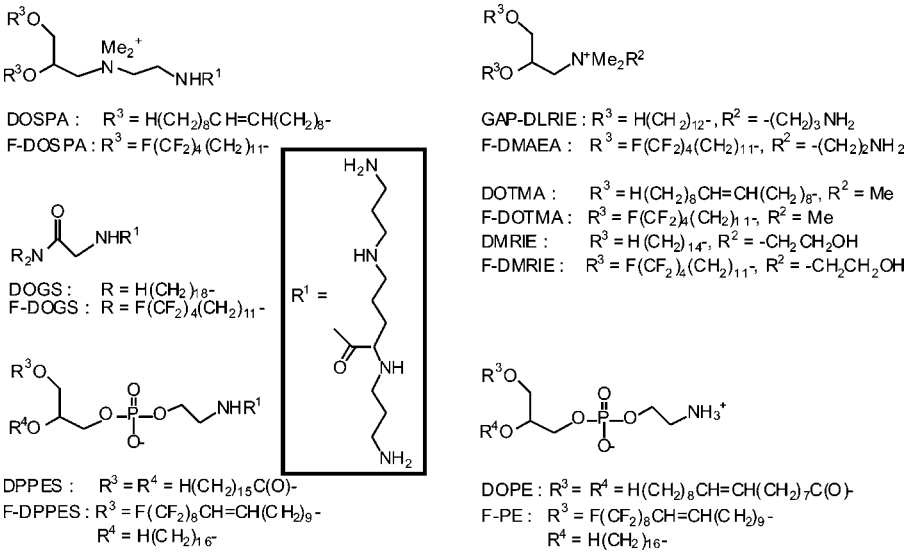


Figure 1. Chemical structure and code name of the fluorinated and conventional cationic and helper) lipids used and/or mentioned in this study. F-DOSPA, F-DMAEA, F-DOGS (*14*), F-DOTMA, F-DMRIE, F-DPPES (*13*), and F-PE (*15*, *17*) are fluorinated analogues of conventional DOSPA (*19*), GAP-DLRIE (*18*), DOGS (*25*), DOTMA (*26*), DMRIE (*27*), DPPES (*28*), and DOPE, respectively.

goals of this study were to extend the library of fluorinated cationic lipids that enable gene transfer and expression and to confirm or infirm the transfection potential of fluorinated cationic lipoplexes in the presence of surfactants (*16*). As the use of helper lipids (HL) enhances the transfection activity of most (poly)cationic lipids (including the fluorinated analogues of DOGS) (*14*, *17*), we report on the transfection efficacy of these new fluorinated cationic lipids (CL) used in conjunction with DOPE or F-PE, a fluorinated analogue of DOPE (see structure in Figure 1) which was found in vitro and in vivo to be a more efficient helper lipid than DOPE (*15*, *17*). In this paper, we show that, in the presence of STC, the cationic fluorinated F-DOSPA/F-PE lipoplexes display a greater stability with respect to detergent-triggered disintegration and DNA accessibility, and a significantly larger in vitro transfection potential than conventional lipoplexes formulated with Lipofectamine.

MATERIALS AND METHODS

General Experimental and Analytical Conditions. Most of the reactions were performed in anhydrous solvents under dry and oxygen-free nitrogen. Anhydrous solvents were prepared by standard methods. Purifications by column chromatography were carried out using silica gel 60 (Merck, 70−230 mesh) and chloroform ($CHCl_3$), dichloromethane (CH_2Cl_2), methanol (MeOH), or mixtures thereof as indicated. Unless noted otherwise, the ratios describing the composition of solvent mixtures represent relative volume. Advancement of the reaction was followed by thin-layer chromatography (TLC) on silica plates F254 (Merck). The following developing systems were used: UV light, $KMnO_4$, H_2SO_4/EtOH, Dragendorff reagent, ninhydrin reagent (Sigma). Tetra-*N*,*N*′,*N*″,*N*‴-(*tert*-butyloxycarbonyl)-spermine-5-carboxylic acid [(Boc)4SperCOOH] and *N*-[1-(2,3-di-11-(*F*-butyl)-undecyloxy)-propyl]-*N*-[2-hydroxyethyl]-*N*,*N*-dimethylammonium bromide [F-DMHEA] were synthesized according to published procedures (*13*, *14*). *rac*-3-[11-(*F*-Octyl)undec-10-enyl]-2-(hexadecyl)glycero-1-phosphoethanolamine, F-PE, was from our laboratory (*15*, *17*). 1,2-Dioleoyl-sn-glycero-3-phosphoethanolamine (DOPE) was purchased from Sigma. All other organic chemicals were purchased from Sigma, Aldrich, or Fluka. Lipofectamine was purchased from Invitrogen (Cergy Pontoise, France). ^1H, ^{13}C, and ^{19}F NMR spectra were recorded at 200, 50.3, and 188.3 MHz, respectively, on a Bruker AC-200. Chemical shifts were measured relative to $CHCl_3$ (δ 7.26 ppm) or CH_3OD (δ 3.31 ppm) for ^1H, relative to $CDCl_3$ (δ 77.1 ppm) for ^{13}C and expressed indirectly in relation to TMS, and relative to CCl_3F as internal reference for ^{19}F. The following abbreviations are used to describe the signal multiplicities: s (singlet), d (doublet), t (triplet), q (quadruplet), and m (multiplet). Chemical shifts are expressed in parts per million and listed as follows: shift in parts per million (multiplicity, coupling, integration, and attribution). Electrospray ionization mass spectrometry (ESI-MS) in positive mode was performed on a Finnigan MAT LCQ equipped with an atmospheric pressure ionization (API) source.

Synthesis of the Fluorinated Cationic Lipids. Synthesis of *N*-[1-(2,3-di-11-(*F*-butyl)undecyloxy)-propyl]-*N*,*N*-dimethyl-*N*-(2-aminoethyl)ammonium hydroxide [F-DMAEA].

To a solution of F-DMHEA (*13*) (600 mg, 0.6 mmol) in THF (20 mL) were added 0.7 mL of a freshly prepared 1.6 M solution of hydrazoic acid (HN_3, 1.1 mmol) in chloroform followed by 0.22 mL of a THF solution of diisopropyl azodicarboxylate (DIAC, 1.1 mmol) and then 10 mL of a THF solution of triphenylphosphine (0.52 g, 2 mmol) (*20*). The resulting mixture was stirred at 50 °C overnight. Water (1 mL) was added, and the temperature was maintained at 50 °C for 3 h. After evaporation in vacuo of the solvents, the residue was dissolved in dichloromethane. The organic phase was washed three times with water and then dried over Na_2SO_4. Flash chromatography of the residue obtained after evaporation over a silica gel column (60 g, from $CHCl_3$/MeOH 9/1 to $CHCl_3$/MeOH 8/2 and then $CHCl_3$/MeOH/NH_4OH 8/2/0.2) led to 0.27 g (0.27 mmol, 45%) of a white powder consisting into F-DMAEA as its hydroxide. TLC ($CHCl_3$/MeOH/NH_4OH, 8/2/0.2 v/v; H_2SO_4, Dragendorff, ninhydrin): $R_f = 0.35$. ^1H NMR ($CDCl_3$/CD_3OD): δ 1.02−1.31 (s large, 28H, $CF_2(CH_2)_2(CH_2)_7$); 1.31−1.55 (m, 8H, CF_2-CH_2CH_2, CH_2CH_2O); 1.90 (tt, ^3J = 8.3 Hz, $^3J_{HF}$ = 18.8 Hz, 4H, CF_2CH_2); 2.93−3.09 (m, 2H,CH_2NH_2); 3.09−3.19 (s large, 6H, CH_3); 3.23−3.61 (m, 10H, CH_2O, CH_2NCH_2); 3.80−3.95 (m, 1H, CH). ^{13}C NMR ($CDCl_3$/CD_3OD): δ 19.9 (t, $^3J_{CF}$ = 3.7 Hz, $CF_2CH_2CH_2$); 25.9, 26.0 ($CH_2(CH_2)_2O$); 28.9, 29.0, 29.2, 29.3, 29.4 ($CF_2(CH_2)_2(CH_2)_6$); 29.9 (CH_2-

CH_2O); 30.6 (t, $^2J_{CF} = 22.3$ Hz, CF_2CH_2); 35.4 (CH_2NH_2); 52.3, 52.9 (CH_3); 66.4 (CH_2NCH_2); 68.6, 69.3, 71.9 (CH_2O); 73.0 (CH).^{19}F NMR ($CDCl_3/CD_3OD$): δ −78.2 (3F, CF_3); −111.1 (2F, CF_2CH_2); −129.4 (2F, $CF_2CF_2CH_2$); −127.5 (2F, CF_3CF_2). MS (ESI+): $m/z = 907.6$ $[M]^+$, in agreement with the mass calculated for $[M]^+ = C_{37}H_{61}F_{18}N_2O_2$.

Synthesis of *N*-[1-(2,3-Di-11-(*F*-butyl)undecyloxy)-propyl]-*N*-[2-(sperminecarboxamido)ethyl]-*N*,*N*-dimethylammonium as a Trifluoroacetate Salt, [F-DOSPA]. To a solution of (Boc)4SperCOOH (*14*) (212 mg, 0.33 mmol) in 15 mL of CH_2Cl_2 were added *N*-hydroxysuccinimide (HOSu) (49 mg, 0.43 mmol) and dicyclohexylcarbodiimide (DCC) (88 mg, 0.43 mmol) with a few drops of THF. The mixture was stirred at room temperature during 12 h and was then cooled to 0 °C and filtered. Then, 270 mg (0.27 mmol) of F-DMAEA and 75 μL (0.54 mmol) of triethylamine were added, and the resulting mixture was stirred at room temperature during 12 h. The organic phase was washed with 5% sodium carbonate, 5% citric acid, and water until neutrality and then dried over Na_2SO_4. Flash chromatography over a silica gel column of the residue obtained after evaporation (20 g, CH_2Cl_2/MeOH: from 99/1 to 90/10 then CH_2Cl_2/MeOH/NH_4OH, 8/2/0.2 v/v) led to 200 mg (0.12 mmol, 46%) of a colorless oil consisting of *N*-[1-(2,3-di-11-(*F*-butyl)undecyloxy)propyl]-*N*-[2-(tetrabutoxycarbonyl-sperminecarboxamido)ethyl]-*N*,*N*-dimethylammonium hydroxide [F-DOSPA(Boc)]. TLC ($CHCl_3$/MeOH/ NH_4OH: 8/2/0.2; Dragendorff, ninhydrin): $R_f = 0.51$. ^{1}H NMR ($CDCl_3/CD_3OD$): δ 0.74−1.83 (m, 80H, $CF_2CH_2(CH_2)_9$, CH_3(Boc), CH_2CH_2N(H)Boc, CH_2CH_2NBoc, CH_2CHC(O)); 1.97 (tt, $^3J_{HH} = 7.5$ Hz and $^3J_{HF} = 19.1$ Hz, 4H, CF_2CH_2); 2.92−4.26 (m, 30H, $N(CH_3)_2$, CH_2O, CHO, CH_2N, CHC(O)NH). ^{13}C NMR ($CDCl_3/CD_3OD$): δ 20.1 (t, $^3J_{CF} = 3.7$ Hz, CF_2-CH_2CH_2); 26.1, 26.2 ($CH_2(CH_2)_2O$); 28.5 (CH_3(Boc); 29.1, 29.3, 29.4, 29.6, 29.7, 30.0 ($CF_2(CH_2)_2(CH_2)_6$, CH_2CH_2O, CH_2CH_2NBoc, CH_2CHNBoc); 30.8 (t, $^2J_{CF} = 22.3$ Hz, CF_2CH_2); 38.3, 44.0, 46.4, 46.7 (CH_2NBoc); 52.6 (CH_2-NHC(O)); 53.3, 53.5 ($N(CH_3)_2$); 60.6 (CHC(O)NH); 68.6, 69.5, 72.1 (CH_2O, $CHCH_2NCH_2$); 73.3 (CHO); 78.9, 79.6, 80.7 ($C(CH_3)_3$); 155.6, 155.7, 156.2 (C(O)). ^{19}F NMR ($CDCl_3/CD_3OD$): δ −81.6 (3F, CF_3); −115.1 (2F, CF_2CH_2); −125.0 (2F, $CF_2CF_2CH_2$); −126.6 (2F, CF_3CF_2). MS (ESI+): $m/z = 1536$ $[M]^+$, in agreement with the calculated mass for $[M]^+ = C_{68}H_{117}F_{18}N_6O_{11}$.

The Boc-deprotection of F-DOSPA(Boc) was quantitatively achieved in a large excess of a TFA/CH_2Cl_2 mixture during 1 h at room temperature. The excess TFA was removed by coevaporation with cyclohexane yielding F-DOSPA as a TFA salt (2.6 TFA according to ^{19}F NMR). ^{1}H NMR (CD_3OD): δ 1.22−2.29 (m, 48H, $CF_2(CH_2)_{10}$, CH_2CH_2NH, CH_2CHC(O)); 2.84−3.81 (m, 29H, $N(CH_3)_2$, CH_2O, CHO, CH_2N); 4.01−4.17 (m, 1H, CHC(O)NH). ^{13}C NMR (CD_3OD): δ 21.2 (t, $^3J_{CF} = 3.8$ Hz, $CF_2CH_2CH_2$); 23.1 (CH_2CHC(O)); 25.3 ($CH_2(CH_2)_2OCH_2$); 26.3 (CH_2-$(CH_2)_2$OCH); 27.2, 27.3, 28.6, 29.4, 30.1, 30.4, 30.5, 30.6, 30.7, 31.1 ($CF_2(CH_2)_2(CH_2)_6$, CH_2CH_2O); 31.6 (t, $^2J_{CF} = 22.4$ Hz, CF_2CH_2); 34.5 ($CH_2CH_2NH_2$); 37.8 (CH_2NHC-(O)); 38.5, 45.3, 45.9, 48.4 (CH_2NH, CH_2NH_2); 52.8, 53.1 ($N(CH_3)_2$); 61.6 (CHC(O)NH); 64.4, 67.4, 70.1, 70.2 (CH_2O, $CHCH_2NCH_2$); 72.8 (CHO); 163.1 (q, $^2J_{CF} = 34.5$ Hz, CF_3COO^-); 171.9 (C(O)NH).^{19}F NMR (CD_3OD): δ −77.2 (8F, CF_3COO^-); −83.0 (3F, CF_3); −116.1 (2F, CF_2CH_2); −125.9 (2F, $CF_2CF_2CH_2$); −127.7 (2F, CF_3CF_2). MS (ESI+): $m/z = 1135.7$ and m/2z = 568.6 in agreement with the calculated mass for $[M]^+ = C_{48}H_{85}F_{18}N_6O_3$ and $[M + H]^{2+}/2$, respectively.

Preparation of the DNA Complexes. The plasmid pTG11236 (pCMV-SV40-luciferase-SV40pA) used for the preparation of the DNA complexes and for transfection assays was produced by Transgène (Strasbourg, France). It is a plasmid of 5739 bp. The endotoxin content of the plasmid preparation was checked using a Limulus Amebocyte Lysat kit (Biogenic, France). This value was below 1 endotoxin unit/mg of plasmid, hence below the 5 e.u./mg of DNA recommended for in vivo protocols.The quantities of lipids used for the *N*/*P* 5 lipoplexes were calculated according to the DNA concentration of 0.1 mg/mL in the lipoplex preparation, the molar weight, and the number of amino groups in the selected cationic lipid (CL is F-DMAEA, F-DOSPA or DOSPA). The *N*/*P* ratio of 5 corresponds to the molar amount of CL necessary to have a ratio of five amino group nitrogens (for 1 mol CL) per one phosphate in the DNA (330 Da mean MW), as described elsewhere (*13*−*17*).

Liposomal dispersions containing CL and DOPE (or F-PE) as helper lipid (HL) at a [CL]/[HL] 60/40 molar ratio and at a CL concentration of 1.0 mg/mL in a 5% glucose solution were first prepared. Thus, for the preparation of *N*/*P* 5 F-DOSPA/HL/DNA complexes, 100 μL of a F-DOSPA solution (10 mg/mL in $CHCl_3$/MeOH 9/1) and 34.8 μL of DOPE or 54.7 μL of F-PE solutions (10 mg/mL in $CHCl_3$ or $CHCl_3$/MeOH 9/1, respectively) were transferred to a borosilicate glass tube. The solvents were evaporated in a Rotavap evaporation system (45 °C, 0.2 bar, 40 rotations/min). Then, 1.0 mL of a 5% glucose solution was added to the film obtained. The preparation was vortexed for 12 h and then sonicated for 5 min to yield a liposomal preparation. The F-DOSPA/HL/DNA lipoplexes were then formulated by adding 64.8 μL of the F-DOSPA/HL liposomal preparation to 85.2 μL of a DNA solution in glucose 5% (0.176 mg/mL) to reach a final DNA concentration of 0.1 mg/mL. This preparation was vortexed for 10 s and was used within 1 h for particle size measurements, agarose gel electrophoresis, ethidium bromide (BET) exclusion, and/or in vitro transfection experiments.

Measurement of the Size of the Lipoplexes. The average sizes were measured by photon correlation spectroscopy using a Coulter N4Plus particle size analyzer, as described elsewhere (*14*).

Agarose Gel Electrophoresis. Each sample of the above-described lipoplex preparation (0.5 μg of plasmid) was electrophoresed for about 30 min under 150 V, through a 0.8% agarose gel in TAE 1 x (Tris-acetate-EDTA) buffer and stained by spreading a 1 μL/mL BET solution in TAE buffer. The absence of BET-stained DNA bands after photographing on a UV transilluminator confirmed that all the DNA was complexed. Its integrity was confirmed by electrophoresis after disrupting the lipoplexes with a large excess of sodium dodecyl sulfate, following procedures described elsewhere (*14*).

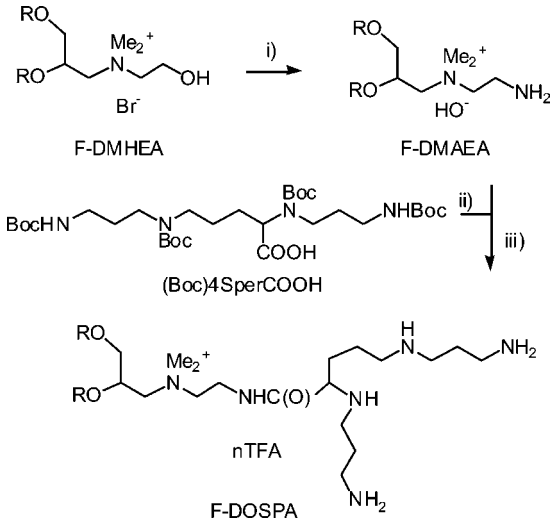
Lipoplex Stability in the Presence of Sodium Taurocholate Dye-Exclusion Assays. The BET intercalation into the *N*/*P* 5 lipid-complexed DNA at a concentration of 15.0 μM for F-DOSPA or DOSPA (respectively 37.5 μM for F-DMAEA) and 15 μM DNA phosphate in the presence of various concentrations of STC (from 0 to 60 mM) was assessed by fluorescence monitoring at 2.5 μM BET which correspond to a BET:nucleotide ratio of 1:6. Under these conditions, the fluorescence of BET intercalated into DNA was found to be directly proportional to the percentage of accessible DNA (*21*). The above-described lipoplex preparation (0.1 mg DNA/mL) (75 μL) in a 5% glucose solution was added to 750 μL of BET (5 μM in a 5% glucose solution) and to 675 μL of STC in glucose 5% to reach a final concentration of STC in the 0−60 mM range. The resulting

preparations were incubated at 37.0 ± 0.5 °C in a thermoregulated cell with magnetic stirring for 10 min. Then, the fluorescence F was measured using a Perkin-Elmer Spectrofluorometer LS 50B (excitation at 306 nm, emission at 622 nm, and a 530 nm emission cutoff filter). The fluorescence signal, F_{max}, which corresponds to 100% BET intercalation, was determined for each detergent concentration tested on a 2.5 μM BET and naked DNA 0.1 mg/mL glucose solution. The fluorescence of each sample was corrected for the background fluorescence F0 of BET in the absence of DNA and in the presence of STC at each concentration tested. The percentage of accessible DNA to BET for each sample and for each detergent concentration was calculated from the equation $(F - F_0)/(F_{max} - F_0)$. This percentage can exceed 100% owing to diffusion background fluorescence resulting from the presence of lipospermine-based aggregates (in the present experiments F could not be corrected for this effect). The given means were calculated from at least three independent experiments.

In Vitro Transfection of A549 Cells. For in vitro transfection, A549 cells (epithelial cells derived from human pulmonary carcinoma) were grown 24 h before the experiments in Dulbeco-modified Eagle culture medium (DMEM) (Gibco-BRL), containing 10% foetal calf serum, FCS (Sigma), in 96-well plates (2×10^4 cells per well), in a wet (37 °C) and 5% CO_2/95% air atmosphere. Five microliters of CL/HL/DNA lipoplex preparation was diluted to 50 μL in DMEM. Ten minutes before addition to the cells, this dispersion was diluted with 50 μL of STC in DMEM to obtain the desired detergent concentration (from 0 to 17.5 mM). The cell culture medium was removed and replaced with this 100 μL of lipoplex/detergent/DMEM solution which corresponds to a DNA concentration of 0.5 μg and a lipid concentration of 15.1 μM for F-DOSPA and 37.9 μM for F-DMAEA in each well. After 4 and 24 h, 50 and 100 μL of DMEM supplemented with 30% and 10% FCS, respectively, were added. Forty-eight hours after transfection, the culture medium was discarded and the cells were washed twice with 100 μL of phosphate-buffered saline (PBS) and then lysed with 50 μL of lysis buffer (Promega, Charbonnières, France). The lysates were frozen at −40 °C awaiting for luciferase activity analysis. This measurement was done for 10 s on 10 μL of lysis mixture in a LB96P luminometer (Berthold, Evry, France) in dynamic mode, using the 'Luciferase' determination system (Promega) in 96-well plates. The total protein concentration per well was determined by the BCA test (Pierce, Montluçon, France). For cells grown in the absence of lipoplexes or STC, a well contained approximately 30−50 μg of proteins. Luciferase activity was calculated as femtograms (fg) of luciferase per milligram (mg) of proteins. The percentage cell viability of the lipoplexes (without or with STC) and of STC was calculated as the ratio of the total protein per well of the transfected cells (without or with STC) relative to that measured for untreated cells or for cells incubated with the detergent × 100%, respectively. The given means ± SEM were calculated from three independent experiments.

Statistical Analysis. Statistical tests were performed with STATGRAPHICS Plus5.1 software. Analysis of variance (Anova) was run on the logarithmic transformation of transfection levels (log10(fg luciferase/mg protein)) and on the cell viability to fit normal distributions of the data. One factor, i.e., the nature of the formulation, for a given amount of STC added (in the 0−60 mM range) was analyzed as source of the variation of cell viability percentages and of logarithmic transformation of the transfection levels using a one-way comparison procedure. The Tukey's honestly significant difference (HSD) method was used to discriminate among the means of cell viability percentages and the logarithmic transformations of luciferase expression levels.

Scheme 1. Synthetic Route to F-DMAEA and F-DOSPA[a]



[a] Reagents: (i) HN_3, PPh_3, DIAC; (ii) DCC, HOSu, CH_2Cl_2/THF; (iii) excess TFA/CH_2Cl_2. R represents $F(CF_2)_4(CH_2)_{11}$.

RESULTS AND DISCUSSION

Our main objectives were to extend the library of fluorinated cationic lipids and lipoplex formulations that enable gene transfer and expression (*13*, *14*) and to confirm the most promising transfection potential of fluorinated cationic lipoplexes in the presence of a powerful anionic surfactant (e.g. sodium taurocholate, STC) (*16*). Therefore, we (i) performed the synthesis of F-DMAEA and F-DOSPA, (ii) evaluated, as compared with control lipoplexes formulated with the commercially available DOSPA/DOPE Lipofectamine mixture, their ability to maintain, in the presence of STC, the integrity (in terms of DNA accessibility) of fluorinated lipoplexes they form, and (iii) explored their potential as gene transfer vectors and the impact of their hydrophobic and lipophobic character on detergent-triggered transfection inhibition.

The fluorinated F-DMAEA and F-DOSPA lipids were designed according to previous studies conducted in our laboratory on fluorinated analogues of DOGS (*14*, *16*). Their framework consists of a hydrophobic part which includes two $F(CF_2)_4(CH_2)_{11}$ chains. These chains were shown to lead to one of the most efficient gene transfer agent in the fluorinated DOGS series (*14*, *16*).

Synthesis. The synthesis of the fluorinated polycationic lipid F-DOSPA relies on F-DMAEA which himself relies on F-DMHEA precursor previously reported by our laboratory (Scheme 1) (*13*). The transformation of F-DMHEA into F-DMAEA consisted of a Mitsunobu reaction which converts the alcohol function into an amine (*20*). This was achieved by the use of hydrazoic acid (HN_3) in the presence of diisopropyl azodicarboxylate (DIAC) and triphenylphosphine. The conversion of F-DMAEA into F-DOSPA (isolated as its 2.6TFA salt as attested by ^{19}F NMR) was then performed using a conventional two-step coupling/deprotection procedure consisting into DCC/HOSu activation of tetra-*tert*-butoxycarbonylspermine-5-carboxylic acid (*14*) and condensation with F-DMAEA, followed by the quantitative removal of the Boc-protect-

ing groups with TFA. The chemical structure of the fluorinated F-DMAEA and F-DOSPA lipids was clearly attested by ESI/MS as well as by ^{1}H, ^{13}C, and ^{19}F NMR.

Lipoplex Formation and Characterization. The fluorinated lipoplexes were formulated at a *N*/*P* ratio of 5 with the fluorinated cationic lipid F-DOSPA or F-DMAEA in conjunction with a helper lipid (HL = DOPE or F-PE). These lipids were used at a molar ratio of 60/40 as for the control ones formulated with commercial Lipofectamine (i.e. DOSPA/DOPE 60/40). These studies were performed with pTG11236 plasmid also used for the detergent-triggered disintegration and the in vitro transfection assays (see below). The procedure applied for the lipoplex preparation relies on the dilution from liposomal CL/HL 60/40 dispersion in 5% glucose, using a *N*/*P* ratio of 5. All the lipoplex preparations consisted into a single population of stable DNA particles of mean diameters in the 120 (50) to 300 (150) nm range, as shown by light scattering measurements (data not shown). These formulations were also analyzed by gel electrophoresis (results not shown) which indicated the presence of fully complexed plasmid (not accessible to ethidium bromide intercalation). It should be mentioned that only *N*/*P* 5 lipoplexes were formulated and analyzed. We selected this *N*/*P* ratio as we found that in our transfection protocol and among the control *N*/*P* 0.8 to 10 Lipofectamine lipoplexes tested, the *N*/*P* 5 ones led to the highest level of luciferase expression (see Transfection section below).

Lipoplex Stability in the Presence of the Detergent. To evaluate the ability of the fluorinated lipids, as compared to Lipofectamine, to prevent lipoplex disintegration in the presence of surfactants, we examined the effects of STC on BET intercalation into the complexed plasmid. We used the fluorescence monitoring of BET intercalation into DNA which has been reported for characterizing DNA complexes (*21*) and applied for the first generation of fluorinated lipoplexes (*16*). When DNA is not accessible to BET, as in the *N*/*P* 5 lipoplexes, a fluorescence signal of very weak intensity (F0) corresponding to the free dye in solution is measured upon mixing BET with the lipoplexes. When surfactant-triggered dissociation of the lipoplexes occurs and all the BET intercalation sites of DNA become accessible, BET fluorescence is enhanced. For naked DNA, an approximately 40-fold fluorescence enhancement is obtained upon intercalation into DNA, the maximal fluorescence intensity (F_{max}) being measured for a BET:nucleotide ratio of 1:6. The intensity varies further linearly between F_0 and F_{max} for accessible DNA between zero and six nucleotides per BET. This allows the degree of DNA accessibility to be observed fluorometrically.

Figure 2 shows the evolution of the percentage of DNA accessibility to BET from the CL/HL (CL = F-DOSPA, or F-DMAEA; HL = DOPE or F-PE) and control Lipofectamine *N*/*P* 5 lipoplexes with the detergent/lipid [STC]/([CL]+[HL]) molar ratio. The percentage of DNA accessibility was seen to increase for all formulations when the STC concentration and, consequently, the detergent/lipid ratio were raised. However, lipoplexes formulated with the fluorinated or conventional pentaamino DOSPA were substantially more resistant to the lytic activity of STC than those formulated with the diamino F-DMAEA lipid. Indeed, for the F-DMAEA-based lipoplexes, a STC concentration of only 5 to 10 mM (which corresponds to a detergent/lipid molar ratio of 80−160) was sufficient to promote 80 to 100% of DNA accessibility (hence almost complete disintegration), whereas for the Lipofectamine and F-DOSPA-based lipoplexes and these STC concentrations (which correspond to detergent/lipid molar ratios of 200−400), only 40−45% of the DNA intercalation sites became accessible to BET. Furthermore, much higher STC concentrations (50 and 60 mM, respectively), which correspond to detergent/lipid molar ratios of 2000−2400, were necessary to disintegrate actively these latter lipoplexes. Interestingly, our data show further that the stability of the lipoplexes, with respect to the lytic activity of STC, is increasing along the sequence Lipofectamine < F-DOSPA/DOPE < F-DOSPA/F-PE, indicating that the higher the fluorination degree of the lipoplexes, the higher their stability. These results are in line with the pioneering study from this laboratory which highlighted a greater resistance to STC-triggered disintegration of lipoplexes formulated with fluorinated analogues of Transfectam (or DOGS) rather than with Transfectam itself (*16*). They confirm that the enhanced lipophobic and hydrophobic character of the fluorinated cationic or helper lipids, and consequently of the fluorinated lipoplexes they form, prevents these lipoplexes from disintegration by the detergent and, consequently, prevents DNA from degradation and from interactions with lipophilic and hydrophilic biocompounds. The main impact of the fluorinated lipids likely stems from the reduction of the detergent solubility into the film they form which surrounds DNA, owing to the very low miscibility between hydrocarbon (e.g. STC) and fluorinated lipids (*22*−*24*).

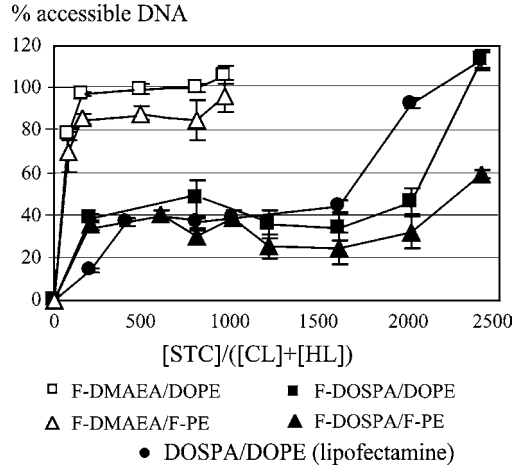


Figure 2. Evolution of the percentage of DNA accessibility to ethidium bromide (BET) from various lipoplexes with the [STC]/([CL]+[HL])] molar ratio (STC = sodium taurocholate; CL = cationic lipid = DOSPA, F-DOSPA, or F-DMAEA; HL = helper lipid DOPE or F-PE). The lipoplexes prepared in 5% glucose solution were made of the cationic lipids and helper lipids (structure shown in Figure 1) and plasmid pTG11236 (DNA) for a *N*/*P* ratio of 5 and for a [CL]/[HL] molar ratio of 60/40. The BET intercalation into lipid-complexed DNA at a concentration of 15.0 μM for F-DOSPA or DOSPA (respectively 37.5 μM for F-DMAEA) and 15 μM DNA phosphate in the presence of various concentrations of STC (from 0 to 60 mM) was assessed by fluorescence monitoring at 2.5 μM BET and at a BET:nucleotide ratio of 1:6. The given means ± SEM were calculated from at least three independent experiments. For more details, see Materials and Methods.

Transfection. The transfection potential of F-DOSPA and F-DMAEA with DOPE or F-PEhelper lipid was assayed in vitro on A549 cells, a commonly used cell model for in vitro gene delivery. These assays were performed by incubating the *N*/*P* 5 lipoplexes (at a DNA dose of 0.5 μg/well) with the cells in the presence of 10% fetal calf serum for 24 h and in the presence of increasing concentrations of STC (from 0 to 17.5 mM) and, consequently, of various detergent/lipid molar ratios (from 0

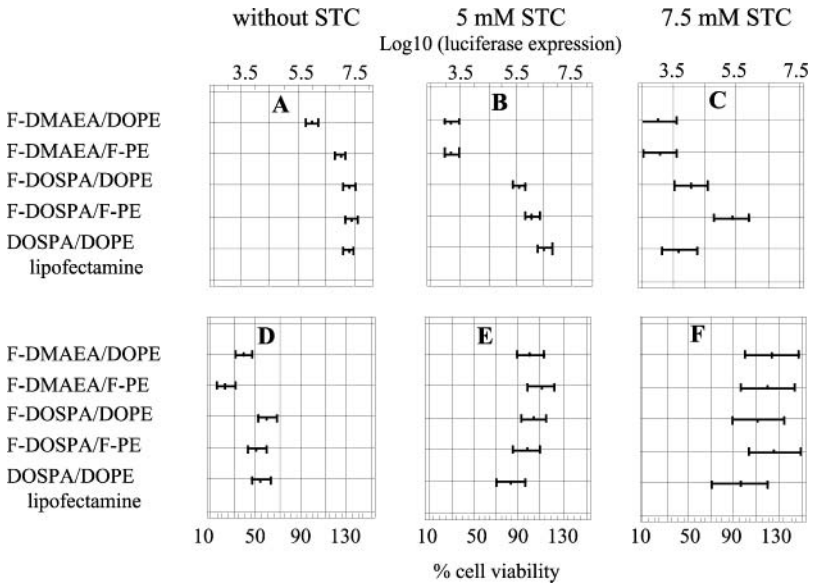


Figure 3. Means and 95.0% Tukey HSD intervals of the logarithmic transformation of transfection levels (log10(fg luciferase/mg protein); panels A−C) and of the percentage of cell viability (panels D−F) for the fluorinated F-DMAEA- or F-DOSPA-based *N*/*P* 5 lipoplexes coformulated with DOPE or F-PE, and for control *N*/*P* 5 formulations made with lipofectamine and incubated without STC (panels A and D), with 5 mM STC (panels B and E) or with 7.5 mM STC (panels C and F). Luciferase expression and percentage of cell viability were determined in A549 cells for a DNA dose of 0.5 μg per well. For the F-DMAEA-based lipoplexes, a STC concentration of 5 and 7.5 mM corresponds to a [STC]/[lipid] molar ratio of 80 and 120, respectively. For the (F-)DOSPA-based lipoplexes, a STC concentration of 5 and 7.5 mM corresponds to a [STC]/[lipid] molar ratio of 200 and 300, respectively. For more details, see Materials and Methods.

to 693 for (F-)DOSPA and 0 to 277 for F-DMAEA). Their transfection efficiency (expressed in femtograms (fg) of luciferase/mg of protein) was further evaluated as compared to naked DNA and to reference *N*/*P* 5 lipoplexes based on Lipofectamine. These conditions (*N*/*P* 5 and DNA dose of 0.5 μg/well) were shown to give the highest luciferase expression level and percentage of cell viability for the transfection of A549 cells with the control lipoplexes formulated with Lipofectamine among the *N*/*P* 0.8 to 10 ratio and DNA dose of 0.5 and 1 μg/well tested (data not shown). Cells treated with naked DNA under equivalent conditions showed expression levels of about 10^{2-3} fg of luciferase/mg of protein. The cell viability of the lipoplexes without and with STC at the different concentrations tested was also checked by determining the total protein amount per well of the transfected cells relative to that measured for untreated cells (for which the total protein amount per well is in a 30−60 μg/well range).

Figure 3 represents a variance analysis of (i) the logarithmic transformation of the transfection levels (panels A−C) and (ii) the percentage cell viability (panels D−F) obtained with the various *N*/*P* 5 lipoplexes without or with increasing amounts of STC. Although analysis was performed throughout the 0−17.5 mM STC concentration range, only data for a 0−7.5 mM STC concentration range are presented. For a STC concentration higher than 7.5 mM, cell toxicity of the lipoplexes and of STC was indeed too important to allow an unambiguous interpretation of the transfection results. However, it should be noted that in the presence of a STC concentration of 5 and 7.5 mM, cell viability of the lipoplexes was improved as compared with that of the lipoplexes alone (see Figure 3, panel E and F vs panel D). This indicates likely that, in this STC concentration range, STC neutralizes the deleterious effects on cells of the cationic lipids present in excess in the *N*/*P* 5 lipoplexes.

Concerning the transfection experiments performed in the absence of surfactant (Figure 3, panel A), our data show that the *N*/*P* 5 lipoplexes formulated with the fluorinated lipospermine F-DOSPA (whether used with DOPE or the fluorinated F-PE helper lipid) and the control Lipofectamine-based lipoplexes display comparable transfection efficiencies. This indicates that there is no benefit from using F-DOSPA/DOPE (or F-PE) instead of DOSPA/DOPE for transfecting A549 cells and is in line with the data obtained in our laboratory for fluorinated analogues of DOGS/DOPE (*14*). It can be further observed that the lipoplexes coformulated with the dicationic fluorinated F-DMAEA lipid and DOPE are less efficient for transfecting A549 cells than those formulated with the pentacationic lipospermine (F-)DOSPA and DOPE. Moreover, coformulation of the F-DMAEA lipoplexes with the fluorinated F-PE analogue of DOPE resulted in a substantial enhancement of transfection efficiency, confirming the remarkable transfection helper properties of F-PE (*15*, *17*). This transfection increase is however accompanied by a substantial decrease of cell viability (Figure 3, panel D). It should further be noticed that the *N*/*P* 5 F-DMAEA-based lipoplexes exhibit a lower cell viability than their respective lipospermine-based ones. This is likely related to the fact that, for a given *N*/*P* ratio, the concentration of the lipids in the transfection wells is 2.5-fold higher for a dicationic (e.g. F-DMAEA) than for a pentacationic lipid (e.g. (F-)DOSPA).

More importantly, concerning the transfection experiments performed in the presence of STC (Figure 3, panels B and C), and based on the stability study described in the precedent section, lipofection was expected to be inhibited by the detergent for all the lipoplexes but to a lesser extent (i) for any of the (F-)DOSPA lipoplexes as compared with the F-DMAEA-based ones, and (ii) for the fluorinated F-DOSPA lipoplexes as compared with the Lipofectamine controls and particularly with increasing the fluorination degree of the formulation. These were the observed trends as can be seen in Figure 3 (panels B and C vs panel A). Indeed, lipofection when mediated by the *N*/*P* 5 F-DMAEA-based lipoplexes was fully inhibited for a STC concentration of 5 mM which corresponds to a

[STC]/[lipid] molar ratio of 80. By contrast, only a 6-, 15-, and 50-fold inhibition of transfection ($p < 0.05$) was observed for the *N*/*P* 5 DOSPA/DOPE, F-DOSPA/F-PE, and F-DOSPA/DOPE formulations, respectively, although for these latter formulations a STC concentration of 5 mM corresponds to a higher [STC]/[lipid] molar ratio (i.e. 200). For a STC concentration of 7.5 mM (panel C), lipofection mediated with complexes formulated with both the fluorinated F-DOSPA and helper lipid F-PE was significantly higher than with Lipofectamine (nearly 50-fold, $p < 0.05$) or even with F-DOSPA/DOPE (nearly 30-fold, $p < 0.05$). It is thus the formulation displaying the highest fluorination degree of the formulations investigated here which possesses the largest lipofection potential in the presence of STC. That F-DOSPA/F-PE lipoplexes are more efficient for transfecting A549 cells than the F-DOSPA/DOPE ones illustrates again the remarkable helper properties of F-PE, a fluorinated analogue of DOPE.

The present study which demonstrates the improved lipofection capability of fluorinated lipoplexes in the presence of a powerful surfactant is in line with a previous study from this laboratory which was performed with *N*/*P* 5 lipoplexes made from fluorinated DOGS analogues (*16*). However, for these fluorinated DOGS formulations higher detergent concentrations (up to 17.5 mM vs 10 mM for F-DOSPA/F-PE) and higher [STC]/[lipid] molar ratios (up to 462 vs 400 for F-DOSPA/F-PE, data not shown) were necessary to inhibit lipofection of A549 cells. The lower cell transfection ability of F-DOSPA/F-PE (or DOPE) lipoplexes in the presence of STC as compared with that of the fluorinated DOGS analogues is likely related to the presence of the helper lipid (DOPE or F-PE) for the former formulations. STC displays a greater miscibility with DOPE and even with the mixed-chain F-PE (which contains a fluorinated and hydrocarbon chain) than with the fluorinated DOGS which contain two fluorocarbon chains (*22*−*24*). One expects therefore a lower stability (with respect to disintegration) in the presence of STC for the F-DOSPA/F-PE (or DOPE) lipoplexes than for the lipoplexes formulated only with fluorinated double-chain DOGS analogues.

Within the [STC]/[lipid] molar ratio range of 0−300, only subtle differences in disintegration of the (F-)-DOPSA-based lipoplexes were observed by the dye-exclusion assay (Figure 2), while more drastic differences were observed in transfection. This is due to the different experimental conditions employed for each assay type, as discussed elsewhere (*16*).

CONCLUSION

The extent of gene therapy using synthetic vectors depends on the development of new approaches to improve the features of lipoplexes aimed at facilitating their use in vivo. This study, which shows improved stability of fluorinated lipoplexes and higher levels of lipofection with fluorinated lipoplexes in the presence of surfactants, definitely confirms that fluorinated lipoplexes display a most promising potential as gene transfer vectors, and that they constitute a very attractive alternative to their more conventional homologues. The data reported here, together with the higher in vivo lung transfection efficiency found for fluorinated lipoplexes (*15*), suggest that their enhanced lipophobic and hydrophobic character prevents them from disintegration and, consequently, DNA from degradation and from interactions with lipophilic and hydrophilic biocompounds responsible for lipofection inhibition.

ACKNOWLEDGMENT

We wish to thank TRANSGENE, SA (Strasbourg, France) for the generous gift of pcTG11236.

LITERATURE CITED

(1) Tranchant I., Thompson, B., Nicolazzi, N., Mignet, N., and Scherman, D. (2004) Physicochemical optimisation of plasmid delivery with cationic lipids. *J. Gene Med. 6*, S24−S35.

(2) Liu, D., Ren, T., and Gao, X. (2003) Cationic transfection lipids. *Curr. Med. Chem. 10*, 1307−1315.

(3) Miller, A. D. (2003) The problem with cationic liposome/micelle-based nonviral vector systems for gene therapy. *Curr. Med. Chem. 10*, 1195−1211.

(4) Niculescu-Duvaz, D., Heyes, J., and Springer, C. J. (2003) Structure−activity relationship in cationic lipid mediated gene transfection. *Curr. Med. Chem. 10*, 1233−1261.

(5) Ilies, M. A., Seitz, W. A., and Balaban, A. T. (2002) Cationic lipids in gene delivery: principles, vector design and therapeutical applications. *Curr. Pharm. Des 8*, 2441−2473.

(6) Kichler, A. (2004) Gene transfer with modified polyethylenimines. *J. Gene Med.* 6, S3−S10.

(7) Merdan, T., Kopecek, J., and Kissel, T. (2002) Prospects for cationic polymers in gene and oligonucleotide therapy against cancer. *Adv. Drug Delivery Rev. 54*, 715−758.

(8) Merlin, J. L., N'Doye, A., Bouriez, T., and Dolivet, G. (2002) Polyethylenimine Derivatives as Potent Nonviral Vectors for Gene Transfer. *Drug News Perspect. 15*, 445−451.

(9) Raczka, E., Kukowska-Latallo, J. F., Rymaszewski, M., Chen, C., and Baker, J. R., Jr. (1998) The effect of synthetic surfactant Exosurf on gene transfer in mouse lung in vivo. *Gene Ther. 5*, 1333−1339.

(10) Duncan, J. E., Whitsett, J. A., and Horowitz, A. D. (1997) Pulmonary surfactant inhibits cationic liposome-mediated gene delivery to respiratory epithelial cells in vitro. *Hum Gene Ther. 8*, 431−438.

(11) Tsan, M. F., Tsan, G. L., and White, J. E. (1997) Surfactant inhibits cationic liposome-mediated gene transfer. *Hum Gene Ther. 8*, 817−825.

(12) Ernst, N., Ulrichskotter, S., Schmalix, W. A., Radler, J., Galneder, R., Mayer, E., Gersting, S., Plank, C., Reinhardt, D., and Rosenecker, J. (1999) Interaction of liposomal and polycationic transfection complexes with pulmonary surfactant. *J. Gene Med. 1*, 331−340.

(13) Gaucheron, J., Santaella, C., and Vierling, P. (2002) Transfection with fluorinated lipoplexes based on fluorinated analogues of DOTMA, DMRIE and DPPES. *Biochim. Biophys. Acta 1564*, 349−358.

(14) Gaucheron, J., Santaella, C., and Vierling, P. (2001) Highly fluorinated lipospermines for gene transfer: synthesis and evaluation of their in vitro transfection efficiency. *Bioconjugate Chem. 12*, 114−128.

(15) Boussif, O., Gaucheron, J., Boulanger, C., Santaella, C., Kolbe, H. V. J., and Vierling, P. (2001) Enhanced in vitro and in vivo cationic lipid-mediated gene delivery with a fluorinated glycerophospho-ethanolamine helper lipid. *J. Gene Med. 3*, 109−114.

(16) Gaucheron, J., Santaella, C., and Vierling, P. (2001) Improved in vitro gene transfer mediated by fluorinated lipoplexes in the presence of a bile salt surfactant. *J. Gene Med. 3*, 338−344.

(17) Gaucheron, J., Boulanger, C., Santaella, C., Sbirrazzuoli, N., Boussif, O., and Vierling, P. (2001) In vitro cationic lipid-mediated gene delivery with fluorinated glycerophospho-ethanolamine helper lipids. *Bioconjugate Chem. 12*, 949−963.

(18) Wheeler, C. J., Felgner, P. L., Tsai, Y. J., Marshall, J., Sukhu, L., Doh, S. G., Hartikka, J., Nietupski, J., Manthorpe, M., Nichols, M., Plewe, M., Liang, X., Norman, J., Smith, A., and Cheng, S. H. (1996) A novel cationic lipid greatly enhances plasmid DNA delivery and expression in mouse lung. *Proc. Natl. Acad. Sci. U.S.A. 93*, 11454−11459.

(19) Hawley-Nelson, P., Ciccarone, V., Gebeyehu, G., Jessee, J., and Felgner, P. L. (1993) Lipofectamine reagent: a new, higher efficiency polycationic liposome transfection reagent. *Focus* 73−79.
(20) Fabiano, E., Golding, B. T., and Sadeghi, M. M. (1987) A simple conversion of alcohols into amines. *Synthesis* 190−192.
(21) Eastman, S. J.; Siegel, C.; Tousignant, J.; Smith, A. E.; Cheng, S. H.; and Scheule, R. K. (1997) Biophysical characterization of cationic lipid: DNA complexes. *Biochim. Biophys. Acta 1325*, 41−62.
(22) Gadras, C., Santaella, C., and Vierling, P. (1999) Improved stability of highly fluorinated phospholipid-based vesicles in the presence of bile salts. *J. Controlled Release 57*, 29−34.
(23) Vierling, P., Santaella, C., Riess J. G. (1995) Fluorinated Liposomes. *Liposomes: New Systems and New Trends in their Applications* (Puisieux, F., Couvreur, P., Delattre J., and Devissaguet J. P., Eds.) Editions de Santé, Paris, pp 295−313.
(24) Vierling, P., Santaella, C., and Greiner, J. (2001) Highly fluorinated amphiphiles as drug and gene carrier and delivery systems. *J. Fluorine Chem. 107*, 337−354.
(25) Remy, J. S., Abdallah, B., Zanta, M. A., Boussif, O., Behr, J. P., and Demeneix, B. A. (1998) Gene transfer with lipospermines and polyethylenimines. *Adv. Drug Delivery Rev. 30*, 85−95.
(26) Felgner, P. L., Gadek, T. R., Holm, M., Roman, R., Chan, H. W., Wenz, M., Northrop, J. P., Ringold, G. M., and Danielsen, M. (1987) Lipofection: a highly efficient, lipid-mediated DNA-transfection procedure. *Proc. Natl. Acad. Sci. U.S.A. 84* 7413−7417.
(27) Felgner, J. H., Kumar, R., Sridhar, C. N., Wheeler, C. J., Tsai, Y. J., Border, R., Ramsey, P., Martin, M., and Felgner, P. L. (1994) Enhanced gene delivery and mechanism studies with a novel series of cationic lipid formulations. *J. Biol. Chem. 269*, 2550−2561.
(28) Behr, J.-P., Demeneix, B., Loeffler, J. P., and Perez-Mutul, J. (1989) Efficient gene transfer into mammalian primary endocrine cells with lipopolyamine-coated DNA. *Proc. Natl. Acad. Sci. U.S.A. 86*, 6982−6986.

BC049942+

Fluorescent Vasotocin Conjugate for Identification of the Target Cells for Brain Actions of Vasotocin

Christine M. Lewis,[†] E. Kurt Dolence,[†,§] Zhaojie Zhang,[‡] and James D. Rose[†,‡,*]

Neuroscience Program, School of Pharmacy, and Department of Zoology and Physiology, University of Wyoming, Laramie, Wyoming 82071-3166. Received March 19, 2004; Revised Manuscript Received May 5, 2004

The effects of neuropeptides on the brain are a major focus of neuroendocrine research, and little progress has been made in the identification of the target neurons for many neuropeptides. Arginine[8]-vasotocin (AVT) is a neurohypophyseal peptide present in nonmammalian vertebrates that controls many neural and behavioral functions. Here we describe synthesis and functional characterization of an AVT-Oregon green conjugate **1** (AVT−OG **1**) that can be used in vivo to identify AVT target neurons. Application of AVT−OG **1** to the brainstem of an amphibian produces rapid, endosome-like internalization together with typical AVT-like neurophysiological effects. Thus, preparation of AVT−OG **1**, which preserves the peptide's neurophysiological effects, is useful as a fluorescent marker for AVT target neurons. Consequently, AVT−OG **1** conjugate will have considerable utility for analyzing the neural actions of AVT in the intact brain.

INTRODUCTION

Vasopressin-like and oxytocin-like peptides are members of a family of highly related neurohypophyseal nonapeptides that are present in all animals. Arginine[8]-vasotocin (AVT) is the specific peptide that serves antidiuretic and pressor functions in all vertebrate taxa except mammals, most of which produce arginine[8]-vasopressin (AVP) for these functions (*1*). These two neuropeptides differ only in that AVP has phenylalanine rather than isoleucine in position 3 (*2*). In addition to the antidiuretic and pressor effects of these neuropeptides, AVT and AVP appear to act in the vertebrate brain and spinal cord to mediate a diverse array of complex functions, particularly regulation of reproductive behaviors (*3, 4*). In addition, neural development and control of cellular responses to neuronal injury may be influenced by vasopressin-like neuropeptides (*5, 6*).

Numerous studies of mammalian and nonmammalian vertebrate species suggest that the neurobehavioral effects of AVT and AVP are mediated by V_1-like receptors in the central nervous system (*3, 7*−*10*). Agonist activation of G-protein-coupled receptors, such as the receptors mediating AVT and AVP behavioral effects, triggers a cascade of events, including internalization of the ligand−receptor complex (*11, 12*). This internalization may modulate cell responsiveness by causing the loss of receptors from the cell surface, making them inaccessible to continued ligand challenge (*13, 14*).

Current understanding of the cellular actions of vasopressin-like neuropeptides is very uneven, ranging from a detailed account of the target cells and mechanisms of action for antidiuretic functions involving the kidney, to much less complete mechanistic understanding of neural and behavioral actions. A limiting factor in elucidation of cellular mechanisms underlying neural−behavioral effects of vasopressin-like neuropeptides has been the absence of a means to identify the specific target neurons for AVT or AVP. Although receptors for these neuropeptides have been localized in certain neurons, the demonstration of receptors, per se, does not reveal the functional effects mediated by such receptors or even guarantee that histologically demonstrated receptors are functional. In addition, the diversity of structural and functional phenotypes of neurons in the brain, unlike structurally simpler peripheral target tissues such as the kidney, further complicates the matter of relating neuropeptide target cells to a role in neural function.

The purpose of the present paper is to document the preparation of a fluorescent Oregon Green 488 AVT conjugate **1** (AVT−OG **1**), validate its functional effects on neurons, and demonstrate its utility as a means of identifying the neuronal target cells for AVT. These steps in validating the utility of the fluorescent AVT conjugate will permit the use of this conjugate in the elucidation of this neuropeptide's mechanism of neurobehavioral action.

Research in this laboratory uses a comparatively simple model for analysis of the neurobehavioral actions of AVT. Roughskin newts (*Taricha granulosa*) exhibit a highly stereotyped pattern of mating behavior in which the male clasps the female with all four legs from a dorsal approach for a period of hours as an obligatory step in the courtship process leading to fertilization (*15*). It has been established that AVT is one of the hormones normally facilitating this behavior and the lower brainstem is the key brain region for AVT action in facilitating clasping (*4*). In addition, we have shown that the clasp-facilitating neural action of AVT appears to entail an enhancement of the responsiveness of medullary neurons to sensory stimuli applied to various locations on the body surface (*16*).

To visualize peptide internalization in endosome-like vesicles, previous studies of peripheral tissues have utilized fluorescent AVT (*17*), fluorescent AVP (*12*), and

* To whom correspondence should be addressed: Department of Zoology and Physiology, Box 3166, University of Wyoming, Laramie, WY 82071-3166. E-mail: trout@uwyo.edu, Phone: 307-766-6719 Fax: 307-766-2921.

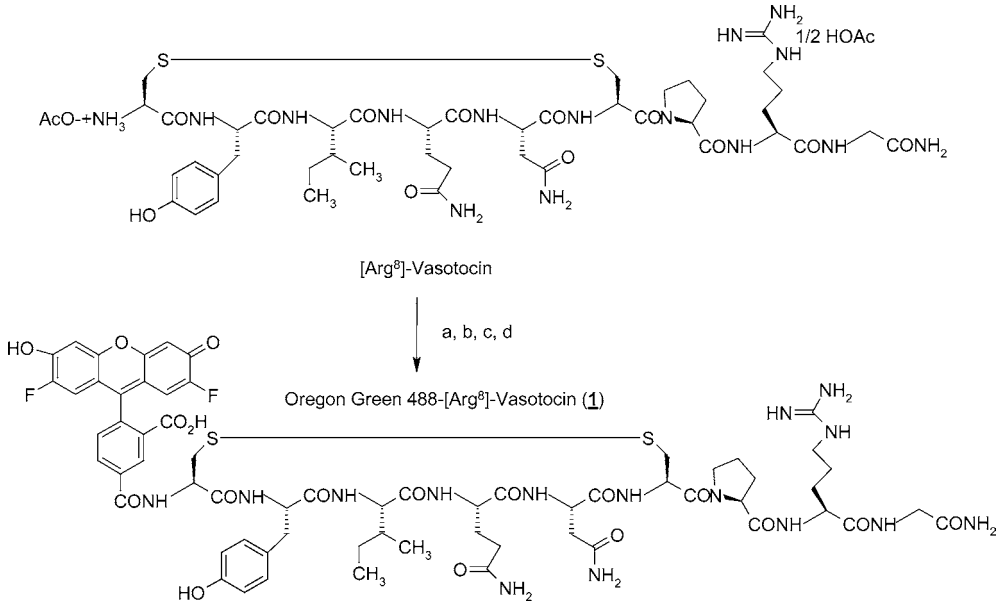
[†] Neuroscience Program.

[§] School of Pharmacy.

[‡] Department of Zoology and Physiology.

10.1021/bc049928x CCC: $27.50 © 2004 American Chemical Society
Published on Web 06/19/2004

Scheme 1. Synthesis of Oregon Green 488−[Arg^8]-Vasotocin Conjugate AVT−OG (1)[a]



[a] (a) 5′-Isomer Oregon Green 488, DMF, *N*OHSu, EDC·HCl, 21 h, 22 °C; (b) [Arg^8]-vasotocin, 0.1 M aq $NaHCO_3$, 24 h, 22 °C; (c) lyophilization; (d) C_{18} RP-TLC followed by preparative C_{18} RP-HPLC.

fluorescent receptor agonists or antagonists (*18*). However, the use of such conjugates has been confined to in vitro studies of nonneural cells (*11*, *12*, *14*, *17*−*20*). The most significant aspect of our use of this fluorescent vasopressin-like neuropeptide AVT−OG **1** is in vivo application to the brain in such a way that specific neuronal target cells can be visualized while the concurrent neuronal effects of AVT are neurophysiologically monitored. In addition, the fluorescent AVT−OG **1** that we are presenting appears to be comparable in neuropotency to unlabeled AVT and retains excellent fluorescence. Using this approach, we aim, for the first time, to connect the functional effects of AVT with the neuropeptide's specific target neurons and their structural characteristics. The analytic power of this in vivo use of the fluorescent neuropeptide AVT−OG **1**, particularly in the roughskin newt model, is considerable, in that it can also be used in conjunction with real-time techniques such as optical imaging of signaling events.

EXPERIMENTAL PROCEDURES

Synthesis of Oregon Green 488 Conjugated Arginine^8-Vasotocin 1 (AVT−OG 1) (Scheme 1). *Reagents.* Unless otherwise stated, reagents and solvents were obtained from commercial sources without further purification. Distilled deionized water was obtained from a Millipore NanoPure system. C_{18} reverse phase TLC was conducted using Merck RP-18 F_{254} glass-backed TLC plates. Preparative C_{18} RP-HPLC was conducted using a Phenomenex Juptiter 10 μm 300A 250 × 21.2 mm column while monitoring at both 254 and 494 nm with a flow rate of 1.0 mL/min. ESI mass spectrometry was obtained using a mixture of 50:50 CH_3CN:H_2O containing 0.1% TFA.

*Oregon Green 488−[Arg^8]-Vasotocin Conjugate (**1**) (AVT−OG **1**).* The 5′-isomer of Oregon Green 488 (0.5 mg, 1.1 μM, Molecular Probes) was dissolved in DMF (56 μL) in a foil-covered vial. To this solution was added 22 μL (2.2 μmol) of a stock solution of *N*-hydroxysuccinimide (0.1 μM in DMF) and 22 μL (2.2 μmol) of a stock solution of 1-[3-(dimethylamino)propyl]-3-ethylcarbodiimide hydrochloride (0.1 μM in DMF). This mixture was stirred at 22 °C for 21 h. This active ester solution was transferred to the manufacturer's vial of [Arg^8]-vasotocin acetate salt (1.0 mg, 1.0 μM Sigma, free base MW 1050.2) dissolved in 100 μL of 0.1 M aq $NaHCO_3$ with the aid of 100 μL of DMF and 100 μL of 0.1 M aq $NaHCO_3$. The vial was covered with foil, and this mixture was stirred vigorously for 24 h at 22 °C. At this time, the mixture was transferred to a 25 mL pear shaped round-bottom flask with the aid of water, frozen, and lyophilized to afford a yellow film. This film was applied using 50:50 CH_3CN:H_2O containing 0.1% TFA to one 20 × 20 cm RP-18 F_{254} TLC plate and eluted with 40:60 CH_3CN:H_2O containing 0.1% TFA. The major yellow band (R_f 0.31) was removed by scraping and eluted with 50:50 CH_3CN:H_2O containing 0.1% TFA, and the solvents were removed by evaporation in vacuo. This material was further purified by gradient preparative RP-HPLC (5% CH_3CN:H_2O containing 0.1% TFA (5 min) followed by a gradient over 40 min to a composition of 80:20 CH_3CN:H_2O containing 0.1% TFA) (t_R = 26.3 min). This afforded 0.6 mg (41% yield) of **1** as a water soluble yellow film. ESI mass spectrometry calcd for $C_{64}H_{75}N_{15}O_{18}S_2F_2$ $(M + H)^+$ *m*/*z* 1444.5 found: $C_{64}H_{75}N_{15}O_{18}S_2F_2$ $(M + H)^+$ *m*/*z* 1444.3.

Neurophysiological Validation of the Physiological Activity of AVT−OG 1. Adult male roughskin newts (*Taricha granulosa*) were held in community tanks supplied with continuously flowing, aerated well water. The animals were fed chopped beef heart and maintained on a natural photoperiod. The University of Wyoming Animal Care and Use Committee approved all procedures involving animals.

Procedures used for recording and analysis of neuronal activity were similar to those previously reported (*16*) and will be only briefly described here. Newts were anesthetized by immersion in 0.1% MS-222 (tricaine methanesulfonate). The rostral medulla was surgically exposed, and the head was stabilized with a support system attached to the skull. After surgical preparation was complete, the newt was removed from the anesthetic and partially immersed in fresh, aerated well water with the skin covered by wet tissue paper to facilitate transcutaneous respiration. For electrophysiological recording, newts were immobilized by administration of 2% solution of gallamine triethiodide in Ringer's solution (0.2 mL, ip).

Recording began after sufficient time elapsed for the newt to recover from the anesthetic (approximately 2−4 h). Single neuron activity was recorded with 50 μm Diamel-insulated stainless steel microelectrodes (impedances of 100−500 kΩ) placed on the surface of the rostromedial medulla in the lower brainstem. At most recording sites, spikes were recorded simultaneously from two to five neurons. Two AVT-sensitive parameters of neuronal function were evaluated: spontaneous firing rates and responses to skin stimulation. Sensory responsiveness was tested by application of light pressure (4 s) to locations on the face, individual feet, and trunk with a cone-shaped probe mounted on a piano wire stylus to ensure constant force of stimuli. The stylus was fixed to a pressure transducer to record stimulus onset, duration, and offset. Stimuli were administered at 3 min intervals throughout each experiment. Prior to administration of a peptide or vehicle, four trials of stimulation were done to establish a baseline neuronal response. All newts received hormone or vehicle administration in 4 μL of physiological saline administered directly to the surface of the medulla via microsyringe.

Neuronal activity, pressure transducer recordings, and a voice narrative were recorded on videotape in pulse code-modulated format by means of a Neurodata Neurocorder for later analysis. Firing by individual neurons was identified with Spike II software (Cambridge Electronic Designs). The criterion required for identification of neuronal sensory responses and the assessment of hormone effects on neuronal sensory responses and activity levels were similar to those described previously (*16*). Changes in activity were assessed by comparison of prehormone and posthormone response magnitudes. In order for a neuron's spontaneous firing to be considered changed by AVT−OG **1**, or AVT, it's second-by-second firing rate after the neuropeptide application had to be above or below each of the four prepeptide samples of firing by at least 30%. Likewise for a neuron's response to a sensory stimulus to be considered increased, its second-by-second firing rate during a sensory stimulus after the neuropeptide application had to be above or below the four prepeptide records of firing during the same stimulus by at least 30%.

In addition to evaluating the neurophysiological effectiveness of AVT−OG **1**, we examined three aspects of the conjugate's internalization by neurons: time course, minimally effective dose, and specificity. To this end, 4 μL of physiological saline containing one of three doses of AVT−OG **1** (10 ng, 40 ng, or 80 ng), AVT (80 ng), or vehicle alone were administered to the surface of the medulla and rinsed at the end of 30 min ($n = 4$ newts for each group). To assess time course of internalization, two additional groups of newts ($n = 4$) received 80 ng of AVT−OG **1** for 5, 30, or 60 min prior to rinsing. Small numbers of additional newts received 80 ng of AVT−OG **1** for various exposure times between 5 and 60 min (e.g. 15, 45 min) to provide a more complete qualitative picture of the time course of internalization. These dosages of the peptide and application volumes of vehicle were based on previous neurophysiological and behavioral experiments showing that a 4 μL volume of solution containing AVT in these relative concentrations and applied directly to the surface of the medulla produced reliable neurophysiological effects (*16*). To determine the specificity of neuronal internalization of AVT−OG **1** the medulla was pretreated with 4 μL of physiological saline containing either unlabeled AVT or Manning compound (*21*, *22*), a V_1-receptor antagonist. For each treatment condition ($n = 4$), 1.76 mg of Manning compound (d(CH_2)$_5$-[Tyr(Me)^2]AVP), or physiological saline (VEH) was administered followed 30 min later by 80 ng of AVT−OG **1** in 4 μL of physiological saline.

Histological Localization of Fluorescent AVT−OG 1 Internalization by Neurons. After completion of each experimental treatment, the surface of the medulla was rinsed twice with ice cold PBS (1−4 °C), the newt was immediately decapitated, and the head was rinsed for 30 s twice in ice-cold PBS (1−4 °C) before being placed in ice-cold 30% sucrose−formalin (1−4 °C) for a minimum of 24 h. Brains were removed, embedded in Tissue Tek OCT compound, and transversely sectioned using a cryostat. Sections cut through the medulla were selected at 100 μm intervals, beginning just caudal to the cerebellum, thaw-mounted on microscope slides, and dried for a minimum of 8 h at room temperature.

Neuronal labeling by AVT−OG **1** was examined and digital images collected with a Leica TCS SP2 confocal laser-scanning microscope in the University of Wyoming Microscopy Core as well as with a conventional epifluoresence microscope (Olympus BX40, FITC filter set, and Optronics digital video camera system). Neuronal AVT−OG **1** internalization was determined by counting the number of nucleated neurons with 10 or more fluorescent endosomes in sections through the rostral medulla. This value is consistent with other studies in which endosomes have been counted for quantification of target cells (*13*, *17*−*20*). An endosome was defined as a spot of fluorescence greater than 0.1 μm but less than 0.5 μm in diameter (*12*). In each transverse section, neurons were counted from a zone extending from the lateral border of the medulla to the midline. This encompassed an area 1800 μm in width and 600 μm in depth in each section. Neurons were counted from sections every 100 μm in a zone extending from 0 μm to 2000 μm caudal to the posterior extent of the cerebellum. Numbers of labeled neurons were compared across treatment conditions with analysis of variance followed by Bonferroni critical value procedure.

RESULTS

Neuronal Internalization of AVT−OG 1. Application of AVT−OG **1** to the surface of the medulla produced a time- and dose-dependent internalization of fluorescence (Figure 1) that exhibited properties consistent with previously reported (*12*, *14*) demonstrations of neuropeptide internalization. When viewed by confocal microscopy, the intracellular labeling consisted of endosome-like foci of fluorescence approximately 0.2 μm in diameter (Figure 1b). The nuclei of labeled neurons were always devoid of labeling (Figures 1a and 1c).

The endosome-like uptake of fluorescence was evident in numerous medullary neurons of all sizes, particularly those in the medial reticular nuclei. The labeled neurons tended to be in clusters that were separated by unlabeled ones (Figures 1c and 1e). Fluorescently labeled cells were present at the lowest AVT−OG **1** dose examined (10 ng); however, these cells were present primarily at the most dorsal aspects of the tissue section examined. At both 40 ng and 80 ng doses, the number of labeled cells increased, but consistent labeling throughout the depth of the medulla appeared only after administration of 80 ng of AVT−OG **1** (Figure 2). Exposure of medullary neurons to AVT−OG **1** for durations of 5, 30, or 60 min revealed intracellular fluorescent labeling, but the pattern of labeling differed significantly across the three time intervals ($p < 0.01$) (Figure 3). At 5 min, labeled cells were present, but the mean number of cells for the group

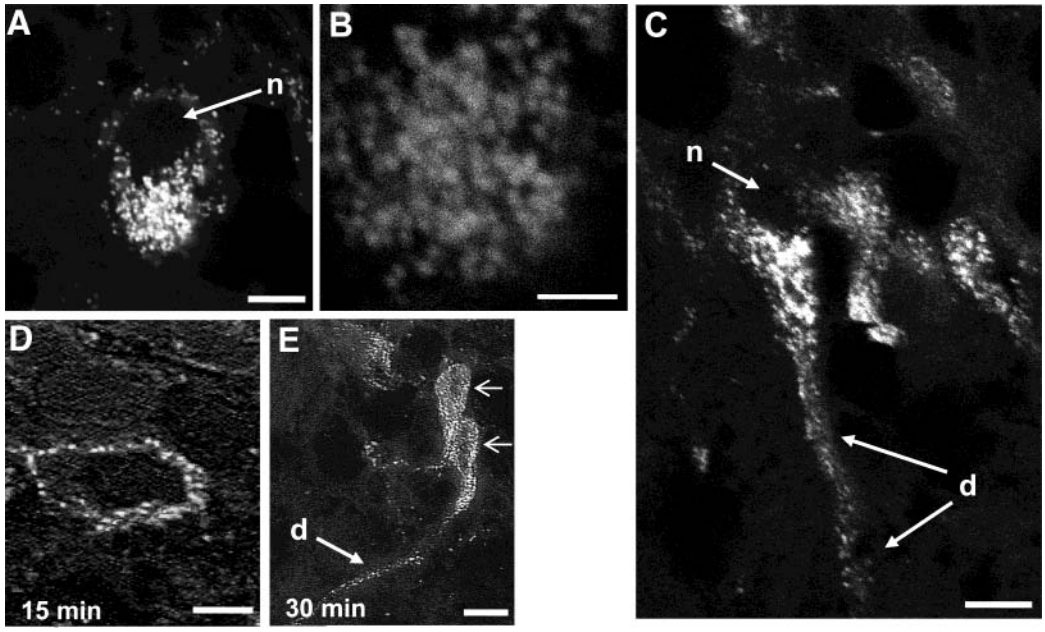


Figure 1. Confocal and epifluorescent images of rostromedial medullary neurons showing AVT−OG **1** internalization. (A and C) Single confocal optical scans (2 μm) illustrating the distribution of labeling within neurons. The cytoplasm of the cell body and a proximal dendrite (d) were intensely labeled but not the nucleus (n) (scale bar = 10 μm). (B) Confocal image of internalized AVT−OG **1** localized in puncta similar in size and appearance to endosomes (scale bar = 5 μm). (D and E) Epifluorescence images illustrating peripheral distribution of puncta in a neuronal cell body (D) at 15 min after AVT−OG **1** administration and redistribution of puncta throughout the cytoplasm of two neurons (E; small arrows) and a dendrite (d) at 30 min after AVT−OG **1** administration (scale bar = 10 μm).

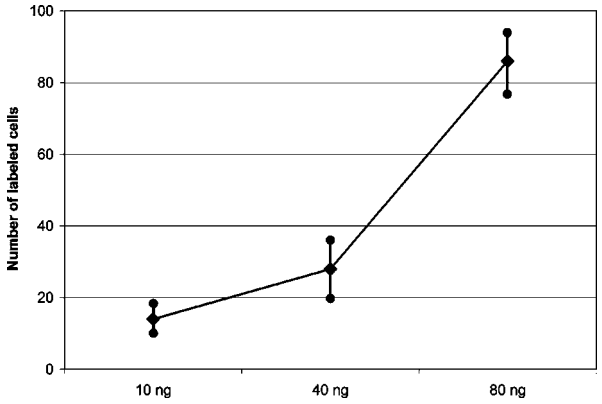


Figure 2. Mean number of labeled neurons in each group of newts as a function of dose after AVT−OG **1** administration (10 ng, 40 ng, or 80 ng) to the medulla. Neurons with AVT−OG **1** internalization were present at the lowest dose (10 ng) and the number of labeled cells increased substantially at the highest dose examined (80 ng).

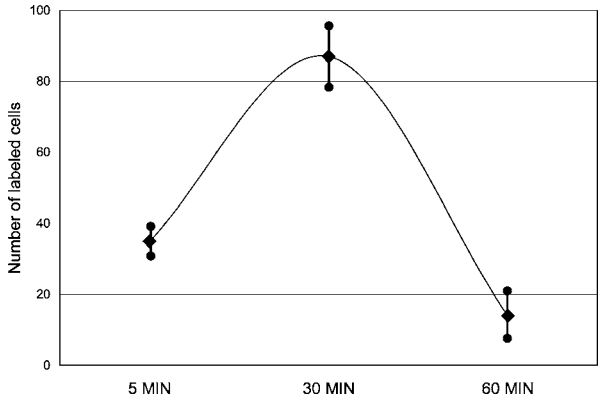


Figure 3. Mean number of labeled neurons in each group of newts as a function of time after AVT−OG **1** administration. AVT−OG **1** was applied to the medulla and rinsed after 5, 30, or 60 min. Neurons with AVT−OG **1** internalization were present at 5 min and the number of labeled cells peaked at 30 min.

of newts was significantly less (mean = 34.75) than at 30 min of exposure (mean = 85.75; $p < 0.01$) when the number of fluorescently labeled neurons was highest. Labeling was typically clustered at the periphery of the neuronal cell bodies at 15 min (Figure 1d) but at 30 min was distributed throughout the cytoplasm of each cell as well as proximal portions of primary dendrites (Figure 1e). Labeling of fine diameter processes thin enough to be axons was not evident. The number of fluorescently labeled cells peaked at 30 min and was significantly lower by 60 min of exposure (mean = 15.25).

AVT−OG 1 Internalization Is Specific and Blocked by AVT Receptor Ligands. Fluorescent labeling of medullary neurons appeared to be specific to AVT receptors in that it differed significantly across pretreatment competition conditions (Figure 4). Labeling was greatly diminished by pretreatment with either unlabeled AVT ($p < 0.01$) or Manning compound ($p < 0.01$), a specific V_1-receptor antagonist. Vehicle pretreatment had no effect on AVT−OG **1** internalization and Oregon Green, by itself, did not label cells.

AVT−OG 1 Internalization Is Associated with AVT-like Neurophysiological Effects. Application of AVT−OG **1** to the medulla produced changes in neuronal activity and sensory responsiveness (Figure 5) of the same types and magnitudes as previously seen with unlabeled AVT. For the AVT−OG **1** dose used in the present study (80 ng), most recorded neurons showed a pronounced increase in spontaneous firing within 3 min. Most of these neurons showed complete reversal of spontaneous firing to pretreatment values within 32−54 min of hormone administration. The majority (60.5%) of these neurons showed increased magnitudes of response to somatic sensory stimuli applied to various body locations after hormone administration. These changes in spontaneous activity and sensory responsiveness were

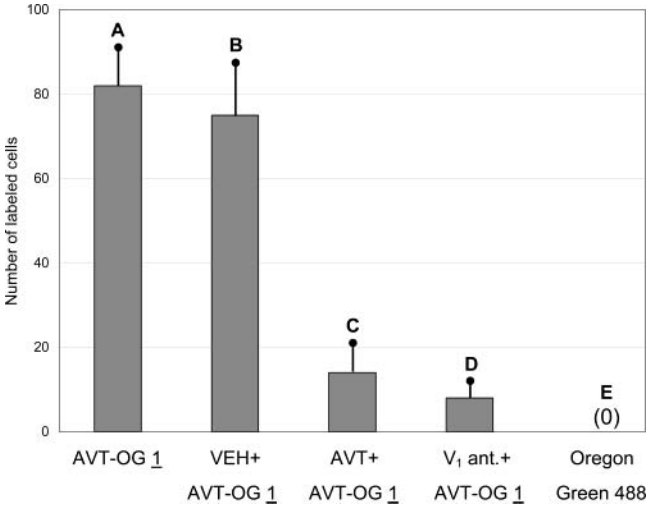


Figure 4. Competition of AVT−OG **1** neuronal labeling due to pretreatment with AVT or Manning compound. Unlabeled AVT or the specific V_1 receptor antagonist, Manning compound, administered immediately prior to AVT−OG **1**, significantly decreased the mean number of labeled cells, whereas vehicle pretreatment had no effect on AVT−OG **1** internalization. Significant differences were found in comparisons between A vs E, B vs C, and B vs D. Oregon Green 488 alone (E) did not produce any labeling.

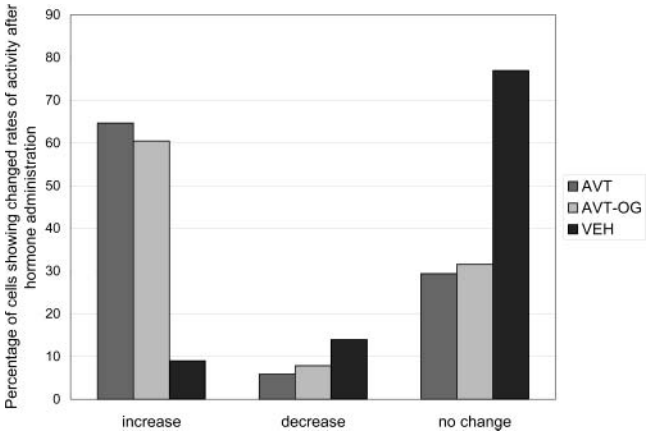


Figure 5. Both AVT and AVT−OG **1** caused significant increases in neuronal sensory responses rapidly after hormone administration. Sensory responsiveness increased in 22 of 34 neurons after administration of AVT and 23 of 38 neurons increased in sensory responsiveness after AVT−OG **1** administration. Changes of this magnitude were not seen after vehicle administration ($n = 22$).

not observed after vehicle application to the medulla (Figure 5). Collectively, these neurophysiological effects of AVT−OG **1** are essentially the same as those we have observed previously with unlabeled AVT, were similar to changes seen after administration of unconjugated AVT (Figure 5), and showed that the conjugate was functionally effective with a time course paralleling the process of internalization.

DISCUSSION

The fluorescent conjugate AVT−OG **1** described here provides a significant new tool for analysis of this neuropeptide's functions in cellular systems. One of the most active areas of investigation concerns AVT effects on brain functions, particularly those controlling behavior. Our results show that the AVT−OG conjugate **1** effectively labels target neurons for the neuropeptide and concurrently initiates the usual physiological actions of AVT. The potent enhancement of neuronal spontaneous activity and responsiveness to somatic sensory stimuli were essentially identical to results previously obtained (*16*) with a comparable dose of unlabeled AVT.

The cytological pattern of AVT−OG **1** uptake is consistent with an endosome-like pattern of internalization, like that previously described for toad bladder (*18, 19*) with an AVT agonist conjugate and for vasopressin agonist conjugates (*11, 12, 14*) in nonneuronal cells. The time course of AVT−OG **1** uptake and dispersal in endosome-like foci of fluorescence began in the perimeter of the cell body and progressed through the extranuclear cytoplasm of the neuronal somata and proximal dendrites. This pattern is also consistent with endosome formation.

Our results are compatible with a V_1 receptor-based process of AVT−OG **1** internalization. In the intact brain, competition by pretreatment with unlabeled AVT or a specific V_1 receptor antagonist blocked AVT−OG **1** uptake, thus verifying the specificity of action of the conjugate. In addition, the fact that Manning compound pretreatment produced very pronounced blockade of AVT−OG **1** uptake shows that the neurons in the newt medulla may have predominantly V_1 receptors. This result validates the utility of this conjugate **1** for investigations of neural effects of AVT due to the fact that V_1-like receptors mediate such neural effects (*4*, *7*).

In summary, this is the first use of a fluorescent AVT conjugate to investigate neuroendocrine function. In addition, we have verified that the AVT−OG conjugate **1** retains its receptor specificity and physiological effects. The availability of this fluorescent AVT makes new and analytically powerful investigations of neural and other cellular actions of AVT more feasible.

ACKNOWLEDGMENT

This research was made possible by NIH-NCRR grant P20 RRO15553 to J.D.R. and the University of Wyoming's Center of Biomedical Research Excellence in Cellular Signaling and NIH grant GM062139-01 to E.K.D. This research was also supported by the University of Wyoming COBRE Microscopy Core and the Department of Chemistry's ESI-MS facilities.

Supporting Information Available: ESI-MS and reverse phase HPLC for compound **1**. This material is available free of charge via the Internet at http://pubs.acs.org/BC.

LITERATURE CITED

(1) Norris, D. O. (1997) *Vertebrate Endocrinology*, pp 157−240, Academic Press, San Diego.

(2) Moore, F. L. (1992) Evolutionary precedents for behavioral actions of oxytocin and vasopressin. *Ann. N. Y. Acad. Sci. 652*, 156−165.

(3) Goodson, J. L., and Bass, A. H. (2001) Social behavior functions and related anatomical characteristics of vasotocin/vasopressin systems in vertebrates. *Brain Res. Rev. 35*, 246−265.

(4) Rose, J. D., and Moore, F. L. (2002) Behavioral Neuroendocrinology of vasotocin and vasopressin and the sensorimotor processing hypothesis. *Front. Neuroendocrinol. 23*, 317−341.

(5) Tribollet, E., Arsenijevic, Y., Marguerat, A., Barberis, C., and Dreifuss, J. J. (1994) Axotomy induces the expression of vasopressin receptors in cranial and spinal motor nuclei in the adult rat. *Proc. Natl. Acad. Sci. U.S.A. 91*, 9636−9640.

(6) Oz, M., Kolaj, M., and Renaud, L. P. (2001) Electrophysiological evidence for vasopressin V(1) receptors on neonatal motoneurons, premotor and other ventral horn neurons. *J. Neurophys. 86*, 1202−1210.
(7) Albers, H. E., Pollock, J., Simmons, W. H., and Ferris, C. F. (1986) A V1-like receptor mediates vasopressin-induced flank marking behavior in hamster hypothalamus. *J. Neurosci. 6*, 2085−2089.
(8) Iwata, T., Toyoda, F., Yamamoto, K., and Kikuyama, S. (2000) Hormonal control of urodele reproductive behavior. *Comp. Biochem. Physiol. B 126*, 221−229.
(9) Insel, T. R., Winslow, J. T., Wang, Z., and Young, L. J. (1998) Oxytocin, vasopressin, and the neuroendocrine basis of pair bond formation. *Adv. Exp. Med. Biol. 449*, 215−224.
(10) Miller, F. L. and Moore, L. J. (1983) Arginine vasotocin induces sexual behavior of newts by acting on cells in the brain. *Peptides 4*, 97−102.
(11) Briner, V. A., Williams, B., Tsai, P., and Schrier, R. W. (1992) Demonstration of processing and recycling of biologically active V1 vasopressin receptors in vascular smooth muscle. *Proc. Natl. Acad. Sci. U.S.A. 89*, 2854−2858.
(12) Lutz, W., Salisbury, J. L., and Kumar, R. (1991) Vasopressin receptor-mediated endocytosis: current view. *Am. J. Physiol. 261*, F1−F13.
(13) Tsao, P., Cao, T., and von Zastrow, M. (2001) Role of endocytosis in mediating downregulation of G-protein-coupled receptors. *Trends. Pharmacol. Sci. 22*, 91−96.
(14) Innamorati, G., Le Gouill, C., Balamotis, M., and Birnbaumer, M. (2001) The long and the short cycle: Alternative intracellular routes for trafficking of G-protein-coupled receptors. *J. Biol. Chem. 276*, 13096−13103.
(15) Propper, C. R. (1991) Courtship in the roush-skinned newt *Taricha granulosa*. *Animal Behav. 41*, 547−554.
(16) Rose, J. D., Kinnaird, J. R. and Moore, F. L. (1995) Neurophysiological effects of vasotocin and corticosterone on medullary neurons: Implications for hormonal control of amphibian courtship behavior. *Neuroendocrinology 62*, 406−417.
(17) Eggena, P., and Buku, A. (1989) Synthesis and characterization of a long-acting fluorescent analog of vasotocin. *Biol. Cell 66*, 1−6.
(18) Eggena, P., Lu, M., and Buku, A. (1990) Internalization of fluorescent vasotocin-receptor agonist and antagonist in the toad bladder. *Am. J. Physiol. 259*, C462− C470.
(19) Eggena, P., Ma, C.-L., Lu, M., and Buku, A. (1990) A fluorescent analogue of hydrin 1: a new probe for vasotocin receptors. *Am. J. Physiol. 259*, E524-E528.
(20) Buku, A., Masur, S., and Eggena, P. (1989) Synthesis and characterization of fluorescein- and rhodamine-labeled probes for vasotocin receptors. *Am. J. Physiol. 257*, E804−E808.
(21) Sawyer, W. H., and Manning, M. (1984) The development of vasopressin antagonists. *Fed. Proc. 43*, 87−90.
(22) Tripp, S. K., and Moore, F. L. (1988) Autoradiographic characterization of binding sites labeled with vasopressin in the brain of a urodele amphibian. *Neuroendocrinology 48*, 87−92.

BC049928X

Conjugation of a Hairpin Pyrrole-Imidazole Polyamide to a Quinone Methide for Control of DNA Cross-Linking

Dalip Kumar, Willem F. Veldhuyzen, Qibing Zhou,† and Steven E. Rokita*

Department of Chemistry and Biochemistry, University of Maryland, College Park, Maryland 20742. Received April 1, 2004; Revised Manuscript Received April 22, 2004

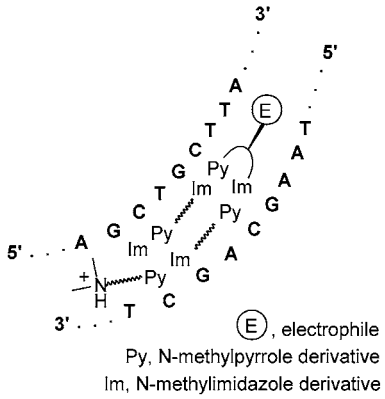
A series of quinone methide precursors designed for DNA cross-linking were prepared and conjugated to a pyrrole-imidazole polyamide for selective association to the minor groove. Although reaction was only observed for DNA containing the predicted recognition sequence, yields of strand alkylation were low. Interstrand cross-linking was more efficient than alkylation but still quite modest and equivalent to that generated by a comparable conjugate containing the N-mustard chlorambucil. Varying the length of the linker connecting the polyamide and quinone methide derivative did not greatly affect the yield of DNA cross-linking. Instead, intramolecular trapping of the quinone methide intermediate by nucleophiles of the attached polyamide appears to be the major determinant that limits its reaction with DNA. Self-adducts of the quinone methide conjugate form readily and irreversibly as detected by a combination of chromatography and mass spectroscopy. This result is unlike comparable self-adducts observed for oligonucleotide conjugates that form more slowly and remain reversible. Equivalent intramolecular alkylation of a polyamide by its attached chlorambucil mustard was not observed under similar condition. The presence of DNA, however, did facilitate hydrolysis of this mustard conjugate.

INTRODUCTION

Distamycin continues to inspire development of new compounds with a highly precise and predictable ability to recognize an extended series of base pairs in duplex DNA since its original discovery over 40 years ago (*1*). This natural product is composed of three *N*-methylpyrrole rings attached through amide bonds to create a molecule that complements the bend of DNA's minor groove and offers hydrogen bonding to its preferred target region rich in A/T pairs (*2*). Such selectivity has since been conferred to a number of reagents with covalent reactivity by conjugating the appropriate appendages to distamycin or related derivatives (*3*−*5*). Included in this series are a variety of alkylating agents. For example, a distamycin−benzoic acid N-mustard conjugate, tallimustine, was prepared and tested clinically as an anticancer drug candidate (*6*, *7*). Variations of tallimustine have also been synthesized and examined under a range of biological conditions (*8*−*11*). Other alkylating and cross-linking agents have similarly been attached to distamycin including a bis(hydroxylmethyl)pyrrole (*12*), a methyl alkyl sulfate (*13*), mitomycin (*14*), a pyrrolobenzodiazepine derivative reminiscent of tomamycin (*15*), and a cyclopropylpyrroloindole group related to CC-1065 and duocarmycin (*16*).

Once distamycin and its conjugates were found to bind as a dimer in the minor groove (*17*), polyamides containing the equivalents of a dimer structure were constructed (*18*). As predicted, these new hairpin-shaped derivatives bound tightly and precisely to chosen sequences of DNA. Inclusion of additional heterocyclic substituents allowed for distinct recognition of each base pair (*4*, *19*, *20*). Further derivatization of such compounds with cyclopropylpyrroloindole and chlorambucil appendages provided additional efficiency and selectivity for alkylating and cross-linking DNA (Scheme 1) (*21*−*23*). Success with the pyrrole-imidazole polyamides created an extremely attractive system for directing the chemistry of quinone methides to the minor groove of DNA.

Scheme 1



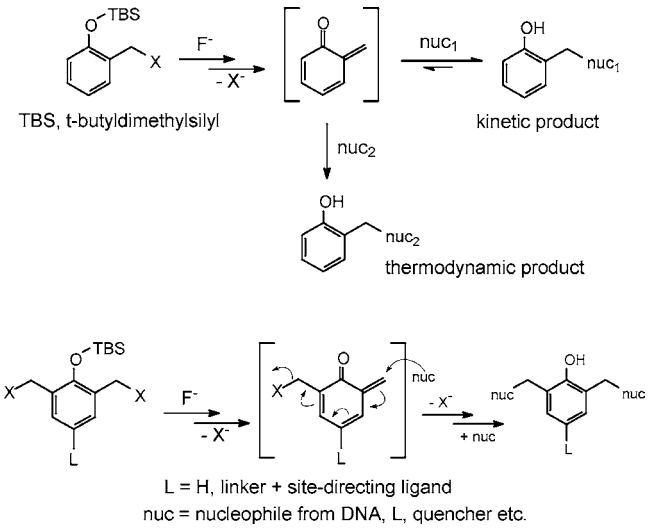
Quinone methides are highly electrophilic and transient intermediates that are implicated in alkylation of DNA by drugs such as mitomycin (*24*) and tamoxifen (*25*), food additives such as butylated hydroxytoluene (BHT) (*26*), and certain natural products (*27*, *28*). Our laboratory has prepared and studied a series of simple precursors and their bioconjugates that form *o*-quinone methide intermediates. Activation of these precursors is easily controlled by addition of fluoride, a species that is otherwise rarely encountered under chemical and biological conditions (Scheme 2). The products formed by quinone methide reaction with strongly nucleophilic groups in DNA tend to be unstable and readily reverse so that only adducts formed by the weakly nucleophilic exo amino groups of G and A are often isolated (nuc_1 vs nuc_2, respectively in Scheme 2) (*29*−*34*).

* To whom correspondence should be addressed. E-mail: rokita@umd.edu.

† Current address: Department of Chemistry, Virginia Commonwealth University, Richmond, VA 23284.

10.1021/bc049941h CCC: $27.50 © 2004 American Chemical Society
Published on Web 06/04/2004

Scheme 2



The tendency for an *o*-quinone methide to accumulate only irreversible adducts can be overridden by attachment of a DNA ligand that is capable of maintaining close proximity between a reactive nucleophile−electrophile pair. Reversibility of addition is not affected by this strategy. Rather, diffusion of the regenerated intermediate is inhibited and consequently shielded from exposure to the weak nucleophiles forming irreversible adducts. This is best illustrated by the ability of a quinone methide−acridine conjugate to act as a highly efficient and persistent cross-linker of duplex DNA through reaction primarily at G N7 in the major groove, a site that would otherwise form only an unstable and transient adduct (*35*). The ratio of monoalkylation to cross-linking of this reagent is significantly smaller than that for an equivalent conjugate formed by chlorambucil. This desirably low ratio might also derive from the reversibility of quinone methide addition if the conjugate is able to migrate from sites allowing only monoalkylation to sites capable of cross-linking. Certainly, an equivalent reversibility in product formation is responsible for converting oligonucleotide−quinone methide self-adducts from inactive and undesirable side products to highly valuable target-promoted alkylating agents (*36*). A series of conjugates between a pyrrole-imidazole polyamide and quinone methide precursors has now been prepared and examined as described here to investigate whether a similar synergy could be realized between a distamycin-based ligand, a quinone methide intermediate, and the minor groove of DNA.

MATERIALS AND METHODS

General. Solvents, chemicals, and reagents were obtained in the highest purity commercially available and used without additional purification unless described below. Chlorambucil, 4-(4′-methoxyphenyl)butyric acid and monomethyl adipoyl chloride were purchased from ICN Biomedicals, Aldrich Chemical Co. and Fluka Chemical Corporation, respectively. Boc-*β*-alanine-Pam resin and (*R*)-2-Fmoc-4-Boc-diaminobutyric acid were purchased from Peptides International. Diisopropylethylamine (DIEA) and *N*,*N*-(dimethylamino)propylamine were distilled from calcium hydride (CaH_2) and stored over NaOH pellets. Fuming nitric acid was prepared by distillation of a 50:50 solution of concentrated sulfuric acid and 70% nitric acid. Dimethylformamide (DMF) was distilled from P_2O_5 and stored over molecular sieves, and acetonitrile was distilled from CaH_2. Pyridine was freshly distilled over NaOH pellets, and ethanol (EtOH) was dried by distillation over magnesium and iodine (10:1 w/w). Both methylene chloride (CH_2Cl_2) and toluene were distilled from CaH_2 prior to use. All aqueous solutions were prepared with water purified to a resistivity of 17.8−18.0 MΩ.

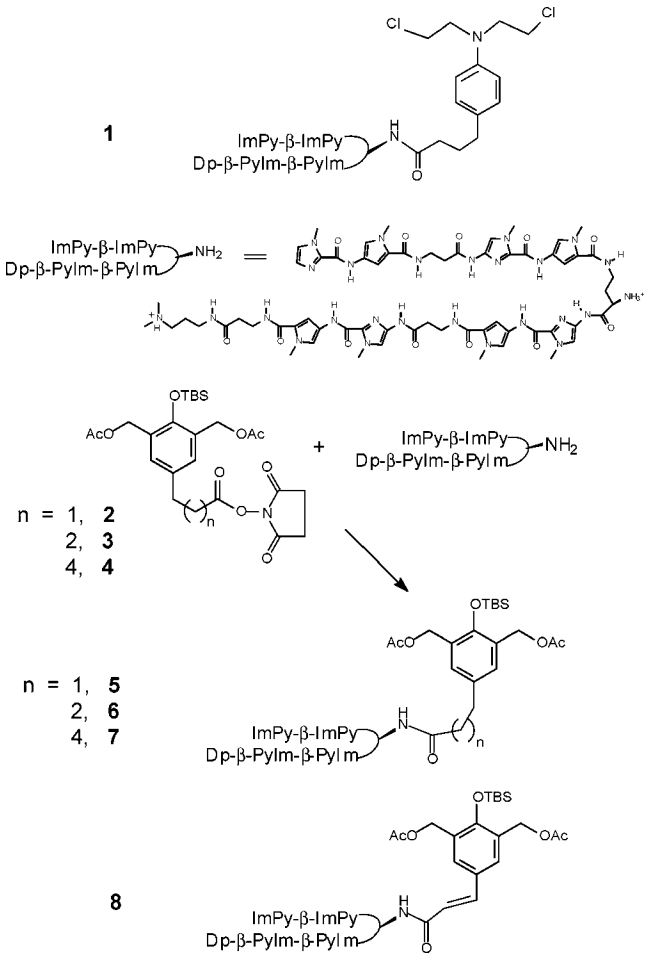
Silica gel for flash chromatography (230−400 mesh) was purchased from EM Sciences. Reverse phase C-18 chromatography was performed using analytical (Varian Microsorb-MV C-18, 300 C particle size, 250 mm × 4.6 mm) and semipreparative (Alltech Econosphere C-18, 10 um particle size, 250 mm × 10 mm) columns and a Jasco PU-980 HPLC equipped with a Jasco MD-1510 UV−Vis photodiode array detector.

^1H and ^{13}C spectra were recorded on a Bruker 400 MHz spectrometer. All NMR chemical shifts (δ) are reported in parts per million (ppm) and were determined relative to the standard values of the solvent (Cambridge Isotope Laboratories). Coupling constants (J) are reported in hertz (Hz). UV absorption spectra were obtained with a Hewlett-Packard 8453 UV−Vis spectrophotometer. Low resolution (LRMS) and high resolution (HRMS) mass spectra were determined on a VG7070E instrument using EI and FAB. Electrospray ionization mass spectrometry was performed with a Finnigan LCQ system equipped with a quadrupole ion trap.

Synthetic Procedures. *N*-Succinimidyl esters of 3-[4′-*tert*-butyldimethylsilyloxy-3′,5′-bis(acetoxymethyl)phenyl]-propionate (**2**), the related unsaturated derivative, and its conjugate **8** were prepared as described previously (*35*, *37*). The pyrrole-imidazole polyamide ImPy-*β*-ImPy-(R)*γ*-ImPy-*β*-ImPy-*β*-Dp and its chlorambucil conjugate **1** were synthesized as first reported by Wurtz and Dervan (*22*) (Scheme 3), and all of the monomeric components necessary for this were prepared as described by Baird and Dervan (*38*).

4-[4′-*tert*-Butyldimethylsilyloxy-3′,5′-bis(*tert*-butyldimethylsilyloxymethyl)phenyl]butanoic Acid (10a). Formaldehyde (37%, 11.1 mL) was added to an aqueous solution of NaOH (25%, 7.7 mL) containing *p*-hydroxyphenylbutanoic acid **9a** (2.0 g, 12 mmol) and methanol (6 mL) at 0 °C. The resulting mixture was heated to 37 °C, stirred for 48 h, and then diluted with acetone (80 mL). The orange aqueous phase was isolated, diluted with methanol (10 mL), and again added to acetone (125 mL). The resulting white precipitate was isolated by filtration, washed with acetone, and dried. This crude product (1.40 g, 4.93 mmol) was directly silylated by addition of DMF (15 mL), *tert*-butyldimethylsilyl chloride (TBS-Cl, 3.94 g, 26.1 mmol), and imidazole (4.00 g, 59.2 mmol). The reaction mixture was stirred at room temperature for 20 h, diluted with water (100 mL), and extracted with ether (3 × 50 mL). The organic phases were combined, dried with $MgSO_4$, and evaporated under reduced pressure. The residue was dissolved in methanol (40 mL), and potassium carbonate (2.0 g) was added in one portion. The solution was stirred for 40 min at room temperature, neutralized with 2 M HCl (150 mL), and extracted with ether (3 × 50 mL). The organic phase was dried ($MgSO_4$) and concentrated to yield a residue that was subject to silica gel flash chromatography using EtOAc/hexanes (1:9). The desired product was isolated as a colorless solid. Yield 56%; mp 78 °C. ^1H NMR ($CDCl_3$): δ 0.00 (s, 12H, $Si(CH_3)_2$), 0.07 (s, 6H, $Si(CH_3)_2$), 0.92(s, 18H, $C(CH_3)_3$), 1.01 (s, 9H, $C(CH_3)_3$), 1.92−1.96 (m, 2H, CH_2), 2.36 (t, J = 8.0 Hz, 2H, CH_2), 2.63 (t, J = 8.0 Hz, 2H, CH_2), 4.68 (s, 4H, CH_2), 7.16 (s, 2H, Ar−H). ^{13}C NMR ($CDCl_3$): δ 0.00, 18.4, 18.8, 26.0, 26.1, 26.2,

Scheme 3



33.3, 34.6, 60.6, 125.9, 131.5, 134.1, 146.2, 179.7. HRMS (FAB): calcd for $C_{30}H_{58}O_5Si_3$ $(M)^+$ 582.3592, found 582.2138.

4-[4′-*tert*-Butyldimethylsilyloxy-3′,5′-bis(acetoxymethyl)phenyl]butanoic Acid (11a). Solid ferric chloride (0.030 g, 0.19 mmol) was added to a stirred suspension of **10a** (0.33 g, 0.57 mmol) at 0 °C. The reaction mixture was maintained at this temperature and stirred for 0.5 h before adding ice-cold water (100 mL). This mixture was extracted with ether (3 × 10 mL). The organic layer was evaporated, and the residue was suspended in water (50 mL). This was extracted with hexanes (3 × 10 mL). The organic phase was dried with $MgSO_4$ and concentrated under reduced pressure. The resulting residue was subjected to silica gel column chromatography using EtOAc:hexanes (1:9), and the desired product (viscous oil) was isolated in 81% yield. ^{1}H NMR ($CDCl_3$): δ 0.17 (s, 6H, $Si(CH_3)_2$), 1.00 (s, 9H, $C(CH_3)_3$), 1.89 (m, 2H, CH_2), 2.08 (s, 6H, $COCH_3$), 2.35 (t, 2H, CH_2), 2.58 (t, 2H, CH_2), 5.05 (s, 4H, CH_2), 7.09 (s, 2H, Ar−H). ^{13}C NMR ($CDCl_3$): δ 18.9, 21.0, 25.8, 26.2, 33.3, 34.1, 61.9, 126.8, 130.3, 134.6, 149.6, 171.0. HRMS (FAB): calcd for $C_{22}H_{34}O_7SiNa$ $(M + Na)^+$ 461.1972, found 461.1962.

***N*-Succinimidyl 4-[4′-*tert*-Butyldimethylsilyloxy-3′,5′-bis(acetoxymethyl)phenyl]butanoate (3).** A mixture of **11a** (0.050 g, 0.11 mmol), *N*-hydroxysuccinimide (0.048 g, 0.42 mmol), and 1-(3-dimethylaminopropyl)-3-ethylcarbodiimide hydrochloride (EDC) (0.080 g, 0.42 mmol) in DMF (5 mL) was stirred at room temperature for 12 h. The reaction mixture was poured into cold water (100 mL) and extracted with ether (3 × 10 mL). The organic phase was dried with $MgSO_4$, and solvent was removed at reduced pressure. The resulting residue was subjected to preparative thin-layer chromatography using EtOAc:hexanes (2:3) to afford the desired product as a viscous oil. Yield 67%. ^{1}H NMR ($CDCl_3$): δ 0.17 (s, 6H, $Si(CH_3)_2$), 1.00 (s, 9H, $C(CH_3)_3$), 2.01−2.05 (m, 2H, CH_2), 2.09 (s, 6H, $COCH_3$), 2.60 (t, J = 7.0 Hz, 2H, CH_2), 2.09 (t, J = 7.0 Hz, 8.0 Hz, 2H, CH_2), 2.83 (s, 4H, CH_2), 5.06 (s, 4H, CH_2), 7.11(s, 2H, ArH). ^{13}C NMR ($CDCl_3$): δ −3.7, 18.6, 21.0, 25.60, 25.88, 26.22, 30.23, 33.77, 61.90, 127.00, 130.30, 134.00, 149.80, 168.40, 169.10, 171.0. HRMS (EI): calcd for $C_{26}H_{37}NO_9Si$ $(M)^+$, 535.2238, found 535.2227.

6-[4′-*tert*-Butyldimethylsilyloxy-3′,5′-bis(*tert*-butyldimethylsilyloxymethyl)phenyl]hexanoic Acid (10b). This was prepared equivalently to that described for **10a** starting from **9b** (0.52 g, 2.5 mmol). Yield 44%; mp. 82 °C. ^{1}H NMR ($CDCl_3$): δ 0.06 (s, 12H, $Si(CH_3)_2$), 0.13 (s, 6H, $Si(CH_3)_2$), 0.92 (s, 18H, $C(CH_3)_3$), 1.00 (s, 9H, $C(CH_3)_3$), 1.37−1.38 (m, 2H, CH_2), 1.59−1.67 (m, 4H, CH_2), 2.32 (t, J = 8.0 Hz, 2H, CH_2), 2.56 (t, J = 8.0 Hz, 2H, CH_2), 4.67 (s, 4H, CH_2), 7.13 (s, 2H, Ar−H). ^{13}C NMR ($CDCl_3$) δ 18.4, 18.72, 24.58, 25.94, 26.02, 28.67, 30.96, 33.96, 35.21, 60.6, 125.8, 131.2, 135.3, 179.7. HRMS (FAB): calcd for $C_{32}H_{61}O_5Si_3$ $(M - H)^-$ 609.3827, found 609.3826.

6-[4′-*tert*-Butyldimethylsilyloxy-3′,5′-bis(acetoxymethyl)phenyl]hexanoic Acid (11b). This was prepared equivalently to that described for **11a** starting from **10b** (025 g, 041 mmol). Yield 69% (viscous oil). ^{1}H NMR ($CDCl_3$): δ 0.18 (s, 6H, $Si(CH_3)_2$), 1.01 (s, 9H, $C(CH_3)_3$), 1.38−1.42 (m, 2H, CH_2), 1.57−1.71 (m, 4H, CH_2), 2.06 (s, 6H, $OCOCH_3$), 2.44 (t, J = 7.0, J = 8.0 Hz, 2H, CH_2), 2.54 (t, J = 8.0 Hz, 2H, CH_2), 5.06 (s, 4H, CH_2), 7.08 (s, 2H, Ar−H). ^{13}C NMR ($CDCl_3$): δ -3.8, 18.6, 21.0, 22.1, 23.9, 24.4, 25.8, 28.4, 30.9, 34.7, 35.0, 61.9, 126.6, 130.2, 135.7, 149.4, 169.2, 170.9. HRMS (FAB): calcd For $C_{24}H_{37}O_7Si$ $(M - H)^-$ 465.2309, found 465.2293.

***N*-Succinimidyl 6-[4′-*tert*-Butyldimethylsilyloxy-3′,5′-bis(acetoxymethyl)phenyl]hexanoate (4).** This was prepared equivalently to that described for **3** starting from **11b** (0.10 g, 0.21 mmol). Yield 66% (liquid). ^{1}H NMR ($CDCl_3$): δ 0.16 (s, 6H, $Si(CH_3)_2$), 0.99 (s, 9H, $C(CH_3)_3$), 1.43−1.45 (m, 2H, CH_2), 1.61−1.63 (m, 2H, CH_2), 1.74−1.77 (m, 2H, CH_2), 2.08 (s, 6H, $OCOCH_3$), 2.52−2.81 (m, 4H, CH_2), 2.82 (s, 4H, CH_2), 5.05 (s, 4H, CH_2), 7.08 (s, 2H, Ar−H). ^{13}C NMR ($CDCl_3$): δ −3.8, 18.6, 21.0, 24.4, 25.5, 25.8, 28.3, 30.8, 34.7, 61.9, 126.6, 130.2, 135.7, 149.4, 168.5, 169.1, 170.9. HRMS (FAB): calcd for $C_{28}H_{41}LiNO_9Si$ $(M + Li)^+$ 570.2711, found 570.2698.

Polyamide−Quinone Methide Conjugate (5). A solution of *N*-succinimidyl-3-[4′-*tert*-butyldimethylsilyloxy-3′,5′-bis(acetoxymethyl)phenyl]propionate **2** (10 mg, 19 μmol) in CH_3CN (100 μL) was added to a solution of ImPy-β-ImPy-(R)γ-ImPy-β-ImPy-β-Dp (4 mg, 3 μmol) in DMF (320 μL). Reaction was initiated by addition of DIEA (200 μL) and stirred for 10 min at room temperature. The desired product was purified by preparative HPLC using a solvent gradient of 25% CH_3CN:0.1% (v/v) aq TFA to 50% CH_3CN:0.1% (v/v) aq TFA over 40 min (5 mL/min). Solvent was removed by lyophilization to yield a white powder (0.3 mg, 6%). This yield was measured by A_{306} based on the extinction coefficient of the polyamide-chlorambucil conjugate **1** (69 500 M^{-1} cm^{-1}) (*22*). LRMS (electrospray) *m/z* calcd for $C_{83}H_{111}N_{26}O_{18}Si$ $(M + H)^+$ 1787.8, found 1787.7.

Polyamide−Quinone Methide Conjugate (6). This product was prepared equivalently to that described for conjugate **5** starting from **3** (4 mg, 8 μmol). Yield 3%;

LRMS (electrospray) *m*/*z* calcd for $C_{84}H_{113}N_{26}O_{18}Si$ $(M + H)^+$ 1801.8, found 1801.7.

Polyamide−Quinone Methide Conjugate (7). This product was prepared equivalently to that described for conjugate **5** starting from **4** (4 mg, 8 μmol). Yield 2%; LRMS (electrospray) *m*/*z* calcd for $C_{86}H_{117}N_{26}O_{18}Si$ $(M + H)^+$ 1829.8, found 1829.5.

DNA Preparation and Analysis. Oligonucleotides were synthesized by Invitrogen Life Technologies (Rockville, MD) and purified by gel electrophoresis under standard conditions (*39*). Oligonucleotides were labeled at their 5′ terminus with [γ-^{32}P]-ATP (New England Biolabs, Beverly, MA) as directed by the supplier. Typically, a 5′-[^{32}P] radiolabeled oligonucleotide (100 pmol, 640 nCi), its unlabeled equivalent (200 pmol), and its complementary strand (330 pmol) were annealed in a solution of Tris (20 mM, pH 7) by placing the mixture (total volume 200 μL) in a microfuge tube. The tube was placed in a water bath (90° C), and the bath and the tube were allowed to cool to room temperature over 3−4 h to afford a 2 μM solution of labeled duplex DNA.

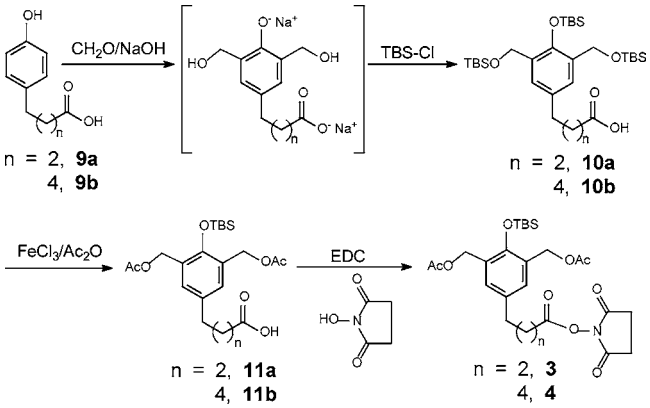
DNA Alkylation and Cross-Linking by Polyamide Conjugates. Typically, 10 μL of the DNA solutions described above (2 μM, 20 mM Tris, pH 7) were mixed with water (2 μL) and a 15% aqueous acetonitrile solution (4 μL) of conjugate **1**, **5**, **6**, **7**, or **8** (15 μM) in a microfuge tube. After addition of 4 μL of a salt solution (15 mM NaCl, 10 mM $MgCl_2$, 5 mM $CaCl_2$, ± 5 mM NaF), the resulting mixture (20 μL, 10 mM Tris, pH 7) of DNA (1 μM), reactant (3 μM), and salts (3 mM NaCl, 2 mM $MgCl_2$, 1 mM $CaCl_2$, ± 1 mM NaF) was incubated (37 °C) for 12 h. Aliquots (3 μL) were removed from the reaction mixtures and combined with a formamide loading solution (10 μL, 0.05% bromophenol blue and 0.05% xylene cyanol FF) and analyzed by 20% polyacrylamide (19:1 acrylamide:bisacrylamide) gel electrophoresis under denaturing conditions (8 mM urea). DNA was detected and analyzed by phosphoimagery.

RESULTS AND DISCUSSION

Design and Synthesis of the Quinone Methide Precursors and Their Conjugates. A bis-functional precursor designed for cross-linking DNA through sequential formation of two quinone methide intermediates had previously been coupled to an acridine derivative and a triplex-forming oligonucleotide for delivery to the major groove (Scheme 2) (*35*, *40*). This same precursor has now also been attached to a pyrrole-imidazole polyamide for its complementary delivery to the minor groove. This new conjugate additionally allowed for comparison to a related derivative prepared previously by Wurtz and Dervan containing the N-mustard chlorambucil (**1**) (*22*) (Scheme 3). This original conjugate was designed to bind in the minor groove of helical DNA containing 5′-(A/T)GC(A/T)GC(A/T)-3′ and cross-link neighboring sequences with its N-mustard attached to a central γ-aminobutyric acid (*22*). Synthesis of the polyamide was first accomplished by manual solid-phase synthesis (*22*, *38*) and repeated in our laboratory in comparable yield. The N-mustard was also coupled to this polyamide as described by Wurtz and Dervan (*22*).

Coupling between the available quinone methide precursor **2** and the polyamide yielded a conjugate (**5**) that contained one less methylene unit in its linker than **1** (Scheme 3). Consequently, a series of additional quinone methide precursors were also prepared to more closely mimic the distance between the polyamide and its attached N-mustard in **1**. First, the alkyl chain connecting the polyamide and quinone methide precursor was extended by one carbon (**6**) to match the distance between the polyamide and aromatic ring of chlorambucil. Second, a longer extension (**7**) was generated to approach more closely the 11-atom distance between the polyamide of **1** and the site of nucleophilic addition by DNA on the N-mustard. In all cases, the linkers provided conformational flexibility for sampling numerous sites of potential reactivity. A contrasting analogue containing a conjugated vinyl linker was additionally prepared (**8**) as described previously (*37*) since this type of linkage had demonstrated great effectiveness in other polyamide conjugates (*16*, *41*, *42*).

Scheme 4



The activated esters **3** and **4** used for coupling to the polyamide were constructed using the same strategy developed for the original bis-functional quinone methide precursor **2** (*35*). The starting material **9a** was formed by demethylation of 4-(4′-methoxyphenyl)butyric acid, and **9b** was obtained from a Friedel−Craft acylation of phenol by monomethyl adipoyl chloride and subsequent Clemmensen reduction (*43*, *44*). These materials were hydroxymethylated with formaldehyde under basic conditions and then silylated with *tert*-butyldimethylsilyl chloride (TBS-Cl) under standard conditions to yield **10a**,**b** (Scheme 4) (*35*). The benzylic positions were selectively substituted with acetate by treatment with acetic anhydride and $FeCl_3$ (*45*), and finally the carboxylic acids were converted to their *N*-hydroxysuccinimide esters **3** and **4** in the presence of EDC. These activated esters were condensed with the polyamide in a mixture of CH_3CN, DMF, and DIEA to yield the desired conjugates capable of generating quinone methide intermediates. Analysis by reverse phase (C-18) HPLC indicated that all polyamide amine was consumed in the presence of the *N*-hydroxysuccinimide esters within 1 h and more than 50% had already reacted within the first 10 min. This analysis also indicated that the conjugate formed in yields of up to 65%. However, product recovery after reverse-phase chromatography was quite low and suggested problems with the final steps of isolation. This method of purification still generated sufficient material for the studies below, and consequently these procedures were not optimized. The molecular weights of each conjugate were confirmed by electrospray mass spectroscopy.

Alkylation and Cross-Linking of a Target DNA Using N-Mustard and Quinone Methide Conjugates. The original N-mustard chlorambucil conjugate **1** was targeted for selective reaction on either side of the TATA box of a HIV promoter and tested with a restriction fragment of DNA that offered a range of sequence variants (*22*). Indeed, the predicted sites were alkylated

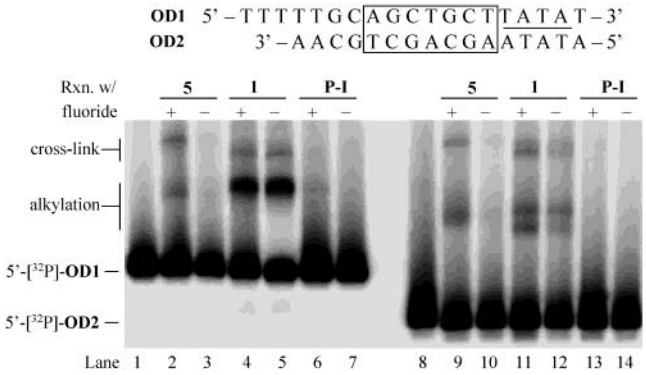


Figure 1. Alkylation and cross-linking of DNA by pyrrole-imidazole polyamide conjugates. 5′-[^{32}P]-**OD1** (30 nCi, 1.0 μM) and **OD2** (1.1 μM) (lane 1) or 5′-[^{32}P]-**OD2** (30 nCi, 1.0 μM) and **OD1** (1.1 μM) (lane 8) were incubated for 12 h (37 °C) in a solution of 5% aqueous acetonitrile (3 mM NaCl, 2 mM $MgCl_2$, 1 mM $CaCl_2$, 10 mM Tris, pH 7) in the added presence of conjugate **5** (10 μM, lanes 2, 3, 9, and 10), conjugate **1** (10 μM, lanes 4, 5, 11, and 12), or the polyamide ImPy-β-ImPy-(R)γ-ImPy-β-ImPy-β-Dp (**P**−**I**) (10 μM, lanes 6, 7, 13, and 14). Reactions were alternatively incubated in the presence of fluoride (1 mM NaF, lanes 2, 4, 6, 9, 11, and 13) or in its absence (lanes 3, 5, 7, 10, 12, and 14). The yields of alkylation and cross-linked products were determined relative to the total material per experiment.

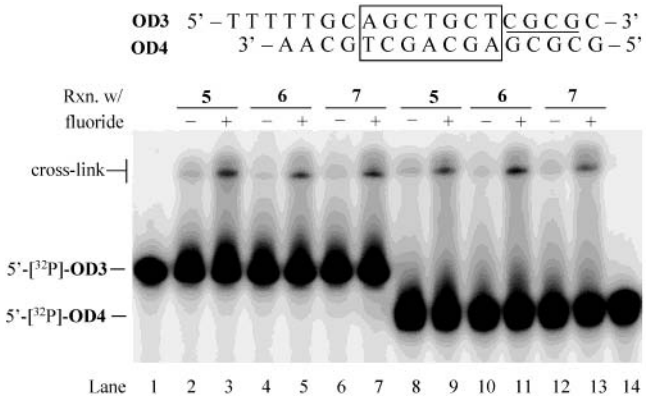


Figure 2. The effect of varying the linker length between a quinone methide precursor and its attached pyrrole-imidazole polyamide on the efficiency of DNA cross-linking. 5′-[^{32}P]-**OD3** (30 nCi, 1.0 μM) and **OD4** (1.1 μM) (lane 1) or 5′-[^{32}P]-**OD4** (30 nCi, 1.0 μM) and **OD3** (1.1 μM) (lane 14) were incubated for 12 h (37 °C) in a solution of 5% aqueous acetonitrile (3 mM NaCl, 2 mM $MgCl_2$, 1 mM $CaCl_2$, 10 mM Tris, pH 7) in the added presence of conjugate **5** (3 μM, lanes 2, 3, 8, and 9), conjugate **6** (3 μM, lanes 4, 5, 10, and 11), or conjugate **7** (3 μM, lanes 6, 7, 12, and 13). Reactions were alternatively incubated in the absence of fluoride (lanes 2, 4, 6, 8, 10, and 12) or in its presence (1 mM NaF, lanes 3, 5, 7, 9, 11, and 13). The yields of alkylation and cross-linked products were determined relative to the total material per experiment.

with greatest efficiency as expected for minor groove recognition. One of these sites has now been reproduced in the model formed by **OD1**·**OD2** to focus on the relative efficacy of alkylation by the contrasting electrophiles of a N-mustard and quinone methide. The length of **OD1** was extended beyond that of **OD2** to allow for easy differentiation of products formed by monoalkylation and interstrand cross-linking (bis-alkylation) using gel electrophoresis. Attempts to utilize the same ionic conditions as first reported by Wurtz and Dervan (*22*) led to precipitation after either KF or NaF (10 mM) was added to initiate quinone methide formation. Dilution of the NaCl (3 mM), $MgCl_2$ (2 mM), $CaCl_2$ (1 mM) and NaF (1 mM) was sufficient to avoid detectable precipitation. The initial precipitate was most likely due to the limited solubility of CaF_2. Although polyamides also exhibit low solubility, the conjugates described here appear to remain in solution at concentrations below 10 μM.

The chlorambucil- and quinone methide-containing conjugates **1** and **5** both yielded strand alkylation and cross-linking. Alkylation resulted in products that migrated in a strand specific manner (**OD1** vs **OD2**) and cross-linking resulted in a product that migrated equivalently regardless of which strand was labeled (Figure 1). Consistent with the mechanisms of each conjugate, fluoride was required to initiate reaction of the quinone methide precursor (Figure 1, lanes 2 and 9 vs lanes 3 and 10) whereas fluoride was not required for the N-mustard conjugate **1** (Figure 1, lanes 4, 5, 11, and 12). The slowly migrating products in both cases appear dependent on the reactive appendages since the polyamide alone did not generate equivalent species (Figure 1, lanes 6, 7, 13, and 14). Additionally, no reaction was detected when conjugate **5** was incubated with a DNA duplex formed by 5′-TTTTGCAGGTGGTGCCGC-3′ and a complementary strand that lacked the optimal sequence for polyamide recognition in the minor groove (5′-(A/T)GC(A/T)GC(A/T)-3′).

The expected site of reaction within **OD1**/**OD2** (*22*), 5′...TATA...3′/3′...ATAT...5′ adjacent to the polyamide binding site does not offer the preferred nucleophile for either a N-mustard or quinone methide. The intrinsic specificity of chlorambucil lacking a site-directing ligand is the N7 group of guanosine located in the major groove (*46*). Likewise, the most commonly reported adduct of simple quinone methides form with the 2-amino group of guanosine in the minor groove (*26*, *30*, *34*). Still, the N-mustard had been shown to alkylate the N3 position of A when held in the minor groove (*22*). Alkylation of the duplex by conjugate **1** proceeded in a yield of ∼18% for one strand (**OD1**, Figure 1, lanes 4 and 5) and ∼10% for the other (**OD2**, Figure 1, lanes 11 and 12). Cross-linking was less efficient (∼4%) but still detectable (Figure 1, lanes 4, 5, 11, and 12). The conjugate **5** containing the quinone methide precursor also reacted with this DNA after addition of fluoride and produced cross-linked DNA in a yield equivalent to that of the N-mustard (4%, Figure 1, lanes 2 and 9 vs 4, 5, 11 and 12). In contrast, strand alkylation by the quinone methide conjugate proceeded in only 5% and 8% yields for **OD1** and **OD2**, respectively (Figure 1, lanes 2 and 9). The DNA products formed by conjugate **1** generated strand fragmentation at A16 of **OD1** and A6 of **OD2** after heat treatment as expected for alkylation at their N3 positions (*22*). In contrast, no fragmentation was observed after comparable treatment of the DNA products formed by conjugate **5**. This suggests that reaction of the quinone methide may instead have involved the 2-amino group of G residues within the recognition site of the polyamide.

The efficiency of quinone methide-dependent cross-linking was next examined with an alternative DNA (**OD3/OD4**, Figure 2) that retained the polyamide recognition sequence but contained 5′-CGCG-3′ as a new target for reaction. This change placed a 2-amino of G proximal to the bound conjugate and supplied the preferred sequence (5′-CG-3′) for cross-linking in the minor groove by a quinone methide-like intermediate formed by mitomycin (*24*). Previously, the quinone methide precursor within conjugate **5** had been directed to the major groove by attachment to an acridine ligand with great success (*35*) although a related conjugate based on a triplex-forming oligonucleotide exhibited only modest activity (*40*). The major site of reaction, the N7 of G,

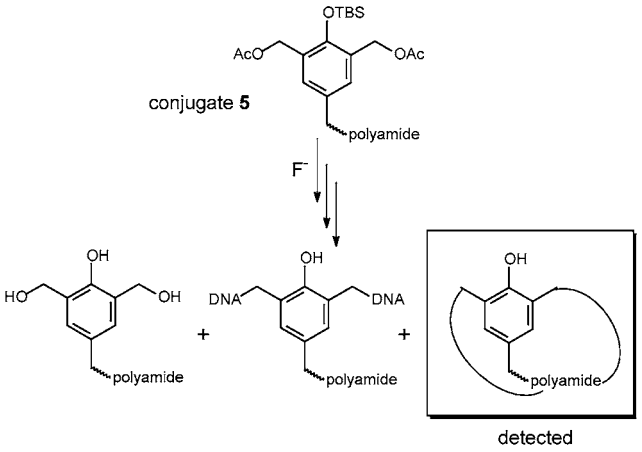
forms a reversible adduct. Alternative delivery of the quinone methide to the minor groove was expected to support high levels of reaction due to the potential advantages of localizing the quinone methide proximal to the 2-amino group of guanosine that generates a stable adduct irreversibly (*30*, *31*). Surprisingly, the quinone methide conjugate **5** also cross-linked its new target **OD3/OD4** with a low yield (~5%) and did not generate monoalkylation products detectably (Figure 2, lanes 3 and 9).

Many parameters could have impeded activity of the polyamide conjugate including the length and flexibility of the linker. While a long molecular spacer may allow access to many potential sites of reaction, the principle conformers of the spacer may not necessarily coincide with those most reactive. In contrast, a short and restricted spacer may stabilize a single conformer, but this may or may not necessarily represent the most reactive alignment. Certainly, the various linkers used for attaching N-mustards to ligands such as acridine (*47*) and triplex-forming oligonucleotides (*40*, *48*) dramatically affected target alkylation, and hence additional quinone methide conjugates were prepared for more precise comparison with the related polyamide−N-mustard conjugate **1**. The quinone methide conjugate **5** was extended by one carbon unit to form conjugate **6** containing the same four carbon link to the aromatic ring as that in the original N-mustard conjugate **1**. Another quinone methide conjugate **7** was prepared to mimic more closely the 11 atom spacing between the sites of ligand attachment and DNA alkylation of **1**. Surprisingly, neither change effected the apparent activity of the attached quinone methide. Conjugates **6** and **7** both cross-linked **OD3/OD4** in low yield (3−6%) and no monoalkylated derivatives were apparent in either case (Figure 2).

A short and rigid acrylamide linker has also been used to join various reactive appendages to the termini of distamycin-like ligands (*16*, *41*, *42*). The successes achieved with this design prompted construction of an equivalent quinone methide derivative (**8**) linked to the hairpin rather than terminal region of the polyamide as used previously (*37*). However, incubation of conjugate **8** under conditions equivalent to those used for conjugates **1** and **5**−**7** generated no observable alkylation or cross-linking of **OD3/OD4** (data not shown). This may reflect a decrease in the stability of the TBS-protected precursor relative to its saturated derivative **5** (*37*). Alternatively, the modest activity of the pyrrole-imidazole polyamide conjugates **5**−**7** and even the lack of reaction of **8** might instead have originated from a common characteristic shared by all of these quinone methide derivatives.

Intramolecular Trapping of the Quinone Methide Limits Its Reaction with DNA. Quinone methide intermediates are highly unstable and have the potential to react with a range of nucleophiles including those present in the attached site-directing ligand. Such intramolecular trapping would typically suppress reaction with the intended target, but the reversible nature of the quinone methide self-adducts formed with DNA allows subsequent transfer of the reactive intermediate from an intra- to intermolecular position (*36*). This process of reversible intramolecular trapping now serves a very beneficial role in an appealing new strategy for target promoted alkylation. The nucleophilic groups of the polyamide like those of DNA may also form intramolecular adducts with the attached quinone methide. Whether reaction with the polyamide suppresses or maintains target selective alkylation of DNA depends on the reversibility of possible self-adducts. The lack of efficient cross-linking and alkylation of DNA by the conjugates

Scheme 5



5−**8**, however, began to suggest that intramolecular adducts were forming and not capable of regenerating the quinone methide.

Reaction between the quinone methide of conjugate **5** and its pyrrole-imidazole polyamide were consequently examined by HPLC and electrospray mass spectrometry in a manner equivalent to that used to detect the self-adducts of an oligonucleotide−quinone methide conjugate (*36*). Within 12 h, conjugate **5** was completely consumed in the presence, but not absence, of 10 mM KF under neutral conditions, and several new products were detected by HPLC. Each exhibited a *m*/*z* of 1554 which is consistent with loss of the silyl protecting group and substitution of both benzylic acetate groups with internal nucleophiles. No additional products were indicated by mass spectroscopy including no ions consistent with a single intramolecular substitution and addition of one water (*m*/*z* 1572), addition of two waters (*m*/*z* 1590), or other possible products (Scheme 5) (Supporting Information). HPLC-MS analysis was also repeated using very high concentrations of fluoride (1 M KF) in order to monitor the deprotected quinone methide precursor (− TBS) and its transformation to the self-adducts (Figure 3). Under these conditions, ~60% of conjugate **5** converted within 50 s to a transient intermediate that is consistent with its deprotected derivative. Within 5 min, signals of the self-adducts appeared and by 60 min the profile of self-adducts remained constant. Self-adduct formation within the polyamide conjugate occurred much more rapidly than that observed for related oligonucleotide conjugates (*36*). Both types of conjugates appear to form a diversity of self-adducts that likely result from reaction with various nucleophiles along the attached DNA ligand.

Generation of self-adducts of conjugate **5** would not necessarily preclude subsequent reaction with a target DNA as long as the adducts formed reversibly and the polyamide self-adducts could still recognize the target DNA. Conformational constraints created by intramolecular nucleophilic addition are likely to inhibit selective binding but affinity should be regained upon quinone methide regeneration. Without such regeneration, neither binding nor alkylation of DNA would likely be possible. First, the stability of the polyamide self-adducts in the presence of a stoichiometric concentration of duplex DNA (0.3 μM, **OD3/OD4**) was monitored over 3 days. No change in the profile or quantity of self-adducts was detected by HPLC, and concurrently no alkylation or cross-linking of DNA was detected by gel electrophoresis. Next, the self-adducts were incubated in the presence of

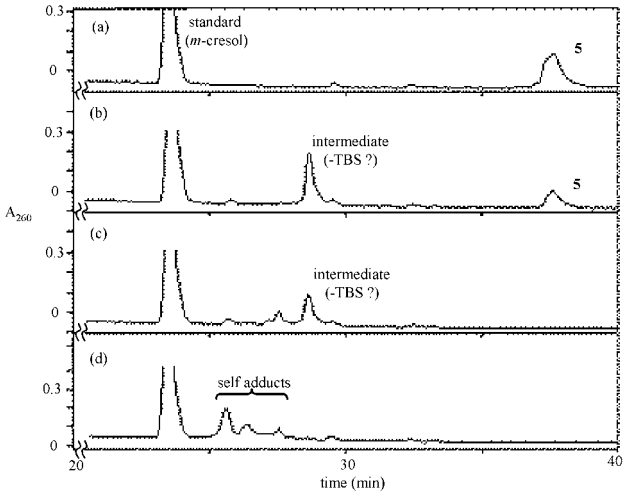
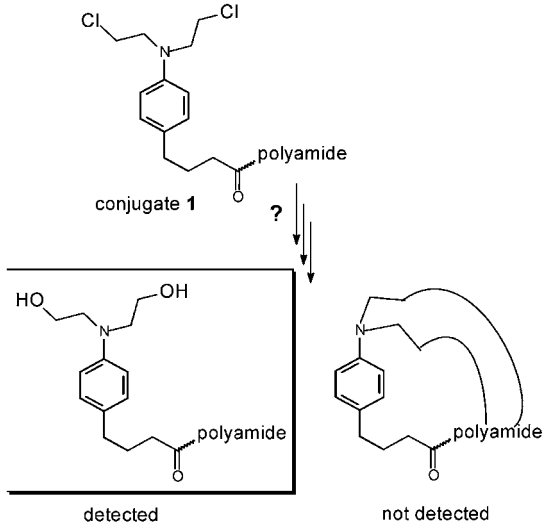


Figure 3. Formation of self-adducts from a quinone methide containing conjugate based on **5**. (a) Reaction of conjugate **5** in MES (10 mM, pH 7) and 16% acetonitrile was initiated by addition of KF (1.0 M) in the presence of a chromatographic standard *m*-cresol. Product formation was then monitored after (b) 50 s, (c) 5 min, and (d) 60 min by reverse phase (C-18) chromatography using a gradient of 5% to 70% acetonitrile in 0.1% aq TFA over 45 min at 1 mL/min.

Scheme 6



10 mM β-mercaptoethanol for 24 h, and again these adducts appeared inert. Thus, the polyamide self-adducts seem to form irreversibly and in high yield at the expense of DNA alkylation. The nonmethylated imidazole nitrogens most likely participate in self-adduct formation. This functional group is quite nucleophilic but does not exhibit a leaving group ability that is comparable to the functional groups of DNA already known to form quinone methide adducts reversibly (*31*, *33*, *34*).

N-Mustards have the potential to undergo reversible nucleophilic substitution as well, although such observations were not found in the literature. Accordingly, self-adduct formation by the polyamide−mustard conjugate **1** was investigated. Little consumption of conjugate **1** was observed after a 4 h incubation in the absence of **OD3/OD4**, and no self-adduct was detected in the presence or absence of this DNA (Supporting Information). However, ca. 60% of conjugate **1** was consumed in the presence of DNA over an equivalent period. This result can be attributed to DNA alkylation as evident by the change in chromatographic signals assigned to the DNA and hydrolysis of the dichloro mustard to its hydrolyzed diol product (Supporting Information). Thus, DNA appears to promote alkylation by and hydrolysis of the mustard containing conjugate without formation of self-adducts (Scheme 6).

CONCLUSION

The target selectivity of a quinone methide designed for cross-linking DNA was enhanced after its conjugation to a pyrrole-imidazole polyamide (*35*, *49*). However, reaction efficiency was only mildly enhanced. Yields of DNA cross-linking by the polyamide conjugates **5**−**7** were greater than similar reaction of the nonconjugated derivative at 20-fold higher concentration but still much lower than that of an acridine conjugate. The length of the linker used to attach the quinone methide to the polyamide did not affect target reaction in a significant manner. Instead, the conjugates were controlled by a dominant and irreversible formation of self-adducts by intramolecular nucleophilic addition to the transient quinone methide. A similar process was also suggested to explain a decrease in activity of mitomycin C when linked to an increasing number of *N*-methylpyrrole units (*14*). The propensity for generating intramolecular self-adducts will become advantageous rather than detrimental for target-directed alkylation once such self-adducts can be designed to form reversibly. Under these conditions, reaction selectivity, and efficiency can be achieved through a target-promoted mechanism (*36*)

ACKNOWLEDGMENT

We thank Drs. Qingping Zeng and Praveen Pande for their initial efforts on related bioconjugates. This research was supported in part by the National Institutes of Health (CA-81571).

Supporting Information Available: Electrospray mass spectrum of the self-adduct formed by conjugate **5**, the hydrolysis product of conjugate **1**, and the stability of conjugate **1** in the presence and absence of DNA. This material is available free of charge via the Internet at http://pubs.acs.org.

LITERATURE CITED

(1) Arcamone, F. M., Penco, S., Orezzi, P., Nicolella, V., and Pirelli, A. (1964) Structure and synthesis of Distamycin A. *Nature 203*, 1064−1065.

(2) Bailly, C., and Chaires, J. B. (1998) Sequence-specific DNA minor groove binders. Design and synthesis of netropsin and distamycin analogues. *Bioconjugate Chem. 9*, 513−538.

(3) Sondhi, S. M., Reddy, B. S. P., and Lown, J. W. (1997) Lexitropsin conjugates: action on DNA targets. *Curr. Med. Chem. 4*, 313−358.

(4) Dervan, P. B., and Edelson, B. S. (2003) Recognition of the DNA minor groove by pyrrole-imidazole polyamides. *Curr. Opin. Struct. Biol. 13*, 284−299.

(5) Baraldi, P. G., Tabrizi, M. A., Preti, D., Fruttarolo, F., Avitabile, B., Bovero, A., Pavani, G., del Carmen Nunez Carretero, M., and Romagnoli, R. (2003) DNA minor-groove binders. Design, synthesis and biological evaluation of ligands structurally related to CC-1065, distamycin and anthramycin. *Pure Appl. Chem., 75*, 187−194.

(6) Arcamone, F. M., Animati, F., Barbieri, B., Configliacchi, E., D'Alession, R., Geroni, C., Giuliani, C., Lazzari, E., Menozzi, M., Mongelli, N., Penco, S., and Verini, M. A. (1989) Synthesis, DNA-binding properties, and antitumor activity of novel distamycin derivatives. *J. Med. Chem. 32*, 774−778.

(7) Weiss, G. R., Poggesi, I., Rocchetti, M., Demaria, D., Hooneyham, T., Reilly, D., Vitek, L. V., Whaley, F., Patricia, E., Von Hoff, D. D., and O'dwyer, P. (1998) A phase I and pharmacokinetic study of tallimustine in patients with advanced cancer. *Clin. Cancer Res. 4*, 53−59.

(8) Wyatt, M. D., Lee, M., and Hartley, J. A. (1997) The sequence specificity of alkylation for a series of benzoic acid mustard and imidazole-containing distamycin analogues: the importance of local sequence conformation. *Nucleic Acids Res. 25*, 2359−2364.
(9) Brooks, N., McHugh, P. J., Lee, M., and Hartley, J. A. (2000) Alteration in the choice of DNA repair pathway with increasing sequence selective DNA alkylation in the minor groove. *Chem. Biol. 7*, 659−668.
(10) Baraldi, P. G., Romagnoli, R., Pavani, M. G., del Carmen Nunez, M., Bingham, J. P., and Hartley, J. A. (2002) Benzoyl and cinnamoyl nitrogen mustard derivatives of benzoheterocyclic analogues of the tallimustine: synthesis and antitumour activity. *Bioorg. Med. Chem. 10*, 1611−1618.
(11) Wang, Y., Wright, S. C., and Larrick, J. W. (2003) Synthesis and preliminary cytotoxicity of nitrogen mustard derivatives of distamycin A. *Bioorg. Med. Chem. Lett. 13*, 459−461.
(12) Woo, J., Sigurdsson, S. T., and Hopkins, P. B. (1993) DNA interstrand cross-linking reactions of pyrrole-derived bifunctional electrophiles: evidence of a common target site in DNA. *J. Am. Chem. Soc. 115*, 3407−3415.
(13) Encell, L., Shuker, D. E. G., Foiles, P. G., and Gold, B. (1996) The in vitro methylation of DNA by a minor groove binding methyl sulfonate ester. *Chem. Res. Toxicol. 9*, 563−567.
(14) Paz, M. M., Das, A., and Tomasz, M. (1999) Mitomycin C linked to DNA minor groove binding agents: synthesis, reductive activation, DNA binding and cross-linking properties and in vitro antitumor activity. *Bioorg. Med. Chem. 7*, 2713−2726.
(15) Damayanthi, Y., Reddy, B. S. P., and Lown, J. W. (1999) Design and synthesis of novel pyrrolo[2.1-c][1,4]benzodiazepine-lexitropsin conjugates. *J. Org. Chem. 64*, 290−292.
(16) Fregeau, N. L., Wang, Y., Pon, R. T., Wylie, W. A., and Lown, J. W. (1995) Characterization of a CPI-lexitropsin conjugate-oligonucleotide covalent complex by ^{1}H NMR and restrained molecular dynamics simulation. *J. Am. Chem. Soc. 117*, 8917−8925.
(17) Pelton, J. G., and Wemmer, D. E. (1989) Structural characterization of a 2: 1 distamycin A−d(CGCAAATTGGC) complex by two-dimensional NMR. *Proc. Natl. Acad. Sci. U.S.A. 86*, 5723−5727.
(18) Dervan, P. B. (2001) Molecular recognition of DNA by small molecules. *Bioorg. Med. Chem. 9*, 2215−2235.
(19) Kielkopf, C. L., Baird, E. E., Dervan, P. B., and Rees, D. C. (1998) Structural basis for G−C recognition in the DNA minor groove. *Nat. Struct. Biol. 5*, 104−109.
(20) Kielkopf, C. L., White, S., Szewczyk, J. W., Turner, J. M., Baird, E. E., Dervan, P. B., and Rees, D. C. (1998) A structural basis for recognition of A−T and T−A base pairs in the minor groove of B-DNA. *Science 282*, 111−115.
(21) Tao, Z.-F., Fujiwara, T., Saito, I., and Sugiyama, H. (1999) Rational design of sequence-specific DNA alkylating agents based on Duocarmycin A and pyrrole-imidazole hairpin polyamides. *J. Am. Chem. Soc. 121*, 4961−4967.
(22) Wurtz, N. R., and Dervan, P. B. (2000) Sequence specific alkylation of DNA by hairpin pyrrole-imidazole polyamide conjugates. *Chem. Biol. 7*, 153−161.
(23) Chang, A. Y., and Dervan, P. B. (2000) Strand selective cleavage of DNA by diastereomers of hairpin polyamide−*seco*-CBI conjugates. *J. Am. Chem. Soc. 122*, 4865−4864.
(24) Tomasz, M. (1995) Mitomycin C: small, fast and deadly (but very selective). *Chem. Biol. 2*, 575−579.
(25) Fan, P. W., Zhang, F., and Bolton, J. L. (2000) 4-Hydroxylated metabolites of the antiestrogens tamoxifen and toremifene are metabolized to unusually stable quinone methides. *Chem. Res. Toxicol. 13*, 45−52.
(26) Lewis, M. A., Yoerg, D. G., Bolton, J. L., and Thompson, J. A. (1996) Alkylation of 2′-deoxynucleosides and DNA by quinone methides derived from 2,6-di-*tert*-butyl-4-methylphenol. *Chem. Res. Toxicol. 9*, 1368−1374.
(27) Morris, B. D., and Prinsep, M. R. (1998) Euthyroideones, novel brominated quinone methides from the Bryozoan *Euthyroides episcopalis*. *J. Org. Chem. 63*, 9545−9547.
(28) Zjawiony, J. K., Bartyzel, P., and Hamann, M. T. (1998) Chemistry of puupehenone: 1,6-conjugate addition to its quinone methide system. *J. Nat. Prod. 61*, 1502−1508.
(29) Pande, P., Shearer, J., Yang, J., Greenberg, W. A., and Rokita, S. E. (1999) Alkylation of nucleic acids by a model quinone methide. *J. Am. Chem. Soc. 121*, 6773−6779.
(30) Veldhuyzen, W., Lam, Y.-f., and Rokita, S. E. (2001) 2-Deoxyguanosine reacts with a model quinone methide at multiple sites. *Chem. Res. Toxicol. 14*, 1345−1351.
(31) Veldhuyzen, W. F., Shallop, A. J., Jones, R. A., and Rokita, S. E. (2001) Thermodynamic versus kinetic products of DNA alkylation as modeled by reaction of deoxyadenosine. *J. Am. Chem. Soc. 123*, 11126−11132.
(32) Zhou, Q., and Turnbull, K. D. (2001) Quinone methide phosphodiester alkylation under aqueous conditions. *J. Org. Chem. 66*, 7072−7077.
(33) Freccero, M., Di Valentin, C., and Sarzi-AmadP, M. (2003) Modeling H-bonding and solvent effects in the alkylation of pyrimidine bases by prototype quinone methide. A DFT study. *J. Am. Chem. Soc. 125*, 3544−3553.
(34) Freccero, M., Gandolfi, R., and Sarzi-AmadP, M. (2003) Selectivity of purine alkylation by a quinone methide. Kinetic or thermodynamic control? *J. Org. Chem. 68*, 6411−6423.
(35) Veldhuyzen, W. F., Pande, P., and Rokita, S. E. (2003) A transient product of DNA alkylation can be stabilized by binding localization. *J. Am. Chem. Soc. 125*, 14005−14013.
(36) Zhou, Q., and Rokita, S. E. (2003) A general strategy for target-promoted alkylation in biological systems. *Proc. Natl. Acad. Sci. U.S.A. 100*, 15452−15457.
(37) Kumar, D., and Rokita, S. E. (2004) Synthesis of a hairpin pyrrole-imidazole polyamide conjugate containing a quinone methide precursor and vinyl linking group. *Tetrahedron Lett. 45*, 2887−2889.
(38) Baird, E. E., and Dervan, P. B. (1996) Solid-phase synthesis of polyamides containing imidazole and pyrrole amino acids. *J. Am. Chem. Soc. 118*, 6141−6146.
(39) Ellington, A., and Pollard, J. D. (1998) in *Current Protocols in Molecular Biology* (Ausuble, F. M., Brent, R., Kingston, R. E., Moore, D. D., Seidman, J. G., Smith, J. A., and Struhl, K., Eds.) section 2.12, John Wiley and Sons, New York.
(40) Zhou, Q., Pande, P., Johnson, A. E., and Rokita, S. E. (2001) Sequence-specific delivery of a quinone methide intermediate to the major groove of DNA. *Bioorg. Med. Chem. 9*, 2347−2354.
(41) Tao, Z.-F., Saito, I., and Sugiyama, H. (2000) Highly cooperative DNA dialkylation by the homodimer of imidiazole-pyrrole diamide-CPI conjugate with vinyl linker. *J. Am. Chem. Soc. 122*, 1602−1608.
(42) Bando, T., Narita, A., Saito, I., and Sugiyama, H. (2002) Molecular design of a pyrrole-imidazole hairpin polyamides for effective DNA alkylation. *Chem. Eur. J. 8*, 4781−4790.
(43) Chu, L., Hutchins, J. E., Weber, A. E., Lo, J.-L., Yang, Y.-T., Cheng, K., Smith, R. G., Fisher, M. H., Wyvratt, M. J., and Goulet, M. T. (2001) Initial structure−activity relationship of a novel class of nonpeptidyl GnRH receptor antagonists: 2-arylindoles. *Bioorg. Med. Chem. Lett. 11*, 509−513.
(44) Aultz, D. E., and McFadden, A. R. (1977) Dibenz[*b*,*e*]-oxepinalkanoic acids as nonsteroidal antiinflammatory agents. 3. ω-(6,11-dihydro-11-oxodibenz[*b*,*e*]oxepin-2-yl)alkanoic acids. *J. Med. Chem. 20*, 1499−1501.
(45) Ganem, B., and Small, V. R. (1974) Ferric chloride in acetic anhydride. A mild and versatile reagent for the cleavage of ethers. *J. Org. Chem. 39*, 3728−3730.
(46) Kohn, K. W., Hartley, J. A., and Mattes, W. B. (1987) Mechanisms of DNA sequence selective alkylation of guanine-N7 positions by nitrogen mustards. *Nucleic Acids Res. 15*, 10531−10549.
(47) Boritzki, T. J., Palmer, B. D., Coddington, J. M., and Denny, W. A. (1994) Identification of the major lesion from the reaction of an acridine-targeted aniline mustard with DNA as an adenine N1 adduct. *Chem. Res. Toxicol. 7*, 41−46.
(48) Reed, M. W., Lukhtanov, E. A., Gorn, V., Dutyavin, I., Gall, A., Wald, A., and Meyer, R. B. (1998) Synthesis and reactivity of aryl nitrogen mustard-oligodeoxyribonucleotide conjugates. *Bioconjugate Chem. 9*, 64−71.
(49) Zeng, Q., and Rokita, S. E. (1996) Tandem quinone methide generation for cross-linking DNA. *J. Org. Chem. 61*, 9080−9081.

BC049941H

TECHNICAL NOTES

Carbohydrate Conjugates for Molecular Imaging and Radiotherapy: ^{99m}Tc(I) and ^{186}Re(I) Tricarbonyl Complexes of *N*-(2′-Hydroxybenzyl)-2-amino-2-deoxy-D-glucose

Simon R. Bayly,[†,‡] Cara L. Fisher,[†,‡] Tim Storr,[†] Michael J. Adam,*[,‡] and Chris Orvig*[,†]

Department of Chemistry, University of British Columbia, 2036 Main Mall, Vancouver, British Columbia, V6T 1Z1, Canada, and TRIUMF, 4004 Wesbrook Mall, Vancouver, British Columbia, V6T 2A3, Canada. Received January 26, 2004; Revised Manuscript Received April 28, 2004

An approach to a new class of potential radiopharmaceuticals is demonstrated by the labeling of a glucosamine derivative with the tricarbonyls of ^{99m}Tc and ^{186}Re. The proligand H**L²** (*N*-(2′-hydroxybenzyl)-2-amino-2-deoxy-d-glucose) was produced by hydrogenation of the corresponding Schiff base and reacted with $[NEt_4]_2[Re(CO)_3Br_3]$ to form the neutral complex $[(\mathbf{L^2})Re(CO)_3]$ in 40% yield. ^{1}H and ^{13}C NMR spectra indicate that the $\{Re(CO)_3\}$ core is bound in a tridentate fashion via the amino N, phenolato O, and C-3 hydroxyl O atoms of the ligand. At the tracer-level, labeling of H**L²** with $[^{99m}Tc(CO)_3(H_2O)_3]^+$ and $[^{186}Re(CO)_3(H_2O)_3]^+$ was achieved in aqueous conditions in 95 ± 2% and 94 ± 3% average radiochemical yields, respectively.

INTRODUCTION

2-[^{18}F]-Fluoro-2-deoxy-D-glucose (FDG) is the preeminent radiotracer used in positron emission tomography (*1*). Because the production of ^{18}F requires a cyclotron and the isotope has a short (110 min) half-life, its utility is somewhat limited compared to that of single photon emitters in nuclear medicine. By comparison, ^{99m}Tc, the isotope most commonly used in single photon emission computed tomography (SPECT), is produced in the form of $Na^{99m}TcO_4$ from a ^{99}Mo generator; hence, it is widely available and relatively inexpensive (*2*). The third row transition metal analogue of technetium, rhenium, has similar chemistry to that of technetium and has particle-emitting radioisotopes with physical properties applicable to therapeutic nuclear medicine (*3*). For these reasons, we seek a ^{99m}Tc SPECT tracer that will mimic the biodistribution of FDG and the therapeutic potential of the analogous rhenium compounds. Our approach is to attach to glucose a chelating ligand that, in a subsequent reaction, will bind the radioisotope ^{99m}Tc or $^{186/188}$Re. A metal-chelate could be preformed and then attached to glucose. To mimic the properties of FDG it is imperative that the effects of the tracer group on the properties of the glucose molecule are minimized. Existing ^{99m}Tc labeled glucose derivatives fail this criterion: they are either ionic or have relatively high molecular weight (i.e. carry two glucose moieties) (*4*).

We elected to use the versatile low valent *fac*-$\{M(CO)_3\}$ core (M = ^{99m}Tc^{I} or ^{186}Re^{I}), whose recent chemistry has been pioneered by Alberto and co-workers (*5*). The facially coordinated carbonyl ligands stabilize the Tc +1 oxidation state, obviating the elaborate, often macrocyclic, polydentate structures required to stabilize other intermediate oxidation states of Tc and Re. In neutral complexes with simple N,O donors the *fac*-$\{M(CO)_3\}$ core possesses intermediate lipophilicity, an advantage in living systems (*6*).

Glucosamine (2-amino-2-deoxy-D-glucose) is a highly attractive scaffold for a glucosyl ligand, because the amine acts both as a potential coordination site and as a useful target for further functionalization. Furthermore, there is much evidence in the literature to suggest that N-functionalized glucosamines show activity with GLUTs (glucose transporters) and hexokinase—the enzymes that are most closely associated with the metabolism of FDG—even when the functional group is large (*7*).

EXPERIMENTAL PROCEDURES

All solvents and chemicals (Fisher, Aldrich) were reagent grade and used without further purification unless otherwise specified. H**L¹** (*8*) and $[NEt_4]_2[Re(CO)_3Br_3]$ (*9*) were prepared according to previously published procedures. ^{1}H and ^{13}C NMR spectra were recorded on a Bruker AV-400 instrument at 400.132 and 100.623 MHz, respectively. Assigned chemical shifts for the compounds prepared are recorded in Table 1. Mass spectra (+ ion) were obtained on dilute methanol solutions using a Macromass LCT (electrospray ionization, ESI). Elemental analyses were performed at the University of British Columbia Chemistry Department by Mr. M. Lakha (Carlo Erba analytical instrumentation). HPLC analyses were performed on Knauer Wellchrom K-1001 HPLC equipped with a K-2501 absorption detector, a Kapintek radiometric well counter, and a Synergi 4 μm C-18 Hydro-RP analytical column with dimensions 250 × 4.6 mm. The

* Corresponding authors. E-mail: adam@triumf.ca and orvig@chem.ubc.ca.
† University of British Columbia.
‡ TRIUMF.

10.1021/bc0499681 CCC: $27.50 © 2004 American Chemical Society
Published on Web 06/10/2004

Table 1. ^{1}H and ^{13}C{^{1}H} NMR Data (DMSO-d_6) (δ in ppm) for the α-Anomers of HL^2 and [(L^2)Re(CO)$_3$]

	^{1}H NMR (δ in ppm)			^{13}C{^{1}H} NMR (δ in ppm)		
	H**L**^{2}	[(**L**^{2})Re(CO)$_3$]	$\delta_{complex} - \delta_{ligand}$	H**L**^{2}	[(**L**^{2})Re(CO)$_3$]	$\delta_{complex} - \delta_{ligand}$
C-1	5.11	5.22	0.11	90.4	87.5	−2.9
C-2	2.34	2.37	0.03	61.3	58.0	−3.3
C-3	3.52	3.66	0.14	72.4	79.8	7.4
C-4	3.06	3.20	0.14	71.0	70.6	−0.4
C-5	3.39	3.43	0.04	72.4	71.8	−0.6
C-6	3.4, 3.6	3.4, 3.6		61.5	59.8	−1.7
C-7	3.80	3.85, 4.30		48.7	51.1	2.4
C-8				124.8	119.4	−5.4
C-9				157.5	163.2	5.7
C-10	6.7	6.35	−0.35	119.6	120.3	0.7
C-11	7.05	6.80	−0.25	128.9	129.1	0.2
C-12	6.7	6.45	−0.25	116.1	114.1	−2.0
C-13	7.05	6.95	−0.10	129.6	130.6	1.0

HPLC solvent consisted of 0.1% trifluoroacetic acid in water (solvent A) and acetonitrile (solvent B). Samples were analyzed with a linear gradient method (100% solvent A to 100% solvent B over 30 min).

Synthesis. *N-(2′-Hydroxybenzyl)-2-amino-2-deoxy-*D*-glucose (H**L**^{2}).* H**L**^{1} (1.00 g, 3.53 mmol) was dissolved in MeOH (60 mL), and 10% Pd/C w/w (50 mg) was added. The mixture was stirred under a pressurized H_2 atmosphere (50 bar) for 24 h. The reaction mixture was clarified by filtration and the solvent evaporated to give H**L**^{2} (0.98 g, 98%). ESI-MS: 286 ([M + H]$^+$). Anal. Calcd for $C_{13}H_{19}NO_6 \cdot H_2O$: C, 51.48; H, 6.98; N, 4.62. Found: C, 51.50; H, 6.81; N, 4.60.

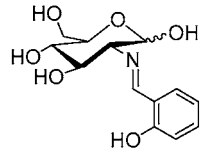
*Tricarbonyl(N-(2′-Hydroxybenzyl)-2-amino-2-deoxy-*D*-glucose)rhenium(I) (Re**L**^{2}(CO)$_3$).* [NEt$_4$]$_2$[Re(CO)$_3$Br$_3$] (200 mg, 0.26 mmol), H**L**^{2} (74 mg, 0.26 mmol), and sodium acetate trihydrate (40 mg, 0.32 mmol) were dissolved in H_2O (7 mL) and heated with stirring to 50 °C for 2 h. The solvent was then removed in vacuo and the residue dissolved in CH_2Cl_2 (10 mL) for 30 min. On standing, a brown residue was recovered by decanting off the solvent. This was purified to an off-white powder (58 mg, 0.10 mmol, 40%) by column chromatography (silica, 5:1CH_2Cl_2:CH_3OH). ESI-MS: 556, 554 ([M + H]$^+$), 578, 576 ([M + Na]$^+$). Anal. Calcd for $C_{16}H_{18}NO_9Re \cdot H_2O$: C, 33.57; H, 3.52; N, 2.45. Found: C, 33.55; H, 3.53; N, 2.75.

Radiolabeling. [^{99m}Tc(CO)$_3$(H$_2$O)$_3$]$^+$ was prepared from a saline solution of Na[^{99m}TcO$_4$] (1 mL, 100 MBq) using an "Isolink" boranocarbonate kit generously donated by Mallinckrodt Inc. Due to the increased chemical inertness and lower redox potential of rhenium, [^{186}Re(CO)$_3$(H$_2$O)$_3$]$^+$ was not accessible by the kit preparation used for technetium. [^{186}Re(CO)$_3$(H$_2$O)$_3$]$^+$ was prepared by addition 4.5 μL of 85% H_3PO_4 to a saline solution of Na[^{186}ReO$_4$] (0.5 mL, 100 MBq), followed by addition of this solution to 3 mg of borane ammonia complex that had been flushed with CO for 10 min. The mixture was heated at 60 °C for 15 min and then cooled to room temperature. Labeling was achieved by mixing an aliquot of one of the above final solutions (0.5 mL) with a 1 mM solution of H**L**^{2} in PBS (pH 7.4, 1 mL) and incubating at 75 °C for 30 min.

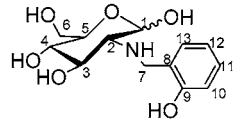
Stability Evaluation. [(**L**^{2})^{99m}Tc(CO)$_3$(H$_2$O)] (100 μL, 10 MBq, 1 mM in H**L**^{2}) was added to 900 μL of either 1 mM histidine or 1 mM cysteine in PBS. The solutions were incubated at 37 °C and aliquots were removed at 1, 4, and 24 h, at which time HPLC analysis was run. Histidine labeling was achieved by adding a solution containing [^{99m}Tc(CO)$_3$(H$_2$O)$_3$]$^+$ to a 1 mM solution of histidine in PBS (pH 7.4, 1 mL) and incubating at 75 °C for 30 min. HPLC analysis confirmed the formation of a single radiolabeled product.

Scheme 1

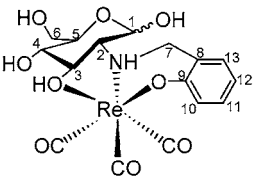
H**L**^{1}



H**L**^{2}



[(**L**^{2})Re(CO)$_3$]



RESULTS AND DISCUSSION

The Schiff base formed by condensation of glucosamine with salicylaldehyde H**L**^{1} (Scheme 1) has been previously investigated as a ligand for transition metals, including ^{99}Tc(V) (*8*). Using the starting material [NEt$_4$]$_2$[Re(CO)$_3$Br$_3$] (*9*) as a "cold" surrogate for [M(CO)$_3$(H$_2$O)$_3$]$^+$ (M = ^{99m}Tc or ^{186}Re), we synthesized the complex [(**L**^{1})Re(CO)$_3$] (as observed by ESIMS (+)); however, both the imine and the complex are unstable to hydrolysis and proved to be unsuitable for aqueous radiolabeling chemistry.

To circumvent the hydrolysis problem, we reduced H**L**^{1} to the more hydrolytically robust amine phenol H**L**^{2} (*N*-(2′-hydroxybenzyl)-2-amino-2-deoxy-D-glucose, Scheme 1). Catalytic hydrogenation of H**L**^{1} provided H**L**^{2} in 98% yield, with sufficient purity for subsequent radiolabeling studies. The reaction of H**L**^{2} with [NEt$_4$]$_2$[Re(CO)$_3$Br$_3$] and NaOAc in H_2O produced the compound [(**L**^{2})Re(CO)$_3$] in 40% yield after column chromatographic purification. The molecular ion was identified as [((**L**^{2})Re(CO)$_3$) + H]$^+$ by ESIMS, and the formulation of the bulk sample was confirmed by elemental analysis. Comparison of the anomeric ratio (α/β) observed in the ^{1}H NMR spectrum (CD_3OD) showed a change from 1.9 for H**L**^{2} to 1.1 for the complex, indicating that complexation has decreased the difference in thermodynamic stability between the two anomers. For solubility reasons full NMR studies were carried out in DMSO-d_6 solution (Table 1). The ^{1}H NMR spectrum (DMSO-d_6) of the complex is highly convoluted, but the shifting and broadening out of the aromatic resonances compared to those of H**L**^{2} signify that the phenol "arm" participates, as desired, in the binding of the {Re^I(CO)$_3$} moiety. The splitting of the methine

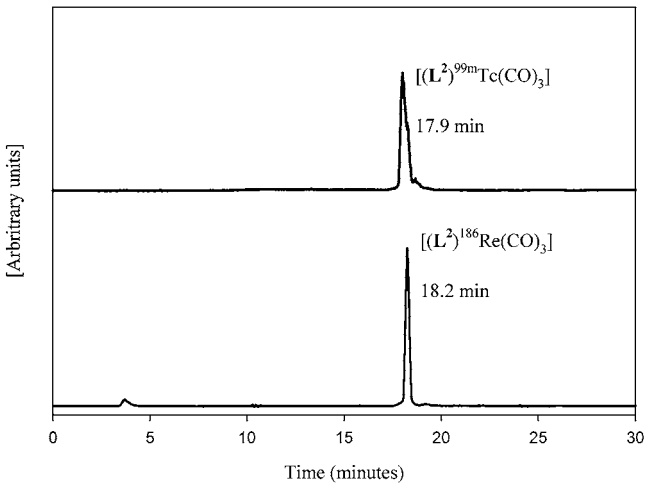


Figure 1. Radiation traces and retention times from HPLC analysis using a C18 column eluting with the gradient 100% 0.1% trifluoroacetic acid buffer to 100% acetonitrile over 30 min.

proton signals into two doublets for each anomer indicates the methine proton inequivalence on formation of the complex. Binding of the ligand N and O donor atoms incorporates the methine in a ring, rigidly holding the two protons in diastereotopic chemical environments. Signals due to the sugar C1 protons were shifted downfield in both anomers compared to those of H**L²**. Peaks due to the sugar C2 protons are also well-resolved and compared to those of H**L²** are also shifted slightly downfield in both anomers. Small extraneous peaks in the spectrum also indicate that at least one other minor species is present. When kept overnight in CD_3OD or DMSO-d_6 solution, samples of the complex become visibly brown and the relative intensities of these peaks increase, indicating that they arise from decomposition products. The signals do not correlate with the chemical shifts of uncomplexed H**L²**. Minor species are also detected by UV/visible spectroscopy in the HPLC of the complex and become more significant over time.

The $^{13}C\{^1H\}$ NMR spectrum (d_6-DMSO) of the complex was fully assigned for the α-anomer, and partially assigned for the β-anomer (Table 1). The Re carbonyls show three sharp resonances at 196−198 ppm as expected due to the lack of symmetry. In both anomers, peaks due to the phenol CO and the CH_2 linker are shifted significantly downfield from their values of H**L²**, giving a clear indication that the Re is bound both by the phenol O and glucosamine N (*10*). The C1 and C2 signals of both anomers are shifted upfield on complexation, presumably reflecting some slight conformational change in the hexose skeleton. The result of this could be destabilization of the α-anomer and hence the changed anomeric ratio compared to that of H**L²** itself. In the α-anomer the C3 signal has shifted downfield 7.4 ppm, suggesting that the C3 glucosamine hydroxyl is binding to the Re center in place of the predicted solvent molecule (*11*). Unfortunately, C3 for the β-anomer could not be assigned, due to the lower concentration of the anomer in DMSO solution. Less polar than water or methanol, DMSO is unable to stabilize the unfavorable dipole moments present in the β-anomer (*12*). It is unlikely that the stereochemistry at C1 can have any effect on the geometry-dependent propensity of the C3 hydroxyl to coordinate to Re, thus both anomers are predicted to bind Re in a similar tridentate manner.

Labeling H**L²** with $[^{99m}Tc(CO)_3(H_2O)_3]^+$ and $[^{186}Re(CO)_3(H_2O)_3]^+$ was achieved in 95 ± 2% and 94 ± 3% average radiochemical yields, respectively, as measured by HPLC (Figure 1). The identities of the radiolabeled complexes were confirmed to be $[(\mathbf{L^2})^{99m}Tc(CO)_3]$ (t_R = 17.9 min) and $[(\mathbf{L^2})^{186}Re(CO)_3]$ (t_R = 18.2 min) by coinjection of the radiolabeled product with the authentic "cold" Re complex (t_R = 17.9 min.). To make a preliminary assessment of the potential in vivo stability of the ^{99m}Tc complex, cysteine/histidine challenge experiments were performed. In a typical test, the radiolabeled complex was incubated at 37 °C in aqueous phosphate buffer solution (pH 7.4) containing either 1 mM cysteine or 1 mM histidine, and aliquots were removed at 1, 4, and 24 h (Table 2). HPLC analysis showed the complex to be stable in either histidine or cysteine solution but only in the short term; by 4 h, less than 30% of the complex remained intact. Histidine-labeled $[^{99m}Tc(CO)_3(H_2O)_3]^+$ was determined to be the major decomposition product of the histidine challenge experiments. The complex instability may be due to the relatively weak binding ability of the donor atoms, especially the secondary amino group and the carbohydrate hydroxyl. When considering modifications to increase complex stability, the fortuitous tridentate binding has directed us to investigate purposely tridentate ligands, and those containing binding groups with higher affinities for the soft $\{M(CO)_3\}$ center.

Table 2. Percentage of $[(L^2)^{99m}Tc(CO)_3]$ Remaining after Incubation at 37 °C in 1 mM Cysteine or Histidine for 1, 4, and 24 h

	% of $[(L^2)^{99m}Tc(CO)_3]$ remaining		
	1 h	4 h	24 h
incubation in cysteine	88	28	not detected
incubation in histidine	50	24	4

In summary, neutral, low molecular weight ^{99m}Tc- and ^{186}Re-labeled carbohydrate complexes were produced in high radiochemical yield from a simple functionalized glucosamine. H**L²** is in trials as a ligand for $^{62/64}Cu$ and $^{67/68}Ga$, and other carbohydrate-containing ligands for ^{99m}Tc and $^{186/188}Re$ are under study.

ACKNOWLEDGMENT

We acknowledge NSERC for a Strategic Grant and a Postgraduate Scholarship (T.S.), Mallinckrodt Inc. for the Isolink kits, the UBC Hospital Department of Nuclear Medicine for $Na^{99m}TcO_4$, and MDS Nordion Inc. for $Na^{186}ReO_4$.

LITERATURE CITED

(1) Fowler, J. S., and Wolf, A. P. (1997) Working Against Time: Rapid Radiotracer Synthesis and Imaging the Human Brain. *Acc. Chem. Res. 30*, 181−188.

(2) Jurisson, S. S., and Lydon, J. D. (1999) Potential Technetium Small Molecule Radiopharmaceuticals. *Chem. Rev. 99*, 2205−2218.

(3) Volkert, W. A., and Hoffman, T. J. (1999) Therapeutic Radiopharmaceuticals. *Chem. Rev. 99*, 2269−2292.

(4) (a) Petrig, J., Schibli, R., Dumas, C., Alberto R., and Schubiger, P. A. (2001) Derivatization of Glucose and 2-Deoxyglucose for Transition Metal Complexation: Substitution Reactions with Organometallic ^{99m}Tc and Re Precursors and Fundamental NMR Investigations. *Chem. Eur. J. 7*, 1868−1873. (b) Yang, D. J., Kim, C. G., Schechter, N. R., Azhdarinia, A., Yu, D. F., Oh, C. S., Bryant, J. L., Won, J. J., Kim, E. E., and Podoloff, D. A. (2003) Imaging with ^{99m}Tc ECDG Targeted at the Multifunctional Glucose Transport System: Feasibility Study with Rodents. *Radiology 226*, 465−473.

(5) (a) Alberto, R., Schibli, R., Waibel, R., Abram, U., and Schubiger, P. A. (1999) Basic Aqueous Chemistry of $[M(OH_2)_3(CO)_3]^+$ (M = Re, Tc) Directed Towards Radiopharmaceutical

Application. *Coord. Chem. Rev. 190*−*192*, 901−919. (b) Schibli, R., Schwarzbach, R., Alberto, R., Ortner, K., Schmalle, H., Dumas, C., Egli, A., and Schubiger, P. A. (2002) Steps Toward High Specific Activity Labeling Biomolecules for Therapeutic Application: Preparation of Precursor $[^{188}Re(H_2O)_3(CO)_3]+$ and Synthesis of Tailor-Made Bifunctional Ligand Systems. *Bioconjugate Chem. 13*, 750−756.

(6) Zhang, M., Zhang, Z., Blessington, D., Li, H., Busch, T. M., Madrak, V., Miles, J., Chance, B., Glickson, J. D., and Zheng, G. (2003) Pyropheophorbide 2-Deoxyglcoseamide: a New Photosensitizer Targeting Glucose Transporters. *Bioconjugate Chem. 14*, 709−714, and references within.

(7) Schibli, R., La Bella, R., Alberto, R., Garcia-Garayoa, E., Ortner, K., Abram, U., and Schubiger, P. A. (2000) Influence of the Denticity of Ligand Systems on the In Vitro and In Vivo Behavior of ^{99m}Tc(I)-Tricarbonyl Complexes: A Hint for the Future Functionalization of Biomolecules. *Bioconjugate Chem. 11*, 345−351.

(8) (a) Adam, M. J., and Hall, L. D. (1982) Synthesis of Metal-Chelates of Amino Sugars: Schiff's Base Complexes. *Can. J. Chem. 60*, 2229−2237. (b) Duatti, A., Marchi, A., Magon, L., Deutsch, E., Bertolasi, V., and Gilli, G. (1987) Synthesis and Structure of an Amino Sugar Schiff Base Complex of Technetium(V) Containing Salicylaldehyde in an Unusual Coordination Mode. *Inorg. Chem. 26*, 2182−2186.

(9) Alberto, R., Egli, A., Abram, U., Hegetschweiler, K., Gramlich, V., and Schubiger, P. A. (1994) Synthesis and reactivity of $[NEt_4][ReBr_3(CO)_3]$. Formation and structural characterization of the clusters $[NEt_4][Re_3(\mu^3\text{-}OH)(\mu\text{-}OH)_3(CO)_9]$ and $[NEt_4][Re_2(\mu\text{-}OH)_3(CO)_6]$ by alkaline titration. *J. Chem. Soc., Dalton Trans.* 2815−2820.

(10) Klufers, P., and Kunte, T. (2001) A Transition Metal Complex of D-glucose. *Angew. Chem., Int. Ed. 40*, 4210−4212.

(11) (a) Andrews, M. A., Voss, E. J., Gould, G. L., Klooster, W. T., and Koetze, T. F. (1994) Regioselective Complexation of Unprotected Carbohydrates by Platnium(II): Synthesis, Structure, Complexation Equilibria and Hydrogen-Bonding in a Carbonate Derived Bis(phosphine) Platnium(II) Diolate and Alditolate Complexes. *J. Am. Chem. Soc. 116*, 5730−5740. (b) Klufers, P., and Kunte, T. (2003) Palladium(II) Complexes of the Reducing Sugars d-Aribinose, D-Ribose, rac-Mannose, and D-Galactose. *Chem. Eur. J. 9*, 2013−2018. (c) Klufers, P., Oswald, K., and Ossberger, M. (2002) Oxorhenium(V) Complexes of Carbohydrate Ligands. *Eur. J. Inorg. Chem. 2002*, 1919−1923.

(12) Prayly, J. P., and Lemieux, R. U. (1987) The Influence of Solvent on the Anomeric Effect. *Can. J. Chem. 65*, 213−223.

BC0499681

Labeling of Steroids on Solid Phase

Jari Peuralahti, Katriina Suonpää, Kaj Blomberg, Veli-Matti Mukkala, and Jari Hovinen*

PerkinElmer Life and Analytical Sciences, Turku Site, P.O. Box 10, FIN-20101 Turku, Finland.
Received March 19, 2004; Revised Manuscript Received May 27, 2004

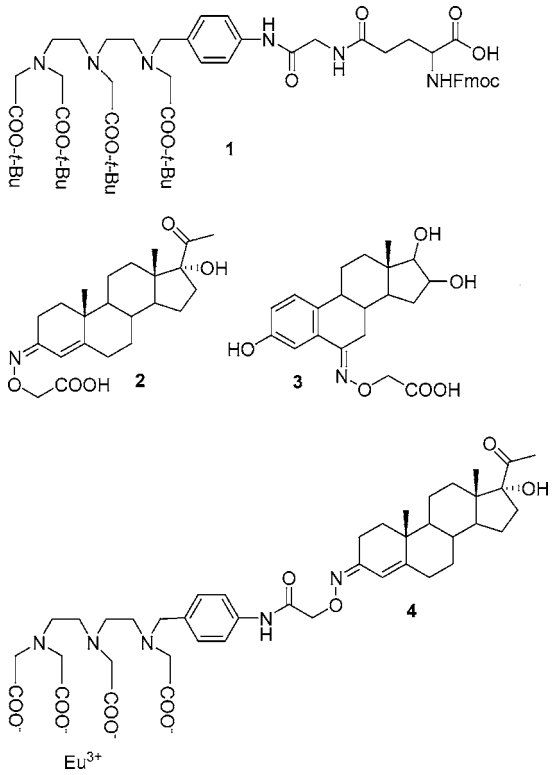
Up to four tetra-*tert*-butyl-1-[4-aminoacetamido)benzyl]diethylenetriaminetetrakis(acetato) derivatives of Fmoc glutamic acid (**1**) were attached to two steroids (17α-hydroxyprogesterone-3-*O*-carboxymethyloxime **2** and 1,3,5(10)-estratriene-3,16α,17*β*-triol-6-one-6-*O*-carboxymethyloxime, **3**)) on solid phase using an oligopeptide synthesizer. Upon deprotection and conversion to the corresponding europium(III) chelates, these steroid conjugates were used in DELFIA-based competitive fluoroimmunoassays. The more chelates conjugated to 17-α-hydroxyprogesterone, the more diluted antiserum could be used in an immunoassay for 17-α-hydroxyprogesterone, without any alteration of the measurement range. Hence, 17-α-hydroxyprogesterone tracers with several chelates are useful when a high serum dilution factor is desired i.e., when only a limited quantity of antiserum is available. The result demonstrates the suitability and usefulness of lanthanide(III) chelates as multilabels in bioaffinity assays.

INTRODUCTION

Steroids with additional functional groups are often needed for biological, microbiological and medicinal applications (*1*). For example, in competitive immunoassays, haptens coupled to a label molecule are used as tracers (*2*, *3*). Most commonly, a spacer arm with a reactive *ω*-substituent (amino or thiol) is introduced to the steroid structure before the labeling reaction, which is performed in solution between the hapten and an isothiocyanato, haloacetyl, or 3,5-dichloro-2,4,6-triazinyl derivative of the label molecule. Steroids tethered to a carboxylic acid group, in turn, are coupled to labels bearing an amino function using carbodiimide (*4*). The solution-phase labeling has been used in the preparation of haptens labeled with up to two europium(III) chelates (*5*). Because in all of these cases the labeling reaction is performed in the presence of an excess of an activated label or an activator, laborious purification procedures cannot be prevented. Especially, when attachment of several label molecules is needed, purification and characterization of the desired biomolecule conjugate may be extremely difficult. The purification problems can be avoided by performing the labeling reaction on solid phase. Hence, most of the impurities can be removed by washings when the biomolecule conjugate is still anchored to the solid support, and after release to the solution, only one chromatographic purification is needed.

Fluorescent label molecules attached to monomers for solid-phase synthesis are often organic dyes. Although organic chromophores can be utilized in several applications, these labels and labeled biomolecules suffer from many known drawbacks, such as Raman scattering, low water solubility, and especially concentration quenching. In addition, the sensitivity is compromised by the phosphorescence of the microtitration plates. Instead, the unique properties of lanthanide(III) chelates (*6*−*9*) such as long decay-time luminescence make them ideal labels for microtitration plate-based assays. Furthermore, large

Chart 1



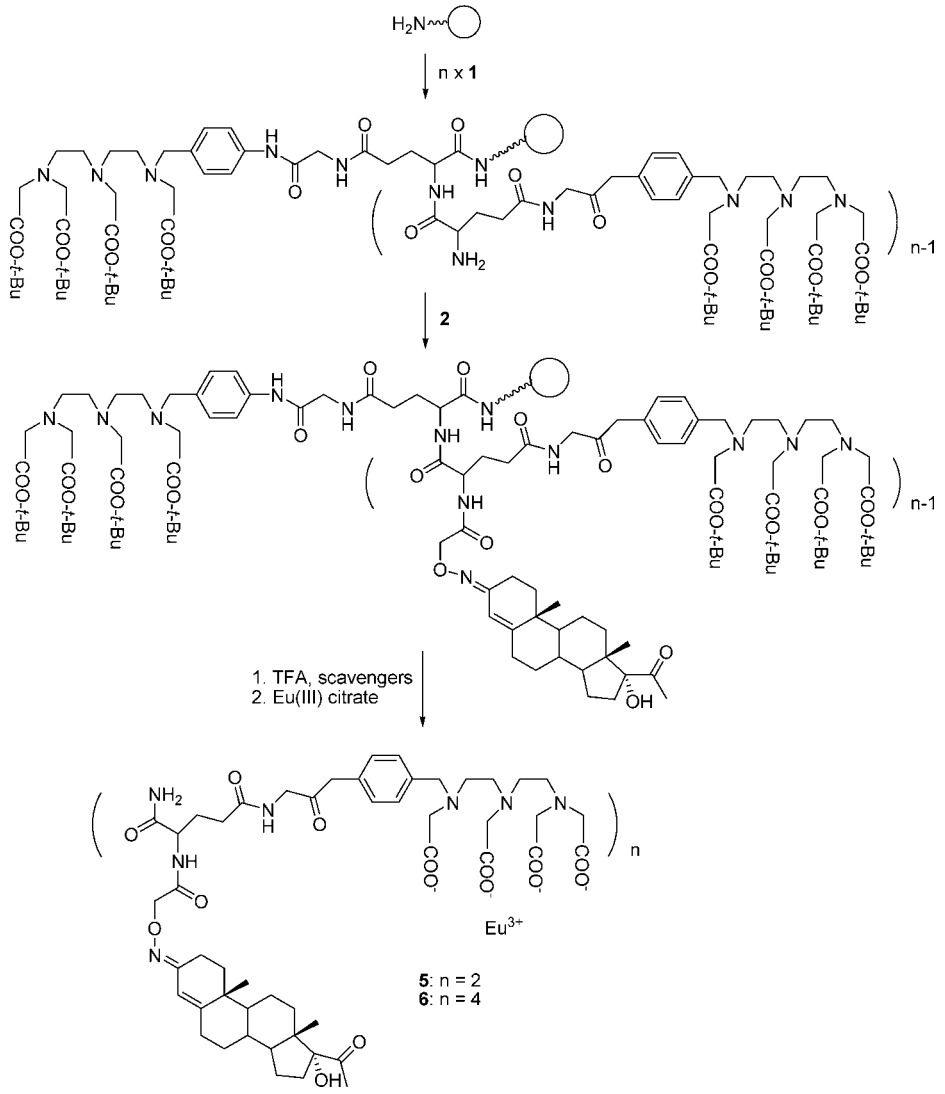
Stokes shift and very sharp emission bands enable the simultaneous use of four lanthanides (i.e. Eu, Tb, Dy, and Sm). Thus, the heterogeneous DELFIA technique is widely applied in assays where exceptional sensitivity and robustness is required (*6*, *7*).

Quite recently, we reported a solid-phase method for the labeling of oligopeptides (*10*) and oligonucleotides (*11*, *12*). The approach involves synthesis of oligonucleotide and oligopeptide building blocks, which can be introduced to the biomolecule structure using commercial oligonucleotide and oligopeptide synthesizers by phosphoramidite and Fmoc chemistry, respectively. Upon comple-

* To whom correspondence should be addressed. Tel: + 358 2 2678 513, fax: + 358 2 2678 380, e-mail: jari.hovinen@perkinelmer.com.

10.1021/bc049929p CCC: $27.50 © 2004 American Chemical Society
Published on Web 06/25/2004

Scheme 1. Labeling of Steroids on Solid Phase



tion of the chain assembly, the oligomer is deprotected and finally treated with the appropriate lanthanide(III) citrate to give rise to the desired biomolecule conjugate. Here the strategy is exploited in multilabeling of steroids using a peptide synthesizer. Accordingly, several tetra-*tert*-butyl-1-[4-aminoacetamido)benzyl]diethylenetriaminetetrakis(acetato) derivatives of Fmoc glutamic acid (**1**; Chart 1) were coupled to steroids tethered to a carboxyl acid function (**2**, **3**). Upon deprotection and conversion to the corresponding europium(III) chelate, these steroid conjugates were used in competitive fluoroimmunoassays based on DELFIA technology. The fluorescence signal was approximately proportional to the number of chelates attached to the steroids: the signal with 17-α-hydroxyprogesterone tethered to two or four europium(III) chelates was two and a half and five times higher, respectively, compared to the monolabeled derivative, **4**, demonstrating the suitability of lanthanide(III) chelates to multilabeling.

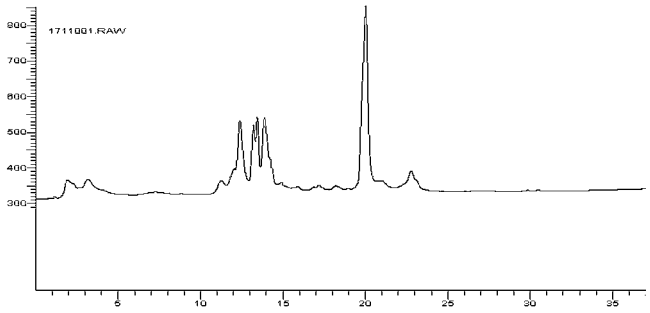


Figure 1. Reversed-phase HPLC profile (crude reaction mixture) of 17-α-hydroxyprogesterone labeled with four nonluminescent europium(III) chelates synthesized in the aid of block **1** and the steroid analogue **2** detected at 240 nm. The peak at t_R 20.06 min is the desired product. For chromatographic conditions, see Experimental Procedures.

EXPERIMENTAL PROCEDURES

General. The steroid compounds (**2** and **3**) were purchased from Steraloids (Newport, RI). The nonluminescent block, **1**, was synthesized as described previously (*10*). 17-α-OHP-3-CMO−Eu (**4**), rabbit anti-17-α-OHP antiserum, and the time-resolved fluorometer VICTOR^{2}V were products of PerkinElmer LAS. Anti-rabbit coated microtitration plates, blood spot standards, assay buffer, wash solution, and enhancement solution were from the DELFIA Neonatal 17-α-OH-progesterone kit 1244−039 (PerkinElmer LAS). HPLC analyses were performed on a PerkinElmer LC 2000 instrument using a reversed-phase column (LiChrocart 125−3 Purospher RP-18e, 5 μm). The mobile phase used was the following: Buffer A: 0.02 M TEAA (pH 7.5); Buffer B: A in 50% (v/v) acetonitrile. Gradient: from 0 to 1 min 95% A, from 1 to

Table 1. Tracers Synthesized and Their Observed and Calculated Molecular Weights

tracer[a]	$[M - nH]^{n-}/n$ calculated	$[M - nH]^{n-}/n$ observed
17-α-OHP-3-CMO-Eu_2 (**5**)	957.3 ($n = 2$)	957.7 ($n = 2$)
17-α-OHP-3-CMO-Eu_4 (**6**)	1143.3 ($n = 3$)	1143.5 ($n = 3$)
E3−6-CMO−Eu_2 (**7**)	944.2 ($n = 2$)	944.2 ($n = 2$)

[a] 17-α-OHP = 17-α-hydroxyprogesterone; E3 = estriol. CMO = carboxymethyloxime.

30 min from 95% A to 100% B. Flow rate was 0.6 mL min^{-1}. Electrospray ionization time-of-flight mass spectra (ESI-TOF MS) were recorded on an Applied Biosystems Mariner instrument on negative detection mode.

Synthesis of the Steroid Conjugates. The synthesis was performed in 10 μmol scale on an Applied Biosystems 433A instrument using Fmoc chemistry and recommended procedures (*O*-benzotriazol-1-yl-*N*,*N*,*N*′,*N*′-tetramethyluronium hexafluorophosphate (HBTU)/1-hydroxybentzotriazole (HOBt) activation; no capping), except the coupling time was increased to 2 h. 35 μmol of **1** was used in all coupling reactions. The last coupling was performed with 15 μmol of **2** or **3**. When the chain assembly was completed, the resin was treated with the mixture of crystalline phenol (75 mg), ethanethiol (25 μL), thioanisole (50 μL), water (50 μL), and trifluoroacetic acid (1 mL) for 3 h. The resin was removed by filtration, and the crude steroid conjugate was precipitated with diethyl ether. The precipitate was redissolved in water and treated with aqueous europium(III) citrate (5 equiv/ligand) Purification was performed on HPLC. The steroid conjugates were characterized on ESI-TOF mass spectrometry.

Time-Resolved Fluoroimmunoassays. The 17-α-hydroxyprogesterone derivatives synthesized were tested in a time-resolved fluoroimmunoassay. Standards (3.1 mm disks) punched from blood spots on filter paper were incubated in the wells of anti-rabbit coated microtitration plates with various concentrations of rabbit anti-serum to 17-α-hydroxyprogesterone and 300 pmol/L 17-α-hydroxyprogesterone-Eu tracers in a total volume of 200 μL, for 2 h. Bound and free 17-α-hydroxyprogesterone-Eu fractions were separated by washing, and bound Eu was measured, after addition of 200 μL of DELFIA enhancement solution, into which Eu dissociates and in which it forms highly fluorescent complexes. The fluorescence was measured in a 1420 Victor²V multilabel counter.

RESULT AND DISCUSSION

Tracer Synthesis. The present approach for solid-phase steroid derivatization is outlined in Scheme 1. Accordingly, two or four building blocks **1** were coupled to an amide resin in 10 μmol scale using Fmoc chemistry. A prolonged coupling time (2 h instead of 30 min) but otherwise standard conditions (3.5 equiv of **1**; HBTU/HOBt as an activator) were used. After the desired number of blocks was introduced, a steroid analogue tethered to a carboxylic acid function (1.5 equiv of **2** or **3**) was coupled using similar conditions. When the reaction was completed, the steroid conjugate was released from the resin and deprotected followed by precipitation from diethyl ether. Treatment of the deblocked conjugate with europium(III) citrate converted it to the corresponding lanthanide(III) chelate.

The labeled steroids were purified on reversed-phase HPLC and characterized on ESI-TOF mass spectrometry. A typical HPLC profile (crude reaction mixture) is shown in Figure 1 as an illustrative example. In all of the cases, the observed molecular weights were in accordance with the proposed structures (Table 1).

The DELFIA Assay. In the DELFIA assay set up for 17-α-hydroxyprogesterone, it is clearly seen that the signal goes up more than what is anticipated from the number of chelates attached to the steroid structure and that an increasing number of chelates makes the analytical sensitivity of the assay somewhat worse (Table 2). The shift of the standard curve to the right as well as the 5-fold increase in signal level when the number of Eu-chelates rises from 1 to 4 indicate that the antiserum has a higher affinity to tracers with more Eu-chelates. However, in 17-α-hydroxyprogesterone assays with these three tracers (**4**−**6**) the same sensitivity was observed when 17-α-hydroxyprogesterone antiserum and tracer dilutions were chosen to give the same signal in all three assays (Table 3). Thus, the more chelates conjugated to 17-α-hydroxyprogesterone, the more diluted antiserum could be used. Hence, 17-α-hydroxyprogesterone tracers

Table 2. Dose−Response Values and Analytical Sensitivity with the Three 17-α-Hydroxyprogesterone Tracers (4−6) Tested in an Immunoassays for 17-α-OH-progesterone at Constant Tracer and Anti-Serum Concentrations

tracer	tracer (pmol/L)	antiserum (dilution factor)	B_0[a] (fluorescence counts)	standard curve (nmol/L) at B/B_0[b] = 0.20	$B/B_0 = 0.50$	$B/B_0 = 0.80$	analytical sensitivity[c] (nmol/L)
4	300	60000	27500	36	6.4	1.4	0.6
5	300	60000	70000	95	12	2.5	1.0
6	300	60000	146500	160	20	3.5	1.34

[a] B_0 was the fluorescence signal from tracer bound to antiserum at zero 17-α-OH-progesterone dose. The background signal, measured from wells containing all reagents except tracer, was between 500 and 1000 in all assays. [b] *B* was the fluorescence signal from tracer with 17-α-OH-progesterone present and B/B_0 is their ratio. [c] The analytical sensitivity was defined as the dose calculated from a response 3 SD below the B_0 signal ($n = 4$).

Table 3. Dose−Response Values and Analytical Sensitivity with the Three 17-α-Hydroxyprogesterone Tracers Tested in an Immunoassays for 17-α-OH-Progesterone at Constant Signal Level

tracer	tracer (pmol/l)	antiserum dilution factor	B_0[a] (fluorescence counts)	standard curve (nmol/L) at B/B_0[b] = 0.20	$B/B_0 = 0.50$	$B/B_0 = 0.80$	analytical sensitivity[c] (nmol/L)
4	300	60000	20252	42	7.5	2.2	0.9
5	300	120000	25428	65	9.9	2.5	1.0
6	150	240000	24114	62	8.6	2.3	1.0

[a] B_0 was the fluorescence signal from tracer bound to antiserum at zero 17-α-OH-progesterone dose. The background signal, measured from wells containing all reagents except tracer, was between 500 and 1000 in all assays. [b] *B* was the fluorescence signal from tracer with 17-α-OH-progesterone present and B/B_0 is their ratio. [c] The analytical sensitivity was defined as the dose calculated from a response 3 SD below the B_0 signal ($n = 4$).

with several chelates are useful when a high serum dilution factor is desired i.e., when only limited quantities of antibody is available. This is usually the case in immunoassay applications for steroids of which many are widely used in clinical routine laboratories. Thus, when required, considerable amounts of antiserum can be saved and the lifetime of an assay prolonged by attachment of several chelates to the tracer. By contrast, if the labeling were performed using organic chromophores such as fluorescein or cyanine dyes, these dyes in close proximity will partially quench each other and further dilution of antiserum would be impossible.

In summary, a straightforward method for labeling of steroids on solid phase is demonstrated. Although an increasing number of biomolecule conjugates are nowadays synthesized entirely on solid phase (*13*), according to our knowledge, no method for solid phase labeling of steroids have been reported, excluding solid-phase synthesis of steroid−oligonucleotide conjugates. Although only labeling of carboxymethyloxime derivatives of estriol and 17-α-hydroxyprogesterone with several lanthanide(III) chelates is demonstrated, in all likelihood, the method is applicable to other haptens tethered to a carboxylic acid group as well.

LITERATURE CITED

(1) Pratt, J. J. (1978) Steroid immunoassay in clinical chemistry. *Clin. Chem. 24*, 1869−1890.

(2) Mikola, H., Sundell, A.-C., and Hänninen, E. (1993) Labeling of estradiol and testosterone alkyloxime derivatives with a europium chelate for time-resolved fluoroimmunoassay. *Steroids 58*, 330−334.

(3) Meltola, N., Jauria, P., Saviranta, P., and Mikola, H. (1999) Synthesis of novel europium-labeled estradiol derivatives for time-resolved fluoroimmunoassays. *Bioconjugate Chem. 10*, 325−331.

(4) Takalo, H., Mukkala, V.-M., Mikola, H., Liitti, P., and Hemmilä, I. (1994) Synthesis of europium(III) chelates suitable for labeling of bioactive molecules. *Bioconjugate Chem. 5*, 278−282.

(5) Mikola, H., and Hedlöf, E. (1997) Synthesis of europium-labeled digoxin derivatives and their use in time-resolved fluoroimmunoassay. *Steroids 59*, 472−478.

(6) Hemmilä, I. (1991) Applications of Fluorescence in Immunoassays, in *Chemical Analysis: A Series of Monographs on Analytical Chemistry and Its Applications*, Vol. 117, John Wiley & Sons, Inc., New York.

(7) Hemmilä, I., Ståhlberg, T., and Mottram, P., Eds. (1994) *Bioanalytical Applications of Labelling Technologies*, Chapter 9, Wallac Oy, Turku.

(8) Hemmilä, I., Dakubu, S., Mukkala, V.-M., Siitari, H., and Lövgren, T. (1984) Europium as a label in time-resolved immunofluorometric assays. *Anal. Biochem. 137*, 335−343.

(9) Hemmilä, I., and Mukkala, V.-M. (2001) Time-resolution in fluorometry technologies, labels and applications. *Crit. Rev. Clin. Lab. Sci. 38*, 441−519.

(10) Peuralahti, J., Hakala, H., Mukkala, V.-M., Hurskainen, P., Mulari, O., and Hovinen, J. (2002) Introduction of lanthanide(III) chelates to oligopeptides on solid phase. *Bioconjugate Chem. 13*, 870−875.

(11) Hovinen, J., and Hakala, H. (2001) Versatile strategy for oligonucleotide derivatization. Introduction of lanthanide(III) chelates to oligonucleotides. *Org. Lett. 3*, 2473−2476.

(12) Hakala, H., Ollikka, P., Degerholm, J., and Hovinen, J. (2002) Oligonucleotide conjugates based on acyclonucleosides and their use in DNA hybridization assays. *Tetrahedron 58*, 8771−8777.

(13) Virta, P., Katajisto, J., Niittymäki, T., and Lönnberg, H. (2003) Solid-supported synthesis of oligomeric bioconjugates. *Tetrahedron 59*, 5137−5174.

BC049929P

Synthesis and Characterization of Dextran−Peptide−Methotrexate Conjugates for Tumor Targeting via Mediation by Matrix Metalloproteinase II and Matrix Metalloproteinase IX

Ying Chau, Frederick E. Tan, and Robert Langer*

Massachusetts Institute of Technology, Cambridge, Massachusetts 02142. Received April 4, 2004; Revised Manuscript Received May 30, 2004

We designed and synthesized new dextran−peptide−methotrexate conjugates for tumor-targeted delivery of chemotherapeutics via the mediation of matrix metalloproteinase II (MMP-2) and matrix metalloproteinase IX (MMP-9), both being widely known tumor-associated enzymes. A robust and flexible synthesis procedure and process monitoring chromatography assays were developed. The linker chemistry and the backbone charge were optimized to allow high sensitivity of the conjugates toward the targeted enzymes. The optimal conjugate carries Pro-Val-Gly-Leu-Ile-Gly as the peptide linker, and the charge on the dextran backbone is fully neutralized. In the presence of the targeted enzymes, the peptide was cleaved and peptidyl methotrexate was released, with a k_{cat}/K_m value of 1.21×10^5 M^{-1} s^{-1} for MMP-2 and 3.60×10^3 M^{-1} s^{-1} for MMP-9, respectively. Satisfactory stability of the new conjugates was demonstrated in serum containing conditions, suggesting the conjugates can remain intact in systemic circulation. These findings supported the tumor targeting capability of the new conjugates and warranted further investigation with in vivo study.

INTRODUCTION

Since conventional chemotherapy is nonspecific, it causes severe side effects and the treatment can be compromised due to dose-limiting toxicity. Recent advances in the understanding of tumor environment have prompted the current research to investigate a new approach to improve the biodistribution of chemotherapeutics. For tumors to survive, grow and metastasize, the expressions of a number of enzymes in high levels are required in the extracellular space. Among the many tumor-associated enzymes, we have selected to focus on matrix metalloproteinase II (MMP-2) and matrix metalloproteinase IV (MMP-9). These enzymes are extensively studied members of a family of zinc-dependent enzyme. They are elevated in a number of human epithelial cancers, including breast (*1*), prostate (*2*),colon (*3*), ovary (*4*), bladder (*5*) and gastric carcinoma (*6*). In fact, for tumor cells to invade and metastasize, the first barrier to overcome is the basement membrane (*7*, *8*) which is composed of type IV collagen and is susceptible to the degradation by MMP-2 and MMP-9. New functions of these MMPs have been recently reviewed (*9*). MMP-2 and MMP-9 can release growth factors sequestered in the extracellular matrix, expose binding sites for cell adhesion molecules, and activate growth factors and angiogenesis factors by cleaving their precursors. Their functions thus involve promoting tumor cell growth, upregulating angiogenesis and triggering tumor cell motility. They are either produced by the tumor cells or by the surrounding stromal cells, as extracellular or membrane-bound enzymes in the tumor's vicinity.

Polymer−drug conjugates are showing emerging potential in tumor targeting (*10*−*12*). The appropriate polymeric carriers are biocompatible and water-soluble. Covalent attachment of drug molecules to the macromolecular carrier solves the problem of poor solubility. Polymer of high molecular weight (with size near or above the renal excretion limit) is of special interest in tumor targeting due to two reasons. First, the half-life of the polymer−drug conjugates in the circulation is much longer than the free drugs. The decreased total body clearance of the polymer−drug conjugate increases the amount of drug delivered to the tumor site (*13*). Second, there is enhanced permeation and retention of the polymer−drug conjugates to the tumor site because solid tumor has leaky blood vessels and poor lymphatic drainage (*14*).

At the tumor site, as conjugates are internalized by nonspecific endocytosis, active drug molecules are released by either acid or intracellular enzymatic hydrolysis. However, fluid phase endocytosis is a slow process (*15*) and is not specific to tumor cells. Drug uptake by tumor cells can be enhanced by increasing the extent of binding of conjugates to the tumor cells. This route, selective endocytosis, has been investigated by the attachment of targeting ligands to the polymeric carriers (*10*, *16*−*19*). Alternatively, tumor uptake can be improved by increasing the extent of extracellular drug release in the tumor vicinity. This route is being explored in the current research by linking drug molecules to the polymeric carriers with peptide sequences. The specific peptide sequences are labile to the cleavage by tumor-associated enzymes in the extracellular space, enabling the release of drug molecules from the polymeric carriers.

The covalent attachment of a chemotherapeutic drug molecule to a peptide sequence susceptible to tumor-associated enzyme has produced prodrug that is activated by the enzyme of interest. Notably, the work on doxorubicin−peptide prodrug has demonstrated selective in vitro cytotoxicity for tumor cells producing prostate-specific antigen and in vivo antitumor efficacy (*20*). Sequences susceptible to cleavage by matrix metalloproteases (MMP) have also been used to increase tumor

* To whom correspondence should be addressed. Address: 77 Massachusetts Ave., E25-342, Cambridge, MA 02139. Phone: (617)253-3107. Fax: (617)258-8827. E-mail: rlanger@mit.edu.

10.1021/bc0499174 CCC: $27.50 © 2004 American Chemical Society
Published on Web 06/29/2004

selectivity of cytotoxins. Protective protein of anthrax toxin was mutated to contain a MMP recognizable sequence in order to be activated by the enzymes via a cleavage event on the cell surface (*21*). However, the tumor targeting efficiency of the above strategies is limited by the short circulation half-life of the active components.

We intend to combine the concepts of polymer−drug conjugate and peptide prodrug in our new conjugate and exploit the presence of MMP in tumor vicinity to release active drug molecules. We select dextran as the polymeric carrier because of its biocompatibility (*22*) and biodegradability (*23*). The hydroxyl groups on the dextran backbone provide possible functional sites for drug linkage. Previously, dextran of MW 70 000 was conjugated to doxorubicin via an acid-labile linkage for intratumoral delivery (*24*). Methotrexate is a folic acid analogue which inhibits dihydrofolate reductase and thus hinders the synthesis of RNA and DNA. Like most chemotherapeutic drugs, it is toxic to all fast growing cells. It is used as the model drug candidate in our conjugate. This molecule has been used for cancer treatment for many years and is effective against a number of tumors, including lymphoblastic leukemia in children, chriocarcinoma and related trophoblastic tumors in women, osteosacroma and carcinomas of the breast, head, neck, ovary and bladder. The major side effect is toxicity in gastrointestinal tract and bone marrow (*25*). Chemically, methotrexate has two carboxyl groups available for covalent linkage. The drug activity is relatively preserved when the gamma-carboxyl is chemically modified whereas the alpha-carboxyl has much less bulk tolerance (*26*). The peptide linker composition is based upon the work of Turk and co-workers (*27*) in which the authors constructed a combinatorial library of oligopeptides as MMP substrates. They scored all possible amino acids at each of the position from P4 to P4′. The highest-scoring amino acids without functional side chains are selected in our conjugate to form the optimal hexapeptide linker.

We report here a method to synthesize new dextran−peptide−methotrexate conjugates. The synthesis route is easily modified to prepare conjugates with different peptide linkers and different backbone charges. By tuning these parameters, the new conjugate is optimized in terms of sensitivity against MMP-2 and MMP-9. The conjugates also demonstrated excellent stability in serum-containing conditions, suggesting their capability to remain intact in systemic circulation.

EXPERIMENTAL PROCEDURES

Materials. Dextran T-70 with a nominal molecular weight of 70 000 was ordered from Pharmacia. 1-Ethyl-3-(3-dimethylaminopropyl)carbodiimide hydrochloride (EDC) and ethanolamine were obtained from Alfa Aesar. *O*-Bis(aminoethyl)ethylene glycol trityl resin, PyBop and HOBT were obtained from Nova Biochem. Glutamic acid-α-OtBu was purchased from Bachem. Trifluoroacetic acid (TFA), dimethylformamide (DMF), dimethyl sulfoxide (DMSO), acetonitrile (ACN), ethyl acetate, ether and 10× phosphate-buffered saline were obtained from EM Science. Methanol, sodium chloride and sodium phosphate were from Mallinckrodt. Tris was purchased from Boehringer Mannheim. Chloroacetic acid, *N*,*N*′-diisopropyl-(ethylamine) (DIPEA), BOP, 4-amino-4-deoxy-N^{10}-methylpteroic acid (APA), calcium chloride and phorbol 12-myristate 13-acetate (PMA) were from Sigma. Concanavalin A (ConA) was ordered from Calbiochem.

Purified active human MMP-2 and MMP-9 were purchased from Calbiochem. Precast protein gels with 10% gelatin and reagents for gelatin zymography were obtained from Biorad. Plasmocin was ordered from Invivogen. All other cell culture media and reagents as well as EDTA solution pH 8.0 were ordered from Gibco. Human tumor cell lines HT-1080 and BT-20 were obtained from American Type Cell Culture.

Preparation of Carboxymethyl Dextran (CM-dextran) (structure iv, Scheme 1). This procedure was based on the method by Nogusa for activating pullulan (*28*). Dextran T-70 (10 g) was dissolved in 100 mL of 6 N sodium hydroxide solution. Chloroacetic acid (30.2 g) was added to the solution and held at 70 °C for 2−3 h. Elevated temperature was necessary for this reaction. The reaction mixture was removed from heat and checked for pH. Acetic acid was used to neutralize the pH if necessary. The solution was then dialyzed against DI water using Spectrapor regenerated cellulose membrane with molecular weight cutoff at 3000−8000 for 2 days at 4 °C and lyophilized for storage. Degree of carboxymethyl substitution was determined by analysis of sodium content. Atomic absorption analysis to determine sodium content was performed by Quantitative Technologies Inc. (Whitehouse, NJ). The degree of substitution was consistently at 50% (±2%).

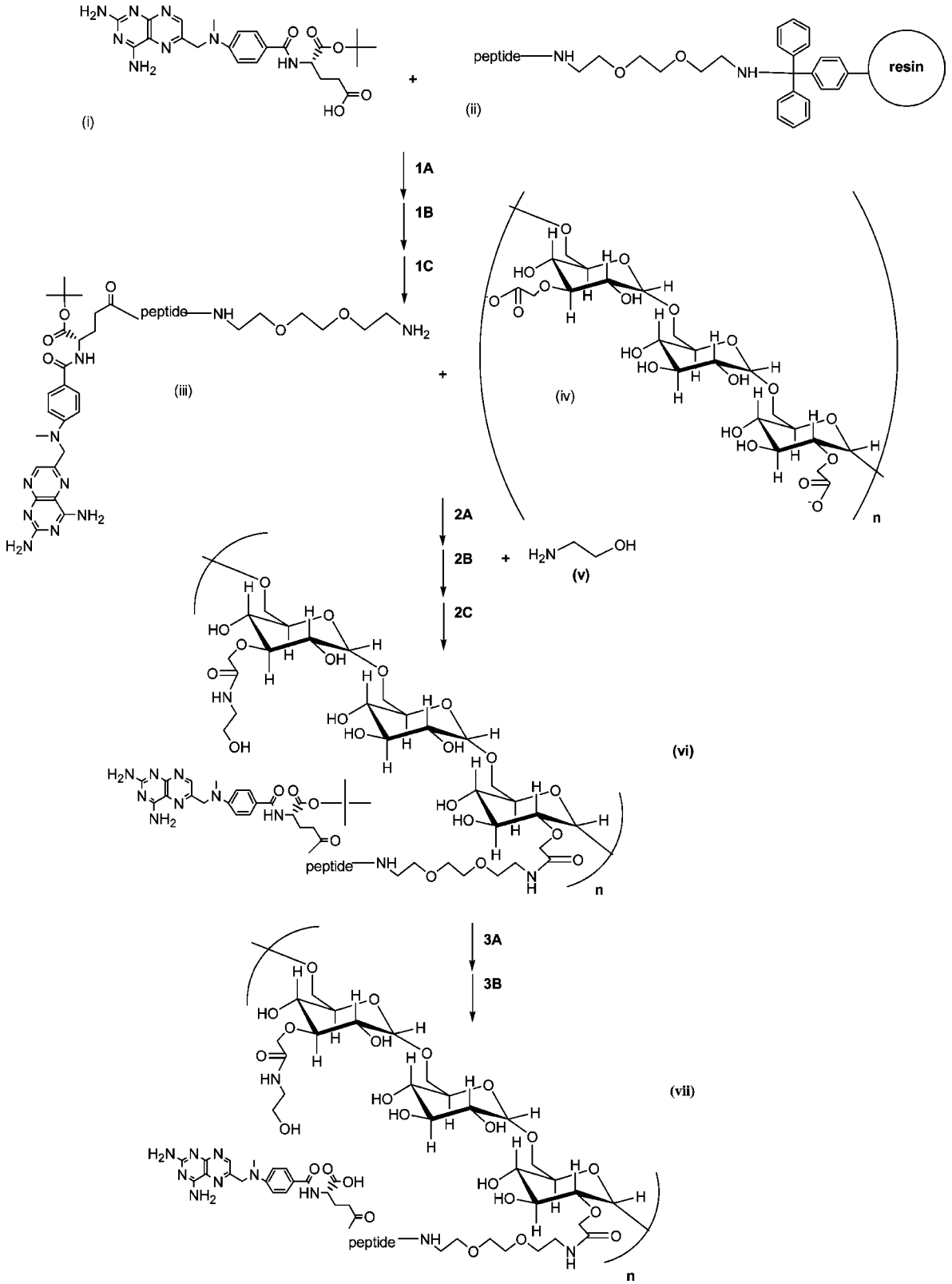
Synthesis and Purification of Methotrexate-alpha-OtBu (structure i, Scheme 1). Methotrexate-alpha-OtBu (MTX(OtBu)) was prepared from 4-amino-4-deoxy-N^{10}-methylpteroic acid (APA) and glutamic acid-α-OtBu using BOP as the conjugating reagent, following the procedure of Nagy (*29*). Crude MTX(OtBu) was precipitated by centrifugation in a 1:1 mixture of cold ether/ethyl acetate. The material was further purified by HPLC on a 95 mL C18 preparative scale column (Grace Vydac, Hesperia, CA) using a gradient from 0−100% acetonitrile with 0.2% TFA. The organic solvent in the product fractions was removed by rotoevaporation and the purified material was subsequently lyophilized. Product purity was confirmed to be ≥95% and the amount was quantified by the analytical scale reversed-phase HPLC. The average retention factor was 6.14.

Synthesis of Jeffamine−Peptide−Methotrexate-(OtBu) (structure iii, Scheme 1). Standard FMOC peptide synthesis in solid phase was carried out on *O*-Bis-(aminoethyl)ethylene glycol trityl resins by Biopolymer Lab at Massachusetts Institute of Technology. As in the conventional peptide synthesis, the peptide chain grew from the carboxyl to the amino terminal. After the last amino acid was loaded to the chain, FMOC was removed and the peptide with a free amino terminal was exposed whereas the carboxyl remained attached to the solid resin via a short six-carbon poly(ethylene oxide) spacer.

To couple MTX-α-OtBu to the amino terminal of the peptide chain, MTX-α-OtBu (2.5 equiv to the amount of peptide) was dissolved in DMF containing DIPEA (2.5 equiv). PyBop (2.5 equiv), HOBT (2.5 equiv) and additional DIPEA (2.5 equiv) were used to activate the γ-carboxyl of MTX-α-OtBu for about 15 min. More DMF was added such that the final concentration of MTX-α-OtBu was about 0.1 M. The mixture was combined with the resins loaded with peptide and stirred at room-temperature overnight. The reaction was confirmed for completeness the next day by ninhydrin test. Excessive reactants were washed away from the resins with DMF, DCM and methanol. The resins were then dried thoroughly.

Jeffamine−peptide−MTX(OtBu) was cleaved from trityl resins by suspending the resins in DCM containing 2% TFA for 10 min. This step was repeated three times. To collect all the cleaved product, the resins were further

Scheme 1. Schematics of the Synthesis Procedure of the New Dextran−Peptide−Methotrexate[a]



[a] Reactants and scales: (i) methotrexate with alpha carboxyl protected (MTX(OtBu)); typical scale = 1.25 mmol MTX equiv = 2.5 molar excess of peptide; (ii) peptide on *O*-bis(aminoethyl)ethylene glycol trityl resin; (iii) jeffamine−peptide−MTX(OtBu); typical scale= 0.35 mmol MTX equiv; (iv) carboxymethyl dextran with degree of substitution of CM groups at ∼50% and nominal MW 70 000; (v) ethanolamine; (vi) modified dextran−peptide−MTX(OtBu) with degree of modification at ∼50% and degree of drug loading at ∼1%; typical scale = 0.14 mmol MTX equiv; (vii) modified dextran−peptide−MTX with degree of modification ∼50% and with degree of drug loading∼1%; typical scale = 0.11 mmol MTX equiv. Reaction conditions and step yields*:* 1A: PyBop/HOBT/DIPEA coupling in DMF; 1B: dilute trifluoroacetic acid cleavage from resin.; 1C: reversed phase HPLC purification; typical yield for step 1= ∼70% yield. 2A: coupling with EDC in H_2O; 2B: charge neutralization by EDC/ethanolamine in excess; 2C: methanol precipitation; typical yield for step 2 = ∼40%. 3A: strong trifluoroacetic acid cleavage to deprotect *tert*-butyl group from MTX; 3B: diafiltration against DI water; typical yield for step 3 = ∼80%.

washed with DCM and methanol and the step was repeated until no further yellow color was observed (the yellow color was indicative of the presence of the MTX-(OtBu)-containing product). Organic solvent was subsequently removed by rotoevaporation from the collected product. The crude material was resuspended in water and purified by HPLC over a 0−100% acetonitrile gradient with 0.2% TFA using a 95 mL C18 preparative column. Product fractions were lyophilized after the organic solvent was removed by rotoevaporation. Product purity was found to be ≥95%, and the amount was quantified by analytical scale reversed phase HPLC.

The average retention factor on HPLC for MTX(OtBu)-Pro-Val-Gly-Leu-Ile-Gly-jeffamine was 6.71. Mass spectroscopy confirmed the identity of this intermediate product (structure iii in Scheme 1): Calc: 1177.3; Found: 1177.7. [^{1}H NMR (400 MHz, D_2O): δ 8.59 (s, H-7 of methotrexate, 1H), 7.62 (d, 3′,5′-H of methotrexate, 2H), 6.81 (d, 2′6′-H of methotrexate, 2H), 4.86 (s, H-9 of methotrexate, ∼2H, overlapping with H_2O), 4.33 (m, Hα of methotrexate, ∼1H, overlapping with H-2 of Pro) 1.8−2.0 (m,Hβ of methotrexate, 2H, overlapping with 3,4-H of Pro), 2.6 (m, Hγ of methotrexate, ∼2H), 1.41 (s, CH_3 of *tert*-butyl, ∼9H, overlapping with 3,4-H of Leu), 3.21 (s, CH_3-11 of methotrexate, 3H, overlapping with jeffamine EDR 148), 3.18−3.74 (m, H of jeffamine EDR 148, ∼12H, overlapping with H-5 of proline and CH_3-11 of methotrexate), 4.33 (m, H-2 of Pro, ∼1H, overlapping with Hα of methotrexate), 3.87−4.35 (m, H-2 of Val, Gly, Leu, Ile, Gly, 7H), 3.4−3.6 (m, H-5 of Pro, ∼2H, overlapping with jeffamine EDR 148), 2.1−2.3 (m, 3-H of Val, 3H of Ile, 2H), 1.8−2.1 (m, 3,4-H of Pro, 4H, overlapping with Hβ of methotrexate), 1.2−1.54 (m, 3,4-H of Leu, ∼3H, overlapping with CH_3 of *tert*-butyl), 0.78−0.93 (m, 3′,4-H of Val, 4′5-H of Leu, 3′4,5-H of Ile, 20H)].

The average retention factor of MTX(OtBu)-Gly-Ile-Val-Gly-Pro-Leu-jeffamine on our reversed-phase HPLC assay was 6.59. Mass spectroscopy confirmed the identity of this intermediate product (structure iii in Scheme 1): Calc: 1177.3; Found: 1177.1 [^{1}H NMR (400 MHz, D_2O): δ 8.59 (s, H-7 of methotrexate, 1H), 7.60−7.62 (d, 3′,5′-H of methotrexate, 2H), 6.78−6.80 (d, 2′6′-H of methotrexate, 2H), 4.85 (s, H-9 of methotrexate, ∼2H, overlapping with H_2O), 4.35 (m, Hα of methotrexate, ∼1H, overlapping with H-2 of Pro), 1.7−2.1 (m, Hβ of methotrexate, ∼2H, overlapping with 3,4-H of Pro), 2.45 (m, Hγ of methotrexate, 2H), 1.41 (s, CH_3 of *tert*-butyl, ∼9H, overlapping with 3,4-H of Leu), 3.20 (s, CH_3-11 of methotrexate, 3H, overlapping with jeffamine EDR 148), 3.16−3.74 (m, H of jeffamine EDR 148, ∼12H, overlapping with H-5 of proline and CH_3-11 of methotrexate), 4.35 (m, H-2 of Pro, 1H, overlapping with Hα of methotrexate), 3.84−4.25 (m, H-2 of Val, Gly, Leu, Ile, Gly, 7H), 3.3−3.5 (m, H-5 of Pro, ∼2H, overlapping with jeffamine EDR 148), 2.1−2.3 (m, 3-H of Val, 3H of Ile, 2H), 1.7−2.1 (m, 3,4-H of Pro, ∼4H, overlapping with Hβ of methotrexate), 1.1- - - 1.7 (m, 3,4-H of Leu, ∼3H, overlapping with CH_3 of *tert*-butyl), 0.74−0.88 (m, 3′,4-H of Val, 4′5-H of Leu, 3′4,5-H of Ile, 20H)]

Synthesis of Jeffamine−Methotrexate(OtBu) (iii′, structure not shown). The procedure was similar to above for the synthesis of (iii) except that no peptide was loaded onto the resin. MTX-α-OtBu was directly coupled to *O*-bis(aminoethyl)ethylene glycol trityl resin using the same protocol. Product found to be ≥ 95% by reversed-phase HPLC. The average retention factor of jeffamine−MTX(OtBu) was 5.81. Mass spectroscopy confirmed the identity of this intermediate product (iii′): Calc: 640.6; Found:640.6..

Synthesis and Purification of Dextran−Peptide−MTX (structure vii, Scheme 1). To couple jeffamine−peptide−MTX(OtBu) to CM-dextran, jeffamine−peptide−MTX(OtBu) (0.5 mMol) dissolved in DI water (1.9 mL) was combined with CM-dextran (4 g) dissolved in DI water (6.7 mL). EDC (4.7 g) was added to the mixture while stirring. The reaction was held overnight at room temperature. Another aliquot of EDC (4.7 g) was added the next day, and the reaction was held overnight to form CM-dextran−peptide−MTX(OtBu) (structure vi of Scheme 1).

To block the unreacted carboxymethyl groups on the dextran backbone, ethanolamine (30 mL) was first neutralized to pH 6−7 using 5 N HCl in dibasic phosphate buffer on ice. This mixture was added to (vi) followed by the reaction with EDC (47 g). It was held stirring at room-temperature overnight. The modified dextran−peptide−MTX(OtBu) was precipitated by centrifugation in methanol.

To remove the protection group OtBu, modified dextran−peptide−MTX(OtBu) was resuspended in 40 mL of strong trifluroacetic acid by vigorous stirring and held at room temperature for 3 h. This deprotection step was quenched by diluting the acidic mixture with 0.1 M phosphate buffer and neutralizing the pH with 5 N sodium hydroxide on ice. Extensive diafiltration was performed using Pellicon XL membrane cassettes of regenerated cellulose with 10 000 MWCO (Millipore, Billerica, MA) to remove excessive reactants and byproducts of the reaction. After purification, the product in the retentate was concentrated and then lyophilized for storage. The product purity was confirmed to be ≥99% by size-exclusion HPLC. The drug loading density was estimated by HPLC to be at 1.0 ± 0.2% (mol % per glucose unit).

Synthesis and Purification of Dextran−MTX (structure vii′, structure not shown). This procedure comprised of steps similar to those for the synthesis and purification of dextran−peptide−MTX (structure vii of Scheme 1), with the exception that jeffamine−MTX-(OtBu) was used instead of jeffamine−peptide−MTX-(OtBu).

Zeta Potential Measurement. Dextran and dextran−peptide−MTX conjugates were dissolved in DI water at 10 mg/mL. Measurement was performed with Zeta-analyzer (Brookhaven Instruments Co., Holtsville, NY).

Measurement of Kinetic Parameters for MMP-2 and MMP-9 Digestion of Conjugates. The kinetics of enzymatic digestion of the conjugates by MMP-2 and MMP-9 was modeled by the classical Michaelis−Menten equation:

$$\frac{1}{V_i} = \frac{1}{k_{cat}E_{total}} + \left(\frac{K_m}{k_{cat}E_{total}}\right)\frac{1}{S_o}$$

where V_i is the initial reaction velocity, S_o is the substrate concentration and E_{total} is the total enzyme concentration, including both bound and nonbound forms. K_m is the Michaelis−Menten constant and k_{cat} is the turnover rate of the substrate−enzyme complex to product. The ratio k_{cat}/K_m is widely used in the literature, termed as specificity constant, as a measure of how fast enzymatic digestion occurs. Conjugates of interest were dissolved in assay buffer (10 mM $CaCl_2$, 0.2 M NaCl in 50 mM Tris pH 7.5) at various concentrations: 5, 10, 20, 50 and 100 μM. For each substrate concentration, active MMP-2 or MMP-9 at a final concentration of 10 nM was added and the mixture was incubated at 37 °C. At specific time

points, the reaction mixture was quenched with EDTA solution at a final concentration of 20mM. The mixture was assayed by two-column size-exclusion HPLC (assay details are included in the next paragraph) and the cleavage product peak was quantified to calculate the reaction rate. Initial rate was defined as the rate for the cleavage of the first 20% of the conjugate. Triplicate measurements were made at each time point for each substrate concentration. Linear regression was performed on a double reciprocal plot of $1/V_i$ versus $1/S_o$ to determine the specificity constant k_{cat}/K_m.

HPLC Analytical Methods. *Reversed Phase Analytical Assay for Online Monitoring of Process Yield and Product Purity.* A silica C18 0.21 mm (ID) × 25 cm (L) column (Grace Vydac, Hesperia, CA) was connected to a HPLC solvent delivery system equipped with a UV detector (1100 series, Agilent Technologies, Palo Alto, CA). The method was run at 0.5 mL/min with mobile phase A as 0.2% trifluoroacetic acid (TFA) in water and mobile phase B as 0.2% TFA in acetonitrile. A sample of 10 μL was injected onto a preequilibrated column followed by 5 min of wash with mobile phase A. A gradient ramped from 0%B to 100%B in 20 min. Detection for methotrexate-containing moieties was made by UV absorbance at 307 nM. A calibration curve was constructed correlating the peak areas in the chromatograms and the concentrations of methotrexate standards.

Two-Column Size-Exclusion Assay for Enzyme Kinetics Study. A PW3000 7.8 mm (ID) × 30 cm (L) column followed by PW2000 7.5 mm (ID) × 30 cm (L) column (Tosohaas, Montgomeryville, PA) were connected to a HPLC solvent delivery system equipped with a UV detector (Agilent Technologies).The method consisted of an isocratic elution with 20% acetonitrile and 3.6× phosphate-buffered saline in water at 0.8 mL/min. Detection for methotrexate-containing moieties was made by UV detection at 307 nM or 390 nM. The default sample injection volume was set at 10 μL. A calibration curve was constructed correlating the peak areas in the chromatograms and the concentrations of methotrexate standards.

One-Column Size-Exclusion Assay for Online Monitoring of Process Yield and Product Purity. A PW3000 7.8 mm (ID) × 30 cm (L) column (Tosohaas) was connected to a HPLC solvent delivery system equipped with a UV detector (Agilent Technologies). The method consisted of an isocratic elution with 20% acetonitrile and 3.6× phosphate-buffered saline in water at 0.8 mL/min. Detection for methotrexate-containing moieties was made by UV detection at 307 nM. The default sample injection volume was set at 10 μL. A calibration curve was constructed correlating the peak areas in the chromatograms and the concentrations of methotrexate standards.

Maintenance of Cell Culture. Human tumor cells HT-1080 and BT-20 were maintained using DMEM low glucose media supplemented with 2 mM L-glutamine, 1× glutamine−penicillin−streptomycin (GPS), 25 μg/mL plasmocin, and 10% fetal bovine serum.

Zymography of Cell Conditioned Media. HT-1080 and BT-20 were grown to about 70% confluence before the growth media was exchanged to the serum-free media (DMEM low glucose containing 2 mM L-glutamine, 1× GPS, and 12.5 ng/mL of PMA) The culture was grown in serum-free media for another 3 days. Cell-conditioned media were analyzed with gelatin zymography according to a previously described procedure (*30*, *31*). Briefly, samples were separated with electrophoresis in a 10% polyacrylamide gel containing gelatin. After renaturing the gel in 2.5% Triton X-100 solution, it was incubated overnight in a development buffer to allow the digestion of the gelatin by MMP-2 or MMP-9. White clear bands in a blue background after Coomassie Blue staining indicated the presence of the enzymes.

In Vitro Digestion Experiments of Conjugates. To assess the stability of the conjugate MTX−PVGLIG−dextran (PVGLIG is the shorthand notation of the peptide Pro-Val-Gly-Leu-Ile-Gly) in serum-containing conditions, it was incubated at 37 °C and 5% CO_2 with various media for 24 h. The percentage cleavage of the conjugate was determined by the two-column size-exclusion HPLC assay.

To demonstrate that the specificity of release of peptidyl drug from the conjugate in cell culture was MMP-2 and MMP-9 dependent, HT-1080 and BT-20 were grown in 12-well-plates to about 80% confluence and growth media was exchanged to serum-free media containing 12 ng/mL of PMA or 10 μg/mL of ConA. PMA and ConA were used to activate pro-MMP-2 and pro-MMP-9 to their active forms. After 2 days, the conjugate MTX−PVGLIG−dextran was added to the cell culture and incubated for 6 h. Media samples were analyzed by two-column size-exclusion HPLC assay to determine the percentage peptidyl drug released from the conjugate.

Cytotoxicity Assay. (3-(4,5-Dimethylthiazol-2-yl)-2,5-diphenyl-2*H*-tetrazolium bromide) assay (MTT assay) was used to measure the drug cytotoxicity according to a previously described procedure with modifications (*32*). Cells were seeded in serum-containing growth media to 96-well-plates at 10 000 cells/well. After 1 day, the growth media was exchanged to serum-free media and the drug solutions at specified concentrations were added. After another 2 days of drug exposure, MTT solution was added and the plates were incubated at 37 °C for 2 h, followed by overnight incubation with extraction solution (10% SDS in DMF/H_2O pH 4.7). Plates were read at 570 nM, and the readings of the absorbance corresponded to the number of living cells. Percentage survival was calculated using the formula listed in the website of National Cancer Institute (http://dtp.nci.nih.gov/branches/btb/ivclsp.html):

$$[(T_i - T_z)/(C - T_z)] \times 100 \text{ for concentrations for which } T_i \geq T_z$$

$$[(T_i - T_z)/T_z] \times 100 \text{ for concentrations for which } T_i < T_z$$

where T_z is the reading at time zero prior to the addition of drug solutions, T_i is the reading at the assay end-point at each of the drug concentration level, and C is reading at the assay end-point for the control growth (with no drug addition).

Growth inhibition of 50% (GI50) was calculated from $[(T_i - T_z)/(C - T_z)] \times 100 = 50$, which was the drug concentration resulting in a 50% reduction in the net increase in the number of viable cells (as measured by MTT assay) compared to control growth.

RESULTS

Synthesis of the New Conjugates. We have developed a robust process to synthesize and purify the new dextran−peptide−methotrexate conjugates. The process flowchart is shown in Scheme 1. To help us monitor and optimize the synthesis process, we have also established a reversed-phase and two size-exclusion HPLC assays.

The drug molecule to be attached to the new conjugate, methotrexate, has some bulk tolerance at the γ-carboxyl group. It is important that the α-carboxyl, the less

Table 1. Conjugation Yield of the Reaction Step between Carboxymethyl Dextran and Jeffamine−Peptide−MTX(OtBu), Varying the Amine and the Carboxyl Concentration

amine concn (M)	carboxyl concn (M)	conjugation yield (%)
0.02	0.66	76
0.02	0.18	41
0.02	0.09	29
0.02	0.02	15
0.01	0.66	25

tolerable functional group, is protected throughout the synthesis process. Thus methotrexate-alpha-(OtBu) (structure i, Scheme 1) was prepared from APA. This protected methotrexate was first conjugated to the peptide in a solid-phase reaction. Trityl resins were chosen as the solid-phase supports since the products synthesized on the resins could be released using a dilute acid thus leaving the *tert*-butyl group on methotrexate unaffected. This protection group was eventually removed in the last reaction step (step 3A, Scheme 1).

We have chosen a special trityl resin, *O*-bis(aminoethyl)ethylene glycol trityl resin (structure ii, Scheme 1), as the solid support. This enables the peptide to be attached to jeffamine, a short poly(ethylene oxide) chain. After detaching from the solid support, the peptide remains attached to jeffamine. Jeffamine aids in the coupling between the peptide−drug and carboxymethyl dextran (structure iv, Scheme 1). Our MMP-recognizable peptide sequence is composed of hydrophobic amino acids (Pro-Val-Gly-Leu-Ile-Gly). The protected drug MTX-α-(OtBu) also has limited aqueous solubility. On the other hand, carboxymethyl dextran is hydrophilic. In our attempts to couple peptide−drug to carboxymethyl dextran in the presence of EDC, we have found that the concentration of the amine component and the concentration of the carboxyl component are critical factors in determining conjugation yield. Table 1 lists the conjugation yield when we varied the amine or the carboxyl concentration in the coupling step, keeping all other reaction conditions identical. This observation is explained by the relatively short half-life of the EDC-activated carboxyl. If unable to encounter an amine component for reaction, the active ester becomes inactivated (*33*). Because of the hydrophilic character of the jeffamine spacer that improves aqueous solubility, higher concentration of jeffamine−peptide−MTX(OtBu) (structure iii, Scheme 1) can be attained and the conjugation in aqueous phase results in a reasonable yield (Step 2A, Scheme 1).

MMP-Mediated Drug Release Requires an Optimized Peptide Linker. We have prepared three different conjugates: (1) MTX−PVGLIG−dextran, with the peptide linker composition optimized for MMP-2 recognition; (2) MTX−GIVGPL−dextran, with a scrambled peptide linker; (3) MTX−dextran, without a peptide linker. The extents of drug release from these conjugates in the presence of MMP-2 and MMP-9 were compared in Figure 1 and Figure 2.

Similar trends were observed for both MMP-2 and MMP-9. MTX−PVGLIG−dextran conjugate released 89% of peptidyl methotrexate in the presence of MMP-2 and 61% in the presence of MMP-9 after 24 h. In contrast, conjugates without any peptide linker or carrying the scrambled peptide linker did not show any significant release. Without the MMP recognizable peptide linker, the conjugate was stable even in the presence of a high concentration of MMP-2 or MMP-9. We isolated the small molecular weight cleavage product from the digest of

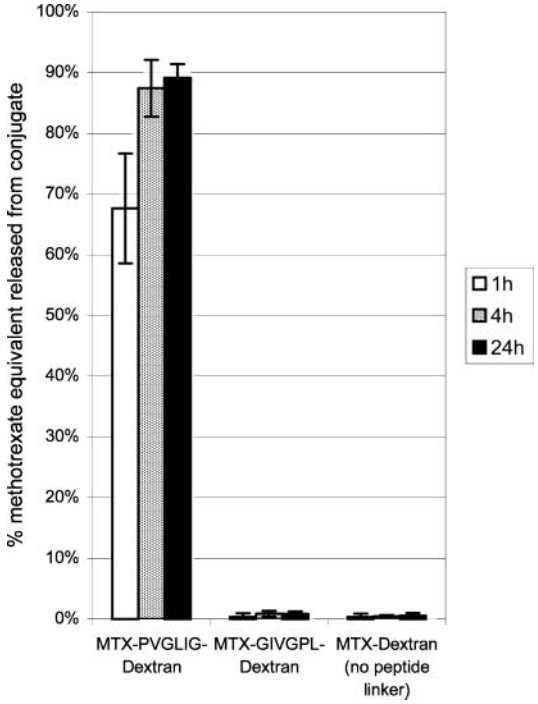


Figure 1. Extent of methotrexate equivalent released from different conjugates in the presence of MMP-2. Conjugates of different linkers were incubated with 10 nM of MMP-2 in assay buffer at 37 °C and measured for percentage cleavage at specified time points by size exclusion. Peptidyl methotrexate analogues were the expected products released from the dextran−peptide−methotrexate conjugates upon cleavage. Methotrexate was the expected product released from the dextran−methotrexate conjugate upon cleavage. Cleavage of the conjugate by MMP-2 was dependent on the linker composition.

MTX−PVGLIG−dextran on size-exclusion column and analyzed the product fraction by mass spectroscopy. The molecular weight found was 707.5 and was consistent with the notion that methotrexate−proline-valine-Gly (MTX−PVG) was the released product. This can be predicted by the scissile site of MMP-2 and MMP-9 on the peptide (*27*).

Preparation of Conjugates with Varying Backbone Negative Charges. To investigate the effect of the net charge on the dextran backbone, we prepared different conjugates by reacting the excess carboxymethyl with ethanolamine using different conditions. Ethanolamine is a simple, neutral and hydrophilic molecule (structure v and step 2B, Scheme 1). The charges on the resulting conjugates were characterized by its zeta potential. We first experimented with just carboxymethyl dextran (structure iv, Scheme 1) and found that the negative charge could be partially or fully neutralized using appropriate reaction conditions (Table 2).

By tuning the amount of EDC and ethanolamine, we prepared MTX−PVGLIG−dextran conjugates with varying negative charges and examined the charge effect on the kinetics of digestion by MMP-2 and MMP-9 (Table 3). As seen in Table 3, the charge on the conjugate backbone has a significant effect on the rate of MMP-2 cleavage. The value of k_{cat}/K_m is varied by an order of magnitude depending on the charge. The conjugate most sensitive to MMP-2 (Conjugate C) has its excess carboxymethyl groups completely masked by ethanolamine and is neutral in charge. It has a similar kinetic constant toward MMP-2 digestion as the optimal peptide found by Turk (*27*). In his report, Ile-Pro-Val-Ser-Leu-Arg-Ser has a k_{cat}/K_m value of 0.82×10^5 M^{-1} s^{-1}. On the other

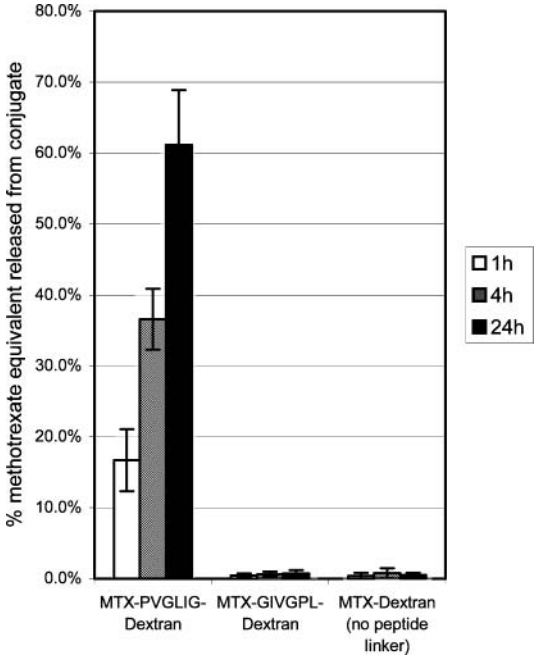


Figure 2. Extent of methotrexate equivalent released from different conjugates in the presence of MMP-9. Conjugates of different linkers were incubated with 10 nM of MMP-9 in assay buffer at 37 °C and measured for percentage cleavage at specified time points by size exclusion. Peptidyl methotrexate analogues were the expected products released from the dextran−peptide−methotrexate conjugates upon cleavage. Methotrexate was the expected product released from the dextran−methotrexate conjugate upon cleavage, if any. Cleavage of conjugate by MMP-9 was dependent on the linker composition.

hand, the kinetics of enzymatic digestion by MMP-9 was much less sensitive to the charge difference on our conjugate backbone. Taken together, the conjugate with its carboxymethyl groups masked and hence least negatively charged has the highest sensitivity toward MMP-2 and MMP-9.

Stability in Serum-Containing Conditions. We used fetal bovine serum and serum spiked with active human MMP-2 and MMP-9 to approximate the physiological conditions encountered by the conjugates in systemic circulation. In contrast to the conditions without serum, we found no significant cleavage even in serum spiked with high concentration of MMP-2 and MMP-9 (Figure 3). These results showed that the peptide linker within the conjugate was shielded from the exopeptidases in serum. Furthermore, the two MMPs were inactivated in serum.

Specificity of Release in Tumor Cell Culture. HT-1080 is a human fibrosacroma cell line that is known to express MMP-2 and MMP-9. BT-20, a human breast cancer cell line, is known to be negative in MMP-2 and MMP-9. These features were confirmed by zymography of the cell-conditioned media from these cell lines (Figure 4). In HT-1080 cell conditioned media, the prominent band at 68kD indicates the presence of active MMP-2 and the band at 86 kDa the presence of MMP-9. In BT-20 conditioned media, only a faint band is present at 72 kDa showing a relatively small amount of pro-MMP-2.

The conjugates MTX−PVGLIG−dextran were incubated for 6 h with these two types of cell culture. The digest showed no detectable cleavage of the conjugates in BT-20 culture. In contrast, 14% cleavage was observed in HT-1080 culture (Table 4). The in vitro experiments indicated that the extracellular release of peptidyl methotrexate from the conjugate was associated with the presence of active MMP-2 and MMP-9.

Cytotoxicity of the Released Peptidyl Methotrexate toward Tumor Cells. The released product from the new conjugate is a peptidyl methotrexate analogue (MTX−PVG) and has three amino acids attached to the free drug. The cytotoxicity of MTX−PVG was measured and compared with free methotrexate using MTT assay. For both tumor cell lines, HT-1080 and BT-20, peptidyl methotrexate was cytotoxic with GI50 on the order of 10 μM. Compared to free methotrexate, the potency of the drug was lowered by 2 orders of magnitude (Figures 5 and 6).

DISCUSSION

We have developed a robust and flexible synthesis procedure to prepare new dextran−peptide−methotrexate conjugates. Reaction and purification steps are monitored by HPLC to confirm high purity and reasonable yield. We have combined solid-phase and solution-phase synthesis to make the process more flexible. Peptide synthesis on solid supports is now a highly automated process, and peptide sequences of varying length or composition can be readily prepared in a short time. The advance of this current technology lets us accommodate any change in the peptide sequence for our conjugate's linker. This is valuable when we expand the current approach to target other tumor-associated enzymes, which are made up of a diverse group of proteases. A few examples include prostate-specific antigens (*34*), urokinase-type plasminogen activator (*35*), and cathepsin-L (*36*). We have also devised a method to modify the magnitude of negative charge on the dextran backbone, another factor that can be tailored to different enzymes of interest in order to optimize conjugate sensitivity. We have chosen a special trityl resin, *O*-bis(aminoethyl)-ethylene glycol trityl resin (structure ii, Scheme 1), as the solid support. This enables the ready incorporation of a 10-atom long jeffamine spacer adjacent to the specific peptide. Our original concept was to use the spacer to prevent steric hindrance posed by the dextran polymer backbone on the enzymatic cleavage of the specific peptide. This hydrophilic spacer is actually important in ensuring the robustness of the synthesis process. It improves the solubility of the peptide and hence increases the concentration of the amine component in the conjugation reaction, giving consistent and reasonable yield in this key reaction step.

We intend our new conjugates to release the active drug molecules in the presence of the tumor-associated enzymes MMP-2 and MMP-9. A peptide linker labile to enzymatic digestion is important to achieve this purpose. We selected the most preferable amino acids for MMP-2 from Turk's work (*27*) to fill the substrate positions from P3 to P3′. From our experience in developing dextran−peptide−doxorubicin conjugates (*37*), these six positions are necessary for recognition by MMP-2 and MMP-9. This observation is consistent with reports in the literature (*38*). We showed that the cleavage of the new dextran−peptide−methotrexate conjugate depended on the presence of the optimal peptide, as conjugates with scrambled peptide or no peptide linker did not respond to even a high concentration of MMP-2 or MMP-9 (Figures 1 and 2). Although the peptide PVGLIG shows a high cleavage rate by MMP-2 and MMP-9, this peptide is not sensitive exclusively to these two enzymes. Because of the similarity among members in the family of matrix metalloproteinases (*27*, *39*), this peptide is expected to be cleavable by other MMPs albeit with lower rates.

In our previous experience with dextran−peptide−doxorubicin conjugates, we observed that the rate of

Table 2. Zeta Potentials of Dextran and Modified Dextran Samples

sample	zeta potential (mV)
dextran T70 (neutral)	−6.6
carboxymethyl dextran CM−dextran (degree of substition ~50% determined by atomic absorption sodium analysis)	−47.4
ethanolamine neutralized CM−dextran A (EDC at 2-fold excess and ethanolamine at 10-fold excess of glucose units present on dextran)	−36.25
ethanolamine neutralized CM−dextran B (EDC at 10-fold excess and ethanolamine at 20-fold excess of glucose units present on dextran)	−1.06

Table 3. MTX−PVGLIG−Dextran Conjugates with Varying Negative Backbone Charge Show Significantly Different Sensitivity toward MMP-2 Cleavage but Similar Sensitivity toward MMP-9

conjugate ID	backbone negative charge masked with ethanolamine?	zeta potential (mV)	k_{cat}/K_m (M^{-1} s^{-1}) by MMP-2 digestion[a]	k_{cat}/K_m (M^{-1} s^{-1}) by MMP-9 digestion[b]
A	none	−43.7	$2.12 \times 10^4 \pm 3.33 \times 102$	$7.09 \times 10^3 \pm 5.52 \times 10^2$
B	partially	−27.8	$1.10 \times 10^4 \pm 9.66 \times 10^2$	$3.09 \times 10^3 \pm 5.04 \times 10^2$
C	fully	−12.2	$1.21 \times 10^5 \pm 4.11 \times 10^3$	$3.60 \times 10^3 \pm 4.14 \times 10^2$

[a,b] The average values and standard deviations of three replicates are reported.

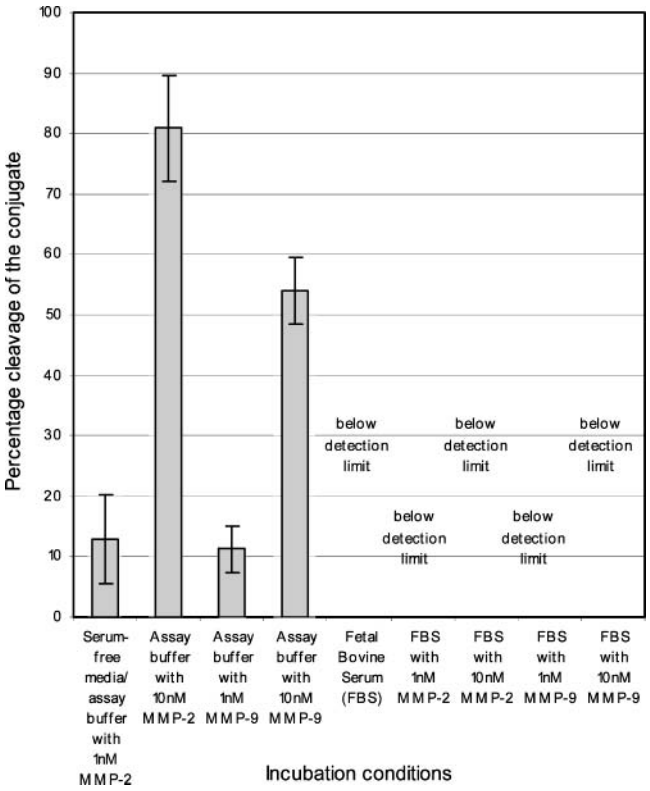


Figure 3. Stability of conjugate MTX−PVGLIG−dextran in various media conditions. Conjugates were incubated with the specified conditions for 24 h at 37 °C and assayed by size-exclusion HPLC to determine the percentage cleavage of the conjugate. The conjugate released peptidyl drug in serum-free conditions but remained intact in all the serum-containing conditions. The average values from three replicates with standard deviations as error bars are shown.

MMP-2 cleavage increased with higher ionic strength in the digestion media. In accordance with Debye−Hückel theory, we reasoned that this phenomenon could be explained by the electrostatic repulsion between the enzyme and the negatively charged conjugate (*37*). In the current report, we investigated the relationship between the negative charge on the dextran backbone and the enzyme kinetics of conjugate digestion. We confirmed our previous suspicion that MMP-2 was repulsive to negative charge. Blocking the excess negative charge on the dextran backbone improved the enzyme kinetics significantly (Table 3). Interestingly, MMP-9 is relatively insensitive to charge modification on the dextran backbone. MMP-2 and MMP-9 are similar in structure. Both

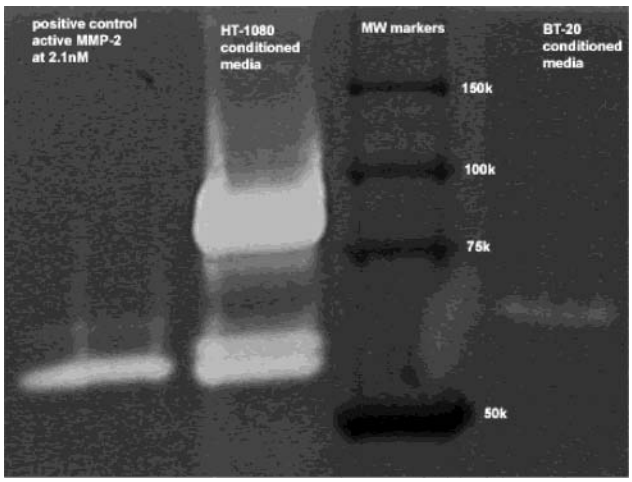


Figure 4. Gelatin zymography of HT-1080 and BT-20 cell conditioned media. The white bands in the dark backgrounds indicate the presence of gelatinases (MMP-2 and MMP-9). Active MMP-2 (68kD) and active MMP-9 (86kD) were expressed by HT-1080. Only a faint band of pro-MMP-2 (72kD) was found in BT-20.

Table 4. Susceptibility of the MTX−PVGLIG−Dextran Conjugate to Cleavage in Tumor Cell-Conditioned Media

cell culture	expression of active MMP-2	expression of active MMP-9	% cleavage of the conjugate[a]
HT-1080	+	+	14.2% ± 0.07
BT-20	-	-	none detected

[a] The average value of two experiments and the standard deviation are reported.

have three repeats of fibronectin type II domain (*39*). Categorized together as gelatinases, these two enzymes are also reported to have similar biological substrates and specificity (*38*).We compared the amino acid sequences of the active form of human MMP-2 and MMP-9, taken from the Swiss-Prot database (P08253 and P14780 for their precursors). The net charge of MMP-2 is 10 times more negative than MMP-9. This difference is consistent with our current experimental observation that MMP-2 exhibits significantly more electrostatic repulsion toward the negatively charged dextran backbone.

Our new conjugates are intended for systemic delivery. To be able to target tumor sites, the conjugates must remain stable in the blood circulation and the drug molecules should stay attached to the polymer backbone prior reaching the tumor tissues. We demonstrated that our conjugates were satisfactory in meeting the stability

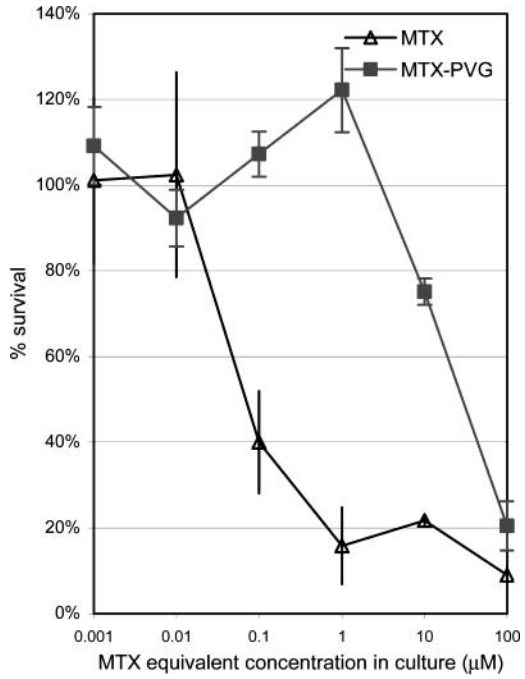


Figure 5. Cytotoxic effect of methotrexate and methotrexate-Pro-Val-Gly on HT-1080 cell culture measured by MTT assays. The average values of three replicates with standard deviations as error bars are shown.

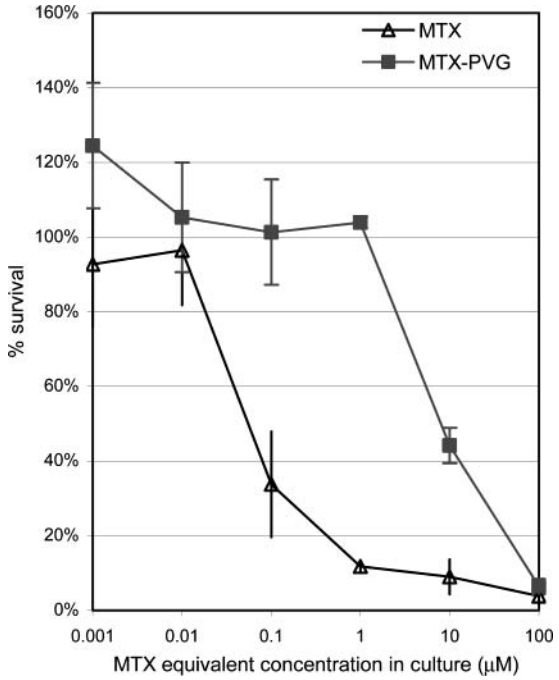


Figure 6. Cytotoxic effects of methotrexate and methotrexate-Pro-Val-Gly on BT-20 cell culture measured by MTT assays. The average values of three replicates with standard deviations as error bars are shown.

criteria—they did not show any significant cleavage in serum-containing conditions (Figure 3). The peptide linker is covalently joined to the methotrexate molecule on one end and to the dextran backbone on the other, thus being protected from the exopeptidases present in the serum. Other than pure serum, we also tested the conjugate's stability in serum spiked with MMP-2 or MMP-9. These conditions are intended to mimic the physiological environments in which tumor growth is present in the body. When tumor tissues overexpress MMP-2 and MMP-9, the enzyme levels are also elevated in the blood stream (*40*). However, protease activities of these MMPs in the systemic circulation are greatly reduced because of the inhibition by serum proteins. One of these inhibitors is α2-macroglobulin, a large serum protein with molecular weight of about 800 kDa that offers the proteases a bait region. Once the bait region is cut, α2-macroglobulin changes shape to entrap the MMP (*39*). This inhibitory effect was clearly demonstrated in our experiments. While the conjugate MTX−PVGLIG−dextran was sensitive to MMP-2 or MMP-9 in assay medium that was serum free, releasing a significant amount of peptidyl methotrexate, it did not respond to the same enzymes at equivalent concentrations when serum was present.

We provided evidence that the conjugates were able to be cleaved in the tumor culture and the release of peptidyl drug was due to the presence of MMP-2 and MMP-9 (Figure 4 and Table 4). In these cell cultures, no serum was present. The absence of serum protein was intended to mimic the conditions in the tumor vicinity in vivo. Because of the large sizes of the serum protease inhibitors such as α2-macroglobulin, they are unable to cross the capillary endothelium and therefore are absent in the interstitial fluid. In the tumor tissues, the activities of MMP-2 and MMP-9 are not inhibited by serum proteins although they are regulated more specifically by tissue inhibitors of metalloproteinases (TIMPs) (*39*).

Because of the requirement of P3 to P3′ sites for substrate recognition by MMP-2 and MMP-9, the released product from the conjugate contains three amino acids attached to the free drug. Although methotrexate exhibits some bulk tolerance at the gamma-carboxyl site, we are concerned about the therapeutic effect of the released product. Cytotoxicity assays showed that the released product was still effective in inhibiting the proliferation of tumor cells but the potency was lower than the free methotrexate. This is the biggest concern of the current approach, namely, the drug is not released in the original free form. However, the loss in cytotoxicity in vitro may not translate to the loss in antitumor efficacy in vivo. The sensitivity of the new conjugates to the tumor-associated enzymes MMP-2 and MMP-9, as well as their capability of remaining stable in the systemic circulation, suggests that the new conjugates can passively and actively target the tumor tissue. We predict that these qualities will improve both the circulation half-life of the conjugate and the percentage dose accumulated in the tumor tissue. While these effects can bring about improvement in antitumor efficacy in vivo but cannot be measured in cell culture assays, further investigation in animal models is warranted.

ACKNOWLEDGMENT

The authors thank Dr. Sanyong Jon for the collection and the interpretation of NMR data. We are grateful for Dr. Dane Wittrup's advice on charge optimization of the conjugates and Dr. Marsha Moses's advice on biochemical characterization of MMP. Y. Chau is supported by a Whitaker Fellowship. This research is funded by Amgen Inc.

LITERATURE CITED

(1) Davies, B., Miles, D. W., Happerfield, L. C., Naylor, M. S., Bobrow, L. G., Rubens, R. D., and Balkwill, F. R. (1993) Activity of Type-IV Collagenases in Benign and Malignant Breast Disease. *Br. J. Cancer 67*, 1126−1131.

(2) Hamdy, F. C., Fadlon, E. J., Cottam, D., Lawry, J., Thurrell, W., Silcocks, P. B., Anderson, J. B., Williams, J. L., and Rees, R. C. (1994) Matrix Metalloproteinase-9 Expression in Pri-

mary Human Prostatic Adenocarcinoma and Benign Prostatic Hyperplasia. *Br. J. Cancer 69*, 177−182.
(3) Levy, A. T., Cioce, V., Sobel, M. E., Garbisa, S., Grigioni, W. F., Liotta, L. A., and Stetlerstevenson, W. G. (1991) Increased Expression of the Mr 72, 000 Type-IV Collagenase in Human Colonic Adenocarcinoma. *Cancer Res. 51*, 439−444.
(4) Naylor, M. S., Stamp, G. W., Davies, B. D., and Balkwill, F. R. (1994) Expression and Activity of MMPs and Their Regulators in Ovarian-Cancer. *Int. J. Cancer 58*, 50−56.
(5) Davies, B., Waxman, J., Wasan, H., Abel, P., Williams, G., Krausz, T., Neal, D., Thomas, D., Hanby, A., and Balkwill, F. (1993) Levels of Matrix Metalloproteases in Bladder-Cancer Correlate with Tumor Grade and Invasion. *Cancer Res. 53*, 5365−5369.
(6) Derrico, A., Garbisa, S., Liotta, L. A., Castronovo, V., Stetlerstevenson, W. G., and Grigioni, W. F. (1991) Augmentation of Type-Iv Collagenase, Laminin Receptor, and Ki67 Proliferation Antigen Associated with Human Colon, Gastric, and Breast-Carcinoma Progression. *Modern Pathol. 4*, 239−246.
(7) Fidler, I. J., and Radinsky, R. (1990) Genetic-Control of Cancer Metastasis. *J. Natl. Cancer Inst. 82*, 166−168.
(8) Liotta, L. A., Steeg, P. S., and Stetlerstevenson, W. G. (1991) Cancer Metastasis and Angiogenesis − an Imbalance of Positive and Negative Regulation. *Cell 64*, 327−336.
(9) Egeblad, M., and Werb, Z. (2002) New functions for the matrix metalloproteinases in cancer progression. *Nat. Rev. Cancer 2*, 161−174.
(10) Duncan, R., Seymour, L. W., O'Hare, K. B., Flanagan, P. A., Wedge, S., Hume, I. C., Ulbrich, K., Strohalm, J., Subr, V., and Spreafico, F. (1992) Preclinical evaluation of polymer-bound doxorubicin. *J. Controlled Release 19*, 331−346.
(11) Kopecek, J., Rejmanova, P., Strohalm, J., Ulbrich, K., Rihova, B., Chytry, V., Lloyd, J. B., and Duncan, R. (1986) Synthetic polymeric drugs. Eur. Pat. Appl. (Ceskoslovenska Akademie Ved, Czech.; Carlton Medical Products Ltd.) 70 pp., Ep.
(12) Matsumura, Y., and Maeda, H. (1986) A New Concept for Macromolecular Therapeutics in Cancer-Chemotherapy − Mechanism of Tumoritropic Accumulation of Proteins and the Antitumor Agent Smancs. *Cancer Res. 46*, 6387−6392.
(13) Nishikawa, M., Takakura, Y., and Hashida, M. (1996) Pharmacokinetic evaluation of polymeric carriers. *Adv. Drug Delivery Rev. 21*, 135−155.
(14) Maeda, H., Wu, J., Sawa, T., Matsumura, Y., and Hori, K. (2000) Tumor vascular permeability and the EPR effect in macromolecular therapeutics: a review. *J. Controlled Release 65*, 271−284.
(15) Hashida, M., and Takakura, Y. (1994) Pharmacokinetics in Design of Polymeric Drug-Delivery Systems. *J. Controlled Release 31*, 163−171.
(16) Pechar, M., Ulbrich, K., Jelinkova, M., and Rihova, B. (2003) Conjugates of antibody-targeted PEG multiblock polymers with doxorubicin in cancer therapy. *Macromol. Biosci. 3*, 364−372.
(17) Seymour, L. W., Ferry, D. R., Anderson, D., Hesslewood, S., Julyan, P. J., Poyner, R., Doran, J., Young, A. M., Burtles, S., and Kerr, D. J. (2002) Hepatic drug targeting: Phase I evaluation of polymer-bound doxorubicin. *J. Clin. Oncol. 20*, 1668−1676.
(18) Tang, A. J., Kopeckova, P., and Kopecek, J. (2003) Binding and cytotoxicity of HPMA copolymer conjugates to lymphocytes mediated by receptor-binding epitopes. *Pharm. Res. 20*, 360−367.
(19) Flanagan, P. A., Duncan, R., Subr, V., Ulbrich, K., Kopeckova, P., and Kopecek, J. (1992) Evaluation of Protein-N−(2-Hydroxypropyl)Methacrylamide Copolymer Conjugates as Targetable Drug-Carriers 0.2. Body Distribution of Conjugates Containing Transferrin, Antitransferrin Receptor Antibody or Anti-Thy 1.2 Antibody and Effectiveness of Transferrin-Containing Daunomycin Conjugates against Mouse L1210 Leukemia in Vivo. *J. Controlled Release 18*, 25−37.
(20) Garsky, V. M., Lumma, P. K., Feng, D. M., Wai, J., Ramjit, H. G., Sardana, M. K., Oliff, A., Jones, R. E., DeFeo-Jones, D., and Freidinger, R. M. (2001) The synthesis of a prodrug of doxorubicin designed to provide reduced systemic toxicity and greater target efficacy. *J. Med. Chem. 44*, 4216−4224.
(21) Liu, S., Netzel-Arnett, S., Birkedal-Hansen, H., and Leppla, S. H. (2000) Tumor Cell-selective Cytotoxicity of Matrix Metalloproteinase-activated Anthrax Toxin. *Cancer Res. 60*, 6061−6067.
(22) Sgouras, D., and Duncan, R. (1990) Methods for the Evaluation of Biocompatibility of Soluble Synthetic-Polymers Which Have Potential for Bio-Medical Use. 1. Use of the Tetrazolium-Based Colorimetric Assay (MTT) as a Preliminary Screen for Evaluation of in Vitro. Cytotoxicity. *J. Mater. Sci.-Mater. Med. 1*, 61−68.
(23) Vercauteren, R., Schacht, E., and Duncan, R. (1992) Effect of the Chemical Modification of Dextran on the Degradation by Rat-Liver Lysosomal-Enzymes. *J. Bioactive Compatible Polym. 7*, 346−357.
(24) Munechika, K., Sogame, Y., Kishi, N., Kawabata, Y., Ueda, Y., Yamanouchi, K., and Yokoyama, K. (1994) Tissue Distribution of Macromolecular Conjugate, Adriamycin Linked to Oxidized Dextran, in Rat and Mouse Bearing Tumor-Cells. *Biol. Pharm. Bull. 17*, 1193−1198.
(25) Chamber, B. A., Ryan, D. P., Paz-Ares, L., Garcia-Carbonero, R., and Calabresi, P. (2001) *Goodman and Gilman's The Pharmacological Basis of Therapeutics* (Hardman, J. G., Limbird, L. E., and Gilman, A. G., Eds.) pp 1389, The McGraw-Hill Companies, Inc., New York.
(26) Rosowsky, A., Forsch, R., Uren, J., and Wick, M. (1981) Methotrexate Analogues. 14. Synthesis of New Gamma-Substituted Derivatives as Dihydrofolate-Reductase Inhibitors and Potential Anticancer Agents. *J. Med. Chem. 24*, 1450−1455.
(27) Turk, B. E., Huang, L. L., Piro, E. T., and Cantley, L. C. (2001) Determination of protease cleavage site motifs using mixture-based oriented peptide libraries. *Nat. Biotechnol. 19*, 661−667.
(28) Nogusa, H., Yano, T., Okuno, S., Hamana, H., and Inoue, K. (1995) Synthesis of Carboxymethylpullulan Peptide Doxorubicin Conjugates and Their Properties. *Chem. Pharm. Bull. 43*, 1931−1936.
(29) Nagy, A., Szoke, B., and Schally, A. V. (1993) Selective Coupling of Methotrexate to Peptide-Hormone Carriers through a Gamma-Carboxamide Linkage of Its Glutamic-Acid Moiety − Benzotriazol-1-Yloxytris(Dimethylamino)Phosphonium Hexafluorophosphate Activation in Salt Coupling. *Proc. Natl. Acad. Sci. U. S. A. 90*, 6373−6376.
(30) Hibbs, M. S., Hasty, K. A., Seyer, J. M., Kang, A. H., and Mainardi, C. L. (1985) Biochemical and immunological characterization of the secreted forms of human neutrophil gelatinase. *J. Biol. Chem. 260*, 2493−2500.
(31) Yan, L., Moses, M. A., Huang, S., and Ingber, D. E. (2000) Adhesin-dependent control of matrix-metalloproteinase-2 activation in human capillary endothelial cells. *J. Cell Sci. 113*, 3979−3987.
(32) Denizot, F. L., R. (1986) Rapid colorimetric assay for cell growth and survival. Modifications to the tetrazolium dye procedure giving improved sensitivity and reliability. *J. Immunol. Methods 89*, 271.
(33) Hermanson, G. T. (1996) *Bioconjugate Techniques*, Academic, New York.
(34) Denmeade, S. R., Lou, W., Lovgren, J., Malm, J., Lilja, H., and Isaacs, J. T. (1997) Specific and efficient peptide substrates for assaying the proteolytic activity of prostate-specific antigen. *Cancer Res. 57*, 4924−4930.
(35) Marutsuka, K., Suzumiya, J., Kataoka, H., Komada, N., Koono, M., and Sumiyoshi, A. (1991) Correlation between Urokinase-Type Plasminogen-Activator Production and the Metastatic Ability of Human Rectal-Cancer Cells. *Invasion Metastasis 11*, 181−191.
(36) Heidtmann, H. H., Salge, U., Havemann, K., Kirschke, H., and Wiederanders, B. (1993) Secretion of a Latent, Acid Activatable Cathepsin-L Precursor by Human Nonsmall Cell Lung-Cancer Cell-Lines. *Oncol. Res. 5*, 441−451.
(37) Chau, Y., and Langer, R. S. (2003) Important factors in designing targeted delivery of cancer therapeutics via MMP-2 mediation. *J. Controlled Release 91*, 239−240.
(38) Netzel-Arnett, S., Sang, Q. X., Moore, W. G. I., Navre, M., Birkedalhansen, H., and Vanwart, H. E. (1993) Comparative Sequence Specificities of Human 72-kDa and 92-kDa Gelati-

nases (Type-IV Collagenases) and Pump (Matrilysin). *Biochemistry 32*, 6427−6432.
(39) Woessner, J. F., and Nagase, H. (2000) *Matrix Metalloproteinases and TIMPs*. Oxford University Press, New York.
(40) Kuyvenhoven, J. P., van Hoek, B., Blom, E., van Duijn, W., Hanemaaijer, R., Verheijen, J. H., Lamers, C., and Verspaget, H. W. (2003) Assessment of the clinical significance of serum matrix metalloproteinases MMP-2 and MMP-9 in patients with various chronic liver diseases and hepatocellular carcinoma. *Thrombosis Haemostasis. 89*, 718−725.

BC0499174

Bacteriorhodopsin Conjugates as Anchors for Supported Membranes

Manoj K. Sharma, Harsha Jattani, and M. Lane Gilchrist, Jr.*

Departments of Chemical and Biomedical Engineering, The City College of the City University of New York, 140th Street and Convent Avenue, New York, New York 10031. Received December 26, 2003; Revised Manuscript Received April 23, 2004

The sophistication of supported lipid bilayer membranes has increased steadily as new applications are being explored. In general, tethered lipids are used to anchor the lipid bilayer to the substrate. Here we describe a new type of anchoring system for supported lipid bilayers that is based on biotin−PEG_{3400}−bacteriorhodopsin conjugates. Amine-based coupling was used to construct the polymer conjugates, followed by fluorophore labeling to enable confocal imaging. The bacteriorhodopsin-based anchoring system was used to construct solid-supported vesicles from streptavidin-coated microspheres. This method could provide a new route for the stability enhancement of supported lipid bilayer membrane assemblies.

The means of constructing supported membranes for the immobilization of membrane proteins has progressed rapidly from simple physical adsorption of lipid bilayers to more sophisticated approaches involving polymer tethering (*1*−*6*). In the cases involving tether-supported membranes, a wide variety of tethering molecules have been employed, ranging from polymers to peptides (*1*, *5*). Thus far, primarily single lipid moieties connected at the end of tethers have been used to anchor membranes to solid supports (*7*−*10*). In the present study, our aim was to construct biotin−PEG_{3400}−bacteriorhodopsin (bR) conjugates and use them to anchor lipid bilayer membranes to streptavidin-coated microspheres.[1]

As our ultimate goal is to construct robust, supported membrane particles for immobilization of membrane proteins such as biocatalysts, the potential benefits of bacteriorhodopsin anchoring are multifold and linked to greater control over the stability of supported bilayers. Shown schematically in Figure 1, the use of bacteriorhodopsin (26.5 kDa without retinal) as a building block provides a means for more extensive anchor−membrane interactions relative to lipid-mediated tethering. The energetics of the removal of the tethered lipophilic moiety from the membrane are expected to be more highly unfavorable for the case of bR relative to a lipid anchor. This can be argued on the basis of anchor to membrane interaction surface area differences. Supported membrane assemblies on surfaces and particles fabricated in this fashion should exhibit greater stability under shear or processing flows. In addition, due to the increase in anchoring efficiency that could be obtained from the bR anchor, it is conceivable that fewer tethering points would be needed for a given supported membrane area. This would allow for greater native lipid areas for the introduction of membrane proteins into supramolecular assemblies of this type. A further benefit of bR anchoring is that reactive sites on the outer surface of the bR opposite the tether can be exploited to further stabilize the assemblies via cross-linking or by ligating large hydrophilic polymers such as glycans.

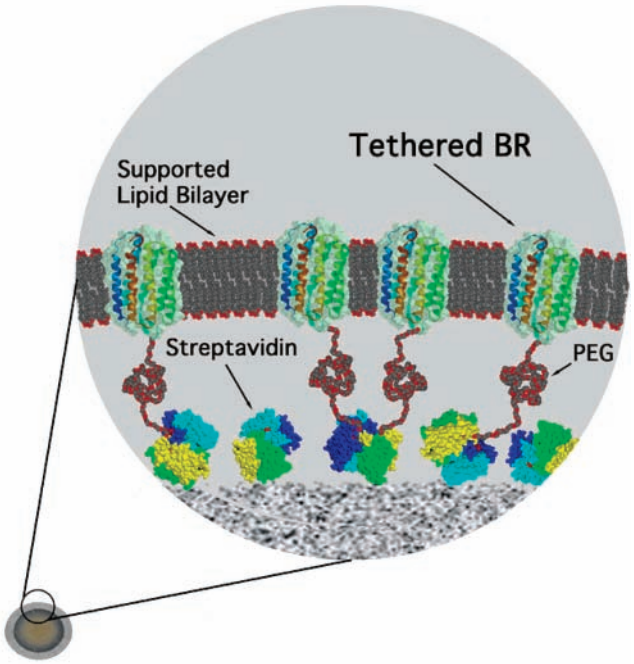


Figure 1. Schematic diagram of solid-supported vesicles that integrate bacteriorhodopsin conjugates as lipid bilayer membrane anchors.

There are a few precedents related to the present study that have involved bacteriorhodopsin or rhodopsin conjugation that warrant mention here. In one such study, Sirokman and Fasman explored the amine-based PEGylation of bR in conferring water solubility to the protein, providing an analysis of likely conjugation sites (*11*). In addition, their studies indicated that PEG_{5000}−bR retained similar proton-pumping activity relative to that

[1] Abbreviations: bR, bacteriorhodopsin; PEG, polyethylene glycol; NHS, *N*-hydroxylsuccinimide; SPA, succinimidyl propionate; DMSO, dimethyl sulfoxide; TR, Texas Red; POPC, L-α-phosphatilylcholine; DOPG, 1,2-dioleoyl-*sn*-glycero-3-[phospho-*rac*-(1-glycerol)] (sodium salt); OG, octyl β-glucoside; SSV, solid-supported vesicle or spherically supported vesicle; MALDI-TOF-MS, matrix-assisted laser desorption/ionization time-of-flight mass spectrometry.

10.1021/bc034231h CCC: $27.50 © 2004 American Chemical Society
Published on Web 07/03/2004

of unlabeled bR when the conjugate was reconstituted into lipid bilayers. In more recent work, Puu et al. utilized biotinylation of bR to allow for the localization of the protein in surface-deposited proteoliposomes, which was verified via AFM imaging of streptavidin−colloidal gold probes (*4*). Also related to the present study is the work of Bieri et al. in which rhodopsin that was biotinylated at the extracellular glycan moiety was used to tether the protein in a specific orientation in a biosensor microarray (*12*). While these studies demonstrate the feasibility of conjugation of bR and tethering via closely related rhodopsin, our work explores the first use of bR as a building block for a potentially improved means to anchor supported membranes.

This paper describes the construction and use of biotin−PEG_{3400}−bacteriorhodopsin conjugates in the formation of solid-supported membranes on particles. We have used amine-based coupling to conjugate biotin−PEG_{3400} to bR. The conjugates were characterized using sodium dodecyl sulfate−polyacrylamide gel electrophoresis (SDS−PAGE) and matrix-assisted laser desorption ionization mass spectrometry (MALDI-MS) after purification. The PEG−bR conjugate was further labeled with Texas Red to facilitate localization via fluorescence imaging. Supported membranes containing biotin−PEG_{3400}−bacteriorhodopsin were constructed through self-assembly onto streptavidin-coated beads to form solid-supported vesicles (SSVs). Confocal microscopy was used to image these supramolecular complexes, establishing the use of biotin−PEG_{3400}−bacteriorhodopsin as a membrane anchor.

MATERIALS AND METHODS

Materials. Bacteriorhodopsin was obtained as lyophilized powder of the Purple Membrane from *Halobacterium salinarum* strain S9 (Munich Innovative Biomaterials (MIB) GmbH, Germany). Biotin−PEG−SPA (MW 3400) was obtained from Nektar Therapeutics, Huntsville, AL. OG was obtained from Pierce Biotechnology Inc., Rockford, IL. Texas Red-X, succinimidyl ester, and β-BODIPY 530/550 C5−HPC were obtained from Molecular Probes, Eugene, OR. Sephadex G-50 was obtained from Amersham Biosciences Inc, Piscataway, NJ. Streptavidin-coated silica beads (3.18 μm diameter) were obtained from Bangs Laboratories Inc., Fishers, IN. Lipids POPC (egg, chicken), DOPG, and cholesterol (>98% pure) were purchased from Avanti Polar Lipids, Inc. Alabaster, AL. Bio-Beads SM-2 adsorbents were obtained from Bio-Rad Laboratories, Hercules, CA. Sequencing-grade trypsin (Bovine Pancreatic) was obtained from Roche Allied Science, Indianapolis, IN. RapiGest was purchased from Waters Corp., Waltham, MA.

Labeling of bR with Biotin−PEG and Texas Red. Purple membrane (3.45 mg bR) and biotin−PEG−SPA (38.2 mg) were each dissolved in 200 μL of 50 mM Na_2HPO_4 buffer stocks, pH 9.0 with 100 mM OG. The two solutions were mixed together and incubated at room temperature with gentle shaking for 2 h. TR-X succinimidyl ester stock (16.7 mg/mL) was prepared in DMSO and 30 μL was added to 200 μL of the reaction mixture. The remaining reaction mixture was saved for SDS−PAGE and MALDI-TOF-MS analysis after the addition of 15 μL of hydroxylamine (1.5 M) stop reagent. TR-X-containing reaction mixture was further incubated in the dark at room temperature for 2 h before the addition of 15 μL of hydroxylamine (1.5 M) stop reagent. Excess reactants were separated over a Sephadex G-50 column (1 cm × 50 cm) equilibrated with 50 mM Na_2HPO_4 buffer without any OG. bR fractions (labeled and unlabeled) collected from the first peak were pooled together and concentrated using Amicon Ultra-15 filters (30 kDa cutoff, 2800*g*, 30 min). bR aggregates formed on filter membrane were resolubilized using 100 mM OG. To achieve greater purification, traces of excess fluorescent probe TR and unattached biotin−PEG were further removed by another G-50 column. bR fractions from the first peak were pooled together again and exchanged with Hepes buffer A (Hepes, 20 mM; EDTA, 1 mM; NaCl, 100 mM, pH 7.5) using Amicon Ultra-15 filters (2800*g*, 30 min) in three rinse−spin cycles. The final retentate contained both labeled and unlabeled bR, was redissolved in 100 mM OG (25 μM protein, 600 μL total volume), and was stored at 4 °C until required.

Tethering of TR-Labeled Biotin−PEG−bR to Streptavidin-Coated Silica Microspheres. A 200 μL microsphere stock solution (~2 mg microspheres, biotin binding capacity 0.032 μg/mg microspheres) was washed three times with Hepes buffer A with 100 mM OG and centrifuged (200*g*, 10 min). After the third spin cycle the microspheres were mixed with 50 μL of the stock containing TR and biotin−PEG-labeled bR and incubated at room temperature for 3 h with gentle shaking. Biotin−PEG−bR tethered beads were centrifuged (200*g*, 10 min) to remove excess unattached bR complexes and rinsed with Hepes buffer A containing 100 mM OG. This wash−spin cycle was repeated three times to completely remove any nonspecifically adsorbed molecules from the microsphere surface.

Formation of Solid-Supported Vesicles. POPC, DOPG, and cholesterol were mixed in molar ratio 9:1:7 in chloroform (total lipid concentration 10 mg/mL). Green β-BODIPY 530/550 C5−HPC lipid probe was also added to the mixture at a ratio of 1:500 (probe:lipid). The lipid solution was subdivided in 250 μL parts in 4 mL vials and solvent was evaporated using a vacuum. The vials containing the lipid films were then stored under argon at −20 °C until required. For SSV preparation, one lipid formulation containing 2.5 mg of lipids was dissolved in 500 μL of Hepes buffer A with 100 mM OG. This lipid suspension was then used to resuspend the centrifuged biotin−PEG−bR tethered beads that were fabricated in previous steps. The mixture was incubated at 5 °C for 1 h. To remove detergent and form SSVs, 80 mg of wet Bio-Beads was added to the mixture kept at 5 °C with gentle shaking. After 3 h, a fresh lot of 80 mg of Bio-Beads was added and mixture was incubated for additional 2 h. Bio-Beads were then decanted from the solution containing regular and solid-supported lipid vesicles (SSVs). SSVs were centrifuged (200*g*, 10 min) and washed with Hepes buffer A.

Other Methods. MALDI-TOF mass spectrometry analysis was conducted at the Columbia University Protein Core Facility on a Perceptive Biosystems delayed-extraction reflector instrument. Trypsin digestion was carried out overnight at 37 °C in 0.5% RapiGest SF, at concentrations of bR and sequencing-grade trypsin of 0.5 and 0.05 mg/mL, respectively. The detergent was removed via ultrafiltration and a 10 min, 100 °C denaturing step preceded the digestion. SDS−PAGE was done on Bio-Rad Mini PROTEAN II apparatus using 4−15% *Linear Gradient Ready Gel* Tris-HCl Gels. Bio-Safe Coomassie stain from Bio-Rad Laboratories was used to detect protein bands. Gel densitomograms were obtained using a 16 bit Umax flatbed scanner, with image processing carried out using Igor Pro 4.0 (Wavemetrics, Inc). UV−Vis analysis was done on a Hitachi U-3010 spectrophotometer. The extent of fluorophore labeling was

determined by comparison of the Texas Red absorbance relative to protein concentration. Samples were imaged using a Leica TCS-SP four channel confocal microscope at the Mt. Sinai School of Medicine, using 488 nm excitation for β-BODIPY lipid probe and 568 nm for the Texas Red. The transmittance confocal channel was used to position the imaging plane at the center of the microspheres. Image analysis of confocal data was carried out with Igor Pro 4.0 (Wavemetrics, Inc).

RESULTS AND DISCUSSION

Our strategy to conjugate bacteriorhodopsin for anchoring membranes was adapted from the earlier work of Sirokman and Fasman (*11*) with a distinctly different aim. In our application, predominantly single-site labeling is desired. Furthermore, low yield is tolerable, because only the biotinylated bR conjugates will be assembled into the supramolecular complexes. Therefore, in contrast to the earlier bR PEGylation study, in which moderate double labeling was obtained, we did not employ two reaction cycles nor include nonreactive PEG to increase the reactivity of the protein (*11*). The first step of the conjugation was carried out at pH 9 at a 90-fold molar excess of biotin−PEG_{3400}−SPA. To enable fluorescence imaging of the biotin−PEG_{3400}−bR conjugates, an amine-based labeling (at 5-fold molar excess) with Texas-Red succinimidyl ester was conducted after PEGylation, also at pH 9. Separation of the excess reactants was carried out using gel filtration followed by ultrafiltration to remove all traces of Texas Red dye, thus minimizing artifacts in the confocal imaging studies. Figure 2 displays MALDI-TOF-MS traces of the bR starting material (trace A), the bR−PEG_{3400}−biotin conjugate (trace B), and the biotin-PEG_{3400}−bR−Texas Red conjugate (trace C). The inset of Figure 2 displays SDS−PAGE densitomograms that correspond to the MALDI-TOF-MS traces: bacteriorhodopsin starting material (trace A′), the bR−PEG_{3400} conjugate (trace B′), and the molecular weight markers (trace M). Traces B (MALDI-TOF-MS) and B′ (SDS−PAGE) each contain two peaks, a lower molecular weight peak from the unreacted bR and an additional peak of higher molecular weight that we assign to the conjugate. In trace B, we assign the conjugate peak (denoted by an asterisk (*)) to the broad band located approximately 3400 Da higher in molecular weight. A very weak band that appears to correspond to bR−(PEG_{3400}−biotin)$_2$ is evidenced near 34 100 Da in trace B. We assign this feature to a small amount of double labeling of bR. As MALDI-TOF characterization does not provide direct quantitative information about conjugate yield due to differences in desorption of various species, SDS−PAGE studies were also employed. SDS−PAGE densitomograms were obtained for separate bioconjugation trials. Multipeak fitting gave estimated yields of the bR−PEG_{3400}−biotin conjugates that ranged from 13 to 25%.

Figure 3 shows a schematic of the amino acid sequence of bR, with reference to the secondary structures of bR as determined by X-ray crystallography in recent work by Belrhali et al. (1999; PDB 1qhj) (*13*). The seven lysine residues are indicated by the circles, and the residues that comprise the transmembrane helices are located inside the rectangles. We note that the N-terminus is posttranslationally modified and does not contain a primary amine (*14*). The most likely polymer conjugation sites are Lys 129 and Lys 159 (indicated by arrows), as these are found on loops interconnecting the transmembrane helices and are solvent accessible to bulky reactants such as the SPA−PEG_{3400}−biotin employed here

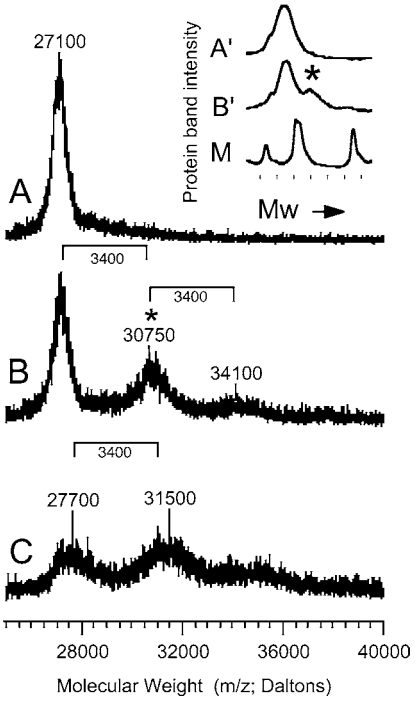


Figure 2. MALDI-TOF-MS and SDS−PAGE gel densitometry results for the biotin−PEG_{3400}−bacteriorhodopsin conjugate. Trace A was obtained from the bR starting material. Trace B was obtained from the biotin−PEG_{3400}−bR conjugate. The peak denoted by the asterisk (*) in the main figure and inset is assigned to the biotin-PEG_{3400}−bacteriorhodopsin conjugate. Trace C was obtained from the biotin−PEG_{3400}−bR−Texas Red conjugate. In the inset, SDS−PAGE gel densitometry results are shown for samples corresponding to traces A and B of the MALDI-TOF-MS results. Trace A′ was obtained from the bR starting material. Trace B′ was obtained from the biotin−PEG_{3400}−bR conjugate. Trace M was from the molecular weight markers (20, 25, and 37 kDa, left to right).

(*11*). Furthermore, in aforementioned studies carried out by Sirokman and Fasman with amine-reactive PEG_{5000}, chymotrypsin digestion studies were consistent with loop lysine labeling (*11*). Their findings were further bolstered by cogent arguments also based on the structure of bR. Early work with small-molecule labeling indicated that Lys 129 was the most likely site (*15, 16*).

To address this question directly, we have performed a trypsin digestion of the bR−PEG_{3400}−biotin conjugate, followed by MALDI-TOF-MS characterization of the resulting fragments. The degree of difficulty of trypsin fragmentation is especially high for membrane proteins such bR, as most cleavage sites are buried and, in addition, give rise to highly hydrophobic peptides (*14*). Furthermore, the addition of detergents to expose cleavage sites dramatically reduces trypsin activity. To obtain greater digestion yields, we employed a new, acid-cleavable denaturant (RapiGest SF, Waters Corp.) that does not greatly inhibit proteases and allows for higher trypsin reaction yields. In our experiments, run over a wide set of conditions, including ranges of RapiGest SF concentration and trypsin:bR ratio, we obtained peptides with missed cleavages almost exclusively. Table 1 lists the tryptic digest fragments detected that contain either K129 or K159. The corresponding MALDI-TOF-MS traces are shown in Figure 4. Trace A is from bR (control) and traces B and B′ (3 × B) are from the bR−PEG_{3400}−biotin conjugate. Prominent in trace A are the peaks at 17 578 and 24 856 *m*/*z*, assigned to 1−159 and 1−227, respectively, formed from loop site cleavage. Inspection of the bR−PEG_{3400}−biotin conjugate trace magnified 3× shows

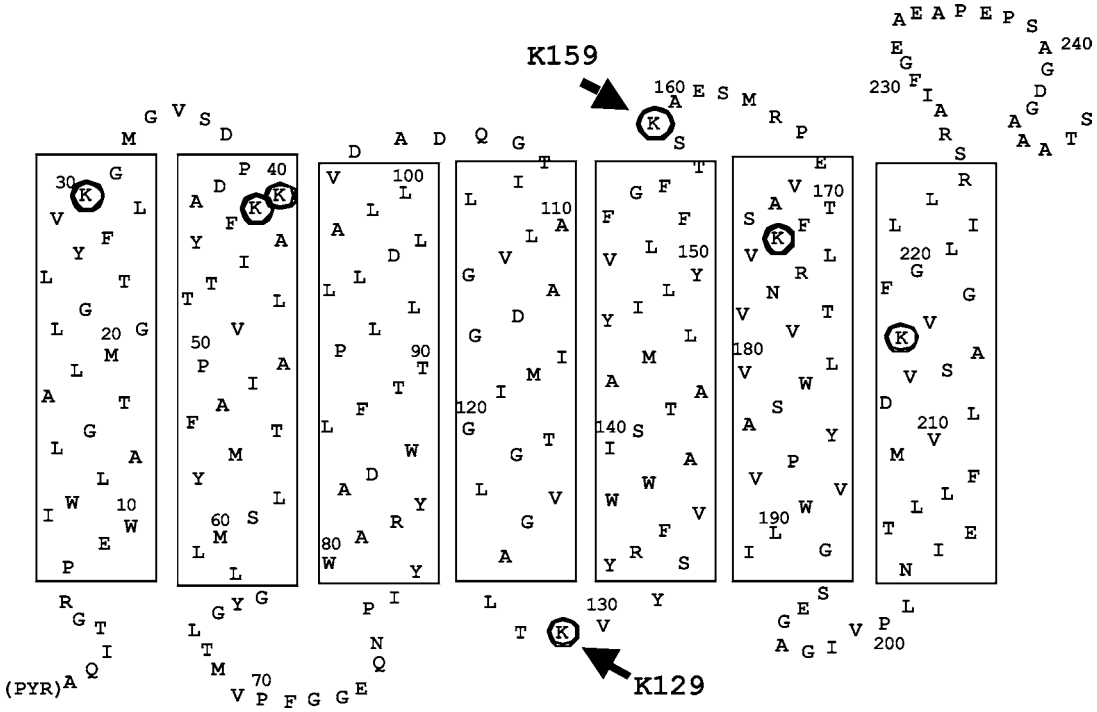


Figure 3. Schematic diagram of the structure of bacteriorhodopsin. The amino acid residues located in transmembrane helices are indicated by the rectangular boxes.

Table 1. Trypsin Fragments of Bacteriorhodopsin Detected That Contain Potentially Accessible Lysines

trypsin fragment no.	bR obsd (m/z)[a]	bR−PEG_{3400}−biotin observed (m/z)[a]	assigned sequence or conjugate (expected MW, species)
T6-7	3 566	3 600	130−159 (3 645, $[M + H]^+$)
T5-7	8 479	8 481	83−159 (8 470, $[M + H]^+$)
T1-7	9 025	9 017	1−159 (9 034, $[M + H]^{+2}$)
T1-7−PEG_{3400}−biotin		10 826	1−159−PEG_{3400}−biotin (9 034, $[M + H]^{+2}$)
T1-12	12 355	12 432	1−227 (24 882, $[M + H]^{+2}$)
T3-7	13 262	13 307	41−159 (13 198, $[M + H]^+$)
T1-7	17 578	17 662	1−159 (17 487, $[M + H]^+$)
T1-7−PEG_{3400}−biotin		21 200	1−159−PEG_{3400}−biotin (20 870, $[M + H]^+$)
T1-12	24 856	24 885	1−227 (24 882, M^+)
T1-12−PEG_{3400}−biotin		28 551	1−227−PEG_{3400}−biotin (28 282, $[M + H]^+$)

[a] The moderate errors in m/z relative to the expected MWs are attributed to external calibration of the spectra and some degree of amino acid side reactions such as methionine oxidation.

broad peaks shifted over by approximately 3400 Da from peaks assigned to sequences 1−159 and 1−227. These peaks are assigned to 1−159−PEG_{3400}−biotin and 1−227−PEG_{3400}−biotin conjugated fragments. The doubly charged 1−159−PEG_{3400}−biotin species was also detected as a broad peak centered at 10 826 m/z. We were unable to detect any other PEGylated species, including conjugates of 83−159 and 41−159, a consequence, presumably, of lower yields of intrahelical site cleavage that precluded detection. Due to the high yield of 1−159−PEG_{3400}−biotin species in the trypsin digest, we infer that the predominant PEG_{3400}−biotin conjugation site is K129, as PEG_{3400}−biotin labeling at K159 would be expected to inhibit trypsin due to steric hindrance.

The other five lysines are thought to be less solvent accessible and are the likely sites of conjugation of the hydrophobic Texas Red fluorophore. Evidence for successful fluorophore labeling was first seen in the SDS−PAGE gels, as the bands from bR labeled with Texas Red generated a different hue due to the colorimetric properties of this chromophore combined with the bromophenol blue protein stain. MALDI-TOF-MS of the biotin−PEG_{3400}−bR−Texas Red conjugate is shown in trace C of Figure 2. Two broad peaks with complex line shapes were evidenced, centered at approximately 27 700 and 31 500 Da. These features are shifted by over 600 Da from the corresponding peaks arising from bR and the bR−PEG_{3400}−biotin conjugate (found in trace B). These shifts are consistent with the successful conjugation of Texas Red (ligated molecular weight 702 Da) to a fraction of both the unreacted bR starting material and the bR−PEG_{3400}−biotin conjugate, giving rise to broad composite

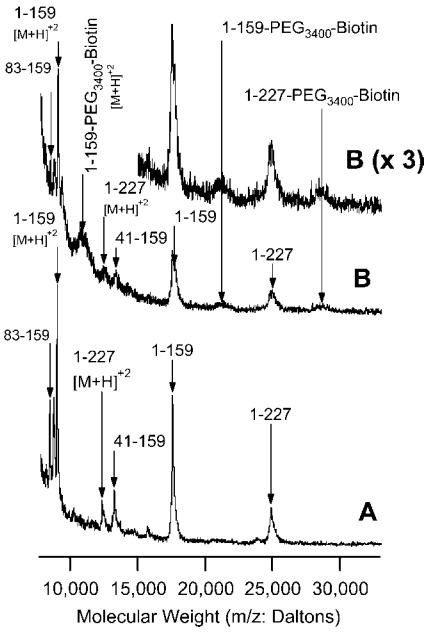


Figure 4. MALDI-TOF-MS results for the tryptic digest reaction products of the biotin−PEG_{3400}−bacteriorhodopsin conjugate. Trace A was obtained from a tryptic digest of the bR starting material. Trace B was obtained from a tryptic digest of biotin−PEG_{3400}−bR conjugate, conducted under the same conditions as in trace A. For closer examination, the region from 15 000 to 32 000 of trace B is shown magnified three times in the top trace.

peaks comprised of fluorophore-labeled and unlabeled molecules. Furthermore, UV−Vis analysis of the conjugate revealed that approximately 1−2 Texas Red fluorophores were conjugated to each protein molecule. This was based on protein concentration determined by UV absorption, combined with the Texas Red absorption intensity of the conjugate.

To demonstrate the use of bR in membrane anchoring, we have constructed solid supported vesicles (SSVs) based on streptavidin-coated silica microspheres (nominal size 3.18 μm). The first step in SSV assembly is to bind the biotin−PEG_{3400}−bR−Texas Red conjugates to the microspheres via biotin−streptavidin complex formation. In these experiments, the biotinylated conjugates were added in excess of a 1:1 molar ratio of the total number of streptavidin sites (from manufacturer's specifications) to aim for complete coverage. Removal of excess bR and bR conjugates is facilitated by the ease of settling the particles by low-speed centrifugation. To demonstrate formation of the supported bilayers on the particles, a green fluorescent phosphatidylcholine analogue (β-BODIPY 530/550 C5−HPC) was incorporated into the supported bilayer phospholipids. This reagent was incorporated in the formulation of negatively charged phospholipids (at a 1:500 probe:lipid ratio) that was combined with the bR-terminated particles. The phospholipids mixture also contained octyl glucoside detergent at 100 mM, which is above the concentration at which membranes become completely solublized and lipids form mixed micelles with detergent (*17, 18*). The final reconstitution steps were to form supported lipid bilayers on the particle surface upon removal of detergent by Bio-Beads (adsorbent), followed by centrifugation/washing steps to remove excess regular liposomes.

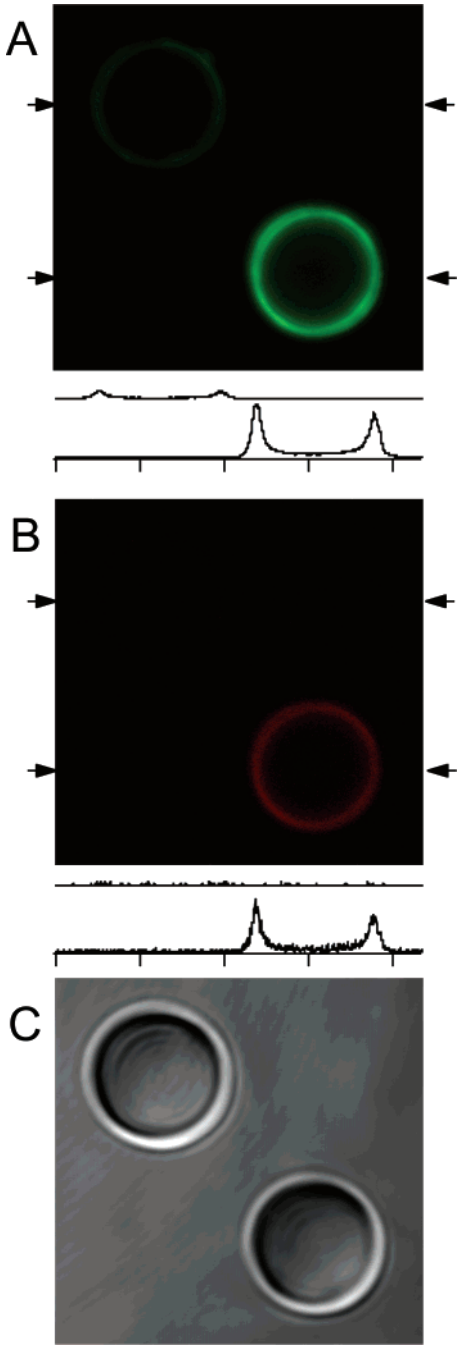


Figure 5. Confocal microscopy of solid-supported vesicles (SSVs) doped with a green fluorescent phosphatidylcholine analogue (β-BODIPY 530/550 C5−HPC) anchored by biotin−PEG_{3400}−bR−Texas Red conjugates. The images were obtained in a single *XY* imaging plane (~0.2 μm thickness) at the center of the particles. The top left particle is the nonspecific adsorption negative control, and the desired bR-anchored SSV particle is at the bottom right. The particles are each shown in three channels: β-BODIPY 530/550 (top panel A, excitation 488 nm, detection 500−570 nm), Texas red (middle panel B, excitation 568 nm, detection 580−660 nm), and reflectance mode (bottom panel C). Shown below the emission images are intensity profiles taken from horizontal slices bisecting the images at the positions of the arrows.

Confocal imaging results from a single *XY* plane obtained from bR-anchored, solid-supported vesicles (right, bottom) and a nonspecific adsorption control (left, top) are shown in Figure 5. These images were obtained from a region of the slide that contained both a (nonspecific adsorption) control particle and a desired bR-anchored SSV particle. The β-BODIPY 530/550 (green) emission

image is shown in panel A and the Texas Red emission image is shown below in panel B. For reference, the reflectance mode confocal image is given in panel C. Intensity profiles, taken horizontally from the images at the position of the arrows, are shown immediately below each dye emission image. At this resolution, the bR-anchored, solid-supported vesicle (right, bottom) exhibits colocalization of Texas Red and β-BODIPY 530/550 emissions in an approximately homogeneous ring around the particle. The presence of this pattern suggests that we have formed the bR anchored SSVs as intended in the design, with spatially overlapping emissions from the biotin−PEG_{3400}−bR−Texas Red conjugate and β-BODIPY 530/550 from the lipid layer. As a negative control, we also probed the nonspecific adsorption of β-BODIPY 530/550 containing lipids to the streptavidin microspheres under conditions similar to bR-anchored, SSV formation. In this case no tethering to the microspheres was employed. In general, nonspecific adsorption of the green fluorescent lipids was evidenced on average at lower levels than for the desired bR-anchored, solid-supported vesicles. This is reflected in the comparison of the intensities of representative particles shown in cross section in panel A. Moreover, the control microsphere in panel B (left, top) shows no Texas Red emission, as expected. This attribute was used to distinguish SSV particles from control particles on the same slide.

CONCLUSIONS

Bacteriorhodopsin−PEG_{3400}−biotin conjugates were constructed via primary amine coupling. The conjugates were characterized with MALDI-TOF-MS; single-site labeling occurred predominantly under these conditions. In cases in which the bR−PEG_{3400}−biotin conjugates were subsequently labeled with Texas Red for imaging, one or two sites per protein were tagged. Lysine 129, situated on an interhelical loop, was the most likely site for conjugation, as determined by trypsin digestion studies.

The confocal imaging results provide direct evidence that we have formed supported bilayers anchored with bacteriorhodopsin conjugates over a majority of the surfaces of the particles. In addition, β-BODIPY 530/550 containing lipid was localized on the particle surface, providing further evidence for supported vesicle formation mediated by the bR anchor formation. The present use of bR as an anchoring moiety may provide a new direction in the goal of enabling greater control over the stability of supported membranes positioned onto particles or onto surfaces. Continuing with this approach, we aim to fabricate particles that provide highly robust, yet nativelike microenvironments for the immobilization of membrane proteins. Further studies are currently underway to assess enhancements in stability relative to lipid tethering and to construct assemblies with varying amounts of bilayer tethering. In parallel, we are working to co-localize other membrane proteins in bR-anchored bilayers and examine retention of native function of the protein and activity in the assemblies.

ACKNOWLEDGMENT

Confocal microscopy was performed at the Mt. Sinai Medical School-Microscopy Shared Research Facility, supported, in part, with funding from NIH-NCI shared resources grant (1 R24 CA095823-01). Mary Ann Gawinowicz of the Columbia University Protein Core Facility is gratefully acknowledged for vital guidance in the tryptic digestion and MALDI-MS analysis.

LITERATURE CITED

(1) Cheng, Y., Ogier, S. D., Bushby, R. J., and Evans, S. D. (2000) Discrete membrane arrays. *J. Biotechnol. 74* (3), 159−74.

(2) Groves, J. T., Ulman, N., and Boxer, S. G. (1997) Micropatterning fluid lipid bilayers on solid supports. *Science 275* (5300), 651−3.

(3) Kalb, E., Frey, S., and Tamm, L. K. (1992) Formation of supported planar bilayers by fusion of vesicles to supported phospholipid monolayers. *Biochim. Biophys. Acta. 1103* (2), 307−16.

(4) Puu, G., Artursson, E., Gustafson, I., Lundstrom, M., and Jass, J. (2000) Distribution and stability of membrane proteins in lipid membranes on solid supports. *Biosens. Bioelectron 15* (1−2), 31−41.

(5) Sackmann, E. (1996) Supported membranes: Scientific and practical applications. *Science 271* (5245), 43−8.

(6) Tamm, L. K., and McConnell, H. M. (1985) Supported phospholipid bilayers. *Biophys J 47* (1), 105−13.

(7) Wagner, M. L., and Tamm, L. K. (2000) Tethered polymer-supported planar lipid bilayers for reconstitution of integral membrane proteins: Silane−poly(ethylene glycol)−lipid as a cushion and covalent linker. *Biophys. J. 79* (3), 1400−14.

(8) Wagner, M. L., and Tamm, L. K. (2001) Reconstituted syntaxin1a/SNAP25 interacts with negatively charged lipids as measured by lateral diffusion in planar supported bilayers. *Biophys. J. 81* (1), 266−75.

(9) Shen, W. W., Boxer, S. G., Knoll, W., and Frank, C. W. (2001) Polymer-supported lipid bilayers on benzophenone-modified substrates. *Biomacromolecules 2* (1), 70−9.

(10) Kiessling, V., and Tamm, L. K. (2003) Measuring distances in supported bilayers by fluorescence interference-contrast microscopy: polymer supports and SNARE proteins. *Biophys. J. 84* (1), 408−18.

(11) Sirokman, G., and Fasman, G. D. (1993) Refolding and proton pumping activity of a poly(ethylene glycol)−bacteriorhodopsin water-soluble conjugate. *Protein Sci. 2* (7), 1161−70.

(12) Bieri, C., Ernst, O. P., Heyse, S., Hofmann, K. P., and Vogel, H. (1999) Micropatterned immobilization of a G protein-coupled receptor and direct detection of G protein activation. *Nat. Biotechnol. 17* (11), 1105−8.

(13) Belrhali, H., Nollert, P., Royant, A., Menzel, C., Rosenbusch, J. P., Landau, E. M., and Pebay-Peyroula, E. (1999) Protein, lipid and water organization in bacteriorhodopsin crystals: A molecular view of the purple membrane at 1.9 A resolution. *Structure Fold Des. 7* (8), 909−17.

(14) Gerber, G. E., Gray, C. P., Wildenauer, D., and Khorana, H. G. (1977) Orientation of bacteriorhodopsin in *Halobacterium halobium* as studied by selective proteolysis. *Proc. Natl. Acad. Sci. U.S.A. 74* (12), 5426−30.

(15) Henderson, R., Jubb, J. S., and Whytock, S. (1978) Specific labeling of the protein and lipid on the extracellular surface of purple membrane. *J. Mol. Biol. 123* (2), 259−74.

(16) Heberle, J., and Dencher, N. A. (1992) Surface-bound optical probes monitor protein translocation and surface potential changes during the bacteriorhodopsin photocycle. *Proc. Natl. Acad. Sci. U.S.A. 89* (13), 5996−6000.

(17) Paternostre, M. T., Roux, M., and Rigaud, J. L. (1988) Mechanisms of membrane protein insertion into liposomes during reconstitution procedures involving the use of detergents. 1. Solubilization of large unilamellar liposomes (prepared by reverse-phase evaporation) by Triton X-100, octyl glucoside, and sodium cholate. *Biochemistry 27* (8), 2668−77.

(18) Ollivon, M., Eidelman, O., Blumenthal, R., and Walter, A. (1988) Micelle-vesicle transition of egg phosphatidylcholine and octyl glucoside. *Biochemistry 27* (5), 1695−703.

BC034231H

CORRECTIONS

Volume 15, Number 3, May/June, 2004.

Christie L. Hunter and Gerd G. Kochendoerfer*

NATIVE CHEMICAL LIGATION OF HYDROPHOBIC PEPTIDES IN LIPID BILAYER SYSTEMS

Page 437. An incorrect spelling of "Hydrophobic" in the manuscript title appears in the print-published manuscript. The Web-published manuscript was corrected June 4, 2004.

BC040291R

10.1021/bc040291r
Published on Web 06/17/2004

SEPTEMBER/OCTOBER 2004
Volume 15, Number 5

© *Copyright 2004 by the American Chemical Society*

Bioconjugate Chemistry

COMMUNICATIONS

Ruthenium(II)−Phenanthroline−Biotin Complexes: Synthesis and Luminescence Enhancement upon Binding to Avidin

Mohamed Slim and Hanadi F. Sleiman*

Department of Chemistry, McGill University, 801 Sherbrooke Street West, Montreal, QC H3A 2K6 Canada.
Received March 31, 2004; Revised Manuscript Received July 22, 2004

We report the synthesis, characterization, and avidin-binding properties of two novel ruthenium complexes, $[Ru(bpy)_2(phen\text{-}biotin)][PF_6]_2$ **1** and $[Ru(phen)_2(phen\text{-}biotin)][PF_6]_2$ **2** (bpy = 2,2′-bipyridine; phen = 1,10-phenanthroline, phen-biotin = 5-(10-amidobiotinyl)-1,10-phenanthroline)). We demonstrate that both biotinylated compounds bind to avidin through their biotin moieties with high affinity and in a 4:1 ratio. The binding of compounds **1** and **2** to avidin results in an enhancement in luminescence intensity (∼1.4×, ∼1.6×, respectively), relative to the unbound biotinylated ruthenium complexes. This behavior is markedly different from biotinylated organic dyes, whose fluorescence is quenched upon binding to avidin. Thus, ruthenium−biotin complexes **1** and **2** can form the basis of new, simplified biotin−avidin assays, which involve luminescence detection of the relevant biotinylated molecule through cross-linking with avidin.

INTRODUCTION

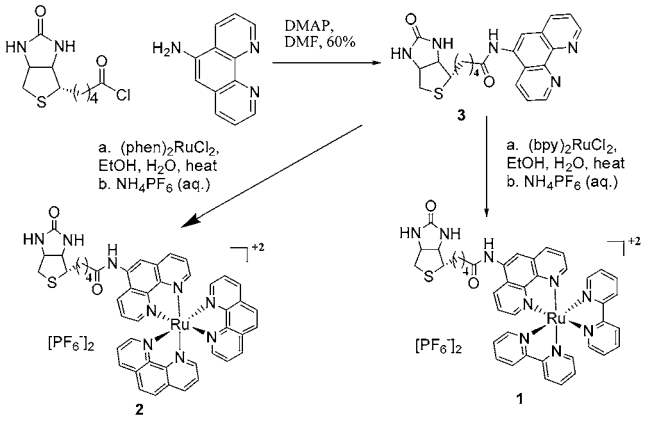
The binding of biotin to (strept)avidin has found widespread applications in biomolecule detection, medical diagnostics, immunoassays, cytochemistry, and nanoscience (*1*−*7*). This is primarily due to the strength of the interaction between the ligand and the protein ($K_d = 1.3 \times 10^{-15}$ M) and to the presence of four binding sites for biotin on avidin, which in turn allows for the cross-linking of different biotinylated molecules (*1*). Bioanalytical applications based on the biotin/avidin interaction have typically used enzymatic reactions, radiolabeling techniques, and fluorescence for detection/visualization (*8*−*12*). Of these, fluorescence-based assays are some of the most straightforward and rapid detection techniques (*13*−*16*). The simplest design for these biotin−avidin assays would be covalent attachment of the fluorescent dye to biotin, followed by fluorescence detection of the relevant biotinylated molecule through cross-linking with avidin. However, biotinylated organic dyes have been shown to lose their luminescence intensity upon binding to avidin, likely through resonance energy transfer mechanisms (*17*−*22*). To overcome this problem, long spacers, such as poly(ethylene glycol), have been used to maximize the distance between the biotin-conjugated organic dyes and the avidin binding site (*17*, *18*). As a result of these difficulties, most fluorescence-based detection methods have relied on the more difficult conjugation of the organic dyes to the protein itself, rather than simple attachment to biotin (*18*, *19*).

Among many inorganic chromophores, ruthenium(II) bipyridyl or phenanthroline complexes have recently

* To whom correspondence should be addressed. E-mail: hanadi.sleiman@mcgill.ca.

10.1021/bc049919o CCC: $27.50 © 2004 American Chemical Society
Published on Web 08/24/2004

Scheme 1. Synthesis of Ru(II)−Phenanthroline−Biotin Complexes 1 and 2



emerged as promising candidates for a variety of bioanalytical applications (*13*, *23*−*26*). These complexes present some unique photophysical properties, which distinguish them from their organic counterparts, including their chemical inertness and photostability, the tunability of their photophysical characteristics, the relative insensitivity of their photophysical properties to environmental changes, their large Stokes shifts, and their long excited-state lifetimes (*13*). We here report the facile synthesis of ruthenium complexes **1** and **2**, where a $(bpy)_2Ru(phen)^{2+}$ or $(phen)_3Ru^{2+}$ center is conjugated to a biotin moiety (bpy = 2,2′-bipyridine, phen = 1,10-phenanthroline). Unlike organic dyes, binding of these Ru(II)−biotin complexes to avidin results in an enhancement in their luminescence intensity, thus making them useful tools for fluorescence-based biotin−avidin assays.

The synthesis of complexes **1** or **2** was carried out by first coupling 5-amino-1,10-phenanthroline (*27*, *28*) with the acyl chloride (*29*) derivative of biotin, to give the biotin−phenanthroline ligand **3**. The target complexes **1** and **2** were then obtained by refluxing ligand **3** with $Ru(bpy)_2Cl_2$ or $Ru(phen)_2Cl_2$ (*30*) in good yield (70−80%) and were isolated as their PF_6^- salts (Scheme 1) (*46*).

The UV/vis absorbance spectrum of ruthenium−biotin complexes **1** and **2** in CH_2Cl_2 shows bands at 450 nm, assigned to Ru(II) dπ−π* metal-to-ligand charge transfer (MLCT) transitions (Figure 1) (*46*). In addition, more intense bands at 250−300 nm were assigned to ligand-centered π−π* transitions. These absorbances and assignments are consistent with a number of related complexes in the literature (*13*, *30*). Steady-state emission spectra were recorded for complexes **1** and **2** in dichloromethane and showed strong luminescence at 589 nm for **1** and 580 for **2**, upon excitation of the MLCT band at 450 nm (Figure 1). The emission wavelength showed a slight increase with increasing solvent polarity, likely due to the stabilization of the MLCT state with polar solvents (*46*).

The binding properties of the Ru−biotin complexes **1** and **2** to avidin were first examined using the 4′-hydroxyazobenzene-2-carboxylic acid (HABA) assay (*32*, *46*). HABA can bind to avidin at the same binding site as biotin, with an association constant of 10^7 M^{-1} and with the same stoichiometry as unmodified biotin (4:1). Upon binding to avidin, HABA displays a new peak in its absorption spectrum at 500 nm. When biotin or biotinylated molecules are added, the displacement of HABA from avidin results in the reduction of this HABA−avidin absorption at 500 nm. The HABA−avidin complex was thus generated and was then titrated with the Ru−biotin complex **1**. An immediate decrease in the absorption at 500 nm was detected, and a new peak at ca. 450 nm, corresponding to the ruthenium complex **1**, was observed. The titration required exactly 4 mol equiv of complex **1** to avidin, after which no further changes in the absorption peak at 500 nm were detected (*46*). These results are consistent with immediate displacement of HABA from avidin and concomitant binding of Ru−biotin complex **1** to the protein. Similar results were obtained when the HABA−avidin complex was titrated with complex **2** (*46*). Thus, complexes **1** and **2** bind to avidin in a 4:1 ratio and with greater affinities than the HABA-avidin interaction.

To investigate the luminescence changes of complexes **1** and **2** in the presence of avidin, an avidin solution (in buffer A, containing 100 mM NaCl, 50 mM NaH_2PO_4, 1 mM EDTA, pH adjusted to 7.5 using NaOH) was titrated with complex **1** (16 μM), and luminescence at 615 nm was monitored (Figure 2, curve II). In addition, a blank buffer solution was titrated with complex **1** (16 μM, Figure 2, curve I). These experiments were repeated using complex **2** (Figure 3). Comparison of the titration curves I and II revealed that the luminescence of the Ru−biotin complexes is *enhanced* upon binding to avidin (*33*).

The emission intensity of the Ru−biotin complex **1** fully bound to avidin (4:1) ratio was measured to be ca. 1.4 times greater than unbound complex **1**, and complex **2** showed a greater enhancement of 1.6 (Figure 4). As a control experiment, the titration of avidin with $Ru(bpy)_3^{2+}$, which has similar structural and photophysical properties to complexes **1** and **2**, but lacks a biotin moiety, showed no detectable change in its luminescence intensity. Thus, complexes **1** and **2** bind to avidin through their biotin moiety in a 4:1 ratio and show luminescence enhancement as a result of this interaction. This is in marked contrast with the behavior of biotinylated organic

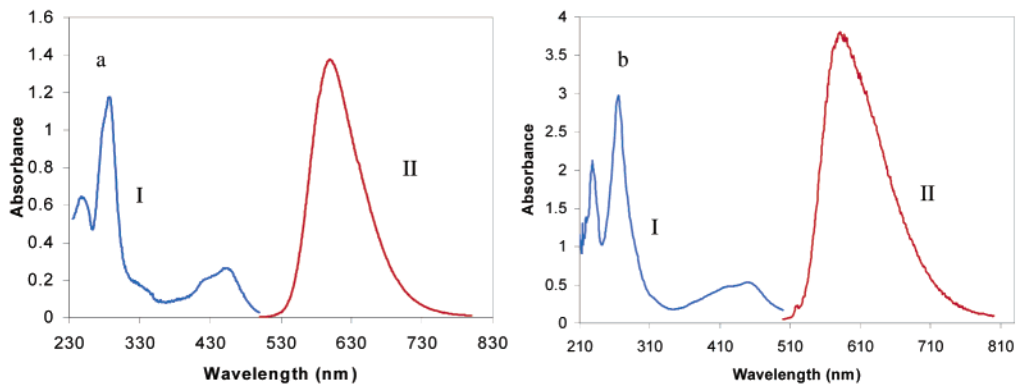


Figure 1. Electronic absorption (I) and emission (II) spectra of complexes **1** (a) and **2** (b) in CH_2Cl_2 at ambient temperature.

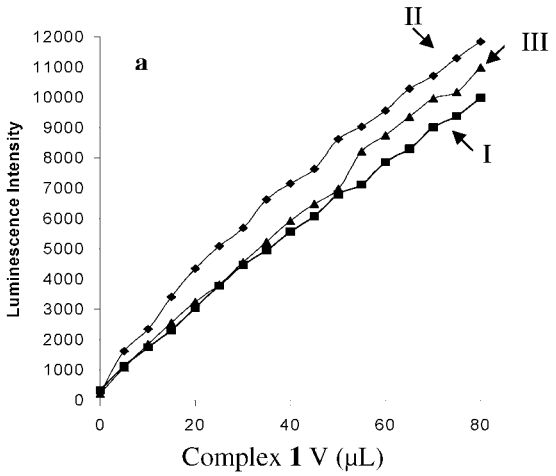


Figure 2. Luminescence titration curves for the titrations of (I) a blank buffer A solution with complex **1**, (II) an avidin solution (20 nmol) with complex **1**, (III) a preformed complex of avidin (20 nmol), and biotin (80 nmol) with complex **1** (16 M); the time delay between each addition was approximately 8 min.

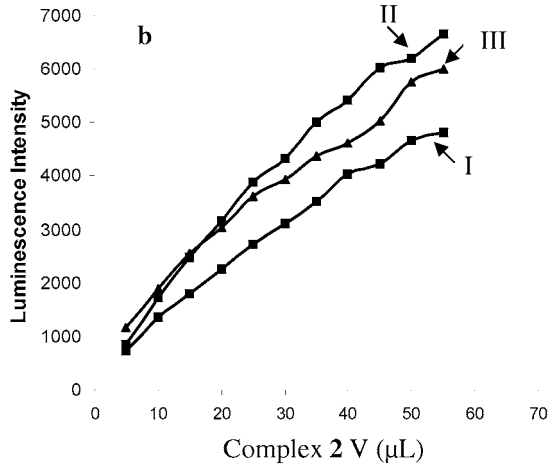


Figure 3. Luminescence titration curves for the titrations of (I) a blank buffer A solution with complex **2**, (II) an avidin solution (10 nmol) with complex **2**, (III) a preformed complex of avidin (10 nmol), and biotin (40 nmol) with complex **2** (16 M) the time delay between each addition was approximately 8 min.

fluorophores, whose fluorescence is quenched upon binding to avidin. The increase in luminescence intensity of the ruthenium complexes may be a result of the positioning of these chromophores in a more hydrophobic environment upon binding to avidin. Indeed, Ru(II) polypyridine complexes show a higher luminescence quantum yield in organic solvents, compared to water (*34*−*36*). Interestingly, preliminary experiments performed on the interaction of complex **2** with streptavidin, which is more hydrophobic and less positive in charge than avidin, showed a greater luminescence enhancement of ∼1.9 (*9*, *47*). To our knowledge, there is only one previous report describing a rhenium−biotin complex, which binds to avidin with luminescence enhancement (*37*). The tris-chelated Ru-complexes **1** and **2** are expected to display greater stability than the rhenium complex, which possesses monodentate pyridine and carbonyl ligands (*38*). In addition, ruthenium (II) bipyridine complexes are redox active, and can be used for electrochemiluminescence experiments, with a significant amplification of their luminescence signals (*41*).

To compare the avidin binding affinity of the Ru−biotin complexes to that of biotin itself, a complex of avidin−biotin in a 1:4 ratio was generated. This sample was then titrated with Ru−biotin complexes **1** (or **2**) (16 μM), and the luminescence intensity at 615 nm was monitored (Figures 2 and 3, titration curves III). Complex **2** showed consistently higher luminescence intensity than unbound Ru−biotin (curve I in Figure 3). This suggests partial displacement of biotin from avidin by molecule **2** and concomitant binding of this complex to avidin, resulting in an increase in its luminescence intensity. Complex **1**, on the other hand, showed similar luminescence intensity to that of unbound Ru−biotin, which increased only when relatively high concentrations were attained (curve III in Figure 2). Thus, the binding constant of complex **2** to avidin is likely higher than that of complex **1**. A similar preliminary experiment was performed with streptavidin, where 4 equiv of molecule **2** were added to a preformed streptavidin:biotin complex. In this case, an enhancement of ∼1.8 was noticed, consistent with an even greater binding affinity of complex **2** to streptavidin (*47*).

A final experiment was carried out, where a preformed complex of avidin−Ru−biotin in a 4:1 ratio was generated and then titrated with a solution of biotin (16 μM). The titration curves for both complexes **1** and **2** showed a steady decrease in luminescence intensity, until a ratio of biotin:avidin of approximately 4:1 was reached, upon which the luminescence intensity of the ruthenium complexes was unchanged with further biotin addition (*46*). This result is consistent with displacement of complexes **1** and **2** from avidin by biotin itself, suggesting that biotin binds to avidin with a higher affinity than complexes **1** and **2**. Thus, complexes **1** and **2** showed a relatively high binding affinity to avidin, albeit lower than biotin itself (K_d = 10^{-15} M), with a 4:1 binding stoichiometry and concomitant luminescence enhance-

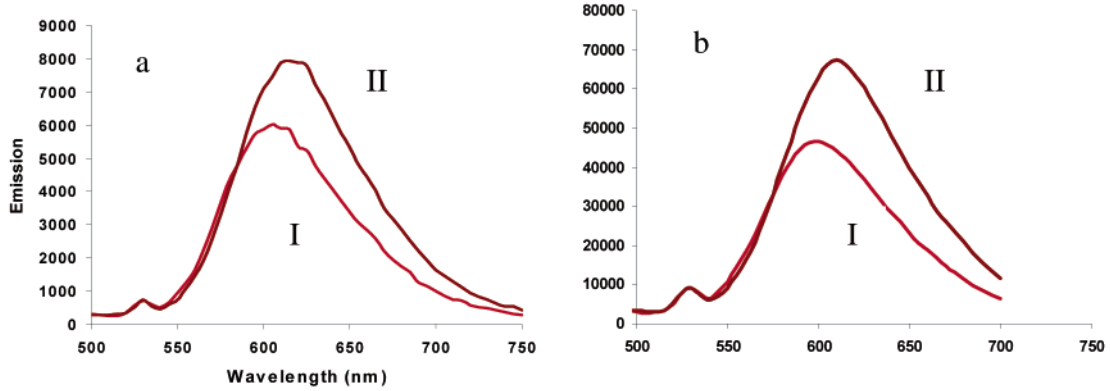


Figure 4. (a) Emission of complex **1** in buffer A (I) and in buffer A with avidin (II) (4:1 ratio). (b) Emission of complex **2** in buffer A (I) and in buffer A with avidin (II) (4:1 ratio).

ment. Interestingly, when a similar experiment was performed using streptavidin instead of avidin, the addition of 4 equiv of biotin to a preformed complex of streptavidin:molecule **2** did not cause any decrease in luminescence intensity, even after 12 h. This is consistent with little displacement of complex **2** from avidin by biotin and again suggests higher binding affinity of complex **2** to streptavidin, as compared to avidin (*47*).

In conclusion, we have generated a new class of ruthenium complexes, where $(bpy)_2Ru(phen)^{2+}$ or $(phen)_3Ru^{2+}$ centers are conjugated to a biotin moiety. These complexes bind to avidin and streptavidin through their biotin moiety with high affinity, in a 4:1 ratio, and with concomitant enhancement in their fluorescence intensity. This is in marked contrast with organic dyes, which lose their fluorescence upon binding to avidin. Thus, these new ruthenium−biotin complexes can form the basis of new, simplified biotin−avidin assays, which consist of cross-linking the unknown biotinylated molecule and the ruthenium−biotin complex to avidin, for luminescence detection. Ru(II) polypyridine complexes present other advantages over the currently used chromophores, including their photostability and resistance to photobleaching, and their large Stokes shifts, which allow many of these chromophores to be linked to the protein for signal amplification, without quenching their luminescence (*19*, *21*, *39*−*45*). Further work is in progress in our laboratory to extend the applications of these and related transition metal−biotin complexes to more selective bioassays.

ACKNOWLEDGMENT

We thank the Natural Sciences and Engineering Research Council of Canada (NSERC), the Canada Foundation for Innovation, the Centre for Self-Assembled Chemical Structures, the Research Corporation, and the NSERC Strategic Grant program for financial support. H. F. Sleiman is a Cottrell Scholar of the Research Corporation.

Supporting Information Available: Synthesis of the phenanthroline−biotin ligand. Synthesis of complex **1** $[Ru(bpy)_2(phen\text{-}biotin)](PF_6)_2$. Synthesis of complex **2** $[Ru(phen)_2(phen\text{-}biotin)](PF_6)_2$. Electronic absorption and emission data for complexes **1** and **2**. Binding specificity of complexes **1** and **2** toward avidin:HABA assays. Competitive binding assay: titration of Ru−biotin−avidin complexes **1** and **2** with biotin. This material is available free of charge via the Internet at http://pubs.acs.org.

LITERATURE CITED

(1) Wilchek, M., and Bayer, E. A. (1990) *Methods of Enzymology*; Vol. 184, Academic Press, San Diego.

(2) Weizmann, Y., Patolsky, F., Katz, E., and Willner, I. (2003) Amplified DNA Sensing and Immunosensing by the Rotation of Functional Magnetic Particles. *J. Am. Chem. Soc. 125* (12), 452−3454.

(3) Rivera, V. R., Merrill, G. A., White, J. A., and Poli, M. A. (2003) An Enzymatic Electrochemiluminescence Assay for the Lethal Factor of Anthrax. *Anal. Biochem. 312* (1), 125−130.

(4) Guggiero, F. P., and Sheffield, J. B. (1998) The Use Of Avidin as a Probe for the Distribution of Mitochondrial Carboxylases in Developing Chick Retina. *J. Histochem. Cytochem. 46* (2), 177−183.

(5) Richter, J., Adler, M., and Niemeyer, C. M. (2003) Monte Carlo Simulation of the Assembly of bis-Biotinylated DNA and Streptavidin. *ChemPhysChem. 4* (1), 79−83.

(6) Cao, R., Gu, Z., Hsu, L., Patterson, G. D., and Armitage, B. A. (2003) Synthesis and Characterization of Thermoreversible Biopolymer Microgels Based on Hydrogen Bonded Nucleobase Pairing. *J.* Am. *Chem. Soc. 125* (35), 10250−10256.

(7) Caswell, K. K., Wilson, J. N., Bunz, U. H. F., and Murphy, C. J. (2003) Preferential End-to-End Assembly of Gold Nanorods by Biotin-Streptavidin connectors. *J. Am. Chem. Soc. 125* (46), 13914−13915.

(8) Hermanson, G. T. (1996) *Bioconjugate Techniques*; Academic Press, San Diego.

(9) Schetters, H. (1999) Avidin and Streptavidin in Clinical Diagnostics. *Biomol. Eng. 16* (1−4), 73−78.

(10) Lo, K. K.-W., Chung, C.-K., Lee, T. K.-M., Lui, L.-H., Tsang, K. H.-K., and Zhu, N. (2003). New Luminescent Cyclometalated Iridium(III) Diimine Complexes as Biological Labeling Reagents. *Inorg. Chem. 42* (21), 6886−6897.

(11) Hadour, N., Gondran, C., and Cosnier, S. (2004) A New Biotinylated tris Bipyridinyl Iron(II) Complex as Redox Biotin-Bridge for the Construction of Supramolecular Biosensing Architectures. *Chem. Commun.* (3), 324−325.

(12) Adamczyk, M., Mattingly, P. G., Moore, J. A., and Pan, Y. (2003) Regiodependent Luminescence Quenching of Biotinylated *N*-Sulfonyl-acridinium-9-carboxamides by Avidin. *Org. Lett. 5* (21), 3779−3782.

(13) Lakowicz, J. R. (1999) *Principles of Fluorescence Spectroscopy,* 2nd ed.; Kluwer Academic and Plenum Publishers, New York.

(14) Fang, X., Liu, X., Schuster, S., and Tan, W. (1999) Desiging a Novel Molecular Beacon for Surface-Immobilized DNA Hybridization Studies. *J. Am. Chem. Soc., 121* (12), 2921−2922.

(15) Sueda, S., Yuan, J., and Matsumoto, K. (2002) A Homogeneous DNA Hybridization System by Using A New Luminescence Terbium Chelate. *Bioconjugate Chem. 13* (2), 200−205.

(16) Kumer, J. M., Wolfbeis, O. S., and Klimant, I. (2002) Homogeneous Luminescence Decay Time-Based Assay Using Energy Transfer from Nanospheres. *Anal. Chem. 74* (9), 2151−2156.

(17) Gruber, H. J., Marek, M., Schindler, H., and Kaiser, K. (1997) Biotin−Fluorophore Conjugates with Poly(ethylene glycol) Spacers Retain Intense Fluorescence after Binding to Avidin and Streptavidin. *Bioconjugate Chem. 8* (4), 552−559.

(18) Marek, M., Kaiser, K., and Gruber, H. J. (1997) Biotin−Pyrene Conjugates with Poly(ethylene glycol) Spacers are convenient Fluorescence Probes for Avidin and Streptavidin. *Bioconjugate Chem. 8* (4), 560−566.

(19) Gruber, H. J., Hahn, C. D., Kada, G., Riener, C. K., Harms, G. S., Ahrer, W., Dax, T. G., and Knaus, H.-G. (2000) Anomalous Fluorescence Enhancement of Cy3 and Cy3.5 versus Anomalous Fluorescence Loss of Cy5 and Cy7 Upon Covalent Linking to IgG and Noncovalent Binding to Avidin. *Bioconjugate Chem. 11* (5), 696−704.

(20) Marmé, N., Knemeyer, J.-P., Sauer, M., and Wolfrum, J. (2003) Inter- and Intramolecular Fluorescence Quenching of Organic Dyes by Tryptophan. *Bioconjugate Chem. 14* (6), 1133−1139.

(21) Kada, G., Falk, H., and Gruber, H. J. (1999) Accurate Measurement of Avidin and Streptavidin in Crude Biofluids with a New, Optimized Biotin-Fluorescein Conjugate. *Biochim. Biophys. Acta 1427*, 33−43.

(22) Buschmann, V., Weston, K. D., and Sauer, M. (2003) Spectroscopic Study and Evaluation of Red-Absorbing Fluorescent Dyes. *Bioconjugate. Chem. 14* (1), 195−204.

(23) Megan, N. E., and Barton, J. K. (2000) Probing DNA Charge Transport with Metallointercalators. *Curr. Opin. Chem. Biol. 4* (2), 199−206.

(24) Szmacinski, H., Terpetschnig, E., and Lakowicz, J. R. (1996) Synthesis and Evaluation of Ru−Complexes as Anisotropy Probes for Protein Hydrodynamics and Immunoassays of High-Molecular-Weight Antigens. *Biophys. Chem. 62* (1−3), 109−120.

(25) Terpetschnig, E., Dattelbaum, J. D., Szmacinski, H., and Lakowicz, J. R. (1997) Synthesis and Spectral Characterization of a Thiol-Reactive Long-Lifetime Ru(II) Complex. *Anal. Biochem. 251* (2), 241−245.

(26) Zhou, M., Roovers, J., Robertson, G. P., and Grover, C. P. (2003) Multilabeling Biomolecules at a Single Site. 1- Synthesis and Characterization of a dendrotoc Label for Electrochemiluminescence Assays. *Anal. Chem. 75* (23), 6708−6717.
(27) Smith, G. F., and Cagle, F. W., Jr. (1947) The Improved Synthesis of 5-Nitro-1,10-Phenanthroline *J. Org. Chem. 12*, 781−784.
(28) Lecomte, J.-P., Kirsch-De Mesmaeker, A., Demeunynck, M., and Lhomme, J. (1993) Synthesis and Characterisation of a New DNA-Binding Bifunctional Ruthenium(II) Complex. *J. Chem. Soc., Faraday Trans. 89* (17), 3261−3269.
(29) Crapatureanu, S., Serbanescu, R., Brevitt, S. B., and Kluger, R. (1999) Molecular Necklaces. Cross-Linking Hemoglobin with Reagents Containing Covalently Attached Ligands. *Bioconjugate Chem. 10* (6), 1058−1067.
(30) Sullivan, B. P., Salmon, D. J., and Meyer, T. J. (1978) Mixed Phosphine 2,2′-Bipyridine Complexes of Ruthenium. *Inorg. Chem. 17* (12), 3334−3341.
(31) In addition, the slope of the avidin titration curve before the equivalence point ([Ru]:[avidin] = 4:1), i.e., as the Ru−biotin complex binds to avidin, was found to be greater (ca. 1.5 times for **1**, 1.7 times for **2**) than after the equivalence point. After the equivalence point, this slope coincides with the slope of unbound Ru−biotin. (Figure 2, titration curves I and II).
(32) Green, N. M. (1965) A Spectrophotometric Assay for Avidin and Biotin Based on Binding of Dyes by Avidin. *Biochem. J. 94*, 23c−24c.
(33) Our results indicate that the luminescence enhancement of the ruthenium−biotin molecules **1** and **2**, when complexed with avidin, is retained for at least 12 h, and thus their dissociation kinetics from avidin are slow.
(34) Durham, B., Caspar, J. V., Nagle, J. K., and Meyer, T. J. (1982) Photochemistry of $Ru(bpy)_3^{2+}$. *J. Am. Chem. Soc. 104* (18), 4803−4810.
(35) Caspar, J. V., and Meyer, T. J. (1983) Photochemistry of $Ru(bpy)_3^{2+}$. Solvent Effects. *J. Am. Chem. Soc. 105* (17), 5583−5590.
(36) Hartmann, P., Leiner, M. J. P., Draxler, S., and Lippitsch, M. E. (1996) Specific Solvent Effects of Linear Alcohols on the Spectrum and the Excited-State Decay of Tris(2,2′-bipyridyl)ruthenium(II). *Chem. Phys. 207* (1), 137−146.
(37) Lo, K. K.-W., Hui, W.-K., and Ng, D. C.-M. (2002) Novel Rhenium Polypyridine Biotin Complexes That Show Luminescence Enhancement and Lifetime Elongation upon Binding to Avidin. *J. Am. Chem. Soc. 124* (32), 9344−9345.
(38) Wallace, L., and Rillema, D. P. (1993) Photophysical Properties of Rhenium(I) Tricarbonyl Complexes Containing Alkyl- and Aryl-Substituted Phenanthroline as Ligands. *Inorg. Chem. 32* (18), 3836−3843.
(39) Towe, B. C., and Flechsig, S. (1996) A Recirculating-Flow Fluorescence Oxygen Sensor. *Biosens. Bioelectron. 11* (8), 799−803.
(40) Levi, S. A., Mourran, A., Spatz, J. P., van Veggel, F. C. J. M., Reinhoud, D. N., and Möller, M. (2002) Fluorescence of Dyes Adsorbed on Highly Organized, Nanostructured Gold Surfaces. *Chem. Eur. J. 8* (8), 3808−3814.
(41) Staffilani, M., Höss, E., Giesen, U., Schneider, E., Hartl, F., Josel, H.-P., and De Cola, L. (2003) Multimetallic Ruthenium(II) Complexes as Electrochemiluminescence Labels. *Inorg. Chem. 42* (24), 7789−7798.
(42) Zhou, M., and Roovers, J. (2001) Dendritic Supramolecular Assembly with Multiple Ru(II) Tris(bipyridine) Units at the Periphery: Synthesis, Spectroscopic, and Electrochemical Study. *Macromolecules 34* (2), 244−252.
(43) Murfee, H. J., Thoms, T. P. S., Greaves, J., and Hong, B. (2000) New Metallodendrimers Containing an Octakis(diphenylphosphino)-Functionalized Silsesquioxane Core and Ruthenium(II)-Based Chromophores. *Inorg. Chem. 39* (23), 5209−5217.
(44) Muheim, A., Todd, R. J., Casimiro, D. R., Gray, H. B., and Arnold, F. H. (1993) Ruthenium-Mediated Protein Cross-Linking and Stabilization. *J. Am. Chem. Soc. 115 (12)*, 5312−5313.
(45) Kise, K. J., Jr., and Bowler, B. E. (2002) A Ruthenium(II) Tris(bipyridil) Amino Acid: Synthesis and Direct Incorporation into an α-Helical Peptide by Solid-phase Synthesis. *Inorg. Chem. 41* (2), 379−386.
(46) See Supporting Information.
(47) We are carrying out further investigations on the interaction of complexes **1** and **2** with streptavidin, and these will be reported in a future contribution.

BC049919O

ARTICLES

Facile Synthesis of Chain-End Functionalized Glycopolymers for Site-Specific Bioconjugation

Sijian Hou,[†] Xue-Long Sun,*[,†] Chang-Ming Dong,[†] and Elliot L. Chaikof*[,†,‡]

Laboratory for Biomolecular Materials Research, Departments of Surgery and Biomedical Engineering, Emory University School of Medicine, Atlanta, Georgia 30322, and School of Chemical and Biomolecular Engineering, Georgia Institute of Technology, Atlanta, Georgia 30320. Received March 19, 2004; Revised Manuscript Received June 22, 2004

A series of derivatized arylamine initiators were used to generate chain-end functionalized glycopolymers by cyanoxyl-mediated free-radical polymerization. Significant features of this strategy include the capacity to produce polymers of low polydispersity (PDI < 1.5) under aqueous conditions using unprotected monomers bearing a wide range of functional groups. In addition, the presence of a phenyl ring simplifies calculation of polymer saccharide content and molar mass by ^{1}H NMR. It is particularly noteworthy, however, that derivatized arylamine initiators in conjunction with the presence of a terminal cyanate group provide a convenient approach for synthesizing polymers with a variety of distinct functional groups at α and ω chain ends. In the process, the capacity to label glycopolymers or otherwise conjugate them to proteins or other molecules is greatly enhanced.

INTRODUCTION

Polymers containing carbohydrate moieties as pendant groups, referred to as "glycopolymers", have potential applications in medicine and biotechnology. In particular, glycopolymers potentiate multivalent protein−carbohydrate interactions, which lead to biomolecular recognition events that are dramatically different from those elicited by monovalent interactions (*1*−*3*). In the past decade, considerable efforts have focused on the application of living/controlled polymerization strategies for the production of glycopolymers that exhibit low fluctuation in size and composition. Examples include cationic polymerization (*4*−*7*), ring-opening polymerization (*8*, *9*), ring-opening metatheses polymerization (*10*, *11*), and nitroxide-mediated radical polymerization (*12*−*16*). Likewise, recent reports have also demonstrated the efficacy of transition metal-catalyzed atom transfer radical polymerization (ATRP) for the synthesis of carbohydrate-bearing polymers (*17*−*21*).

Recently, the potential utility of glycopolymers in bio- and immunochemical assays (*22*−*25*), as biocapture reagents (*26*, *27*), and as glycosurfaces (*28*, *29*) has been investigated by the addition of functional anchoring groups either pendant to the backbone or at the chain end. In this regard, a chain-end functionalized glycopolymer facilitates site-specific immobilization required for generating a uniformly oriented multivalent array of carbohydrates (*25*). However, the desire to generate glycopolymers with oligosaccahride units of increasing functional complexity poses a number of significant challenges, including a requirement for serial protection−deprotection steps or further polymer derivatization after initial synthesis. We have previously reported that cyanoxyl (OCN)-mediated free radical polymerization of unprotected glycomonomers can be conducted in aqueous solution, is tolerant of a broad range of functional groups including −OH, −NH_2, −COOH, and SO_3^- moieties, and can yield glycopolymers with low polydispersity (PDI < 1.5) (*29*−*31*). In the present study, we describe a straightforward approach to synthesize chain-end functionalized glycopolymers (Figure 1) using functionalized arylamine initiators in conjunction with cyanoxyl-mediated polymerization. As a model system, copolymerization of acrylamide with either lactose or sulfated lactose acrylamide monomer was performed. Notably, polyacrylamide-based neoglycoconjugates have been used as diagnostic reagents (*32*) or as solid-phase coatings in enzyme-linked immunosorbent assays (ELISA) (*22*, *33*).

EXPERIMENTAL PROCEDURES

Chemicals. *p*-Anisidine(4-methoxyaniline), 2-(4-aminophenyl) ethylamine, 4-aminobenzoic hydrazide, 4-aminophenylacetic acid, *N*-(9-fluorenymethoxycarbonyloxy) succinimide, piperidine, sodium nitrite, fluoroboronic acid (48% aqueous solution), sodium cyanate, tetrahydrofuran (THF), acrylamide (AM), peracetyl lactose, dimethylformamide (DMF), methanol, trifluoron boron in ether (BF_3·OEt_2), sodium azide, acryloyl chloride, platinum oxide, sodium methoxide, and triethylamine were used as received, unless otherwise specified. Lactose acrylamide monomer (**2**) and sulfated lactose acrylamide monomer (**3**) were synthesized as previously described (*31*).

Cyanoxyl-Mediated Free-Radical Polymerization of Acylamide-Derived Glycomonomers with Acrylamide Initiated by $RC_6H_4N{\equiv}N^+BF_4^-$/NaOCN

* To whom correspondence should be addressed. Mailing address: 1639 Pierce Drive 5105 WMB, Emory University, Atlanta, GA 30322. Phone: (404) 727-8027. Fax: (404) 727-3660. E-mail addresses: xsun@emory.edu or echaiko@emory.edu.
[†] Emory University School of Medicine.
[‡] Georgia Institute of Technology.

10.1021/bc0499275 CCC: $27.50 © 2004 American Chemical Society
Published on Web 08/12/2004

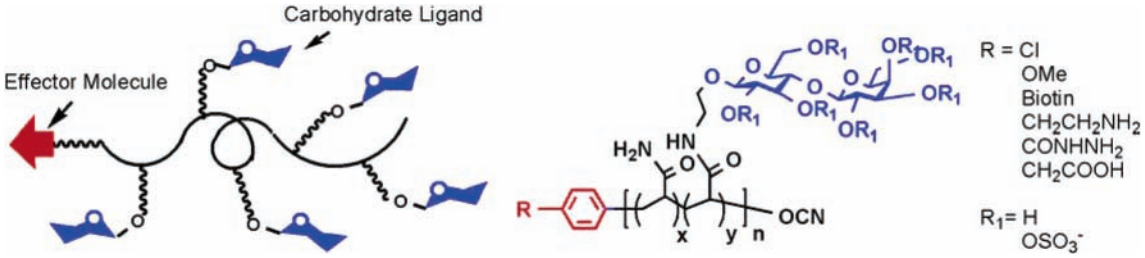
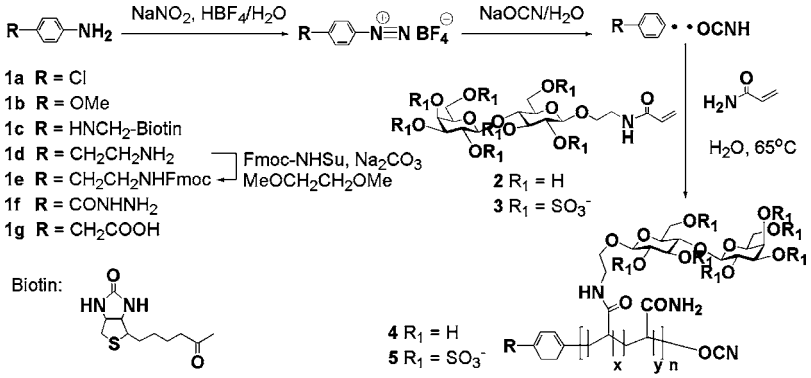


Figure 1. Schematic structure of chain-end functionalized glycopolymer.

Scheme 1: Synthesis of Chain-End Functionalized Glycopolymers via Cyanoxyl-Mediated Free Radical Polymerization



(Scheme 1). In a three-neck flask, 6.03×10^{-5} mol of arylamine was reacted with 17 mg of HBF_4 (48 wt % aqueous solution, 9.04×10^{-5} mol) in 2 mL of water at 0 °C and under an Ar atmosphere. The diazonium salt $RC_6H_4N^+{\equiv}NBF_4^-$ was then generated by adding 5 mg (7.2×10^{-5} mol) of sodium nitrite ($NaNO_2$) to the reaction medium. After 30 min, a degassed mixture of 225 mg (6.03×10^{-4} mol) of glycomonomer (2/3), 171 mg (2.41×10^{-3} mol) of acrylamide, and 4 mg (6.03×10^{-5} mol) of NaOCN dissolved in 1 mL of water were introduced into the flask containing the diazonium salt. The polymerization solution was then heated to 65 °C for 16 h to yield statistical copolymers (**4**/**5**) after quenching the reaction and dialysis for 2 days at room temperature to remove inorganic salt and impurities. The conversions were determined by weight for the resultant glycopolymers.

Complex Formation of Biotin Chain-End Functionalized Glycopolymer with Streptavidin. The biotin chain-end functionalized glycopolymer **4c**/**5c** (1.33×10^{-4} mmol) dissolved in PBS (0.2 mL) was incubated with streptavidin (1.67×10^{-5} mmol) at room temperature for 2 h. UV−vis spectroscopy was performed before and after adding 4′-hydroxyazo-benzene-2-carboxylic acid (HABA, 1.33×10^{-4} mmol). All spectra were acquired on a Cary 50 Bio UV−visible spectrophotometer (Varian).

Conversion of Cyanate (OCN) of Glycopolymer 4b to a Hydroxyl End Group. Pyridine (0.5 mL) was added to a solution of glycopolymer **4b** (16 mg, 2.1×10^{-3} mmol) in water (2 mL). The mixture was stirred at room temperature for 2 h, followed by dialysis against water at room temperature for 2 days to remove excess pyridine and glutaconic aldehyde. Infrared spectra of **4b** and **6b** were acquired using a Digilab/BioRad FTS-4000 Fourier transform infrared (FT-IR) spectrometer (Randolf, MA) equipped with a wide band MCT detector, collected with 512 backgrounds scans, triangular apodization, and 4 cm^{-1} resolutions.

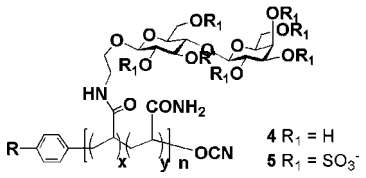
Synthesis of Fmoc-Protected Arylamine 1e. 2-(4-Aminophenyl) ethylamine (**1d**) (220 mg, 1.615 mmol) was dissolved in a sodium carbonate aqueous solution (10%, 7 mL) and was stirred 30 min at room temperature. A solution of *N*-(9-fluorenylmethoxycarbonyloxy) succinimide (Fmoc-NHS, 545 mg, 1.615 mmol) in 1,2-dimethoxyethane (7 mL) was slowly added, and the reaction mixture was stirred overnight at room temperature. A white solid in the reaction mixture was removed by filtration. The filtrate was evaporated to yield a residue, which was dissolved in ethyl acetate, washed three times with distilled water, and then concentrated. The resulting residue was purified by silica gel column chromatography using chloroform/methanol (95/5) as eluent to obtain **1e** (265 mg, yield 46%). ^{1}H NMR ($CDCl_3$) δ ppm: 7.75 (2H, d, J = 7.5 Hz), 7.6 (2H, d, J = 7.2 Hz); 7.40 (2H, t, J = 7.2 Hz), 7.30 (2H, t, J = 4.8 Hz), 6.95 (2H, d, J = 4.8 Hz), 6.60 (2H, d, J = 8.1 Hz), 4.40 (2H, d, J = 6.6 Hz), 4.2 (1H, t, J = 6.9 Hz), 3.4 (2H, m), 2.70 (2H, t, J = 6.9 Hz). MS/FAB, m/z: 358 $(M + Li)^+$.

Removal of Fmoc Protecting Group of Glycopolymer 5e. Fmoc-protected glycopolymer **5e** (50 mg) was dissolved in 3 mL of DMF. Piperidine (3 mL) was dropped into the polymer solution, which was stirred overnight at room temperature. The reaction mixture was dialyzed using a cellulose membrane for 2 days and then extracted three times using chloroform. The solution was freeze-dried using a lyophilizer to give glycopolymer **5d** (33 mg).

RESULTS AND DISCUSSION

Previous investigations have demonstrated that cyanoxyl (OCN)-mediated free-radical polymerization of acrylamide glycomonomers could be conducted in aqueous solution to yield glycopolymers of low polydispersity. In this polymerization scheme, cyanoxyl radicals are generated by an electron-transfer reaction between cyanate anions ($^-OC{\equiv}N$) from a NaOCN aqueous solution and aryl-diazonium salts ($RC_6H_4N{\equiv}N^+BF_4^-$) prepared in situ through a diazotization reaction of arylamine in water. In addition to cyanoxyl persistent radicals, aryl-type active radicals were simultaneously produced, and only the latter species is capable of initiating chain growth. Therefore, we hypothesized that chain-end functionalized

Table 1. Free-radical Copolymerization of Nonsulfated and Sulfated Lactose Glycomonomers 2/3 (GM) with Acrylamide (AM)[a]



initiator	R	glycomonomer (GM)	GM/AM (mol)	$[M]_0/[I]_0$	glycopolymer	yield (%)	polymer composition (x/y)[b]	M_n[b] (g/mol)
1a	Cl	**2**	1/7	20	**4a**	71	1/6	9 000
1b	MeO	**2**	1/7	48	**4b**	78	1/9	7 500
1c	biotin-$NHCH_2$	**2**	1/7	20	**4c**	75	1/7	11 000
1a	Cl	**3**	1/1	10	**5a**	80	1/10	9 300
1b	MeO	**3**	1/8	25	**5b**	65	1/11	11 100
1c	biotin-$NHCH_2$	**3**	1/7	20	**5c**	61	1/8	16 000
1d	$H_2NCH_2CH_2$	**3**	1/5	12	**5d**	25	1/6	11 300
1e	Fmoc-**1d**	**3**	1/7	28	**5e**	57	1/9	15 900
1f	H_2NHNCO	**3**	1/5	22	**5f**	35	1/6	12 800
1g	$HOOCCH_2$	**3**	1/1	10	**5g**	57	1/1	10 800

[a] Polymerizations were performed for 16 h at 65 °C. [b] Mass content of saccharide and molecular weight were determined by ^1H NMR analysis (in D_2O).

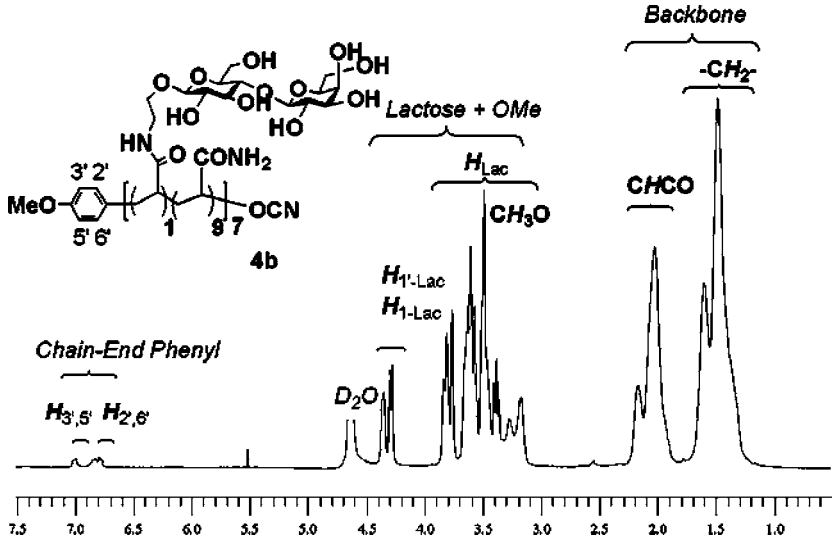


Figure 2. ^1H NMR spectrum of methoxyl phenyl chain-ended glycopolymer **4b** in D_2O.

glycopolymers could be obtained if functionalized arylamines could act as efficient initiators for polymerization. A series of 4-substituted phenylamines (**1a**−**1g**) were investigated as initiators of cyanoxyl-mediated copolymerization of nonsulfated and sulfated lactose acrylamide monomers (**2**/**3**) with acrylamide. Consequently, a series of chain-end functionalized glycopolymers of varying molecular weight were prepared by altering either monomer conversion or the initial ratio of monomer to initiator concentrations ($[M]_0/[I]_0$). As shown in Scheme 1 and summarized in Table 1, copolymerization of lactosyl acrylamide (**2**/**3**) and acrylamide generated a series of expected chain-end functionalized glycopolymers (**4**/**5**). Of note, carboxylic acid, amine, and hydrazine end groups will facilitate glycopolymer conjugation with amine-, acid-, and aldehyde-containing molecules, respectively, while the biotin end group facilitates glycopolymer binding to streptavidin (*29*), and the methoxyl phenyl end group provides an activated aromatic ring for radiohalogenation of the glycopolymer (*34*).

The resultant glycopolymers were characterized by NMR spectroscopy. It is noteworthy that the phenyl group at the end of the glycopolymer provides a convenient mechanism for calculating carbohydrate content and the molar mass through comparison of integrated phenyl proton peaks with those of carbohydrate and backbone protons, respectively. For example, as illustrated in Figure 2, comparison of the integrated signals produced from the chain-end phenyl protons ($H_{2',6'}$ and $H_{3',5'}$) with those due to the anomeric protons of lactose ($H_{1'-Lac}$ and H_{1-Lac}) and the backbone protons indicated that the average composition of the methoxylphenyl chain-end functionalized glycopolymer **4b** was seven lactose units and 63 acrylamide units with M_n of 7500. In addition, downfield shift of end phenyl protons $H_{2',6'}$ of resultant glycopolymers confirmed C−C bond formation between phenyl and the polymer backbone (Table 2).

When compared to chlorine-, methoxyl-, carboxylic-, and biotin-containing arylamine initiators, amine- and hydrazine-derivatized arylamines (**1d** and **1f**) afforded the corresponding glycopolymers (**5d** and **5f**) in lower yield. This may be a result of quaternization of the amino group, limiting subsequent radical formation. Therefore, Fmoc-protected arylamine (**1e**) initiated polymerization was investigated providing an amine-protected chain-end

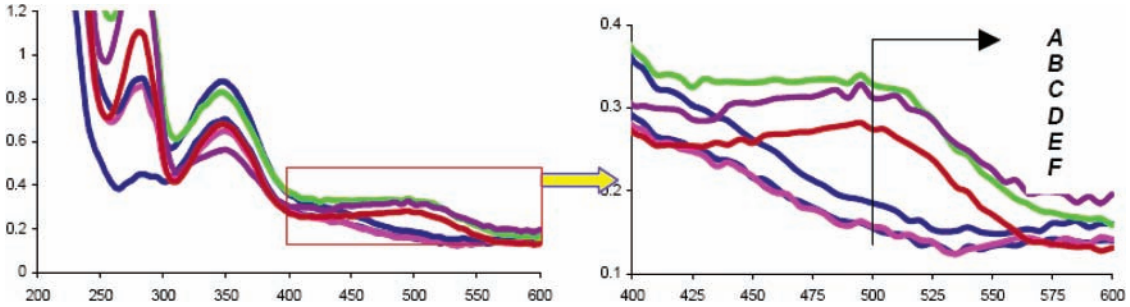


Figure 3. Monitoring of streptavidin−biotin−glycopolymer (**4c**/**5c**) interactions by UV−vis spectroscopy: (A) streptavidin + **4a** + HABA; (B) streptavidin + **5a** + HABA; (C) streptavidin + HABA; (D) streptavidin + biotin + HABA; (E) streptavidin + **4c** + HABA; (F) streptavidin + **5c** + HABA.

Scheme 2. Representitive Scheme of Glycopolymer−Protein Hybrid Fabrication

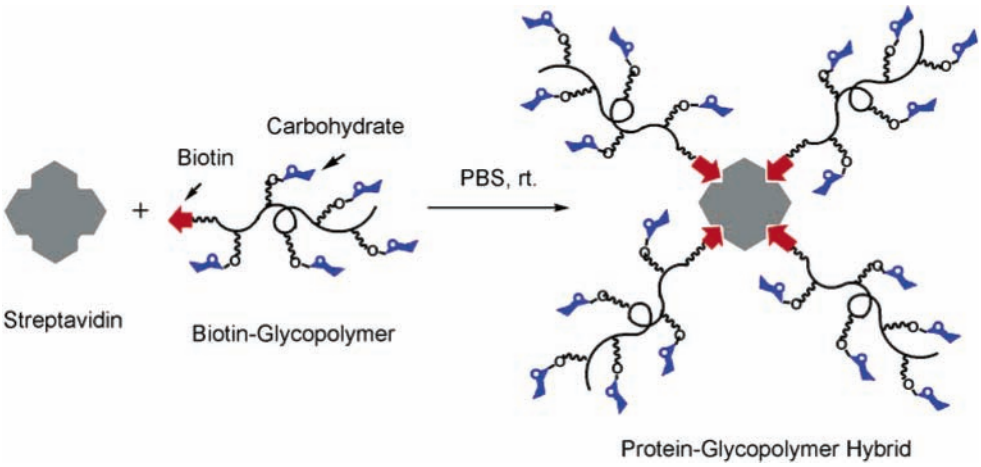


Table 2. Chemical Shifts of Phenyl Protons of Initiators and Polymers (ppm)[a]

		initiator		polymer[b]		
initiator	ending group	$H_{3',5'}$	$H_{2',6'}$	$H_{3',5'}$	$H_{2',6'}$	polymer
1a	Cl−	7.10	6.60	7.10	7.20	**4a**
1b	MeO−	6.70	6.60	6.80	7.00	**4b**
1c	Biotin-$NHCH_2$−	7.13	6.78	7.08	7.06	**4c**
1d	$H_2NCH_2CH_2$−	6.95	6.60	7.10	7.10	**5d**
1f	H_2NHNCO−	7.55	6.60	7.80	7.20	**5f**
1e	$HOOCCH_2$−	7.85	7.35	7.10	7.10	**5g**

[a] ^{1}H NMR spectra were recorded in D_2O (4.65 ppm of DHO as standard) at room temperature. [b] Broad, 2H, polymeric phenyl protons.

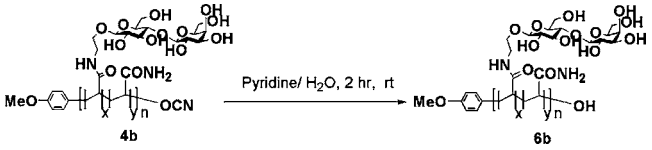
functionalized glycopolymer (**5e**) in high conversion yield. ^{1}H NMR comfirmed that piperidine completely deprotected the Fmoc groups producing an amine chain-end functionalized glycopolymer.

High-affinity binding of biotin to streptavidin (ca. 10^{13-15} M^{-1}) has led to the use of streptavidin as a molecular adapter in diverse applications (*35*). For example, polymers with biotinylated end groups have been found to be significant for a self-organizing protein−polymer hybrid amphiphile that uses the molecular recognition between streptavidin and biotin (*36*). In the present study, glycopolymer-based noncovalent neoglycoproteins were produced by incubation of streptavidin with biotin chain-end functionalized polymers **4c** and **5c** (Scheme 2). The ability of biotin−glycopolymers to specifically bind streptavidin was accessed using a HABA−streptavidin assay (*37*). HABA ′ (λ_{max} 350 nm) changes color from yellow to red (λ_{max} 500 nm) upon binding to streptavidin (Figure 3, trial C). When HABA was added to a solution of streptavidin saturated with free biotin or biotin glycopolymers **4c** and **5c**, a red shift was not observed (Figure 3, trials D, E, and F). In contrast, a color change was noted when HABA was added to a solution of streptavidin with non-biotin-containing glycopolymers **4a** and **5a** (Figure 3, trials A and B). These results demonstrate glycopolymer−protein hybrid formation through specific binding of chain-end biotin of glycopolymers **4c** and **5c** to streptavidin. In principle, streptavidin has four free biotin-binding sites. However, the HABA assay revealed an average occupancy of 3.0−3.6 glycopolymer chains per streptavidin molecule. Full occupancy may be limited as a result of steric factors.

Another significant feature of cyanoxyl (OCN)-mediated polymerization is the presence of a terminal cyanate group at the opposing chain end (Scheme 1). Cyanate-based ligand immobilization via specific reaction with an amine group to form an isourea bond has proven to be a useful tool in bioconjugate chemistry (*38*, *39*). As such, the OCN end group provides a second feasible reaction pathway for conjugation of glycopolymers with amine-containing surfaces and molecules (*40*). Consequently, this scheme establishes a facile approach for producing α,ω asymmetric bifunctional chain-terminated polymers. Moreover, the potential to conjugate glycopolymers that have been selectively labeled with a chromophore, fluorophore, or radiotracer is apparent. It is also noteworthy that desired the cyanate group can be converted to a hydroxyl group (Scheme 3) by treatment with pyridine in water (*41*). IR spectroscopy demonstrated that the OCN absorption band at 2157 cm^{-1} disappeared after pyridine treatment of glycopolymer **4b** to **6b** thereby confirming complete hydrolysis of the cyanoxyl group. Further ^{1}H NMR of **6b** indicated that this hydrolysis reaction did not induce any further structural changes.

In summary, a straightforward approach for the synthesis of a series of α,ω chain-end functionalized glyco-

Scheme 3. Conversion of Terminal Glycopolymer Cyanate Group (OCN) to a Hydroxyl Moiety



polymers via cyanoxyl-mediated free-radical polymerization has been presented. Significantly, a variety of arylamine derivatives proved to be acceptable initiators for cyanoxyl-mediated free-radical polymerization yielding chain-end functionalized glycopolymers that can be successfully conjugated or otherwise linked to a variety of molecules or surfaces.

ACKNOWLEDGMENT

This work was supported by grants from the NIH and NSF. The authors acknowledge the Emory University NMR and Mass Spectrometry Centers for use of their facilities and Dr. Keith Faucher for assistance with IR spectroscopy.

LITERATURE CITED

(1) Lee, Y., and Lee, R. T. (1995) Carbohydrate-protein interactions: basis of glycobiology. *Acc. Chem. Res. 28*, 321.

(2) Strong, L. E., and Kiessling, L. L. (1999) A general synthetic route to defined, biologically active multivalent arrays. *J. Am. Chem. Soc. 121*, 6193.

(3) Lundquist, J. J., and Toone, E. J. (2002) The cluster glycoside effect. *Chem. Rev. 102*, 555.

(4) D'Agosto, F., Charreyye, M. T., Pichot, C., and Mandrand, B. (2002) Polymer of controlled chain length carrying hydrophilic galactose moieties for immobilization of DNA probes. *Macromol. Chem. Phys.* 203, 146.

(5) D'Agosto, F., Charreyye, M. T., Delolme, F., Dessalces, G., Cramail, H., Deffieux, A., and Pichot, C. (2002) Kinetic study of the "living" cationic polymerization of a galactose carrying vinyl ether. MALDI-TOF MS analysis of the resulting glycopolymers. *Macromolecules 35*, 7911.

(6) Yamada, K., Minoda, M., and Miyamoto, T. (1999) Controlled synthesis of amphiphilic block copolymers with pendant *N*-acetyl-D-glucosamine residues by living cationic polymerization and their Interaction with WGA lectin. *Macromolecules 32*, 3553.

(7) Yamada, K., Minoda, M., and Miyamoto, T. (1997) Controlled synthesis of glycopolymers with pendant D-glucosamine residues by living cationic polymerization. *J. Polym. Sci., Part A: Polym. Chem. 35*, 751.

(8) Tsutsumiuchi, K., Aoi, K., and Okada, M. (1997) Synthesis of polyoxazoline-(Glyco)peptide block copolymers by ring-opening polymerization of (Sugar-Substituted) α-amino acid *N*-carboxyanhydrides with polyoxazoline macroinitiators. *Macromolecules 30*, 4013.

(9) Aoi, K., Tsutsumiuchi, K., and Okada, M. (1994) Glycopeptide synthesis by an alpha-amino acid *N*-carboxyanhydride (NCA) method: ring-opening polymerization of a sugar-substituted NCA. *Macromolecules 27*, 875.

(10) Nomura, K., and Schrock, R. R. (1996) Preparation of "sugar-coated" homopolymers and multiblock ROMP copolymers. *Macromolecules 29*, 540.

(11) Fraser, C., and Grubbs, R. U. (1995) Synthesis of glycopolymers of controlled molecular weight by ring-opening metathesis polymerization using well-defined functional group tolerant ruthenium carbene catalysts. *Macromolecules 28*, 7248.

(12) Gotz, H., Horth, E., Schiller, S. M., Frank, C. W., Knoll, W., and Hawker, C. J. (2002) Synthesis of lipo-glycopolymer amphiphiles by nitroxide-mediated living free-radical polymerization. *J. Polym. Sci., Part A: Polym. Chem. 40*, 3379.

(13) Chen, Y. M., and Wulff, G. (2001) Synthesis of poly(styryl sugar)s by TEMPO mediated free radical polymerization. *Macromol. Chem. Phys. 202*, 3426.

(14) Chen, Y. M., and Wulff, G. (2001) Amphiphilic block copolymers with pendent sugar as hydrophilic segments and their surface properties. *Macromol. Chem. Phys. 202*, 3273.

(15) Narumi, A., Matsuda, T., Kaga, H.; Satoh, T., and Kakuchi, T. (2001) Glycoconjugated polymer II. Synthesis of polystyrene-*block*-poly(4-vinylbenzyl glucoside) and polystyrene-*block*-poly(4-vinylbenzyl maltohexaoside) via 2,2,6,6-tetramethylpiperidine-1-oxyl-mediated living radical polymerization. *Polym. J. 33*, 939.

(16) Ohno, K., Tsujii, Y., Miyamoto, T., Fukuda, T., Goto, M., Kobayashi, K., and Akaike, T. (1998) Synthesis of a well-defined glycopolymer by nitroxide-controlled free radical polymerization. *Macromolecules 31*, 1064.

(17) Chen, Y. M., and Wulff, G. (2002) ABA and star amphiphilic block copolymers composed of polymethacrylate bearing a galactose fragment and poly(ϵ-caprolactone). *Macromol. Rapid Commun. 23*, 59.

(18) Li, Z. C., Liang, Y. Z., Chen, G. Q., and Li, F. M. (2000) Synthesis of amphiphilic block copolymers with well-defined glycopolymer segment by atom transfer radical polymerization. *Macromol. Rapid Commun. 21*, 375.

(19) Haddleton, D. M., and Ohno, K. (2000) Well-defined oligosaccharide-terminated polymers from living radical polymerization. *Biomacromolecules 1*, 152.

(20) Ohno, K., Tsujii, Y., and Fukuda, T. (1998) Synthesis of a well-defined glycopolymer by atom transfer radical polymerization. *J. Polym. Sci., Part A: Polym. Chem. 36*, 2473.

(21) Okada, M. (2001) Molecular design and syntheses of glycopolymers. *Prog. Polym. Sci. 26*, 67.

(22) Roy, R., Tropper, F. D., and Romanowska, A. (1992) Custom-designed glycopolymer syntheses by terpolymerizations. *J. Chem. Soc., Chem. Commun*. 1611.

(23) Thoma, G., Patton, J. T., Magnani, J. L., Ernst, B., Öhrlein, R., and Duthaler, R. O. (1999) Versatile functionalization of polylysine: synthesis, characterization, and use of neoglycoconjugates. *J. Am. Chem. Soc. 121*, 5919.

(24) Gorden, E. J., Gestwicki, J. E., Strong, L. E. and Kiessling, L. L. (2000) Synthesis of end-labeled multivalent ligands for exploring cell-surface-receptor−ligand interactions. *Chem. Biol. 7*, 9.

(25) Gestwicki, J. E., Cairo, C. W., Mann, D. A., and Kiessling, L. L. (2002) Selective immobilization of multivalent ligands for surface plasmon resonance and fluorescence microscopy. *Anal. Biochem. 305*, 149.

(26) Rye, P. D., and Bovin, N. V. (1997) Selection of carbohydrate-binding cell phenotypes using oligosaccharide-coated magnetic particles. *Glycobiology 7*, 179.

(27) Bundy, J. L., and Fenselau, C. (2001) Lectin and carbohydrate affinity capture surfaces for mass spectrometric analysis of microorganisms. *Anal. Chem. 73*, 751.

(28) Yoshizumi, A., Kanayama, N., Maehara, Y., Ide, M., and Kitano, H. (1999) Self-assembled monolayer of sugar-carrying polymer chain: Sugar balls from 2-methacryloyloxyethyl D-glucopyranoside. *Langmuir 15*, 482.

(29) Sun, X. L., Faucher, K. M., Houston, M., Grande, D., and Chaikof, E. L. (2002) Design and synthesis of biotin chain-terminated glycopolymers for surface glycoengineering. *J. Am. Chem. Soc. 124*, 7258.

(30) Grande, D., Baskaran, S., Basakaran, C., Gnanou, Y., and Chaikof, E. L. (2000) Glycosaminoglycan-mimetic biomaterials. 1. Nonsulfated and sulfated glycopolymers by cyanoxyl-mediated free-radical polymerization. *Macromolecules 33*, 1123.

(31) Sun X. L., Grande, D., Baskaran, S., and Chaikof, E. L. (2002) Glycosaminoglycan mimetic biomaterials. 4. Synthesis of sulfated lactose-based glycopolymers that exhibit anticoagulant activity. *Biomacromolecules 3*, 1065.

(32) Sigal, G. B., Mammen, M., Dahmann, G., and Whitesides, G. M. (1996) Polyacrylamides bearing pendant α-sialoside groups strongly inhibit agglutination of erythrocytes by influenza virus: The strong inhibition reflects enhanced binding through cooperative polyvalent interactions. *J. Am. Chem. Soc. 118*, 3789.

(33) Bovin, N. V. (1998) Polyacrylamide-based glycoconjugates as tools in glycobiology. *Glycoconjugate J. 15*, 431.
(34) March, J. (1985) Aromatic electrophilic substitution. *Adv. Org. Chem*. 447−511.
(35) Weber, P. C., Ohlendore, D. H., Wendoloski, J. J., and Salemme, F. R. (1989) Structural origins of high-affinity biotin binding to streptavidin. *Science 243*, 85.
(36) Hanink, J. M., Cornelissen, J. L. M., Farrera, J. A., Foubert, P. De Schryver, F. C., Sommerdijk, N. A. J. M., and Nolte, R. J. M. (2001) Protein-polymer hybrid amphiphiles. *Angew. Chem, Int. Ed. 40*, 4732.
(37) Weber, P. C., Wendoloski, J. J., Pantoliano, M. W., and Salemme, F. R. (1992) Crystallographic and thermodynamic comparison of natural and synthetic ligands bound to streptavidin. *J. Am. Chem. Soc. 114*, 3197.
(38) Axen, R., Porath, J., and Ernback, S. (1967) Chemical coupling of peptides and proteins to polysaccharides by means of cyanogen bromide. *Nature 214*, 1302.
(39) Wilchek, M., and Miron, T. (1999) Thirty years of affinity chromatography. *React. Funct. Polym. 41*, 263.
(40) Lees, A., Nelson, B. L., and Mond, J. J. (1996) Activation of soluble polysaccharides with 1-cyano-4-dimethylaminopyridiniumtetrafluoroborate for use in protein-polysaccharide conjugate vaccines and immunological reagents. *Vaccine 14*, 190.
(41) Kohn, J., and Wilchek, M. (1978) A colorimetric method for monitoring activation of sepharose by cyanogen bromide. *Biochem. Biophys. Res. Commun. 84*, 7.

BC0499275

Novel Hyperbranched Dendron for Gene Transfer in Vitro and in Vivo

Pallab Banerjee, Wilfried Reichardt, Ralph Weissleder, and Alexei Bogdanov, Jr.*

Center for Molecular Imaging Research, Massachusetts General Hospital, Charlestown, Massachusetts 02129.
Received November 13, 2003; Revised Manuscript Received May 19, 2004

Novel hyperbranched dendron (HD) polymers were synthesized using a low molecular weight poly(ethyleneimine) core (BPEI). Using successive attachment of ethyleneimine moieties to the PEI core, the relative ratio of linear-to-branched structures was lowered from 1.17 to 0.70. We found that the more extensive branching of PEI enables the condensation of plasmid DNA into nanostructures with a size of 70−100 nm. The obtained complexes were stable at least for 3 weeks at 4 °C. The HD−DNA complexes prepared using secondary and tertiary amine-containing dendrons exerted a very low cytotoxicity in vitro during a coincubation with cells for 48 h. Using firefly luciferase as a marker of protein expression, we established that HD complexes were efficient in transfecting cells in the presence of serum. Under optimized conditions, the transfection activity at a nitrogen-to-phosphate (N/P) ratio of 6 was approximately six times higher than that of the commercially available polycationic transfection reagent. Bioluminescent imaging of in vivo gene expression using a luciferase reporter gene showed the increase of the signal in the liver and in submandibular lymph nodes in live mice. Our preliminary in vivo gene expression data demonstrates the potential of HD polymers as in vivo transfection agents that could be potentially useful for lymph node gene delivery.

INTRODUCTION

Nonviral gene transfer is frequently regarded as a potentially safer alternative to viral gene delivery (*1*−*5*). However, nonviral gene transfer to mammalian cells usually lacks the efficiency typical to that of viral transduction and requires substantial improvement (*6*). Nonviral delivery of DNA usually requires condensation with positively charged lipids or polycations to enable binding of polyionic complexes to plasma membrane and further internalization by the cells. The condensation ideally yields complexes that could release DNA after the internalization. In recent years several cationic polymers that readily form complexes with DNA (e.g. polylysine, poly(ethyleneimine), or various types of block and graft copolymers) have been investigated as potential nonviral vectors that enable transfer of DNA into mammalian cells (*7*−*12*). The binding of a polycation to DNA results in a formation of very compact colloidal complexes which are unstable in solution (*13*). Properties of these complexes that define their size and stability depend heavily on chemical structure as well as on physical properties of the polycation (*14, 15*).

As the use of synthetic carriers for DNA delivery expands beyond the traditional in vitro experiments, various polycations, including branched poly(ethyleneimine) (BPEI),[1] starburst polyamidoamine (PAMAM) dendrimers (*16*−*19*), and hyperbranched polymers (*20, 21*) are now being closely investigated. Some of the above polycations have shown high levels of gene transfer in mammalian cell culture. High transfection efficiency of BPEI and PAMAM compared to other polycations is explained by the "proton sponge" effect (*22*). This effect is supposedly caused by the protonation of tertiary amines present in the core of those polymers in the acidic milieu of endosomes. Godbey et al. (*23*) reported that the protonated form of branched PEI or PAMAM may perturb endosomes probably due to membrane disruption or as a result of osmotic effects (*23*). Haensler et al. (*16*) reported that dendrimers show a high level of transfection in a wide variety of cells in culture with low concomitant cytotoxicity. The transfection activity of PAMAM improved dramatically after random degradation by heat treatment in a solvolytic solvent (*24*), suggesting that polydisperse "fractured" dendrimers are more flexible than monodisperse PAMAM enabling "fractured" dendrimer to form compact complex with DNA. Interestingly, fractured dendrimers are able to swell when released from DNA (*24*). Recently, Lim et al. (*20, 21*) reported biodegradable hyperbranched poly(amino esters) with high transfection efficiency and low cytotoxicity in vitro.

The majority of PEI-mediated transfections utilize a low-branched polymer having a MW from 25 kDa to 800 kDa (*22, 25, 26*). Unfortunately, high molecular weight PEI has high cytotoxicity that limits the scope of potential applications in vivo. To decrease the cytotoxicity and to increase water solubility of DNA polymer complex, poly(ethylene glycol)-grafted PEI has been synthesized having lower transfection efficiency and low cytotoxicity at high N/P ratios (*27*). Alternatively, linear PEI (LPEI) has been suggested for in vitro and in vivo gene delivery (*28*−*30*)

* To whom correspondence should be addressed at Center for Molecular Imaging Research, Rm. 5420, Massachusetts General Hospital, Bldg. 149, 13th St., Charlestown, MA 02129. Telephone (617) 726−5788; fax (617) 726−5708. E-mail: abogdanov@helix.mgh.harvard.edu.

[1] Abbreviations: DMEM, Dublecco's Modified Eagle's Medium; SEC, size exclusion chromatography; HD, hyperbranched dendron polymer; BPEI, low molecular weight ethyleneimine; CMV, cytomegalovirus; ip, intraperitoneally; CEA, 2-chloroethylamine; PAMAM, polyamidoamine dendrimer; BPEI, branched ethyleneimine; LPEI, linear polyethylneimine; PDI, polydispersity index; N/P, nitrogen/phosphorous.

10.1021/bc0342128 CCC: $27.50 © 2004 American Chemical Society
Published on Web 07/22/2004

since tertiary and secondary amine groups of LPEI causes less toxic effects than primary amines.

However, none of above nontoxic polycations appears to form sufficiently stable submicron complexes with DNA that could be useful for gene transfer in the presence of serum. The preservation of transfectability in serum is critical for in vivo gene delivery. Therefore, the goal of this research was to test a novel polymers that (1) would form nanosized, stable complexes with plasmid DNA, (2) would be efficient at low N/P ratios in the presence of serum, (3) would have low cytotoxicity, and (4) would be useful for in vivo gene delivery.

MATERIALS AND METHODS

Materials and Analytical Methods. Poly(ethyleneimine) (BPEI) (average molecular weight 10 kD) was obtained from Polysciences, Inc. (Warrington, PA) and purified by ultrafiltration using 30K NMWC cartridge (UFP-30, Amersham Biosciences). Gel permeation chromatography (GPC) was used to determine the molecular mass and molecular weight distribution. GPC analysis was carried out using PL aquagel-OH 40 8 μm column (Polymer Laboratories Inc, Amherst, MA) eluted at 1 mL/min with 100 mM ammonium acetate (pH 7) on Varian ProStar HPLC coupled with two detectors, UV−vis and differential refractive index (RI) detector at 30 °C. Molecular mass was measured using poly(ethylene oxide)s as standards. Twelve polyethylenoxide standards with molecular mass range from 5 kDa to 920 kDa were used for column calibration. The weight average molecular mass was computed from the refractive index data. Proton and ^{13}C NMR were recorded using D_2O solutions by Spectral Data Service (Champaign, IL) at 400 MHz for ^{1}H and 100 MHz for ^{13}C spectra, respectively. The quantitative ^{13}C were recorded using inverse gated decoupling pulse sequences. The spectra was obtained using ∼0.5 g/mL solution at 30 °C. The data were acquired with an 80° pulse and 10 s recycle delay. D-Luciferin was purchased from Xenogen (Alameda, CA).

Synthesis of PEI-Dendron. *Hyperbranched Dendron 2 (HD2).* Ten grams (0.086 mol) of 2-chloroethylamine hydrochloride (CEA, Acros, Pittsburgh, PA) was dissolved in 25 mL of water; 5 g (0.125 mol) of sodium hydroxide was added to this solution, stirred at the room temperature, and added dropwise into the condenser-equipped reaction flask containing a 10% water solution of 10 g of BPEI. The reaction mixture was stirred for 1 h at 50 °C. Sodium hydroxide solution (25%, 10 mL) was then added to the reaction mixture, and the temperature was raised to 90 °C, refluxed for 5 h, and stirred another 12 h at room temperature. The low molecular weight HD2 was purified by ultrafiltration using 30K NMWC cartridge (A/G Technology Co, Framingham MA) and freeze-dried. *Hyperbranched Dendrons 3 and 4 (HD3 and HD4).* HD2 (3.5 g) was reacted with 10 g of CEA in the presence of sodium hydroxide as described above. The purified product (HD3) was used in further experiments and as a core for HD4 synthesis. HD4 was prepared by repeating the procedure above using HD3 as a starting material.

Preparation of Dendron−DNA Complexes. The reporter plasmid, pCMV−Luc (3.2 MDa, 5.12kb), encoding firefly luciferase, was propagated in *E. coli*, DH5α and purified using Megaprep columns (Qiagen, Valencia, CA). Plasmid integrity was confirmed by gel electrophoresis in agarose. DNA concentration and purity were determined by measuring absorbance at 260 and 280 nm. The complex was prepared using 1 μg of pCMV−Luc plasmid DNA with varying amounts of polymers in TE buffer at pH 7.1 for 1 h before loading onto a 0.7% agarose gel. Ethidium bromide displacement titration studies were performed using F-4500 Fluorescence spectrophotometer (Hitachi, Danbury, CT). The excitation and emission wavelengths for ethidium bromide was 366 and 591 nm, respectively. Briefly, 10 μg of DNA and 2 μg of ethidium bromide solution (0.4 mg/mL) were mixed in 2 mL of TE buffer (pH 7.1). Polymer solution was added in 4−5 μL aliquots (1.06 mg polymer/mL). After adding polymer solution, the mixture was incubated at room temperature for 3 min for equilibration and the fluorescence intensity was measured. Two consecutive measurements were performed, and intensity values were averaged.

The size of the complexes was determined using Zetasizer 1000HSA (Malvern Instruments Inc, Southborogh, MA) using a 633 nm laser source at a fixed angle of 90°. Complexes were prepared in 0.25 M sucrose. All complexes were made by adding respective amount of dendron solution (∼3 mg/mL 0.25 M sucrose solution) to 20 μg/mL DNA in TE buffer. The particle size was measured using 500 μL of complex solution at 25 °C. Data were collected after two consecutive measurements. The change of particle size was measured for 3 weeks. All complexes were stored at 4 °C.

Cell Culture. COS-1 cells were propagated in Dulbecco's modified Eagle's medium with 4 mM L-glutamine, 1% penicillin−streptomycin, and 10% fetal bovine serum. Neuroprogenitor-derived cells, C17.2 (a generous gift of Dr. E. Snyder, Harvard Medical School), were propagated as described (*31*). Human umbilical venous endothelial cells (HUVEC) were cultured using EGM2 (Cambrex Bio Science, Baltimore, MD).

Transfection Experiments. HD polymers were dissolved in 0.25 M sucrosee solutions (∼3 mg/mL) and stored at 4 °C. Polymer−DNA complexes were formed by adding polymer solutions to DNA solutions. The maximum volume for the complex was adjusted to 50 μL by adding 0.25 M sucrose solution. Weight ratios of hyperbranched dendron-to-nucleic acid were based on the calculation of total charge present in each component, taking into account the molecular masses and degree of polymerization, i.e., the number of total nitrogen present in hyperbranched polymer vs the number of phosphates present in the nucleic acid. For example, 1 μg of plasmid DNA solution (0.74 mg/mL) was assumed to have 0.19×10^{16} negative charges. One microgram of HD4 solution (3.3 mg/mL stock solution in 0.25 M sucrose) was assumed to have 1.35×10^{16} positive charges. To obtain the theoretical charge ratio N/P = 1, we mixed 0.15 μg of HD4 solution, prepared by dilution polymer stock solution (3 mg/mL), with one μg of DNA (0.74 mg DNA/mL). We calculated N/P ratio assuming that total nitrogen (i.e. primary, secondary, and tertiary amines) contained within a single HD molecule, as well as all phosphates of DNA are taking part in the complex formation. Superfect cell transfection reagent (Qiagen, Valencia, CA) was used as a standard in our experiments. Superfect reagent and DNA complexes with Superfect were diluted using a 0.25 M sucrose solution.

Cell Transfection. Transfections with HD-plasmid DNA complexes were performed, and the results were analyzed using standard assay for luciferase activity expression (Luciferase assay reagent, Promega, Madison, WI). Various amounts of hyperbranched polymer in 0.25 M sucrose were added to the plasmid solution (0.5 μg of pCMV-luc DNA in 30 μL of 0.1 TE buffer), mixed, and incubated at room temperature for 30 min. Cells were plated at a density of 10 000 cells/well in 96-well plates,

24 h prior to transfection. Before the addition of complexes, medium was replaced by fresh 100 μL of serum-containing media. The complexes were then added to each well. The total volume did not exceed 150 μL/ well. The transfection was carried for either 4 or 48 h at 37 °C. In the case of 4 h transfection, the complete growth medium was replaced with the fresh serum-containing medium followed by another 48 h incubation. In the case of 48 h transfection, no medium change was performed. Luciferase activity in cell lysates was determined using Microlumat LB96P (EG&G Berthold) by adding 50 μL of luciferin substrate (Promega, Madison, WI) to 25 μL of cell lysate in each well using an automated injector (n = 3 independent experiments for each transfection reagent). Luciferase activity was integrated over 10 s with 2 s intervals. The protein concentration was measured in the rest of 25 μL of cell lysate using standard protein assay reagent Pierce-Endogen, Rockford, IL). Results were expressed in relative light units per mg of cell protein.

Transfection after Storage. The complexes of hyperbranched polymer were prepared at the same ratio as in the case of conventional transfection. Complexes were incubated 20 min at room temperature and then stored at 4 °C for 3 weeks. After 3 weeks, complexes were used for transfection, which was carried out in the same way as described above. As a control, freshly made complexes were used.

Cytotoxicity. Cells were plated at the same density as above at 24 h before the experiment. Medium was replaced by fresh 150 μL of serum-containing medium before the addition of complexes. Fifty microliters of complex solution was then added to each well and incubated at 48 h, 37 °C. Cytotoxicity assays (n = 4 experiments) were performed using standard CytoTox 96 Nonradioactive cytotoxicity assay (Promega, Madison, WI), i.e., a colorimetric method based on lactate dehydrogenase release (LDH). The absorbance at 490 nm was measured using a 96-well ELISA plate reader. The background absorbance was minimized using phenol red free cell growth media. Nontreated cells were used as controls. The percent cell death was calculated using the formula: % cytotoxicity = experimental LDH release (OD_{490})/maximum LDH release (OD_{490}).

Flow Cytometry. Various amounts of HD polymers in 0.25 M sucrose solution were added to the plasmid solution (1.5 μg of pCMV-GFP plasmid in 30 μL of 0.1 TE buffer (*32*), mixed, and incubated at room temperature for 30 min. Cells were plated at 40 000 cells/well in 12-well plates, 24 h prior to transfection. Before the addition of complexes, medium was replaced by fresh 800 μL of serum-containing medium. One hundred microliters of complex-containing solution was then added to each well. The total volume did not exceed 900 μL/well. After 4 h, the complete growth medium was replaced with the fresh serum-containing medium followed by another 48 h incubation. Cells were trypsinized and resuspended in 4% formalin−PBS solution for flow cytometry analysis (FACSCalibur, Beckton-Dickinson, Lexington, KY).

In Vivo CCD Camera Imaging of Luciferase Reporter Gene Expression. Hyperbranched polymers (HD4 and HD3) were used for complex formation with 50 μg of plasmid DNA at N/P 6.3 and 9.1, respectively, in 200 μL of 5% glucose containing 20 mM HEPES (pH 5.5). A complex with BPEI was obtained at N/P 6.3. The complexes were injected intravenously via the tail vein of 4−6 week old *nu*/*nu* mice. A negative control group of animals did not receive DNA injections. Animals (n= 3) were imaged for 7 d beginning at 1-day post iv injection. For imaging, animals were anesthetized ip using ketamine/xylazine. After anesthesia, the animals were injected ip with 200 μL of 4.5 mg/mL D-luciferin in saline. After 5 min, the animals were placed in the imaging chamber equipped with a CCD camera system (Roper Scientific, Trenton, NJ). A light image of the animal was obtained using polychromatic illumination. The luciferase activity within animal was then measured by recording the CCD photon counts for 15 min. Following data acquisition, postprocessing was performed using image display and analysis suite developed in IDL (Research Systems Inc., Boulder, CO). Regions of interest were defined using an automatic intensity contour procedure to identify bioluminescence signals with intensities significantly greater than the background. For visualization purposes, bioluminescence images were fused with the corresponding white light images in a transparent pseudocolor overlay, permitting correlation of areas of bioluminescence with the anatomy.

Ex Vivo Luciferase Activity. After the third day of imaging, HD4 complex-injected animals were sacrificed, and the major organs were harvested for luminescence analysis as in (*33*). The relative light measurements were normalized per organ weight. All results were reported as mean ± SEM.

Histology. Submandibular lymph nodes were dissected for histology 3 days postinjection. The tissue rinsed with PBS and frozen using Histo Prep (Fisher Scientific). Frozen sections (thickness, 6 μm) were cut and treated using anti- luciferase goat polyclonal antibody conjugated with horseradish peroxidase (AbCam, Cambridge MA) according to the manufacturer's protocol. The sections were counterstained using hematoxylin and eosin prior to mounting and microscopy.

RESULTS

Synthesis and Characterization. Hyperbranched PEI synthesis (Figure 1A) resulted in polymers that were characterized using ^{1}H and ^{13}C NMR (Figure 1B,C). Proton NMR spectra showed the characteristic 2.5−2.8 ppm peak due to the methylene group (CH_2) of the backbone (not shown). Since different amine substitutions could not be efficiently separated for quantitative analysis of ^{1}H NMR spectra, we used inversely gated decoupling pulse sequences to obtain ^{13}C spectra for quantitation (Figure 1B,C). All structural elements showed well-separated signals in the chemical shift range (37−58 ppm), peaks 1−8. Using the previously described (*34*, *35*) formula, we determined that commercially available branched BPEI has the ratio of secondary-to-tertiary amine of 1.17 (Table 1). The molecular mass of 9.5 kDa measured by GPC is in agreement with the 10 kDa value provided by the manufacturer. After the first round of reaction of HD polymer with 2-chloroethylamine, the molecular mass of the product increased to 11.7 kDa and PDI was 2.34 (HD2). The increase of molecular mass was due to the conjugation of approximately 50 ethyleneimine groups. In the case of dendron 3 (HD3, mol mass 13.7 kDa, PDI 2.32) and hyperbranched dendron 4 (HD4, mol mass 15 kDa, PDI 2.25), the number of ethyleneimine groups increased to 98 and 128, respectively. The final HD4 had the secondary-to-tertiary amine ration of 0.71. Since size exclusion chromatography (SEC) tends to underestimate the true molecular masses of branched polymers, the molecular masses measured in our studies (Table 1) were somewhat lower than the true molecular mass (*36*). Physical properties of the material changed from a liquidlike (low molecular weight branched PEI, BPEI) to a semisolid (HD4) at room temperature.

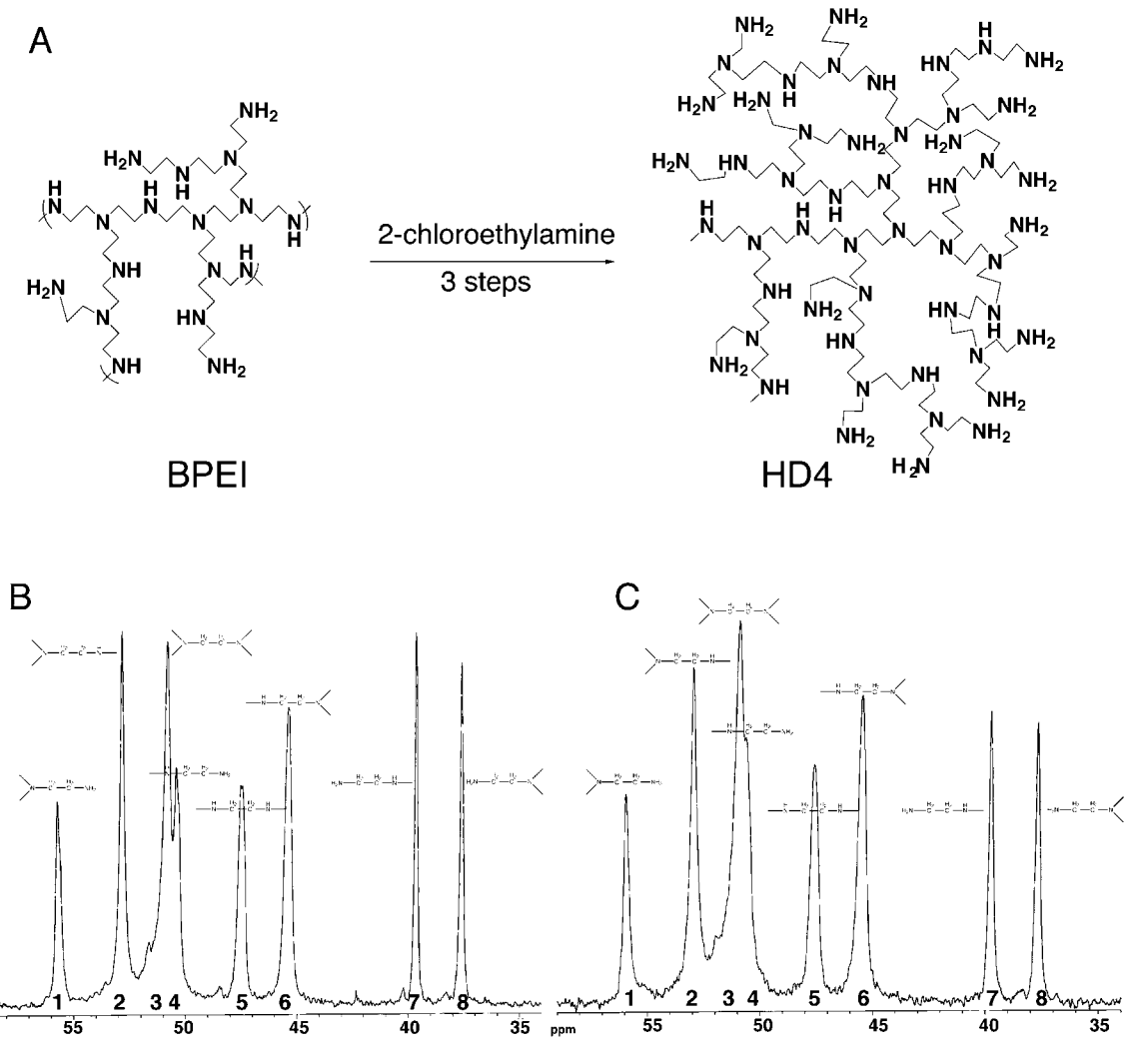


Figure 1. (A) A schematic representation of branched poly(ethyleneamine) BPEI and the hyperbranched dendron (HD4) obtained using consecutive aminoethylation of the core BPEI; (B) ^{13}C NMR spectrum of BPEI, (C) ^{13}C NMR spectrum of HD4. The spectra were analyzed as described in Results and Table 1.

Table 1. Properties of Branched Poly(ethyleneimine) and Hyperbranched Dendrons

polymer	MW[a] (KD)	PDI[b]	primary:secondary:tertiary amine[c]
BPEI	9.5	2.46	1.28:1.17:1
HD2	11.7	2.34	0.96:1.06:1
HD3	13.7	2.32	0.81:0.90:1
HD4	15	2.25	0.80:0.70:1

[a] MW = weight average molecular mass. GPC data was used for molecular mass determination. [b] PDI = polydispersity index. [c] Ratio of primary:secondary:tertiary amino groups calculated from ^{13}C NMR spectra.

Cytotoxicity. Figure 2 shows the cytotoxicity results obtained using branched PEI (BPEI) and synthesized hyperbranched dendrons. All cytotoxicity measurements were performed after 48 h of transfection with polymer−DNA complexes without medium changes. In all cases, the toxicity was low even after a 48-h incubation. For hyperbranched polymers in the moderate range of polymer concentrations (0.05 to 0.5 mg/mL), a maximum of 15% cell death was observed which is significantly lower than in the case of BPEI.

Complex Formation. The formation of complexes was monitored by fluorescence microscopy using ethidium bromide displacement method. At the N/P ratio of 2.30, the relative fluorescence decreased by approximately 50% for BPEI (Figure 3). In case of hyperbranched

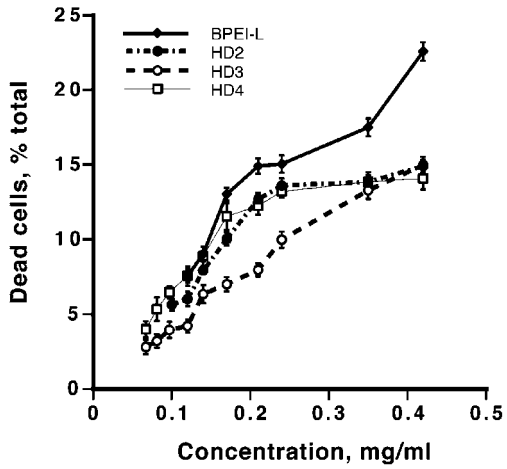


Figure 2. Polymer cytotoxicity measured in COS-1 cell culture as a function of concentration. Complexes were added to cells with growth medium and incubated for 48 h without changing the medium. Results represent the average of four independent experiments. Diamonds, BPEI; filled circles, HD2; open circles, HD3; squares, HD4.

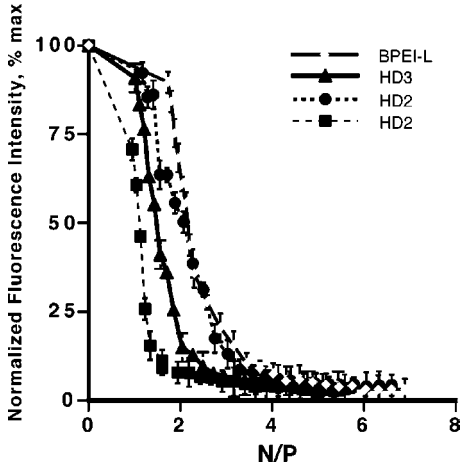


Figure 3. Ethidium bromide displacement from hyperbranched polymer−DNA complexes. The legend denotes complexes formed between BPEI (diamonds), HD4 (closed squares), HD3 (closed triangles), and HD2 (closed circles). The averages of three separate experiments are shown.

dendron 2 (HD2), the same 50% decrease was achieved at N/P of 2.27. In the case of hyperbranched dendron 3 (HD3) a 50% fluorescence intensity decrease was observed at the N/P of 1.70, and for hyperbranched dendron 4 (HD4) a similar decrease was observed at N/P ratio of 1.23 (Figure 3). To investigate the mobility of complexes, we studied the interaction between the positively charged polymers and the plasmid at the different charge ratio using electrophoresis. Figure 4 shows the migration of DNA complexes obtained using different hyperbranched polymers. The migration of DNA was partially retarded by branched BPEI at N/P 4.4, and at the higher N/P ratios there was no detectable migration of the complex. In the case of hyperbranched dendron, the partial retardation of the migration was observed at N/P 2.9, 2.6, and 1.8, respectively, for HD2, HD3, and HD4 complexes. The electrophoretic migration of complexes stored for 3 weeks at 4 °C was almost unchanged (data not shown).

In isotonic sucrose and glucose solutions the particle size of DNA−BPEI complexes at all N/P ratios ranged between 50 and 120 nm. A similar behavior was observed for all HD complexes (Figure 5A). For HD4 complexes, particle size showed an increase from 90 to 160 nm when N/P ratio was decreased from 18 to 1. In the case of HD3 complex, the lowest particle size was observed at N/P ratio of 9.1, otherwise it varied slightly at different N/P. Figure 5B shows the stability of the complexes measured for 3 weeks. In 150 mM NaCl solution complexes were not stable and usually coagulated within 3 h. In the case of 5% glucose with 20 mM HEPES, complexes were more stable and usually smaller (approximately 40−60 nm) than in isotonic sucrose solution (data not shown).

Transfection Efficiency. To examine the potential of hyperbranched polymer for gene transfer to cells, we compared the transfection efficiency of BPEI and HDs with the standard commercially available dendrimer-based reagent (Superfect, Qiagen, Valencia, CA). Superfect (fractured dendrimer) is a very efficient transfection agent, especially in absence of serum in the cell culture medium (*24*). Since our main objective was to investigate the potential of hyperbranched polymers for the future in vivo gene delivery, we performed all transfections using 10% serum-containing media. The transfection efficiency was evaluated by luciferase reporter gene assay. We used various N/P ratio for optimization of the transfection efficiency of hyperbranched polymer and Superfect. Hyperbranched dendron 4 (HD4) showed a very high transfection efficiency compared to other polymers in the presence of serum. When transfection efficiencies of the different HDs and branched polymers were compared, we found that HD4-mediated transfection was very high at N/P ∼9 while BPEI showed maximum transfection efficiency at N/P ratio of ∼33. Transfection efficiency of HD at 4 h in absence of serum was at least 1 order of magnitude higher than transfection in the presence of serum (data not shown). To obtain the further insight into the cytotoxicity effect and transfection efficiency, we carried out the transfection for 48 h without changing cell culture media. Figure 6A shows the optimized N/P ratios based on 48 h transfection. Our data suggested that even after a prolonged coincubation, the transfection efficiency was still 5−6-fold higher than in the case of Superfect. All HDs as well as the branched PEI (BPEI) had higher transfection efficiencies in the presence of serum than with positive control transfection agent. The 48 h transfection data suggested that for HD4 at N/P = 6.3 the highest transfection has been achieved, whereas for BPEI the best results were achieved at N/P = 23.4 (Figure 6A). Transfection efficiencies of freshly prepared complexes and complexes stored for 3 weeks were then compared (Figure 6B). A comparison of transfection efficiencies at the optimized N/P ratios after a conventional 4 h transfection demonstrated that freshly prepared complexes have lower transfection efficiency than those stored for 3 weeks. At 48 h time point, HD4 and HD3 showed the highest transfection efficiency at N/P = 13 whereas the transfection efficiencies reached the highest levels at N/P ∼23 and 19 for HD2 and BPEI, respectively (Figure 6B). In all cases prolonged storage of complexes in sucrose solution resulted in ∼8-fold higher transfection efficiencies.

Flow ytometry. To test the transfection efficacy of hyperbranched polymers in cells other than COS-1, we tested transfection efficiency in neuroprogenitor-derived C17.2 cells and human endothelial cell cultures. We used green fluorescent protein as a marker (Table 2). Both HD4 and HD3 were capable of transfecting 20−25% C17.2 and HUVEC cells compared to 40% cells in the case of COS-1.

In Vivo Gene Expression. To test the in vivo gene delivery efficacy we relied on long-term transfection results in selecting N/P ratios. In preliminary experiments we determined that HD4 and HD3 showed the highest transfection efficiency at N/P 6.3 and 9.1, respec-

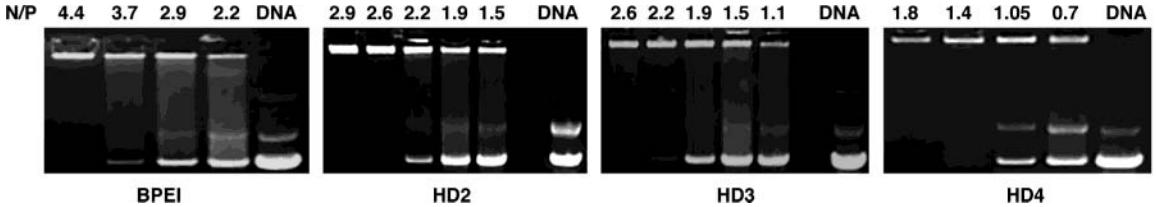


Figure 4. Agarose gel electrophoresis of pCMV−Luc plasmid complexes with BPEI HD2, HD3, and HD4 obtained at the different nitrogen-to-phosphate (N/P) ratios.

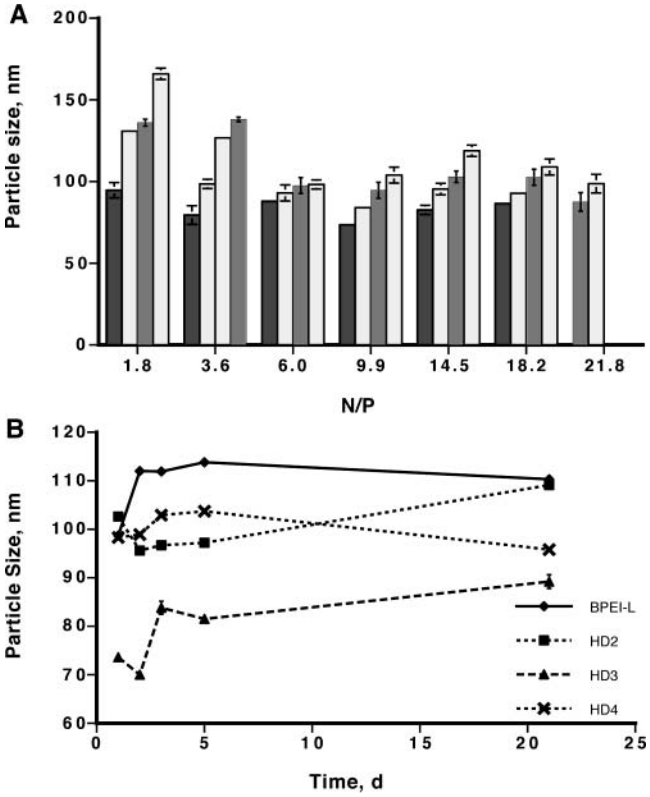


Figure 5. (A) Particle sizes of pCMV−Luc plasmid complexes prepared using HD4, HD3, HD2 and BPEI at different nitrogen-to-phosphate (N/P) ratios. (B) Variation of particle size with time. The legend denotes BPEI (diamonds) at N/P 21.83, HD4 (crosses) at N/P 6.03, HD3 (triangles) at N/P 9.9, and HD2 (squares) at N/P 18.18. Average sizes obtained in four experiments are shown.

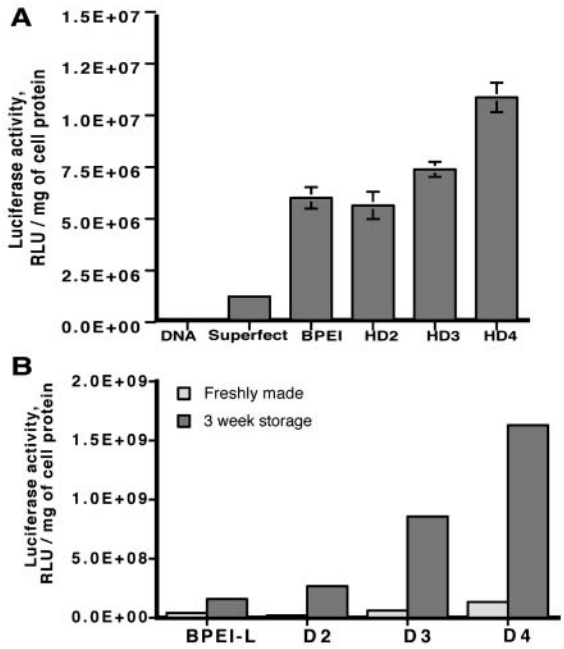


Figure 6. (A) In vitro luciferase expression in vitro after transfection using hyperbranched polymers, BPEI and Superfect. COS-1 were transfected by adding complexes in the presence of growth medium for 48 h. All results shown are the averages of three separate experiments obtained using complexes at the optimized N/P ratios. (B) In vitro luciferase activity in COS-1 cells transfected for 48 h using complexes that were either freshly prepared or stored for three weeks at 4 °C before use.

Table 2. Percent of Transfected Cells Measured Using Flow Cytometry

polymer[a]	COS-1[b]	C17.2[b]	HUVEC[b]
HD4	∼40	∼20−25	∼20−25
HD3	∼30−40	∼20−25	∼20−25

[a] Cells were transfected with pCMV-GFP -polymer complex as described in Materials and Methods. [b] Histograms were analyzed using CellQuest software (10 000 cells/analysis were used).

tively. These N/P ratios were chosen for preparing a complex with 50 μg of apyrogenic pCMV−Luc plasmid DNA in 20 mM HEPES/5% glucose solution. In the case of BPEI, we noticed that the complex prepared at the optimized N/P= 23 showed a profound toxicity after the injection. Since it is known that BPEI (molar mass 25 kDa) usually shows less toxicity and better transfection in animals at N/P 6−8 (*30*, *37*−*39*), in further animal experiments we selected N/P ratio of 6.3. Figure 7A shows the luciferase marker gene expression profile in vivo obtained by using noninvasive whole body bioluminescence imaging. We monitored the expression profile in the same group of animals repeatedly for 7 days. As pseudo-color maps demonstrate, gene expression was the highest in the case of HD4 complex. The major "hot spots" of luciferase expression were found in the liver and neck, as well as in the submandibular lymph node region. BPEI-based complex and "naked" DNA alone showed a much lower expression profile than hyperbranched dendron-based complexes. Figure 7B shows the change of photon counts over a period of 7 days. Both HD4 and HD3 showed the highest photon counts at 3−5 days either around the liver or in the neck regions. Figure 7C shows the luciferase assay performed in animals injected with the HD4-based complex. Luminescence measured over liver and lymph node regions showed a correlation with the gene expression profile obtained by luminescence imaging. Other organs did not show any measurable luciferase activity. Histology of lymph node frozen sections showed many immunoperoxidase-positive cells located on the periphery of lymph nodes, mainly around the follicle area (Figure 7D, image 1). The positive cells were absent in lymph nodes of control animals or in animals injected with plasmid DNA only (Figure 7D, image 2).

DISCUSSION

The compaction of DNA by positively charged molecules (e.g. polymers or lipids) into nanosized particles plays a crucial role for achieving high transfection efficiencies. Unfortunately, most of the polymer vectors reported so far are efficient mainly for in vitro cell transfection because of the inhibitive effects of serum and/or high in vivo toxicity. To reduce toxicity, several groups achieved limited success by using derivatization of polycations with poly (ethylene glycol) resulting in vectors with low cytotoxicity but also with lower transfection efficacy (*27*, *40*).

We hypothesized that the optimization of the balance between the cationic charge density of the polymer vector and phosphate groups of the DNA could potentially result in efficient DNA compaction and low cytotoxicity. We synthesized novel flexible hyperbranched polymers (dendrons, HD) by controlling branching of the initial PEI core polymers. Although hyperbranched dendrons and dendrimers are similar in that both are branched, other structural aspects are quite dissimilar (Figure 1). During HD synthesis, 2-chloroethylamine reacts with primary or secondary amines of the PEI core, resulting in a

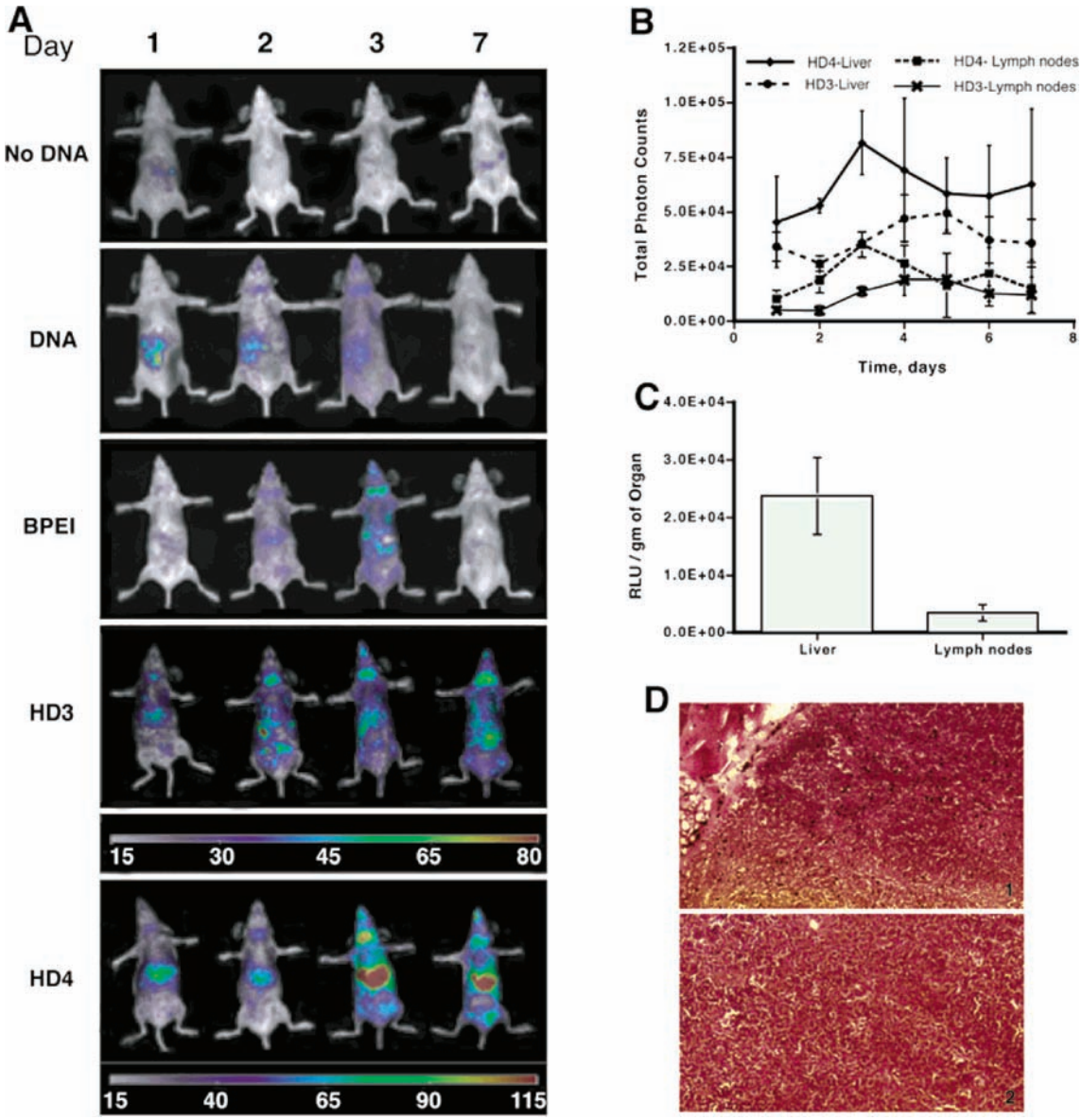


Figure 7. (A) Bioluminescence imaging of luciferase expression in living mice using a CCD camera performed at the time intervals indicated above the images. The image shows the best representative of the group ($n = 3$). Fifty micrograms pCMV−Luc was used for iv injections in all cases. All images were taken for 15 min and shown using two pseudocolor scales: one for HD4 and other for rest of the groups. (B) The change of the total photon counts integrated for 15 min imaging over 7 days in the case of HD4 and HD3 groups. The photon counts are averaged for three animals. Data presented as mean ± SD. (C) Ex vivo luciferase activity of lymph nodes and livers of animals injected with HD4-based complex. The results are presented as mean ± SD ($n = 3$). (D) Immunohistology of lymph nodes after the administration of HD4/DNA complex (image 1) or naked DNA (image 2) intravenously. Fifty micrograms of DNA was used to prepare complexes at N/P 6.3. Animals were sacrificed 3 days after injection. Polyclonal goat anti-luciferase antibody−peroxidase conjugate was used to identify luciferase-positive cells followed by a hematoxylin/eosin counterstaining. Brown dots (image 1) represent luciferase-positive cells. Magnification, 30-fold.

random, treelike branched structure. As demonstrated previously, the reactivity of the chain end of a dendrimer is higher than the chain end reactivity of a hyperbranched polymer (*41*). To increase the rate of reaction between the functional end groups and chloroethylamine, we used a large excess of 2-chloroethylamine in alkaline conditions (*42*). The excess of 2-chloroethylamine or its cyclic byproduct (*43*, *44*) was removed later using ultrafiltration.

It is known that that highly branched, commercially available PEI with the high molar mass ranging from 25 kDa to 800 kDa have tertiary-to-secondary amine ratio of less than 0.75 (*35*). The above ratio measured in hyperbranched dendrons suggested that successive aminoethylation resulted in an increase of branching order (Table 1). Thus, the increased branching enables the incorporation of more secondary and tertiary amino groups than initially present in commercially available PEI core polymers. In HD4 this ratio is 2 times higher than in BPEI.

Partially hydrolyzed (∼53%) linear PEI (LPEI) has a lower toxicity than BPEI because of the high content of tertiary amines present in the backbone of LPEI (*45*). Therefore, we expected that the increase in branching, i.e., the increase of tertiary amine content, could result in a reduction of cytoxicity. In our experiments, hyperbranched polymers (HD2 to HD4) showed low toxicity (10% cell death, Figure 2). Better survival of cells in the presence of HD could be a result of a high secondary and tertiary amine content of HD polymer.

We further hypothesized that flexible architecture of HD polymers enables efficient condensation of plasmid

DNA (*46*). We found that the increase of ethyleneimine content in HD resulted in similar titration behavior of HDs in ethidium bromide displacement experiments with the exception of the position of the neutralizing point (Figure 3). Therefore, at any specific fixed concentration, different "generations" of HDs had different surface charges because of the branching order variations. This resulted in a measurable change of N/P ratio corresponding to a half-maximal displacement of ethidium bromide since more ethyleneimine moieties were present in HD than in BPEI. The hydrodynamic diameter of the complexes was approximately 100 nm and, in contrast to BPEI, the diameter increased at a much slower rate or remained almost constant over long periods of time (Figure 5). These results were relevant for further transfection experiments suggesting that the HD−DNA complex could tolerate the presence of serum proteins. This was not the case if a high molecular mass PEI was used in the presence of the serum (*22*).

It has been reported before that branched cationic polymers transfect cells because of the high buffering capacity of the amines present on these polymers, which leads to the release of DNA from the endosome (*16*, *22*, *47*). Such agents have been observed to induce osmotic swelling and lysis in response to the endosomal local pH drop (*48*). Hyperbranched dendrons contain all three different types of amine nitrogen, allowing the polymer to collapse, or to swell, depending on the magnitude of local pH change. This could explain the observation of a higher transfection efficiency of HD4 at low N/P ratios compared to a less branched core BPEI (Figure 6).

Since the complex of HD with plasmid vectors showed exceptional stability during storage, we decided to test whether during storage the complex retains the ability to transfect cells (Figure 6). Our results suggest that that the "aged" complex attains a more compact structure (*49*) which could help in preserving its transfection efficacy. Previous research suggested that DNA−carrier interactions can strengthen with time. For example, it is known that a time-dependent maturation process of lipid−DNA results in increased serum resistance (*49*, *50*). It is possible that during the storage, HD chains, due to segmental flexibility, could achieve strong multipoint interaction with negatively charged DNA, resulting in particles that are more compact (hydrodynamic diameter was approximately 10 nm lower than that of the complex formed immediately). A more compact structure would yield better stability in serum-containing medium, resulting in more efficient transfection.

Finally, we addressed the question whether stable complexes of plasmids with HD polymers would be efficient in gene transfer in vivo. Previously, in vivo bioluminescent imaging was used to detect gene expression after nonviral gene delivery (*51*). In our experiments, seven consecutive days of luciferase imaging suggested that HD4 could induce a prolonged gene expression, which reaches a maximum at 72 h in the liver and lymph nodes (Figure 7). Both HD4 and HD3 appear to be more efficient than either BPEI or "naked" DNA. Since complexes with HD bear a weak positive charge (zeta potential of HD4 complex at N/P $\sim$ 6.3 is 6.9 mV), we expected less interaction with blood components and lung endothelium. Indeed, we observed low expression of luciferase in the lung. Correlative luciferase activity measurements in tissue extracts (Figure 7C) and immunohistology pointed to expression of luciferase in the lymph node cells, with the majority of positive cells located on the periphery and around germinal centers (Figure 7D). The distribution of positive cells in the tissue argues for the ability of HD-based complexes to transfect organs located at the sites distant to the injection site, presumably because of the small size and weak positive charge.

In conclusion, we demonstrated that it is feasible to "tune" the molecular structure of PEI by attaching additional secondary and tertiary amino groups to commercially available ethyleneimine core. The "tuning" results in a substantial increase of transfection efficacy with the concomitant lower cytotoxicity in vitro. The advantage of HD polymers as gene delivery carriers are (1) the high transfection efficiency at low N/P ratios, (2) the formation of small stable complexes with DNA, (3) the tolerance of serum, and (4) overall low toxicity at the transfection conditions, as the amounts of HD needed to achieve high transfection efficiency were low. Finally, our preliminary in vivo studies suggested that HD-based complexes have a potential for transfection of lymph node cells in vivo.

ACKNOWLEDGMENT

This study was supported in part by NIH grant P50 CA86355. W.R. received support from German National Academy Foundation (Studienstiftung).

LITERATURE CITED

(1) Felgner, P. L. (1997) Nonviral strategies for gene therapy. *Sci. Am. 276*, 102−106.

(2) Felgner, P. L. (1998) DNA vaccines. *Curr. Biol. 8*, R551−R553.

(3) Ghosh, S. S., Takahashi, M., Thummala, N. R., Parashar, B., Chowdhury, N. R., and Chowdhury, J. R. (2000) Liver-directed gene therapy: promises, problems and prospects at the turn of the century. *J. Hepatol. 32*, 238−252.

(4) Sandhu, J. S., Keating, A., and Hozumi, N. (1997) Human gene therapy. *Crit. Rev. Biotechnol. 17*, 307−326.

(5) Wolff, J. A. (1997) Naked DNA transport and expression in mammalian cells. *Neuromusc. Disord. 7*, 314−318.

(6) Mahato, R. I. (1999) Nonviral peptide-based approaches to gene delivery. *J Drug Target. 7*, 249−68.

(7) Zauner, W., Ogris, M., and Wagner, E. (1998) Polylysine-based transfection systems utilizing receptor- mediated delivery. *Adv. Drug Delivery Rev. 30*, 97−113.

(8) Wagner, E., Cotten, M., Foisner, R., and Birnstiel, M. L. (1991) Transferrin Polycation DNA Complexes − the Effect of Polycations on the Structure of the Complex and DNA Delivery to Cells. *Proc. Natl. Acad. Sci. U.S.A. 88*, 4255−4259.

(9) Zhou, X., and Huang, L. (1994) DNA transfection mediated by cationic liposomes containing lipopolylysine: characterization and mechanism of action. *Biochim. Biophys. Acta 1189*, 195−203.

(10) Wolfert, M. A., Schacht, E. H., Toncheva, V., Ulbrich, K., Nazarova, O., and Seymour, L. W. (1996) Characterization of vectors for gene therapy formed by self- assembly of DNA with synthetic block copolymers. *Hum. Gene Ther. 7*, 2123−2133.

(11) Nguyen, H. K., Lemieux, P., Vinogradov, S. V., Gebhart, C. L., Guerin, N., Paradis, G., Bronich, T. K., Alakhov, V. Y., and Kabanov, A. V. (2000) Evaluation of polyether-polyethyleneimine graft copolymers as gene transfer agents. *Gene Ther. 7*, 126−138.

(12) Rolland, A., and Felgner, P. L. (1998) Nonviral gene delivery systems − Preface. *Adv. Drug Delivery Rev. 30*, 1−3.

(13) Pelta, J., Livolant, F., and Sikorav, J. L. (1996) DNA aggregation induced by polyamines and cobalthexamine. *J. Biol. Chem. 271*, 5656−62.

(14) Radler, J. O., Koltover, I., Salditt, T., and Safinya, C. R. (1997) Structure of DNA-cationic liposome complexes: DNA intercalation in multilamellar membranes in distinct interhelical packing regimes. *Science 275*, 810−814.

(15) Dunlap, D. D., Maggi, A., Soria, M. R., and Monaco, L. (1997) Nanoscopic structure of DNA condensed for gene delivery. *Nucleic Acids Res. 25*, 3095−3101.
(16) Haensler, J., and Szoka, F. C. (1993) Polyamidoamine Cascade Polymers Mediate Efficient Transfection of Cells in Culture. *Bioconjugate Chem. 4*, 372−379.
(17) Ohsaki, M., Okuda, T., Wada, A., Hirayama, T., Niidome, T., and Aoyagi, H. (2002) In vitro gene Transfection using dendritic poly(L-lysine). *Bioconjugate Chem. 13*, 510−517.
(18) KukowskaLatallo, J. F., Bielinska, A. U., Johnson, J., Spindler, R., Tomalia, D. A., and Baker, J. R. (1996) Efficient transfer of genetic material into mammalian cells using Starburst polyamidoamine dendrimers. *Proc. Natl. Acad. Sci. U.S.A. 93*, 4897−4902.
(19) Choi, J. S., Joo, D. K., Kim, C. H., Kim, K., and Park, J. S. (2000) Synthesis of a barbell-like triblock copolymer, poly(L-lysine) dendrimer-*block*-poly(ethylene glycol)-*block*-poly(L-lysine) dendrimer, and its self-assembly with plasmid DNA. *J. Am. Chem. Soc. 122*, 474−480.
(20) Lim, Y. B., Kim, S. M., Lee, Y., Lee, W. K., Yang, T. G., Lee, M. J., Suh, H., and Park, J. S. (2001) Cationic hyperbranched poly(amino ester): A novel class of DNA condensing molecule with cationic surface, biodegradable three- dimensional structure, and tertiary amine groups in the interior. *J. Am. Chem. Soc. 123*, 2460−2461.
(21) Lim, Y. B., Kim, S. M., Suh, H., and Park, J. S. (2002) Biodegradable, endosome disruptive, and cationic network-type polymer as a highly efficient and nontoxic gene delivery carrier. *Bioconjugate Chem. 13*, 952−957.
(22) Boussif, O., Zanta, M. A., and Behr, J. P. (1996) Optimized galenics improve in vitro gene transfer with cationic molecules up to 1000-fold. *Gene Ther. 3*, 1074−1080.
(23) Godbey, W. T., Wu, K. K., and Mikos, A. G. (1999) Tracking the intracellular path of poly(ethylenimine)/DNA complexes for gene delivery. *Proc. Natl. Acad. Sci. U.S.A. 96*, 5177−5181.
(24) Tang, M. X., Redemann, C. T., and Szoka, F. C. (1996) In vitro gene delivery by degraded polyamidoamine dendrimers. *Bioconjugate Chem. 7*, 703−714.
(25) Fischer, D., Bieber, T., Li, Y. X., Elsasser, H. P., and Kissel, T. (1999) A novel nonviral vector for DNA delivery based on low molecular weight, branched polyethylenimine: Effect of molecular weight on transfection efficiency and cytotoxicity. *Pharm. Res. 16*, 1273−1279.
(26) Godbey, W. T., Wu, K. K., and Mikos, A. G. (1999) Poly-(ethylenimine) and its role in gene delivery. *J. Controlled Release 60*, 149−160.
(27) Petersen, H., Fechner, P. M., Martin, A. L., Kunath, K., Stolnik, S., Roberts, C. J., Fischer, D., Davies, M. C., and Kissel, T. (2002) Polyethylenimine-graft-poly(ethylene glycol) copolymers: Influence of copolymer block structure on DNA complexation and biological activities as gene delivery system. *Bioconjugate Chem. 13*, 845−854.
(28) Ferrari, S., Moro, E., Pettenazzo, A., Behr, J. P., Zacchello, F., and Scarpa, M. (1997) ExGen 500 is an efficient vector for gene delivery to lung epithelial cells in vitro and in vivo. *Gene Ther. 4*, 1100−1106.
(29) Goula, D., Remy, J. S., Erbacher, P., Wasowicz, M., Levi, G., Abdallah, B., and Demeneix, B. A. (1998) Size, diffusibility and transfection performance of linear PEI/DNA complexes in the mouse central nervous system. *Gene Ther. 5*, 712−717.
(30) Goula, D., Benoist, C., Mantero, S., Merlo, G., Levi, G., and Demeneix, B. A. (1998) Polyethylenimine-based intravenous delivery of transgenes to mouse lung. *Gene Ther. 5*, 1291−1295.
(31) Snyder, E. Y., Deitcher, D. L., Walsh, C., Arnoldaldea, S., Hartwieg, E. A., and Cepko, C. L. (1992) Multipotent Neural Cell-Lines Can Engraft and Participate in Development of Mouse Cerebellum. *Cell 68*, 33−51.
(32) Simonova, M., Weissleder, R., Sergeyev, N., Vilissova, N., and Bogdanov, A., Jr. (1999) Targeting of green fluorescent protein expression to the cell surface. *Biochem. Biophys. Res. Commun. 262*, 638−42.
(33) Manthorpe, M., Cornefert-Jensen, F., Hartikka, J., Felgner, J., Rundell, A., Margalith, M., and Dwarki, V. (1993) Gene therapy by intramuscular injection of plasmid DNA: studies on firefly luciferase gene expression in mice. *Hum. Gene Ther. 4*, 419−31.
(34) Pierre, T. S., and Geckle, M. (1985) C-13-Nmr Analysis of Branched Polyethyleneimine. *J. Macromol. Sci.-Chem., A22* 877−887.
(35) von Harpe, A., Petersen, H., Li, Y. X., and Kissel, T. (2000) Characterization of commercially available and synthesized polyethylenimines for gene delivery. *J. Controlled Release 69*, 309−322.
(36) Flory, P. J. (1953) *Principles of polymer chemistry*, Cornell University Press, Ithaca.
(37) Bragonzi, A., Dina, G., Villa, A., Calori, G., Biffi, A., Bordignon, C., Assael, B. M., and Conese, M. (2000) Biodistribution and transgene expression with nonviral cationic vector/DNA complexes in the lungs. *Gene Ther. 7*, 1753−60.
(38) Kircheis, R., Schuller, S., Brunner, S., Ogris, M., Heider, K. H., Zauner, W., and Wagner, E. (1999) Polycation-based DNA complexes for tumor-targeted gene delivery in vivo. *J. Gene Med. 1*, 111−20.
(39) Wightman, L., Kircheis, R., Rossler, V., Carotta, S., Ruzicka, R., Kursa, M., and Wagner, E. (2001) Different behavior of branched and linear polyethylenimine for gene delivery in vitro and in vivo. *J. Gene Med. 3* 362−72.
(40) Petersen, H., Kunath, K., Martin, A. L., Stolnik, S., Roberts, C. J., Davies, M. C., and Kissel, T. (2002) Star-shaped poly(ethylene glycol)-*block*-polyethylenimine copolymers enhance DNA condensation of low molecular weight polyethylenimines. *Biomacromolecules 3*, 926−936.
(41) Frechet, J. M. J., Hawker, C. J., and Wooley, K. L. (1994) The Convergent Route to Globular Dendritic Macromolecules − a Versatile Approach to Precisely Functionalized 3-Dimensional Polymers Amd Novel Block-Copolymers. *J. Macromol. Sci.-Pure Appl. Chem. A31*, 1627−1645.
(42) Kuo, P. L., Ghosh, S. K., Liang, W. J., and Hsieh, Y. T. (2001) Hyperbranched polyethyleneimine architecture onto poly(allylamine) by simple synthetic approach and the chelating characters. *J. Polym. Sci. Pol. Chem. 39*, 3018−3023.
(43) Detar, D. F., and Brooks, W. (1978) Cyclization and Polymerization of Omega- (Bromoalkyl)Dimethylamines. *J. Org. Chem. 43*, 2245−2248.
(44) Detar, D. F., and Luthra, N. P. (1980) Quantitative-Evaluation of Steric Effects in Sn2 Ring-Closure Reactions. *J. Am. Chem. Soc. 102*, 4505−4512.
(45) Jeong, J. H., Song, S. H., Lim, D. W., Lee, H., and Park, T. G. (2001) DNA transfection using linear poly(ethylenimine) prepared by controlled acid hydrolysis of poly(2-ethyl-2-oxazoline). *J. Controlled Release 73*, 391−399.
(46) Bielinska, A. U., KukowskaLatallo, J. F., and Baker, J. R. (1997) The interaction of plasmid DNA with polyamidoamine dendrimers: mechanism of complex formation and analysis of alterations induced in nuclease sensitivity and transcriptional activity of the complexed DNA. *Biochim. Biophys. Acta-Gene Struct. Expression 1353*, 180−190.
(47) Boussif, O., Lezoualch, F., Zanta, M. A., Mergny, M. D., Scherman, D., Demeneix, B., and Behr, J. P. (1995) A Versatile Vector for Gene and Oligonucleotide Transfer into Cells in Culture and in-Vivo − Polyethylenimine. *Proc. Natl. Acad. Sci. U.S.A. 92*, 7297−7301.
(48) Raczka, E., Kukowska-Latallo, J. F., Rymaszewski, M., Chen, C., and Baker, J. R. (1998) The effect of synthetic surfactant Exosurf on gene transfer in mouse lung in vivo. *Gene Ther. 5*, 1333−1339.
(49) Cherng, J. Y., Talsma, H., Crommelin, D. J., and Hennink, W. E. (1999) Long-term stability of poly((2-dimethylamino)-ethyl methacrylate)-based gene delivery systems. *Pharm. Res. 16*, 1417−23.
(50) Yang, J. P., and Huang, L. (1998) Time-dependent maturation of cationic liposome-DNA complex for serum resistance. *Gene Ther. 5*, 380−7.
(51) Hildebrandt, I. J., Iyer, M., Wagner, E., and Gambhir, S. S. (2003) Optical imaging of transferrin targeted PEI/DNA complexes in living subjects. *Gene Ther. 10*, 758−64.

BC0342128

Targeted Protein Functionalization Using His-Tags

Gavin D. Meredith,*,† Hayley Y. Wu, and Nancy L. Allbritton*

Department of Physiology & Biophysics, University of California - Irvine, Irvine, California 92697-4560
Received May 1, 2004; Revised Manuscript Received July 6, 2004

With the impressive growth in gene sequence data that has become available, recombinant proteins represent an increasingly vast source of molecular components, with unique functional and structural properties, for use in biotechnological applications and devices. To facilitate the use, manipulation, and integration of such molecules into devices, a controllable method for their chemical modification was developed. In this approach, a trifunctional labeling reagent first recognizes and binds a His-tag on the target protein's surface. After binding, a photoreactive group on the trifunctional molecule is triggered to create a covalent linkage between the reagent and the target protein. The third moiety on the labeling reagent can be varied to bring unique chemical functionality to the target protein. This approach provides: (1) specificity in that only His-tagged targets are modified, (2) regio-specific control in that the target is modified proximal to the His-tag, the position of which can be varied, and (3) stoichiometric control in that the number modifications is limited by the binding capacity of the His-tag. Two such labeling reagents were designed, synthesized, and used to modify both N- and C-terminally His-tagged versions of the enzyme murine dihydrofolate reductase (mDHFR). The first reagent biotinylated the enzyme,while the second served to attach an oligonucleotide to yield a protein−DNA conjugate. In all cases, modification in this manner brings new functionality to the protein while leaving the enzymatic activity intact. The protein−DNA conjugate was used to specifically immobilize the active enzyme through DNA hybridization onto polystyrene microspheres, a step toward creating a functional protein microarray.

INTRODUCTION

Reagents and methods to selectively chemically modify proteins are becoming increasingly important for the study and utilization of protein functions and interactions, particularly due to the explosive growth in our knowledge of protein sequences from genome sequencing efforts and the drive to conduct proteomic research. Robust technologies for the rational chemical modification of proteins are needed for subsequent immobilization to create protein arrays for screening of function and interactions. The chemical attachment of prosthetic groups is also important for the creation of new protein-based biosensors and reporter molecules for life science research, biodetection assays, and therapeutics. Looking further ahead, controllable modification of proteins should help to foster a new era in biomaterials design and manufacture and semi-synthetic molecular engineering.

In general, when chemically modifying a protein, the goal is to introduce novel chemical functionality while preserving its native function and properties. Ideally, one would be able to covalently attach a precise number of unique chemical groups to one or more specific locations on the surface of any target protein in solution. This would provide maximal versatility and control over subsequent handling of the target while minimizing the likelihood of disrupting its native function. It is also important that the approach integrate with established technologies for recombinant protein production. Currently, the most general approach is to use electrophilic reagents that can react with nucleophilic groups on the surface of a target protein; however, this approach tends to yield a heterogeneous mixture of products since almost all proteins carry a number of nucleophilic groups on their surfaces. The thiol side-chain of cysteine is the most nucleophilic group that naturally occurs on a protein's surface and thiol-specific modifying reagents are numerous. Hence, to date, the best approach to engineer a site for selective chemical modification into a protein has been to genetically introduce a non-native cysteine at the desired site. After production and purification, the recombinant protein is covalently modified through thiol-specific chemistry. This approach is often successful, but can fail for a number of reasons. Foremost, the number and positions of native cysteines can be vitally important for the structural or functional integrity of many proteins; insertion of a non-native cysteine or removal of native cysteine can lead to misfolding or loss of function. Similarly, inappropriately modified native cysteines can lead to protein inactivation. This is particularly likely for enzymes that utilize a cysteine in their active site, including cysteine-based oxidoreductases, dehydrogenases, proteases, and some metal-binding proteins (*1*). Similar difficulties can arise from methods that rely on reaction between a terminal cysteine and a terminal thioester as typified by the native chemical ligation and expressed protein ligation approaches (*2*, *3*). In general, the site of modification by these elegant methods is restricted to a protein terminus; however, there are examples where multistep syntheses have permitted the introduction of modifications at internal positions (*4*, *5*). Oxidation-mediated protein labeling is also generally restricted to the termini (*6*−*8*). Another strategy to engineer sites for specific chemical modification in pro-

* Corresponding authors. G.D.M.: phone (760) 476-6127; fax (508) 546-7742; e-mail Gavin.Meredith@invitrogen.com. N.L.A.: phone (949) 824-6493; fax (949) 824-8540; e-mail nlallbri@uci.edu.

† Current Address: Invitrogen Corporation, 1600 Faraday Avenue, Carlsbad, CA 92008.

10.1021/bc0498929 CCC: $27.50 © 2004 American Chemical Society
Published on Web 08/10/2004

teins has been to develop expression systems that allow for the incorporation of unnatural amino acids that can serve as unique targets for covalent modification; however, these strategies have yet to prove widely applicable (*9*−*11*).

An alternative strategy to alter a protein's surface chemistry involves introducing unique non-native stretches of amino acids into a recombinant protein's native sequence (*12*). Such stretches of amino acids serve as integral "tags" that provide novel chemical functionality or can serve as targets for molecular recognition. A number of such tags have been described; they have been used principally for noncovalent immobilization or to allow antibody recognition. One notable exception has been the development of a tag that can serve as the target for novel biarsenical labeling reagents (*13*). Another genetic-engineering based approach is to link the sequence of two (or more) protein domains to yield novel recombinant "fusion" or "chimeric" proteins. In general, such tags have not provided a means for further covalent modification; however, recently a specific 207-amino-acid fusion tag has been developed that can serve as a site for selective covalent modification (*14*, *15*).

In protein research, the most versatile and widely used genetically encoded tag is the "polyhistidine" or "His-tag", which typically consists of a string of 2−6 consecutive histidine residues (*16*, *17*). Introduction of a His-tag at either the N- or C-terminus of a recombinant protein was first described as a convenient and generally nonperturbative means to facilitate purification of recombinant protein by immobilized metal-affinity chromatography. Functional His-tags can also be placed internally within the sequence of recombinant proteins, their sequences can be varied to include nonhistidine residues, and they can even take the form of engineered histidine "patches", consisting of histidines that are close in space though not in sequence within a folded protein structure (*18*−*23*). Immobilization takes place through coordination of two or more of the histidine residues with a metal ion (usually Ni(II)) that is incompletely coordinated by a substrate-attached chelating group such as nitrilotriacetic acid (NTA). Since its introduction, variants of this basic molecular recognition technology have been developed and utilized for a number of applications beyond protein purification; examples include sensitive target protein detection, protein structure studies, and protein immobilization for binding studies using surface plasmon resonance or atomic force microscopy (*24*−*28*). Since in its simplest form, as either an N- or C-terminal extension, the His-tag can be easily incorporated into expression vectors, genome-scale expression libraries of His-tagged proteins have been generated (*29*−*33*). In a groundbreaking study by Snyder and co-workers, 5800 different His-tagged yeast proteins, corresponding to about 80% of the yeast proteome, were expressed, purified, and arrayed on nickel-coated glass slides for subsequent probing (*32*). While this noncovalent immobilization served the purposes of the investigators, we reason that such arrays could be made more robust if the His-tag could serve as the target for covalent surface attachment. One solid-phase based approach to such affinity-directed covalent capture has been reported by Guisan and colleagues where His-tagged proteins have been bonded to chromatography resins that simultaneously carry metal-chelating groups and reactive epoxide groups (*34*).

We envision a broader use of the His-tag as a unique affinity target to direct proximal covalent bonding to a recombinant protein in solution. Solution-phase chemical modification is important to allow subsequent handling of the modified proteins and is required for the creation of protein-based reagents such as soluble therapeutic antibody−enzyme conjugates used in antibody-directed enzyme prodrug therapy (*35*). We judge the His-tag to have the best ensemble of features since as noted it is small relative to the size of most proteins of interest, it is generally nondisruptive to its host protein's structure and function, it can be placed at either terminus and even internally within its host's sequence, and it is widely used, particularly in the construction of expression libraries. Similar reasoning has led others to use the His-tag as a solution-phase target for the noncovalent tethering of bifunctional NTA-containing conjugates to protein (*36*, *37*). To direct covalent modification in solution, we have synthesized two different water-soluble trifunctional molecules based on shared design principles.

Ultimately, we envision this as a step toward the creation of encoded libraries of proteins (*38*) and a competitive technology for the creation of self-assembling protein arrays, engineered protein-containing molecular assemblies and nanostructures, and the integration of proteins into devices such as biosensors.

EXPERIMENTAL PROCEDURES

Instrumentation. The following instrumentation was used: an Agilent (Palo Alto, CA) 1050 and an 1100 HPLC system, each equipped with quartenary gradient pump, UV absorbance detector, fluorescence detector, and Chemstation software, a Cary 20 UV/vis absorbance spectrophotometer with kinetics software (Varian, Palo Alto, CA), a PerSeptive Voyager STR-DE Biospectrometry matrix-assisted laser deionization time-of-flight (MALDI-TOF) mass spectrometer (Applied Biosystems, Foster City, CA), a Micromass LCT electrospray ionization mass spectrometer (Waters Corp., Milford, MA), a DRX-500 nuclear magnetic resonance spectrometer (Bruker Biospin, Rheinstetten, Germany), a Perseptive Cytofluor 4000 microplate reader (Applied Biosystems), a Rotavaporator R-200 (Büchi, Flawil, Switzerland) with vacuum pump (Fisher Scientific, Hampton, NH), a Blak-ray B-100AP handheld long-UV lamp, a French-press, a Beckman preparative J-21 centrifuge (Beckman Coulter, Fullerton, CA), a Sorvall ultracentrifuge and tabletop low-speed centrifuge (Kendro, Asheville, NC), a tabletop 5415C microcentrifuge (Eppendorf AG, Hamburg, Germany), a mini-Protean II gel apparatus with Powerpac 300 power supply (Bio-Rad, Hercules, CA), and a Milli-Q water purification system (Millipore, Billerica, MA). The following columns were used: 250 × 4.60 mm Jupiter C4 packed with 5 μm beads, 250 × 10 mm Jupiter C4 packed with 15 μm beads, 250 × 4.60 mm Jupiter C18 packed with 5 μm beads, and a 250 × 10 mm Jupiter C18 packed with 10 μm beads with a 50 × 10 mm guard column. All Jupiter columns had 300 Å pores and were from Phenomenex (Torrance, CA). Also used: a 4.6 × 250 mm Zorbax GF-250 column with 4 μm beads (Agilent) and a HiPrep 16/60 Sephacryl S-100 HR column (Amersham Biosciences, Buckinghamshire, England).

Materials. DHFR expression plasmids, *Escherichia coli* host strains, Ni-NTA resins, and DAPase were all obtained from Qiagen (Valencia, CA). Bacterial culture media, IPTG, and ampicillin came from USBiological (Swampscott, MA). Buffers, salts, chemicals, biochemicals, and solvents were obtained from Sigma-Aldrich (St. Louis, MO) unless otherwise noted. Herring sperm DNA was from Promega (Madison, WI). HPLC solvents and methanol were purchased from EM Sciences (Hatfield, PA). *N*-(5-amino-1-carboxypentyl)iminodiacetic acid (NTA-

amine) came from Toronto Research Chemicals (North York, On., Canada). Sulfo-SBED, monomeric avidin, D-biotin, Immunopure HABA, Coomassie protein assay reagent, Gelcode Blue stain, and Gelcode SilverSNAP stain were from Pierce Chemical (Rockford, IL). β-Maleimido-proprionic acid was purchased from Molecular Biosciences (Boulder, CO). SPOS resin, PyBOP, and HOBt were from NovaBiochem (EMD Biosciences, San Diego, CA). Fmoc-Bpa-OH was purchased from Bachem (Bubendorf, Switzerland). NAP-10 gel filtration columns were from Amersham. Centricon Plus-20 PLGC devices and ZipTips came from Millipore. Precast minigels and protein electrophoresis standards were from Bio-Rad. Polymeric microspheres were from Polysciences (Warrington, PA). DNA-bind plates were from Corning (Corning, NY). Plastic, untreated, flat-bottom 96-well plates were from Nalge Nunc (Rochester, NY).

The following synthetic modified oligonucleotides were obtained from Integrated DNA Technologies (Coralville, IA); all linkers were C_6-type. Modifications included 5′-terminal thiol (SH-) groups, 5′-terminal amine (NH_2-) groups, 3′-terminal biotin, and terminal carboxyfluorescein (FAM) or hexachlorofluorescein (HEX) fluorophores.

Thiolated oligonucleotides used for protein labeling (the "sense" sequence is underlined):

$Oligo_{biotin}$: 5′SH-TTTTTCGTTGATAACCTGTCCATCTCTA-biotin

$Oligo_{FAM}$: 5′SH-TTTTTCGTTGATAACCTGTCCATCTCTA-FAM

Aminated oligonucleotides used to create capture surfaces:

Complementary: 5′ NH_2-TTTTTTTTTTAGAGATGGACAGGT

Noncomplementary: 5′ NH_2-TTTTTTTTTCCCTAAGAAGACGGA

Fluorescent oligonucleotides used to test capture surfaces:

FAM-sense: 5′ FAM-ACCTGTCCATCTCTA

HEX-anti-noncomplementary: 5′ HEX-TCCGTCTTCTTAGGG

Expression and Purification of N- or C-terminally His-Tagged Murine Dihydrofolate Reductase (His_6-mDHFR and mDHFR-His_6, Respectively) and Tagless Murine Dihydrofolate Reductase (mDHFR). To produce the His_6-mDHFR and mDHFR-His_6 proteins, competent *E. coli* (M15 [pREP4]) were separately transformed with the respective expression constructs pQE-40 and pQE-16 using the source company's protocols. The amino acid sequence of His_6-mDHFR differs from the sequence that can be obtained from the Swissprot database, DYR_MOUSE (accession number P00375), in that it has 14 additional residues at its N-terminus, MRGSHHHHHHGSGI-, has the C-terminal aspartate replaced by 17 residues, -GSRSACGTPGRPAAKLN, and has the cysteine in the seventh position replaced by a serine. The amino acid sequence of mDHFR-His_6 differs from DYR_MOUSE in that it has six additional residues at its N-terminus, MRGSGI-, has the C-terminal aspartate replaced by 10 residues, -GSRSHHHHHH, and has the cysteine in the seventh position replaced by a serine. Large-scale cultures were grown in LB medium containing neomycin (25 μg/mL) and ampicillin (100 μg/mL) at 37 °C, induced with 1 mM IPTG, harvested by centrifugation for 15 min at 6000 rpm in a Beckman J-10 rotor in a Beckman JA-21 centrifuge, frozen, and stored at −70 °C based on the Qiagen protocol. For protein purification 20−30 g of pelleted cells were resuspended and brought to a volume of 100 mL in lysis buffer (50 mM potassium phosphate (pH 8.9), 300 mM NaCl, 10 mM imidazole, 1× protease inhibitors). The cells were passed through a French press twice at a pressure of 1200−1600 psi. Cleared cellular lysate was obtained after centrifugation at 4 °C at 100000*g* for 1 h using an F-28/36 rotor in a Sorvall ultracentrifuge. Protease inhibitors were added at 1× concentration to the cleared lysate prior to loading onto a 10 mL Ni-NTA Superflow column. The column was preequilibrated in lysis buffer and peristaltically pumped at 1.2 mL/min at 4 °C. Following loading, the column was washed with 50 mL of low-imidazole buffer (20 mM imidazole, 300 mM NaCl, 50 mM potassium phosphate (pH 8.3)). Both His-tagged mDHFRs elute as a single peak at approximately 100 mM imidazole in a linear gradient of increasing imidazole. Peak fractions were pooled, dialyzed against mDHFR buffer (20 mM NaCl, 20 mM sodium phosphate (pH 7.6), 20% glycerol), and stored at 4 °C. Untagged mDHFR was generated from His_6-mDHFR by proteolytic digest with the enzyme DAPase followed by repurification on NTA-agarose resin according to the manufacturer's protocols.

Assay of Enzyme Activity in Solution. At room temperature, the oxidation of β-NADPH to $NADP^+$ that is coupled with reduction of DHFA to tetrahydrofolate (THFA) by mDHFR, was monitored as a decrease in absorbance at 340 nm with a Cary 20 UV/vis spectrophotometer (*39*). The reaction buffer, prepared immediately before use, consisted of either DHFA and β-NADPH at 67 μM with 13 mM β-mercaptoethanol and 1 mg/mL BSA, or DHFA and β-NADPH at 50 μM with 20 mM β-mercaptoethanol and 1 mg/mL BSA, in degassed 100 mM potassium phosphate buffer (pH 7.5). After recording the steady absorbance of 1 mL of the reaction buffer alone over 2 min, 1−2 μg of mDHFR or mDHFR−oligo conjugate was added to the cuvette, mixed by several inversions, and returned to the spectrophotometer. Changing absorbance at 340 nm was recorded for >10 min. Reaction velocities were determined from a 4-min linear portion of the recordings that typically began 30 s to 3 min after mixing. Activities were compared based on reaction velocity per microgram of added mDHFR.

Synthesis and Purification of NAB. The synthesis of NAB is shown in Scheme 2. NTA-amine (4 mg, 15 μmol) was dissolved/suspended in 1 mL of 50% anhydrous, deaminated dimethyl formamide (DMF), 50% anhydrous dimethyl sulfoxide (DMSO) containing triethylamine (TEA) (10 μL, 69 μmol). To this was added Sulfo-SBED (10 mg, 11 μmol) dissolved in 1:1 DMF/DMSO. The reaction was stirred under nitrogen overnight, in the dark, at room temperature. After the reaction, the mixture was reduced to a yellowish oily concentrate under high vacuum. The concentrate was redissolved in DMF or dimethyl acetamide (DMA) and purified by RP-HPLC using a C4 column (250 × 4.6 mm) pumped at 1 mL/min. Solvent A was water/0.01% trifluoroacetic acid (TFA) and solvent B was acetonitrile/0.01% TFA. The column was loaded and pumped for 10 min in 10% solvent B, followed by a brief linear gradient, from 10 to 27% solvent B over 5 min, then followed by 15 min at 27% solvent B. NAB elutes as the second major peak with a retention time of 28.5 min. Since NAB is light sensitive, preparative purification was conducted with the detector light sources turned off. Peak fractions were identified by UV absorbance spectroscopy of samples diluted into water. Peak fractions were pooled and dried down or used immediately in labeling reactions. The yield under these conditions was 50%.

Synthesis and Purification of NBzM. The solid-phase synthesis of NBzM is shown in Scheme 3. All steps were at room temperature unless otherwise noted. All

amine deprotection and coupling steps were monitored with the TNBS test as described in the NovaBiochem catalog (TNBS is 2,4,6-trinitrobenzenesulfonic acid). In a 25-mL manual peptide synthesis reaction vessel, Fmoc-Lys(Mtt)-Wang resin (2.75 g, 1.98 mmol) was swollen in dichloromethane (DCM) for 1 h. Fmoc deprotection was effected by six successive 15 min treatments of the resin with 20% piperidine in DCM. After deprotection, the resin was washed extensively with DCM. To the washed resin was added a 20-fold excess of *tert*-butyl-bromoacetate (6.4 mL, 40 mmol) with an equal amount of diisopropylethylamine (DIPEA) (7.2 mL, 41 mmol) and 2 mL of DCM. This reaction vessel was shaken at 350 rpm at 45 °C for 27 h. At this point, a TNBS test indicated that there were some residual free amines present on the resin beads. Fresh reagents were added and the vessel was further incubated at 45 °C with shaking for 18.5 h. The beads were washed successively with DCM, ethyl acetate, and DCM again. The Mtt group was removed by five 3-min treatments with 10 mL of 1% TFA, 5% triisopropyl silane (TIS) in DCM. After extensive washing with DCM, the beads were washed twice with 10 mL of 1:1 DCM/DMA. Fmoc-BPA-OH (1.95 g, 3.96 mmol), PyBOP (2.06 g, 3.96 mmol), HOBt (0.606 g, 3.96 mmol), and DIPEA (1.38 mL, 7.92 mmol) were added to the beads in 10 mL of 1:2 DCM/DMA. The beads were agitated with bubbling dry nitrogen for 17.5 h. Fresh reagents were added in half the previous amounts and allow to further react for 3 h. The beads were washed with DCM/DMA followed by DCM prior to Fmoc deprotection as previously carried out. After washing with DCM, the beads were washed twice with 10 mL of 1:1 DCM/DMA. β-Maleimido-proprionic acid (0.375 g, 2.22 mmol), PyBOP (1.155 g, 2.22 mmol), HOBt (0.340 g, 2.22 mmol), and DIPEA (780 μL, 4.44 mmol) were added to the beads in 12 mL of 1:2 DCM/DMA. The beads were allowed to react with agitation for ~48 h. After washing of the sample, an equivalent amount of fresh reagents were added and allowed to react for seven more hours. The beads were washed successively with DCM, ethyl acetate, methanol, DCM again, and dried briefly under vacuum. Products were cleaved from the resin with several 5-min treatments with 10 mL of 95% TFA, 5% anisole. The material was reduced to near dryness with rotary evaporation, precipitated with ice-cold diethyl ether, and dried under high vacuum.

The dried off-white material was dissolved in DMA and purified by semipreparative RP-HPLC over a Jupiter C18 column (50 × 10 mm guard, 250 × 10 mm main) pumped at 2.5 mL/min. Solvent A was water/0.01% TFA and solvent B was acetonitrile/0.01% TFA. The column was loaded in 10% solvent B and immediately linearly ramped up to 28.7% solvent B over 5 min. This was followed by a shallow linear gradient from 28.7 to 29.3% solvent B over 20 min, followed by a 5-min linear ramp to 95%. NBzM elutes as the forth major peak that starts to elute after 24 min. Peak fractions were pooled, dried by lyophilization, and stored dry in the dark. The yield, relative to the amount of Fmoc-Lys(Mtt) on the resin, was 12%.

Coupling of NBzM to Thiolated Oligonucleotides. Prior to reaction with NBzM, thiolated synthetic oligonucleotides were dissolved in Milli-Q water and reduced by overnight incubation with 2% TEA (v/v) and 50 mM DTT as recommended by the manufacturer. After reduction, thiolated oligonucleotides were separated from small molecules by gel filtration over a NAP-10 column preequilibrated with 50 mM sodium phosphate (pH 7.0), 300 mM NaCl. A 30-fold excess of dry, weighed NBzM was immediately added to the reduced thiolated oligonucleotide and allowed to react at room temperature overnight. Reduced thiolated oligonucleotide was almost entirely converted to NBz−oligo and was purified by RP-HPLC at neutral pH with a semipreparative C4 column (250 × 10 mm) pumped at 2.5 mL/min (*40*). Solvent A was 100 mM ammonium acetate (pH 7.0), and solvent B was pure acetonitrile. The column was loaded in 5% solvent B and immediately linearly ramped to 20% B over 30 min. NBz−oligo$_{FAM}$ elutes as the second major peak with a retention time of 25.2 min. MALDI-MS was used to confirm the mass of the NBz−oligo product. The peak fractions that contained the desired mass were pooled, lyophilized to dryness, and resuspended in sterile, Milli-Q water. The concentration of conjugate was determined by absorbance at 260 nm and a calculated extinction coefficient based on the nucleotide sequence and adjusted to account for the presence of benzophenone (*41*). Yields were typically ~50% relative to the amount of starting thiolated oligo. To charge the conjugate molecules with Ni(II), concentrated MOPS buffer, pH 7.9, was added to 20 mM followed by addition of $NiSO_4$ to 1.1-fold excess over the conjugate concentration (typically, 0.5−1 mM) (*24*). Ni(II) charged conjugates (Ni:NBz−oligo) were allowed to equilibrate at room temperature for several hours and then stored at 4 °C.

Photocrosslinking. For photoconjugation, purified target protein (10−200 μM) was preincubated from 1 to 12 h at 4 °C with an equimolar amount of trifunctional labeling reagent in 20 mM sodium phosphate (pH 7.6−8.0) and 300 mM NaCl. Following preincubation, the mixture was adjusted to 10 mM imidazole by addition of 1 M imidazole (pH 8.0) 30−60 min prior to irradiation. The reaction mixture, typically 50−500 μL, was contained in an uncapped microcentrifuge tube tightly sealed with Saran-wrap affixed by an elastic band. The tube(s) were placed in a cooled aluminum block and irradiated with long-UV light (Blak-Ray B-100AP lamp, ~365 nm) from above (~6 cm from source) at 4 °C for 3−18 h with stirbar agitation. This corresponded to an irradiation energy of 0.28−1.7 MJ/cm^2.

Purification of Protein Conjugates. Biotinylated protein conjugates, either NAB-labeled or NBz−oligo$_{biotin}$-labeled, were purified at room temperature by batch affinity chromatography using an Immunopure Immobilized Monomeric Avidin kit as per the manufacturer's instructions. Eluted biotinylated proteins were dialyzed, using Spectropore 10 kDa M_w cutoff membranes, extensively against 20 mM NaCl, 20 mM sodium phosphate, 20% glycerol for storage. After photoconjugation, mDHFR−oligo$_{FAM}$ conjugates were purified at room temperature by size-exclusion chromatography on a HiPrep 16/60 Sephacryl S-100 HR column installed on an Agilent 1100 series HPLC system equipped with a quartenary pump and UV−visible variable wavelength absorbance and fluorescence detectors. The column was equilibrated and run in 600 mM NaCl, 50 mM sodium phosphate (pH 7.6) at 0.25 mL/min. One-milliliter fractions were collected. Peak fractions were pooled and concentrated and exchanged into storage buffer by centrifugal ultrafiltration using Centricon Plus-20 PLGC devices in a room temperature tabletop centrifuge as per the manufacturer's instructions.

Absorbance Spectroscopy. All concentrations were determined based on absorbance measurements made with a quartz cuvette in a Cary-20 UV−visible spectrophotometer. The amount of biotin present in a pure sample of NAB was determined by a spectrophotometric assay using HABA and avidin (*42*). This quantity was

used along with absorbance measurements to determine a molar extinction coefficient at 270 nm, ϵ_{270}, of NAB in water. This extinction coefficient was used for all subsequent determinations of NAB concentration. Oligonucleotide concentrations were determined according to Beer's law based on absorbance at 260 nm and sequence-dependent calculated extinction coefficients provided by Integrated DNA Technologies. Pure mDHFR concentrations were determined from absorbance measurements at 280 nm in a quartz cuvette and a calculated extinction coefficient ($\epsilon_{280} = 25\,440$) based on amino acid content (*43*). mDHFR−oligo conjugate concentrations were determined by a microscale Bradford assay using a commercial Coomassie Protein Assay reagent and calibrated relative to staining of pure mDHFR with the same reagent; the oligo portion did not stain with this reagent.

Mass Spectrometry of Proteins, Oligos, and Conjugates. Protein samples were desalted using $ZipTip_{C18}$ devices as per the manufacturer's instructions. Proteins were eluted in ~2 μL, diluted to 10 μL in sinapinic acid solution (as per the instrument manual), and spotted directly onto a sample plate for interrogation with a Voyager-DE STR MALDI mass spectrometer. Oligonucleotides and NBz−oligo conjugates were desalted using $ZipTip_{C4}$ devices and spotted with 3-hydroxypicolinic acid as the matrix. For positive-ion ESI-MS, pure NAB, Ni:NAB, NBzM, and Ni:NBzM were dissolved in pure water, neutralized with ammonium bicarbonate buffer (pH 8.0), and diluted 5-fold with neat spectroscopic-grade methanol.

NMR. For NMR spectroscopy, approximately 22 mg of pure NBzM was dissolved in ~800 μL of DMSO-d_6. ^{1}H and ^{13}C NMR spectra were collected.

Polyacrylamide Gel Electrophoresis. Precast Tris-HCl Ready Gel mini-gels were run using a Mini-Protean II apparatus with a PowerPac 300 power supply at 200 V in 25 mM Tris, 192 mM glycine, and 0.1% SDS. For reducing conditions, protein samples were suspended and heat-denatured in 1× Laemmli buffer supplemented with 100 mM DTT; for nonreducing conditions no DTT was added. Prestained protein standards were either Precision- or Precision Plus-type from Bio-Rad. Carboxyfluorescein fluorescence from unstained gels was imaged, with a 2 s exposure, onto Polaroid type 667 film using a SYBR-Gold (Molecular Probes, Eugene, OR) gelatin filter with a Polaroid camera mounted over a UV transilluminator. Gels were stained using either GelCode Blue Stain or GelCode SilverSNAP.

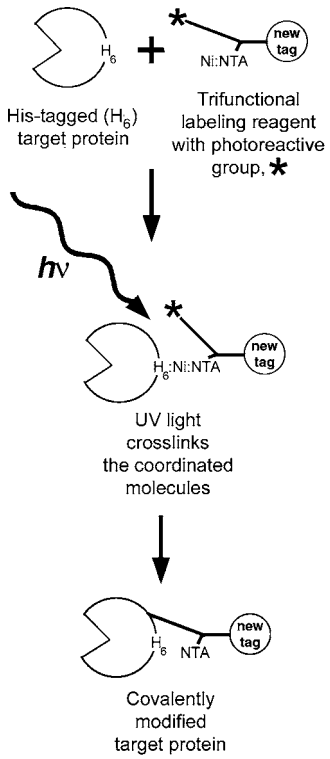
Preparation of DNA-Modified Microplate Wells. The wells of DNA-bind plates were modified with aminated oligonucleotides as per the manufacturer's protocol. Oligonucleotides were used at a concentration of 200 pmol per well and were coupled over 3 h at 37 °C. Ethanolamine was used for blank wells and blocking. Plates were washed and stored in 50 mM sodium phosphate, pH 7.4, 150 mM NaCl and 0.02% sodium azide at 4 °C. Specificity of hybridization was confirmed with the fluorescent oligonucleotides FAM-sense and HEX-anti-noncomplementary.

Hybridization of Protein−Oligo Conjugate on Microplate Wells. mDHFR−oligo conjugate and unmodified mDHFR were diluted with water and 2× plate hybridization buffer (1.2 M NaCl, 120 mM sodium citrate, 0.02% Tween-20, 20 mM EDTA, 1 mg/mL Ac−BSA, 0.2 mg/mL Herring Sperm DNA, 100 mM TrisCl (pH 7.5)) to 500 nM in 1× plate hybridization buffer. Specificity of hybridization was confirmed by using the fluorescent oligonucleotides FAM-sense and HEX-anti-noncomplementary similarly diluted to 1 μM. Three separate 100 μL volumes of each sample type were dispensed into microplate wells modified with either 5′-aminated complementary, noncomplementary, or no capture oligonucleotide. On-plate hybridization occurred overnight at 37 °C in a shaking-platform incubator. After hybridization, supernatants were removed and saved, and the microwells were washed once with 200 μL of plate wash buffer (300 mM NaCl, 30 mM sodium citrate, 0.01% Tween-20, 50 mM TrisCl (pH 7.5)), again with 150 μL of the same buffer, and finally with 150 μL of 50 mM TrisCl (pH 7.5), 150 mM NaCl, 0.01% Tween-20. Each wash step was at 37 °C for 5 min. After washing, the microwells were filled with 100 μL of 50 mM sodium phosphate (pH 7.0), 100 mM NaCl, and the fluorescence was measured at room temperature with a Cytofluor 4000 fluorescence microplate reader. FAM fluorescence was measured using a 485/20 excitation filter and a 530/25 emission filter. HEX fluorescence was measured using a 530/25 excitation filter and a 620/40 emission filter.

Preparation of DNA-Modified Microspheres. Polybead carboxylate microspheres (4.34 ± 0.24 μm diameter) were modified with 5′-aminated oligonucleotides by one-step coupling as described by Weimer and colleagues (*44*). Briefly, ~81 mg of microspheres were washed twice with 10 mM NaOH, three times with Millipure water, three times with freshly prepared 100 mM MES (pH 4.7), and divided equally into three microcentrifuge tubes. After removing excess buffer, each of the ~27 mg portions of microspheres was resuspended to 600 μL with 100 mM 1-ethyl-3-(3-dimethylaminopropyl)-carbodiimide (EDAC) in 100 mM MES (pH 4.7). At this point, 100 μL of 1 mM aminated oligonucleotide in water, or for blank microspheres, 100 mM ethanolamine in 100 mM MES (pH 4.7), was added to each portion of microspheres. The microfuge tubes of microspheres were then incubated in the dark, at room temperature, with mixing by rotation for ~72 h. This was followed by a 1 h exposure to 10 mM ethanolamine in 50 mM sodium phosphate, 1 mM EDTA (pH 8.5). The microspheres were washed 4 times with storage buffer (50 mM TrisCl, pH 7.5, 50 mM NaCl, 10 mM EDTA, 0.01% Tween-20, 0.02% sodium azide) and stored in the same buffer at ~25 mg/mL at 4 °C. The beads were characterized for their binding capacity by hybridization with fluorescently labeled complementary oligonucleotides and measurement of the residual fluorescence left in solution.

Hybridization of Protein−Oligo Conjugate on Microspheres. For mDHFR−$oligo_{FAM}$ conjugate hybridization experiments, three separate 50 μL aliquots (~1.25 mg) of each type of microsphere (bearing complementary, noncomplementary, or no DNA) were pelleted by centrifugation at 14 000 rpm at 4 °C in an Eppendorf 5415C microcentrifuge, resuspended, and incubated for 30 min with mixing, at room temperature in 100 μL of prehybridization solution (22.5 mM NaCl, 25 mM TrisCl (pH 7.5), 10 mM sodium phosphate, 2.5 mM EDTA, 0.01% Tween-20, 10% glycerol, 1 mg/mL acetylated bovine serum albumin (Ac−BSA)). Following repelleting of the sample, and removal of 40 μL of supernatant, the microspheres were resuspended with 20.4 μL of BSA buffer (25 mM NaCl, 50 mM TrisCl (pH 7.5), 5 mM EDTA, 0.02% Tween-20, 2 mg/mL Ac−BSA). To these suspensions was added 20.4 μL of mDHFR−oligo conjugate (100 pmol). Parallel incubations of conjugate without microspheres served as controls. Hybridization occurred at room temperature with mixing by rotation over 20 min. After hybridization and repelleting, supernatants (~40 μL) were removed carefully to avoid drying any of the microspheres. The microspheres were washed once

Scheme 1



for 5 min at room temperature with 100 μL of prehybridization solution, repelleted, and resuspended in 40 μL of fresh prehybridization solution after removal of the wash solution. The resultant ~50 μL suspensions of microspheres, along with 50 μL samples of supernatants, wash solutions, and control reactions, were pipetted into separate wells of a flat-bottom, untreated, 96-well microplate for fluorescence measurement and mDHFR activity assay with a Cytofluor 4000 fluorescence microplate reader. FAM fluorescence was measured using a 485/20 excitation filter and a 530/25 emission filter.

Assay of mDHFR Activity on Immobilized on Microspheres. All measurements were obtained at room temperature. After recording the FAM fluorescence, 50 μL of reaction buffer (100 μM β-NADPH, 100 μM DHFA, 20 mM β-mercaptoethanol in prehybridization solution) was added to the microplate wells. The final concentration of both substrate (DHFA) and cofactor (β-NADPH) was 50 μM, well above their sub-micromolar K_m values (*45*). Mixing of microspheres and substrates for 30 s every cycle was achieved using the instrument's built-in agitation mechanism. The fluorescence due to β-NADPH was periodically measured from each well at a frequency of once every 97 s (*46*). Fluorescence was measured using a 360/40 excitation filter and a 460/40 emission filter. Fluorescence measurements were averaged between three wells and background corrected for total fluorescence at $t = 8.1$ min. Linear fitting was error weighted and calculated using the program Origin 7.0 (OriginLab Corp., Northampton, MA).

RESULTS

The goal of this work was to develop reagents that can covalently label recombinant proteins selectively in solution. The strategy, involving a trifunctional labeling reagent that recognizes the His-tag, is illustrated in Scheme 1. First, the labeling reagent noncovalently coordinates to the His-tag on the protein through its Ni:NTA group. After this, long-wavelength UV light is used to create a covalent bond between the juxtaposed photoreactive group and protein surface. Affinity-driven docking of the labeling reagent ensures that the covalent bond is made proximal to the His-tag. Principal reaction products are expected to be selectively monofunctionalized proteins that retain native activity.

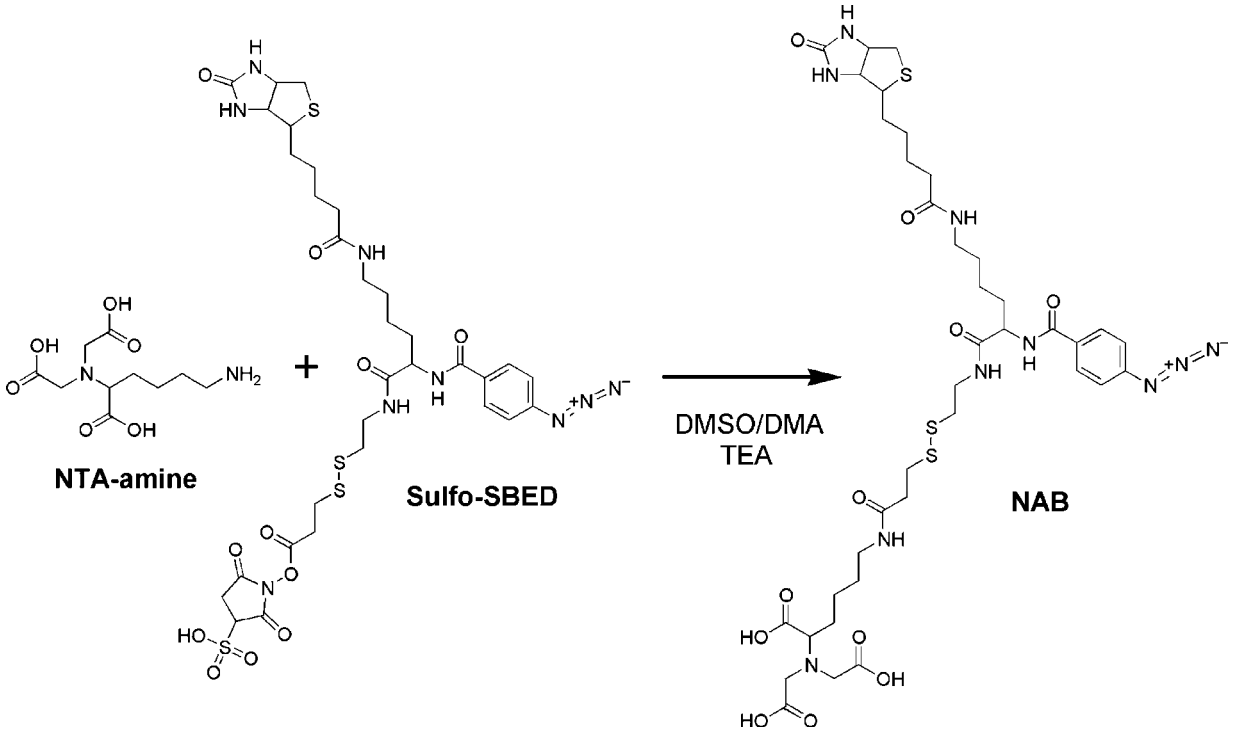
Design and Synthesis of NAB. To test whether a protein's His-tag could serve as a recognition element to guide a subsequent photoconjugation reaction, a trifunctional labeling reagent was synthesized in one step from commercially available precursors (Scheme 2). It is designated NAB since its three branches end in an **N**TA His-tag targeting group, a phenyl **A**zide photoreactive group, and a **B**iotin functional group. Electrospray ionization mass spectrometry (ESI-MS) of RP-HPLC purified NAB demonstrated masses at 925.3 and 947.3 corresponding to the protonated, $[M + H]^+$, and sodiated, $[M + Na]^+$, molecular ions. High-resolution ESI-MS of NAB following incubation with an excess of Ni(II) at pH 8.0 yielded a mass of 981.2538 as compared to an expected mass of 981.2567, corresponding to $[(M - 2H + Ni) + H]^+$ molecular ions; thus each NAB molecule can coordinate a Ni(II) ion to form a 1:1 complex. The molar extinction coefficient at 270 nm, ϵ_{270}, of NAB in water is ~26 900 M^{-1} cm^{-1} based on a quantitative assay of D-biotin.

Labeling of mDHFR with NAB and Characterization. NAB coordinated to Ni(II) was assayed for its capacity to selectively biotinylate His-tagged proteins. mDHFR was chosen as a test enzyme for modification by NAB. This small, ~23 kDa, monomeric enzyme is equally active when expressed with a His-tag at either its N-terminus or C-terminus and it is easily assayed in solution. A crystallographically determined model of the atomic structure of the highly homologous (87% sequence identity) human version of this enzyme shows that both termini occur at the surface of the molecule and are remote from its active-site (*47*). Thus, we reason that targeted modification of mDHFR guided by a His-tag at either the N- or C-terminus will leave the enzyme active.

Upon exposure to UV light, reactions of NAB with either N- or C-terminally His-tagged mDHFR (His_6-mDHFR and mDHFR-His_6, respectively) produce singly and doubly modified enzyme molecules. Under identical conditions, NAB fails to label untagged mDHFR. NAB-modified proteins could be detected by a small shift in mobility on nonreducing SDS−PAGE gels (data not shown). The covalent attachment of biotin to mDHFR could also be detected on Western blots (data not shown). Matrix-assisted laser desorption and ionization mass spectrometry (MALDI-MS) confirmed the presence of singly and doubly labeled species (Figure 1). Since a His-tag of six consecutive histidines was used, the occurrence of doubly modified mDHFR molecules may have resulted from the simultaneous or sequential coordination of two NAB molecules on a single His-tag; only two appropriately positioned histidine residues are necessary to coordinate a Ni:NTA moiety. We intend to test whether shorter His-tags change the distribution of modified products in future studies.

Characterization of NAB-Labeled mDHFR. NAB-labeled mDHFR remained active and its covalently attached biotin group was accessible by avidin. During purification by biotin-affinity chromatography, covalently NAB-labeled mDHFR remained immobilized on avidin-coated particles in the presence of 200 mM imidazole, a concentration sufficient to disrupt the noncovalent NTA:Ni(II):His-tag interaction. Elution of NAB-labeled mDHFR from the avidin-coated support yielded mixed popu-

Scheme 2



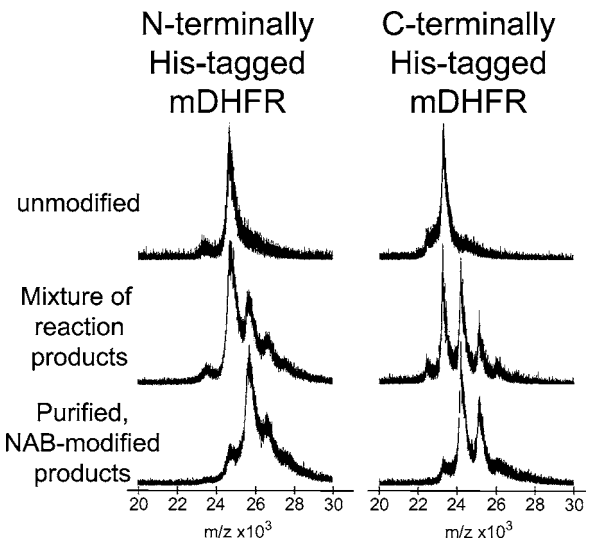
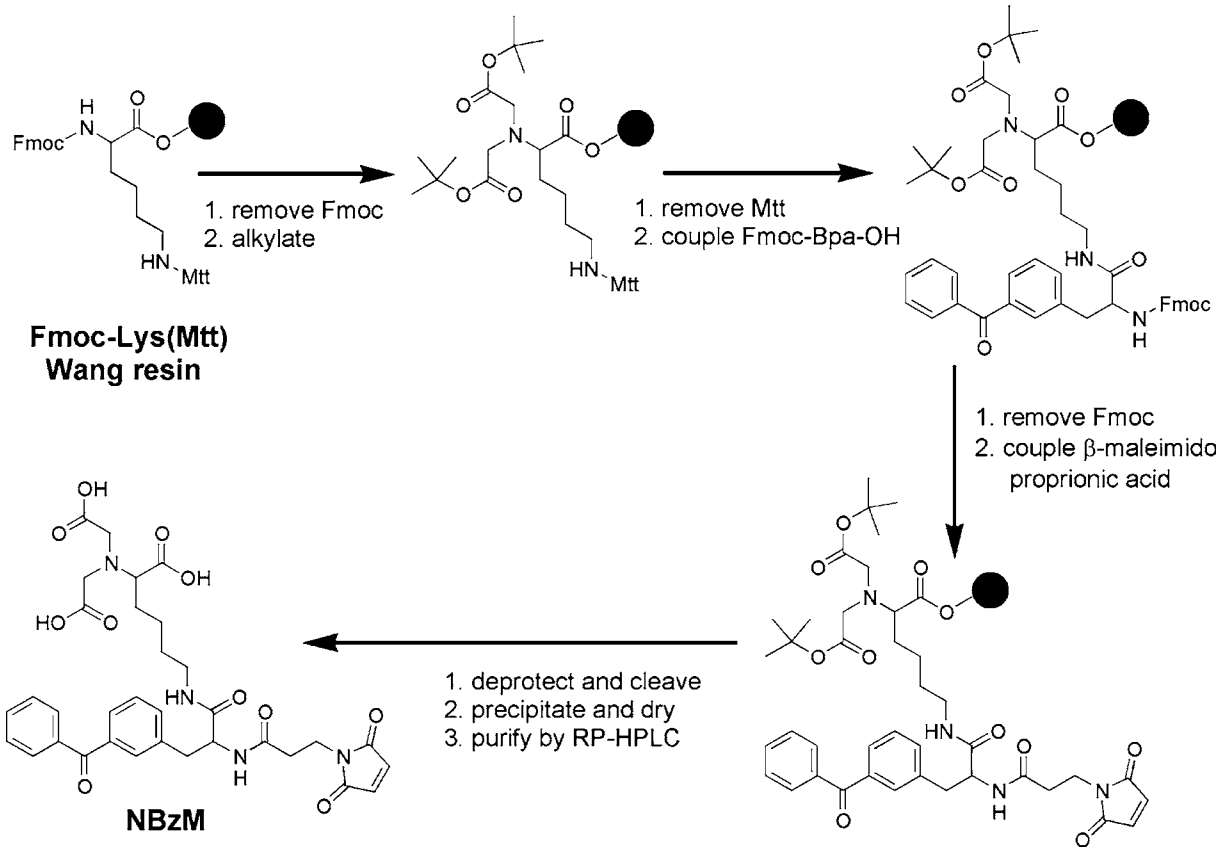


Figure 1. MALDI mass spectrometry of NAB-modified mDHFRs. Depicted are linear-mode MALDI-TOF spectra of both N- and C-terminally His-tagged versions of mDHFR prior to labeling with NAB (top), after labeling but before purification (middle) and after affinity purification of biotinylated species (bottom). Discrete peaks corresponding to singly and doubly modified mDHFR molecules are clearly present in both reactions demonstrating that labeling can be directed through a His-tag on either terminus of this enzyme. Affinity purification yields samples of almost entirely modified enzyme. The specific activity of both preparations remained close to that of the unmodified enzyme (see text).

lations of singly and doubly modified protein molecules containing very little (<5%) unmodified protein (Figure 1). Under the conditions used, approximately 20% of the mDHFR molecules were labeled by NAB. The modified mDHFR molecules remained highly active; relative to unmodified controls, NAB−His_6-mDHFR retained 89% of its specific activity, and NAB−mDHFR-His_6 retained 96% of its specific activity ($n = 3$). No further efforts were made toward optimizing the yield of these conjugates.

Design and Synthesis of NBzM. To further explore the potential of the His-tag as a guide for the selective modification of proteins, we decided to design and test a more general trifunctional reagent. This reagent is called NBzM since its three branches end in an **N**TA affinity-directing group, a **B**enzophenone photoconjugating group, and a **M**aleimide functional group. The maleimide group provides a means to generate a series of related compounds since it can react specifically with a thiol-bearing compound under mild conditions. A straightforward solid-phase synthesis of this trifunctional molecule was developed as shown in Scheme 3. It should be noted that since introduction of the maleimide moiety occurs penultimate to cleavage, any of a variety of groups can substitute for it at this point to produce reagents attached to the same NTA-benzophenone molecular scaffold. Apart from replacement of the biotin group with maleimide, the structure of NBzM differs from NAB in three significant ways. Foremost, benzophenone was chosen as the photoreactive group since it is resistant to chemical reduction by thiols, and because its photolysis creates a reactive intermediate that, in the presence of oxygen, can decay back to the original photosensitive structure in the absence of covalent bond formation (*41*, *48*). Benzophenone has been used as the photoreactive group in many protein photolabeling studies (*49*). Second, the number of successive interatomic bonds between the photoreactive center and the tertiary nitrogen of NTA was shortened to 14 from 21. Simple modeling, where the mDHFR molecule is considered to be a sphere of uniform density, $\rho = 1.3$ g/cm^3, and the labeling compound is fully extended from a point on the protein surface, indicates that NBzM could form a covalent linkage near the His-tag in a region corresponding to ~15% of the surface area of mDHFR whereas the longer NAB could attach anywhere within an area of ~37% of the protein's surface. Finally, the disulfide bond that occurs in the NAB structure was eliminated.

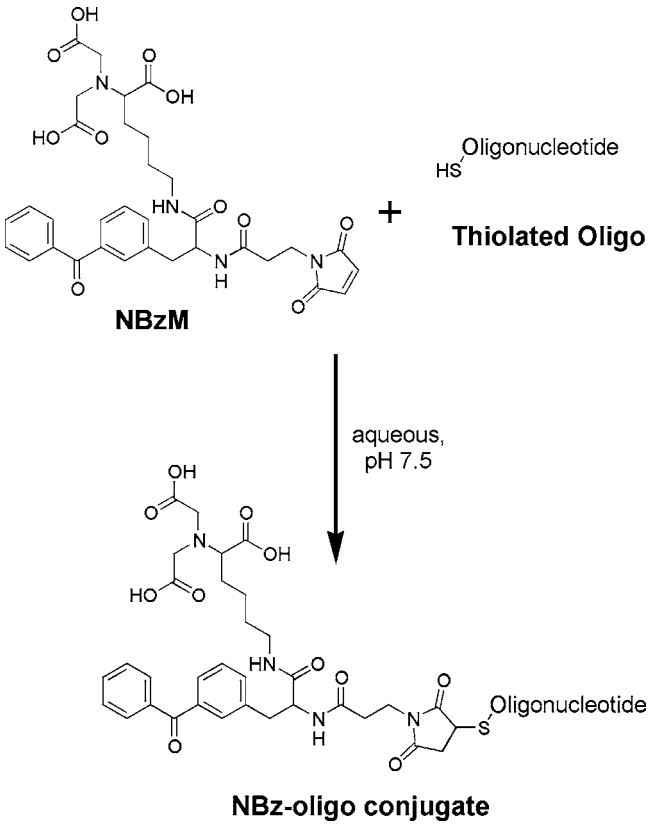
Scheme 3



Pure NBzM is resolved as a single peak by analytical RP-HPLC. Hi-resolution ESI-MS of pure NBzM yielded a mass of 665.2481 as compared to an expected mass of 665.2459, corresponding to the protonated, $[M+H]^+$ molecular ion. Incubation with an excess of Ni(II) at pH 8.0 biased the ESI-MS peaks to a cluster starting at a mass of 721.3 corresponding to $[(M - 2H + Ni) + H]^+$ molecular ions indicating that NBzM can coordinate a Ni(II) ion to form a 1:1 complex. ^1H and ^{13}C NMR measurements in DMSO-d_6 are consistent with the structure of NBzM shown in Scheme 3.

Conjugation of NBzM to Thiol Oligos. We were particularly interested in testing whether NBzM could be used as a reagent for the preparation of protein−DNA conjugates. Protein−nucleic acid conjugates have been used as synthetic nucleases, as hybridization probes, for antisense directed delivery, for protein library encoding, for in vitro selection, and as immune stimulants (*50*−*56*). Protein−nucleic acid conjugates are also of increasing interest as elements for the production of self-assembling protein arrays (*57*−*59*). The overall strategy consists of first coupling NBzM through its maleimide group to a terminal thiol group on a synthetic DNA oligonucleotide (Scheme 4) then using the NTA group of this NBz−oligo molecule to guide a subsequent photoconjugation to a His-tagged protein. As determined by RP-HPLC and MALDI-MS, reduced thiolated oligos could be almost entirely converted to NBz−oligo conjugates by reaction with excess NBzM. Similar results were obtained with four different 5′- or 3′-thiolated oligonucleotides ranging from 15 to 28 bases in length. Ni(II) could be added to NBz−oligo conjugates at 1.1-fold excess over NTA groups; however, greater excesses were found to cause precipitation of oligos and the conjugates. Precipitation of DNA by Ni(II) has been observed and studied in other contexts (*60*−*62*). Given a stability constant of

Scheme 4



$10^{11.5}$ for the coordination of Ni(II) by NTA, when both Ni(II) and NBz−oligo are present at 10 μM, >99.99% of the conjugates will be coordinated to Ni(II) at equilibrium (*63*).

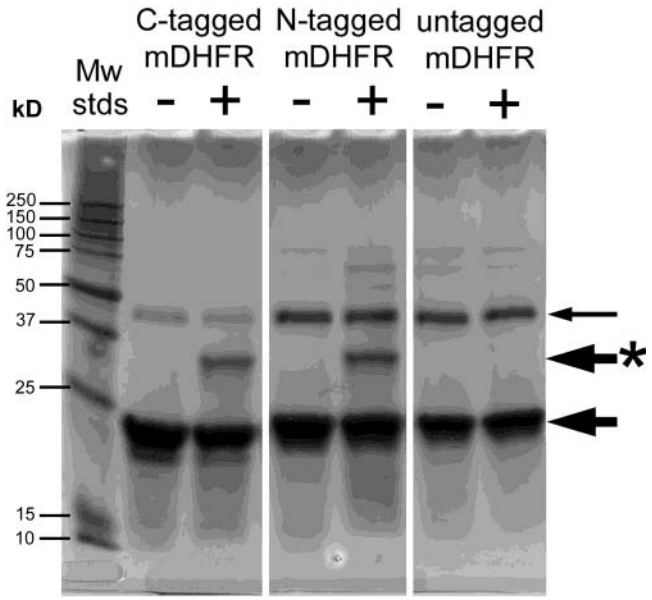


Figure 2. NBz−oligo labeling of mDHFR is selective for the presence of the His-tag. Hybrid molecules of covalently linked protein and DNA, the products of photoconjugation between NBz−oligo and His-tagged mDHFR in solution, are resolved as a discrete species on reducing and denaturing 12% polyacrylamide gels by SDS−PAGE. Shown are lanes from the same silver-stained gel (irrelevant lanes have been excised) where labeling reactions (+) between C- and N-terminally His-tagged mDHFRs are separated parallel to control reactions lacking NBz−oligo. The final two lanes are from reactions with mDHFR lacking a His-tag. The middle arrow, marked with an asterisk, indicates the position of the shifted species with a mobility equivalent to that of a 35 kDa protein. In similar experiments in which the oligo carries a terminal fluorophore, the fluorescence of this shifted band can be detected on unstained gels. The lower arrow indicates the mobility of the unmodified mDHFR molecules, with molecular masses ranging from 23.3 kDa for the C-tagged species to 24.7 kDa for the N-tagged species. All mDHFR preparations contain, to a variable extent, the ~50 kDa protein (small arrow) as a contaminant.

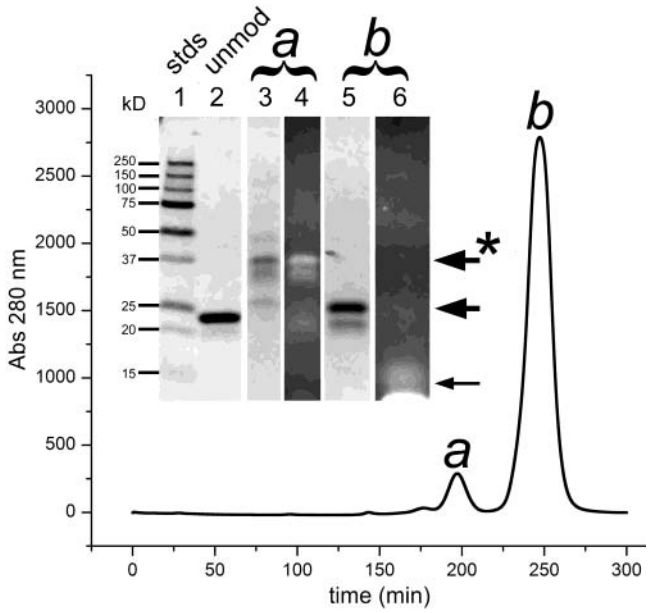


Figure 3. Size-exclusion chromatography allows purification of NBz−oligo-modified mDHFR. A 100 nmol scale reaction between C-terminally His-tagged mDHFR and the fluorescently labeled modification reagent NBz−oligo$_{FAM}$ was separated by high-resolution size exclusion chromatography. The elution profile is shown as a function of absorbance at 280 nm, a wavelength absorbed by protein and DNA. Collected fractions across peaks a and b were pooled separately and concentrated by ultrafiltration. The inset shows Coomassie-blue protein staining (lanes 2, 3, and 5) of reducing SDS−PAGE separations of unmodified C-tagged DHFR and the concentrated components of peaks a and b, respectively. Lanes 4 and 6, fluorescent images of the lanes 3 and 5, respectively, show the fluorescent species visible prior to staining. All lanes are from the same gel. Peak a is highly enriched with a fluorescent protein of high molecular weight (lanes 3 and 4): the NBz−oligo$_{FAM}$−mDHFR conjugate, indicated by the uppermost arrow labeled with an asterisk. Peak b appears to be a mixture of unmodified mDHFR (lane 5, middle arrow) and unattached fluorescent NBz−oligo (lane 6, lowest arrow). When assayed for mDHFR activity, peak a demonstrated a specific activity of about 80% that of unmodified mDHFR, while peak b had a specific activity equivalent to that of unmodified mDHFR.

Ni:NBz−Oligo Labeling of mDHFRs. NBz−oligo coordinated to Ni(II) was assayed for its capacity to label mDHFR. Reactions of Ni:NBz−oligo with both His$_6$-mDHFR and mDHFR-His$_6$ yielded protein molecules linked to a single oligo, while reactions with mDHFR lacking a His-tag showed no evidence of modification (Figure 2). Reactions between Ni:NBz−oligo and His-tagged mDHFR were significantly inhibited by the presence of either 150 mM imidazole or 5 mM EDTA (data not shown). Oligo-modified proteins could be detected by a significant shift in mobility on reducing SDS−PAGE gels (Figure 2). In all such labeling reactions, the NBz−oligo carried an additional label, either biotin or 6-carboxyfluorescein (FAM), linked to the end of the oligo opposite the NBz-group. When NBz−oligo$_{biotin}$ was used, biotin on the shifted protein was detected on Western blots (data not shown) and when NBz−oligo$_{FAM}$ was used, the fluorescence of the shifted protein was observed directly in the unstained gel (inset, Figure 3). No suitable conditions could be found to measure the molecular weight of these oligo−protein molecules by mass spectrometry.

Characterization of Oligo-Labeled mDHFR. Preparative-scale conjugation reactions were conducted between mDHFR-His$_6$ and either NBz−oligo$_{biotin}$ or NBz−oligo$_{FAM}$. Although the incorporation of biotin permitted significant enrichment of mDHFR−oligo conjugates over unmodified mDHFR through biotin affinity chromatography, size-exclusion methods permitted purification to near homogeneity (Figure 3). Under the conditions tested, NBz−oligo labeling yields were low, from 1 to 2%. In solution, purified mDHFR−oligo conjugates exhibited on average 72% (n = 4 preparations, ranging from 56 to 81%) of the specific activity of unmodified mDHFR indicating that the covalent attachment of oligo and subsequent manipulations did not greatly reduce the enzyme's native activity. When mDHFR−oligo conjugate molecules were incubated with either complementary or noncomplementary fluorescently labeled oligos in solution, analytical HPLC gel-filtration experiments showed the presence of new high-mobility species only with the complementary DNA (data not shown). This suggests that the mDHFR−oligo conjugate molecules could specifically hybridize with a complementary DNA oligonucleotide in solution. Under identical conditions, there was no evidence of hybridization to either of two different noncomplementary oligonucleotides.

To test whether the protein−oligo conjugates can be used to make self-assembling protein arrays their capacity to specifically hybridize to DNA-coated surfaces was assayed. For these experiments, the DNA portion of the conjugate was 28 bases long and linked to the mDHFR through its 5′ end. The 3′ end of the DNA consisted of a 15-base hybridization sequence termed "sense", end-

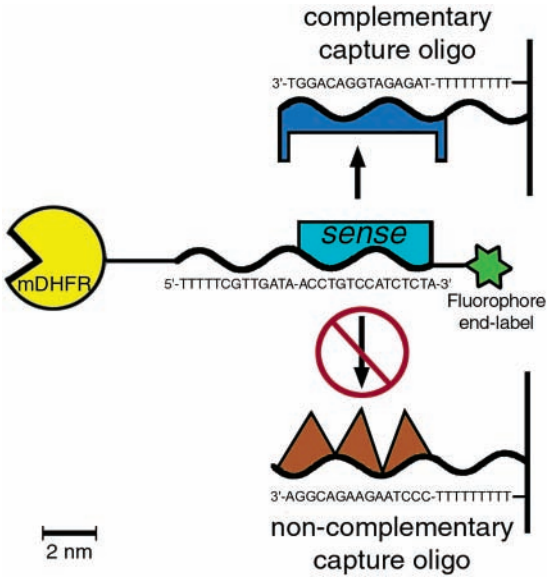


Figure 4. Scale cartoon of mDHFR−oligo conjugate used in hybridization experiments. The mDHFR−$oligo_{FAM}$ conjugate and its capture partners are depicted as fully extended molecules where the DNA segments have the length expected for duplex B-DNA. In the hybridization/immobilization experiments described, the conjugate is presented with either a complementary or noncomplementary capture strand that has been affixed through its 5′-end to a substrate. A 9-base spacer of thymidine residues links the capture sequences to the substrate to minimize crowding and to accommodate the fluorescent end-label of the conjugate. The nonspacer 15-base capture sequences are shown as shapes that either match or fail to match the shape of the conjugate 15-base "sense" sequence.

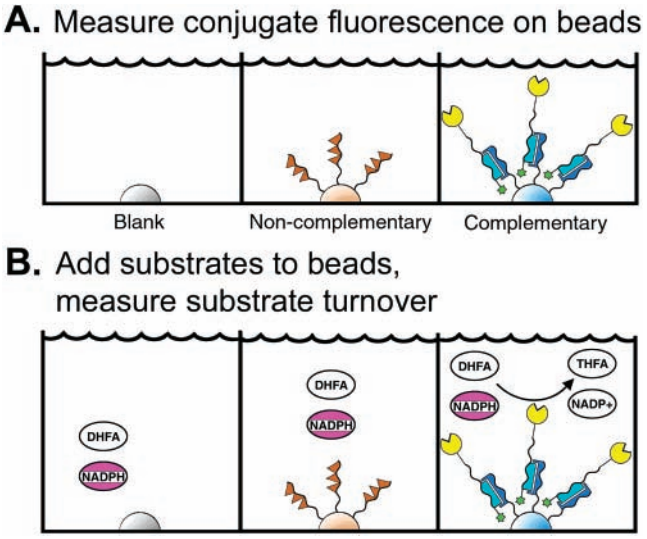


Figure 5. Schematic diagram of experiment to measure the enzyme activity of specifically immobilized conjugates. (A) The various microsphere types, either blank (non-DNA bearing), noncomplementary, or complementary beads are schematically shown in separate microplate wells under buffer, after having been incubated with mDHFR−$oligo_{FAM}$ conjugate (see Figure 4) and washed. The conjugate fluorescence is measured at this point. (B) A concentrated mixture of the substrate, DHFA, and cofactor β-NADPH are added to the wells. The enzyme mDHFR couples the oxidation of β-NADPH to $NADP^+$ with the reduction of DHFA to THFA.

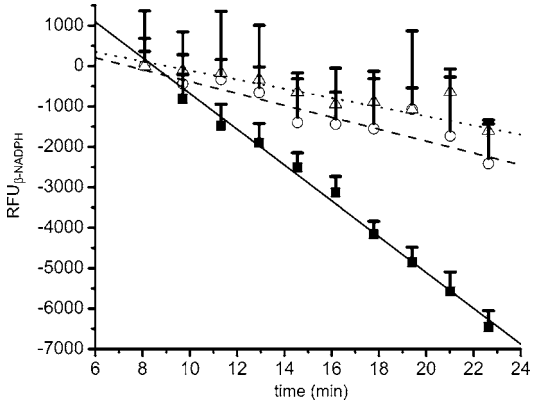


Figure 6. mDHFR immobilized through sequence-specific hybridization shows significant activity. Measurements of β-NADPH fluorescence were recorded as described in the methods and depicted in Figure 5. Filled squares, ■, correspond to complementary DNA-coated microspheres after hybridization to mDHFR−$oligo_{FAM}$ conjugate. Open circles, ○, correspond to noncomplementary DNA-coated microspheres after identical treatment. Open triangles, △, correspond to uncoated microspheres treated likewise. Linear least-squares fitting yielded the respective solid, dashed, and dotted lines. Subtracting the slope of the line for the unmodified beads from the slopes of the lines of the DNA-coated beads indicates that the activity difference due to sequence specificity is approximately 10-fold. Each datapoint is the average of measurements from three separate microwells. Error bars correspond to standard error of the mean. The mean background fluorescence of the first time-point used (t = 8.1 min after addition of substrates) was subtracted from all points for each dataset. Prior to the first time point used, there was significant scatter, most likely due to settling of the beads and inefficient mixing within the microplate reader.

labeled with a FAM fluorescent group (Figure 4). This design was chosen to allow the sense sequence to extend well away from the protein surface, to minimize self-complementarity, and to allow the conjugates to be directly detected by fluorescence measurements. To prepare surfaces that display capture DNA in the best orientation for hybridization, synthetic 5′-aminated oligos were coupled through primary amine-specific chemistry. Following the 5′-terminal amine, the capture oligo sequences consisted of nine deoxythymidine residues, which serve as an economical spacer sequence, followed by 15 bases that were complementary (5′-TAG AGA TGG ACA GGT-3′) or noncomplementary (5′-CCC TAA GAA GAC GGA-3′). To preserve the structure and activity of the mDHFR, the capture sequences were chosen to allow hybridization to their respective complementary sequences at room temperature at low ionic strength. The sequences were also selected to minimize self- and cross-complementarity. Specific hybridization of mDHFR−oligo conjugates could be observed on both oligo-modified flat plastic microwell surfaces and polymer microspheres. On microplate, noncomplementary wells captured only 12.1% as much conjugate, as measured by fluorescence, as did complementary ones (n = 3). Similarly, noncomplementary microspheres retained only 1.4% as much FAM fluorescence as compared to microspheres coated with complementary capture oligo (n = 3). Precise determination of the changes in fluorescence due to interaction with the microspheres is not within the scope of the current work.

To measure the enzymatic activity of the immobilized conjugates, the amount of mDHFR activity retained on microspheres after hybridization and washing was measured. In the assay, oxidation of the cofactor β-NADPH to β-$NADP^+$, which is coupled to the reduction of dihydrofolate (DHFA) to tetrahydrofolate (THFA), is monitored as a decrease in the fluorescence attributable to β-NADPH. The assay is depicted schematically in Figure 5. The amount of conjugate retained on the microspheres after hybridization was determined by measuring the FAM fluorescence of the supernatants and wash solutions

Table 1. Quantitative Results from Microsphere-Immobilized mDHFR−Oligo Conjugates

microsphere type	measured quantity of mDHFR−oligo remaining in solution (pmol)	calculated quantity of mDHFR−oligo retained on microspheres (pmol)	apparent mass equivalent activity, relative to nonimmobilized conjugate (pmol)
complementary	58.5	41.5	13.9
non-complementary	100	0	1.4

and comparing this to the fluorescence of known amounts of conjugate in the same buffer solution (Table 1). This was done because binding to the beads clearly altered the fluorescence of the conjugate molecules. By this measure, aliquots of 1.25 mg of complementary DNA-modified microspheres retained an average of 41.5 pmol of mDHFR−oligo conjugate, whereas equivalent aliquots of noncomplementary DNA-modified and unmodified microspheres failed to retain quantifiable amounts of conjugate. This value closely matches estimates of the binding capacity of the microspheres, 28−40 pmol/mg, as determined with fluorescent complementary oligonucleotides. Addition of the substrate DHFA and the cofactor β-NADPH at concentrations well above their respective K_m values allowed the activity of the immobilized mDHFR to be measured over time (Figure 6). With this assay, microspheres carrying specifically immobilized mDHFR showed approximately 10-fold greater activity than control microspheres (Table 1). The activity of the specifically immobilized mDHFR−oligo conjugate is 33.5% of that determined for an equivalent amount of conjugate in solution; this decrease may be due to nonideal mixing, molecular crowding and steric effects, or limits to substrate diffusion to a surface. No effort was made to optimize the kinetic behavior of the immobilized conjugate, nor was the long-term stability or reusability of the immobilized conjugate assessed.

DISCUSSION

This is the first report demonstrating the use of the His-tag as a guide for the covalent modification of a protein in solution. This approach has several advantages over conventional labeling methods in that (i) it utilizes the widely used His-tag, making it compatible with common expression systems and established libraries of His-tagged proteins, (ii) it presumably restricts the point of modification to the proximity of the His-tag, (iii) it restricts the stoichiometry of modification to yield largely 1:1 conjugates, (iv) the recognition element used, the His-tag, can be located at either protein terminus and possibly at internal sites, (v) a wide spectrum of modifications, from small molecules to macromolecules, are possible. We have shown that when this strategy is used to link a DNA oligonucleotide to a model enzyme, the protein's functionality remains intact both in solution and upon immobilization through sequence-specific hybridization. Thus, this technology may serve in the future creation of self-assembling, functional protein arrays.

With regard to the attachment of nucleic acid to protein for the creation of protein arrays, it should be noted that others have made progress using alternative methods. Such a goal was first expressed by Niemeyer and co-workers who chemically linked oligonucleotides to streptavidin (*64*). The oligo−streptavidin conjugate molecules were subsequently coupled to functional biotinylated antibodies through the strong noncovalent streptavidin−biotin interaction. Using this approach, the authors demonstrated the "translation", via hybridization, of a microtiter plate-based DNA array into a functional antibody array. Recently, the same group used expressed protein ligation to produce covalent conjugates between polyamide nucleic acid (PNA) and Ras protein and between PNA and the Ras binding domain of the c-Raf-1 protein (*59*). The authors showed that these C-terminally linked PNA−protein conjugates could hybridize to convert a simple glass-slide based DNA microarray into a protein array with retention of specific protein binding properties; however, no immobilized catalytic activity was demonstrated. Kuimelis and colleagues used mRNA−protein fusions to convert a DNA microarray chip to a simple protein microarray (*57*). The methodology described relies on in vitro translation and is restricted to fusions between the C-terminus of the protein and the 3′-end of its encoding mRNA. The array produced consisted of fragments of full-length proteins that were functional only in that they could be detected by specific antibodies. The approach we describe uses more readily produced biologically expressed full-length proteins, provides for modification in a variety of positions, and is compatible with many different sequences of the more chemically robust DNA or other nucleic acid analogues. Furthermore, the enzyme we immobilized was shown to retain catalytic activity.

More recently, Oleinikov and co-workers also used cell-free biosynthesis to produce lysine-biotinylated proteins (*58*). A series of steps allowed these researchers to produce protein−streptavidin−oligo conjugates that could be used to produce a simple self-assembled protein array. Importantly, both the proteins used, enhanced green fluorescent protein and the enzyme luciferase, retained their described functions. This approach is promising but also depends on the products of in vitro translation reactions. The biotinylation results we describe using the NAB reagent offer an alternative to this cell-free approach that could be easily integrated with their subsequent steps. The random incorporation of biotinylated-lysines by Oleinikov and colleagues eliminates the possibility of controlling the orientation of the proteins within the array. With our strategy, one can imagine varying the position of the His-tag in a given protein to control its resultant orientation upon modification and immobilization. Since protein arrays are sought largely as tools for the screening of molecular interactions, orientational control may prove very important. Further, orientational control is considered important for optimal functionality of immobilized enzymes (reviewed in ref *65*).

There are a number of ways that our results may be extended and improved. Foremost, greater efficiency of the photoreaction is expected if the affinity of the labeling reagent for the His-tag were to be increased. Drawing a lesson from the results of Ebright and co-workers, the affinity can be expected to be increased 10−100 fold simply by incorporation of two appropriately spaced NTA groups into the labeling reagent (*37*). Chemistries that yield covalent bonds other than through photolysis may increase efficiency as well. Combinatorial methods may allow co-optimization of the labeling reagent and variations of the His-tag that improve both specificity and affinity. Mapping the exact locations of protein modification produced with these reagents should shed light on their degree of regioselectivity. Other affinity-tag-directed cross-linking reagents are envisioned, such as one that incorporates glutathione to target the commonly used glutathione-*S*-transferase (GST) fusion tag. Use of this oligo-labeling strategy against a battery of proteins will allow a true self-assembling protein array, either bead- or chip-based to be demonstrated.

Of particular interest is the prospect of harnessing this molecular recognition based technology to achieve an unprecedented degree of control over the artificial assembly of molecular complexes. In recent years, it has become increasingly apparent that biological processes are mediated largely by exquisitely organized assemblies of functional macromolecules (*66*). Typically, such assemblies are multifunctional molecular machines capable of carrying out a series of physical and chemical transactions in a coordinated and efficient manner. Examples include the transcriptional apparatus that synthesizes RNA from genomic DNA in a highly regulated and processive manner, the ribosome which synthesizes proteins from mRNA also in a regulated and processive manner, and G-protein coupled receptor complexes which assemble and disassemble in response to signals at the cell-surface. In these systems, the identities, number, and relative orientations of the proteins are precisely defined, but by architectural rules that are currently poorly understood. The engineered assembly of proteins into higher-order multifunctional molecular machines requires a means to simplify these rules. Along these lines, significant progress in molecular assembly, programmed through the rules of nucleic acid interaction, has developed over the last two decades (see refs *67* and *68* for recent reviews). With this approach, remarkable molecular objects have been created from both DNA alone and protein−DNA conjugates. It is believed that the technology presented here may offer a predictable and practical means to modify recombinant proteins with precision sufficient to enable the design and assembly of novel multifunctional molecular machines held together and organized by structural elements such as nucleic acid. This or a similar approach, coupled with our ever-increasing knowledge of protein sequences, structures, and functions may form the basis for new engineered semi-synthetic biomolecular materials, catalysts, and nanobiotechnological devices.

ACKNOWLEDGMENT

This work was supported by NIH Grants F32NS11063 (G.D.M.) and GM57015 (N.L.A.). The authors thank John Greaves for help with mass spectrometry, Philip Dennison for NMR spectroscopy, Dennis Ta and Larry Vickery for help with molecular biology, J. Denis Heck for microarray support, Stephen Hou for help with bead-based fluorescence measurements, David van Vranken, Casey McComas, Josh Yoburn, and Frank Rossi for advice and help with organic synthesis, and Joseph Soughayer and Kwan Ng for helpful discussions.

LITERATURE CITED

(1) Jacob, C., Giles, G. L., Giles, N. M., and Sies, H. (2003) Sulfur and selenium: The role of oxidation state in protein structure and function. *Angew. Chem., Int. Ed. 42*, 4742−4758.

(2) Dawson, P. E., Muir, T. W., Clark-Lewis, I., and Kent, S. B. H. (1994) Synthesis of Proteins by Native Chemical Ligation. *Science 266*, 776−779.

(3) Muir, T. W., Sondhi, D., and Cole, P. A. (1998) Expressed protein ligation: A general method for protein engineering. *Proc. Natl. Acad. Sci. U.S.A. 95*, 6705−6710.

(4) Cotton, G. J., Ayers, B., Xu, R., and Muir, T. W. (1999) Insertion of a Synthetic Peptide into a Recombinant Protein Framework: A Protein Biosensor. *J. Am. Chem. Soc. 121*, 1100−1101.

(5) Becker, C. F. W., Hunter, C. L., Seidel, R. P., Kent, S. B. H., Goody, R. S., and Engelhard, M. (2001) A sensitive fluorescence monitor for the detection of activated Ras: total chemical synthesis of site-specifically labeled Ras binding domain of c-Raf1 immobilized on a surface. *Chem. Biol. 8*, 243−252.

(6) Geoghegan, K. F., and Stroh, J. G. (1992) Site-Directed Conjugation of Nonpeptide Groups to Peptides and Proteins Via Periodate-Oxidation of a 2-Amino Alcohol−Application to Modification at N-Terminal Serine. *Bioconjugate Chem. 3*, 138−146.

(7) Fancy, D. A., and Kodadek, T. (1997) Site-directed oxidative protein cross-linking. *Tetrahedron 53*, 11953−11960.

(8) Gaertner, H. F., Rose, K., Cotton, R., Timms, D., Camble, R., and Offord, R. E. (1992) Construction of Protein Analogues by Site-Specific Condensation of Unprotected Fragments. *Bioconjugate Chem. 3*, 262−268.

(9) van Hest, J. C. M., and Tirrell, D. A. (1998) Efficient introduction of alkene functionality into proteins in vivo. *FEBS Lett. 428*, 68−70.

(10) Cornish, V. W., Hahn, K. M., and Schultz, P. G. (1996) Site-specific protein modification using a ketone handle. *J. Am. Chem. Soc. 118*, 8150−8151.

(11) Sharma, N., Furter, R., Kast, P., and Tirrell, D. A. (2000) Efficient introduction of aryl bromide functionality into proteins in vivo. *FEBS Lett. 467*, 37−40.

(12) Johnsson, N., and Johnsson, K. (2003) A fusion of disciplines: Chemical approaches to exploit fusion proteins for functional genomics. *ChemBioChem 4*, 803−810.

(13) Griffin, B. A., Adams, S. R., and Tsien, R. Y. (1998) Specific covalent labeling of recombinant protein molecules inside live cells. *Science 281*, 269−272.

(14) Keppler, A., Gendreizig, S., Gronemeyer, T., Pick, H., Vogel, H., and Johnsson, K. (2003) A general method for the covalent labeling of fusion proteins with small molecules in vivo. *Nat. Biotechnol. 21*, 86−89.

(15) Kindermann, M., George, N., Johnsson, N., and Johnsson, K. (2003) Covalent and selective immobilization of fusion proteins. *J. Am. Chem. Soc. 125*, 7810−7811.

(16) Hochuli, E., Dobeli, H., and Schacher, A. (1987) New Metal Chelate Adsorbent Selective for Proteins and Peptides Containing Neighboring Histidine-Residues. *J. Chromatogr. 411*, 177−184.

(17) Hochuli, E., Bannwarth, W., Dobeli, H., Gentz, R., and Stuber, D. (1988) Genetic Approach to Facilitate Purification of Recombinant Proteins with a Novel Metal Chelate Adsorbent. *Bio/Technol. 6*, 1321−1325.

(18) Lu, Z. J., DiBlasio-Smith, E. A., Grant, K. L., Warne, N. W., LaVallie, E. R., Collinsracie, L. A., Follettie, M. T., Williams, M. J., and McCoy, J. M. (1996) Histidine patch thioredoxins−mutant forms of thioredoxin with metal chelating affinity that provide for convenient purifications of thioredoxin fusion proteins. *J. Biol. Chem. 271*, 5059−5065.

(19) Lin, J. T., Kormanec, J., Homerova, D., and Kinne, R. K. H. (1999) Probing transmembrane topology of the high-affinity sodium/glucose cotransporter (SGLT1) with histidine-tagged mutants. *J. Membr. Biol. 170*, 243−252.

(20) Voss, J., Salwinski, L., Kaback, H. R., and Hubbell, W. L. (1995) A method for distance determination in proteins using a designed metal ion binding site and site-directed spin labeling: Evaluation with T4 lysozyme. *Proc. Natl. Acad. Sci. U.S.A. 92*, 12295−12299.

(21) Bailey, J., and Manoil, C. (2002) Genome-wide internal tagging of bacterial exported proteins. *Nat. Biotechnol. 20*, 839−842.

(22) *BD HAT Protein Expression and Purification System User Manual*, pp 1−31, Clontech, 2002.

(23) Xu, Z., and Lee, S. Y. (1999) Display of Polyhistidine Peptides on the *Escherichia coli* Cell Surface by Using Outer Membrane Protein C as an Anchoring Motif. *Appl. Environ. Microbiol. 65*, 5142−5147.

(24) McMahan, S. A., and Burgess, R. R. (1996) Single-step synthesis and characterization of biotinylated nitrilotriacetic

acid, a unique reagent for the detection of histidine-tagged proteins immobilized on nitrocellulose. *Anal. Biochem 236*, 101−106.

(25) Kubalek, E. W., LeGrice, S. F. J., and Brown, P. O. (1994) Two-Dimensional Crystallization of Histidine-Tagged, HIV-1 Reverse Transcriptase Promoted by a Novel Nickel-Chelating Lipid. *J. Struct. Biol. 113*, 117−123.

(26) O'Shannessy, D. J., O'Donnell, K. C., Martin, J., and Brigham-Burke, M. (1995) Detection and Quantification of Hexa-Histidine-Tagged Recombinant Proteins on Western Blots and by a Surface Plasmon Resonance Biosensor Technique. *Anal. Biochem 229*, 119−124.

(27) Sigal, G. B., Bamdad, C., Barberis, A., Strominger, J., and Whitesides, G. M. (1996) A Self-Assembled Monolayer for the Binding and Study of Histidine-Tagged Proteins by Surface Plasmon Resonance. *Anal. Chem 68*, 490−497.

(28) Schmitt, L., Ludwig, M., Gaub, H. E., and Tampe, R. (2000) A Metal-Chelating Microscopy Tip as a New Toolbox for Single-Molecule Experiments by Atomic Force Microscopy. *Biophys. J. 78*, 3275−3285.

(29) Christendat, D., Yee, A., Dharamsi, A., Kluger, Y., Gerstein, M., Arrowsmith, C. H., and Edwards, A. M. (2000) Structural proteomics: prospects for high throughput sample preparation. *Prog. Biophys. Mol. Biol. 73*, 339−345.

(30) Heinemann, U., Frevert, J., Hofmann, K. P., Illing, G., Maurer, C., Oschkinat, H., and Saenger, W. (2000) An integrated approach to structural genomics. *Prog. Biophys. Mol. Biol. 73*, 347−362.

(31) Bussow, K., Nordhoff, E., Lubbert, C., Lehrach, H., and Walter, G. (2000) A human cDNA library for high-throughput protein expression screening. *Genomics 65*, 1−8.

(32) Zhu, H., Bilgin, M., Bangham, R., Hall, D., Casamayor, A., Bertone, P., Lan, N., Jansen, R., Bidlingmaier, S., Houfek, T., Mitchell, T., Miller, P., Dean, R. A., Gerstein, M., and Snyder, M. (2001) Global analysis of protein activities using proteome chips. *Science 293*, 2101−2105.

(33) Heyman, J. A., Cornthwaite, J., Foncerrada, L., Gilmore, J. R., Gontang, E., Hartman, K. J., Hernandez, C. L., Hood, R., Hull, H. M., Lee, W. Y., Marcil, R., Marsh, E. J., Mudd, K. M., Patino, M. J., Purcell, T. J., Rowland, J. J., Sindici, M. L., and Hoeffler, J. P. (1999) Genome-scale cloning and expression of individual open reading frames using topoisomerase I-mediated ligation. *Genome. Res. 9*, 383−392.

(34) Mateo, C., Fernandez-Lorente, G., Cortes, E., Garcia, J. L., Fernandez-Lafuente, R., and Guisan, J. M. (2001) One-step purification, covalent immobilization, and additional stabilization of poly-His-tagged proteins using novel heterofunctional chelate-epoxy supports. *Biotech. Bioeng. 76*, 269−276.

(35) Melton, R. G., and Sherwood, R. F. (1996) Antibody-enzyme conjugates for cancer therapy. *J. Natl. Cancer Inst. 88*, 153−165.

(36) Hainfeld, J. F., Liu, W. Q., Halsey, C. M. R., Freimuth, P., and Powell, R. D. (1999) Ni−NTA-gold clusters target his-tagged proteins. *J. Struct. Biol. 127*, 185−198.

(37) Kapanidis, A. N., Ebright, Y. W., and Ebright, R. H. (2001) Site-specific incorporation of fluorescent probes into protein: Hexahistidine-tag-mediated fluorescent labeling with (Ni^{2+}: Nitrilotriacetic acid)(n)-fluorochrome conjugates. *J. Am. Chem. Soc. 123*, 12123−12125.

(38) Brenner, S., and Lerner, R. A. (1992) Encoded Combinatorial Chemistry. *Proc. Natl. Acad. Sci. U.S.A. 89*, 5381−5383.

(39) Hillcoat, B. L., and Blakely, R. L. (1966) Dihydrofolate Reductase of *Streptococcus faecalis*. *J. Biol. Chem. 241*, 2995−3001.

(40) Becker, C. R., Efcavitch, J. W., Heiner, C. R., and Kaiser, N. F. (1985) Use of a C-4 Column for Reversed-Phase High-Performance Liquid-Chromatographic Purification of Synthetic Oligonucleotides. *J. Chromatogr. 326*, 293−299.

(41) Bosca, F., and Miranda, M. A. (1998) Photosensitizing drugs containing the benzophenone chromophore. *J. Photochem. Photobiol. B 43*, 1−26.

(42) Savage, M. D., Mattson, G., Desai, S., Nielander, G. W., Morgensen, S., and Conlin, E. J. (1996) *Avidin−Biotin Chemistry: A Handbook*, Pierce Chemical Co., Rockford, IL.

(43) Pace, C. N., Vajdos, F., Fee, L., Grimsley, G., and Gray, T. (1995) How to measure and predict the molar absorption coefficient of a protein. *Protein Sci. 4*, 2411−2423.

(44) Walsh, M. K., Wang, X., and Weimer, B. C. (2001) Optimizing the immobilization of single-stranded DNA onto glass beads. *J. Biochem. Biophys. Methods 47*, 221−231.

(45) Blakely, R. L. (1995) Eukaryotic Dihydrofolate Reductase. *Adv. Enzymol. 70*, 23−102.

(46) Held, P. (2001) Determination of NADH or NADPH Concentrations with the FL600 using Fluorescence or Absorbance Modes. *Bio-Tek Application Note*, http://www.biotek.com/products/tech_res_detail.php?id=57.

(47) Lewis, W. S., Cody, V., Galitsky, N., Luft, J. R., Pangborn, W., Chunduru, S. K., Spencer, H. T., Appleman, J. R., and Blakley, R. L. (1995) Methotrexate-resistant variants of human dihydrofolate reductase with substitutions of leucine 22−kinetics, crystallography, and potential as selectable markers. *J. Biol. Chem. 270*, 5057−5064.

(48) Hermanson, G. T. (1996) *Bioconjugate Techniques*, Academic Press, San Diego.

(49) Dorman, G., and Prestwich, G. D. (1994) Benzophenone photophores in biochemistry. *Biochemistry 33*, 5661−5673.

(50) Corey, D. R., and Schultz, P. G. (1987) Generation of a Hybrid Sequence-Specific Single-Stranded Deoxyribonuclease. *Science 238*, 1401−1403.

(51) Ghosh, S. S., Kao, P. M., and Kwoh, D. Y. (1989) Synthesis of 5′-Oligonucleotide Hydrazide Derivatives and Their Use in Preparation of Enzyme Nucleic-Acid Hybridization Probes. *Anal. Biochem 178*, 43−51.

(52) Roberts, R. W., and Szostak, J. W. (1997) RNA-peptide fusions for the in vitro selection of peptides and proteins. *Proc. Natl. Acad. Sci. U.S.A. 94*, 12297−12302.

(53) Doi, N., and Yanagawa, H. (1999) STABLE: protein-DNA fusion system for screening of combinatorial protein libraries in vitro. *FEBS Lett. 457*, 227−230.

(54) Tighe, H., Takabayashi, K., Schwartz, D., Marsden, R., Beck, L., Corbeil, J., Richman, D. D., Eiden, J. J., Spiegelberg, H. L., and Raz, E. (2000) Conjugation of protein to immunostimulatory DNA results in a rapid, long-lasting and potent induction of cell-mediated and humoral immunity. *Eur. J. Immunol. 30*, 1939−1947.

(55) Rajur, S. B., Roth, C. M., Morgan, J. R., and Yarmush, M. L. (1997) Covalent protein-oligonucleotide conjugates for efficient delivery of antisense molecules. *Bioconjugate Chem. 8*, 935−940.

(56) Kurz, M., Gu, K., Al-Gawari, A., and Lohse, P. A. (2001) cDNA-protein fusions: covalent protein-gene conjugates for the in vitro selection of peptides and proteins. *ChemBioChem 2*, 666−672.

(57) Weng, S., Gu, K., Hammond, P. W., Lohse, P., Rise, C., Wagner, R. W., Wright, M. C., and Kuimelis, R. G. (2002) Generating addressable protein microarrays with PROfusion (TM) covalent mRNA-protein fusion technology. *Proteomics 2*, 48−57.

(58) Oleinikov, A. V., Gray, M. D., Zhao, J., Montgomery, D. D., Ghindills, A. L., and Dill, K. (2003) Self-assembling protein arrays using electronic semiconductor microchips and in vitro translation. *J. Proteome Res. 2*, 313−319.

(59) Lovrinovic, M., Seidel, R., Wacker, R., Schroeder, H., Seitz, O., Engelhard, M., Goody, R. S., and Niemeyer, C. M. (2003) Synthesis of protein-nucleic acid conjugates by expressed protein ligation. *Chem. Commun. 2003*, 822−823.

(60) Shih, H. C., Kassahun, H., Burrows, C. J., and Rokita, S. E. (1999) Selective association between a macrocyclic nickel complex and extrahelical guanine residues. *Biochemistry 38*, 15034−15042.

(61) Hansma, H. G., Pietrasanta, L. I., Golan, R., Sitko, J. C., Viani, M. B., Paloczi, G. T., Smith, B. L., Thrower, D., and

Hansma, P. K. (2000) Recent highlights from atomic force microscopy of DNA. *J. Biomol. Struct. Dyn.* 271−275.
(62) Abrescia, N. G. A., Huynh-Dinh, T., and Subirana, J. A. (2002) Nickel-guanine interactions in DNA: crystal structure of nickel-d. *J. Biol. Inorg. Chem. 7*, 195−199.
(63) Dawson, R. M. C., Elliot, D. C., Elliot, W. H., and Jones, K. M. (1986) *Data for Biochemical Research*, Clarendon Press, Oxford.
(64) Niemeyer, C. M., Sano, T., Smith, C. L., and Cantor, C. R. (1994) Oligonucleotide-directed self-assembly of proteins: semisynthetic DNA-streptavidin hybrid molecules as connectors for the generation of macroscopic arrays and the construction of supramolecular bioconjugates. *Nucleic Acids. Res. 22*, 5530−5539.
(65) Turkova, J. (1999) Oriented immobilization of biologically active proteins as a tool for revealing protein interactions and function. *J. Chromatogr. B 722*, 11−31.
(66) Baumeister, W., and Steven, A. C. (2000) Macromolecular electron microscopy in the era of structural genomics. *Trends Biol. Sci. 25*, 624−631.
(67) Seeman, N. (2003) At the Crossroads of Chemistry, Biology, and Materials: Structural DNA Nanotechnology. *Chem. Biol. 10*, 1151−1159.
(68) Niemeyer, C. M., and Adler, M. (2002) Nanomechanical Devices Based on DNA. *Angew Chem, Int. Ed. 41*, 3779−3783.

BC0498929

Detection of Apoptosis Using the C2A Domain of Synaptotagmin I

Hyo-il Jung,[†] Mikko I. Kettunen, Bazbek Davletov,[‡] and Kevin M. Brindle*

Department of Biochemistry, University of Cambridge, Tennis Court Road, Cambridge CB2 1GA, U.K.
Received April 24, 2004; Revised Manuscript Received July 8, 2004

Binding of annexin V or the C2A domain of synaptotagmin I to phosphatidylserine expressed on the surface of apoptotic cells can, when labeled with appropriate probe molecules, be used to detect the presence of apoptosis using radionuclide, magnetic resonance, and optical imaging techniques. The preparation of a biotinylated C2A−GST fusion protein is described, and its capability, when used in conjunction with fluorescein-labeled streptavidin, of detecting apoptotic cells by flow cytometry is compared directly with the performance of a commercial preparation of fluorescein-labeled annexin V. Biotinylated C2A−GST, when used in conjunction with streptavidin-conjugated superparamagnetic iron oxide nanoparticles or Gd−chelate−avidin conjugates, was shown to be capable of detecting apoptotic cells using T_2-weighted or T_1-weighted magnetic resonance imaging experiments, respectively.

INTRODUCTION

Apoptosis, or programmed cell death, is a highly regulated process that results in the selective elimination of cells during normal tissue homeostasis and differentiation (*1*). Apoptosis can also occur in tumors following chemotherapy, where the extent of apoptosis and the speed of onset have been shown to be good prognostic indicators for the outcome of treatment (*2*−*5*). For this reason we have been interested in identifying markers of tumor cell apoptosis that could be detected noninvasively in the clinic using magnetic resonance spectroscopy and imaging techniques (*6*, *7*). There are a number of markers that can be used to identify apoptotic cells, including morphological changes, DNA fragmentation, and caspase activation (*8*). A relatively early event in the process is the flipping of phosphatidylserine from the inner leaflet of the plasma membrane bilayer to the outer surface (*9*), which can be detected by binding of the protein annexin V to surface phosphatidylserine (*10*). This has led to the development of a number of annexin V based probes for detecting apoptotic cells, including technetium-labeled (*11*) and near-infrared fluorochrome-labeled-proteins (*12*), which have allowed the detection of apoptotic cells in vivo using radionuclide and optical imaging techniques, respectively. We have demonstrated previously that the C2A domain of the protein synaptotagmin I, which binds to negatively charged phospholipids in a Ca^{2+}-dependent manner, can be used to detect apoptotic cells in vitro using flow cytometry. We also showed that when labeled with superparamagnetic iron oxide nanoparticles (SPIO)[1] the protein domain could be used to detect apoptotic cells, in vitro and in vivo, using T_2-weighted magnetic resonance imaging experiments (*13*). We describe here the synthesis of a biotinylated protein that, when used in conjunction with appropriately labeled avidin or streptavidin molecules, which bind very tightly to biotin ($K_d \approx 10^{-15}$ M), can be used to detect apoptotic cells by flow cytometry or by T_1- or T_2-weighted ^{1}H magnetic resonance imaging. Flow cytometric detection of apoptotic cells using C2A was compared with detection using a commercial preparation of the more widely used annexin V.

EXPERIMENTAL PROCEDURES

Protein Purification. *E. coli* BL21(DE3) cells transformed with a pGEX vector (Amersham Biosciences) expressing a C2A−GST fusion protein (*14*) were grown at 37 °C in 2xTY medium (2 L) supplemented with 50 μg/mL ampicillin until the A_{600} was between 0.5 and 0.8. The cells were then induced with IPTG (final concentration of 0.1 mM) and incubated for a further 3 h before harvesting by centrifugation at 6000*g* for 30 min. The cells were resuspended in 40 mL of BugBuster protein extraction reagent (Novagen) and incubated for 20 min at 25 °C. Cell debris was removed by ultracentrifugation at 20000*g* for 30 min, the supernatant was applied to glutathione sepharose 4B beads (Amersham Biosciences) preequilibrated with phosphate-buffered saline (PBS), and the protein was purified according to the manufacturer's instructions. The protein, which ran as a single band in sodium dodecyl sulfate polyacrylamide gel electrophoresis (SDS−PAGE), was dialyzed against PBS and concentrated using a Vivaspin filter (Vivascience, Germany). The protein can be produced in very high yield using this system (∼40 mg/L *E. coli* culture), which is an advantage given the relatively large amounts required for magnetic resonance (MR) imaging experiments.

The C2A domain was prepared by thrombin cleavage of the fusion protein and purified using glutathione

* To whom correspondence should be addressed. Phone: +44 (0)1223 333674. Fax: +44 (0)1223 766002. E-mail: kmb@mole.bio.cam.ac.uk.

[†] Present address: Department of Mechanical Engineering, Yonsei University, South Korea.

[‡] Neurobiology Division, MRC Laboratory of Molecular Biology, Hills Road, Cambridge CB2 2QH.

[1] SPIO, superparamagnetic iron oxide; C2A, C2A domain of synaptotagmin I; GST, glutathione S-transferase; PS, phosphatidylserine; PC, phosphatidylcholine; DTPA, diethylenetriaminepentaacetate; HBS, HEPES-buffered saline; SulfoNHS−LC−biotin, sulfosuccinimidyl-6-(biotinamido) hexanoate; PI, propidium iodide; MALDI-TOF MS, matrix assisted laser desorption ionization time-of-flight mass spectrometry; NTA, *N*,*N* bis(carboxymethyl)glycine; RU, response unit; SPR, surface plasmon resonance; MRI, magnetic resonance imaging; SDS−PAGE, sodium dodecyl sulfate polyacrylamide gel electrophoresis.

10.1021/bc049899q CCC: $27.50 © 2004 American Chemical Society
Published on Web 08/12/2004

sepharose 4B beads. Briefly, 400 μg of C2A−GST fusion protein were mixed with 10 units of thrombin in PBS and incubated for 20 h at 25 °C. Glutathione sepharose 4B beads were added to the reaction mixture and incubated for a further 10 min before the solution was centrifuged at 300*g* for 5 min to collect the supernatant, which contained the C2A domain. The bead-bound GST was eluted using a reduced glutathione solution.

Surface Plasmon Resonance Analysis. Liposomes were prepared from brain phospholipids (Avanti Polar Lipids Co.). Samples containing 2.6 μmol of a PS/PE/PC mixture (molar ratio 35:50:15) in chloroform were dried under a stream of nitrogen and resuspended in 2.6 mL of buffer (20 mM HEPES, 100 mM NaCl, pH 7.4) by vigorous vortexing. A milky suspension was created, indicating the formation of large multilamellar vesicles (LMV). Small unilamellar vesicles (SUV) were obtained by sonication of the LMV until the solution cleared. To determine the binding affinity of the C2A domain for the liposomes, surface plasmon resonance analysis was performed using a Biacore 2000 system (Biacore, Uppsala, Sweden) and L1 chips. The sensor chips were coated with 40 μL of a suspension of SUV containing 1 mM phospholipid at a flow rate of 5 μL/min. The resulting response was about 3000 RU. To remove any multilamellar material from the lipid surface, 5 μL of 50 mM NaOH was injected, which resulted in a stable baseline (∼2000 RU) corresponding to the lipid bilayer linked to the chip surface. The C2A domain was allowed to interact with the sensor surface for 10 min (association phase) at five different concentrations, increasing from 150 to 550 nM. All the experiments were conducted in a buffer containing 10 mM HEPES, pH 7.4, 150 mM NaCl, and 2 mM $CaCl_2$ at a flow rate of 5 μL/min and at 25 °C and were repeated three times. To regenerate the phospholipid bilayer surface after the dissociation phase, 10 μL of 50 mM NaOH solution was used. The binding data were evaluated using BIAevaluation software, version 3.1 (BIAcore AB, Uppsala, Sweden).

Biotinylation of the C2A−GST Fusion Protein. The protein was biotinylated using an *N*-hydroxysulfosuccinimide (NHS) ester derivative of biotin, which modifies primary amine groups. Since the Ca^{2+}-dependent PS binding sites on C2A contain two Lys residues (Lys200 and Lys236) (*20*), we sought to protect these by first binding the protein to an SP sepharose column. The protein binds tightly to the negatively charged SP sepharose resin in a Ca^{2+}-dependent manner, via binding sites that likely overlap those for PS. Purified C2A−GST (6 mg/mL, 1 mL) was loaded onto an SP column (HiTrap SP FF, 1 mL volume, Amersham Biosciences) equilibrated with HEPES-buffered saline containing 20 mM HEPES, pH 7.4, 150 mM NaCl, and 0.2 mM $CaCl_2$. After extensive washing, sulfoNHS−LC−biotin (Pierce) (1.8 mg/mL, 1 mL, 40-fold excess of biotin) in the same buffer was injected into the column and the flow-through fraction was collected and reinjected. After four cycles of reinjection, the column was left at 25 °C for 15 min and then washed with 10 bed volumes of HEPES−Ca^{2+} buffer. The biotinylated protein was eluted using buffer lacking $CaCl_2$ and containing 10 mM EDTA. The collected fractions were pooled and dialyzed against PBS for 24 h to remove EDTA.

The biotinylation sites in C2A−GST were investigated by cleaving the fusion protein at the thrombin cleavage site. To estimate the number of moles of biotin conjugated per mole of C2A−GST and to identify the region of the protein modified (C2A versus GST), the biotin-conjugated protein (0.4 mL of a 1 mg/mL solution in PBS) was mixed with a thrombin solution (10 μL of a 1 U/μL solution in PBS) and incubated at 25 °C for 20 h. The resulting mixture of two protein fragments and the intact fusion protein were analyzed by SDS−PAGE and MALDI-TOF mass spectrometry. The binding activity of biotinylated C2A−GST for PS was assessed using a liposome binding assay described previously (*21*). Briefly, the biotinylated protein was mixed with the liposomes and then centrifuged.

Flow Cytometry. Murine lymphoma cells (EL4) were grown in RPMI 1640 medium supplemented with 10% heat-inactivated fetal bovine serum, 2 mM L-glutamine, 100 U/mL penicillin, and 0.1 mg/mL streptomycin. The cells were treated with 15 μM etoposide for 16 h to induce apoptosis, collected by centrifugation, and then washed in ice-cold PBS. The washed cells were suspended in C2A-binding buffer (10 mM HEPES, 140 mM NaCl, 2.5 mM $CaCl_2$, pH 7.4), and the cell density was adjusted to 1×10^6 cells/mL. To 100 μL of cell suspension, 1 μL of biotin−C2A−GST protein (30 μM protein), 1 μL of propidium iodide (PI) (100 μg/mL), and 5 μL of streptavidin−FITC (Sigma) (1 mg/mL) were added, and the mixture was incubated for 5 min at 25 °C. The resulting mixture was then subjected to flow cytometry (FACScan, Becton Dickinson, U.K.). For each sample 20 000 cells were counted. Apoptosis was also detected using a commercially available preparation of annexin V-FITC (Molecular Probes), which was used according to the manufacturer's instructions.

Preparation of Contrast Agents and Magnetic Resonance Imaging. Avidin−GdDTPA conjugates were prepared as described in (*15*). Briefly, purified avidin (Sigma) was incubated with 20-fold excess DTPA anhydride (Sigma) for 24 h at 4 °C. After extensive dialysis against 100 mM sodium citrate buffer, pH 6.5, a 40-fold excess of $Gd(NTA)_2$ was added to the avidin−DTPA solution. After incubation for 24 h at 4 °C, the resulting mixture was dialyzed extensively against PBS and stored at −20 °C before use. The T_1 relaxivity of this modified protein at 9.4 T was about 60 mM^{-1} s^{-1}. For T_2-weighted ^1H MR imaging, commercially available strepavidin-conjugated SPIO nanoparticles were used (Miltenyi Biotec). Etoposide-treated cells were incubated with different concentrations (1.5, 4.5, 15 μM) of the biotinylated C2A−GST protein at 25 °C for 5 min. The protein concentration was determined by amino acid analysis. After being washed, cells were incubated with avidin−GdDTPA conjugates (80 μM protein) or streptavidin−SPIO nanoparticles (30 ng/mL of Fe) at 25 °C for 5 min. After washing, 10^7 cells were mixed with 50 μL of 4% bovine gelatin and then immediately loaded into a 5 mm NMR tube. T_1- (repetition time, TR = 0.2 s; spin−echo time, TE = 15 ms) and T_2- (TR = 4 s, TE = 40 ms) weighted ^1H MR images of the samples were acquired at 9.4 T using a two-dimensional spin−echo imaging sequence, a 25 mm diameter proton probe, and a Varian UnityPlus spectrometer.

RESULTS

Measurement of the Affinity of C2A for Phosphatidylserine-Containing Liposomes Using Surface Plasmon Resonance. Small unilamellar vesicles were immobilized on an L1 sensor chip, which allows retention of the lipid bilayer structure (*16*). A representative sensorgram is shown in Figure 1, showing the association of the C2A domain with phosphatidylserine on the surface of the sensor chip and its subsequent dissociation. The C2A domain bound to the surface of the

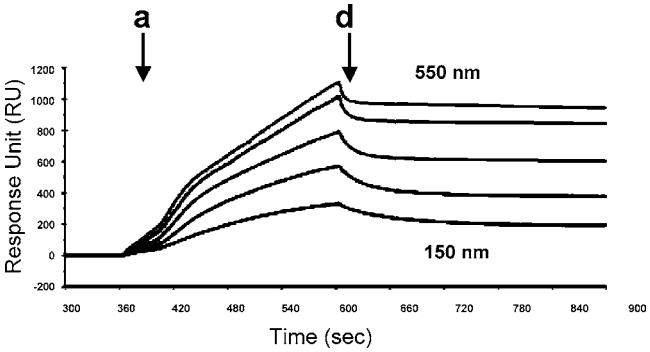


Figure 1. SPR sensorgram (relative response vs time) for the C2A domain. The L1 sensor chip was coated with PS-containing liposomes, and the C2A domain was injected at a series of increasing concentrations (150, 250, 350, 450, and 550 nM). The start of the association and dissociation phases are indicated by the symbols a and d, respectively.

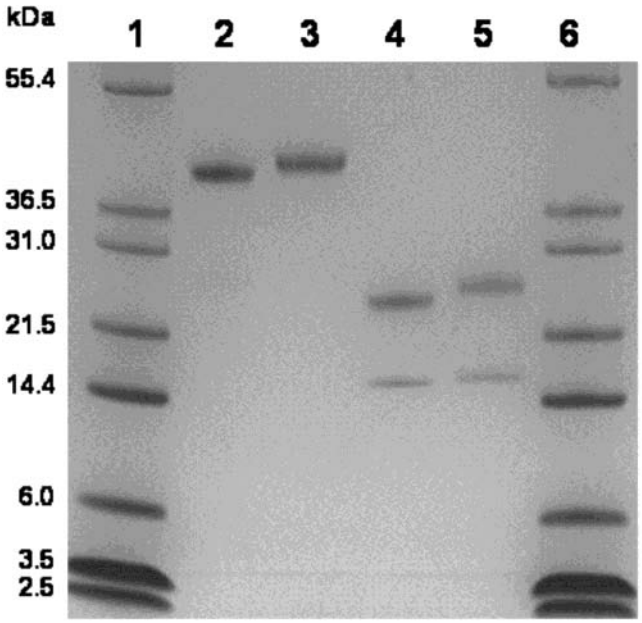


Figure 2. Analysis of the biotinylation of C2A−GST by SDS−PAGE: (1) size markers; (2) intact C2A-GST; (3) biotinylated C2A-GST; (4) thrombin-cleaved C2A−GST; (5) thrombin-cleaved biotinylated C2A-GST; (6) size markers. The relative molecular mass of GST is 26 kDa, and that of the C2A domain is 16 kDa. Both the GST and C2A bands from the biotinylated protein are retarded when compared to the unmodified protein, indicating that both domains of the fusion protein are biotinylated.

sensor chip in the presence of 2 mM $CaCl_2$ but had no affinity when free Ca^{2+} was depleted by the addition of 10 mM EDTA (data not shown). The calculated dissociation constant is in the nanomolar range ($(17.1 \pm 0.5) \times 10^{-9}$ M) and comparable to a value of 115×10^{-9} M for the binding of C2A−GST to a lipid monolayer (*17*) determined by surface plasmon resonance and to a value of 40×10^{-9} M for the binding of C2A to phospholipid vesicles (25% PS/75% PC) determined using intrinsic fluorescence measurements (*18*). However, the affinity of C2A for phosphatidylserine-containing membranes is lower than that of annexin V, for which a dissociation constant of $<0.1 \times 10^{-9}$ M was measured for its binding to phospholipid vesicles (20% PS/80% PC) at an ionic strength of 0.15 M (*19*).

Biotinylation of C2A−GST. The biotinylation sites in C2A−GST were investigated by cleaving the fusion protein at the thrombin cleavage site and analyzing the resulting two fragments and the intact fusion protein

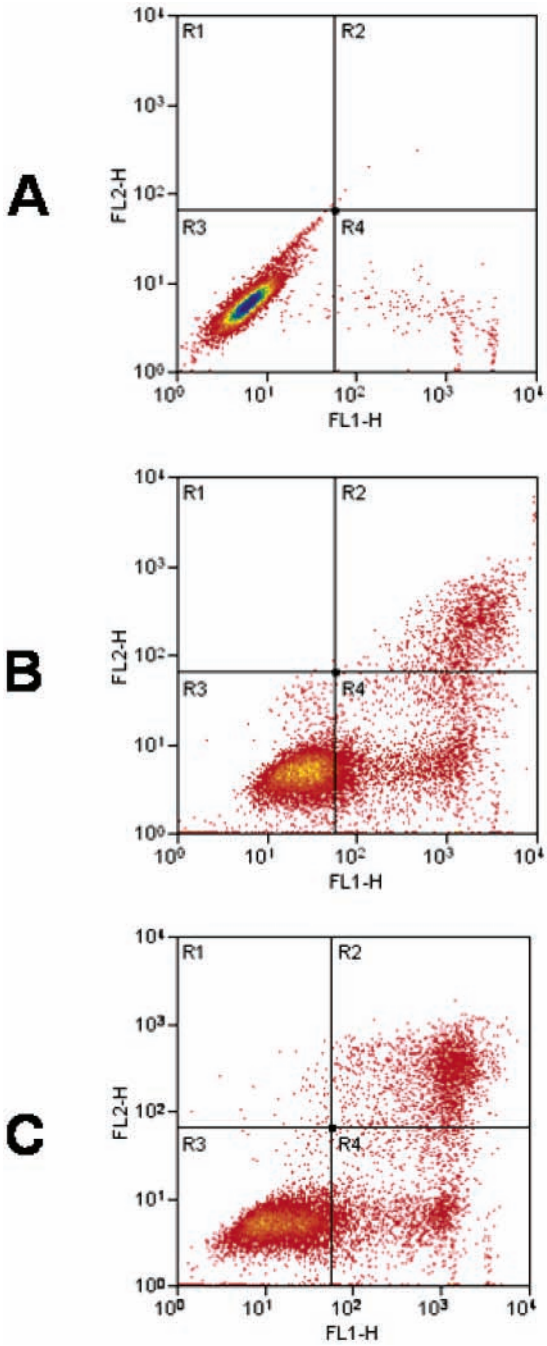


Figure 3. The capability of biotinylated C2A−GST to bind to apoptotic cells was assessed by flow cytometry: (A) apoptotic EL4 cells (1×10^6 cells/mL); (B) apoptotic EL4 cells (1×10^6 cells/mL) incubated with biotin−C2A−GST + streptavidin−FITC + PI; (C) apoptotic EL4 cells (1×10^6 cells/mL) + annexin V-FITC + PI.

using SDS−PAGE and MALDI-TOF mass spectrometry. As shown in Figure 2, the gel bands for biotinylated C2A−GST, C2A, and GST were retarded when compared with the unmodified proteins. MALDI-TOF mass spectrometry showed that GST contained between five and six biotin moieties and the C2A domain contained between zero and three. There are 14 lysine residues in C2A and 21 in GST. A liposome binding assay indicated that the modified protein was pulled down by the liposomes, demonstrating that it retained a strong binding affinity for PS (data not shown).

Flow Cytometry. The capability of biotinylated C2A−GST to detect apoptotic cells was assessed by using flow

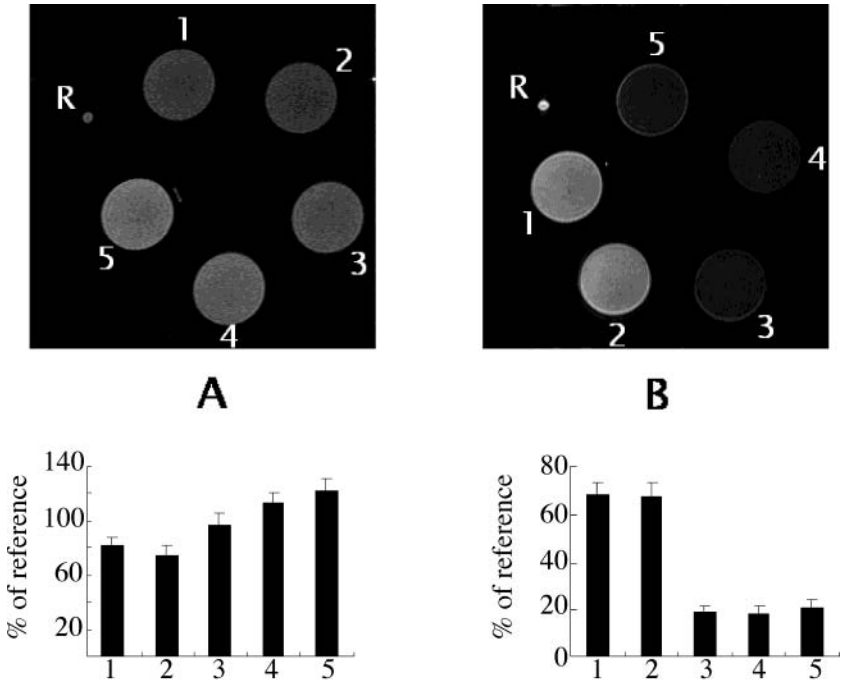


Figure 4. MR imaging of apoptotic cells in vitro. Apoptotic EL4 cells were incubated with biotin−C2A−GST at the specified concentration, washed, and then subsequently incubated with avidin−GdDTPA (80 μM protein) or streptavidin−SPIO (30 ng of Fe/mL), washed again, and then suspended in 4% gelatin in PBS and loaded into 5 mm diameter NMR tubes for T_1-weighted (A) or T_2-weighted (B) ^{1}H MR images. The tubes contained the following: (1) apoptotic cells; (2) apoptotic cells + avidin−GdDTPA (A) or streptavidin−SPIO (B); (3−5) apoptotic cells + biotin−C2A−GST + avidin−GdDTPA (A) or streptavidin−SPIO (B). The concentrations of biotinylated C2A−GST increased from tube 3 to tube 5 (tube 3, 1.5 μM; tube 4, 4.5 μM; tube 5, 15 μM). The signal intensities (mean pixel intensities ± SD) of the tubes relative to the reference (R) are shown at the bottom of each image.

cytometry in conjunction with fluoroscein-labeled streptavidin (streptavidin−FITC). Murine lymphoma cells (EL4) were induced to undergo apoptosis by treatment with etoposide and then stained with a combination of biotinylated C2A−GST, streptavidin−FITC, and propidium iodide (PI). PI stains the nuclei of necrotic cells. The same apoptotic cell preparation was also stained with FITC-labeled annexin V and PI for comparison (Figure 3). The annexin V-FITC was used according to the manufacturer's instructions. The biotinylated C2A−GST preparation allowed a distinction to be made between live cells (69%, quadrant labeled R3 in Figure 3B), apoptotic cells (21%, quadrant labeled R4 in Figure 3B), and necrotic cells (10%, quadrant labeled R2 in Figure. 3B). Despite the lower affinity of C2A for PS, similar results were obtained using annexin V, which detected 64% live cells, 16% apoptotic cells, and 20% necrotic cells (Figure 3C).

The single C2A domain was also biotinylated using the same conjugation procedure described above. The modified protein contained between two and six biotins, as determined by mass spectrometry. However, this protein showed no activity in the streptavidin−FITC flow cytometric assay most likely because the streptavidin−FITC interfered with binding of the biotinylated C2A to the cell membrane.

Magnetic Resonance Imaging. Figure 4 shows T_1-(A) and T_2-weighted (B) images obtained from apoptotic EL4 cells that had been incubated with biotinylated C2A−GST, washed, and then incubated with either avidin−GdDTPA or streptavidin-SPIO, before being washed again and then immobilized in gelatin. Apoptotic cells incubated with progressively increasing concentrations of C2A−GST and then either avidin−GdDTPA or streptavidin−SPIO showed progressively increasing or decreasing image intensities, respectively.

DISCUSSION

We had already shown that the C2A−GST fusion protein, when directly conjugated to SPIO nanoparticles, could be used to detect apoptotic tumor cells in vitro and in vivo using T_2-weighted magnetic resonance imaging experiments (*13*). Annexin V conjugated to a superparamagnetic complex has also been used for apoptosis detection by MRI (*22*). However, the SPIO label, although very sensitive to MRI detection, has two major limitations. The label is relatively large (we used particles 20−30 nm in diameter), which restricts extravasation of the agent from the vasculature into the tumor interstitium, and it gives rise to signal loss, or negative contrast in the MR image. Since there are many factors that can give rise to negative contrast in tumors, which show highly heterogeneous and temporally variable image contrast, this can make the label difficult to detect. Artemov et al. (*15*) have shown recently that they could detect the Her2-neu receptor in breast cancer cells with MRI by using a biotinylated antibody directed against the receptor in conjunction with either streptavidin−SPIO or avidin−GdDTPA conjugates in T_2-weighted or T_1-weighted imaging experiments respectively (*15*, *23*). This approach has the virtue that the imaging reagent is assembled in situ on the surface of the cell from smaller components, thus potentially overcoming the problems associated with the limited vascular permeability of larger agents, and in the case of the Gd conjugate, the agent gives rise to positive contrast in T_1-weighted images. Furthermore, it allows for the production of generic labeling agents based on avidin/streptavidin, which can be used in conjunction with specific, biotinylated, targeting agents. The experiments presented here (Figure 4) have demonstrated the feasibility of imaging apoptosis in vivo with a biotinylated targeting agent, C2A−GST, and a generic labeling agent based on either avidin or streptavidin conjugated to SPIO

or Gd−DTPA. Whereas SPIO gave relatively large decreases in image intensity in T_2-weighted images, the intensity increases produced by avidin−GdDTPA in the T_1-weighted images were more modest (Figure 4). For this reason it would be desirable to increase the amount and/or relaxivity of the Gd conjugates attached to the avidin/streptavidin. This may be achieved, for example, by attaching polyamidoamine dendrimers, conjugated to GdDTPA (*24*), to avidin/streptavidin. However, a drawback of the avidin/streptavidin system is the immunogenecity of these proteins (*25*), which may limit their application in the clinic. In this case, it may be preferable to conjugate high-relaxivity Gd-based agents directly to C2A−GST.

ACKNOWLEDGMENT

This work was supported by Cancer Research U.K. [CUK], Grant C197/A3514. M.I.K. thanks The Ella and Georg Ehrnrooth Foundation, The Emil Aaltonen Foundation, The Finnish Cultural Foundation of Northern Savo, and the University of Kuopio for their support.

LITERATURE CITED

(1) Heemels, M.-T. (2000) Apoptosis. *Nature 407*, 769.
(2) Meyn, R. E., Stephens, L. C., Ang, K. K., Hunter, N. R., Brock, W. A., Milas, L., and Peters, L. J. (1993) Heterogeneity in apoptosis development in irradiated murine tumours of different histologies. *Int. J. Radiat. Biol. 64*, 583−591.
(3) Meyn, R. E., Stephens, L. C., Hunter, N. R., and Milas, L. (1995) Apoptosis in murine tumours treated with chemotherapy agents. *Anti-Cancer Drugs 6*, 443−450.
(4) Chang, J., Ormerod, M., Powles, T. J., Allred, D. C., Ashley, S. E., and Dowsett, M. (2000) Apoptosis and proliferation as predictors of chemotherapy response in patients with breast carcinoma. *Cancer* 2145−2152.
(5) Dubray, B., Breton, C., Delic, J., Klijanienko, J., Maciorowski, Z., Vielh, P., Forquet, A., Dumont, J., Magdelenat, H., and Cosset, J. M. (1998) In vitro radiation-induced apoptosis and early response to low-dose radiotherapy in non-Hodgkin's lymphomas. *Radiother. Oncol. 46*, 185−191.
(6) Hakumäki, J. M., and Brindle, K. M. (2003) Visualising apoptosis by nuclear magnetic resonance. *Trends Pharmacol. Sci. 24*, 146−149.
(7) Brindle, K. M. (2002) Detection of apoptosis using magnetic resonance imaging and spectroscopy. *Adv. Enzyme Regul. 42*, 101−112.
(8) Saraste, A., and Pulkki, K. (2000) Morphologic and biochemical hallmarks of apoptosis. *Cardiovasc. Res. 45*, 528−537.
(9) Martin, S. J., Reutelingsperger, C. P. M., McGahon, A. J., Rader, J. A., Vanschie, R. C. A. A., LaFace, D. M., and Green, D. R. (1995) Early redistribution of plasma-membrane phosphatidylserine is a general feature of apoptosis regardless of the initiating stimulus−Inhibition by overexpression of Bcl-2 and Abl. *J. Exp. Med. 182*, 1545−1556.
(10) Vermes, I., Haanen, C., Steffens-Nakken, H., and Reutelingsperger, C. (1995) A novel assay for apoptosis. Flow cytometric detection of phosphatidylserine expression on early apoptotic cells using fluorescein labelled Annexin V. *J. Immunol. Methods 184*, 39−51.
(11) Blankenberg, F. G., Katsikis, P. D., Tait, J. F., Davis, R. E., Naumovski, L., Ohtsuki, K., Kopiwoda, S., Abrams, M. J., Darkes, M., Robbins, R. C., Maecker, H. T., and Strauss, H. W. (1998) In vivo detection and imaging of phosphatidylserine expression during programmed cell death. *Proc. Natl. Acad. Sci. U.S.A. 95*, 6349−6354.
(12) Petrovsky, A., Schellenberger, E., Josephson, L., Weissleder, R., and Bogdanov, A. (2003) Near-infrared fluorescent imaging of tumor apoptosis. *Cancer Res. 63*, 1936−1942.
(13) Zhao, M., Beauregard, D. A., Loizou, L., Davletov, B., and Brindle, K. M. (2001) Non-invasive detection of apoptosis using magnetic resonance imaging and a targeted contrast agent. *Nat. Med. 7*, 1241−1244.
(14) Davletov, B. A., and Sudhof, T. C. (1993) A single C2 domain from synaptogamin I is sufficient for high affinity Ca^{2+}/phospholipid binding. *J. Biol. Chem. 268*, 26 386−26 390.
(15) Artemov, D., Mori, N., Ravi, R., and Bhujwalla, Z. (2003) Magnetic resonance molecular imaging of the HER-2/neu receptor1. *Cancer Res 63*, 2723−2727.
(16) Saenko, E., Sarafanov, A., Ananyeva, N., Behre, E., Shima, M., Schwinn, H., and Josic, D. (2001) Comparison of the properties of phospholipid surfaces formed on HPA and L1 biosensor chips for the binding of the coagulation factor VIII. *J. Chromatogr. 921*, 49−56.
(17) Lu, Y.-J., He, Y., and Sui, S.-f. (2002) Inositol hexakisphosphate (INsP6) can weaken the Ca^{2+}-dependent membrane binding of C2AB domain of synaptotagmin. *FEBS Lett. 527*, 22−26.
(18) Davis, A., Bai, J., Fasshauer, D., Wolowick, M., Lewis, J., and Chapman, E. (1999) Kinetics of synaptotagmin responses to Ca^{2+} and assembly with the core SNARE complex onto membranes. *Neuron 24*, 363−376.
(19) Tait, J., Gibson, D., and Fujikawa, K. (1989) Phospholipid binding properties of human placental anticoagulant protein-I, a member of the lipocortin family. *J. Biol. Chem. 264*, 7944−7949.
(20) Zhang, X., Rizo, J., and Sudhof, T. (1998) Mechanism of phospholipid binding by the C2A-domain of synaptotagmin I. *Biochemistry 37*, 12395−12403.
(21) Davletov, B., Perisic, O., and Williams, R. L. (1998) Calcium-dependent membrane penetration is a hallmark of the C2 domain of cytosolic phospholipase A2 whereas the C2A domain of synaptotagmin binds membranes electrostatically. *J. Biol. Chem. 273*, 19093−19096.
(22) Schellenberger, E., Bogdanov, A., Hogemann, D., Tait, J., Weissleder, R., and Josephson, L. (2002) Annexin V-CLIO: a nanoparticle for detecting apoptosis by MRI. *Mol. Imaging 1*, 102−107.
(23) Artemov, D., Mori, N., Okollie, B., and Bhujwalla, Z. M. (2003) MR molecular imaging of the Her-2/neu receptor in breast cancer cells using targeted iron oxide nanoparticles. *Magn. Reson. Med. 49*, 403−408.
(24) Wiener, E. C., Brechbiel, M. W., Brothers, H., Magin, R. L., Gansow, O. A., Tomalia, D. A., and Lauterbur, P. C. (1994) Dendrimer-based metal chelates: A new class of magnetic resonance imaging contrast agents. *Magn. Reson. Med. 31*, 1−8.
(25) Paganelli, G., Bartolomei, M., Ferrari, M., Cremonesi, M., Broggi, G., Maira, G., Sturiale, C.; Grana, C., Prisco, G., Gatti, M., Caliceti, P., and Chinol, M. (2001) Pre-targeted locoregional radioimmunotherapy with 90Y-biotin in glioma patients: Phase I study and preliminary therapeutic results. *Cancer Biother. Radiopharm. 16*, 227−235.

BC049899Q

Evaluation of ^{64}Cu- and ^{125}I-Radiolabeled Bitistatin as Potential Agents for Targeting $\alpha_v\beta_3$ Integrins in Tumor Angiogenesis

Paul McQuade,[†] Linda C. Knight,*[,‡] and Michael J. Welch[†]

Mallinckrodt Institute of Radiology, Washington University School of Medicine, St. Louis, Missouri 63110, and Department of Diagnostic Imaging, Temple University School of Medicine, Philadelphia, Pennsylvania 19140.
Received February 18, 2004; Revised Manuscript Received July 19, 2004

The formation of new blood vessels (angiogenesis) is a feature common to all solid tumors. The integrin receptor $\alpha_V\beta_3$, which is found on endothelial cells lining newly growing blood vessels at a higher density than on mature blood vessels, is being explored as a marker for tumor angiogenesis. Bitistatin, a member of the disintegrin family of polypeptides, has affinity for $\alpha_V\beta_3$ integrins. To determine whether radiolabeled bitistatin could target tumors, its biodistribution was tested in tumor-bearing mice. For initial validation studies, ^{125}I-bitistatin was injected into BALB/c mice bearing EMT-6 mouse mammary carcinoma tumors, a model that is highly vascular but which lacks $\alpha_V\beta_3$ directly on tumor cells. Tumor uptake reached maximal values (11.7 ± 4.6 %ID/g) at 2 h. Co-injection of 200 μg of unlabeled bitistatin reduced tumor uptake 62%, suggesting that the binding of ^{125}I-bitistatin is receptor-mediated. This work was extended to include the β^+-emitting radionuclide ^{64}Cu, which was attached to bitistatin via 1,4,7,10-tetraazacyclododecane-*N*,*N*′,*N*″,*N*‴-tetraacetic acid (DOTA). This modification did not significantly alter receptor binding in vitro. MicroPET images obtained with ^{64}Cu-DOTA-bitistatin showed that the tumor could easily be identified 4 h after administering the radiopharmaceutical. The biodistribution of ^{64}Cu-DOTA-bitistatin differed from the ^{125}I analogue, in that maximum tumor uptake was nearly 8-fold lower and took at least 6 h to reach maximal binding (1.6 ± 0.2 %ID/g). As with ^{125}I-labeled bitistatin, the ^{64}Cu conjugate showed a 50% reduction in tumor uptake with the co-injection of 200 μg of unlabeled bitistatin (0.8 ± 0.2 %ID/g). Competition studies with integrin-specific peptides indicated that the tumor uptake was related to both $\alpha_v\beta_3$ and $\alpha_{IIb}\beta_3$ integrin binding. To see if tumor uptake could be improved upon, ^{64}Cu was tethered to bitistatin using bromoacetamidobenzyl-1,4,7,-10-tetraazacyclododecane-*N*,*N*′,*N*″,*N*‴-tetraacetic acid (BAD). Tumor uptake for ^{64}Cu-BAD-2IT-bitistatin was higher than the DOTA conjugate at all time points, reaching a maximum at least 6 h postinjection (5.2 ± 0.6 %ID/g); however, this was accompanied by higher uptake in nontarget organs at all time points. Radiolabeled ligands of this type may be useful in the targeting of tumor angiogenesis, but the choice of radiolabeling approach has a significant impact on the in vivo properties of the radioligand.

INTRODUCTION

Detecting cancer early enough to improve patient prognosis remains a difficult problem. Typically, solid tumors must be larger than 10 mm to be reliably detected by anatomic imaging techniques such as computed tomography (CT). In a similar fashion, traditional nuclear medicine techniques are limited to detection of larger tumors, so many lesions are missed. Thus, there is a need to develop new techniques for the early detection of tumors, so that treatment can be started earlier and improve patient prognoses. One of the ways this can be achieved is by targeting the evolving vasculature that nourishes a growing tumor.

As has been documented, the expansion of a tumor beyond a few cubic millimeters is dependent on the formation of new blood vessels (angiogenesis) to provide nutrients and oxygen needed by the growing tumor (*1*). The vasculature of the tumor differs from that found in the rest of the body in that it is relatively immature and contains large numbers of receptors involved in vessel growth (*2*). The unique character of tumor vasculature therefore would be a good target for pharmaceuticals in both the detection and treatment of a wide variety of cancerous tumors, as all solid tumors are dependent on angiogenesis. It is possible that targeting of tumor vasculature could allow monitoring of smaller tumors than can be detected with the present nuclear medicine radiotracers.

One marker of tumor angiogenesis that may be a suitable target is $\alpha_V\beta_3$, also known as the vitronectin receptor (*3*). It is a member of the integrin family of receptors which are involved in adhesion and signaling of many types of cells (*4*−*6*), and binds ligands containing an Arg-Gly-Asp (RGD) motif. Molecules containing this RGD motif are of interest as antagonists of angiogenesis. One such family of molecules is the disintegrins, which were first reported as $\alpha_{IIb}\beta_3$ antagonists isolated from the venoms of various snakes (*7*). These low molecular mass (5−9 kDa), cysteine-rich polypeptides are constrained by internal disulfide linkages into multiloop structures and

* Author for Correspondence: Linda C. Knight, Ph.D., Department of Diagnostic Imaging, Temple University School of Medicine, 3401 N. Broad St., Philadelphia, PA 19140. Phone (215) 707 4940. (215) 707 8110 (FAX). E-mail: lknight@temple.edu.

[†] Washington University School of Medicine.

[‡] Temple University School of Medicine.

10.1021/bc049961j CCC: $27.50 © 2004 American Chemical Society
Published on Web 08/13/2004

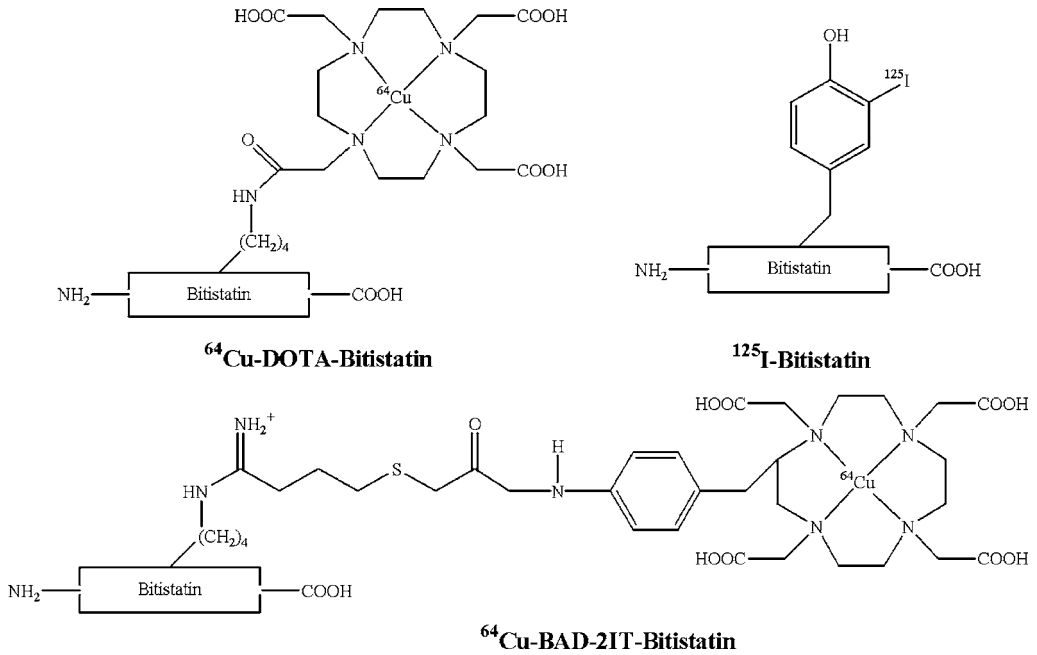


Figure 1. Structures of ^{64}Cu-DOTA-, ^{125}I-, and ^{64}Cu-BAD-2IT-labeled bitistatin.

are the most potent known inhibitors of integrin function. A common feature of the disintegrins is that they contain an RGD or analogous sequence at the apex of one of these loops.

The disintegrin bitistatin was selected for initial evaluation as a marker for tumor angiogenesis. When labeled with ^{123}I or ^{99m}Tc, bitistatin has been shown to be a promising agent for in vivo imaging of experimental pulmonary emboli (PE) and deep venous thrombi (DVT) (*8*−*11*). In a canine model, labeled bitistatin images were characterized by high uptake in thrombi and emboli and low background in muscle and most other tissues except for kidneys and spleen. Bitistatin has been shown to bind to both $\alpha_V\beta_3$ and $\alpha_{IIb}\beta_3$ integrins (*12*). We hypothesize that binding to both integrins may be advantageous, as bitistatin's reversible binding to $\alpha_{IIb}\beta_3$ on blood platelets may increase the blood residence time and therefore the bioavailability for delivery of radioligand to $\alpha_V\beta_3$ on endothelial cells. This approach differs significantly from previous studies that have focused on small cyclic RGD-containing peptides which were designed to have the highest possible affinity for $\alpha_V\beta_3$, while minimizing platelet binding with the lowest possible affinity for $\alpha_{IIb}\beta_3$ (*13*−*16*).

Molecular modeling studies have shown that the five lysine residues of bitistatin are located on the opposite side of the molecule from the putative binding domain (*10*). This suggests that bitistatin could be conjugated to bifunctional chelators (BFC) for labeling with radiometals without affecting the binding domain, and this has been successfully accomplished with Hynic modification for ^{99m}Tc labeling. The positron-emitting isotope ^{64}Cu ($t_{1/2}$ = 12.7 h, β^+ = 0.655 MeV (19.3%), β^- = 0.573 MeV (39.6%)) is an attractive radionuclide and has found use both as a diagnostic agent by utilizing the high sensitivity of PET imaging, and also as a radiotherapy agent (*17*). Large quantities of high-specific activity ^{64}Cu can be produced on demand using a biomedical cyclotron (*18*). In this study, bitistatin was first labeled with ^{125}I by direct radioiodination methods and then with ^{64}Cu to test whether it could be used for PET imaging of tumors.

EXPERIMENTAL PROCEDURES

General Methods and Materials. All chemicals unless otherwise stated were purchased from Sigma-Aldrich Chemical Co. (St. Louis, MO). Water was distilled and then deionized (18 MΩ/cm^2) by passing through a milli-Q water filtration system (Millipore Corp., Milford, MA). Reversed-phase HPLC separation was achieved using a Dynamax C_{18}, 12 μm, 300 Å, 4.6 × 250 mm column (Rainin Instruments, Woburn, MA), eluted with a linear gradient of 0−60% acetonitrile in 0.1% trifluoroacetic acid over 30 min at a flow rate of 1.0 mL/min. FPLC analysis was performed using a Sephadex G-25 column equilibrated and eluted with 0.1 M NaCl/HEPES buffer pH 7.4 at a flow rate of 1 mL/min. ^{64}Cu was produced on a CS-15 biomedical cyclotron at Washington University School of Medicine, using published methods (*18*). Radioactivity was counted with a Beckman Gamma 8000 counter containing a NaI crystal (Beckman Instruments, Inc., Irvine, CA). Bitistatin was purified from the crude venom of Bitis arietans (Miami Serpentarium Laboratories, Punta Gorda, FL) by ion-exchange chromatography followed by RP-HPLC yielding a single peak (*8*, *19*). Mass spectrometry and partial amino acid sequence analysis were used to confirm the identity of bitistatin.

^{125}I-Bitistatin (Figure 1). Bitistatin (30 μg; 3.3 nmol) in 0.2 M Tris buffer, pH 7.8 was combined with 750 μCi ^{125}I (Perkin-Elmer Life Sciences, N. Billerica, MA) containing 1 nmol of NaI. The mixture was transferred to a tube containing 20 μg of IodoGen (Pierce Chemical Co, Rockford, IL). After 25 min at room temperature, the reaction was removed from the vial, diluted with saline, and allowed to stand for 5 min without addition of reductant. Unreacted ^{125}I was removed by gel filtration on a Econo-Pak 10DG column (Bio-Rad Laboratories, Hercules, CA) (*8*). The product had radiochemical purity of greater than 99% as determined by reversed phase HPLC.

^{64}Cu-DOTA-Bitistatin (Figure 1). The activation of 1,4,7,10-tetraazacyclododecane-*N*,*N*′,*N*″,*N*‴-tetraacetic acid (DOTA) and subsequent conjugation to bitistatin was carried out as described previously (*20*). Briefly, activa-

tion of DOTA with EDC (1-ethyl-3-[3-(dimethylamino)-propyl]carbodiimide) and sulfo-NHS (*N*-hydroxy-sulfo-succinimide) was carried out at 4 °C for 30 min. A 10-fold excess of DOTA and sulfo-NHS over EDC was used to ensure only one carboxylic acid moiety per DOTA was activated. The pH was then adjusted to 8.5 and enough bitistatin was added to generate a bitistatin:NHS-DOTA ratio of 1:100. The reaction vessel was then kept at 4 °C for 15 h, with continuous end-over-end mixing. The conjugated peptide was then purified using a Centricon-3 centrifugal filter (MW cutoff 3000; Millipore, Billerica, MA). The average number of DOTA units attached to bitistatin was found to be 1.76, as determined by TLC (*21*).

The conjugated bitistatin was labeled with ^{64}Cu as follows: bitistatin-DOTA (25−40 μg) was combined with $^{64}CuCl_2$ (6−8 mCi) in 0.03 M ammonium citrate buffer (pH 6.5), to give a total volume of 150 μL. The reaction mixture was heated at 55 °C for 40 min, after which diethylenetriaminepentaacetic acid (DTPA) was added to challenge nonbound radiometals. The radiolabeled peptide was purified with a Bio-Spin 6 column (Bio-Rad, Hercules, CA) centrifuged at 2500 rpm for 6 min. Using this method, specific activities of 250 μCi/g were typically obtained, with radiopurity of around 96% as determined by FPLC.

^{64}Cu-BAD-2IT-Bitistatin (Figure 1). The activation of bromoacetamidobenzyl-1,4,7,10-tetraazacyclododecane-*N*,*N*′,*N*″,*N*‴-tetraacetic acid (BAD) (Macrocyclics, Dallas, TX) and subsequent conjugation to bitistatin was carried out as described previously (*22*). To a solution of bitistatin (0.1 M ammonium phosphate, pH 8.0) was added in this order: excess BAD in aqueous solution and freshly prepared 2-iminothiolane (2IT) in 50 mM triethanolamine hydrochloride, pH 8.7. The overall bitistatin/BAD/2IT ratio was 1:100:20, and the pH of the resulting solution was adjusted to 8.0. The reaction was then incubated at 37 °C for 40 min. The conjugated peptide was purified using a Centricon-3 centrifugal filter (MW cutoff 3000). The average number of BAD units attached to bitistatin was found to be 0.55, as determined by TLC (*21*).

The conjugated bitistatin was labeled with ^{64}Cu in a similar manner as the DOTA analogue. Briefly, BAD-2IT-bitistatin (120 μg) was combined with $^{64}CuCl_2$ (10−12 mCi) in 0.1 M ammonium citrate buffer (pH 6.5), to give a total volume of 150 μL. The reaction mixture was heated at 55 °C for 40 min, after which DTPA was added to challenge nonbound radiometals. The radiolabeled peptide was purified via gel filtration with a PD-10 column. Specific activities of 50 μCi/μg were obtained, with a radiopurity of 90% as determined by FPLC.

Stability of Radiolabel. To measure the in vivo stability of ^{64}Cu-DOTA-bitistatin in mice, plasma samples obtained at 1 h were purified by size exclusion chromatography and the fractions obtained were counted on a gamma counter. In an analogous in vitro experiment, ^{64}Cu-DOTA-bitistatin was incubated with human serum albumin (HSA) at 37 °C for 20 h, after which the solution was then separated by size exclusion chromatography to determine the amount of ^{64}Cu that remained bound to DOTA-bitistatin.

Inhibition of Platelet Aggregation In Vitro. Blood was obtained from aspirin-free human donors and anticoagulated with 0.1 vol of 3.8% sodium citrate. The blood was centrifuged at 160*g* for 12 min to obtain platelet-rich plasma (PRP). The concentration of platelets in human PRP was determined using a hemacytometer, and then diluted with the donor's own plasma to obtain a platelet concentration of 300 000/μL. For each measurement, 400 μL of adjusted PRP was placed in a cuvette and stirred at 37 °C. Vehicle (saline) or various concentrations of peptide was added in a volume of 10 μL and stirred at 37 °C for 1 min while recording light transmission. ADP was then added (final concentration 10 μM) to induce platelet aggregation. Platelet aggregation was determined by change in light transmission through the PRP, which was recorded for 5 min after ADP addition. The IC_{50} was determined (by least-squares fitting) as the concentration of peptide required to produce 50% inhibition of the response to ADP in the presence of the vehicle. Results were normalized to the results for the tetrapeptide Arg-Gly-Asp-Ser (RGDS).

Biodistribution Studies. All animal experiments were conducted in compliance with the Guidelines for the Care and Use of Research Animals established by Washington University's Animal Studies Committee. Biodistribution studies were carried out on female BALB/c mice (20−25 g) that had been implanted with 1×10^6 EMT-6 cells subcutaneously into the nape of the neck. This cell line was chosen as the resulting tumor is fast growing, and presumably contains vasculature that is rich in $\alpha_V\beta_3$ integrins, while the cells themselves are devoid of RGD binding receptors (*23*). EMT-6 murine mammary carcinoma cells were obtained from the Yale Cancer Center. Tumors were allowed to grow for 10 days after implantation of cells, after which time the animals received either 1 μCi of ^{125}I-bitistatin (1.1 pmol), 7 μCi ^{64}Cu-DOTA-bitistatin (3.1 pmol), or 5 μCi ^{64}Cu-BAD-2IT-bitistatin (11 pmol), in 125 μL of saline via lateral tail vein injection. In an analogous experiment to monitor the effect excess bitistatin would have on tumor uptake, 200 μg (22 nmol) of unlabeled bitistatin was injected into mice implanted with EMT-6 cells immediately prior to administering ^{125}I- or ^{64}Cu-DOTA-labeled bitistatin. This represents a 20 000- and 7100-fold increase over the mass of peptide injected with ^{125}I- and ^{64}Cu-DOTA-bitistatin respectively as compared to the nonblocked biodistribution studies. Animals were then euthanized at desired time points (30 min, 2 and 4 h for ^{125}I-bitistatin, 2, 4, and 6 h for ^{64}Cu-DOTA-bitistatin, 30 min, 2 h, 4 h, and 6 h for ^{64}Cu-BAD-2IT-bitistatin). Tissues and organs of interest were then removed and weighed and radioactivity was measured in a gamma counter. The percent dose per gram (%ID/g) was then calculated.

Because bitistatin can bind to both $\alpha_V\beta_3$ and $\alpha_{IIb}\beta_3$ integrins, a separate study was carried out to determine the effect blocking each integrin individually would have on tumor uptake. BALB/c mice bearing EMT-6 tumors were injected with 7 μCi of ^{64}Cu-DOTA-bitistatin (3.1 pmol) in 125 μL of saline via lateral tail vein injection. Immediately prior to injection of the radiopharmaceutical 40 μg (70 nmol) of the $\alpha_V\beta_3$-specific peptide cyclo[RGDfV] (*24*) (Bachem Bioscience Inc, King of Prussia, PA), or 55 μg (66 nmol) of the $\alpha_{IIb}\beta_3$-specific peptide eptifibatide (*25*) (GL Biochem (Shanghai) Ltd, Shanghai, China), was injected. After 2 h the animals were euthanized and their organs were counted.

Cell Binding Studies. The extent of platelet binding in vivo was assessed by collecting blood samples by cardiac puncture in mice pretreated with ^{64}Cu-DOTA-bitistatin and immediately layering over 100 μL of 30% sucrose in a microfuge tube. After centrifugation at 13000*g* for 5 min, the plasma was carefully removed by pipet to a clean tube for counting. The tip of the microfuge tube containing the cell pellet was snipped off into a second tube for counting. The percentage of total counts in the cell pellet was calculated.

To determine the extent of cell binding directly to EMT-6 cells, ^{64}Cu-DOTA-, ^{64}Cu-BAD-2IT-, and ^{125}I-bitistatin were incubated with EMT-6 cells in vitro. EMT-6 cells were suspended to a concentration of 5×10^6 cells/mL in PBS. Cell number was determined with a hemocytometer, and viability was determined by trypan blue exclusion. For the assay, the cell suspension was supplemented with $CaCl_2$ and $MnCl_2$ (final concentration 0.5 mM each), then radiolabeled bitistatin was added to a final concentration of 2 nM. Nonspecific binding was determined in the presence of 2.5 mM Na_4EDTA to chelate divalent cations which are needed for integrin function (*6*, *9*). After 1 h at 37 °C, 100 μL aliquots of the cell suspension were layered over 100 μL of a 30% sucrose solution in a microfuge tube. The cells were then pelleted from the media by centrifuging at 13000*g* for 3 min. The supernatant was transferred into a clean tube for counting and the tip containing the cell pellet was snipped from the microfuge tube and placed in a second tube for counting. Both supernatant and pellet were counted, and the percentage of the radioactivity associated with the cells was calculated. This was done in triplicate for each incubation condition.

MicroPET Imaging. Whole body microPET images were obtained on a microPET-R4 system (Concorde Microsystems, Knoxville, TN) (*26*). Imaging studies were carried out on BALB/c mice that had received an implant of EMT-6 cells (1×10^6 cells) in the nape of the neck ($n = 14$), with each mouse receiving 250 μCi of ^{64}Cu-DOTA-bitistatin (0.1 nmol). At each time point (4, 6, and 15 h) half of the animals were given 200 μg (22 nmol; 200-fold mass increase over ^{64}Cu-DOTA-bitistatin injected) of unlabeled bitistatin prior to the radiopharmaceutical to monitor the effect it would have on tumor uptake and clearance. The mice were imaged in pairs (blocked vs unblocked) side by side, and standardized uptake values (SUV) for the tumor, kidneys, and liver were obtained at all time points. The SUVs were determined by drawing regions of interest (ROI) around the target tissue to generate the radioactive concentration, which was decay corrected to the time of injection, multiplied by the mouse body weight (grams), and divided by the injected dose (nCi) to give the normalized tissue uptake to injected dose per body weight (*27*).

Statistical Methods. To compare differences between the ^{64}Cu- and ^{125}I-labeled bitistatin, a Student's *t*-test was performed. Differences at the 95% confidence level ($p < 0.05$) were considered significant.

RESULTS

Stability of ^{64}Cu-DOTA-Bitistatin. When ^{64}Cu-DOTA-bitistatin was incubated with HSA at 37 °C for 20 h, 90% of the radiopharmaceutical remained in its original form (no breakdown or plasma protein binding) (Figure 2). Size exclusion chromatography of plasma samples obtained from mice at 1 h did not contain enough radioactivity for accurate assessment by the in-line detector. However, subsequent counting of the fractions on a gamma counter showed that in both blocked and unblocked mice >95% of ^{64}Cu in mouse plasma samples was in the form of ^{64}Cu-DOTA-bitistatin. From these results, we can infer that ^{64}Cu-DOTA-bitistatin has a high in vivo stability in plasma.

Platelet Binding Studies. To determine whether conjugation of DOTA to bitistatin affected its ability to bind to $\alpha_{IIb}\beta_3$ integrin, DOTA-bitistatin and unmodified bitistatin were compared for their ability to inhibit human platelet aggregation via binding to $\alpha_{IIb}\beta_3$. The IC_{50}

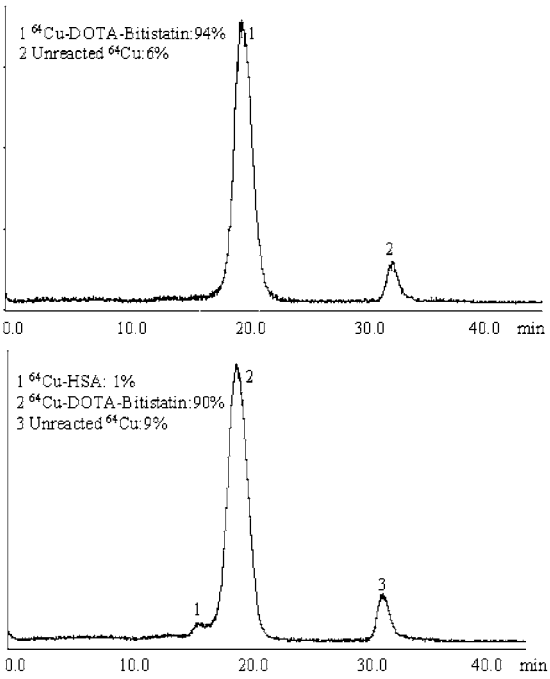


Figure 2. Radioactive profile of ^{64}Cu-DOTA-bitistatin before (top) and after (bottom) incubation in HSA for 20 h. The Sephadex G-25 column was eluted with 0.1 M NaCl/HEPES buffer, pH 7.4, at 1 mL/min.

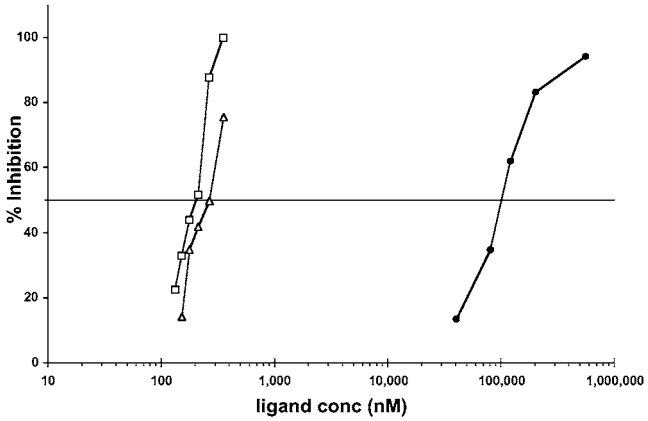


Figure 3. Inhibition of ADP-induced human platelet aggregation by unmodified bitistatin (open squares), DOTA-bitistatin (gray filled triangles), and Arg-Gly-Asp-Ser tetrapeptide (filled circles).

for inhibition of human platelet aggregation was 163 ± 27 nM for DOTA-bitistatin, compared with 140 ± 11 nM for the same lot of bitistatin before modification (Figure 3). There was no significant difference between these groups ($p = 0.46$).

Binding of ^{64}Cu-DOTA-bitistatin to platelets in vivo was found to be about 60% of the total blood activity in blood samples drawn at 1 h after injection. This is similar to the percentage of platelet binding of ^{125}I-bitistatin (64%) found in mice at 1 h. In mice which also received 200 μg of unlabeled bitistatin, the level of platelet-bound ^{125}I-bitistatin was reduced to 21%.

EMT-6 Binding Studies. Binding of ^{125}I-, ^{64}Cu-DOTA-, and ^{64}Cu-BAD-2IT-bitistatin to EMT-6 cells in vitro is shown in Figure 4. Binding of ^{125}I-bitistatin (6.4 ± 0.7%) was not significantly higher than nonspecific binding (4.3 ± 1.7%; $p = 0.22$). Similar results were found for both ^{64}Cu-DOTA-bitistatin (control 9.8 ± 0.8%, nonspe-

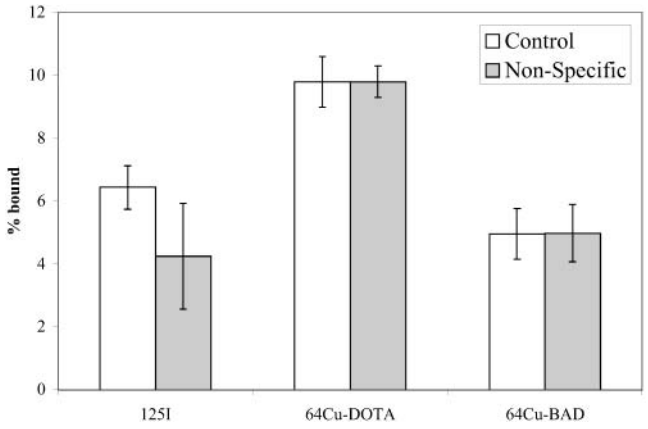


Figure 4. Binding of ^{64}Cu-DOTA-, ^{125}I-, and ^{64}Cu-BAD-2IT-labeled bitistatin to EMT-6 cells after incubation at 37 °C for 1 h. Nonspecific binding was determined in the presence of EDTA. Each point is based on triplicate samples, with error bars representing standard deviations.

Table 1. Biodistribution Data for ^{125}I-Bitistatin in BALB/c Mice Implanted with EMT-6 Tumors[a]

	30 min	2 h	2 h blk	4 h
blood	7.31 ± 1.69	5.16 ± 1.78	2.32 ± 1.03	2.21 ± 0.45
lung	14.09 ± 8.80	9.89 ± 5.25	2.29 ± 0.89	2.69 ± 0.43
liver	4.25 ± 1.26	2.35 ± 0.91	1.14 ± 0.44	0.97 ± 0.26
spleen	12.35 ± 2.78	8.19 ± 2.18	2.98 ± 0.63	2.91 ± 0.29
kidney	57.60 ± 31.08	14.44 ± 6.46	10.14 ± 4.35	4.45 ± 0.70
muscle	2.13 ± 0.39	1.77 ± 0.46	1.62 ± 0.61	0.83 ± 0.25
fat	3.28 ± 0.56	1.79 ± 0.68	0.95 ± 0.41	0.97 ± 0.21
heart	2.95 ± 3.09	3.22 ± 3.88	0.76 ± 0.37	0.81 ± 0.75
tumor	6.19 ± 2.02	11.68 ± 4.56	4.39 ± 2.75	5.35 ± 1.97
abd aorta	6.84 ± 2.10	5.76 ± 0.62	3.33 ± 2.77	1.77 ± 0.33
thyroid	14.15 ± 3.19	128.4 ± 74.16	105.36 ± 36.42	235.22 ± 93.48

[a] Blocked animals given 200 μg of bitistatin. Data presented as %ID/g ± SD (n = 5).

Table 2. Biodistribution Data for ^{64}Cu-DOTA-Bitistatin in BALB/c Mice Implanted with EMT-6 Tumors

	2 h	4 h	6 h	6 h blk
blood	0.53 ± 0.11	0.50 ± 0.03	0.53 ± 0.04	0.22 ± 0.05
lung	1.61 ± 0.03	1.36 ± 0.13	1.98 ± 0.07	1.06 ± 0.37
liver	2.60 ± 0.09	3.45 ± 0.64	4.66 ± 0.44	2.63 ± 0.70
spleen	2.42 ± 0.13	2.29 ± 0.13	3.07 ± 0.28	1.39 ± 0.14
kidney	41.27 ± 4.74	61.27 ± 6.20	57.93 ± 9.91	62.70 ± 5.65
muscle	0.23 ± 0.04	0.24 ± 0.02	0.33 ± 0.03	0.18 ± 0.05
heart	0.45 ± 0.02	0.64 ± 0.04	0.85 ± 0.03	0.45 ± 0.12
tumor	1.13 ± 0.07	1.03 ± 0.25	1.55 ± 0.19	0.78 ± 0.18
abd. aorta	2.10 ± 2.15	1.04 ± 0.21	1.43 ± 0.22	0.51 ± 0.13

[a] Blocked animals given 200 μg of bitistatin. Data presented as %ID/g ± SD (n = 4).

cific 9.8 ± 0.5%; p = 0.94) and ^{64}Cu−BAD-2IT-bitistatin (control 5.0 ± 0.9%, nonspecific 5.0 ± 0.8%; p = 0.99).

Biodistribution Studies. For ^{125}I-bitistatin, tumor uptake reached a maximum at 2 h postinjection (11.7 ± 4.6 %ID/g) and then decreased (5.4 ± 2.0 %ID/g) after 4 h (Table 1). Co-injection of 200 μg of unlabeled bitistatin reduced tumor uptake at 2 h to 4.4 ± 2.8 %ID/g (p = 0.01), indicating receptor-mediated uptake. At 30 min, kidney uptake was high (57.6 ± 31.1 %ID/g) but cleared rapidly and after 4 h was 4.4 ± 0.7 %ID/g. As with other biomolecules directly radiolabeled with iodine, accumulation in the thyroid was observed.

In the studies undertaken with ^{64}Cu-DOTA-bitistatin, the biodistribution differed from that of the ^{125}I analogue in that the maximum tumor uptake was lower (1.6 ± 0.2 %ID/g, p < 0.001) and was achieved 6 h postinjection (Table 2). As with ^{125}I-bitistatin, the co-injection of 200 μg of unlabeled bitistatin reduced tumor uptake 2-fold

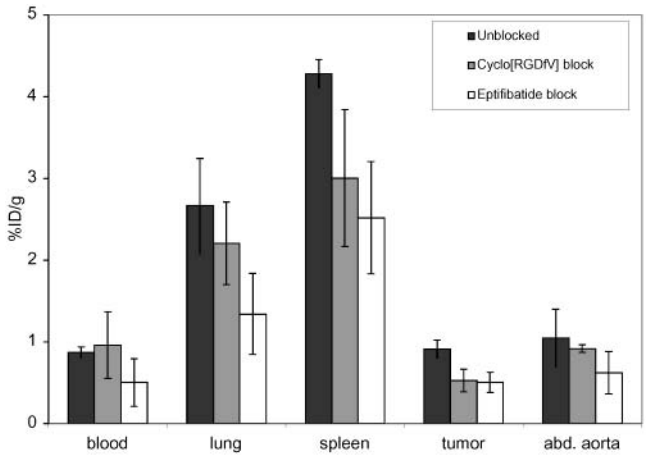


Figure 5. Comparative uptake of ^{64}Cu-DOTA-bitistatin in select organs, obtained from BALB/c mice implanted with EMT-6 tumors at 2 h. Control animals received only ^{64}Cu-DOTA-bitistatin, while blocked animals received either 40 μg of cyclo[RGDfV] or 55 μg of eptifibatide immediately prior to administering tracer. Data presented as %ID/g ± SD (n = 4).

(0.78 ± 0.18 %ID/g) at 6 h (p = 0.007). The clearance properties of ^{64}Cu-DOTA-bitistatin also differed significantly from those observed for the ^{125}I analogue. Initially kidney uptake was high (41.3 ± 4.7 %ID/g), and continued to increase up to 4 h (61.3 ± 6.2 %ID/g) before reaching a plateau.

Binding to integrins $\alpha_V\beta_3$ and $\alpha_{IIb}\beta_3$ was selectively blocked with the integrin specific peptides cyclo[RGDfV] and eptifibatide. A comparison of tissue uptake in selected organs is shown in Figure 5. Blocking of $\alpha_V\beta_3$ integrin with cyclo[RGDfV] had no effect on blood level (0.7 ± 0.2 %ID/g) or uptake in blood rich organs such as the lung (2.2 ± 0.5 %ID/g) or abdominal aorta (0.9 ± 0.1 %ID/g) at 2 h compared to controls. Tumor uptake however was significantly reduced (p = 0.009) to 0.5 ± 0.1 %ID/g, an approximate 2-fold reduction compared to control values. When the $\alpha_{IIb}\beta_3$ selective peptide eptifibatide was administered, significant reductions (p < 0.01) were seen in blood (0.6 ± 0.1 %ID/g), lung (1.3 ± 0.5 %ID/g), aorta (0.5 ± 0.2 %ID/g), and spleen (2.5 ± 0.7 %ID/g) levels at 2 h compared to the control mice. This was accompanied by a similar 2-fold reduction in tumor uptake (0.5 ± 0.1 %ID/g; p = 0.003), similar to the effect seen with cyclo[RGDfV]. Unexpectedly, kidney levels in the mice receiving eptifibatide (21.5 ± 6.2 %ID/g) was significantly lower (p = 0.01) than in mice that had not received competing peptide (36.7 ± 5.6 %ID/g) or in the mice that had received cyclo[RGDfV] (35.9 ± 9.9 %ID/g).

Because tumor localization of ^{64}Cu-DOTA-bitistatin was lower than expected, a different ^{64}Cu conjugate was tested to see if tumor targeting could be improved. Tumor uptake for ^{64}Cu-BAD-2IT-bitistatin was higher than the DOTA conjugate at all time points examined (p < 0.001), reaching a maximum 6 h postinjection (5.2 ± 0.6 %ID/g) (Table 3). At 6 h kidney and liver uptake had reached 221 ± 63 and 19.1 ± 4.1 %ID/g, respectively. Uptake in these nontarget organs was higher than those seen with the DOTA conjugate and substantially higher than those obtained for ^{125}I-bitistatin (p < 0.001).

MicroPET Imaging. Transaxial slices showing the localization of ^{64}Cu-DOTA-bitistatin in EMT-6 tumors as determined by microPET imaging are shown in Figure 6. Four hours after administering ^{64}Cu-DOTA-bitistatin no statistical difference (p = 0.98) in tumor SUV data was observed between the control (0.15 ± 0.03) and blocked mice (0.15 ± 0.03). It was not until 6 h postin-

Table 3. Biodistribution Data for ^{64}Cu-BAD-2IT-Bitistatin in BALB/c Mice Implanted with EMT-6 Tumors

	30 min	2 h	4 h	6 h
blood	3.86 ± 2.07	1.36 ± 0.30	1.61 ± 0.95	1.51 ± 0.28
lung	3.54 ± 0.93	3.46 ± 1.02	4.32 ± 2.46	5.09 ± 0.89
liver	9.79 ± 3.66	15.33 ± 6.24	15.69 ± 5.89	19.24 ± 4.12
spleen	3.95 ± 1.72	4.12 ± 0.55	4.66 ± 2.40	4.80 ± 0.97
kidney	168.33± 79.67	229.43± 52.04	184.96± 23.00	221.15± 63.36
muscle	1.50 ± 0.69	1.19 ± 0.31	1.21 ± 0.66	1.07 ± 0.15
fat	1.48 ± 1.06	1.12 ± 0.27	1.34 ± 1.40	0.97 ± 0.10
heart	1.56 ± 0.54	1.65 ± 0.28	1.91 ± 0.77	2.39 ± 0.43
tumor	3.57 ± 1.11	4.70 ± 1.61	4.76 ± 2.23	5.18 ± 0.60
abd aorta	4.16 ± 1.52	3.86 ± 0.64	4.45 ± 1.11	6.00 ± 5.12

[a] Data presented as %ID/g ± SD (n = 4).

jection that tumor uptake in the control and blocked animals were statistically different: SUV = 0.17 ± 0.02 and 0.09 ± 0.01, respectively (p < 0.02). After 15 h, tumor SUV in the control animals was 0.19 ± 0.01, while in the blocked animals tumor SUV was significantly lower (0.12 ± 0.01, p < 0.001). These data agree with qualitative examination of Figure 6, where blocking is observed at 6 and 15 h. Significant uptake of ^{64}Cu-DOTA-bitistatin in the liver and kidneys was observed at all time points.

DISCUSSION

Previous studies for the detection of angiogenesis have focused on small cyclic RGD-containing peptides which bind selectively to $\alpha_V\beta_3$ integrins, with the goal of minimizing platelet binding via $\alpha_{IIb}\beta_3$ (*13*−*16*). This approach usually results in fast blood clearance and is usually accompanied by low tumor uptake, possibly because of inadequate contact time with the target receptors. In this study, we have taken the opposite approach by utilizing a ligand that has affinity for $\alpha_v\beta_3$ integrins, allowing binding to receptors involved in angiogenesis and to $\alpha_{IIb}\beta_3$ integrins, prolonging the bioavailability of the radioligand.

A source of naturally occurring high-affinity ligands for integrins is found in the family of molecules known as disintegrins. These cysteine-rich peptides were first isolated from viper venoms and to date close to 50 have been isolated (*28*). Of these peptides, bitistatin was chosen as the targeting molecule for these studies, as previous work has shown that it binds to both $\alpha_{IIb}\beta_3$ and $\alpha_v\beta_3$, and has been successfully used for in vivo imaging when directly radiolabeled with ^{123}I (*8*, *9*), or when labeled with ^{99m}Tc via hydrazinonicotinate (Hynic) linker (*10*, *11*). In studies in a canine model, labeled bitistatin exhibited high uptake in thrombotic lesions and very low uptake in most background tissues. Another characteristic of bitistatin is that it is displaced slowly from the activated $\alpha_{IIb}\beta_3$ receptor (*9*), and it was hoped that this slow off-rate would be observed on the $\alpha_v\beta_3$ integrin as well. It should be noted that other disintegrins have been reported to have higher affinity and selectivity for $\alpha_v\beta_3$ than bitistatin, and thus may be better for tumor angiogenesis targeting. Studies with these peptides are ongoing.

Both in vitro and in vivo studies were performed using EMT-6 murine mammary carcinoma cells. This cell line was chosen as the cells themselves are devoid of RGD binding receptors (*23*, *29*), while immunohistochemical staining of untreated EMT-6 tumors have shown a high concentration of vascular endothelial growth factor (VEGF) (*30*). This is important as it has been shown that VEGF directly activates $\alpha_v\beta_3$ leading to an increased concentration of this integrin on endothelial cells (*31*). It would be desirable to perform immunohistochemical staining of EMT-6 tumors to confirm the presence of $\alpha_v\beta_3$; however, at present the available antibodies for $\alpha_v\beta_3$ do not crossreact with murine tissue.

When the three labeled conjugates of bitistatin were incubated with EMT-6 cells, there was no significant binding of any of the conjugates above nonspecific levels, confirming that there is no integrin receptor binding of these conjugates to EMT-6 cells. Slight differences in the level of nonspecific binding were observed, however. The higher binding of the ^{64}Cu-DOTA-bitistatin conjugate may be explained by hydrogen bonding of the negatively charged carboxylate arms present on DOTA to positively charged moieties on the cell surface. It is possible that this was not seen for the BAD conjugate because the number of conjugates attached was 3-fold lower, 1.76 vs 0.55, respectively. In other investigations, the ability of bitistatin to bind to cells expressing $\alpha_v\beta_3$ has been demonstrated by the finding that ^{99m}Tc- or ^{125}I-bitistatin binds in vitro to cultured human endothelial cells and to two $\alpha_v\beta_3$ receptor positive tumor cell lines, and that this binding is completely abolished by competition with cyclo-[RGDfV] (*32*).

In most previously published studies, the ability of radiolabeled RGD-containing peptides to image tumor angiogenesis was obscured by the fact that the tumors were grown from cell lines that express $\alpha_v\beta_3$ directly on the tumor cells. In these cases, it was impossible to determine whether targeting was to the tumor vasculature or directly to the tumor cells themselves. In this study, we have provided evidence for targeting of tumor vasculature without targeting the tumor cells directly. This is likely to be a more challenging task, because the density of the target receptors may be much lower due to the lower number of tumor-associated endothelial cells compared to the number of tumor cells in the tumor mass.

The tumor uptakes achieved in this study (11.7 %ID/g at 2 h for ^{125}I-bitistatin and 5.18 %ID/g at 6 h for ^{64}Cu-BAD-2IT-bitistatin) compare favorably with uptakes of small RGD-containing peptides which have been evaluated in models employing $\alpha_v\beta_3$-positive tumor cell lines such as murine osteosarcoma, M21 melanoma, and OVCAR-3 ovarian carcinoma (*33*). It is notable that studies with an ^{18}F-labeled glycosylated cyclo[RGDfK], one of the most promising synthetic peptide radioligands, showed good uptake in $\alpha_v\beta_3$-positive M21 tumors in mice, but imaging showed no focal tracer accumulation in control tumors using $\alpha_v\beta_3$-negative M21-L cells (*34*). Although the tumor/background ratios obtained with bitistatin conjugates are not as high as have been reported with other tracers binding to tumor cell membranes and definitely could be improved upon, it is encouraging that adequate targeting to vasculature was achieved to enable focal imaging at 4−15 h.

Biodistribution studies carried out with ^{125}I-bitistatin in mice implanted with EMT-6 cells showed that maximum tumor uptake was observed 2 h postinjection, with elevated uptake in blood-rich organs such as the lung, spleen, and heart. This appeared to be related to receptor binding, as the co-injection of 200 μg of unlabeled bitistatin substantially reduced uptake in these organs. This work was then extended to positron emitting nuclides so that the sensitivity and high resolution of PET could be used to visually identify tumors. For these studies, ^{64}Cu was chosen due to its availability, energy of positron emission, and the stability of the final product. However, unlike iodine it must be attached via a bifunctional chelator (BFC) which is covalently bound to lysine side chains (*35*−*38*). 1,4,7,10-Tetraazacyclododecane-*N*,*N*′,*N*″,*N*‴-tetraacetic acid (DOTA) was chosen as the

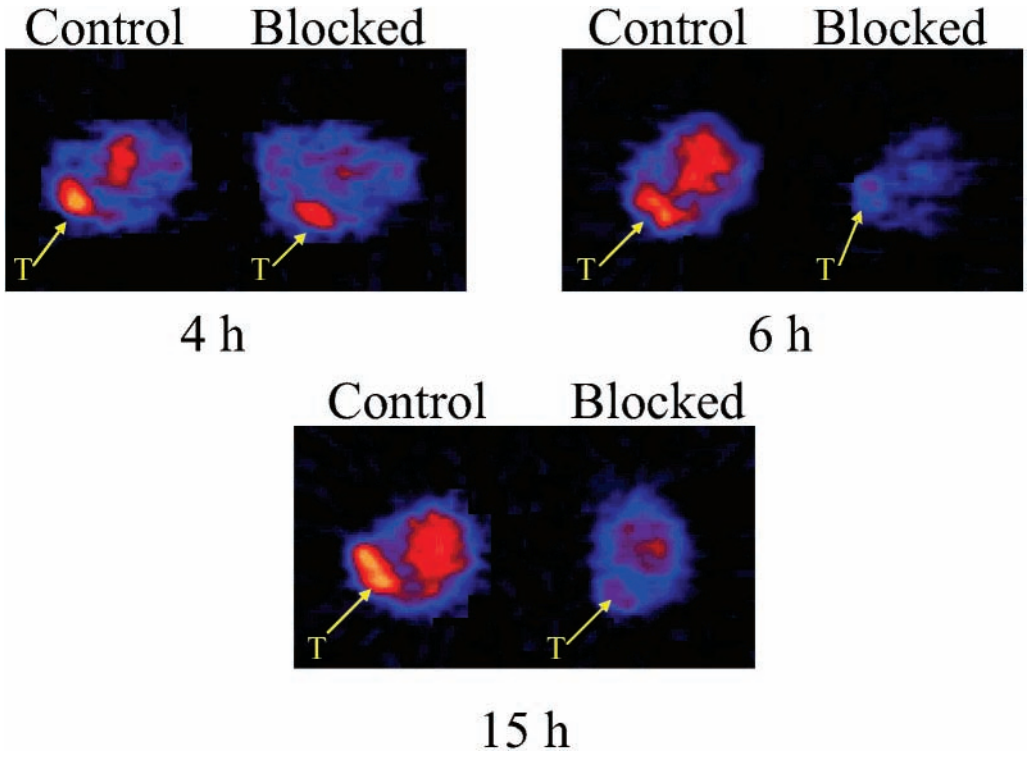


Figure 6. Transaxial images of BALB/c containing EMT-6 murine mammary carcinoma tumors 4, 6, and 15 h after tail vein injection of 250 μCi of ^{64}Cu-DOTA-bitistatin. Blocked mice were co-injected with 200 μg of bitistatin (T = tumor).

metal chelating agent due to its commercial availability and its flexibility to bind a variety of metal ions including Ga^{3+}, In^{3+}, and Y^{3+}. MicroPET images obtained with ^{64}Cu-DOTA-bitistatin showed that EMT-6 tumors could be identified after 4 h. As with ^{125}I-bitistatin, the co-injection of 200 μg of bitistatin reduced uptake in the tumor and blood-rich organs, indicating receptor mediated uptake. However, tumor uptake of ^{64}Cu-DOTA-bitistatin was 87% lower than the ^{125}I analogue and did not reach a maximum until at least 6 h postinjection. In addition, the percentage of ^{64}Cu-DOTA-bitistatin found in blood-rich organs was lower than observed for the ^{125}I analogue. This was surprising as the ^{64}Cu-DOTA conjugate appeared to be stable both in vitro and in vivo, with no significant change in potency for inhibition of human platelet aggregation by DOTA-bitistatin as compared unmodified bitistatin. Furthermore, although total blood levels for ^{125}I-bitistatin and ^{64}Cu-DOTA-bitistatin were different at 1 h postinjection, for both tracers a similar percentage of blood activity was bound to platelets in vivo at this time.

A possible explanation of this is that during conjugation of DOTA to bitistatin, some of the conjugation locations resulted in unfavorable alterations in bitistatin's receptor binding. These alterations may be more pronounced after labeling, which was not tested in the platelet assay in vitro. Conjugates that have impaired binding to platelets may leave the blood faster by renal clearance. At 1 h, if these forms have been substantially cleared, total blood activity would be lower, but the percent of total blood activity which is platelet-bound could be the same as for the ^{125}I-labeled bitistatin. Studies with site-directed mutagenesis to alter the locations of attachment of bifunctional chelating agents to bitistatin have shown that conjugation of Lys35 with Hynic followed by ^{99m}Tc labeling results in a slight loss of binding to $\alpha_{IIb}\beta_3$ (*39*). Unfortunately, we were unable to test for differences among the conjugates for binding to $\alpha_v\beta_3$ in vitro in this study because the EMT-6 cells do not express the receptor. Future studies with $\alpha_v\beta_3$ positive cells or purified integrin will need to be done.

These observations suggest that modification of lysine residues thought to be far from the binding domain could have an effect on bitistatin's pharmacokinetics. To investigate this further, the BFC bromoacetamidobenzyl-1,4,7,10-tetraazacyclododecane-*N*,*N*′,*N*″,*N*‴-tetraacetic acid (BAD) was examined. This chelator was chosen because the copper binding domain of BAD is identical to DOTA, but the linker unit between the macrocycle and the lysine residue is longer, and any steric interactions that may occur are minimized. As with the DOTA conjugate, maximum tumor uptake did not occur until 6 h postinjection; however, tumor levels were 3−4-fold higher at all time points. This demonstrates that modifying the same lysine residues along the polypeptide backbone with differing conjugates can have a profound effect on the pharmokinetics, which alter not only receptor-mediated uptake but also uptake in clearance organs, as can be seen with elevated uptake in nontarget tissue compared to the DOTA analogue. Despite the increased tumor uptake compared to ^{64}Cu-DOTA-bitistatin, the overall tumor-to-tissue ratios obtained with ^{64}Cu-BAD-2IT-bitistatin were similar to those obtained with the ^{64}Cu-DOTA analogue (Table 4).

Kidney uptake and retention of both ^{64}Cu-DOTA- and ^{64}Cu−BAD-2IT-bitistatin was substantial. Initially, like ^{125}I-bitistatin, kidney uptake was high, but unlike the ^{125}I analogue they were retained and levels increased over time. The ^{125}I direct label was not as stable in vivo as evidenced by the thyroid uptake. It is possible that reaching maximal uptake in tumor at 2 h reflects the instability of the iodine label in blood preventing higher uptake beyond that time. More work is needed to select the optimal labeling method for best tumor targeting and background clearance.

Table 4. Comparison of Selected Tumor-to-Tissue Ratios (%ID/g) of ^{64}Cu-DOTA and ^{64}Cu-BAD-2IT-Labeled Bitistatin in BALB/c Mice Bearing EMT-6 Tumors

	^{6}4Cu-DOTA			^{64}Cu-2IT-BAD		
	2 h	4 h	6 h	2 h	4 h	6 h
tumor/blood	2.2 ± 0.5	2.1 ± 0.7	2.9 ± 0.2	3.4 ± 0.4	3.2 ± 0.7	3.5 ± 0.4
tumor/liver	0.4 ± 0.1	0.3 ± 0.02	0.3 ± 0.1	0.3 ± 0.03	0.3 ± 0.03	0.3 ± 0.02
tumor/kidney	0.03 ± 0.006	0.02 ±0.003	0.03 ± 0.008	0.02 ± 0.002	0.03 ± 0.01	0.03 ± 0.007
tumor/muscle	3.2 ± 1.5	4.3 ± 0.8	4.7 ± 0.8	4.0 ± 0.7	4.0 ± 0.3	4.9 ± 0. 9

These studies demonstrated that tumor uptake of ^{125}I- and ^{64}Cu-DOTA-bitistatin was dependent on binding both to $\alpha_v\beta_3$ integrins on endothelial cells and $\alpha_{IIb}\beta_3$ integrins found in circulating blood platelets. Selectively blocking $\alpha_v\beta_3$ with cyclo[RGDfV] or $\alpha_{IIb}\beta_3$ with eptifibatide, an antithrombotic drug, each reduced tumor uptake of ^{64}Cu-DOTA-bitistatin. Blocking with eptifibatide also led to reductions in radiotracer levels in blood and blood-rich organs such as spleen and lung. Blocking with cyclo-[RGDfV] led to reductions only in tumor and spleen, an organ that has previously been reported to take up $\alpha_V\beta_3$-targeted peptides (*13*). These data indicate that while tumor uptake is indeed mediated by $\alpha_V\beta_3$ receptor binding, the increased blood retention caused by binding to $\alpha_{IIb}\beta_3$ has an equivalently large effect, suggesting that the observed tumor uptake of labeled bitistatin is dependent on both $\alpha_v\beta_3$ and $\alpha_{IIb}\beta_3$ integrins.

Unexpectedly kidney uptake in the mice receiving eptifibatide was significantly lower ($p = 0.01$) than controls or in the mice that had received cyclo[RGDfV]. One possible explanation is that eptifibatide or some metabolite inhibits the tubular reabsorption of ^{64}Cu-DOTA-bitistatin, similar to the effect seen when an infusion of amino acids is given (*40*).

In summary, bitistatin, when directly labeled with ^{125}I or with ^{64}Cu via the BFCs DOTA and BAD was shown to accumulate in tumors in which the tumor cells themselves do not express $\alpha_V\beta_3$ integrin. Uptake was determined to be receptor-mediated by a combination of $\alpha_{IIb}\beta_3$ and $\alpha_V\beta_3$ integrins. ^{125}I-bitistatin achieved a higher tumor uptake than bitistatin labeled with ^{64}Cu using a BFC. The biodistribution data suggest a different time−activity profile for uptake and washout of ^{125}I-bitistatin from the tumor as compared to its ^{64}Cu analogue. This along with the differing tumor and renal uptake for DOTA and BAD conjugated bitistatin suggest that modification of the side chains can have a dramatic affect on the distribution, stability, and clearance properties of radiolabeled bitistatin. Even though tumor uptake of ^{64}Cu-DOTA-bitistatin was significantly lower than that seen with ^{125}I-bitistatin, microPET imaging showed the tumor could be identified as quickly as 4 h. Therefore, radiolabeled ligands of this type may be useful in the targeting of tumor angiogenesis, but as demonstrated here the choice of radiolabeling approach has a significant impact on the in vivo properties of the radioligand.

ACKNOWLEDGMENT

The authors thank Jan E. Romano for purification of bitistatin and for performing platelet aggregation assays. Preparation of cells for implantation and uptake studies was done by Susan Adams. MicroPET imaging and evaluation was performed by John A Engelbach and Jerrel R. Rutlin, with biodistribution studies done with the assistance of Terry Sharp, Lynne Jones, and Nicole Fettig. This work was supported by NIH R24 CA86307 (M.J.W.), NIH R01 CA96792 (L.C.K.), and NIH R01 HL54578 (L.C.K.). We would also like to thank the Small Animal Imaging Core of the Alvin J. Siteman Cancer Center at Washington University and Barnes-Jewish Hospital in St. Louis, Missouri for additional support of the microPET imaging and the Statistics Core for statistical analysis. The Core is supported by an NCI Cancer Center Support Grant #1 P30 CA91842. The production of copper radionuclides is supported by a grant from the National Cancer Institute (CA86307).

LITERATURE CITED

(1) Folkman, J. (1971) Tumor angiogenesis: therapeutic implications. *N. Engl. J. Med. 285*, 1182−1186.

(2) Keshet, E., and Ben-Sasson, S. A. (1999) Anticancer drug targets: approaching angiogenesis. *J. Clin. Invest. 104*, 1497−1501.

(3) Harris, T. D., Kalogeropoulos, S., Nguyen, T., Liu, S., Bartis, J., Ellars, C., Edwards, S., Onthank, D., Silva, P., Yalamanchili, P., Robinson, S., Lazewatsky, J., Barrett, J., and Bozarth, J. (2003) Design, synthesis, and evaluation of radiolabeled integrin alpha v beta 3 receptor antagonists for tumor imaging and radiotherapy. *Cancer Biother. Radiopharm. 18*, 627−641.

(4) Hynes, R. O. (1992) Integrins: versatility, modulation, and signaling in cell adhesion. *Cell 69*, 11−25.

(5) Ruoslahti, E. (1991) Integrins. *J. Clin. Invest. 87*, 1−5.

(6) Cox, D., Aoki, T., Seki, J., Motoyama, Y., and Yoshida, K. (1994) The pharmacology of the integrins. *Med. Res. Rev. 14*, 195−228.

(7) Dennis, M. S., Henzel, W. J., Pitti, R. M., Lipari, M. T., Napier, M. A., Deisher, T. A., Bunting, S., and Lazarus, R. A. (1990) Platelet glycoprotein IIb-IIIa protein antagonists from snake venoms: evidence for a family of platelet-aggregation inhibitors. *Proc. Natl. Acad. Sci. U.S.A. 87*, 2471−2475.

(8) Knight, L. C., Maurer, A. H., and Romano, J. E. (1996) Comparison of iodine-123-disintegrins for imaging thrombi and emboli in a canine model. *J. Nucl. Med. 37*, 476−482.

(9) Knight, L. C., Romano, J. E., and Maurer, A. H. (1998) In vitro platelet binding compared with in vivo thrombus imaging using alpha(IIb)beta3-targeted radioligands. *Thromb. Haemostasis 80*, 845−851.

(10) Knight, L. C., Baidoo, K. E., Romano, J. E., Gabriel, J. L., and Maurer, A. H. (2000) Imaging pulmonary emboli and deep venous thrombi with 99mTc-bitistatin, a platelet-binding polypeptide from viper venom. *J. Nucl. Med. 41*, 1056−1064.

(11) Knight, L. C. (2001) Radiolabeled peptide ligands for imaging thrombi and emboli. *Nucl. Med. Biol. 28*, 515−526.

(12) Pfaff, M., McLane, M. A., Beviglia, L., Niewiarowski, S., and Timpl, R. (1994) Comparison of disintegrins with limited variation in the RGD loop in their binding to purified integrins alpha IIb beta 3, alpha V beta 3 and alpha 5 beta 1 and in cell adhesion inhibition. *Cell Adhes. Commun. 2*, 491−501.

(13) Ogawa, M., Hatano, K., Oishi, S., Kawasumi, Y., Fujii, N., Kawaguchi, M., Doi, R., Imamura, M., Yamamoto, M., Ajito, K., Mukai, T., Saji, H., and Ito, K. (2003) Direct electrophilic radiofluorination of a cyclic RGD peptide for in vivo alpha-(v)beta3 integrin related tumor imaging. *Nucl. Med. Biol. 30*, 1−9.

(14) Pfaff, M., Tangemann, K., Muller, B., Gurrath, M., Muller, G., Kessler, H., Timpl, R., and Engel, J. (1994) Selective recognition of cyclic RGD peptides of NMR defined conformation by alpha IIb beta 3, alpha V beta 3, and alpha 5 beta 1 integrins. *J. Biol. Chem. 269*, 20233−20238.

(15) Koivunen, E., Restel, B. H., Rajotte, D., Lahdenranta, J., Hagedorn, M., Arap, W., and Pasqualini, R. (1999) Integrin-binding peptides derived from phage display libraries. *Methods Mol. Biol. 129*, 3−17.

(16) Haubner, R., Wester, H. J., Reuning, U., Senekowitsch-Schmidtke, R., Diefenbach, B., Kessler, H., Stocklin, G., and Schwaiger, M. (1999) Radiolabeled alpha(v)beta3 integrin antagonists: a new class of tracers for tumor targeting. *J. Nucl. Med. 40*, 1061−1071.

(17) Blower, P. J., Lewis, J. S., and Zweit, J. (1996) Copper radionuclides and radiopharmaceuticals in nuclear medicine. *Nucl. Med. Biol. 23*, 957−980.

(18) McCarthy, D. W., Shefer, R. E., Klinkowstein, R. E., Bass, L. A., Margeneau, W. H., Cutler, C. S., Anderson, C. J., and Welch, M. J. (1997) Efficient production of high specific activity 64Cu using a biomedical cyclotron. *Nucl. Med. Biol. 24*, 35−43.

(19) Knight, L. C., Maurer, A. H., Ammar, I. A., Shealy, D. J., and Mattis, J. A. (1988) Evaluation of indium-111-labeled anti-fibrin antibody for imaging vascular thrombi. *J. Nucl. Med. 29*, 494−502.

(20) Lewis, M. R., Kao, J. Y., Anderson, A. L., Shively, J. E., and Raubitschek, A. (2001) An improved method for conjugating monoclonal antibodies with N-hydroxysulfosuccinimidyl DOTA. *Bioconjugate Chem. 12*, 320−324.

(21) Meares, C. F., McCall, M. J., Reardan, D. T., Goodwin, D. A., Diamanti, C. I., and McTigue, M. (1984) Conjugation of antibodies with bifunctional chelating agents: isothiocyanate and bromoacetamide reagents, methods of analysis, and subsequent addition of metal ions. *Anal. Biochem. 142*, 68−78.

(22) Meares, C. F., Moi, M. K., Diril, H., Kukis, D. L., McCall, M. J., Deshapnde, S. V., DeNardo, S. J., Snook, D., and Epenetos, A. A. (1990) Macrocyclic chelates of radiometals for diagnosis and therapy. *Br. J. Cancer Suppl. 10*, 21−26.

(23) Allen, C. M., Sharman, W. M., La Madeleine, C., Weber, J. M., Langlois, R., Ouellet, R., and van Lier, J. E. (1999) Photodynamic therapy: tumor targeting with adenoviral proteins. *Photochem. Photobiol. 70*, 512−523.

(24) Wermuth, J., Goodman, S. L., Jonczyk, A., and Kessler, H. (1997) Stereoisomerism and biological activity of the selective and superactive alpha(v)beta(3) integrin inhibitor cyclo(-RGDfV-) and its retro-inverso peptide. *J. Am. Chem. Soc. 119*, 1328−1335.

(25) Scarborough, R. M., Naughton, M. A., Teng, W., Rose, J. W., Phillips, D. R., Nannizzi, L., Arfsten, A., Campbell, A. M., and Charo, I. F. (1993) Design of potent and specific integrin antagonists. Peptide antagonists with high specificity for glycoprotein IIb-IIIa. *J. Biol. Chem. 268*, 1066−1073.

(26) Knoess, C., Siegel, S., Smith, A., Newport, D., Richerzhagen, N., Winkeler, A., Jacobs, A., Goble, R. N., Graf, R., Wienhard, K., and Heiss, W. D. (2003) Performance evaluation of the microPET R4 PET scanner for rodents. *Eur. J. Nucl. Med. Mol. Imaging 30*, 737−47.

(27) Kim, C. K., Gupta, N. C., Chandramouli, B., and Alavi, A. (1994) Standardized uptake values of FDG: body surface area correction is preferable to body weight correction. *J. Nucl. Med. 35*, 164−167.

(28) Calvete, J. J., Jurgens, M., Marcinkiewicz, C., Romero, A., Schrader, M., and Niewiarowski, S. (2000) Disulphide-bond pattern and molecular modelling of the dimeric disintegrin EMF-10, a potent and selective integrin alpha5beta1 antagonist from Eristocophis macmahoni venom. *Biochem. J. 345 Pt 3*, 573−581.

(29) Allen, C. M., Sharman, W. M., La Madeleine, C., van Lier, J. E., and Weber, J. M. (2002) Attenuation of photodynamically induced apoptosis by an RGD containing peptide. *Photochem. Photobiol. Sci. 1*, 246−254.

(30) Kanamori, S., Nishimura, Y., Okuno, Y., Horii, N., Saga, T., and Hiraoka, M. (1999) Induction of vascular endothelial growth factor (VEGF) by hyperthermia and/or an angiogenesis inhibitor. *Int. J. Hyperthermia 15*, 267−278.

(31) Byzova, T. V., Goldman, C. K., Pampori, N., Thomas, K. A., Bett, A., Shattil, S. J., and Plow, E. F. (2000) A mechanism for modulation of cellular responses to VEGF: activation of the integrins. *Mol. Cell 6*, 851−860.

(32) Knight, L. C., Romano, J. E., Marcinkiewicz, C., Iqbal, N., and Cosenza, S. (2004) Binding of 99mTc-disintegrins to avb3 on cultured tumor and vascular cells. *J. Nucl. Med. 45*, 113P.

(33) Haubner, R., Wester, H. J., Weber, W. A., and Schwaiger, M. (2003) Radiotracer-based strategies to image angiogenesis. *Q. J. Nucl. Med. 47*, 189−199.

(34) Haubner, R., Wester, H.-J., Weber, W. A., Mang, C., Ziegler, S. I., Goodman, S. L., Senekowitsch-Schmidtke, R., Kessler, H., and Schwaiger, M. (2001) Noninvasive imaging of $\alpha_v\beta_3$ integrin expression using ^{18}F-labeled RGD-containing glycopeptide and positron emission tomography. *Cancer Res. 61*, 1781−1785.

(35) Wang, M., Caruano, A. L., Lewis, M. R., Meyer, L. A., VanderWaal, R. P., and Anderson, C. J. (2003) Subcellular localization of radiolabeled somatostatin analogues: implications for targeted radiotherapy of cancer. *Cancer Res. 63*, 6864−6869.

(36) Lewis, M. R., Wang, M., Axworthy, D. B., Theodore, L. J., Mallet, R. W., Fritzberg, A. R., Welch, M. J., and Anderson, C. J. (2003) In vivo evaluation of pretargeted 64Cu for tumor imaging and therapy. *J. Nucl. Med. 44*, 1284−1292.

(37) Zimmermann, K., Grunberg, J., Honer, M., Ametamey, S., Schubiger, P. A., and Novak-Hofer, I. (2003) Targeting of renal carcinoma with 67/64Cu-labeled anti-L1-CAM antibody chCE7: selection of copper ligands and PET imaging. *Nucl. Med. Biol. 30*, 417−427.

(38) Lewis, M. R., Boswell, C. A., Laforest, R., Buettner, T. L., Ye, D., Connett, J. M., and Anderson, C. J. (2001) Conjugation of monoclonal antibodies with TETA using activated esters: biological comparison of 64Cu-TETA-1A3 with 64Cu−BAT-2IT-1A3. *Cancer Biother. Radiopharm. 16*, 483−494.

(39) Knight, L. C., Romano, J. E., and Gabriel, J. L. (2003) Selection of radiolabeling sites by site-directed mutagenesis. *J. Labelled Compd. Radiopharm. 46*, S24.

(40) Behr, T. M., Becker, W. S., Sharkey, R. M., Juweid, M. E., Dunn, R. M., Bair, H. J., Wolf, F. G., and Goldenberg, D. M. (1996) Reduction of renal uptake of monoclonal antibody fragments by amino acid infusion. *J. Nucl. Med. 37*, 829−33.

BC049961J

Specific Antitumor Targetable β-Cyclodextrin−Poly(ethylene Glycol)−Folic Acid Drug Delivery Bioconjugate

Stefano Salmaso, Alessandra Semenzato, and Paolo Caliceti*

Department of Pharmaceutical Sciences, University of Padua, Via F. Marzolo, 5-35131 Padova, Italy

Johan Hoebeke

UPR CNRS 9021, Immunologie et Chimie Thérapeutiques, I.B.M.C., Université de Strasbourg, 67084 Strasbourg, France

Fabio Sonvico, Catherine Dubernet, and Patrick Couvreur

Physico-Chimie-Pharmacotechnie-Biopharmacie, Faculté de Pharmacie, UMR CNRS 8612, Université Paris-Sud XI, 5, Rue Jean Baptiste Clément, 92296 Châtenay-Malabry, France. Received October 8, 2003; Revised Manuscript Received June 30, 2004

The tumor targeting properties of a new drug carrier synthesized by bioconjugation of folic acid (FA) to β-cyclodextrins through a poly(ethylene glycol) (PEG) spacer (CD−PEG−FA) were investigated. Surface plasmon resonance demonstrated that CD−PEG−FA specifically interacts with immobilized folate binding protein (FBP) while the naked β-cyclodextrins do not display any specific interaction. In vitro studies demonstrated that CD−PEG−FA was devoid of cell toxicity. [^{3}H]-folic acid/CD−PEG−FA competition binding investigations performed with folate receptor overexpressing human epidermal carcinoma KB cells showed that CD−PEG−FA had about 14 times lower tumor cell binding capacity than free folic acid. The carrier cell trafficking properties were investigated using rhodamine-B as fluorescent probe, which possesses 3000 and 4580 M^{-1} inclusion constants for CD−PEG−FA and β-cyclodextrins, respectively. Cell-associated fluorescence measurements showed that CD−PEG−FA does not promote the rhodamine-B uptake into non-folate receptor expressing human lung carcinoma MCF7 cells while 19% higher accumulation in KB cells was found with respect to rhodamine-B loaded β-cyclodextrins. Confocal laser scanning microscopy indicated the presence of cytosolic red fluorescent spots after 2 h of incubation of KB cells with rhodamine-B included CD−PEG−FA. The fluorescent dye resided primarily in small spots, namely, endosomes and multivesicular bodies. At 1 h after pulsed incubation, wider red fluorescent cellular structures appeared as a fusion of previous structures.

INTRODUCTION

Cyclodextrins are cyclic oligosaccharides forming molecular inclusion complexes with a wide range of hydrophobic molecules. The ability to allocate active molecules into the oligosaccharide hydrophobic core offers several opportunities in drug solubility, stability, and bioavailability optimization (*1*−*3*). However, aside from γ-cyclodextrins, which have been used in parenteral drug administration, systemic application of natural cyclodextrins, namely α- and β-cyclodextrins, entails the risk of toxic effects such as hemolysis and nephrotoxicity (*4*−*5*). Aimed at reducing the toxicity and enhancing the biopharmaceutical properties of cyclodextrins, semisynthetic derivatives were prepared by introduction of hydroxyalkyl or sulfoalkyl functions or by conjugation to water-soluble polymers (*3*, *6*).

Although cyclodextrins possess interesting properties for delivery of therapeutics with high pharmacological activity, low therapeutic index, and poor physicochemical properties, they cannot be used for active drug targeting because they are devoid of any specificity for biological structures. To exploit cyclodextrins as targetable drug delivery systems, the oligosaccharide structure should be properly functionalized with targeting moieties such as peptides, hormones, vitamins, antibody fragments, etc.

Folic acid is a vitamin that binds selectively the folate receptor (FR), a glycosylphosphatidylinositol-anchored cell surface receptor that is overexpressed in many human tumors, including ovarian, endometrial, colorectal, breast, lung, renal, neuroendocrine carcinomas, and brain metastases (*7*). Upon receptor interaction, the folic acid−FR complex is taken up by cells and moves through many organelles involved in endocytic trafficking, providing for cytosolic disposition (*8*).

The folate receptor mediated endocytosis was largely investigated to expand the therapeutic value of drugs by increasing delivery to the target tissue as well as the target/nontarget tissue ratio. Examples of targetable drug delivery carriers functionalized by folic acid conjugation include radionuclide deferoxamine−folate complexes for radiopharmaceutical imaging, liposome−folate encapsulated drugs, liposome−folate encapsulated polylysine−DNA, cytotoxin−folate conjugates and folic acid decorated nanoparticles (*9*−*13*).

* To whom correspondence should be addressed. Phone: 049 8275695. Fax: 049 8275366. E-mail: paolo.caliceti@unipd.it.

10.1021/bc034186d CCC: $27.50 © 2004 American Chemical Society
Published on Web 08/25/2004

Recently, we synthesized a new targetable drug delivery system by folic acid conjugation to β-cyclodextrins through a 700 Da poly(ethylene glycol) (PEG) spacer arm. Preliminary studies demonstrated that the derivative possesses suitable properties for drug delivery: high solubility, ability to form inclusion complexes with few drug models, and negligible hemolytic activity (*14*).

In the present study the biological and biopharmaceutical properties of the new β-cyclodextrin−PEG−folic acid bioconjugate were investigated. The affinity of the bioconjugate for the immobilized folate binding protein (FBP) and for the cell membrane folate receptor was determined by Biacore and cultured tumor folate receptor overexpressing KB cells, respectively. The ability of the conjugate to be taken up by folate receptor overexpressing and nonexpressing cells was also investigated, and its intracellular localization was determined.

MATERIALS AND METHODS

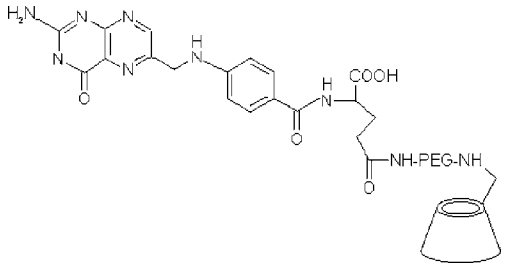
β-Cyclodextrins, folic acid (FA), and *O*,*O*′-bis(2-aminopropyl)poly(propylene glycol)-*block*-poly(ethylene glycol)-*block*-poly(propylene glycol) (Jeffamine or PEG) were purchased from Fluka Chemika (Buchs, Switzerland). Tissue culture products were obtained from GIBCO (Grand Island, NY).

Rhodamine-B and methylene blue were from Aldrich (Steinheim, Germany), and [^{3}H]-folic acid was from Amersham (Little Chalfont, U.K.). Folate binding protein (FBP) was furnished by Sigma (St. Louis, MO), FluorSave reagent was obtained from Calbiochem (San Diego, CA), fluorescein−DHPE was from Molecular Probes (Eugene, OR), and the Bio-Rad protein assay was from Bio-Rad Laboratories (Richmond, CA). Surface plasmon measurements were carried out with Biacore 3000 (Biacore AB, Uppsala, Sweden). CM 5 sensorchips and coupling reagents were furnished by Biacore.

Human nasopharyngeal epidermal carcinoma KB cells were cultured as a monolayer at 37 °C in a humidified atmosphere containing 5% CO_2 in folate-deficient Dulbecco's modified Eagle's medium (DMEM) supplemented with 10% (v/v) heat-inactivated fetal calf serum, 2 mM glutamine, 100 IU/mL penicillin, and 100 μg/mL streptomycin. Lung human carcinoma MCF7 cells were cultured in normal RPMI-1640 medium, supplemented with 15% fetal calf serum, 2 mM glutamine, 100 IU/mL penicillin, and 100 μg/mL streptomycin. The folic acid concentration in the normal RPMI media was 2.26 μM. Cells were routinely treated with a 500 μg/mL trypsin and 200 μg/mL EDTA solution in Ca^{2+} and Mg^{2+} free phosphate buffered saline (PBS).

Synthesis of 6-Mono{folic acid-γ-[*O*,*O*′-bis(2-aminopropyl)poly(propylene glycol)-*block*-poly(ethylene glycol)-*block*-poly(propylene glycol)]}-β-cyclodextrin. 6-Mono{folic acid-γ-[*O*,*O*′-bis(2-aminopropyl)polypropylene glycol-*block*-poly(ethylene glycol)-*block*-polypropylene glycol]}-β-cyclodextrin (CD−PEG−FA) was prepared according to a two-step procedure reported elsewhere (14). Briefly, 6-mono[*O*,*O*′-bis(2-aminopropyl)poly(propylene glycol)-*block*-poly(ethylene glycol)-*block*-poly(propylene glycol)]-β-cyclodextrin (CD−PEG−NH_2) was prepared by reaction of 6-mono-(*p*-toluenesulfonyl)-β-cyclodextrin (0.995 g, 0.772 mmol) with *O*,*O*′-bis(2-aminopropyl)poly(propylene glycol)-*block*-poly(ethylene glycol)-*block*-poly(propylene glycol) (53.34 mmol) in DMF (*15*). The mixture was refluxed for 8−9 h at 80 °C under argon. The 6-mono[*O*,*O*′-bis(2-aminopropyl)poly(propylene glycol)-*block*-poly(ethylene glycol)-*block*-poly(propylene glycol)]-β-cyclodextrin conjugate was precipitated in 250 mL of acetone, washed several times with the same solvent, collected by centrifugation, and desiccated under vacuum. The final product was characterized by thin layer chromatography, NMR, and ESI-TOF mass spectrometry, and the iodine test and *p*-anisaldehyde were for PEG and cyclodextrin determination, respectively (*16*, *17*).

Chart 1. Main Isomer Formed by Bioconjugation Reaction of CD−PEG−NH_2 to Folic Acid (λ Carboxyl Folic Acid isomer): 6-Mono{folic acid-γ-[*O*,*O*′-bis-(2-aminopropyl)poly(propylene glycol)-*block*-poly(ethylene glycol)-*block*-poly(propylene glycol)]}-β-cyclodextrin (CD−PEG−FA).



6-Mono{folic acid-γ-[*O*,*O*′-bis(2-aminopropyl)polypropylene glycol-*block*-poly(ethylene glycol)-*block*-polypropylene glycol]}-β-cyclodextrin was obtained by reaction of 6-mono-[*O*,*O*′-bis(2-aminopropyl)poly(propylene glycol)-*block*-poly(ethylene glycol)-*block*-poly(propylene glycol)]-β-cyclodextrin (0.791 g, 0.438 mol) with the *N*-hydroxy-
succinimide ester of folic acid (2.884 g, 5.356 mmol) in 50 mL of anhydrous DMSO (*10*). TEA (320 μL, 0.2295 mmol) was added to the reaction mixture, and pH 9.0 was maintained by addition of the same base. The reaction mixture was stirred under dark and anhydrous conditions for 40 h. The solution was poured dropwise into 500 mL of cold acetone, and the precipitate was washed with 50 mL of the same solvent and dried under vacuum. The dry product was dissolved in 100 mL of 0.1 M borate buffer, pH 8.3, and fractionated by gel permeation chromatography using Sephadex G25 superfine column, eluting with 10 mM ammonium carbonate buffer, pH 8.0. The eluted volume was analyzed by UV at 363 nm, iodine test, and *p*-anisaldehyde. The bioconjugate was isolated and further purified by preparative RP-C18 column (2.5 cm × 22 cm), eluting in a gradient mode, using 10 mM ammonium acetate pH 6.5 (eluent A) and acetonitrile (eluent B). The peak corresponding to the conjugate was collected, concentrated, and analyzed by RP-C18 chromatography, UV−vis for folate determination (*18*), iodine test, mass spectrometry, and ^{1}H NMR.

The reaction procedure reported above yields two isomers where folic acid is conjugated at the α or λ carboxyl group of glutamate residue, respectively. According to the literature data (*19*), the conjugation takes place preferentially at the level of the λ carboxyl group. Chart 1 reports the chemical structure of the more abundant isomer (folic acid λ carboxyl derivative): 6-mono-{folic acid-γ-[*O*,*O*′-bis(2-aminopropyl)poly(propylene glycol)-*block*-poly(ethylene glycol)-*block*-poly(propylene glycol)]}-β-cyclodextrin (CD−PEG−FA).

Host−Guest Inclusion Constant Determination. Five sample series were prepared by addition of β-cyclodextrins (sample A), PEG (sample B), folic acid (sample C), β-cyclodextrins/PEG/folic acid 1:1:1 molar ratio mixture (sample D), and CD−PEG−FA conjugate (sample E) to 5 mL volumes of 10 mM phosphate buffer, 0.15 M NaCl, pH 7.2, containing 5 μM rhodamine-B. The solutions were prepared in order to obtain β-cyclodextrins/

rhodamine-B, PEG/rhodamine-B, folic acid/rhodamine-B, [β-cyclodextrins/PEG/folic acid]/rhodamine-B, or CD−PEG−FA/rhodamine-B molar ratios in the range of 0−200. The fluorescence of the samples was determined using a Perkin-Elmer LS 50 B spectrofluorimeter in a conventional 96-well plate. The instrument was set up using 2.5 nm excitation and emission slits, 543 nm excitation, and 580 nm emission wavelengths. Inclusion constants were calculated from fluorescence emission values according to the procedure reported in the literature (*20*, *21*).

Surface Plasmon Resonance Measurements. Surface plasmon resonance measurements were carried out using Biacore 3000. Cow milk folate-binding protein (FBP) was immobilized on the sensor chip surface of a carboxylated dextran-coated gold film (CM 5 sensor chip) activated according to the general procedure for immobilization by amine coupling recommended by the supplier (*22*, *23*). The flow channel of Biacore was equilibrated with HBS buffer (10 mM Hepes, 150 mM NaCl, 0.05% surfactant P20, pH 7.4), and then the following samples were successively injected into the system: (a) 0.1 M *N*-hydroxysuccinimide/0.4 M *N*′-(3-dimethylaminopropyl)-*N*-ethylcarbodiimide solution (1/1, v/v) to obtain an activated carboxylated dextran; (b) 1 mg/mL of FBP in 100 mM potassium phosphate buffer, 4 mM mercaptoethanol, 10% v/v glycerol, pH 7.0; (c) 1 M ethanolamine, pH 8.5, to deactivate residual *N*-hydroxysuccinimidyl esters on the sensor chip. FBP immobilization was carried out using a flow rate of 5 μL/min. The receptor bound to the chip surface was 1.5 ng/mm^2 per channel. Four-hundred nanomolar samples of β-cyclodextrins or β-cyclodextrin-equivalent samples of β-cyclodextrins/PEG 1:1 molar ratio mixture or CD−PEG−FA solutions in HBS were injected in the Biacore flow channel at a flow rate of 30 μL/min and allowed to interact with the immobilized receptor for 3 min.

CD−PEG−FA in the presence of 10 μM free folic acid was also injected under the operative conditions reported above.

HBS solutions containing CD−PEG−FA in the range 50−400 nM were injected into the system and allowed to interact for 3 min to study the kinetic parameters of interaction.

Cytotoxic Assays. KB cells were seeded in 96-well tissue culture plates at a density of 5 × 10^4 cells/well. After 24 h, the culture medium was replaced with 200 μL of medium containing increasing concentrations (0−4 mM) of β-cyclodextrins, PEG, folic acid, β-cyclodextrins/PEG/folic acid 1:1:1 molar ratio mixture, or CD−PEG−FA. After 6 h of incubation, the medium was removed and the cells were washed three times with 200 μL of PBS, pH 7.4. An amount of 100 μL of a 0.25% (w/v) methylene blue in 50% (v/v) methanol/water solution was added to each well. After 30 min of incubation at room temperature, the plates were washed four times with PBS. The plates were dried at 55 °C for 30 min, and stained cells were immediately dissolved by addition of 200 μL/well of 0.1 M HCl. The absorbance was measured at 620 nm after overnight gentle stirring.

Cell Binding Studies. KB cells were seeded in 33 mm well culture plates at a concentration of 5 × 10^5 cells/well. After 24 h, the wells were washed twice with PBS, pH 7.4, and then the plates were incubated at 37 °C for 30 min with 1 mL of folic acid free DMEM medium containing 0.1 μM [^{3}H]-folic acid and CD−PEG−FA or β-cyclodextrins/PEG 1:1 molar ratio mixtures at concentrations ranging from 0 to 100 μM. After incubation, the plates were washed four times with PBS and the cells were lysed by overnight incubation with 1 mL/well aqueous solution containing 0.1% Triton-X100. The amount of radioactivity in the lysate was determined by addition of scintillation cocktail, and the radioactivity values were referenced to a standard radioactivity curve. All measures were carried out in triplicate. Plates preincubated with medium and serum without cells were used for residual plate radioactivity determination according to the procedure reported in the literature (*19*).

Cell Uptake Studies. KB or MCF7 cells were seeded in 33 mm culture wells (6 × 10^5 and 7 × 10^5 cells/well, respectively). After 24 h, the wells were washed with PBS, pH 7.4, and incubated with 1 mL of folic acid free DMEM containing free rhodamine-B (1 μM) or the same rhodamine-B concentration in the presence of β-cyclodextrins or β-cyclodextrins/PEG 1:1 molar ratio mixture or β-cyclodextrins/PEG/folic acid 1:1:1 molar ratio mixture or CD−PEG−FA (100 μM). After 2 h of incubation at 37 °C, the wells were washed four times with PBS and then subjected to addition of 300 μL of Ca^{2+} and Mg^{2+} free phosphate buffer containing 500 μg/mL of trypsin, 200 μg/mL of EDTA. The released cells were washed twice with PBS and lysed by overnight treatment with 0.667 mL of 0.1% Triton-X 100 water solution. The cell-associated rhodamine-B was determined by fluorescence analysis as reported above. The number of cells in the wells was estimated by a Bio-Rad protein assay, and the relative fluorescence obtained with the samples was normalized on the basis of the cell number.

Confocal Studies. KB and MCF7 cells (5 × 10^4 and 8 × 10^4 cells in 1 mL, respectively) were seeded into a 24-well culture plate containing one glass coverslip/well (1 mL of suspension per well). After 72 h, the wells were washed with PBS, pH 7.4, and the wells were incubated with 0.5 mL of a folic acid free DMEM medium containing 1 μM of rhodamine-B in free solution or in the presence of 100 μM β-cyclodextrins or 100 μM β-cyclodextrins/PEG 1:1 molar ratio mixture or 100 μM CD−PEG−FA. After 2 h of incubation, coverslips were taken, washed four times with cold PBS, placed in empty wells, and treated with 0.5 mL of 4% paraformaldehyde in PBS for 15 min at 4 °C. After two additional PBS washings, the cells on the coverslips were treated with 50 μL of a 20 μg/mL fluorescein−DHPE [*N*-(fluorescein-5-thiocarbamoyl)-1,2-dihexadecanoyl-*sn*-glycerol-3-phosphoethanolamine, triethylammonium salt] solution in PBS, washed three times with PBS, and mounted on glass slides by FluorSave reagent. Coverslips were maintained at 4 °C in the dark overnight and analyzed by a Zeiss LSM-510 confocal scanning laser microscope equipped with a 25 mW argon ion laser and an ×63 (oil) objective with a numerical aperture of 1.4. Green fluorescence was observed with a 505−550 nm band-pass emission filter under 488 nm laser illumination, and red fluorescence was observed with a 560 nm band-pass emission filter under 543 nm laser illumination.

For cell trafficking studies KB and MCF7 cell samples were treated according to the procedure reported in the previous section. The cells were incubated for 1 h with 0.5 mL of a folic acid free DMEM medium containing 1 μM of rhodamine-B and 100 μM CD−PEG−FA. After 1 h of incubation, the wells and coverslips were washed four times with PBS and incubated with 1 mL of folic acid free DMEM medium. At scheduled times, the coverslips were treated as reported above for cell fixing and analyzed by a Zeiss LSM-510 confocal scanning laser microscope.

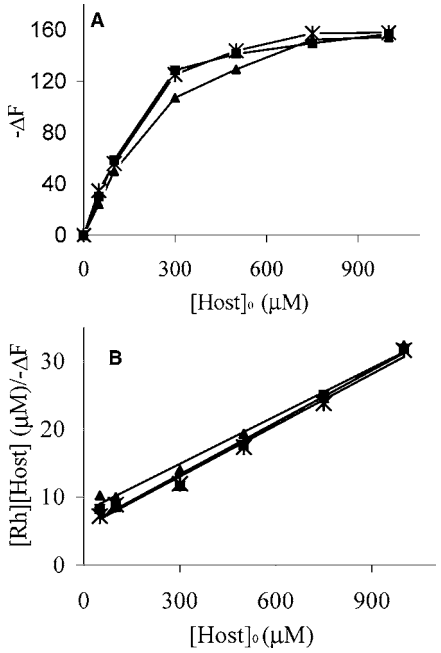


Figure 1. (A) Fluorescence quenching curve-fitting of rhodamine-B with β-cyclodextrins (×), β-cyclodextrins/PEG/folic acid 1:1:1 molar ratio mixture (■), and CD−PEG−folic acid (▲). (B) Modified Benesi−Hildebrand plots of rhodamine-B complexation with β-cyclodextrins (×), β-cyclodextrins/PEG/folic acid 1:1:1 molar ratio mixture (■), and CD−PEG−FA (▲).

RESULTS

Host−Guest Inclusion Constant Determinations. The formation of β-cyclodextrins and CD−PEG−FA inclusion complexes with rhodamine-B was investigated by fluorimetric titration (*24*).

Figure 1A shows the quenching profiles of rhodamine-B in the presence of different concentrations of β-cyclodextrins, β-cyclodextrins/PEG/folic acid 1:1:1 molar ratio mixture, and CD−PEG−FA. Figure 1B reports the quenching value elaboration used to calculate the inclusion constants of rhodamine-B for β-cyclodextrins, β-cyclodextrins in the presence of PEG and folic acid and CD−PEG−FA. The complex stability constants were determined according to the modified Benesi−Hildebrand equation (*20*, *21*) assuming a 1:1 rhodamine-B/cyclodextrin stoichiometry described by the following equation:

$$\mathrm{CDs} + \mathrm{RhB} \rightleftarrows \mathrm{CDs{\cdot}RhB}$$

$$\frac{[\mathrm{RhB}]_0[\mathrm{CDs}]_0}{F - F_0} = \frac{[\mathrm{CDs}]_0[\mathrm{RhB}]}{F_\infty - F_0} + \frac{[\mathrm{RhB}]}{(F_\infty - F_0)K_s}$$

where $[RhB]_0$ and $[CDs]_0$ are the initial guest (rhodamine-B) and host (β-cyclodextrin or CD−PEG−FA) concentrations, respectively, F_0 and F are the fluorescence intensities in the absence and in the presence of host, respectively, F_∞ is the fluorescence intensity limit when all rhodamine-B was included in the β-cyclodextrins, and K_s is the inclusion constants for 1:1 complex.

The complex stability constants of rhodamine-B for β-cyclodextrins, β-cyclodextrins/PEG/folic acid, and CD−PEG−FA were calculated to be 4580, 4500, and 3000 M^{-1}, respectively. Importantly, the calculated inclusion constant of rhodamine-B for β-cyclodextrins corresponds fairly to the value reported in the literature (*20*).

Surface Plasmon Resonance Measurements. The selective interaction of CD−PEG−FA with the cow milk folate binding protein (FBP) was investigated by surface plasmon resonance analysis.

The surface plasmon resonance profiles relative to β-cyclodextrins, β-cyclodextrins/PEG, and CD−PEG−FA reported in Figure 2 display a low signal/noise ratio typical of low molecular weight compounds, which elicit a weak signal. The signal variation (RU) at the injection time was due to irregularities induced by the injection of a solution with different refractive index compared to that of the solvent. To avoid this abnormality, the association curves were analyzed with a delay time of 9.9 s.

Despite the high noise, the surface plasmon resonance profiles reported in Figure 2A show differences among CD−PEG−FA, β-cyclodextrins, and the β-cyclodextrins/PEG mixture. The CD−PEG−FA bioconjugate elicits a signal due to a specific interaction with the FBP immobilized on the sensor chip, whereas the unconjugated β-cyclodextrins, either in the presence or in the absence of PEG, elicit a very weak signal indicating that no binding takes place.

The plasmon resonance signal/noise ratio did not allow for an accurate evaluation of the CD−PEG−FA apparent dissociation constant for FBP. However, the bioconjugate was estimated to have approximately 400 times lower affinity constant for FBP compared to the free folic acid value reported in the literature (*25*).

Specific binding of CD−PEG−FA to immobilized FBP was also demonstrated by injection of the conjugate in the presence of an excess of free folic acid (CD−PEG−FA/folic acid 1:25 molar ratio). The plasmon resonance profiles obtained with CD−PEG−FA in the absence or in the presence of free folic acid reported in Figure 2B indicate that the amount of CD−PEG−FA bound to FBP was sensibly lower in the case of folic acid co-injection, suggesting that the free folic acid competes with CD−PEG−FA for FBP binding.

Cell Toxicity Investigations. Aimed at setting up proper cell culture protocols for evaluating the cell binding and uptake, investigations were undertaken by incubation of PEG, folic acid, β-cyclodextrins, β-cyclodextrins/PEG/folic acid 1:1:1 molar ratio mixture, and CD−PEG−FA with folate receptor overexpressing KB cells or folate receptor nonexpressing MCF7 cells. As expected, samples containing free folic acid displayed enhanced cell proliferation while PEG did not have any effect on cell viability. Also, neither β-cyclodextrins nor CD−PEG−FA was found to affect the cell viability under the experimental conditions.

Competition Binding Studies. [^{3}H]-folic acid/CD−PEG−FA or [^{3}H]-folic acid/[β-cyclodextrins/PEG 1:1 molar mixture] binding competition studies were undertaken using KB cells to evaluate the CD−PEG−FA affinity for the cell folate receptor. The [^{3}H]-folic acid binding competition profiles reported in Figure 3 show that β-cyclodextrins/PEG do not compete with [^{3}H]-folic acid for the cell receptor. The maximal cell-associated radioactivity due to [^{3}H]-folic acid binding to the cell receptors was in fact retained at high [β-cyclodextrins/PEG mixture] concentrations (log [host], μM). In contrast, the cell-associated radioactivity decreased as the CD−PEG−FA concentration increased, indicating that the bioconjugate displaced the [^{3}H]-folic acid from the cell receptor. Since 50% of cell-associated radioactivity was obtained with 1.4 μM CD−PEG−FA and 0.1 μM [^{3}H]-folic acid, CD−PEG−FA was estimated to maintain 7% of the residual affinity for cell folate receptor.

Cell Uptake Investigations. Cell uptake studies were carried out by incubation of free rhodamine-B,

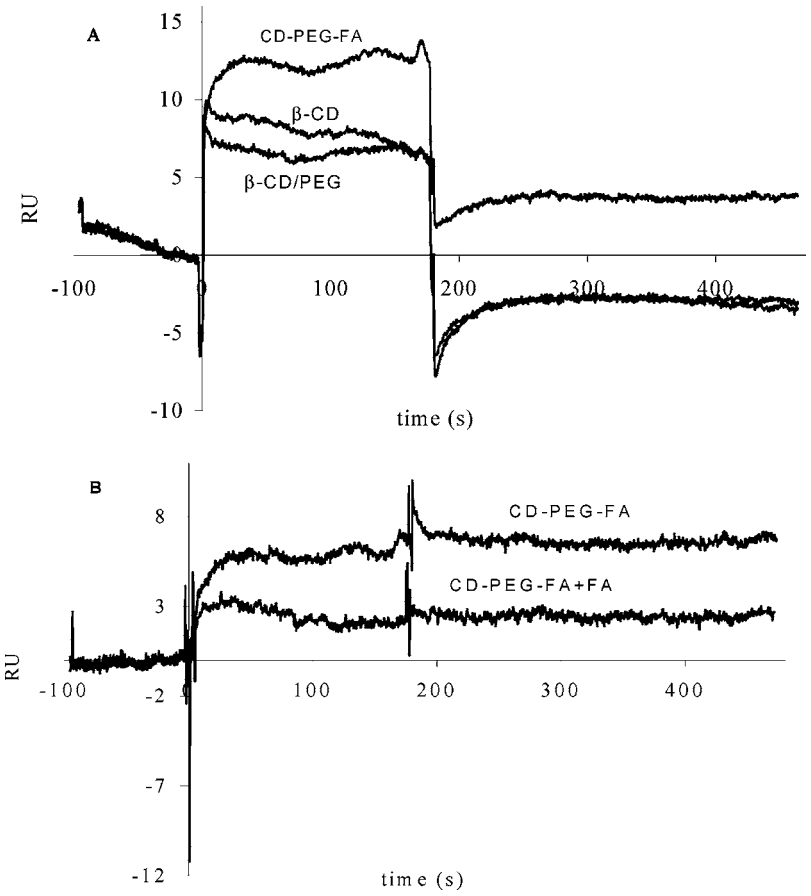


Figure 2. Surface plasmon resonance behavior of interaction with immobilized FBP: (A) binding profiles of CD−PEG−FA, β-cyclodextrins, and β-cyclodextrins/PEG 1:1 molar ratio mixture; (B) binding competition profiles in the absence and in the presence of free folic acid. RU = resonance units.

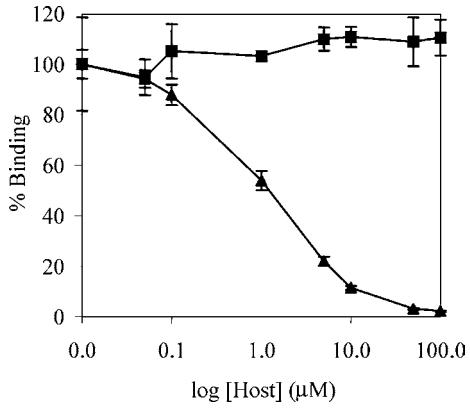


Figure 3. [^{3}H]-folic acid competition binding profiles of cellular folate receptor obtained with monolayer KB cells incubated with cyclodextrin/PEG 1:1 molar ratio (■) and CD−PEG−FA (▲). The mean values and standard deviations were calculated on the basis of five experiments.

rhodamine-B included in CD−PEG−FA, and various mixtures of the individual components (β-cyclodextrin, PEG, folic acid, and rhodamine-B) with folate receptor overexpressing KB cells or folate receptor not expressing MCF7 cells. According to the results reported in Figure 1A, 1:100 rhodamine-B/β-cyclodextrin molar ratio was chosen to guarantee over 90% of rhodamine-B inclusion into β-cyclodextrins or into CD−PEG−FA.

The enzymatic cell detachment procedure avoided fluorescence interferences due to unspecific rhodamine-B absorption on the plastic material. Rhodamine-B concentrations below 2 μM were used to prevent rhodamine-B related cell toxicity. Finally, methylene blue assay used to evaluate the cell viability avoided absorbance interferences observed with the MTT assay (*26*).

Figure 4A shows the KB cell-associated fluorescence values obtained after incubation with free rhodamine-B or rhodamine-B included in β-cyclodextrins/PEG, β-cyclodextrins/PEG/folic acid, and CD−PEG−FA. The data reported in the figure were obtained by subtracting the values obtained with rhodamine-B loaded β-cyclodextrins, which displayed the lower cell-associated fluorescence.

The increase of cell-associated fluorescence obtained with free rhodamine-B indicates that the passive penetration of the probe into the cells is prevented by inclusion into naked β-cyclodextrins. PEG and folic acid were found to enhance the cell uptake of rhodamine-B loaded β-cyclodextrins. The uptake of rhodamine-B loaded CD−PEG−FA was significantly higher ($P < 0.02$) compared to that under other experimental conditions: 19% higher with respect to rhodamine-B loaded β-cyclodextrins, 12% higher compared to free rhodamine-B, more than 10% higher compared to β-cyclodextrins/PEG and β-cyclodextrins/PEG/folic acid mixtures.

The bioconjugate selectivity for the folate receptor overexpressing cells was confirmed by using MCF7 cells, a human lung carcinoma cell line that lacks the folate receptor. The test was carried out under the same conditions reported above for the KB cell studies. Figure 4B shows that low cell-associated fluorescence is observed after incubation with free rhodamine-B and with rhodamine-B complexed with β-cyclodextrins/PEG or with β-cyclodextrins/PEG/folic acid, as well as after incubation with rhodamine-B loaded CD−PEG−FA. These results

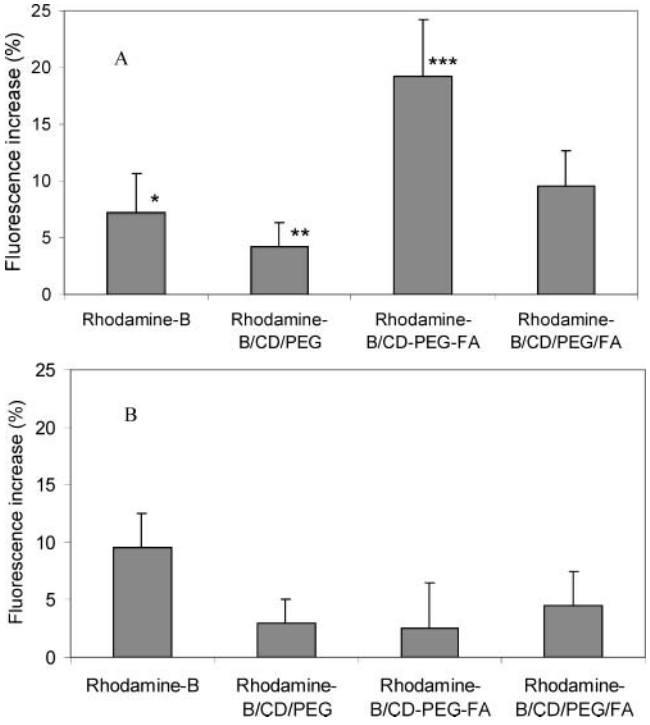


Figure 4. Rhodamine-B uptake by KB cells (A) and MCF7 cells (B). Fluorescence increase after cell incubation with free rhodamine-B and rhodamine-B complexed with β-cyclodextrins/PEG 1:1 molar ratio mixture, CD−PEG−FA, and β-cyclodextrins/PEG/folic acid 1:1:1 molar ratio mixture. The fluorescence increase is referenced to the values obtained with β-cyclodextrin complexed rhodamine-B. The mean values and the standard deviations were calculated on the basis of five experiments: $P < 0.02$ (***); $P < 0.05$ (**); $P < 0.5$ (*).

indicate that in this case the fluorophore was not taken up actively by cells.

Figure 5 shows the confocal laser-scanning microscopy images obtained after cell incubation with rhodamine-B loaded CD−PEG−FA and rhodamine-B loaded β-cyclodextrins/PEG/folic acid. The cell membranes were green-stained by fluorescein−DHPE, while red fluorescence was related to taken-up rhodamine-B.

Figure 5A shows that CD−PEG−FA promotes the rhodamine-B localization into KB cell tubular endosomal structures, some of them having a thickness of about 1−2 μm similar to those reported by other authors (*27*). Also, multivesicular bodies with predominant perinuclear fluorophore disposition were observed. Very weak diffuse fluorescence was detected in the cytosolic compartment and without localization into the nuclei. In contrast, the images obtained after KB or MCF7 cell incubation with free rhodamine-B, rhodamine-B loaded β-cyclodextrins/PEG, and β-cyclodextrins/PEG/folic acid mixtures or after MCF7 cell incubation with rhodamine-B loaded CD−PEG−FA did not show specific rhodamine-B localization into tubular endosomal structures and multivesicular bodies. In these cases, a diffused fluorescence in the cyctosolic compartment was observed. As an example, Figure 5B reports the image obtained with KB cells incubated with rhodamine-B loaded β-cyclodextrins/PEG/folic acid.

To get more information about intracellular trafficking of delivered rhodamine-B, KB cells were incubated for 1 h of pulse contact with medium containing rhodamine-B included CD−PEG−FA. Figure 5C shows that red fluorescence in dispersed cytosolic small spots, probably corresponding to small endosomes, was detectable soon after incubation. After 1 h, larger cytosolic fluorescent areas were observed (Figure 5D) indicating that the endosomes migrate and are localized in proximity of the Golgi apparatus as reported in the literature (*8*).

DISCUSSION

β-Cyclodextrins, folic acid, and PEG were properly assembled to obtain a supramolecular carrier system for active drug delivery. The delivery system was designed in order to exploit the physicochemical and biological properties of the various components; the β-cyclodextrin unit can host drugs with low solubility and stability, folic acid allows for active targeting to folate receptor over-expressing tumor cells, and PEG was used as a spacer between β-cyclodextrin and folic acid. PEG confers to the targeting moiety a certain flexibility that overcomes problems related to steric hindrance of β-cyclodextrin. Furthermore, PEG endows a derivative with higher solubility compared to the naked β-cyclodextrin or folic acid. The solubility of the new construct in water is, in fact, about 100 mg/mL, while the solubility of β-cyclodextrins and folic acid is 18.5 and 0.0016 mg/mL, respectively.

The bioconjugate was found to maintain high affinity for rhodamine-B used as the fluorescent probe in the present study. This result is in agreement with the data relative to estradiol already published (*14*). Similarly to estradiol, the rhodamine-B affinity constants for naked β-cyclodextrins and CD−PEG−FA were in the same order. However, the slight decrease in affinity obtained with CD−PEG−FA may be attributable to the chemical modification of the oligosaccharide ring or to the presence of the bound PEG that can interfere with the drug association, though the PEG and folic acid physically mixed with the β-cyclodextrins were not found to affect significantly the rhodamine-B affinity constant.

It should be noted that drugs with high-affinity constants are probably necessary to exploit the carrier properties of CD−PEG−FA because high drug/carrier affinity avoids the drug release before reaching the target. Aimed at selecting suitable drug models, an in silico drug design study is in progress.

Cell culture studies demonstrated that CD−PEG−FA was devoid of cytotoxicity, which represents a prerequisite for its pharmaceutical application. High cell viability was, in fact, observed by incubating both KB and MCF7 cells with high CD−PEG−FA concentration solutions. Also, previous studies demonstrated that this new derivative displays negligible hemolytic activity compared to the naked β-cyclodextrins, which confirms the good biocompatibility and low toxicity of this new macromolecular carrier.

The targeting properties of the bioconjugate were demonstrated by both the Biacore technique and cell culture investigations. Though the plasmon resonance signal/noise ratio did not allow for accurate affinity constant evaluation, CD−PEG−FA displayed a lower affinity for the cow milk folate binding protein compared to the free folic acid constant affinity reported in the literature (K_a = 50 pM). However, the free folic acid affinity constant reported in the literature was determined by using a different evaluation method with respect to the method adopted in this study. In the surface plasmon resonance assay, FBP is immobilized on a solid substrate while the affinity constant of free folic acid reported in the literature was evaluated by using FBP in solution, which prevents evaluation problems due to the solid matrix hindrance (*25*). Also, it is important to note that a certain decrease in affinity of the biocon-

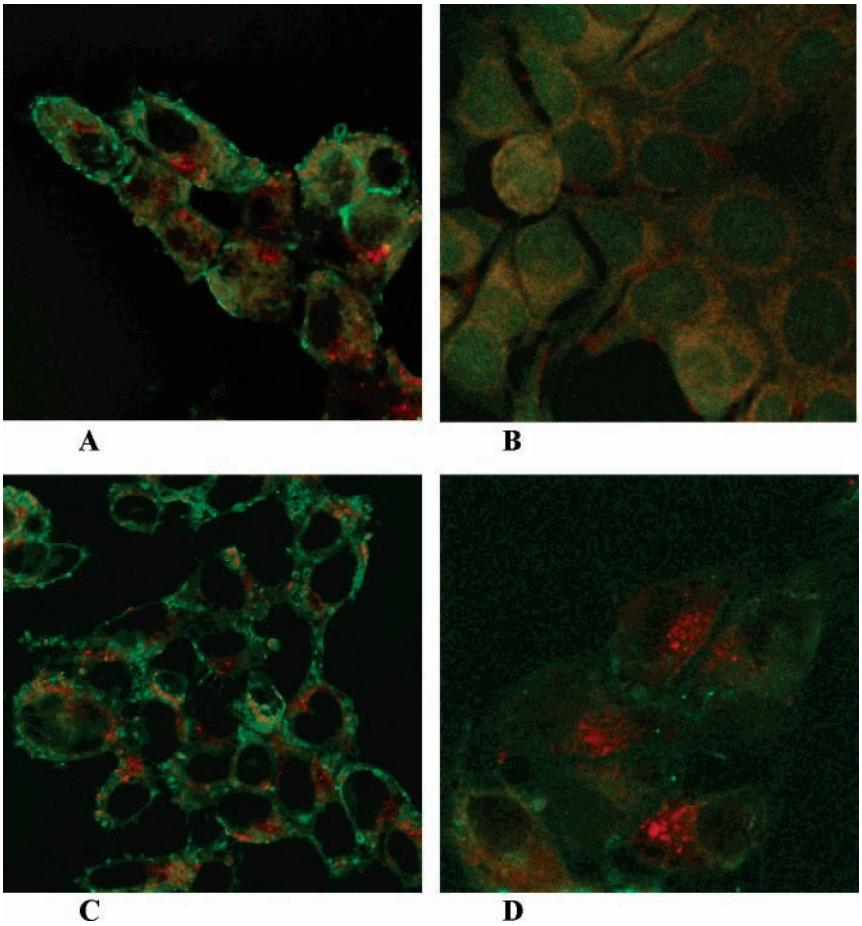


Figure 5. Confocal images obtained by incubation of 1 μM rhodamine-B with KB cells under different conditions: after 2 h of incubation with rhodamine-B loaded CD−PEG−FA (A); after 2 h of incubation with rhodamine-B loaded β-cyclodextrins/PEG/folic acid 1:1:1 molar ratio mixture (B); after 1 h of incubation with rhodamine-B loaded CD−PEG−FA (C); after 1 h from 1 h of incubation with rhodamine-B loaded CD−PEG−FA (D).

jugated folate was expected because about 20% of the folic acid was linked to PEG through the α-carboxylic group which is involved in the receptor recognition (*19*).

[^{3}H]-folic acid competition experiments performed using folate receptor overexpressing KB cells confirmed the specific recognition of CD−PEG−FA for the biological target. Although the folate affinity for the cell folate receptor decreased after conjugation to β-cyclodextrin−PEG, the conjugate was found to maintain high receptor affinity to guarantee its applicability in drug targeting similar to that reported for the folic acid−PEG 2000 Da bioconjugate used for liposome decoration (*19*).

The folate interaction with the folic acid receptor is known to promote a receptor-mediated internalization of the carrier into cells through a potocytosis pathway (*28*). The intracellular delivery of CD−PEG−FA was verified by cell culture studies using the fluorescent probe rhodamine-B. Confocal measurements showed that CD−PEG−FA provides for active transport of the probe into localized cell multivesicular bodies. Partial but unspecific rhodamine-B penetration was also observed when folate receptor overexpressing KB cells were incubated with free rhodamine-B or rhodamine-B loaded β-cyclodextrins/PEG or β-cyclodextrins/PEG/folic acid mixtures. Slight internalization was also obtained by incubation of folate receptor not-expressing MCF7 cells with free rhodamine-B, rhodamine-B included β-cyclodextrins/PEG/FA, or rhodamine-B included in CD−PEG−FA. Probably PEG partially disorganizes the biological membranes favoring passive rhodamine-B diffusion into the cells while folic acid promotes the rhodamine-B uptake from bulk solution by stimulating the cell potocytosic activity in folate receptor overexpressing cells.

Although the rhodamine-B uptake obtained using CD−PEG−FA was not massive, it was significantly higher compared to the other samples. Furthermore, it is worth noting that the simultaneous presence of folic acid and drug-loaded β-cyclodextrins in the same construct can guarantee the in vivo uptake of the carrier into the target cells where the drug can be released by environmental changes. The pH-induced ionization, for example, can take place in lysosomes or other cytosolic sites that display acidic pH and can provoke an affinity decrease that can result in drug release.

CONCLUSIONS

The supramolecular carrier obtained by β-cyclodextrins, PEG 700 Da, and folic acid bioconjugation possesses interesting properties for active tumor targeting. The copresence of the three components in the same construct enhances the drug solubility and stability and promotes drug targeting to the disease site, receptor recognition, and intracellular delivery. The drug release into the cells occurs by physical displacement, which represents a further advantage of this delivery system because chemical or enzymatic mechanisms usually required for drug release from polymer therapeutics often entail ineffective drug release.

Interestingly, the physicochemical and biopharmaceutical properties of this new class of bioconjugates can be optimized by the proper choice of the construct compo-

nents over a wide range of materials: cyclodextrins, polymeric spacer arms, and targeting moieties. Furthermore, according to the physicochemical properties of the drug and the target disease, tailor-made supramolecular carriers can be prepared.

ACKNOWLEDGMENT

This research was supported by the MIUR (PRIN 2002) and University of Padua grant programs.

LITERATURE CITED

(1) Szejtli, J. (1994) Medicinal applications of cyclodextrins. *Med. Res. Rev. 14*, 353−386.

(2) Szente, L., and Szejtli, J. (1999) Highly soluble cyclodextrin derivatives: chemistry, properties, and trends in development. *Adv. Drug Delivery Rev. 36*, 17−28.

(3) Hirayama, F., and Uekama, K. (1999) Cyclodextrin-based controlled drug release system. *Adv. Drug Delivery Rev. 36*, 125−141.

(4) Michaelis, M., Cinatl, J., Vogel, J. U., Pouckova, P., Driever, P. H., and Cinatl, J. (2001) Treatment of drug-resistant human neuroblastoma cells with cyclodextrin inclusion complexes of aphidicolin. *Anti-Cancer Drugs 12*, 467−473.

(5) Ohtani, Y., Irie, T., Uekama, K., Fukunaga, K., and Pitha, J. (1989) Differential effects of alpha-, beta- and gamma-cyclodextrins on human erythocytes. *Eur. J. Biochem. 186*, 17−22.

(6) Topchieva, I. N., Mischnick, P., Kuhn, G., Polyakov, V. A., Elezkaya, S. V., Bystryzky, G. I., and Karezin, K. I. (1998) Novel derivatives of cyclodextrins, modified with poly(ethylene oxide) and their complexation properties. *Bioconjugate Chem. 9*, 676−682.

(7) Garin-Chesa, P., Campbell, I., Saigo, P. E., Lewis, J. L., Jr., Old, L. J., and Rettig, W. J. (1993) Trophoblast and ovarian cancer antigen LK26. Sensitivity and specificity in immunopathology and molecular identification as a folate-binding protein. *Am. J. Pathol. 142*, 557−567.

(8) Turek, J. J., Leamon, C. P., and Low, P. S. (1993) Endocytosis of folate−protein conjugates: ultrastructural localization in KB cells. *J. Cell. Sci. 106*, 423−430.

(9) Wang, S., Lee, R. J., Mathias, C. J., Green, M. A., and Low, P. S. (1996) Synthesis, purification, and tumor cell uptake of ^{67}Ga−deferoxamine−folate, a potential radiopharmaceutical for tumor imaging. *Bioconjugate Chem. 7*, 56−62.

(10) Lee, R. J., and Low, P. S. (1994) Delivery of liposomes into cultured KB cells via folate receptor-mediated endocytosis. *J. Biol. Chem. 269*, 3198−3204.

(11) Gottschalk, S., Cristiano, R. J., Smith, L. C., and Woo, S. L. (1994) Folate receptor mediated DNA delivery into tumour cells: potosomal disruption results in enhanced gene expression. *Gene Ther. 1*, 185−191.

(12) Leamon, C. P., and Low, P. S. (1994) Selective targeting of malignant cells with cytotoxin−folate conjugates. *J. Drug Targeting 2*, 101−112.

(13) Stella, B., Arpicco, S., Pernacchia, M. T., Desmaele, D., Hoebeke, Renoir, J., D'Angelo, M. J., Cattel, L., and Couvreur, P. (2000) Design of folic acid-conjugated nanoparticles for drug targeting. *J. Pharm. Sci. 89*, 1452−1464.

(14) Caliceti, P., Salmaso, S., Fornasier, R., Carofiglio, T., Pricl, S., Fermeglia, M., and Ferrone, M. (2003) Synthesis and physico-chemical characterization of folate−cyclodextrin bioconjugate for active drug delivery. *Bioconjugate Chem. 14*, 899−908.

(15) Petter, R. C., Salek, J. S., Sikorski, C. T., Kumaravel, G., and Lin, F.-T. (1990) Cooperative binding by aggregated mono-6-(alkylamino)-β-cyclodextrins. *J. Am. Chem. Soc. 112*, 3860−3868.

(16) Sims, G. E. C., and Snape, T. J. (1980) A method for estimation of poly(ethylene glycol) in plasma protein fractions. *Anal. Biochem. 107*, 60−63.

(17) Carofiglio, T., Fornasier, R., Lucchini, V., Simonato, L., and Tonellato, U. (2000) Synthesis, characterizatoion and supramolecular properties of a hydrophilic porphyrin−β-cyclodexrin conjugate. *J. Org. Chem. 65*, 9013−9021.

(18) Kranz, D. M., Patrick, T. A., Brigle, K. E., Spinella, M. J., and Roy, J. (1995) Conjuagates of folate and anti-T-receptor antibodies specifically target folate−receptor-positive tumour cells for lysis. *Proc. Natl. Acad. Sci. U.S.A. 92*, 9057−9061.

(19) Gabizon, A., Horowitz, A., Goren, D., Tzemach, D., Mandelbaum-Shavit, F., Qazen, M. M., and Zalipsky, S. (1999) Targeting folate receptor with folate linked to extremities of poly(ethylene glycol) grafted liposomes: in vitro studies. *Bioconjugate Chem. 10*, 289−298.

(20) Yu, L., Lan, J., and Shi-Xin, S. (2000) Molecular recognition studies on supramolecular systems. 26. Inclusion complexation of natural and amino acid modified β-cyclodextrins with model substances: ANS and RhB molecules. *Microchem. J. 64*, 59−65.

(21) Benesi, H. A., and Hildebrand, J. H. (1949) A spectrophotometric investigation of the interaction of iodine with aromatic hydrocarbons. *J. Am. Chem. Soc. 71*, 2703−2707.

(22) Löfås, S., and Johnsson, B. (1990) A novel hydrogel matrix on gold surfaces plasmon resonance sensors for fast and efficient covalent immobilization of ligands. *J. Chem. Soc., Chem. Commun. 21*, 1526−1528.

(23) Johnsson, B., Löfås, S. S., and Lindquist, G. (1991) Immobilization of proteins to a carboxymethyldextran-modified gold surface for biospecific interaction analysis in surface plasmon resonance sensors. *Anal. Biochem. 198*, 268−277.

(24) Yu, L., Bao-Hang, H., Shi-Xin, S., Takehiko, W., and Yoshihisa, I. (1999) Molecular recognition study on supramolecular systems. 20. Molecular recognition and enantioselectivity of aliphatic alcohols by L-tryptophan-modified β-cyclodextrin. *J. Org. Chem. 64*, 1487−1493.

(25) Salter, D. N., Scott, K. J., Slade, H., and Andrews, P. (1981) The preparation and properties of folate-binding protein from cow's milk. *Biochem. J. 193*, 469−476.

(26) Mosdam, T. (1983) Rapid colorimetric assay for cellular growth and survival: application to proliferation and cytotoxic assay. *J. Immunol. Methods 65*, 55−63.

(27) Finlay, G. J., Baguley, B. C., and Wilson, W. R. (1984) A semiautomated microculture method for investigating growth effects of cytotoxic compounds on exponentially growing carcinoma cells. *Anal. Biochem. 139*, 272−277.

(28) Leamon, C. P., and Low, P. S. (1991) Delivery of macromolecules into living cells: A method that exploits folate receptor endocytosis. *Proc. Natl. Acad. Sci. U.S.A. 88*, 5572−5576.

(29) Anderson, R. G. W., Kamen, B. A., Rothberg, K. G., and Lacy, S. W. (1992) Potocytosis: sequestration and transport of small molecules by caveolae. *Science. 255*, 410−411.

BC034186D

C-Terminal Site-Specific PEGylation of a Truncated Thrombomodulin Mutant with Retention of Full Bioactivity

Chrystelle S. Cazalis,[†] Carolyn A. Haller,[†] Lisa Sease-Cargo,[†] and Elliot L. Chaikof*[,†,‡]

Laboratory for Biomolecular Materials Research, Departments of Surgery and Biomedical Engineering, Emory University School of Medicine, Atlanta, Georgia 30322, and School of Chemical and Biomolecular Engineering, Georgia Institute of Technology, Atlanta, Georgia 30332. Received April 16, 2004; Revised Manuscript Received June 24, 2004

Addition of poly(ethylene glycol) to bioactive proteins (PEGylation) improves their plasma half-life, enhances stability against proteolytic cleavage, and may also decrease protein immunogenicity. Characteristically, PEGylation usually involves a reaction to available lysine amino groups, some of which may be within or near a bioactive site. Thus, most protocols are nonspecific and result in a loss of protein activity. We report herein a strategy for site-specific PEGylation of a thrombomodulin (TM) derivative at the C terminus. A truncated TM mutant consisting of epidermal growth factor (EGF)-like domains 4−6 was expressed in *Escherichia coli* with a C-terminal azido-methionine. The TM mutant was site-specifically conjugated to a methyl-PEG-triarylphosphine compound via the Staudinger reaction. Enzymatic activity of the TM construct before and after PEGylation was unchanged, which confirms the utility of this site-specific PEGylation scheme.

INTRODUCTION

Addition of poly(ethylene glycol) to bioactive proteins (PEGylation) increases both their molecular size and steric hindrance, which results in an increase of protein plasma half-life and resistance to proteolytic cleavage. In addition, protein immunogenicity may be decreased (*1*, *2*). Characteristically, PEGylation usually involves a reaction to available lysine amino groups, some of which may be within or near a bioactive site. Thus, most protocols are nonspecific and result in a loss of protein activity (*3*, *4*). For example, Han et al. (*5*) conjugated TM to PEG via trichlorotriazine as a coupling agent for immobilization onto a glass surface. Despite successful immobilization, reduced TM activity was noted presumably because of the alteration of protein conformation after PEGylation. To overcome the limitations of current conjugation strategies, several approaches have been proposed. Site-specific PEGylation can be achieved through the introduction of a cysteine residue in engineered proteins with a free thiol available for conjugation reactions (*6*, *7*). As a consequence, several PEG derivatives have been developed for that purpose (*8*−*11*). The efficacy of this approach is compromised, however, by a low yield of PEGylated protein and often by a substantial loss of activity if abnormal protein folding is induced by the introduction of the cysteine residue (*12*). As an alternative strategy, Yamamoto et al. (*13*) reported site-specific PEGylation of a lysine-deficient tumor necrosis factor-α (TNFα) at its N terminus. The corresponding bioconjugate showed higher bioactivity in vitro and greater antitumor potency than a randomly mono-PEGylated TNFα.

We report herein the use of a strategy for site-specific PEGylation of human thrombomodulin. This transmembrane protein is a critical regulator of the protein C pathway and represents a major anticoagulant mechanism that is operative under physiologic conditions in vivo (*14*, *15*). Thrombomodulin (TM) is a cofactor for thrombin-catalyzed activation of protein C, enhancing the rate of the reaction by 1000-fold (*16*). To closely mimic the TM structure as it appears at the cell surface (*17*, *18*) and consequently preserve its bioactivity, we investigated the PEGylation at the C terminus. Using a genetically directed synthesis in *Escherichia coli*, we first expressed a short TM construct containing epidermal growth factor (EGF)-like domains 4−6 and an azido-functionalized methionine analogue (*19*) as a C-terminal linker. The PEGylation was then achieved through Staudinger ligation (*20*) with a suitably engineered PEG derivative.

EXPERIMENTAL PROCEDURES

Materials. All chemical reagents were obtained from Sigma Chemical Corp. (St. Louis, MS). The methyl-PEG-amine 5000 was purchased from Netkar Corp. (Hunstville, AL). The *Bam*H I and Shrimp Alkaline Phosphatase enzymes were obtained from New England Biolabs, Inc. (Beverly, MA). The Quikchange Site-Directed Mutagenesis kit was from Stratagene (La Jolla, CA). *E. coli* strain B834 (DE3), plasmid pET-39b(+), S-Tag Rapid Assay kit, and Site-Specific Enterokinase Cleavage and Capture kits were from Novagen (Madison, WI). All plasmid purification kits were purchased from QIAGEN Inc. (Chatsworth, CA). The mouse monoclonal antibody to human TM was from COVANCE Corp. (Richmond, CA). Synthetic oligonucleotides were purchased from Integrated DNA Technologies, Inc. (Coralville, IA). Purified recombinant human PC and human α thrombin were from Haematologic Technologies Inc. (Essex Junction, VT). Human anti-thrombin, recombinant human TM

* To whom correspondence should be addressed: 1639 Pierce Drive 5105 WMB, Emory University, Atlanta, GA 30322. Phone: (404) 727-8027. Fax: (404) 727-3660. E-mail: echaiko@emory.edu.

[†] Emory University School of Medicine.

[‡] Georgia Institute of Technology.

10.1021/bc049903y CCC: $27.50 © 2004 American Chemical Society
Published on Web 08/28/2004

(soluble truncated form of TM that lacks the putative transmembrane and the cytoplasmic domains, with an approximate weight of 68 kD), and chromogenic substrate Spectrozyme PCa were purchased from American Diagnostica Inc. (Stamford, CT). All reagents for manipulating DNA and bacteria were sterilized by autoclave.

Instrumentation. MALDI−TOF mass spectrometry data were performed on an Applied Biosystem Voyager-DE STR Biospectrometry Workstation MALDI−TOF mass spectrometer using an 2-(4-hydroxy-phenylazo)-benzoic acid matrix. ^{1}H, ^{13}C, and ^{31}P NMR spectra were recorded at 600 MHz (^{1}H and ^{13}C) and 242 MHz (^{31}P) on a Varian INOVA in $CDCl_3$ (internal Me_4Si and H_3PO_4, respectively, δ ppm). Optical density was recorded on a Varian Cary 50 Bio UV−visible spectrophotometer.

Synthetic Gene Construction. A DNA fragment encoding for EGF (4−6) domains of human TM was obtained by polymerase chain reaction using primers 5′-TACCCTAACTACGACCTGGTG-3′ and 5′-TATGAGCAAGCCCGAATG-3′. Through a series of intermediate constructs, this fragment was used to generate a gene containing a leucine (Leu) substitution for methionine-388 (Met-388), N- and C-terminal *Bam*H I sites, and a C-terminal linker GlyGlyMet using site-directed mutagenesis. The final construct (TM_{GGM}) was then inserted using the *Bam*H I site of the expression plasmid pET-39b(+). All mutations were verified through sequence analysis.

Protein Expression and Purification. pET39b(+)-TM_{GGM} was transformed into the *E. coli* methionine auxotroph B834(DE3). M9 minimal medium (500 mL), supplemented with 1 mM $MgSO_4$, 0.4 wt % glucose, 1 mg/L thiamine chloride, 0.1 mM $CaCl_2$, kanamycin (30 mg/L), and all proteinogenic amino acids (40 mg/L), was inoculated with 20 mL of an overnight culture of the transformed cells. When the turbidity of the culture reached an OD_{600} of 0.8, protein expression was induced by addition of isopropyl-β-D-thiogalactopyranoside (IPTG) to a final concentration of 0.5 mM. After 5 min, the medium was exchanged to remove methionine, cells were sedimented (4000*g* for 20 min), and the cell pellet was washed twice with 200 mL of 1× M9 salts. Cells were resuspended in 500 mL of the M9 minimal medium described above, without methionine but supplemented with 100 mg/L of azido-functionalized methionine analogue (*19*). A culture lacking methionine served as the negative control. Cultures were grown for 4.5 h at 37 °C. The expression of the TM protein was analyzed by 4−20% gradient SDS−PAGE gel electrophoresis and visualized by Western blot analysis using a mouse monoclonal antibody to human TM. The target protein was expressed as a N-terminal Dsba enzyme fusion to a leader sequence containing an enterokinase cleavage site, hexahistidine, and S tags (protein TM_A). S-Tag Rapid Assay was used to quantify the protein concentration and therefore the expression yield, which averaged 17 mg/L of cell culture. TM_A was purified from the cell pellet by using immobilized metal-affinity chromatography on TALON resin (Clontech Laboratories, Inc.) under native conditions using an imidazole gradient for elution of the target polypeptide. The cells were first harvested by centrifugation at 4 °C at 10000*g* for 30 min and resuspended in 25 mL of lysis buffer (300 mM NaCl, 50 mM NaH_2PO_4, 10% glycerol, 1 mg/mL lysozyme, and 10 μg/mL PMSF at pH 8). After incubation on ice for 30 min, the cell lysate was clarified by centrifugation at 10000*g* for 20 min. The soluble extract was then loaded onto a column containing TALON metal-affinity resin (25 mL), which had been pre-equilibrated with lysis buffer. The weakly binding proteins were removed by rinsing the column with 125 mL of wash buffer (300 mM NaCl, 50 mM NaH_2PO_4, 10% glycerol, and 20 mM imidazole at pH 8). TM_A was eluted by the addition of 50 mL of elution buffer (300 mM NaCl, 50 mM NaH_2PO_4, 10% glycerol, and 250 mM imidazole at pH 8). The chromatographic fractions were analyzed by 4−20% gradient SDS−PAGE gel electrophoresis and visualized by Western blot analysis using mouse monoclonal antibody to human TM. The nitrocellulose membrane was developed using the ECL plus Western blotting detection kit (Amersham Biosciences, U.K.). Enterokinase cleavage removed the fusion tag and generated the target protein (TM_B). N-terminal sequencing, amino acid compositional, and mass analysis (SELDI−TOF) confirmed the integrity of TM_B, [mass detected (m/z) = 16 545.2 D (calculated = 16 540.1 D)].

Synthesis of Methyl-PEG-triarylphosphine (2). 1,3-Dicyclohexylcarbodiimide (DCC) (5.7 mg, 27 μmol) was added to a solution of phosphino reagent (**1**) (10.3 mg, 28 μmol) in anhydrous $CHCl_3$ (2 mL) at room temperature under argon. The mixture was stirred for 1 h, followed by the addition of methyl-PEG-amine [m-PEG-NH_2 (M_n = 5 kD)] (120 mg, 24 μmol) dissolved in $CHCl_3$ (2 mL). The mixture was subsequently agitated for 2.5 days under argon. The methyl-PEG-triarylphosphine conjugate was recovered by precipitation in cold diethyl ether (200 mL) and filtration. The precipitate was dissolved in water. The aqueous solution was filtrated and lyophilized to afford the final product with 50% substitution. The product was used in the Staudinger reaction without further purification. ^{1}H NMR (600 MHz, $CDCl_3$) δ: 3.38 [s, 3H, OCH_3 (PEG)], 3.45−3.90 [m, 448 H, OCH_2 (PEG)], 7.47−7.55 (m, 6H), 7.67−7.70 (m, 5H), 7.91−7.94 (m, 1H), 8.12−8.13 (m, 1H). ^{13}C NMR (150 MHz, $CDCl_3$) δ: 40.0, 41.3, 52.5, 59.3, 70.2, 70.6, 71.1, 72.0, 128.5, 128.7, 128.8, 130.5, 131.0, 131.3, 132.0, 133.3, 134.1, 137.7, 138.1, 166.5, 166.7. ^{31}P NMR (242 MHz, $CDCl_3$) δ: −3.11. MALDI−TOF: 6034 D (calculated = 6014 D).

TM−PEG Conjugation. To a solution of TM_B in phosphate-buffered saline (PBS) at pH 7.4 (300−500 nM, 100 μL) was added a large excess (1 mg) of lyophilized methyl-PEG-triarylphosphine, and the mixture was subsequently heated at 37 °C for 36 h to obtain maximum conjugation. The mixture was divided in half and two sets of reactions were subjected to SDS−PAGE in parallel. Proteins from the first gel were transferred to nitrocellulose membrane and visualized by Western blot analysis using a mouse monoclonal antibody to human TM. This procedure monitored the presence of TM_B proteins that had reacted with the phosphine and were therefore PEG-labeled, as well as unreacted TM_B. The second gel was stained with barium chloride/iodine solutions to reveal PEGylated molecules only (*21*).

TM Enzymatic Activity Assay. A saturated concentration of TM_B in 20 μL of assay buffer (20 mM Tris-HCl at pH 7.5, 100 mM NaCl, and 2.5 mM $CaCl_2$) was incubated for 30 min at 37 °C with 10 nM human α thrombin and varying amounts of human protein C (0−8 μM). Reactions were quenched by addition of 5 μL of human antithrombin (10.7 μM) and incubation for 5 min at room temperature. The amount of activated protein C (APC) formed was determined by addition of 275 μL of Spectrozyme PCa (218 μM), followed by incubation for 20 min at room temperature. Spectrozyme PCa is a chromogenic substrate used for the quantification of APC in solution. A total of 1 mol of the substrate is hydrolyzed by APC producing 1 mol of *p*-nitroaniline (pNA). The pNA concentration was determined by UV spectro-



Figure 1. Schematic structure of the targeted truncated TM, whose amino acid sequence is encoded by the gene TM_{GGM}.

phometry at 407 nm using the equation

$$OD_{407nm} = -0.0014 + 0.0096[pNA] \quad (1)$$

where eq 1 was obtained by optical density measurements of pNA solutions of known concentrations. The corresponding rate (mol/min) of *p*-nitroaniline formed (R_{pNA}) was obtained by dividing the pNA concentration by the 20-min assay time.

A second standard plot was used to determine the APC concentration from R_{pNA}, where

$$R_{pNA} = -0.059 + 0.0671[APC] \quad (2)$$

To obtain eq 2, commercial APC was dissolved in the assay buffer at various concentrations and incubated with Spectrozyme PCa for 20 min at room temperature. The corresponding rate (mol/min) of APC formed (R_{APC}) by the TM−thrombin complex was obtained by dividing the observed APC concentration by the 30-min assay time.

Values obtained for control experiments without TM were subtracted to give final rates of APC produced. Michaelis−Menten parameters (k_{cat} and K_m) were calculated from a plot of R_{APC} versus the protein C concentration.

RESULTS AND DISCUSSION

It is now well-established that the three consecutive EGF-like domains 4−6 (EGF4−6) of human TM exhibit full cofactor activity (*22*). The corresponding amino acid sequence contains only one methionine residue (Met-388), which is not vital for protein bioactivity (*23, 24*). In fact, prior studies have demonstrated that mutation of Met-388 to Leu results in a construct that is more resistant to oxidative inactivation and exhibits greater enzymatic activity than the native TM protein (*25*). Thus, we postulated that a truncated TM fragment containing EGF4−6 with the insertion of a C-terminal nonnatural methionine analogue would provide a good target for site-specific PEGylation. Indeed Kiick et al. (*19*) have recently reported the incorporation of an azide function into recombinant proteins via the use of a methionine analogue, which facilitated chemoselective modification by Staudinger ligation.

To create a short recombinant bioactive TM mutant, we first used the DNA fragment encoding for the amino acid sequence 349−492 to generate a gene containing a Met-388−Leu substitution and a C-terminal linker GlyGlyMet using site-directed mutagenesis (Figure 1). The final construct (TM_{GGM}) was then inserted in the expression plasmid pET-39b(+). This plasmid contains a leader gene sequence coding for the Dsba enzyme, which is a periplasmic enzyme catalyzing the formation and isomerization of disulfide bonds of expressed proteins. Therefore, we expected the target TM mutant to possess all disulfide bonds required for proper protein folding and enzyme activity. Expression under the induction of IPTG using the *E. coli* methionine auxotroph B834 (DE3)/pET39b(+)−TM_{GGM} in cultures depleted of methionine and supplemented with an azido-functionalized methionine analogue, azidohomoalanine (*19*), afforded the target protein as a N-terminal Dsba enzyme fusion

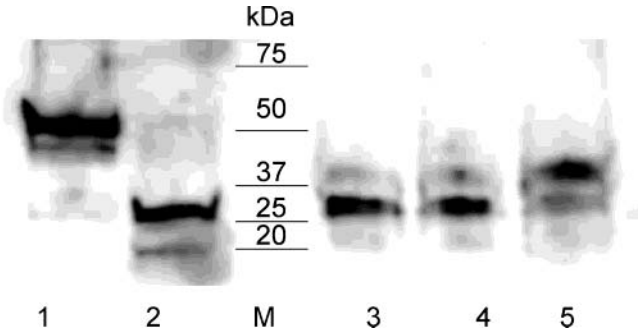


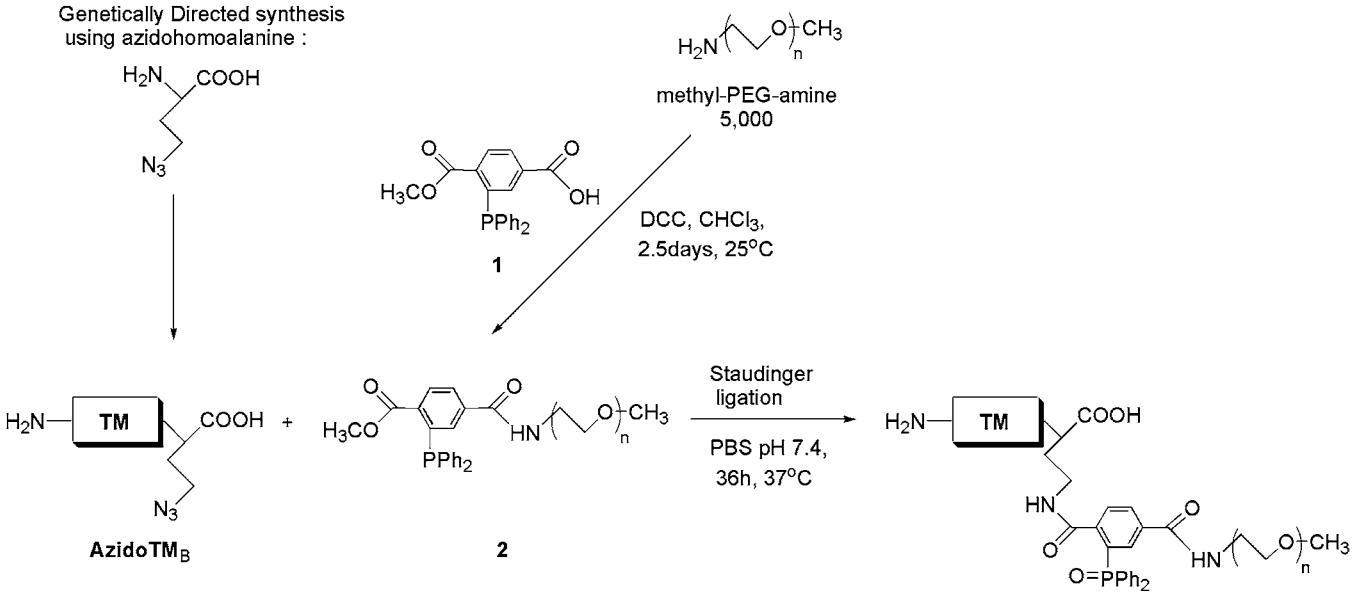
Figure 2. Western blot analysis of TM derivatives (4−20% SDS−PAGE gel). (1) Purified TM_A. (2) Enterokinase cleavage of TM_A leading to the target protein TM_B. (3−5) Conjugation of **2** to TM_B over time at 4, 8, and 24 h, respectively. M = molecular-weight marker proteins.

to a leader sequence containing enterokinase recognition sequence, hexahistidine, and S tags. Protein expression was monitored by SDS−PAGE analysis and visualized by Western blot analysis. The target protein was not observed in the negative control culture, whereas TM fused to the leader sequence (TM_A) was clearly detected in the positive control cultures supplemented with azidohomoalanine. The accumulation of TM_A was taken as preliminary evidence for incorporation of the nonnatural amino acid. TM_A was purified from the cell pellet by using immobilized metal-affinity chromatography with stepwise imidazole-gradient elution under native conditions. Enterokinase cleavage removed the fusion tag and generated the target proteins (TM_B). N-terminal sequencing, amino acid compositional, and mass analysis (mass detected = 16 545 D) confirmed the integrity of TM_B. TM_B was characterized by a band at 33 kD on Western blot analysis (Figure 2), which is consistent with prior reports that TM associates into dimers even under denaturing conditions (*25*).

Having expressed an azide-modified form of TM, we then investigated the selective Staudinger ligation of this protein with a methyl-PEG-triarylphosphine conjugate **2** (Scheme 1). We choose this ligation protocol to minimize the risk of side reactions that might alter the TM structure and activity. Indeed, in its classical form, the Staudinger reaction meets many of the criteria required of a chemoselective ligation in a cellular enviroment. The phosphine and the azide react rapidly, selectively, and in high yield, in water at room temperature. Kiick et al. (*19*) prepared a triarylphosphine compound **1** that was used for the preparation of a protein-flag conjugate, as well as for labeling cell-surface azide-bearing sialic acids with a biotinylated phosphine (*20*). In a similar manner, we used **1** in the synthesis of methyl-PEG-triarylphosphine conjugate **2**. The carboxylic acid group of **1** was reacted with the amino group of a commercially available derivative, m-PEG-NH_2 (5 kD), with amide-bond formation (Scheme 1). The incorporation of a phosphino group in PEG was assessed by ^1H, ^{13}C, and ^{31}P NMR, as well as by MALDI−TOF spectroscopy (Figure 3). The average molecular weight of 6034 D observed for the methyl-PEG-triarylphosphine conjugate **2** is consistent with an expected mass increase of 346 D, as a result of linking the phosphino compound **1** to m-PEG-NH_2 (average molecular weight observed = 5668 D).

The addition of m-PEG-NH_2 to **1** dramatically enhances the water solubility of the hydrophobic phosphino group. A large excess of lyophilized methyl-PEG-triarylphosphine conjugate **2** (1 mg) was added to 100 μL of an aqueous solution of TM_B in PBS at pH 7.4, and

Scheme 1. Synthesis of the Methyl-PEG-triarylphosphine Conjugate 2 and Its Conjugation to Azido-Functionalized TM_B



Staudinger ligation was performed at 37 °C for 24 h. The formation of the TM_B−PEG conjugate was followed by Western blot analysis of the reaction mixture over time (Figure 2). The gel shows a band at a higher molecular weight than the initial TM_B with a simultaneous disappearance of the TM_B band. These results indicate that the Staudinger reaction proceeded efficiently with incorporation of the PEG polymer into the TM construct. Because the reaction was not complete after 24 h, we allowed it to proceed for an additional 12 h. Western blot analysis (Figure 4a) and barium chloride/iodine staining (Figure 4b) of SDS−PAGE gels were performed in parallel to monitor the formation of the TM_B−PEG conjugate. Disappearance of the band characteristic of the unconjugated TM_B revealed that bioconjugation of TM_B to PEG was 100% complete. The SDS gel run in parallel under identical conditions but stained with barium chloride/iodine confirmed the presence of PEG in the bioconjugate. The presence of a low molecular-weight band represents unreacted methyl-PEG-triarylphosphine **2**.

Enzyme activity was assessed to determine the effect of PEGylation on TM cofactor activity (Table 1). We initially investigated the activity of the TM_A and TM_B mutants, as well as a commercial recombinant human TM mutant consisting solely of the extracellular domain (American Diagnostica Inc.). As previously noted, Clarke et al. (*23*) have reported that the Met-388−Leu mutation results in a 2-fold increase in k_{cat} for the activation of protein C by a thrombin−TM fragment complex. Although we were unable to observe this enhancement of activity, Michaelis−Menten parameters were similar for

Table 1. Michaelis−Menten Parameters for Protein C Activation by TM Derivatives

	TM_A	TM_B	PEG−TM_B	commercial TM
K_M (μM)	0.9 ± 0.2	1.0 ± 0.5	1.0 ± 0.5	0.7 ± 0.1
k_{cat} (min^{-1})	0.22 ± 0.05	0.16 ± 0.05	0.20 ± 0.05	0.14 ± 0.02
k_{cat}/K_M ($min^{-1}\,\mu M^{-1}$)	0.26 ± 0.10	0.16 ± 0.05	0.20 ± 0.05	0.21 ± 0.05

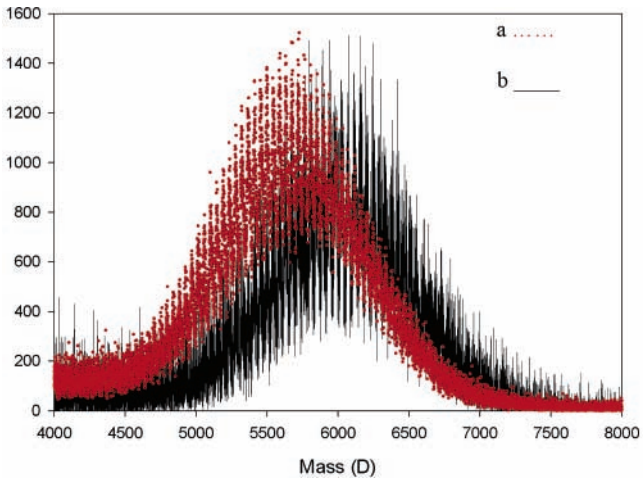


Figure 3. MALDI−TOF mass spectra of (a) the starting polymer m-PEG-NH_2 (average molecular weight detected = 5668 D) and (b) the methyl-PEG-triarylphosphine conjugate **2** [average molecular weight detected = 6034 D, (calculated = 6014 D)].

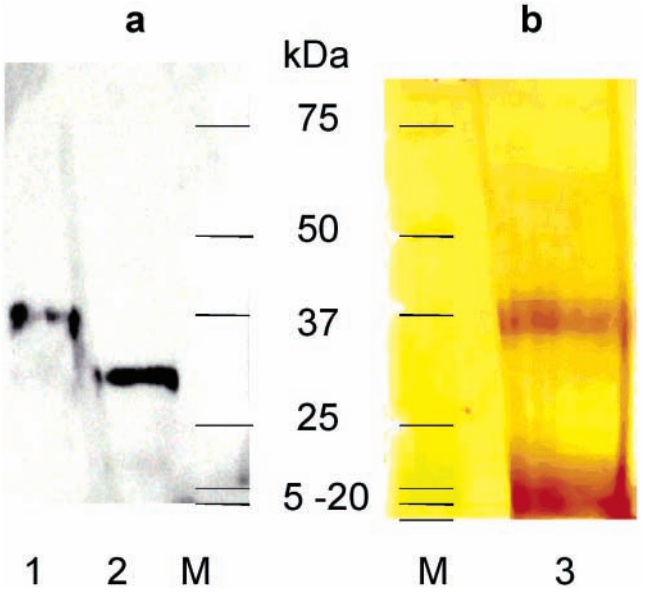


Figure 4. (a) Western blot analysis and (b) barium chloride/iodine staining of a 10% SDS−PAGE gel. (1 and 3) Reaction mixture of the bioconjugation of **2** to TM_B after 36 h. (2) Initial azido-functionalized TM_B. M = molecular-weight marker proteins.

TM_A and TM_B, as well as for the commercial human TM protein. We inferred that the generated TM mutants exhibited the requisite conformation and structure necessary for proper thrombin binding and protein C activation. Significantly, the incorporation of PEG into TM_B did not affect cofactor activity, indicating that this site-specific PEGylation scheme did not interfere with thrombin binding and protein C activation. Parenthetically, despite a concerted effort by our group, previous attempts to generate an enzymatically active truncated TM mutant with a C-terminal cysteine, as a potential bioconjugation site, were unsuccessful using both yeast and *E. coli* expression systems. We speculate that an additional terminal cysteine likely interfered with normal protein folding dependent upon the presence of native disulfide loops in the EGF sequences.

CONCLUSIONS

A human TM derivative containing EGF(4−6)-like domains designed with an azido-functionalized methionine C-terminal linker was successfully synthesized via a genetic engineering strategy. The protein exhibited bioactivity toward protein C that was comparable to native human TM. The TM construct was successfully conjugated to a novel engineered methyl-PEG-triarylphosphine compound via the Staudinger reaction under mild conditions. The cofactor activity assay before and after PEGylation was unchanged, confirming successful application of this site-specific PEGylation scheme. To our knowledge, this report is the first to describe site-specific PEGylation of a TM mutant with the retention of full bioactivity.

ACKNOWLEDGMENT

This work was supported by grants from the NIH and JDRF.

LITERATURE CITED

(1) Veronese, F. M. (2001) Peptide and protein PEGylation: A review of problems and solutions, *Biomaterials 22*, 405−417.
(2) Roberts, M. J., Bentley, M. D., and Harris, J. M. (2002) Chemistry for peptide and protein PEGylation, *Adv. Drug Delivery Rev. 54*, 459−476.
(3) Katre, N. V. (1993) The conjugation of proteins with polyethylene glycol and other polymers. Altering properties of proteins to enhance their therapeutic potential, *Adv. Drug Delivery Rev. 10*, 91−114.
(4) Monkarsh, S. P., Ma, Y. M., Aglione, A., Bailon, P., Ciolek, D., DeBarbieri, B., Graves, M. C., Hollfelder, K., Michel, H., Palleroni, A., Porter, J. E., Russoman, E., Roy, S., and Pan, Y. C. E. (1997) Positional isomers of monopegylated interferon α2a: Isolation, characterization, and biological activity, *Anal. Biochem. 247*, 434−440.
(5) Han, H.-S., Yang, S.-L., Yeh, H.-Y., Lin, J.-C., Wu, H.-L., and Shi, G.-Y. (2001) Studies of a novel human thrombomodulin immobilized substrate: Surface characterization and anticoagulation activity evaluation, *J. Biomater. Sci., Polym. Ed. 12*, 1075−1089.
(6) Tsutsumi, Y., Onda, M., Nagata, S., Lee, B., Kreitman, R. J., and Pastan, I. (2000) Site-specific chemical modification with polyethylene glycol of recombinant immunotoxin anti-Tac(Fv)-PE38 (LMB-2) improves antitumor activity and reduces animal toxicity and immunogenicity, *Proc. Natl. Acad. Sci. U.S.A. 97*, 8548−8553.
(7) He, X. H., Shaw, P. C., Xu, L. H., and Tam, S. C. (1999) Site-directed polyethylene glycol modification of trichosanthin: Effects on its biological activities, pharmacokinetics, and antigenicity, *Life Sci. 64*, 1163−1175.
(8) Goodson, R. J., and Katre, N. V. (1990) Site-directed pegylation of recombinant interleukin-2 at its glycosylation site, *Biotechnology 8*, 343−346.
(9) Kogan, T. P. (1992) The synthesis of substituted methoxypoly(ethylene glycol) derivatives suitable for selective protein modification, *Synth. Commun. 22*, 2417−2424.
(10) Morpurgo, M., Veronese, F. M., Kachensky, D., and Harris, J. M. (1996) Preparation and characterization of poly(ethylene glycol) vinyl sulfone, *Bioconjugate Chem. 7*, 363−368.
(11) Woghiren, C., Sharma, B., and Stein, S. (1993) Protected thiol-polyethylene glycol: A new activated polymer for reversible protein modification, *Bioconjugate Chem. 4*, 314−318.
(12) Kuan, C. T., Wang, Q. C., and Pastan, I. (1994) *Pseudomonas* exotoxin A mutants. Replacement of surface-exposed residues in domain II with cysteine residues that can be modified with polyethylene glycol in a site-specific manner, *J. Biol. Chem. 269*, 7610−7616.
(13) Yamamoto, Y., Tsutsumi, Y., Yoshioka, Y., Nishibata, T., Kobayashi, K., Okamoto, T., Mukai, Y., Shimizu, T., Nakagawa, S., Nagata, S., and Mayumi, T. (2003) Site-specific PEGylation of a lysine-deficient TNF-α with full bioactivity, *Nat. Biotechnol. 21*, 546−552.
(14) Weiler, H., and Isermann, B. H. (2003) Thrombomodulin, *J. Thromb. Haemostasis 1*, 1515−1524.
(15) Kalafatis, M., Egan, J. O., Van't Veer, C., Cawthern, K. M., and Mann, K. G. (1997) The regulation of clotting factors, *Crit. Rev. Eukaryotic Gene Expression 7*, 241−280.
(16) Esmon, N. L., Owen, W. G., and Esmon, C. T. (1982) Isolation of a membrane-boud cofactor for thrombin-catalyzed activation of protein-C, *J. Biol. Chem. 257*, 859−864.
(17) Esmon, C. T. (1992) The regulation of clotting factors, *Arterioscler. Thromb. 12*, 135−145.
(18) Sadler, J. E. (1997) Thrombomodulin structure and function, *Thromb. Haemostasis 78*, 392−395.
(19) Kiick, K. L., Saxon, E., Tirrell, D. A., and Bertozzi, C. R. (2002) Incorporation of azides into recombinant proteins for chemoselective modification by the Staudinger ligation, *Proc. Natl. Acad. Sci. U.S.A. 99*, 19−24.
(20) Saxon, E., and Bertozzi, C. R. (2000) Cell surface engineering by a modified Staudinger reaction, *Science 287*, 2007−2010.
(21) Kurfurst, M. M. (1992) Detection and molecular weight determination of polyethylene glyol-modified hirudin by staining after sodium dodecyl sulfate−polyacrylamide gel electrophoresis, *Anal. Biochem. 200*, 244−248.
(22) Parkinson, J. F., Nagashima, M. M., Kuhn, I., Leonard, J., and Morser, J. (1992) Structure−function studies of the epidermal growth-factor domains of human thrombomodulin, *Biochem. Biophys. Res. Commun. 185*, 567−576.
(23) Clarke, J. H., Light, D. R., Blasko, E. J., Parkinson, F., Nagashima, M., McLean, K., Vilander, L., Andrews, W. H., Morser, J., and Glaser, C. B. (1993) The short loop between epidermal growth factor-like domain-4 and domain-5 is critical for human thrombomodulin function, *J. Biol. Chem. 268*, 6309−6315.
(24) Nagashima, M., Lundh, E., Leonard, J. C., Morser, J., and Parkinson J. F. (1993) Alanine-scanning mutagenesis of the epidermal growth factor-like domains of human thrombomodulin identifies critical residues for its cofactor activity, *J. Biol. Chem. 268*, 2888−2892.
(25) Glaser, C. B., Morser, J., Clarke, J. H., Blasko, E., McLean, K., Kuhn, I., Chang, R. J., Lin, J.-H., Vilander, L., Andrews, W. H., and Light, D. R. (1992) Oxidation of a specific methionine in thrombomodulin by activated neutrophil products blocks cofactor activity. A potential rapid mechanism for modulation of coagulation, *J. Clin. Invest. 90*, 2565−2573.

BC049903Y

Novel Chemoselective Linkage Chemistry toward Controlled Loading of Ligands to Proteins through In Situ Real-Time Quantification of Conjugate Formation

Nicholas S. Flinn, Martin Quibell, William G. Turnell,§ Tracy P. Monk, and Manoj K. Ramjee*

Amura Therapeutics Limited, Horizon Park, Barton Road, Comberton, CB3 7AJ, United Kingdom
Received March 15, 2004; Revised Manuscript Received June 11, 2004

'Linkage chemistry', which encompasses the science of chemical attachment of a ligand molecule to a carrier moiety, plays a crucial role in a wide range of biochemical and biophysical disciplines. In particular, the production of synthetic vaccines, where quality assurance criteria are an essential part of the approvals procedure for development of medicines, is reliant upon reproducible linkage chemistries. Herein, we describe novel 2-hydroxybenzaldehyde-based quaternary amine containing chemoselective linkers that provide a simple and robust linkage process that overcomes the deficiencies present in state-of-the-art linkage chemistries. The 2-hydroxybenzaldehyde groups undergo a pH-dependent absorbance change that enabled its nondestructive quantification, even when covalently attached to a wide range of proteins. Additionally, formation of a hydrazone bond between the benzaldehyde group and a range of ligand hydrazides resulted in a second reversible absorbance change enabling the forward (ligand loading) and reverse (ligand release for analysis) reactions of ligand-loaded proteins to be monitored in situ and quantified in real time. Incorporation of the quaternary amine moiety into our improved linkage chemistries was found to increase the relative solubility of protein conjugates and enabled significantly higher loading of proteins with linker and subsequent ligands, while retaining aqueous solubility, when compared to standard methods.

INTRODUCTION

The covalent crosslinking of chemical and biological moieties is an essential process used in many diverse biophysical and biochemical applications (*1*−*4*). Each application requires the covalent attachment of an active moiety (i.e., a ligand) to a soluble or insoluble 'carrier' via an appropriately functionalized chemical linker. However, the diversity in the nature of the ligands (*4*−*8*) and carriers (*9,10*) has meant that each application has required an empirical solution for the successful production of conjugates. In this respect, perhaps one of the most challenging and yet promising areas has been the development of synthetic conjugate vaccines as medicines (*6*).

Small molecules and peptides, identified as epitopes for vaccine development, usually require conjugation to carrier proteins to provide a construct with which to provoke an immune response to the immunogen in vivo. An ideal vaccine construct would contain a high surface coverage of conjugated epitope on the carrier protein while retaining high aqueous solubility. Conjugation has traditionally been facilitated by the use of chemically reactive linkers, for which a number of reagents have been described (*11,12*). Although homobifunctional linkers were the first to be exploited, heterofunctional linkers became prominent as a means to circumvent ligand-to-ligand and carrier-to-carrier crosslinking. However, even with the improved control afforded by heterofunctional linkers, various practical issues, such as aqueous stability of the reactive species, conjugate solubility and stability, chemoselectivity, and ease of conjugate analysis still need to be solved empirically using laborious methods. Furthermore, the use of disulfide-bond constrained peptide loops as structural epitope mimics as well as the presence of certain functional groups within the epitope may also exclude the use of certain linkers since they provide sensitive or alternative reactive centers (*13*). To overcome these and other limitations, more selective aqueous compatible chemoselective linkage strategies have been developed. One such linkage chemistry is based on the formation of the acyl−hydrazone bond.

Hydrazides, being weak bases, form stable acyl−hydrazone bonds with an aldehyde functionality at mildly acidic pH (*14,15*). As such, hydrazone formation has been employed for various selective conjugation reactions (*16*−*19*) and this methodology has led to the development of a marketed product (Gemtuzumab Ozogamicin-Mylotarg) (*6*). Nevertheless, some basic practical issues remain for the routine production and quality assurance of conjugates. For example, highly loaded protein conjugates are in most cases unobtainable, due to the low and unpredictable solubility observed as the ratio of ligand to carrier protein increases (*20*). Additionally, the linkage created between the carrier protein and epitope would ideally be immunogenically inert and not involve residues or functionalities critical to epitope recognition (*13*). Also, for the production of medicines, quality assurance criteria are crucial as part of the FDA approvals procedure, for which some of the basic requirements are the quantitative assessment of linker loading of carrier as well as the extent of ligand coupling of the derivatized protein; both of which can be arduous tasks (*13*). These types of issues have made the production of synthetic vaccines a semi-empirical process, hampering the rapid development of

* To whom correspondence should be addressed. Tel: +44(0)1223-264211. Fax: +44(0)01223−265662. E-mail: manoj.ramjee@amura.co.uk.

§ Current address: MediVas LLC, 6350 Nancy Ridge Drive, Suite 103, San Diego, CA 92121.

10.1021/bc0499329 CCC: $27.50 © 2004 American Chemical Society
Published on Web 08/26/2004

therapeutic vaccines. Therefore, the development of linkers that overcome the existing limitations would be of great benefit.

Here we describe the synthesis and characterization of 2-hydroxybenzaldehyde-based reversible chemoselective linkers that provide a number of practical advantages over conventional linkage technologies. First, the linkers could be quantified spectrophotometrically in a nondestructive manner in the absence or presence of various proteins. Second, elaboration of the protein-bound linker with a ligand via hydrazone formation resulted in a quantifiable absorbance change, enabling the forward (ligand loading) and reverse (ligand release for analysis) reactions of linker-loaded proteins to be monitored in situ. The linker was also designed to contain a quaternary amine moiety as a means of primarily compensating the loss of surface charge upon coupling of the linker onto the surface-exposed primary amines of proteins. This feature enabled relatively higher linker loading of proteins while retaining solubility.

EXPERIMENTAL PROCEDURES

General Biochemistry. All reagents were of the highest commercially available quality and were used as received. Unless otherwise stated, all chemicals and biochemicals were purchased from the Sigma Chemical Company (Poole, Dorset, United Kingdom). Unless otherwise stated, routine protocols were carried out at room temperature and kinetic experiments at 25 °C. Protein concentrations were determined using Bradford reagent (Sigma) according to the manufacturer's instructions using BSA as the standard. Absorbance measurements were carried out in 384-well microtiter plates (Corning Costar 3702 plates, Fisher Scientific, Loughborough, United Kingdom), flat-bottomed 96-well plates (Spectra; Greiner Bio-One Ltd., Stonehouse, Gloucestershire, United Kingdom) or standard 1-mL quartz cuvettes, using a SpectraMax PLUS384 plate reader (Molecular Devices, Crawley, United Kingdom). Fluorescence measurements were carried out in either 384-well microtiter plates (Corning Costar 3705 plates, Fisher Scientific) or 96-well 'U' bottomed Microfluor W1 microtiter plates (Thermo Labsystems, Ashford, Middlesex, United Kingdom). Fluorescence assays were monitored using a SpectraMax Gemini fluorescence plate reader (Molecular Devices). In all cases SOFTmax Pro 3.1.2 software was used for data collection and handling (Molecular Devices). All spectra were collected at a resolution of 2 nm. Gel and membrane images were captured using a Hewlett-Packard C7710A scanner employing HP Precision ScanPro 3.02 software on default settings. Images were routinely scanned at a minimum resolution of 600 dpi in gray scale mode (32 bit). Images were marked with legends employing Powerpoint (Microsoft Corp., Seattle, WA). Image analysis and processing was carried out using ImageJ software (*21*).

General Chemistry. All solid-phase synthesis was performed using an "Fmoc/tBu" procedure (*22*) following standard solid-phase synthesis resin washing protocols. Standard Fmoc amino acids were obtained from Chem-Impex International (Wood Dale, IL) and Merck Biosciences (Nottingham, United Kingdom) with the exception of Fmoc *N*-ϵ-trimethyl-l-lysine, which was purchased from Bachem UK Ltd. (St. Helens, United Kingdom). The 2-chlorotrityl-resin (Product 04-12-2800) was obtained from Merck Biosciences (Nottingham, United Kingdom). The PS-carbodiimide resin was obtained from Argonaut Technologies (Muttenz, Switzerland). All solvents were purchased from Romil (Cambridge, United Kingdom). Solid-phase syntheses were performed manually in a polypropylene syringe fitted with a polypropylene frit to allow filtration under vacuum. Analytical HPLC was performed on Agilent 1100 series instruments including a G1311A quaternary pumping system, with a G1322A degassing module and a G1365B multiple wavelength UV−vis detector. Data were collected and integrated with Chemstation 2D software. Analytical HPLC analyses were performed on a Zorbax, 5-μm, C8 reverse phase column (150 × 4.6 mm i.d.), at a flow rate of 1.5 mL/min, monitoring at 215 and 254 nm. Eluents used were (A) 0.1% trifluoroacetic acid in water and (B) 90% acetonitrile/10% eluent A. They were used to run a gradient starting at 10% B, increasing to 90% B over 7 min, holding for 1 min, returning to 10% B over 1 min, and then remaining at initial conditions for a further 4 min to allow column reequilibration. Compounds were purified by semipreparative HPLC, using a Phenomenex Jupiter C4 reverse phase column (250 × 10 mm i.d.) at a flow rate of 4 mL/min, using the equipment and eluents described above. Compound molecular ions were determined on an Agilent 1100 series LC/MSD electrospray mass spectrometer.

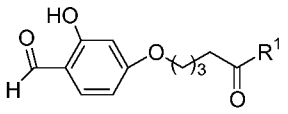
Amine Determination. The amine concentrations were determined using fluorescamine (Fluram; Fluka) (*23*), employing Ac−Lys−NH_2 (Bachem) as the calibration control. Routinely, 10 μL of test sample was diluted into 85 μL 50 mM sodium phosphate; pH 10 and 5 μL 10 mM Fluram (in 100% acetonitrile) were added. The Fluram solutions were freshly prepared prior to use. The reactions were mixed and incubated at room temperature for 30 min prior to measuring the fluorescence (390-nm excitation, 485-nm emission).

SDS−PAGE and Western Blot Analysis. The SDS−PAGE and Western blot components were obtained from Invitrogen, Paisley, United Kingdom. For denatured protein analysis, samples were routinely analyzed by SDS−PAGE using the NuPAGE system employing 4−12% bis-tris NuPAGE gels. Unless otherwise stated, all gels were run in MES running buffer. For native protein analysis, samples were analyzed by PAGE using the NuPAGE system employing the 4−12% bis-tris NuPAGE gels, 7% NuPAGE tris-acetate, or 3−8% tris-acetate gels with the appropriate buffers. The POWEREASE system was used to carry out electrophoresis employing protocols embedded in the unit's software. Proteins were visualized with SimplyBlue stain kits or SilverExpress stain kits according to manufacturers' protocols. After staining, gels were dried using DryEase gel drying solution and cellophane membranes.

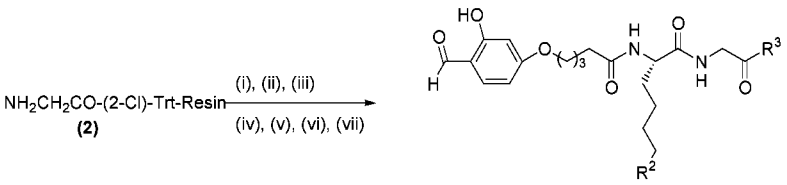
For Western blot analysis of conjugates, the proteins were transferred from the gel onto a PVDF membrane using the manufacturer's (Invitrogen) reagents and protocols. The PVDF membranes were blocked by gentle agitation in 50 mL phosphate buffered saline containing 1% Tween 20 (PBST; Sigma) plus 1% (w/v) BSA for 15 min. The recovered membranes were washed three times, by gentle agitation, in 100 mL PBST for 5 min per cycle. Following this, the membranes were incubated in 50 mL PBST containing a 1 in 5000 dilution of ExtrAvidin-

[1] Abbreviations: BSA, bovine serum albumin; HBV, hepatitis B virus; DCM, dichloromethane; DMF, dimethylformamide; DMSO, dimethyl sulfoxide; DTNB, 5,5′-dithio-bis-(2-nitrobenzoic acid); HEWL, hen egg-white lysozyme; HOBt, 1-hydroxybenzotriazole; HBTU, 2-(1*H*-benzatriazole-1-yl)-1,1,3,3′-tetramethyluronium hexafluorophosphate; NMM, *N*-methylmorpholine; OSu, *N*-hydroxysuccinamide ester; PBS, phosphate buffered saline; PFP, pentafluorophenol.

Scheme 1



(**1a**) R^1 = OH
(**1b**) R^1 = OSu
(**1c**) R^1 = NH-X (where X = BSA)



(3,4,5a-k,6,7,8)

(**3**) R^3 = OH, R^2 = $N^+(CH_3)_3$
(**4**) R^3 = N-hydroxysuccinimide, R^2 = $N^+(CH_3)_3$
(**5a**) R^3= NH-BSA, R^2 = $N^+(CH_3)_3$
(**5b**) R^3= NH-aprotinin, R^2 = $N^+(CH_3)_3$
(**5c**) R^3= NH-HEWL, R^2 = $N^+(CH_3)_3$
(**5d**) R^3= NH-carbonic anhydrase, R^2 = $N^+(CH_3)_3$
(**5e**) R^3= NH-OVA, R^2 = $N^+(CH_3)_3$
(**5f**) R^3= NH-apo-transferrin, R^2 = $N^+(CH_3)_3$
(**5g**) R^3= NH-holo-transferrin, R^2 = $N^+(CH_3)_3$
(**5h**) R^3= NH-phosphorylase B, R^2 = $N^+(CH_3)_3$
(**5i**) R^3= NH-β-galactosidase, R^2 = $N^+(CH_3)_3$
(**5j**) R^3= NH-myosin, R^2 = $N^+(CH_3)_3$
(**5k**) R^3= NH-HBV core delta-Ag, R^2 = $N^+(CH_3)_3$
(**6**) R^3 = OH, R^2 = $NHC(O)CF_3$
(**7**) R^3 = N-hydroxysuccinimide, R^2 = $NHC(O)CF_3$
(**8**) R^3= NH-BSA, R^2 = $NHC(O)CF_3$

(i) 3 eq. *N*-α-Fmoc-Lys(Me)$_3$−COOH **(9)** or *N*-α-Fmoc-Lys(Tfa)−OH **(10)**, 3 eq. HBTU, 3 eq. HOBt, 6 eq. NMM, DMF, 2 × 6 h. (ii) 20% Piperidine/DMF (v/v), 1 × 15 min. (iii) 3 eq 5-(4-Formyl-3-hydroxyphenoxy)pentanoic acid (*19*) **(1a)**, 3 eq. HBTU, 3 eq. HOBt, 6 eq. NMM, DMF, 2 × 2 h. (iv) 20% Piperidine/DMF (v/v), 1 × 20 min. (v) 5% Trifluoroacetic acid/DCM (v/v), 5 × 5 min, then RP-HPLC purification, lyophilization. (vi) 1.1 eq. acid **(3)** or **(6)**, 1 eq. PS-carbodiimide resin **(11)**, 0.95 eq. *N*-hydroxysuccinimide **(12)**, DMF/DCM (1:5, v/v), rt, 5 h. (vii) Protein conjugation conditions (see main text).

Peroxidase (Sigma) for 30 min, washed as before in PBST, and allowed to partially drip dry. Regions of peroxidase activity were visualized by addition of a 3,3′,5,5′-tetramethylbenzidine (TMB) liquid substrate (Sigma) onto the static membrane. After appropriate exposure, the membrane was recovered, washed in water, and air-dried prior to scanning, analysis, and storage.

Diafiltration. Routinely, Amicon Ultra-4 (≤4 mL) or Ultra-15 (≤15 mL) centrifugal filter units (10 000 mwco; Millipore, Watford, United Kingdom) were used for diafiltration. Each cycle consisted of diluting the protein sample approximately 10-fold with exchange buffer and concentrating the sample by centrifugation back to its original volume. Cycles were repeated as required for quick and highly efficient equilibration/washing of protein samples. Routinely six cycles were completed for each diafiltration step.

Synthesis of 5-(4-Formyl-3-hydroxyphenoxy)pentanoic Acid (*19*) **(Scheme 1: 1a).**Spray-dried potassium fluoride (8.4 g, 0.144 mol) and 2,4-dihydroxybenzaldehyde (10 g, 0.072 mol) were stirred vigorously at 60 °C for 20 min in anhydrous acetonitrile (150 mL). Methyl-5-bromovalerate (42.3 g, 0.216 mol) was added in one portion and the mixture brought to a gentle reflux for 5 h. The reaction was allowed to cool to room temperature and the solvent was removed in vacuo. The residue was partitioned between water (100 mL) and ethyl acetate (50 mL). The aqueous portion was washed twice more with ethyl acetate (2 × 30 mL) and the combined organic layers were back-washed with water, dried over anhydrous magnesium sulfate, filtered, and evaporated to dryness. The resulting red oil was recrystallized from ether (30 mL) and heptane (20 mL). The methyl ester obtained was dissolved in tetrahydrofuran (120 mL) and stirred vigorously at room temperature. To this solution was added lithium hydroxide (3.7 g, 0.088 mol) dissolved in water (60 mL) and the mixture was stirred for 4 h. The solvent was reduced in vacuo and the resultant oily residue was diluted with water (30 mL), washed twice with methyl *tert*-butyl ether (2 × 50 mL), acidified to pH 2 with concentrated hydrochloric acid, and extracted with ethyl acetate (4 × 30 mL). The combined ethyl acetate fractions were dried over anhydrous magnesium sulfate, filtered, and evaporated to dryness to give a white solid product. Yield: 9.86 g, 0.041 mol, 57%. ^{1}H NMR ($CDCl_3$) δ: 11.26 (2H, brs), 9.69 (1H, s), 7.41 (1H, d, J = 8.6 Hz), 6.51 (1H, dd, J = 8.6, 2.2 Hz), 6.40 (1H, d, J = 2.2 Hz), 4.02 (2H, t, J = 5.9 Hz), 2.44 (2H, t, J = 7.0 Hz), 1.84 (4H, m). mp: 88−91 °C. ESI−MS *m*/*z*: 239.1 (calc. for M + H^+ 239.08). HPLC retention time: 5.34 min.

Synthesis of 5-(4-Formyl-3-hydroxyphenoxy)pentanoic Acid 2,5-Dioxopyrrolin-1-yl Ester (Scheme 1: 1b). PS-carbodiimide resin (**11**) (4.2 g, 5.5 mmol) was suspended in dichloromethane (45 mL) stirred for 5 min to swell the resin. Compound **1a** (1.0 g, 4.2 mmol) was added and dissolved in dichloromethane (10 mL); the resin mixture stirred for a further 20 min before the addition of *N*-hydroxysuccinimide (**12**) (0.46 g, 4.0 mmol) dissolved in dimethylformamide (4 mL). The reaction was then stirred and monitored by HPLC until completion (18 h). The resin was removed by filtration, the solvent was removed in vacuo, and the final product was recrystallized from 2-propanol. Yield: 1.3 g, 3.8 mmol, 92%. ESI−MS *m*/*z*: 336.1 (calc. for M + H^+ 336.1). HPLC retention time: 6.18 min.

Synthesis of {5*S*-(Carboxymethyl-carbamoyl)-5-[5-(4-formyl-3-hydroxyphenoxy)pentanoyl Aminopentyl}trimethylammonium (Scheme 1: 3). (a) Resin derivatized with a 2-chlorotrityl linker (0.19 g, 0.19 mmol), preloaded with glycine (**2**) (substitution: 1.0

mmol/g), was added to a polypropylene syringe fitted with a polypropylene filter frit (which allowed filtration of the resin under vacuum) and washed with DMF (5 × 5 mL) to swell the resin. *N*-α-Fmoc-Lys(Me)$_3$−OH (*9*) (0.25 g, 0.57 mmol) was dissolved in DMF (5 mL) along with 2-(1*H*-benzotriazole-1-yl)-1,1,3,3-tetramethyluronium hexafluorophosphate (HBTU, 0.22 g, 0.57 mmol), 1-hydroxybenzotriazole (HOBt, 0.09 g, 0.57 mmol), and *N*-methylmorpholine (NMM, 125 μL, 1.14 mmol) and mixed thoroughly for 30 s, allowing in situ formation of the acyloxyuronium intermediate. This solution was then added to the glycyl resin and left for 6 h at room temperature with gentle agitation. After washing the resin with DMF (5 × 5 mL), the coupling procedure was repeated as above. Following washing of the resin with DMF (10 × 5 mL), the *N*-α-Fmoc group of the covalently attached trimethyllysine was removed by a 15 min treatment with 20% piperidine in DMF under continuous flow, followed by further washing of the resin with DMF (10 × 5 mL).

(b) 5-(4-Formyl-3-hydroxyphenoxy)pentanoic acid **(Scheme 1: 1a)** (0.14 g, 0.57 mmol) was double coupled to the trimethyl-L-lysyl-glycyl resin, using the same HBTU/HOBt activation protocol as described for *N*-α-Fmoc-Lys(Me)$_3$−OH, differing only in the reaction time (2 × 2 h). Following washing of the resin with DMF (10 × 5 mL), a final 20% piperidine in DMF treatment was carried out, to remove any unwanted ester that may have formed by reaction of the phenolic hydroxyl group with activated acid species, followed by a further DMF wash (10 × 5 mL).

(c) Final cleavage from the resin was performed by 5 × 5 min treatments of the peptidyl resin with 5% trifluoroacetic acid in dichloromethane (40 mL/g). The spent resin was removed by filtration and the pooled filtrate was concentrated by sparging with nitrogen. The crude product was precipitated and washed with cold methyl *tert*-butyl ether, before being redissolved in 30% aq. acetonitrile and lyophilized. The crude residue was purified by semipreparative RP-HPLC and the pure fractions were pooled and lyophilized to yield **3** (yield 35 mg, 0.075 mmol, 39%; HPLC retention time: 3.75 min). ^{1}H NMR (500 MHz, d_6-DMSO at 300 K): δ 1.21−1.75 (m, $OCH_2CH_2CH_2$ + $OCH_2CH_2CH_2$ + $NHCHCH_2CH_2$ + $NHCHCH_2CH_2$ + $(CH_3)_3N^+CH_2CH_2$, 10H), 2.19 (t, J = 7.20 Hz, CH_2CH_2CO, 2H), 3.01 (s, $CH_2N^+(CH_3)_3$, 9H), 3.19−3.24 (m, $CH_2N^+(CH_3)_3$, 2H), 3.66−3.80 (m, $NHCH_2$-CO, 2H), 4.02 (t, J = 6.10 Hz, OCH_2CH_2, 2H), 4.33 (m, $NHCHCH_2$, 1H), 6.46 (d, J = 2.30 Hz, $HOCCHCOCH_2$, 1H), 6.54 (dd, J = 2.25, 8.60 Hz, $CHCHCOCH_2$, 1H), 7.59 (d, J = 8.75 Hz, $CHCHCOCH_2$, 1H), 8.02 (d, J = 8.30 Hz, $NHCHCH_2$, 1H), 8.24 (t, J = 5.80 Hz, $NHCH_2CO$,-1H), 9.98 (s, *CH*O, 1H), 11.04 (s, *H*O, 1H), 12.30−12.80 (bs, COO*H*, 1H); calculated accurate mass for $C_{23}H_{36}N_3O_7$ (M^+): 466.2548, observed mass 466.2551 (+0.77 ppm).

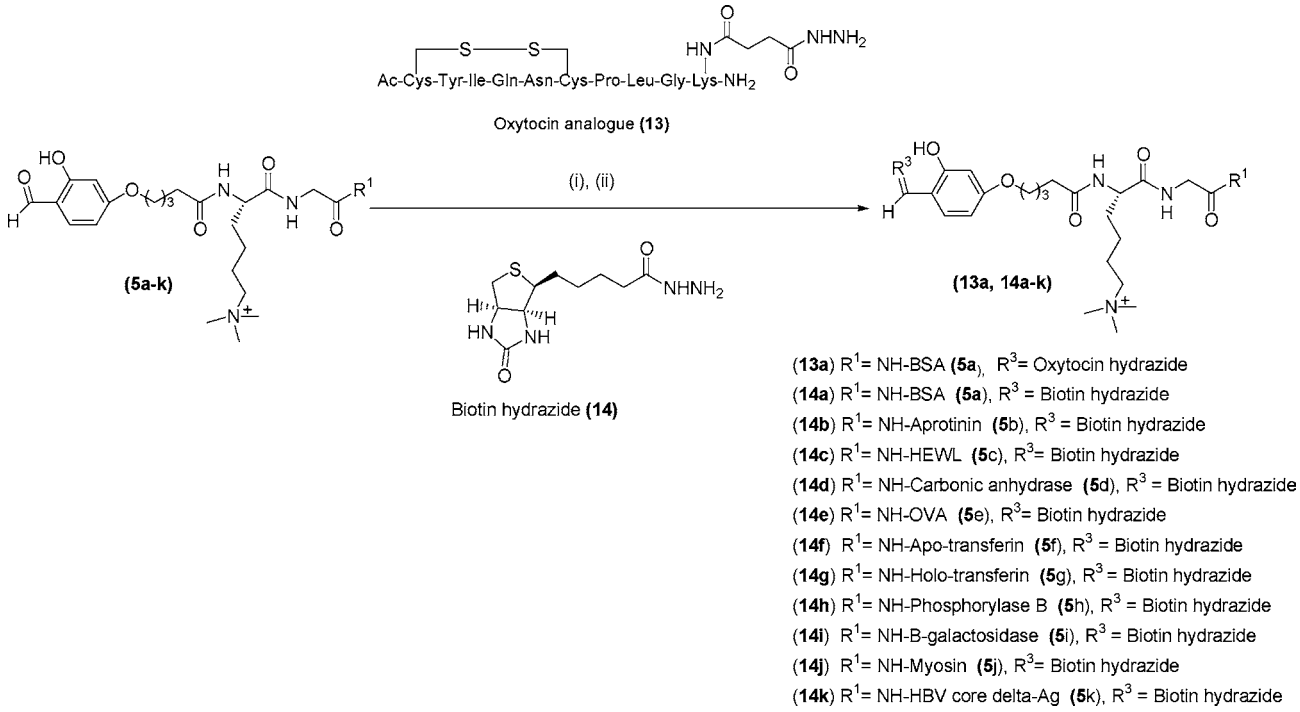
Synthesis of {5*S*-(Carboxymethylcarbamoyl)-5-[5-(4-formyl-3-hydroxyphenoxy)pentanoylamino] pentyl}trifluoroacetic Acid (Scheme 1: 6). Synthesis of **(6)** was carried out in an analogous manner to **(3)** except that *N*-α-Fmoc-Lys(Tfa)−OH **(10)** was used in place of *N*-α-Fmoc-Lys(Me)$_3$−OH **(9)** (see above) (yield 49 mg, 0.095 mmol, 32%; HPLC retention time: 5.12 min). ^{1}H NMR (500 MHz, d_6-DMSO at 300 K): δ 1.20−1.70 (m, $OCH_2CH_2CH_2$ + $OCH_2CH_2CH_2$ + $NHCHCH_2CH_2$ + $NHCHCH_2CH_2$ + $CF_3CONHCH_2CH_2$, 10H), 2.15 (m, CH_2CH_2CO, 2H), 3.12 (m, $CH_2NHCOCF_3$, 2H), 3.65−3.78 (m, $NHCH_2CO$, 2H), 4.00 (t, J = 6.10 Hz, OCH_2CH_2, 2H), 4.27 (m, $NHCHCH_2$, 1H), 6.44 (d, J = 2.30 Hz, $HOCCH$-$COCH_2$, 1H), 6.53 (dd, J = 2.30, 8.70 Hz, $CHCHCOCH_2$, 1H), 7.58 (d, J = 8.75 Hz, $CHCHCOCH_2$, 1H), 7.93 (d, J = 8.25 Hz, $NHCHCH_2$, 1H), 8.17 (t, J = 5.90 Hz, $NHCH_2$-CO,1H), 9.37 (t, J = 5.50 Hz, $CH_2NHCOCF_3$,1H), 9.97 (s, *CH*O, 1H), 10.97 (s, *H*O, 1H), 12.51 (s, COO*H*, 1H); calculated accurate mass for $C_{22}H_{28}N_3O_8F_3$ (MNa^+): 542.1721, observed mass 542.1712 (−1.62 ppm).

Preparation of {5*S*-[(2,5-Dioxopyrrolidin-1-yloxycarbonylmethyl)carbamoyl]-5-[5-(4-formyl-3-hydroxyphenoxy)pentanoylamino]pentyl}trimethylammonium (Scheme 1: 4). Compound **3** (35 mg, 0.075 mmol) was dissolved in DMF (2 mL) and added to a stirred solution of PS-carbodiimide (**11**) (288 mg, 0.375 mmol) in DCM (10 mL). The mixture was stirred for 20 min before the addition of *N*-hydroxysuccinimide (**12**) (9 mg, 0.075 mmol) in DMF (1 mL). The reaction was then stirred at room temperature and monitored by HPLC until completion (5 h). The resin was removed by filtration, the solvent was removed in vacuo, and the compound was used without further purification (yield 38 mg, 0.068 mmol, 90%; HPLC retention time: 4.16 min). Calculated accurate mass for $C_{27}H_{39}N_4O_9$ (M^+): 563.2712, observed mass 563.2721 (+1.70 ppm).

[2S-[5-(4-Formyl-3-hydroxyphenoxy)pentanoylamino]-6-(2,2,2-trifluoroace tylamino)hexanoylamino]-acetic Acid 2,5-dioxopyrrolinin-1-yl Ester (Scheme 1: 7). Synthesis of **7** was carried out in an analogous manner to **4** except that **6** was used as the starting material (see above). The product was used without further purification (yield 55 mg, 0.089 mmol, 93%; HPLC retention time: 5.64 min). Accurate calculated mass for $C_{26}H_{31}N_4O_{10}F_3$ (MNa^+): 639.1884, observed mass 639.1885 (+0.07 ppm).

Synthesis of Oxytocin Analogue (Scheme 1: 13). The oxytocin analogue Acetyl-CYIQNCPLGK($COCH_2$-$CH_2CONHNH_2$)−NH_2 was synthesized manually using the Fmoc/*t*Bu protection strategy on TGR resin (0.25 g, 0.05 mmol, substitution: 0.2 mmol/g; Merck Biosciences). Coupling of the Fmoc amino acids was accomplished with an HBTU/HOBt method using DMF as the solvent, using 3 eq. of amino acid and coupling reagents with respect to the loading of the resin. The Fmoc group was removed by a 15-min treatment with 20% piperidine in DMF. The C-terminal lysine residue was introduced with Dde side-chain protection to allow orthogonal deprotection at a later stage in the synthesis. After Fmoc deprotection of the final residue, the N-terminus was acetylated using acetic anhydride (48 μL, 0.5 mmol) and diisopropylethylamine (43 μL, 0.25 mmol) in DMF for 2 h and the Dde protection of the lysine side chain was removed with 2% hydrazine in DMF for 15 min. The free amine of the lysine side chain was extended by reaction with succinic anhydride (50 mg, 0.5 mmol) and diisopropylethylamine (43 μL, 0.25 mmol) in DMF for 2 h and then hydrazine, coupled as a 10% solution in DMF using HBTU/ HOBt (in excess) for 3 h (A more efficient method to incorporate the hydrazide functionality has since been developed and involves the use of Boc-$NHNHCO(CH_2)_2COOH$ introduced onto the *N*-ϵ amine of lysine, using the HBTU/ HOBt protocols already described.). Final cleavage of the peptide from the resin was performed with 92.5% trifluoroacetic acid/2.5% triisopropylsilane/2.5% water/2.5% ethanedithiol (40 mL/g resin) for 75 min. The resin was removed by filtration and the filtrate was concentrated by sparging with nitrogen. The crude product was precipitated and washed with cold methyl *tert*-butyl ether (3 × 50 mL), before being redissolved in 50% (aq.) acetonitrile and lyophilized. The peptide was redissolved in ammonium bicarbonate (0.1 M, pH 8) to a concentration of 100 μM and oxidized using hydrogen peroxide (1.5

Scheme 2. Conjugation of Oxytocin Hydrazide or Biotin Hydrazide to a Wide Range of Protein Carriers



(i) 0.1 M sodium formate pH 4.5/DMSO. (ii) Dialysis.

eq) for 45 min. The reaction was monitored by LC−MS and by reaction with Ellman's reagent and was finally quenched with 10% (aq.) acetic acid (in excess). The mixture was lyophilized once more and the desired product was purified by semipreparative RP-HPLC (yield 24 mg, 0.019 mmol, 37%), ESI−MS *m/z*: 1291.3 (calc. for M + H^+ 1291.5), HPLC retention time 3.44 min.

General Method for Preparation of Linker-modified Proteins 1c, 5a−j, and 8. Aprotonin (cat # A4520), Hen egg-white lysozyme (HEWL; cat # L6876), carbonic anhydrase (cat # C2273), ovalbumin (OVA; cat # A7642), bovine serum albumin (BSA; cat # A7638), apo-transferrin (cat # T4382); holo-transferrin (cat #T4132); phosphorylase B (cat # P4649), β-galactosidase (β-gal; cat # G8511), and myosin (MYO; cat # M3889) were obtained from Sigma and made up to 1 mg/mL in either 0.1 M sodium acetate, pH 7.25, or 50 mM potassium phosphate, pH 9.3. The reactive amine concentration for each protein sample was determined and these data used as the basis for determining the reactive amine stoichiometry for each protein.

A fivefold excess over reactive amine content of **1b**, **4**, or **7** (from a 10 mM stock in DMSO) was added to an aliquot (200 μL) of each protein sample and the reactions were incubated at room temperature for 1−3 h followed by overnight incubation in the fridge (∼8 °C). Each reaction mixture was dialyzed against three changes of 1800 mL of either 10 mM ammonium bicarbonate, pH 8; 10 mM sodium acetate, pH 7.25; or 0.1 M sodium formate, pH 4.0, for 2 h, depending upon the desired application. The samples were recovered and stored in the fridge until required and, where necessary, were analyzed by SDS−PAGE.

General Method for Preparation of Protein Conjugates 13a and 14a−j (Scheme 2). A 5 molar excess of either oxytocin−hydrazide (**13**) or biotin−hydrazide **(14)** (Fluka cat # 14403; from a 10 mM stock in DMSO) over the reactive lysine content in the protein was added to the sodium formate dialyzed samples of each of the linker-derivatized proteins **5a−e** and **5h−j**. The DMSO concentration was then adjusted to 10−40% (depending upon the protein being used) and the samples were incubated at room temperature for 2−4 h and then stored overnight in the fridge (∼8 °C).

Since compounds **14f** and **14g** had been previously dialyzed into 50 mM potassium phosphate; pH 9.0 buffer, both compounds were mixed with equal volumes of 0.2 M sodium formate, pH 4.0, to obtain pH 4.5 for the conjugation reaction. The samples were then reacted with a 5 M excess of biotin−hydrazide, as above, at room temperature for 2 h and then overnight at ∼8 °C. After incubation, the reaction mixtures were recovered and each was dialyzed against 4 L of either 20 mM sodium acetate, pH 7.4, or 10 mM ammonium bicarbonate, pH 8, for 2 h at room temperature. The samples were recovered and stored in the fridge for further analysis.

Preparation of HBV Core Delta Ag-linker-Biotin Conjugate (14k). Recombinant HBV core delta Ag, strain ayw, was purchased from Advanced ImmunoChemical Inc., Long Beach, CA. To 75μL of a 1 mg/mL solution of HBVcore delta Ag was added 7.5 μL 0.5 M sodium phosphate, pH 9.3. The sample was mixed and, from this pool, an aliquot (55 μL) was removed and 5.5 μL of **4** (10 mM in DMSO) was added to it. The sample was then mixed again by pipetting and incubated at room temperature for 2 h to give linker-protein **5k**. After this incubation period, a further 27.5 μL was removed and 2 μL 2.65 M formic acid was added to the sample. The sample was mixed, 1.37 μL of 10 mM biotin−hydrazide was added, and the sample was incubated at room temperature for 60 min and then overnight at ∼8 °C. The protein samples were analyzed without dialysis.

Solubility Measurements of BSA-linker Constructs (1c, 5a, and 8). For measurement of solubility at pH 8, aliquots (1 mL) of the BSA-linker constructs **1c**, **5a**, and **8** in ammonium bicarbonate buffer were concentrated to approximately a fifth of their original volume by diafiltration and the protein concentration was determined. The concentration of constructs **1c** and **5a** was adjusted to 5 mg/mL while the concentration of construct

8 was adjusted to 4 mg/mL. Aliquots (40 μL) of each solution were transferred into the wells (in triplicate) of a 384-well microtiter plate and the samples were double diluted to produce a dilution series. The samples were allowed to equilibrate for 30 min at room temperature before the turbidity was measured at 650 nm. For measurement of solubility at pH 4.5, aliquots (1 mL) of the BSA-linker constructs in ammonium bicarbonate buffer were diafiltered for six cycles into 0.1 M sodium formate buffer, pH 4.5, and turbidity measurements were carried out as described above.

Monitoring the Conjugation of Biotin-hydrazide (14) to 5a and 5b. To an aliquot (100 μL) of ~1 mg/mL **5a** and **5b** in 0.1 M sodium formate, pH 4.5, was added 100 μL 10 mM biotin−hydrazide in 100 mM sodium formate, pH 4.5. The sample was mixed and then split into two 100 μL aliquots; one portion was used for collection of the absorption spectra and the other portion was used for concomitant sampling. These aliquots were quenched in sample-loading buffer (Invitrogen) followed by snap freezing in dry ice. Samples were stored at −20 °C and thawed as required prior to analysis by ELISA, SDS−PAGE, and Western blot.

ELISA Analysis of 14a and 14b. The enzyme-linked immunosorbent assays (ELISAs) of **14a** and **14b** were carried out as follows. Aliquots (1 μL) of each of the quenched samples were diluted into 500 μL 10 mM phosphate buffered saline (PBS; Sigma) and 100 μL of this was dispensed into a 96-well Immulon 2HB microtiter plate (Thermo Life Sciences, Basingstoke, United Kingdom). The plate was covered and incubated at 37 °C for 60 min, after which it was washed three times with 200 μL of PBS-Tween 20 (PBST). The wells were blocked by the addition of 100 μL PBST containing 1% (w/v) BSA followed by incubation at 37 °C for 60 min. The plate was washed as before, 100 μL of 1-in-5000 dilution of ExtrAvidin-HRP conjugate (Sigma) in PBST added to each well and incubated at 37 °C for 30 min. The plate was recovered and washed as before, was dried by shaking, and 100 μL OPD reagent (Sigma) was added to each well. The color was allowed to develop by eye; the reaction was stopped by addition of 100 μL 0.1 M sulfuric acid and the plates read at 492 nm.

General Method for Acid-catalyzed Cleavage of Hydrazone Bond. The acid-catalyzed release of the ligand, via cleavage of the hydrazone bond, was carried out by addition of HCl to a final concentration of 1 M. This was routinely facilitated by either addition of concentrated HCl or addition of an equal volume of 2 M HCl to an aliquot of sample.

RESULTS

Synthesis and Characterization of Linkers. Synthesis of the oxytocin analogue **13** and the linkers **1a**, **3,** and **6** proceeded smoothly using standard solution chemistry and Fmoc solid-phase techniques (*22*), to provide the desired compounds in good yield and purity. The linkers were stored as the free acids and the activated succinimidyl ester of the linkers (**1b**, **4**, and **7**) were freshly prepared when required.

The utilization of 2-hydroxybenzaldehyde within the linker provided a moiety that exhibited a pH-dependent change in its absorbance spectrum (Figure 1). The change in absorbance spectra as a function of pH produced three distinct regions of change with isosbestic points at 255 and 333 nm. The pK_a and wavelength maxima for the absorbance transitions were measured as 7.7 at 280 nm, 7.8 at 316 nm, and 8.3 at 364 nm (Figure 1 inset). Of

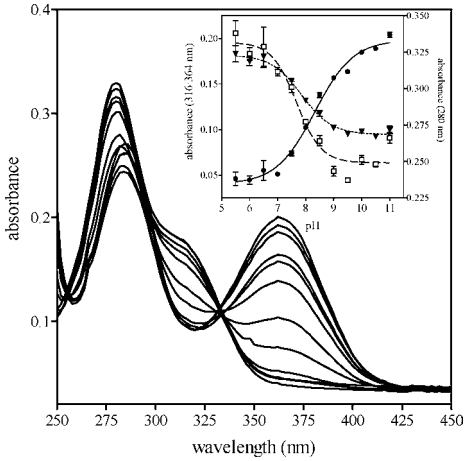


Figure 1. UV absorbance spectra of **3** (100 μM) as a function of pH. Spectra were collected with 100 μL of sample in 50 mM potassium phosphate buffer using Spectra 96-well plates. Inset: plot of the absorbance values versus pH at 280 nm (□), 316 nm (▼), and 364 nm (●). The lines represent sigmoidal fits to a single pK_a.

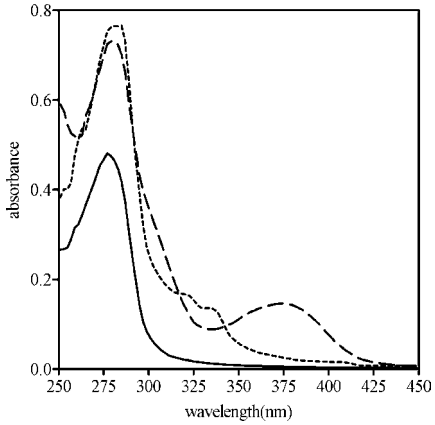


Figure 2. UV/visible absorbance spectra of 0.9 mg/mL BSA (solid line) and **5a** in 50 mM potassium phosphate, pH 9.5 (long-dashed line) and 0.1 M sodium formate, pH 4.0 (short-dashed line). Absorbance spectra were collected in 1-mL quartz cuvettes and background corrected using the respective buffers. Only one spectrum for BSA is presented since the spectra were superimposed in both buffers.

these absorbance transitions, the change at 364 nm proved to be the most accurate since the transitions at the other wavelengths were accompanied by spectral shifts. In 50 mM potassium phosphate, pH 10, compound **3** had a maximum extinction coefficient of 4685 $M^{-1}cm^{-1}$ at 364 nm ($\epsilon_{364\ nm}$ 4685 $M^{-1}cm^{-1}$), which routinely enabled as low as 5−10 μM of the linker to be quantified spectrophotometrically. Quantification could also be carried out in microtiter plates, making the system amenable to high throughput applications. Additionally, since proteins in general do not have any significant absorbance above 300 nm, this region of the spectrum also proved useful for quantification of the linker when covalently attached to a protein. Derivatization of BSA to produce linker-derivatized BSA (**5a**) demonstrated that linker loading could be quantified in situ without sample destruction (Figure 2). Although in most cases it was observed that, upon covalent attachment of **3** (*via* active ester **4**) to protein, the visible region absorbance maxima did not change significantly, in some cases slight shifts were observed (Figures 1 and 2). In all cases the extinction coefficient determined for compound **3** was used to calculate the protein-bound linker concentration. It was found that these calculated values were in good agree-

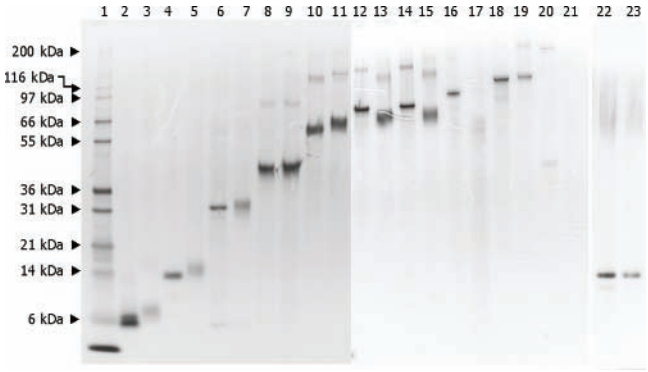


Figure 3. SDS−PAGE analysis of underivatized and linker-derivatized protein samples. Lane 1, Mark 12 molecular weight markers; lane 2 aprotinin; lane 3, **5b**; lane 4, HEWL; lane 5, **5c**; lane 6, carbonic anhydrase; lane 7, **5d**; lane 8, OVA; lane 9, **5e**; lane 10, BSA; lane 11, **5a**; lane 12, apo-transferrin; lane 13, **5f**; lane 14, holo-transferrin; lane 15, **5g**; lane 16, phosphorylase B; lane 17, **5h**; lane 18, β-gal; lane 19, **5i**; lane 20, myosin; lane 21, **5j**; lane 22, HBV core delta Ag; lane 23, **5k**.

ment with titrations carried out for amine determination before and after linker derivatization. The novel linker **3** therefore provided a method for the nondestructive in situ quantification of linker loading of proteins, afforded by a simple change in buffer pH.

Derivatization of Proteins with Linker 3. To exemplify the practical applications of the linker for protein conjugation, in particular amine functionalization, the acid form of the linker **3** was activated to produce the active ester **4**. Although the NHS ester was used to exemplify much of the protein work, because of its favorable solubility properties, we found application of the pentafluorophenol (Pfp) ester to be comparable. Compound **4** was applied to a wide variety of proteins from viral, bacterial, plant, and animal sources ranging in molecular weight form from ∼6 to ∼300 kDa. Upon reaction, most of the proteins displayed slightly diffuse bands, most likely due to heterogeneous labeling of surface amines. In most cases the protein SDS−PAGE migration of the derivatized proteins were similar to the native proteins. Of the proteins tested, only phosphorylase B (∼97 kDa) and myosin (∼205 kDa) displayed a significant change in electrophoretic mobility upon derivatization, with derivatized phosphorylase B (**5h**) migrating significantly faster (∼60 kDa) and derivatized myosin (**5j**) migrating as a broad diffuse band (Figure 3). Dimeric (homo-) and multimeric (homo- and hetero-) proteins have also being derivatized using **4**, with varying results depending on the protein. In some cases the proteins did not migrate any differently to the underivatized proteins as judged by SDS−PAGE, whereas in other cases, especially with heteromultimeric proteins, marked differences were observed (data not shown). Similarly, an analysis of the native molecular weights of linker-derivatized proteins, as judged by gel permeation chromatography and native-PAGE, produced analogous trends in that linker-derivatized monomeric proteins generally displayed little or no change whereas multimeric proteins varied in their elution profile (data not shown). Once again, depending on the protein, HPLC analysis produced somewhat similar results. Nevertheless, in all cases the amount of conjugated linker could be quantified spectrophotometrically, even with proteins that had a significant UV/visible absorbance (e.g., holo-transferrin). Since the amount of linker could be quantified and related to the changes in migration or elution profiles, the extent of linker conjugation could easily be modified to optimize linker loading and yet minimize protein denaturation.

Elaboration of Linker-derivatized Proteins. During the characterization of the absorbance spectra of test samples, we observed marked differences between the spectra of a protein alone, a linker-derivatized protein (Figure 2) and a linker-hydrazone-protein conjugate (Figure 4A). Further investigation revealed that treatment of linker-derivatized proteins (e.g., BSA and aprotinin constructs **5a** and **5b**) with biotin−hydrazide (**14**), providing protein conjugates **14a** and **14b**, resulted in an increase in the absorbance spectra between ∼295 nm and ∼350 nm, with the maximum change being observed at 324 nm (Figure 4A).

To verify whether the absorbance changes were due to hydrazone formation, as a result of the reaction of biotin−hydrazide (**14**) with the aldehyde moiety of the linker, concomitant analysis of the reaction mixtures by absorbance, ELISA, SDS−PAGE, and Western blot were carried out (Figures 5, 6A, and 6B). The results clearly showed that as the absorbance at 324 nm increased (Figures 4A and 4B), the amount of biotin detected also increased (Figures 5 and 6B). Additionally the relative differences between the absorbance changes for the BSA **(5a)** and aprotinin **(5b)** samples were reflected in the final relative amounts of biotin detected (Figure 5). Additionally, the BSA and aprotinin samples were co-loaded onto the SDS−PAGE/Western blot gels to directly compare and relate the data to that from the ELISA analysis. It was clear that the observed absorbance

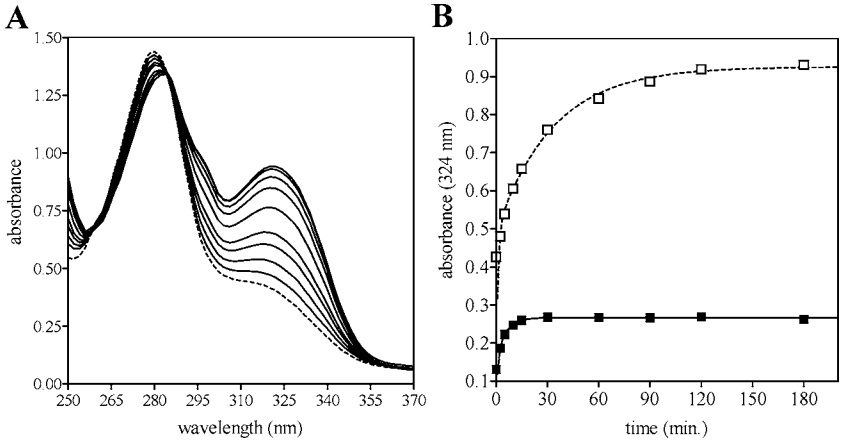


Figure 4. A: Time dependent change in UV/visible absorbance spectra of **5a** upon reaction with biotin−hydrazide (**14**) in 100 mM sodium formate, pH 4.0. **B**: Increase in absorbance at 324 nm while monitoring reaction of biotin−hydrazide (**14**) with **5a** (□) and **5b** (■). The solid lines represent nonlinear regression fits using two-phase exponential analysis.

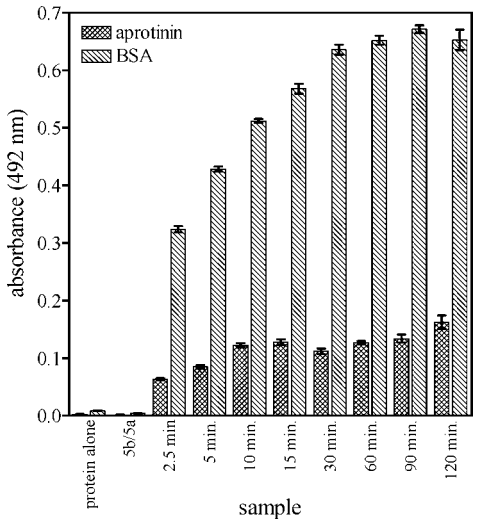


Figure 5. ELISA data for time-dependent elaboration of **5a** and **5b** with biotin−hydrazide (**14**). The respective samples as described in Figures 4 and 6 were used for this analysis.

changes upon addition of biotin hydrazide (**14**) to **5a** and **5b** were due to hydrazone formation (Analogous observations were also made when other linker-derivatized proteins were treated with a wide range of hydrazides (e.g., peptide−hydrazides, acetic acid hydrazide, BODIPY-hydrazide, etc.)). A repeat of the biotin conjugation reaction on a range of protein samples, followed by analysis by ELISA, SDS−PAGE, and Western blot (Figure 7), demonstrated that the conjugation chemistry was reproducible and that the hydrazone linkage was stable not only to the prolonged procedures associated with these protocols, but also to extensive dilution associated with the copious washing cycles. Thus, UV monitoring of the novel linker protein-bound constructs **5a**−**k** has provided a nondestructive real-time in situ method to follow the formation of the hydrazone bond during ligand conjugation processes.

The Effect of Positive-charged Linker (3) on Conjugate Solubility. Based on the hypothesis that charge balancing would enable relatively higher linker loading with the maintenance of conjugate solubility, one aspect of the design of the novel linker **(3)** was to incorporate a quaternary amine as a means to compensate for the loss of charge upon derivatization of the surface accessible amines, in particular the *N*-ϵ-amines of lysine residues. On this basis, the ability of the quarternary ammonium moiety of **3** to enhance the water solubility of protein conjugates, was tested along with comparable noncharged linkers (**1a** and **6**). With linker **1a**, it was not possible to obtain more than 55% loading (100% surface loading was determined by Fluram titration and equated to 22 mol amine per mol of diafiltered BSA (cat# A7638, Sigma) protein.) of BSA without catastrophic precipitation of the linker-derivatized product (**1c**$^{55\%}$) even with large-scale dilution, changing the buffer composition, or adding organic solvent (e.g., DMSO). A loading of 85% was possible with linker **6**, providing protein construct **8**, and this product could be solubilized by dilution or a change in buffer composition. An 85% loading of BSA was also achievable with linker **3**, providing protein construct **5a**, but with the added benefit of a superior solubility profile over the pH range tested (Figures 8A and 8B). Similarly, when **1c**$^{55\%}$, **5a**$^{85\%}$, and **8**$^{85\%}$ were elaborated with oxytocin−hydrazide (**13**), the conjugate **13a** was found to be the most soluble in PBS (data not shown).

Monitoring the Reversibility of the Hydrazone Bond. Having already established that conjugation of hydrazide derivatives to protein modified with novel linker **3** resulted in an absorbance change, we sought to use the same absorbance-based monitoring to assess the chemical reversibility of the reaction. This was demonstrated by treatment of conjugate **13a** with acid (1 M HCl final), which resulted in a return of the absorbance spectra to that observed prior to hydrazone formation, along with the concomitant release of ligand (**13**) from the protein conjugate. This time dependent release of the intact disulfide loop peptide (i.e., oxytocin−hydrazide (**13**)) could be spectrophotometrically monitored and the released product characterized by HPLC and mass spectrometry (Figure 9). Although the treatment with 1 N hydrochloric acid may be considered too harsh for more

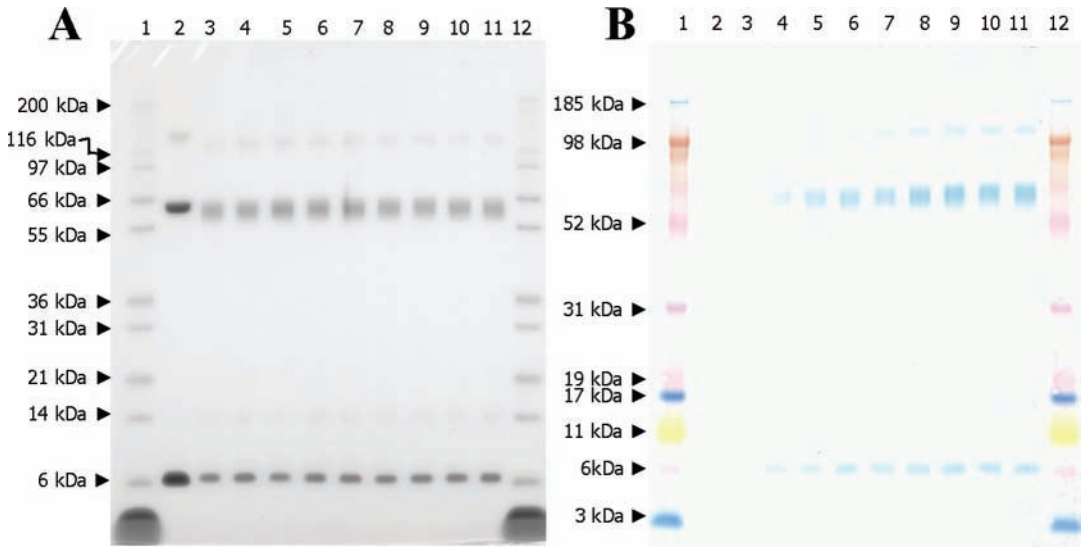


Figure 6. Concomitant SDS−PAGE (**A**) and Western blot (**B**) for time-dependent elaboration of **5a** and **5b** with biotin−hydrazide (**14**) as described in Figures 4 and 5. To directly compare the Western blot band intensities, the BSA and Aprotinin conjugates **14a** and **14b** were coloaded onto each of the gels. Lane 1 and 12: Mark 12 (SDS−PAGE) and Rainbow (Western) molecular weight markers; lane 2: untreated protein samples (BSA and Aprotinin); lane 3: **5a** and **5b** samples; lane 4: 2.5-min samples; lane 5: 5-min samples; lane 6: 10-min samples; lane 7: 15-min samples; lane 8: 30-min samples; lane 9: 60-min samples; lane 10: 90-min samples; lane 11: 120-min samples.

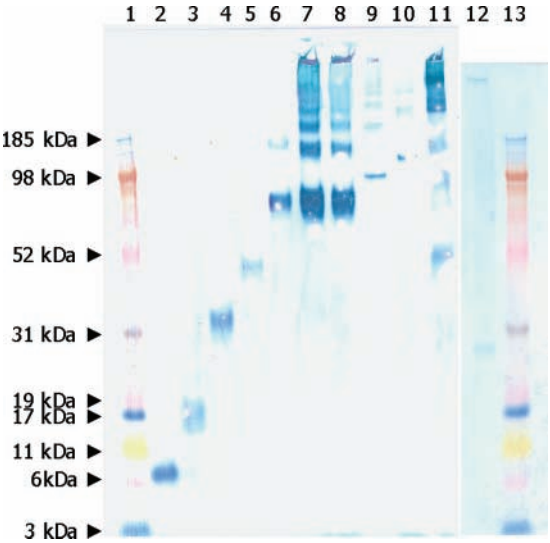


Figure 7. Western blot analysis of protein−biotin conjugates (**14a**−**k**). Lane 1 and 13, Rainbow molecular weight markers; lane 2 aprotinin−biotin (**14b**); lane 3, HEWL−biotin (**14c**); lane 4, carbonic anhydrase−biotin (**14d**); lane 5, OVA−biotin (**14e**); lane 6, BSA−biotin (**14a**); lane 7, apo-transferrin−biotin (**14f**); lane 8, holo-transferrin−biotin (**14g**); lane 9, phosphorylase B−biotin (**14h**); lane 10, β-gal−biotin (**14i**); lane 11, myosin−biotin (**14j**); lane 12, HBV core delta Ag−biotin (**14k**).

sensitive ligands and/or carriers, an added facet of the novel linker is the option to modify the acid liability by substitution within the aromatic ring (*24*−*26*). Also, since the acidolytic release feature was used simply to monitor the quality of the attached ligand, only a representative sample and not a full release of the ligand was required for analysis. A similar treatment of the conjugates **14a** and **14b** with acid (1 M HCl final) also resulted in a return of the absorbance spectra to that observed prior to hydrazone formation, along with the concomitant loss of the biotin label as judged by SDS−PAGE/Western blot analysis (data not shown).

DISCUSSION

Our initial goals in the design and synthesis of new linkage chemistry were to produce a chemoselective reagent that, when compared to existing methodologies, enabled controlled and relatively higher loading of proteins with ligands, while maintaining adequate aqueous solubility. When considering these requirements, the advantages afforded by aldehyde (*14*,*15*), benzaldehyde (*16*), and more specifically 2-hydroxybenzaldehyde (*19*) moieties as part of chemoselective reversible linkers has been well documented in the literature. However, in the first aspect of our design process, we have now demonstrated that known 2-hydroxybenzaldehyde chemistries further enable the in situ real-time spectrophotometric quantification of protein-linker formation and subsequent ligand-hydrazone formation in a nondestructive and reversible manner. The reaction monitoring is simple, is robust, and has been exemplified using a number of protein carriers and a variety of hydrazide-based ligands, illustrating the general wide utility of the process (Spectrophotometric changes upon protein−ligand interactions are known in nature; for example, enzymes that use a pyridoxal phosphate cofactor display characteristic absorbance changes associated with formation of different covalent adducts between substrate, cofactor and/or enzyme (*27*)).

In comparison to the existing nonspecific protocols of conjugation, which rely on post-reaction analysis using relatively laborious electrophoretic techniques (*11*, *12*), this simple but effective method of spectrophotometric monitoring permits fine control of the conjugation process, allowing immediate intervention to alter a reaction profile where necessary. In addition, the process is reversible under acidic conditions, thus enabling simple qualitative and quantitative quality control of the released ligand. This is particularly important, since the structural integrity of a ligand is paramount to its interaction with a target protein and any undesirable chemical modifications occurring during the conjugation process could result in a change or complete loss of recognition. These two features provide significant technical and practical advantages over the current state-of-the-art linkers.

In the second aspect of our design process, we have incorporated a quaternary amine as part of the linkage chemistry in the form of an N-ϵ-trimethyl-l-lysine residue. The incorporation of this moiety was based on the premise that linkers containing this group would compensate for the loss of protein surface charge that occurs upon derivatization of the surface amines of proteins, in particular the N-ϵ-amine of surface-exposed lysine residues. The use of quaternary amines as solubilizing agents has been well documented (*28*,*29*). One aspect of their use has been their incorporation into detergents and nondetergent solubilizing and renaturation agents (*29*).

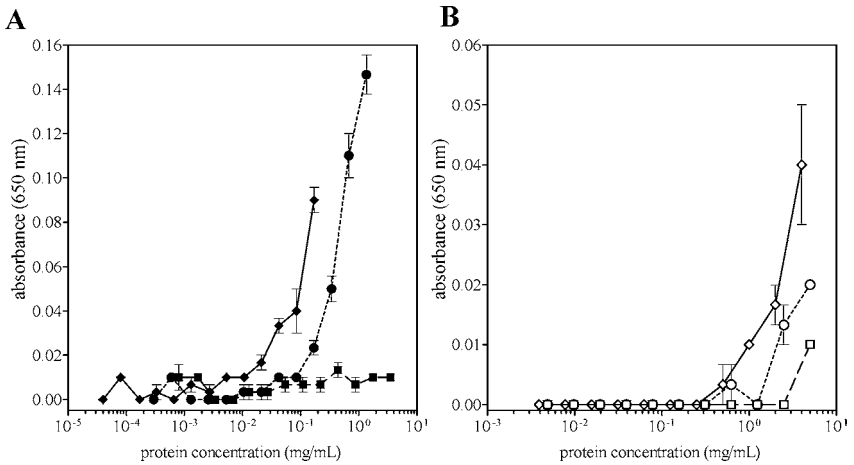


Figure 8. Relative solubility of linker-conjugated BSA samples tested in **A**: 100 mM sodium formate, pH 4.5 (left ordinate) for **5a**$^{85\%}$ (■), **1c**$^{55\%}$ (●), and **8**$^{85\%}$ (◆) and **B**: in 10 mM ammonium bicarbonate; pH 8.0 (right ordinate) for **5a**$^{85\%}$ (□), **1c**$^{55\%}$ (O), and **8**$^{85\%}$ (◇).

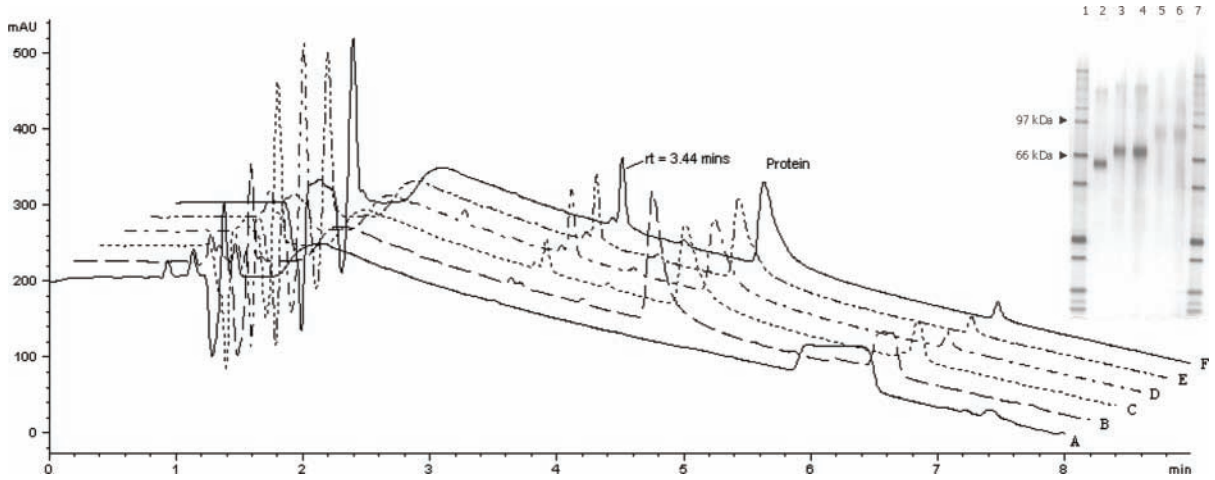


Figure 9. Time-dependent removal of oxytocin−hydrazide (**13**)from **13a**. Protein conjugate **13a** was acidified and aliquots were analyzed over time by HPLC (215 nm). The chromatograms relate to the blank buffer (negative) control (A), **13a** (positive) control (B), 15 min (C), 30 min (D), 45 min (E), and 60 min (F) incubation samples. The peak at 3.44 min was identified as free oxytocin−hydrazide (**13**) (ESI−MS *m*/*z*: 1291.3; calc. for M + H^+ 1291.5) and the inset shows the silver-stained gel of BSA (lane 2); **5a** (lanes 3 and 4) and **13a** (lanes 5 and 6).

Since protein solubility is a complex function of various factors (e.g., protein isoelectric point (p*I*), protein concentration, solvent temperature, surface accessible amino acids, solvation (hydrodynamic entropy), protein hydrophobicity, solvent pH, protein molecular weight, solvent ionic strength, protein conformation, etc.), the use of quaternary amines as protein solubilizing agents has primarily been empirical. Nevertheless, a resurgence of interest in the subject of protein solubility has been prompted by studies of protein crystallography and the underlying principles and themes have been extensively reviewed elsewhere (*30*−*33*). In relation to the role of surface-accessible lysine residues on protein solubility, various studies have been reported. For example, it has been demonstrated that chemical modification of surface lysine residues in goat serum albumin (GSA) with acetic anhydride increased the Stokes radii of the derivatized proteins, causing a change in protein conformation and a reduction in solubility (*20*). However, since acetylation of surface lysine residues by a neutral reagent would have also produced a change in surface charge, derivatization of the protein may have destabilized the native protein structure by increasing the electrostatic free energy of the protein and decreasing the favorable free energy of solvation associated with the positively charged amino acids (*20*). A major drawback to the chemical modification studies was that modifications were usually heterogeneous and uncontrolled. More recently, recombinant DNA technology, site directed mutagenesis, and protein crystallography have converged in order to better understand the criteria affecting protein solubility as a means to expedite protein crystallization. To this end, a number of studies have been carried out, not only to prevent protein precipitation but also to promote protein desolution as an aid to crystallization. For example, replacement of surface lysine with alanine in the cytosolic regulator RhoGDI resulted in a less-soluble protein, promoting protein crystallization (*34*). However, these studies were relatively focused on the production of material amenable to crystallization. Nevertheless, they show the importance of surface accessible lysine to solubility. A perhaps somewhat more comprehensive study was based on the selective replacement of glutamate and aspartate residues in ribonuclease Sa with lysine (*35*). Upon mutation, the more acidic isoelectric point for the wild-type protein (∼pH 3.5) was altered to ∼pH 6.5 for a three-lysine replacement mutant protein and ∼pH 10.2 for a five-lysine replacement mutant protein. The study concluded that the pH of minimum solubility varied with p*I* whereas the pH of maximum activity or stability did not (*35*). However, the data indicated that neither protein solubility nor the conformational stability was significantly affected by these changes. These and other studies only emphasize the difficulties in trying to rationalize the criteria that govern protein solubility other than categorizing gross effects. With this in mind we have not attempted to over-rationalize the effects of the quaternary amine on protein solubility other than to directly compare the relative solubility of conjugates using analogous linkers under the same conditions (Figures 8A and 8B). Our results clearly demonstrate that under similar conditions the quaternary amine enhances the solubility of protein-linker conjugates and, more importantly, protein-linker-carrier conjugates. We are in the process of fully characterizing the nature of this effect under a range of conditions employing an assortment of conjugates.

In summary, we have developed a chemoselective linkage technology, which enables highly loaded protein conjugates to be produced, while maintaining aqueous solubility. Spectral properties of the linker allow real-time monitoring of the conjugation reaction in situ and the reversible nature of the hydrazone bond under acidic conditions provides a simple means of quality control. This linker technology is now being used within applications such as conjugate vaccine production and the same basic design chemistry used in affinity purification strategies, micro-array design, and bio-active materials development.

ACKNOWLEDGMENT

We thank staff at Amura Therapeutics Limited for technical assistance, advice and manuscript review. Patent WO 03/087824 covers certain aspects of the work described in this publication.

LITERATURE CITED

(1) Wong, S. S. (1991) *Chemistry of Protein Conjugation and Cross-Linking*, CRC Press
(2) http://www.piercenet.com/.
(3) Cuatrecasas, P., and Anfinsen, C. B. (1971) in *Methods in Enzymology* (Fleischer, S., Sies, H., Kaplan, N., and Colowick, N., Eds.) Vol. 31, pp. 345−378, Academic Press Inc., New York.

(4) Haugland, R. P. (2002) in *Handbook of fluorescent probes and research chemicals*, Molecular Probes, Inc., Eugene.
(5) Akbarzadeh, A., Mehraby, M., Zarbakhsh, M., and Farzaneh, H. (1999) Design and synthesis of a morphine-6-succinyl-bovine serum albumin hapten for vaccine development. *Biotechnol. Appl. Biochem. 30 (Pt 2),* 139−146.
(6) Hamann, P. R., Hinman, L. M., Beyer, C. F., Lindh, D., Upeslacis, J., Flowers, D. A., and Bernstein, I. (2002) An anti-CD33 antibody-calicheamicin conjugate for treatment of acute myeloid leukemia. Choice of linker. *Bioconjugate Chem. 13*, 40−46.
(7) Arano, Y., Matsushima, H., Tagawa, M., Koizumi, M., Endo, K., Konishi, J., and Yokoyama, A. (1991) A novel bifunctional metabolizable linker for the conjugation of antibodies with radionuclides. *Bioconjugate Chem. 2*, 71−76.
(8) CHOI, J. S., LEE, E. J., CHOI, Y. H., JEONG, Y. J., AND PARK, J. S. (1999) POLY(ETHYLENE GLYCOL)-BLOCK-poly(l-lysine) dendrimer: novel linear polymer/dendrimer block copolymer forming a spherical water-soluble polyionic complex with DNA. *Bioconjugate Chem. 10*, 62−65.
(9) Boas, U., Sontjens, S. H., Jensen, K. J., Christensen, J. B., and Meijer, E. W. (2002) New dendrimer-peptide host−guest complexes: towards dendrimers as peptide carriers. *Chembiochem. 3*, 433−439.
(10) Yan, M., Cai, S. X., Wybourne, M. N., and Keana, J. F. (1994) N-hydroxysuccinimide ester functionalized perfluorophenyl azides as novel photoactive heterobifunctional crosslinking reagents. The covalent immobilization of biomolecules to polymer surfaces. *Bioconjugate Chem. 5*, 151−157.
(11) Ji, T. H. (1983) Bifunctional reagents. *Methods Enzymol. 91*, 580−609.
(12) Means, G. E. and Feeney, R. E. (1990) Chemical modifications of proteins: history and applications. *Bioconjugate Chem. 1*, 2−12.
(13) Briand, J. P., Muller, S., and Van Regenmortel, M. H. (1985) Synthetic peptides as antigens: pitfalls of conjugation methods. *J. Immunol. Methods 78*, 59−69.
(14) Reeves, R. L. (1966) in *The chemistry of the carbonyl group* (Patai, S., Ed.), pp 600−614, Interscience, London.
(15) Jencks, W. P. (1959) *J. Am. Chem. Soc. 81*, 475−481.
(16) King, T. P., Zhao, S. W., and Lam, T. (1986) Preparation of protein conjugates via intermolecular hydrazone linkage. *Biochemistry 25*, 5774−5779.
(17) Rose, K., Vilaseca, L. A., Werlen, R., Meunier, A., Fisch, I., Jones, R. M., and Offord, R. E. (1991) Preparation of well-defined protein conjugates using enzyme-assisted reverse proteolysis. *Bioconjugate Chem. 2*, 154−159.
(18) Gaertner, H. F., Rose, K., Cotton, R., Timms, D., Camble, R., and Offord, R. E. (1992) Construction of protein analogues by site-specific condensation of unprotected fragments. *Bioconjugate Chem. 3*, 262−268.
(19) Flinn, N. S., and Johnson, T. (2001) in *Patent Cooperation Treaty (PCT) WO 01/45745 A2*, Acambis Research Limited; Smith*kl*ine Beecham Biologicals S. A.
(20) Qamar, S., Islam, M., and Tayyab, S. (1993) Probing the determinants of protein solubility with amino acid modification. *J. Biochem. (Tokyo) 114*, 786−792.
(21) http://rsb.info.nih.gov/ij/index.html.
(22) Atherton, E. and Sheppard, R. C. (1989) *Solid-Phase Peptide Synthesis: A Practical Approach*, IRL Press, Oxford.
(23) Udenfriend, S., Stein, S., Bohlen, P., Dairman, W., Leimgruber, W., and Weigele, M. (1972) Fluorescamine: a reagent for assay of amino acids, peptides, proteins, and primary amines in the picomole range. *Science 178*, 871−872.
(24) Nguyen, R. and Huc, I. (2003) Optimizing the reversibility of hydrazone formation for dynamic combinatorial chemistry. *Chem. Commun. (Camb)* 942−943.
(25) Flinn, N. S., Quibell, M., Turnell, W. G., and Ramjee, M. K. (2003) in *Patent Cooperation Treaty (PCT) WO 03/087824*, Amura Therapeutics Limited.
(26) Kaneko, T., Willner, D., Monkovic, I., Knipe, J. O., Braslawsky, G. R., Greenfield, R. S., and Vyas, D. M. (1991) New hydrazone derivatives of adriamycin and their immunoconjugates—a correlation between acid stability and cytotoxicity. *Bioconjugate Chem. 2*, 133−141.
(27) Capitani, G., McCarthy, D. L., Gut, H., Grutter, M. G., and Kirsch, J. F. (2002) Apple 1-aminocyclopropane-1-carboxylate synthase in complex with the inhibitor l-aminoethoxyvinylglycine. Evidence for a ketimine intermediate. *J. Biol. Chem. 277*, 49735−49742.
(28) Yamada, H., Seno, M., Kobayashi, A., Moriyama, T., Kosaka, M., Ito, Y., and Imoto, T. (1994) An S-alkylating reagent with positive charges as an efficient solubilizer of denatured disulfide-containing proteins. *J. Biochem. (Tokyo) 116*, 852−857.
(29) Bhairi, S. M. (1997) *Detergents. A guide to the properties and uses of detergents in biological systems*, Calbiochem-Novabiochem Corporation, San Diego.
(30) Cohn, E. J. and Edsall, J. T. (1943). Protein, Amino Acids and Peptides as Ions and Dipolar Ions (Cohn, E. J., and Edsall, J. T., Eds.), Hafner, New York.
(31) Ries-Kautt, M. and Ducruix, A. (1997) *Macromolecular Crystallography, Part A*. Methods in Enzymology (Carter, C. J., Sweet, R., Abelson, J., and Simon, M., Eds.), 276, Elsevier.
(32) Tanford, C. and Reynolds, J. A. (1976) Characterization of membrane proteins in detergent solutions. *Biochim. Biophys. Acta 457*, 133−170.
(33) Tanford, C. (2003) 'Cohn and Edsall': physical chemistry conclusively supports a protein model. *Biophys. Chem. 100*, 81−90.
(34) Longenecker, K. L., Garrard, S. M., Sheffield, P. J., and Derewenda, Z. S. (2001) Protein crystallization by rational mutagenesis of surface residues: Lys to Ala mutations promote crystallization of RhoGDI. *Acta Crystallogr., Sect. D 57*, 679−688.
(35) Shaw, K. L., Grimsley, G. R., Yakovlev, G. I., Makarov, A. A., and Pace, C. N. (2001) The effect of net charge on the solubility, activity, and stability of ribonuclease Sa. *Protein Sci. 10*, 1206−1215.

BC0499329

Adapter Protein for Site-Specific Conjugation of Payloads for Targeted Drug Delivery

Marina V. Backer,*,† Timur I. Gaynutdinov,† Vimal Patel,† Brian T. Jehning,† Eugene Myshkin,‡ and Joseph M. Backer†

Rammelkamp Center for Research, Case Western Reserve University School of Medicine, Cleveland, Ohio 44109, and SibTech, Inc., Newington, Connecticut 06111. Received March 3, 2004; Revised Manuscript Received July 21, 2004

High-affinity interactions of two fragments of human RNase I (1−15-aa Hu-tag and 21−125-aa HuS adapter protein) can be used for assembly of targeting drug delivery complexes. In this approach, a targeting protein is expressed as a fusion protein with a 15-aa Hu-tag, while HuS is conjugated to a drug (or a drug carrier) creating a "payload" module, which is then bound noncovalently to the Hu-tag of the targeting protein. Although this approach eliminates chemical modifications of targeting proteins, the payload modules are still constructed by random cross-linking of drugs or drug carriers to an adapter protein that might lead to functional heterogeneity of the complexes. To avoid this problem, we engineered an adapter protein HuS(N88C) with an unpaired cysteine in position 88 that can be directly modified without interference with activity of assembled targeting complexes. HuS(N88C) binds Hu-tagged annexin V with K_D of 50 ± 6 nM, which is comparable to that of wild-type HuS. To demonstrate the utility of HuS(N88C) for developing uniform payload modules, we constructed a HuS(N88C)−lipid conjugate and inserted it into preformed liposomes loaded with a fluorescent dye. Targeting proteins, Hu-tagged vascular endothelial growth factor or Hu-tagged annexin V, were docked to liposomes decorated with HuS, and the assembled complexes delivered liposomes selectively to target cells.

INTRODUCTION

Efficient technology for loading drugs or drug carriers onto targeting proteins is necessary for targeted drug delivery (*1*). Currently, loading is largely based on random chemical conjugation of a cargo, such as drugs, drug carriers, or adapters for drug carriers, directly to targeting proteins. Chemical modifications of targeting proteins often damage their ability to bind to cellular targets, require expensive custom development, and yield heterogeneous preparations. To solve these problems, we have recently proposed to link a cargo to a standardized adapter protein that binds noncovalently to a docking tag engineered into a targeting protein (*2*). Our current adapter/docking tag pair is based on interactions between two fragments of human RNase I (*3*). As an adapter protein, we are using a 21−127-amino acid (aa) fragment of human RNase I, named HuS, while its N-terminal 1−15-aa fragment fused to a targeting protein serves as a docking tag, named Hu-tag. In the first application of this approach in vivo, we imaged a small mouse tumor using assembled complexes of Tc^{99m}-radiolabeled HuS and Hu-tagged vascular endothelial growth factor (*4*).

Although this approach eliminates chemical modifications of targeting proteins, assembled complexes are still structurally (and, potentially, functionally) heterogeneous because an adapter protein is still loaded via random cross-linking. Furthermore, random chemical modifications of adapter protein, particularly with large cargos such as liposomes or nanoparticles, decrease a proportion of molecules retaining full tag-binding activity. To solve these problems, we engineered an adapter protein with an unpaired cysteine in position 88, HuS(N88C), that can be directly modified without interference with activity of assembled targeting complexes. In this work, a PEGylated lipid was cross-linked to C88 in HuS(N88C), and the resulting conjugate was used to decorate liposomes (Figure 1). Hu-tagged vascular endothelial growth factor, or Hu-tagged annexin V, was docked to HuS−liposomes, and assembled complexes delivered liposomes selectively to target cells.

MATERIALS AND METHODS

Construction and Purification of Chimeric BH−RNase Mutants. Construction of chimeric $^{1-29}$B/$^{30-127}$H-RNase (BH-RNase) consisting of a 1−29 aa fragment of bovine RNase A and a 30−127 aa fragment of human RNase I has been described recently (*5*). The N88C and G68C amino acid substitutions were introduced separately in the pET29/$^{1-29}$B/$^{30-127}$H-RNase plasmid DNA by site-directed mutagenesis (Gene-Tailor site-directed mutagenesis kit, Invitrogen, Carlsbad, CA). The following primers were used for mutagenesis: 5′-TC ACT GAC TGC CGT CTT ACT TGC GGA TCC CGT T (sense, mutation underlined) and 5′-AGT AAG ACG GCA GTC AGT GAT ATG CAT AGA A (antisense) for the N88C mutation and 5′-AG AAG GTT ACC TGC AAA AAT TGC CAG GGT AAC TG (sense, mutation underlined) and 5′-ATT TTT GCA GGT AAC CTT CTC TTG GAA GCA A (antisense) for the G68C mutation. Both mutations were confirmed by sequencing. BH-RNase(G68C) and BH-RNase(N88C) were expressed in BL21(DE3) *Escherichia coli* (Novagen,

* To whom correspondence should be addressed. Mailing address: SibTech, Inc., 705 North Mountain Road, Newington, CT 06111. Phone: (860) 953-1753. Fax: (860) 953-1317. E-mail: mbacker@sibtech.com.

† SibTech, Inc.

‡ Case Western Reserve University School of Medicine.

10.1021/bc0499477 CCC: $27.50 © 2004 American Chemical Society
Published on Web 08/24/2004

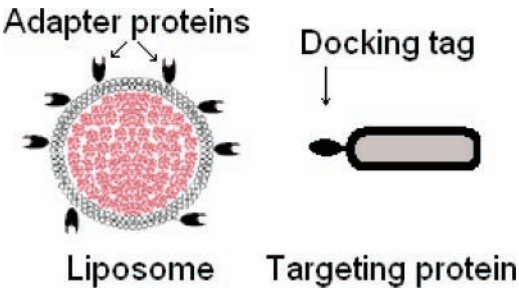


Figure 1. Assembly of targeting complexes for drug delivery.

Madison, WI), refolded from inclusion bodies, and purified by ion-exchange chromatography on HiTrap SP Sepharose Fast Flow (1-mL prepacked columns, Amersham Biosciences, Piscataway, NJ) as described for BH-RNase (*5*). Free SH-groups in proteins were detected by reaction with *N*-(1-pyrene)-maleimide (Molecular Probes, Eugene, OR) as described (*6*). Briefly, *N*-(1-pyrene)-maleimide dissolved in DMSO was added to an assayed protein at the molar ratio of 10:1 and incubated for 1 h at RT (conditions yielding no modification in wild-type BH-RNase). The reaction mixture was analyzed by reverse-phase high-performance liquid chromatography (RP HPLC) on a C4 Alltech MACROSPHERE 300 5 μm column (150 mm × 4.6 mm) with elution at 0.75 mL/min with 0.1% TFA (v/v) and a linear gradient of acetonitrile (5−50% over 15 min) with detection at 216 and 340 nm.

Purification of HuS Mutants. To release 21−127-aa HuS(N88C) and HuS(G68C) proteins, the corresponding BH-RNase mutants were digested with subtilisin (Sigma, St. Louis, MD) at the protein to protease w/w ratio of 50:1. After a 1-hr digestion at 4 °C, the reactions were stopped by ice-cold TFA (a final concentration of 1%), and HuS mutants were purified by affinity chromatography on a column carrying CA-extended Hu-peptide (**CA**-KESRAKKFQRQHMDS synthesized by Genemed Synthesis, Inc., South San Francisco, CA) as described (*5*). Bound HuS mutants were eluted with 0.1 M citric acid, neutralized with 1 M Na_2HPO_4, and stored at −70 °C in small aliquots. Purified proteins were analyzed by RP HPLC on C18 Waters Nova-Pack 5 μm column (150 mm × 3.9 mm) with elution at 0.75 mL/min with 0.1% TFA (v/v) and a linear gradient of acetonitrile (5−50% over 20 min). The concentrations of HuS mutants were calculated using 216-nm integral absorption in HPLC profiles with bovine S-protein (Sigma) serving as a standard.

To obtain HuS(N88C) with a free C88 SH-group, BH-RNase(N88C) was incubated at 4 °C for 16 h in the presence of 1.5-fold molar excess of DTT and 0.5 M NDSB-221 (Novagen) followed by subtilisin digestion and affinity purification as described above. To assign the free SH group, deprotected HuS(N88C) was labeled with *N*-(1-pyrene)-maleimide (Molecular Probes) and digested with endopeptidase Arg-C (Roche) according to the manufacturer's instructions. The digest was separated on RP HPLC C4 column, and a single peak containing 87% of incorporated pyrene was collected and analyzed by electrospray mass spectrometry at Yale Cancer Center Mass Spectrometry Resources and the W. M. Keck Foundation Biotechnology Resource Laboratory (New Haven, CT).

Modification of HuS(N88C) with Poly(ethylene glycol)−α-Distearoyl Phosphatidylethanolamine−ω-maleimide (mPEG−DSPE−maleimide). Twenty milligrams of BH-RNase(N88C) was incubated at 4 °C for 16 h in the presence of 1.5-fold molar excess of DTT and 0.5 M NDSB-221 (Novagen) and then digested with subtilisin (w/w ratio of 50:1) for 2 h at 4 °C. Subtilisin digestion was stopped by ice-cold TFA (a final concentration of 1%), and the reaction mixture was loaded onto a HiTrap SP Sepharose column equilibrated with 20 mM NaOAc, 0.2 M NaCl, and 0.5% TFA. Subtilisin was completely removed from the column with 0.2 M NaCl, 20 mM NaOAc, while digested BH-RNase was eluted with 0.6 M NaCl, 20 mM NaOAc, pH 6.5. Eluted protein was incubated with mPEG−DSPE−maleimide (FW 3400, Shearwater Polymers, Huntsville, AL) at the molar protein-to-lipid ratio of 1:10 for 2 h at RT. The reaction mixture was then passed through a Hu-peptide affinity column. The mixture of HuS(N88C)−DSPE and unmodified HuS(N88C) bound to the column was eluted with 0.1 M citric acid, neutralized with 1 M Na_2HPO_4, and analyzed by RP HPLC on a Vydac Diphenyl (219TP5415) column (250 mm × 4.6 mm) with elution at 0.75 mL/min with 50 mM thriethylamine phosphate, pH 2.8, 20% 2-propanol with a linear gradient of acetonitrile (0−70% over 30 min). The eluted mixture was stored in liquid nitrogen in small aliquots.

Preparation of HuS−Liposomes. Liposomes containing 1,2-dioleoyl-s*n*-glycero-3-phosphocholine (DOPC, FW 786.15, Avanti, Alabaster, AL) and cholesterol (FW 386.7, Sigma) at the ratio of 65:35 (%) were prepared as described (2). A fluorescent dye, 8-hydroxypyrene-1,3,6-trisulfonic acid, trisodium salt (HPTS, Sigma), was added to the lipid hydration mixture at a concentration of 35 mM. Free HPTS was separated from liposomes by chromatography on Sepharose CL-4B (Sigma). The HPTS-loaded liposomes were incubated with 2.5 μM HuS(N88C)−DSPE at 37 °C for 16 h in a volume of 1 mL, and then passed again through Sepharose CL-4B column. The efficiency of HuS(N88C)−DSPE insertion was analyzed by RP HPLC on a Vydac Diphenyl (219TP5415) column (250 mm × 4.6 mm) with elution at 0.75 mL/min with 50 mM thriethylamine phosphate, pH 2.8, and 20% tetrahydrofuran with a linear gradient of acetonitrile (0−70% over 25 min). In four independent preparations, concentration of liposomal HuS(N88C) determined by RP HPLC was 2 ± 0.4 μM. The HPTS content determined fluorometrically at λ_{ex} = 485 nm/λ_{em} = 520 nm was 230 ± 30 μM. The phospholipid content was determined by the ferrithiocyanate method according to the protocol from Analytical Control Systems, Inc. (Fishers, IL). Briefly, chloroform, ferrithiocyanate reagent (23.03 g of ferric chloride hexahydrate and 30.4 g of ammonium ferrothiocynate per 1 L of water), and liposomes were mixed at vol/vol ratio of 2:2:0.1, vigorously mixed on a vortex for 60 s, and centrifuged to separate layers. Phospholipid content of the lower chloroform layer was determined by absorbance at 488 nm using DOPC as a standard. The liposomal phospholipid content was 6 ± 1.5 mM. The liposome average size of 93 nm (SD 11) at 26.3° and 105 nm (SD 14) at 35.2° was determined by DELSA 440SX (Coulter-Beckman, Miami, FL). Assembled liposomes retained the same HPTS concentration and ribonuclease activity of HuS after a 1-week storage on ice.

Construction of the pET/Hu$(G_4S)_3$ Vector. The pET29/Hu-tag vector (a derivative of the pET29a(+) bacterial expression vector, Novagen) for expressing recombinant proteins with an N-terminal Hu-peptide was described recently (*3*). To optimize the vector, a DNA fragment encoding an 8-aa linker between the Hu-tag sequence and the multiple cloning site (MCS) was replaced with a DNA fragment encoding a $(G_4S)_3$ peptide

as follows. Two single-stranded DNA fragments (synthesized by GeneLink, Thornwood, NY) were mixed in equimolar concentrations and annealed at room temperature (RT): 5′-pC GGT AGT GGT GGT GGC GGT TCA GGC GGA GGT GGC TC and 5′-pCAT GGA GCC ACC TCC GCC TGA ACC GCC ACC ACC ACT AC-C GGT AC. The annealed DNA fragment containing overhangs compatible with *Nco*I and *Kpn*I sites was ligated into *Nco*I−*Kpn*I of the pET29/Hu-tag vector. The *Kpn*I site has been destroyed then by site-directed mutagenesis (Gene-Tailor site-directed mutagenesis kit, Invitrogen) using primers: 5′- GT CAA CAC ATG GAC TCT GGT GGC GGC GGT AGT GGT GG (sense, mutation underlined) and 5′-ACC AGA GTC CAT GTG TTG ACG TTG AAA TTT TTT AGC (antisense). In the resulting pET/Hu$(G_4S)_3$ vector, an N-terminal 15-aa Hu-tag located immediately after the initiator methionine is connected to the MCS region via a $(G_4S)_3$ peptide linker.

Construction and Expression of Hu-Tagged Targeting Proteins. A 121-aa isoform of human vascular endothelial growth factor (VEGF) and human annexin V coding sequences were amplified by PCR using primers introducing *Nco*I sites (underlined) and cloned separately into the *Nco*I site of the pET/Hu$(G_4S)_3$ vector. VEGF was amplified from the pET29/Hu−VEGF plasmid (*3*) with primers 5′-CAC AAG CCA TGG CAC CCA TGG CAG AAG GAG GA (sense) and 5′-AC TAC CCA TGG TCA CCG CCT CGG CTT GTC AC (antisense). Human annexin V was amplified from the pPAP1-1.6 plasmid (kindly provided by Dr. J. Tait, University of Washington School of Medicine, Seattle, WA) with primers 5′-CAC AAG CCA TGG CAC AGG TTC TCA GAG (sense) and AC TAC CCA TGG TTA GTC ATC TTC TCC ACA GAG C (antisense). Clones with ORF correct orientations were selected by PCR using a T7-based sense primer. Both Hu-tagged proteins, Hu−VEGF and Hu−annexin, were expressed in *E. coli* strain BL21(DE3) (Novagen) grown in LB medium (Q-Biogen, Carlsbad, CA). The expression was induced by 1 mM IPTG at the optical density of 0.5−0.7 unit at 600 nm. After induction, the cultures were grown for 2 h at 37 °C with shaking at 300 rpm, then harvested by centrifugation. Hu−VEGF was refolded from inclusion bodies and purified as described (*3*). The yield of Hu−VEGF was 5 mg/L, purity was >95% by SDS−PAGE followed by SimplyBlue Safe Stain (Invitrogen), and dimer content was no less than 95% as estimated by nonreducing SDS−PAGE. Hu−annexin was expressed in a soluble cytoplasmic form and purified as described (*7*) with minor modifications. Briefly, bacterial pellets were resuspended in 50 mM Tris-HCl, 15 mM $CaCl_2$, pH 7.2, in the presence of Protease Inhibitor Cocktail Set II (Calbiochem, La Jolla, CA), then opened by sonication and centrifuged at 15 000*g* for 10 min. The pellet was resuspended in 50 mM Tris-HCl, 30 mM EDTA, pH 7.2, and centrifuged at 17 000*g* for 10 min. The supernatant containing Hu−annexin was dialyzed against 100 volumes of 20 mM Tris-HCl, pH 8.0, for 20 h. Hu−annexin was purified from the dialyzed supernatants by ion-exchange chromatography on HiTrap Q Sepharose Fast Flow (1-mL prepacked columns, Amersham). The yield of Hu−annexin was 15 mg/L, and purity was >95% by SDS−PAGE followed by SimplyBlue Safe Stain (Invitrogen). Both Hu−VEGF and Hu−annexin were stored at −70 °C in small aliquots.

Ribonuclease Activity. Ribonuclease activities of wild-type and mutant BH-RNases and reconstituted ribonuclease activities of assembled complexes were assayed as previously described (*2*, *3*, *5*, *6*). Briefly, varying amounts of RNase or preformed complex were added to a buffer containing 20 mM Tris-HCl, 100 mM NaCl, pH 7.5, 0.1 mg/mL poly C, and incubated for 5 min at RT. Ribonuclease activity was measured by 280-nm absorbance of the reaction mixtures cleared from TCA-precipitated material. One optical unit of TCA-soluble material released from poly C under these conditions was defined as one relative unit of ribonuclease activity.

HuS/Hu-tag Binding Assay. The equilibrium dissociation constant (K_D) values for complexes of HuS mutants and Hu-tagged proteins were determined as previously described (*3*, *5*, *6*). Briefly, HuS(N68C) and HuS(N88C) at final concentrations of 0.1, 0.2, or 0.3 nM were mixed separately with varying amounts of Hu−annexin. Reconstituted ribonuclease activity was measured as described above. Calculations of the K_D values were performed assuming that the initial rate of the hydrolysis is proportional to the concentration of reconstituted ribonuclease. DYNAFIT software was used for the global fitting with numeric iteration and calculation of the K_D values (*8*).

Hu-VEGF Assays. HEK293 human transformed embryonic kidney cells (CRL-1573) were from American Type Culture Collection (Rockville, MD). 293/KDR cells expressing 2.5×10^6 VEGFR-2/cell were described elsewhere (*9*). Cells were grown in DMEM with 10% fetal bovine serum (FBS), 2 mM L-glutamine, and antibiotics at 37 °C, 5% CO_2. HEK293 and 293/KDR cells were plated on 24-well plates, 17.5×10^4 cells/well, shifted to starvation medium (DMEM/0.5% FBS) 6 h later, and incubated in this medium for 16 h at 37 °C, 5% CO_2. For liposome binding experiments, cells were used directly after starvation. For VEGFR-2 autophosphorylation, cells after starvation were shifted to serum-free DMEM with 0.5 mM sodium vanadate for 20 min at 37 °C, then stimulated with Hu−VEGF for 10 min at 37° C, lysed, and analyzed by Western blotting using anti-phosphotyrosine RC20 conjugated to horseradish peroxidase (BD Transduction Labs, San Diego, CA).

Hu−Annexin Erythrocyte Binding Assay. The affinity of Hu−annexin for cell membranes with exposed phosphatidylserine was assayed by its ability to compete with FITC−annexin V (Sigma) for binding to erythrocytes as described (*7*, *10*). Briefly, 10^6 erythrocytes of stabilized human blood (4C Plus Cell Control, Beckman Coulter) were incubated with varying amounts of Hu−annexin in the presence of 5 nM FITC−annexin V in binding buffer (10 mM HEPES, pH 7.4, 136 mM NaCl, 2.5 mM $CaCl_2$) for 15 min at RT. Cells were spun down, resuspended in a binding buffer supplemented with 5 mM EDTA, and spun down again. FITC fluorescence in the supernatants was measured at $\lambda_{ex} = 485$ nm/$\lambda_{em} = 520$ nm.

RESULTS

BH-RNase(G68C) and BH-RNase(N88C) Mutants. On the basis of analysis of a 3D-structure of human RNase I (*11*), we have chosen two residues for introducing unpaired cysteines: N88 and G68. Modeling experiments with RNase I indicated that putative C68 and C88 would be oriented away from HuS domains involved in interactions with Hu-tag (Figure 2A) and therefore expected to be available for chemical cross-linking. Both mutant BH-RNases were expressed in BL21(DE3) *E. coli*, refolded from inclusion bodies, and purified to more than 95% pure proteins with yields of 22 mg/L for BH-RNase(G68C) and 45 mg/L for BH-RNase(N88C). Somewhat surprisingly, both mutants displayed decreased ribonuclease activity (Figure 2B) suggesting either subtle effects of the

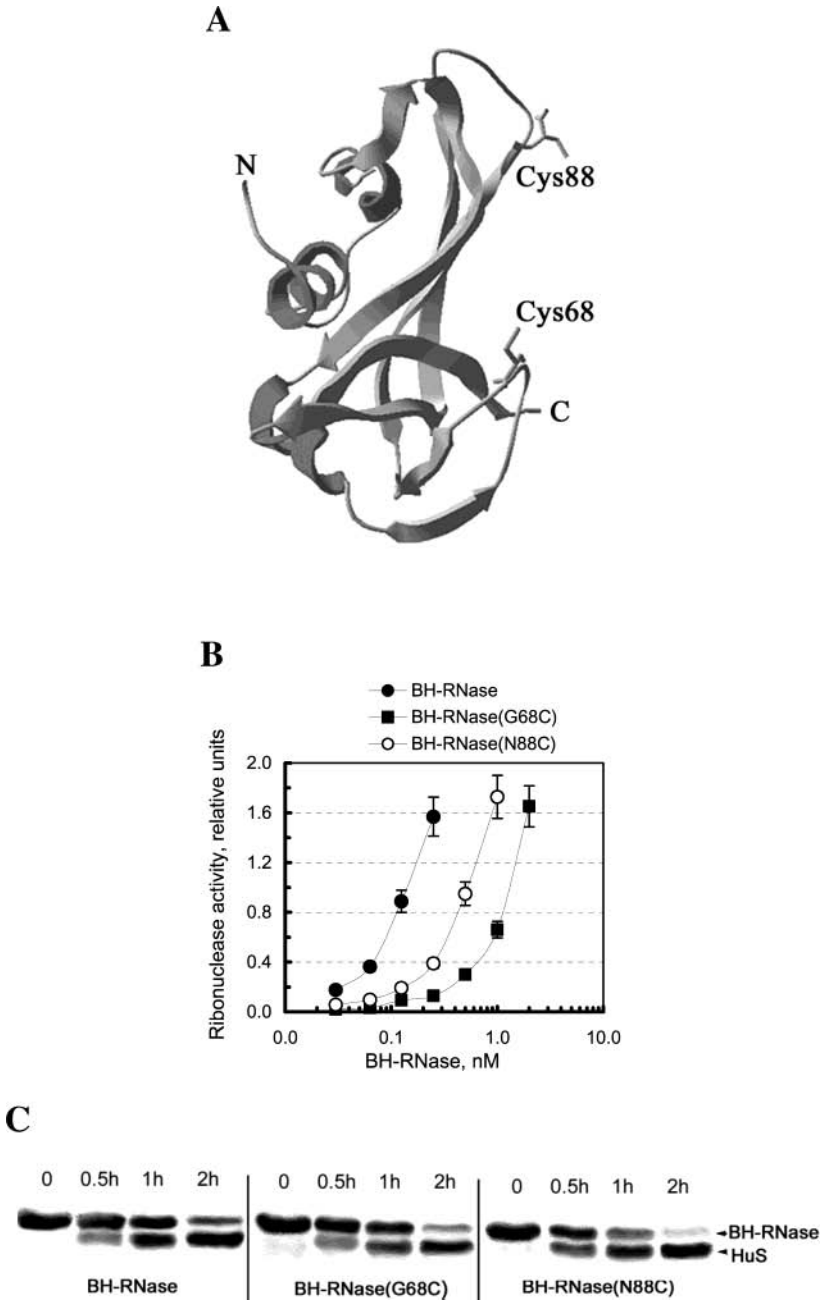


Figure 2. BH-RNase mutants with unpaired cysteines. In panel A, the backbone structure of human RNase I (1E21) is displayed with SWISS-PDB viewer. N- and C-termini and unpaired cysteines in positions 68 and 88 are indicated. Panel B presents the enzymatic activity of BH-RNase mutants. In panel C, wild-type HuS, HuS(G68C), and HuS(N88C) are released from the corresponding BH-RNases by limited digestion with subtilisin at the protease to BH-RNase w/w ratio of 1:50. Digestion reactions were incubated for 0.5, 1, and 2 h at 4 °C and analyzed then by reducing SDS−PAGE on 17.5% gels followed by Simply Blue Safe Stain (Invitrogen).

substitutions on the structure of the active center or the presence of the misfolded mutant BH-RNases in final protein preparations. However, the rates of subtilisin digestion for mutant proteins were comparable to that for wild-type BH-RNase (Figure 2C).

HuS(G68C) and HuS(N88C) Mutants. BH-RNase-(G68C) and BH-RNase(N88C) were digested with subtilisin and mutant HuS proteins were purified on a Hu-peptide affinity column as described for wild-type HuS (*5*). To characterize the affinity of purified mutant HuS proteins to Hu-peptide, we used Hu−annexin. A ribbon model of the HuS/Hu−annexin complex is shown in Figure 3A. Reconstituted ribonuclease activity in HuS/Hu−annexin mixtures was measured under conditions of equilibrium between free and bound HuS, and the data were used to calculate the equilibrium dissociation constant (K_D) values for these complexes as described (*3*, *5*, *6*). We found that affinities of HuS(G88C) and HuS-(N88C) to Hu−annexin were characterized by the K_D values of 123 ± 26 and 50 ± 6 nM, respectively (Figure 3B,C). Taking into account that BH-RNase(N88C) was recovered as a more active enzyme with a higher yield and its HuS(N88C) fragment displayed higher Hu-tag affinity comparable to that of wild-type HuS (K_D = 29 ± 3 nM (*5*)), further experiments were performed with this mutant.

Availability of C88 for Site-Specific Modification. Since BH-RNase(N88C) mutant was refolded in the presence of reduced/oxidized glutathiones (Red/Ox buffer), we have expected that an unpaired cysteine would be

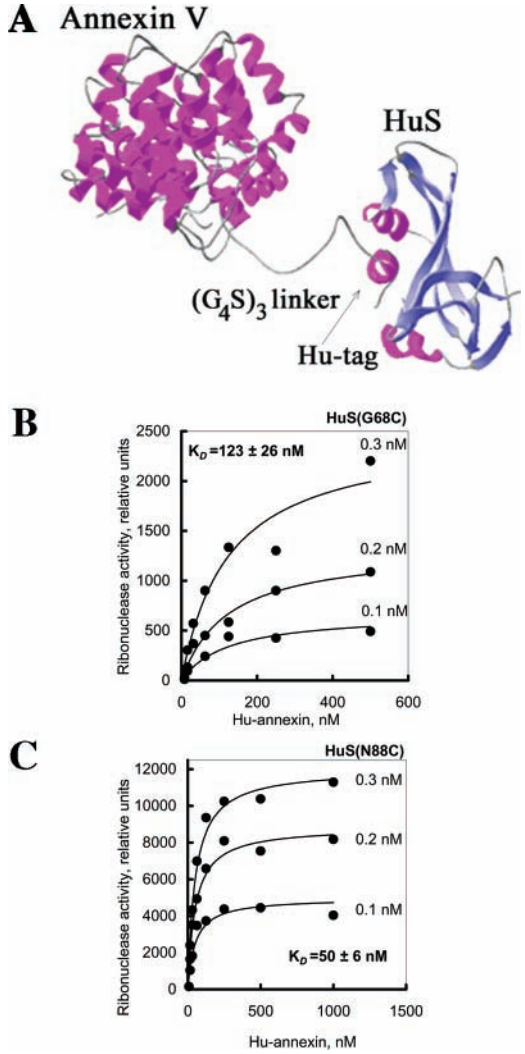


Figure 3. Affinity of HuS mutant proteins for Hu−annexin. Panel A shows the Hu−annexin/HuS complex. The Hu-peptide and $(G_4S)_3$ linker in random orientation were built using SWISS-PDB viewer and linked to the annexin V structure. The Hu−annexin/HuS complex was minimized using the SANDER module of the AMBER software package. Panels B and C show the affinity of HuS/Hu-tag interactions. Fixed amounts (0.1, 0.2, and 0.3 nM) of HuS(G68C) mutant (B) and HuS(N88C) mutant (C) were mixed separately with varying amounts of Hu−annexin. The K_D values for the resulting complexes were calculated as described (*5, 6*).

involved in a mixed disulfide with glutathione. Mixed disulfides were reported for other recombinant proteins with odd numbers of cysteines refolded in Red/Ox buffers including a mutant bovine S-protein with an engineered cysteine in position 122 (*6, 12*). Indeed, modification of freshly isolated BH-RNase(N88C) mutant protein with a sulfhydryl-directed reagent *N*-(1-pyrene)-maleimide indicated that only a fraction of unpaired cysteines was accessible for modification, varying from 5% to 35% in different preparations of BH-RNase(N88C). However, after a mild DTT treatment of BH-RNase(N88C) that did not affect RNase activity (1.5-fold molar excess DTT at 4 °C in the presence of 0.5 M NDSB-221 to prevent protein aggregation), the fraction of unpaired cysteines accessible for pyrene modification reached 95−98% indicating release from mixed disulfide (data not shown). To establish the position of a cysteine with a free SH-group, pyrene-modified HuS(N88C) was digested with endoproteinase Arg-C, and the digest was fractionated by RP HPLC. The major pyrene-containing peak (87% of incorporated pyrene) was found to be a single peptide with a mass of 951.43 as provided by electrospray mass spectrometric analysis. This mass corresponded to the theoretical mass of the expected peptide, Leu_{86}-Thr-Cys-(*N*-1-pyrene)-Gly-Ser-Arg_{92} (933.43 kDa) containing C88 modified with pyrene. The remaining pyrene (13%) was incorporated in several minor peaks that were not further analyzed.

Site-Specific Modification of HuS(N88C). To demonstrate utility of HuS(N88C) for developing uniform "payload" modules, we constructed a HuS(N88C)−lipid conjugate and inserted it into HPTS-loaded liposomes. Site-directed modification of C88 with mPEG−DSPE−maleimide included several steps. First, BH-RNase-(N88C) was "deprotected" from mixed disulfides (as described above). Second, it was cleaved with subtilisin, and subtilisin was removed from the reaction mixture by ion-exchange chromatography on an SP-column. Third, digested BH-RNase(N88C) was modified with mPEG−DSPE−maleimide, and the final product was purified on Hu-peptide affinity column (Figure 4A). The latter step removed undigested BH-RNase(N88C) and yielded a mixture of HuS(N88C)−DSPE conjugate and unmodified HuS(N88C). The extent of lipid modification of HuS-(N88C) eluted from affinity column varied from 70% to 85% as judged by RP HPLC analysis (Figure 4B). Two peaks of HuS−DSPE eluted at 23 and 23.6 min were products of conjugation with two forms of mPEG−DSPE−maleimide that are initially present in the reagent and the traces of which, eluted at 25 and 25.6 min, are still detectable in purified HuS−DSPE (Figure 4B). The mixture of HuS(N88C) and HuS(N88C)−DSPE conjugate retained the same ribonuclease activity after several months of storage in liquid nitrogen (data not shown).

For insertion in HPTS-loaded liposomes, the mixture of HuS(N88C)−DSPE conjugate and HuS(N88C) was incubated with liposomes for 16 h at 37 °C, followed by purification on Sepharose 4B and characterization of the size and composition as described in Materials and Methods. The efficiency of HuS(N88C)−DSPE insertion was determined by RP HPLC analysis of purified liposomes (Figure 4C, note that the RP HPLC system is different from the one described in Figure 4B; the peak eluted at 24 min corresponds to liposomal lipids). Based on this analysis, the amount of inserted HuS(N88C)−DSPE varied from 80% to 95% from experiment to experiment.

Hu-Tagged Targeting Proteins. The pET29/Hu-tag vector for bacterial expression of recombinant proteins with an N-terminal Hu-tag has been described recently (*3*). In the new pET$(G_4S)_3$Hu vector constructed for this work, a random 8-aa linker connecting Hu-tag and MCS region of the pET29/Hu-tag vector has been replaced with a standard $(G_4S)_3$ linker designed for fusion of heavy and light chains of monoclonal antibodies (*13*) and widely used since then for construction of single-chain recombinant antibodies (*14, 15*). Using the pET$(G_4S)_3$Hu vector, we have expressed two targeting proteins, Hu−VEGF and Hu−annexin.

Functional activity of Hu−annexin was determined as its ability to compete with FITC−annexin for binding to phosphatidylserine-displaying erythrocytes of stabilized human blood (*7*). In this assay, annexin is bound to erythrocytes in the presence of Ca^{2+} and released in the presence of EDTA. We found that Hu−annexin displaced FITC−annexin in a dose-dependent manner with IC_{50} of 11 ± 3 nM (Figure 5A). Since correct size recombinant

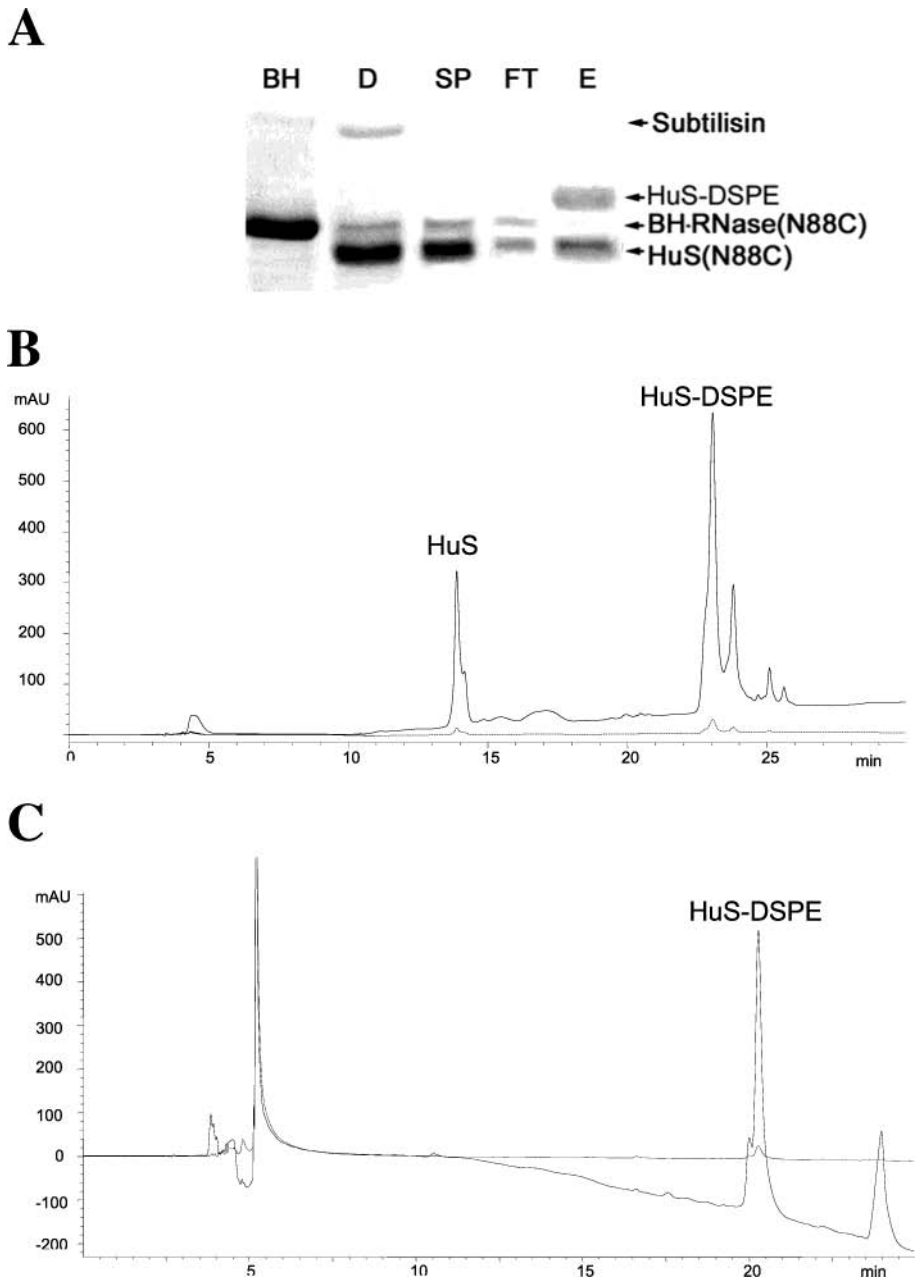


Figure 4. HuS88C−DPDE cross-linking and insertion into liposomes. Panel A shows SDS−PAGE analysis of HuS(N88C)−DSPE conjugate synthesis and purification: lane BH, BH-RNase(N88C); lane D, digestion of BH-RNase(N88C) with subtilisin; lane SP, SP-column purification; lane FT, affinity Hu-column flow-through; lane E, elution from affinity Hu-column. Samples were analyzed by reducing SDS−PAGE on 17.5% gels followed by Simply Blue Safe Stain (Invitrogen). In panel B, HuS(N88C)−DSPE was affinity purified and analyzed by RP HPLC (50 mM thriethylamine phosphate, pH 2.8, 20% 2-propanol with a linear gradient of acetonitrile 0−70% over 30 min). The yield of modified product was calculated as a ratio of integral peak intensities for HuS(N88C)−DSPE conjugate and unmodified HuS(N88C); in this case, modification is 77%. In panel C, the HuS(N88C)−DSPE conjugate was inserted in liposomes (16 h at 37 °C) and then analyzed by RP HPLC (50 mM thriethylamine phosphate, pH 2.8, and 20% tetrahydrofuran with a linear gradient of acetonitrile 0−70% over 25 min).

annexin V displayed a similar activity in this assay (IC_{50} of 9 ± 4 nM, (*7*)), we concluded that fusion of the Hu-tag did not disturb annexin V functional activity.

Functional activity of Hu−VEGF was tested in a VEGFR-2 autophosphorylation assay (Figure 5B). Hu−VEGF induced VEGFR-2 tyrosine autophosphorylation in 293/KDR cells, which was detectable at 0.04 nM Hu−VEGF and reached plateau at 0.4 nM (Figure 5B). Since similar activities were reported for the previous version of Hu−VEGF with a random 8-aa linker and also for recombinant human $VEGF_{165}$ (*3*), we concluded that the extension of the linker from 8-aa to 15-aa did not have detrimental effects on VEGF functional activity.

Targeted Delivery of HuS−Liposomes. Targeting proteins were mixed with HPTS-containing HuS−liposome at equimolar Hu-tagged protein to HuS ratio, and the HuS/Hu-tag association was detected by reconstituted ribonuclease activity. We found that dose-dependencies of ribonuclease activity of complexes with liposome-bound HuS were similar to that obtained with free HuS (Figure 6A). Targeting of HuS−Lip/Hu−annexin was tested in an erythrocyte binding assay. HuS−liposomes were used as a control for a nonspecific binding. We found that Hu−annexin/HuS−liposome complexes bound to erythrocytes in a dose-dependent manner, and the levels of binding

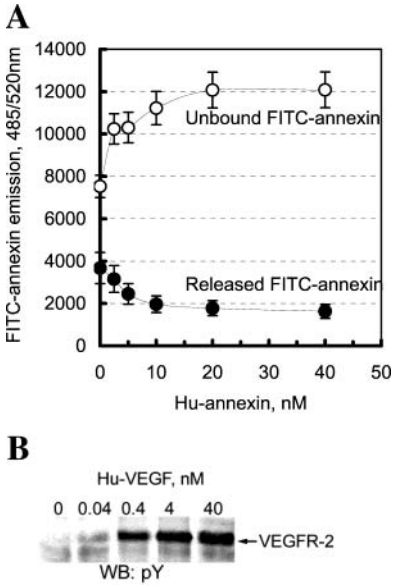


Figure 5. Hu-tagged targeting proteins are functionally active. In panel A, Hu−annexin competes with FITC−annexin for binding to erythrocytes with exposed phosphatidylserine. Unbound FITC−annexin was found in the supernatants after binding with erythrocytes; released FITC−annexin was found in the supernatants after resuspension of erythrocytes in EDTA-containing buffer. In panel B, Hu−VEGF activates VEGFR-2 in 293/KDR cells.

were significantly higher amounts than that for untargeted HuS−liposomes (Figure 6B).

Targeting of HuS−Lip/Hu−VEGF was tested in a binding assay with 293/KDR cells expressing 2.5×10^6 VEGFR-2/cell (9). HuS−liposomes were used as a control for a nonspecific binding. In addition, HEK293 cells lacking VEGFR-2 were used as a control for non-VEGFR-2-mediated binding. We found that 293/KDR cells internalized VEGF-driven HuS−liposomes significantly better than nontargeted HuS−liposomes (Figure 6C). In contrast, both targeted and nontargeted liposomes were internalized to the same extent by HEK293 cells lacking VEGFR-2 (Figure 6C).

DISCUSSION

To eliminate random chemical modification of targeting proteins currently used for targeted delivery of therapeutics and diagnostics, we have recently proposed to link a cargo to a standardized adapter protein that binds noncovalently to a docking tag engineered into a targeting protein (Figure 1). This approach however still yielded heterogeneous targeted drug delivery complexes because of a random cross-linking of a cargo to the adapter protein. Here we report development of a novel HuS(N88C) adapter protein for assembly of targeting drug delivery complexes (Figure 1). This mutant carries an unpaired cysteine in position 88 available for site-directed conjugations of drugs or drug carriers.

We have recently developed a high-yield system for production of HuS protein by subtilisin digestion of a chimeric recombinant BH-RNase containing an appropriate subtilisin cleavage site (*5*). BH-RNase is easily refolded into a functionally active conformation and yielded highly active HuS after subtilisin digestion. Therefore, to develop HuS mutants with unpaired cysteines, we mutated BH-RNase and then recovered HuS mutants by subtilisin digestion of the corresponding BH-RNases. The positions for the G68C and N88C substitutions have been chosen on the basis of 3-D structure of human RNase I (*11*) with the goal to minimize possible interference of cross-linked constructs with tag/adapter interactions. We report here that both mutant HuS proteins are readily recovered from the corresponding mutant BH-RNases by subtilisin digestion followed by affinity purification. We found that HuS(N88C) is a better candidate for further development because of its higher yield and higher affinity to Hu-tag, which is close to that of wild-type HuS (Figure 3 B,C (*5*)). A point mutation in position 88 of bovine RNase A was shown to decrease RNase affinity to ribonuclease inhibitor (RI) and enhances cytotoxic activity of RNase A (*16*). However, mutations in positions 88, 89, or 90 of highly homologous RNase I had little, if any, effect on cytotoxicity of this protein (*17*). Nevertheless, one could expect that cross-linking of bulky compounds to C88 still could decrease affinity of the reconstituted RNase to RI providing the assembled complexes with intrinsic cytotoxicity, which would be an additional benefit in a case of delivery of cytotoxic drugs.

Using maleimide chemistry, we cross-linked a PEGylated lipid to HuS(N88C). HuS−lipid conjugate was inserted into preformed unilamellar liposomes yielding 20−30 adapter proteins per liposome, which is consistent with previously published data on immunoliposome construction (*18*). HuS−liposomes readily bind Hu-tagged proteins as judged by reconstitution of RNase activity upon HuS/Hu-tag interaction. Furthermore, liposomes linked to HuS via C88 did not affect adapter/tag interactions, since complexes reconstituted with both liposomal and free HuS protein displayed similar ribonuclease activities. No significant interference with adapter/tag interactions was also observed in our preliminary experiments with various bulky constructs, such as magnetic beads (Dynal Biotech Corp., Lake Success, NY) or Dexferrum magnetic particles, (American Regent Lab., Shirley, NY) linked to HuS via C88.

Assembled drug delivery complexes might be developed for therapeutic applications only if their cargo does not interfere with targeting protein/receptor interaction. We report here that two different targeting proteins, Hu−annexin V and Hu−VEGF, significantly enhance HuS−liposome binding to the corresponding cells. Thus, liposomes do not interfere with binding of these targeting proteins to their cellular targets. Since annexin V and VEGF are vastly different proteins with even more different targets, we expect that HuS−liposomes developed in this work can be used as a standardized payload module for delivery by various targeting proteins. Although assembly of targeting complexes described in this work requires production of a modified adapter protein, this approach provides significant advantages over traditional drug loading via direct conjugation to targeting proteins. First, the same modified adapter would be suitable for assembly with different targeting proteins. Second, since the site-specifically modified adapter retains the ability to bind targeting proteins, we expect that various drugs or drug carriers can be cross-linked to C88 via standardized chemistries. We therefore expect that the benefits associated with the elimination of both the damage to the targeting proteins and the heterogeneity of the final products would stimulate acceptance of assembled complexes for targeted drug delivery. Experiments are in progress to establish whether selectivity provided by assembled targeting complexes is sufficient for therapeutic and diagnostic applications.

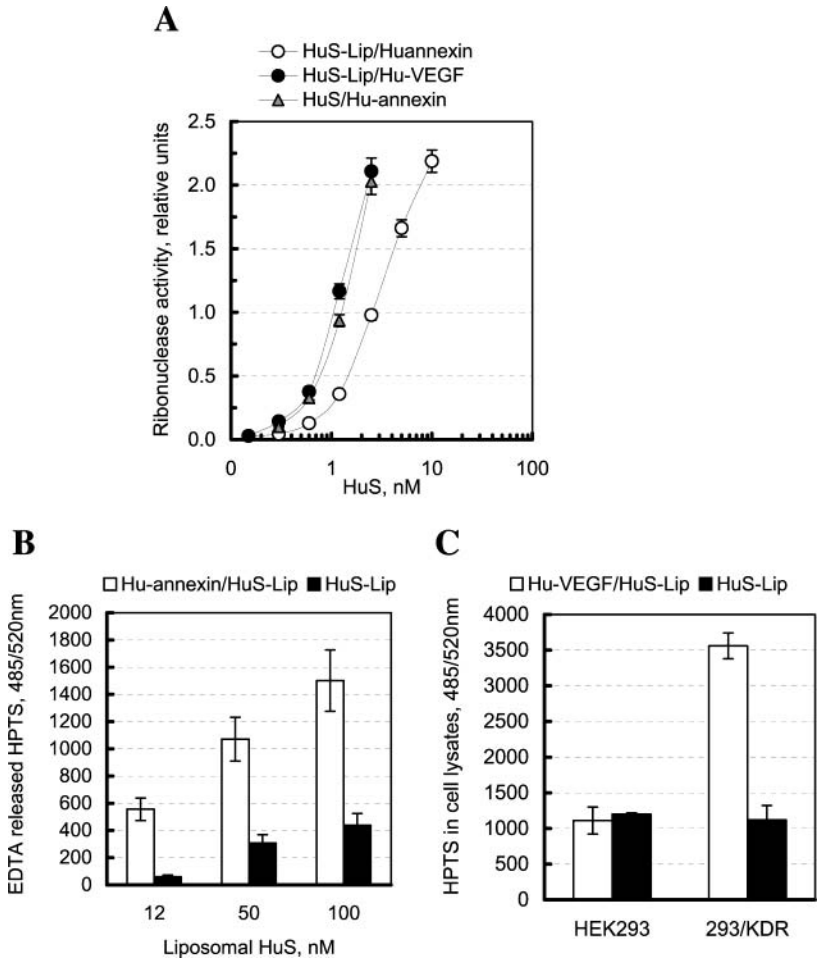


Figure 6. Targeted delivery of HiS−liposomes. Hu-tagged targeting proteins were mixed separately with HuS−liposomes at the liposomal HuS to Hu-tagged protein molar ratio of 1:1. For the liposome alone control (HuS−Lip), equal volumes of protein storage buffer were added to liposomes. All complexes were incubated on ice for 15 min and then added to cells. HPTS fluorescence was measured at λ_{ex} = 485 nm/λ_{em} = 520 nm. Liposome delivery experiments were done in duplicate and repeated twice. In panel A, Hu−annexin and Hu−VEGF bind HuS−liposomes with restoration of ribonuclease activity. In panel B, Hu−annexin-driven liposomes were added to erythrocytes in binding buffer at indicated liposomal HuS concentrations, incubated for 15 min at RT, and then spun down. The pellets were washed twice with binding buffer prior to resuspension in EDTA-containing buffer, then spun down again. HPTS fluorescence was measured in the supernatants. In panel C, Hu−VEGF-driven liposomes were added to starved HEK/293 and 293/KDR cells to final concentrations of 60 nM complex HuS/dimer VEGF. Cells were incubated 45 min at 4 °C and then moved to 37 °C to allow internalization of complexes. After 45 min at 37 °C, cells were washed twice with PBS and once with PBS containing 0.4 M NaCl and lysed in PBS with 1% NP-40. HPTS fluorescence was measured in the clarified cell lysates.

ACKNOWLEDGMENT

This work was supported by Grants DAMD17-03-C-0011 from Department of Defense and DE-FG02-02ER83520 from Department of Energy.

LITERATURE CITED

(1) Dubowchik, G. M, and Walker, M. A. (1999) Receptor-mediated and enzyme-dependent targeting of cytotoxic anticancer drugs. *Pharmacol. Ther. 83*, 67−123.

(2) Backer, M. V., Aloise, R., Przekop, K., Stoletov, K., and Backer, J. M. (2002) Molecular vehicles for targeted drug delivery. *Bioconjugate Chem. 13*, 462−467.

(3) Backer, M. V., Gaynutdinov, T. I., Gorshkova, I. I., Crouch, R. J., Hu, T., Aloise, R., Arab, M., Przekop, K., and Backer, J. B. (2003) Humanized docking system for assembly of targeting drug delivery complexes. *J. Controlled Release, 89*, 499−511.

(4) Blankenberg, F. G., Mandl, S., Cao, Y.-A., O'Connell-Rodwell, C., Contag, C., Mari, C., Gaynutdinov, T. I., Vanderheyden, J.-L., Backer, M. V., and Backer, J. M. (2004) Tumor imaging using a standardized radiolabeled adapter protein docked to vascular endothelial growth factor (VEGF). *J. Nucl. Med. 45*, 1373−1380.

(5) Gaynutdinov, T. I., Myshkin, E., Backer, J. M., and Backer, M. V. (2003) Chimeric ribonuclease as a source of human adapter protein for targeted drug delivery. *Prot. Eng. 16*, 771−775.

(6) Backer, M. V., Gaynutdinov, T. I., Aloise, R., Przekop, K., and Backer, J. (2002) Engineering S-protein fragments of bovine ribonuclease A for targeted drug delivery. *Protein Expression Purif. 26*, 455−461.

(7) Tait, J. F., Smith, C., and Gibson, D. F. (2002) Development of annexin V mutants suitable for labeling with Tc(I)-carbonyl complex. *Bioconjugate Chem. 13*, 1119−1123.

(8) Kuzmic, P. (1996) Program DYNAFIT for the analysis of enzyme kinetic data: Application to HIV proteinase. *Anal. Biochem. 237*, 260−273.

(9) Backer, M. V., and Backer, J. M. (2001) Functionally active VEGF fusion proteins. *Protein. Expression Purif. 23*, 1−7.

(10) Tait, J. F., Engelhardt, S., Smith, C., and Fujikawa, K. (1995) Pourokinase-annexin V chimeras. Construction, expression, and characterization of recombinant proteins. *J. Biol. Chem. 270*, 21594−21599.

(11) Pous, J., Mallorquí-Fernández, G., Peracaula, R., Terzyan, S. S., Futami, J., Tada, H., Yamada, H., Seno, M., de Llorens,

R., Gomis-Rüth, F. X., and Coll, M. (2001) Three-dimensional structure of human RNase 1 delta N7 at 1.9 Å resolution. *Acta Crystallogr., Sect. D.: Biol. Crystallogr. 57*, 498−505.

(12) Proba, K., Honneger, A., and Pluckthun, A. (1997) A natural antibody missing a cysteine in Vh: consequences in thermodynamic stability and folding. *J. Mol. Biol. 265*, 161−172.

(13) Huston, J. S., Levinson, D., Mudgett-Hunter, M., Tai, M. S., Novotný, J., Margolies, M. N., Ridge, R. J., Bruccoleri, R. E., Haber, E., and Crea, R. (1988) Protein engineering of antibody binding sites: recovery of specific activity in an anti-digoxin single-chain Fv analogue produced in *Escherichia coli*. *Proc. Natl. Acad. Sci. U.S.A. 85*, 5879−5883.

(14) Shan, D., Press, O. W., Tsu, T. T., Hayden, M. S., and Ledbetter, J. A. (1999) Characterization of scFv-Ig constructs generated from the anti-CD20 mAb 1F5 using linker peptides of varying lengths. *J. Immunol. 162*, 6589−6595.

(15) Feng, J., Xie, Z., Guo, N., and She, B. (2003) Design and assembly of anti-CD16 ScFv antibody with two different linker peptides. *J. Immunol. Methods 282*, 33−43.

(16) Leland, P. A., L. Schultz, W., Kim, B.-M., and Raines, R. T. (1998) Ribonuclease A variants with potent cytotoxic activity. *Proc. Natl. Acad. Sci. U.S.A. 95*, 10407−10412.

(17) Gaur, D., Swaminathan, S., and Batra, J. K. (2001) Interaction of Human Pancreatic Ribonuclease with Human Ribonuclease Inhibitor. *J. Biol. Chem. 276*, 24978−24984.

(18) Spragg, D. D., Alford, D. R., Greferath, R., Larsen, C. E., Lee, K.-D., Gurtner, G. C., Cybulsky, M. I., Tosi P. F., Nicolau, C., and Gimbrone, M. A., Jr. (1997) Immunotargeting of liposomes to activated vascular endothelial cells: A strategy for site-selective delivery in the cardiovascular system. *Proc. Natl. Acad. Sci. U.S.A. 94*, 8795−8800.

BC0499477

Synthesis and Characterization of a Photocleavable Cross-Linker and Its Application on Tunable Surface Modification and Protein Photodelivery

Funing Yan,[†,§] Liaohai Chen,*[,§] Qiling Tang,[†] and Rong Wang*[,†]

Illinois Institute of Technology, Chicago, Illinois 60616, and Argonne National Laboratory, Argonne, Illinois 60439. Received April 21, 2004; Revised Manuscript Received June 29, 2004

A heterobifunctional photocleavable cross-linker based on an *o*-nitrobenzyl ester moiety was synthesized. The cross-linker has *N*-hydroxysuccinimidyl and disulfide groups attached at each end and thus can anchor a protein to a gold-coated substrate surface. Steady-state spectroscopic studies suggest that the cross-linker undergoes a clean C−O fragmentation upon irradiation with a quantum yield of 0.1. Consequently, immobilized proteins (such as avidin or antibodies) on a substrate surface can be released efficiently (>95%) under UV irradiation (λ > 300 nm) without degrading the protein functionality. We also demonstrated protein delivery via bioconjugation of protein molecules to a gold-coated atomic-force microscope (AFM) tip. When the proteins are photoreleased from the AFM tip, they are delivered to the substrate surface as protein clusters of uniform size. This has been confirmed using both AFM and fluorescence microscopy. The application of bioconjugation in this study opens a new avenue for tunable surface modification and controllable protein delivery in studies of biological systems on the nanometer scale.

INTRODUCTION

Substrate surface modification with proteins is essential in bioassaying, bioengineering, and biotechnology (*1*). While many efforts are focused on the covalent linkage of proteins on a substrate surface (*2*, *3*), it is important to develop methods for detaching the anchored proteins from the substrate surface as desired. One of the practices commonly used to achieve this goal is the use of a reactive enzyme (*4*) to cleave the bond that holds the protein to the substrate surface. This approach may be cumbersome because it involves multiple steps and requires accommodation of enzyme working conditions. An alternative is to anchor proteins to a substrate surface using a photocleavable bond (*5*), so that the proteins can be detached by a photofragmentation reaction. Unlike the enzyme method, the photodetachment of proteins is clean and easy to carry out. No reagents are needed. More importantly, since light can be focused to a small spot (100−400 nm in diameter, depending on the diffraction limitation), the photofragmentation reaction can be achieved in a confined area, allowing detachment of proteins at a precise local position. Immobilization of proteins using a heterobifunctional and photoactivatable cross-linker will open new avenues for manipulating the attachment and detachment of biomolecules to a surface.

Among the photocleavable moieties used to cross-link proteins to a substrate surface, the *o*-nitrobenzyl group is popular due to unique properties that include stability under ambient light, clean cleavage upon exposure to UV irradiation, and fast fragmentation reactions (within nanoseconds) upon photoexcitation (*6*, *7*). This group has been used in myriad solid-phase synthesis, protein isolation, and protein purification experiments (*8*−*12*). In this paper, we report the development of a heterobifunctional photocleavable cross-linker that uses the *o*-nitrobenzyl ester moiety as a core. One terminal of the cross-linker, *N*-hydroxysuccinimidyl, allows a protein to be conjugated. The other terminal, a disulfide group, allows chemical bonding to a gold-coated substrate. The clean C−O photofragmentation was confirmed by our steady-state spectroscopic studies. Proteins (such as avidin or antibodies) anchored to a gold substrate surface by the cross-linker can be efficiently (>95%) photodetached under UV irradiation without degrading protein functions. We also demonstrated that proteins anchored to the AFM tip can be photodelivered to a substrate surface. As a complement to other protein delivery methods such as Dip-pen technology (*13*, *14*), the method developed in this paper allows for precise and controllable protein delivery.

EXPERIMENTAL SECTION

Materials. Reagent grade solvents were used without any purification unless specified; chemicals including 5-hydroxy-2-nitrobenzyl alcohol, 3,4-dihydro-2*H*-pyran, *p*-toluenesulfonic acid, *N*,*N*′-dicyclohexylcarbodiimide (DCC), thioctic acid, succinic anhydride, dimethyl aminopyridine (DMAP), N-hydroxy succinimide, and general organic solvents were purchased from the Sigma-Aldrich Chemical Co. (St. Louis, MO). THF was distilled before use. *N*-Succinimidyl 3-(2-pyridyldithio)propionate (SPDP) and Alexa Fluoro 488 biocytin were purchased from Molecular Probes, Inc. (Benertin, OR).

Synthesis of Photolabile Cross-Linker. *Synthesis of 4-Nitro-3-(tetrahydropyran-2-yloxymethyl)phenol (**2**).* Nitrobenzyl alcohol (3.4 g, 0.02 mol) and *p*-toluenesulfonic acid (0.02 g, 0.1 mmol) were dissolved in 30 mL of dried THF. Under N_2 protection, 2.7 mL of 3,4-dihydro-2*H*-pyran was added dropwise. After the reaction was refluxed for 10 h, THF was evaporated under vacuum. The residue was chromatographed on silica gel using ethyl acetate/*n*-hexane (1:4) and yielded a white crystal-

* Address correspondence to these authors. e-mail: lhchen@anl.gov or wangr@iit.edu.

[†] Illinois Institute of Technology.

[§] Argonne National Laboratory.

10.1021/bc049901d CCC: $27.50 © 2004 American Chemical Society
Published on Web 08/24/2004

line solid. Recrystallization in ethyl acetate/*n*-hexane (1:1) resulted in 4.3 g of **2** (yield 86%). Mp 141−143 °C, ^{1}H NMR (300 MHz, $CDCl_3$): δ 8.13 (d, 1H), 7.36 (d, 1H), 6.79 (d, 1H), 5.18 (m, 2H), 4.80 (t, 1H), 3.98 (m, 1H), 3.60 (m, 1H), 1.90 (m, 2H), 1.60 (m, 4H).

*Synthesis of 5-[1,2]-Dithiolan-3-ylpentanoic Acid 4-Nitro-3-(tetrahydropyran-2-yloxymethyl)phenyl Ester (**3**).* **2** (1.0 g, 4 mmol), thioctic acid (1.65 g, 8 mmol), and DCC (1.65 g, 8 mmol) were dissolved in 20 mL of dried THF. After the reaction was refluxed under N_2 protection for 12 h, the resulting suspension was filtered out and the THF was then evaporated under vacuum. The residue was chromatographed on silica gel using dichloromethane/*n*-hexane (5:1) to give 1.5 g of **3** (yield 85%). Yellow gel, ^{1}H NMR (300 MHz, $CDCl_3$): δ 8.16 (d, 1H), 7.53 (d, 1H), 7.18 (d, 1H), 5.00 (m, 2H), 4.76 (t, 1H), 3.85 (m, 1H), 3.57 (m, 2H), 3.11 (m, 2H), 2.60 (t, 2H), 2.42 (m, 1H), 1.92 (m, 1H), 1.90−1.50 (m, 12H).

*Synthesis of 5-Thioctic Acid 3-Hydroxymethyl-4-nitrophenyl Ester (**4**)* **3**. (2.2 g, 5 mmol) was dissolved in dilute hydrochloride H_2O/THF solution (0.2 M, 1:2 V/V) and stirred overnight at room temperature. Then the mixture was poured into ethyl acetate followed by washing three times with 1% aqueous $NaHCO_3$ solution. After normal workup, the organic phase was chromatographed on silica gel using dichloromethane to give 1.6 g of **4** (yield 90%). Yellow gel, ^{1}H NMR (300 MHz, $CDCl_3$): δ 8.20 (d, 1H), 7.58 (d, 1H), 7.20 (d, 1H), 5.01 (s, 2H), 3.60 (m, 1H), 3.18 (m, 2H), 2.61 (t, 2H), 2.40 (m, 1H), 1.78 (m, 4H), 1.58 (t, 2H).

*Synthesis of Succinic Acid Mono-[5-(5-[1,2]dithiolan-3-yl-pentanoyloxy)-2-nitrobenzyl] Ester (**5**).* **4** (0.7 g, 2 mmol), succinic anhydride (0.4 g, 4 mmol), and 4-dimethylaminopyridine (DMAP) (0.12 g, 1 mmol) were dissolved in 15 mL of dichloromethane and refluxed under N_2 protection for 10 h. The mixture was washed three times by distilled water followed by normal workup and chromatographed on silica gel using dichloromethane/methanol (9:1) to give 0.7 g of **5** (yield 75%). Yellow gel, ^{1}H NMR (300 MHz, $CDCl_3$): δ 8.20 (d, 1H), 7.39 (d, 1H), 7.21 (d, 1H), 5.59 (s, 2H), 3.60 (m, 1H), 3.18 (m, 2H), 2.72 (t, 2H), 2.61 (t, 2H), 2.45 (m, 1H), 1.97 (m, 1H), 1.78 (m, 4H), 1.58 (t, 2H).

*Synthesis of Succinic Acid Succinimidyl Ester 5-Thioyloxy-2-nitrobenzyl Ester (SSTN) (**6**).* **5** (0.9 g, 2 mmol), *N*-hydroxysuccinimide (0.35 g, 3 mmol), and DCC (0.4 g, 2 mmol) were dissolved in 20 mL of dichloromethane. After the reaction was refluxed under N_2 protection for 12 h, the resulting suspension was filtered out and dichloromethane was then evaporated under vacuum. The residue was chromatographed on silica gel using dichloromethane/methanol (9:1) to give a white solid and recrystallized by ethyl acetate/*n*-hexane (6/1) to give 0.7 g of **6** (yield 65%). Mp 85−87 °C, ^{1}H NMR (300 MHz, $CDCl_3$): δ 8.21 (d, 1H), 7.39 (d, 1H), 7.12 (d, 1H), 5.60 (s, 2H), 3.61 (m, 1H), 3.08 (m, 2H), 2.99 (t, 2H), 2.89 (t, 2H), 2.82 (t, 4H), 2.62 (t, 2H), 2.50 (m, 1H), 1.95 (m, 1H), 1.75 (m, 4H), 1.56 (m, 2H); ^{13}C NMR (500 MHz, $CDCl_3$): δ 24.34, 25.53, 25.53, 26.23, 28.62, 28.66, 34.03, 34.51, 38.50, 40.24, 56.24, 63.20, 121.71, 121.76, 126.96, 134.36, 144.12, 154.59, 167.57, 168.82, 168.82, 170.23, 170.92. Anal. Calcd: C 49.82, H 4.69, N 5.05, S 11.55, O 28.88, Found: C 50.05, H 4.69, N 5.17, S 11.08, O 28.82; MS (APCI): 589 (SSTN + Cl).

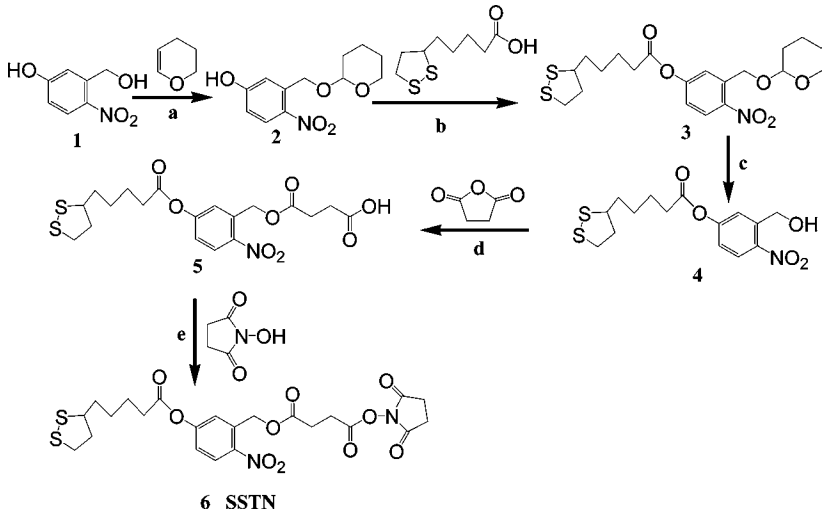
Instruments and Methods. TLC was performed with Analtech silica gel FG TLC plates (250 μm). Flash chromatography was carried out using Aldrich silica gel (60 mesh). ^{1}H NMR spectra were measured on a GE NMR-OMEGA (300 MHz), and ^{13}C NMR spectra were measured on a 500 MHz Bruker DMX. Elemental analysis was done by Atlantic Microlab Inc., Atlanta, GA. Mass spectra (GC/MS) were recorded at the University of Chicago.

A UV−vis absorption spectrometer was used to follow the changes in absorbance of SSTN fragmentation products during the photolysis. The UV−vis spectra were measured on a Hewlett-Packard 8453A diode-array spectrophotometer with a wavelength range from 190 to 1100 nm and a 1 nm bandwidth. The steady-state emission spectral measurements were carried out using 1 cm × 1 cm quartz cells in a PTI C60 spectrofluorimeter with a 75 W mercury lamp as an irradiation source. The detector was a thermoelectrically cooled photomultiplier. A right-angle configuration was used for emission and excitation. The protein-immobilized substrate was placed at an angle of 30° with respect to the excitation light in order to reduce the reflection of excitation light. The surface was covered with 30 μL of PBS during the measurement.

A multimode Nanoscope IIIa AFM (Digital Instruments, Santa Barbara, CA) was used to carry out and examine protein delivery. BSA or anti-human IgG antibody was immobilized on a gold-coated AFM tip via SSTN. The gold coating of the AFM cantilever was created using a thermal evaporator (Denton Vacuum, Moorestown, NJ). A gold-coated AFM tip (3 nm precoated titanium and 50 nm gold) was immersed in a 1.64×10^{-4} M SSTN solution in DMF at room temperature under nitrogen protection, generating a monolayer of SSTN on the tip via Au−S linkage, as routinely performed in the lab (*15*, *16*). After being thoroughly rinsed, the modified tip was immersed in a 10^{-6} M BSA or anti-human IgG antibody solution (in PBS buffer) overnight at room temperature under nitrogen protection. This allowed the chemical bonding of proteins onto the AFM tip. The unbound proteins were removed by thoroughly rinsing the tip in PBS and deionized water. For local functionalization of proteins at the tip end, we used an SSTN-modified AFM tip to approach a thin layer of protein solution on a mica surface. The approaching process was manually controlled using the positioner of the AFM setup and was carefully monitored using the optical microscope equipped with the AFM to allow only the tip end to contact the protein solution. After a 1-h incubation, the tip was withdrawn and thoroughly rinsed in PBS and deionized water to remove any unbound residue. A fluorescence microscope (Olympus IX-70) was used to confirm the local protein functionalization when a fluorescein-labeled anti-human IgG was employed. Photocontrollable protein delivery was performed on either a freshly cleaved mica microscope cover slide surface or a thoroughly cleaned glass microscope cover slide surface. AFM images were acquired in a contact mode using a triangular Si_3N_4 tip.

Photochemical Reactions. Photolysis was performed with a 3.6×10^{-4} M SSTN solution in CH_3CN using a quartz cuvette. The irradiation was carried out at room temperature using a 100 W high-pressure mercury lamp (Oriel Model 68700) with a UV 297 interference filter (Andover Corporation Optical Filter). Irradiation time-dependent photolysis was monitored by periodically taking the absorption spectra of SSTN to quantify the reaction quantum yield. To identify the photoreaction products, the sample was irradiated for 40 min. After the solvents were removed under vacuum, the residues were chromatographed on silica gel using chloroform to give yellow **7** in gel form (0.04 g, 60%). ^{1}H NMR (300 MHz, $CDCl_3$): δ 9.85 (s, 1H), 8.12 (d, 1H), 7.45 (d, 1H), 7.05 (d,

Scheme 1. Synthetic Scheme for Succinic Acid Succinimidyl Ester 5-Thioyloxy-2-nitrobenzyl Ester (SSTN)[a]



[a] Solvents and catalysts: (a) THF, *p*-toluenesulfonic acid, 86%; (b) THF, DCC, 85%; (c) 0.2 M HCl/H_2O/THF (1:2 v/v) rt, 90%; (d) CH_2Cl_2, DMAP, rt, 75%; (e) CH_2Cl_2, DCC, rt, 65%.

1H), 3.61 (m, 1H), 3.08 (m, 2H), 2.62 (t, 2H), 2.50 (m, 1H), 1.95 (m, 1H), 1.70 (m, 4H), 1.56 (m, 2H).

Actinometry and Quantum Yield Measurement. Potassium ferrioxalate actinometry was used as a reference to determine the incident light intensity (*17*). Potassium ferrioxalate was recrystallized from warm water in the dark and dried in a vacuum oven. The concentration of the ferrioxalate was 0.006 M in water. The photoreaction of potassium ferrioxalate was followed by UV−visible absorption. The amount of the product can be directly determined and then converted to determine the quantity of photons delivered (in Einstein). The quantum yield of the photoreaction of SSTN in acetonitrile can then be calculated using the following equation and the lamp flux value:

$$\varphi = \frac{\text{moles of product} \times C}{\text{lamp flux} \times \text{irradiation time (s)}}$$

The amount of product is determined by the absorbance change from UV−vis. C is a value that corrects the incomplete light absorption at the excitation wavelength. $C = 1/(1 - T)$, where T is the transmittance of SSTN before the irradiation.

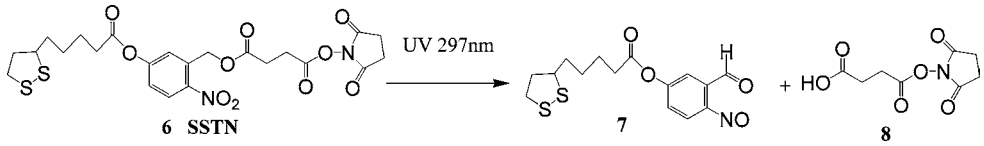
Photocleavable Protein Immobilization. A microscope cover slide (Fisher) was used as a substrate. After being cleaned with H_2O_2/H_2SO_4 solution, the slide was coated with a 100 nm layer of gold on top of 10 nm of precoated titanium. The gold-coated slides were then immersed into SSTN/CH_3CN solution (3.6×10^{-4} M) overnight at room temperature under nitrogen protection (*5*). After being thoroughly rinsed using CH_3CN and then water, the substrates were then incubated in avidin solution (0.5 mg/mL in 0.1 M $NaHCO_3$, pH 8.5) for 4 h at room temperature. After being rinsed with PBS buffer, the avidin-immobilized substrates were immersed in an Alexa 488 biotin solution (2.56×10^{-4} M) for 1 h, followed by multiple rinsings of the substrate to remove any unbound biotin. The immobilization of avidin on the gold substrate surface was confirmed by the strong fluorescence of the coverslips (data not shown). To investigate the photocleavage of avidin from the substrate, emission spectra of the protein-functionalized surface after irradiation and thorough washing were recorded at 2-min intervals in PBS buffer solution. A control experiment was carried out by replacing SSTN with the conventional cross-linker succinimidyl 3-2(2-pyridyldithio)propionate (SPDP) under the same experimental conditions.

RESULTS AND DISCUSSION

Synthesis of Succinic Acid Succinimidyl Ester 5-Thioyloxy-2-nitrobenzyl Ester. The synthesis of succinic acid succinimidyl ester 5-thioyloxy-2-nitrobenzyl ester (SSTN, **6**) was achieved using 5-hydroxy-2-nitrobenzyl alcohol and thioctic acid (1,2-dithiolane-3-pentanoic acid) as starting materials (Scheme 1). The main challenge of this synthetic route was to selectively synthesize **4** without the competitive reactions of the two hydroxyl groups presented in **1** with thioctic acid. This was achieved using 3,4-dihydro-2*H*-pyran as the specific primary hydroxyl protection reagent. Since electrons on phenol oxygen are conjugated with π electrons and are strongly withdrawn by the nitro group, the electron density of the phenol group is much higher than that of the primary hydroxyl group. Therefore, the nucleophilic addition reaction in the first step should be highly selective toward the primary hydroxyl group when compared to the phenol group (*18*). In brief, the primary hydroxyl group of **1** was selectively protected by reacting with 3,4-dehydro-2*H*-pyran (*19, 20*) in the THF in the presence of *p*-toluenesulfonic as the catalyst (yield of 86%). Esterification of the phenol group with thioctic acid was carried out in THF using DCC as the catalyst and yielded nitrobenzyl thioctate derivative **3** (yield of 85%). Deprotection of the hydroxyl group was achieved in dilute hydrochloride H_2O/THF solution (0.2 M, 1:2 V/V), and then tetrahydropyran was removed to yield the primary hydroxyl group **4**, which further reacted with succinic anhydride in dichloromethane to yield 75% of hemisuccinic acid **5**. The final product was synthesized by esterifying **5** with *N*-hydroxysuccinimide in dichloromethane, using DCC as a catalyst with a yield of 65%. The overall yield was 32%. The structures of the final compound and the intermediate products were confirmed by ^{1}H NMR, ^{13}C NMR, mass spectrometry, and elemental analysis.

Photophysics and Photochemistry of the Cross-Linker. Steady-state spectroscopic studies revealed that SSTN contains a major absorption peak (n−σ*) at 274 nm. As with other nitro-aromatic molecules, SSTN has a very weak fluorescence peak at 427 nm. It has been established that α-substituted 2-nitrobenzyl photophore

Scheme 2. Photolysis of SSTN



can undergo a highly efficient and fast photofragmentation reaction (*21*). Indeed, upon irradiation ($\lambda = 297$ nm) of 7 mM of SSTN in deuterated chloroform, a thin-layer chromatograph experiment indicated that two major products were formed when visualized in an iodine chamber. To identify the photoreaction products, the reaction was followed using NMR spectroscopy. Benzyl hydrogen presented in SSTN exhibited a characteristic singlet peak at 5.60 ppm, which disappeared when the SSTN solution (3.6×10^{-4} M) was irradiated with 297 nm light. Another characteristic singlet peak centered at 9.85 ppm emerged as the photoreaction proceeded, suggesting a clean C−O bond cleavage and the formation of nitrosobenzaldehyde and succinic acid monosuccinimidyl ester. On the basis of TLC and NMR experimental results, we conclude that the reaction pathway is as shown in Scheme 2. The reaction scheme matches the reported reaction mechanism of the photolysis of other similar α-substituted 2-nitrobenzyl compounds (*21*).

The photofragmentation reaction can also be monitored using UV−vis absorption spectroscopy. As shown in Figure 1, the product nitrosobenzaldehyde **7** has a $\pi-\pi^*$ transition centered at 334 nm (the other product **8** has no absorption peak above 300 nm), 60 nm red-shifted when compared to the major absorption peak at 274 nm from the starting material. The occurrence of the photofragmentation reaction was made evident by the decrease of SSTN absorption at 274 nm and the increase of nitrosobenzaldehyde absorption at 334 nm.

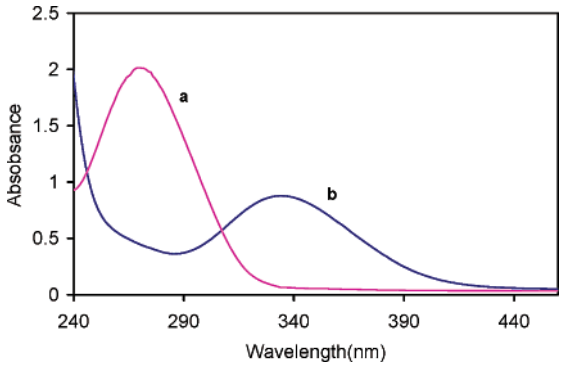


Figure 1. UV−vis spectra of **6** (3.0×10^{-4} M in acetonitrile) (a) and **7** (2.2×10^{-4} M in acetonitrile) (b).

Figure 2 demonstrates the absorption spectrum change of SSTN after the reaction solution (SSTN in acetonitrile, 9.0×10^{-5} M) was irradiated by 297 nm light for a short irradiation time (2-min interval). The insert of Figure 2 shows the absorption spectrum change of the SSTN solution (3.6×10^{-4} M) when irradiated for a longer time (30 min). The presence of an isosbestic point at 298 nm indicates a clean conversion from *o*-nitrobenzyl ester to nitrosobenzaldehyde. The progress of the reaction was followed quantitatively by noting the appearance of nitrosobenzaldehyde, as indicated by an absorption peak at 334 nm. A standard working curve for the absorption of pure nitrosobenzaldehyde as a function of concentration in the presence of the same concentration of starting material was used as a reference to quantify the product. The result of a control experiment, in which pure **7** in acetonitrile was irradiated using the same light source, suggests that **7** is very stable under the photoreaction conditions. Thus, the increase at 334 nm is correlated to the formation of **7**. After the photoflux using potassium ferrioxalate actinometry was determined, the quantum yield of the photoreaction with excitation at 297 nm was calculated to be 0.10 ± 0.04, comparable to the value reported in the literature (*22*). It was also found that the quantum efficiency remains the same in the degassed solvent; thus, oxygen most likely does not play any role in the photofragmentation reaction.

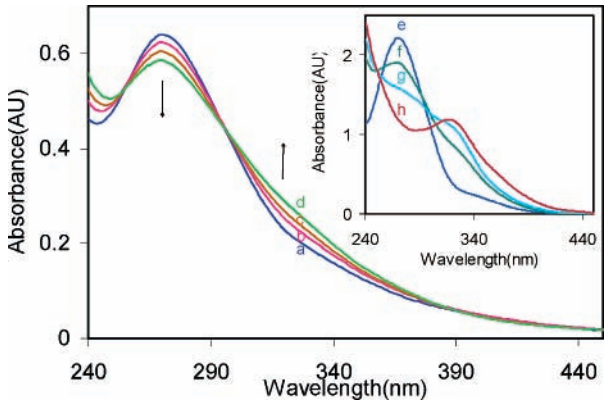


Figure 2. Absorption spectra of SSTN (9.0×10^{-5} M) under photolysis with shorter time interval. a: before irradiation; b: 2 min irradiation; c: 4 min irradiation; d: 6 min irradiation. Insert absorption spectra of SSTN (3.6×10^{-4} M) under photolysis with longer time interval. e: before irradiation; f: 18 min irradiation; g: 24 min irradiation; h: 30 min irradiation.

The mechanism of photolysis of *o*-nitrobenzyl alcohol derivatives (esters) involves a photoinduced intramolecular hydrogen abstraction and redox rearrangement that forms an *o*-quinonoid intermediate, followed by the release of the carboxylic acid and the formation of nitrosobenzaldehyde (*23*). Thus, the low quantum yield observed for the photoreaction is due to the low efficiency of the intramolecular hydrogen abstraction. Two approaches can be used to further increase photoefficiency: (1) introduce an additional *o*-nitro group to improve the chances of hydrogen abstraction by the excited nitro group; (2) introduce an α substitute to the photophore to enhance the efficiency of hydrogen abstraction and thus increase the overall reaction efficiency. Both approaches involve more steps to synthesize the desired cross-linkers. These approaches will be explored in our future study.

Photocontrollable Protein Surface Modification. We used the biotin−avidin model system to demonstrate phototunable protein immobilization using the SSTN cross-linker. The extremely high affinity of the biotin molecule to avidin protein (association constant of 10^{15} M^{-1}) has been well documented in the literature (*24*). As illustrated in Figure 3a, a monolayer of SSTN was self-assembled onto a gold-coated glass slide (*25, 26*). Nonspecifically bound SSTN was extensively washed away. After 4 h of incubation of the modified surface with avidin, the proteins were conjugated on the surface by the reaction of the amine groups of lysines in the avidin

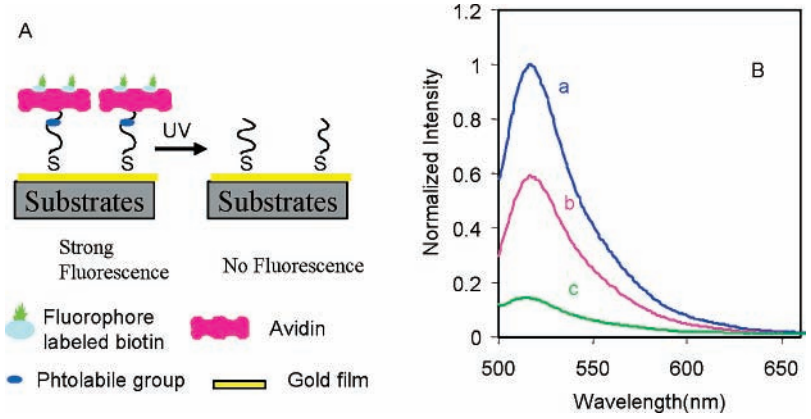


Figure 3. A. Scheme of photocontrollable protein immobilization. B. Fluorescence spectra of the substrates anchored with Alexa 488 biotin−avidin complex by photocleavable SSTN cross-linker, a: before irradiation; b: 2 min irradiation; c: 30 min irradiation.

with hydroxysuccinimidyl in the SSTN to form amide bonds. Again, any nonspecifically bound avidin was extensively washed away. As a control experiment, we also anchored avidin to a gold-coated substrate using succinimidyl 3-2(2-pyridyldithio)propionate (SPDP), a conventional cross-linker. Both substrates were then exposed to the Alexa-488-biotin solution (0.5 mg/mL) for 1 h, and unbound species were washed away with PBS buffer. Emission spectra of both substrates were recorded. The strong fluorescence at 520 nm indicated the formation of biotin−avidin complex on both substrates. Subsequently, both substrates were irradiated with UV light (297 nm) at 2-min intervals, followed by thorough washing steps (three times) before the recording of the fluorescence spectra of the substrates in the PBS buffer solution. Figure 3b demonstrates the changes to the normalized fluorescence intensities of the SSTN-immobilized substrate with different illumination times. The SSTN-immobilized surface lost its fluorescence almost completely after 30 min of UV irradiation. On the other hand, the fluorescence of the SPDP-immobilized surface decreased less than 10% after 30 min of UV irradiation and maintained this level with longer irradiation times (data not shown here).

Consistent with the result of photolysis of SSTN (shown in Figure 2), we conclude that the decrease of the fluorescence on the substrate is due to the break of the C−O bond of SSTN and the release of avidin−biotin-dye complex from the substrate to the solution. This is confirmed by the maintained, strong fluorescence on the SPDP-immobilized substrate even after long-term irradiation. Thus, we can establish that SSTN is an efficient photocleavable cross-linker that can be used to attach and detach protein molecules on a surface in a controllable fashion. Importantly, the 297 nm UV light does not alter the binding affinity between biotin and avidin, as demonstrated in the control experiment.

Photocontrollable Protein Delivery. Photocontrollable protein immobilization on an AFM tip provides an opportunity to deliver protein molecules to a desired location on a substrate. As shown in Figure 4a, we anchored BSA on a gold-coated silicon nitride cantilever using an SSTN cross-linker. The surface of the freshly cleaved mica was imaged using this tip in air contact mode. As shown in Figure 4b, the surface is flat and lacks any features. While the tip was maintained at the same location, UV irradiation (297 nm) was applied to the cantilever for 30 min. The same area of mica surface was then imaged by the same tip (image is shown in Figure 4c). Numerous particles with an average diameter of 50 ± 10 nm and average height of 4 ± 1 nm appeared on

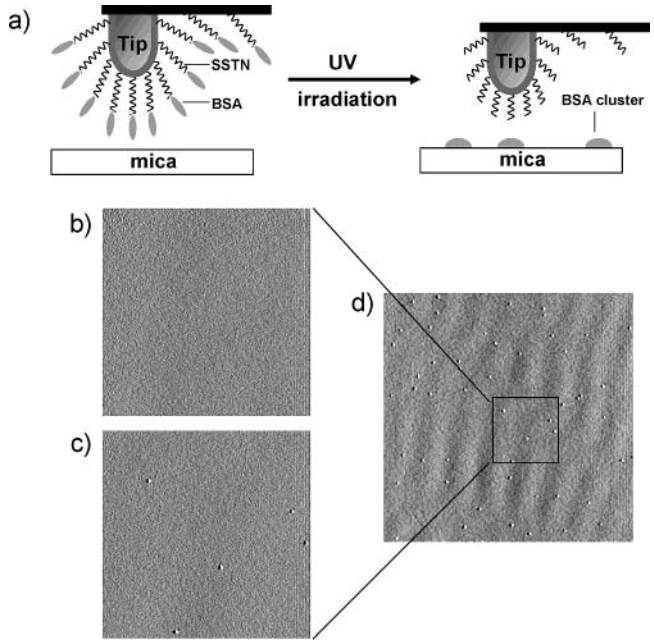


Figure 4. (a) Schematic illustration of AFM tip functionalization with BSA and photocleavage of BSA from the tip. (b) 5 μm × 5 μm contact mode image of newly cleaved mica surface before UV irradiation. (c) 5 μm × 5 μm image collected at the same region with the same tip right after UV irradiation for 1 h. (d) 18 μm × 18 μm image under the same conditions as c.

the surface. A larger scale image (Figure 4d) illustrates the distribution of the particles with uniform size. Note that the wavy parallel lines are result of optical interference due to the flatness of the mica surface and are not surface-relevant features. A control experiment was performed under the same conditions, except that UV irradiation was removed by keeping the sample in the dark for the same time period. In this case, a featureless mica surface was revealed using the AFM. This indicates the particles we observed in Figure 4c are BSA delivered from the AFM cantilever upon photocleavage of SSTN. BSA has an ellipsoidal structure with a short axis of 4 nm and a long axis of 14 nm. Thus, the particles appearing on the mica are clusters of single-layered BSA lying down on the substrate. Each cluster contains approximately 35−50 BSA molecules. High-resolution images indicated that there were no individual protein molecules present on the surface other than the clusters. To further confirm that the species dropped on the substrate are proteins, we used fluorescein (FITC)-labeled anti-human IgG antibody to repeat the experi-

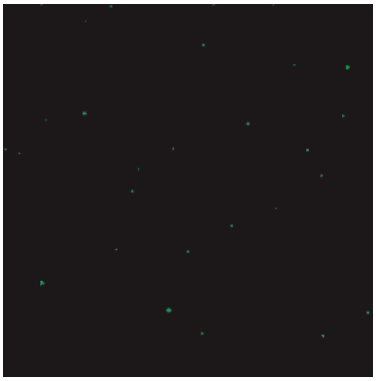


Figure 5. Fluorescence image of clusters of fluorescein-labeled anti-human IgG delivered from an AFM tip.

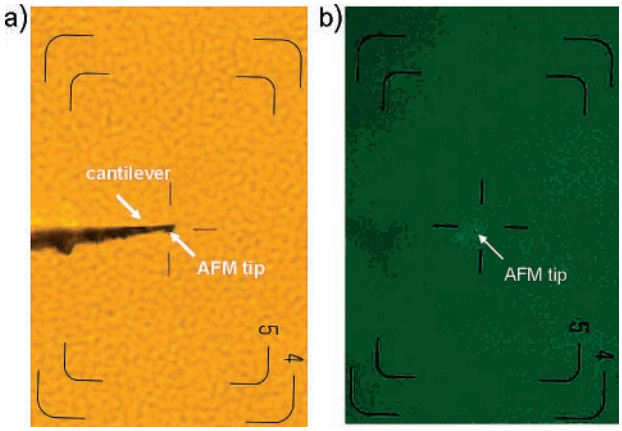


Figure 6. (a) Bright field image of an AFM tip; (b) fluorescence image of the AFM tip modified with FITC-labeled anti-IgG.

ment. Again, the AFM images showed that the antibody fell to the substrate as clusters with a uniform diameter of 70 ± 10 nm. Since the approximate size of intact IgG is 15 nm × 8 nm, each cluster may contain ~32−42 IgG molecules. Taking advantage of the fluorescein label of the antibody molecules, we were able to identify the protein clusters on the substrate using the fluorescence image, as shown in Figure 5.

It was a surprise to observe that proteins fell to the substrate as uniform clusters. We propose that after photocleavage, the proteins remain on the surface of the cantilever due to surface adhesion. Protein−protein attraction drives the proteins to accumulate and form clusters. When the proteins accumulate to a certain size, the gravity of the protein cluster is comparable to the adhesive force and the cluster falls to the substrate. A detailed mechanism is currently under investigation in our labs.

Because tip modification was achieved by incubating the cantilever in protein aqueous solution, proteins were immobilized on the entire cantilever (Figure 4a). When UV irradiation was applied, numerous protein clusters were delivered onto the surface. To accurately control the location of protein delivery, we modified protein molecules exclusively at the tip end. This was achieved by precisely controlling the tip to approach the protein solution, allowing only the tip end to contact the solution for incubation. The success of local tip modification was confirmed by examining the fluorescence image of a tip modified by fluorescein-labeled anti-human IgG antibody in this manner. Figure 6 shows the optical image (Figure 6a) and the fluorescence image (Figure 6b) of the AFM tip on its cantilever, achieved subsequently at the fixed tip position. Fluorescence was detected exclusively at the



Figure 7. Single BSA cluster delivered by AFM tip (4 μm × 4 μm).

tip end. After this tip was exposed to UV irradiation, a single protein cluster was observed at the position right underneath the tip, as shown in the AFM image (Figure 7) acquired using the same tip right after protein photocleavage. The conclusion is 2-fold: (1) proteins can be precisely delivered to a desired position; (2) an AFM tip can serve for both protein delivery and local imaging to examine the consequence of protein delivery.

A challenging task in bioscience is to directly monitor a protein function at local regions in their natural environment. This creates an urgent requirement for a general approach for delivering a ligand to a precise position, with a precise quantity. Our protein delivery approach employed UV light as a remote switch to control both timing and the position of protein delivery. To the best of our knowledge, this is the only approach that can offer the capability to deliver uniform small granules of proteins to a substrate. We also demonstrated that the same tip can be used after photocleavage to image the same local area, which is critical to achieving information on the nanometer scale. Using this approach, we expect to be able to deliver ligand clusters to a cell surface. Guided by the specific interaction via force mapping (*15*, *16*, *27*) using the ligand-functionalized tip, cell membrane receptors will be registered. The ligand will then be delivered to a receptor-rich area in order to in-situ monitor the living cell's localized response to the ligand−receptor binding on the nanometer scale. The feasibility has been demonstrated by our preliminary study in a model system involving the interaction between cholera toxin B oligomer (CTB) and its receptor ganglioside GM1. This approach will open an avenue for answering questions such as how individual ligand−receptor interactions trigger the cell signaling pathways in a living cell and why an inhibitor needs to be delivered to certain protein complexes in order to block protein activity.

CONCLUSION

A photocleavable cross-linker, succinic acid succinimidyl ester 5-thioyloxy-2-nitrobenzyl ester (SSTN), was synthesized in five steps using 5-hydroxy-2-nitrobenzyl-alcohol and thioctic acid (1,2-dithiolane-3-pentanoic acid) as starting materials. Upon photoexcitation, SSTN undergoes a fragmentation reaction to produce carboxylic acid and nitrosobenzaldehyde with a quantum yield of 0.1. SSTN can covalently anchor protein molecules to a gold-coated substrate, and those protein molecules can subsequently be efficiently (>95%) released under UV irradiation. By immobilizing the protein molecules on a gold-coated AFM tip, the protein molecules can be delivered as uniform clusters to the substrate via photolysis, and subsequently imaged at the same local region. Thus, this approach provides an important tool for tunable surface modification and precise protein delivery on the nanometer scale. We also expect that the results obtained in this study will lead to a new avenue

for generating protein patterns. In this case, the cross-linker will function as a "photoresister". When irradiation is applied to the protein-functionalized surface through a conventional photomask, as used in photolithography, the corresponding protein patterns can be easily generated.

ACKNOWLEDGMENT

F. Yan thanks the support from Kilpatrick fellowship of IIT. We also thank Dr. Brian Kay at Argonne National Laboratory for reviewing the manuscript and insightful comments. This work is supported by ANL LDRD and NSF (IBN-0103080).

LITERATURE CITED

(1) For review, Subrahmanyam, S., Piletsky, S. A., and Turner, A. P. F. (2002) Application of natural receptors in sensors and assays. *Anal. Chem. 74* (16), 3942−3951.

(2) Rao, S. V., Anderson, K. W., and Bachas, L. G. (1998) Oriented immobilization of proteins. *Mikrochim. Acta 128*, 127−143.

(3) Kindermann, M., George, N., Johnsson, N., and Johnsson, K. (2003) Covalent and Selective Immobilization of Fusion Proteins. *J. Am. Chem. Soc. 125* (26), 7810−7811.

(4) Cao, R., Gu, Z., Patterson, G. D., and Armitage, B. A. (2004) A recoverable enzymatic microgel based on biomolecular recognition. *J. Am. Chem. Soc. 126* (3), 726−727.

(5) For review, Dormán, G., and Prestwich, G. D. (2002) Using photolabile ligands in drug discovery and development. *Trends Biotechnol. 18*, 64−77.

(6) Smet, M., Liao, L. X., Dehaen, W., and Dominic, V. M. (2000) Photolabile dendrimers using *o*-nitrobenzyl ether linkages. *Org. Lett. 2* (4), 511−513.

(7) Sternson, S. M., and Schreiber, S. L. (1998) An acid- and base-stable *o*-nitrobenzyl photolabile linker for solid-phase organic synthesis. *Tetrahedron Lett. 39*, 7451−7454.

(8) Holmes, C. P., and Jones, D. G. (1995) Reagents for combinatorial organic synthesis: development of a new *o*-nitrobenzyl photolabile linker for solid phase synthesis. *J. Org. Chem. 60*, 2318−2319.

(9) Teague, S. (1996) Facile synthesis of a *o*-nitrobenzyl photolabile linker for combinatorial chemistry. *Tetrahedron Lett. 37* (32), 5751−5754.

(10) Rock, R. S., and Chan, S. I. (1996) Synthesis and photolysis properties of a photolabile linker based on 3′-methoxybenzoin. *J. Org. Chem. 61*, 1526−1529.

(11) Olejnik, J., Sonar, S., Krzymañsk-Olejnik, E., and Rothschild, K. J. (1995) Photocleavable biotin derivatives: A versatile approach for the isolation of biomolecules. *Proc. Natl. Acad. Sci. U.S.A. 92*, 7590−7594.

(12) Ottl, J., Gabriel, D., and Marriott, G. (1998) Preparation and photoactivation of caged fluorophores and caged proteins using a new class of heterobifunctional, photocleavable cross-linking reagents. *Bioconjugate Chem. 9* (2), 143−151.

(13) Rozhok, S., Piner, R., and Mirkin, C. A. (2003) Dip-pen nanolithography: what controls ink transport? *J. Phys. Chem. B. 107* (3), 751−757.

(14) Pena, D. J., Raphael, M. P., and Byers, J. M. (2003) "Dip-pen" nanolithography in registry with photolithography for biosensor development. *Langmuir 19* (21), 9028−9032.

(15) Wang, R., Vengasandra, S., and Yan, F. (2001) Probing the nature of cholera toxin b oligomer by the atomic force microscopy. *Chem. Lett. 11*, 1170−1171.

(16) Vengasandra, S., Sethumadhavan, G., Yan, F., and Wang, R. (2003) Studies on the protein-receptor interaction by atomic force microscopy. *Langmuir 19* (26), 10940−10946.

(17) Murov, S. L., Carmichael, I., and Hug, G. L. (1993) *Handbook of Photochemistry*, 2nd ed.,pp 298−305, Marcel Dekker Inc., New York.

(18) Smith, M. B., and March, J. (2001) *March's Advanced Organic Chemistry*, 5th ed.,pp 994-998, Wiley-Interscience, New York.

(19) Yu, J., Orfino, F. P., and Holdcroft, S. (2001) Structural order in conjugated organic films prepared by catalytic deprotection of self-assembled polymers. *Chem. Mater. 13*, 526−529.

(20) Yu, J., and Holdcroft, J. (2000) Solid-state thermolytic and catalytic reactions in functionalized regioregular polythiophenes. *Macromolecules 33*, 5073−5079.

(21) Pearson, A. J., and Roush, W. R. (1999) *Handbook of Reagents for Organic Synthesis: Activating Agents and Protecting Groups*, pp 287−289, John Wiley & Sons Ltd., New York.

(22) Houlihan, F. M., Shugard, A., Gooden, R., and Reichmanis, E. (1988) Nitrobenzyl ester chemistry for polymer processes involving chemical amplification. *Marcromolecules 21*, 2001−2006.

(23) Yip, R. W., Sharma, D. K., Giasson, R., and Gravel, D. (1985) Photochemistry of the *o*-nitrobenzyl system in solution: evidence for singlet-state intramolecular hydrogen abstraction. *J. Phy. Chem. 89*, 5328−5330.

(24) Laitinen, O. H., Marttila, A. T., Airenne, K. J., Kulik, T., Livnah, O., Bayer, E. A., Wilchek, M., and Kulomaa, M. S. (2001) Biotin Induces tetramerization of a recombinant monomeric avidin. *J. Biol. Chem. 276*, 8219−8224.

(25) Maya, L. (2000) Polymer-mediated assembly of gold nanoclusters. *Langmuir 16*, 9151−9154.

(26) Dong, Y., and Shannon, C. (2000) Heterogeneous immunosensing using antigen and antibody monolayers on gold surfaces with electrochemical and scanning probe detection. *Anal. Chem. 72*, 2371−2376.

(27) Gad, M., Itoh, A., and Ikai, A. (1997) Mapping cell wall polysaccharides of living microbial cells using atomic force microscopy. *Cell Biol. Int. 21*, 697−706.

(28) Chada, V. G. R., Malinowska, K., Menhart, N., and Wang, R. Identification of TrkA on living PC12 cells by the atomic force microscopy, *Biochim. Biophys. Acta*, submitted.

BC049901D

Reduction of Methemoglobin via Electron Transfer from Photoreduced Flavin: Restoration of O_2-Binding of Concentrated Hemoglobin Solution Coencapsulated in Phospholipid Vesicles

Hiromi Sakai, Yohei Masada, Hiroto Onuma, Shinji Takeoka, and Eishun Tsuchida*

Advanced Research Institute for Science and Engineering, Waseda University, Tokyo 169-8555, Japan. Received April 9, 2004; Revised Manuscript Received July 31, 2004

Ferric methemoglobin is reduced to its ferrous form by photoirradiation either by direct photoexcitation of the heme portion to induce electron transfer from the surrounding media (Sakai at al. (**2000**) *Biochemistry 39*, 14595−14602) or by an indirect electron transfer from a photochemically reduced electron mediator such as flavin. In this research, we studied the mechanism and optimal condition that facilitates photoreduction of flavin mononucleotide (FMN) to $FMNH_2$ by irradiation of visible light, and the succeeding reduction of concentrated metHb in phospholipid vesicles to restore its O_2 binding ability. Visible light irradiation (435 nm) of a metHb solution containing FMN and an electron donor such as EDTA showed a significantly fast reduction to ferrous Hb with a quantum yield (Φ) of 0.17, that is higher than the method of direct photoexcitation of heme ($\Phi = 0.006$). Electron transfer from a donor molecule to metHb via FMN was completed within 30 ns. Native-PAGE and IEF electrophoresis indicated no chemical modification of the surface of the reduced Hb. Coencapsulation of concentrated Hb solution (35 g/dL) and the FMN/EDTA system in vesicles covered with a phospholipid bilayer membrane (Hb-vesicles, HbV, diameter: 250 nm) facilitated the metHb photoreduction even under aerobic conditions, and the reduced HbV restored the reversible O_2 binding property. A concentrated HbV suspension ([Hb] = 8 g/dL) was sandwiched with two glass plates to form a liquid layer with the thickness of about 10 μm (close to capillary diameter in tissue, 5 μm), and visible light irradiation (221 mW/cm^2) completed 100% metHb photoreduction within 20 s. The photoreduced $FMNH_2$ reacted with O_2 to produce H_2O_2, which was detected by the fluorescence measurement of the reaction of H_2O_2 and *p*-nitrophenylacetic acid. However, the amount of H_2O_2 generated during the photoreduction of HbV was significantly reduced in comparison with the homogeneous Hb solution, indicating that the photoreduced $FMNH_2$ was effectively consumed during the metHb reduction in a highly concentrated condition inside the HbV nanoparticles.

INTRODUCTION

Photoinduced electron transfer is an essential reaction in biological systems especially during photosynthesis by the chlorophyll−protein complex (*1*). Hemoproteins such as hemoglobin (Hb) and myoglobin (Mb) are originally not related to the photoreaction in a biological system; however, photoexcitation and the resulting electron transfer reactions have been extensively studied (*2*−*6*). In our previous report, we clarified the mechanism of reduction of ferric methemoglobin (metHb) to its ferrous form by the direct excitation of the porphyrin N band in the UVA region (*7*). The reduction proceeds by charge transfer from the porphyrin ring to the central ferric iron to form the porphyrin π cation radical and ferrous iron by the N band excitation, and the contribution of the amino acid residues in the globin chain as an electron donor or an electron pathway. Another photochemical process to reduce metHb is an electron transfer from photochemically reduced flavin derivatives. The precise photoreduction mechanism of a flavin derivative to its reduced form has been extensively studied (*8*−*10*), and this has contributed to the understanding of the mechanism of the electron transfer of flavoproteins (*11*−*17*) and their function in the biological systems such as bacterial photosynthesis (*18*) and visual organs (*19*). Irrespective of the flavoproteins, the photoreduction of metMb and metHb by the externally added photoreduced form of the flavin mononucleotide (FMN) was first reported by Brwon and Synder (*20*) and Yubisui et al. (*21*, *22*), respectively.

We have paid special attention to the reduction of hemoproteins that will be applicable to Hb-based artificial red cells (*23*). We focus on the liposome-encapsulated Hb; a concentrated Hb solution is encapsulated in phospholipid vesicles to form Hb-vesicles (HbV)[1] with a particle size of about 250 nm (*24*, *25*). Ferrous state Hb binds oxygen to form HbO_2; however, it gradually converts to ferric metHb and superoxide anion and loses its oxygen binding property both in vivo and in vitro (*26*). A series of thiols was studied as a reductant for metHb,

* To whom correspondence should be addressed. Phone, +81-3-5286-3120; Fax, +81-3-3205-4740; e-mail, eishun@waseda.jp.

[1] Abbreviations: HbV, Hb-vesicles; FMN, flavin mononucleotide; SOD, superoxide dismutase; EDTA, ethylenediamine tetraacetic acid; DTPA, diethylenetriamine pentaacetic acid; IEF, isoelectric focusing; Native-PAGE, Native-polyacrylamide gel electrophoresis; PEG, poly(ethylene glycol); DPPC, 1,2-dipalmitoyl-*sn*-glycero-3-phosphatidylcholine; DHSG, 1,5-*O*-dihexadecyl-*N*-succinyl-L-glutamate; PEG-DSPE, 1,2-distearoyl-*sn*-glycero-3-phosphatidylethanolamine-*N*-PEG_{5000}; HbCO, carbonylhemoglobin; $[FMN]_{in}$, concentration of FMN in HbV; $[EDTA]_{in}$, concentration of EDTA in HbV; $[heme]_{in}$, concentration of heme in HbV; PHA, *p*-hydroxyphenylacetic acid; DBDA, 6,6′-dihydroxy-(1,1′-biphenyl)-3,3′-diacetic acid, FMN*, triplet FMN; $FMNH_2$, reduced form of FMN;

10.1021/bc049913z CCC: $27.50 © 2004 American Chemical Society
Published on Web 08/26/2004

which is coencapsulated in the vesicles (*27*, *28*). As a result, the functional half-life of the Hb-vesicles is doubled by coencapsulation of the DL-homocysteine and active oxygen scavengers (*27*, *29*). To retard metHb formation, bioconjugation of enzymes such as catalase or superoxide dismutase (SOD) (*30*) and coencapsulation of RBC enzymes including the metHb reductase system, carbonic anhydrase, SOD, or catalase (*29*, *31*) have also been reported.

To restore the O_2 binding property of HbV, we tested utilization of the photoreduction system: the indirect excitation of an externally added electron mediator (*32*), or the direct excitation of metHb absorption in the UV region (*7*). In this study, we have made significant efforts to find out a condition that facilitates metHb reduction by a photoreduced flavin mononucleotide (FMN), because this system was well characterized by Everse (*32*), and the advantages of this system are visible light irradiation and high quantum yield (*9*, *10*). We analyzed the influence of electron donors to FMN, dissolved gases, etc., to find the facilitating condition and elucidate the mechanism for the facilitation of the metHb photoreduction in the HbV nanoparticles, a structure similar to that in red blood cells (RBCs), and this may also help understand the underlying mechanism of the reaction of NADPH-flavin reductase and metHb in RBCs.

EXPERIMENTAL PROCEDURES

Preparation of metHb. Carbonylhemoglobin (HbCO) was purified from outdated donated blood offered by the Hokkaido Red Cross Blood Center as previously reported (*33*, *34*). MetHb was prepared by reacting HbCO with an excess amount of potassium ferricyanide. The unreacted ions and ferrocyanide ions were removed twice by stirring with a mixed bed ion-exchange resin (Bio Rad AG 501-X8), and the solution was then permeated through 0.22 μm-filters (Advantec Co.). The metHb conversion was 99.8% measured by the cyanomethemoglobin method.

Chemicals. Amino acids (Met, Gln, Arg, Glu, Phe, Lys, Tyr, and Trp) were purchased from the Kanto Chem. Co (Tokyo). Peptides (Met-Met and Met-Gly) were from Sigma, and saccharides (mannitol, maltotriose, dextran, glucoseamine, glucron amide), methanol, citric acid sodium salt, ethylenediamine tetraacetic acid (EDTA), and diethylenetriamine pentaacetic acid (DTPA) were from the Kanto Chem. Co. All the chemicals were used without purification.

Photoreduction of FMN in the Presence of an Electron Donor. Three milliliters of phosphate-buffered saline (10 mM PBS, pH 7.4) with an electron donor (e.g., amino acids, peptides, sugars, as listed above, 20 mM) was sealed in a cuvette (2 mm width) with a butyl rubber cap. The solution was bubbled with N_2 for 30 min. A stock solution of FMN prepared in the dark was added at a concentration of 10 μM. The light source was a super high-pressure mercury lamp (USH-250D, 250W, Ushio Co., Tokyo) with a cutoff filter (L-42 and HA-50, Hoya Co., Tokyo) to obtain a single beam with the maximum wavelength of about 435 nm, which is close to λ_{max} of FMN (450 nm). The cuvette was located 2.5 cm away from the light source, and the light intensity was 221 mW/cm^2 that was measured with a power meter (PSV-3102, Gentec Co.). The conversion of the reduction, FMN to $FMNH_2$, was calculated from the reduction of absorbance at 450 nm, measured with an UV/vis spectrophotometer (V-560, Jasco, Tokyo).

Photoreduction of metHb in the Presence of FMN and an Electron Donor. Three milliliters of phosphate-buffered saline (10 mM PBS, pH 7.4) with an electron donor and FMN was sealed in a cuvette (2 mm width) with a butyl rubber cap. The solution was bubbled with N_2 gas for 30 min. A concentrated metHb stock solution deaerated by a gentle N_2 flowing in another bottle (about 3 mM, 10 μL) was injected into the cuvette. This procedure avoided bubbling of a metHb solution that might induce foaming and metHb denaturation. The final concentration of heme was 0.1 mM. The cuvette was exposed to the same visible light (435 nm) as described above. The conversion of the metHb reduction was calculated from the ratio of the Soret band absorption at 405 nm (λ_{max} of metHb) versus 430 nm (deoxyHb) or 415 nm (HbO_2).

A laser flash photolysis system (Tokyo Instr. Co.) was used for the transient spectrum measurement of the reduction of FMN and the succeeding metHb (*7*). The sample solutions were excited at 450 nm with a Pulsed Nd:YAG laser (SL803G-10, Spectron Laser Systems, Ltd.) equipped with an optical parametric oscillator. One irradiation time was 5−8 ns (fwhm) and the interval was 100 ms. A total of 100 accumulations were collected to get an acceptable signal-to-noise ratio. The transient spectra were recorded between 350 and 550 nm using a spectrophotometer (MS257, Oliel Instr. Co.) equipped with an ICCD detector (DH520−18F−WR, ANDOR Technol. Co.). A sample solution was placed in a 10 mm quartz cuvette and purged with N_2. The fastest time point of the measurements was 30 ns. A solution of FMN (100 μM)/Met (20 mM) in a 10 mM phosphate-buffered saline (pH 7.4), and a solution of FMN (5 μM)/Met (20 mM)/metHb ([heme] = 10 μM) in the phosphate-buffered saline were tested.

Quantum Yield Measurement. The ferroioxalate actinometer of $K_3[Fe(C_2O_4)_3]\cdot 3H_2O$ was used to measure the quantum yield (Φ) of metHb photoreduction (*7*, *35*, *36*). In the actinometer, Φ of the photoreduction of Fe^{3+} to Fe^{2+} was assumed to be 1.11 (*35*), and this value was used to calculate the total photons absorbed by the sample solution and Φ of the metHb photoreductions.

Isoelectric Focusing (IEF) and Native Polyacrylaminde Gel Electrophoresis (Native-PAGE). IEF and native-PAGE were performed on PhastGel IEF 3−9 (pH 3−9) and PhastGel Gradient 8−25 (PAGE content, 8−25%) (Amersham Pharmacia Biotech), respectively, with the PhastSystem (Pharmacia). The photoreduced Hbs in N_2 and air in the presence of FMN/EDTA was compared with metHb and the purified HbO_2.

IEF. Forty microliters of sample (1 mg/mL) per one lane was applied on the gel. This was focused and then stained with PhastGel Blue R (Coomassie brilliant blue) in the development unit of the PhastSystem. The marker was the p*I* calibration kit 3−10 (Pharmacia).

Native-PAGE. The samples were applied on the gel and the electrophoresis was automatically performed. The gel was stained with PhastGel Blue R. The marker was HMW Kit E (Parmacia).

Restoration of Oxygen Binding Property. The photoreduced deoxyHb solution ([heme] = 20 mM, [FMN] = 5 μM, [EDTA] = 10 mM) in an Ar atmosphere was bubbled with oxygen, and the UV/vis spectroscopy was measured. The photoreduced Hb solution was permeated through a column of Sephadex G-25 (Pharmacia) to remove FMN, the oxygen equilibrium curve of the obtained Hb solution was obtained at 37 °C with a Hemox Analyzer (TCS Products Inc.), and the oxygen affinity (P_{50}) and Hill number were measured. The Hb samples were diluted in a Hemox phosphate buffer (TCS Products Inc.).

Preparation of Hb-Vesicles Coencapsulating FMN and EDTA, and the Photoreduction of metHb. HbVs were prepared as previously reported (*24*, *34*, *37*). The purified HbO_2 solution (35 g/dL, [heme] = 21.7 mM) contained FMN (5, 10, or 50 mM) and EDTA (10, 20, 30, 50, or 200 mM), this was mixed with the lipid mixtures, and the resulting multilamellar vesicles were extruded through filters to regulate the vesicular size. The lipid bilayer was composed of a mixture of 1,2-dipalmitoyl-*sn*-glycero-3-phosphatidylcholine (DPPC), cholesterol, and 1,5-*O*-dihexadecyl-*N*-succinyl-L-glutamate (DHSG) at the molar ratio of 5/5/1 (Nippon Fine Chem. Co., Osaka), and 1,2-distearoyl-*sn*-glycero-3-phosphatidylethanolamine-*N*-PEG_{5000} (PEG-DSPE, NOF Co., Tokyo) (*38*). Thus the vesicular surface was covered with PEG chains. The molar composition of the DPPC/cholesterol/DHSG/PEG-DSPE was 5/5/1/0.033. HbVs were suspended in a physiologic salt solution at [Hb] = 10 g/dL. The suspension was incubated in the dark at 40 °C for 48 h to facilitate the metHb formation and to prepare metHbV. The concentrations of FMN, EDTA, and heme of Hb in HbV, expressed as $[FMN]_{in}$, $[EDTA]_{in}$, and $[heme]_{in}$, respectively, are assumed to be identical to the fed concentrations for the HbV preparation.

Photoreduction of metHbV was performed in the same manner with a metHb solution in a relatively diluted condition ([heme] = 10 μM) in a 2 mm quartz cuvette. At a higher concentration ([heme] = 5 mM) under aerobic condition, the suspension of metHbV was sandwiched between two glass plates. The optical path length was 10 μm.

Measurement of H_2O_2 in the metHb Photoreduction. The reaction of *p*-hydroxyphenyl acetic acid (PHA) and H_2O_2 to generate a fluorescent dimer, 6,6′-dihydroxy (1,1′-biphenyl)-3,3′-diacetic acid (DBDA), was used to detect H_2O_2 generated during the metHb photoreduction in the metHbV and metHb solutions. During the photoreduction of metHb or metHbV ([heme] = 20 μM in a cuvette) in the presence of FMN (5 μM)/EDTA (50 μM), 1 mL of sample was pipetted out and immediately mixed with horseradish peroxidase (Sigma, 3.7 μM), and PHA (5.8 mM). The mixture was ultracentrifuged in a tube with a filter (Cut off Mw. 30 kDa, Ultrafree, Amicon) at 12 000 rpm for 20 min to remove Hb or HbV and to obtain the filtrate solution. The fluorescence of the filtrate was measured with a fluorometer (JASCO, Ex: 317 nm, Em: 404 nm). The calibration curve was obtained by analysis of a diluted standard H_2O_2 solution (Kanto Chem., Co).

RESULTS

Photoreduction of FMN with an Electron Donor. Figure 1 shows the time course of the conversion of FMN to $FMNH_2$ by irradiation of visible light (435 nm). FMN primarily converts to the photoexcited triplet FMN* and this reacts with two electron donors (D) to generate $FMNH_2$. The reduction can be confirmed by the decrease in the absorption of the characteristics peaks at 370 and 450 nm. Without an addition of an electron donor, photoreduction gradually proceeds (baseline, initial reduction rate = 12 μM/min) (Table 1). A ribityl group in a FMN molecule of itself can be an electron donor. However, further irradiation should induce decomposition that was evident from the phenomena that the spectroscopic curves did not coincide at the isosbestic point. A significantly fast reduction was observed by the addition of EDTA and DTPA that were 88 and 84 times faster than the condition without the addition of an electron donor. Among the amino acids, Met showed the fastest

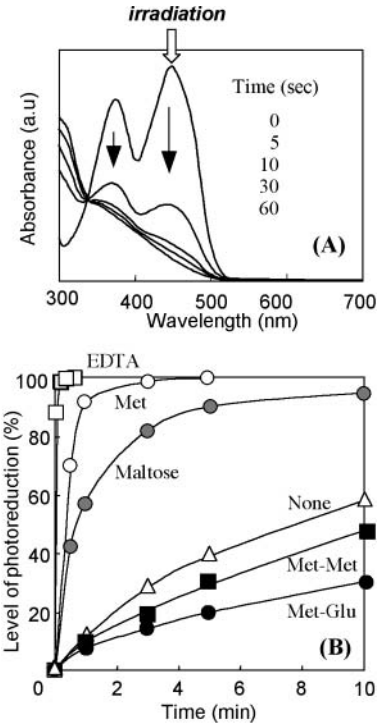


Figure 1. (A) Time course of the spectral changes during the conversion of FMN to $FMNH_2$ in the presence of EDTA (20 mM) by visible light irradiation (435 nm). The characteristic two peaks disappeared with the photoreduction conversion. (B) Time course of the conversion of FMN to $FMNH_2$ with various electron donors. EDTA and Met showed fast photoreduction rate. On the other hand, Met-Met and Met-Glu retarded the reaction. [FMN] = 100 μM, [electron donor] = 20 mM, pH = 7.4, in N_2 atmosphere.

Table 1. Initial Rates of the Photoreduction of FMN to $FMNH_2$ with Various Electron Donors (10 mM)

electron donor	mw	initial reduction rate (μM/min)	comparison with baseline
EDTA	292	1056	88
DTPA	393	1008	84
Met	149	140	11.7
Met-Met (10 mM)	280	5	0.2
Met-Met (20 mM)	280	10	0.8
Met-Glu	278	7	0.6
Arg	174	124	10.3
Phe	165	118	9.8
Lys	146	104	8.7
Gln	146	58	4.8
Glu	147	46	3.8
mannitol	182	45	3.8
maltotriose (10 unit mM)	504	47	3.9
dextran (10 unit mM)	5×10^6	45	3.6
glucoseamine	216	100	8.3
glucron amide	193	72	6.0
methanol	32	42	3.5
citric acid sodium salt	294	40	3.3
hydrogen	2	82	6.8
none (baseline)	- - -	12	1.0

reduction rate (140 μM/min, 12 times faster than the baseline), while Arg, Phe, Lys, Glu, and Gln showed moderate facilitation. On the other hand, Tyr and Trp showed slower rates of photoreduction. Unexpectedly, Met-Met and Met-Glu lowered the reduction rate. As for the saccharides, mannitol, maltotriose, dextran, glucosamine, and glucron amide showed similar facilitation at the same glucose units. However, they are much slower than Met and EDTA. The presence of H_2 gas

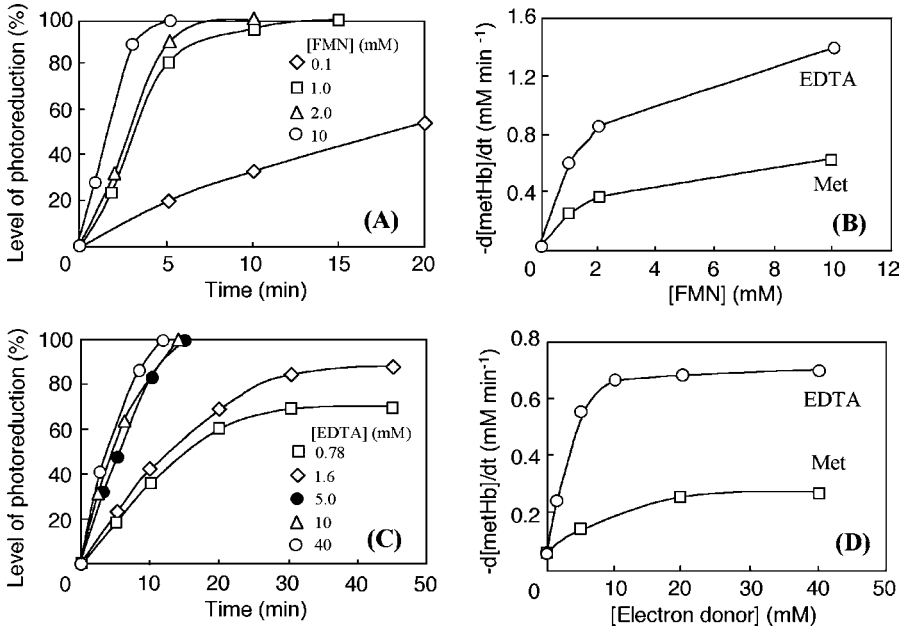


Figure 2. Influence of the concentrations of FMN and EDTA on the rate of metHb reduction. The time course of the level of photoreduction and the initial reaction rates are summarized. (A, B): Influence of the FMN concentration at a constant [EDTA] (20 mM). [FMN] was at 0.1, 1.0, 2.0, or 10 mM. (C, D): Influence of [EDTA] at the constant [FMN] (1.0 mM). [EDTA] was at 0.78, 1.6, 5.0, 10, or 40 mM. The data for the Met addition were inserted as a reference. [heme] = 3.1 mM.

slightly facilitated the reduction. Citric acid and methanol showed a slight facilitation. From these results, EDTA and Met were mainly studied as electron donors.

Reduction of metHb by the Photoreduced FMNH_2. The reduction of metHb by the photoreduced FMNH_2 was evident from the spectroscopic change of λ_{max} in the Soret and Q-bands. The influence of the concentration of FMN was examined at constant concentrations of metHb (5 g/dL, [heme] = 3.1 mM) and EDTA (20 mM) (Figure 2A). The presence of 100 μM FMN showed 50% reduction of metHb at 20 min; however, 1 mM FMN completed the reduction at 15 min. The influence of the EDTA concentration was examined at constant concentrations of metHb ([heme] = 3.1 mM) and FMN (1.0 mM) (Figure 2B). Without EDTA, the metHb photoreduction proceeded since a ribityl group of FMN and probably globin of Hb can be an electron donor. When the EDTA concentration was less than that of the heme concentration, the reduction rate was very slow, and the reduction could not be completed. However, 5 mM EDTA and higher showed a faster rate and the reduction was completed within 15 min. Similar results were obtained with Met; however, the initial rates were much slower than with EDTA.

The transient spectrum of the photoreduction of FMN in the presence of Met after laser flash irradiation showed the reduction of the absorbances at 445 and 373 nm at 30 ns, and the spectral profile was the same at 5 ms (data not shown here). Therefore, the photoreduction of FMN to FMNH_2 was completed within 30 ns. In the presence of metHb, a total of 30 ns was enough to observe the reduced deoxyHb (λ_{max} = 430 nm) and the spectrum was the same for 5 ms.

The influence of the presence of O_2 was examined (Figure 3). The metHb photoreduction in the presence of EDTA and FMN in the N_2 atmosphere completed the reduction within 15 min. The metHb photoreduction under the aerobic conditions became slightly slower, and the level of reduction reached 95% and then showed a plateau. In the case of the addition of Met, the reduction was completed within 40 min in the N_2 atmosphere that

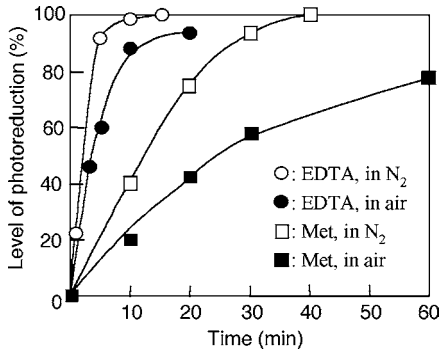


Figure 3. The influence of the presence of O_2 on the rate of photoreduction of metHb ([heme] = 3.1 mM) with FMN (1.0 mM) and an electron donor (20 mM) at pH 7.4. The data for Met addition (1.0 mM) were also inserted as a reference. The presence of O_2 retarded the metHb photoreduction.

was much slower in comparison with the EDTA addition. Under the aerobic condition, the reduction in the presence of Met was significantly slow and did not reach 80% at 60 min.

Native-PAGE of the photoreduced Hb both in the N_2 and aerobic atmospheres showed identical bands with the normal oxyHb and meHb (Figure 4A). Even though the Mw of Hb is 64.5 kDa, it showed a higher relative Mw than albumin (67 kDa) as one of the markers in the Native-PAGE in the absence of sodium dodecyl sulfate, SDS, because the surface charge of the protein directly affect on the traveling distance during the electrophoresis. IEF of the photoreduced Hbs showed the presence of HbO_2 at pI = 7.0 as a dense band and a weak band at pI = 7.2 of a partially reduced Hb (Figure 4B). There was no band at 7.4 that corresponds to metHb.

The oxygen dissociation curve of the photoreduced Hb was identical with that of the normal HbO_2 (Data not shown here). The P_{50} and Hill number of the photoreduced Hb were 10.5 Torr and 1.8, respectively, and they were almost identical with the normal HbO_2 (11 Torr and 1.7, respectively).

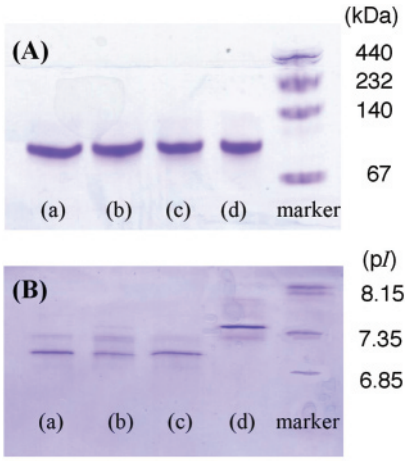


Figure 4. Native-PAGE (A) and IEF (B) of the photoreduced Hb in the presence of EDTA and FMN both in N_2 and aerobic atmospheres: (a) photoreduced Hb in N_2, (b) photoreduced Hb in air, (c) oxyHb, (d) metHb. In A, there was no change in the molecular weight of the Hb subunits. Since Native-PAGE does not include sodium dodecyl sulfate, the surface property of the protein directly affect on the traveling distance during electrophoresis. Therefore, Mw of Hb (Mw = 64.5 kDa) seemed much larger than albumin marker (Mw = 67 kDa). In B, the band at 7.4, which corresponded to metHb, almost disappeared in lanes a and b. No other bands were observed.

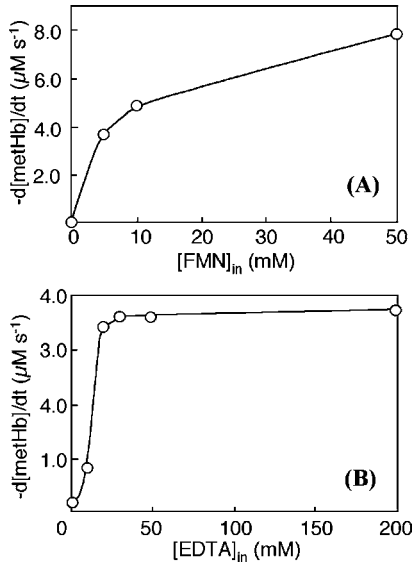


Figure 5. Influence of the concentrations of FMN and EDTA inside HbV on the initial rate of metHb reduction. (A) Influence of $[FMN]_{in}$ at the constant $[EDTA]_{in}$ = 20 mM. (B) Influence of $[EDTA]_{in}$ at the constant $[FMN]_{in}$ = 5 mM. [heme] = 10 μM in the cuvette, $[heme]_{in}$ = 21.7 mM. When $[EDTA]_{in}$ was higher than $[heme]_{in}$, the initial rate of metHb reduction was plateau.

Reduction of metHb in Hb-Vesicles. At first a diluted metHbV suspension ([heme] = 10 μM in a cuvette; $[heme]_{in}$ = 21.7 mM) was tested for photoreduction to analyze the kinetics. The initial rate of metHb reduction increased with increasing $[FMN]_{in}$ at a constant $[EDTA]_{in}$ (20 mM); however, the initial rate at $[FMN]_{in}$ = 10 mM was lower than twice that at $[FMN]_{in}$ = 5 mM (Figure 5A). At a constant $[FMN]_{in}$ (5 mM), increasing the $[EDTA]_{in}$ significantly facilitated the metHb photoreduction, however, the photoreduction rate did not increase above 20 mM (Figure 5B). This critical concentration is almost identical to $[heme]_{in}$ (21.7 mM). From these results, the rate-determining step of this system should be the electron transfer from an electron donor to the photoexcited FMN.

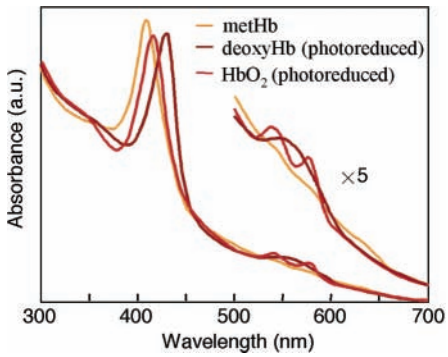


Figure 6. UV−visible spectra of HbV before irradiation (metHb), after photoreduction (deoxyHb), and its oxygenated form (HbO_2). $[EDTA]_{in}$ = 50 mM, $[FMN]_{in}$ = 5 mM, $[heme]_{in}$ = 21.7 mM. These spectra indicate the successful restoration of O_2-binding property of HbV.

The absorption spectra of the metHbV and the photoreduced HbV (λ_{max} = 430 nm) are shown in Figure 6. Due to the light scattering effect of the HbV particles, the turbidity was higher at a lower wavelength (*39*). Bubbling with an O_2 gas in a photoreduced HbV solution reversibly converted deoxyHb to HbO_2 with a characteristic shift of λ_{max} from 430 to 415 nm, indicating that the oxygen binding ability was successfully restored.

The concentration of [heme] in an HbV suspension for the intravenous infusion should be estimated to about 3−6 mM, which is significantly higher in comparison with 10 μM in a cuvette for the absorption spectral analysis. To test the photoreduction at a practical Hb concentration, a metHbV suspension ([heme] = 5.0 mM) was sandwiched between two glass plates and irradiated with visible light. The photoreduction proceeded quite promptly (Figure 7). Due to the thin liquid layer (ca. 10 μm in thickness), the effect of light scattering seen in Figure 6 is minimized. At the constant $[FMN]_{in}$ (5 mM) condition, the $[EDTA]_{in}$ of 10 and 20 mM were not enough to complete the reduction. At $[EDTA]_{in}$ = 50 mM, the photoreduction was significantly fast and the reaction was completed within 20 s with the characteristic λ_{max} of deoxyHb (430 nm). At $[FMN]_{in}$ = 100 mM and $[EDTA]_{in}$ = 20 mM, the initial reduction rate was the fastest; however, the reduction was not completed which was evident from the fact that the absorption at 430 nm in the Soret band was not high enough. The value of $[EDTA]_{in}$ should at least be higher than $[heme]_{in}$ (21.7 mM).

Quantum Yield of the Photoreduction Reactions. Table 2 summarizes the quantum yield, Φ, of various photoreduction conditions. The combination of metHb/FMN/EDTA showed the highest value (0.17) in an Ar atmosphere at [heme] = 0.1 mM. This was about 28 times higher than that for the photoreduction by the direct excitation of the N-band irradiating by near UV light (365 nm, Φ = 0.003−0.006) (*7*), and 4 times higher than the condition without an electron donor (0.04). In the case of HbV that coencapsulates FMN and EDTA, the concentrations of the components in the cuvette were much smaller, however, the concentrations in the nanoparticles (HbV) are much higher and the Φ for HbV was also very high (0.09−0.11). Probably due to the light scattering effect of HbV, Φ for HbV is slightly lower than that for the homogeneous Hb solution, but significantly higher than that for the N-band excitation (0.003−0.006).

Measurement of H_2O_2 in the metHb Photoreduction. Visible light irradiation to metHb([heme] = 20 μM)/FMN(5 μM)/EDTA(50 μM) under aerobic conditions

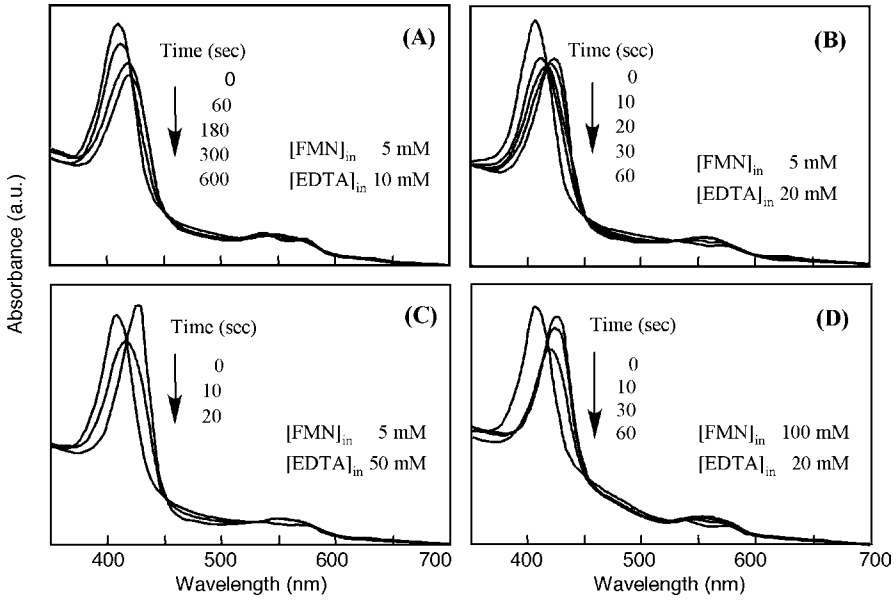


Figure 7. UV−visible spectral changes of HbV in a liquid layer sandwiched between two glass plates during photoreduction under aerobic conditions. The thickness of the layer was approximately 10 μm. Condition (C) ($[FMN]_{in} = 5$ mM, $[EDTA]_{in} = 50$ mM) showed the fastest rate of photoreduction, and the reaction was completed within 20 s. The arrows indicate the decrease in absorbance at 405 nm of MetHb with irradiation time.

Table 2. Quantum Yield (Φ) of Photoreduction of metHb and metHbV

	heme (mM)	FMN (mM)	electron donor (mM)	condition	λ_{ex} (nm)	Φ
metHb	0.1	0.01	EDTA (20)	in Ar	435	0.17
	0.1	0.01	Met (20)	in Ar	435	0.11
	0.1	0.01	no addition	in Ar	435	0.04
metHbV	0.01 (21.7)[a]	2.3×10^{-3} (5)[a]	EDTA (9.2×10^{-3}) (20)[a]	in Ar	435	0.09
	0.01 (21.7)[a]	46×10^{-3} (100)[a]	EDTA (9.2×10^{-3}) (20)[a]	in Ar	435	0.11
metHb	0.01	−	Trp (1.0)	in Ar	365	0.006[b]
	0.01	−	mannitol (100)	in CO	365	0.006[b]
	0.01	−	no addition	in CO	365	0.003[b]

[a] Concentrations of the components inside HbV; $[heme]_{in}$, $[FMN]_{in}$, $[EDTA]_{in}$. [b] Data from ref 7.

produced H_2O_2, and the fluorescent intensity of DBDA ($\lambda_{em} = 404$ nm) significantly increased (Figure 8a). The amount of H_2O_2 reached 40 μM at 120 s (Figure 8b). Irradiation to FMN alone produced 100 μM H_2O_2 for 120 s without any formation of $FMNH_2$. We confirmed that the irradiation to metHb alone did not produce H_2O_2 (data not shown here). The level of metHb photoreduction was less than 20% at 120 s (Figure 8c). A significant suppression of H_2O_2 generation was confirmed for the irradiation to metHbV and the H_2O_2 generation decreased to less than 20 μM, and the level of metHb photoreduction reached 50% at 120 s. A further increase in the level of photoreduction to 80% was confirmed when the partial oxygen pressure in the cuvette was regulated to 40 Torr; however, the amount of H_2O_2 could not be significantly reduced.

DISCUSSION

We found for the first time that the coencapsulation of concentrated Hb solution and the FMN/EDTA system in phospholipid vesicles (HbV) significantly facilitated the reduction of metHb by visible light irradiation (435 nm). This was evident from the Φ of the reaction, i.e., 0.17 for the Hb solution and 0.10 for the HbV suspension. The lowered Φ for HbV in comparison with that for a Hb solution is probably due to the light scattering of the illuminated visible light due to the particle of HbV (diameter, 250 nm) (*39*). However, they are much higher than that for the metHb photoreduction via direct photoexcitation of the N-band of the porphyrin ring in the UVA region (Φ = 0.006) (*7*). Even though the concentrations of the components in the cuvette were much lower for HbV than for the homogeneous Hb solution as shown in Table 2, the concentrations inside HbV were significantly higher and this condition facilitated the desired reactions (photoreduction of FMN and metHb) and suppressed the unwanted side reactions (generation of active oxygen species).

The reaction mechanism is that the photoexcited triplet FMN* rapidly receives an electron from the donor molecule, EDTA, to transform to the semiquinone followed by disproportionation to the two electron reduced form, $FMNH_2$. They are effective reducing agent to offer an electron to metHb. According to Yubisui et al., $FMNH_2$ reduces metHb with the rate constant of 5.5×10^6 M^{-1} s^{-1} (*22*), which is significantly faster than do glutathione (rate constant = 2.5×10^{-3} M^{-1} s^{-1}) (*27*) and ascorbic acid (3.0×10^{-3} M^{-1} s^{-1}) (*22*). The transient spectrum of the reduction of metHb by the photoreduced form of FMN demonstrated the completion of the reaction at 30 ns. Our result may be plausible because it is reported that a flavocytochrome showed complete photoreduction within 100 ns (*14*), measured by a laser flash-induced transient absorption difference spectra. The externally added FMN should more freely access to the protoporphyrin IX (heme) in the Hb molecule and would show a faster electron transfer. It is reported that the direct chemical conjugation of flavin to the propionic acid residue of heme significantly facilitates the electron transfer from flavin to heme in a reconstituted myoglobin (*40*, *41*). Therefore,

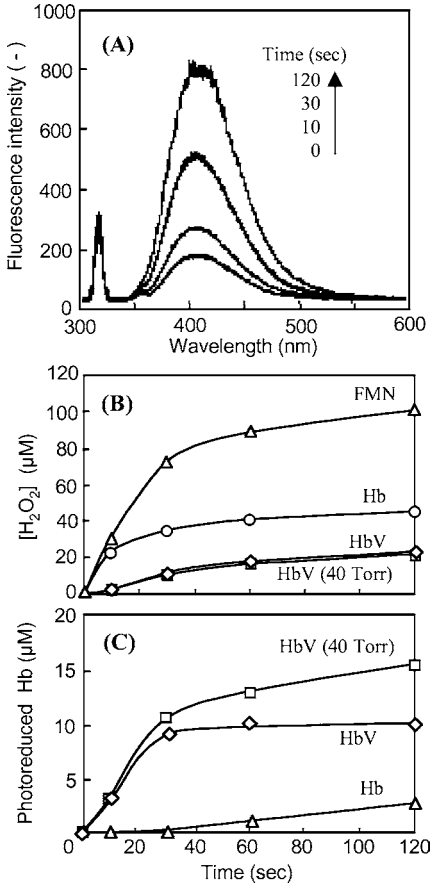


Figure 8. Detection of H_2O_2 using the fluorescence of DBDA during the photoreduction of Hb and HbV in the presence of FMN and EDTA. (A) An example of the fluorescence spectroscopy of the DBDA. The fluorescence intensity (λ_{em} = 404 nm) increased with time during the photoreduction of metHb solution under aerobic conditions (pO_2= 150 Torr). (B) Time course of the generation of H_2O_2 during the photoreduction of Hb and HbV under aerobic conditions (pO_2= 150 Torr), and HbV at pO_2 = 40 Torr. Irradiation to FMN alone was also tested as a reference (top curve) that produced 100 μM H_2O_2 for 120 s. Liberation of H_2O_2 from HbV was significantly suppressed in comparison with Hb solution. (C) The levels of metHb photoreduction during the measurement of H_2O_2 generation. The concentrations of heme (20 μM), FMN (5 μM), and EDTA (50 μM) in the cuvette were identical between the metHb solution and HbV suspension. For HbV, $[heme]_{in}$ = 21.6 mM, [FMN]in = 5 mM, and $[EDTA]_{in}$ = 50 mM.

two propionic acid groups of a heme that directly face the outer aqueous phase of an Hb molecule should contribute to the electron transfer from the externally added FMN to the heme.

The side reaction of $FMNH_2$ is the reaction with O_2 to generate singlet O_2 ($^1O_2$) or H_2O_2 (*11*, *42*), due to the low redox potential of reduced flavin (E_m = −209 mV). However, according to the quantitative measurement of H_2O_2, photoreduction of metHbV significantly reduced the side reaction in comparison with the metHb solution. This effect is due to the highly concentrated condition inside metHbV: the photoexcited FMN* readily reacts with EDTA to generate $FMNH_2$, and it also readily reacts with concentrated metHb inside the HbV nanoparticle. However, for the complete removal of H_2O_2, further coencapsulation of catalase would be effective (*29*) in the presence of O_2. Of course, in the absence of O_2, only the metHb reduction proceeds.

We tried to find other optimal electron donors instead of EDTA, because it has been reported that the oxidized and decomposed EDTA elements contain acetaldehyde that might react with the lysine residues on a protein molecule (*10*), and EDTA is a strong chelator of Ca^{2+} as an anticoagulant and may require caution when using a large dosage. We confirmed that Met was effective secondary to EDTA, as reported by other researchers (*9*, *32*). Arg was also effective, but it was not stable against oxidation during incubation under aerobic conditions at 37 °C for 3 days. Met was stable against oxidation. However, the small amino acid, Met (Mw = 149), gradually leaks out from the HbV across the phospholipid bilayer membrane (data not shown). To minimize the leakage of an electron donor, larger molecules, Met-Met and Met-Glu, were tested. Unexpectedly, they did not show any contribution as an electron donor and retarded the reduction of FMN. The ribityl phosphate group in the FMN molecule can be an electron donor, because the photoreduction of FMN proceeds without the addition of an electron donor. The retardation by the peptides should be probably due to some interaction of these peptides with the ribityl phosphate group that may hinder the electron transfer to the isoalloxazine ring. Other amino acids such as Phe and Lys, and saccharides such as mannitol or maltotoriose, are effective as an electron donor; however, their reduction rates of FMN were much lower in comparison with EDTA. Interestingly, methanol and gaseous H_2 also showed facilitation. DTPA, a structure similar to EDTA, showed an effectiveness comparable with EDTA. EDTA is a well-known electron donor, and its larger size (Mw = 292) and four negative charges prevent leakage from the vesicles. We could not find a more effective electron donor in our study, but confirmed that IEF and native-PAGE did not demonstrate any change in the chemical modification of the photoreduced Hb in the presence of EDTA/FMN, and the O_2 binding property was successfully restored. Therefore, we tested coencapsulation of FMN/EDTA in HbV for the other studies.

When HbV is intravenously infused for the substitution of blood, the concentrations of Hb and the heme of HbV in plasma should reach 5 g/dL and 3.1 mM, respectively, or higher (*43*). These are much higher than the experimental conditions in Figures 1−4, and it is impossible to test such a highly concentrated solution in a cuvette because of the strong light scattering by the particles and absorption by Hbs. We thus tested sandwiching the solution with two glass plates, thus making a thin liquid layer between the glass plates. The thickness of the liquid membrane is approximately 10 μm, about twice the capillary diameter in in vivo peripheral tissues. Irradiation of visible light onto the liquid membrane of HbV coencapsulating FMN and EDTA showed significantly fast rates for the metHb photoreduction. Especially, the coencapsulation of FMN (5 mM) and EDTA (50 mM) completed the metHb photoreduction within only 20 s. This significantly fast photoreduction system would be applicable to the transcutaneous irradiation of visible light to the body for the rejuvenation of HbV when the metHb content increased after the infusion of HbV.

In our study we established an efficient photoreduction system in a nanoparticle as shown in Figure 9. The illuminated visible light excites FMN to convert it to FMN*, and this reacts with an electron donor and transforms to $FMNH_2$, that subsequently reduces ferric metHb to its ferrous form. The reduced Hb can then reversibly bind O_2. Irrespective of the blood substitutes, one advantage of coencapsulation in a nanoparticle is that the concentrations of the components in the vesicles (nanoenvironment) are very high. Accordingly, the desired reactions are significantly accelerated and the

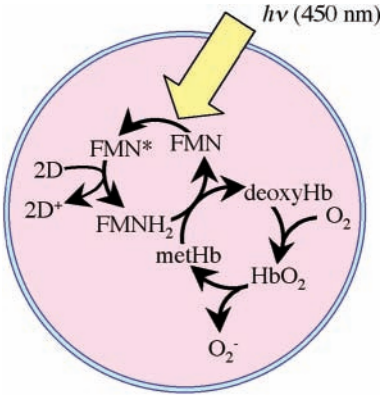


Figure 9. MetHb photoreduction system in a nanoparticle (HbV) using FMN and an electron donor (D), and recovery of the O_2-binding property.

unwanted side reaction is minimized in comparison with the homogeneous solution. To completely eliminate the side reaction of $FMNH_2$ and O_2, photoreduction under anaerobic conditions or coencapsulation of a radical scavenger, such as catalase, would be effective (*29*, *30*). RBC contains NADPH-flavin reductase to reduce metHb (*21*), and the reduced form of flavin is susceptible to react with O_2 as a side reaction. However, our results imply that the highly concentrated condition in RBCs and well-organized radical scavenging system should contribute to the effective metHb reduction in RBCs.

ACKNOWLEDGMENT

Supported by Health Sciences Research Grants (Research on Pharmaceutical and Medical Safety, Artificial Blood Project), the Ministry of Health and Welfare, Japan, 21 COE "Practical Nano-Chemistry" from MEXT, Japan, and Grants in Aid for Scientific Research from the Japan Society for the Promotion of Science (B16300162).

LITERATURE CITED

(1) Tracewell, C. A., Cua, A., Stewart, D. H., Bocian, D. F., and Brudvig, G. W. (2001) Characterization of carotenoid and chlorophyll photooxidation in photosystem II. *Biochemistry 40*, 193−203.

(2) Vorkink, W. P., and Cusanovivh, M. A. (1974) Photoreduction of horse heart cytochrome *c*. *Photochem. Photobiol. 19*, 205−215.

(3) Adar, F., and Yonetani, T. (1978) Resonance Raman spectra of cytochrome oxidase. Evidence for photoreduction by laser photons in resonance with the Soret band. *Biochim. Biophys. Acta 502*, 80−86.

(4) Kitagawa, T., and Nagai, K. (1979) Quaternary structure-induced photoreduction of haem of haemoglobin. *Nature 281*, 503−504.

(5) Kitagawa, T., Chihara, S., Fushitani, K., and Morimoto, H. (1984) Resonance Raman study of subunit assembly dependent photoreduction of heme of extracellular giant hemoglobin. *J. Am. Chem. Soc. 106*, 1860−1862.

(6) Pierre, J., Bazin, M., Debey, P., and Santus, P. (1982) One-electron photoreduction of bacterial cytochrome P-450 by ultraviolet light. *Eur. J. Biochem. 124*, 533−537.

(7) Sakai, H., Onuma, H., Umeyama, M., Takeoka, S., and Tsuchida E. (2000) Photoreduction of methemoglobin by irradiation in the near-ultraviolet region. *Biochemistry 39*, 14595−14602.

(8) McCormick, D. B., Koster, J. F., and Veeger, C. (1967) On the mechanism of photochemical reductions of FAD and FAD-dependent flavoproteins. *Eur. J. Biochem. 2*, 387−391.

(9) Heelis, P. F., Parsons, B. J., Phillips, G. O., and McKellar, J. F. (1979) The photoreduction of flavins by amino acids and EDTA. A continuous and flash photolysis study. *Photochem. Photobiol. 30*, 343−347.

(10) Traber, R., Kramer, H. E. A., and Hemmerich, P. (1982) Mechanism of light-induced reduction of biological redox centers by amino acids. A flash photolysis study of flavin photoreduction by ethylenediaminetetraacetate and nitrilotriacetate. *Biochemistry 21*, 1687−1693.

(11) Massey, V., Strickland, S., Mayhew, S. G., Howell, L. G., Engel, P. C., Matthews, R. G., Schuman, M., and Sullivan, P. A. (1969) The production of superoxide anion radicals in the reaction of reduced flavins and flavoproteins with molecular oxygen. *Biochem. Biophys. Res. Commun.* 36, 891−897.

(12) Massey, V., Stankovich, M., and Hemmerich, P. (1978) Light-mediaated reduction of flavoproteins with flavins as catalyst. *Biochemistry 17*, 1−8.

(13) Cusanovich, M. A., Meyer, T. E., and Tollin, G. (1985) Flavocytochrome *c*: Transient kinetics of photoreduction by flavin analogues. *Biochemistry 24*, 1281−1287.

(14) Sharp, R. E., Moser, C. C., Rabanal, F., and Dutton, P. L. (1998) Design, synthesis, and characterization of a photoactivatable flavocytochrome molecular maquette. *Proc. Natl. Acad. Sci. U.S.A.* 95, 10465−10470.

(15) Hazzard, J. T., Govindaraj, S., Poulos, T. L., and Tollin, G. (1997) Electron transfer between the FMN and heme domains of cytochrome P450 μ_B-3. *J. Biol. Chem. 272*, 7922−7926.

(16) Shumyantseva, V. V., Bulko, T. V., Schmid, R. D., and Archakov, A. I. (2002) Photochemical properties of a riboflavins/cytochrome P450 2B4 comples. *Biosensors Bioelecronics 17*, 233−238.

(17) Shumyantseva, V. V., Bulko, T. V., Schmid, R. D., and Archakov, A. I. (2000) Flavocytochrome P450 2B4 photoreduction. *Biophysics 45*, 982−987 (Translated from *Biofizika*).

(18) Masuda, S., and Bauer, C. E. (2002) AppA is a blue light photoreceptor that antirepresses photosynthesis gene expression in Rhodobacter sphaeroides. *Cell 110*, 613−623.

(19) Tsubota, K., Laing, R. A., and Kenyon, K. R. (1987) Noninvasive measurements of pyridine nucleotide and flavoprotein in the lens. *Invest. Ophthalmol. Vis. Sci. 28*, 785−789.

(20) Brown, W. D., and Synder, H. E. (1969) Nonenzymatic reduction and oxidation of myoglobin and hemoglobin by nicotinamide adenine dinucleotides and flavins. *J. Biol. Chem. 244*, 6702−6706.

(21) Yubisui, T., Takeshita, M., and Yoneyama, Y. (1980a) Reduction of methemoglobin through flavin at the physiological concetration by NADPH-flavin reductase of human erythrocytes. *J. Biochem. 87*, 1715−1720.

(22) Yubisui, T., Matsukawa, S., and Yoneyama, Y. (1980b) Stopped flow studies on the nonenzymatic reduction of methemoglobin by reduced flavin mononucleotide. *J. Biol. Chem. 255*, 11694−11697.

(23) Tsuchida, E. (1998) *Blood Substitutes: present and future perspectives* (Tsuchida, E., Ed.) Elsevier Science, New York.

(24) Takeoka, S., Ohgushi, T., Ohmori, T., Terase, T., and Tsuchida, E. (1996) Layer controlled hemoglobin vesicles by interaction of hemoglobin with phospholipid assembly. *Langmuir 12*, 1775−1779.

(25) Sakai, H., Takeoka, S., Park, S. I., Kose, T., Nishide, H., Izumi, Y., Yoshizu, A., Kobayashi, K., and Tsuchida, E. (1997) Surface modification of hemoglobin vesicles with poly(ethyleneglycol) and effects on aggregation, viscosity, and blood flow during 90% exchange transfusion in anesthetized rats. *Bioconjugate Chem. 8*, 23−30.

(26) Szebeni, J., Hauser, H., Eskelson, C. D., Watson, R. R., and Winterhalter, K. H. (1988) Interaction of hemoglobin derivatives with liposomes. Membrane cholesterol protects against the changes of hemoglobin. *Biochemistry 27*, 6425−6434,

(27) Takeoka, S., Sakai, H., Kose, T., Mano, Y., Seino, Y., Nishide, H., and Tsuchida, E. (1997) Methemoglobin formation in hemoglobin vesicles and reduction by encapsulated thiols. *Bioconjugate Chem. 8*, 539−544.

(28) Sakai, H., Tomiyama, K., Sou, K., Takeoka, S., and Tsuchida, E. (2000) Poly(ethyleneglycol)-conjugation and

deoxygenation enable long-term preservation of hemoglobin vesicles as oxygen carriers. *Bioconjugate Chem. 11*, 425−432
(29) Teramura, Y., Kanazawa, H., Sakai, H., Takeoka, S., and Tsuchida, E. (2003) The prolonged oxygen -carrying ability of Hb vesicles by coencapsulation of catalase in vivo. *Bioconjugate Chem. 14*, 1171−1176.
(30) D'Agnillo, F., and Chang, T. M. (1998) Polyhemoglobin-superoxide dismutase-catalase as a blood substitute with antioxidant properties. *Nat. Biotechnol. 16*, 667−71.
(31) Chang, T. M., Powanda, D., and Yu WP. (2003) Analysis of polyethylene-glycol-polylactide nano-dimension artificial red blood cells in maintaining systemic hemoglobin levels and prevention of methemoglobin formation. *Artif. Cells Blood Substitutes Immobilization Biotechnol. 31*, 231−47.
(32) Everse, J. (1994) Photochemical reduction of methemoglobin and methemoglobin derivatives. *Methods Enzymol. 231*, 524−536.
(33) Sakai, H., Takeoka, S., Yokohama, H., Seino, Y., Nishide, H., and Tsuchida, E. (1993) Purufication of concentrated Hb using organic solvent and heat treatment. *Protein Expression Purif. 4*, 563−569.
(34) Sakai, H., Yuasa, M., Onuma, H., Takeoka, S., and Tsuchida, E. (2000) Synthesis and physicochemical characterization of a series of hemoglobin-based oxygen carriers: objective comparison between cellular and acellular types. *Bioconjugate Chem. 11*, 56−64.
(35) Hatchard, C. G., and Parker, C. A. (1956) A new sensitive chemical actinometer II. Potasium ferrioxalate as a standard chemical actinometer. *Proc. R. Soc. London 235*, 518−536.
(36) Wegner, E. E., and Adamson, A. W. (1966) Photochemistry of complex ions. III. Absolute quantum yields for the photolysis of some aqueous chromium (III) complexes. Chemical actinometry in the long wavelength visible region. *J. Am. Chem. Soc. 88*, 394−404.
(37) Sou, K., Naito, Y., Endo, T., Takeoka, S., and Tsuchida, E. (2003) Effective encapsulation of proteins into size-controlled phospholipid vesicles using freeze−thawing and extrusion. *Biotechnol. Prog. 19*, 1547−1552.
(38) Sou, K., Endo, T., Takeoka, S., and Tsuchida, E. (2000) Poly(ethylene glycol)-modification of the phospholipid vesicles by using the spontaneous incorporation of poly(ethylene glycol)-lipid into the vesicles. *Bioconjugage Chem. 11*, 372−379.
(39) Sakai, H., Tomiyama, K., Masada, Y., Takeoka, S., Horinouchi, H., Kobayashi, K., and Tsuchida, E. (2003) Pretreatment of serum containing Hb-vesicels (oxygen carriers) to avoid interference in clinical laboratory tests. *Clin. Chem. Lab. Med. 41*, 222−231.
(40) Hamachi, I., Nomoto, K., Tanaka, S., Tajiri, Y., and Shinkai, S. (1994) Self-sufficient electron injection from NADH to the active center of flavin-pendant myoglobin. *Chem. Lett. 1994*, 1139−1142.
(41) Matsuo, T., Hayashi, T., and Hisaeda, Y. (2002) Reductive activation of dioxygen by a myoglobin reconstituted with a flavohemin.*J. Am. Chem. Soc. 124*, 11234−11235.
(42) Frati, E., Khatib, A., Front, P., Panasyuk, A., Aprile, F., and Mitrovic, D. R. (1997) Degradation of hyaluronic acid by photosensitized riboflavin in vitro. Modulation of the effect by transition metals, radical quenchers, and metal chelators. *Free Rad. Biol. Med. 22*, 1139−1144.
(43) Sakai, H., Horinouchi, H., Masada, Y., Yamamoto, M., Takeoka, S., Kobayashi, K., Tsuchida, E. (2004) Hemoglobin-vesicles suspended in recombinant human serum albumin for resuscitation from hemorrhagic shock in anesthetized rats. *Crit. Care Med. 32*, 539−545.

BC049913Z

Highly Efficient Technetium-99m Labeling Procedure Based on the Conjugation of *N*-[*N*-(3-Diphenylphosphinopropionyl)glycyl]cysteine Ligand with Poly(ethylene glycol)

Roberta Visentin,† Gianfranco Pasut, Francesco Maria Veronese,* and Ulderico Mazzi*

Department of Pharmaceutical Sciences, University of Padova, 35131 Padova, Italy. Received April 28, 2004; Revised Manuscript Received June 30, 2004

The PN_2S *N*-(*N*-(3-diphenylphosphinopropionyl)glycyl)cysteine ligand was conjugated to methoxy-poly(ethylene glycol)-amino (mPEG-NH_2) 5 and 20 kDa to yield PN_2S(Trt)-PEG_{5000} **1** and PN_2S(Trt)-PEG_{20000} **2**, and then detritylated to PN_2S-PEG_{5000} **4** and PN_2S-PEG_{20000} **5**. When an acidic solution of $^{99m}TcO_4^-$ is added to **4** or **5** in solid form, a quantitative yield in a single labeled species, ^{99m}Tc-labeled PN_2S-PEG_{5000} **9** and ^{99m}Tc-labeled PN_2S-PEG_{20000} **10**, respectively, is obtained. The reaction occurs in less than 15 min at room temperature for **4** and 35 °C for **5**. This labeling procedure avoids the use of an external reducing agent, and it is based on the amphiphilic properties of PN_2S-PEGs. Once in water, **4** and **5** self-assemble in micelles, which catalyze the metal reduction by means of an electron pair transfer from the phosphorus to technetium. The $[^{99m}TcO]^{3+}$ species is then coordinated, and at micelle level, both the (P)ON_2S and the PN_2S coordinations are possible, as demonstrated by reacting ^{99m}Tc-gluconate and $ReOCl_3(PPh_3)_2$ with **4** and **5** and with the oxidized analogous (P)ON_2S-PEG_{5000} **6**. Compounds **9** and **10** exhibited a high stability both in vitro and in vivo. Biodistribution studies in mice also indicated that PN_2S linking and ^{99m}Tc labeling do not modify PEG behavior in water and in vivo since the polymer dictates the fate of the conjugate.

INTRODUCTION

In the last decades, a large number of techniques have been developed to label biomolecules with ^{99m}technetium and $^{186/188}$rhenium (*1*, *2*). In the most popular approach, namely, the bifunctional approach, the radionuclide is bound to the targeting molecule by means of a bifunctional chelating agent (BFCA) (*3*, *4*). The BFCA comprises a donor atom set to strongly coordinate the radiometal and a functional group to be covalently attached to the targeting molecule, either directly or through a linker. Among the available BFCAs, *N*-(*N*-(3-diphenylphosphinopropionyl)glycyl)-*S*-tritylcysteine, bearing a PN_2S set, was previously labeled with ^{99m}Tc leading to the penta-coordinated $^{99m}TcO[PN_2S]-OH$ (*5*). The labeled compound exhibited high stability in human plasma and in vivo, although the biodistribution was characterized by high hepatobiliary excretion, due to the lipophilicity of the complex. This suggested the need for chemical modification of the ligand to achieve a pharmacokinetics that favors renal clearance.

Attempts to overcome the problems related to radiopharmaceutical in vivo behavior may include the use of polymeric linkers acting as pharmacokinetic modifiers. Among the available polymers, poly(ethylene glycol) (PEG) is the most successfully used in pharmaceutical science (*6*, *7*). Thanks to its unique characteristics, like absence of immunogenicity and toxicity and high solubility either in aqueous or in organic solvents, PEG is extensively used for conjugation to proteins, peptides, and small drugs. It is able to transfer its properties to the conjugated molecules, and the products usually become less antigenic, less immunogenic, and more soluble with respect to the parent molecules. PEGylation also prevents recognition by antibodies and degradation by proteolitic enzymes and decreases renal clearance of small water-soluble molecules, prolonging the half-life of biomolecules. More recently, it was demonstrated that PEG gives to drugs passive tumor targeting by enhanced permeability and retention (EPR) effect (*8*).

These considerations prompted us to synthesize a novel class of PEG conjugates bearing the PN_2S chelating agent (PN_2S-PEGs) and to investigate the coordination with ^{99m}technetium and cold rhenium. During this study, a new labeling method based on the amphiphilic character of PN_2S-PEGs and avoiding the use of an external reducing agent was discovered. In vivo studies are also reported to evaluate the change to the biodistribution of ^{99m}Tc-complex afforded by PEGylation.

EXPERIMENTAL SECTION

Materials. All chemicals were reagent grade and used without further purification. Amino acids and reagents were purchased from Novabiochem (Laufelfingen, Switzerland) and Fluka (Sigma-Aldrich, Milan, Italy); 3-diphenylphosphinopropionic acid succinimide ester was provided from Argus Spechem S.a.s. (Prato, Italy); mPEG-NH_2[1] (MW 5 and 20 kDa) were purchased from Nektar Co. (Huntsville, AL). Rhenium was purchased from Sigma-Aldrich (Milan, Italy) as $KReO_4$, and the precursor $ReOCl_3(PPh_3)_2$ was synthesized according to the literature procedure (*9*). The synthesis of the *N*-[*N*-(3-diphenylphosphinopropionyl)glycyl]-*S*-trityl-L-cysteine (PN_2S-(Trt)-OH) ligand was performed according to the previously reported procedure (*10*). The syntheses of ligands

* To whom correspondence should be addressed. Prof. U. Mazzi: Tel +39 049 827 5342; fax +39 049 827 5366; e-mail ulderico.mazzi@unipd.it. Prof. F. M. Veronese: Tel +39 049 827 5694; fax +39 049 827 5366; e-mail francesco.veronese@unipd.it.
† E-mail address: roberta.visentin@unipd.it.

10.1021/bc049896d CCC: $27.50 © 2004 American Chemical Society
Published on Web 08/19/2004

and complexes were carried out under an argon atmosphere using solvents degassed and tested for peroxides before use.

Solvents for syntheses and analysis and HPLC eluents were purchased from Fluka (Sigma-Aldrich, Milan, Italy) and Carlo Erba Reagenti (Div. Antibioticos, Milan, Italy); MilliQ water was obtained from a Millipore system (Millipore, Vimodrone, Milan, Italy). $CDCl_3$ for ^{1}H NMR, ^{13}C NMR, and ^{31}P NMR analysis was purchased from Sigma-Aldrich (Milan, Italy).

$Na^{99m}TcO_4$ was eluted from a commercial Drytec Sorin ^{99}Mo/^{99m}Tc generator (Nycomed Amersham Sorin, Saluggia, Vercelli, Italy). *Caution!* ^{99}Tc is a weak β^--emitter ($E = 0.292$ MeV, $t_{1/2} = 1.12 \times 10^5$ years). All manipulations were carried out in laboratories approved for low-level radioactivity use. Handling milligram amounts of ^{99}Tc does not present a serious health hazard since common laboratory glassware provides adequate shielding and all work is performed in approved and monitored hoods and gloveboxes. Bremsstrahlung is not a significant problem due to the low energy of the β^- particles; however, proper radiation safety procedures must be followed at all times, and particular care should be taken when handling solid samples.

Analytical Methods. ^{1}H NMR spectra were obtained on a Bruker 300 MHz spectrometer, and chemical shifts (ppm) were referenced to tetramethylsilane (TMS). ^{31}P NMR were recorded on a Bruker AC-200 spectrometer using 85% aqueous H_3PO_4 as external reference. Multiplicities were reported as s (singlet), d (doublet), dd (doublet of doublets), t (triplet), q (quadruplet), m (multiplet), and b (broad signal).

RP-HPLC analysis was performed on a LKB−Bromma system (Pharmacia, Cologno Monzese, Italy) comprising a binary LKB 2249 programmable gradient pumps controlled by a gradient controller 680 automated equipped with a LKB−Bromma 2140 tunable absorbance detector (Pharmacia, Cologno Monzese, Italy) set at 215 nm, a Beckman model 170 radioisotope detector system (Beckman, Milano, Italy), and a data module integrating recorder. The UV chromatograms were elaborated by using the WAVESCAN EG software (Pharmacia, Cologno Monzese, Italy), and the UV−RA (radioactive) chromatograms were elaborated by using the PE Nelson 900 series interface software (Pharmacia, Cologno Monzese, Italy). For analytical injections, a Hamilton PRP-1 column (4.1 mm × 250 mm, Alltech Italia, Sedriano, Milan, Italy) was used with a 20 μL injection loop and equipped with a Hamilton PRP-1 precolumn (Alltech Italia, Sedriano, Milan, Italy). The elution method consisted of a linear gradient (0−3 min, 20% solvent B; 3−28 min, 20−60% solvent B; 28−30 min, 60−100% solvent B; 30−33 100% solvent B; 33−35 min, 100−20% solvent B) using a mobile phase of 0.1% TFA in water (solvent A) and 0.05% TFA in MeCN (solvent B) at a flow rate of 1 mL min^{-1}.

Mass spectra were obtained on a Voyager-DE matrix-assisted laser desorption ionization time-of-flight (MALDI-TOF) mass spectrometry system (PerSeptive Biosystems Inc, Framingham, MA). Data for 2 ns pulses of the 337 nm nitrogen laser were averaged for each spectrum in a linear mode, and a positive ion TOF detection was performed using an accelerating voltage of 25 kV. Synapinic acid was used as matrix.

Labeling efficiency and radiochemical purity (RCP) were assessed by reverse-phase high-performance liquid chromatography (RP-HPLC) and thin-layer chromatography (TLC). The RP-HPLC peak of the labeled compound was recovered, and the activity of the collected fraction was measured with a dose calibrator M2361 Messelektronik (Dresden, Germany). RCP was expressed as the percent of injected activity. TLC was performed on Merck silica F_{254s} plates. Ten microliters of the sample was applied at the application point 1 cm from the bottom and eluted over a distance of 7 cm from the bottom. Plates were then cut 4 cm above the application point and the activity of each part was measured using the above-mentioned dose calibrator. The absence of free pertechnetate ($^{99m}TcO_4^-$) in ^{99m}Tc-gluconate solution was assessed using acetone as eluent ($^{99m}TcO_4^-$ $R_F = 1$; ^{99m}Tc-gluconate $R_F = 0$; ^{99m}Tc-colloid $R_F = 0$), whereas determination of reduced-hydrolyzed ^{99m}Tc (colloid) in the same solution was performed using saline (^{99m}Tc-gluconate $R_F = 0.9-1$; ^{99m}Tc-colloid $R_F = 0$). The percentage of colloid (C) was calculated with the following formula: $C = [(A_{Tot} - A_{gluc})/A_{Tot}] \times 100$. Radiochemical purity of ^{99m}Tc-labeled PEGylated compounds was determined by eluting the TLC with saline ($R_F = 0.5$) and calculated with the following formula: $RCP = [(A_{Tot} - A_{gluc})/A_{Tot}] \times 100 - C$. Alternatively, the absence of ^{99m}Tc colloid was verified by subsequent analysis of the labeling mixture via HPLC to ensure a quantitative elution of activity from the column.

PN_2S(Trt)-PEG_{5000} (1). To a chilled solution (4 °C) of PN_2S(Trt)-OH (198 mg, 0.30 mmol) in CH_2Cl_2 (10 mL) were added NHS (51 mg, 0.45 mmol) and DCC (185 mg, 0.90 mmol). The mixture was warmed to room temperature and stirred for 5 h under an argon atmosphere. Then $mPEG_{5000}-NH_2$ (1.00 g, 0.20 mmol) previously dissolved in CH_2Cl_2 (4 mL) and TEA (41 μL, 0.30 mmol) were added. The reaction was left to proceed for 10 h at room temperature. The mixture was then filtered, and the solution was dropped into EtOAc (150 mL) and cooled at 0 °C for 3 h. On cooling, the product precipitated, and the excess of PN_2S(Trt)-OH remained in solution. The product collected on a funnel was dried under vacuum and purified by recrystallization from EtOAc. Yield: 90% (1.01 g, 0.18 mmol). ^{1}H NMR ($CDCl_3$): 2.24−2.85 (m, $P(CH_2)_2$, Cys-βCH_2), 3.38 (s, OCH_3, PEG), 3.64 (bs, $(OCH_2CH_2)_n$, PEG), 4.25 (m, Cys-αCH), 7.24−7.52 (m, ArH). ^{31}P NMR ($CDCl_3$): −14.49. MALDI-TOF MS: bell-shaped spectrum centered at 5701 Da (theory 5642 Da). HPLC: $t_R = 24.73$ min.

PN_2S(Trt)-PEG_{20000} (2). The same procedure was followed as for the synthesis of compound **1**, except for the following changes: PN_2S(Trt)-OH (49 mg, 0.07 mmol); NHS (13 mg, 0.11 mmol); DCC (45 mg, 0.22 mmol); TEA (9 μL, 0.07 mmol); $mPEG_{20000}-NH_2$ (1.00 g, 0.05 mmol). Yield: 91% (0.94 g, 0.04 mmol).^{1}H NMR ($CDCl_3$): 2.32−2.87 (m, $P(CH_2)_2$, Cys-βCH_2), 3.42 (s, OCH_3, PEG), 3.71 (bs, $(OCH_2CH_2)_n$, PEG), 7.20−7.47 (m, ArH). ^{31}P NMR ($CDCl_3$): −14.74. MALDI-TOF MS: bell-shaped spectrum centered at 20 986 Da (theory 20 642 Da). HPLC: $t_R =$ 23.48 min.

(P)ON_2S(Trt)-PEG_{5000} (3). The procedure for the synthesis of compound **1** was followed, except for the following changes: (P)ON_2S(Trt)-OH (203 mg, 0.30 mmol).

[1] Abbreviations: CH_2Cl_2, dichloromethane; $CHCl_3$, chloroform; DCC, *N*,*N*′-dicyclohexylcarbodiimide; EtOAc, ethyl acetate; EtOH, ethanol; Et_2O, diethyl ether; $KReO_4$, potassium perrhenate; mPEG-NH_2, methoxy-PEG-amino; MeCN, acetonitrile; Na-gluconate, sodium gluconate; $mPEG_{5000}-NH_2$, methoxy-PEG-amino MW 5 kDa; $mPEG_{20000}-NH_2$, methoxy-PEG-amino MW 20 kDa; $Na^{99m}TcO_4^-$, sodium pertechnetate; PBS, phosphate buffer solution; NHS, *N*-hydroxysuccinimide; $ReOCl_3(PPh_3)_2$, *trans*-oxotrichloro bistriphenylphosphine rhenium(V); saline, physiological solution (0.9% NaCl); $SnCl_2$, tin(II) chloride; TEA, triethylamine; TFA, trifluoroacetic acid.

Yield: 94% (1.06 g, 0.18 mmol). ^{1}H NMR ($CDCl_3$): 2.48−2.90 (m, $P(CH_2)_2$, Cys-βCH_2), 3.37 (s, OCH_3, PEG), 3.68 (bs, $(OCH_2CH_2)_n$, PEG), 4.32 (m, Cys-αCH), 7.17−7.88 (m, ArH). ^{31}P NMR ($CDCl_3$): 33.46. MALDI-TOF MS: bell-shaped spectrum centered at 5700 Da (theory 5658 Da). HPLC: t_R = 24.75 min.

PN_2S-PEG_{5000} (4). Compound **1** (100 mg, 1.7×10^{-2} mmol) was dissolved in CH_2Cl_2 (1 mL) and TFA (7 mL). Triethylsilane was added until the solution became colorless, and the final mixture was stirred for 45 min. TFA was removed under vacuum, and the resulting residue was crystallized as a white powder upon addition of cold EtOAc. Yield: 92% (88 mg, 1.6×10^{-2} mmol). ^{1}H NMR ($CDCl_3$): 2.31−2.89 (m, $P(CH_2)_2$, Cys-βCH_2), 3.25 (s, OCH_3, PEG), 3.68 (bs, $(OCH_2CH_2)_n$, PEG), 4.56 (m, Cys-αCH), 7.38−7.64 (m, ArH). ^{31}P NMR ($CDCl_3$): −15.02. HPLC: t_R = 19.53 min.

PN_2S-PEG_{20000} (5). The procedure was followed as in the synthesis of compound **4**, except for the following changes: compound **2** (100 mg, 0.5×10^{-2} mmol); TFA (15 mL). Yield: 90% (89 mg, 0.4×10^{-2} mmol). ^{1}H NMR ($CDCl_3$): 2.27−2.78 (m, $P(CH_2)_2$, Cys-βCH_2), 3.36 (s, OCH_3 PEG), 3.72 (bs, $(OCH_2CH_2)_n$, PEG), 7.35−7.51 (m, ArH). ^{31}P NMR ($CDCl_3$): −14.91. HPLC: t_R = 20.02 min.

$(P)ON_2S-PEG_{5000}$ (6). The same procedure for the synthesis of compound **4** was followed, except for the following change: compound **3** (100 mg, 1.7×10^{-2} mmol). Yield: 89% (85 mg, 1.5×10^{-2} mmol). ^{31}P NMR ($CDCl_3$): 36.76. HPLC: t_R = 19.77 min.

$ReO[PN_2S]$-PEG_{5000} (7). To a solution of **4** (250 mg, 4.6×10^{-2} mmol) in degassed CH_2Cl_2 (5 mL) was added a solution of $ReOCl_3(PPh_3)_2$ (38 mg, 4.4×10^{-2} mmol) in the same solvent (3 mL). TEA was added to the mixture to pH 9, resulting in a reddish-brown solution. The final complex was crystallized by adding Et_2O to the solution previously concentrated under vacuum. HPLC: t_R = 21.34 min. UV−vis (nm, $CHCl_3$): 507. ^{1}H NMR ($CDCl_3$): 2.28−2.99 (m, $P(CH_2)_2$), 3.23 (s, OCH_3, PEG), 3.71 (bs, $(OCH_2CH_2)_n$, PEG), 4.30 (dd, ^3J = 11.1, Cys-βCH, anti isomer), 4.51 (d, ^3J = 20.4, Gly-CH, anti isomer), 4.71 (d, ^3J = 21.0, Gly-CH, syn isomer), 4.82 (d, ^3J = 20.4, Gly-CH, anti isomer), 4.88 (d, ^2J = 21.0, Gly-CH, syn isomer), 5.25 (d, Cys-αCH, anti isomer), 5.66 (dd, ^3J = 8.4, Cys-αCH, syn isomer), 7.40−7.74 (m, ArH).

$ReO[(P)ON_2S]$-PEG_{5000} (8). To a solution of **6** (50 mg, 0.9×10^{-2} mmol) in degassed CH_2Cl_2 (3 mL) was added a solution of $ReOCl_3(PPh_3)_2$ (7 mg, 0.9×10^{-2} mmol) in the same solvent (2 mL). TEA was added to the mixture to pH 7, resulting in an orange solution. The final complex was crystallized by adding Et_2O to the solution previously concentrated under vacuum.

^{99m}Tc-labeled PN_2S-PEG_{5000} (9). $^{99m}TcO_4^-$ solution freshly eluted from generator was acidified to pH 2 (0.1 M HCl). One hundred microliters of the solution (1−2 mCi) was added to compound **4** (2 mg, 3.7×10^{-4} mmol) in a 1.5 mL eppendorf vial, and the final mixture was kept at room temperature for 10−15 min. Labeling yield > 95%. HPLC: t_R = 21.19 min.

^{99m}Tc-labeled PN_2S-PEG_{20000} (10). The same procedure was followed as in the synthesis of compound **9**, except for the following changes: compound **5** (8 mg, 3.9×10^{-4} mmol); incubation at 37 °C for 10−15 min. Labeling yield > 95%. HPLC: t_R = 21.91 min.

^{99m}Tc-gluconate. ^{99m}Tc-gluconate was prepared by adding 100 μL of freshly eluted $^{99m}TcO_4^-$ (5−10 mCi) to 10 μL of 0.01 M Na-gluconate (saline) and 1 μL of 0.1 M $SnCl_2$ (0.1 M HCl). The product was purified by Sep-pak chromatography. HPLC: t_R = 2.05 min.

$^{99m}TcO[PN_2S]$-PEG_{5000} (11). To a sample of compound **4** (2 mg, 3.7×10^{-4} mmol) was added a solution of purified ^{99m}Tc-gluconate (50 μL, 1−2 mCi) diluted with absolute EtOH (250 μL). The pH was increased to 9−10 by addition of 0.1 M NaOH, and the mixture was kept at 37 °C for 45 min. Labeling yield > 95%. HPLC: t_R = 20.96.

$^{99m}TcO[PN_2S]$-PEG_{20000} (12). The labeling of compound **5** (8 mg, 3.9×10^{-4} mmol) was performed following the same procedure described for the synthesis of compound **11**. Labeling yield > 95%. HPLC: t_R = 21.45.

$^{99m}TcO[(P)ON_2S]$-PEG_{5000} (13). The labeling of compound **6** (2 mg, 3.7×10^{-4} mmol) was performed following the same procedure described for the synthesis of compound **11**. Labeling yield > 95%. HPLC: t_R = 20.67.

Light Scattering Measurements. The tendency of **4** and **5** to self-associate in micellar aggregates in aqueous solutions was evaluated by dynamic light scattering (DLS) experiments performed at 25 °C using a Nicomp 170 computing autocorrelator (Pacific Scientific, Silver Spring, MD) equipped with a Spectra Physics Stabilite 2017 (Spectra Physics, Mountain View, CA; polarized argon laser 496 nm). A solid sample of the compound was directly dissolved in PBS (pH 4, 7.4, and 10) or in saline (pH 2, 0.1 M HCl) to a final concentration of 20 mg/mL for **4** and 80 mg/mL for **5**. DLS analysis was also employed to assess the presence of micellar aggregates in the labeling mixtures containing compounds **9** and **10**.

Critical Micellar Concentration. Critical micellar concentration of **4** and **5** was evaluated by fluorescence experiments using pyrene as fluorescence probe following a literature procedure (*11*). An amount of PEGylated compound was added to a volumetric flask, and degassed saline (pH 2, 0.1 M HCl) was added to give a final concentration of 20.0 g/L. The solution was diluted to yield stock solutions at different conjugate concentrations from 20.0 to 0.05 g/L. A known amount of pyrene in acetone was added to each of a series of 10 mL volumetric flasks, and the acetone was removed by evaporation. The amount of pyrene was chosen to give a final concentration of 6×10^{-7} M, close to the saturation solubility of pyrene in water at 22 °C, or 1.2×10^{-7} M. To each flask, a stock solution (10 mL) of PEGylated compound was then added. The closed flasks were heated for 3 h at 65 °C to equilibrate pyrene and micelles and subsequently allowed to cool overnight in the dark at room temperature. For measurements, 3 mL of each solution was placed in a quartz cuvette, and the fluorescence (λ_{ex} = 339 nm) and excitation (λ_{em} = 390 nm) spectra were recorded on a Shimatzu RF-540 spectrofluorophotometer at 25 °C and accumulated with an integration time of 1s/0.5 nm.

Specific Activity Determination. To $^{99m}TcO_4^-$ solution freshly eluted from generator (100 μL, 1−2 mCi) was added a standard solution of $^{99}TcO_4^-$ (^{99}Tc is the carrier) in saline (9 μL). The final mixture was acidified to pH 2 (0.1 M HCl) and added to **4** (2 mg, 3.7×10^{-4} mmol) in a 1.5 mL eppendorf vial. The solution was kept at room temperature for 10−15 min. The experiment was performed using 3.95×10^{-2}, 3.95×10^{-3}, and 3.95×10^{-4} M $^{99}TcO_4^-$ solutions to have a ^{99}Tc/PN_2S-PEG_{5000} molar ratio of 1:1, 1:10, and 1:100. The specific activity was determined with the following formula: specific activity = A (MBq)/PN_2S-PEG_{5000} (μmol), where A is the activity when no free $^{99m}TcO_4^-$ is detectable in the labeling mixture assuming the whole Tc (^{99m}Tc and ^{99}Tc) present in the solution as ^{99m}Tc, since ^{99m}Tc and ^{99}Tc are chemically indistinguishable. The amount of generator eluate ^{99m}Tc being negligible, A can be calculated by using the following formula: $A = [(n_{Tc}N_{AV})/N_t] \times 37$, where n_{Tc} =

^{99}Tc moles, N_{AV} = Avogadro's number (6.022×10^{23}), N_t = number of ^{99m}Tc atoms that correspond to 1 mCi of activity (1.16×10^{12}), and 37 is the conversion factor between mCi and MBq (1 mCi = 37 MBq).

In Plasma Stability. The stability of **9** and **10** was evaluated in human plasma. Aliquots of the labeling mixture (30 μL, 500 μCi) were diluted with freshly prepared human plasma from healthy donors (250 μL) and incubated at 37 °C for various times (1, 2, 4, and 6 h). After incubation, protein fractions in the samples were precipitated with MeCN/EtOH (1/1, 50 μL) and centrifuged (4 °C, 6000 rpm). After repeated precipitation and centrifugation, the supernatant was analyzed by RP-HPLC. Data are expressed as percentage of activity corresponding to intact complex and are means ± SD of five experiments. The stability was assessed in the presence and in the absence of micelles. To reach a final concentration of **4** and **5** in the plasma sample under the critical micellar concentration, the labeling mixture was conveniently diluted before incubation.

In Vivo Biodistribution. Compounds **9** and **10** were studied in vivo. All animal experiments were carried out in accordance with national regulations. Male Swiss mice (25−28 g) were from our department. Animals were anaesthetized by intraperitoneal injection of 100 μL of a solution containing tiletamine hydrochloride/zolazepam hydrochloride (1/1, 40 mg/kg) and xilazine (2 mg/kg). The biodistribution was evaluated by intravenous administration of labeled compounds via the tail vein (n = 3). Before injection, the labeling mixture was neutralized (1 M NaOH) and diluted with saline to a final concentration in PEGylated compound of 5 and 20 mg/mL for **4** and **5**, respectively. The biodistribution was evaluated by administration of about 700 μCi/100 μL. Scintigraphic images were collected using a YAP-camera, a γ-camera optimized to perform experiments on small animals with a spatial resolution of 1.0−1.2 and a 40 × 40 mm^2 field of view (*12*). Acquisition of images started 5 min post-injection and images of 1 min were acquired for a total time of 40 min and 3 h after administration of **9** and **10**, respectively. Collected images were elaborated in 10 min images using the Scion Image program. After scintigraphic analysis, tissues and organs were excised from the sacrificed animals and weighed, and the radioactivity counts were determined with a dose calibrator. The blood was withdrawn from the heart through a syringe immediately after sacrifice and counted. Data are expressed as percentage of injected dose (% ID) and of injected dose per gram of tissue (% ID/g). The activity in whole blood was estimated assuming a blood volume of 6.5% of the total body weight.

RESULTS AND DISCUSSION

Synthesis of PEGylated Ligands. The PEGylation of the PN_2S(Trt)-OH ligand and of the oxidized analogous (P)ON_2S(Trt)-OH was achieved at the level of the cysteine carboxylic group, following DCC/NHS activation in dichloromethane to couple to mPEG-NH_2 5 and 20 kDa. PN_2S-(Trt)-PEG_{5000} **1**, PN_2S(Trt)-PEG_{20000} **2**, and (P)ON_2S(Trt)-PEG_{5000} **3** (Figure 1) were obtained in high yield (>90%).

The conjugates showed high solubility in water where both PN_2S(Trt)-OH and (P)ON_2S(Trt)-OH and detritylated derivatives were insoluble. The purity and the identity of the products were assessed by RP-HPLC, MALDI-TOF spectrometry, ^{1}H NMR, and ^{31}P NMR. Laser desorption mass spectrometry gave a bell-shaped spectrum centered at 5701 Da for **1**, at 20 986 Da for **2**, and at 5700 Da for **3** with a family of adjacent peaks at 44 ± 1 Da (the ethylene oxide unit) due to the polydispersity of PEG. The ^{31}P NMR spectra showed a singlet at −14.49 ppm for **1** and at −14.74 ppm for **2**, characteristic of a phosphine phosphorus, and at 33.46 ppm for **3**, confirming the presence of completely oxidized phosphorus. The ^{1}H NMR signals of the PN_2S or (P)ON_2S set protons were detectable despite the broadness of PEG methylene signal, the ligand proton resonances being upshielded or deshielded with respect to PEG chemical shifts. The RP-HPLC chromatogram, as revealed at 215 nm, showed a single homogeneous peak at 24.73, 23.48, and 24.75 min for **1**, **2** and **3**, respectively.

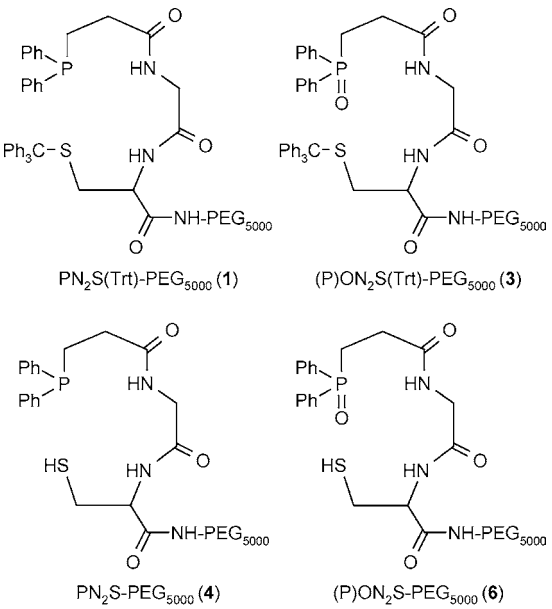


Figure 1. Structures of PEGylated PN_2S (**1**) and (P)ON_2S (**3**) ligands and structures of detritylated derivatives (**4** and **6**) used for ^{99m}Tc-labeling and Re-coordination studies.

To perform the complexation reactions with ^{99m}technetium and $^{185/187}$rhenium, the conjugates were detritylated with trifluoroacetic acid and triethylsilane (*13*) to yield PN_2S-PEG_{5000} **4**, PN_2S-PEG_{20000} **5**, and (P)ON_2S-PEG_{5000} **6**. The products were crystallized from degassed ethyl acetate to avoid the oxidation of phosphorus or the dimerization of cysteine. The purity of compounds was assessed by RP-HPLC, showing a single homogeneous peak at 19.49, 20.02, and 19.77 min for **4**, **5**, and **6**, respectively.

Direct Labeling of $PN_2S-PEGs$. The use of phosphine ligands as reducing agents for $^{99m}TcO_4^-$ is reported in the literature (*14*, *15*), but the reaction usually requires harsh conditions in terms of time and heating. Instead, it was observed that when an acidic solution of $^{99m}TcO_4^-$ (pH 2) is added to compound **4** or **5** in solid form, a quantitative yield in a single labeled species, **9** and **10**, respectively, is obtained, and the reaction occurs in less than 15 min at room temperature for **4** and 35 °C for **5**. The chromatograms depicted in Figure 2 are related to the labeling of **4** 10 min after TcO_4^- addition. The peak revealed by UV at 19.49 min, the same of **4** before labeling, indicates the stability of PEGylated PN_2S ligand under reaction conditions. The unique peak in the RA chromatogram at 21.19 min indicates the radiochemical purity of the labeled compound **9** and the absence of free $^{99m}TcO_4^-$ ($t_R \approx 3$ min). The higher retention time observed for **9** is in agreement with the increased lipophilicity of the labeled species due to metal coordination. Compound **9** is not assessable by UV detector since ^{99m}Tc concentration in the labeling mixture is in the range of picomoles.

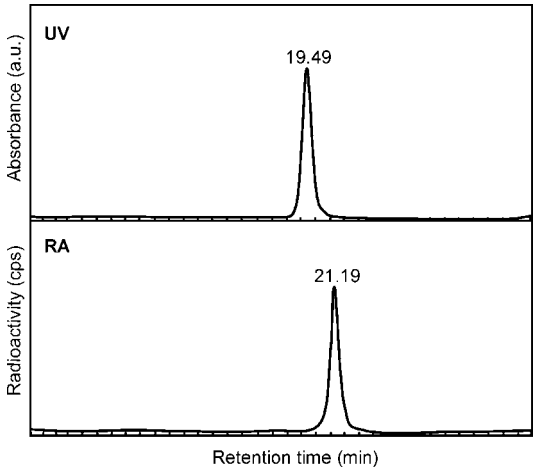


Figure 2. Direct labeling of PN_2S-PEG_{5000} **4**. RP-HPLC analysis of the labeling mixture 10 min after addition of TcO_4^- (pH 2) to solid **4** at room temperature is presented. The peak in the UV chromatogram is related to compound **4**. The RA chromatogram indicates the presence of a single labeled species **9** and the absence of free TcO_4^- ($t_R \approx 3$ min).

Table 1. Dynamic Light Scattering Analysis (25 °C, λ = 496 nm) of PN_2S-PEG_{5000} 4 (20 mg/mL) and PN_2S-PEG_{20000} 5 (80 mg/mL) in Saline (pH 2, 0.1 M HCl), PBS (pH 4, 7.4, and 10), and the Labeling Mixture (pH 2) Leading to ^{99m}Tc-Labeled PN_2S-PEG_{5000} 9 and ^{99m}Tc-Labeled PN_2S-PEG_{20000} 10, Respectively[a]

pH	**4**	**4**[b]	**5**	**5**[b]
2	316.7	125.7	2854.4	2057.3
4	325.2		3029.1	
7.4	318.8		2757.6	
10	391.6		2591.9	

[a] Values represent the mean diameter (nm) of micellar aggregates. [b] Labeling mixture.

Similar chromatograms were obtained when the direct labeling of compound **5** was performed.

It was observed that no labeling takes place if $^{99m}TcO_4^-$ is added to the unconjugated PN_2S-OH ligand or to a mixture of the ligand and mPEG-NH_2 non-covalently bound. Furthermore, the presence of phosphorus as phosphine and the integrity of the PN_2S set are essential, since the labeling does not occur when the conjugate is oxidized to **6** or dimerized through a disulfide bridge.

It was also found that the mixing conditions of TcO_4^- with the PEGylated ligand are very critical: the reaction is faster when the TcO_4^- solution is added to PN_2S-PEG in solid state than when the two reagents are solubilized separately and mixed. In this case, the labeling was still incomplete after 1 day.

A reasonable explanation of all these results is that the reduction and coordination of the metal take place thanks to a micellar catalysis due to self-aggregation of PN_2S-PEGs in water.

In fact, the conjugates have an amphiphilic character, the PN_2S moiety being highly lipophilic and the polymeric PEG chain being highly hydrophilic, and it is well-known that micelles can catalyze redox reactions (*16*). Light scattering measurements indicated that **4** and **5** effectively aggregate in water solutions to yield micelles (Table 1) with a cmc in the range 1−0.5 g/L. The cmc was determined in acidic saline to resemble the labeling reaction conditions using pyrene as a fluorescent probe in the presence of increasing concentrations of PN_2S-PEG conjugate (*11*). The characteristic feature of pyrene excitation spectra, namely, the (0,0) band shift from 334 to 337 nm upon probe partition into the inner core of micelles, was considered to be indicative of cmc achievement (Figure 3).

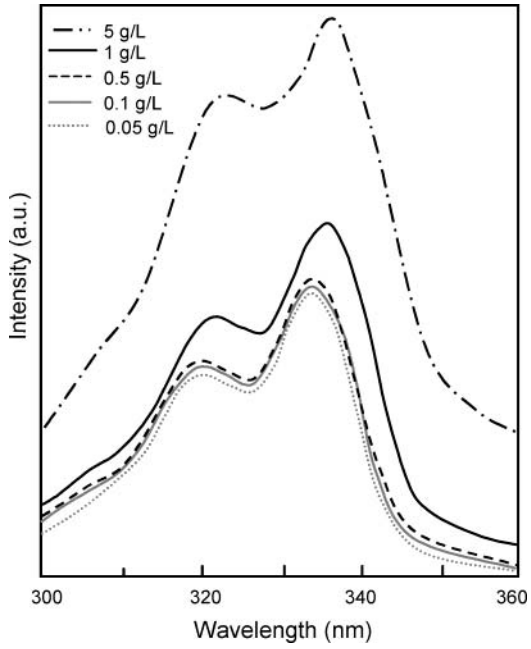


Figure 3. Determination of critical micellar concentration of PN_2S-PEG_{5000} **4** using physically entrapped pyrene as a fluorescent probe. The excitation spectra of pyrene, monitored at 390 nm in saline (pH 2) at 25 °C in the presence of increasing concentrations of **4**, show the shift in the (0,0) band as pyrene partitions between aqueous and micellar environments.

PN_2S-PEG micelles were found to easily disassemble by dilution. By dilution of the concentrated solutions below the cmc just before fluorescence analysis, the shift of the (0,0) band from 337 to 334 nm was observed, in agreement with a rapid disaggregation of micelles.

Micelles were also present in the labeling mixtures (Table 1), and the micellar state of the conjugate is necessary since no technetium labeling was obtained below the cmc. On the other hand, when $^{99m}TcO_4^-$ is added to previously solubilized PN_2S-PEG, the reaction occurs but at much lower rate since the PN_2S moiety, forming the inner lipophilic core of the already shaped micelles, is not available for the reduction and coordination of the metal. However, since micelles are in fluxional equilibrium with monomers, $^{99m}TcO_4^-$ can still be loaded into micelles where the redox reaction rapidly takes place, but this internalization process is slow and difficult to complete.

Furthermore, the catalytic effect mediated by micelles explains the efficiency of the labeling reaction, quantitative in less than 15 min, and the possibility to perform the reaction at acid pH. This pH, although favoring the redox reaction, is not as convenient as the alkaline usually required for the deprotonation of peptide ligand amides (*17*).

Finally, the metal is not simply entrapped into micelles as $^{99m}TcO_4^-$ but is strictly bound to PN_2S-PEG by coordination followed by reduction, since $^{99m}TcO_4^-$ is not released through micelle dissociation below the cmc, as detected under HPLC conditions.

In conclusion, we may state that when $^{99m}TcO_4^-$ is added to the solid **4** or **5**, the conjugate dissolves, associating into micelles, while the anion $^{99m}TcO_4^-$ binds to the phosphine phosphorus through an electrostatic interaction, since at acidic pH the phosphorus is present as phosphonium, as depicted in Figure 4.

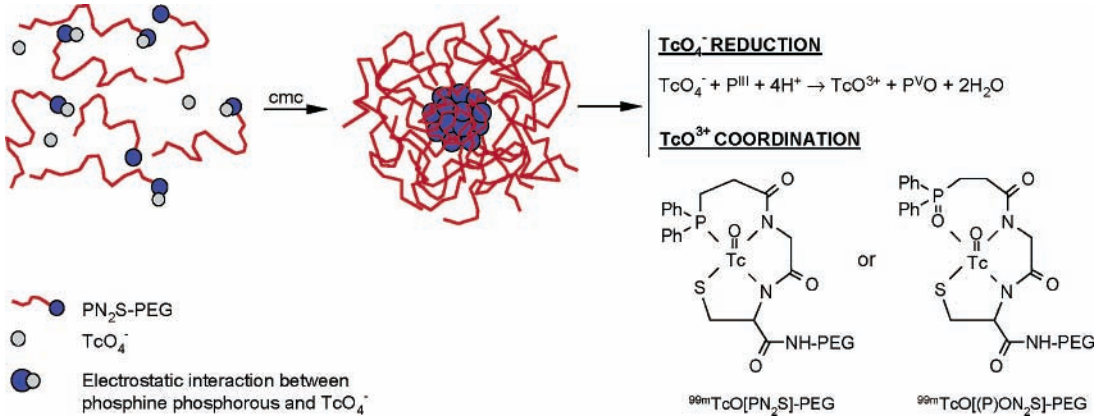


Figure 4. Direct labeling of PEGylated PN_2S ligands. A drawing of the mechanism of ^{99m}Tc reduction−coordination mediated by PN_2S−PEG micelle aggregation with the two possible coordination species is shown.

The Coulombic interaction favors the metal accumulation in the micelle environment where the reduction reaction occurs by means of an electron pair transfer from the phosphine phosphorus to technetium to give the $[^{99m}TcO]^{3+}$ species. It is presumed that the ligand acts as a formal two-electron reducing agent in the presence of $Tc^{VII}O_4^-$ and that, upon reduction of Tc^{VII} to Tc^V, the P^{III} center is oxidized to the corresponding phosphine oxide, P^V. The reduction is then followed by the coordination. The $[^{99m}TcO]^{3+}$ core could be coordinated by the same ligand molecule involved in the redox reaction by means of the new (P)ON_2S set, or alternatively, it could be coordinated through the PN_2S set of a second ligand molecule not involved in the reduction and included in the same micelle.

Transchelation Labeling of PN_2S−PEGs. To evaluate the above-reported coordination hypotheses, both **4** and **5** and the oxidized analogous **6** were employed in the labeling reaction with ^{99m}Tc-gluconate. In this case, the reaction involves the reduction of $^{99m}TcO_4^-$ to $[^{99m}TcO]^{3+}$ by Sn(II) in the presence of sodium gluconate to form the intermediate ^{99m}Tc-gluconate, which later exchanges with the ligand of interest to give the final complex.

Preliminary studies indicated the need to purify ^{99m}Tc-gluconate from technetium-hydrolyzed species leading to unspecific absorption to PEG chain. On the other hand, no interaction between ^{99m}Tc-gluconate and mPEG-NH_2 was observed.

The labeling reaction carried out by the addition of ^{99m}Tc-gluconate to **4** or **5** dissolved in water or in the solid state at a final concentration above the cmc was found to proceed but with a slow rate, since it was still incomplete after 4 h. This indicated that micelles interfere with the exchange ligand reaction, since the PN_2S moiety, which forms the lipophilic core, is less available for the coordination. This was not the case for the reaction carried out in water/EtOH 1:5 (v/v) to avoid micelle formation, a condition that yielded in 35−45 min to a single homogeneous peak detected by HPLC at 20.85 and 21.45 min for **4** and **5**, respectively. The peaks were attributed to ^{99m}TcO[PN_2S]-PEG_{5000} **11** and ^{99m}TcO[PN_2S]-PEG_{20000} **12** obtained from the transchelation between ^{99m}Tc-gluconate and the PN_2S set. The reaction performed using compound **6** led to analogous results with a single labeled species detected at 20.67 min. In this case, the $[^{99m}TcO]^{3+}$ core is supposed to be coordinated by the (P)ON_2S set with the phosphine oxide oxygen bound to the metal center instead of the phosphine phosphorus, leading to the ^{99m}TcO[(P)ON_2S]-PEG_{5000} complex **13**.

These results confirmed that at micelle level both coordinations may take place.

Rhenium Coordination Studies. To further confirm the two coordination possibilities, PEGylated PN_2S and (P)ON_2S were reacted with rhenium. In analogy to a previously reported method for the synthesis of the ReO-[PN_2S]-OMe complex (*10*), the reaction of **4** was performed in dichloromethane using $ReOCl_3(PPh_3)_2$ as rhenium^V oxo starting material. As observed with the PN_2S−OMe ligand, the solution, initially orange-green, turned to reddish-brown by triethylamine addition to reach alkalinity. This demonstrated that PN_2S−PEG_{5000} coordinates $[ReO]^{3+}$ leading to the pentacoordinated complex ReO[PN_2S]-PEG_{5000} **7**. The ^{1}H NMR analysis indicated that both the syn and the anti ReO[PN_2S]-PEG_{5000} complexes are formed, although the HPLC did not separate the two isomers. In the range 4−6 ppm, the signals related to cysteine (Cys) and glycine (Gly) protons were clearly assigned and found to be close to those detected in the syn and anti ReO[PN_2S]-OMe spectra. The Cys α protons were detected at 5.25 and 5.66 ppm for anti and syn isomer, respectively. As for the ReO-[PN_2S]-OMe anti isomer, the splitting pattern of anti isomer Cys α proton appeared as a doublet, indicating that it was at a nearly right angle to one of the β protons, thereby giving no coupling constant. On the other hand, syn isomer Cys α proton appeared as a doublet of doublets indicating that the torsion angles between the Cys α and β protons were different from those in the anti isomer. The Gly α proton signals were detected as two doublets (4.51 and 4.82 ppm, anti isomer; 4.71 and 4.88 ppm, syn isomer), with a geminal coupling of 20.4 and 21.0 Hz for anti and syn isomer, respectively. The β protons of the Cys residue were overlapped to the broad signal of PEG methylene, except for one detected as a doublet at 4.30 ppm and related to anti isomer. Different from ReO[PN_2S]-OMe isomers, always obtained in a 1:1 molar ratio, PN_2S−PEG coordination reaction led to a preference for the anti isomer (70−75%). It is reasonable that the presence of the PEG chain favors, by steric hindrance, one of the diastereomers.

The $ReOCl_3(PPh_3)_2$ precursor was reacted also with oxidized **6**, and the ReO[(P)ON_2S]-PEG_{5000} **8** complex was obtained and found to be stable both in the solid state and in solution. The yield was significantly lower than that achieved with **7**, and unfortunately, we did not succeed to remove the large amount of unreacted PN_2S−PEG_5 by diethyl ether crystallization. This made a good characterization of the product impossible, since in the ^{1}H NMR spectrum the strong intensity of PEG OCH_3 and

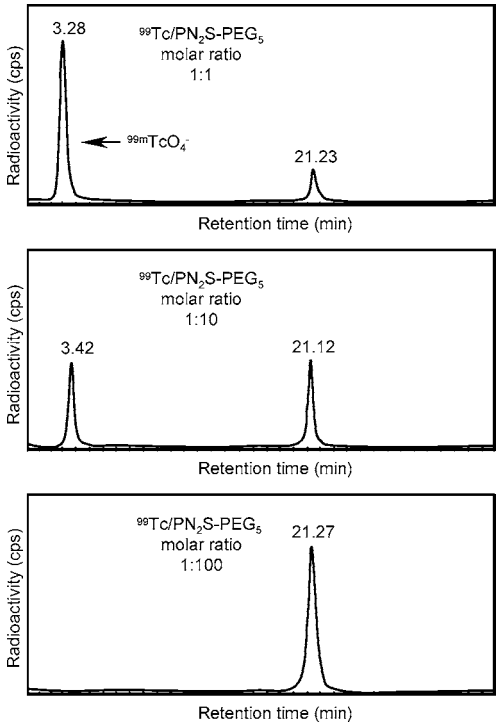


Figure 5. Direct labeling of PEGylated PN_2S ligands: determination of ^{99m}Tc-labeled PN_2S-PEG_{5000} specific activity through carrier added (^{99}Tc) experiments. At the ^{99}Tc/PN_2S-PEG_{5000} molar ratio 1:100, the $^{99m}TcO_4^-$ peak disappears suggesting that all the pertechnetate present in the labeling mixture ($^{99}TcO_4^-$ and $^{99m}TcO_4^-$) is reduced and coordinated. A 1.9 TBq/μmol specific activity was calculated considering the whole Tc present in the solution as ^{99m}Tc.

$CO(CH_2)_2-CO$ signals at 3.27 and 3.62 ppm, respectively, hampered the detection of the peaks related to coordinated Gly-Cys moiety. On the other hand, the same coordination events, initial green solution, which changed to orange by addition of TEA, were observed by reacting the $(P)ON_2S-OMe$ ligand with $[ReO]^{3+}$ as for $(P)ON_2S-PEG_{5000}$ (unpublished results).

In agreement with the results obtained with ^{99m}Tc-gluconate, rhenium-oxo studies confirmed that at micelle level both the PN_2S and $(P)ON_2S$ coordinations are possible.

Specific Activity Determination. The specific activity of **9** was evaluated by means of carrier-added experiments.

Different amounts of $^{99}TcO_4^-$ were added as carrier to $^{99m}TcO_4^-$ solution. The final mixtures were acidified to pH 2 and added to **4** in the solid state. The solutions were kept at room temperature for 10−15 min. The experiment was performed in triplicate using 3.95×10^{-2}, 3.95×10^{-3}, and 3.95×10^{-4} M $^{99}TcO_4^-$ solutions to have a ^{99}Tc/PN_2S-PEG_{5000} molar ratio of 1:1, 1:10, and 1:100. Figure 5 indicates that, when the molar ratio was in the range 1:1−1:10, the labeling reaction did not occur completely, since $^{99m}TcO_4^-$ is still detectable at about 3 min. Instead, at the molar ratio 1:100, the $^{99m}TcO_4^-$ peak disappeared, and it was assumed that all of the pertechnetate present in the labeling mixture ($^{99}TcO_4^-$ and $^{99m}TcO_4^-$) was reduced and coordinated. Based on the fact that ^{99m}Tc and ^{99}Tc are chemically indistinguishable, the specific activity was calculated considering the whole Tc present in the solution as ^{99m}Tc, yielding the considerably high value of 1.9 TBq/μmol.

In Vitro Plasma Stability. The in plasma stability of **9** obtained through the direct labeling procedure was evaluated by incubation at two concentrations, above and below the PN_2S-PEG_5 critical micellar concentration. The results depicted in Figure 6 demonstrated that **9** incubated in absence of micelle exhibited a stability analogous to those already observed for unPEGylated $^{99m}TcO[PN_2S]$-OH and $^{99m}TcO[PN_2S]$-OMe (*5*), while in the presence of micelles, the degradation was markedly reduced. As for the unPEGylated labeled compounds, the decomposition of **9** is due to the release of TcO_4^- and not to byproducts of backbone fragmentation, as demonstrated by RP-HPLC analysis. These experiments demonstrated that PEGylation did not affect the ability of the coordination set to stabilize $[TcO]^{3+}$ toward oxidation or exchange reactions and that micelles further protect the complex by inclusion in the inner core.

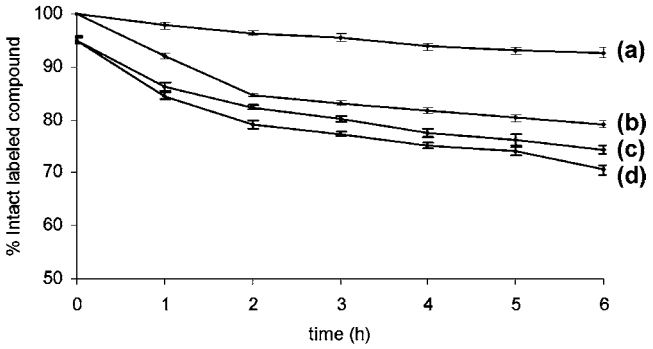


Figure 6. In human plasma stability of ^{99m}Tc-labeled PN_2S-PEG_{5000} **9** after incubation at 37 °C at a concentration above (a) and below (b) the PN_2S-PEG_{5000} cmc, compared with the stability of unPEGylated $^{99m}TcO[PN_2S]$-OMe (c) and $^{99m}TcO[PN_2S]$-OH (d). Values represent the means ± SD ($n = 5$) of the percentage of intact labeled compound.

In Vivo Biodistribution. The labeled compounds **9** and **10** obtained by direct labeling were studied in vivo to evaluate stability, blood residence time, and biodistribution. In Figure 7, the scintigraphic images related to the their biodistribution are depicted.

Scintigraphic images related to **9** were collected for 40 min and showed a rapid and efficient clearance from the bloodstream mainly by the urinary system, also confirmed by ex vivo counting of activity in organs and tissues (Table 2). Those data indicated that the biodistribution of labeled PN_2S-PEG_{5000} is analogous to that reported in the literature for free PEG_{5000} (*18*, *19*) and that the PEGylation of the PN_2S ligand drastically reduces its clearance through the hepatobiliary route (*5*).

For the biodistribution of **10**, the image acquisition time was extended to 3 h. A slow clearance from the blood pool was found, in agreement with a high retention of activity in organs and tissues, as confirmed by the ex vivo counting (Table 3). Also in this case, the biodistribution of labeled PN_2S-PEG_{20000} was similar to that reported for free PEG_{20000} (*18*, *19*), demonstrating that PN_2S linking and labeling do not modify the polymer behavior and that the polymer dictates the fate of the conjugate.

The observed biodistribution of both $^{99m}Tc-PN_2S-PEG$ 5000 and 20000 strictly correlates with that of the unmodified PEG with the same molecular weight, indicating that the excreted species are monomeric. This is also in agreement with the high degree of dilution in the blood pool, which causes micelle disaggregation.

The low activity found in the stomach and the recovery of unmodified labeled conjugates in urine further demonstrated the high affinity of the coordination set for technetium and the stability toward degradation, also due to the shielding effect afforded by PEG to enzymatic

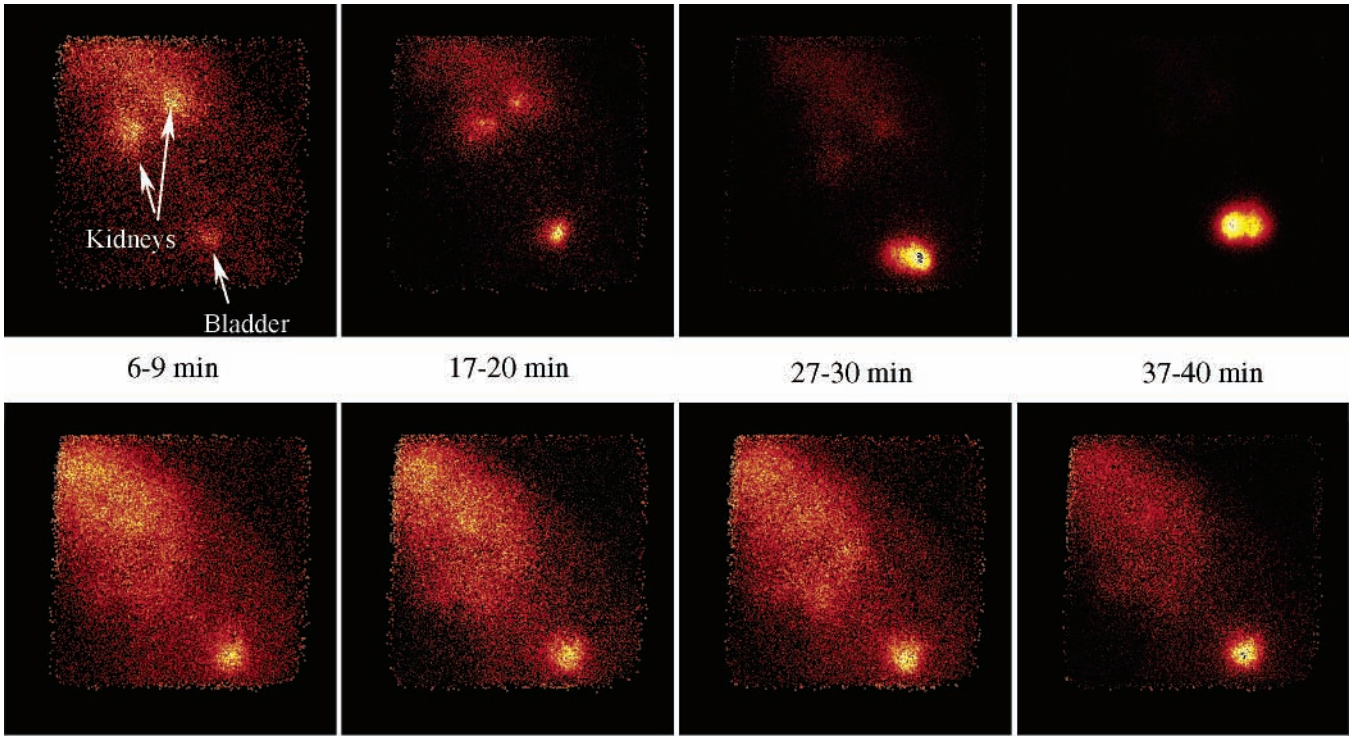


Figure 7. Scintigraphic images related to in mouse biodistribution of ^{99m}Tc-labeled PN_2S-PEG_{5000} **9** (top) and ^{99m}Tc-labeled PN_2S-PEG_{20000} **10** (bottom) obtained through the direct labeling method.

Table 2. Biodistribution in Mice of ^{99m}Tc-Labeled PN_2S-PEG_{5000} 9 at 40 min Postinjection[a]

organ	% ID	% ID/g
right kidney	1.84 ± 0.42	8.58 ± 2.46
left kidney	1.86 ± 0.34	9.00 ± 1.46
bladder	47.21 ± 4.19	
heart	0.42 ± 0.06	2.52 ± 0.41
blood[b]	13.36 ± 1.02	6.73 ± 0.27
stomach	0.55 ± 0.07	0.86 ± 0.35
intestines	4.73 ± 0.11	4.38 ± 1.33
liver	3.89 ± 0.48	2.42 ± 0.36
lungs	0.59 ± 0.19	2.20 ± 0.60
spleen	0.21 ± 0.03	2.91 ± 0.53

[a] Values represent means ± SD ($n = 3$) of the percent of injected dose (% ID) and of injected dose per gram (% ID/g) of tissue. [b] Total blood was estimated to be 6.5% of the body weight.

Table 3. Biodistribution in Mice of ^{99m}Tc-Labeled PN_2S-PEG_{20000} 10 at 3 h Postinjection[a]

organ	% ID	% ID/g
right kidney	1.59 ± 0.12	7.30 ± 0.70
left kidney	1.52 ± 0.07	7.28 ± 0.74
bladder	29.93 ± 1.93	
heart	0.65 ± 0.19	3.85 ± 1.03
blood[b]	20.88 ± 1.76	11.47 ± 1.66
stomach	0.84 ± 0.26	1.84 ± 0.60
intestines	8.03 ± 0.89	7.23 ± 1.77
liver	5.83 ± 1.58	3.54 ± 0.52
lungs	1.17 ± 0.16	4.32 ± 0.50
spleen	0.16 ± 0.05	1.19 ± 0.26

[a] Values represent means ± SD ($n = 3$) of the percent of injected dose (% ID) and of injected dose per gram (% ID/g) of tissue. [b] Total blood was estimated to be 6.5% of the body weight.

cleavage of amide bonds or hydrolysis by water often observed in PEG−peptide drugs.

CONCLUSIONS

The PEGylation of the PN_2S ligand allows a new simple, clean, and efficient ^{99m}Tc-labeling procedure and avoids the use of an external reducing agent. The mechanism of labeling is based on a supramolecular assembly of the PN_2S−PEG conjugates in aqueous solution to yield micelles that favor the reduction and coordination of technetium. The labeling does not modify the polymer behavior in water, and PEG may still convey to the labeled conjugates its pharmacokinetic properties, thanks also to the great in vivo stability of the complex. This novel method can therefore represent an useful tool to further improve the potential of technetium-99m in diagnosis and of rhenium-186/188 in radiotherapy through the labeling of targeting biomolecules conjugated to the PN_2S set via a bifunctional PEG. Studies are now directed to (i) verify the accumulation of monofunctional PEG conjugates in solid tumors exploiting the EPR effect taking advantage of the high steric hindrance of the molecules and (ii) evaluate the new labeling procedure in bioconjugates with the PN_2S set bound to specific targeting peptides using heterobifunctional PEGs.

ACKNOWLEDGMENT

The work originated from collaboration within the program COST-B12 WG-5. Gianfranco Pasut was supported by University of Padova Grant CPDG034599 “Progetto Giovani Ricercatori 2003”. The authors thank Dr. Fabrizio Mancin for assistance with light scattering analysis, Dr, Lorena Giovagnini for ^{31}P NMR spectra, Mr. Michele Bello for scintigraphic images elaboration, and Dr. Guido Bordignon for MALDI-TOF spectrometry.

LITERATURE CITED

(1) Liu, S., and Edwards, S. D. (1999) ^{99m}Tc-Labeled small peptides as diagnostic radiopharmaceuticals. *Chem. Rev. 99,* 2235−2268.

(2) Hom, R. K., and Katzenellenbogen, J. A. (1997) Technetium-99m-labeled receptor-specific small-molecule radiopharmaceuticals: recent developments and encouraging results. *Nucl. Med. Biol. 24,* 485−498.

(3) Jurisson, S. S., and Lydon, J. D. (1999) Potential technetium small molecule radiopharmaceuticals. *Chem. Rev. 99*, 2205−2218.
(4) Fichna, J., and Janecka, A. (2003) Synthesis of target-specific radiolabeled peptides for diagnostic imaging. *Bioconjugate Chem. 14*, 3−17.
(5) Visentin, R., Giron, M. C., Bello, M., and Mazzi, U. (2004) Technetium-99m labeling of N-[N−(3-Diphenylphosphinopropionyl)glycyl]cysteine (PN_2S−OH) and its methyl ester derivative (PN_2S−OMe). *Nucl. Med. Biol. 31*, 655−662.
(6) Harris, J. M., and Chess, R. B. (2003) Effect of PEGylation on pharmaceuticals. *Nat. Rev. Drug Discoveries 2*, 214−221.
(7) Pasut, G., Guiotto, A., and Veronese, F. M. (2004) Protein, peptide and non-peptide drug PEGylation for therapeutical application: a review. *Expert Opin. Ther. Pat. 14*, 859−894.
(8) Seymour, L. W., Ulbrich, K., Steyger, P. S., Brereton, M., Subr, V., Strohalm, J., and Duncan, R. (1994) Tumouritropism and anticancer efficacy of polymer-based doxorubicin prodrugs in the treatment of subcutaneous murine B16F10 melanoma. *Br. J. Cancer 70*, 636−641.
(9) Chatt, J., and Rowe, G. A. (1962) Complex compounds of tertiary phosphines and a tertiary arsine with rhenium(V), rhenium(III), and rhenium(II). *J. Chem. Soc.* 4019−4033.
(10) Visentin, R., Rossin, R., Giron, M. C., Dolmella, A., Bandoli, G., and Mazzi, U. (2003) Synthesis and characterization of rhenium(V)-oxo complexes with *N*-[*N*-(3-diphenylphosphinopropionyl)glycyl]cysteine methyl ester. X-ray crystal structure of {ReO[$Ph_2P(CH_2)$2C(O)-Gly-Cys-OMe,(P,N,N,S)]}. *Inorg. Chem. 42*, 950−959.
(11) Wilhelm, M., Zhao, C., Wang, Y., Xu, R., Winnik, M. A., Mura, J., Riess, G., and Croucher, M. (1991) Poly(styrene-ethylene oxide) block copolymer micelle formation in water: A fluorescence probe study. *Macromolecules 24*, 1033−1040.
(12) Vittori, F., Malatesta, T., and de Notaristefani, F. (1997) The YAP Camera: an accurate gamma camera particularly suitable for new radiopharmaceuticals research. *IEEE Trans. Nucl. Sci. 44*, 47−53.
(13) Pearson, D. A., Blanchette, M., Baker, M. L., and Guindon, C. A. (1989) Trialkylsilanes as scavengers for the trifluoroacetic acid deblocking of protecting groups in peptide synthesis. *Tetrahedron Lett. 30*, 2739−2742.
(14) Smith, C. J., Katti, K. V., Higginbotham, C., and Volkert, W. A. (1997) In vitro and in vivo characterization of novel water-soluble dithio-bisphosphine ^{99m}Tc complexes. *Nucl. Med. Biol. 24*, 685−691.
(15) Freiberg, E., Davis, W. M., Nicholson, T., Davison, A., and Jones, A. G. (2002) Reduction of the pertechnetate anion with bidentate phosphine ligands. *Inorg. Chem. 41*, 5667−5674.
(16) Tascioglu, S. (1996) *Micellar solutions as reaction media. Tetrahedron 52*, 11113−11152.
(17) Vanbilloen, H. P., Bormans, G. M., De Roo, M. J., and Verbruggen, A. M. (1995) Complexes of technetium-99m with tetrapeptides, a new class of ^{99m}Tc-labeled agents. *Nucl. Med. Biol. 22*, 325−338.
(18) Working, P. K., Newman, M. S., Johnson, J., and Cornacoff, J. B. (1997) Safety of Poly(ethylene glycol) and Poly(ethylene glycol) derivatives. *Poly(Ethylene Glycol): Chemistry and Biological Applications* (Harris, J. M., and Zalipsky, S., Eds.) pp 44−57, American Chemical Society Symposium Series 680, American Chemical Society, Washington, DC.
(19) Yamaoka, T., Tabata, Y., and Ikada, Y. (1994) Distribution and tissue uptake of poly(ethylene glycol) with different molecular weights after intravenous administration to mice. *J. Pharm. Sci. 83*, 601−606.

BC049896D

Mechanism for High Stability of Liposomal Glucose Oxidase to Inhibitor Hydrogen Peroxide Produced in Prolonged Glucose Oxidation

Makoto Yoshimoto,[†] Yuya Miyazaki,[†] Mitsunobu Sato,[†] Kimitoshi Fukunaga,[†] Ryoichi Kuboi,[‡] and Katsumi Nakao*[,†]

Department of Applied Chemistry and Chemical Engineering, Faculty of Engineering, Yamaguchi University, 2-16-1 Tokiwadai, Ube 755-8611, Japan, and Department of Chemical Science and Engineering, Graduate School of Engineering Science, Osaka University, 1-3 Machikaneyama-cho, Toyonaka 560-8531, Japan. Received April 13, 2004; Revised Manuscript Received July 13, 2004

Glucose oxidase (GO) was encapsulated in the liposomes composed of POPC (1-palmitoyl-2-oleoyl-*sn*-glycero-3-phosphocholine) to increase the enzyme stability through its decreased inhibition because of hydrogen peroxide (H_2O_2) produced in the glucose oxidation. The GO-containing liposomes (GOLs) were completely free of the inhibition even in the complete conversion of 10 mM glucose at 25 °C because the H_2O_2 concentration was kept negligibly low both outside and inside liposomes throughout the reaction. It was interestingly revealed that the H_2O_2 produced was decomposed not only by a slight amount of catalase originally contained in the commercially available GO but also by the lipid membranes of GOL. As compared to the GOL-catalyzed reaction, the free GO-catalyzed reaction more highly accumulated H_2O_2 because of the more rapid glucose conversion despite containing free catalase, leading to the completely inhibited GO before reaching a sufficient glucose conversion. This suggested that only the liposomal catalase could continue to catalyze the H_2O_2 decomposition. The effect of the glucose oxidation rate, i.e., the H_2O_2 production rate on the liposomal GO inhibition, was also examined employing the various GOLs with different permeabilities to glucose present in their external phase. It was concluded that the liposomal GO free of the inhibition could be obtained when the GOL-catalyzed H_2O_2 formation rate was limited by such a suitable lipid bilayer as POPC membrane so that the rate was well-balanced with the sum of the above two H_2O_2 decomposition rates. The highly stable GOL obtained in the present paper was shown to be a useful biocatalyst for the prolonged glucose oxidation.

INTRODUCTION

Glucose oxidase (GO)-catalyzed glucose oxidation producing gluconic acid and hydrogen peroxide (H_2O_2) has been utilized for glucose quantification (*1*, *2*), sterilization (*3*, *4*), textile bleaching (*5*), removal of oxygen from foods (*6*) and a large-scale production of gluconic acid (*7*). Immobilization of GO in the various solid supports has been studied for increasing physical stability and reusability of the enzyme (*1*, *2*, *5*−*7*). However, it is usually difficult to obtain the stable glucose oxidase free of the product (H_2O_2) inhibition to the enzyme in a prolonged glucose oxidation (*8*). Even though catalase is added to the reaction solution for catalyzing the decomposition of H_2O_2, the inhibitory effect to catalase also needs to be taken into consideration (*9*). Therefore, the key to develop a durable and biocompatible system for the prolonged glucose oxidation is considered to be regulating the behavior of H_2O_2 produced throughout the reaction period with such a biological mean as maintaining the initial activities of both enzymes.

We have studied liposomes (phospholipids vesicles) in modulating the reactivity and selectivity of the liposomal enzyme to the externally added substrates (*10*, *11*), refolding denatured enzyme in the presence of liposomes (*12*), and using the liposomal enzyme in a gas−liquid two-phase flow in a bubble column (*13*). These contributions are for developing the nanoscaled biofunctional materials applicable to bioprocesses. These unique features of liposomes are mainly attributed to the selective permeability of the membranes to substrate molecules (*10*, *11*, *13*) and the electrostatic and hydrophobic interactions between partially unfolded enzyme and lipid bilayer membranes (*12*, *14*). On the basis of such functions of liposomes as above, we recommended the liposomal GO as a stable biocatalyst for the air oxidation of glucose in an external loop airlift bioreactor. In particular, it is practically important that the commercially available GO encapsulated in liposomes can catalyze a prolonged air oxidation of glucose with remarkably higher stability than free GO (*13*). This indicates that the enzyme inhibition because of H_2O_2 produced in the oxidation is effectively suppressed in the liposomal system. However, the mechanism for this phenomenon has so far remained unclear.

In the present paper, a mechanism for an increase in the stability of liposomal GO is examined on the basis of the quantitative determination of the H_2O_2 produced in the glucose oxidations catalyzed by the different types of liposomal GO under the various conditions. The results obtained clearly show that an appropriate liposomal encapsulation of GO can give an extraordinary stable system for the simultaneous glucose oxidation and H_2O_2 decomposition with negligible formation of the inhibited enzymes.

* To whom correspondence should be addressed. Telephone: +81-836-85-9271. Fax: +81-836-85-9201. E-mail: knakao@yamaguchi-u.ac.jp.

[†] Yamaguchi University.

[‡] Osaka University.

10.1021/bc049909n CCC: $27.50 © 2004 American Chemical Society
Published on Web 08/11/2004

EXPERIMENTAL PROCEDURES

Materials. GO from *Aspergius niger* (EC 1.1.3.4, 429 units/mg, $M_r \cong 180\,000$, pI = 4.44) was purchased from Sigma (St. Louis, MO). The GO from Sigma was nominally low in catalase, with the catalase content of less than 0.1 units/mg protein according to the specification. GO (147 units/mg) was also obtained from Toyobo Co. Ltd. (Osaka, Japan). POPC (1-palmitoyl-2-oleoyl-*sn*-glycero-3-phosphocholine) with purity more than 99% was from Avanti Polar Lipids Inc. (Alabaster, AL). β-D-Glucose, H_2O_2 solution (35.1%), 3-AT (3-amino-1,2,4-triazole), DLPC (L-α-phosphatidylcholine, dilauroyl), DMPE (L-α-phosphatidylcholine, dimyristoyl), and sodium cholate were from Wako Pure Chemical Industries, Ltd. (Osaka, Japan).

Preparation of GO-Containing Liposomes (GOL). The GOL was prepared by the extrusion technique as reported previously (*10*), essentially based on the method of Mayer et al. (*15*) as follows. The lipid (30−100 mg) was at first solubilized in chloroform in a round-bottom flask followed by removal of the solvent by using a rotary evaporator. This procedure was repeated twice using diethyl ether as the second solvent. The lipid film obtained was dried under reduced pressure (<10 Pa) using a freeze dryer (FRD-50M, Asahi Techno Glass Corp., Funabashi, Japan) in the dark for 2 h to remove the residual solvent in the lipid layers. The dry lipid film was hydrated with 50 mM Tris-HCl/100 mM NaCl buffer (pH 7.4) (denoted as Tris buffer) containing 1.3 mg/mL GO. The water used for the Tris buffer preparation was deionized to remove metal ions by passing through an ion-exchange resin column. The multilamellar vesicles (MLVs) formed were frozen at −80 °C in dry ice/ethanol and thawed at 35 °C 7 times to transform a fraction of the small liposomes into the larger MLVs. The MLVs were extruded through the two stacked polycarbonate membranes with a nominal pore diameter of 100 nm using an extruding devise (Liposofast from Avestin Inc.) (*16*). Nonentrapped GO molecules were separated from the GOL using the gel-permeation chromatography (GPC) with a sepharose 4B column ($\phi 1 \times 20$ cm). The dehydration−rehydration vesicle method (DRV) (*17*−*19*) was used for preparing the various GOLs with different GO contents in liposomes as follows. The next freezing and drying treatment was performed for the GOL prepared as described above except that the GOL was not passed through the GPC column. The dry liposome−GO mixture obtained was rehydrated with a smaller quantity of deionized water than that in the first hydration. The GO content in the GOL was altered by changing the amount of water used in this rehydration step. Then, the GOL was frozen and thawed and extruded again followed by the same GPC treatment as above to obtain the GOL with different GO content. The lipid concentration was measured enzymatically using a kit from Wako Pure Chemical Industries, Ltd. In the following, the GOL stands for the GO-containing POPC liposomes without the DRV treatment unless otherwise described.

Determination of Activity of Liposomal and Free GO. Enzymatic activity of GO was measured by using the same colorimetric method (*20*) as reported previously (*10*). The activity efficiency (*E*) of the liposomal GO was defined as the observed GOL activity ([lipid] = 75 μM) with the external addition of 10 mM glucose at 25 °C relative to the intrinsic one measured after solubilization of the liposomes with an excess amount of cholate.

Glucose Oxidation Catalyzed by Liposomal and Free GO. The glucose oxidation was performed in the Tris buffer at the reaction volume of 2.0−3.0 mL in a glass test tube capped with cotton. The reaction was initiated with the GOL ([lipid] = 1.0 mM, and [GO] = 2.7 μg/mL) or free GO (2.7 μg/mL) at the initial glucose concentration of 10 mM in a water bath thermostated at 25 ± 0.3, 27 ± 0.3, or 40 ± 0.3 °C. An aliquot of the reaction solution was withdrawn periodically for quantification of the remaining glucose and accumulated H_2O_2 concentrations (see below). The glucose conversion was calculated from the remaining glucose concentration relative to the initial one. The reaction was also carried out in the presence of catalase inhibitor 3-AT at 250 mM. Prior to the reaction with it, either free GO or the GOL was incubated with 3-AT at 25 °C overnight.

Measurement of the Glucose Concentration in the Reaction Solution. The glucose concentration in the reaction mixture was measured either enzymatically or by the Somogyi−Nelson method. The former and latter methods were performed by using the kits from Toyobo Co. Ltd. (Osaka, Japan) and Nacalai Tesque, Inc. (Kyoto, Japan), respectively. The enzymatic method was used for the sample containing a negligible amount of H_2O_2 because it essentially measures H_2O_2 produced from glucose. The Somogyi−Nelson method was used for quantification of glucose in the presence of a relatively high concentration of H_2O_2 in the absence of lipids, i.e., in the reaction catalyzed by free GO. In the case of the reaction catalyzed by the liposomal GO with a high concentration of H_2O_2 accumulated, the glucose concentrations measured with the enzymatic method above were corrected using a calibration curve based on the separately measured H_2O_2 accumulated in the reaction mixtures (see below).

Measurement of the H_2O_2 Concentration in the Reaction Solution. H_2O_2 was quantified based on the oxidation of 3,3-dimethoxybenzidine dihydrochloride (*o*-dianiisidine) with H_2O_2 catalyzed by horseradish peroxidase (HRP) as follows. A total of 50 μL of a H_2O_2-containing sample with the GOL was mixed with 1450 μL of the Tris buffer solution (pH 7.4) to give the final concentrations of 5.0 μM for HRP and 3.3 mM for *o*-dianiisidine. To the above sample, 10−40 mM cholate was added for complete solubilization of liposomes to release the H_2O_2 in liposomes and to decrease the turbidity of the assay solution. The value of A_{460} was then measured immediately using a spectrophotometer (UV-1200, Shimazdu, Japan) in a quartz cell with a 0.5-cm optical length at 25 °C. Decomposition of H_2O_2 in the presence and absence of the various additives was measured at 25 °C for the initial H_2O_2 concentration of 10 mM in the Tris buffer (pH 7.4) of 0.5−3.0 mL in volume in a glass test tube capped with cotton. Then, the time course of the H_2O_2 concentration was measured with the enzymatic method as described above.

Determination of the Remaining Activity of Liposomal GO. The remaining GO activity in the GOL was measured after separating the GOL from the reaction mixture by using the GPC. The GO activity in the GOL fractions was measured after complete liposome solubilization with 40 mM cholate. The remaining GO activity was calculated as the enzyme activity detected in the GOL fractions relative to that determined for the GOL before the glucose oxidation.

RESULTS AND DISCUSSION

Characteristics of Prolonged Glucose Oxidation Catalyzed by Liposomal GO. The mean number of active GO molecules in a GOL used in the present paper

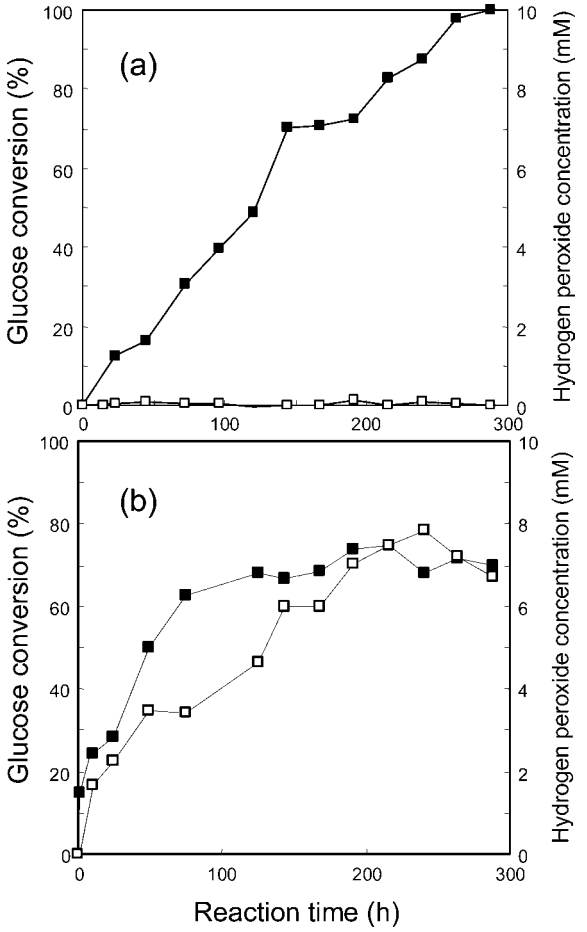


Figure 1. Time course of glucose conversion (■) and H_2O_2 concentrations (□) in glucose oxidation catalyzed by (a) GOL ([POPC] = 1.0 mM, and $[GO]_{overall}$ = 2.7 μg/mL) and (b) free GO ([GO] = 2.7 μg/mL). The initial glucose concentration was 10 mM in 50 mM Tris-HCl/100 mM NaCl buffer (pH 7.4) at 25 °C. The GO from Sigma was used.

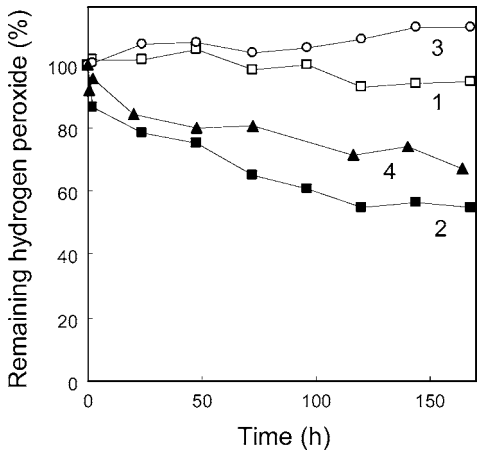


Figure 2. Time course of H_2O_2 concentrations in (1) 50 mM Tris-HCl/100 mM NaCl buffer (pH 7.4), (2) the Tris buffer containing free GO from Sigma ([GO] = 1.3 mg/mL), (3) the buffer containing 1.3 mg/mL free GO from Sigma plus 250 mM 3-AT, and (4) the buffer containing free GO from Toyobo Co. Ltd. ([GO] = 1.3 mg/mL) without 3-AT. All of the experiments were carried out under the initial H_2O_2 concentration of 10 mM at 25 °C.

was 1.7, unless otherwise stated. The values could be determined with the assumptions that the mean liposome diameter is 115 nm (*12*), the bilayer thickness of the POPC liposomes is 3.7 nm, and the mean area of the POPC headgroup is 0.72 nm^2 (*21*). The liposomal GO was found to have the initial apparent activity efficiency *E* of 0.03, that is, to show a very low reactivity with the external addition of glucose because of the limited permeability of glucose through the POPC membranes. Figure 1 shows the typical time courses of the GOL- and free GO-catalyzed glucose oxidation. The initial reaction rate catalyzed by the GOL (Figure 1a) is lower in comparison with that by free GO (Figure 1b). This corresponds to the small *E* value of the GOL. The critical difference in the observed time courses between the GOL- and free GO-catalyzed reactions is that almost no H_2O_2 is accumulated in the former case (Figure 1a), while the H_2O_2 concentration increases with increasing glucose conversion in the latter case (Figure 1b). The GO activity remaining in the GOL was 97% at the reaction time reaching almost complete conversion of glucose. Therefore, negligible GO leakage was found to occur during the reaction, suggesting that the high membrane integrity of the liposome was maintained throughout the reaction. The reason for such a remarkably stable GO activity of the GOL during the prolonged glucose oxidation (for 300 h) is that the H_2O_2 concentration even inside liposomes is kept low enough to give almost no inhibitory effect of H_2O_2 produced on the liposomal GO activity. In contrast, the free GO-catalyzed reaction is stopped because of the formation of an almost completely inhibited GO by H_2O_2 accumulating at a high concentration (*8*) even though unconverted glucose still remains, as seen in the result of Tzanov et al. (*5*). In the following, the highly stable liposomal GO free of the inhibition is analyzed and discussed in detail.

Activity of Free Catalase Contained in GO. Figure 2 shows the time courses of the H_2O_2 decomposition reaction in the four different Tris buffers (pH 7.4) at 25 °C. As shown in the figure, the self-decomposition of H_2O_2 in the Tris buffer (pH 7.4) is negligible (run 1) in agreement with the result of Qiang et al. (*22*). This suggests that the effect of trace metal ions such as Fe^{2+} and Cu^{2+} possibly contained in the water used or on the wall of the glass test tube can be negligible because these metal ions may cause the H_2O_2 decomposition through the formation of radical species such as a hydroxyl radical (*23*). The above result shows that the self-decomposition of H_2O_2 plays a rather minor role in the H_2O_2 behavior observed in the GOL-catalyzed reaction (Figure 1a). It is also seen in Figure 2 that the decomposition of H_2O_2 is enhanced in the free GO solutions (runs 2 and 4 for the GO from Sigma and Toyobo Co. Ltd., respectively). The H_2O_2 decomposition in the solution of free GO from Sigma was inhibited completely by the addition of 250 mM 3-AT (run 3). No decomposition of H_2O_2 was also observed in the solution of free GO from Toyobo Co. Ltd. in the presence of the same concentration of 3-AT (data not shown). Because 3-AT is a typical inhibitor for catalase (*9*, *24*), these results mean that the commercially available GO contains catalase as an impurity. The GO activity in the presence of 3-AT at 250 mM was approximately 90% of the original GO activity. It should be noted that pretreatment of the GOL incubated with 3-AT overnight gives almost completely inhibited catalase in liposomes with negligible GO leakage and deactivation of the GOL because of a sufficiently high permeability of 3-AT through the POPC bilayer membranes. The catalase activity in the free GO is seen to be deactivated progressively even in the absence of 3-AT leading to the stopping of the H_2O_2 decomposition reaction (run 2). This means

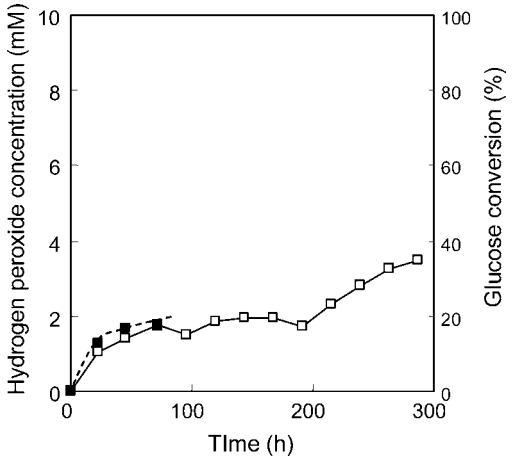


Figure 3. Time course of H_2O_2 concentration (□) and glucose conversion (■) in glucose oxidation catalyzed by GOL ([POPC] = 1.0 mM, and $[GO]_{overall}$ = 2.7 μg/mL) in the presence of 250 mM 3-AT under the initial glucose concentration of 10 mM in the Tris buffer (pH 7.4) at 25 °C.

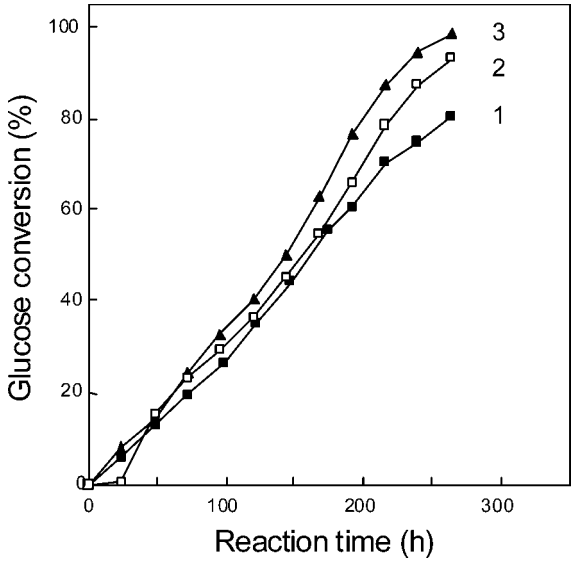


Figure 4. Time course of glucose conversion in glucose oxidation catalyzed by the GOL ([POPC] = 1.0 mM) with the different number of GO molecules in a liposome of 8.9 (1), 4.9 (2), and 2.1 (3). The initial glucose concentration was 10 mM in the Tris buffer (pH 7.4) at 25 °C. The remaining GO activities of the three GOLs at 250 h were 76% (1), 73% (2), and 94% (3). The GO from Sigma was used.

that a relatively high concentration of H_2O_2 causes the deactivation of catalase as reported previously (*9*).

Effects of Catalase Contained in GO on GOL-Catalyzed Glucose Oxidation. The GOL reaction was carried out in the presence of 250 mM 3-AT. Figure 3 shows the time courses of the H_2O_2 produced and the glucose conversion during the GOL-catalyzed glucose oxidation reaction. It is seen in the figure that H_2O_2 is accumulated with an increasing reaction time in contrast to the case of the reaction without 3-AT (Figure 1a). Therefore, it is evident that the liposomal GO is highly stabilized at least through the H_2O_2 decomposition catalyzed by the liposomal catalase. In Figure 3, the amount of glucose converted is slightly higher than that of H_2O_2 accumulated in the initial stage of the reaction. The result together with that of Figure 1a reveals that the liposomal catalase plays a crucial role in decomposing H_2O_2 produced. In Figure 3, the reaction rate is remarkably lowered with an increase in the amount of H_2O_2 accumulated because of its inhibitory effect on the activity of liposomal GO under an extremely limited supply of glucose to the enzyme in liposomes. The very low glucose concentration relative to the H_2O_2 concentration may lead to an almost complete inactivation of GO in liposomes in an earlier stage of the reaction as shown in Figure 3. On the other hand, no sufficient catalase activity is observed in the free GO-catalyzed reaction in the presence of catalase contained in GO, i.e., without addition of 3-AT (Figure 1b). Free catalase is thus suggested to be unstable in a sufficiently high concentration of H_2O_2 in agreement with the result shown in Figure 2 (run 2). The factors that may cause a significant difference in the activity stability between the liposomal and free catalase are considered to be as follows. First, the encapsulation of catalase in liposomes should affect the stability of the enzyme molecular structure essential for catalytic activity of catalase as reported for the other liposomal enzyme system (*25*). Because catalase requires four subunits to express its activity, the dilution-induced dissociation of the tetrameric catalase into subunits occurs in the case of free catalase (*26*). The liposomal encapsulation of an even very low concentration of catalase as in the case of the present GOL preparation, however, results in preventing effectively the tetrameric catalase from the dissociation, that is, giving the liposomal catalase with its high conformational stability. Considering that the amount of catalase is much lower than that of GO and one liposome contains approximately two GO molecules, only a very small fraction of the GOLs should contain a catalase molecule. Because H_2O_2 is much more permeable through the liposome membranes than glucose, the H_2O_2 produced in the catalase-free GOL is readily released into the bulk aqueous phase to be accessible to the liposomes containing catalase. Second, an interaction of liposomes with H_2O_2 possibly induces a change in the chemical stability of H_2O_2. Our preliminary study on the H_2O_2 stability in the GO-free liposome suspension suggests that the presence of intact lipid membranes causes a slightly enhanced decomposition of H_2O_2; i.e., liposomes possess a weak catalase-like function (Yoshimoto et al., unpublished results). The detailed mechanism for this phenomenon is unclear at the moment. Third, the relatively slow H_2O_2 formation in the GOL because of the limited glucose permeability through liposome membranes should have relevance to the H_2O_2 behavior and hence to activities of both GO and catalase in the liposomal system. This is because the amount of H_2O_2 accumulated should be determined by the kinetic balance between the formation and decomposition of H_2O_2. Concerning this point, the various GOLs, which differed in the GO content in liposomes, as well as the membrane permeability to glucose, were prepared and their performances were examined in the glucose oxidation as described below.

Effects of the Glucose Oxidation Rate on H_2O_2 Behavior. Figure 4 shows the time courses of the glucose conversion catalyzed by the various GOLs with the different mean numbers of GO molecules (*2*−*9*) in a GOL in the presence of catalase as an impurity, i.e., without addition of 3-AT. It can be seen in the figure that the initial rate of glucose conversion is not significantly dependent on the GO content in the GOL. This means that the permeation of glucose through the POPC membranes is the rate-controlling step in the GOL reaction in agreement with the results reported previously (*10*). The remaining GO activity was more than 70% for these GOLs (see the caption of Figure 4). The GOLs prepared

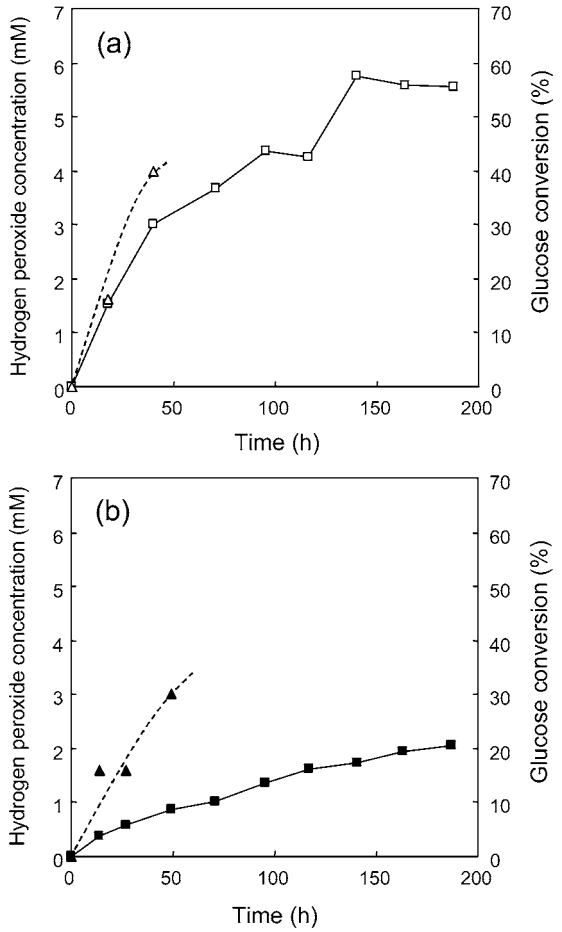


Figure 5. Time courses of H_2O_2 concentration (□ and ■) and glucose conversion (△ and ▲) in glucose oxidation catalyzed by (a) the GOL with DLPC membranes at 25 °C and (b) the GOL with POPC membranes at 40 °C. The initial glucose concentration was 10 mM in the Tris buffer (pH 7.4). The lipid concentration in the reaction was 1.0 mM. The GO from Sigma was used.

by the DRV method tend to show a slightly lower remaining activity. This may be because the GO molecules are partly trapped in the outer surface of the GOL membranes prepared by the DRV method. Such GO molecules may lead to the decreased stability of GO during the glucose oxidation as suggested by the low stability of free GO in the glucose oxidation (Figure 1b). From a practical point of view, the rate of the GOL reaction to consume glucose should be increased while keeping a sufficient GO stability in the GOL. Thus, the membrane permeability of the GOL to glucose was modulated. Figure 5 shows the H_2O_2 formation as well as the glucose conversion in the reaction catalyzed by the GOLs with the *E* values being different from the above GOL with POPC membranes at 25 °C without 3-AT. It can be seen in Figure 5a that the reaction catalyzed by the GOL with the DLPC membranes having much higher permeability to glucose ($E = 0.56$) than that with the POPC membranes ($E = 0.03$) results in the enhanced accumulation of H_2O_2 with an increasing reaction time. The initial rate of glucose conversion is seen to be high because of the considerably higher membrane permeability and hence higher activity efficiency of the liposomal enzyme. In this case, the liposomal catalase could not function enough because the initial production rate of H_2O_2 is significantly high. Consequently, the rate of glucose conversion will be significantly lowered in the later stage of the reaction because of the increasing inhibitory effect of H_2O_2 accumulated on the liposomal GO, as suggested in the reaction catalyzed by the free GO (Figure 1b). H_2O_2 was also accumulated in the reaction catalyzed by the GOL with POPC membranes at 40 °C, corresponding to the optimal temperature for GO activity as shown in Figure 5b. In the figure, the initial rate of glucose conversion is higher than that at 25 °C (Figure 1a) because of the enhanced membrane permeability of glucose at the higher temperature. In addition, the amount of glucose converted is seen to be higher than that of H_2O_2 accumulated, showing that the liposomal catalase decomposed a considerable amount of H_2O_2 produced. In the later stage of the reaction, however, the reaction rate should be lowered as opposed to the case at 25 °C because of an increase in the H_2O_2 concentration with time. Furthermore, Table 1 summarizes the results on the glucose oxidation catalyzed by the GOL with the POPC/DMPE membranes. The DMPE-incorporated GOL was used for the covalent immobilization of GOL into the chitosan gel beads (*13*). It can be seen in the table that the GOLs prepared have the *E* values of 0.07−0.10 and are stable enough to give a sufficient glucose conversion. For all of the cases, almost no H_2O_2 accumulation is observed at the reaction time of 240 h when the high glucose conversion indicated is obtained. These results suggest that the rate of the H_2O_2 formation catalyzed by the liposomal GO should be limited by keeping the *E* value of the GOL adequate enough to decompose the H_2O_2 produced ($E \leq 0.10$) when using the commercially available GO. In other words, the productivity of H_2O_2 in the GOL reaction can be controlled on the basis of the *E* value. The GOL with the POPC membranes at 25 °C showed such a suitable *E* value as the rate of the H_2O_2 formation catalyzed by the liposomal GO, which was well-balanced with that of the H_2O_2 decomposition catalyzed by the catalase contained as an impurity in the commercially available GO and lipid membranes. Therefore, the H_2O_2 concentration in the GOL is considered to be maintained low enough to cause no enzyme deactivation or possibly even activation of the enzyme (*27*). It was previously reported that the GOLs could be used for sterilization in the presence of glucose by producing H_2O_2 on the cell surface (*3*, *4*). The liposomal GO producing H_2O_2 was also utilized for quantification of a high concentration of glucose (*1*, *2*). In these cases, the membrane permeability to glucose corresponding to the *E* value in the present paper may be increased because of an interaction of the liposomes with the cell or solid surface so that the produced H_2O_2

Table 1. Glucose Oxidation Catalyzed by GOLs with POPC/DMPE Membranes[a]

lipid composition (POPC/DMPE in molar ratio)	number of GO molecules in a liposome	initial *E* value	reaction time (h)	H_2O_2 accumulated in the reaction solution (mM)	glucose conversion (%)	remaining GO activity (%)
100:0	2.2	0.07	240	0.1	84	94
95:5	2.0	0.08	240	0.09	85	87
90:10	2.1	0.10	240	0.1	78	82

[a] The GO used was from Toyobo Co. Ltd. The glucose oxidation was performed at 27 °C under the initial glucose and lipid concentrations of 10 and 1.0 mM, respectively.

can be accumulated enough as suggested by the results shown in Figure 5.

CONCLUDING REMARKS

The results obtained in the present paper are summarized as follows. (1) The GOLs efficiently catalyzed the prolonged glucose oxidation to give almost complete conversion of the initially added 10 mM glucose with negligible inhibition of GO due to the H_2O_2 produced because little H_2O_2 was accumulated throughout the reaction. (2) The GOL-catalyzed glucose oxidation with the catalase inhibitor 3-AT revealed that the catalase originally contained in the commercially available GO played a significant role in decomposing the H_2O_2 produced in the reaction. For the free GO-catalyzed reaction, H_2O_2 was significantly accumulated despite the presence of catalase as an impurity. Therefore, it was suggested that the liposomal encapsulation of both GO and catalase was effective to obtain a remarkably stable enzyme system for the glucose oxidation as well as H_2O_2 decomposition. (3) The activity of the commercially available GO with catalase as an impurity encapsulated in the POPC liposomes at 25 °C was suggested to be highly stabilized because the H_2O_2 formation catalyzed by the liposomal GO was kinetically balanced well with the H_2O_2 decomposition catalyzed by the catalase in liposomes as well as the lipid membranes of GOL. The glucose oxidation catalyzed by the GOL with a sufficiently high membrane permeability to glucose resulted in the H_2O_2 accumulation. In the liposomal reaction system, it was shown that the liposome membranes play a crucial role in regulating the activity of encapsulated catalase for an effective H_2O_2 decomposition.

All of the results obtained in the present paper show that the liposomal encapsulation of GO containing a slight amount of catalase remarkably improves the efficiency and durability of both enzymes in comparison with the free GO plus catalase system. It is quite meaningful that such a slight amount of catalase as contained in the commercially available GO is enough for the continuous decomposition of H_2O_2 in the liposomal glucose oxidation. The interactions between the lipid bilayer membranes, catalase contained in a slight amount, and H_2O_2 produced should be examined in detail to fully understand the mechanism of the H_2O_2 decomposition observed in the GOL. Nevertheless, the liposomal GO almost completely free of the inhibition would be a useful biocatalyst in the practical bioreactor operated under oxidative conditions.

ACKNOWLEDGMENT

This work was supported by the Grant-in-Aid for Scientific Research (15206089 and 14750638) of the Ministry of Education, Culture, Sports, Science, and Technology of Japan and The Mazda Foundation's Research Grant.

LITERATURE CITED

(1) Taylor, M. A., Jones, M. N., Vadgama, P. M., and Higson, S. P. J. (1995) The characterization of liposomal glucose oxidase electrodes for the measurement of glucose, *Biosens. Bioelectron. 10*, 251−260.

(2) Memoli, A., Annesini, M. C., Mascini, M., Papale, S., and Petralito, S. (2002) A comparison between different immobilized glucose oxidase-based electrodes, *J. Pharm. Biomed. Anal. 29*, 1045−1052.

(3) Hill, K. J., Kaszuba, M., Creeth, J. E., and Jones, M. N. (1997) Reactive liposomes encapsulating a glucose oxidase-peroxidase system with antibacterial activity, *Biochim. Biophys. Acta 1326*, 37−46.

(4) Jones, M. N., Hill, K. J., Kaszuba, M., and Creeth, J. E. (1998) Antibacterial reactive liposomes encapsulating coupled enzyme, *Int. J. Pharm. 162*, 107−117.

(5) Tzanov, T., Costa, S. A., Gübitz, G. M., and Cavaco-Paulo, A. (2002) Hydrogen peroxide generation with immobilized glucose oxidase for textile bleaching, *J. Biotechnol. 93*, 87−94.

(6) Isaksen, A., and Adler-Nissen, J. (1997) Antioxidative effect of glucose oxidase nad catalase in mayonnaises of different oxidative susceptibility. I. Product trials, *Lebensm.-Wiss. Technol. 30*, 841−846.

(7) Nakao, K., Kiefner, A., Furumoto, K., and Harada, T. (1997) Production of gluconic acid with immobilized glucose oxidase in airlift reactors, *Chem. Eng. Sci. 52*, 4127−4133.

(8) Bao, J., Furumoto, K., Yoshimoto, M., Fukunaga, K., and Nakao, K. (2003) Competitive inhibition by hydrogen peroxide produced in glucose oxidation catalyzed by glucose oxidase, *Biochem. Eng. J. 13*, 69−72.

(9) Putnam, C. D., Arvai, A. S., and Bourne, Y. (2000) Active and inhibited human catalase structures: Ligand and NADPH binding and catalytic mechanism, *J. Mol. Biol. 296*, 295−309.

(10) Yoshimoto, M., Wang, S., Fukunaga, K., Walde, P., Kuboi, R., and Nakao, K. (2003) Preparation and characterization of reactive and stable glucose oxidase-containing liposomes modulated with detergent, *Biotechnol. Bioeng. 81*, 695−704.

(11) Yoshimoto, M., Wang, S., Fukunaga, K., Treyer, M., Walde, P., Kuboi, R., and Nakao, K. (2004) Enhancement of apparent substrate selectivity of proteinase K encapsulated in liposomes through a cholate-induced alteration of the bilayer permeability, *Biotechnol. Bioeng. 85*, 222−233.

(12) Kuboi, R., Yoshimoto, M., Walde, P., and Luisi, P. L. (1997) Refolding of carbonic anhydrase assisted by 1-palmitoyl-2-oleoyl-*sn*-glycero-3-phosphocholine liposomes, *Biotechnol. Prog. 13*, 828−836.

(13) Wang, S., Yoshimoto, M., Fukunaga, K., and Nakao, K. (2003) Optimal covalent immobilization of glucose oxidase-containing liposomes for highly stale biocatalyst in bioreactor, *Biotechnol. Bioeng. 83*, 444−453.

(14) Yoshimoto, M., Kuboi, R., Yang, Q., and Miyake, J. (1998) Immobilized liposome chromatography for studies of protein−membrane interactions and refolding of bovine carbonic anhydrase, *J. Chromatogr., B 712*, 59−71.

(15) Mayer, L. D., Hope, M. J., and Cullis, P. R. (1986) Vesicles of variable sizes produced by extrusion procedure, *Biochim. Biophys. Acta 858*, 161−168.

(16) MacDonald, R. C., MacDonald, R. I., Menco, B. Ph. B. M., Takeshita, K., Subbarao, N. K., and Hu, L. (1991) Small-volume extrusion apparatus for preparation of large, unilamellar vesicles, *Biochim. Biophys. Acta 1061*, 297−303.

(17) Kirby, C., and Gregoriadis, G. (1984) Dehydration−rehydration vesicles: A simple method for high yield drug entrapment in liposomes, *Biotechnology 2*, 979−984.

(18) Deamer, D. W., and Barchfeld, G. L. (1982) Encapsulation of macromolecules by lipid vesicles under simulated prebiotic conditions, *J. Mol. Evol. 18*, 203−206.

(19) Walde, P. (2003) Preparation of vesicles (liposomes), in *Encyclopedia of Nanoscience Nanotechnology* (Nalwa, H. S. Ed.) Vol. 10, American Scientific Publishers: Steven Ranch, CA; pp 1−37.

(20) Huggett, A. S. T., and Nixon, D. A. (1957) Use of glucose oxidase, peroxidase, and *o*-dianisidine in determination of blood and urinary glucose, *Lancet 273*, 368−370.

(21) Dorovska-Taran, V., Wick, R., and Walde, P. (1996) A ^{1}H nuclear magnetic resonance method for investigating the phospholipase D-catalyzed hydrolysis of phosphatidylcholine, *Anal. Biochem. 240*, 37−47.

(22) Qiang, Z., Chang, J.-H., and Huang, C.-P. (2002) Electrochemical generation of hydrogen peroxide from dissolved oxygen in acidic solutions, *Water Res. 36*, 85−94.

(23) Takeoka, S., Teramura, Y., Atoji, T., and Tsuchida, E. (2002) Effect of Hb-encapsulated vesicles on H_2O_2 reaction and lipid peroxidation, *Bioconjugate Chem. 13*, 1302−1308.

(24) Margoliash, E., Novogrodsky, A., and Schejter, A. (1960) Irreversible reaction of 3-amino-1:2:4-triazole and related inhibitors with the protein of catalase, *Biochem. J. 74*, 339−348.
(25) Rodriguez-Nogales, J. M. (2004) Kinetic behavior and stability of glucose oxidase entrapped in liposomes, *J. Chem. Technol. Biotechnol. 79*, 72−78.
(26) Betancor, L., Hidalgo, A., Fernández-Lorente, G., Mateo, C., Fernández-Lafuente, R., and Guisan, J. M. (2003) Preparation of a stable biocatalyst of bovine liver catalase using immobilization and postimmobilization techniques, *Biotechnol. Prog. 19*, 763−767.
(27) Schallreuter, K. U., Elwary, S. M. A., Gibbons, N. C. J., Rokos, H., and Wood, J. M. (2004) Activation/deactivation of acetylcholinesterase by H_2O_2: More evidence for oxidative stress in vitiligo, *Biochem. Biophys. Res. Commun. 315*, 502−508.

BC049909N

Magneto/Optical Annexin V, a Multimodal Protein

Eyk A. Schellenberger,[†,‡] David Sosnovik,[†] Ralph Weissleder,[†] and Lee Josephson*[,†]

Center for Molecular Imaging Research, Massachusetts General Hospital, Building 149, 13th Street, Charlestown, Massachusetts 02129, and Harvard Medical School, 25 Shattuck Street, Boston, Massachusetts 02115. Received April 14, 2004; Revised Manuscript Received June 15, 2004

Multimodal proteins, or proteins labeled with both fluorescent and magnetic reporter groups, can be used in a wide range of applications including FACS or fluorescence microscopy, MRI and or near-infrared based optical imaging, or to fractionate cells by magnetic cell sorting. A problem with multimodal proteins, however, is the need to maximize bioactivity, often achieved by minimizing the number of modification points of the protein, while attaching fluorescent and magnetic labels. Here we describe the synthesis of a magneto/optical form of annexin V, achieved by reacting the amino-CLIO nanoparticle with Cy5.5 and SPDP, to produce a fluorescent, sulfhydryl reactive nanoparticle. A single reactive sulfhydryl group was added to annexin V by reaction with SATA that preserved the protein's ability to bind apoptotic Jurkat T cells. Reacting SATAylated annexin V with an SPDP activated nanoparticle yielded Anx-CLIO−Cy5.5, a magneto/optical form of annexin V. The binding of Anx-CLIO−Cy5.5 was specific for apoptotic Jurkat T cells and had an EC_{50} of 3.66 nM. This was comparable to the strength of the interaction of unmodified annexin V with apoptotic cells, measured as the displacement of FITC−annexin by annexin V (2.4 nM). Our conjugation strategy preserves the strength of the interaction between annexin V and apoptotic cells, while yielding a probe, Anx-CLIO−Cy5.5, that is readily detectable by standard MR imaging or NIRF optical methods.

INTRODUCTION

Programmed cell death or apoptosis plays a crucial role during development (embryogenesis), for the maintenance of cellular homeostasis in the adult, and in the pathology of a wide range of diseases. Apoptosis is a central feature in diseases such as AIDS, neurodegenerative disorders (e.g., Alzheimer's disease), in myelodysplastic syndromes such as aplastic anemia and thalassemia, in progressive heart failure, for chronic hepatitis, and for transplant rejection (*1*−*3*). As cells proceed along pathways to apoptosis, phosphatidylserine (PS), a lipid normally facing the cytoplasm, flips and faces the extracellular fluid (*4*, *5*). The human protein annexin V (36 kDa) binds PS strongly and specifically, which is a reflection of a biological role as an anticoagulant (*6*, *7*). The binding of annexin V to PS is an attractive method for determining apoptosis in organs and tissues since PS is expressed early in the commitment to apoptosis (*4*, *8*) and is a feature of apoptotic cells regardless of how apoptosis is induced (*7*).

The ability of annexin V to recognize PS has led to the development of fluorescent or magnetic annexins that are useful in a variety of applications. Annexin V labeled with FITC is a widely used for identifying apoptotic cells by FACS (*9*, *10*), while a Cy5.5 labeled annexin V has been used for the NIRF/optical imaging of chemotherapy-induced apoptosis (*11*, *12*). Magnetic annexin V's are useful reagents for the removal of apopotic cells (*13*, *14*).

Here we describe the development of a magneto/optical annexin V that retains its binding activity for apoptotic cells, while being detectable by both fluorescent and magnetic resonance imaging modalities. Unlike earlier modified annexin V's, which are based on the direct attachment of fluorochromes to annexin V, or the conjugation of annexin V to magnetic particles, the magneto/optical annexin V is based on the attachment of annexin V to a nanoparticle that is both magnetic and fluorescent. The multimodal annexin V can be used with cell-based, fluorescence methods to identify apoptotic cells (FACS or fluorescent microscopy), with small animal optical imaging, or by MRI.

MATERIALS AND METHODS

Synthesis of Magneto/Optical Annexin V. The synthesis of magneto/optical annexin V consisted of three steps. First, the amino-CLIO (cross-linked iron oxide) nanoparticle was labeled with Cy5.5 and activated with SPDP, to yield a compound termed 2PySS−CLIO−Cy5.5. Second, annexin V was reacted with SATA in a manner that preserved its affinity for apoptotic cells Third, SATAylated annexin V was reacted with 2PySS−CLIO−Cy5.5 to yield the multimodal nanoparticle Anx-CLIO−Cy5.5.

Amino-CLIO was prepared as described (*15*, *16*). To 3.5 mL of amino-CLIO (∼10 mg Fe) we added 2.36 mL of 0.1 M sodium bicarbonate, pH 8.5. The buffered nanoparticle was then added to 1.75 mg of the monofunctional *N*-hydroxysuccinimde ester of Cy5.5 (Amersham-Pharmacia, Piscataway, NJ) dissolved in 0.175 mL of DMSO and incubated for 2 h at room temperature. We then added 0.6 mL of 120 mM SPDP (*N*-succinimidyl 3-(2-pyridyldithio) propionate) in DMSO and incubated for an additional 2 h. Unreacted Cy5.5 and SPDP were removed by gel filtration (Sephadex G-25 column equilibrated with 0.02 M Na citrate, 0.02 M Na borate, 0.9 M NaCl, pH 8.5). The number of Cy5.5 per nanoparticle was

* To whom correspondence should be addressed. Center for Molecular Imaging Research, Massachusetts General Hospital, Building 149, 13th Street, Room 5406, Charlestown, Massachusetts 02129. Fax: (617) 726-5708. E-mail: ljosephson@partners.org.

[†] Massachusetts General Hospital, Harvard Medical School.

[‡] Present address: Department of Radiology, Charité − Universitätmedizin Berlin, Campus Charité Mitte, Berlin, Germany.

10.1021/bc049905i CCC: $27.50 © 2004 American Chemical Society
Published on Web 08/19/2004

determined from the concentrations of iron (*16*) and Cy5.5 dye, the later being determined spectrophotometrically (E_{678} = 250 000), and by assuming 2064 iron atoms per nanoparticle (*17*). The number of 2PySS groups per nanoparticle was determined after the release of 2-pyridine-thione (2-PT) with dithiothreitol (*18*). The resulting nanoparticle, termed 2PySS−CLIO−Cy5.5, was stored at 4 °C until needed.

Annexin V was obtained from Theseus Imaging Corporation (Worcester, MA). To 1 mL of annexin V (3 mg) was added 600 μL of 0.1 M sodium bicarbonate, pH 8.6, and 12 μL of 10.8 mM SATA (*N*-succinimidyl 3-(2-pyridylthio)propionate, S-acetylthioactetate) dissolved in DMSO. After 1 h at room temperature under argon, 220 μL of a solution of 0.01 M hydroxylamine, 0.01 M EDTA (pH 8) was added. The mixture was incubated for 40 min at room temperature under argon, and unreacted SATA separated from annexin V by spin separation (Biogel P6 columns equilibrated with 0.1 M sodium bicarbonate, pH 8).

We then added 200 μL of 2Py-SS−CLIO−Cy5.5 to the SATAylated annexin V and allowed the mixture to stand overnight at room temperature under argon. Unreacted annexin V was removed by gel filtration (Sephadex G-150 equilibrated in 0.02 citrate 0.15 M NaCl, pH 8). Protein content of the resulting nanoparticle was determined by the BCA method (Pierce Chemical, Rockford, IL). Size of the nanoparticle was determined by light scattering using a Zetasizer (Malvern Instruments, Westboro, MA). Relaxivities were measured at 0.47 T and 40 °C using a relaxometer (Bruker Instruments, Braintree, MA).

Interaction of Anx-CLIO−Cy5.5 with Apoptotic Cells. Jurkat T cell cells (Clone E6−1, ATCC #TIB-152) grown in RPMI 1640 medium with 10% fetal bovine serum (Vitacell #30−2021, ATCC, Manassas VA) changed every 2 or 3 days were used in all studies. Apoptosis was induced by the addition of 7 μL of camptothecin (1 mM in DMSO) per milliliter of culture medium for 5−6 h at 37 °C. Induction of apoptosis was verified by staining with propidium iodide and FITC−annexin V using a calcium-containing binding buffer (1.8 mM $CaCl_2$, 10 mM HEPES, 150 mM NaCl, 5 mM KCl, 1 mM $MgCl_2$, pH 7.4). The cells were then analyzed with a FACS−Calibur cytometer (Becton Dickinson, San Jose, CA).

Competition Experiments. The dye-annexin V's we employed (Cy5.5 or FITC) had one mole of dye per mole of annexin V and were prepared as described (*11*, *12*). To assess the bioactivity of annexin V SATAylated to various extents, the ability to block the binding of FITC−annexin V to apoptotic cells was determined by FACS (*11*). Camptothecin-treated Jurkat T cells (10^4−10^5 cells) were incubated with different SATAylated annexin V's (1.0 μg in 200 μL binding buffer) for 5 min at room temperature. FITC−annexin V (0.1 μg) was then added for an additional 10 min at room temperature. Binding of FITC−annexin V to apoptotic cells was determined from the medians of the highest peaks from the FACS analysis as described (*11*). The relative FITC−annexin V fluorescence (Figure 1) was obtained by dividing the median value obtained of SATAylated annexin V's by that median value with no SATAylated annexin, that is by normalization to the binding in the absence of a SATAylated annexin V. IC_{50} values of Anx-CLIO−Cy5.5, annexin V, and Cy5.5−annexin V were determined by the ability to displace FITC−annexin V (4.1 nM or 0.03 μg/500 μL) in the assay above. The direct binding of Anx-CLIO−Cy5.5 to apoptotic cells was assessed by determining the relative cell associated fluorescence in the Cy5.5 channel of the apoptotic cell fraction for camptothecin-treated Jurkat T cells over a range of probe concentrations. The data were fitted to sigmoidal dose−response curves to obtain EC_{50}'s, IC_{50}'s, values of the Hill coefficient (*n*), and the correlation coefficient (R^2), indicating the goodness of fit, using Prism 4 (GraphPad Software, San Diego, CA).

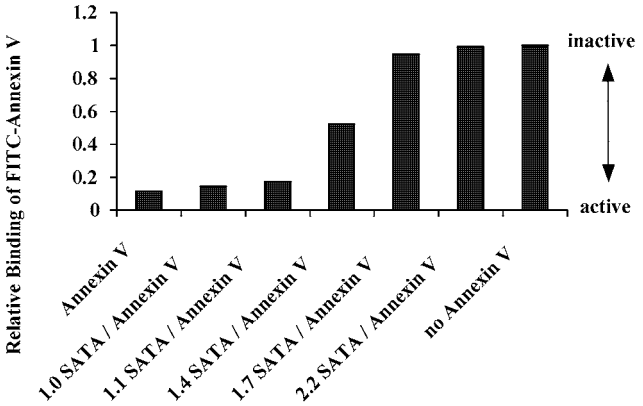


Figure 1. Binding of SATA−annexin V conjugates to camptothecin treated Jurkat T cells. Active SATA-annexin V's displace FITC-annexin V to yield a low Relative Binding by FACS. Inactive SATA-annexin V's, or no annexin V, fail to displace yielding a high Relative Binding. Relative binding is obtained by normalizing to the median fluorescence of the apoptotic cell fraction by FACS.

Table 1. Properties of Anx-CLIO−Cy5.5

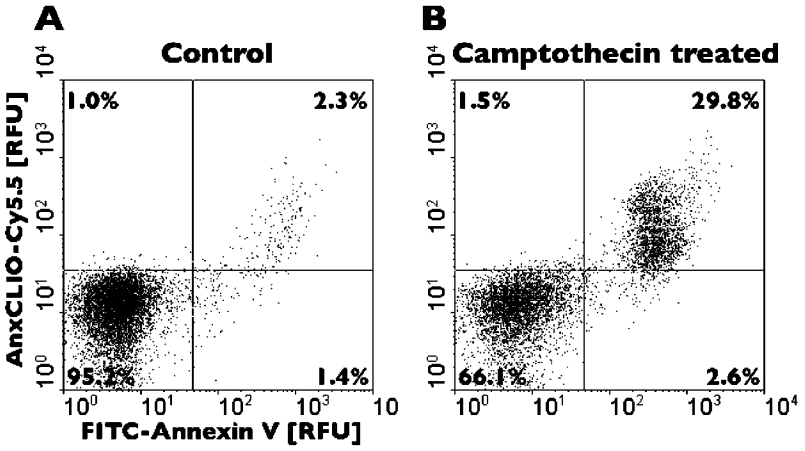
moles of annexin V per CLIO	3.5
moles of Cy5.5 dyes per CLIO	1.8
size [nm]	50
R1 [$mM^{-1}\,s^{-1}$]	19
R2 [$mM^{-1}\,s^{-1}$]	48

Optical and Magnetic Imaging With Anx-CLIO−Cy5.5. Jurkat T cells were incubated with Anx-CLIO−Cy5.5 (1 μg Fe/mL) for 10−15 min and washed twice with calcium binding buffer. Cell pellets in 300 μL tubes were prepared by centrifugation and imaged for surface reflectance fluorescence as described (*19*). MR imaging was performed on a 4.7 T Bruker BioSpin scanner. Transverse relation times (T2's) were determined by fitting signal intensity data (TE = 10−200 ms and TR = 2000 ms) to the spin echo signal intensity equation (*20*). A T2 weighted image was also taken at TE = 50/TR = 2000 (Figure 4).

RESULTS

Synthesis of Magneto/Optical Annexin V. The amino-CLIO nanoparticle was reacted with the NIRF dye Cy5.5 and then with the bifunctional reagent SPDP, followed by a single gel filtration step to remove all low molecular weight impurities. The nanoparticle, 2PySS−CLIO had 71 2PySS groups per nanoparticle, assuming 2064 Fe/nanoparticle (*17*). 2PySS−CLIO−Cy5.5 could be stored at 4 °C and is a general reagent for converting sulfhydryl-bearing proteins in to magneto/optical probes. The properties of the dual modality nanoparticle Anx-CLIO−Cy5.5 are summarized in Table 1.

The sensitivity of annexin V to modification of its amino groups by SATA using a FACS displacement assay is shown in Figure 1. The assay indicates that the attachment of one SATA per mole of annexin V does not affect binding to apoptotic cells. On the basis of these results, annexin V with on average one SATA per mole was reacted with the SPDP-activated amino-CLIO. The resulting nanoparticle had 3.5 annexin V's per nanoparticle with R1 and R2's of 19 and 48 $mM^{-1}\,s^{-1}$, respec-



(C) Cells Binding FITC-annexinV and/or Anx-CLIO-C Y5.5

Treatment	% Cells binding neither FITC-Annexin nor Anx-CLIO-Cy5.5	% Cells binding both FITC-Annexin & Anx-CLIO-Cy5.5	Total % Cells binding FITC-Annexin & Anx-CLIO-Cy5.5 similarly
None	95.2	2.3	97.5
Camptothecin	66.1	29.8	95.9

Figure 2. Dual wavelength FACS analysis with Anx-CLIO−Cy5.5 and FITC−annexin V. Untreated cells (A) and camptothecin-treated cells (B) are shown. Results from (A) and (B) are tabulated in (C).

tively, and a diameter of 50 nm by light scattering, which are values similar to CLIO nanoparticles functionalized with other types of biomolecules (*15*, *21*, *22*).

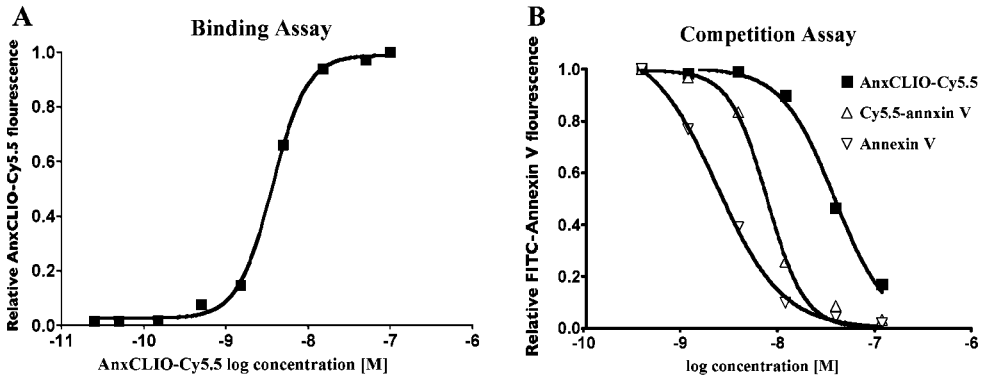
Binding of Magneto/Optical Annexin V, Anx-CLIO−Cy5.5, to Apoptotic Cells. Dual wavelength FACS with FITC−annexin as a reference is an excellent method for examining the specificity of probes such as Anx-CLIO−Cy5.5 for apoptotic cells. Anx-CLIO−Cy5.5 and FITC−annexin V bound in a similar manner to individual cells with populations of normal (Figure 2A) or camptothecin-treated cells (Figure 2B). The binding of probes to cells was in a similar manner at least 95% of the time (Figure 2C). Thus, the conjugation of annexin V to CLIO preserves the specificity of the annexin V interaction with apoptotic cells.

We next examined the strength of the interaction of Anx-CLIO−Cy5.5 with apoptotic cells as shown in Figure 3, using both direct binding and displacement assays. Using the direct binding assay for Anx-CLIO−Cy5.5, we obtained an EC_{50} of 3.66 nM per mole of annexin V, which can be compared to values expressed as dissociation constants as low as 0.1 nM (*23*) or as high as 7 nM (*24*). The conjugation of annexin V to Anx-CLIO−Cy5.5 preserves the strength of the interaction between annexin V and apoptotic cells. However, when the ability of Anx-CLIO−Cy5.5 to displace FITC−annexin was examined, an IC_{50} of 39 nM was obtained which was higher than the IC_{50} for annexin V (2.40 nM) or Cy5.5-annexin (7.8 nM). The multimodal probe Anx-CLIO−Cy5.5 thus interacts with apoptotic cells specifically (Figure 2) and with an affinity similar to native annexin V (3.66 versus 2.40 nM). However, the Anx-CLIO−Cy5.5 nanoparticle, and annexin V protein may interact with the phosphatidylserine in a somewhat different fashion, based on their differing ability to displace FITC−annexin (Anx-CLIO−Cy5.5 IC_{50} = 39 nM; annexin V IC_{50} = 2.4 nM). The presence of 3.5 annexin V's presented on a single 50-nm nanoparticle may bind PS somewhat differently from the 36 kDa annexin V molecule.

Optical and Magnetic Imaging With Anx-CLIO−Cy5.5. We next examined the detection of cells labeled with Anx-CLIO−Cy5.5 by both NIRF and MR imaging modalities. A high signal intensity NIRF signal was observed with apoptotic but not normal cells (Figure 4B) and a corresponding decrease in signal intensity (darkening) of cells was obtained with a T2 weighted MR image (Figure 4C). T2's were 76 ms for the control and 37 ms for the camptothecin-treated cells.

DISCUSSION

Multimodal, or fluorescent and magnetic, nanoparticles have numerous advantages over single modality based probe designs (*25*−*27*). During the research phase of probe development, fluorescence can be used with FACS or fluorescence microscopy to characterize the specificity of interactions with cells or study intracellular processing. Small animal NIRF based imaging for assessing probe targeting is often more convenient and cheaper than MRI. Fluorescence permits the use of multiple, optically distinct fluorochrome probes in conjunction with FACS, microscopy, or animal imaging devices (*19*, *25*). However, despite the rapid advances in small animal optical imaging technology and possible translation of small animal to human imaging (*28*, *29*), the development



(C) Binding of Anx-CLIO-Cy5.5 To Apoptotic Cells			
	Anx-CLIO-Cy5.5	Cy5.5Annexin V	Annexin V
EC_{50} [nM]	3.66	Not Obtained	Not Obtained
n	2.1		
R^2	0.99		
IC_{50} [nM]	39	7.8	2.4
n	1.6	2.3	1.3
R^2	0.99	0.99	0.99

Figure 3. Anx-CLIO−Cy5.5 binding to apoptotic Jurkat T cells. (A) Direct binding assay where Anx-CLIO−Cy5.5 binding is obtained by normalizing the median fluorescence of apoptotic T cells (camptothecin treated) obtained by flow cytometry. (B) Competition assay showing the displacement of FITC-Annexin V by Anx-CLIO−Cy5.5, Cy5.5−annexin V or annexin V. (C) Results from (A) and (B) are tabulated.

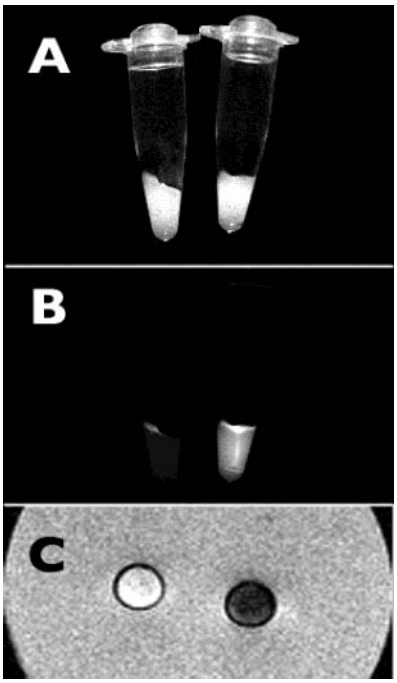


Figure 4. Multimodal imaging of Anx-CLIO−Cy5.5 binding to apoptotic cells. (A) White light image of pellets of control cells (left) and camptothecin-treated cells (right). Control cells (left) were 7.2% apoptotic, while camptothecin-treated cells were 55.3% apoptotic by FACS using FITC−annexin V. (B) NIRF image of the tubes from (A) show high fluorescence of apoptotic cells (C) MRI of cells in (B) shows camptothecin-treated cells (right) had a lower signal intensity, i.e., were dark, compared with the untreated cells.

and distribution of NIRF based clinical imaging systems lie well in the future while MRI is an established imaging modality.

The strategy we have employed for the design of Anx-CLIO−Cy5.5 yields a multimodal (magnetic and fluorescent) form of annexin V that differs from earlier fluorescent, radioactive, or magnetic annexin V's (*10*, *11*, *30*, *31*). First, we preserved the PS binding activity of annexin V by optimizing the reaction between annexin V and SATA (Figure 1). Annexin V loses its PS binding activity if more than 1 lysine per mole is modified by either SATA or fluorochromes (*32*), and appears to be highly sensitive to modification. We then attached SATAylated annexin V (36 kDa) to the SPDP-activated CLIO, which was about 1000 kDa (or about 30 nm). The nanoparticle had 2064 Fe atoms and 1.8 Cy5.5 dyes per nanoparticle. The resulting Anx-CLIO−Cy5.5 probe was highly active compared to the parent annexin V (Figure 3). Anx-CLIO−Cy5.5 is a PS-binding magneto/optical form of annexin V that is about 1000 kDa rather than 36 kDa, featuring 590 Fe atoms per annexin V (2064/3.5) for MR detection and 0.5 Cy5.5 molecules per annexin V (1.8/3.5) for detection by fluorescence.

The low molecular weight, predominant renal elimination, and short blood half-life of the 36 kDa form of annexin V may limit its ability to bind its target PS. Annexin V shows predominant renal elimination with a blood half-life 24 min in humans (*33*) and less than 10 min in mice (*34*, *35*). Radiolabeled PEGylated annexin V's have been developed in an effort to increase blood half-life and improve PS targeting (*36*), but based on the sensitivity of annexin V to modification, the attachment of PEG and DTPA to a single annexin V poses a considerable risk of inactivating the PS binding activity. Anx-CLIO−Cy5.5 is too large to undergo renal elimination and may have a longer blood half-life than annexin V.

Magneto/optical nanoparticles have been successfully used in several in vivo imaging applications. A fluorescent nanoparticle was used to image the cathepsin B activity of lymph nodes in live mice by simple surface reflectance and to obtain high-resolution MR images of nanoparticle disposition (*27*). We have shown that intra-

venously injected Cy5.5 labeled CLIO is internalized by microglia cells, and can be used as a preoperative MR contrast agent for the visualization of brain tumor in an animal model (*26*). The agent also can be seen by NIRF surface reflectance after removal of the cranium, and provides a method of determining tumor margins intraoperatively. Multimodal probes utilizing dextran rather than nanoparticle carriers have employed gadolinium and (fluorochrome), and have been used to study stem cell migration (*37*, *38*).

The addition of a fluorochrome to the magnetic nanoparticle permits FACS analysis or fluorescent microscopy to determine the disposition of the MR contrast agent. The near-infrared fluorescence of Anx-CLIO−Cy5.5 is distinct from many fluorochromes such as fluorescein or Alexafluor 488, which can be used in colabeling studies to characterize the subpopulation of cells binding the multimodal nanoparticle by FACS analysis, without spillover or compensation. With tissue sections and fluorescent microscopy, there is considerably less background with NIRF probes because mammals do not synthesize near-infrared fluorochromes. Other approaches to visualizing nanoparticles, such as iron staining or histochemical methods, require specific staining reagents and can suffer from higher backgrounds.

The fluorescent and magnetic character of Anx-CLIO−Cy5.5 is not only well suited to the determination of probe behavior in vitro and preclinically, but also offers multiple pathways to the development of a clinical diagnostic agent. First, the fluorochrome can be dropped and an annexin V-polymer coated superparamagnetic iron oxide could be used as an MR contrast agent. Polymer-coated iron oxides are used as MR contrast agents for the liver, lymph nodes, and gastrointestinal tract, and are also used to treat anemia. Although optical imaging is undergoing rapid development (*39*, *40*), MRI currently has the advantages of wide clinical availability and the ability to visualize probe accumulation deep within the human body. Second, the targeting biomolecule, in this case annexin V, and NIRF fluorochromes might be attached to a fluorochrome loaded polymeric molecules such as dextran, to yield a high molecular weight form of annexin V for optical imaging. Annexin V at 36 kDa undergoes renal elimination (*33*, *35*), while higher molecular weight forms may have substantially different and, in some applications, improved pharmacokinetics.

The ability to image apoptotic cells in vivo would likely be of significant value in both the diagnosis and treatment of many diseases and treatments. However, in many organs only a small fraction cells undergo apoptosis at any given moment, and thus probes with an optimized conjugation and labeling chemistry may be needed. Future studies will determine the ability of Anx-CLIO−Cy5.5 to detect apoptosis as the percentage of apoptotic cells by MRI and NIRF imaging methods and compare the 36 kDa Dye-annexin V conjugates and Anx-CLIO−Cy5.5 nanoparticle as optical imaging agents.

ACKNOWLEDGMENT

Work was supported by NIH Grants RO1CA86782, P50CA86355, R24 CA92782, and CA91807. E.A.S. was funded by a grant from the "Deutsche Akademie der Naturforscher und Mediziner Lepoldina." D.S. was supported by a Research Fellow Award from the Radiological Society of North America.

LITERATURE CITED

(1) Thompson, C. B. (1995) Apoptosis in the pathogenesis and treatment of disease. *Science 267*, 1456−1462.

(2) Peter, M. E., Heufelder, A. E., and Hengartner, M. O. (1997) Advances in apoptosis research. *Proc. Natl. Acad. Sci. U.S.A. 94*, 12736−12737.

(3) Bursch, W., Oberhammer, F., and Schulte-Hermann, R. (1992) Cell death by apoptosis and its protective role against disease. *Trends Pharmacol. Sci. 13*, 245−251.

(4) Martin, S. J., Reutelingsperger, C. P., McGahon, A. J., Rader, J. A., van Schie, R. C., and LaFace, D. M. et al. (1995) Early redistribution of plasma membrane phosphatidylserine is a general feature of apoptosis regardless of the initiating stimulus: inhibition by overexpression of Bcl-2 and Abl. *J. Exp. Med. 182*, 1545−1556.

(5) Schlegel, R. A., and Williamson, P. (2001) Phosphatidylserine, a death knell. *Cell Death Differ. 8*, 551−563.

(6) Funakoshi, T., Heimark, R. L., Hendrickson, L. E., McMullen, B. A., and Fujikawa, K. (1987) Human placental anticoagulant protein: isolation and characterization. *Biochemistry 26*, 5572−5578.

(7) van Engeland, M., Nieland, L. J., Ramaekers, F. C., Schutte, B., and Reutelingsperger, C. P. (1998) Annexin V-affinity assay: a review on an apoptosis detection system based on phosphatidylserine exposure. *Cytometry 31*, 1−9.

(8) Hammill, A. K., Uhr, J. W., and R. H. Scheuermann (1999) Annexin V staining due to loss of membrane asymmetry can be reversible and precede commitment to apoptotic death. *Exp. Cell Res. 251*, 16−21.

(9) Bossy-Wetzel, E., and Green, D. R. (2000) Detection of apoptosis by annexin V labeling. *Methods Enzymol 322*, 15−18.

(10) Vermes, I., Haanen, C., Steffens-Nakken, H., and Reutelingsperger, C. (1995) A novel assay for apoptosis. Flow cytometric detection of phosphatidylserine expression on early apoptotic cells using fluorescein labeled Annexin V. *J Immunol. Methods 184*, 39−51.

(11) Schellenberger, E., Bogdanov, A. J., Petrovsky, A., Ntziachristos, V., Weissleder, R., and Josephson, L. (2003) Optical imaging of apoptosis as a biomarker of tumor response to chemotherapy. *Neoplasia 5*, 187−192.

(12) Petrovsky, A., Schellenberger, E., Josephson, L., Weissleder, R., and Bogdanov, A., Jr. (2003) Near-infrared fluorescent imaging of tumor apoptosis. *Cancer Res. 63*, 1936−42.

(13) Sestier, C., Da-Silva, M. F., Sabolovic, D., Roger, J., and Pons, J. N. (1998) Surface modification of superparamagnetic nanoparticles (Ferrofluid) studied with particle electrophoresis: application to the specific targeting of cells. *Electrophoresis 19*, 1220−1226.

(14) Halbreich, A., Roger, J., Pons, J. N., Geldwerth, D., Da Silva, M. F., Roudier, M., et al. (1998) Biomedical applications of maghemite ferrofluid. *Biochimie 80*, 379−390.

(15) Josephson, L., Perez, J. M., and Weissleder, R. (2001) Magnetic nanosensors for the detection of oligonucleotide sequences. *Angew. Chem. Int. Ed. 40*, 3204−3206.

(16) Josephson, L., Tung, C. H., Moore, A., and Weissleder, R. (1999) High-efficiency intracellular magnetic labeling with novel superparamagnetic-Tat peptide conjugates. *Bioconjugate Chem. 10*, 186−191.

(17) Shen, T., Weissleder, R., Papisov, M., Bogdanov, A., Jr., and Brady, T. J. (1993) Monocrystalline iron oxide nanocompounds (MION): physicochemical properties. *Magn. Reson. Med. 29*, 599−604.

(18) Zhao, M., Kircher, M. F., Josephson, L., and Weissleder, R. (2002) Differential conjugation of tat Peptide to superparamagnetic nanoparticles and its effect on cellular uptake. *Bioconjugate Chem. 13*, 840−844.

(19) Mahmood, U., Tung, C. H., Bogdanov, A., Jr., and Weissleder, R. (1999) Near-infrared optical imaging of protease activity for tumor detection. *Radiology 213*, 866−870.

(20) Schellenberger, E., Bogdanov, A., Högemann, D., Tait, J. L., Weissleder, R., and Josephson, L. (2002) Annexin V-CLIO: A nanoparticle for detecting apoptosis by MRI. *Mol. Imaging 1*, 1−6.

(21) Perez, J. M., Josephson, L., O'Loughlin, T., Hogemann, D., and Weissleder, R. (2002) Magnetic relaxation switches capable of sensing molecular interactions. *Nat. Biotechnol. 20*, 816−20.

(22) Zhao, M., Josephson, L., Tang, Y., and Weissleder, R. (2003) Magnetic sensors for protease assays. *Angew. Chem. Int. Ed. Engl. 42*, 1375−1378.

(23) Ravanat, C., Archipoff, G., Beretz, A., Freund, G., Cazenave, J. P., and Freyssinet, J. M. (1992) Use of annexin-V to demonstrate the role of phosphatidylserine exposure in the maintenance of haemostatic balance by endothelial cells. *Biochem. J. 282 (Pt 1)*, 7−13.

(24) Blankenberg, F. G., Katsikis, P. D., Tait, J. F., Davis, R. E., Naumovski, L., Ohtsuki, K., et al. (1999) Imaging of apoptosis (programmed cell death) with 99mTc annexin V. *J. Nucl. Med. 40*, 184−191.

(25) Kircher, M. F., Josephson, L., and Weissleder, R. (2002) Ratio imaging of enzyme activity using dual wavelength optical reporters. *Mol. Imaging 1*, 1−7.

(26) Kircher, M. F., Mahmood, U., King, R. S., Weissleder, R., and L. Josephson (2003) A multimodal nanoparticle for preoperative magnetic resonance imaging and intraoperative optical brain tumor delineation. *Cancer Res. 63*, 8122−8125.

(27) Josephson, L., Kircher, M. F., Mahmood, U., Tang, Y., and Weissleder, R. (2002) Near-Infrared Fluorescent Nanoparticles as Combined MR/Optical Imaging Probes. *Bioconjugate Chem. 13*, 554−560.

(28) Ntziachristos, V., Tung, C. H., Bremer, C., and Weissleder, R. (2002) Fluorescence molecular tomography resolves protease activity in vivo. *Nat. Med. 8*, 757−760.

(29) Ntziachristos, V., Ripoli, J., and Weissleder, R. (2002) Would near-infrared fluorescence signals propagate through large human organs for clinical studies? *Opt. Lett. 27*, 333−335.

(30) Gorczyca, W., Melamed, M. R., and Darzynkiewicz, Z. (1998) Analysis of apoptosis by flow cytometry. *Methods Mol. Biol. 91*, 217−238.

(31) Kuypers, F. A., Lewis, R. A., Hua, M., Schott, M. A., Discher, D., Ernst, J. D., et al. (1996) Detection of altered membrane phospholipid asymmetry in subpopulations of human red blood cells using fluorescently labeled annexin V. *Blood 87*, 1179−1187.

(32) Schellenberger, E. A., Weissleder, R., and Josephson, L. (2004) Optimal modification of annexin V with fluorescent dyes. *ChemBioChem 5*, 271−274.

(33) Kemerink, G. J., Boersma, H. H., Thimister, P. W., Hofstra, L., Liem, I. H., Pakbiers, M. T., et al. (2001) Biodistribution and dosimetry of 99mTc−BTAP-annexin-V in humans. *Eur. J. Nucl. Med. 28*, 1373−1378.

(34) Tait, J. F., Cerqueira, M. D., Dewhurst, T. A., Fujikawa, K., Ritchie, J. L., and Stratton, J. R. (1994) Evaluation of annexin V as a platelet-directed thrombus targeting agent. *Thromb. Res. 75*, 491−501.

(35) Ohtsuki, K., Akashi, K., Aoka, Y., Blankenberg, F. G., Kopiwoda, S., Tait, J. F., et al. (1999) Technetium-99m HYNIC-annexin V: a potential radiopharmaceutical for the in-vivo detection of apoptosis. *Eur. J. Nucl. Med. 26*, 1251−1258.

(36) Ke, S., Wen, X., Wu, Q. P., Wallace, S., Charnsangavej, C., Stachowiak, A. M., et al. (2004) Imaging taxane-induced tumor apoptosis using PEGylated, 111In-labeled annexin V. *J. Nucl. Med. 45*, 108−115.

(37) Modo, M., Cash, D., Mellodew, K., Williams, S. C., Fraser, S. E., Meade, T. J., et al. (2002) Tracking transplanted stem cell migration using bifunctional, contrast agent-enhanced, magnetic resonance imaging. *Neuroimage 17*, 803−811.

(38) Huber, M. M., Staubli, A. B., Kustedjo, K., Gray, M. H., Shih, J., Fraser, S. E., et al. (1998) Fluorescently detectable magnetic resonance imaging agents. *Bioconjugate Chem 9*, 242−249.

(39) Ntziachristos, V., Bremer, C., Graves, E. E., and Weissleder, R. (2002) In-vivo tomographic imaging of near-infrared fluorescent probes. *Mol. Imaging, 1*.

(40) Ntziachristos, V., Bremer, C., and Weissleder, R. (2003) Fluorescence imaging with near-infrared light: new technological advances that enable in vivo molecular imaging. *Eur. Radiol. 13*, 195−208.

BC049905I

Design and Synthesis of a Short-Chain Bitistatin Analogue for Imaging Thrombi and Emboli

Kwamena E. Baidoo,*,† Linda C. Knight,‡ Kuo-Shyan Lin,† Jerome L. Gabriel,§ and Jan E. Romano‡

Department of Environmental Health Sciences, 615 North Wolfe Street, Rm. E6632, Baltimore, Maryland 21205, Department of Diagnostic Imaging, Temple University School of Medicine, Broad and Ontario Streets, Philadelphia, Pennsylvania 19140, and Biochemistry Department, Temple University School of Medicine, Broad and Ontario Streets, Philadelphia, Pennsylvania 19140. Received February 24, 2004; Revised Manuscript Received June 10, 2004

Previously, we showed that labeled bitistatin analogues possessed excellent characteristics for imaging both deep-vein thrombosis and pulmonary embolism. We hypothesized that the N-terminal amino acid sequence of bitistatin, which is different from other disintegrins, likely interacts with the binding site of platelets to confer desirable properties to bitistatin for imaging. In this study, we present the design, synthesis, and initial biological testing of a short-chain analogue of the native 83-amino-acid bitistatin sequence. Our initial molecular modeling of the binding loop of bitistatin showed that the minimal sequence that represented the binding region was a cyclic 10 amino acid sequence *cyclo*[*Cys*−Arg−Ile−Ala−Arg−Gly−Asp−Trp−Asn−*Cys(S)*]. Systematic modeling of a truncated N-terminal sequence of bitistatin fused with the optimized binding region having a thioether sequence through a *Gaba* spacer ultimately yielded the 24-amino acid peptide, *cyclo*-[CH_2CO−Arg−Ile−Ala−Arg−Gly−Asp−Trp−Asn−Cys(S−)]−*Gaba*−Gly−Asn−Glu−Ile−Leu−Glu−Gln−Gly−Glu−Asp−Ser−Asp−Ser−Lys−OH, **1**. The peptide was then coupled to the hydrazino-nicotinic acid bifunctional chelating agent and the purified adduct labeled with ^{99m}Tc using tricine as a coligand. Binding of the unlabeled and labeled peptide to stimulated human platelets was assayed in vitro. The ^{99m}Tc labeling yield was > 90%. The in vitro binding assays showed that the IC_{50} for inhibition of platelet aggregation was 3694 nM, while the Kd of the ^{99m}Tc labeled peptide was 185 nM, indicating moderate affinity for the receptor. The ^{99m}Tc-labeled peptide was able to identify sites of experimental thrombi and emboli in a canine model. The results suggest initial success in attempting to mimic the behavior of bitistatin for imaging thrombi and emboli.

INTRODUCTION

Bitistatin[1] is an 83-amino-acid peptide (Figure 1) isolated from the venom of *Bitis arietans* (*1*). The peptide binds to the αIIbβ3 (Glycoprotein IIb/IIIa) receptor on platelets that is involved in the process of platelet aggregation (*2*). Previously, we showed that radiolabeled analogues of bitistatin gave positive images of deep-vein thrombosis and pulmonary embolism in a single test (*3*, *4*). Deep-vein thrombosis and pulmonary embolism are often different halves of the same thromboembolic disease since a clot in the extremities can dislodge and relocate to the lungs. A test that can provide complete information on thromboembolic disease relatively quickly and noninvasively, as can be provided by radiolabeled bitistatin analogues through scintigraphy, would greatly impact patient management. For this reason, many efforts have been made to develop radiolabeled tracers for imaging thromboembolic disease. Many of these have been reviewed in a recent article (*5*). None of the tracers to date consistently provide high-contrast images of both deep-vein thrombosis and pulmonary embolism in a single test. Because of the great potential of labeled bitistatin, it would be greatly beneficial if short-chain synthetic analogues that mimic the natural peptide were available. In this study, we have designed and synthesized a 24-amino acid analogue, labeled it with technetium-99m, and evaluated its ability to image experimental deep-vein thrombosis and pulmonary emboli.

EXPERIMENTAL SECTION

General Methods and Materials. All chemicals were obtained from either the Aldrich Chemical Co. (Milwaukee, WI) or Sigma Chemical Company (St. Louis, MO). Solvents and chemicals were reagent grade and used as received without further purification. The bifunctional chelating agent, succinimidyl-6-hydrazinopyridine-3-carboxylic acid, was synthesized according to literature procedures (*6*).

* To whom correspondence should be addressed: Telephone: (410)-955-7706. Fax: (410) 955-6222. E-mail: kbaidoo@jhsph.edu.
† The Johns Hopkins Medical Institutions.
‡ Department of Diagnostic Imaging, Temple University School of Medicine.
§ Biochemistry Department, Temple University School of Medicine.

[1] Abbreviations: Boc−Lys(2Cl-Z)−PAM resin = N^{α}-*t*−Boc-N^{ϵ}-(2-chloro-benzyloxycarbonyl)-L-lysine−PAM resin; Boc−Ala−OH = N^{α}-*t*-Boc−L-alanine; Boc−Arg(Tos)−OH = N^{α}-*t*-Boc−N^{γ}-tosyl−L-arginine; Boc−Asn(Xan)−OH = N^{α}-*t*-Boc−N^{β}-xanthyl−L-asparagine; Boc−Asp(OcHx)−OH = N^{α}-*t*-Boc−L-aspartic acid β-cyclohexyl ester; Boc−Cys(Mbzl)−OH = N^{α}-*t*-Boc−S-*p*-methoxybenzyl−L-cysteine; Boc−*Gaba*−OH = *t*-Boc−4-aminobutanoic acid (*t*-Boc gamma aminobutanoic acid); Boc−Gln(Xan)−OH = N^{α}-*t*-Boc−γ -xanthyl−L-glutamine; Boc−Glu(OcHx)−OH = N^{α}-*t*-Boc−L-glutamic acid γ-cyclohexyl ester; Boc−Gly−OH = N^{α}-*t*-Boc−glycine; Boc−Ile−OH = N^{α}-*t*-Boc−L-isoleucine; Boc−Leu−OH = N^{α}-*t*-Boc−L-leucine; Boc−Ser(Bzl)−OH = N^{α}-*t*-Boc−O-benzyl−L-serine; Boc−Trp(CHO)−OH = N^{α}-*t*-Boc−N^{α}-formyl-L-tryptophan; Gaba = gamma aminobutanoic acid; *t*-Boc− = *tert*-butyloxycarbonyl−.

10.1021/bc049954v CCC: $27.50 © 2004 American Chemical Society
Published on Web 08/28/2004

```
          10         20         30         40         50         60         70         80
           .          .          .          .          .          .    ***   .          .
rBitistatin
G SPPVCGNEIL EQGEDCDCGS PANCQDQCCN AATCKLTPGS QCNHGECCDQ CKFKKARTVC RIARGDWNDD YCTGKSSDCP WNH

Bitistatin
  SPPVCGNEIL EQGEDCDCGS PANCQDQCCN AATCKLTPGS QCNHGECCDQ CKFKKARTVC RIARGDWNDD YCTGKSSDCP WNH

Barbourin
             EAGEECDCSS PEN---PCCD AATCKLRPGA QCADGLCCDQ CRFMKKGTVC RVAKGDWNDD TCTGQSADCP GLYG

Kistrin
             --GKECDCSS PEN---PCCD AATCKLRPGA QCGEGLCCEQ CKFSRAGKIC RIPRGDMPDD RCTGQSADCP RYH

Echistatin
                                                ECESGPCCRN CKFLKEGTIC KRARGDDMDD YCNGKTCDCP RNPHKGPAT
```

Abbreviations (14):

A= Ala	C= Cys	D= Asp	E= Glu	F= Phe
G= Gly	H= His	I= Ile	K= Lys	L= Leu
M= Met	N= Asn	P= Pro	Q= Gln	R= Arg
S= Ser	T= Thr	V= Val	W= Trp	Y= Tyr

Figure 1. Amino acid sequences of selected disintegrins. The sequences are aligned so that RGD domains (shown in bold, KGD for Barbourin) are aligned with bitistatin. Asterisks (***) indicate the position of the RGD or analogue.

Male CD-1 mice were purchased from the Charles River Laboratories (Charles River, MA). Amino acid analyses and MALDI mass-spectral analyses were performed by AnaSpec, Inc. (San Jose, CA). HPLC was performed with a Waters Chromatography Division (Milford, MA) HPLC System equipped with two model 510EF pumps, a model 680 automated gradient controller, a model 490 UV absorbance detector, and a Bioscan NaI scintillation detector connected to a Bioscan Flow-count System. The output from two channels of the UV detector and the output from the Flow-count system were fed into a Gateway 2000 P5−133 computer fitted with an IN/US System, Inc. (Tampa, FL) computer card. HPLC acquisition and analysis were performed with the Winflow software from IN/US. The semipreparative column (C18 Novapak cartridge, 25 mm × 10 cm, 6 μm), the analytical column (C18 Novapak cartridge, 8 mm × 10 cm, 4 μm), and the C18 Light Sep-Pak cartridges were purchased from Waters Chromatography Division. Reversed-phase HPLC solvents consisted of acetontrile containing 0.1% trifluoroacetic acid (solvent A) and water containing 0.1% trifluoroacetic acid (solvent B). The ^{99m}Tc activity of tissues from biodistribution studies was counted on an automated gamma counter (Pharmacia-Wallac model 1282). The ^{99m}Tc activity for synthetic reactions and doses for biodistribution was measured in a Capintec CRC-7 Dose Calibrator.

Molecular Modeling. All molecular modeling was performed on a Silicon Graphics Personal IRIS 4D/25 workstation using Biograf (Accelrys, San Diego, CA), which incorporates the DREIDING II all atom force field. All peptides were constructed using the peptide builder, while all nonpeptide components were similarly constructed using the organic builder; both routines are contained within the main Biograf program. Partial charges for each atom used in calculating the electrostatic energy contribution of the total energy for each structure were derived by the charge equilibration method of Rappe and Goddard (*7*). Energy calculations for each peptide or construct consisted of energy minimization and quenched molecular dynamics calculations for 50 ps., followed by energy minimization of the lowest-energy structure obtained from the molecular dynamics simulation.

The model of bitistatin used has previously been described (*4*). Briefly, the model was developed by homology modeling with kistrin, another disintegrin, whose structure has been determined by NMR and chemical analysis. The amino acid sequence of bitistatin is 63% identical and 75% similar to the sequence of kistrin (Figure 1). The amino acid sequences of bitistatin and kistrin were aligned, and then the NMR-derived coordinates of the backbone atoms of kistrin were used as a starting point. Computer site-directed mutagenesis was used to replace each amino acid side chain of kistrin with the homologous side chain of bitistatin. Residues present in bitistatin, but not present in kistrin, were added to the model. The pairing of cysteine residues in kistrin was assumed to be the same in bitistatin. The two additional cysteines present in bitistatin at positions 5 and 24 were assumed to form a crosslink. Subsequent disulfide mapping studies confirmed these disulfide pairings in bitistatin (*8*). The part of the molecule that is identical to kistrin was kept constant while the domains added as bitistatin were subjected to energy minimization calculations. The entire molecule was then subjected to energy minimization.

The RGD loop of bitistatin ranges from C60 to C79, and contains another Cys residue at position 72 branching to an adjacent disulfide loop (*4*). According to the previous model of bitistatin, a flattened loop structure stretches from A56 to T73 (*4*). For initial modeling, the minimum number of amino acids needed to simulate the native binding site was determined from systematic deletion of amino acids from either end of the binding loop of native bitistatin. A series of disulfide-constrained

56 73
C R T V A R I A **R G D** W N D D Y A C Native Bitistatin Binding Sequence
C R T V A R I A **R G D** W N D D Y C
C T V A R I A **R G D** W N D D Y C
C V A R I A **R G D** W N D D Y C
C V A R I A **R G D** W N D D C
C A R I A **R G D** W N D D C
C A R I A **R G D** W N D C
C R I A **R G D** W N D C
C R I A **R G D** W N C.....Best match by modeling
C I A **R G D** W N C
C I A **R G D** W C
C A **R G D** W C

Figure 2. Minimum binding sequence of bitistatin. The underlined residue in each sequence has been deleted in the subsequent peptide.

peptides was modeled, retaining Cys on each end for cyclization. Starting with the sequence found in native bitistatin, C−R−I−A−R−G−D−W−N−D−D−Y−C, the series of peptides shown in Figure 2 was modeled.

To select peptides or constructs for further study, each modeled structure was overlaid onto the structure of the corresponding amino acids of our model of natural Bitistatin shown in Figure 3A (*4*) while calculating the root-mean-square standard deviation (rms value) between the modeled structures. Structures with the lowest rms value, suggesting the best "goodness of fit", were selected for further study.

In addition to the RGD-containing loop, bitistatin contains an N-terminal domain of 10−12 amino acids that other related disintegrins lack as depicted in Figure 1. We hypothesized that this N-terminal domain may be responsible for the improved binding properties of bitistatin in vivo. Thus, a second domain was modeled to mimic this section of bitistatin. In native bitistatin, the sequence of the N-terminal domain is S−P−P−V−C-G−N−E−I−L and it is attached to the rest of the molecule by the intervening 47 amino acids and a disulfide bond between C5 and C24. Modeling was used to design a domain that would contain a minimum of amino acids, which could be attached to the single RGD-containing loop peptide modeled above, and which would simulate the tertiary structure of the native N-terminal domain relative to the native RGD-containing domain.

Molecular modeling resulted in the 24 amino acid sequence **1** (Scheme 1), the model of which is depicted in Figure 3B, as a good fit to the structure of bitistatin.

Molecular modeling was also performed on the bifunctional chelator-modified peptide, with and without technetium and tricine, to confirm that these modifications did not adversely affect the orientation of the peptide domains (Figure 4).

Synthesis of the Short Chain Bitistatin Analogue. *cyclo*-[CH_2CO−Arg−Ile−Ala−Arg−Gly−Asp−Trp−Asn−Cys(S−)]−*Gaba*−Gly−Asn−Glu−Ile−Leu−Glu−Gln−Gly−Glu−Asp−Ser−Asp−Ser−Lys−OH, **1**, was synthesized using the BOC technology on an Advanced ChemTech ACT90 automated peptide synthesizer starting with 1.75 g (1.4 mmol, 0.8 mmol/g) Boc−Lys(2Cl−Z)−PAM resin according to Scheme 1. Each Boc-protected amino acid (9 mmol), including Boc−Ser(Bzl)−OH, Boc−Asp(OcHx)−OH, Boc−Glu(OcHx)−OH, Boc−Gly−OH, Boc−Gln(Xan)−OH, Boc−Leu−OH, Boc−Ile−OH, Boc−Asn(Xan)−OH, Boc−*Gaba*−OH, Boc−Cys(Mbzl)−OH, Boc−Trp(CHO)−OH, Boc−Arg(Tos)−OH, and Boc−Ala−OH was reacted with an equimolar mixture of N-hydroxybenzotriazole (HOBt) and 1,3-diisopropylcarbodiimide (DIC) before coupling to the growing sequence. Deprotection of the Boc group was performed in the presence of 35% trifluoroacetic acid, 3% anisole, 0.2% dithiothreitol in dichloromethane (2 times; first time 5 min, second time 25 min). The coupling time per cycle was 30 min. Coupling was repeated if necessary after a ninhydrin test was performed to ascertain completeness of the reaction. The coupling of bromoacetic acid to the sequence followed similar procedures for the amino acids, but used only 1,3-diisopropylcarbodiimide for activation. At the end of chain lengthening, the resin was dried by high vacuum and the peptide was cleaved from the resin with condensed hydrogen fluoride in the presence of *p*-cresol at 0 °C for 1.5 h. The HF was removed under a stream of nitrogen and the residue was washed with ether (3 × 30 mL), then dissolved with 10% acetic acid (100 mL), followed by filtration and lyophilization.

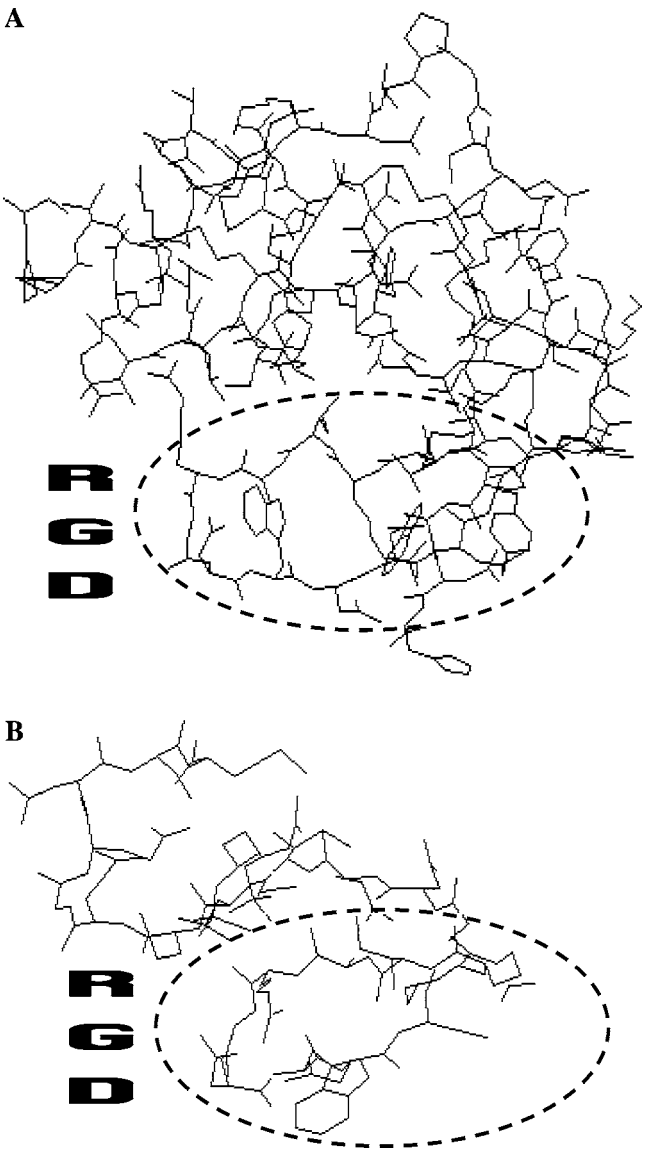
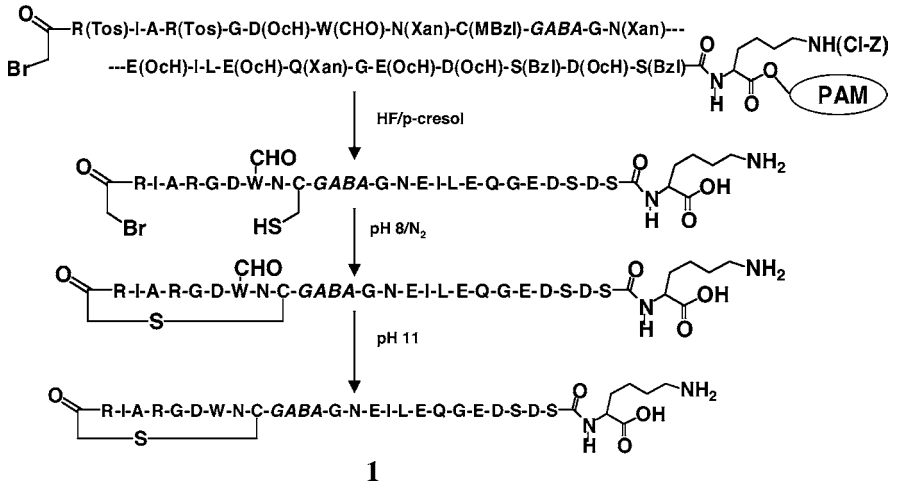


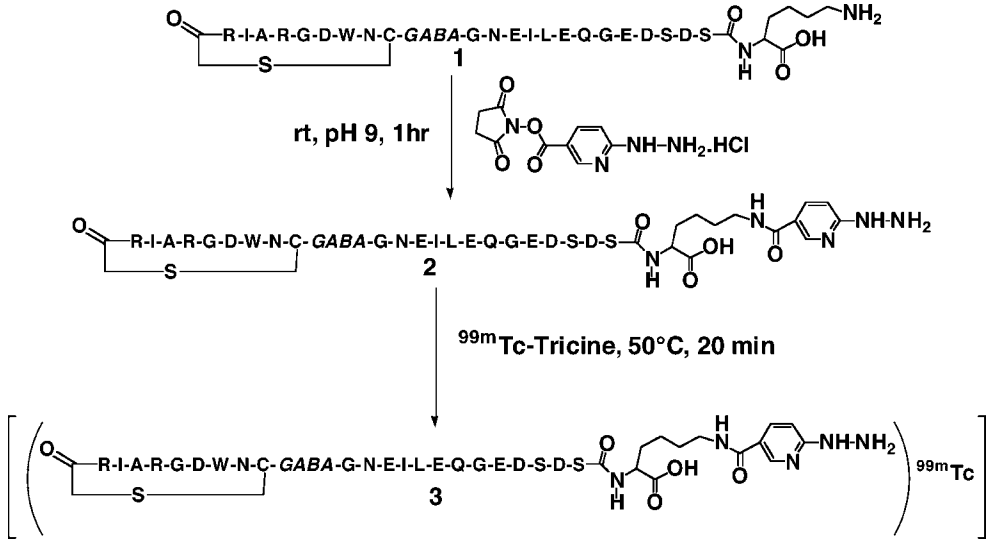
Figure 3. Molecular model of bitistatin (A) compared to the peptide bitistatin analogue (B). The dashed area shows the binding domain.

Cyclization was performed by dissolving 0.5 g of lyophilized powder in 1000 mL water, adjusting the pH to 8.2 with 2 M ammonium hydroxide, and stirring the mixture under nitrogen at room temperature for 24 h. The mixture was then lyophilized again. To remove the formyl (CHO) group on Trp, the mixture was dissolved in water and the pH was adjusted to 11 with 2.5 N sodium hydroxide for 5 min and then readjusted to 7 with 3 N hydrochloric acid. The resulting peptide was purified

Scheme 1. Synthesis of the Target Peptide



Scheme 2. Synthesis of the ^{99m}Tc Labeled Peptide



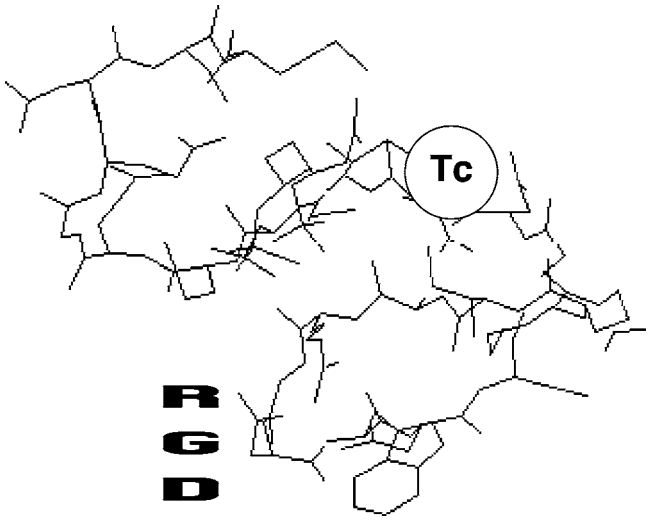


Figure 4. Design of fusion peptide allows for placement of Tc complex on the opposite side of molecule from binding face.

by semipreparative reversed-phase HPLC. The yield was 18%. MALDI MS: calc. MW for expected product 2716.2, found $[M + H]^+$ 2717.1.

Amino acid analysis: calc./found Asp (5/5.03), Ser (2/1.42*), Glu (4/4.29), Gly (3/2.77), Arg (2/2.24), Ala (1/0.93), Cys (1/0.03*), Lys (1/1.0), Ile (2/1.84), Leu (1/ 0.95), Trp (1/0**), and *Gaba* (1/1.0). (*Ser and Cys were partially destroyed during hydrolysis. **Trp was completely destroyed during hydrolysis).

Coupling of the Peptide to Succinimidyl-6-hydrazinopyridine-3-carboxylic Acid. The bifunctional chelating agent, succinimidyl-6-hydrazinopyridine-3-carboxylic acid (6), was coupled to the peptide according to Scheme 2. A DMF solution of succinimidyl-hydrazinonicotinate·HCl (210 mg/mL, 100 μL) was added to a solution of compound **1** (5 mg, 1.8 μmol) in borate buffer (0.4 mL, 0.1 M, pH 9) and the pH was adjusted to 9 with triethylamine. The mixture was incubated at room temperature for 1 h and then extracted with ether (3 × 2 mL). The aqueous fraction was chromatographed by HPLC with a linear gradient from solvent B (100%) to solvent A (80%)/solvent B (20%) over the course of 60 min at a flow rate of 6 mL/min using the semipreparative column monitored on-line for UV absorption at 220 nm.

^{99m}Tc Labeling of the Peptide. The ^{99m}Tc derivative of ***cyclo*-[CH_2CO−Arg−Ile−Ala−Arg−Gly−Asp−Trp−Asn−Cys(S−)]−*Gaba*−Gly−Asn−Glu−Ile−Leu−Glu−Gln−Gly−Glu−Asp−Ser−Asp−Ser−Lys−OH**, was synthesized according to Scheme 2. To a solution of the coupled peptide in ethanol (10 μg in 0.2 mL) a solution of tricine in water (50 mg, 0.4 mL) was added followed by a solution of freshly prepared stannous chloride

dissolved in HCl(aq) (20 μg in 20 μL 0.1 M HCl). The mixture was vortexed for 1 min. To this mixture was added ^{99m}Tc-pertechnetate in saline solution (10 mCi, 0.4 mL) and the reaction mixture was vortexed for an additional 1 min followed by incubation at 50 °C for 20 min. The product was purified by solid-phase extraction using a C-18 Sep-Pak cartridge. The Sep-Pak cartridge was first washed with ethanol (5 mL) followed by a solution of ammonium acetate (0.05 M, 5 mL). The reaction mixture containing the ^{99m}Tc-labeled ***cyclo*-[CH_2CO−Arg−Ile−Ala−Arg−Gly−Asp−Trp−Asn−Cys(S−)]−*Gaba*−Gly−Asn−Glu−Ile−Leu−Glu−Gln−Gly−Glu−Asp−Ser−Asp−Ser−Lys−OH** was diluted five times with ammonium acetate (0.05 M) and then passed through the Sep-Pak cartridge. The Sep-Pak cartridge was washed with an ammonium acetate solution (0.05 M, 5 mL) followed by elution of the ^{99m}Tc-labeled ***cyclo*-[CH_2CO−Arg−Ile−Ala−Arg−Gly−Asp−Trp−Asn−Cys(S−)]−*Gaba*−Gly−Asn−Glu−Ile−Leu−Glu−Gln−Gly−Glu−Asp−Ser−Asp−Ser−Lys−OH** with ethanol (300 μL). The yield of product was >90%.

Inhibition of Platelet Aggregation. Blood was obtained from anonymous aspirin-free human donors according to an approved Institutional Review Board protocol and anticoagulant (0.1 vol, 3.8% sodium citrate) was added. The blood was centrifuged (160 x g, 12 min) to obtain platelet-rich plasma. The concentration of platelets in human platelet-rich plasma was determined using a hemacytometer, then diluted with the donor's own plasma to obtain a platelet concentration of 300 000/μL. For each measurement, 400 μL of diluted platelet-rich plasma was placed in a cuvette and stirred at 37 °C. Vehicle (saline) or various concentrations of peptide were added in a volume of 10 μL and stirred at 37 °C for 1 min while recording visible light transmission. ADP was then added (final concentration of 10 μM) to induce platelet aggregation. Platelet aggregation was determined by change in light transmission through the platelet-rich plasma, which was recorded for 5 min after ADP addition. The IC_{50} was determined (by least-squares fitting) as the concentration of peptide required to produce 50% inhibition of the response to ADP in the presence of the vehicle. Results were normalized to the results for the tetrapeptide Arg-Gly-Asp-Ser (RGDS).

Equilibrium Platelet Binding Assay. Platelet-rich plasma was obtained as described above. Plasma proteins were then removed by filtering the platelets through Sepharose 2B (80 × 25 mm equilibrated with an elution buffer containing 137 mM NaCl, 2.7 mM KCl, 0.1% glucose, 0.2% bovine serum albumin, 0.4 mM NaH_2PO_4, 12 mM $NaHCO_3$, and 10 mM HEPES, pH 7.45). Fractions containing the highest concentrations were pooled, diluted to a concentration of 10^8 platelets/mL, and used within 1 h of preparation. Aliquots of the platelets were stimulated with 19 μM ADP, combined with a radioligand (^{99m}Tc labeled peptide or ^{125}I labeled rBitistatin) over a range of concentrations, and then incubated for 1 h at 37 °C. Nonspecific binding was determined in the presence of 9 mM EDTA (*3*). Platelet-bound radioligand was separated from free radioligand by centrifuging (13 000 x g, 3 min) the suspension through 30% (W/V) sucrose. Scatchard analysis was used to analyze the data (*9*).

Biodistribution. The ethanolic solution of ^{99m}Tc-labeled peptide from the Sep Pak separation was diluted with physiologic saline to make a final injectate (10 μCi/mL) containing < 0.5% ethanol.

Normal male CD-1 mice weighing 24.8 ± 1.3 g were used for biodistribution studies. The labeled peptide (2 μCi, 200 μL) was injected into mice via the tail vein. At 15, 30, 60, and 180 min postinjection, four mice for each time point were euthanized by cervical dislocation. Major organs were dissected, weighed, and counted in an automated gamma counter with aliquots of the injectate (as standards) counted at the same time. The percent injected dose per organ (% ID/organ) and the percent injected dose per gram (% ID/gram) were calculated. The % ID in blood was estimated with the assumption that the total blood volume is 6.5% of the body weight (*10*).

Imaging Experimental Thrombi. Radiolabeled peptide was evaluated in a standardized canine model of deep-vein thrombosis and pulmonary embolism (*3*, *4*). Briefly, under isoflurane anesthesia, an 8-mm embolization coil was placed in the femoral vein of the dog for deep-vein thrombosis while two 5-mm coils were released in the inferior vena cava for pulmonary embolism. The lesions were allowed to develop and mature for 24 h. The ^{99m}Tc-labeled-peptide (8 mCi) was injected through a foreleg vein. Imaging of ^{99m}Tc was performed for 4 h using a large-field-of-view camera (General Electric Medical Systems, Milwaukee) interfaced to a Macintosh computer (Apple, Cupertino, CA) and a data acquisition and processing board (NucLear Mac, Scientific Imaging, Denver, CO). Regions of interest were drawn around the thrombus in the leg and compared to a region of about the same size around adjacent muscle, and also around the vessel in the opposite leg corresponding to the location of the thrombus. The average counts per pixel in each region were computed for the calculation of the following ratios: thrombus:muscle and thrombus:contralateral site. Similarly, for the chest images, regions for embolus, adjacent lung, heart, and muscle (behind the lungs, near the vertebral column) were drawn to obtain embolus:lung, embolus:heart, and embolus-to-muscle ratios. The presence of clots in the lungs and leg were confirmed at autopsy.

RESULTS AND DISCUSSION

Bitistatin exhibits superior imaging characteristics among radioiodinated disintegrins evaluated for the imaging of experimental thrombosis (*3*). The ^{123}I-labeled analogue showed high thrombus uptake, low soft-tissue uptake, and high thrombus and embolus-to-blood and thrombi and emboli-to-soft-tissue differentiation. The ^{99m}Tc analogue showed the highest thrombus-to-blood and thrombus-to-soft-tissue ratios of any ^{99m}Tc-labeled thrombus and/or embolus imaging agent studied (*4*). Radiolabeled bitistatin analogues, therefore, offer the unique potential to generate radiopharmaceuticals capable of rapid positive imaging of both pulmonary emboli and deep-vein thrombosis in a single test. Because native bitistatin is 83 amino acids long and has multiple internal disulfide crosslinks, chemical synthesis is difficult. Thus, we embarked on an effort to generate a short chain analogue that could more conveniently be synthesized.

Bitistatin contains seven internal disulfide bridges that help to maintain its tertiary structure. Initial molecular modeling of the native bitistatin sequence shown in Figure 3A (*4*) indicated that the required RGD binding motif is presented at the turn of a loop represented by the sequence C−R−I−A−R−G−D−W−N−D−D−Y−C (Figure 2). Systematic sequential deletion of single residues from either end resulted in the cyclic decapeptide sequence *C−R−I−A−R−G−D−W−N−C* as the best match of the native binding sequence.

One major difference between bitistatin and other disintegrins is a highly charged domain of additional

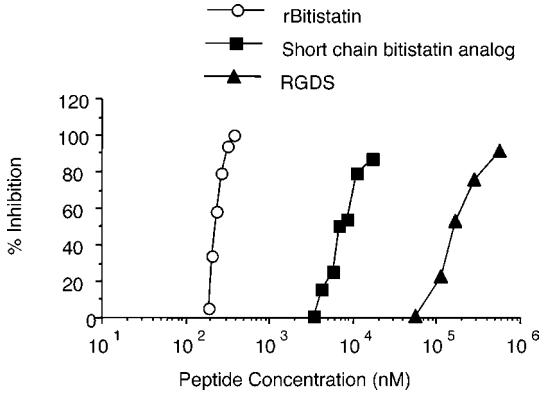


Figure 5. Inhibition of platelet aggregation by the peptides.

amino acids at the N-terminal region. In the model of native bitistatin, this N-terminal sequence appears to be parallel to the binding loop. We hypothesized that this sequence could be interacting with the receptor in some fashion to confer the desirable imaging properties to the molecule. Molecular modeling was performed of components of the N-terminal region fused with the minimal binding site. To confer greater stability to the anticipated peptide and to allow compatibility to a wide variety of bifunctional chelating agents for radiometalation, we replaced the disulfide bridge with the more stable thioether bridge. Furthermore, we attached a Lys residue at the C-terminal to afford the attachment of bifunctional chelating agents to the epsilon amino group. The final molecule having the best fit to the model of bitistatin was the 24-residue peptide *cyclo*-[CH_2CO−Arg−Ile−Ala−Arg−Gly−Asp−Trp−Asn−Cys(S−)]−*Gaba*−Gly−Asn−Glu−Ile−Leu−Glu−Gln−Gly−Glu−Asp−Ser−Asp−Ser−Lys−OH (Scheme 1) whose model is shown in Figure 3B in comparison to the model of bitistatin (Figure 3A). Figure 4 shows that after Tc derivatization, the Tc chelate would be located far from the RGD binding site and thus is not expected to interfere with receptor binding.

Synthesis of the target peptide was performed on an Advanced ChemTech synthesizer ACT90 using the BOC technology as shown in Scheme 1. The final HPLC-purified product was chemically characterized by amino acid analysis and MALDI Mass Spect. Results of in vitro assays of the ability of the new peptide to inhibit platelet aggregation are shown in Figure 5 comparing the activity of the new peptide with a short straight-chain RGD peptide RGDS and recombinant bitistatin (rbitistatin). The IC_{50} of the recombinant bitistatin, the new peptide, and RGDS were 114, 3694, and 100 000 nM, respectively. Thus, while the biological activity of the new peptide was 27-fold better than the RGDS peptide, it was 32-fold less active than recombinant bitistatin.

Table 1. Biodistribution of the ^{99m}Tc Labeled Peptide, *Cyclo*-[CH_2CO−Arg−Ile−Ala−Arg−Gly−Asp−Trp−Asn−Cys(S−)]−*Gaba*−Gly−Asn−Glu−Ile−Leu−Glu−Gln−Gly−Glu−Asp−Ser−Asp−Ser−Lys−OH in Normal Mice

	% injected dose/g[a]			
Organ	15 min	30 min	1 h	3h
blood	7.67 ± 0.27	5.50 ± 0.45	4.14 ± 0.63	1.94 ± 0.35
brain	0.35 ± 0.03	0.21 ± 0.04	0.15 ± 0.03	0.06 ± 0.01
heart	2.62 ± 0.14	1.96 ± 0.24	1.77 ± 0.13	1.21 ± 0.20
lung	4.17 ±0.60	3.06 ± 1.00	2.99 ± 0.56	1.80 ± 1.00
kidneys	73.40 ± 3.95	88.36 ± 7.71	98.26 ± 4.51	112.31 ± 12.10
spleen	2.04 ± 0.37	1.75 ± 0.37	1.92 ± 0.33	1.45 ± 0.18
pancreas	2.38 ± 0.19	1.73 ± 0.18	1.48 ± 0.44	1.06 ± 0.40
stomach	7.81 ± 2.59	10.16 ± 4.10	7.34 ± 1.37	4.12 ± 1.74
intestines	1.63 ± 0.09	1.58 ± 0.17	1.73 ± 0.19	1.77 ± 0.08
liver	4.73 ± 0.52	4.03 ± 0.65	4.47 ± 0.78	3.84 ± 0.45
muscle	1.73 ± 0.21	1.06 ± 0.18	0.71 ± 0.05	0.56 ± 0.24

[a] Average ± 1 SD, $n = 4$.

To label the peptide with ^{99m}Tc, coupling with the hydrazinonicotinamidyl bifunctional chelating agent was performed (Scheme 2). After removal of excess uncoupled reagent by HPLC, the modified peptide was labeled in high yield with ^{99m}Tc using tricine as the coligand. As shown in the Scatchard analysis of in vitro binding studies depicted in Figure 6, the Kd of the peptide was 185 nM with a Bmax of 117 000 sites/cell compared to a Kd of 8 nM and Bmax of 80 000 sites/cell for ^{125}I−rbitistatin. The Kd for ^{99m}Tc-labeled bitistatin from a previous study was 32 nM (*4*). Thus, the ^{99m}Tc-labeled peptide has moderate affinity for the receptor.

Biodistribution studies in normal CD-1 mice showed that the peptide cleared rapidly from the blood and all normal tissues except the kidneys where a substantial amount of the activity accumulates over an extended period of time (Table 1). At 3 h postinjection, there was still significant soft tissue uptake. The highest soft tissue uptake was in the kidneys, which tends to accumulate ^{99m}Tc-labeled small peptides. Varying levels of kidney activity have been associated with ^{99m}Tc−hydrazinonicotinyl−tricine conjugates. The levels of activity exhibited here are higher than usual but similar to those obtained in the kidneys for a ^{99m}Tc-labeled polypeptide, EPI−HNE−2 (*11*), using a similar procedure. The high kidney activity levels may be related to the peptide itself in conjunction with the labeling methodology.

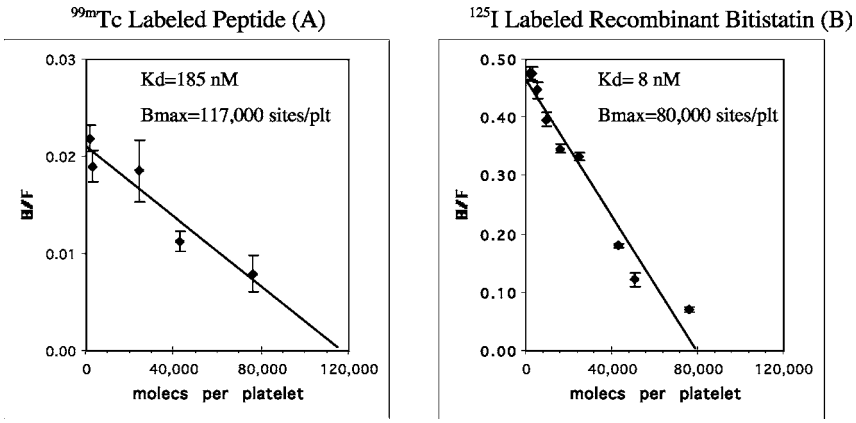


Figure 6. Scatchard plots of the binding of the ^{99m}Tc-Labeled Peptide (A) compared to the ^{125}I-Labeled Recombinant Bitistatin (B). B/F = Bound Ligand/Free Ligand, molecs = molecules.

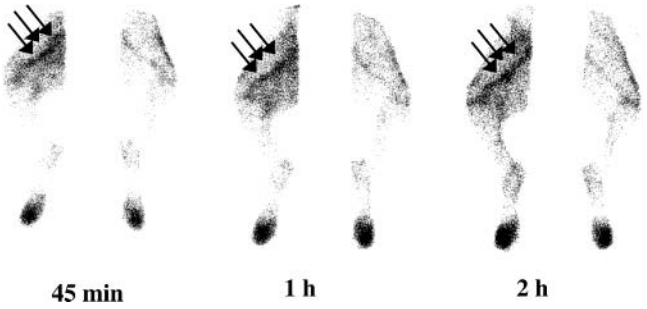


Figure 7. Images of experimental Deep-Vein Thrombosis in a canine model using the ^{99m}Tc-labeled peptide. The images show the hind legs of the dog with the arrows pointing to the clots.

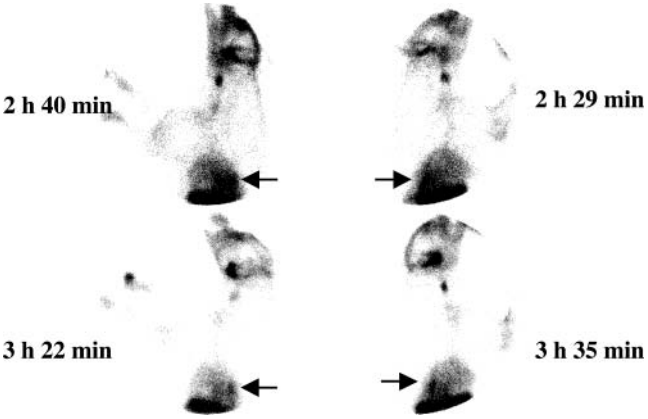


Figure 8. Images of experimental Emboli in the lungs of a dog using the ^{99m}Tc-labeled peptide. The images represent lateral positions of the head, neck, and upper torso. The arrows point to the position of the clots in the lungs. The heart is also in the field of view.

Table 2. Region-of-Interest Analysis of ^{99m}Tc−Short-Chain Bitistatin Analogue Images

	legs		
time postinjection	45 min	1 h	2 h
thrombus: muscle	1.56	1.42	1.57
thrombus: contralateral site	1.68	1.47	1.80

	chest	
time postinjection	2 h 29 min right lateral	3 h 35 min right lateral
embolus: lung	1.15	1.30
embolus: muscle	4.08	3.91
embolus: heart	1.53	1.44
time postinjection	2 h 40 min left lateral	3 h 22 min left lateral
embolus: lung	1.13	1.33
embolus: muscle	3.05	3.04
embolus: heart	1.31	1.47

To investigate the utility of the ^{99m}Tc-labeled peptide for imaging thrombi and emboli, we performed imaging of experimental deep-vein thrombosis and pulmonary emboli in a dog. Figures 7 and 8 show representative images obtained for the deep-vein thrombus and the emboli in lungs of the same dog, respectively. There appeared to be two clots in the lung and one main clot in the leg. The clots in the lung and the leg were discernible within the 4-h imaging period. The clot in the leg could be seen earlier within 45 min postinjection. The target-to-nontarget ratios obtained from the image are presented in Table 2. Comparison of results obtained with bitistatin labeled with ^{99m}Tc in the same fashion (*4*) indicated that the peptide under study was less effective than the native peptide for imaging thrombi and emboli. The lower contrasts obtained with this peptide may be due to the lower affinity of the labeled peptide compared to labeled bitistatin.

Currently, ^{99m}Tc−Apcitide, a small peptide containing a surrogate for RGD constrained in a small loop, is an approved radiopharmaceutical for imaging deep-vein thrombosis. The thrombus uptake of ^{125}I−bitistatin or ^{99m}Tc−bitistatin in the standardized canine model has been consistently much higher than that of ^{99m}Tc−Apcitide. In the same animal model, ^{99m}Tc−Apcitide had image-derived thrombus:contralateral vessel and thrombus:muscle ratios of 2.0 and 1.9 at 4 h postinjection (*12*). The short-chain peptide analogue of bitistatin described here did not exhibit an advantage over ^{99m}Tc−Apcitide with respect to imaging deep-vein thrombosis. However, the bitistatin analogue was able to produce images of pulmonary embolism. No images of pulmonary embolism have previously been reported for ^{99m}Tc−Apcitide.

The RGD-containing loop in bitistatin is very large (more than 13 amino acids). Because of its size, it is inherently flexible and probably depends on the rest of the bitistatin molecule to maintain its orientation. In contrast, the small tetrapeptide loop structure in Apcitide is fairly rigid. Although molecular modeling in this report predicted that a loop structure of 10 amino acids containing RGD would be the best match to the binding loop of bitistatin, it is possible that in the physiologic environment this loop is very flexible and does not have adequately high affinity in all configurations. Previous studies in this animal model with a ^{99m}Tc-labeled linear RGD-containing peptide (*13*) (based upon the binding sequence of an antiplatelet monoclonal antibody) resulted in poorer thrombus binding than the short-chain bitistatin analogue reported here. In this study, we have attempted to simulate the environment created by the N-terminal domain of bitistatin to create the short chain peptide. Other regions of bitistatin may be required to generate a bitistatin analogue that provides the appropriate environment to constrain the orientation of the binding loop. We are currently investigating other structural features of native bitistatin to incorporate in a shorter peptide that would still be amenable to synthesis.

ACKNOWLEDGMENT

The authors would like to thank Dr. Alan Maurer for creating the model of experimental thrombi and emboli. This work was supported in part by NIH grant HL-54578 (L.C.K.).

LITERATURE CITED

(1) Shebuski, R. J., Ramjit, D. R., Bencen, G. H., and Polokiff, M. A. (1989) Characterization and platelet inhibitory activity of bitistatin, a potent arginine-glycine-aspartic acid containing peptide from the venom of the viper *Bitis arietans*. *J. Biol. Chem. 264*, 21550−21556.

(2) McLane, M. A., Kowalska, M. A., Silver, L., Shattil, S. J., and Niewiarowski, S. (1994) Interaction of disintegrins with the alpha IIb beta 3 receptor on resting and activated human platelets. *Biochem. J. 301*, 429−436.

(3) Knight, L. C., Maurer, A. H., and Romano, J. E. (1996) Comparison of Iodine-123-disintegrins for imaging thrombi and emboli in a canine model. *J. Nucl. Med. 37*, 476−482.

(4) Knight, L. C., Baidoo, K. E., Romano, J. E. Gabriel, J. L., and Maurer, A. H. (2000) Imaging pulmonary eemboli and deep venous thrombi with ^{99m}Tc−Bitistatin, a platelet-binding polypeptide from viper venom, *J. Nucl. Med. 41*, 1056−1064.

(5) Knight, L. C. (2001) Radiolabeled peptide ligands for imaging thrombi and emboli. *Nucl. Med. Biol. 28*, 515−526.

(6) Abrams, M. J., Juweid, M., tenKate, C. I., Schwartz, A. D., Hauser, M. M., Gaul, F. E., Fucello, A. J., Rubin, R. H., Strauss, H. W., and Fischman, A. J. (1990) Technetium-99m-

human polyclonal IgG radiolabeled via the hydrazino nicotinamide derivative for imaging focal sites of infection in rats. *J. Nucl. Med. 31*, 2022−2028.

(7) Rappe, A. K. and Goddard, W. A. (1994) "Biograf Reference Manual", Chapter 3, Molecular Simulations, Inc; pp 25.

(8) Calvete, J. J., Schrader, M., Raida, M., McLane, M. A., Romero, A., and Niewiarowski, S. (1997) The disulphide bond pattern of bitistatin, a disintegrin isolated from the venom of the viper Bitis arietans. *FEBS Lett. 416*, 197−202.

(9) Burt, D. R. (1986) Receptor binding methodology and analysis. In *Receptor Binding in Drug Research*. (R. A. O'Brien, Ed.) pp 4−29, Marcel Dekker, New York.

(10) Diehl, K−H., Hull, R., Morton, D., Pfister, R., Rabemampianina, Y., Smith, D., Vidal, J−M., and Van De Vorstenbosch, C. (2001) A good practice guide to the administration of substances and removal of blood, including routes and volumes *J. Appl. Toxicol. 21*, 15−23.

(11) Rusckowski, M., Qu, T., Gupta, S., Ley, A., and Hnatowich, D. J. (2001) A comparison of ^{99m}Tc Labeled to a peptide by 4 methods. *J. Nucl. Med. 42*, 1870−1877.

(12) Lister-James, J., Knight, L. C., Maurer, A. H., Bush, L. R., Moyer, B. T., and Dean, R. T. (1996) Thrombus imaging with a technetium-99m-labeled, activated platelet receptor-binding peptide. *J. Nucl. Med. 37*, 775−781.

(13) Knight, L. C., Radcliffe, R., Maurer, A. H., Rodwell, J. D., and Alvarez, V. L. (1994) Thrombus imaging with technetium-99m synthetic peptides based upon the binding domain of a monoclonal antibody to activated platelets. *J. Nucl. Med. 35*, 282−288.

(14) Lehninger, A. L., Nelson, D. L., and Cox, M. M. (1992) Amino acids and peptides. *Principles of Biochemistry, 2nd edition*. pp 111−133. Chapter 5. Worth Publishers, New York.

BC049954V

Poly(ethylene glycol) Prodrugs of the CDK Inhibitor, Alsterpaullone (NSC 705701): Synthesis and Pharmacokinetic Studies

Richard B. Greenwald,* Hong Zhao, Jing Xia, Dechun Wu, Stephen Nervi, Sherman F. Stinson,*,† Eva Majerova,† Chris Bramhall,† and Daniel W. Zaharevitz†

Enzon Pharmaceuticals Inc., Research & Development Division, 20 Kingsbridge Road, Piscataway, New Jersey 08854 and Developmental Therapeutics Program, NCI, Frederick, Maryland 21702.
Received April 14, 2004; Revised Manuscript Received June 22, 2004

Two methods were devised to conjugate PEG to alsterpaullone (NSC 705701) via the N of the indole ring portion of the molecule. In the first approach, activation of the indole was accomplished by reaction with *p*-nitrophenyl chloroformate to produce a reactive carbamate that was then condensed with a mono blocked diamine to form a urea bond followed by deblocking and conjugation to PEG. The second route used the anion of the indole and produced a carbamate bond. Both compounds were highly water soluble, were stable in buffer, and released alsterpaullone in vitro and in vivo. Studies were conducted in mice to investigate the influence of PEGylation on the plasma pharmacokinetics of alsterpaullone. The total plasma clearance rate was decreased up to 32-fold, and the biological halflife lengthened up to 8-fold when alsterpaullone was injected *i.v.* as a PEG-conjugate and compared to injection of the unconjugated compound. The most pronounced effect on the pharmacokinetics of alsterpaullone was produced by a 40-kDa PEG urea-linked conjugate. When the 40- and 20-kDa urea-linked conjugates were administered by *i.p.* injection, high relative bioavailability (46% and 99%, respectively) of alsterpaullone was observed.

INTRODUCTION

The cyclin-dependent kinases (CDKs) are a group of enzymes that are involved in cell cycle progression regulation (*1*). The CDKs activate host proteins through phosphorylation on serine or threonine using adenosine triphosphate as a phosphate donor (*2*). CDKs have attracted much attention as potential therapeutic targets, especially in treating cancer, because they are key players in the control of cell proliferation. Recently, a novel class of small molecule CDK/cyclin B inhibitors, the paullones, containing a four ring fused system were synthesized, and antitumor activity was demonstrated in vitro (*3*). Structure activity studies yielded 9-nitropaullone (alsterpaullone, **1**) as one of the lead compounds in the series; however, due to its poor aqueous solubility (2 μg/mL), **1** could not be easily formulated, and this precluded in vivo testing. Since PEG prodrugs of molecular weight (mw) > 20 000 have been shown to solubilize and release small molecules in a predictable fashion (*4*), we sought to find means by which PEG could be used in a similar manner with **1**, which has only indole and amide N−H functionalities available for attachment to PEG. A successful conjugation would thus solubilize alsterpaullone and permit intravenous (*i.v.*) or interperatoneal (*i.p.*) administration. To this end, we have developed two methods based on indole modification that yielded PEG prodrugs and produced usable levels of **1** in vivo as evidenced by pharmacokinetic (PK) studies.

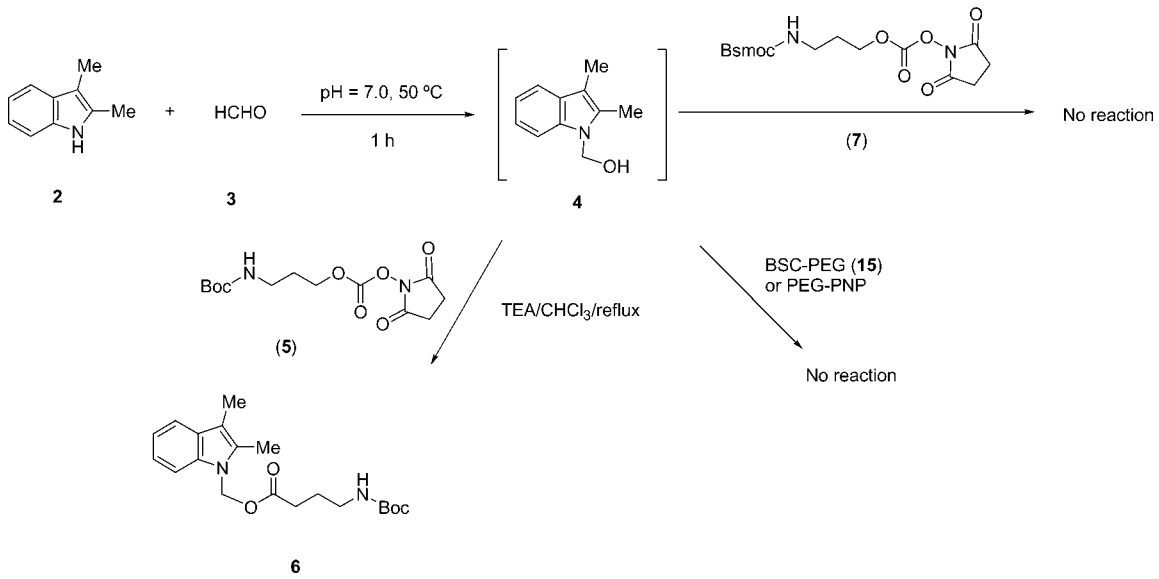
Chemistry. Synthetic approaches to indole functionalization of alsterpaullone were initiated by attempting reactions with 40 000 mw PEG−isocyanate (*5*) and with SC−PEG (PEG succinimidyl carbonate) (*5*). In no case was any reaction detected. We therefore turned to using a model compound, 2,3-dimethylindole (**2**), hoping to define reaction conditions that would lead to the desired modifications. Reaction was achieved in two different instances. First, condensation of formaldehyde (**3**) with **2** gave the hydroxymethyl derivative **4** in situ, in essentially quantitative yield (monitored by HPLC), which was then coupled to the Boc-protected succinimidyl carbonate, **5**, producing the modified indole **6** (Scheme 1). Unfortunately, deprotection of **6** with TFA caused decomposition to the unmodified indole. Unexpectedly, no reaction with **4** was observed using the base labile Bsmoc (1,1-Dioxobenzo[*b*]thiophene-2-ylmethyloxycarbonyl) (*6*) protected amine **7**, or activated PEG linkers such as N-hydroxyphthalimido PEG (BSC−PEG, **15**). However, when using **1** as the substrate**,** it was found that the formaldehyde reaction would proceed to form **8** in only 50% yield (HPLC). Generally, **8** was not isolated but reacted directly with the bifunctional activated carbonate **5**, to give the indole carbamate, **9**, in about 15% yield (Scheme 2). Again, attempts to remove the Boc protecting group with TFA led to decomposition. Finally, using model compound **2** the activation of the NH bond by carbonyldiimidazole (CDI) and conversion to the activated derivative **11** could be accomplished in almost quantitative yield (Scheme 3). This compound was found to be stable in solution, but was unstable toward silica gel; therefore, it was used in the next step without purification. Reaction of crude CDI derivative **11** with the Boc-protected amine **12** produced urea **13**. TFA deprotection followed by condensation with **15** yielded the PEG derivative of 2,3-dimethylindole, **16**. A similar reaction using **1** gave the desired CDI derivative in only 20% yield. Clearly, the model results were not reflective

* To whom correspondence should be addressed. Phone: (732) 980-4924. Fax: (732) 885-2950. E-mail: richard.greenwald@enzon.com. Phone: (301)-846−1118. Fax: (301) 846−6910. E-mail: stinson@dtpax2.ncifcrf.gov.

† NCI.

10.1021/bc049906a CCC: $27.50 © 2004 American Chemical Society
Published on Web 08/14/2004

Scheme 1



of those obtained for the more highly hindered alsterpaullone, and further use of **2** was abandoned in favor of alternative approaches to modification of **1**.

Using the more reactive reagent, *p*-nitrophenyl chloride (PNP-Cl) condensation with **1** in the presence of DMAP in THF solution yielded the activated carbamate **17** (Scheme 4). This was condensed directly with **12** to give the desired Boc indole urea intermediate **18**. In this case deprotection was successfully accomplished with 33% TFA in DCM to give **19**. PEGylation of **19** proceeded smoothly using **15** to give **20**. Alternatively, **19** was conjugated with PEG acid (**21**) in the presence of EDC to yield **22.** A second strategy that was successfully developed is shown in Scheme 5. Reaction of **1** with KOH in THF/DMF produced the potassium salt (not isolated), which was directly condensed with **23,** yielding the Boc-protected carbamate, **24**. Deprotection under acid conditions proceeded smoothly, to the amine salt (**25**) that was conjugated with **14** and **21** to give the indole carbamate PEG conjugated paullones **26** and **27** respectively.

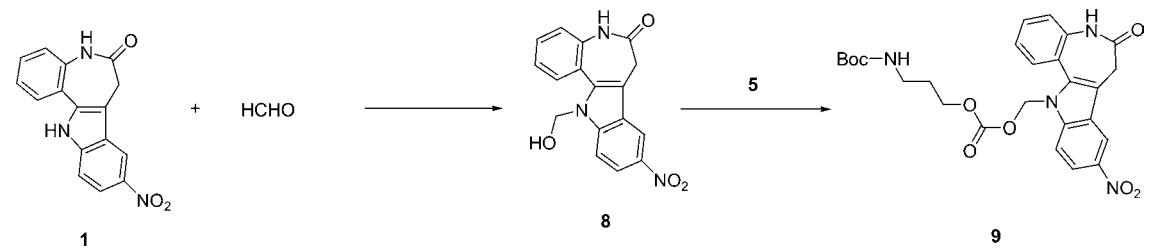
EXPERIMENTAL SECTION

Materials and Methods. *Pharmacokinetics Studies.* Male, young adult (average body weight approximately 27 g) CD2F1 mice (Harlan Sprague−Dawley, Frederick, MD) were used for all studies. The animals were maintained on hardwood chip bedding in temperature-controlled rooms (20 °C) with a 12 h light-dark cycle. Standard diet (Rat and Mouse 18% Protein Diet, PMI Nutrition International, Inc., Brentwood, MO) and water were provided ad libitum. Housing, animal care, and all experimental procedures and manipulations were carried out in strict compliance with the National Institutes of Health guidelines for the care and use of laboratory animals.

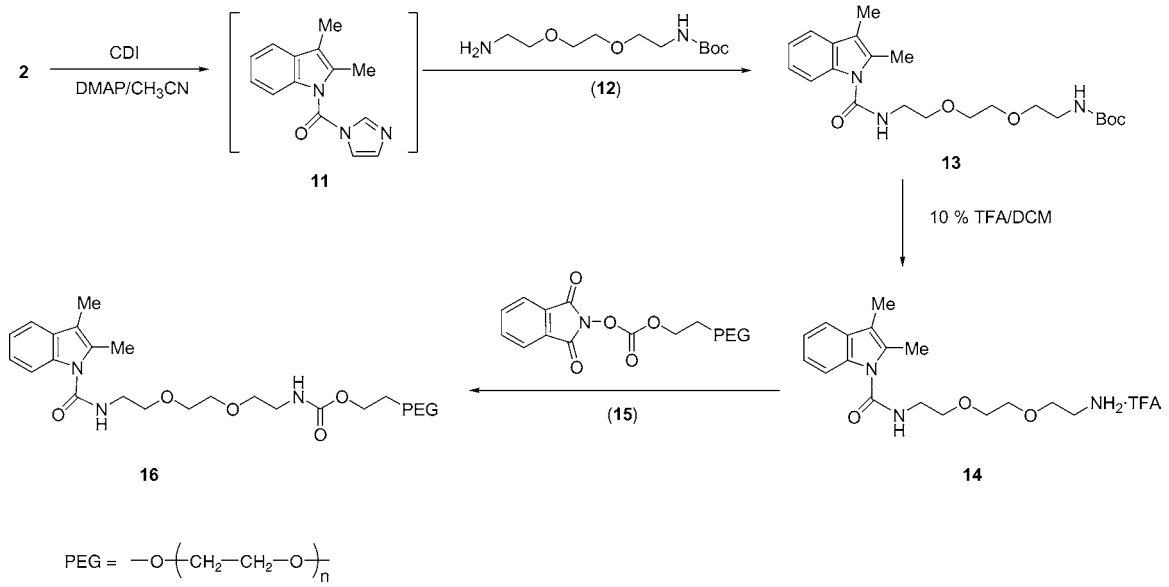
An effort was made to administer all agents at the highest dose possible. Alsterpaullone was given at its maximum tolerated dose (10 mg/kg). Viscosity, rather than toxicity, was the factor limiting the maximum dose of the 40-kDa conjugates; 1000 mg/kg was the greatest concentration resulting in a dosing solution that was workable. The dose of the 20-kDa conjugates (500 mg/kg) was selected so that the alsterpaullone dose would be comparable to that for the 40 kDa studies. The plasma pharmacokinetics of alsterpaullone was investigated following a 0.5 min *i.v.* infusion at a dose of 10 mg/kg, dissolved in a vehicle of DMSO and administered in a dose volume of 1 mL/kg. The conjugates were studied following a short (0.5 min) *i.v.* infusion, or bolus *i.p.* injection (except NSC 723780, compound **26**, and NSC 726143, compound **27**, for which only an *i.v.* study was conducted). The 40-kDa conjugates were given at a dose of 1000 mg/kg dissolved in sterile water (100 mg/mL), in a dose volume of 10 mL/kg. The 20-kDa conjugates were injected at a dose of 500 mg/kg, using the same vehicle and concentration, but in a dose volume of 5 mL/kg. The equivalent dose of alsterpaullone in each case was approximately 14 mg/kg. At selected intervals through 24 h (6 h for the *i.v.* study with alsterpaullone) groups of three mice were lightly anesthetized with methoxyfluorane and were exsanguinated via the retro-orbital sinus. Blood was collected into heparinized microfuge tubes that were then chilled in an ice bath for 1 min, and centrifuged under refrigeration (4 °C) at 13 000 × *g* for 3 min. Plasma was separated and the concentrations of alsterpaullone were immediately assayed by HPLC.

Aliquots (50 μL) of mouse plasma samples were prepared for analysis by precipitation of plasma proteins with 150 μL of chilled (−20 °C) methanol. Samples were vortexed vigorously for 30 s, maintained at −20 °C for

Scheme 2



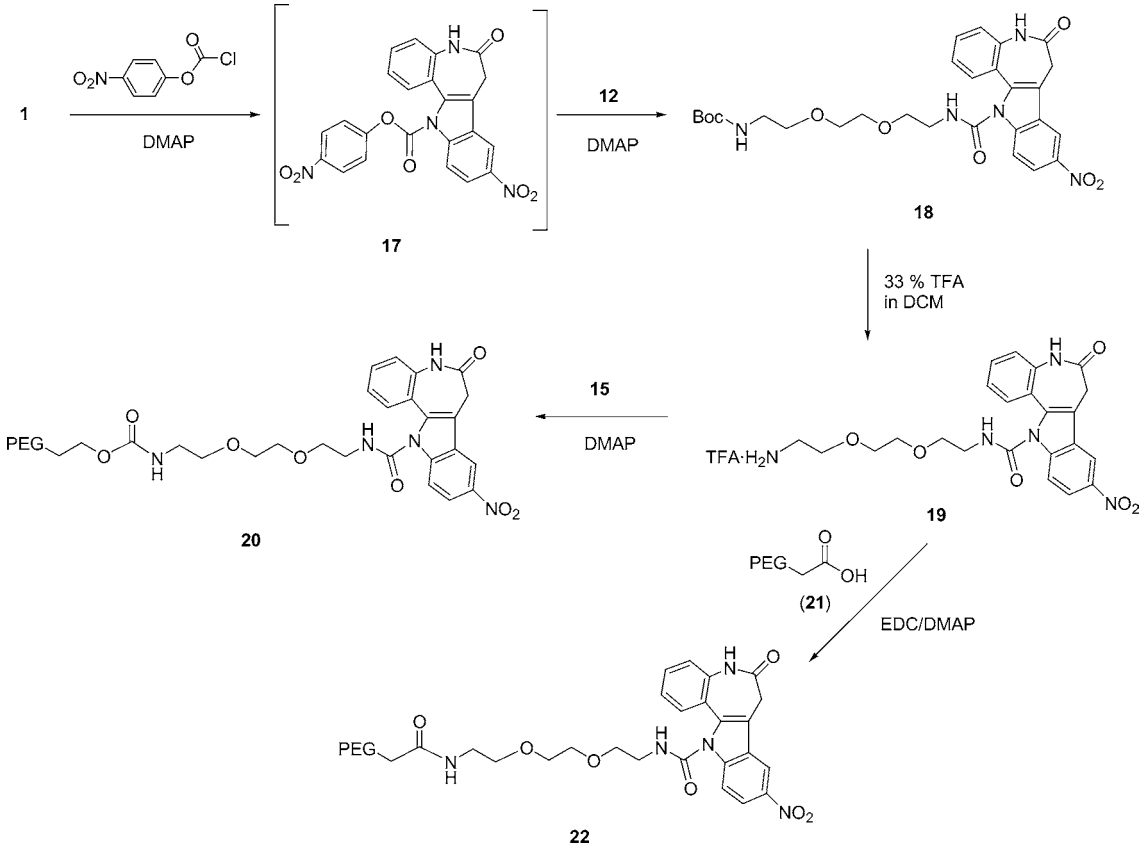
Scheme 3



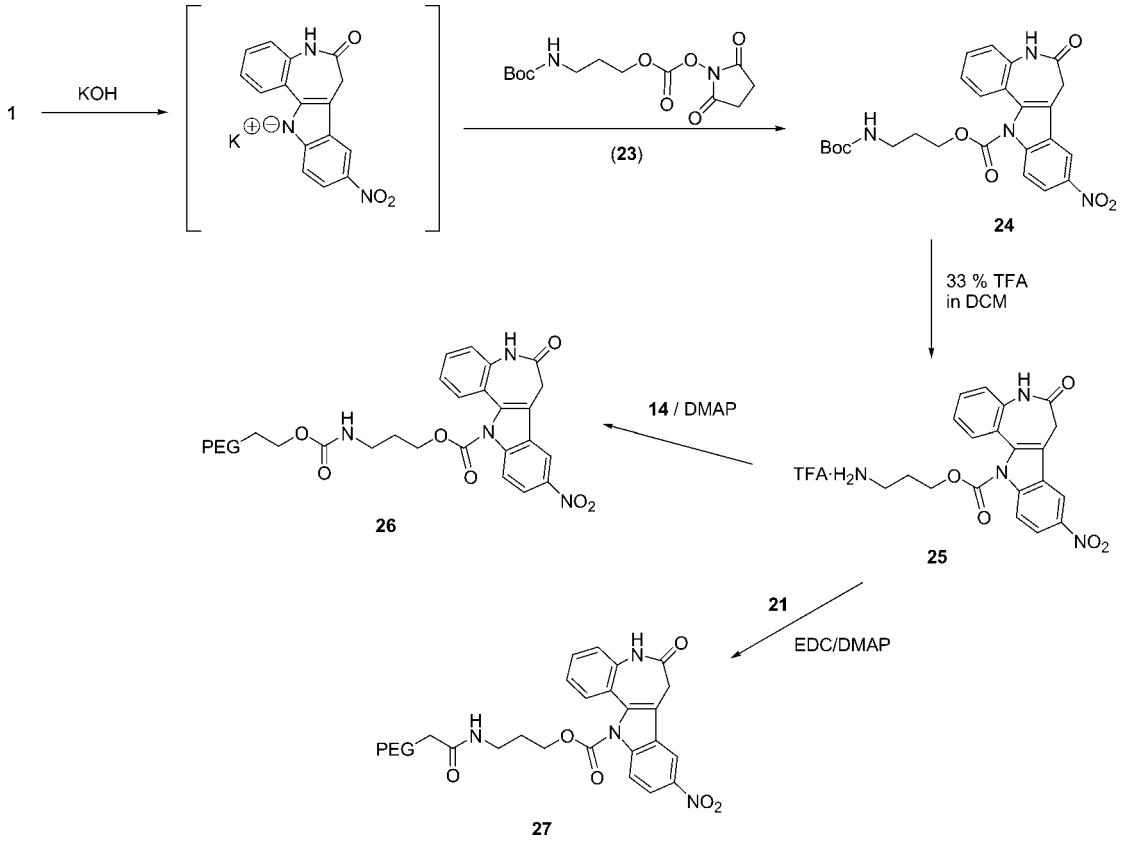
50 min, and centrifuged under refrigeration at 13 000 × g for 12 min. Next, 180 μL of the supernatant was combined with an equal volume of 0.05 M formate buffer (pH 3.0), and 330 μL of the mixture was injected on column. The analytical system consisted of a Hewlett-Packard (Palo Alto, CA) model 1050 pump, a refrigerated autosampler (4 °C), and a variable wavelength ultraviolet absorbance detector with associated software for system control and chromatogram and spectrum analysis. The system was equipped with a stainless steel 4.6 × 150 mm column containing 4 μm J'Sphere ODS H-80 packing (YMC, Inc., Wilmington, NC). Chromatography was performed with an isocratic flow rate of 1.0 mL/min using a mobile phase of acetonitrile/0.05 M, pH 3.0 ammonium formate buffer (38:62, v/v). The column eluent was monitored at 300 nm. Under these conditions, conversion of the conjugates to alsterpaullone during sample preparation and assay was negligible (<2%). The retention time for alsterpaullone was 12 min, the absolute recovery was greater than 90%, and the lower limit of quantitation was 10 nM.

Calibration curves were constructed by plotting the chromatographic peak area of the compounds against the known alsterpaullone concentration in plasma standards. Linear least-squares regression analysis was performed to determine the slope and *y*-intercept of the best-fit line.

Scheme 4



Scheme 5



Analyte concentrations in unknown samples were calculated by interpolation from the regression line. Each unknown sample was assayed in triplicate. The average of the closest two determinations was used for pharmacokinetic analysis.

Plasma concentration vs time profiles were constructed using the geometric mean of the plasma concentrations for the individual animals at each time point, as well as the mean of the times of collection. The data were analyzed by noncompartmental methods. The line of best fit was determined by nonlinear regression analysis, and pharmacokinetic parameters were calculated by standard equations as previously described (*7*).

SYNTHESIS

Compound 12. To a solution of di-*tert*-butyl dicarbonate (15 g, 0.086 mol) in 1,4-dioxane (150 mL) cooled to 5 °C in an ice bath was added a solution of 2,2′-(ethylenedioxy)bis(ethylamine) (25.85 g, 174.4 mmol) in 1,4-dioxane (100 mL), dropwise over a period of 1 h. The reaction mixture was allowed to warm to room temperature and was stirred for two more hours. The solvent was removed under reduced pressure and the residue dissolved in methylene chloride (DCM, 150 mL), washed with water (3 × 150 mL), dried ($MgSO_4$), and filtered; the solvent was evaporated under reduced pressure to yield **12** (13.84 g, mmol, 80%). ^{13}C NMR (75.5 MHz, $CDCl_3$) δ 28.4, 40.1, 70.1, 73.5, 79.0, 115.8.

Compound 14. A solution of **2** (0.10 g, 0.69 mmol), 1,1′-carbonyldiimidazole (CDI, 0.14 g, 0.862 mmol), and a catalytic amount of 4-(dimethylamino)pyridine (DMAP, 2 mg, 0.97 mmol) in anhydrous acetonitrile (10 mL) was refluxed for 16 h. The reaction was cooled to 25 °C, **12** (0.36 g, 1.46 mmol) was added, and the mixture was refluxed for 48 h. The reaction was cooled to 25 °C and the solvent was removed under reduced pressure. The residue was dissolved in methylene chloride (DCM, 10 mL) and washed with 0.25 N HCl (3 × 10 mL);. The organic layer was dried ($MgSO_4$) and filtered; the solvent was removed under reduced pressure to yield crude product **13** (0.26 g, 0.62 mmol, 90%), which was dissolved in 10% trifluoroacetic acid/DCM (6 mL) and stirred at 25 °C for 20 min. The solvents were then removed in vacuo and the residue was dissolved in DCM (5 mL) and then washed with water (3 × 5 mL). The pH of the combined aqueous layers was adjusted to 9.0 by the addition of 1 N NaOH and then extracted by DCM (3 × 15 mL). The combined organic layers were dried ($MgSO_4$) and filtered, and the solvent was removed under reduced pressure to give pure **14** (0.09 g, 0.30 mmol, 48%). ^{13}C NMR (67.8 MHz, $CDCl_3/CD_3OD$) δ 152.8, 134.3, 130.6, 129.1, 121.3, 120.0, 116.9, 110.8, 110.6, 71.2, 69.3, 69.1, 68.4, 39.9, 39.6, 10.1, 8.9.

Compound 16. A solution of **14** (0.08 g, 0.27 mmol), PEG (40,000) linker **15** (2.69 g, 0.066 mmol), and DMAP (0.033 g, 0.27 mmol) in anhydrous DCM (40 mL) was stirred at 25 °C for 16 h. The solution was concentrated under reduced pressure and the PEG conjugate was precipitated by ethyl ether, filtered, and rinsed with additional ether (5 × 100 mL). The solid was crystallized from 2-propanol (IPA, 200 mL) to yield **16** (2.6 g, 0.060 mmol, 91%). ^{13}C NMR (67.8 MHz, $CDCl_3$) δ 155.8, 152.0, 134.3, 131.6, 129.66, 121.9, 120.8, 117.7, 111.3, 74.0−69.4 (PEG), 63.4, 40.3, 11.8, 8.3.

Compound 18. To a suspension of alsterpaullone (1.50 g, 5.11 mmol) in anhydrous tetrahydrofuran (THF, 600 mL) was added 4-nitrophenyl chloroformate (3.082 g, 15.29 mmol) and DMAP (3.736 g, 30.57 mmol) and the reaction mixture was stirred at room temperature for 2 h. Compound **12** (12.54 g, 50.97 mmol) was added and stirring continued for an additional 12 h. The solvent was removed under reduced pressure, the residue was dis-

Table 1. Properties of PEG Alsterpaullone Conjugates

compound	MW[a]	$t_{1/2}$ (PBS)[b] 25 °C	$t_{1/2}$ (rat plasma)[b] 37 °C	% active	solubility of conjugates (mg/mL)	solubility of alsterpaullone equivalent (mg/ mL)
20	40 988	48 h	23 min	1.44	153	2.20
22	21 012	>24 h	1.0 h	2.80	189	5.30
26	40 842	>48 h	19.9 h	1.44	172	2.48
27	20 754	>48 h	50 h	2.88	186	5.36

[a] Average mw was used for PEG. [b] All experiments were done in duplicate. Standard deviation of measurements = ± 10%.

solved in DCM (300 mL), filtered, and finally washed with 0.25 N HCl (3 × 300 mL). The organic layer was dried ($MgSO_4$) and filtered, and the solvent was removed under reduced pressure. The residue was further purified by column chromatography to yield **18** (1.18 g, 2.08 mmol, 40.6%). ^{13}C NMR (75.5 MHz, $CDCl_3$) δ 28.4, 29.7, 31.6, 40.1, 41.0, 68.9, 70.0, 70.3, 79.5, 113.9, 115.1, 116.9, 119.9, 121.7, 123.0, 124.4, 126.4, 129.1, 129.6, 133.9, 135.6, 140.9, 143.4, 150.8, 155.9, 172.9. HRMS: *m/z* calcd for $C_{28}H_{33}N_5O_8$ (M^+ + Na) 590.2227, found 590.2213.

Compound 19. To a mixture of trifluoroacetic acid (TFA, 2 mL) and anhydrous DCM (18 mL) was added compound **18** (1.0 g, 1.76 mmol) and the reaction mixture was stirred for 45 min at room temperature. The solvents were removed under reduced pressure and the crude product was washed with ethyl ether to give **19** (1.02 g, 1.76 mmol, 99%). ^{13}C NMR (75.5 MHz, $CDCl_3$/DMSO-d_6) δ 30.4, 38.8, 40.0, 66.0, 68.3, 69.3, 69.5, 112.1, 114.4, 115.2, 118.4, 121.4, 122.3, 123.6, 125.8, 127.7, 128.6, 134.4, 135.0, 139.9, 142.5, 151.2, 172.4. HRMS: *m/z* calcd for $C_{23}H_{25}N_5O_6$ (free base M^+ + Na) 490.1703, found 490.1708.

Compound 20. To a solution of **19** (0.102 g, 0.176 mmol) in anhydrous dimethylformamide (DMF, 3 mL) and DCM (37 mL) was added 40 kDa PEG linker **15** (2.36 g, 0.059 mmol) and DMAP (0.022 g, 0.176 mmol). The reaction was stirred at room temperature for 12 h, the solution was concentrated under reduced pressure, and the PEG derivative was precipitated with ethyl ether (150 mL). The crude product was crystallized from IPA, (200 mL) to give **20** (2.0 g, 0.05 mmol, 87%). ^{13}C NMR (75.5 MHz, $CDCl_3$) δ 31.2, 40.2, 40.5, 63.5, 68.6, 69.0, 70.1−74.0 (PEG), 113.3, 114.6, 116.3, 119.2, 121.3, 122.9, 123.7, 126.0, 128.4, 128.9, 135.4, 140.3, 142.8, 150.5, 155.9, 171.6.

Compound 22. To a solution of **19** (0.765 g, 1.64 mmol) in anhydrous DMF (20 mL) and DCM (90 mL) was added 20 kDa PEG diacid **21** (7.5 g, 0.37 mmol), 1-[3-(dimethylamino)-propyl]-3-ethylcarbodiimide hydrochloride (EDC, 0.315 g 1.64 mmol), and DMAP (0.364 g, 2.98 mmol), and the mixture was stirred at room temperature for 12 h. The solvent was removed under reduced pressure and the residue was crystallized from IPA (200 mL) to give **22** (7.2 g, 0.343 mmol, 93%). ^{13}C NMR (75.5 MHz, $CDCl_3$) δ 31.2, 38.0, 40.5, 68.5−74.0 (PEG), 113.3, 114.6, 116.2, 119.1, 121.2, 122.9, 123.6, 126.0, 128.4, 128.9, 133.8, 135.5, 140.3, 142.8, 150.4, 169.8, 171.6.

Compound 23. To a solution of *tert*-butyl *N*-(3-hydroxypropyl)-carbamate (5.0 g, 28.57 mmol), *N,N′*-disuccinimidyl carbonate (DSC, 9.6 g, 37.5 mmol) in chloroform (125 mL) was added pyridine (3.0 mL, 37.0 mmol) and the reaction mixture was stirred at room temperature for 12 h. The mixture was washed with 0.5 N HCl (60 mL), dried ($MgSO_4$) and filtered, and solvent was removed under reduced pressure to give compound **23** (8.2 g, 25.92 mmol, 90.7%). ^{13}C NMR (75.5 MHz, $CDCl_3$) δ 25.5, 28.4, 28.9, 36.8, 68.9, 79.4, 151.4, 155.8, 168.5. HRMS: *m/z* calcd for $C_{13}H_{30}N_2O_7$ (M^+ + Na) 339.1168, found 339.1163.

Compound 24. Compound **23** (0.81 g, 2.6 mmol) was added to a reaction mixture of **1** (0.25 g, 0.85 mmol) and finely ground potassium hydroxide (KOH, 0.114 g, 2.03 mmol) in DMF/THF (20 mL/100 mL) previously stirred for 1 h at 0 °C in an ice-salt bath, and the resulting reaction mixture was gradually warmed to room temperature and stirred for 24 h. The solvent was removed under reduced pressure, and the residue was dissolved in DCM (100 mL), filtered, and washed with 0.25 N HCl (2 × 200 mL). The organic layer was dried ($MgSO_4$) and filtered, and the solvent was removed under reduced pressure. The residue was further purified by column chromatography to yield **24** (0.340 g, 0.706 mmol, 83%). ^{13}C NMR (75.5 MHz, $CDCl_3$) δ 25.7, 28.4, 29.0, 31.4, 37.0, 65.5, 68.0, 76.6, 79.6, 114.8, 115.8, 119.4, 120.7, 122.8, 123.9, 128.0, 128.2, 129.9, 134.7, 141.1, 144.3, 150.8, 155.6, 172.7. HRMS: *m/z* calcd for $C_{25}H_{26}N_4O_7$ (M^+ + Na) 517.1699, found 517.1708.

Compound 25. To a solution of **24** (0.15 g, 0.30 mmol) in DCM (3 mL) cooled to 0 °C using an ice-salt bath was added TFA (3 mL) dropwise over 1 h with stirring. The solvents were removed under reduced pressure to give **25** (0.146 g, 0.295 mmol, ~100%). HRMS: *m/z* calcd for $C_{20}H_{18}N_4O_5$ (free base M^+ + H) 395.1355, found 395.1365.

Compound 26. To a solution of **25** (0.15 g, 0.30 mmol) in anhydrous DMF/DCM (6 mL/9 mL) was added 40 kDa PEG linker **15** (2.98 g, 0.074 mmol) and DMAP (0.072 g, 0.60 mmol). The reaction mixture was stirred at room temperature for 12 h, diluted with DCM, and washed with 0.1 N HCl (2 × 20 mL) and brine (20 mL). Removal of the solvent under reduced pressure gave the crude product, which was crystallized from DMF/ethanol (45 mL/45 mL) to give **26** (2.5 g, 0.061 mmol, 83%). ^{13}C NMR (75.5 MHz, $CDCl_3$) δ 28.1, 31.4, 38.6, 63.7, 67.1, 69.4, 69.9, 70.1, 70.3−73.5 (PEG), 114.6, 115.4, 119.3, 120.4, 123.1, 123.2, 127.7, 129.0, 129.3, 135.3, 140.9, 144.0, 150.4, 155.6, 171.8.

Compound 27. A solution of **25** (0.46 g, 0.92 mmol) and 20kDa PEG diacid **21** (4.6 g, 0.23 mmol) in anhydrous DMF (30 mL) and DCM (46 mL) was cooled to 0 °C. Next, EDC (0.177 g, 0.922 mmol) and DMAP (0.562 g, 4.6 mmol) were added all at once and the reaction mixture was stirred at room temperature for 12 h. The solution was washed by 0.1 N HCl (2 × 30 mL) and brine (30 mL), dried ($MgSO_4$), and filtered. The solvent was removed under reduced pressure, and the residue was crystallized from IPA (100 mL) to give **27** (4.26 g, 0.205 mmol, 89%). ^{13}C NMR (75.5 MHz, $CDCl_3$) δ 28.1, 31.1, 34.9, 65.2, 68.5−73.5 (PEG), 114.4, 115.4, 118.9, 120.1, 122.7, 123.1, 127.5, 128.7, 129.4, 134.8, 135.3, 140.6, 143.8, 150.3, 169.6, 171.8.

RESULTS

In Vitro Measurements. The solubility of all PEG derivatives was determined by the previously described (*8*) procedure. Rates of hydrolysis in saline and rat plasma of **16**, **23**, **26**, and **27** were carried out as described earlier (*5*). These values are presented in Table 1.

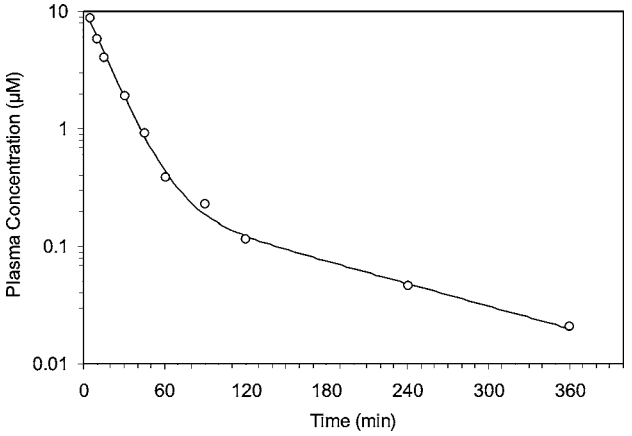


Figure 1. Geometric mean plasma concentrations and lines of best fit observed following *i.v.* administration of **1** to CD2F1 mice at a dose of 10 mg/kg.

Table 2. Selected Pharmacokinetic Parameters Derived from Nonlinear Least Squares Regression Analysis of Alsterpaullone (1) Plasma Concentration vs. Time Data Obtained Following *i.v.* Injection of 10 Mg/kg Body Weight in CD2F1 Mice

parameter	value
$t_{1/2,1}$	11.2 min
$t_{1/2,z}$	1.6 hr
MRT	0.6 hr
CL	9.7 l/hr/kg
V_1	3.1 l/kg
V_z	6.2 l/kg
$AUC_{0-\infty}$	3.5 μM × hr
AUC_1	82%
AUC_z	18%

$t_{1/2,1}$ and $t_{1/2,z}$ = half-lives for the initial and terminal disposition phases, MRT = mean residence time, CL = total plasma clearance rate, V_1 = apparent volume of the central compartment, V_z = apparent volume of distribution, $AUC_{0-\infty}$= area under the plasma concentration−time curve extrapolated to infinity, AUC_1 and AUC_z = percentage of $AUC_{0-\infty}$ represented by the initial and terminal disposition phases.

Pharmacokinetics Studies. Nonlinear regression analysis indicated that plasma concentrations of alsterpaullone declined in a biexponential manner following *i.v.* administration of 10 mg/kg, from nearly 10 μM at 5 min to 20 nM by 6 h (Figure 1). The half-lives for the initial and terminal disposition phases were 11 and 94 min, respectively (Table 2). The total plasma clearance rate (CL) was 9.7 l/hr/kg. The high ratio of the proportion of the area under the plasma concentration−time curve ($AUC_{0-\infty}$) represented by the initial phase relative to that of the terminal phase (82% and 18% respectively) suggests that tissue distribution rather than elimination is a controlling factor in the in vivo disposition of alsterpaullone.

Administration of PEGylated alsterpaullone by the *i.v.* route resulted in a 3 to 32-fold reduction in the CL of unconjugated alsterpaullone (Table 3, Figure 2). The urea linkage was associated with the largest reduction in the CL. The 40- and 20-kDa urea-linked conjugates produced CL values for alsterpaullone (0.3 and 0.7 L/hr/kg, respectively), which were three to four times lower than those found with corresponding carbamate-linked conjugates of equal molecular weight. The biological halflife of alsterpaullone was also three to four times longer with the urea-linked conjugates. The CL of alsterpaullone was one-third to one-half slower, and the biological halflife two to three times longer with the 40-kDa conjugates when compared to corresponding 20-kDa conjugates. The relative bioavailability of alsterpaullone when the urea-linked conjugates were given by the *i.p.* route was 46% for the 40-kDa compounds and 99% for the 20-kDa compounds. Peak plasma concentrations of 4 and 7 μM were achieved 6 h after administration. Levels then declined with halflives of 9 and 3 h for the 40-kDa and 20-kDa conjugates, respectively. Asterpaullone was not detected in the plasma following *i.p.* injection of the 20-kDa carbamate-linked conjugate. An *i.p.* study was not conducted with the corresponding 40-kDa conjugate.

DISCUSSION

PEG has been extensively used due to its ability to increase the solubility, circulating life, safety, and permeable tissue accumulation level for small molecule prodrug platforms (*9*). The use of prodrug design has been applied to numerous therapeutic areas with the goal to improve the pharmacologic properties of drugs. A prodrug is a biologically inactive derivative of a parent drug molecule that usually requires an enzymatic or chemical transformation within the body in order to release the active drug, and has improved delivery properties over the parent molecule (*10*). Essential to drug delivery with a prodrug is the rate of release of the active drug. A rapid breakdown of the prodrug can result in spiking of the parent drug and possible toxicity, while too slow a release rate will compromise the drug's effectiveness. The linkages between the active drug and the carrier molecule can theoretically be chosen so that either pH or enzymatic degradation can mediate prolonged drug release. Therefore, the effectiveness of prodrug delivery is dependent on the stability of the drug conjugate linkage and its potential for controlled degradation. PEG conjugated to

Table 3. Selected Pharmacokinetic Data Derived from Alsterpaullone (1) Plasma Concentration Time Curves Obtained Following *i.v.* or *i.p.* Administration of PEG−conjugates in CD2F1 Mice

	NSC 723779 (**20**)	NSC 723780 (**26**)	NSC 726142 (**22**)	NSC 726143 (**27**)
molecular weight	40 998	40 842	21 012	20 754
linker	urea	carbamate	urea	carbamate
dose (mg/kg)	1000	1000	500	500
alsterpaullone equivalent dose (mg/kg)	14.3	14.3	13.9	14.1
i.v. studies				
$AUC_{0-\infty}$ (μM x hr)	149	54	73	17
CL (l/hr/kg)	0.3	0.9	0.7	2.9
$t_{1/2,z}$ (hr)	12.9	4.8	6.6	1.8
i.p. studies				
$AUC_{0-\infty}$ (μM x hr)	69	nd	72	bld
$t_{1/2,z}$ (hr)	9.2	−	3.1	−
F (%)	46	−	99	−

$AUC_{0-\infty}$ = area under the curve extrapolated to infinity, CL = total plasma clearance rate, $t_{1/2,z}$ = terminal disposition phase halflife, F = relative bioavailable fraction, nd = study not done, bld = below the limit of detection.

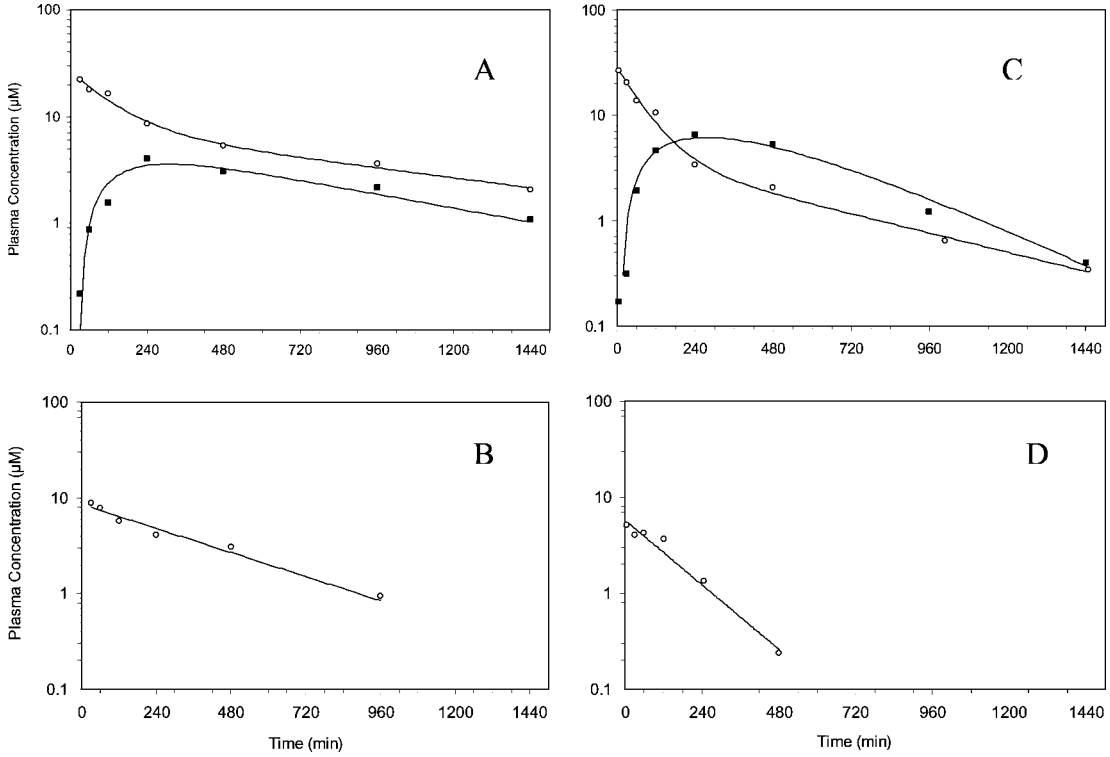


Figure 2. Geometric mean plasma concentrations of **1** and lines of best fit observed following i.v. (○) or i.p. (■) administration of PEG−conjugates to CD2F1 mice at doses equivalent to 14 mg/kg **1** (A, **20**, B, **26**; C, **22**; D, **27**).

amino prodrugs that function via a 1,4- or 1,6-elimination has been demonstrated to be a feasible methodology to deliver anticancer drugs (*5*). Another approach based on PEG technology also has now been proven to be useful for the delivery of insoluble indole-containing systems. PEG linkers were designed to target the indole N−H bond and resulted in a PEG-linked-drug bipartate system that provided alteration of plasma pharmacokinetics, while providing substantial aqueous solubility to the modified alsterpaullone.

The synthetic program conducted for this initial investigation of PEG−alsterpaullone prodrugs provided two distinct types of PEG−alsterpaullone prodrugs: those formed with a carbamate linker and those with a urea connection. These PEG conjugates were highly soluble in saline, (>2.2 mg/mL), and both of these systems demonstrated prolonged stability (>24 h) in saline at 25 °C; thus, physically the conjugates have potential clinical utility as injectable agents.

Alsterpaullone is a potent CDK inhibitor and produces cytotoxicity in sensitive human tumor cell lines exposed to 6 uM concentrations for brief periods (0.75 to 1.5 h) (*11*). An important objective of this investigation was to determine the feasibility of producing effective concentrations of alsterpaullone in vivo. When given to mice at its maximum tolerated dose, plasma concentrations of alsterpaullone were in the effective range for only 10 min. In contrast, when the 20- and 40-kDa urea conjugates were administered, alsterpaullone concentrations exceeded effective levels for 3 or 8 hours, respectively. Furthermore, administration of **1** as a PEG conjugate significantly reduced its plasma clearance rate and lengthened its biological halflife, thereby greatly increasing the in vivo residence time of **1**, and enhancing its potential for producing a therapeutic effect. Thus, this investigation revealed that PEG conjugated to **1** via an indole results in prodrugs that demonstrate significant in vivo release of **1** (Tables 2 and 3).

In vivo investigations of these PEG prodrugs are currently in progress. The results will be reported at a later date.

ACKNOWLEDGMENT

We would like to thank Drs. Laurent Meijer and Conrad Kunick for general discussions of the paullones, and Carol Aitken for her assistance in preparing this manuscript.

LITERATURE CITED

(1) Kunick, C., Schultz, C., Lemcke, T., Zaharevitz, D. W., Gussio, R., Jalluri, R. K., Sausville, E. A., Leost, M., and Meijer, L. (2000) 2-Substituted Paullones: CDK1/Cyclin B−Inhibiting Property and In Vitro Antiproliferative Activity. *Bioorg. Med. Chem. Lett.* 567−569.

(2) Sielecki, T. M., Boylan, J. F., Benfield, P. A., and Trainor, G. L. (2000) Cyclin-Dependent Kinase Inhibitors: Useful Targets in Cell Cycle Regulation. *J. Med. Chem. 42*, 1−18.

(3) Schultz, C., Link, A., Leost, M., Zaharevitz, D. W., Gussio, R., Sausville, E. A., Meijer, L., and Kunick, C. (1999) Paullones, a Series of Cyclin-Dependent Kinase Inhibitors: Synthesis, Evaluation of CDK1/Cyclin B Inhibition, and in vitro Antitumor Activity. *J. Med. Chem. 42*, 2909−2919.

(4) Greenwald, R. B., Choe, Y. H., McGuire, J., and Conover, C. (2003) Effective Drug Delivery by PEGylated drug conjugates. *Adv. Drug Delivery Rev. 55*, 217−250.

(5) Greenwald, R. B., Pendri, A., Conover, C. D., Zhao, H., Choe, Y. H., Martinez, A., Shum, K., and Guan, S. (1999) Drug Delivery Systems Employing 1, 4- or 1, 6-Elimination: Poly (ethylene glycol) Prodrugs of Amine-Containing Compounds. *J. Med. Chem. 42*, 3657−3667.

(6) Carpino, L. A., Ismail, M., Truran, G. A., Mansour, E. M. E., Iguchi, S., Ionescu, D., El-Faham, A., Riemer, C., and Warass, R. (1999) The 1,1-dioxobenzo[*b*]thiophene-2-ylmethyloxycarbonyl (Bsmoc) amino protecting group. *J. Org. Chem. 64*, 4324−4328.

(7) Stinson, S. F., House, T., Bramhall, C., Saavedra, J. E., Keefer, L. K., and Nims, R. W. (2002) Plasma Pharmacoki-

netics of a Liver-Selective Nitric Oxide-Donating Diazeniumdiolate in the Male C57BL/6 Mouse. *Xenobiotica 3*, 339−347.
(8) Conover, C. D., Zhao, H., Longley, C., Shum, K. L., and Greenwald, R. B. (2003) The Utility of Poly (ethylene glycol) Conjugation to Create Prodrugs of Amphotericin B. *Bioconjugate Chem. 14*, 661−666.
(9) Greenwald, R. B., Conover, C. D., and Choe, Y. H. (2001) Poly (ethylene glycol) Conjugated Drugs and Prodrugs: A Comprehensive Review. *Crit. Rev. Ther. Drug 17*, 101−161.
(10) Stella, V. J., Charman, W. N., and Naringrekar, V. H. (1985) Prodrugs, Do They Have Advantages in Clinical Practice? *Drugs 29*, 455−473.
(11) Sausville, E. A., Johnson J., Alley M., Zaharevitz D., and Senderowicz A. M. (2000) Inhibition of CDKs as a therapeutic modality. *Ann. N.Y. Acad. Sci. 910*, 207−221.

BC049906A

First Synthetic Probe for the Detection and Quantification of a Protein with a Potential α,(2→8)Sialyltransferase Activity

Gabriele D'Andrea,* Anna Rita Lizzi, and Arduino Oratore

Department of Biomedical Sciences and Technologies, University of L'Aquila, Coppito 2, Via Vetoio, I-67100 L'Aquila, Italy. Received January 23, 2004; Revised Manuscript Received July 9, 2004

There is considerable interest in monitoring α,(2→8)sialyltransferase (ST8) levels; however, there are few specific and sensitive methods to directly detect and quantitate the protein. This paper reports the development of a synthetic probe composed of oxidized colominic acid coupled to biotinyl-L-lysine hydrazide to detect and quantify ST8 with putative "initiase" activity and its use in three solid-phase applications. The detection limit observed for ST8 purified from K562 cells was ∼2 pg by dot-blot analysis. In Western blots the probe bound and specifically recognized a protein band corresponding to ST8. In ELISA a linear dose response was obtained for pure protein in the range of 50−200 pg. Analysis of 3′-azido-3′deoxythymidine-treated cells by all three methods showed a reduction in ST8 compared to control cells; treated cells had 73% of control levels by ELISA. This probe will be useful for studies on the expression ST8 and its role in glycoconjugate biosynthesis.

INTRODUCTION

A large number of sialyltransferases (STs)[1] are required to terminally add sialic acid on glycoconjugates (*1*, *2*). In the case of humans, the genome encodes probably more than 20 different STs, but up until now about 15 different human ST cDNAs have been encoded and characterized (see the web site given in ref *3*). Among the various ST activities, two of them, namely, ST8Sia II (also known as STX or "initiase") and ST8Sia IV (also known as PST or "elongase"), mediate the so-called polysialylation process, a unique type of modification in which tens of sialic acid residues are joined through an α,(2→8) linkage in a linear array (*4*); usually, polysialic acid (PSA) chains formed by ST8Sia IV are longer than those synthesized by ST8Sia II (*5*−*7*). Due to these interesting and actual observations, remarkable efforts have been directed to develop simple, reliable, inexpensive, and specific assays for different STs in general, but at the moment none is available for the direct detection and quantification of ST8 viewed just as a protein. On the other hand, specific assays in which fluoresceinyl- or radiolabeled CMP−NeuAc is used as donor and asialoglycoproteins or gangliosides are used as acceptors, allow the determination of ST8 enzymatic activity (*8*−*15*). In addition, it has been also possible to set up a protocol for parallel screening of several samples using microtiter filtration plates (*16*). However, due to the heterogeneity of putative acceptor sites, assays that make use of labeled donors hardly discriminate the different ST activities. Nevertheless, the enzyme previously cloned by Livingstone and Paulson (*17*), as well as the subsequent ST8 purified from CHP-134 neuroblastoma cells (*18*), and the affinity-purified ST8 we isolated from K562 cells (*10*, *11*) all recognize solely fetuin as substrate (and not asialofetuin), suggesting that sialyl residues in either the α,(2→3) or α,(2→6) linkage are required for the enzymatic activity: for this reason the enzyme we purified is supposed to possess a potential ST8Sia II activity. Starting from these latter pieces of evidence and taking into strict account our recent studies (*10*, *11*), we report very sensitive and easy assays for the direct detection and quantification of a putative ST8Sia II in cell lysates such as the ones obtained from both control and AZT-treated K562 erythroleukemia human cells.

To this purpose a synthetic probe was prepared comprising oxidized colominic acid coupled to biotinyl-L-lysine hydrazide. In particular, the probe was successfully used in dot-blot, Western blot, and ELISA applications. Thus, many different samples supposed to contain a putative ST8 displaying "initiase"-like activity (ST8Sia II) could be inexpensively screened simultaneously with high sensitivity and specificity in a minimum of time.

EXPERIMENTAL PROCEDURES

Probe Synthesis. Colominic acid (poly[2,8-(*N*-acetylneuraminic acid sodium salt)]; $(C_{11}H_{16}NNaO_8)_n$, Fluka code 27698) was dissolved in 0.1 M sodium *m*-periodate (100 mM sodium acetate, pH 5.5; 2.5 mg/10 mL), and the solution was left at room temperature for 20 min in the dark. Glycerol 86−88% (250 μL) was added to stop the reaction (room temperature for 20 min in the dark). Four dialysis changes against PBS-cations (20 mM potassium phosphate buffer, pH 7.2, containing 0.15 M NaCl, 1 mM each $CaCl_2$ and $MgCl_2$) were then carried out. Subsequently, N_ϵ-(+)biotinyl-L-lysinehydrazide hydrochloride

* Author to whom correspondence should be addressed (e-mail gadan@cc.univaq.it; telephone +39-862-433464; fax +39-862-433433).

[1] Abbreviations: AZT, 3′-azido-3′-deoxythymidine; BCIP, 5-bromo-4-chloro-3-indolyl phosphate *p*-toluidine salt; BSA, bovine serum albumin; MET buffer: 50 mM MES buffer, pH 6.0, containing 1 mM dithiothreitol; NBT, nitro blue tetrazolium chloride; PBS-cations: 20 mM potassium phosphate buffer, pH 7.2, containing 0.15 M NaCl and 1 mM each $CaCl_2$ and $MgCl_2$; PBS-T, 20 mM potassium phosphate buffer, pH 7.2, containing 0.15 M NaCl and 0.05% (w/v) Tween-20; PSA, polysialic acid; PVDF, poly(vinylidene difluoride); SDS−PAGE, sodium dodecyl sulfate−polyacrylamide gel electrophoresis; ST, sialyltransferase; ST8, α,(2→8)sialyltransferase; ST8Sia II or STX, α,(2→8)-sialyltransferase displaying "initiase" activity; ST8Sia IV or PST, α,(2→8)sialyltransferase displaying "elongase" activity; TTBS, 0.05 M Tris-HCl buffer, pH 7.5, containing 150 mM NaCl and 0.05% (w/v) Tween-20.

10.1021/bc049970s CCC: $27.50 © 2004 American Chemical Society
Published on Web 08/07/2004

($C_{16}H_{30}N_6O_3S$·HCl; Fluka code 14415; 2.5 mg/2 mL PBS-cations) was added and the solution incubated at room temperature for 16 h. After the solution had cooled at 0 °C and an equal volume of 30 mM sodium cyanoborohydride (Fluka code 71435) had been added, incubation at 0 °C for 45 min followed. Last, a dialysis step as above was carried out and the solution stored at 4 °C in the presence of 0.02% (w/v) sodium azide.

Cell Cultures. Human erythroleukemia cells (K562), kindly supplied by Dr. L. Di Renzo (Laboratory of Experimental and Pathologic Medicine, University of Rome 'La Sapienza'), were grown as already described (*10*).

Cell Homogenate Preparation and ST8 Purification. K562 cells (6.5×10^8) incubated alone or with 20 μM AZT for 3 h were washed twice with PBS (20 mM potassium phosphate buffer, pH 7.2, containing 150 mM NaCl), resuspended in 1.45 mL of 50 mM MES buffer, pH 6.0, containing 1 mM dithiothreitol (MET buffer), and then homogenized. Sonication for 10 s × 10 and centrifugation at 1120g for 15 min followed. The supernatant solution was centrifuged at 23000*g* for 1 h and the pellet suspended in 500 μL of 0.1% (w/v) Triton CF-54 in MET buffer, pH 6.0, sonicated for 10 s × 10, and centrifuged at 23000*g* for 30 min. This second supernatant solution was used in all types of analyses.

ST8 was purified from K562 as already reported (*10*).

Dot-Blot. Different amounts of protein homogenates from control and AZT-treated samples, or pure ST8, were separately loaded into each well. The PVDF membrane was then washed in TTBS [0.05 M Tris-HCl buffer, pH 7.5, containing 150 mM NaCl and 0.05% (w/v) Tween-20] for 10 min and blocked with 1% (w/v) BSA. After three washes, the membrane was soaked in 25 mM HCl for 20 min, washed again, and then incubated with the probe solution (1.3 μg/mL, 1 h, 25 °C). Further washing steps were carried out, and incubation for 1 h with alkaline phosphatase−Extravidine conjugate (Sigma, Milan, Italy) diluted 1:300 000 followed. Blots were developed by using 10 mL of substrate solution composed of 9.9 mL of TBS, 45 μL of BCIP (13 mg/mL in dimethylformamide), and 55 μL of NBT [20 mg/mL in 70% (v/v) dimethylformamide].

SDS−PAGE and Western Blot. Aliquots of the second supernatant solution (8 μg) and pure ST8 (1 μg) were assayed by SDS−PAGE on a 10% gel according to the method of Laemmli (*19*); bands were visualized by Coomassie brilliant blue staining (Figure 2A). Cell lysates and pure ST8, prepared as above and resolved by SDS−PAGE, were blotted onto PVDF membranes as described elsewhere (*20*), with slight modifications. The membrane was washed, blocked, and treated as reported under Dot-Blot.

ELISA. Cell homogenates (100 μL), or the pure enzyme solutions, diluted in 0.08 M carbonate buffer, pH 9.6, were loaded to the wells of a plastic 96-well microtiter plate and left for 3 h at 37 °C. Wells were then washed four times with PBS-T [20 mM potassium phosphate buffer, pH 7.2, containing 0.15 M NaCl and 0.05% (w/v) Tween-20] followed by incubation with 25 mM HCl for 20 min. After a washing step, 100 μL of probe solution (1.3 μg/mL) was added to each well, and the reaction was allowed to go on for 1 h at 37 °C. The wells were then again washed four times with PBS-T before incubation (1 h at 37 °C) with alkaline phosphatase−Extravidine conjugate (Sigma, Milan, Italy) diluted 1:10 000. After the last washes, 100 μL of 1 mg/mL 4-nitrophenyl phosphate bis(cyclohexylamine) salt in 0.1 M glycine, pH 9.4, was poured into each well, and the absorbance was read at 415 nm after 1 h.

Protein Determination. Total protein concentration was determined according to the Bio-Rad protein assay (*21*).

RESULTS AND DISCUSSION

Polysialic acid (PSA) is a linear homopolymer ($n = \sim 8$ to >100) of α,(2→8)-linked sialic acid joined, most of the time, to an N-linked carbohydrate core (*22*), although a novel member of α,(2→8)sialyltransferase (ST8Sia VI) that sialylates preferentially *O*-glycans has been recently identified (*23*).

However, at the moment it is not clear if the so-called "initiase" activity and the so-called "elongase" activity, both necessary to synthesize PSA, may be subsumed by the two above-mentioned enzymes or are the province of distinct sialyltransferases. It has been reported that cell lines from colon cancer express polysialyltransferases (mainly ST8 IV) without concomitant expression of PSA (*24*). Although different experimental approaches made possible the study on PSA biology (*22*, *25*−*27*), the cellular mechanism by which PSA affects cell interactions has not yet been defined. On the other hand, at present, specific and sensitive assays for ST8 displaying "initiase" activity are scarcely available except the one that makes use of fetuin as glycoprotein substrate acceptor (*10*, *11*, *18*). In the present study we report the first synthetic probe for the direct detection and quantification of a protein displaying a potential, putative ST8Sia II activity. To this purpose some typical methods such as dot-blot, Western blot, and ELISA were set up.

In particular, starting from the evidence that it is possible to purify ST8 basically by colominic acid/polyacrylohydrazido-agarose affinity chromatography (*10*, *11*, *18*), colominic acid was first oxidized and the reaction stopped by incubation with glycerol. Then, after dialysis, the colominic acid solution was recovered and reacted with a biotinylating compound such as biotinyl-L-lysine hydrazide that shows a better solubility in aqueous solution than either biotin hydrazide or biotin LC-hydrazide (*28*). Subsequently, the adduct solution was incubated with sodium cyanoborohydride to further stabilize the bond between the hydrazide and the aldehyde (produced after colominic acid oxidation) (*29*). An additional dialysis step was carried out to remove unbound material and the adduct solution stored a 4 °C. Because our recent studies have been focused on K562 cells expressing an ST8 consistent with an "initiase"-like activity sensitive to AZT (*10*, *11*), this cell system was used to check the ability of our synthetic adduct to recognize ST8Sia II, permitting both the detection and quantitation of the enzymatic protein. To this purpose, three different typical and basic methodological approaches were explored (i.e., dot-blot, Western blot, and ELISA). In all cases, protein extracts obtained after solubilization in Triton CF-54, from both control and AZT-treated K562 cells, were appropriately prepared and analyzed. In dot-blot format the same range of total proteins from both control and AZT-treated cells was exploited (from 0.5 to 20 μg). As shown in Figure 1, the sensitivity limit found for our ST8 purified from K562 cells was ∼2 pg (row ST8). Although by dot-blot analysis it was possible to determine the sensitivity limit of our probe, a different quantitative expression of ST8 between control cells and AZT-treated cells could be only slightly visually appreciated (Figure 1, rows C and T, respectively); furthermore, normal human serum did not give

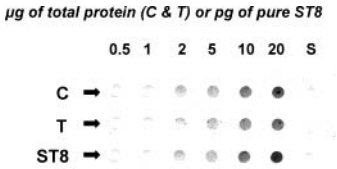


Figure 1. Dot-blot of control (C), AZT-treated (T) K562 cells, and α,(2→8)sialyltransferase (ST8) purified from K562 cells (*10*). S, normal human serum 1:250, 100 μL.

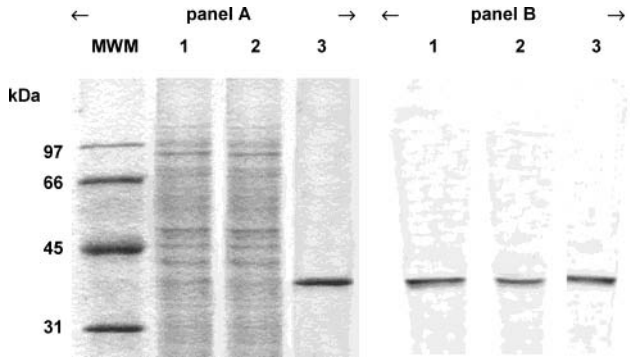


Figure 2. SDS−PAGE (A) and Western blot (B) analyses: (lane 1) control K562 cells; (lane 2) AZT-treated K562 cells; (lane 3) ST8 purified from K562 cells (*10*). MWM, molecular weight markers.

any reaction, indicating the lack of nonspecific binding of our probe at least toward human serum proteins (Figure 1, lane S).

After SDS−PAGE (Figure 2A), samples were blotted onto a PVDF membrane and revelation carried out as reported under Experimental Procedures (Figure 2B). Thus, when the same types of samples were analyzed by Western blot, a specific binding was observed for the protein band that showed a molecular mass of ∼40 kDa and corresponding to ST8, as previously reported (*10*). Interestingly, although the same amount of total proteins was loaded for both types of samples, control sample showed a higher intensity than AZT-treated sample, not only after SDS−PAGE (Figure 2A, lane 1) but also, and much more evidently, after Western blot (Figure 2B, lane 1). Moreover, apart from the net positive reaction observed for ST8, all other protein bands present in cell homogenates did not react with the probe (Figure 2B, lanes 1 and 2). Furthermore, control experiments carried out with different pure commercial sialyltransferases, that is, α,(2→3) (N), α,(2→3) (O), α,(2→6) (N) (Calbiochem), and loaded at the same amount of our pure ST (i.e., 1 μg) did not react versus our probe (data not shown). Eventually, when the pure protein (enzyme) was analyzed by ELISA, a linear dose-dependent response was obtained in the range of 50−200 pg (Figure 3, inset). A similar linear response was observed also for both control and AZT-treated samples, but these latter showed a decrease (73% of control) as calculated from the slope (Figure 3). Remarkably, the value of this decreased amount of protein (73% of control) strictly paralleled the decrease of ST8 activity we previously found in K562 cells treated with 20 μM AZT (75% of control) (*11*). Confirmatory evidence that the probe response in ELISA correlated with ST8 enzymatic activity was achieved through a "reverse" ELISA-like experiment. Briefly, streptavidin-coated microtiter plates (Molecular Probe) were first incubated with our probe and then with K562 cell homogenates from control or AZT-treated cells or with the pure ST8. After intermediate washing steps, elution-in-well by using colominic acid (25 mM) followed. The

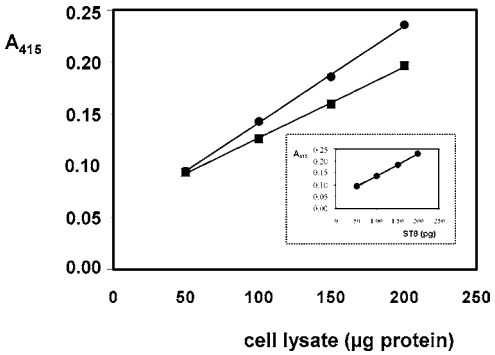


Figure 3. ELISA: absorbance values at 415 nm as a function of cell lysate protein amount in control (●) and AZT-treated (■) K562 cells. (Inset) Standard curve obtained with the pure enzyme ST8 purified from K562 cells (*10*). Data are means of three separate determinations with SD < 3%.

recovered solution was subsequently dialyzed, concentrated, assayed for its enzymatic activity (*10*, *11*), and subjected to dot-blot, Western blot, and ELISA. In all cases, compared to the ST8 enzyme affinity purified, superimposed results were obtained (data not shown). Of course, for an absolute quantitation in other cell systems, the pure protein is required.

It is worth noting that all data here reported, representing the best results achieved, were obtained when incubation with the probe was carried out after incubation with 25 mM HCl (20 min, room temperature). In our opinion this "acidic step" improved all assays probably because the enzymatic protein was freed of some bound anionic compound. This view is partly supported by the evidence that ST8 displaying "initiase"-like activity (ST8Sia II) strongly recognizes and binds to a highly negatively charged molecule such as colominic acid (coupled to polyacrylohydrazido-agarose) and it is eluted from the affinity column by using high colominic acid concentration (*10*, *11*, *18*). However, it should be underscored that although colominic acid binds to ST8Sia II, it does not serve as substrate (*10*, *18*). Last, independently from the analyses we carried out (dot-blot, Western blot, ELISA), the decreased amount of the putative ST8 we found in AZT-treated cells, compared to control cells, was in line with our recent study (*11*).

At the moment further studies are in progress to better characterize the synthetic probe we obtained, mainly from the spectroscopic point of view.

In conclusion, because considerable efforts have been directed to developing simple, reliable, specific, and inexpensive assays for different STs in general, but at present none is available for the direct detection and quantitation of ST8, especially in cell homogenates, we have developed a promising synthetic probe for the direct, rapid, inexpensive, and sensitive detection and quantitation of ST8. Our probe combines the advantage and detection technology of solid-phase reaction, being versatile and capable of simultaneous processing of multiple samples. The probe we synthesized could represent an attractive alternative to the currently used approaches to study ST8, and it is predicted to be a powerful tool for further investigation of ST8.

ACKNOWLEDGMENT

We thank Prof. A. Bozzi for helpful advice during manuscript preparation. This work was supported by MURST (Ministero dell'Università e della Ricerca Scientifica e Tecnologica, Rome, Italy).

LITERATURE CITED

(1) Kornfeld, R., and Kornfeld, S. (1985) Assembly of asparagine-linked oligosaccharides. *Annu. Rev. Biochem. 54*, 631−664.

(2) Reuter, G., and Schauer, R. (1994) Determination of sialic acids. *Methods Enzymol. 230*, 168−199.

(3) http://www.gene.ucl.ac.uk/nomenclature/genefamily/SIAT.shtml.

(4) Inoue, S., and Inoue, Y. (2001) Developmental profile of neural cell adhesion molecule glycoforms with a varying degree of polymerization of polysialic acid chains. *J. Biol. Chem. 276*, 31863−31870.

(5) Angata, K., Nakayama, J., Fredette, B., Chong, K., Ranscht, B., and Fukuda, M. (1997) Human STX polysialyltransferase forms the embryonic form of the neural cell adhesion molecule. Tissue-specific expression, neurite outgrowth, and chromosomal localization in comparison with another polysialyltransferase, PST. *J. Biol. Chem. 272*, 7182−7190.

(6) Angata, K., Suzuki, M., and Fukuda, M. (1998) Differential and cooperative polysialylation of the neural cell adhesion molecule by two polysialyltransferases, PST and STX. *J. Biol. Chem. 273*, 28524−28532.

(7) Kitazume-Kawaguchi, S., Dohmae, N., Takio, K., Tsuji, S., and Colley, K. J. (1999) The relationship between ST6Gal I Golgi retention and its cleavage-secretion. *Glycobiology 9*, 1397−1406.

(8) Gross, H. J., Sticher, U., and Brossmer, R. (1990) A highly sensitive fluorometric assay for sialyltransferase activity using CMP-9-fluoresceinyl-NeuAc as donor. *Anal. Biochem. 186*, 127−134.

(9) Brossmer, R., and Gross, H. J. (1994) Fluorescent and photoactivatable sialic acids. *Methods Enzymol. 247*, 177−193.

(10) D'Andrea, G., Di Ciccio, L., Brindelli, F., D'Alessandro, A. M., Bozzi, A., and Oratore, A. (2001) Purification and partial characterization of an α-2,8-sialyltransferase from human erythroleukemia K562 cells. *Prepr. Biochem. Biotechnol. 31*, 355−368.

(11) D'Andrea, G., Lizzi, A. R., Brisdelli, F., D'Alessandro, A. M., Bozzi, A., and Oratore, A. (2003) Protein glycans alteration and a different distribution of some enzymatic activities involved in glycan processing are found in AZT-treated K562 cells. *Mol. Cell. Biochem. 252*, 45−51.

(12) Paulson, J. C., Beranek, W. E., and Hill, R. L. (1977) Purification of a sialyltransferase from bovine colostrum by affinity chromatography on CDP-agarose. *J. Biol. Chem. 252*, 2358−2362.

(13) Weinstein, J., de Souza-e-Silva, U., and Paulson, J. C. (1982) Purification of a Galβ(1→4)GlcNAcα(2→6) sialyltransferase and a Galβ(1→3(4))GlcNAcα (2→3) sialyltransferase to homogeneity from rat liver. *J. Biol. Chem. 257*, 13835−13844.

(14) Hooper, L. V., and Baenziger, J. U. (1993) Sulfotransferase and glycosyltransferase analyses using a 96-well filtration plate. *Anal. Biochem. 212*, 128−133.

(15) Gosselin, S., Alhussaini, M., Streiff, M. B., Takabayashi, K., and Palcic, M. M. (1994) A continuous spectrophotometric assay for glycosyltransferases. *Anal. Biochem. 220*, 92−97.

(16) Laroy, W., Maras, M., Fiers, W., and Contreras, R. (1997) A radioactive assay for sialyltransferase activity using 96-well mu1tiscreen filtration plates. *Anal. Biochem. 249*, 108−111.

(17) Livingston, B. D., and Paulson, J. C. (1993) Polymerase chain reaction cloning of a developmentally regulated member of the sialyltransferase gene family. *J. Biol. Chem. 268*, 11504−11507.

(18) Stoykova, L. I., and Glick, M. C. (1995) Purification of an α-2,8-sialyltransferase, a potential initiating enzyme for the biosynthesis of polysialic acid in human neuroblastoma cells. *Biochem. Biophys. Res. Commun. 217*, 777−783.

(19) Laemmli, U. K. (1970) Cleavage of structural proteins during assembly of the head of bacteriophage T4. *Nature 227*, 680−685.

(20) Towbin, H., Staehelin, T., and Gordon, J. (1979) Electrophoretic transfer of proteins from polyacrylamide gels to nitrocellulose sheets. Procedure and some applications. *Proc. Natl. Acad. Sci. U.S.A. 76*, 4350−4354.

(21) Bradford, M. M. (1976) A rapid and sensitive method for the quantitation of microgram quantities of protein utilizing the principle of protein−dye binding. *Anal. Biochem. 72*, 248−254.

(22) Roth, J., Rutishauser, U., and Troy, F. A. (1992) *Polysialic Acid*, Birkhauser Verlag, Basel, Switzerland.

(23) Takashima, S., Ishida, H. K., Inazu, T., Ando, T., Ishida, H., Kiso, M., Tsuji, S., and Tsujimoto, M. (2002) Molecular cloning and expression of a sixth type of α-2,8-sialyltransferase (ST8Sia VI) that sialylates *O*-glycans. *J. Biol. Chem. 277*, 24030−24038.

(24) Jimbo, T., Nakayama, J., Akahane, K., and Fukuda, M. (2001) Effect of polysialic acid on the tumor xenografts implanted into nude mice. *Int. J. Cancer 94*, 192−199.

(25) Vimr, E. R., McCoy, R. D., Vollger, H. F., Wilkison, N. C., and Troy, F. A. (1984) Use of prokaryotic-derived probes to identify poly(sialic acid) in neonatal neuronal membranes. *Proc. Natl. Acad. Sci. U.S.A. 81*, 1971−1975.

(26) Finne, J., and Makela, P. H. (1985) Cleavage of the polysialosyl units of brain glycoproteins by a bacteriophage endosialidase. Involvement of a long oligosaccharide segment in molecular interactions of polysialic acid. *J. Biol. Chem. 260*, 1265−1270.

(27) Acheson, A., Sunshine, J. L., and Rutishauser, U. (1991) NCAM polysialic acid can regulate both cell−cell and cell−substrate interactions. *J. Cell. Biol. 114*, 143−153.

(28) Hermanson, G. T. (1996) *Bioconjugate Techniques*, Chapter 8, pp 390−393, Academic Press, New York.

(29) Hermanson, G. T. (1996) *Bioconjugate Techniques*, Chapter 2, p 159, Academic Press, New York.

BC049970S

Carbostyril Derivatives as Antenna Molecules for Luminescent Lanthanide Chelates

Pinghua Ge[†] and Paul R. Selvin*[,†,‡]

Department of Physics and Center for Biophysics and Computational Biology, University of Illinois, Urbana, Illinois 61801. Received April 6, 2004; Revised Manuscript Received June 18, 2004

Luminescent lanthanide complexes consisting of a lanthanide-binding chelate and organic-based antenna molecule have unusual emission properties, including millisecond excited state lifetimes and sharply spiked spectra, compared to standard organic fluorophores. We have previously used carbostyril (cs124, 7-amino-4-methyl-2(1*H*)-quinolinone) as an antenna molecule (Li and Selvin, *J. Am. Chem. Soc.*, 1995) attached to a polyaminocarboxylate chelate such as DTPA. Here, we report the chelate syntheses of DTPA conjugated with cs124 derivatives substituted on the 1-, 3-, 4-, 5-, 6-, and 8-position. Among them, the DTPA chelate of cs124-6-SO_3H has similar lifetime and brightness for both Tb^{3+} and Eu^{3+} compared to the corresponding DTPA−cs124 complexes, yet it is significantly more soluble in water. The Tb^{3+} complex of DTPA−cs124-8-CH_3 has significantly longer lifetime compared to DTPA−cs124 (1.74 vs 1.5 ms), indicating higher lanthanide quantum yield resulting from the elimination of back emission energy transfer from Tb^{3+} to the antenna molecule. Thiol-reactive forms of chelates were made for coupling to proteins. These lanthanide complexes are anticipated to be useful in a variety of fluorescence-based bioassays.

INTRODUCTION

Carbostyril (cs124, 7-amino-4-methyl-2(1*H*)-quinolinone) and its derivatives have been used as antenna molecules to absorb light and to transfer excitation energy to lanthanide ions, which significantly increases the fluorescence efficiency of lanthanides (*1*−*4*). To achieve this energy transfer, cs124 or its derivatives are attached to a chelate backbone (such as diethylenetriaminepentaacetic acid, DTPA), which is the site that ligates lanthanide ions. If placed in close range, energy transfer from cs124 (or derivatives) to lanthanide ions is achieved. The chelate backbone site can be further attached to either a thiol-reactive or amine-reactive group for attachment to biomolecules such as DNA and proteins. The advantages of such fluorescence complexes include high solubility in aqueous solution, long fluorescence lifetime (milliseconds), high quantum yields, large Stokes shifts, and sharply spiked emission spectra. These properties make lanthanide complexes attractive probes for fluorescence studies of biomolecules. Such complexes have been used in energy transfer experiments on the muscle protein myosin (*5*−*8*) and on ion channels (*9*).

Most of these lanthanide chelates have used carbostyril as the sensitizer (*10*−*14*). Rarely, a carbostyril derivative was used as a sensitizer (*15*). Because of complex photophysics, the mechanisms of energy transfer from sensitizer to lanthanides have not been fully understood (*16*−*19*). Therefore, it is difficult to rationally design the structures of carbostyril-based lanthanide sensitizers. Given the versatile synthetic possibilities of modifying the cs124 structure (Figure 1), it is interesting to explore how the structural modification can effect the chemical, physical, and photophysical properties of lanthanide chelates. We report the syntheses of new lanthanide chelates with carbostyril derivatives with substitutes on the 1-, 3-, 4-, 5-, 6-, and 8-position as sensitizer, their photophysical properties, and their reactivity to biomolecules.

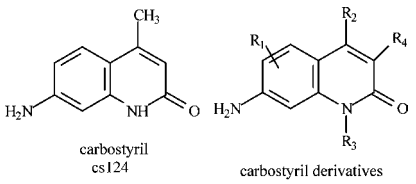


Figure 1. Structures of carbostyril and its derivatives.

EXPERIMENTAL METHODS

Chemicals and Materials. The following were purchased from Sigma-Aldrich: diethylenetriaminepentaacetic acid dianhydride (caDTPA), 3′-aminoacetanilide, 2,4-diaminobenzenesulfonic acid, 3,5-diaminobenzyl alcohol dihydrochloride, ethylenediamine (EDA), anhydrous dimethyl sulfoxide (DMSO, in sure seal bottle), and triethylamine (for reaction). DMSO and triethylamine were dried over activated molecular sieves before use. Glacial acetic acid, methanol, and triethylamine (for making triethylammonium acetate (TEAA) buffer) were purchased from Fisher Scientific. *β*-Maleimidopropionic acid hydrazide·TFA (EMPH·TFA) and *N*-hydroxysuccinimidyl bromoacetate were purchased from Molecular Biosciences (Boulder, CO). *N*-(*ϵ*-Maleimidocaproic acid) hydrazide (EMCH) was purchased from Pierce (Rockford, IL). Maltose binding protein (MBP) was a gift from Panvera Inc. (Madison, WI). Distilled and deionized (18 MΩ cm^{-1}) water was used throughout. All glassware was washed

* To whom correspondence should be addressed. Address: Department of Physics, 1110 W. Green Street, University of Illinois, Urbana, IL 61801. Phone: (217) 244-3371. Fax: (217) 244-7559. E-mail: selvin@uiuc.edu.

[†] Department of Physics.

[‡] Center for Biophysics and Computational Biology.

10.1021/bc049915j CCC: $27.50 © 2004 American Chemical Society
Published on Web 08/20/2004

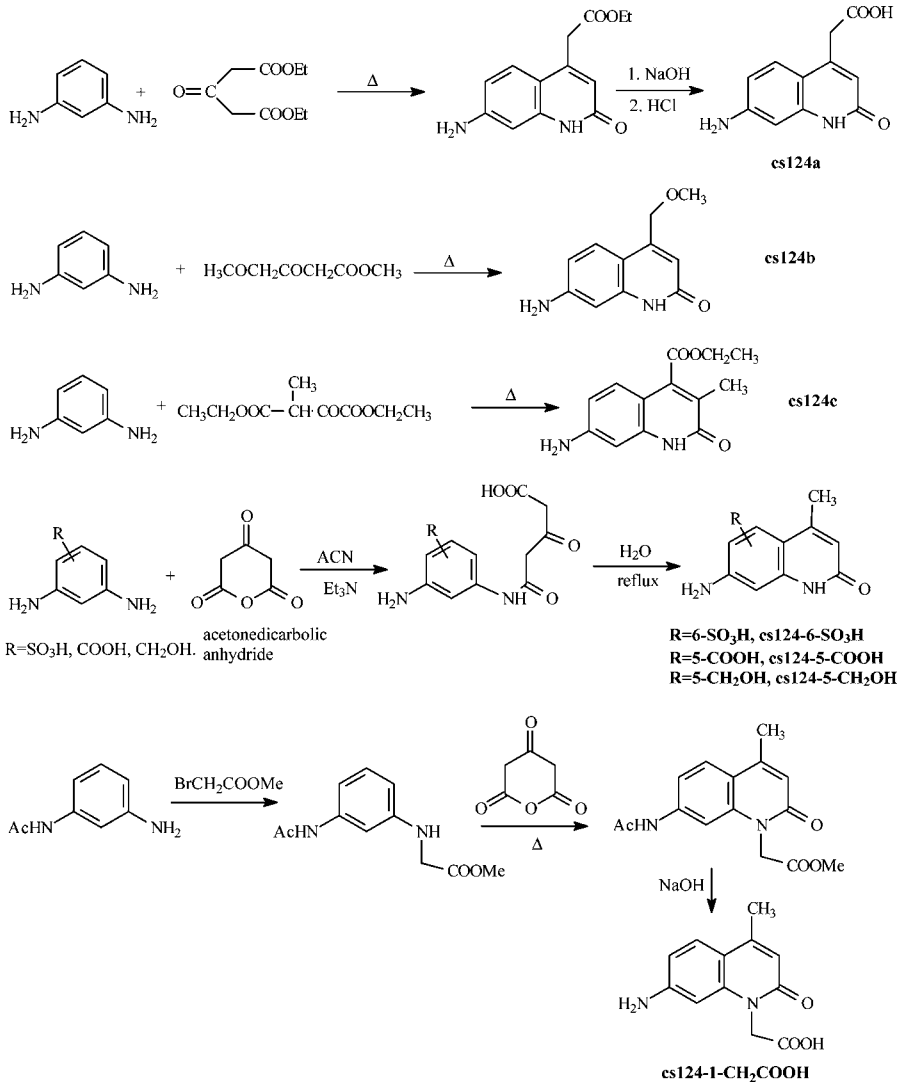


Figure 2. Syntheses and structures of 7-aminoquinolinone derivatives.

with a mixed acid solution and thoroughly rinsed with deionized, distilled water. All plastic labware was purchased from Bio-rad (metal-free). All chemicals were of the purest grade available.

Acetonedicarboxylic anhydride was synthesized according to published method (*20*). 7-Amino-4,8-dimethyl-2-(1*H*)-quinolinone (carbostyril 124-8-methyl, cs124-8-CH_3) was purchased from SPECS & BioSPECS (Rijswijk, The Netherlands). The syntheses of 7-amino-4,6-dimethyl-2-(1*H*)-quinolinone (carbostyril 124-6-methyl, cs124-6-CH_3) and 7-amino-4-methyl-6-sulfonic acid-2-(1*H*)-quinolinone (carbostyril 124-6-SO_3H, cs124-6-SO_3H) had been reported (*21*). In this report, a different synthetic method for cs124-6-SO_3H was used.

Purification. Reverse-phase high-performance liquid chromotography was performed at room temperature on a Waters model 600 system with a Dynamax 60 Å C_{18} column (10 or 25 mm i.d. × 250 mm, Rainin, at 8 mL/min, respectively) using a linear gradient (solvent A = 0.1 M triethylammonium acetate (TEAA), pH 6.5; solvent B = methanol or acetonitrile) over 40 min. The eluted fractions were monitored with a UV detector at a wavelength of 328 nm.

Spectroscopy. NMR spectra were recorded on a Varian Unity 400 spectrometer. Time-resolved and gated luminescence measurements were made on a laboratory-built spectrometer described previously, employing a 5 ns excitation pulse at 337 nm followed by time-resolved detection of lanthanide emission (*22*).

Syntheses of cs124 Derivatives (Figure 2). *Synthesis of 7-Amino-1,2-dihydro-2-oxo-4-quinoline Acetic Acid (cs124a).* 1,3-Diaminobenzene (200 mg, 1.85 mmol) was mixed with diethyl 1,3-acetonedicarboxylate (410 mg, 2.03 mmol). The mixture was heated at ∼160 °C for 24 h under N_2. A brown solid formed at the end. The solid was refluxed with acetone for 1 h. After the mixture was cooled to room temperature, the insoluble material was collected by filtration and washed with acetone. The collected solid was stirred with 5 mL of 10% NaOH for 5 h. Most of the solid dissolved. HCl and acetic acid were used to adjust the pH to ∼9. The solution was filtered through Celite. The filtrate was subjected to HPLC purification with a 20−40% linear gradient of MeOH/TEAA. The peak with the retention time of 12 min was collected. The solvent was removed to afford 7-amino-1,2-dihydro-2-oxo-4-quinoline acetic acid (trace amount, yield <1%). MS, *m/z*: 217 (M^- − 1, ESI). ^{1}H NMR (ppm, DMSO-d_6): 11.13 (s, 1H), 7.42 (d, 1H), 6.39 (d, 1H), 6.34 (s, 1H), 5.87 (s, 1H), 5.65 (s, br, 2H), 3.32 (s, 2H). ^{13}C NMR (ppm, DMSO-d_6): 171.72, 162.27, 151.06, 145.19, 141.00, 125.58, 116.11, 114.56, 110.51, 109.80, 96.74.

7-Amino-4-(methoxymethyl)-2(1H)-quinolinone (cs124b). 1,3-Diaminobenzene (200 mg, 1.85 mmol) was mixed with

methyl 4-methoxyacetoacetate (297 mg, 2.03 mmol). The mixture was heated at ~160 °C for 24 h under N_2, after which a brownish solid formed. The solid was washed with acetone and collected by filtration. The solid was further purified by recrystallization in EtOH to afford a pale-yellow solid, cs124b (232 mg, 69% yield). MS, *m/z*: 205 ($M^+ + 1$, ESI). Anal. Calcd for $C_{11}H_{12}N_2O_2$: C, 64.69; H, 5.92; N, 13.72. Found: C, 63.43; H, 5.93; N, 13.41. ^{1}H NMR (ppm, DMSO-d_6): 11.24 (s, 1H), 7.29 (d, 1H), 6.42 (d, 1H), 6.36 (s, 1H), 6.06 (s, 1H), 5.76 (s, 2H), 4.51 (s, 2H), 3.33 (s, 3H). ^{13}C NMR (ppm, DMSO-d_6): 162.35, 151.05, 147.25, 141.05, 124.96, 112.70, 110.46, 108.06, 96.78, 70.46, 57.99.

7-Amino-1,2-dihydro-2-oxo-3-methyl-4-quinoline Carboxylic Acid Ethyl Ester (cs124c). 1,3-Diaminobenzene (350 mg, 3.24 mmol) was mixed with diethyl oxalpropionate (719 mg, 3.56 mmol). The mixture was heated at ~160 °C for 24 h under N_2. A brownish solid formed and was dissolved in boiling ethyl acetate. The hot solution was cooled in an ice bath, causing yellow crystals to form. The solid was collected by filtration and further purified by passing through a silica gel column with ethyl acetate as the eluent to afford a yellow compound, cs124c (464 mg, 58% yield). MS, *m/z*: 247 ($M^+ + 1$, ESI). Anal. Calcd for $C_{13}H_{14}N_2O_3$: C, 63.40; H, 5.73; N, 11.38. Found: C, 63.15; H, 5.80; N, 11.07. ^{1}H NMR (ppm, acetone-d_6): 10.85 (s, br, 1H), 7.13 (d, 1H), 6.60 (s, 1H), 6.57 (d, 1H), 5.38 (s, br, 2H), 4.47 (q, 2H), 2.03 (s, 3H), 1.40 (t, 3H).

General Procedure for the Syntheses of cs124-6-SO_3H, cs124-5-COOH, and cs124-5-CH_2OH. To a suspension of substituted diaminobenzene dihydrochloride in anhydrous acetonitrile, 1 equiv of Et_3N was added at 0 °C under N_2. The mixture was stirred for 30 min. Acetonedicarboxylic anhydride, 1.2 equiv, was added to the above mixture. The reaction mixture was stirred for 8 h during which the temperature was warmed to room temperature. The organic solvent was removed under reduced pressure. The residue was dissolved in H_2O. $NaHCO_3$ was added until no CO_2 bubbles were released. The aqueous solution was refluxed under N_2 for 36 h. The solution was acidified with HCl and acetic acid to pH ~3−4. Precipitates formed during this process. The solution was allowed to stay overnight to complete the crystallization process. The solid was collected and further purified by recrystallization in ethanol.

cs124-6-SO_3H: yellow solid, 55% yield. MS, *m/z*: 253 ($M^- - 1$, ESI). ^{1}H NMR (ppm, DMSO-d_6): 11.16 (s, 1H), 7.73 (s, 1H), 6.38 (s, 1H), 5.95 (s, 1H), 2.27 (s, 3H).

cs124-5-COOH: white solid, 26% yield. MS, *m/z*: 219 ($M^+ + 1$, FAB). ^{1}H NMR (ppm, DMSO-d_6): 11.29 (s, 1H), 6.39 (s, 2H), 5.96 (s, 1H), 5.90 (s, 2H), 2.28 (s, 3H). ^{13}C NMR (ppm, DMSO-d_6): 172.08, 161.61, 149.79, 147.12, 141.68, 117.00, 109.82, 106.02, 97.56, 20.53.

cs124-5-CH_2OH: white solid, 18% yield. MS, *m/z*: 205 ($M^+ + 1$, FAB). ^{1}H NMR (ppm, DMSO-d_6): 11.15, (s, 1H), 6.58 (s, 1H), 6.30 (s, 1H), 5.88 (s, 1H), 5.73 (s, 2H), 3.34 (s, 2H), 2.54 (s, 3H). ^{13}C NMR (ppm, DMSO-d_6): 161.59, 149.88, 149.36, 142.65, 141.05, 116.60, 112.64, 108.76, 96.65, 63.28, 23.42.

Synthesis of cs124-1-CH_2COOH. 3′-Aminoacetanilide (500 mg, 3.33 mmol) was added to the aqueous solution containing 300 mg (3.57 mmol) of $NaHCO_3$. Methyl bromoacetate (560 mg, 3.66 mmol) was added to the mixture. The reaction mixture was refluxed for 4 h. The solution was cooled to room temperature and stirred overnight. The white solid of *N*-(3′-aminophenyl)glycine methyl ester was formed during the process. The solid was collected by filtration and dried. This solid was used for the next step without further purification.

The synthesized *N*-(3′-aminophenyl)glycine methyl ester (300 mg, 1.35 mmol) was mixed with acetonedicarboxylic anhydride (200 mg, 1.56 mmol) under N_2. The mixture was heated at ~160 °C for 24 h. The resulting deep-red solid was mixed with 3 mL of acetone. The mixture was refluxed for 30 min, then cooled to 0 °C. A precipitate formed during this process and was collected by filtration and washed with cold acetone to yield pale-reddish solid. The solid was further purified by recrystallization in EtOH to afford white 7-acetamide−cs124-1-CH_2COOCH_3 (152 mg, 39% yield). MS, *m/z*: 289 ($M^+ + 1$, FAB).

The obtained 7-acetamide−cs124-1-CH_2COOCH_3 was stirred in 10% NaOH for 8 h under N_2. A clear solution was formed. The solution was acidified with dilute HCl to pH ~3−4. A white precipitate formed during the process. The precipitate was collected and washed with H_2O. The solid was further purified by recrystallization in EtOH to afford 7-amino-*N*-(acetic acid)-2-quinolinone (47 mg, 37% yield). MS, *m/z*: 231 ($M^- - 1$, ESI). ^{1}H NMR (ppm, DMSO-d_6): 7.43 (d, 1H), 6.51 (d, 1H), 6.31 (s, 1H), 6.09 (s, 1H), 5.86 (s, br, 2H), 4.78 (s, 2H), 2.31 (s, 3H). ^{13}C NMR (ppm, DMSO-d_6): 169.85, 161.28, 151.66, 147.50, 141.11, 126.65, 113.51, 110.94, 109.90, 96.54, 43.07, 18.59.

Syntheses of DTPA-Based Lanthanide Chelates (Figure 3). *Gerneral Procedure for the Syntheses of Lanthanide Chelates from cs124 Derivatives.* An amount of 1 equiv of DTPA dianhydride was dissolved in a mixture of DMSO and 5 equiv of Et_3N under N_2. An amount of 0.7 equiv of cs124 derivative dissolved in DMSO was added slowly to the above solution with vigorous stirring. The reaction mixture was stirred at room temperature for 2 h. The solution was saved for the following steps.

If non-thiol-reactive chelates were to be synthesized, the above solution was quenched by addition of acetic acid and 0.1 M TEAA buffer (pH 6.5). The products were purified by reverse-phase HPLC with a linear gradient (typically 20−40% MeOH/TEAA, pH 6.5, over 40 min). The yield varies from ~20% to ~50%, as judged from the HPLC profiles (Table 1).

If the maleimide form of thiol-reactive chelates were to be synthesized, the above solution was transferred rapidly to a DMSO solution containing 1.3 equiv of EMPH·TFA (or EMCH) under N_2. The reaction mixture was stirred at room temperature for 4 h. Acetic acid and 0.1 M TEAA (pH 6.5) were added to quench the reaction. The product was purified by reverse-phase HPLC with a linear gradient (typically 20−40% MeOH/TEAA, pH 6.5, over 40 min). The yield varies from ~15% to 40%, as judged from the HPLC profiles (Table 2).

DTPA−cs124-8-CH_3−EDA-Br was prepared with a procedure similar to that used for DTPA−cs124−EDA-Br (*11*). DTPA dianhydride was reacted with cs124-8-CH_3 and EDA sequentially. The intermediate compound, DTPA−cs124-8-CH_3−EDA, was purified by HPLC. The pH of the concentrated aqueous solution of DTPA−cs124-8-CH_3−EDA was adjusted to ~8.5 by addition of Et_3N. *N*-Hydroxysuccinimidyl bromoacetate (3 equiv) was added to the solution. The reaction mixture was stirred at room temperature for 1 h. The product, DTPA−cs124-8-CH_3−EDA-Br, was purified by HPLC.

Addition of Metals. $TbCl_3$ or $EuCl_3$ was added to the chelate in a 1:2 molar ratio usually at >0.5 mM concentration at pH 6−7, usually in 0.1 M TEAA, pH 6.5 buffer, and allowed to stand for 30 min at room temperature before use.

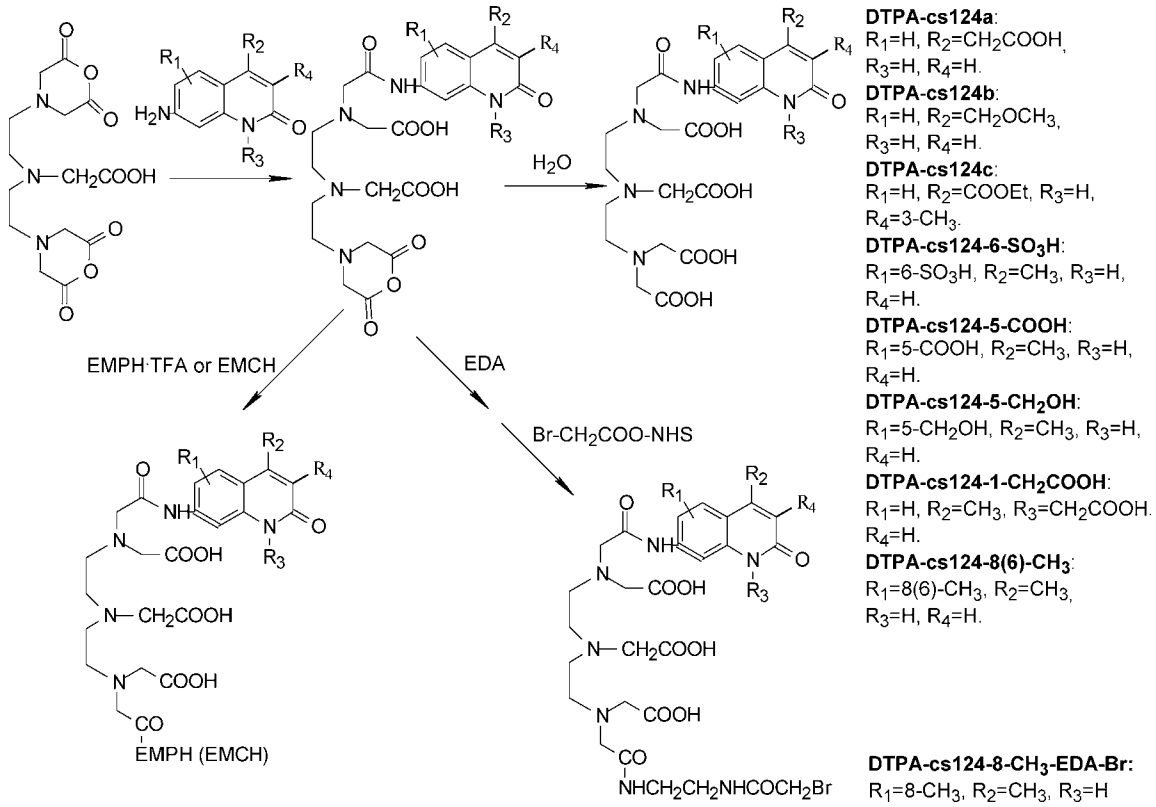


Figure 3. Syntheses of lanthanide chelates from cs124 derivatives.

Table 1. Non-Thiol Reactive Lanthanide Chelates

non-thiol-reactive DTPA chelates	linear gradients	retention time (min)	yield (%)	ESI-MS, $M^- - 1$ (m/z)
DTPA−cs124a	20−40% MeOH/TEAA	13.5	20	592
DTPA−cs124b	20−40% MeOH/TEAA	19	50	578
DTPA−cs124c	30−50% MeOH/TEAA	30.5	36	620
DTPA−cs124-6-SO_3H	30−50% MeOH/TEAA	13.5	20	628
DTPA−cs124-5-COOH	20−40% MeOH/TEAA	15.0	40	592
DTPA−cs124-5-CH_2OH	30−50% MeOH/TEAA	13.0	20	578
DTPA−cs124-1-CH_2COOH	30−50% MeOH/TEAA	13.5	40	606
DTPA−cs124-8-CH_3	30−50% MeOH/TEAA	13.4	30	562
DTPA−cs124-6-CH_3	20−40% MeOH/TEAA	17.2	40	562

Table 2. Thiol-Reactive Lanthanide Chelates

thiol-reactive chelates	linear gradients	retention time (min)	yield (%)	ESI-MS, $M^- - 1$ (m/z)
DTPA−cs124a−EMPH	20−40% MeOH/TEAA	20.6	25	757
DTPA−cs124-6-SO_3H−EMCH	30−50% MeOH/TEAA	19.5	40	835
DTPA−cs124-8-CH_3−EMCH	30−50% MeOH/TEAA	27.0	20	769
DTPA−cs124-8-CH_3−EDA-Br	30−50% MeOH/TEAA	21.5	95	725
DTPA−cs124-6-CH_3−EMCH	30−50% MeOH/TEAA	26.2	15	769
DTPA−cs124-5-CH_2OH−EMPH	30−50% MeOH/TEAA	18.3	15	743
DTPA−cs124-1-CH_2COOH−EMPH	30−50% MeOH/TEAA	16.5	30	771

Coupling to Biomolecules. The labeling conditions for conjugation to muscle protein (S1 fragment of smooth muscle myosin containing a single cysteine at position 208) have been described previously (*5*, *11*). The procedure for labeling Shaker K^+ ion channels in Xenopus oocytes has also been published (*9*). The maleimide chelates were coupled to muscle protein or to maltose binding protein (MBP, a 65 kDa protein containing a single cysteine) at a typical ratio of 10:1 with a protein concentration of ~15 μM. The coupling reaction was carried out on ice overnight in 20 mM 3-(*N*-morpholino)-propanesulfonic acid, pH 7.0, 5 mM $MgCl_2$. The excess lanthanide chelates were removed by passing the reaction mixture through a Sephadex G-50 size-exclusion column.

RESULTS AND DISCUSSION

Syntheses. The key step in synthesizing carbostyril and its derivatives is the formation of the 2-quinolinone ring. 1,3-Diaminobenzene and its derivatives reacted with β-diketone compounds to form intermediate β-diketone amido compounds, which further underwent ring closure to form the products. The compounds cs124a, cs124b, and cs124c were synthesized by reacting 1,3-diaminobenzene with the corresponding β-diketone esters at high temperature (usually >150 °C). A good yield was obtained for cs124b and cs124c, but a trace amount of cs124a was isolated after hydrolysis. The vast undesired byproducts were not identified.

Compounds cs124-6-SO_3H, cs124-5-COOH, cs124-5-CH_2OH, and cs124-1-CH_2COOH were synthesized with

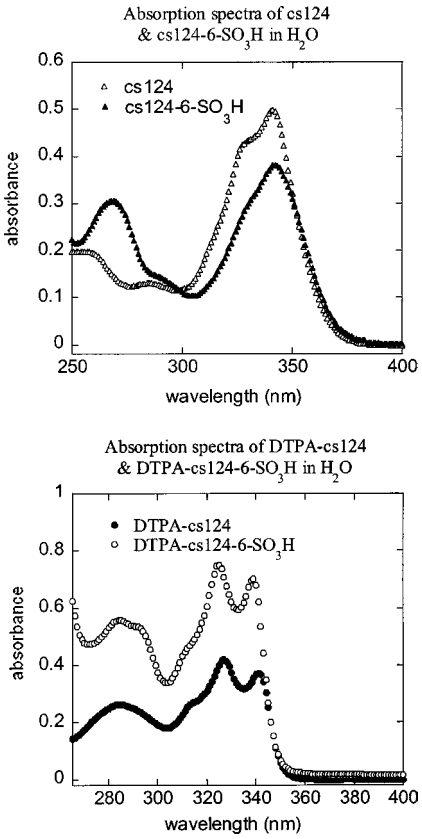


Figure 4. Comparison of the absorption spectra of cs124 and cs124-6-SO_3H and their lanthanide chelates.

a modified method. 1,3-Diaminobenzene derivatives were reacted with 1 equiv of acetonedicarboxylic anhydride at room temperature. The intermediates formed were then refluxed under milder conditions (100 °C) to undergo ring closure. The −COOH group in the intermediates from acetonedicarboxylic anhydride was easily lost to produce the 4-CH_3 group. The advantage of this method is that it does not require as high a temperature as the synthesis using β-diketone esters. This is especially important when the 1,3-diaminobenzene derivatives are not thermally stable. We note that acetonedicarboxylic anhydride had been used to synthesize quinolinone acetic acid compound (*20*). Our efforts in using this method to synthesize cs124a showed that mainly the −COOH depleted product, cs124, was formed.

The luminescent lanthanide chelates were synthesized in a way similar to that in previously reported work (*10*, *11*, *14*). DTPA dianhydride was reacted with cs124 derivatives to form monoanhydride intermediates (Figure 3). These intermediates can be either hydrolyzed or reacted with EMPH (or EMCH) to form thiol-reactive maleimide chelates. The chelates were purified by reverse-phase linear gradient HPLC. The syntheses are straightforward, and the yields are satisfactory.

Absorption Spectra. All of the synthesized cs124 derivatives and their DTPA lanthanide chelates exhibit similar or almost identical absorption spectra to those of cs124 and its DTPA lanthanide chelate. As an example, the UV−vis spectra of cs124-6-SO_3H and DTPA−cs124-6-SO_3H were compared to that of cs124 and DTPA−cs124 (Figure 4).

These absorption spectra were taken in aqueous media. Both of the absorption spectra of free cs124 and cs124-6-SO_3H exhibit the most intense absorption at 342 nm. A shoulder peak appears at ∼326 nm. After the coupling

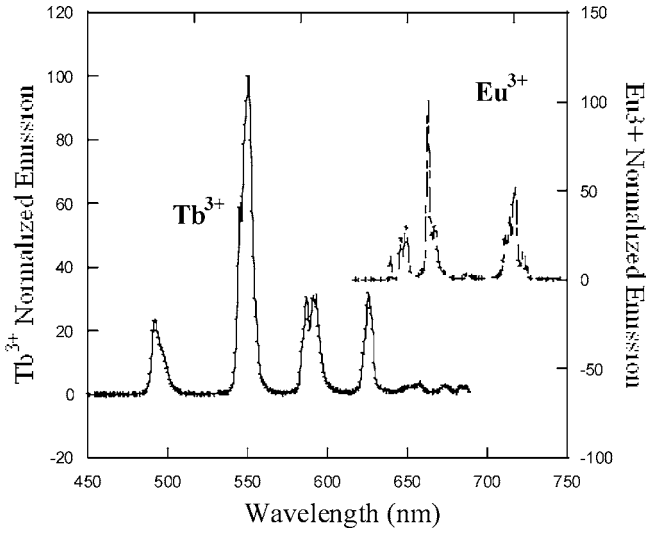


Figure 5. Normalized Tb^{3+} and Eu^{3+} emission spectra in DTPA−cs124-6-SO_3H in 0.1 M TEAA, pH 6.5, at a concentration of 1 μM. Tb^{3+} and Eu^{3+} display their characteristic sharply spiked spectra. Pulsed excitation was at 40 Hz, 3.5 μJ/pulse for Eu^{3+}, 3.0 μJ/pulse for Tb^{3+}. The integration time is 1 s for Tb^{3+} and 10 s for Eu^{3+}.

to DTPA, these two absorption peaks are well resolved, and the absorption at ∼326 nm becomes the most intense peak. These are the characteristic features of carbostyril and its DTPA lanthanide chelates. Such features were also observed for all cs124 derivatives and their lanthanide chelates.

Emission Spectroscopy of Lanthanide Complexes. All the Tb^{3+} and Eu^{3+} complexes exhibit their characteristic sharply spiked emission spectra as demonstrated by their DTPA−cs124-6-SO_3H complexes (Figure 5). Table 3 lists the excited-state lifetimes of Tb^{3+} and Eu^{3+} measured for their complexes with the chelates. Table 4 lists the excited state lifetimes of Tb^{3+} and Eu^{3+} measured for their complexes with the chelates labeled to proteins (smooth muscle myosin, maltose binding protein (MBP), and Xenopus oocytes). Generally, the Tb^{3+} and Eu^{3+} complexes of these chelates have emission brightness comparable to that of the benchmark chelate, DTPA−cs124. By introduction of hydrophilic groups to the sensitizers, the chelates derived from cs124a, cs124-6-SO_3H, cs124-5-COOH, cs124-5-CH_2OH, and cs124-1-CH_2COOH possess increased solubility in water, especially in the case of cs124-6-SO_3H. Although they show emission brightness comparable to that of the reference complex, DTPA−cs124, they often have shorter lifetimes. Contrary to this trend, Tb^{3+}−DTPA−cs124-6-SO_3H shows a slightly longer lifetime, and its brightness is about 62% that of Tb^{3+}−DTPA−cs124. Clearly, the introduction of 6-SO_3H on cs124 has no dramatic effect on the emission properties of its lanthanide complex.

The Tb^{3+} complexes with the chelates of 6- or 8-CH_3 cs124 derivatives, especially the 8-CH_3 derivative, have longer lifetimes than DTPA−cs124 (1.74 vs 1.53 ms). This suggests that a higher lanthanide quantum yield was achieved in these complexes. Increased lanthanide quantum yield could result from either a decrease in solvent quenching or a decrease in energy back transfer to the antenna. We measured the number of solvent molecules coordinated to the lanthanide ion in Tb^{3+}−DTPA−cs124-8-CH_3 using the method of Horrocks and Sudnick (*23*). Lifetimes of Tb^{3+}−DTPA−cs124 and Tb^{3+}−DTPA−cs124-8-CH_3 were measured in both H_2O and D_2O (Table 5). For both molecules, 1.1 H_2O molecules coordinated to

Table 3. Brightness and Lifetimes of Tb^{3+} and Eu^{3+} Complexes of DTPA−cs124 Derivative Chelates

chelate	relative brightness (%)	lifetimes (ms)
	Complexes with Tb^{3+}	
DTPA−cs124 (benchmark)	100	1.53
DTPA−cs124-6-SO_3H	62	1.58
DTPA−cs124-6-SO_3H−EMCH	72	1.86 76%; 0.44 24%
DTPA−cs124-8-CH_3	80	1.74
DTPA−cs124-8-CH_3−EMCH	58	2.16 82%; 0.92 18%
DTPA−cs124-8-CH_3−EDA-Br	64	1.68
DTPA−cs124-5-CH_2OH	79	0.93 45%; 0.65 55%
DTPA−cs124-5-CH_2OH−EMPH	37	0.82 85%; 0.37 15%
DTPA−cs124-5-COOH	36	0.82 24%; 0.50 76%
DTPA−cs124-6-CH_3	87	1.63
DTPA−cs124-6-CH_3−EMCH	4	1.85 59%; 0.25 41%
DTPA−cs124a	80	1.38
DTPA−cs124b	100	1.09
DTPA−cs124c	N/A	N/A
DTPA−cs124-1-CH_2COOH	77	1.29
DTPA−cs124-1-CH_2COOH−EMCH	20	1.43 74%; 0.41 26%
	Complexes with Eu^{3+}	
DTPA−cs124 ("benchmark")	100	0.61
DTPA−cs124-6-SO_3H	77	0.605
DTPA−cs124-6-SO_3H−EMCH	22	0.42 76%; 0.14 24%
DTPA−cs124-8-CH_3	100	0.603
DTPA−cs124-8-CH_3−EMCH	26	0.57 60%; 0.12 40%
DTPA−cs124-8-CH_3−EDA-Br	43	0.60
DTPA−cs124-5-CH_2OH	38	0.64 68%; 0.41 32%
DTPA−cs124-5-CH_2OH−EMPH	34	0.55 75%; 0.11 25%
DTPA−cs124-5-COOH	75	0.60
DTPA−cs124-6-CH_3	60	0.605
DTPA−cs124-6-CH_3−EMCH	N/A	N/A
DTPA−cs124a	52	0.60
DTPA−cs124b	173	0.60
DTPA−cs124c	152	0.53
DTPA−cs124-1-CH_2COOH	100	0.60
DTPA−cs124-1-CH_2COOH−EMCH	10	0.44 68%; 0.11 32%

Tb^{3+}, demonstrating that there is no difference in solvent quenching. Clearly, the higher quantum yield is achieved from the decrease of energy back transfer from excited Tb^{3+} to cs124-8-CH_3. Such lanthanide to ligands back energy transfer has been observed for other lanthanide complexes (*24*).

Interestingly, the thiol-reactive (maleimide form) chelates with 6- or 8-CH_3 cs124 derivatives exhibit significantly different emission properties. The Tb^{3+} complexes of DTPA−cs124-8-CH_3−EMCH is about 60% as bright as Tb^{3+}−DTPA−cs124 and is biexponential with an ∼80% long lifetime component (2.16 ms) and a ∼20% short lifetime component (0.92 ms). The Eu^{3+} complexes of DTPA−cs124-8-CH_3−EMCH is also biexponential with the brightness about 25% that of Eu^{3+}−DTPA−cs124. In contrast, the Tb^{3+} complex of DTPA−cs124-6-CH_3−EMCH is only 4% as bright as Tb^{3+}−DTPA−cs124 and is biexponential with a reduced population for the long lifetime component (1.85 59%, 0.25 41%). The Eu^{3+} complexes of DTPA−cs124-6-CH_3−EMCH is emission-silent.

The 3-CH_3 substituted chelate, DTPA−cs124c, is fluorescently effective only for Eu^{3+}. With Tb^{3+}, no emission was observed. This is consistent with our previous observation that with a substituent on the 3-position of cs124, its lanthanide chelate was fluorescent only for Eu^{3+} but not for Tb^{3+} (*25*).

In all cases, thiol-reactive chelates with the maleimide functional group are both biexponential and often dimmer compared to the benchmark chelate, DTPA−cs124. In contrast, DTPA−cs124-8-CH_3−EDA-Br is single exponential with both Tb^{3+} and Eu^{3+}. The intensity is about half of that of DTPA−cs124. Its Tb^{3+} complex has a longer lifetime than that of Tb^{3+}−DTPA−cs124 (1.68 vs 1.53 ms). After reaction to glutathione, the lifetimes remain single exponential and did not change.

The maleimide form of chelates have been successfully coupled to proteins and Xenopus oocytes cells. Both Tb^{3+} and Eu^{3+} complexes are biexponential. The Tb^{3+} complexes have a predominant long lifetime (>1 ms) component. Among them, the long lifetime components of Tb^{3+}−DTPA−cs124-8-CH_3−EMCH and Tb^{3+}−DTPA−cs124-6-SO_3H−EMCH have lifetimes significantly longer than the reference, Tb^{3+}−DTPA−cs124.

CONCLUSIONS

New light-harvesting quinolinone chromophors with the modification on the 1-, 3-, 4-, 5-, 6-, and 8-position of cs124 have been synthesized. Generally, their lanthanide chelates have similar brightness and lifetimes to the reference compound, DTPA−c124. The 6- or 8-methyl, especially 8-methyl, derived chelates have even longer lifetimes indicating higher lanthanide quantum yields. The 6-SO_3H derived chelate has similar luminescent properties to the reference compound while possessing dramatically increased water solubility. The thiol-reactive chelates made from these derivatives show promising physical and chemical properties.

ACKNOWLEDGMENT

This work is supported by NIH Grant AR44420, NSF Grant 9984841, and the U.S. Department of Energy, Division of Materials Sciences under Award No. DEFG02-91ER45439, through the Frederick Seitz Materials Re-

Table 4. Brightness and Lifetimes of Tb^{3+} and Eu^{3+} Complexes of Thiol-Reactive DTPA−cs124 Derivative Chelates Labeled to Proteins

chelate	protein	lifetimes (ms)
	Complexes with Tb^{3+}	
DTPA−cs124-8-CH_3−EMCH	smooth muscle myosin HC208[a]	2.19 77%; 1.21 23%
	Shaker K^+ channels in oocyte cells[b]	2.17 93%; 0.63 7%
DTPA−c124-6-SO_3H−EMCH	MBP[c]	1.86 78%; 0.72 22%
DTPA−c124-5-CH_2OH−EMPH	MBP[c]	0.97 79%; 0.36 21%
DTPA−c124-8-CH_3−EDA-Br	glutathione[d]	1.67
	Complexes with Eu^{3+}	
DTPA−c124-8-CH_3−EMCH	smooth muscle myosin HC208[a]	0.69 35%; 0.12 65%
DTPA−c124-6-SO_3H−EMCH	MBP[c]	0.42 45%; 0.14 55%
DTPA−c124-5-CH_2OH−EMPH	MBP[c]	0.63 40%; 0.19 60%
DTPA−c124-8-CH_3−EDA-Br	glutathione[d]	0.59

[a] Subfragment 1 (100 kDa) of smooth muscle myosin with a single cysteine at position 208 of the heavy chain. [b] Details of ion channel expression can be found in the following: Cha. (1999) *Nature 402*, 809−813. [c] Maltose binding protein. [d] Purified by HPLC after labeling.

Table 5. Lifetimes of Tb^{3+}−DTPA−c124 and Tb^{3+}−DTPA−c124-8-CH_3 Measured in H_2O and D_2O and the Number of H_2O Molecules Coordinated to Tb^{3+}

	lifetimes		
compd	H_2O (ms)	D_2O (ms)	no. of H_2O
Tb^{3+}−DTPA−c124	1.55	2.64	1.1
Tb^{3+}−DTPA−c124-8-CH_3	1.73	3.20	1.1

search Laboratory at the University of Illinois at Urbana−Champaign. We thank Baigen Mei, Marie Christenson, and Kurt Vogel from Panvera Corp. for the generous gift of MBP protein. The labeling experiments to oocytes expressing Shaker ion channels were done by David Posson. The mass spectrometry experiments were performed by the Mass Spectrometry Center, University of Illinois at Urbana−Champaign. The elemental analyses were performed by Microanalysis Laboratory, University of Illinois at Urbana−Champaign.

LITERATURE CITED

(1) Soini, E., and Lövgren, T. (1987) Time-resolved fluorescence of lanthanide probes and applications in biotechnology. *CRC Crit. Rev. Anal. Chem. 18*, 104−154.

(2) Sammes, P. G., and Yahioglu, G. (1996) Modern Bioassays using Metal Chelates as Luminescent Probes. *Nat. Prod. Rep. 13*, 1−28.

(3) Selvin, P. R. (2002). Principles and Biophysical Applications of Luminescent Lanthanide Probes. *Annu. Rev. Biophys. Biomol. Struct. 31*, 275−302.

(4) Selvin, P. R. (2003) Lanthanide-labeled DNA. *Topics in Fluorescence Spectroscopy, Vol 7*, (Lakowicz, J., Ed.) pp 177−212, Kluwer Academic/Plenum, New York.

(5) Burmeister-Getz, E., Cooke, R., and Selvin, P. R. (1998) Luminescence resonance energy transfer measurements in myosin. *Biohys. J. 75*, 2451−2458.

(6) Xiao, M., Li, H., Snyder, G. E., Cooke, R. G., Yount, R., and Selvin, P. R. (1998) Conformational changes between the active-site and regulatory light chain of myosin as determined by luminescence resonance energy transfer: The effect of nucleotides and actin. *Proc. Natl. Acad. Sci. U.S.A. 95*, 15309−15314.

(7) Chakrabarty, T., Xiao, M., Cooke, R., and Selvin, P. R. (2000) Structure and dynamics of the myosin dimer measured by fluorescence and luminescence resonance energy transfer. *Biohys. J. 78*, 233A.

(8) Xiao, M., Reifenberger, J. G., Wells, A. L., Baldacchino, C., Chen, L. Q., Ge, P., Sweeney, H. L., and Selvin, P. R. (2003) An actin-dependent conformational change in myosin. *Nat. Struct. Biol. 10*, 402−408.

(9) Cha, A., Snyder, G. E., Selvin, P. R., and Bezanilla, F. (1999) Atomic scale movement of the voltage sensing region in a potassium channel measured via spectroscopy. *Nature 402*, 809−813.

(10) Li, M., and Selvin, P. R. (1997). Amine-reactive forms of a luminescent DTPA chelate of terbium and europium: Attachment to DNA and energy transfer measurements. *Bioconjugate Chem. 8*, 127−132.

(11) Chen, J., and Selvin, P. R. (1999) Thiol-reactive luminescent lanthanide chelates. *Bioconjugate Chem. 10*, 311−315.

(12) Kapanidis, A. N., Ebright, Y. W., Ludescher, R. D., Chan, S., and Ebright, R. H. (2001) Mean DNA bend angle and distribution of DNA bend angles in the CAP-DNA complex in solution. *J. Mol. Biol. 312*, 453−68.

(13) Takalo, H., Mukkala, V.-M., Mikola, H., Liitti, P., and Hemmila, I. (1994) Synthesis of Europium(III) Chelates Suitable for Labeling of Bioactive Molecules. *Bioconjugate Chem. 5*, 278−282.

(14) Ge, P., and Selvin, P. (2003). Thio-reactive lanthanide chelates, II. *Bioconjugate Chem. 14*, 870−876.

(15) Chen, J., and Selvin, P. R. (2000) Synthesis of 7-amino-4-trifluoromethyl-2-(1*H*)-quinolinone and its use as an antenna molecule for luminescent europium polyaminocarboxyllates chelates. *J. Photochem. Photobiol., A 135*, 27−32.

(16) Crosby, G. A., Whan, R. E., and Alire, R. M. (1961) *J. Chem. Phys. 34* 743.

(17) Abusalch, A., and Meares, C. (1984). *Photochem. Photobiol. 39*, 763−769.

(18) Kirk, W. R., Wessels, W. S., and Prendergast, F. G. (1993) *J. Phys. Chem. 97*, 10326−10340.

(19) Alpha, B., Ballardini, R., Lehn, J.-M., Perathoner, S., and Sabbatini, N. (1990). *Photochem. Photobiol. 52*, 299−306.

(20) Kiang, A. K., Tan, S. F., Wong, W. S. (1971). Reactions of acetonedicarboxylic anhydride (3-oxoglutaric anhydride) and its mono- and diacetyl derivatives with amines. *J. Chem. Soc. C* (15), 2721−2726.

(21) Spathe, H. (1957) 7-Amino-2-hydroxy-4-methylquinolines. DE 958647 19570221.

(22) Xiao, M., and Selvin, P. R. (1999) An Improved instrument for measuring time-resolved lanthanide emission and resonance energy transfer. *Rev. Sci. Instrum. 70*, 3877−3881.

(23) Harrocks, W. D., Jr., and Sudnick, D. R. (1979) Lanthanide ion probes of structure in biology. Laser-induced luminescence decay constants provide a direct measure of the number of metal-coordinated water molecules. *J. Am. Chem. Soc. 123*, 7067−7073.

(24) Lis, S., Elbanowski, M., Makowska, B., Hnatejko, Z. (2002). Energy transfer in solution of lanthanide complexes. *J. Photochem. Photobiol. 150*, 223−247.

(25) Chen, J., and Selvin, P. R. Unpublished data.

BC049915J

Gene-Transferring Efficiencies of Novel Diamino Cationic Lipids with Varied Hydrocarbon Chains

Hong Sung Kim,[†] Jaeho Moon,[†] Keun Sik Kim,[†] Myung Min Choi,[†] Ji Eun Lee,[†] Yeon Heo,[‡] Dae Hyan Cho,[‡] Doo Ok Jang,[‡] and Yong Serk Park*[,†]

Department of Biomedical Laboratory Science and Department of Chemistry, Yonsei University, Wonju 220-710, Korea. Received March 13, 2004

Utilizing three biocompatible components, a series of novel cationic lipids has been chemically synthesized and tested for their gene-transferring capabilities in 293 transformed kidney cells and B16BL6 mouse melanoma cells. The synthesized cationic lipids consisting of a core of lysine and aspartic acid with hydrocarbon chains of varied length were assigned the acronyms DLKD (*O*,*O*′-dilauryl *N*-lysylaspartate), DMKD (*O*,*O*′-dimyristyl *N*-lysylaspartate), DPKD (*O*,*O*′-dipalmityl *N*-lysylaspartate), and DSKD (*O*,*O*′-distearyl *N*-lysylaspartate). The gene-transferring capabilities of these cationic lipids were found to be dependent on the hydrocarbon chain length. Under similar experimental conditions, the order of gene transfection efficiency was DMKD > DLKD > DPKD > DSKD. Addition of cholesterol or dioleoyl phosphatidylethanolamine (DOPE) as a colipid did not change this order. Colipid addition affected the transfection efficiency positively or negatively depending on the length of the cationic lipid acyl chain. On the whole, the length of the hydrophobic carbon chain was a major factor governing the gene-transferring capabilities of this series of cationic lipids. The observed differences in transfection efficiency may be due to differing binding affinities to DNA molecules as well as differences in the surface charge potential of the liposome−DNA complexes (lipoplexes) in the aqueous environment.

INTRODUCTION

Cationic liposomes have become established as one of the leading nonviral gene transfer systems for both clinical and nonclinical purposes. The ease and rapidity of preparation of liposome−DNA complexes (lipoplexes) coupled with their relative safety, demonstrated in a number of preclinical and clinical tests, has expanded their applications despite relatively low transfection efficiency as compared to that of viral vector systems (*1*). The low transfection efficiency is related to the biophysical characteristics of cationic liposomes as well as the biological activity of plasmid DNA inside mammalian cells (*2*). Compared with viral infection, internalization of DNA vectors mediated by cationic lipids is a less specific and less active process. In addition, plasmid DNA transferred into the cytoplasm is incapable of self-replication and is vulnerable to intracellular degradation. However, starting from the initial interactions of lipoplexes with cells and ending with gene expression, the many obstacles encountered along the way suggest that, if they can be resolved, additional possibilities for clinical application of this delivery system may lie in the future.

Potential clinical applications of cationic liposome-mediated gene delivery have been demonstrated in disease models of various cancers (*3*,*4*) and some genetic diseases such as cystic fibrosis (*5*,*6*). However, at present, the low transfection efficiency of cationic lipidic vectors has hindered their application in those areas of gene therapy such as genetic diseases that require persistent gene expression at a therapeutic level. Hence, a great deal of effort, including synthesis of new cationic lipids (*7*) and providing lipoplexes with new characteristics (*8*), has been expended in the search for more effective cationic lipid vectors.

A number of preclinical and clinical studies have claimed that lipoplexes are safe when delivered locally in relatively low doses (*9*). However, it has been reported that, in a mouse model, intravenous administration of high doses of lipolexes induces acute toxicity (*10*). Several groups have been working on establishment of a structure−function relationship to define the requirements for the safe and efficient gene transfection of cationic lipids (*11*).

To begin to address transfection efficiency and safety concerns, we synthesized a series of novel cationic lipids incorporating the biocompatible and biodegradable components, lysine, aspartate, and fatty acyl chains. In this series of cationic lipids based on lysylaspartate (KD), diacyl derivatives with hydrocarbon chains of differing length (C_{12}, C_{14}, C_{16}, and C_{18}) exhibited different DNA-binding affinities which could be correlated with their different in vitro gene-transferring capabilities. The KD derivatives with the short acyl chains (C_{12} and C_{14}) exhibited stronger DNA-binding affinity and more efficient transfection than ones with long acyl chains. Biocompatible cationic liposomes of the type described here may be more suitable for preclinical and clinical applications.

EXPERIMENTAL PROCEDURES

Reagents. Dioleoyl phosphatidylethanolamine (DOPE) and *N*-[1-(2,3-dioleoyloxy)]-*N*,*N*,*N*-trimethylammonium propane methyl sulfate (DOTAP) were purchased from Avanti Polar Lipids (Alabaster, AL). Cholesterol was

* To whom correspondence should be addressed. Phone: +82-33-760-2448. Fax: +82-33-763-5224. E-mail: yspark@dragon.yonsei.ac.kr.

[†] Department of Biomedical Laboratory Science.

[‡] Department of Chemistry.

10.1021/bc049934t CCC: $27.50 © 2004 American Chemical Society
Published on Web 08/14/2004

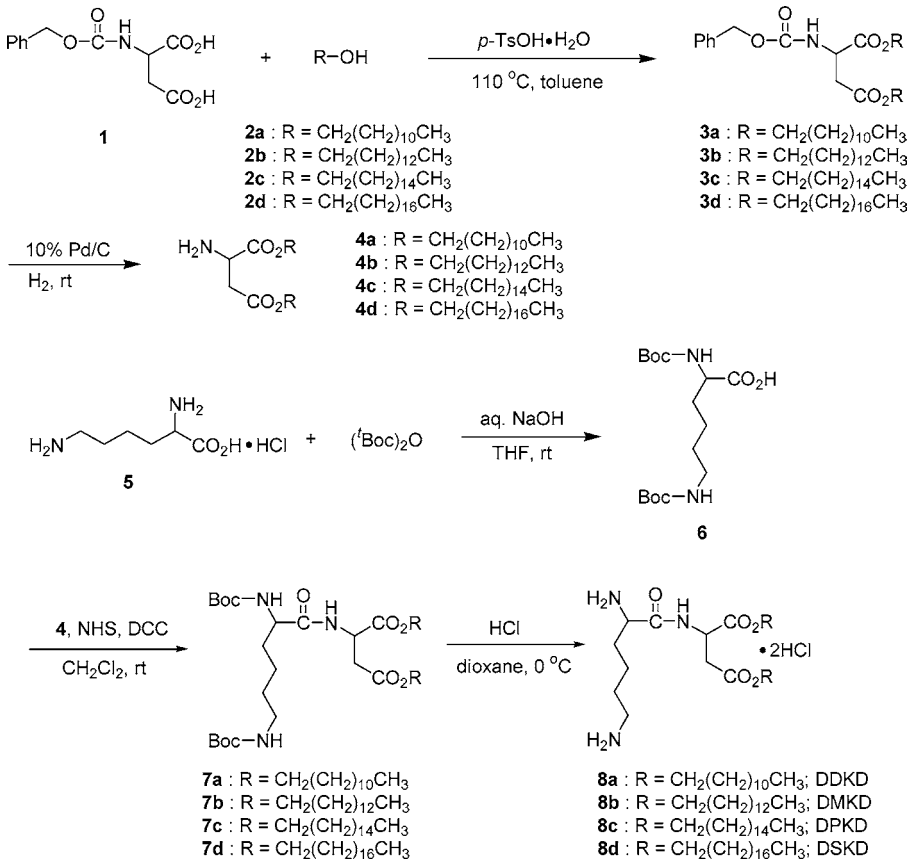


Figure 1. Synthetic outline for the KD series of cationic lipids

purchased from Sigma (St. Louis, MO). All organic reagents employed in the synthesis of cationic lipids were obtained from Aldrich (Milwaukee, WI) and used as received.

Synthesis of Dialkyl *N*-Carbobenzyloxy-L-aspartate (3a−d). Chemical synthesis of the KD series of cationic lipids is outlined in Figure 1. A solution of *N*-carbobenzyloxy-L-aspartic acid (**1**) (500 mg, 1.87 mmol), 1-dodecanol (**2a**) (1.06 mL, 4.68 mmol), and *p*-toluenesulfonic acid monohydrate (71 mg, 0.37 mmol) in toluene (30 mL) was heated at reflux with a Dean−Stark trap. After 16 h, the solution was washed with water and dried over anhydrous $MgSO_4$. After filtration, the solvent was removed in vacuo and the residue purified by column chromatography over silica gel (eluent: hexane−EtOAc = 9.5:0.5) to afford 960 mg of **3a** (85%). ^{1}H NMR ($CDCl_3$) δ 0.90−1.90 (m, 50H), 2.99 (m, 2H), 4.17 (m, 4H), 4.94 (m, 1H), 5.40 (m, 2H), 5.65 (m, 1H), 7.30−7.45 (m, 5H). Compounds **3b**, **3c**, and **3d** were synthesized using the same method as described above for compound **3a** in 66, 62, and 65% yields, respectively. **3b**: ^{1}H NMR ($CDCl_3$) δ 0.93−2.00 (m, 54H), 3.11 (m, 2H), 4.19 (m, 4H), 4.94 (m, 1H), 5.43 (m, 2H), 5.60 (m, 1H), 7.26−7.38 (m, 5H). **3c**: ^{1}H NMR ($CDCl_3$) δ 0.95−1.60 (m, 62H), 2.99 (m, 2H), 4.26 (m, 4H), 4.60 (m, 1H), 5.53 (s, 2H), 5.80 (m, 1H), 7.3−7.5 (m, 5H). **3d**: ^{1}H NMR ($CDCl_3$) δ 0.82−1.84 (m, 70H), 2.99 (m, 2H), 4.18 (m, 4H), 4.60 (m, 1H), 5.21 (s, 2H), 5.80 (m, 1H), 7.3−7.5 (m, 5H).

Synthesis of Dialkyl L-Aspartate (4a−d). A solution of compound **3a** (523 mg, 0.87 mmol) and 10% Pd/C (523 mg, 0.49 mmol) in THF (20 mL) was stirred at room temperature under a hydrogen atmosphere until the reaction was complete. The catalyst was filtered off through a Celite pad and the filtrate concentrated and purified by flash column chromatography on silical gel (eluent: hexane−EtOAc = 8:2) to afford 387 mg of **4a** (95%). ^{1}H NMR ($CDCl_3$) δ 0.78−1.71 (m, 50H), 2.72 (m, 2H), 3.80 (m, 1H), 4.12 (m, 4H). Compounds **4b**, **4c**, and **4d** were synthesized using the same method as described above for compound **4a** in 94, 91, and 92% yields, respectively. **4b**: ^{1}H NMR ($CDCl_3$) δ 0.82−1.72 (m, 54H), 2.74 (m, 2H), 3.81 (m, 1H), 4.12 (m, 4H). **4c**: ^{1}H NMR ($CDCl_3$) δ 0.67−1.63 (m, 62H), 2.39 (m, 2H), 3.39 (m, 1H), 4.11 (m, 4H). **4d**: ^{1}H NMR ($CDCl_3$) δ 0.82−1.62 (m, 70H), 2.74 (m, 2H), 3.80 (m, 1H), 4.12 (m, 4H).

Synthesis of Bis(*N,N′*-*tert*-butoxycarbonyl)aspartic Acid (6). L-Lysine monohydrochloride (200 mg, 1.01 mmol) was dissolved in aqueous NaOH solution (131.5 mg of NaOH in 3 mL of H_2O) followed by addition of a THF (3 mL) solution of di-*tert*-butyl dicarbonate (477.9 mg, 2.19 mmol). The mixture was stirred at room temperature overnight and then was neutralized with 1 M HCl aqueous solution and extracted with CH_2Cl_2. The organic layer was dried over anhydrous $MgSO_4$ and concentrated to give 311 mg of **6** (82%). ^{1}H NMR ($CDCl_3$) δ 1.21−1.91 (m, 24H), 3.12 (m, 2H), 3.76 (m, 1H), 4.28 (br, 1H), 6.03 (br, 1H).

Synthesis of 2-(2,6-Bis-*tert*-butoxycarbonylaminohexanoylamino) Succinic Acid Dialkyl Ester (7a−d). A solution of compound **6** (260 mg, 0.75 mmol), *N*-hydroxysuccinimide (87 mg, 0.75 mmol), and 1,3-dicyclohexylcarbodiimide (388 mg, 1.88 mmol) in THF (30 mL) was stirred for 1 h at room temperature. Compound **4a** (294 mg, 0.63 mmol) was added to the above solution, and the resulting mixture was stirred for an additional 6 h. The reaction mixture was washed with water, dried, and concentrated. The residue was purified by column chromatography on silica gel (eluent: hexane−EtOAc = 8:2) to furnish 377 mg of **7a** (75%). ^{1}H NMR ($CDCl_3$) δ 0.80−1.58 (m, 74H), 2.73−3.12 (m, 4H), 4.15 (m, 4H), 4.64 (br, 1H), 4.82 (m, 2H), 5.15 (br, 1H), 6.91 (br, 1H). Compounds **7b**, **7c**, and **7d** were synthesized using the

same method as described above for compound **7a** in 62, 61, and 62% yields, respectively. **7b**: ^{1}H NMR ($CDCl_3$) δ 0.82−1.58 (m, 78H), 2.76−3.14 (m, 4H), 4.14 (m, 4H), 4.65 (br, 1H), 4.86 (m, 2H), 5.15 (br, 1H), 6.91 (br, 1H). **7c**: ^{1}H NMR ($CDCl_3$) δ 0.96−1.62 (m, 82H), 2.74−3.11 (m, 4H), 4.07 (m, 4H), 4.65 (br, 1H), 4.68 (m, 2H), 5.13 (br, 1H), 6.90 (br, 1H). **7d**: ^{1}H NMR ($CDCl_3$) δ 0.82−1.83 (m, 86H), 2.77−3.16 (m, 4H), 4.17 (m, 4H), 4.69 (br, 1H), 4.91 (m, 2H), 5.14 (br, 1H), 6.91 (br, 1H).

Synthesis of 2-(2,6-Bis-*tert*-butoxycarbonylamino-hexanoylamino) Succinic Acid Dialkyl Ester Dihydrochloride (8a−d). Compound **7a** (494 mg, 0.62 mmol) was dissolved in THF (10 mL) and treated with 4 M HCl in 1,4-dioxane (10 mL) at 0 °C. After 6 h, the reaction mixture was concentrated and the residue was washed with Et_2O, affording 344 mg of **8a** (93%). Similarly, **8b**, **8c**, and **8d** were prepared in 93, 94, and 92% yields, respectively.

Cells and Cell Culture. Transformed kidney cells (293 cells) were purchased from the American Type Culture Collection (ATCC, Manassa, VA). The 293 cells were grown at 37 °C under a 5% CO_2 atmosphere in Dulbecco's Modified Eagle Medium (DMEM) (Gibco, Tulsa, OK), supplemented with 10% fetal bovine serum, 1 mM sodium bicarbonate, 50 μg/mL streptomycin, and 500 U/mL penicillin. Highly metastatic B16BL6 mouse melanoma cells were provided by Dr. Fidler (M. D. Anderson Cancer Center, Houston, TX). The melanoma cells were grown in Minimum Essential Medium Eagle (MEM) supplemented with 5% FBS, 100 μM vitamin solution, 100 μM sodium pyruvate, 10 μM nonessential amino acid, and penicillin/streptomycin antibiotics.

Preparation of Plasmid DNA−Lipid Complexes. The plasmid used in this study was pAAVCMV (prepared by Dr. M. J. During, Jefferson Medical College, Philadelphia, PA) containing a luciferase gene under the control of adeno-associated virus inverted terminal repeats and the cytomegalovirus promoter. The plasmid was prepared with a plasmid maxiprep kit (QIAGEN, Germany).

Appropriate amounts of cationic lipids (DLKD, DSKD, DPKD, DMKD, or DOTAP) alone or with helper lipids (DOPE or cholesterol) were mixed in chloroform. The organic solvent was evaporated under a stream of N_2 gas. Vacuum desiccation for about 2 h ensured removal of the residual organic solvent. The dried lipid films were hydrated in an appropriate amount of saline and then vigorously mixed with a vortex mixer for 5 min. Varied amounts of plasmid DNA in saline were gently mixed with appropriate amounts of the prepared liposomal solution. To provide stable lipoplex formation, the lipid−DNA mixtures were incubated at room temperature for 30 min before they were added to cultured cells.

Gel Retardation Analysis of Lipoplexes. Various amounts of cationic liposomes (0.3−12 nmol in 50 μL of saline) were added to 1 μg of DNA in 50 μL of saline, which were then incubated at room temperature for 30 min. A small aliquot of ethidium bromide (EtBr) solution was added to 20 μL of the lipoplex solution, which was run on 0.7% agarose gel and visualized by UV illumination (Fluor-S MultiImage, Bio-Rad, Herculus, CA).

ζ-Potential Measurement. The ζ-potentials of the lipoplexes were measured using a zetasizer (Zetasizer4, Malvern, U.K.). The lipoplex suspensions in Hepes buffer (pH 7.5) were loaded in the capillary cell mounted on the zetasizer, and their ζ-potentials were measured five times per sample at 25 °C.

In Vitro Gene Transfection. The 293 cells (1×10^5 cells/well) were plated onto 24-well plates and incubated at 37 °C under 5% CO_2 for 24 h. The various lipoplex formulations were added onto the 293 or B16BL6 cells in serum-free media, which were then incubated further for 4 h. After transfection, the cell culture medium containing the lipoplexes was replaced with a fresh serum-containing medium and the transfected cells were incubated for an additional 48 h. After removal of the culture medium by aspiration, the transfected cells in each well were carefully washed twice with 3 mL of PBS. The cells were lysed with 100 μL of lysis buffer (0.1 M Tris-HCl, 2 mM EDTA, and 0.1% Triton X-100, pH 7.8). The luciferase activity in a 10 μL aliquot of the cell lysate was measured with a luminometer (Minilumat LB9506, EG&G, Germany) and a luciferase assay kit (Promega, Madison, WI). The protein concentration of each cell lysate was determined by a standard protein assay (Bio-Rad Protein Assay, Bio-Rad, Hercules, CA). The luciferase activity in each sample was normalized to the relative light unit (RLU) per microgram of protein.

Cytotoxicity of Cationic Liposomes. The cytotoxicity of cationic liposomes was determined by MTT assay (*12*). The B16BL6 cells were plated into 96-well plates (5×10^3 cells per well) and cultured for 24 h. The cells were treated with various concentrations of cationic liposomes and then cultured for 24 h. Fifty microliters of MTT solution (1 mg/mL) was added to the cells, which were further cultured for 4 h. After the media containing MTT were removed, 100 μL of DMSO was added to solubilize the MTT−formazan product. The absorbance at 540 nm was measured with a microplate reader (Molecular Devices, Sunnyvale, CA).

RESULTS

Synthesis of Diacyl Lysylaspartate Cationic Lipids. We have synthesized a series of biocompatible cationic lipids that exhibit potent gene-transferring capability. These KD cationic lipids, composed of three biocompatible molecular moieties, lysine (the cationic headgroup), aspartic acid (the anchor), and two acyl chains (the hydrophobic tails), were synthesized as outlined in Figure 1.

Esterification of *N*-carbobenzyloxy-L-aspartic acid (**1**) with alcohols **2a−d** in the presence of *p*-toluenesulfonic acid monohydrate was carried out to obtain the corresponding diesters **3a−d** in 62−85% yields. Deprotection of the *N*-carbobenzyloxy group of the diesters **3a−d** with 10% Pd/C under hydrogen atmosphere gave the dialkyl aspartates **4a−d**. L-Lysine monohydrochloride (**5**) was transformed into **6** with di-*tert*-butyl dicarbonate, which was coupled with the compounds **4a−d** in the presence of NHS (*N*-hydroxysuccinimide) and DCC at room temperature, affording compounds **7a−d** in 61−75% yields. The desired cationic lipids **8a−d** were prepared by treatment of **7a−d** with 4.0 M HCl in dioxane at 0 °C.

Formation of DLKD-, DSKD-, DPKD-, and DMKD-Based Lipoplexes and Their Surface Charges. (DLKD = *O*,*O*′-dilauryl *N*-lysylaspartate, DMKD = *O*,*O*′-dimyristyl *N*-lysylaspartate, DPKD = *O*,*O*′-dipalmityl *N*-lysylaspartate, and DSKD = *O*,*O*′-distearyl *N*-lysylaspartate.) It has been well documented that electronic interactions between the headgroups of the cationic lipids and DNA molecules cause the formation of liposome−DNA complexes, called "lipoplexes". However, the strength of these interactions is dependent on the biophysical characteristics of the cationic lipids and the polymorphism of the liposomal membranes.

The gel retardation assay is a simple method that can be used to show the relative strength of electric interac-

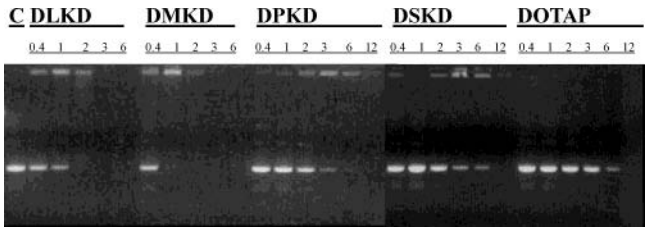


Figure 2. Gel retardation of pDNA complexed to KD liposomes. An aliquot of EtBr solution was added to plasmid DNA complexed to DLKD, DMKD, DPKD, DSKD, and DOTAP liposomes at various charge ratios. The lipoplexes were run on agarose gel and visualized by UV illumination.

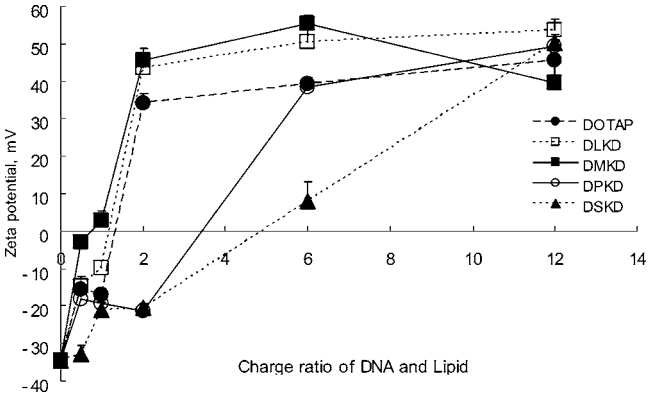


Figure 3. ζ-potentials of KD lipoplexes. The DLKD, DMKD, DPKD, DSKD, and DOTAP lipoplexes were prepared at various charge ratios of lipid to pDNA and loaded into the capillary cell mounted on a zetasizer. The numbers given were calculated from five measurements at 25 °C.

tions between cationic liposomes and DNA molecules. In this assay, a cationic liposome suspension and a DNA solution are mixed in various charge ratios from 0.4:1 to 12:1 (lipid/DNA) and run on an agarose gel. Stable lipoplexes do not penetrate into the agarose gel, but free pDNA, not complexed to cationic liposomes, localizes in the same pattern as the control of pDNA in the absence of cationic liposomes (Figure 2). The DMKD liposomes and DLKD liposomes were able to complete complex formation at approximately 1:1 and 2:1 charge ratios of lipid to DNA, respectively. Meanwhile, the DPKD liposomes and DSKD liposomes completed complex formation at charge ratios higher than 6:1. The DNA-binding affinity of DOTAP liposomes, one of the well-established cationic liposomes, was similar to that of the DPKD liposomes. It is possible that the configuration of cationic charges on the DMKD liposomes and DLDK liposomes confers an advantage in binding pDNA and lipoplex formation over that of the other liposomes.

ζ-potential measurement of cationic liposome−DNA complexes also indicates completion of lipoplex formation, as well as the resulting surface charge, another major parameter governing gene transfection activity. The DMKD lipoplexes exhibited a positively charged surface at a 1:1 (lipid/DNA) charge ratio (Figure 3). The DLKD and DOTAP lipoplexes became positively charged at charge ratios higher than 1:1, and their patterns of surface charge change were similar to each other. However, The DPKD and DSKD lipoplexes exhibited their positive surface charge at a 6:1 charge ratio. These results also indicate that DMKD and DLKD liposomes form stable lipoplexes more effectively than the other liposomes, as was suggested previously (Figure 2).

In Vitro Transfection Activities of KD Cationic Liposomes. To evaluate the transfection efficiencies of KD liposomes, various lipoplex formulations were prepared and tested in 293 transformed human kidney cells and B16BL6 mouse melanoma cells. After a 4 h transfection and an additional 24 h incubation, luciferase expression in the cells was measured by a luciferase activity assay. As is shown in Figure 4, the DMKD liposomes clearly have the most potent transfection efficiency among the series of KD liposomes, and the DLKD liposomes are next. When various amounts of pDNA complexed to the DMKD or DLKD liposomes (1:6, DNA wt/lipid wt) were added to 293 and B16BL6 cells in 24 well plates (Figure 4A and C), luciferase expression was nearly maximal at 0.5 μg of pDNA and saturated at higher DNA concentrations. Transfection with 5 μg of pDNA greatly diminished the luciferase expression in 293 cells. The gene expression pattern by the DPKD and DSKD was different from that by the DMKD and DLKD liposomes. The overall level of gene expression mediated by the DPKD and DSKD liposomes in the two cell lines was significantly lower than that by the DMKD liposomes and was not saturated up to 5 μg of pDNA.

Meanwhile, 293 cells and B16BL6 cells were transfected with 1 μg of pDNA complexed to various amounts of the KD series of cationic lipids to find the optimal ratio for in vitro transfection. In both cell lines, luciferase expression mediated by the DMKD liposomes was maximal at a 1:3−1:6 weight ratio of DNA and lipid and then decreased slightly on addition of more cationic lipids (Figure 4B and D). At all ratios tested, the DMKD liposomes exhibited a transfection efficiency superior to that of the other cationic liposomes including DOTAP liposomes. Under the same transfection conditions, the DLKD liposomes exhibited a similar transfection pattern to that of the DMKD liposomes but a lower transfection activity. In both cell lines, transfection by the DPKD or DSKD liposomes was not saturated up to the ratio 1:9, but their transfection efficiencies were far lower than those of any of the DMKD or DLKD liposomes. Under the best transfection conditions for each liposomal formulation, the order of transfection activities was DMKD > DLKD > DOTAP > DPKD > DSKD. These results implied that the optimal transfection conditions were dependent on the type of cationic liposomes as well as the characteristics of the cell lines.

It has been well documented that helper lipids, such as cholesterol and DOPE, generally enhance the transfection activity of cationic lipids (*13*). We prepared a series of the KD cationic liposomes containing cholesterol or DOPE (50 mol %) and compared their transfection activities in 293 and B16BL6 cells with those of liposomes consisting of only KD lipids. The transfection patterns of the helper lipid-containing liposomes were similar in both cell lines (Figure 5). Addition of cholesterol enhanced the transfection activities of the DSKD and DPKD liposomes 2.6- and 4.0-fold in 293 cells and 10.4- and 6.3-fold in B16BL6 cells, respectively. However, the DMKD and DLKD liposomes containing cholesterol exhibited 5.8- and 2.2-fold lower transfection activity in 293 cells and 4.5- and 2.1-fold lower activity in B16Bl6 cells, respectively. Meanwhile, addition of DOPE further enhanced the transfection activities of the DSKD liposomes (19.8-fold in 293 cells and 33.5-fold in B16BL6 cells) and DPKD liposomes (20.0-fold in 293 cells and 19.1-fold in B16BL6 cells). However, DOPE addition reduced the transfection activities of the DMKD liposomes (28.4-fold in 293 cells and 2.1-fold in B16BL6 cells) and the DLKD liposomes (10.9-fold in 293 cells and 1.3-fold in B16BL6 cells). These results indicated that addition of the helper lipids cholesterol or DOPE could affect the transfection

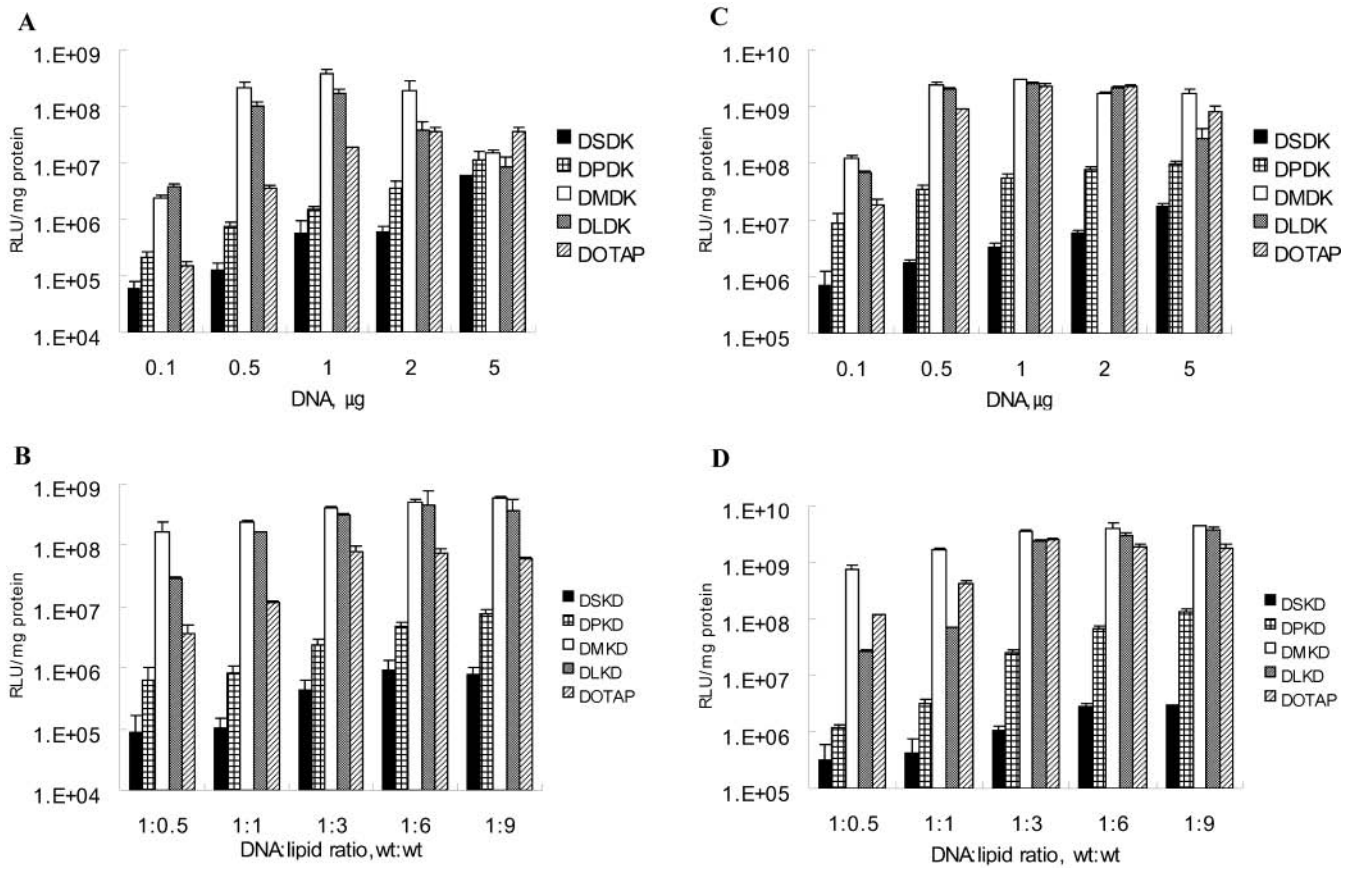


Figure 4. Transfection activities of KD lipoplexes in 293 and B16BL6 cells. Various amounts of pDNA complexed to KD liposomes and DOTAP liposomes (1:6 wt ratio of DNA and lipid) were added to 293 cells (A) and B16BL6 cells (C). Also 1 μg of pDNA complexed to KD liposomes and DOTAP liposomes at various weight ratios was added to 293 cells (B) or B16BL6 cells (D). The cells were transfected for 4 h and incubated for an additional 24 h. The luciferase activity of the cell lysate was measured with a luminometer and a luciferase assay kit. The mean luciferase activity was calculated from three different measurements.

activities of cationic liposomes positively or negatively, depending on the type and characteristics of the cationic lipids.

Cell Toxicity of KD Cationic Liposomes. The B16BL6 cells were incubated in the presence of various concentrations of KD liposomes and DOTAP liposomes to measure their cell toxicities and compare them to each other. In the ranges of lipid concentration for in vitro transfection <10 mg/mL, DMDK, DLKD, DSKD, and DOTAP liposomes did not severely damage the cultured B16BL6 cell, exhibiting over 75% cell viability. However, generally the KD liposomes were more cytotoxic than the DOTAP liposomes at the higher lipid concentrations (see Figure 6).

DISCUSSION

In designing a preclinical or clinical research study in gene therapy, a number of options must be considered in order to ensure effective gene transfer and efficient gene expression. The most important decision affecting transgene expression is whether to employ a viral or a nonviral gene delivery system. Depending on the characteristics of the disease state to be treated and the biological functions of therapeutic genes, a decision can be made as to which system is more desirable. Among the viral systems, one may have certain advantages over others, depending on the specific characteristics of the virus, such as the type of genetic material, life cycle, and so on. When safety and easy application are desired, nonviral gene transfer systems can be a primary choice and, among these, lipofection (gene transfection mediated by cationic liposomes) can be the first consideration.

Since the first report of liposomal gene transfection (*14*), a number of cationic lipids have been synthesized and tested in various cell culture models and animal models (*7*). The knowledge accumulated to date indicates that the transfection activity of a cationic lipid is determined by the chemical structure of the lipid, the charge number and strength, and the physical integrity of the liposomes when complexed to DNA (*2*). To achieve the best results in clinical applications, the transfection efficiency of gene-transferring vehicles must be a primary concern. Among the series of cationic lipids prepared in this study, DLKD and DMKD may satisfy the requirements for an efficient lipidic gene-transferring system.

Even though these synthesized cationic lipids all have a common backbone structure and differ only in the length of the hydrocarbon chains, they exhibited very different DNA-binding capabilities, lipoplex surface charges, and in vitro gene-transferring capability. The cationic lipids with shorter hydrocarbon chains exhibited the stronger DNA binding. The DMKD (C_{14}) liposomes were able to complete lipoplex formation at an approximately 1:1 charge ratio of lipid to DNA, which implied that all of the available cationic lipids are efficiently involved in DNA binding. At a 1:1 charge ratio, all of the pDNA molecules were completely covered by the DMKD cationic liposomal membranes, as indicated by no penetration and binding of EtBr. However, at this charge ratio, the DSKD (C_{18}), DPKD (C_{16}), and DOTAP liposomes were not able to bind all available pDNA molecules and they had to be added in much larger amounts to complete the lipoplex formation. Interest-

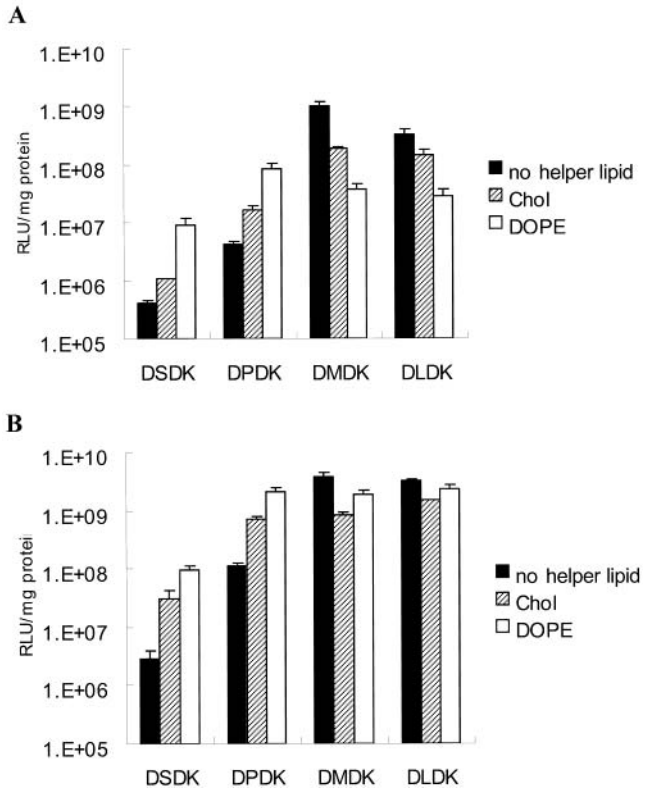


Figure 5. Effects of cholesterol and DOPE on the transfection activity of KD liposomes in 293 and B16BL6 cells. One microgram of pDNA complexed to KD liposomes, KD/cholesterol (50 mol %) liposomes, or KD/DOPE (50 mol %) liposomes at a 1:6 wt ratio of pDNA and lipid was added to each well containing 293 cells (A) or B16BL6 cells (B). The cells were transfected for 4 h and incubated for an additional 24 h. The luciferase activity of the cell lysate was measured with a luminometer and a luciferase assay kit. The mean luciferase activity was calculated from three different measurements.

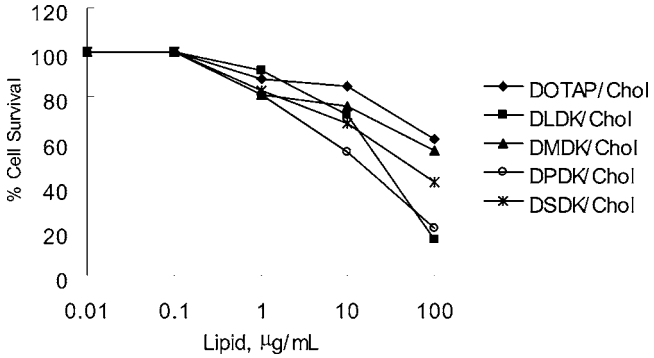


Figure 6. Cell toxicity of KD cationic liposomes. The B16BL6 cells were treated with various concentrations of cationic liposomes and then cultured for 24 h. Cell viability was measured by the MTT assay.

ingly, DLKD (C_{12}) also needs more addition to complete lipoplex formation and has a positive surface charge. These results imply that C_{14} is the optimal length of the hydrocarbon chain of the KD lipid derivatives for effective gene transfection.

Gene transfection activities of the KD cationic liposomes appear to be directly related to their DNA-binding affinities as well as the surface charge of the formed lipoplexes. As stated above, the KD cationic liposomes consisting of longer (C_{16} and C_{18}) or shorter (C_{12}) hydrocarbon chains had to be added more to complete lipoplex formation and to reach a positive ζ-potential. This also implied that the positively charged headgroups of the cationic lipids were not able to participate as effectively in lipoplex formation. Previously, it has been suggested that shorter hydroxyethyl quaternary ammonium lipid derivatives showed better transfection efficiency than longer ones. The order of efficiency was dimyristyl > dipalmytyl > distearyl (*15*). These results and those previously reported strongly indicate that cationic lipid polymorphism and liposomal membrane integrity affect the DNA-binding affinity of cationic liposomes. Even though the mechanism is not fully understood, there is a certain optimal membrane fluidity of liposomal bilayers for more suitable binding and accommodation of pDNA molecules, which may be more effective in interaction with cellular membranes due to proper lipid mixing.

It has been well documented that addition of cholesterol (*16*) or DOPE affects lipid polymorphism in liposomal membranes (*17*,*18*). Liposomal membrane fluidity can be controlled by the amount of cholesterol added (*19*). The addition of DOPE, a typical phospholipid that prefers a non-bilayer hexagonal phase, increases the fusogenic properties of the liposomes (*18*). Generally, incorporation of these two ingredients enhances the transfection activity of cationic liposomes (*20*,*21*). However, their effects on the transfection activities of the KD liposomes were varied depending on the structure of the individual cationic lipids. As is shown in Figure 5, addition of cholesterol or DOPE can interfere with the transfection activity of the DMKD and DLKD liposomes. However, their addition affected the transfection activities of the DSKD and DPKD liposomes both positively. At this moment it is not clear how these two molecules affect the membrane integrity and polymorphism of KD cationic liposomes. However, it can be stated that better gene transfection by cationic liposomes is derived from optimization of the membrane integrity and maximization of their surface charge. Also, the conditions for transfection by cationic liposomes can be changed depending on the characteristics of the target cells.

The KD series of cationic liposomes was expected to exhibit less cytotoxicity than other commercially available cationic liposomes, such as DOTAP-based liposomes, because they consist of lysine, aspartic acid, and two acyl hydrocarbon chains. Unexpectedly, the KD cationic liposomes were relatively more cytotoxic than the DOTAP liposomes. We speculated that the cytotoxicity of the KD liposomes may be due to physical membrane damage induced by detergent-like cationic lipid molecules and not to biochemical damage because their components are all biocompatible and their degradation does not produce any toxic end products in the cell.

In summary, among the KD series of cationic liposomes, the DMKD liposomes were the most effective in gene transfection into 293 and B16BL6 cells, and the DLKD liposomes were next. Since the DMKD liposomes needed much smaller amounts of pDNA and lipid to reach maximal gene transfection than the DOTAP liposomes, it can be stated that the DMKD liposomes are superior to the DOTAP liposomes. The potent transfection activity observed may be attributed to the strong DNA-binding affinity and effective distribution of positive surface charge on the lipoplex surface, which may mediate efficient interactions between cells and the lipoplexes. We have now undertaken in vivo transfection studies using the KD series of cationic lipids. KD liposome transfection systems optimized in vivo will be utilized for preclinical or clinical applications.

ACKNOWLEDGMENT

The authors wish to acknowledge the financial support of the Korea Ministry of Commerce, Industry, and Energy given in the program year of 2002.

LITERATURE CITED

(1) Huang, L., and Viroonchatanpan, E. (1999) *Nonviral vectors for gene therapy* (Huang, L., et al., Eds.) pp 3−22, Academic Press, San Diego, CA.

(2) Lasic, D. D. (1999) *Nonviral vectors for gene therapy* (Huang, L., et al., Eds.) pp 69−89, Academic Press, San Diego, CA.

(3) Hui, K. M., Ang, P. T., Huang, L., and Tay, S. K. (1997) Phase I study of immunotherapy of cutaneous metastases of human carcinoma using allogeneic and xenogeneic MHC DNA-liposome complexes. *Gene Ther. 8* 783−790.

(4) Rini, B. I., Selk, L. M., and Vogelzang, N. J. (1999) Phase I study of direct intralesional gene transfer of HLA-B7 into metastatic renal carcinoma lesions. *Clin. Cancer Res. 5,* 2766−2772.

(5) Hyde, S. C., Southern, K. W., Gileadi, U., Fitzjohn, E. M., Mofford, K. A., Waddell, B. E., Gooi, H. C., Goddard, C. A., Hannavy, K., Smyth, S. E., Egan, J. J., Sorgi, F. L., Huang, L., Cuthbert, A. W., Evans, M. J., Colledge, W. H., Higgins, C. F., Webb, A. K., and Gill, D. R. (2000) Repeat administration of DNA/liposomes to the nasal epithelium of patients with cystic fibrosis. *Gene Ther. 7,* 1156−1165.

(6) Noone, P. G., Hohneker, K. W., Zhou, Z., Johnson, L. G., Foy, C., Gipson, C., Jones, K., Noah, T. L., Leigh, M. W., Schwartzbach, C., Efthimiou, J., Pearlman, R., Boucher, R. C., and Knowles, M. R. (2000) Safety and biological efficacy of a lipid-CFTR complex for gene transfer in the nasal epithelium of adult patients with cystic fibrosis. *Mol. Ther. 1,* 105−114.

(7) Liu, D., Ren, T., and Gao, X. (2003) Cationic transfection lipids. *Curr. Med. Chem. 10,* 1005−1013.

(8) Hofland, H. E., Masson, C., Iginla, S., Osetinsky, I., Reddy, J. A., Leamon, C. P., Scherman, D., Bessodes, M., and Wils, P. (2002) Folate-targeted gene transfer in vivo. *Mol. Ther. 5,* 739−744.

(9) Stewart, M. J., Plautz, G. E., Del Buono, L., Yang, Z. Y., Xu, L., Gao, X., Huang, L., Nabel, E. G., and Nabel, G. J. (1992) Gene transfer in vivo with DA-liposome complexes: Safety and acuty toxicity in mice. *Hum. Gene Ther. 3,* 267−275.

(10) Song, Y. K., Liu, F., Chu, S., and Liu, D. (1997) Characterization of cationic liposome-mediated gene transfer in vivo by intravenous administration. *Hum. Gene Ther. 8,* 1585−1594.

(11) Choi, J. S., Lee, E. J., Jang, H. S., and Park, J. S. (2001) New cationic liposomes for gene transfer into mammalian cells with high efficiency and low toxicity. *Bioconjugate Chem. 12,* 108−113.

(12) Carmichael, J., deGraff, W. G., Gazdar, A. F., Minna, J. D., and Mitchel, J. B. (1987) Evaluation of a tetrazolium-based semiautomated colorimetric assay: assessment of radio sensitivity. *Cancer Res. 47,* 936−942.

(13) Hui, S. W., Langner, M., Zhao, Y. L., Ross, P., Hurley, E., and Chan, K. (1996) The role of helper lipids in cationic liposome-mediated gene transfer. *Biophys. J. 71,* 590−599.

(14) Felgner, P. L., Gadek, T. R., Holm, M., Roman, R., Chan, H. W., Wenz, M., Northrop, J. P., Ringold, G. M., and Danielsen, M. (1987) Lipofection: a highly efficient, lipid-mediated DNA-transfection procedure. *Proc. Natl. Acad. Sci. U.S.A. 84,* 7413−7417.

(15) Felgner, J. H., Kumar, R., Sridhar, C. N., Wheeler, C. J., Tsai, Y. J., Border, R., Ramsey, P., Martin, M., and Felgner, P. L. (1994) Enhanced gene delivery and mechanism studies with a novel series of cationic lipid formulations. *J. Biol. Chem. 269,* 2550−2561.

(16) Tilcock, C. P. (1986) Lipid polymorphism. *Chem. Phys. Lipids 40,* 109−125.

(17) Smisterova, J., Wagenaar, A., Stuart, M. C., Polushkin, E., ten Brinke, G., Hulst, R., Engberts, J. B., and Hoekstra, D. (2001) Molecular shape of the cationic lipid controls the structure of cationic lipid/dioleylphosphatidylethanolamine-DNA complexes and the efficiency of gene delivery. *J. Biol. Chem. 276,* 47615−47622.

(18) Bentz, J., Ellens, H., Lai, M. Z., and Szoka, F. C., Jr. (1985) On the correlation between H_{II} phase and the contact-induced destabilization of phosphatidylethanolamine-containing membranes. *Proc. Natl. Acad. Sci. U.S.A. 82,* 5742−5745.

(19) Spector, A. A., and Yorek, M. A. (1985) Membrane lipid composition and cellular function. *J. Lipid Res. 26,* 1015−1035.

(20) Li, S., Tseng, W. C., Stolz, D. B., Wu, S. P., Watkins, S. C., and Huang, L. (1999) Dynamic changes in the characteristics of cationic lipidic vectors after exposure to mouse serum: implications for intravenous lipofection. *Gene Ther. 6,* 585−594.

(21) Regelin, A. E., Fankhaenel, S., Gurtesch, L., Prinz, C., von Kiedrowski, G., and Massing, U. (2000) Biophysical and lipofection studies of DOTAP analogues. *Biochim. Biophys. Acta 1464,* 151−164.

BC049934T

Temperature Sensitization of Liposomes by Use of *N*-Isopropylacrylamide Copolymers with Varying Transition Endotherms

Keisuke Yoshino, Atsushi Kadowaki, Toru Takagishi, and Kenji Kono*

Department of Applied Materials Science, Graduate School of Engineering, Osaka Prefecture University, 1-1, Gakuen-cho, Sakai, Osaka 599-8531, Japan. Received November 6, 2003; Revised Manuscript Received May 28, 2004

Three kinds of copolymers of *N*-isopropylacrylamide (NIPAM) with the same conformational transition temperature and varying transition endotherms were synthesized with *N*-acryloylpyrrolidine (APr), *N*,*N*-dimethylacrylamide (DMAM), and *N*-isopropylmethacrylamide (NIPMAM) as the comonomers. Two dodecyl groups were incorporated into the termini of these copolymers as an anchor for the fixation to a liposomal membrane. Egg yolk phosphatidylcholine liposomes having these copolymers were prepared and their temperature-sensitive contents release and association properties were investigated. While these copolymer exhibited a conformational transition at ca. 40 °C, ΔH for the transition increased in the order of poly(APr-*co*-NIPAM) < poly(DMAM-*co*-NIPAM) < poly(NIPMAM-*co*-NIPAM). The liposomes containing poly(NIPMAM-*co*-NIPAM) showed a drastic release enhancement of entrapped calcein above the transition temperature, whereas the liposomes with poly(DMAM-*co*-NIPAM) and those with poly(APr-*co*-NIPAM) exhibited moderate and slight enhancement of calcein release above that temperature, respectively. On the contrary, the liposomes containing poly(APr-*co*-NIPAM) showed significant aggregation above the transition temperature, but the aggregation was hardly observed for the liposomes having poly(NIPMAM-*co*-NIPAM), indicating that poly(APr-*co*-NIPAM) more efficiently made the liposome surface hydrophobic. Thus, we concluded that the copolymer with a large ΔH is suitable for obtaining functional liposomes with a temperature-sensitive contents release property, whereas the copolymer with a small ΔH is appropriate for preparing functional liposomes with a temperature-sensitive surface property.

1. INTRODUCTION

Liposomes have been considered to be a highly attractive material as drug carriers, because of their merits, such as biocompatibility, ability to encapsulate both hydrophilic and hydrophobic drugs, and size controllability (*1*). To increase their usefulness as drug carriers, many efforts have been made to provide liposomes with various functions. pH-Sensitive (*2*−*4*), light-sensitive (*5*−*8*), and temperature-sensitive (*9*−*11*) liposomes have been extensively studied as functional liposomes, which are useful for site-specific and/or cytoplasmic drug delivery.

While several approaches have been employed for the production of functional liposomes, modification of the liposomes with functional polymers is one of the most effective methods (*12*−*14*). For example, Tirrell and coworkers (*3*, *13*) have achieved the sensitization of egg yolk phosphatidylcholine (EYPC) liposomes to pH by the conjugation of a pH-sensitive polymer, poly(2-ethylacrylic acid), which strongly binds to lipid membranes and permeabilizes them. In addition, various synthetic polymers and peptides containing carboxyl groups have been used to render stable liposomes pH-sensitive (*15*−*17*).

Recently, the temperature sensitization of liposomes has been actively attempted by use of thermosensitive polymers, such as poly(*N*-isopropylacrylamide) [poly(NIPAM)] (*14*, *18*−*21*). Poly(NIPAM) is known to exhibit a lower critical solution temperature (LCST) at ca. 32 °C (*22*). This polymer is hydrophilic and soluble in water below the LCST. However, it becomes hydrophobic and forms an insoluble aggregate above this temperature due to hydrophobic interactions and hydrogen bonding. At the molecular level, it undergoes a coil-to-globule transition at the LCST. We have shown that when a homopolymer and copolymers of NIPAM are fixed onto the liposome surface, contents release from the liposome can be triggered by increasing the temperature above their LCST (*18*, *20*, *23*). In addition, it has been demonstrated that surface modification with these thermosensitive polymers provides liposomes with temperature-sensitive surface properties. For example, the hydrophobicity and surface charge density of the thermosensitive polymer-modified liposomes were shown to be controlled by the ambient temperature (*24*, *25*).

The functions of the thermosensitive polymer-modified liposomes are generated through the interaction between the fixed thermosensitive polymer and the liposome membrane. Their performance should be affected by the mechanism and strength of their interaction. The ability of thermosensitive polymers to sensitize liposome membranes should depend on their structures and characteristics. Therefore, for the development of functional liposomes with high temperature sensitivity, it is important to know what characteristics of the thermosensitive polymers will affect their ability to sensitize liposomes.

In this study, three kinds of NIPAM copolymers, which undergo a conformational transition at the same temperature but exhibit different transition endotherms, were synthesized with *N*-acryloylpyrrolidine (APr), *N*,*N*-

* Corresponding author: Tel +81-72-254-9330; fax +81-72-254-9913; e-mail kono@ams.osakafu-u.ac.jp.

10.1021/bc034205j CCC: $27.50 © 2004 American Chemical Society
Published on Web 08/21/2004

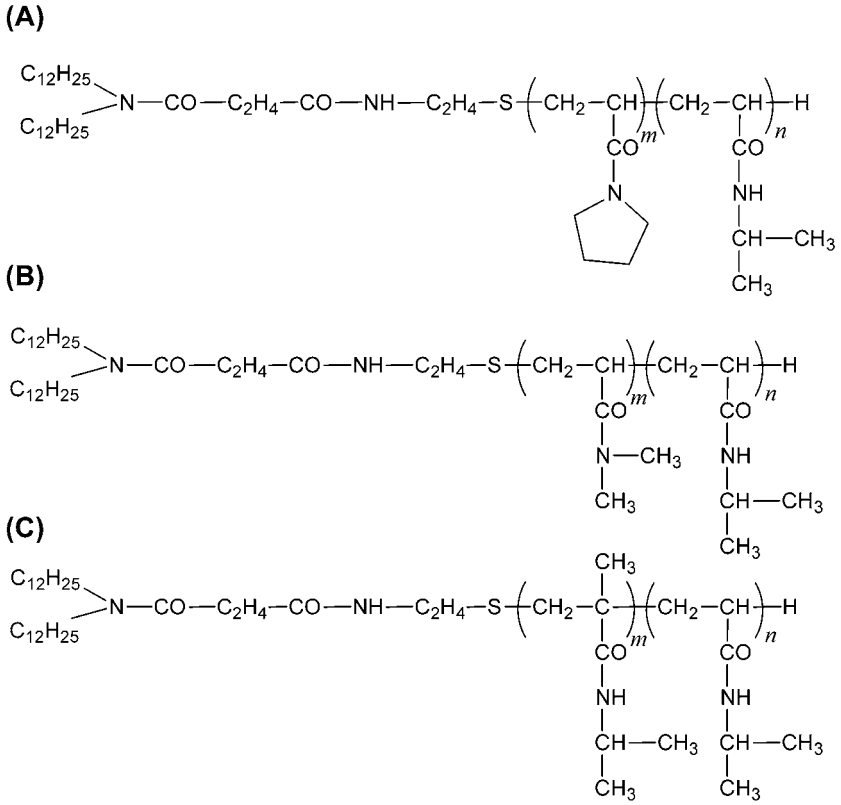


Figure 1. Structures of $2C_{12}$-poly(APr-*co*-NIPAM) (A), $2C_{12}$-poly(DMAM-*co*-NIPAM) (B), and $2C_{12}$-poly(NIPMAM-*co*-NIPAM) (C).

dimethylacrylamide (DMAM), and *N*-isopropylmethacrylamide (NIPMAM) as comonomers. Two dodecyl groups were connected to the chain end of these copolymers as an anchor to a liposomal membrane. These anchor-bearing copolymers are termed $2C_{12}$-poly(APr-*co*-NIPAM), $2C_{12}$-poly(DMAM-*co*-NIPAM), and $2C_{12}$-poly(NIPMAM-*co*-NIPAM) (Figure 1). The close correlation between the transition enthalpies of the copolymers and their ability to sensitize liposomes has been described.

2. EXPERIMENTAL SECTION

2.1. Materials. EYPC was kindly donated by Nippon Oil and Fats Co. (Tokyo, Japan). NIPAM, 2-aminoethanethiol, and Triton X-100 were supplied from Tokyo Kasei (Tokyo, Japan). Calcein, 1,6-diphenyl-1,3,5-hexatriene (DPH), 8-anilino-1-naphthalenesulfonic acid (ANS), and 1-pyrenecarboxaldehyde (PyCHO) were obtained from Sigma−Aldrich Japan (Tokyo, Japan). 1-Ethyl-3-(3-dimethylaminopropyl) carbodiimide (EDC) was obtained from Wako Pure Chemical Industries (Osaka, Japan). Azobis(isobutyronitrile) (AIBN), tris(hydroxymethyl)aminomethane (Tris), *N*,*N*-dimethylformamide (DMF), and ethylenediamineteraacetic acid disodium salt (EDTA) were from Kishida Chemical (Osaka, Japan). NIPAM and AIBN were purified by crystallization from benzene−*n*-hexane and methanol, respectively. APr was prepared as previously reported (*26*). NIPMAM was synthesized according to the method reported by Jordan et al. (*27*). *N*,*N*-Didodecylsuccinamic acid was synthesized according to the method of Okahata and Seki (*28*).

2.2. Synthesis of NIPAM Copolymers with Anchor. Three kinds of NIPAM copolymers having two dodecyl groups at the chain end, $2C_{12}$-poly(APr-*co*-NIPAM), $2C_{12}$-poly(DMAM-*co*-NIPAM), and $2C_{12}$-poly(NIPMAM-*co*-NIPAM) (Figure 1), were prepared according to the method previously reported (*25*, *29*). In brief, for the synthesis of $2C_{12}$-poly(APr-*co*-NIPAM), APr (15.7 mmol), NIPAM (12.8 mmol), 2-aminoethanethiol (0.4 mmol), and AIBN (0.03 mmol) were dissolved in freshly distilled DMF (12 mL) and then the solution was heated at 75 °C for 15 h in N_2 atmosphere. The copolymer was recovered by precipitation with diethyl ether and further purified on a Sephadex LH-20 column eluted with methanol. The obtained poly(APr-*co*-NIPAM) having an amino group (1.5 g) at the terminus was reacted with *N*,*N*-didodecylsuccinamic acid (3.3×10^{-4} mol) in DMF (50 mL) with 1-ethyl-3-(3-dimethylaminopropyl) carbodiimide (3.3×10^{-4} mol) for 48 h at 4 °C. The copolymer having a didodecyl group, $2C_{12}$-poly(APr-*co*-NIPAM), was purified by an LH-20 column eluting with methanol (yield 1.1 g). The $2C_{12}$-poly(DMAM-*co*-NIPAM) was prepared according to the above method. DMAM (2.4 mmol), NIPAM (9.4 mmol), 2-aminoethanethiol (0.5 mmol), and AIBN (0.13 mmol) were dissolved in DMF (7.5 mL) and then the solution was heated at 75 °C for 15 h in N_2 atmosphere. The obtained poly(DMAM-*co*-NIPAM) having an amino group (0.5 g) at the terminal was reacted with *N*,*N*-didodecylsuccinamic acid (1.5×10^{-4} mol) in DMF (15 mL) with 1-ethyl-3-(3-dimethylaminopropyl) carbodiimide (1.5×10^{-4} mol) for 48 h at 4 °C. The copolymer having a didodecyl group, $2C_{12}$-poly(DMAM-*co*-NIPAM), was purified as described above (yield 0.25 g). The $2C_{12}$-poly(NIPMAM-*co*-NIPAM) was synthesized by the same method. NIPMAM (15.7 mmol), NIPAM (19 mmol), 2-aminoethanethiol (1.15 mmol), and AIBN (0. 3 mmol) were dissolved in DMF (20 mL) and then the solution was heated at 75 °C for 15 h in N_2 atmosphere. The obtained poly(NIPMAM-*co*-NIPAM) having an amino group (1.5 g) at the terminus was reacted with *N*,*N*-didodecylsuccinamic acid (3.3×10^{-3} mol) in DMF (50 mL) with 1-ethyl-3-(3-dimethylaminopropyl) carbodiimide (3.3×10^{-3} mol) for 48 h at 4 °C. The copolymer having a didodecyl group, $2C_{12}$-poly(NIPMAM-*co*-NIPAM), was purified as described above (yield 1.1 g).

2.3. Liposome Preparation. The liposomes were prepared as previously reported (*20*, *29*). EYPC in chloroform solution (10 mg/mL, 1 mL) and the copolymer in chloroform solution [10 mg/mL, 1 mL for $2C_{12}$-poly(NIPMAM-*co*-NIPAM) and $2C_{12}$-poly(APr-*co*-NIPAM) or 4 mL for $2C_{12}$-poly(DMAM-*co*-NIPAM)] were mixed in a flask and the solvent was removed by evaporation. The obtained thin lipid/copolymer mixed membrane was further dried under vacuum overnight and dispersed in 1.5 mL of an aqueous calcein solution (63 mM). The obtained liposome suspension was extruded through a polycarbonate membrane with a pore diameter of 100 nm in an ice-cooled water bath. The free calcein and free copolymer were removed by gel-permeation chromatography (GPC) on a Sepharose 4B column at 4 °C in a 10 mM Tris-HCl-buffered solution containing 140 mM NaCl and 1 mM EDTA solution at pH 7.4. The calcein-loaded liposomes were kept at 5 °C until the measurement.

2.4. Calcein Release from Liposome. The release measurements were performed according to the method previously reported (*26*, *29*). An aliquot of dispersion of the calcein-loaded liposomes was added into 2 mL of 10 mM Tris-HCl, 140 mM NaCl, and 1 mM EDTA solution (pH 7.4) in a quartz cell (final concentration of the lipids 10 μM) at a given temperature, and the fluorescence intensity of the solution was monitored on a spectrofluorometer (Shimadzu RF-5000). The excitation and monitoring wavelengths were 490 and 520 nm, respectively. The percent release of calcein from the liposomes was defined as

$$\% \text{ release} = (F^t - F^i)/(F^f - F^i) \times 100$$

where F^i and F^t mean the initial and intermediary fluorescence intensities of the liposome suspension, respectively. F^f is the fluorescent intensity of the liposome suspension after the addition of Triton X-100 (final concentration 0.15%).

2.5. Estimation of the Amount of Copolymer Bound to Liposome. The amount of the copolymer bound to the liposome was estimated by use of high-performance liquid chromatography as previously reported (*24*, *29*). The liposomes bearing the copolymer were dried under vacuum and then dissolved in methanol/water (7:3 v/v). The solution was filtered through a poly(tetrafluoroethylene) membrane with a pore size of 0.25 μm. The filtrate (20 μl) was injected into an SB-803 column (Showa Denko) and the effluent was monitored by the absorbance at 220 nm on a UV detector (Jasco, UV-790). The amount of copolymer was estimated from the absorbance of the separated copolymer. Also, the lipid amount was determined by the method of Bartlett (*30*).

2.6. Fluorescence Measurements. Emission spectra of PyCHO were obtained on a spectrofluorometer with excitation at 365.5 nm. Fluorescence polarization (P) of DPH and ANS was measured as reported previously (*31*). ANS and DPH were excited at 395 and 360 nm, respectively, and the fluorescence intensities of ANS and DPH were monitored at 467 and 428 nm, respectively. The P value was evaluated by use of

$$P = (I_p - I_v)/(I_p + I_v)$$

where I_p and I_v represent the intensities of parallel polarized fluorescence and vertically polarized fluorescence, respectively.

2.7. Other Methods. The size of liposomes was evaluated by dynamic light scattering on a Nicomp 380 ZLS instrument (Particle Sizing Systems). The weight-average molecular weight (M_w) and the number-average molecular weight (M_n) of the polymers were estimated by gel-permeation chromatography on a system equipped with a Shodex KD-803 column (Showa Denko) with differential refractive index detection (Jasco, RI-930) with DMF as an eluent and poly(ethylene glycol) as the standard. Differential scanning calorimetry (DSC) was performed with a DSC 120 microcalorimeter (Seiko Electronics).

3. RESULTS AND DISCUSSION

3.1. Characterization of Copolymer and Copolymer-Modified Liposomes. It is known that the LCST of poly(NIPAM) can be controlled by copolymerization with comonomers having varying degrees of hydrophilicity/hydrophobicity (*32*). In this study, we used three kinds of comonomers, APr, DMAM, and NIPMAM, to obtain NIPAM copolymers that have different structures but exhibit the same LCST. Because the most attractive application of temperature-sensitive liposomes is the drug delivery application, we chose 40 °C as the LCST of the copolymers. Such temperature-sensitive liposomes can deliver drugs by specifically releasing them at the target site, which is mildly heated above that temperature (*2*). APr and DMAM have already been used to obtain NIPAM copolymers with an LCST around the physiological temperature (*26*, *27*).

Copolymerization of NIPAM and these comonomers was performed in the presence of the chain transfer reagent 2-aminoethanethiol to introduce an amino group at one terminus of the copolymer chain (*34*), which can be used for the attachment of a hydrophobic moiety for the fixation of the copolymer chain to the liposome membrane. The compositions of the copolymers were estimated from the integral ratios of signals derived from NIPAM and the comonomer units in the ^{1}H NMR spectra (Figure 2). Also, the number-average molecular weight (M_n), the weight-average molecular weight (M_w), and polydispersity index (M_w/M_n) of the copolymers were evaluated by gel-permeation chromatography with poly(ethylene glycol) as the standard. The results for the copolymers used in this study are listed in Table 1.

The cloud point measurement was performed to determine the LCST of the copolymer before the conjugation of the anchor. Figure 3 shows the transmittance of the aqueous solutions of these copolymers. The solutions were transparent below 38 °C, indicating that these copolymers were soluble in water below 38 °C. However, the solution became turbid around 40 °C, showing that these copolymers became water-insoluble around this temperature. The LCSTs of poly(APr-*co*-NIPAM), poly(DMAM-*co*-NIPAM), and poly(NIPMAM-*co*-NIPAM) were estimated from Figure 3 and are listed in Table 2.

It is known that the LCST of poly(NIPAM) can be determined by DSC (*22*, *35*). Thus, we examined the calorimetric detection of LCST for these copolymer solutions. Figure 4 depicts the typical DSC curves of these copolymer solutions. These curves exhibited an endotherm centered at approximately the same temperature, 40 °C, which agrees well with their LCST determined from the cloud point measurement. However, the amplitude of the endotherm significantly varies among these copolymers. As shown in Table 2, ΔH for the phase separation increases in the order poly(APr-*co*-NIPAM) < poly(DMAM-*co*-NIPAM) < poly(NIPMAM-*co*-NIPAM). Because the endotherm is mainly related to the destruction of water around the hydrophobic groups (*32*), this result suggests that the poly(NIPMAM-*co*-NIPAM) forms

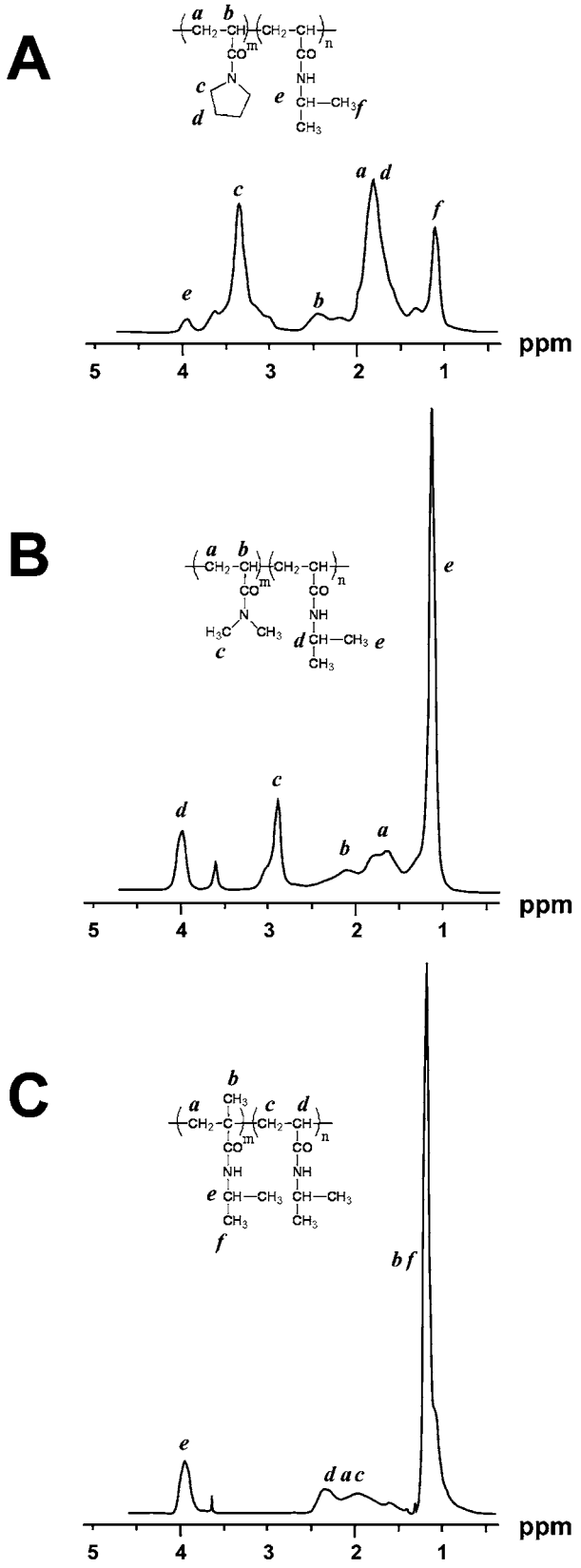


Figure 2. ^{1}H NMR spectra for poly(APr-*co*-NIPAM) (A), poly(DMAM-*co*-NIPAM) (B), and poly(NIPMAM-*co*-NIPAM) (C) in $CDCl_3$.

the most hydrophobic domain above the LCST, whereas poly(APr-*co*-NIPAM) forms the least hydrophobic domain among these copolymers.

Many studies have shown that a variety of hydrophilic polymers with hydrophobic anchor moieties can be fixed

Table 1. Characterization of the NIPAM Copolymers

copolymer	composition[a] comonomer/ NIPAM (mol/mol)	M_n[b]	M_w[b]	M_w/M_n[b]
poly(APr-*co*-NIPAM)	81/19	4100	9200	2.2
poly(DMAM-*co*-NIPAM)	28/72	4600	12800	2.8
poly(NIPMAM-*co*-NIPAM)	46/54	4850	7550	1.6

[a] Estimated by ^{1}H NMR. [b] Estimated by GPC.

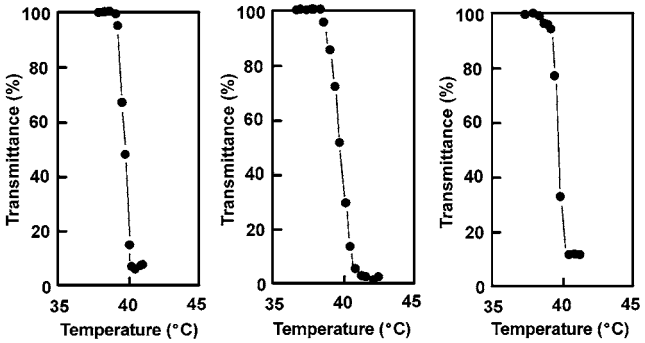


Figure 3. Cloud point curves for aqueous solutions of copoly(NIPAM-APr) (A), poly(DMAM-*co*-NIPAM) (B), and $2C_{12}$-poly(NIPMAM-*co*-NIPAM) (C).

Table 2. LCST of Copolymers

copolymer	cloud point (°C)	T_{max}[a] (°C)	ΔH (J/g)
poly(APr-*co*-NIPAM)	38.6	39.0	1.4
poly(DMAM-*co*-NIPAM)	39.8	41.1	11.8
poly(NIPMAM-*co*-NIPAM)	39.4	39.6	26.8

[a] Temperature of peak maximum of calorimetric endotherm.

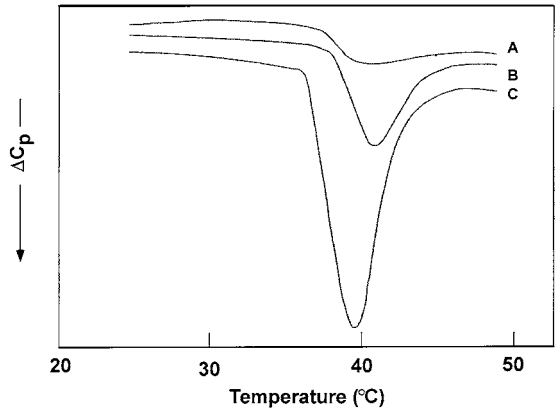


Figure 4. Microcalorimetric endotherms for copoly(NIPAM-APr) (A), poly(DMAM-*co*-NIPAM) (B), and poly(NIPMAM-*co*-NIPAM) (C).

to liposome membranes by a hydrophobic interaction between the hydrophobic moieties and liposome membranes (*12*, *15*, *36*). Since these copolymers have an amino group at one terminus of the chain, two dodecyl groups were introduced to the chain end by reacting didodecylsuccinamic acid with the terminal amino group. We have already shown that the didodecyl group can act as an anchor for the fixation of the NIPAM copolymers to the liposome membranes (*26*, *29*, *31*).

Liposomes modified with the copolymers bearing the anchor, $2C_{12}$-poly(APr-*co*-NIPAM), $2C_{12}$-poly(DMAM-*co*-NIPAM), and $2C_{12}$-poly(NIPMAM-*co*-NIPAM), were prepared by hydration of a mixture of EYPC and the copolymer and subsequent extrusion through a polycarbonate membrane with a pore size of 100 nm. The free

copolymer, which was not bound to the liposome membrane, was removed by GPC. The mean diameters and the standard deviations of the EYPC liposomes modified with $2C_{12}$-poly(APr-*co*-NIPAM), $2C_{12}$-poly(DMAM-*co*-NIPAM), and $2C_{12}$-poly(NIPMAM-*co*-NIPAM) were estimated by dynamic light scattering to be 125.7 ± 1.4, 106.6 ± 11.4, and 95.8 ± 3.8 nm, respectively, at 20 °C. It is apparent that these copolymer-modified liposomes possess diameters close to the pore size of the polycarbonate membrane used to prepare the liposomes. The amounts of the fixed copolymer were found to be 0.66, 0.44, and 0.58 mg/mg of liposomal lipid for liposomes modified with $2C_{12}$-poly(APr-*co*-NIPAM), $2C_{12}$-poly(DMAM-*co*-NIPAM), and $2C_{12}$-poly(NIPMAM-*co*-NIPAM), respectively, indicating that these copolymer-modified liposomes contain similar amounts of the copolymers. As indicated in the Experimental Section, the amounts of $2C_{12}$-poly(APr-*co*-NIPAM), $2C_{12}$-poly(DMAM-*co*-NIPAM), and $2C_{12}$-poly(NIPMAM-*co*-NIPAM) mixed with the lipid (10 mg) were 10, 40, and 10 mg, respectively, for the preparation of the liposomes. Thus, their binding efficiencies are calculated to be 66%, 11%, and 58%, respectively. The contents of the didodecylsuccinamic acid residues in these copolymers were estimated to be 0.6, 0.4, and 1.0 mol %, respectively, from ^{1}H NMR spectra for these anchor-bearing copolymers. Therefore, the low content of the anchor moiety and relatively high polydispersity (Table 1) of $2C_{12}$-poly(DMAM-*co*-NIPAM) may produce the low fixation efficiency.

3.2. Calcein Release from Copolymer-Modified Liposomes. We have already demonstrated that liposomes modified with thermosensitive polymers hardly release their contents below the LCST of the polymer but enhance the contents release above the LCST (*10*, *25*). Figure 5A shows profiles of calcein release from EYPC liposomes modified with these NIPAM copolymers at 25 and 42 °C. As is apparent in Figure 5A, all of the copolymer-modified liposomes did not release calcein at 25 °C. Because these copolymers showed an LCST around 40 °C, this result indicates that well-hydrated chains of these copolymers do not destabilize the liposomal membrane, despite the difference in their molecular structures. In contrast, at 42 °C, an enhancement of the contents release was seen for all of the copolymer-modified liposomes, but the extent of the enhancement was quite different among them. The liposomes modified with $2C_{12}$-poly(APr-*co*-NIPAM) showed only a limited extent of calcein release. However, the liposomes modified with $2C_{12}$-poly(DMAM-*co*-NIPAM) moderately promoted the contents release, and a very rapid and intensive release was observed for the liposomes modified with $2C_{12}$-poly(NIPMAM-*co*-NIPAM).

Figure 5B represents the percent release of calcein from these copolymer-modified liposomes as a function of temperature. For all of the liposomes, the calcein release was enhanced around 40 °C, indicating that the enhancement is triggered by the dehydration of the copolymers above their LCST. For the liposomes modified with $2C_{12}$-poly(APr-*co*-NIPAM), the release gradually increased with increasing temperature above 40 °C. This may be because dehydration of the copolymer chain proceeds with temperature even after its conformational transition. However, even at 50 °C, only 20% of the entrapped calcein molecules were released from the $2C_{12}$-poly(APr-*co*-NIPAM)-modified liposomes. Similarly, for the $2C_{12}$-poly(DMAM-*co*-NIPAM)-modified liposomes, an enhancement in the contents release occurred above 40 °C and the release was promoted by temperature, although the extent of the release was higher than the case

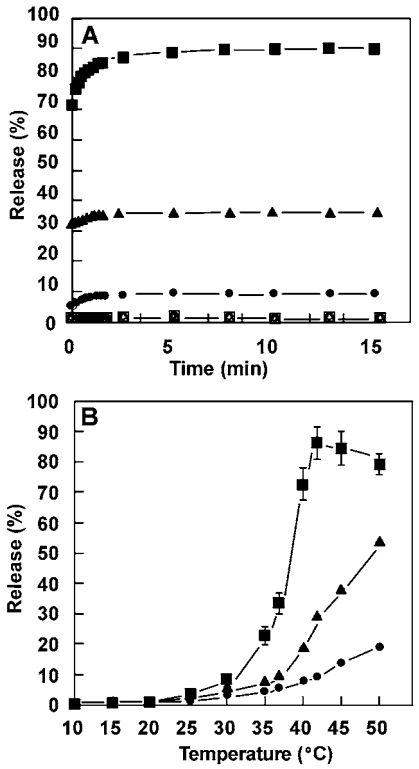


Figure 5. Release of calcein from $2C_{12}$-poly(APr-*co*-NIPAM)-modified (○, ●), $2C_{12}$-poly(DMAM-*co*-NIPAM)-modified (△, ▲), and $2C_{12}$-poly(NIPMAM-*co*-NIPAM)-modified EYPC liposomes (□, ■) in 10 mM Tris-HCl and 140 mM NaCl solution (pH 7.4). (A) Time course of calcein release at 25 °C (open symbols) and 42 °C (solid symbols). (B) Percent release after 15-min incubation as a function of temperature.

of the $2C_{12}$-poly(APr-*co*-NIPAM)-modified liposomes. For the $2C_{12}$-poly(NIPMAM-*co*-NIPAM)-modified liposomes, an intensive promotion of the release is seen around 40 °C, indicating that this copolymer chain strongly destabilizes the liposome membrane when dehydrated. A certain degree of contents release was also observed at 35 and 37 °C, although these temperatures are below the LCST. As seen in Figure 4, the DSC curve for the poly(NIPMAM-*co*-NIPAM) solution exhibits a large endotherm between 35 and 45 °C. This fact indicates that partial dehydration occurs even below the LCST. Thus, it is likely that the dehydrated segments of the copolymer chain interact with the liposome membrane and induce the contents release to some extent (*29*).

As mentioned above, the extent of partitioning of the copolymers onto the liposome increased in the order of $2C_{12}$-poly(DMAM-*co*-NIPAM) < $2C_{12}$-poly(NIPMAM-*co*-NIPAM) < $2C_{12}$-poly(APr-*co*-NIPAM), although the amounts of the bound copolymer were in the range of 0.44−0.66 mg/mg of lipid and not very different among these copolymer-modified liposomes. Therefore, the observed difference in their degree of contents release behavior cannot be explained from the difference in the extent of the copolymer partitioning. Thus, the ability of the dehydrated copolymer chain to induce the contents release could vary depending on their molecular structures.

3.3. Association of Copolymer-Modified Liposomes. Because the surface of the liposomes is covered by the hydrated copolymer chains below the LCST, these copolymer chains would enhance hydration of the liposome surface. However, above the LCST, dehydration of the copolymer chains would cause binding of the dehydrated copolymer chains onto the liposome surface,

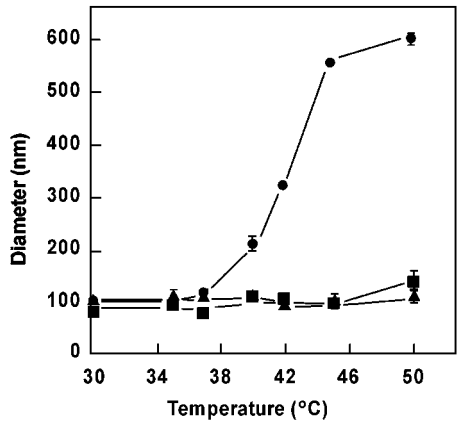


Figure 6. Diameters of $2C_{12}$-poly(APr-*co*-NIPAM)-modified (●), $2C_{12}$-poly(NIPMAM-*co*-NIPAM)-modified (■), and unmodified (▲) EYPC liposomes in 10 mM Tris-HCl and 140 mM NaCl solution (pH 7.4) as a function of temperature.

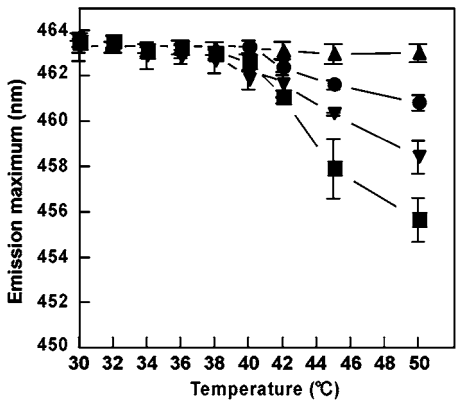


Figure 7. Emission maxima for PyCHO in the absence (▲) or presence of poly(APr-*co*-NIPAM) (●), poly(DMAM-*co*-NIPAM) (▼), and poly(NIPMAM-*co*-NIPAM) (■) in water. The concentrations of PyCHO and the copolymers were 1 μM and 0.4 mg/mL, respectively.

resulting in an increase in hydrophobicity of the liposome surface. Such a temperature-dependent alteration of the characteristic of the copolymer chain on the liposome surface could generate a new type of functional liposome whose surface property is controlled by temperature (*24*). As already shown, from the viewpoint of contents release, $2C_{12}$-poly(NIPMAM-*co*-NIPAM) exhibited the highest ability to sensitize liposomes, whereas $2C_{12}$-poly(APr-*co*-NIPAM) showed the lowest ability among the copolymers prepared in this study. Thus, we examined the temperature-dependent association of the copolymer-modified liposomes for these copolymers.

Figure 6 depicts the apparent diameters of the copolymer-modified and the unmodified EYPC liposomes as a function of temperature. The unmodified liposomes showed essentially the same diameter of ca. 100 nm throughout the experimental temperature range. Both the $2C_{12}$-poly(APr-*co*-NIPAM)-modified and the $2C_{12}$-poly(NIPMAM-*co*-NIPAM)-modified liposomes also exhibited almost the same diameter below the LCST. However, above the LCST, an increase in diameter was observed for both copolymer-modified liposomes, although the extent of the diameter increase is considerably different between them. The $2C_{12}$-poly(APr-*co*-NIPAM)-modified liposomes exhibited a significant increase in the diameter above the LCST, indicating that the dehydrated polymer chains fixed to the liposome made the liposome surface highly hydrophobic and induced aggregation of the liposomes through a hydrophobic interaction. Since the $2C_{12}$-poly(NIPMAM-*co*-NIPAM)-modified liposomes strongly enhanced the contents release above the LCST (Figure 5), we expected that these liposomes would show a more significant association above the LCST. However, the $2C_{12}$-poly(NIPMAM-*co*-NIPAM)-modified liposomes exhibited only a slight increase in the diameter at 50 °C, suggesting that this copolymer does not have the ability to provide a hydrophobic nature to the liposome surface.

3.4. Interaction of Copolymers with Liposome Membrane. Since the NIPAM copolymers exhibited an LCST at ca. 40 °C, these copolymers take on a dehydrated globule above this temperature. However, these copolymers induced the contents release from the liposomes and the association of the liposomes in a very different manner. Because these behaviors of the liposomes might be provided by the hydrophobic nature of the copolymers, the above results imply that the hydrophobicity is different among these copolymers taking on a dehydrated state. Thus, we investigated the hydrophobicity of a domain formed by these copolymers using PyCHO. This molecule is known to change the wavelength of the emission maximum (λ_{max}) of the fluorescence, depending on polarity of the solvent (*37*). By using this property of PyCHO, Schild and Tirrell (*38*) detected collapse of the backbone of the homopolymer and copolymers of NIPAM.

Figure 7 depicts λ_{max} of PyCHO dissolved in an aqueous solution with or without the copolymers. In the absence of the copolymers, λ_{max} did not change in the experimental temperature range. In contrast, in the presence of the copolymers, a marked blue shift above the LCST was observed. However, the extent of the change in λ_{max} was quite different among these copolymers. For poly(APr-*co*-NIPAM), λ_{max} was 463 nm below the LCST but slightly decreased above 40 °C, indicating that the collapsed copolymer chain formed a hydrophobic domain. In the case of poly(DMAM-*co*-NIPAM), however, λ_{max} decreased more significantly above the LCST. The most remarkable blue shift of λ_{max} was observed in the presence of poly(NIPMAM-*co*-NIPAM). Because the λ_{max} of PyCHO linearly increases with dielectric constant of the environment (*37*), this result suggests that poly(NIPMAM-*co*-NIPAM) formed a domain with the highest hydrophobicity, whereas poly(APr-*co*-NIPAM) formed a domain with the lowest hydrophobicity.

To obtain information about their interaction with lipid membranes, we next examined their influence on the membrane fluidity of the liposomes using ANS and DPH (Figure 8). The fluorescence probes ANS and DPH have been frequently used to evaluate membrane fluidity and are known to provide information about the surface and the hydrophobic region of the membrane, respectively (*39*). The inverse polarization of fluorescence probes ($1/P$) was taken as an indication of the membrane fluidity (*39*).

Figure 8A−D depicts the temperature dependence of the membrane fluidities of the EYPC liposomes modified with the copolymers and the unmodified EYPC liposomes as monitored by ANS. For the unmodified liposomes (panel A), the membrane fluidity monotonically increased with the increasing temperature. Similarly, the membrane fluidity of the $2C_{12}$-poly(APr-*co*-NIPAM)-modified liposomes (panel B) increased with temperature and no change in the temperature dependence of the membrane fluidity was observed around the LCST. For the $2C_{12}$-poly(DMAM-*co*-NIPAM)-modified liposomes (panel C), a similar increase in the membrane fluidity was seen between 10 and 40 °C. However, the change in the membrane fluidity was slightly suppressed around the LCST. For the $2C_{12}$-poly(NIPMAM-*co*-NIPAM)-modified

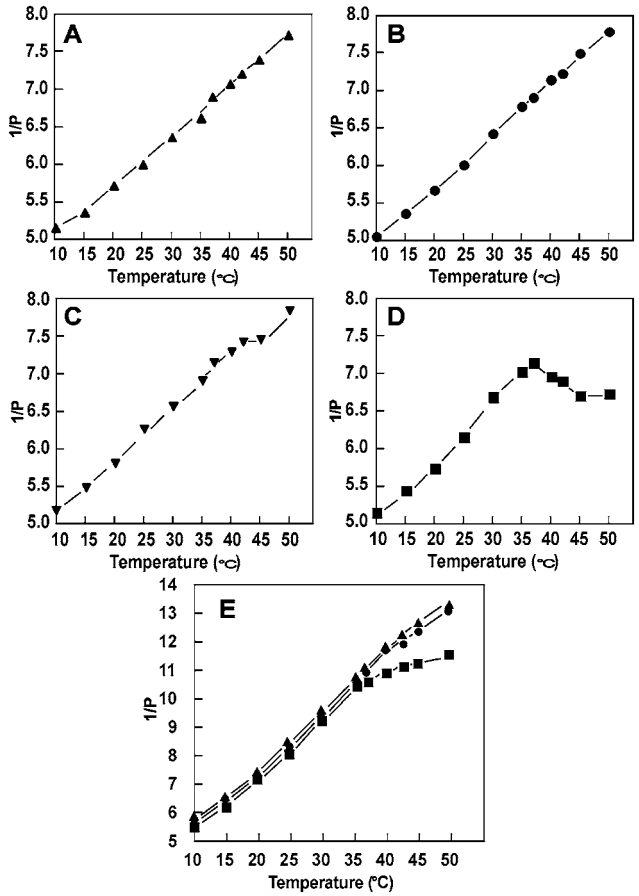


Figure 8. Temperature dependence of membrane fluidity (1/*P*) of $2C_{12}$-poly(APr-*co*-NIPAM)-modified (●), $2C_{12}$-poly(DMAM-*co*-NIPAM)-modified (▼), $2C_{12}$-poly(NIPMAM-*co*-NIPAM)-modified (■), and unmodified (▲) EYPC liposomes in 10 mM Tris-HCl and 140 mM NaCl solution (pH 7.4) as monitored by ANS (A−D) and DPH (E). The concentrations of EYPC, ANS, and DPH were 0.4 mM, 4.4 μM, and 0.44 μM, respectively.

liposomes (panel D), a marked change in the membrane fluidity took place at the LCST. In this case, the membrane fluidity decreased with temperature above the LCST.

A similar tendency can be seen in the temperature dependence of the membrane fluidity monitored by DPH. As seen in Figure 8E, the membrane fluidity of the $2C_{12}$-poly(APr-*co*-NIPAM)-modified liposomes (●) and that of the unmodified liposomes (▲) increased in almost the same manner. However, for the $2C_{12}$-poly(NIPMAM-*co*-NIPAM)-modified liposomes (■), a remarkable change in the temperature dependence of the membrane fluidity was seen above the LCST. These results indicate that, when hydrated, the chains of these copolymers hardly interact with the lipid membrane. However, when dehydrated, these polymer chains interact with the lipid membrane quite differently. The poly(APr-*co*-NIPAM) chain hardly affected the membrane fluidity even above the LCST, suggesting that their interaction is weak. The poly(DMAM-*co*-NIPAM) chain slightly influenced the membrane fluidity around the LCST, and hence, the copolymer moderately interacts with the membrane. In contrast, poly(NIPMAM-*co*-NIPAM) decreased the membrane fluidity of both the surface and the hydrophobic regions at and above the LCST, indicating that the dehydrated chain of this copolymer strongly interacts with the lipid membrane.

As already described, ΔH for the conformational transition was quite different among these NIPAM copolymers and increased in the order poly(APr-*co*-NIPAM) < poly(DMAM-*co*-NIPAM) < poly(NIPMAM-*co*-NIPAM) (Figure 4). Because this endotherm is related to the destruction of water around the hydrophobic groups (*32*), it is postulated that the copolymer, which exhibits a large ΔH, forms a domain with a higher hydrophobocity after the transition. In fact, the fluorometric measurement with PyCHO clearly demonstrated that the hydrophobicity of a domain formed by the dehydrated copolymer chain increases in the same order (Figure 7). The copolymer with the higher hydrophobicity, indeed, strongly interacts with the lipid membrane. This is consistent with the result of the membrane fluidity measurement, which showed that poly(NIPMAM-*co*-NIPAM) strongly reduced the fluidities of both the surface and the hydrophobic regions of the lipid membrane (Figure 8). Thus, poly(NIPMAM-*co*-NIPAM) could induce a significant contents release, whereas poly(DMAM-*co*-NIPAM) and poly(APr-*co*-NIPAM) provided the liposomes with moderate and weak contents release properties, respectively.

Since poly(NIPMAM-*co*-NIPAM) strongly enhanced the contents release from the liposomes above the LCST (Figure 5), we expected that these liposomes would show more significant associations above the LCST. However, contrary to our expectation, the liposomes having poly(NIPMAM-*co*-NIPAM) chains exhibited only a slight increase in the diameter at 50 °C (Figure 6). Rather, poly(APr-*co*-NIPAM) enhanced the aggregation of the liposomes much more strongly. As is seen in Figure 8D, the dehydrated chain of poly(NIPMAM-*co*-NIPAM) affected the fluidity of the hydrophobic region of the lipid membrane. This fact implies that this copolymer chain deeply penetrates into the lipid membrane and, hence, is buried in the membrane. In contrast, the poly(APr-*co*-NIPAM) chain did not decrease the membrane fluidity even after the conformational transition, suggesting that the dehydrated copolymer chain still exists on the surface of the liposome. Thus, the dehydrated copolymer chains of poly(APr-*co*-NIPAM) could efficiently cover the liposome surface and make its surface hydrophobic.

4. CONCLUSIONS

In this study, we prepared three kinds of NIPAM copolymers with the same conformational transition temperature and varying transition endotherms, and then we investigated their ability to sensitize EYPC liposomes to temperature. We found that their abilities correlated with their ΔH values for the transition. The copolymer with a large ΔH is suitable for obtaining functional liposomes that drastically release contents above the LCST, whereas the copolymer with a small ΔH is appropriate for preparing functional liposomes whose surface becomes hydrophobic above the LCST. These liposomes can release the encapsulated drugs at, or bind to, a target site that is heated above the LCST. Therefore, these liposomes may have potential usefulness for site-specific drug delivery.

ACKNOWLEDGMENT

This work was partly supported by the Grant-in Aid from Japanese Ministry of Education, Culture, Sports, Science and Technology and Terumo Life Science Foundation.

LITERATURE CITED

(1) Lasic, D. D. (1993) *Liposomes, from physics to applications*, Elsevier, Amsterdam.

(2) Yatvin, M. B., Kretz, W., Horwitz, B. A., and Shinitzky, M. (1980) pH-Sensitive liposomes: possible clinical implications. *Science 210*, 1253−1255.
(3) Maeda, M., Kumano, A., and Tirrell, D. A. (1988) H^+-induced release of contents of phosphatidylcholine vesicles bearing surface-bound polyelectrolyte chains. *J. Am. Chem. Soc. 110*, 7455−7459.
(4) Rui, Y., Wang, S., Low, P. S., and Thompson, D. H. (1998) Diplasmenylcholine-folate liposomes: An efficient vehicle for intracellular drug delivery. *J. Am. Chem. Soc. 120*, 11213−11218.
(5) Pidgeon, C., and Hunt, C. A. (1983) Light sensitive liposomes. *Photochem. Photobiol. 37*, 491−494.
(6) Anderson, V. C., and Thompson, D. H. (1992) Triggered release of hydrophilic agents from plasmalogen liposomes using visible light or acid. *Biochim. Biophys. Acta 1109*, 33−42.
(7) Mueller, A., Bondurant, B., and O'Brien, D. F. (2000) Visible-light-stimulated destabilization of PEG-liposomes. *Macromolecules 33*, 4799−4804.
(8) Sato, T., Kijima, M., Shiga, Y., and Yonezawa Y. (1991) Photochemically controlled ion permeability of liposomal membrane containing amphiphilic azobenzene. *Langmuir 7*, 2330−2335.
(9) Yatvin, M. B., Weinstein, J. N., Dennis, W. H., and Blumenthal, R. (1978) Design of liposomes for enhanced local release of drugs by hyperthermia. *Science 202*, 1290−1293.
(10) Kono, K., and Takagishi, T. (2004) Temperature-sensitive liposomes. *Methods Enzymol. 387*, 73−82.
(11) Needham, D., Anyarambhatla, G., Kong, G., and Dewhirst, M. W. (2000) A new temperature-sensitive liposome for use with mild hyperthermia: characterization and testing in a human tumor xenograft model. *Cancer Res. 60*, 1197−1201.
(12) Ringsdorf, H., Schlarb, B., and Venzmer, J. (1988) Molecular architecture and function of polymeric oriented systems: models for the study of organization, surface recognition, and dynamics of biomembranes. *Angew. Chem., Int. Ed. Engl. 27*, 113−158.
(13) Thomas, J. L., and Tirrell, D. A. (1992) Polyelectrolyte-sensitized phospholipid vesicles. *Acc. Chem. Res. 25*, 336−342.
(14) Kono, K. (2001) Thermosensitive polymer-modified liposomes. *Adv. Drug Delivery Rev. 53*, 307−319.
(15) Kono, K., Zenitani, K., and Takagishi, T. (1994) Novel pH-sensitive liposomes: liposomes bearing a poly(ethylene glycol) derivative with carboxyl groups. *Biochim. Biophys. Acta 1193*, 1−9.
(16) Meyer, O., Papahadjopoulos, D., and Leroux, J.-C. (1998) Copolymers of *N*-isopropylacrylamide can trigger pH sensitivity to stable liposomes. *FEBS Lett. 421*, 61−64.
(17) Bailey, A. L., Monck, M. A., and Cullis, P. R. (1997) pH-Induced destabilization of lipid bilayers by a lipopeptide derived from influenza hemagglutinin. *Biochim. Biophys. Acta 1324*, 232−244.
(18) Kono, K., Hayashi, H., and Takagishi, (1994) Temperature-sensitive liposomes: liposomes bearing poly(*N*-isopropylacrylamide). *J. Control. Release 30*, 69−75.
(19) Kitano, H., Maeda, Y., Takeuchi, S., Ieda, K., and Aizu, Y. (1994) Liposomes containing amphiphilic poly-(*N*-isopropylacrylamides) prepared by using a lipophilic radical initiator. *Langmuir 10*, 403−406.
(20) Hayashi, H., Kono, K., and Takagishi, T. (1999) Temperature sensitization of liposomes using copolymers of *N*-isopropylacrylamide. *Bioconjugate Chem. 10*, 412−418.
(21) Chandaroy, P., Sen, A., and Hui, S. W. (2001) Temperature-controlled content release from liposomes encapsulating Pluronic F127. *J. Control. Release 76*, 27−37.
(22) Heskins, M., and Guillet, J. E. (1968) Solution properties of poly(*N*-isopropylacrylamide). *J. Macromol. Sci., Chem. A2*, 1441−1455.
(23) Hayashi, H., Kono, K., and Takagishi, T. (1996) Temperature-controlled release property of phospholipid vesicles bearing a thermo-sensitive polymer. *Biochim. Biophys. Acta 1280*, 127−134.
(24) Hayashi, H., Kono, K., and Takagishi, T. (1998) Temperature-dependent associating property of liposomes modified with a thermosensitive polymer. *Bioconjugate Chem. 9*, 382−389.
(25) Kono, K., Henmi, A., and Takagishi, T. (1999) Temperature-controlled interaction of thermo-sensitive polymer-modified cationic liposomes with negatively charged phospholipid membranes. *Biochim. Biophys. Acta 1421*, 183−197.
(26) Kono, K., Nakai, R., Morimoto, K., and Takagishi, T. (1999) Thermosensitive polymer-modified liposomes that release contents around physiological temperature. *Biochim. Biophys. Acta 1416*, 239−250.
(27) Jordan, E. F., Jr., Riser, G. R., Parker, W. E., and Wrigley, A. N. (1966) Mechanical properties and transition temperatures for copolymers of N-*n*-alkylacrylamides and acrylonitrile. *J. Polym. Sci.: Part A-2 4*, 975−996.
(28) Okahata, Y., and Seki, T. (1984) pH-Sensitive capsule membranes. Reversible permeability control from the dissociative bilayer-coated capsule membrane by an ambient pH change. *J. Am. Chem. Soc. 106*, 8065−8070.
(29) Kono, K., Yoshino, K., and Takagishi, T. (2002) Effect of poly(ethylene glycol) grafts on temperature-sensitivity of thermosensitive polymer-modified liposomes. *J. Control. Release 80*, 321−332.
(30) Bartlett, G. R. (1959) Phosphorus assay in column chromatography. *J. Biol. Chem. 234*, 466−468.
(31) Kono, K., Henmi, A, Yamashita, H., Hayashi, H., and Takagishi, T. (1999) Improvement of temperature-sensitivity of poly(*N*-isopropylacrylamide)-modified liposomes, *J. Control. Release 59*, 63−75.
(32) Feil, H., Bae, Y. H., Feijen, and Kim, S. W. (1993) Effect of comonomer hydrophilicity and ionization on the lower critical solution temperature of *N*-isopropylacrylamide copolymers. *Macromolecules 26*, 2496−2500.
(33) Chung, J. E., Yokoyama, M., Aoyagi, T., Sakurai, Y., and Okano, T. (1998) Effect of molecular architecture of hydrophobically modified poly(*N*-isopropylacrylamide) on the formation of thermoresponsive core−shell micellar drug carriers. *J. Control. Release 53*, 119−130.
(34) Kaneko, Y., Sakai, K., Kikuchi, A., Yoshida, R., Sakurai, Y., and Okano, T. (1995) Influence of freely mobile grafted chain length on dynamic properties of comb-type grafted poly-(*N*-isopropylacrylamide) hydrogels. *Macromolecules 28*, 7717−7723.
(35) Schild, H. G., and Tirrell, D. A. (1990) Microcalorimetric detection of lower critical solution temperatures in aqueous polymer solutions. *J. Phys. Chem. 94*, 4352−4356.
(36) Kitano, H., Akatsuka, Y., and Ise, N. (1991) pH-Responsive liposomes which contain amphiphiles prepared by using lipophilic radical initiator. *Macromolecules 24*, 42−46.
(37) Kalyanasundaram, K., and Thomas, J. K. (1977) Solvent-dependent fluorescence of pyrene-3-carboxaldehyde and its applications in the estimation of polarity at micelle−water interfaces. *J. Phys. Chem. 81*, 2176−2180.
(38) Schild, H., and Tirrell, D. A. (1991) Microheterogeneous solutions of amphiphilic copolymers of *N*-isopropylacrylamide. *Langmuir 7*, 1319−1324.
(39) Ohtoyo, T., Shimagaki, M., Otoda, K., Kimura, S., and Imanishi, Y. (1988) Change in membrane fluidity induced by lectin-mediated phase separation of the membrane and agglutination of phospholipids vesicles containing glycopeptides. *Biochemistry 27*, 6458−6463.

BC034205J

Different Immune Response of Mice Immunized with Conjugates Containing Multiple Copies of Either Consensus or Mixotope Versions of the V3 Loop Peptide from Human Immunodeficiency Virus Type 1

Luis J. Cruz,[†] Enrique Iglesias,[‡] Julio C. Aguilar,[‡] Ania Cabrales,[‡] Osvaldo Reyes,[‡] and David Andreu*[,§]

Institut de Recerca Biomèdica de Barcelona, Parc Científic de Barcelona−Universitat de Barcelona, Josep Samitier 1, E-08028 Barcelona, Spain, Centro de Ingeniería Genética y Biotecnología, Apdo 6162, Cubanacán, Habana 10600, Cuba, and Departament de Ciències Experimentals i de la Salut, Universitat Pompeu Fabra, Doctor Aiguader 80, E-08003, Barcelona, Spain. Received March 5, 2004; Revised Manuscript Received May 28, 2004

The critical role that antibody responses to the V3 loop epitope play in human immunodeficiency virus type 1 (HIV-1) neutralization has caused this peptide to be used in many HIV-1 vaccine candidates. To enhance cross-reactivity toward several V3 sequences, a database of 50 peptides of the V3 region from HIV-1 subtype A was used to design both a consensus peptide and a combinatorial peptide (mixotope) library representative of these sequences. The two immunogens (consensus and mixotope) were incorporated into multiple antigen peptide (MAP) constructions, conjugated to a recombinant surface antigen from hepatitis B virus (HbsAg) carrier protein, and inoculated to mice in combination with a C4 (CD4-binding) peptide MAP construction, also conjugated to HBsAg. The respective responses and cross-reactivity to several V3 loop sequences of both types of immunogens were compared. Mice inoculated with the V3 consensus-MAP−HBsAg + C4-MAP−HBsAg mixture elicited higher antibody responses than those given the V3 mixotope-MAP−HBsAg + C4-MAP−HBsAg mixture. In addition, pooled serum from the first group of immunogens analyzed at dilution 1:100 had higher cross-reactivity against V3 peptides on cellulose membranes than those from mice given the combinatorial immunogen. Fine epitope mapping of both consensus and C4 peptide by the spot synthesis technique showed that sera of the first group strongly recognized both sequences in their entirety, whereas mice immunized with the mixotope library recognized only the N-terminal region of V3. These results seem to suggest that the V3 consensus peptide is superior to the combinatorial strategy in inducing potent and cross-reactive responses to HIV.

INTRODUCTION

The complexity of the HIV[1] life cycle, with high mutation rates and resulting polymorphism, its different mechanisms of evading the immune system, and the absence of suitable animal infection models, have so far combined to forestall the development of successful vaccines. These difficulties notwithstanding, recent advances in the study of HIV entry mechanisms and of structure/function relationships for envelope proteins gp120 and gp41 (*1*) still offer good possibilities for the development of vaccines with preventive and/or therapeutic properties (*2*). Most vaccine prototypes designed so far involve these two targets (*3*). Such prototypes include recombinant proteins (*4*), naked DNA (*5*), and synthetic peptides (*6*).

Several recombinant multiepitope HIV peptide constructions have been described (*7*). For instance, TAB9, which includes six V3 loop peptides (isolates LR150, JY1, RF, MN, IIIB, and BRVA), was used in a phase I clinical study (*8*). The recombinant protein was immunogenic and induced high levels of antibody neutralization, but the immune response was mainly directed at JY1 and LR150 and only weakly at MN, suggesting the need for considerable improvement (*9*). The problem with chimeric polypeptides of this type is that they adopt unpredictable 3D structures that favor the exposure of some epitopes, at the expense of others that in practice remain silent. Alternative strategies, such as synthetic MAP dendrimer constructs, have been proven more effective in achieving more balanced epitope presentations (*10*).

Naked DNA technology has not progressed as far or as fast as expected, largely because no suitable delivery routes have yet been devised. In addition, the long-range collateral effects associated with this approach have not

* Corresponding author: Phone (+34) 935422934; fax (+34) 93542280; e-mail david.andreu@upf.edu.

[†] Parc Científic de Barcelona−Universitat de Barcelona.

[‡] Centro de Ingeniería Genética y Biotecnología.

[§] Universitat Pompeu Fabra.

[1] Abbreviations: AAA, amino acid analysis; AcOH, acetic acid; Boc, *t*-butyloxycarbonyl; Bzl, benzyl; BSA, bovine serum albumin; CFA, complete Freund's adjuvant; DIPC, *N*,*N*′-diisopropylcarbodiimide; DTT, dithiothreitol; DCM, dichloromethane; DMF, *N*,*N*-dimethylformamide; DIEA, *N*,*N*-diisopropylethylamine; EDTA, ethylenediaminetetraacetic acid; EDAC, 1-ethyl-3-(dimethylaminopropyl)carbodiimide; Fmoc, 9-fluorenylmethoxycarbonyl; HOBt, 1-hydroxybenzotriazole; HPLC, high-performance liquid chromatography; IFA, incomplete Freund's adjuvant; MAP, multiple antigenic peptide; MeCN, acetonitrile; MS, mass spectrometry; PBS, phosphate-buffered saline; RP, reverse phase; TFA, trifluoroacetic acid; TBTU, 2-(1*H*-benzotriazol-1-yl)-1,1,3,3-tetramethyluronium tetrafluoroborate.

10.1021/bc049944u CCC: $27.50 © 2004 American Chemical Society
Published on Web 08/19/2004

been adequately clarified. On the other hand, plasmid DNA vaccines, initially regarded as promising, have failed to provide a sufficiently protective response against either HIV or simian immunodeficiency virus (SIV) in primates. Viral mutants escaping plasmid DNA-induced CTL (cytotoxic T lymphocytes) responses have recently been described (*11*).

The synthetic peptide approach makes it possible, in principle, to select only the epitopes of interest and thus largely circumvent problems such as viral variability, unwanted immunosuppression, etc., by focusing on selected segments of envelope proteins such as gp41 and gp120, directly involved in HIV entry and widely regarded as ideal targets for blocking the first step of viral replication. One particular envelope protein, gp120, includes the V3 loop, one of the most widely studied motifs, which defines epitopes for both antibodies and lymphocytes (*12*) and also has a crucial role in viral tropism and pathogenesis (*13*). Consequently, the V3 loop is featured in almost all vaccine candidates currently under evaluation. A recent U.S. clinical trial for a mixture of five V3 peptides showed decreased HIV levels even in patients with strains differing in two or three residues from those used for immunization (*14*). Another relevant gp120 motif, the fourth conserved (C4) domain, is a major player in the binding of HIV to its primary receptor, CD4, leading to virus−cell fusion and replication; a single amino acid change in C4 results in loss of infectivity (*15*).

As is well-known, the V3 region of HIV-1, containing the principal determinant of neutralization, is highly variable. To overcome this difficulty, consensus peptides preserving those amino acid positions more consistently repeated in field or clinical isolates have been explored (*16*). A competing approach, aimed at covering a broad spectrum of V3 sequences, is the generation of combinatorial libraries, named mixotopes (*17*−*19*), representing the more variable positions of the V3 loop. Promising results from this type of strategy have recently been reported (*20*, *21*).

In the present study we have decided to compare both types of strategies. To this end, both consensus and mixotope versions of V3 were synthesized as MAP constructs and conjugated to an HBsAg carrier protein to find out which of the two approaches provides better results in terms of immunogenicity and cross-reactivity. To enhance the immune response, the two kinds of V3 conjugates were coadministered with HBsAg conjugates of a MAP version of the C4 (CD4-binding) sequence. The antibody responses generated by the two types of immunogens were analyzed against several V3 representative peptides, and fine epitope mapping of both groups of sera were performed.

EXPERIMENTAL PROCEDURES

Chemicals and Biologicals. Boc-protected amino acids and other reagents for peptide synthesis were purchased from Bachem (Bubendorf, Switzerland). *p*-Methylbenzhydrylamine (MBHA) resin was from Fluka (Buchs, Switzerland). Solvents for peptide synthesis (DCM, 2-propanol, DMF) were obtained from Merck (Darmstadt, Germany). The recombinant surface antigen from hepatitis B virus (HBsAg) was produced at CIGB (Habana, Cuba). Succinic anhydride was from Sigma (Milwaukee, WI).

MAP Synthesis. All MAPs were prepared by manual stepwise solid-phase synthesis methods (*22*) on *p*-methylbenzhydrylamine (MBHA) resin. The protecting group scheme was based on the Boc group for the α-NH_2 terminus, and the side chains of trifunctional amino acids were protected as benzyl (Asp, Glu, Ser, Thr), 2-chlorobenzyloxycarbonyl (Lys), dichlorobenzyl (Tyr), 2,4-dinitrophenyl (His), formyl (Trp), 4-methoxybenzyl (Cys), and tosyl (Arg) derivatives. The three Lys residues making up the tetravalent dendrimer core were incorporated onto the β-Ala-Cys-MBHA resin as Boc-Lys(Boc) derivatives, by use of TBTU/HOBt/DIEA for the coupling. Cleavage of the Boc group was done with 40% TFA in DCM followed by neutralization with 5% DIEA in DCM. Double couplings with a 10-fold excess of Boc-amino acid and DIPC/HOBt or TBTU/HOBt/DIEA were used for most residues of the V3 epitope. When required by the Kaiser test (*23*), capping steps were performed with 4% acetic anhydride and 1% DIEA in DMF. After low−high HF cleavage and deprotection, the MAPs were extracted into 0.1 M Tris-HCl (pH 8.0) containing 8 M urea, dialyzed against 2 M urea in 0.1 M Tris-HCl (pH 8.0) for 24 h, and then stirred in the same solvent in an open vessel to promote dimerization by disulfide bond formation, until a negative Ellman test (*24*) was obtained. The homodimeric MAPs were then dialyzed against 1 M AcOH, to remove all the urea, and lyophilized.

For the V3 mixotope, a similar synthetic scheme was followed, except that at high-variability positions a representative mixture of the corresponding amino acids (in equimolar proportion) was coupled by means of TBTU/DIEA in DMF under substoichiometric conditions for long reaction times, as previously described (*17*).

Characterization of MAPs. For analytical purposes only, the homodimeric MAP constructs were converted to the monomer form. Lyophilized material was redissolved at 5 mg/mL concentration in 0.3 M Tris-HCl, 6 M guanidinium chloride, and 3 mM EDTA (pH 8.5), a 20-fold molar excess of DTT over Cys residues was added, and the solution was flushed with nitrogen and incubated for 2 h at 37 °C. A 2-fold molar excess of iodoacetic acid over DTT was next added and the solution was kept at room temperature for 1 h in the dark. Modified MAPs were characterized by RP-HPLC on Baker C_8 wide-pore (100 × 4.6 mm) columns in a system consisting of a Pharmacia model 2150 dual pump coupled to a Knauer (FRG) variable-wavelength UV detector. Linear gradients of MeCN (+0.05% TFA) into water (+0.1% TFA) were used for the separation, at 0.8 mL/min flow rate. Optical density was monitored at 226 nm. Data were processed with the BioCrom program (CIGB, Cuba). Electrospray MS analysis was done in a hybrid quadrupole time-of-flight (Q-TOF) instrument (Micromass, Manchester, U.K.) fitted with a Z-spray nano flow ion source (*25*). The mass spectrometer was operated with a source temperature of 80 °C and a drying gas flow rate of 50 L/h. RP-HPLC-purified MAPs were dissolved in a 50% (v/v) water/MeCN solution containing 1% acetic acid, to an approximate concentration of 5 pmol/μL. The MAP solution was infused at 3 μL/ min into the mass spectrometer by use of a syringe pump (Harvard Apparatus, Holliston, MA). The capillary and cone voltage were set to 3 kV and 35 V, respectively. Data acquisition and processing were performed with the Micromass MassLynx package.

For amino acid analysis, samples of S-carboxymethylated MAPs were hydrolyzed with 6 M HCl containing 0.1% phenol and 0.1% 2-mercaptoethanol for 24 h in vacuum-sealed ampules. After evaporation, amino acids in the hydrolysate were determined in a Pharmacia-LKB Alpha Plus 4151 analyzer with a sodium buffer system and *o*-phthalaldehyde derivatization for fluorescence detection. All samples were analyzed in triplicate.

Table 1. Immunization Protocols[a]

group	dose (μg)
A: HBsAg	10
B: C4-MAP−HBsAg	10
C: C4-MAP−HBsAg and consensus MAP−HBsAg	5 + 5
D: C4-MAP−HBsAg and library MAP−HBsAg	5 + 5

[a] All immunogens formulated in CFA (100 μL, day 0) and IFA (days 14, 28, 56). Each group consisted of eight mice.

Conjugation of MAPs to Carrier Protein. Homodimeric, octavalent MAPs were coupled to HBsAg as described by Deen et al. (*26*) (see Figure 1 also). Briefly, 5 mg of HBsAg was dissolved in 5 mL of 0.2 M K_2HPO_4 (pH 8.0), solid succinic anhydride (1 mg) was added, and the solution was stirred until all anhydride was dissolved, with occasional dropwise addition of 3 M NaOH as required to keep the pH at 8−8.5. The activated protein was next exhaustively dialyzed against dilute HCl (pH 4.5), mixed with 7 mg of EDAC, and stirred for 10 min at 25 °C. Then, 5 mg of octavalent MAP dissolved in 1 mL of 3 M guanidine hydrochloride in PBS was added and the mixture was gently stirred for 3 h at 25 °C. The conjugates were purified by gel filtration through Sephadex CL-4B (Pharmacia, Uppsala, Sweden) eluted with PBS. The front-eluting fractions were pooled and quantitated by the Coomassie method (*27*).

Immunizations. Groups of eight female Balb/c mice, 6−8 weeks old (Cenpalab, Cuba), were inoculated subcutaneously on days 0, 14, 28, and 56 with 100 μL of a suspension containing 10 μg of antigens (Table 1) emulsified in either CFA (day 0) or IFA (other days). Animals were bled 10 days after the fourth dose.

Enzyme-Linked Immunosorbent Assay against Synthetic Peptides. ELISA of anti-peptide sera was done as previously described (*28*). Briefly, 96-well (Costar high binding) polystyrene plates (Corning Biosciences, Acton, MA) were coated with 100 μL of 10 μg/mL solutions of consensus or C4 peptides (as BSA conjugates) or of the MAP library and incubated overnight at 4 °C. After three washings with 0.05% Tween 20 in PBS, plates were blocked with 2% milk in PBS (blocking solution) for 1 h at 37 °C. Serum samples were diluted with 0.05% Tween 20−5% sheep serum in blocking solution and incubated for 2 h at 37 °C. After four washings, an anti-mouse IgG peroxidase conjugate (Amersham, Little Chalfont, U.K.) was added and the mixture was incubated for 1 h at 37 °C. The color reaction with *o*-phenylenediamine was allowed to develop for 10 min and then stopped with 3 M H_2SO_4 solution (50 μL), and the absorbance at 492 nm was determined in a SensIdent Scan (Merck). Results were expressed as log titer, determined by interpolation of OD values at fixed serum dilutions into a standard curve of a serum with known titer. Titer was defined as the logarithm of the highest dilution giving twice the absorbance of negative control sera. Titers are given as the geometric mean ± SD of the titers of individual sera.

Epitope Mapping by Use of Cellulose-Bound Peptides. The spot synthesis technique previously described by Frank (*29*) was used. The Whatman 540 paper support (Whatman, Maidstone, U.K.) was functionalized by esterification of Fmoc-β-Ala-OH, activated by DIPC and *N*-methylimidazole in dry DMF, at defined positions to give a spot array suitable to the required number of sequence peptides. All subsequent residues in the different V3 loop sequences were incorporated manually by standard Fmoc/tBu chemistry. All peptides were acetylated at the N-terminus at the end of the synthesis program.

Table 2. V3 Loop Sequences of 50 HIV-1 Subtype A V3 Isolates Used to Define the Consensus Sequence

#	Accession number[a].	Amino acid sequence
-	consensus	SVRIGPGQAFYATGDIIGDIRQ
1	AAC37794	--HM---R----------
2	AAC37804	--HM---KT----------
3	AAB87297	-M------T----------
4	AAC37825	-I----------
5	AAB34131	-IHI-P-Q------A-------
6	AAP37302	----------
7	CAA50920	--N----------
8	CAA50937	--H---------R---------
9	CAA50942	-L------T----------
10	AAO20500	--H----------
11	AAC55823	--------T----------
12	AAG48444	GIH----SAI----------
13	CAC15292	GIH-----T-----E---N---
14	AAS18950	--------T-----A-------
15	AAD05114	--------T---A---------
16	AAF67679	----------TR-
17	AAD24257	-IHF----TL----N-------
18	AAD42826	-I---S-TS---------N--E
19	CAA91881	GIH----R------Q-T-----
20	AAC42384	-I----------T-----N---
21	AAQ83975	-IH----------N---
22	AAC55896	-I------T---------N---
23	CAD36394	-I----------T---T-----
24	AAB58169	-IH----------S--------
25	AAK85213	-I---------T----------
26	AA020437	--H----------N---
27	AAA70070	-AN----------E-------
28	AAA70078	GIH-----S-----S-V-N---
29	AAS19003	-I------T-----E---N---
30	AAC16336	G-H----------
31	AAF02185	-I------S-H----------
32	CAB00597	--H----------V------
33	AAF02186	G----------G-------
34	AAK98157	--H-----TS----------
35	AAD03181	-IHL---R----------
36	AAC42562	----------N---
37	CAD87155	--H---------R---------
38	AA048836	-IH---------R----N----
39	AAA44006	--HI----------E-------
40	CAA08527	--------T---------N---
41	AAA44019	--H----K------G-V-----
42	AAA44029	--H----------A---S---
43	AAA43985	-IG-----T---ADN-------
44	AAB58176	--------S----------K-
45	AAS17820	-IS----R-F----------
46	AAA78796	GIHM----IL----S-------
47	AAA78797	-I------V-TN----------
48	AAB34131	-IH-A---------A-------
49	AAB34136	GIHL---------NA-------
50	AAB58169	-IH----------

[a] Accession numbers are from the National Center for Biotechnology Information (BLAST Program).

Paper-Based Peptide Enzyme Immunoassay. Washing steps and incubations were performed at 25 °C with Tris-buffered saline (TBS) containing 0.05% Tween-20. Blocking of free binding sites was performed by overnight incubation with 5% skim milk in TBS. Spots were next incubated with sera for 3 h, washed, and incubated for 2 h with alkaline phosphatase-conjugated anti-mouse IgG (Sigma). Detection of bound antibody was achieved with 5-bromo-4-chloro-3-indolyl phosphate (Sigma) in substrate buffer [0.1 M Tris (pH 8.9), 0.1 M NaCl, and 2 mM $MgCl_2$]. Washing with PBS stopped staining. The peptide-bearing cellulose sheets were regenerated and prepared for the next run as described by Frank (*29*).

Statistical Analysis. All ELISA OD values were transformed to the natural logarithm to get a normal distribution in the immunized groups. An *F*-test was performed to assess variance homogeneity between groups and a Student's *t*-test was done ($p < 0.05$ was considered statistically significant).

Table 3. HIV-1 Amino Acid Sequences Used for the Immunogens

Peptide	Sequence synthesized[a]
C4	KQIINMWQEVGKAMYA
Consensus	KSVRIGPGQAFYATGDIIGDIRQA
Combinatorial mixotope[b]	KXXXIGPGQXFYATGXIIGXIRQA SVR A D D GMH T A N LN S E S IG V G AS I S N Q

[a] In the consensus and mixotope sequences, a non-native N-terminal Lys residue was added to facilitate conjugation to the carrier protein. The N-terminal Lys of the C4 sequence is native. [b] In the mixotope top sequence, the Xs denote combinatorial sites, where mixtures of the residues shown below have been incorporated.

RESULTS

Design and Synthesis of V3 Consensus and Combinatorial MAPs. Fifty sequences (Table 2) from the V3 region of HIV-1, subtype A, with (i) reasonable chemical diversity, (ii) adequate geographical representation, and (iii) demonstrated infectivity were manually selected out of ca. 7000 sequences available at the time at the National Center for Biotechnology Information (BLAST program) and used to design a 24-residue consensus sequence, where the most frequent amino acid among the isolates was chosen for each position. The same database was used to build a mixotope combinatorial library (*18*) in which sites with over 90% conservation among the 50 isolates were represented by a single residue, while at more degenerate positions an amino acid mixture representative of the different mutations was incorporated (Table 3).

The design of our immunogens started (Figure 1A) with the incorporation of either the consensus single peptide, or the mixotope library, or of another HIV peptide sequence (C4) known to play a major role in viral binding to the CD4 primary receptor, into tetravalent MAP platforms. The original approach of Tam (*30*) was followed, with two minor modifications: (i) a Lys residue was added at the N-terminus of both consensus and mixotope sequence to facilitate conjugation to carrier protein (the C4 peptide already has a native Lys at the N-terminus), and (ii) a Cys residue was placed at the C-terminus of the entire MAP dendrimer, to allow dimerization by disulfide formation. The resulting octavalent constructions would next be conjugated to HBsAg (see next section and Figure 1B).

All three MAPs were prepared by Boc-based methods of solid-phase synthesis and, after cleavage from the resin with HF, were solubilized under denaturing conditions and dialyzed to remove synthesis and cleavage byproducts while in situ air oxidation was allowed to proceed. The reaction was monitored by HPLC gel filtration and the Ellman test (data not shown). Once shown to be complete by HPLC (see Supporting Information), the dimeric MAPs were dialyzed against 1 M AcOH and lyophilized. MAP dimers were found to be stable at or below pH 7, room temperature, in aqueous solution, with or without chaotropic additives. To further evaluate their quality, an aliquot was reduced, S-carboxymethylated, and characterized by both reverse-phase HPLC and MS (Figure 2). As expected, the HPLC profile corresponding to the combinatorial MAP, containing an estimated mixture of over 5000 different peptide sequences, was a rather broad peak. For the two single-sequence MAPs, the HPLC profiles showed a main fraction that was analyzed by electrospray MS and found to correspond very well with the expected theoretical mass: 11 318.87 Da for the consensus V3-MAP (found *m*/*z* 11 319.63) and 8824.56 Da for C4-MAP (found *m*/*z* 8824.25). In this latter case, the broad elution band overlapping the main peak was attributed to byproducts resulting from Trp degradation during the HF deprotection step. The MAPs were further characterized by amino acid analysis, which in all three cases showed compositions consistent with the expected structure (Table 4).

MAP−HBsAg Conjugates. To further enhance the immunogenicity of the homodimeric MAPs, they were conjugated to recombinant HBsAg, a polymeric protein of about 2000 kDa (*31*, *32*). Our choice of HBsAg was based on its high molecular weight, proven stability, and high immunogenicity and because it is known to act as an effective and safe vaccine in humans. The conjugations were performed with a succinic acid cross-linking between Lys amino groups of the MAP epitopes and the carrier. Thus, HBsAg was first succinylated under mildly alkaline conditions, followed by dialysis to remove excess succinic anhydride and thus avoid unwanted cross-linking. The carboxyl groups on the modified HBsAg were next activated with EDAC (a soluble carbodiimide) and

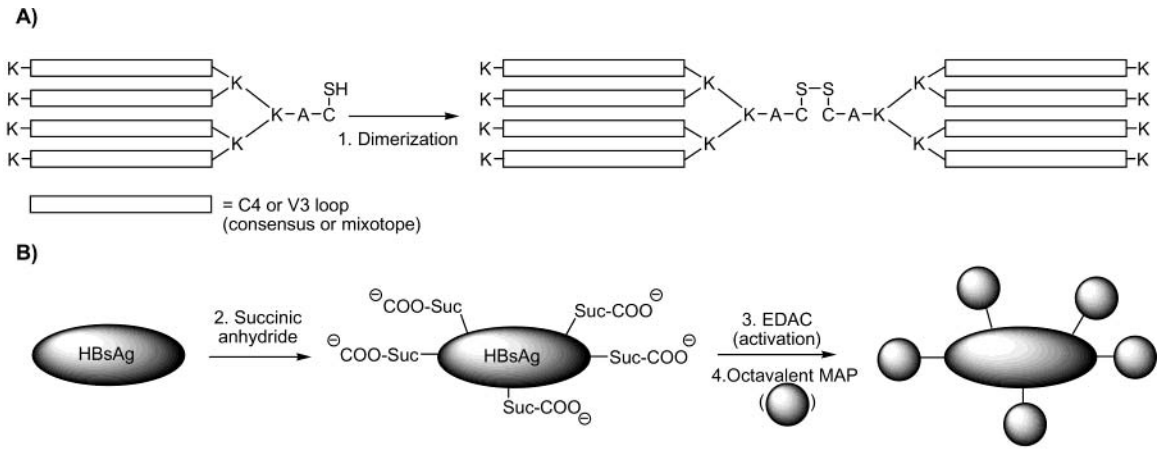


Figure 1. Synthetic strategy for MAP conjugates of C4 and the V3 loop of HIV. (A) Octavalent MAP constructs result from dimerization (1) of synthetic tetravalent MAP through disulfide formation. (B) Amino groups in HBsAg are converted to carboxyls (2) by succinylation and then activated (3) with water-soluble carbodiimide to allow conjugation (4) with the octavalent MAP.

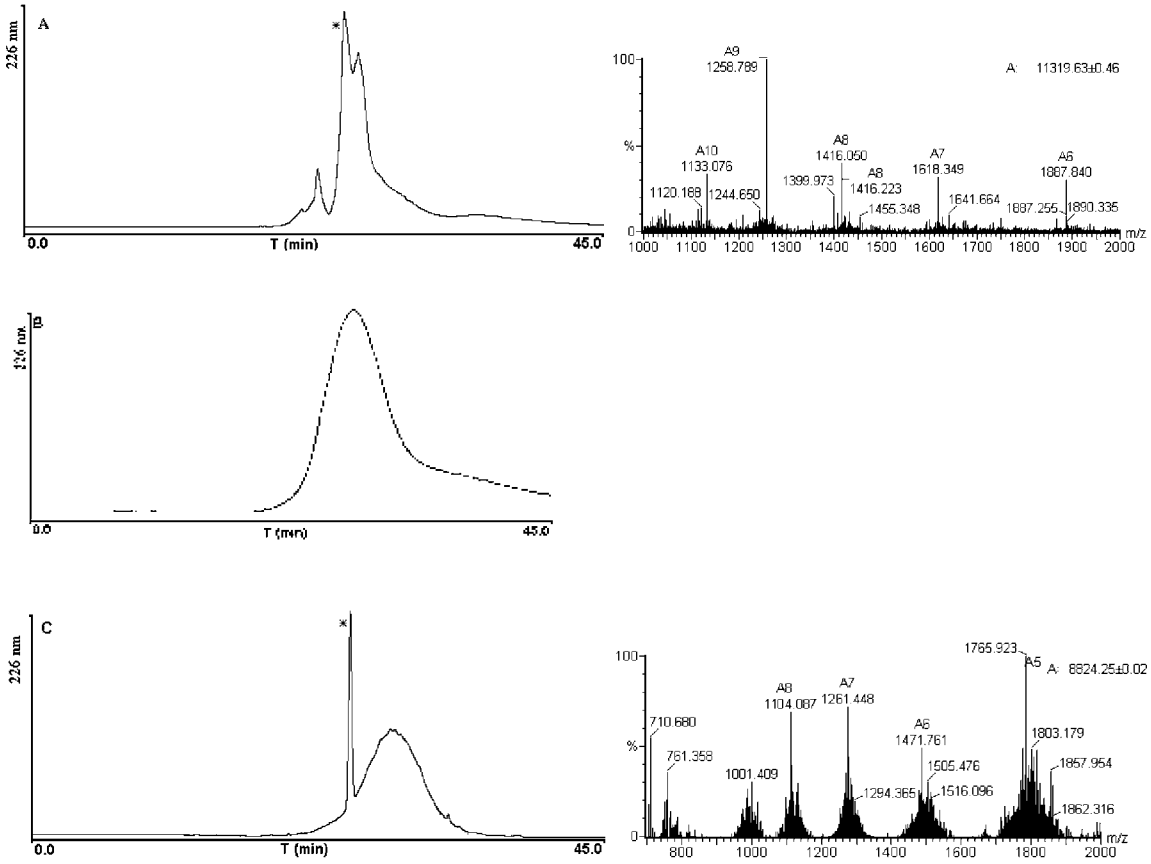


Figure 2. HPLC analysis of tetravalent MAP constructs corresponding to the V3 loop in consensus (A) and mixotope (B) form and (C) to C4. Profiles show the product resulting from reduction and S-carboxymethylation of the synthetic octavalent dimer. In panels A and C, the ESI mass spectrum of the main fraction (marked with an asterisk) is shown at the right of the chromatogram. For the consensus V3 loop MAP, calculated MW 11 318.87 Da; found, *m*/*z* 11 319.63. For the C4 MAP, calculated MW 8824.56 Da; found, *m*/*z* 8824.25.

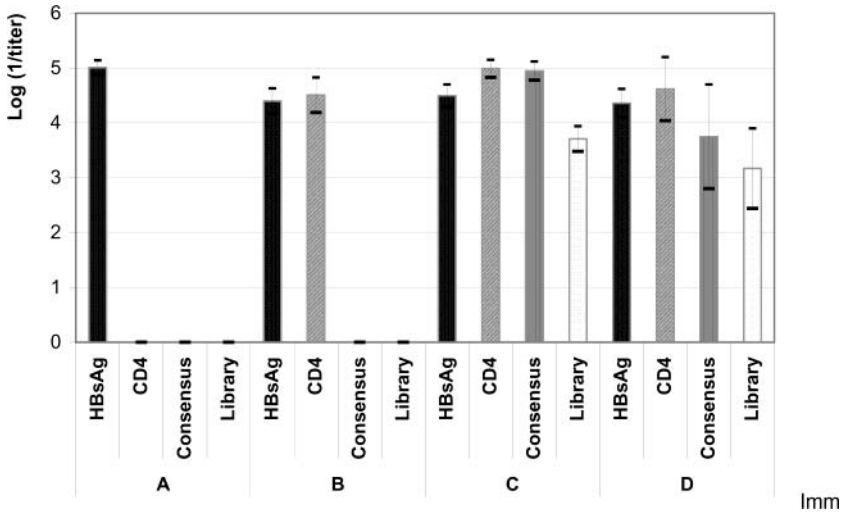


Figure 3. Antibody titers of mice after immunization with four doses of (A) HbsAg, 10 μg; (B) C4-MAP−HBsAg conjugate, 10 μg; (C) mixture of C4-MAP−HBsAg and consensus V3-MAP−HBsAg conjugates, 10 μg; and (D) mixture of C4-MAP−HBsAg and V3 mixotope-MAP−HBsAg, 10 μg. Titers are the geometric mean ± SD of eight mouse antisera.

allowed to react with the free amino grups of each MAP (Figure 1B). The conjugates were purified by gel filtration on Sephadex CL-4B to remove excess carbodiimide and MAP. Since amino acid analysis of HBsAg is notoriously unreliable, no attempt was made to determine MAP-to-HBsAg molar ratios by this method. Instead, a qualitative estimation of the efficiency of epitope incorporation to the conjugates was obtained by ELISA (see Supporting Information).

Analysis of Antibody Response in Mice Immunized with MAP Conjugates. Groups of eight Balb/c mice were inoculated subcutaneously to evaluate the anti-MAP antibody responses against the different immunogens. For coimmunizations, appropriate formulations of each individual conjugate were prepared and mixed before inoculation. All four groups of animals gave anti-HBsAg responses (Figure 3), which were predictably more pronounced in the control group A. Responses to

Table 4. Amino Acid Compositions and Mass Spectrometry of MAPs[a]

amino acid	C4	consensus	mixotope
Asx	3.26 (4)	8.71 (8)	3.27 (4.4)
Thr		3.31 (4)	3.80 (4.8)
Ser		2.56 (4)	4.53 (3.5)
Glx	11.83 (12)	8.19 (8)	8.16 (9.7)
Gly	12.15 (12)	23.99 (24)	27.49 (26.6)
Ala	8.90 (8)	12.88 (12)	6.67 (6.6)
Val	3.16(4)	1.66 (4)	0.72 (1.7)
Met	5.77(8)		0.86 (0.8)
Ile	7.56(8)	15.38 (16)	16.36 (17.8)
Leu			1.07 (0.8)
Tyr	2.60(4)	3.25(4)	3.52 (4)
Phe		3.02(4)	3.30 (4)
His			0.29 (0.8)
Lys	12.71(11)	7.66 (7)	8.47 (7)
Arg		7.10 (8)	1.98 (4.8)
Cys	0.89(1)	0.9(1)	0.94(1)
β-Ala[b]	(1)	(1)	(1)
Trp	3.4 (4)		
Pro		2.08 (4)	3.08 (4)

[a] Data are expressed as number of residues per molecule. Experimental values represent the mean of three independent determinations. The theoretical values calculated from MAP sequences are in parentheses. Asx = Asp + Asn; Glx = Glu + Gln. [b] β-Ala not determined.

C4 were also comparable in the three groups immunized with the corresponding MAP−HBsAg conjugate. Co-immunization of C4-MAP−HBsAg with either the V3 consensus MAP−HBsAg or the V3 mixotope-MAP−HBsAg conjugates produced antibody responses against both (V3 and C4) types of B-cell epitopes. Interestingly, animals receiving the consensus V3 immunogen recognized the mixotope somewhat better than those given the mixotope itself. From Figure 3 it is clear that the antibody responses against all three types of immunogen (C4, consensus, and mixotope) were significantly higher for group C mice (inoculated with consensus V3-MAP−HBsAg + C4-MAP−HBsAg) than for group D (V3 mixotope instead of consensus V3 peptide). From these results we conclude that, at least in this particular case, co-administration of two immunogens is advantageous in terms of obtaining a dual antibody response. Such an approach should be valuable for generating bivalent vaccines when the carrier protein is per se a vaccine immunogen such as HBsAg.

Analysis of Cross-reactivity with Peptides Synthesized on Cellulose Membrane. Cross-reactivity of the different antisera was evaluated (Figure 4) against a panel of 50 cellulose-bound peptides corresponding to different isolates of the V3 loop of HIV-1, subtype A. After the third booster, pooled sera from group D (immunized with C4-MAP−HBsAg and V3 mixotope-MAP−HBsAg) at 1:100 dilution recognized 26% (13/50) of the test peptides, 53% (7/13) of them with high reactivity. In contrast, pooled sera from group C (given C4-MAP−HBsAg and consensus V3-MAP−HBsAg) recognized 72% (36/50) of the same peptide panel same peptides panel, 50% (18/36) with high reactivity. Thus, somewhat counterintuitively with the use of a single sequence, the consensus immunogen gives rise not only to higher titers but also to broader cross-reactivities.

Fine Epitope Mapping of Anti-V3 Sera. Given the substantial differences in cross-reactivity observed for antibody responses to either consensus or mixotope strategies, it seemed appropriate to perform a fine epitope mapping of both types of antisera. For this we resorted again to the spot synthesis technique, using 18 and 10 overlapping heptapeptides to cover the sequences of the consensus and the C4 peptides, respectively (Figure 5). ELISA of pooled sera from groups C and D at a 1:100 dilution showed that the former group (immunized with consensus V3-MAP−HBsAg) strongly recognized the N-terminal (KSVRIGP and RIGPGQA), central (FYATGDII), and C-terminal (IGDIRQA) regions of the immunogen. In contrast, mice immunized with the combinatorial mixotope only recognized heptapeptides from the N-terminal region (KSVRIGP and RIGPGQA). Again, a more satisfactory antibody response was found for mice immunized with the V3 consensus MAP.

Spot	Peptide Sequence	Immunogen group			
		A	B	C	D
1	SVHMGPGRAFYATGDIIGDIRQ				
2	SVHMGPGKTFYATGDIIGDIRQ				
3	SMRIGPGQTFYATGDIIGDIRQ				
4	SIRIGPGQAFYATGDIIGDIRQ				
5	SIHIAPRQAFYATGAIIGDIRQ				
6	SVRIGPGQAFYATGDIIGDIRQ				
7	SVNIGPGQAFYATGDIIGDIRQ				
8	GVHIGPGQAFYARGDIIGDIRQ				
9	SLRIGPGQTFYATGDIIGDIRQ				
10	SVHIGPGQAFYATGDIIGDIRQ				
11	SVRIGPGQTFYATGDIIGDIRQ				
12	GIHIGPGSAIYATGDIIGDIRQ				
13	GIHIGPGQTFYATGEIIGNIRQ				
14	SVRIGPGQTFYATGAIIGDIRQ				
15	SVRIGPGQTFYAAGDIIGDIRQ				
16	SVRIGPGQAFYATGDIIGDTRQ				
17	SIHFGPGQTLYATGNIIGDIRQ				
18	SIRIGSGQTSYATGDIIGNIRE				
19	GIHIGPGRAFYATGQITGDIRQ				
20	SIRIGPGQAFYATGDIIGNIRQ				
21	SIHIGPGQAFYATGDIIGNIRQ				
22	SIRIGPGQTFYATGDIIGNIRQ				
23	SIRIGPGQAFYATGDITGDIRQ				
24	SIHIGPGQAFYATSDIIGDIRQ				
25	SIRIGPGQAFYTTGDIIGDIRQ				
26	SVHIGPGQAFYATGDIIGNIRQ				
27	SANIGPGQAFYATGEIIGDIRQ				
28	GIHIGPGQSFYATGSIVGNIRQ				
29	SIRIGPGQTFYATGEIIGNIRQ				
30	GVHIGPGQAFYATGDIIGDIRQ				
31	SIRIGPGQSFHATGDIIGDIRQ				
32	SVHIGPGQAFYATGDVIGDIRQ				
33	GVRIGPGQAFYATGGIIGDIRQ				
34	SVHIGPGQTSYATGDIIGDIRQ				
35	SIHLGPGRAFYATGDIIGDIRQ				
36	SVRIGPGQAFYATGDIIGNIRQ				
37	SVHIGPGQAFYARGDIIGDIRQ				
38	SIHIGPGQAFYARGDIIGNIRQ				
39	SVHIGPGQAFYATGEIIGDIRQ				
40	SVRIGPGQTFYATGDIIGNIRQ				
41	SVHIGPGKAFYATGGIVGDIRQ				
42	SVHIGPGQAFYATGAIIGSIRQ				
43	SIGIGPGQTFYAADNIIGDIRQ				
44	SVRIGPGQSFYATGDIIGDIKQ				
45	SISIGPGRAFFATGDIIGDIRQ				
46	GIHMGPGQILYATGSIIGDIRQ				
47	SIRIGPGQVFYTNGDIIGDIRQ				
48	SIHIAPGQAFYATGAIIGDIRQ				
49	GIHLGPGQAFYATNAIIGDIRQ				
50	SIHIGPGQAFYATGDIIGDIRQ				

Figure 4. Cross-reactivity analysis of anti-V3 loop-MAP antibodies against heterologous V3 peptides displayed on cellulose membrane. Pooled sera (after initial inoculation + three boosters) from different immunization groups (A−D as in Figure 3) were analyzed. Boxes are coded as follows: white, no recognition; light gray, weak recognition; dark gray, intermediate recognition; black, strong recognition.

DISCUSSION

Different strategies have been proposed to deal with the challenge that highly variable antigenic sites, such as the V3 loop of HIV-1, pose to synthetic peptide-based vaccination schemes (*33*). Most of these strategies have relied on the use of combinations of several representa-

Peptide	Spot	Sequence	A	B	C	D
Consensus	1	KSVRIGP				
	2	SVRIGPG				
	3	VRIGPGQ				
	4	RIGPGQA				
	5	IGPGQAF				
	6	GPGQAFY				
	7	PGQAFYA				
	8	GQAFYAT				
	9	QAFYATG				
	10	AFYATGD				
	11	FYATGDI				
	12	YATGDII				
	13	ATGDIIG				
	14	TGDIIGD				
	15	GDIIGDI				
	16	DIIGDIR				
	17	IIGDIRQ				
	18	IGDIRQA				
C4	19	KQIINMW				
	20	QIINMWQ				
	21	IINMWQE				
	22	INMWQEV				
	23	NMWQEVG				
	24	MWQEVGK				
	25	WQEVGKA				
	26	QEVGKAM				
	27	EVGKAMY				
	28	VGKAMYA				

Figure 5. Epitope mapping of consensus and C4 peptides by the spot synthesis technique. The first 18 overlapping heptapeptides correspond to the consensus V3 loop sequence; the other 10 peptides, to C4. Pooled sera (after initial inoculation + three boosters) from different immunization groups (A−D as in Figure 3) were analyzed. Boxes are coded as follows: white, no recognition; light gray, weak recognition; dark gray, intermediate recognition; black, strong recognition.

tive peptide variants. We had earlier shown that V3 loop-based peptide cocktails, in the form of MAP dendrimers, were a good strategy of epitope presentation (*9*).

In the present study we have compared two alternative approaches to the variability problem, namely, (i) the use of a rationally derived consensus sequence where each position is occupied by the statistically most relevant residue or (ii) the mixotope concept, which not only reproduces a broad spectrum of reported, characteristic mutations, as done before with peptide cocktails (*9*), but additionally merges them in combinatorial fashion. Although our study is confined to basic features of the responses elicited by these two different immunogen types, it provides nonetheless sufficient evidence that the first approach is to be preferred if a strong, cross-reactive, and representative immune response to the V3 loop is wished. Our choice of antigenic presentation, i.e., homodimeric MAPs conjugated to HBsAg, relied on previous data (*32*) demonstrating its enhancing effect on peptide immunogenicity and may have influenced the strength of the immune response (e.g., relative to immunization with free peptides) but would predictably have had parallel effects on both consensus and mixotope formulations and thus little or no effect on the differences we have observed.

In contrast to the report by Resnick et al. (*34*), here we demonstrate that the mixotope strategy did not generate higher levels of cross-reactivity against several V3 peptides than those of the consensus strategy. The fine epitope mapping showed that the anti-peptide antibody response elicited by the consensus MAP was more complete than that generated by the MAP library. The fact that the latter is composed of some 5000 different sequences may account for the substantial reduction in global immune response and may also explain why the antibodies raised against the mixotope library tend to target mainly on the conserved regions of the V3 loop (Figure 5), which are better represented than the variant ones. In conclusion, our data support the hypothesis that, for highly variable antigens, a rationally designed consensus sequence, such as the one derived here for the V3 loop of gp120, may be a valid approach for synthetic vaccine development, providing desirable cross-reactivity and therapeutic advantage.

ACKNOWLEDGMENT

This work was supported by the Center for Genetic Engineering and Biotechnology, La Habana, Cuba. Work at Barcelona was supported by the Spanish Ministry of Science and Technology (Grants PB97-0873 and BIO2002-04091-C03-01, to D.A.), and by the Spanish Agency for International Cooperation (Cuban−Spanish joint research program, to D.A.).

Supporting Information Available: Data on the preparation and stability of MAP dimers and on the purification and characterization of MAP−HBsAg conjugates. This information is available free of charge via the Internet at http://pubs.acs.org.

LITERATURE CITED

(1) Poignard, P., Saphire, E. O., Parren, P. W., and Burton, D. R. (2001) gp120: Biologic aspects of structural features. *Annu. Rev. Immunol. 19*, 253−274.

(2) Birx, D. L., Loomis-Price, L. D., Aronson, N., Brundage, J., Davis, C., Deyton, L., Garner, R., Gordin, F., Henry, D., Holloway, W., Kerkering, T., Luskin-Hawk, R., McNeil, J.,

Michael, N., Foster, P. P., Poretz, D., Ratto-Kim, S., Renzullo, P., Ruiz, N., Sitz, K., Smith, G., Tacket, C., Thompson, M., Tramont, E., Yangco, B., Yarrish, R., and Redfield, R. R. (2000) Efficacy testing of recombinant human immunodeficiency virus (HIV) gp160 as a therapeutic vaccine in early-stage HIV-1-infected volunteers. rgp160 Phase II Vaccine Investigators. *J. Infect. Dis. 181*, 881−889.

(3) Girard, M., Yue, L., Barre-Sinoussi, F., van der Ryst, E., Meignier, B., Muchmore, E., and Fultz, P. N. (1996) Failure of a human immunodeficiency virus type 1 (HIV-1) subtype B-derived vaccine to prevent infection of chimpanzees by an HIV-1 subtype E strain. *J. Virol. 70*, 8229−8233.

(4) Vazquez-Blomquist, D., Gonzalez, S., and Duarte, C. A. (2002) Effect of promoters on cellular immune response induced by recombinant fowlpox virus expressing multi-epitope polypeptides from HIV-1. *Biotechnol. Appl. Biochem. 36*, 171−179.

(5) Kim, J. J., Yang, J. S., Manson, K. H., and Weiner, D. B. (2001) Modulation of antigen-specific cellular immune responses to DNA vaccination in rhesus macaques through the use of IL-2, IFN-gamma, or IL-4 gene adjuvants. *Vaccine 19*, 2496−2505.

(6) Lambert, J. S., Keefer, M., Mulligan, M. J., Schwartz, D., Mestecky, J., Weinhold, K., Smith, C., Hsieh, R., Moldoveanu, Z., Fast, P., Forrest, B., and Koff, W. (2001) A Phase I safety and immunogenicity trial of UBI microparticulate monovalent HIV-1 MN oral peptide immunogen with parenteral boost in HIV-1 seronegative human subjects. *Vaccine 19*, 3033−3042.

(7) Aguilar, A., Carrazana, Y., and Duarte, C. A. (2001) Impact of epitope permutations in the antibody response of mice to a multi-epitope polypeptide of the V3 loop of human immunodeficiency virus type 1. *Biomol. Eng. 18*, 117−124.

(8) Toledo, H., Baly, A., Castro, O., Resik, S., Lamerte, J., Rolo, F., Navea, L., Lovaina, L., Cruz, O., Miguez, J., Serrano, T., Sierra, B., Perez, L., Ricardo, M. E., Debed, M., Lubian, A. L., Blanco, M., Millan, J. C., Ortega, A., Iglesias, E., Penton, E., Martin, Z., Perez, J., Diaz, M., and Duarte, C. A. **(**2001) A phase I clinical trial of a multi-epitope polypeptide TAB9 combined with Montanide ISA 720 adjuvant in non-HIV-1 infected human volunteers. *Vaccine 19*, 4328−4336.

(9) Cruz, L. J., Quintana, D., Iglesias, E., García, Y., Huerta, V., Garay, H. E., Duarte, C., and Reyes, O. (2000) Immunogenicity Comparison of a Multi-antigenic Peptide Bearing V3 Sequences of the Human Immunodeficiency Virus Type 1 with TAB9 Protein in Mice. *J. Peptide Sci. 6*, 217−224.

(10) Nardelli, B., Lu, Y. A., Shiu, D. R., Delpierre-Defoort, C., Profy, A. T., and Tam, J. P. (1992) A chemically defined synthetic vaccine model for HIV-1. *J. Immunol. 148*, 914−920.

(11) Barouch, D. H., and Letvin, N. L. (2000) Cytokine-induced augmentation of DNA vaccine-elicited SIV-specific immunity in rhesus monkeys. *Dev. Biol. 104*, 85−92.

(12) Lifson, J. D., and Martin, M. A. (2002) One step forwards, one step back. *Nature 415*, 272−273.

(13) Moore, J. P., and Nara, P. L. (1991) The role of the V3 loop in HIV infection. *AIDS 5*, 521−533.

(14) Lenz, J., Su, M., Mizrachi, Y., Burke, M., and Rubinstein, A. (2001) V3 variation in HIV-seropositive patients receiving a V3-targeted vaccine. *AIDS 15*, 577−581.

(15) Cardonnier, A., Montagnier, L., and Emerman, M. (1989) Single amino acid changes in HIV envelope affect viral tropism and receptor binding. *Nature 340*, 571−574.

(16) Tian, H., Lan, C., and Chen, Y. H. (2002) Sequence variation and consensus sequence of V3 loop on HIV-1 gp120. *Immunol. Lett. 83*, 231−233.

(17) Masse, H. G., Ameisen, J. C., Boutillon, C., Rouaix, F., Bossus, M., Deprez, B., Neyrinck, J. L., Capron, A., and Tartar, A. (1992) Synthetic Vaccines and HIV-1 hypervariability: a "mixotope" approach. *Pept. Res. 5*, 211−215.

(18) Estaquier, J., Gras-Masse, H., Boutillon, C., Ameisen, J. C., Capron, A., Tartar, A., and Auriault, C. (1994) The mixotope: a combinatorial peptide library as a T cell and B cell immunogen. *Eur. J. Immunol. 24*, 2789−2795.

(19) Gras-Masse, H., Boutillon, C., Dieses, E., Deprez, B., and Tartar, A. (1997) Confronting the degeneracy of convergent combinatorial immunogens, or "mixotopes", with the specificity of recognition of the target sequences. *Vaccine 15*, 1568−1578.

(20) Neurath, A. R., and Strick, N. (1990) Confronting the hypervariability of an immunodominant epitope eliciting virus neutralizing antibodies from the envelope glycoprotein of human immunodeficiency virus type 1 (HIV-1) *Mol. Immunol. 27*, 539−549.

(21) Smith, A. D., Geisler, S. C., Chen, A. A., Resnick, D. A., Roy, B. M., Lewi, P. J., Arnold, E., and Arnold, G. F. (1998) Human rhinovirus type 14: human immunodeficiency virus type 1 (HIV-1) V3 loop chimeras from a combinatorial library induce potent neutralizing antibody responses against HIV-1. *J. Virol. 72*, 651−659.

(22) Houghten, R. A., Graw, S. T., and Bray, M. K. (1986) Simultaneous multiple peptide synthesis: The rapid preparation of large numbers of discrete peptides for biological, immunological and methodological studies. *BioTechniques 4*, 522−526.

(23) Kaiser, E., Colescott, R. L., Bossinger, C. D., and Cook, P. I. (1970) Color test for detection of free terminal amino groups in solid-phase synthesis of peptides. *Anal. Biochem. 34*, 595−598.

(24) Ellman, G. L. (1959) Tissue sulfhydryl groups. *Arch. Biochem. Biophys. 82*, 70−77.

(25) Mo, W., Sakamoto, H., Nishikawa, A., Kagi, N., Langridge, J. I., Shimonishi, Y., and Takao, T. (1999) Structural characterization of chemically derivatized oligosaccharides by nanoflow electrospray ionization mass spectrometry. *Anal. Chem. 71*, 4100−4106.

(26) Deen, C., Claassen, E., Gerritse, K., Zegers, N. D., and Boersma, W. J. A. (1990) A novel carbodiimide coupling method for synthetic peptides: Enhanced antipeptide antibody responses. *J. Immunol. Methods 129*, 119−125.

(27) Bradford, M. M. (1976) A rapid and sensitive method for the quantitation of microgram quantities of proteins utilizing the principle of protein−dye binding. *Anal. Biochem. 72*, 248−254.

(28) Gómez, C. E., López-Campistrous, A. E., and Duarte, C. A. (1998) An immunoassay with bovine serum albumin coupled peptides for the improved detection of anti V3 antibodies in HIV-1 + Human sera. *J. Virol. Methods 71*, 7−16.

(29) Frank, R. (1992) Spot-Synthesis: An easy technique for the positionally addressable, parallel chemical synthesis on a membrane support. *Tetrahedron 48*, 9217−9232.

(30) Tam, J. P. (1988) Synthetic peptide vaccine design: synthetic and properties of a high-density multiple antigenic peptide system. *Proc. Natl. Acad. Sci. U.S.A. 86*, 5409−5413.

(31) Cruz, L. J., Iglesias, E., Aguilar, J. C., Quintana, D., Garay, H. E., Duarte, C., and Reyes, O. (2001) Study of different coupling agents in the conjugation of a V3-based synthetic MAP to carrier proteins. *J. Pept. Sci. 7*, 511−518.

(32) Cruz, L. J., Iglesias, E., Aguilar, J. C., Gonzalez, L. J., Reyes, O., Albericio, F., and Andreu, A. (2004) A comparative study of different presentation strategies for an HIV peptide immunogen. *Bioconjugate Chem. 15*, 112−120.

(33) Hewer, R., and Meyer, D. (2003) Peptide immunogens based on the envelope region of HIV-1 are recognized by HIV/AIDS patient polyclonal antibodies and induce strong humoral immune responses in mice and rabbits. *Mol. Immunol. 40*, 327−335.

(34) Resnick, D. A., Smith, A. D., Gesiler, S. C., Zhang, A., Arnold, E., and Arnold, G. F. (1995) Chimeras from a human rhinovirus 14−human immunodeficiency virus type 1 (HIV-1) V3 loop seroprevalence library induce neutralizing responses against HIV-1. *J. Virol. 4*, 2406−2411.

BC049944U

On-Resin Assembly of a Linkerless Lanthanide(III)-Based Luminescence Label and Its Application to the Total Synthesis of Site-Specifically Labeled Mechanosensitive Channels

Christian F. W. Becker,[†] Daniel Clayton,[‡] George Shapovalov,[‡] Henry A. Lester,[‡] and Gerd G. Kochendoerfer*[,†]

Gryphon Therapeutics, 600 Gateway Boulevard, South San Francisco, California 94080, and Division of Biology, California Institute of Technology, Pasadena, California 91125. Received May 19, 2004; Revised Manuscript Received July 15, 2004

A synthesis strategy for the on-resin assembly of luminescent lanthanide chelates from commercially available compounds was developed. Advantages of the approach include the absence of spacers between the metal ion and the attachment site, and the compatibility with typical chemical protein synthesis protection schemes. Methoxycoumarin-labeled lysine and tris(*tert*-butyl)-DOTA were consecutively coupled with high efficiency to a free amino group in otherwise fully protected peptide segments using standard peptide synthesis methods. Addition of stoichiometric amounts of Tb^{3+} to the modified, cleaved, and purified peptides yielded the desired lanthanide chelate. Incorporation of this label into a chemically synthesized, full-length mechanosensitive channel of large conductance (MscL) of *E. coli* and subsequent reconstitution into vesicles resulted in a functional mechanosensitive channel of comparable conductance to the wild-type channel. However, this channel required increased suction to gate. Excitation of the antenna molecule methoxycoumarin at 336 nm resulted in an emission spectrum typical for Tb^{3+} and a luminescence lifetime of 0.67 ms. The location of the probe close to the backbone of this protein may provide precise information about conformational changes during channel opening from LRET studies.

INTRODUCTION

Lanthanide(III)-based chelates are used increasingly for spectroscopy applications, in particular luminescence resonance energy transfer (LRET),[1] due to the unique luminescence properties of the chelated ions (*1*−*9*). LRET is a type of luminescence assay where a lanthanide donor (Tb^{3+} or Eu^{3+}) transfers excitation energy to an organic fluorescent acceptor in a distance-dependent manner, thus yielding static or dynamic distance information. The unique advantages of lanthanide complexes for this application include luminescence lifetimes in the millisecond range, very sharp emission spectra, high quantum yields, and, in most cases, unpolarized emission (*10*). The advantage of long-lasting fluorescence or luminescence lies in the less costly instrumentation that can be used to detect the emitted signal when compared to measurements of dyes with lifetimes in the nanosecond range. An additional advantage, in particular in the study of highly scattering solutions such as detergent micelle and liposome containing solutions, is the ability to gate the detection in order to reject stray-light. Finally, in the case of oligomeric proteins such as ion channels with multiple distances between nonequivalent positions on identical subunits, the ease of fitting emission decays of long-lived emitters to multiple decay constants allows straightforward deconvolution of these distances (*2*, *7*).

Luminescent lanthanide(III)-based chelates have been principally developed to label folded proteins or DNA. Therefore, they typically utilize flexible linkers with thiol- or amine-reactive groups, and in many cases the sensitizer itself, to distance the chelator moieties from the amino acid side chains of peptides or proteins (*1*, *3*, *11*−*14*). Whereas the presence of a spacer may be desirable for efficient labeling of folded proteins under mild conditions for steric reasons, and in cases where the bulk of the chelate label may interfere with function, such linkers may considerably reduce the accuracy of distance measurements that can be achieved through LRET by introducing additional flexibility to the system.

Our design strategy focused on the fast and facile assembly of a luminescent label that is located close to the backbone of the respective peptide or protein. The label is prepared from commercially available starting materials, DOTA as chelator and methoxycoumarine-labeled lysine as the antenna moiety in protected forms. Commercial availability of these starting materials frees the nonorganic chemist from the solution synthesis steps required for preparation of lanthanide labels described previously in the literature (*1*, *3*, *6*, *11*, *12*, *14*, *15*). The label can be introduced in a straightforward fashion during solid-phase synthesis employing either Boc or Fmoc protecting group strategies. After establishing our approach by preparing a labeled test peptide consisting of 32 amino acids using Boc-chemistry, we extended it to the assembly of multiple luminescent variants of the

* Corresponding author. E-mail: gerd@gryphonrx.com. Phone: 650-360-1418. Fax: 650-952-3055.

[†] Gryphon Therapeutics.

[‡] California Institute of Technology.

[1] Abbreviations: Acm, acetamidomethyl; CPS, chemical protein synthesis; DBU, 1,8-diazabicyclo[5.4.0]undec-7-ene; DOTA, 1,4,7,10-tetraazacyclododecane-1,4,7,10-tetraacetic acid; DPC, dodecylphosphocholine; Dpr, L-1,2-diaminopropionic acid; ESI-MS, electrospray ionization mass spectrometry; LRET, luminescence resonance energy transfer; Mca, methoxycoumarin; MscL, mechanosensitive channel of large conductance; TTHA, triethylenetetraminehexaacetic acid; TM, transmembrane domain.

10.1021/bc0498828 CCC: $27.50 © 2004 American Chemical Society
Published on Web 08/24/2004

mechanosensitive channel of large conductance from *E. coli*. Loading of the DOTA chelator with Tb^{3+} was accomplished following successful synthesis and purification of the test peptide and MscL proteins, respectively, and yielded a lanthanide complex with the desired features for biophysical measurements.

EXPERIMENTAL PROCEDURES

The following reagents were obtained from the indicated sources: Boc-protected amino acids (Midwest Biotech, Fishers, IN); Fmoc-protected amino acids (Novabiochem, San Diego, CA); trifluoroacetic acid (Halocarbon, River Edge, NJ); DIEA (*N*,*N*-diisopropylethylamine) (Applied Biosystems, Foster City, CA); HBTU (2-(1*H*-benzotriazol-1-yl)-1,1,3,3-tetramethyluronium hexafluorophosphate) (Spectrum, Gardena, CA); acetonitrile (Burdick & Jackson, Gardena, CA). Other chemicals were obtained from Sigma (St. Louis, MO) or Aldrich (Milwaukee, WI) and were used as received.

Peptide Synthesis and Purification. Peptides were synthesized at a 0.2 mmol scale on a custom-modified Applied Biosystems 433A peptide synthesizer using S-DVB (stryrene−divinylbenzene) resin carrying an $-OCH_2-$PAM linker (Applied Biosystem, Foster City, CA) or a thioester-generating linker, respectively, following an in-situ neutralization protocol for machine-assisted Boc (*tert*-butoxycarbonyl) chemistry (*16*, *17*). Side-chain protecting groups were Arg(Tos), Asn(Xan), Asp(OcHx), Cys(pMeBzl), Glu(OcHx), His(Dnp), Lys(2ClZ), Ser(Bzl), Thr(Bzl), Trp(CHO), and Tyr(2BrZ). The amino acid sequence of the 32mer test peptide used to prototype the DOTA-Mca-label synthesis: H-CAVVFVTRKNRQVSANPEKKAVREYINSLELL-OH(MW: 3676 Da) was derived from the chemokine CCL5 (RANTES). The sequence and assembly of the peptide backbone of the MscL peptide segments (MscL1-55, MscL56-102, and MscL103-136) was as described previously (*18*).

Assembly of the Luminescent DOTA-Mca Label. The label was introduced on-resin into the N-terminus of the test peptide, and into the N-terminus and positions Val16 and Leu47 in the N-terminal peptide segment MscL1-55. For attachment to the N-terminus, the N-terminal Boc group was removed by treatment with 100% TFA for 2 × 1min cycles. For attachment to positions Val16 and Leu47, the side chain Fmoc protecting group of diaminopropionic acid incorporated at the desired position was removed by 3 × 3 min treatments with 3% DBU (1,8-diazabicyclo[5.4.0]undec-7-ene) in DMF. Fmoc-Lys(Mca)-OH (Novabiochem, San Diego, CA) was coupled to the respective free amino group by using a 5-fold excess of the fluorescent amino acid activated with an equimolar amount of HBTU in DMF in the presence of 10% DIEA (*17*). The Fmoc protecting group on the Lys(Mca) label was removed by 3 × 3 min treatments with 3% DBU in DMF, and 1,4,7,10-tetraazacyclododecane-1,4,7-tris(acetic acid-*tert*-butyl ester)-10-acetic acid (DOTA-tris(*tert*-butyl ester) (Macrocyclics, Dallas, TX) was coupled to the resulting free amine using HBTU/DIEA activation as described for Fmoc-Lys(Mca)-OH. The peptides were then deprotected and simultaneously cleaved from the resin support using HF (*16*). MscL peptides were purified as previously described (*18*).

Assembly of Ec-MscL. The total chemical synthesis and refolding of MscL was performed as previously described (*18*). Briefly, MscL protein was produced by consecutive native chemical ligation of three unprotected, purified peptide segments (MscL1-55, MscL56-102, and MscL103-136) to form the full-length protein. Ligations were performed at a reactant concentration of ~0.1 mM in a solution containing 17 mg/mL dodecyphosphocholine (DPC), 8 M urea, and 100 mM NaP_i, pH 7.5, at 40 °C. Peptides were dissolved in this buffer at 40 °C for 5 min and sonicated for 3−5 min. Ligation reactions were initiated by addition of 0.5% thiophenol, and the progress of the reaction was monitored by analytical RP-HPLC and ESI-MS (electrospray ionization mass spectrometry) analysis. Prior to purification, ligation solutions were worked up at 40 °C in a 5-fold excess of a solution of 20% β-mercaptoethanol in 8 M urea containing 17 mg/mL DPC. Following purification of the first ligation intermediate MscL56-136, the Acm (acetamidomethyl) protecting group was removed from the side chain of the N-terminal cysteine residue in preparation for the final ligation step (*19*). After the final ligation, free cysteine residues were modified by adding DPC to a final concentration of >2 mg/mL to the HPLC pool and subsequent reaction with a 30-fold molar excess of bromoacetamide for 30 min at room temperature. The full-length protein containing the label was then purified. Loading of the chelator with Tb^{3+} was achieved by addition of $TbCl_3$ to the protein solution.

Electrophysiological Characterization. DOTA-Mca-labeled Ec-MscL channel protein was reconstituted into artificial liposomes as described (*18*). Single-channel recordings were made at 20−22 °C on the reconstituted labeled as well as recombinant wt protein at a bandwidth of 20 kHz at 50 mV (intracellular medium is negative) in symmetrical 250 mM KCl, 1 mM $MgCl_2$, 5 mM HEPES (pH 7.1) solution. Currents were acquired with an Axopatch 200B amplifier (Axon Instruments, Union City, CA) and digitized with an Axon Digidata 1322A digitizer. Conductance recordings were analyzed using Axon pCLAMP 8 software. The probability of opening (P_{open}) vs suction curves were generated using software developed by one of the authors (G.S.). Boltzmann functions were fitted to the dose−response relations using the Microcal Origin 6.0 software, yielding activation midpoints and gradients.

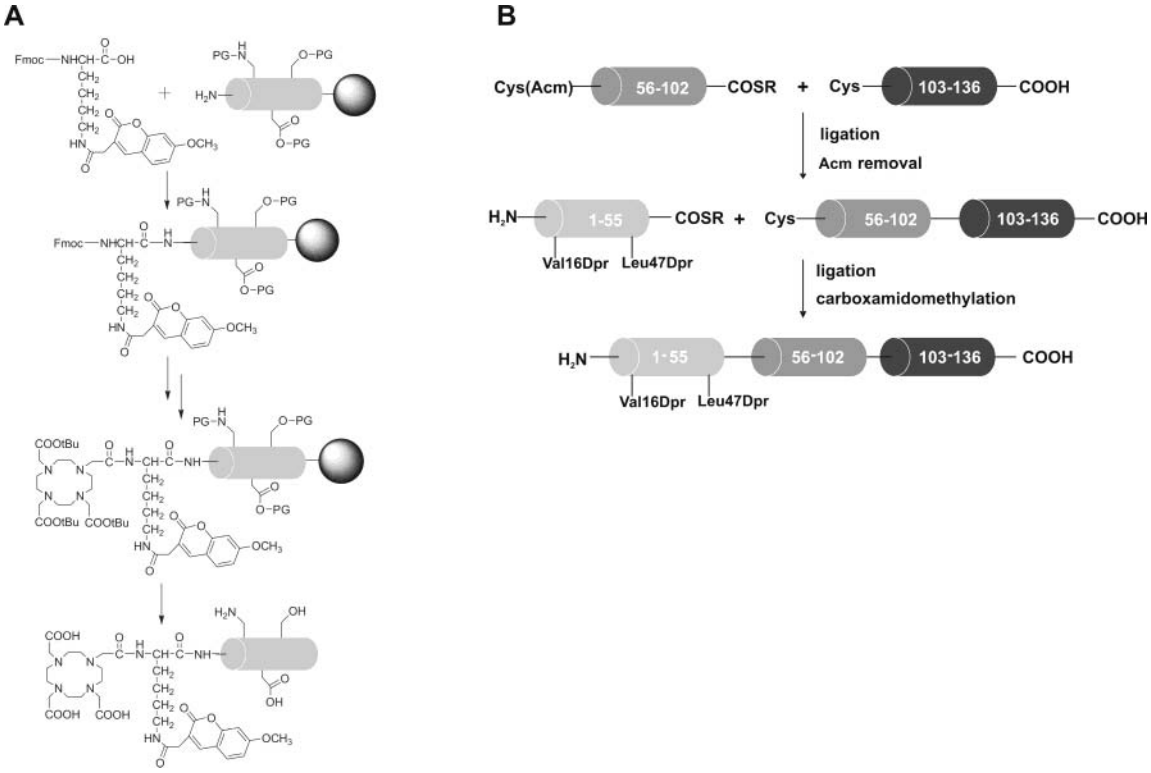
Fluorescence Spectroscopy. Fluorescence spectroscopy was performed with a FluoroLog-3 system (Jobin Yvon, Edison, NJ) equipped with a Xenon-lamp for continuous excitation and a pulsed Xenon lamp for time-resolved measurements using the phosphorimeter setup. Typical settings were an excitation wavelength of 336 nm for the Mca fluorophore, a delay of the detection window relative to the flash pulse of 50 μs, number of flashes 10 (at 20 Hz), and a scanning range of 370 to 700 nm. Data obtained from lifetime measurements were fitted with a single-exponential equation using Kaleidagraph (Synergy Software).

Mass Spectrometry. All crude, purified, and ligated peptides were identified by ESI-MS using ABI-150 or API−III mass spectrometers (Applied Biosystems, Foster City, CA).

RESULTS AND DISCUSSION

Our objective was to develop a simple and efficient procedure to label synthetic peptides and chemically synthesized proteins site-specifically with luminescent labels during solid-phase peptide synthesis. In our design, the lanthanide ion that ultimately determines the experimental distance in LRET experiments is close to the backbone of the peptide or protein since a lysine branch is employed to scaffold the attachment sites of the chelator and the antenna fluorophore (See Scheme 1). The more distant ϵ-amino group of this lysine carries the coumaryl sensitizer, while the DOTA chelator is attached

Scheme 1. (A) On-Resin Assembly of the DOTA-Mca Label; (B) Total Chemical Synthesis of Ec-MscL[a]



[a] DOTA-Mca labeling sites are indicated at the N-terminus and at amino acid positions Val16 and Leu47, respectively. Abbreviations: Acm (acetamidomethyl), Dpr (L-1,2-diaminopropionic acid).

to the proximal α-amino group. The lysine scaffold is either attached to the peptide's N-terminus or to a noncoded diaminopropionic acid residue that is incorporated into the sequence of the target peptide or protein in order to minimize the distance to the backbone. As a result, the lanthanide ion is placed at a maximum distance of 10 Å from the backbone as determined by molecular modeling. By contrast, most other luminescent chelates, such as polyaminocarboxylate−coumarin complexes, were mostly designed to employ long alkyl chains as linkers between peptide and lanthanide complex, which results in larger distances between the label and its attachment site (*1, 3, 11*−*14*).

The assembly of the luminescent probe was initiated by coupling Fmoc-Lys(Mca)-OH either to an unprotected α-amino group of the peptide or a side chain amino group of diaminopropionic acid in an otherwise fully protected peptide linked to a solid support (Scheme 1). Deprotection of the α-amino group was achieved by Boc removal with TFA. The side chain amino group of diaminopropionic acid was specifically deprotected by removing an Fmoc group with a sterically hindered base such as DBU. Activation and in situ neutralization using a 5-fold excess of Fmoc-Lys(Mca)-OH gave excellent coupling yields and no further optimization was needed (*17*). Subsequently, the Fmoc group was removed from the Lys(Mca) moiety by treatment with 3% DBU in DMF for 3 × 3 min and a protected DOTA was coupled to the free α-amino group. DOTA has been extensively used as a chelator for radionuclides in imaging and therapy (*20*−*23*). In our case, DOTA was *tert*-butyl protected at three out of its four carboxyl groups to overcome solubility problems that we encountered with unmasked DOTA in all solvents compatible with solid-phase synthesis such as DMF, DMSO, NMP, and DCM. The 4th carboxyl group was used to form a stable amide bond between the chelator DOTA and the peptide. A 3- to 4-fold excess of tris-(*tert*-butyl)-DOTA was sufficient to obtain fully modified peptides using HBTU/DIEA activation.

This synthesis strategy was initially tested on a 32 amino acid peptide by attaching the label to its unblocked N-terminus and later extended toward a C-terminal α-thioester peptide consisting of the 55 N-terminal amino acid residues of Ec-MscL. Subsequently, the purified peptide was used in the total chemical synthesis of Ec-MscL (*18*) to demonstrate compatibility with native chemical ligation strategies (see Scheme 1B). The assembly of the label gave high yields in each case. In all cases, deletion peptides missing either the coumaryl group or the DOTA group were not observed as significant side products, as determined by RP-HPLC and ESI-MS analysis of the crude cleavage products. As a result, coupling yields are estimated to be >95% overall for both coupling steps, and labeled peptides could be obtained in comparable yields to the unlabeled peptides.

Purification of the test peptide from the crude cleavage mixture by RP-HPLC was followed by lyophilization and transfer into an aqueous buffer containing 10% acetonitrile and reconstitution with $TbCl_3$. Successful complexation of the lanthanide ion by the DOTA label was verified by ESI-MS since the affinity between DOTA and Tb^{3+} was strong enough to survive the ionization process (*24*). Figures 1A and 1B show the electrospray mass spectra of the peptide before and after addition of $TbCl_3$ and desalting by RP-HPLC. The mass difference of +158 Da directly demonstrates binding of a single terbium ion to the peptide, presumably to the DOTA chelator (Figure 1B). Since excess $TbCl_3$ was removed by the desalting column, unspecific binding of Tb^{3+} to the peptide is unlikely to be the cause of the mass gain.

After this proof of principle, we proceeded to assemble labeled variants of the mechanosensitive ion channel of *E. coli* (Ec-McL). The recent total chemical synthesis of Ec-MscL allowed the direct, site-specific introduction of

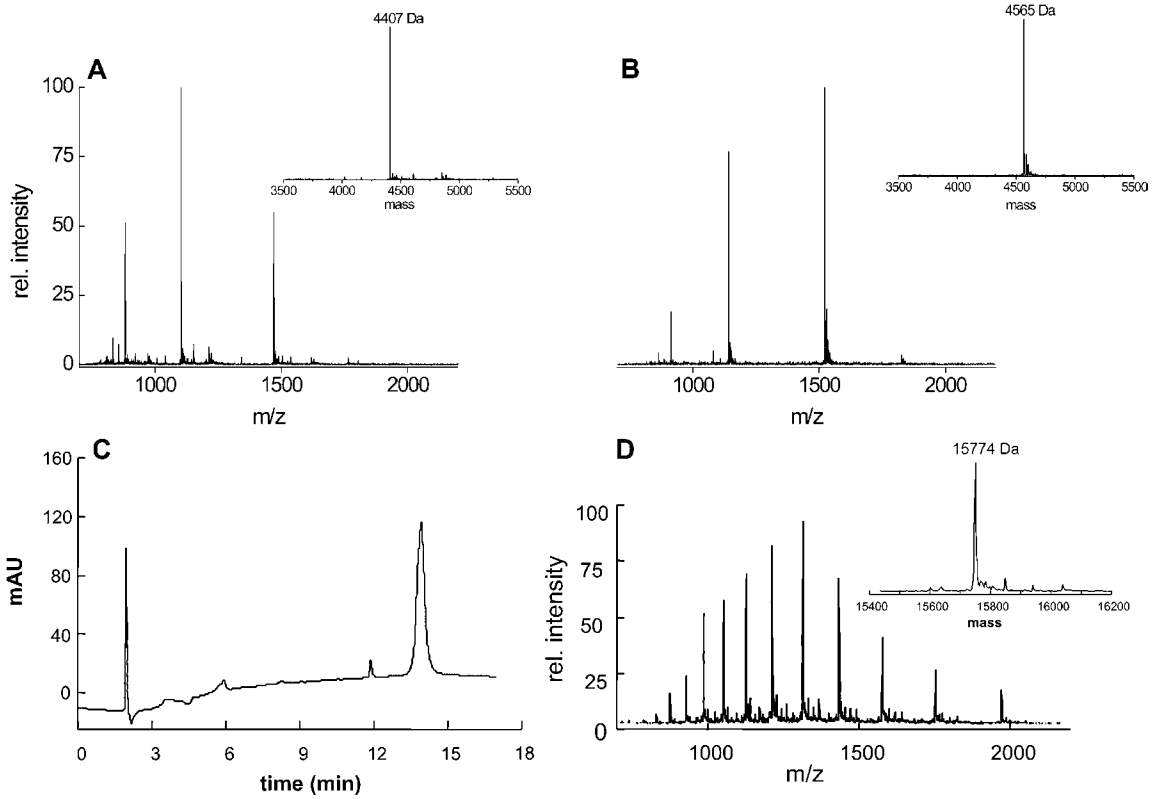


Figure 1. (A) ESI-MS of purified test peptide bearing the DOTA-Mca label (prior to Tb^{3+} addition); (B) ESI-MS of purified test peptide bearing the DOTA-Mca label (after Tb^{3+} addition); (C) RP-HPLC of purified N-terminally DOTA-Mca-labeled Ec-MscL; (D) ESI-MS of purified N-terminally DOTA-Mca-labeled Ec-MscL.

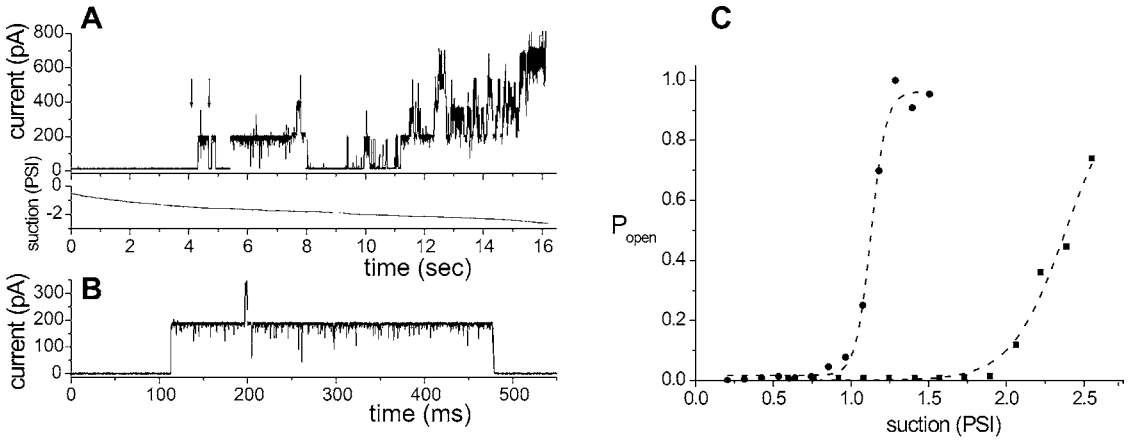


Figure 2. Electrophysiological analysis of vesicle-reconstituted N-terminally DOTA-Mca-labeled Ec-MscL. (A) Current trace (top) showing channel activity on the application of suction (bottom). The sudden increase of current at ~16 s corresponds to breakage of the patch. (B) Expanded time axis in the region of panel A indicated by arrows (suction of approximately −2.0 psi). (C) Sample opening probability curves of wt Ec-MscL (circles) and N-terminally biotinylated DOTA-Mca-labeled Ec-MscL (squares). In this experiment, activation thresholds were determined to be 1.0 psi and 2.4 psi, respectively, by using a Boltzmann fit (dashed lines).

spectroscopic labels at distinct positions of this protein during the peptide assembly stage. Since the open pore of Ec-MscL is predicted to be around 30 Å in diameter (*25*−*29*), LRET studies employing sensitized lanthanide chelates that exhibit large Förster distances and are typically most sensitive for distances between 20 and 100 Å (*8*) are uniquely suited to monitor conformational changes associated with channel opening and are not limited by the small dynamic range of EPR studies (*28*, *30*). Accordingly, a single lanthanide chelate was incorporated into three distinct positions of Ec-MscL, the N-terminus, position Val16 at the cytoplasmic end of the first membrane spanning helix of MscL, and position Leu47 in the loop region between TM1 and TM2 (Scheme 1B). Three positions were chosen in order to get a set of distances in LRET studies after transfer of luminescence to an appropriate acceptor such as TAMRA (tetramethylrhodamine).

After assembly and labeling of the respective N-terminal peptides of Ec-MscL, purification from the crude cleavage mixtures was achieved by RP-HPLC and yielded pure peptides that were used for initial testing of the fluorescent and luminescent properties of the synthetic molecule (data not shown) and as starting materials for the assembly by native chemical ligation. Yields from a synthesis at 0.2 mmol scale on the peptide level were typically 15−20 mg for unlabeled and 10−15 mg for labeled peptide. Assembly of the full-length channel protein largely followed the published procedures (*18*). The assembly process was closely monitored by RP-HPLC

and ESI-MS and was performed in the absence of lanthanide ions. Chemical protein synthesis by native chemical ligation, modification of cysteine ligation sites by bromoacetamide to mask the unnatural cysteine residues, and Acm removal from the ligation intermediates did not modify or alter the label, suggesting that it is fully compatible with the chemical synthesis approach.

Figures 1C and 1D show the HPLC trace and ESI-MS of purified N-terminally DOTA-Mca labeled Ec-MscL (experimental mass: 15 774 Da (±2 Da), theoretical mass: 15 772.9 Da) after assembly (*31*). All other variants could be prepared with comparable purity, and about 1 mg of each variant was prepared in this fashion. The ESI-MS spectra of the intermediate and the final construct also demonstrate that the *tert*-butyl group of the chelator is completely removed prior to protein assembly.

The labeled channel proteins were characterized electrophysiologically in order to ensure correct folding and function. Reconstitution of the synthesized ion channel into artificial liposomes was performed as previously described (*18*) and yielded patches with resistances in the range of 5−20 GΩ. Application of suction produced characteristic single-channel activity that disappeared upon suction release. Figure 2A shows sample activity of the synthesized channel. The single-channel conductance and presence of multiple substates (Figure 2B) correspond to that of the recombinant channel (*18*); however, greater suction was required to open the DOTA-Mca-labeled channel. Figure 2C compares dose−response (P_{open} vs suction) curves for the synthetic (squares) and recombinant (circles) channels. Boltzmann fits to the dose−response curves yielded average activation thresholds of 1.3 ± 0.1 psi (9 ± 1 kPa) for wt and 2.4 ± 0.2 psi (17 ± 1 kPa) for the synthetic channel. It should be noted, however, that the higher activation threshold of DOTA-Mca-labeled channel was similar to the suction at which the liposome membrane in the patches regularly ruptured. Thus, the reported activation midpoint for the DOTA-Mca-labeled channel gives a lower boundary estimate of the value.

Overall, the electrophysiology data confirm that the described synthesis and ligation steps yielded the properly folded and functional protein. However, the introduction of the N-terminal DOTA-Mca label seems to alter channel function either by interfering with the transfer of tension from the bilayer to the channel or by stabilizing the closed-state or destabilizing the open-state. Others have also observed that modifications to the N-terminus can affect the pressure sensitivity of Ec-MscL (*32*). Unfortunately, no reproducible MscL-like conductance could be measured for the MscL variants labeled at positions Val16 and Leu47. In hindsight, this could be rationalized by the location of the label at the membrane−water interface, which might be important for transducing mechanical tension into protein conformational change (*33*). The exploration of alternative labeling sites is ongoing.

To assess the luminescent properties of the resulting protein constructs after reconstitution into a TFE/water mixture (4:1), the methoxycoumarin ring of the label was excited at 336 nm, inducing a strong fluorescence with a maximum intensity at 393 nm due to spontaneous fluorescence of the sensitizer. In the absence of lanthanide ions such as Tb^{3+}, no luminescence signal could be detected. However, after additon of an aqueous solution of $TbCl_3$ to this solution, Tb^{3+} luminescence was detected (Figure 3A). This emission was partially hidden by the stronger Mca background fluorescence. When

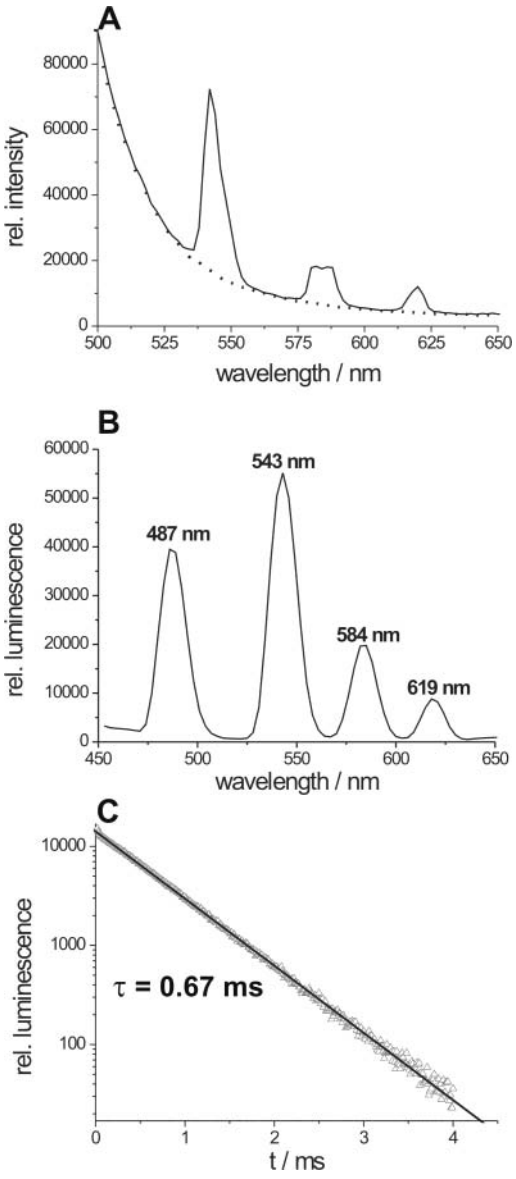


Figure 3. Luminescence of DOTA-Mca-labeled Ec-MscL after excitation at 336 nm. (A) Emission of DOTA-Mca-labeled Ec-MscL with (solid line) and without (dashed line) Tb^{3+} after CW excitation and detection; (B) Tb^{3+} luminescence, after pulsed excitation with a 10 μs pulse and gated detection (50 μs delay); (C) semilogarithmic plot of Tb^{3+}-luminescence decay.

using a phosphorimeter set up that allowed time-gated measurements, a 50 μs delay between excitation of the sample and the starting point for detection of the emission was sufficient to obtain a completely independent Tb^{3+} luminescence signal (Figure 3B). The Tb^{3+} emission showed typical, sharp maxima at 487, 543, 584, and 619 nm, with the strongest emission around 543 nm. The decay was monoexponential, and the luminescence lifetime was determined as 0.67 ms from a semilogarithmic plot of the decreasing luminescence intensity. 0.67 ms is about half of the lifetime found for DOTA-carbostyril-based Tb^{3+} chelates ($\tau \sim 1.5$ ms) in solution (Figure 3C) (*34*). The reduced lifetime may be attributed to less efficient shielding of the Tb^{3+} ion when bound to its DOTA chelator in the context of this chelate. The coordination of water, which might result in nonradiative de-excitation processes, might be facilitated in this chelate. The intrinsic quantum yield for the terbium chelate was estimated by taking the ratio of the luminescence lifetime of Tb^{3+} in the DOTA-Mca chelate and the

intrinsic lifetime of Tb^{3+} (4.75 ms) (*35*, *36*). The resulting estimated luminescence quantum yield of DOTA-chelated terbium in our label is thus 14%. More detailed studies may be needed to investigate the cause of the reduced lifetime and provide a more exact luminescence quantum yield. Nonetheless, the observed luminescence lifetime of the DOTA-Mca chelate is sufficient for LRET experiments.

CONCLUSIONS

We have demonstrated that membrane proteins, site-specifically labeled with a luminescent lanthanide(III)-based chelate, can be prepared by chemical protein synthesis. Preparation of the sensitized chelate from commercial starting materials is a significant improvement to previously reported labels. Introduction of the label close to the protein backbone may allow highly precise measurements of distance changes during the opening of mechanosensitive channels by luminescence resonance energy transfer. Taken together, CPS and LRET provide a powerful combination of techniques for studying the structure−function relationship of membrane proteins such as Ec-MscL.

ACKNOWLEDGMENT

This work was supported by an NIH Program Project Grant, GM-062532.

LITERATURE CITED

(1) Mathis, G. (1995) Probing molecular interactions with homogeneous techniques based on rare earth cryptates and fluorescence energy transfer. *Clin. Chem. 41*, 1391−1397.

(2) Cha, A., Snyder, G. E., Selvin, P. R., and Bezanilla, F. (1999) Atomic scale movement of the voltage-sensing region in a potassium channel measured via spectroscopy. *Nature 402*, 809−813.

(3) Chen, J., and Selvin, P. R. (1999) Thiol-reactive luminescent chelates of terbium and europium. *Bioconjugate Chem. 10*, 311−315.

(4) Heyduk, T. (2002) Measuring protein conformational changes by FRET/LRET. *Curr. Opin. Biotechnol. 13*, 292−296.

(5) Li, M., and Selvin, P. R. (1997) Amine-reactive forms of a luminescent diethylenetriaminepentaacetic acid chelate of terbium and europium: attachment to DNA and energy transfer measurements. *Bioconjugate Chem. 8*, 127−132.

(6) Selvin, P. R., and Hearst, J. E. (1994) Luminescence energy transfer using a terbium chelate: improvements on fluorescence energy transfer. *Proc. Natl. Acad. Sci. U.S.A. 91*, 10024−10028.

(7) Selvin, P. R. (2002) Principles and biophysical applications of lanthanide-based probes. *Annu. Rev. Biophys. Biomol. Struct. 31*, 275−302.

(8) Selvin, P. R. (2000) The renaissance of fluorescence resonance energy transfer. *Nat. Struct. Biol. 7*, 730−734.

(9) Jares-Erijman, E. A., and Jovin, T. M. (2003) FRET imaging. *Nat. Biotechnol. 21*, 1387−1395.

(10) Reifenberger, J. G., Snyder, G. E., Baym, G., and Selvin, P. R. (2003) Emission polarization of europium and terbium chelates. *J. Phys. Chem. B 107*, 12862−12873.

(11) Heyduk, E., and Heyduk, T. (1997) Thiol-reactive, luminescent Europium chelates: luminescence probes for resonance energy transfer distance measurements in biomolecules. *Anal. Biochem. 248*, 216−227.

(12) Ge, P., and Selvin, P. R. (2003) Thiol-reactive luminescent lanthanide chelates: part 2. *Bioconjugate Chem. 14*, 870−876.

(13) Peuralahti, J., Puukka, K., Hakala, H., Mukkala, V. M., Mulari, O., Hurskainen, P., and Hovinen, J. (2002) Synthesis of nonluminescent lanthanide(III) chelates tethered to an aminooxy group and their applicability to biomolecule derivatization. *Bioconjugate Chem. 13*, 876−880.

(14) Peuralahti, J., Hakala, H., Mukkala, V. M., Loman, K., Hurskainen, P., Mulari, O., and Hovinen, J. (2002) Introduction of lanthanide(III) chelates to oligopeptides on solid phase. *Bioconjugate Chem. 13*, 870−875.

(15) Weibel, N., Charbonniere, L. J., Guardigli, M., Roda, A., and Ziessel, R. (2004) Engineering of Highly Luminescent Lanthanide Tags Suitable for Protein Labeling and Time-Resolved Luminescence Imaging. *J. Am. Chem. Soc. 126*, 4888−4896.

(16) Camarero, J. A., and Muir, T. W. (1999) Chemical Ligation of Polypeptides, in *Current Protocols in Protein Science*, 18.4.1−18.4.21, John Wiley & Sons, Inc., New York.

(17) Schnölzer, M., Alewood, P., Jones, A., Alewood, D., and Kent, S. B. H. (1992) In situ neutralization in Boc-chemistry solid phase peptide synthesis. Rapid, high yield assembly of difficult sequences. *Int. J. Pept. Protein Res. 40*, 180−193.

(18) Clayton, D., Shapovalov, G., Maurer, J. A., Dougherty, D. A., Lester, H. A., and Kochendoerfer, G.G. (2004) Total chemical synthesis and electrophysiological characterization of mechanosensitive channels from Escherichia coli and Mycobacterium tuberculosis. *Proc. Natl. Acad. Sci. U. S. A. 101*, 4764−4769.

(19) Canne, L. E., Botti, P., Simon, R. J., Chen, Y. J., Dennis, E. A., and Kent, S. B. H. (1999) Chemical protein synthesis by solid-phase ligation of unprotected peptide segments. *J. Am. Chem. Soc. 121*, 8720−8727.

(20) Runge, V. M., Carollo, B. R., Wolf, C. R., Nelson, K. L., and Gelblum, D. Y. (1989) Gd DTPA: a review of clinical indications in central nervous system magnetic resonance imaging. *Radiographics 9*, 929−958.

(21) Froidevaux, S., and Eberle, A. N. (2002) Somatostatin analogues and radiopeptides in cancer therapy. *Biopolymers 66*, 161−183.

(22) Valdes Olmos, R. A., Hoefnagel, C. A., Bais, E., Boot, H., Taal, B., de Kraker, J., and Vote, P. A. (2001) [Therapeutic advances of nuclear medicine in oncology]. *Rev. Esp. Med. Nucl. 20*, 547−557.

(23) Cutler, C. S., Smith, C. J., Ehrhardt, G. J., Tyler, T. T., Jurisson, S. S., and Deutsch, E. (2000) Current and potential therapeutic uses of lanthanide radioisotopes. *Cancer Biother. Radiopharm. 15*, 531−545.

(24) Loncin, M. F., Desreux, J. F., and Merciny, E. (1986) Coordination of Lanthanides by Two Polyamino Polycarboxylic Macrocycles: Formation of Highly Stable Lanthanide Complexes. *Inorg. Chem. 25*, 2646−2648.

(25) Perozo, E., and Rees, D. C. (2003) Structure and mechanism in prokaryotic mechanosensitive channels. *Curr. Opin. Struct. Biol. 13*, 432−442.

(26) Sukharev, S., Betanzos, M., Chiang, C. S., and Guy, H. R. (2001) The gating mechanism of the large mechanosensitive channel MscL. *Nature 409*, 720−724.

(27) Sukharev, S., Durell, S. R., and Guy, H. R. (2001) Structural models of the MscL gating mechanism. *Biophys. J. 81*, 917−936.

(28) Perozo, E., Cortes, D. M., Sompornpisut, P., Kloda, A., and Martinac, B. (2002) Open channel structure of MscL and the gating mechanism of mechanosensitive channels. *Nature 418*, 942−948.

(29) Ajouz, B., Berrier, C., Garrigues, A., Besnard, M., and Ghazi, A. (1998) Release of thioredoxin via the mechanosensitive channel MscL during osmotic downshock of Escherichia coli cells. *J. Biol. Chem. 273*, 26670−26674.

(30) Perozo, E., Kloda, A., Cortes, D. M., and Martinac, B. (2001) Site-directed spin-labeling analysis of reconstituted Mscl in the closed state. *J. Gen. Physiol. 118*, 193−206.

(31) Dawson, P. E., Muir, T. W., Clark-Lewis, I., and Kent, S. B. H. (1994) Synthesis of proteins by native chemical ligation. *Science 266*, 776−779.

(32) Hase, C. C., Le Dain, A. C., and Martinac, B. (1997) Molecular dissection of the large mechanosensitive ion channel (MscL) of E. coli: mutants with altered channel gating and pressure sensitivity. *J. Membr. Biol. 157*, 17−25.

(33) Chang, G., Spencer, R. H., Lee, A. T., Barclay, M. T., and Rees, D. C. (1998) Structure of the MscL homologue from *Mycobacterium tuberculosis*: a gated mechanosensitive ion channel. *Science 282*, 2220−2226.

(34) Li, M., and Selvin, P. R. (1997) Luminescent Polyaminocarboxylate Chelates of Terbium and Europium − The Effect of Chelate Structure. *J. Am. Chem. Soc. 117,* 8132−8138.
(35) Drake, S. K., Zimmer, M. A., Kundrot, C., and Falke, J. J. (1997) Molecular tuning of an EF-hand-like calcium binding loop. Contributions of the coordinating side chain at loop position 3. *J. Gen. Physiol. 110,* 173−184.
(36) Vazquez-Ibar, J. L., Weinglass, A. B., and Kaback, H. R. (2002) Engineering a terbium-binding site into an integral membrane protein for luminescence energy transfer. *Proc. Natl. Acad. Sci. U.S.A. 99,* 3487−3492.

BC0498828

Novel Monoclonal Antibodies with Specificity for Chelated Uranium(VI): Isolation and Binding Properties

Robert C. Blake II,[‡] Andrey R. Pavlov,[§,||] Mehraban Khosraviani,[§,⊥] Harry E. Ensley,[⊗] Garry E. Kiefer,[#] Haini Yu,[§] Xia Li,[§,▽] and Diane A. Blake[§,*]

Division of Basic Pharmaceutical Sciences, College of Pharmacy, Xavier University of Louisiana, New Orleans, Louisiana, Department of Biochemistry, Tulane University Health Sciences Center, New Orleans, Louisiana, Department of Chemistry, Tulane University, New Orleans, Louisiana, Dow Chemical Company, Freeport, Texas, and Beijing Vegetable Research Institute, Beijing, China. Received May 7, 2004; Revised Manuscript Received August 2, 2004

A derivative of 1,10-phenanthroline that binds to UO_2^{2+} with nanomolar affinity was found to be a very effective immunogen for the generation of antibodies directed toward chelated complexes of hexavalent uranium. This study describes the synthesis of 5-isothiocyanato-1,10-phenanthroline-2,9-dicarboxylic acid and its use in the generation and functional characterization of a group of monoclonal antibodies that recognize the most soluble and toxic form of uranium, the hexavalent uranyl ion (UO_2^{2+}). Three different monoclonal antibodies (8A11, 10A3, and 12F6) that recognize the 1:1 complex between UO_2^{2+} and 2,9-dicarboxy-1,10-phenanthroline (DCP) were produced by the injection of BALB/c mice with DCP−UO_2^{2+} covalently coupled to a carrier protein. Equilibrium dissociation constants for the binding of DCP−UO_2^{2+} to antibodies 8A11, 10A3, and 12F6 were 5.5, 2.4, and 0.9 nM, respectively. All three antibodies bound the metal-free DCP with roughly 1000-fold lower affinity. The second-order rate constants for the bimolecular association of each antibody with soluble DCP−UO_2^{2+} were in the range of 1 to 2 × 10^7 M^{-1} s^{-1}. Binding studies conducted with structurally related chelators and 21 metal ions demonstrated that each of these three antibodies was highly specific for the soluble DCP−UO_2^{2+} complex. Detailed equilibrium binding studies conducted with three other derivatives of DCP, either complexed with UO_2^{2+} or metal-free, suggested that the antigen binding sites on the three antibodies have significant functional and structural similarities. Biomolecules that bind specifically to uranium will be at the heart of any new biotechnology developed to monitor and control uranium contamination. The three antibodies described herein possess sufficient affinity and specificity to support the development of immunoassays for hexavalent uranium in environmental and clinical samples.

INTRODUCTION

The mining and processing of uranium ores have contaminated significant quantities of soil and groundwater in the US, Europe, and Russia (*1*−*3*). In the US alone, more than 200 million metric tons of mine tailings and other waste have been identified for cleanup and disposal (*4*). The health effects associated with oral or dermal exposure to natural and depleted uranium appear to be solely chemical in nature and not related to uranium's radiological properties (*5*). The toxicity of natural uranium varies according to its chemical form, and the more soluble, hexavalent form has been shown to be the most potent systemic toxicant (*6*). Uranium is absorbed from the intestine or the lungs. Although most uranium is rapidly excreted in the urine, a small percentage is deposited in the tissues, predominantly kidney, muscle, and bone (*7, 8*). Chronic exposure to uranium in drinking water is weakly associated with altered proximal tubulus function without a clear threshold, which suggests that even low uranium concentrations in drinking water can cause nephrotoxic effects (*9*). Current research suggests that the safe concentration of uranium in drinking water may be close to the value proposed by the US Environmental Protection Agency, 30 μg/L or ∼130 nM (*10*).

As part of an ongoing effort in our laboratories to develop immunoassays for heavy metals in environmental and clinical samples, we have produced and characterized a growing number of monoclonal antibodies directed toward epitopes of metal−chelate complexes (*11*−*17*). Although other laboratories have described the generation and properties of monoclonal and recombinant antibodies directed toward chelated metal ions (*18*−*23*), a detailed characterization of antibodies directed toward an epitope that includes some form of ionic uranium has not been reported. Previous attempts by our laboratories to generate antibodies to chelated hexavalent uranium using bifunctional acyclic polyaminocarboxylate chelators available from similar studies were not successful. These failed attempts led us to hypothesize that bifunctional chelators derived from EDTA and DTPA did not coordi-

* To whom correspondence should be addressed at 1430 Tulane Ave., SL-43, New Orleans, LA 70112. E-mail: blake@tulane.edu; Tel: 504-988-2478; Fax: 504-988-2684.

‡ Xavier University of Louisiana.

§ Department of Biochemistry, Tulane University Health Sciences Center.

⊗ Department of Chemistry, Tulane University.

Dow Chemical Company.

▽ Beijing Vegetable Research Institute.

|| Current address: Fidelity Systems Inc., Gaithersburg, MD 20879.

⊥ Current address: Amgen Incorporated, Thousand Oaks, CA 91320.

10.1021/bc049889p CCC: $27.50 © 2004 American Chemical Society
Published on Web 08/20/2004

nate hexavalent uranium with an affinity high enough to preserve the metal−chelate complex during immune processing in the injected animal.

This paper describes the generation and binding properties of three different monoclonal antibodies directed toward an epitope comprised of the hexavalent UO_2^{2+} and a novel bifunctional derivative of 2,9-dicarboxy-1,10-phenanthroline (DCP)[1]. DCP bound to UO_2^{2+} with an affinity approximately 5 orders of magnitude greater than that determined for EDTA or DTPA. Each of the three monoclonal antibodies produced using this new amine-reactive chelator bound to the soluble DCP−UO_2^{2+} complex with an equilibrium dissociation constant in the low nM range. Equilibrium and kinetic binding studies conducted with different chelators and metal ions indicated that each of these three antibodies possessed sufficient specificity and affinity to create an immunoassay for soluble natural uranium in the concentration range currently proposed by the US Environmental Protection Agency for drinking water (*10*).

EXPERIMENTAL PROCEDURES

Materials. 2,9-Dicarboxy-1,10-phenanthroline (DCP) was synthesized (*24*) or purchased from Alfa Aesar (Wood Hill, MA). 1,10-Phenanthroline, 2,9-dimethyl-1,10-phenanthroline, and 4-(2-pyridylazo)resorcinol (PAR) were products of Aldrich, Inc. (Milwaukee, WI). The 2,9-diphosphonatomethyl-, 2,9-dicarboxymethyl ester-, 2,9-dihydroxymethyl-, and 2,9-ditrichloromethyl-substituted 1,10-phenanthrolines were generously provided by Dow Chemical Co. (Freeport, TX). Uranyl diacetate (ACS-grade) was a product of Mallinckrodt Chemical Works (St. Louis, MO). Other metals (atomic absorption grade) were obtained from Perkin-Elmer (Norwalk, CT). Prepacked Sephadex G-25 columns (PD-10) were products of Pharmacia, Inc. (Piscataway, NJ). Centricon filters were purchased from Amicon (Beverly, MA). Keyhole limpet hemocyanin (KLH) was purchased from CalBiochem (LaJolla, CA). BALB/c inbred mice were obtained from Charles River Laboratories (Wilmington, MA). SP 2/0-Ag14 myeloma cells were from the American Type Culture Collection (Rockville, MD). RIBI and TiterMax adjuvants were purchased from RIBI Immunochemicals (Hamilton, MT) and CyxRx (Norcross, GA). Culture media and other reagents for the preparation of hybridoma cells were obtained from Stem Cell Technologies (Vancouver, BC, Canada). An IsoStrip mouse monoclonal antibody isotyping kit was purchased from Boerhinger-Mannheim (Indianapolis, IN) and used according to the manufacturer's instructions. Fetal bovine serum (low IgG) was the product of Hyclone Laboratories (Logan, UT). 3,3′,5,5′-Tetramethylbenzidine peroxidase substrate (TMB Microwell Substrate) was from Kirkegaard-Perry Laboratories (Gaithersburg, MD). Microwell plates for ELISA (high-binding, flat bottom) and standard tissue culture plasticware were from Corning/Costar (Cambridge, MA). CellLine culture flasks were distributed by Fisher Chemical Co. (Houston, TX). Polystyrene beads (98 micron diameter) for binding studies were purchased from Sapidyne Inc (Boise, ID). HRP- and Cy5-labeled goat anti-mouse IgG were products of Jackson Immunoresearch Laboratories (West Grove, PA). Ethylenediaminetetraacetic acid (EDTA), diethylenetriaminepentaacetic acid (DTPA), pristane, HEPES, RPMI medium, L-glutamine, antibiotics, bovine serum albumin (fraction V, metal-free), and antibodies specific for mouse IgG1, IgG2a IgG2b, IgG3, IgM, and IgA were purchased from Sigma Chemical Co. (St. Louis, MO). The DTPA analogue, *N*-(2-aminoethyl)-*trans*-1,2-diaminocyclohexane-*N*,*N*′,*N*″-pentaacetic acid (CHXDTPA), was available from a previous study (*16*). Elemental analyses were performed by Atlantic Microlab, Inc., Norcross, GA.

Determination of Dissociation Constants for the Interaction of Chelators with UO_2^{2+}. The binding of uranyl ion to colorimetric and noncolorimetric chelators was determined by spectrophotometric titrations performed on an OLIS-14 renovated Cary Spectrophotometer (On-Line Instruments, Inc. Bogart, GA). Visible absorbance spectra of 26 μM PAR in HEPES-buffered saline (HBS, 137 mM NaCl, 3 mM KCl, 10 mM HEPES, pH 7.4) were performed in the absence and presence of varying concentrations of uranyl ions (5−50 μM), and values of Δ absorbance were determined as differences in the spectrum of the metal-free chelator versus the spectrum of the chelator in the presence of uranyl ions. For determination of the dissociation constants of noncolorimetric chelators with uranyl ion, the concentrations of PAR and uranyl ion were fixed at 26 and 30 μM, respectively, and spectra were obtained after adding varying concentrations of the noncolorimetric chelator to the preformed complex. Data were fit to the equations described in Results to obtain equilibrium dissociation constants.

Synthesis of Bifunctional Chelator for UO_2^{2+}. Synthesis of 5-isothiocyanato-1,10-phenanthroline-2,9-dicarboxylic acid was performed in four steps, as shown in Figure 1.

5-Nitro-2,9-dimethyl-1,10-phenanthroline (**2** in Figure 1). To a mixture of 5 mL of nitric acid and 10 mL of sulfuric acid was added 0.5 g (2.4 mmol) of 2,9-dimethyl-1,10-phenanthroline (**1** in Figure 1), and the solution was heated at 115 °C for 1 h. The solution was poured onto 100 g of ice, and the mixture was adjusted to pH 8 with a concentrated solution of NaOH. The precipitate was filtered and dried at 110 °C to give 248 mg of **2** (0.98 mmol, 41% yield); mp 201−203 °C, 1H NMR δ 2.97 (3H, s), 2.99 (3H, s), 7.66 2H, app t, J = 8.5 Hz), 8.26 (1H, d, J = 8.3 Hz), 8.60 (1H, s) 8.91 (1H, d, J = 8.7 Hz).

5-Nitro-1,10-phenanthroline-2,9-carboxylic Acid (**4** in Figure 1). A mixture of compound **2** (1.0 g, 3.6 mmol) and selenium dioxide (1.0 g, 9.0 mmol) was dissolved in 5 mL of dioxane containing 4% water and heated at reflux for 3 h, then filtered through a pad of Celite while hot. The dialdehyde **3** was isolated from the filtrate as a yellow-red precipitate in 64% yield. Anal. ($C_{14}H_7N_3O_4$) C, H, N.

The dialdehyde was subsequently oxidized to the dicarboxylic acid using 10 mL of 80% nitric acid under reflux for 3 h. The solution was then cooled and poured into ice. The resulting precipitate was collected and recrystallized from aqueous THF to give 580 mg of the bis-acid **4** (1.9 mmol, 46% from **2**); mp 217−220° C; IR 3100 and 1733 cm^{-1}, ^{1}H NMR δ 8.47 (1H, d, J = 8.0 Hz), 8.95 (1H, d, J = 8.0 Hz), 9.04 (1H, d, J = 8.8 hz), 9.17 (1H, s). Anal. ($C_{14}H_7N_3O_6$-1/2 H_2O) C, H, N.

5-Isothiocyanato-1,10-phenanthroline-2,9-dicarboxylic Acid (**5** in Figure 1). Compound **4** (110 mg, 0.3 mmol) was hydrogenated in 5 mL of ethanol at 60 psi in the presence of 15 mg of 10% Pd/C. On exposure to air, the initially yellow solution became bright red. Therefore, the

[1] The following abbreviations are used in the text: BSA, bovine serum albumin; CHXDTPA, *trans*-*N*-(2-aminoethyl)-1,2-diaminocyclohexane-*N*,*N*′,*N*″-pentaacetic acid; DCP, 2,9-dicarboxy-1,10-phenanthroline; DHM, 2,9-dihydroxymethyl-1,10-phenanthroline; DME, 2,9-dicarboxymethyl ester-1,10-phenenthroline; DPP, 2,9-diphosphonatomethyl-1,10-phenanthroline; DTPA, diethylenetriaminepentaacetic acid; EDTA, ethylenediaminetetraacetic acid; PAR, 4-(2-pyridylazo)resorcinol.

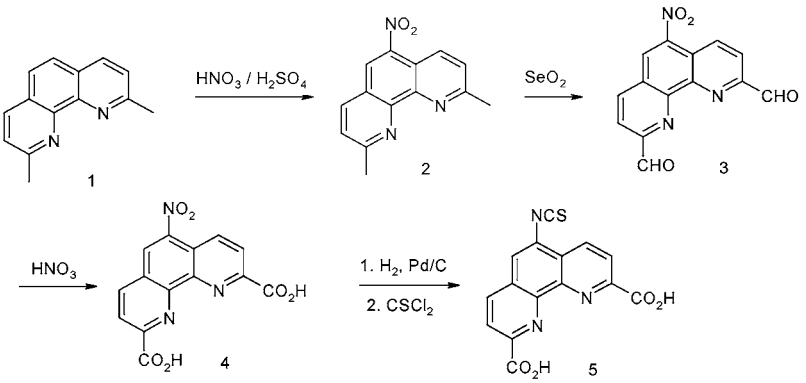


Figure 1. Synthesis of 5-isothiocyanato-1,10-phenanthroline-2,9-dicarboxylic acid. Scheme for the synthesis of 5-isothiocyanato-1,10-phenanthroline-2,9-dicarboxylic acid in from 2,9-dimethyl-1,10-phenanthroline.

amine was directly converted to the isothiocyanate. 3 N HCl (10 mL) was added, and the solution was filtered to remove the catalyst. The ethanol was evaporated at reduced pressure, and the solution was cooled to 0 °C. Thiophosgene (5 mL of a 10% solution in chloroform) was then added with rapid stirring, which was continued overnight at room temperature in a chemical hood. Evaporation of the two-phase mixture under reduced pressure gave a solid that was washed with 10 mL of cold water and dried under vacuum to give 98 mg (0.30 mmol, 86% from **4**) of **5**. The isothiocyanate derivative could be used immediately or stored for up to 3 months at −20 °C.

Synthesis of Protein−Chelate Conjugates. 5-Isothiocyanato-1,10-phenanthroline-2,9-dicarboxylic acid (7.1 mg or 22 μmol, ∼equal molar with respect to total lysine residues in these proteins) was suspended in 1.0 mL of 0.1 M HEPES buffer, pH 9.0, containing 20 mg of BSA or KLH. The pH of the reaction mixture was readjusted to 9.0 if necessary with KOH, and the reactions were stirred overnight at room temperature. The supernatant from this reaction mixture was desalted by filtration through a prepacked Sephadex G-25 column equilibrated with HEPES-buffered saline (HBS, 137 mM NaCl, 3 mM KCl, 10 mM HEPES, pH 7.4). The protein−DCP conjugates eluted in the void volume of the column and could be further concentrated (if necessary) by ultrafiltration in Centricon filters (30 000 mol. wt. cutoff). The concentration of the conjugates was determined using the BCA protein assay kit (Pierce Chemical Co., Rockford, IL) with supplied BSA standards. The degree of lysine substitution in the conjugates was estimated by a modification of a literature method (*25*). The original procedure required additional background measurements because the conjugates had significant absorbance at 345 nm. Protein−chelate conjugates prepared by this method were estimated to have between 20% and 80% lysine substitution (depending upon the preparation) and were light yellow-brown in color when present at a concentration > 2.5 mg/mL.

Mouse Immunization, Hybridoma Production, and Purification of Monoclonal Antibodies. The KLH−DCP conjugate (80% substitution, 0.7 mg in 0.28 mL of HBS) was mixed 0.07 mL of 10× HBS and 0.07 mL of uranyl diacetate (62.5 mM solution in dilute acetic acid, 3.5 μmol), followed by immediate addition of 0.05 mL of KOH (1.8 M aqueous solution) to bring the pH of the mixture to 7.0. The mixture was diluted by the addition of 0.15 mL of water, the pH was adjusted to 7.0, and the final volume of the solution was brought to 0.7 mL. This mixture was emulsified with an equal volume of RIBI or TiterMax adjuvant. The components of this preparation were not fully soluble, but produced homogeneous emulsions with both adjuvants. The final immunogen contained 0.5 mg/mL of the KLH−DCP conjugate and 2.5 mM uranyl diacetate.

Three 6-week old female BALB/c mice were each injected intraperitoneally with 0.1 mL of the prepared immunogen (2 with RIBI and 1 with TiterMax). The injections were repeated after 3 weeks, and the polyclonal antibody responses were measured by indirect ELISA as described below. The mouse with the best polyclonal antibody response to uranium-loaded BSA−DCP was given a final intraperitoneal injection of 50 μg of KLH−DCP with 2.5 mM uranyl diacetate in HBS, and after 72 h the animal was sacrificed and its spleen was removed. Hybridomas were prepared by fusion of splenocytes and SP 2/0-Ag14 myeloma cells using the reagents provided by Stem Cell Technologies and plated into a semisolid growth medium also provided by this manufacturer. After incubation at 37 °C in 95% air/5% CO_2, hybridoma cell colonies began to grow out in 7−10 days. These colonies, visible to the naked eye, were individually transferred to the wells of 96-well plates that contained 0.15 mL of culture medium and incubated for several days. The culture supernatants were assayed for antibody production by indirect and competitive ELISA (described below) and representative cells were cloned twice by limiting dilution before storage in liquid nitrogen.

Ascites fluid was produced in pristane-primed BALB/c mice. For some experiments, large quantities of antibodies were prepared by hybridoma culture in 1-L CellLine culture flasks, used according to the manufacturer's instructions. Monoclonal antibodies were purified by affinity chromatography on protein G as previously described (*11*). The homogeneity of the purified proteins was checked by gel electrophoresis in the presence of sodium dodecyl sulfate and β-mercaptoethanol (*26*). The concentration of the antibodies was determined using the BCA protein assay, and the immunoglobulin subclass was determined and quantified by sandwich ELISA using antibodies specific for IgG1, IgG2a, IgG2b, IgG3, IgM, and IgA. Light chain isotype was identified by using the IsoStrip antibody isotyping kit according to the manufacturer's instructions.

Indirect and Competitive ELISA. Addition of uranyl diacetate to concentrated solutions of the DCP−protein conjugates (>100 μg/mL) caused precipitation. This precipitation could be avoided either by dilution of the conjugate to concentrations less that 10 μg/mL before addition of uranyl ion, or by immobilizing metal-free DCP−protein conjugate onto the ELISA plate and sub-

sequently incubating the plate with a solution of uranyl diacetate. Both procedures gave equivalent results in control experiments (data not shown). ELISA plates were incubated with 2−5 μg/mL of DCP−BSA in HBS amended with 5 μM uranyl diacetate for at least 1 h at 37 °C or overnight at 4 °C. The plates could be stored for several weeks in this coating buffer with no loss of activity. Immediately before use, the plates were washed three times with PBS-Tween (137 mM NaCl, 3 mM KCl, 10 mM phosphate, pH 7.4, and 0.05% Tween-20), blocked for 15 min with 3% BSA in HBS, and washed again three times with PBS-Tween.

For indirect ELISA, diluted serum or hybridoma culture supernatant was incubated for 1 h at room temperature in the coated wells. After three washes in PBS-Tween, the amount of primary antibody bound on the plate was quantified using an HPR-conjugated goat anti-mouse antibody and TMB microwell substrate (see refs 11 and 12 for a more detailed description). For competitive ELISA, diluted hybridoma culture supernatants were incubated in microwell plates coated with BSA−DCP−UO_2^{2+} in the presence of one of the following: 12.5 μM DCP in HBS or 12.5 μM DCP + 5 μM uranyl diacetate in HBS. The binding of the antibodies in HBS alone served as a control in the competitive ELISA's. The amount of primary antibody bound to the plate was quantified as described for indirect ELISA.

Equilibrium Binding Studies and Kinetic Analyses. Equilibrium binding studies and measurements of association rate constants were performed using a KinExA 3000 (Sapidyne Instruments Inc, Boise, ID) flow fluorimeter. The general procedures have been described in detail elsewhere (*11*, *27*, *28*). For these experiments, polystyrene beads coated with UO_2^{2+}−DCP−BSA were used as the capture reagent. Polystyrene beads (98 μm, 200 mg) were incubated with 1 mL of 100 μg/mL DCP−BSA for 1 h at 37 °C. The beads were washed two times with 1 mL of HBS, then any remaining binding sites were blocked by incubation for 1 at 37 °C with BSA (10 mg/mL in HBS containing 0.03% NaN_3.) Beads could be stored in this blocking solution for up to 2 months at 4 °C. Immediately before use, the beads were diluted into 30 mL of HBS amended with 30 μM uranyl diacetate to saturate the immobilized DCP with UO_2^{2+}. The excess uranyl ions were washed away when the coated beads were packed into the capillary observation cell.

RESULTS

Binding of Uranyl Ions to Chelators. Our laboratories have successfully isolated and characterized monoclonal antibodies to chelated forms of ionic cadmium and lead using bifunctional derivatives of EDTA (*11*), CHXDTPA (*16*), and DTPA (*14*) to create metal-binding epitopes on appropriate carrier proteins. In all cases to date, the resulting covalent complexes of chelated metal ions appeared to be weak immunogens, since only a few clones out of hundreds assayed actually produced antibodies that exhibited acceptable specificity for the chelated metal ion in question. In the present case, initial efforts to generate monoclonal antibodies directed against chelated forms of UO_2^{2+} utilized bifunctional acyclic polyaminocarboxylate chelators (DTPA and CHXDTPA). Not a single clone (out of approximately 2000 examined) produced an antibody with acceptable affinity and specificity for chelated ionic uranium (*29*).

One hypothesis to account for these observations is that the affinity of DTPA and CHXDTPA for uranyl ions was insufficient to maintain the intact chelated uranium complex for the period of time necessary to elicit an immune response to the chelated metal. To test this hypothesis, the binding affinity of various chelators for uranyl ions was determined by competitive uranyl binding experiments conducted in the presence of 2-(4-pyridylazo)resorcinol (PAR), a spectrophotometric complexiметric indicator for cationic metal ions (*30*, *31*), including UO_2^{2+}. Figure 2A shows representative absorbance spectra of PAR obtained in the absence and presence of different concentrations of UO_2^{2+}. As the concentration of UO_2^{2+} increased, the absorbance peak of the metal-free PAR at 410 nm decreased concomitantly as a new absorbance peak at 520 nm increased. These UO_2^{2+}-dependent changes in the absorbance spectrum of PAR were exploited to determine the equilibrium dissociation constant for the binding of UO_2^{2+} to the colorimetric chelator. Differences in the spectra were quantified as follows: for the interval from 340 to 453 nm, the area under the spectrum obtained in the presence of UO_2^{2+} was subtracted from the area under the spectrum obtained in the absence of UO_2^{2+}; for the interval from 455 to 640 nm, the area under the spectrum obtained in the absence of UO_2^{2+} was subtracted from that obtained in the presence of UO_2^{2+}; the values of the resulting two quantities were then combined to create the values represented on the ordinate of Figure 2B.

Figure 2B shows the dependence of the spectral changes extracted from the primary data in Figure 2A on the concentration of total uranyl ion. The *dashed lines* represent the theoretical curve anticipated for a 1:1 stoichiometric binding event with infinite affinity. The actual data points clearly conform to a model where PAR binds a single uranyl ion with relatively high affinity. The value of the equilibrium dissociation constant for the binding of UO_2^{2+} to PAR, K_{PAR-U}, was obtained from a nonlinear regression fit of quadratic equation 1 where [P] and [U] are the concentrations of total PAR and UO_2^{2+}, respectively. Equation 1 corresponds to a 1:1 homogeneous binding model where the binding event causes a significant depletion in the concentrations of both of the free, uncomplexed reagents. The value of K_{PAR-U} that provided the best fit of eq 1 to the data in Figure 2B was $4.0 \pm 0.3 \times 10^{-7}$ M.

The next experiment was to study the binding of UO_2^{2+} to a noncolorimetric chelator by quantifying the effects that the colorless chelator had on the interaction of UO_2^{2+} with the colorimetric chelator, PAR. When different concentrations of DTPA (a colorless chelator) were equilibrated with a preformed complex of PAR−UO_2^{2+}, uranyl ions transferred from the PAR to the DTPA, thus regenerating the metal-free form of the colored chelator (primary data not shown). Figure 2C shows the dependence of the spectral changes taken from these 3-component competition experiments on the concentration of total DTPA. The value of the equilibrium dissociation constant for the binding of UO_2^{2+} to DTPA, K_{DTPA-U}, was obtained from a nonlinear regression fit of quadratic equation 2 where [D] is the concentration of total DTPA. Equation 2 differs from eq 1 only in that the concentration of total uranyl ion is divided by the factor $(1 + [D]/K_{DTPA-U})$, which represents the influence of UO_2^{2+} complexation with DTPA on the concentration of

$$\text{fraction of PAR occupied with } UO_2^{2+} = \frac{([P] + [U] + K_{PAR-U}) - \{([P] + [U] + K_{PAR-U})^2 - 4[P][U]\}^{1/2}}{2} \quad (1)$$

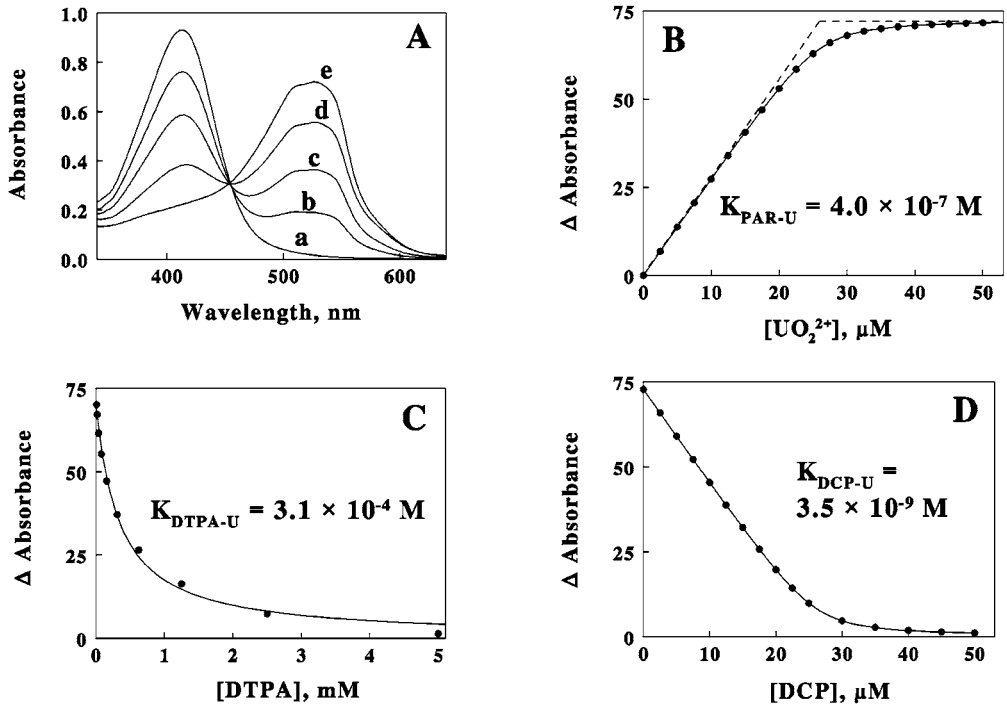


Figure 2. Determination of binding constants for uranyl ion to colorimetric and noncolorimetric chelators. A, visible absorbance spectra of 26 μM 4-(2-pyridazo)resorcinol (PAR) in the absence (a) and presence of 5.0 (b), 12.5 (c), 20 (d), and 50 (e) μM uranyl ion. B, dependence of the changes in the absorbance of 26 μM PAR as a function of the concentration of uranyl ion. The values of Δ absorbance were determined as the differences in the spectrum of the metal-free chelator versus the spectrum of the chelator observed in the presence of uranyl ions. C, dependence of the changes in the absorbance of the PAR−uranyl ion complex as a function of the concentration of DTPA. The concentrations of PAR and uranyl ion were 26 and 30 μM, respectively. The values of Δ absorbance were determined as the differences in the spectrum of the PAR−uranyl complex in the absence of DTPA versus the spectrum of the complex observed in the presence of DTPA. D, dependence of the changes in the absorbance of the PAR-uranyl ion complex as a function of the concentration of DCP. The conditions were the same as those described in C, except that DCP was substituted for DTPA. The parameters for the *curves* drawn through the data points in B, C, and D were determined by nonlinear regression analyses using eqs 1, 2, and 3, respectively, in the text.

Table 1. Equilibrium Dissociation Constants for Uranyl Ion with Selected Complexants

chelator[a]	equilibrium dissociation constant, M
PAR	$4.0 \pm 0.3 \times 10^{-7}$
DTPA	$3.1 \pm 0.2 \times 10^{-4}$
EDTA	$2.4 \pm 0.2 \times 10^{-4}$
CHXDTPA	$3.3 \pm 0.3 \times 10^{-4}$
DCP	$3.5 \pm 0.4 \times 10^{-9}$

[a] Abbreviations are as follows: PAR, 4-(2-pyridylazo)resorcinol; DTPA, diethylenetriaminepentaacetic acid; EDTA, ethylenediaminetetraacetic acid; CHXDTPA, *trans*-*N*-(2-aminoethyl)-1,2-diaminocyclohexane-*N*,*N*′,*N*″-pentaacetic acid; DCP, 2,9-dicarboxy-1,10-phenanthroline.

free UO_2^{2+} that is available to bind to the PAR. The value of K_{DTPA-U} that provided the best fit of eq 2 to the data in Figure 2C was $3.1 \pm 0.2 \times 10^{-4}$ M. Analogous competition experiments were conducted with two other colorless chelators, EDTA and CHXDTPA (primary data not shown). The values of the corresponding equilibrium dissociation constants for the binding of UO_2^{2+} to each of these chelators are summarized in Table 1. These competition experiments provided uranium complexation data consistent with the hypothesis that the low affinity of DTPA and CHXDTPA for UO_2^{2+} was the most probable origin of the failure to identify antibodies directed against the corresponding chelator−uranyl ion complexes.

Figure 2D shows the dependence of spectral changes taken from analogous competition experiments on the concentration of 2,9-dicarboxy-1,10-phenanthroline (DCP), an alternative colorless chelator examined as part of an effort to identify chelators that bound to UO_2^{2+} with higher affinities. Unlike DTPA, where millimolar concentrations of the colorless chelator were required to effectively compete with 26 μM PAR, concentrations of DCP stoichiometric with that of PAR were sufficient to remove UO_2^{2+} from its complex with the colored chelator. The value of the equilibrium dissociation constant for the binding of UO_2^{2+} to DCP, K_{DCP-U}, was obtained from a nonlinear regression fit of quadratic equation 3 where [DCP] is the concentration of total DCP. Equation 3 corresponds to a competition binding model where the

$$\text{fraction of PAR occupied with } UO_2^{2+} = \frac{([P] + [U]/(1+[D]/K_{DTPA-U}) + K_{PAR-U}) - \{([P] + [U]/(1+[D]/K_{DTPA-U}) + K_{PAR-U})^2 - 4[P][U]/(1+[D]/K_{DTPA-U})\}^{1/2}}{2} \quad (2)$$

$$\text{fraction of PAR occupied with } UO_2^{2+} = \frac{(2K_{DCP-U}[P] + K_{PAR-U}[DCP] - K_{PAR-U}[P]) - \{(2K_{DCP-U}[P] + K_{PAR-U}[DCP] - K_{PAR-U}[P])^2 - 4(K_{DCP-U} - K_{PAR-U})K_{DCP-U}[P]^2\}^{1/2}}{2 \times (K_{DCP-U} - K_{PAR-U})} \quad (3)$$

transfer of UO_2^{2+} from PAR to DCP causes significant changes in the concentrations of the metal-free forms of both chelators. Since the concentrations of both chelators were significantly higher than their respective dissociation constants for their binding with UO_2^{2+}, the concentration of free, uncomplexed UO_2^{2+} was assumed to be negligibly small. In addition, all of the PAR initially present in the absence of DCP was assumed to be coordinated with UO_2^{2+}. The value of K_{DCP-U} that provided the best fit of eq 3 to the data in Figure 2D was $3.5 \pm 0.4 \times 10^{-9}$ M. A summary of the equilibrium dissociation constants determined for these complexants at the pH and ionic strength dictated by the immunization protocol is provided in Table 1.

Hybridoma Production and Screening. Clearly, the DCP chelator was superior to EDTA, DTPA, or derivatives thereof in its ability to bind strongly to the UO_2^{2+} ion at the pH and ionic strength required by the immunization protocol. The UO_2^{2+}−DCP complex should therefore be better at eliciting a metal-specific immune response than the forms of chelated UO_2^{2+} previously employed as immunogens. However, this complex was not of sufficient size to generate an immune response, and the chelator needed to be covalently coupled to a carrier protein to be an effective immunogen. Bifunctional derivatives of DCP were not commercially available, and the synthesis of 5-isothiocyanato-1,10-phenanthroline-2,9-dicarboxylic acid from 2,9-dimethyl-1,10-phenanthroline was performed in four steps, as shown in Figure 1. The isothiocyanato derivative of DCP was subsequently coupled to a carrier protein and injected into mice. After a 4-week injection series, all the animals showed high serum titers of antibodies with the ability to bind immobilized UO_2^{2+}−DCP−BSA (data not shown). The animal with the highest titer was given an intraperitoneal boost of antigen, and its spleen was used 72 h later for the preparation of hybridoma cells.

A novel culture procedure that utilized semisolid media (see Experimental Procedures) resulted in the isolation of 1146 individual hybridoma colonies from a single fusion. The culture supernatants from these hybridomas were initially screened for their ability to bind to UO_2^{2+}−DCP−BSA immobilized in 96-well plates, and 486 clones (42.4%) secreted antibodies with reactivity toward uranium-loaded DCP−BSA (defined as an $absorbance_{450\ nm} > 0.3$ in indirect ELISA). When these 486 supernatants were rescreened by competitive ELISA (shown in Figure 3), 89.9% of the reactive supernatants (437/486) or 36.8% (437/1186) of the total hybridomas generated in these experiments were inhibited by soluble UO_2^{2+}−DCP. Of the remaining 49 clones, 2.3% (11/486) were more strongly inhibited by metal-free DCP, and 7.8% (38/486) could not be inhibited by either metal-free DCP or UO_2^{2+}−DCP and were assumed to be directed toward the thioureido group that linked the chelator to the carrier protein.

Three of these clones, 8A11, 10A3, and 12F6, were chosen for further experiments because they had desirable growth characteristics, showed the least reactivity to metal-free DCP, and/or produced supernatants with high specific titers at limiting dilutions (data not shown). These hybridomas were subcloned by limiting dilution to confirm homogeneity. All three hybridomas secreted antibodies of the IgG1 subtype with a κ light chain. Production of antibody for subsequent characterization was performed either by culture as an ascites in pristine-primed BALB/c mice or by in vitro culture in a specialized tissue culture apparatus, followed by purification on protein G. Monoclonal antibodies prepared by these two

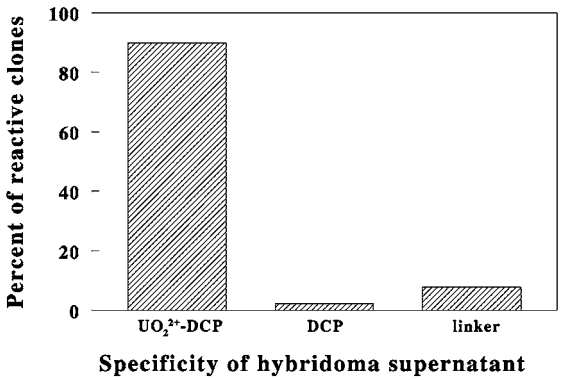


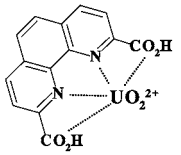
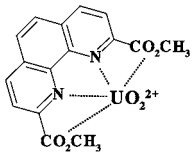
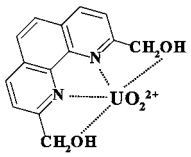
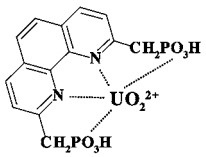
Figure 3. Specificity of antibodies synthesized by hybridomas. The 486 reactive hybridoma ($abs_{450nm} > 0.3$ when tested against immobilized BSA−DCP−UO_2^{2+}) were rescreened by competitive ELISA as described in Methods. Of the 486 supernatants examined in theses experiments, 437 (89.9%) of the hybridomas synthesized antibodies with a primary specificity for DCP−UO_2^{2+}, and 11 (2.2%) showed specificity for metal-free DCP. A small number (38, 7.8%) of the antibodies in hybridoma supernatants bound to immobilized BSA−DCP−UO_2^{2+} but not to immobilized BSA and could not be competitively inhibited by either DCP−UO_2^{2+} or DCP; these antibodies were assumed to be directed toward the linker region between the DCP and the carrier protein.

culture methods showed identical binding properties for metal-free DCP and UO_2^{2+}−DCP (data not shown).

Binding Specificity. The binding specificity of each of the three anti-uranium monoclonal antibodies was investigated by conducting equilibrium binding measurements on a KinExA 3000 immunoassay instrument. The KinExA is a flow fluorimeter designed to achieve the rapid separation and quantification of free, unbound antibody present in reaction mixtures of antibody, antigen, and antibody−antigen complexes; its operation has been described in detail elsewhere (*11*, *27*, *28*). The equilibrium binding data presented in Figure 4 demonstrate that each of the three anti-uranium antibodies bound to the DCP−UO_2^{2+} complex with much higher affinity than it bound to the metal-free DCP. The low affinity binding curves in each panel of Figure 4 were obtained with metal-free DCP, while the corresponding high affinity binding curves were obtained with different concentrations of DCP in the presence of a constant total concentration of UO_2^{2+} of 1.0 μM. Given the affinity of DCP for UO_2^{2+} as determined above, these solution conditions dictated that greater than 99.6% of the DCP was present as the 1:1 complex with UO_2^{2+}; control experiments indicated that 1.0 μM UO_2^{2+} alone did not inhibit the binding of any of the antibodies to the immobilized antigen. In all cases in Figure 4, the value of the equilibrium dissociation constant, K_d, for the binding of the antibody to the soluble ligand was obtained as previously described (*11*, *27*, *28*). Values for the dissociation constants thus obtained are given in Table 2. Antibody 12F6 had the highest affinities for both the metal-free DCP and the DCP−UO_2^{2+} complex; antibody 8A11 had the lowest affinities for the same ligands. Antibody 10A3 showed the highest level of discrimination between the metal-free DCP and the DCP−UO_2^{2+} complex; the difference in Gibbs free energy between the binding of DCP−UO_2^{2+} and metal-free DCP to 10A3 was −4.2 kcal/mol. However, the least discriminatory antibody, 8A11, still exhibited a corresponding difference in Gibbs free energy of −3.9 kcal/mol between its affinity for DCP−UO_2^{2+} versus that for the metal-free chelator.

Each of the three anti-uranium antibodies exhibited appreciable affinity for other chelators that bore a close

Table 2. Equilibrium Dissociation Constants for the Binding of Selected Phenanthroline Derivatives in the Presence and Absence of Uranyl Ion to Monoclonal Antibodies 12F6, 10A3, and 8A11

	Value of K_d, M		
Chelator complex	**12F6**	**10A3**	**8A11**
DCP-UO_2^{2+} 	$9.1 \pm 0.7 \times 10^{-10}$	$2.4 \pm 0.2 \times 10^{-9}$	$5.5 \pm 0.2 \times 10^{-9}$
DME-UO_2^{2+} 	$2.5 \pm 0.1 \times 10^{-9}$	$7.6 \pm 0.2 \times 10^{-9}$	$1.2 \pm 0.1 \times 10^{-8}$
DHM-UO_2^{2+} 	$7.5 \pm 0.4 \times 10^{-9}$	$3.3 \pm 0.1 \times 10^{-7}$	$8.6 \pm 0.3 \times 10^{-8}$
DPP-UO_2^{2+} 	$4.5 \pm 0.3 \times 10^{-6}$	$6.3 \pm 0.2 \times 10^{-6}$	$8.7 \pm 0.6 \times 10^{-6}$
DCP, metal free	$7.5 \pm 0.5 \times 10^{-7}$	$2.8 \pm 0.1 \times 10^{-6}$	$3.7 \pm 0.2 \times 10^{-6}$
DME, metal free	$8.7 \pm 0.6 \times 10^{-7}$	$3.4 \pm 0.3 \times 10^{-6}$	$4.4 \pm 0.2 \times 10^{-6}$
DHM, metal free	$1.9 \pm 0.2 \times 10^{-5}$	$5.1 \pm 0.4 \times 10^{-5}$	$6.7 \pm 0.3 \times 10^{-5}$

structural resemblance to DCP. Table 2 contains values of the equilibrium dissociation constants for the binding of each antibody to the dimethyl ester of DCP in the presence and absence of excess UO_2^{2+}. In general, esterification of the two carboxyl groups on DCP had only a small (<2- to 3-fold) negative influence on the measured affinity of each antibody, regardless of whether UO_2^{2+} was absent or present. Table 2 also contains values of the equilibrium dissociation constants of the binding of each antibody to a derivative of DCP where the two carboxyl groups were replaced with two hydroxymethyl groups. The affinities of 12F6 and 8A11 for the DHM−UO_2^{2+} complex were moderately lower than those for the corresponding DCP−UO_2^{2+} complex (8- and 16-fold, respectively), while the affinity of 10A3 for DHM−UO_2^{2+} was over 120-fold lower than that for DCP−UO_2^{2+}. All three antibodies bound to the metal-free DHM with significantly lower affinities than they did to the metal-free forms of DCP or DME. Finally, Table 2 contains values of the equilibrium dissociation constants for the binding of each antibody to a derivative of DCP where the two carboxyl groups were replaced with two methylphosphonate groups. This substitution lowered the affinity of each antibody for the DPP−UO_2^{2+} complex by roughly 3 orders of magnitude compared with those observed with the corresponding DCP complex. Binding of the metal-free form of DPP to each of the three antibodies was not detected. Similarly, none of the three antibodies showed detectable affinity for unsubstituted 1,10-phenanthroline, the 2,9-dimethyl derivative (neocuproine), or 2,9-ditrichloromethyl-substituted 1,10-phenanthroline, either in the absence or presence of excess UO_2^{2+} (data not shown). In general, all of the antibodies exhibited negligible affinity for other types of metal chelators such as EDTA, DTPA, and CHXEDTA, regardless of whether excess UO_2^{2+} was present or absent. The one exception to this generalization was 12F6, which bound to PAR in the absence and presence of UO_2^{2+} with equilibrium dissociation constants of 1.1×10^{-6} M and 8.7×10^{-7} M, respectively (primary data not shown). Binding of PAR or PAR−UO_2^{2+} to either 10A3 or 8A11 was not detected.

All three antibodies displayed a high degree of specificity for UO_2^{2+} in the DCP−metal ion complex. The data in Table 3 summarize the binding properties of each antibody to DCP−metal complexes that contained metal ions other than UO_2^{2+}. The limiting reagent in each assay was DCP, which was held at a fixed concentration of 2.0 μM; in all cases the concentration of the individual metal ion exceeded 2.0 μM. Thus each response in Table 3 represents a range over which the 2.0 μM DCP−metal complex appeared to inhibit the binding of the soluble

Table 3. Metal Ion Specificity of Monoclonal Antibodies 8A11, 10A3, and 12F6[a]

metal ion	12F6	10A3	8A11
Hg(II)	+	−	−
Ti(III)	−	−	+
Au(III)	−	+	+
Cu(II)	++	++	++
Al(III)	+	−	−
Mo(VI)	+	−	−

[a] Individual KinExA assays were conducted with each antibody amended with 1.0 μg/mL of each metal ion in the presence and absence of 2.0 μM DCP. A '−' response indicates that the assays in the presence and absence of DCP were within ± 5% of each other; a single '+" response indicates that the assays in the presence of DCP were inhibited from 5 to 15% of the assays in the absence of DCP; a double '++' response indicates that the assays in the presence of DCP were inhibited from 15 to 25% of assays in the absence of DCP. For the following metal-DCP complexes, the assays in the presence and absence of metal were within + 5% of each other for all three monoclonal antibodies: Ca(II), Mg(II), Mn(II), Cd(II), Pb(II), Sr(II), Fe(III), Co(II), In(III), Ag(I), Ni(II), Y(III), Pr(III), Er(III), and Zn(II).

antibody to the immobilized DCP−UO_2^{2+} complex in the KinExA instrument. Cupric ion was the only metal ion that weakly inhibited all three antibodies when it was presented in a complex with DCP. The apparent equilibrium dissociation constant for the binding of each antibody to the DCP−Cu(II) complex fell in the range of 6 to 11 μM, greater than 3 orders of magnitude lower affinity than the comparable binding to DCP−UO_2^{2+}. A similar calculation for those responses in Table 3 represented by a single positive sign indicates that those DCP−metal complexes bound to their respective antibodies with a range of calculated K_d values from 11 to 38 μM.

Interference from Bovine Serum Albumin. Preliminary studies to characterize the equilibrium binding properties of the three anti-uranium antibodies provided clear evidence that BSA interfered with the binding interaction between the antibody and the DCP−UO_2^{2+} complex. When different concentrations of BSA were added to antibody−antigen reaction mixtures to minimize the binding of dilute antibodies to surfaces, demonstrably different results were obtained for the binding of DCP or its UO_2^{2+} complex to the antibody. Examples of the effects of BSA on the binding of the DCP−UO_2^{2+} complex to antibodies 12F6 and 8A11 are shown in Figure 5A and B, respectively. Figure 5A shows the decrease in the fraction of occupied binding sites on 12F6 as a function of BSA concentration at a constant concentration of DCP−UO_2^{2+}, while Figure 5B shows the results of the same experiment using antibody 8A11. In both cases the data were consistent with the hypothesis that BSA could bind the DCP−UO_2^{2+} and compete with the antibody for the chelator−metal complex. The values of the apparent equilibrium inhibition constants for the competitive, BSA-dependent loss of DCP−UO_2^{2+} from the antibody−DCP−UO_2^{2+} complex, K_{app}, were obtained from nonlinear regression fits of the following empirical equation to the data in Figures 5A and 5B:

$$\varphi = \left(\frac{[\text{DCP}-\text{U}]}{[\text{DCP}-\text{U}] + K_{\text{DCP}-\text{U}}}\right)\left(1 - \frac{[\text{B}]}{[\text{B}] + K_{\text{app}}}\right) \quad (4)$$

where φ is the fraction of antibody binding sites that are occupied with the soluble antigen DCP−U, [B] and [DCP−U] are the total concentrations of BSA and the DCP−UO_2^{2+} complex, respectively, and $K_{\text{DCP}-\text{U}}$ is the equilibrium dissociation constant for the binding of the

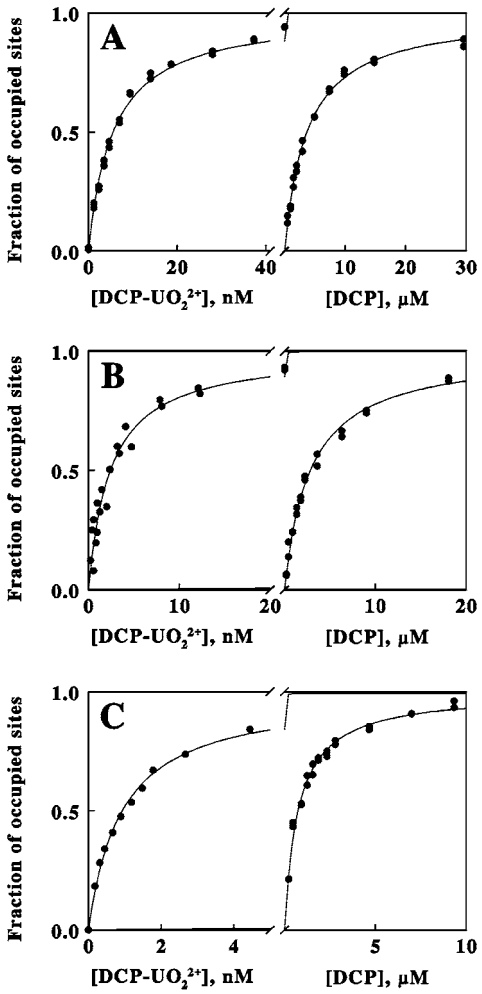


Figure 4. Equilibrium data for the binding of 2,9-dicarboxy-1,10-phenanthroline (DCP) in the presence and absence of uranyl ion to monoclonal antibodies 8A11 (A), 10A3(B), and 12F6 (C). The concentrations of occupied antibody binding sites, determined from kinetic exclusion assays as described in the text, were expressed as a fraction of the concentration of total antibody binding sites and plotted versus the concentration of the total soluble antigen in the mixture. The parameters for the *curves* drawn through the data points were determined by nonlinear regression analyses as described in refs 11, 27, 28.

DCP−UO_2^{2+} complex to the antibody. The values of K_{app} thus obtained are given in the figures.

It was evident that the value of K_{app} was a complex function of the concentration of the total DCP−UO_2^{2+} and the equilibrium dissociation constant of the individual antibody. Using simple one-site homogeneous binding models for the interactions of DCP−UO_2^{2+} with both the antibody and with BSA, the following equation was obtained:

$$[\text{B}]\,\varphi = K_{\text{BSA}-\text{DCP}-\text{U}}\left(1 + \frac{[\text{DCP}-\text{U}]}{K_{\text{DCP}-\text{U}}}\right)(1 - \varphi) - 1 \quad (5)$$

where $K_{\text{BSA}-\text{DCP}-\text{U}}$ is the equilibrium dissociation constant for the binding of the DCP−UO_2^{2+} complex with BSA. The additional assumptions employed in obtaining eq 5 were that (i) the concentration of the antibody−DCP−UO_2^{2+} complex was much less the total concentration of DCP−UO_2^{2+} and (ii) the total concentration of the BSA−DCP−UO_2^{2+} complex was much less than that of the total BSA. Both assumptions were valid under the conditions of the experiments presented in Figures 5A and 5B (see

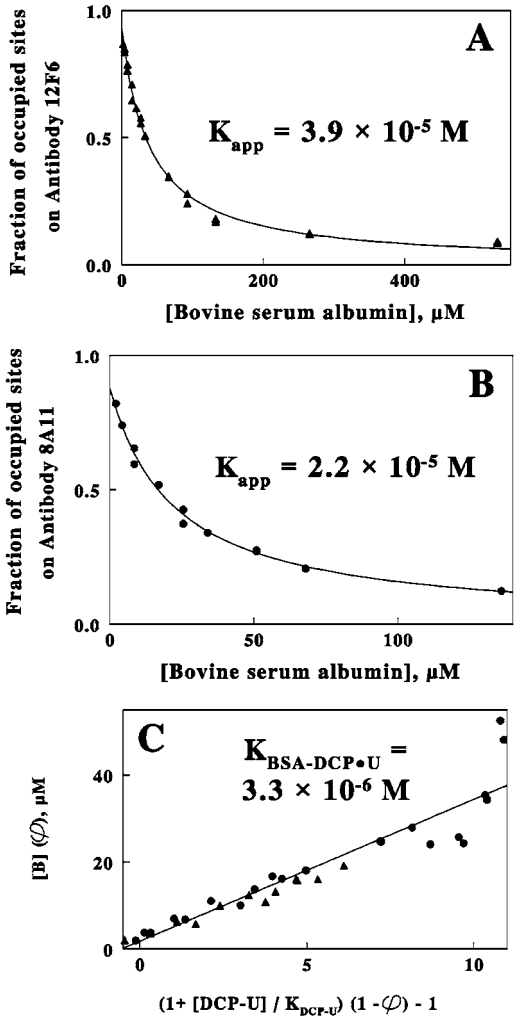


Figure 5. Equilibrium data for the binding of the DCP−uranyl ion complex to BSA. A and B, the fraction of binding sites occupied with the DCP−UO_2^{2+} complex on antibodies 12F6 and 8A11, respectively, as a function of the concentration of BSA. The concentration of DCP−UO_2^{2+} was 11 and 40 nM in A and B, respectively. The parameters for the *curves* drawn through the data points in both panels were determined by nonlinear regression analyses using eq 4 in the text. *C*, a linear plot, according to eq 5 in the text, of the data replotted from *A* and *B*. The *closed circles* and *triangles* represent binding data obtained with antibodies 8A11 and 12F6, respectively. The values of [B], [DCP−U], K_{DCP-U}, and φ were taken from the data in the respective figures. The line drawn through the data points was determined by a linear regression analysis; the value of the slope yielded the value of the equilibrium dissociation constant for the BSA−DCP−UO_2^{2+} complex.

legend to Figure 5). Figure 5C shows a linear plot according to eq 5 of the combined data taken from Figures 5A and 5B. Even though the two sets of data were obtained with different antibodies and a different set concentration of total DCP−UO_2^{2+}, the replotted data in Figure 5*C* appeared to describe a straight line that passed through the origin of the graph. A value of 3.3 × 10^{-6} M was obtained for the equilibrium dissociation constant for the binding of DCP−UO_2^{2+} to BSA from a linear regression fit of eq 6 to the data in Figure 5C. Analogous experiments and analyses were conducted with antibodies 8A11, 12F6, and metal-free DCP (data not shown). The equilibrium dissociation constant for the binding of metal-free DCP to BSA was determined to be 2.9 × 10^{-6} M.

Kinetic Rate Constants. The object of these experiments was to determine values for the kinetic rate

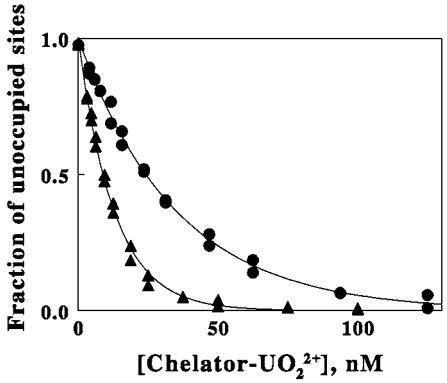


Figure 6. Determination of association rate constants for the bimolecular combination of DCP−UO_2^{2+} (circles) and DME−UO_2^{2+} (triangles) with the 10A3 monoclonal antibody. Antibody (1.5 nM in binding sites) and the chelated uranium complex were incubated for 7 s before separation of the antibody into occupied and unoccupied fractions. The value of the bimolecular association rate constant for each reaction was obtained from a nonlinear regression fit of the data in each curve to the single-exponential function of ligand concentration given by eq 6 in the text. Each determination was performed in duplicate; in some cases the error in the data was less than the diameter of the plotted points.

constants for the binding of those chelator−uranyl ion complexes (DCP−UO_2^{2+} and DME−UO_2^{2+}) that exhibited the greatest affinity for each of the three anti-uranium antibodies. Accordingly, kinetic exclusion assays were conducted to separate and quantify the unoccupied antibody binding sites that remained in reaction mixtures that were far from equilibrium, as has been previously described (*11*, *27*, *28*). Figure 6 shows the dependence of the fraction of unoccupied binding sites that remained on antibody 10A3 at 7 s after mixing on the concentration of either DCP−UO_2^{2+} or DME−UO_2^{2+}. The value of the association rate constant, k_1, for the bimolecular binding of 10A3 with each chelated uranium complex was obtained from a nonlinear regression fit of the kinetic data to the following single-exponential function of ligand concentration:

$$[A] = [A]_0 e^{-k_1[L]t} \quad (6)$$

where [A] is the concentration of unoccupied antibody binding sites at ligand concentration [L], $[A]_0$ is the total concentration of antibody binding sites when no ligand is present, and t is 7 s. Equation 6 represents the time- and ligand concentration-dependent progress of a binding reaction conducted under pseudo first-order conditions where the value of the unimolecular rate constant, k_2, for the dissociation of the antibody−antigen complex is negligible compared with the value of the k_1[L] multiplicand. Values for k_1 of 1.1 × 10^7 M^{-1} s^{-1} and 4.1 × 10^6 M^{-1} s^{-1} were obtained from the data in Figure 6 for the bimolecular association rate constants for the binding of DCP−UO_2^{2+} and DME−UO_2^{2+}, respectively, with antibody 10A3. Analogous kinetic experiments were conducted with antibodies 8A11 and 12F6, and the values of all of the bimolecular association rate constants thus obtained are summarized in Table 4. Table 4 also contains the values of the corresponding unimolecular dissociation rate constants for each reversible binding reaction calculated from the identity $K_d = k_2/k_1$.

A comparison of the kinetic and equilibrium binding data in Tables 2 and 4, respectively, indicated that the differences in equilibrium affinity between the binding of DCP−UO_2^{2+} and DME−UO_2^{2+} to either 8A11 or 10A3

Table 4. Individual Kinetic Rate Constants for the Binding of Chelated Uranyl Ion to Monoclonal Antibodies 8A11, 10A3, and 12F6

antibody	chelator−uranium complex	bimolecular association rate constant, $M^{-1}\ s^{-1}$	unimolecular dissociation rate constant, s^{-1}
8A11	DCP−UO_2^{2+}	$1.9 \pm 0.1 \times 10^7$	$1.0 \pm 0.1 \times 10^{-1}$
8A11	DME−UO_2^{2+}	$6.8 \pm 0.2 \times 10^6$	$8.2 \pm 0.1 \times 10^{-2}$
10A3	DCP−UO_2^{2+}	$1.1 \pm 0.1 \times 10^7$	$2.6 \pm 0.2 \times 10^{-2}$
10A3	DME−UO_2^{2+}	$4.1 \pm 0.1 \times 10^6$	$3.1 \pm 0.2 \times 10^{-2}$
12F6	DCP−UO_2^{2+}	$2.0 \pm 0.1 \times 10^7$	$1.8 \pm 0.2 \times 10^{-2}$
12F6	DME−UO_2^{2+}	$3.0 \pm 0.2 \times 10^7$	$7.5 \pm 0.4 \times 10^{-2}$

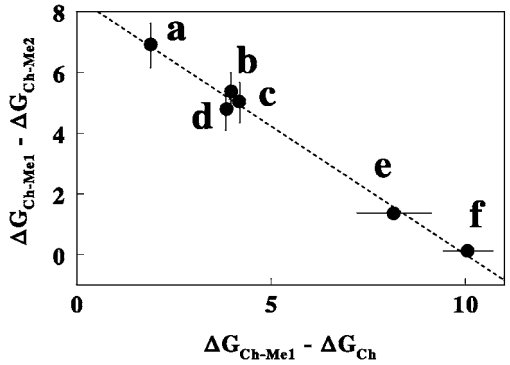


Figure 7. Relationship between metal ion specificity and the relative affinity for metal-free chelator exhibited by six anti-metal monoclonal antibodies. Free energies of binding to antibody: ΔG_{Ch}, chelator in the absence of metal ions; ΔG_{Ch-Me1}, complex of chelator and the metal ion that was used to select the corresponding clone; ΔG_{Ch-Me2}, complex of chelator and the alternative metal ion that elicited the next highest affinity in comparison with the primary metal ion in its interaction with the antibody. Antibody and primary chelator−metal specificity: a, 2C12 and CHXDTPA-Pb(II); b, 12F6 and DCP−U(VI); c, 10A3 and DCP−U(VI); d, 8A11 and DCP−U(VI); e, 15B4 and DTPA-Zn(II); and f, 2A81G5 and EDTA-Cd(II). The *solid lines* represent conservative error estimates; the *dashed line* was generated from a linear regression analysis.

were primarily due to differences in the respective bimolecular association rate constants to form the complex, while the difference observed in the affinity of the two ligands binding to 12F6 was due primarily to a difference in the unimolecular rate constant for the dissociation of the complex. The former observations obtained with 10A3 and 8A11 are inconsistent with the generalization that the value of the equilibrium dissociation constant for an antibody is primarily dependent on the value of the rate constant for the unimolecular dissociation of the antibody−antigen complex; that is, that the bimolecular association of free antibody and antigen to form a complex is close to diffusion controlled and that the corresponding bimolecular rate constant does not vary much from antigen to antigen for the same antibody.

DISCUSSION

With the addition of the three anti-uranium antibodies described herein, our laboratories have now conducted detailed equilibrium binding studies on the affinity and specificity of eight different anti-metal monoclonal antibodies (*11*−*16*). The principal metal ions recognized by these antibodies include Pb(II), U(VI), Zn(II), and Cd(II), while the corresponding chelators are comprised of CHXDTPA, DCP, DTPA, and EDTA, respectively. Despite the diversity in the molecular and ionic properties of these individual chelators and metal ions, the structure−function activity relationship presented in Figure 7 was constructed from the binding data obtained with six of these antibodies. The *abscissa* in Figure 7 represents the difference in free energy between the binding of the antibody to the chelator−metal ion complex that was used to elicit the corresponding clone and the binding of the antibody to the metal-free chelator. A large numerical value on the abscissa signifies that the affinity of the antibody for the metal-free chelator was many orders of magnitude less than that observed for the corresponding complex of chelator and principal metal ion. A small numerical value signifies that the affinity of the antibody for the metal-free chelator was much closer to that observed for the corresponding complex of chelator and principal metal ion. The *ordinate* in Figure 7 represents the difference in free energy between the binding of the antibody to the chelated metal ion that was used to elicit the clone and the binding to the chelated metal ion that exhibited the next highest affinity compared to that of the principal metal ion in its interaction with the antibody. Thus a large numerical value on the ordinate signifies a high degree of metal ion specificity, while a small value signifies a low degree of metal ion specificity. It is evident from the linear relationship in Figure 7 that those antibodies that exhibited the greatest specificities for particular metal ions also exhibited the least differences in their affinities for metal-loaded versus metal-free chelator and vice versa.

For those antibodies that show a relatively high affinity for the metal-free chelator (such as 2C12 binding to CHXEDTA, datum *a* in Figure 7), one hypothesis is that the majority of the amino acid residues that comprise the antigen binding site are devoted to complementing the structure of the chelator itself, regardless of whether a metal ion is coordinated by the chelator. Since the majority of the free energy for binding the chelator−metal complex appears to be dependent on the identity of the chelator and not on the presence of the metal ion, one might reasonably expect such an antibody to show a relatively lower degree of specificity for the metal ion in question. This is certainly not the case with 2C12 and the three anti-uranium antibodies described herein. One means whereby an antibody could provide a high degree of specificity for a particular metal ion could be direct ligation of the metal ion using appropriately positioned amino acid side chains in the antigen binding site. Previous investigations have clearly indicated a role for histidine residues in the binding of aminobenzyl-EDTA−In(III) and EDTA−Cd(II) to their respective monoclonal antibodies (*17*, *19*). In the former case, substitution of a histidine residue at the antigen binding site with leucine dramatically weakened the binding of chelated Cd(II) to the antibody. In the latter case, X-ray crystallographic studies revealed that a histidine residue served as the sixth coordination ligand for chelated In(III), but was prohibited on steric grounds from similarly coordinating with chelated Fe(III). Perhaps there are similar direct ligation reactions that occur at the antigen binding sites of antibodies 8A11, 10A3, and 12F6.

For those antibodies that show a relatively low affinity for the metal-free chelator (such as 2A81G5 binding to

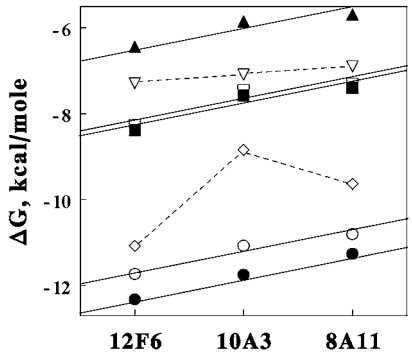


Figure 8. Evidence that the antigen binding sites of antibodies 12F6, 10A3, and 8A11 share common features for the binding of selected ligands. The free energy of dissociation was plotted for all combinations of antibodies and soluble ligands studied herein. Each anti-uranium antibody was assigned an arbitrary position on the abscissa to facilitate a comparison of the curves. Ligands: DCP−UO_2^{2+}, *closed circles*; DME−UO_2^{2+}, *open circles*; DHM-UO_2^{2+}, *open diamonds*; metal-free DCP, *solid squares*; metal-free DME, *open squares*; DPP−UO_2^{2+}, *open triangles*; and metal-free DHM, *open triangles*. The five *solid lines* have identical slopes that represent the average value of the five slopes that were determined individually for each respective ligand. The two *dashed lines* simply connect the data points that were obtained with the other two ligands.

EDTA, datum *f* in Figure 7), one hypothesis is that the majority of the amino acid residues that comprise the antigen binding site are devoted to complementing the complex of the chelator with the metal ion, not the chelator itself. Previous modeling studies have revealed that the only discernible differences among individual EDTA−metal complexes are the subtle ways in which the arms of the chelator encircle the metal ion (*15*). Given that the distance differences between any two analogous atoms in the structures of the antigens are less than 0.6 Å, it is extraordinary that an antibody can actually distinguish among individual complexes of EDTA and different metal ions. It is likely that the metal ion specificity that is achieved by antibodies such as 2A81G5 is due to the sum of many small, additive effects that are achieved by an antigen binding site that must encompass and complement the overall structure of the chelator−metal ion complex.

A second interesting linear free energy relationship was obtained from the equilibrium dissociation data presented in Table 2. The corresponding free energy for dissociation was calculated for each equilibrium dissociation constant in Table 2. These 21 free energy values were then plotted in three vertical columns corresponding to the three anti-uranium antibodies, as illustrated in Figure 8. Each vertical column was placed at an arbitrary position on the abscissa to facilitate the comparison of the data. The relative affinities of the three antibodies for DCP, DCP−UO_2^{2+}, DME, DME−UO_2^{2+}, and DHM−UO_2^{2+} appeared to follow the same pattern of reactivity. That is, antibody 12F6 appeared to bind each of these five antigens with 0.69 ± 0.12 and 0.94 ± 0.11 kcal/mol greater free energies than did antibodies 10A3 and 8A11, respectively. This pattern of behavior is represented in Figure 8 using five parallel solid lines to link the corresponding 15 values of the free energies. It is tempting to hypothesize that each of these five antigens presents approximately the same general conformation in solution, a conformation that is complemented by the antigen binding sites of antibodies 12F6, 10A3, and 8A11 in the same relative manner regardless of the identity of the antigen. In contrast, the values of the free energies for the dissociation of DHM and DPP−UO_2^{2+} from the three antibodies did not follow the same pattern as that observed for each of the other five antigens. Perhaps DHM and DPP−UO_2^{2+} assume general conformations in solution that are different from that hypothesized for the other five antigens, and the antigen binding sites of the three antibodies complement these different antigen conformations in ways that are unique to each antibody. It would be of interest to obtain molecular models of these chelators both in their metal-free forms and chelated with UO_2^{2+} to test these hypotheses regarding the solution conformations of the antigens.

In terms of the eventual application of any of these anti-uranium antibodies to create one or more accurate, sensitive immunoassays for soluble UO_2^{2+}, it is evident that the affinity, metal-ion specificity, and rate of complex formation exhibited by each antibody under the solution conditions of the assay are all crucial parameters in determining the performance characteristics of the assay, regardless of the assay format. Probably the most productive approach for future assay development activities is that each antibody must be analyzed on the assumption that it will exhibit at least some unique feature in its kinetic or equilibrium behavior. Detailed comparisons among the anti-uranium antibodies that appear to express different equilibrium and kinetic behavior may provide the opportunity to deduce the advantages and disadvantages of each for individual assay formats or platforms.

Elemental Analyses. Elemental analyses were performed by Atlantic Microlab, Inc., Norcross, Ga. Elemental analysis for the dialdehyde was as follows: $C_{14}H_7N_3O_4$; C calcd 59.79, found 59.58; H calcd 2.51, found 2.66; N calcd 14.94 found 14.67. Elemental analysis for the diacid (calculated as the hemihydrate) was as follows: $C_{14}H_7N_3O_6 \cdot {}^1/_2H_2O$; C calcd 52.18, found 52.42; H calcd 2.50, found 2.46; N calcd 13.04, found 13.09. Both were within the 0.3% limit.

ACKNOWLEDGMENT

This research was supported by Grant Nos. DE-FG02-98ER62704 and DE-FG02-02ER63459 (D.A.B.) from the Office of Science (BER), U.S. Department of Energy, by Grant No. 82799(3CEN) from the U.S. Department of Energy EMSP (D.A.B.), and by DE-FC02-02-EW15254 (R.C.B.) from the United States Department of Energy.

LITERATURE CITED

(1) Gongalsky, K. B. (2003) Impact of pollution caused by uranium production on soil macrofauna. *Environ. Monit. Assess. 89*, 197−219.

(2) Noubactep, C., Meinrath, G., Deitrich, P., and Merkel, B. (2003) Mitigating uranium in groundwater: prospects and limitations. *Environ. Sci. Technol. 37*, 4304−4308.

(3) Vandenhove, H. (2002) European sites contaminated by residues from the ore-extracting and -processing industries. *Int. Congr. Ser.* (High Levels of Natural Radiation and Radon Areas) *1225*, 307−315.

(4) DOE (1995) Estimating the Cold War Mortgage: The 1995 Baseline Environmental Management Report (2 vol.). DOE/EM-0230.

(5) Agency for Toxic Substances and Disease Registry, ATSDR Public Health Statement: Uranium, Atlanta: ATSDR, December 1990.

(6) Dygert, H. P. (1949) *Pharmacology and Toxicology of Uranium Compounds*, McGraw-Hill, New York.

(7) Ortega, A., Domingo, J. L., Llobet, J. M., Tomas, J. M., and Paternain, J. L. (1989) Evaluation of the oral toxicity of uranium in a 4-week drinking-water study in rats. *Bull. Environ. Contam. Toxicol. 42*, 935−941.

(8) Dang, H. S., Pullat, V. R., and Sharma, R. C. (1995) Distribution of uranium in human organs of an urban Indian population and its relationship with clearance half-lives**.** *Health Phys. 68*, 328−31.
(9) Kurttio, P., Auvinen. A., Salonen. L., Saha, H., Pekkanen, J., Makelainen, I., Vaisanen, S. B., Penttila, I. M., and Komulainen. H. (2002) Renal effects of uranium in drinking water. *Environ. Health Perspect. 110*, 337−342.
(10) Environmental Protection Agency (2000) National Primary Drinking Water Regulations; Radionuclides: Final Rule. *Fed. Reg.* Vol. 65, No. 236, pp 76707−70814, EPA, Washington, D.C.
(11) Blake, D. A., Chakrabarti, P., Khosraviani, M., Hatcher, F. M., Westhoff, C. M., Goebel, P., Wylie, D. E., and Blake, R. C., II. (1996) Metal binding properties of a monoclonal antibody directed towards metal-chelate complexes. *J. Biol. Chem. 271*, 27677−27685.
(12) Blake, D. A., Blake, R. C., II, Khosraviani, M., and Pavlov, A. R. (1998) Metal ion immunoassays. *Anal. Chim. Acta 376*, 13−19.
(13) Blake, D. A., Pavlov, A. R., Yu, H., Khosraviani, M., Ensley, H. E., and Blake, R. C., II. (2001) Antibodies and antibody-based assays for hexavalent uranium. *Anal. Chim. Acta 444*, 3−11.
(14) Blake, R. C., II., Delehanty, J. B., Khosraviani, M., Yu, H., Jones, R. M., and Blake, D. A. (2003) Allosteric binding properties of a monoclonal antibody and its Fab fragment. *Biochemistry 42*, 497−508.
(15) Jones, R. M., Yu, H., Delehanty, J. B., and Blake, D. A. (2002) Monoclonal antibodies that recognize minimal differences in the 3-dimensional structures of metal−chelate complexes. *Bioconjugate Chem. 13*, 408−415.
(16) Khosraviani, M., Blake, R. C., II., Pavlov, A. R., Lorbach, S. C., Yu, H., Delehanty, J. B., Brechbiel, M. W., and Blake, D. A. (2000) Binding properties of a monoclonal antibody directed toward lead−chelate complexes. *Bioconjugate Chem. 11*, 267−277.
(17) Delehanty, J. B., Jones, R. M., Bishop, T. C., and Blake, D. A. (2003) Identification of important residues in metal−chelate recognition by monoclonal antibodies. *Biochemistry 42*, 14173−17183.
(18) Reardan, D. T., Meares, C. F., Goodwin, D. A., McTigue, M., David, G. S., Stone, M. R., Leung, J. P., Bartholomew, R. M., and Frincke, J. M. (1985) Antibodies against metal chelates. *Nature 316*, 265−268.
(19) Love, R. A., Villafranca, J. E., Aust, R. M., Nakamura, K. K., Jue, R. A., Major, J. G., Jr., Radhakrishnan, R., and Butler, W. F. (1993) How the anti-(metal chelate) antibody CHA255 is specific for the metal ion of its antigen: X-ray structures for two Fab'/hapten complexes with different metals in the chelate. *Biochemistry 32*, 10950−10959.
(20) Boden, V., Colin, C., Barbet, J., Le Doussal, J. M., and Vijayalakshmi, M. (1995) Preliminary study of the metal binding site of an anti-DTPA-indium antibody by equilibrium binding immunoassays and immobilized metal ion affinity chromatography. *Bioconjugate Chem. 6*, 373−379.
(21) Feng, X., Pak, R. H., Kroger, L. A., Moran, J. K., DeNardo, D. G., Meares, C. F., DeNardo, G. L., and DeNardo, S. J. (1998) New anti-Cu-TETA and anti-Y-DOTA monoclonal antibodies for potential use in the pre-targeted delivery of radiopharmaceuticals to tumors. *Hybridoma 17*, 125−132.
(22) Westhoff, C. M., Lopez, O., Goebel, P., Carlson, L., Carlson, R. R., Wagner, F. W., Schuster, S. M., and Wylie, D. E. (1999) Unusual amino acid usage in the variable regions of mercury-binding antibodies. *Proteins 37*, 429−440.
(23) DeNardo, S. J., DeNardo, G. L., Brush, J., and Carter, P. (1999) Phage library-derived human anti-TETA and anti-DOTA ScFv for pretargeting RIT. *Hybridoma 18*, 13−21.
(24) Chandler, C. J., Deadly, L. W., and Reiss, J. A. (1981) Macrocyclic polyether and polythioeter diesters and dithioesters from 1, 10-phenanthroline-2,9-dicarboxylic acid. *J. Heterocycl. Chem. 18*, 599−601.
(25) Habeeb, A. F. (1966) Determination of free amino groups in proteins by trinitrobenzenesulfonic acid. *Anal. Biochem. 14*, 328−336.
(26) Hames, B. D. (1981) An introduction to polyacrylamide gel electrophoresis, in *Gel Electrophoresis of Proteins: A Practical Approach* (Hames, B. D., and Rickwood, D., Eds.) pp 1−92, IRL Press, Washington, D.C.
(27) Blake, R. C., II., Pavlov, A. R., and Blake, D. A. (1999) Automated kinetic exclusion assays to quantify protein binding interactions in homogeneous solution. *Anal. Biochem. 272*, 123−134.
(28) Blake, R. C., II., and Blake, D. A. (2003) Kinetic exclusion assay to study high-affinity binding interactions in homogeneous solutions, in *Methods in Molecular Biology, Vol. 248: Antibody Engineering: Methods and Protocols*, (Lo, B. K. C., Ed.) pp 417−430, Humana Press, Totowa, NJ.
(29) Pavlov, A. R., Khosraviani, M., Chaiban, J. E., and Blake, D. A. (1997) Strategies and problems in the isolation of metal-specific monoclonal antibodies, in *Antibody Engineering II: New Technology, Application and Commercialization*. Vol II, pp 5.1.1−5.1.20, IBC USA Publishing, Southborough, MA.
(30) Florence, T. M., and Farrar, Y. (1963) Spectrophotometric determination of uranium with 4-(2-pyridylazo)resorcinol. *Anal. Chem. 35*, 1613−16.
(31) Gao, H.-W. (1995) Determination of a metal chelate's characteristic parameters by dual-wavelength beta-correction spectroscopy. *Anal. Proc. 32*, 479−480.

BC049889P

A Conjugate of a Tumor-Targeting Ligand and a T Cell Costimulatory Antibody To Treat Brain Tumors

Ute Gawlick,[†] David M. Kranz,[‡] Victor D. Schepkin,[§] and Edward J. Roy*[,†]

Neuroscience Program and Department of Biochemistry, University of Illinois, Urbana, Illinois 61801, and Center for Molecular Imaging, University of Michigan, Ann Arbor, Michigan 48109. Received April 9, 2004; Revised Manuscript Received July 22, 2004

T cell immunotherapy is a potential strategy for the treatment of brain tumors because it offers a high degree of specificity, the ability to extravasate into solid tumors, and the potential for eliciting a long-term protective immune response. Various approaches have been developed to overcome T cell immune tolerance to cancer, including the use of cytokines and bispecific antibodies. T cell stimulation with the proinflammatory cytokine IL-12 can elicit antitumor immunity. T cell activation can be increased using bispecific antibodies against activating molecules on the surface of T cells and a tumor antigen. We studied the effects of systemic IL-12 administration in combination with a conjugate of an anti-CD28 antibody and a ligand for the folate receptor. The high affinity folate receptor is expressed on endogenously arising choroid plexus tumors of SV11 mice, which are transgenic for large T antigen under the control of the SV40 promoter. SV11 mice are immunocompetent, yet immunologically tolerant to large T antigen expressed by choroid plexus tumors. MRI analysis showed that the administration of IL-12 and anti-CD28 Fab/folate significantly slowed tumor growth. Proliferating $CD8^+$ T cells were found in choroid plexus tumors of treated animals. Treatment of animals with IL-12 + anti-CD28 Fab/folate prolonged survival compared to IL-12 alone. Cytokine treatment combined with tumor-targeted costimulation may be a useful adjunct treatment.

INTRODUCTION

One goal of immunotherapy against cancer is to induce a response that will lead to cytotoxic T lymphocytes (CTLs) with specificity for the tumor. A major obstacle in the activation of antitumor T cells is the process involving self-tolerance to tumor epitopes, a consequence of several processes, including clonal deletion of higher affinity self-reactive T cells during thymic development and exposure to antigens in a noninflammatory context. T cell activation and proliferation usually requires at least two signals: one in the form of the interaction of the peptide/major histocompatibility complex (pepMHC) on the antigen-presenting cell with the T cell antigen receptor (TCR) on the T cell, the other the engagement of the costimulatory receptor CD28 on the T cell with its ligand B7 (*1*, *2*). Increasing evidence suggests that the dependence of CTL activation on CD28 costimulation is related to surface levels of the pepMHC antigen, affinity of the TCR:pepMHC interaction, and duration of the cell to cell interaction (*3*−*5*). Immunogenic tumors may elicit a T cell response to a viral peptide presented by class I MHC or to an antigen expressed at higher levels that are sufficient to overcome self-tolerance (*6*). In some cases, where there is a higher affinity TCR (e.g. with K_D values below 1 μM), tumors can be eradicated in the apparent absence of ligation of CD28 (*7*). In other cases, nonimmunogenic tumors can stimulate a CTL response when they are transfected with B7, the ligand for CD28 (*8*). Hence, strengthening the CD28 signal would be expected to increase activation of CTLs, particularly those with lower affinity TCRs. The approach described here is to strengthen the activating signals received by T cells by targeting a costimulatory receptor with an antibody conjugated to a tumor-selective ligand.

In addition to CD28 costimulation, IL-12 has emerged as a third signal for CTL activation and a potent cancer therapeutic (*9*). IL-12 is a proinflammatory cytokine that can reverse antigen specific tolerance by affecting signaling through B7 expressed by antigen presenting cells (*10*). Exogenous IL-12 has been demonstrated to be effective in mice for the elimination of P815 tumors in DBA/2 mice (*11*). Furthermore, the coadministration of soluble IL-12 with peptide pulsed dendritic cells induced peptide specific CTLs and protection in mice challenged with P815 tumor cells (*12*). Tumor cell lines that are otherwise nonimmunogenic were rejected when transfected with the IL-12 gene (*13*).

To combine the effects of IL-12 and stimulation through CD28 in the generation of an antitumor CTL response, the costimulatory signals should be linked to the recognition of tumor antigens by the TCR. The high affinity folate receptor (FR) (K_D = 1 nM) has been used as a target because it is expressed at high levels on several types of cancer. Although the low affinity folate binding protein (K_D = 1−100 μM) is widely expressed on normal tissues, the high-affinity folate receptor is more selectively expressed on normal tissues and tumors. FR is expressed on over 90% of ovarian carcinomas, choroid plexus tumors, and ependymomas (*14*, *15*). In the present studies, folate was conjugated to an anti-CD28 antibody in order to link signaling through CD28 to the engagement of tumor cells. In this approach, activaton of the T cell would require recognition by the TCR of pepMHC antigens expressed by the same tumor cell.

* Address correspondence to: Edward J. Roy, Department of Biochemistry, University of Illinois, 600 S. Mathews Ave., Urbana, IL 61801. e-roy@uiuc.edu. Phone: 217-333-3375. Fax: 217-244-5858.

[†] Neuroscience Program, University of Illinois.

[‡] Department of Biochemistry, University of Illinois.

[§] University of Michigan.

10.1021/bc049911e CCC: $27.50 © 2004 American Chemical Society
Published on Web 08/19/2004

FR is expressed on human choroid plexus tumors and ependymomas, and it is expressed in murine tumors of a similar origin. SV11 mice are transgenic for large T antigen (Tag) of simian virus 40 (SV40) on a C57BL/6 background (*16*−*18*). With the large T antigen (Tag) gene under the SV40 promoter, these mice develop endogenous choroid plexus tumors, with some level of Tag expression in the thymus. Tag of SV40 is processed into several specific peptides that are presented by class I MHC and these pepMHC antigens can activate CTLs (*19*). In the mouse, Tag has been shown to contain four peptide epitopes that serve as targets for CTLs that interact with the $H2^b$ MHCs that are found in C57BL/6 mice and SV11 mice (*20*). Epitope V is immunorecessive while epitopes I, II/III, and IV are immunodominant. Tolerance to Tag epitopes in SV11 mice has been demonstrated by the failure of CTL to develop after immunization with Tag transformed cells or Tag expressed by a recombinant vaccinia virus (rVV) (*21*). In SV11 mice receiving adoptively transferred C57BL/6 splenocytes, epitope IV specific CTLs are implicated as the chief mediators of immunity against Tag-expressing choroid plexus tumors (*21*). SV11 mice are tolerant to Tag epitopes, either due to deletion of T cells in the thymus or a mechanism of peripheral tolerance following high levels of expression of Tag in tumors (*22*). Nevertheless, a population of low avidity T cells specific for epitope V of the T antigen does exist in SV11 mice and can be expanded ex vivo by stimulating splenocytes with cells that express large T antigen (*23*).

In an attempt to stimulate a T cell response against endogenous choroid plexus tumors in SV11 mice, we treated mice with a combination therapy of systemic IL-12 and anti-CD28/Folate bispecific conjugate. We found that anti-CD28 Fab/Folate treatment synergizes with systemic IL-12 to increase survival of choroid plexus tumor bearing animals. MRI analysis revealed that the treatment strongly inhibited tumor growth over a 21 day period. Flow cytometry and immunohistochemistry of the tumor revealed activated T cells consistent with a role of CTLs in the therapeutic immune response.

MATERIALS AND METHODS

Mice. SV11 heterozygous mice transgenic for SV40 large T antigen (obtained from Dr. T. A. Van Dyke, University of North Carolina, Chapel Hill, NC) were mated with C57BL/6 females (obtained from Jackson Laboratory, Bar Harbor, ME). Genotyping was done as previously described using PCR for large T antigen gene (*24*). Seven days prior to experiments, animals were placed on folate free chow in order to reduce competition of endogenous folate with the anti-CD28 Fab/Folate. RAG/TCR mice are RAG-1 knockout mice transgenic for 2C T cell (*7*). Animals were housed in animal facilities at the University of Illinois, and all studies were approved by the Institutional Animal Care and Use Committee.

Reagents and Cells. PV-1 hybridoma was obtained from Dr. Jeff Bluestone (University of California, San Francisco). Recombinant murine IL-12 was obtained from Dr. Stan Wolf (Genetics Institute, Cambridge, MA). *N*-α-Pteroyl-*N*-ε-(4′-fluoresceinthiocarbamoyl)-L-lysine (PLF) purchased from T. P. McAlinden (*25*). PV-1 IgG was biotinylated at a concentration of 1 mg/mL using biotinamidocaproate *N*-hydroxysuccinimide ester following standard procedures. Anti-TCR Fab/Folate was made in our laboratory as previously described (*26*). Antibodies and fluorophores used were CY-labeled anti-CD8, CY-labeled anti-CD3, FITC-labeled anti-CD25, PE-labeled anti-hamster IgG (Pharmingen); rat anti-CD8 IgG (Leinco); biotinylated goat anti-rat IgG mouse adsorbed (Vector), anti-BrdU (Becton-Dickinson); SA-594 and SA-488 (Molecular Probes). Flow cytometry was performed at the Flow Cytometry Facility at the University of Illinois. Primary splenocytes were obtained from spleens of euthanized animals and dissociated through wire mesh. Red blood cells were depleted using lysis buffer (0.14 M NH_4-Cl, 0.017 M Tris, pH 7.2) and cells were washed and counted for experiments. Tumor cells lines KB (human) and EL-4 (mouse $H\text{-}2^b$) were maintained in folate free RPMI (Gibco). Culture media contained 10% heat inactivated FCS (Hyclone), 1.3 mM L-glutamine, 50 mM 2-mercaptoethanol, 100 unit/mL penicillin (Gibco), and 100 units/mL streptomycin (Gibco). Cells were grown at 37 °C in 5% CO_2 in a humidified incubator.

Preparation of Anti-CD28 Fab/Folate. Anti-CD28 IgG antibody was purified from ascites fluid generated by the hybridoma PV-1 (*27*). Anti-CD28 IgG was purified by lipid removal, ammonium sulfate precipitation, DEAE column chromatography, and protein A column chromatography. Fab fragments were produced by 24 h incubation with papain conjugated beads (Pierce) at 37 °C on a shaker. Fab fragments were purified over a protein A column, and purity was examined by 10% SDS−PAGE. Anti-CD28 Fab fragments were concentrated to 1 mg/mL and covalently linked to folic acid using the standard EDC (1-ethyl-3-(3-dimethylaminopropyl)carbodiimide) reaction at a molar ratio of 50 folates per one Fab fragment. Labeled fragments were purified over a size exclusion column, dialyzed into phosphate-buffered saline (PBS), and concentrated to 1 mg/mL.

Anti-CD28 Fab/Folate Flow Cytometry Inhibition Assays. To assess binding of anti-CD28 Fab/folate preparations to the FR, a competitive inhibition assay was performed. KB cells were incubated with various concentrations of anti-CD28 Fab/folate at 37 °C for 20 min in 0.01% PBS−BSA. The fluorescent folic acid analogue, *N*-α-pteroyl-*N*-ε-(4′-fluoresceinthiocarbamoyl)-L-lysine, PLF, was added at the indicated concentrations to the cells and incubated at 37 °C for an additional 20 min. To assess binding of anti-CD28 Fab/folate preparations to CD28, a different competitive inhibition assay was performed. Primary C57BL/6 splenocytes were incubated for 20 min at 37 °C with indicated concentrations of anti-CD28 Fab/folate. Biotinylated anti-CD28 IgG was added to the cells and incubated at 37 °C for an additional 20 min. Cells were incubated with SA:PE in 0.01% PBS−BSA for 20 min at 4 °C. Cells were washed 3× in 0.01% PBS−BSA before analysis using a Coulter EPICS XL instrument.

^{3}H-Thymidine Incorporation Assay. KB cells were treated with mitomycin C at 1 mg/mL for 2 h at 37 °C. 10^4 KB cells were incubated with 10^5 TCR/RAG splenocytes in folate-free RPMI and various concentrations of a conjugate of an anti-TCR antibody (KJ16 Fab) with folate (to stimulate the TCR) and various concentrations of anti-CD28 Fab/folate. Cells were cultured in 96-well flat bottom plates for 48 h at 37 °C and 5% CO_2. Cells were pulsed with ^{3}H-thymidine (ICM Pharmaceuticals) for 16 h and harvested using a PHD cell harvester. Thymidine incorporation was assessed using a Beckman LS1801 beta-scintillation counter.

MRI Analysis. Mice were anesthetized using 100 mg/kg ketamine and 15 mg/kg xylazine. MRI data acquisition used a single loop small coil with 14 mm diameter placed around the mouse head and proton MR signals were detected using 4.7 T Varian MR scanner at 200 MHz. Coronal MR images of mouse brain were obtained using SEMS pulse sequence with interleaved slice acquisition. Twenty slices were acquired without gap during each

scan using slice thickness of 0.5 mm. Repetition time TR was 750 ms and echo time TE was 25 ms. Data matrix had 256 × 128 complex points and FOV was 30 × 30 mm. Duration of each MRI experiment was 6.4 min using NEX = 4. Data processing of MR raw data and images was performed using V and TkViewit software packages (BMRL, University of Illinois) and ImageJ (version 1.28). For volume measurements following the sc injection of anti-CD28 Fab/folate, the number of animals (*n*) equaled 9 (IL-12), 12 (IL-12 + anti-CD28 Fab/folate), and 6 (PBS). For volume measurements of intracerebroventricular (ICV) treated animals, *n* = 5 (IL-12), 4 (IL-12 + anti-CD28 Fab/Fol), and 4 (PBS). Data from mice that received IL-12 alone and IL-12 + ICV PBS were combined, as no significant differences were found between these groups. Statistical analysis was done using SAS JMP software.

IL-12 and Anti-CD28 Fab/Folate Treatments and Survival Analysis. $SV11^+$ tumor mice were treated for 10 days starting at day 85 of age with intraperitoneal (ip) injections of either 100 μL of 1% normal mouse serum (NMS) in PBS or 0.1 μg (5 μg/kg) murine IL-12 in 100 μL of 1% NMS in PBS. Anti-CD28 Fab/folate was delivered by one of four routes: iv (2 μg (0.1 mg/kg) on days 4, 7, 9 of IL-12 treatment); sc (2 μg on days 4, 7, 9); ICV as a single injection (5 μg (0.25 mg/kg) on day 6); or ICV as a continuous infusion (a total of 25 μg (1.5 mg/kg) infused from an osmotic minipump on days 6−21). Control mice were injected with PBS for each route of anti-CD28 Fab/folate delivery. Mice were checked daily for health status and weight. If mice were lethargic or weighed less than 75% of their baseline body weight they were euthanized. Survival statistics were analyzed by Kaplan−Meier estimates and log-rank test using SAS JMP software.

Intracerebroventricular (ICV) Injections and Cannula Implantations with Minipumps. For ICV injections and infusions, the tip of the needle or cannula was stereotaxically placed into the lateral ventricle; from bregma: 0.8 mm lateral, 0.5 mm posterior, and 3.1−3.3 mm ventral. Animals were anesthetized using 100 mg/kg ketamine and 15 mg/kg xylazine. The exposed skull was trephined with a 26G needle. For ICV injections, a 27G Hamilton syringe was used to inject 5 μg/5 μL anti-CD28 Fab/folate or PBS. Cannulas (Plastics One) were held in place with Lock-tite and attached with vinyl tubing to an osmotic minipump (Alzet). The pump was implanted subcutaneously at the nape of the neck and filled with 25 μg anti-CD28 Fab/folate in PBS or PBS alone. MRI imaging was used to test whether the osmotic minipump was able to deliver fluid to the indwelling cannula implanted into the lateral ventricle. A Teflon cannula was implanted into the lateral ventricle of a nontumor mouse using the same coordinates as the ICV injections and connected to an osmotic minipump filled with gadolinium. As visualized by MRI, the gadolinium in the pump was delivered to the ventricles and infused the surrounding brain tissue (data not shown).

Immunohistochemistry (IHC). Animals were injected with 50 μg BrdU/g 2 h before sacrifice. Brains were dissected, embedded in Cryomatrix, and frozen at −80 °C. Ten micrometer sections were cut on a cryostat and fixed using 95% ethanol at −20 °C. Slides were rehydrated and washed between incubations in PBS-0.1%Tween20 (PBST). Sections were blocked with Superblock (Pierce) for 1.5 h. Primary anti-CD8 antibody was incubated at room temperature for 30 min. Slides were incubated with secondary biotinylated goat anti-rat antibody at room temperature for 20 min and incubated with SA-488 for 15 min. Sections were coverslipped or incubated in cold 2.7% formaldehyde-0.01% Tween20 at 4 °C for 45 min. Slides washed 2× in PBST, 1× in $NaCl/MgCl_2$ buffer, and incubated 45 min in DNase I, 50 U/150 μL in $NaCl/MgCl_2$ buffer. Slides were blocked in MOM blocker (Vector), 5 min, and incubated in primary anti-BrdU antibody at 4 °C overnight. Secondary biotinylated anti-mouse antibody was incubated for 10 min at room temperature and visualized using SA-594 stained 15 min.

RESULTS

Construction and Characterization of Anti-CD28 Fab/Folate. To eliminate potential complications of tumor-independent, Fc-receptor-mediated activation of T cells, Fab fragments of the anti-CD28 antibody PV-1 were used in these studies. Fab fragments, prepared by digestion with papain coated beads, were run over a protein A column to remove undigested IgG and F_c regions. Fab fragments were labeled with folic acid using the EDC reaction, which links carboxyl groups of folic acid to primary amine groups on the protein. Fab fragments and folate-labeled Fab fragments were examined by SDS−PAGE (Figure 1A). The Fab/folate preparation (lane 3) migrated slightly slower than the Fab fragment (lane 2) suggesting that the protein was successfully coupled to folic acid molecules, given that the molecular weight of folate is 441.

The bispecific conjugate was tested for binding capability to its respective ligands using competition assays and flow cytometry. FR binding of anti-CD28 Fab/folate was tested using *N*-α-pteroyl-*N*-ϵ-(4′-fluoresceinthiocarbamoyl)-L-lysine (PLF), a fluorescein derivative of the lysine analogue of folic acid (*25*). Anti-CD28 Fab/folate was able to inhibit the binding of PLF in a dose dependent manner, retaining its ability to bind FR after EDC coupling (Figure 1B and data not shown). Conjugation of the folate to the larger antibody substantially reduced its affinity, by approximately 2 orders of magnitude on a molar basis. Flow cytometry was used to test CD28 binding of anti-CD28 Fab/folate conjugate. Anti-CD28 Fab/folate conjugate blocked the binding of biotinylated anti-CD28 IgG to C57Bl/6 mouse splenocytes, as detected with PE-labeled streptavidin (Figure 1C). Together, these results indicate that anti-CD28 Fab/folate is functional and can bind both FR and CD28.

Cross-linking of the tumor cell with CD28 on a T cell by the bispecific conjugate is required for CD28-mediated activation and signaling. The ability of the Fab/folate conjugate to costimulate T cells was assessed using ^{3}H-thymidine incorporation into primary splenocytes, upon activation with an anti-TCR Fab/folate conjugate. Primary splenocytes from a Vβ8+ TCR/RAG mouse were cultured with the tumor cell line KB (mitomycin C treated) that expresses the high affinity folate receptor. In the presence of an anti-Vβ8 Fab fragments conjugated to folate (KJ16 Fab/folate) (*26*), T cells proliferated in a dose dependent manner by cross-linking of the TCR to the FR (Figure 2A). Cultures were treated with a concentration of KJ16 Fab/folate (10 ng/mL) below maximal stimulation and various concentrations of anti-CD28 Fab/folate. As predicted from many other studies with anti-CD28 antibodies, anti-CD28 Fab/folate synergized with the KJ16 Fab/folate (Figure 2B). Anti-CD28 Fab/Fol by itself had no effect on proliferation, as expected (data not shown). Taken together, these results indicate that the binding and cross-linking of the anti-CD28 Fab/folate is functional and the conjugate is biologically active.

Systemic Administration Routes of Anti-CD28 Fab/Folate. In previous studies, we found that a 10 day

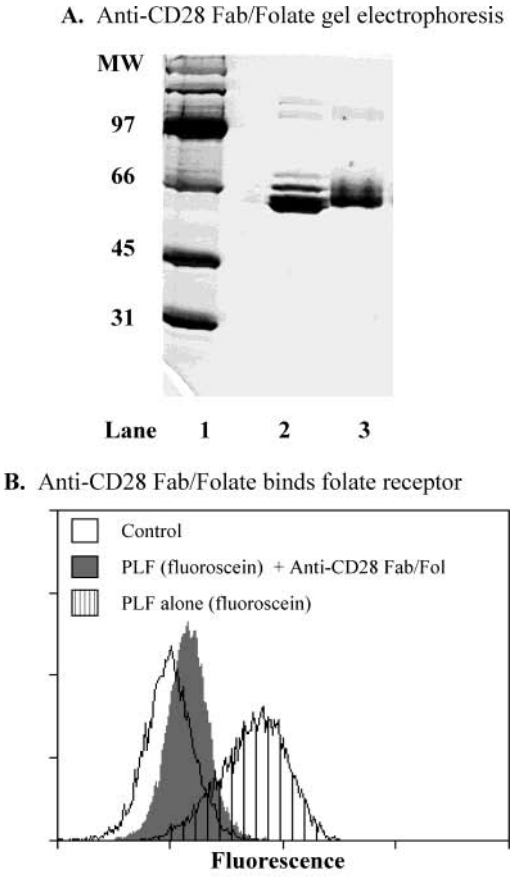


Figure 1. Anti-CD28 Fab/Folate preparation. (A) SDS−PAGE gel of unreduced anti-CD28 Fab preparation. Lane 1, MW standards. Lane 2, anti-CD28 Fab. Lane 3, conjugated anti-CD28 Fab/folate. (B) Flow cytometric analysis demonstrating that anti-CD28 Fab/folate (2×10^{-6} M) inhibits binding of the folic acid analogue PLF (*N*-α-pteroyl-*N*-ϵ-(4′-fluoresceinthiocarbamoyl)-L-lysine, 10^{-8} M). (C) Flow cytometric analysis showing folate conjugated anti-CD28 Fab (2×10^{-6} M) can inhibit binding of divalent anti-CD28 IgG (7×10^{-8} M) to CD28.

course of IL-12 leads to a modest, but significant, increase in survival of SV11 mice (*28*). After IL-12 treatment, T cells were found to migrate into the brain tumor. We reasoned that by providing daily IL-12 intraperitoneal (ip) injections, followed by anti-CD28 Fab/folate treatments beginning on day 4, enhanced costimulatory signals could be delivered to infiltrating lymphocytes in the choroid plexus tumor. SV11 mice were treated with IL-12 and various systemic routes of delivery (intraperitoneal, intravenous, and subcutaneous) of anti-CD28 Fab/folate. SV11 animals received anti-CD28 Fab/folate on days 4, 7, and 10 after onset of IL-12 treatment.

A regimen of three sc injections of anti-CD28 Fab/folate resulted in enhancement of survival and was further

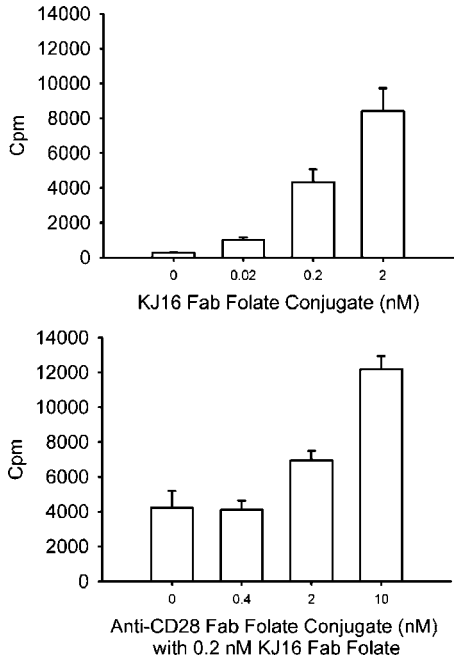


Figure 2. Functional activity of conjugated anti-CD28 Fab/Folate. ^{3}H-Thymidine incorporation into splenocytes after incubation with the folate receptor expressing cell line KB, with varying concentrations of anti-TCR antibody−ligand conjugate (KJ16 Fab/folate) and anti-CD28 Fab/folate. A. Increasing stimulation of the TCR increases proliferation. B. At a given concentration of KJ16 Fab/folate, increasing concentrations of Anti-CD28 Fab/folate stimulated increased splenocyte proliferation.

studied with MRI-based volumetric analysis as the endpoint. Subcutaneous anti-CD28 Fab/folate administration (2 μg × 3 days) in combination with daily IL-12 (0.1 μg ip for 10 days) increased mouse survival from an average of 106 days with PBS alone ($n = 37$), to 115 days with IL-12 alone ($n = 55$, $p < 0.001$ versus PBS), to 121 days with the combination of IL-12 and anti-CD28 Fab/folate ($n = 44$, $p < 0.05$ versus IL-12 alone, Figure 3A).

The 10 day tumor progression from day 85 to day 95 was followed using MRI (Figure 3B and 3C). Volume reconstruction of images was used to assess tumor growth. Tumors of PBS treated animals ($n = 6$) increased by 263% while tumors of IL-12 treated animals ($n = 9$) increased only 81% ($p < 0.05$, Figure 3B). Animals treated with IL-12 in conjunction with anti-CD28 Fab/folate ($n = 9$) decreased tumor growth even further, growing only 8% over 10 days ($p < 0.05$ versus IL-12 alone, Figure 3B).

Intracerebroventricular (ICV) Injection of Anti-CD28 Fab/Folate. It is possible that relatively short circulating lifetime of Fab fragments minimizes their benefits because most of the conjugate does not reach the brain tumor. Thus, the effects of direct administration of anti-CD28 Fab/folate into the brain were investigated. Animals were treated daily for 10 days ip with PBS or IL-12. To allow for T cell infiltrate into choroid plexus tumors mediated by IL-12, ICV anti-CD28 Fab/folate injection was administered on day 6. Figure 4A shows that animals treated with a single administration of 5 μg of anti-CD28 Fab/folate ICV in combination with daily IL-12 ip survived an average of 122 days ($n = 17$), while animals treated with IL-12 alone or IL-12 plus ICV PBS ($n = 14$) survived 114 days ($p < 0.02$). Mice treated with anti-CD28 Fab/folate but without IL-12 pretreatment ($n = 3$) did not survive longer than PBS controls ($n = 7$). The increase in survival in animals treated with the combination of IL-12 and anti-CD28 Fab/folate is com-

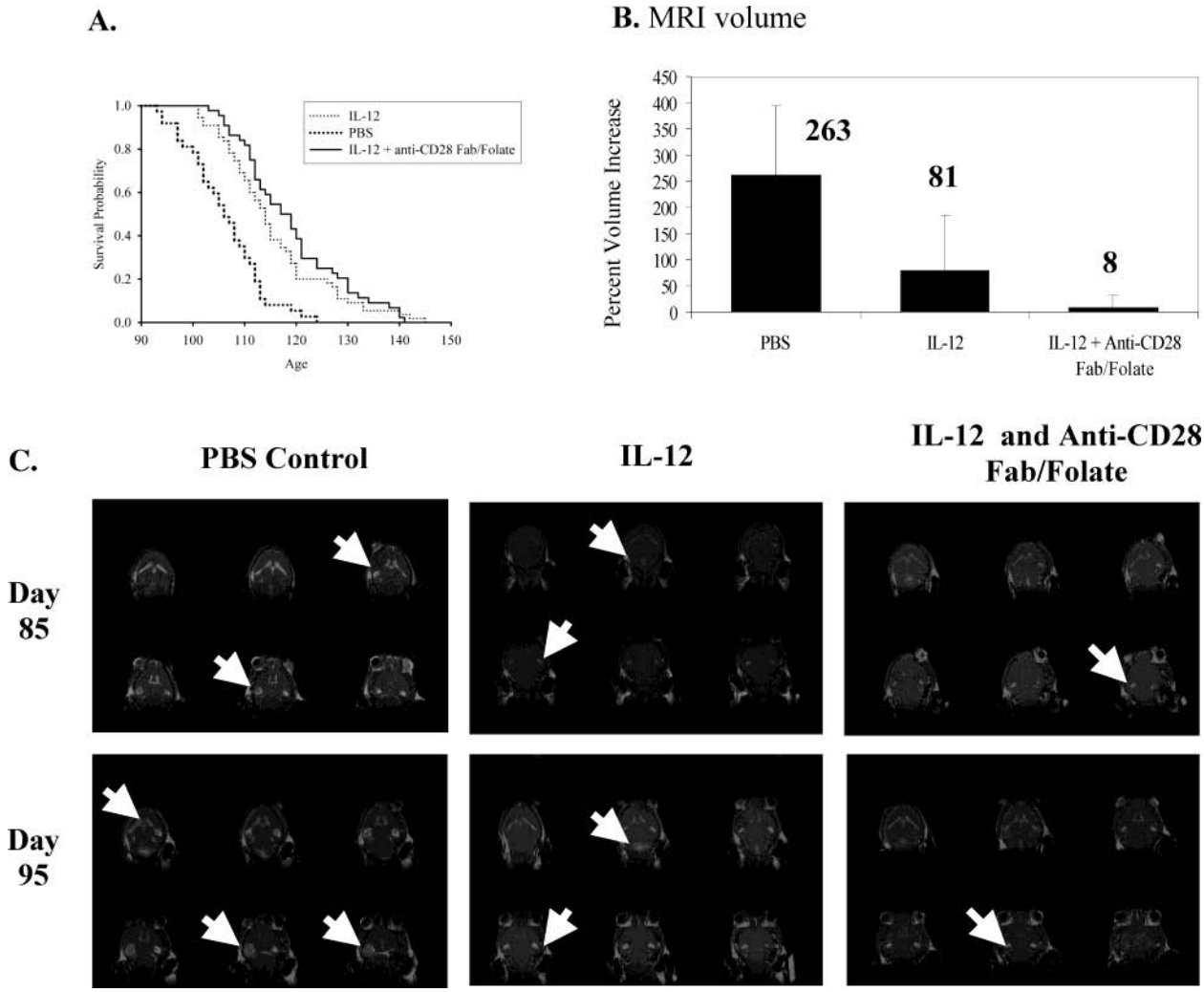


Figure 3. Response to subcutaneous administration of anti-CD28 Fab/folate. (A) Kaplan−Meier survival curves of three treatment groups showing longest survival time for animals treated with IL-12 in combination with Anti-CD28 Fab/folate ($p < 0.02$ versus IL-12 alone). (B) MRI analysis showing percent volume increase in choroid plexus tumor size over 10 day treatment. Mice treated with IL-12 + anti-CD28 Fab/folate had smaller increases than mice treated with IL-12 alone ($p < 0.05$). PBS ($n = 6$), IL-12 ($n = 9$), IL-12 + anti-CD28 Fab/folate ($n = 9$). (C) Representative MRI images showing 10 day tumor progression of tumors in mice treated with PBS, IL-12, and IL-12 plus 3 sc injections of Anti-CD28 Fab/folate conjugate. Arrows point to choroid plexus tumors.

parable to experiments described above using three sc injections of 2 μg anti-CD28 Fab/folate (Figure 3A), indicating that a single direct administration of bispecific conjugate to the site of the tumor can produce similar therapeutic effects. The average survival of untreated animals was 106 days, 21 days past start of treatment.

Immunohistochemistry of brain sections from ICV injected animals revealed a proliferating T cell infiltrate. To evaluate the proliferative state of both the tumor and T cells, animals in treatment groups were injected with BrdU 2 h before sacrifice and brain sections stained for BrdU. To examine whether cytotoxic T cells are present in the infiltrate, double staining was also performed with an anti-CD8 antibody. Consistent with the rapid growth observed by MRI, tumor cells were highly proliferative. Within the 2 h window of BrdU exposure, 15−20% of tumor cells were found to be proliferating. In addition, a double positive CD8 and BrdU population was found in anti-CD28 Fab/folate treated animals (Figure 4B), indicative of a tumor-reactive CTL infiltrate into choroid plexus tumors.

Continuous Delivery of Anti-CD28 Fab/Folate. The effect of a 14 day continuous ICV infusion of anti-CD28 Fab/folate through an osmotic minipump was tested in combination with daily IL-12 ip injections. To control for tumor variability inherent in the SV11 model, mice were imaged by MRI for tumors and matched for tumor size among treatment groups at the start of the experiment. Animals received anti-CD28 Fab/folate into the right lateral ventricle, through an indwelling cannula connected to a surgically implanted osmotic minipump. The animals received 0.25 μL/h for 14 days of either PBS or a total dose of 25 μg anti-CD28 Fab/folate. Mice were analyzed by MRI (Figure 5A) on day 1 of treatment and 21 days after treatment (in contrast to MRI analyses after 10 days of treatment described earlier). The PBS treated animals ($n = 4$) had a significant increase in tumor size, 73 mm^3 within the 21 day period (Figure 5B). The IL-12 treated tumors ($n = 5$) grew 30 mm^3, while IL-12 and anti-CD28 Fab/folate treated tumors (= 4) had little growth, 2 mm^3 ($p < 0.05$ versus IL-12, Figure 5B). After anti-CD28 Fab/folate and IL-12 treatments were stopped, tumors rapidly progressed. Both treated groups survived significantly longer than PBS controls ($p < 0.05$, data not shown), but the slower growth of the tumors in mice treated with anti-CD28 Fab/folate did not translate into survival benefit, compared to IL-12 alone. The smaller sample sizes in this experiment (n's = 4 and 5) may have contributed to the lack of effect on survival.

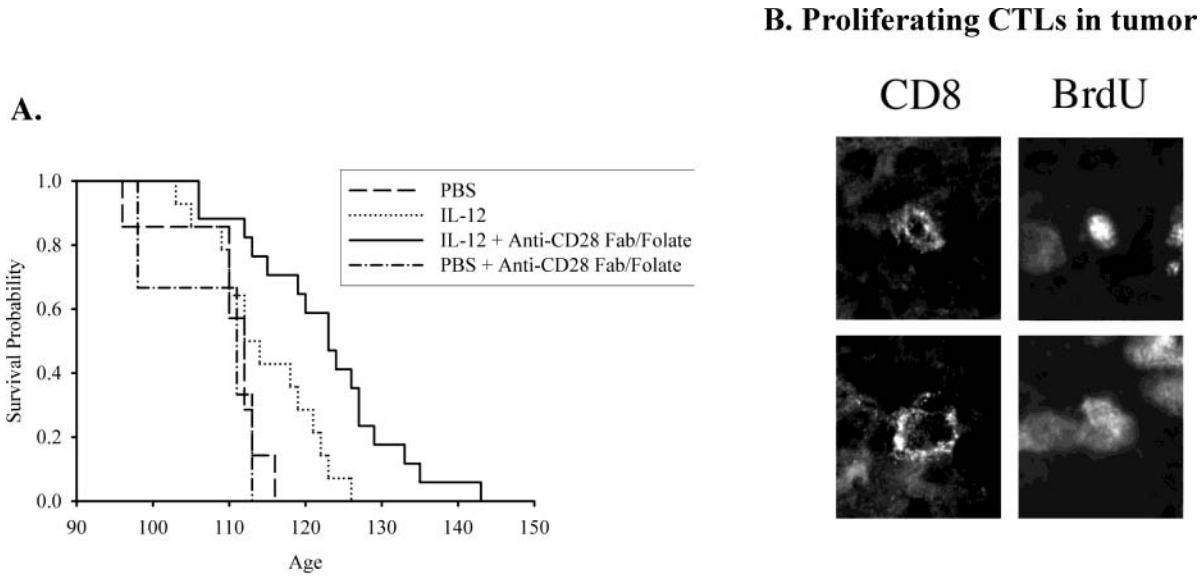


Figure 4. Response to intracerebroventricular (ICV) administration of anti-CD28 Fab/folate. (A) Kaplan−Meier survival curves of four treatment groups showing longest survival for mice treated with IL-12 in combination with anti-CD28 Fab/folate ($p < 0.02$ versus IL-12 alone). (B) Immunohistochemistry of tumor sections from ICV injected animals. $CD8^+$/BrdU double positive cells can be seen within the choroid plexus tumors (60× magnification, IL-12 and anti-CD28 Fab/folate treated animal).

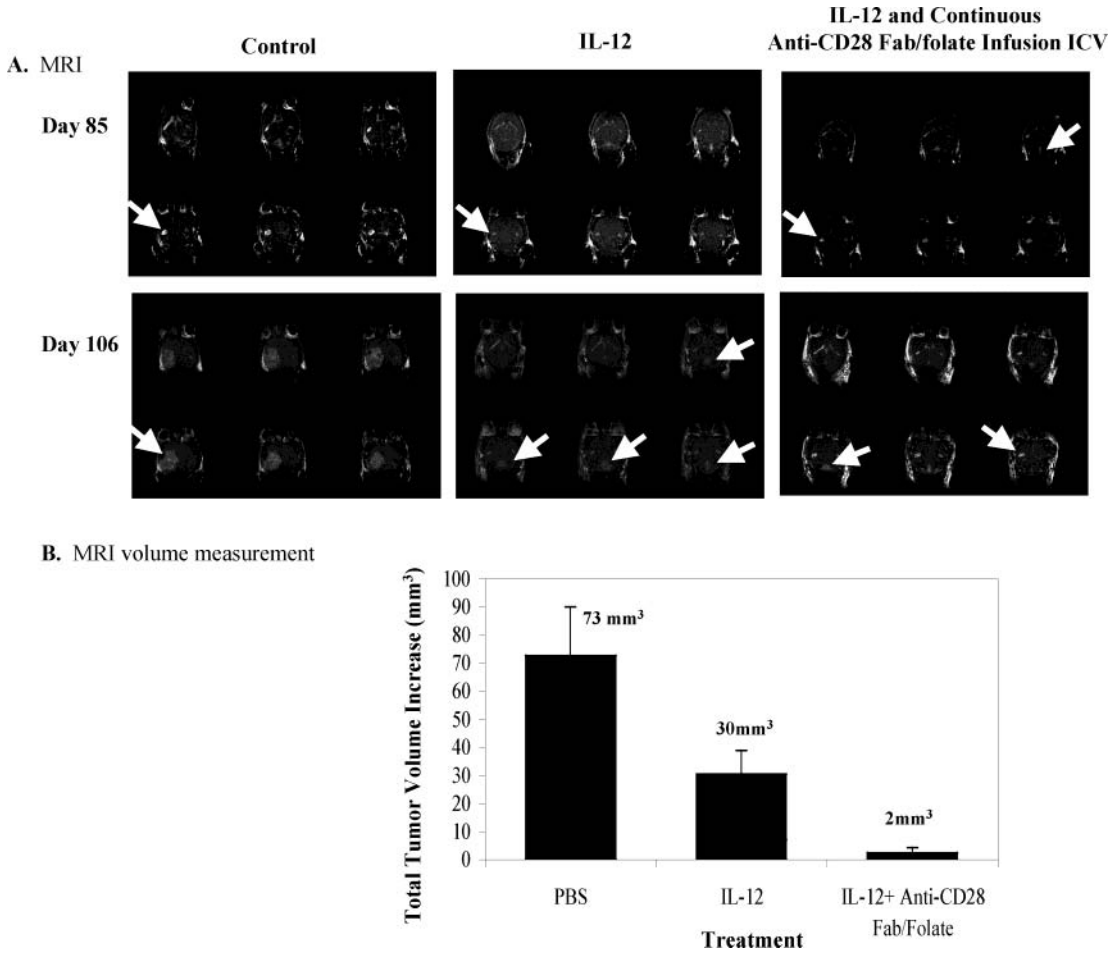


Figure 5. Response to continuous ICV infusion with anti-CD28 Fab/folate. (A) Representative MRI images showing 21 day treatment and progression of tumors after treatment with PBS, IL-12 ip, IL-12 ip + ICV PBS infusion, or IL-12 ip + ICV anti-CD28 Fab/folate infusion. Arrows point to choroid plexus tumors. (B) MRI analysis of tumor volume growth over 21 day treatment. Volumes expressed as mm^3 of tumor growth. PBS ($n = 4$), IL-12 ip ($n = 5$), IL-12 ip + anti-CD28 Fab/folate ICV infusion ($n = 4$).

DISCUSSION

Although immune responses can be readily elicited within transplanted tumor models, attempts at eliciting native host immune responses against endogenously arising tumors have been less successful (*29*, *30*). Among the challenges posed by endogenously arising tumors are that host T cells are tolerant to the tumor. During thymic education, self-reactive T cells undergo apoptosis as the

normal developmental pathway which protects against autoimmunity. However, the process of central tolerance is not complete and allows the escape of low-affinity self-reactive T cells. The T cell repertoire in tumor bearing SV40 transgenic mice is shaped by clonal deletion, as a consequence of the fact that tumor antigens are expressed at low levels in the thymus (*31*). Even though SV40 transgenic mice undergo central tolerance through the expression of Tag during thymic selection, a population of low-avidity autoreactive immune CTLs can escape thymic deletion (*23*, *32*). The polyclonal population of self-reactive T cells which escape deletion during negative selection has been related to T cell avidity (*33*). Highest affinity T cells are deleted in thymus while lower affinity, immunorecessive epitopes persist and offer opportunity for immune-based therapy (*34*).

The effectiveness of a CTL response in the control of SV40 tumors is dependent on the degree of central tolerance and the degree of SV40 antigen expression. Positively selected T cells can also be anergized peripherally as a result of weak stimulating signals received by immature dendritic cells expressing low amounts of pMHC or presentation of pMHC to a low affinity TCR in the absence of costimulatory signals such as B7. T cells with low avidity TCRs are not necessarily deficient in proliferative capacity and can be effectively stimulated by altered peptide ligands with higher affinity for the TCR (*35*). A higher affinity ligand promoted the expansion of these low-avidity self-reactive T cells with increased magnitude of response and maintenance of effector function upon immunization with the peptide. This suggests that the defect in tolerized or anergic CTL responses is not an intrinsic problem but rather a defect in T cell activation (*35*). T cell survival is based upon total strength of stimulation consisting of quantity and affinity for antigen, duration of stimulation, degree of costimulation, and T cell cytokine responsiveness (*36*), and thus additive avenues of activation are most likely needed for a long-term response.

We have previously found that IL-12 stimulates a T cell response against endogenous SV11 tumors (*28*). The present study demonstrates that the antitumor effect of IL-12 is enhanced when combined with the bispecific ligand-antibody conjugate, anti-CD28 Fab/folate. Anti-CD28 Fab/folate targets CD28 on T cells and the FR on tumor cells to enhance a specific an antitumor CTL response. To promote tumor specificity and infiltration, the bispecific antibody conjugate was constructed from an anti-CD28 Fab fragment and directly conjugated to folic acid**.** After chemical conjugation, both CD28 and FR binding were retained and anti-CD28 Fab/folate was able to induce T cell proliferation in vitro in combination with an anti-TCR/folate antibody conjugate.

The dosing schedule and route of administration of anti-CD28 Fab/folate influenced the effectiveness of the treatment in vivo. Although intravenous administration of anti-CD28 Fab/folate in combination with daily intraperitoneal injections of IL-12 did not significantly prolong survival, an increase in infiltrating activated T cells in the tumors suggested that peripheral administration of anti-CD28 Fab/folate was effective in activating T cells focally within the area of the tumor (data not shown). Subcutaneous administration would be expected to provide a more sustained delivery of the agent to the brain, compared to intravenous administration. Consistent with this idea, subcutaneous administration of anti-CD28 Fab/folate in combination with daily intraperitoneal injections of IL-12 over a 10 day period resulted in increased survival and a dramatic decrease in tumor growth as assessed by MRI. Given the fact that choroid plexus epithelium is on the blood side of the blood-CSF barrier and the finding that the tumors enhanced with gadolinium, peripheral injections would be expected to have access to the tumors. However, the relatively short circulating lifetime of Fab fragments, and the possibility that FR+ macrophages are in the periphery, may reduce the effective concentration Fab/folate conjugates that make it to the brain.

The possibility that the bispecific agent acts in the local tumor environment to enhance costimulation of infiltrating T cells was supported by the observations that local administration of anti-CD28 Fab/folate at the site of the choroid plexus tumors was also effective. The survival of mice treated with a single ICV injection of anti-CD28 Fab/folate was comparable to results seen with three subcutaneous injections of the bispecific antibody conjugate. This is significant considering that at the start of treatment, tumors in these animals have rapid tumor growth with high levels of large-T antigen and highly neoplastic pathology (*21*, *37*). The strongest effect on tumor growth assessed by MRI was achieved through the 2 week continuous local ICV administration of anti-CD28 Fab/folate. Choroid plexus tumors in animals treated with anti-CD28 Fab/folate exhibited little or no growth 21 days after initiation of treatment.

Proliferating $CD8^+$ T cells were seen in brain sections of animals treated with IL-12 in combination with ICV injections of anti-CD28 Fab/folate. In efforts to examine whether the specificity of the CD8+ tumor infiltrating cells are specific for the most dominant SV40 Tag epitope (epitope IV bound to K^b), we examined splenocytes with tetramers of epitope IV/K^b. However, we were unable to detect significant binding (data not shown), consistent with findings of Schell that the T antigen specific T cells stimulated in SV11 mice by a T antigen vaccine are specific for epitope V (*23*). Thus, if the T cells stimulated by IL-12 and anti-CD28 Fab/folate are specific for large T antigen, it is possible that they are specific for the immunorecessive epitope V.

Two other SV40 transgenic tumor models have shown recently that strong activating signals are required to overcome T cell tolerance. SV40 under an α-amylase promoter produces endogenously arising osteosarcomas; naïve SV40 epitope I specific T cells adoptively transferred into these SV40 tumor-expressing mice lacked effector function due to peripheral T cell anergy (*38*). However, treatment with an agonist antibody against CD40 in addition to the adoptively transferred CTLs prevented the development of T cell tolerance and promoted the development of CTL effector function, clonal expansion, and memory cell development (*38*). Upon CD40 ligation, dendritic cells upregulate B7 expression as well as secrete IL-12. In contrast, in an SV40 prostate mouse model, CD40 ligation in combination CpG injections failed to reverse SV40 T cell tolerance, but CTLs against the subdominant Tag epitope V could be elicited (*39*).

Overcoming self-tolerance for activation of naïve low-affinity antitumor CTLs requires a considerable synergistic engagement of a variety of receptors on naïve T cells. Increasing evidence points to a three signal model for T cell activation. While the TCR/pMHC interaction confers antigenic specificity, CD28 and IL-12 are needed to amplify the low-affinity activation. While both CD28 and IL-12 can stimulate T cell proliferation and cytokine secretion, growing evidence indicates that CD28 is needed for the development of CTL effector function and IL-12 is needed for T cell memory formation. In the develop-

ment of antitumor immunotherapies, a specific and strong immune response must be elicited to activate tumor-tolerized T cells. The most successful treatment will most likely comprise a combination of therapies that stimulate signaling pathways needed to activate and sustain a specific antitumor T cell response.

ACKNOWLEDGMENT

We thank Laurie Rund and Lori Carr for technical assistance, and Dr. Todd Schell for comments on the manuscript. Supported by NIH grants CA77499 (E.J.R.) and AI3599 (D.M.K.).

LITERATURE CITED

(1) Harding, F. A., McArthur, J. G., Gross, J. A., Raulet, D. H., and Allison, J. P. (1992) CD28-mediated signaling costimulates murine T cells and prevents induction of anergy in T-cell clones. *Nature 356*, 607−609.

(2) Shahinian, A., Pfeffer, K., Lee, K. P., Kundig, T. M., Kishihara, K., Wakeham, A., Kawai, K., Ohashi, P. S., Thompson, C. B., and Mak, T. W. (1993) Differential T cell costimulatory requirements in CD28-deficient mice. *Science 261*, 609−612.

(3) Bachmann, M. F., McKall-Faienza, K., Schmits, R., Bouchard, D., Beach, J., Speiser, D. E., Mak, T. W., and Ohashi, P. S. (1997) Distinct roles for LFA-1 and CD28 during activation of naive T cells: adhesion versus costimulation. *Immunity 7*, 549−557.

(4) Salomon, B., and Bluestone, J. A. (2001) Complexities of CD28/B7: CTLA-4 costimulatory pathways in autoimmunity and transplantation. *Annu. Rev. Immunol. 19*, 225−252.

(5) Kundig, T. M., Shahinian, A., Kawai, K., Mittrucker, H. W., Sebzda, E., Bachmann, M. F., Mak, T. W., and Ohashi, P. S. (1996) Duration of TCR stimulation determines costimulatory requirement of T cells. *Immunity 5*, 41−52.

(6) Morgan, D. J., Kreuwel, H. T., Fleck, S., Levitsky, H. I., Pardoll, D. M., and Sherman, L. A. (1998) Activation of low avidity CTL specific for a self-epitope results in tumor rejection but not autoimmunity. *J. Immunol. 160*, 643−651.

(7) Manning, T. C., Rund, L. A., Gruber, M. M., Fallarino, F., Gajewski, T. F., and Kranz, D. M. (1997) Antigen recognition and allogeneic tumor rejection in CD8+ TCR transgenic/RAG-(-/-) mice. *J. Immunol. 159*, 4665−4675.

(8) Townsend, S. E., and Allison, J. P. (1993) Tumor rejection after direct costimulation of CD8+ T cells by B7-transfected melanoma cells. *Science 259*, 368−370.

(9) Curtsinger, J. M., Lins, D. C., and Mescher, M. F. (2003) Signal 3 determines tolerance versus full activation of naive CD8 T cells: dissociating proliferation and development of effector function. *J. Exp. Med. 197*, 1141−1151.

(10) Ushio, H., Tsuji, R. F., Szczepanik, M., Kawamoto, K., Matsuda, H., and Askenase, P. W. (1998) IL-12 reverses established antigen-specific tolerance of contact sensitivity by affecting costimulatory molecules B7−1 (CD80) and B7−2 (CD86). *J. Immunol. 160*, 2080−2088.

(11) Fallarino, F., Uyttenhove, C., Boon, T., and Gajewski, T. F. (1996) Endogenous IL-12 is necessary for rejection of P815 tumor variants in vivo. *J. Immunol. 156*, 1095−1100.

(12) Fallarino, F., Uyttenhove, C., Boon, T., and Gajewski, T. F. (1999) Improved efficacy of dendritic cell vaccines and successful immunization with tumor antigen peptide-pulsed peripheral blood mononuclear cells by coadministration of recombinant murine interleukin-12. *Int. J. Cancer 80*, 324−333.

(13) Hallez, S., Detremmerie, O., Giannouli, C., Thielemans, K., Gajewski, T. F., Burny, A., and Leo, O. (1999) Interleukin-12-secreting human papillomavirus type 16-transformed cells provide a potent cancer vaccine that generates E7-directed immunity. *Int. J. Cancer 81*, 428−437.

(14) Ross, J. F., Chaudhuri, P. K., and Ratnam, M. (1994) Differential regulation of folate receptor isoforms in normal and malignant tissues in vivo and in established cell lines. Physiologic and clinical implications. *Cancer 73*, 2432−2443.

(15) Garin-Chesa, P., Campbell, I., Saigo, P. E., Lewis, J. L., Jr., Old, L. J., and Rettig, W. J. (1993) Trophoblast and ovarian cancer antigen LK26. Sensitivity and specificity in immunopathology and molecular identification as a folate-binding protein. *Am. J. Pathol. 142*, 557−567.

(16) Brinster, R. L., Chen, H. Y., Messing, A., van Dyke, T., Levine, A. J., and Palmiter, R. D. (1984) Transgenic mice harboring SV40 T-antigen genes develop characteristic brain tumors. *Cell 37*, 367−379.

(17) Van Dyke, T., Finlay, C., and Levine, A. J. (1985) A comparison of several lines of transgenic mice containing the SV40 early genes. *Cold Spring Harb. Symp. Quant. Biol. 50*, 671−678.

(18) Palmiter, R. D., Chen, H. Y., Messing, A., and Brinster, R. L. (1985) SV40 enhancer and large-T antigen are instrumental in development of choroid plexus tumours in transgenic mice. *Nature 316*, 457−460.

(19) Schirmbeck, R., Zerrahn, J., Kuhrober, A., Deppert, W., and Reimann, J. (1993) Immunization of mice with the N-terminal (1−272) fragment of simian virus 40 large T antigen (without adjuvants) specifically primes cytotoxic T lymphocytes. *Eur. J. Immunol. 23*, 1528−1534.

(20) Mylin, L. M., Schell, T. D., Roberts, D., Epler, M., Boesteanu, A., Collins, E. J., Frelinger, J. A., Joyce, S., and Tevethia, S. S. (2000) Quantitation of CD8(+) T-lymphocyte responses to multiple epitopes from simian virus 40 (SV40) large T antigen in C57BL/6 mice immunized with SV40, SV40 T-antigen-transformed cells, or vaccinia virus recombinants expressing full-length T antigen or epitope minigenes. *J. Virol. 74*, 6922−6934.

(21) Schell, T. D., Mylin, L. M., Georgoff, I., Teresky, A. K., Levine, A. J., and Tevethia, S. S. (1999) Cytotoxic T-lymphocyte epitope immunodominance in the control of choroid plexus tumors in simian virus 40 large T antigen transgenic mice. *J. Virol. 73*, 5981−5993.

(22) Webb, S., Morris, C., and Sprent, J. (1990) Extrathymic tolerance of mature T cells: clonal elimination as a consequence of immunity. *Cell 63*, 1249−1256.

(23) Schell, T. D. (2004) In vivo expansion of the residual tumor antigen-specific CD8+ T lymphocytes that survive negative selection in simian virus 40 T-antigen-transgenic mice. *J. Virol. 78*, 1751−1762.

(24) Patrick, T. A., Kranz, D. M., Zachary, J. F., and Roy, E. J. (1998) Intracerebral bispecific ligand-antibody conjugate increases survival of animals bearing endogenously arising brain tumors. *Int. J. Cancer 78*, 470−479.

(25) McAlinden, T. P., Hynes, J. B., Patil, S. A., Westerhof, G. R., Jansen, G., Schornagel, J. H., Kerwar, S. S., and Freisheim, J. H. (1991) Synthesis and biological evaluation of a fluorescent analogue of folic acid. *Biochemistry 30*, 5674−5681.

(26) Cho, B. K., Roy, E. J., Patrick, T. A., and Kranz, D. M. (1997) Single-chain Fv/folate conjugates mediate efficient lysis of folate-receptor-positive tumor cells. *Bioconjugate Chem. 8*, 338−346.

(27) Abe, R., Vandenberghe, P., Craighead, N., Smoot, D. S., Lee, K. P., and June, C. H. (1995) Distinct signal transduction in mouse CD4+ and CD8+ splenic T cells after CD28 receptor ligation. *J. Immunol. 154*, 985−997.

(28) Roy, E. J., Gawlick, U., Orr, B. A., Rund, L. A., Webb, A. G., and Kranz, D. M. (2000) IL-12 treatment of endogenously arising murine brain tumors. *J. Immunol. 165*, 7293−7299.

(29) Schell, T. D., and Tevethia, S. S. (2001) Control of advanced choroid plexus tumors in SV40 T antigen transgenic mice following priming of donor CD8(+) T lymphocytes by the endogenous tumor antigen. *J. Immunol. 167*, 6947−6956.

(30) Cordaro, T. A., de Visser, K. E., Tirion, F. H., Schumacher, T. N., and Kruisbeek, A. M. (2002) Can the low-avidity self-specific T cell repertoire be exploited for tumor rejection? *J. Immunol. 168*, 651−660.

(31) Zheng, X., Gao, J. X., Zhang, H., Geiger, T. L., Liu, Y., and Zheng, P. (2002) Clonal deletion of simian virus 40 large T antigen-specific T cells in the transgenic adenocarcinoma of mouse prostate mice: an important role for clonal deletion in shaping the repertoire of T cells specific for antigens overexpressed in solid tumors. *J. Immunol. 169*, 4761−4769.

(32) Oehen, S. U., Ohashi, P. S., Burki, K., Hengartner, H., Zinkernagel, R. M., and Aichele, P. (1994) Escape of thymocytes and mature T cells from clonal deletion due to limiting tolerogen expression levels. *Cell Immunol. 158*, 342−352.

(33) Bouneaud, C., Kourilsky, P., and Bousso, P. (2000) Impact of negative selection on the T cell repertoire reactive to a self-peptide: a large fraction of T cell clones escapes clonal deletion. *Immunity 13*, 829−840.

(34) Ohlen, C., Kalos, M., Hong, D. J., Shur, A. C., and Greenberg, P. D. (2001) Expression of a tolerizing tumor antigen in peripheral tissue does not preclude recovery of high-affinity CD8+ T cells or CTL immunotherapy of tumors expressing the antigen. *J. Immunol. 166*, 2863−2870.

(35) de Visser, K. E., Cordaro, T. A., Kessels, H. W., Tirion, F. H., Schumacher, T. N., and Kruisbeek, A. M. (2001) Low-avidity self-specific T cells display a pronounced expansion defect that can be overcome by altered peptide ligands. *J. Immunol. 167*, 3818−3828.

(36) Gett, A. V., Sallusto, F., Lanzavecchia, A., and Geginat, J. (2003) T cell fitness determined by signal strength. *Nat. Immunol. 4*, 355−360.

(37) Van Dyke, T. A., Finlay, C., Miller, D., Marks, J., Lozano, G., and Levine, A. J. (1987) Relationship between simian virus 40 large tumor antigen expression and tumor formation in transgenic mice. *J. Virol. 61*, 2029−2032.

(38) Staveley-O'Carroll, K., Schell, T. D., Jimenez, M., Mylin, L. M., Tevethia, M. J., Schoenberger, S. P., and Tevethia, S. S. (2003) In vivo ligation of CD40 enhances priming against the endogenous tumor antigen and promotes CD8+ T cell effector function in SV40 T antigen transgenic mice. *J. Immunol. 171*, 697−707.

(39) Grossmann, M. E., Davila, E., and Celis, E. (2001) Avoiding Tolerance Against Prostatic Antigens With Subdominant Peptide Epitopes. *J. Immunother. 24*, 237−241.

BC049911E

TECHNICAL NOTES

Engineering Surfaces for Bioconjugation: Developing Strategies and Quantifying the Extent of the Reactions

Virginie Gauvreau,[†] Pascale Chevallier,[†,‡] Karine Vallières,[†,‡] Éric Petitclerc,[†,§] René C.-Gaudreault,[†,§] and Gaétan Laroche*[,†,‡]

Unité de Biotechnologie et de Bioingénierie, Centre de Recherche de l'Hôpital Saint-François d'Assise, C.H.U.Q., 10 rue de l'Espinay, Québec, Québec, Canada, G1L 3L5, Département de Génie des Mines, de la Métallurgie et des Matériaux, Centre de Recherche en Science et en Ingénierie des Macromolécules, Faculté des sciences et génie, Université Laval, Québec, Québec, Canada, G1K 7P4, and Département de Médecine, Faculté de Médecine, Université Laval, Québec, Québec, Canada, G1K 7P4. Received June 18, 2004

This study presents two-step and multistep reactions for modifying the surface of plasma-functionalized poly(tetrafluoroethylene) (PTFE) surfaces for subsequent conjugation of biologically relevant molecules. First, PTFE films were treated by a radiofrequency glow discharge (RFGD) ammonia plasma to introduce amino groups on the fluoropolymer surface. This plasma treatment is well optimized and allows the incorporation of a relative surface concentration of approximately 2−3.5% of amino groups, as assessed by chemical derivatization followed by X-ray photoelectron spectroscopy (XPS). In a second step, these amino groups were further reacted with various chemical reagents to provide the surface with chemical functionalities such as maleimides, carboxylic acids, acetals, aldehydes, and thiols, that could be used later on to conjugate a wide variety of biologically relevant molecules such as proteins, DNA, drugs, etc. In the present study, glutaric and *cis*-aconitic anhydrides were evaluated for their capability to provide carboxylic functions to the PTFE plasma-treated surface. Bromoacetaldehyde diethylacetal was reacted with the aminated PTFE surface, providing a diethylacetal function, which is a latent form of aldehyde functionality. Reactions with cross-linkers such as sulfo-succinimidyl derivatives (sulfo-SMCC, sulfo-SMPB) were evaluated to provide a highly reactive maleimide function suitable for further chemical reactions with thiolated molecules. Traut reagent (2-iminothiolane) was also conjugated to introduce a thiol group onto the fluoropolymer surface. PTFE-modified surfaces were analyzed by XPS with a particular attention to quantify the extent of the reactions that occurred on the polymer. Finally, surface immobilization of fibronectin performed using either glutaric anhydride or sulfo-SMPB activators demonstrated the importance of selecting the appropriate conjugation strategy to retain the protein biological activity.

INTRODUCTION

Nowadays, biomolecule grafting onto polymer surfaces is often used for biological detection involving viruses, DNA, proteins, etc. (*1*−*5*), as well as for improving biomaterial surface properties such as hemocompatibility and biocompatibility (*6*−*16*). Most of the time, the conjugation procedures involve the chemical modification of the biomolecules to be grafted with appropriate functionalities and subsequent reactions involving reactive groups on the surface (*1*−*4*). However, such biomolecule chemical modifications often lead to denaturation or polymerization phenomena that alter or nullify their biological activity. It seems therefore more suitable to modify the surface onto which the molecule should be conjugated with appropriate chemical functionalities and thereafter proceed to the conjugation of the native and optimally active biomolecule. The first step of the latter strategy involves polymer surface modification with reactive functionalities for further chemical reaction with various reagents that will provide the moieties able to bind biomolecules. In this context, radiofrequency glow discharge (RFGD) plasma treatment was proven in the past to be a technique of choice as it allows the incorporation of reactive moieties onto the polymer surfaces with no modification to the bulk material (*17*, *18*). This approach was successfully used to functionalize the surface of polymers such as polyethylene, polypropylene, polyesters, and poly(tetrafluoroethylene) (PTFE) (*19*−*32*).

Because of some favorable properties such as high electrical resistivity and good thermal and chemical stability, PTFE has been the subject of several investigations to modify its surface through plasma treatments in order to benefit from its bulk characteristics while modulating its surface behavior (*19*, *21*, *22*, *24*, *26*−*35*). In the 1960s, Hansen and Schonhorn were the first to employ plasma treatments to modify the hydrophobic PTFE surface and succeeded in rendering it hydrophilic (*32*). In addition, plasma surface modifications enable the introduction of new chemical functionalities onto the surface depending on the gases employed. For example,

* Corresponding author. Phone: (418) 656-2131 ext. 7983. Fax: (418) 656−5343. E-mail: gaetan.laroche@gmn.ulaval.ca.
[†] Centre de Recherche de l'Hôpital Saint-François d'Assise.
[‡] Département de Génie des Mines, Université Laval.
[§] Département de Médecine, Université Laval.

10.1021/bc049858u CCC: $27.50 © 2004 American Chemical Society
Published on Web 08/20/2004

ammonia is used to provide amino groups (*20*, *24*, *28*, *31*, *36*, *37*) as well as other nitrogen-containing moieties on the modified surface. Plasma treatments involving CO_2, H_2O, and CO_2/H_2O, to introduce carboxylic acid groups onto the surface, were also largely utilized as well as treatments with H_2/H_2O, O_2/H_2O and H_2/O_2 leading to alcohols and other oxygen-containing functionalities (*19*, *23*, *38*, *39*). However, performing plasma treatments with different gases requires exhaustive optimization of the reaction parameters such as gas pressure and flow, treatment time, power of the radiofrequency field, to maximize the reactive moieties surface concentration while minimizing surface damages. The optimization of these plasma treatments requires extensive characterization of the modified surfaces, control of the plasma composition, and the plasma−polymer interaction through the use of in-situ plasma spectroscopic quantifications and X-ray photoelectron spectroscopy (XPS) surface analyses.

In this context, our strategy to introduce various chemical functionalities onto the PTFE surface consists of treating the polymer using a fully optimized radiofrequency glow discharge (RFGD) ammonia plasma reactor during the first step of the procedure (*31*). Using appropriate experimental conditions, this protocol allows the maximization of the amino group surface concentration while almost completely eliminating surface damages. In addition, this surface treatment was proven to be noncytotoxic (*36*, *37*), therefore enabling its use in several biological applications where living tissues are involved. The nucleophilic surface amino groups are further used for the covalent binding of various chemical reagents which, in turn, allow the grafting of useful functionalities such as maleimides, carboxylic acids, thiols, acetals and aldehydes. The presence of these reactive surface functionalities on the polymer opens the door to a wide variety of biomolecule conjugation strategies.

In this study, glutaric anhydride was used to introduce carboxylic groups at the surface of the ammonia plasma-treated PTFE films. Likewise, *cis*-aconitic anhydride was reacted with the aim to double the surface concentration of carboxylic groups obtained as compared to glutaric anhydride grafting. Following appropriate activation, acidic moieties are able to react with amino groups to form stable amide bonds. Moreover, reaction with bromoacetaldehyde diethylacetal (BADEA) was also evaluated to provide ethylacetal functionalities on the PTFE ammonia plasma-treated surface. Acetals are commonly used as latent protecting groups for aldehydes (*40*). Once the acetal group is removed, the regenerated aldehyde can react swiftly with aminated entities. Additionally, the reaction of sulfo-succinimidyl-4-(*N*-maleidomethyl)-cyclohexane-1-carboxylate (S-SMCC) and similarly the reaction of sulfo-succinimidyl-4-(*p*-maleimidophenyl)butyrate (S-SMPB) with the surface amino moieties were assessed to provide a maleimide functionality suitable to carry out further chemical conjugations of thiolated molecules such as fibronectin (*41*). Finally, 2-iminothiolane was used to introduce a thiol function onto the fluoropolymer surface that can be used afterward for the coupling of either S-SMCC- or S-SMPB-modified molecules.

Particular attention was paid to quantify the extent of the chemical reactions performed on the polymer surface. Along with calculations originating from surface derivatization strategies, X-ray photoelectron spectroscopy is particularly well suited to perform such measurements. This spectroscopic technique was also very useful for the detection of specific functionalities present through peak fitting of core level spectra, especially that of the carbon 1s orbitals. This spectral region presents a relatively good sensitivity and a wide literature associating the various binding energies to the corresponding carbon binding states (*42*).

EXPERIMENTAL PROCEDURE

Materials. Poly(tetrafluoroethylene) (Teflon) films were purchased from Goodfellow (Huntingdon, England). Phosphate-buffer-saline (PBS, pH 7.4) was purchased from VWR Canlab (Ville Mont-Royal, QC, Canada) while 2-(*N*-morpholino)ethanesulfonic acid buffer (MES, pH 4.75) was obtained from Sigma-Aldrich (Milwaukee, WI). Molecules to be grafted such as glutaric anhydride, *cis*-aconitic anhydride, bromoacetaldehyde diethylacetal, sulfo-SMCC, 1-ethyl-3-(3-dimethylaminopropyl)carbodiimide hydrochloride (EDC), Lys-Lys dimer, human fibronectin, and reagents such as 5-bromosalicylaldehyde and sodium cyanoborohydride were obtained from Sigma-Aldrich (Milwaukee, WI). Other molecules to be immobilized onto PTFE such as 2-iminothiolane (Traut reagent) and sulfo-SMPB were acquired from Pierce (Brockville, ON, Canada). Buffer solutions were prepared in filtered, deionized water (Nanopure system) at 0.2 M. Fine adjustments of the pH (7.4 or 8.0, depending on the reaction to be performed) were made by adding either 0.1 M of HCl or NaOH to reach the desired value. All chemicals were of commercial grades of highest purity and were used without further purification. The cell culture experiments were performed with the HT1080 human fibrosarcoma cell line (American Type Cell Culture, Manassas, VA) in Dulbecco's modified Eagle's Medium (DMEM) (Sigma-Aldrich, Milwaukee, WI) supplemented with penicillin, streptomycin, and glutamine (Life Technologies, St Paul, MN) using 96-well tissue culture plates (Fisher Scientific, Whitby, ON, Canada).

Methods. *Preparation of PTFE Surfaces.* PTFE surfaces of 3 cm × 3 cm were cleaned ultrasonically for 10 min successively after immersion in high purity methanol, deionized water, and acetone. The films were then air-dried and kept under vacuum until use. The cleaning procedure was validated by XPS showing the presence of only carbon and fluorine in the appropriate stoichiometric ratio.

Plasma Treatment. The ammonia plasma treatment and system apparatus were described elsewhere (*22*, *31*). Briefly, the treatments were performed at a power of 20 W and a pressure of 300 mTorr for 250 s using high purity ammonia gas. The PTFE films were held by a Teflon-made circular sample holder and treated in a cylindrical plasma chamber. Only the internal side of the film was treated using such a plasma configuration and geometry.

Characterization. Immediately following the ammonia plasma treatment, the aminated-PTFE film was cut into nine one-cm^2 samples in a glovebox purged with dry nitrogen in order to minimize the surface oxygen uptake. Three samples, one coming from each row and column, were analyzed by XPS without delay to assess the exact atomic composition of the surface following the plasma treatment. The XPS spectra were recorded using a PHI 5600-ci spectrometer (Physical Electronics, Eden Prairie, MN). A monochromatic aluminum X-ray source (1486.6 eV) at 400 W with neutralizer was used to record the survey spectra while high-resolution spectra were obtained using the monochromatic magnesium X-ray source (1253.6 eV) at 400 W without charge neutralization. The

detection was performed at 45° with respect to the surface normal.

Three other samples were used to quantify the amine surface concentration through vapor-phase chemical derivatization using 5-bromosalicylaldehyde as described previously (*31*). Briefly, the reaction was performed at 85 °C for 2 h in a sealed glass tube in which a 1 cm-thick bed of soda-lime glass beads was used to separate the reagent from the reactive surface. The surfaces were then vacuum-dried overnight at 40 °C and analyzed by XPS. Taking into account the nine newly bonded atoms upon reaction of 5-bromosalicylaldehyde with the surface amino groups, the amine surface concentration can be determined through eq 1.

$$[\%NH_2] = [\%Br]/(100 - 9 \times [\%Br]) \times 100 \quad (1)$$

Yield Calculations. The atomic percentages following plasma treatment and the amine surface concentration are essential to calculate the theoretical atomic percentages expected for any given chemical reaction aiming at providing a new chemical functionality on the ammonia plasma-treated PTFE. Basically, the efficiency of a surface chemical reaction may be calculated from the knowledge of the surface concentration variation for any atom present on the surface before and after the chemical grafting reaction as determined from XPS as described in eq 2.

$$[\%A] = \frac{[A]_0 + y \times [NH_2]_0}{100 + w \times [NH_2]_0} \times 100 \quad (2)$$

In this equation, A is the atom for which the surface concentration is measured by XPS, $[A]_0$ is the surface concentration of the atom A on the plasma-treated film surface measured readily after the plasma treatment, $[NH_2]_0$ is the amine surface concentration determined from the vapor-phase chemical derivatization, *y* and *w* are the number A-type atoms and the total number of atoms in the newly bonded molecule, respectively. The conversion factor, *x*, is equal to 0 in the case where no reaction occurs and 1 in the case of a complete reaction. The denominator in the right term takes into account for the total number of newly added atoms coming from the reagent as well as the atoms lying underneath and probed by the XPS analyses.

The yields of the chemical reactions were obtained from the ratio between the experimental atomic percentage measured by XPS analyses and the calculated theoretical atomic percentage for a particular atom. Indeed, one would expect the atom A experimental relative surface concentration to increase following a chemical reaction with a molecule containing a higher atom A concentration ratio than that measured on the ammonia plasma-treated PTFE surface.

Chemical Reactions. The last three samples to be grafted with the various chemical reagents were placed individually in three 5 mL polypropylene tubes in such a manner to avoid mechanical overlay of the samples that would interfere with the chemical reaction.

For each of the three PTFE-amino modified samples grafted with a molecule, five punctual areas were analyzed by XPS. Moreover, each grafting was made in triplicate to ensure that the values presented therein are statistically significant.

Grafting of Anhydrides. A solution of 55 mg/mL of glutaric anhydride in acetone was prepared in a glovebox under a dry nitrogen atmosphere. The reaction was performed for 60 min at room temperature under mechanical agitation. After 20 and 40 min, the concentration of glutaric anhydride was raised to 65 and 75 mg/mL respectively, to ensure completion of the reaction. Similarly, acetonic solution of *cis*-aconitic anhydride at a concentration of 100 mg/mL was prepared in a glovebox purged with nitrogen. The reaction mixture was mechanically agitated at room temperature for 120 min. After 30 and 60 min, the concentration of *cis*-aconitic anhydride in the solution was increased to 125 and finally 150 mg/mL. One cm^2 films were reacted with 1 mL of the anhydride acetonic solution.

Grafting of BADEA. Plasma-treated films were also reacted with bromoacetaldehyde diethylacetal. The aminated-PTFE samples were immersed individually in 1 mL of pure bromoacetaldehyde diethylacetal and agitated for 2 h at room temperature. To ascertain the success of the reaction, the diethylacetal function was further hydrolyzed afterward in a 10% HCl solution stirred at room temperature for 2 h (*40*). The films were then thoroughly washed with deionized water and the aldehyde functionality was used for the subsequent grafting of the dipeptide Lys-Lys. A solution of 4 mg of Lys-Lys in 1 mL PBS at pH 7.4 was stirred for 5 min at room temperature, and the imine bond formed was immediately reduced to amine by adding 8 mg of $NaBH_3CN$ to the reaction mixture that was stirred for 3 h at room temperature.

Grafting of Maleimide Derivatives. Sulfo-SMCC and sulfo-SMPB were reacted with the ammonia plasma-treated film samples in 1 mL of 3 mg/mL solutions of reagent in PBS at pH 7.4. The reactions were then allowed to proceed for 2 h under a nitrogen atmosphere and under low light intensity to protect the reactants.

Generation of Thiolated Functionalities. Finally, 2-iminothiolane was also reacted with the aminated-PTFE surface immediately after the plasma treatment. The samples were reacted in solutions containing 30 mg/mL of 2-iminothiolane in PBS at pH 8.0. The reaction was allowed to proceed under constant agitation for 2 h under a nitrogen atmosphere. Meanwhile, to ascertain the completion of the reaction, the cross-linking agent S-SMPB was conjugated to Lys-Lys in a solution containing 5 mg of S-SMPB (1.09 mmol) and 7.6 mg of Lys-Lys (2.18 mmol) in 1 mL of PBS at pH 7.4 (41). Lys-Lys was added in excess to ensure that all the terminal succinimidyl groups would react exclusively with the dipeptide's amino groups instead of unreacted amines on the PTFE surface if there were any. This mixture was stirred for 2 h at room temperature. The rinsed thiolated films were then immersed in the solution containing the S-SMPB-derived dipeptide and the reaction allowed to proceed for 2 h under constant mechanical agitation at room temperature.

Grafted films were all washed thoroughly with deionized water. BADEA grafted films were first washed with methanol and then with deionized water. Afterward, the films were vacuum-dried overnight at ambient temperature before analysis by XPS.

Fibronectin Grafting. Prior to the immobilization of human fibronectin, glutaric anhydride-grafted films were activated with a solution containing 3 mg/mL of EDC in MES buffer (0.1 M, pH 4.75). Two subsequent additions of 3 mg of EDC were made to this solution every 10 min during 20 min at room temperature and under stirring (for a total reaction time of 30 min) to minimize the effect of the water-induced hydrolysis of the activator on the grafting efficiency. These films were then extensively washed with the MES buffer. Both the glutaric anhydride-

Table 1. Average Atomic Percentages, Amine Surface Concentration, and Atomic Ratios as Probed by XPS for Virgin PTFE and Plasma-Treated PTFE Films

films	%C	%F	%N	%O	$\%NH_2$[a]	*F/C*	*O/C*	*N/C*
virgin	32.2	66.6	–	1.2	–	2.07	0.04	–
plasma-treated	46.6 ± 2.9	38.8 ± 4.6	11.2 ± 1.8	2.9 ± 0.9	2.5 ± 0.6	0.83	0.06	0.24

[a] Determined through vapor-phase chemical derivatization using 5-bromosalicylaldehyde.

grafted films activated with EDC and the S-SMPB grafted films were reacted with a PBS solution containing 10 μg/mL of human fibronectin at pH 7.4 for 3 h under mechanical agitation. They were washed five times with deionized water and cut in 5.9 mm diameter circles with an awl to fit in a 96-well tissue culture plate.

Cell Adhesion Experiments. *Cell Culture.* The HT1080 human fibrosarcoma cell line was used for all the experimentation. The culture medium was Dulbecco's modified Eagle's Medium (DMEM) with 10% fetal bovine serum, 100 U/mL penicillin, 100 μg/mL streptomycin, 0.3 mg/mL glutamine, 100 μM citrate, and 0.1% BSA. The cells were cultured at 37 °C and 98% humidity in air containing 5% CO_2.

Cell Adhesion on Modified PTFE. To check the availability of the cell interaction sites on the PTFE bound fibronectin, adhesion tests were performed with HT1080 cells known for their strong affinity to adhesion sequences of the protein. 5.9 mm diameter circles of clean PTFE, ammonia plasma-treated PTFE, ammonia plasma-treated PTFE conjugated with glutaric anhydride, fibronectin conjugated on ammonia plasma-treated PTFE through glutaric anhydride, ammonia plasma-treated PTFE conjugated with S-SMPB, and fibronectin conjugated on ammonia plasma-treated PTFE through S-SMPB were prepared and put in a 96-well tissue culture plate, with the treated face up. Human fibronectin (10 μg/mL in PBS at pH 7.4) was coated 2 h at 37 °C in five empty wells and washed twice with PBS. All wells were blocked with 1% BSA overnight at 4 °C, to prevent any nonspecific cell adhesion, and washed twice with PBS. The HT1080 cells in culture were harvested with trypsin, counted, and diluted in 10% DMEM serum and 0.1% BSA to reach a final concentration of 250 000 cells/mL. An amount of 50 000 cells was seeded in each well, and the plate was incubated for 10 min at 37 °C. The wells were then washed twice with DMEM without serum, and cells were stained with violet crystal for 20 min. After washing, all wells were photographed and the number of cells per square millimeter was counted. Statistical analysis of the difference between each group was performed using the analysis of variance (ANOVA) followed by Dunnett's test where appropriate. *P* values lower than 0.01 were considered significant and all data were expressed as mean ± standard error (SE).

RESULTS

Surface Composition of the Plasma-Treated Surface. The relative surface concentrations of carbon, fluorine, nitrogen and oxygen atoms as well as the amine concentration were determined for each sample to control the efficiency of each reaction step. The relative atomic percentage of nitrogen detected on the PTFE surface film after plasma treatment was 11.2% on average. Among these nitrogen-containing species, approximately one-fifth were shown to be amino moieties as measured by derivatization with 5-bromosalicylaldehyde (Table 1). These results are in agreement with those already available from the literature (*22, 27, 31*).

Selection of the Atom Used as XPS Probe To Follow the Extent of Surface Reaction. For the purpose of this study, it seemed that in all cases the oxygen content probed at the modified surface by XPS analyses was the best choice for calculating the yield of the reactions. Indeed, the surface concentration of this atom is only slightly affected upon exposure to solvents such as PBS as demonstrated in Figure 1. In addition, the molecules grafted on the PTFE surface are heavily loaded with oxygen atoms. In fact, the newly bonded molecules contained between one and five oxygen atoms. The ratio *O/n* (where n is the total number of newly bonded atoms) were of 3/8 or 38% for glutaric anhydride, 5/11 or 45% for *cis*-aconitic anhydride, 2/8 or 25% for BADEA, 1/6 or 17% for 2-iminothiolane, 3/16 or 19% for SMCC, and finally 3/18 or 17% for SMPB, respectively. The relative oxygen concentration of these molecules is by far higher than that measured on the plasma-treated PTFE surfaces exposed to PBS. In addition, our XPS data (not shown) demonstrated that, once grafted with the various molecules investigated, the surfaces were stable over time. It should be pointed out, on one hand, that both fluorine and carbon surface concentrations, despite leading to less relative variations than those measured for oxygen upon molecule conjugation, provided very similar evaluation of the reaction yields. On the other hand, nitrogen is clearly a less suitable probe, as some of the nitrogen-containing species, other than amino groups, were shown to be readily removed from the surface upon exposure to water, which is the solvent used to perform some of the reactions presented therein. Possible explanations of this phenomenon are related to displacement of polar groups from the surface into the bulk, hydrolysis of surface imine moieties also created during the ammonia plasma treatment, and dissolution in water of low molecular weight fragments known to be formed during the plasma process (*22, 31*). Therefore, this leads to an overestimation (more than 80% in the present case) of the initial nitrogen surface concentration, required to perform an accurate calculation of the reaction

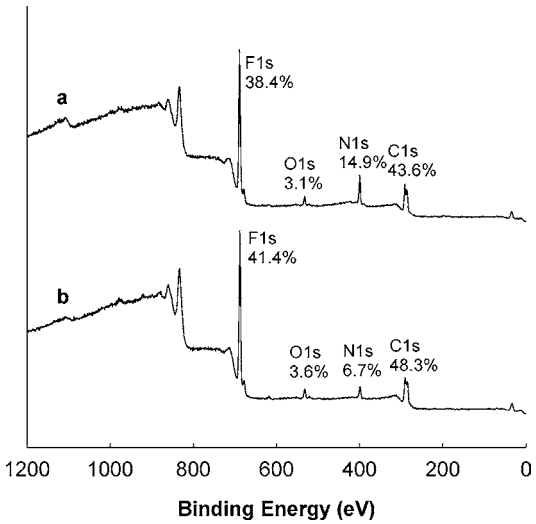


Figure 1. Typical XPS spectra of ammonia plasma-treated PTFE surfaces before (a) and after (b) immersion in PBS, showing that the oxygen surface concentration is only slightly affected upon contact with the aqueous solution.

Table 2. Glutaric Anhydride Grafting. The $[NH_2]_0$ Average for These Plasma Treatments Was 2.4%

	%C	%F	%N	%O
plasma treatment	47.1 ± 1.3	39.7 ± 3.0	11.3 ± 1.1	1.9 ± 0.2
glutaric anhydride	52.5 ± 0.6	35.1 ± 1.8	5.1 ± 0.9	7.3 ± 0.7
theoretical values	49.6	33.3	9.5	7.6
Δ experimental	+5.4	−4.6	−6.2	+5.4
Δ expected	+2.5	−6.4	−1.8	+5.7
% yield	106 ± 3	95 ± 9	54 ± 9	96 ± 6

yields. As XPS probes relative surface concentrations, the loss of nitrogen (8.2% from Figure 1) is mainly reported in the relative concentrations of both carbon and fluorine (Figure 1) and therefore leads to less important relative overestimations, as the surface concentration of these two atoms is inherently higher than that of nitrogen.

Grafted Molecules. These latter observations are further supported through the XPS data recorded in the case of glutaric anhydride conjugation on ammonia plasma-treated PTFE (Table 2). As depicted in Table 2, the oxygen surface concentration increased by 5.4% upon glutaric anhydride grafting. Therefore, based on this atom surface concentration, it can be confirmed that the glutaric anhydride grafting is very successful, the yield of the reaction being near 100%. Both carbon and fluorine XPS signals, with surface variations of +5.4% and −4.6%, respectively, lead to similar conclusions with calculated reaction yields reasonably close to 100% (106 ± 3% and 95% ± 9 using the carbon and fluorine XPS signal, respectively). Performing the calculations with the nitrogen signal leads to a very different trend with an extent of reaction of 54 ± 9%, in agreement with the fact that the initial nitrogen surface concentration is overestimated due to the removal of some of the nitrogen-containing species upon exposure to water.

The successfulness of this reaction is confirmed more visually by the comparison of the XPS spectrum for each steps of the glutaric anhydride grafting process (Figure 2). Nitrogen is obviously not observed on the virgin PTFE surface and presents a surface concentration of 11.3% immediately after the ammonia plasma treatment. The amino group surface concentration on this particular aminated-surface was assessed to be 2.4% through surface derivatization and allowed the grafting of glutaric anhydride thereafter raising the carbon and oxygen peaks from 47.1% and 1.9% to 52.5% and 7.3%, respectively, while diminishing the fluorine and nitrogen peaks from 39.7% and 11.3% to 35.1% and 5.1%, respectively.

The conjugation of glutaric anhydride to aminated-PTFE being successful, further studies were made using *cis*-aconitic anhydride. Reaction of *cis*-aconitic anhydride with the amino groups provides two free carboxylic groups for every grafted molecule (Figure 3a), hence theoretically doubling the density of carboxylic acid group surface concentration as compared to the glutaric anhydride conjugation. In addition, *cis*-aconitic anhydride is recognized to form labile amide bonds with drugs such as daunorubicin that slowly hydrolyze in aqueous solutions to release the drug in its native form (*43*). On the basis of the oxygen surface concentration, the *cis*-aconitic anhydride yielded to a 76% reaction with the amines. The expected 2-fold increase of the carboxylic acid functionalities was therefore not reached. Instead, conjugation with *cis*-aconitic anhydride allows adding approximately 1.5 times more carboxylic acid moieties onto the polymer surface as compared to the aforementioned grafting of glutaric anhydride. As predicted from the molecular structure of *cis*-aconitic anhydride, XPS spectra showed an increase in carbon and oxygen atomic content, from 47.2% and 3.0% to 54.4% and 9.7%, respectively, whereas

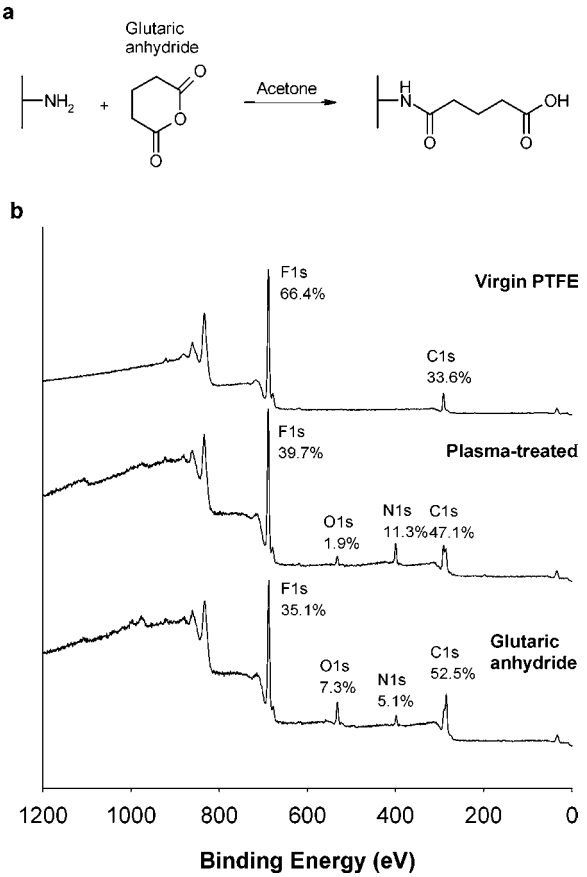


Figure 2. (a) Synthetic scheme of glutaric anhydride grafting onto an ammonia plasma-treated PTFE film. (b) Spectra for plasma-treated PTFE film and glutaric anhydride-grafted PTFE film. $[NH_2]_0$ was 2.4% and the yield of the reaction 96 ± 6% based on the oxygen surface concentration.

the fluorine and nitrogen content decreased along from 35.6% and 13.8% to 30.5% and 5.3%, respectively (Figure 3b).

Grafting of both anhydrides was successful, and thereafter the free carboxylic groups generated could further be activated by several carboxyl-activating agents (*5*, *10*, *41*, *44*) such as *N*-hydroxysuccinimide (NHS), 1-ethyl-3-(3-(dimethylamino)propyl)carbodiimide (EDC), and carbonyldiimidazole (CDI) to conjugate numerous organic or biologic molecules containing amine functionalities, therefore leading to the formation of an amide link between the biomolecule and the polymer surface.

Bromoacetaldehyde diethylacetal (BADEA) also allows the conjugation of amino group-containing biomolecules. However, in this case, the reaction of the imine group generated in the reaction between the PTFE-aldehyde and the amine-bearing biological molecule with the borohydride leads to the formation of a substituted amine, which is stable to hydrolysis. Grafting of BADEA was also successful, with a reaction yield of 57% according to the oxygen surface concentration (Figure 4). Although the atomic percentages obtained from XPS seem to point toward at least a partially grafted surface,

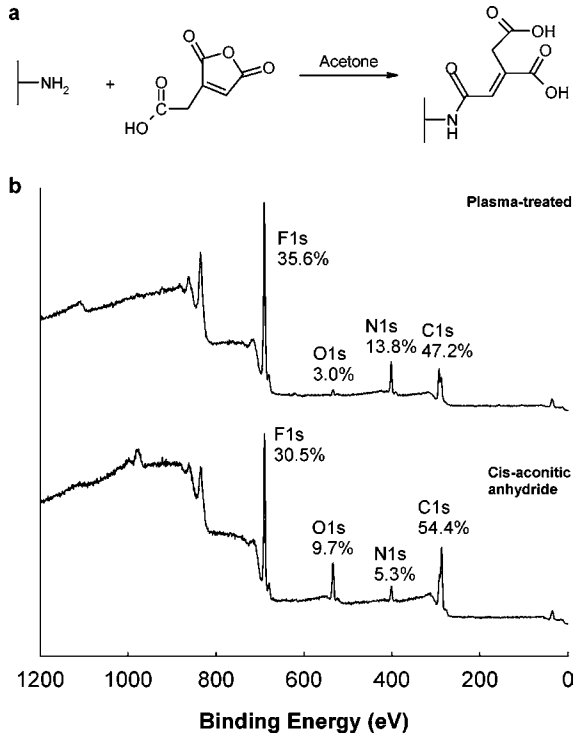


Figure 3. (a) Synthetic scheme of *cis*-aconitic anhydride grafting onto an ammonia plasma-treated PTFE film. (b) Spectra for plasma-treated PTFE film and *cis*-aconitic anhydride-grafted PTFE film. $[NH_2]_0$ was 2.7% and the yield of the reaction 76 ± 15%.

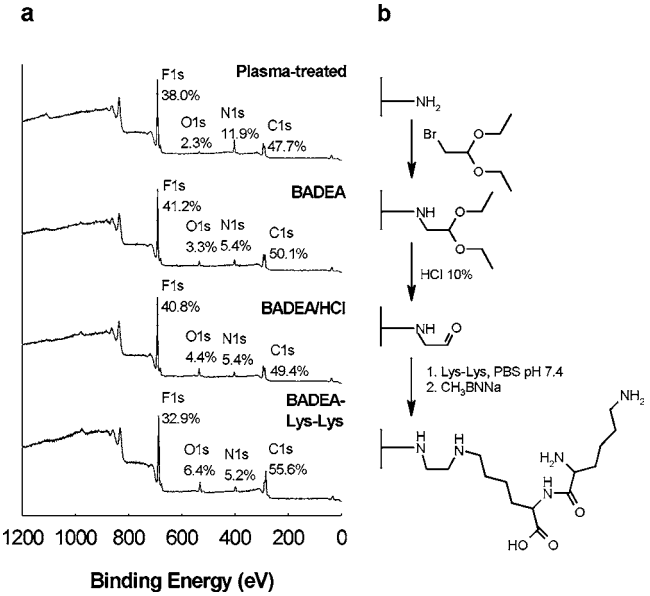


Figure 4. (a) XPS spectra for each step of bromoacetaldehyde diethylacetal grafting and subsequent reaction with dipeptide Lys-Lys. (b) Synthetic scheme of bromoacetaldehyde diethylacetal grafting onto an ammonia plasma-treated PTFE film, subsequent reduction of the diethylacetal into aldehyde functionality, and further conjugation with Lys-Lys. $[NH_2]_0$ was 2.5% and the yield of the reaction of BADEA with the amino groups 57 ± 8%

the reaction was not complete enough to ascertain the grafting. Therefore, to establish whether the BADEA grafting was successful and provided ethylacetal functionality, this functionality was hydrolyzed into the more nucleophilic aldehydic group. The aldehyde moiety provides only three newly bonded atoms to the PTFE surface compared to the plasma-treated analyzed surface. In other words, hydrolysis of the ethylacetal functionality decreases by five the number of atoms as compared to the surface grafted with BADEA before the hydrolysis that is too small to ascertain its presence on the surface. Thus, it was further reacted with the dipeptide Lys-Lys, and immediately the imine group was reduced into a stable amine using sodium cyanoborohydride (Figure 4b). This reaction provides 18 supplementary atoms on the analyzed surface, well enough to confirm its presence and therefore provided indirect solid evidences for the bromoacetaldehyde diethylacetal grafting successfulness. This is confirmed by the atomic percentages obtained at each step of the process and more visually by the XPS spectra of each of these steps (Figure 4a). The oxygen content increases from 3.3% to 4.4% upon hydrolysis of the diethylacetal moieties and finally to 6.4% after conjugation of Lys-Lys to the BADEA-grafted surface. The small increase of the relative atomic oxygen percentage upon hydrolysis of the acetal groups, despite being surprising is normal because the relative oxygen content increases from 25% (two oxygen atoms out of eight atoms total) to 33% (one oxygen atom out of three atoms total).

Grafting of sulfo-succinimidyl-4-(*N*-maleidomethyl)-cyclohexane-1-carboxylate (sulfo-SMCC) on the aminated-PTFE (Figure 5a) was also studied in order to bind the biomolecules through their thiol groups (*41*). It appeared that the reaction between sulfo-SMCC and the amine moieties present at the surface of the PTFE plasma-treated film was very successful, with a quantitative reaction yield, considering the experimental error. The efficacy of the reaction is depicted in Figure 5c: the carbon content increased from 46.1% to 54.5% while the oxygen content increased from 2.2% to 7.9%. Accordingly, the fluorine and nitrogen content decreased from 42.1% and 9.7% to 30.9% and 6.0%, respectively.

The ability of sulfo-succinimidyl-4-(*p*-maleimidophenyl)butyrate (sulfo-SMPB) to react with the amine moieties (Figure 5b) was also tested since, as a cross-linker, it provides the same double bond functionality as S-SMCC with a longer spacer arm, allowing to conjugate a second molecule further apart from the PTFE surface. XPS analyses showed the presence of 0.6% of sulfur (Figure 5d). These sulfur atoms must be originating from the sulfo group of the cross-linker. As aforementioned, sulfur exhibits a low XPS sensibility index and its presence added to an oxygen content superior than expected indicates that a competitive and unexpected reaction takes place. This reaction would allow the SO_3 part of S-SMPB to be grafted or adsorbed on the polymer surface, hence increasing the oxygen and sulfur content. The oxygen atomic percentage reported is therefore widely increased by this unknown reaction that explains the 163% yield calculated according to the oxygen content. Nevertheless the S-SMPB reaction is successful and the double bond function is available for subsequent reactions with for example sulfhydryl containing proteins such as fibronectin, which is known for enhancing cellular adhesion (*45*).

The C1s high-resolution spectra for SMCC and SMPB (Figure 5e) were curve-fitted into four components at 291.1, 288.4, 285.9, and 284.8 eV which were assigned to CF_2 components, $C{=}O$ groups, CN groups, and CH_x, CC, and $C{=}C$ moieties, respectively (*27, 46*). These spectra clearly indicate, either qualitatively and quantitatively, that both SMCC and SMPB are bonded to the PTFE surface. From a qualitative point of view, the relative peak area of the CF_2 components is largely reduced compared to that measured for the plasma-treated surface as the contribution of the other carbon

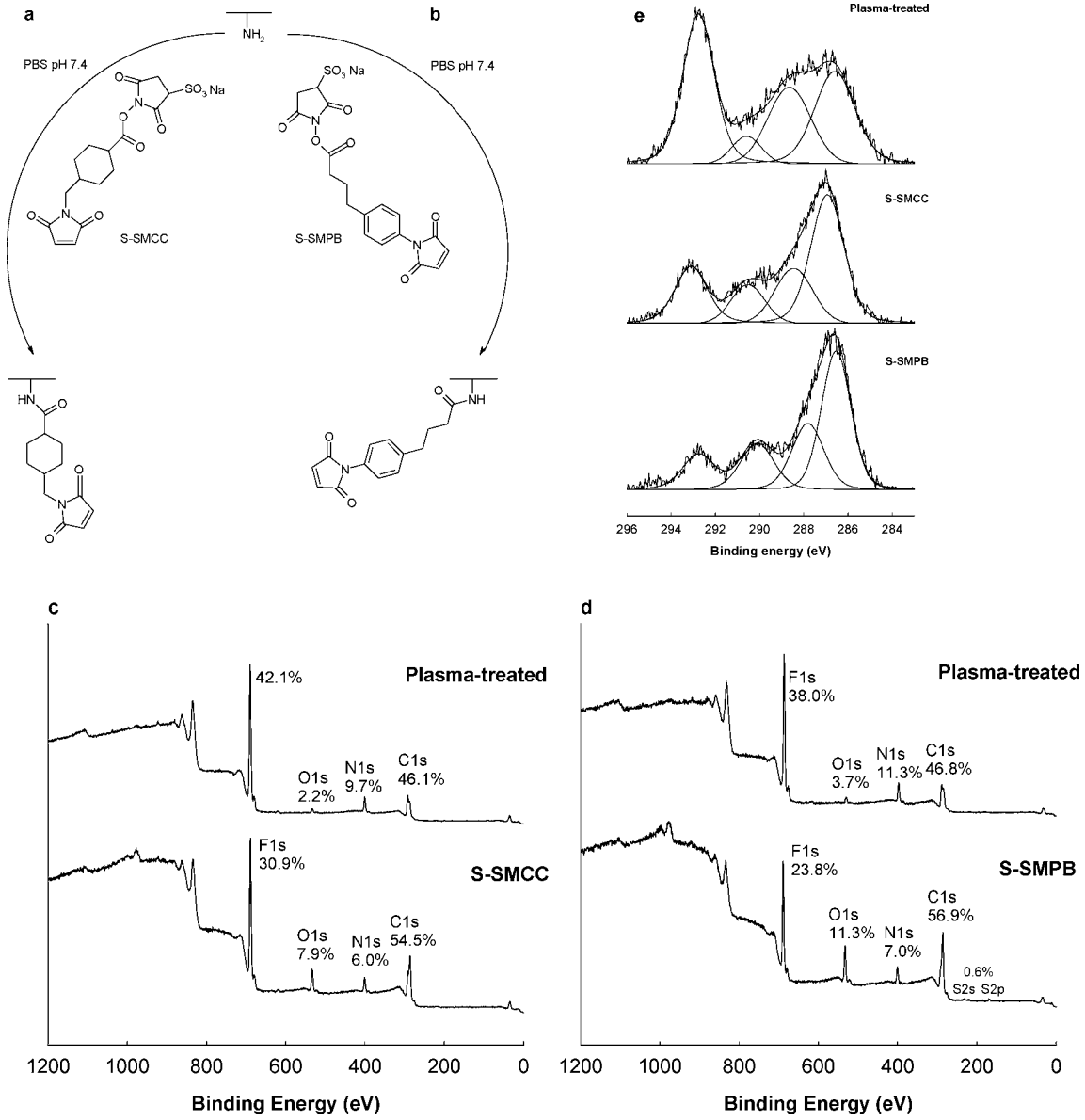


Figure 5. Synthetic schemes for S-SMCC (a) and S-SMPB (b) grafting on an ammonia plasma-treated PTFE film. Spectra for plasma-treated PTFE films and for SMCC- (c) and SMPB- (d) grafted PTFE films. $[NH_2]_0$ was 2.8% for the S-SMCC reaction and 1.9% in the case of S-SMPB grafting reaction. The former reaction presents a yield of 114 ± 25% and the latter reaction 163 ± 20%. C1s high-resolution spectrum (e) for S-SMCC and S-SMPB grafting. Panel e (top to bottom) shows the curve fits of the C1s XPS spectra of the ammonia plasma-treated PTFE surface and S-SMCC and S-SMPB PTFE-grafted surfaces, respectively.

spectral components increases when the cross-linkers are bonded to the surface. Quantitatively, the relative peak area of the curve fittings matches closely with the stoichiometric ratios of the carbon components in the grafted molecules. Moreover, the area of the *C*═O band located at 288.4 eV is useful to calculate the yield of the reactions. In the case of SMCC grafting, the *C*═O component corresponds to 17.0% of the total carbon contribution on the surface. Combining this value with the carbon content of 54.5% measured from the XPS survey spectrum lead to conclude that 9.3% of the atoms on the modified surface are *C*═O groups. As one SMCC-grafted molecule to an amino group provides three carboxylic groups, it means that the initial amino group surface concentration should be one-third of 9.3% that is 3.1%. This simplistic calculation closely matches with the value of 2.8% of amino groups determined through vapor-phase chemical derivatization and leads to a SMCC grafting reaction yield of 111% (3.1/2.8), which is in good agreement with the value of 114 ± 25% presented in Figure 4c. A similar calculation may be performed for the SMPB grafting reaction, as the *C*═O component at 288.4 eV correspond to 18.0% of the 56.9% carbon atom contribution after SMPB grafting. Again, if three *C*═O groups are covalently attached to the surface for every SMPB molecule, there would be 3.4% $[NH_2]_0$ on the plasma-treated PTFE film. For this plasma-treated film, derivatization with 5-bromosalicylaldehyde allowed measurement of an amino group surface concentration of 1.9%, therefore leading to a reaction yield of 179%, in fairly good agreement with the value reported in Figure 5d and therefore confirming the hypothesis of the occurrence of a competitive and unexpected reaction. Nevertheless, as aforementioned, this competitive reaction does not impede further conjugation of other molecules.

Grafting of the 2-iminothiolane was also performed since a successful grafting would provide a thiol functionality on the PTFE-ammonia plasma-treated surface ready to further react with a maleimidyl-containing molecule (*47*) (Figure 6a). Our XPS analysis first revealed

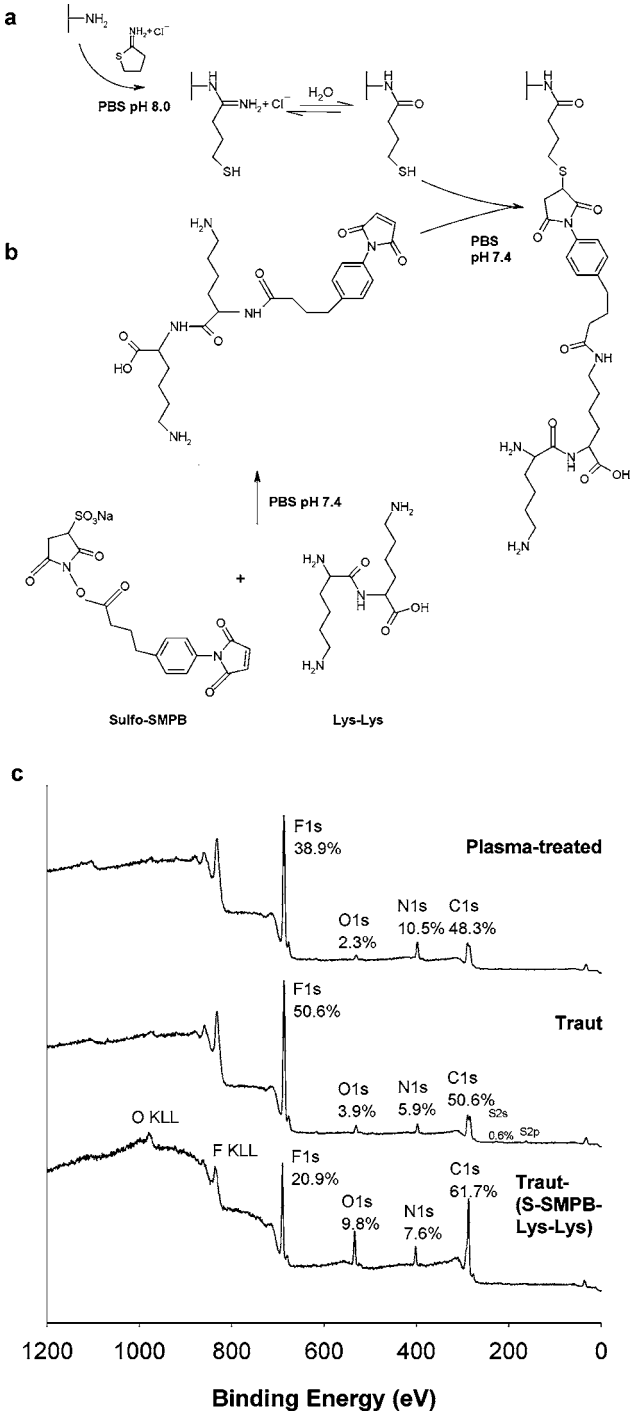


Figure 6. (a) Synthetic scheme of 2-iminothiolane grafting on an ammonia plasma-treated PTFE film and hydrolysis of the $C{=}NH_2^+Cl^-$ into an amide bond. (b) Synthetic scheme of the conjugation of sulfo-SMPB to the dipeptide Lys-Lys and reaction of the succinimidyl moiety of the cross-linker to the thiol function resulting from the reaction of 2-iminothiolane to the aminated-PTFE. (c) Spectra for plasma treated-PTFE film, 2-iminothiolane grafted-PTFE film and 2-iminothiolane-SMPB-Lys-Lys grafted-PTFE film. $[NH_2]_0$ was 2.7%. The yield of the reaction of 2-iminothiolane with the amino groups is 94 ± 12%, and the yield of the conjugation of SMPB-Lys-Lys to the thiol group of 2-iminothiolane is 82 ± 6%

that only 0.6% of sulfur was detected, and since this atom is hardly perceived by XPS spectroscopy, having a very low atomic sensitivity factor of 0.570 (*48*), we proceeded the same way as we did for bromoacetaldehyde diethylacetal to verify the presence of 2-iminothiolane on the plasma-treated PTFE surface. The thiol function was

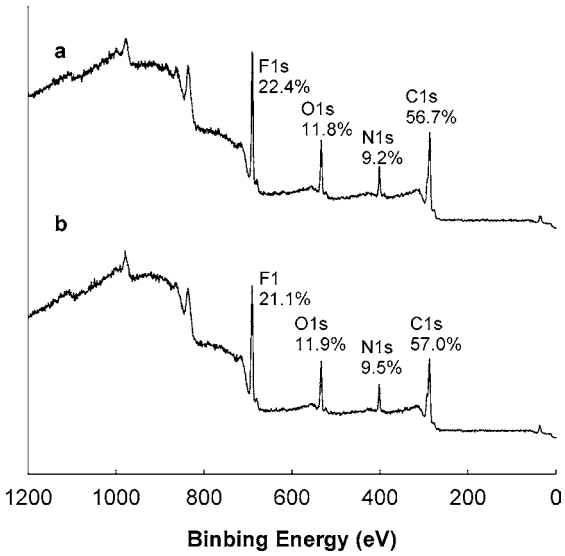


Figure 7. XPS spectra of fibronectin conjugated on ammonia plasma-treated PTFE previously activated with S-SMPB (a) or glutaric anhydride (b).

reacted with the maleimide functionality of sulfo-succinimidyl-4-(*p*-maleimidophenyl)butyrate (sulfo-SMPB) previously conjugated to Lys-Lys (Figure 6b). The increase of the molecular weight of the molecule grafted on the PTFE surface allows ascertaining the successfulness of the Traut reagent conjugation through XPS, as it provides 43 new atoms upon conjugation to the surface. The spectra and the atomic percentages obtained from XPS analyses clearly indicate that the reaction occurred (Figure 6c). 2-Iminothiolane was grafted on the fluoropolymer surface with a yield of reaction estimated to 94% according to the oxygen content, taking into account that the oxygen atom considered in the percentage yield equation comes from hydrolysis of $C{=}NH_2^+Cl^-$ groups into amide moieties. This estimate is also supported by the atomic percentages obtained following the grafting of the 43-atom molecule where again, if this latter reaction is complete, we get a higher than 80% yield for 2-iminothiolane grafting and the subsequent reaction with the dipeptide. The conjugation reaction of 2-iminothiolane to SMPB-lysine-lysine is a two-step reaction, where sulfo-SMPB first reacts with the dipeptide and then reacts with 2-iminothiolane, and both reactions may not be complete. Therefore, it is once more reasonable to assert a 94% yield for the grafting reaction of 2-iminothiolane to the plasma-treated PTFE film.

Grafting Fibronectin on Plasma-Treated PTFE Surfaces: Influence of the Conjugation Strategy on Cell Adhesion. A convincing example of the usefulness of the conjugation strategies and quantification methods presented above is seen through the immobilization of fibronectin on PTFE surfaces. The attachment of this protein on various material surfaces was shown to promote cell attachment and proliferation (*9*). In this context, fibronectin was covalently attached on plasma-treated PTFE samples previously reacted either with glutaric anhydride or S-SMPB. The XPS-spectra (Figure 7) of both surface samples clearly put in evidence that the same amount of protein was grafted with either surface activator, therefore eliminating the possibility of a fibronectin surface concentration effect on the cell adhesion experiments. However, using these surfaces in cell adhesion experiments leads to very different behaviors. As illustrated in Figure 8, a clean PTFE surface does not support cell adhesion. On the other hand, fibronectin

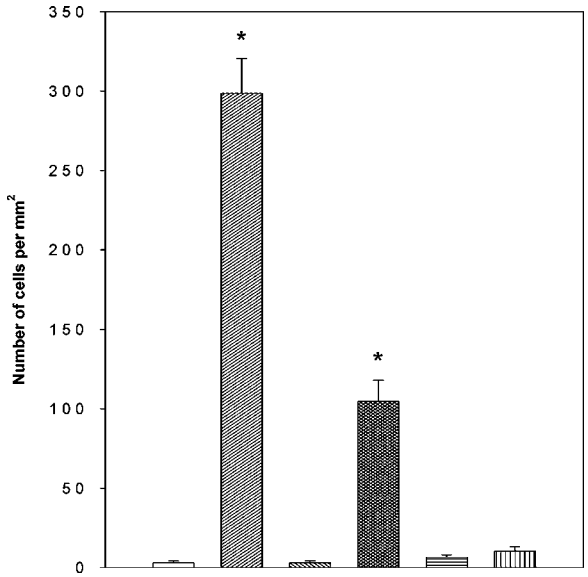


Figure 8. Adhesion of human endothelial vascular cells on a clean PTFE surface (□), in a well coated with fibronectin (right diagonal stripe), on ammonia plasma-treated PTFE conjugated with glutaric anhydride (left diagonal stripe), on fibronectin conjugated on ammonia plasma-treated PTFE through glutaric anhydride (dotted), on ammonia plasma-treated PTFE conjugated with S-SMPB (horizontal stripe), and on fibronectin conjugated on ammonia plasma-treated PTFE through S-SMPB (vertical stripe). (*) indicates a significant difference with respect to the clean PTFE surface with $p < 0.01$ according to Dunnett's test.

conjugated on ammonia plasma-treated PTFE through glutaric anhydride clearly supports cell adhesion, with about one-third of the cells observed for a well coated with fibronectin. In the opposite way, immobilization of fibronectin on ammonia plasma-treated PTFE using S-SMPB as activator gives rise only to slightly more cell adhesion than the clean PTFE surface. This surprising result tends to demonstrate that an inappropriate surface conjugation strategy of fibronectin may lead to conformational changes and/or hiding of biologically relevant protein adhesion sites.

DISCUSSION

Many research groups have focused their efforts for the past decades on modifying polymer surfaces using different types of plasma treatments (*19*, *20*, *28*, *30*, *38*, *49*). However, these treatments require sustained work of characterization over prolonged periods of time in order to determine the most effective plasma treatment conditions for a particular plasma apparatus and a specific polymer. The plasma procedure used in the present study has been the subject of a complete set of characterization while treating PTFE surfaces (*22*, *31*). These previously published data demonstrated that the surface plasma treatments were homogeneous and that it was possible to exert a control over the amine surface concentration through an appropriate selection of experimental parameters such as ammonia gas pressure and flow, treatment time, and radiofrequency power. From these works and considering various parameters intrinsic to the XPS analytical technique (such as the surface elements electron mean free path), it can be concluded that the 2−3.5% amino group relative surface concentration corresponds to about 0.5 to 2 amine every nm^2. This amino surface concentration is by far sufficient to conjugate biological molecules such as proteins, enzymes, or growth factors, considering that the surface plasma modification occurs on the first atomic layers of the polymer surface (*50*). For example, albumin, with a molecular weight of 66 kDa, has an elliptical shape and can cover 12 nm^2 in the best conditions (*51*). It means that one HSA molecule could cover between 6 and 24 amino groups on the PTFE surface, depending on the protein orientation on the surface, therefore showing that the amine surface concentration reached through radiofrequency glow discharge is by far sufficient to allow the grafting of molecules of biological interest.

This study reports a solid proof-of-concept for biotechnological applications of modified polymer-surfaces since only one type of plasma treatment is now required to optimally enable further reaction with chemical reagents and generation of chemical functionalities for biomolecule conjugation. Moreover, it appears that most of the chemical reactions that we have studied are very simple, straightforward, and easily performed using readily available reagents.

Conjugation of molecules onto polymer surfaces is commonly used in various spheres of biotechnology such as biochips and biomaterials fabrication. Most of the time, the developments in these fields are based on the awareness of the biological function and activity of biomolecules and on the assumption that they should preserve their characteristics once conjugated onto surfaces. However, such reasoning does not take into account some important aspects of biomolecule interactions with the surrounding environment. Indeed, the surface concentration of the conjugated biomolecule may play a key role to ensure the proper function of the surface-engineered material. Surface grafting of the vascular endothelial growth factor (VEGF) for improving vascular prostheses self-endothelialization is a good example of this assertion, as one of the characteristics of this molecule regulatory pathway is a cellular down-regulation in response to an excess of the growth factor (*52*, *53*). This issue points toward the fact that the construction of biotechnologically relevant surfaces requires the knowledge and control over the concentration of the linking arms aimed at binding the biomolecules. To our knowledge, the present study is the first to provide quantitative data on the reaction yields and chemical functionality surface concentrations obtained after chemical synthesis on surfaces.

The importance of accurately measuring the surface concentration of chemical moieties on surfaces raises the question of the choice of the surface analytical technique to perform a quantitative characterization. During the course of this study, the potential of other spectroscopic techniques, namely FTIR-ATR and Raman confocal spectroscopies, was also investigated in order to reach our objectives. On one hand, it turned out that FTIR-ATR allowed the measurement of spectral characteristics of the moieties grafted onto the plasma treated PTFE; however, the signal-to-noise ratio was too poor to allow any quantitative analyses. On the other hand, Raman confocal spectroscopy completely failed to provide any data because of the difficulty of precisely focusing the laser beam on the modified layer surface for which the thickness does probably not exceed a few nanometers. In this context, surface derivatization strategies coupled with the surface sensitivity of X-ray photoelectron spectroscopy, that probes about 10 nm in depth, despite being cumbersome, remains one of the best techniques to perform quantitative analyses on surfaces.

The second constraint to overcome upon conjugation of biomolecules onto surfaces is the ability of proteins, enzymes, or nucleic acids to retain their active confor-

mational structure during the surface grafting process. In this context, it is strategically more relevant to perform the first steps of the conjugation protocol on the polymer surface, as these procedures often require the utilization of harsh reaction conditions such as the use of organic solvents, hydrolysis in acidic aqueous solution, or direct contact with chemical reagents. Performing the surface conjugation through the reaction of the biomolecule with the cross-linker as the first step of the reaction may lead (and in fact often lead) to a complete loss of the biomolecule-targeted activity.

In connection with this idea, the various surface conjugation schemes presented in this publication open the way to the possibility of selecting appropriate synthetic pathways for preserving molecules bioactivity. Indeed, the endothelial cell adhesion data presented therein on fibronectin-grafted PTFE surfaces are good examples of the importance of selecting appropriate strategies for grafting biologically active molecules in an attempt to preserve their function. Most of the time, biological molecules are grafted on surfaces without any consideration for the conjugation scheme with the assumption that they will continue to play their biological roles. The Sheardown's group was the first to demonstrate that the surface orientation of cell signaling peptides such as RGD are of prime importance for promoting cell adhesion (*54*). The present publication goes a step further by unambiguously demonstrating that even larger molecules require to be conjugated with appropriate orientation/conformation on surfaces to ensure their biological function.

CONCLUSION

In this study, surface modification strategies for PTFE surfaces were developed to provide various chemical functionalities for further molecule immobilization. In a first step, a radiofrequency glow discharge (RFGD) ammonia plasma treatment was applied to PTFE films to covalently bind amino groups onto their surface. In a second step, various chemical reactions were performed, generating carboxylic acid, thiol, maleimide, ethylacetal, and aldehyde functionalities on the PTFE surfaces. The grafting reactions were carefully controlled at each step by XPS analyses, allowing quantifying the yield of each reaction. Some examples were also provided to confirm the accessibility and the reactivity of these new functional groups used also as a linking arm for relevant proteins, aiming at increasing the compatibility/function of the grafted material.

ACKNOWLEDGMENT

This study was supported by the National Science and Engineering Research Council (NSERC) of Canada and the Fonds pour la Recherche en Santé du Québec (FRSQ) (G.L.). V. Gauvreau acknowledges a postgraduate scholarship from NSERC.

LITERATURE CITED

(1) Wang, C. C., Seo, T. S., Li, Z., Ruparel, H., and Ju, J. (2003). Site-specific fluorescent labeling of DNA using staudinger ligation. *Bioconjugate Chem. 14*, 697−701.

(2) Zhu, H. W., Xu, C. L., Wu, D. H., Wei, B. Q., Vajtai, R., and Ajayan, P. M. (2002). Direct synthesis of long single-walled carbon nanotube strands. *Science (Washington, D. C.) 296*, 884−886.

(3) Kumar, P., and Gupta, K. C. (2003). A rapid method for the construction of oligonucleotide arrays. *Bioconjugate Chem. 14*, 507−512.

(4) Skrzypczynski, Z., and Wayland, S. (2003). New reagents for the introduction of reactive functional groups into chemically synthesized DNA probes. *Bioconjugate Chem. 14*, 642−652.

(5) Wagner, P., Kernen, P., Hegner, M., Ungewickell, E., and Semenza, G. (1994). Covalent anchoring of proteins onto gold-directed NHS-terminated self-assembled monolayers in aqueous buffers: SFM images of clathrin cages and triskelia. *FEBS Lett. 356*, 267−271.

(6) Allain, L. R., Askari, M., Stokes, D. L., and Vo-Dinh, T. (2001). Microarray sampling-platform fabrication using bubble-jet technology for a biochip system. *Fresenius' J. Anal. Chem. 371*, 146−150.

(7) Blawas, A. S., and Reichert, W. M. (1998). Protein patterning. *Biomaterials 19*, 595−609.

(8) Chandy, T., Das, G. S., Wilson, R. F., and Rao, G. H. R. (2000). Use of plasma glow for surface-engineering biomolecules to enhance blood compatibility of Dacron and PTFE vascular prosthesis. *Biomaterials 21*, 699−712.

(9) Chen, C. S., Mrksich, M., Huang, S., Whitesides, G. M., and Ingber, D. E. (1998). Micropatterned surfaces for control of cell shape, position, and function. *Biotechnol. Prog. 14*, 356−363.

(10) Favia, P., Palumbo, F., D'Agostino, R., Lamponi, S., Magnani, A., and Barbucci, R. (1998). Immobilization of heparin and highly sulfated hyaluronic acid onto plasma-treated polyethylene. *Plasmas Polym. 3*, 77−96.

(11) Ito, Y. (1999). Surface micropatterning to regulate cell functions. *Biomaterials 20*, 2333−2342.

(12) Keusgen, M., Glodek, J., Milka, P., and Krest, I. (2001). Immobilization of enzymes on PTFE surfaces. *Biotechnol., Bioeng. 72*, 530−540.

(13) Levesque, S., Thibault, J., Castonguay, M., C.-Gaudreault, R., and Laroche, G. (2002). Modification of lipid transport through a microporous PTFE membrane wall grafted with poly(ethylene glycol). *Colloids Surf., B: Biointerf. 25*, 205−217.

(14) Massia, S. P., and Stark, J. (2001). Immobilized RGD peptides on surface-grafted dextran promote biospecific cell attachment. *J. Biomed. Mater. Res. 56*, 390−399.

(15) Reichmuth, P., Sigrist, H., Badertscher, M., Morf, W. E., de Rooij, N. F., and Pretsch, E. (2002). Immobilization of biomolecules on polyurethane membrane surfaces. *Bioconjugate Chem. 13*, 90−96.

(16) Zhang, Q., Wang, C., Babukutty, Y., Ohyama, T., Kogoma, M., and Kodama, M. (2002). Biocompatibility evaluation of ePTFE membrane modified with PEG in atmospheric pressure glow discharge. *J. Biomed. Mater. Res. 60*, 502−509.

(17) Ratner, B. D., Chilkoti, A., and Lopez, G. P. (1990). Plasma deposition and treatment for biomedical applications, in *Plasma Deposition, Treatment, and Etching of Polymers* (D'Agotino, R., Ed.) p 463, Academic Press, New York.

(18) Ratner, B. D. (1993). New ideas in biomaterials science. A path to engineered biomaterials. *J. Biomed. Mater. Res. 27*, 837−850.

(19) Da, Y., Griesser, H. J., Mau, A. W. H., Schmidt, R., and Liesegang, J. (1991). Surface modification of poly(tetrafluoroethylene) by gas plasma treatment. *Polymer 32*, 1126−1130.

(20) Gengenbach, T. R., Xie, X., Chatelier, R. C., and Griesser, H. J. (1994). Evolution of the surface composition and topography of perfluorinated polymers following ammonia-plasma treatment. *J. Adhes. Sci., Technol. 8*, 305−328.

(21) Inagaki, N., Tasaka, S., Narushima, K., and Teranishi, K. (2002). Surface modification of poly(tetrafluoroethylene) with pulsed hydrogen plasma. *J. Appl. Polym. Sci. 83*, 340−348.

(22) Mantovani, D., Castonguay, M., Pageau, J. F., Fiset, M., and Laroche, G. (1999). Ammonia RF-plasma treatment of tubular ePTFE vascular prostheses. *Plasmas Polym. 4*, 207−228.

(23) Médard, N., Soutif, J.-C., and Poncin-Epaillard, F. (2002). CO_2, H_2O, and CO_2/H_2O plasma chemistry for polyethylene surface modification. *Langmuir 18*, 2246−2253.

(24) Pringle, S. D., Joss, V. S., and Jones, C. (1996). Ammonia plasma treatment of PTFE under known plasma conditions. *Surf. Interface Anal. 24*, 821−829.

(25) Ramires, P. A., Mirenghi, L., Romano, A. R., Palumbo, F., and Nicolardi, G. (2000). Plasma-treated PET surfaces improve the biocompatibility of human endothelial cells. *J. Biomed. Mater. Res. 51*, 535−539.

(26) Wilson, D. J., Williams, R. L., and Pond, R. C. (2001). Plasma modification of PTFE surfaces Part II: plasma-treated surfaces following storage in air or PBS. *Surf. Interface Anal. 31*, 397−408.

(27) Wilson, D. J., Williams, R. L., and Pond, R. C. (2001). Plasma modification of PTFE surfaces Part I: surfaces immediately following plasma treatment. *Surf. Interface Anal. 31*, 385−396.

(28) Xie, X., Gengenbach, T. R., and Griesser, H. J. (1992). Changes in wettability with time of plasma-modified perfluorinated polymers. *J. Adhes. Sci., Technol. 6*, 1411−1431.

(29) Yamada, Y., Yamada, T., Tasaka, S., and Inagaki, N. (1996). Surface Modification of Poly(tetrafluoroethylene) by Remote Hydrogen Plasma. *Macromolecules 29*, 4331−4339.

(30) Yu, Q. S., Reddy, C. M., Meives, M. F., and Yasuda, H. K. (1999). Surface modification of poly(tetrafluoroethylene) by a low-temperature cascade arc torch and radiofrequency plasmas. *J. Polym. Sci., Part A: Polym. Chem. 37*, 4432−4441.

(31) Chevallier, P., Castonguay, M., Turgeon, S., Dubrulle, N., Mantovani, D., McBreen, P. H., Wittmann, J. C., and Laroche, G. (2001). Ammonia RF-plasma on PTFE surfaces: chemical characterization of the species created on the surface by vapor-phase chemical derivatization. *J. Phys. Chem. B 105*, 12490−12497.

(32) Hansen, R. H., and Schonhorn, H. (1966). A new technique for preparing low surface energy polymers for adhesive bonding. *J. Polym. Sci. 4*, 203−209.

(33) Inagaki, N., Tasaka, S., and Umehara, T. (1999). Effects of surface modification by remote hydrogen plasma on adhesion in poly(tetrafluoroethylene)/copper composites. *J. Appl. Polym. Sci. 71*, 2191−2200.

(34) Inagaki, N., Tasaka, S., and Goto, Y. (1997). Surface modification of poly(tetrafluoroethylene) film by plasma graft polymerization of sodium vinylsulfonate. *J. Appl. Polym. Sci. 66*, 77−84.

(35) Kim, S. R. (2000). Surface modification of poly(tetrafluoroethylene) film by chemical etching, plasma, and ion beam treatments. *J. Appl. Polym. Sci. 77*, 1913−1920.

(36) Sipehia, R. (1990). The enhanced attachment and growth of endothelial cells on anhydrous ammonia gaseous plasma modified surfaces of polystyrene and poly(tetrafluoroethylene). *Biomat. Art. Cells, Art. Org. 18*, 437−446.

(37) Sipehia, R. (1993). Enhanced attachment and growth of human endothelial cells derived from umbilical veins on ammonia plasma modified surfaces on PTFE and ePTFE synthetic vascular graft biomaterials. *Biomat., Art. Cells Immob. Biotech. 21*, 455−468.

(38) Vargo, T. G., Gardella, J. A., Jr., Meyer, A. E., and Baier, R. E. (1991). Hydrogen/liquid vapor radio frequency glow discharge plasma oxidation/hydrolysis of expanded poly(tetrafluoroethylene) (ePTFE) and poly(vinylidene fluoride) (PVDF) surfaces. *J. Polym. Sci., Part A: Polym. Chem. 29*, 555−570.

(39) Vargo, T. G., Bekos, E. J., Kim, Y. S., Ranieri, J. P., Bellamkonda, R., Aebischer, P., Margevich, D. E., Thompson, P. M., Bright, F. V., and Gardella, J. A., Jr. (1995). Synthesis and characterization of fluoropolymeric substrata with immobilized minimal peptide sequences for cell adhesion studies. I. *J. Biomed. Mater. Res. 29*, 767−778.

(40) Baldwin, S. W., Aube, J., and McPhail, A. T. (1991). Studies directed at the synthesis of optically active pretazettine via intramolecular nitrone/alkene cycloaddition reactions. *J. Org. Chem. 56*, 6546−6550.

(41) Hermanson, G. T. (1996). *Bioconjugate Techniques*, Academic Press, San Diego.

(42) Beamson, G., and Briggs, D. (1992). *High-Resolution XPS of Organic Polymers: The Scienta ESCA300 Database*, John Wiley & Sons, New York.

(43) Shen, W. C., and Ryser, H. J. (1981). cis-Aconityl spacer between daunomycin and macromolecular carriers: a model of pH-sensitive linkage releasing drug from a lysosomotropic conjugate. *Biochem. Biophys. Res. Commun. 102*, 1048−1054.

(44) Vermette, P., and Meagher, L. (2002). Immobilization and characterization of poly(acrilyc acid) graft layers. *Langmuir 18*, 10137−10145.

(45) Dekker, A., Reitsma, K., Beugeling, T., Bantjes, A., Feijen, J., and van Aken, W. G. (1991). Adhesion of endothelial cells and adsorption of serum proteins on gas plasma-treated poly(tetrafluoroethylene). *Biomaterials 12*, 130−138.

(46) Stile, R. A., Barber, T. A., Castner, D. G., and Healy, K. E. (2002). Sequential robust design methodology and X-ray photoelectron spectroscopy to analyze the grafting of hyaluronic acid to glass substrates. *J. Biomed. Mater. Res. 61*, 391−398.

(47) Leggett, G. J., Roberts, C. J., Williams, P. M., Davies, M. C., Jackson, D. E., and Tendler, S. J. B. (1993). Approaches to the immobilization of proteins at surfaces for analysis by scanning tunneling microscopy. *Langmuir 9*, 2356−2362.

(48) Moulder, J. F., Stickle, W. F., Sobol, P. E., and Bomben, K. D. (1992). *Handbook of X-ray Photoelectron Spectroscopy*, Perkin-Elmer Corporation, Physical Electronics Division, Eden Prairie.

(49) Hook, D. J., Vargo, T. G., Gardella, J. A., Jr., Litwiler, K. S., and Bright, F. V. (1991). Silanization of radio frequency glow discharge modified expanded poly(tetrafluoroethylene) using (aminopropyl)triethoxysilane. *Langmuir 7*, 142−151.

(50) Gerenser, L. J. (1987). *J. Adhesion Sci. Technol. 1*, 303−318.

(51) Sukhishvili, S. A., and Granick, G. (1999). *J. Chem. Phys. 110*, 10153−10161.

(52) Tassiopoulos, A. K., and Greisler, H. P. (2000). Angiogenic mechanisms of endothelialization of cardiovascular implants: a review of recent investigative strategies. *J. Biomater. Sci. Polym. Ed. 11*, 1275−1284.

(53) Crombez, M., and Mantovani, D. (2003). Biomaterials in tissue engineering and repair − Progresses in synthetic vascular prostheses: toward the endothelialization, in *Tissue engineering, stem cells and gene therapies* (Elçin, M. Y., Ed.) Kluwer Academic Publishers, New York.

(54) McMillan, R., Meeks, B., Bensebaa, F., Deslandes, Y., and Sheardown, H. (2001). *J. Biomed. Mater. Res.* 54, 272−283.

BC049858U

Bioconjugate Chemistry

NOVEMBER/DECEMBER 2004
Volume 15, Number 6

© *Copyright 2004 by the American Chemical Society*

EDITORIAL: Special Section on Imaging Chemistry

A Symposium on Chemistry and Biological Applications of Imaging Agents and Molecular Beacons, organized by Samuel Achilefu and Darryl Bornhop, was held at the spring 2004 National Meeting of the American Chemical Society. The work presented there inspired a series of reviews and other articles that, along with directly submitted manuscripts, have been collected into a special section on imaging chemistry that appears in this issue of the journal (on pages 1376−1502). A second installment is planned for a later issue.

Claude F. Meares

Editor-in-Chief

BC049742Y

10.1021/bc049742y CCC: $27.50 © 2004 American Chemical Society
Published on Web 11/17/2004

COMMUNICATIONS

Synthesis of Phosphate-Branched Oligonucleotides

Petri Heinonen* and Harri Lönnberg

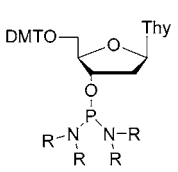
Department of Chemistry, University of Turku, FIN-20014 Turku, Finland. Received July 1, 2004; Revised Manuscript Received September 16, 2004

A solid-phase synthesis for phosphate-branched oligonucleotides is described. The method is based on coupling of a single nucleoside phosphorodiamidite to terminal hydroxyl functions of two solid-supported oligonucleotides. After oxidation of the phosphite triester obtained to a phosphate triester, the third branch is assembled by conventional phosphoramidite chemistry.

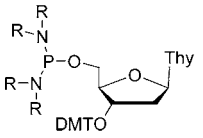
Phosphate-branched nucleic acids have recently received interest for the reason that two small nuclear RNAs (U2 and U6 snRNA) participating in splicing of pre-mRNA have been suggested to form an X-shaped phosphotriester structure by an attack of the 2′-hydroxy group of an adenosine residue of U2 snRNA on an ApG phosphodiester bond of U6 snRNA (*1*). The results obtained by simple ribonucleoside 3′-dialkyl phosphates (*2*−*6*) suggest that such a triester, although susceptible to a facile nucleophilic attack by the neighboring 2′-hydroxy function of the 3′-linked adenosine moiety, may still exist under physiological conditions. For firm conclusions, studies on reactions of oligomeric substrates that more closely mimic the structure of X-shaped RNA are needed. Unfortunately, no methodology for the solid-phase synthesis of phosphate-branched oligonucleotides has been described. The present paper is aimed at partly filling this gap.

Appropriately protected nucleoside phosphorodialkylamidites were introduced in late 1980s as alternative building blocks for the solid-phase synthesis of oligodeoxyribonucleotides (*7*, *8*) and their thioate, (*7*) amidate (*8*), and triester (*7*, *9*) analogues. In addition, they were shown to form 3′,5′-internucleosidic hydrogen-phosphonate (*10*) and phosphorodithioate (*11*) linkages in solution. Since then, phosphorodialkylamidites have rarely found a place in published applications, mainly because of the unfavorable balance between reactivity and hydrolytic stability. These building blocks, however, exhibit one attractive feature. They allow two subsequent couplings and, hence, enable construction of phosphate-branched oligonucleotides. We now report on the use of nucleoside 3′- (**1**) and 5′-phosphorodiamidites (**2**, **3**) as building blocks in solid-phase syntheses of such oligomers.

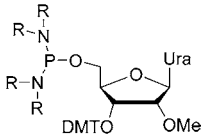
Phosphorodialkylamidites **1**−**3** may in principle be used in two different ways to obtain phosphate-branched oligonucleotides. Either two solid-supported oligonucleotides are reacted through their terminal hydroxyl functions with a single phosphorodialkylamidite monomer



1a R = Me
1b R = Et
1c R = i-Pr



2 R = Et



3 R = Et

(Reaction A in Scheme 1), or an internucleosidic phosphoramidite linkage of a solid-supported oligonucleotide is converted to a phosphite triester by nucleophilic attack of a monomeric nucleoside hydroxyl function (Reaction B in Scheme 1). The rest of the branches are then assembled, after oxidation of the phosphite triester to a phosphate ester, by conventional phosphoramidite chemistry. As mentioned above, five different nucleoside phoshorodialkylamidite building blocks (**1**−**3**) were prepared, and the coupling reactions indicated in Scheme 1 were studied.

5′-*O*-(4,4′-Dimethoxytrityl)thymidine 3′-*N,N,N′,N′*-tetraethylphosphorodiamidite (**1b**) and its tetraisopropyl analogue (**1c**) were prepared by phosphitylating 5′-*O*-(4,4′-dimethoxytrityl)thymidine with an appropriate bis-(dialkylamino)chlorophosphine, as described previously (*9*, *10*). The corresponding tetramethylphosphorodiamidite (**1a**) was obtained by phosphitylating the same nucleoside with tris(dimethylamino)phosphine, using tetrazole as an activator (*12*, *13*). Formation of **1a** was accompanied by appearance of a ^{31}P NMR resonance at 138.9 ppm**.** The compound was not isolated, but the reaction mixture was used immediately for the solid-phase synthesis. Phosphitylation of 3′-*O*-(4,4′-dimethoxytrityl)thymidine and 3′-*O*-(4,4′-dimethoxytrityl)-2′-*O*-methyluridine with bis(diethylamino)chlorophosphine gave **2** (^{31}P NMR 135.8 ppm) and **3** (^{31}P NMR 133.7 ppm), respectively.

It is essential to note that phosphorodialkylamidites are far more prone to hydrolysis than normal phosphoramidites. The sensitivity to hydrolysis depends on the size of the alkyl group. While chromatographic purification of building block **1a** was impossible, compound **1c** was

* To whom correspondence should be addressed. Tel: +358 2 333 7631. e-mail: petheino@utu.fi.

10.1021/bc049845g CCC: $27.50 © 2004 American Chemical Society
Published on Web 10/08/2004

Scheme 1. Key Steps in Branching of Oligonucleotides Using Phosphorodialkylamidites as Building Blocks

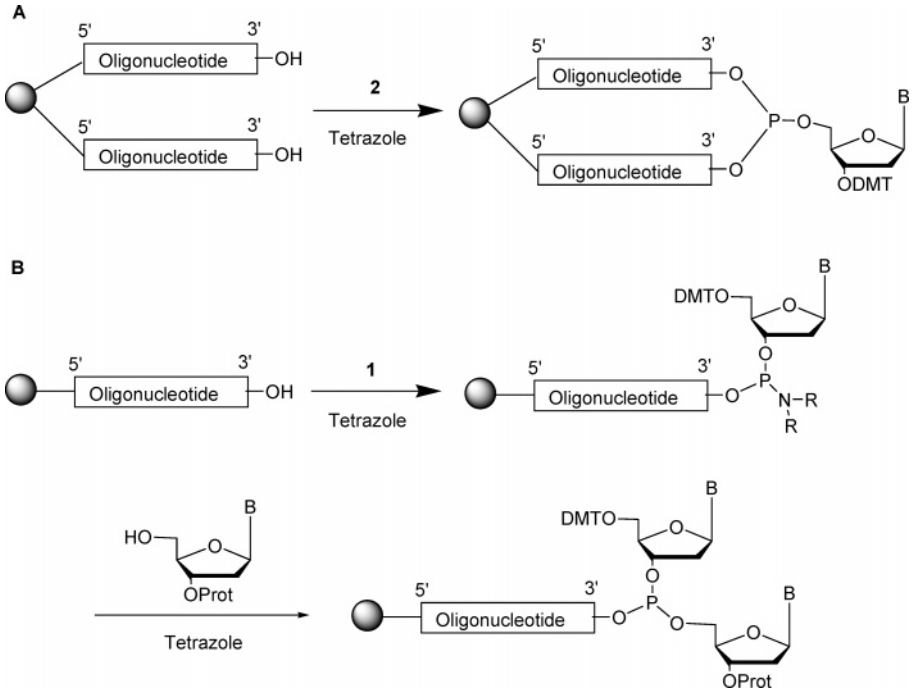


Table 1. Structures, Yields, and HPLC/MS Characterization of the Branched Oligonucleotides Synthesized

Entry	Structure	Yield[a] /%	t_R (HPLC)[b] /min	MS[c] obs.	MS calc.
1	HO-5'-T-T-T-3'-O, HO-5'-T-T-T-3'-O, P(=O), O-3'-T-T-T-5'-OH **4**	70	12.75	2594.51	2595.84
2	HO-5'-T-T-T-3'-O, HO-5'-T-T-T-3'-O, P(=O), O-5'-T-T-T-3'-OH **5**	50	11.96	2594.51	2595.84
3	HO-5'-T-T-dC-3'-O, HO-5'-T-T-dC-3'-O, P(=O), O-5'-T-dA-dG-3'-OH **6**	35	12.06	2599.84	2599.88
4	HO-5'-T-T-2'OMeU-3'-O, HO-5'-T-T-2'OMeU-3'-O, P(=O), O-5'-2'OMeU-T-T-3'-OH **7**	20	12.44	2643.42	2643.84

[a] According to HPLC. [b] Hypersil ODS column (4 × 15 mm), 50 mmol L^{-1} ammonium acetate to 50% MeCN in 50 mmol L^{-1} ammonium acetate buffer in 30 min. [c] Applied Biosystems Mariner System 5272, ES ionization mode, negative ion polarity.

easy to handle under normal laboratory conditions, and it withstood silica gel column chromatography. In fact, **1a** did not allow reproducible solid-phase synthesis, owing to its extreme hydrolytic instability, although the same compound had successfully been exploited in a related solution-phase synthesis (*12*, *13*). *N*,*N*,*N*′,*N*′-Tetraisopropylphosphorodiamidite (**1c**), in turn, proved to be too unreactive to be used in a solid-phase synthesis of oligonucleotide triesters. Accordingly, main attention was paid to *N*,*N*,*N*′,*N*′-tetraethylphosphordiamidite (**1b**) representing a reasonable compromise between reactivity and hydrolytic stability.

The applicability of ethyl-substituted phosphorodiamidites **1b**, **2**, and **3** was demonstrated by assembling four branched 9-mers (**4**−**7**) on a succinyl linker. Accordingly, T_3 sequences were first assembled in an inverse (5′→3′) direction, and the support was then treated with **1b** or **2** in small portions in excess of tetrazole, which resulted in coupling of a single thymidine phosphorodiamidite to the 3′-hydroxy group of two solid-supported T_3-chains. After oxidation to a phosphate ester, the third branched was assembled by the normal or inverted (5′→3′) phosphoramidite chemistry to obtain **4** and **5**, respectively (Reaction A in Scheme 1). The HPLC chromatograms of the crude reaction mixtures showed that the desired 9-mers had been formed in a 70% (**4**) and 50% (**5**) overall yield (Figure 1, Table 1). A structural analogue of **5** containing dC, dA, and dG in addition to T (**6**) was obtained similarly in a 35% yield. Expectedly, the reaction of a 5′-phosphorodiamidite (**3**) with the 3′-hydroxy function of a solid-supported 2′-*O*-methylribonucleoside was less efficient, but it still allowed preparation of a branched 9-mer (**7**), having an all-ribonucleoside structure at the branching site, in a pure state in more than 20% yield. Both CPG and Tentagel were used as a support. Somewhat surprisingly the support material and a loading on the support had only a marginal effect on the yield of the phosphorotriester product. The phosphotriesters (**4**−**7**) were remarkably stable to the overnight ammonolysis at 55 °C used to cleave the product from the support and to remove the standard benzoyl and isobutyryl protection groups of the base moieties.

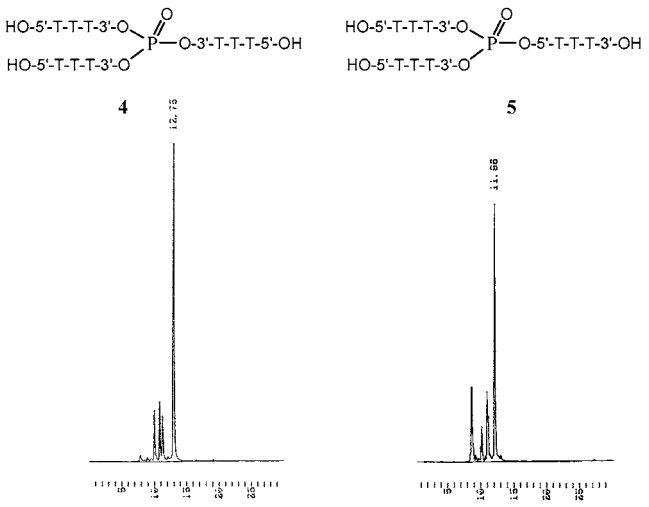


Figure 1. HPLC chromatograms of crude reaction mixtures of phosphate-branched oligonucleotide trimesters obtained by Reaction A in Scheme 1. Hypersil ODS column (4 × 15 mm), 50 mmol L^{-1} ammonium acetate to 50% MeCN in 50 mmol L^{-1} ammonium acetate buffer in 30 min.

Recation B in Scheme 1 represents a more flexible approach to the preparation of phosphate-branched oligonucleotides, since each of the three branches may in principle be elongated independently. Oligonucleotides containing isopropyl triester linkages at selected positions have previously been prepared by displacing the diethylamino ligand of an internucleosidic phosphoramidite linkage with 2-propanol (*9*). Also in our hands the reaction worked; an isopropyl triester was obtained in an 87% yield. Unfortunately, no similar reaction took place on using 3′-*O*-levulinylthymidine as a nucleophile instead of 2-propanol. Accordingly, this approach was not studied in more detail.

ACKNOWLEDGMENT

Financial aid from the Academy of Finland is gratefully acknowledged.

Supporting Information Available: Experimental details. This material is available free of charge via the Internet at http://pubs.acs.org.

LITERATURE CITED

(1) Valadkhan, S., and Manley, J. L. (2003) Characterization of the catalytic activity of U2 and U6 snRNAs. *RNA 9*, 892−904.

(2) Kosonen, M., Oivanen, M., and Lönnberg, H. (1994) Hydrolysis and interconversion of the dimethyl esters of 5′-*O*-methyluridine 2′- and 3′-monophosphates: Kinetics and mechanism. *J. Org. Chem. 59*, 3704−3708.

(3) Kosonen, M., and Lönnberg, H. (1995) General and specific acid/base catalysis of the hydrolysis and interconversion of ribonucleoside 2′- and 3′-phosphotriesters: kinetics and mechanisms of the reactions of 5′−O-pivaloyluridine 2′- and 3′-dimethylphosphates. *J. Chem. Soc., Perkin Trans. 2*, 1203−1209.

(4) Kosonen, M., Hakala, K., and Lönnberg, H. (1998) Hydrolysis and intramolecular transesterification of ribonucleoside 3′-phosphotriesters: the effect of alkyl groups on the general and specific acid−base-catalyzed reactions of 5′-O-pivaloyluridin-3′-yl dialkyl phosphates. *J. Chem. Soc., Perkin Trans. 2*, 663−670.

(5) Kosonen, M., Yousefi-Salakdeh, E., Strömberg, R., and Lönnberg, H. (1998) pH- and buffer-independent cleavage and mutual isomerization of uridine 2′- and 3′-alkyl phosphodiesters: implications for the buffer catalyzed cleavage of RNA. *J. Chem. Soc., Perkin Trans. 2*, 1589−1595.

(6) Kosonen, M., Seppänen, R., Wickmann, O., and Lönnberg, H. (1999) Hydrolysis and intramolecular transesterification of ribonucleoside 3′-phosphotriesters: comparison of structural effects in the reactions of asymmetric and symmetric dialkyl esters of 5′-O-pivaloyl-3′-uridylic acid. *J. Chem. Soc., Perkin Trans. 2*, 2433−2439.

(7) Uznanski, B., Wilk, A., and Stec, W. J. (1987) Deoxyribonucleoside 3′-phosphordiamidites as substrates for solidsupported synthesis of oligodeoxyribonucleotides and their phosphorothioate and dna-triester analogues. *Tetrahedron Lett. 28*, 3401−3404.

(8) Yamana, K, Nishijima, Y., Oka, A., Nakano, H., Sangen, O., Ozaki, H., and Shimidzu, T. (1989) A simple preparation of 5′-O-dimethoxytrityl deoxyribonucleoside 3′-O-phosphorbisdiethylamidites as useful intermediates in the synthesis of oligodeoxyribonucleotides and their phosphorodiethylamidate analogs on a solid support. *Tetrahedron 45*, 4135−4140.

(9) Yamana, K., Nishijima, Y., Negishi, K., Yashiki, T., Nishio, K., Nakano, H., and Sangen, O. (1991) Deoxyribonucleoside 3′-phosphorobisamidites in the synthesis of isopropyl phosphotriester oligodeoxyribonucleotide analogues. *Tetrahedron Lett. 32*, 4721−4734.

(10) Marugg, J. E., Burik, A., Tromp, M., van der Marel, G. A., and van Bom, J. H. (1986) A new and versatile approach to the preparation of valuable deoxynucleoside 3′-phosphite intermediates. *Tetrahedron Lett. 27*, 2271−2274.

(11) Nielsen, J., Brill, W. K.-D., and Caruthers, M. H. (1988) Synthesis and characterization of dinucleoside phosphorodithioates. *Tetrahedron Lett. 29*, 2911−2914.

(12) Lönnberg, T., and Mikkola, S. (2004) Hydrolysis of 2′,3′-*O*-methyleneadenos-5′-yl bis(2′,5′-di-*O*-methylurid-3′-yl) phosphate, a sugar O-alkylated trinucleoside 3′,3′,5′-monophosphate: Implications for the mechanism of large ribozymes. *J. Org. Chem. 69*, 802−810.

(13) Poijärvi, P., Oivanen, M., and Lönnberg, H. (2004) Towards oligonucleotide pro-drugs: 2,2-bis(ethoxycarbonyl) and 2-(alkylaminocarbonyl)-2-cyano substituted 3-(pivaloyloxy)propyl groups as biodegradable protecting groups for internucleosidic phosphoromonothioate linkages. *Lett. Org. Chem. 1*, 183−188.

BC049845G

Targeting Malaria with Polyamines

Andrew J. Geall,*,† John A. Baugh,‡ Mark Loyevsky,§ Victor R. Gordeuk,§ Yousef Al-Abed,|| and Richard Bucala⊥

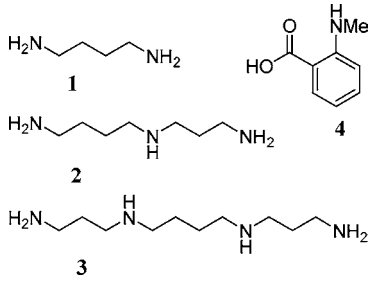
Vical Inc., 10390 Pacific Center Court, San Diego, California 92121, The Conway Institute of Biomolecular and Biomedical Research, University College Dublin, Belfield, Dublin 4, Ireland, Center for Sickle Cell Disease/ Department of Microbiology, Howard University College of Medicine, Washington, D.C. 20012, Laboratory of Medicinal Chemistry, North Shore-LIJ Research Institute, Manhasset, New York 10030, and Department of Medicine, and Pathology, Yale University School of Medicine, P.O. Box 208031, New Haven, Connecticut 06520.
Received February 21, 2004; Revised Manuscript Received September 13, 2004

During the asexual cycle of *Plasmodium falciparum* within the host erythrocyte, the parasite induces a stage-dependent elevation in the levels of polyamines by increased metabolism and uptake of extracellular pools. Polyamine amides of *N*-methylanthranilic acid have been synthesized which have embedded within them putrescine, spermidine, or spermine and from a charge perspective mimic natural polyamines. The interaction of these polyamine conjugates with human erythrocytes infected with malaria is described using fluorescent microscopy. The fluorescent spermine mimic was the only probe to show measurable intracellular accumulation. This was observed in late stage development but not in the ring stages or in uninfected erythrocytes.

INTRODUCTION

Putrescine **1**, spermidine **2**, and spermine **3** (Chart 1) are naturally occurring polyamines present in all mammalian cell types and are known to be essential for cell growth (*1*, *2*). Changes in the concentration of intracellular polyamine pools are achieved by regulation of a biosynthetic pathway, a catabolic pathway, and an active transport system (*1*–*4*). Human erythrocytes contain only trace amounts of polyamines and lack the biosynthetic enzymes for their production (*5*, *6*) but are capable of polyamine transport in vitro (*7*). During the asexual cycle of *Plasmodium falciparum*, the parasite induces numerous biochemical, structural, and functional changes in the host erythrocyte. In particular, the parasite induces a stage-dependent elevation in the levels of polyamines by increased metabolism (*5*, 6) and uptake of extracellular pools (*6*, *8*). Polyamine metabolism by *Plasmodium* differs from the metabolism in mammalian cells (*6*). A bifunctional enzyme, ornithine decarboxylase-*S*-adenosylmethionine decarboxylase, has been characterized (*9*), and in the plasmodial resource database, PlasmoDB (http://plasmoDB.org), a putative spermidine synthase (gene PF_0301), has been identified (*10*). The existence of deoxyhypusine synthase and homospermidine synthase has also been established (*11*); these enzymes are involved in spermidine metabolism in *P. falciparum*. The biosynthetic steps for the synthesis of putrescine and spermidine have therefore been identified, but the presence of the enzyme spermine synthase and the ability to synthesize spermine is questionable (*6*), although the parasitized erythrocytes contain appreciable amounts of this polyamine (*5*).

Chart 1. Structures of Putrescine 1, Spermidine 2, Spermine 3, and *N*-Methylanthranilic Acid 4

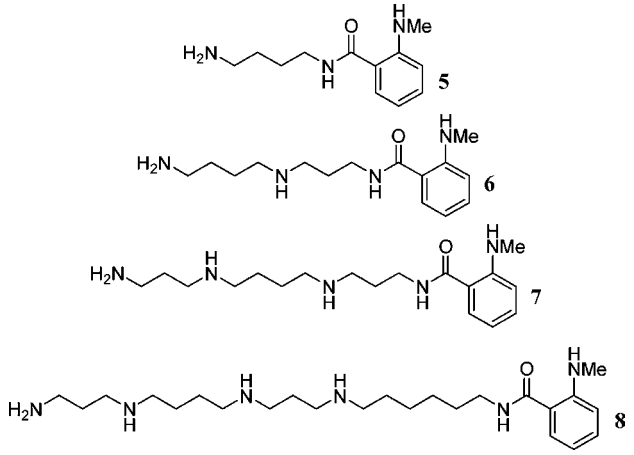


During the growth of a malarial parasite, the membrane transport characteristics of the host erythrocyte are modified (*6*, *8*, *12*). Increasing evidence suggests that targeting the parasite's polyamine biosynthetic pathway to inhibit growth, while attractive pharmacologically, may be problematic because of an influx of polyamine from extracellular pools (*3*, *5*, *6*, *8*, *12*). This polyamine transport system remains poorly characterized and it is unclear if the parasite is using the endogenous erythrocytic system or a parasite-derived pathway, although a simian putrescine transporter has been reported in *Plasmodium knowlesi*-infected erythrocytes (*8*). The presence of a spermine transport pathway seems likely considering the elevated levels of this polyamine during proliferation (*5*) and the inability of the parasite to synthesize the molecule biosynthetically. The mammalian polyamine transporter appears to tolerate a degree of structural substrate diversity, but it is quite distinct from systems transporting other cellular components, such as amino acids. Generally, the number of charges, the natural polyamine spacing (propylene or butylene), and a nonbranched structure correlate with high affinity for the transporter (*4*, *13*–*16*). Fluorescent polyamine conjugates (*13*, *17*) are promising leads for

* To whom correspondence should be addressed. Tel: 858 646 1260. Fax: 858 646 1150. E-mail: ageall@vical.com.
† Vical Inc.
‡ University College Dublin.
§ Howard University College of Medicine.
|| North Shore-LIJ Research Institute.
⊥ Yale University School of Medicine.

10.1021/bc0499578 CCC: $27.50 © 2004 American Chemical Society
Published on Web 10/07/2004

Chart 2. Structures of the Target Polyamine Amide *N*-Methylanthranilic Acid Conjugates 5−8



probing and understanding the polyamine transporter for targeted drug delivery.

Herein we report the design and controlled synthesis of fluorescent polyamine amides **6**−**8** (Chart 2) of 2-methylaminobenzoic acid **4** (*N*-methylanthranilic acid or MANT, Chart 1) that mimic both the charge and regiochemical distribution of natural polyamine substrates **1**−**3** (Chart 1). We also report the synthesis of fluorescent conjugate **5** (Chart 2), which contains a single primary amine and can be used along with MANT **4** (Chart 1) as non-polyamine controls. The uptake, via the mammalian polyamine transporter, of conjugates **4**−**8** into a rapidly proliferating leukemic T-cell line is characterized and shown to be consistent with the literature (*13*). Transport of conjugates **4**−**8** into malaria-infected erythrocytes at different stages of maturation is described using fluorescent microscopy.

EXPERIMENTAL PROCEDURES

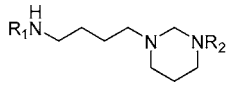
Materials. Analytical grade reagents were purchased from major suppliers.

Methods. Details of NMR, fluorescent, and mass spectroscopy are supplied as Supporting Information. Chemical analysis data for compounds **4**−**8** are supplied as Supporting Information.

Cell Culture. Jurkat T cells were cultured at a density of 0.2−0.8 million per milliliter in RPMI 1640 media supplemented with 10% fetal bovine serum (FBS) under an atmosphere of 5% CO_2−95% air at a temperature of 37 °C. Intracellular accumulation of MANT conjugates was determined in viable Jurkat cells using a FACS Vantage SE flow cytometer. UV excitation coupled with a 424/44 band-pass detection filter allowed visualization of fluorescence on the FL5 channel. Cells were cultured overnight in the presence of the fluorescent probes (50 μM). Prior to FACS analysis, nonspecific membrane-associated compounds were dissociated by incubation for 2 min in 1 mM free spermine (TFA salt) followed by repeated washing in PBS.

^{3}H-Hypoxanthine Proliferation Assay. The in vitro antimalarial activity of compounds **4**−**8** was evaluated on the growth of ring-stage-synchronized *Plasmodium falciparum* (7G8 strain) malaria cultures[1] by incorporation of ^{3}H-hypoxanthine. Erythrocyte suspensions with ring-stage-synchronized parasites were distributed into 24-well plates at 2% parasitemia and 2% hematocrit and compounds **4**−**8** were added at 1, 10, and 100 μm concentrations in triplicate. The plates were incubated in a candle jar at 37 °C for 24 h. ^{3}H-Hypoxanthine was

Chart 3. Structures of the Intermediates in the Synthesis of Polyamine Amide *N*-Methylanthranilic Acid Conjugates 6



9 R_1 = H R_2 = H
10 R_1 = $COCF_3$ R_2 = H
11 R_1 = $COCF_3$ R_2 = MANT
12 R_1 = H R_2 = MANT

then added to each well at a final activity of 5 μCi/mL. After an additional 24-h incubation period, the cells were harvested onto filters, dried in the oven, transferred to vials with the scintillation fluid, Fluosafe (Fisher Scientific Co., Norcross, GA), and counted on a Beckman LS5000CE scintillation counter.

Fluorescent Microscopy. Fluorescent microscopy was used to visualize the intracellular accumulation of the fluorescent probes **4**−**8** in in vitro *Plasmodium falciparum* (7G8) cultures[1] at 2% hematocrit, 8% parasitemia. Compounds **4**−**8** at 5 μM concentrations were incubated for 17 h and then separated on a Percoll gradient into mature, ring-infected and -uninfected erythrocytes. Cells were fixed with 4% paraformaldehyde and 0.05% glutaraldehyde and air-dried on polylysine-coated slides. The slides were washed in 1 mM unlabeled spermine in PBS (20 min) and PBS (10 min) to remove nonspecifically bound fluorochrome and mounted using Vectashield (Vector Laboratories, Burlingame, CA). Images were then taken using a 100× oil immersion objective with an Olympus IX70 inverted microscope. A 360/40 band-pass excitation filter was used in conjunction with a multipass emission filter which allowed visualization of the 435 nm emission of MANT.

(2-Methylaminobenzoyl)-4-amino-4-aza-butane (5). Putrescine **1** (Chart 1) was selectively N^1-acylated with MANT **4** (Chart 1) (1.0 equiv), mediated by DCC (1.5 equiv) and catalytic 1-hydroxybenzotriazole (HOBt) (0.2 equiv, DCM, 25 °C, 72 h), and purified by RP-HPLC over Supelcosil ABZ+Plus (25 cm × 10 mm, 5 μm) (solvent A: 0.1% TFA in MeCN, solvent B: 0.1% aq TFA, gradient elution, 100% A to 65% A, over 20 min, λ = 340 nm) to afford, after lyophilization, the polytrifluoroacetate salt of polyamine amide **5** (Chart 2, 27%).

(2-Methylaminobenzoyl)-1,8-diamino-4-azaoctane (6). Spermidine **2** (Chart 1) was protected as the hexahydropyrimidine **9** (Chart 3), in quantitative yield, as previously described (*18*). The free primary amino functional group was then orthogonally protected with ethyl trifluoracetate (1.2 equiv, in MeOH, at −78 °C for 1 h and then warmed to room temperature over 1 h) to afford, without purification, the N^1-trifluoroacetamide intermediate **10** (Chart 3). N-Acylation, with MANT **4**

[1] *P. falciparum* strain 7G8 was used in all experiments. Parasites were maintained in cultures of RPMI-1640 medium supplemented with 25 mM HEPES, 23 mM $NaHC0_3$, 10 mM glucose, 10% (v/v) heat-inactivated human plasma (0^+ or A^+), and washed human erythrocytes (A^+) at 2% hematocrit. The growth medium was replaced daily and cultures were gassed with a mixture of 90% N_2, 5% CO_2, and 5% O_2. The morphological characteristics of the parasites and the level of parasitemia were determined by microscopic examination of Giemsa-stained thin blood smears. Alanine lyses erythrocytes infected with the trophozoite stage parasite, leaving intact only erythrocytes with ring-stage parasites. Synchronization to the ring stage was therefore achieved by lysis of cells bearing mature parasites with isoosmotic solution containing 300 mM alanine, 10 mM Tris-HCl, pH 7.4.

(Chart 1) afforded, after purification over silica gel (DCM-MeOH 25:1 to 20:1 v/v), the fully protected acylated spermidine intermediate **11** (Chart 3, 81.6%). The TFA protecting group was then cleaved by stirring in concentrated methanolic ammonia (25 °C, 48 h) to afford, after purification over silica gel (DCM−MeOH−concentrated NH_4OH 50:10:1 to 40:10:1 v/v/v), the hexahydropyrimidine intermediate **12** (Chart 3, 53%). Treatment with malonic acid (3.6 equiv) and pyridine (3.1 equiv, dry MeOH, reflux, 2 h) (*19*), afforded, after purification by RP-HPLC, the polytrifluoroacetate salt of polyamine amide **6** (Chart 2, 60%). This deprotection step resulted in a change of retention time by RP-HPLC from 11.5 (compound **12**) to 7.6 min (compound **6**) (Supelcosil ABZ+Plus, 5 μm, 15 cm × 4.6 mm, solvent A:0.1% TFA in MeCN, solvent B:0.1% aq. TFA, gradient elution 100% A to 65% A over 20 min, 1.5 mL/min, $\lambda = 340$ nm) loss of the required mass by mass spectroscopy and a ^{13}C NMR spectrum consistent with the required unsymmetrical polyamine amide (*20*).

(2-Methylaminobenzoyl)-1,12-diamino-4,9-diazadodecane (7). N^1,N^2,N^3-Tri-*tert*-Boc-spermine was synthesized as previously described (*21*). N-Acylation with MANT **4** afforded, after purification over silica gel (petroleum ether−EtOAc 80:20 to 50:50 v/v), the Boc-protected acylated spermine intermediate (74%). Deprotection with TFA (50:50 TFA-DCM v/v, 25 °C, 2 h) gave, after RP-HPLC purification and lyophilization, the polytrifluoroacetate salt of polyamine amide **7** (Chart 2, 65%).

(2-Methylaminobenzoyl)-1,16-diamino-4,8,13-triazahexadecane (8). Incorporation of an intact spermine moiety was achieved using a previously described spermine desymmetrization protocol (*22*) by reductive alkylation of N^1,N^2,N^3-tri-*tert*-Boc-spermine with 6-benzyloxycarbonylaminohexanal to afford (N^1,N^4,N^9,N^{13}-tetra-*tert*-Boc)-1,19-diamino-4,9,13-triazanonadecane. N-Acylation (88%), poly-Boc deprotection, RP-HPLC purification, and lyophilization afforded the polytrifluoroacetate salt of polyamine amide **8** (Chart 2, 65%). The pK_as of polyamines are a function of the interamine distance as well as their substituents (*18*), so a six-carbon spacer rather than the previously described three-carbon spacer was introduced using aminohexanal.

RESULTS

Polyamine amides **5**−**8** (Chart 2) are homogeneous by RP-HPLC and have been characterized by electrospray MS, ^1H, ^{13}C, and HETCOR NMR, and the polyamine substituents were consistent with previously published spectroscopic data of polyamine amides and carbamates (*21*, *22*). The flow cytometry data are shown in Figure 1 and indicate that compounds **6**−**8** (Chart 2) are all sequestered into viable Jurkat cells. The population shift indicates that approximately 95% of all cells within each population are actively accumulating the fluorescent polyamine analogues. In accord with these data, we have shown that the remaining 5% of the cell population is accounted for by dying cells, as determined by propidium iodide uptake using flow cytometery (data not shown). As approximately 100% of live cells were shown to actively sequester the polyamine analogues, we have used the measure of mean fluorescence intensity (MFI) to give a quantifiable comparison of the degree of uptake of each of the test compounds. These data, Table 1, show that the dicationic putrescine mimic, compound **6**, is the most highly sequestered (MFI 372.26), followed by the spermine mimic, compound **8** (MFI 359.69) and then to a lesser degree the spermidine mimic, compound **7** (MFI 204.65). According to flow cytometery, accumulation of

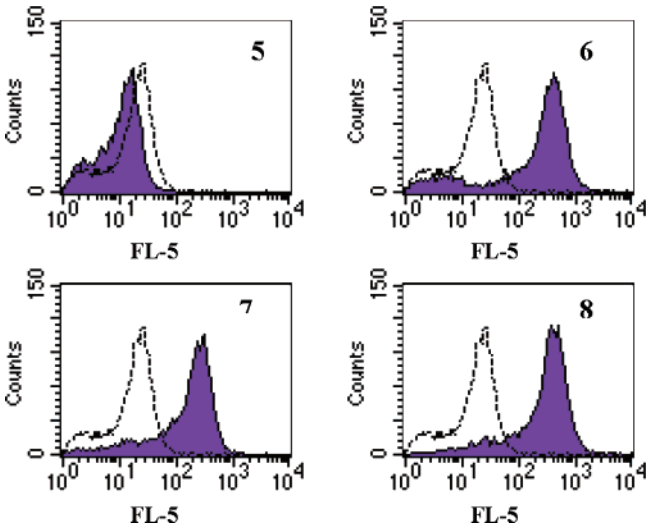


Figure 1. FACS analysis of polyamine amide *N*-methylanthranilic acid conjugates **5**−**8** uptake in Jurkat cells. The figure shows fluorescence of MANT conjugate in solid purple with control fluorescence of free MANT-treated cells overlaid in the broken line.

Table 1. Mean Fluorescence Intensity of Viable Jurkat Cells

compound	mean fluorescence Intensity
4	22.51
5	12.23
6	372.26
7	204.65
8	359.69

the monocationic amine **5** and unconjugated MANT **4** is at background levels. These data are consistent with our results obtained with fluorescence microscopy and fluorimetric analysis of cell lysates (see Supporting Information). Fluorimetry was also used to show that uptake of conjugate **6** was energy-, time-, and concentration-dependent and was competitive with the natural substrates (see Supporting Information). The indication of an active transport system, rather than passive diffusion across a lipid membrane (*4*), correlates with literature reports of polyamine−MANT conjugates using the polyamine transport pathway (*13*).

The in vitro antimalarial activity of compounds **4**−**8** was evaluated on the growth of ring-stage-synchronized *Plasmodium falciparum* (7G8 strain) malaria cultures[1] by incorporation of ^3H-hypoxanthine. Figure 2 shows that none of the compounds had antimalarial activity, and microscopic examination of Giemsa-stained, thin blood smears showed normal morphological characteristics of

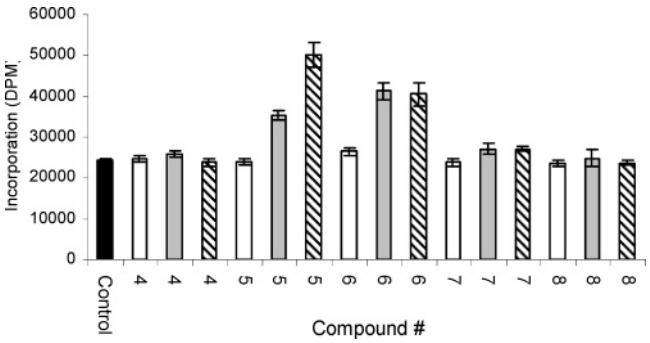


Figure 2. In vitro incorporation of ^3H-hypoxanthine into ring-stage synchronized *Plasmodium falciparum* (7G8 strain) for compounds **4**−**8**: (open) 1 μM, (grey) 10 μM, (hashed) 100 μM as compared to control (black).

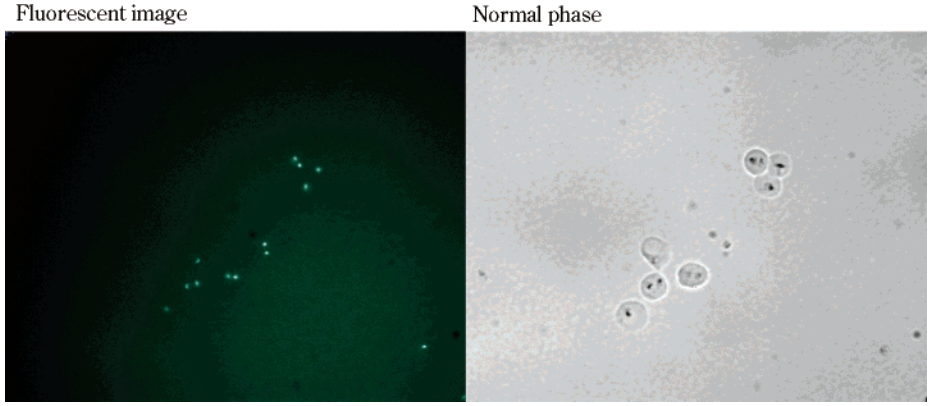


Figure 3. Uptake of polyamine MANT conjugate **8** by intraerythrocytic *P. falciparum* trophozoites as visualized by fluorescent microscopy.

the parasites (data not shown). Thus, these fluorescent polyamine conjugates do not interfere with the normal metabolic function of the malaria parasite within the host erythrocyte and are therefore ideal probes.

Fluorescence microscopy was then used to visualize the intracellular accumulation of the fluorescent probes. Compounds **4**−**7** showed no intracellular accumulation at any of the stages of development of the parasite. However, using fluorescent microscopy, the spermine mimic **8** showed intracellular accumulation in late stage development but not in the ring stages or in uninfected erythrocytes. Figure 3 (right panel) shows the normal phase photograph of trophozoite-infected erythrocytes. The parasites are unstained but the hemozoin within the food vacuole can be seen. The fluorescent image (Figure 3, left panel) shows accumulation of the probe within the cytoplasm of the parasite, which is colocalized with the hemozoin.

DISCUSSION

Previously, the uptake of polyamine-*N*-methylanthranilic acid conjugates into mammalian cells via the polyamine transporter has been characterized (*13*). The MANT fluorophore shows λ_{max} 250 nm (ϵ 5400) and 333 nm (ϵ 2100) and an emission frequency of 436 nm (excitation 341 nm) and is unlikely to perturb the interactions and subsequent distribution of the polyamine analogue (*13*). We have synthesized polyamine amide conjugates that have embedded within them putrescine, spermidine, or spermine, and from a charge perspective mimic the natural polyamines. We have characterized their uptake into a human leukemic T-cell line (rapidly proliferating, metabolically active leukemia of lymphoid origin) and shown them to be consistent with literature reports of uptake via the polyamine transporter for MANT conjugates (*13*). Fluorescence microscopy studies with malaria infected erythrocytes showed only measurable accumulation of the spermine mimic (**8**). Malaria parasites are capable of synthesizing spermidine and putrescine (*5*, *6*, *8*, *9*), but it is questionable whether they are capable of synthesizing spermine (*6*). This fluorescent probe, from a charge perspective, is a mimic of spermine, and we speculate that its accumulation is via the polyamine transporter, although more extensive studies will be required to confirm this. These fluorescent probes will find considerable use in the evaluation of this transport system in malaria for targeted drug therapy.

ACKNOWLEDGMENT

We thank Dr. Simon Carrington (University of Bradford, U.K.) for some useful synthetic discussions. Studies were supported by NIH 1RO1AI051306 (R.B.), RO1AI44857-04 (V.R.G.), UH1-HL03679-05 from National Heart, Lung and Blood Institute, the Office of Research on Minority Health, and by the Howard University General Clinical Research Center Grant M01-RR10284.

Supporting Information Available: Experimental details. This material is available free of charge via the Internet at http://pubs.acs.org.

LITERATURE CITED

(1) Tabor, C. W., and Tabor, H. (1984) Polyamines. *Annu. Rev. Biochem. 53*, 749−790.
(2) Kramer, D. I., Miller, J. T., Bergeron, R. J., Khomutov, R., Knomutov, A., and Porter, C. W. (1993) regulation of polyamine transport by polyamines and polyamine analogs. *J. Cell Physiol. 155*, 399−407.
(3) Marton, L. J., and Pegg, A. E. (1995) Polyamines as targets for therapeutic intervention. *Annu. Rev. Pharmacol. Toxicol. 35*, 55−91.
(4) Seiler, N., Delcros, J. G., and Moulinoux, J. P. (1996) Review: Polyamine transport in mammalian cells. *Int. J. Biochem. Cell Biol. 28*, 843−861.
(5) Assaraf, Y. G., Golenser, J., Spira, D. T., and Bachrach, U. (1984) Polyamine levels and the activity of their biosynthetic enzymes in human erythrocytes infected with the malaria parasite, *Plasmodium falciparum*. *Biochem. J. 222*, 815−819.
(6) Müller, S., Coombs, G. H., and Walter, R. D. (2001) Targeting polyamines of parasitic protozoa in chemotherapy. *Trends Parasitol. 17*, 242−249.
(7) Moulinoux, J.-P., Le Calve, M., Quemener, V., and Quash, G. (1984) In vitro studies on the entry of polyamines into normal red blood cells. *Biochimie 66*, 385−393.
(8) Singh, S., Puri, S. K., Singh, S. K., Srivastava, R., Gupta, R C., and Pandey, V. C. (1997) Characterization of simian malarial parasite (*Plasmodium falciparum*)-induced putrescine transport in rhesus monkey erythroctes. *J. Biol. Chem. 272*, 13506−13511.
(9) Muller, S., Da'dara, A., Luersen, K., Wrenger, C., Das Gupta, R., Madhubala, R., and Walter, R. D. (2000) In the human malaria parasite *Plasmodium falciparum*, polyamines are synthesized by a bifunctional ornithine decarboxylase, s-adenosylmethionine decarboxylase. *J. Biol. Chem. 11*, 8097−8102.
(10) Le Roch, K. G., Zhou, Y., Blair, P. L., Grainger, M., Moch, J. K., Haynes, J. D., De La Vega, P., Holder, A. A., Batalov, S., Carucci, D. J., and Winzeler, E. A. (2003) Discovery of gene function by expression profiling of the malaria parasite life cycle. *Science 301*, 1503−1508.
(11) Kaiser, A., Gottwald, A., Maier, W. and Seitz, H. M. (2003) Targeting enzymes involved in spermidine metabolism of parasitic protozoa − a possible new strategy for anti-parasitic treatment. *Parasitol. Res. 91*, 508−516.
(12) Ginsburg, H., and Kirk, K. (1998) Membrane Transport in the Malaria-infected Erythrocyte. *Malaria: Parasite Biol-*

ogy, Pathogenesis, and Protection (Sherman, I. W., Ed.) pp 219−232, ASM Press, Washington, DC.
(13) Cullis, P. M., Green, R. E., Merson-Davies, L., and Travis, N. (1999) Probing the mechanism of transport and compartmentalization of polyamines in mammalian cells. *Chem. Biol. 6*, 717−729.
(14) Porter, C. W., Miller, J., and Bergeron, R. J. (1984) Aliphatic chain-length specificity of the polyamine transport-system in ascites L1210 leukemia-cells. *Cancer Res. 44*, 126−128.
(15) Bergeron, R. J., McManis, J. S., Weimar, W. R., Schreier, K. M., Gao, F., Wu, Q., Oritiz-Ocasio, J., Luchetta, G. R., Porter, C., and Vinson, J. R. T. (1995) The role of charge in polyamine analogue recognition. *J. Med. Chem. 38*, 2278−2285.
(16) Wang, C., Delcros, J.-G., Cannon, L., Konate, F., Carias, H., Biggerstaff, J., Gardner, R. A., and Phanstiel, O., IV. (2003) Defining the molecular requirements for selective delivery of polyamine conjugates into cells containing active polyamine transporters. *J. Med. Chem. 46*, 5129−5138.
(17) Aziz, S. M., Yatin, M., Worthen, D. R., Lipke, D. W., and Crooks, P. A. (1998) A novel technique for visualizing the intracellular localization and distribution of transported polyamines in cultured pulmonary artery smooth muscle cells. *J. Pharm. Biomed. Anal. 17*, 307−320.
(18) Ganem, B., and Chantrapromma, K. (1983) Preparation of thermospermine. *Methods Enzymol. 94*, 416−418.
(19) Lurdes, M., Almeida, S., Grehn, L., and Ragnarsson, U. (1988) Selective protection of polyamines: Synthesis of model compounds and spermidine derivatives. *J. Chem. Soc., Perkin Trans. 1* 1905−1911.
(20) -1,8-diamino-4-azaoctane (**6**). Purified by RP-HPLC (poly-TFA salt, t_R = 7 min, Supelcosil ABZ+Plus, 5 μm, 25 cm × 10 mm, solvent A: 0.1% TFA in MeCN, solvent B: 0.1% aq. TFA, gradient elution 100% A to 65% A over 20 min, 6.0 mL/min, λ = 340 nm) as a white powder. ^{13}C NMR 67.9 MHz, [^{2}H]$_6$-DMSO, 23.2 (7-CH_2); 24.7 (6-CH_2); 26.5 (2-CH_2); 29.9 (CH3); 36.6 (1-CH_2); 38.8 (8-CH_2); 45.4 (5-CH_2); 46.6 (3-+CH_2); 111.2 (1′-C); 114.6 (3′-CH_2); 115.4 (5′-CH_2); 128.8 (6′-CH_2); 133.0 (4′-CH_2); 150.5 (2′-C); 170.0 (*C*ONH). ESI/MS found 279, (M^+ + 1), $C_{15}H_{27}N_4O_1$ requires M^+ + 1 = 279.
(21) Geall, A. J., Taylor, R. J., Earll, M. E., Eaton, M. A. W., and Blagbrough, I. S. (2000) Synthesis of cholesteryl polyamine carbamates: pK_a studies and condensation of calf thymus DNA. *Bioconjugate Chem. 11*, 314−326.
(22) Geall, A. J., and Blagbrough, I. S. (2000) Homologation of polyamines in the rapid synthesis of lipospermine conjugates and related lipoplexes. *Tetrahedron 56*, 2449−2460.

BC0499578

ARTICLES

Cytosolic Delivery of Macromolecules. 3. Synthesis and Characterization of Acid-Sensitive Bis-Detergents

Aravind Asokan and Moo J. Cho*

Division of Drug Delivery & Disposition, School of Pharmacy, University of North Carolina at Chapel Hill, Chapel Hill, North Carolina 27599. Received May 20, 2004; Revised Manuscript Received August 9, 2004

A serious limitation that precludes utilization of single-tailed, pH-sensitive detergents for the cytosolic delivery of macromolecules is their low limit of incorporation in stable liposomal formulations. To address this issue, we have prepared two Gemini surfactants or 'bis-detergents' by cross-linking the headgroups of single-tailed, tertiary amine detergents through oxyethylene (**BD1**) or acid-labile acetal (**BD2**) moieties. The membrane-bound pK_a of the twin tertiary amine headgroups was determined to be 6.37 ± 0.36 using a fluorescence-based assay. As evidenced by thin-layer chromatography, **BD2** was hydrolyzed under acidic conditions (pH 5.0) with an approximate half-life of 3 h at 37 °C, while **BD1** remained stable. Low pH-induced collapse of liposomes containing acid-labile **BD2** into micelles was more facile than that of **BD1**. With **BD1**, the process appeared to be reversible in that aggregation of micelles was observed at basic pH. The irreversible lamellar-to-micellar transition observed with **BD2**-containing liposomes can possibly be attributed to acid-catalyzed hydrolysis of the acetal cross-linker, which generates two detergent monomers within the bilayer. Liposomes composed of 75 mol % bis-detergent and 25 mol % phosphatidylcholine were readily prepared and could entrap macromolecules such as polyanionic dextran of MW 40 kDa with moderate efficiency. The ability of **BD2**-containing liposomes to promote efficient cytosolic delivery of antisense oligonucleotides was confirmed by (a) their diffuse intracellular distribution seen in fluorescence micrographs, and (b) the up-regulation of luciferase in an antisense functional assay. The low pH-responsive, bis-detergent constructs described herein are suitable for triggered release strategies targeted to acidic intracellular or interstitial environments.

INTRODUCTION

Lipid-based drug carriers often promote membrane fusion or permeabilization by virtue of their inherent bilayer-perturbing conformations. As a result, incorporation of sufficient concentrations of such lipids in stable liposomal formulations poses a formidable challenge. For example, the utility of fusogenic lipids such as dioleoylphosphatidylethanolamine (DOPE) that preferentially adopt the hexagonal phase has been compromised by their low limit of incorporation into liposomal bilayers (*1*−*3*). To address this issue, Guo and Szoka (*4*) have devised an acid-cleavable ortho ester−poly(ethylene glycol) (PEG) conjugate of distearoyl glycerol. The PEGylated lipid not only serves to stabilize DOPE in bilayer vesicles, but also prolongs circulation half-life of the liposomal formulation in vivo. Cleavage of PEG in an acidic environment promotes lamellar-to-hexagonal transition of the liposomal formulation, which in turn results in release of contents and membrane fusion.

A similar problem pertaining to liposomal incorporation of micelle-favoring, pH-sensitive detergents remains unsolved (*5*). Liposomes containing detergent-to-phospholipid ratios greater than 1:3 are inherently unstable (*6*, *7*). Stabilization of such formulations with bilayer-favoring lipids such as cholesterol is counterproductive, in that it compromises their delivery potential (*5*, *8*). As a result, concentrations of pH-sensitive detergents required to promote efficient liposomal collapse and permeabilization of the endosomal membrane remain unattainably high (*9*).

A chemical solution to this problem is to mask the membrane-disrupting ability of such detergents by conjugating a second lipid tail to the detergent headgroup (*10*) or cross-linking two single-tailed detergents with a cleavable moiety (*11*). Unlike conventional detergents, the latter bis-detergents (BD) or Gemini surfactants tend to behave more like phospholipids than surfactants (*12*). Hence, while single-chain detergents tend to adopt micellar structures, bis-detergents due to their cylindrical shape can be incorporated with relative ease in vesicle bilayers (*11*, *13*). More importantly, such constructs allow for in situ generation of single-tailed detergents within stable bilayers upon exposure to specific stimuli, acidic pH in the present case.

On the basis of the above rationale, we have developed a two-step strategy for the cytosolic delivery of macromolecules using cleavable detergent dimers that possess an acid-labile acetal linker between their polar headgroups (Figure 1). Ortho ester, acetal, and vinyl ether groups are stable under neutral conditions but hydrolyze rapidly at acidic pH due to stabilization of the intermedi-

* Corresponding author: Moo J. Cho, CB # 7360, School of Pharmacy, University of North Carolina at Chapel Hill, Chapel Hill, NC 27599-7360, tel. no: 919-966-1345, fax no: 919-966-7778, e-mail: m_j_cho@unc.edu.

10.1021/bc049880n CCC: $27.50 © 2004 American Chemical Society
Published on Web 09/29/2004

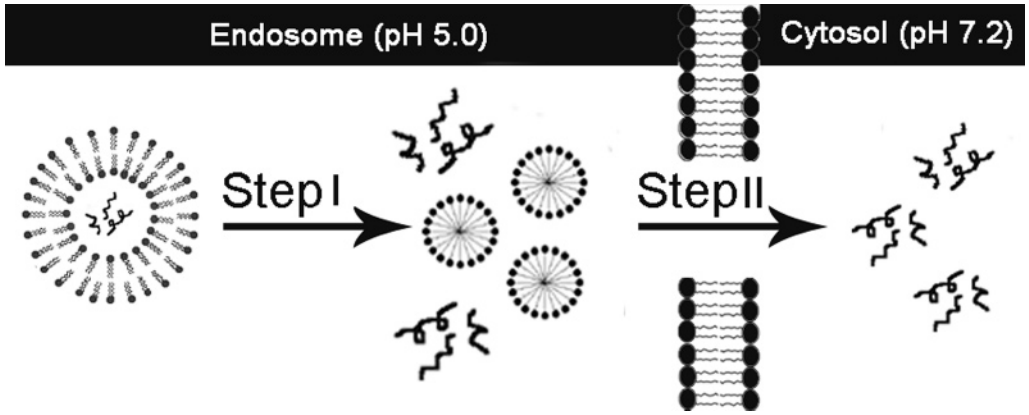


Figure 1. Two-step strategy for cytosolic delivery of macromolecules utilizing liposomes containing acid-labile bis-detergents such as **BD2** in Scheme 1. The proposed two-step mechanism of action is as follows: In Step I, acid-catalyzed hydrolysis of the acetone acetal cross-linker in the bis-detergent within the endosome is expected to generate single-tailed detergents within the liposomal bilayer. Upon reaching a critical concentration, these tertiary amine detergents would promote liposomal collapse into micelles and triggered release of entrapped contents. In Step II, the detergent-containing micelles are expected to form stable or transient pores in the endosomal membrane, which in turn will facilitate cytosolic delivery of initially entrapped contents.

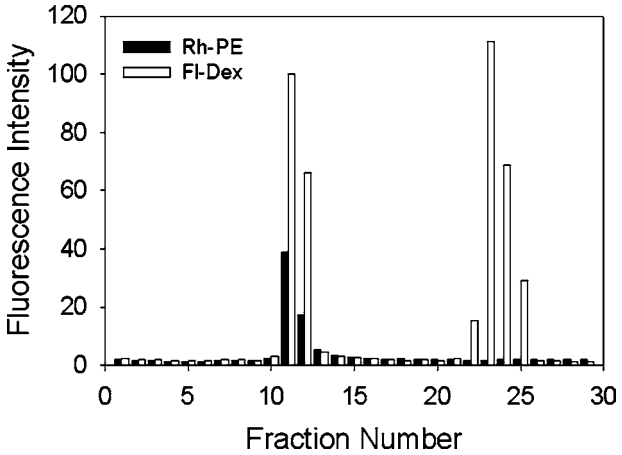


Figure 2. Size exclusion chromatography of **BD1**-containing liposomes encapsulating fluorescein-labeled, polyanionic dextran (MW 40 kDa) using a Sephadex CL-6B column. Rhodamine-labeled liposomes coelute with dextran in fractions no. 11 and 12 confirming entrapment. Later fractions (no. 22−25) contained unentrapped dextran.

ate carbonium ion by electron-donating groups (*14*, *15*). In the current study, as an example of cleavable and noncleavable bis-detergents, we report the synthesis and characterization of **BD1** and **BD2**, respectively (Figure 2). We demonstrate the ability of such agents to promote vesicle-to-micelle transition under acidic conditions and facilitate the endosome-to-cytosol translocation of macromolecules.

EXPERIMENTAL PROCEDURES

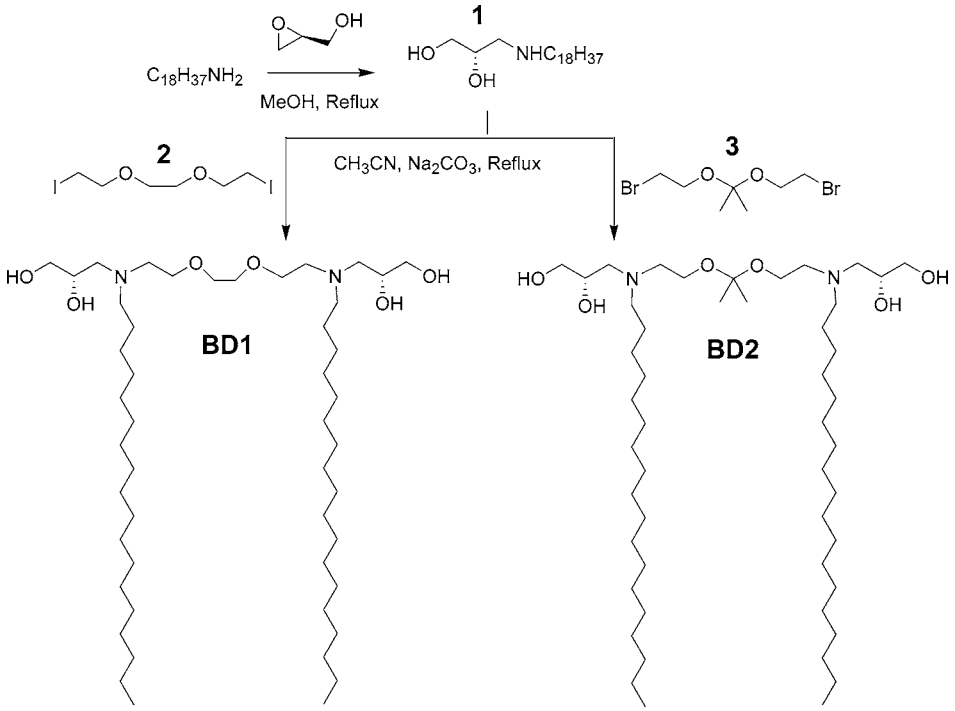
Lipids and Chemicals. All chemicals and solvents were purchased from Aldrich (Milwaukee, WI) and used without further purification. Glass thin-layer chromatography (TLC) plates were also purchased from Aldrich. Egg phosphatidylcholine (PC), cholesterol, and 1,2-dioleoyl-sn-glycero-3-phosphoethanolamine-*N*-(lissamine rhodamine B sulfonyl) (Rh-PE) were obtained from Avanti Polar Lipids (Alabaster, AL). Triton X-100 and *p*-toluidinyl naphthalene sulfonic acid (TNS) was obtained from Sigma (St. Louis, MO). Fluorescein-labeled, polyanionic dextran of MW 40 kDa (Fl-Dex) was purchased from Molecular Probes (Eugene, OR). Antisense 18-mer oligonucleotides (5′-CCU CUU ACC UCA GUU ACA-3′, ON-705) with 2′-*O*-Me phosphorothioate backbones were prepared by The Midland Certified Reagent Company, Inc. (Midland, TX). An unrelated sequence of Texas red-labeled oligonucleotides (TR-ON) was a generous gift from Professor Ryszard Kole (Lineberger Cancer Center, UNC-CH).

Synthesis of Bis-Detergents. The overall synthetic scheme is shown in Scheme 1. Compound **1** was synthesized by reacting (*S*)-glycidol with octadecylamine (*16*). Briefly, 3 g of octadecylamine (12 mmol) was dissolved using a heat gun in anhydrous methanol (5 mL) and transferred to a round-bottomed flask (round-bottom flask, 25 mL) fitted with a reflux condenser. A solution of (*S*)-glycidol (280 mg, 3 mmol) in 5 mL of methanol was then added dropwise to the round-bottom flask with continuous stirring and heat (60 °C). Reaction progress was monitored using TLC, and solvents were removed under vacuum after 1 h. The white residue was dissolved in hexane (50 mL) using a heat gun and allowed to cool, upon which a white precipitate (**1**) was formed. This process was repeated several times, following which the white precipitate was filtered and redissolved in 1 mL of $CHCl_3$:MeOH:aq NH_4OH (80:18:2). The clear solution was loaded onto a silica gel column (115 g) and purified using the same eluent system ($R_f \sim 0.4$). Pure compound **1** was obtained at ~60% yield (600 mg).

Compound **2** was purchased from Aldrich, while compound **3** was prepared by the method of Lorette and Howard (*17*). Briefly, a mixture of 2-bromoethanol (0.6 mol, 75 g), 2,2-dimethoxypropane (0.25 mol, 26 g), benzene (100 mL), and *p*-toluenesulfonic acid (0.2 g) were added into a 500 mL round-bottom flask connected to a fractional distillation apparatus fitted with a vacuum pump. The reaction mixture was distilled until the benzene−methanol azeotrope (~100 mL) boiling between 57 and 60 °C was completely removed. The contents were then cooled below the boiling temperature, and a solution of 0.5 g of sodium methoxide in 20 mL of methanol was added with stirring to achieve nearly instantaneous neutralization of acid. Distillation was resumed under vacuum (7 mmHg) upon which three fractions were collected: 28−30 °C (50 mL, fraction I); 65−75 °C (10 mL, fraction II); and 75−80 °C (2 mL, III). ^{1}H NMR ($CDCl_3$, 300 MHz): δ 1.39 (s, 6H), 3.45 (t, 4H), and 3.8 (t, 4H) confirmed pure symmetric acetone acetal (**3**) in fraction III.

Bis-detergent **BD1** was prepared by subjecting a mixture of compounds **1** (200 mg, 0.6 mmol), **2** (37 mg,

Scheme 1. Synthetic Scheme for Preparation of Bis-Detergents BD1 and BD2



0.1 mmol), and Na_2CO_3 (100 mg) in 20 mL of CH_3CN to reflux overnight. The solvents were then removed under high vacuum, and the residue was resuspended in $CHCl_3$ and filtered using a sintered glass funnel. The concentrated filtrate was then loaded onto a silica gel column (115 g) and eluted using $CHCl_3$:MeOH:aq NH_4OH (80:18:2, $R_f \sim 0.6$). Compound **BD1** was obtained in good yield (65 mg, ~80%). ^1H NMR ($CDCl_3$, 300 MHz, chemical shifts relative to TMS signal): δ 0.88 (t, 6H), 1.25 (br, 60H), 1.48 (br, 4H), 2.6−2.77 (m, 10H), 2.87−2.94 (m, 2H), 3.27 (br, 4H), and 3.49−3.84 (m, 14H), respectively. ESI-MS, calculated 801.76, found $[M + Na]^+$ 824.7 (22%), 750.1 (72%), and 454.5 (6%).

Bis-detergent **BD2** was prepared in a similar fashion by subjecting a mixture of compounds **1** (335 mg, 1 mmol), **3** (70 mg, 0.2 mmol), and Na_2CO_3 (500 mg) in 20 mL of CH_3CN to reflux overnight. A total of 72 mg (~60% yield) of compound **BD2** was obtained after silica gel chromatography using $CHCl_3$:MeOH:aq NH_4-OH (80:18:2, $R_f \sim 0.6$). ^1H NMR ($CDCl_3$, 300 MHz, chemical shifts relative to TMS signal): δ 0.88 (t, 6H), 1.25 (br, 60H), 1.38 (d, 6H), 1.45 (br, 4H), 2.5−2.8 (m, 10H), 2.85−2.95 (m, 2H), 3.45−3.53 (m, 10H), and 3.7−3.76 (m, 4H), respectively. ESI-MS, calculated 814.76, found $[M + Na]^+$ 837.7 (12.5%), 763.7 (1%), 450.4 (37.5%), and 410.3 (49%).

Preparation of Liposomes. Blank liposomes were prepared by generating a thin dry film composed of 7.5 mg of bis-detergent and 2.5 mg of PC in a 10 mL round-bottom flask by removing $CHCl_3$ in vacuo. The film was hydrated using 1 mL of Tris-buffered saline (TBS, pH 8.0) or phosphate-buffered saline (PBS, pH 7.0) and alternatively vortexed and sonicated for 15 min. Vesicles were then extruded 10 times through a 0.22 μm polycarbonate membrane (Millipore) using an extruder (Lipex Biomembranes, Vancouver, CA). The size of vesicles formed was determined using a Nicomp 370 particle sizer (Particle Sizing Systems, CA).

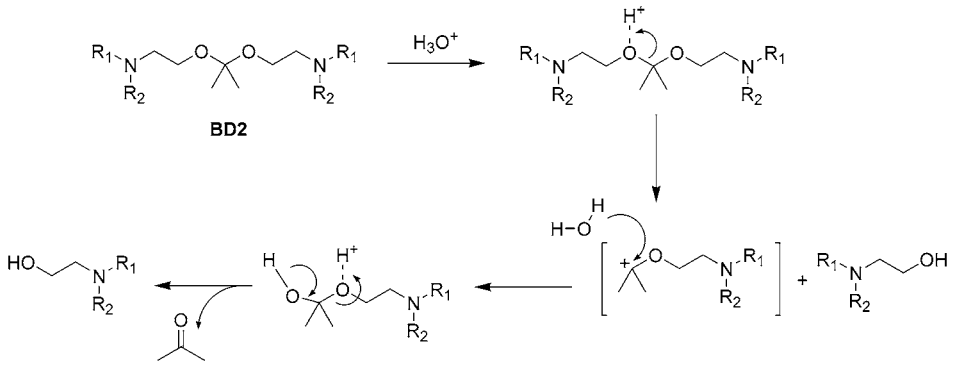
All macromolecules (fluorescently labeled or otherwise) were entrapped within liposomes using the minimum volume entrapment method (*18*). Briefly, a thin dry lipid film containing **BD1** or **BD2** with PC (75:25), generated by removing chloroform under high vacuum, was hydrated with a 100 μL aliquot of TBS or PBS containing a high concentration of oligonucleotides (50 μM) or Fl-Dex (10 μM), respectively, and vortexed at room temperature for 15 min. Vesicles formed were diluted to 1 mL with corresponding buffer and extruded (Lipex Biomembranes) 10 times through a 0.22 μm polycarbonate filter (Millipore) at a pressure of approximately 400 psi.

Finally, unencapsulated solutes were separated from liposomal fractions by elution with TBS/PBS through Sepharose CL-6B (Sigma) or DEAE-Sepharose fast flow anion exchange (Pharmacia) resins packed in a 20 cm × 1 cm glass column. Liposomal fractions were identified by monitoring coelution of Rh-PE as a lipid marker and Fl-Dex (MW 40 kDa) as a fluid-phase marker, respectively. Encapsulation efficiency was determined by dissolving a 10 μL aliquot of liposomes in 100 μL of 2-propanol, diluting to 1 mL with PBS, and measuring the fluorescence intensity/absorbance of the sample. Final concentrations were calculated using the extinction coefficient of oligonucleotides or from a standard curve generated with known concentrations of Fl-Dex.

Membrane-Bound pK_a and Acid-Catalyzed Hydrolysis of Bis-Detergents. Membrane-bound pK_a value of **BD1** (10 mol %) incorporated into PC:cholesterol (70:20) liposomes was determined using TNS (*19*). Acid-catalyzed hydrolysis of the acetone acetal cross-linker in **BD2**, which generates two, single-tailed lysosomotropic detergents and acetone (Scheme 2) was monitored by thin-layer chromatography. Briefly, 2 μL aliquots of **BD2**:PC (75:25) liposomes suspended in low ionic strength buffers of pH 4.0, 5.0, 6.0, and 7.0 were spotted at different time intervals onto silica gel TLC plates and eluted with $CHCl_3$:MeOH:aq NH_4OH (80:18:2). Spots corresponding to **BD2** ($R_f \sim 0.6$) and single-tailed, tertiary amine detergent monomers ($R_f \sim 0.3$) were identified using ninhydrin.

UV Light Scattering. Acid-induced collapse of **BD1**- or **BD2**-containing liposomes into micelles was monitored for approximately 10 min using a Shimadzu Model

Scheme 2. Mechanism of Specific Acid-Catalyzed Hydrolysis of Bis-Detergent BD2 into Tertiary Amine Detergent Monomers and Acetone. The Formation of Stabilized Carbonium Ion Intermediate Is Thought To Be Rate-Determining (*15*)



UV2401-PC UV/Vis spectrophotometer. Briefly, a 30 μL aliquot of blank liposomes containing BD:PC (75:25) was suspended in 3 mL of Tris-buffered saline (pH 8.0) taken in a quartz cuvette and the decrease in absorbance (turbidity) monitored under different conditions at a wavelength of 350 nm. The buffer was acidified or alkalinized by quickly injecting a 10 μL aliquot of acetic acid or 10 μL aliquots of aq NH_4OH into the cuvette. A 100 μL aliquot of 0.1% Triton X-100 injected at the end of the experiment served as positive control.

Cytosolic Delivery of Antisense Oligonucleotides. For fluorescence microscopy experiments, HeLa Luc-705 cells obtained from Professor Ryszard Kole's lab (Lineberger Cancer Center, UNC-CH) were cultured in two-well glass culture slides (2×10^5/well) using Dulbecco's modified eagle's medium (DMEM-H, Gibco), 10% fetal bovine serum, 100 units/mL penicillin, and 100 μg/mL streptomycin under 5% CO_2 humidified atmosphere at 37 °C. The cells were incubated for a period of 6 h with serum-free DMEM-H containing TR-ON (0.1 μM) in (a) free solution, (b) complexed with Lipofectamine (GIBCO, manufacturer specifications), (c) entrapped in **BD1**:PC (75:25) liposomes, or (d) entrapped in **BD2**:PC (75:25) liposomes. The formulations were replaced with serum-containing media and incubated for a further 18 h after which the slides were washed thrice with cold phosphate-buffered saline (PBS) and fixed using 2% paraformaldehyde in PBS. Cells were then examined immediately under a Leica Diaplan fluorescence microscope (25× magnification) equipped with a Texas red filter and a Hamamatsu camera.

For the antisense functional assay (*20*), HeLa Luc-705 cells were seeded in 12-well plates at 10^5 cells per well in DMEM-H containing 10% fetal bovine serum, 100 units/mL penicillin, and 100 μg/mL streptomycin and allowed to adhere overnight in a 5% CO_2 humidified atmosphere at 37 °C. The cells were incubated for a period of 6 h with serum-free DMEM-H containing ON-705 (0.1 μM) in (a) free solution, (b) complexed with Lipofectamine (manufacturer specifications), (c) entrapped in **BD1**:PC (75:25) liposomes, or (d) entrapped in **BD2**:PC (75:25) liposomes. In a separate experiment, Hela Luc-705 cells were incubated with **BD1**:PC or **BD2**:PC liposomes containing ON-705 under similar conditions, but in serum-containing media to reduce apparent toxicity associated with such formulations. All formulations were then replaced with serum-containing media and incubated for a further 18 h after which the wells were washed thrice with Hank's balanced salt solution (HBSS) without calcium/magnesium ions.

An aliquot of 200 μL of cell lysis buffer (BD Pharmingen, San Diego, CA) was then added to each well, and the cells were dislodged using a cell scraper (Costar, Corning, NY), following which the plates were incubated for 15 min at room temperature. The cell lysates were quickly spun down using a microcentrifuge to remove cell debris and a small aliquot used from each for determining protein content using the Bradford assay. Luminescence measurements were performed in a luminometer (Analytical Luminescence Laboratory, Ann Arbor, MI) using a Luciferase assay kit (BD Pharmingen, manufacturer specifications). Luciferase expression was expressed in relative light units (RLU) per μg of cellular protein.

RESULTS

Entrapment of Macromolecules by Bis-Detergent-Containing Liposomes. Liposomes containing **BD1**:PC:Rh-PE (75:24:1) were used to entrap Fl-Dex of MW 40 kDa in PBS (pH 7.0) using the minimum volume entrapment procedure. Following extrusion, liposomes and unentrapped solute were separated by size exclusion chromatography with PBS as eluent. The coelution of rhodamine-labeled liposomes ($\lambda_{ex} = 530$ nm; $\lambda_{em} = 590$ nm) with Fl-Dex ($\lambda_{ex} = 490$ nm; $\lambda_{em} = 515$ nm) in fractions no. 11 and no. 12 seen in Figure 2 indicates successful encapsulation. Un-entrapped Fl-Dex elutes in later fractions (no. 22−25). The average size of purified liposomes was 238 ± 69 nm with ~40% encapsulation efficiency. Liposomes containing **BD1** or **BD2** with PC (75:25) entrapping oligonucleotides were prepared in a similar fashion and separated from unentrapped oligonucleotides by ion exchange chromatography. Encapsulation efficiencies of polyanionic oligonucleotides (~6 kDa) and dextran (40 kDa) in BD-containing liposomes ranged from ~10% in TBS to 40% in PBS.

Membrane-Bound pK_a of BD1 Incorporated into Liposomal Bilayers. The membrane-bound pK_a of **BD1** was determined using the TNS assay. Briefly, increasing membrane potential of **BD1**-containing liposomes with decreasing pH results in increased partitioning and intensity of TNS in liposomal bilayers. No pH-dependent change in membrane potential is seen with liposomes lacking **BD1**. As determined from Figure 3, the twin, tertiary amine headgroups have an average pK_a of 6.37 ± 0.36.

Acid-Catalyzed Hydrolysis of BD2 Embedded in Liposomes. To quickly estimate the sensitivity of the acetone acetal in **BD2** toward acidic conditions relevant to an endosomal/lysosomal setting, a simple TLC assay was used. Briefly, ninhydrin was used to detect products of **BD2** hydrolysis, i.e., detergent monomers upon incubation for different time intervals at 37 °C in buffers of

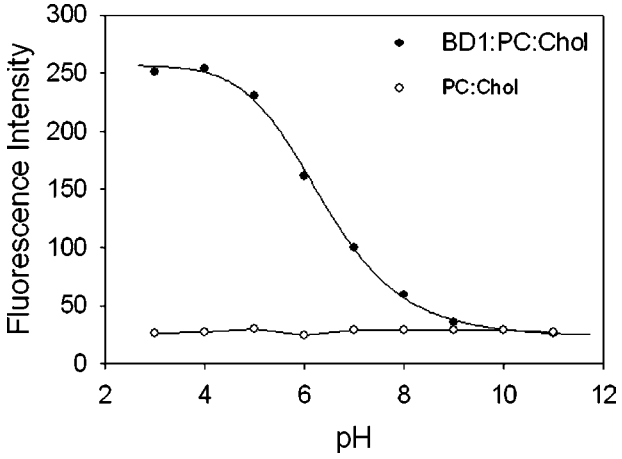


Figure 3. Membrane-bound pK_a of **BD1** determined using the TNS assay described previously. Liposomes containing PC/Chol with 10 mol % **BD1** (●) and without **BD1** (○) served as test and control, respectively. A pK_a of 6.37 ± 0.36 was obtained from triplicate experiments with **BD1**-containing liposomes.

different pH. As shown in Figure 4, **BD2** appears stable at 10 min in all buffers as indicated by the single spot at $R_f \sim 0.6$. However, after an hour, detergent monomers are detectable at pH 4.0 and 5.0 ($R_f \sim 0.3$), but not at pH 6.0 or 7.0. After 3 h, substantial hydrolysis of **BD2** is seen in pH 4.0 buffer and about 50% of starting material is hydrolyzed at pH 5.0. Detergent monomers are also detectable at pH 6.0, but not at pH 7.0. Finally, after 6 h, the detergent dimers are almost completely hydrolyzed at pH 4.0, but still remain intact at pH 7.0. Thus, **BD2** appears to degrade with a $t_{1/2}$ of ~3 h at pH 5.0 at 37 °C.

Low pH-Induced Collapse of BD-Containing Liposomes into Micelles. Liposomal formulations containing 75 mol % of **BD1** or **BD2** were characterized at 37 °C for changes in turbidity by monitoring their UV absorption spectra at 350 nm. This wavelength is the region where changes in particle size will have a large effect on the optical density due to light scattering without any interference from lipid absorbance (*20*). UV spectra were obtained over a time interval of approximately 10 min during which liposomal suspensions in pH 8.0 buffer were (a) acidified to pH 4.2, (b) neutralized to pH 7.1, followed by addition of base increasing pH to 9.0, and (c) finally disrupted completely to micelles with 0.1% Triton X-100.

As seen in Figure 5, addition of acetic acid to a final pH of 4.2 to liposomes containing **BD1** (upper curve) results in ~70% collapse into micelles. When the system was neutralized to pH 7.1, no changes in light scattering were apparent. In contrast, micellar aggregates were formed as suggested by the increase in turbidity observed at pH 9.0. The acidification of **BD2**-containing liposomal suspension (lower curve) resulted in nearly 90% collapse into micelles. Interestingly, neither neutralization nor alkalinization to pH 9.0 had an effect on turbidity. Addition of Triton X-100, which resulted in complete liposomal collapse into micelles served as reference.

Cytosolic Delivery of Antisense Oligonucleotides. The intracellular disposition of Texas red-labeled oligonucleotides (TR-ON) was monitored using fluorescence microscopy (Figure 6). As seen in Panel 6C, liposomes containing acid-stable **BD1** display large punctate spots against a partially diffuse background similar to that seen with Lipofectamine in Panel 6B. Such a distribution pattern suggests a moderate ability of **BD1**-containing liposomes to promote cytosolic delivery of oligonucleotides. In contrast, liposomes containing acid-labile **BD2** show a largely diffuse pattern of fluorescence seen in Panel 6D. This observation is consistent with efficient endosomal permeabilization and cytosolic delivery of oligonucleotides by **BD2**-containing liposomes. Pinocytic uptake of free TR-ON, which is seen as a predominantly punctate pattern, served as control (Panel 6A).

The ability of bis-detergent-containing liposomes to promote the cytosolic delivery of ON-705, an 18-mer oligonucleotide was also confirmed using an antisense functional assay based on luciferase up-regulation in HeLa Luc-705 cells (*20*). Briefly, the assay involves corrective splicing of aberrantly spliced luciferase precursor mRNA (pre-mRNA) to mRNA by ON-705 resulting in up-regulation of luciferase. It is noteworthy to mention that such corrective splicing strategies require backbone-modified antisense oligomers that function via RNase-H independent mechanism. Thus, oligomers with nuclease-resistant backbones, i.e., polyanionic 2′-*O*-methyl phosphorothioate (2′-*O*-Me) were used in this study. As seen in Figure 7, free ON-705 is unable to correct splicing and induce luciferase expression. On the other hand, as evidenced by similar levels of luciferase expression, liposomal formulations containing 75 mol % of **BD1** or **BD2** appear to be as efficient as Lipofectamine in promoting cytosolic delivery of oligonucleotides. In ad-

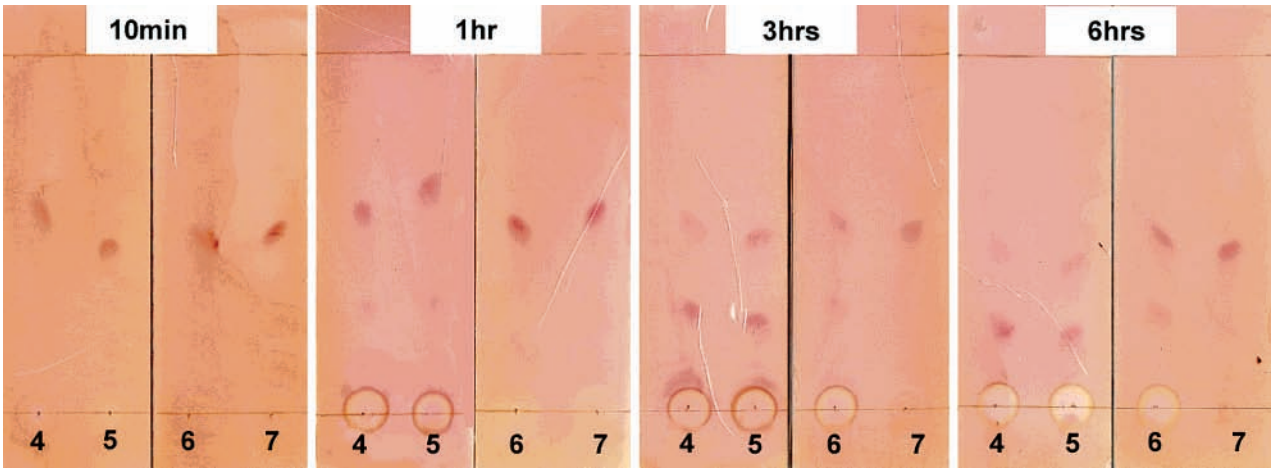


Figure 4. Acid-catalyzed hydrolysis of **BD2**, which generates single-tailed lysosomotropic detergents monitored by thin-layer chromatography. Briefly, 2 μL aliquots of **BD2**:PC (75:25) liposomes suspended in low ionic strength buffers of pH 4.0, 5.0, 6.0, and 7.0 were spotted at different time intervals onto silica gel TLC plates and eluted with $CHCl_3$:MeOH:aq NH_4OH (80:18:2). Spots corresponding to **BD2** ($R_f \sim 0.6$) and single-tailed, tertiary amine detergent monomers ($R_f \sim 0.3$) were identified using ninhydrin.

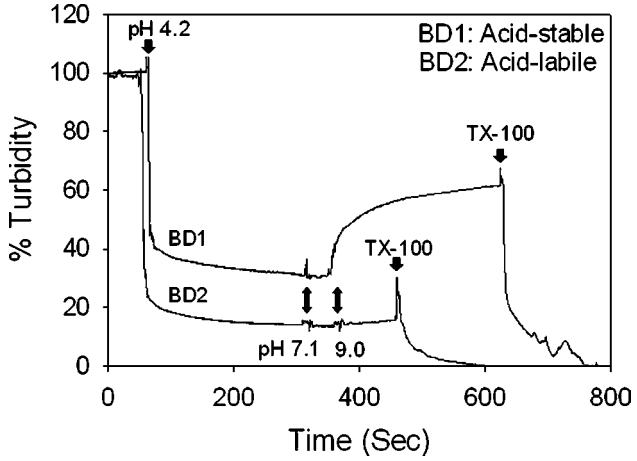


Figure 5. Light scattering by **BD1**:PC (75:25) liposomes (upper curve) and **BD2**:PC (75:25) liposomes (lower curve) at 350 nm. Liposomal formulations were suspended in 3 mL Tris-buffered saline (pH 8.0) in a quartz cuvette and acidified to pH 4.2 with a 10 μL aliquot of acetic acid. Two 10 μL aliquots of aq NH_4OH were added at ~325 s and 375 s increasing the pH to 7.1 and 9.0, respectively. Finally, 100 μL of 0.1% Triton X-100 was used to disrupt vesicles completely (TX-100). All experiments were performed in duplicate.

dition, the ability of **BD2**-containing liposomes to deliver ON-705 to the cytosol and hence up-regulate luciferase expression appears to improve in the presence of serum in comparison with formulations containing the acid-stable **BD1**.

DISCUSSION

The bis-detergents characterized in this study were designed to overcome the issue of low levels of incorporation of single-tailed detergents in stable liposomal drug delivery systems. The strategy involves in situ generation of micelles within the endosome and subsequent cytosolic delivery of initially entrapped contents. Synthesis of the constructs is rather straightforward, although cross-linker **3** is often obtained in low yield. The acetone acetal linker in **BD2** was chosen based on well-established chemistry and examples in the literature (*17*, *22*).

The kinetics of hydrolysis of **BD2** incorporated in liposomes was assessed in a semiquantitative fashion using TLC. The acid-catalyzed hydrolysis of the acetone acetal spacer was rather sluggish ($t_{1/2} \sim 3$ h; pH 5.0) as opposed to that reported in the literature ($t_{1/2} \sim 15$ min; pH 5.0, (*22*)). Such a decrease in rate of hydrolysis can be attributed in part to the lower H_3O^+ activity at the bilayer-water interface in comparison to the bulk aqueous phase. In addition, the acquisition of cationic charge upon protonation of tertiary amine headgroups of **BD2** can further deplete H_3O^+ activity at the liposomal surface due to electrostatic charge repulsion (*15*, *23*, *24*). Indeed, the headgroups of bis-detergents in this study were shown to have an average pK_a of 6.37, thus supporting the near-complete protonation of both tertiary amines at pH 5.0 or so. A detailed, quantitative analysis of the mechanism of acid-catalyzed hydrolysis of **BD2** is currently in progress.

Bis-detergents have been shown to form stable vesicles and more recently, been used to entrap macromolecules such as plasmid DNA (*25*). In the current study, lipid films containing 75 mol % detergent dimers and 25 mol % PC formed vesicles capable of entrapping macromolecules such as dextran. The higher entrapment efficiency in PBS can possibly be attributed to electrostatic interactions between polyanionic dextran and the partially protonated bis-detergent headgroups at neutral pH. This is further supported by the relatively lower encapsulation efficiency of formulations prepared at a higher pH in TBS (pH 8.0) when cationic charge on bis-detergent headgroups is negligible.

We have observed that macromolecular probes such as dextran (MW 10kDa) can be delivered to the cytosol simply upon coincubation with micelles containing single-tailed, pH-sensitive detergents (unpublished data). Such data in conjunction with other published results (*5*, *9*) suggest that acid-induced collapse of liposomes into micelles within the endosome is a prerequisite for endosomal permeabilization and macromolecular escape into the cytosol. Results from the UV light scattering experiment shown in Figure 5, confirm the ability of bis-detergents to promote liposomal collapse into micelles under acidic conditions. Although this set of data does not allow interpretation of the observation at the molecular level, it is likely that the collapse was largely due to repulsion between the protonated twin headgroups of each bis-detergent. Such electrostatic repulsion between twin headgroups of a similar Gemini surfactant has been shown to promote lamellar-to-micellar transition (*25*). However, such low pH-induced vesicle-to-micelle transition appears to be reversible, presumably due to reaggregation of micelles at basic pH (*26*). In contrast, the acid-triggered collapse of liposomes containing acid-labile **BD2** appears irreversible. In summary, it is tempting to speculate that the irreversible, acid-catalyzed hydrolysis of **BD2** into two single-tailed detergents might well be responsible for such efficient liposomal collapse and micelle formation. Pilot studies were therefore conducted to investigate the hypothesis that **BD2** could promote endosomal escape more efficiently than its noncleavable counterpart, **BD1**.

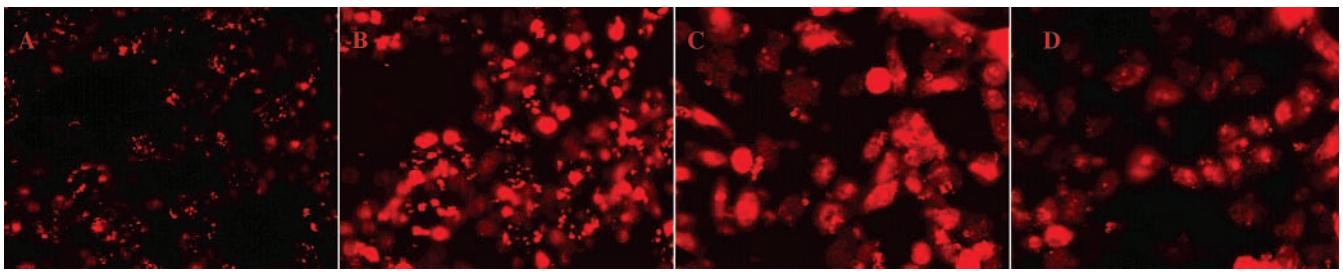


Figure 6. Intracellular distribution of different formulations containing Texas red-labeled oligonucleotides (TR-ON). HeLa Luc-705 cells grown in slide wells were incubated for a period of 6 h with serum-free DMEM-H containing TR-ON (0.1 μM) in (A) solution, (B) complexed with Lipofectamine (GIBCO, manufacturer specifications), (C) entrapped in **BD1**:PC (75:25) liposomes, or (D) entrapped in **BD2**:PC (75:25) liposomes. Formulations were replaced with serum-containing media and cells incubated for 18 h after which slides were washed thrice with cold PBS and fixed using 2% paraformaldehyde in PBS. Slides were immediately examined under a Leica Diaplan fluorescence microscope (25× magnification) equipped with a Hamamatsu camera.

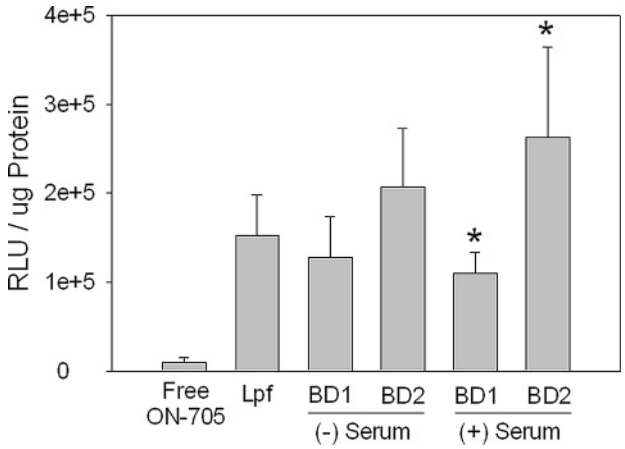


Figure 7. Upregulation of luciferase upon cytosolic delivery of antisense oligonucleotides (ON-705) using different formulations. HeLa Luc-705 cells seeded in 12-well plates were treated for 6 h with serum-free DMEM-H containing ON-705 (0.1 μM) in: solution (n = 6); complexed with Lipofectamine (n = 6, manufacturer specifications); entrapped in **BD1**:PC (75:25) liposomes (n = 3); entrapped in **BD2**:PC (75:25) liposomes (n = 3); or in serum-containing DMEM-H with **BD1**:PC or **BD2**:PC liposomes (n = 3 each). Formulations were replaced with serum-containing media and luciferase expression measured after 24 h in a luminometer using a Luciferase assay kit (manufacturer specifications). Luciferase expression is expressed in relative light units (RLU) per μg of cellular protein (mean ± SD, p < 0.05).

The cytosolic delivery potential of bis-detergent formulations was assessed qualitatively by monitoring the intracellular distribution of initially entrapped TR-ON through fluorescence microscopy. The predominantly diffuse pattern seen in HeLa cells treated with formulations containing acid-labile **BD2** contrasts the partially aggregated fluorescence pattern seen in cells treated with **BD1**-containing liposomes or Lipofectamine. These results are consistent with the notion that acid-labile bis-detergents are likely more efficient in promoting endosome-to-cytosol translocation of macromolecules than noncleavable detergent dimers or cationic lipids.

The delivery efficiency of aforementioned formulations was quantitatively assessed using an antisense functional assay. In the absence of serum, formulations of ON-705 prepared with bis-detergents were as efficient as Lipofectamine in promoting luciferase upregulation. Interestingly, addition of serum, which is known to completely inhibit Lipofectamine-mediated transfection (*27*, *28*) did not attenuate cytosolic delivery potential of **BD1**- or **BD2**-containing liposomes. More importantly, liposomes containing acid-labile **BD2** are presumably more efficient at promoting cytosolic delivery of ON-705 than liposomes containing acid-stable **BD1** in the presence of serum. In summary, acid-labile bis-detergents such as **BD2** appear to offer a dual advantage, i.e., the formulation of stable liposomes at neutral pH as well as in situ generation of membrane-disrupting, single-tailed detergents that promote efficient liposomal collapse into micelles in acidic environments. Such a system can potentially be exploited for cytosolic delivery of macromolecular drugs such as proteins, oligonucleotides, and genes in vitro and in vivo.

CONCLUSION

Two detergent dimer constructs, also referred to as 'bis-detergents' in the present study, with noncleavable (**BD1**) or acid-labile (**BD2**) spacers were synthesized. The bis-detergents were characterized for their ability to form stable liposomes at concentrations as high as 75 mol %, for the pH-dependent protonation of their headgroups and the ability of **BD2**, in particular to hydrolyze under acidic conditions. Liposomes composed of 75% **BD1** or **BD2** and 25% PC collapsed into micelles at mildly acidic pH similar to that found in endosomes/lysosomes. The collapse of **BD2**:PC liposomes was more efficient than that of **BD1**:PC liposomes presumably due to acid-catalyzed hydrolysis of the acetal spacer. Such can be attributed to the accumulation of single-tailed, micelle-favoring detergent species within the liposomal bilayer. Bis-detergent-containing liposomes were utilized to encapsulate antisense oligonucleotides and promote delivery of entrapped contents into the cytosol of HeLa cells. The efficiency of cytosolic delivery was comparable to Lipofectamine and substantially improved in the presence of serum. Further improvements in the cytosolic delivery potential of acid-sensitive bis-detergents can possibly be achieved by incorporation of biodegradable linkers and systematic characterization of formulations thereof. These studies are currently in progress.

ACKNOWLEDGMENT

We would like to thank Professors Rudy Juliano, Hal Kohn, Jeff Krise, Barry Lentz, and Ed LeCluyse for their helpful suggestions on this study. We would also like to acknowledge NIH GM071040 for research support.

LITERATURE CITED

(1) Cullis, P. R., and De Kruijff, B. (1978) The polymorphic phase behaviour of phosphatidylethanolamines of natural and synthetic origin. A 31P NMR study. *Biochim Biophys Acta 513* (1), 31−42.

(2) Tari, A., and Huang, L. (1989) Structure and function relationship of phosphatidylglycerol in the stabilization of the phosphatidylethanolamine bilayer. *Biochemistry 28* (19), 7708−7712.

(3) Winterhalter, M., and Lasic, D, D. (1993) Liposome stability and formation: experimental parameters and theories on the size distribution. *Chem. Phys. Lipids 64* (1−3), 35−43.

(4) Guo, X., and Szoka, F. C. (2001) Steric stabilization of fusogenic liposomes by a low-pH sensitive PEG- -diortho ester—lipid conjugate. *Bioconjugate Chem. 12* (2), 291−300.

(5) Asokan, A., and Cho, M. J. (2003) Cytosolic delivery of macromolecules. II. Mechanistic studies with pH-sensitive morpholine lipids. *Biochim. Biophys. Acta 1611* (1−2), 151−160.

(6) Bhamidipati, S. P., and Hamilton, J.A (1995) Interactions of lyso 1-palmitoylphosphatidylcholine with phospholipids: a 13C and 31P NMR study. *Biochemistry 34* (16), 5666−5677.

(7) Sun, C., Hanasaka, A., Kashiwagi, H., and Ueno, M. (2000) Formation and characterization of phosphatidylethanolamine/lysophosphatidylcholine mixed vesicles. *Biochim. Biophys. Acta 1467* (1), 18−26.

(8) Liang, E., and Hughes, J. A. (1998) Membrane fusion and rupture in liposomes: effect of biodegradable pH-sensitive surfactants. *J. Membr. Biol. 166* (1), 37−49.

(9) Asokan, A., and Cho, M. J. (2004) Cytosolic delivery of macromolecules: IV. Mechanism of membrane destabilization by pH-sensitive detergents. *Biochim. Biophys. Acta* (under review).

(10) Boomer, J. A., and Thompson, D. H. (1999) Synthesis of acid-labile diplasmenyl lipids for drug and gene delivery applications. *Chem. Phys. Lipids 99* (2), 145−153.

(11) Jaeger, D. A., Li, B., and Clark, T. (1996) Cleavable double-chain surfactants with one cationic and one anionic headgroup that form vesicles. *Langmuir 12* (18), 4314−4316.

(12) Yaroslavov, A. A., Udalykh, O., Melik-Nubarov, N. S., Kabanov, V. A., Ermakov, Y. A., Azov, A. V., and Menger, F. M. (2001) Conventional and gemini surfactants embedded within bilayer membranes: contrasting behavior. *Chem.−Eur. J. 7* (22), 4835−4843.

(13) Menger, F. M., and Peresypkin, A. V. (2003) Strings of vesicles: flow behavior in an unusual type of aqueous gel. *J. Am. Chem. Soc. 125* (18), 5340−5345.
(14) Fife, T. H., and Jao, L. K. (1965) Substituent effects in acetal hydrolysis. *J. Org. Chem. 30* (5), 1492−1495.
(15) Cordes, E. H., and Bull, H. G. (1974) Mechanism and catalysis for hydrolysis of acetals, acetals and orthoesters. *Chem Rev. 74* (5), 581−603.
(16) Vollhardt, D., and Gehlert, U. (2002) Chiral discrimination in 1-stearylamine-glycerol monolayers. *J. Phys. Chem. B. 106* (17), 4419−4423.
(17) Lorette, N. B., and Howard, W. L. (1960) Preparation of ketals from 2,2-dimethoxypropane. *J. Org. Chem. 25* (4), 521−525.
(18) Thierry, A. R., Rahman, A., and Dritschilo, A. (1993) Overcoming multidrug resistance in human tumor cells using free and liposomally encapsulated antisense oligodeoxynucleotides. *Biochem. Biophys. Res. Commun. 190* (3), 952−960.
(19) Bailey, A. L., and Cullis, P. R. (1994) Modulation of membrane fusion by asymmetric transbilayer distributions of amino lipids. *Biochemistry 33* (42), 12573−12580.
(20) Kang, S. H., Cho, M. J., and Kole, R. (1998) Up-regulation of luciferase gene expression with antisense oligonucleotides: implications and applications in functional assay development. *Biochemistry 37* (18), 6235−6239.
(21) Ollivon, M., Eidelman, O., Blumenthal, R., and Walter, A. (1988) Micelle-vesicle transition of egg phosphatidylcholine and octyl glucoside. *Biochemistry 27* (5), 1695−1703.
(22) Srinivasachar, K., and Neville, D. M., Jr. (1989) New protein cross-linking reagents that are cleaved by mild acid. *Biochemistry 28* (6), 2501−2509.
(23) Adamson, A. W., and Gast, A. P. (1997) Electrical aspects of surface chemistry. *Physical chemistry of surfaces,* 6th ed., pp 169−179, John Wiley & Sons, New York.
(24) Guo, X., MacKay, J. A., and Szoka, F. C., Jr. (2003) Mechanism of pH-triggered collapse of phosphatidylethanolamine liposomes stabilized by an ortho ester poly(ethylene glycol) lipid. *Biophys. J. 84* (3), 1784−1795.
(25) Fielden, M. L., Perrin, C., Kremer, A., Bergsma, M., Stuart, M. C., Camilleri, P., and Engberts, J. B. (2001) Sugar-based tertiary amino gemini surfactants with a vesicle-to-micelle transition in the endosomal pH range mediate efficient transfection in vitro. *Eur. J. Biochem. 268* (5), 1269−1279.
(26) Johnsson, M., Wagenaar, A., and Engberts, J. B. (2003) Sugar-based gemini surfactant with a vesicle-to-micelle transition at acidic pH and a reversible vesicle flocculation near neutral pH. *J. Am. Chem. Soc. 125* (3), 757−760.
(27) Felgner, P. L., Gadek, T. R., Holm, M., Roman, R., Chan, H. W., Wenz, M., Northrop, J. P., Ringold, G. M., and Danielsen, M. (1987) Lipofection: a highly efficient, lipid-mediated DNA-transfection procedure. *Proc. Natl. Acad. Soc. 84* (21), 7413−7417.
(28) Yang, J. P., and Huang, L. (1997) Overcoming the inhibitory effect of serum on lipofection by increasing the charge ratio of cationic liposome to DNA. *Gene Ther. 4* (9), 950−960.

BC049880N

Synthesis and in Vitro Testing of J591 Antibody–Dendrimer Conjugates for Targeted Prostate Cancer Therapy

Anil K. Patri,[§] Andrzej Myc,[§] James Beals,[§] Thommey P. Thomas,[§] Neil H. Bander,[‡] and James R. Baker, Jr.[§,*]

Center for Biologic Nanotechnology, Department of Internal Medicine, Division of Allergy, University of Michigan, 9220 MSRB III, Box 0648, Ann Arbor, Michigan 48109, and Department of Urology, New York Presbyterian Hospital-Weill Medical College of Cornell University, 525 E. 68th Street, New York, New York 10021. Received April 9, 2004; Revised Manuscript Received August 16, 2004

Targeted therapeutics using antibodies are an attractive option over conventional cancer chemotherapeutics due to their potential to deliver a therapeutic specifically to cancer tissue without damaging normal tissue. However, there are known problems with immunoconjugates such as decreased immunoreactivity and poor solubility. Using dendrimers as carriers for these agents has the potential to resolve these issues. We synthesized J591 anti-PSMA (prostate specific membrane antigen) antibody dendrimer conjugates containing fluorophores on the dendrimer. The in vitro studies of these conjugates show that they specifically bind to cells expressing PSMA. Confocal microscopy experiments document the binding and internalization of these conjugates. This research encourages the further study of antibody–dendrimer–drug conjugates for use in targeted therapeutics.

INTRODUCTION

Targeted therapy for cancer offers potential improvements over existing chemotherapy regimens since the drug is preferentially delivered to the cancer tissue. The side effects associated with chemotherapy can be minimized by targeted drug delivery. Moreover, a prodrug attached to a carrier and a targeting agent would further reduce general cytotoxicity as the drug does not become active until it is released in the targeted tissue.

Monoclonal antibodies (mAb) are useful for the targeted delivery of therapeutics (*1*), imaging agents, and radiotherapy to tumors. For targeted therapy, identifying an antigen that is uniquely expressed or overexpressed on tumor cells is of crucial importance since this is essential to target the delivery of drugs to tumors while sparing normal tissue. One such antigen for prostate cancer is the prostate-specific membrane antigen (PSMA) (*2*, *3*). PSMA is a 100-kDa, type II membrane glycoprotein highly expressed by all prostate cancers as well as by nonprostatic tumor neovasculature and the vascular endothelium of virtually all solid sarcoma and carcinoma tumors (*4*). Important to note is that it is not expressed on normal vascular endothelium. Several anti-PSMA mAbs that bind the extracellular PSMA domain might be useful in targeting tumor cells have been developed (*5*). These antibodies define two distinct, noncompeting epitopes on the extracellular domain of PSMA. They induce and increase the rate of internalization of PSMA. The internalized antibodies accumulate in endosomes (*6*). This has led to in vitro and in vivo investigations of these antibodies for immunotherapy (*7*) and radioimmunotherapy (*8*–*11*) for which these antibodies are ideally suited.

* Corresponding author: Prof. James R. Baker, Jr., M.D. Phone: (734) 647-2777. Fax: (734) 936-2990. Email: jbakerjr@umich.edu.

[§] University of Michigan.

[‡] New York Presbyterian Hospital–Weill Medical College of Cornell University.

Dendrimers (*12*, *13*) are synthetic, nanometer-sized macromolecules that can be modified to suit a specific application. Several types of dendrimers are commercially available, among which PAMAM dendrimers are the most extensively studied for biological applications (*14*, *15*). They have a unique architecture based on β-alanine subunits with primary amine groups on the surface that are available for the attachment of several types of biological material (*16*). Their aqueous solubility and biocompatibility are well suited to carry ligands, fluorochromes, and drugs for targeting, imaging (*17*), and drug delivery (*18*–*21*). Some of the issues associated with immunoconjugates, such as decreased solubility and reduced binding efficiency, can be addressed using dendrimers as carrier molecules attached to antibodies (*22*). Several groups have studied the conjugation of dendrimers to antibodies for targeting applications (*17*, *23*–*25*). Antibody–dendrimer conjugates have been used for radiolabeling (*26*) with minimal loss of immunoreactivity (*23*). The current work shows that the anti-PSMA antibody J591 (*27*), when conjugated to a dendrimer containing a fluorochrome, can be used for targeting prostate cancer and has potential as an efficient delivery system for therapeutics and imaging agents.

EXPERIMENTAL PROCEDURES

Materials. The anti-PSMA antibody, J591, which binds with high affinity to the extracellular domain of PSMA, was used in binding and uptake studies (*28*). Goat anti-mouse IgG-FITC antibody was purchased from Jackson ImmunoResearch Laboratories (West Grove, PA). Generation 5 PAMAM dendrimers were synthesized in our lab by Dr. Douglas Swanson and characterized by ^{1}H and ^{13}C NMR, GPC, and MALDI-TOF mass spectrometry. Fluorescein isothiocyanate (FITC), dithiothreitol (DTT), *N*-ethylmaleimide, acetic anhydride, triethylamine, methanol, and dimethyl sulfoxide were purchased from Aldrich (St. Louis, MO). 6-Carboxytetramethylrhodamine succinimidyl ester (6-TAMRA SE) was pur-

10.1021/bc0499127 CCC: $27.50 © 2004 American Chemical Society
Published on Web 10/08/2004

chased from Molecular Probes (Eugene, OR). The water soluble heterobifunctional cross linkers sulfosuccinimidyl 4-(*N*-maleimidomethyl)cyclohexane-1-carboxylate (Sulfo-SMCC) and sulfosuccinimidyl 6-[3′(2-pyridyldithio)propionamido]hexanoate (Sulfo-LC-SPDP) were purchased from Pierce (Rockford, IL). Prepacked sephadex G-25 PD-10 columns were purchased from Amersham Pharmacia Biotech (Piscataway, NJ) and equilibrated with eluting buffer before sample introduction. Pellicon, microcon, and centricon devices were purchased from Millipore (Bedford, MA). HiPrep Sephacryl S-100, S-200, and S-300 columns were purchased from Amersham Pharmacia Biotech and used in conjunction with the Isco LPLC system with type 11 (254 nm) or type 12 (214 nm) detectors for purification of dendrimer and antibody conjugates. Novex 4−20% trisglycine gels were used for PAGE with trisglycine SDS running buffer. UV measurements were carried out on a Perkin-Elmer Lambda 20 spectrometer. NMR measurements were carried out on a Bruker 500 MHz spectrometer. The PC-3 and LNCaP.FGC cell lines were purchased from American Type Cell Collection (ATCC, Manassas, VA) and grown in RPMI medium supplemented with penicillin (100 units/mL), streptomycin (100 μg/mL), 50 mM L-glutamine, and 10% heat-inactivated FBS as the monolayer at 37 °C and 5% CO_2.

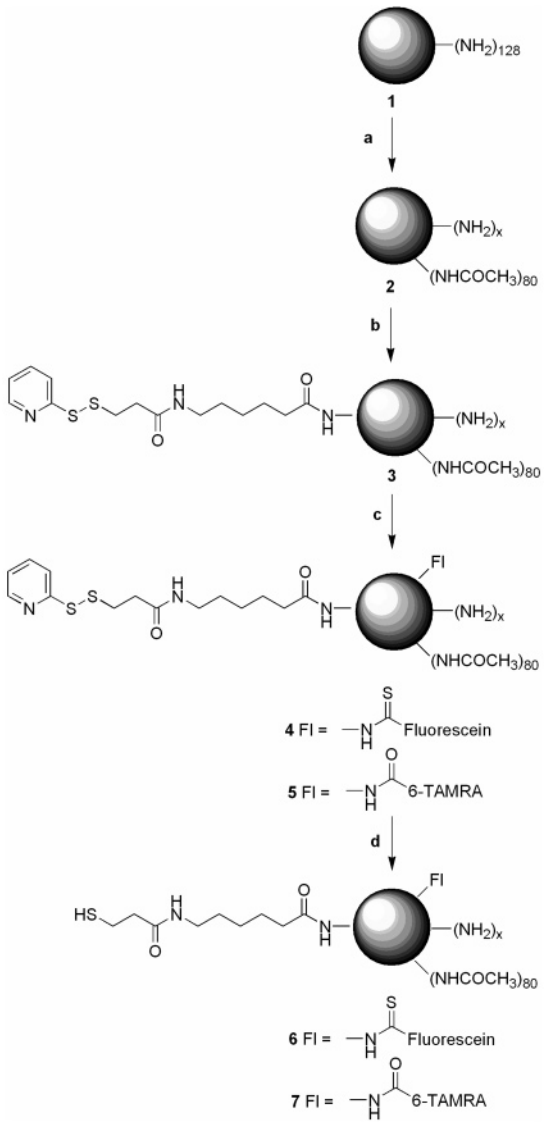
Cell Staining Assay. Approximately 80% confluent cells were washed once with PBS, trypsinized, washed again, and resuspended in 0.1% bovine serum albumin in PBS (washing buffer). One million cells in 100 μL of washing buffer were incubated on ice either with the J591 antibody or with the isotype control antibody at a concentration of 1 μg/mL for 30 min and then washed twice in washing buffer and stained with anti-mouse IgG-FITC antibody for 30 min. In some experiments the cells were incubated with conjugates **12**, **13** (see Scheme 3) or respective control nanodevices either on ice or at 37 °C for 30 min. After incubation, the cells were washed, resuspended in washing buffer, and analyzed using flow cytometry.

Flow Cytometry Analysis. Single cell suspensions of cells incubated with fluorescent compounds were washed with washing buffer. Samples were run on a Coulter EPICS-XL MCL Beckman-Coulter flow cytometer, and data were analyzed using Expo32 software (Beckman-Coulter, Miami, FL).

Microscopy Analysis. To determine the bleaching rate of FITC and 6-TAMRA dendrimer conjugates, 1 μL of 1 M solutions of each of the dendrimer conjugates was placed on a slide coated with gelatin and dried. Appropriate filter and lasers were used for imaging. For the FITC conjugate, a 488 nm 60% neutral density filter with a 505−530 band-pass emission filter was used, and for the 6-TAMRA conjugate, a 543 nm 0% neutral density filter with a 650−615 nm band-pass emission filter was used. The gain was set to within 10% of each other (686−700), and the laser intensity was adjusted with the neutral density filter to saturate the detector. Two line scans from the center to the edge of the sample drop were imaged and averaged. This was repeated 999 times.

Three-dimensional imaging was done with a Zeiss 510 Meta LSCM. A Zeiss 40× Plan apo 1.2 NA was used at 4× digital zoom. Both fluorescence and differential interference contrast images were acquired simultaneously using a 543 nm HeNe laser. An image stack was acquired using confocal fluorescence with a 1 airy unit pinhole with appropriate laser and filters for 6-TAMRA (543 nm laser, 560 nm long pass filter). The image stack size, resolution, and sampling rate settings assured that an individual cell could be rendered in 3D with enough detail to discern internalization of the nanodevice. There were 31 optical sections in a 512 × 512 pixel image stack. Each optical section was 1.5 μm thick. The image stacks were imported into Volocity (Improvision, Inc.) for deconvolution and 3D reconstruction. The deconvolution used an iterative maximum entropy algorithm and a theoretical confocal point spread function run to achieve 85% confidence level. Three-dimensional rendering enabled us to select, measure, and identify individual endocytosed vesicles.

Scheme 1. Synthesis of Dendrimer Conjugates by Terminal Group Modifications on Generation 5 PAMAM Dendrimer[a]



[a] Reagents and conditions: (a) Acetic anhydride, Et_3N, methanol, rt, 16 h; (b) Sulfo-LC-SPDP, PBS, rt, 3 h; (c) FITC or 6-TAMRA SE, DMSO; (d) DTT, PBS−EDTA.

Synthesis of Dendrimer Conjugates. To a methanolic solution of generation 5 PAMAM dendrimer **1** (1.85 g; 72 μmol) (Scheme 1) under nitrogen, triethylamine (0.56 g; 5.5 mmol), and acetic anhydride (0.552 g; 5.4 mmol) were added dropwise while stirring (*20*). Stirring continued at an ambient temperature for 16 h. Methanol was removed in vacuo, and the residue was ultrafiltered using a Pellicon Device (10K MWCO), washing initially with a pH 8.0 PBS buffer and then for several recirculations with deionized water. The partially acetylated

dendrimer conjugate **2** was lyophilized; 1.5 g was recovered. To a solution of conjugate **2** (0.2 g; 7 μmol) in PBS (20 mL), sulfo-LC-SPDP (21 mg; 40 μmol) was added. The unreacted reagents and byproduct were separated after 3 h. by ultrafiltration using a 10K MWCO Pelicon device, washing initially with PBS and then with DI water. The conjugate was lyophilized to give 115 mg of disulfide conjugate **3** as an off-white powder.

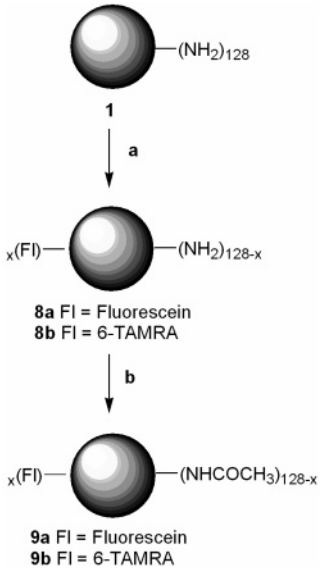
To the dendrimer disulfide conjugate **3** (45 mg; 1.5 μmol) in DMSO (5 mL), a solution of FITC (3.4 mg; 8.7 μmol) in DMSO (0.5 mL) was slowly added while stirring over a period of 30 min in darkness under nitrogen at ambient temperature. Stirring continued for 16 h. The reaction mixture was cooled on an ice bath, water was added, and the solution was dialyzed in a 15K MWCO regenerated cellulose bag in the dark. The initial buffer exchanges were with PBS and later with deionized water. The resultant purified dendrimer−FITC−disulfide conjugate was lyophilized to yield 35 mg of conjugate **4**. Similarly, 6-TAMRA succinamidyl ester (5 mg; 9.4 μmol) in DMSO (0.5 mL) was slowly added to dendrimer conjugate **3** (41 mg; 1.4 μmol) in DMSO (5 mL) at room temperature and stirred in the dark under nitrogen for 16 h. The reaction mixture was then dialyzed in a 15 K MWCO regenerated cellulose membrane. The initial red permeate fractions releasing free 6-TAMRA faded, and the dialysis continued until the permeate fractions were colorless. After dialyzing further in deionized water, the retentate was lyophilized to give 25 mg of dendrimer−6-TAMRA−disulfide conjugate **5** as an amorphous red powder.

The disulfide bonds on dendrimer conjugates **4** and **5** (2 mg each; 64 nmol) were reduced by using 10 mM DTT in degassed PBS-EDTA buffer (0.5 mL) at RT under argon to provide the corresponding dendrimer−thiol conjugates **6** and **7**. These conjugates were purified by gel filtration, eluting with PBS-EDTA buffer under nitrogen on a PD-10 column to remove excess reagents and byproducts, and were immediately used for subsequent antibody conjugation.

Dendrimer conjugates without antibody, for in vitro control experiments, were prepared by treating G5 PAMAM dendrimer **1** (100 mg; 4 μmol) with a 6-fold molar excess of FITC (9 mg; 24 μmol) or 6-TAMRA (12.6 mg; 24 μmol) dropwise in DMSO (10 mL) under an inert atmosphere of nitrogen in the dark (Scheme 2). The conjugates were purified by dialysis using a 10K MWCO regenerated cellulose membrane. The resultant conjugates **8a** and **8b** (25 mg each; 0.94 μmol) were then acetylated in a 1:1 mixture of PBS:DMSO (5 mL) at pH 8.0 using an excess of acetic anhydride (15.3 mg; 150 μmol) with equimolar triethylamine (15.1 mg; 150 μmol). The pH was readjusted to 8 after 3 h, and another 1 equiv of acetic anhydride was added. The resultant conjugates were purified by dialysis after 12 h as before and lyophilized to give completely acetylated dendrimer conjugates **9a** (G5−FITC) and **9b** (G5−6-TAMRA).

Antibody Conjugation. Modification of J591 anti-PSMA mAb (Scheme 3). The J591 antibody (**10**) was provided in 5 mg/mL concentration in PBS buffer and used without dilution. A thiol reactive maleimide group was introduced on the antibody by reacting the J591 mAb with sulfo-SMCC in PBS at ambient temperature for 2 h to give conjugate **11** using standard protocols (*29*). The excess reagent was removed by gel filtration on a Sephadex G-25 column. This maleimide-linked antibody conjugate **11** was then concentrated on a microcon YM50 and immediately reacted with dendrimer thiolates **6** or **7** in degassed PBS-EDTA buffer at an ambient temperature for 2 h under an inert atmosphere. Excess thiol groups on the dendrimer were then quenched using *N*-ethylmaleimide to minimize dimer formation. The products were then concentrated by centrifugal ultrafiltration using YM100 microcon devices to remove excess dendrimer and other reagents. They were further purified on a S-200 Sephacryl column to give conjugates **12** and **13**.

Scheme 2. Dendrimer Labeled with FITC or 6-TAMRA for Control Experiments



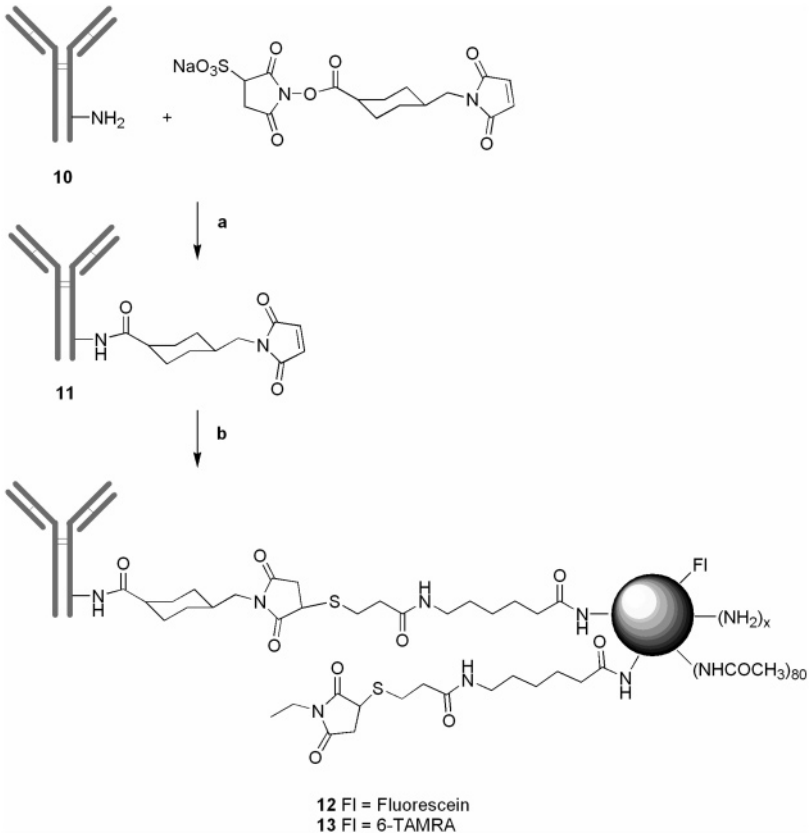
[a] Reagents and conditions: (a) DMSO, FITC or 6-TAMRA SE; (b) acetic anhydride, Et_3N, PBS−DMSO, rt, 12 h.

RESULTS AND DISCUSSION

Dendrimer Conjugate Characterization. The dendrimer terminal group modification is shown in Scheme 1. Amine-terminated PAMAM dendrimers can nonspecifically bind to cells due to the positive surface charge. To improve targeting efficacy and decrease nonspecific interactions, the generation 5 PAMAM dendrimer **1** was partially acetylated. The use of 80 times molar excess of acetic anhydride leaves some amines unreacted on the dendrimer for further conjugation. Acetylation also decreases the intermolecular interactions, minimizing aggregate formation and solubility problems. Initially using pH 7.4 PBS, for ultrafiltration, removes loosely bound side products that would otherwise be retained if ultrafiltered only against water. The purity of the conjugate **2** and the extent of acetylation can be measured (*30*) and monitored by ^{1}H NMR, which shows a distinct signal for the terminal NHCOCH_3 protons of the dendrimer at δ 1.85. If acetic acid contamination is detected upfield at δ 1.80, it can be removed by repeated dialysis in PBS and water.

To introduce a disulfide group, the water-soluble heterobifunctional cross-linking agent sulfo-SPDP was conjugated to the partially acetylated dendrimer **2** to provide a protected thiol in the form of a disulfide, which is later cleaved with DTT. The extent of disulfide modification can be monitored by UV spectroscopy, using the pyridine-2-thione assay (Figure 1) by adding DTT to a measured quantity of dendrimer and recording the absorbance of the released 2-thiopyridine at 343 nm. On the basis of this measurement, it was calculated that there are an average of two disulfide groups per dendrimer in conjugate **3** in agreement with values obtained by ^{1}H NMR by comparing the integration values of the

Scheme 3. Antibody–Dendrimer Conjugation[a]



[a] Reagents and conditions: (a) PBS, pH 7.4, rt, 2 h; (b) conjugate **6** or **7**, PBS-EDTA, pH 7.4, rt, 2 h, *N*-ethylmaleimide.

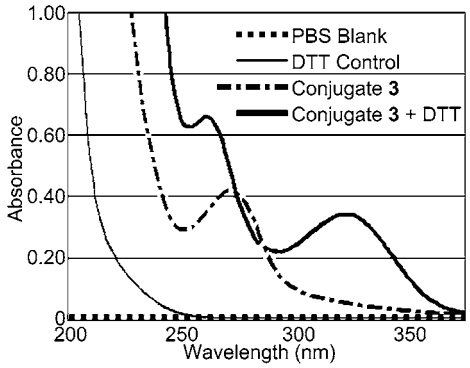


Figure 1. Pyridine-2-thione assay. The increase in absorbance at 343 nm for the conjugate is due to the release of 2-thiopyridine.

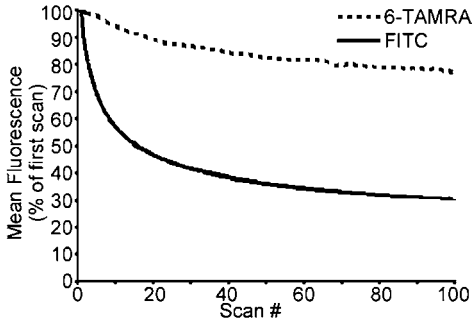


Figure 2. Comparison of photobleaching of FITC and 6-TAMRA labeled dendrimer conjugates (**9a** and **9b**) in the confocal microscope. A rapid decrease of 50% fluorescence in dendrimer conjugated to FITC was observed after 25 scans. The fluorescence decreased by only 10% for dendrimer–6-TAMRA conjugate after 25 scans.

heteroaromatic signals of the pyridine and the aliphatic signals of the dendrimer.

Imaging of cells by flow cytometry or confocal microscopy requires a detectable fluorescent probe. We have investigated the use of different fluorescent probes on the dendrimer for this purpose. Remarkably, up to 20 times molar excess of these probes, which have aromatic groups, can be conjugated to the dendrimer while still having the conjugate remain soluble in aqueous buffers. To retain complete solubility but still provide an imaging source for these studies, the amount of FITC labeling was decreased to six per dendrimer. The UV spectrum of conjugate **4** shows absorption for the fluorescein at λ_{max} 498 nm. The ^{1}H NMR of the conjugate shows overlapping signals in the aromatic region for both the fluorescein and the pyridine ring from the disulfide linker apart from the expected aliphatic signals for the dendrimer. The fluorescein label is ideally suited for flowcytometry experiments for in vitro studies; it, however, photobleaches under confocal microscopy conditions. For the confocal microscopy experiments, we tested 6-TAMRA, a dye with a higher quantum yield and with minimal photobleaching compared to FITC.

We tested the rate of photobleaching in dendrimer conjugates with FITC and 6-TAMRA (Figure 2). A rapid decrease of 50% fluorescence in the FITC-labeled dendrimer conjugate was observed as compared to a 10% decrease in fluorescence on the 6-TAMRA dendrimer conjugate using the confocal microscope. Hence, the antibody–dendrimer conjugate with 6-TAMRA was used for confocal microscopy experiments to detect binding and internalization. Therefore we synthesized the corresponding dendrimer conjugate **5** with 6-TAMRA. Even though the conjugation efficiency of the 6-TAMRA succinamidyl ester is less than that of the FITC, using a

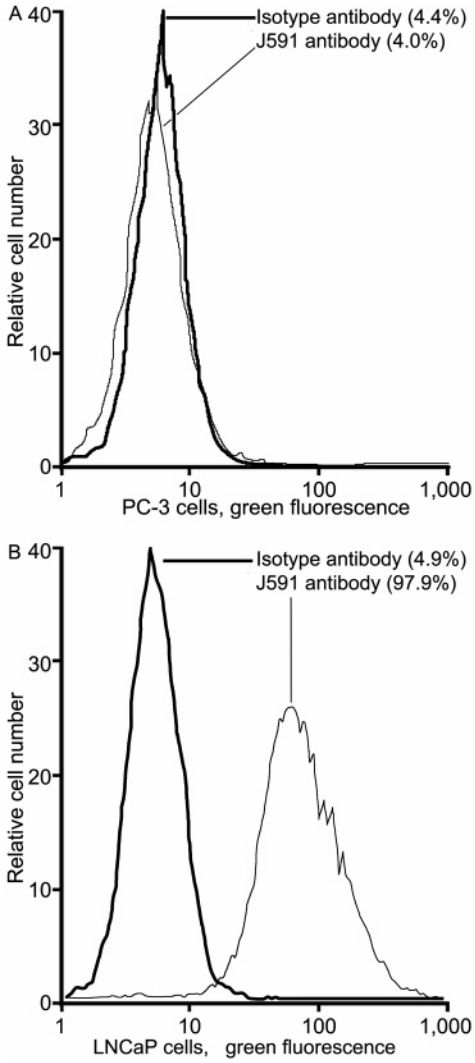


Figure 3. PC-3 (a) and LNCaP.FGC (b) cells were incubated either with isotype control or J591 antibodies (1 μg/mL), for 30 min. on ice, and then stained with anti-mouse IgG-FITC antibody, and green florescence was analyzed on FCM.

slight excess resulted in a stable conjugate that is water soluble. The reduction of disulfide bonds on dendrimer conjugates **4** and **5** was carried out by using DTT. The resultant dendrimer thiols **6** and **7** can undergo oxidation and hence the reactions were carried out and purified carefully under an inert atmosphere in degassed PBS−EDTA buffer.

For in vitro control experiments, G5 PAMAM dendrimer was labeled with FITC and 6-TAMRA. The ^{1}H NMR of the purified conjugates **8a** and **8b** showed additional signals in the aromatic region between δ 6−8 ppm. The UV−vis spectrum of **8a** had absorption at λ_{max} 498 nm for the conjugate. The conjugates **8a** and **8b** were then completely acetylated with excess acetic anhydride in the presence of triethylamine at pH 8 to give conjugates **9a** and **9b**. An additional peak at δ 1.8 for the CH_3 of the terminal acetyl group and the merging of methylene proton signals α to the NH_2 in the starting material confirms the complete acetylation of the terminal amines.

A thiol reactive maleimide group was introduced on the antibody with water soluble sulfo-SMCC using standard protocols and the resultant conjugate was purified by gel filtration. To minimize the free antibody, 5-fold molar excess of dendrimer conjugates was used in the antibody−dendrimer conjugation; the unreacted thiols

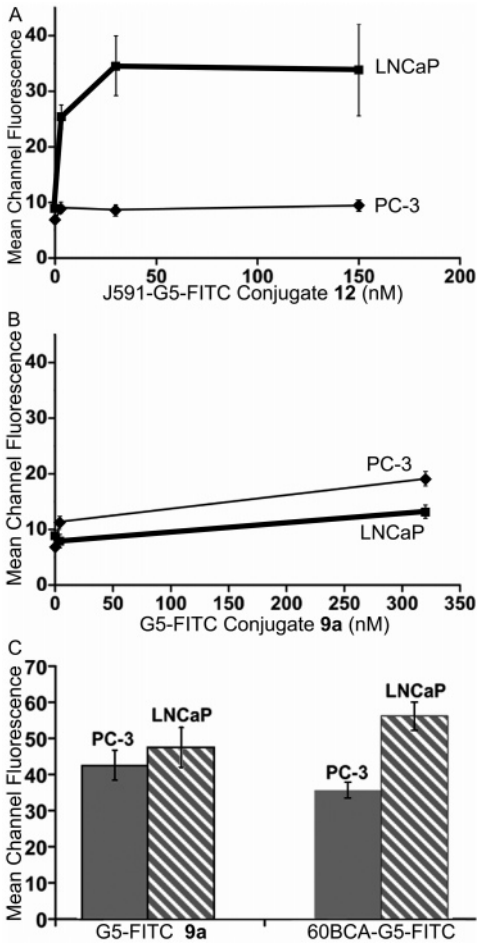


Figure 4. PC-3 and LNCaP.FGC cells were stained with increasing concentrations of J591-G5-FITC conjugate (**12**) (a, top panel), G5-FITC (**9a**) (b, middle panel) or 150 nM of irrelevant 60BCA-G5-FITC antibody−dendrimer conjugate (c, bottom panel) and analyzed on FCM.

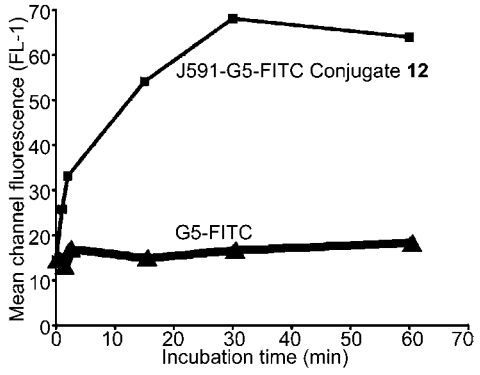


Figure 5. Kinetics of binding J591-G5-FITC dendrimer to LNCaP.FGC cells. The cells were incubated with a 50 nM concentration of **12** or control G5-FITC dendrimer (**9a**) for the indicated periods of time at rt. After incubation, cells were washed and the mean channel fluorescence of stained cells was determined by FCM.

were quenched with *N*-ethylmaleimide to minimize dimer formation due to cross-linking of dendrimer to antibodies. Free unreacted dendrimer was removed initially by filtration with a 100K MWCO microcon. Further purification on a S-200 Sephacryl column removed any residual free dendrimer. The resultant conjugates **12** and **13** were analyzed using PAGE, which shows a band above the antibody band that confirms the conjugation and an absence of a band for the free dendrimer. The fluores-

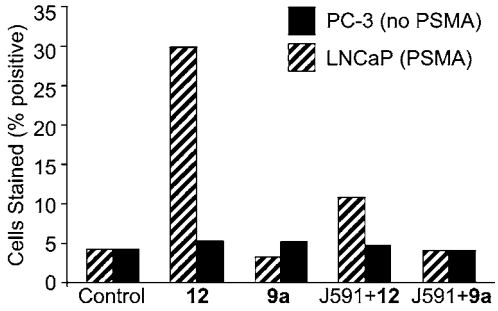


Figure 6. The specific binding of J591–G5–FITC conjugate to LNCaP.FGC cells. The PSMA positive and negative cells were preincubated in the absence or presence of free J591 antibody and further incubated with either **12** or **9a**. The 'control' represents cells that have not undergone any treatment. After washing, the stained cells were analyzed on FCM.

cence of the conjugates gives an indirect proof of conjugation since the fluorescent probe was conjugated to the dendrimer.

Targeting PSMA-Positive Prostate Cancer Cells with Monoclonal Antibody. To confirm the specificity of the J591 antibody toward the extracellular domain of PSMA, live PSMA-positive LNCaP.FGC cells and PSMA-negative PC-3 cells were incubated with J591 antibody and stained with anti IgG-FITC. The J591 antibody shows a great specificity against PSMA antigen. More than 97% of LNCaP.FGC cells were positively stained with J591 mAb (Figure 3b) compared to a nonspecific stain with the isotype antibody. The PC-3 cells showed (Figure 3a) only background-level staining with both antibodies (J591 and isotype) and no specificity. This confirms that the J591 antibody specifically binds to the LNCaP.FGC cells, and the binding is highly specific (*27*).

Targeting PSMA-Positive Prostate Cancer Cells Using Monoclonal Antibody–Dendrimer Conjugates. Dendrimer conjugation to the antibody can alter the binding characteristics of the antibody since it has the potential to block the binding sites. To ascertain whether the targeting efficacy and specificity of the antibody–dendrimer conjugate toward PSMA is maintained, three types of conjugates were tested, conjugates **9**, **12**, and another antibody dendrimer conjugate, 60BCA-G5-FITC, as a control (a dendrimer conjugated to an irrelevant antibody). At a 3 nM concentration of **12** (J591-G5-FITC), the LNCaP.FGC reached approximately 25 units of mean channel fluorescence (MCF) (Figure 4a). At 10 times higher concentration, the fluorescence reached an upper plateau at 35 MCF. Staining with a similar concentration (4 nm) of the G5-FITC control dendrimer conjugate **9a** (without the antibody) yielded less than 15 MCF (Figure 4b). The MCF never exceeded 20 units even at a 300 nm concentration of conjugate **9a**. Both conjugates (**9a** and **12**) have nonspecific staining of PC-3 cells equal to the background (Figure 4) fluorescence. The irrelevant antibody (same class) conjugate (60BCA-G5-FITC) did not bind significantly to either cell line (Figure 4c).

We have also examined the kinetics of the binding of conjugate **12** and control dendrimer **9a** to LNCaP.FGC cells. The binding of **12** to LNCaP.FGC cells reached a plateau after 30 min. of incubation. The mean fluorescence of cells stained with **12** increased from 14.5 to 68.1 MCF, while the mean fluorescence increase of cells stained with **9a** was insignificant (Figure 5). To further prove the specific binding of the dendrimer–antibody conjugate, LNCaP.FGC and PC-3 cells were preincubated with free J591 antibody at 750 ng/mL concentration for 15 min. on ice to block the receptor sites. Dendrimer conjugates **12** and **9a** (48 nM) were added, and the cells were incubated for an additional 30 min and then washed and subjected to FCM analysis. Free J591 antibody

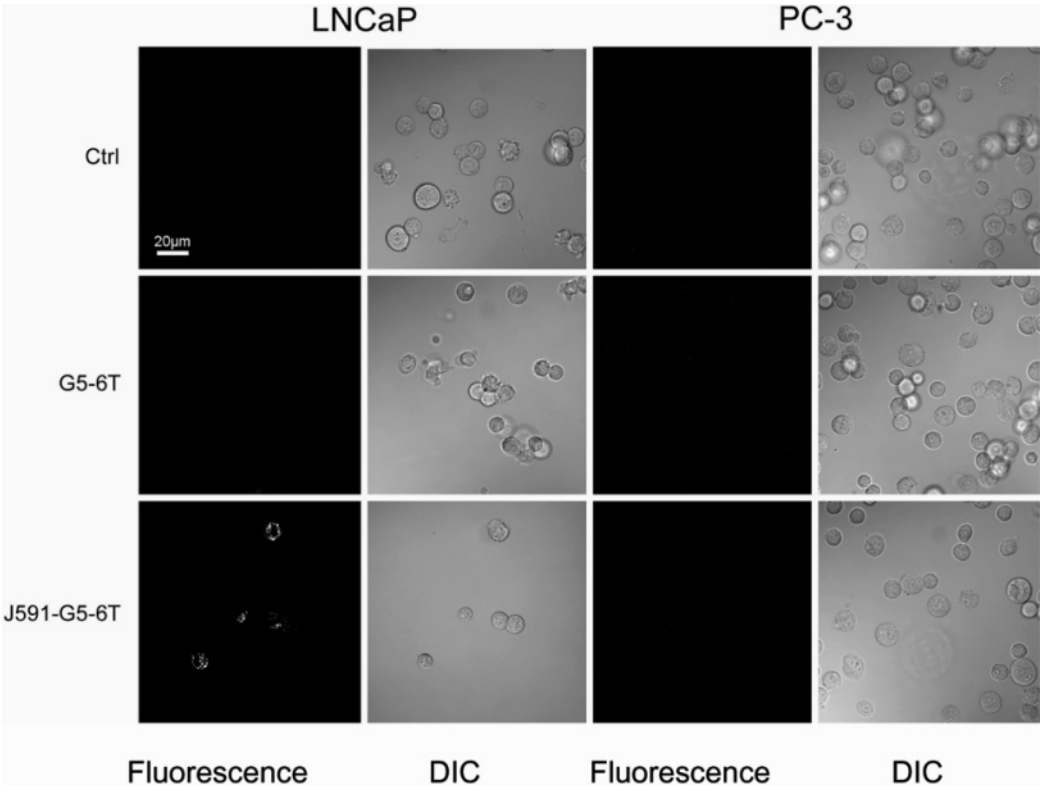


Figure 7. LNCaP.FGC and PC-3 cells were incubated with either J591–G5–6T (conjugate **13**; bottom row) or G5–6T (conjugate **5**; middle row) or with the vehicle (PBS; top row) for 60 min. at 37 °C, washed, and analyzed under the confocal microscope. The antibody–dendrimer conjugate **13** shows intracellular localization in the LNCaP.FGC cells, but not in the PC-3 cells. The control dendrimer (G5–6T) failed to associate with both cell lines.

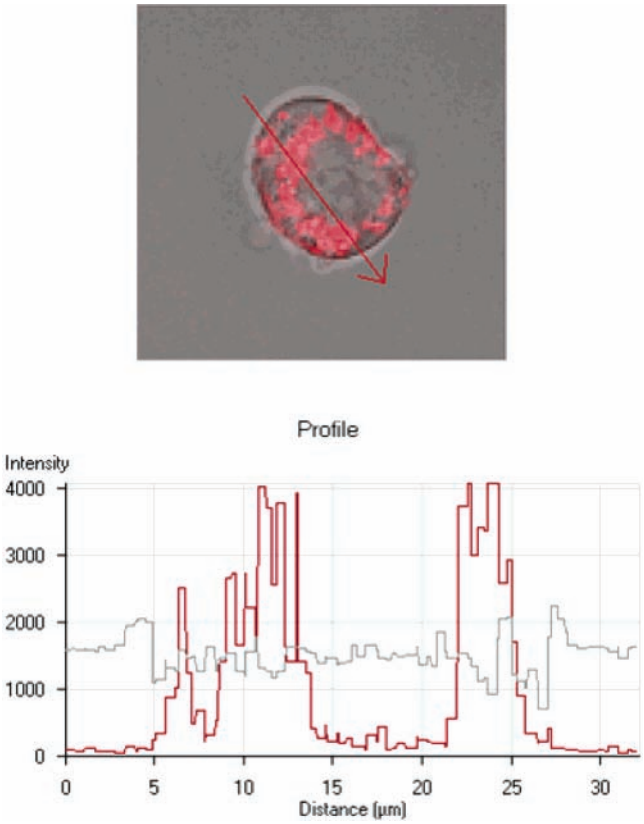


Figure 8. Confocal microscopy demonstration of internalization of J591 antibody dendrimer conjugate **13**. An optical section (top) from an image stack showing a medial 0.7 μm slice of a single cell. The fluorescence intensity profile (bottom) taken along the line shown by the arrow.

inhibited the binding of the conjugate to LNCaP.FGC cells by more than 71%, while nonspecific binding to PSMA-negative cells remained unchanged (Figure 6). This blocking experiment proves that the antibody−dendrimer conjugate retains specific binding to PSMA.

Internalization of the Dendrimer Conjugates by PSMA-Positive Cells. Free J591 antibody is readily internalized by LNCaP.FGC cells (*6*). We examined whether the antibody−dendrimer retains this ready internalization. Initial confocal microscopy studies with the dendrimer conjugate **12** and live cells provided inconclusive results due to the photobleaching of the FITC and background autofluorescence. Changing the fluorescent probe on the dendrimer to 6-TAMRA gave a better signal-to-noise ratio which allowed conclusive measurements. The PC-3 and LNCaP.FGC cells were trypsinized, washed, and incubated with conjugate **13** for 1 h. at 37 °C and then washed and analyzed.

LNCaP.FGC cells yielded the highest fluorescence when stained with conjugate **13** (Figure 7). We observed minimal fluorescence in PC-3 cells stained with conjugate **13**. To analyze the fluorescence intensity in both cell types quantitatively, we selected 3D-rendered images of representative LNCaP.FGC and PC-3 cells and determined the number of fluorescent voxels per cell. The LNCaP.FGC yielded 12 520 voxels, while PC-3 yielded only 1156. Since both LNCaP and PC-3 are human prostate cell lines grown under identical conditions and they are very similar in size, the order of magnitude difference in the number of fluorescent voxels can be attributed to differences in dendrimer uptake. The confocal images were further analyzed by taking optical sections to determine internalization of the conjugate. Medial optical scans (Figure 8) clearly show internalization of the antibody−dendrimer conjugate **13** into the PSMA-positive LNCaP.FGC cells. The fluorescence profile shows increased intensity in the cytoplasm but not inside the nucleus.

CONCLUSION

Dendrimers are useful as carrier macromolecules for targeting, imaging, and drug delivery agents. Terminal group functionalization of water-soluble PAMAM dendrimers with different aromatic and hydrophobic molecules allows delivery of many types of drugs but may significantly reduce the aqueous solubility of the conjugates. Altering the surface amine functionality to a more neutral acetylated surface reduces the formation of aggregates and retains the water solubility of the conjugates. The acetylated terminal groups also decreased the nonspecific binding to the cells (*20*). The conjugation of the targeting J591 antibody to surface-modified G5 dendrimers has been achieved. Flow cytometry experiments showed that the antibody−dendrimer conjugate is specifically bound by the PSMA-positive LNCaP.FGC cell line but does not bind to the PC-3 cell line which does not express PSMA. Dendrimers not conjugated to an antibody did not show any significant binding. Confocal microscopy studies also confirmed the binding and internalization of the antibody−dendrimer conjugate, while the dendrimer alone did not show significant binding or uptake into the cells. Studies are under way to synthesize a multifunctional dendrimer conjugate with drug, fluorochrome, and antibody for targeted drug delivery and imaging.

ACKNOWLEDGMENT

This project has been funded in whole or in part with Federal Funds from the U.S. Army Medical Research and Material Command, Department of Defense, under grant DAMD17-02-1-0096, National Cancer Institute, National Institutes of Health, under Contract #NOI-CO-97111, and the S.P.O.R.E. National Institutes of Health, under grant 2-P50-CA69568-04.

LITERATURE CITED

(1) Guillemard, V., and Saragovi, H. U. (2001) Taxane-Antibody Conjugates Afford Potent Cytotoxicity, Enhanced Solubility, and Tumor Target Selectivity. *Cancer Res. 61*, 694−699.
(2) Chang, S. S., Gaudin, P. B., Reuter, V. E., and Heston, W. D. W. (2000) Prostate-specific membrane antigen: Present and future application. *Urology 55*, 622−629.
(3) Fair, W. R., Israeli, R. S., and Heston, W. D. W. (1997) Prostate-specific membrane antigen. *Prostate 32*, 140−148.
(4) Chang, S. S., O'Keefe, D. S., Bacich, D. J., Reuter, V. E., Heston, W. D., and Gaudin, P. B. (1999) Prostate-specific membrane antigen is produced in tumor-associated neovasculature. *Clin. Cancer Res. 5*, 2674−2681.
(5) Liu, H., Moy, P., Kim, S., Xia, Y., Rajasekaran, A., Navarro, V., Knudsen, B., and Bander, N. H. (1997) Monoclonal antibodies to the extracellular domain of prostate-specific membrane antigen also react with tumor vascular endothelium. *Cancer Res. 57*, 3629−3634.
(6) Liu, H., Rajasekaran, A. K., Moy, P., Xia, Y., Kim, S., Navarro, V., Rahmati, R., and Bander, N. H. (1998) Constitutive and antibody-induced internalization of prostate-specific membrane antigen. *Cancer Res. 58*, 4055−4060.
(7) Fracasso, G., Bellisola, G., Cingarlini, S., Castelletti, D., Prayer-Galetti, T., Pagano, F., Tridente, G., and Colombatti, M. (2002) Antitumor effects of toxins targeted to the prostate specific membrane antigen. *Prostate 53*, 9−23.
(8) McDevitt, M. R., Barendswaard, E., Ma, D., Lai, L., Curcio, M. J., Sgouros, G., Ballangrud, A. M., Yang, W. H., Finn, R.

D., Pellegrini, V., Geerlings, M. W., Jr., Lee, M., Brechbiel, M. W., Bander, N. H., Cordon-Cardo, C., and Scheinberg, D. A. (2000) An alpha-particle emitting antibody ([213Bi]J591) for radioimmunotherapy of prostate cancer. *Cancer Res. 60*, 6095−6100.

(9) McDevitt, M. R., Ma, D., Lai, L. T., Simon, J., Borchardt, P., Frank, R. K., Wu, K., Pellegrini, V., Curcio, M. J., Miederer, M., Bander, N. H., and Scheinberg, D. A. (2001) Tumor therapy with targeted atomic nanogenerators. *Science 294*, 1537−1540.

(10) Smith-Jones, P. M., Vallabahajosula, S., Goldsmith, S. J., Navarro, V., Hunter, C. J., Bastidas, D., and Bander, N. H. (2000) In vitro characterization of radiolabeled monoclonal antibodies specific for the extracellular domain of prostate-specific membrane antigen. *Cancer Res. 60*, 5237−5243.

(11) Smith-Jones, P. M., Vallabhajosula, S., Navarro, V., Bastidas, D., Goldsmith, S. J., and Bander, N. H. (2003) Radiolabeled monoclonal antibodies specific to the extracellular domain of prostate-specific membrane antigen: preclinical studies in nude mice bearing LNCaP human prostate tumor. *J. Nucl. Med. 44*, 610−617.

(12) Newkome, G. R., Moorefield, C. N., and Vogtle, F. (2001) Dendrimers and Dendrons: Concepts, Syntheses, Applications, Wiley-VCH, Weinheim, Germany.

(13) Fréchet, J. M. J., and Tomalia, D. A. (2002) Dendrimers and other dendritic polymers, Wiley, Chichester, UK.

(14) Patri, A. K., Majoros, I., and Baker, J. R., Jr. (2002) Dendritic polymer macromolecular carriers for drug delivery. *Curr. Opin. Chem. Biol. 6*, 466−471.

(15) Cloninger, M. J. (2002) Biological applications of dendrimers. *Curr. Opin. Chem. Biol. 6*, 742−748.

(16) Singh, P. (1998) Terminal groups in Starburst dendrimers: activation and reactions with proteins. *Bioconjugate Chem. 9*, 54−63.

(17) Wu, C., Brechbiel, M. W., Kozak, R. W., and Gansow, O. A. (1994) Metal-chelate-dendrimer-antibody constructs for use in radioimmunotherapy and imaging. *Bioorg. Med. Chem. Lett. 4*, 449−454.

(18) Kojima, C., Kono, K., Maruyama, K., and Takagishi, T. (2000) Synthesis of polyamidoamine dendrimers having poly(ethylene glycol) grafts and their ability to encapsulate anticancer drugs. *Bioconjugate Chem. 11*, 910−917.

(19) Esfand, R., and Tomalia, D. A. (2001) Poly(amidoamine) (PAMAM) dendrimers: from biomimicry to drug delivery and biomedical applications. *Drug Discovery Today 6*, 427−436.

(20) Quintana, A., Raczka, E., Piehler, L., Lee, I., Myc, A., Majoros, I., Patri, A. K., Thomas, T., Mule, J., and Baker, J. R., Jr. (2002) Design and function of a dendrimer-based therapeutic nanodevice targeted to tumor cells through the folate receptor. *Pharm. Res. 19*, 1310−1316.

(21) Baker, J. R., Quintana, A., Piehler, L. T., Banazak-Holl, M., Tomalia, D., and Raczka, E. (2001) The synthesis and testing of anti-cancer therapeutic nanodevices. *Biomed. Microdevices 3*, 61−69.

(22) Ong, K. K., Jenkins, A. L., Cheng, R., Tomalia, D. A., Durst, H. D., Jensen, J. L., Emanuel, P. A., Swim, C. R., and Yin, R. (2001) Dendrimer enhanced immunosensors for biological detection. *Anal. Chim. Acta 444*, 143−148.

(23) Kobayashi, H., Sato, N., Saga, T., Nakamoto, Y., Ishimori, T., Toyama, S., Togashi, K., Konishi, J., and Brechbiel, M. W. (2000) Monoclonal antibody-dendrimer conjugates enable radiolabeling of antibody with markedly high specific activity with minimal loss of immunoreactivity. *Eur. J. Nucl. Med. 27*, 1334−1339.

(24) Barth, R. F., Adams, D. M., Soloway, A. H., Alam, F., and Darby, M. V. (1994) Boronated Starburst Dendrimer-Monoclonal Antibody Immunoconjugates: Evaluation as a Potential Delivery System for Neutron Capture Therapy. *Bioconjugate Chem. 5*, 58−66.

(25) Wu, G., Barth, R. F., Yang, W., Chatterjee, M., Tjarks, W., Ciesielski, M. J., and Fenstermaker, R. A. (2004) Site-specific conjugation of boron-containing dendrimers to anti-EGF receptor monoclonal antibody cetuximab (IMC-C225) and its evaluation as a potential delivery agent for neutron capture therapy. *Bioconjugate Chem. 15*, 185−194.

(26) Roberts, J. C., Adams, Y. E., Tomalia, D. A., Mercer-Smith, J. A., and Lavallee, D. K. (1990) Using Starburst Dendrimers as Linker Molecules to Radiolabel Antibodies. *Bioconjugate Chem. 1*, 305−308.

(27) Patri, A. K., Thomas, T., Baker, J. R., Jr. and Bander, N. H. (2002) Antibody-dendrimer conjugates for targeted prostate cancer therapy. *Polym. Mater. Sci. Eng. 86*, 130.

(28) Chang, S. S., Reuter, V. E., Heston, W. D., Bander, N. H., Grauer, L. S., and Gaudin, P. B. (1999) Five different anti-prostate-specific membrane antigen (PSMA) antibodies confirm PSMA expression in tumor-associated neovasculature. *Cancer Res. 59*, 3192−3198.

(29) Hermanson, G. T. (1996) Heterobifunctional Cross-linkers, in *Bioconjugate Techniques*, pp 228−286, Elsevier Science, San Diego, CA.

(30) Majoros, I. J., Keszler, B., Woehler, S., Bull, T., Baker, Jr., J. R. (2003) Acetylation of Poly(amidoamine) Dendrimers. *Macromolecules 36*, 5526−5529.

BC0499127

Synthesis and Evaluation of a Triplex-Forming Oligonucleotide–Pyrrolobenzodiazepine Conjugate

Zhanna V. Zhilina,[†] Amy J. Ziemba,[†] John O. Trent,[‡] Michael W. Reed,[§,||] Vladimir Gorn,[§] Qun Zhou,[†,⊥] Wenhu Duan,[†,⊥] Laurence Hurley,[†] and Scot W. Ebbinghaus[†,*]

Arizona Cancer Center, University of Arizona, Tucson, Arizona 85724-5024, James Graham Brown Cancer Center, University of Louisville, Louisville, Kentucky 40202, and Epoch Biosciences, Bothell, Washington 98021. Received June 9, 2004; Revised Manuscript Received August 25, 2004

In most cases, unmodified oligonucleotides designed as antigene molecules are incapable of binding to DNA with sufficient stability to prevent gene expression. To stabilize binding to a polypurine tract in the HER-2/neu promoter, a triplex forming oligonucleotide (TFO) was conjugated to a pyrrolo[1,4]-benzodiazepine (PBD), desmethyltomaymycin, and site-specific DNA binding was evaluated. An activated ester of the PBD moiety was conjugated by an acylation reaction to a free primary amine on a 50-atom aliphatic linker at the 5′ end of the TFO. This long aliphatic linker was designed to provide a bridge from the major groove binding site of the TFO to the minor groove binding site of the PBD. Triplex formation by the resulting TFO–PBD conjugate occurred more slowly and with a nearly 30-fold lower affinity compared to an unconjugated TFO. PBD binding to the triplex target was demonstrated by protection from restriction enzyme digestion, and covalent binding to the exocyclic amino group of guanine was inferred by substituting specific guanines with inosines. Although the binding of the TFO was less efficient, this report demonstrates that in principle, TFOs can be used to direct the binding of a PBD to specific location. Further optimization of TFO–PBD conjugate design, likely involving optimization of the linker and perhaps placing a PBD at both ends of the TFO, will be needed to make gene modification robust.

INTRODUCTION

The sequence-specificity of triplex forming oligonucleotides (TFOs[1]) gives these molecules tremendous potential as tools to alter gene expression (*1*). TFOs can potentially regulate gene expression by several different mechanisms including recombination, mutagenesis, and inhibition of RNA transcription (*2*, *3*). Interstrand DNA triplex formation occurs through the binding of a TFO in the major groove of a polypurine:polypyrimidine tract of DNA (*4*, *5*) by forming base specific Hoogsteen hydrogen bonds (*6*, *7*). While TFOs have been successfully used to regulate gene expression in several model systems, a number of cellular barriers still limit the ability of TFO to inhibit target gene expression in living cells. One of these barriers is removal of the TFO by the DNA repair machinery or by DNA helicases (*8*–*11*). To improve the stability of triplex formation within cells, DNA-reactive agents can be conjugated to the ends of TFOs to covalently bind the third strand to the target sequence (*12*). For example, psoralen, reactive minor groove binders (MGBs), bromoacetyl, nitrogen mustard, and aziridinyl quinone residues have been conjugated with TFOs and shown to react with target sites (*13*–*17*).

The HER-2/neu oncogene is a good target for triplex formation because it has two polypurine tracks capable of triplex formation with a third strand (*18*, *19*) and because HER-2/neu directed therapies have established the principle that preventing the expression or function of the HER-2/neu gene product can induce the regression of metastatic tumors that overexpress HER-2/neu (*20*, *21*). The HER-2/neu promoter has served as a good model for evaluating triplex formation by TFO–alkylator conjugates in previous studies (*11*, *22*) as well as in the present report. The triplex target site is located from −218 to −245 upstream of the first codon (+1) in a region of HER-2/neu promoter that is necessary for the efficient initiation of HER-2/neu transcription (Figure 1). Previous studies demonstrated that a preformed triple helix with an unmodified DNA oligonucleotide as the third strand was undetectable 24 h after transfection of a reporter plasmid bearing the target sequence, demonstrating the limited stability of the triple helix in cells. Conjugation to nitrogen mustards greatly improved the stability of third strand binding, and a TFO conjugated to phenylacetic acid mustard (PAM) at both ends efficiently suppressed HER-2/neu expression from a reporter plasmid. The ability of DNA unwinding by polymerases and

* Corresponding author: Scot W. Ebbinghaus, 1515 North Campbell Ave., Tucson, AZ 85724-5024. Tel: (520) 626-3424. Fax: (520) 626-3754. E-mail: sebbinghaus@azcc.arizona.edu.
[†] University of Arizona.
[‡] University of Louisville.
[§] Epoch Biosciences.
[||] Current affiliation: Bioconjugate Consulting, Seattle, WA.
[⊥] Current affiliation: Shanghai Institute of Materia Medica, Chinese Academy of Sciences, Shanghai, China.

[1] Abbreviations: TFO, triplex forming oligonucleotide; PAM, phenylacetic acid mustard; PBD, pyrrolo[1,4]benzodiazepine; 5′Pu-G-Pu, purine-guanine-purine; MGB, minor groove binding compounds; CPI, cyclopropapyrroloindoles; PEG, poly(ethylene glycol) wraparound linker; MALDI, matrix-assisted laser desorption/ionization; TOF, time-of-flight; FAB, fast atom bombardment; TFA, trifluoroacetic acid; PDA, photodiode array; ODN, oligodeoxyribonucleotide; DMSO, dimethyl sulfoxide; TEA, triethylammonium; PAM, phenyl acetic acid mustard; PPG, the pyrazolopyrimidine analogue of guanine; EMSA, electrophoretic mobility shift assay; TBM, tris-borate-magnesium buffer; K_d, dissociation constant; DMS, dimethyl sulfate; MPE-Fe, methidiumpropyl EDTA-Fe(II).

10.1021/bc0498673 CCC: $27.50 © 2004 American Chemical Society
Published on Web 10/30/2004

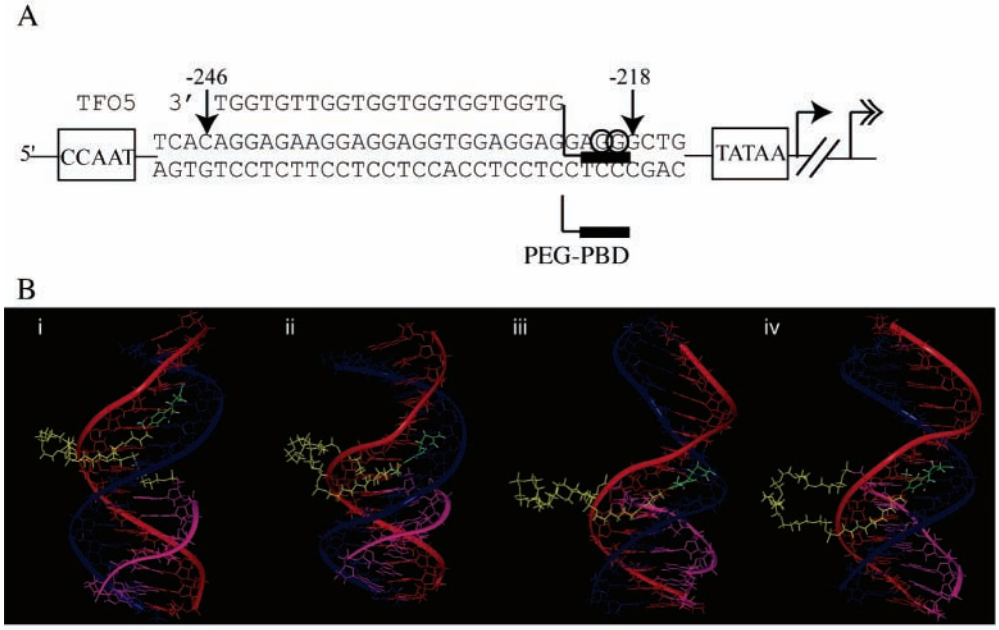


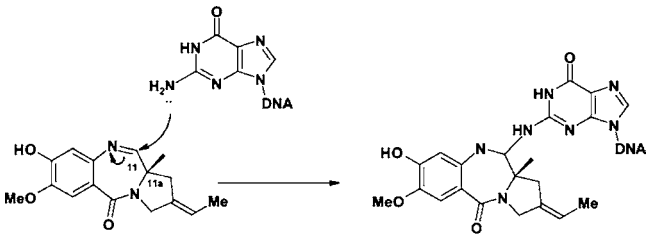
Figure 1. Triplex formation in the HER-2/neu promoter with TFO5. (A) Schematic representation of the HER-2/neu promoter with the triplex target sequence located from −245 to −218 relative to the first codon. TFO5 is an antiparallel GT motif TFO conjugated to desmethyltomamycin (PBD) with a PEG wraparound linker that allows the PBD to bind in the minor groove at an adjacent 5′Pu-G-Pu site. TFO5 is designed to direct PBD binding to the AGG (−219 to −221) or the GGG (−218 to −220) sequences that are just downstream of the triple helix, which ends at −223. A covalent adduct is formed with the central guanine in the PBD binding site (circled). Additional PBD binding sites at the GGA (−221 to −223) or the AGG (−222 to −224) at the duplex−triplex junction are also predicted by molecular modeling studies. (B) Molecular models of triplex formation and PBD binding to the HER-2/neu promoter. The models consists of 15 bp of the HER-2/neu promoter from −215 to −229 (purine strand, red; pyrimidine strand, blue) with seven base triplets from the 5′ end of the TFO (−223 to −229, magenta), the PEG wraparound linker (yellow), and the PBD (atom colors) binding in the minor groove and forming adducts with guanines at positions (i) −219, (ii) −220, (iii) −222, or (iv) −223.

helicases to displace a TFO has been reported and can be prevented by triplex formation coupled with covalent modification of the DNA (*8*, *9*, *11*, *19*, *23*−*30*).

Nitrogen mustards have a mechanism of DNA alkylation involving the spontaneous formation of a highly reactive aziridinium cation intermediate in aqueous solution followed by the electrophilic attack of the relatively nucleophilic N7 of guanine (*31*). Short TFOs conjugated to a nitrogen mustard can drive DNA alkylation to near completion, as shown by the site-specific alkylation of an isolated genomic DNA target using 12-mer TFOs (*32*). The electrophilic aziridinium cation can also react with other nucleophiles or with water to give degradation products that are incapable of guanine alkylation, and in permeabilized cells or isolated nuclei, triplex directed alkylation by a nitrogen mustard is much less efficient (*32*, *33*). The short half-life of the aziridinium cation in aqueous solution presents a potential barrier to the effectiveness of a TFO conjugated to nitrogen mustard in gene targeting in living cells (*34*).

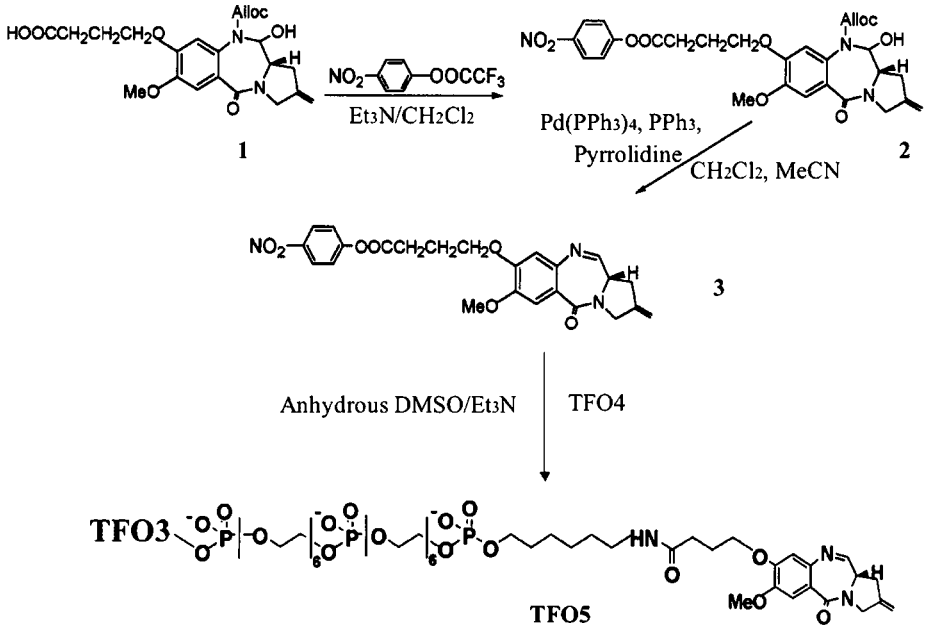
In the present report, we wished to develop TFO−alkylator conjugates with an alkylating agent that does not become inactive in aqueous solution. We selected the pyrrolo[1,4]benozdiazepines (PBDs) as a class of DNA alkylating agents that would not be as unstable in water as the nitrogen mustards. Anthramaycin, tomaymycin, sibiromycin, and the neothramycins are members of a potent group of antitumor antibiotics, the PBDs, initially isolated from various *Streptomyces* species (*35*). The DNA binding reaction of the PBDs initially proceeds through reversible, noncovalent binding in the minor groove of DNA that positions the reactive C11 of the B ring of the PBD facing into the minor groove for covalent binding to the exocyclic amino group of a guanine (Scheme 1). The aminal bond that forms is labile and potentially reversible to regenerate an active PBD (*36*). The formation of a PBD−DNA adduct at purine-guanine-purine (5′Pu-G-Pu) sequences has been shown to block RNA polymerase, and anthramycin and tomaymycin are the most potent blockers of transcription (*37*). The formation of a DNA−PBD adduct can interfere with the linear translocation of DNA-processing enzymes or inhibit their recognition of specific DNA sequences (*38*). The cytotoxicity and antitumor activity of the PBDs is related to their ability to inhibit DNA and RNA synthesis; however, the binding of PBDs at the large number of 5′Pu-G-Pu sites throughout the genome may explain the high level of toxicity observed with this class of compounds. For this reason, several groups have investigated ways to improve the site-specificity of PBD binding by using PBD dimers, PBDs conjugated to other MGBs, or PBDs conjugated to polyamides (*39*−*42*). In the current report, we have taken advantage of potential PBD binding sites in the polypurine tract of the HER-2/neu promoter to use a TFO to direct the binding of a PBD to a specific location adjacent to the triple helix (Figure 1). TFOs conjugated to PBDs could have some advantages over TFOs conjugated to spontaneously reactive nitrogen mustards and improve the specificity of the PBD.

Scheme 1. Covalent Adduct Formation by a PBD with the 2-Amino Group of Guanine



Tomaymycin

Scheme 2. Synthesis of Desmethyltomaymycin−TFO Conjugate, TFO5



A challenge for the design and synthesis of TFO−PBD conjugates is the fact that the TFO binds in the major groove while the PBD binds in the minor groove. In other studies of TFOs conjugated to MGBs such as cyclopropapyrroloindoles (CPI), this challenge was addressed with a long, poly(ethylene glycol) "wrap-around" linker (PEG) to form a bridge from the major groove to the minor groove (*43*, *44*). The long flexible linker will allow the MGB to wrap around the DNA duplex to find a binding site within 4−8 bp of the TFO terminus. In this report we describe the design and synthesis of a novel bioconjugate of desmethyltomaymycin to a DNA TFO and demonstrate the site-specific interaction of the PBD with the intended target site in the HER-2/neu promoter.

EXPERIMENTAL PROCEDURES

Materials. Solvents and chemicals obtained from commercial sources were analytical grade or better and were used without further purification. Solvents for HPLC analysis were obtained as HPLC grade and were filtered (0.2 μM) prior to use.

Spectral Analysis. ^{1}H NMR spectra were obtained on a Bruker AVANCE (300 MHz) instrument. Matrix-assisted laser desorption/ionization (MALDI) mass spectra of oligonucleotides were measured on a Bruker-Reflex-III MALDI-time-of-flight (MALDI-TOF) mass spectrometer. 3-Hydroxypicolinic acid (0.1 M) with 0.1% ammonium tartrate was used as the matrix, and a conventional N_2 laser (337 nm) was used to generate ions. Fast atom bombardment (FAB) mass spectra of desmethyltomaymacin were determined on a JEOL HX110A instrument using a matrix of 50% glycerol, 25% thioglycerol, and 25% *m*-nitrobenzyl alcohol containing 0.1% of trifluoroacetic acid (TFA). Preparative HPLC purification was performed on a Varian ProStar system equipped with a photodiode array (PDA) detector.

Molecular Modeling. Modeling of triplex formation and PBD binding was performed using methods that have been previously described (*45*, *46*). Briefly, molecular mechanics and dynamics were performed using Macromodel 7.0 (*47*) with an implicit solvent algorithm (GB/SA water solvation) using the AMBER* force field. The models were initially minimized (1000 steps steepest decents followed by 1000 steps Polak-Ribier conjugate gradient) followed by molecular dynamics simulations (100 ps equilibrium phase and 500 ps production phase, 1.5 fs time step, 300 K, followed by averaging 25 samples of the last 50 ps, with subsequent minimization as above). Models of the HER-2/neu promoter triple helix and PBD binding site included 15 bp of the target duplex, d(G-GAGGAGGAGGGCTG)-d(CAGCCCTCCTCCTCC) and seven bases of the TFO from the 5′ end, d(GGTGGTG). Multiple simulations were completed using the chiral *S* configuration of the PBD based on a reported structure (*48*). Covalent adducts of the PBD with G-223, G-222, G-220, and G-219 are illustrated in Figure 1B.

Synthesis of Desmethyltomaymycin *p*-Nitrophenyl Ester. The C8 substituted tomaymycin analogue **1** (Scheme 2) was synthesized starting from vanillic acid and using the thioacetal method described by Thurston and co-workers (*49*). The intermediate compound **1** was then converted to the active *p*-nitrophenyl ester **2**, deprotected with $Pd(PPh_3)_4$, PPh_3, and pyrrolidine to afford compound **3** in 60% yield as a yellow oil, and crystallized from Et_2O to afford **3** as a yellow solid. ^{1}H HMR (d_6-acetone) δ2.32 (m, 2H, $(CH_2)_3$), 2.87 (t, 2H, $(CH_2)_3$, J = 6.7), 2.94 (d, 1H, H1a, J = 16.1), 3.12 (dd, 1H, H1b, J = 15.8, J = 8.3), 3.87−3.89 (m, 1H, H11a), 3.93 (s, 3H, OCH_3), 4.18 and 4.22 (2m, 2H, H3), 4.29 (s, 2H, $(CH_2)_3$), 5.17 and 5.20 (2x br s, 2H, C=CH_2), 6.84 (s, 1H, H9), 7.30 (d, 2H, Ph, J = 8), 7.52 (s, 1H, H6), 7.70 (d, 1H, H11), 8.27 (d, 2H, Ph, J = 8); *m/z* (FAB) 466 (M + 1).

Synthesis and Purification of Oligonucleotides. DNA oligonucleotides (ODNs) used for conjugation to the PBD (TFO3, TFO4, and TFO5) were prepared by our group (TFO sequences are given in Table 1). ODNs were synthesized on an Expedite System Model 8909 synthesizer using 1 μmol phosphoramidite protocols supplied by the manufacturer and phosphoramidite reagents from Glen Research. TFO5 also contained a 3′ hexanol modification, introduced into TFO4 and TFO5 during automated DNA synthesis using a hexanol-modified CPG support from Glen Research. The linker was composed of hexa(ethylene glycol) phosphate groups and a C6-amino group (Scheme 2), synthesized by adding two

Table 1. Triplex Forming Oligonucleotides Used in This Report[a]

Name	Sequence
TFO1	5'GGGAGGAGGAGGCGGAGGAGGAAGAGGA
TFO2	5'PAM-GGAGGAGGAGGCGGAGGAGGAAGAG-PAM
TFO3	5'GTGGTGGTGGTGGTGGTTGTGGT
TFO4	5'PEG-GTGGTGGTGGTGGTGGTTGTGGT
TFO5	5'PBD-PEG-GTGGTGGTGGTGGTGGTTGTGGT

[a] PAM, phenylacetic acid mustard; PEG, poly(ethylene glycol) wraparound linker; PBD, pyrrolo[1,4]benzodiazepine; *G*, pyrazolopyrimidine analogue of guanine (underlined).

Spacer Phosphoramidite 18 groups and an N-MMT-hexanolamine phosphoramidite to the 5′ end of the oligonucleotide during automated synthesis (linker phosphoramidites were from Glen Research). ODNs were cleaved and deprotected in ammonium hydroxide, purified by HPLC, detritylated, precipitated, and suspended in deionized water. The concentrations of all ODNs were determined from UV absorbance at 260 nm in water. MALDI-TOF MS analysis of starting TFO4 for $C_{260}H_{351}N_{89}O_{166}P_{25}$ $[M + H]^+$: calculated 8154.5, found 8154.4. All ODNs were analyzed by reverse phase HPLC (C_{18} HPLC) using a 250 × 4.6 mm C_{18} column equipped with a guard column (Alltech Adsorbosil, 5 μm particle size). A gradient of 2 to 60% solvent B over 20 min was used. Solvent B was acetonitrile (flow rate 1 mL/min), and solvent A was 0.1 M triethylammonium acetate in water (pH 7.5). The triethylammonium (TEA) salt of the ODN was eluted from the column. Detection was carried out by UV absorbance at 260 nm. All ODNs were greater than 95% pure by C_{18} HPLC. TFO2 was synthesized with the pyrazolopyrimidine analogue of guanine (PPG, 8-aza-7-deazaguanine) in place of guanines and was conjugated at both ends to phenylacetic acid mustard (PAM) as previously described (*11*). Unmodified ODNs (TFO1 and synthetic target sequences) were purchased from commercial sources and gel-purified before use. The sequences of the synthetic duplex DNA target sequences are HNP36 d(TCACAGGAGAAGGAGGAGGTGGAGGAGGAGGGCTGC)-d(GCAGCCCTCCTCCTCCTCCACCTCCTCCTTCTCCTGTGA); HNP40-ApaI d(TCACAGGAGAAGGAGGAGGTGGAGGAGGAGGGCCCCTTGA)-d(TCAAGGGGCCCTCCTCCTCCTCCACCTCCTCCTTCTCCTGTGA); HNP40-inosine d(TCACAGGAGAAGGAGGAGGTGGAGGAGGAIIICTGCTTGA)-d(TCAAGCAGCCCTCCTCCTCCTCCACCTCCTCCTTCTCCTGTGA).

Synthesis of the ODN−PBD Conjugate. TFO4 (37 nmol, 0.3 mg), bearing the PEG wraparound linker ending in a C6-amino group, was redried, and the residue was dissolved in 0.1 mL of dimethyl sulfoxide (DMSO) with 15 μL of triethylamine. A 2 mg/100 μL solution of **3** in DMSO was prepared, and 17 μL (0.34 mg, 7.4 μmol) was added to the ODN. The mixture was incubated for 21 h at 37 °C with occasional shaking. The product was precipitated with $NaClO_4$/acetone, the pellet was sonicated with 2 mL of acetone, recentrifuged, and dried in a vacuum, and the crude product was stored at −20 °C. The product then was analyzed by C_{18} HPLC using the gradient described above. The product peak was collected and precipitated with ethanol, and the pellet was sonicated with 2 mL of ethanol, recentrifuged, and dried in a vacuum. The purified ODN−PBD conjugate, TFO5, was dissolved in water. MALDI-TOF MS analysis of TFO5 for $C_{278}H_{369}N_{91}O_{170}P_{25}$ $[M + H]^+$: calculated 8483.1, found 8483.8. The yield of TFO5 was 41% (0.12 mg).

Electrophoretic Mobility Shift Assay (EMSA) Analysis of Triplex DNA Formation. TFOs were incubated with the 36-base pair HER-2/neu duplex target sequence end-labeled on the pyrimidine strand. Reaction mixtures included increasing concentrations of the TFO with 0.01 μM target duplex in 1× TBM buffer (90 mM Tris pH 7.4, 90 mM borate, 10 mM $MgCl_2$) for 24, 48, and 72 h at 37 °C before nondenaturing gel electrophoresis with 1× TBM in both the gel and running buffer. Dissociation constants (K_d) were calculated to compare binding affinities of the TFOs by plotting the fractional yield (y) of triplex [triplex/(triplex + duplex)] as a function of the oligonucleotide concentration (*45*). It should be mentioned that the K_d is not a true dissociation constant for a reversible reaction at steady state, since the PBD may form a covalent bond with guanine, but remains a useful numerical representation of these data. Roughly, K_d is a TFO concentration under which 50% formation of triplex occurred; that is why we decided not to use the term K_d but use C_{50} instead.

Restriction Enzyme Protection Reactions. Triplex formation was performed as described above, but with a 40-base pair HER-2/neu duplex that was mutated to contain an ApaI site (5′GGGCTG3′→ 5′GGGCCC3′) adjacent to the polypurine tract and PBD binding site. Triplex mixtures (5 μL) were digested with ApaI for 2 h at 37 °C by adding 30 units of ApaI, restriction enzyme buffer (final concentration 10 mM Tris, pH 7.5, 10 mM $MgCl_2$), and water to bring reaction volumes up to 50 μL. Reactions were terminated with 30 μL of formamide loading buffer, denaturated for 2′ at 95 °C, and separated on a 12% denaturing gel.

Chemical and Enzymatic Footprinting. A 250 bp PstI/XmaI fragment of the pGL3/HNP410 plasmid containing a 410 bp HER-2/neu promoter within the PGL3 basic luciferase promoter plasmid (Promega) was used to create an end-labeled template by Klenow filling. To compare native versus inosine-substituted PBD binding sites, synthetic oligonucleotides were 5′-labeled on the purine-rich strand, annealed, and gel-purified prior to use. Triplex formation was performed in 1× TBM at 37 °C for 24 h. For dimethyl sulfate (DMS) footprinting, samples (10 μL) were mixed with 4 μg of sonicated salmon sperm DNA and treated with 0.5 μL of 10% ethanol solution of dimethyl sulfate (DMS) for 5 min. The reaction was stopped by the addition of 5 μL of DMS stop solution mixture. The DNA samples were ethanol-precipitated and lyophilized. Piperidine cleavage was performed by heating the DNA pellet with 50 μL of 10% piperidine for 20 min at 90 °C followed by ethanol-precipitation. Samples were suspended in water and an equal volume of formamide gel loading buffer and denatured at 95 °C for 2 min before electrophoresis. For DNaseI footprinting, samples (10 μL) were mixed with 2 μL poly(dI-dC)(1 mg/mL), 4 μL DNaseI binding buffer (Roche), and 15 μL of a mixture of 10 mM $CaCl_2$ and 10 mM $MgCl_2$. The samples were digested with 1 μL of Dnase I (0.1 U/μL) for 30 s, and the reactions were stopped by adding 25 μL formamide gel loading buffer and heating to 95 °C for 2 min. Footprinting reactions were separated on 10% denaturing gels.

Transient Transfections. HeLa cells were obtained from the American Type Culture Collection and cultured according to supplier guidelines. The pGL3/HNP410 plasmid (2 μg) containing the HER-2/neu promoter was incubated in 1× TBM at 37 °C with 10 μM TFO1, TFO3, or TFO5 for 48 h or with 1 μM of TFO2 for 4 h. Unbound

TFO was removed using 1× TBM equilibrated Chromaspin-100 columns (Clontech). Transfection was accomplished with Lipofectamine 2000 (Invitrogen) and included 20 ng of an internal control plasmid (pRL/SV40, Promega). Cell lysates were obtained at 24 h, and dual luciferase assays (Promega) were performed. Data from at least three assays were averaged, were normalized for transfection efficiency, and are presented as a percentage of luciferase activity from plasmid without TFO treatment.

RESULTS

Design of the TFO−PBD Conjugate. The ODN selected for conjugation to a PBD is a 23-mer GT antiparallel motif TFO, TFO3, that will form a triple helix with the polypurine tract in the HER-2/neu promoter, but will leave the last 5 bp of the tract available adjacent to the end of the triple helix for PBD binding (Figure 1). TFO sequences are given in Table 1. A 28-mer GA motif TFO (TFO1, Table 1) was shown to bind with high affinity to that region and prevent transcription in vitro (Ebbinghaus 1993), but required modification at both ends with a nitrogen mustard (TFO2, Table 1) to suppress the expression of HER-2/neu from a reporter plasmid in tumor cells (*11*). Substitution of guanines with the pyrazolopyrimidine analogue of guanine (PPG) in TFO2 prevents self-association of guanine rich oligonucleotides and improves triplex formation in physiological buffers (*32*). Studies comparing GA and GT motif TFOs for this target sequence showed similar binding affinities slightly favoring the GT motif (*45*). Tomaymycin is one of the most potent representatives of the PBD antitumor antibiotic family, and like all PBDs, it has a sequence preference for 5′Pu-G-Pu and forms a covalent bond with the exocyclic amino group of the central guanine of its binding sequence (Scheme 1). There are multiple potential PBD binding sites in the polypurine tract, and we selected a site at the downstream end of the polypurine tract for PBD binding. The synthetic PBD compound used in this study is structurally similar to the naturally occurring tomaymycin, but lacking a methyl group at the unsaturated C2-exo position. The unsaturation at the C2-exo position causes a flattening of the C ring and leads to a better fit in the minor groove. At the same time, an alkyl substituent at the C8-position of the A ring might reduce both DNA-binding affinity and cytotoxicity by a small degree (*50*), but this modification provides the bridge for conjugation with the ODN. Two hexa(ethylene glycol) chain linkers with one internal phosphodiester bond in each plus a 6-aminohexyl tail were introduced at the 5′end of TFO3 (resulting in TFO4, Table 1) to make a linker that is 50 atoms in length to allow for effective interaction of the PBD with the minor groove adjacent to the triple helix (Figure 1). The molecular models in Figure 1B show the triple helix, wraparound linker, and PBD bound to 5′Pu-G-Pu sites in the duplex region adjacent to the triple helix (Figure 1B, i and ii), or the duplex−triplex junction (Figure 1B, iii and iv) forming a covalent adduct with G-219 (i), G-220 (ii), G-222 (iii), or G-223 (iv). These models predict that triplex formation by the TFO−PBD conjugate (TFO5, Table 1) with the relatively long flexible linker will allow the PBD to reach the minor groove by wrapping around one DNA strand to bind at nearby 5′Pu-G-Pu binding sites.

Conjugation of the PBD to an Oligonucleotide. A mild method to introduce a nucleophilic alkylamine group on the end of the ODN for conjugation with an electrophilic derivative of the drug was employed, using DMSO as the solvent (*51*). The TEA salt of the ODN is soluble in DMSO and allows the lipophilic PBD moiety to be successfully conjugated in an organic solvent. The amine-containing linker was added to the growing ODN sequence during automated synthesis, resulting in TFO4. The TEA salt of the HPLC purified ODN was modified with the PBD as shown in Scheme 2. The *p*-nitrophenyl ester of desmethyltomaymycin was chosen as the activated moiety of the PBD for conjugation. *p*-Nitrophenyl esters are traditionally used in acylation reaction with amine-containing molecules to give amide bonds. *p*-Nitrophenyl esters can be purified by column chromatography and have slow rates of hydrolysis compared to some other activated esters. The activated ester of desmethyltomaymycin **3** was prepared as shown in Scheme 2. Anhydrous DMSO is a polar aprotic solvent that is useful for ODN conjugation chemistry. Generally the conjugation process requires an aqueous base to dissolve the ODN and to increase the nucleophilicity of the alkylamine linker. At the same time an organic cosolvent is needed in the system to increase the solubility of the liphophilic electrophiles. Although the PBD is stable in aqueous conditions, deactivation of the ester moiety might result in a lower yield of conjugation reaction and require a large excess of the PBD. In addition, desmethytomaymycin is lipophilic and has poor solubility in aqueous solutions. For these reasons, anhydrous conditions were used for synthesis of the ODN−PBD conjugate.

The progress of the conjugation reaction was monitored by HPLC and UV absorbance as shown in Figure 2. A PDA detector simplifies analysis because the PBD is a unique chromophore. The absorption spectra of the *p*-nitrophenyl ester of desmethyltomaymycin has a broad absorbance maximum at 225−240 nm.The HPLC chromatogram (Figure 2A) shows that 25 min after beginning, the reaction mixture contains an excess of starting unconjugated PBD (retention time 21 min), TFO4 (unconjugated ODN-linker), and a small peak of conjugated product, TFO5, close to TFO4 (retention time 13.3 and 12.9 min, respectively). After 21 h of incubation, the amount of unconjugated PBD is considerably decreased while the conjugated product, TFO5, represents the major peak in the chromatogram. UV absorbance monitoring (Figure 2B) demonstrates a very unique absorbance curve for the conjugated product, and the intensity of the absorbance of TFO5 is increased dramatically after 6 h of incubation. After 21 h of incubation, TFO5 was precipitated from the DMSO by adding sodium perchlorate in acetone. The resulting crude mixture was purified by reverse phase HPLC, and the identity of the conjugate was confirmed by mass spectral analysis.

Detection of Triplex Formation and Calculation of Binding Affinities by EMSA. The binding of TFO5 to the triplex target site in the HER-2/neu promoter was evaluated by EMSA (Figure 3A). Triplex mixtures were incubated in 1× TBM buffer for 24−72 h. After 24 h, triplex formation with TFO5 proceeds with a $C_{50} = 3.2$ μM that is very poor compared to TFO3 ($C_{50} = 0.015$ μM). Longer incubation with TFO5 improves the binding so that after 48 h the formation of triplex proceeds with $C_{50} = 2.1$ μM, and after 72 h with $C_{50} = 0.9$ μM. This experiment demonstrates that the presence of the PBD on the end of the TFO slows the process of triplex formation, but also shows that the PBD remains active for at least 72 h. The TFO itself may have potential PBD binding sites, and intramolecular interaction of the PBD with the TFO or self-association of the guanine rich oligonucleotides might account for the poor binding to the

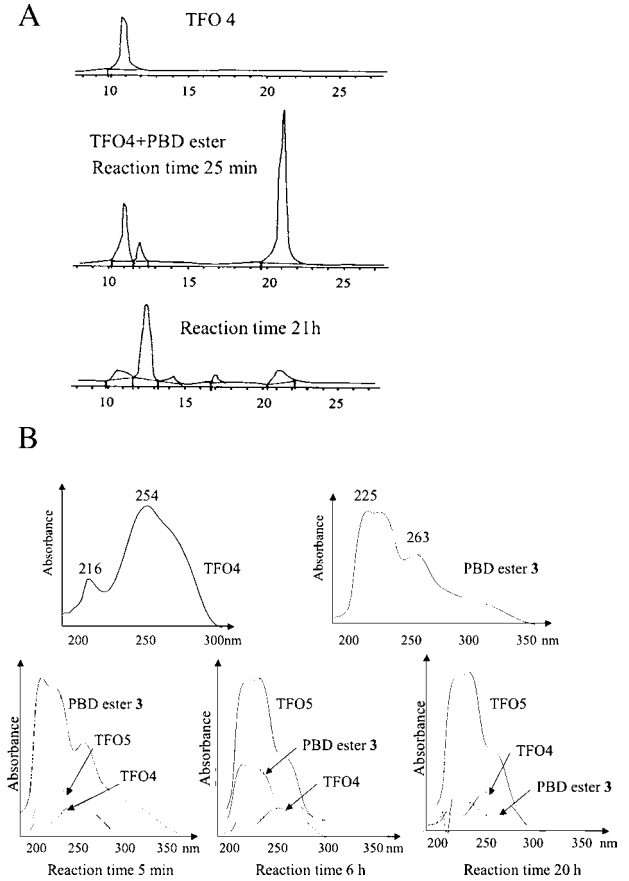


Figure 2. HPLC and UV monitoring of the TFO–PBD conjugation reaction. (A) HPLC analysis monitoring the conjugation between TFO4 and PBD ester **3**. The top chromatogram shows unconjugated TFO4 at time zero, t_R = 12.9 min. The middle chromatogram shows the reaction mixture after 25 min with a large peak for the unconjugated PBD ester **3**, t_R = 21 min, and a small peak for TFO5, t_R = 13.3 min. The bottom chromatogram shows the reaction mixture after 21 h, with a large peak for TFO5 at 13.3 min. (B) UV monitoring of the conjugation reaction between TFO4 and the PBD ester **3**. Top panels, UV spectra of TFO4 (left) and the PBD *p*-nitrophenyl ester **3** (right). Bottom panels, UV spectra of the conjugation reaction at monitoring of progress in conjugation reaction at 5 min, 6 h, and 20 h.

target sequence. EMSAs were performed with increasing concentrations of TFO5 alone for up to 72 h, and no self-association of TFO5 was observed by methylene blue staining (not shown). Because the triplex target sequence contains many potential PBD binding sites, we speculate that the process of PBD docking in the minor groove in the triplex target sequence is interfering with the formation of the triple helix within major groove. The structure and length of the TFO and linker might cause sterical obstacles for positioning the drug in the desired location adjacent to the TFO binding site and may be amenable to further optimization (*44*).

Enzymatic and Chemical Footprinting. To precisely determine the binding site for TFO5, we used DNase I footprinting. DNase I has been used extensively to footprint TFOs and some MGBs such as distamycin, netropsin, Hoechst 33258, and berenil. These MGBs cause clear changes in the DNase I digestion patterns, but no simple footprints (*52*). In contrast, the PBD analogue DC-81 does not alter DNase I cleavage patterns, and among the PBDs, tomaymycin binding produces the least distortion of the duplex (*39*, *53*). Our DNaseI footprinting experiment with TFO3, TFO4 (not shown), and TFO5 demonstrated that all three TFOs protect the

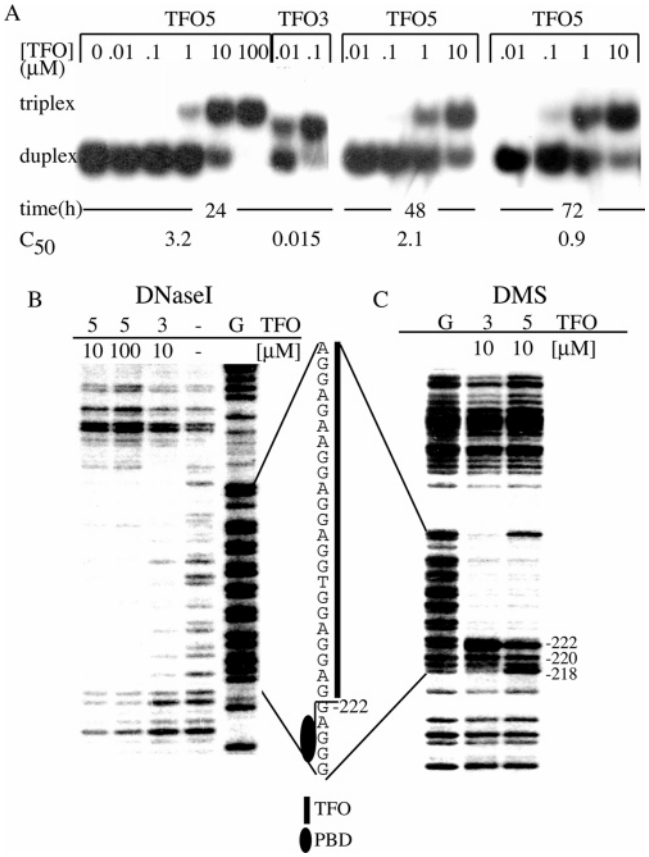


Figure 3. Triplex formation by TFOs with and without PBD. (A) EMSAs showing triplex formation at 24, 48, and 72 h. Apparent dissociation constants (K_d) for TFO3 and TFO5 calculated from these EMSAs are shown below each time point. (B) DNaseI footprints showing the binding of TFO3 and TFO5 to the HER-2/neu promoter. A stronger footprint is observed for TFO5. (C) DMS footprints showing the binding of TFO3 and TFO5 to the triplex target sequence. Note the hypersensitivity of G(−222) at the duplex–triplex junction in the absence of PBD binding with TFO3, and the hypersensitivity of G(−218) in the presence of PBD binding with TFO5. Also note partial protection of G(−219) and G(−220) in the presence of PBD binding with TFO5.

duplex from cleavage by DNase I, with identical binding sites for the TFO with and without the PBD conjugate (Figure 3B). We do not observe an altered cleavage pattern due to the PEG linker or PBD interaction with the DNA template, in accord with previous observations of the absence of altered DNase I cleavage patterns produced by tomaymycin. At the same time, these footprints demonstrate that TFO5 provides greater protection of the duplex than TFO3, suggesting that PBD binding stabilizes triplex formation between duplex and TFO5 conjugate.

Triplex formation was also evaluated with DMS footprinting (Figure 3C). DMS can be used to determine the accessibility of the N7 position of guanines, and protection from DMS alkylation occurs due to the Hoogsteen bonds formed by the TFO. DMS cleavage patterns can also reflect changes in the nucleophilicity of the N7 of guanine, which can be influenced by flanking bases and drug binding to DNA in the vicinity of the guanine (*54*). Thus, although the PBD binds in the minor groove and reacts with the exocyclic amino group of guanine, changes in the DMS cleavage pattern adjacent to the triple helix would be indicative of PBD binding. The DMS footprints in Figure 3C show that both TFO3 and TFO5 protect the guanines in the triple helix. TFO3 binding produces a hypersensitive guanine immediately adjacent to the triple

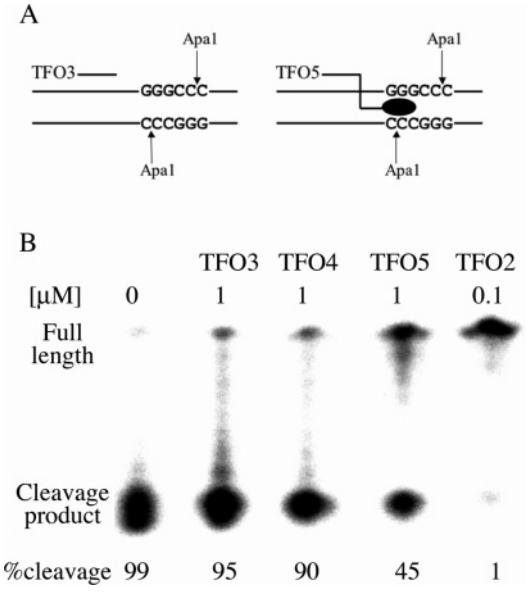


Figure 4. PBD binding adjacent to the triple helix protects the target sequence from restriction enzyme digestion with ApaI. (A) Schematic representation of the location of the engineered ApaI site in the HER-2/neu promoter relative to the triple helix formed by TFO3, TFO4, and TFO5. (B) The cleavage products of ApaI digestion before and after triplex formation by TFO2−TFO5 were resolved on a denaturing gel and quantified by densitometry.

helix at G(−222) that is not observed with the binding of TFO5, indicating that either the wraparound linker blocks the accessibility of the N7 of this guanine to DMS or that PBD binding alters its reactivity to DMS. TFO5 binding also decreases the reactivity of G(−220) and G(−219) while inducing a hypersensitive guanine at G(−218). Interestingly, a guanine at the opposite end of the triple helix from the expected PBD binding site, G(−244), is also more reactive with TFO5 compared to TFO3, perhaps due to a 3′ hexanol modification in TFO5. Agents that bind to the minor groove have been shown to alter DMS cleavage patterns over a fairly long range so that assignment of explicit drug binding sites is difficult (*54*). Nonetheless, these footprints suggest that the PBD moiety of TFO5 binds to either the AGG (−221 to −219) or the GGG (−220 to −218) 5′Pu-G-Pu PBD binding sites adjacent to the triple helix.

Restriction Endonuclease Protection Analysis. To provide further evidence for PBD binding adjacent to the triple helix formed by TFO5, we evaluated the ability of PBD binding to prevent restriction endonuclease cleavage adjacent to the triple helix (Figure 4). For this assay, we modified two bp of the HER-2/neu promoter downstream of the polypurine tract to form an ApaI (native sequence: 5′GGGCTG3′→ ApaI mutant sequence: 5′GGGCCC3′) so that PBD binding would protect this sequence from ApaI cleavage (Figure 4A). TFO3, TFO4, and TFO5 were added to the ApaI mutant sequence at a final concentration of 1 μM and incubated for 48 h, while TFO2 was incubated with the duplex for 4 h at a concentration of 0.1 μM. Figure 4B shows the cleavage products of ApaI digestion after triplex formation with TFOs with and without a PBD conjugate. Of these, only TFO5 containing the PBD conjugate inhibited ApaI digestion. The triple helix itself does not prevent ApaI cleavage, since nearly complete digestion is seen with TFO3 (unmodified TFO). Similarly, the 50-atom linker does not appear to sterically inhibit ApaI recognition or cleavage, since nearly complete digestion is seen with TFO4 (TFO with the linker). TFO2, a slightly longer TFO conjugated to PAM, completely prevented ApaI digestion, while restriction endonuclease protection by TFO5 was incomplete, suggesting that PBD binding at the ApaI site is either less efficient or less stable than PAM binding; however, it is important to note that the triple helix formed by TFO2 overlaps the ApaI site, whereas the triple helix formed by TFO5 does not, and ODN binding in the major groove may more effectively block the restriction site than PBD binding in the minor groove. PBD binding to DNA has been previously demonstrated by methidiumpropyl EDTA-Fe(II) (MPE-Fe) cleavage (*37*, *53*), but our attempts to obtain a differential cleavage pattern between TFOs with and without the PBD (TFO3 and TFO5) using MPE-Fe were not successful, perhaps because tomaymycin produces the least distortion of the double helix of any member of the PBD family. Nonetheless, the combination of DMS footprinting and endonuclease protection studies clearly demonstrates that TFO5 directs the binding of the PBD moiety to a PBD binding site adjacent to the triple helix.

DMS Footprints with an Inosine-Substituted PBD Binding Site. The 2-amino (exocyclic amino) group of guanine is a critical element in the sequence-specific recognition of DNA through the minor groove, where most small molecules bind (*55*, *56*). For this reason, footprinting studies performed on DNA fragments containing inosine in place of guanine are useful for demonstrating minor groove binding by proteins and small molecules. Inosine (I) is a guanine analogue that lacks the exocyclic amino group (Figure 5A) and is therefore not able to donate a hydrogen bond nor form a covalent bond with a PBD. Inosine-substituted oligonucleotides were used in studies that showed the aminal bond formed between the C11 of tomamycin and the exocyclic amino group of guanine (*57*). We compared the DMS footprints produced by TFO3, TFO4, and TFO5 in a duplex target with three inosine substitutions I(−218), I(−219), and I(−220) in the PBD binding site. EMSA analysis demonstrates that inosine substitution at these positions does not significantly alter the ability of the TFOs to form a triple helix with the target sequence (Figure 5B). The DMS cleavage pattern adjacent to the triple helix again demonstrates that PBD binding in the native sequence greatly reduces the reactivity of a hypersensitive guanine, G-222, at the duplex−triplex junction (Figure 5C, left panel). In contrast, in the inosine-substituted sequence, the DMS reactivity of G-222 is essentially identical for TFO3, TFO4, and TFO5 (Figure 5C, right panel). In addition, the DMS reactivity of the guanine at −218 is again reduced by PBD binding to the native sequence, while the DMS reactivity of all three inosine bases is essentially identical for TFO3, TFO4, and TFO5. These data clearly demonstrate the interaction between the PBD molecule and the guanines adjacent to the triple helix and, taken together with prior studies (*57*), provide inferential evidence for a covalent PBD interaction with a guanine in the PBD binding site.

Transient Transfection Assays. To determine whether PBD binding sufficiently stabilized triplex formation to prevent HER-2/neu transcription initiation, we performed transient transfection assays with a HER-2/neu promoter-luciferase reporter plasmid. Triple helix formation by TFOs with and without 5′ and 3′ PAM groups (TFO1 and TFO2) was compared to triplex formation by TFOs with and without a 5′PBD (TFO3 and TFO5). For these experiments, the plasmid was treated with the TFO under ideal binding conditions, purified from unbound, excess TFO by column chromatography, and transfected into HeLa cells. Figure 6 shows HER-2/

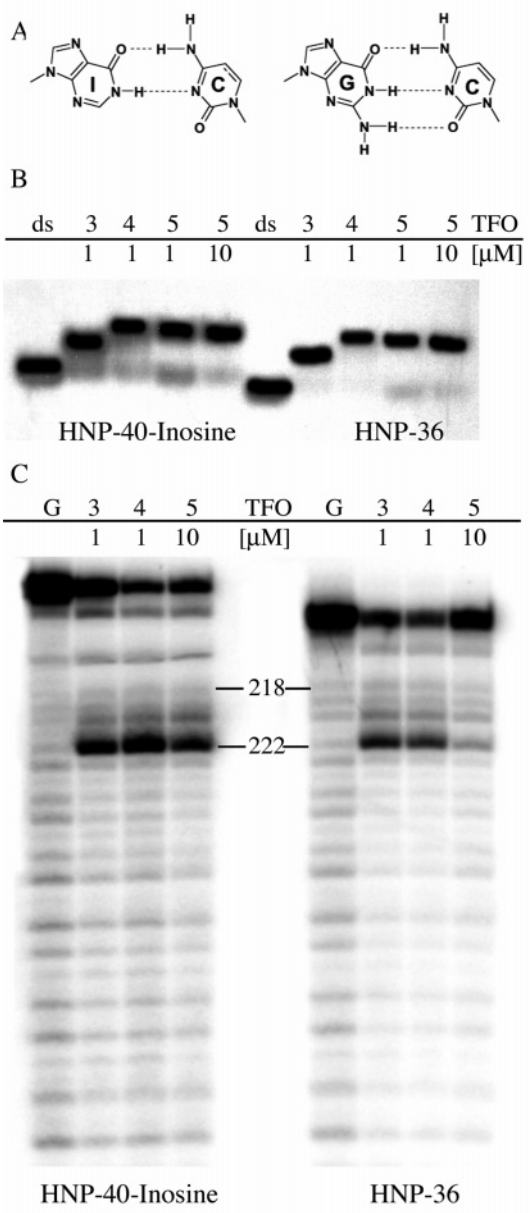


Figure 5. The PBD binding site adjacent to the triple helix was demonstrated with DMS footprints on an inosine-substituted, synthetic HER-2/neu promoter fragment. (A) Structure of hydrogen-bonded guanine-cytosine and guanine-inosine base pairs. (B) EMSA demonstrating that the amount of triplex formation by TFO3−TFO5 is equivalent between the inosine-substituted (HNP-40-inosine) and native (HNP-36) synthetic HER-2/neu promoter fragments. Inosines were substituted for guanines at the putative PBD binding site (−218 to −220). (C) DMS footprints demonstrating identical cleavage patterns for TFOs with (TFO5) and without (TFO3, TFO4) a PBD in the inosine-substituted HER-2/neu promoter fragment. Note the hypersensitivity of G(−222) at the duplex−triplex junction in the absence of PBD binding seen with all TFOs in the inosine-substituted sequence, but only for TFO3 and TFO4 in the native sequence.

neu driven luciferase activity at 24 h after treatment with TFOs, presented as relative expression compared to untreated plasmid and normalized for transfection efficiency by a cotransfected reporter plasmid. These data demonstrate that triplex formation by itself (TFO1 and TFO3) is incapable of preventing HER-2/neu transcription, while triplex formation and covalent adduct formation at both ends of the triple helix with a nitrogen mustard (TFO2) is capable of suppressing transcription from the HER-2/neu promoter by approximately 60% and

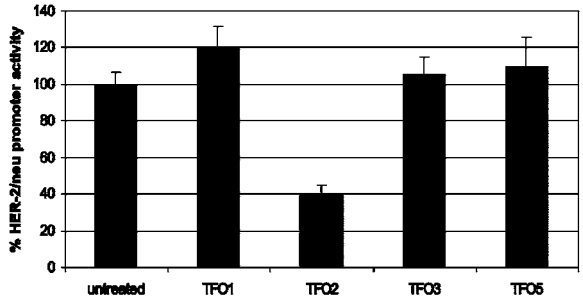


Figure 6. Transient transfection analysis of the effects of triplex formation by unmodified TFOs (TFO1 and TFO3) and TFO conjugates (TFO2 and TFO5) on HER-2/neu expression. HeLa cells were transfected with a firefly luciferase plasmid controlled by a 410 bp HER-2/neu promoter and treated with TFOs prior to transfection, and luciferase activity was measured at 24 h.

reproduce our earlier findings (*11*). Triplex formation and PBD binding (TFO5) failed to suppress HER-2/neu transcription in these studies, even though the binding conditions for TFO5 in this experiment were shown to yield complete binding to the target sequence by the TFO and at least reasonably efficient binding by the PBD in other assays. We have previously shown that guanine adduct formation at only one end of the triple helix by a nitrogen mustard was inefficient at preventing HER-2/neu transcription in this assay system, and the present results are in accord with our findings that covalent binding at both ends of the HER-2/neu triplex target sequence is probably needed to prevent HER-2/neu transcription by a TFO in cells.

DISCUSSION

We report the synthesis of a novel oligonucleotide−pyrrolo[1,4]benzodiazepine conjugate by a versatile method. This TFO−PBD conjugate is capable of forming a triple helix with the HER-2/neu promoter and directing the site-specific binding of the PBD adjacent to the triple helix. Conceptually, this strategy could improve the binding of the TFO and direct the biological activity of the PBD to a single gene of interest. However, our results demonstrate some of the challenges to this strategy that may be amenable to further optimization.

First, the presence of the PBD moiety on the TFO slows the process of triplex formation, since the TFO alone completely binds to the target sequence after 4 h at 37 °C. PBDs are known to initially bind slowly and reversibly to DNA, and binding may be incomplete even after 48 h at 37 °C (*58*−*60*). Alternately, the linker between the major groove binding TFO and the minor groove binding PBD may be critical to the activity of the conjugate. The long, flexible linker used in this study may allow the PBD to bind to any available PBD binding site before the TFO binds, until an optimal TFO−PBD binding site is finally encountered. The HER-2/neu promoter is rich in potential PBD binding sites, and we speculate that reversible PBD binding at unintended PBD binding sites prevents binding by the TFO and initially slows binding by the TFO−PBD conjugate. Once the TFO binds, the high local concentration of the PBD adjacent to the triple helix may actually improve covalent bond formation by the PBD and improve overall binding by the conjugate.

Conjugation of the PBD to a minor groove binding polyamide carrier improves PBD binding to DNA and antiproliferative activity in tissue culture, suggesting that the presence of the alkylating moiety and the carrier

in the same minor groove of DNA can create a more stable drug−DNA interaction (*39*, *61*). The CPIs are another class of MGBs that have been tethered to TFOs. CPIs appear to bind more rapidly, and in the context of a TFO−CPI conjugate, triplex formation is the rate-limiting step in the binding of the conjugate (*43*). Studies of TFO−CPI conjugates also demonstrate the importance of the linker between the major groove and the MGB and suggest that an aromatic molecule capable of intercalating into the DNA and threading the duplex may be a more robust means of using a TFO to direct the site of the MGBs (*44*).

Second, the interaction of the TFO−PBD conjugate with the HER-2/neu promoter is not sufficient to prevent HER-2/neu expression from a reporter plasmid. It is likely that the triple helix formed by the TFO−PBD conjugate is not sufficiently stable in cells, even though the TFO−PBD conjugate produces a stronger DNaseI and DMS footprint, indicative of an improvement in binding, compared to the unconjugated TFO. Our previous studies with TFOs conjugated to PAM at one or both ends demonstrated that a mono-conjugate was practically inactive at suppressing transcription within cells, while a bis-conjugate significantly suppressed HER-2/neu expression in this assay system and was the least susceptible to displacement by a recombinant DNA helicase (*11*). Similarly, TFO−psoralen conjugates that create a single locus of DNA damage are efficiently repaired in cells while triplex-directed cross-links at both ends of the triple helix are not (*62*).

Helicase activity is present in many of the enzymes that process DNA, including replication, transcription, and repair. DNA interactive small molecules differ in their ability to inhibit DNA helicase translocation and unwinding, and nogalamycin is one of the most potent helicase inhibitors, because it intercalates and binds in both the major and minor grooves into both grooves of DNA (*63*). MGBs including distamycin and netropsin can also block DNA helicase (*64*). PBD−DNA adducts, however, are stable only as long as the double helix structure of DNA is maintained (*65*) and thus may be unable to remain bound to DNA in the face of an advancing helicase. C8 linked PBD dimers, which form interstrand cross-links, are able to resist the repair process in cells for more than 48 h (*66*). A single tomaymycin molecule on the end of the TFO may be unable to resist displacement by helicases, and conjugation to a PBD dimer capable of forming cross-links or to a PBD molecule at both ends of the TFO would likely be more active in this regard.

In conclusion, we report the first example of an ODN−PBD conjugate and demonstrate that triplex formation by the ODN directs the PBD to a specific location adjacent to the triple helix. Although our studies did not directly demonstrate covalent PBD binding to the target sequence, the lack of PBD binding to an inosine-substituted target sequence demonstrates the need for the exocyclic amino group of guanine in accord with previous data that demonstrate covalent PBD binding to guanine. This study demonstrates the conceptual feasibility of site-specific PBD targeting by a TFO, but shows that further optimization of the design of this bioconjugate will be needed to address the obstacles of slow binding to DNA and instability of the interaction within cells.

ACKNOWLEDGMENT

This work was supported by grants from the NIH (CA85306) and the Flinn Foundation (1580). The authors gratefully acknowledge the Lajos Szabo for assistance with HPLC analysis and David Milesi for assistance with the conjugation reactions.

NOTE ADDED AFTER ASAP POSTING

In the version of the manuscript posted October 30, 2004, “Pyrrolobenzodiazepine” replaces “Tomaymycin” in the manuscript title. In line 19 of the first paragraph of the Results section, “Desmethyltomaymycin” is replaced by “Tomaymycin”. In line 29 of the same paragraph, the phrase “but lacking a methyl group at the unsaturated C2-exo position” is inserted. Finally, a corrected Scheme 1 has been inserted into the second page. The corrected version of the manuscript was posted November 9, 2004.

LITERATURE CITED

(1) Knauert, M. P., and Glazer, P. M. (2001) Triplex forming oligonucleotides: sequence-specific tools for gene targeting. *Hum. Mol. Genet. 10*, 2243−2251.

(2) Praseuth, D., Guieysse, A. L., and Helene, C. (1999) Triple helix formation and the antigene strategy for sequence-specific control of gene expression. *Biochim. Biophys. Acta 1489*, 181−206.

(3) Vasquez, K. M., and Glazer, P. M. (2002) Triplex-forming oligonucleotides: principles and applications. *Q. Rev. Biophys. 35*, 89−107.

(4) Le Doan, T., Perrouault, L., Praseuth, D., Habhoub, N., Decout, J. L., Thuong, N. T., Lhomme, J., and Helene, C. (1987) Sequence-specific recognition, photocrosslinking and cleavage of the dna double helix by an oligo-[alpha]-thymidylate covalently linked to an azidoproflavine derivative. *Nucleic Acids Res. 15*, 7749−7760.

(5) Moser, H. E., and Dervan, P. B. (1987) Sequence-specific cleavage of double helical dna by triple helix formation. *Science 238*, 645−650.

(6) Frank-Kamenetskii, M. D., and Mirkin, S. M. (1995) Triplex DNA structures. *Annu. Rev. Biochem. 64*, 65−95.

(7) Felsenfeld, G., Davies, D. R., and Rich, A. (1957) Formation of a three-stranded polynucleotide molecule. *J. Am. Chem. Soc. 79*, 2023−2024.

(8) Maine, I. P., and Kodadek, T. (1994) Efficient unwinding of triplex DNA by a DNA helicase. *Biochem. Biophys. Res. Commun. 204*, 1119−1124.

(9) Brosh, R. M., Jr., Majumdar, A., Desai, S., Hickson, I. D., Bohr, V. A., and Seidman, M. M. (2001) Unwinding of a DNA triple helix by the Werner and Bloom syndrome helicases. *J. Biol. Chem. 276*, 3024−3030.

(10) Vasquez, K. M., Christensen, J., Li, L., Finch, R. A., and Glazer, P. M. (2002) Human XPA and RPA DNA repair proteins participate in specific recognition of triplex-induced helical distortions. *Proc. Natl. Acad. Sci. U. S. A 99*, 5848−5853.

(11) Ziemba, A. J., Reed, M. W., Raney, K. D., Byrd, A. B., and Ebbinghaus, S. W. (2003) A bis-alkylating triplex forming oligonucleotide inhibits intracellular reporter gene expression and prevents triplex unwinding due to helicase activity. *Biochemistry 42*, 5013−5024.

(12) Asseline, U. (1999) in *Triple Helix Forming Oligonucleotides* (Malvy, C., Harel-Bellan, A., and Pritchard, L. L., Eds.) pp 63−73, Kluwer Academic Publishers, Boston.

(13) Reed, M. W., Wald, A., and Meyer, R. B. (1998) Triplex-Directed Interstrand DNA Cross-Linking by Diaziridinylquinone-Oligonucleotide Conjugates. *J. Am. Chem. Soc. 120*, 9729−9734.

(14) Lukhtanov, E. A., Podyminogin, M. A., Kutyavin, I. V., Meyer, R. B., and Gamper, H. B. (1996) Rapid and efficient hybridization-triggered cross-linking within a DNA duplex by an oligodeoxyribonucleotide bearing a conjugated cyclopropapyrroloindole. *Nucleic Acids Res. 24*, 683−687.

(15) Vasquez, K. M., Wensel, T. G., Hogan, M. E., and Wilson, J. H. (1996) High-efficiency triple-helix-mediated photocross-linking at a targeted site within a selectable mammalian gene. *Biochemistry 35*, 10712−10719.

(16) Povsic, T. J., Strobel, S. A., and Dervan, P. B. (1992) Sequence-specific double-strand alkylation and cleavage of DNA mediated by triple-helix formation. *J. Am. Chem. Soc. 114*, 5934−5941.

(17) Kutyavin, I. V., Gamper, H. B., Gall, A. A., and Meyer, R. B. (1993) Specific intrastrand cross-linking of double stranded DNA by a chlorambucil-modified triplex forming oligonucleotide. *J. Am. Chem. Soc. 115*, 9303−9304.

(18) Ebbinghaus, S. W., Gee, J. E., Rodu, B., Mayfield, C. A., Sanders, G., and Miller, D. M. (1993) Triplex formation inhibits HER-2/neu transcription in vitro. *J. Clin. Invest 92*, 2433−2439.

(19) Ebbinghaus, S. W., Fortinberry, H., and Gamper, H. B., Jr. (1999) Inhibition of transcription elongation in the HER-2/neu coding sequence by triplex-directed covalent modification of the template strand. *Biochemistry 38*, 619−628.

(20) Agus, D. B., Bunn, P. A., Jr., Franklin, W., Garcia, M., and Ozols, R. F. (2000) HER-2/neu as a therapeutic target in non-small cell lung cancer, prostate cancer, and ovarian cancer. *Semin. Oncol. 27*, 53−63.

(21) Meric, F., Hung, M. C., Hortobagyi, G. N., and Hunt, K. K. (2002) HER2/neu in the management of invasive breast cancer. *J Am. Coll. Surg. 194*, 488−501.

(22) Ziemba, A., Derosier, L. C., Methvin, R., Song, C. Y., Clary, E., Kahn, W., Milesi, D., Gorn, V., Reed, M., and Ebbinghaus, S. (2001) Repair of triplex-directed DNA alkylation by nucleotide excision repair. *Nucleic Acids Res. 29*, 4257−4263.

(23) Young, S. L., Krawczyk, S. H., Matteucci, M. D., and Toole, J. J. (1991) Triple helix formation inhibits transcription elongation in vitro. *Proc. Natl. Acad. Sci. U.S.A. 88*, 10023−10026.

(24) Sastry, S. S., and Hearst, J. E. (1991) Studies on the interaction of T7 RNA polymerase with a DNA template containing a site-specifically placed psoralen cross- link. II. Stability and some properties of elongation complexes. *J. Mol. Biol. 221*, 1111−1125.

(25) Sastry, S. S., and Hearst, J. E. (1991) Studies on the interaction of T7 RNA polymerase with a DNA template containing a site-specifically placed psoralen cross- link. I. Characterization of elongation complexes. *J. Mol. Biol. 221*, 1091−1110.

(26) Duval-Valentin, G., Thuong, N. T., and Helene, C. (1992) Specific inhibition of transcription by triple helix-forming oligonucleotides. *Proc. Natl. Acad. Sci. U.S.A. 89*, 504−508.

(27) Skoog, J. U., and Maher, L. J. (1993) Relief of triple-helix-mediated promoter inhibition by elongating rna polymerases. *Nucleic Acids Res. 21*, 4055−4058.

(28) Samadashwily, G. M., and Mirkin, S. M. (1994) Trapping DNA polymerases using triplex-forming oligodeoxyribonucleotides. *Gene 149*, 127−136.

(29) Diviacco, S., Rapozzi, V., Xodo, L., Helene, C., Quadrifoglio, F., and Giovannangeli, C. (2001) Site-directed inhibition of DNA replication by triple helix formation. *FASEB J. 15*, 2660−2668.

(30) Kopel, V., Pozner, A., Baran, N., and Manor, H. (1996) Unwinding of the third strand of a DNA triple helix, a novel activity of the SV40 large T-antigen helicase. *Nucleic Acids Res. 24*, 330−335.

(31) Povirk, L. F., and Shuker, D. E. (1994) DNA damage and mutagenesis induced by nitrogen mustards. *Mutat. Res. 318*, 205−226.

(32) Belousov, E. S., Afonina, I. A., Kutyavin, I. V., Gall, A. A., Reed, M. W., Gamper, H. B., Wydro, R. M., and Meyer, R. B. (1998) Triplex targeting of a native gene in permeabilized intact cells: covalent modification of the gene for the chemokine receptor CCR5. *Nucleic Acids Res. 26*, 1324−1328.

(33) Ebbinghaus, S. W., Vigneswaran, N., Mayfield, C. A., Curiel, D. T., and Miller, D. M. (1999) in *Triple Helix Forming Oligonucleotides* (Malvy, C., Harel-Bellan, A., and Pritchard, L. L., Eds.) pp 117−127, Kluwer Academic Publishers, Boston.

(34) Reed, M. W., Lukhtanov, E. A., Gorn, V. V., Kutyavin, I. V., Gall, A. A., Wald, A., and Meyer, R. B. (1998) Synthesis and reactivity of aryl nitrogen mustard- oligodeoxyribonucleotide conjugates. *Bioconjugate Chem. 9*, 64−71.

(35) Hurley, L. H. (1994) The minor groove covalent reactive drugs anthramycin and (+)-CC-1065 and their interstrand cross-linking derivatives. *IARC Sci. Publ.* 295−312.

(36) Hurley, L. H., Reck, T., Thurston, D. E., Langley, D. R., Holden, K. G., Hertzberg, R. P., Hoover, J. R., Gallagher, G., Jr., Faucette, L. F., Mong, S. M., and. (1988) Pyrrolo[1,4]-benzodiazepine antitumor antibiotics: relationship of DNA alkylation and sequence specificity to the biological activity of natural and synthetic compounds. *Chem. Res. Toxicol. 1*, 258−268.

(37) Puvvada, M. S., Forrow, S. A., Hartley, J. A., Stephenson, P., Gibson, I., Jenkins, T. C., and Thurston, D. E. (1997) Inhibition of bacteriophage T7 RNA polymerase in vitro transcription by DNA-binding pyrrolo[2,1-*c*][1,4]benzodiazepines. *Biochemistry 36*, 2478−2484.

(38) Kamal, A., Rao, M. V., Laxman, N., Ramesh, G., and Reddy, G. S. (2002) Recent developments in the design, synthesis and structure−activity relationship studies of pyrrolo[2,1-c][1,4]benzodiazepines as DNA-interactive antitumour antibiotics. *Curr. Med. Chem. Anti. −Canc. Agents 2*, 215−254.

(39) Baraldi, P. G., Balboni, G., Cacciari, B., Guiotto, A., Manfredini, S., Romagnoli, R., Spalluto, G., Thurston, D. E., Howard, P. W., Bianchi, N., Rutigliano, C., Mischiati, C., and Gambari, R. (1999) Synthesis, in vitro antiproliferative activity, and DNA-binding properties of hybrid molecules containing pyrrolo[2,1-*c*][1,4]benzodiazepine and minor-groove-binding oligopyrrole carriers. *J. Med. Chem. 42*, 5131−5141.

(40) Reddy, B. S., Sharma, S. K., and Lown, J. W. (2001) Recent developments in sequence selective minor groove DNA effectors. *Curr. Med. Chem. 8*, 475−508.

(41) Mountzouris, J. A., Wang, J. J., Thurston, D., and Hurley, L. H. (1994) Comparison of a DSB-120 DNA interstrand cross-linked adduct with the corresponding bis-tomaymycin adduct: an example of a successful template-directed approach to drug design based upon the monoalkylating compound tomaymycin. *J. Med. Chem. 37*, 3132−3140.

(42) Kumar, R., and Lown, J. W. (2003) Recent developments in novel pyrrolo[2,1-c][1,4]benzodiazepine conjugates: synthesis and biological evaluation. *Mini. Rev. Med. Chem. 3*, 323−339.

(43) Lukhtanov, E. A., Mills, A. G., Kutyavin, I. V., Gorn, V. V., Reed, M. W., and Meyer, R. B. (1997) Minor groove DNA alkylation directed by major groove triplex forming oligodeoxyribonucleotides. *Nucleic Acids Res. 25*, 5077−5084.

(44) Dempcy, R. O., Kutyavin, I. V., Mills, A. G., Lukhtanov, E. A., and Meyer, R. B. (1999) Linkers designed to intercalate the double helix greatly facilitate DNA alkylation by triplex-forming oligonucleotides carrying a cyclopropapyrroloindole reactive moiety. *Nucleic Acids Res. 27*, 2931−2937.

(45) Basye, J., Trent, J. O., Gao, D., and Ebbinghaus, S. W. (2001) Triplex formation by morpholino oligodeoxyribonucleotides in the HER-2/neu promoter requires the pyrimidine motif. *Nucleic Acids Res. 29*, 4873−4880.

(46) Trent, J. O. (2001) Molecular modeling of drug−DNA complexes: an update. *Methods Enzymol. 340*, 290−326.

(47) Mohamadi, F., Richards, N. G., Guida, W. C., Liskamp, R., Lipton, M., Caufield, C., Chang, G., Hendrickson, T., and Still, W. C. (1990) MacroModel − an integrated software system for modeling organic and bioorganic molecules using molecular mechanics. *J. Comput. Chem. 11*, 440−455.

(48) Jenkins, T. C., Hurley, L. H., Neidle, S., and Thurston, D. E. (1994) Structure of a covalent DNA minor groove adduct with a pyrrolobenzodiazepine dimer: evidence for sequence-specific interstrand cross-linking. *J. Med. Chem. 37*, 4529−4537.

(49) Thurston, D. E., Bose, D. S., Thompson, A. S., Howard, P. W., Leoni, A., Croker, S. J., Jenkins, T. C., Neidle, S., Hartley, J. A., and Hurley, L. H. (1996) Synthesis of Sequence-Selective C8−Linked Pyrrolo[2,1-c][1,4]benzodiazepine DNA Interstrand Cross-Linking Agents. *J. Org. Chem. 61*, 8141−8147.

(50) Thurston, D. E., Bose, D. S., Howard, P. W., Jenkins, T. C., Leoni, A., Baraldi, P. G., Guiotto, A., Cacciari, B., Kelland, L. R., Foloppe, M. P., and Rault, S. (1999) Effect of A-ring

modifications on the DNA-binding behavior and cytotoxicity of pyrrolo[2,1-*c*][1,4]benzodiazepines. *J. Med. Chem. 42*, 1951−1964.
(51) Milesi, D., Kutyavin, I., Lukhtanov, E. A., Gorn, V. V., and Reed, M. W. (2000) Synthesis of oligonucleotide conjugates in anhydrous dimethyl sulfoxide. *Methods Enzymol. 313*, 164−173.
(52) Brown, P. M., and Fox, K. R. (1996) Minor groove binding ligands alter the rotational positioning of DNA fragments on nucleosome core particles. *J. Mol. Biol. 262*, 671−685.
(53) Hertzberg, R. P., Hecht, S. M., Reynolds, V. L., Molineux, I. J., and Hurley, L. H. (1986) DNA sequence specificity of the pyrrolo[1,4]benzodiazepine antitumor antibiotics. Methidiumpropyl-EDTA-iron(II) footprinting analysis of DNA binding sites for anthramycin and related drugs. *Biochemistry 25*, 1249−1258.
(54) Shelton, C. J., Harding, M. M., and Prakash, A. S. (1996) Enzymatic and chemical footprinting of anthracycline antitumor antibiotics and related saccharide side chains. *Biochemistry 35*, 7974−7982.
(55) Bailly, C., Mollegaard, N. E., Nielsen, P. E., and Waring, M. J. (1995) The influence of the 2-amino group of guanine on DNA conformation. Uranyl and DNase I probing of inosine/diaminopurine substituted DNA. *EMBO J. 14*, 2121−2131.
(56) Waring, M. J., and Bailly, C. (1994) The purine 2-amino group as a critical recognition element for binding of small molecules to DNA. *Gene 149*, 69−79.
(57) Boyd, F. L., Stewart, D., Remers, W. A., Barkley, M. D., and Hurley, L. H. (1990) Characterization of a unique tomaymycin-d(CICGAATTCICG)2 adduct containing two drug molecules per duplex by NMR, fluorescence, and molecular modeling studies. *Biochemistry 29*, 2387−2403.
(58) Hurley, L. H. (1977) Pyrrolo(1,4)benzodiazepine antitumor antibiotics. Comparative aspects of anthramycin, tomaymycin and sibiromycin. *J. Antibiot. (Tokyo) 30*, 349−370.
(59) Hurley, L. H., Gairola, C., and Zmijewski, M. (1977) Pyrrolo(1,4)benzodiazepine antitumor antibiotics. In vitro interaction of anthramycin, sibiromycin and tomaymycin with DNA using specifically radiolabelled molecules. *Biochim. Biophys. Acta 475*, 521−535.
(60) Farmer, J. D., Jr., Gustafson, G. R., Conti, A., Zimmt, M. B., and Suggs, J. W. (1991) DNA binding properties of a new class of linked anthramycin analogs. *Nucleic Acids Res. 19*, 899−903.
(61) Kumar, R., and Lown, J. W. (2003) Design, synthesis and in vitro cytotoxicity studies of novel pyrrolo [2,1][1,4] benzodiazepine-glycosylated pyrrole and imidazole polyamide conjugates. *Org. Biomol. Chem. 1*, 3327−3342.
(62) Sandor, Z., and Bredberg, A. (1995) Deficient DNA repair of triple helix-directed double psoralen damage in human cells. *FEBS Lett. 374*, 287−291.
(63) Tuteja, N., Phan, T. N., Tuteja, R., Ochem, A., and Falaschi, A. (1997) Inhibition of DNA unwinding and ATPase activities of human DNA helicase II by chemotherapeutic agents. *Biochem. Biophys. Res. Commun. 236*, 636−640.
(64) Soderlind, K. J., Gorodetsky, B., Singh, A. K., Bachur, N. R., Miller, G. G., and Lown, J. W. (1999) Bis-benzimidazole anticancer agents: targeting human tumour helicases. *Anticancer Drug Des. 14*, 19−36.
(65) Hurley, L. H., Chandler, C., Garner, T. F., Petrusek, R., and Zimmer, S. G. (1979) DNA binding, induction of unscheduled DNA synthesis, and excision of anthramycin from DNA in normal and repair-deficient human fibroblasts. *J. Biol. Chem. 254*, 605−608.
(66) Smellie, M., Kelland, L. R., Thurston, D. E., Souhami, R. L., and Hartley, J. A. (1994) Cellular pharmacology of novel C8-linked anthramycin-based sequence-selective DNA minor groove cross-linking agents. *Br. J. Cancer 70*, 48−53.

BC0498673

Influence of Pendant Arms Bearing Ligating Groups on the Structure of Bismuth Porphyrins: Implications for Labeling Immunoglobulins Used in Medical Applications

Zakaria Halime,[†,‡] Lydie Michaudet,[†] Mohammed Lachkar,[‡] Pierre Brossier,[§] and Bernard Boitrel*[,†]

Institut de Chimie, Université de Rennes1, UMR CNRS 6509, 35042 Rennes Cedex, France, Faculté des Sciences Dhar El Mehraz, Laboratoire d'Analyses, d'Essais et d'Environnement (L.A.E.E), Université Sidi Mohammed Ben Abdellah, B.P. 1796 (Atlas), 30000 Fès, Morocco, and Laboratoire de microbiologie médicale et moléculaire, Facultés de médecine et pharmacie, Université de Bourgogne, 7 Bd Jeanne d'Arc, 21000 Dijon, France. Received July 2, 2004; Revised Manuscript Received September 3, 2004

The synthesis of two picket bismuth(III) porphyrins is reported, and their crystal structures are compared. The influence of the nature of the pickets, as well as their number, is discussed in terms of stability, kinetics of metalation, structure, and distortion of the porphyrin. Unexpectedly, the results indicate that the coordination sphere of bismuth is not affected by different types of distortion nor is the stability of the complex. For both types of complexes, the X-ray crystallography revealed that a single arm is actually in direct interaction with the bismuth cation, thereby allowing further functionalization on the porphyrin core as the linkage with immunoglobulins or anti-rabbit antibodies (both noted IgG), which have been used in diagnostic or therapeutic applications.

INTRODUCTION

Bismuth coordination has long been represented by bismuth citrate because of its activity in the treatment of gastric ulcers (*1*, *2*). Very recently, the structure of colloidal bismuth subcitrate has also been investigated in dilute acidic medium (*3*). Additionally, compounds containing radioactive isotopes of bismuth such as ^{213}Bi are now under investigation due to the potential of α-emitting nuclides in radioimmunotherapy (*4*, *5*). However, a major issue remains the stable in vivo binding of the metal to the ligand without any leakage because it has been shown, for instance, that the binding constant of bismuth to human serum albumin is 10^{11} and that its binding to transferrin is even stronger (*6*). Different types of cyclic structures have also been investigated as potential chelates of bismuth. Among them, one can cite crown-ethers, tetraazamacrocyles and porphyrins (*7*−*11*). Until the early 1980s, few reports dealing with the complexation of bismuth into porphyrins had been published, presumably because of their instability (*12*). On the other hand, during the past decade, various studies led to a better understanding of the coordination of bismuth in porphyrins, whether in organic or aqueous medium (*13*−*17*). Our group has also investigated the potential of picket porphyrins as bismuth chelates, targeting on one hand a better knowledge of the coordination of bismuth and on the other hand the preparation of bifunctional linkers ready to be linked on biological proteins such as immunoglobulins (IgG). We have published the solid-state structures of two related porphyrins (*18*, *19*), as well as an evaluation of the length of the picket bearing an ethyl ester group (*20*).

In this study, we report the detailed preparation of these two bismuth porphyrins, a precise comparison of the corresponding X-ray structures, its implications for the transformation of the initial chelates in several analogous bifunctional linkers, and their reactivity toward IgG by means of different spacers.

EXPERIMENTAL PROCEDURES

General. Unless otherwise stated, the analytical facilities were provided by the Université de Bourgogne (C.S.M.) in Dijon. ^{1}H (500.13 or 300.14 MHz) and ^{13}C (125.05 or 75.47 MHz) NMR spectra were recorded on Bruker Avance DRX 500 or Avance 300 spectrometers and referenced with respect to the residual protonated solvents. Mass spectra were performed on a MS/MS ZABSpec TOF spectrometer at the University of Rennes I (C.R.M.P.O.). UV/vis spectra were recorded on a Varian Cary 1E spectrometer, λ/nm (10^{-3} ϵ, M^{-1} cm^{-1}). IR spectra were recorded on a Bruker IFS 66 spectrometer in cm^{-1}. All solvents (ACS for analysis) were purchased from Carlo Erba. THF was distilled over potassium metal. CH_2Cl_2 was used as received. Triethylamine was distilled over CaH_2. The starting materials were generally used as received (Acros, Aldrich) without any further purification. All reactions were performed under an argon atmosphere and monitored by TLC (silica, CH_2Cl_2/CH_3-OH). Column flash chromatography was performed on silica gel (Merck TLC-Kieselgel 60H, 15 μm). Immunoglobulins and anti-rabbit antibodies were purchased from Sigma.

Syntheses. α-*5,10,15,20-Tetrakis{2-[3-(ethoxycarbonyl)propionylamido] phenyl} Porphyrin,* ***1****.* αααα-Tetra-*ortho*-aminophenyl Porphyrin (TAPP) (0.2 g, 0.3 mmol) was dissolved in 20 mL of freshly distilled THF under argon. Ten equivalents of anhydrous Et_3N was added, and the mixture was cooled to 0 °C. Ethyl succinyl chloride (5 equiv) was then added, and the solution was stirred overnight. Solvent was evaporated to dryness, and the residue was dissolved in a minimum amount of CH_2-

* Corresponding author. Fax: 02 2323 5637. Tel: 02 2323 5856. E-mail: Bernard.Boitrel@univ-rennes1.fr.
† Université de Rennes1.
‡ Université Sidi Mohammed Ben Abdellah.
§ Université de Bourgogne.

10.1021/bc049844o CCC: $27.50 © 2004 American Chemical Society
Published on Web 10/30/2004

Cl_2 to be poured on a silica gel chromatography column. Product was eluted with a 0.1% CH_3OH/CH_2Cl_2 mixture and obtained in 93% yield (330 mg, 0.28 mmol). Microanalysis, $C_{68}H_{66}N_8O_{12}\cdot CH_3OH$, found (calcd): C, 68.25 (67.97); H, 4.44 (4.79); N, 9.33 (9.19)%. FAB-MS: *m/z* = 1187.8 $[M + H]^+$. FTIR (KBr, cm^{-1}): 1731 $(CO)_{ester}$, 1694 $(CO)_{amide}$. UV−vis (CH_2Cl_2, λ nm, 10^{-3} ϵ, M^{-1} cm^{-1}): 419 (337), 514 (20.9), 546 (5.8), 588 (6.7), 643 (3.7). ^1H NMR ($CDCl_3$, 323 K, 500 MHz): δ_H 8.86 (8H, s, β-pyr), 8.59 (4H, d, J = 7.1 Hz, aro), 8.00 (4H, d, J = 7.5 Hz, aro), 7.86 (4H, t, J = 7.6 Hz, aro), 7.55 (4H, t, J = 7.2 Hz, aro), 7.19 (4H, s, −NHCO), 3.44 (8H, br s, $-CH_2CH_3$), 2.18 (8H, t, J = 6.7 Hz, $-CH_2CH_2$), 1.70 (8H, br s, $-CH_2CH_2$), 0.79 (12H, br s, $-CH_2CH_3$), −2.59 (2H, s, −NH pyr). ^{13}C NMR ($CDCl_3$, 300 K, 125 MHz): δ_C 172.6, 170.1, 138.7, 135.4, 132.1, 130.3, 123.9, 122.9, 115.5, 60.7, 31.5, 29.0, 14.1.

α-*5,10,15,20-Tetrakis{2-[3-(ethoxycarbonyl)propionylamido] phenyl} Porphyrin Bismuth(III) Nitrate,* ***1BiNO$_3$***. In a 50 mL flask, **1** (26 mg, 0.02 mmol) was dissolved in 7 mL of pyridine. This solution was warmed to 55 °C before $Bi(NO_3)_3\cdot 5H_2O$ (100 mg, 0.2 mmol) was added. After the solution was heated for 2 h, the solvent was evaporated, and the residue was dissolved in a minimum amount of CH_2Cl_2 to be poured on a silica gel chromatography column. The product was eluted with a 1.2% CH_3OH/CH_2Cl_2 mixture and obtained in 85% yield (25 mg, 0.017 mmol). Microanalysis, $C_{68}H_{64}BiN_9O_{15}\cdot 2H_2O$, found (calcd): C, 55.16 (54.73); H, 4.47 (4.59); N, 8.27 (8.45)%. FAB-MS: *m/z* = 1393.8 $[M - NO_3]^+$. UV−vis (CH_2Cl_2, λ nm, 10^{-3} ϵ, M^{-1} cm^{-1}): 354 (42.4), 472 (176.9), 598 (9.8), 644 (8.3). FTIR (KBr, cm^{-1}): 1732 $(CO)_{ester}$, 1695 $(CO)_{amide}$, 1384 (NO_3), 991 (Bi−Np). ^1H NMR ($CDCl_3$, 300 K, 500 MHz): δ 9.24 (8H, s, β-pyr), 8.68 (4H, br s, aro), 8.22 (3H, br s, −NHCO), 8.13 (1H, br s, −NHCO), 7.89 (4H, m, aro), 7.90 (4H, t, aro), 7.56 (4H, br s, aro), 3.46 (2H, br s, $-\mathbf{CH_2}CH_3$), 3.32 (6H, br s, $-\mathbf{CH_2}CH_3$), 2.04 (8H, br s, $-CH_2CH_2$), 1.92 (8H, br s, $-CH_2CH_2$), 0.96 (3H, br s, $-CH_2\mathbf{CH_3}$), 0.87 (9H, s, $-CH_2\mathbf{CH_3}$). ^{13}C NMR ($CDCl_3$, 300 K, 125 MHz): δ_C 173.5, 170.8, 149.3, 140.4, 134.9, 133.5, 131.3, 130.6, 123.6, 123.1, 122.7, 119.3, 60.8, 31.5, 29.5, 14.1.

α-*5,10,15-Tris(2-(acetylamido)phenyl)-*α*-20-{2-[3-(ethoxycarbonyl)propionylamido] phenyl} Porphyrin,* ***3***. Compound **2** (0.37 g, 0.4 mmol), prepared as previously described, was dissolved in 30 mL of freshly distilled THF under argon. Ten equivalents of anhydrous Et_3N (0.3 mL, 4 mmol) was added, and the mixture was cooled to 0 °C. Ethyl succinyl chloride (21.60 μL, 0.15 mmol) was then added, and this mixture was stirred overnight. The solvent was evaporated to dryness, and the residue was dissolved in a minimum amount of CH_2Cl_2. The compound was purified by chromatography on a silica gel column. The product was eluted with a 0.8% CH_3OH/CH_2Cl_2 mixture and obtained in 92% yield (407 mg, 0.37 mmol). Microanalysis, $C_{56}H_{48}N_8O_6\cdot CH_3OH\cdot H_2O$, found (calcd): C, 70.02 (69.92); H, 5.14 (5.56); N, 10.83 (11.44)%. FAB−HRMS: calcd *m/z* = 929.3775 $[M + H]^+$, found 929.3763. FTIR (KBr, cm^{-1}): 1741 $(CO)_{ester}$, 1679 $(CO)_{amide}$. UV−vis (CH_2Cl_2, λ nm, 10^{-3} ϵ, M^{-1} cm^{-1}): 419 (337.4), 514 (17.5), 547 (4.4), 587 (5.5), 643 (1.6). ^1H NMR ($CDCl_3$, 300 K, 300 MHz): δ_H 8.87 (8H, s, β-pyr), 8.71 (4H, br s, aro), 7.8 (8H, br s, aro), 7.55 (4H, br s, aro), 6.97 (4H, s, −NHCO), 3.55 (2H, q, J = 6.4 Hz, $-\mathbf{CH_2}CH_3$), 2.19 (2H, br s, $-CH_2CH_2-$), 1.60 (2H, br s, $-CH_2CH_2-$), 1.30 (9H, br s, $-CH_3$), 0.87 (3H, t, J = 6.4 Hz, $-CH_2\mathbf{CH_3}$), −2.71 (2H, s, −NH pyr). ^{13}C NMR ($CDCl_3$, 300 K, 75 MHz): δ_C 135.1, 130.1, 123.2, 123.4, 121.9, 121.5, 80.0, 77.3, 60.6, 31.1, 28.5, 24.1.

α-*5,10,15-Tris(2-(acetylamido)phenyl)-*α*-20-{2-[3-(hydroxycarbonyl)propionylamido]phenyl} Porphyrin,* ***4***. Compound **3** (100 mg, 0.09 mmol) was dissolved in THF to which was added KOH in ethanol (0.09 mmol in 5 mL). The mixture was heated at 50 °C for 4 h, cooled, and evaporated. The crude product was filtered in ethylic ether dissolved in water. Upon addition of HCl (6 M), precipitation occurred. The solid was neutralized by washing with water. The yield was quantitative. Microanalysis, $C_{54}H_{44}N_8O_6\cdot CH_3OH\cdot H_2O$, found (calcd): C, 69.58 (69.46); H, 4.87 (5.30); N, 11.42 (11.78)%. HR-MS (ESI): *m/z* 939.3017 $[(M + K)^+$, 100%]. ^1H NMR (500 MHz, DMSO-d_6, 298 K): δ_H 11.85 (s, 1H, −COOH), 8.81 (br s, 2H, −NHCO), 8.78 (br s, 2H, −NHCO), 8.70 (s, 8H, β-pyr), 8.14 (d, J = 7.5 Hz, 4H, aro), 8.10 (d, J = 7.5 Hz, 2H, aro), 7.94 (d, J = 7.0 Hz, 4H, aro), 7.83 (t, J = 8 Hz, 4H, aro), 7.57 (t, J = 6.5 Hz, 4H, aro), 1.99 (t, J = 5 Hz, 2H, $-CH_2CH_2-$), 1.64 (br s, 2H, $-CH_2CH_2-$), 1.24 (s, 3H, $-CH_3$), 1.22 (s, 6H, $-CH_3$), −2.72 (s, 2H, −NH pyr).

α-*5,10,15-Tris(2-(acetylamido)phenyl)-*α*-20-{2-[3-(carboxylate)propionylamido]phenyl} Porphyrin Bismuth(III),* ***4Bi***. The procedure described for preparation of **1BiNO$_3$** was applied without the silicagel chromatography column. The reaction was instantaneous with 1.1 equiv of bismuth nitrate in pyridine at room temperature. The compound was precipitated in a THF/ethylic ether mixture. HR-MS (ESI): *m/z* 1129.2863 $[(M + Na)^+$, 100%]. UV−vis (CH_2Cl_2): λ_{max}/nm (log ϵ, dm^2 mol^{-1} cm^{-1}): 350 (4.8), 472 (13.5), 598 (1.7), 646 (1.5). FTIR (of crystals, KBr, cm^{-1}): 1670 (CO); 990 ρ(Bi−Np). ^1H NMR (500 MHz, DMSO-d_6, 300 K): δ_H 9.03 (d, J = 4.5 Hz, 2H, β-pyr), 9.03 (d, J = 4.5 Hz, 2H, β-pyr), 8.99 (d, J = 8 Hz, 6H, pyr), 8.97 (d, J = 5 Hz, 2H, β-pyr), 8.89 (d, J = 5 Hz, 2H, β-pyr), 8.72 (br s, 4H, aro), 8.55 (t, J = 7 Hz, 3H, pyr), 8.33 (br s, 1H, aro), 8.33−8.26 (m, 2H, aro), 8.07 (t, J = 6.6 Hz, 1H, aro), 7.99 (t, J = 7.8 Hz, 6H, pyr), 7.90 (m, 3H, aro), 7.73 (br s, 1H, aro), 7.45 (br s, 4H, −NHCO), 7.36 (t, J = 7 Hz, 2H, aro), 7.16 (m, 2H, aro), 1.87 (br s, 2H, $-CH_2-$), 1.63 (br s, 2H, $-CH_2-$), 1.49 (s, 9H, $-CH_3$).

α-*5,10,15-Tris{2-[3-(ethoxycarbonyl)propionamido]-phenyl)}:* α-*20-(2-Aminophenyl) Porphyrin,* ***5***. Under argon, 0.37 g (0.4 mmol) of porphyrin single trityl TAPP (TrTAPP) was dissolved in 30 mL of THF. Ten equivalents of triethylamine and 0.23 mL (1.6 mmol) of ethyl succinyl chloride were added. The mixture was stirred overnigth at room temperature. It was evaporated and dissolved again in methylene chloride. Two milliliters of trifluoroactic acid was added to this solution. After 30 min of stirring, the solution was neutralized with gaseous ammonia, purified by silica gel chromatography column, and eluted with 0.8% $MeOH/CH_2Cl_2$ (yield = 76%, 320 mg, 0.30 mmol). Microanalysis, $C_{62}H_{58}N_8O_9\cdot CH_3OH$, found (calcd): C, 69.53 (69.34); H, 4.61 (4.73); N, 10.27 (10.27)%. MALDI-TOF-MS: *m/z* = 1059.1 $[M + H]^+$. UV−vis (CH_2Cl_2): λ_{max}/nm (log ϵ, dm^2 mol^{-1} cm^{-1}): 419 (289); 514 (18.4); 548 (4.7); 588 (5.7); 643 (1.8). ^1H NMR (500 MHz, $CDCl_3$, 323 K): δ_H 9.01 (d, J = 4.5 Hz, 2H, β-pyr); 8.85 (s, 6H, β-pyr); 8.67 (d, J = 8.1 Hz, 2H, aro); 8.61 (d, J = 7.9 Hz, 1H, aro); 8.05 (d, J = 7.0 Hz, 1H, aro); 8.01 (d, J = 7.0, 2H, aro); 7.90−7.87 (m, 4H, aro); 7.66 (td, J = 1.5 Hz, J = 7.9 Hz, 1H, aro); 7.57 (t, J = 7.0 Hz, 1H, aro); 7.55 (t, J = 7.3 Hz, 2H, aro); 7.22 (td, J = 1.1 Hz, J = 7.4 Hz, 1H, aro); 7.17 (dd, J = 0.8 Hz, J = 8.1 Hz, 1H, aro); 7.09 (s, 3H, −NHCO); 3.64 (large s, 2H, $-NH_2$); 3.53 (m, 4H, $-\mathbf{CH_2}CH_3$); 3.36 (br q, J = 6.7 Hz, 2H, $-\mathbf{CH_2}CH_3$); 2.28−2.13 (m, 6H, $-CH_2CH_2$); 1.70−1.63 (m, 6H, $-CH_2CH_2$); 0.86 (t, J = 6.7 Hz, 6H, $-CH_2\mathbf{CH_3}$); 0.75 (t, J = 6.7 Hz, 3H, $-CH_2\mathbf{CH_3}$); −2.65 (s, 2H). ^{13}C NMR ($CDCl_3$, 300 K, 125 MHz): δ_C 172.5; 170.0; 146.8; 138.7;

135.4; 132.0; 131.8; 130.5; 130.2; 126.5; 123.7; 122.4; 122.3; 118.3; 117.9; 115.9; 115.0; 60.7; 31.7; 29.1; 29.0; 14.2; 14.1.

α-*5,10,15-Tris{2-[3-(ethoxycarbonyl)propionamido]-phenyl}:* α-*20-[2-(Acrylamido)phenyl] Porphyrin,* ***6***. Porphyrin **5** (110 mg, 0.1 mmol) was dissolved in 20 mL of THF under argon at room temperature. Triethylamine (0.2 mL) and acryloyl chloride (25 μL) were added to this solution. After 12 h of stirring, the mixture was evaporated, and the compound was purified by chromatography on a silica gel column. The desired compound was obtained in a 78% yield (78 mg, 0.07 mmol). Microanalysis, $C_{62}H_{58}N_8O_9 \cdot CH_3OH$, found (calcd): C, 68.66 (68.35); H, 5.45 (5.82); N, 9.26 (9.52)%. FAB-MS: $m/z = 1113.0$ $[M]^{+\bullet}$. UV−vis (CH_2Cl_2): λ_{max}/nm (log ϵ, $dm^2\ mol^{-1}\ cm^{-1}$): 419 (350.8); 513 (19.6); 547 (4.6); 587 (6.0); 642 (1.6). ^1H NMR (500 MHz, $CDCl_3$, 323 K): δ_H 8.88 (m, 8H, β-pyr); 8.74 (d, $J = 7.3$ Hz, 1H, aro); 8.62 (d, $J = 7.9$ Hz, 3H, aro); 8.02 (m, 4H, aro); 7.87 (m, 4H, aro); 7.57 (m, 4H, aro); 7.22 (s, 1H, −NHCO); 7.15 (s, 3H, −NHCO); 5.9 (d, $J = 16.8$ Hz, 1H, $-CHCH_2$); 5.2 (large s, 1H, $-CHCH_2$); 5.1 (d, $J = 16.8$ Hz, 1H, $-CHCH_2$); 3.42 (large s, 6H, $-CH_2CH_3$); 2.19 (m, 6H, $-CH_2CH_2$); 1.73 (large s, 6H, $-CH_2CH_2$); 0.78 (m, 9H, $-CH_2CH_3$); −2.55 (s, 2H). ^{13}C NMR ($CDCl_3$, 300 K, 125 MHz): δ_C 172.4; 169.9; 163.3; 147.5; 138.8; 135.4; 132.1; 130.9; 130.2; 127.4; 123.8; 122.7; 115.6; 60.5; 31.6; 29.1; 14.0.

α-*5,10,15-Tris{2-[3-(ethoxycarbonyl)propionamido]-phenyl}:* α-*20-{2-[3-(Carboxy)propionamido]phenyl} Porphyrin,* ***7***. Porphyrin **5** (140 mg, 0.13 mmol) was heated at 50 °C in ethanol. Succinic anhydride (27 mg, 0.26 mmol, 2 equiv) was added to this solution. The mixture was stirred for 48 h, an additional 2 equiv of succinic anhydride was added, and the mixture was stirred again for 3 h. The desired compound was purified by chromatography on a silica gel column and eluted with 6% of MeOH/CH_2Cl_2 (yield = 85%, 170 mg, 0.15 mmol). Microanalysis, $C_{66}H_{62}N_8O_{12} \cdot CH_2Cl_2$, found (calcd): C, 64.48 (64.68); H, 5.05 (5.18); N, 8.58 (9.01)%. FAB-MS: $m/z = 1159.0$ $[M]^{+\bullet}$. ^1H (500 MHz, $CDCl_3$, 323 K): δ_H 11.9 (large s, 1H, −OH); 8.84 (s, 8H, β-pyr); 8.5 (large s, 2H, aro); 8.44 (d, $J = 6.8$ Hz, 2H, aro); 8.05 (d, $J = 6.1$ Hz, 2H, aro); 8.00 (d, $J = 7.1$ Hz, 2H, aro); 7.86 (t, $J = 7.3$ Hz, 4H, aro); 7.80 (large s, 4H, −NHCO); 7.58 (m, 4H, aro); 4.02 (large s, 2H, $-CH_2CH_3$); 3.64 (large s, 2H, $-CH_2CH_3$); 3.57 (large s, 2H, $-CH_2CH_3$); 2.17 (t, $J = 6.2$ Hz, 2H, $-CH_2CH_2$); 2.04 (large s, 6H, $-CH_2CH_2-$); 1.66 (large s, 4H, $-CH_2CH_2$); 1.61 (large s, 4H, $-CH_2CH_2$); 0.96 (s, 3H, $-CH_3$); 0.89 (s, 6H, $-CH_3$); −2.73 (s, 2H). ^{13}C NMR ($CDCl_3$, 300 K, 125 MHz): δ_C 172.9; 170.8; 170.2; 138.8; 138.6; 135.4; 132.1; 130.1; 124.3; 123.9; 123.2; 115.7; 60.9; 31.1; 29.2; 28.9; 14.1.

Cross-Linking Reactions with the IgG. The employed IgG was provided from an antiserum (whole molecule) developed in goat using rabbit IgG as the immunogen (Sigma product no. R-1131). The antiserum has been treated to remove lipoproteins. Only the protein concentration was determined (the antiserum contains 17.2 mg of specific IgG per milliliter). The F(ab)′ fragment was obtained after reduction of the disulfide bridges of F(ab)′2 fragment (Sigma product no. R-9130) resulting from pepsin-digested antiserum (Sigma product no. R-1131).

Different solutions were prepared to be employed in the linking experimental procedures.

Buffered Solution A. The solution contains 0.1 M sodium phosphate dihydrate ($NaH_2PO_4 \cdot 2H_2O$) and 5 mM ethylenediamine tetraacetic acid dihydrate ($H_4EDTA \cdot 2H_2O$) in distilled water. The pH of the solution was tuned to 6 by addition of sodium hydroxide.

Buffered Solution B. The solution contains 0.1 M sodium phosphate dihydrate ($NaH_2PO_4 \cdot 2H_2O$), 1 mM ethylenediamine tetraacetic acid dihydrate ($H_4EDTA \cdot 2H_2O$), and 1 mM sodium chloride in distilled water. The pH of the solution was tuned to 7.5 by addition of hydrochloric acid.

Buffered Solution C. The solution contains 50 mM sodium tetraborate decadihydrate ($Na_2B_4O_7 \cdot 10H_2O$) and 5 mM ethylenediamine tetraacetic acid dihydrate ($H_4EDTA \cdot 2H_2O$) in distilled water. The pH of the solution was tuned to 8.3 by addition of diluted chlorohydric acid.

N-Succinimidyl(4-iodoacetyl)aminobenzoic Acid (SIAB) Solution. SIAB (1.4 mg, 0.003 mmol) was dissolved in 1 mL of DMSO.

Solution of Porphyrin ***5***. Porphyrin **5** (1.2 mg) was dissolved in 0.12 mL of DMSO to obtain a concentration of 9.44 mM.

Solution of Porphyrin ***6***. Porphyrin **6** (3.7 mg, 50 equiv relative to the antibody) was dissolved in 0.38 mL of DMSO to obtain a concentration of 8.5 mM.

Coupling Reaction of Porphyrin 5 with Fab′ Fragments Activated with SIAB, Fab′−SIAB−5. SIAB solution (10 μL, 5 equiv/protein) was added to the solution of reduced IgG. The mixture was then incubated in the dark at room temperature during 1 h. This solution of the activated Fab′ was purified by gel filtration chromatography over a Sephadex G25 column and eluted with buffered solution C. To the solution of purified Fab′−SIAB, 38 μL of the solution of **5** (50 equiv/protein) was added. The mixture was incubated for 1 h in the dark at room temperature to allow complete coupling of the Fab′. The solution of the final conjugate was purified again by gel filtration chromatography over a Sephadex G25 column and eluted with buffered solution C. A second chromatography did not change the ratio porphyrin/antibody.

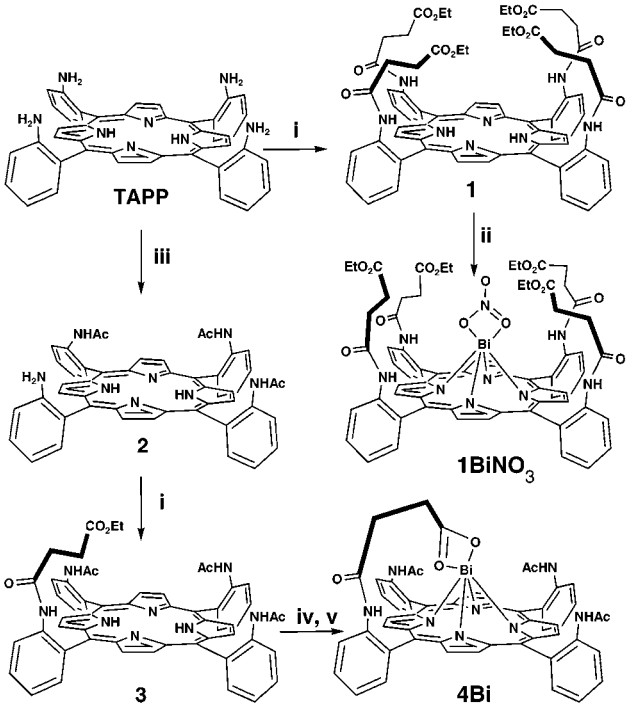
Coupling Reaction of Porphyrin 6 with a Reduced IgG Fragment, Fab′−6. As a test reaction, the same porphyrin has been coupled with thiophenol, and the resulting porphyrin led to consistent analytical data. In a hemolysis tube, 2.5 mg of IgG was dissolved in 1 mL of buffered solution A. 2-Mercaptoethanolamine (MEA, 6.6 mg) was added, leading to a MEA concentration of 50 mM. The mixture was then stirred at 37 °C for 1 h, 30 min. Buffered solution B (2.5 mL) was added, and the Fab′ fragments were purified by gel filtration chromatography over a Sephadex G25 column (NAP-10 Pharmacia, Sweden). The reduced IgG were dissolved in 2.5 mL of buffered solution B, and 100 μL of solution of porphyrin **6** was added; then the mixture was stirred at room temperature. The conjugate was purified by gel filtration chromatography over a Sephadex G25 column and eluted with buffered solution B.

Coupling Reaction of Porphyrin 7 with Anti-Rabbit Antibodies, Ab−7. Porphyrin **7** was dissolved in THF together with *N*-hydroxysuccinimide and dicyclohexylcarbodiimide (DCC) under an argon atmosphere. After 24 h of stirring, the reaction mixture was filtered to remove the precipitate due to formation of DCU, evaporated and used without any further purification. The activated porphyrin was dissolved in DMSO, and 50 equiv/protein was employed. The same experimental procedure as above was applied.

RESULTS AND DISCUSSION

Obviously, the porphyrinic macrocycle is attractive owing to its coordination properties but also because it

Scheme 1: Synthetic Pathway for the Preparation of Succinylamido Picket Porphyrins[a]



[a] Reagents and conditions: (i) $ClCO(CH_2)_2CO_2Et$ (5 equiv for **1** or 1.1 equiv for **3**), NEt_3, THF; (ii) $Bi(NO_3)_3{\cdot}5H_2O$ (10 equiv), 55 °C, pyridine, 2 h; (iii) CH_3COCl (3 equiv), NEt_3, THF; (iv) KOH, EtOH, 55°C → **4**; (v) $Bi(NO_3)_3{\cdot}5H_2O$ (1.2 equiv), rt, pyridine, 10 min.

represents a relatively rigid and disk-shaped structure suitable as a framework to build up new types of artificial chelators. Furthermore, meso-ortho-substituted phenyl porphyrins, owing to their possible atropisomerization, provide another interesting property that allows preorganization on a specific side of the macrocycle. We have taken advantage of this particularity by performing very simple reactions on αααα-tetra-*ortho*-aminophenyl porphyrin (TAPP). The initial idea consisted in supplementing the porphyrin by four ester pickets, assuming that one or several pickets would bend over the porphyrin ring to complete and satisfy the coordination sphere of the metal, making it inaccessible to dissociation (*21*). Besides, in compound **1BiNO$_3$**, the picket fence could protect the metal from any intermolecular interaction. In a second step, we have prepared the single carboxylic acid picket porphyrin **4**, keeping in mind that, bismuth being trivalent, the carboxylate function would lead to a neutral complex. The synthesis of these two ligands is detailed in Scheme 1.

Where porphyrin **1** bearing four ethyl succinyl pickets (4ES) is obtained by a straigthfoward acylation of the αααα atropisomer of TAPP with ethyl succinyl chloride, the preparation of **4** requires several extra steps to reach the single succinic acid compound (1SA). Indeed, the first step of the synthesis requires the protection of three amino groups of TAPP with acetyl chloride in dry THF. The optimization of the yield (55%) toward the three-protected porphyrin **2** requires the use of 3 equiv of the acylation reagent, and the separation of undesired compounds such as the tetra- and diacylated porphyrins was performed on a silica gel chromatography (*20*). The remaining amino group was functionalized with 1.1 equiv of ethyl succinyl chloride to obtain **3** (89%) the ester group of which was hydrolyzed with KOH, leading to **4**. So far, we performed the metal insertion by heating at 50 °C

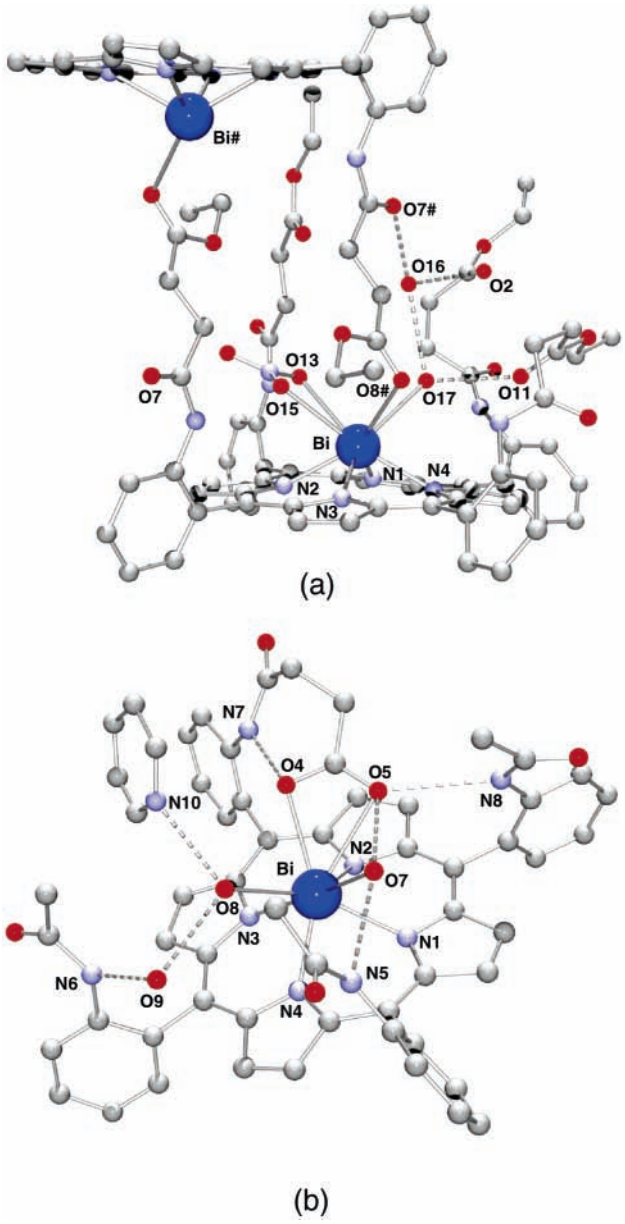


Figure 1. Ball and stick representation of the crystal structure of (a) **1BiNO$_3$** and (b) **4Bi**.

the free-base porphyrin with bismuth nitrate in pyridine. Actually, we found out that this complexation is achieved after stirring for 10 min at room temperature. Both complexes led to an X-ray structure, and the detailed comparison of these structures (Figure 1) is instructive both in terms of differences and similarities.

In both complexes, the Bi(III) is eight coordinate with an approximate square antiprismatic geometry. One square is formed by the four nitrogen atoms from the porphyrin, the other one being composed of four oxygen atoms. Two of them come from the bidentate counteranion, whether nitrate in **1BiNO$_3$** or carboxylate for **4Bi**. The third bound oxygen atom comes from a water molecule included in a hydrogen bonding net: O17 in **1BiNO$_3$**; O7 in **4Bi**. In **1BiNO$_3$**, the fourth bound oxygen comes from a carbonyl oxygen atom O8# of the terminal ester group belonging to an arm attached to a symmetrically related macrocycle, forming in this way, a centrosymmetric dimer. For **4Bi**, which exhibits a mononuclear structure—the first major difference between the two structures, a second water molecule represents the fourth oxygen atom O8. For both compounds, only one

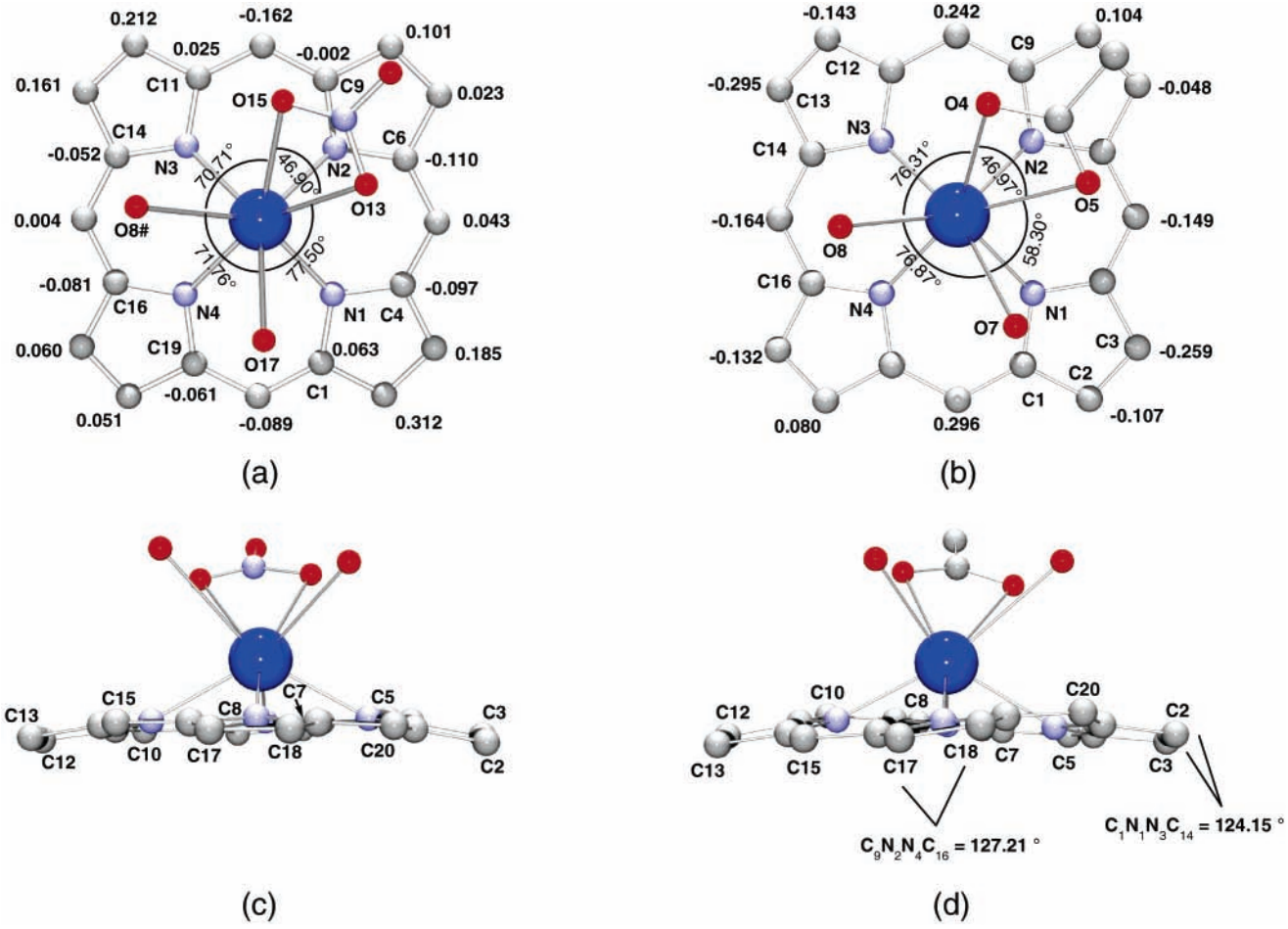


Figure 2. Ball and stick polyhedron coordination top views of (a) **1BiNO$_3$** and (b) **4Bi** and side views of (c) **1BiNO$_3$** and (d) **4Bi**. All the deviations refer to the mean porphyrin plane.

arm is in direct interaction with the metal, either in an intermolecular fashion in **1BiNO$_3$** or in an intramolecular scorpionate-like coordination in **4Bi**. Indeed, for the dimer, two other ester pickets are taking part to the hydrogen bonding net including the water molecule O17. But the fourth picket seems to have no function in the stability of the complex: this detail is worth underlining and will be discussed later in terms of further functionalization of the ligand. In the monomer, the amide function from the three acetyl pickets belongs to the hydrogen bonding net, which also includes the two bismuth-bound water molecules O7 and O8. However, the major driving force of this structure is undoubtely the carboxylate group, which binds in a bidentate fashion the metal, occupying two coordination sites and leading to a neutral complex. In organic solvents, this tailed carboxylate group allows porphyrin **4** to complex bismuth almost instantaneously. This represents a significant improvement in the kinetics of metalation relative to its ester picket analogue for which heating the ligand at 50 °C was necessary to obtain a complete metalation (*20*).

In both structures, the bismuth cation is largely displaced out of the N_4 plane of the porphyrin, 1.125 and 1.145 Å in **1BiNO$_3$** and **4Bi**, respectively. In the binuclear structure of **1BiNO$_3$**, the intermetallic distance is 10.61 Å. Our preliminary study was in favor of a monomeric structure in solution (*20*). However, this conclusion was reached for the compound dissolved in an organic solvent. In terms of therapeutic applications, and so in aqueous medium, if this binuclear edifice was maintained, it would be possible to deliver not one but two radioactive nuclei per complex. This would represent a simple and efficient method to directly increase the amount of α particles around the targeted cells.

Two other significant differences between these two complexes are exhibited in Figure 2, which outlines the coordination sphere of bismuth (panels a and b), as well as a side view of the porphyrin plane (panels c and d). The first one concerns the antiprismatic coordination sphere, which is almost regular in **1BiNO$_3$** but severly distorted in **4Bi**. For example, the angle in the dimer between O13−Bi and Bi−O17 is 77.5°, but the angle is only 58.3° in the monomer between O5−Bi and Bi−O7. A possible explanation for this distortion in which a labile water molecule takes part could be that O7, to be stabilized, requires being equidistant between O5 and N5, but the length of the hydrogen bonds O5−O7 (2.821 Å) and O7−N5 (3.053 Å) are not very consistent with this explanation. In fact, the angle between the oxygen atom−Bi bonds of the bidentate ligand is the only one to be identical in the two complexes.

The second main distortion to be observed concerns the porphyrin core itself. Indeed, porphyrins are known to adopt various conformations according to the bound metal and the steric hindrance or the electronic properties of its substituents. Chiefly, to identify this distortion, the displacement of the four meso carbon atoms, as well as the eigth β-pyrrolic carbon atoms, in respect to the 24 atom mean porphyrin plane is calculated. The mean porphyrin plane refers to the least-squares mean plane calculated for the 24 atom macrocycle and not that for the four coordinating nitrogen atoms, the metal being not included in the calculations. The Cα−N−N−Cα torsion angle is also taken into account to quantify the degree

of ruffling. According to these displacements, it appears that the porphyrin in the dimer is domed (*22*, *23*), whereas it is both ruffled (*24*, *25*) and saddled (*26*, *27*) in the monomer. The former distortion is quite usual in most of the previously reported X-ray structures of bismuth porphyrins (*15*, *17*) and could be attributed to the out-of-plane coordination of the metal itself. Typically, the domed conformation is only observed when the porphyrin is coordinated to a large central metal ion, usually with one or more axial ligands. Indeed, in Figure 2a, it is clear that all the β carbons are on one side (below with a positive displacement) of the porphyrin mean plane where the meso carbons are in or near the plane. All the α carbons but two, C1 and C11, and the nitrogens are located above the mean porphyrin plane with negative displacements, on the same side as the metal (*28*).

On the other hand, the unusual mixed conformation of the monomer is presumably due to the nonsymmetrical substitution pattern of the porphyrin. Indeed, the carbon atoms in the opposite meso positions (5,15 and 10,20) are not located in the 24-atom least-squares plane but above or below. More precisely, the deviations (Cm) from the mean porphyrin plane of these atoms are 0.296, −0.149, 0.242, and −0.164 Å, leading to an average absolute value of 0.213 Å. This is expected for a ruffle conformation and not for a saddled macrocycle. But in the former conformation, the β carbons of the same pyrrolic subunit should be on opposite sides of the porphyrin mean plane. This distribution is not regularly observed for **4Bi** because C2 and C3 as well as C12 and C13 are located on the same side of the macrocyle. However, the torsion angles C9N2N4C16 and C1N1N3C14 are found to be equal to 127.21° and 124.15°, respectively, representing the signature of a ruffled macrocycle. Moreover, the tilts of the pyrrole planes against each other are 8° and 17°, confirming clearly this significant ruffling. This conformation has been found in porphyrins with small metal ions such as Ni(II) owing to the Ni−N bond shortening (*29*, *30*) but to the best of our knowledge was unkown for a large cation with a crystalline radius of 1.31 Å (for a coordination of 8) (*31*). These two major distortions seem also to be the result of a too short length of the coordinating arm because the latter has to pull the meso carbon on which it is tethered to be able to coordinate the metal. Nevertheless, it is worth noting that **4Bi**, bearing a single coordinating picket and exhibiting significative distortions, is as stable as **1BiNO$_3$** in organic solvents. Of course, this situation may be altered in aqueous medium because our final objective remains to link these chelates on a protein. A direct consequence of this observation is that by replacing the succinyl motif by a longer coordinating arm it should be possible to obtain an even more stable complex with a planar, or at least a less distorted, porphyrin core.

In light of both X-ray structures, we have verified that this type of porphyrin could be further functionalized without interfering with the key features of the coordination sphere. This is the reason, as a test reaction, we have chosen to transform ligand **1** in a bifunctional linker (*32*) ready to react with immunoglobulins (IgG). Indeed, for future applications with the radioactive isotope, the free carrier, and not the metalled complex, will be attached to the IgG.

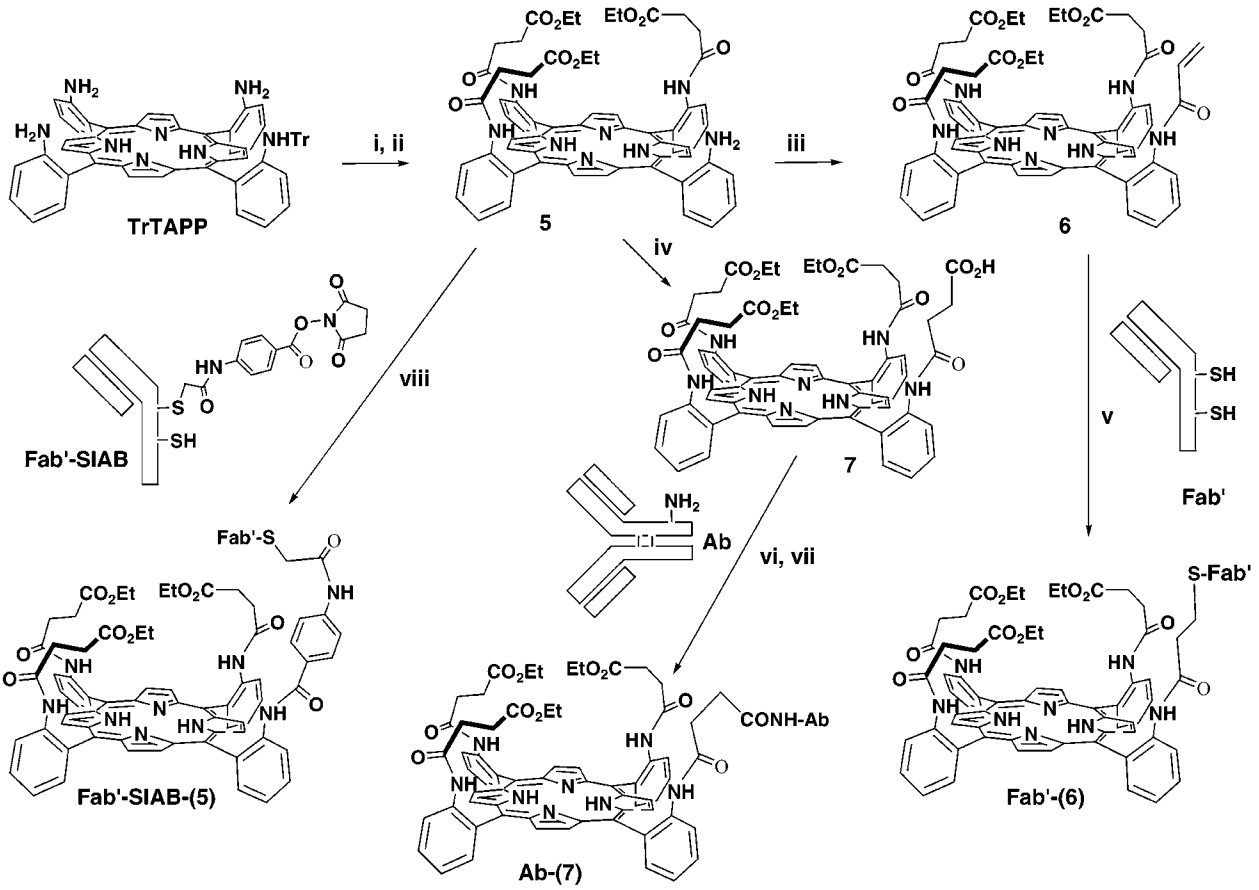
As earlier mentioned, in **1BiNO$_3$**, only one picket does not seem to be decisive in the stability of the complex. We reasoned that this ethylsuccinyl picket could be replaced by a linker properly designed without perturbing considerably the coordination properties of the ligand. The synthesis consists of sparing one amino function of TAPP by employing the single trityl TAPP (TrTAPP), prepared as previously described (*33*). The further steps then introduce a reactive function for either primary amines of the lysine residues or thiol groups from the cysteine and particularly those obtained after reduction of the disulfide bridges of immunoglobulins, which leads to the Fab′ fragments (Scheme 2) (*34*). The reaction targeting coupling with thiol groups of the Fab′ was performed from the reduced fragment of the IgG obtained according to the usual methodology with 2-mercaptoethanolamine. Thus, porphyrin **5**, easily synthesized from TrTAPP and bearing only three succinyl pickets, was transformed in porphyrin **6** and porphyrin **7** by reaction with acryloyl chloride and succinic anhydride, respectively. In the first case, the sulfhydryl groups of the reduced IgG are known to react with the acrylamide function according to a 1,4 addition creating a stable thioether bond (*34*). In the second case, the resulting porphyrin **7** bearing a four-carbon spacer was activated by the *N*-hydroxysuccinimide (NHS) method and then coupled with the complete IgG via formation of amide bonds. Because of the lack of precise methods such as γ emission counting, only a rough evaluation of the porphyrin/IgG ratios was possible. Indeed, because the porphyrin absorbs around 420 nm with an average ϵ of 350 000 M^{-1} cm^{-1} and the protein (IgG) absorbs at 280 nm with an ϵ = 195 000 M^{-1} cm^{-1}, this evaluation was performed by UV−visible spectroscopy. This methodology has already been successfully employed with a sulfonated aluminum phthalocyanine bearing a 6-aminohexanoic acid spacer and a murine anti-CEA monoclonal antibody (*35*). Additionally, in our case, it is also expected to be convenient for future in vivo studies with the bismuth complex, which absorbs at 470 nm.

A typical UV−visible spectrum is illustrated by the coupling of porphyrin **7** to an antibody (Figure 3). The molar protein concentration, C_{ab}, and molar porphyrin concentration, C_p, are given by the following equations: $A_{280\ nm}/(l\epsilon_{ab}) = C_{ab}$ and $A_{428\ nm}/(l\epsilon_p) = C_p$. This calculation allows one to obtain an approximate number of dye molecules per antibody molecule.

We first investigated the coupling of porphryin **6** to Fab′ fragments. With an excess of 50 equiv of this porphyrin and ϵ_p = 350 800 M^{-1} cm^{-1}, only 40% of the Fab′ were found to be conjugated to the porphyrin. When the excess of porphyrin was decreased to 25 equiv, only 15% of the Fab′ were labeled. The same type of measurement was performed to evaluate the coupling between IgG and porphyrin **7** according to the activated ester method, but the result was as disapointing as that for the previous one. Indeed, only 20% of the protein was linked to the porphyrin. In fact, although the two reactions cannot be compared, these two results are consistent with one another and could be explained by a too short length of the spacers (3−4 atom-length). Indeed, it has been reported that the approach of the reactive functions from the antibodies can be sensitive to the steric hindrance of the chelate (*36*).

This prompted us to reinvestigate this conjugation by using a commercially available spacer. We have chosen the *N*-succinimidyl(4-iodoacetyl)aminobenzoic acid (SIAB) for two reasons. First, the length of this spacer is greater than the two previous ones with a value of 10.6 Å. Second, the activated ester function of the spacer allows the direct coupling of the Fab′ on porphyrin **5** without any other reaction or purification step on it. The iodoactetyl function of this heterobifunctional cross-linker will react with the thiol groups of the reduced IgG (Fab′). According to the same method, the ratio C_p/C_{ab} is found to equal 1.5.

Scheme 2: Synthesis of Different Bifunctional Ligands Related to 1 and Their Coupling with an Antibody (Ab) or Reduced Antibody (Fab′)[a]



[a] Reagents and conditions: (i) $ClCO(CH_2)_2CO_2Et$ (4 equiv), NEt_3, THF; (ii) TFA, CH_2Cl_2; (iii) $ClCOCH{=}CH_2$ (1.5 equiv), NEt_3, THF; (iv) succinic anhydride (2 equiv), EtOH, 50 °C, 48 h; (v) reduced antibody (Fab′); (vi) NHS/DCC; (vii) antibody; (viii) SIAB-activated reduced antibody.

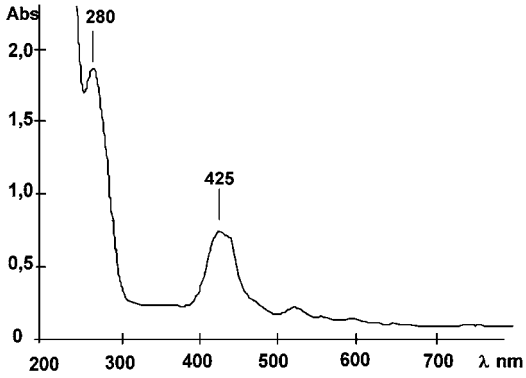


Figure 3. UV−vis spectrum of the immunoconjugate **Ab**−**7**.

If one considers that the Fab′ is completely labeled, 50% is attached to one porphyrin whereas the other 50% is doubly marked. This third coupling test reaction clearly indicates that with a chelate such as picket porphyrins, the length of the linker becomes critical in comparison with other ligands such as nonaromatic tetraazamacrocycles.

CONCLUSIONS

In summary, we have shown that both bismuth complexes for which the solid-state structures are known are valid molecules for further investigations in radioimmunotherapy applications. For the dimeric complex, three pickets among the four available are included in the structure of the complex. Interestingly, if the dimeric structure is maintained in aqueous medium with the hot radioisotope, this type of edifice could carry two radioactive nuclei instead of one, thereby delivering a higher dose of high linear energy emission. For the monomer, the scorpionate built-in tail guarantees the neutrality of the complex without any exogenous counteranion and a faster complexation of the bismuth. Various bifunctional chelates have been synthesized by introducing usual reactive groups for linking these ligands with immunoglobulins (IgG) or reduced IgG (Fab′). Our results indicate that the length of the spacer between the chelate and the IgG or reduced IgG is a crucial parameter. Work is in progress to investigate the immunological properties of these conjugates toward the rabbit IgG immunogen before and after the complexation of the radioactive isotope of bismuth.

ACKNOWLEDGMENT

We gratefully acknowledge La Ligue contre le cancer, Région Bretagne, and the CNRS for financial support. We are particularly indebted to the Comité des Côtes-d′Armor de La Ligue contre le cancer for his generous help to Z.H.

LITERATURE CITED

(1) Herrmann, W. A., Herdtweck, E., and Pajdla, L. (1991) "Colloidal Bismuth Subcitrate" (CBS): Isolation and Structural Characterization of the Active Substance against *Helicobacter pylori*, a causal Factor of Gastric Diseases. *Inorg. Chem. 30*, 2579−2581.

(2) Asato, E., Katsura, K., Mikuriya, M., Fujii, T., and Reedijk, J. (1993) Synthesis, Structure, and Spectroscopic Characterization of Bismuth Citrate Compounds and Bismuth-Containing Ulcer Healing Agent Colloidal Bismuth Subcitrate (CBS). 3. Crystal and Solution Structures of $K(NH_4)[Bi_2(cit)_2(H_2O)_2]\cdot(H_2O)_x$ ($x = 2, 4$). *Inorg. Chem. 32*, 5322−5329.

(3) Li, W., Jin, L., Zhu, N., Hou, X., Deng, F., and Sun, H. (2003) Structure of Colloidal Bismuth Subcitrate (CBS) in Dilute HCl: Unique Assembly of Bismuth Citrate Dinuclear Units ($[Bi(cit)_2Bi]^{2-}$). *J. Am. Chem. Soc. 125*, 12408−12409.

(4) Brechbiel, M. W., Gansow, O. A., Pippin, C. G., Rogers, R. D., and Planalp, R. P. (1996) Preparation of the Novel Chelating Agent *N*-(2-Aminoethyl)-*trans*-1,2-diaminocyclohexane-*N*,*N*′,*N*″-pentaacetic Acid $(H_5CyDTPA)^{2-}$ and $Bi^{III}(H_2$-DTPA) Complexes. *Inorg. Chem. 35*, 6343−6348.

(5) Yao, Z., Zhang, M., Garmestani, K., Axworthy, D. B., Mallett, R. W., Fritzberg, A. R., Theodore, L. J., Plascjak, P. S., Eckelman, W. C., Waldmann, T. A., Pastan, I., Paik, C. H., Brechbiel, M. W., and Carrasquillo, J. A. (2004) *Clin. Cancer Res. 10*, 3137−3146.

(6) Sun, H., and Szeto, K. Y. (2003) Binding of bismuth to serum proteins: implication for targets of Bi(III) in blood plasma. *J. Inorg. Biochem. 94*, 114−120.

(7) Alcock, N. W., Ravindran, M., and Willey, G. (1989) Crown Ether Complexes of Bi^{III}. Synthesis and Crystal and Molecular Structures of $BiCl_3$.12-Crown-4 and $2BiCl_3$.18-Crown-6. *J. Chem. Soc., Chem. Commun.* 1063−1064.

(8) Rogers, R. D., Bond, A. H., Aguinaga, S., and Reyes, A. (1992) Complexation Chemistry of Bismuth(III) Halides with Crown Ethers and Polyethylene Glycols. Structural Manifestations of a Stereochemically Active Lone Pair. *J. Am. Chem. Soc. 114*, 2967−2977.

(9) Luckay, R., Reibenspies, J. H., and Hancock, R. D. (1995) Synthesis and Structure of a Complex of Bismuth(III) with a Nitrogen Donor Macrocycle. *J. Chem. Soc., Chem. Commun.* 2365−2366.

(10) Luckay, R., Cukrowski, I., Mashishi, J., Reibenspies, J. H., Bond, A. H., Rogers, R. D., and Hancock, R. D. (1997) Synthesis, stability and structure of the complex of bismuth-(III) with the nitrogen-donor macrocycle 1,4,7,10-tetraazacyclododecane. The role of the lone pair on bismuth(III) and lead(II) in determining coordination geometry. *J. Chem. Soc., Dalton Trans.* 901−908.

(11) Buchler, J. W., and Lay, K. L. (1974) Arsen-, Antimon- und Wismutkomplexe des Octaäthylporphins. *Inorg. Nucl. Chem. Lett. 10*, 297−300.

(12) Treibs, A. (1969) Metallkomplexe von Porphyrinen. *Justus Liebigs Ann. Chem. 728*, 115−148.

(13) Sayer, P., Gouterman, M., and Connell, C. R. (1982) Metalloid Porphyrins and Phathalocyanines. *Acc. Chem. Res. 15*, 73−79.

(14) Barbour, J., Belcher, W. J., Brothers, P. J., Rickard, C. E. F., and Ware, D. C. (1992) Preparation of Group 15 (Phosphorus, Antimony, and Bismuth) Complexes of *meso*-Tetra-*p*-tolylporphyrin (TTP) and X-ray Crystal Structure of $[Sb(TTP)(OCH(CH_3)_2)_2]Cl$. *Inorg. Chem. 31*, 746−754.

(15) Michaudet, L., Fasseur, D., Guilard, R., Ou, Z., Kadish, K. M., Dahoui, S., and Lecomte, C. (2000) Synthesis, characterization and electrochemistry of bismuth porphyrins. X-ray crystal structure of $(OEP)Bi(SO_3CF_3)$. *J. Porphyrins Phthalocyanines 4*, 261−270.

(16) Chacko, G.-P., and Hambright, P. (1994) Acid-, Anion-, and Base-Catalyzed Solvolysis Reactions of a Water Soluble Bismuth(III) Porphyrin. *Inorg. Chem. 33*, 5595−5597.

(17) Boitrel, B., Breede, M., Brothers, P. J., Hodgson, M., Michaudet, L., Rickard, C. E. F., and Al Salim, N. (2003) Bismuth porphyrin complexes: syntheses and structural studies. *Dalton Trans.* 1803−1807.

(18) Michaudet, L., Richard, P., and Boitrel, B. (2000) Synthesis and crystal structure of an unprecedented bismuth porphyrin containing ester pendant arms. *Chem. Commun.* 1589−1590.

(19) Boitrel, B., Halime, Z., Michaudet, L., Lachkar, M., and Toupet, L. (2003) Structural characterisation of the first mononuclear bismuth porphyrin. *Chem. Commun.* 2670−2671.

(20) Halime, Z., Michaudet, L., Razavet, M., Ruzié, C., and Boitrel, B. (2003) Synthesis, characterisation, and properties of bismuth(III) ester pendant arms picket porphyrins. *Dalton Trans.* 4250−4254.

(21) Hancock, R. D., Maumela, H., and S. de Sousa, A. (1996) Macrocyclic ligands with pendent amide and alcoholic oxygen donor groups. *Coord. Chem. Rev. 148*, 315−347.

(22) Ryu, S., Whang, D., Kim, J., Yeo, W., and Kim, K. (1993) Synthesis, Characterization and Crystal Structures of Novel Hafnium Porphyrins. *J. Chem. Soc., Dalton Trans.* 205−209.

(23) Dawson, D. Y., Brand, H., and Arnold, J. (1994) Tantalum Porphyrin Chemistry. Synthesis and Reactivity of Organometallic Derivatives and the X-ray Crystal Structure of the Sandwich Compound $[Ta(OEP)_2][TaCl_6]$. *J. Am. Chem. Soc. 116*, 9797−9798.

(24) Medforth, C. J., Senge, M. O., Smith, K. M., Sparks, L. D., and Shelnutt, J. A. (1992) Nonplanar Distortion Modes for Highly Substituted Porphyrins. *J. Am. Chem. Soc. 114*, 9859−9869.

(25) Senge, M. O., Ema, T., and Smith, K. M. (1995) Crystal structure of a remarkably ruffled nonplanar porphyrin (pyridine)[5,10,15,20-tetra(*tert*-butyl)porphyrinato]zinc(II). *J. Chem. Soc., Chem. Commun.* 733−734.

(26) Sparks, L. D., Medforth, C. J., Park, M. S., Chamberlain, J. R., Ondrias, M. R., Senge, M. O., Smith, K. M., and Shelnutt, J. A. (1993) Metal Dependence of the Nonplanar Distortion of Octaalkyltetraphenylporphyrins. *J. Am. Chem. Soc. 115*, 581−592.

(27) Barkigia, K. M., Renner, M. W., Furenlid, L. R., Medforth, C. J., Smith, K. M., and Fajer, J. (1993) Crystallographic and EXAFS studies of conformationally designed nonplanar nickel(II) porphyrins. *J. Am. Chem. Soc. 115*, 3627−3635.

(28) For an interactive introduction to porphyrin distortions and more details about the deviations of each atom, see: http://www-chem.ucdavis.edu/groups/smith/chime/chime_index.html.

(29) Brennan, T. D., Scheidt, W. R., and Shelnutt, J. A. (1988) New crystalline phase of (octaethylporphinato)nickel(II): effects of π-π interactions on molecular structure and resonance Raman spectra. *J. Am. Chem. Soc. 110*, 3919−3924.

(30) Richard, P., Rose, E., and Boitrel, B. (1998) Characterization and crystal structure of a chiral ruffled basket-handle porphyrin. *Inorg. Chem. 37*, 6532−6534.

(31) Shannon, R. D. (1976) Revised Effective Ionic Radii and Systematic Studies of Interatomic Distances in Halides and Chalcogenides. *Acta Crystallogr. A32*, 751−753.

(32) Liu, S., and Edwards, D. S. (2001) Bifunctional chelators for therapeutic lanthanide radiopharmaceuticals. *Bioconjugate Chem. 12*, 7−34.

(33) Collman, J. P., Bröring, M., Fu, L., Rapta, M., Schwenninger, R., and Straumanis, A. (1998) Novel protecting strategy for the synthesis of porphyrins with different distal and proximal superstructures. *J. Org. Chem. 63*, 8082−8083.

(34) Hermanson, G. T. (1996) *Bioconjugate Techniques*, Academic Press, New York.

(35) Carcenac, M., Larroque, C., Langlois, R., Van Lier, J. E., Artus, J. C., and Pèlegrin, A. (1999) Preparation, Phototoxicity and Biodistribution Studies of Anti-Carcinoembryonic Antigen Monoclonal Antibody-Phthalocyanine Conjugates. *Photochem. Photobiol. 70*, 930−936.

(36) Bedel-Cloutour, C. H., Maneta-Peyret, L., Pereyre, M., and Bezian, J. H. (1991) Synthesis of a Monoclonal Antibody-Indium-111-Porphyrin Conjugate. *J. Immunol. Methods 144*, 35−41.

BC049844O

Synthetic Biocompatible Cyclodextrin-Based Constructs for Local Gene Delivery to Improve Cutaneous Wound Healing

Nathalie C. Bellocq,[†] David W. Kang,[‡] Xuehui Wang,[†] Gregory S. Jensen,[†] Suzie H. Pun,[†,⊥] Thomas Schluep,[‡] Monica L. Zepeda,[‡] and Mark E. Davis*[,§]

Insert Therapeutics, Inc., 2585 Nina Street, Pasadena, California 91107, Canji Inc., 3525 John Hopkins Court, San Diego, California 92121, and Chemical Engineering, California Institute of Technology, Pasadena, California 91125. Received August 2, 2004; Revised Manuscript Received October 2, 2004

The localized, sustained delivery of growth factors for wound healing therapy is actively being explored by gene transfer to the wound site. Biocompatible matrices such as bovine collagen have demonstrated usefulness in sustaining gene therapy vectors that express growth factors in local sites for tissue repair. Here, new synthetic biocompatible materials are prepared and shown to deliver a protein to cultured cells via the use of an adenoviral delivery vector. The synthetic construct consists of a linear, β-cyclodextrin-containing polymer and an adamantane-based cross-linking polymer. When the two polymers are combined, they create an extended network by the formation of inclusion complexes between the cyclodextrins and adamantanes. The properties of the network are altered by controlling the polymer molecular weights and the number of adamantanes on the cross-linking polymer, and these modifications and others such as replacement of the β-cyclodextrin (host) and adamantane (guest) with other cyclodextrins (hosts such as α, γ, and substituted members) and inclusion complex forming molecules (guests) provide the ability to rationally design network characteristics. Fibroblasts exposed to these synthetic constructs show proliferation rates and migration patterns similar to those obtained with collagen. Gene delivery (green fluorescent protein) to fibroblasts via the inclusion of adenoviral vectors in the synthetic construct is equivalent to levels observed with collagen. These in vitro results suggest that the synthetic constructs are suitable for in vivo tissue repair applications.

INTRODUCTION

The enhancement of dermal and epidermal regeneration is a significant goal for the treatment of chronic wounds. Studies aimed at understanding the complex cascade of wound healing have shown that the use of growth factors may be a useful therapeutic strategy, and several growth factors in the form of proteins have been evaluated as therapeutics agents (*1*, *2*). A significant limitation for direct use of proteins is their fast degradation when exposed to an in vivo environment. This loss in activity makes it difficult to maintain therapeutic protein levels within treatment sites (*3*, *4*). One approach to potentially bypass this issue is to use localized gene therapy to promote the continuous production of the desired growth factor at a specific tissue site.

A major challenge in localized gene delivery is to determine the best means to introduce the therapeutic gene into a site such that cells can be transduced and express it. Gene transfer with naked DNA was one of the earliest methods investigated. It has been shown that naked DNA can be successfully transferred to the skin by direct injection (*5*, *6*). Recently, in an effort to increase transgene expression in skin wounds, a new technique called microseeding was developed (*7*, *8*). This method delivers naked DNA by microneedles that are inserted directly into the healing wound. The depth of penetration can be determined by the needle design, and by variation of the DNA concentration and the amount loaded into the needles, the magnitude of gene expression can be affected. Cationic liposome-mediated gene transfer to wounds has also been accomplished (*9*, *10*). Sun et al. administered a plasmid coding for an acidic fibroblast growth factor (FGF-1) to the skin of diabetic mice with incisional wounds by either topical or subcutaneous injection (*9*). It was found that FGF-1 improved wound treatment when compared to controls. A drawback to liposomal vectors is their low in vivo transfection efficiencies. Low transfection efficiencies can be overcome with the use of viral vectors. Adenoviral vectors are known to be very effective for both in vitro and in vivo gene transfer. Adenoviral gene transfer of platelet-derived growth factor-B (PDGF-B) to ischemic rabbit excisional wounds enhanced granulation tissue volume and re-epithelialization of the wound (*11*). Transgene expression was observed for up to 2 weeks in that study.

Although gene therapy appears promising for wound healing, the need for effective ways to deliver genes at the desired site with high level of gene transfer and cellular expression remains. A number of delivery systems have been designed to increase transfection efficiency. A particle-mediated device for gene transfer, the gene gun technology, was one of the earliest delivery techniques used to transfer naked DNA into the skin (*12*−*14*). The technique uses physical force to penetrate the cellular membranes and to deliver DNA that is adhered to microscopic particles. This approach has been used to deliver genes encoding PDGF-B (*15*) and keratinocyte growth factor-1 (*16*) for wound repair. Low

* To whom correspondence should be addressed. E-mail: mdavis@cheme.caltech.edu.
[†] Insert Therapeutics, Inc.
[‡] Canji Inc.
[⊥] Current address: Bioengineering, University of Washington, Seattle, WA.
[§] California Institute of Technology.

10.1021/bc0498119 CCC: $27.50 © 2004 American Chemical Society
Published on Web 10/26/2004

transfection rates and cellular damage due to the consequences of the method of introducing the particles were the major limitations of this technique.

Various biomaterials have been developed to achieve localized, sustained delivery of the genes. Collagen was initially investigated and is a readily available component that allows cell infiltration and proliferation (*17*). Fang et al. were the first to explore and successfully demonstrate the possibility of using collagen sponges as implantable carriers for naked plasmid DNA (pDNA) (*18*). Collagen was used to generate a so-called gene-activated matrix (GAM), since the collagen matrix physically entraps pDNA. GAM has been used in a variety of tissues including skin (*19*), bone (*20*), nervous system (*21*), and blood vessels (*22*). Collagen has also been employed as a carrier of nonviral DNA vectors (*23*−*25*). Adenoviruses delivered in collagen matrices have also been evaluated in dermal wound healing studies (*26*, *27*). The adenoviral delivery of the gene encoding PDGF-B induced a wound healing cascade that culminated in complete regeneration of skin. Further enhancements of the wound repair response have been achieved by combining matrix-enabled gene transfer with molecular targeting where the adenovirus was conjugated to a basic fibroblast growth factor ligand (FGF-2) (*28*, *29*). Adenoviruses delivered in collagen matrices have also demonstrated promising results for repair of bone defects (*30*).

These studies have shown that through the application of matrix-mediated delivery to gene therapy, the DNA vector as well as the transgene product is retained within the defect site, and this leads to an increase in efficacy. However, collagen is an animal-derived protein and its use may raise discussions about safety. The GAM concept can be extended to materials other than collagen. Synthetic materials represent another promising approach for the delivery of pDNA.

Matrices of poly(lactide-*co*-glycolide) (PLGA) loaded with plasmids that encode rhPDGF-B showed a significant increase in the thickness of granulation tissue and neovascularization in rats after transfection (*31*). Recently, triblock copolymers, poly[ethylene glycol-*b*-(D,L-lactic acid-*co*-glycol acid)-*b*-ethylene glycol] (PEG−PLGA−PEG) have been used to effectively deliver genes into skin cells (*32*). The PEG−PLGA−PEG polymers form thermosensitive biodegradable hydrogels that are able to deliver pDNA in a sustained fashion. These encouraging results indicate the potential use of synthetic materials for therapies of skin disorders and wound healing.

Wide and diverse ranges of polymer compositions have been used to prepare hydrogels and other types of matrices (*33*), and many cross-linking methods to create these materials (including chemical or physical cross-linking methods) have been investigated (*34*). In recent years, there has been increasing interest in physically cross-linked gels obtained via noncovalent interactions, ionic interactions, hydrophobic interactions, crystallization, etc. Recently, a new strategy based on inclusion complex formation has been described in which supramolecular structures have been prepared by noncovalent host−guest interactions. Cyclodextrins have been extensively studied as host molecules since they can form inclusion complexes with a wide variety of guest molecules ranging from small hydrophobic compounds to polymers (*35*−*37*). Huh et al. have reported the formation of supramolecular hydrogel based on inclusion complexation between α-cyclodextrin and poly(ethylene glycol)-grafted dextran (*38*) or poly(ethylene glycol)-modified chitosan (*39*). Li et al. have also developed polymer inclusion complex-based supramolecular hydrogels between pluronics (commercial triblock copolymers of poly(ethylene oxide)−poly(propylene oxide)−poly(ethylene oxide) (PEO−PPO−PEO) and α-cyclodextrin (*40*). This strategy for preparing polymer inclusion complex hydrogels is promising but is available for a limited combination of polymers and cyclodextrins. Amiel and co-workers have reported another associating system that involves inclusion complex interactions between hydrophobically modified poly(ethylene oxide) (PEO) and β-cyclodextrin polymers formed by randomly linking the cyclodextrins with epichlorohydrine (*41*, *42*). PEO was end-capped with adamantyl and naphthyl hydrophobic moieties since they are known to form stable inclusion complexes with β-cyclodextrins. These polymers induced interesting associative properties; however, this type of network formation may be difficult to control because the β-cyclodextrin polymer preparation is also difficult to control and can lead to gel formation by itself (*43*). β-cyclodextrin polymers formed by polycondensation of β-cyclodextrin with epichlorohydrin give a highly random conformation because epichlorohydrin can react with any of the 21-hydroxyl groups of the cyclodextrin cup (Figure 1).

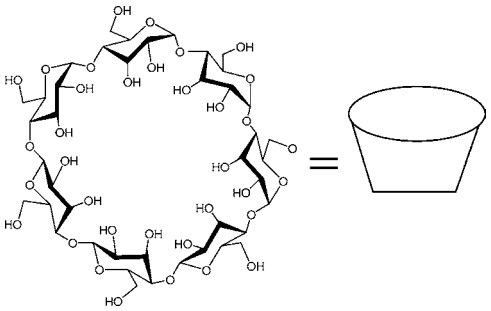


Figure 1. Schematic illustration of β-cyclodextrin.

Over the past few years, our group has demonstrated the use of cyclodextrins as building blocks for the preparation of a suite of linear, cyclodextrin-based polymers for systemic gene delivery (*44*−*46*). In this study, we develop cyclodextrin-based constructs that consist of a linear, cyclodextrin-containing polymer and a cross-linking agent that contains adamantane groups. The constructs are prepared by inclusion complex formation when the two components are combined. If the synthetic components are mixed together in the presence of adenovirus, the construct can serve as a gene carrier for local controlled gene delivery. Here, the preparation and characterization of linear cyclodextrin-based poly(ethylene glycol) polymers and their inclusion complex formation with adamantane end-capped poly(ethylene glycol) polymers is described. We report the influence of polymer structure and size on the construct properties and evaluate the feasibility of using these biodegradable inclusion complex cyclodextrin-based constructs to formulate adenovirus vectors that carry genes encoding growth factors.

EXPERIMENTAL PROCEDURES

Material Preparation and Characterization. *Linear Cyclodextrin-based Poly(ethylene glycol) Polymers (CD*−*PEG).* CD−PEG polymers (Figure 2) were prepared by the polymerization of a difunctionalized β-cyclodextrin (CD) monomer (A) with a difunctionalized poly(ethylene glycol) comonomer (B) to give an ABAB product. 6A,6D-Dideoxy-6A,6D-di(2-aminoethanethio)-β-cyclodextrin (denoted dicysteamine-β-cyclodextrin) (**1**) was synthesized according to previously described procedures (*44*, *47*). Disuccinimidyl propionate poly(ethylene glycol) (PEG−

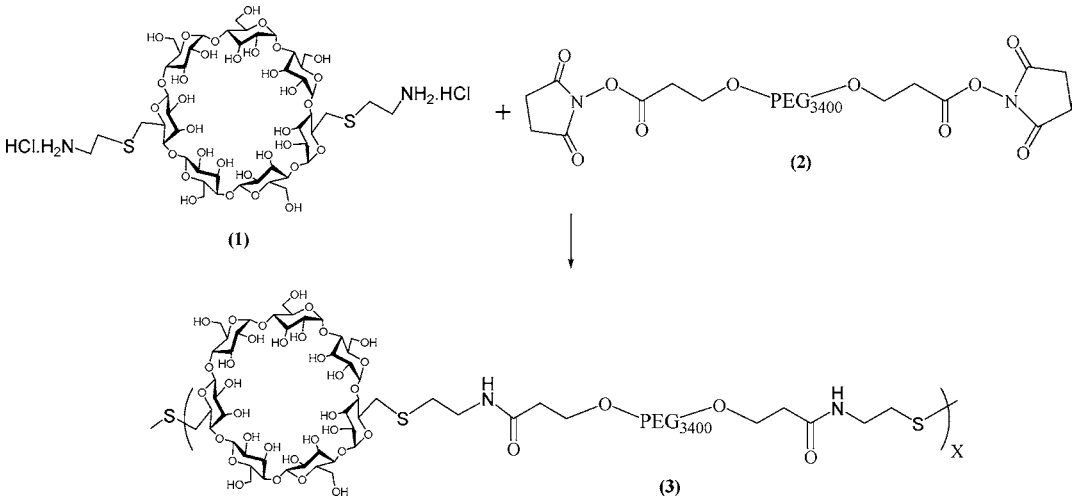


Figure 2. Synthesis of linear, cyclodextrin-based poly(ethylene glycol) polymers (CD−PEG).

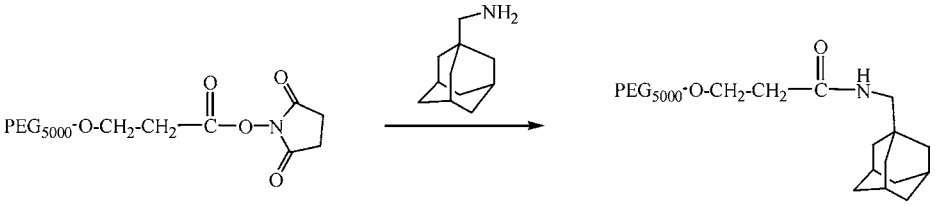


Figure 3. Synthesis of adamantane−poly(ethylene glycol) conjugate (ADA−PEG).

diSPA, MW 3400) (**2**) was purchased from Nektar (Huntsville, AL). In a typical experiment, (**1**) (0.4 g, 0.32 mmol) was acidified with HCl, precipitated with acetone, and then dried under vacuum for 14 h. PEG−diSPA (1.08 g, 0.32 mmol) and anhydrous DMSO (8 mL) were added under argon. After 10 min of stirring, anhydrous diisopropylethylamine (DIEA) (254 μL, 1.46 mmol) was added under argon. The resulting mixture was then allowed to stir at room temperature under argon. The reaction was followed over time (2, 15, 30, 60, 180, and 300 min), addition of DIEA being at time zero. At the end of the reaction, the solution was transferred to a 10 000 MWCO membrane (Spectra/Por 7, Spectrum Laboratories Inc., Rancho Dominguez, CA) and dialyzed against deionized water for 48 h. The solution was then lyophilized to dryness. The polymer samples were analyzed on a Hitachi D6000 HPLC system equipped with a ERC-7512 RI detector, a Precision Detectors PD2020/DLS static light scattering detector, and a PL aquagel-OH 30 (Polymer Laboratories, Amherst, MA) column using phosphate-buffered saline (PBS, 150 mM) as eluant at a 0.7 mL/min flow rate. The specific refractive index increment, dn/dc, was measured in PBS (Cellgro, Mediatech, Inc, Herndon, VA) using a Bausch & Lomb ABBE-3L refractive index detector.

Adamantane−Poly(ethylene glycol) (ADA−PEG). ADA−PEG (Figure 3) was synthesized according to published procedures (*45*). In brief, succinimidyl propionate poly(ethylene glycol) (Nektar) (PEG−SPA, MW 5000, 2 g, 0.4 mmol) was reacted with 1-adamantane-methylamine (Aldrich, Milwaukee, WI; 142 μL, 0.8 mmol) dissolved in dichloromethane. The resulting solution was stirred at room temperature for 4 h. The solvent was removed under vacuum, and water was added to the remaining solution. The solution was centrifuged at 15 000 rcf for 15 min to remove unreacted 1-adamantane-methylamine. The aqueous portion was collected and dialyzed (Slide-A-Lyzer MWCO 3500, Pierce, Rockford, IL) for 24 h against water. The dialyzed solution was then lyophilized to dryness to give ADA−PEG in 97% yield. The product was analyzed on a Beckman Coulter Gold HPLC system equipped with a Richards Scientific Sedere evaporative light scattering detector and a C18 reversed phase column (Hichrom HIRPB-4438, Richards Scientific) using a gradient of water and acetonitrile at 1 mL/min. The product was found to be pure (retention time of PEG−SPA, 10.7 min; retention time of ADA−PEG, 12.1 min). The product was also confirmed by mass spectroscopy matrix-assisted laser desorption ionization time-of-flight (MALDI-TOF) analysis (Voyager DE-PRO, Applied Biosystems, Foster City, CA).

Adamantane−Poly(ethylene glycol)−Adamantane (2-ADA−PEG). Disuccinimidyl propionate poly(ethylene glycol) (Nektar) (PEG-diSPA, MW 3400) (2 g, 0.59 mmol) was reacted with 1-adamantane-methylamine (Aldrich) (219 μL, 1.24 mmol) dissolved in dichloromethane (Figure 4). The resulting solution was stirred at room temperature for 4 h. The solvent was removed under vacuum, and water was added to the remaining solution. The solution was centrifuged at 15 000 rcf for 15 min to remove unreacted 1-adamantane-methylamine. The aqueous portion was collected and dialyzed (Slide-A-Lyzer MWCO 1000, Pierce) for 24 h against water. The dialyzed solution was then lyophilized to give 2-ADA−PEG in 95% yield. The product was analyzed using the same HPLC technique as that for ADA−PEG. The product was found to be pure (retention time of PEG−diSPA, 10.4 min; retention time of 2-ADA−PEG, 13.4 min). The product was also confirmed by mass spectroscopy MALDI-TOF analysis (Voyager DE-PRO, Applied Biosystems).

Tetraadamantane−Poly(ethylene glycol) (4-ADA−PEG). 1-Adamantane-methylamine (0.069 g, 0.44 mmol, Aldrich) was added to 1 g of four-arm poly(ethylene glycol) succinimidyl succinate (PEG-(ss)$_4$, MW 10 000) (SunBio, Inc., Anyang City, S. Korea) (0.1 mmol) previously dissolved in 10 mL of dichloromethane (Figure 5). The resulting solution was stirred at room temperature overnight. The solvent was evaporated under vacuum,

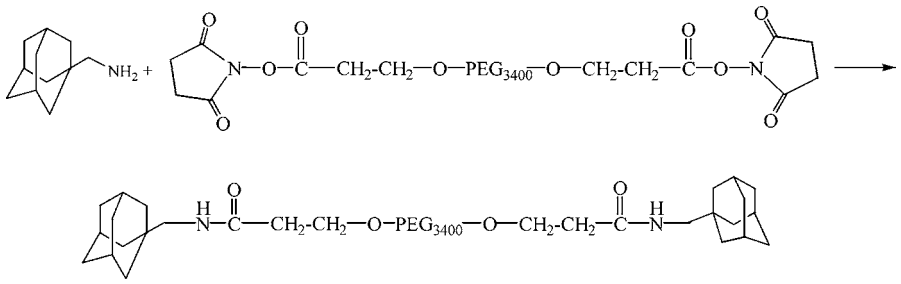


Figure 4. Synthesis of diadamantane−poly(ethylene glycol) cross-linker (2-ADA−PEG).

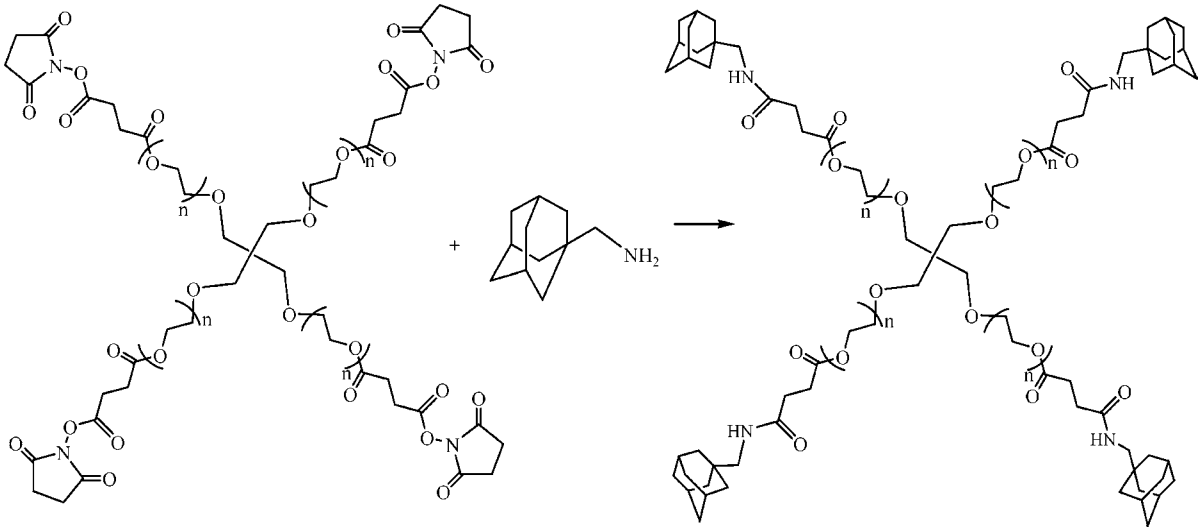


Figure 5. Synthesis of tetraadamantane−poly(ethylene glycol) cross-linker (4-ADA−PEG).

and the resulting polymer was precipitated with ether. The resulting solid was dried and analyzed using the same HPLC technique as that for ADA−PEG. The product was found to be pure (retention time of PEG-$(ss)_4$, 11.4 min; retention time of 4-ADA−PEG, 15.1 min). The product was also confirmed by mass spectroscopy MALDI-TOF analysis (Voyager DE-PRO, Applied Biosystems).

Synthetic Construct Preparation and Characterization. *Preparation of Polymeric Inclusion Complex-Based Construct between Cyclodextrin-Based Poly(ethylene glycol) Polymer (CD-PEG) and Adamantane-Containing Poly(ethylene glycol) Cross-Linker (CD-ADA Matrix).* Cyclodextrin-based poly(ethylene glycol) polymer was dissolved at 250 mg/mL in water. PBS (10×) and adamantane-containing poly(ethylene glycol) cross-linker (2-ADA−PEG) dissolved in water were then added such that the resulting complex had a CD−PEG concentration of 100 mg/mL and a 1/1 adamantane/cyclodextrin ratio (39.5 mg/mL) in 1x PBS, pH 7.2 (Figure 6). The resulting mixture was mixed vigorously to form a homogeneous solution. An increase in the viscosity was observed in about 1 min. For comparison, the mono- and the tetraadamantane poly(ethylene glycol) derivatives (ADA−PEG and 4-ADA−PEG, respectively) were tested at the same concentration as 2-ADA−PEG (39.5 mg/mL). For cell culture studies, 5% dextrose in water (D5W) was used instead of 1× PBS.

Rheology Study. Oscillatory rheological measurements were performed on an RFS 3 (TA Instruments, New Castle, DE) with a parallel plate geometry equipped with a Peltier temperature element. A sequence of three tests was performed for each sample. First, a time sweep at a frequency of 10 rad/s and 0.5% strain was performed for

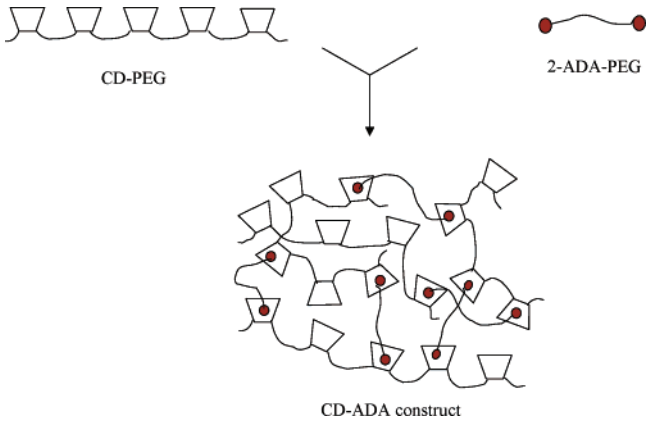


Figure 6. Schematic illustration of the structure of the polymer inclusion complex-based contruct between cyclodextrin−poly(ethylene glycol) polymer (CD−PEG) and adamantane−poly(ethylene glycol) polymer (2-ADA−PEG or 4-ADA−PEG).

1800 s. Second, a frequency sweep from 1 to 100 rad/s was performed at 0.5% strain. Third, a strain sweep from 0.02% strain to 100% strain was performed at a frequency of 10 rad/s. The reported loss factor, tan δ, and complex viscosity, η^*, were determined as the respective means of the constant portion in the strain sweep at 10 rad/s.

Recombinant Adenovirus (rAd) Construction and Purification. rAd-GFP is an E1-, E3-, and pIX-deleted adenoviral vector containing the eGFP (Clontech, Palo Alto, CA) expression cassette driven by a human CMV promoter. Homologous recombination in 293 cells (Microbix Biosystems, ON, Canada) was used to generate infectious virus (*49*). Virus was grown in 293 cells, purified by column chromatography (*50*), and quantitated by anion-exchange HPLC (*51*).

Cell Culture and Cellular Studies. *Cell Viability.* Human skin fibroblasts, CCD-1074sk (1×10^4 cells, ATCC, Manassas, VA) in DMEM media (Cambrex Bio Science, Walkersville, MD) containing 10% fetal bovine serum (JRH Biosciences, Lenexa, KS) and 1% penicillin−streptomycin solution (Invitrogen Life Technologies, Carlsbad, CA) were placed on top of 400 μL of either 2.4 mg/mL Cell Prime liquid bovine collagen (Cohesion, Palo Alto, CA) or 100 mg/mL CD−ADA matrix in a 24-well tissue culture plate (Becton Dickinson, Franklin Lakes, NJ) and incubated at 37 °C. Forty-eight hours later, the cells were examined under phase contrast using an inverted microscope (Nikon, Melville, NY).

Cell Mobility through Matrix. Two hundred microliters of 100 mg/mL CD−ADA matrix containing 10 ng/mL hPDGF-BB protein (Chemicon, Temecula, CA) was placed in an 8.0 μm pore FluoroBlokTM insert (Becton Dickinson, Franklin Lakes, NJ) for a 24-well plate. CCD-1074sk cells (1×10^4 cells) were stained for 30 min with 5 μM Calcein-AM, a fluorescent dye that labels viable cells (Molecular Probes, Eugene, OR), washed, and resuspended in DMEM media containing 10% FBS and 1% penicillin−streptomycin solution and then seeded on top of the CD−ADA matrix containing hPDGF-BB. Media containing 50 ng/mL hPDGF-BB protein was placed in the lower chamber to provide a chemoattractant gradient to stimulate cell migration through the FluoroBlokTM pores. Seventy-two hours later, the FluoroBlokTM inserts were photographed at 100× magnification under GFP fluorescence using an inverted microscope (Nikon) to look for cell migration through the insert pores.

In Vitro Transduction Studies. A total of 1×10^9 particle numbers (PN) per well of rAd-GFP was mixed with either 100 μL of DMEM media containing 10% FBS alone (no matrix), 100 μL of CD−ADA matrix at a concentration of 100 mg/mL, or 100 μL of collagen at a concentration of 2.4 mg/mL and plated onto a 24-well flat bottom tissue culture plate, in duplicate, then incubated at 37 °C for 30 min. CCD-1074sk cells (1×10^4 cells) in 0.4 mL media were layered over the above matrix/virus or media/virus mixture and incubated for 48 h at 37 °C and 5% CO_2, then photographed at 100× magnification under identical GFP fluorescence settings for all samples.

Fluorometric Analyses. A total of 1×10^9 PN/well of rAd-GFP was mixed with either 50 μL of DMEM media containing 10% FBS alone (no matrix), 50 μL of CD−ADA construct at a concentration of 100 mg/mL, or 50 μL of collagen at a concentration of 2.4 mg/mL and plated onto a 96-well flat bottom tissue culture plate, in triplicate, then incubated at 37 °C for 30 min. CCD-1074sk cells (5×10^3 cells) in 150 μL of media were layered over the matrix/virus or media/virus mixture and incubated for 48 h at 37 °C and 5% CO_2, then read on a fluorometer (PerSeptive Biosystems, Foster City, CA) to measure expression of rAd-GFP transduction (excitation = 485 nm; emission = 530 nm). Results are reported in fluorescence intensity (FI) units.

Cell Proliferation Assay. CCD-1074sk cells (5×10^3 cells) were plated in media alone, CD−ADA construct, or collagen as described above (fluorometric analysis) but without any virus added. After 48 h at 37 °C and 5% CO_2, 40 μL of a MTS-based dye [MTS = (3-(4,5-dimethylthiazol-2-yl)-5-(3-carboxymethoxyphenyl)-2-(4-sulfophenyl)-2*H*-tetrazolium] (Cell Titer 96 Aqueous One, Promega, Madison, WI) was added to each well, incubated for an additional 3 h, and read on a spectrophotometer (Molecular Devices, Sunnyvale, CA) to determine cell proliferation (λ_1 = 490 nm minus λ_2 = 630 nm). Results are reported in optical density (OD).

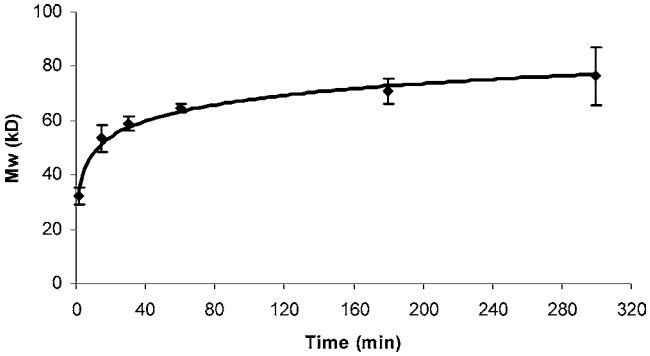


Figure 7. Molecular weight of CD−PEG as a function of polymerization time. The results shown are mean ± SD for three experiments.

RESULTS

CD-PEG Synthesis and Characterization. CD−PEG polymers were synthesized by reacting dicysteamine-β-cyclodextrin−2HCl comonomer with PEG−diSPA in anhydrous DMSO solution under argon. The viscosity of the polymerization solutions increased dramatically after the addition of a nonnucleophilic organic base such as DIEA. DIEA deprotonated the amino groups of **1** to render them more nucleophilic for coupling with PEG−diSPA. Polymerization of **1** with PEG−diSPA typically produced polymers in yields greater than 90%. The polymer MW, determined by light scattering, increased to around 80 kD over a 5 h time course (Figure 7) with a polydispersity index of 1.5. This polymerization is thus a fast but reproducible reaction. Polymers with MW ranging from 30 to 80 kD can be easily obtained by controlling the polymerization time. These polymers are highly soluble in aqueous solution. They can be easily dissolved in water or PBS at concentrations of at least 100 mg/mL. The polymers with high MW go into solution more slowly.

CD-ADA Construct Preparation and Characterization. Hydrophobically modified poly(ethylene glycol) polymers were obtained by reaction between the succinimidyl propionate or succinimidyl succinate termini of the PEG molecules with 1-adamantane-methylamine. The structural formulas of the polymers obtained are schematically illustrated in Figures 3−5. CD−PEG polymers with a molecular weight of 30, 65, or 85 kD were dissolved in PBS at 100 mg/mL and were mixed with these adamantane-containing poly(ethylene glycol) derivatives (39.5 mg/mL).

The macroscopic properties of the constructs are probed via rheological measurements, and the direct consequences of the formation of cross-linking inclusion complexes observed in the data (Table 1). Oscillatory rheology measurements were performed on an RFS 3 (TA Instruments) using a parallel plate geometry. Figure 8 shows measured values of the storage modulus (G') and the loss modulus (G'') vs frequency for a mixture of CD−PEG (85 kD MW) polymer and 2-ADA−PEG (A). In the frequency range from 1 to 100 rad/s, G' is found to be much smaller than G''. The same behavior is observed at various polymer lengths and temperatures and using different cross-linkers with increasing functionality (2-ADA−PEG, 4-ADA−PEG). In fact, using a monovalent ADA−PEG control, the behavior is similar. A summary of the observed ratios of G'' to G', that is, the loss factor, tan δ, is shown in Table 1. A high value of tan δ indicates that the polymer sample behaves more like a viscous fluid rather than a typical gel that would show a tan δ smaller

Table 1: Rheological Characterization of CD−PEG Polymer (30, 65, and 85 kD) at 100 mg/mL Mixed with ADA−PEG, 2-ADA−PEG, or 4-ADA−PEG (39.5 mg/mL) Compared to a Bovine Collagen Matrix[a]

polymer	MW [kD]	×-linker	temp [°C]	tan δ	slope G'	η^* [Pa s]	fold increase in viscosity
CD−PEG_{3400}	30	ADA−PEG	20	1.51	*b*	0.046	1
CD−PEG_{3400}	30	2-ADA−PEG	20	34.00	0.880	0.723	16
CD−PEG_{3400}	30	4-ADA−PEG	20	50.20	1.55	4.320	94
CD−PEG_{3400}	30	ADA−PEG	35	6.14	*b*	0.022	1
CD−PEG_{3400}	30	2-ADA−PEG	35	17.90	*b*	0.223	10
CD−PEG_{3400}	30	4-ADA−PEG	35	23.70	0.854	1.400	64
CD−PEG_{3400}	65	ADA−PEG	20	18.56	*b*	0.044	1
CD−PEG_{3400}	65	2-ADA−PEG	20	55.10	1.46	3.290	75
CD−PEG_{3400}	65	4-ADA−PEG	20	30.30	1.61	8.300	189
CD−PEG_{3400}	65	ADA−PEG	35	20.40	*b*	0.035	1
CD−PEG_{3400}	65	2-ADA−PEG	35	54.00	1.30	1.120	32
CD−PEG_{3400}	65	4-ADA−PEG	35	38.30	1.29	2.500	71
CD−PEG_{3400}	85	ADA−PEG	20	5.58	*b*	0.074	1
CD−PEG_{3400}	85	2-ADA−PEG	20	16.82	1.46	5.606	76
CD−PEG_{3400}	85	4-ADA−PEG	20	13.15	1.68	18.620	252
CD−PEG_{3400}	85	ADA−PEG	35	5.12	*b*	0.064	1
CD−PEG_{3400}	85	2-ADA−PEG	35	13.33	1.34	2.194	34
CD−PEG_{3400}	85	4-ADA−PEG	35	12.01	1.18	6.990	109
collagen	*b*	*b*	35	0.0489	0.0517	3.293	*b*

[a] The loss factor, tan δ, is the ratio of loss modulus G'' to storage modulus G' (>1 for mostly viscous behavior and <1 for mostly elastic behavior). Slope of G' (2 for ideally elastic and 0 for ideally viscous fluids), complex viscosity, η^*, and increase in viscosity after cross-linking are also shown. In certain cases no slope of G' could be determined because the frequency sweep resulted in measurements below sensitivity range of the instrument. [b] Not applicable.

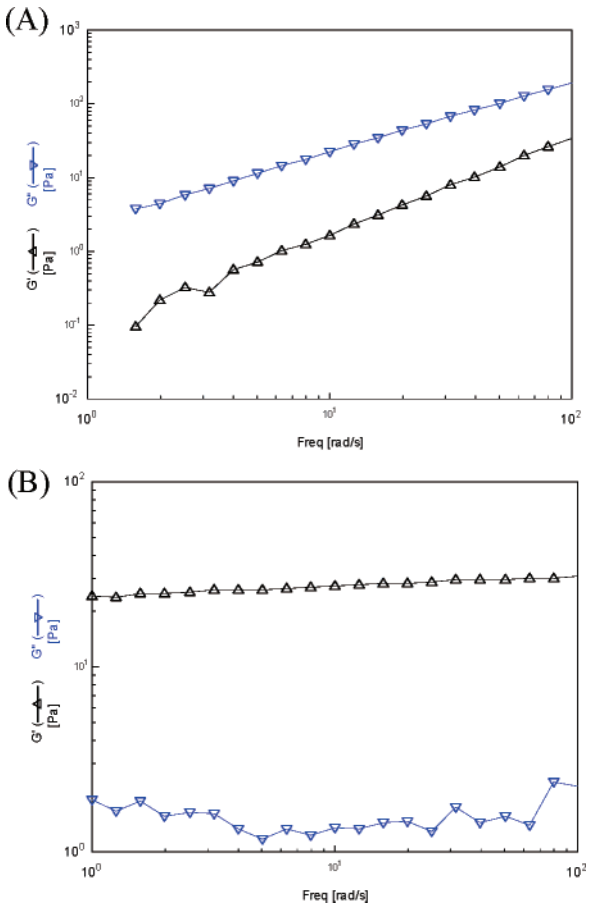


Figure 8. G' and G'' vs frequency for CD−ADA construct (A) and bovine collagen (B) at 35 °C.

than one. For comparative purposes, Figure 8B gives a frequency scan of G' and G'' for bovine collagen, a matrix previously used for gene delivery to wounds (*27*). At 35 °C, G' is significantly larger than G'' over the frequency range observed, resulting in a tan δ value $\ll 1$. In the frequency range studied, G' and G'' do not cross each other.

Another measure that characterizes the viscoelastic behavior of the sample is the slope of G' vs frequency, which is close to 2 for ideally viscous and zero for ideally elastic materials. While the slopes of G' are between 0.9 and 1.7 for CD−PEG polymer samples (Table 1), indicating mostly viscous behavior, the slope of G' is 0.052 for the bovine collagen matrix, indicating strong elastic behavior.

Figure 9 shows the complex viscosity of the CD−ADA as a function of CD−PEG polymer molecular weight at both 20 (A) and 35 °C (B) using 2- and 4-ADA−PEG as cross-linkers. Monovalent ADA−PEG is used as control. The viscosity increases with the MW of the polymer and with the functionality of the cross-linker. The viscosity is noticeable lower at 35 than at 20 °C.

In Vitro Biocompatibility Study. Biocompatibility of the CD−ADA construct was assessed by visually monitoring cell viability (Figure 10). CCD-1074sk cells were placed on top of either collagen (Figure 10A) or the CD−ADA construct (Figure 10B) and examined 48 h later under phase contrast. Figure 10 shows that CCD-1074sk cells are not affected by the presence of CD−ADA construct (cells are viable and have the appropriate morphology); thus, the CD−ADA construct is biocompatible with cells.

To test whether CCD-1074sk cells can migrate through the CD−ADA material, cell-migration assays, using the FluoroBlokTM insert system, were carried out (Figure 11). CCD-1074sk cells, labeled with the fluorescent dye Calcein-AM, were placed on the CD−ADA construct containing a low concentration of hPDGF-BB protein in the top chamber of the insert. hPDGF-BB protein was also placed in the lower chamber at a higher concentration to provide a chemoattractant gradient and stimulate cell migration through the FluoroBlokTM pores (Figure 11A). Figure 11B shows fluorescence from cells migrating through the pores 72 h after plating, demonstrating that the CD−ADA construct supports migration of CCD-1074sk cells.

In Vitro Transgene Expression Study. rAd-GFP was mixed with media alone (no matrix), the CD−ADA construct, or collagen and placed onto a 24-well flat bottom tissue culture plate. After 30 min at 37 °C, CCD-

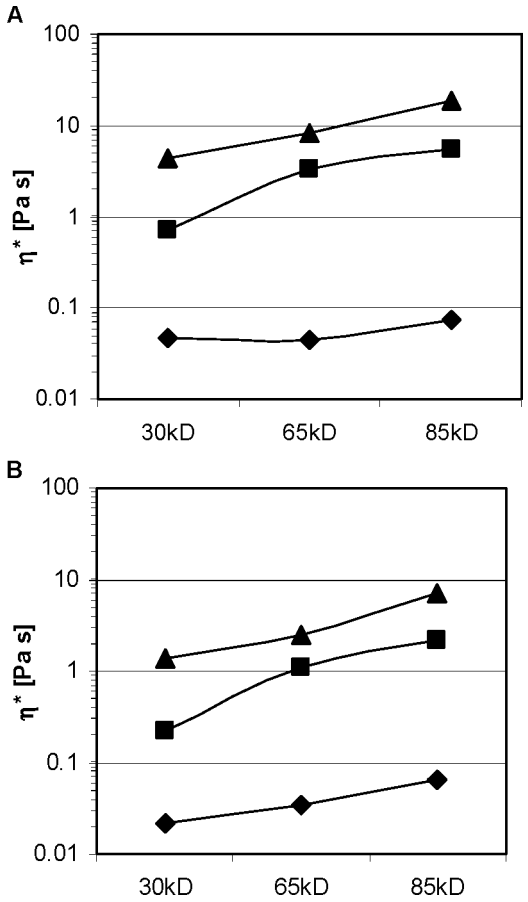


Figure 9. Complex viscosity of CD−ADA construct as a function of CD−PEG polymer molecular weight at 20 (A) and 35 °C (B) using various cross-linker functionalities (2-ADA−PEG (■) and 4-ADA−PEG (▲)). Monofunctionalized ADA−PEG (◆) is included to establish a baseline for a non-cross-linked polymer solution.

1074sk cells were layered over the virus/matrix or virus/media mixtures and incubated for 48 h. The cells from the various treatment groups were examined and photographed at 100× magnification under an inverted microscope using identical settings for all samples (Figure 12). All cells, regardless of the type of matrix or media, appeared to be healthy by visual inspection (phase contrast view). Wells treated with virus had cells that were positive to rAd-GFP transduction when viewed under a fluorescent light source, while cells that were not treated with virus showed no GFP signal (data not shown). Cells in the CD−ADA construct appeared to be more numerous in cell count than cells in collagen.

The visual GFP expression results were corroborated when the plates were quantitatively analyzed with a fluorometer (Figure 13A). At 48 h, cells in the CD−ADA construct have the highest average fluorescent intensity, followed by cells in media alone (no matrix) then cells in the collagen matrix (5455, 5280, and 4659 avg FI units, respectively). However, observed differences in fluorescence were not statistically significant ($p > 0.1$, unpaired two-tailed t-test). The CD−ADA complex therefore allows for adenoviral transduction of dermal fibroblast cells in vitro at levels comparable to collagen or media alone.

The MTS-based cell proliferation assay shows that plating in media alone resulted in the highest number of viable cells after 48 h (0.85 OD), followed by cells in collagen (0.37 OD) and cells in CD−ADA construct (0.27 OD) (Figure 13B). However, statistical analysis (unpaired two-tailed t-test) shows that the observed differences between the CD−ADA construct and collagen were not significant ($p > 0.1$).

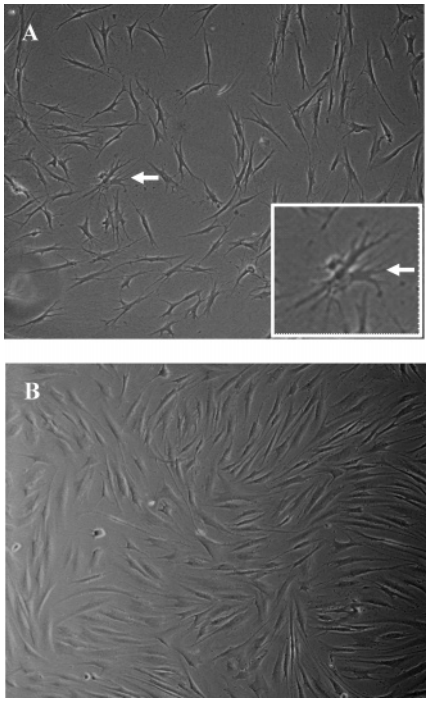


Figure 10. Biocompatibility of CCD-1074sk cells with collagen (A) or CD−ADA construct (B). The picture was taken at 100× magnification. The inset in panel A is a 200× magnification of a skin fibroblast cell marked by an arrow. Filopodia, a morphological feature associated with cell migration, are indicated by an arrow in the inset.

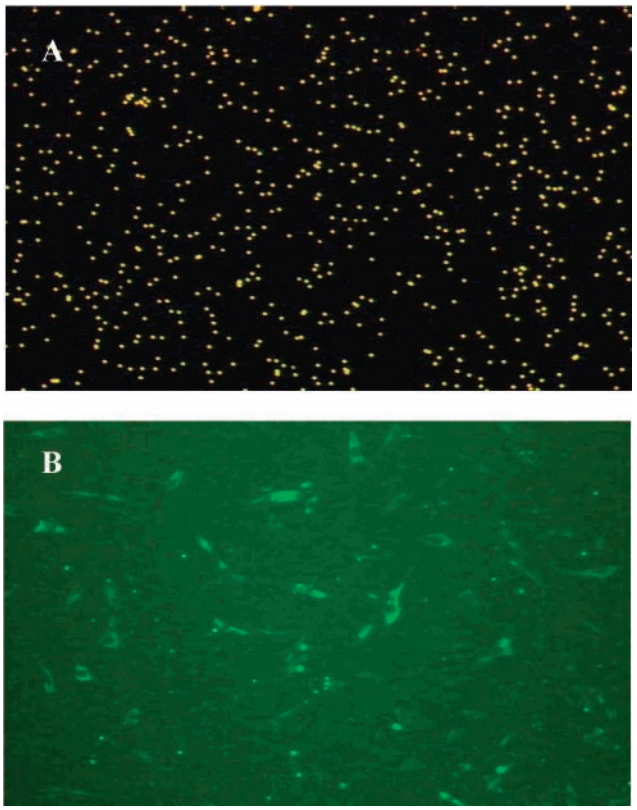


Figure 11. Migration of CCD-1074sk cells through CD−ADA contruct: (A) brightfield image of 8.0 μm pores of the FluoroBlok insert at 100× magnification; (B) fluorescent image of CCD-1074sk cells that have migrated through the FluoroBlok pores at 100× magnification.

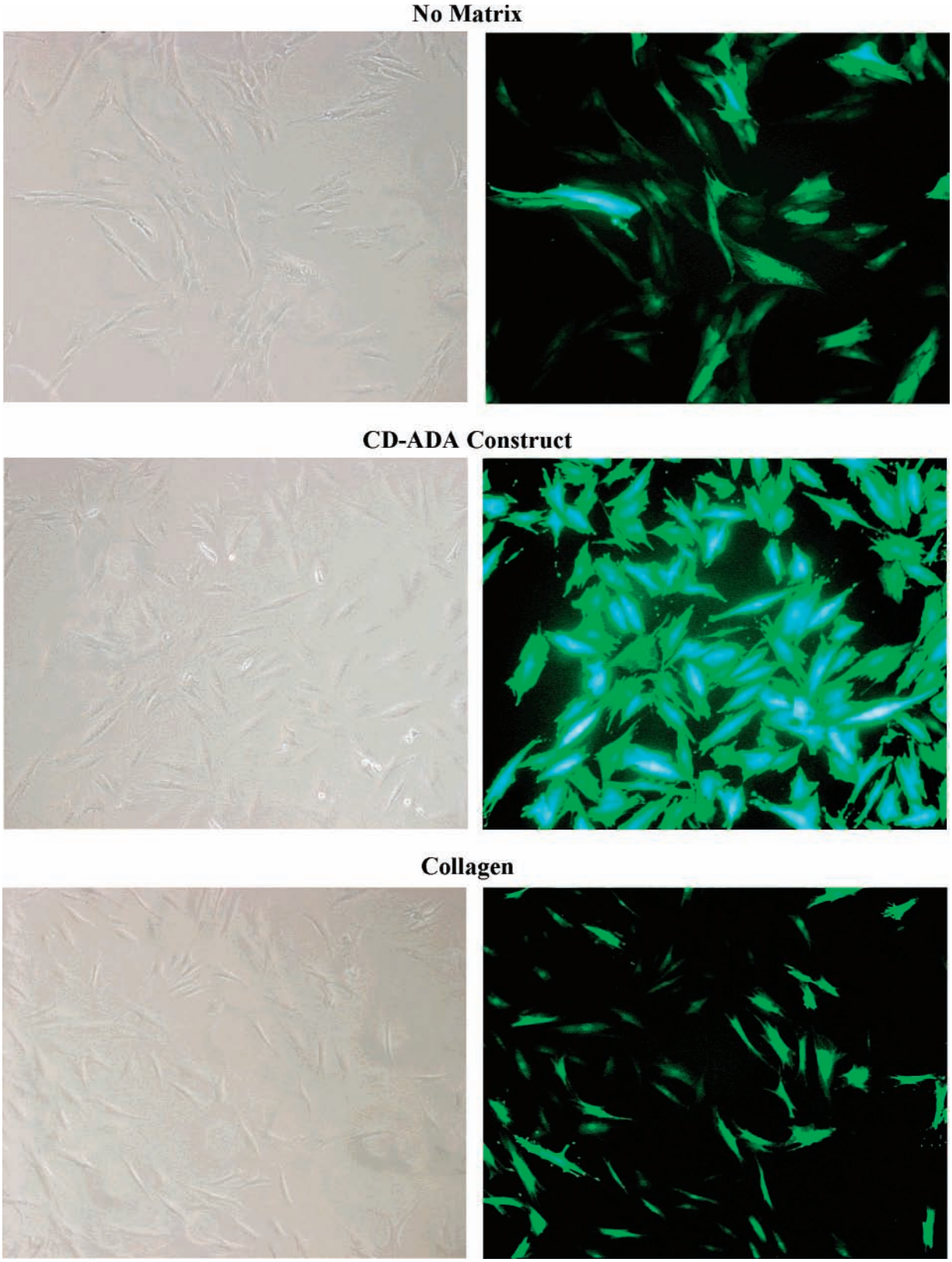


Figure 12. In vitro transduction of CCD-1074sk cells with rAd-GFP: left photos, phase contrast; right photos, fluorescence. All images are at 100× magnification.

DISCUSSION

The objective of this study is to synthesize and evaluate a new type of construct for use in gene transfer in cutaneous wound repair. The complete construct consists of three components, a linear, cyclodextrin-containing polymer, an adamantane-containing polymer that is used as a cross-linking agent, and a recombinant adenovirus. The assembly of the construct involves the mixing of two polymers: a hydrophobically end-capped poly(ethylene glycol) and a β-cyclodextrin-based polymer that create an associating network via inclusion complex formation between the cyclodextrins and adamantanes. The inter-

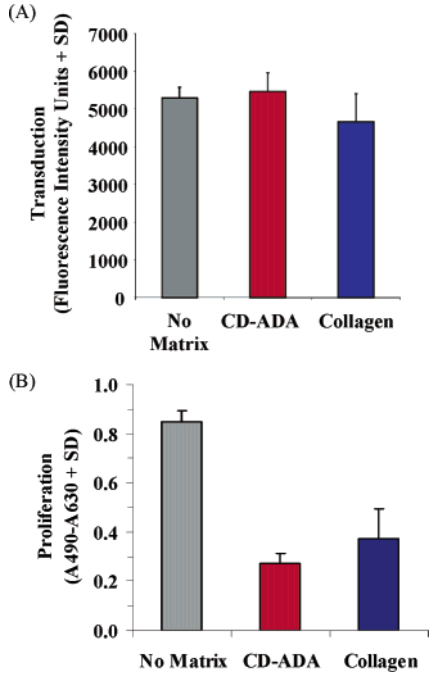


Figure 13. Fluorometric (A) and MTS (B) analyses of CCD-1074sk cells after transduction with rAd-GFP in three formulations: no matrix, CD−ADA construct, and collagen. The graphs represent values after the background (wells containing only media alone, CD−ADA, or collagen, respectively) is subtracted.

actions between these two types of polymers have been previously described (*42*), but the β-cyclodextrin polymer used in that study was prepared by polycondensation with epichlorohydrin. One of the drawbacks in the use of epichlorohydrin is the highly random conformation of the resulting β-cyclodextrin polymer since the reaction can occur on any of the 21 exterior hydroxyl groups of the cyclodextrin cavity (7 primary hydroxyl at one rim and 14 secondary hydroxyl at the other rim) (Figure 1) (*43*). Here, only two of the 21 hydroxyls are converted to diamino cyclodextrin derivatives (dicysteamine-β-cyclodextrin (**1**)), and well-defined and controlled syntheses of linear, cyclodextrin-based polymers are achieved. The rational control over polymer properties is necessary to have control over the characteristics of the final construct formed.

Linear cyclodextrin-based poly(ethylene glycol) polymers were synthesized by reacting **1** with an activated difunctionalized derivative. Due to the bulky size of the CD, disuccinimide groups separated by a relatively long distance were used to minimize the steric hindrance between cyclodextrin cups in the construction of polymers chains. PEG−diSPA was thus used as comonomer for the polymerization. Linear, CD-based polymers with MWs greater than 50 kD can be easily synthesized in a reproducible manner using this method (Figure 7). Since β-CD does not form complexes with PEG (*36*), no cross-linking was observed in these polymers.

Hydrophobically modified PEGs were obtained by reacting succinimide-functionalized PEG with 1-adamantane-methylamine (Figures 3−5). Adamantane is a hydrophobic moiety known for its ability to form stable inclusion complexes with β-CD. The hydrophobic molar ratio was varied by using a four-arm branched PEG (Figure 5). Monofunctionalized ADA−PEG was included as a control since it cannot cross-link.

The general strategy for the design of the cyclodextrin-containing constructs is illustrated in Figure 6. The association between the adamantane and cyclodextrin components was investigated by rheology measurements (for a comprehensive presentation on rheology see ref *48*). In the frequency range from 1 to 100 rad/s, G' was found to be much smaller than G'' for the CD−PEG samples. However, with collagen, G' was significantly larger than G'' over the frequency range observed (tan δ value $\ll 1$). This result indicates that the CD−ADA complex behaves more like a viscous liquid than an elastic gel such as collagen. A possible explanation for the behavior of the CD−PEG samples is the reversible nature of the inclusion complex formation between adamantane and β-cyclodextrin as proposed by Amiel and Sebille (*41*). Another possible explanation could be that aggregates of limiting size are formed instead of an extended network. In the frequency range studied, G' and G'' did not cross one another. In the "Maxwell model", the crossover frequency is the inverse of the average relaxation time that is characteristic for the transient network (*48*). By using the model of Tanaka and Edwards, the relaxation time can be related to the dissociation kinetics between the chemical groups forming the network (*48*). For the CD−PEG samples, the crossover frequency (if it exists) was found to be higher than 100 rad/s. It is of interest that in the case of a highly elastic network such as bovine collagen, no G'/G'' crossover was observed in the same frequency range (Figure 8B).

The CD−PEG polymer length and cross-linker functionality influences the viscosity of the resulting polymer solutions. The complex viscosity increases as a function of both molecular weight of the CD−PEG polymer and cross-linker functionality (Figure 9). Significant increases in viscosity over the baseline established with monovalent ADA−PEG were observed after addition of cross-linker (Table 1). As expected, the viscosities are higher at 20 vs 35 °C, but the same type of behavior is observed at both temperatures.

In vitro biocompatibility studies show that human skin fibroblasts are viable in both the collagen and CD−ADA matrices, as indicated by the presence of elongated and translucent cells (morphologies typically observed with healthy fibroblasts). Cells in collagen appear to be in a migratory phenotype at 48 h because lamellipodia and filopodia fingerlike structures that extend from the appendages of the cells are observed (Figure 10, inset) (*52*). It is known that dermal fibroblasts plated on collagen are stimulated to migrate (*53*, *54*). Cells in CD−ADA did not appear to be in a migratory phenotype. However, we have shown that CCD-1074sk cells will also migrate through the CD−ADA matrix when stimulated to do so by a chemo-attractant gradient such as rhPDGF−BB (Figure 11). Evaluation of these migratory cells at higher magnification also shows the presence of lamellipodia and filopodia at the appendages (data not shown).

In vitro transgene expression studies show that a recombinant adenovirus encoding GFP formulated in the CD−ADA construct can efficiently transduce CCD-1074sk cells. While fluorescent pictures suggest that the CD−ADA construct enables higher levels of expression than collagen or media alone, fluorometric data indicate that the observed differences are not statistically significant.

Cell proliferation is significantly higher ($p < 0.05$) in the media alone group compared to collagen and the CD−ADA matrix. It has been reported that floating collagen matrices have an inhibitory effect on proliferation of fibroblasts (*55*). Cells in floating collagen matrices also exhibit distinct morphological characteristics generally described as an extended dendritic network (*56*). In our

observations, fibroblasts plated on collagen show a proliferation pattern and morphology similar to what is observed in floating collagen matrices. Fibroblasts in the CD−ADA construct proliferate at a rate comparable to cells in the collagen matrix but have a slightly different morphological appearance than cells plated in either media alone or collagen. This is not unexpected, since a mainly PEG-based polymer will not provide the same signaling to cells as collagen, nor will it provide the rigid attachment points for cells found on a plastic surface.

Taken together, these results indicate that the CD−ADA construct can serve as a highly tunable and biocompatible matrix for recombinant adenovirus-mediated gene delivery to local wound sites. The properties of the network can be altered by controlling the polymer molecular weights and the number of adamantanes on the cross-linking polymer, and these modifications and others such as replacement of the β-cyclodextrin (host) and adamantane (guest) with other cyclodextrins (hosts such as α, γ, and substituted members) and inclusion complex forming molecules (guests) provide the ability to rationally design network characteristics. The CD−ADA constructs are highly biocompatible and will thus be useful for in vivo applications. We have successfully employed these constructs in wound healing animal models and will report our results elsewhere.

LITERATURE CITED

(1) Lynch, S. E., Colvin, R. B., and Antoniades, H. N. (1989) Growth factors in wound healing. Single and synergistic effects on partial thickness porcine skin wounds. *J. Clin. Invest*. *84*, 640−646.

(2) Deuel, T. F., Kawahara, R. S., Mustoe, T. A., and Pierce, A. F. (1991) Growth factors and wound healing: platelet-derived growth factor as a model cytokine. *Annu. Rev. Med*. *42*, 567−584.

(3) Pierce, G. F., and Mustoe, T. A. (1995) Pharmacologic enhancement of wound healing. *Annu. Rev. Med*. *46*, 467−481.

(4) Greenhalgh, D. G. (1996) The role of growth factors in wound healing. *J. Trauma 41*, 159−167.

(5) Hengge, U. R., Chan, E. F., Foster, R. A., Walker, P. S., and Vogel, J. C. (1995) Cytokine gene expression in epidermis with biological effects following injection of naked DNA. *Nat. Genet*. *10*, 161−166.

(6) Hengge, U. R., Walker, P. S., and Vogel, J. C. (1996) Expression of naked DNA in human, pig, and mouse skin. *J. Clin. Invest*. *97*, 2911−2916.

(7) Eriksson, E., Yao, F., Svensjo, T., Winkler, T., Slama, J., Macklin, M. D., Andree, C., McGregor, M., Hinshaw, V., and Swain, W. F. (1998) In vivo gene transfer to skin and wound by microseeding. *J. Surg. Res*. *78*, 85−91.

(8) Eriksson, E. (2000) Gene transfer in wound healing. *Adv. Skin Wound Care 13*, 20−22.

(9) Sun, L., Xu, L., Chang, H., Henry, F. A., Miller, R. M., Harmon, J. M., and Nielsen, T. B. (1997) Transfection with aFGF cDNA improves wound healing. *J. Invest. Dermatol*. *108*, 313−318.

(10) Jeschke, M. G., Herndon, D. N., Baer, W., Barrow, R. E., and Jauch, K. W. (2001) Possibilities of nonviral gene transfer to improve cutaneous wound healing. *Curr. Gene Ther*. *1*, 267−278.

(11) Liechty, K. W., Nesbit, M., Herlyn, M., Radu, A., Adzick, N. S., and Crombleholme, T. M. (1999) Adenoviral-mediated overexpression of platelet-derived growth factor-B corrects ischemic impaired wound healing. *J. Invest. Dermatol*. *113*, 375−383.

(12) Andree, C., Swain, W. F., Page, C. P., Macklin, M. D., Slama, J., Hatzis, D., and Eriksson, E. (1994) In vivo transfer and expression of a human epidermal growth factor gene accelerates wound repair. *Proc. Natl. Acad. Sci. U.S.A*. *91*, 12188−12192.

(13) Benn, S. I., Whitsitt, J. S., Broadley, K. N., Nanney, L. B., Perkins, D., He, L., Patel, M., Morgan, J. R., Swain, W. F., and Davidson, J. M. (1996) Particle-mediated gene transfer with transforming growth factor-beta1 cDNAs enhances wound repair in rat skin. *J. Clin. Invest*. *98*, 2894−2902.

(14) Eming, S. A., Whitsitt, J. S., He, L., Krieg, T., Morgan, J. R., and Davidson, J. M. (1999) Particle-mediated gene transfer of PDGF isoforms promotes wound repair. *J. Invest. Dermatol*. *112*, 297−302.

(15) Kuwahara, H., Mitchell, A. T., Macklin, M. D., Zhao, J., Listengarten, D., and Phillips, L. G. (2000) Transfer of platelet-derived growth factor-BB gene by gene gun increases contraction of collagen lattice by fibroblasts in diabetic and nondiabetic human skin. *Scand. J. Plast. Reconstr. Surg. Hand Surg*. *34*, 301−307.

(16) Byrnes, C. K., Khan, F. H., Nass, P. H., Hatoum, C., Duncan, M. D., and Harmon, J. W. (2001) Success and limitations of a naked plasmid transfection protocol for keratinocyte growth factor-1 to enhance cutaneous wound healing. *Wound Repair Regen*. *9*, 341−346.

(17) Ruszczak, Z. (2003) Effect of collagen matrices on dermal wound healing. *Adv. Drug Deliv. Rev*. *55*, 1595−1611.

(18) Fang, J., Zhu, Y. Y., Smiley, E., Bonadio, J., Rouleau, J. P., Goldstein, S. A., McCauley, L. K., Davidson, B. L., and Roessler, B. J. (1996) Stimulation of new bone formation by direct transfer of osteogenic plasmid genes. *Proc. Natl. Acad. Sci. U.S.A*. *93*, 5753−5758.

(19) Tyrone, J. W., Mogford, J. E., Chandler, L. A., Ma, C., Xia, Y., Pierce, G. F., and Mustoe, T. A. (2000) Collagen-embedded platelet-derived growth factor DNA plasmid promotes wound healing in a dermal ulcer model. *J. Surg. Res*. *93*, 230−236.

(20) Bonadio, J., Smiley, E., Patil, P., and Goldstein, S. (1999) Localized, direct plasmid gene delivery in vivo: prolonged therapy results in reproducible tissue regeneration. *Nat. Med*. *5*, 753−759.

(21) Berry, M., Gonzalez, A. M., Clarke, W., Greenlees, L., Barrett, L., Tsang, W., Seymour, L., Bonadio, J., Logan, A., and Baird, A. (2001) Sustained effects of gene-activated matrices after CNS injury. *Mol. Cell. Neurosci*. *17*, 706−716.

(22) Kyriakides, T. R., Hartzel, T., Huynh, G., and Bornstein, P. (2001) Regulation of angiogenesis and matrix remodeling by localized, matrix-mediated antisense gene delivery. *Mol. Ther*. *3*, 842−849.

(23) Pakkanen, T. M., Laitinen, M., Hippelainen, M., Hiltunen, M. O., Alhava, E., and Yla-Herttuala, S. (2000) Periadventitial lacZ gene transfer to pig carotid arteries using a biodegradable collagen collar or a wrap of collagen sheet with adenoviruses and plasmid-liposome complexes. *J. Gene Med*. *2*, 52−60.

(24) Scherer, F., Schillinger, U., Putz, U., Stemberger, A., and Plank, C. (2002) Nonviral vector loaded collagen sponges for sustained gene delivery in vitro and in vivo. *J. Gene Med*. *4*, 634−643.

(25) Cohen-Sacks, H., Elazar, V., Gao, J., Golomb, A., Adwan, H., Korchov, N., Levy, R. J., Berger, M. R., and Golomb, G. (2004) Delivery and expression of pDNA embedded in collagen matrices. *J. Controlled Release 95*, 309−320.

(26) Doukas, J., Chandler, L. A., Gonzalez, A. M., Gu, D., Hoganson, D. K., Ma, C., Nguyen, T., Printz, M. A., Nesbit, M., Herlyn, M., Crombleholme, T. M., Aukerman, S. L., Sosnowski, B. A., and Pierce, G. F. (2001) Matrix immobilization enhances the tissue repair activity of growth factor gene therapy vectors. *Hum. Gene Ther*. *12*, 783−798.

(27) Gu, D. L., Nguyen, T., Gonzalez, A. M., Printz, M. A., Pierce, G. F., Sosnowski, B. A., Phillips, M. L., and Chandler, L. A. (2004) Adenovirus encoding human platelet-derived growth factor-B delivered in collagen exhibits safety, biodistribution, and immunogenicity profiles favorable for clinical use. *Mol. Ther*. *9*, 699−711.

(28) Doukas, J., Blease, K., Craig, D., Ma, C., Chandler, L. A., Sosnowski, B. A., and Pierce, G. F. (2002) Delivery of FGF genes to wound repair cells enhances arteriogenesis and myogenesis in skeletal muscle. *Mol. Ther*. *5*, 517−527.

(29) Lanciotti, J., Song, A., Doukas, J., Sosnowski, B., Pierce, G., Gregory, R., Wadsworth, S., and O'Riordan, C. (2003)

Targeting adenoviral vectors using heterofunctional poly-(ethylene glycol) FGF2 conjugates. *Mol. Ther*. *8*, 99−107.
(30) Schek, R. M., Hollister, S. J., and Krebsbach, P. H. (2004) Delivery and protection of adenoviruses using biocompatible hydrogels for localized gene therapy. *Mol. Ther*. *9*, 130−138.
(31) Shea, L. D., Smiley, E., Bonadio, J., and Mooney, D. J. (1999) DNA delivery from polymer matrices for tissue engineering. *Nat. Biotechnol*. *17*, 551−554.
(32) Li, Z., Ning, W., Wang, J., Choi, A., Lee, P. Y., Tyagi, P., and Huang, L. (2003) Controlled gene delivery system based on thermosensitive biodegradable hydrogel. *Pharm. Res*. *20*, 884−888.
(33) Hoffman, A. S. (2002) Hydrogels for biomedical applications. *Adv. Drug Deliv. Rev*. *54*, 3−12.
(34) Hennink, W. E., and van Nostrum, C. F. (2002) Novel crosslinking methods to design hydrogels. *Adv. Drug Deliv. Rev*. *54*, 13−36.
(35) Wenz, G. (1994) Cyclodextrins as building-blocks for supramolecular structures and functional units. *Angew Chem., Int. Ed. Engl*. *33*, 803−822.
(36) Harada, A. (1996) Preparation and structures of supramolecules between cyclodextrins and polymers. *Coord. Chem. Rev*. *148*, 115−133.
(37) Szejtli, J. (1998) Introduction and General Overview of Cyclodextrin Chemistry. *Chem. Rev*. *98*, 1743−1754.
(38) Huh, K. M., Ooya, T., Lee, W. K., Sasaki, S., Kwon, I. C., Jeong, S. Y., and Yui, N. (2001) Supramolecular-structured hydrogels showing a reversible phase transition by inclusion complexation between poly(ethylene glycol) grafted dextran and α-cyclodextrin. *Macromolecules 34*, 8657−8662.
(39) Huh, K. M., Cho, Y. W., Chung, H., Kwon, I. C., Jeong, S. Y., Ooya, T., Lee, W. K., Sasaki, S., and Yui, N. (2004) Supramolecular hydrogel formation based on inclusion complexation between poly(ethylene glycol)-modified chitosan and α-cyclodextrin. *Macromol. Biosci. 4*, 92−99.
(40) Li, J., Li, X., Zhou, Z., Ni, X., and Leong, K. W. (2001) Formation of supramolecular hydrogels induced by inclusion complexation between pluronics and α-cyclodextrin. *Macromolecules 34*, 7236−7237.
(41) Amiel, C., and Sebille, B. (1999) Association between amphiphilic poly(ethylene oxide) and β-cyclodextrin polymers: aggregation and phase separation. *Adv. Colloid Interface Sci*. *79*, 105−122.
(42) Sandier, A., Brown, W., Mays, H., and Amiel, C. (2000) Interaction between an adamantane end-capped poly(ethylene oxide) and a β-cyclodextrin polymer. *Langmuir 16*, 1634−1642.
(43) Renard, E., Deratani, A., Volet, G., and Sebille, B. (1997) Preparation and characterization of water soluble high molecular weight β-cyclodextrin-epichlorohydrin polymers. *Eur. Polym*. *33*, 49−57.
(44) Hwang, S. J., Bellocq, N. C., and Davis, M. E. (2001) Effects of structure of beta-cyclodextrin-containing polymers on gene delivery. *Bioconjugate Chem*. *12*, 280−290.
(45) Pun, S. H., and Davis, M. E. (2002) Development of a nonviral gene delivery vehicle for systemic application. *Bioconjugate Chem*. *13*, 630−639.
(46) Davis, M. E., Pun, S. H., Bellocq, N. C., Reineke, T. M., Popielarski, S. R., Mishra, S., and Heidel, J. D. (2004) Self-assembling nucleic acid delivery vehicles via linear, water-soluble, cyclodextrin-containing polymers. *Curr. Med. Chem*. *11*, 179−197.
(47) Gonzalez, H., Hwang, S. J., and Davis, M. E. (1999) New class of polymers for the delivery of macromolecular therapeutics. *Bioconjugate Chem*. *10*, 1068−1074.
(48) Larson, R. G. (1999) *The structure and rheology of complex fluids*, Oxford University Press, New York, Oxford, U.K.
(49) Cheney, I. W., Johnson, D., Vaillancourt, M., Avanzini, J., Morimoto, A., Demers, B., Willis, K., Shabram, P., Bolen, J. B., Tavtigian, S. V., and Bookstein, R. (1998). Suppression of tumorigenicity of glioblastoma cells by adenovirus-mediated MMACl/TREN gene transfer. *Cancer Res. 58*, 2331−2334.
(50) Huyghe, B. G., and Liu, S., et al. (1995). Purification of a type 5 recombinant adenovirus encoding human p53 by column chromatography. *Hum. Gene Ther. 6*, 1403−1416.
(51) Shabram, P. W., and Giroux, D. D., et al. (1997). Analytical Anion-Exchange HPLC of Recombinant Type-5 Adenoviral Particles. *Hum. Gene Ther. 8*, 453−465.
(52) Parker, K. K., and Lepre Brock, A., et al. (2002). Directional control of lamellipodia extension by constraining cell shape and orienting cell tractional forces. *FASEB 16*, 1195−1204.
(53) Li, W., and Fan, J. et al. (2004). Mechanism of human dermal fibroblast migration by type I, collagen and platelet-derived growth factor-BB. *Mol. Biol. Cell 15* (1), 294−309.
(54) Roy, P., and Petroll, W. M. (1999). Effect of cell migration on the maintenance of tension on a collagen matrix. *Ann. Biomed. Eng. 27* (6), 721−730.
(55) Grinnell, F. (1994). Fibroblasts, Myofibroblasts, and Wound Contraction, *J. Cell Biol. 124*, 401−404.
(56) Grinnell, F. (2003). Fibroblast biology in three-dimensional collagen matrices. *Trends Cell Biol. 13* (5), 264−269.

BC0498119

Poly(3-guanidinopropyl methacrylate): A Novel Cationic Polymer for Gene Delivery

Arjen M. Funhoff, Cornelus F. van Nostrum, Martin C. Lok, Marjan M. Fretz, Daan J. A. Crommelin, and Wim E. Hennink*

Department of Pharmaceutics, Utrecht Institute for Pharmaceutical Sciences (UIPS), Utrecht University, P.O. Box 80082, 3508 TB, Utrecht, The Netherlands. Received June 11, 2004; Revised Manuscript Received September 15, 2004

A cationic polymethacrylate with a guanidinium side group was designed in order to create a polymer with cell membrane-penetrating properties such as Tat or other arginine-rich peptides. The polymer, poly(3-guanidinopropyl methacrylate), abbreviated as pGuaMA, was synthesized by free radical polymerization. The DNA-condensing properties of pGuaMA (Mw 180 kDa) were investigated via dynamic light scattering and zeta potential measurements, and small, positively charged particles (110 nm, +37 mV) were found. It was shown that polyplexes based on pGuaMA were able to transfect COS-7 cells efficiently in the absence of serum, while under the same conditions poly(arginine) (pArg) polyplexes did not show detectable transfection levels. Addition of a membrane-disrupting peptide, INF 7, derived from the influenza virus, to preformed pGuaMA polyplexes did result in ~2 times increased transfection levels. DLS, zeta potential measurements, gel electrophoresis, and ethidium bromide displacement measurements indicated that serum induced aggregation of the polyplexes at high polymer/plasmid ratios, while at low polymer/plasmid ratios the polarity of the polyplexes reversed likely due to adsorption of negatively charged proteins on their surface. Likely, the unfavorable interactions of pGuaMA polyplexes with serum proteins is the reason for the absent transfection activity of these polyplexes in the presence of serum. Confocal laser scanning microscopy indicated cellular internalization via endocytosis of both polyplexes and free polymer. Thus, pGuaMA polyplexes enter cells, as reported for other polyplexes, by endocytosis and not, as hypothesized, via direct membrane passage.

INTRODUCTION

The use of genetic material as medicines to cure life-threatening diseases is currently under investigation. Several potential vehicles for gene delivery (called vectors) into target cells are investigated, each with its own advantages and disadvantages. There exist however a number of physical and biological barriers (*1*–*5*) which limit the potential transfection activity of the presently investigated nonviral (= synthetic) gene delivery systems. It is widely accepted that complexes of the carrier system and DNA (called polyplexes in the case of polymers or polypeptides (such as pEI, pDMAEMA, or pLL), and lipoplexes in the case of lipids (such as DOTAP)) (*6*–*9*), are taken up by cells via endocytosis (*2*) and end up in endosomes/lysosomes. The content of the endosomes/lysosomes is eventually degraded by the enzymes present in these organelles. Therefore, poly-/lipoplexes have to escape from the endosomes/lysosomes before this degradation occurs. The overall efficiency of this process is usually low, resulting in low gene-expression levels, but it has been demonstrated that the transfection efficiency of polyplexes can be increased using endosomal escape agents (*10*). However, completely circumventing endocytosis as the pathway of uptake and making use of an alternative route to enter the cell cytoplasm is an attractive strategy to improve the overall efficiency of nonviral gene delivery systems.

In the past few years, it was reported that some peptides are taken up by cells by a route other than endocytosis. Uptake of these peptides is seemingly receptor- or protein-independent and already occurs at 4 °C, although the actual mechanism is not clarified. These peptides are called cell-penetrating peptides or protein transduction domains, as they easily pass cellular membranes. Two examples of such peptides are the basic domain from the HIV-1 Tat protein (*11*) and a sequence from the *Drosophila melanogaster* antennapedia protein (Ant) (*12*). A common feature of these two peptides is that they consist of a large number of positively charged amino acids, mainly arginine and lysine. It was shown that other arginine-rich peptides (*13*) as well as oligoarginines (*14*) show the same cellular uptake as the Tat peptide. These peptides were coupled to macromolecular therapeutics to facilitate the cellular uptake of these compounds. The group of Kopeçek showed that when the Tat peptide was coupled to a *N*-(2-hydroxypropyl)-methacrylamide copolymer, cellular uptake and nuclear localization of the copolymer was substantially improved (*15*). Coupling of the Tat or the Ant peptide to antisense oligonucleotides also increased the cellular uptake (*16*). It was even shown that if the backbone of peptide nucleic acids (PNAs) was modified with guanidinium groups, cellular uptake of the PNAs was much higher and directed toward the nucleus (*17*).

Since the guanidinium group is highly basic (pK_a = 12.5), it is fully protonated at physiological pH. Therefore, synthetic polymers (e.g., poly(meth)acrylates) bearing guanidinium side chains should be able to complex and

* Corresponding author. Tel. +31-30.2536964. Fax +31−30.2517839. E-mail address: W.E.Hennink@pharm.uu.nl.

10.1021/bc049864q CCC: $27.50 © 2004 American Chemical Society
Published on Web 10/23/2004

condense DNA into small particles. On the basis of the above-mentioned literature, we initially expected that such polymers and/or polyplexes based thereon will be taken up by cells via another pathway than endocytosis and localize in the nucleus. This may result in increased transfection levels. For poly(arginine), the ability to condense DNA into small particles has been shown by Pouton et al. (*18*). However, the transfection efficiency of poly(arginine)-based polyplexes was the lowest of the tested cationic polypeptides. When compared to polymethacrylates, polypeptides have a much lower transfection efficiency (*19*), thus changing the backbone of poly(arginine) to a methacrylate may be advantageous.

In more recent publications the spontaneous passage of arginine-rich peptides over the plasma membrane has been questioned. Richard et al. (*20*) suggested that the observed 'spontaneous' membrane passage by these peptides might be an artifact created by the fixation of the cells with formaldehyde, as diffuse fluorescence in the cytosol was only found when cells were fixated, whereas a punctuate distribution was found in living cells. Krämer et al. reported that the Tat peptide is not able to penetrate the lipid bilayer of liposomes or the cell membrane of living cells (*21*). Both Richard et al. and Krämer et al. concluded therefore that endocytosis is the main pathway of internalization of these cationic peptides. Although the cell-penetrating properties of these peptides are questionable, they may still be useful for drug delivery purposes. Console et al. showed that the Ant or Tat peptide promotes cellular uptake of macromolecules and liposomes through endocytosis (*22*). The amount of internalized FITC-labeled avidin or streptavidin was higher when it was bound to biotinylated Ant or Tat peptide. Thus, although our initial approach to synthesize a polymer with cell membrane-translocating properties is probably not feasible, an increase in cellular uptake can also promote the transfection efficiency and may therefore be of interest.

This paper reports on the synthesis of the monomer 2-methacrylic acid 3-guanidinopropyl ester and the corresponding polymer. The transfection activity and mechanism of cellular uptake of polyplexes based on this polymer are studied as well.

EXPERIMENTAL PROCEDURES

Materials. The following materials were used as received: 3-amino-1-propanol (Janssen Chimica), 2-ethyl-2-thiopseudourea hydrobromide (Aldrich), *N*-(aminopropyl)methacrylamide hydrochloride (Polysciences), rhodamine B isothiocyanate (Aldrich), poly(L-aspartic acid) sodium salt (pAspA) (Sigma), poly(L-arginine hydrochloride) (pArg) (Sigma, $M_w = 42.4$ kDa). Methacryloyl chloride purum ≥ 97% (Fluka) was distilled before use. The plasmid pCMVLacZ, containing a bacterial LacZ gene preceded by a nuclear localization signal under control of a CMV promoter, was purchased from Sanvertech (Heerhugowaard, The Netherlands). INF-7, a 24 amino acid containing peptide with fusogenic activity derived from the influenza virus, was synthesized via standard Fmoc solid-phase synthesis (*23*). The reference polymers: poly((dimethylamino)ethyl methacrylate) (pDMAEMA, $M_n = 92$ kg/mol) was synthesized via radical polymerization (*24*), and PEI (branched 25 kDa) was purchased from Sigma.

Synthesis of 2-Methacrylic Acid 3-Guanidinopropyl Ester (GuaMA). 2-Guanidinopropanol was synthesized according to Fishbein and Gallaghan (*25*). In detail, 3-aminopropanol (0.641 g, 8.54 mmol) was added dropwise to 2-ethyl-2-thiopseudourea hydrobromide (1.58 g, 8.54 mmol) in a 10 mL flask. After 5 min of stirring, 1 mL water was added. The resulting solution was stirred overnight at room temperature. Next, water was removed under reduced pressure to obtain a white solid, which was further dried (yield 1.67 g, 8.43 mmol, 99.8%). NMR spectra were recorded on a Varian G-300 300 MHz spectrometer (Varian, Palo Alto, CA). ^{1}H NMR (DMSO): $\delta = 7.6-6.6$ (multiple bs, 4H, NH's), 4.7 (bs, 1H, OH), 3.44 (t, 2H, HOCH_2CH$_2$CH$_2$N), 3.14 (t, 2H, HOCH$_2$-CH$_2$CH_2N), 1.60 (dt, 2H, HOCH$_2$CH_2CH$_2$N). ^{13}C NMR (DMSO): $\delta = 157.1$ (CH$_2$NH*C*(NH)NH$_2$), 58.0 (HO*C*H$_2$-CH$_2$CH$_2$), 38.2 (CH$_2$*C*H$_2$NHC), 31.6 (CH$_2$*C*H$_2$CH$_2$NH).

2-Methacrylic acid 3-guanidinopropyl ester was synthesized as follows. Methacryloyl chloride (0.892 g, 8.50 mmol) was added to guanidinopropanol (1.67 g, 8.43 mmol) dissolved in acetonitrile (10 mL) and stirred at room temperature for 2 days. Acetonitrile was removed under reduced pressure, resulting in a white solid. The crude product was purified by column chromatography over silica (eluent EtOAc/EtOH 1/1, $R_f = 0.68$), and the solvent from the pooled fractions with the desired product was removed under reduced pressure, resulting in a white solid, the HCl salt of the monomer. This was recrystalized in EtOAc, yielding 1.04 g (46%). ^{1}H NMR (DMSO): $\delta = 7.6$ and 7.2 (bs, 4H, NH's), 6.04 (s, 1H, H_2C=C), 5.68 (s, 1H, H_2C=C), 4.12 (t, 2H, OCH_2CH$_2$), 3.19 (m, 2H, CH$_2$CH_2NHC), 1.87 (s, 3H, C=C(CH_3)), 1,82 (m, 2H, CH$_2$CH_2CH$_2$). ^{13}C NMR (DMSO): $\delta = 157.4$ (CH$_2$NH*C*(NH)NH$_2$), 136.4 (H$_2$C=*C*), 126.6 (H$_2$*C*=C), 62.3 (O*C*H$_2$CH$_2$), 38.3 (CH$_2$*C*H$_2$NC), 28.3 (CH$_2$*C*H$_2$CH$_2$NH), 18.6 (C=C(*C*H$_3$)).

Polymerization. pGuaMA was synthesized via radical polymerization as described before for pDMAEMA (*24*). In brief, 0.500 g of monomer was dissolved in 2 mL of 1 M hydrochloric acid, and the pH was adjusted to 5. Polymerization was carried out under a nitrogen atmosphere at 60 °C overnight with ammonium peroxodisulfate as initiator at a M/I ratio of 100. After cooling to room temperature, the solution was poured into a dialysis tube (MWCO 3.5 kDa) and extensively dialyzed against water. The polymer was collected as a white fluffy solid after freeze-drying (yield 0.366 g, 73%). Molecular weights were determined via gel permeation chromatography (GPC) relative to dextran standards (Fluka) (*24*). GPC measurements were performed with two thermostated (30 °C) columns in series (Shodex OHpak K80P and KB-80M, Showa, Denko, Japan) on a system consisting of a pump Model 600, an autoinjector Model 486, and a refractive index detector Model 410 (all Waters Associates, Milford, MA). The eluent was an aqueous solution of 0.7 M $NaNO_3$, 0.1 M Tris (pH 7.2), and the flow rate was 1 mL/min.

A fluorescently labeled polymer was synthesized by copolymerization of GuaMA with 5 mol % *N*-(aminopropyl)methacrylamide using the same synthetic procedure as described above. Rhodamine isothiocyanate (1 mg, 1.87 μmol) was coupled to the free amines of the polymer (50.0 mg, 17.3 μmol free NH_2) in 2.50 mL of 20 mM HEPES buffer, pH 7.4, overnight at 4 °C. Unreacted rhodamine was removed by gel permeation chromatography over a Sephadex G25 column (Pharmacia) using water as an eluent. The fractions with the polymer were collected, and the fluorescently labeled polymer was obtained via lyophilization of the combined fractions (yield 39.7 mg, 78%).

Physical Characterization of Polyplexes. Polyplexes with different polymer-to-plasmid ratios (expressed as *N*/*P* ratios, where *N* is the amount of protonated nitrogens in the polymer (for pGuaMA/pArg: one

per side chain) in moles and *P* is the amount of plasmid phosphate in moles) were made by adding a pGuaMA or pArg solution (700 μL, various concentrations) in buffer (HEPES (20 mM) buffered saline (HBS) for particle size measurements, 20 mM HEPES buffer pH 7.4 for ζ-potential measurements) to a plasmid DNA solution (175 μL, 75 μg/mL). After incubation of the polyplex dispersions for 30 min at room temperature, *Z*-average diameters were measured with dynamic light scattering at 25 °C with a Malvern 4700 system using an argon-ion laser (488 nm) operating at 10.4 mW (Uniphase) and PCS (photon correlation spectrometry) software for Windows version 1.34 (Malvern, UK). Viscosity and refractive index of pure water at 25 °C were used. The system was calibrated with an aqueous dispersion of polystyrene particles with a 100 nm diameter. The ζ-potential of the polyplexes was determined at 25 °C in a DTS5001 cell with a Zetasizer 2000 unit (Malvern). The instrument was calibrated with a polystyrene dispersion with known ζ-potential.

In Vitro Transfection and Cell Viability Studies. Transfection and cell viability studies were performed in COS-7 cells as described before (*26*). The plasmid pCMVLacZ was used as reporter gene. Plates (96-well) were seeded with 3×10^4 cells/cm^2 24 h before transfection. At the day of transfection, 250 μL pGuaMA/pArg polyplex dispersions in HBS were made essentially as described above with the exception that the DNA concentration used was 50 μg/mL (instead of 75 μg/mL). INF-7 coated pGuaMA polyplexes were made by mixing 150 μL of polymer solution and 50 μL of DNA solution in HBS. After 30 min of incubation, 50 μL of INF-7 solution (150 μg/mL in HBS) was added, and the polyplexes were incubated for an additional 15 min. Previous studies showed that positively charged polyplexes were coated with the negatively charged INF-7 peptide (*27*). After washing of the cells with HBS, 100 μL of polyplex dispersion and 100 μL of culture medium (with or without fetal bovine serum) were applied to the cells for 1 h, after which the cells were washed and fresh culture medium was applied. All studies were performed in two identical series in two different 96-well plates. After 48 h of incubation, one plate was evaluated for reporter gene (β-galactosidase) expression with *o*-nitrophenyl-β-D-galactopyranoside, the other plate was used to determine cell viability using a XTT colorimetric assay (*28*). As a reference, pDMAEMA and PEI polyplexes prepared at the same DNA concentration and an *N*/*P* ratio of 6 were used. The transfection activity of the pDMAEMA polyplex formulation was set at one.

Influence of Serum on the Biophysical Properties of Polyplexes. To determine the effect of serum on the biophysical properties of the polyplexes, their size in the presence or absence of serum was measured. In detail, 500 μL polyplex dispersions in HBS were made as described above. After 30 min incubation, the polyplex dispersions were split into two equal volumes and 1 to 1 diluted with either buffer solution or buffer solution containing 10% serum. These dispersions were incubated for another hour before *Z*-average diameters were measured using DLS. For zeta potential measurements, a 2.5 mL polyplex dispersion (30 μg/mL DNA) in 20 mM HEPES buffer, pH 7.4, was diluted with 2.5 mL of 20 mM HEPES buffer containing 10% serum.

To study whether serum proteins induced polyplex dissociation, two different tests were performed. In the first test, DNA condensation (by pGuaMA/pArg) and poly(aspartic acid) (pAspA)-mediated dissociation of the formed complexes in the absence or presence of 5% serum was monitored using agarose gel electrophoresis. Polyplexes were made by mixing 10 μL plasmid solution (80 μg/mL in HBS) with 10 μL of polymer solution (various concentrations in HBS), and the dispersions were incubated for 30 min at room temperature. Next, 5 μL of buffer or buffer containing 30% serum was added, and the dispersions were incubated for 15 min. Subsequently, 5 μL of pAspA (10 mg/mL) (or 5 μL buffer as a control) was added, and the dispersions were incubated for another 30 min. After addition of 3 μL of sample buffer (containing bromophenol blue 0.4% (w/v), 10 mM EDTA, and 50% (v/v) glycerol in water), 30 μL of this mixture was applied onto a 0.7% agarose gel containing 0.5 μg/mL ethidium bromide. After development of the gel, DNA was visualized with a UV lamp using a GelDoc system (BioRad) (*26*).

In the second test, free DNA was detected via fluorescence with ethidium bromide that was added to a DNA solution (25 μg/mL in HBS) in a 1:10 molar ratio to the DNA phosphates. A solution of pGuaMA (400 μL, various concentrations in HBS) was added to 100 μL of DNA, vortexed for 5 s, and incubated for 30 min. This was done in two identical series. To one series, 500 μL buffer was added, and to the other series 500 μL of buffer containing 10% serum. The dispersions were incubated at room temperature for 1 h after which the fluorescence was measured using a Spex Fluorlog III spectrofluorimeter (Spex, Edison, NJ). The excitation and emission wavelength were 520 and 600 nm, respectively, and the slits were 1.26 and 4.52 nm, respectively. The relative fluorescence (F_r) values were determined as follows:

$$F_r = (F_{obs} - F_e)/(F_0 - F_e)$$

where F_{obs} is the fluorescence of the polyplex dispersion, F_e is the fluorescence of ethidium bromide in the absence of DNA, and F_0 is the initial fluorescence of DNA/ethidium bromide in the absence of pGuaMA.

Cellular Uptake of Polyplexes and Free Polymer. The cellular uptake of polyplexes and free polymer was investigated via confocal laser scanning microscopy (CLSM) in living cells in the absence or presence (only polyplexes) of an endocytosis inhibitor (1 mM iodoacetamide) or at 4 °C. DNA was labeled with AlexaFluor 647 C_2 maleimide (Molecular Probes) using the Fasttag FL labeling kit from Vector Laboratories. Polyplexes were made with the rhodamine-labeled polymer, and for experiments in the presence of inhibitor nonlabeled DNA was used. In a 16-well glass plate, cells were seeded (3×10^4 cells/cm^2) and culture medium was added. The cells were grown at 37 °C in a humidified 5% CO_2-containing atmosphere. Twenty-four or 47 h after seeding, 100 μL of serum-free culture medium and 100 μL of either polyplexes with an N/P ratio of 2.7 (10 μg/mL DNA, polymer 15 μg/mL) or free pGuaMA (15 μg/mL) were applied for 1 h to the cells. As control, pDMAEMA based polyplexes (N/P = 6) were applied to the cells 24 h after seeding. Thereafter, the polyplex dispersion and the free polymer were removed and culture medium was applied. The cells were cultured for 48 h in total after seeding, after which the cells were rinsed with PBS, and covered with a glass slide. Directly afterward, fluorescent and transmitted light microscope images were taken simultaneously on a Leica TCS−SP microscope equipped with an argon 488 nm, a krypton 568 nm and a HeNe 647 nm laser and were analyzed with Leica TCS−SP Power Scan software (Leica Microsystems, Rijswijk, The Netherlands).

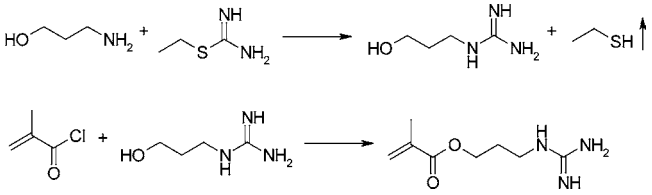


Figure 1. Synthetic route toward 2-methylacrylic acid 3-guanidinopropyl ester.

RESULTS AND DISCUSSION

Monomer and Polymer Synthesis. The synthesis of 2-methacrylic acid 3-guanidino-propyl ester (GuaMA) was performed in two steps (Figure 1). In the first step, 3-aminopropanol was converted into guanidinopropanol using 2-ethyl-2-thiopseudourea hydrobromide with the release of ethanethiol (*25*). This reaction yielded the desired product in quantitative yield and good purity (>97% by NMR). In the second step, guanidinopropanol was esterified with methacryloyl chloride and purified via column chromatography and recrystallization from ethyl acetate. This resulted in the desired monomer in reasonable yield (46%) and good purity (>97% by NMR, melting point 65 °C). Free radical polymerization of this monomer in an aqueous HCl solution and subsequent dialysis and lyophilization gave poly(3-guanidinopropyl methacrylate) (yield 73%) with a weight average molecular weigh (M_w) of 180 kDa and a number average molecular weight (M_n) of 25 kDa as determined with GPC relative to dextran standards. A pGuaMa M_w 180 kDa was synthesized since high molecular weight cationic polymers have, generally speaking (as demonstrated, for example, for pDMAEMA (*24*)), the best DNA-condensing properties.

Biophysical Characterization of Polyplexes. The biophysical properties of pArg- or pGuaMA-based polyplexes were investigated by DLS and zeta potential measurements. Figure 2 shows the average size and zeta potential of these polyplexes as a function of the polymer-to-DNA ratio (in the absence of serum proteins). As can be seen in Figure 2A, pArg was able to condense DNA in small particles of approximately 80 nm at all tested *N*/*P* ratios. Zeta potential measurements showed negatively charged polyplexes at low *N*/*P* ratios. With increasing *N*/*P* ratios the zeta potential of the polyplexes raised to approximately + 20 mV. As shown in Figure 2B, pGuaMA condensed DNA into small particles of approximately 100 nm when an excess of the polymer was used. The particles have a zeta potential of approximately +37 mV at these ratios, which is rather high when compared to the pArg polyplexes and other polyplexes (*29*−*31*). This might suggest that under the conditions where small and stable particles are formed (*N*/*P* > 5) DNA binds more pGuaMA than pArg in a polyplex. pGuaMA polyplexes prepared at an *N*/*P* ratio of 2 were neutral, and consequently, due to the absence of electrostatic repulsion, large aggregates were formed in the polyplex formulation. At lower ratios negatively charged polyplexes were formed. Similar DNA condensation behavior has been found for other cationic polymers (*29*−*31*).

In Vitro Transfection and Cell Viability Studies. Transfection studies were performed in COS-7 cells (Figure 3). The transfection activity and cytotoxicity of the pGuaMA/pArg polyplexes was compared with those of pDMAEMA and PEI systems. When serum was present during the incubation of the polyplexes and the cells, no transfection was found for both pGuaMA- and pArg-based polyplexes. Compared to pDMAEMA-based

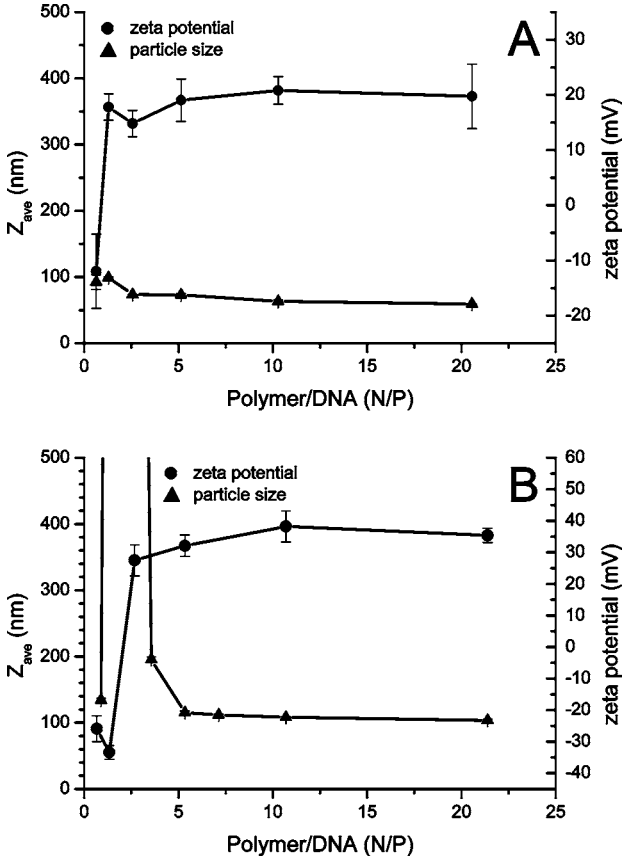


Figure 2. Physical characteristics of pArg (A)- and pGuaMA (B)-based polyplexes: particle size (▲) and zeta potential (●) as a function of the *N*/*P* ratio. All experiments were done in triplicate.

polyplexes, the pGuaMA and pArg polyplexes had a low toxicity since the concentration of polymer resulting in 50% cell death was 100 μg/mL for pArg and 150 μg/mL for pGuaMA (Table 1), respectively, whereas it was 30 μg/mL for pDMAEMA. For the pGuaMA polyplexes prepared at *N*/*P* ratios above 22, it was observed by visual inspection that a precipitate was deposited onto the cells. These precipitates likely are aggregates of the free pGuaMA present in the polyplex formulation and serum proteins (see section 'Influence of Serum on pGuaMA Based Polyplexes'). Therefore, transfection experiments were also done in the absence of serum. As can be seen in Figure 3 and Table 1, this had a major effect on both the transfection activity and the cytotoxicity of the pGuaMA polyplexes. Transfection efficiencies of 0.20 relative to the reference polymers (pDMAEMA and PEI) were found at an *N*/*P* ratio of 5.4. As has been found for other polymer (*24*, *30*), small, positively charged polyplexes were formed at ratios where transfection occurred. Above an *N*/*P* ratio of 5.4, the transfection levels decreased most likely due to the increasing toxicity of the polyplexes as can be seen in Figure 3B. Thus serum proteins mask the toxicity of the polyplexes, as has been observed previously for other polyplex systems (*31*, *32*). In contrast, omitting serum proteins did not result in detectable transfection levels or polyplexes based on pArg, while the cytotoxicity of the polyplexes was comparable to pGuaMA-based polyplexes (Figure 3). Pouton et al. compared different cationic polypeptides, among which pArg and poly(L-lysine) (pLL), as vectors for gene delivery in B16 cells and they showed that pArg had the lowest transfection efficiency (*18*). It is known that different polymers, albeit having related structures, may

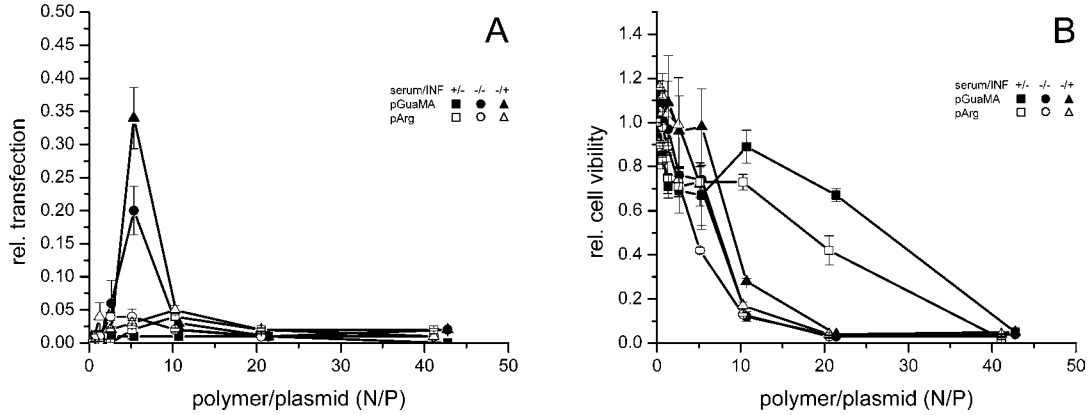


Figure 3. Transfection efficiency (A) and cell viability (B) of pGuaMA (closed symbols)- and pArg (open symbols)-based polyplexes in the presence (square) or absence (circle) of serum and of pGuaMA-based polyplexes in the absence of serum and presence of INF-7 (triangle) in COS-7 cells. All experiments were done in triplicate. Both reference polyplex formulations (pDMAEMA or PEI/DNA 6/1 (*N/P*) had comparable transfection activity, respectively 1.0 (pDMAEMA) and 1.05 (PEI), in the absence of serum.

Table 1. IC_{50} Values of pGuaMA and pArg Polyplexes under Different Transfection Conditions[a]

	transfection conditions		
polymer	+ serum − INF	− serum − INF	− serum + INF
pGuaMA	152 ± 5	42 ± 8	51 ± 4
pArg	105 ± 5	26 ± 2	42 ± 4

[a] The IC_{50} value is defined as the concentration polymer (in μg/mL) resulting in 50% cell death.

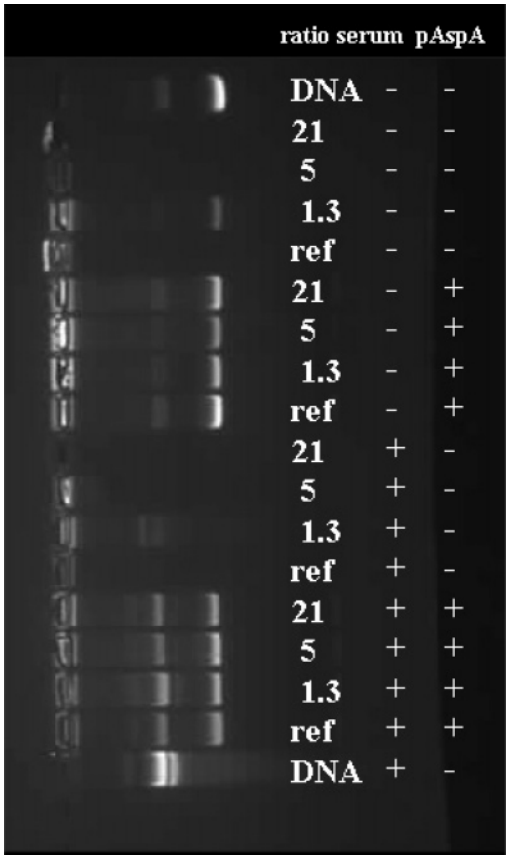


Figure 4. Gel electrophoresis of pGuaMA-based polyplexes in the absence (−) or presence (+) of serum or poly(aspartic acid) at various *N/P* ratios. Ref = pDMAEMA-based polyplexes at *N/P* = 6.

show substantial differences in transfection activity (*33*). Probably, changes in the polymeric backbone, such as from amino acid (pArg) to methacrylate (pGuaMA) can also affect the transfection activity.

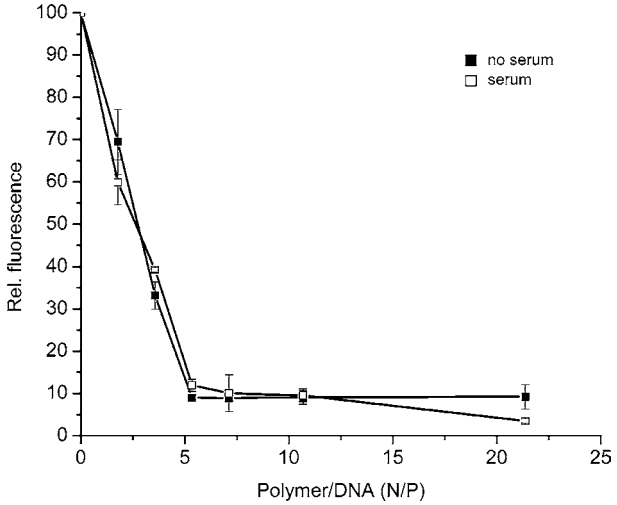


Figure 5. Ethidium bromide fluorescence (relative intensity) of pGuaMA-based polyplexes in the absence (■) or presence (□) of 5% serum. All experiments were done in triplicate.

Figure 3 shows that when the membrane-disrupting peptide INF-7 was added to pGuaMA-based polyplexes, an increase in transfection was observed by a factor of approximately 2. In contrast, addition of the peptide to pArg-based polyplexes did not result in increased transfection levels (data not shown). Probably, one of the following processes (e.g., polyplex destabilization, nuclear uptake) in gene delivery is rate limiting. As observed for other polyplexes (*30*, *33*, *34*), the cell viability was not influenced by the addition of the peptide. To investigate whether an endocytosis inhibitor had effect on the transfection, experiments in the presence of 1 mM iodoacetamide were performed. However, no detectable expression of the transgene was found at all pGuMA/DNA ratios tested. Both experiments indicated that the polyplexes are taken up via endocytosis rather than direct membrane passage.

Influence of Serum on pGuaMA-Based Polyplexes. Free polymer present in the polyplex dispersions prepared at high *N/P* ratios probably binds to negatively charged serum proteins, causing large aggregates, as has been demonstrated for pDMAEMA polyplexes (*35*). Incubating free polymer with serum in the same concentrations indeed resulted in large aggregates (data not shown). Because the pGuaMA polyplexes did not show

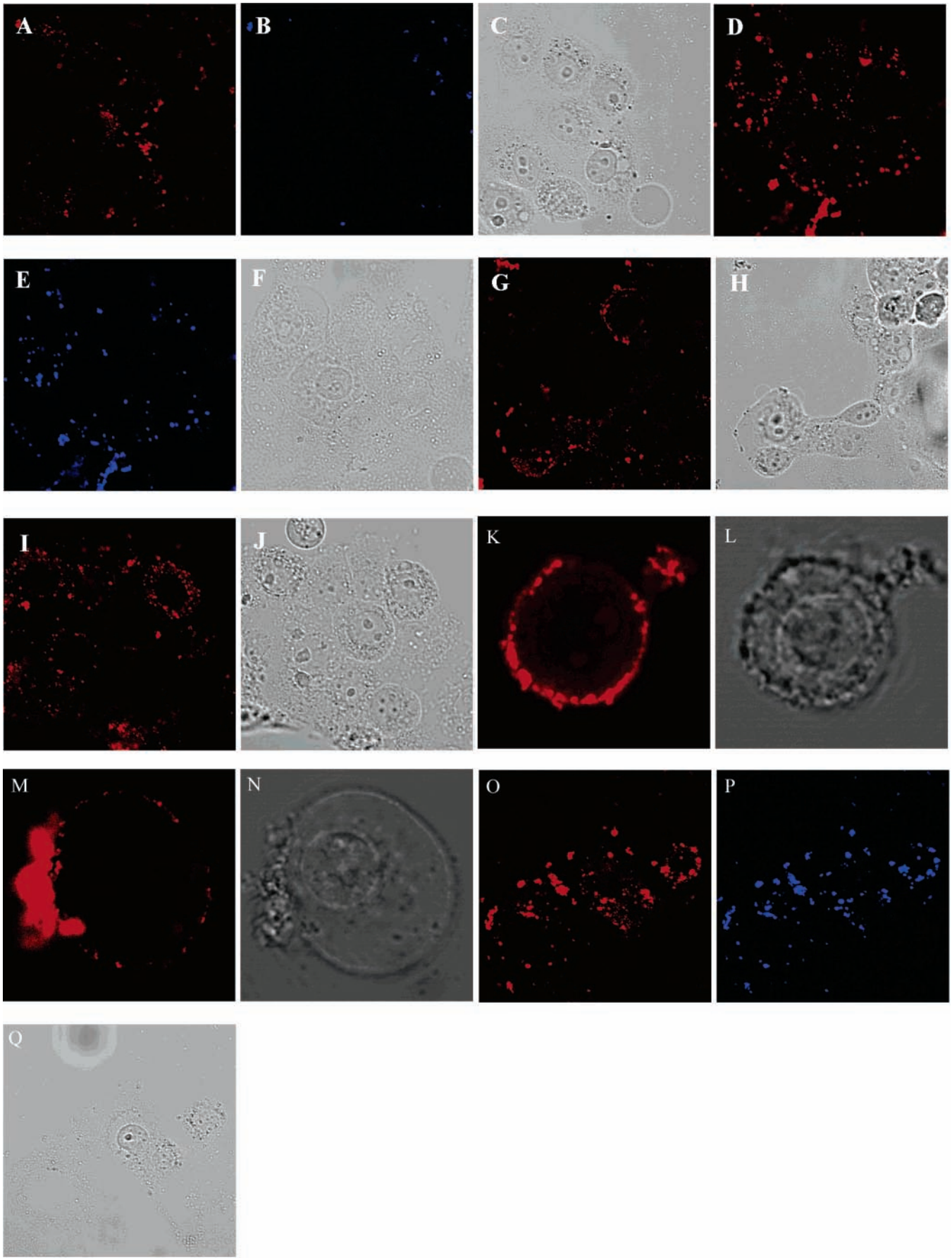


Figure 6. CLSM pictures of pGuaMA-based polyplexes (*N*/*P* ratio of 2.7) (A−C 1 h, D−F 24 h) and free polymer (15 μg/mL) (G−H 1 h, I−J 24 h) in the absence and polyplexes in the presence (K, L) of endocytosis inhibitor or at 4 °C (M, N). pDMAEMA-based polyplexes (*N*/*P* ratio of 6) (O−Q, 24 h) were used as control.

detectable transfection in COS cells and simultaneously large aggregates were visible, possible adverse interactions of serum with these polyplexes were investigated. It is known that serum proteins can cause aggregation of polyplexes or cause polyplex destabilization (*36*, *37*).

DLS measurements showed that polyplexes prepared at *N*/*P* ratios <10 did not show an increase in size when incubated with serum (data not shown). Zeta potential measurements, however, revealed that independent of the *N*/*P* ratio, pGuaMA polyplexes had a negative surface charge (zeta potential −14 mV) when serum was present. A substantial increase in particles size from 70 nm to >1 μm was observed when pGuaMA polyplexes (*N*/*P* > 10) were incubated with serum. At this ratio free polymer is probably present. When serum was added to a pGuaMA solution with the same concentration as used for the preparation of the *N*/*P* = 10 polyplexes, large aggregates were formed. Thus serum proteins adsorb on the positively charged polyplexes by which their zeta potential becomes negative. It has been shown before that polyplexes with a negative zeta potential had low aspecific cellular binding and consequently low transfection activity (*33*). Moreover, it has been reported that serum proteins can also induce polyplex destabilization (*36*, *37*). Figure 4 shows the gel electrophoretic patterns of pGuaMA polyplexes prepared at three different *N*/*P* ratios in the presence or absence of serum and poly(aspartic acid) (pAspA), a known and strong polyplex destabilization agent (*26*, *38*) pDMAEMA-based polyplexes (*N*/*P* = 6) were used as a reference. In the absence of pAspA, all DNA was found in the starting slots at *N*/*P* ratios 5 and 21, demonstrating that the DNA was bound to the polymer. A small amount of free DNA could be detected at an *N*/*P* ratio of 1.3. This is in agreement with DLS data (Figure 2), which showed small, positively charged particles at *N*/*P* ratios of 5 and 21, but aggregates at *N*/*P* ratio of 1.3. The electrophoretic patterns in the presence of serum gave the same results, suggesting that serum was not able to dissociate the polyplexes. When pAspA was present, free DNA could be detected at all ratios, indicating that the polyplexes were dissociated. Also here, no influence of serum was found.

Figure 5 shows the change in ethidium bromide fluorescence when pGuaMA is added to DNA in the absence or presence of serum. This figure shows that serum does not affect the complex formation between DNA and pGuaMA. Considering all the data, it can be concluded that not polyplex destabilization but interaction of serum proteins with the polyplexes is probably the main reason for the low transfection activity of the pGuaMA polyplexes in the presence of serum. These adverse interactions of polyplexes with serum proteins may be prevented by pegylation of the polyplexes. Moreover, pegylation of polyplexes has the additional advantage that the circulation times in vivo are increased, thereby increasing the accumulation of the polyplexes at the desired site (*39*−*41*).

Cellular Uptake of Polyplexes. Polyplexes based on previously described polymers (e.g., pDMAEMA, pEI) are taken up by cells via endocytosis (*2*). As pointed out in the Introduction, for Tat and other arginine-rich peptides another pathway than endocytosis that leads to the direct introduction of the peptide in the cytoplasm, has been suggested. However, this has been questioned in latter publications and uptake by endocytosis was suggested for these peptides. To investigate the pathway by which pGuaMA polyplexes are taken up by cells, confocal laser scanning microscopy (CLSM) studies were done in living cells, to avoid fixation artifacts (*20*, *21*). Cells in serum-free medium were incubated with polyplexes made with a red fluorescent labeled polymer and (blue labeled) DNA, or with free labeled polymer. CLSM and transmission pictures are shown in Figure 6. From these photographs it can be seen that the polyplexes and free polymer were associated with the cellular membrane 1 h after polyplex addition, whereas hardly any fluorescence was observed intracellularly, in agreement with previous observations (*33*). Twenty-four hours after administration, the polyplexes and free polymer were intracellularly located in small, punctuated spots lying around the nucleus of the cells. These spots most likely represent endosomes or lysosomes, as has also been found for other cationic polymers (*30*, *33*). When iodoacetamide, an endocytosis inhibitor, was added during incubation of the polyplexes with cells, or when the cells were incubated at 4 °C, only membrane binding of the polyplexes was found. The diffuse fluorescent pattern in the cytoplasm, due to cell membrane passage found for Tat peptide (conjugates) in the studies mentioned in the Introduction, was not observed in our experiments. This indicates that the route of uptake of pGuaMA polyplexes is, as for other polyplexes, mainly endocytosis.

As pGuaMA-based polyplexes do transfect cells to some extent, escape from the endosomes has to occur. For some cationic polymeric gene delivery systems, the 'proton sponge mechanism' has been proposed as an explanation for their endosomal escape (*42*, *32*). However, this mechanism is suggested for polymers having a buffering capacity around physiological and lysosomal pH. As pGuaMA is already fully protonated at physiological pH (pK_a = 12.5) and consequently does not have buffering capacity, the proton sponge mechanism cannot be the reason for endosomal escape for polyplexes based on this polymer. However, indications that the proton sponge mechanism is not generally valid were reported recently because polymers having buffering capacities around physiological pH were not able to transfect cells after endosomal uptake (*30*, *43*). Still, pGuaMA-based polyplexes, because they give transfection, obviously can escape from the endosomes and thus must have some membrane destabilizing activity.

CONCLUSION

A new polymethacrylate with a guanidinium side group, abbreviated as pGuaMA, was synthesized. The polymer was able to transfect cells, but only when serum was absent during transfection, as absorption of serum proteins changed the polarity of the polyplexes. When compared to the polypeptide analogue pArg, a substantial better transfection was observed. Polyplexes based on pGuaMA were internalized in small, punctuate spots as visualized via CLSM. No evidence was found with CLSM that polyplexes were taken up via an endocytosis-independent way, as has been suggested for arginine-rich peptides and other guanidine-containing structures, but disputed in recent publications.

ACKNOWLEDGMENT

This research was supported by a grant from the Dutch ministry of Economic Affairs (project number: BTS-98150).

LITERATURE CITED

(1) Zabner, J., Fasbender, A. J., Moninger, T., Poellinger, K. A., and Welsh, M. J. (1995) Cellular and molecular barriers to gene transfer by a cationic lipid. *J. Biol. Chem. 270*, 18997−19007.

(2) Wiethoff, C. M., and Middaugh, C. R. (2003) Barriers to nonviral gene delivery. *J. Pharm. Sci. 92*, 203−217.
(3) Ruponen, M., Honkakoski, P., Ronkko, S., Pelkonen, J., Tammi, M., and Urtti, A. (2003) Extracellular and intracellular barriers in nonviral gene delivery. *J. Controlled Release 93*, 213−217.
(4) Miller, A. D. (2003) The problem with cationic liposome/micelle-based nonviral vector systems for gene therapy. *Curr. Med. Chem. 10*, 1195−1211.
(5) Wagner, E. (2004) Strategies to improve DNA polyplexes for in vivo gene transfer: will "artificial viruses" be the answer? *Pharm. Res. 21*, 8−14.
(6) Godbey, W. T., and Mikos, A. G. (2001) Recent progress in gene delivery using nonviral transfer complexes. *J. Controlled Release 72*, 115−125.
(7) Merdan, T., Kopecek, J., and Kissel, T. (2002) Prospects for cationic polymers in gene and oligonucleotide therapy against cancer. *Adv. Drug Delivery Rev. 54*, 715−758.
(8) De Smedt, S. C., Demeester, J., and Hennink, W. E. (2000) Cationic polymer based gene delivery systems. *Pharm. Res. 17*, 113−126.
(9) Brown, M. D., Schatzlein, A. G., and Uchegbu, I. F. (2001) Gene delivery with synthetic (non viral) carriers. *Int. J. Pharm. 229*, 1−21.
(10) Cho, Y. W., Kim, J. D., and Park, K. (2003) Polycation gene delivery systems: escape from endosomes to cytosol. *J. Pharm. Pharmacol. 55*, 721−734.
(11) Vivès, E., Brodin, P., and Lebleu, B. (1997) A truncated HIV-1 Tat protein basic domain rapidly translocates through the plasma membrane and accumulates in the cell nucleus. *J. Biol. Chem. 272*, 16010−16017.
(12) Derossi, D., Calvet, S., Trembleau, A., Brunissen, A., Chassaing, G., and Prochiantz, A. (1996) Cell internalization of the third helix of the Antennapedia homeodomain is receptor-independent. *J. Biol. Chem. 271*, 18188−18193.
(13) Suzuki, T., Futaki, S., Niwa, M., Tanaka, S., Ueda, K., and Sugiura, Y. (2002) Possible existence of common internalization mechanisms among arginine-rich peptides. *J. Biol. Chem. 277*, 2437−2443.
(14) Wender, P. A., Mitchell, D. J., Pattabiraman, K., Pelkey, E. T., Steinman, L., and Rothbard, J. B. (2000) The design, synthesis, and evaluation of molecules that enable or enhance cellular uptake: Peptoid molecular transporters. *Proc. Nat. Acad. Sci. U.S.A. 97*, 13003−13008.
(15) Nori, A., Jensen, K. D., Tijerina, M., Kopečková, P., and Kopeček, J. (2003) Tat-conjugated synthetic macromolecules facilitate cytoplasmic drug delivery to human ovarian carcinoma cells. *Bioconjugate Chem. 14*, 44−50.
(16) Astriab-Fisher, A., Sergueev, D., Fisher, M., Ramsay Shaw, B., and Juliano, R. L. (2002) Conjugates of antisense oligonucleotides with the tat and antennapedia cell-penetrating peptides: effects on cellular uptake, binding to target sequences, and biologic actions. *Pharm. Res. 19*, 744−754.
(17) Zhou, P., Wang, M., Du, L., Fisher, G. W., Waggoner, A., and Ly, D. H. (2003) Novel binding and efficient cellular uptake of guanidine-based peptide nucleic acids (GPNA). *J. Am. Chem. Soc. 125*, 6878−6879.
(18) Pouton, C. W., Lucas, P., Thomas, B. J., Uduehi, A. N., Milroy, D. A., and Moss, S. H. (1998) Polycation−DNA complexes for gene delivery: a comparison of the biopharmaceutical properties of cationic polypeptides and cationic lipids. *J. Controlled Release. 53*, 289−299.
(19) Verbaan, F. J., Bos, G. W., Snel, C., Oussoren, C., Woodle, M. C., Hennink, W. E., and Storm, G. (2004) A comparative study of different cationic transfection agents for in vivo gene delivery after intravenous administration. *J. Drug Delivery Sci. Tech. 14*, 1−7.
(20) Richard, J. P., Melikov, K., Vives, E., Ramos, C., Verbeure, B., Gait, M. J., Chernomordik, L. V., and Lebleu, B. (2003) Cell-penetrating peptides, a reevaluation of the mechanism of cellular uptake. *J. Biol. Chem. 278*, 585−590.
(21) Krämer, S. D., and Wunderli-Allenspach, H. (2003) No entry for TAT(44−57) into liposomes and intact MDCK cells: novel approach to study membrane permeation of cell-penetrating peptides. *Biochim. Biophys. Acta 1609*, 161−169.
(22) Console, S., Marty, C., Garcia-Echeverria, C., Schwendener, R., and Ballmer-Hofer, K. (2003) Antennapedia and HIV transactivator of transcription (TAT) "protein transduction domains" promote endocytosis of high molecular weight cargo upon binding to cell surface glycosaminoglycans. *J. Biol. Chem. 278*, 35109−25114.
(23) Plank, C., Oberhauser, B., Mechtler, K., Koch, C., and Wagner, E. (1994) The influence of endosome-disruptive peptides on gene-transfer using synthetic virus-like gene-transfer systems. *J. Biol. Chem. 269*, 12918−12924.
(24) van de Wetering, P., Cherng, J. Y., Talsma, H., and Hennink, W. E. (1997) Relation between transfection efficiency and cytotoxicity of poly(2-(dimethylamino)ethyl methacrylate/plasmid complexes. *J. Controlled Release 49*, 59−69.
(25) Fischbein, L., and Gallaghan, J. A. (1954) Some new 1-(nitroxyalkyl)-3-nitroguanidines and their cyclic products. *J. Am. Chem. Soc. 76*, 3217−3219.
(26) Arigita, C., Zuidam, N. J., Crommelin, D. J. A., and Hennink, W. E. (1999) Association and dissociation characteristics of polymer/DNA complexes used for gene delivery. *Pharm. Res. 16*, 1534−1541.
(27) Zuidam, N. J., Posthuma, G., de Vries, E. T. J., Crommelin, D. J. A., and Hennink, W. E. (2000) Effects of physicochemical characteristics of poly(2-(dimethylamino)ethyl methacrylate)-based polyplexes on cellular association and internalization. *J. Drug Target. 8*, 51−66.
(28) Scudiero, D. A., Shoemaker, R. H., Paull, K. D., Monks, A., Tierney, S., Nofziger, T. H., Currens, M. J., Seniff, D., and Boyd, M. R. (1988) Evaluation of a soluble tetrazolium formazan assay for cell-growth and drug sensitivity in culture using human and other tumor-cell lines. *Cancer Res. 48*, 4827−4833.
(29) van de Wetering, P., Schuurmans-Nieuwenbroek, N. M. E., Steenbergen, M. J., Crommelin, D. J. A., and Hennink, W. E. (2000) Copolymers of 2-(dimethylamino)ethyl methacrylate with ethoxytriethylene glycol methacrylate or N-vinyl-pyrrolidone as gene transfer agents. *J. Controlled Release 64*, 193−203.
(30) Funhoff, A. M., van Nostrum, C. F., Koning, G. A., Schuurmans-Nieuwenbroek, N. M. E., Crommelin, D. J. A., and Hennink, W. E. (2004) Endosomal escape of polymeric gene delivery complexes is not always enhanced by polymers buffering at low pH. *Biomacromolecules 5*, 32−39.
(31) Luten, J., van Steenis, J. H., van Someren, R., Kemmink, J., Schuurmans Nieuwenbroek, N. M. E., Koning, G. A., Crommelin, D. J. A., van Nostrum, C. F., and Hennink, W. E. (2003) Polyphosphazenes as biodegradable nonviral vector systems. *J. Controlled Release 89*, 483−497.
(32) Gonzalez, H., Hwang, S. J., and Davis, M. E. (1999) New class of polymers for the delivery of macromolecular therapeutics. *Bioconjugate Chem. 10*, 1068−1074.
(33) van de Wetering, P., Moret, E. E., Schuurmans-Nieuwenbroek, N. M. E., van Steenbergen, M. J., and Hennink, W. E. (1999) Structure−activity relationships of water-soluble cationic methacrylate/methacrylamide polymers for nonviral gene delivery. *Bioconjugate Chem. 10*, 589−597.
(34) Funhoff, A. M., van Nostrum, C. F., Janssen, A. P. C. A., Fens, M. H. A. M., Crommelin, D. J. A., and Hennink, W. E. (2004) Polymer side-chain degradation as a tool to control the destabilization of polyplexes. *Pharm. Res. 21*, 170−176.
(35) Cherng, J. Y., van de Wetering, P., Talsma, H., Crommelin, D. J. A., and Hennink, W. E. (1996) Effect of size and serum proteins on transfection efficiency of poly ((2-dimethylamino)-ethyl methacrylate)-plasmid nanoparticles. *Pharm. Res. 13*, 1038−1042.
(36) Audouy, S., Molema, G., de Leij, L., and Hoekstra, D. (2000) Serum as modulator of lipoplex-mediated gene transfection: dependence of amphiphile, cell type and complex stability. *J. Gene Med. 2*, 465−476.
(37) Yang, J. P., and Huang, L. (1997) Overcoming the inhibitory effect of serum on lipofection by increasing the charge ratio cationic liposome to DNA. *Gene Ther. 4*, 1−10.
(38) Katayose, S., and Kataoka, K. (1997) Water-soluble polyion complex associates of DNA and poly(ethylene glycol)-poly(L-lysine) block copolymer. *Bioconjugate Chem. 8*, 702−707.

(39) Verbaan, F. J., Oussoren, C., Snel, C. J., Crommelin, D. J. A., Hennink, W. E., and Storm, G. (2004) Steric stabilization of poly(2-(dimethylamino)ethyl methacrylate) based polyplexes mediates prolonged circulation and tumor targeting in mice. *J. Gene Med. 6*, 64−75.

(40) Ogris, M., Brunner, S., Schuller, S., Kircheis, R., and Wagner, E. (1999) PEGylated DNA/transferrin-PEI complexes: reduced interaction with blood components, extended circulation in blood and potential for systemic gene delivery. *Gene Ther. 6*, 595−605.

(41) Kakizawa, Y., and Kataoka, K. (2002) Block copolymer micelles for delivery of gene and related compounds. *Adv. Drug Delivery Rev. 54*, 203−222.

(42) Boussif, O., Lezoualch, F., Zanta, M. A., Mergny, M. D., Scherman, D., Demeneix, B., and Behr, J.-P. (1995) A versatile vector for gene and oligonucleotide transfer into cells in culture and in vivo: polyethylenimine. *Proc. Nat. Acad. Sci. U.S.A. 92*, 7297−7301.

(43) Dubruel, P., Christiaens, B., Rosseneu, M., Vandekerckhove, J., Grooten, J., Goossens, V., and Schacht, E. (2004) Buffering properties of cationic polymethacrylates are not the only key to successful gene delivery. *Biomacromolecules 5*, 379−388.

BC049864Q

Hydrotropic Dendrimers of Generations 4 and 5: Synthesis, Characterization, and Hydrotropic Solubilization of Paclitaxel

Tooru Ooya,[†] Jaehwi Lee,[‡] and Kinam Park*,[‡]

School of Materials Science, Japan Advanced Institute of Science and Technology, 1-1 Asahidai, Tatsunokuchi, Ishikawa 923-1292, Japan, and Departments of Pharmaceutics and Biomedical Engineering, Purdue University, West Lafayette, Indiana 47907. Received August 1, 2004; Revised Manuscript Received October 1, 2004

Polyglycerol dendrimers (PGDs) with 4−5 generations were synthesized and used to investigate the effect of dendritic architecture and its generation on aqueous solubilization of paclitaxel (PTX), a poorly water-soluble drug. Chemical and physical properties of the PGDs were characterized by NMR, MALDI-TOF mass, GPC, viscosity, and dynamic light scattering measurements. The PTX solubility in all the solutions of PGDs, even below 10 wt %, was much higher than that in PEG400 that is commonly used as a cosolvent or a hydrotropic agent. Increase in the PTX solubility by PGDs was dependent on the dendrimer generation. The dendritic structure was the reason for the enhanced solubility of PTX even at low concentrations. ^{1}H NMR spectra of PTX before and after mixing with PGDs in D_2O suggested that the aromatic rings and some methyne groups of PTX were surrounded by PGDs. PGDs, which do not require hydrophobic segment as in polymeric micelles, provide an alternative method of hydrotropic solubilization of poorly soluble drugs.

INTRODUCTION

Formulation of poorly water-soluble drugs has been one of the most important problems in drug delivery. Previous formulations have utilized surfactant and polymeric micelles, micro- or nanoparticles, solid dispersion, complexation with cyclodextrin, and cosolvents (*1*). Cosolvent methods have been widely used because of easy processing for fabricating oral as well as injectable formulations (*2*, *3*). The U.S. Food and Drug Administration has approved six water-miscible cosolvents: glycerin, poly(propylene glycol), poly(ethylene glycol) (PEG), *N*,*N*-dimethylformamide, Cremophor, and ethanol (*1*). Use of such organic solvents is limited because of their toxicities. In commercially available formulations, paclitaxel is formulated in a 50:50 mixture of Cremophor EL (castor oil modified with PEG-35) and ethanol, which is diluted in normal saline or dextrose solution (to make 5 wt % paclitaxel concentration) before administration (*4*). This formulation can cause fatal hypersensitivity reactions mainly due to cytototoxity of the amphiphilic compound and the organic solvent (*5*). For this reason, safer vehicles for delivery of paclitaxel have been explored.

PEGs have been frequently used for increasing the water-solubility of poorly soluble drugs. PEG with molecular weight of 400 g/mol (PEG400) has been used as a cosolvent for various poorly water-soluble drugs (*6*, *7*). PEG400 increases the solubility of β-estradiol 4−5 orders of magnitude when its concentration is 80 wt % and higher (*6*). The majority of PEG400 are capable of self-association through hydrogen bonding at higher concentration regions (over 80 wt %). Such associations may alter water structure to influence the water-solubility of poorly soluble drugs (*8*). A high density of PEG400 or ethylene glycol units is the key factor in increasing the solubility of poorly water-soluble drugs.

In our previous studies, graft and star-shaped graft copolymers of PEG400 were examined as solubilizers of paclitaxel (*9*). These molecular architectures enhanced the aqueous solubility of paclitaxel. In addition to graft and star-shaped graft copolymers of PEG400, polyglycerol dendrimers (PGDs) were examined for their ability to increase the water-solubility of paclitaxel. Well-defined hyperbranched polyglycerols were synthesized by ring-opening multibranching polymerization (*10*) and used as biocompatible materials (*11*, *12*). PGD with generation 3 was synthesized by step-by-step allylation and dihydroxylation (*13*). The density of ethylene glycol units in PGDs is expected to be higher than that of linear PEGs. PGDs have a good potential as biomaterials because of their high water solubility, chemical reactivity, and structural similarity to PEG with high density of the ethylene glycol unit. PGDs increased solubilization of paclitaxel more than the graft and star-shaped graft copolymers did. Although the PGDs have a good potential as a drug solubilizer, PGDs with 4 and 5 generations were not characterized, and the mechanism of the solubility enhancement of paclitaxel was not examined. In this study, PGDs with 4 and 5 generations were synthesized and characterized in terms of chemical structure, solution properties, and solubility mechanism of paclitaxel.

MATERIALS AND METHODS

Materials. Tetrabutylammonium bromide (TBAB), 50 wt % of sodium hydroxide solution, allyl chloride, magnesium sulfate ($MgSO_4$), silica gel, *N*-methylmorpholine *N*-oxide (NMO), and aqueous (4 wt %) OsO_4 solution were purchased from Aldrich (Milwaukee, WI) and used without further purification. *t*-Butanol (*t*-BuOH) and

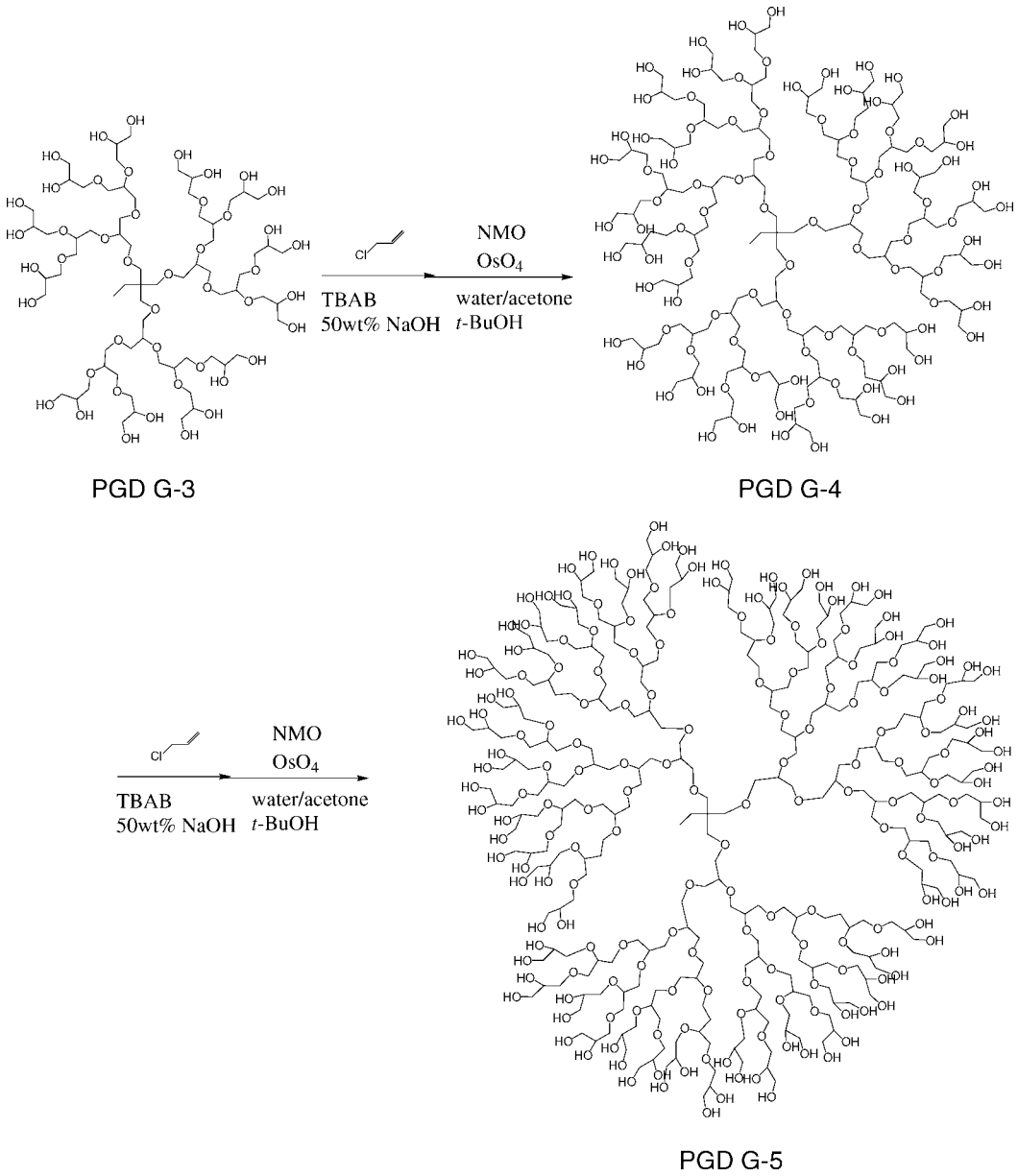
* To whom correspondence should be addressed. Professor Kinam Park, Purdue University, School of Pharmacy, 575 Stadium Mall Drive, Room G22, West Lafayette, IN 47907-2091. Tel: 765) 494-7759. Fax: 765) 496-1903. E-mail: kpark@purdue.edu.

[†] Japan Advanced Institute of Science and Technology.

[‡] Purdue University.

10.1021/bc049814l CCC: $27.50 © 2004 American Chemical Society
Published on Web 10/22/2004

Scheme 1. Synthesis of Polygrycerol Dendrimers (PGDs)[a]



[a] TBAB: tetrabutylammonium bromide, NMO: *N*-methylmorpholine *N*-oxide, OsO_4: osmium oxide 4 wt % aqueous solution.

N,*N*-dimethylformamide (DMF, HPLC grade) were purchased from Fisher. Benzylated cellulose membrane (MWCO 1000) was purchased from Sigma (St. Louis, MO). Paclitaxel was obtained from Samyang Genex Corp. (Taejeon, South Korea). Acetone, petroleum ether, ethyl acetate, toluene, and methanol were of a reagent grade.

Synthesis of Polyglycerol Dendrimers (PGDs) Started from Generation 3 (Scheme 1). PGDs (generations 4 and 5) were synthesized according to the report of Haag et al. (*13*). Each generation of the dendrimer was synthesized by a two-step process based on allylation of alcohols and catalytic dihydroxylation. A part of the purification process was modified.

PGD with Generation 3 (PGD G-3). PGD G-3 was synthesized in the same method of Haag et al. (*13*). ^{1}H NMR (300 MHz, CD_3OD): 4.85 (s, O*H*), 3.90−3.31 (m, 105H), 3.31 (s, 6H, C(C*H*$_2$)$_3$), 1.42 (q, 2H, C*H*$_2$CH$_3$), 0.89 (t, J = 7.20 Hz, 3H, C*H*$_3$); ESI-MS (4.52 kV, positive) calcd for $C_{69}H_{140}O_{45}$ 1688.9, found 1689.5, 1711.9 (+ Na).

Allylated PGD with Generation 3 (PGD G-3.5). In a three-neck flask, PGD G-3 (10.1 g, 5.98 mmol, OH groups: 143.5 mmol) was dissolved in 50 wt % of sodium hydroxide (57 mL) with heating. To the solution, TBAB (4.6 g, 14.3 mmol) was added and dispersed under vigorous stirring using a mechanical stirrer. Then, allyl chloride (75.7 mL, 930 mmol) was added over 20 h at 45 °C under vigorous stirring using the mechanical stirrer. After the addition of 143 mL of toluene to the mixture, the organic phase was separated from the other phase, dried over $MgSO_4$, filtered, and concentrated using a rotary evaporator. The crude was further purified by column chromatography (silica gel, petroleum ether/ethyl acetate 10:1 to 1:1) to obtain colorless oil. Oxygen was removed by flowing N_2 gas during the whole process. Yield: 11.1 g, ^{1}H NMR (300 MHz, $CDCl_3$): 5.88 (m, 24H, C*H*=CH$_2$), 5.18 (m, 48H, CH=C*H*$_2$), 4.14 (d, J = 5.40 Hz, 24H, CHOC*H*$_2$CH=CH$_2$), 3.99 (d, J = 5.40 Hz, 24H, CH$_2$-OC*H*$_2$CH=CH$_2$), 3.67−3.39 (m, 105H, C*H*$_2$C*H*(OR)C*H*$_2$O), 3.26 (s, 6H, C(C*H*$_2$)$_3$), 1.38 (q, 2H, CH$_3$C*H*$_2$), 0.84 (t, J = 7.21 Hz, 3H, C*H*$_3$); ^{13}C NMR (75 MHz, $CDCl_3$): 135.7 (CHOCH$_2$*C*H=CH$_2$), 135.2 (CH$_2$OCH$_2$*C*H=CH$_2$), 117.1 (CH$_2$OCH$_2$CH=*C*H$_2$), 116.9 (CHOCH$_2$CH=*C*H$_2$), 78.0

($CH_2CH(OR)CH_2$), 77.6 ($CH_2CH(OCH_2CH{=}CH_2)CH_2$), 72.6 ($CH_2CH(OR)CH_2$), 72.5 ($CH_2OCH_2CH{=}CH_2$), 71.6 ($CH_2OCH_2CH{=}CH_2$), 70.7 ($CHOCH_2CH{=}CH_2$), 43.6 ($C(CH_2)_4$), 23.6 ($CH_2CH_3$), 8.3 ($CH_2CH_3$); ESI-MS (4.52 kV, positive) calcd for $C_{141}H_{236}O_{45}$ 2649.6 found 2649.4.

PGD with Generation 4 (PGD G-4). In a one-neck flask, PGD G-3.5 (10.9 g, 5.42 mmol, 130 mmol allyl equivalents) and *N*-methylmorpholine *N*-oxide (NMO) (16.8 g, 143 mmol) were added to a mixture of acetone (65 mL), distilled water (65 mL), and *t*-BuOH (13 mL). Aqueous (4 wt %) OsO_4 solution (2.6 mL) was added and stirred for 20 h at room temperature. Then, all volatile compounds were removed in vacuo. The crude products were further purified by dialysis in methanol using benzylated cellulose membrane (MWCO 1000). The solution was concentrated in vacuo, and water was added to the obtained pale yellow oils. Water-insoluble impurity was removed by passing through a microfilter (pore size: 0.45 μm). Finally, the solute was lyophilized to obtain pure PGD G-4 as pale yellow oils. Yield: 11.7 g, ^{1}H NMR (300 MHz, CD_3OD): 4.85 (s, O*H*), 3.89−3.42 (m, 231H), 3.35 (s, 6H, $C(CH_2)_3$), 1.44 (q, 2H, CH_2CH_3), 0.92 (t, J = 6.92 Hz, 3H, CH_3); ^{13}C NMR (75 MHz, CD_3OD): 80.3 ($(CH_2)_2CH_2C$(H)OR), 74.5 ($CH_2OCH_2CH(OH)CH_2OH$), 73.4 ($C(CH_2)_3$), 72.9 ($ROCH_2C$(H)(OR)CH_2OR), 72.6 ($CHOCH_2CH(OH)CH_2OH$), 71.7 ($CHOCH_2CH(OR)CH_2OR$), 64.9 (CH_2OH), 45.1 ($C(CH_2)_4$), 25.2 (CH_2CH_3), 9.0 (CH_2CH_3); MALDI-TOF MS calcd for $C_{144}H_{290}O_{93}$ 3507.8 found 3507.4 +H, 3491.7 $-H_2O$.

Allylated PGD with Generation 4 (PGD G-4.5). In a three-neck flask, PGD G-4 (8.3 g, 2.63 mmol, OH groups: 126.2 mmol) was dissolved in 50 wt % of sodium hydroxide (45 mL) with heating (viscous gum was sometimes observed). To the solution, TBAB (3.65 g, 11.3 mmol) was added and dispersed under vigorous stirring using a mechanical stirrer. Then, allyl chloride (64.4 mL, 791 mmol) was added over 20 h at 45 °C under vigorous stirring using the mechanical stirrer. After the addition of 126 mL of toluene to the mixture, the organic phase was separated from the other phase, dried over $MgSO_4$, filtered, and concentrated using a rotary evaporator. The crude was further purified by column chromatography (silica gel, petroleum ether/ethyl acetate 10:1 to 1:1) to obtain colorless oil. Oxygen should be removed via flowing N_2 gas during the whole process. Yield: 5.84 g, ^{1}H NMR (300 MHz, $CDCl_3$): 5.90 (m, 48H, $CH{=}CH_2$), 5.24 (m, 96H, $CH{=}CH_2$), 4.15 (d, J = 5.10 Hz, 48H, $CHOCH_2CH{=}CH_2$), 4.00 (d, J = 5.10 Hz, 24H, $CH_2OCH_2CH{=}CH_2$), 3.67−3.30 (m, 231H, $CH_2CH(OR)CH_2O$), 3.33 (brs, 6H, $C(CH_2)_3$), 1.44 (brq, 2H, CH_3CH_2), 0.86 (brt, 3H, CH_3); ^{13}C NMR (75 MHz, $CDCl_3$): 135.7 ($CHOCH_2CH{=}CH_2$), 135.3 ($CH_2OCH_2CH{=}CH_2$), 117.2 ($CH_2OCH_2CH{=}CH_2$), 117.1 ($CHOCH_2CH{=}CH_2$), 77.9 ($CH_2CH(OR)CH_2$), 77.5 ($CH_2CH(OCH_2CH{=}CH_2)CH_2$), 72.7 ($CH_2CH(OR)CH_2$), 72.7 ($CH_2OCH_2CH{=}CH_2$), 71.7 ($CH_2OCH_2CH{=}CH_2$), 70.7 ($CHOCH_2CH{=}CH_2$), 43.4 ($C(CH_2)_4$), 23.5 ($CH_2CH_3$), 8.2 ($CH_2CH_3$).

PGD with Generation 5 (PGD G-5). In a one-neck flask, PGD G-4.5 (5.84 g, 1.1 mmol, 52.8 mmol allyl equivalents) and *N*-methylmorpholine *N*-oxide (NMO) (6.72 g, 57.2 mmol) were added to a mixture of acetone (26 mL), distilled water (26 mL), and *t*-BuOH (5.2 mL). Aqueous (4 wt %) OsO_4 solution (1.1 mL) was added and stirred for 20 h at room temperature. Then, all volatile compounds were removed in vacuo. The crude products were further purified by dialysis in methanol using benzylated cellulose membrane (MWCO 1000). The solution was concentrated in vacuo, and water was added to the obtained pale yellow oils. Water-insoluble impurity was removed by passing through a microfilter (pore size: 0.45 μm). Finally, the solute was lyophilized to obtain pure PGD G-5 as pale yellow oils. Yield: 6.1 g, ^{1}H NMR (300 MHz, CD_3OD): 4.85 (s, O*H*), 3.79−3.42 (m, 477H), 3.35 (s, 6H, $C(CH_2)_3$), 1.45 (brq, 2H, CH_2CH_3), 0.94 (brt, 3H, CH_3); ^{13}C NMR (75 MHz, CD_3OD): 80.3 ($(CH_2)_2CH_2C$(H)OR), 74.4 ($CH_2OCH_2CH(OH)CH_2OH$), 73.4 ($C(CH_2)_3$), 72.9 ($ROCH_2C$(H)(OR)CH_2OR), 72.6 ($CHOCH_2CH(OH)CH_2OH$), 71.7 ($CHOCH_2CH(OR)CH_2OR$), 64.9 (CH_2OH), 45.1 ($C(CH_2)_4$), 25.2 (CH_2CH_3), 9.0 (CH_2CH_3); MALDI-TOF MS calcd for $C_{291}H_{584}O_{189}$ 7103.6 found 6769.2 +H, 6959.2 −H.

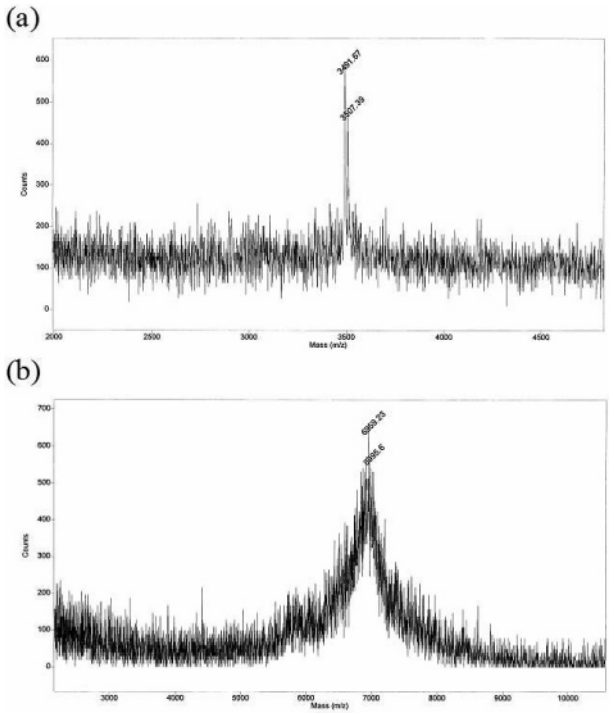


Figure 1. MALDI-TOF mass spectra of (a) PGD G-4 and (b) PGD G-5.

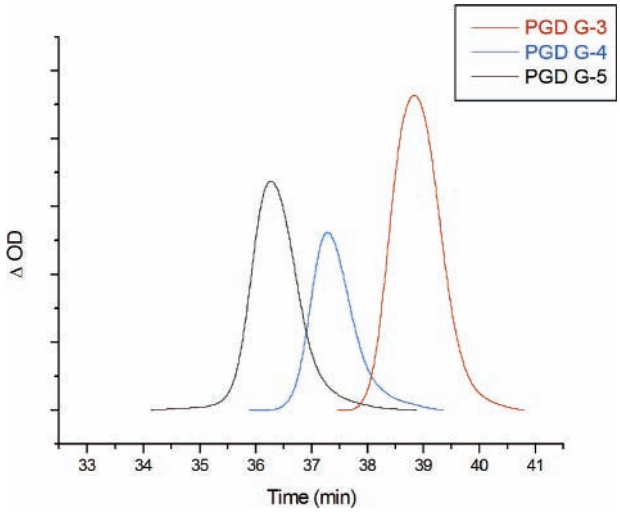


Figure 2. GPC charts of PGDs (G-3, G-4, and G-5). Eluent: DMF; flow rate: 0.6 mL/min; detectot: reflactive index.

Characterization of PGDs. *NMR Spectroscopy*. ^{1}H and ^{13}C NMR spectra were obtained on a Bruker ARX300 spectrometer at 300 and 75 MHz, respectively. For the analysis of the interaction between PGDs and paclitaxel in a solubilized state in D_2O, a 750 MHz NMR apparatus (Varian, Unity plus, CA) was used.

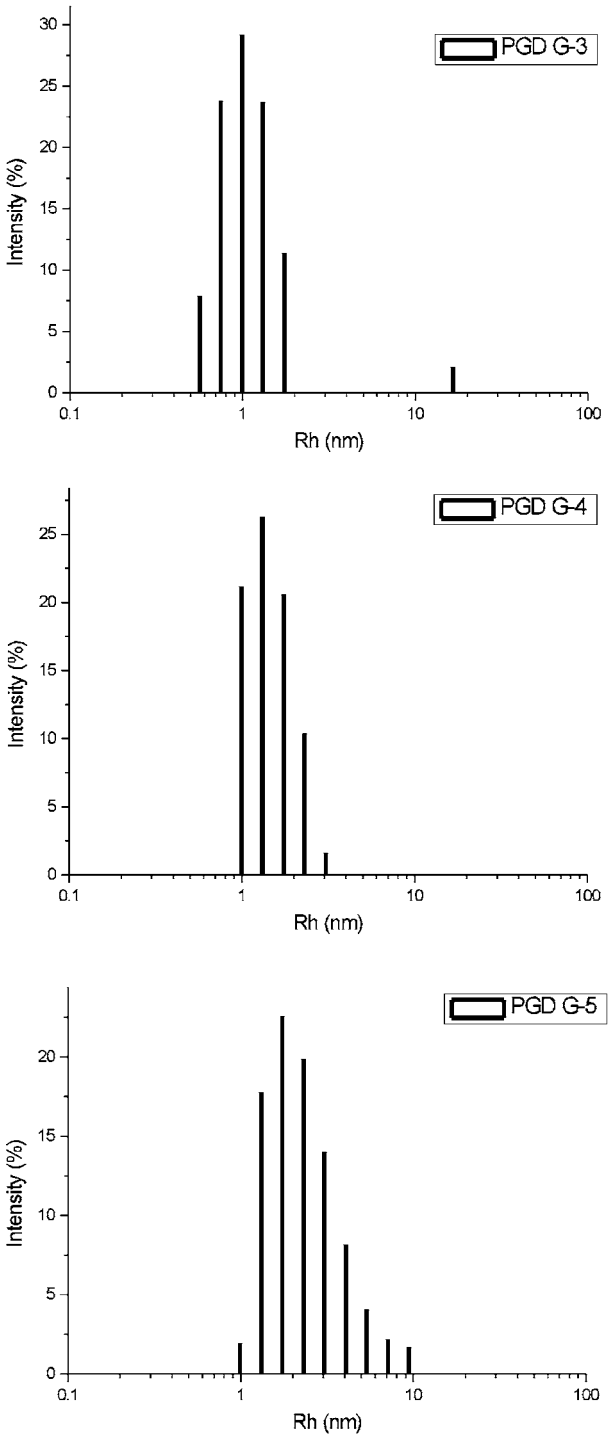


Figure 3. Regularization histgrams of PGDs on DLS. (a) G-3, (b) G-4, and (c) G-5.

Mass Spectroscopy. Electrospray ionization mass spectrometry (ESI-MS) assay was carried out on a Finnigan-MAT LCQ (ThermoFinnigan Corp, San Jose, CA). The electrospray needle voltage was set at 4.5 kV, the heated capillary voltage was set to 10 V, and the capillary temperature was set to 225 °C. Typical background source pressure was 1.2×10^{-5} Torr as read by an ion gauge. The sample flow rate was approximately 10 μL/min. The drying gas was nitrogen. The LCQ was scanned to 2000 amu for these experiments. Matrix-assisted laser desorption ionization (MALDI) mass spectroscopy was carried out using a PerSeptive Biosystems Voyager mass spectrometer (Framingham, MA) in linear mode. Samples were prepared by casting the matrix compound (2,5-dihydroxyacetophenone) with PGDs (~0.2 mg/mL in methanol) onto the slide, and the solvent was evaporated. Ionization was accelerated with 20 kV in the positive ion mode.

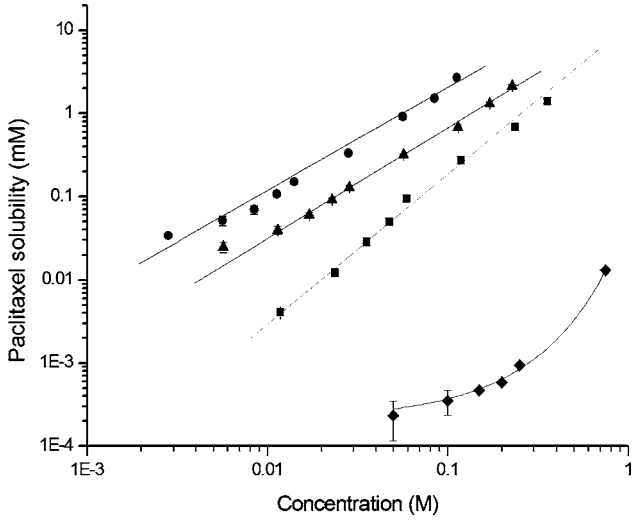


Figure 4. Aqueous paclitaxel solubility as a function of the PGD concentration (mean ± SD, $n = 3$). (circle) G-5, (triangle) G-4, (square) G-3, and (diamond) PEG400.

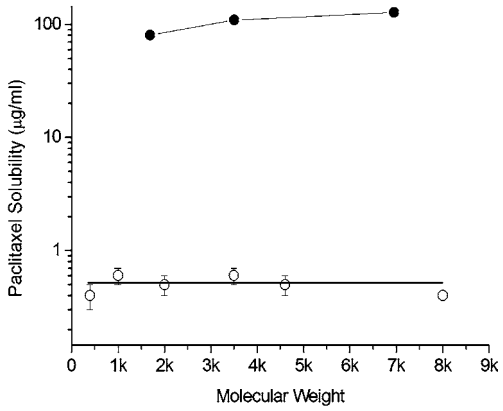


Figure 5. Dependence of molecular weight of PGDs (closed circle) and PEG (open circle) on the aqueous paclitaxel solubility. The concentration of PDGs and PEG was 10 wt%.

Gel permeation Chromatography (GPC). The molecular weight and molecular weight distribution were analyzed by GPC equipped with an Agilent 1100 series RI detector, quaternary pump, and PL aquagel-OH columns with pore sizes of 30, 40, and 50 Å (Agilent Technologies, Wilmington, DE). The eluent was DMF, and flow rate was 0.6 mL/min. The molecular weights are calibrated with poly(ethylene oxide) standards.

Dynamic Light Scattering (DLS) Measurements. Hydrodynamic radius (R_h) of the PGDs was measured by DLS using a DynaPro 99 (Protein Solutions, Inc.) at a fixed angle (90°). The wavelength of the laser source was 826 nm. The membrane filter with Watman Anotop 10 attachment and the pore diameter 20 nm was used, and 0.15 mL of PGD-dissolved 0.2 M NaCl aqueous solution was injected into a cell. Solution concentration was 1 wt %.

Viscosity Measurements. The viscosity of PGDs in water was measured at 25 °C using a Cannon-Manning Semi-Micro Viscometer (Size: 50 C286, Cannon Instrument Co., PA). Specific viscosity (η_{sp}) of PGDs was calculated by the following equation:

$$\eta_{sp} = (\eta - \eta_0)/\eta_0 = (t - t_0)/t_0$$

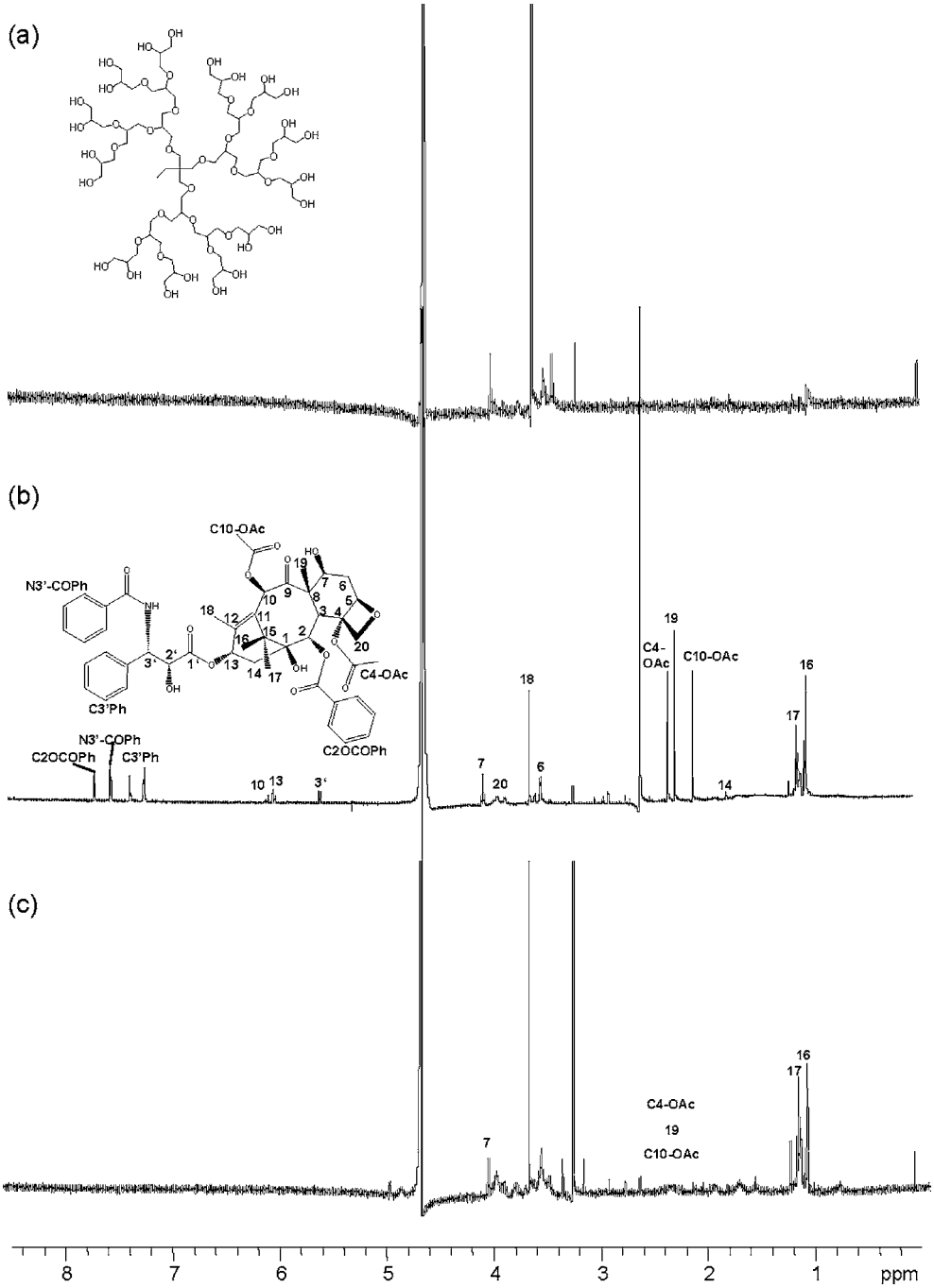


Figure 6. ^{1}H NMR spectra measured using a 750 MHz NMR apparatus in D_2O. (a) PGD G-3 (0.35 μM), (b) paclitaxel (0.35 μM), and (c) mixture of PGD G-3 and paclitaxel.

where η is the solution viscosity, η_0 the viscosity of water, t the measuring time of the solution, and t_0 the measuring time of water. From Huggins plot, [η] of PGDs was determined.

Solubility Test of Paclitaxel. Excess paclitaxel (~10 mg/mL) was added to screw-capped vials containing fixed volume of PGD solutions. This mixture in the vials was stirred using a magnetic stirring bar at 37 °C. The samples were taken after 24 h, filtered through a 0.2 μm nylon membrane, and analyzed for paclitaxel using HPLC. The concentration of paclitaxel was determined by an isocratic reverse-phase HPLC (Agilent 1100 series, Agilent Technologies, Wilmington, DE) using a Symmetry column (Water Corp., Milford, MA) at 25 °C. The mobile phase consisted of acetonitrile−water (45:55 v/v) with a flow rate of 1.0 mL/min. A diode array detector was set at 227 nm and linked to ChemStation software for data analysis. The paclitaxel concentrations in the samples were obtained from a calibration curve.

RESULTS AND DISCUSSION

Synthesis and Structural Characterization of PGD G-4 and G-5. The obtained PGDs were characterized by NMR, mass, GPC, DLS, and viscosity measurements (Table 1). The ^{1}H and ^{13}C NMR spectra of PGD G-3.5 and G-4.5 were attributed to allyl group [e.g., 5.88 (CH=CH_2), 5.18 (CH=CH_2) on the ^{1}H NMR spectra, and 135.2 (CH_2OCH_2CH=CH_2), 116.9 ($CHOCH_2CH$=CH_2) on the ^{13}C NMR sperctra]. The ^{1}H and ^{13}C NMR spectra of PGD G-4 and G-5 were also attributed to the monomer units. The M_w of the G-4 and G-5 dendrimers were determined by MALDI TOF-MS. As shown in Figure 1a, two peaks were observed at m/z 3507.4 +H, 3491.7 $-H_2O$, indicating that successful synthesis of PGD G-4. As for

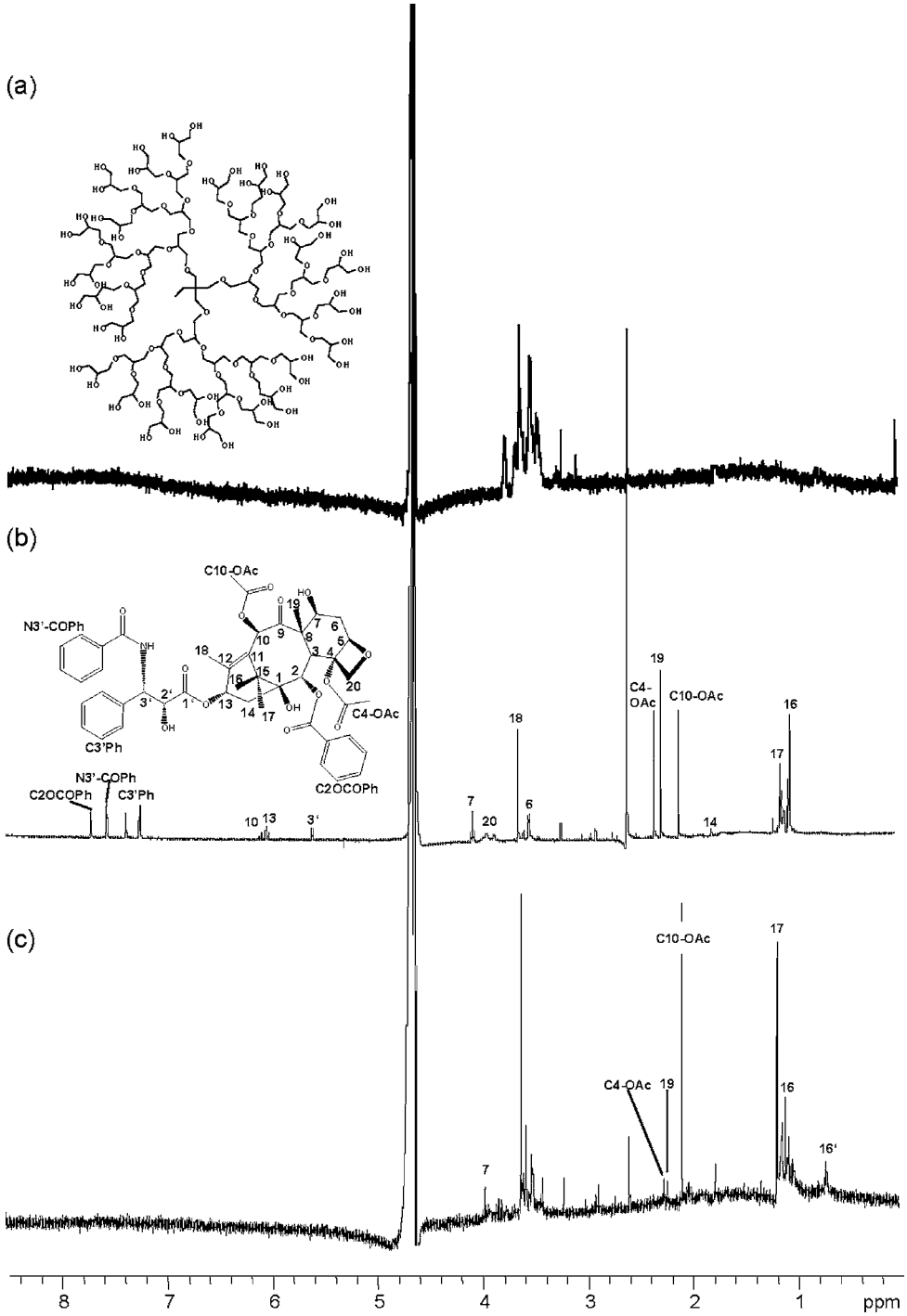


Figure 7. ^{1}H NMR spectra measured using a 750 MHz NMR apparatus in D_2O. (a) PGD G-4 (0.35 μM), (b) paclitaxel (0.35 μM), and (c) mixture of PGD G-4 and paclitaxel.

Table 1. Results of MALDI-MS, GPC, DLS, and Viscosity of PGDs

sample code	MALDI		GPC			DLS	[η]
	M_{theo}[a]	M_w[b]	M_w[c]	M_n[c]	M_w/M_n	R_h (nm)	(mL·g^{-1})
PGD G-3	1689	1690	2309	2356	1.02	1.1	1.89
PGD G-4	3508	3507	3764	3841	1.02	1.9	3.90
PGD G-5	7104	6959	5312	5450	1.03	2.4	3.06

[a] Theoretical molecular weight. [b] Determined by MALDI-TOFF mass measurements. [c] Determined by GPC using DMF as an eluent with calibration curve of poly(ethylene oxide) standards.

the PGD G-5, two peaks were observed at 6769.2 +H, 6959.2 −H (Figure 1b). These values were smaller than the calculated value (7103.6), so that there was structural defect. Steric hindrance of crowded hydroxyl groups of PGD G-4 is thought to be the reason for decreased conversion of allylation and/or dihydroxylation. The molecular weight and molecular weight distribution (M_w/M_n) were also analyzed by GPC. As shown in Figure 2, retention time of the PGDs on the GPC charts became shorter with increasing the generation. This order was consistent with the results of mass spectroscopy. As expected, M_w/M_n was close to 1.00, indicating that the molecular weight distribution of these PGDs was very narrow. The observed molecular weights of G-3, G-4, and G-5 were found to be larger, a little bit larger, and smaller, respectively, than the calculated values. These results, along with MALDI mass, indicate that the PGDs

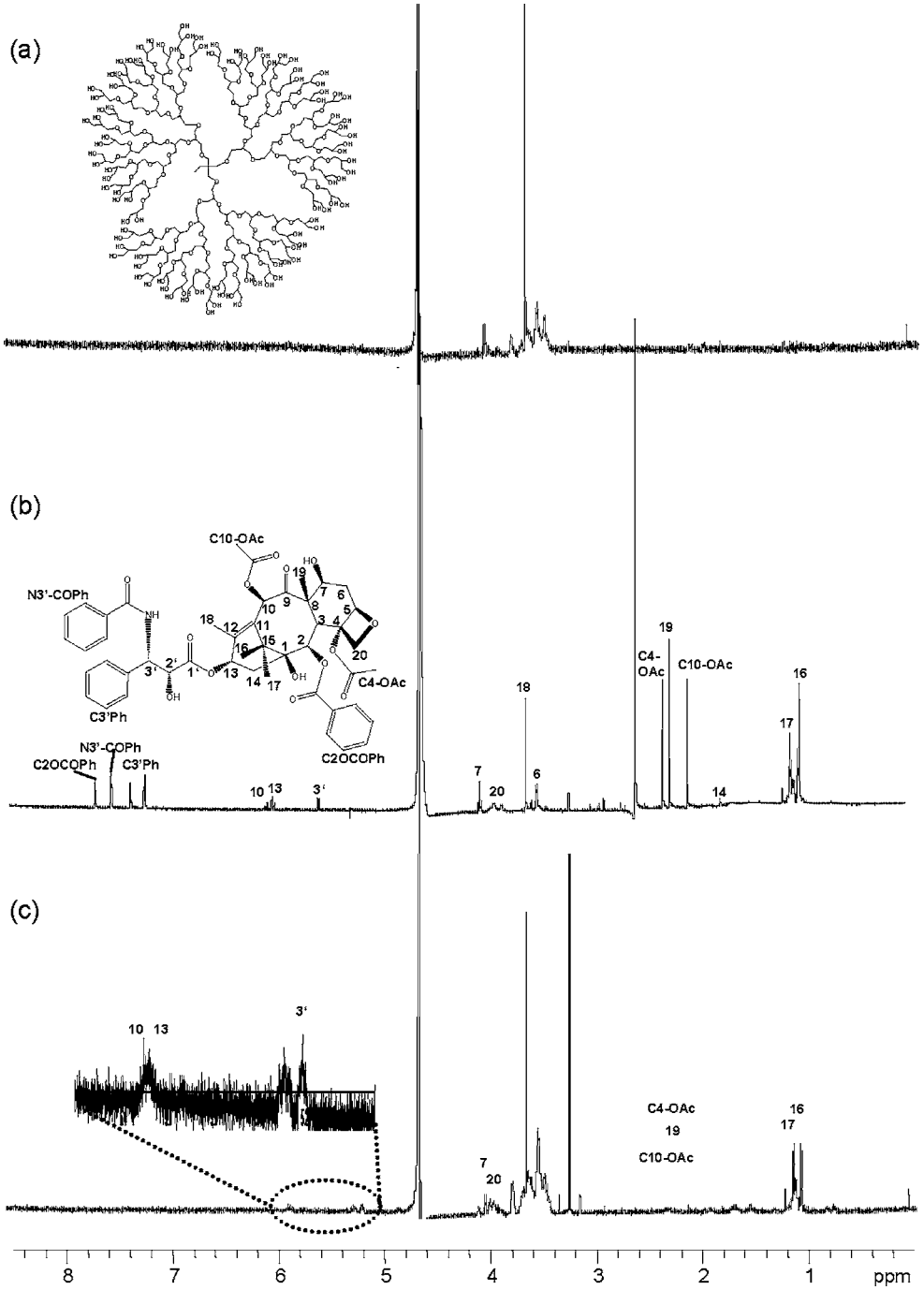


Figure 8. ^{1}H NMR spectra measured using a 750 MHz NMR apparatus in D_2O. (a) PGD G-5 (0.35 μM), (b) paclitaxel (0.35 μM), and (c) mixture of PGD G-5 and paclitaxel.

became compact with increasing the generation. This compacted state of dendrimers was consistent with starburst dendrimers (*14*). Hydrodynamic radius (R_h) of the PGDs was measured by DLS. As shown in Figure 3, the regularization histograms indicate very narrow distribution of those R_h values. The mean R_h values of PGD G-3, G-4 and G-5, calculated by cumulant analysis, were ca. 1.1, 1.9 and 2.4 nm, respectively. [η] values of PGD G-3, G-4 and G-5 were 1.89, 3.90 and 3.06 mL/g, respectively. Since [η] value of PEG 400 was 4.36 (data not shown), the PGDs seemed to behave as low-molecular-weight compounds in single molecule state in water. These results were also consistent with the GPC results that suggest the compact state of PGDs.

The Effect of PGD G-4 and G-5 on Paclitaxel Solubility. The effect of PGD G-4 and G-5 on paclitaxel solubilization in water was examined by measuring the concentration of solubilized paclitaxel using HPLC. Paclitaxel solubilities in all the solutions of PGDs (including G-3) were much higher than those of PEG400 (Figure 4). Since the molecular weights of PGDs were much higher than PEG400, the molecular weight should be considered as one of the important factors. To estimate the effect of molecular weight and the dendritic structure, paclitaxel solubilities in various PEGs with different molecular weights were measured and compared with those in PGD solutions (Figure 5). The paclitaxel solubilities in 10 wt % of PEG (M_n: 400 $\sim$ 8000) aqueous solutions were found to be 0.4−0.6 μg/mL, which was similar to the paclitaxel solubility in water (0.3 μg/mL) (*15*). On the other hand, the paclitaxel solubilities in 10 wt % of PGDs (M_n: 1690−6960) were 80−128 μg/mL,

which were 3 orders of magnitude higher than that in pure water. These results suggest that the increased solubility is due to the dendritic architecture. Since the concentration of PGDs required for solubilization of paclitaxel was 30−5000 times higher than the concentration of paclitaxel (Figure 4), it is likely that paclitaxel might not be incorporated into the dendrimer core and PGDs provide hydrotropic effect by providing local high concentrations of ethylene glycol units (*16*). The ability to enhance the paclitaxel solubility was in the order of G-5 > G-4 > G-3, which is understandable from the hydrotropic effect of dendrimers.

Proposed Mechanism of the Hydrotropic Solubilization. The hydrotropic solubilization of paclitaxel by the PGDs was examined in more detail. Since ^{1}H NMR data provide valuable information on direct interactions between dendrimer and hydrophobic compounds (*17*), the chemical shifts of paclitaxel in D_2O before and after mixing with PGD G-3, G-4, and G-5 were examined (Figures 6−8). The 750 MHz NMR apparatus made us to obtain the spectra of paclitaxel even in the lower concentration in D_2O (0.35 μM). The measurements at much higher concentration of paclitaxel in the presence of PGD G-4 (Figure 4) were tried, but several hundred times higher concentration of PGD G-4 hindered observing the spectra of paclitaxel. Therefore, the concentration of paclitaxel was fixed to be maximum concentration (0.35 μM), and the same molar amounts of PGDs G-3, G-4, and G-5 were dissolved in the solution to observe the chemical shifts. Before mixing paclitaxel with PGDs, the peaks of all the aromatic rings (C2OCOPh, N3′-COPh, and C3′-Ph) and methyne groups of C10, C13, and C3′ were observed at 7.69, 7.53, 7.35−7.21, 6.05, 6.01, and 5.94, respectively (Figures 6−8b). When mixing with the same concentration of PGDG-3, those peaks of all the aromatic rings, methyne groups were suppressed (Figure 6c). In addition, the peaks of C4−OAc (2.25 ppm), methyl of C19 (2.21 ppm) and C10−OAc (2.06 ppm) in Figure 6b were broadened (Figure 6c). Similar tendency of the peak suppression has been reported in the case of hydrophilic−hydrophobic block copolymers (*18*) and dendrimers (*19*): the peaks of hydrophobic parts were suppressed in D_2O when the polymers form micelles with core−shell structure. Thus, the results suggest that the aromatic rings, methyne groups, and acetyl groups of paclitaxel are surrounded by the PGD G-3. The methyl peaks of C17 and 16 (1.11−1.0 ppm) were clearly observed after the mixing, suggesting that the whole paclitaxel molecules could not be incorporated in the PGD core. Similar tendency in the case of PGD G-4 was observed, but the peaks of C7 methyne (3.99 ppm), C4−OAc (2.25 ppm), methyl of C19 (2.21 ppm), C10−OAc (2.06 ppm), and the methyl peaks of C17 and 16 were observed after the mixing, as shown in Figure 7c. Interestingly, when mixing with PGD G-5, the methyne peaks of C10, C13, and C3′ were observed with some chemical shift change to higher magnetic fields (Figure 8c). These results suggest that the way of intermolecular interactions for the hydrotropic solubilization is changeable with increasing the generation of PGDs. Presumably, the increased number of hydroxyl groups participates hydrogen bonds with amide, ester, and/or hydroxyl group of paclitaxel. Since PGDs did not have any hydrophobic core like the dendritic unimolecular micelles composed of many aromatic rings (*19*), the solubilization ability without using the hydrophobic region (such as aromatic rings) suggests a new mechanism of solubilization. Our ongoing study shows that the solubilized paclitaxel is amorphous, but the chemical structure was stable in the solubilized states over several months.

CONCLUSION

Polyglycerol dendrimers (PGDs) with 4−5 generations were synthesized and characterized by NMR, MALDI-TOF mass, GPC, viscosity, and dynamic light scattering measurements. Polydispersity of the obtained PGDs was very narrow, and the PGDs in water exist in compacted states. The paclitaxel solubility was increased with the higher generation of PGD, and the effect was due to the dendritic architecture. PGDs increased the paclitaxel solubility by surrounding aromatic rings and some methyne groups of paclitaxel. The hydrotropic solubilization by PGDs does not require a hydrophobic segment as in polymeric micelles, and it provides an alternative approach of increasing the solubility of poorly soluble drugs.

ACKNOWLEDGMENT

This study was supported in part by National Institute of Health through grant GM 65284, Samyang Corp., and Japanese Government through Monbukagakusho grant for visiting research scholar. The authors would like to thank Mr. Koichi Higashimine (JAIST) for 750 MHz ^{1}H NMR measurements.

LITERATURE CITED

(1) Sweetana, S., and Akers, M. J. (1996) Solubility principle and practices for parental drug dosage form development. *PDA J. Pharm. Sci. Technol. 50*, 330−342.
(2) Thelly, T., Isel, H., and Mountfield, R. J. (2000) The impact of cosolvents and the composition of experimental formulations on the pump rate of the ALZET osmotic pump. *Int. J. Pharm. 205*, 195−198.
(3) Boylan, J. C. (1987) Liquids, in *The Theory and Practice of Industrial Pharmacy* (Lachman, L., Lieberman, H. A., Kanig, J. L., Eds.) pp 460−461, Varghese Publishing House, Bombay.
(4) Singla, A. K., Garg, A., and Aggarwal. (2002) Paclitaxel and its formulations. *Int. J. Pharm. 235*, 179−192.
(5) Dye, D., and Watkins, J. (1980) Suspected anaphylactic reaction to cremophor EL. *Br. Med. J. 280*, 1353.
(6) Groves, M. J., Bassett, B., and Sheth, V. (1984) The solubility of 17 β-oestradiol in aqueous poly(ethylene glycol) 400. *J. Pharm. Pharmacol. 36*, 799−802.
(7) Tejwani, R. W., Joshi, H. N., Varia, S. A., and Serajuddin, A. T. M. (2000) Study of phase behavior of poly(ethylene glycol)-polysorbate 80 and poly(ethylene glycol)-polysorbate 80-water mixtures. *J. Pharm. Sci. 89*, 946−950.
(8) Sato, T., Niwa, H., and Chiba, A. (1998) Dynamical structure of oligo(ethylene glycol)s-water solutions studied by time domain reflectometry. *J. Chem. Phys. 108*, 4138−4147.
(9) Ooya, T., Lee, J., and Park, K. (2003) Effects of ethylene glycol-based graft, star-shaped, and dendritic polymers on solubilization and controlled release of paclitaxel. *J. Controlled Release 93*, 121−127.
(10) Sunder, A., Hanselmann, R., Frey, H., and Mulhaupt, R. (1999) Controlled synthesis of hyperbranched polyglycerols by ring-opening multibranching polymerization. *Macromolecules 32*, 4240−4246.
(11) Frey, H., and Haag, R. (2002) Dendritic polyglycerol: a new versatile biocompatible material. *Rev. Mol. Biotech. 90*, 257−267.
(12) Siegers, C., Biesalski, M., and Haag, R. (2004) Self-assembled monolayers of dendritic polyglycerol derivatives on gold that resist the adsorption of proteins. *Chem.−Eur. J. 10*, 2831−2838.
(13) Haag, R., Sunder, A., and Stumbe, J.-F. (2000) An approach to glycerol dendrimers and pseudo-dendritic polyglycerols. *J. Am. Chem. Soc. 122*, 2954−2955.
(14) Tomalia, D. A., Naylor, A. M., and Goddard, W. A., III (1990) Starburst dendrimers: molecular-level control of size,

shape, surface chemistry, topology, and flexibility from atoms to macroscopic matter. *Angew. Chem., Int. Ed. Engl. 29*, 138−175.

(15) Lee, J., Lee, S. C., Acharya, G., Chang, C.-J., and Park, K. (2003) Hydrotropic solubilization of paclitaxel: Analysis of chemical structures for hydrotropic property. *Pharm. Res. 20*, 1022−1030.

(16) Srinivas, V., Rodley, G. A., Ravikumar, K., Robinson, W. T., Turnbull, M. M., and Balasubramanian, D. (1997) Molecular organization in hydrotrope assemblies. *Langmuir 13*, 3235−3239.

(17) Morgan, M. T., Carnahan, M. A., Immoos, C. E., Ribeiro, A. A., Finkelstrin, S., Lee, S. J., and Grinstaff, M. W. (2003) Dendritic molecular capsules for hydrophobic compounds. *J. Am. Chem. Soc. 125*, 15485−15489.

(18) Jeong, Y.-I., Nah, J.-W., Lee, H.-C., Kim, S.-H., and Cho, C.-S. (1999) Adriamycin release from flower-type polymeric micelle based on star-block copolymer composed of poly(g-benzyl L-glutamate) as the hydrophobic part and poly-(ethylene oxide) as the hydrophilic part. *Int. J. Pharm. 188*, 49−58.

(19) Liu, M., Kono, K., and Fréchet, J. M. J. (2000) Water-soluble dendritic unimolecular micelles: Their potential as drug delivery agents. *J. Controlled Release 65*, 121−131.

BC049814L

Tuning of Intercalation and Electron-Transfer Processes between DNA and Acridinium Derivatives through Steric Effects

Joshy Joseph,[†] Elizabeth Kuruvilla,[†] Asha T. Achuthan,[†] Danaboyina Ramaiah,*[,†] and Gary B. Schuster[‡]

Photosciences and Photonics Division, Regional Research Laboratory (CSIR), Trivandrum 695019, India, and School of Chemistry and Biochemistry, Georgia Institute of Technology, Atlanta, Georgia 30332-0400. Received July 23, 2004; Revised Manuscript Received September 27, 2004

A series of acridinium derivatives **1**−**6**, wherein steric factors have been varied systematically through substitution at the 9 position of the acridine ring, have been synthesized and their DNA interactions have been investigated by various biophysical techniques. The unsubstituted and methylacridinium derivatives **1** and **2** and the *o*-tolylacridinium derivative **6** exhibited high fluorescence quantum yields ($\Phi_f \cong 1$) and lifetimes (τ = 35, 34, and 25 ns, respectively), when compared with the arylacridinium derivatives **3**−**5**. The acridinium derivatives **1** and **2** showed high DNA binding affinity ($K = 7.3-7.7 \times 10^5\ M^{-1}$), when compared to the arylacridinium derivatives **3**-**5** ($K = 6.9-10 \times 10^4\ M^{-1}$). DNA melting and viscosity studies establish that in the case of the aryl-substituted systems, the efficiency of DNA binding is in the order, phenyl > *p*-tolyl > *m*-tolyl ⋙ *o*-tolyl derivative. The increase in steric crowding around the acridine ring hinders the DNA binding interactions and thereby leads to negligible binding as observed in the case of **6** (*o*-tolyl derivative). These results indicate that a subtle variation in the substitution pattern has a profound influence on the photophysical and DNA interactions. Further, they demonstrate that π-stacking interactions of the ligands with DNA are essential for efficient electron transfer between the DNA bases and the ligands. These water soluble and highly fluorescent molecules which differ in their DNA binding mode can act as models to study various DNA−ligand interactions.

INTRODUCTION

The study of interactions of various ligands with DNA has been the subject of considerable interest because of its importance in the design of drugs targeted to DNA as well as in understanding the electron and energy transfer properties of DNA (*1*−*10*). Of the various types of interactions, the intercalative interactions of ligands with DNA is particularly important because of the fact that many anticancer drugs and antibiotics exert their biological activity through DNA intercalation (*11*−*14*). A better understanding of the factors that govern the binding mode of ligands with DNA is not only essential for the design of efficient drugs targeted to DNA and development of probes for various DNA structures but also for the use of DNA in electronic materials applications (*15*).

To investigate how steric and conformational factors influence the mode and extent of binding of small molecules with DNA, we have chosen systems based on the acridine chromophore for study. Acridines are a special class of compounds not only because of their interesting chemical and physical properties but also due to their immense utility in the pharmaceutical and dye industries (*16*, *17*). Acridines were the first chromophore that was extensively studied for its noncovalent DNA interactions. These studies led to the concept of intercalation. The study of the steric and conformational effects on the DNA binding properties of acridine chromophores has received less attention (*11*, *12*, *18*, *19*). In this context, we have designed a series of acridinium derivatives **1**−**6**, wherein we have systematically varied the steric factors through substitution at the 9 position of the acridinium ring (Figure 1) to assess the energetics and nature of their DNA binding interactions. The results of these investigations indicate that subtle variation in the substitution pattern on the acridinium chromophore has a profound influence on their photophysical and DNA binding interactions. These results demonstrate that these water soluble and highly fluorescent molecules can act as models to study various DNA interactions.

EXPERIMENTAL PROCEDURES

The equipment and procedure for spectral recordings are described elsewhere (*19*). The fluorescence lifetimes were measured on an IBH picosecond single photon counting system using a 401 nm IBH NanoLED source and a Hamamatsu C4878−02 MCP detector. The fluorescence decay profiles were deconvoluted using IBH Data Station software V2.1, fitted with a mono-, bi-, or triexponential decay and minimizing the χ^2 values of the fit to 1 ± 0.1. The oligonucleotides (**DNA1**: 5′-CGT GGA CAT TGC ACG GTA C-3′; **DNA2**: 5′-GTA CCG TGC AAT GTC CAC G-3′) were synthesized on an Applied Biosystems DNA Synthesizer as described earlier (*20*). Solution of calf thymus DNA (CT DNA, Pharmacia Biotech, USA) in phosphate buffer was sonicated for 1 h and filtered through a 0.45 μM Millipore filter. The concentrations of the CT DNA solutions were determined by using the average extinction coefficient value of 6600 $M^{-1}\ cm^{-1}$ for a single nucleotide at 260 nm (*21*). Polynucleotides (Amersham Pharmacia Biotech Inc.) were dissolved in phosphate buffer, and the concentrations were deter-

* To whom correspondence should be addressed. Fax: (+91) 471-2490186, E-mail: d_ramaiah@rediffmail.com or rama@csrrltrd.ren.nic.in.

[†] Regional Research Laboratory (CSIR).

[‡] Georgia Institute of Technology.

10.1021/bc0498222 CCC: $27.50 © 2004 American Chemical Society
Published on Web 10/28/2004

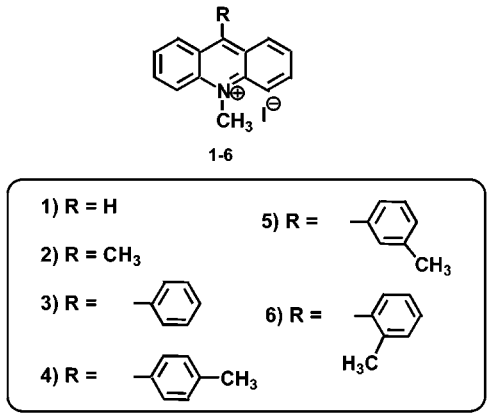


Figure 1. Structures of acridinium derivatives **1**−**6** under study.

mined by using the average extinction coefficient value of 7400 M^{-1} cm^{-1} at 253 nm for poly(dG).poly(dC) and 6000 M^{-1} cm^{-1} at 260 nm for poly(dA).poly(dT) (*21*). The absorption and fluorescence titrations of the acridinium derivatives with DNA were carried out by adding small aliquots of DNA solution containing the same concentration of the compound as that in the test solution. The binding affinities were calculated using fluorescence quantum yields, according to the method of McGhee and von Hippel by using the data points of the Scatchard plot (*22*−*24*).

Preparation of the Acridinium Derivatives 1−6. The acridine derivatives **8b**−**f** were synthesized by a modified Bernthsen procedure as shown in Scheme 1 (*25*). The condensation reaction of diphenylamine with the corresponding carboxylic acid in the presence of anhydrous $ZnCl_2$ yielded the acridine derivatives **8b**−**f** in 50−60% yields. The quarternization of these acridine derivatives with methyl iodide gave the corresponding acridinium derivatives **1**−**6** in quantitative yields, which were recrystallized from a mixture (4:1) of acetonitrile and methanol (*26*).

10-Methylacridinium iodide (1): 79%; mp 230−232 °C; ^{1}H NMR (300 MHz, DMSO-d_6) δ 4.87 (3H, s), 8.05 (2H, t, J = 7.5 Hz), 8.48 (2H, t, J = 8 Hz), 8.63 (2H, d, J = 8.4 Hz), 8.79 (2H, d, J = 9.2 Hz), 10.21 (1H, s); ^{13}C NMR (75 MHz, DMSO-d_6) δ 150.96, 141.69, 139.43, 131.98, 128.15, 126.60, 119.36, 39.44. Elemental analysis calcd (%) for $C_{14}H_{12}IN$: C, 52.36; H, 3.77; N, 4.36. Found: C, 52.36; H, 3.51; N, 4.53.

9,10-Dimethylacridinium iodide (2): 76%, mp 248−249 °C; ^{1}H NMR (300 MHz, DMSO-d_6) δ 3.48 (3H, s), 4.77 (3H, s), 8.01 (2H, t, J = 7.2 Hz), 8.41 (2H, t, J = 7.4 Hz), 8.72 (2H, d, J = 9.2 Hz), 8.89 (2H, d, J = 8.2 Hz); ^{13}C NMR (75 MHz, DMSO-d_6) δ 149.76, 138.85, 136.22, 127.42, 125.55, 124.71, 120.51, 39.59, 15.36. Elemental analysis calcd (%) for $C_{15}H_{14}IN$: C, 53.75; H, 4.21; N, 4.18. Found: C, 53.87; H, 4.07; N, 4.18.

9-Phenyl-10-methylacridinium iodide (3): 71%; mp 201−202 °C; ^{1}H NMR (300 MHz, DMSO-d_6) δ 4.93 (3H, s), 7.54−7.56 (2H, m), 7.75−7.80 (3H, m), 7.92 (4H, d, J = 3.7 Hz), 8.44−8.49 (2H, m), 8.88 (2H, d, J = 9.2 Hz); ^{13}C NMR (75 MHz, DMSO-d_6) δ 160.95, 141.76, 138.97, 133.66, 130.67, 130.35, 130.06, 129.41, 128.49, 126.08, 119.81, 39.52. Elemental analysis calcd (%) for $C_{20}H_{16}IN$: C, 60.47; H, 4.06; N, 3.53. Found: C, 60.55; H, 4.03; N, 3.27.

9-(4-Methylphenyl)-10-methylacridinium iodide (4): 71%; mp 228−230 °C; ^{1}H NMR (300 MHz, DMSO-d_6) δ 2.54 (3H, s), 4.93 (3H, s), 7.47 (2H, d, J = 8 Hz), 7.58 (2H, d, J = 7.9 Hz), 7.90−7.99 (4H, m), 8.46 (2H, t, J = 7.7 Hz), 8.85 (2H, d, J = 9.3 Hz). ^{13}C NMR (75 MHz, DMSO-d_6) δ 161.26, 141.67, 140.41, 138.88, 130.66, 130.40, 130.11, 129.92, 128.35, 126.09, 119.75, 39.62, 21.54. Elemental analysis calcd (%) for $C_{21}H_{18}IN$: C, 61.33; H, 4.41; N, 3.41. Found: C, 61.60; H, 4.39; N, 3.48.

9-(3-Methylphenyl)-10-methylacridinium iodide (5): 68%; mp 220−222 °C; ^{1}H NMR (300 MHz, DMSO-d_6) δ 1.86 (3H, s), 4.95 (3H, s), 7.36 (1H, d, J = 7.5 Hz), 7.57 (1H, t, J = 7.3 Hz), 7.63−7.72 (2H, m), 7.78 (2H, d, J = 8.6 Hz), 7.95 (2H, t, J = 7.6 Hz), 8.48 (2H, t, J = 7.9 Hz), 8.90 (2H, d, J = 9.2 Hz); ^{13}C NMR (75 MHz, DMSO-d_6) δ 160.72, 141.76, 139.04, 136.33, 133.30, 131.16, 130.72, 129.92, 129.40, 128.75, 126.78, 125.96, 120.03, 39.63, 19.76. Elemental analysis calcd (%) for $C_{21}H_{18}IN$: C, 61.33; H, 4.41; N, 3.41. Found: C, 61.08; H, 4.18; N, 3.51.

9-(2-Methylphenyl)-10-methylacridinium iodide (6): 60%; mp 224−225 °C; ^{1}H NMR (300 MHz, DMSO-d_6) δ 1.87 (3H, s), 4.97 (3H, s), 7.36 (1H, d, J = 7.5 Hz), 7.57 (1H, t, J = 7.3 Hz), 7.63−7.72 (2H, m), 7.78 (2H, d, J = 8.6 Hz), 7.95 (2H, t, J = 7.6 Hz), 8.48 (2H, t, J = 7.9 Hz), 8.90 (2H, d, J = 9.2 Hz); ^{13}C NMR (75 MHz, DMSO-d_6) δ 160.72, 141.76, 139.04, 136.33, 133.30, 131.16, 130.72, 129.92, 129.40, 128.75, 126.78, 125.96, 120.03, 39.63, 19.76. Elemental analysis calcd (%) for $C_{21}H_{18}IN$: C, 61.33; H, 4.41; N, 3.41. Found: C, 61.55; H, 4.17; N, 3.62.

RESULTS AND DISCUSSION

The photophysical properties of the acridinium derivatives were investigated under different conditions, and these results are summarized in Table 1. The acridinium derivatives **1**, **2** and the *o*-tolylacridinium derivative **6** exhibited quantitative fluorescence quantum yields ($\Phi_f \cong 1$) with an emission maximum around 500 nm. In contrast, the fluorescence quantum yields of the arylacridinium derivatives **3**−**5** (Φ_f = 0.09, 0.05, and 0.11, respectively) were found to be significantly quenched. The acridinium derivative **1** exhibits a single-exponential decay with a lifetime of 35 ns, whereas the *o*-tolylacridinium derivative **6** shows a reduced lifetime of 25 ns (Table 1). When compared to **1**, **2**, and **6**, unusually low lifetimes were observed for the arylacridinium derivatives **3**−**5** (τ = 1.3, 0.6, and 1.7 ns, respectively). The lower values of the fluorescence quantum yields and lifetimes observed for the arylacridinium derivatives **3**−**5** can be attributed to enhanced nonradiative decay pathways due to the rotation between the acridinium and the phenyl ring and the favorable quenching of the singlet excited state by the aryl group through an electron-transfer mechanism (*26*, *30*, *31*). Interestingly, the excited-state properties of the *o*-tolylacridinium derivative **6**, is very similar to that of the simple acridinium derivatives **1** and **2**, probably because of the steric constraints offered by the *o*-methyl substituent.

The acridinium derivatives **1**−**6** can in principle interact with DNA through intercalation and/or electrostatic modes. Figure 2 shows the change in the absorption spectra of the acridinium derivative **2** with increasing DNA concentrations. The addition of CT DNA to a solution of **2** results in a strong decrease in the absorption of the acridinium chromophore, along with a red shift of around 3 nm. Furthermore, with the increase in DNA concentration, a strong quenching of the acridinium fluorescence emission is observed as shown in Figure 3. Similar changes in absorption and fluorescence emission

Scheme 1

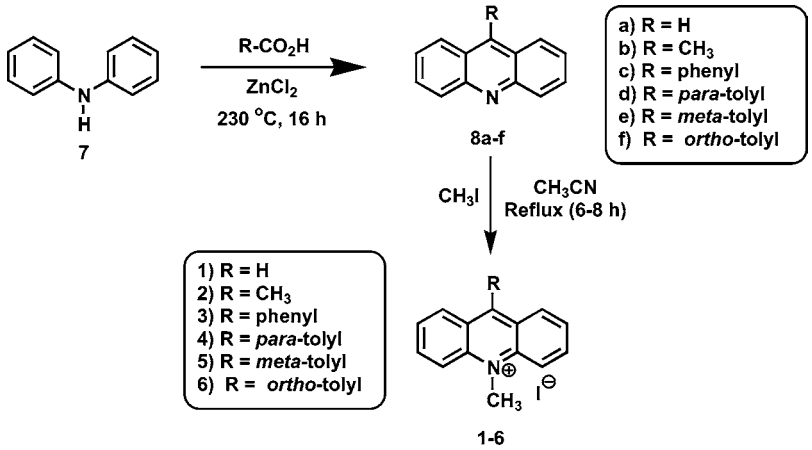


Table 1. Photophysical and DNA Binding Properties of the Acridinium Derivatives 1−6[a]

compound	λ_{em}, nm	Φ_f[b]	τ, ns	K (M^{-1})[c]	n[d]	k_{DNA} (s^{-1})[e]
1	491	1	35	7.7×10^5	2.5	1.2×10^{10}
2[f]	493	1	34	7.3×10^5	2.5	1.1×10^{10}
3	508	0.09	1.3	1.1×10^5	6	5×10^{10}
4	508	0.05	0.6	7.1×10^4	7	6.5×10^{10}
5	508	0.11	1.7	6.9×10^4	6.5	3×10^{10}
6	501	1	25	*g*	*g*	*g*

[a] Average of more than two experiments and error ca. ±5%. The photophysical and DNA binding properties were examined in water and phosphate buffer (10 mM, pH 7.4), respectively. [b] Fluorescence quantum yields were calculated using 10-methylacridium trifluoromethane sulfonate as the standard (Φ_f = 1) (*26*, *27*). [c] DNA association constants determined by the Scatchard analysis of fluorescence titration data. [d] Number of nucleotides occluded by a bound ligand. [e] Rate of static quenching by DNA calculated as reported earlier (*28*, *29*). [f] Compound **2**, under similar conditions exhibited DNA association constants (K) 8.5×10^5 M^{-1} and 4.12×10^5 M^{-1} and electron-transfer rate constants (k_{DNA}) 3.8×10^{10} s^{-1}, and 0.24×10^{10} s^{-1} with poly(dG).poly(dC) and poly(dA).poly(dT), respectively. [g] Negligible binding.

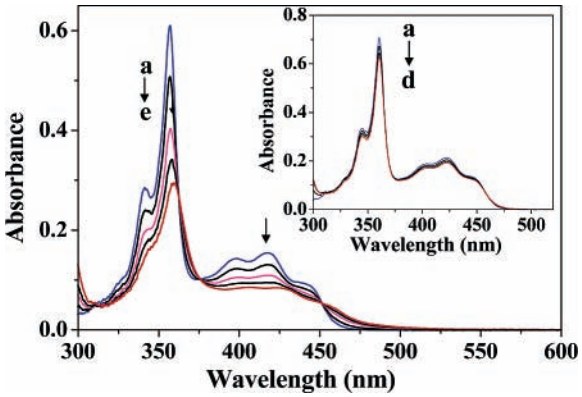


Figure 2. Change in absorption spectra of **2** (32 μM) in phosphate buffer (10 mM; pH 7.4) with increasing concentration of CT DNA. [DNA] (a) 0, (b) 0.05, (c) 0.12, (d) 0.19, and (e) 0.34 mM. Inset shows the change in absorption spectra of **6** (42.5 μM) in phosphate buffer (10 mM; pH 7.4) with increasing concentration of CT DNA. [DNA] (a) 0, (b) 0.17, (c) 0.34, and (d) 0.42 mM.

spectra were observed for the acridinium derivatives **1** and **3**−**5** (Supporting Information; Figures S1−S4). Among all the acridinium derivatives, the *o*-tolylacridinium derivative **6** showed an interesting variation. Insets of Figures 2 and 3 show the changes in the absorption and fluorescence emission spectra of **6**, respectively, with increasing concentration of DNA. Both the absorption

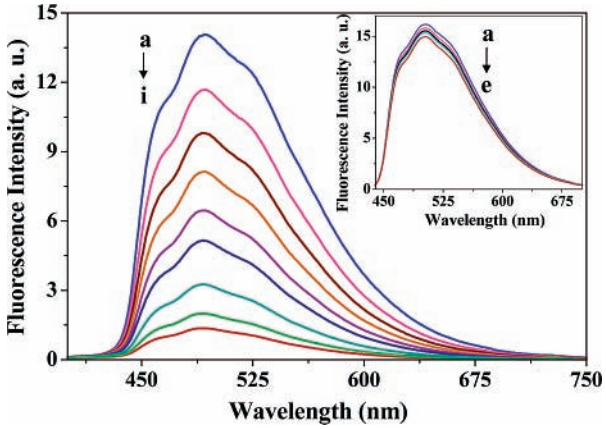


Figure 3. Change in fluorescence spectra of **2** (32 μM) in phosphate buffer (10 mM; pH 7.4) with increasing concentration of CT DNA. [DNA] (a) 0, (b) 0.05, (c) 0.09, (d) 0.12, (e) 0.16, (f) 0.19, (g) 0.26, (h) 0.34, and (i) 0.42 mM. Inset shows the change in fluorescence spectra of **6** in phosphate buffer (10 mM; pH 7.4) with increasing concentration of CT DNA. [DNA] (a) 0, (b) 0.17, (c) 0.34, (d) 0.42, and (e) 1 mM. Excitation wavelength, 363 nm.

and fluorescence studies indicate that the ortho-derivative **6** exhibits negligible interactions with DNA.

With a view to understanding the effect of various DNA sequences, we have investigated the interaction of the acridinium derivatives with polynucleotides such as poly(dG)·poly(dC) and poly(dA)·poly(dT). The addition of poly(dG)·poly(dC) to a solution of **2** resulted in a strong decrease in the absorption of the acridinium chromophore, along with a red shift of around 5 nm with an isosbestic point at 450 nm. Similar observations were made with poly(dA)·poly(dT) and with other acridinium derivatives (Supporting Information; Figure S5). Furthermore, with the increase in poly(dG)·poly(dC) concentration, a strong quenching of the acridinium fluorescence emission is observed as shown in Figure 4. The poly(dG).poly(dC) exhibits an efficient fluorescence quenching of the acridinium derivative **2** when compared to CT DNA and poly(dA)·poly(dT) (inset of Figure 4), indicating thereby the preferential interactions of these molecules with DNA rich in guanosine sequences.

The DNA association constants (K) of the complexes formed between the acridinium derivatives **1**−**5** and DNA were determined based on fluorescence titration experiments, according to the method of McGhee and von Hippel by using the data points of the Scatchard plot (*9*) and are reported in Table 1. For example, 10-methylacridinium (**1**) shows a binding constant of 7.7×10^5 M^{-1},

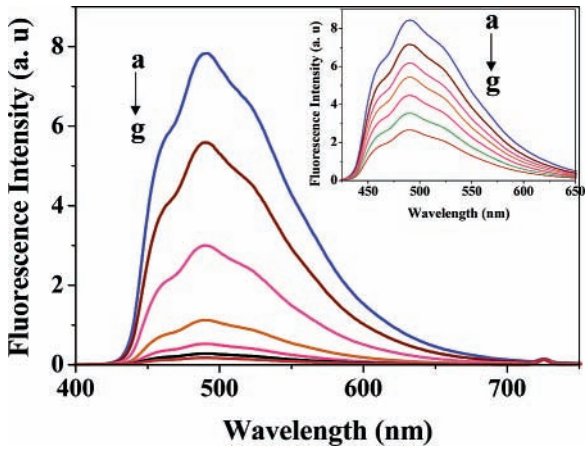


Figure 4. Change in fluorescence spectra of **2** (32 μm) in phosphate buffer (10 mM; pH 7.4) with increasing concentration of poly(dG).poly (dC). [poly(dG).poly(dC)] (a) 0, (b) 0.08, (c) 0.16, (d) 0.24, (e) 0.30, (f) 0.38, (g) 0.5 mM. Inset shows the change in fluorescence spectra of **2** in phosphate buffer (10 mM, pH 7.4) with increasing concentration of poly(dA).poly(dT). [poly(dA).poly-(dT)] (a) 0, (b) 0.08, (c) 0.17, (d) 0.25, (e) 0.33, (f) 0.48, (g) 0.63 mM. Excitation wavelength, 363 nm.

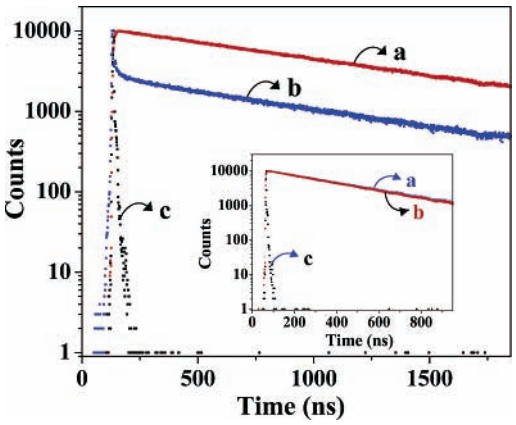


Figure 5. Fluorescence decay profiles of **2** (32 μM) in the presence and absence of DNA in phosphate buffer (10 mM; pH 7.4). [DNA] (a) 0 and (b) 0.34 mM. Inset shows the fluorescence decay profiles of **6** in the presence and absence of DNA under similar conditions. [DNA] (a) 0 and (b) 0.34 mM. Excitation wavelength, 401 nm.

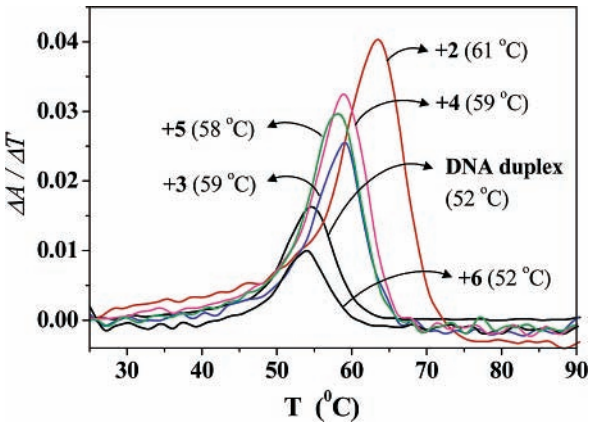


Figure 6. First derivative plots for the thermal denaturation curves of the DNA duplex, **DNA1.DNA2** in the presence and absence of the acridinium derivatives **1**−**6** (20 μM) in 10 mM phosphate buffer (pH 7.4). **DNA1:** 5′-CGT GGA CAT TGC ACG GTA C-3′; **DNA2:** 5′-GTA CCG TGC AAT GTC CAC G-3′.

whereas the arylacridinium derivatives **3**−**5** show relatively lower values of DNA association constants. These association constants were also found to be sensitive to the DNA sequences. For example, the association constant of the acridinium derivative **2** with poly(dG)·poly-(dC) was found to be around 1.2 and 2 times greater than that of CT DNA and poly(dA)·poly(dT).

Interestingly, the binding site size (n) was found to be greater for the arylacridinium derivatives **3**−**5** ($n = 6-7$) than the acridinium derivatives **1** and **2** ($n = 2.5$). Thus, a comparison of the DNA binding constants indicate that the acridinium derivatives **1** and **2** bind to DNA by nearly one order greater efficiently when compared with the arylacridinium derivatives **3**−**5**. In the case of the aryl-substituted derivatives, the efficiency was found to be in the order, phenyl > *p*-tolyl > *m*-tolyl ⋙ *o*-tolyl, wherein the increase in steric factors around the acridine ring hinders the DNA binding interactions and finally leads to a negligible binding as observed in the case of the *o*-tolylacridinium derivative **6**.

Picosecond time-resolved fluorescence studies in the presence and absence of DNA indicate that the acridinium derivative **2** exhibits a single-exponential decay in buffer with a fluorescence lifetime of 34 ns (Figure 5), while in the presence of DNA it shows a triexponential decay with lifetimes of 35 ps, 0.8 ns and 33 ns. The short lifetimes observed (35 ps and 0.8 ns) may be attributed to the intercalative binding of the acridinium chromophore at two different base sequence environments, whereas the third lifetime could be due to the unbound molecules. On the other hand, the ortho-derivative **6**, having a fluorescence lifetime of 25 ns in buffer, exhibited negligible changes in the presence of DNA (inset of Figure 5). These observations confirm that the acridinium chromophore in the case of **6** undergoes neither intercalative nor groove binding interactions with DNA.

Figure 6 shows the first derivative plots for the thermal denaturation curves obtained for the duplex **DNA1** and **DNA2** in the presence and absence of the acridinium derivatives **2**−**6**. The oligonucleotide duplex melts at 52 °C in the absence of ligands, whereas the presence of 20 μM of acridinium derivative **2** stabilizes the duplex by 9 °C. As expected, the arylacridinum derivatives **3**−**5**, under similar conditions, stabilize the duplex less (6−7 °C), whereas, the ortho-derivative **6** provides negligible stabilization to the DNA duplex. The absorbance changes observed at 260 nm, corresponding to DNA during the thermal denaturation of DNA in the presence and absence of the acridinium derivatives, clearly reflect the extent and nature of binding interactions of these derivatives with DNA. Similar absorption changes were observed when monitored at 355 nm corresponding to the acridinium chromophore, which further supports the binding trends observed in the case of the substituted acridinium derivatives.

Figure 7 shows the results of the viscometry studies of representative examples which indicate that the viscosity of DNA increases proportionally with the binding affinity of the acridinium derivatives **2** and **4**, whereas negligible viscosity changes are observed for the ortho-derivative **6**. The change in viscosity could be attributed to the π-stacking of the acridinium derivatives between DNA base pairs, which results in the increase in the viscosity of DNA as in the case of typical intercalators (*32*, *33*). On the other hand, the ortho-derivative **6** shows negligible binding with DNA by intercalation as reflected from the physical and spectroscopic studies. The intercalative interactions of several acridinium conjugates with DNA have been well characterized in the literature by various biophysical and NMR techniques (*34*−*37*).

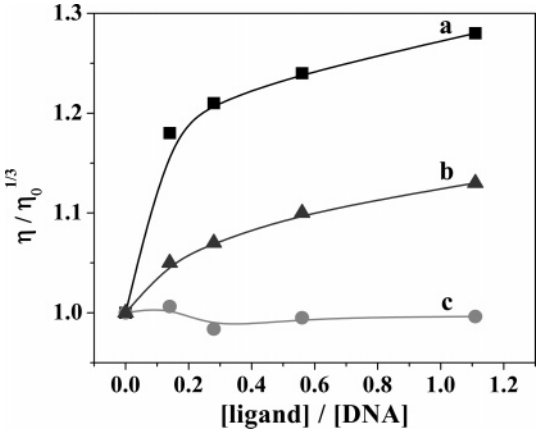


Figure 7. Effect of increasing concentrations of the acridinium derivatives **2** (a), **4** (b), and **6** (c) on the relative viscosity of CT DNA (0.7 mM) at 26 ± 0.2 °C in phosphate buffer (10 mM, pH 7.4).

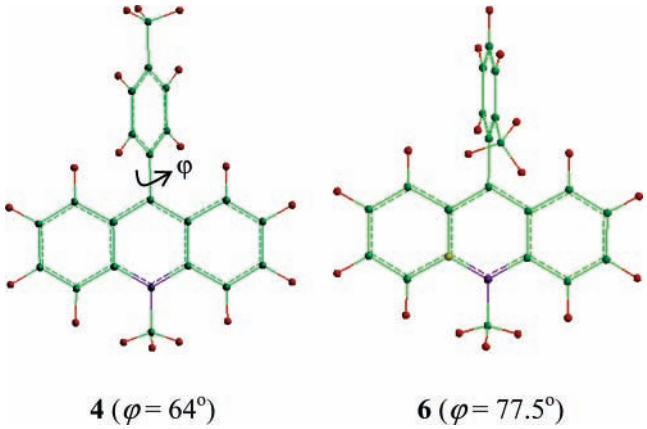


Figure 8. Minimum energy conformations of *p*- and *o*-tolylacridinium derivatives **4** and **6**, obtained by AM1 calculations.

The differences observed in DNA binding affinity of these acridinium derivatives could be rationalized in terms of the steric effects offered by the substituents. The structural analysis of the arylacridinium derivatives reveals that the acridinium as well as the aryl substituent are out of plane to each other and the dihedral angle (φ) according to the minimum energy conformations for **3**−**6** are 64.8°, 64°, 64.7°, and 77.5° (Figure 8) (*38*). To achieve effective intercalation of the acridinium chromophore, the aryl group has to undergo a rotation during the process of intercalation. The feasibility of this rotation is the deciding factor in effective binding of these molecules to DNA. In the case of the ortho-derivative **6**, the rotation of the tolyl group is sterically hindered and hence no significant binding with DNA was observed.

The π-stacking of the acridinium chromophore between the DNA bases as in the case of the simple acridinium derivatives **1** and **2** and arylacridinium derivatives **3**−**5** causes a strong quenching of the fluorescence of the molecule due to the possible electron-transfer processes from DNA bases (*39*). Whereas, in the case of the ortho-derivative **6**, which does not intercalate, the electron transfer is not an efficient process and hence the fluorescence emission properties remain unchanged in the presence of DNA. On the basis of the limiting fluorescence intensity (under conditions where >99% of the substrate is bound to DNA), the rate constant for the static quenching of the singlet excited state of the acridinium chromophore by DNA (k_{DNA}) could be evaluated using eq 1,

$$I_o/I = 1 + k_{DNA}/k_{SI} \quad (1)$$

where I_o and I are the fluorescence intensities in the absence and presence of DNA and k_{SI} is the sum of rate constants ($k_r + k_{nr}$) of the singlet excited-state deactivation (*28*, *29*). As shown in Table 1, for the acridinium derivatives **1**−**5**, which bind with DNA through intercalation, the rate constant for static quenching was found to be in the order of 10^{10} s^{-1}. This observation confirms that the intercalative mode of binding is crucial to observe an efficient quenching of fluorescence of ligands through the electron transfer process from the DNA bases. Moreover, the electron transfer rate constant in the case of the polynucleotide enriched with GC content, poly(dG)·poly(dC), was found to be around 3.5 and 16 times greater than that of CT DNA and poly (dA)·poly(dT), respectively (Table 1). This can be explained in terms of lower oxidation potential of guanosine (*39*) and hence greater feasibility of electron transfer from guanosine to the singlet excited state of the acridinium moiety.

In conclusion, we have demonstrated that by introducing subtle steric factors one may alter the DNA binding properties of acridinium derivatives. It was observed that the unsubstituted and methylacridinium derivatives **1** and **2** bind with DNA by nearly one order more efficiently when compared to the bulky arylacridinium derivatives **3**−**5**. In the case of the aryl-substituted derivatives, the efficiency of binding was found to be in the order, phenyl > *p*-tolyl > *m*-tolyl ⋙ *o*-tolyl, wherein the increase in steric factors around the acridine ring hinders the DNA binding interactions and finally leads to a negligible binding as observed in the case of the *o*-tolylacridinium derivative **6**. Furthermore, these results support the fact that intercalative π-stacking interactions of the ligands with DNA are essential for observing efficient electron transfer reactions between the DNA bases and the ligands. Studies related to the use of these highly fluorescent molecules for the recognition of various DNA structures and duplexes containing mismatches and base bulges are in progress in our laboratory.

ACKNOWLEDGMENT

This work was supported by the Council of Scientific and Industrial Research (CSIR) and the Department of Science and Technology (DST), India, and National Science Foundation (NSF), USA. We acknowledge the National Centre for Ultrafast Processes (NCUFP), Chennai, for lifetime measurements. This is contribution number RRLT-PPD(PRU)-177 from the Regional Research Laboratory, Trivandrum.

Supporting Information Available: Absorption and emission spectra. This material is available free of charge via the Internet at http://pubs.acs.org.

LITERATURE CITED

(1) Waring, M. J. (1981) DNA modification and cancer. *Annu. Rev. Biochem. 50*, 159−192.

(2) Tomasz, M. (1994) The mitomycins: Natural cross-linkers of DNA. *Molecular Aspects of Anticancer-Drug Interactions* (Neidle, S., and Waring, M., Eds.) Vol. 2, pp 312−349, CRC Press, Boca Raton, FL.

(3) Wilson, W. D. (1999) DNA intercalators. *DNA and Aspects of Molecular Biology* (Kool, E., Ed.) Vol. 7 in *Comprehensive Natural Products Chemistry* (Barton, D., and Nakanishi, K., Eds.), Chapter 12, Pergamon Press, Elsevier.

(4) *Small Molecule DNA and RNA Binders: From Synthesis to Nucleic Acid Complexes* (Demeunynck, M., Bailly, C., and Wilson, W. D., Eds.) p 336, Vols. 1 and 2, Wiley-VCH, Weinheim.
(5) Schuster, G. B. (2000) Long-range charge transfer in DNA: Transient structural distortions control the distance dependence. *Acc. Chem. Res. 33*, 253−260.
(6) Kelley, S. O., Holmlin, R. E., Stemp, E. D. A., and Barton, J. K. (1997) Photoinduced electron transfer in ethidium modified DNA duplexes: dependence on distance and base stacking. *J. Am. Chem. Soc. 119*, 9861−9870.
(7) Lewis, F. D., and Wu, Y. (2001) Dynamics of superexchange photoinduced electron transfer in duplex DNA. *J. Photochem. Photobiol. C: Photochem. Rev. 2*, 1−16.
(8) Armitage, B. (1998) Photocleavage of nucleic acids. *Chem. Rev*. *98*, 1171−1200.
(9) Kochevar, I. E., and Dunn, D. A., (1990) Photosensitized reactions of DNA: Cleavage and addition. *Bioorganic Photochemistry: Photochemistry and the Nucleic Acids* (Morrison, H., Ed.) pp 273−315, Vol. 1, John Wiley and Sons, New York.
(10) Giese, B. (2000) Long-distance charge transport in DNA: The hopping mechanism. *Acc. Chem. Res. 33*, 631−636.
(11) Waring, M. J. (1970) Variation of the supercoils in closed circular DNA by binding of antibiotics and drugs. Evidence for molecular models involving intercalation. *J. Mol. Biol*. *54*, 247−279.
(12) Lerman, L. S. (1961) Structural considerations in the interaction of deoxyribonucleic acid and acridines. *J. Mol. Biol. 3*, 18−30.
(13) Pindur, U., Haber, M., and Sattler, K. (1993) Antitumor active drugs as intercalators of deoxyribonucleic acid: Molecular models of intercalation complexes. *J. Chem. Educ. 70*, 263−272.
(14) Gao, Q., Williams, L. D., Egli, M., Rabinovich, D., Chen, S.-L., Quigley, G. J., and Rich, A. (1991) Drug-induced DNA repair: X-ray structure of a DNA-ditercalinium complex. *Proc. Natl. Acad. Sci. U.S.A. 88*, 2422−2426.
(15) Di Ventra, M., and Zwolak, M. (2004) DNA electronics. *Encyclopedia of Nanoscience and Nanotechnology* (Nalwa, H. S., Ed.) pp 475−493, Vol. 2, American Scientific Publishers, Stevenson Ranch, CA.
(16) Albert, A. (1966) *The acridines: Their preparation, physical, chemical, and biological properties and uses*, Edward Arnold Ltd., London.
(17) Zittoun, R. (1985) m-AMSA: a review of clinical data. *Eur. J. Cancer Clin. Oncol. 21*, 649−653.
(18) Eldho, N. V., Joseph, J., and Ramaiah, D. (2001) Steric and conformational effects on the photophysical and DNA binding properties of novel viologen linked tolylacridines. *Chem. Lett.*, 438−439.
(19) Joseph, J., Eldho, N. V., and Ramaiah, D. (2003) Control of electron-transfer and DNA binding properties by the tolyl spacer group in viologen linked acridines. *J. Phys. Chem. B 107*, 4444−4450.
(20) Gasper, S. M., and Schuster, G. B. (1997) Intramolecular photoinduced electron transfer to anthraquinones linked to duplex DNA: The effect of gaps and traps on long-range radical cation migration. *J. Am. Chem. Soc. 119*, 12762−12771.
(21) Baguley, B. C., and Falkenhaug, E. M. (1978) The interaction of ethidium with synthetic double-stranded polynucleotides at low ionic strength. *Nucleic Acids Res. 5*, 161−171.
(22) Scatchard, G. (1949) The attraction of proteins for small molecules and ions. *Ann. N. Y. Acad. Sci. 51*, 660−672.
(23) McGhee, J. D., and Von Hippel, P. H. (1974) Theoretical aspects of DNA-protein interactions. Cooperative and noncooperative binding of large ligands to a one-dimensional homogeneous lattice. *J. Mol. Biol. 86*, 469−489.
(24) Adam, W., Cadet, J., Dall'Acqua, F., Epe, B., Ramaiah, D., and Saha-Moeller, C. R. (1995) Photosensitized formation of 8-hydroxy-2′-deoxyguanosine in salmon testes DNA by furocoumarin hydroperoxides: A novel, intercalating "Photo-Fenton" reagent for oxidative DNA damage. *Angew. Chem., Int. Ed. Engl. 34*, 107−110.
(25) Eldho, N. V., Saminathan, M., and Ramaiah, D. (1999) One pot synthesis of acridinylalkanoic acids and novel bisacridines. *Synth. Commun. 29*, 4007−4014.
(26) Jonker, S. A., Ariese, F., and Verhoeven, J. W. (1989) Cation complexation with functionalized 9-arylacridinium ions: Possible applications in the development of cation-selective optical probes. *Recl. Trav. Chim. Pays-Bas 108*, 109−115.
(27) Weber, G., and Teale, F. W. J. (1957) Determination of the absolute quantum yield of fluorescent solutions. *Trans. Faraday Soc. 53*, 646−655.
(28) Rogers, J. E., Le, T. P., and Kelly, L. A. (2001) Nucleotide oxidation mediated by naphthalimide excited states with covalently attached viologen cosensitizers. *Photochem. Photobiol. 73*, 223−229.
(29) Joseph, J., Eldho, N. V., and Ramaiah, D. (2003) Design of photoactivated DNA oxidizing agents: Synthesis and study of photophysical properties and DNA interactions of novel viologen-linked acridines. *Chem. Eur. J. 9*, 5926−5935.
(30) Sosonkin, I., M., Subbotin, V. A., Charushin, V. N., and Chupakhin, O. N. (1976) Mechanism of nucleophilic substitution of hydrogen. Electron transfer in the oxidation of substituted 9, 10-dihydroacridines. *Dokl. Akad. Nauk. SSSR 229*, 888−891.
(31) Jones, G., II, Farahat, M. S., Greenfield, S. R., Gosztola, D. J., and Wasielewski, M. R. (1994) Ultrafast photoinduced charge-shift reactions in electron donor−acceptor 9-arylacridinium ions. *Chem. Phys. Lett. 229*, 40−46.
(32) Reinert, K. E. (1983) Anthracycline-binding induced DNA stiffening, bending and elongation; stereochemical implications from viscometric investigations. *Nucleic Acids. Res. 11*, 3411−3430.
(33) Breslin, D. T., Coury, J. E., Anderson, J. R., McFail-Isom, L., Kan, Y.,; Williams, L. D., Bottomley, L. A., and Schuster, G. B. (1997) Anthraquinone photonuclease structure determines its mode of binding to DNA and the cleavage chemistry observed. *J. Am. Chem. Soc. 119*, 5043−5044.
(34) Bostock-Smith, C. E., Gimenez-Arnau, E., Missailidis, S., Laughton, C. A., Stevens, M. F. G., and Searle, M. S. (1999) Molecular recognition between a new pentacyclic acridinium salt and DNA sequences investigated by optical spectroscopic techniques, proton nuclear magnetic resonance spectroscopy, and molecular modelling. *Biochemistry 38*, 6723−6731.
(35) Barry, C. G., Baruah, H., and Bierbach, U. (2003) Unprecedented monofunctional metalation of adenine nucleobase in guanine- and thymine- containing dinucleotide sequences by a cytotoxic platinum-acridine hybrid agent. *J. Am. Chem. Soc. 125*, 9629−9637.
(36) Tan, J. D., Farinas, E. T., David, S. S., and Mascharak, P. K. (1994) NMR evidence of sequence specific DNA binding by a cobalt(III)-bleomycin analogue with tethered acridine. *Inorg. Chem. 33*, 4295−4308.
(37) Lancelot, G., and Thuong, N. T. (1986) Nuclear magnetic resonance studies of complex formation between the oligonucletide d(TATC) covalently linked to an acridine derivative and its complementary sequence d(GATA). *Biochemistry 25*, 5357−5363.
(38) Minimum energy conformations were obtained by AM1 calculations using Titan Version 1 software from Wavefunction, Inc.; 18401, Von Karman, Suite 370, Irvine, CA 92612.
(39) Change in free energy values calculated for electron transfer from DNA bases to the singlet excited state of acridinium are $\Delta G = -0.89$, -0.76, -0.58, and -0.48 for guanosine, adenosine, pyridine, and thymidine, respectively; for nucleoside oxidation potentials, S. Steenken, S., and Jovanovich, S. V. (1997) How easily oxidizable is DNA? One-electron reduction potentials of adenosine and guanosine radicals in aqueous solution. *J. Am. Chem. Soc*. *119*, 617−618 and reduction potential of acridinium moiety (−0.57 eV vs SCE) was taken from C. K. Mann, K. K. Barnes (1970) *Electrochemical Reactions in Nonaqueous Systems*, Marcel Dekker, Inc., New York.

BC0498222

Binding Behavior of Aliphatic Oligopeptides by Bridged and Metallobridged Bis(*β*-cyclodextrin)s Bearing an Oxamido Bis(2-benzoic) Carboxyl Linker

Yu Liu,* Yan-Li Zhao, Yong Chen, Fei Ding, and Guo-Song Chen

Department of Chemistry, State Key Laboratory of Elemento-Organic Chemistry, Nankai University, Tianjin 300071, P. R. China. Received June 3, 2004; Revised Manuscript Received August 31, 2004

β-Cyclodextrin dimers bearing an oxamido bis(2-benzoic) carboxyl linker (**1**) or its metal complexes (**2** and **3**) were newly synthesized, and their inclusion complexation behavior with a series of representative aliphatic oligopeptides, i.e., Leu-Gly, Gly-Leu, Gly-Pro, Glu-Glu, Gly-Gly, Gly-Gly-Gly, and Glu(Cys-Gly), was elucidated by means of UV/vis, circular dichroism, fluorescence, and 2D NMR spectroscopy in Tris-HCl buffer solution (pH 7.4) at 25 °C. The results obtained indicated that metallobridged bis(*β*-cyclodextrin)s **2** or **3** could significantly enhance the original molecular binding abilities of parent bis(*β*-cyclodextrin) **1** toward model substrates through the cooperative binding of two cyclodextrin moieties and the additional chelation effect supplied by the coordinated metal centers. It is interesting that hosts **2** and **3** displayed an entirely different fluorescence behavior upon complexation with guest oligopeptides. Among the guest peptides examined, **3** showed the highest complex formation constant of 68 200 M^{-1} for Glu-Glu, up to 510-fold as compared with **1** (135 M^{-1}), while **1** gave excellent molecular selectivity for Glu(Cys-Gly)/Glu-Glu pair, up to 51-fold. The molecular binding ability and selectivity were discussed from the viewpoints of the induced-fit and multiple recognition mechanism between host and guest.

INTRODUCTION

Over the past three decades, numerous efforts have been devoted to molecular recognition studies of binding of biological molecules to various synthetic receptors, and among them, peptide recognition has become an exciting topic (*1*−*10*). These investigations potentially promote our insights into the selective binding between a designed molecular receptor (host) and a recognition target (guest). As one of the most successful receptors for peptide recognition and separation, cyclodextrins (CDs), a class of cyclic oligosaccharides with 6−8 glucopyranose units, and their derivatives have been widely applied due to their hydrophobic cavities capable of binding guest molecules through simultaneous contributions of several noncovalent interactions (*11*−*20*). Breslow et al. (*11*) studied the binding behavior of *β*-CD derivatives with some peptides using combinatorial chemistry, microcalorimetric titration, and a capillary electrophoresis approach, which showed that modified *β*-CDs could be used as sequence-selective peptide-cleaving reagents. Moroder et al. (*12*) linked the heptapeptide amide to mono(6-succinylamino-6-deoxy)-*β*-CD to analyze the effect of the bulky cyclic carbohydrate moiety on both the recognition of peptides by the G-protein-coupled CCK-B/gastrin receptor and their signal transduction potencies. Recently, Inoue et al. (*14*) reported chiral recognition thermodynamics of dipeptides with native *γ*-CD as studied by microcalorimetry, discussing the effects of length, bulkiness, and flexibility of the tether connecting the two aromatic moieties in a guest. These studies were not only directed toward an understanding of the thermodynamic aspects of binding and chiral/molecular discrimination of CDs, but also provided valuable information on the effects of changes in functionality and chirality, which attempt to elucidate the nature of molecular recognition between CDs and peptide guests.

It is interesting to note that a CD dimer (bis-CDs) connected with a linker of different length and structure, which possesses dual hydrophobic cavities in close proximity, can bind diverse molecules to form supramolecular sandwich complexes and thus give much higher binding abilities and molecular selectivities than those exhibited by parent CD. Furthermore, their metal complexes can extend the binding affinity of bis-CDs through the electrostatic interaction and/or cooperative chelation between ligated metal and accommodated guest molecule. Accordingly, a number of bis-CDs linked by functional tethers have recently been designed and synthesized to gain insights into the factors and mechanism controlling the inclusion complexation phenomena (*21*−*25*). However, the molecular recognition of metal-coordinated bridged bis-CDs to small peptides, especially aliphatic peptides, have not been well investigated so far (*11a*), although these studies are very important to elucidate the molecular recognition mechanism and control the binding behavior of biological receptors. In the present paper, we wish to report our investigation results on the binding behavior of bridged oxamide bis(2-benzoic) carboxyl linked bis(*β*-CD) (**1**) and its metal copper(II) (**2**) or nickel(II) (**3**) complexes (Scheme 1) with some representative oligopeptides (Chart 1) in Tris-HCl buffer solution (pH 7.4). The results obtained indicated that hosts **2** and **3** significantly enhanced the original binding abilities of parent bis(*β*-CD) (**1**) toward oligopeptides. Interestingly, **2** and **3** were found to induce different fluorescence behaviors upon addition of guest oligopeptides; that is, the fluorescence intensity of **2** or **3** gradually decreased upon addition of Glu(Cys-Gly) or Glu-Glu, but increased

* To whom correspondence should be addressed. Tel: +86-22-23503625, Fax: +86-22-23503625, E-mail: yuliu@public.tpt.tj.cn.

10.1021/bc049870m CCC: $27.50 © 2004 American Chemical Society
Published on Web 10/30/2004

Scheme 1. Schematic Representation of the Formation of Hosts 1−3

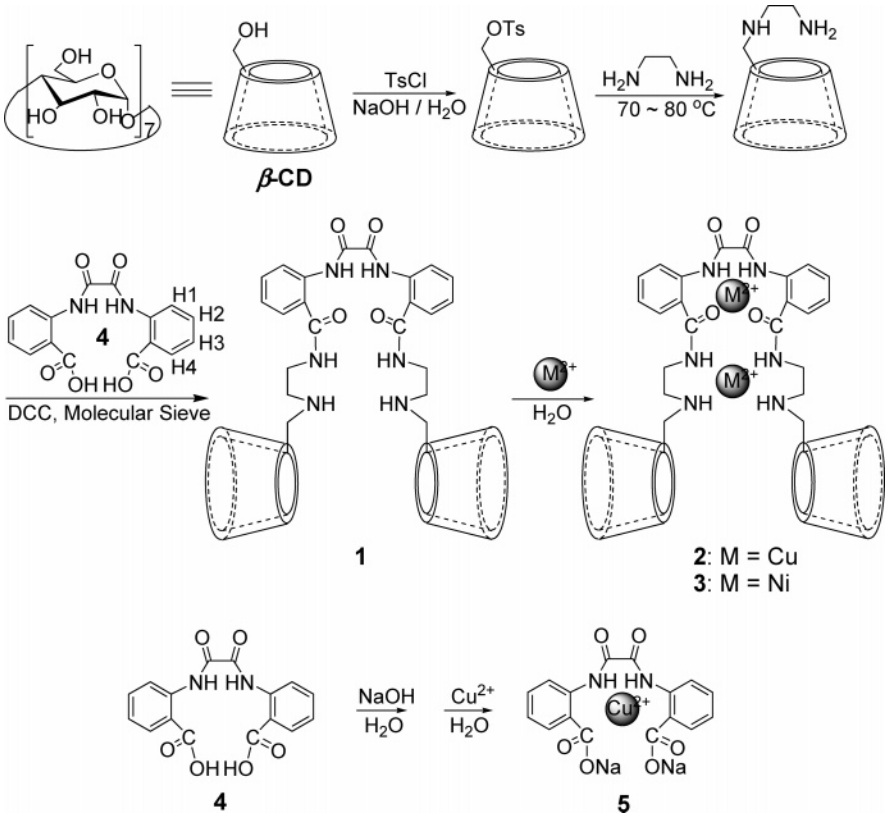
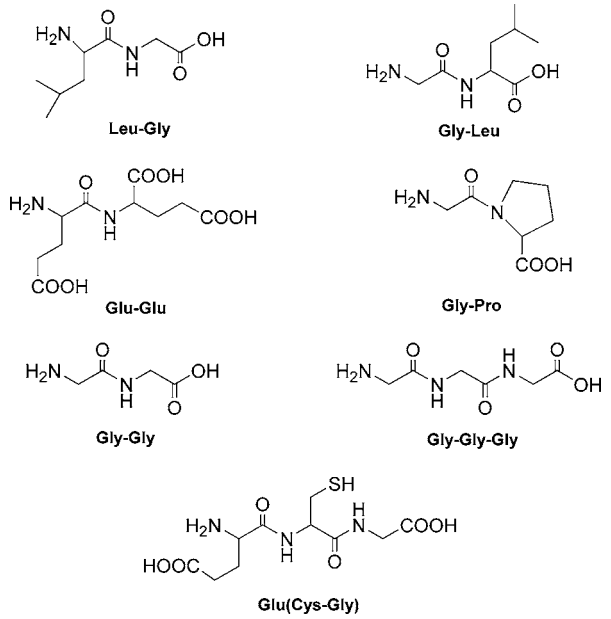


Chart 1. Structures of the Di- and Tripeptides Employed



with addition of other guests, which enabled these metallobridged bis(β-CD)s to be efficient fluorescence probes for the recognition of peptides. On the basis of the investigation of circular dichroism and 2D NMR spectroscopy, the molecular binding mode and complex formation constants (K_S) of substrates with bridged bis(β-CD)s **1**−**3** were discussed from the viewpoints of cooperative chelation and molecular multiple recognition between the host and guest. It is our special interest to examine the molecular recognition mechanism of oligopeptides by β-CD oligomers with ligated metal centers, which will serve our further understanding of this recently developing, but less investigated, area of metallobridged bis(β-CD)s.

EXPERIMENTAL PROCEDURES

Materials. β-CD of reagent grade was recrystallized twice from water and dried in vacuo at 95 °C for 24 h prior to use. *N*,*N*-Dimethylformamide (DMF) was dried over calcium hydride for 2 days and then distilled under reduced pressure prior to use. The oligopeptides Leu-Gly, Gly-Leu, Gly-Pro, Glu-Glu, Gly-Gly, Gly-Gly-Gly, and Glu(Cys-Gly) were commercially available and used without further purification. Oxamido bis(2-benzoic) acid (**4**) and its Cu(II) complex (**5**) were prepared according to the procedure reported by Kahn et al. (*26*). Mono[6-*O*-(*p*-toluenesulfonyl)]-β-cyclodextrin (6-OTs-β-CD) was prepared by the reaction of *p*-toluenesulfonyl chloride with β-CD in alkaline aqueous solution (*27*). Then, 6-OTs-β-CD was converted to mono(6-aminoethylamino-6-deoxy)-β-CD in 70% yield upon heating in excess ethylenediamine at 70 °C for 7 h (*28*, *29*).

Instruments. Circular dichroism and UV/vis spectra were recorded in a conventional quartz cell (light path 10 mm) on a JASCO J-715S spectropolarimeter or a Shimadzu UV-2401PC spectrophotometer equipped with a PTC-348WI temperature controller to keep the temperature at 25 °C. Fluorescence spectra were recorded in a conventional quartz cell (10 × 10 × 45 mm) at 25° C on a JASCO FP-750 fluorescence spectrometer with excitation and emission slits of 10 nm width. Elemental analysis was performed on a Perkin-Elmer 2400C instrument. NMR spectra were recorded on a Varian Mercury VX300 spectrometer.

[Oxamido bis(2-benzoic)acylamide]ethyleneamino-6,6′-deoxy-bis(β-CD)s 1. Mono(6-aminoethylamino-6-deoxy)-β-CD (1 mmol) was dissolved in DMF (30 mL) in the presence of a small amount of 4 Å molecular sieves, and then DCC (1 mmol) and **4** (0.5 mmol) were added.

The mixture was stirred for 2 days in an ice bath and another 2 days at room temperature and then allowed to stand for 5 h until no more precipitate deposited. The precipitate was removed by filtration, and the filtrate was evaporated to dryness under reduced pressure. The residue was dissolved in a minimum amount of hot water and then poured into 150 mL of acetone, and the precipitate formed was collected by filtration. This procedure was repeated several times. The crude product obtained was purified on a column of Sephadex G-25 with water as eluent. After the residue was dried in vacuo, a pure sample **1** was obtained in 27% yield. UV/vis λ_{max} (H_2O)/nm (log ϵ): 305.8 (3.62). ^{1}H NMR (D_2O, TMS, ppm): δ 2.54∼2.95 (m, 8H); 3.34∼3.79 (m, 84H); 4.85∼4.87 (m, 14H); 7.15∼7.20 (m, 2H); 7.43∼7.48 (m, 2H); 7.88∼8.04 (m, 2H); 8.39∼8.42 (m, 2H). IR (KBr, cm^{-1}): ν 3336.0, 2927.8, 2362.7, 2061.9, 1672.5, 1584.4, 1503.7, 1434.0, 1365.5, 1202.8, 1155.2, 1078.6, 1029.7, 944.9, 846.7, 756.7, 705.6, 578.2. Anal. Calcd for $C_{104}H_{160}O_{72}N_6 \cdot 8H_2O$: C, 44.76; H, 6.36; N, 3.01. Found: C, 44.65; H, 6.47; N, 2.87.

Bis(β-CD)−Copper(II) Complex 2. Bis(β-CD) **1** was added dropwise to a dilute aqueous solution of slightly excess copper(II) perchlorate in an ice/water bath. Several drops of chloroform were further added, and the resultant solution was kept at 5 °C for 2 days. Then, the solution was evaporated under reduced pressure, and the precipitate formed was collected by filtration, washed successively with a small amount of ethanol and diethyl ether, and then dried in vacuo to give complex **2** as a blue solid in 63% yield. UV/vis λ_{max} (H_2O)/nm (log ϵ): 306.8 (3.55). IR (KBr, cm^{-1}): ν 3351.4, 2930.4, 2051.0, 1637.0, 1581.1, 1449.5, 1426.1, 1364.2, 1333.6, 1152.1, 1118.4, 1080.2, 1029.0, 944.5, 846.0, 757.2, 706.3, 627.5, 577.8, 529.6, 415.3. Anal. Calcd for $C_{104}H_{160}O_{72}N_6 \cdot 2Cu(ClO_4)_2 \cdot 11H_2O$: C, 37.07; H, 5.44; N, 2.49. Found: C, 37.31; H, 5.23; N, 2.61.

Bis(β-CD)−Nickel(II) Complex 3. Bis(β-CD)−nickel(II) complex **3** was prepared, according to procedures similar to those in the synthesis of **2**, as a green solid (yield 58%). UV/vis λ_{max} (H_2O)/nm (log ϵ): 307.4 (3.55). ^{1}H NMR (D_2O, TMS, ppm): δ 2.96∼3.20 (m, 8H); 3.35∼3.86 (m, 84H); 4.94 (s, 14H); 7.21∼7.24 (m, 2H); 7.48∼7.52 (m, 2H); 8.01∼8.05 (m, 2H); 8.40∼8.43 (m, 2H). IR (KBr, cm^{-1}): ν 3336.0, 2931.0, 2044.0, 1665.9, 1587.6, 1506.9, 1439.9, 1334.1, 1299.5, 1240.9, 1152.7, 1079.6, 1029.8, 946.7, 843.6, 756.7, 706.6, 626.8, 578.2, 411.0. Anal. Calcd for $C_{104}H_{160}O_{72}N_6 \cdot 2Ni(ClO_4)_2 \cdot 13H_2O$: C, 36.78; H, 5.52; N, 2.47. Found: C, 36.96; H, 5.38; N, 2.56.

RESULTS AND DISCUSSION

Metal Coordination and Stoichiometry. As shown in Scheme 1, the metallobridged bis(β-CD)s **2** and **3** were prepared from bis(β-CD)s **1** by the coordination reaction with copper(II) and nickel(II) in aqueous solution, respectively. In addition to the elemental analysis data, the ^{1}H NMR, IR, and UV/vis spectra provided additional evidence about the formation of the **2** and **3**. Since the paramagnetic disturbance caused by the ligated copper(II) complex makes the ^{1}H NMR spectrum of **2** unavailable to measure, we compared the ^{1}H NMR spectra of **1** and its nickel(II) complex **3**. Some changes in the chemical shift of the aromatic protons of **3** were observed relative to those in **1**: the H1, H2, H3, and H4 protons shifted downfield ca. 0.07, 0.05, 0.05, 0.01 ppm, respectively, which indicated that a complex had formed between the **1** and nickel(II). The IR spectra of **1**−**3** showed that the stretching vibration of carbonyl groups

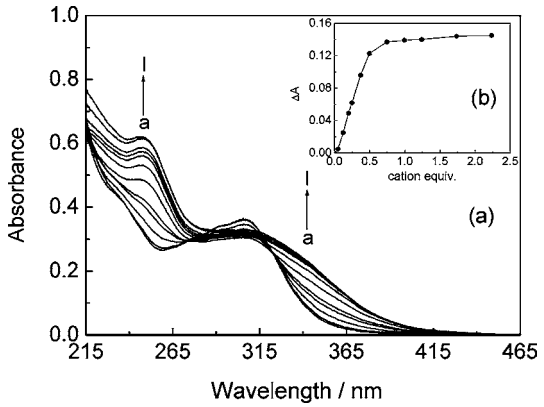


Figure 1. (a) UV/vis spectral change of **1** upon addition of copper(II) perchlorate in aqueous solution. ([**1**] = 7.8 × 10^{-5} mol dm^{-3}, [Cu^{2+}] = 0 to 1.7 × 10^{-4} mol dm^{-3} from *a* to *l*). (b) Absorbance changes of **1** at 350 nm with the addition of copper(II) ion in aqueous solution.

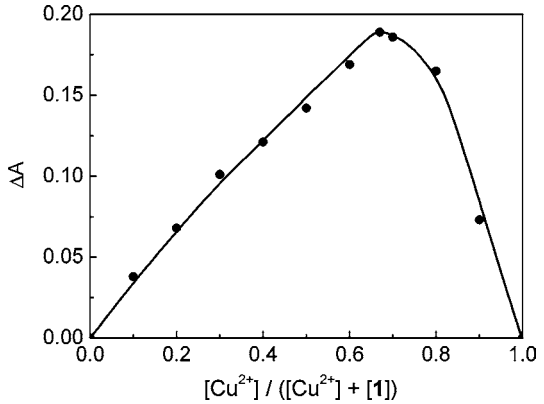


Figure 2. Job's plot of **1**/Cu(II) system at 350.0 nm. ([**1**] + [Cu(II)] = 2.0 × 10^{-4} mol dm^{-3}).

shifted from 1672.5 cm^{-1} for **1** to 1637.0 cm^{-1} for **2** and 1650.9 cm^{-1} for **3**, which could also be ascribed to the coordination of metal ions. Additionally, a weak absorption at 627.5 cm^{-1} for **2** (626.8 cm^{-1} for **3**), which may be assigned to a weakly coordinated perchlorate, was also observed, and indicated that the copper(II) or nickel(II) ion was coordinated to the bridged bis(β-CD) to form metallobridged bis(β-CD)s.

To compare the coordination behavior of bis(β-CD)s **1** with metal ions, spectrophotometric titrations of **1** with copper(II) or nickel(II) ions have been performed at 25 °C in aqueous solution. A typical titration curve of **1** with copper(II) ion was illustrated in Figure 1a. As can be seen in Figure 1a, the absorption intensity of **1** at 259 and 350 nm gradually increased with the addition of varying amounts of copper(II) perchlorate, accompanying an obvious bathochromic shift of absorption peaks. In the control experiments, UV/vis spectra of copper(II) ion within measurement concentration range displayed no appreciable change at 200−400 nm under comparable experimental conditions. Figure 1b showed the absorbance changes of **1** at 350 nm with the addition of copper(II) perchlorate. Furthermore, Job's experiments were also performed to explore the coordination stoichiometry of the bis(β-CD)−metal(II) complex in aqueous solution. The results obtained indicated that the complex stoichiometry was 1:2 for both **2** and **3**. A representative Job's plot for the coordination of **1** with copper(II) perchlorate was shown in Figure 2. The plot for the **1**/Cu(II) system showed a maximum at 0.67 which corresponded to the 1:2 **1**/Cu(II) stoichiometry. This result indicated that one

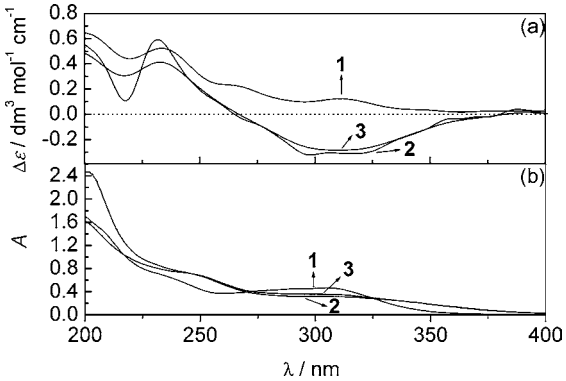


Figure 3. Circular dichroism (a) and absorption (b) spectra of **1** (1.1×10^{-4} mol dm^{-3}), **2** (8.9×10^{-5} mol dm^{-3}), and **3** (1.0×10^{-4} mol dm^{-3}) in aqueous solution at 25 °C.

bis(β-CD) **1** could bind two copper(II) ions, as illustrated in Scheme 1. According to the spectrophotometric titration and the Job's experiments, we can deduce that the coordination of **1** with Cu(II) should be a two-step process. The spectra from *a* to line *f* (Figure 1), which gave two isosbestic points at 273.8 and 322.2 nm, might refer to the coordination process of **1** with the first metal ion, while the spectra from line *g* to line *l* (Figure 1) might point to the coordination process of the second metal ion. Therefore, as an overall illustration of this two-step process, the spectra of absorption titration of **1** with Cu(II) did not give clear isosbestic points.

Conformations of Hosts 1−3. Achiral organic compounds can show an induced circular dichroism (ICD) signal around their corresponding transition bands in cases where there is a chiral microenvironment. Therefore, to deduce the conformation of interaction between the achiral chromophoric compound and the β-CD chiral cavity, ICD spectra of **1**−**3** were measured at 25 °C in aqueous solution. As can be seen from Figure 3, the circular dichroism spectrum of **1** showed two positive Cotton effects around 233.0 nm ($\Delta\epsilon = 0.52$ dm^{-3} mol^{-1} cm^{-1}) and 311.0 nm ($\Delta\epsilon = 0.12$ dm^{-3} mol^{-1} cm^{-1}), respectively. Interestingly, host **2** gave a positive Cotton effect around 232.0 nm ($\Delta\epsilon = 0.59$ dm^{-3} mol^{-1} cm^{-1}) and a negative Cotton effect around 298.0 nm ($\Delta\epsilon = -0.32$ dm^{-3} mol^{-1} cm^{-1}), while **3** gave a positive Cotton effect around 233.0 nm ($\Delta\epsilon = 0.41$ dm^{-3} mol^{-1} cm^{-1}) and a negative Cotton effect around 310.0 nm ($\Delta\epsilon = -0.28$ dm^{-3} mol^{-1} cm^{-1}). According to the pioneering studies (*24*, *30*, *31*) on the ICD phenomena of cyclodextrin complexes, we can deduce that the oxamide bis(2-benzoic) carboxyl group of **1** was shallowly included in the β-CD cavity with an acclivous orientation to form the self-included complexes. After the metal coordination, the linker group was located outside the β-CD cavity, leading to an opposite ICD signal around 300 nm for **2** or **3**. In addition to the ICD experiments, the 2D NMR experiments gave the primary evidence of inside−outside movement of the linker group, which is described below.

2D NMR spectroscopy has recently become an important method for the investigation of not only the interaction between host CDs and guest molecules, but also the self-included mode between the CD cavity and its substituent groups, since the NOE cross-peaks between the protons that are closer than 0.4 nm in space will be observed in the NOESY or ROESY spectrum and the relative intensities of these cross-peaks depend on the spaces between the corresponding protons. The height and the diameter of the β-CD cavity are about 0.79 ± 0.01 nm and 0.60−0.65 nm, respectively. Therefore, while

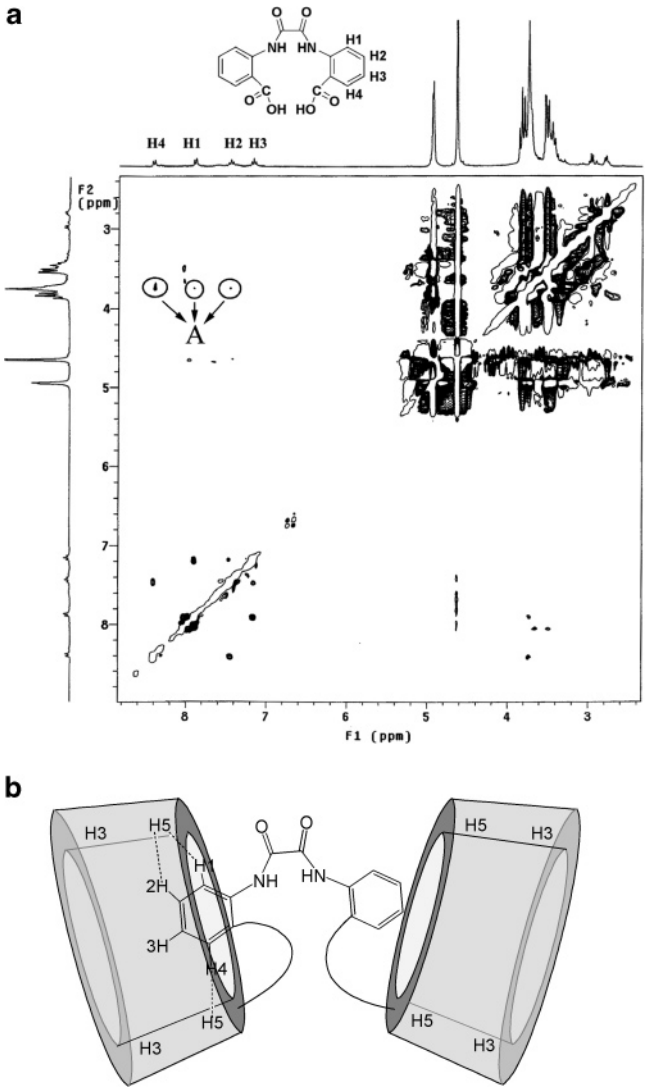


Figure 4. (a) ^{1}H ROESY spectrum of **1** (3.8×10^{-3} mol dm^{-3}) in D_2O at 25 °C with a mixing time of 400 ms, (b) possible conformation of **1**.

the substituent group is included into the β-CD cavity, the NOE correlations between the protons of the substituent group and the inner protons of the β-CD cavity (H-3 and H-5) will be measured. On the other hand, according to the relative intensity of these cross-peaks (*32*), it is possible to estimate the orientation of the substituent group within the β-CD cavity. To obtain further evidence about the original conformation of **1**−**3**, 2D NMR spectroscopy experiments were performed in D_2O solution. As shown in Figure 4a, the ROESY spectrum of **1** displayed clear NOE cross-peaks between the H5 of β-CD and the H1, H2, and H4 protons of oxamide bis(2-benzoic) carboxyl group (peaks A), which indicated distinctly that the linker group of **1** was shallowly self-included into the hydrophobic cavity from the primary side of β-CD. According to these results, a possible conformation of **1** was shown in Figure 4b. At the same time, the NOE cross-peaks between the β-CD's H5 and/or H3 and the protons of the linker group were not found in the ROESY spectrum of **3** (Figure 5), which indicated that the linker group of **3** should be located outside the β-CD cavity. Therefore, the results of the ROESY experiments not only further supported the ICD investigation results on the conformations of bridged bis(β-CD)s **1**−**3**, but also may serve to establish correlation

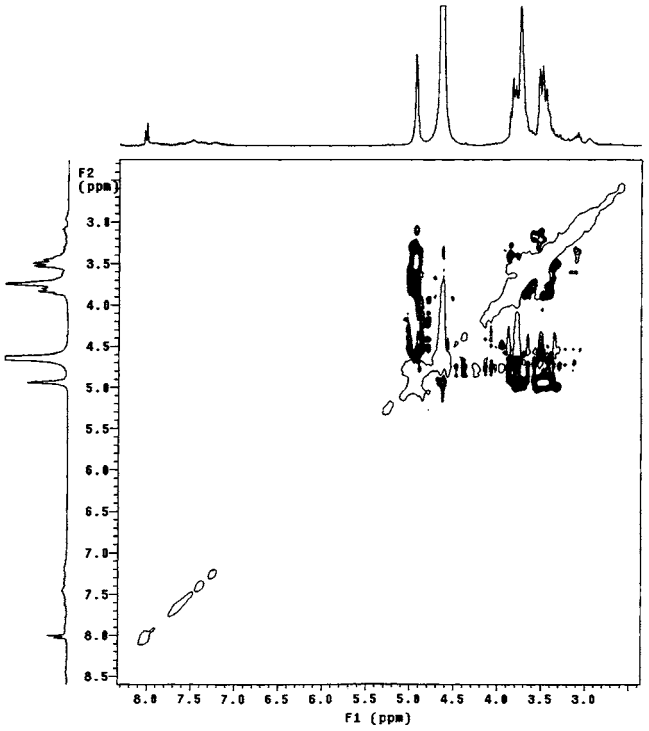


Figure 5. ^{1}H ROESY spectrum of **3** (3.5×10^{-3} mol dm^{-3}) in D_2O at 25 °C with a mixing time of 400 ms.

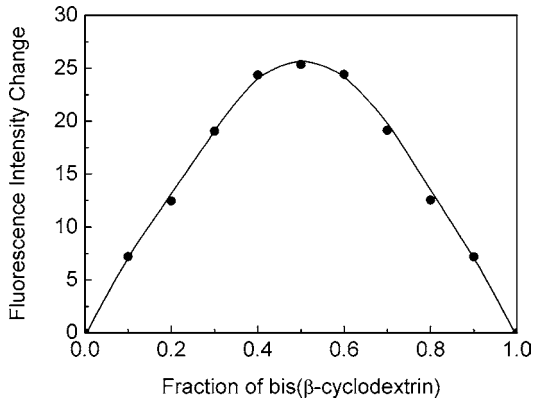


Figure 6. Job's plot of **2**/Glu-Glu system at 408.0 nm. ([**2**] + [Glu-Glu] = 1.0×10^{-5} mol dm^{-3}).

between the original conformation of modified β-CDs and their molecular recognition ability.

Spectral Titration. As elucidated above, the oxamide bis(2-benzoic) carboxyl group was either shallowly included in the β-CD cavity to form the self-included complexes (the case of **1**) or located on the edges of the β-CD cavity (the case of **2** and **3**). Therefore, the linker group might suffer substantial conformational change upon guest inclusion and thus result in the relevant spectral changes, which allows the bis(β-CD) to function as a spectral probe to obtain binding constants in differential fluorescence spectrometry. Herein, we chose some representative aliphatic oligopeptides, i.e., Leu-Gly, Gly-Leu, Gly-Pro, Glu-Glu, Gly-Gly, Gly-Gly-Gly, and Glu(Cys-Gly), to determine their binding behavior with hosts **1**−**3** by spectral titration experiments. Figure 6 illustrated a representative Job's plot for **2**/Glu-Glu system in Tris-HCl buffer solution (pH 7.4) at 25 °C. In the used concentration range, the plot for metallobridged bis(β-CD) showed a maximum at a molar fraction of 0.5, indicating the 1:1 inclusion complexation between the host and guest. The same results were obtained in the

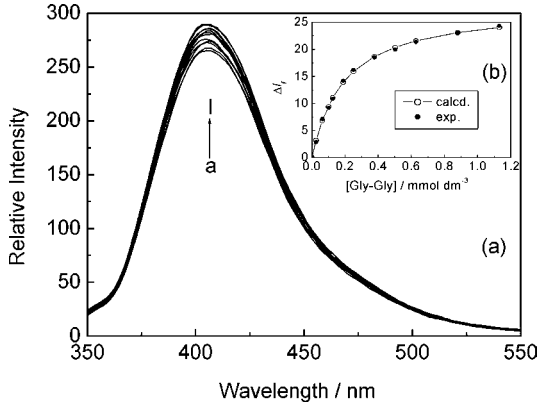


Figure 7. (a) Fluorescence spectral changes of host **3** (1.0×10^{-5} mol dm^{-3}) upon addition of Gly-Gly (0 to 1.13×10^{-3} mol dm^{-3} from *a* to *l*) in Tris-HCl buffer solution (pH 7.4) at 25 °C. (b) the nonlinear least-squares analysis of the differential intensity (ΔI_f) to calculate the complex formation constant (K_S). ($\lambda_{ex} = 314.0$ nm, $\lambda_{em} = 406.0$ nm).

cases of the inclusion complexation of other bis(β-CD)s with selected oligopeptide guests.

Using 1:1 host/guest stoichiometry, where the two β-CD moieties in **1**−**3** were treated as one unit, the complexation of the oligopeptide guest (OP) with the bis(β-CD) host (CD) can be expressed by eq 1.

$$\mathrm{CD} + \mathrm{OP} \overset{K_S}{\rightleftharpoons} \mathrm{CD{\cdot}OP} \qquad (1)$$

The relative fluorescence intensity change of host unit (ΔI_f) upon addition of guest molecule, where $\Delta I_f = I_f$ (with guest molecule) − I_f (without guest molecule), was assumed to be proportional to the concentration of inclusion complex formed by bis(β-CD) unit with model substrate, i.e., $\Delta I_f = \alpha[\mathrm{CD{\cdot}OP}]$. The proportionality coefficient α was taken as a sensitivity factor for the fluorescence change upon inclusion complexation. Then, the effective complex formation constant (K_S) (*33*, *34*) can be expressed by eq 2:

$$K_S = \frac{[\mathrm{CD{\cdot}OP}]}{[\mathrm{CD}][\mathrm{OP}]} = \frac{[\mathrm{CD{\cdot}OP}]}{([\mathrm{CD}]_0 - [\mathrm{CD{\cdot}OP}])([\mathrm{OP}]_0 - [\mathrm{CD{\cdot}OP}])} = \frac{\Delta I_f/a}{([\mathrm{CD}]_0 - \Delta I_f/a)([\mathrm{OP}]_0 - \Delta I_f/a)} \qquad (2)$$

where $[\mathrm{CD}]_0$ and $[\mathrm{OP}]_0$ denoted the initial concentrations of bis(β-CD) host and oligopeptide guests, respectively. Subsequently, eq 2 can be solved for ΔI_f to give eq 3:

$$\Delta I_f = \{\alpha([\mathrm{CD}]_0 + [\mathrm{OP}]_0 + 1/K_S) - \sqrt{\alpha^2([\mathrm{CD}]_0 + [\mathrm{OP}]_0 + 1/K_S)^2 - 4\alpha^2[\mathrm{OP}]_0[\mathrm{CD}]_0}\}/2 \qquad (3)$$

Using the nonlinear least squares curve-fitting method according to eq 3 (*35*), we obtained the complex formation constant for each host−guest combination from the analysis of the sequential changes of fluorescence intensity (ΔI_f) at various guest concentrations. Figure 7b illustrated a typical curve-fitting plot for the titration of Gly-Gly with **3**, which showed excellent fits between the experimental and calculated data obtained. A good correlation between the experimental and calculated result indicated the reliability of the obtained complex formation constants. The complex formation constants (K_S) and

Table 1. Complex Formation Constant (K_S) and Gibbs Free Energy Change ($-\Delta G°$) for the Inclusion Complexation of Bis(β-CD)s 1−3 with Oligopeptide Guests in Tris-HCl Buffer Solution (pH 7.4) at 25 °C

host	guest	K_S/M^{-1}	log K_S	$-\Delta G°$/kJ mol^{-1}
1	Leu-Gly	1450	3.16	18.04
	Gly-Leu	740	2.87	16.38
	Glu-Glu	135	2.13	12.16
	Gly-Pro	647	2.81	16.04
	Gly-Gly	890	2.95	16.83
	Gly-Gly-Gly	1400	3.15	17.96
	Glu(Cys-Gly)	6850	3.84	21.89
2	Leu-Gly	4470	3.65	20.83
	Gly-Leu	2160	3.33	19.03
	Glu-Glu	17900	4.25	24.27
	Gly-Pro	3820	3.58	20.45
	Gly-Gly	1260	3.10	17.70
	Gly-Gly-Gly	3770	3.58	20.42
	Glu(Cys-Gly)	12750	4.11	23.41
3	Leu-Gly	22000	4.34	24.79
	Gly-Leu	5260	3.72	21.24
	Glu-Glu	68200	4.83	27.59
	Gly-Pro	18100	4.26	24.30
	Gly-Gly	5370	3.73	21.29
	Gly-Gly-Gly	7270	3.86	22.04
	Glu(Cys-Gly)	42000	4.62	26.39

Gibbs free energy changes ($-\Delta G°$) obtained for the complexation of bis(β-CD)s **1**−**3** with oligopeptide guests were compiled in Table 1. When repeated measurements were made, the K_S values were reproducible within an error of ±5%.

Binding Mode. It is well-known that the competitive inclusion, cooperative binding, and induced-fit generally occur in the molecular binding process of modified β-CDs, and therefore it is very important to investigate the inclusion modes between host β-CDs and guest molecules for elucidating the mechanism of molecular recognition. In our previous research by means of ^{1}H NMR, circular dichroism, and fluorescence spectroscopy as well as CPK model examination (*24*), we found that a multiple sandwich binding mode was operative in the association of the guest molecule with bridged bis(β-CD); that is, upon inclusion complexation with bis(β-CD), two side groups of the guest molecule were embedded into the hydrophobic β-CD cavities from the primary side of β-CD to form a sandwich host−guest inclusion complex. In the present paper, we wish to establish the possible binding mode of bridged and metallobridged bis(β-CD)s **1**−**3** with oligopeptides according to the results of circular dichroism, ^{1}H NMR, and fluorescence spectral experiments.

For the self-included CD hosts, there should exist a competition between the substituent group of host and guest upon inclusion complexation with the CD cavity, and this competitive inclusion may be verified by the circular dichroism spectral studies. Typically, a series of ICD signals of **2** in the presence of different amounts of Gly-Gly were shown in Figure 8. As can be seen from Figure 8, the ICD intensity of host **2** around 310 nm increased gradually upon the addition of increasing amounts of Gly-Gly. However, the corresponding absorption intensity around 340 nm decreased gradually, accompanied by the appearance of an isobestic point at 309 nm. Since Gly-Gly displayed no ICD signal in the range of 210−400 nm, one possible explanation for these spectral phenomena was that, during the inclusion complexation, the guest molecule was cooperatively bound by two β-CD cavities from the primary side, which forced the linker group of bis(β-CD) away from the β-CD cavity and thus gave the weak ICD signals.

Interestingly, the **2** and **3** were found to show different fluorescence behaviors upon complexation of guest peptides. The gradual addition of Glu-Glu or Glu(Cys-Gly) to a dilute solution of **2** or **3** significantly decreased the fluorescence intensity (Figure 9). However, fluorescence intensity for **2** or **3** gradually enhanced with the stepwise addition of other peptides under comparable conditions. In a control experiment, neither disodium oxamidobis-(2-benzoxylate) nor its Cu(II) complex **5** exhibited appreciable fluorescence change upon the addition of oligopeptides. In additional control experiments, the formation constant (K_S) of disodium oxamido bis(2-benzoxylate) with Cu(II) ion was also determined by means of UV−vis spectral titration, and the obtained K_S value was 27930 ± 1390 M^{-1}, which indicated a strong association of oxamido bis(2-benzoxylate) with Cu(II). Moreover, we also compared the NMR spectra of disodium oxamido bis-(2-benzoxylate) ([**4**−Na] = 4.6 × 10^{-4} mol dm^{-3}), a 1:1 complex of **4**−Na with Ni(II) ([**4**−Na/Ni] = 3.8 × 10^{-4} mol dm^{-3}), and a 1:1 mixture of **4**−Na/Ni with Glu-Glu ([**4**−Na/Ni] = [Glu-Glu] = 3.9 × 10^{-4} mol dm^{-3}). The reason for choosing Ni(II) as metal ion was to avoid the paramagnetic disturbance caused by Cu(II). As can be seen in Figure 10, several changes of the δ values of the aromatic protons in the **4**−Na/Ni system were observed as compared with those in **4**−Na; that is, the δ values of H1, H2, H3, and H4 protons shifted downfield ca. 0.11, 0.08, 0.07, and 0.04 ppm, respectively, indicating that the Ni(II) ion was coordinated to the oxamido bis(2-benzoxy-

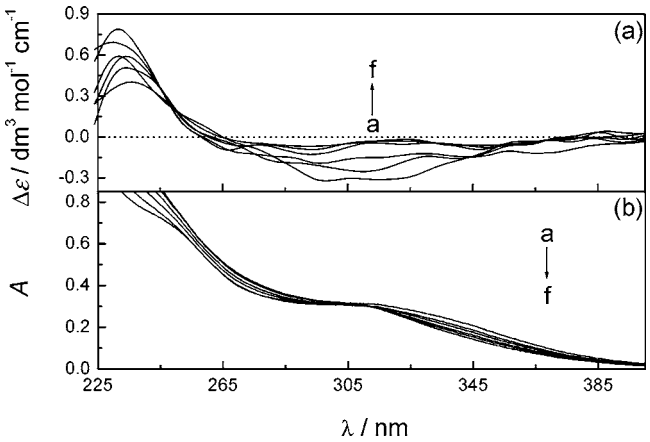


Figure 8. Circular dichroism (a) and absorption (b) spectra of **2** (8.9 × 10^{-5} mol dm^{-3}) upon addition of Gly-Gly (0 ∼ 9.13 × 10^{-3} mol dm^{-3} from *a* to *f*) in Tris-HCl buffer solution (pH 7.4) at 25 °C.

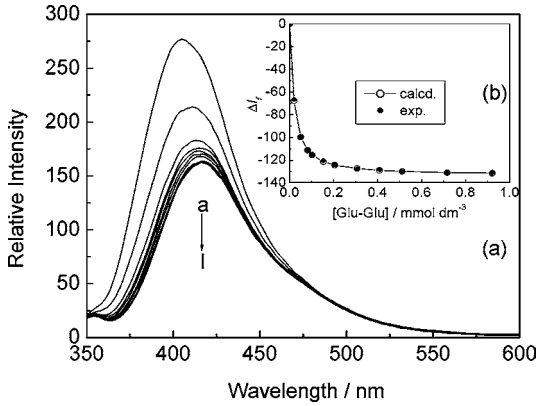


Figure 9. (a) Fluorescence spectral changes of host **3** (1.1 × 10^{-5} mol dm^{-3}) upon addition of Glu-Glu (0∼0.92 × 10^{-3} mol dm^{-3} from *a* to *l*) in Tris-HCl buffer solution (pH 7.4) at 25 °C and (b) the nonlinear least-squares analysis of the differential intensity (ΔI_f) to calculate the complex formation constant (K_S). (λ_{ex} = 314.0 nm, λ_{em} = 405.0 nm).

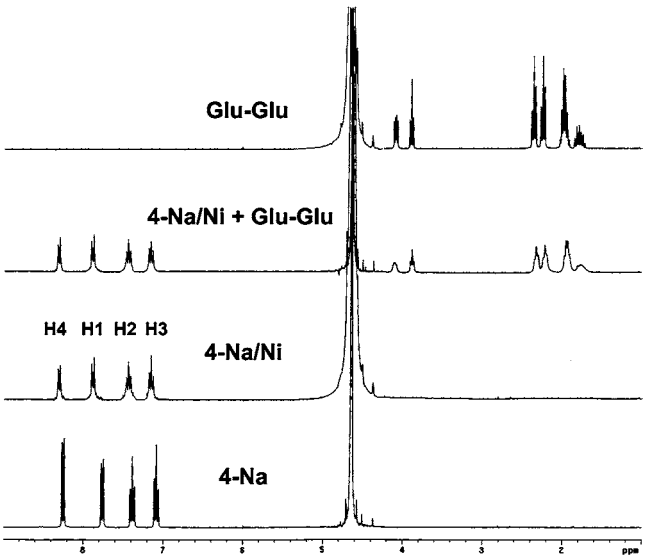


Figure 10. The ^{1}H NMR spectra of **4**−Na (4.6×10^{-4} mol dm^{-3}), a 1:1 complex of **4**−Na with Ni(II) ([**4**−Na/Ni] = 3.8×10^{-4} mol dm^{-3}), a 1:1 mixture of **4**−Na/Ni with Glu-Glu ([**4**−Na/Ni] = [Glu-Glu] = 3.9×10^{-4} mol dm^{-3}), and Glu-Glu (4.2×10^{-4} mol dm^{-3}) in D_2O at 25 °C.

late) ligand. However, the δ values of the aromatic protons in **4**−Na/Ni did not show any appreciable changes after adding Glu-Glu. These unchanged δ values before and after adding guest oligopeptides may indicate that the metal ion was still bound to the oxamido bis(2-benzoxylate) ligand in the presence of guest oligopeptides, because the demetalation of **4**−Na/Ni by the guest would make the δ values of the aromatic protons in **4**−Na/Ni shift upfield to the original position. The results of these control experiments jointly indicated that the increased or decreased fluorescence of hosts **1**−**3** upon the addition of guests was mainly attributed to the inclusion complexation, not just to the simple enhancing/quenching effect of the linker group or the demetalation of metallobridged bis(β-CD) by the guest. That is to say, such contrasting fluorescence behavior indicated that the different binding modes were operative in the inclusion complexations of Glu-Glu with **1** and **3**. The increased fluorescence intensity could be rationalized by the increased microenvironmental hydrophobicity and/or steric shielding around the fluorophore arising from the cooperative interactions between the host and guest (*36*). Therefore, the fluorescent group of the host could be efficiently shielded from the deactivating water attack by the formation of a sandwich inclusion complex, which consequently contributed to the fluorescence enhancement of the host (Figure 11b). On the other hand, for guests Glu-Glu or Glu(Cys-Gly), their branch groups (amino and carboxyl groups for Glu-Glu, amino and sulfydryl for Glu(Cys-Gly)) could interact strongly with the coordinated metal center of host **2** or **3** through the cooperative chelation effect (Figure 12b) (*6*, *37*), which led to the degressive fluorescence intensity of **2** or **3** upon inclusion complexation.

To obtain direct evidence to further elucidate the origin of these opposite fluorescence behaviors, ^{1}H ROESY experiments of **1** and **3** with the representative guest Glu-Glu were performed in D_2O at 25 °C. As illustrated in Figure 11a, the ^{1}H ROESY spectrum of a mixture of host **1** with guest Glu-Glu in D_2O displayed sophisticated NOE cross-peaks, which came from not only the intermolecular interactions between β-CD and Glu-Glu, but also the intramolecular interactions of **1** or Glu-Glu. Among these

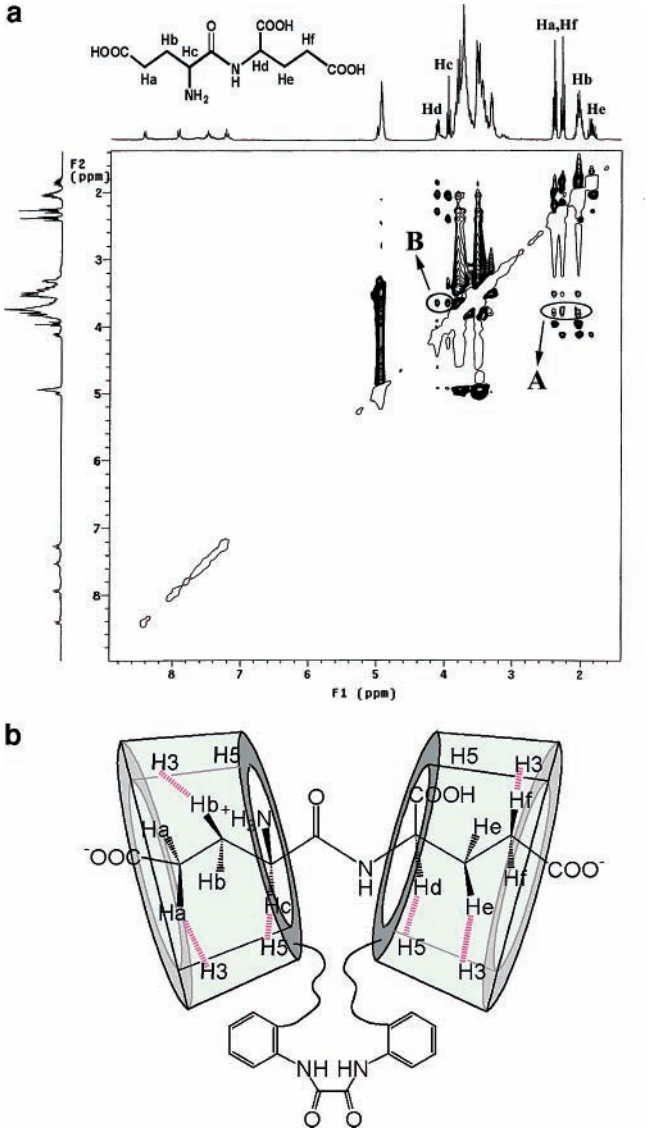


Figure 11. (a) ^{1}H ROESY spectrum of a mixture of **1** (2.5×10^{-3} mol dm^{-3}) with Glu-Glu (2.9×10^{-3} mol dm^{-3}) in D_2O at 25 °C with a mixing time of 400 ms; (b) possible complex structure of **1** with Glu-Glu.

signals, the NOE cross-peaks between the protons in the linker group of **1** and the H5/H3 protons of β-CD as well as the protons of Glu-Glu were not found, but the correlations between Ha, Hb, Hf protons of Glu-Glu and H3 protons of β-CD (peaks A), and the correlations between Hc, Hd protons of Glu-Glu and H5 protons of β-CD (peaks B), were clearly observed. These phenomena indicated that the Glu-Glu molecule was located in the β-CD cavity, while the linker group of **1** outside. According to the 2D NMR experimental results, a possible conformation of host **1** with Glu-Glu was shown in Figure 11b.

Figure 12a showed the ^{1}H ROESY spectrum of a mixture of **3** with Glu-Glu. Although the NOE correlation peaks between the H3/H5 of β-CD and the protons of Glu-Glu (peaks A) were not clear enough to estimate their relative intensity, we could deduce unambiguously that there did exist the corresponding NOE correlations. Simultaneously, the correlation peaks between the H3/H5 of β-CD and the protons of the linker group in **3** were not observed, which indicated that Glu-Glu was located in the β-CD cavities but the linker group outside the cavities (Figure 12b).

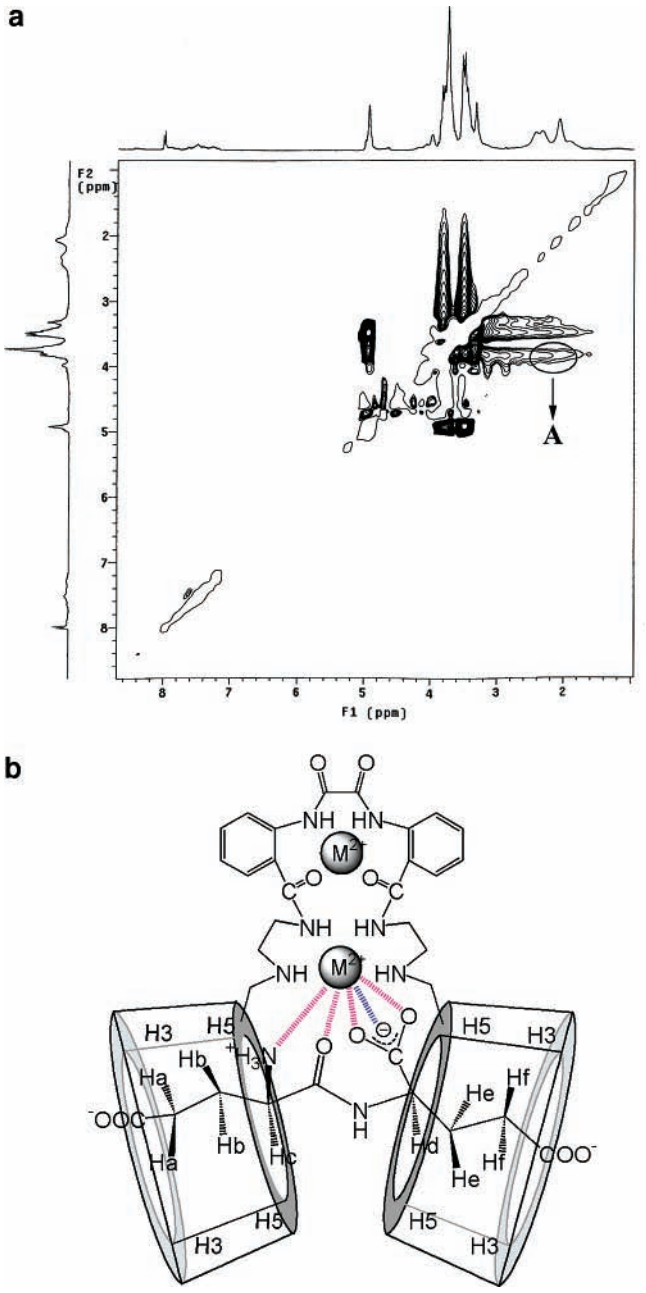


Figure 12. (a) ^{1}H ROESY spectrum of a mixture of **3** (2.7×10^{-3} mol dm^{-3}) with Glu-Glu (3.1×10^{-3} mol dm^{-3}) in D_2O at 25 °C with a mixing time of 400 ms; (b) possible complex structure of **3** with Glu-Glu.

Binding Ability and Molecular Selectivity. Native and simply modified CDs afford only very small binding constants to model substrates, probably due to the weak hydrophobic interactions between the host and guest. Bridged bis(β-CD), however, can enhance the original binding ability through cooperative binding of two adjacent cavities and potential multiple recognition ability. It is significantly noted that the introduction of the metal ions alters not only the original conformation of the linker group but also the distance and orientation of two β-CD cavities in bridged bis(β-CD). As compared with monomeric and dimeric CDs, metallobridged bis(β-CD)s can afford much more stable inclusion complexes with model substrates, owing to a fixed conformation by metal ligation, and additional cooperative chelation, electrostatic interaction, and/or electron transfer between ligated metal and accommodated guest. Furthermore, investigations on the inclusion complexation conformation of bridged and metallobridged bis(β-CD)s with guests also indicate that the cooperative binding and metal coordination can dominate the stability of complex formed between bis(β-CD)s and model substrate, leading to stronger van der Waals and hydrophobic interactions, since these interactions are closely related to the distance and contacting surface area between the host and guest. As can be seen from Table 1, the complex formation constants (K_S) for **1** with oligopeptides were variable according to the guest structures. Among the guest peptides examined, host **1** afforded the highest complex formation constant of 6850 M^{-1} for the inclusion complexation with Glu(Cys-Gly) and the largest molecular selectivity for Glu(Cys-Gly)/Glu-Glu pair ($K_S^{Glu(Cys-Gly)}/K_S^{Glu-Glu} = 51$). This may be attributed to the strict size/shape fitting relationship between the longest guest Glu(Cys-Gly) and the long-tethered bis(β-CD) **1**, which fully enjoyed the cooperative binding of two β-CD cavities with one guest molecule. However, possessing three carboxyl groups, Glu-Glu was more hydrophilic than other guests, which reduced the hydrophobic interactions as well as the extent of desolvation upon inclusion complexation and thus resulted in poor association with bis(β-CD).

Furthermore, metallobridged bis(β-CD)s **2** and **3** showed significantly enhanced binding abilities and molecular selectivities upon inclusion complexation with oligopeptides as compared with those of parent bis(β-CD) **1**. It can be seen from Table 1 that the coordination of the linker group to the metal ions further enhanced the binding abilities of **1** for guest peptides by a factor of 1.4−510. This further enhancement may point to a mechanism concerning a multiple recognition behavior of metallobridged bis(β-CD)s toward model substrates. Upon complexation with guest molecules, the metallobridged bis(β-CD)s not only afforded two hydrophobic binding sites (two β-CD cavities) cooperatively associating with a guest but also provided additional binding interactions between the heteroatoms of peptides and the coordinated metal center. Thus, as a cumulative result of these factors, metallobridged bis(β-CD)s displayed significantly enhanced binding abilities toward guest peptides as compared with parent bis(β-CD).

It is also interesting to compare the molecular selectivity sequence of hosts **1**−**3**. The complex formation constants (K_S) for the inclusion complexation of hosts **1**−**3** with oligopeptides decreased in the following order:

For **1**: Glu(Cys-Gly) > Leu-Gly > Gly-Gly-Gly > Gly-Gly > Gly-Leu > Gly-Pro > Glu-Glu

For **2**: Glu-Glu > Glu(Cys-Gly) > Leu-Gly > Gly-Pro > Gly-Gly-Gly > Gly-Leu > Gly-Gly

For **3**: Glu-Glu > Glu(Cys-Gly) > Leu-Gly > Gly-Pro > Gly-Gly-Gly > Gly-Gly > Gly-Leu

It can be seen that, different from parent bis(β-CD), metallobridged bis(β-CD)s showed the highest binding ability for Glu-Glu. This is because, besides the cooperative binding of two adjacent β-CD cavities and the heteroatom−metal chelation effects, the electrostatic interactions between the cationic metal center and the anionic carboxyl group located in the middle of Glu-Glu (blue line in Figure 12b) also contributed to the strong inclusion complexation of Glu-Glu with metallobridged bis(β-CD)s, since the carboxyl groups in peptides should exist as anions in this medium (pH = 7.4).

Another intriguing finding is the relatively high sequence selectivity of hosts **1**−**3** upon complexation of guest peptides. As can be seen in Table 1, hosts **1**−**3** could differentiate the sequence of dipeptide, with the selectivity as high as 2.0−4.2 for the Leu-Gly/Gly-Leu pair and

1.4−3.0 for the Gly-Gly-Gly/Gly-Gly pair. This sequence recognition ability of bis(β-CD)s could be accounted for in terms of the size/shape fit between host and guest. Possessing a quasi-linear structure, Leu-Gly was more favorable to the cooperative binding of two β-CD cavities than Gly-Leu that possessed a large isobutyl branch. On the other hand, the longer guest Gly-Gly-Gly was a better fit to the intercavity distance of bis(β-CD)s than Gly-Gly, which in turn led to stronger host−guest inclusion complexation.

As a whole, we can see that the host selectivity sequence of bis(β-CD)s **1**−**3** for each oligopeptide guests was **3** > **2** > **1**. This indicated that nickel(II)-coordinated bis(β-CD) **3** could give stronger binding abilities to oligopeptides than parent bis(β-CD) and its copper(II) complex, which may be helpful to select the appropriate metal ion as the coordination center in the design of the functional β-CD dimers and their metal complexes.

CONCLUSIONS

In summary, novel bridged bis(β-CD)s **1** can recognize the size and hydrophobicity of guest peptides through the cooperative binding of two CD cavities, having higher binding abilities toward relatively long peptides. Especially, its metal complexes effectively enhanced the original binding ability and sequence selectivity of parent **1** through a simultaneous contribution of the multiple chelation effects and/or the electrostatic interactions between the coordinated metal center and the guest peptide. On the other hand, the metal coordination can switch the fluorescence behavior of the parent bis(β-CD) for special substrates, which potentially enabled these novel bis(β-CD)s to function as fluorescence sensors for the molecular recognition of biological guests.

ACKNOWLEDGMENT

This work was supported by NNSFC (Nos. 90306009 and 20272028) and the Tianjin Natural Science Fund (No. 043604411), which are gratefully acknowledged. We also thank the reviewers for their highly valuable suggestions regarding the revision.

LITERATURE CITED

(1) (a) Peczuh, M. W., and Hamilton, A. D. (2000) Peptide and Protein Recognition by Designed Molecules. *Chem. Rev. 100*, 2479−2494. (b) Albert, J. S., Goodman, M. S., and Hamilton, A. D. (1995) Molecular Recognition of Proteins: Sequence-selective Binding of Aspartate Pairs in Helical Peptides. *J. Am. Chem. Soc. 117*, 1143−1144.

(2) Fischer, G. (2000) Chemical Aspects of Peptide Bond Isomerisation. *Chem. Soc. Rev. 29*, 119−127.

(3) Yaffe, M. B., Schutkowski, M., Shen, M., Zhou, X. Z., Stukenberg, P. T., Rahfeld, J.-U., Xu, J., Kuang, J., Kirschner, M. W., Fischer, G., Cantley, L. C., and Lu, K. P. (1997) Sequence-specific and Phosphorylation-dependent Proline Isomerization: A Potential Mitotic Regulatory Mechanism. *Science 278*, 1957−1960.

(4) Chen, C.-T., Wagner, H., and Still, W. C. (1998) Fluorescent, Sequence-selective Peptide Detection by Synthetic Small Molecules. *Science 279*, 851−853.

(5) (a) Fessmann, T., and Kilburn, J. D. (1999) Identification of Sequence-selective Receptors for Peptides with a Carboxylic Acid Terminus. *Angew. Chem., Int. Ed. 38*, 1993−1996. (b) Braxmeier, T., Demarcus, M., Fessmann, T., McAteer, S., and Kilburn, J. D. (2001) Identification of Sequence Selective Receptors for Peptides with a Carboxylic Acid Terminus. *Chem. Eur. J. 7*, 1889−1898. (c) Henley, P. D., and Kilburn, J. D. (1999) A Synthetic Receptor for the Cbz-*L*-Ala-*L*-Ala-OH Dipeptide Sequence. *Chem. Commun.* 1335−1336. (d) Botana, E., Ongeri, S., Arienzo, R., Demarcus, M., Frey, J. G., Piarulli, U., Potenza, D., Gennari, C., and Kilburn, J. D. (2001) Enantioselective Binding of Dipeptides Using Acyclic Receptos. *Chem. Commun.* 1358−1359.

(6) Aït-Haddou, H., Wiskur, S. L., Lynch, V. M., and Anslyn, E. V. (2001) Achieving Large Color Changes in Response to the Presence of Amino Acids: A Molecular Sensing Ensemble with Selectivity for Aspartate. *J. Am. Chem. Soc. 123*, 11296−11297.

(7) Morii, T., Tanaka, T., Sato, S.-i., Hagihara, M., Aizawa, Y., and Makino, K. (2002) A General Strategy to Determine a Target DNA Sequence of a Short Peptide: Application to a D-Peptide. *J. Am. Chem. Soc. 124*, 180−181.

(8) Sirish, M., and Schneider, H.-J. (1999) Porphyrin Derivatives as Water-soluble Receptors for Peptides. *Chem. Commun.* 907−908.

(9) Tsubaki, K., Kusumoto, T., Hayashi, N., Nuruzzaman, M., and Fuji, K. (2002) Sequence-selective Visual Recognition of Nonprotected Dipeptides. *Org. Lett. 4*, 2313−2316.

(10) Douteau-Guével, N., Perret, F., Coleman, A. W., Morel, J.-P., and Morel-Desrosiers, N. (2002) Binding of Dipeptides and Tripeptides Containing Lysine or Arginine by *p*-Sulfonatocalixarenes in Water: NMR and Microcalorimetric Studies. *J. Chem. Soc., Perkin Trans. 2* 524−532.

(11) (a) Maletic, M., Wennemers, H., McDonald, Q. D., Breslow, R., and Still, W. C. (1996) Selective Binding of the Dipeptides *L*-Phe-*D*-Pro and *D*-Phe-*L*-Pro to β-Cyclodextrin. *Angew. Chem., Int. Ed. Engl. 35*, 1490−1492. (b) Breslow, R., Yang, Z., Ching, R., Trojandt, G., and Odobel, F. (1998) Sequence Selective Binding of Peptides by Artificial Receptors in Aqueous Solution. *J. Am. Chem. Soc. 120*, 3536−3537. (c) Wilson, D., Perlson, L., and Breslow, R. (2003) Helical Templating of Oligopeptides by Cyclodextrin Dimers. *Bioorg. Med. Chem. 11*, 2649−2653. (d) Leung, D. K., Yang, Z., and Breslow, R. (2000) Selective Disruption of Protein Aggregation by Cyclodextrin Dimers. *Proc. Natl. Acad. Sci. U.S.A. 97*, 5050−5053.

(12) Schaschke, N., Fiori, S., Weyher, E., Escrieut, C., Fourmy, D., Müller, G., and Moroder, L. (1998) Cyclodextrin as Carrier of Peptide Hormones. Conformational and Biological Properties of β-Cyclodextrin/Gastrin Constructs. *J. Am. Chem. Soc. 120*, 7030−7038.

(13) Ueoka, R., Matsumoto, Y., Harada, K., Akahoshi, H., Ihara, Y., and Kato, Y. (1992) Cyclodextrin-mediated Deacylation of Peptide Esters with Marked Stereoselectivity. *J. Am. Chem. Soc. 114*, 8339−8340.

(14) Rekharsky, M. V., Yamamura, H., Kawai, M., and Inoue, Y. (2003) Complexation and Chiral Recognition Thermodynamics of γ-Cyclodextrin with *N*-Acetyl- and *N*-Carbobenzyloxy-dipeptides Possessing Two Aromatic Rings. *J. Org. Chem. 68*, 5228−5235.

(15) Fukahori, T., Ugawa, T., and Nishikawa, S. (2002) Molecular Recognition Kinetics of Leucine and Glycyl-leucine by β-Cyclodextrin in Aqueous Solution in Terms of Ultrasonic Relaxation. *J. Phys. Chem. A 106*, 9442−9445.

(16) (a) Hossain, M. A., Mihara, H., and Ueno, A. (2003) Novel Peptides Bearing Pyrene and Coumarin Units with or without β-Cyclodextrin in Their Side Chains Exhibit Intramolecular Fluorescence Resonance Energy Transfer. *J. Am. Chem. Soc. 125*, 11178−11179. (b) Matsumura, S., Sakamoto, S., Ueno, A., and Mihara, H. (2000) Construction of α-Helix Peptides with β-Cyclodextrin and Dansyl Units and Their Conformation and Molecular Sensing Properties. *Chem. Eur. J. 6*, 1781−1788. (c) Furukawa, S., Mihara, H., and Ueno, A. (2003) Sensing Behavior of Fluorescence Cyclodextrin/Peptide Hybrids Bearing a Macrocyclic Metal Complex. *Macromol. Rapid Commun. 24*, 202−206.

(17) Hacket, F., Simova, S., and Schneider, H.-J. (2001) The Complexation of Peptides by Aminocyclodextrins. *J. Phys. Org. Chem. 14*, 159−170.

(18) (a) Süss, F., Poppitz, W., de Griend, C. E. S.-V., and Scriba, G. K. E. (2001) Influence of the Amino Acid Sequence and Nature of the Cyclodextrin on the Separation of Small Peptide Enantiomers by Capillary Electrophoresis Using Randomly Substituted and Single Isomer Sulfated and Sulfonated Cyclodextrin. *Electrophoresis 22*, 2416−2423. (b) Süss, F., Kahle, C., Holzgrabe, U., and Scriba, G. K. E. (2002) Studies

on the Chiral Recognition of Peptide Enantiomers by Neutral and Sulfated β-Cyclodextrin and Heptakis-(2,3-di-*O*-acetyl)-β-cyclodextrin Using Capillary Electrophoresis and Nuclear Magnetic Resonance. *Electrophoresis 23*, 1301−1307.

(19) (a) Cheng, J., Khin, K. T., Jensen, G. S., Liu, A., and Davis, M. E. (2003) Synthesis of Linear, β-Cyclodextrin-based Polymers and Their Camptothecin Conjugates. *Bioconjugate Chem. 14*, 1007−1017. (b) Bellocq, N. C., Pun, S. H., Jensen, G. S., and Davis, M. E. (2003) Transferrin-containing, Cyclodextrin Polymer-based Particles for Tumor-targeted Gene Delivery. *Bioconjugate Chem. 14*, 1122−1132.

(20) Liu, Y., Chen, G.-S., Chen, Y., Ding, F., Liu, T., and Zhao, Y.-L. (2004) Molecular Binding Behavior of Pyridine-2,6-dicarboxamide-bridged Bis(β-cyclodextrin) with Oligopeptides: Switchable Molecular Binding Mode. *Bioconjugate Chem. 15*, 300−306.

(21) (a) Veneme, F., Rowan, A. E., and Nolte, R. J. M. (1996) Binding of Porphyrins in Cyclodextrin Dimers. *J. Am. Chem. Soc. 118*, 257−258. (b) Nelissen, H. F. M., Feiters, M. C., and Nolte, R. J. M. (2002) Synthesis and Self-inclusion of Bipyridine-spaced Cyclodextrin Dimers. *J. Org. Chem. 67*, 5901−5906. (c) Nelissen, H. F. M., Kercher, M., de Cola, L., Feiters, M. C., and Nolte, R. J. M. (2002) Photoinduced Electron Transfer between Metal-coordinated Cyclodextrin Assemblies and Viologens. *Chem. Eur. J. 8*, 5407−5414.

(22) Petter, R. C., Sikorski, C. T., and Waldeck, D. H. (1991) Inclusion Complexation by Bis(cyclodextrin) in the Presence of Phospholipid Vesicles. *J. Am. Chem. Soc. 113*, 2325−2327.

(23) de Jong, M. R., Engbersen, J. F. J., Huskens, J., and Reinhoudt, D. N. (2000) Cyclodextrin Dimers as Receptor Molecules for Steroid Sensors. *Chem. Eur. J. 6*, 4034−4040.

(24) (a) Liu, Y., Li, L., Zhang, H.-Y., and Song, Y. (2003) Synthesis of Novel Bis(β-cyclodextrin)s and Metallobridged Bis(β-cyclodextrin)s with 2, 2′-Diselenobis(benzoyl) Tethers and Their Molecular Multiple Recognition with Model Substrates. *J. Org. Chem. 68*, 527−536. (b) Liu, Y., Chen, Y., Li, B., Wada, T., and Inoue, Y. (2001) Cooperative Multipoint Recognition of Organic Dyes by Bis(β-cyclodextrin)s with 2,2′-Bipyridine-4,4′-dicarboxy Tethers. *Chem. Eur. J. 7*, 2528−2535.

(25) Park, J. W., Song, H. E., and Lee, S. Y. (2003) Homodimerization and Heteroassociation of 6-*O*-(2-Sulfonato-6-naphthyl)-γ-cyclodextrin and 6-Deoxy-(pyrene-1-carboxamino)-β-cyclodextrin. *J. Org. Chem. 68*, 7071−7076.

(26) Nakatani, K., Carriat, J. Y., Journaux, Y., Kahn, O., Lloret, F., Renard, J. P., Pei, Y., Sletten, J., and Verdaguer, M. (1989) Chemistry and Physics of the Novel Molecular-based Compound Exhibiting a Spontaneous Magnetization below T_c = 14 K, MnCu(obbz)·1H_2O (obbz = Oxamidobis(benzoato)). Comparison with the Antiferromagnet MnCu(obbz)·5H_2O. Crystal Structure and Magnetic Properties of NiCu(obbz)·6H_2O. *J. Am. Chem. Soc. 111*, 5739−5748.

(27) Petter, R. C., Salek, J. S., Sikorski, C. T., Kumaravel, G., and Lin, F.-T. (1990) Cooperative Binding by Aggregated Mono-6-(alkylamino)-β-cyclodextrin. *J. Am. Chem. Soc. 112*, 3860−3868.

(28) Tabushi, I., Shimizu, N., Sugimoto, T., Shiozuka, M., and Yamamura, K. (1977) Cyclodextrin Flexibly Capped with Metal Ion. *J. Am. Chem. Soc. 99*, 7100−7102.

(29) May, B. L., Kean, S. D., Easton, C. J., and Lincoln, S. F. (1997) Preparation and Characterization of 6^A-Polyaminomonosubstituted β-Cyclodextrin. *J. Chem. Soc., Perkin Trans. 1* 3157−3160.

(30) Kajtár, M., Horvath-Toro, C., Kuthi, E., and Szejtli, J. (1982) A Simple Rule for Predicting Circular Dichroism Induced in Aromatic Guests by Cyclodextrin Hosts in Inclusion Complexes. *Acta Chim. Acad. Sci. Hung. 110*, 327−355.

(31) (a) Zhang, X., and Nau, W. M. (2000) Chromophore Alignment in a Chiral Host Provides a Sensitive Test for the Orientation-intensity Rule of Induced Circular Dichroism. *Angew. Chem., Int. Ed. 39*, 544−547. (b) Mayer, B., Zhang, X., Nau, W. M., and Marconi, G. (2001) Co-conformational Variability of Cyclodextrin Complexes Studied by Induced Circular Dichroism of Azoalkanes. *J. Am. Chem. Soc.* **2001**, *123*, 5240−5248.

(32) Schneider, H.-J., Hacker, F., Rüdiger, V., and Ikeda, H. (1998) NMR Studies of Cyclodextrins and Cyclodextrin Complexes. *Chem. Rev. 98*, 1755−1785.

(33) Benesi, H. A., and Hildebrand, J. H. (1949) A Spectrophotometric Investigation of the Interaction of Iodine with Aromatic Hydrocarbons. *J. Am. Chem. Soc. 71*, 2703−2707.

(34) Becker, H.-C., and Norden, B. (1997) DNA Binding Properties of 2,7-Diazapyrene and Its *N*-Methylated Cations Studied by Linear and Circular Dichroism Spectroscopy and Calorimetry. *J. Am. Chem. Soc. 119*, 5798−5803.

(35) (a) Liu, Y., Li, B., Wada, T., and Inoue, Y. (1999) Enantioselective Recognition of Aliphatic Amino Acids by Organoselenium Modified β-Cyclodextrin. *Supramol. Chem. 10*, 173−184. (b) Liu, Y., Han, B.-H., Sun, S.-X., Wada, T., and Inoue, Y. (1999) Molecular Recognition Study on Supramolecular Systems. 20. Molecular Recognition and Enantioselective of Aliphatic Alcohols by L-Tryptophan-modified β-Cyclodextrin. *J. Org. Chem. 64*, 1487−1493.

(36) Liu, Y., Song, Y., Wang, H., Zhang, H.-Y., Wada, T., and Inoue, Y. (2003) Selective Binding of Steroids by 2,2′-Biquinoline-4,4′-dicarboxamide-bridged bis(β-cyclodextrin): Fluorescence Enhancement by Guest Inclusion. *J. Org. Chem. 68*, 3687−3690.

(37) Tobey, S. L., and Anslyn, E. V. (2003) Energetics of Phosphate Binding to Ammonium and Guanidinium Containing Metallo-receptors in Water. *J. Am. Chem. Soc. 125*, 14807−14815.

BC049870M

Protein Cargo Delivery Properties of Cell-Penetrating Peptides. A Comparative Study

Pille Säälik,[†] Anna Elmquist,[‡] Mats Hansen,[‡] Kärt Padari,[†] Külliki Saar,[‡] Kaido Viht,[§] Ülo Langel,[‡] and Margus Pooga*[,†]

Estonian Biocentre, 23 Riia Street, 51010 Tartu, Estonia, Department of Neurochemistry and Neurotoxicology, Arrhenius Laboratories, Stockholm University, S-10691 Stockholm, Sweden, and Institute of Organic and Bioorganic Chemistry, University of Tartu, 2 Jakobi Street, 51014 Tartu, Estonia. Received March 12, 2004; Revised Manuscript Received August 19, 2004

Application of cell-penetrating peptides for delivering various hydrophilic macromolecules with biological function into cells has gained much attention in recent years. We compared the protein transduction efficiency of four cell-penetrating peptides: penetratin, Tat peptide, transportan, and pVEC and studied the effects of various medium parameters on the uptake. Depletion of cellular energy and lowering of temperature strongly impaired the internalization of protein complexed with cell-penetrating peptides, confirming the endocytotic mechanism of peptide-mediated protein cellular transduction. Peptide-induced protein association with HeLa cells decreased 3−6-fold in energy-depleted cells. Inhibition of clathrin-dependent endocytosis by the hyperosmolar medium decreased the uptake of peptide-avidin complexes 1.5−3-fold and the removal of cholesterol from the plasma membrane 1.2−2-fold, suggesting that both clathrin-dependent and independent endocytosis were involved in peptide-induced cellular delivery of avidin. However, even under conditions of cellular energy depletion, ceasing of cellular traffic, and partial depolarization of plasma membrane, peptide−protein complexes associated with HeLa cells, as observed by FACS analysis and spectrofluorimetry. Among the studied peptides, pTat and transportan revealed higher protein transduction efficiency than penetratin or pVEC.

INTRODUCTION

Discovery and design of various cell-penetrating peptides (CPP) (for reviews see ref 1) have opened a possibility of introducing different hydrophilic macromolecules into cells (*2*, *3*). These peptides show a capability to enter cells in culture even at low temperature and in the presence of endocytosis inhibitors. Although the primary structure of CPPs is highly variable, some general features, envisaged to be essential for efficient cell entry, can be outlined. An abundance of positive charges, especially from arginines (*4*−*6*) and the presence of amino acids with a bulky hydrophobic side-chain (*7*) in the peptide sequence have been suggested to be crucial for efficient cellular uptake. The ability of a peptide to form an amphipathic helix is in correlation with cellular uptake efficacy for some peptides (*8*), whereas for most CPPs, folding into an α-helical structure is not required.

Recently we compared the carrier properties of the four most widely used CPPs, loading them with a small model peptide as a cargo (*9*). The obtained results enabled the division of the peptides into two major classes, based on cargo delivery efficiency and membrane disturbance. Tat peptide (pTat) and penetratin had no adverse effect on plasma membrane permeability in high concentration, but possessed lower cargo delivery efficiency. The model amphipathic peptide (MAP) and transportan, on the contrary, showed higher delivery yield but induced stronger plasma membrane leakage (*9*).

* To whom correspondence should be addressed. Tel: (372−7) 375 023, Fax: (372−7) 420 286. E-mail: mpooga@ebc.ee.
[†] Estonian Biocentre.
[‡] Stockholm University.
[§] University of Tartu.

It was recently suggested that some arginine-rich peptides share a common mechanism of cell entry (*10*). On the other hand, different cellular uptake mechanisms for the arginine-rich pTat and its protein conjugates were demonstrated (*11*). However, translocation of fluoresceinyl-penetratin and -pTat into living cells was questioned lately (*12*, *13*). The uptake detected at higher concentrations was ascribed to membrane perturbation and the toxic effects of labeled peptides. Still, the conjugates of the respective CPPs with PNA oligomers internalized efficiently (*12*). The uptake of fluorescein-labeled pTat and Arg_9 was suggested to proceed mainly by the endocytic pathway (*13*). In addition, internalization of lipid-interacting peptides SynB5 and penetratin was also shown to proceed by absorptive endocytosis rather than by temperature-independent translocation (*14*, *15*). The characteristic diffuse localization of CPPs in the cytoplasm reported in numerous studies earlier was suggested to stem from the fixation and permeabilization of cells (*13*, *16*). On the other hand, the uptake of pTat and Arg_7 by living cells under endocytosis-blocking conditions was demonstrated recently (*17*), and the authors suggested the presence of an additional nonendocytic pathway. Later the observed diffuse localization of CPPs in the cytoplasm associated with the nonendocytic internalization was suggested to be caused by the escape of peptides from endosomal structures, since the inhibition of acidification of endosomes blocked the translocation of CPPs into cytoplasm (*18*, *19*). Cellular uptake of heterologous fusion proteins comprising Tat or its protein transduction domain and EGFP is shown to proceed by a cholesterol- and cellular-energy-dependent caveolae-mediated pathway (*20*, *21*). The cellular uptake of Cre-

10.1021/bc049938y CCC: $27.50 © 2004 American Chemical Society
Published on Web 10/01/2004

Table 1. Sequences and Molecular Masses of Studied Peptides

peptide (abbreviation)	sequence[a]	calculated Mw	obtained Mw	+biotin (calcd)	+biotin (obt)
Penetratin (pAntp)	R*QIKIWFQNRRMKWKK amide	2246	2249.2	2473	2473.9
pTat	G*RKKRRQRRRPPQ amide	1718	1719	1945	1945.2
pVEC	L*LIILRRRIRKQAHAHSK amide	2209	2208.7	2436	2435
Transportan (TP)	GWTLNSAGYLLGK*INLKALAA LAKKIL amide	2842	2841.1	3069	3066.7

[a] *Amino acid labeled with biotin; the peptides (except transportan) are tagged at the N-terminus of the peptide; transportan is labeled at N^{ϵ}-lysine.

recombinase fusion protein with the pTat, however, was very recently demonstrated to occur by caveolin-independent macropinocytosis of lipid rafts (*22*).

The present study characterizes the ability of CPPs (see Table 1 for structures) to target a protein cargo into HeLa cells. We studied the impact of low temperature, endocytosis inhibitors, modulation of the plasma membrane composition and culture medium on the protein cellular transduction efficiency. Inhibition of relevant cellular processes affects the cargo delivery efficiency of different CPPs in a divergent manner. We assume that the observed changes in protein delivery may help elucidate the mechanism by which the four studied peptides facilitated the cellular uptake of proteins.

MATERIALS AND METHODS

Peptide Synthesis. The peptides (Table 1) were synthesized as described earlier (*23*, *24*) on a peptide synthesizer (Applied Biosystems model 431A, USA) in a stepwise manner in a 0.1-mmol scale using the *t*-Boc strategy of solid-phase peptide synthesis. *tert*-Butyloxycarbonyl amino acids were coupled as hydroxybenzotriazole (HOBt) esters to a *p*-methylbenzylhydrylamine (MBHA) resin (Neosystem, Strasbourg, France) to obtain C-terminally amidated peptides.

Biotin was coupled manually to the N-terminus (or to $N^{\epsilon 13}$-Lys in transportan) of the peptide by adding a 3-fold excess of HOBt and *o*-benzotriazol-1-yl-*N*,*N*,*N*′,*N*′-tetramethyluronium tetrafluorborate (TBTU) activated biotin (Chemicon, Hampshire, UK) in DMF to the peptidyl-resin. Deprotection of the dinitrophenyl group was carried out by treatment with 20% thiophenol in DMF for 1 h at room temperature. Deformylation was carried out by treatment with 20% piperidine in DMF for 40 min at room temperature. The peptides were finally cleaved from the resin with liquid HF at 0 °C for 1 h in the presence of *p*-cresol. Purification of peptides with reverse-phase HPLC was carried out with a Supelcosil LC-18 preparative column (25 cm × 21.2 mm, 5 μm) (Sigma Aldrich Chemie, Steinheim, Germany) using water–acetonitrile, both containing 0.1% CF_3COOH, gradient from 20 to 100%. The purity of peptides was >98% as demonstrated by HPLC on an analytical Nucleosil 120-3 C-18 RP-HPLC column (0.4 × 10 cm). Correct molecular masses were obtained by using a MALDI-TOF mass spectrometer (Voyager-DE STR, Applied Biosystems, Foster City, CA) (Table 1).

Cell Culture. HeLa cells (ATCC CCL-2) were cultivated in Iscove's Modified Dulbecco's Medium (IMDM) supplemented with 100 IU/mL penicillin, 100 μg/mL streptomycin, and 10% fetal calf serum (FCS) at 37 °C in humidified atmosphere containing 5% CO_2. Effects of CPPs on plasma membrane integrity were assayed by measuring the LDH release using the CytoTox-ONE Assay (Promega Corp. Madison, WI). In parallel, the MTT-assay was also performed.

Uptake Experiments. The cells were incubated with fluorescein-labeled avidin complexed with biotinyl-CPPs in IMDM containing 10% FCS if not stated otherwise. The CPP–avidin complexes were preformed by associating fluorescein-labeled avidin with biotinyl-CPP at room temperature in a minimal volume for 5 min and applied to the cells after dilution with the culture medium to the concentration of 0.15 μM and 0.5 μM, respectively. Incubation was carried out at 37 °C or on ice, and the incubation time was varied from 15 min to 24 h, depending on the experiment. For experiments at low temperature, the cells were preincubated on ice for 15 min. Depletion of cellular energy was achieved by inhibiting oxidative phosphorylation and glycolysis with 0.5 or 1% sodium azide and 25 or 50 mM 2-deoxyglucose (DOG), respectively, either alone or in combination (*25*) prior to the application of complexes. The hyperosmolar medium was prepared by dissolving sucrose at a concentration of 0.4 M in IMDM, and solutions containing deoxyglucose were prepared in Dulbecco's PBS. The cells were treated with a solution containing the respective agent for 30 min, and then avidin or CPP–avidin complexes in the same solution were applied and the uptake was measured after 30 min incubation. Organization of plasma membrane lipids was modified by incubating the cells in serum-free IMDM with 10 mM methyl β-cyclodextrin, which extracts cholesterol from the cells' plasma membrane (*26*), leads to the disappearance of rafts and caveolae and inhibits their re-formation (*27*).

FACS Analysis. The cells were seeded in six-well plates to a density of 250 000 cells per well in 2.5 mL medium and used for experiments 1 day after seeding at 70–90% confluence. After incubation with peptide–protein complexes, the cells were rinsed twice with PBS and detached from the plastic by incubating with trypsin solution (0.5 mg/mL in PBS containing 0.2 mg/mL EDTA) at 37 °C for 3, 15, or 30 min, respectively. Trypsinized cells were suspended, collected by centrifugation at 250*g* for 5 min at 4 °C, and resuspended in PBS. The intactness of the cells was estimated by resuspending the cells' pellet in PBS containing 1 μg/mL of propidium iodide. In the flow cytometry analysis 30 000 cells per sample were counted by the FACS Calibur, using Cell Quest software (BD Biosciences, Heidelberg, Germany). Each value represents a mean of three separate determinations.

Spectrofluorimetric Quantification of Internalized Avidin. The cells were treated with the complexes as described in uptake experiments and trypsinized for 15 min, and the washed cell pellet was dissolved in 1 mL 0.1 M NaOH. The fluorescence signal in the obtained solution was measured in a 10 × 10 mm cuvette at 520 nm using excitation at 490 nm by a F-4500 fluorescence spectrophotometer (Hitachi, Japan). Quantitative data analysis was performed by MS Excel.

Confocal Scanning Microscopy. HeLa cells in eight-well chambered coverglasses (Nalge Nunc International, Rochester, NY) were incubated with 0.15 μM Alexa Fluor 488 labeled avidin (Molecular Probes, Leiden, Netherlands) and 0.5 μM biotinyl-CPP in 10% of FCS containing

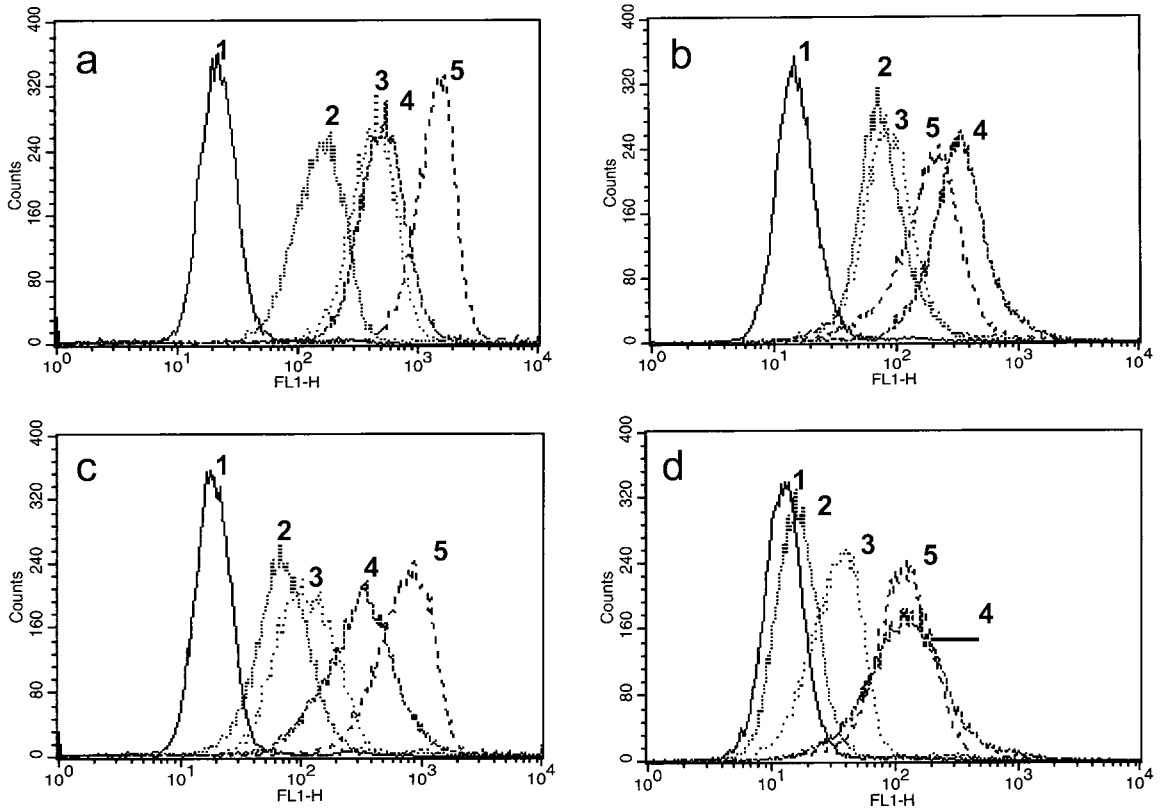


Figure 1. Cellular uptake of FITC-labeled avidin complexes with different biotinyl-CPPs. HeLa cells were incubated with complexes of 0.15 μM FITC-labeled avidin and 0.5 μM biotinyl-CPP for 30 min at 37 °C (a, c) or 4 °C (b, d) and thereafter treated with trypsin for 3 min (a, b) or 15 min (c, d). The cells were incubated with FITC-labeled avidin (1) or complexed with biotin-tagged penetratin (2), pVEC (3), pTat (4), or transportan (5). The number of cells (*y*-axis) is plotted against the fluorescence signal of cells (*x*-axis).

IMDM for 45 min at 37 °C. The medium with the complexes was removed, the cells were rinsed twice with PBS, covered with PBS (containing 1 mM of $CaCl_2$ and 0.5 mM $MgCl_2$), and the serial images were recorded using the laser confocal scanning microscope MRC-1024 (Bio-Rad Laboratories, Hercules, CA). After recording the images, an equal volume of 8% (w/v) paraformaldehyde in PBS was added. The images from the cells were obtained in the course of fixation with 4% PFA every 10 min using the identical settings of the microscope.

RESULTS

Peptides. All peptides were synthesized and biotinylated by using conventional peptide synthesis protocols. Orthogonal protection group strategy was used for the labeling of transportan at the 13th position with biotin (*23*, *28*). The studied peptides (Table 1) at the used concentrations were not toxic in the applied conditions and did not impair the viability of cells, judged by the standard methods for measuring cell viability, using a MTT-based assay and plasma membrane integrity by the LDH leakage assay (data not shown).

Protein Transduction Ability of CPPs Differs. Addition of fluorescein-labeled avidin into the culture medium and incubation for 30 min led to negligible, if any, detectable increase in the fluorescence of HeLa cells (Figure 1a). Coapplication of FITC-labeled avidin with 0.5 μM biotinyl-CPP led to a marked increase in the cells' fluorescence that ranged from about a 10-fold gain with biotinyl-penetratin to a more than a 100-fold rise with biotinyl-transportan (Figure 1a). The effect of biotinyl-derivatives of pTat and pVEC peptides lay between these limits (Figure 1a). Although the total gain of fluorescence intensity widely varied for avidin−FITC complexes with different biotinyl-CPPs, the uptake of each complex is rather uniform, i.e., all cells were labeled and only one cell population was present.

Lowering the incubation temperature from 37 to 4 °C led to a remarkable drop in fluorescence intensity, showing a decreased association/uptake of biotinyl-CPP−avidin complexes with/into cells (Figure 1b). Still, all the cells were stained and the order of potency among the four CPPs was the same as at the physiological temperature. Protein delivery with the Tat peptide was less affected upon lowering the incubation temperature as compared to complexes with the other studied CPPs.

The avidin−biotinyl-CPP complexes loosely bound at the plasma membrane may interfere with the FACS analysis (*13*). After a prolonged trypsin treatment for 15 min, cells incubated with biotinyl-CPP−avidin complexes revealed markedly lower fluorescence intensity, showing that a significant fraction of complexes is still accessible to extracellularly applied trypsin (Figure 1c). The amount of cell-associated protein complexes with biotinyl-penetratin and biotinyl-pVEC was more and complexes with biotinyl-pTat and biotinyl-transportan less affected upon a prolonged trypsin treatment, revealing lower accessibility of the latter to the enzyme. However, the changes induced by prolonged trypsin treatment did not change the principal order of delivery efficiency of the studied CPPs (Figure 1c). Analogous results were obtained with complexes of FITC-labeled streptavidin and the respective CPPs. When the biotin moiety was coupled to the CPP via an aminohexanoic acid spacer, the uptake of avidin complex was identical with the spacer-free biotinyl-CPPs (data not shown).

The avidin−CPP complexes, associated with cells at low temperature, were highly accessible and a substan-

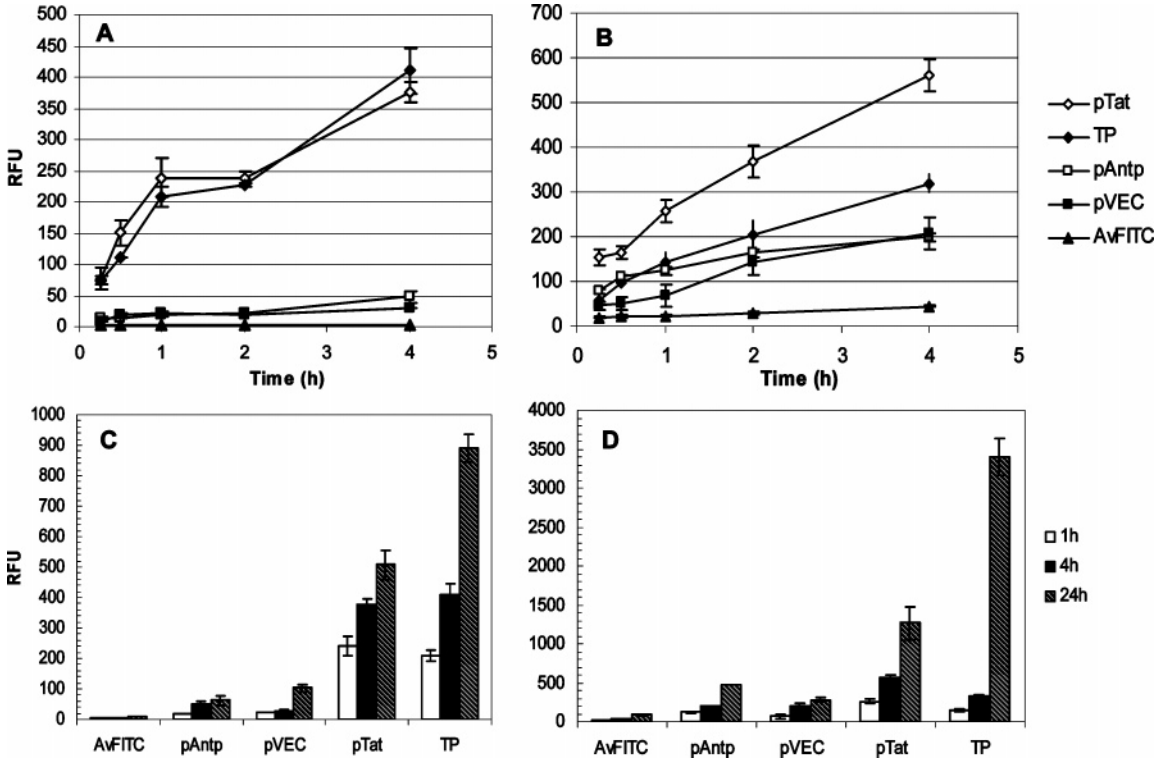


Figure 2. Cell association kinetics of CPP−avidin complexes. HeLa cells were incubated with 0.15 μM FITC-labeled avidin or its complexes with the respective 0.5 μM biotinyl-CPP and fluorescence was measured by FACS (a, c) in live cells or by spectrofluorimetry (b, d) in cell lysates. Association kinetics of complexes during the first 4 h (a, b) and from 1 to 24 h (c, d). Each value is the mean ± SD of three separate determinations. The fluorescence intensity in the cells is expressed as a ratio to the fluorescence of untreated control cells.

tial fraction of complexes was removed by trypsin. The association of avidin complexes with penetratin was more and complexes with pTat less affected in comparison with other peptides. Probably the penetratin−avidin complexes remained loosely bound to the cell surface at low temperatures. Stable association of penetratin−avidin complexes with HeLa cells seems to be more temperature-dependent than that of other studied CPPs.

Lowering of the incubation temperature or the prolongation of trypsin treatment did not cause any detectable increase in the number of cells taking up propidium iodide as compared to untreated control cells (data not shown). Therefore, we believe that the barrier function of the cells plasma membrane was not compromised and the integrity of the cells was not impaired by these treatments.

Uptake Kinetics of CPP−Avidin Complexes. Marked reduction in the fluorescence signal under an extended trypsin treatment implies that after 30 min a substantial fraction of biotinyl-CPP complexes with FITC-labeled avidin are still located on the cell surface. The uptake of complexes was measured in a serum-containing culture medium in order to maintain favorable conditions for cells. Prolongation of incubation time with CPP−avidin complexes from 15 min to 4 h led to a gradual increase in cell-associated fluorescence (Figure 2a).

Analogous time-dependency of internalization was observed for all the biotinyl-CPP complexes studied. However, in the serum-supplemented culture medium the uptake of complexes with transportan was reduced and slightly less efficient than that of Tat complexes.

Although the protein transduction efficiency of the studied CPPs is different, the initial stable association is very fast and already in 15 min a substantial amount of complexes is stably associated with the cells. Cellular fluorescence increases linearly during the first hour. After 2-h incubation a deceleration in the uptake was observed, followed by a new fast increase (Figure 2a), and the internalization of CPP−avidin complexes continued for at least 24 h at this peptide concentration (Figure 2c). Uptake of fluorescein-labeled avidin shows a rather similar time-dependence, though at a markedly lower level. Spectrofluorimetry did not reveal any deceleration in the uptake of fluorescent CPP−avidin complexes after 1 h, but a continuous increase during the first 4 h. While the FACS analysis shows an approximately 10-fold difference in transduction efficiency between the Tat and penetratin peptides, comparison by spectrofluorimetry reveals less than a 3-fold difference after 4 h incubation (Figure 2b). Prolonged incubation of cells with complexes from 4 to 24 h approximately doubles the intracellular concentration of the labeled complex (Figure 2c). Surprisingly, the cellular uptake of transportan−avidin complexes did not slow after 4 h incubation but continued increasing at high speed. Growing accumulation of transportan−avidin complexes in HeLa cells from 4 to 24 h was detected by both, FACS and spectrofluorimetry (Figure 2c, d). Perforation of the plasma membrane and free entrance into cells is not the reason for the observed accumulation since the integrity of cells is not compromised as confirmed by the exclusion of propidium iodide.

Constituents of Serum and Tissue Culture Medium Slightly Modulate the Uptake of CPP−Avidin Complexes. It is usually considered that the cellular uptake of CPPs and their cargoes is reduced in the presence of serum. However, the uptake of CPP−avidin complexes by HeLa cells was more efficient in a serum containing medium and less efficient in PBS (Figure 3). Transportan was an exception, inducing the internalization of a higher amount of avidin in a serum-free than serum containing medium (Figure 3). On the other hand, a less efficient uptake of transportan−avidin complexes

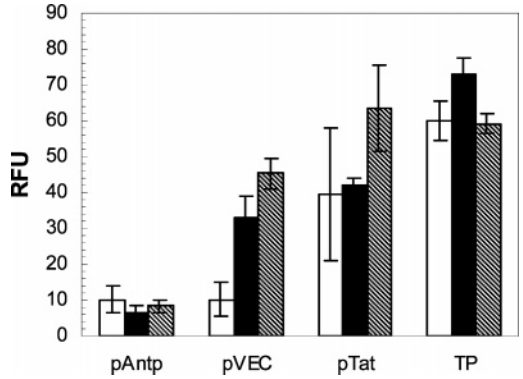


Figure 3. Effect of culture medium on protein cellular uptake. HeLa cells were incubated with complexes of 0.15 μM FITC-labeled avidin with the respective 0.5 μM biotinyl-CPP in PBS (empty bars), serum-free IMDM (black bars), or serum-containing IMDM (striped bars) for 30 min at 37 °C. Fluorescence intensity in the cells is expressed as a ratio to the fluorescence of control cells that were incubated with FITC-labeled avidin.

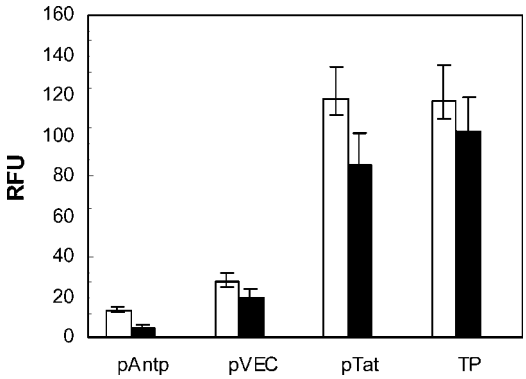


Figure 4. Inhibition of the cellular uptake of CPP−avidin complexes in hyperosmolar cell culture medium. HeLa cells were incubated with 0.15 μM FITC-labeled avidin with the respective 0.5 μM biotinyl-CPPs in isotonic IMDM (empty bars) or hyperosmolar culture medium containing 0.45 M sucrose (black bars).

in the presence of serum was observed only with short incubation times of 15 to 30 min. In less than 1 h the uptake of complexes with transportan was equal both in serum-containing and serum-free media (data not shown). After longer incubations, the internalization of transportan−avidin complexes followed the rule: a higher uptake took place in the presence of serum.

Role of Clathrin-Mediated Endocytosis in the Uptake of CPP−Avidin Complexes. The cellular uptake of FITC-labeled avidin complexed with biotinylated CPPs decreased under hyperosmolar conditions, which inhibits clathrin-dependent endocytosis as compared to a normal isotonic medium. The uptake of avidin complexes formed with penetratin decreased about 3-fold under hyperosmolar conditions, but the uptake could not be completely blocked by inhibiting clathrin-dependent endocytosis (Figure 4). The uptake of pTat-avidin, transportan−avidin, and pVEC−avidin complexes by HeLa cells decreased in the hyperosmolar medium only slightly, about 1.5-fold, pointing at a possible different mode of interaction at the plasma membrane and the internalization pathway for penetratin.

Depletion of Cellular Energy Minimizes the Association of Peptide−Protein Complexes with HeLa Cells. Deprivation of cellular energy strongly impaired the uptake of avidin complexed with any of the four CPPs (Figure 5). Sodium azide inhibited the uptake of CPP−avidin complexes more, reducing the fluorescence signal about 2−5-fold, while the change from glucose to DOG

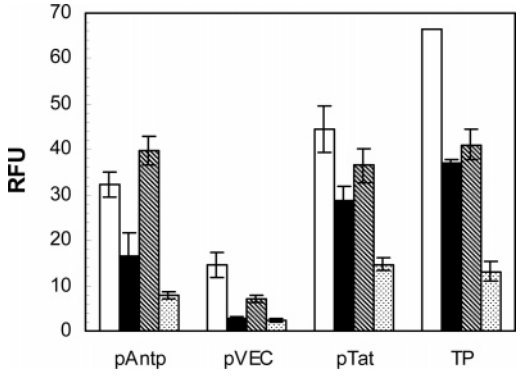


Figure 5. Inhibition of uptake of avidin−CPP complexes by depletion of cellular energy. Uptake in the presence of 0.5% NaN_3 in IMDM (black bars), 25 mM 2-deoxyglucose in PBS (striped bars), or both inhibitors in PBS (dotted bars). Control cells were incubated in IMDM (empty bars). HeLa cells were treated with the respective inhibitors for 30 min at 37 °C, and then the complexes of 0.15 μM FITC-labeled avidin with the respective 0.5 μM biotinyl-CPPs in the same solution were applied and incubated for additional 30 min at 37 °C.

had almost no effect as with penetratin−avidin complexes, or a small inhibitory effect of 1.2−2-fold. Coapplication of inhibitors had an additive effect, and the fluorescence signal associated with the cells was reduced about 3−6-fold, depending on the CPP examined. Identical reduction in the uptake was obtained with 1% sodium azide (i.e., by doubling the concentration) alone. Increase in the DOG concentration from 25 to 50 mM slightly (about 1.5-fold) enhanced its inhibitory effect (not shown). Still, a clearly detectable fraction of CPP−avidin complexes stably associated with cells in the presence of both inhibitors with all the tested peptides. This residual fluorescence could not be eliminated by extensive treatment with trypsin or pronase (not shown).

In the absence of cellular energy, about 2- to 5-fold more FITC-labeled avidin associated with cells when complexed to a biotinyl-CPP than without a carrier peptide. This is in the line with the results obtained at low temperature, suggesting that by energy depletion the stable association of CPPs with the cells was not completely blocked.

Organization of Membrane Lipids is Essential for CPP-Mediated Protein Delivery. Extraction of cholesterol from cells leads to the disappearance of caveolae, flattening of the plasma membrane, and the loss of rafts and abolishes staining with filipin as observed in electron microscopy (*27*). Treatment of HeLa cells with methyl-β-cyclodextrin removed more than 2/3 of cholesterol from the plasma membrane as indicated the staining of cells with filipin. Cholesterol-depleted HeLa cells took CPP−avidin complexes up less avidly than the untreated cells. However, a drop in the uptake of complexes was not uniform for all the four CPPs examined (Figure 6). Uptake of avidin, complexed with penetratin or pVEC decreased about 2-fold, while that of transportan and pTat complexes by only about 20%.

Intracellular Localization of CPP−Avidin Complexes. Incubation of cells with complexes of any used biotinyl-CPP and fluorescently labeled avidin for more than 15 min led to an intense labeling of all cells in the culture as revealed by fluorescence microscopy. The complexes appeared first as punctuate structures on the plasma membrane and of spherical or tubular shape in cortical cytoplasm. Later the complexes shifted more centrally and were detectable also in the perinuclear region of HeLa cells (Figure 7). The punctuate pattern

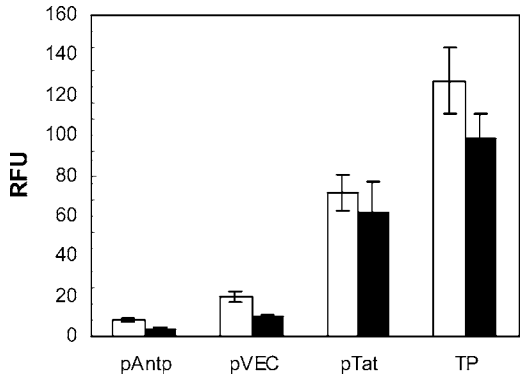


Figure 6. Effect of cholesterol removal from the plasma membrane on the uptake of avidin−CPP complexes. Cholesterol was extracted from the HeLa plasma membranes by incubating cells for 30 min in the medium with 10 mM methyl-β-cyclodextrin. The complexes of 0.15 μM FITC-labeled avidin with the respective 0.5 μM biotinyl-CPPs were applied in the same solution and incubated for additional 30 min at 37 °C. Uptake by cholesterol-depleted HeLa cells (black bars) and control cells (empty bars).

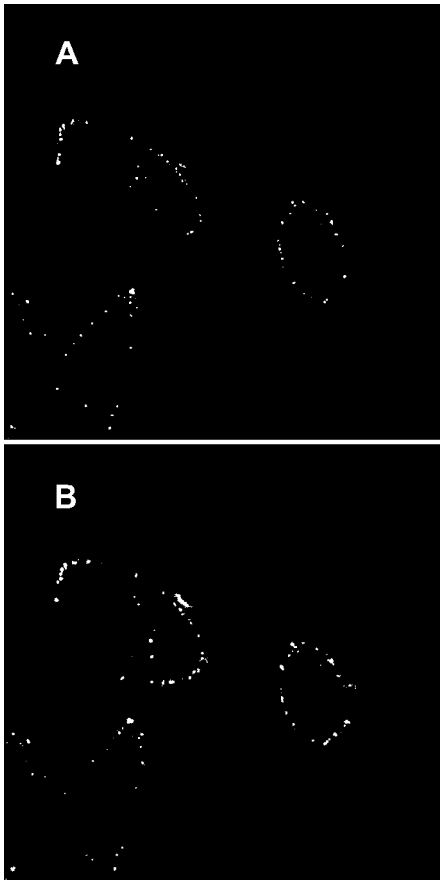


Figure 7. Localization of avidin−FITC complexes with biotinylated transportan in living and fixed HeLa cells. Confocal fluorescence microscopy images of HeLa cells (equatorial view) incubated with 0.5 μM biotinyl-transportan and 0.15 μM avidin−Alexa Fluor 488 for 45 min before (A) and after fixation (B) in 4% paraformaldehyde for 15 min.

of staining of HeLa cells prevailed also after 4 h incubation, suggesting the localization of avidin−CPP complexes mainly in vesicular structures. However, some uniform diffuse staining of cytoplasm was also detectable after at least 30 min incubation.

Distribution of fluorescein-labeled CPPs from the plasma membrane into intracellular structures upon fixation leading to an artifactual staining pattern was demonstrated recently (*12*, *13*, *16*). To study the redistribution, we assessed the localization of fluorescent CPP−avidin complexes in the course of fixation with 4% paraformaldehyde by confocal scanning microscopy during 40 min. No marked redistribution of avidin−CPP complexes upon fixation was observed within this time period (Figure 7a,b).

DISCUSSION

We estimated the ability of different CPPs to target/deliver proteins into cells by following the cellular uptake of fluorescein-labeled avidin complexed with biotinylated peptides by fluorescence microscopy, flow cytometry and spectrofluorimetry. Transduction of fluorescently labeled avidin and/or streptavidin into cells after complexing with biotinylated transportan (*29*), pVEC (*24*), pTat, penetratin (*15*), and proline-rich peptides (*30*) was demonstrated recently. Therefore, instead of synthesizing a multitude of CPP−protein covalent conjugates, we used the complexes of a respective biotinyl-CPP with fluorescein-labeled avidin. Tagging of a peptide with biotin could introduce conformational constraints and interfere with association with avidin or influence the translocation activity. We assumed that biotinylation restrains peptides analogously and all the studied CPPs complexed with fluorescein-labeled avidin and induced its cellular uptake under physiological conditions. The biotin moiety associating a peptide with avidin, on the other hand, may be considered as a spacer reducing constraints posed by a cargo to CPP activity.

Penetratin, pTat, transportan, and pVEC were chosen as representatives of the respective CPP families. The motifs that are considered to be essential for cell penetration are, in general, arginines for pTat (*5*, *31*), positively charged amino acids (*32*) and tryptophan for penetratin (*33*), hydrophobic N-terminal region for pVEC (A. Elmquist personal communication), and the amphipathic carboxyterminal part for transportan (*34*). A multitude of molecular determinants necessary for the cellular uptake of particular peptides suggests that different CPPs may vary in cellular penetration ability (*35*).

The four CPPs studied here were capable of targeting the complexed FITC-labeled avidin to the HeLa cell plasma membrane and inducing cellular uptake. Transportan and pTat were more efficient in the transduction of complexed avidin than penetratin and pVEC. A substantial fraction of CPP−avidin complexes was not internalized but tightly bound extracellularly and removed only by extending trypsin treatment to 15 min. Extensive trypsin treatment affected the amount of cell-bound penetratin−avidin complexes more, implying a slower passage across the plasma membrane into cytoplasm or better accessibility to the enzyme in the plasma membrane. Lower avidin/streptavidin delivery efficiency with biotinyl-penetratin compared to biotinylated Tat peptide has been observed also earlier (*15*). Avidin cargo may introduce conformational constraints on a penetratin and pVEC molecule, leading to a reduced uptake as suggested for a human calcitonin-derived peptide (*36*). On the other hand, the interaction of penetratin and pVEC with the plasma membrane of cells might be more dependent on the concentration of peptide, temperature, and cellular energy. Tryptophan in the sixth position of pAntp has been shown to serve as a membrane anchor and induce cellular transduction (*37*); therefore, higher stiffness of plasma membrane at lower temperatures might impede stable association of penetratin with HeLa cells and subsequent translocation.

The amount of internalized CPP−avidin complexes increased rapidly in physiological conditions during the first 4 h. Spectrofluorimetry showed an about 2−3-fold difference in the transduction potential between pTat and penetratin, whereas the FACS analysis suggested an almost 10-fold difference. Discrepancy between the obtained results could be explained by the sensitivity of fluorescein emission to the microenvironment and partial quenching in the endosomal structures of living cells used for the FACS analysis (*19*). Transportan or pTat might disrupt the acidic vesicular structures and escape into cytoplasm more efficiently than penetratin or pVEC. By analogy, a relative deceleration in the cellular uptake of complexes observed by FACS may also be caused by the translocation of complexes into acidic vesicular structures. The uptake of complexes did not cease after 4 h and continued slowly for three studied peptides for 24 h. Transportan−avidin complexes continued to concentrate intracellularly after 4 h incubation at high speed, suggesting that transportan could stimulate the uptake by modulating intracellular processes without compromising the intactness of cells (*38*).

The lowering of temperature decreases plasma membrane permeability and partially depolarizes the cells leading to a dramatically reduced internalization of CPPs (*14*). CPP-mediated protein cellular delivery decreased even more, suggesting that the uptake process was energy-dependent and the stiffening of the plasma membrane minimized the uptake. About 80−90% of FITC-labeled avidin associated with HeLa cells by biotinyl-CPPs was removed by an extensive trypsin treatment, demonstrating that at low temperature the majority of complexes remained in the plasma membrane and were not internalized. Cellular energy deficiency reduced the uptake of CPP−avidin complexes even more strongly. Still, a small fraction of CPP−protein complexes associated with energy-deficient cells and association took place also at low temperature, suggesting a stable association or uptake. This might imply that the initial interaction of CPPs with the plasma membrane was not dependent on cellular metabolic energy and activity.

All endocytic processes, clathrin-dependent and -independent endocytosis, micro- and macropinocytosis, are blocked at low temperature and in energy-deficient cells (*39*). Hyperosmolar medium, which inhibits clathrin-mediated endocytosis, led to a minor inhibition of the internalization of avidin−CPP complexes, showing a small role of this mechanism in the uptake and a prevalence of other, clathrin-independent endocytic processes. Detergent resistant membrane fractions (DRM) that are rich in cholesterol and sfingolipids form "rafts" and caveolae in the plasma membrane are necessary for clathrin-independent endocytosis to occur (*40*). Caveolae are suggested to mediate Tat-phage internalization into COS-1 cells (*41*) and EGFP fusion proteins with the Tat protein or peptide into HeLa cells (*20*, *21*). On the other hand, it has been recently shown that caveolae are highly immobile plasma membrane microdomains that are not involved in constitutive endocytosis (*42*), and the raft regions might mediate the uptake. Uptake of avidin complexed with the tested CPPs by HeLa cells was strongly impaired after removing cholesterol from the plasma membrane by methyl-β-cyclodextrin. Cell transducible fusion proteins with Tat are suggested to enter HeLa cells by caveolar endocytosis (*20*, *21*) and mouse lymphocytes by macropinocytosis (*22*). Both these processes are cholesterol-dependent and start from lipid rafts. Our data do not enable us to distinguish between these two pathways of cellular uptake. However, in our earlier studies with fixed cells we detected transportan−protein conjugates and complexes at the plasma membrane in structures of various size and volume but not in highly uniform and morphologically defined caveolae.

The potential application of CPP-mediated transport in vivo necessitates knowledge about the influence of serum and other medium constituents on the cellular uptake of particular CPPs. Serum is usually considered to reduce the cellular uptake of CPPs and their cargoes but the protein delivery efficiency of the studied CPPs was slightly enhanced in the presence of serum. Potentiation of cargo delivery by the presence of serum could give CPP-mediated cell transduction an advantage over lipofection, for example, for in vivo use.

In conclusion, all four studied peptides are capable of promoting the cellular delivery of avidin. Although these peptides are classified as cell-penetrating, their protein delivery potential differs substantially. Changes in experimental conditions such as temperature, medium composition and osmolarity, cellular energy, and plasma membrane composition affect protein transduction by these peptides in a rather similar manner. This suggests that the four studied transport peptides could share a common mechanism to promote the cellular uptake by endocytosis. The peptide-mediated cellular transduction of proteins comprises several subsequent steps of binding to the cellular surface, interaction at the plasma membrane, and translocation into and traffic inside the cell. Probably, various interaction modes at the plasma membrane cause most of the observed differences in the internalization efficiency of CPP−protein complexes (*43*, *44*).

ACKNOWLEDGMENT

We are grateful to Dr. U. Soomets for peptide synthesis and discussions. This work was supported by grants from the European Community (QLK3-CT-2002-01989), the Estonian Science Foundation (ESF 4007 and 5588), the Swedish Institute Visby Program, Swedish Royal Academy of Sciences, and Swedish Research Councils TFR and NFR.

LITERATURE CITED

(1) Langel, Ü. (2002) *Cell-Penetrating Peptides, Processes and Applications*, CRC Press, Boca Raton.
(2) Lindsay, M. (2002) Peptide-mediated cell delivery: application in protein target validation. *Curr. Opin. Pharmacol. 2*, 587−594.
(3) Schwarze, S. R., and Dowdy, S. F. (2000) In vivo protein transduction: intracellular delivery of biologically active proteins, compounds and DNA. *Trends. Pharmacol. Sci. 21*, 45−48.
(4) Futaki, S., Suzuki, T., Ohashi, W., Yagami, T., Tanaka, S., Ueda, K., and Sugiura, Y. (2001) Arginine-rich peptides. An abundant source of membrane-permeable peptides having potential as carriers for intracellular protein delivery. *J. Biol. Chem. 276*, 5836−5840.
(5) Mitchell, D. J., Kim, D. T., Steinman, L., Fathman, C. G., and Rothbard, J. B. (2000) Polyarginine enters cells more efficiently than other polycationic homopolymers. *J. Pept. Res. 56*, 318−325.
(6) Wender, P. A., Mitchell, D. J., Pattabiraman, K., Pelkey, E. T., Steinman, L., and Rothbard, J. B. (2000) The design, synthesis, and evaluation of molecules that enable or enhance cellular uptake: peptoid molecular transporters. *Proc. Natl. Acad. Sci. U.S.A. 97*, 13003−13008.
(7) Derossi, D., Chassaing, G., and Prochiantz, A. (1998) Trojan peptides: the penetratin system for intracellular delivery. *Trends Cell Biol. 8*, 84−87.
(8) Scheller, A., Oehlke, J., Wiesner, B., Dathe, M., Krause, E., Beyermann, M., Melzig, M., and Bienert, M. (1999) Structural

requirements for cellular uptake of alpha-helical amphipathic peptides. *J. Pept. Sci. 5*, 185−194.
(9) Hällbrink, M., Florén, A., Elmquist, A., Pooga, M., Bartfai, T., and Langel, Ü. (2001) Cargo delivery kinetics of cell-penetrating peptides. *Biochim. Biophys. Acta 1515*, 101−109.
(10) Suzuki, T., Futaki, S., Niwa, M., Tanaka, S., Ueda, K., and Sugiura, Y. (2002) Possible existence of common internalization mechanisms among arginine-rich peptides. *J. Biol. Chem. 277*, 2437−2443.
(11) Silhol, M., Tyagi, M., Giacca, M., Lebleu, B., and Vivés, E. (2002) Different mechanisms for cellular internalization of the HIV-1 Tat- derived cell penetrating peptide and recombinant proteins fused to Tat. *Eur. J. Biochem. 269*, 494−501.
(12) Koppelhus, U., Awasthi, S. K., Zachar, V., Holst, H. U., Ebbesen, P., and Nielsen, P. E. (2002) Cell-dependent differential cellular uptake of PNA, peptides, and PNA- peptide conjugates. *Antisense Nucleic Acid Drug Dev. 12*, 51−63.
(13) Richard, J. P., Melikov, K., Vivés, E., Ramos, C., Verbeure, B., Gait, M. J., Chernomordik, L. V., and Lebleu, B. (2003) Cell penetrating peptides: a reevaluation of the mechanism of cellular uptake. *J. Biol. Chem. 278*, 585−590.
(14) Drin, G., Cottin, S., Blanc, E., Rees, A. R., and Temsamani, J. (2003) Studies on the internalization mechanism of cationic cell-penetrating peptides. *J. Biol. Chem. 278*, 31192−31201.
(15) Console, S., Marty, C., Garcia-Echeverria, C., Schwendener, R., and Ballmer-Hofer, K. (2003) Antennapedia and HIV transactivator of transcription (TAT) "protein transduction domains" promote endocytosis of high molecular weight cargo upon binding to cell surface glycosaminoglycans. *J. Biol. Chem. 278*, 35109−35114.
(16) Lundberg, M., and Johansson, M. (2002) Positively charged DNA-binding proteins cause apparent cell membrane translocation. *Biochem. Biophys. Res. Commun. 291*, 367−371.
(17) Thorén, P. E., Persson, D., Isakson, P., Goksör, M., Önfelt, A., and Nordén, B. (2003) Uptake of analogs of penetratin, Tat(48−60) and oligoarginine in live cells. *Biochem. Biophys. Res. Commun. 307*, 100−107.
(18) Potocky, T. B., Menon, A. K., and Gellman, S. H. (2003) Cytoplasmic and nuclear delivery of a TAT-derived peptide and a beta-peptide after endocytic uptake into HeLa cells. *J. Biol. Chem. 278*, 50188−50194.
(19) Fischer, R., Köhler, K., Fotin-Mleczek, M., and Brock, R. (2004) A stepwise dissection of the intracellular fate of cationic cell-penetrating peptides. *J. Biol. Chem. 279*, 12625−12635.
(20) Fittipaldi, A., Ferrari, A., Zoppe, M., Arcangeli, C., Pellegrini, V., Beltram, F., and Giacca, M. (2003) Cell membrane lipid rafts mediate caveolar endocytosis of HIV-1 Tat fusion proteins. *J. Biol. Chem. 278*, 34141−34149.
(21) Ferrari, A., Pellegrini, V., Arcangeli, C., Fittipaldi, A., Giacca, M., and Beltram, F. (2003) Caveolae-mediated internalization of extracellular HIV-1 tat fusion proteins visualized in real time. *Mol. Ther. 8*, 284−294.
(22) Wadia, J. S., Stan, R. V., and Dowdy, S. F. (2004) Transducible TAT-HA fusogenic peptide enhances escape of TAT-fusion proteins after lipid raft macropinocytosis. *Nat. Med. 10*, 310−315.
(23) Soomets, U., Lindgren, M., Gallet, X., Hällbrink, M., Elmquist, A., Balaspiri, L., Zorko, M., Pooga, M., Brasseur, R., and Langel, Ü. (2000) Deletion analogues of transportan. *Biochim. Biophys. Acta 1467*, 165−176.
(24) Elmquist, A., Lindgren, M., Bartfai, T., and Langel, Ü. (2001) VE-cadherin-derived cell-penetrating peptide, pVEC, with carrier functions. *Exp. Cell. Res. 269*, 237−244.
(25) Sandvig, K., and Olsnes, S. (1982) Entry of the toxic proteins abrin, modeccin, ricin, and diphtheria toxin into cells. I. Requirement for calcium. *J. Biol. Chem. 257*, 7495−4503.
(26) Torgersen, M. L., Skretting, G., van Deurs, B., and Sandvig, K. (2001) Internalization of cholera toxin by different endocytic mechanisms. *J. Cell. Sci. 114*, 3737−3747.
(27) Thyberg, J. (2002) Caveolae and cholesterol distribution in vascular smooth muscle cells of different phenotypes. *J. Histochem. Cytochem. 50*, 185−195.
(28) Pooga, M., Hällbrink, M., Zorko, M., and Langel, Ü. (1998) Cell penetration by transportan. *FASEB J. 12*, 67−77.
(29) Pooga, M., Kut, C., Kihlmark, M., Hällbrink, M., Fernaeus, S., Raid, R., Land, T., Hallberg, E., Bartfai, T., and Langel, Ü. (2001) Cellular translocation of proteins by transportan. *FASEB J. 15*, 1451−1453.
(30) Sadler, K., Eom, K. D., Yang, J. L., Dimitrova, Y., and Tam, J. P. (2002) Translocating proline-rich peptides from the antimicrobial peptide bactenecin 7. *Biochemistry 41*, 14150−14157.
(31) Vivés, E., Brodin, P., and Lebleu, B. (1997) A truncated HIV-1 Tat protein basic domain rapidly translocates through the plasma membrane and accumulates in the cell nucleus. *J. Biol. Chem. 272*, 16010−16017.
(32) Fischer, P. M., Zhelev, N. Z., Wang, S., Melville, J. E., Fåhraeus, R., and Lane, D. P. (2000) Structure−activity relationship of truncated and substituted analogues of the intracellular delivery vector Penetratin. *J. Pept. Res. 55*, 163−172.
(33) Derossi, D., Joliot, A. H., Chassaing, G., and Prochiantz, A. (1994) The third helix of the Antennapedia homeodomain translocates through biological membranes. *J. Biol. Chem. 269*, 10444−10450.
(34) Pooga, M., Hällbrink, M., and Langel, Ü. (2002) Transportans. In *Cell-Penetrating Peptides, Processes and Applications* (Langel, Ü. ed) pp 53−70, CRC Press, Boca Raton.
(35) Gräslund, A., and Eriksson, G. (2002) Biophysical studies of cell-penetrating peptides. In *Cell-Penetrating Peptides, Processes and Applications* (Langel, Ü., Ed.) pp 223−244, CRC Press, Boca Raton.
(36) Krauss, U., Müller, M., Stahl, M., and Beck-Sickinger, A. G. (2004) In vitro gene delivery by a novel human calcitonin (hCT)-derived carrier peptide. *Bioorg. Med. Chem. Lett. 14*, 51−54.
(37) Christiaens, B., Grooten, J., Reusens, M., Joliot, A., Goethals, M., Vandekerckhove, J., Prochiantz, A., and Rosseneu, M. (2004) Membrane interaction and cellular internalization of penetratin peptides. *Eur. J. Biochem. 271*, 1187−1197.
(38) Lindgren, M. E., Hällbrink, M. M., Elmquist, A. M., and Langel, Ü. (2004) Passage of cell-penetrating peptides across a human epithelial cell layer in vitro. *Biochem. J. 377*, 69−76.
(39) Dunn, W. A., Hubbard, A. L., and Aronson, N. N., Jr. (1980) Low temperature selectively inhibits fusion between pinocytic vesicles and lysosomes during heterophagy of ^{125}I-asialofetuin by the perfused rat liver. *J. Biol. Chem. 255*, 5971−5978.
(40) Nichols, B. J., and Lippincott-Schwartz, J. (2001) Endocytosis without clathrin coats. *Trends Cell Biol. 11*, 406−412.
(41) Eguchi, A., Akuta, T., Okuyama, H., Senda, T., Yokoi, H., Inokuchi, H., Fujita, S., Hayakawa, T., Takeda, K., Hasegawa, M., and Nakanishi, M. (2001) Protein transduction domain of HIV-1 Tat protein promotes efficient delivery of DNA into mammalian cells. *J. Biol. Chem. 276*, 26204−26210.
(42) Thomsen, P., Roepstorff, K., Stahlhut, M., and van Deurs, B. (2002) Caveolae are highly immobile plasma membrane microdomains, which are not involved in constitutive endocytic trafficking. *Mol. Biol. Cell 13*, 238−250.
(43) Gruenberg, J. (2001) The endocytic pathway: a mosaic of domains. *Nat. Rev. Mol. Cell Biol. 2*, 721−730.
(44) Conner, S. D., and Schmid, S. L. (2003) Regulated portals of entry into the cell. *Nature 422*, 37−44.

BC049938Y

Acetals as pH-Sensitive Linkages for Drug Delivery

Elizabeth R. Gillies, Andrew P. Goodwin, and Jean M. J. Fréchet*

Center for New Directions in Organic Synthesis, Department of Chemistry, University of California, Berkeley, California 94720-1460. Received June 24, 2004; Revised Manuscript Received August 11, 2004

pH-Sensitive linkages designed to undergo hydrolysis at mildly acidic pH can trigger the release of therapeutics selectively at targets such as tumor and inflammatory tissues and in the endosomes and lysosomes of cells. Acetals have the potential to be used as linkages for a range of alcohol functionalities, and, by altering their chemical structure, it is possible to tune their hydrolysis rate. The syntheses of four conjugates of model drug molecules with PEO using acetals of varying chemical structure are described herein. Primary and secondary alcohols, as well as syn-1,2-diols, were incorporated in the conjugates. The hydrolysis kinetics were investigated by HPLC, and the conjugates had half-lives ranging from less than 1 min to several days at pH 5.0, with slower hydrolysis at pH 7.4 in all cases. These acetal linkages are therefore promising for use in a variety of drug delivery applications ranging from polymer−drug conjugates to pH-sensitive micelles and nanoparticulate systems.

INTRODUCTION

Research has revealed that numerous pH gradients exist in both normal and pathophysiological conditions. For example, tumor (*1*, *2*) and inflammatory tissue (*3*) have a pH slightly more acidic than the blood and normal tissue. In addition, although the endocytic pathway of cells begins near the physiological pH of 7.4, it drops to a lower pH of 5.5−6.0 in endosomes and approaches pH 4.5−5.0 in lysosomes (*4*). Therefore, pH-responsive systems can potentially be exploited in a broad range of drug delivery applications. It has been shown for example that attachment of anticancer drugs to high molecular weight polymers can significantly improve their solubility, circulation half-lives, and tumor targeting (*5*). However, as the drug is often not active in its conjugated form, it is necessary to design methods to release the drug selectively in tumor tissue or upon uptake of the polymer therapeutic by endocytosis. Furthermore, for the delivery of biomacromolecules such as proteins and DNA that are sensitive to enzymatic degradation in lysosomes, researchers have been working to develop systems that are capable of rapidly releasing biomolecules from mildly acidic endosomes prior to reaching lysosomes (*6*−*8*).

To successfully engineer systems that release therapeutic molecules under the mildly acidic conditions accessible physiologically, it is necessary to have a set of linkages available that can be used with a variety of functional groups and that are responsive to subtle changes in pH. Several acid-sensitive linkages have been tested in recent years for the development of polymer−drug or antibody−drug conjugates. For example, Greenfield and co-workers (*9*, *10*) have investigated various hydrazone linkages for the conjugation of the ketone group of doxorubicin to hydrazides. These hydrazones have also been exploited by several other groups (*11*−*14*). They typically have half-lives of several hours at pH 4.5, depending on the specific structure. *cis*-Aconityl linkages have been used for conjugation of the amino group of doxorubicin onto polymers and antibodies (*15*−*17*). The reported half-life of this linkage is 3 h at pH 4 (*15*). Trityl groups have also been used for the conjugation of amine-containing moieties onto carriers with variable half-lives ranging from 2 to 26 h at pH 5.4 depending on the substitution on the aromatic groups of the trityl linkage (*18*, *19*). Ortho esters have been used for the preparation of acid-sensitive polymers (*20*) and lipids (*21*), and as protein cross-linking agents (*22*).

Acetals are promising candidates for the development of acid-sensitive linkages for hydroxyl groups because their hydrolysis is generally first order relative to the hydronium ion, making the expected rate of hydrolysis 10 times faster with each unit of pH decrease (*23*). In addition, acetals can be formed using a variety of types of hydroxyl groups including primary, secondary, tertiary, and syn-1,2- and -1,3-diols, and the rate of hydrolysis can be tuned by varying the structure of the acetal. Despite this, there are only a few reports of acetals applied as protein cross-linking agents (*22*, *24*) and as pH-sensitive protecting groups masking anticancer drug activity (*25*−*27*). Therefore, the goal of this work is to broadly explore the usefulness of acetals as pH-sensitive linkages for drug delivery. In particular, we are interested in developing methods for the conjugation of drug hydroxyl groups to polymers. Here we report the design, synthesis, and hydrolysis studies of four different acetal-based conjugates using model drugs and polymers. These conjugates are composed of various acetal structures, different types of alcohol groups and display a broad range of hydrolysis rates at mildly acidic pH.

MATERIALS AND METHODS

General Procedures and Materials. Unless otherwise noted, materials were obtained from commercial suppliers and used without further purification. THF was distilled from Na/benzophenone, and CH_2Cl_2 and pyridine were distilled from CaH_2 prior to use. NMR chemical shifts are reported in ppm and calibrated against residual solvent signals of $CDCl_3$ (δ 7.26, 77.2). All coupling constants are reported in Hz. For NMR spectra of compounds containing acid-sensitive groups, the $CDCl_3$

* To whom correspondence should be addressed. E-mail: frechet@cchem.berkeley.edu.

10.1021/bc049853x CCC: $27.50 © 2004 American Chemical Society
Published on Web 10/09/2004

was dried and neutralized by filtering over activated basic alumina immediately prior to use. FT-IR spectroscopic analyses were performed using a thin film from CH_2Cl_2 on a reflective mirror surface and are reported in cm^{-1}. FAB mass spectrometry was performed at the UC Berkeley Mass Spectrometry Facilities. MALDI-TOF MS was performed on a Voyager-DE from PerSeptive Biosystems using *trans*-3-indoleacrylic acid as a matrix. Elemental analyses were performed at the UC Berkeley Micro-Mass Facilities.

5-Hydroxymethyldihydrofuran-2-one (2). Pentenoic acid (4.0 g, 1.0 equiv, 40 mmol) was added to a stirring biphasic mixture of 30% hydrogen peroxide (6.3 mL, 1.4 equiv, 56 mmol) in water, 125 mL of chloroform, and methyltrioxorhenium (VII) (0.30 g, 0.03 equiv, 1.2 mmol). The reaction was stirred at room temperature for 40 h, during which time the yellow solution became colorless. A saturated solution of sodium carbonate in water (50 mL) was added, and the aqueous layer was extracted with chloroform/2-propanol (1:1). The organic layers were dried with $MgSO_4$, filtered, and evaporated yielding 4.1 g (89%) of **2** as a colorless oil. Spectral data agreed with those previously reported in the literature (*28*).

Benzoic Acid 5-Oxotetrahydrofuran-2-ylmethyl Ester (3). Benzoyl chloride (0.79 g, 1.2 equiv, 5.6 mmol) was added to a solution of **2** (0.54 g, 1.0 equiv, 4.7 mmol) in dry pyridine (8 mL) at 0 °C. The mixture was stirred at room temperature for 30 min and then heated at reflux for 90 min. The solution was then diluted with CH_2Cl_2 and washed twice with 1 M $NaHSO_4$, twice with a 10% Na_2CO_3, and then saturated brine. The organic layers were dried with $MgSO_4$, filtered, and evaporated. The resulting product was diluted with dichloromethane and filtered through a silica gel plug. Evaporation of the solvent provided 0.92 g (89%) of **3** as a colorless oil. Spectral data agreed with those previously reported in the literature (*29*).

Benzoic Acid 5-Methoxytetrahydrofuran-2-ylmethyl Ester (4). A solution of **3** (0.52 g, 2.4 mmol) in 6 mL of dry THF was cooled to −78 °C, and then 4.25 mL of 1 M diisobutylaluminum hydride in hexane was added dropwise over 1 h with the temperature not exceeding −70 °C. The reaction mixture was stirred for 30 min, and then water was added slowly to the mixture until bubbling ceased followed by 2 mL of 6 M HCl to dissolve solids. The product was warmed to room temperature and extracted twice with diethyl ether. The ether solution was dried over $MgSO_4$, filtered, and evaporated. Immediately, the colorless liquid was dissolved in a 0.2% solution of HCl in methanol and stirred for 30 min. The solution was neutralized by addition of a 5% solution of KOH in methanol and then concentrated in vacuo. The product was taken up in benzene, filtered, and concentrated again. The residue was then purified via silica gel chromatography using hexane/ethyl acetate (19:1) as an eluent to yield 0.78 g (68%) of **4** as a mixture of cis and trans diastereomers (approximately 1:1) as a colorless oil. Spectral data agreed with those previously reported in the literature (*30*).

4-Nitrophenyl Carbonate-Activated PEO (7). Poly(ethylene glycol) monomethyl ether (**6**) (2.0 g, 1.0 equiv, 1.0 mmol) with a peak MW of 2100 according to MALDI-TOF MS was dissolved in 20 mL of dry CH_2Cl_2. Dry pyridine (0.64 mL, 8.0 equiv, 8.0 mmol) was added, followed by 4-nitrophenyl chloroformate (0.80 g, 4.0 equiv, 4.0 mmol). The reaction mixture was stirred at room temperature overnight and then precipitated into 200 mL of diethyl ether two times. The product was dissolved in benzene, pyridinium salts were filtered off, and the resulting solution was precipitated again into diethyl ether to provide 1.5 g (75%) of **7** as a white powder. IR: 3115, 3075, 1767, 1510. ^1H NMR (500 MHz, $CDCl_3$): δ 3.29 (s, 3H), 3.56 (br s, 190H), 4.35−4.37 (m, 2H), 7.30−7.37 (m, 2H), 8.19−8.22 (m, 2H). MS calcd for $[M]^+$ based on the peak MW of the starting material: 2266. Found: (MALDI-TOF MS): 2266.

Tetrahydrofuranylmethyl Acetal-Activated PEO (8). Acetal **4** (0.15 g, 0.64 mmol) was added to a 1.0 wt % solution of KOH in methanol and the solution stirred at room temperature for 1 h. The methanol was removed gently under vacuum, and the resulting oil was partitioned between dichloromethane and water. The aqueous layer was extracted with CH_2Cl_2, and the combined organic layers were dried over $MgSO_4$, filtered, and evaporated. Without further purification, the oil (**5**) (75 mg, 1.5 equiv, 0.57 mmol) was dissolved in 3 mL of dry CH_2Cl_2. To this solution were added carbonate **7** (0.82 g, 1.0 equiv, 0.38 mmol) and *N*,*N*-dimethyl-4-aminopyridine (0.66 g, 1.4 equiv, 0.54 mmol). The solution was stirred at room temperature for 72 h, and then the product was precipitated into cold diethyl ether providing 0.68 g (83%) of **8** as a mixture of cis and trans diastereomers (approximately 1:1) as a white powder. IR: 1746. ^1H NMR (500 MHz, $CDCl_3$): δ 1.55−2.08 (m, 4), 3.24 (s, 2H), 3.26 (s, 1H), 3.30 (s, 3H), 3.41−3.74 (m, 190H), 4.01−4.13 (m, 2H), 4.20−4.27 (m, 4H), 4.91 (br d, 0.4H, J = 4.5), 4.97 (br d, 0.6H, J = 4.5). MS calcd for $[M + Na]^+$ based on the peak MW of the starting material: 2282. Found: (MALDI-TOF MS): 2284.

Podophyllotoxin−PEO Acetal Conjugate (10). Podophyllotoxin (**9**) (30 mg, 72 μmol) and **8** (0.12 g, 56 μmol) were dissolved in 1 mL of dry toluene. The solution was heated to 110 °C, and then *p*-toluenesulfonic acid (0.50 mg, 0.05 equiv, 3.0 μmol) was added. The mixture was stirred for 3 h at 110 °C with a distillation head for azeotropic removal of methanol, and then the reaction was quenched by addition of 100 μL of NEt_3. The solvent was removed in vacuo, and the resulting solid was purified by silica gel chromatography using ethyl acetate/methanol (80:20) with 2% NEt_3 as an eluent to yield 0.11 g (80%) of **10** as a mixture of stereoisomers as a white powder. IR: 3510, 1775, 1747. ^1H NMR (400 MHz, $CDCl_3$): δ 1.58−2.28 (m, 4), 2.68−2.82 (m, 1), 2.97−3.09 (m, 1), 3.30−3.78 (m, 400), 3.98−4.25 (m, 8), 4.40−4.59 (m, 2), 4.80−5.44 (m, 1), 5.88−5.95 (m, 2), 6.32 (d, 2, J = 4), 6.44 (d, 1, J = 4), 6.82−7.27 (m, 1). MS calcd for $[M + Na]^+$ based on the peak MW of the starting material: 2664. Found: (MALDI-TOF MS): 2665.

2-(7-Methoxyoct-6-enyl)-isoindole-1,3-dione (14). A suspension of the phosphonium salt **12**, prepared as previously reported (*31*) (0.45 g, 1.5 equiv, 1.3 mmol) in 5 mL of dry THF, was cooled to −43 °C under nitrogen in a dry ice/acetonitrile bath. 0.52 mL (1.0 equiv, 0.84 mmol) of a 1.6 M solution of ^{n}BuLi in hexanes was added dropwise resulting in a deep red color. The reaction mixture was stirred at −43 °C for 1 h, and then a solution of 6-bromohexanal (**11**) (*32*) (0.15 g, 1.0 equiv, 0.84 mmol) in 2.5 mL of dry THF was added. The reaction mixture was stirred for 10 min before allowing it to come to room temperature. It was then diluted with diethyl ether and extracted with water, and the aqueous layer was extracted two times with diethyl ether. The ether layers were combined and dried with $MgSO_4$, filtered, and evaporated. The crude product was partially purified by silica gel chromatography using hexanes with 2% triethylamine as an eluent to provide 136 mg of the enol ether **13** containing a triphenylphosphine impurity. The

product was taken to the next step without further purification.

The enol ether was dissolved in 1 mL of DMF, and potassium phthalimide (0.34 g, 3.0 equiv, 1.8 mmol) was added. The reaction mixture was stirred at room temperature overnight and then was diluted with CH_2Cl_2 and washed with water to remove DMF. The organic phase was dried with $MgSO_4$ and then evaporated. The resulting material was purified by silica gel chromatography using hexanes/ethyl acetate (95:5) with 2% triethylamine as an eluent to provide 155 mg (27% yield over two steps) of **14** as a mixture of *E* and *Z* stereoisomers (approximately 1:1) as a colorless oil. IR: 1772, 1710, 1615. ^{1}H NMR (400 MHz, $CDCl_3$): δ 1.33−1.38 (m, 4H), 1.62−1.67 (m, 2H), 1.73 (s, 1.6H), 1.77 (s, 1.4H), 1.92−2.06 (m, 2H), 3.44 (s, 1.6H), 3.50 (s, 1.4H), 3.63−3.68 (m, 2H), 4.31 (t, 0.6H, J = 7.3 Hz), 4.36 (td, 0.4H, J = 1.0, 7.2), 7.67−7.72 (m, 2H), 7.79−7.84 (m, 2H). ^{13}C NMR (100 MHz, $CDCl_3$): δ 16.2, 17.5, 24.5, 26.4, 26.6, 26.8, 28.6, 29.6, 30.5, 38.1, 38.2, 54.0, 55.7, 96.4, 108.4, 123.2, 123.3, 132.29, 132.31, 133.9, 134.0, 151.1, 153.4, 168.5. MS calcd $[M]^+$ ($C_{17}H_{21}NO_3$): 287. Found: (FABLR) 287. Anal. Calcd for $C_{17}H_{21}NO_3$: C, 71.06; H, 7.37; N, 4.87. Found: C, 70.85; H, 7.24; N, 4.86.

5-Flouro-2′-deoxyuridine Acetal Conjugate (16). 5-Fluoro-2′-deoxyuridine **15** (10 mg, 1.0 equiv, 40 μmol) and the enol ether **14** were dissolved in dry THF and 100 μL of a 3.5 mg/mL solution of *p*-toluenesulfonic acid were added. The reaction was stirred at room temperature for 15 min and then quenched with 100 μL of NEt_3. The solvent was evaporated and the product was purified by silica gel chromatography using CH_2Cl_2 with 2% MeOH and 2% NEt_3 as an eluent and then again using EtOAc with 2% MeOH and 2% NEt_3 to provide 11 mg (50%) of the acetal **16** as a mixture of diastereomers (approximately 1:1) along with a small amount of triethylamine salt. IR: 3444, 3200, 3064, 1770, 1711. ^{1}H NMR (400 MHz, $CDCl_3$): δ 1.32−1.36 (m, 9H), 1.62−1.73 (m, 4H), 2.19−2.25 (m, 1H), 2.43−2.48 (m, 1H), 3.21 (s, 3H), 3.61−3.74 (m, 4H), 4.14−4.17 (m, 1H), 4.51−4.59 (m, 1H), 6.36 (t, 1H, J = 6.2), 7.71−7.74 (m, 2H), 7.84−7.86 (m, 2H), 8.24 (d, 1H, J = 6.4). ^{13}C NMR (100 MHz, $CDCl_3$): δ 14.4, 15.0, 21.3, 21.5, 23.9, 24.2, 26.7, 26.8, 28.3, 28.5, 29.1, 29.4, 36.8, 36.9, 38.0, 38.1, 41.5, 45.9, 48.7, 59.9, 60.1, 71.5, 71.8, 85.7, 86.4, 102.7, 123.4, 123.5, 124.8 (d, J = 34), 132.2, 132.3, 134.1, 134.2, 140.8 (d, J = 238 Hz), 149.1, 149.2, 157.2 (d, J = 27), 168.7, 168.9. MS calcd $[M + H]^+$ ($C_{26}H_{32}FN_3O_8$): 534. Found: (FABLR) 534.

5-Flouro-2′-deoxyuridine−PEO Acetal Conjugate (18). The phthalimide **16** (22 mg, 41 μmol) was dissolved in 5 mL of 0.2 M hydrazine in MeOH containing 0.1 mL of NEt_3. The reaction was stirred at room temperature overnight, and then the volatile compounds were removed under vacuum. Without further purification, the resulting amine **17** (1.5 equiv) was combined with **7** (60 mg, 1.0 equiv, 28μmol), *N*,*N*-(dimethylamino)pyridine (1.0 mg, 0.30 equiv, 8.3 μmol) and NEt_3 (4.5 mg, 1.6 equiv, 44 μmol) in 2 mL of 1:1 Benzene/DMF and the reaction was stirred at room temperature overnight. The solvents were then removed under vacuum and the product was purified by silica gel chromatography using CH_2Cl_2 containing 2% MeOH and 2% NEt_3 as an eluent to provide 30 mg (45%) of **18** as a glassy solid. IR: 3335, 1707, 1522, 1466. ^{1}H NMR (500 MHz, $CDCl_3$): δ 1.26−1.33 (m, 11H), 1.56−1.68 (m, 2H), 2.11−2.17 (m, 1H), 2.37−2.44 (m, 1H), 3.18 (s, 3H), 3.35 (s, 3H), 3.51−3.53 (m, 2H), 3.62 (br s, 190H), 4.09−4.12 (m, 2H), 4.13−4.18 (m, 2H), 4.46−4.49 (m, 1H), 4.93−5.01 (m, 0.5H), 5.08−5.14 (m, 0.5H), 5.53 (s, 1H), 6.216.31 (m, 1H), 8.18−8.27 (m, 1H). MS calcd for $[M]^+$ based on the peak MW of the starting material: 2530. Found: (MALDI TOF MS): 2529.

2-(7-Methoxyhept-6-enyl)isoindole-1,3-dione (21). This enol ether was prepared using the same procedure as for the preparation of **14**, except that (methoxymethyl)-triphenylphosphonium chloride (**19**) was used in place of **12** to provide **21** (33% over 2 steps) as a mixture of *E* and *Z* stereoisomers (approximately 1:1) as a colorless oil. IR: 3468, 3033, 1773, 1710, 1653, 1617. ^{1}H NMR (500 MHz, $CDCl_3$): δ 1.28−1.39 (m, 4H), 1.60−1.70 (m, 2H), 1.89−1.92 (m, 1H), 2.00−2.06 (m, 1H), 3.48 (s, 1.5 H), 3.56 (s, 1.5 H), 3.67 (t, 2H, J = 7.5), 4.31 (dd, 0.5 H, J = 7.3, 13.8), 4.66−4.72 (m, 0.5H), 5.85 (d, 0.5H, J = 6.0), 6.26 (d, 0.5 H, J = 13.0), 7.69−7.71 (m, 2H), 7.82−7.84 (m, 2H). ^{13}C NMR (125 MHz, $CDCl_3$): δ 23.6, 26.1, 26.4, 27.4, 28.35, 28.40, 29.2, 30.2, 37.9, 38.1, 55.8, 59.4, 102.7, 106.5, 123.08, 123.10, 132.11, 132.13, 133.77, 133.80, 146.2, 147.1, 168.4. MS calcd $[M + H]^+$ ($C_{16}H_{20}NO_3$): 274. Found: (FABLR) 274. Anal. Calcd for $C_{16}H_{19}NO_3$: C, 70.31; H, 7.01; N, 5.13. Found: C, 70.13; H, 7.19; N, 5.00%.

Tri(ethylene glycol)-Derivatized Estradiol (24). Estradiol (**22**) (0.30 g, 1.1 mmol, 1.0 equiv) was dissolved in 5 mL of DMF, and the chloride **23** (*33*) (0.30 g, 1.7 mmol, 1.5 equiv) was added followed by K_2CO_3 (0.30 g, 2.2 mmol, 2.0 equiv) and a catalytic amount of KI. The reaction mixture was heated at 110 °C overnight, cooled, diluted with CH_2Cl_2, and washed three times with 0.1 M NaOH. The organic phase was dried with $MgSO_4$, filtered, and evaporated. The product was purified by silica gel chromatography using a gradient from 70:30 to 50:50 hexanes/ethyl acetate to provide 0.26 g (57%) of **24** as a colorless oil. IR: 3460, 1725, 1607, 1500. ^{1}H NMR (500 MHz, $CDCl_3$): δ 0.76 (s, 3H), 1.13−1.20 (m, 1H), 1.24−1.51 (m, 7H), 1.64−1.72 (m, 1H), 1.79 (s, 1H), 1.84−1.88 (m, 1H), 1.91−1.95 (m, 1H), 2.05−2.12 (m, 1H), 2.13−2.18 (m, 1H), 2.27−2.31 (m, 1H), 2.78−2.88 (m, 2H), 3.37 (s, 3H), 3.53−3.55 (m, 2H), 3.64−3.74 (m, 7H), 3.83 (t, 2H, J = 4.8), 4.09 (t, 2H, J = 5.0), 6.63 (d, 1H, J = 2.5), 6.70 (dd, 1H, J = 2.5, 8.5), 7.17 (d, 1H, J = 8.5). ^{13}C NMR (125 MHz, $CDCl_3$): δ 11.2, 23.2, 26.4, 27.4, 29.9, 30.6, 36.8, 38.9, 43.3, 44.0, 50.1, 59.1, 67.4, 69.9, 70.7, 70.8, 70.9, 72.0, 81.9, 112.2, 114.7, 126.4, 132.9, 138.0, 156.7. MS calcd $[M + H]^+$ ($C_{25}H_{39}O_5$): 419. Found: (FABLR) 419. Anal. Calcd for $C_{25}H_{38}O_5$: C, 71.74; H, 9.15. Found: C, 71.40; H, 9.39%.

Estradiol Acetal Conjugate (25). Estradiol derivative **24** (115 mg, 0.28 mmol, 1.0 equiv) and enol ether **21** (150 mg, 0.55 mmol, 2.0 equiv) were dissolved in dry THF, and *p*-toluenesulfonic acid (5.0 mg, 0.030 mmol, 0.1 equiv) was added. The reaction mixture was stirred at room temperature overnight under nitrogen and then quenched by addition of 100 μL of NEt_3. The solvent was evaporated, and then the product was purified by silica gel chromatography using gradient from 90:8:2 to 70:28:2 hexanes/ethyl acetate/triethylamine to provide 80 mg (42%) of **25** as a mixture of diastereomers (approximately 1:1) as a colorless oil. IR: 3030, 1770, 1712, 1614. ^{1}H NMR (500 MHz, $CDCl_3$): δ 0.78 (s, 3H), 1.13−1.19 (m, 1H), 1.24−1.69 (m, 18H), 1.83−1.86 (m, 1H), 1.89−1.94 (m, 1H), 1.97−2.03 (m, 2H), 2.13−2.17 (m, 1H), 2.23−2.27 (m, 1H), 2.78−2.88 (m, 2H), 3.27 (s, 1.5 H), 3.29 (s, 1.5 H), 3.37 (s, 3H), 3.53−3.55 (m, 2H), 3.57−3.67 (m, 7H), 3.71−3.73 (m, 2H), 3.82 (t, 2H, J = 5.0), 4.09 (t, 2H, J = 5.0), 4.43 (t, 0.5H, J = 5.5), 4.46 (t, 0.5H, J = 5.5), 6.62 (d, 1H, J = 2.5), 6.69 (d, 1H, J = 8.8), 7.16 (dd, 1H, J = 2.5, 8.8), 7.68−7.70 (m, 2H), 7.81−7.84 (m, 2H). ^{13}C NMR (125 MHz, $CDCl_3$): δ 23.2, 23.3, 24.7, 24.9, 26.4, 26.9, 27.3, 27.4, 28.2, 28.7, 28.9, 29.19, 29.25, 29.9, 33.6,

33.9, 37.4, 37.7, 38.1, 38.7, 38.8, 43.1, 43.5, 44.06, 44.14, 50.05, 50.12, 51.8, 52.0, 59.2, 67.5, 69.9, 70.7, 70.8, 70.9, 72.1, 84.6, 86.3, 102.7, 104.4, 112.22, 112.24, 114.7, 123.3, 126.4, 132.3, 133.0, 133.1, 134.0, 138.1, 156.71, 156.73, 168.6. MS calcd $[M]^+$ ($C_{41}H_{57}NO_8$): 691. Found: (FABLR) 691. Anal. Calcd for $C_{41}H_{57}NO_8$: C, 71.17; H, 8.30; N, 2.02. Found: C, 70.95; H, 8.64; N, 1.97%.

Estradiol−PEO Acetal Conjugate (26). The same procedure was used as for the preparation of **18** to provide **26** (62%) as a glassy solid. IR: 3500, 3330, 1720, 1500. ^{1}H NMR (500 MHz, $CDCl_3$): δ 0.78 (s, 3H), 1.14−1.19 (m, 1H), 1.24−1.73 (m, 18H), 1.83−2.08 (m, 4H), 2.13−2.19 (m, 1H), 2.26−2.29 (m, 1H), 2.78−2.88 (m, 2H), 3.14−3.17 (m, 2H), 3.29 (s, 1.5 H), 3.30 (s, 1.5 H), 3.37 (s, 3H), 3.48−3.51 (m, 2H), 3.48−3.78 (m, 190H), 3.83 (t, 2H, J = 5.0), 4.09 (t, 2H, J = 5.0), 4.20 (m, 2H), 4.44 (t, 0.5H, J = 5.5), 4.46 (t, 0.5H, J = 5.5), 4.82 (s, 1H), 6.63 (d, 1H, J = 2.5), 6.69 (d, 1H, J = 8.8), 7.16 (d, 1H, J = 8.8). MS calcd for $[M + Na]^+$ based on the peak MW of the starting material: 2675. Found: (MALDI TOF MS): 2675.

2,6-Dimethoxy-4-bromooctyloxybenzaldehyde (28). 2,6-Dimethoxy-4-hydroxybenzaldehyde (**27**), prepared as previously reported (*34*) (0.50 g, 1.0 equiv, 2.7 mmol), was dissolved in 10 mL of DMF and 1,8-dibromooctane (5.1 mL, 10 equiv, 27 mmol) was added, followed by K_2CO_3 (0.45 g, 1.2 equiv, 3.3 mmol). The reaction was stirred at room temperature overnight, diluted with CH_2Cl_2, and washed with 0.1 M NaOH four times and then water. The organic phase was dried with $MgSO_4$, filtered, and evaporated. The resulting material was purified by silica gel chromatography using hexanes/ethyl acetate (60:40) as an eluent to provide 0.69 g (68%) of **28** as an off-white solid. mp: 82.5−83.5 °C. IR: 1673, 1601, 1573. ^{1}H NMR (500 MHz, $CDCl_3$): δ 1.28−1.48 (m, 8H), 1.73−1.79 (m, 2H), 1.79−1.86 (m, 2H), 3.37 (t, 2H, J = 6.8), 3.83 (s, 6H), 3.98 (t, 2H, J = 6.5), 6.03 (s, 2H). ^{13}C NMR (125 MHz, $CDCl_3$): δ 26.0, 28.1, 28.7, 29.1, 29.2, 32.8, 34.1, 56.1, 68.3, 90.7, 108.7, 164.2, 166.0, 187.8. MS calcd $[M]^+$ ($C_{17}H_{25}O_4Br$): 373. Found: (FABLR) 373. Anal. Calcd for $C_{17}H_{25}O_4Br$: C, 54.70; H, 6.75. Found: C, 54.78; H, 6.80%.

2,6-Dimethoxy-4-phthalimidooctyloxybenzaldehyde (29). The bromide **28** (0.55 g, 1.0 equiv, 1.5 mmol) was dissolved in 4 mL of DMF, and potassium phthalimide (0.82 g, 3.0 equiv, 4.4 mmol) was added. The reaction mixture was stirred at room temperature overnight, diluted with CH_2Cl_2, and washed with 0.1 M NaOH four times and then with water. The organic phase was dried with $MgSO_4$, filtered, and evaporated to provide 0.65 g (100%) of **29** as a white solid. MP: 116.5−118 °C. IR: 1770, 1700, 1677, 1600, 1575. ^{1}H NMR (500 MHz, $CDCl_3$): δ 1.29−1.36 (m, 6H), 1.39−1.46 (m, 2H), 1.61−1.68 (m, 2H), 1.71−1.78 (m, 2H), 3.64 (t, 2H, J = 7.5), 3.84 (s, 6H), 3.97 (t, 2H, J = 6.5), 6.03 (s, 2H), 7.65−7.69 (m, 2H), 7.77−7.81 (m, 2H). ^{13}C NMR (125 MHz, $CDCl_3$): δ 26.0, 26.8, 28.6, 29.09, 29.12, 29.2, 38.1, 56.1, 68.4, 90.7, 108.7, 123.2, 132.2, 134.0, 164.2, 166.0, 168.6, 187.8. MS calcd $[M + H]^+$ ($C_{25}H_{29}NO_6$): 440. Found: (FABLR) 440. Anal. Calcd for $C_{25}H_{29}NO_6$: C, 68.32; H, 6.65; N, 3.19. Found: C, 68.12; H, 6.78; N, 3.14%.

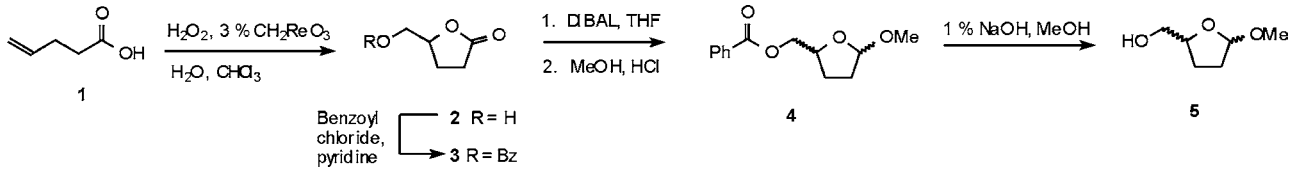
5-Fluorouridine Acetal Conjugate (31). The aldehyde **29** (91 mg, 1.0 equiv, 0.19 mmol) was dissolved in 5 mL of dry THF, and 5-fluorouridine (**30**) (100 mg, 2.0 equiv, 0.38 mmol) was added, followed by 1.5 g of 5 Å molecular sieves and *p*-toluenesulfonic acid (10 mg, 0.30 equiv, 57 μmol). The reaction was stirred at room temperature overnight and then quenched with 100 μL of NEt_3. The reaction mixture was filtered, and the filtrate was evaporated. The resulting product was purified by silica gel chromatography using a gradient from EtOAc with 2% NEt_3 to EtOAc/MeOH (95:5) with 2% NEt_3 to provide 76 mg (58%) of **31** as a mixture of diastereomers (approximately 1:1) along with a small amount of triethylamine salt. IR: 3490, 3233, 3065, 1770, 1720, 1608, 1592. ^{1}H NMR (500 MHz, $CDCl_3$): δ 1.28−1.37 (m, 6H), 1.37−1.45 (m, 2H), 1.61 (m, 2H), 1.68 (m, 2H), 3.65 (t, 2H, J = 7.5), 3.76 (s, 3H), 3.78−3.86 (m, 4H), 3.87−3.98 (m, 3H), 4.26−4.29 (m, 0.5H), 4.50−4.53 (m, 0.5H), 4.83−4.88 (m, 1H), 4.96 (dd, 0.5 H, J = 6.0, 2.5), 5.10 (t, 0.5H, J = 5.3), 6.06 (s, 1H), 5.76 (d, 0.5 H, J = 2.5), 6.06 (s, 1H), 6.08 (s, 1H), 6.14 (d, 0.5 H, J = 2.0 Hz), 6.52 (s, 0.5H), 6.75 (s, 0.5H), 7.67−7.69 (m, 2.5H), 7.80−7.84 (m, 2.5H). ^{13}C NMR (125 MHz, $CDCl_3$): δ 26.0, 26.9, 28.7, 29.2, 29.3, 29.2, 38.1, 55.9, 56.1, 62.5, 63.0, 64.6, 68.1, 70.6, 80.2, 81.7, 83.9, 84.3, 84.8, 86.1, 91.5, 91.6, 93.6, 100.3, 102.7, 102.9, 104.5, 123.3, 126.5 (d, J = 34), 126.7 (d, J = 34), 132.22, 134.1, 140.6 (d, J = 235), 149.5, 149.7, 157.7 (d, J = 26), 157.6 (d, J = 26), 160.6, 160.9, 162.2, 162.5, 168.7. MS calcd $[M + H]^+$ ($C_{34}H_{38}N_3O_{11}F$): 684. Found: (FABLR) 684.

5-Fluorouridine−PEO Acetal Conjugate (32). The same procedure was used as for the preparation of **18** to provide **32** (68%) as a glassy solid. IR: 3515, 3068, 1711, 1671, 1592. ^{1}H NMR (500 MHz, $CDCl_3$): δ 1.25−1.48 (m, 10H), 1.71−1.77 (m, 2H), 3.06−3.14 (m, 2H), 3.35 (s, 3H), 3.51−3.54 (m, 2H), 3.62 (br s, 200H), 3.73−3.85 (m, 8H), 3.88−3.98 (m, 2H), 4.16−4.19 (m, 2H), 4.27−4.30 (m, 0.5H), 4.52−4.54 (m, 0.5H), 4.84−4.91 (m, 1H), 4.94 (dd, 0.5H, J = 6.0, 3.0), 5.07−5.09 (m,0.5H), 5.81 (d, 0.5H, J = 1.0), 6.06 (s, 1H), 6.09 (s, 1H), 6.18 (s, 0.5H), 6.53 (s, 0.5H), 6.77 (s, 0.5H), 7.77 (d, 0.5H, J = 6.0), 7.91 (d, 0.5H, J = 6.0). MS calcd for $[M + Na]^+$ based on the peak MW of the starting material: 2704. Found: (MALDI TOF MS): 2705.

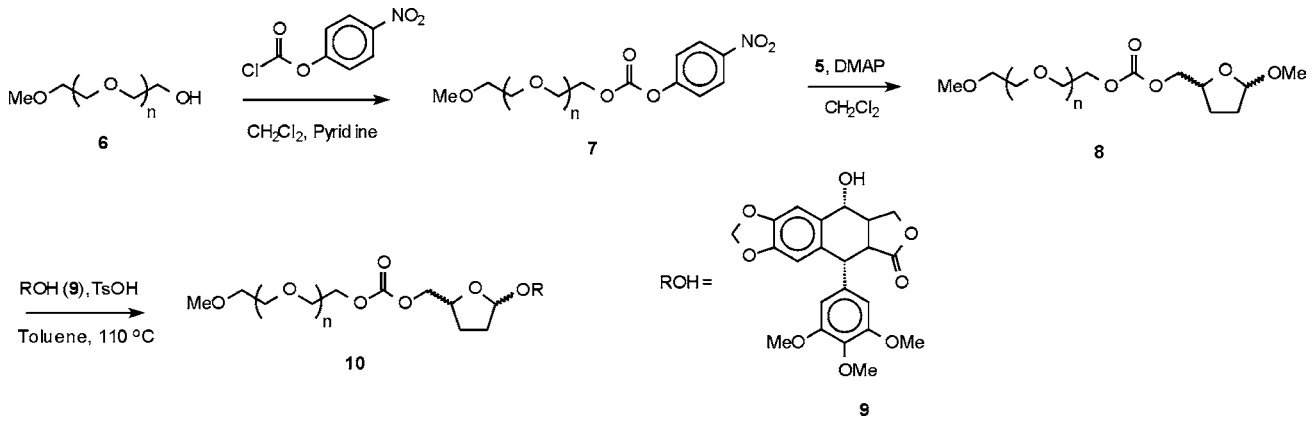
Determination of the Hydrolysis Rate for Conjugate 18. For determination of the hydrolysis rate at pH 7.4, a solution of conjugate **18** (25 μg/mL drug equiv) was incubated in 10 mM pH 7.4 phosphate buffer at 37 °C. Aliquots were removed at time points ranging from 10 min to 8 h, and the extent of hydrolysis was determined by HPLC. For determination of the hydrolysis rate at pH 5.0, a solution of conjugate **18** (250 μg/mL) was incubated in 10 mM pH 5.0 acetate buffer at 37 °C. At time points ranging from 30 s to 1 h, aliquots were removed and the hydrolysis was slowed by 10-fold dilution with 10 mM pH 7.4 buffer, followed by freezing at −4 °C. Following completion of the hydrolysis, the samples were thawed one at a time and the extent of hydrolysis was determined by HPLC. HPLC was performed at 25 °C on an Agilent 1100 series HPLC system (Agilent Technologies, Palo Alto, CA) equipped with a diode array detector and an Eclipse XDB−C8 column (4.6 × 150 mm, Agilent Technologies). The injection volume was 50 μL, the flow rate was 1 mL/min, and a gradient from 10 mM pH 7.4 phosphate buffer in H_2O to buffer/acetonitrile (35:65) over 5 min. was used as the eluent. Detection was by absorbance at 270 nm, and the % hydrolysis was determined using peak area. Errors on peak area measurements were about ±4%.

Determination of the Hydrolysis Rate for Conjugate 26. **26** was dissolved in 10 mM pH 7.4 (phosphate) or pH 5.0 (acetate) buffer at a concentration of 0.5 mg/mL drug equiv and one Eppendorf tube containing 100 μL of solution was prepared for each time point. At the desired time point, 100 μL of CH_3CN was added to the solution to dissolve any released estradiol derivative that had precipitated. The extent of hydrolysis was deter-

Scheme 1



Scheme 2



mined by HPLC as described above but using a gradient from MeOH/water (80:20) to 100% MeOH over 4 min, and detection was at 280 nm.

Determination of the Hydrolysis Rate for Conjugate 32. The hydrolysis rate for the 5-fluorouridine conjugate **32** was determined at pH 7.4 and pH 5.0 by HPLC using the same method used for **18** at pH 7.4.

RESULTS AND DISCUSSION

Design and Synthesis. The design of acetal linkages sensitive to mildly acidic conditions is facilitated by the fact that acetals are commonly used protecting groups for alcohols in organic synthesis, and their hydrolysis rates have generally been well studied and reported in the literature (*35*). However, whereas protecting groups are simply capping agents, a pH-sensitive linkage used to conjugate a polymer with a drug must be bifunctional. Thus one goal of this work was to select promising acetal candidates and to develop synthetic methods that accommodate the required bifunctional character of the linkage in order to achieve orthogonal coupling to drug on one side and polymer on the other.

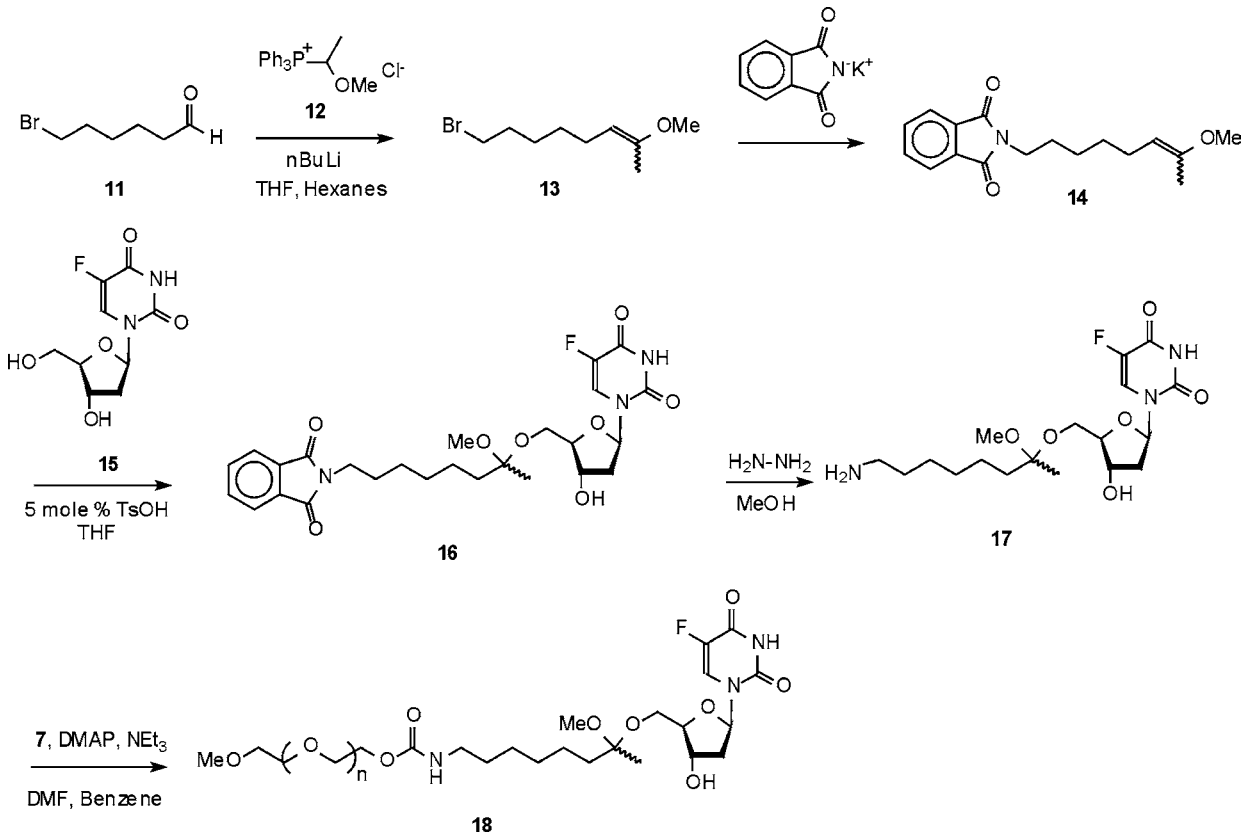
Our initial investigation of tetrahydrofuranyl (THF) acetals as drug linkages was motivated by reports in the literature of a half-life of 75 min for a THF-protected secondary alcohol at pH 5.0 and 20 °C (*36*). We proposed that acetals of this structure could be adapted for polymer conjugation by introduction of a functional handle on the 5 position of the furan ring. Thus, the synthesis of this linkage was initiated by the cyclization of 4-pentenoic acid **1** to the lactone **2** via rhenium(VII)-catalyzed oxidation as shown in Scheme 1. The free alcohol was then protected by esterification to form the benzoate **3** (Scheme 1). The lactone was reduced to the hemiacetal, which, following removal of solvent, was treated immediately with acidic methanol to provide methyl acetal **4** in an approximately 1:1 cis:trans ratio according to ^{1}H NMR spectroscopy. The benzoate could then be saponified under basic conditions to give the alcohol **5**, which was used directly in the polymer coupling step due to its relatively high volatility.

Poly(ethylene oxide) (PEO) was chosen as a model polymer because of its high water solubility and its extensive use in drug delivery applications (*37*). Poly(ethylene glycol) monomethyl ether (MW 2000 g/mol) (**6**) was first functionalized by addition of 4-nitrophenyl chloroformate to form the activated carbonate **7** as shown in Scheme 2. This carbonate could then be reacted with **5** in the presence of 4-(dimethylamino)pyridine (DMAP) to give **8**. Podophyllotoxin (**9**), an anticancer drug precursor having a secondary alcohol, was chosen as a model drug for attachment to the linker. Acid-catalyzed transacetalization conditions were employed with azeotropic removal of methanol from the reaction mixture to afford **10** as a mixture of diastereomers. The identity of **10** was confirmed by NMR spectroscopy, using comparisons with both starting materials, and by MALDI-TOF MS. Although multiple peaks exist in the mass spectrum of **10** due to the initial polydispersity of the starting PEO, end group analysis of various peaks by mass difference from the starting material, as well as a shift in the peak MW from the starting material, verifies the presence of the linkage and drug on the polymer.

The next target linkage was pursued based on literature reports of the rapid hydrolysis rates of acetals of aliphatic ketones such as acetone (*38*). Therefore, an acetal derived from acetone and a primary alcohol is expected to hydrolyze very rapidly with a half-life of about 90 s at pH 5.0 and 6 h at pH 7.4 at 25 °C. Such a fast hydrolyzing acetal would be most applicable to systems where targeting to tissues such as the tumors is quite rapid, and it should be possible to release the drug even at the very mildly acidic extracellular tumor pH.

The synthesis of this highly acid-sensitive linkage began with conversion of 6-bromohexanal **11** (*32*) to the enol ether **13** by a Wittig reaction using the phosphonium salt **12** (*31*) as shown in Scheme 3. The bromide was subsequently converted to a phthalimide by reaction with potassium phthalimide to provide **14**, containing a masked amine group for coupling to the polymer. The anticancer compound 5-fluoro-2′-deoxyuridine (**15**) was then conjugated to **14** by acid-catalyzed electrophilic addition to the enol ether to form the acetal **16** with selective reaction of the primary alcohol over the secondary alcohol of the drug. Two diastereomers of the acetal were produced in

Scheme 3



approximately a 1:1 ratio according to ^{1}H NMR spectroscopy. The phthalimide protecting group was then removed by treatment with hydrazine in MeOH containing 2% NEt_3 to give an amine **17** which was reacted with the activated polymer **7** to provide the desired conjugate **18**. The identity of the compound was verified by NMR spectroscopy and MALDI-TOF MS as for conjugate **11**. The fact that the drug was stable to the phthalimide deprotection and polymer conjugation conditions was verified by liberation of the free drug from an acidic D_2O solution and comparison of the ^{1}H NMR spectrum with that of an authentic sample of 5-fluoro-2′-dexoyuridine.

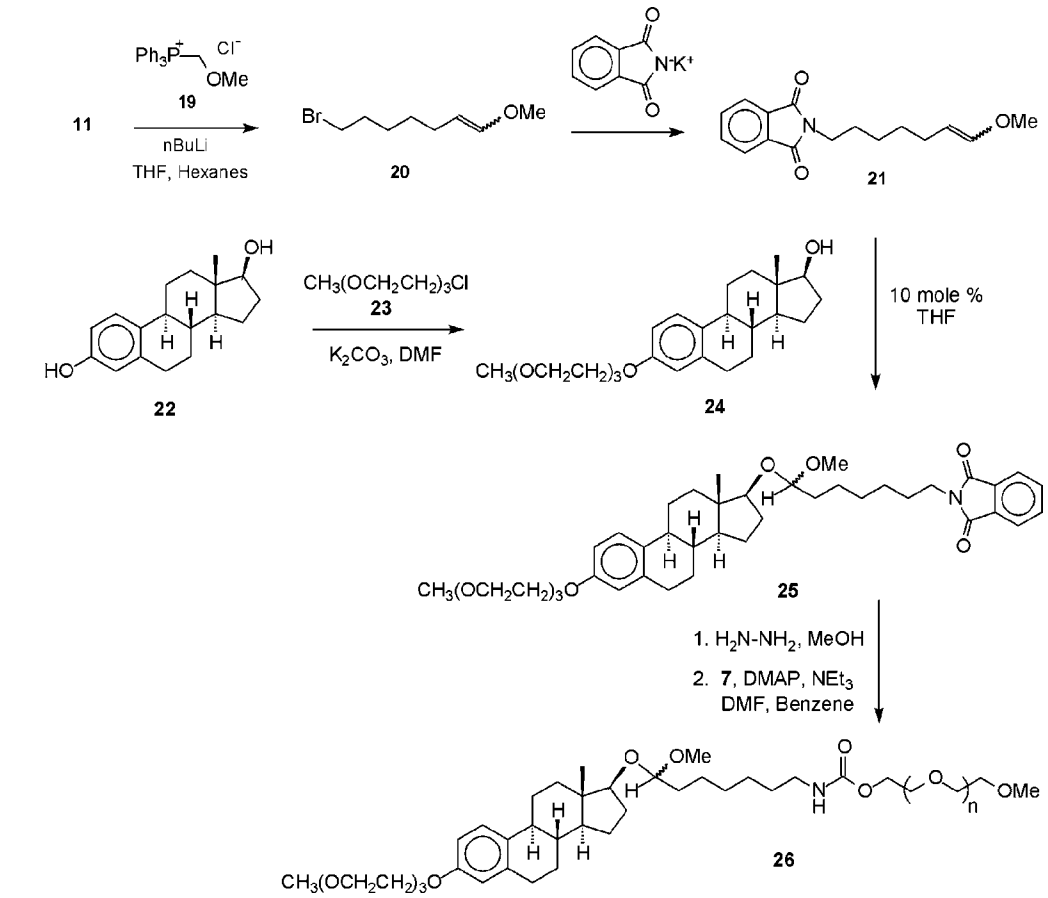
Because of the absence of the second electron-donating methyl group to stabilize the carbocation intermediate during hydrolysis, acetals of aldehydes generally hydrolyze much more slowly than those of ketones. For example, based on previous work, an acetal obtained from acetaldehyde and primary alcohols is expected to have a hydrolysis half-life of about 100 h at pH 5.0 and about 3 years at pH 7.4. (*38*). Therefore, such acetals could be useful for applications where stability over prolonged period at pH 7.4 is required. In addition, as acetals with structure **18** are too unstable to be used for the conjugation of secondary alcohols, it was hypothesized that the use of this more stable acetal might be useful for secondary alcohols and may show increased hydrolysis rates relative to those reported for primary alcohols.

To prepare this class of acetals, the enol ether **21** was prepared by a synthetic route (Scheme 4) analogous to that used for the preparation of **14**. To prepare a model drug having a secondary alcohol, the phenol of estradiol **22** was reacted with chloride **23** (*33*) to provide **24**. A tri(ethylene glycol) monomethyl ether moiety was introduced both to protect the phenol from interfering in the coupling of the secondary alcohol and also to provide enhanced water solubility to the product, a feature that would be beneficial in the subsequent kinetic study. The secondary alcohol of **24** was then smoothly conjugated to enol ether **21** in the presence of acid to provide the acetal **25** as a mixture of two diastereomers (approximately 1:1). The phthalmide protecting group was then removed, and the resulting amine was conjugated to **7** to provide the target acetal **26**.

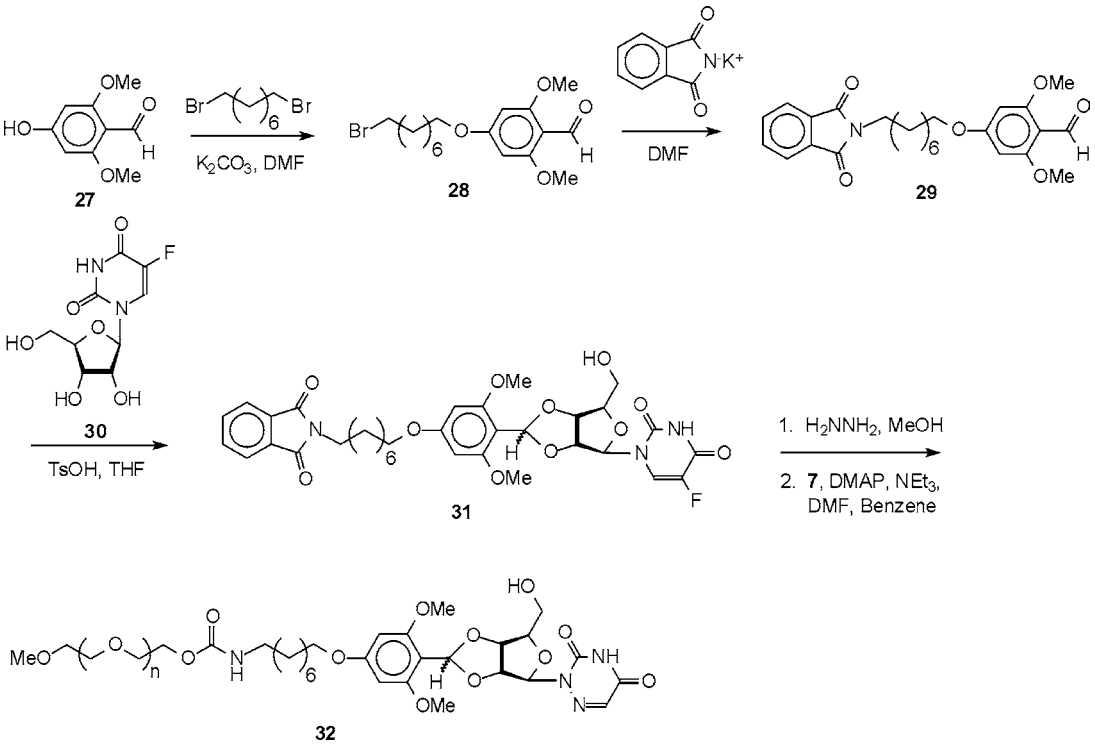
To demonstrate the versatility of acetals in the development of pH-sensitive linkages, we were also interested in preparing sensitive cyclic acetals from syn-1,2- and -1,3-diols. However, cyclic acetals based on five- and six-membered rings are known to hydrolyze very slowly relative to their acyclic counterparts (*23*). In previous work we have prepared cyclic benzylidene acetals from 1,3-diols and have found that introduction of electron-donating methoxy groups in the 2, 4, and 6 positions of the aromatic rings accelerates the rate of hydrolysis to provide a half-life of 1 h at pH 5.0 and several days at pH 7.4 (*39*). Therefore, we were interested in exploring the use of this type of cyclic acetal to prepare polymer−drug conjugates.

The synthesis of a cyclic acetal conjugate was initiated by reaction of 2,6-dimethoxy-4-hydroxybenzaldehyde (**27**) with excess 1,8-dibromooctane to provide **28**, and then the bromide was converted to a phthalimide group by reaction with potassium phthalimide, giving **29** as shown in Scheme 5. The anticancer compound 5-fluorouridine (**30**) was selected as a model drug containing a syn-1,2 diol and was converted to the cyclic acetal **31** by reaction with the aldehyde **29** in dry THF containing catalytic *p*-toluenesulfonic acid and 5 Å molecular sieves. Both cis- and trans-diastereomers were produced in approximately a 1:1 ratio. After removal of the phthalimide protecting group, the amine was coupled to the activated polymer **7** to provide the target **32**. As for all previous conjugates, the identity of this conjugate was verified by NMR and MALDI-TOF MS.

Scheme 4



Scheme 5



Determination of Acetal Hydrolysis Rates. The hydrolysis of the podophyllotoxin−PEO conjugate **10** was initially investigated by ^{1}H NMR at pH 5.0 using an acetate buffer in D_2O. Surprisingly, after 24 h at 37 °C, the NMR spectrum still showed unchanged conjugate, and no peaks corresponding to the free drug were observed. In addition, no free drug was observed by TLC after the same time period. After 11 h, a very small amount of hydrolysis was observed by TLC at pH 4.0 and somewhat more at pH 3.0, but the acetal was clearly too stable to undergo hydrolysis under the mildly acidic conditions accessible physiologically. The discrepancy

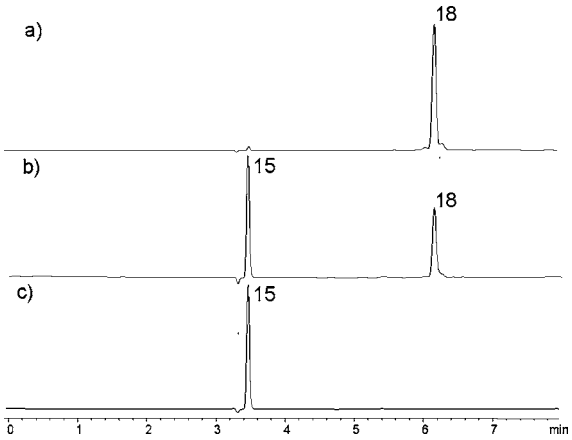


Figure 1. HPLC chromatograms of (a) conjugate **18** prior to hydrolysis; (b) conjugate **18** after 1 min. at pH 5.0; (c) 5-fluoro-2′-deoxyuridine (**15**).

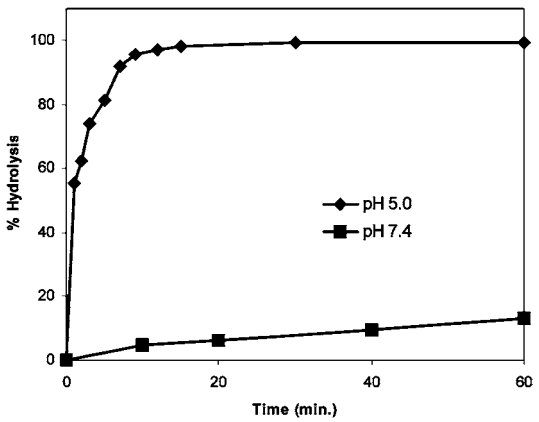


Figure 2. Hydrolysis rates for conjugate **18** at pH 5.0 and pH 7.4.

between these results and those previously reported in the literature may be due to the fact that the previous kinetic studies were performed in 1:1 THF/H_2O with HCl added to adjust to pH 5.0 (*36*). It is possible that these conditions do not extrapolate appropriately to a fully aqueous buffer system.

After initial verification by NMR spectroscopy that conjugate **18** underwent substantial hydrolysis at pH 5.0 after 10 min to afford free 5-fluoro-2′-deoxyuridine (**15**), a more detailed HPLC study of the hydrolysis rate was undertaken. Samples of **18** were dissolved in aqueous buffers of pH 7.4 and pH 5.0 and were incubated at 37 °C. Aliquots of the sample at pH 7.4 were withdrawn and directly injected into the HPLC instrument. Due to the very rapid rate of hydrolysis at pH 5.0 relative to the time required for the HPLC separation, aliquots at pH 5.0 were first neutralized by dilution with pH 7.4 buffer and then frozen until HPLC injection to prevent undesired hydrolysis prior to chromatographic analysis. An HPLC chromatogram of conjugate **18** and its hydrolysis products after 1 min at pH 5.0 is compared to a chromatogram of free drug **15** in Figure 1. Chromatographic analysis confirms that intact drug is indeed released upon hydrolysis, and that the hydrolysis rate is rapid at pH 5.0 with a half-life of less than 1 min. A comparison of the hydrolysis rates at pH 7.4 and pH 5.0 is shown in Figure 2. The results indicate that hydrolysis is nearly complete at pH 5.0 after 20 min, whereas at pH 7.4 less than 15% hydrolysis had occurred after 1 h. The observed hydrolysis rate is therefore consistent with that previously reported for acetals of similar structure (*38*).

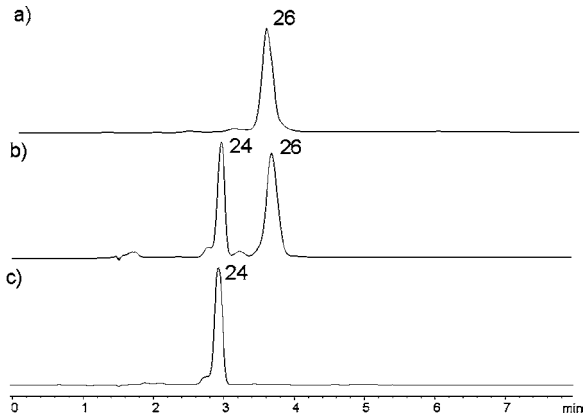


Figure 3. HPLC chromatograms of (a) conjugate **26** prior to hydrolysis; (b) conjugate **26** after 70 h at pH 5.0; (c) estradiol derivative **24**.

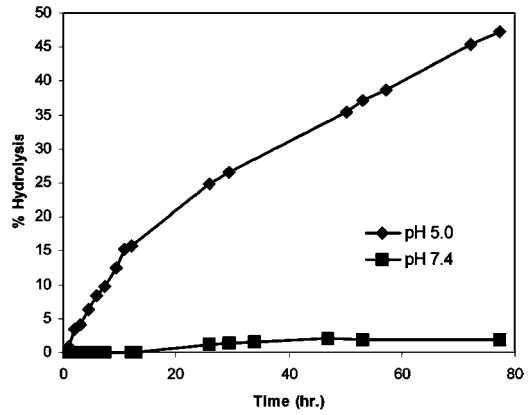


Figure 4. Hydrolysis rates for conjugate **26** at pH 5.0 and pH 7.4.

The hydrolysis of acetal **26** at pH 5.0 and 7.4 at 37 °C was also investigated by HPLC. In Figure 3, HPLC chromatograms of conjugate **26** prior to hydrolysis and after 70 h at pH 5.0 are compared to that of the estradiol derivative **24**, illustrating the gradual release of the model drug. A comparison of the hydrolysis rates at pH 7.4 and pH 5.0, as shown in Figure 4 illustrates that only a negligible amount of hydrolysis occurs at pH 7.4 over 80 h, while at pH 5.0 the half-life was found to be 88 ± 3 h. These results are also close to those reported in the literature for acetals of acetaldehyde with primary alcohols (*38*), and this work therefore shows that the rate of hydrolysis of these acetals is not significantly accelerated by conjugation of secondary rather than primary alcohols. This may be explained by the lack of steric hindrance, a factor that may contribute to accelerating the hydrolysis of other secondary alcohol derivatives.

HPLC chromatograms of the cyclic acetal conjugate **32** prior to hydrolysis, **32** after 7 h at pH 5.0 and 37 °C, and of a pure sample of 5-fluorouridine (**30**) are shown in Figure 5, and a comparison of the hydrolysis rates at pH 7.4 and pH 5.0 is shown in Figure 6. At pH 5.0, more than 70% of the drug is released after 30 h., while at pH 7.4, less than 2% of the drug is released over the same time period. A half-life of 17.6 ± 0.4 h at pH 5.0 and on the order of weeks at pH 7.4 was determined using the kinetic data. Interestingly, the hydrolysis rate of this five-membered ring cyclic acetal is significantly slower than that of the six-membered ring analogues formed from 1,3-diols such as serinol and 1,1,1-tris(hydroxymethyl)ethane that we have previously investigated (*39*). Presumably, this is due to entropic reasons associated with the five-

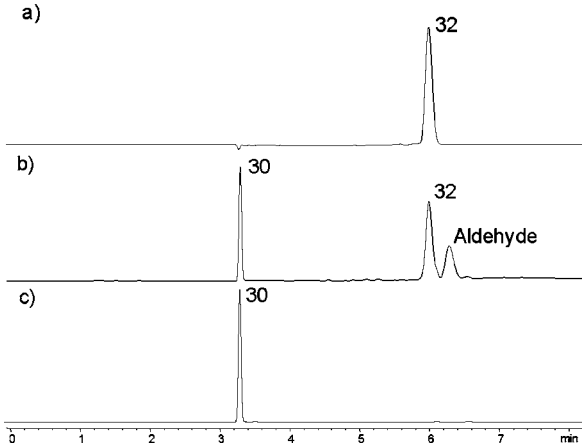


Figure 5. HPLC chromatograms of (a) conjugate **32** prior to hydrolysis; (b) **32** after 7 h. at pH 5.0; (c) 5-fluorouridine (**30**).

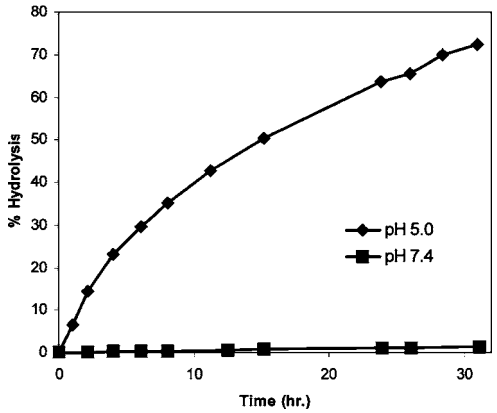


Figure 6. Hydrolysis of conjugate **32** at pH 5.0 and pH 7.4 monitored by HPLC.

membered ring and also because, for this system, free rotation about the carbon−carbon bond between alcohol groups is not permitted, in contrast to the situation that prevailed with previously investigated systems.

CONCLUSIONS

Acetals of varying chemical structure were investigated for their potential as pH-sensitive linkages in drug delivery applications. Several conjugates of model drug molecules with PEO were successfully prepared, illustrating that acetals can be applied for the conjugation of primary and secondary alcohols as well as diols. The hydrolysis rates were investigated by HPLC and half-lives ranging from less than 1 minute to several days at pH 5.0 were determined for the conjugates. In each case the conjugates showed significantly higher stability at pH 7.4. These acetals can therefore be applied as polymer−drug linkages in a variety of drug delivery applications, ranging from situations where rapid hydrolysis is desired in mildly acidic endosomes or tumor tissue to those where high stability at neutral pH accompanied by gradual drug release at acidic pH is necessary. In addition, these acetals can potentially be applied to the development of other pH-sensitive systems including micelles and nanoparticles designed to undergo pH dependent release of low MW drugs as well as proteins and DNA.

ACKNOWLEDGMENT

We thank the National Institute of Health (GM 65361 and EB 002047) for support of this research. The Center for New Directions in Organic Synthesis is supported by Bristol-Myers Squibb as a Sponsoring Member and Novartis Pharma as Supporting Member.

LITERATURE CITED

(1) Engin, K., Leeper, D. B., Cater, J. R., Thistlethwaite, A. J., Tupchong, L., and McFarlane, J. D. (1995) Extracellular pH distribution in human tumors. *Int. J. Hypertherm. 11*, 211−216.

(2) Ojugo, A. S. E., Mesheehy, P. M. J., McIntyre, D. J. O., McCoy, C., Stubbs, M., Leach, M. O., Judson, I. R., and Griffiths, J. R. (1999) Measurement of the extracellular pH of solid tumors in mice by magnetic resonance spectroscopy: a comparison of exogenous 19F and 31P probes. *NMR Biomed. 12*, 495−504.

(3) Gallin, J. I., Goldstein, I. M., and Snyderman, R. E. (1992) *Inflammation − basic principles and clinical correlates*, 2nd ed., pp 511−533.

(4) Mellman, I., Fuchs, R., and Helenius, A. (1986) Acidification of the endocytic and exocytic pathways. *Annu. Rev. Biochem. 55*, 773−700.

(5) Duncan, R. (2003) The dawning era of polymer therapeutics. *Nature Rev. 2*, 347−360.

(6) Murthy, N., Xu, M., Schuck, S., Kunisawa, J., Shastri, N., and Fréchet, J. M. J. (2003) A macromolecular delivery vehicle for protein-based vaccines: acid-degradable protein-loaded microgels. *Proc. Nat. Acad. Sci. 100*, 4995−5000.

(7) Davis, M. (2002) Nonviral gene delivery systems. *Curr. Opin. Biotechnol. 13*, 128−131.

(8) Wiethoff, C. M., and Middaugh, C. R. (2003) Barriers to Nonviral Gene Delivery. *J. Pharm. Sci. 92*, 203−217.

(9) Greenfield, R. S., Kaneko, T., Daues, A., Edson, M. A., Fitzgerald, K. A., Olech, L. J., Grattan, A., Spitalny, G. L., and Brawslawsky, G. R. (1990) In vitro evaluation of adriamycin immunoconjugates synthesized using an acid-sensitive hydrazone linker. *Cancer Res. 50*, 6600.

(10) Kaneko, T., Willner, D., Monkovic, I., Knipe, J. O., Braslawsky, G. R., Greenfield, R. S., and Dolatrai, M. V. (1991) New hydrazone derivatives of Adriamycin and their immunoconjugates − a correlation between acid stability and cytotoxicity. *Bioconjugate Chem. 2*, 133−141.

(11) Etrych, T., Jelínková, M., Rihová, B., and Ulbrich, K. (2001) New HPMA copolymers containing doxorubicin bound via pH-sensitive linkage: synthesis and preliminary in vitro and in vivo biological properties. *J. Controlled Release 73*, 89−102.

(12) Kruger, M., Beyer, U., Schumacher, P., Unger, C., Zahn, H., and Kratz, F. (1997) Synthesis and stability of four maleimide derivatives of the anticancer drug doxorubicin for the preparation of chemoimmunoconjugates. *Chem. Pharm. Bull. 45*, 399−401.

(13) Rodrigues, P. C. A., Beyer, U., Schumacher, P., Roth, T., Fiebig, H. H., Unger, C., Messori, L., Orioli, P., Paper, D. H., Mulhaupt, R., and Kratz, F. (1999) Acid-sensitive polyethylene glycol conjugates of doxorubicin: preparation, in vitro efficacy and intracellular distribution. *Bioorg. Med. Chem. 7*, 2517−2524.

(14) Padilla De Jesús, O. L., Ihre, H. R., Gagne, L., Fréchet, J. M. J., and Szoka, F. C. J. (2002) Polyester Dendritic Systems for Drug Delivery Applications: In Vitro and In Vivo Evaluation. *Bioconjugate Chem. 13*, 453−461.

(15) Shen, W. C., and Ryser, H. J. P. (1981) cis-Aconityl spacer between daunomycin and macromolecular carriers − a model of pH-sensitive linkage releasing drug from a lysosomotropic conjugate. *Biochem. Biophys. Res. Commun. 102*, 1048−1054.

(16) Choi, W. M., Kopecková, P., Minko, T., and Kopecek, J. (1999) Synthesis of HPMA copolymer containing adriamycin bound via and acid-labile spacer and its activity toward human ovarian carcinoma cells. *J. Bioact. Compat. Polym. 14*, 447−456.

(17) Hudecz, F., Ross, H., Price, M. R., and Baldwin, R. W. (1990) Immunoconjugate design: a predictive approach for coupling of daunomycin to monoclonal antibodies. *Bioconjugate Chem. 1*, 197−204.

(18) Patel, V. F., Hardin, J. N., Mastro, J. M., Law, K. L., Zimmerman, J. L., Ehlhardt, W. J., Woodland, J. M., and Starling, J. J. (1996) Novel acid labile COL1 trityl-linked

difluoronucleoside immunoconjugate: synthesis, characterization, and biological activity. *Bioconjugate Chem. 7*, 497−510.
(19) Patel, V. F., Hardin, J. N., Starling, J. J., and Mastro, J. M. (1995) Novel trityl linked drug immunoconjugates for cancer-therapy. *Bioorg. Med. Chem. Lett. 5*, 507−512.
(20) Heller, J., Barr, J., Ng, S. Y., Abdellauoi, K. S., and Gurny, R. (2002) Poly(ortho esters): synthesis, characterization, properties and uses. *Adv. Drug Delivery Rev. 54*, 1015−1039.
(21) Guo, X., and Szoka, F. C. J. (2001) Steric stabilization of fusogenic liposomes by a low-pH sensitive PEG-diortho ester-lipid conjugate. *Bioconjugate Chem. 12*, 291−300.
(22) Srinivasachar, K., and Neville, D. M. (1989) New protein cross-linking reagents that are cleaved by mild acid. *Biochemistry 28*, 2501−2509.
(23) Fife, T., and Jao, L. (1965) Substituent effects in acetal hydrolysis. *J. Org. Chem. 30*, 1492−1495.
(24) Neville, D. M., Srinivasachar, K., Stone, R., and Scharff, J. (1989) Enhancement of immunotoxin efficacy by acid-cleavable cross-linking agents utilizing diphtheria-toxin and toxin mutants. *J. Biol. Chem. 264*, 14653−14661.
(25) Tietze, L. F., Neumann, M., Möllers, T., Fischer, R., Glüsenkamp, K.-H., Rajewsky, M. F., and Jähde, E. (1989) Proton-mediated liberation of aldophosphamide from a non-toxic prodrug: a strategy for tumor-selective activation of cytocidal drugs. *Cancer Res. 49*, 4179−4184.
(26) Jähde, E., Glüsenkamp, K.-H., Klünder, I., Hülser, D. F., Tietze, L. F., and Rajewsky, M. F. (1989) Hydrogen ion-mediated enhancement of cytotoxicity of bis-chloroethylating drugs in rat mammary carcinoma cells in vitro. *Cancer Res. 49*, 4179−4184.
(27) Tietze, L. F., Beller, M., Fischer, R., Lögers, M., Jähde, E., Glüsenkamp, K.-H., and Rajewsky, M. F. (1990) Development of tailor-made cytostatics activable by acid-catalyzed hydrolysis for selective tumor therapy. *Angew. Chem., Int. Ed. Engl. 29*, 782−783.
(28) Tan, H., and Espenson, J. H. (1999) Regioselective hydroxylactonization of γ,δ-unsaturated carboxylic acids with hydrogen peroxide catalyzed by methyltrioxorhenium. *J. Mol. Catal. A 142*, 333−338.
(29) Mihelic, D., Jakse, R., Svete, J., Stanovnik, B., and Grdadolnik, S. G. (2001) Synthesis of (S)-3-heteroaryl-2-hydroxy-1-propylbenzoates by "ring switching" methodology. *J. Heterocycl. Chem. 38*, 1307−1312.
(30) Lee-Ruff, E., Xi, F., and Qie, J. H. (1996) Enantioselective preparation of 2′, 3′-dideoxynucleosides and their analogues from ring expansion of cyclobutanones. 2. Synthesis of 2′, 3′-dideoxyribosides and (1S, 3R)-1-amino-3-(hydroxymethyl)-cyclopentane. *J. Org. Chem. 61*, 1547−1550.
(31) Coulson, R. D. (1964) New synthesis of methyl ketones. *Tetrahedron Lett.* 3323−3326.
(32) Khanapure, S. P., Kim, S., Penrose, J. F., Austen, K. F., Powell, W. S., and Rokach, J. (2002) An efficient approach to the synthesis of LTB_4 and w-substituted LTB_4 metabolites. *Tetrahedron Lett. 43*, 6063−6066.
(33) Loth, H., and Foltin, U. (1998) Methoxy-polyethoxy side-chain silastomers as materials controlling drug delivery by diffusion flux. *J. Controlled Release 54*, 273−282.
(34) Albericio, F., Kneib-Cordonier, N., Biancalana, S., Gera, L., Masada, R. I., Hudson, D., and Barany, G. (1990) Preparation and application of the 5-(4-(9-fluorenylmethyloxycarbonyl)aminomethyl-3,5-dimethoxyphenoxy)-valeric acid (PAL) handle for the solid-phase synthesis of C-terminal peptide amides under mild conditions. *J. Org. Chem. 55*, 3730−3743.
(35) Greene, T. W., and Wuts, P. G. M. (1999) Protective groups in organic synthesis, 3rd ed., pp 57−58.
(36) Kruse, C. G., Jonkers, F. L., Dert, V., and van der Gen, A. (1979) Synthetic applications of 2-chlorotetrahydrofuran: protection of alcohols as tetrahydro-2-furanyl (THF) ethers. *Recl. Trav. Chim. Pays-Bas. 98*, 371−380.
(37) Greenwald, R. B., Conover, C. D., and Choe, Y. H. (2000) Poly(ethylene glycol) conjugated drugs and prodrugs: a comprehensive review. *Crit. Rev. Ther. Drug 17*, 101−161.
(38) Kreevoy, M. M., and Taft, R. W. J. (1955) The evaluation of inductive and resonance effects on reactivity. I. Hydrolysis rates of acetals of nonconjugated aldehydes and ketones. *J. Am. Chem. Soc. 77*, 5590−5595.
(39) Gillies, E. R., and Fréchet, J. M. J. (2003) A new approach towards acid sensitive copolymer micelles for drug delivery. *Chem. Commun.* 1640−1641.

BC049853X

Site-Specifically Traced Drug Release and Biodistribution of a Paclitaxel–Antibody Conjugate toward Improvement of the Linker Structure[1]

Ahmad Safavy,*[,†,‡] Gunda I. Georg,[||] David Vander Velde,[||] Kevin P. Raisch,[†,‡] Kamellia Safavy,[⊥] Mark Carpenter,[#] Wenquan Wang,[‡,▽] James A. Bonner,[†,‡] M. B. Khazaeli,[†,‡] and Donald J. Buchsbaum[†,‡]

Departments of Radiation Oncology and Medicine, Biostatistics and Bioinformatics Unit, and Comprehensive Cancer Center, University of Alabama at Birmingham, Birmingham, Alabama 35294, Department of Medicinal Chemistry, University of Kansas, Lawrence, Kansas 66045, and Department of Discrete and Statistical Science, Auburn University, Auburn, Alabama 36849. Received June 8, 2004; Revised Manuscript Received August 16, 2004

Tumor-directed drug delivery is a promising strategy in cancer treatment, and in this field, monoclonal antibodies constitute an important class of targeting vehicles. A critical issue in the design of targeting conjugates is the timing of the release of the cytotoxic payload, with the ideal situation being the release at the maximum tumor uptake of the targeting molecule. A site-specific radiolabeling technique was used to elucidate the biodistribution and in vivo drug release pattern of an antibody conjugate of paclitaxel (PTX, **1**, Figure 1) in which the drug and the antibody moieties were connected by a succinate (SX) linker. In this new method, a metabolite of PTX, 3′-(4-hydroxyphenyl)paclitaxel (3′-OH-PTX, **2**, Figure 1) was used as a tyrosine mimic for the synthesis of the drug site-labeled conjugate (DSL, [^{125}I]-3′-OH-PTXSXC225). This was achieved by iodogen ^{125}I-labeling of 3′-OH-PTXSX and subsequent conjugation to C225. The antibody site-labeled conjugate (ASL, PTXSX-[^{125}I]-C225) was prepared by direct radioiodination of PTXSXC225. Biodistribution of these compounds was studied in *Balb/c* nude mice bearing DU-145 human prostate carcinoma xenografts. While the 4 and 24 h tumor uptake (in percent injected dose per gram of tissue, %ID/g) for [^{125}I]-3′-OH-PTXSXC225 were 3.3 ± 1.5 and 1.7 ± 0.6%ID/g, the PTXSX–[^{125}I]-C225 showed tumor uptake values of 3.8 ± 4.2 and 14.8 ± 4.2%ID/g at these time points. This difference in the tumor uptake over time indicates an early cleavage of the drug with respect to the antibody tumor localization. This was further confirmed by an in vitro drug release kinetics study leading to a half-life of about 2 h for PTXSXC225 under physiological conditions. To increase the stability of the PTX–MAb bond, a new conjugate (PTXGLC225) with glutaric acid (GL) as the linker was synthesized. Under the same conditions, the PTXGLC225 showed a 16-fold increase in the half-life ($t_{1/2}$) of the drug release. The effect of the increased $t_{1/2}$ of this compound on the antitumor activity of the conjugate was tested in a DU-145 human prostate tumor-implanted mouse model. In comparison to a previous similar experiment with PTXSXC225, better antitumor activity was observed for the PTXGLC225 conjugate as compared to controls. These results demonstrated the first time use of radioiodinated 3′-OH-PTX for in vivo tracing of a paclitaxel conjugate and application of the resulting information to the design of a therapeutically more useful PTX–MAb linker.

INTRODUCTION

Monoclonal antibodies (MAbs)[2] are being utilized in tumor-targeted cancer treatment due to the potential of this strategy for efficient and specific delivery of tumoricidal agents (*1*–*5*). MAb-mediated targeted drug delivery usually involves covalent conjugation of the antitumor agent to the MAb with the latter to guide the construct for tumor localization (*6*–*8*). The benefits of this targeted strategy are expected to be 2-fold: Enhancing the antitumor efficacy of the drug due to its targeted, tumor-specific delivery, and ameliorating the systemic toxicity and side-effects due to the possibilities of reduced dosing.

* To whom correspondence should be addressed. Ahmad Safavy, Ph.D., University of Alabama at Birmingham, 1824 6th Ave. South, WTI 674, Birmingham, AL 35294-6832. E-mail: safavy@uab.edu.

† Department of Radiation Oncology, University of Alabama at Birmingham.

⊥ Department of Medicine, University of Alabama at Birmingham.

▽ Biostatistics and Bioinformatics Unit, University of Alabama at Birmingham.

‡ Comprehensive Cancer Center, University of Alabama at Birmingham.

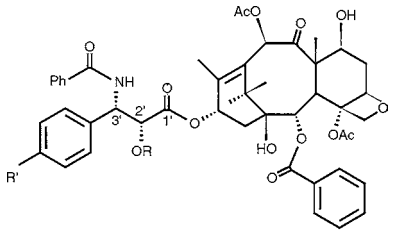
|| University of Kansas.

Auburn University.

[1] Presented in part at the AACR/NCI/EORTC conference, Boston, MA, November 17–21, 2003.

[2] Abbreviations: ASL, antibody site-labeled; DIEA, *N,N*-diisopropylethylamine; DMF, *N,N*-dimethylformamide; DSL, drug site-labeled; EEDQ, 2-ethoxy-1-ethoxycarbonyl-1, 2-dihydroquinoline; ESMS, electrospray mass spectrometry; GL, glutaric acid or glutarate; IgG, immunoglobulin; EGFR, epidermal growth factor receptor; MAb, monoclonal antibody; MALDI MS, matrix-assisted laser desorption/ionization mass spectrometry; NHS, *N*-hydroxysuccinimide; 3′-OH-PTX, 3′-(4-hydroxyphenyl)-pacliaxel; PBS, phosphate-buffered saline; PEG, poly(ethylene glycol); PTX, paclitaxel; RP-HPLC, reveresed-phase HPLC.; SX, succinic acid or succinate; SE-HPLC, size-exclusion HPLC; TAX, taxane.

10.1021/bc049868v CCC: $27.50 © 2004 American Chemical Society
Published on Web 10/08/2004



1, PTX : R = H, R' = H
2, 3'-OH-PTX : R = H, R' = OH
3, PTXSX : R = -CO(CH$_2$)$_2$CO$_2$H, R' = H

Figure 1. Structures of paclitaxel (PTX), 3′-(4-hydroxyphenyl)-paclitaxel (3′-OH-PTX) and paclitaxel-2′-succinate (PTXSX).

These seemingly straightforward expectations could not, however, be taken for granted, as important hurdles may be encountered in practice. Two important issues to be considered in the design of drug-delivering conjugates are the in vivo rate of the release of the drug from the conjugate, and the tissue distribution pattern prior to that release. An early and premature release of the drug will result in lowered or totally compromised drug efficacy. This may be particularly true of conjugates with large molecular weights such as antibodies. The observed maximum tumor uptake time for an IgG monoclonal antibody has been reported to be over 24 h (*9*−*12*). The drug segment of a conjugate intended for tumor targeting, and released within a narrower time window, therefore, will have a smaller chance of being delivered tumor-specifically. Lowered drug efficacies may be also experienced if the drug has too slow a cleavage mechanism, that is, release of the drug after the peak tumor uptake period and after the catabolism and clearance of the antibody. The latter scenario would be particularly harmful to the performance of *prodrug* conjugates, compounds in which the native drug will resume full antitumor efficacy only after cleavage from the tumor-targeting vehicle (*13*−*16*). Information on the in vivo behavior of a drug−MAb conjugate in terms of the rate of the release of the drug and the extent of tissue uptake of the targeting molecule may be, therefore, of critical importance in the design of conjugates with intended therapeutic applications. We have previously reported the synthesis and biological evaluation of conjugates of PTX to a bombesin receptor-recognizing peptide, and to the anti-EGFR MAb C225 (*17*−*19*), in which succinic acid was used as the drug−MAb linker. Improved cytotoxicities were observed for PTX in these conjugates as compared to its free, "untargeted" form in both types of conjugates. However, while compared to untreated control both C225 and PTXSXC225 showed higher antitumor activity, there was no significant advantage between C225 and the conjugate. We hypothesized that one reason could be an untimely in vivo release of the drug as a result of the low stability of the succinate linker (*19*). The aim of the present study was to design more in-depth in vitro and in vivo experiments to test this hypothesis and to compile information for the development of PTX−MAb conjugates suitable for therapeutic applications. Accordingly, comparative drug release and biodistribution studies were conducted with succinate- and glutarate-linked PTXC225 conjugates leading to the selection of the latter linker for further antitumor activity experiments. In this report, we describe the results of this investigation.

EXPERIMENTAL PROCEDURES

General. The paclitaxel-2′-*mono*-succinate (PTXSX) and -glutarate (PTXGL) were prepared according to the procedure of Deutsch et al. (22) with slight modifications as described in Results and Discussion. 3′-(4-Hydroxyphenyl)paclitaxel and C225 (Erbitux) were donated as gifts by Tapestry Pharmaceuticals, Inc. (Boulder, CO) and ImClone Systems (New York, NY), respectively. Amino poly(ethyleneglycol) carboxylate was purchased from Nektar (Huntsville, AL). [^{14}C]-2′-Benzoylpaclitaxel (50 μCi) and sodium [^{125}I]-iodide were obtained from Moravek Biochemicals (Brea, CA) and NEN Life Sciences (Boston, MA), respectively. Gel filtration chromatography was performed in PD-10 Sephadex G-25 M columns (Amersham Pharmacia AB, Uppsala, Sweden) equilibrated and eluted with phosphate-buffered saline (PBS, 10 mM, pH 6.5). Taxol was supplied by Bristol-Myers Squibb (Princeton, NJ). Radioactivity monitoring was carried out in Packard (Shelton, CT) Minaxi-Gamma (5000 Series) gamma and Packard (Meriden, CT) TRI-CARB 1900 TR scintillation counters. HPLC analyses were performed with a Beckman System Gold instrument consisting of a SG 125 solvent module and a SG 166 UV/vis detector, operated by Beckman 32 Karat Version 5.0 software. Analytical UV/radiodetected HPLC experiments used a Bio-Rad (Hercules, CA) Model 2800 solvent delivery system operated by Bio-Rad ValueChrome software and a UV-1806 UV/vis detector connected in series to a Beckman Model 170 radioisotope detector. Reversed-phase (RP) HPLC used either a 4.6 × 250 mm C18 column (Vydac, Hesperia, CA) for analytical separations or a Vydac 10 × 250 mm C18 column for semipreparative separations. Columns were eluted with 0.1% TFA/water (solvent A) and a 10% to 90% gradient of 0.1:60:40, TFA: CH_3CN:H_2O (v/v) (solvent B). Retention times (t_R) in minutes are reported for each compound, with the corresponding percent purities in parentheses. For analytical SE-HPLC, a 7.5 mm × 25 cm G3000SW column (TosoHaas, Montgomeryville, PA) was used. A 10 mM PBS containing 10 mM Na_2SO_4 at pH 6.7 was used as solvent. Sep-Pak C18 cartridges were obtained from Waters (Milford, MA). Mass spectra in ES mode were recorded either on an API VI triple quadruple mass spectrometer (PE-Sciex, Toronto, Ontario) or Micromass Platform LCZ mass spectrometer (Beverly, MA). MALDI MS were analyzed in the positive mode on a Voyager Elite mass spectrometer with delayed extraction technology (PerSeptive Biosystems, Framingham, MA). Sinapinic acid was used as matrix, and samples were prepared in a 50:50 (v/v) mixture of 0.1% TFA/acetonitrile. A 1 pmol/L solution of bovine serum albumin was added as an internal standard. NMR spectra were acquired on a Varian Inova 600, operating at 599.7 MHz for ^{1}H and at 150.8 MHz for ^{13}C, or a Bruker DRX-500, operating at 500.13 MHz for ^{1}H and at 125.78 MHz for ^{13}C. Female *Balb/c* nude mice were obtained from the National Cancer Institute Frederick Research laboratory (Frederick, MD). Procedures to minimize discomfort, pain, and distress were in accord with the Animal Resource Program at the University of Alabama at Birmingham, accredited by the American Association for Accreditation of Laboratory Animal Care.

3′-(4-Hydroxyphenyl)paclitaxel-2′-succinate (3′-OH-PTXSX). 3′-(4-Hydroxyphenyl)paclitaxel (76.3 mg, 87.7 μmol) and succinic anhydride (52.6 mg, 526.2 μmol) were dissolved in dry pyridine (1.5 mL), and the solution was kept at room temperature and under argon for 10 h. TLC of the reaction mixture (10:90, methanol:chloroform, v/v) showed complete disappearance of the starting material and formation of a new compound. The solvent was distilled off in high vacuum, and the residue was purified in a silica gel column using chloroform and a

0% to 3% methanol gradient to afford the pure 3′-OH-PTXSX as a white crystalline solid (72 mg, 84.6%). RP-HPLC t_R: 23.3 min (98%); ^{1}H NMR ($CDCl_3$, 599.7 MHz): 1.13 (s, 3H), 1.22 (s, 3H), 1.68 (s, 3H), 1.88 (m, 1H), 1.91 (s, 3H), 2.22 (s, 3H), 2.25 (m, 1H), 2.38 (m, 1H), 2.39 (s, 3H), 2.55 (m, 1H), 2.72−2.62 (m, 2H), 2.74 (br, 2H), 3.79 (d, J = 7.0 Hz, 1H), 4.20 (AB, J = 7.0 Hz, 1H), 4.31 (AB, J = 7.0 Hz, 1H), 4.42 (dd, J = 6.7, 10.8 Hz, 1H), 4.99 (dd, J = 1.8, 9.5 Hz, 1H), 5.58 (d, J = 3.0 Hz, 1H), 5.69 (d, J = 7.0 Hz, 1H), 5.90 (dd, J = 3.0, 9.1 Hz, 1H), 6.24 (br t, J = 8.7 Hz, 1H), 6.29 (s, 1H), 6.75 (d, J = 8.5 Hz, 2H), 7.03 (d, J = 9.1 Hz, 1H), 7.16 (d, J = 8.5 Hz, 2H), 7.41 (t, J = 7.7 Hz, 2H), 7.50 (t, J = 7.7 Hz, 1H), 7.50 (t, J = 7.7 Hz, 2H), 7.60 (t, J = 7.7 Hz, 1H), 7.75 (d, J = 9.0 Hz, 2H), 8.13 (d, J = 7.3 Hz, 2H). ^{13}C NMR (150.8 MHz): 9.66, 14.89, 20.84, 22.05, 22.61, 26.87, 28.72, 28.96, 35.54, 35.57, 43.14, 45.67, 52.25, 58.54, 71.93, 72.19, 74.19, 75.05, 75.64, 76.46, 79.11, 81.24, 84.37, 115.90 (2C), 127.17 (2C), 127.93 (2C), 128.31, 128.76 (2C), 128.78 (2C), 129.14, 130.22 (2C), 132.12, 132.88, 133.44, 133.73, 142.68, 156.16, 167.03, 167.44, 168.13, 170.31, 171.32, 171.37, 174.6, 203.72. ESMS: *m/z* 971 $(M + H)^+$.

[^{125}I]-3′-OH-PTXSX. The iodogen method (*20, 21*) was used with slight modification. Briefly, 3′-OH-PTXSX was dissolved in DMF and the solution was mixed with 200 mM PBS at pH 7.6. Poly(styrene) beads coated with iodogen (1,3,4,6-tetrachloro-3a,6a-diphenylglyguril, IODOGEN, Pierce, Rockford, IL), and Na [^{125}I]-I (500 μCi) were added, and the mixture was shaken at room temperature for 10 min after which time it was diluted with 400 μL of 200 mM ammonium acetate buffer (pH 4.2). The mixture was loaded in a C18 Sep-Pak cartridge, prewashed sequentially with 3 mL each $H_2O/CH_3CN/H_2O$. The cartridge was washed with the acetate buffer (2 mL) and water (2 mL) and was eluted with 6 × 500 μL fractions of CH_3CN. Radioactivity of the eluted fractions was measured in a gamma counter. Fractions 1 and 2 showed 98.5% of the loaded activity. These were pooled and used for conjugation to C225 as described in the general procedure above.

PTXSX-[^{125}I]-C225. The indogen bead procedure was used. A solution of the conjugate (100 μL, 500 mg/mL) was mixed with 400 μL PBS (200 mM, pH 7.6) and iodogen beads (4/mg of the conjugate) were added. A solution of Na [^{125}I]-I (1.5 mCi) in 0.1 M sodium hydroxide (5 μL) was added, and the mixture was gently shaken for 5 min. The labeled conjugate was purified by gel filtration chromatography using a PD-10 column, eluted with 10 mM PBS, pH 6.5. This procedure afforded the PTX−[^{125}I]-C225 conjugate with a specific activity of 2 mCi/mg.

Iodo-3′-OH-PTXSX. Iodogen (0.22 mg, 0.51 μmol) was dissolved in methylene chloride (500 μL) in a poly(propylene) centrifuge tube, and the solvent was evaporated under argon and was replaced with 400 μL of phosphate buffer (50 mM, pH 7.3). With stirring, a solution of 3′-OH-PTXSX (3.8 mg, 3.9 μmol) in DMF (20 μL) was added followed by the addition of 8 × 3.5 μL of a solution of sodium iodide (2.0 mg, 13.3 μmol) in water, which developed a light yellow color. The addition of NaI was done over a period of 8 h in approximately 1 h intervals. The heterogeneous mixture was stirred vigorously at room temperature, and the reaction progress was monitored by analytical RP-HPLC. Formation of two new compounds was observed with gradual fading of the yellow color. The new products, as well as the unreacted starting material 3′-OH-PTXSX, were separated and purified by RP-HPLC using solvents A and B. This procedure afforded 1.2 mg and 0.37 mg of *mono*-iodo-3′-OH-PTXSX (28%) and *di*-iodo-3′-OH-PTXSX (7.7%), respectively.

3′-(4-Hydroxy-3-iodophenyl)paclitaxel-2′-succinate. RP-HPLC t_R: 25.1 min (96%); ^{1}H NMR ($CDCl_3$, 599.7 MHz): 1.13 (s, 3H), 1.23 (s, 3H), 1.68 (s, 3H), 1.89 (m, 1H), 1.92 (s, 3H), 2.19 (m, 1H), 2.23 (s, 3H), 2.34 (dd, J = 9.3, 15.3 Hz, 1H), 2.43 (s, 3H), 2.56 (m, 1H), 2.82−2.68 (m, 4H), 3.80 (d, J = 7.0 Hz, 1H), 4.19 (AB, J = 7.0 Hz, 1H), 4.32 (AB, J = 7.0 Hz, 1H), 4.42 (dd, J = 6.7, 10.8 Hz, 1H), 4.98 (dd, J = 1.8, 9.5 Hz, 1H), 5.47 (d, J = 3.0 Hz, 1H), 5.68 (d, J = 7.0 Hz, 1H), 5.85 (dd, J = 3.0, 9.1 Hz, 1H), 6.23 (br t, J = 8.7 Hz, 1H), 6.29 (s, 1H), 6.94 (d, J = 8.5 Hz, 1H), 7.02 (d, J = 9.1 Hz, 1H), 7.24 (dd, J = 2.0, 8.5 Hz, 2H), 7.42 (t, J = 7.7 Hz, 2H), 7.53 (t, J = 7.7 Hz, 1H), 7.53 (t, J = 7.7 Hz, 2H), 7.61 (t, J = 7.7 Hz, 1H), 7.67 (d, J = 2.0 Hz, 1H), 7.77 (d, J = 9.0 Hz, 2H), 8.13 (d, J = 7.3 Hz, 2H). ^{13}C NMR (150.8 MHz): 9.83, 15.05, 21.06, 22.27, 22.88, 27.07, 28.67, 29.11, 35.73, 35.78, 43.42, 45.84, 52.01, 58.73, 72.27, 72.41, 74.40, 75.24, 75.79, 76.68, 79.35, 81.41, 84.63, 86.04, 115.71, 127.44 (2C), 128.67, 128.99 (2C), 129.01 (2C), 129.31, 130.45 (2C), 131.11, 132.47, 133.13, 133.45, 133.98, 136.98, 142.76, 155.47, 167.30, 167.53, 167.98, 170.22, 171.33, 171.52, 174.74, 203.92. ESMS: *m/z* 1097 $(M + H)^+$.

3′-(4-Hydroxy-3,5-diiodophenyl)paclitaxel-2′-succinate. RP-HPLC t_R: 26.6 min (95%); ^{1}H NMR ($CDCl_3$, 599.7 MHz): 1.13 (s, 3H), 1.22 (s, 3H), 1.67 (s, 3H), 1.88 (m, 1H), 1.91 (s, 3H), 2.16 (m, 1H), 2.23 (s, 3H), 2.32 (dd, J = 9.3, 15.3 Hz, 1H), 2.45 (s, 3H), 2.56 (m, 1H), 2.82−2.68 (m, 4H), 3.79 (d, J = 7.0 Hz, 1H), 4.20 (AB, J = 7.0 Hz, 1H), 4.33 (AB, J = 7.0 Hz, 1H), 4.43 (dd, J = 6.7, 10.8 Hz, 1H), 4.98 (dd, J = 1.8, 9.5 Hz, 1H), 5.39 (d, J = 3.0 Hz, 1H), 5.68 (d, J = 7.0 Hz, 1H), 5.78 (dd, J = 3.0, 9.1 Hz, 1H), 5.84 (br, 1H), 6.23 (br t, J = 8.7 Hz, 1H), 6.29 (s, 1H), 7.02 (d, J = 9.1 Hz, 1H), 7.43 (t, J = 7.7 Hz, 2H), 7.52 (t, J = 7.7 Hz, 1H), 7.54 (t, J = 7.7 Hz, 2H), 7.62 (t, J = 7.7 Hz, 1H), 7.69 (s, 2H), 7.76 (d, J = 9.0 Hz, 2H), 8.13 (d, J = 7.3 Hz, 2H).^{13}C NMR (125.7 MHz): 9.58, 14.80, 20.83, 22.06, 22.63, 26.85, 28.42, 28.98, 35.50, 35.54, 43.18, 45.59, 51.30, 58.52, 72.13, 72.15, 74.18, 74.97, 76.42, 76.80, 79.13, 81.19, 82.65, 84.39, 127.25 (2C), 128.78 (2C), 128.82 (2C), 129.03, 130.20 (2C), 132.30, 132.97, 133.02, 133.78, 137.58 (2C), 137.65, 139.38, 142.41, 153.92, 167.05, 167.10, 167.49, 169.86, 170.93, 171.27, 173.73, 203.69. ESMS: *m/z* 1222 (M + H). RP-HPLC analyses on samples of the purified [^{125}I]-3′-OH-PTXSX and 3′-(4-hydroxy-3-iodophenyl)-PTXSX were performed in an analytical C18 column, both individually and as a mixture, all showing a t_R of 19.9 ± 0.14 min.

[^{14}C]-PTXSXC225. Paclitaxel (19.6 mg, 23 μmol) was spiked with [^{14}C]-2′-benzoylpaclitaxel (50 μCi), and the mixture was used for the synthesis of the [^{14}C]-PTXSXC225 conjugate according to the general procedure described below. Radiochemical analyses determined a [^{14}C]-PTXSX:C225 molar ratio of 1.3:1.

General Procedure for the Synthesis of PTXSXC225 and PTXGLC225 Conjugates. The previously reported protocol was employed (*19*). Briefly, the taxane (TAX), i.e., paclitaxel or its 3′-hydroxy derivative, was converted to the corresponding succinate (TAXSX) or glutarate (TAXGL) according to the procedure described above for 3′-OH-PTXSX. The PTXSX and PTXGL were identified by ESMS and by comparison to the reported analytical data (*22*). The 3′-OH-PTXSX was identified by ESMS and by ^{1}H and ^{13}C NMR as shown above.

The carboxylated taxanes ($TAXCO_2H$) thus prepared were used for the preparation of the antibody conjugates as follows: A solution of $TAXCO_2H$ (1 equiv) in DMF was treated with NHS (2 equiv) and EEDQ (1.25 equiv) for 30 min, and the resulting solution was added to that of C225 in PBS (pH 8.1) at a 10:1, TAX:C225, molar ratio. The solution was gently stirred at 0 °C for 1 h, and the conjugate was purified by SE-HPLC.

Drug Release Kinetics of [^{14}C]-PTXSXC225. Equal volumes of the [^{14}C]-PTXSXC225 and freshly prepared human serum were mixed, and a 20-μL aliquot was withdrawn and quenched by shock freezing in a dry ice–methanol bath and stored in a −20 °C freezer. The remaining mixture was incubated at 37 °C in an incubator. Two-hundred-microliter aliquots were withdrawn at 0.5, 1, 1.5, 2, 3, 4, and 6.5 h, at which time the beginning of the plateau portion of the decay curve was indicated. The reaction solution was then kept incubated to yield an equilibrium concentration of the cleaved [^{14}C]-PTX at 22.5 h postincubation. Samples were extracted with ethyl acetate (0.5 mL per aliquot) by vortexing the immiscible layers. The organic layers were separated and stored at −20 °C. The ethyl acetate extracts were individually mixed with 10 mL of scintillation cocktail and were counted in a scintillation counter. The end-point of the run was the equilibrium at which no further increase in the concentration of the cleaving [^{14}C]-PTX was observed. The increasing radioactivity counts were then plotted against sampling times.

PTXSXPEGCO$_2$H. To a solution of the PTXSX (1.5 equiv) in dry DMF (250 μL/mg) were added NHS (2.5 equiv), EEDQ (1.5 equiv), and DIEA (2 equiv), and the mixture was stirred at room temperature for 30 min under argon. A solution of H_2N-PEG-CO_2H·HCl (1 equiv) and DIEA (2 equiv) was then added, and the clear solution was stirred for another 6 h. The DMF was removed in a vacuum, and the residue was mixed with 500 μL of ice-cold ammonium acetate buffer (0.2 M, pH 4.2). The suspension was transferred into a dialysis membrane with a 1000 MW cutoff and was dialyzed against 3 × 2 L of purified (18.2 MΩ) water at 4 °C and for 24 h. Lyophylization afforded a white solid product. Yield: 78%. MALDI: 4750. HPLC t_R: 23.30 min (98%).

PTXGLPEGCO$_2$H. The same procedure as for PTXSXPEGCO$_2$H was used, with PTXGL as the starting material, to afford a white solid product after lyophylization. Yield: 84%. MALDI: 4700. HPLC t_R: 24.0 min (96%).

Drug Release Kinetics of PTXPEG Conjugates. The PEG conjugate (PTXSXPEGCO$_2$H or PTXGLPEGCO$_2$H, 5 mg) was dissolved in DPBS (250 μL), and the solution was mixed with an equivalent volume of freshly prepared normal human serum at 0 °C. A 50-μL aliquot was immediately withdrawn and quenched by shock freezing at −72 °C to serve as the time-zero HPLC reference. The conjugate solution was incubated at 37 °C with occasional stirring. At certain time intervals, 50-μL aliquots were withdrawn and analyzed in an RP-HPLC system. At equilibrium (no further growth in the PTX peak, predetermined with an authentic PTX sample), the percent area under the peak (%AUC) for the decomposing conjugate and the forming PTX in each aliquot were plotted against time.

This experiment was repeated with the PTXGLPEGCO$_2$H conjugate in 100 mM acetate buffer at pH 5.0 containing an equal volume of human serum and also in 100 mM acetate buffer at pH 4.0, both at 37 °C.

Biodistribution Studies. Four groups (one group/conjugate/time point) of female *Balb/c* nude mice (6/group) were inoculated *subcutaneously* with the androgen-independent DU-145 human prostate carcinoma cells (1×10^7 cells/animal). With tumor sizes around 7 mm in diameter, the mice were injected *intraveneously* with 2 μCi each of purified [^{125}I]-3′-OH-PTXSXC225 or PTXSX-[^{125}I]-C225. The mice were sacrificed at 4 and 24 h postinjection, weighed samples of the tumors and normal organs were resected, washed with saline, and blotted dry, and the radioactivity associated with each sample was counted in a gamma counter. Tissue uptake of the radioactivity in %ID/g were then calculated from the raw activity counts for blood (BL), heart (HT), lung (LU), liver (LI), stomach (ST), small intestine (SI), spleen (SP), kidney (KD), bone (BN), muscle (MU), lining of abdominal cavity (AB), uterus (UT), pancreas (PA), and tumor (TU).

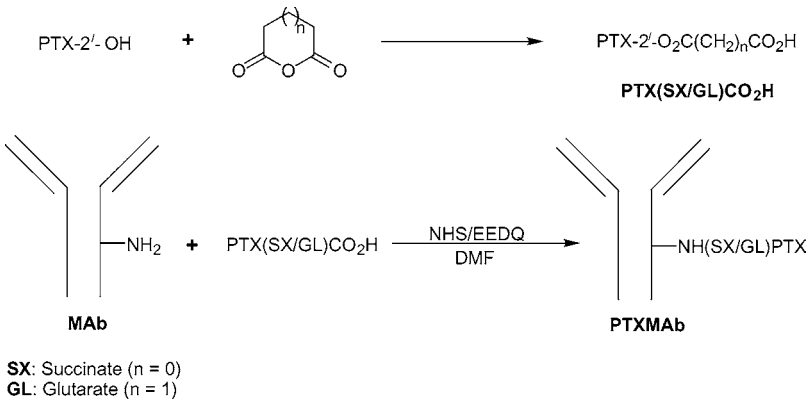
Antitumor Activity Studies. *Balb/c* mice were inoculated sc with DU-145 cells (2×10^7 cells per mouse) and were randomized into three groups of eight when the tumor sizes reached around 7 mm in diameter. The mice were treated by 6 i.v. injections every 72 h as follows (administered doses are shown in parentheses in mg/kg body weight/injection/mouse): Group 1, saline; Group 2, Taxol + C225 (0.22 + 12.5); Group 3, PTXGLC225 conjugate (0.22/12.5). The PTXGLC225 conjugate had a drug:MAb ratio of 3.1 by MALDI. The mice were observed daily for survival and tumors were measured three times a week by vernier calipers.

Statistical Analyses. The three treatment groups, saline (7 animals), Taxol + C225 (8 animals), and conjugate (8 animals), were compared with respect to in vivo antitumor efficacy over time using two statistical methods. In the first method, the tumor sizes were modeled over time through a mixed linear model growth curve analysis, using the MIXED procedure in the Statistical Analysis System (SAS). The second approach defined inhibition of tumor growth as extension of tumor tripling times. In this method, the number of days at which the tumors tripled in surface area (product of two diameters, mm^2) relative to baseline on day 10 after tumor cell injection was used in the tripling time analysis. Only one tumor from the conjugate group had not tripled by the last day of experiment. The tripling time for this tumor was treated as censored in the analysis, and the last day in the experiment (105 days) was substituted as the tumor's day of tripling. One animal from the saline group died before its tumor size tripled. In this case, the day of death was substituted as the tumor's day of tripling and that value was treated as censored in the analysis. The tumor tripling time data were analyzed using one-way analysis of variance (ANOVA), the nonparametric Kruskal–Wallis test, and log-rank test on the survival curves. The Kaplan–Meier survival curves were also plotted. All statistical analyses were conducted in SAS using the MIXED, GLM, NPAR1WAY, and LIFETEST procedures.

RESULTS AND DISCUSSION

Synthesis. Paclitaxel and its 3′-(4-hydroxyphenyl) derivative were conjugated to the anti-EGFR receptor antibody C225 according to Scheme 1. A two-step procedure was used starting with 2′-hemisuccinylation (Scheme 1, $n = 0$) or 2′-hemiglutarylation (Scheme 1, $n = 1$) of these taxanes through a previously reported reaction (*22*). Slight modifications in this procedure (lower succinic anhydride:PTX molar ratio and silica gel chromatography instead of the acetone/water recrystalization reported in ref 22) significantly improved the yield and purity of

Scheme 1



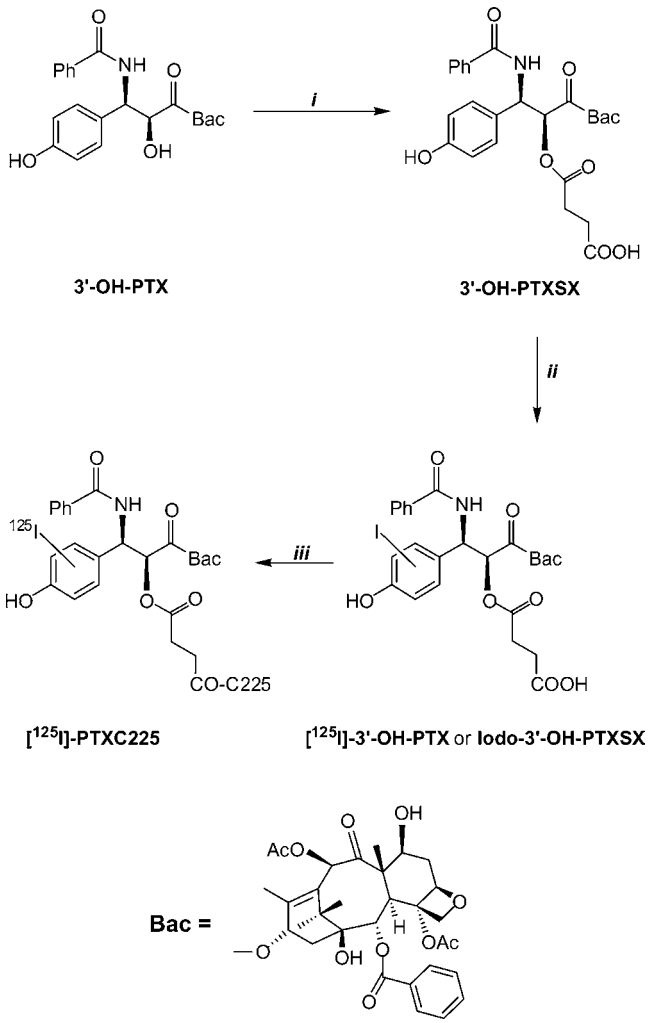
PTXSX in our hands. This procedure produced in good yield the 2′-hemisuccinate of the 3′-(4-hydroxyphenyl) derivative without protection of the phenolic oxygen, which in turn, was due to scarcity of this starting material. Evidence for this observation was provided by unambiguous ESMS of the purified product and information from the NMR integration data. Should the phenolic hydroxy group have the same, or higher, activity toward hemisuccinylation as the 2′-hydroxyl group, an exposure of the phenolic derivative to excess succinic anhydride would have been expected to form a *di-succinylated* derivative with readily detected analytical characteristics. This was not observed to any detectable scale in this synthesis.

To further support these findings, we carried out a model succinylation reaction, using as the substrate, Fmoc-tyrosine,[3] which shares the same 4-hydroxyphenyl function with the 3′-(4-hydroxyphenyl)-PTX.[3] Chromatographic (TLC, HPLC) and MS analyses determined formation of no *O*-succinylated products and the starting tyrosine was still present intact.

Conjugation of the PTX to the MAb was carried out by the NHS/EEDQ method (Scheme 1) as described previously (*19*). This protocol produced batches of conjugate with a PTX:C225 molar ratio of 3 ± 0.2 as determined by MALDI-TOF mass spectrometry. Not exceeding this drug-to-MAb ratio is critical as precipitation of the higher conjugates were observed due to low aqueous solubility of the PTX nucleus (*19*).

To demonstrate the drug site-specific radioiodination of the 3'-OH-PTXSX conjugate, a nonradioactive iodination reaction of the drug was carried out to allow for the chromatographic comparison of the products and establishing an analytical correlation between these and the product formed by the radioiodination procedures. Iodination of the succinylated PTX-3'-OH and conjugation of the product to C225 are shown in Scheme 2. In the nonradioactive procedure, a 25 mol % excess of iodogen and 300 mol % excess of sodium iodide resulted in complete conversion of the 3′-OH-PTXSX to the *di*-iodo product within 30 min. On the other hand, an excess (300 mol %) of NaI with respect to the substrate, and only 13 mol % of iodogen, resulted in the formation of the *mono*-iodo compound as the major (28%) and the *di*-iodo derivative as the minor (7.7%) products. The products were identified by the observation of the right molecular

Scheme 2[a]



[a] (i) Succinic anhydride/dry pyridine; (ii) Na [^{125}I]-I or NaI/iodogen; (iii) (a) [^{125}I]-3′-OH-PTXSX/NHS/EEDQ/DMF, (b) C225/PBS/pH 8.1.

weights in ESMS as well as by ^{1}H and ^{13}C NMR spectroscopy. We did not pursue optimization of the reaction conditions to achieve a higher *mono*:*di* product ratio, since in this work the compounds were needed only as controls and in small quantities, and also due to significant limitations in the supply of the 3′-OH-PTX starting material. The HPLC purities of these compounds (95−98%), however, were suitable for the comparative radiolabeling and conjugation studies reported here. The *mono*-iodo-3′-OH-PTXSX thus prepared was used for comparative RP-HPLC analyses with [^{125}I]-3′-OH-PTX.

[3] Fmoc-Tyrosine was incubated with a 6 molar excess of succinic anhydride in dry pyridine, and at room temperature for 10 h. The solution was then analyzed by TLC (in two solvent systems) and RP-HPLC (C18 column). No detectable reaction was observed.

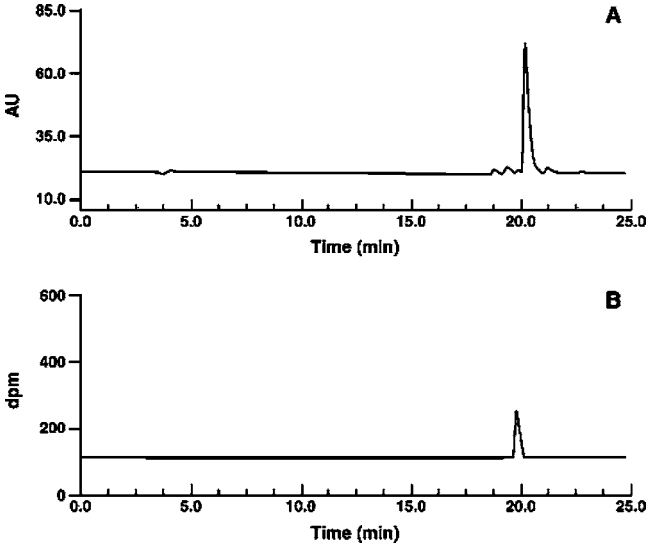


Figure 2. RP−HPLC UV (A) and radioactivity (B) traces of *mono*-iodo-3′-OH-PTXSX (A) and [^{125}I]-3′-OH-PTXSX (B). These and a *mixed* trace (not shown) measured a t_R of 19.9 ± 0.14 min showing the same chemical identity for the two isotopically different compounds. The slight difference in retention times is due to the in-series connection of the two detectors.

The RP-HPLC traces on the two compounds, both individually and as a mixture, showed identical retention times in dually (radioactivity and UV) detected analyses (Figure 2). These experiments demonstrated that the radioiodinated species detected in the [^{125}I]-radiolabeling of 3′-OH-PTXSX was indeed the expected 3′-(4-hydroxy-3-[^{125}I]-iodo)-phenyl paclitaxel hemisuccinate. In this iodination reaction, the PTX metabolite functions similar to a tyrosine side-chain in direct radioiodination reactions (*23*) of proteins. This procedure may be, therefore, useful in tracing studies of paclitaxel derivatives, particularly the nonprotein polymeric constructs (see following section) (*24*−*26*).

Antibody Radiolabeling and Biodistribution Studies. Originally, biodistribution of the drug site- and antibody site-labeled conjugate was attempted with [^{125}I]-labeled [^{14}C]-PTXSXC225. This would have had the advantage of simultaneous ^{14}C/^{125}I-traced biodistribution studies. To this end, the [^{14}C]-PTXSX-[^{125}I]-C225 conjugate was synthesized, through Scheme 1 by the use of commercially supplied [^{14}C]-PTX, and subsequent antibody iodination of the intermediate [^{14}C]-PTXSXC225 product. However, in biodistribution analysis, we found that the ^{14}C activities in all tissues, after resection and workup, were too low to be detected, particularly in the presence of the ^{125}I with some spillover effect. The latter problem jeopardized an unbiased independent tracing of the two radioisotopes and led to the use of only radioiodinated conjugates described here.

3′-(4-Hydroxyphenyl)paclitaxel (3′-OH-PTX), was isolated as a metabolite of paclitaxel from treated patients (27) and was later synthesized by Reddy et al. (*28*). We reasoned that the presence of the 4-hydroxyphenyl ring would render the molecule a tyrosine mimic, and thereby, would allow for direct radiolabeling of the conjugate through standard oxidative radioiodination protocols. To test this, 3′-OH-PTXSX was treated with nonradioactive NaI in the presence of iodogen, a condition similar to that of a standard radioiodination protocol (*20, 21*). Mass spectral and HPLC analyses of the products confirmed the presence of a *mono*-iodinated 3′-OH-PTXSX, and the compound was selected for the two-step synthesis of the DSL conjugate (Scheme 2). This approach, in which the drug segment was radioiodinated before conjugation to the antibody, ensured the placement of ^{125}I on the PTX nucleus and thus allowed for an exclusively PTX-traced biodistribution analysis. Indeed, preconjugation radioiodination of 3′-OH-PTXSX proceeded in good (75%) yield (see the preceding section). The resulting [^{125}I]-3′-OH-PTXSX product was purified by reversed-phase filtration and was conjugated to C225 by the EEDQ/NHS procedure (*19*). In a separate experiment, the ASL conjugate (PTXSX-[^{125}I]-C225) was prepared in a standard iodogen reaction for the antibody-traced in vivo distribution experiments.

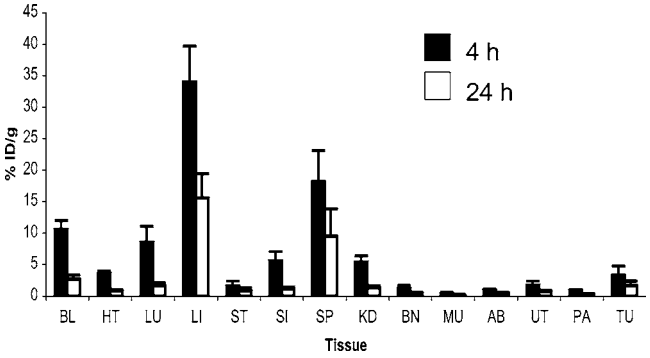


Figure 3. Biodistribution of the DSL conjugate [^{125}I]-3′-OH-PTXSXC225 in Balb/c nude mice bearing sc DU-145 human prostate carcinoma xenografts at 4-h and 24-h time points.

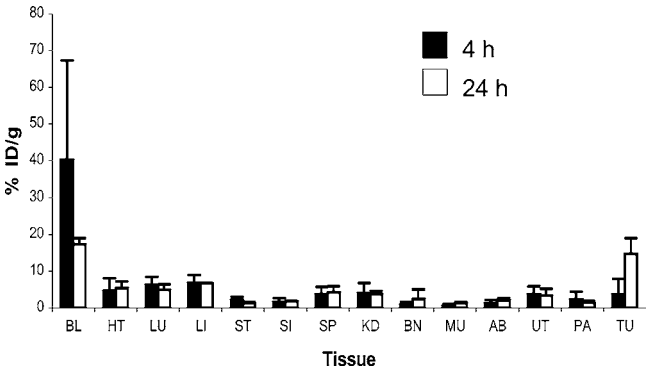


Figure 4. Biodistribution of the ASL conjugate PTXSX-[^{125}I]-C225 in Balb/c nude mice bearing sc DU-145 human prostate carcinoma xenografts at 4-h and 24-h time points.

The labeled conjugates were used for biodistribution studies in *Balb/c* nude mice implanted sc with DU-145 human prostate carcinoma cells. Each mouse received an *iv* injection of the labeled compound and the biodistribution analyses were performed at 4-h and 24-h time points. The results of these experiments are shown in Figures 3 and 4 for [^{125}I]-3′-OH-PTXSXC225 and PTXSX-[^{125}I]-C225, respectively.

The 24-h serum clearance rate of the DSL ([^{125}I]-PTXSX-C225) was about twice as fast as that for the ASL (PTXSX-[^{125}I]-C225). On the other hand, while the ASL conjugate had an increase (from 3.8 ± 4.2%ID/g to 14.8 ± 4.2%ID/g) in tumor uptake from 4 to 24 h postinjection, the DSL conjugate showed a decrease (from 3.3 ± 1.5%ID/g to 1.7 ± 0.6%ID/g) within this time interval. This pattern of biodistribution of DSL may point to the behavior of a molecule with a smaller overall size than a typical IgG conjugate such as the PTXC225. This is further supported by the liver activity of DSL, which decreased by around 50% from 4 to 24 h (34.0 ± 5.7%ID/g to 15.6 ± 3.8%ID/g), while that of ASL was almost constant within this time (6.7 ± 2.1%ID/g to 6.6 ± 1.2%ID/g), indicating a more rapid metabolism/clearance

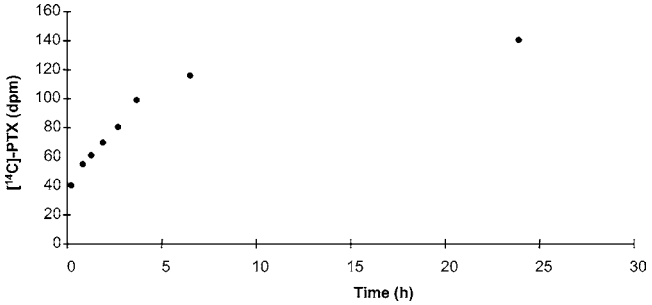


Figure 5. Drug release profile for [^{14}C]-PTXSXC225 at 37 °C and pH 7.4 PBS and in the presence of human serum. Each data point is the average of values from two independent runs.

Table 1. Half-Lives ($t_{1/2}$) of Hydrolysis for Different PTX-2′-Succinate Conjugates at 37 °C and at pH 7.4

conjugate[a]	condition	$t_{1/2}$ (min)	ref
2′-PTX		54	29
2′-PTX−*di*-PEG^{5K,8K,9K}	hSe[b]	60	30
2′-PTX−PEG$^{3.4K}$−BBN[7−13]	hSe[b]	113	18
[^{14}C]-PTXSXC225	hSe[b]	165	

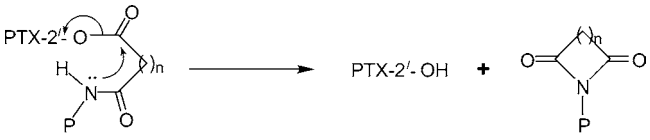
[a] Superscripted numbers indicate PEG molecular weights. [b] Reaction medium included human serum.

process for DSL than for ASL. Also, the kidney activities were 5.5 ± 1.0%ID/g (4 h) to 1.3 ± 0.2%ID/g (24 h) and 4.0 ± 2.9%ID/g (4 h) to 3.8 ± 0.7%ID/g (24 h) for DSL and ASL, respectively, which parallel the serum clearance for these conjugates. Collectively, and considering that both conjugates were of the same molecular size, the biodistribution results clearly demonstrate an early release of the drug from the PTXSXC225 conjugate with respect to the peak tumor uptake of the antibody.

Furthermore, the loss of label due to lysosomal dehalogenation of the conjugates (29, 30) was not taken into account in this experiment. It is not known, therefore, whether the observed tumor uptake could be higher, had it not been for such a postinternalization catabolism. On the other hand, since only a comparison of biodistribution of the conjugates with respect to each drug and antibody segments was of interest, exclusion of the dehalogenation mechanisms might still be a safe practice.

Drug Release Kinetics. To further validate the findings of biodistribution experiments, a direct (in vitro) determination of the timing of PTX cleavage from C225 was carried out. Since the choice of either ^{14}C- or ^{125}I-labeled conjugate carried no advantage over each other for an in vitro experiment, and due to the availability of [^{14}C]-PTXSXC225, this conjugate was selected for this release study. Thus [^{14}C]-PTXSXC225 was incubated at 37 °C in PBS containing freshly prepared human serum. The increase in the cleaved PTX was monitored at certain time intervals by a quench/extract/count procedure using ethyl acetate as the PTX-extracting solvent. The radioactivity of the extracted aliquots was then measured in a scintillation counter. Plotting the counts against time afforded the PTX release profile for this conjugate (Figure 5). Using this profile, a drug release half-life ($t_{1/2}$) of 2.7 h was estimated for this conjugate. For comparison, the $t_{1/2}$ values of PTX release from this and various other conjugates are shown in Table 1 (*31, 32*). Although in some studies, including this work, $t_{1/2}$ evaluations are performed under *physiological* conditions and in the presence of human serum, it should be emphasized that these half-lives are still in vitro measurements and the actual in vivo times may be somewhat different. The in vitro release times are, nevertheless, useful guides for formulation considerations and design of the therapy protocols.

Scheme 3

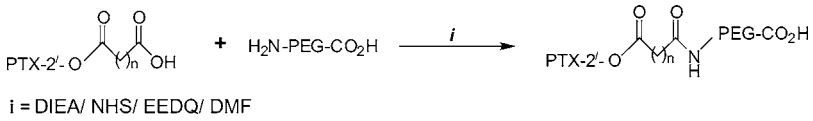


Although the corresponding half-lives of Table 1 seem to be highly structure- and condition-related, they demonstrate relatively short cleavage time windows for *2′*-succinylated PTX conjugates and are in agreement with our present findings on the PTXSXC225. While for low-MW tumor-targeting conjugates, such as those derived from small-molecule peptides (*18*), shorter cleavage times may be an advantage, it could be a significant disadvantage for antibody-conjugated drugs. For a drug−MAb conjugate with a drug release $t_{1/2}$ of 2 h, for example, more than 96% of the originally conjugated drug could be released and cleared from the circulatory system at the peak tumor antibody uptake time of 24 h. Accordingly, PTX−MAb linkers with higher physiological stabilities than that of the succinate may be required for an effective targeted delivery of this drug.

Since our work with the tumor-targeting PTX conjugates had used succinic acid as the *lead* linker, we naturally were interested in examining different derivatives of this molecule in our search for high-stability linkers. We anticipated that the cleavage of PTX from conjugates was a one-step ring-closing reaction with the formation of an imide resulting from the PTX displacement by the N-terminal nitrogen of the peptide or protein residue as shown in Scheme 3. It has been shown that in such processes, the change in the entropy of the reaction transition state ($\Delta S^{\ddagger}$) is a rate-determining factor, with the five-membered ring structures (Scheme 3, $n = 2$) presenting a rate constant 2 and 3 orders of magnitude faster than the four- ($n = 1$) and six-membered ($n = 3$) ring closures, respectively (*33*). Accordingly, we reasoned that a PTX−MAb conjugate with glutaric acid as a linker might have the desired longer $t_{1/2}$ of drug release. Prior to the synthesis of glutarate-linked antibody conjugates, however, we set out to test this by an in vitro release kinetics study on the direct comparison of the two linkers under the same conditions. Thus, conjugates of PTX to an amino-PEG, using the succinate ($n = 2$) and glutarate ($n = 3$) linkers, were synthesized as shown in Scheme 4. The rationale for the incorporation of the amino PEG was 2-fold: The water-solubilizing effect of this polymer on the otherwise insoluble drug, and the pseudo-anchimeric assistance, which might be expected from the amino PEG nitrogen atom in cleaving the PTX nucleus as shown in Scheme 3. The latter situation was expected to be similar to that of an actual PTX−MAb conjugate where the PTX-linker is attached to the ϵ-amino groups of the MAb lysine residues. Although the free carboxylic acid functions of both PTXSX and PTXGL might have generated solubility by conversion to their corresponding salts, we elected to avoid this route of solubilization, as a pH too basic for the PTX-linker bond might have resulted. This high pH could cleave the drug from the linkers before a timed study could be performed.

As shown in Figures 6 and 7, the glutarate conjugate has a considerably longer cleavage $t_{1/2}$ than the succi-

Scheme 4



nate, that is, ~2.6 h and ~44 h, for PTXSXPEG and PTXGLPEG, respectively, indicating the better compatibility of the former linker with MAb-mediated PTX delivery. Furthermore, Figure 6 also shows excellent agreement between the release $t_{1/2}$ of the PEG conjugate with that of the PTXSXC225 shown in Figure 5.

On the basis of a previous report on the limited stability of the PTX–glutarate bond in a low-pH acetate buffer (100 mM, pH 4) (*34*), we investigated the stability of the PTXGLPEG conjugate in the same buffer as well as in a pH 5 acetate buffer with human serum. No detectable amount of released PTX was noticed under either condition and after at least 24 h (pH 5) and several days (pH 4) of incubation at 37 °C.

These findings justified the use of glutaric acid instead of succinic acid as the PTX–MAb linker for a drug release timing which matches with that of the peak tumor uptake of the conjugate. The PTXGLC225 was prepared by the same method as for the succinate congener (Scheme 2) and was used for a preliminary antitumor activity study described below.

Antitumor Activity Studies. The first clue on the finding that the SX might not have been a suitable linker for in vivo MAb-targeted PTX delivery came from the observation that the conjugate showed only very modest antitumor activity in several experiments (data not shown). This was also despite high (in vitro) cytotoxic activity of the PTXSXC225 conjugate as compared to the free PTX in several human carcinoma cell lines. With the development of the cleavage kinetics data, it was anticipated that the antitumor activity of the conjugate might improve by the use of a linker with a higher release $t_{1/2}$. To this end, a therapy experiment using the PTXGLC225 conjugate and in a mouse model with DU-145 human prostate carcinoma implants was initiated. Injections were given iv and every 72 h. The 72-h timing of injections was selected based on the tumor %ID/g values in the biodistribution experiments (i.e., unlikelihood of tumor saturation), the expected 24-h tumor uptake peak, the 24-h blood half-life, and the slow release $t_{1/2}$ of the glutarate linker. Increase in the surface area (product of two diameters) was used as a measure of tumor growth.

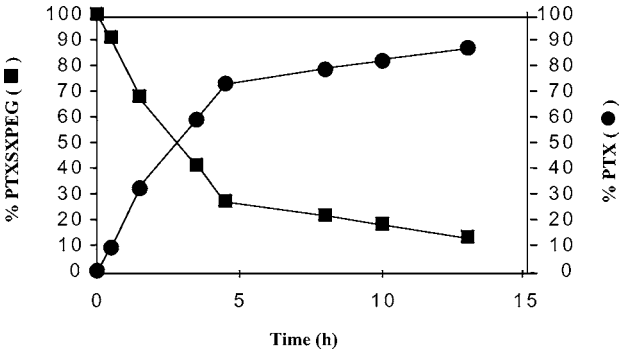


Figure 6. Drug release profile for PTXSXPEG at 37 °C in pH 7.4 PBS containing normal human serum. Each point is the average of values from two independent runs.

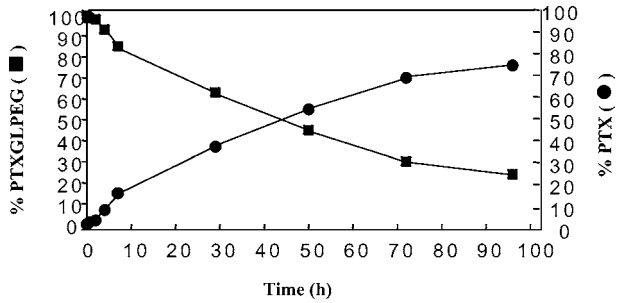


Figure 7. Drug release profile for PTXGLPEG at 37 °C in pH 7.4 PBS containing normal human serum. Each point is the average of values from two independent runs.

In this experiment, and based on the two statistical analyses described in Experimental Procedures, the conjugate group showed significantly better antitumor efficacy over time as compared to the saline and Taxol + C225 mixture. The mixed linear model on the raw (tumor size over time) growth curves, using the MIXED procedure in SAS, showed (Figure 8) a significantly slower rate of growth over time (on average a smaller slope in the growth curves) for the conjugate group as compared to the Taxol + C225 and saline groups ($p < 0.001$). In the tumor tripling time analysis, we recorded the time during which tumors had tripled in surface area. All but two of the 23 tumors had tripled by the end of study. Three separate statistical analyses, including one that takes into account censoring (Kaplan–Meier and associated log-rank test), resulted in the same statistical conclusions. The tumors were fast growing tumors which doubled on average quite quickly, with over half of the Taxol + C225 and conjugate groups having doubled within 48 and 52 days (6/7 of the saline group tumors doubled by 25 days and 7/7 of them doubled by 43 days). On the basis of this, we concluded that tripling time analysis was more appropriate in this situation. In addition to the tripling time analysis, the tumor sizes were modeled over time through a mixed linear model growth curve analysis, which resulted in the same conclusions as the tripling time analysis. Therefore, although doubling time is traditionally used in these types of analyses, the tripling time analysis seemed to be appropriate and accurately reflected the differences in tumor growth inhibition. Table 2 contains the statistics summarizing the tumor tripling times per group. Based on Analysis of Variance (ANOVA), there were overall significant mean differences in tripling times between groups ($p = 0.001$). Subsequent multiple comparisons indicated that the conjugate group had significantly longer mean tumor-tripling times than the Taxol + C225 and saline groups and that the Taxol + C225 group had significantly longer tumor tripling times over the saline group. The nonparametric Kruskal–Wallis test confirmed this result. The Kaplan–Meier curves for the time-to-tumor-tripling, shown in Figure 9, clearly demonstrate superior tumor growth inhibition in the treated groups over the saline control group, and the associated log-rank test confirms that the time-to-tumor-tripling for the PTXGLC225 was significantly extended as compared to the Taxol + C225 groups ($p = 0.018$) and the saline control group ($p = 0.008$).

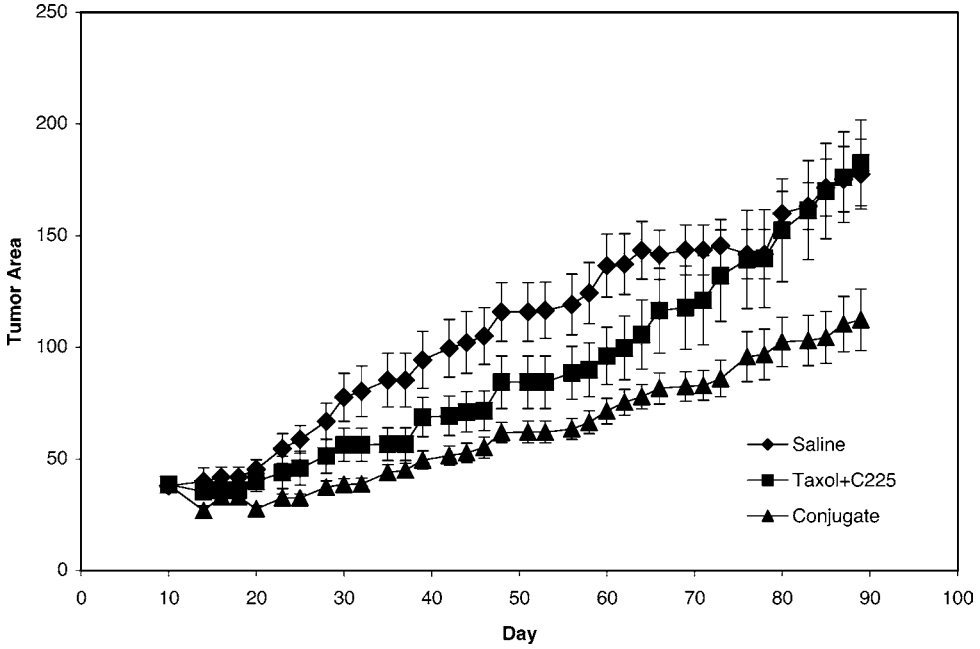


Figure 8. Tumor growth inhibition induced by the PTXGLC225 conjugate in *Balb/c* nude mice bearing sc DU-145 human prostate carcinoma tumors. Saline and a physical mixture of Taxol and C225 were used as controls.

Table 2. Summary Statistics on the Times-to-Tumor Tripling[a]

group	*N*	number of nontripled tumors	mean (days)	median (days)	standard error (days)
saline	7	1	38.4	39.0	7.3
Taxol + C225	8	0	60.6	59.5	5.0
conjugate	8	1	77.6	79.0	4.6

[a] Based on ANOVA, the conjugate group had significantly longer mean tumor-tripling times than the Taxol + C225 and saline groups, and the Taxol + C225 group had significantly longer tumor-tripling times over the saline group.

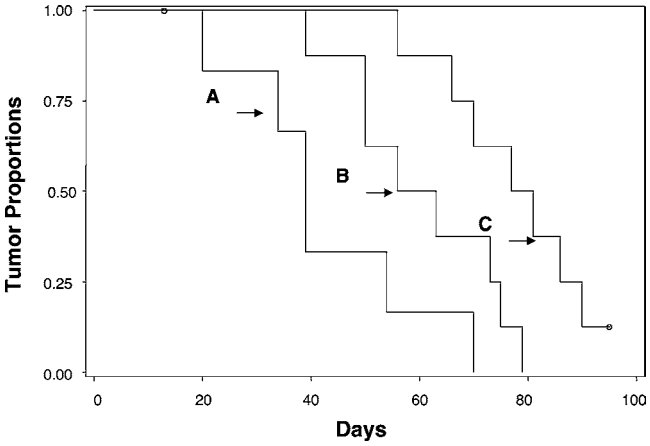


Figure 9. Kaplan-Meier tumor tripling time curves in *Balb/c* nude mice bearing sc DU-145 human prostate carcinoma tumors and treated with either Taxol + C225 mixture (B) or the PTXGLC225 conjugate (C) as compared to the untreated controls (A). The ordinate represents the estimated proportion of tumors that tripled over time (shown in days on the abscissa). The circles indicated censored values.

CONCLUSIONS

While an early cleavage of the drug molecule from the conjugate will reduce the possibility of its tumor-targeted delivery, too slow a release may result in an unsuccessful therapy outcome as well. The latter would be particularly harmful to the performance of prodrug conjugates, which may require a timely drug cleavage/activation mechanism. Information on the kinetics of the release would be, therefore, critical in designing drug−antibody conjugates with useful therapeutic features. In the work described here, drug-site and antibody-site radioiodinated PTXSXC225 conjugates were synthesized and were used to study the in vivo fate of both the drug and the antibody segments. These experiments were performed in DU-145 tumor-implanted *Balb/c* nude mice and demonstrated that the time of cleavage of the PTX from the succinic acid-linked conjugate (PTXSXC225) was shorter than the time required for C225 tumor localization. This finding was further supported by an in vitro drug release rate estimation experiment, which indicated half-times of 2.75 and 2.6 h for the cleavage of PTX from [^{14}C]-PTXSXC225 and PTXSXPEG conjugates, respectively. According to the biodistribution results, however, less than 4%ID/g of the PTXSXC225 localized in the tumor at 4 h postinjection. On the other hand, a glutaric acid-linked conjugate showed a significantly longer drug release mechanism and was selected for a therapy study in DU-145-bearing mice. As compared to the previously performed therapy experiments with the PTXSXC225 conjugate, better antitumor activity was observed with the PTXGLC225 in this controlled experiment. In addition to the introduction of a new method for the synthesis of drug-site radiodinated PTX−MAb conjugates, the results presented in this article demonstrate the effect of the PTX−antibody linkers on the overall antitumor activity of the conjugate. These results are being utilized in an ongoing work toward the design and synthesis of PTX−MAb conjugates with optimal therapeutic features.

ACKNOWLEDGMENT

The generous donations of 3′-OH-PTX and C225 by Tapestry Pharmaceuticals (Boulder, CO) and ImClone Systems (New York, NY), respectively, are greatly acknowledged. The authors would like to thank the UAB Comprehensive Cancer Center Mass Spectrometry Shared Facility for MW determinations, and Sheila Bright and Cherlene Hardy for assisting in the biodistribution experiments. Soneshia McMillan and Dr. Abhijit Roy-

cowdhury are thanked for preparing the manuscript and the synthetic schemes, respectively. Supported by Department of the Army Award Numbers DAMD17-02-1-0004 and DAMD17-02-1-2068.

LITERATURE CITED

(1) Pietersz, G. A., and McKenzie, I. (2002) The use of drug-monclonal antibody conjugates for the treatment of cancer, in *Tumor Targeting in Cancer Therapy* (Pagé, M, Ed.) pp 179−196. Humana Press, Totowa, NJ.

(2) Safavy, A., and Buchsbaum, D. J. (2002) ^{188}Rhenium-Labeled Trisuccin-Δ*C*H2HuCC49 as a Radioimmunotherapy Model in Nude Mice, in *Drug Targeting in Cancer Therapy* (Pagé, M, Ed.) pp 257−275, The Human Press Inc., Totowa, NJ.

(3) Illidge, T. M., and Brock, S. (2000). Radioimmunotherapy of cancer: using monoclonal antibodies to target radiotherapy. *Curr. Pharm. Des. 6,* 1399−1418.

(4) Kousparou, C. A., Deonarain, M. P., and Epenetos, A. A. (2000). Advances in tumour targeting. *J. Int. Soc. Tumor Target. 1,* 55−69.

(5) Doronina, S. O., Toki, B. E., Torgov, M. Y., Mendelsohn, B. A., Cerveny, C. G., Chace, D. F., DeBlanc, R. L., Gearing, R. P., Bovee, T. D., Siegall, C. B., Francisco, J. A., Wahl, A. F., Meyer, D. L., and Senter, P. D. (2003). Development of potent monoclonal antibody auristatin conjugates for cancer therapy. *Nat. Biotechnol. 21,* 778−784.

(6) Griffiths, G. L., Mattes, M. J., Stein, R., Govindan, S. V., Horak, I. D., Hansen, H. J., and Goldenberg, D. M. (2003). Cure of SCID Mice Bearing Human B-Lymphoma Xenografts by an Anti-CD74 Antibody-Anthracycline Drug Conjugate. *Clin. Cancer Res. 9,* 6567−6571.

(7) Hamann, P. R., Hinman, L. M., Beyer, C. F., Lindh, D., Upeslacis, J., Flowers, D. A., and Bernstein, I. (2002). An anti-CD33 antibody-calicheamicin conjugate for treatment of acute myeloid leukemia. Choice of linker. *Bioconjugate Chem. 13,* 40−46.

(8) Stan, A. C., Radu, D. L., Casares, S., Bona, C. A., and Brumeanu, T. D. (1999). Antineoplastic efficacy of doxorubicin enzymatically assembled on galactose residues of a monoclonal antibody specific for the carcinoembryonic antigen. *Cancer Res. 59,* 115−121.

(9) Jekunen, A., Kairemo, K., and Karnani, P. (1996). In vivo modulators of antibody kinetics. *Acta Oncol. 35,* 267−271.

(10) Palm, S., Enmon, R. M., Jr., Matei, C., Kolbert, K. S., Xu, S., Zanzonico, P. B., Finn, R. L., Koutcher, J. A., Larson, S. M., and Sgouros, G. (2003). Pharmacokinetics and Biodistribution of ^{86}Y-Trastuzumab for ^{90}Y dosimetry in an ovarian carcinoma model: correlative MicroPET and MRI. *J. Nucl. Med. 44,* 1148−1155.

(11) Lee, F. T., Rigopoulos, A., Hall, C., Clarke, K., Cody, S. H., Smyth, F. E., Liu, Z., Brechbiel, M. W., Hanai, N., Nice, E. C., Catimel, B., Burgess, A. W., Welt, S., Ritter, G., Old, L. J., and Scott, A. M. (2001). Specific localization, gamma camera imaging, and intracellular trafficking of radiolabeled chimeric anti-G(D3) ganglioside monoclonal antibody KM871 in SK-MEL-28 melanoma xenografts. *Cancer Res. 61,* 4474−4482.

(12) Reist, C. J., Archer, G. E., Wikstrand, C. J., Bigner, D. D., and Zalutsky, M. R. (1997). Improved targeting of an anti-epidermal growth factor receptor variant III monoclonal antibody in tumor xenografts after labeling using *N*-succinimidyl 5-iodo-3-pyridinecarboxylate. *Cancer Res. 57,* 1510−1515.

(13) Florent, J. C., Dong, X., Gaudel, G., Mitaku, S., Monneret, C., Gesson, J. P., Jacquesy, J. C., Mondon, M., Renoux, B., Andrianomenjanahary, S., Michel, S., Koch, M., Tillequin, F., Gerken, M., Czech, J., Straub, R., and Bosslet, K. (1998). Prodrugs of anthracyclines for use in antibody-directed enzyme prodrug therapy. *J. Med. Chem. 41,* 3572−3581.

(14) Wrasidlo, W., Gaedicke, G., Guy, R. K., Renaud, J., Pitsinos, E., Nicolaou, K. C., Reisfeld, R. A., and Lode, H. N. (2002). A novel 2′-(*N*-methylpyridinium acetate) prodrug of paclitaxel induces superior antitumor responses in preclinical cancer models. *Bioconjugate Chem. 13,* 1093−1099.

(15) Wong, B. K., DeFeo-Jones, D., Jones, R. E., Garsky, V. M., Feng, D. M., Oliff, A., Chiba, M., Ellis, J. D., and Lin, J. H. (2001). PSA-specific and non-PSA-specific conversion of a PSA-targeted peptide conjugate of doxorubicin to its active metabolites. *Drug Metab. Dispos. 29,* 313−318.

(16) DeFeo-Jones, D., Garsky, V. M., Wong, B. K., Feng, D. M., Bolyar, T., Haskell, K., Kiefer, D. M., Leander, K., McAvoy, E., Lumma, P., Wai, J., Senderak, E. T., Motzel, S. L., Keenan, K., Van Zwieten, M., Lin, J. H., Freidinger, R., Huff, J., Oliff, A., and Jones, R. E. (2000). A peptide-doxorubicin 'prodrug' activated by prostate-specific antigen selectively kills prostate tumor cells positive for prostate-specific antigen in vivo. *Nat. Med. 6,* 1248−1252.

(17) Safavy, A. Taxane derivatives for targeted therapy of cancer. US Patent 6,191,290, 2001.

(18) Safavy, A., Raisch, K. P., Khazaeli, M. B., Buchsbaum, D. J., and Bonner, J. A. (1999). Paclitaxel derivatives for targeted therapy of cancer: Toward the development of smart taxanes. *J. Med. Chem. 42,* 4919−4924.

(19) Safavy, A., Bonner, J. A., Waksal, H., Buchsbaum, D. J., Gillespie, G. Y., Khazaeli, M. B., Arani, R. B., Chen, D. T., Carpenter, M., and Raisch, K. P. (2003). Synthesis and biological evaluation of paclitaxel-C225 conjugate as a model for targeted drug delivery. *Bioconjugate Chem. 14,* 302−310.

(20) Salacinski, P. R., McLean, C., Sykes, J. E., Clement-Jones, V. V., and Lowry, P. J. (1981). Iodination of proteins, glycoproteins, and peptides using a solid-phase oxidizing agent, 1,3,4,6-tetrachloro-3alpha, 6alpha-diphenylglycoluril. *Anal. Biochem. 117,* 136−146.

(21) Fraker, P. J., and Speck, J. C. (1978). Protein and cell membrane iodinations with a sparingly soluble chloroamide, 1, 3, 4, 6-tetrachloro-3α, 6α-diphenylglycoluril. *Biochem. Biophys. Res. Commun. 80,* 849−857.

(22) Deutsch, H., Glinski, J., Hernandez, M., Haugwitz, R., Narayanan, V., Suffness, M., and Zalkow, L. (1989). Synthesis of congeners and prodrugs: Water soluble prodrugs of taxol with potent antitumor activity. *J. Med. Chem. 32,* 788−792.

(23) Bhargava, K. K., and Acharya, S. A. (1989). Labeling of monoclonal antibodies with radionuclides. *Semin. Nucl. Med. 19,* 187−201.

(24) Auzenne, E., Donato, N. J., Li, C., Leroux, E., Price, R. E., Farquhar, D., and Klostergaard, J. (2002). Superior therapeutic profile of poly-L-glutamic acid-paclitaxel copolymer compared with taxol in xenogeneic compartmental models of human ovarian carcinoma. *Clin. Cancer Res. 8,* 573−581.

(25) Luo, Y., and Prestwich, G. D. (1999). Synthesis and selective cytotoxicity of a hyaluronic acid-antitumor bioconjugate. *Bioconjugate Chem. 10,* 755−763.

(26) Sharma, A., Mayhew, E., Bolcsak, L., Cavanaugh, C., Harmon, P., Janoff, A., and Bernacki, R. J. (1997). Activity of paclitaxel liposome formulations against human ovarian tumor xenografts. *Int. J. Cancer 71,* 103−107.

(27) Sparreboom, A., Huizing, M. T., Boesen, J. J., Nooijen, W. J., van Tellingen, O., and Beijnen, J. H. (1995). Isolation, purification, and biological activity of mono- and dihydroxylated paclitaxel metabolites from human feces. *Cancer Chemother. Pharmacol.* 36*,* 299−304.

(28) Krishna Reddy, S. H., Lee, S., Datta, A., and Georg, G. I. (2001). Efficient synthesis of the 3′-phenolic metabolite of paclitaxel. *J. Org. Chem. 66,* 8211−8214.

(29) Press, O. W., Shan, D., Howell-Clark, J., Eary, J., Appelbaum, F. R., Matthews, D., King, D. J., Haines, A. M. R., Hamann, P., Hinman, L., Shochat, D., and Bernstein, I. D. (1996). Comparative metabolism and retention of iodine-125, yttrium-90, and indium-111 radioimmunoconjugates by cancer cells. *Cancer Res. 56,* 2123−2129.

(30) Geissler, F., Anderson, S. K., Venkatesan, P., and Press, O. (1992). Intracellular catabolism of radiolabeled anti-mu antibodies by malignant B-cells. *Cancer Res. 52,* 2907−2915.

(31) Li, C., Yu, D., Inoue, T., Yang, D. J., Milas, L., Hunter, N. R., Kim, E. E., and Wallace, S. (1996). Synthesis and evaluation of water-soluble polyethylene glycol-paclitaxel conjugate as a paclitaxel prodrug. *Anticancer Drugs 7,* 642−648.

(32) Greenwald, R. B., Gilbert, C. W., Pendri, A., Conover, C. D., Xia, J., and Martinez, A. (1996). Drug delivery systems:

Water soluble taxol 2′-poly(ethylene glycol) ester prodrugs-design and in vivo effectiveness. *J. Med. Chem. 39,* 424−431.
(33) Mandolini, L. (1978). Ring-closure reactions. The activation parameters for the formation of four to six-membered lactones from w-Bromoalkanoate ions. The role of the entropy factor in small- and common-ring formation. *J. Am. Chem. Soc. 100,* 550.
(34) Guillemard, V., and Saragovi, H. U. (2001). Taxane-antibody conjugates afford potent cytotoxicity, enhanced solubility, and tumor target selectivity. *Cancer Res. 61,* 694−699.

BC049868V

Sequence-Selective Cleavage of Oligoribonucleotides by 3d Transition Metal Complexes of 1,5,9-Triazacyclododecane-Functionalized 2′-*O*-Methyl Oligoribonucleotides

Teija Niittymäki and Harri Lönnberg*

Department of Chemistry, University of Turku, FIN-20014 Turku, Finland. Received July 14, 2004; Revised Manuscript Received September 10, 2004

2′-*O*-Methyl oligoribonucleotides bearing a 3′-[2,6-dioxo-3,7-diaza-10-(1,5,9-triazacyclododec-3-yl)decyl phospate conjugate group have been shown to cleave in slight excess of Zn^{2+} ions complementary oligoribonucleotides at the 5′-side of the last base-paired nucleotide. The cleavage obeys first-order kinetics and exhibits turnover. The acceleration compared to the monomeric Zn^{2+} 1,5,9-triazacyclododecane chelate is more than 100-fold. In addition, 2′-*O*-methyl oligoribonucleotides having the 1,5,9-triazacyclododec-3-yl group tethered to the anomeric carbon of an intrachain 2-deoxy-β-D-*erythro*-pentofuranosyl group via a 2-oxo-3-azahexyl, 2,6-dioxo-3,7-diazadecyl, or 2,9-dioxo-3,10-diazatridecyl linker have been studied as cleaving agents. These cleave as zinc chelates a tri- and pentaadenyl bulge opposite to the conjugate group approximately 50 times as fast as the monomeric chelate and show turnover. The cleavage rate is rather insensitive to the length of linker. Interestingly, a triuridyl bulge remains virtually intact in striking contrast to a triadenyl bulge. Evidently binding of the zinc chelate to a uracil base prevents its catalytic action. Replacement of Zn^{2+} with Cu^{2+} or Ni^{2+} retards the cleaving activity of all the cleaving agents tested.

INTRODUCTION

Oligonucleotide conjugates that sequence-selectively cleave complementary RNA targets have attracted considerable attention during the past decade (*1*–*5*). Such cleaving agents may enable chemical tailoring of RNA and, hence, serve as artificial restriction enzymes for RNA in vitro. In addition, they may possibly find applications in chemotherapy as chemically reactive antisense oligonucleotides that are able to destroy their target mRNA and exhibit RNase H independent turnover. The feasibility of such of an approach has been demonstrated by in vitro studies on cell lines (*6*, *7*), although not in vivo.

Most of the artificial ribonucleases described are conjugates of metal ion chelates having a lanthanide ion (*8*–*15*), Cu^{2+} (*16*–*19*), or Zn^{2+} (*20*–*22*) as the central ion. In addition, conjugates of peptidelike oligomers have been reported to catalyze sequence-selective phosphodiester hydrolysis, but their catalytic activity is still low compared to that of the metal ion-dependent cleavers (*23*–*31*). Since certain macrocyclic polyamines, the so-called azacrowns, bind 3d transition metal ions very tightly (*32*–*33*), in fact more tightly than many of the previously described metal-ion-dependent cleaving agents, and since some of these chelates, above all 1,5,9-tirazacyclododecane ([12]aneN_3, **1**), have been shown to promote the hydrolysis of RNA fragments rather efficiently (*34*–*37*), azacrown-functionalized oligonucleotides may be regarded as viable candidates of artificial RNases. For this purpose, we have recently prepared 2′-*O*-methyl oligoribonucleotides bearing a 1,5,9-triazacyclododec-3-yl group tethered either to the 3′-terminus of the oligonucleotide or to an intrachain abasic sugar unit (*38*). We now report on evaluation of the applicability of their Zn^{2+} complexes as artificial RNases. A detailed kinetic analysis of the cleavage reaction has been carried out by using synthetic oligoribonucleotides as targets. The influences of the concentration of the target and cleaving agent, the structure of the linker connecting the azacrown to the oligonucleotide, and the size and base content of the bulge created on the target upon hybridization have been studied. In addition, some comparative measurements with Cu^{2+} and Ni^{2+} complexes have been carried out.

EXPERIMENTAL PROCEDURES

Materials. Preparation of the azacrown-functionalized 2′-*O*-methyl oligoribonucleotides **2**–**4** and **6** has been described previously (*38*). Conjugate **5** was obtained as reported for **6**, and its authenticity was verified by ESI-MS. MS(ESI) for **5**: *m/z* 587.6 (8%) $[M - 8H]^{8-}$, 671.9 (30%) $[M - 7H]^{7-}$, 783.8 (76%) $[M - 6H]^{6-}$, 940.7 (100%) $[M - 5H]^{5-}$, 1175.9 (94%) $[M - 4H]^{4-}$, 1568.0 (44%) $[M - 3H]^{3-}$. M_{obs} 4708.5, M_{calcd} 4707.4.

The chimeric 2′-*O*-methylribo/ribo oligonucleotides (**7**–**17**) used as targets were assembled from commercially available 2′-*O*-methyl and 2′-*O*-triisopropylsilyloxymethyl (2′-*O*-TOM) protected 2-cyanoethyl-*N*,*N*-diisopropylphosphoramidite building blocks (Glen Research) by conventional phosphoramidite strategy using a 1.0 μmol scale and following the standard RNA-coupling protocol of Applied Biosystems 392 DNA/RNA Synthesizer.

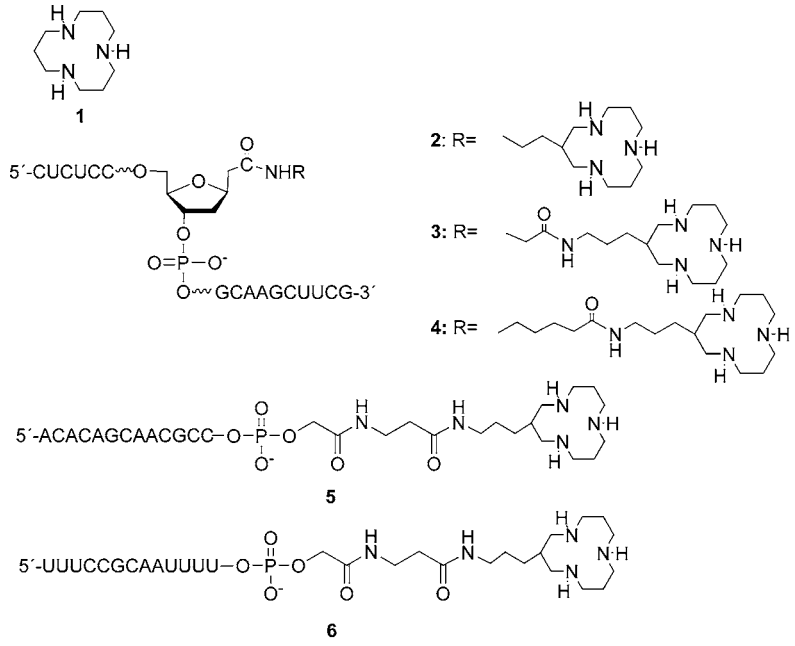
The buffer reagents and salts employed were of reagent grade. All buffer solutions were prepared in sterilized water, and sterilized equipments were used for their handling.

Kinetic Measurements. The reactions were carried out in Eppendorf tubes immersed in a water bath, the

* To whom correspondence should be addressed. E-mail: harlon@utu.fi.

10.1021/bc0498323 CCC: $27.50 © 2004 American Chemical Society
Published on Web 11/02/2004

Chart 1. Structures of Cleaving Agents (1−6), Targets (7−11), and Potential Product Oligonucleotides (12−17)[a]



7: 3′-GAGAG**GAAACG**UUCGAAGC-5′

8: 3′-GAGAG**GAAAAACG**UUCGAAGC-5′

9: 3′-GAGAG**GUUUCG**UUCGAAGC-5′

10: 3′-UGUGUCGUU**GCGGACAACAA**-5′

11: 3′-AAAGGCGUU**AAAAUCUUCAU**-5′

12: 3′-UGUGUCGUU**G**-5′

13: 3′-UGUGUCGUU**GC**-5′

14: 3′-UGUGUCGUU**GCG**-5′

15: 3′-UGUGUCGUU**GCGG**-5′

16: 3′-UGUGUCGUU**GCGGA**-5′

17: 3′-UGUGUCGUU**GCGGAC**-5′

[a] Bold letters refer to ribonucleotides, the rest to 2′-*O*-methylribonucleotides.

temperature of which was maintained at 35.0 ± 0.1 °C. The volume of the reaction mixture was 200 μL. The pH was adjusted to 7.3 with a HEPES buffer (0.1 mol L^{-1}). The Zn^{2+}, Cu^{2+} and Ni^{2+} ions were added as nitrates to give a total metal ion concentration of 50 μmol L^{-1}, and the ionic strength was adjusted to 0.1 mol L^{-1} with sodium nitrate. The concentration of the azacrown-functionalized oligonucleotides and their targets was varied from 9 to 36 μmol L^{-1} and 18 to 36 μmol L^{-1}, respectively. *p*-Nitrobenzenesulfonate ion was used as an internal standard.

Aliquots of 20 μL were withdrawn at suitable intervals and immediately cooled to 0 °C. The reaction was quenched by adding aqueous hydrogen chloride (1.0 μL of 1.0 mol L^{-1} solution). The samples were analyzed immediately.

Analysis of Samples. The samples were analyzed by capillary zone electrophoresis (CZE; Beckman Coulter P/ACE MDQ CE System) using a fused silica capillary (50 μm inner diameter, 60.2 cm total length, 50 cm effective length). The inverted polarity and citrate buffer (0.2 mol L^{-1}, pH 3.1) were used. The voltage applied was −30 kV. The temperature of the capillary was kept at 25 °C. The samples were injected using hydrodynamic injection with 2 psi for 8 s. The capillary was flushed with water, 10 mmol L^{-1} aqueous hydrogen chloride, and the background electrolyte buffer (for 3 min each) between every analytical run. UV-detection at 254 nm was applied to quantify the oligonucleotides and the internal standard.

Calculation of Rate Constants. First-order rate constants for the cleavage of the target oligonucleotides were calculated by applying the integrated first-order rate law to the disappearance of the starting material. The peak area was first normalized by dividing the area by the migration time and then by the similarly normalized area of the internal standard.

Determination of the Cleavage Site. The cleavage site within target **10** was determined by spiking with standards **12**−**17**. Each of the standards was added one after another to an aliquot of the reaction mixture, which contained the cleaved target **10**, and the mixtures were analyzed by CZE as described above. Standards **13**, **14**, and **17** did not comigrate with the cleavage products. Standard **16** comigrated with the minor product of the cleavage reaction. Standards **12** and **15** both comigrated with the major product. For this reason, those mixtures were additionally analyzed by an otherwise similar CZE method but using a different background electrolyte, viz. iminodiacetic acid (50 mmol L^{-1}, pH 2.3). Measurements in this more acidic buffer revealed standard **15** to be identical with the major cleavage product.

RESULTS AND DISCUSSION

Structure of the Cleaving Agents and Their Target Oligonucleotides. Chart 1 shows the cleaving agents studied (**2**−**6**), their target oligonucleotides (**7**−**11**), and the oligonucleotide standards used for the determination of the cleavage site (**12**−**17**). The cleaving agents are fully 2′-*O*-methylated oligoribonucleotides bearing the catalytically active [12]aneN_3 chelate tethered either to an abasic sugar unit within the chain (**2**−**4**) or to the 3′-terminal hydroxy function (**5**, **6**). The

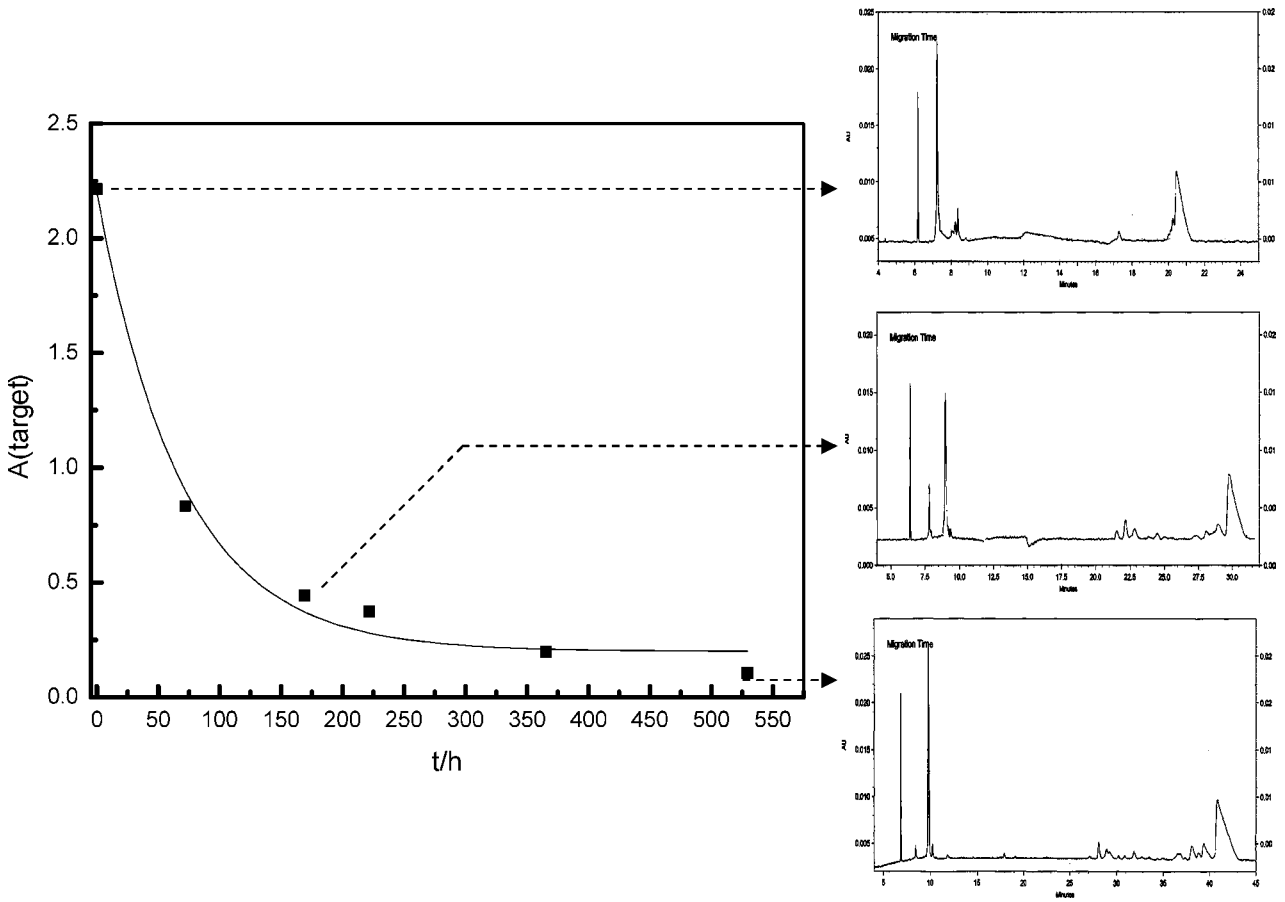


Figure 1. Cleavage of chimeric 2′-*O*-methylribo/ribo oligonucleotide **10** by sequence-selective cleaving agent **5** in 0.1 mol L^{-1} HEPES buffer at pH 7.3 and 35 °C (I = 0.1 mol L^{-1} with $NaNO_3$), and the electropherograms obtained at time 0, 165, and 530 h. The initial concentration of both the target oligonucleotide and the cleaving agent is 36 μmol L^{-1}.

targets are chimeric 2′-*O*-methylribo/ribo oligonucleotides containing several unsubstituted ribo units in the vicinity of the expected cleavage site, i.e. either 6 or 8 ribonucleosides in the middle of an 2′-*O*-methylribonucleotide chain (**7**−**9**) or 11 ribonucleosides at the 5′-end of a 2′-*O*-methylribonucleotide chain (**10**, **11**). The base sequences are selected so that upon hybridization of the cleaving agent with target, either a tri- or pentanucleotide bulge is formed on the target sequence (binding of **2**−**4** to **7**−**9**) or the sequence of the cleaving agent is fully complementary with the 3′-terminal sequence of the target (binding of **5** to **10** or **6** to **11**). Creation of a bulge to achieve intrachain cleavage is essential, since it has been shown that [12]aneN_3 cleaves oligoribonucleotide within a bulged region, even at a single nucleotide bulge, but it is unable to cleave phosphodiester bonds within a double helical region (*36*, *37*). Insertion of 2′-*O*-methylribonucleosides in the target sequence facilitates the synthesis and ensures high affinity of the target to the cleaving agent, preserving the A-type duplex structure (*39*).

Cleavage by the 3′-Tethered Conjugates. Figure 1 shows as an illustrative example the cleavage of target **10** by conjugate **5** in 0.1 mol L^{-1} HEPES buffer at pH 7.3 and 35.0 ± 0.1 °C. The concentration of both oligomers (**5**,**10**) was 36 μmol L^{-1} and that of Zn^{2+} somewhat higher, about 50 μmol L^{-1}, to ensure complete complexing [the stability constant for Zn^{2+}[12]aneN_3 is $10^{8.6}$ L mol^{-1} (*33*)]. Increasing of the Zn^{2+} concentration to 150 μmol L^{-1} did not, however, have any influence on the cleavage rate. The ionic strength was adjusted to 0.1 mol L^{-1} with $NaNO_3$. The progress of the reaction was followed by determining the composition of the aliquots withdrawn at suitable intervals by capillary electrophoresis. To facilitate the quantification, *p*-nitrobenzenesulfonate was used as an internal standard. As seen from the electropherograms in Figure 1, the target **10** entirely disappeared and a product oligonucleotide appeared at a longer retention time. First-order kinetics were reasonably well obeyed.

The cleavage site within target **10** was determined by spiking the product mixture with the potential cleavage products, i.e. with separately synthesized chimeric 2′-*O*-methylribo/ribo oligonucleotide standards **12**−**17**. Each of the standards was mixed separately with an aliquot of the reaction mixture containing the cleaved target **10**. The major product of the cleavage reaction, representing about 80% of the total cleavage, was observed to be **15**, the minor product being **16**. Accordingly, target **10** is predominantly cleaved at the 5′-side of the last base-paired nucleotide and to a minor extent at the phosphodiester bond one nucleotide toward the 5′-end.

The cleavage reaction also shows turnover. As seen from Figure 2, the target oligonucleotide is entirely cleaved obeying first-order kinetics, even when the target is present in a 4-fold excess compared to the cleaving agent. Cleaving agent **6** that contains only three cytosine bases and one guanine base and, hence, binds to its target (**11**) less firmly than **5** that forms eight CG base-pairs with **10**, exhibits under these turnover conditions 5-fold cleaving activity compared to **5**. Most likely the enhanced cleavage does not, however, result from the reduced affinity to the target, but from the fact that an 5′-UpA-3′ bond is cleaved instead of an 5′-ApG-3′. It is known that

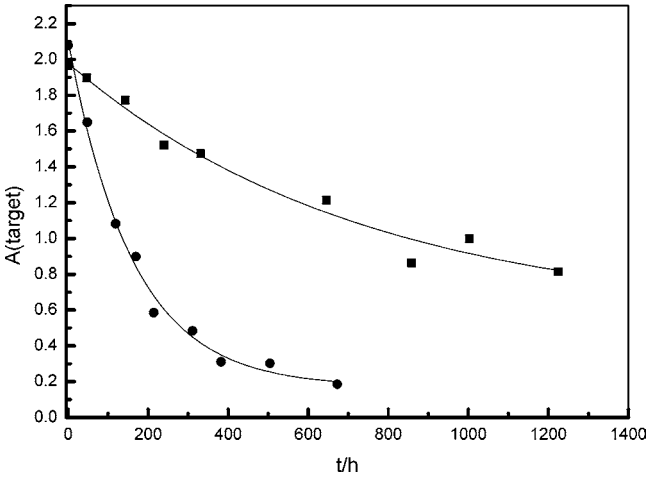


Figure 2. Cleavage of chimeric 2′-*O*-methylribo/ribo oligonucleotide **10** by cleaving agent **5** (squares) and **11** by **6** (circles). The concentration of the target oligonucleotides (**10**,**11**) is 36 μmol L^{-1} and that of the cleaving agents (**5**,**6**) 9 μmol L^{-1}. For the conditions, see the legend of Figure 1.

Table 1. First-order Rate Constants for the Cleavage of Targets 10 and 11 by Metal Ion Chelates of Conjugates 5 and 6, Respectively, in 0.10 Mol L^{-1} HEPES Buffer at pH 7.3 and 35 °C (I = 0.1 Mol L^{-1} with NaNO$_3$)[a]

cleaving agent	target	M^{2+}	c (cleaving agent), μmol L^{-1}	c (target), μmol L^{-1}	k, 10^{-6} s^{-1}
5	**10**	Zn^{2+}	36	36	1.5 ± 0.2
			18	18	1.4 ± 0.1
			18	36	0.31 ± 0.02
			9	36	0.20 ± 0.02
5	**10**	Cu^{2+}	18	18	0.49 ± 0.01
5	**10**	Ni^{2+}	18	18	0.71 ± 0.03
6	**11**	Zn^{2+}	18	36	0.77 ± 0.06
			9	36	1.0 ± 0.1
6	**11**	Cu^{2+}	9	36	0.62 ± 0.08
6	**11**	Ni^{2+}	9	36	0.71 ± 0.03

[a] The total concentration of M^{2+} was 50 μmol L^{-1}. Even at [M^{2+}] = 150 μmol L^{-1} the cleavage rate, however, remained unchanged.

within many sequences, the inherent hydrolytic stability of the 5′-UpA-3′ bond is lower than that of the other phosphodiester bonds (*40*).

Table 1 records the first-order rate constants obtained for the cleavage of targets **10** and **11** with conjugates **5** and **6**, respectively. With the more stable pair of the cleaving agent and target, **5/10**, the reaction rate is increased with the increasing concentration of **5**. Although the reaction at each concentration of **5** shows turnover, the rate is not strictly proportional to the concentration of **5**, but the rate constants obtained in excess of the target **10** are only half of the values expected on the basis of first-order dependence of the rate on the concentration of **5**. The reaction possibly is subject to moderate product inhibition, suggesting that the cleaving agent hybridizes slightly more efficiently with the product oligonucleotides **15**, **16** than with the target **10**. This inhibition is not, however, sufficiently strong to markedly deviate the cleavage from first-order kinetics. At 1:1 concentration ratio of the cleaving agent **5** and target **10**, the cleavage rate is independent of the concentration, as shown by the fact that the rate constants obtained at 36 and 18 μmol L^{-1} are equal within the limits of experimental error. Evidently in this concentration range the duplex formation is virtually quantitative. Surprisingly, the less efficiently hybridizing cleaving agent/target pair **6/11** behaved quite differently. Increasing the concentration of the cleaving agent from 9 to 18 μmol L^{-1} did not accelerate the cleavage of **11** on keeping the concentration of the latter constant (36 μmol L^{-1}). A possible, but still fully tentative, explanation is that **6**, containing two sequences of contiguous uracil bases, tends at higher concentrations to undergo intermolecular association by mutual interaction between the zinc chelate in one conjugate and a uracil sequence in another. For comparison, simultaneous binding of two Zn^{2+} chelates of 1,4,7,10-tetraazacyclododecane to two thymine bases has been shown to exhibit stability constants in micromolar range (*41*).

Table 2. First-Order Rate Constants for the Cleavage of Targets 7−9 by Zn^{2+} Chelates of Conjugates 2−4 in 0.10 Mol L^{-1} HEPES Buffer at pH 7.3 and 35 °C (I = 0.1 Mol L^{-1} with NaNO$_3$)[a]

cleaving agent	target	c (cleaving agent), μmol L^{-1}	c (target), μmol L^{-1}	k, 10^{-6} s^{-1}
2	**7**	18	18	0.74 ± 0.06
2	**8**	18	18	1.2 ± 0.08
2	**9**	9	36	<0.1
3	**7**	18	18	0.64 ± 0.06
		9	36	0.48 ± 0.02
3	**8**	18	18	1.1 ± 0.06
		9	36	0.37 ± 0.02
3	**9**	9	36	0.12 ± 0.02
4	**7**	18	18	0.51 ± 0.01
		9	36	0.46 ± 0.02
4	**8**	18	18	0.92 ± 0.04
		9	36	0.41 ± 0.03
4	**9**	9	36	0.11 ± 0.01

[a] The total concentration of Zn^{2+} was 50 μmol L^{-1}. Even at [Zn^{2+}] = 150 μmol L^{-1} the cleavage rate, however, remained unchanged.

Table 3. First-Order Rate Constants for the Cleavage of Targets 7 and 8 by Metal Ion Chelates of Conjugates 3 and 4 in 0.10 Mol L^{-1} HEPES Buffer at pH 7.3 and 35 °C (I = 0.1 Mol L^{-1} with NaNO$_3$)[a]

cleaving agent	target	M^{2+}	c (cleaving agent), μmol L^{-1}	c (target), μmol L^{-1}	k, 10^{-6} s^{-1}
3	**7**	Zn^{2+}	18	36	0.96 ± 0.05
		Cu^{2+}	18	36	0.25 ± 0.01
		Ni^{2+}	18	36	0.17 ± 0.02
3	**8**	Zn^{2+}	18	36	0.88 ± 0.04
		Cu^{2+}	18	36	0.55 ± 0.08
		Ni^{2+}	18	36	0.26 ± 0.02
4	**7**	Zn^{2+}	18	36	0.60 ± 0.04
		Cu^{2+}	18	36	0.20 ± 0.02
		Ni^{2+}	18	36	0.12 ± 0.01
4	**8**	Zn^{2+}	18	36	0.96 ± 0.05
		Cu^{2+}	18	36	0.44 ± 0.06
		Ni^{2+}	18	36	0.14 ± 0.01

[a] The total concentration of M^{2+} was 50 μmol L^{-1}.

In addition to Zn^{2+}, some comparative measurements were carried out with Cu^{2+} and Ni^{2+}. As seen from Table 1, both of these accelerated the cleavage of **10** by **5** and **11** by **6** less efficiently than Zn^{2+}.

Cleavage by the Intrachain Conjugates. Three targets, **7**−**9**, differing with respect to the size and base content of the bulge formed upon hybridization with the cleaving agent, were subjected to cleavage by metal ion chelates of three oligonucleotide conjugates, **2**−**4**, bearing the 1,5,9-triazacyclododecan-3-yl group in an intrachain position. The cleaving agents employed differed only with respect to the length of the tether by which the 1,5,9-triazacyclododecan-3-yl group was attached to the *C*1-β-carboxymethyl group of the abasic sugar unit. Tables 2 and 3 record the rate constants obtained.

Cleavage by the intrachain conjugates **2**−**4** shows turnover without any indication of product inhibition. In other words, the disappearance of the target is complete and obeyes first-order kinetics throughout a kinetic run, even when used in 4-fold excess compared to the cleaving agent. The cleavage rate is proportional to the concentration of the cleaving agent, as long as the target is present in excess and its concentration remains constant (36 μmol L^{-1}).

Somewhat unexpectedly, the length of the tether appears to play only a minor role. The cleavage of target **7**, forming a trinucleotide A_3-bulge upon hybridization, is retarded by 30% on going from the shortest (**2**) to the longest tether (**4**), when the target and cleaving agent are used in 1:1 concentration ratio (18 μmol L^{-1}). With target **8** forming a pentanucleotide A_5-bulge, the differences in the cleavage rate are even smaller (Table 2).

The more flexible pentanucleotide A_5-bulge is cleaved 1.6 to 1.8 times as fast as the trinucleotide A_3-bulge. Similar differences in the hydrolytic stability of pentanucleotide and trinucleotide bulges have previously been observed on using monomeric Zn^{2+}[12]aneN_3 as a cleaving agent (*37*). Interestingly, a trinucleotide U_3-bulge is considerably more stable than its A_3-counterpart. One may tentatively assume that the well-established tendency of Zn^{2+} azacrown chelates to bind uracil bases (*41*) prevents the interaction with internucleosidic phosphodiester bonds and, hence, the catalytic action is impeded.

Table 3 lists the first-order rate constants for the cleavage reactions on using Cu^{2+} or Ni^{2+} as a catalytic species instead of Zn^{2+}. As with the 3′-terminal conjugates, the Cu^{2+} and Ni^{2+} chelates of the oligonucleotide conjugates are less efficient cleaving agents than the Zn^{2+} chelates. However, the Cu^{2+} chelate is now more efficient than the Ni^{2+} chelate, while the situation with the 3′-terminal chelates is the opposite. It has been shown (*42*) that monomeric Zn^{2+}[12]aneN_3 cleaves polyuridylic acid 20 times more readily than the corresponding Ni^{2+} chelate. With the sequence-selective cleaving agents of the present study, the difference in the catalytic activity is less marked.

Cleaving Activity Compared to Other Zn^{2+}-Based Cleaving Agents. We have previously studied the cleavage of phosphodiester bonds within chimeric 2′-*O*-methylribo/ribo oligonucleotides using monomeric Zn^{2+}[12]aneN_3 as a catalyst (*37*). For example, the first-order rate constant for the cleavage of a 5′-UpA-3′ bond within a linear single strand in 5 mmol L^{-1} Zn^{2+} chelate solution at pH 7.4 and 35 °C is 4.2×10^{-6} s^{-1}. As seen from Table 1, the first-order rate constant for the cleavage of a 5′-UpA-3′ bond by cleaving agent **6** at 9 μmol L^{-1} concentration is 1.0×10^{-6} s^{-1} at pH 7.3. Accordingly, the acceleration compared to a monomeric chelate is 130-fold. Comparison of the rate constants observed for the cleavage of a A_3-bulge by cleaving agent **2** at 18 μmol L^{-1} concentration (0.74×10^{-6} s^{-1}) and by the monomeric Zn^{2+} chelate at 5 mmol L^{-1} concentration (4.5×10^{-6} s^{-1}) gives, in turn, a 46-fold acceleration. A comparable rate-enhancement compared to a monomeric cleaving agent has been previously obtained by tethering 2,9-dimethylphenanthroline to *C*5 of an intrachain uracil base (*18*, *22*). These dimethylphenanthroline conjugates cleave their complementary targets about 1 order of magnitude faster than the azacrown conjugates described in the present paper, because the Zn^{2+} complex of 2,9-dimethylphenanthroline is a more efficient cleaving agent than Zn^{2+}[12]aneN_3. The azacrown functionalized oligonucleotides have, however, one major advantage over the dimethylphenanthroline conjugates. The stability constant for the Zn^{2+} complex of 1,5,9-triazacyclododecane is $10^{8.6}$ L mol^{-1} (*33*), whereas the Zn^{2+} complex of 2,9-dimethylphenanthroline is more than 4 orders of magnitude less stable. Accordingly, while the dimethylphenanthroline conjugates are more efficient cleaving agents in excess of Zn^{2+}, the situation in all likelihood is the opposite at low metal ion concentrations and, hence, under intracellular conditions.

ACKNOWLEDGMENT

Financial support from the Academy of Finland is gratefully acknowledged.

LITERATURE CITED

(1) Travick, B. N., Daniher, A. T., and Bashkin, J. K. (1998) Inorganic mimics of ribonucleases and ribozymes: from random cleavage to sequence-specific chemistry to catalytic antisense drugs. *Chem. Rev. 98*, 939−960.
(2) Häner, R., Hall, J., Pfützer, A., and Hüsken, D. (1998) Development of artificial nucleases. *Pure Appl. Chem. 70*, 111−116.
(3) Komiyama, M., Sumaoka, J., Kuzuya, A., and Yamamoto, Y. (2001) Sequence-selective artificial ribonucleases. *Methods Enzymol. 341*, 455−468.
(4) Cowan, J. A. (2001) Chemical Nucleases. *Curr. Opin. Chem. Biol. 5*, 634−642.
(5) Häner, R. (2001) Artificial ribonucleases. *Chimia 55*, 1035−1037.
(6) Ushijima, K., Shirakawa, M., Kagoshima, K., Park, W.-S., Miyano-Kurosaki, N., and Takaku, H. (2001) Anti-HIV-1 activity of an antisense phosphorothioate oligonucleotide bearing imidazole and primary amine groups. *Bioorg. Med. Chem. 9*, 2165−2169.
(7) Baker, B. F., Lot, S. S., Kringel, J., Cheng-Flournoy, S., Villiet, P., Sasmor, H. M., Siwskowski, A. M., Chappel, L. L., and Morrow, J. M. (1999) Oligonucleotide -europium complex conjugate designed to cleave the 5′-cap structure of the ICAM-1 transcript potentiates antisense activity in cells, *Nucleic Acids Res. 27*, 1547−1551.
(8) Hall, J., Hüsken, D., Pieles, U., Moser, H. E., and Häner, R. (1994) Efficient sequence-specific cleavage of RNA using novel europium complexes conjugated to oligonucleotides. *Chem. Biol. 1*, 185−190.
(9) Hall, J., Hüsken, D., and Häner, R. (1996) Towards artificial ribonucleases: the sequence specific cleavage of RNA in a duplex. *Nucleic Acids Res. 24*, 3522−3526.
(10) Häner, R., and Hall, J. (1997) The sequence-specific cleavage of RNA by artificial chemical ribonucleases. *Antisense Nucleic Acid Drug Dev. 7*, 423−430.
(11) Canaple, L., Hüsken, D., Hall, J., and Häner, R. (2002) Artificial ribonucleases: efficient and specific in vitro cleavage of human *c-raf-1* RNA. *Bioconjugate Chem. 13*, 945−951.
(12) Magda, D., Miller, R. A., Sessler, J. L., and Iverson, B. L. (1994) Site-specific hydrolysis of RNA by europium(III) texapyrin conjugated to a synthetic oligodeoxyribonucleotide. *J. Am. Chem. Soc. 116*, 7439−7440.
(13) Magda, D., Wright, M., Crofts, S., Lin, A., and Sessler, J. L. (1997) Metal complex conjugates of antisense DNA which display ribozyme-like activity. *J. Am. Chem. Soc. 119*, 6947−6948.
(14) Huang, L., Chappell, L. L., Iranzo, O., Baker, B. F., and Morrow, J. R. (2000) Oligonucleotide conjugates of Eu(III) tetraazamacrocycles with pendent alcohol and amide groups promote sequence-specific RNA cleavage. *J. Biol. Inorg. Chem. 5*, 85−92.
(15) Matsumura, K., Endo, M., and Komiyama, M. (1994) Lanthanide complex-oligo-DNA hybrid for sequence-selective hydrolysis of RNA. *J. Chem. Soc., Chem. Commun.* 2019−2020.
(16) Bashkin, J. K., Frolova, E. I., and Sampath, U. (1994) Sequence-specific cleavage of HIV mRNA by a ribozyme mimic. *J. Am. Chem. Soc. 116*, 5981−5982.
(17) Trawick, B. N., Osiek, T. A., and Bashkin, J. K. (2001) Enhancing sequence-specific cleavage of RNA within a duplex

region: incorporation of 1,3-propanediol linkers into oligonucleotide conjugates of serinol-terpyridine. *Bioconjugate Chem. 12*, 900−905.
(18) Putnam, W. C., Daniher, A. T., Trawick, B. N., and Bashkin, J. K. (2001) Efficient new ribozyme mimics: direct mapping of molecular design principles from small molecules to macromolecular, biomimetic catalysis. *Nucleic Acids Res. 29*, 2199−2204.
(19) Sakamoto, A., Tamura, T., Furukawa, T., Komatsu, Y., Ohtsuka, E., Kitamura, M., and Inoue, H. (2003) Highly efficient catalytic RNA cleavage by the cooperative action of two Cu(II) complexes embodied within an antisense oligonucleotide. *Nucleic Acids Res. 31*, 1416−1425.
(20) Hovinen, J., Guzaev, A., Azhayeva, E., Azhayev, A., and Lönnberg, H. (1995) Imidazole tethered oligodeoxyribonucleotides: synthesis and RNA cleaving activity. *J. Org. Chem.* **1995**, *60*, 2205−2209.
(21) Matsuda, S., Ishikubo, A., Kuzuya, A., Yashiro, M., and Komiyama, M. (1998) Conjugates of a dinuclear zinc(II) complexes and DNA oligomers as novel sequence-selective artificial ribonucleases. *Angew. Chem., Int. Ed. 37*, 3284−3286.
(22) Åström, H., Williams, N. H., and Strömberg, R. (2003) Oligonucleotide based artificial nuclease (OBAN) systems. Bulge size dependence and positioning of catalytic group in cleavage of RNA-bulges. *Org. Biomol. Chem. 1*, 1461−1465.
(23) Reynolds, M. A., Beck, T. A., Say, P. B., Schwartz, D. A., Dwyer, B. P., Daily, W. J., Vaghefi, M. M., Metzler, M. D., Klem, R. E., and Arnold, L. J., Jr. (1996) Antisense oligonucleotides containing an internal nonnucleotide-based linker promote site-specific cleavage of RNA. *Nucleic Acids Res. 24*, 760−765.
(24) Komiyama, M., and Inokawa, T. (1994) Selective hydrolysis of tRNA by ethylenediamine bound to a DNA oligomer. *J. Biochem. 116*, 719−720.
(25) Endo, M., Azuma, Y., Saga, Y., Kuzuya, A., Kawai, G., and Komiyama, M. (1997) Molecular design for a pinpoint RNA scission. Interposition of oligoamines between two DNA oligomers. *J. Org. Chem. 62*, 846−852.
(26) Beloglazova, N. G., Silnikov, V. N., Zenkova, M. A., and Vlassov, V. V. (2000) Cleavage of yeast $tRNA^{Phe}$ with complementary oligonucleotide conjugated to a small ribonuclease mimic. *FEBS Lett. 481*, 277−280.
(27) Beloglazova, N. G., Epanchintsev, A. Yu., Silnikov, V. N., Zenkova, M. A., and Vlassov, V. V. (2002) Highly efficient site-directed RNA cleavage by imidazole-containing conjugates of antisense oligonucleotides. *Mol. Biol. 36*, 581−588.
(28) Mironova, N. L., Pyshnyi, D. V., Ivanova, E. M., Zenkova, M. A., Gross, H. J., and Vlassov, V. V. (2004) Covalently attached oligodeoxyribonucleotides induce RNase activity of a short peptide and modulate its base specificity. *Nucleic Acids Res. 32*, 1928−1936.
(29) Ushijima, K., Gouzu, H., Hosono, K., Shirakawa, M., Kagosima, K., Takai, K., and Takaku, H. (1998) Site-specific cleavage of tRNA by imidazole and/or primary amine groups bound at the 5′-end of oligodeoxyribonucleotides. *Biochim. Biophys. Acta 1379*, 217−223.
(30) Verheijen, J. C., Deiman, B. A. L. M., Yeheskiely, E., van der Marel, G. A., and van Boom, J. H. (2000) Efficient hydrolysis of RNA by a PNA-diethylenetriamine adduct. *Angew. Chem., Int. Ed. 39*, 369−372.
(31) Petersen, L., de Konig, M. C., van Kuik-Romeijn, P., Weterings, J., Pol, C. J., Platenburg, G., Overhand, M., van der Marel, G. A., and van Boom, J. H. (2004) Synthesis and in vitro evaluation of PNA-peptide-DETA conjugates as potential cell penetrating artificial ribonucleases. *Bioconjugate Chem. 15*, 576−582.
(32) Zompa, L. J. (1978) Metal complexes of cyclic triamines. 2. Stability and electronic spectra of nickel(II), copper(II), and zinc(II) complexes containing nine- through twelve-membered cyclic triamine ligands. *Inorg. Chem. 17*, 2531−2536.
(33) Kodama, M., and Kimura, E. (1977) Equilibria and kinetics of complex-formation between zinc(II), lead(II), and cadmium-(II), and 12-membered, 13-membered, 14-membered and 15-membered macrocyclic tetra-amines. *J. Chem. Soc., Dalton Trans.* 2269−2276.
(34) Kuusela, S., and Lönnberg, H. (1993) Metal ions that promote the hydrolysis of nucleoside phosphoesters do not enhance the intramolecular phosphate migration. *J. Phys. Org. Chem. 6*, 347−356.
(35) Kuusela, S., and Lönnberg, H. (1994) Metal ion promoted hydrolysis of polyuridylic acid. *J. Chem. Soc., Perkin Trans. 2* 2301−2306.
(36) Zagorowska, I., Kuusela, S., and Lönnberg, H. (1998) Metal ion-dependent hydrolysis of RNA phosphodiester bonds within hairpin loops. A comparative kinetic study on chimeric ribo/2′-*O*-methylribo oligonucleotides. *Nucleic Acids Res. 26*, 3392−3396.
(37) Kaukinen, U., Bielecki, L., Mikkola, S., Adamiak, R. W., and Lönnberg, H. (2001) The cleavage of phosphodiester bonds within small RNA bulges in the presence and absence of metal ion catalysts: towards artificial RNases. *J. Chem. Soc., Perkin Trans. 2* 1024−1031.
(38) Nittymäki, T., Kaukinen, U., Virta, P., Mikkola, S., and Lönnberg, H. (2004) Preparation of azacrown-functionalized 2′-*O*-methyl oligoribonucleotides, potential artificial RNases. *Bioconjugate Chem. 15*, 174−184.
(39) Popenda, M., Biala, E., Milecki, J., and Adamiak, R. W. (1997) Solution structure of RNA duplexes containing alternationg CG base pairs: NMR study of $r(CGCGCG)_2$ and 2′-*O*-$Me(CGCGCG)_2$ under low salt conditions. *Nucleic Acids Res. 25*, 4589−4598.
(40) Kaukinen, U., Lyytikäinen, S., Mikkola, S., and Lönnberg, H. (2002) The reactivity of phosphodiester bonds within linear single stranded oligoribonucleotides is strongly dependent on the base sequence. *Nucleic Acids Res. 30*, 468−474.
(41) Kimura, E., Kikuchi, M., Kitamura, H., and Koike, T. (1999) Selective and efficient recognition of thymidylylthymidine (TpT) by bis(Zn^{II}-cyclen) and thymidylylthymidylylthymidine (TpTpT) by tris(Zn^{II}-cyclen) at neutral pH in aqueous solution. *Chem. Eur. J. 5*, 3113−3123.
(42) Kuusela, S., and Lönnberg, H. (1994) Metal-ion-promoted hydrolysis of polyuridylic acid. *J. Chem. Soc., Perkin Trans. 2* 2301−2306.

BC0498323

Acid-Degradable Particles for Protein-Based Vaccines: Enhanced Survival Rate for Tumor-Challenged Mice Using Ovalbumin Model

Stephany M. Standley,[†,‡] Young Jik Kwon,[†,‡] Niren Murthy,[†,‡,§] Jun Kunisawa,[∥] Nilabh Shastri,[∥] Steven J. Guillaudeu,[†,‡] Lana Lau,[‡] and Jean M. J. Fréchet*[,†,‡,§]

Center for New Directions in Organic Synthesis and Departments of Chemistry and Molecular and Cellular Biology, University of California, Berkeley, California 94720-1460, and Materials Sciences Division, Lawrence Berkeley National Laboratory, Berkeley, California 94720. Received February 22, 2004; Revised Manuscript Received September 12, 2004

Acid-degradable protein-loaded polymer particles show promise for antigen-based vaccines due to their ability to activate cytotoxic T lymphocytes (CTLs) in vitro. Protein loadings and cytotoxic T lymphocyte activation efficiencies have now been enhanced through novel delivery vehicle designs. In particular, the use of a more hydrophilic acid-degradable cross-linker leads to increased water dispersibility and increased protein loading efficiency for the particles. A 2.5-fold increase in protein encapsulation allows the delivery of more protein antigen to antigen presenting cells (APCs) leading to a 20-fold rise in antigen presentation levels. The mechanism by which APCs internalize these particles was explored using the phagocytosis inhibitor, cytochalasin B. In addition, preliminary in vivo experiments were conducted to investigate the ability of the protein-loaded particles to provide immunity against tumors in mice, and an enhanced survival rate over the use of protein alone was observed, indicating that this vaccine delivery strategy has great practical potential.

INTRODUCTION

Traditional vaccine strategies have been ineffective at generating vaccines against diseases such as AIDS and hepatitis C, largely due to the high toxicity of the associated live attenuated viruses (*1*). Therefore, new vaccine strategies based on protein antigens are being investigated and have considerable promise due to their low toxicity and widespread applicability (*2*). Protein antigens have been identified for a number of different diseases, such as prostatic acid phosphatase for prostate cancer and gp120 and Tat for HIV, but the effectiveness of each of these would require the development of a more effectual vaccination strategy (*3*, *4*). Efficient protein-based vaccines must be able to activate CTLs, which play a central role in combating viral infections and tumors and generating immunity (*5*, *6*).

A key step in activating CTLs is the delivery of antigens into the cytoplasm of professional APCs, which process these cytoplasmic proteins by degrading them into peptides that are then assembled with major histocompatibility complex (MHC) class I molecules. These MHC class I peptide complexes are transported to the cell surface where they are recognized by antigen specific CTLs, which then become activated and primed to recognize and kill cells that have been infected with that particular antigen.

Therefore, a major challenge in generating this CTL response is to create a vaccine system that can efficiently deliver proteins into the cytoplasm of APCs in order to induce protective immunity against a specific disease. A delivery system is needed because exogenous antigens, proteins not synthesized in the cytoplasm, cannot efficiently reach the cytoplasm of APCs when administered alone as a vaccine because they are taken up through endocytosis and are sequestered and degraded in endosomes or lysosomes of the cell (*7*).

One class of protein delivery systems that is able to introduce exogenous proteins into the cytoplasm of APCs and has shown potential in vaccine research is polymer particles. One advantage of using particles as delivery vehicles is that they can be easily targeted to professional APCs by adjusting their size since it is known that APCs phagocytose particles that are 0.5−3 μm in diameter and cross-linked polymer beads of this size range have been shown to successfully encapsulate proteins (8-11). In theory, these particles could deliver a variety of protein antigens making this technology applicable to many diseases. In addition, encapsulation of proteins inside of the particles protects them from inactivation and unfavorable immune reactions that may occur during delivery.

Antigens associated with particles, such as proteins adsorbed onto polycaprolactone or polystyrene beads, as well as proteins covalently linked to the surface of iron oxide beads, have been shown to present peptides via the MHC class I pathway (*12*, *13*). Also, proteins encapsulated inside poly(lactide-*co*-glycolide) particles have been used to activate CTLs (*14*). These particle-based systems have demonstrated the validity of this method of protein delivery as a useful vaccination strategy. They were thought to weakly disrupt endosomes of APCs after internalization, which allowed a fraction of the protein to be delivered to the cytoplasm. However, while these particles were capable of being taken up by APCs, there

* To whom all correspondence should be addressed. Fax (510) 643-3079. E-mail: frechet@cchem.berkeley.edu.

[†] Center for New Directions in Organic Synthesis, University of California.

[‡] Department of Chemistry, University of California.

[§] Material Sciences Division, Lawrence Berkeley National Laboratory.

[∥] Department of Molecular and Cellular Biology, University of California.

10.1021/bc049956f CCC: $27.50 © 2004 American Chemical Society
Published on Web 10/22/2004

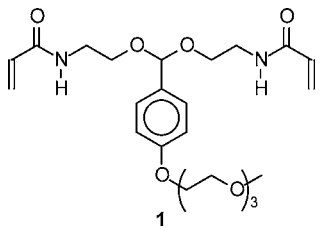


Figure 1. Acid-degradable cross-linker.

was no well-defined mechanism for the transfer of protein from endosomal compartments to the cytoplasm.

To improve upon the cytoplasmic delivery using polymer-based systems, we have reported previously a particle system that was designed to be strongly endosomal disruptive (*15*, *16*). These particles release encapsulated protein in a pH-dependent manner. They are stable at the physiological pH of 7.4 but degrade quickly in the pH 5.0 environment of endosomes, freeing the protein. The rationale for this design, known as the colloid osmotic mechanism (*7*, *17*), is to generate a quick degradation of the particles into many molecules, thus increasing the osmotic pressure within the endosome, leading to a rapid influx of water across the membrane resulting in its disruption. Rupture of the endosomal compartment affords the viral antigen an outlet to the cytoplasm of the cell while also circumventing the possible degradation of the protein by hydrolytic enzymes present in the mildly acidic endosome.

The acid-sensitive protein-loaded particles were synthesized by copolymerizing an acid-degradable cross-linker, **1** (Figure 1) and acrylamide in the presence of a protein using an inverse emulsion polymerization technique. Preliminary experiments have demonstrated that these particles were nontoxic and were capable of MHC class I presentation and CTL activation in vitro, which was determined by the LacZ assay (*16*). Although this system showed promise for applications in vaccine development, this new strategy had not been optimized or evaluated using in vivo experiments.

In this report the protein-loading capacity and enhanced water dispersibility of the particle system are investigated. In addition, we present in vitro studies evaluating the CTL activation levels of the optimized particles and discuss the mechanism by which the particles are internalized by APCs. Finally, preliminary in vivo experiments testing the ability of the protein delivery vehicle to provide a protective immunity against tumors using an ovalbumin model are presented.

EXPERIMENTAL PROCEDURES

General Procedures and Materials. Tetrahydrofuran was distilled under a nitrogen atmosphere from Na/benzophenone immediately prior to use. *p*-Toluenesulfonic acid was dehydrated and then recrystallized from toluene. *N*-(2-Hydroxyethyl)-2,2,2-trifluoroacetamide and acryloyl chloride were freshly distilled before each use. Combined organic layers after extractions were dried over anhydrous $MgSO_4$. Solvents were removed under reduced pressure using a rotary evaporator. Merck Kieselgel plates coated with silica gel 60 F_{254} were used for thin-layer chromatography, and compounds were visualized by UV activity. Flash column chromatography was done with Merck Kieselgel 60 silica gel (230−400 Mesh). Mice were purchased from Jackson Laboratory, and cells were purchased from the ATCC. The SIINFEKL peptide was purchased from the Synpep Corporation. The antibody 25.D1-16 was produced from the hybridoma cells generously provided by Dr. Ronald Germain of NIAID, and the goat anti-mouse antibody labeled with R-phycoethrin (PE) was purchased from Pharmingen.

Characterization. ^{1}H NMR spectra were recorded at 300 or 400 MHz, and ^{13}C spectra were recorded at 100 MHz. NMR chemical shifts are reported in ppm relative to tetramethylsilane (TMS) and are calibrated against residual solvent peaks: $CDCl_3$ (δ 7.26, δ 77.23) or DMSO-d_6 (δ 2.49, δ 39.51). All coupling constants are reported in Hz. High-resolution fast atom bombardment mass spectrometry (FAB-HRMS) experiments were performed at the UC−Berkeley mass spectrometry facility. FT-IR spectroscopic analyses were performed using a thin film cast from $CHCl_3$ on a reflective mirror surface. Elemental analyses were performed by M-H-W Laboratories or at the UC−Berkeley Analytical Laboratory.

***N,N′*-Diacryloyl-bis(2-aminoethoxy)-[4-(1,4,7,10-tetraoxaundecyl)phenyl]methane (1).** This compound was prepared according to literature procedure (*16*).

1-Chloro-3,6,9,12-tetraoxatridecane (3). This compound was prepared according to the reaction conditions reported by Schafheute et. al. used to prepare 1-chloro-3,6,9,12,15-pentaoxahexadecane (*18*). This procedure was modified by using dichloroethyl ether as the dichloride compound. The product was isolated by short path distillation (106 °C/2 mmHg). IR (cm^{-1}): 2875 (s), 1149 (s). ^{1}H NMR (300 MHz, $CDCl_3$): δ 3.38 (s, 3), 3.55 (t, 2, J = 4.6), 3.75 (t, 2, J = 5.9), 3.60−3.67 (m, 12). ^{13}C NMR ($CDCl_3$): δ 42.36, 58.60, 70.11, 70.19, 70.21, 70.24, 70.96, 71.55. Calcd: $[M + H]^+$ ($C_9H_{20}O_4Cl$) m/z = 227.1050. Found FAB-HRMS: $[M + H]^+$ m/z = 227.1045. Anal. Calcd. for $C_9H_{19}O_4$: C, 47.68; H, 8.45. Found: C, 47.83; H, 8.62.

***p*-(1,4,7,10,13-Pentaoxatetradecyl)benzaldehyde (4).** Chloride **3** (13.3 g, 58.6 mmol, 1.5 equiv) and *p*-hydroxybenzaldehyde (4.78 g, 39.1 mmol, 1 equiv) were dissolved in dry THF (15 mL). K_2CO_3 (5.4 g, 39.1 mmol, 1 equiv) was added followed by 18-crown-6 (103 mg, 0.39 mmol, 0.01 equiv) and KI (64.9 mg, 0.39 mmol, 0.01 equiv). The reaction mixture was stirred at reflux for 48 h. The resulting mixture was cooled to room temperature, and water (150 mL) was added. The product was extracted with three 150 mL portions of ethyl acetate, and the combined organic layers were dried and concentrated. The oil was loaded onto a silica gel column and eluted with a 1:1 mixture of ethyl acetate/hexane to afford 11.8 g (97%) of **4** as a clear oil. IR (cm^{-1}): 1693 (s), 1132 (s). ^{1}H NMR (300 MHz, $CDCl_3$): δ 3.33 (s, 3), 3.50 (t, 2, J = 4.5), 3.72−3.58 (m, 10), 3.86 (t, 2, J = 4.8), 4.18 (t, 2, J = 4.8), 6.99 (d, 2, J = 8.7), 7.79 (d, 2, J = 8.6), 9.80 (s, 1). ^{13}C NMR ($CDCl_3$): δ 58.82, 67.59, 69.26, 70.32, 70.41, 70.43, 70.69, 71.73, 114.70, 129.84, 131.74, 163.68, 190.59. Calcd: $[M + H]^+$ ($C_{16}H_{25}O_6$) m/z = 313.1651. Found FAB-HRMS: $[M + H]^+$ m/z = 313.1643.

***N,N′*-Bis(trifluoroacetyl)-bis(2-aminoethoxy)-[4-(1,4,7,10,13-pentaoxatetradecyl)phenyl]methane (5).** Aldehyde **4** (6.65 g, 21.3 mmol, 1 equiv) and *N*-(2-hydroxyethyl)-2,2,2-trifluoroacetamide (25.4 g, 161.8 mmol, 7.6 equiv) were dissolved in dry THF (40 mL). *p*-Toluenesulfonic acid (586 mg, 3.4 mmol, 0.16 equiv) and 5 Å molecular sieves (52 g) were added. The reaction mixture was stirred overnight and then quenched with triethylamine (3.8 mL, 27.7 mmol, 1.3 equiv). The reaction mixture was filtered, and water (150 mL) was added to the filtrate. The product was extracted with five 150 mL portions of ethyl acetate, and the solvent was evaporated. To remove the excess alcohol, benzoyl chloride (16.3 mL, 140.4 mmol, 1 equiv), triethylamine (40.0 mL, 280.8 mmol, 2 equiv), and dry THF (100 mL) were

added. The reaction mixture was stirred at room temperature for 1 h. Water (250 mL) was added and the product was extracted with five 250 mL portions of ethyl acetate, and the solvent was evaporated. The remaining oil was loaded onto a silica gel column and eluted with a 3:7 mixture of ethyl acetate/hexane, followed by a 4:1 mixture of ethyl acetate/hexane to afford 10.4 g (82%) of **5** as a white solid. MP: 74.6−75.0 °C. IR (cm^{-1}): 3292 (br), 1701 (s), 1560 (m), 1209 (s), 1178 (s). ^1H NMR (400 MHz, DMSO-d_6): δ 3.21 (s, 3), 3.34−3.41 (m, 6), 3.46−3.58 (m, 14), 3.72 (t, 2, $J = 4.6$), 4.07 (t, 2, $J = 4.6$), 5.52 (s, 1), 6.91 (d, 2, $J = 8.4$), 7.29 (d, 2, $J = 8.4$), 9.53 (t, 2, $J = 5.6$). ^{13}C NMR (DMSO-d_6): δ 39.22, 58.01, 62.56, 67.12, 68.89, 69.56, 69.76, 69.81, 69.91, 71.26, 100.54, 113.92, 115.19 (q, $J = 288$), 127.72, 130.25, 156.38 (q, $J = 36$), 158.51. Calcd: $[M]^+$ ($C_{24}H_{34}F_6N_2O_9$) $m/z = 608.2168$. Found FAB-HRMS: $[M]^+$ $m/z = 608.2153$. Anal. Calcd. for $C_{24}H_{34}F_6N_2O_9$: C, 47.37; H, 5.63; N, 4.60. Found: C, 47.20; H, 5.84; N, 4.54.

***N,N′*-Diacryloyl-bis(2-aminoethoxy)-[4-(1,4,7,10,-13-pentaoxatetradecyl)phenyl]methane (2).** Compound **5** (0.40 g, 0.66 mmol, 1 equiv) and 6 M NaOH (2.8 mL) were added to dioxane (1.8 mL), and the reaction mixture was stirred at room temperature for 3.5 h. Upon complete removal of the acetamide groups, as determined by TLC using ninhydrin staining, the reaction mixture was cooled to 0 °C and triethylamine (0.6 mL) was added. Acryloyl chloride (1.1 mL, 14 mmol, 21 equiv) and triethylamine (5.6 mL, 40.0 mmol, 61 equiv) were added in small alternating portions while periodically monitoring the pH to maintain it above 7. A 10% K_2CO_3 in water solution (40 mL) was added, and the reaction was stirred for 10 min before extracting the product with six 40 mL portions of ethyl acetate. The organic layers were dried and concentrated to afford a yellow oil. The crude product was purified by column chromatography and eluted with a 2:1 mixture of ethyl acetate/hexane, followed by ethyl acetate, and a 1:9 mixture of methanol/ethyl acetate to afford 0.20 g (58%) of **2** as a white solid. MP: 62.0−63.0 °C. IR (cm^{-1}): 3302 (br), 1657 (s), 1541 (m), 1102 (s). ^1H NMR (300 MHz, DMSO-d_6): δ 3.21 (s, 3), 3.29 (t, 2, $J = 4.5$), 3.39−3.55 (m, 18), 3.72 (t, 2, $J = 4.6$), 4.07 (t, 2, $J = 4.6$), 5.49 (s, 1), 5.56 (dd, 2, $J = 10$, $J = 2$), 6.10 (dd, 2, $J = 17$, $J = 2$), 6.30 (dd, 2, $J = 17$, $J = 10$), 6.90 (d, 2, $J = 8.6$), 7.32 (d, 2, $J = 8.6$), 8.20 (t, 2, $J = 5.5$). ^{13}C NMR (DMSO-d_6): δ 38.67, 58.01, 63.77, 67.07, 68.88, 69.54, 69.74, 69.78, 69.89, 71.24, 100.80, 113.88, 125.06, 127.83, 130.60, 131.67, 131.87, 158.42, 164.68. Calcd: $[M + Li]^+$ ($C_{26}H_{40}N_2O_9Li$) $m/z = 531.2893$. Found FAB-HRMS: $[M + Li]^+$ $m/z = 531.2883$. Anal. Calcd. for $C_{26}H_{40}N_2O_9$: C, 59.53; H, 7.69; N, 5.34. Found: C, 59.19; H, 7.63; N, 5.04.

Inverse Emulsion Polymerization. To generate protein-loaded particles, an inverse emulsion polymerization technique was used. The organic phase consisted of hexane (5 mL) and 150 mg of surfactants. A 3:1 weight ratio of Span 80 (sorbitan monooleate) and Tween 80 (poly(ethylene glycol)−sorbitan monooleate) was used. The oxygen dissolved in the organic phase was removed by sparging with nitrogen for 10 min. The aqueous phase consisted of acrylamide and cross-linker (250 mg combined in a range of ratios) dissolved in 300 mM sodium phosphate-buffered water (pH 8, 500 μL). The oxygen dissolved in the aqueous phase was removed by purging with nitrogen for 1 min. Free radical initiator, potassium peroxodisulfate (12 mg), and ovalbumin (labeled with cascade blue dye or unlabeled) were added to the aqueous phase and then emulsified with the organic phase by sonicating for 30 s. Polymerization was initiated by the addition of *N,N,N′,N′*-tetramethylethylenediamine (TMEDA) and stirred for 10 min at room temperature. The mixture was centrifuged at 2800 rpm for 10 min, and the supernatant was decanted. The particles were washed with two 20 mL portions of hexane, followed by four 20 mL portions of acetone, and finally centrifuged. The solvent was decanted, and the purified particles were dried in vacuo overnight.

Nondegradable particles were prepared using the method described above using *N,N′*-methylene-bis-acrylamide as the cross-linker. The mole percent of cross-linker and total weight of monomer and cross-linker combined were the same as above.

Scanning Electron Microscopy. The particles were dried in vacuo to remove residual water, sputter-coated with a 20 nm gold layer, and viewed in a scanning electron microscope (WDX ISI-ds130C, Microspec Corporation, Inc.). Photographs were taken at 15 kV.

Protein Encapsulation Measurements. A small amount of each particle sample (2 mg) containing ovalbumin labeled with cascade blue was dispersed in 300 mM sodium phosphate-buffered water (pH 8, 500 μL). The samples were then centrifuged for 5 min, and the supernatant was removed. The pellet was then redispersed into 300 mM sodium acetate buffered water (pH 1.6, 500 μL). Once completely hydrolyzed, the fluorescence emission of the aqueous solution was measured at 405 nm with an excitation at 355 nm. The unknown protein concentration of each particle sample was calculated by fitting the emission to a calibration curve made from known concentrations of ovalbumin labeled with cascade blue. The background emission of the buffer was measured and subtracted from all of the readings. Each sample was done in triplicate.

The protein determination of the nondegradable particles was performed differently since they do not degrade in acidic conditions. The samples were weighed and washed in a pH 8 buffer. The solid was then redispersed into 6 M NaOH to hydrolyze the protein−cascade blue into smaller pieces that could diffuse out of the particles. After 1 day, the solid was removed by centrifugation and the fluorescence emission of the aqueous solution was measured at 405 nm with an excitation at 355 nm. The unknown protein concentration of each microparticle sample was calculated by fitting the emission to a calibration curve made from known concentrations of ovalbumin−cascade blue that had been dissolved in 6 M NaOH for the same period of time. Each sample was done in triplicate, and degradable particles were also analyzed at the same time in this fashion for direct comparison. Although the amount of protein measured for the degradable samples using this method was higher than found for the method above, a relative comparison between the samples was performed.

Class I Antigen Presentation Assay. The class I antigen presentation assay (LacZ assay) was performed using the OVA-derived SIINFEKL peptide/K^b-specific B3Z T cell hybridoma and RAW 309.1 CR antigen presenting cells. RAW cells were plated at 5×10^4 cells per well in a 96-well plate and allowed to grow overnight. Ovalbumin loaded particles were dispersed in DMEM medium (5 mg/mL) and sonicated for 5 min. An appropriate amount of the particle stock solution was added to the cells, in a 100 μL volume. The RAW cells were incubated with the particles for 6 h at 37 °C and then washed several times with DMEM medium. B3Z cells (1×10^5) were added to the RAW cells, and the two cell lines were incubated together for 16 h in RPMI media at 37 °C. LacZ activity was measured as the absorbance at 595 nm of the cleavage product of chlorophenol red-β-D-

galactopyranoside. All samples were performed in triplicate.

For each antigen presentation assay performed, a standard peptide curve was prepared by incubating the RAW cells with a series of SIINFEKL concentrations alongside the particle samples. The absorbance at 595 nm was plotted against the log of the peptide concentration. The resulting curve was sigmoidal, but only the optimal concentrations were used for the linear standard so high and low concentrations were deleted. The trendline equation was then used to quantify the amount of peptide presented using the absorbance values.

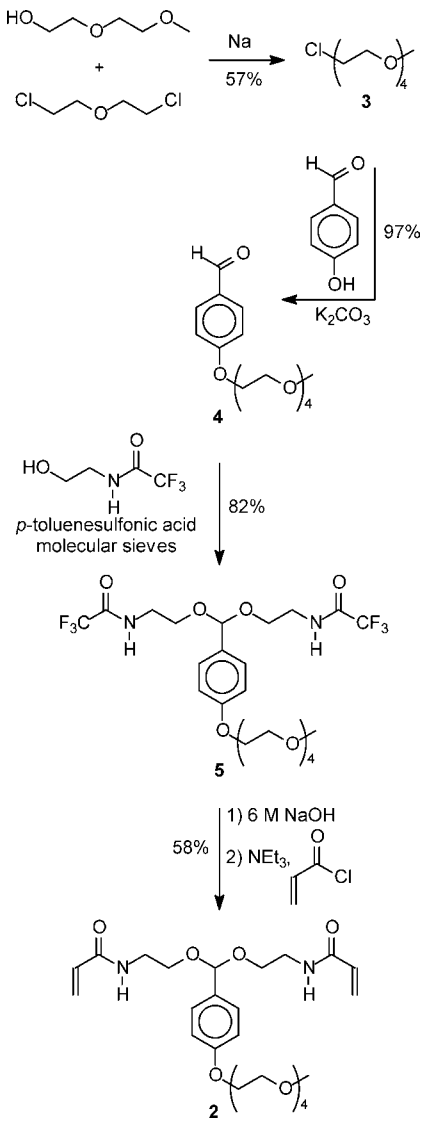
Cytochalasin B Assay. To inhibit phagocytosis, RAW cells were incubated in a 17 μM solution of cytochalasin B in DMEM 2 h before the particle samples were added. Identical particle samples were added to both the inhibited and uninhibited groups of cells in triplicate. The remainder of the experiment was the same as described above for the class I antigen presentation assay.

In Vivo Tumor Protection Experiment. Experiments were performed with female C57BL/6 mice and all immunizations were administered by subcutaneous injections using 26 gauge needles. There were three groups (15 mice per group): control mice injected with saline (200 μL); mice injected with free ovalbumin in saline (50 μg in 200 μL); and mice injected with ovalbumin encapsulated in particles (Sample D) dispersed in saline (1.13 mg particles, corresponds to 50 μg ovalbumin, in 200 μL). A second identical immunization was delivered 2 weeks after the first. Then 10 days after the second immunization, tumors were established by administering an injection of 1×10^6 EG7-OVA tumor cells in 100 μL saline into the shaved left flank of each mouse. One week prior to injection, the EG7 cells were stained with the anti-SIINFEKL/K^b monoclonal antibody 25.D1-16 and the secondary goat anti-mouse antibody labeled with R-phycoethrin (PE). Then highly ovalbumin-expressing cells were collected using flourescence-activated cell sorting (FACS) and proliferated. After injection, the tumor growth was monitored by measuring two perpendicular axes using digital calipers. Tumor volume was then calculated using the equation, volume = 0.5 $\times$ length $\times$ width^2, with the length being the longest diameter and the width being the shortest diameter of the two perpendicular measurements. Once the tumor reached 1.5 cm in average diameter, the mouse was removed from the experiment and euthanized according to guidelines set by the UC−Berkeley Animal Care and Use Committee. Mice were also removed if they showed other signs of pain or distress such as a lack of cleaning, eating, or mobility. A log rank test was used to determine *p*-values. A *p*-value of 0.05 or less was considered to be statistically significant.

RESULTS AND DISCUSSION

Controlling the Hydrophilicity of the Cross-Linker. The dispersibility of particles made with cross-linker **1**, while sufficient for proof-of-concept experiments, required further improvement, as the particles it afforded as a white powder could be suspended in an aqueous solution, but they readily aggregated and formed a precipitate. For practical application as a vaccine, the material should be uniformly dispersed in solution, enabling it to be used by injection. Covering the particle surface with a long hydrophilic oligoethylene glycol layer would be expected to enhance the colloidal properties of the particles in water due to greater hydration and steric stabilization afforded by the layer (*19*−*21*). However, the use of high molecular weight poly(ethylene glycol) chains was not pursued since it has been shown that a 5 kDa poly(ethylene glycol) surface on poly(lactic-*co*-glycolic acid) particles diminished the recognition of particles by phagocytic cells, and this would clearly be detrimental in our target application (*20*). To balance the need for enhanced hydrophilicity and the requirements of inverse microemulsion polymerization (*16*), we prepared cross-linker **2** in which the solubilizing group is extended by one ethylene oxide unit over that of our earlier cross-linker **1**.

Scheme 1. Synthesis of Cross-Linker



This target molecule **2** was prepared in four steps as shown in Scheme 1. 1-Chloro-3,6,9,12-tetraoxatridecane, **3**, was prepared and coupled to *p*-hydroxybenzaldehyde and K_2CO_3 to afford **4** in 97% yield. Intermediate **5** was synthesized in 82% yield by reaction of **4** with *N*-(2-hydroxyethyl)-2,2,2-trifluoroacetamide in the presence of a catalytic amount of *p*-toluenesulfonic acid and a drying agent to shift the equilibrium toward the acetal product. To install the polymerizable handles, the primary amine groups of **5** were deprotected with 6 M NaOH and coupled to acryloyl chloride in dioxane using biphasic conditions, affording **2** in 58% yield. Triethylamine was added in the final step to quench any HCl byproduct in order to avoid any possible and untimely degradation of the acid labile acetal.

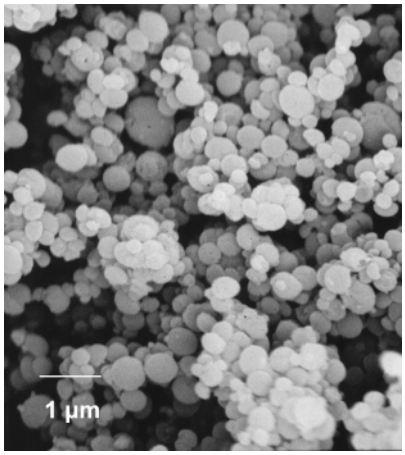


Figure 2. SEM image of particles prepared with cross-linker 2.

Inverse Emulsion Polymerization with Cross-Linker 2. Cross-linked protein-loaded particles were synthesized using **2** and acrylamide as the monomers in an inverse microemulsion polymerization process (*16*, *22*). First, **2** and acrylamide were dissolved in buffered water, and ovalbumin and the polymerization initiator, potassium peroxodisulfate, were then added. The aqueous phase was dispersed into an organic phase, which consisted of a 3:1 blend of Span 80 and Tween 80 surfactants in hexane. Span 80 and Tween 80 were chosen because they are nonionic and nontoxic. The emulsion was created by sonication and polymerization was initiated upon addition of TMEDA. After polymerization, the particles were isolated by centrifugation, washed, and dried to remove residual hexane and surfactants. The particle size ranged from 250 to 500 nm in diameter, as determined by Figure 2, and we observed that the particles were readily dispersible in water unlike particles synthesized with the less hydrophilic cross-linker **1**.

Protein Loading Studies. Increasing the amount of protein encapsulated in the particles was an important step in developing an effective and better controlled delivery system. Ideally, the amount of protein delivered to an APC per particle would be large enough to produce efficient MHC class I presentation. This is especially important for in vivo experiments where a smaller number of particles per cell would be taken up as compared to tissue culture. In initial studies with cross-linker **1** (*16*), it was noted that the protein loading did not change with the degree of cross-linking. Therefore, protein loading studies were carried out using a fixed amount of cross-linker **1** (12.8%) and acrylamide in the polymerization mixture, varying only the concentration of ovalbumin labeled with cascade blue. Following inverse microemulsion polymerization, the amount of protein encapsulated was determined for each sample by hydrolyzing the particles in acidic conditions until the solution became completely clear and then measuring the fluorescence of the released ovalbumin in solution.

Protein loading increased with initial ovalbumin concentration in the polymerization mixture as shown in Table 1. For example, when the initial amount of protein in the polymerization was tripled from 5.4 mg to 16.8 mg, the amount of ovalbumin encapsulated doubled from 9.5 μg/mg to 22.0 μg/mg as illustrated by samples A (*16*) and B in Table 1. Also, when the initial amount was 33.2 mg, the final ovalbumin loading increased 6-fold from 9.5 to 62.6 μg/mg as shown in sample C. The appearance and stability of the particles remained the same even though more protein had been encapsulated. The maximum ovalbumin encapsulation achieved with this system using cross-linker **1** was 62.6 μg/mg particles for sample C. The use of higher initial protein concentrations in reaction mixtures involving this set of monomers and polymerization conditions resulted in a large amount of aggregation and precipitation during the polymerization.

Table 1. Particle Samples with Increased Protein Loading

sample	cross-linker	initial amount of cascade blue-labeled ovalbumin (mg)	encapsulated ovalbumin/particles (μg/mg)
A	1	5.4	9.5
B	1	16.8	22.0
C	1	33.2	62.6
D	2	5.2	44.3
E	2	33.0	135.6
F	2	45.6	154.8

The same experiments were performed using the new, more hydrophilic, cross-linker **2** with the same mole percent of cross-linker (12.8%), keeping the total amount of monomers (acrylamide and **2**) constant. The concentration of ovalbumin labeled with cascade blue in the initial polymerization mixture was varied as shown in Table 1. Unexpectedly, higher protein encapsulation efficiencies were achieved using the more hydrophilic **2**. This increase in efficiency may be due to increased stabilization of the particles and protein in the emulsion or aqueous solution causing less protein aggregation and precipitation. The protein encapsulation efficiency of particles made with **2** was over twice that of particles made with **1**. For example, when 33 mg of ovalbumin was added to the initial mixture, the loading of particles made with **1** was 62.6 μg ovalbumin/mg particles (sample C), whereas the loading of particles made with **2** was 135.6 μg protein/mg particles (sample E). The maximum protein encapsulation obtained with cross-linker **2** was 154.8 μg ovalbumin/mg particles in sample F. Therefore, our goals of increasing the hydrophilicity of the particles while achieving better control over their protein content were met with the development and application of cross-linker **2**.

Antigen Presentation Experiments with Highly Loaded Particles. LacZ antigen presentation assays, developed by Karttunen et al., were performed to determine if the increased encapsulation of protein in the acid-degradable particles resulted in enhanced cytoplasmic delivery of protein to APCs, leading to higher MHC class I presentation levels and CTL activation (*23*). To demonstrate CTL activation, the particles were first incubated at various concentrations with the antigen presentation cell line, RAW 309.1 CR, for 6 h. After removal of extracellular particles, the APCs were incubated with ovalbumin specific B3Z cells. These B3Z cells are CTLs engineered to secrete β-galactosidase after binding to the ovalbumin-derived SIINFEKL peptide in a MHC class I (K^b)-restricted manner. This allows T cell activation to be quantified by β-galactosidase activity. Higher β-galactosidase activity, quantified by absorbance measurements at 595 nm due to release of a dye, infers greater antigen presentation and CTL activation levels. The measured absorbance values at 595 nm can then be converted into the corresponding concentration of SIINFEKL peptide presented using a standard peptide curve.

An antigen presentation assay was run testing samples A, B, C, and E since they displayed a range of protein loadings. Figure 3 illustrates that higher ovalbumin loadings lead to greater antigen presentation levels as

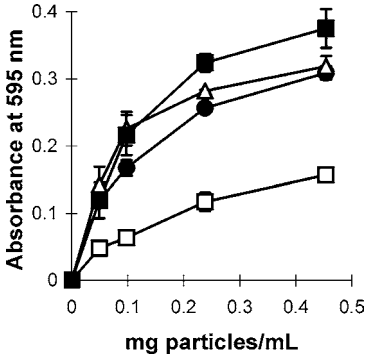


Figure 3. Antigen presentation assay testing particles with varied protein loadings. Sample A (□); sample B (●); sample C (△); sample E (■).

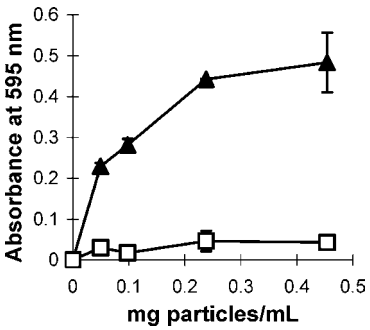
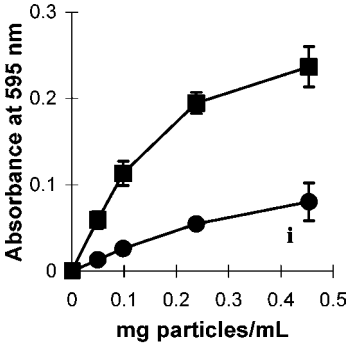


Figure 4. Effect of degradability on antigen presentation. Degradable (▲); nondegradable (□).

indicated by higher β-galactosidase activity. Also, increasing sample concentration leads to greater antigen presentation levels. These trends are likely due to the rise in the amount of ovalbumin delivered to the cytoplasm of the APCs, leading to more SIINFEKL peptide presentation. For example, at a sample concentration of 0.45 mg particles/mL, after conversion of absorbance values to presented peptide concentration, sample E shows a 20-fold enhancement over sample A which we reported previously in our proof-of-concept system (*16*).

To determine if the acid-degradable characteristic of the particles enhanced MHC class I presentation, a nondegradable ovalbumin-loaded particle sample was synthesized using *N*,*N*′-methylene-bis-acrylamide as the stable cross-linker. An antigen presentation study was then performed comparing nondegradable and degradable particles with similar protein content. Figure 4 clearly demonstrates that the degradable particles enhance MHC class I presentation, suggesting that the hydrolysis of the cross-linker and release of small molecules in the lysosome may help to destabilize the membrane resulting in the transport of protein into the cytoplasm for processing.

Phagocytosis-Mediated Antigen Delivery into MHC Class I Presentation. To help determine if the particles enter APCs through the process of phagocytosis, antigen presentation assays were performed in the presence of a phagocytosis inhibitor, cytochalasin B (*13*). Cytochalasin B inhibits phagocytosis by preventing actin polymerization and the interaction of actin filaments. Figure 5i shows that the antigen presentation levels for the cells incubated with the inhibitor are greatly reduced as compared to the cells that were not. For example, at the highest particle concentration, the calculated concentration of presented peptide for cells incubated with the inhibitor is only 30% of the peptide presented as calculated for the cells incubated without cytochalasin B. This finding is consistent with a process in which the particles undergo phagocytosis. Another key point is that the peptide presentation levels of the cells incubated without cytochalasin B are very close to the concentration of presented peptide at saturation (Figure 5ii). The saturation concentration is determined from the standard peptide curve, which is prepared by adding free SIINFEKL peptide to the RAW cells in various concentrations. This free peptide is not delivered to the cytoplasm of the RAW cells, but instead directly binds to MHC class I molecules that are on the surface of the cells. These SIINFEKL complexes can also activate the B3Z cells. The concentration of free SIINFEKL at which the absorbance at 595 nm levels off is considered to represent the saturation concentration of presented peptide, which was 2 nM in this experiment (Figure 5ii). For the particle sample, at 0.45 mg particles/mL the concentration of peptide presented without the phagocytosis inhibitor is 1.7 nM of peptide (Figure 5i), which is near the saturation level. This study suggests that this acid-sensitive particle system is very efficient for in vitro delivery of the protein antigen into the MHC class I presentation pathway.



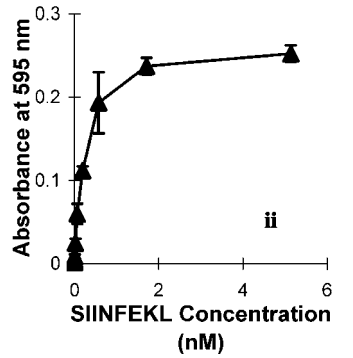


Figure 5. (i) Antigen presentation assay with phagocytosis inhibitor. Sample D (■); sample D with cytochalasin B (●). (ii) Antigen presentation assay of SIINFEKL peptide.

In Vivo Tumor Protection. To assess the ability of the acid-degradable protein-loaded particles to deliver protein to the cytoplasm of APCs and activate CTLs and provide a protective immunity in vivo, a preliminary tumor protection experiment was performed using the EG7 tumor model (*24*, *25*). EG7 is a derivative of the thymoma EL4, which was transfected with the ovalbumin gene, making it a target cell for CTLs activated against ovalbumin. Sample D was chosen for this experiment because it had the best dispersibility of all of the samples in Table 1, an important consideration for the study since the particles had to be suspended in saline and injected into animals. Samples E and F, although also prepared with cross-linker **2**, were somewhat more difficult to suspend than Sample D, most likely due to a degree of particle aggregation as a result of higher ovalbumin content.

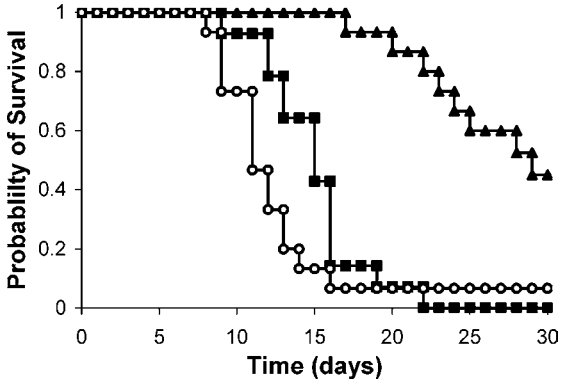


Figure 6. Kaplan−Meier survival plot. Saline (○); free ovalbumin (■); ovalbumin in particles (▲).

The experiment involved three groups of animals as follows: mice immunized with free ovalbumin, mice immunized with an equal amount of ovalbumin encapsulated in the particles (Sample D), and a control group receiving only saline. Each mouse received two subcutaneous immunizations that were 2 weeks apart. Ten days after the final immunization, EG7 tumor cells that had been previously sorted into a set of highly ovalbumin expressing cells were injected subcutaneously into each mouse, and tumor growth was then monitored, with Day 1 being the first day of tumor establishment. Tumors were visible on almost all of the mice in the saline and free ovalbumin groups 7 days after the EG7 injection, whereas 13 out of 15 mice in the particle group did not show any visible tumors until Day 16. In general, tumor growth in the saline control group occurred early in the experiment and was very rapid, resulting in the removal of all but 1 mouse by Day 16. The free ovalbumin group also demonstrated tumor growth early in the experiment but at a slower rate resulting in the removal of all mice from the study by Day 21. For the mice receiving particles, EG7 tumors were not observed until midway through the experiment, and the growth was slower in comparison to the other groups. At the completion of the study, Day 30, five mice in the particle group had yet to be removed from the experiment, although they did have tumors. The trends seen in tumor growth also correlated with the survival rates. This can be seen in the Kaplan−Meier survival plot (Figure 6). The slope of the saline and free ovalbumin series is much steeper than the particle series. The mice that received the particles had a survival rate of 100% after 17 days versus approximately 14% and 7% for the free ovalbumin and saline groups, respectively. The probability of survival eventually dropped to 0% for the free ovalbumin mice by Day 22 while the saline group remained at 7% while the particle group only fell to 45% by the end of the experiment. There was a statistically significant difference between the particle group and the other two groups (compared to saline $p < 0.0001$; compared to ovalbumin alone $p < 0.00001$), but there was no difference between the ovalbumin and saline groups ($p > 0.1$). These encouraging preliminary results suggest that the particles can stimulate an immune response against EG7 tumor cells that is more effective than ovalbumin alone, indicating that the particles can provide a protective immune response against tumor cells in vivo. Future experiments will seek to improve these results by taking advantage of the synthetic flexibility of the system through incorporation of APC targeting and immunostimulatory groups such as mannose and CpG DNA into the particles (*6*, *26*−*28*). Additional studies will also test samples with varied doses and protein loadings to determine if these variables have the same effect in vivo as they do in vitro.

CONCLUSION

This study confirms that tuning the hydrophilicity of acid-degradable cross-linkers such as **2** can be used to enhance the potential of antigen-loaded particles for the delivery of vaccines. Particles prepared with this cross-linker have higher protein loading efficiencies and better dispersibility in aqueous solution than our earlier proof-of-concept system. The MHC class I presentation levels achieved with these particles are vastly enhanced as a result of their ability to deliver more protein into the cytoplasm of APCs. Experiments involving the addition of cytochalasin B, which significantly reduces MHC class I antigen presentation levels provide support for our assumption of a phagocytosis mechanism for the internalization of these particles. Initial animal studies showed promising results with the demonstration that these acid-sensitive particles can stimulate the immune system against an injected protein resulting in the enhanced rejection of EG7 tumor cells in vivo. This new protein delivery system should find applications in vaccines targeted against viruses and tumors, where the activation of CTLs is required for the generation of immunity.

ACKNOWLEDGMENT

We thank Ann Fischer (UC Berkeley Cell Culture Facility) for help with the cell culture studies and Lindsey Jennings (UC Berkeley Animal Facility) for help with the animal studies. We thank the U.S. Department of Energy (Grant DE-ACO3-76SF00098) for funding the development of biocompatible acid-degradable particles and the National Institute of Health (Grant RO1EB002047) for funding the biological studies. Jun Kunisawa is a Research Fellow of the Japan Society for the Promotion of Science. The Center for New Directions in Organic Synthesis is supported by Bristol-Myers Squibb as the Sponsoring Member and Novartis as a Supporting Member.

LITERATURE CITED

(1) Blower, S. M., Koelle, K., Kirschner, D. E., and Mills, J. (2001) Live attenuated HIV vaccines: predicting the tradeoff between efficacy and safety. *Proc. Natl. Acad. Sci. U.S.A. 98*, 3618−3623.

(2) Berzofsky, J. A., Ahlers, J. D., and Belyakov, I. M. (2001) Strategies for designing and optimizing new generation vaccines. *Nat. Rev. Immunol. 1*, 209−219.

(3) Fong, L., and Engleman, E. G. (2000) Dendritic cells in cancer imunnotherapy. *Annu. Rev. Immunol. 18*, 245−273.

(4) Goldstein, G. (1996) HIV-1 Tat protein as a potential AIDS vaccine. *Nat. Med. 1*, 960−964.

(5) Letvin, N. L., Barouch, D. H., and Montefiori, D. C. (2002) Prospects for vaccine protection against HIV-1 infections and AIDS. *Annu. Rev. Immunol. 20*, 73−99.

(6) Merad, M., Sugie, T., Engleman, E. G., and Fong, L. (2002) In vivo manipulation of dendritic cells to induce therapeutic immunity. *Blood 99*, 1676−1682.

(7) Moore, M. W., Carbone, F. R., and Bevan, M. J. (1988) Introduction of soluble protein into the class I pathway of antigen processing and presentation. *Cell 54*, 777−785.

(8) Seymour, L., Schacht, E., and Duncan, R. (1991) The effect of size of polystyrene particles on their retention within the rat peritoneal compartment, and on their interaction with rat peritoneal macrophages in vitro. *Cell Biol. Int. Rep. 15*, 277−286.

(9) O′Hagan, D. T., Palin, K., Davis, S. S., Artursson, P., and Sjöholm, I. (1989) Microparticles as potentially orally active immunological adjuvants. *Vaccine 7*, 421−424.
(10) Ekman, B., Lofter, C., and Sjöholm, I. (1976) Incorporation of macromolecules in microparticles: preparation and characteristics. *Biochemistry 15*, 5115−5120.
(11) Edman, P., Ekman, B., and Sjöholm, I. (1980) Immobilization of proteins in microspheres of biodegradable polyacryldextran. *J. Pharm. Sci*. *69*, 838−842.
(12) Oh, Y., Harding C. V., and Swanson, J. A. (1997) The efficiency of antigen delivery from macrophage phagosomes into cytoplasm for MHC class I-restricted antigen presentation. *Vaccine 15*, 511−518.
(13) Kovacsovics-Bankowski, M., Clark, K., Benacerraf, B., and Rock K. L. (1993) Efficient major histocompatibility complex class I presentation of exogenous antigen upon phagocytosis by macrophages. *Proc. Natl. Acad. Sci. U.S.A. 90*, 4942−4946.
(14) Moore, A., McGuirk, P., Adams, S., Jones W. C., McGee, J. P., O′Hagan, D. T., and Mills, K. H. G. (1995) Immunization with a soluble recombinant HIV protein entrapped in biodegradable microparticles induces HIV-specific $CD8^+$ cytotoxic T lymphocytes and $CD4^+$ Th1 cells. *Vaccine 13*, 1741−1749.
(15) Murthy, N., Thng, Y. X., Schuck, S., Xu, M., and Fréchet, J. M. J. (2002) A novel strategy for encapsulation and release of proteins: hydrogels and microgels with acid-labile acetal cross-linkers. *J. Am. Chem. Soc*. *124*, 12398−12399.
(16) Murthy, N., Xu, M., Schuck, S., Kunisawa, J., Shastri, N., and Fréchet, J. M. J. (2003) A macromolecular delivery vehicle for protein-based vaccines: acid-degradable protein-loaded microgels. *Proc. Natl. Acad. Sci. U.S.A. 100*, 4995−5000.
(17) Okada, C. Y., and Rechsteiner, M. (1982) Introduction of macromolecules into cultured mammalian cells by osmotic lysis of pinocytic vesicles. *Cell 29*, 33−41.
(18) Schafheutle, M. A., and Finkelmann, H. (1988) Shapes of micelles and molecular geometry: synthesis and studies on the phase behaviour, surface tension and rheology of rigid rodlike surfactants in aqueous solutions. *Liq. Cryst. 3*, 1369−1386.
(19) Riley, T., Govender, T., Stolnik, S., Xiong, C. D., Garnett, M. C., Illum, L., and Davis, S. S. (1999) Colloidal stability and drug incorporation aspects of micellar-like PLA-PEG nanoparticles. *Colloids Surf., B 16*, 147−159.
(20) Li, Y. P., Pei, Y. Y., Zhang, X. Y., Gu, Z. H., Zhou, Z. H., Yuan, W. F., Zhou, J. J., Zhu, J. H., and Gao, X. J. (2001) PEGylated PLGA nanoparticles as protein carriers: synthesis, preparation and biodistribution in rats. *J. Controlled Release 71*, 203-211.
(21) Kanaras, A. G., Kamounah, F. S., Schaumburg, K., Kiely, C. J., and Brust, M. (2002) Thioalkylated tetraethylene glycol: a new ligand for water soluble monolayer protected gold clusters. *Chem. Commun*. *20*, 2294−2295.
(22) Kriwet, B., Walter, E., and Kissel, T. (1998) Synthesis of bioadhesive poly(acrylic acid) nano- and microparticles using an inverse emulsion polymerization method for the entrapment of hydrophilic drug candidates. *J. Controlled Release 56*, 149−158.
(23) Karttunen, J., and Shastri, N. (1991) Measurements of ligand induced activation in single viable T-cells using the lacZ reporter gene. *Proc. Natl. Acad. Sci. U.S.A. 88*, 3972−3976.
(24) El-Shami, K., Tirosh, B., Bar-Haîm, E., Carmon, L., Vadai, E., Fridkin, M., Feldman, M., and Eisenbach, L. (1999) MHC class I-restricted epitope spreading in the context of tumor rejection following vaccination with a single immunodominant CTL epitope. *Eur. J. Immunol*. *29*, 3295−3301.
(25) Kim, T. S., Chung, S. W., and Hwang, S. Y. (2000) Augmentation of antitumor immunity by genetically engineered fibroblast cells to express both B7.1 and interleukin-7. *Vaccine 18*, 2886−2894.
(26) Diebold, S. S., Lehrmann, H., Kursa, M., Wagner, E., Cotten, M., and Zenke, M. (1999) Efficient gene delivery into human dendritic cells by adenovirus polyethylenimine and mannose polyethylenimine transfection. *Hum. Gene Ther. 10*, 775−786.
(27) Fukasawa, M., Shimizu, Y., Shikata, K., Nakata, M., Sakakibara, R., Yamamoto, N., Hatanaka, M., and Mizuochi, T. (1998) Liposome oligomannose-coated with neoglycolipid, a new candidate for a safe adjuvant for induction of $CD8^+$ cytotoxic T lymphocytes. *FEBS Lett. 441*, 353−356.
(28) Sparwasser, T., Koch, E., Vabulas, R. M., Heeg, K., Lipford, G. B., Ellwart, J. W., and Wagner, H. (1998) Bacterial DNA and immunostimulatory CpG oligonucleotides trigger maturation and activation of murine dendritic cells. *Eur. J. Immunol. 28*, 2045−2054.

BC049956F

Enhanced Anti-Rotavirus Action of Human Cystatin C by Site-Specific Glycosylation in Yeast

Soichiro Nakamura,[†,*] Junya Hata,[‡] Makoto Kawamukai,[‡] Hideyuki Matsuda,[‡] Masahiro Ogawa,[§] Kosuke Nakamura,[§] Hao Jing,[†] David D. Kitts,[§] and Shuryo Nakai[§]

Department of Life and Environmental Science and Department of Life Science and Biotechnology, Shimane University, Shimane, Japan 690-8504, and Food, Nutrition and Health, University of British Columbia, Vancouver, BC, Canada V6T 1Z4. Received July 9, 2004; Revised Manuscript Received September 10, 2004

The cDNA encoding human cystatin C (HCC) was subjected to site-specific substitution of alanine for serine at the position 37, to obtain the Asn_{35}-Lys_{36}-Ser_{37} sequence that is a signal for asparagine-linked (*N*-linked) glycosylation of protein in eukaryotes, and was transformed into *Pichia pastoris* X33. As a result, 1.2 mg/L oligomannosyl HCC with a carbohydrate chain of $Man_{10}GlcNAc_2$ was produced by the *Pichia* transformant. The oligomannosyl HCC was more stable at the low ionic strength condition of 50 mM potassium phosphate buffer, pH 7.0, than the wild-type. In addition, the oligomannosylation substantially improved the molecular stability of cystatin against an aspartic proteinase, cathepsin D, in which the susceptibility decreased to less than 50% of nonglycosylated one. The anti-rotavirus activity of HCC was substantially enhanced by the site-directed glycosylation using the yeast expression system. A MA-104 cell line was used as a host cell for human rotavirus type-2 *Wa* strain in this study, to which both the wild-type and oligomannosyl HCCs did not show cytotoxicity at a concentration of 100 μg/mL. More than 80% viability of the host cell infected with 1.0×10^5 PFU/mL of rotavirus was conserved under the condition coexisting with 75 μg/mL of the oligomannosyl HCC, which was 15.2% higher than that of wild-type HCC. Thus, the in vitro anti-rotavirus assay indicated that the supplement of a proper amount of the oligomannosyl HCC could be used as an anti-rotavirus agent.

INTRODUCTION

Human cystatin C, a monomeric cysteine protease inhibitor consisting of 120 amino acid residues with two disulfide bonds, belonging to family II of the cystatin superfamily (*1*), is known to be ubiquitous in tissues and body fluids and has a well-defined molecular structure (*2*−*4*). This proteinaceous inhibitor has been investigated for potential application as antivirus medication for inhibiting replication of picornaviruses (*5*), coronaviruses (*6*, *7*), and herpes simplex type 1 virus (*8*, *9*). It has also been reported that brewer yeast polysaccharides had protective effects against bacterial infections (*10*, *11*). Therefore, if carbohydrate chains are attached to the protein molecule, functionality of human cystatin C will be improved for potential application for food or pharmaceutical aid. Our previous study has reported that mouse cystatin C, with a possible site for N-linked glycosylation, was successfully glycosylated and expressed in both *Saccharomyces cerevisiae* and *Pichia pastoris* (*12*); hereby, we intended to employ human cystatin C instead of mouse cystatin C as a template for biosynthesis using the yeast expression system. While most of the family II cystatins including human cystatin C have no recognition site for asparagine-linked (N-linked) glycosylation on their DNA sequences (*13*), we introduced an Asn-X-Thr/Ser sequence, using a site-specific glycosylation technique, and were able to produce glycosylated human cystatin C in the *Pichia* transformant expression system (*14*).

We have already identified the most possible introduction sites for glycosylation of cystatins belonging to family II for improving stability without any severe loss in their bioactivities (*15*) based on the information from rodent cystatin C and kininogens (*2*, *16*−*18*). The prospective sites for glycosylation in human cystatin C include amino acid residues at the positions 35, 36, and 79 (*15*). Since there were some reports in that the efficiency of the glycosylation decreases with the distance of the glycosylation signal from the N-terminus (*14*, *19*−*21*), we chose the glycosylation site at the position 35 in the molecule. Thus, a mutant human cystatin C, A37S, in which the alanine residue was replaced by serine residue at the position 37 in order to obtain Asn_{35}-Lys_{36}-Ser_{37} sequence, was constructed.

The main objective here was to determine physicochemical properties and anti-rotavirus activity of the mutant human cystatin C with an oligomannnosyl chain on its molecular surface. This study also investigates molecular stability of the oligomannosyl human cystatin C.

MATERIALS AND METHODS

Materials. *Escherichia coli* DH5α and *Epicurian coli* XL1-Blue were used as routine plasmid amplification and host cell for site-directed mutagenesis, respectively. *Pichia pastoris* X33 was employed as a protein expression host (Invitrogen, Carlsbad, CA). Human rotavirus type-2 *Wa* strain was by courtesy of Dr. O. Nishio, National

* To whom correspondence should be addressed. Tel. +81-852-32-6351, fax: +81-852-32-6351, e-mail: soichiro@edu.shimane-u.ac.jp.

† Department of Life and Environmental Science, Shimane University.

‡ Department of Life Science and Biotechnology, Shimane University.

§ University of British Columbia.

10.1021/bc049838s CCC: $27.50 © 2004 American Chemical Society
Published on Web 11/02/2004

Institute of Public Health (Tokyo, Japan). A cell line derived from embryonic rhesus monkey kidney, MA-104, was obtained from Shimane Prefectural Institute of Public Health and Environmental Science (Matsue, Japan). All tissue culture media and materials were from Nissui Pharmaceutical Co. Ltd. (Tokyo, Japan). EDTA-trypsin and Cell-Banker (BLC-1) were from CosmoBio Co. Ltd. (Tokyo, Japan) and Jujifield Inc. (Tokyo, Japan), respectively. Egg-white cystatin, *N*α-benzoyl-DL-Arg-*p*-nitroanilide (BAPNA)[1] and MTT (3-[4,5-dimethylthiozol-2-yl]-2,5-diphenyltetrazolium bromide) were from Sigma-Aldrich Japan (Tokyo). Other chemicals used were of all analytical grade and from Wako Pure Chemical Industries, Ltd. (Osaka, Japan) and Sigma-Aldrich Japan (Tokyo, Japan).

Synthesis, Mutation and Expression of Human Cystatin C Gene. A synthetic gene encoding the primary amino acids sequence of human cystatin C was prepared as previously described (*15*). The resulting synthetic gene was cut with *Xho* I and *Xba* I and ligated into a *Pichia pastoris* expression vector, pPICZα-A (Invitrogen, Carlsbad, CA). The inserted gene was sequenced on both strands by the dideoxynucleotide protocol in order to confirm that the DNA sequence encoded for the amino acid sequence of human cystatin C. Site-directed mutagenesis for the introduction of Asn_{35}-Lys_{36}-Ser_{37} sequence, A37S mutation, was performed according to QuikChange Site-Directed Mutagenesis Kit (Stratagene, La Jolla, CA). Oligonucleotide primers used for the mutation were 5′-GGTGAGTACAACAAGTCCTC-TAACGACATG-3′, and its antisense pPICZα-A carrying the A37S gene was linearlized with *Dra* I and transformed *P. pastoris* ×33 according to *Pichia* EasyComp Transformation Kit (Invitrogen). Integration of the mutant gene into the yeast genome was confirmed by genomic PCR using 5'AOX1 primer (5′-GACTGGTTC-CAATTGACAAGC-3′) paired with 3'AOX1 primer (5′-GCAAATGGCATTCTGACATCC-3′). A single colony of transformants was inoculated into 2 mL of YPD medium and incubated at 30 °C with shaking at 250 rpm. Cells were grown in 60 mL of YPD. Following collection of cells by centrifugation at 1500*g*, the resultant cell pellet yeast was suspended with 24 mL of BMMY (1% yeast extract, 2% peptone, 100 mM potassium phosphate buffer at pH 7.0, 1.34% yeast nitrogen base, 4×10^{-5} % biotin, and 0.5% methanol as the sole carbon source). Methanol was added to a final concentration of 0.5% every 24 h to maintain induction. After 2-day induction with methanol, the culture was centrifuged at 10 000*g* for 10 min, and then recombinant proteins were purified by hydrophobic interaction chromatography using Hiprep 16/10 Phenyl low-sub column (Amersham Pharmacia Biotech., Japan, Tokyo) followed by size-exclusion chromatography using Superdex 200 HR 10/30 column (Amersham Pharmacia Biotech). Glycosylated protein was prepared by affinity chromatography using concanavalin A-Sepharose (Amersham Pharmacia Biotech). The con-A column was prewashed with 10 bed volumes of 100 mM potassium phosphate (pH 7.0) containing 0.5 M NaCl and washed with the same buffer after loading sample until the washing solution was free from proteins. The absorbed glycoprotein was subsequently eluted with 100 mM α-methylmannoside in the 20 mM Tris-HCl buffer containing 0.5 M NaCl. The glycoprotein solution was dialyzed against 0.1 M NaCl−100 mM potassium phosphate buffer (pH 7.0) and used for further examination,

Endo-H Treatment and SDS−Polyacrylamide Gel Electrophoresis. Endo-β-*N*-acetylglucosaminidase (endo-H) was used to digest the carbohydrate-chain according to the method of Tarentino and Maley (*22*) with slight modifications. Recombinant proteins (0.1 mg/mL) were boiled in 50 mM sodium citrate buffer (pH 5.5) containing 1% SDS and 200 μg/mL of phenylmethylsulfonyl fluoride for 5 min. After cooling, samples were supplemented with an equal volume of either 0.02 unit of endo-H in 50 mM sodium citrate buffer (pH 5.5) or the same buffer without the enzyme and were subsequently incubated at 37 °C for 20 h. After incubation, the samples were analyzed by SDS-polyacrylamide gel electrophoresis (PAGE). SDS−PAGE was conducted according to the method of Laemmli (*23*) using 15% acrylamide separating gel and 5% stacking gel containing 1% SDS. Samples were heated at 100 °C for 5 min in 0.01 M Tris-glycine buffer (pH 8.8) containing 1% SDS and 1% β-mercaptoethanol. Electrophoresis was carried out at a constant current of 10 mA for 5 h using an electrophoretic buffer of Tris-glycine containing 0.1% SDS. After electrophoresis, the gel sheet was stained with 0.025% Coomassie Brilliant Blue R-250.

Analysis of Carbohydrate Moiety. The total sugar content of the glycosylated mutant A37S was estimated using the phenol−sulfuric acid reaction employing mannose as a standard. HPLC analysis serves as a method of identification of the hexose liberated from glycosylated A37S cystatin by hydrolysis with 2 N HCl at 100 °C for 3 h in a sealed glass ample. The hydrolysates were dried, dissolved in water, and chromatographed on an Asahipak NH2P-50 column (Asahi Chemical, Tokyo) in 75% acetonitrile using the Hitachi HPLC system equipped with an RI detector. For the analysis of hexosamine, the hydrolysates with 3 N HCl at 100 °C for 4 h were dried and then analyzed using an amino acid analyzer (Tosoh, HLC 805).

Papain-Inhibitory Activity. Papain-inhibitory activity of recombinant proteins was determined using a synthetic substrate of papain, N^{α}-benzoyl-DL-Arg-*p*-nitroanilide (*24*). The inhibitory activity was expressed as the amount of active inhibitor (AI) present in the aliquot taken for assay: AI (μmol) = {% inhibition/100} × {PA (μg)/23 400 (μg/μmol)} where PA is the amount of papain present in the assay solution. The protein concentration of the solution was determined by Bio-Rad protein assay kit (Bio-Rad Lab., Tokyo) using egg-white cystatin as the protein standard.

Circular Dichroism (CD) Analysis. The far-ultraviolet (190−260 nm) CD spectra of wild-type and mutant proteins were recorded at a protein concentration of 300 μg/mL protein in 50 mM potassium phosphate buffer (pH 7.0) using a spectropolarimeter (JASCO J-720, Tokyo) using a 1.0-cm cuvette. The temperature of the cuvette was maintained at 25 °C with a circulating water bath. The accuracy of the data was improved by averaging 10 scans integrated using the data processor, JASCO Series 700. Accumulation of the CD spectra was initiated within 5 min of recording the absorbance spectra of the samples. The resulting averaged spectra were normalized to molar ellipticities (molar ellipticity [θ] in deg cm^2/dmol).

Molecular Stability. The melting curve of recombinant protein was determined using CD spectroscopy. A 300 μg/mL protein solution prepared as described for the above CD measurement was put into a 1.0-cm cuvette, and the average ellipticity signal in the CD spectra was measured at 222 nm at different temperature. The

[1] Abbreviations: BAPNA, *N*α-benzoyl-DL-Arg-*p*-nitroanilide; CD, circular dichroism; FBS, fetal bovine serum; MEM, Eagle's minimum essential medium; MTT, 3-[4,5-dimethylthiozol-2-yl]-2,5-diphenyltetrazolium bromide; PAGE, polyacrylamide gel electrophoresis; PCR, polymerase chain reaction; SDS, sodium dodecyl sulfate.

temperature of the sample was gradually increased from 40 °C to 90 °C at a rate of 1 °C/min.

The protein solution (300 μg/mL protein) was mixed with potassium phosphate buffer (pH 7.0) containing guanidine hydrochloride (up to 6 M) and incubated at 25 °C for 5 h, and then changes of CD spectra were measured. Unfolding fraction was expressed as the relative ratio at 222 nm. Also we determined changes of the CD spectra and papain-inhibitory activity after 30-day incubation at 4 °C in 50 mM phosphate buffer (pH 7.0) with and without NaCl (up to 0.5 M). Susceptibility of recombinant cystatins to cathepsin D was measured to determine the conformational stability of oligomannosyl cystatin. Five hundred microliters of a 0.1 mg/mL protein solution of cystatin was incubated with an equal volume of 0.5 μM cathepsin D at 37 °C. After a preset time up to 40 min, 100 μL samples were removed and mixed with 1 μM pepstatin A to terminate the enzymatic activity of the cathepsin D. Residual papain-inhibitory activity determined using BAPNA was expressed as percentage of the initial activity.

Cytotoxicity Assay against MA-104 Cells. To assess cytotoxicity of recombinant cystatins, 1.0×10^5 cells/mL MA-104 cells were seeded in Eagle's minimum essential medium (MEM) containing 10% fetal bovine serum (FBS) on a 96-well tissue culture microplate (IWAKI Co, Tokyo) and incubated at 37 °C for 24 h in a CO_2 incubator. Then, 100 μg/mL protein (as a final concentration) sample was added with MEM containing 10% FBS and incubated for 3 days under the 5% CO_2 environment. The number of vial cells was determined using MTT method as described earlier (*25*).

Anti-Rotavirus Assay in Vitro. The inhibitory effects of recombinant cystatins on the replication of rotaviruses were determined by inhibition rate (%) of virus-induced cytotoxicity in MA-104 cells. The cells were grown to confluence in a 96-well plate in the presence of MEM and 10% FBS at 37 °C under 5% CO_2 environment. The cells were washed with serum-free media before use. Aliquots of recombinant cystatins were diluted with MEM and mixed with an equivalent volume of rotavirus *Wa* strain. Thus, the confluent monolayer culture of MA-104 was infected with the final concentration of 1.0×10^5 PFU/mL rotavirus coexistent with various concentrations of recombinant cystatins and then continuously incubated for 3 days in 5% CO_2. After incubation, cell viability was determined by the MTT assay (*25*).

RESULTS

Production of Recombinant Cystatins. The wild-type and A37S human cystatin C's were successfully expressed in *P. pastoris* and purified by hydrophobic interaction chromatography and size-exclusion chromatography. SDS−PAGE results showed that mutant A37S was expressed in two different forms: a major form with apparent molecular mass of 15 kDa and a minor form with 20 kDa. As shown in Figure 1, the 20 kDa band completely disappeared, and the 15 kDa band remained by the deglycosylation with endo-β-*N*-acetylglucosaminidase, suggesting that the 20 kDa cystatin was glycosylated with N-linked carbohydrates and the 15 kDa protein was nonglycosylated. Glycosylated human cystatin C secreted from yeast was separated from nonglycosyl cystatin C by con-A affinity chromatography and determined for the composition of the carbohydrate moiety. Chemical analysis revealed that the oligosaccharide chain consisted of 10 mol of mannose and 2 mol of *N*-acetylglucosamine, indicating that the glycosylated

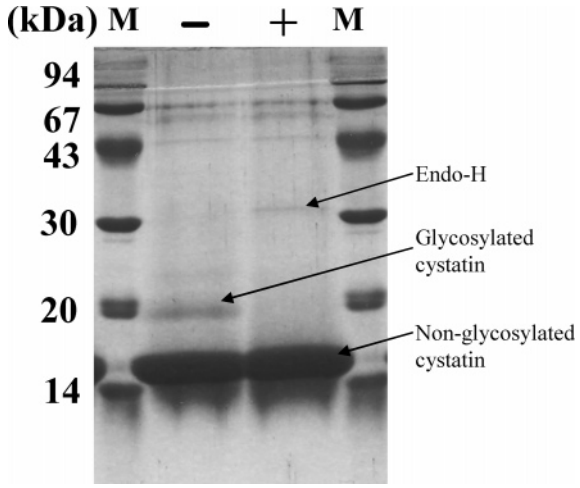


Figure 1. SDS−PAGE patterns of mutant A37S human cystatin C with and without endo-H treatment. A 100 μg/mL protein was boiled for 5 min in a 50 mM sodium citrate buffer (pH 5.5) containing 1% SDS and 200 μg/mL of phenylmethylsulfonyl fluoride. After cooling, an equal volume of either 0.02 unit of endo-H or buffer was added and incubated at 37 °C for 20 h. After incubation, the samples were subjected to SDS−PAGE. *M*, molecular weight marker; -, without endo-H, +, with endo-H.

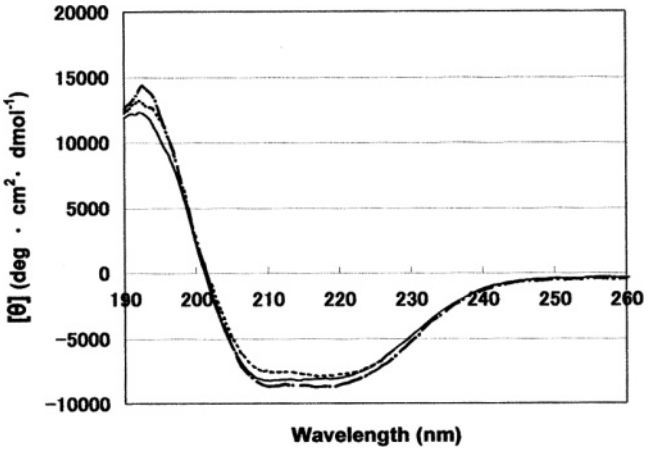


Figure 2. CD spectra of wild-type and mutant cystatins. The CD spectra were recorded at a protein concentration of 300 μg/mL in a 50 mM potassium phosphate buffer (pH 7.0) in a cuvette (1.0 cm) at 25 °C. The spectra are from a representative experiment repeated three times with similar results. —, wild-type cystatin; — · -, oligomannosyl cystatin; - - - -, nonglycosylated cystatin.

cystatin carried $Man_{10}GlcNAc_2$-linked oligomannosyl form. The average secretion amount was 1.2 mg/L culture for oligomannosyl cystatin C, while that of nonglycosyl type was 53 mg/L culture.

Molecular Stability of Oligomannosyl Cystatin C. The effect of the glycosylation on the conformation of human cystatin C was analyzed by CD measurement. As shown in Figure 2, no substantial changes in CD spectra were observed among wild-type, nonglycosylate, and glycosylated human cystatin C, suggesting that no conformational changes occurred with the site-directed mutagenesis as well as the attachment of an oligomannosyl chain.

Heat stability was determined by monitoring changes changes in ellipticity of cystatin C at 222 nm of CD spectra at temperature increments. The structures of all three recombinant cystatins were stable up to 58 °C with T_m value of 68 °C. While wild-type and nonglycosylated cystatins were completely denatured at 74 °C, oligom-

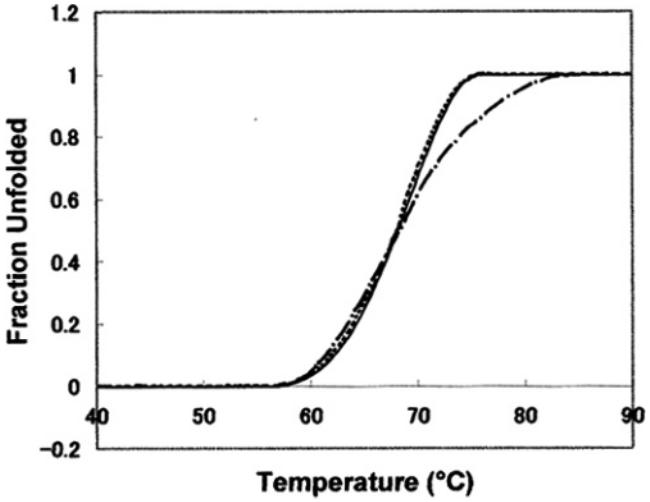


Figure 3. Heat stabilities of recombinant cystatins. A 300 μg/mL protein in a 50 mM potassium phosphate buffer (pH 7.0) was put into a 1.0 cm cuvette, and the average ellipticity signal in the CD spectra was measured at 222 nm at the temperature range of 40−90 °C. Unfolding fraction was expressed as the relative ratio at the wavelength. Data are from a representative experiment repeated three times with similar results. —, wild-type cystatin; — · —, oligomannosyl cystatin; - - - -, nonglycosylated cystatin.

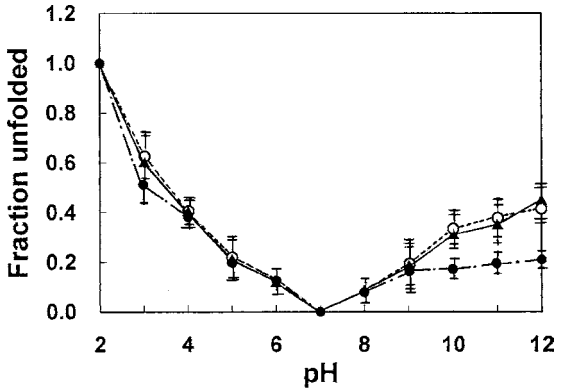


Figure 4. Molecular stability of recombinant cystatins under various pH conditions. A 300 μg/mL protein in a various buffer (pH 2−8, Citrate-Na_2HPO_4 buffer; pH 9 and 10, Tris-HCl buffer; pH 11 and 12, Na_2HPO_4−NaOH buffer) was incubated at 25 °C for 1h, and the average ellipticity signal in the CD spectra was measured at 222 nm. Unfolding fraction was expressed as the relative ratio at the wavelength. All data are expressed as mean ± SD (n = 3). ▲—▲, wild-type cystatin; ●—·—●, oligomannosyl cystatin; ○- - - -○, nonglycosylated cystatin.

annosyl cystatin was completely denatured at 83 °C (Figure 3). Furthermore, the molecular stabilities of recombinant cystatins were assessed under various pH conditions. No substantial changes appeared at pH 1−12 for wild-type and nonglycosylated cystatins; however, structure stability was greatly increased for oligomannosyl cystatin at pH 10−12, as shown in Figure 4.

Measurement of tolerance to guanidine hydrochloride was based on concentration-dependent denaturation. A complete denaturation was observed in wild-type and nonglycosylated cystatins in the salt density of 3 M, whereas that of oligomannosyl cystatin was 4 M, as shown in Figure 5. Interestingly, oligomannosyl cystatin showed a biphase structure transition, in contrast to a monophase transition of wild-type cystatin and nonglycosylated A37S. Effects of the salt existence on molecular stability of recombinant cystatins were also investigated after 1 month storage at 4 °C. According to the CD spectra around 222 nm (220−240 nm), their structures

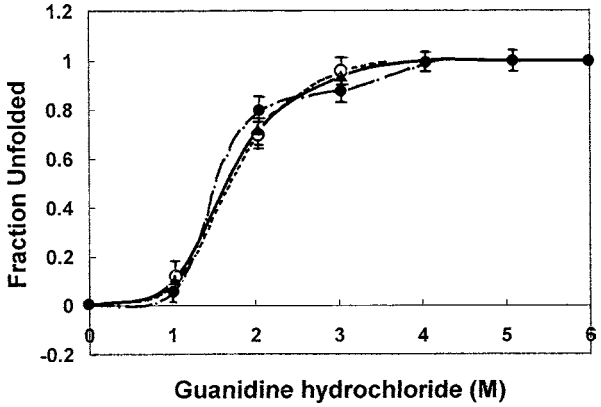


Figure 5. Molecular stability of recombinant cystatins to guanidine hydrochloride. A 300 μg/mL protein in a 50 mM potassium phosphate buffer (pH 7.0) containing guanidine hydrochloride (0−6 M) was incubated at 25 °C for 5 h, and the average ellipticity signal in the CD spectra was measured at 222 nm. Unfolding fraction was expressed as the relative ratio at the wavelength. All data are presented as mean ± SD (n = 3). ▲—▲, wild-type cystatin; ●—·—●, oligomannosyl cystatin; ○- - - -○, nonglycosylated cystatin.

were most stable in 0.5 M NaCl for both wild type and variation types (Figure 6). The phenomena were consistent with the papain-inhibitory activity of the tested cystatins, in that the strongest activities were observed under the 0.5 M NaCl condition. At the lower ionic strength condition of 50 mM potassium phosphate buffer, pH 7.0, without any additional NaCl, activities of wild-type and nonglycosylated cystatin decreased to 61.4 % and 59.8% of original stocks, respectively, while oligomannosyl cystatin maintained 95.7 % activity (Figure 7). Besides, stability of cystatin C to cathepsin D proteolysis was also investigated. Cathepsin D, a typical lysosomal aspartyl proteinase, is widely distributed in all mammalian tissues. Pepstatin A, an inhibitor of aspartyl proteinases, was used to avoid further digestion of recombinant cystatins by cathepsin D after a certain incubation time. As shown in Figure 8, the papain-inhibitory activity was better maintained in the oligomannosyl cystatin than in the wild-type and nonglycosyl ones. The papain-inhibitory activity of the oligomannosyl cystatin retained about 20 % of the initial activity after incubation with cathepsin D for 40 min, while both unglycosylated cystatins were rapidly inactivated with increasing incubation time. It is concluded that the site-directed glycosylation confers cystatin's better conformational stability in various undesirable environmental conditions.

Antivirus Effect of Oligomannosyl Cystatin C. Recombinant cystatins was used at a concentration of 100 μg/mL protein, at which no cytotoxic effect was observed on MA-104 cells. Confluent MA-104 cells were continuously incubated for 3 days at 37 °C in 5% CO_2 under new MEM with and without 1.0×10^5 PFU/mL rotavirus (Figures 9A and 9B). As a result, cells were destroyed, were detached from the well base, and floated in the culture in the rotavirus infection system (Figure 9B). As an extension, preventing effects of recombinant cystatins on rotavirus infection were investigated. On the other hand, many adhered cells were observed in the well base in the coexisting system with 10 μg/mL protein recombinant cystatins, as shown in Figure 9C and 9D. The dose−response relationship showed a greater effect with increasing concentration of cystatins (Figure 10). Furthermore, it revealed that the effect of oligomannosyl cystatin C was more effective than the wild-type coun-

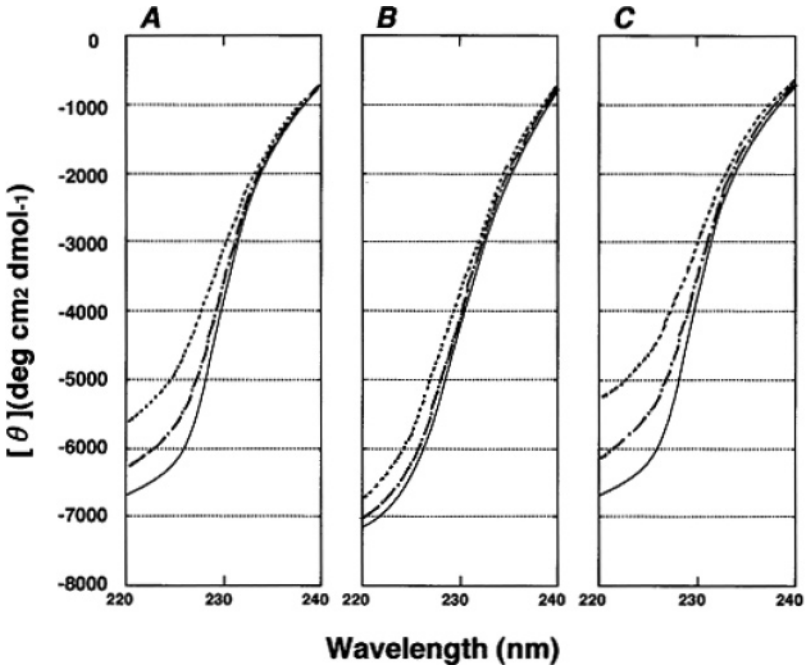


Figure 6. Changes of CD spectra around 222 nm during incubation with and without NaCl. A 300 μg/mL protein in a 50 mM potassium phosphate buffer (pH 7.0) was incubated with NaCl (0.1 and 0.5 M) and without NaCl at 25 °C for 30 days, and the change of CD spectra was measured in a cuvette (1.0 cm) at 25 °C. The spectra are from a representative experiment repeated three times with similar results. —, wild-type cystatin; — · —, oligomannosyl cystatin; - - - -, nonglycosylated cystatin.

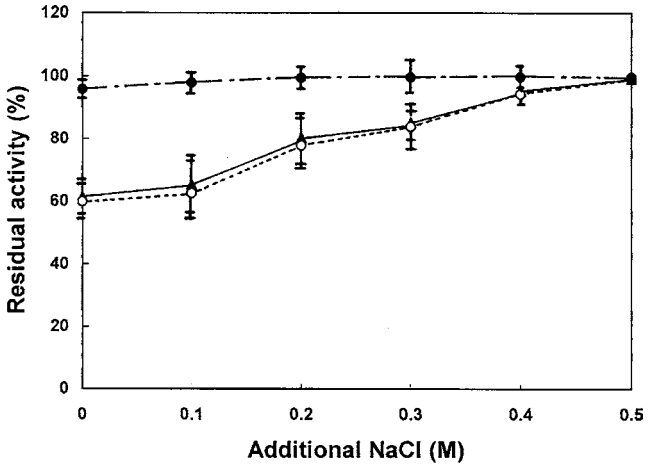


Figure 7. Molecular stability of recombinant cystatins under various NaCl concentrations. A 300 μg/mL protein in a 50 mM potassium phosphate buffer (pH 7.0) containing NaCl (0−0.5 M) was incubated at 25 °C for 30 days. Residual papain-inhibitory activity was expressed as percentage of the initial activity. All data are presented as mean ± SD (n = 3). ▲—▲, wild-type cystatin; ●—·—●, oligomannosyl cystatin; ○- - -○, nonglycosylated cystatin.

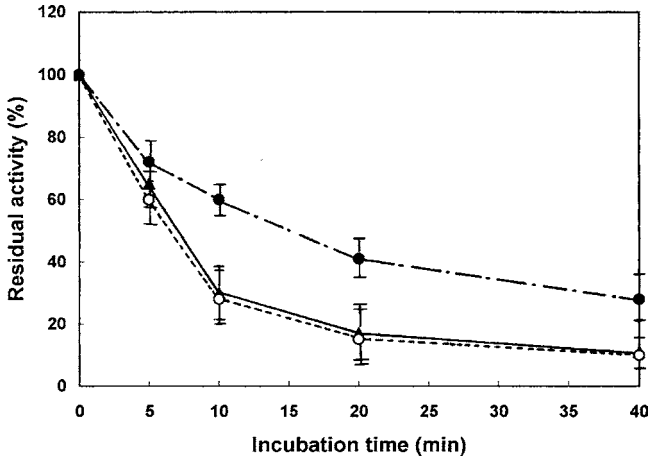


Figure 8. Molecular stability of recombinant cystatins to cathepsin D. A 100 μg/mL protein solution of cystatin was incubated with an equal volume of 0.5 μM cathepsin D at 37 °C for 40 min. Residual papain-inhibitory activity was expressed as percentage of the initial activity. All data are presented as mean±SD (n = 3). ▲—▲, wild-type cystatin; ●—·—●, oligomannosyl cystatin; ○- - -○, nonglycosylated cystatin.

terpart. One hundred μg/mL protein of the glycoprotein retained more than 80% viability of the host cells after a 3-day incubation with a rotavirus.

DISCUSSION

Rotaviruses, nonenveloped and double-stranded RNA viruses belonging to the Reoviridae family, were discovered in 1963 in mice as etiologic agents of acute gastroenteritis (*26*), and human rotaviruses were first identified in 1973 as a cause of infectious gastroenteritis in infants (*27*). Rotavirus infections have been associated with a high rate of infant mortality with more than one million incidents in developing countries (*28*, *29*), and now they are the leading causes of dehydrating diarrhea throughout the world (*30*−*32*). Each year in the United States, rotavirus infections account for an estimated 3.5 million cases of diarrhea and vomiting among children aged less than 5-years old (*33*). Current surveillance reveals that all age groups are regarded as being susceptible to rotavirus infection (*34*−*39*), and a large amount of foodborne diseases are associated with viruses, especially rotaviruses (*40*−*43*). Vaccines have been developed for the prevention of the gastrointestinal virus infections; however, a rotavirus vaccine, rhesus-human reassortant rotavirus tetravalent vaccine licensed by the FDA, has already been withdrawn due to rare but severe complications of intussusception (*44*). There is a growing awareness of the need for the development of new and safe anti-rotavirus medicines.

Thus, a protease inhibitor, human cystatin C, was employed for the template for the prevention and/or

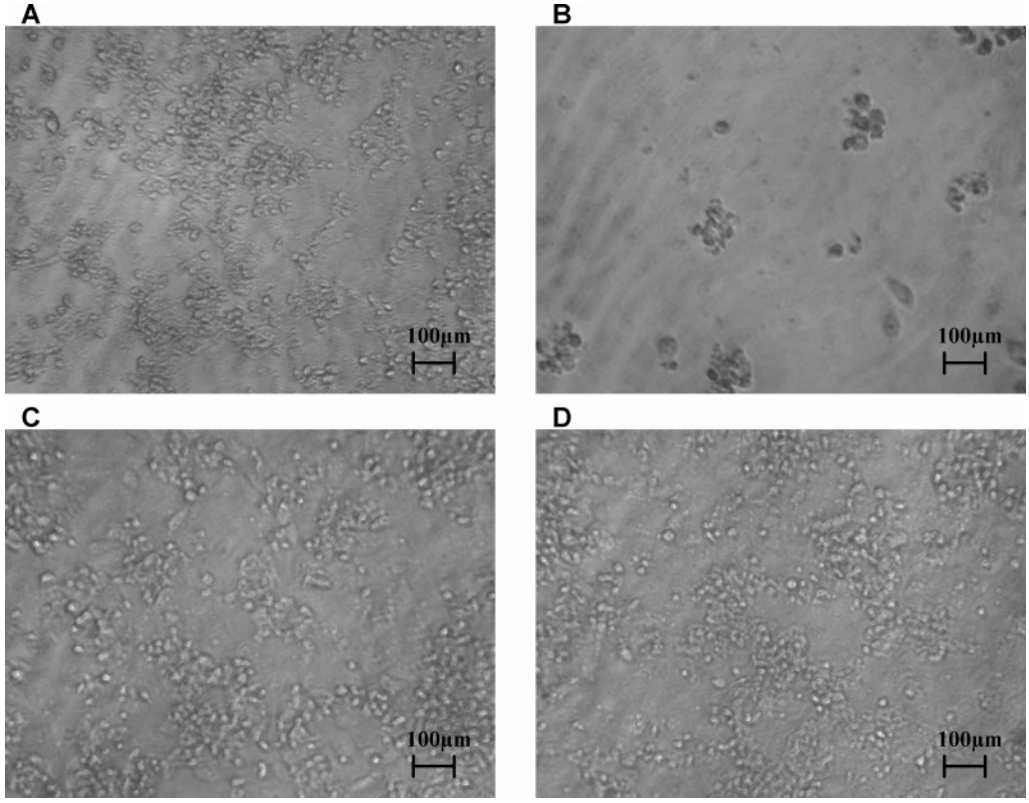


Figure 9. Anti-rotavirus effect of recombinant cystatins. A and B, control without recombinant cystatins; A, without rotavirus; B, with rotavirus; C and D, with recombinant cystatins; C, wild-type cystatin C; D, oligomannosyl cystatin C.

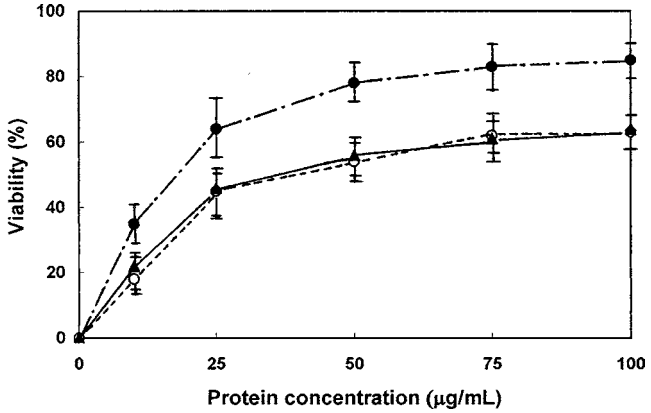


Figure 10. Concentration dependency of anti-virus effects. All data are presented as mean±SD (n = 3). ▲—▲, wild-type cystatin; ●—·—●, oligomannosyl cystatin; ○- - - -○, nonglycosylated cystatin.

treatment agent of rotavirus infections in this study. The result revealed that recombinant cystatins exhibited potential antivirus effects to human rotavirus type-2 *Wa* strain. The anti-rotavirus effect of glycosylated cystatin was stronger than that of wild-type or nonglycosylated cystatin. The improved conformational stability of cystatin due to its oligomannosylation could be attributed to high antiviral activity. As shown in Figures 3−6, the oligomannosyl cystatin was found to be appreciably more stable than unglycosylated controls under various harsh conditions. Although cystatin has a tightly packed conformation (*45*), further enhancement of the molecular stability was observed in the oligomannosyl cystatin. According to our previous work, the reversibility of the denatured glycosyl lysozyme was observed in the DSC, obtained by reheating after heat denaturation (*46*). The oligomannosyl cystatin seems to easily refold due to the excellent reversibility of denaturation. Cathepsin D, a typical lysosomal aspartyl proteinase, is widely distributed in all mammalian tissues, and it is assumed that the protease is responsible for the regulation of sulfhydryl proteinase activity by inactivating cystatin C and kininogen (*47*). As shown in Figure 7, the papain-inhibitory activity was better maintained in the oligomannosyl cystatin than in the unglucosylated controls. The carbohydrate chain probably blocked physical accessibility of cathepsin D to the proteolytic cleavage sites in the oligomannosyl cystatin, and resulting conformational stability of oligomannosyl cystatin might play a key role in the enhancement of antirotavirous effect, compared to nonglucosylated cystatin.

Oligomannosyl cystatin might also prevent rotavirus binding to MA-104 cells and inhibit virus replication in the target cell. As shown in Figure 8, oligomannosyl cystatin was able to keep most host cells intact under the rotavirus coexisting system. Antivirus properties of glycoproteins and protease inhibitors have attracted attention from many researchers (*48*−*55*). In the early 1990s, bovine submaxillary mucin, a glycoprotein, was found to inhibit the replication of rotaviruses. It was suggested that the mucin served as an analogue of the rotaviral receptor and prevented the cell attachment by binding to the virus (*48*). Later, more glycoproteins with various carbohydrate chains, such as ovoalbumin, ovomucoid, and lactoferrin, were found to inhibit rotavirus replication, and the antiviral effect was attributed to prevent virus entry in the host cell, either by blocking cellular receptors or by direct binding to the virus particles (*56*−*59*). Although it well-known that the sialic acid moiety of the oligosaccharides plays an important role in the inhibition of rotaviral infection, there also are some papers that describe carbohydrate chains without sialic acid that could be receptors for rotaviruses (*60*−*62*). It has been reported that polysaccharides from brewer yeast showed antivirus effects against 13 kinds

of DNA and RNA viruses, by protecting host cells from being infected with the tested viruses (*63*). It has been found that rotaviruses had a preference in binding glycoproteins on the cell membrane (*64*), which was possibly associated with its outer capsid glycoprotein components of VP4 and VP7 (*65*). VP7 contains a high-mannose oligosaccharide (*66*). The enhanced antivirus activity of oligomannosylated human cystatin C could be due to the synergetic effect of its improved structure stability and carbohydrate moiety, which might compete with rotavirus caspid glycoproteins for cell receptors and also bind with the rotavirus.

The present study successfully prepared oligomannosylated human cystatin C in the *Pichia* expression system and demonstrated that it had higher anti-rotavirus inhibition effect than nonglycosylated cystatin. It opened the opportunity to prevent rotavirus infection by applying human cystatin C. The highly efficient mechanism of the anti-rotavirus effect of oligomannosyl cystatin could be related to binding of the oligomannosyl chain to the rotavirus. Our finding reveals a new potential avenue for antiviral therapeutics and prophylaxis, targeting specific oligosaccharide-comprised sites in rotaviruses, and certain enveloped viruses, including influenza virus and HIV. Further studies will be performed to investigate mechanisms of enhanced antirotavirus effect of glycosylated cystatin.

ACKNOWLEDGMENT

This work was supported by Grant-in Aid for 11660134 for Science and Culture of Japan.

LITERATURE CITED

(1) Abrahamson, M., Barrett, A. J., Salvesen, G., and Grubb, A. (1986) Isolation of six cysteine proteinase inhibitors from human urine. Their physicochemical and enzyme kinetic properties and concentrations in biological fluids. *J. Biol. Chem. 261*, 11282−11289.

(2) Esnard, A., Esnard, F., Faucher, D., and Gauthier, F. (1988) Two rat homologies of human cystatin C. *FEBS Lett. 236*, 475−478.

(3) Abrahamson, M., Olafsson, I., Palsdottir, A., Ulvsback, M., Lundwall, A., Jensson, O., and Grubb, A. (1990) Structure and expression of the human cystatin C gene. *Biochem. J. 268*, 287−294.

(4) Turk, V., and Bode, W. (1991). The cystatins: Protein inhibitors of cysteine proteinases. *FEBS Lett. 285*, 213-219.

(5) Korant, B. D., Brzin, J., and Turk, V. (1985) Cystatin, a protein inhibitor of cysteine proteases alters viral protein cleavages in infected human cells. *Biochem. Biophys. Res. Commun. 127*, 1072−1076.

(6) Collins, A. R., and Grubb, A. (1991) Inhibitory effects of recombinant human cystatin C on human coronaviruses. *Antimicrob. Agents. Chemother. 35*, 2444−2446.

(7) Collins, A. R., and Grubb, A. (1998) Cystatin D, a natural salivary cysteine protease inhibitor, inhibits coronavirus replication at its physiologic concentration. *Oral Microbiol. Immunol. 13*, 59−61.

(8) Saitoh, E., Minaguchi, K., and Ishibashi, O. (1998) Production and characterization of two variants of human cystatin SA encoded by two alleles at the CST2 locus of the type 2 cystatin gene family. *Arch. Biochem. Biophys. 352*, 199−206.

(9) Bjorck, L., Grubb, A., and Kjellen, L. (1990) Cystatin C, a human proteinase inhibitor, blocks replication of herpes simplex virus. *J. Virol. 64*, 941−943.

(10) Okawa, Y., Okura, Y., Hashimoto, K., Matsumoto, T., Suzuki, S., and Suzuki, M. (1982) Protective effect of D-mannan of bakers' yeast against Staphylococcus aureus infection in mice. *Carbohydr. Res. 108*, 328−334.

(11) Funayama, M., Nishikawa, A., Shinoda, T., and Fukazawa, Y. (1983) Immunochemical determinant of Candida parapsilosis. *Carbohydr. Res. 117*, 229−239.

(12) Nakamura, S., Ogawa, M., and Nakai, S. (1998) Effects of Polymannosylation of recombinant cystatin C in yeast on its stability and activity. *J. Agric. Food Chem. 46*, 2882−2887.

(13) Grubb, A., and Löfberg, H. (1982). Human γ-trace, a basic micoprotein: Amino acid sequence and presence in the adenohypophysis. *Proc. Natl. Acad. Sci. U.S.A. 79*, 3024−3027.

(14) Nakamura, S., Takasaki, H., Kobayashi, K., and Kato, A. (1993) Hyperglycosylation of hen egg white lysozyme in yeast. *J. Biol. Chem. 268*, 12706−12712.

(15) Nakamura, S., Ogawa, M., and Nakai, S. (1999) Production and use of modified cystatins. PCT Application No. CA99/00717.

(16) Cole, T., Dickson, P. W., Esnard, F., Averill, S., Risbridger, G. P., Gauthier, F., and Shreiber, G. (1989) The cDNA structure and expression analysis of the genes for the cysteine proteinase inhibitor cystatin C and for β-microglobulin in rat brain. *Eur. J. Biochem. 186*, 35−42.

(17) Solem, M., Rawson, C., Lindburg, K., and Barnes, D. (1990) Transforming growth factor beta regulates cystatin C in serum-free mouse embryo (SFME) cells. *Biochem. Biophys. Res. Commun. 172*, 945−951.

(18) Barrett, A. J. (1987) The cystatins: a new class of peptidase inhibitors. *Trends Biochem. Sci. 12*, 193−196.

(19) Sheares, B. T. (1988) Site-specific glycosylation in animal cells. Substitution of glutamine for asparagine 293 in chicken ovalbumin does not allow glycosylation of asparagine 312. *J. Biol. Chem. 263*, 12778−12782.

(20) Minamitake, Y., Kodama, S., Katayama, T., Adachi, H., Tanaka, S., and Tsujimto, M. J. (1990) Structure of recombinant human interleukin 5 produced by Chinese hamster ovary cells. *J. Biochem. 107*, 292−297.

(21) Shakin-Eshleman, S. H., Remaley, A. T., Eshleman, J., R., Wunner, W. H, and Spitalnik, S. L. (1992) N-linked glycosylation of rabies virus glycoprotein. Individual sequons differ in their glycosylation efficiencies and influence on cell surface expression. *J. Biol. Chem.* 267, 10690−10698.

(22) Tarentino, A. L., and Maley, F. (1974) Purification and properties of an endo-beta-N-acetylglucosaminidase from Streptomyces griseus. *J. Biol. Chem. 249*, 811−817.

(23) Laemmli, U. K. (1970) Cleavage of structural proteins during the assembly of the head of bacteriophage T4. *Nature 227*, 680−685.

(24) Barrett, A. J. (1981) Cystatin, egg white inhibitor of cystein proteinases. *Methods Enzymol. 80*, 771−778.

(25) DiStefano, D. J., Gould S. L., Munshi, S, and Robinson, D. K. (1995) Titration of human-bovine rotavirus ressortants using a tetrazolium-based colorimetric end-point dilution assay. *J. Virol. Methods 55*, 199−208.

(26) Adams, W. R., and Kraft, L. M. (1963) Epizootic diarrhea of infant mice: Identification of the etiologic agent. *Science 141*, 359−360.

(27) Bishop, R. F., Davidson, G. P., Holmes, I. H., and Ruck, B. J. (1973) Virus particles in epithelial cells of duodenal mucosa from children with acute nonbacterial gastroenteritis. *Lancet 2*, 1281−1283.

(28) Bloom, B. R. (1989) Vaccines for the third world. *Nature 342*, 115−120.

(29) Kaspikian, A. Z., Flores, J., Vesikari, T., Ruuska, T., Madore, H. P., Green, K. Y., and Perez-Schael, I. (1991) Recent advances in development of a rotavirus vaccine for prevention of severe diarrheal illness of infants and young children. *Adv. Exp. Med. Biol. 310*, 255−264.

(30) Tatti, K., Gentsch, J., Shieh, W., Ferebee-Harris, T., Lynch, M., Bresee, J., Jiang, B., Zaki, S., and Glass, R. (2002) Molecular and immunological methods to detect rotavirus in formalin-fixed tissue. *J. Virol. Methods 105*, 305−319.

(31) Fischer, T. K., Valentiner-Branth, P., Steinsland, H., Perch, M., Santos, G., Aaby, P., Molbak, K., and Sommerfelt, H. (2002) Protective immunity after natural rotavirus infection: a community cohort study of newborn children in Guinea-Bissau, west Africa. *J. Infect. Dis. 186*, 593−597.

(32) Rosa, E., Silva, M. L, Pires De Carvalho, I., and Gouvea, V. (2002) 1998−1999 rotavirus seasons in Juiz de Fora, Minas Gerais, Brazil: Detection of an unusual G3P[4] epidemic strain. *J. Clin. Microbiol. 40*, 2837−2842.

(33) Lass, R. I., Kilgore, P. E., Holman, R. C., Jin, S., Smith, J. C., Woods, P. A., Clarke, M. J., Ho, M. S., and Gentsch, J. R. (1996) The epidemiology of rotavirus diarrhea in the United States: surveillance and estimates of disease burden. *J. Infect. Dis. 174*, S5−S11.

(34) Fang, Z. Y., Ye, Q., Ho, M. S., Dong, H., Qing, S., Penaranda, M. E., Hung, T., Wen, L., and Glass, R. I. (1989) Investigation of an outbreak of adult diarrhea rotavirus in China. *J. Infect. Dis. 160*, 948−953.

(35) Dupuis, P., Beby, A., Bourgoin, A., Lussier-Bonneau, M. D., and Agius, G. (1995) Epidemic of viral gastroenteritis in an elderly community. *Presse Med. 24*, 356−358.

(36) Timenetsky, M. C., Gouvea, V., Santos, N., Alge, M. E., Kisiellius, J. J., and Carmona, R. C. (1996) Outbreak of severe gastroenteritis in adults and children associated with type G2 rotavirus. Study Group on Diarrhea of the Instituto Adolfo Lutz. *J. Diarrhoeal. Dis. Res. 14*, 71−74.

(37) Griffin, D. D., Fletcher, M., Levy, M. E., Ching-Lee, M., Nogami, R., Edwards, L., Peters, H., Montague, L., Gentsch, J. R., and Glass, R. I. (2002) Outbreaks of adult gastroenteritis traced to a single genotype of rotavirus. *J. Infect. Dis. 185*, 1502−1505.

(38) Banyai, K., Angyal, M., Kormendi, E., Lakatos, F., Uj, M., and Szucs, G. (2002) Outbreak of human rotavirus infection in an adult community. *Orv. Hetil. 143*, 1347−1352.

(39) Chimura, Y., Annaka, M., Shibazaki, S., Adachi, K., Shinkai, T., Sadamasu, K., Noguchi, Y., Masuda, Y., and Inamatsu, T. (2002) An epidemic of rotavirus infection in a nursing home for the elderly in Japan. *Kansenshogaku Zasshi 76*, 450−454.

(40) Hedberg, C. W., and Osterholm, M. T. (1993) Outbreaks of food-borne and waterborne viral gastroenteritis. *Clin. Microbiol. Rev. 6*, 199−210.

(41) Lees, D. (2000) Viruses and bivalve shellfish. *Int. J. Food Microbiol. 59*, 81−116.

(42) Svensson, L. (2000) Diagnosis of foodborne viral infections in patients. *Int. J. Food Microbiol. 59*, 117−126.

(43) Richards, G. P. (2001) Enteric virus contamination of foods through industrial practices: a primer on intervention strategies. *J. Ind. Microbiol. Biotechnol. 27*, 117−125.

(44) Abramson, J. S., Baker, C. J., Fisher, M. C., Gerber, M. A., Meissner, H. C., Murray, D. L., Overturf, G. D., Prober, C. G., Rennels, M. B., Saari, T. N., Weiner, L. B., and Whitley, R. J. (1999) Possible association of intussusception with rotavirus vaccination. American Academy of Pediatrics. *Comm. Infect. Dis. Pediatr. 104*, 575.

(45) Bode, W., Engh, R., Musil, D., Thiele, U., Huber, R., Karshikov, A., Brzin, J., Kos, J., and Turk, V. (1988) The 2.0 A X-ray crystal structure of chicken egg white cystatin and its possible mode of interaction with cysteine proteinases. *EMBO J. 7*, 2593−2599.

(46) Kato, A., Nakamura, S.: Ban, M., Azakami, H., and Yutani, K. (2000) Enthalpic destabilization of glycolyated lysozyme constructed nby genetic modification. *Biochim. Biophys. Acta 1481*, 88−96.

(47) Lennarcic, I. C. B., Krasovec, M., Ritonja, R., Olafsson, I, and Turk, V. (1991) Inactivation of human cystatin C and kininogen by human cathepsin D. *FEBS Lett. 280*, 211−215.

(48) Yolken, R., Kinney, J., Wilde, J., Willoughby, R., and Eiden, J. (1990) Immunoglobulines and other modalities for the prevention and treatment of enteric viral infection. *J. Clin. Immunol. 10*, 80S-87S.

(49) Yolken, R. H., Willoughby, R., Wee, S. H., Miskuff, R., and Vonderfecht, S. L. (1987) Silalic acid glycoproteins inhibit in vitro and in vivo replication of rotavirus. *J. Clin. Invest. 79*, 148−154.

(50) Keljo, D. J., and Smith, A. K. (1988) Characterization of binding of simian rotavirus SA-11 to cultured epithelial cells. *J. Pediatr. Gastroenterol. Nutr. 7*, 249−256.

(51) Yolken, R. H., Peterson, J. A., Vonderfecht, S. L., Fouts, E. T., Midthun, K., and Newburg, D. S. (1987) Human milk mucin inhibits rotavirus replication and prevents experimental gastroenteritis. *J. Clin. Invest. 79*, 148−154.

(52) Superti, F., Marziano, M. L., Tinari, A., and Donelli, G. (1993) Effect of polyione on the infectivity of SA-11 rotavirus in LLC-MK2 cells. *Comput. Immunol. Microbiol. Infect. Dis. 16*, 55−62.

(53) Koketsu, M., Nitoda, T., Juneja, L. R., Kim, M., Kashimura, N., and Yamamoto, T. (1995) Sialyloligosaccharides from egg yolk as an inhibitor of rotaviral infection. *J. Agric. Food Chem. 43*, 858−861.

(54) Tsuge, Y., Shimoyamada, M., and Watanabe, K. (1996) Differences in hemagglutination inhibition activity against bovine rotavirus and hen Newcastle disease virus based on the subunits in hen egg white ovomucin. *Biosci. Biotech. Biochem. 60*, 1505−1506.

(55) Superti, F., Siciliano, R., Rega, B., Giansanti, F., Valenti, P., and Antonini, G. (2001) Involvement of bovine lactoferrin metal saturation, silaic acid and protein fragments in the inhibition of rotavirus infection. *Biochim. Biophys. Acta 1528*, 107−115.

(56) Vonderfecht, S. L., Miskuff, R. L., Wee, S. B., Sato, S., and Tidwell, R. R. (1988) Protease inhibitors suppress the in vitro and in vivo replication of rotavirus. *J. Clin. Invest. 82*, 2011−2016.

(57) Jayashree, S., Bhan, M. K., Kumar, R., Bhandari, N., and Sazawal, S. (1988) Protection against neonatal rotavirus infection by breast milk antibodies and trypsin inhibitors. *J. Med. Viol. 26*, 333−338.

(58) Ebina, T., and Tsukada, K. (1991) Protease inhibitors prevent the development of human rotavirus-induced diarrhea in sucking mice. *Microbiol. Immunol. 35*, 583−588.

(59) Ketyal, R., Rana, S. V., Ojha, S., Vaiphei, K., Singh, V., and Singh, K. (2001) Soybean trypsin inhibitor confers protection against rotavirus infection in infant mice. *Trop. Gastroenterol. 22*, 207−210.

(60) Willoughby, R. E., Yolken, R. H., and Schnaar, R. L. (1990) Rotaviruses specifically bind to the neutral glycosphingolipid asialo-GM1. *J. Virol. 64*, 4830−4835.

(61) Srnka, C. A., Tiemeyer, M., Gilbert, J. H., Moreland, M., Schweingruber, H., de Lappe, B. W., James, P. G., Gant, T., Willoughby, R. E., and Yolken, R. H. (1992) Cell surface ligands for rotavirus, mouse intestinal glycolipids and synthetic carbohydrate analogs. *Virology 190*, 794−805.

(62) Tsuge, Y., Shimoyamada, M., and Watanabe, K. (1996) Differences in hemagglutination inhibition activity against bovine rotaviruos and hen Newcastle disease virus based on the subunits in hen egg white ovomucin. *Biosci. Biotech. Biochem. 60*, 1505−15016.

(63) Li, F., Shi, Y., Guan, X., Zhang, S., and Tian, T. (1998) Antivirus effect of polysaccharides of brewer yeast in vitro. *Zhongguo Zhong Yao Za Zhi 23*, 171−173

(64) Bass, D. M., Mackow, E. R., and Greenberg, H. B. (1991). Identification and partial characterization of a rhesus rotavirus binding glycoprotein on murine enterocytes. *Virology 183*, 602−10.

(65) Dormitzer, P. R., Sun, Z.-Y. J., Wagner, G., and Harrison, S. C. (2002) The rhesus rotavirus VP4 sialic acid binding domain has a galectin fold with a novel carbohydrate binding site. *EMBO J. 21*, 885−897.

(66) Kang, S. Y., Nagaraja, K. V., and Newman, J. A. (1987) Characterization of viral polypeptides from avian rotavirus. *Avian Dis. 31*, 607−621.

BC049838S

Reversible Photocontrol of Peptide Helix Content: Adjusting Thermal Stability of the Cis State

Nina Pozhidaeva, Marie-Eve Cormier, Anita Chaudhari, and G. Andrew Woolley*

Department of Chemistry, University of Toronto, 80 Saint George Street, Toronto M5S 3H6, Canada. Received June 21, 2004; Revised Manuscript Received September 7, 2004

Cross-linking reagents based on an azobenzene core can be used to reversibly photoregulate secondary structure when introduced as intramolecular bridges in peptides and proteins. Photoisomerization of the azobenzene core in the trans to cis direction is triggered by photon absorption but isomerization from cis to trans occurs thermally as well as photochemically. The rate of the thermal process effectively determines the half-life of the cis form as well as the extent to which the trans form can be recovered. We designed and characterized a series of methanethiosulfonate (MTS)-bearing thiol-reactive azobenzene-based cross-linkers. These cross-linkers are shown to permit photoregulation of helix content in a test peptide with half-lives for the cis conformation ranging from 11 s to 43 h at 25 °C. The cross-linkers described here thus broaden the range of reagents available for reversible photocontrol of peptide and protein conformation.

INTRODUCTION

Upon irradiation at appropriate wavelengths, azobenzene chromophores undergo reversible cis−trans isomerization (*1*). Kumita et al. introduced thiol-reactive azobenzene cross-linkers as tools for the control of peptide conformation (*2*−*4*). They designed a symmetrical reagent 4,4′-bis(iodoacetamide)azobenzene (Figure 1) in which two Cys-reactive iodoacetamide moieties are linked to the azobenzene chromophore. When the reagent was used to intramolecularly cross-link peptides with Cys residues spaced at either i, i+4, i, i+7 or i, i+11 positions, photoisomerization led to predictable changes in peptide secondary structure.

Azobenzene isomerization in the cis-to-trans direction, in addition to being promoted by irradiation with light at >400 nm, occurs thermally. The half-life of the cis isomer of the bis(iodoacetamide)azobenzene cross-linker shown in Figure 1 is approximately 12 min at 25 °C (*3*). Half-lives for thermal isomerization are important for determining the practical usefulness of such photochemical switches. For instance, if structural studies are intended with the cis form, a much longer half-life than 12 min may be desired. Alternatively, if a pulsed conformational change is desired as part of a biochemical switch, then rapid return to the trans state would be preferable. Additionally, a rapid thermal relaxation to the trans form ensures virtually complete conversion to the trans isomer, important where a complete "off" state is desired for a biochemical switch. Because of the overlap in absorption spectra of cis and trans azobenzenes, irradiation never produces only one isomer. We note that natural photoswitches (e.g. photoactive yellow protein, phytochromes) also employ thermal relaxation to reset the switch (*5*).

Several groups have shown that the rate of thermal isomerization of azobenzenes can be varied substantially by altering the nature of substituents on the aromatic rings (e.g. (*6*−*9*)). For instance, thermal stability can be

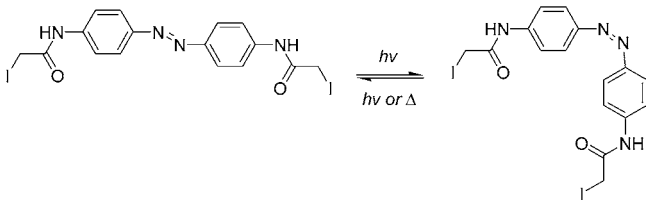


Figure 1. Cis−trans isomerization of 4,4′-bis(iodoacetamide)-azobenzene.



Figure 2. Two resonance forms of a substituted diamino-azobenzene.

adjusted by varying substituents that control the relative contribution of an N−N single bond resonance structure (Figure 2)(*8*, *10*). Precisely how this operates to lower transition state energies is not clear, however, since the mechanism of isomerization (rotation or inversion) remains controversial (*11*).

We wished to create a series of azobenzene cross-linkers analogous to the Kumita compound but showing a range of thermal stabilities. To enhance stability, we designed a derivative with sp^3 carbon atoms in the para positions in the expectation that it would show stability similar to *p*-methyl azobenzene ($\tau^1/_2$ 2−3 days)(*6*). To increase the rate of thermal reversion we designed derivatives in which enhanced delocalization of the *p*-amino group lone pair electrons would be possible. High reactivity and selectivity toward Cys residues was achieved by introducing methanethiosulfonyl groups. These groups enable reversible attachment of the cross-linker to peptides and proteins via disulfide linkages (*12*). The effects of the cross-linkers on the conformation of a test peptide (FK-11)(*3*) were evaluated.

EXPERIMENTAL PROCEDURES

The following includes general experimental procedures, specific details for representative reactions, and

* To whom correspondence should be addressed. E-mail: awoolley@chem.utoronto.ca; telephone/fax: (416) 978-0675.

10.1021/bc049855h CCC: $27.50 © 2004 American Chemical Society
Published on Web 11/02/2004

isolation and spectroscopic information for the new compounds prepared. All ^1H and ^{13}C NMR spectra were recorded using a Varian Unity 400 or a Varian Gemini 300 spectrometer. All chemicals were purchased from Aldrich Chemical Co. except if specified otherwise. High-resolution mass spectra were obtained either by electron impact (EI) or electrospray (ESI) ionization. Peptide mass spectra were obtained either by electrospray (ESI) or MALDI ionization.

Synthesis of 4,4′-Dimethylazobenzene (6). *p*-Toluidine (2.0 g, 18.7 mmol) was dissolved in dichloromethane (160 mL). Potassium permanganate (8.86 g, 56.1 mmol) and cupric sulfate pentahydrate (9.32 g, 37.3 mmol) were added, and the suspension was stirred at room temperature for 48 h. The suspension was filtered through a mixture of Celite and silica and eluted with dichloromethane. The solid obtained after evaporation of the filtrate was redissolved and purified on a silica column with dichloromethane as solvent to give **6** as an orange solid (780 mg, 40%). ^1H NMR (300 MHz, $CDCl_3$) δ 2.43 (s, 6H, CH_3), 7.31 (d, 4H, J = 8.1 Hz, Ar), 7.80 (d, 4H, J = 8.1 Hz, Ar); ^{13}C NMR (100 MHz, $CDCl_3$) δ 21.5, 122.7, 129.7, 141.2, 150.8. HRMS-EI for $C_9H_8O_4S$, calcd 210.1166, found 210.1157.

Synthesis of 4,4′-Dibromomethylazobenzene (7). 4,4′-Dimethylazobenzene (**6**)(202 mg, 0.97 mmol), *N*-bromosuccinimide (343 mg, 1.9 mmol), and benzoyl peroxide (7.0 mg, 0.03 mmol) were suspended in carbon tetrachloride (4 mL) and refluxed for 2 h. Another aliquot of benzoyl peroxide (7.0 mg, 0.03 mmol) was added to the mixture and reflux continued for another 2 h. The mixture was then stirred at room-temperature overnight. The solution was filtered, and the orange solid obtained was redissolved in dichloromethane. The organic layer was then washed with water, dried over $MgSO_4$, and concentrated under vacuum. The product was purified by flash chromatography using hexanes/EtO_2 (1:1) as eluant to give **7** as an orange solid (175 mg, 49%). ^1H NMR (300 MHz, $CDCl_3$) δ 4.58 (s, 4H, CH_2), 7.55 (d, 4H, J = 8.4 Hz, Ar), 7.90 (d, 4H, J = 8.4 Hz, Ar); ^{13}C NMR (100 MHz, $CDCl_3$) δ 32.7, 123.4, 129.9, 140.8, 152.3 HRMS-EI for $C_9H_8O_4S$, calcd 365.9371, found 365.9367.

Synthesis of 4,4′-Diiodomethylazobenzene (8). Sodium iodide (5.83 g, 39 mmol) was dissolved in dry acetone (50 mL) and stirred under nitrogen for 10 min. 4,4′-Dibromomethylazobenzene (**7**)(143 mg, 0.39 mmol) was added to the mixture in dry tetrahydrofuran (14 mL). The mixture was refluxed for 6 h and then stirred at room-temperature overnight. The solvent was evaporated and the solid resuspended in dichloromethane. The excess of sodium iodide and sodium bromide was filtered out, and the solution was evaporated under vacuum to give **8** as an orange solid (173 mg, 96%). ^1H NMR (300 MHz, $CDCl_3$) δ 4.53 (s, 4H, CH_2), 7.52 (d, 4H, J = 8.8 Hz, Ar), 7.84 (d, 4H, J = 8.8 Hz, Ar); ^{13}C NMR (100 MHz, $CDCl_3$) not soluble enough in $CDCl_3$ and DMSO for routine ^{13}C; HRMS-EI for $C_9H_8O_4S$, calcd 461.9090, found 461.9099.

Synthesis of 4,4′-Methanethiosulfonatemethyl-azobenzene (1) (MTS-alkyl-azobenzene). 4,4′-Diiodomethylazobenzene (**8**) (28 mg, 0.062 mmol) and sodium methanethiosulfonate (Toronto Research Chemicals) (42 mg, 0.31 mmol) were dissolved in a mixture of ethanol (2 mL) and dichloromethane (2 mL) and refluxed overnight. Dichloromethane and water were added to the mixture. The organic layer was dried over $MgSO_4$ and evaporated. The product was dissolved in dichloromethane and precipitated with a few drops of pentane to give **1** as an orange solid (12 mg, 45%). ^1H NMR (300 MHz, $CDCl_3$) δ trans isomer 2.99 (s, 6H, CH_3), 4.45 (s, 4H, CH_2), 7.57 (d, 4H, J = 8.4 Hz, Ar), 7.93 (d, 4H, J = 8.4 Hz, Ar); ^{13}C NMR (100 MHz, $CDCl_3$) δ 40.7, 51.6, 123.7, 130.2, 138.6, 152.2; HRMS-ESI for $C_9H_8O_4S$, calcd 431.0222, found 431.0231.

Synthesis of 4,4′-Dichloroacetamide Azobenzene (10). 4,4′-Diaminoazobenzene (**9**) (255 mg, 1.2 mmol) (Lancaster, Pelham NH) was dissolved in anhydrous tetrahydrofuran (20 mL) and stirred under nitrogen for 15 min protected from light. Three equivalents of triethylamine (500 μL, 3.61 mmol) was added, followed by the dropwise addition of 3 equiv of chloroacetyl chloride (287 μL, 3.61 mmol). The reaction mixture was left stirring under nitrogen for 30 min at room temperature. The reaction mixture was filtered via vacuum filtration to remove the precipitate that formed, and the tetrahydrofuran was removed by rotary evaporation. The crude product was redissolved in a solution of tetrahydrofuran and dichloromethane (1:1) and extracted with water acidified with a few drops of 1% HCl. The filtrate was dried over anhydrous $MgSO_4$ and vacuum filtered, and solvents were removed by rotary evaporation producing a yellow-brown solid (**10**) (395 mg, 91%). ^1H NMR (DMSO-d_6, 300 MHz): δ 4.31 ppm (s, 4H), δ 7.79 ppm (d, J = 9.0 Hz, 4H), δ 7.87 ppm, (d, J = 9.0 Hz, 4H), δ 10.65 ppm (s, 2H). ^{13}C NMR (DMSO-d_6, 75 MHz): δ 43.6, 119.6, 123.5, 141.2, 148.0, 165.0; EI−HRMS: ($C_{16}H_{14}Cl_2N_4O_2$), calcd 364.0494, found 364.0498.

Synthesis of 4,4′-Diiodoacetamide Azobenzene (11). Anhydrous acetone (20 mL) and anhydrous tetrahydrofuran (15 mL) were combined and the solvent mixture degassed. Sodium iodide (1 g, 7.1 mmol) was dissolved in the degassed solvent and added to 150 mg (0.71 mmol) of dichloroacetamide azobenzene (**10**). The reaction mixture was stirred for 12 h under nitrogen and protected from light. After filtration to remove NaCl, the solvent was removed by rotary evaporation to produce a yellow-brown solid. The solid was redissolved in a solution of tetrahydrofuran and dichloromethane (1:1), and excess of NaI was removed by vacuum filtration. The filtrate was extracted with water, dried over anhydrous $MgSO_4$, vacuum filtered, and solvents were removed by rotary evaporation to produce a yellow-brown solid (**11**) (330 mg, 85%). ^1H NMR (DMSO-d_6, 300 MHz): δ 3.87 ppm (s, 4H), δ 7.76 ppm (d, J = 9.0 Hz, 4H), δ 7.86 ppm, (d, J = 9.0 Hz, 4H), δ 10.67 ppm (s, 2H); ^{13}C NMR (DMSO-d_6, 100 MHz), δ 1.4, 119.3, 123.5, 141.5, 147.8, 167.0; EI−HRMS: ($C_{16}H_{14}I_2N_4O_2$), calcd 547.9209, found 547.9199.

Synthesis of 4,4′-Methanethiosulfonylacetamide Azobenzene (2). 4,4′-Diiodoacetamide azobenzene (**11**) (90 mg, 0.164 mmol) and sodium methanethiosulfonate (48.4 mg, 0.361 mmol) (Toronto Research Chemicals) were dissolved in a degassed mixture of anhydrous ethanol (15 mL) and anhydrous tetrahydrofuran (15 mL) and refluxed for 12 h. The solvents were removed by rotary evaporation to produce a yellow-brown solid (**2**) that was washed with water to remove excess sodium methanethiosulfonate and dried (77 mg, 85%). ^1H NMR (DMSO-d_6, 300 MHz): δ 3.61 ppm (s, 6H), δ 4.24 ppm (s, 4H), δ 7.78 ppm (d, J = 9.0 Hz, 4H), δ 7.87 ppm, (d, J = 9.0 Hz, 4H), δ 10.72 ppm (s, 2H); ^{13}C NMR (75 MHz, DMSO-d_6), δ 38.4, 50.6, 119.6, 123.5, 141.2, 148.0, 165.6; ESI−HRMS: ($C_{18}H_{21}N_4O_6S_4$)(MH^+), calcd 517.0343, found 517.0338.

Synthesis of 4,4′-*p*-Nitrophenoxyacetamide Azobenzene (12). 4,4′-Diaminoazobenzene (**9**)(80 mg, 0.377 mmol) (Lancaster, Pelham NH) was dissolved in anhydrous dichloromethane (20 mL) and stirred under nitrogen for 15 min protected from light. Four equivalents of *p*-nitrophenyl chloroformate (304 mg, 1.509 mmol) (Flu-

ka) were dissolved in anhydrous dichloromethane (10 mL) and added to the diaminoazobenzene solution, followed by the dropwise addition of 4 equiv of pyridine (121.4 μL, 1.509 mmol). The reaction mixture was stirred under nitrogen at room temperature for 2 h. The volume of the solvent was reduced by half, and the solid precipitate was collected. The precipitate was purified by washing with water, 5% HCl, 5% NaOH, and water again to give **12** as a yellow-brown solid (165 mg, 81%). ^{1}H NMR (DMSO-d_6, 400 MHz): δ 7.58 ppm (d, J = 9.0 Hz, 4H), δ 7.72 ppm, (d, J = 9.0 Hz, 4H), δ 7.89 ppm (d, J = 9.0 Hz, 4H), δ 8.32 ppm (d, J = 9.0 Hz, 4H), δ 10.87 ppm (s, 2H); ^{13}C NMR (100 MHz, DMSO-d_6), δ 118.9, 123.0, 123.6, 125.3, 141.0, 144.7, 147.8, 150.5, 155.3; Molecular ion was not observed with EI-MS.

Synthesis of 4,4′-(Methanethiosulfonate-ethyloxy)-acetamide Azobenzene (3). 4,4′-*p*-Nitrophenoxyacetamide azobenzene (**12**) (15.8 mg, 0.029 mmol) and 2-hydroxyethyl methanethiosulfonate (10 mg, 0.064 mmol) (Toronto Research Chemicals) were combined together and suspended in DMSO (3 mL). Diisopropylethylamine (2.2 equiv, 11.2 μL, 0.064 mmol) was added, and the reaction mixture was stirred at room temperature under nitrogen for 6 h. The solvent was removed under high vacuum. The crude product was washed with water, 5% sodium bicarbonate, and water and dried (10 mg, 60%). ^{1}H NMR (acetone-d_6, 300 MHz): δ 3.470 ppm (s, 6H), δ 3.85 ppm (q, J = 5.7 Hz, 4H), δ 4.31 ppm (t, J = 5.7 Hz, 4H), δ 7.83 ppm (d, J = 8.7 Hz, 4H), δ 7.96 ppm, (d, J = 8.7 Hz, 4H), δ 9.80 ppm (s, 2H). ^{13}C NMR (100 MHz, acetone-d_6), δ 33.7, 38.9, 54.7, 120.7, 122.9, 140.4, 148.1, 154.0. ESI−HRMS: ($C_{20}H_{25}N_4O_8S_4$)(MH^+), calcd 577.0555, found 577.0549.

Synthesis of 4,4′-(Methanethiosulfonate-ethyl-amino)acetamide Azobenzene (4). One equivalent of 4,4′-*p*-nitrophenoxyacetamide azobenzene (**12**) (63 mg, 0.116 mmol) and 2.5 equiv of 2-aminoethyl methanethiosulfonate hydrobromide (68.4 mg, 0.290 mmol) (Toronto Research Chemicals) were combined together and suspended in DMSO (4 mL). Diisopropylethylamine (2.5 equiv, 50 μL, 0.290 mmol) was added, the reaction mixture was stirred at room temperature under nitrogen for 6 h, and then the solvent was removed under high vacuum. The crude product was washed with water, 5% sodium bicarbonate, and water and then dried (53 mg, 80%). ^{1}H NMR (DMSO-d_6, 400 MHz): δ 3.35 ppm (t, J = 6.4 Hz, 4H), δ 3.48 ppm (dt, J_1 = 6.4, J_2=5.6 Hz, 4H), δ 3.57 ppm (s, 6H), δ 6.58 ppm (t, J = 5.6 Hz, 2H), δ 7.58 ppm (d, J = 7.8 Hz, 4H), δ 7.75 ppm, (d, J = 7.8 Hz, 4H), δ 9.04 ppm (s, 2H); ^{13}C NMR (100 MHz, DMSO-d_6), δ 36.0, 38.7, 50.2, 117.7, 123.4, 142.9, 146.5, 154.8; ESI−HRMS: ($C_{20}H_{27}N_6O_6S_4$)(MH^+), calcd 575.0874, found 575.0869.

Cross-Linking of MTS-alkyl-azobenzene to FK-11. A 10 mM solution of the cross-linker **1** in DMSO and a 0.49 mM solution of FK-11 in water were prepared. The peptide solution (1.23 mL, 0.6 μmol), a first aliquot of the cross-linker solution (30 μL, 0.3 μmol), and 410 μL of DMSO were stirred at room temperature, in the dark, for 15 min. Another aliquot of cross-linker was added (30 μL, 0.3 μmol), and the solution was stirred for anther 15 min. The last aliquot of cross-linker (30 μL, 0.3 μmol) was added to the solution, and stirring was continued for another 40 min. The solvent was evaporated under high vacuum. The product was purified by HPLC on a preparative C18-column (Apex, ODS Prepsil, 25 cm 8 μm) with an ACN (0.1% TFA) and H_2O (0.1% TFA) gradient (step 1: 15% to 90% ACN in 45 min; step 2: 90% ACN for 3.0 min; step 3: 90% to 15% ACN in 3.0 min), with detection at 360 nm. The retention time was 24 min (flow rate 10 mL/min). MS/ESI: calcd 2018, found 672.9 (3+), 1009.4 (2+).

Cross-Linking of MTS-amide-azobenzene to FK-11. An 11.6 mM solution of the cross-linker **2** in DMSO and 0.549 mM solution of FK-11 in water were prepared. The peptide solution (1.09 mL, 0.6 μmol) and the first out of three aliquots of the cross-linker solution (55 μL, 0.6 μmol) were combined together followed by addition of extra 400 μL of pure DMSO. The reaction mixture was stirred at room temperature, in the dark, for 15 min. Another aliquot of cross-linker was added (55 μL, 0.6 μmol), and the solution was stirred for another 15 min. The last aliquot of cross-linker (55 μL, 0.6 μmol) was added, and stirring was continued for another 1.5 h. After completion the solvent was removed under high vacuum. The product was purified by HPLC on a semi-preparative SB-C18 column (Zorbax, 9.4 mm ID × 25 cm) with an ACN (0.1% TFA) and H_2O (0.1% TFA) gradient (step 1: from 15% to 90% ACN in 45 min; step 2: 90% ACN for 8 min; step 3: from 90% to 15% ACN in 8 min). Absorbance at 360 nm was monitored, and the pure product was eluted at 50% ACN with a retention time 14 min (flow rate 2.1 mL/min). MALDI-MS [MH^+]: ($C_{81}{}^{13}C_2H_{128}N_{31}O_{26}S_4$) calcd 2106 0.38, found 2106.96, 1053.96 (2+).

Cross-Linking of MTS-carbamate-azobenzene to FK-11. A 4.5 mM solution of the cross-linker **3** in DMSO and a 0.55 mM solution of FK-11 in water were prepared. The peptide solution (1.09 mL, 0.6 μmol) and the first out of three aliquots of the cross-linker solution (132 μL, 0.6 μmol) were combined together followed by addition of extra 200 μL of pure DMSO. The reaction mixture was stirred at room temperature, in the dark, for 15 min. Another aliquot of cross-linker was added (132 μL, 0.6 μmol), and the solution was stirred for another 15 min. The last aliquot of cross-linker (132 μL, 0.6 μmol) was added, and stirring was continued for another 1.5 h. After completion the solvent was removed by high vacuum pumping. The product was purified by HPLC on a semipreparative SB-C18 column (Zorbax, 9.4 mm ID × 25 cm) with an ACN (0.1% TFA) and H_2O (0.1% TFA) gradient (step 1: from 10% to 90% ACN in 45 min; step 2: 90% ACN for 5 min; step 3: from 90% to 10% ACN in 5 min), with monitoring at 360 nm. The pure product was eluted at 44% ACN with the retention time 25 min (flow rate 2.1 mL/min). MALDI-MS [MH^+]: ($C_{83}{}^{13}C_2H_{134}N_{31}O_{28}S_4$) calcd 2166.45, found 2165.97.

Cross-Linking of MTS-urea-azobenzene to FK-11. A 5.92 mM solution of the cross-linker **4** in DMSO and a 0.549 mM solution of FK-11 in water were prepared. The peptide solution (1.09 mL, 0.6 μmol) and the first out of three aliquots of the cross-linker solution (100 μL, 0.6 μmol) were combined together followed by addition of extra 400 μL of pure DMSO. The reaction mixture was stirred at room temperature, in the dark, for 15 min. Another aliquot of cross-linker was added (100 μL, 0.6 μmol), and the solution was stirred for another 15 min. The last aliquot of cross-linker (100 μL, 0.6 μmol) was added, and stirring was continued for another 1.5 h. After completion, the solvent was removed under high vacuum. The product was purified by HPLC on a semipreparative SB-C18 column (Zorbax, 9.4 mm ID × 25 cm) with an ACN (0.1% TFA) and H_2O (0.1% TFA) gradient (step 1: from 35% to 80% ACN in 45 min; step 2: 80% ACN for 5 min; step 3: from 80% to 35% ACN in 5 min) with monitoring at 360 nm. The pure product was eluted at 41% ACN with the retention time 6 min (flow rate 2.1

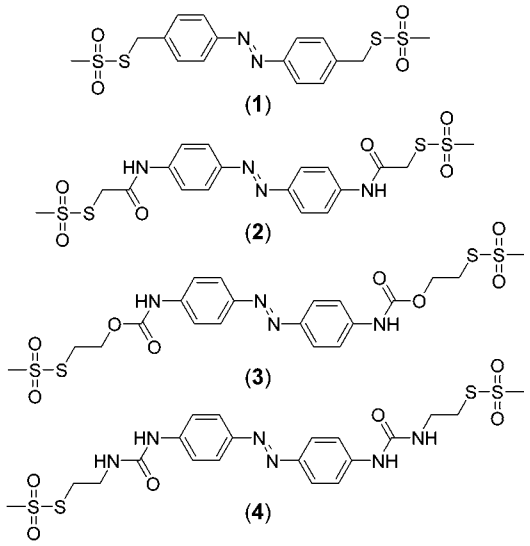


Figure 3. Structures of MTS-azobenzenes synthesized: MTS-alkyl-azobenzene (**1**), MTS-amide-azobenzene (**2**), MTS-carbamate-azobenzene (**3**), MTS-urea-azobenzene (**4**).

mL/min). MALDI-MS [MH^+]: ($C_{83}{}^{13}C_2H_{136}N_{33}O_{26}S_4$) calcd 2164.48, found 2165.07.

Synthesis of Glutathione Derivatives. One equivalent of each cross-linker was dissolved in 500 μL of DMSO. Ten equivalents of γ-glutathione were dissolved in 500 μL of TrisCl buffer (100 mM, pH 8) and added dropwise to each solution of cross-linker in DMSO. The reaction mixture was stirred at room temperature for 2 h in the dark. After completion, the solvent was removed under high vacuum. The products were purified by HPLC on a semipreparative SB-C18 column (Zorbax, 9.4 mm ID $\times$ 25 cm) as described above. Structures were confirmed by MALDI-MS.

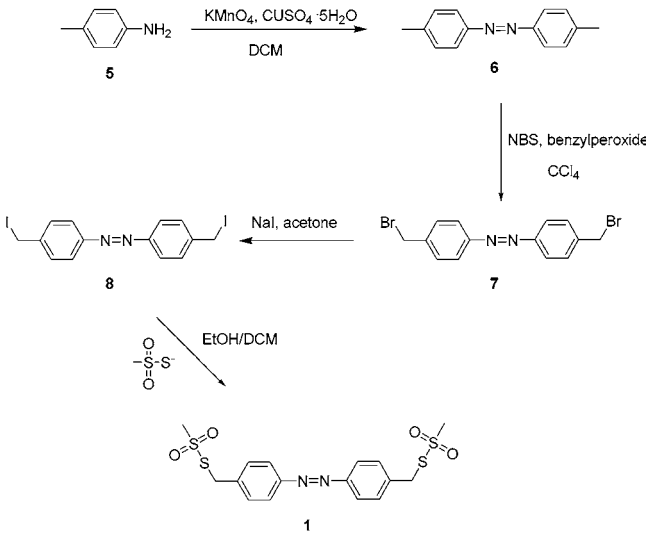
Photoisomerization. A 70 W Metal Halide Tri-Lite Lamp (World Precision Instruments Inc., FL) coupled with either a 340 $\pm$ 10 nm, 370 $\pm$ 10 nm, or 380 $\pm$ 10 nm band-pass filter (Harvard Apparatus Canada, PQ) was used to photoisomerize peptide solutions to the cis isomers. For photoisomerization to the trans isomer, a 455 nm cutoff filter (Harvard Apparatus Canada, PQ) was used coupled to the same lamp. Photoisomerization in both directions was completed within 10 min.

UV/Vis and CD Spectroscopy and Relaxation Curves. Peptide samples were dissolved in a 5 mM phosphate buffer (pH 7). For the relaxation curves experiments, the spectra were taken using a BDS 100 Fiber Deuterium/Tungsten light source, a Quantum Northwest temperature control and an Oceanoptics UBS 2000 diode-array. Quartz cuvettes (0.1 cm path length) were used for the measurements. Relaxation curves were fit to single exponentials and time constants and activation energies evaluated in the standard way.

All the circular dichroism (CD) experiments were performed on a Jasco Model J-710 spectropolarimeter using thermostated quartz cuvettes (0.1 or 1.0 cm path length). The samples were dissolved in a 5 mM phosphate buffer (pH = 7). A 10 nm/min, 1.0 nm bandwidth and a 4 s response time were used. Corrected CD spectra for 100% cis isomers were obtained using the following equation: θ (100% cis) = [θ (observed after irradiation) $-$ (fraction trans $\times$ θ (dark-adapted))]/fraction cis.

Calculations of Absorbance Spectra. Models of each chromophore were built in Spartan 04 for Windows (Wave function Inc.) with structures as shown in Figure 3 except that the $CH_3S(O)_2SCH_2$ unit was replaced by a methyl group. Geometry was optimized using the ab intio HF 6-31G* method in Spartan. Only trans geometries of the azo unit were studied. Wavelengths for absorbance maxima together with oscillator strengths were calculated using the DFT EDF1 6-31G method in Spartan. ZINDO/S calculations were performed on the HF 6-31G* minimized structures using Hyperchem v.6 (Hypercube Inc.).

Scheme 1. Synthesis of MTS-alkyl-azobenzene



RESULTS AND DISCUSSION

Synthesis of MTS-azobenzene Cross-Linkers. A series of azobenzene-based thiol-reactive cross-linkers was synthesized with structures as shown in Figure 3. For convenience we will refer to these compounds according to the type of linkage between the azobenzene group and the thiol-reactive MTS moiety (e.g. MTS-carbamate-azobenzene). It is this linkage that primarily affects the thermal stability of the compounds.

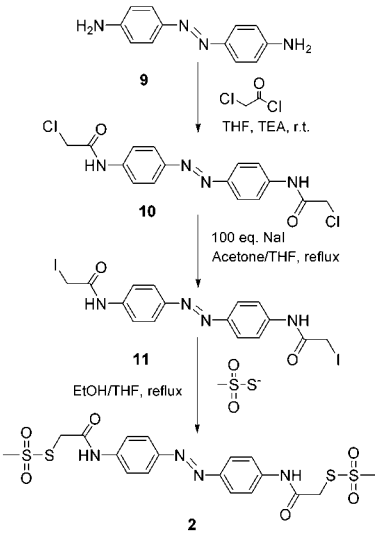
The MTS-alkyl-azobenzene cross-linker (**1**) was obtained in a four-step synthesis (Scheme 1). First, *p*-toluidine **5** was oxidized using a mixture of potassium permanganate and cupric sulfate to give **6**. Bromination of the benzylic methyl groups was achieved through a radical reaction using *N*-bromosuccinimide in carbon tetrachloride with benzoyl peroxide as an initiator. In our first trials, we attempted to install MTS on **7** by displacement of the bromide but the yield of this reaction was low. We therefore carried out a bromo/iodo exchange reaction on **7**. Refluxing **8** in a mixture of dichloromethane and ethanol with the sodium methanethiosulfonate was sufficient to obtain the desired product **1**.

The MTS-amide-azobenzene cross-linker (**2**) was obtained by a simple displacement reaction between Na-MTS and the Kumita cross-linker synthesized as described previously (Scheme 2).

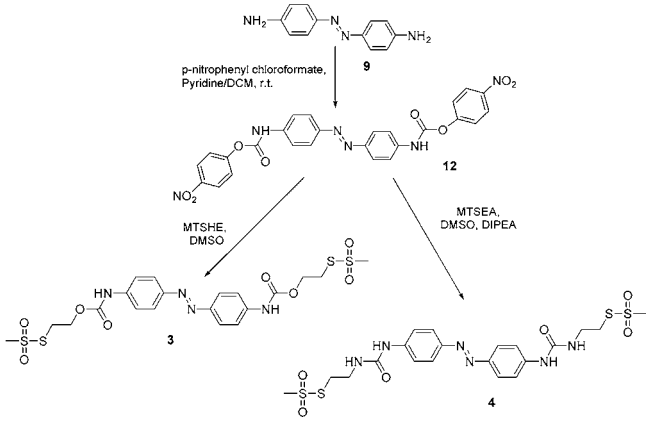
The MTS-carbamate-azobenzene cross-linker (**3**) and MTS-urea-azobenzene cross-linker (**4**) were obtained as outlined in Scheme 3. Reaction of diaminoazobenzene with *p*-nitrophenyl chloroformate produced the carbamate **12**. This reacted rapidly with 2-aminoethyl methanethiosulfonate and more sluggishly with 2-hydroxyethyl methanethiosulfonate with DMSO as solvent to form cross-linkers **3** and **4**, respectively.

Peptide Cross-Linking with MTS-azobenzenes. On the basis of previous studies, we chose the peptide FK-11 (Acetyl-Glu-Ala-Cys-Ala-Arg-Glu-Ala-Ala-Ala-Arg-Glu-Ala-Ala-Cys-Arg-Gln-amide) as a target for photo-

Scheme 2. Synthesis of MTS-amide-azobenzene



Scheme 3. Synthesis of MTS-carbamate-azobenzene and MTS-urea-azobenzene



control (*3*, *13*). FK-11 has cysteine residues spaced 11 residues apart and is known to form stable α-helices in water (*3*, *14*). Molecular models of cross-linked FK-11 indicated that when the peptide is in a helical conformation, the distance between the two Cys residues can accommodate the trans isomer of the cross-linkers with relatively little distortion of the helix. The end-to-end distance of the cis conformation of the cross-linker is less compatible with this Cys residue spacing. Trans-to-cis isomerization is thus is expected to lead to decreased peptide helical content in aqueous solution.

Cross-linking of the peptides was achieved rapidly and efficiently by dissolving the peptide in water and slowly adding a solution of the cross-linker in DMSO. The modified peptides were purified by HPLC. To test for effects of peptide structure on the thermal stability of the cross-linker, the MTS-azobenzene cross-linkers were also reacted with glutathione to furnish a chemically similar adduct without secondary structure.

Spectral Properties and Thermal Stability. Spectra were obtained for each of the MTS-azobenzene peptide conjugates after dark adaptation to produce pure trans isomers (Figure 4). Absorption maxima are collected in Table 1.

The absorption maximum of the trans isomer of the MTS-alkyl-azobenzene is close to that observed for unmodified azobenzene (340 nm) and at a significantly shorter wavelength than that for the amide-, carbamate-, and urea-substituted compounds. The trend in absorption

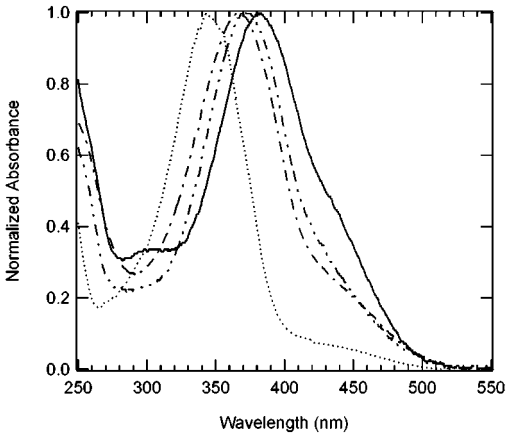


Figure 4. Spectra of dark-adapted (trans isomers) of cross-linked peptides: (···) MTS-alkyl-azobenzene FK-11, (– · –) MTS-amide-azobenzene FK-11, (– ·· –) MTS-carbamate-azobenzene MTS, (—) MTS-urea-azobenzene FK-11.

Table 1. Experimental and Calculated Absorption Maxima of Chromophores

structure	λ_{max}, nm (obsd) (trans)	λ_{max}, nm (ZINDO) (trans)	λ_{max}, nm, DFT EDF1 6-31G* (trans)
alkyl	342	335 (1.018)	330 (0.817)
amide	366	349 (1.190)	379 (1.519)
carbamate	372	349 (1.198)	376 (1.555)
urea	382	350 (1.212)	387 (1.567)

maxima is predicted by the ZINDO semiempirical method (*9*, *15*, *16*) although predicted λ_{max} values are too small, as has been observed in related studies (*16*). The DFT EDF1 method gives a better match to experiment (Table 1). The trend in absorption maxima can be understood in terms of a greater degree of delocalization of electrons associated with the benzylic atom from alkyl through urea structures in the series. Spectra of pure cis forms for the alkyl and amide derivatives were similar to those reported previously for unmodified azobenzene (*17*) and the Kumita compound (*3*). Spectra for the pure cis isomers of the carbamate and urea compounds were not obtained in the present study due to complications arising from the rapid thermal reversion to the trans isomer (vide infra). In contrast to observations with some other some delocalized azobenzene derivatives ((*16*)), however, significant degrees of conversion to the cis isomer were obtained as can be seen from the spectra shown in Figure 5.

Thermal stabilities of the cis isomers of cross-linked FK-11 peptides together with the corresponding glutathione adduct were measured. After irradiation, recovery of the trans form in the dark was monitored by following absorption at 370 nm for series of different temperatures (Figure 6). These data are collected in Table 2 together with calculated activation energies for the thermal isomerization process. As observed previously, half-lives depend on the nature of the attached peptide,i.e. whether it is unstructured glutathione or the highly structured FK-11 peptide (*3*). Nevertheless, a clear correlation is observed between the absorption wavelength maximum of the cross-linker and the thermal stability of the cis form. With more delocalization, absorption maxima increase and half-lives decrease.

Effects of Photoisomerization on Peptide Conformation. Circular dichroism spectroscopy (CD) was employed to determine the effect of cross-linker isomerization on the FK-11 peptide structure. The CD spectrum of dark-adapted MTS-alkyl-azobenzene cross-linked

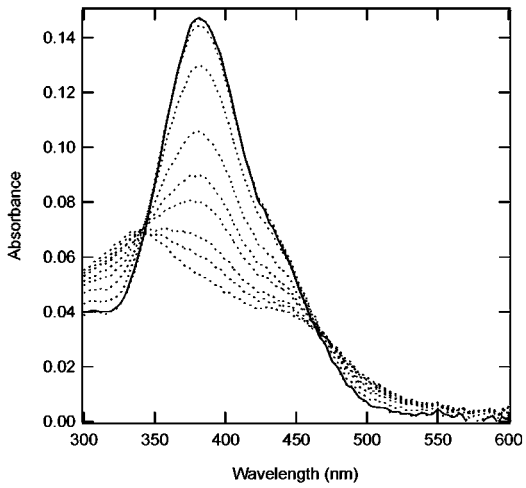


Figure 5. Spectra showing thermal relaxation at 4 °C of MTS-urea-azobenzene FK-11 after irradiation at 370 nm. Spectra were recorded at 0.65, 1.3, 2.0, 3.3, 6.5, 12.3, and 61.3 min (solid line) after irradiation.

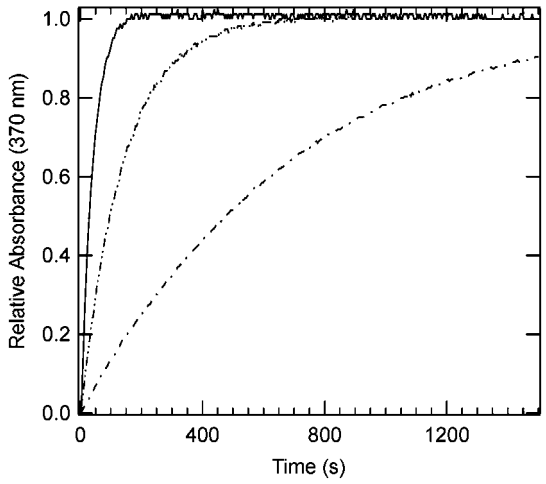


Figure 6. Time courses for thermal relaxation (25 °C) of FK-11 peptides cross-linked with linkers: (– · –) MTS-amide-azobenzene FK-11, (– ·· –) MTS-carbamate-azobenzene MTS, (—) MTS-urea-azobenzene FK-11. The absorbance of the MTS-alkyl-azobenzene cross-linked peptide shows no change over this time period.

Table 2. Half-lives and Activation Energies for Cross-Linked FK-11 Peptides

structure	$\tau_{1/2}$@25 °C	$\tau_{1/2}$@37 °C	E_a (kJ/mol)
alkyl-FK11	43 h	12 h	82
amide-FK11	8 min	3 min	72
carbamate-FK11	96 s	33 s	69
urea-FK11	26 s	10 s	62
alkyl-glutathione	43 h	12 h	82
amide-glutathione	12 min	4 min	76
carbamate-glutathione	80 s	30 s	67
urea-glutathione	11 s	5 s	60

FK-11 peptide at 10 °C shows bands at 208 and 222 nm, characteristic of a helical peptide (Figure 7A). Upon irradiation at 340 nm, the intensity of the two bands decreases, the largest difference being for the band at 222 nm, consistent with a decrease in peptide helical content. The normalized spectrum for the pure cis form (calculated by subtracting the contribution of the remaining trans isomer) is shown in Figure 7A. Upon irradiation at >450 nm, the helical content returns to the level observed for the dark-adapted state. For each of the cross-linked peptides, photoisomerization of the cross-linker from trans to cis causes a decrease in peptide helicity as expected (Figure 7B–D). Thermal relaxation recovered the dark-adapted (trans) spectra.

The size of the effect can be evaluated by measuring the percent change in ellipticity at 222 nm. However, as noted above, rapid thermal relaxation of the MTS-carbamate and MTS-urea derivatives prevents isolation of the cis isomers for determination of their spectra. Nevertheless, the effect of irradiation on the absorption spectra of each of the derivatives is qualitatively similar (Figure 5) so that ~75±5% conversion to the cis isomer is likely occurring in each case. Using this assumption, the change in percent helix content observed upon irradiation for each peptide was calculated (Table 3)

The magnitude of the effect of trans-to-cis isomerization on peptide helix content follows the order MTS-alkyl-azobenzene > MTS-amide-azobenzene > MTS-carbamate-azobenzene ≈ MTS-urea-azobenzene. This pattern can be qualitatively understood by examining distance ranges between atoms corresponding to Cys-γ-S atoms in models of the free linkers (Table 3). The ideal S–S distance range between Cys-γ-S atoms in positions i, i +11 of an α-helix is 14.1 to 19.2 Å. Whereas each linker is able to accommodate this distance range in the trans conformation,

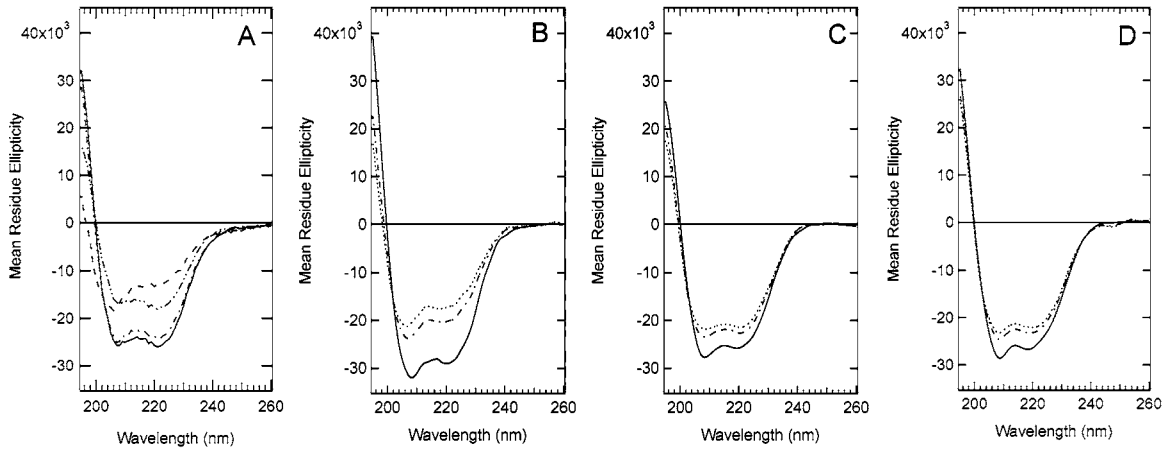


Figure 7. CD spectra of MTS-alkyl-azobenzene cross-linked FK-11 (A), MTS-amide-azobenzene cross-linked FK-11 (B), MTS-carbamate-azobenzene cross-linked FK-11 (C), MTS-urea-azobenzene cross-linked FK-11 (D). For A: Dark-adapted (—); 100% cis (- - -) (after irradiation at 340 nm and corrected for % conversion as described in the methods section); irradiated with a 450 long pass filter (– · –); after treatment with TCEP (– ·· –). For (B–D): Dark-adapted (—); after irradiation at 370 nm (– · –), corrected for 100% cis (- - -). After thermal relaxation the dark-adapted spectra were recovered in each case.

Table 3

structure	% helix change obsd[a]	S−S range, Å (trans)[b]	S−S range, Å (cis)[b]
MTS-alkyl-azo-FK11	45	9.8−17.7	3.3−13.0
MTS-amide-azo-FK11	39	14.3−22.4	3.2−16.5
MTS-carbamate-azo-FK11	14	14.9−26.3	4.0−18.0
MTS-urea-azo-FK11	16	15.1−26.5	3.2−18.9

[a] Calculated as % helix (dark) − % helix (cis), where 100% helix is −30 000 deg·cm^2·dmol^{-1}. [b] S−S range is the distance between Cys-γ-S atoms. In an ideal α-helix this distance range is 14.1−19.2 Å for Cys residues spaced at i, i+11.

the alkyl linker is least compatible with this distance range when in the cis conformation. The MTS-urea-azobenzene and MTS-carbamate-azobenzene cross-linkers, in particular, are long and flexible enough to accommodate a significant part of the optimal distance range between Cys-γ-S atoms even when in the cis conformation. The length of these linkers may make them more suitable (in the trans conformation) for cross-linking between Cys residues spaced more than 11 residues apart in an α-helix. Alternatively, the cis conformations of the linkers may be used to link closely spaced Cys residues (e.g., i, i+4) in peptide sequence. In that case, photoisomerization in the trans-to-cis direction should stabilize an α-helical structure.

Cleavage of the Cross-Linked Peptides. Under standard photoisomerization conditions the peptides appear chemically stable. Mass spectra of the samples after irradiation showed that the cross-linked peptides remained intact during at least 10−20 photocycles. Extensive irradiation at higher temperatures (50 °C) was found to cause some cleavage of the cross-linkers from the peptide.

A possible advantage of the MTS-activated cross-linkers over the Kumita iodoacetamide linker is that they can be removed from the peptide upon addition of thiols or mild reducing agents. Addition of the water-soluble reducing agent triscarboxyethylphosphine (TCEP) to a solution of cross-linked peptide caused rapid and complete removal of the linker. Figure 7A shows the CD spectra obtained for FK-11 after treatment with TCEP. After cleavage, the only peak observed in the electrospray mass spectrum is the molecular ion for the un-cross-linked peptide.

SUMMARY AND CONCLUSIONS

The new azobenzene-based cross-linkers described here can be covalently attached to peptides or proteins through cysteine residues and removed again by reduction using TCEP. When used to cross-link the test peptide FK-11 the linkers enabled photocontrol of peptide helical content in a manner similar to the iodoacetamide based cross-linker introduced by Kumita et al. (*2*, *3*, *18*) but with a large range of thermal stabilities observed for the cis forms from 11 s to 43 h at 25 °C. The cross-linkers described here thus broaden the range of reagents available for reversible photocontrol of peptide and protein conformation.

ACKNOWLEDGMENT

The authors would like to acknowledge the financial support of the Natural Sciences and Engineering Research Council of Canada (NSERC) and the Volkswagen Stiftung (Germany).

LITERATURE CITED

(1) Rau, H. (1990). Photoisomerization of Azobenzenes. In *Photochemistry and Photophysics* (Rabek, J. F., Ed.), vol. II. pp 119−141, CRC Press Inc., Boca Raton, FL.

(2) Kumita, J. R., Smart, O. S., and Woolley, G. A. (2000). Photocontrol of helix content in a short peptide. *Proc. Natl. Acad. Sci. U.S.A. 97*, 3803−3808.

(3) Flint, D. G., Kumita, J. R., Smart, O. S., and Woolley, G. A. (2002). Using an azobenzene cross-linker to either increase or decrease peptide helix content upon trans-to-cis photoisomerization. *Chem. Biol. 9*, 391−397.

(4) Kumita, J. R., Flint, D. G., Smart, O. S., and Woolley, G. A. (2002). Photocontrol of peptide helix content by an azobenzene cross-linker: steric interactions with underlying residues are not critical. *Protein Eng. 15*, 561−569.

(5) Hellingwerf, K. J., Hoff, W. D., and Crielaard, W. (1996). Photobiology of microorganisms: how photosensors catch a photon to initialize signalling. *Mol. Microbiol. 21*, 683−693.

(6) Talaty, E. R., and Fargo, J. C. (1967). Thermal cis−trans isomerization of substituted azobenzenes: a correction of the literature. *J. Chem. Soc.* 65−66.

(7) Le Fevre, R. J. W., and Northcott, J. (1953). The effects of substituents and solvents on the cis−trans change of azobenzene. *J. Chem. Soc.*, 867−870.

(8) Nishimura, N., Sueyoshi, T., Yamanaka, H., Imai, E., Yamamoto, S., and Hasegawa, S. (1976). Thermal cis-to-trans isomerization of substituted azobenzenes II. Substituent and solvent effects. *Bull. Chem. Soc. Jpn. 49*, 1381−1387.

(9) Forber, C. L., Kelusky, E. C., Bunce, N. J., and Zerner, M. C. (1985). Electronic spectra of cis- and trans-azobenzenes: consequences of ortho substitution. *J. Am. Chem. Soc. 107*, 5884−5890.

(10) Yamamoto, S., Nishimura, N., and Hasegawa, S. (1973). The tautomeric equilibria of 4-(dialkylamino)azobenzene derivatives. *Bull. Chem. Soc. Jpn. 46*, 194−198.

(11) Cembran, A., Bernardi, F., Garavelli, M., Gagliardi, L., and Orlandi, G. (2004). On the mechanism of the cis−trans isomerization in the lowest electronic states of azobenzene: S0, S1, and T1. *J. Am. Chem. Soc. 126*, 3234−3243.

(12) Smith, D. J., Maggio, E. T., and Kenyon, G. L. (1975). Simple alkanethiol groups for temporary blocking of sulfhydryl groups of enzymes. *Biochemistry 14*, 766−771.

(13) Chen, E., Kumita, J. R., Woolley, G. A., and Kliger, D. S. (2003). The kinetics of helix unfolding of an azobenzene cross-linked peptide probed by nanosecond time-resolved optical rotatory dispersion. *J. Am. Chem. Soc. 125*, 12443−12449.

(14) Merutka, G., Shalongo, W., and Stellwagen, E. (1991). A model peptide with enhanced helicity. *Biochemistry 30*, 4245−4248.

(15) Bacon, D., and Zerner, M. C. (1979). *Theor. Chim. Acta 53*, 21.

(16) Cisnetti, F., Ballardini, R., Credi, A., Gandolfi, M. T., Masiero, S., Negri, F., Pieraccini, S., and Spada, G. P. (2004). Photochemical and electronic properties of conjugated bis(azo) compounds: an experimental and computational study. *Chem. Eur. J. 10*, 2011−2021.

(17) Zimmerman, G., Chow, L., and Paik, U. (1958). The photochemical isomerization of azobenzene. *J. Am. Chem. Soc. 80*, 3528−3531.

(18) Zhang, Z., Burns, D. C., Kumita, J. R., Smart, O. S., and Woolley, G. A. (2003). A water-soluble azobenzene cross-linker for photocontrol of peptide conformation. *Bioconjugate Chem. 14*, 824−829.

BC049855H

Prediction of the Viscosity Radius and the Size Exclusion Chromatography Behavior of PEGylated Proteins

Conan J. Fee*,† and James M. Van Alstine‡

Department of Materials and Process Engineering, University of Waikato, Private Bag 3105, Hamilton 2020, New Zealand, and Protein Separations, General Electric Healthcare, Bjorkgatan 30, Uppsala 75184, Sweden.
Received July 3, 2004; Revised Manuscript Received September 13, 2004

Size exclusion chromatography (SEC) was used to determine the viscosity radii of equivalent spheres for proteins covalently grafted with poly(ethylene glycol) (PEG). The viscosity radius of such PEGylated proteins was found to depend on the molecular weight of the native protein and the total weight of grafted PEG but not on PEG molecular weight, or PEG-to-protein molar grafting ratio. Results suggest grafted PEG's form a dynamic layer over the surface of proteins. The geometry of this layer results in a surface area-to-volume ratio approximately equal to that of a randomly coiled PEG molecule of equivalent total molecular weight. Two simple methods are given to predict the viscosity radius of PEGylated proteins. Both methods accurately predicted (3% absolute error) the viscosity radii of various PEG-proteins produced using three native proteins, α-lactalbumin (14.2 kDa MW), β-lactoglobulin dimer (37.4 kDa MW), and bovine serum albumin (66.7 kDa MW), three PEG reagents (2400, 5600, and 22500 MW), and molar grafting ratios of 0 to 8. Accurate viscosity radius prediction allows calculation of the distribution coefficient, K_{av}, for PEG-proteins in SEC. The suitability of a given SEC step for the analytical or preparative fractionation of different PEGylated protein mixtures may therefore be assessed mathematically. The methods and results offer insight to several factors related to the production, purification, and uses of PEGylated proteins.

INTRODUCTION

Covalent modification of proteins with poly(ethylene glycol) (PEG) molecules often dramatically improves their clinical efficacy. Terminal end-functionalized PEG molecules are typically used to modify proteins by reacting with protein amine or other (e.g. sulfhydryl) reactive groups (*1*, *2*). PEGylation may (a) mask and reduce immune-recognition and clearance from the body, (b) protect from enzymatic or chemical alteration, and clearance (*3*−*5*), (c) enhance hydrodynamic size and reduce glomerular filtration (*2*). The effectiveness of small therapeutic proteins (<20 kDa) is particularly prone to enhancement through PEGylation (*6*−*8*). Many PEGylated therapeutic proteins are FDA approved, and more are under development as PEGylation increases efficacy, reduces dosage frequency, allows for novel dosage mechanisms, and may prolong shelf life (*4*, *5*, *9*).

The major drawback of PEGylation is that PEGylated proteins are prepared from pure proteins, which are converted to product mixtures of PEG, native protein, and PEG-proteins having varied PEGylation extent (also known as degree of modification or grafting ratio, *N*) and variation in the site(s) of modification. Such PEGylated proteins may vary substantially in both physicochemical and biomedical properties. Low molecular weight byproducts formed during PEGylation and/or hydrolysis of functionalized PEG's also add to product complexity.

The extent of PEGylation must routinely be determined in research, development and production laboratories. The current method of choice for analysis is mass spectrometry, particularly matrix-assisted laser desorption ionization−time-of-flight mass spectrometry (MALDI-TOF MS). Other methods include capillary electrophoresis (*10*) or light scattering (*11*). All such methods are relatively complex, require specialized equipment, and have little direct relationship to the chromatographic, filtration, and other methods used to purify PEGylation reaction product mixtures.

Size exclusion chromatography (SEC) and related methods are attractive for fractionation of native and PEGylated proteins due to the significant increases in protein viscosity radii which result from PEG grafting. In addition, PEGylation may variously alter protein properties and behavior in regard to solubility, electrophoresis, ion exchange, affinity, or other interactions typically used to facilitate their purification.

SEC is also a simple, low-cost technique that has been used for many decades to estimate the molecular weight (MW) of proteins and polymers through the use of calibration curves between molecular weight and the distribution coefficient,

$$K_{av} = \frac{(V_R - V_o)}{(V_c - V_o)} \quad (1)$$

where V_R, V_o, and V_c represent solute elution volume, void volume, and the total bed volume of fluid and SEC media combined, respectively.

Given the above, SEC is attractive for both the purification and characterization of PEG-proteins, and there is a significant need to be able to predict SEC results based only on native protein MW, PEG MW, and *N*. However, proteins and PEG molecules of similar MW differ greatly with respect to their distribution coefficients

* Corresponding author. Phone: +64 7 838 4206, Fax: +64 838 4835. E-mail: c.fee@waikato.ac.nz.
† University of Waikato.
‡ General Electric Healthcare. E-mail: james.van.alstine@amersham.com.

10.1021/bc049843w CCC: $27.50 © 2004 American Chemical Society
Published on Web 10/30/2004

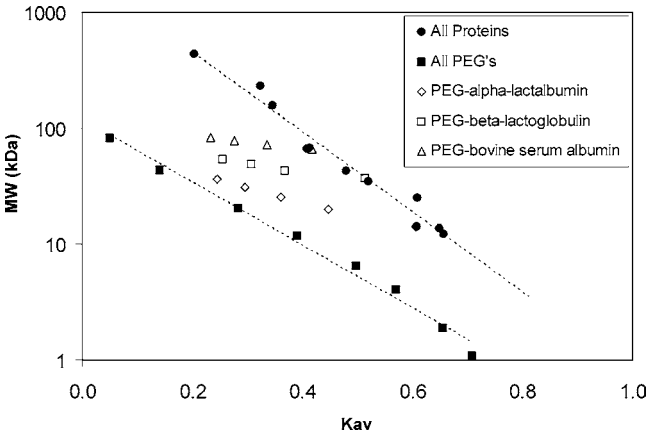


Figure 1. Distribution coefficient, K_{av}, as a function of $\ln(M_r)$ for protein and PEG molecular weight standards in a Superdex 200 HR 10/30 gel filtration column. Also shown are α-lactalbumin, β-lactoglobulin, and BSA, PEGylated to various extents with mPEG-SPA 5000.

in SEC media (*12*). This is illustrated by Figure 1 which shows calibration curves for protein and PEG molecular weight standards in a Superdex 200 HR10/30 SEC column (Amersham Biosciences, Uppsala, Sweden).[1]

PEG-proteins are hybrid molecules, and their SEC column distributions should not necessarily mimic that of either proteins or PEG molecules (*13*). One solution would be to calibrate SEC columns for PEG-proteins using protein MW standards modified with defined types of PEG's at defined degrees of modification. Clearly such calibrations are tedious, expensive, and may not pertain to PEG-proteins produced using novel PEG's or proteins. As such there is a significant need to develop simple methods to predict the SEC behavior of PEG-proteins.

Such a need is supported by previous literature. McGoff et al. (*14*) fractionated samples of PEGylated superoxide dismutase by SEC and concluded that determination of PEG-protein molecular weights based on protein standards was unreliable. Fortier and Laliberté (*15*) used protein MW standards and SEC to estimate the MW's of PEGylated horseradish peroxidase samples. They noted significant deviations from molecular weights estimated by other means, and that use of the SEC results to estimate N gave noninteger values, e.g., ranging from 3.1 to 6.0 against an expected value of 4 (lysines per protein). Christakopoulos et al. (*16*) cautioned about use of SEC to estimate PEG-protein MW's but nevertheless used SEC to relate an average increase of 30 to 40 kDa in the apparent MW of endogluconase to estimate N as 6 to 8 PEG molecules added per protein molecule. Veronese (*17*) noted that elution times of PEGylated proteins in SEC are not directly related to the increase in molecular weight due to the linked PEG, the implication being that SEC is not a useful analysis method for determining the degree of PEGylation. Fee (*13*) recently showed the apparent MW's of α-lactalbumin and β-lactoglobulin PEGylated with 5000 MW PEG increased nonlinearly between 50 and 100 kDa per grafted PEG molecule, when estimated by SEC calibrated with protein MW standards. However, the SEC MW estimates increased linearly by 7 kDa when the column was calibrated with PEG MW standards.

The present work addresses the need for a simple method to predictively model the SEC behavior of PEGylated proteins. The viscosity radii of PEG-proteins were determined using several SEC columns and two models for predicting the viscosity radii (and therefore the distribution coefficients) of PEG-proteins were derived. The first approach is based on a proposed linear relationship between total grafted PEG MW and PEGylated protein size, leading to a simple predictive equation dependent on two experimentally determined constants, a and b. The second approach assumes that PEG-protein size is determined primarily by the conformation of the grafted PEG layer. The resultant model depends only on the viscosity radii of the native protein and PEG's and contains no experimentally determined parameters.

The models were tested experimentally using PEG-protein samples prepared using three different proteins of MW 14 to 67 kDa, three different PEG reagents of MW 2 to 20 kDa, and N values of 1 to 8. Both models provide an accurate prediction of the viscosity radii of PEG-proteins. Both enable the prediction of SEC to separate different PEG-proteins, and the identification of N by SEC using a single calibration curve, based on protein or PEG or a combination of protein and PEG molecular weight standards. In addition to their practical significance, the predictive accuracy of the models suggests they provide insight to the possible behavior of PEG's when grafted to globular protein surfaces.

EXPERIMENTAL METHODS

Apparatus and Materials. Chromatographic experiments were carried out on an AKTAFPLC liquid chromatography system with protein species detected by UV absorbance at 280 nm (Amersham Biosciences, Uppsala, Sweden). PEG and PEG-containing species were detected with a Waters Model 410 Refractive Index detector (Waters Corporation, Milford, MA). The chromatography system was operated using Unicorn software, version 4.1 (Amersham Biosciences, Uppsala, Sweden).

Superdex 200 HR 10/30 and Superdex 75 HR 10/30 prepacked columns (30 cm length × 1.0 cm i.d., nominal $d_p = 13\ \mu m$, $V_c = 23.562$ mL) were obtained from Amersham Biosciences (Uppsala, Sweden).

Phosphate buffered saline (PBS), Tris-HCl, Blue Dextran ($M_r = 2000000$), α-lactalbumin from bovine milk (85% pure by polyacrylamide gel electrophoresis (PAGE)), β-lactoglobulin from bovine milk (90% pure by PAGE), and bovine serum albumin (BSA) from bovine plasma (98% pure by PAGE) were purchased from Sigma (St. Louis, MO). The nominal molecular weights of α-lactalbumin, β-lactoglobulin dimer, and BSA were, respectively, 14.2, 36.0, and 66.0 kDa and were estimated by MALDI-TOF mass spectrometry to be 14.2, 37.4, and 66.7 kDa, respectively. Mono-methoxy-poly(ethylene glycol)-succinimidyl propionate (mPEG-SPA) reagents of nominal molecular weights 2000, 5000, and 20000 Da were purchased from Nektar Therapeutics (Huntsville, AL). The actual molecular weights were estimated by MALDI-TOF mass spectrometry to be 2.4, 5.6, and 22.5 kDa, respectively.

Low Molecular Weight and High Molecular Weight gel filtration calibration kits containing ribonuclease A (M_r 13.7 kDa), chymotrypsinogen A (M_r 25 kDa), ovalbumin (M_r 43 kDa), albumin (M_r 67 kDa), aldolase (M_r 158 kDa), catalase (M_r 232 kDa), and ferritin (M_r 440 kDa) were obtained from Amersham Biosciences (Uppsala, Sweden). Polyethylene glycol 106−20000 MW, and Poly(ethylene oxide) 20000−1000000 MW Size Exclusion Calibration kits, containing molecular weights of 1100, 1900, 4000, 6500, 11800, 20400, 43500, and 82300, were purchased from Polymer Laboratories Ltd (Shropshire, UK).

[1] For ease of comparison, protein and polymer molecular weights determined by various methods are herein referred to in Daltons (Da) or kDa.

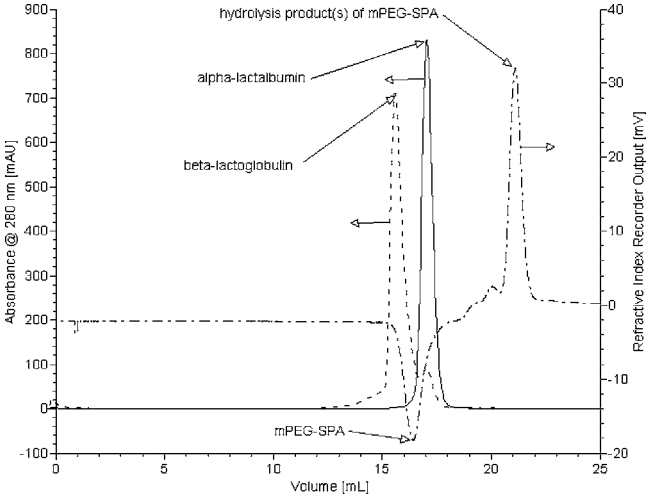


Figure 2. Chromatograms of native protein and mPEG-SPA 5000 reagent species in a Superdex 200 HR 10/30 SEC column.

Methods. Size-exclusion columns were calibrated against protein and PEG molecular weight standards. Individual solutions of each standard were prepared according to the manufacturer's instructions. 50 μL samples were injected onto each size exclusion column, using PBS running buffer at 0.5 mL/min. UV absorbance at 280 nm (protein standards) and refractive index (PEG standards) were used to determine the elution volumes of each standard. V_o was measured by the elution volume of Blue Dextran ($M_r = 2000000$) marker. V_o values were found to be 7.97 and 7.83 mL for the Superdex 200 and the Superdex 75 columns, respectively. K_{av} values were calculated for each column using eq 1 and plotted against molecular weight. Figure 1 shows the calibration curves for the Superdex 200 HR 10/30 column. Similar curves were obtained for the Superdex 75 column (data not shown).

SEC curves for individual samples of α-lactalbumin, β-lactoglobulin (dimer), and BSA proteins, and mPEG-SPA 5000 PEGylation reagent, are plotted in Figure 2. All had retention volumes consistent with their native molecular weights according to corresponding MW calibration curves. Corresponding curves for mPEG-SPA 2000 and mPEG-SPA 20 000 were omitted for clarity, but they exhibited peak maxima at retention volumes consistent with their molecular weights. The UV active peak eluting at about 20 mL is believed to represent *N*-hydroxysuccinimide acid byproduct of the hydrolysis of mPEG-SPA.

Batch PEG grafting was carried out for each protein individually. All solutions were made up in PBS at pH 7.4. Typically 5 mL of 20 mg/mL mPEG-SPA solution was added to 5 mL of 20 mg/mL native protein and stirred in an open 10 mL beaker at room temperature. One sample (approximately 1 mL) was withdrawn immediately after mixing the reactants and further samples were taken at 2, 5, 10, 20, 30, 40, 50, and 60 min. Samples were immediately acidified with three drops of 0.1 M HCl to stop the reaction. 50 μL of each sample was then analyzed separately by SEC under the same conditions as used during column calibration. 100 μL samples were used when collecting fractions for MALDI-TOF analysis. In such cases fractions containing protein were collected in 1 mL samples and exchanged into 20 mM ammonium bicarbonate buffer using a HiTrap desalting column (5 mL) (Amersham Biosciences, Uppsala, Sweden) prior to MALDI-TOF analysis.

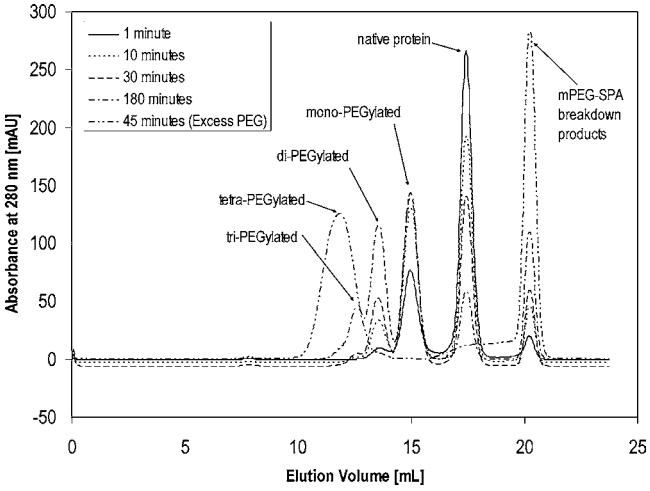


Figure 3. SEC chromatograms for samples withdrawn at intervals from batch PEGylation of α-lactalbumin with mPEG-SPA 5000, showing change in extent of PEGylation with time.

An Ettan II MALDI-TOF mass spectrometer (Amersham Biosciences, Uppsala, Sweden), operated in linear mode at 20 kV, was used to determine the molecular weights of native and PEGylated proteins. The matrix was prepared by saturating a solvent (consisting of 500 μL each of acetonitrile and MilliQ water and 9 μL of trifluoroacetic acid) with sinapic acid. Equal volumes of sample and matrix solution were mixed, and 0.3 μL of the mixture was applied to the sample plates.

RESULTS AND DISCUSSION

Figure 3 shows a representative size exclusion chromatograph obtained in the Superdex 200 column for the products of batch PEGylation of α-lactalbumin by mPEG-SPA 5000. As expected, several products with distinctly different molecular sizes result from the modification of the protein, and there is a shift in the areas of the product peaks with time as the degree of PEGylation increases. Similar results were observed for batch PEGylation of β-lactoglobulin and BSA (data not shown for brevity). Such behavior has been extensively reported in the literature (*5*). The reaction products were tentatively identified as mono-, di-, tri-, and tetra-PEGylated protein by inference from progression of the reaction and the chromatograph in Figure 3. Fractions were then collected in a repeat SEC run with a larger sample, and the molecular weights were confirmed by MALDI-TOF. As noted in the previous section, the peak at 20 mL may represent a low MW byproduct of the grafting reaction.

Similar chromatograms were obtained (data not shown) using a Superdex 200 column for analyzing proteins PEGylated with mPEG-SPA 2000 and 20 000. Peak maxima corresponding to the individual PEG-protein products were not resolved for mPEG-SPA 2000 except for α-lactalbumin. Similar chromatograms were also obtained (data not shown) using a Superdex 75 column for modification of α-lactalbumin with mPEG-SPA 2000 and 5000 and for modification of β-lactoglobulin with mPEG-SPA 2000.

Where peak maxima were clearly resolved, the K_{av} values of each PEG-protein reaction product identified were calculated using eq 1. In Figure 1, values for mPEG-SPA 5000-grafted proteins separated on the Superdex 200 column are plotted against their corresponding molecular weights (calculated from the native protein plus mPEG-SPA molecular weights and confirmed by MALDI-TOF). Comparison of experimental data points

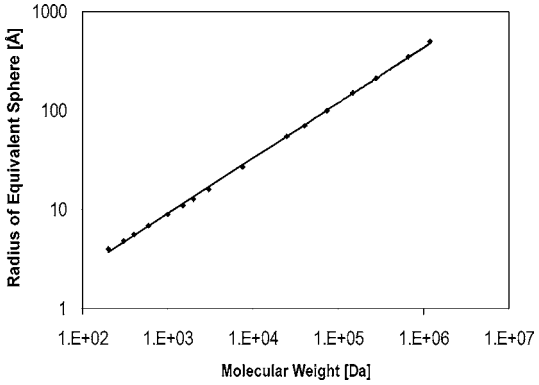


Figure 4. Viscosity radius of PEG molecules versus molecular weight (after Kuga et al. (*21*)).

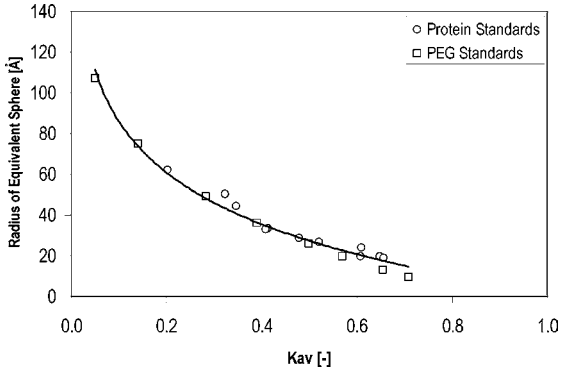


Figure 5. Universal calibration curve, viscosity radius versus K_{av} for PEG and protein molecular weight standards.

with the protein and PEG calibration curves in Figure 1 confirms that PEGylated proteins behave neither as proteins nor as PEG molecules (of similar MW) in size exclusion media. Rather, as more PEG is grafted to a protein, the related K_{av} shifts from the native protein's position on the protein standard curve toward the PEG standard curve (see also Fee (*13*)).

Clearly the distribution coefficients of the PEG-proteins in Figure 1 depend on the molecular weights of both PEG reagents and native proteins, as well as the PEGylation extent. However, the effects of increasing$N$ (and the total mass of PEG grafted) appears to correlate for samples related to each type of native protein. This suggests existence of a general method to relate such distribution coefficients to values for native protein MW, PEG reagent MW, and N.

It is common practice to calibrate SEC columns using molecular weight (M_r) standards and to produce a calibration chart in terms of the K_{av} versus ln(M_r). Normally such a curve is approximately linear over a range of molecular weights for a given SEC media. However, the distribution coefficient in SEC is not governed by molecular weight but, more generally, by the hydrodynamic volume or viscosity radius, R_h, of the molecule (*18*). A universal calibration method, though not in common use for proteins, can be produced for a given SEC media for globular proteins and flexible polymers such as PEG in terms of K_{av} versus viscosity radius (*19*).

For globular proteins, the viscosity radius (in Ångströms) of the molecule (assuming a spherical shape) is related to its molecular weight in Da, by eq 2 (*20*).

$$R_{h,prot} \approx (0.82 \pm 0.02)M_r^{1/3} \quad (2)$$

Kuga (*21*) collated data from 14 authors on the limiting viscosity numbers and diffusion coefficients of a variety of polymers in water, including PEG, and used these to calculate the R_h of the equivalent sphere for each compound. The radii calculated from viscosity and diffusion data agreed well with each other when correlated to MW across 6 orders of magnitude. A subset of Kuga's data for PEG's of MW 0.2 to 1200 kDa yields the following power-law relationship (correlation coefficient $R^2 = 0.9995$) between viscosity radius (Å) and molecular weight (Da) (Figure 4):

$$R_{h,PEG} = 0.1912M_r^{0.559} \quad (3)$$

The viscosity radii of all proteins and PEG's studied were calculated using eqs 2 and 3, respectively, and a universal calibration curve was produced for each SEC column studied. Figure 5 shows the "universal" calibration curve for Superdex 200 HR 10/30. A similar curve was obtained for the Superdex 75 column (data not shown).

Figure 5 shows that, in keeping with Kunitani et al. (*19*), the PEG in water standard data noted above falls on the same universal curve as for protein standards in PBS. Although the relative size of PEG polymer random coils is expected to be affected by aqueous solution temperature, salt concentration, and salt type, one might not expect much difference in hydration radius and SEC behavior between PEG's in PBS and distilled water at room temperature, since both conditions lie far from lower critical solution conditions. Under similar conditions, when characterizing ion exchange media, Hunter and Carta (*22*) showed that ionic strength had no effect on the retention volume of neutral flexible polymers. We therefore conclude that the sizes of PEG's in phosphate-buffered saline are approximately the same as they are in water. Since the viscosity radii of both proteins and PEG molecules lie on the same universal calibration curve for a given SEC media, it is reasonable to expect that PEGylated proteins will also conform to the same curve. It should therefore be possible to experimentally estimate the viscosity radii of PEG-proteins from their elution volumes in an SEC column calibrated in this way.

Tables 1−3 show viscosity radii data for all of the PEG's, proteins, and PEG-proteins studied in this work, as determined from the above universal calibration curves using K_{av} values calculated from experimentally determined elution volumes.

Two methods and related models for predicting the viscosity radii of PEG-proteins will now be described. We must be cautious in interpreting the viscosity radius too literally in terms of an actual physical radius. Chromatography is a stochastic process, so the hydrodynamic radius that is calculated from chromatography data represents an average of many molecular level interactions. The viscosity radius throughout this paper refers to the radius of an equivalent sphere in aqueous solution, whatever the true shape of the molecule. However, as a starting point for analysis we consider the radius, $R_{h,PEGprot}$, of a molecule formed by the conjugation of a protein of radius $R_{h,protein}$ and a PEG molecule of radius $R_{h,PEG}$.

Model 1. We assume that the generally benign effect of PEG grafting on protein activity (and the fact that PEG is a common food additive and is one of the compounds listed by the US Food and Drug Administration as "generally regarded as safe") indicates that the general shape (viscosity radius) of a protein is maintained in the PEG-protein conjugate. Now observe that in the aqueous environments related to this study the experimentally

Table 1. Properties of Proteins PEGylated with mPEG-SPA 2000

protein	*N*	MW expected	MW by MALDI-TOF[a]	R_h predicted (Å) eq 5	R_h predicted (Å) eq 11	R_h expt Superdex 200 (Å)	R_h expt Superdex 75 (Å)	volume of PEG layer (Å^3)	surface area to volume ratio of PEG layer (Å^{-1})
α-lactalbumin	0	14200	14200	-	19.8	20.1	18.4	0	-
	1	16500	16500	27.0	26.2	25.1	23.7	34259	0.232
	2	18800	18800	29.9	30.3	28.6	28.1	76758	0.144
	3	21100	21200	32.8	34.1	31.2	31.0	126459	0.112
β-lactoglobulin	0	37400	18600[b] (37400)	-	27.3	25.7	25.4	0	-
	1	39700	20700[b] (39300)	34.2	33.3	*c*	-	45859	0.272
	2	42000	23100[b] (41700)	37.1	36.9	*c*	34.7	98576	0.158
	3	44300	25400[b] (44000)	39.9	40.1	37.3	-	157552	0.119
BSA	0	66700	66700	-	33.1	34.5	-	0	-
	1	69000	69000	38.4	38.9	*c*	-	55424	0.306
	2	71300	71100	41.1	42.2	39.6	-	116902	0.172
	4	73600	73400	46.3	48.0	44.6	-	256476	0.104
	8	85100	85200	56.9	58.2	57.6	-	594629	0.067

[a] Rounded average values from all fractions assayed. [b] Values correspond to monomer. Values indicated in brackets correspond to the measured value plus the native protein monomer molecular weight. [c] No peak maxima on chromatograms but MALDI-TOF analysis of fractions indicated molecular weights that were consistent with those expected.

Table 2. Properties of Proteins PEGylated with mPEG-SPA 5000

protein	*N*	MW expected	MW by MALDI-TOF[a]	R_h predicted (Å) eq 5	R_h predicted (Å) eq 11	R_h expt Superdex 200 (Å)	R_h expt Superdex 75 (Å)	volume of PEG layer (Å^3)	surface area to volume ratio of PEG layer (Å^{-1})
α-lactalbumin	0	14200	14200	-	19.8	20.1	18.4	0	-
	1	19800	19900	30.8	31.7	31.2	30.2	99668	0.126
	2	25400	15500	37.6	40.1	39.1	38.7	242024	0.084
	3	31000	30800	44.3	47.7	46.2	-	419090	0.068
	4	36600	36700	51.0	54.6	53.0	-	626448	0.058
β-lactoglobulin	0	37400	18600[b] (37400)	-	27.3	26.2	-	0	-
	1	43000	24400[b] (43000)	38.4	38.1	38.2	-	126019	0.136
	2	48600	29900[b] (48500)	45.1	45.3	44.9	-	289379	0.087
	3	54200	35400[b] (54000)	51.8	51.9	51.5	-	484617	0.069
BSA	0	66700	66700	-	33.1	33.7	-	0	-
	1	72300	72500	41.9	43.3	41.7	-	148310	0.146
	2	77900	77900	48.1	49.9	48.7	-	330470	0.090
	3	83500	83500	54.3	55.9	55.0	-	542378	0.070

[a] Rounded average values from all fractions assayed. [b] Values correspond to monomer. Values indicated in brackets correspond to the measured value plus the native protein monomer molecular weight.

Table 3. Properties of Proteins PEGylated with mPEG-SPA 20 000

protein	*N*	MW expected	MW by MALDI-TOF[a]	R_h predicted (Å) eq 5	R_h predicted (Å) eq 11	R_h expt Superdex 200 (Å)	volume of PEG layer (Å^3)	surface area to volume ratio of PEG layer (Å^{-1})
α-lactalbumin	0	14200	14200	-	19.8	19.6	0	-
	1	36600	36500	51.1	54.4	52.3	704985	0.056
	2	59000	58600	78.1	77.6	77.0	1934851	0.039
β-lactoglobulin	0	37400	18600[b] (37400)	-	27.3	26.3	0	-
	1	59800	40700[b] (59300)	58.6	57.9	66.6 58.8[c]	792176	0.056
	2	82200	62600[b] (81200)	85.6	79.6	82.4 77.4[c]	2079600	0.039
BSA	0	66700	66700	-	33.1	33.3	0	-
	1	89100	88600	60.5	61.5	61.7	1022470	0.048
	2	111500	110400	85.3	81.8	84.1	2364463	0.036

[a] Rounded average values from all fractions assayed. [b] Values correspond to monomer. Values indicated in brackets correspond to the measured value plus the native protein monomer molecular weight. [c] Values obtained after fractionating the mono-PEGylated peak and re-running individually.

determined viscosity radius (R_h = 53.0 Å) of α-lactalbumin modified with four mPEG-SPA 5000 molecules (Table 2) is similar to that of α-lactalbumin modified with one mPEG-SPA 20 000 (R_h = 52.3 Å, Table 3). This implies that the final molecular size for each PEG-protein species is determined by native globular protein size and the total amount of PEG grafted, rather than by PEG reagent molecular weight or degree of grafting. We have observed the same behavior for cytochrome C modified with mPEG-NHS reagents of 10 000, 20 000, and 40 000 kDa, wherein PEGylated species with the same total amount of PEG grafted per protein molecule elute during SEC at the same volume, regardless of *N* (data not shown).

It follows from the previous paragraph that the excess (or difference in) viscosity radii between a native protein and PEGylated forms of that protein can be expressed as a function of the total PEG molecular weight, $M_{r,totPEG}$. The simplest function is a linear one such that

$$R_{h,PEGprot} - R_{h,protein} = a + bM_{r,totPEG} \quad (4)$$

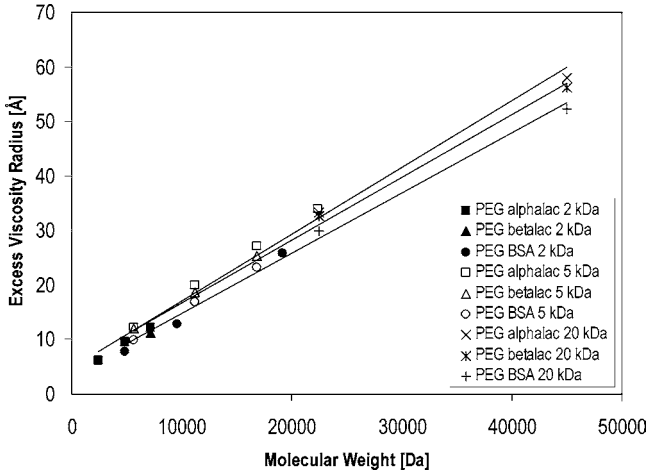


Figure 6. Excess radii of PEGylated proteins versus the total molecular weight of conjugated PEG.

where a and b are constants. Figure 6 shows that a plot of $(R_{h,PEGprot} - R_{h,protein})$ vs $M_{r,totPEG}$ yields the expected linear relationship for each protein, with a regression coefficient $R^2 > 0.99$ in each case. Therefore the viscosity radius (Å) of a PEGylated protein is given by

$$R_{h,PEGprot} = 0.82(M_{r,prot})^{0.33} + a + bM_{r,PEGtot} \quad (5)$$

where a = 4.88, 5.21, and 3.73 Å for α-lactalbumin, β-lactoglobulin, and BSA, respectively, and b = 0.0012 Å/Da for α-lactalbumin and β-lactoglobulin and b = 0.0011 Å/Da for BSA.

Intuitively, we expect the value of a to be 0, i.e., as the molecular weight of total grafted PEG approaches zero, so should the excess radius. It may be that the relationship between excess radius and total PEG molecular weight is actually weakly nonlinear. The above values of a correspond to a discrepancy of approximately 100 to 300 Da. If the relationship is indeed linear, this nonzero intercept might be due to several factors including (a) the length of the amide linkage (MW 43) formed between the PEG and the protein, (b) covalent grafting altering the contribution (via freedom of movement and hydration) of a few ethylene oxide units (CH_2CH_2O, MW 44) to the overall structure, (c) the grafting reaction and localization of PEG at the protein surface slightly altering the protein conformation and thus its contribution to the viscosity radius of the PEG-protein, (d) weak interactions between a few polymer units of the PEG and the protein surface.

Tables 1−3 show that the experimentally determined viscosity radii and those predicted by eq 5 are in excellent agreement (<3% absolute average error) in relation to both the Superdex 75 and 200 SEC column measurements.

In Tables 1−3, experimental values are given only for those cases where individual peak maxima were resolved. In the case of grafting with mPEG-SPA 2000, neither of the two SEC columns was able to resolve individual peaks for PEGylated β-lactoglobulin and BSA that differed by less than $N = 2$. This is not unexpected, as the K_{av} values for species differing by only a 2 kDa PEG are not large enough to obtain peak resolution in these media. However, MALDI-TOF analysis of fractions collected during elution confirmed that the elution volumes of the PEG-protein species corresponded to those expected of molecules with viscosity radii calculated from eq 5 (Table 1).

In all cases, except mPEG-SPA 20 000-grafted β-lactoglobulin, SEC elution volumes corresponded to those expected from molecular species having viscosity radii calculated from eq 5. This occurred even when chromatographed samples contained native protein, several PEG-protein species, unreacted mPEG-SPA reagent, and reaction byproducts. This suggests little interaction between the species when on the column.

In the case of mPEG 20 000-β-lactoglobulin (Table 3) the initial elution volume of the mono-PEGylated protein ($N = 1$) corresponded to a viscosity radius of 66.6 Å, versus 58.6 Å predicted from eq 5. The elution volume for $N = 2$ corresponded to a viscosity radius of 82.4 Å, versus 85.6 Å predicted. Both peaks showed significant tailing. Such results were very reproducible and, when grafting reactions were repeated, the products yielded the same result. MALDI-TOF analysis confirmed the identities of the products in these peaks to be mono- and di-PEGylated β-lactoglobulin dimers (Table 3).

β-Lactoglobulin consists of two 18.7 kDa monomeric chains held together by Ca^{2+}-mediated linkages. It does not appear that PEGylation resulted in multiply PEGylated protein monomers, as SEC determined viscosity radii did not correspond to any possible combinations of PEGylated monomeric β-lactoglobulin proteins.

A new hypothesis suggested that different PEGylated β-lactoglobulin proteins associated weakly with one another in the early regions of the SEC, chromatographing initially as a larger aggregate and then separately during their migration down the column. Fresh PEG-protein samples were run again and the peaks collected separately before being subjected to individual SEC runs. The viscosity radius of the $N = 1$ species (58.8 Å) calculated from the elution volumes agreed well with the 58.6 Å prediction from eq 5. The viscosity radius of the $N = 2$ species (77.4 Å from SEC) was smaller than the eq 5 related value of 85.6 Å. Such discrepancies were only seen with one reagent and one dimeric protein. They are noted here to illustrate that the relations described here may not apply to certain proteins under some circumstances.

Model 2. Although eq 5 appears to accurately predict viscosity radii, and the values of the constants a and b are closely similar between protein species, optimal accuracy demands that unique values of a and b should be determined experimentally for each protein. In developing model 2 we sought a predictive method that does not depend on experimentally determined parameters. We again picture a scenario in which the protein molecule remains unchanged in size and the final size of the conjugate is determined by alterations to the conformation of the PEG molecule alone. Calculating the volume of the equivalent sphere from the viscosity radius and subtracting the volume of the equivalent sphere for the native protein gives the volume that can be attributed to the PEG portion of the conjugated molecule.

The volumes of the equivalent spheres for mPEG-SPA 2000, 5000, and 20 000 in PBS are 13 667 Å^3, 57 263 Å^3, and 582 896 Å^3, respectively. Tables 1−3 show that the volume added to the protein molecule by the first PEG is much larger than the volume of the original PEG molecule in free solution. Also, each successive PEG group added to the conjugate molecule contributes an increasingly larger volume to the conjugate. However, if we examine the outer surface area of the conjugate and the volume contributed by the PEG, we find that the ratio of the surface area of the PEG exposed to the ionic environment to the PEG layer volume remains virtually constant for a given total PEG molecular weight (Tables

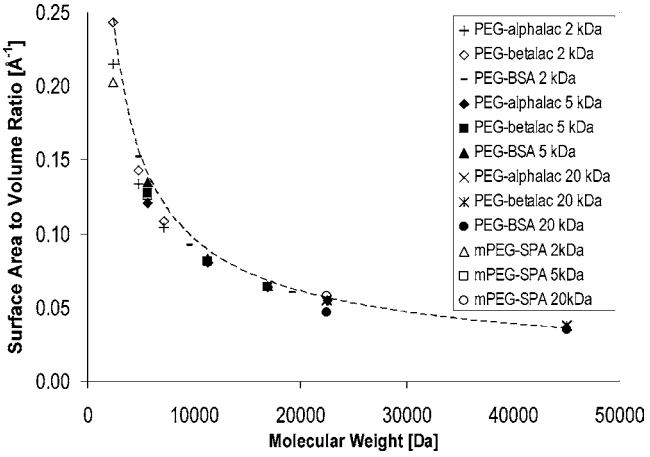


Figure 7. Surface area-to-volume ratio for the PEG molecules and for the PEG layer surrounding PEGylated proteins (line from eq 6).

1−3). Figure 7 shows the surface area-to-volume ratio for a given total molecular weight of PEG is approximately constant both for the individual PEG reagents in free solution and for the PEG layers surrounding all three protein species PEGylated to any extent, although the ratio increases slightly with increasing molecular weight of the native protein.

These observations, together with the fact that the final radius is determined by the total molecular weight of conjugated PEG and not by the number of PEG molecules conjugated, strongly suggests that the PEG forms a continuous layer surrounding the protein and that it adjusts its thickness such that the surface area-to-volume ratio of the layer is approximately the same as that of a PEG molecule with the equivalent molecular weight in free solution. Rather than a rigid coating, we envisage a very dynamic and flexible PEG molecule with enough surface interaction to result in what is in effect a protein with significant surface masking by PEG rather than a PEG spheroid grafted to a protein spheroid. Such a conformation would allow protein surface diffusion and the approach of other molecules, though such movement would be subject to some steric hindrance. The PEG layer mobility would presumably be most constrained near the site of conjugation. The protein would therefore maintain its biological function but with its in vitro activity reduced by an amount dependent on the position(s) of conjugation relative to the active site(s) of the protein. This view is consistent with the widely reported effects of the PEGylation location on protein activity. This is discussed further below.

We can now use the fact that under the low conductivity, room temperature conditions studied, the surface area-to-volume ratio is approximately constant for any given total molecular weight of PEG, to calculate the thickness of the PEG layer surrounding a PEGylated protein and thus its final viscosity radius. The ratio, AV_{PEG}, of surface area to volume of the equivalent sphere for a PEG molecule in free solution is

$$AV_{PEG} = \frac{3}{R_{h,PEG}} \tag{6}$$

and the surface area, $A_{PEGprot}$, of the PEGylated protein exposed to the phosphate buffered saline environment is

$$A_{PEGprot} = 4\pi(R_{h,PEGprot})^2 \tag{7}$$

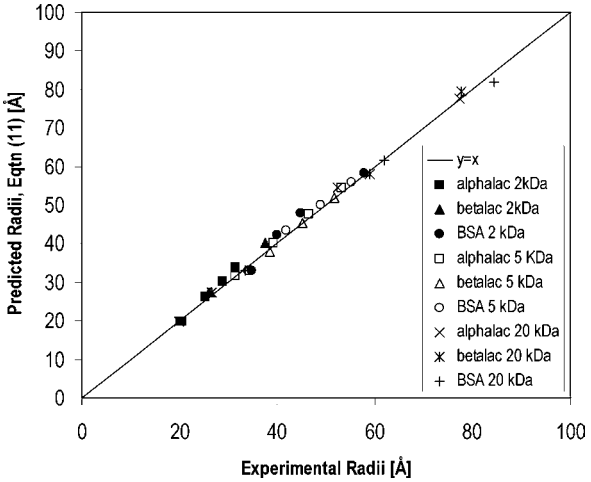


Figure 8. Comparison between experimentally determined viscosity radii of PEGylated proteins and those predicted by eq 11.

where $R_{h,PEGprot}$ is the viscosity radius of the PEGylated protein. The volume of the PEG fraction of the PEGylated protein, assuming that the protein volume is unchanged by PEGylation, is

$$V_{PEGlayer} = \frac{4\pi}{3}({R_{h,PEGprot}}^3 - {R_{h,prot}}^3) \tag{8}$$

The surface area-to-volume ratio of the PEG layer in the PEGylated protein, $AV_{PEGprot}$, is obtained by combining eqs 6−8, noting that $R_{h,PEG}$ is the viscosity radius of the equivalent sphere for a PEG molecule having a molecular weight equal to the total molecular weight of PEG conjugated to the protein, yielding

$$AV_{PEGlayer} = \frac{{R_{h,PEGprot}}^2}{({R_{h,PEGprot}}^3 - {R_{h,prot}}^3)} = \frac{1}{R_{h,PEG}} \tag{9}$$

Equation 9 can be rearranged to give a cubic equation in $R_{h,PEGprot}$

$${R_{h,PEGprot}}^3 - R_{h,PEG}{R_{h,PEGprot}}^2 - {R_{h,prot}}^3 = 0 \tag{10}$$

Equation 10 has only one real root, given by eq 11.

$$R_{h,PEGprot} = \frac{1}{6}[108{R_{h,prot}}^3 + 8{R_{h,PEG}}^3 + 12(81{R_{h,prot}}^6 + 12{R_{h,prot}}^3{R_{h,PEG}}^3)^{1/2}]^{1/3} + \frac{2}{3}\frac{{R_{h,PEG}}^2}{[108{R_{h,prot}}^3 + 8{R_{h,PEG}}^3 + 12(81{R_{h,prot}}^6 + 12{R_{h,prot}}^3{R_{h,PEG}}^3)^{1/2}]^{1/3}} + \frac{1}{3}R_{h,PEG} \tag{11}$$

Equation 11 shows that the viscosity radius of the PEGylated protein is a function only of the viscosity radius of the native protein and that of an equivalent sphere for a PEG molecule having a molecular weight equal to the total PEG molecular weight conjugated to the protein. Using eqs 2 and 3 to substitute for $R_{h,prot}$ and $R_{h,PEG}$ in terms of molecular weight allows eq 11 to be solved for any total amount of PEG added to a given protein. Figure 8 shows the correlation between predictions using eq 11 and experimental measurements for each of the PEGylated species studied. The fit is very good (marginally better than when using eq 5, with average absolute errors of less than 3%). So too, the

values predicted by eq 11 agree well with the experimentally determined values for both mono- and di-PEGylated β-lactoglobulin (with mPEG-SPA 20 000) when these species were analyzed separately (Table 3).

Either eq 5 or eq 11 can be used to calculate $R_{h,PEGprot}$. Equation 5 is simpler to calculate but requires experimental determination of the constants a and b. It is beyond the scope of this paper to determine the dependence of a and b on the protein species but we surmise, based upon our experience with the three proteins used in this study, that these constants are not strongly affected by protein type. Equation 11 possibly represents a more robust model of the physical situation and requires no experimentally determined parameters.

Finally, the K_{av} (and therefore the elution volume) of any PEGylated species may be predicted from either eq 5 or eq 11 together with the universal calibration curve for a given SEC column.

The general shape and size of PEG random coils appear to be dictated by polymer hydration and excluded volume (HEV) effects (*23*, *24*) and to a somewhat lesser degree by interaction with solution ions (*25*). Thus, above a few thousand MW, PEG's take on random coil spherical shapes that, due to weak segment-segment interactions, are more flexible and relatively larger than for proteins of similar MW. It is now well appreciated that PEG segments are capable of assuming conformations with considerable variation in relative hydrophilicity and hydrophobicity (*23*, *26*, *27*). When PEG molecules are attached to a surface, they lose conformational freedom, and in the case of a well-hydrating environment and a surface which does not exhibit strong interactions with the polymer, this is expected to lead to entropic repulsion, such that the PEG chains extend normal to the surface (*23*, *28*). Such surface structures are influenced by polymer MW and surface grafting density (*28*, *29*). Terminally grafted PEG conformations may vary from essentially spherical to extended "brush" conformations depending on grafting density. In the case of PEG's of 5000 to 6000 MW this may involve polymer layer thicknesses of 40 to 100 Å (*29*). Naturally there are conditions (raised salt concentration, temperature, and pressure) where the polymer can be induced to interact more favorably with the surface and affect its surface conformation as well as protein adsorption.

Under the physiological salt, room temperature, and atmospheric pressure conditions of the present study, PEG interactions with proteins might be expected to be dominated by HEV effects and therefore to be repulsive (*23*, *29*−*33*). Such behavior is believed to be responsible for the ability of PEG-coated surfaces to reduce protein adsorption, and for PEGylated proteins to show enhanced biocompatibility, serum circulation lifetime, and resistance to enzymatic degradation. Thus, one might expect low-density single-point conjugation of PEG to a protein to yield a complex product composed of two linked but distinct molecular spheroids.

In contrast, the present study strongly suggests that the protein and conjugated PEG favorably interact to create a single spheroid PEG-protein complex, with the PEG portion forming a layer surrounding the protein. This is supported in particular by the excellent predictions of viscosity radius obtained by eq 11. Also, the viscosity radius of a protein conjugated with distinct PEG spheroids would tend to be increasingly independent of N above a value of 2 or 3, since each additional PEG group added would likely be contained within the swept volume of a rotating protein molecule with a PEG spheroid grafted on opposite sides. Tables 1−3 and Figure 6 clearly show that this is not the case but that the excess radii of PEGylated proteins are linearly related to N for all proteins studied, including up to the case of $N = 8$ for BSA PEGylated with mPEG 2000. The shape and other properties of PEG in the outer layer appear to be influenced by the same HEV factors experienced by free PEG in solution, as the surface area-to-volume ratio of the PEG remains approximately constant between the free solution and conjugated forms. However, the volume of the layer is much larger than that for the free PEG in solution, indicating increased overall hydration (though not necessarily uniform throughout the layer).

Partition of proteins such as BSA and lactalbumin into aqueous phases rich in PEG is well documented (*31*, *34*, *35*) particularly in the presence other polymers such as dextran. We considered the possibility that the Superdex media, being dextran based, might provide a unique partitioning environment that caused the PEG layer to preferentially associate with the protein rather than the matrix. However, we obtained identical results (not shown) when using a Superose 12 SEC media, which is agarose based. While this does not preclude the possibility of such partitioning, it adds confidence to the general relevance of the results obtained in the Superdex media.

It may be wrong to relate the interactions of PEG and protein molecules when each is free in solution to their interactions when conjugated, as the latter case involves a closest point of contact within their mutual hydration shells and double layers. Instead, it is possible to speculate on a variety of favorable PEG to protein interactions such as hydrogen bonding, divalent cation chelation, hydrophobic interactions, and so on (*29*, *31*, *33*).

It is beyond the scope of this paper to model such behavior, but it would be of great interest to know if such a model were theoretically possible and, if so, what would be its implications for the biomedical properties of PEGylated proteins. The concept of PEGylated proteins consisting of conjugated but distinct spheroids is not in keeping with biomedical results (*32*, *36*, *37*) which suggest that PEGylation even with relatively small MW PEG's can dramatically alter a protein's average surface properties. Such results are more in keeping with the single spheroid concept assumed in the present study in deriving eq 11.

CONCLUSIONS

When molecular weight is used to calibrate a SEC column, PEGylated proteins apparently behave differently from both pure proteins and pure PEG molecules in size exclusion media. However, the distribution coefficients of protein and PEG macromolecules in size exclusion chromatography columns are related to their hydrodynamic volumes or viscosity radii such that a single universal calibration curve can be created for each column. The relationship between the distribution coefficient and viscosity radius apparently extends also to PEGylated proteins, and thus the viscosity radii of these proteins can be determined experimentally from a column calibrated with PEG and/or protein standards alone.

The viscosity radius of PEGylated proteins in phosphate-buffered saline is dependent on the native protein size and the total amount of PEG conjugated but is independent of the PEGylation extent, N. There is a linear relationship between the effective radius added to a protein and the total molecular weight of grafted PEG.

On the basis of the assumption that the native protein conformation is unaffected by PEGylation, it is proposed

that the conjugated PEG acts to form a dynamic, hydrated polymer-rich layer at the protein surface whose thickness is such that it maintains an external surface area-to-volume ratio (i.e., the surface area exposed to the external ionic environment divided by the volume of the PEG layer) approximately equal to that of a PEG molecule of equivalent molecular weight in free solution.

Two equations for predicting the viscosity radii of PEGylated proteins in PBS, an ionic environment that closely matches physiological conditions, have been presented. Equation 5, based on the simple assumption that PEG-protein radius is linearly related to the total conjugated PEG molecular weight predicts viscosity radii to within 3% of experimental values. Equation 11 is based on the assumption of a constant protein molecular conformation, together with a constant PEG layer surface area-to-volume ratio. The latter method is more representative of the physical situation and predicts the viscosity radii well, without the need for experimentally determined parameters.

The K_{av} (and therefore the elution volume) of any PEG-protein species may be predicted from either eq 5 or eq 11 together with the universal calibration curve for a given SEC column.

ACKNOWLEDGMENT

The authors gratefully acknowledge the support of Peter Moore and Lars-Erik Nyström, of General Electric Healthcare, and Karin Caldwell, of Uppsala University, in relation to this work.

LITERATURE CITED

(1) Fisher, D., Delgado, C., Selisko, B., Malik, F., Agrawal, A. K., and Francis, G. E. (1995) Covalent attachment of PEG to protein and liposomal surfaces. In *Biopolymer Mixtures* (Harding, S. E., Hill, S. E., and Mitchell, J. R., Eds.) Nottingham University Press, Nottingham.

(2) Fung, W.-J., Porter, J. E., and Bailon, P. (1997) Strategies for the preparation and characterization of poly(ethylene glycol) (PEG) conjugated pharmaceutical proteins. *Polym. Prepr. 38* (1), 565−66.

(3) Abuchowski, A., McCoy, J. R., Palczuk, N. C., Van Es, T., and Davis, F. F. (1977) Effect of covalent attachment of poly-(ethylene glycol) on immunogenicity and circulating life of bovine liver catalase. *J. Biol. Chem. 252*, *(11)*, 3582−86.

(4) Harris, J. M., Ed. (1992) *Poly(ethylene glycol) Chemistry: Biotechnical and Biomedical Applications*, Plenum Press, New York.

(5) Harris, J. M., and Zalipsky, S., Ed.s, (1997) *Poly(ethylene glycol): Chemistry and Biological Applications*, American Chemical Society, Washington, D.C.

(6) Cunningham-Rundles, C., Zhuo, Z., Griffith, B., and Keenan, J. (1992) Biological activities of polyethylene-glycol immunoglobulin conjugates. Resistance to enzymatic degradation. *J. Immunol. Methods 152*, *(2)*, 177−90.

(7) Francis, G. E., Fisher, D., Delgado, C., Malik, F., Gardiner, A., and Neale, D. (1998) PEGylation of cytokines and other therapeutic proteins and peptides: the importance of biological optimization of coupling techniques. *Int. J.Hematol. 68* (1), 1−18.

(8) Gombotz, W. R., and Pettit, D. K. (2000) PEGylation: A tool to enhance protein delivery, in *Controlled Drug Delivery: Designing technologies for the future* (Park, K., and Mrsny, R. J., Eds.) American Chemical Society, Washington, DC.

(9) Fisher, D., Buckley, B., Delgado, C., Francis, G. E., Goodwin, C., Kippen, A., Malik, F., and Marlow, S. (2000) Factors with impact on the success of protein and virus PEGylation. *Polym. Prepr. 41* (1), 1012−3.

(10) Bullock, J., Chowdhury, S., and Johnston, D. (1996) Characterization of poly(ethylene glycol) modified superoxide dismutase: comparison of capillary electrophoresis and matrix-assisted laser desorption/ionization mass spectrometry. *Ann. Chem. 68*, 3258−64.

(11) Kendrick, B. S., Kerwin, B. A., Chang, B. S., and Philo, J. S. (2001) Online size-exclusion high-performance liquid chromatography light scattering and differential refractometry methods to determine degree of polymer conjugation to proteins and protein−protein or protein−ligand association states. *Anal. Biochem. 299* (2), 136−46.

(12) Hellberg, U., Ivarsson, J.-P., and Johansson, B.-L. (1996) Characteristics of Superdex prep grade media for gel filtration of proteins and peptides. *Process Biochem. 31* (2), 163−72.

(13) Fee, C. J. (2003) Size exclusion reaction chromatography (SERC): a new technique for protein PEGylation. *Biotechnol. Bioeng. 82* (2), 200−06.

(14) McGoff, P., Baziotis, A. C., and Masckiewicz, R. (1988) Analysis of poly(ethylene glycol) modified superoxide dismutase by chromatographic, electrophoretic, light scattering, chemical and enzymatic methods. *Chem. Pharm. Bull. 36* (8), 3079−91.

(15) Fortier, G., and Laliberte, M. (1993) Surface modification of horseradish peroxidase with poly(ethylene glycol)s of various molecular masses. *Biotechnol. Appl. Biochem. 17* (1), 115−30.

(16) Christakopoulos, P., Kourentzi, E., Hatzinikolaou, D. G., Claeyssens, M., Kekos, D., and Macris, B. J. (1998) Enhancement of pH-stability of a low molecular mass endoglucanase from *Fusarium* oxysporum by protein PEGylation. *Carbohydr. Res. 314* (1−2), 95−99.

(17) Veronese, F. M. (2001) Peptide and protein PEGylation: a review of problems and solutions. *Biomaterials 22*, 405−17.

(18) Benoit, H., Gallot-Grubisic, Z., Rempp, P., Decker, D., and Zilliox, J. G. (1966) Liquid-phase chromatographic study of branched and linear polystyrenes of known structure. *J. Chim. Phys. 63* (11−12), 1507−14.

(19) Kunitani, M., Dollinger, G., Johnson, D., and Kresin, L. (1991) On-line characterization of poly(ethylene glycol)-modified proteins. *J. Chromatogr. 588*, 125−37.

(20) Hagel, L. (1998) Gel Filtration, in *Protein Purification* (Janson, J.-C., and Rydén, L., Eds) 2nd ed., John Wiley & Sons, New York.

(21) Kuga, S. (1981) Pore size distribution analysis of gel substances by size exclusion chromatography. *J. Chromatogr. 206* (3), 449−61.

(22) Hunter, A. K., and Carta, G. (2001) Protein adsorption on novel acrylamido-based polymeric ion-exchangers III. Salt concentration effects and elution behavior. *J. Chromtogr. A 930*, 79−93.

(23) Karlström, G., and Engkvist, O. (1997)Theory of poly-(ethylene glycol) in solution, in *Poly(ethylene glycol) Chemistry and Biological Applications* (Harris, J. M., and Zalipsky, S., Eds) American Chemical Society, Washington, DC.

(24) Seigou, K., Genji, I., Suzuki, J., Miyahara, A., Kitano, T., and Ito, K. (1997) Aqueous solution properties oligo and poly-(ethylene oxide) by light scattering and intrinsic viscosity. *Polymer 38*, 2885−91.

(25) Yoko, M., and Nakanishi, T. (2002) Ion-Specific Swelling Behaviour of Poly(oxyethylene Oxide) Gel and Correlation to the Intrinsic Viscosity of the Polymer in Salt Solution. *J. Colloid Polym. Sci. 280*, 547−53.

(26) Andersson, M., and Karlstrom, G. (1985) Conformational structure of 1,2-dimethoxyethane in water and other dipolar solvents, studied by quantum chemical, reaction field, and statistical mechanical techniques. *J. Phys. Chem. 89* (23), 4957−62.

(27) Smith, G. D., Bedrov, D., and Borodin, O. (2000) Conformations and chain dimensions of poly(ethylene xoide in aqueous solution. *J. Am. Chem. Soc. 122*, 9548−49.

(28) Fleer, G. J., Stuart, M. A. C., Scheutjens, J. M. H. M., Cosgrove, T., and Vincent, B. (1993) *Polymers at interfaces*, Chapman & Hall, London.

(29) Efremova, N. V., Sheth, S. R., and Leckband, D. E. (2001) Protein-induced changes in poly(ethylene glycol) brushes: molecular weight and temperature difference. *Langmuir 17*, 7628−36.

(30) Emoto, K., Van Alstine, J. M., and Harris, J. M. (1998) Stability of poly(ethylene -glycol) graft coatings. *Langmuir 14*, 2722−29.
(31) Delgado, C., Malmsten, M., and Van Alstine, J. M. (1997) Analytical partitioning of poly(ethylene glycol)-modified proteins. *J. Chromatogr. B 692* (2), 263−72.
(32) Malmsten, M., Emoto, K., and Van Alstine, J. M. (1998) Effect of chain density on inhibition of protein adsorption by poly(ethylene glycol) based coatings. *J. Colloid Interface Sci. 202* (2), 507−17.
(33) Vergara, A., Paduano, L., and Sartorio, R. (2002) Mechanism of protein-poly(ethylene glycol) interaction from a diffusive point of view. *Macromolecules 35*, 1389−98.
(34) Albertsson, P. (1986) *Partition of cell particles and macromolecules*, Wiley, New York.
(35) *35*) Walter, H., and Johansson, G. (1986) Partitioning in aqueous two-phase systems: an overview. *Anal. Chem. 155* (2), 215−42.
(36) *36*) Yamamoto, Y., Tsutsumi, Y., Yoshioka, Y., Nishbata, T., Kobayashi, K., Okamoto, T., Mukai, Y., Shimuzu, T., Nakagawa, S., Nagata, S., and Mayumi, T. (2002) Site-specific, PEGylations of a lysine-deficient TNF-a with full bioactivity. *Nature Biotechnol. 21*, 546−52.
(37) *37*) Na, D. H., Park, M. O., Choi, S. Y., Kim, Y. S., Lee, S. S., Yoo, S. D., Lee, H. S., and Lee, K. C. (2002) Identification of the modifying sites of mono-PEGylated salmon calcitonins by capillary electrophoresis and MALDI-TOF Mass Spectrometry. *J. Chromtogr. B 754*, (259−63).

BC049843W

Peptide Nucleic Acid (PNA) Amphiphiles: Synthesis, Self-Assembly, and Duplex Stability

James P. Vernille, Lara C. Kovell, and James W. Schneider*

Department of Chemical Engineering, Carnegie Mellon University, Pittsburgh, Pennsylvania 15213-3890. Received July 14, 2004

Peptide amphiphiles comprising a class of conjugates of peptide nucleic acid (PNA), natural amino acids, and *n*-alkanes were synthesized and studied. These PNA amphiphiles (PNAA) self-assemble at concentrations between 10 and 50 μM and exhibit water solubilities above 500 μM. The highly specific, stable DNA binding properties of PNAs are preserved by these modifications, with no significant differences between the thermodynamics of DNA binding of the PNA peptide and the PNA amphiphile. Proper solubilization of the PNAA required the attachment of $(Lys)_2$ and $(Glu)_4$ peptides to PNAs, which affected the PNAA–DNA duplex stability by electrostatic interactions between these charged amino acids and the negatively charged DNA backbone. These electrostatic effects did not affect the specificity of DNA binding, however. Electrostatic effects are screened with added salt, in a manner consistent with previous studies of PNA–DNA duplex stability and predictions from a charged-cylinder model for the duplex.

INTRODUCTION

Peptide nucleic acid (PNA) is a structural mimic of DNA that replaces the negatively charged sugar–phosphate backbone of DNA with an uncharged *N*-(2-aminoethyl)glycine backbone with attached nucleobases (*1*, *2*). PNA oligomers bind DNA oligomers in an antiparallel orientation, following Watson–Crick base pairing rules (*3*), but PNA–DNA duplexes are significantly more stable than the corresponding DNA–DNA duplex. The added stability of PNA–DNA duplexes has a largely electrostatic origin and is highest at low ionic strength conditions that destabilize DNA–DNA duplexes (*4*). PNA–DNA duplex stabilities are highly sensitive to sequence mismatches at the single-base level (*5*, *6*). PNA can also bind specific dsDNA targets by triplex formation, even in biological buffers that suppress triplex formation between ssDNA and dsDNA (*7*, *8*). Leveraging these unique DNA-binding properties, PNAs have been implemented in platforms for DNA sensing (*9*–*17*) and separation (*18*–*21*), primarily by linking PNAs to solid surfaces or fluorophores.

The attachment of peptides to lipophilic materials to form "peptide amphiphiles" is a convenient means to functionalize surfaces for cell attachment and proliferation (*22*, *23*) and for the measurement of molecular-level interactions between biomolecules using the atomic force microscope (AFM) (*24*) or surface force apparatus (SFA) (*25*–*27*). Surface functionalization generally requires water-insoluble peptide amphiphiles to enable Langmuir–Blodgett deposition or vesicle formation. Depending on the exact design, water-soluble peptide amphiphiles may self-assemble in solution to form disklike micelles (*28*), rodlike micelles (*29*), or helical ribbons (*30*) above their critical micelle concentration (cmc). Stupp and co-workers have shown that peptide amphiphiles can micellize with pH-dependent reversibility and that the micelles can be formed irreversibly by cross-linking of the peptide headgroups (*31*). We are working on the responsive, controlled self-assembly of peptide amphiphiles for implementation in DNA sensing and separation modalities such as liquid chromatography and capillary zone electrophoresis. With that goal in mind, we have attached *n*-alkanes and natural amino acids to form water-soluble PNA amphiphiles (PNAA). Recently, we have demonstrated that PNAA–DNA duplexes are easily separated from unbound DNA oligomers in hydrophobic interaction chromatography (*32*). The PNAA acts as a nonpolar sequence tag that helps separate target DNA from mixtures of DNA oligomers of up to 60 bases in length. Separation of longer DNA oligomers and dsDNA might be achieved with a better understanding of the binding and micellization properties of PNAA.

Because PNA is uncharged, it is sparingly soluble in water without the attachment of charged groups (*1*, *2*). For biophysical studies, either PNA oligomers are used at low concentration or a single lysine group is attached to confer greater water solubility. We expect that the attachment of *n*-alkane chains will exacerbate the poor water solubility of PNAA. For the design of PNAA, we wish to provide a moderate water solubility while maintaining sequence-specific DNA binding properties. One might expect that both the *n*-alkane and the requisite charged groups would also affect the PNAA–DNA duplex stability. For example, attachment of *n*-alkanes to collagen peptides has resulted in the stabilization of their triplexes (*33*), and the attachment of *n*-alkanes to antimicrobial peptides has been shown to promote their antimicrobial activity (*34*).

In this work, we have synthesized a series of PNAAs and measured their micellization properties and the stability of their duplexes with DNA oligomers. It should be noted that others have synthesized PNAs linked to lipophilic materials, including attachment of rhodamine and fluoroscein for thermodynamic studies (*35*) and the nonpolar group adamantane for improved cellular uptake of PNA (*36*). The distinction here is that our water-soluble PNA peptide amphiphiles have been designed for

* Author to whom correspondence should be addressed (e-mail schneider@cmu.edu).

10.1021/bc049831a CCC: $27.50 © 2004 American Chemical Society
Published on Web 11/02/2004

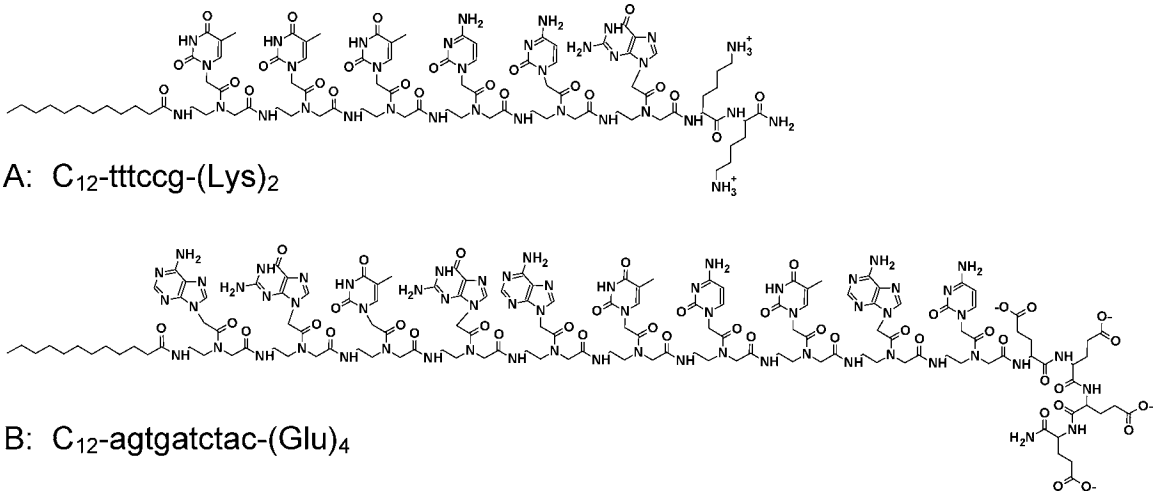


Figure 1. Structures of the PNA amphiphiles (PNAA) C_{12}-agtgatctac-$(Glu)_4$ and C_{12}-tttccg-$(Lys)_2$ used in this study. PNAA names are listed from the N to the C terminus from left to right (same binding properties as the 5′ → 3′ DNA sequence). PNAA nucleobases are in lower case.

a controlled, tunable self-assembly applicable to next-generation bioanalytical devices.

MATERIALS AND METHODS

PNAA Synthesis. All solvents (sequencing grade) were purchased from Fisher Scientific (Pittsburgh, PA), and buffers and salts were purchased from Sigma-Aldrich (St. Louis, MO). PNAAs were synthesized by solid-phase peptide synthesis using Fmoc/Bhoc-protected PNA monomers (Applied Biosystems) (*37*) and Fmoc-protected PAL-PEG-PS resin (Peptides International, Louisville, KY) with a 0.25 mmol/g loading capacity. One hundred milligrams of resin was shaken gently in dichloromethane (DCM) for several hours to expose reactive sites on the resin prior to peptide coupling. The resin was then deprotected three times with 20% piperidine in *N*,*N*-dimethylformamide (DMF) for 5 min to remove the Fmoc protecting group. A 5-fold excess of PNA monomer (based on manufacturer's reported loading capacity) in base solution (Applied Biosystems) and activator solution (Applied Biosystems) was then prepared (*38*), The base solution consists of a mixture of 2,6-lutidine and *N*,*N*-diisopropylethylamine in DMF. The activator is a solution of *O*-(7-azabenzotriazol-1-yl)-1,1,3,3-tetramethyluronium hexafluorophosphate (HATU) in DMF. Following a 2-min activation step, the solution was added to the resin. The initial monomer coupling to resin was allowed to proceed for at least 1 h to ensure complete coupling on the optimal number of resin sites. We found that the longer coupling time was required for high yields. The resin was washed with DCM and DMF following the coupling step and a small fraction collected for a ninhydrin test. Unreacted sites were then capped by a 10-min incubation of the resin with the acetic anhydride. The resin was washed with DCM and DMF, and the process was repeated with 20-min coupling steps until the desired PNA peptide was synthesized. Lauric acid (Sigma-Aldrich) was then coupled to the N terminus of the PNA peptide, also in a 5-fold excess.

The resin was soaked in a mixture of 4:1 trifluoroacetic acid (TFA)/*m*-cresol (total volume = 2 mL) for 2 h to cleave the PNAA from the resin and remove Bhoc side protecting groups. Once cleaved from the support, the PNAA was precipitated by the addition of dry ether (~10-fold excess over PNAA). The precipitated PNAA was cooled for 5 min in a −80 °C freezer to ensure complete precipitation. The solid was separated from the ether by centrifugation (1000*g*) for 5 min. The top phase was decanted off and the pellet resuspended with another addition of dry ether. The cooling and centrifugation process was done in triplicate. Upon completion, the PNAA pellet was dried within a stream of nitrogen and dissolved in deionized water. In many cases, yields of PNAA were improved substantially by foregoing the ether precipitation step and injecting the cleavage cocktail directly into the HPLC for purification.

Semipreparative-scale PNAA purification was performed on a Waters Delta 600 HPLC using a Symmetry300 C_4 column with a particle size of 5 μm. Elution of the PNAA product was achieved using a 30-min linear gradient (0.1% TFA in acetonitrile to 0.1% TFA in water) and a 20 mL/min flow rate. The product eluted as a single peak and following collection was lyophilized to a powder. The yield of the reaction was ~30% (based on the manufacturer's reported resin loading), or 0.0075 mmol of PNAA product. The following $[M + H]^+$ values for PNA peptides and PNAA amphiphiles were obtained: C_{12}-tttccg-$(Lys)_2$, 2050 Da (theoretical: 2049.96); NH_2-tttccg-$(Lys)_2$, 1865.91 Da (theoretical: 1866.71); C_{12}-agtgatctac-$(Glu)_4$, 3425.8 Da (theoretical: 3425.52); NH_2-agtgatctac-$(Glu)_4$, 3242.52 Da (theoretical: 3241.59).

The naming convention we use lists the PNA peptide sequence in the N to C direction from left to right (Figure 1). PNA sequences listed in the N to C direction follow the same Watson−Crick base pairing rules as the corresponding DNA sequence listed in the 5′ to 3′ direction. Note that the resin used here leaves a terminal amine group at the C terminus. PNA nucleobases are in lower case to distinguish them from DNA nucleobases (upper case). The three-letter abbreviation is used for the natural amino acids, and the length of *n*-alkane is the subscript under "C."

Solubility Measurements. PNAA solubilities were measured by centrifugation of saturated PNAA solutions in buffer. A large (>1 mM) amount of PNAA was dissolved in 20 mM sodium phosphate buffer (pH 7.0) and cooled to 4 °C. Samples were then warmed to room temperature and centrifuged (Eppendorf 5415C microcentrifuge) to sediment aggregated or precipitated material. The PNAA concentration in the supernatant was measured spectrophotometrically on a Varian Cary 3 spectrophotometer at 260 nm. PNAA concentrations were calculated from the measured absorbance by Beer's law. Extinction coefficients for the PNAA were calculated by

summing the extinction coefficients for each monomer on the PNA peptide (ϵ_{260} = 13700, 11700, 8600, and 6600 L/mol-cm for A, G, T, and C, respectively.) Absorbance measurements were made at 80 °C to ensure that the nucleobases were completely destacked and that hypochromicity could be neglected.

cmc Measurements. Critical micelle concentrations for the PNAA were obtained by light scattering using a Malvern Zetasizer 3000 system (Malvern Instruments). Solutions of PNAA in 20 mM sodium phosphate buffer (pH 7.0) were prepared and filtered to remove dust or large PNAA aggregates using 0.2-μm syringe filters (Fisher). UV absorbance measurements were made on the filtrate to account for any losses of PNAA during filtration. The filtered solutions were then placed in a 1-mL cuvette and installed in the Zetasizer instrument. The intensity of laser light (532 nm) scattered 90° from incidence was measured using an internal photomultiplier and recorded by the Zetasizer software. Disposable cuvettes were used to obviate any carry-over of PNAA from sample to sample. The cmc was taken to be the PNAA concentration at which the intensity versus [PNAA] plot had a pronounced slope discontinuity.

UV Melting Curves and Circular Dichroism (CD). DNA oligomers were purchased from Integrated DNA Technologies (Coralville, IA) and used as received. DNA purity was assessed using anion-exchange chromatography (Waters Spherisorb S5 SAX column, 80-Å pore size and 5-μm particle size), with a 30-min linear gradient from 20 mM Tris-HCl (pH 8.0) to 20 mM Tris-HCl in 1 M NaCl (pH 8.0). Samples with purity of <95% were rejected. Stock solutions of DNA oligomers were prepared in 20 mM phosphate buffer (pH 7.0) for UV melting analysis.

CD spectra were run on a Jasco J-715 spectropolarimeter equipped with a thermoelectrically controlled single-cell holder. CD spectra for PNAA−DNA mixtures were obtained in 5 mM sodium phosphate buffer (pH 7.0) with 100 mM NaCl and 1 mM EDTA.

UV melting curves were obtained at 260 nm for PNAA−DNA solutions in 20 mM sodium phosphate buffer (pH 7.0) using a Varian Cary 3 spectrophotometer equipped with a thermoelectrically controlled multicell holder using 1-cm quartz cuvettes (Starna, Atascadero, CA). PNAA−DNA mixtures were initially heated to 90 °C and held there for 2 min to equilibrate. The temperature was then lowered at 1.0 °C/min to a lower target value (5−20 °C) and cycled between the upper and lower temperature limits several times.

Melting temperatures and thermodynamic data for all melting curves were determined by a van't Hoff analysis under a two-state model for hybridization

$$S_{PNA} + S_{DNA} \leftrightarrow D_{PNA/DNA} \quad (1)$$

where S denotes single strands and D duplex. The two-state model is considered to be valid for short sequences (4−20 base pairs) (*39*). The absorbance versus temperature plot is converted to a plot of duplex fraction (α) versus temperature. The total absorbance (A) is assumed to be the sum of the absorbance of the single strands (A_S) and the double strands (A_D):

$$A = \alpha A_D + (1 - \alpha)A_S \quad (2)$$

The melting transition temperature (T_m) is taken to be the temperature at which $\alpha = 0.5$. The absorbance values of the single- and double-stranded forms of the DNA and PNA are assumed to vary linearly with temperature and take the form

$$A_S = m_S T + b_S$$
$$A_D = m_D T + b_D \quad (3)$$

As nucleotide length increases, the nucleobase stacking dynamics become more pronounced and the slopes m_S and m_D will deviate from zero.

The equilibrium constant for the hybridization process is

$$K = \frac{[D_{PNA/DNA}]}{[S_A][S_B]} = \frac{2\alpha}{(1 - \alpha)^2 C_T} \quad (4)$$

where C_T is the total concentration of strands, on a single-strand basis. The equilibrium constant, K, versus temperature data can be analyzed using the van't Hoff equation to obtain the enthalpy of hybridization ΔH

$$\frac{d \ln K}{d(1/T)} = \frac{-\Delta H^\circ}{R} \quad (5)$$

where R is the gas constant.

RESULTS AND DISCUSSION

PNAA Synthesis. Most PNA syntheses have been accomplished by solid-phase synthesis using Boc/Z-protected monomers following the protocol of Christensen et al. (*40*). In our case, we were interested in attaching dialkyl chains with ester linkages that are hydrolyzed under the cleavage conditions required for Boc/Z. The milder cleavage conditions required by Fmoc/Bhoc protection have been shown to maintain the ester linkage (*41*), and therefore we used the Fmoc/Bhoc approach. The Fmoc/Bhoc PNA synthesis protocol provided by Egholm and Casale (*42*) was developed for automated PNA synthesis, and it was refined for manual synthesis in our laboratory. The most significant changes were increasing the coupling, capping, and deprotection times and the use of a 5-fold excess of monomer for each coupling. To obtain high yields, we found it necessary to increase the time of the initial resin−monomer coupling to 1 h, but subsequent couplings could be performed for 20 min. Because the alkane-modified PNAs are more nonpolar than the PNA peptides, it was often necessary to inject the cleavage cocktail directly into the HPLC for high-yield purification. The PNAA structures we are mainly concerned with in this paper are listed in Figure 1.

Solubility and cmc Measurements. Unmodified PNAs are sparingly soluble in water and have a tendency to self-aggregate even when the PNAs are apparently solubilized (*2*). A typical approach to improve water solubility is attachment of a C-terminal lysine residue to the sequence, which for the PNA peptide NH_2-t_{10}-Lys confers a water solubility of >1.5 mM in 10 mM sodium phosphate buffer (pH 7.0) (*37*). For PNAA, additional charges need to be added to bring the solubility of PNAA above their cmc, enabling self-assembly. To find an appropriate combination of alkane substitution and charging, we synthesized about 12 variants with different PNA sequences and substitutions. The PNAAs C_{18}-tttccg-Lys, C_{16}-tttccg-Lys, and C_{14}-tttccg-Lys gave a cloudy solution at 1−10 μM concentrations in water or 10 mM sodium phosphate buffer (pH 7.0). C_{12}-tttccg-$(Lys)_2$ had twice the solubility of C_{12}-Lys-tttccg-Lys and was studied in more detail (Figure 1A). For longer PNA sequences, such as C_{12}-t_{10}-$(Lys)_4$ in 20 mM phosphate buffer (pH 7.0),

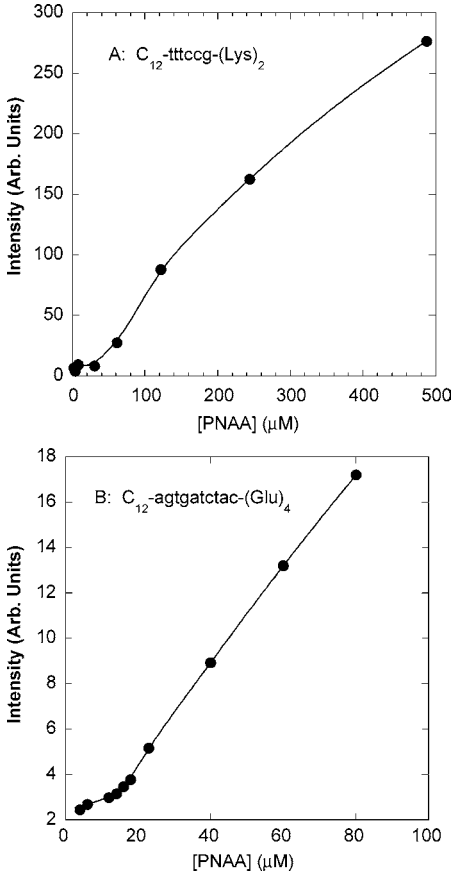


Figure 2. Scattered intensity versus [PNAA] for (A) C_{12}-tttccg-$(Lys)_2$ and (B) C_{12}-agtgatctac-$(Glu)_4$ in 20 mM sodium phosphate buffer (pH 7.0). The cmc is marked by an abrupt increase in scattered intensity (*43*).

Table 1. Solubilities and Critical Micelle Concentrations for PNA Amphiphiles in 20 mM Phosphate Buffer (pH 7.0)

	solubility, 25 °C (μM)	cmc, 25 °C (μM)
C_{12}-tttccg-$(Lys)_2$	1000	40
C_{12}-agtgatctac-$(Glu)_4$	650	15

addition of either complementary or noncomplementary DNA to 20 mM phosphate buffer clouded the solution. The clouding was mitigated by the use of glutamic acid groups to charge the PNAA, the use of a Tris-HCl (pH 7−8) buffer rather than phosphate buffer, or adjusting the pH to pH ∼2−3. The PNAA C_{12}-agtgatctac-$(Glu)_4$ (Figure 1B) has a solubility of 1000 μM in 20 mM sodium phosphate buffer and >1400 μM in 10 mM Tris-HCl (pH 7.0).

Although the effect of tail length, charge amount and type, and length of PNA sequence have not been exhaustively studied, some rules of thumb have emerged. Generally, 6-mer sequences require two charged groups and 10-mer sequences require four charged groups for solubilities on the order of 500−1000 μM. Charged groups placed at the N terminus of the PNA peptide were more effective than those placed between the alkane and the PNA peptide.

cmc measurements were made by a light-scattering method using a laser Doppler velocimetry system in static mode. The cmc is marked by a large increase in scattered intensity as shown in Figure 2 (*43*). The shorter PNAA sequence of C_{12}-tttccg-$(Lys)_2$ gave a slightly higher cmc than C_{12}-agtgatctac-$(Glu)_4$ (Table 1). cmc values for C_{14}-tttccg-$(Lys)_2$ and C_{18}-tttccg-$(Lys)_2$ were similar to that of C_{12}-tttccg-$(Lys)_2$, indicating that the primary driving force

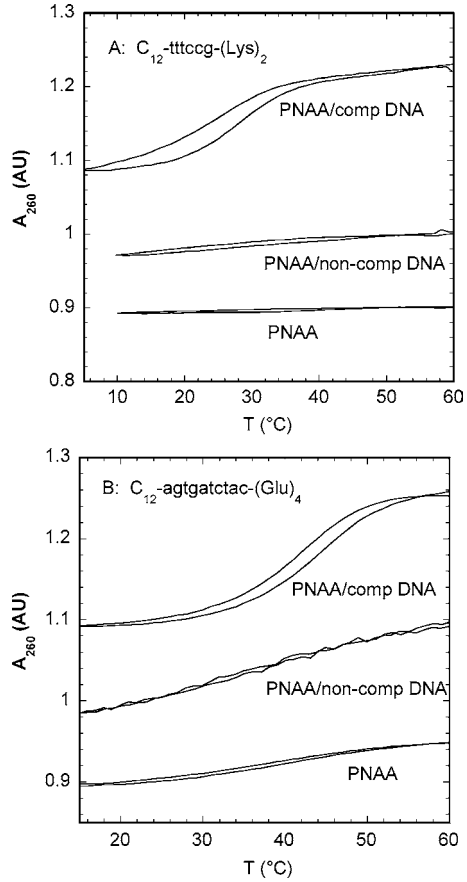


Figure 3. UV melting curves for PNAA with and without DNA: (A) C_{12}-tttccg-$(Lys)_2$ alone, with noncomplementary DNA (5′-ATAGCC-3′), and with complementary DNA (5′-CGGAAA-3′); (B) C_{12}-agtgatctac-$(Glu)_4$ alone, with noncomplementary DNA (5′-TGTACGACTC-3′), and with complementary DNA (5′-GTAGATCACT-3′). For (A) and (B), a ramp rate of 1.0 °C/min and a total strand concentration of 20 μM in 20 mM sodium phosphate at pH 7.0 were used. In each case, the self-melt was shifted up by 0.4 AU and the PNAA/noncompDNA was shifted down by 0.1 AU for clarity.

for micellization is attractive interactions between the PNA peptides. Accordingly, longer sequences tend to lower the cmc. To avoid complications, the measurements presented below were made at concentrations below the cmc for both PNAA.

Hybridization of PNA Amphiphiles with DNA. The substitutions made on the PNA peptide to form PNAA include the *n*-alkane tail and the charged amino acids, and both could potentially affect the specificity of binding to DNA oligomers and the stability of the resulting PNAA−DNA duplex. Figure 3A shows UV melting curves for the PNAA C_{12}-tttccg-$(Lys)_2$ with an equimolar amount of its 6-mer DNA complement (5′-CGGAAA-3′), a noncomplementary 6-mer (5′-ATAGCC-3′), and the PNAA on its own. Significant hypochromicity was observed only for the PNAA/complementary DNA mixture (T_m = 27.6 °C), indicating sequence specificity is preserved. Figure 3B shows UV melting curves for the PNAA C_{12}-agtgatctac-$(Glu)_4$ with an equimolar amount of its 10-mer DNA complement (5′-GTAGATCACT-3′), a noncomplementary 10-mer (5′-TGTACGACTC-3′), and the PNAA on its own. In this case, each of the three curves shows hypochromicity. A van't Hoff analysis of the PNAA/complementary DNA curve gave T_m = 42.0 °C. Other hypochromicities are likely due to self-melt characteristics for the longer DNA and PNAAs of Figure 3B. Self-melts are generally larger for PNAs compared to

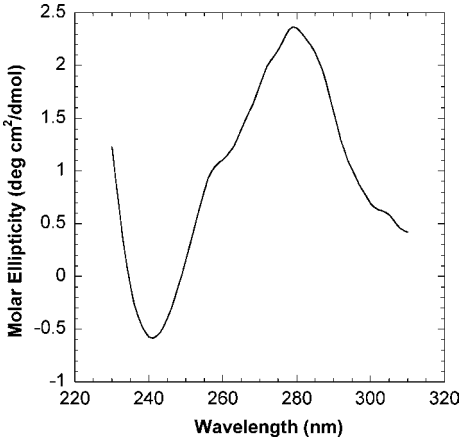


Figure 4. CD spectrum for C_{12}-agtgatctac-$(Glu)_4$ with 5′-GTAGATCACT-3′ at a total strand concentration of 5 μM (averaged over 10 scans) 20 mM sodium phosphate at pH 7.0 (T = 25 °C).

Table 2. Melting Temperatures for PNAA with Complementary DNA Targets (5′-CGGAAA-3′ and 5′-GTAGATCACT-3′) in 20 mM Phosphate Buffer (pH 7.0), along with T_m Predictions from a Nearest-Neighbor Model (*45*)

	T_m (°C),[a] exptl	T_m (°C), theor
NH_2-tttccg-$(Lys)_2$	27.4	24.3
C_{12}-tttccg-$(Lys)_2$	27.6	24.3
NH_2-agtgatctac-$(Glu)_4$	38.9	53.7
C_{12}-agtgatctac-$(Glu)_4$	42.0	53.7

[a] T_m had an associated error of 0.5 °C.

DNAs as the more flexible PNA backbone allows the nucleobases to stack to a greater degree. Because the hypochromicity is comparable for the PNAA and the PNAA with noncomplementary DNA, we conclude that the mixture does not form a duplex or other intermolecular association. This self-structured nature of the C_{12}-agtgatctac-$(Glu)_4$ can be considered a small potential source of error when the melting curve for thermodynamic parameters is analyzed. Note that the self-melt is not evident in the case of the shorter PNAA and DNA 6-mers (Figure 3A). A small hysteresis between the melting and cooling curves was observed in each case. For the C_{12}-agtgatctac-$(Glu)_4$ PNAA−DNA melting curve, the hysteresis decreased from 1.54 to 0.41 °C when the scan rate was slowed from 1 to 0.5 °C/min.

To verify duplex formation, the secondary structure of the PNAA−DNA duplex was confirmed using CD (Figure 4). Hybridization of C_{12}-agtgatctac-$(Glu)_4$ with complementary DNA 5′-GTAGATCACT-3′ shows the formation of a right-handed helix with maxima at 260 and 280 nm and a minimum at 240 nm. These features compare well with those measured by Ratilainen (*35*) for a PNA peptide with a single lysine group attached. CD spectra were not obtained for the duplex of C_{12}-tttccg-$(Lys)_2$ and its 6-mer DNA complement, since the duplex is marginally stable in phosphate buffer at room temperature.

UV melting curves were also obtained for the corresponding PNA peptides without alkylation and are summarized in Table 2. For both PNAAs studied here, the corresponding peptide shows about the same T_m. Similar observations have been made by Griffin and Smith (*44*) for PNAs with attached 8-amino-3,6-dioxaoctadecanoic acid groups and by Ørum et al. (*18*) for PNAs with attached $(His)_6$ peptides. Although alkylation appears to have little effect on the binding, the substantial amount of charged amino acids required for solubilization does.

Table 3. Thermodynamic Parameters for Hybridization of PNAA C_{12}-agtgatctac-$(Glu)_4$ with Complementary DNA (5′-GTAGATCACT-3′) in 10 mM Tris Buffer (pH 7.0, unless Otherwise Indicated) with Increasing Concentrations of NaCl[a]

[NaCl] (mM)	T_m (°C)	ΔH (kJ/mol)	ΔG_{298} (kJ/mol)
0 (pH 4.0)	41.7	−256	−45.7
0	39.7	−274	−45.0
20	42.7	−254	−46.2
40	43.8	−265	−47.8
60	44.5	−277	−49.2
80	45.0	−270	−49.1
100	45.3	−286	−50.3
1000	47.2	−300	−52.9

[a] T_m had an associated error of 0.5 °C, ΔH had an error of 10 kJ/mol, and ΔG had an error of 0.5 kJ/mol.

Giesen et al. (*45*) provided an extension to the nearest-neighbor model of SantaLucia (*46*) for PNA−DNA duplexes. The model claims to be valid over a wide range of ionic strengths and does not include the effects of amino acids or lipids and, hence, serves as a useful reference. Table 2 includes a comparison of the model predictions and the observed T_m and shows that T_m is underpredicted in the case of C_{12}-tttccg-$(Lys)_2$ and overpredicted in the case of C_{12}-agtgatctac-$(Glu)_4$, pointing to an electrostatic contribution to the duplex stability.

To verify the electrostatic nature of the stabilization in the case of C_{12}-tttccg-$(Lys)_2$ and destabilization in the case of C_{12}-agtgatctac-$(Glu)_4$, the effect of added salt on PNAA−DNA duplex stability was determined for C_{12}-agtgatctac-$(Glu)_4$ (Table 3). As the ionic strength was increased (pH 7.0), T_m increased and ΔG decreased as expected. Additionally, the duplex was stabilized by decreasing the pH to 4.0 (no added salt), likely due to the lowering state of charging for the Glu residues, the side-chain carboxylic acid of which has a pK_a of 4.07. Below pH 4.0, UV spectra were excessively noisy due to light scattering from insoluble aggregates of PNAA.

The effect of ionic screening on PNAA−DNA duplex stability can be predicted by a Poisson−Boltzmann-type model (*47*, *48*) that considers the oligomers to behave as charged cylinders with a higher charge density in duplex form than as a single-stranded coil. An increase in bulk cation concentration acts to stabilize the high charge density state, resulting in a higher thermal stability. The change in melting temperature with changing salt concentration can be related to the thermodynamic differential counterion association parameter per phosphate group ($\Delta\psi$) by (*4*, *49*)

$$\frac{dT_m}{d \log [Na^+]} = 0.9\left\{\frac{2.03RT_m^2}{\Delta H}\right\}(N_u\Delta\psi) \qquad (6)$$

where ΔH is the helix-to-coil transition enthalpy, R is the gas constant with units of cal/(mol K), and N_u is the number of charged groups (phosphate, in the case of DNA) per cooperative melting unit. The data of Table 3 have $dT_m/d \log [Na^+]$ for C_{12}-agtgatctac-$(Glu)_4$ of 3.8 K, indicating that counterion association takes place upon PNA−DNA helix formation. From ΔH and T_m values taken from the van't Hoff analysis of the melting curves, the thermodynamic differential counterion association parameter ($\Delta\psi$) was calculated to be 0.059.

Table 4 summarizes these results and compares them to literature values. Because the PNAA C_{12}-tttccg-$(Lys)_2$ has a low T_m, it was difficult to obtain the full sigmoidal curve required for accurate thermodynamic data in the presence of added salt. Instead, we measured melting

Table 4. Salt Concentration Dependence on Duplex Stability for PNAA with Complementary DNA (5′-CGGAAA-3′ and 5′-GTAGATCACT-3′) in 10 mM Tris Buffer (pH 7.0)

duplex	$d(T_m)/d(\log[Na^+])$ (K)	$RT_m^2/\Delta H$ (K)	$\Delta\psi$ (mol/mol of duplex)
C_{12}-tttccg-$(Lys)_2$−DNA	−4.2	1.95	−0.17
C_{12}-agtgatctac-$(Glu)_4$−DNA	3.8	3.10	0.059
PNA−DNA[a]	−3.4	3.52	−0.05
DNA−DNA[a]	15.9	2.74	0.15

[a] Literature values for PNA and DNA decamers and their DNA−decamer complements (*4*).

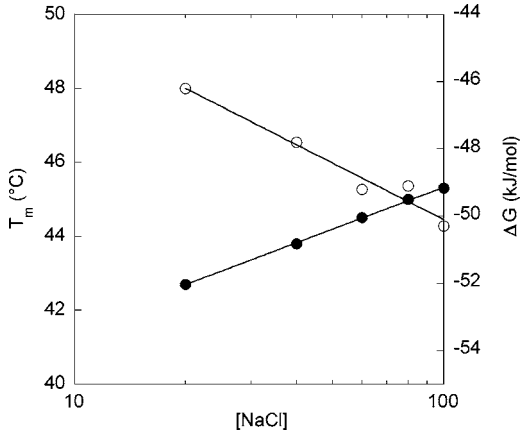


Figure 5. Dependence of T_m (filled circles) and ΔG (open circles) on the concentration of NaCl added to 10 mM Tris buffer for hybridization of PNAA C_{12}-agtgatctac-$(Glu)_4$ with complementary DNA (5′-GTAGATCACT-3′). The T_m data are fit to the equation $T_m = 37.8 + 3.77\log([Na^+])$, and the ΔG data are fit to the equation $\Delta G = -38.9 - 5.58\log([Na^+])$. Regression coefficients are >98% in both cases.

curves in pure water (deemed to have an effective $[Na^+] = 10^{-5}$ M) and compared them to the buffer case (effective $[Na^+] = 2 \times 10^{-2}$ M). In this case, $\Delta\psi = -0.17$, indicating that counterions are released on duplex formation owing to the complexation of positively charged lysine and negatively charged phosphates. Tomac et al. (*4*) made similar measurements and obtained a value of $\Delta\psi = -0.05$ for an unmodified PNA 10-mer with fully complementary DNA and $\Delta\psi = 0.15$ for the corresponding DNA−DNA duplex. This indicates that the addition of 4 Glu residues has the same destabilizing effect as about 2.5 phosphate groups. Although each group carries a negative charge, in principle, this result is reasonable considering the separation between the distal Glu groups and DNA phosphate groups and the possibility of incomplete dissociation of the side-group carboxylic acids at pH 7.0. Figure 5 is a plot of T_m and ΔG with added salt, showing a semilog dependence. Griffin and Smith obtained a value of $d\Delta G/d\log[Na^+] = -1.82$ kJ/mol for fully complementary PNA (unmodified) and DNA 9-mers. The PNA−DNA duplex is stabilized by added salt, because

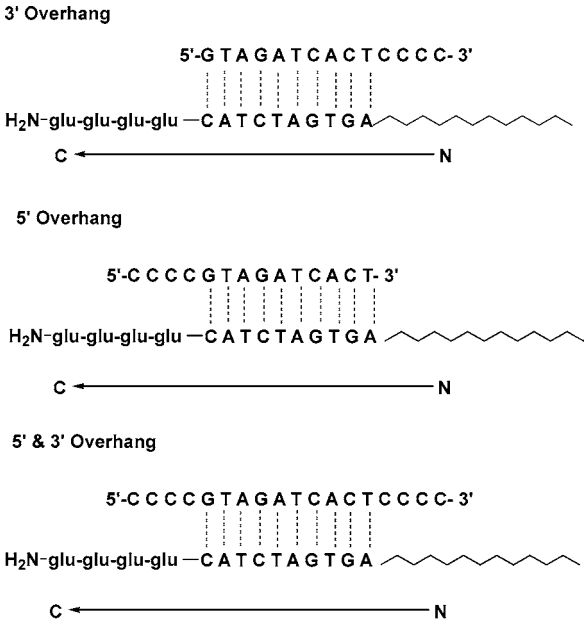


Figure 6. Orientation of the PNAA/DNA duplex with overhanging DNA bases on the 3′, 5′, and 3′ and 5′ ends.

the helix carries a greater charge density than the coil, as described above. We obtained a value of $d\Delta G/d\log[Na^+] = -5.58$ kJ/mol, indicating a much greater free energy penalty for the introduction of $(Glu)_4$ to the duplex than the closer proximity of phosphate charges required for helix formation.

Datta and Armitage have reported a stabilizing effect of overhanging, unbound DNA bases on PNA−DNA duplexes with length asymmetries (*50*). The overhang effect was ascribed to an enthalpic gain provided by stacking of the overhanging DNA bases with those in the PNA−DNA duplex. The effect is more evident in PNA−DNA duplexes than in DNA−DNA duplexes, presumably due to the wider pitch of the PNA−DNA helix that leaves bases more exposed to solvent. To determine if the alkane tail would have any impact on overhang-induced stabilization, we also collected UV-melting data using longer DNA strands, those with overhanging C bases surrounding a 10-mer binding site (Table 5; Figure 6). The first conclusion we draw is that, for overhangs on both sides of the PNAA binding sequence of the DNA, there appears to be no difference for the PNA peptide compared to the PNA amphiphile. Additionally, DNA overhangs on the 3′ end of the binding sequence (closest to the PNAA alkane, Figure 6) stabilize the duplex while those on the 5′ end (closest to the $(Glu)_4$ group, Figure 6) destabilize the PNAA−DNA duplex. Because the thermodynamic data for PNAA−DNA duplexes mirror those for PNA−DNA duplexes, we must presume that the stabilization afforded by the 3′ overhangs is due to the same effect reported by Datta and Armitage, whereas the destabilization by the 5′ overhangs has an electrostatic origin that

Table 5. Effect of Overhang Position on Thermodynamic Parameters for Duplexes of Various DNA Oligomers and the PNA Amphiphile C_{12}-agtgatctac-$(Glu)_4$ or the PNA Peptide NH_2-agtgatctac-$(Glu)_4$[a]

DNA target (3′→5′)	T_m (°C), amph	T_m (°C), peptide	ΔH (kJ/mol), amph	ΔH (kJ/mol), peptide	ΔG_{298} (kJ/mol), amph	ΔG_{298} (kJ/mol), peptide
TCACTAGATG	42.0	38.9	−287	−264	−47.7	−43.7
TCACTAGATG**CCCC**	37.3	38.7	−181	−163	−37.3	−38.7
CCCCTCACTAGATG	47.8	47.7	−298	−292	−53.1	−52.7
CCCCTCACTAGATG**CCCC**	45.0	45.4	−281	−287	−49.8	−50.6
CCCCCCTCACTAGATG**CCCCCC**	50.1		−328		−57.6	
CCCCCCCCTCACTAGATG**CCCCCCCC**	50.4		−329		−58.0	

[a] Overhanging DNA bases are in bold (see Figure 6).

either exists along with an overhang stabilization (but outweighing it) or prevents the molecular arrangements required for overhang stabilization from occurring. Finally, we note that the overhang-induced stabilization appears to saturate with six cytosine bases on each end of the binding sequence, because the stability is not improved with eight bases on each end. This appears to agree with results from Datta and Armitage, who found a significant added stabilization of PNA−DNA duplexes with eight overhanging bases rather than four.

CONCLUSIONS

We have provided details concerning the synthesis and characterization of PNA amphiphiles (PNAA), self-assembling compounds that bind DNA with high selectivity. We have found that the addition of the alkane tail makes self-assembly possible, but does not affect the binding selectivity or the stability of the resulting PNAA−DNA duplex. The incorporation of about four charged amino acids per 10-mer (or two per 6-mer) was required for adequate water solubility. Addition of a $(Glu)_4$ peptide destabilized the duplex, whereas addition of a $(Lys)_2$ peptide stabilized it. Both effects were attenuated with increased ionic strength, indicating an electrostatic mechanism. This electrostatic control over the stability could be useful for the tuning of the duplex melting temperature for future applications of these materials in bioanalytical devices. Stabilization of the PNAA−DNA duplex was also observed when using DNAs with overhanging bases, but this overhang stabilization was not affected by the PNAA alkane.

ACKNOWLEDGMENT

We acknowledge the National Science Foundation (BES-0093538), the Arnold and Mabel Beckman Foundation, and a joint grant from the Air Force Office of Scientific Research and the DARPA SIMBIOSYS program for financial support of this work. We also thank Bruce Armitage and Stu Kushon for helpful discussions.

LITERATURE CITED

(1) Nielsen, P. E. (1999) Peptide nucleic acid. A molecule with two identities. *Acc. Chem. Res. 32*, 624−630.

(2) Uhlmann, E.; Peyman, A.; Breipohl, G.; Will, D. W. (1998) PNA: synthetic polyamide nucleic acids with unusual binding properties. *Angew. Chem., Int. Ed. Engl. 37*, 2796−2823.

(3) Egholm, M.; Buchardt, O.; Christensen, L.; Behrens, C.; Freier, S. M.; Driver, D. A.; Berg, R. H.; Kim, S. K.; Norden, B.; Nielsen, P. E. (1993) PNA hybridizes to complementary oligonucleotides obeying the Watson−Crick hydrogen-bonding rules. *Nature 365*, 566−568.

(4) Tomac, S.; Sarkar, M.; Ratilainen, T.; Wittung, P.; Nielsen, P. E.; Norden, B.; Graslund, A. (1996) Ionic effects on the stability and conformation of peptide nucleic acid complexes. *J. Am. Chem. Soc. 118*, 5544−5552.

(5) Igloi, G. L. (1998) Variability in the stability of DNA-peptide nucleic acid (PNA) single-base mismatched duplexes: real-time hybridization during affinity electrophoresis in PNA-containing gels. *Proc. Natl. Acad. Sci. 95*, 8562−8567.

(6) Ratilainen, T.; Holmén, A.; Tuite, E.; Nielsen, P. E.; Nordén, B. (2000) Thermodynamics of sequence-specific binding of PNA to DNA. *Biochemistry 39*, 7781−7791.

(7) Kim, S. K.; Nielsen, P. E.; Egholm, M.; Buchardt, O.; Berg, R. H.; Norden, B. (1993) Right-handed triplex formed between peptide nucleic acid PNA-T8 and poly(dA) shown by linear and circular dichroism spectroscopy. *J. Am. Chem. Soc. 115*, 6477−6481.

(8) Wittung, P.; Nielsen, P.; Nordén, B. (1996) Direct observation of strand invasion by peptide nucleic acid (PNA) into double-stranded DNA. *J. Am. Chem. Soc. 118*, 7049−7054.

(9) Ørum, H.; Nielsen, P. E.; Egholm, M.; Berg, R. H.; Buchardt, O.; Stanley, C. (1993) Single base pair mutation analysis by PNA directed PCR clamping. *Nucleic Acids Res. 21*, 5332−5336.

(10) Gaylord, B. S.; Heeger, A. J.; Bazan, G. C. (2002) DNA hybridization detection with water-soluble conjugated polymers and chromophore-labeled single-stranded DNA. *J. Am. Chem. Soc. 125*, 896−900.

(11) Komiyama, M.; Ye, S.; Liang, X.; Yamamoto, Y.; Tomita, T.; Zhou, J.-M.; Aburatani, H. (2003) PNA for one-base differentiating protection of DNA from nuclease and its use for SNPs detection. *J. Am. Chem. Soc. 125*, 3758−3762.

(12) Wang, J.; Palecek, E.; Nielsen, P. E.; Rivas, G.; Cai, X.; Shiraishi, H.; Dontha, N.; Luo, D.; Farias, P. A. M. (1996) Peptide nucleic acid probes for sequence-specific DNA biosensors. *J. Am. Chem. Soc. 118*, 7667−7670.

(13) Wang, J.; Nielsen, P. E.; Jiang, M.; Cai, X.; Fernandes, J. R.; Grant, D. H.; Ozsoz, M.; Beglieter, A.; Mowat, M. (1997) Mismatch-sensitive hybridization detection by peptide nucleic acids immobilized on a quartz crystal microbalance. *Anal. Chem. 69*, 5200−5302.

(14) Wang, J.; Rivas, G.; Cai, X.; Chicharro, M.; Parrado, C.; Dontha, N.; Begleiter, A.; Mowat, M.; Palecek, E.; Nielsen, P. E. (1997) Detection of point mutation in the p53 gene using a peptide nucleic acid biosensor. *Anal. Chim. Acta 344*, 111−118.

(15) Myal, Y.; Blanchard, A.; Watson, P.; Corrin, M.; Shiu, R.; Iwasiow, B. (2000) Detection of genetic point mutations by peptide nucleic acid-mediated Polymerase Chain Reaction clamping using paraffin-embedded specimens. *Anal. Biochem. 285*, 169−172.

(16) Ross, P. L.; Lee, K.; Belgrader, P. (1997) Discrimination of single-nucleotide polymorphisms in human DNA using peptide nucleic acid probes detected by MALDI-TOF mass spectrometry. *Anal. Chem. 69*, 4197−4202.

(17) Svanvik, N.; Westman, G.; Wang, D.; Kubista, M. (1999) Light-Up probes: thiazole orange-conjugated peptide nucleic acid for detection of target nucleic acid in homogeneous solution. *Anal. Biochem. 281*, 26−35.

(18) Ørum, H.; Nielsen, P. E.; Jorgensen, M.; Larsson, C.; Stanley, C.; Koch, T. (1995) Sequence-specific purification of nucleic acids by PNA-controlled hybrid selection. *BioTechniques 19*, 472−480.

(19) Seeger, C.; Batz, H.-G.; Ørum, H. (1997) PNA-mediated purification of PCR amplifiable human genomic DNA from whole blood. *BioTechniques 23*, 512−517.

(20) Chandler, D. P.; Stults, J. R.; Cebula, S.; Schuck, B. L.; Weaver, D. W.; Anderson, K. K.; Egholm, M.; Brockman, F. J. (2000) Affinity purification of DNA and RNA from environmental samples with peptide nucleic acid clamps. *Appl. Environ. Microbiol. 66*, 3438−3445.

(21) Chandler, D. P.; Stults, J. R.; Anderson, K. K.; Cebula, S.; Schuck, B. L.; Brockman, F. J. (2000) Affinity capture and recovery of DNA at femtomolar concentrations with peptide nucleic acid probes. *Anal. Biochem. 283*, 241−249.

(22) Winger, T. M.; Ludovice, P. J.; Chaikof, E. L. (1996) Lipopeptide conjugates: biomolecular building blocks for receptor activating membrane-mimetic structures. *Biomaterials 17*, 437−441.

(23) Dori, Y.; Bianco-Peled, H.; Satija, S. K.; Fields, G. B.; McCarthy, J. B.; Tirrell, M. (2000) Ligand accessibility as means to control cell response to bioactive bilayer membranes. *J. Biomed. Mater. Res. 50*, 75−81.

(24) Dillow, A. K.; Ochsenhirt, S. E.; McCarthy, J. B.; Fields, G. B.; Tirrell, M. (2001) Adhesion of $\alpha5\beta1$ receptors to biomimetic substrates constructed from peptide amphiphiles. *Biomaterials 22*, 1493−1505.

(25) Schneider, J.; Berndt, P.; Haverstick, K.; Kumar, S.; Chiruvolu, S.; Tirrell, M. (1998) Force and adhesion measurements between hydrogen-bonded layers of glycine-functionalized amphiphiles. *J. Am. Chem. Soc. 120*, 3508−3509.

(26) Berndt, P.; Kurihara, K.; Kunitake, T. (1995) Measurement of forces between surfaces composed of two-dimensionally organized, complementary and noncomplementary nucleobases. *Langmuir 11*, 3083−3091.

(27) Pincet, F.; Perez, E.; Bryant, G. (1996) Specific forces between DNA bases. *Mod. Phys. Lett. B 10*, 81−99.
(28) Gore, T.; Dori, Y.; Talmon, Y.; Tirrell, M.; Bianco-Peled, H. (2001) Self-assemply of model collagen peptide amphiphiles. *Langmuir 17*, 5352−5360.
(29) Hartgerink, J. D.; Beniash, E.; Stupp, S. I. (2001) Self-assembly and mineralization of peptide-amphiphile nanofibers. *Science 294*, 1684−1688.
(30) Shimizu, T.; Hato, M. (1993) Self-assembling properties of synthetic peptidic lipids. *Biochim. Biophys. Acta 1147*, 50−58.
(31) Hartgerink, J. D.; Beniash, E.; Stupp, S. I. (2002) Peptide-amphiphile nanofibers: a versatile scaffold for the preparation of self-assembling materials. *Proc. Natl. Acad. Sci. U.S.A. 99*, 5133−5138.
(32) Vernille, J. P.; Schneider, J. W. (2004) Sequence-specific oligonucleotide purification using peptide nucleic acid (PNA) amphiphiles in hydrophobic interaction chromatography. *Biotechnol. Prog.* in press.
(33) Yu, Y. C.; Tirrell, M.; Fields, G. B. (1998) Minimal lipidation stabilizes protein-like molecular architecture. *J. Am. Chem. Soc. 120*, 9979−9987.
(34) Chu-Kung, A. F.; Bozzelli, K. N.; Lockwood, N. A.; Haseman, J. R.; Mayo, K. H.; Tirrell, M. V. (2004) Promotion of peptide antimicrobial activity by fatty acid conjugation. *Bioconjugate Chem. 15*, 530−535.
(35) Ratilainen, T.; Holmen, A.; Tuite, E.; Haaima, G.; Christensen, L.; Nielsen, P. E.; Nordén, B. (1998) Hybridization of peptide nucleic acid. *Biochemistry 37*, 12331−12342.
(36) Ljungstrøm, T.; Knudsen, H.; Nielsen, P. E. (1999) Cellular uptake of adamantyl conjugated peptide nucleic acids. *Bioconjugate Chem. 10*, 955−972.
(37) Egholm, M.; Buchardt, O.; Nielsen, P. E.; Berg, R. H. (1992) Peptide nucleic acids (PNA). Oligonucleotide analogues with an achiral peptide backbone. *J. Am. Chem. Soc. 114*, 1895−1897.
(38) Chan, W. C.; White, P. D. (2000) *Fmoc Solid-Phase Peptide Synthesis*, Oxford University Press, New York.
(39) Nielsen, P. E., Egholm, M., Eds. (1999) *Peptide Nucleic Acids Protocols and Applications*, Horizon Scientific Press, Wymondham, U.K.
(40) Christensen, L.; Fitzpatrick, R.; Gildea, B.; Petersen, K. H.; Hansen, H. F.; Koch, T.; Egholm, M.; Buchardt, O.; Nielsen, P. E.; Coull, J. (1995) Solid-phase synthesis of peptide nucleic acids. *J. Pept. Sci. 1*, 185−183.
(41) Berndt, P.; Fields, G. B.; Tirrell, M. (1995) Synthetic lipidation of peptides and amino acids: monolayer structure and properties. *J. Am. Chem. Soc. 117*, 9515−9522.
(42) Egholm, M.; Casale, R. A. (2000) The chemistry of peptide nucleic acids. In *Solid-Phase Synthesis* (Kates, S. A., Albericio, F., Eds.) pp 549−578, Dekker, New York.
(43) Evans, D. F.; Wennerström, H. (1994) *The Colloidal Domain: Where Physics, Chemistry, Biology, and Technology Meet*, VCH Publishers, New York.
(44) Griffin, T. J.; Smith, L. M. (1998) An approach to predicting the stabilities of peptide nucleic acid:DNA duplexes. *Anal. Biochem. 260*, 56−63.
(45) Giesen, U.; Kleider, W.; Berding, C.; Geiger, A.; Ørum, H.; Nielsen, P. E. (1998) A formula for the thermal stability (T_m) prediction of PNA/DNA duplexes. *Nucleic Acids Res. 26*, 5004−5006.
(46) SantaLucia, J.; Allawi, H. T.; Seneviratne, P. A. (1996) Improved nearest-neighbor parameters for predicting DNA duplex stability. *Biochemistry 35*, 3555−3562.
(47) Anderson, C. F.; Record, M. T. (1983) *Structure and Dynamics* ed. (Clementi, E., Sarma, R, Eds.) pp 301−309, Adenine Press, New York.
(48) Bond, J. P.; Anderson, C. F.; Record, M. T. (1994) Conformational transitions of duplex and triplex nucleic acid helixes: thermodynamic analysis of effects of salt concentration on stability using preferential interaction coefficients. *Biophys. J. 67*, 825−836.
(49) Record, M. T.; Anderson, C. F.; Lohman, T. M. (1978) Thermodynamic analysis of ion effects on the binding and conformational equilibriums of proteins and nucleic acids: the roles of ion association or release, screening, and ion effects on water activity. *Q. Rev. Biophys. 11*, 103−178.
(50) Datta, B.; Armitage, B. A. (2001) Hybridization of PNA to structured DNA targets: quadruplex invasion and the overhang effect. *J. Am. Chem. Soc. 123*, 9612−9619.

BC049831A

Synthesis of Poly(ethylene glycol)-Based Saquinavir Prodrug Conjugates and Assessment of Release and Anti-HIV-1 Bioactivity Using a Novel Protease Inhibition Assay

Simi Gunaseelan,[†] Olivia Debrah,[†] Li Wan,[†] Michael J. Leibowitz,[‡,||,§] Arnold B. Rabson,[‡,||] Stanley Stein,[†,||,§] and Patrick J. Sinko*[,†,||,§]

Department of Pharmaceutics, Ernest Mario School of Pharmacy, Rutgers University, Piscataway, New Jersey 08854-0789, Center for Advanced Biotechnology and Medicine, Department of Molecular Genetics, Microbiology, and Immunology, Robert Wood Johnson Medical School, University of Medicine and Dentistry of New Jersey, Piscataway, New Jersey 08854, Cancer Institute of New Jersey, New Brunswick, New Jersey 08903-2681, and New Jersey Center for Drug Targeting and Delivery, Piscataway, New Jersey 08854. Received May 12, 2004; Revised Manuscript Received September 23, 2004

Various poly(ethylene glycol)(PEG)-based prodrug conjugates of the HIV-1 protease inhibitor (PI) saquinavir (SQV) were prepared using several types of chemical groups potentially capable of modifying its pharmacokinetic properties. These prodrug conjugates included SQV−cysteine-PEG3400, SQV−cysteine-PEG3400-biotin, SQV−cysteine(R.I.CK-Tat9) [a cationic retro-inverso-cysteine-lysine-Tat nonapeptide]-PEG3400, and SQV−cysteine(R.I.CK(stearate)-Tat9)-PEG3400. SQV was linked to cysteine to form a releasable SQV−cysteine ester bond in all of the conjugates. The amino group of the cysteine moiety provided an attachment site for a slower-degrading amide bond with *N*-hydroxysuccinimide-activated forms of PEG- and PEG-biotin. Disulfide bonds were used to attach the cationic peptides, R.I.CK-Tat9 and R.I.CK(stearate)-Tat9 to the cysteine moiety in order to provide cell-specific release. An assay was established and validated for measuring the activity of SQV and other protease inhibitors in biological samples. In this assay, cleavage of an internally quenched fluorescent substrate, Arg-Glu(EDANS)-Ser-Gln-Asn-Tyr-Pro-Ile-Val-Gly-Lys(DABCYL)-Arg by HIV-1 protease was inhibited by SQV in a dose-dependent manner at concentrations of 0.05−0.5 μM. All prodrug conjugates were shown to be inactive in this assay until the ester bond was cleaved and active SQV was released. The prodrug reconversion half-lives in 0.1 N HCl, phosphate-buffered saline (PBS) at pH 7.4 and in spiked plasma at 37 °C were 9, 14, and 0.9 h, respectively. The anti-HIV-1 activity (ED_{50}) of the PEG-based SQV prodrug conjugates was evaluated in MT-2 cells using an MTT assay. The activity of conjugated SQV was reduced (ED_{50} = 900 nM) for the PEG only conjugate, but restored with the addition of biotin (ED_{50} = 125 nM), R.I.CK-Tat9 (ED_{50} = 15 nM), and R.I.CK-(stearate)-Tat9 (ED_{50} = 62 nM) as compared to maximum achievable anti-HIV-1 activity (unconjugated SQV, control, ED_{50} = 15 nM), suggesting enhanced cellular uptake of conjugates. Cytotoxicity (LD_{50}) was assessed for all prodrug conjugates using non-HIV-1 infected cells and was found to be in the micromolar range. The difference between the LD_{50} and ED_{50} suggests a favorable therapeutic index for the prodrug conjugates. In conclusion, these promising initial results demonstrate that the reconversion of the conjugate prodrugs was complete and that active SQV was released. Since the major delivery advantages of PEG prodrug conjugates can only be observed in vivo, issues of reconversion and elimination half-lives in plasma will have to be further studied in an in vivo model. The current results also demonstrate that the protease inhibition assay is a simple yet effective bioanalytical tool that can be used to assess the release and anti-HIV-1 activity of HIV-1 PIs from their prodrug forms.

INTRODUCTION

Acquired immunodeficiency syndrome (AIDS) is a degenerative disease of the immune and central nervous systems caused by the human immunodeficiency virus (HIV). HIV-1 protease is the target of the protease inhibitors, a class of drugs commonly used for AIDS therapy. SQV[1] is the first HIV-1-protease inhibitor (PI) to be approved by the U.S. Food and Drug Administration. However, therapeutic use of SQV suffers from problems of low absorptive and high secretory permeability, bioconversion to inactive metabolites, and poor solubility (*1, 2*). The oral bioavailability of SQV in clinical formulations is low and/or variable with limited penetration into the lymphatic and central nervous systems (CNS) (*3*−*6*). While its low and variable bioavailability is primarily attributed to metabolism by cytochrome P-450 3A, recent results published by our group (*7, 8*) and others (*9*) suggest that multiple membrane transporters may also contribute significantly to the observed behavior. The consequence of variable SQV bioavailability can be the development of viral resistance, ultimately resulting in therapeutic failure. Clearly, better drug

* To whom correspondence should be addressed. Tel: +1-732-445-3831*213. Fax: +1-732-445-4271. E-mail: sinko@rci.rutgers.edu.
[†] Rutgers University.
[‡] University of Medicine and Dentistry of New Jersey.
[||] Cancer Institute of New Jersey.
[§] New Jersey Center for Drug Targeting and Delivery.

10.1021/bc0498875 CCC: $27.50 © 2004 American Chemical Society
Published on Web 10/28/2004

delivery methods are required to enhance the bioavailability of SQV and to reduce the associated variability observed in the clinic.

One common drug delivery approach to enhancing bioavailability is to utilize prodrugs. A 'prodrug' approach has the potential advantage of achieving greater drug bioavailability by altering the physicochemical properties of the drug, minimizing processes that would otherwise cause elimination or breakdown of the parent drug, or by increasing cellular uptake. Various ester PI prodrugs derived from SQV, indinavir, or nelfinavir connected to fatty acids, L-valine, L-tyrosine, PEG, or D-glucose (*10, 11*) have been reported. The most encouraging results were obtained with the L-valine PI prodrugs (*12*) which prompted the extension of this series to include L-leucine and L-phenylalanine along with new ester PI prodrugs derived from L-tyrosine or that are linked to diglycerides (*13*). Among the strategies explored up to now, the most successful has been the "hydrophilic" prodrug approach which has led to the discovery of fosamprenavir, a water-soluble phosphate ester prodrug of the sparingly water-soluble amprenavir that was approved in 2003. The absorption enhancement of amprenavir that is observed by using the fosamprenavir prodrug occurs because the water solubility of this poorly soluble drug is dramatically increased and net systemic absorption is greatly enhanced. Unfortunately, prodrugs are rapidly converted back to the parent drug in vivo either in the intestinal environment or on the first pass through the intestine and liver. Therefore, once a prodrug is "absorbed", only the drug appears in the blood and the potential benefits of the prodrug are lost. Since nearly all PIs are faced with poor cellular uptake/retention, metabolism, and protein binding, the maximal therapeutic potential of these agents is not likely to be achieved using a classical prodrug approach since concentrations in target cells such as T4 helper lymphocytes or macrophages will be difficult to control.

In the current report, macromolecular prodrug conjugates were designed to overcome several biopharmaceutical challenges associated with HIV-1 PIs and prodrugs in general including poor solubility, cellular uptake/retention, metabolism/stability, and variable cellular drug concentrations. The conjugate scaffold used in the current study was based on PEG. PEGylation has been shown to significantly enhance the biopharmaceutical properties (i.e., circulation half-life, aqueous solubility, etc.) of drugs resulting in more effective in vivo delivery (*14*−*18*). Enhancing cell association and/or uptake was also an important design element. This was addressed by using biotin (*17,18*), R.I.CK-Tat9 (*19, 20*), or R.I.CK-(stearate)-Tat9 (*21*) to enhance cell uptake. In addition to being an effective cell-penetrating peptide (CPP), R.I.CK-Tat9 is also an anti-HIV-1 agent that acts on nonprotease targets (*22*−*25*) and may be useful in combination therapy. In this report, the design, synthesis, and initial characterization of prototype prodrug conjugates of SQV with PEG-based substituents are described. These substituents were linked to the drug using releasable (ester and disulfide) and nonreleasable (amide) bonds. For these prodrug conjugates, the anti-HIV-1 activity was assessed in HIV-infected MT-2 cells using an MTT assay and compared to the maximal possible in vitro therapeutic potential of unconjugated SQV. Also, a novel HIV-1 protease inhibition assay was used to monitor the release of active drug from the prodrug conjugates.

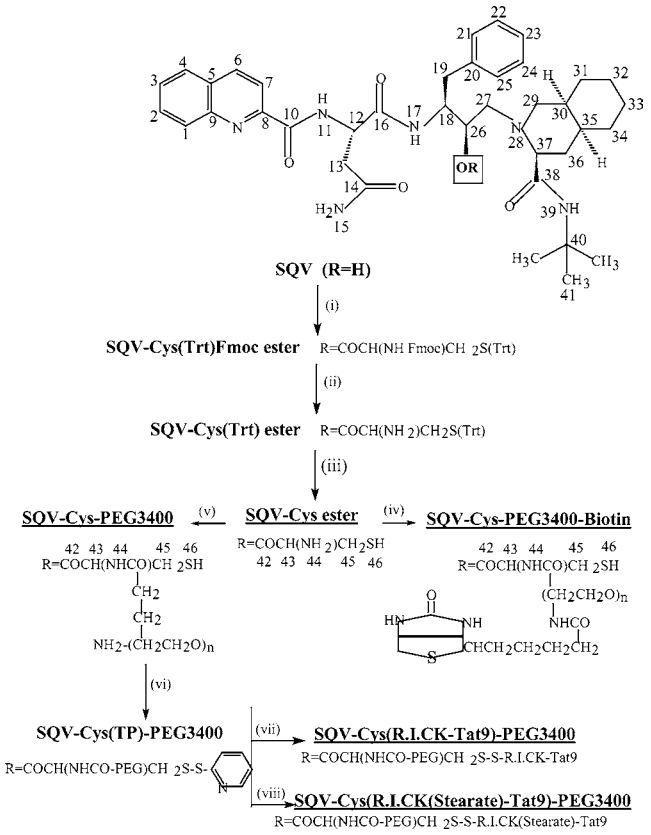
EXPERIMENTAL PROCEDURES

Materials. Fluorenylmethoxycarbonyl (Fmoc)-amino acid derivatives, MBHA Rink amide resin, BOP (benzotriazol-1-yl-oxytris(dimethylamino)phosphonium hexafluorophosphate) and HOBt (*N*-hydroxybenzotriazole) were purchased from Calbiochem-Novabiochem Corp. (La Jalla, CA). Fmoc-PEG-NHS (MW 3400) and biotin-PEG-NHS (MW 3400) were obtained from Nektar Therapeutics AL, Corp. (formerly Shearwater Corp.) (Huntsville, AL). Stearic acid, DIEA (diisopropylethylamine), aldrithiol, piperidine, and hydrazine were obtained from Sigma Chemicals (St. Louis, MO). Acetic anhydride and diethyl ether were purchased from Fischer Chemicals (Pittsburgh, PA). Dde (1-(4,4-dimethyl-2,6-dioxocyclohex-1-ylidene)ethyl), EDT (ethanedithiol), TIS (triisopropyl silane), DMAP (4-(dimethylamino)pyridine), DIPC (1,3-diisopropylcarbodiimide), anhydrous dimethylformamide (DMF), and anhydrous dimethyl sulfoxide (DMSO) were obtained from Aldrich Chemicals (Milwaukee, WI). Dichloromethane (DCM) obtained from Sigma was dried over calcium hydride and freshly distilled prior to use. Trifluoroacetic acid (TFA) obtained from Aldrich was distilled with H_2SO_4 before use. SQV from commercially purchased capsules (Inverase, Roche) was extracted with methanol. Chemical reactions were carried out under a nitrogen atmosphere. The purity of all new compounds was checked by mass spectrometry, TLC, and/or NMR.

Spectral Analyses. UV spectra were recorded on a Shimadzu UV-1201 spectrophotometer. ^1H and ^{13}C NMR spectra were recorded on a Bruker ARX 300. Chemical shifts (δ) were expressed as parts per million (ppm) using tetramethylsilane (TMS) as the internal standard (δ = 0.0 ppm). Coupling constants (J values) are expressed in Hz, and multiplicities are referred to as s (singlet), d (dublet), t (triplet), m (multiplet), bs (broad singlet), and td (triplet dublet). Electrospray ionization mass spectra (ESI-MS) were recorded on a Finnigan MAT TSQ 7000 equipped with an atmospheric pressure ionization source. This method used in positive mode detects either the $(M + H)^+$ and/or $(M + Na)^+$ signal. Mass spectrometry using matrix-assisted-laser-desorption-ionization time-of-flight (MALDI-TOF) was performed on a PE Biosystems Voyager System 6080. $^1H/^{13}C$ NMR and mass spectrometry (ESI-MS and/or MALDI-TOF) data fully confirm the signal assignments and structure of the materials. For atom numbering, see Scheme 1.

[1] Abbreviations: AcOEt, ethyl acetate; AIDS, acquired immunodeficiency syndrome; BOP, benzotriazol-1-yl-oxy-tris(dimethylamino)phosphonium hexafluorophosphate; $CDCl_3$, deuterated chloroform; CH_2Cl_2, methylene chloride; CNS, central nervous system; CPP, cell-penetrating peptide; CPT, camptothecin; Cys, cysteine; DCM, dichloromethane; Dde, 1-(4,4-dimethyl-2,6-dioxocyclohex-1-ylidene)ethyl; DIEA, diisopropylethylamine; DIPC, 1,3-diisopropylcarbodiimide; DMAP, 4-(dimethylamino)-pyridine; DMF, dimethylformamide; DMSO, dimethyl sulfoxide; ED, effective dose; EDT, ethanedithiol; ESI-MS, electrospray ionization mass spectrometry; Et_2O, diethyl ether; FBS, fetal bovine serum; Fmoc, fluorenylmethoxycarbonyl; FRET, fluorescence resonance energy transfer; Gly, glycine; HAART, highly active anti-retroviral therapy; HIV, human immunodeficiency virus; HOBt, *N*-hydroxybenzotriazole; LD, lethal dose; Lys, lysine; MALDI-TOF, matrix-assisted-laser-desorption ionization time-of-flight; MeOH, methanol; MOI, multiplicity of infection; MTT, 3-(4,5-dimethylthiazol-2-yl)-2,5-diphenyltetrazolium bromide; NHS, *N*-hydroxysuccinimide-; NMR, nuclear magnetic resonance; PBS, phosphate-buffered saline; PEG, poly(ethylene glycol); PI, protease inhibitor; PR, protease; R.I.CK-Tat9, retro-inverso-cysteine-lysine-Tat nonapeptide; RP-HPLC, reverse-phase high-performance liquid-chromatography; SQV, saquinavir; TFA, trifluoroacetic acid; TIS, triisopropylsilane; TMS, tetramethylsilane; TP, 2-thiopyridine; Trt, trityl.

Scheme 1. Synthetic Pathway to SQV Prodrug Conjugates[a]



[a] (i) 3 equiv of Fmoc-Cys(S-Trt)-COOH in CH_2Cl_2 with DIPC/DMAP; (ii) 20% piperidine in CH_2Cl_2; (iii) TFA/CH_2Cl_2 (1:1); (iv) 2 equiv of biotin-PEG-NHS in CH_2Cl_2 with DIEA; (v) 2 equiv of Fmoc-PEG-NHS in CH_2Cl_2 with DIEA; (vi) 2 equiv of 2,2′-dithiodipyridine in DMSO; (vii) 2 equiv of R.I.CK-Tat9 in DMSO; (viii) 2 equiv of R.I.CK(stearate)-Tat9 in DMSO.

Chromatography. All reactions were monitored by TLC analysis on precoated silica gel F_{254} plates (Merck) with detection by UV absorption and by charring with 50% methanol−sulfuric acid solution, $KMnO_4$, or ninhydrin. Column chromatographic separations were carried out as flash chromatography using silica gel 60 (Merck, 70−230 mesh). Gel permeation chromatography was done on a Sephadex LH-20 column using dimethylformamide as solvent. The UV absorbance of each fraction obtained from gel permeation chromatography was detected at 239 nm, the absorption maximum for SQV (*26*). Peptide purification was done by HPLC on Vydac protein and peptide preparative column RP-C_{18} (10 μm)-packed column (2.2 × 25 cm) with detection at 220 nm, the maximum absorbance for peptides. The fractions obtained after HPLC purification were dried using a lyophilizer. Amino acid analysis was performed by cation exchange chromatography. Amino acid elution was accomplished by using a two buffer system initially eluting with 0.2 N sodium citrate, pH 3.28, followed by 1.0 N sodium citrate, pH 7.4. The amino acids were detected by on-line postcolumn reaction with ninhydrin. Derivatized amino acids were quantitated by their absorption at 570 nm wavelength. This procedure was performed on an automated Beckman system Gold HPLC amino acid analyzer.

SQV−Cys Ester. Fmoc-Cys(S-Trt)-COOH (0.220 g, 0.375 mmol) was dissolved in 100 mL of anhydrous CH_2Cl_2 at room temperature, and to this solution was added DMAP (0.32 g, 0.265 mmol), DIPC (58.7 μL, 0.375 mmol), and SQV (0.074 g, 0.11 mmol) at 0 °C. The reaction mixture was allowed to warm to room temperature and stirred overnight. The product was washed with 0.1 N HCl, dried over $MgSO_4$, and evaporated under reduced pressure to yield the solid product. The crude residue was chromatographed [silica gel chromatography (eluent: AcOEt)] yielding, 63 mg (85% recovery) of SQV−Cys(Trt)-Fmoc ester as a white powder. TLC (AcOEt/MeOH: 90/10, v/v, UV detection): $R_f = 0.75$. ESI-MS (*m/z*): 1238.5 $(M + H)^+$; 1260.5 $(M + Na)^+$. The Fmoc-protecting group was removed by dissolving the SQV−Cys(Trt)Fmoc ester (50 mg) in a mixture of CH_2Cl_2 and piperidine (80:20) and stirring at room temperature for 2 h. Solvent was evaporated under reduced pressure and the product subjected to silica gel chromatography (eluent: AcOEt) to yield 45 mg (90% recovery) of SQV−Cys(Trt) ester as a white solid. TLC (AcOEt/MeOH: 90/10, v/v, UV detection): $R_f = 0.80$. ESI-MS (*m/z*): 1016.5 $(M + H)^+$; 1038.5 $(M + Na)^+$. The protecting group (Trt) was removed by incubating SQV−Cys(Trt) ester (49 mg) for 3 h in a mixture of CH_2Cl_2 and TFA (trifluoroacetic acid) (50:50). The product was recrystallized from cold ether (Et_2O) and dried under vacuum overnight to give 40 mg (82% recovery) of SQV−Cys ester as a white powder. TLC (AcOEt/MeOH: 90/10, v/v, UV detection): $R_f = 0.85$. ESI-MS (*m/z*): 774.5 $(M + H)^+$; 796.5 $(M + Na)^+$. ^{1}H NMR ($CDCl_3$): δ 9.19 (d, *J* 7.2 Hz, H11); 8.24 (d, *J* 8.8 Hz, H7); 8.14 (d, *J* 8.5 Hz, H6); 8.12 (d, *J* 8.0 Hz, H1); 7.82 (d, *J* 8.1 Hz, H4); 7.74 (td, *J* 1.5 Hz, 8.1 Hz, H2); 7.59 (td, *J* 1.5 Hz, 8.1 Hz, H3); 7.51 (d, *J* 8.8 Hz, H17); 6.89−7.13 (m, H21−25); 6.50 (s, H15); 5.76 (bs, H39); 5.33 (m, H26); 4.81 (m, H12); 4.37 (m, H18); 4.12 (m, H43); 2.61−2.98 (m, H13/19/27/29/30/35/36/37); 2.44 (d, *J* 8.6 Hz, H44); 2.30 (t, *J* 7.6 Hz, H45); 1.92 (t, *J* 7.5 Hz, H46); 1.34−1.81 (m, H31−34); 1.22 (s, H41). ^{13}C NMR ($CDCl_3$): δ 173.7, 173.4 (C14/16); 170.4 (C38); 164.8 (C10); 155.6 (C42); 149.1 (C8); 146.8 (C9); 137.5 (C5); 137.1 (C6); 129.8−130.1 (C1/4); 129.4 (C20); 129.2 (C22/24); 128.5 (C21/25); 128.2 (C2); 127.7 (C3); 126.5 (C23); 118.7 (C7); 73.4 (C26); 70.8 (C37); 59.9 (C29); 57.1 (C27); 51.8 (C12); 51.3 (C43); 51.0 (C40); 49.8 (C18); 37.4 (C13); 36.1 (C45); 35.8 (C30); 35.5 (C19); 33.2 (C35); 30.8 (C36); 28.8 (C41); 30.7, 26.2, 25.8, 20.7 (C31−34).

SQV−Cys-PEG3400. SQV−Cys ester (12.5 mg, 0.016 mmol) and Fmoc-PEG-NHS (3400 molecular mass of PEG) [105.0 mg, 0.031 mmol] were added to CH_2Cl_2 (1.25 mL), and DIEA (12.5 μL) was added to adjust the pH to basic. The reaction was stirred for 3 h at room temperature. The product was recrystallized from cold ether and dried under vacuum overnight. The product obtained as a white powder and after Fmoc removal was subjected to gel permeation chromatography using a Sephadex LH-20 column in DMF, and absorbance was monitored at 239 nm. Two separate peaks were obtained as shown in Figure 1. The first peak corresponded to the purified SQV−Cys-PEG3400 and the second peak to the unreacted SQV−Cys ester. The fractions of first peak were combined and the solvent removed under reduced pressure to obtain SQV−Cys-PEG3400 with 75−80% recovery. Mass spectrometry of the conjugate showed a polydisperse peak at the expected molecular weight [*m/z*(%) 4044.9 Da] using MALDI-TOF (Figure 2). ^{1}H NMR ($CDCl_3$): δ 9.18 (d, *J* 7.6 Hz, H11); 8.27 (d, *J* 8.3 Hz, H7); 8.16 (d, *J* 8.2 Hz, H6); 8.11 (d, *J* 8.0 Hz, H1); 7.86 (d, *J* 8.2 Hz, H4); 7.73 (td, *J* 1.6 Hz, 8.3 Hz, H2); 7.64 (td, *J* 1.6 Hz, 8.3 Hz, H3); 7.51 (d, *J* 8.6 Hz, H17); 7.34 (d, *J* 8.1 Hz, H44); 6.85−7.15 (m, H21−25); 6.52 (s, H15); 5.70 (bs, H39); 5.30 (m, H26); 4.82 (m, H12); 4.32 (m, H18); 4.20 (m, CH_2CH_2); 4.11 (m, H43); 3.57 [bs, $CH_2(OCH_2CH_2)_n$]; 2.63−3.05 (m, H13/19/27/29/30/35/36/37);

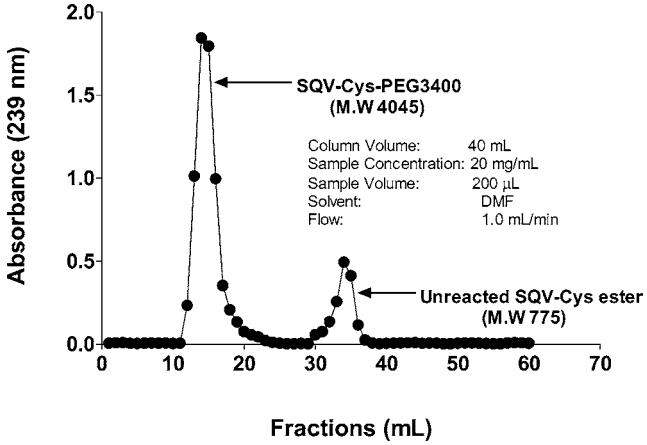


Figure 1. Gel permeation chromatogram showing separation of SQV−Cys-PEG3400 from unreacted SQV−Cys ester using Sephadex LH-20 column in DMF. The absorbance of each fraction was detected at a wavelength of 239 nm, the absorption maximum for SQV.

2.41 [s, NH_2]; 2.33 (t, J 7.4 Hz, H45); 1.92 (t, J 7.6 Hz, H46); 1.36−1.81 (m, H31−34); 1.22 (s, H41). ^{13}C NMR ($CDCl_3$): δ 173.5, 173.1 (C14/16); 172.5 (CH_2CONH); 170.6 (C38); 165.1 (C10); 155.6 (C42); 149.3 (C8); 146.5 (C9); 137.8 (C5); 137.2 (C6); 129.8−130.1 (C1/4); 129.6 (C20); 129.2 (C22/24); 128.6 (C21/25); 128.1 (C2); 127.8 (C3); 126.5 (C23); 118.4 (C7); 73.1 (C26); 72.5 ($OCH_2CH_2)_n$; 70.5 (C37); 59.2 (C29); 57.9 (C27); 55.5 (CH_2CH_2CO); 52.5 (CH_2CH_2CO); 51.9 (C12); 51.3 (C43); 51.3 (C40); 49.5 (C18); 37.9 (C13); 36.1 (C45); 35.7 (C30); 35.3 (C19); 33.0 (C35); 30.5 (C36); 28.5 (C41); 30.3, 26.2, 25.0, 20.8 (C31−34).

SQV−Cys-PEG3400-Biotin. The above process, when applied to NHS-PEG-biotin (3400 molecular mass of PEG) and SQV−Cys ester, followed by gel permeation chromatography in DMF, yielded SQV−Cys-PEG3400-biotin as a white powder with 70% recovery. Mass spectrometry of this conjugate using MALDI-TOF showed a polydisperse peak at 4059.6 Da (m/z) identical to the expected molecular weight. ^{1}H NMR ($CDCl_3$): δ 9.13 (d, J 7.3 Hz, H11); 8.26 (d, J 8.3 Hz, H7); 8.15 (d, J 8.3 Hz, H6); 8.11 (d, J 8.0 Hz, H1); 7.85 (d, J 8.1 Hz, H4); 7.76 (td, J 1.6 Hz, 8.3 Hz, H2); 7.66 (td, J 1.6 Hz, 8.3 Hz, H3); 7.48 (d, J 8.4 Hz, H17); 7.34 (d, J 8.1 Hz, H44); 7.24 (s, NH-CO−NH); 7.20 [s, N$H(CH_2CH_2O)_n$]; 6.84−7.13 (m, H21−25); 6.52 (s, H15); 5.70 (bs, H39); 5.34 (m, H26); 4.84 (m, H12); 4.35 (m, H18); 4.13 (m, biotin aliphatic chain); 4.11 (m, H43); 3.56 [bs, $(OCH_2CH_2)_n$]; 2.61−3.08 (m, H13/19/27/29/30/35/36/37); 2.33 (t, J 7.4 Hz, H45); 1.92 (t, J 7.6 Hz, H46); 1.35−1.84 (m, H31−34); 1.26 (s, H41). ^{13}C NMR ($CDCl_3$): δ 175.8 (NHCONH); 173.6, 173.1 (C14/16); 172.5, 172.9 [CONH $(CH_2CH_2O)_nC$ONH]; 170.6 (C38); 164.9 (C10); 155.7 (C42); 149.6 (C8); 146.3 (C9); 137.9 (C5); 137.2 (C6); 129.8−130.1 (C1/4); 129.5 (C20); 129.2 (C22/24); 128.6 (C21/25); 128.3 (C2); 127.9 (C3); 126.8 (C23); 118.5 (C7); 73.1 (C26); 72.5 ($OCH_2CH_2)_n$; 70.4 (C37); 59.7 (C29); 57.9 (C27); 55.5 (biotin); 52.5 (CH_2CH_2CO); 51.9 (C12); 51.5 (C43); 51.0 (C40); 49.5 (C18); 37.5 (C13); 36.1 (C45); 35.8 (C30); 35.5 (C19); 33.1 (C35); 30.9 (C36); 28.8 (C41); 30.7, 26.3, 25.8, 20.6 (C31−34).

SQV−Cys(R.I.CK-Tat9)-PEG3400. Aldrithiol (2,2′-dithiodipyridine, 1.6 mg, 0.007 mmol) was dissolved in 2.0 mL of DMSO, and to this solution was added 12 mg (0.004 mmol) of SQV−Cys-PEG3400 having a free thiol group on cysteine. The reaction was stirred at room temperature. The completion of the reaction was monitored by measuring the absorbance of 2-thiopyridine (TP) release at 343 nm (*27*) until the absorbance value remained constant. Solvent was evaporated under reduced pressure to yield 9.5 mg (79% recovery) of SQV−Cys(TP)-PEG3400 as a white powder. The retro-inverso-cysteine-lysine-Tat nonapeptide (R.I.CK-Tat9), N-acetyl-CKRRRQRRKKR-NH_2 was synthesized manually on a MBHA Rink Amide resin by Fmoc chemistry in the presence of coupling activating reagents, BOP and HOBt. The two additional residues at the N-terminus, Cys and Lys, were reserved for further conjugations. For acetylation, the assembled peptide on the solid support was allowed to react with acetic anhydride in the presence of BOP, HOBt, and 1% DIEA for 6 h. The peptide was cleaved from the support and deprotected by treatment

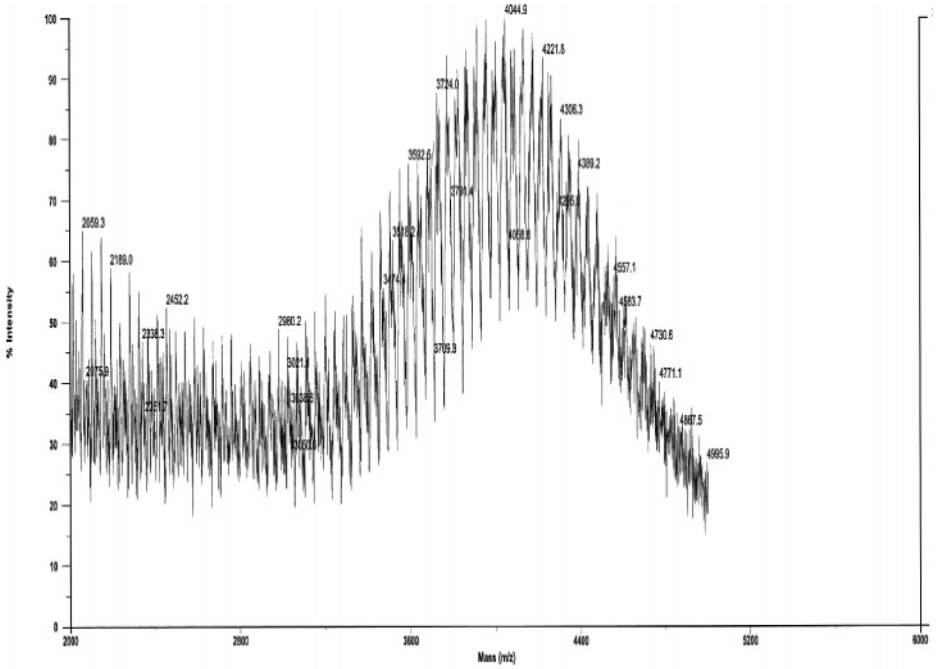


Figure 2. MALDI-TOF (m/z) spectrum of SQV−Cys-PEG3400 showing a polydisperse peak at 4044.9 Da.

with a mixture of 94% TFA, 2.5% water, 2.5% EDT, and 1% TIS for 3 h at room temperature. The crude product was obtained after ether precipitation. The R.I.CK-Tat9 peptide was purified (>95%) by preparative C_{18} reverse-phase high-performance liquid chromatography (RP-HPLC). The fractions obtained after HPLC purification were lyophilized to obtain the dry purified peptide. HPLC: 0.05% TFA (v/v) in water (mobile phase A) and 0.05% TFA (v/v) in a mixture of 10% water, 20% 2-propanol, and 70% acetonitrile (mobile phase B), linear gradient (t = 0 min, 20% B, 80% A; t = 5 min, 20% B, 80% A; t = 35 min, 50% B, 50% A; t = 36 min, 100% B, 0% A, t = 40 min stop), flow rate = 3 mL/min, UV detection = 220 nm, t_R (retention time) = 25 min. ESI-MS: 1613 $(M + H)^+$, 807.4 $[(M + 2H)/2]^+$, 538.5 $[(M + 3H)/3]^+$. R.I.CK-Tat9 peptide concentration was determined by amino acid analysis. R.I.CK-Tat9 (10.0 mg, 0.006 mmol) was dissolved in 2.0 mL of DMSO, and to this solution was added 10.2 mg (0.003 mmol) of SQV−Cys(TP)-PEG3400. The reaction was stirred to completion at room temperature and monitored at 343 nm to measure TP release. Solvent was evaporated under reduced pressure to yield a white microcrystalline powder. This product was subjected to gel permeation chromatography using a Sephadex LH-20 column in DMF, yielding a single sharp peak (absorbance monitored at 239 nm). The fractions of this peak were combined, and the solvent was removed under reduced pressure to obtain SQV−Cys(R.I.CK-Tat9)-PEG3400 with 65% recovery. Mass spectrometry of the conjugate demonstrated a polydisperse peak at the expected molecular weight [m/z(%) 5447.6 Da] using MALDI-TOF.

SQV−Cys(R. I.CK(Stearate)-Tat9)-PEG3400. The synthesis of R.I.CK(stearate)-Tat9 [*N*-acetyl-CK(ϵ-stearate)RRRQRRKKR] entailed the same procedure as R.I.CK-Tat9 except for attachment of fatty acid, stearic acid was coupled to the side chain of the N-terminal lysine residue. To allow this reaction, this N-terminal lysine residue had the ϵ-Dde protecting group, which was selectively removed from the resin-bound peptide using 2% hydrazine in DMF. Thereafter, 3 equiv of stearic acid were dissolved in DMF with coupling agents HOBt and BOP and reacted with peptide on the solid support for 3 h at room temperature. After cleavage from the MBHA Rink amide resin, the peptide was precipitated in precooled ether. The crude peptide was then subjected to HPLC purification, lyophilized, and determined by amino acid analysis and mass spectrometry. HPLC: 0.05% TFA (v/v) in water (mobile phase A) and 0.05% TFA (v/v) in a mixture of 10% water, 20% 2-propanol, and 70% acetonitrile (mobile phase B), linear gradient (t = 0 min, 50% B, 50% A; t = 5 min, 50% B, 50% A; t = 35 min, 100% B, 0% A; t = 40 min, 100% B, 0% A, t = 41 min stop), flow rate = 3 mL/min, UV detection = 220 nm, t_R (retention time) = 32 min. ESI-MS: 1880 $(M + H)^+$, 940.1 $[(M + 2H)/2]^+$, 627.2 $[(M + 3H)/3]^+$. The above process when applied to R.I.CK(stearate)-Tat9 and SQV−Cys(TP)-PEG3400, followed by gel permeation chromatography using Sephadex LH-20 in DMF, yielded SQV−Cys(R.I.CK(stearate)-Tat9)-PEG3400 as a white microcrystalline powder with 68% recovery. Mass spectrometry of this conjugate using MALDI-TOF showed a polydisperse peak at 5716.6 Da (m/z) identical to the expected molecular weight.

Protease Inhibition Assay. An assay developed by Matayoshi and co-workers that is based on intramolecular fluorescence resonance energy transfer (FRET) was adapted and modified (*28*). The assay uses quenched fluorogenic substrates having a peptide sequence derived from a natural processing site for HIV-1 protease (PR). The quenched fluorogenic substrate 1 (obtained from Sigma) was Arg-Glu(EDANS)-Ser-Gln-Asn-Tyr-Pro-Ile-Val-Gly-Lys(DABCYL)-Arg, where EDANS is the fluor and DABCYL the quencher. Recombinant HIV-1 PR was obtained from the NIH AIDS Research and Reference Reagent Program, Division of AIDS, National Institute of Allergy and Infectious Diseases. Incubation of recombinant HIV-1 PR with the fluorogenic substrate at 37 °C results in specific cleavage of a tyrosine-proline bond, causing an increase in fluorescence due to elimination of intramolecular quenching. In the presence of an inhibitor such as SQV, the fluorescence signal is expected to decrease with increasing concentration of inhibitor. Cleavage by the HIV-1 PR occurs at the pseudo-phenylalanine-proline bond in SQV and at the tyrosine-proline bond in substrate 1. Thus, inhibition of HIV-1 PR by SQV in the presence of substrate 1 is observed as a decrease in fluorescence intensity. Therefore, the release of SQV is measured resulting from the hydrolysis of the prodrug SQV−Cys ester. Steady-state fluorescence data were obtained on a Cytofluor Spectrofluorometer (excitation at 340 nm, emission at 490 nm). All data were corrected with blanks. Solutions of HIV-1 PR and substrate 1 were prepared in the HIV-1 protease assay buffer at pH 4.7 using published procedures (*28*). In all of the experiments, the protease was added last to keep the incubation times consistent.

Determination of Hydrolysis Kinetics of SQV−Cys Ester. The fluorogenic protease inhibition assay was used to measure the hydrolysis kinetics of the prodrug, SQV−Cys ester. The chemical stability of the ester was determined in 0.1 N HCl at 37 °C, and the biological stability was determined in PBS at pH 7.4 and in plasma both measured at 37 °C. Initially, different SQV concentrations (0.05−0.5 μM) were taken separately in 0.1 N HCl, in PBS at pH 7.4, and in plasma. Plasma samples (90 μL) were spiked with 10 μL of various concentrations of SQV dissolved in DMSO. For the determination of SQV, plasma samples were deproteinated with 200 μL of ice cold MeOH. The samples were vortexed followed by centrifugation to precipitate the plasma proteins. The clear supernatant was then dried down and reconstituted in protease assay buffer. SQV samples taken in 0.1 N HCl were neutralized with sodium bicarbonate before fluorescence measurements. A fixed amount of substrate 1 (110 μM) and HIV-1 PR (35 nM) were added, and the reaction was carried out for 60 min in the HIV protease assay buffer at pH 4.7 (Figure 3). From the measurement of fluorescence versus SQV concentration, calibration curves were obtained in 0.1 N HCl, in PBS at pH 7.4, and in spiked plasma (Figure 4). Thereafter, the prodrug, SQV−Cys ester (0.15 μM) was incubated separately in 0.1 N HCl, in PBS at pH 7.4, and in spiked plasma at 37 °C, respectively. Aliquots were taken at different time points and measuring the protease inhibitory activity using the fluorogenic assay assessed the release of SQV, resulting from ester bond hydrolysis. Each measurement was done in triplicate. All fluorescence signals were converted to moles of SQV using the calibration curves derived in each medium (Figure 4) to obtain a plot of percentage of released SQV versus incubation time (Figure 5). The rate constant (k) was obtained from the linear plot of $\ln[(SQV)_t - (SQV)_\infty]$ versus incubation time, t (h), where $[SQV]_t$ = concentration of SQV at different incubation times, t, and $[SQV]_\infty$ = concentration of SQV at the last time point, when hydrolysis is complete (Figure 6). The half-life ($t_{1/2}$) for ester hydrolysis was estimated from the relation $t_{1/2} = 0.693/k$ where k is the slope of the linear plot.

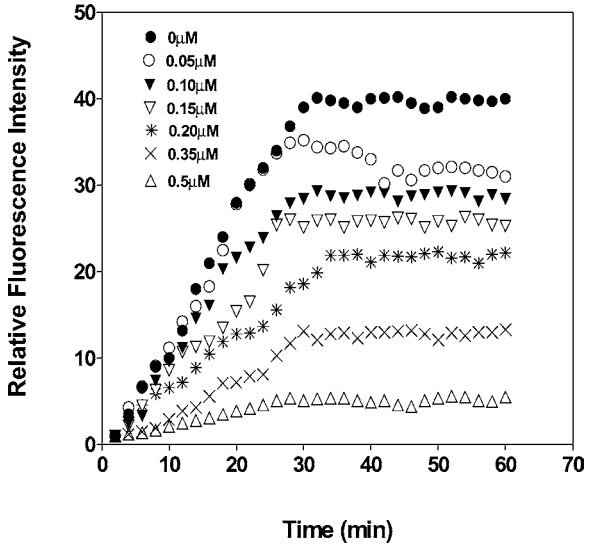


Figure 3. Kinetics of HIV-1 protease (35 nM) cleavage of fluorescence-quenched substrate **1** (110 μM) carried out in the presence of various concentrations of SQV in PBS, pH 7.4 at 37 °C.

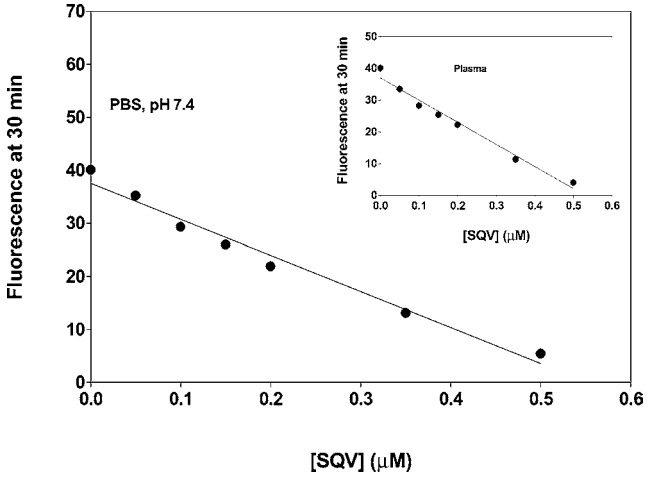


Figure 4. Calibration curve of fluorescence intensity of substrate **1** at 30 min as a function of various concentrations of SQV in PBS, pH 7.4 at 37 °C. Inset. Calibration curve in plasma at 37 °C.

Antiviral Assay. The in vitro antiviral activity of poly(ethylene glycol)(PEG)-based SQV prodrug conjugates was determined using a MTT-based HIV-1 susceptibility assay that was performed using MT-2 cells infected with the HIV-1 strain LAV/LAI (*29*). In this assay, the maximal potential antiviral efficacy was assessed by using unconjugated SQV. SQV remained in the test media for the entire duration of the in vitro test unlike the in vivo situation where SQV is rapidly cleared from cells and the body. Therefore, the in vitro antiviral activity of all conjugates was compared to the maximum achievable effect. The cytotoxicity of the prodrug conjugates was evaluated in parallel to their antiviral activity and was based on the viability of noninfected cells as monitored by the MTT method. The MT-2 cell line is an HTLV-1-transformed human T-cell leukemia cell line isolated from cord blood lymphocytes and cocultured with cells of patients with adult T-cell leukemia. The MT-2 cells were grown in RPMI 1640 DM (Dutch modification) medium, supplemented with 20% FBS, 1% w/v pen−strep, and 1% w/v L-glutamine. The cells were maintained at 37 °C in a humidified atmosphere of 5% CO_2 in air. Every 2−3 days, the growth medium was changed, and

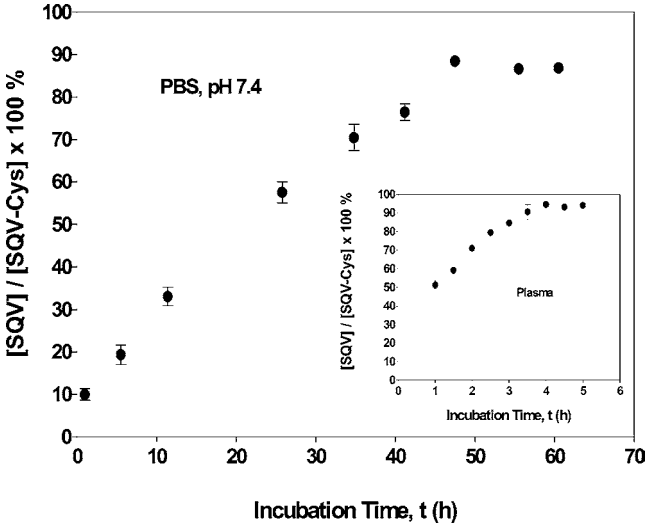


Figure 5. Release of SQV by hydrolysis of the prodrug, SQV−Cys ester (0.15 μM) in PBS, pH 7.4, at 37 °C, using protease assay. Inhibition of protease by released SQV was determined at 37 °C. The ester was hydrolyzed to release SQV as monitored by steady-state fluorescence. The fluorescence measured due to the released SQV was converted to moles of SQV using the calibration curves from Figure 4. All measurements were done in triplicate. Inset. Release of SQV by hydrolysis of SQV−Cys ester (0.15 μM) in plasma at 37 °C.

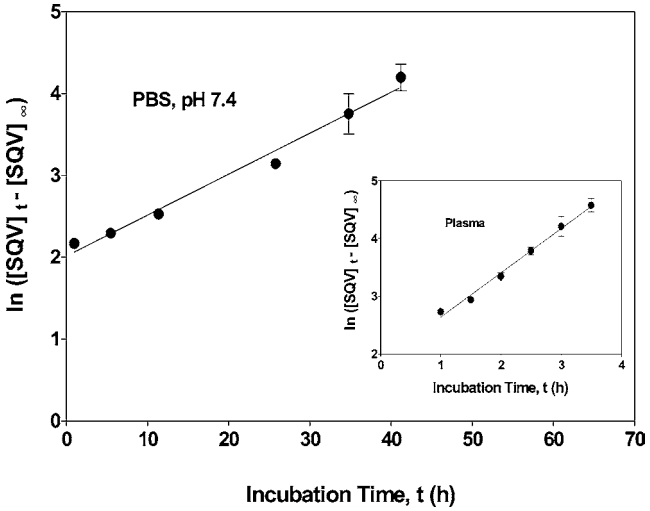


Figure 6. Plot of $\ln[(SQV)_t-(SQV)_\infty]$ (derived from Figure 5) versus incubation time (t) of SQV−Cys ester in PBS, pH 7.4 at 37 °C. The rate constant (k) is the slope of this linear plot. The half-life ($t_{1/2}$) for the ester hydrolysis was calculated using the relation $t_{1/2} = 0.693/k$. Inset**.** Plot of $\ln[(SQV)_t - (SQV)_\infty]$ versus incubation time (t) of SQV−Cys ester in plasma at 37 °C.

the cells were diluted to 2×10^5 cells/mL and recultured. The cultured MT-2 cells were infected using a multiplicity of infection (MOI) of 0.01 (1 viral particle per 100 cells) causing the death of 90% of the cells 5 days later. The tested prodrug conjugates were diluted with RPMI 1640 medium and were added to the cultured MT-2 cells after viral infection. Dosage of each prodrug conjugate was given in terms of SQV concentration, and this was determined by absorbance of prodrug conjugate at 239 nm (λ_{max} of SQV) with a calibration standard of SQV. Each prodrug conjugate was tested in triplicate for its antiviral activity. Cell viability was measured by the colorimetric MTT test, which is based on the capacity of living cells to reduce the yellow colored MTT [3-(4,5-dimethylthiazol-2-yl)-2,5-diphenyltetrazolium bromide] to blue formazan by mitochondrial dehydrogenases. The

quantity of formazan produced (absorbance at 540 nm) is directly proportional to the number of living cells. The percentage protection achieved by different concentrations of the tested prodrug conjugate in HIV-1-infected cells after 5 days of incubation at 37 °C was calculated using the formula:

$$[(A_{TC})_{HIV} - (A_{UC})_{HIV}]/[(A_{UC})_{NHIV} - (A_{UC})_{HIV}] \times 100$$

where $(A_{TC})_{HIV}$ is the absorbance measured for treated HIV-1-infected cells, $(A_{UC})_{HIV}$ is the absorbance measured for untreated HIV-1-infected cells, and $(A_{UC})_{NHIV}$ is the absorbance for untreated noninfected cells. The dose achieving 50% protection according to the above formula is defined as the 50% effective dose (ED_{50}). The prodrug conjugate ED_{50} values were determined from the curves of percentage protection versus prodrug conjugate concentration.

For cytotoxicity, the effect of the prodrug conjugates on cell viability was measured in noninfected cells using the colorimetric MTT test after 5 days of incubation at 37 °C with various concentrations of the tested compounds. The percentage cytotoxicity of the tested prodrug conjugates was calculated using the formula:

$$[(A_{TC})_{NHIV}]/[(A_{UC})_{NHIV}] \times 100$$

where $(A_{TC})_{NHIV}$ is the absorbance measured for treated noninfected cells. The dose achieving 50% toxicity is defined as the 50% lethal dose (LD_{50}). The prodrug conjugate LD_{50} values were determined from the curves of the percentage of living cells against prodrug conjugate concentration.

RESULTS

Synthesis of Prodrug Conjugates. A series of SQV prodrug conjugates, SQV−Cys-PEG3400, SQV−Cys-PEG3400-biotin, SQV−Cys(R.I.CK-Tat9)-PEG3400, and SQV−Cys(R.I.CK(stearate)-Tat9)-PEG3400 was prepared and characterized. In all of these prodrug conjugates, the SQV hydroxyl group was covalently linked to a Cys carboxylic acid group by a releasable ester bond. The two other functional groups on Cys were then used for further derivatization. The thiol group of Cys was used to attach R.I.CK-Tat9 and R.I.CK(stearate)-Tat9 via a releasable disulfide bond. The amino group of Cys was used to attach PEG3400 and PEG3400-biotin via a more stable amide bond.

In the synthesis of the SQV prodrug conjugates (Scheme 1), the active hydroxyl function of SQV was esterified with Fmoc-Cys(S-Trt)-COOH using DIPC/DMAP as coupling reagent. SQV−Cys ester was obtained with 82% yield after Fmoc removal with piperidine, followed by TFA-deprotection of the Trt group. The esterification of the hydroxyl of SQV after silica gel purification was unambiguously confirmed by ESI-MS and ^1H and ^{13}C NMR. Different types of prodrug conjugates were synthesized keeping the SQV−Cys ester as the common prodrug element. PEGylation (using Fmoc-PEG3400-NHS and biotin-PEG3400- NHS) of the SQV−Cys ester was carried out using DIEA/DCM with the formation of relatively more stable amide linkages. The PEGylated products (SQV−Cys-PEG3400 and SQV−Cys-PEG3400-biotin) were purified using gel permeation chromatography (Sephadex LH-20 column in DMF, UV 239 nm) (Figure 2) resulting in 70−80% yield. The formation of these products was confirmed by MALDI-TOF (Figure 3) and ^1H and ^{13}C NMR. In the synthesis of SQV−Cys-(R.I.CK-Tat9)-PEG3400 and SQV−Cys(R.I.CK(stearate)-Tat9)-PEG3400, the thiol group of the Cys in SQV−Cys-PEG3400 was first activated with 2,2′-dithiodipyridine in DMSO to give SQV−Cys(TP)-PEG3400. With the addition of R.I.CK-Tat9 or R.I.CK(stearate)-Tat9 to the activated PEGylated form of SQV, TP release (343 nm) was monitored to confirm reaction completion. The formation of the respective SQV−Cys(R.I.CK-Tat9)-PEG3400 and SQV−Cys(R.I.CK(stearate)-Tat9)-PEG3400 having reversible disulfide bonds in 65−68% yield range was confirmed by MALDI-TOF. Finally, significant increases in water solubility of these PEG-based SQV prodrug conjugates were observed relative to unconjugated SQV.

Chemical and Biological Stability of the Prodrug, SQV−Cys, and Release of SQV. The HIV-1 PR inhibition assay was used for measuring the release of active (i.e., free) SQV resulting from the hydrolysis of the prodrug, SQV−Cys ester. This study was important since the level of HIV-1 inhibition by the prodrug conjugates depends on the apparent hydrolysis kinetics of SQV release. Since the SQV−Cys ester was the common intermediate for all of the synthesized prodrug conjugates, the in vitro stability of the prodrug was the initial focus of the investigation. The chemical stability of SQV−Cys in 0.1 N HCl and the biological stability in PBS at pH 7.4 and in spiked plasma were evaluated at 37 °C.

In the absence of SQV, the incubation of fluorogenic substrate 1 with HIV-1 PR produced a 40-fold increase in fluorescence signal in a reaction that was approximately linear for 30 min (Figure 3). However, SQV inhibited this response in a dose-dependent manner at concentrations of 0.05−0.5 μM as shown in Figure 3. The calibration curves of fluorescence versus concentration of SQV in 0.1 N HCl, PBS at pH 7.4, and plasma were linear with a correlation coefficient (R^2) of 0.9834 for 0.1 N HCl, 0.9779 for PBS at pH 7.4, and 0.9787 for plasma (Figure 4). SQV−Cys ester (0.15 μM) itself did not inhibit fluorescence, suggesting that the SQV prodrug was inactive. The inhibition of fluorescence signal increased with time of hydrolysis of SQV−Cys ester. Therefore, prodrug reconversion is necessary in order for SQV to exert protease inhibition. At the latest time point (31 h in the case of 0.1 N HCl, 47.5 h for PBS at pH 7.4, and 4 h in plasma) there was about a 90% inhibition of enzyme activity by free SQV (Figure 5). Since this level of inhibition is about the same as that produced by 0.15 μM parent drug (Figure 3), the reconversion to active drug was deemed essentially complete. Plots of $\ln[(SQV)_t - SQV)_\infty]$ versus incubation time, t(h), were linear within the concentration range studied with correlation coefficients (R^2) of 0.9939 (for 0.1 N HCl), 0.9834 (for PBS at pH 7.4), and 0.9916 (for plasma), indicating that the hydrolysis is a first-order process with respect to the prodrug (Figure 6). The half-lives of hydrolysis ($t_{1/2}$) obtained from each of the media were calculated from these linear plots. The prodrug reconversion half-lives in 0.1 N HCl, in phosphate-buffered saline (PBS) at pH 7.4, and in spiked plasma at 37 °C were 9, 14, and 0.9 h, respectively. These studies demonstrate that SQV prodrug conjugates with their in-built SQV−Cys ester are inactive until the bond between SQV and cysteine is cleaved.

Biological Activity of Prodrug Conjugates. The HIV-1 inhibition levels and cytotoxicities of PEG-based SQV prodrug conjugates were evaluated against HIV-1 in vitro in MT-2 cells according to an established antiviral assay (*29*). Since the active hydroxyl group of SQV is responsible for its protease inhibitory potency, it is essential that this functional group is free and accessible

Table 1. Anti-HIV-1 Activity (ED_{50}) and Cytotoxicity (LD_{50}) Data for SQV and Its Prodrugs[a] in MT-2 Cells Infected with HIV-1 Strain LAV/LAI (MOI of 0.01)[b]

compound	ED_{50} (μM)	R[c]	LD_{50} (μM)	therapeutic index LD_{50}/ED_{50}
SQV ($MeSO_3H$)	0.015	–	25	1667
SQV−Cys-PEG3400	0.90	60	45	50
SQV−Cys-PEG3400-biotin	0.125	8.3	15	120
SQV−Cys(R.I.CK−Tat9)-PEG3400	0.015	1	12.5	833
SQV−Cys(R.I.CK(stearate)-Tat9)-PEG3400	0.062	4.1	6.3	102

[a] These data reflect the amount of parent drug that was released during the 5 day incubation at 37 °C. [b] Several assays of each compound were done with variations in the virus stock, dosage, and days of incubation. [c] R is the ED_{50} ratio of the prodrug to that of its parent drug, as previously described (*10*).

for antiviral activity. Thus, the level of HIV-1 inhibition of the prodrug conjugates would depend on their hydrolysis kinetics, which in turn reflects the release rate of the active parent drug, SQV. The antiviral activity of the SQV prodrug conjugates was determined by incubating HIV-1-infected MT-2 cells in the presence of different concentrations of prodrug conjugates for 5 days at 37 °C (Table 1). On the basis of the hydrolysis half-lives of the prodrug, SQV−Cys ester, and the antiviral activity results of the prodrug conjugates, it appears that most of the SQV was released during the 5-day incubation period. The appended putative cell uptake promoting groups (PEG3400, PEG3400-biotin, R.I.CK-Tat9, and R.I.CK(stearate)-Tat9) might have influenced the hydrolysis half-lives and/or cell uptake of the prodrug conjugates as measured by differences in antiviral activity (Table 1). The activity of SQV in prodrug conjugates compared to the maximal achievable antiviral efficacy (control, ED_{50} = 15 nM) was reduced (ED_{50} = 900 nM) for PEG alone, but restored with the addition of biotin (ED_{50} = 125 nM), R.I.CK-Tat9 (ED_{50} = 15 nM), or R.I.CK-(stearate)-Tat9 (ED_{50} = 62 nM). Similar results were obtained during repeated assays of each compound with variations in the virus stock, dosage, and days of incubation. The cytotoxicities of the SQV prodrug conjugates were measured by incubating noninfected MT-2 cells in the presence of different concentrations of prodrug conjugates for 5 days at 37 °C. The cytotoxicity (LD_{50}) of all the tested conjugates was in the low micromolar range (6.3−45 μM). Results also show that all the SQV-based prodrug conjugates were less toxic than free SQV. The ratio of LD_{50}/ED_{50} was used as an indicator of the in vitro therapeutic index and is shown in Table 1.

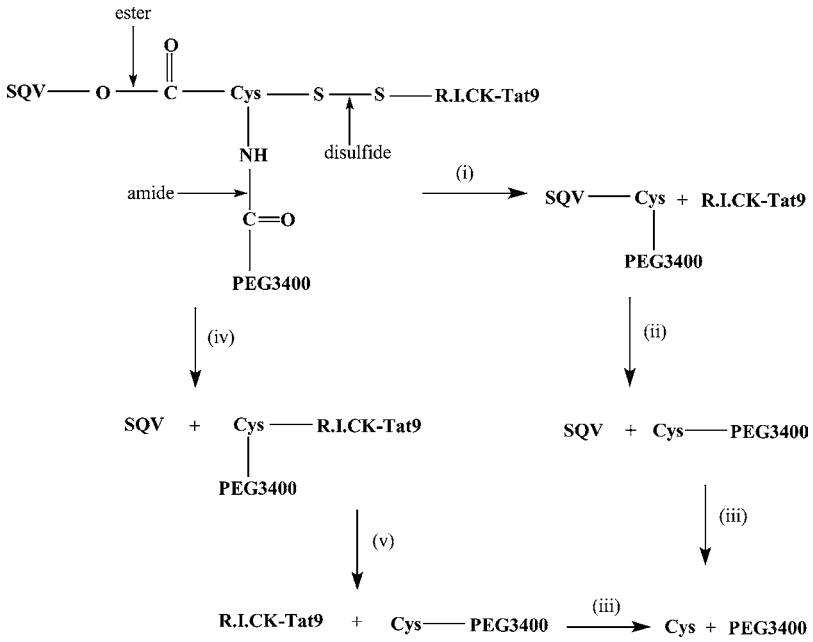
DISCUSSION

HIV-1 protease inhibitors are "peptoids" or "peptidomimetics" that bind and block the active site of the viral proteinase enzyme, thereby inhibiting maturation of the virus. HAART (highly active anti-retroviral therapy) regimens that utilize inhibitors of HIV-1-encoded protease combined with reverse transcriptase inhibitors result in a profound and sustained suppression of viral replication, reduce morbidity, and prolong life in patients with HIV-1 infection (*30*−*32*). Current guidelines recommend that initial treatment of all HIV-1-infected patients include the administration of an HIV-1-protease inhibitor (*33*). However, despite attaining nondetectable viral blood levels, the development of resistance and the inability to ultimately cure HIV-1 infection has raised considerable debate about evaluating treatment efficacy (*34*) and which drugs should be used in optimal combination therapy. The control of HIV-1 infection and the ultimate cure of AIDS will require the development of not only new and more potent therapeutic agents but also of novel pharmacodelivery strategies. The current report represents an initial effort in developing smarter drug delivery strategies to overcome the many biopharmaceutical challenges associated with anti-HIV-1 therapeutic regimens.

In the current study, macromolecular prodrug conjugates have been designed and evaluated. Classical prodrugs are typically designed to overcome problems with solubility, stability, or limited absorption. Some prodrugs of anti-HIV-1 agents have been reported in the literature (*10, 11, 13, 35*). However, these previous efforts have focused on improving absorption by improving the physicochemical properties of these drugs. The current work focuses on a prodrug conjugate approach that attempts to control the kinetics of release and cellular concentrations of SQV at the target sites and protects the "cargo" (i.e., SQV) until it reaches the site of action where it can be released. As a first step toward improving the cellular bioavailability and efficacy of SQV, various prototype prodrug conjuates were designed, based on their known pharmacological properties. PEG-based prodrug conjugates composed of the putative cell uptake enhancing agents, biotin, R.I.CK-Tat9, and R.I.CK(stearate)-Tat9 were synthesized (Scheme 1), characterized. and studied in order to test the hypothesis that improved delivery would result in an enhancement in the pharmacological properties of SQV.

The various components of the conjugates were carefully selected. The rationale for this selection and the results obtained for each conjugate component will be discussed separately. (1) PEG was chosen as a scaffold based on its ability to promote an extended half-life in blood or extracellular fluid and to increase the solubility of SQV (*14, 15*). PEG conjugates are less toxic than free drug (*16*) and have also been found to prevent in vivo binding to plasma proteins, as well as inactivation and rapid elimination from the blood (*36*). The conjugation of PEG to SQV yielded a less active prodrug conjugate, SQV−Cys-PEG3400 (Table 1). In this conjugate, PEG is stably bound to Cys by an amide bond, while the carboxylic acid group of Cys has a reversible ester bond with SQV. The 60-fold lower activity of the conjugate compared to the parent drug could be due to the slow cleavage of the ester bond and/or cell uptake of the conjugate. (2) Biotin was incorporated into the conjugate to enhance the uptake of the conjugates into cells (*17, 18*) since the hydrophobicity of biotin is known to promote cell membrane adhesion and enhanced cellular penetration (*37, 38*). Indeed, about 8-fold greater antiviral activity was observed when biotin was appended to the distal end of the long PEG chain (Table 1). This phenomenon has been observed in other systems as well. For example, the biotinylated form of Tat protein shows better cell uptake and transactivating activity presumably due to increased hydrophobic interactions with the plasma membrane (*39*). We also observed this with a prodrug conjugate of the anticancer drug, camptothecin (CPT), in which an ester bond with the carboxylic acid group of glycine (Gly) has to be cleaved to generate the

Scheme 2. Possible Metabolic Pathways Shown for SQV−Cys(R.I.CK-Tat9)-PEG3400[a]



[a] If the disulfide bond is cleaved first (i), then the product is still an inactive prodrug, which can be further cleaved at the ester bond (ii) to form the active drug, SQV. The remainder of the conjugate might be degraded (iii). Alternatively, if the ester bond is cleaved first, active drug SQV is released (iv). The remainder of the conjugate might be degraded (v). Released Tat might also contribute to antiviral activity (see Discussion).

parent drug (*17*). In that study, the Gly-PEG conjugate of CPT was about 12-fold more potent than CPT alone. However, an additional biotin group appended to the distal end of PEG, CPT-Gly-PEG3400-biotin, gave a further increase in potency of 5-fold, similar to the effect of biotin in the present study (Table 1). (3) R.I.CK-Tat9 was chosen for two reasons. First, it possesses anti-HIV-1 activity and may be useful in combination therapy. Tat analogues have been shown to exert an inhibitory effect by interacting with HIV-1 RNA (*22, 23*) or by binding to the $CXCR_4$ receptor on $CD4^+$ cells (*24, 25*). Second, polycationic peptides such as Tat9 have been reported to facilitate membrane penetration (*19, 20*). The R.I.CK (retro-inverso-cysteine-lysine)-Tat9 consisted of D-amino acids assembled in the reverse order of the natural L-amino acid Tat9 peptide, *N*-acetyl-L-Arg-L-Lys-L-Lys-L-Arg-L-Arg-L-Gln-L-Arg-L-Arg-L-Arg-NH_2. Thus, R.I.CK-Tat9 represents the sequence of all D-amino acids: *N*-acetyl-D-Cys-D-Lys-D-Arg-D-Arg-D-Arg-D-Gln-D-Arg-D-Arg-D-Lys-D-Lys-D-Arg-NH_2. R.I. peptides have similar shapes and charge distributions to the natural L-amino acid peptides but are more stable to proteases and retain pharmacological activity (*40*). The attachment of the Tat peptide by a reversible disulfide linkage to the Cys residue returns the prodrug conjugate to the full antiviral activity of the parent drug, SQV (Table 1). The prodrug conjugate containing Tat peptide could have an even greater interaction with the plasma membrane due to the eight basic amino acids, including five arginines, which could interact with the phosphate headgroups of the lipid bilayer. Thus, immobilization of the conjugate to the plasma membrane might then increase cell uptake, although other factors such as the effect of Tat peptide on hydrolysis rate may be involved in the antiviral activity. Furthermore, the Tat peptide and similar cationic peptides (*23, 25*) also participate in a relatively strong interaction with the chemokine receptor, CXCR4 on T-cells, which is inhibitory to HIV-1 infection (*24, 25*). As a result, SQV−Cys(R.I.CK-Tat9)-PEG3400 might possess two different antiviral activities that are additive in function (Table 1). Further studies will have to be performed to determine the exact mechanism of enhancement. (4) Tat-like peptides appended to fatty acids such as stearic acid have been reported to possess a greater penetrating ability for DNA delivery into cells (*21*). In the present work, the stearate group was initially appended to the Tat peptide in order to combine the hydrophobic and cationic properties and thereby achieve even greater membrane affinity. Instead, the stearate adduct had less activity (Table 1). This could be due to an inhibitory effect on the binding of Tat peptide to the chemokine receptor. Improvements in the ability of cationic peptides to augment drug uptake continue to be published (*41*). (5) The various conjugate components are linked to the scaffold by bonds that control the site and rate of release of the components and SQV from the conjugate. This is an important consideration for improving the delivery properties of SQV since it was previously demonstrated that SQV conjugates with a stable carbamate bond between the hydroxyl group of SQV and an amino group of an amino acid linker did not possess anti-HIV-1 activity (*13*). In contrast, a less stable ester bond with cysteine was used for the conjugates prepared for the current study resulting in releasable SQV conjugates. One mechanism of control utilized in the current studies was a labile ester bond present in the SQV−Cys ester that can be hydrolyzed by cellular esterases to regenerate the parent antiviral drug. Similar ester prodrugs of SQV have been reported (*10, 11, 13, 42*). The in vivo stability of ester bonds in conjugates with other drugs was previously reported by Greenwald and co-workers (*14, 43−45*). Using the fluorescence-based HIV-1 PR inhibition assay, the in vitro release of SQV was assessed (Figures 5, 6). The labile disulfide linkage used for conjugating R.I.CK-Tat9 compounds to SQV−Cys-PEG3400 can be cleaved by glutathione, a physiologically relevant reducing agent. This linkage might be especially useful for drug delivery into cells, due to the stronger reducing environment within cells than in extracellular fluids (*46*). Thus, a disulfide-linked conjugate is expected to be

relatively stable in extracellular fluids or plasma but should be cleaved once inside cells. Previously, disulfide linkages have been successfully used by our group to link PEG-based polymers to a cysteine-containing peptide (*46*). However, cleavage of the disulfide bond is not sufficient to regenerate free SQV. Instead, an inactive prodrug, SQV−Cys-PEG3400, as well as free R.I.CK-Tat9 (or R.I.CK(stearate)-Tat9) are released (Scheme 2). For this particular situation, two consecutive release steps (i.e., cleavage of the disulfide bond followed later by ester bond cleavage) would be valuable since esterases are ubiquitous, and SQV release would occur readily in the blood stream. Hence, these prodrug conjugates would be no more effective than traditional prodrugs. However, the relative stability of the disulfide bond must be designed to protect the ester bond by stearic hindrance or by electron-donating effect and thereby ensure that SQV release would occur preferentially inside cells. A rapid release of SQV inside cells might result in cellular concentrations that are higher than the secretory K_m for transporters such as P-gp and MRP2, resulting in prolonged and more effective cellular drug concentrations.

The HIV-1 MTT assay was used to determine the maximal achievable antiviral activity of free SQV and to determine if all SQV was released from the conjugates in vitro. While the MTT assay format is good for assessing if the conjugates release active SQV, the assay does not yield other mechanistic information that might further suggest differences in the in vivo performance between the various conjugate forms or in comparison to free SQV. The reasons for the limitations relate to the closed nature of the test system and the 5-day time frame of the study. Released SQV is available for the entire 5 days of the assay. For the case of the control, free SQV is present during the entire study, and this therefore represents the maximal achievable antiviral activity. This limitation is not uncommon and was recently demonstrated for PEGylated α-interferon. PEGylated α-interferon is an example of a clinically useful drug conjugate for which an improvement in therapeutic value was not revealed by an in vitro assay (*47*). In that study, the receptor affinity and the specific activity of the PEGylated interferon were substantially lower (about 7%), but the half-life was increased almost 10-fold in vivo after subcutaneous injection. This would lead to a substantial increase in the "area under the curve" (i.e., blood level amounts), and, instead of injecting the patient 3 times each week, the PEGylated protein may be administered weekly, giving nearly constant drug levels (*48*). Furthermore, comparison of the two forms of interferon in a clinical trial of chronic hepatitis C (*49*) demonstrated greater efficacy with PEGylated interferon α-2a. While these examples further point out limitations in the in vitro assay, the assay is a reliable indicator of SQV activity and release. However in vivo studies are needed in order to evaluate delivery system performance and possible in vivo effectiveness.

SUMMARY AND CONCLUSIONS

The current results suggest that SQV bioconjugates can be synthesized and active SQV can be released. This is critical since conjugated SQV is inactive. The in vitro anti-HIV-1 activity of all conjugates was evaluated against an unconjugated SQV control where the drug was 100% available during the entire anti-HIV-1 test. This rigorous test is unlike an in vivo situation where SQV is quickly cleared from target cells and the body; however, it gave an indication of the expected maximum therapeutic potential of SQV in this in vitro system. Appending various putative cell uptake enhancing moieties to the SQV conjugates produced variable effects on anti-HIV-1 activity, and in vitro activity was fully restored compared to nonconjugated SQV with one conjugate. Since conjugated SQV is inactive, the current results suggest that the appended moieties may be significantly modifying the release of SQV from the conjugate. Also, further work is required to ascertain the specific mechanism of enhancement for the Tat-based conjugate since Tat also possesses anti-HIV-1 activity. In conclusion, SQV conjugates were successfully synthesized and chemically characterized. They also show promise since anti-HIV-1 activity is not lost in vitro. However, the major benefits of conjugation are expected to be observed in vivo, and this is the focus of the next set of studies.

ACKNOWLEDGMENT

This work was supported by NIH Grants AI 33789 and 51214. The following reagent was obtained through the NIH AIDS Research and Reference Reagent Program, Division of AIDS, NIAID, NIH: HIV-1HXB2 KIIA Protease, cat. no. 4375 from Drs. David Davis, Stephen Stahl, Paul Wingfield, and Joshua Kaufmann. We acknowledge Dr. Hsin-Ching Lin for assistance in establishment of the HIV assays.

LITERATURE CITED

(1) Aungst, B. J. (1999) P-Glycoprotein, Secretory Transport, and Other Barriers to the Oral Delivery of Anti-HIV Drugs. *Adv. Drug Delivery Rev. 39,* 105−116.

(2) Sinko, P. J., Kunta, J. R., Usansky, H. H., and Perry, B. A. (2004) Differentiation of Gut and Hepatic First Pass Metabolism and Secretion of Saquinavir in Ported Rabbits. *J. Pharmacol. Exp. Ther. 310,* 359−366.

(3) Chun, T. W., Stuyver, L., Mizell, S. B., Ehler, L. A., Mican, J. A., Baseler, M., Lloyd, A. L., Nowak, M. A., and Fauci, A. S. (1997) Presence of an Inducible HIV-1 Latent Reservoir During Highly Active Antiretroviral Therapy. *Proc. Natl. Acad. Sci. U. S. A 94,* 13193−13197.

(4) Flexner, C. (1998) HIV−Protease Inhibitors. *N. Engl. J. Med. 338,* 1281−1292.

(5) Pialoux, G., Fournier, S., Moulignier, A., Poveda, J. D., Clavel, F., and Dupont, B. (1997) Central Nervous System As a Sanctuary for HIV-1 Infection Despite Treatment With Zidovudine, Lamivudine and Indinavir. *AIDS 11,* 1302−1303.

(6) Sawchuk, R. J., and Yang, Z. (1999) Investigation of Distribution, Transport and Uptake of Anti-HIV Drugs to the Central Nervous System. *Adv. Drug Delivery Rev. 39,* 5−31.

(7) Su, Y., Zhang, X., and Sinko, P. J. (2004) Human Organic Anion-Transporting Polypeptide OATP-A (SLC21A3) Acts in Concert With P-Glycoprotein and Multidrug Resistance Protein 2 in the Vectorial Transport of Saquinavir in Hep G2 Cells. *Mol. Pharm. 1,* 49−56.

(8) Williams, G. C., Liu, A., Knipp, G., and Sinko, P. J. (2002) Direct Evidence That Saquinavir Is Transported by Multidrug Resistance-Associated Protein (MRP1) and Canalicular Multispecific Organic Anion Transporter (MRP2). *Antimicrob. Agents Chemother. 46,* 3456−3462.

(9) Jones, K., Bray, P. G., Khoo, S. H., Davey, R. A., Meaden, E. R., Ward, S. A., and Back, D. J. (2001) P-Glycoprotein and Transporter MRP1 Reduce HIV Protease Inhibitor Uptake in CD4 Cells: Potential for Accelerated Viral Drug Resistance? *AIDS 15,* 1353−1358.

(10) Farese-Di Giorgio, A., Rouquayrol, M., Greiner, J., Aubertin, A. M., Vierling, P., and Guedj, R. (2000) Synthesis and Anti-HIV Activity of Prodrugs Derived From Saquinavir and Indinavir. *Antivir. Chem. Chemother. 11,* 97−110.

(11) Rouquayrol, M., Gaucher, B., Greiner, J., Aubertin, A. M., Vierling, P., and Guedj, R. (2001) Synthesis and Anti-HIV Activity of Glucose-Containing Prodrugs Derived From Saquinavir, Indinavir and Nelfinavir. *Carbohydr. Res. 336,* 161−180.

(12) Rouquayrol, M., Gaucher, B., Roche, D., Greiner, J., and Vierling, P. (2002) Transepithelial Transport of Prodrugs of the HIV Protease Inhibitors Saquinavir, Indinavir, and Nelfinavir Across Caco-2 Cell Monolayers. *Pharm. Res. 19,* 1704−1712.

(13) Gaucher, B., Rouquayrol, M., Roche, D., Greiner, J., Aubertin, A. M., and Vierling, P. (2004) Prodrugs of HIV Protease Inhibitors-Saquinavir, Indinavir and Nelfinavir-Derived From Diglycerides or Amino Acids: Synthesis, Stability and Anti-HIV Activity. *Org. Biomol. Chem. 2,* 345−357.

(14) Conover, C. D., Pendri, A., Lee, C., Gilbert, C. W., Shum, K. L., and Greenwald, R. B. (1997) Camptothecin Delivery Systems: the Antitumor Activity of a Camptothecin-20−0-Polyethylene Glycol Ester Transport Form. *Anticancer Res. 17,* 3361−3368.

(15) Davis, S., Abuchowski, A., Park, Y. K., and Davis, F. F. (1981) Alteration of the Circulating Life and Antigenic Properties of Bovine Adenosine Deaminase in Mice by Attachment of Polyethylene Glycol. *Clin. Exp. Immunol. 46,* 649−652.

(16) Greenwald, R. B., Choe, Y. H., McGuire, J., and Conover, C. D. (2003) Effective Drug Delivery by PEGylated Drug Conjugates. *Adv. Drug Delivery Rev. 55,* 217−250.

(17) Minko, T., Paranjpe, P. V., Qiu, B., Lalloo, A., Won, R., Stein, S., and Sinko, P. J. (2002) Enhancing the Anticancer Efficacy of Camptothecin Using Biotinylated Poly(Ethylene Glycol) Conjugates in Sensitive and Multidrug-Resistant Human Ovarian Carcinoma Cells. *Cancer Chemother. Pharmacol. 50,* 143−150.

(18) Ramanathan, S., Qiu, B., Pooyan, S., Zhang, G., Stein, S., Leibowitz, M. J., and Sinko, P. J. (2001) Targeted PEG-Based Bioconjugates Enhance the Cellular Uptake and Transport of a HIV-1 TAT Nonapeptide. *J. Controlled Release 77,* 199−212.

(19) Nori, A., Jensen, K. D., Tijerina, M., Kopeckova, P., and Kopecek, J. (2003) Tat-Conjugated Synthetic Macromolecules Facilitate Cytoplasmic Drug Delivery to Human Ovarian Carcinoma Cells. *Bioconjugate Chem. 14,* 44−50.

(20) Zhang, X., Wan, L., Pooyan, S., Su, Y., Gardner, C. R., Leibowitz, M. J., Stein, S., and Sinko, P. J. (2004) Quantitative Assessment of the Cell Penetrating Properties of RI-Tat-9: Evidence for a Cell Type-Specific Barrier at the Plasma Membrane of Epithelial Cells. *Mol. Pharm. 1,* 145−155.

(21) Futaki, S., Ohashi, W., Suzuki, T., Niwa, M., Tanaka, S., Ueda, K., Harashima, H., and Sugiura, Y. (2001) Stearylated Arginine-Rich Peptides: a New Class of Transfection Systems. *Bioconjugate Chem. 12,* 1005−1011.

(22) Choudhury, I., Wang, J., Rabson, A. B., Stein, S., Pooyan, S., Stein, S., and Leibowitz, M. J. (1998) Inhibition of HIV-1 Replication by a Tat RNA-Binding Domain Peptide Analog. *J. Acquir. Immune. Defic. Syndr. Hum. Retrovirol. 17,* 104−111.

(23) Choudhury, I., Wang, J., Stein, S., Rabson, A., and Leibowitz, M. J. (1999) Translational Effects of Peptide Antagonists of Tat Protein of Human Immunodeficiency Virus Type 1. *J. Gen. Virol. 80,* 777−782.

(24) Montefiori, D. C., Collman, R. G., Fouts, T. R., Zhou, J. Y., Bilska, M., Hoxie, J. A., Moore, J. P., and Bolognesi, D. P. (1998) Evidence That Antibody-Mediated Neutralization of Human Immunodeficiency Virus Type 1 by Sera From Infected Individuals Is Independent of Coreceptor Usage. *J. Virol. 72,* 1886−1893.

(25) Scarlatti, G., Tresoldi, E., Bjorndal, A., Fredriksson, R., Colognesi, C., Deng, H. K., Malnati, M. S., Plebani, A., Siccardi, A. G., Littman, D. R., Fenyo, E. M., and Lusso, P. (1997) In Vivo Evolution of HIV-1 Co−Receptor Usage and Sensitivity to Chemokine-Mediated Suppression. *Nat. Med. 3,* 1259−1265.

(26) Ucpinar, S. D., and Stavchansky, S. (2003) Quantitative Determination of Saquinavir From Caco-2 Cell Monolayers by HPLC−UV. High Performance Liquid Chromatography. *Biomed. Chromatogr. 17,* 21−25.

(27) Riener, C. K., Kada, G., and Gruber, H. J. (2002) Quick Measurement of Protein Sulfhydryls With Ellman's Reagent and With 4,4′-Dithiodipyridine. *Anal. Bioanal. Chem. 373,* 266−276.

(28) Matayoshi, E. D., Wang, G. T., Krafft, G. A., and Erickson, J. (1990) Novel Fluorogenic Substrates for Assaying Retroviral Proteases by Resonance Energy Transfer. *Science 247,* 954−958.

(29) Pauwels, R., Balzarini, J., Baba, M., Snoeck, R., Schols, D., Herdewijn, P., Desmyter, J., and De Clercq, E. (1988) Rapid and Automated Tetrazolium-Based Colorimetric Assay for the Detection of Anti-HIV Compounds. *J. Virol. Methods 20,* 309−321.

(30) Cameron, D. W., Heath-Chiozzi, M., Kravcik, S., Mills, R., Potthoff, A., and Henry. D. (1996) Prolongation of Life and Prevention of AIDS Complications in Advanced HIV Immunodeficiency With Ritonavir: Update, in *Volume 1 of Program and Abstracts of the 11th International Conference on AIDS,* Vancouver, B.C., July 7−12, 24−25*,* abstract*.* 24−25.

(31) Hammer, S. M., Squires, K. E., Hughes, M. D., Grimes, J. M., Demeter, L. M., Currier, J. S., Eron, J. J. Jr., Feinberg, J. E., Balfour, H. H. Jr., Deyton, L. R., Chodakewitz, J. A., and Fischl, M. A. (1997) A Controlled Trial of Two Nucleoside Analogues Plus Indinavir in Persons With Human Immunodeficiency Virus Infection and CD4 Cell Counts of 200 Per Cubic Millimeter or Less. AIDS Clinical Trials Group 320 Study Team. *N. Engl. J. Med. 337,* 725−733.

(32) Salgo, M. P., Beattie, D., Bragman, K., Donatacci, L., Jones, M., and Montgomery, L. (1996) Saquinavir (Invirase) Vs. HIVID (Zalcitabine) Vs. Combination As Treatment for Advanced HIV Infection in Patients Discontinuing/Unable to Take Retrovir (Zidovudine). In *Volume 1 of Program and Abstracts of the 11th International Conference on AIDS,* Vancouver, B.C., July 7−12, 24. abstract 24.

(33) Carpenter, C. C., Fischl, M. A., Hammer, S. M., Hirsch, M. S., Jacobsen, D. M., Katzenstein, D. A., Montaner, J. S., Richman, D. D., Saag, M. S., Schooley, R. T., Thompson, M. A., Vella, S., Yeni, P. G., and Volberding, P. A. (1997) Antiretroviral Therapy for HIV Infection in 1997. Updated Recommendations of the International AIDS Society-USA Panel. *JAMA 277,* 1962−1969.

(34) Thiebaut, R., Chene, G., Jacqmin-Gadda, H., Morlat, P., Mercie, P., Dupon, M., Neau, D., Ramaroson, H., Dabis, F., and Salamon, R. (2003) Time-Updated CD4+ T Lymphocyte Count and HIV RNA As Major Markers of Disease Progression in Naive HIV-1-Infected Patients Treated With a Highly Active Antiretroviral Therapy: the Aquitaine Cohort, 1996−2001. *J. Acquir. Immune. Defic. Syndr. 33,* 380−386.

(35) Vierling, P., and Greiner, J. (2003) Prodrugs of HIV Protease Inhibitors. *Curr. Pharm. Des. 9,* 1755−1770.

(36) Foroutan, S. M., and Watson, D. G. (1997) Synthesis and Characterisation of Polyethylene Glycol Conjugates of Hydrocortisone As Potential Prodrugs for Ocular Steroid Delivery. *Int. J. Pharm. 157,* 103−111.

(37) Israelachvili, J. (1997) The Different Faces of Poly(Ethylene Glycol). *Proc. Natl. Acad. Sci. U. S. A 94,* 8378−8379.

(38) Rassoulzadegan, M., Binetruy, B., and Cuzin, F. (1982) High Frequency of Gene Transfer After Fusion Between Bacteria and Eukaryotic Cells. *Nature 295,* 257−259.

(39) Frankel, A. D., and Pabo, C. O. (1988) Cellular Uptake of the Tat Protein From Human Immunodeficiency Virus. *Cell 55,* 1189−1193.

(40) Fromme, B., Eftekhari, P., Van Regenmortel, M., Hoebeke, J., Katz, A., and Millar, R. (2003) A Novel Retro-Inverso Gonadotropin-Releasing Hormone (GnRH) Immunogen Elicits Antibodies That Neutralize the Activity of Native GnRH. *Endocrinology 144,* 3262−3269.

(41) Siprashvili, Z., Scholl, F. A., Oliver, S. F., Adams, A., Contag, C. H., Wender, P. A., and Khavari, P. A. (2003) Gene Transfer Via Reversible Plasmid Condensation With Cysteine-Flanked, Internally Spaced Arginine-Rich Peptides. *Hum. Gene Ther. 14,* 1225−1233.

(42) Bold, G., Faessler, A., and Lang, M. (1994) Preparation of Antiretroviral Amino Acid Derivatives. Eur. Pat. Appl. 594540*, Chem. Abstr. 121,* 231363.

(43) Greenwald, R. B., Gilbert, C. W., Pendri, A., Conover, C. D., Xia, J., and Martinez, A. (1996) Drug Delivery Systems: Water Soluble Taxol 2′-Poly(Ethylene Glycol) Ester Prodrugs-Design and in Vivo Effectiveness. *J. Med. Chem. 39,* 424−431.

(44) Lee, S., Greenwald, R. B., McGuire, J., Yang, K., and Shi, C. (2001) Drug Delivery Systems Employing 1,6-Elimination: Releasable Poly(ethylene glycol) Conjugates of Proteins. *Bioconjugate Chem. 12,* 163−169.

(45) Greenwald, R. B., Pendri, A., Conover, C. D., Lee, C., Choe, Y. H., Gilbert, C., Martinez, A., Xia, J., Wu, D., and Hsue, M. m. (1998) Camptothecin-20-PEG Ester Transport Forms: the Effect of Spacer Groups on Antitumor Activity. *Bioorg. Med. Chem. 6,* 551−562.

(46) Huang, S. Y., Pooyan, S., Wang, J., Choudhury, I., Leibowitz, M. J., and Stein, S. (1998) A Polyethylene Glycol Copolymer for Carrying and Releasing Multiple Copies of Cysteine-Containing Peptides. *Bioconjugate Chem. 9,* 612−617.

(47) Bailon, P., Palleroni, A., Schaffer, C. A., Spence, C. L., Fung, W. J., Porter, J. E., Ehrlich, G. K., Pan, W., Xu, Z. X., Modi, M. W., Farid, A., Berthold, W., and Graves, M. (2001) Rational Design of a Potent, Long-Lasting Form of Interferon: a 40 KDa Branched Poly(ethylene glycol)-Conjugated Interferon Alpha-2a for the Treatment of Hepatitis C. *Bioconjugate Chem. 12,* 195−202.

(48) Potera, C. (2003) Pegylation for improving polypeptide drugs. *Genet. Eng. News 23*, 58. http://www.genengnews.com.

(49) Zeuzem, S., Feinman, S. V., Rasenack, J., Heathcote, E. J., Lai, M. Y., Gane, E., O'Grady, J., Reichen, J., Diago, M., Lin, A., Hoffman, J., and Brunda, M. J. (2000) Peginterferon Alfa-2a in Patients With Chronic Hepatitis C. *N. Engl. J. Med. 343,* 1666−1672.

BC0498875

Novel NMR Platform for Detecting Gene Transfection: Synthesis and Evaluation of Fluorinated Phenyl β-D-Galactosides with Potential Application for Assessing LacZ Gene Expression†

Jianxin Yu, Pieter Otten, Zhenyi Ma, Weina Cui, Li Liu, and Ralph P. Mason*

Department Radiology, The University of Texas Southwestern Medical Center at Dallas, Dallas, Texas 75390-9058. Received March 12, 2004; Revised Manuscript Received October 1, 2004

Gene therapy holds great promise for the treatment of diverse diseases, but widespread implementation is hindered by difficulties in assessing the success of transfection. The development of noninvasive reporter techniques based on appropriate molecules and imaging modalities may help to assay gene expression. Fluorophenyl-β-D-galactopyranosides provide a novel class of NMR active molecules, which are highly responsive to the action of β-galactosidase (β-gal), the product of the lacZ gene. The reporter molecules are stable in solution and with respect to wild-type cells, but the enzyme causes liberation of the aglycon, a fluorophenol, accompanied by distinct color formation and a ^{19}F NMR chemical shift of 5−10 ppm, depending on pH. Synthetic strategy, experimental methods, and molecular and ^{19}F NMR characteristics are reported for a series of molecules in solution, blood, and tumor cells. This class of molecules presents a new strategy for assaying gene expression with a highly versatile molecular structural platform.

INTRODUCTION

Gene therapy holds great promise for the treatment of diseases including cancer, cystic fibrosis, and immunodeficiency. However, a major hurdle to widespread successful implementation is the need to verify successful transfection, in particular, the spatial distribution of gene expression in the target tissue, together with assays of the longevity of expression. An image-based assay could greatly facilitate optimal gene therapy vector dosing, in a precise temporal and spatial manner.

Two approaches are gaining popularity for reporter genes. One method favors the use of genes producing reporter molecules such as green fluorescent protein, which are directly detectable by physical methods such as fluorescence. The second approach uses genes to produce enzymes, which act upon substrates administered to specifically interrogate gene expression. A critical criterion is that the reporter gene not be normally present or expressed in the cells of interest. The most popular reporter genes today are associated with optical imaging, because this is a cheap modality and is highly sensitive and the results are rapidly available (*1*, *2*). Thus, fluorescent imaging of green fluorescent protein [GFP[1] and longer wavelength variants (*3*)] and bioluminescent imaging (BLI) of luciferase activity on administered D-luciferin (*4*) are popular. These techniques are useful only in superficial tissues and have extensive applications in mice, but application to larger bodies is limited by shallow light penetration.

Several nuclear medicine approaches have been demonstrated by exploiting the action of thymidine kinase on a variety of substrates including iodo- and fluoronucleosides, such as FIAU and gancyclovir, and various radionuclide labels including ^{123}I, ^{124}I, ^{125}I, and ^{18}F (*5*, *6*). For cancer, thymidine kinase has the advantage that not only does the gene serve as a reporter, but the gene products can themselves have therapeutic value. An alternative approach uses the sodium iodine symporter (hNIS), which works well with both iodide and pertechnetate substrates (*7*).

NMR has been applied to cells transfected to express melanin or transferrin resulting in iron accumulation, which produces proton MRI contrast (*8*, *9*). ^{19}F NMR has been used to detect conversion of 5-fluorocytosine to 5-fluorouracil following introduction of cytosine deaminase (*10*).

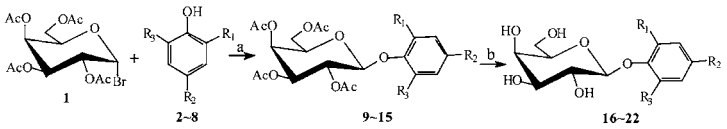
Historically, the bacterial *lac*Z gene, encoding the enzyme β-galactosidase (β-gal, EC 3.2.1.23), has been the most popular reporter gene. The lac operon was the first gene expression system to be well characterized, some 40 years ago by Jacob and Monod (*11*), and it is a recognized tool for the study of problems in cell and molecular biology and the recently emerging fields of genomics and proteomics (*12*). Its induction has become a standard means of assaying clonal insertion and transcriptional activation (*13*). The long-established tests for β-gal based on colorimetric assay of *o*- and *p*-nitrophenyl-β-galactopyranoside hydrolysis to release yellow *o*- or *p*-nitrophenols remain popular (*14*). However, because of the broad substrate specificity of the enzyme, alternate reporter substrates have been proposed (*15*−*19*), and many are commercially available. Fluorogenic galactosides based on fluorescein and resorufin, such as *p*-naphtholbenzein, 1,2-dihydroxyanthraquinone, 4-methylumbeliferone, 5-bromo-4-chloro-3-indoxyl-β-galactopyranoside (X-Gal), and 3,4-cyclohexenoesculetin-β-galactopyranoside (S-Gal) are well established (*16*, *20*−

†Presented in part at the 16th International NMR Spectroscopy Conference, Cambridge, U.K., July 2003.

* Address correspondence to this author at the Department of Radiology, The University of Texas Southwestern Medical Center at Dallas, 5323 Harry Hines Blvd., Dallas, TX 75390-9058 [telephone (214) 648-8926; fax (214) 648-2991; e-mail Ralph.Mason@UTSouthwestern.edu].

[1] Abbreviations: β-gal, β-galactosidase; BLI, bioluminescent imaging; GFP, green fluorescent protein; ONPG, *o*-nitrophenyl-β-galactopyranoside; PFONPG, 4-fluoro-2-nitrophenyl-β-D-galactopyranoside; S-Gal, 3,4-cyclohexenoesculetin-β-galactopyranoside; X-Gal, 5-bromo-4-chloro-3-indoxyl-β-galactopyranoside.

10.1021/bc049936d CCC: $27.50 © 2004 American Chemical Society
Published on Web 10/23/2004



Reaction conditions: (a) CH_2Cl_2-H_2O, pH 8~9, 50 °C, TBAB, ~1 hr, near quantitative yield; (b) NH_3-MeOH, 0 °C→r.t., 24 hr, quantitative yields.

Compounds	R_1	R_2	R_3
2, 9, 16	NO_2	F	H
3, 10, 17	F	NO_2	H
4, 11, 18	F	H	NO_2
5, 12, 19	F	H	H
6, 13, 20	H	F	H
7, 14, 21	Cl	F	H
8, 15, 22	Br	F	H

Figure 1. Reactions and structures of **1**−**22**.

23). The staining methodologies described above are effective for histological specimens and in vitro, but in vivo capabilities would promise new applications to study, and clinically evaluate, gene transfection.

Recently, Louie et al. (*24*) demonstrated an elegant MRI assessment of β-gal activity based on 1-[2-(β-D-galactopyranosyloxy)propyl]-4,7,10-tris(carboxymethyl)-1,4,7,10-tetraazacyclododecane)gadolinium(III) (EgadMe). Access of water to the first coordination sphere of the paramagnetic Gd^{3+} is blocked by a galactopyranose bridge, but β-gal cleaves the bridge, yielding a 20% increase in relaxivity. Whereas EgadMe is a poor substrate for the enzyme (several orders of magnitude less efficient than the colorimetric biochemical agent ONPG) and does not penetrate cells, it facilitated effective investigation of cell lineage following direct intracellular microinjections (*24*). These studies prompted us to consider other NMR active analogues, and it appeared that introduction of a fluorine atom into the popular colorimetric biochemical indicator ONPG could produce a strong candidate molecule. Diverse fluorinated reporter molecules have been successfully applied previously to metabolic and physiological studies (*25*, *26*). ^{19}F-labeled molecules exploit the high NMR visibility of fluorine, the great NMR sensitivity of ^{19}F to the environmental milieu, and the lack of background signal. We recently reported the successful synthesis of a prototype reporter molecule, *p*-fluoro-*o*-nitrophenyl β-D-galactopyranoside (PFONPG; **16**), and demonstrated initial NMR applications (*27*). We have now synthesized and evaluated a series of analogues and provide structural characterization, together with evaluation of their activity in solution and in cell culture, and compare the relative merits of the substrates.

EXPERIMENTAL SECTION

General Methods. NMR spectra were recorded on Varian Inova spectrometers (400 or 600 MHz for ^1H, 100 or 150 MHz for ^{13}C) with $CDCl_3$ (for **9**−**15**) or DMSO-d_6 (for **16**−**22**) as solvents, and ^1H and ^{13}C chemical shifts were referenced to TMS, as internal standard. Compounds were characterized by acquisition of ^1H, ^{13}C, DEPT, ^1H−^1H COSY, or NOESY experiments at 25 °C. ^{19}F NMR (376 MHz) measurements were performed at 25−37 °C in aqueous solution with ^{19}F signals referenced to dilute sodium trifluoroacetate (NaTFA) in a capillary, as an external standard. High-resolution mass spectra were obtained on an ABI Voyager STR MALDI-TOF mass spectrometer in reflector mode (service provided by Dr. Tichy, Department of Chemistry, Texas A&M University).

Reactions requiring anhydrous conditions were performed under nitrogen or argon. Solutions in organic solvents were dried with anhydrous sodium sulfate and concentrated in vacuo below 45 °C. Column chromatography was performed on silica gel (200−300 mesh) with cyclohexane−EtOAc. Analytical TLC (silica gel GF_{254}; Aldrich Chemical Co.) used detection by UV or staining with 5% ethanolic H_2SO_4 at 110 °C for 10 min.

Although many nitrophenol glycosides have been described (*28*, *29*) including nitrophenyl fluorogalactoside (*30*), to our knowledge there have been no published syntheses of the β-D-galactosides **16**−**22**. For the construction of *O*-glycosidic linkages, many strategies are available using anhydrous zinc chloride (for the α anomer) or *p*-toluenesulfonic acid (for the β anomer), but the *p*-nitrophenyl glycosides were usually obtained in low yield (*31*−*33*).

We initially tested the method of Yoon et al. (*30*), which involves the reaction of a potassium salt of an acidic phenol with an α-D-galactopyranosyl bromide. Aryl β-D-galactopyranosides **16** and **17** were prepared by a nucleophilic substitution reaction of a phenolate ion on acetobromo-α-D-galactose **1** followed by saponification of the acetyl groups. We applied two different procedures for generating the phenolate ion, depending on the acidity of the phenol. The brightly colored solid potassium salts of fluoronitrophenols **2** and **3** could be isolated by lyophilizing an aqueous solution of phenol with a slight excess of aqueous KOH. The salts were subsequently used directly in excess for the synthesis of the corresponding fluoronitrophenyl tetra-*O*-acetyl β-D galactopyranosides **9** and **10**. Compounds **9** and **10** were isolated pure in moderate yields (58−77%) after basic extractive workup and flash chromatography. A different strategy had to be applied for the less acidic 2-fluorophenol **5**. The phenolate was generated in situ with K_2CO_3 in refluxing acetone in the presence of a catalytic amount of 18-crown-6 (*34*).

However, given the reported high yields, mild reaction conditions, and high stereospecificity, we ultimately explored phase-transfer catalysis for the synthesis of our desired glycosides (Figure 1) (*30*, *34*).

Fluorophenyl β-D-Galactopyranoside Tetraacetates 9−15. *General Procedure (Figure 1).* A solution of **1** (1 mmol; 2,3,4,6-tetra-*O*-acetyl-α-D-galactopyranosyl bromide, Sigma) in CH_2Cl_2 (5 mL) was added dropwise

to a vigorously stirred solution of fluorophenol **2**−**8** (1.2 mmol) and tetrabutylammonium bromide (0.48 g, 1.5 mmol) in H_2O (5 mL; pH 8−9) at 50 °C in a three-neck round-bottom flask equipped with a condenser and thermometer. After TLC showed complete reaction (∼1 h), the organic layer was separated, washed, dried, evaporated under reduced pressure, and recrystallized (EtOH−H_2O) or purified by column chromatography on silica gel to give fluorinated aryl β-D-galactopyranoside tetraacetates **9**−**15**, as white crystals.

*2-Nitro-4-fluorophenyl 2,3,4,6-tetra-O-acetyl-β-D-galactopyranoside **9**:* 0.5 g, 99%; R_f 0.31 (3:2 cyclohexane−EtOAc); δ_H 7.55 (1H, dd, J = 3.0, 8.4 Hz, Ar−H), 7.42 (1H, dd, J = 4.8, 9.0 Hz, Ar−H), 7.27 (1H, m, Ar−H), 5.04 (1H, d, $J_{1,2}$ = 7.8 Hz, H-1), 5.52 (1H, dd, $J_{2,3}$ = 8.4 Hz, H-2), 5.11 (1H, dd, $J_{3,4}$ = 3.0 Hz, H-3), 5.47 (1H, d, $J_{4,5}$ = 2.6 Hz, H-4), 4.07 (1H, m, H-5), 4.26 (1H, dd, $J_{5,6a}$ = 4.2 Hz, $J_{6a,6b}$ = 11.4 Hz, H-6a), 4.17 (1H, dd, $J_{5,6b}$ = 5.4 Hz, H-6b), 2.20, 2.14, 2.07, 2.02 (12H, 4s, 4 × CH_3CO); δ_C 170.43, 170.31, 170.24, 169.62 (4 × CH_3**C**O), 157.70 (d, J_{F-C} = 164.8 Hz, Ar−C), 145.66 (Ar−C), 141.86 (d, J_{F-C} = 5.7 Hz, Ar−C), 122.68 (d, J_{F-C} = 4.9 Hz, Ar−C), 120.77 (d, J_{F-C} = 15.2 Hz, Ar−C), 112.60 (d, J_{F-C} = 18.3 Hz, Ar−C), 101.40 (C-1), 68.01 (C-2), 70.63 (C-3), 66.86 (C-4), 71.58 (C-5), 61.45 (C-6), 21.25, 21.10, 20.38, 20.25 (4 × **C**H_3CO); HRMS, $[M + Na]^+$, $C_{20}H_{22}NO_{12}FNa$, calcd 510.1024, found 510.1014; $[M + K]^+$, $C_{20}H_{22}NO_{12}FK$, calcd 526.0763, found 526.0751.

*2-Fluoro-4-nitrophenyl 2,3,4,6-tetra-O-acetyl-β-D-galactopyranoside **10**:* 0.5 g, 99%; R_f 0.35(3:2 cyclohexane−EtOAc); δ_H 8.03 (2H, m, Ar−H), 7.32 (1H, m, Ar−H), 5.13 (1H, d, $J_{1,2}$ = 7.8 Hz, H-1), 5.58 (1H, dd, $J_{2,3}$ = 10.2 Hz, H-2), 5.15 (1H, dd, $J_{3,4}$ = 3.6 Hz, H-3), 5.40 (1H, dd, $J_{4,5}$ = 3.6 Hz, H-4), 4.10 (1H, ddd, $J_{5,6a}$ = 4.5 Hz, $J_{5,6b}$ = 5.0 Hz, H-5), 4.26 (1H, dd, $J_{6a,6b}$ = 11.0 Hz, H-6a), 4.19 (1H, dd, H-6b), 2.21, 2.11, 2.08, 2.04 (12H, 4s, 4 × CH_3CO); δ_C 170.45, 170.26, 170.21, 169.44 (4 × CH_3**C**O), 152.23 (d, J_{F-C} = 252.0 Hz, Ar−C), 150.07 (d, J_{F-C} = 10.6 Hz, Ar−C), 120.51 (d, J_{F-C} = 9.2 Hz, Ar−C), 118.53 (d, J_{F-C} = 11.7 Hz, Ar−C), 113.11 (d, J_{F-C} = 23.7 Hz, Ar−C), 100.28 (d, J_{F-C} = 3.1 Hz, C-1), 68.34 (C-2), 70.57 (C-3), 66.81 (C-4), 71.83 (C-5), 61.45 (C-6), 20.80, 20.77, 20.72, 20.33 (4 × **C**H_3CO); HRMS, $[M + Na]^+$, $C_{20}H_{22}NO_{12}FNa$, calcd 510.1010, found 510.1014; $[M + K]^+$, $C_{20}H_{22}NO_{12}FK$, calcd 526.0763, found 526.0751.

*2-Nitro-6-fluorophenyl 2,3,4,6-tetra-O-acetyl-β-D-galactopyranoside **11**:* 0.49 g, 98%; R_f 0.30 (3:2 cyclohexane−EtOAc); δ_H 7.58 (1H, ddd, J = 1.2, 1.4, 8.8 Hz, Ar−H), 7.39 (1H, ddd, J = 1.8, 8.4, 9.8 Hz, Ar−H), 7.29 (1H, m, Ar−H), 5.02 (1H, d, $J_{1,2}$ = 8.0 Hz, H-1), 5.48 (1H, dd, $J_{2,3}$ = 10.4 Hz, H-2), 5.08 (1H, dd, $J_{3,4}$ = 5.4 Hz, H-3), 5.41 (1H, dd, $J_{4,5}$ = 3.6 Hz, H-4), 3.90 (1H, m, H-5), 4.11 (1H, dd, $J_{5,6a}$ = 7.8 Hz, $J_{6a,6b}$ = 10.2 Hz, H-6a), 4.08 (1H, dd, $J_{5,6b}$ = 7.2 Hz, H-6b), 2.20, 2.14, 2.01, 2.00 (12H, 4s, 4 × CH_3CO); δ_C 170.45, 170.19, 169.61 (4 × CH_3**C**O), 155.84 (d, J_{F-C} = 251.8 Hz, Ar−C), 146.01 (Ar−C), 137.17 (d, J_{F-C} = 15.3 Hz, Ar−C), 125.66 (d, J_{F-C} = 7.6 Hz, Ar−C), 121.11 (d, J_{F-C} = 20.6 Hz, Ar−C), 120.22 (d, J_{F-C} = 3.8 Hz, Ar−C), 102.84 (d, J_{F-C} = 2.3 Hz, C-1), 68.75 (C-2), 70.76 (C-3), 66.74 (C-4), 71.41 (C-5), 61.02 (C-6), 20.82, 20.79, 20.70, 20.66 (4 × **C**H_3CO); HRMS, $[M + Na]^+$, $C_{20}H_{22}NO_{12}FNa$, calcd 510.1024, found 510.1011; $[M + K]^+$, $C_{20}H_{22}NO_{12}FK$, calcd 526.0763, found 526.0750.

*2-Fluorophenyl 2,3,4,6-tetra-O-acetyl-β-D-galactopyranoside **12**:* 0.45 g, 98%; R_f 0.40 (3:2 cyclohexane−EtOAc); δ_H 7.48 (1H, dd, J = 2.0, 10 Hz, Ar−H), 7.36 (1H, m, Ar−H), 7.30 (1H, m, Ar−H), 7.22 (1H, m, Ar−H), 5.54 (1H, d, $J_{1,2}$ = 8.4 Hz, H-1), 5.48 (1H, dd, $J_{2,3}$ = 10.0 Hz, H-2), 5.09 (1H, dd, $J_{3,4}$ = 4.4 Hz, H-3), 5.40 (1H, d, $J_{4,5}$ = 3.0 Hz, H-4), 4.24 (1H, m, H-5), 4.18 (1H, dd, $J_{5,6a}$ = 7.5 Hz, $J_{6a,6b}$ = 10.4 Hz, H-6a), 4.08 (1H, dd, $J_{5,6b}$ = 7.0 Hz, H-6b), 2.19, 2.10, 2.04, 2.02 (12H, 4s, 4 × CH_3CO); δ_C 170.66, 170.23, 170.10, 169.58 (4 × CH_3**C**O), 156.14 (Ar−C), 146.01 (d, J_{F-C} = 245.9 Hz, Ar−C), 136.58 (d, J_{F-C} = 14.8 Hz, Ar−C), 126.08 (d, J_{F-C} = 7.9 Hz, Ar−C), 122.33 (d, J_{F-C} = 26.3 Hz, Ar−C), 121.33 (d, J_{F-C} = 6.8 Hz, Ar−C), 101.89 (d, J_{F-C} = 2.6 Hz, C-1), 68.85 (C-2), 70.58 (C-3), 66.79 (C-4), 71.56 (C-5), 61.33 (C-6), 20.77, 20.70, 20.60, 20.58 (4 × **C**H_3CO); HRMS, $[M + Na]^+$, $C_{20}H_{23}NO_{10}FNa$, calcd 465.1173, found 465.1169; $[M + K]^+$, $C_{20}H_{23}NO_{10}FK$, calcd 481.0912, found 481.0907.

*4-Fluorophenyl 2,3,4,6-tetra-O-acetyl-β-D-galactopyranoside **13**:* 0.42 g, 95%; R_f 0.45 (3:2 cyclohexane−EtOAc); δ_H 6.99 (4H, m, Ar−H), 4.98 (1H, d, $J_{1,2}$ = 8.0 Hz, H-1), 5.48 (1H, dd, $J_{2,3}$ = 10.0 Hz, H-2), 5.11 (1H, dd, $J_{3,4}$ = 4.2 Hz, H-3), 5.45 (1H, d, $J_{4,5}$ = 2.4 Hz, H-4), 4.06 (1H, m, H-5), 4.24 (1H, dd, $J_{5,6a}$ = 7.2 Hz, $J_{6a,6b}$ = 10.4 Hz, H-6a), 4.16 (1H, dd, $J_{5,6b}$ = 6.4 Hz, H-6b), 2.19, 2.09, 2.06, 2.02 (12H, 4s, 4 × CH_3CO); δ_C 170.45, 170.36, 170.28, 169.48 (4 × CH_3**C**O), 160.08 (Ar−C), 157.69 (Ar−C), 153.10 (d, J_{F-C} = 20.0 Hz, Ar−C), 118.82−115.97 (m, Ar−C), 100.62 (C-1), 68.68 (C-2), 70.71 (C-3), 66.90 (C-4), 71.06 (C-5), 61.44 (C-6), 20.79, 20.72, 20.68, 20.64 (4 × **C**H_3CO); HRMS, $[M + Na]^+$, $C_{20}H_{23}NO_{10}FNa$, calcd 465.1173, found 465.1170; $[M + K]^+$, $C_{20}H_{23}NO_{10}FK$, calcd 481.0912, found 481.1014.

*2-Bromo-4-fluorophenyl 2,3,4,6-tetra-O-acetyl-β-D-galactopyranoside **14**:* 0.50 g, 97%; R_f 0.48 (3:2 cyclohexane−EtOAc); δ_H 7.28 (1H, ddd, J = 3.2, 2.8, 3.2 Hz, Ar−H), 7.16 (1H, dd, J = 4.8, 9.2 Hz, Ar−H), 6.97 (1H, m, Ar−H), 4.91 (1H, d, $J_{1,2}$ = 8.0 Hz, H-1), 5.56 (1H, dd, $J_{2,3}$ = 10.8 Hz, H-2), 5.10 (1H, dd, $J_{3,4}$ = 3.6 Hz, H-3), 5.46 (1H, d, $J_{4,5}$ = 4.0 Hz, H-4), 4.24 (1H, m, H-5), 4.25 (1H, dd, $J_{5,6a}$ = 7.2 Hz, $J_{6a,6b}$ = 11.4 Hz, H-6a), 4.08 (1H, dd, $J_{5,6b}$ = 6.0 Hz, H-6b), 2.19, 2.11, 2.06, 2.02 (12H, 4s, 4 × CH_3CO); δ_C 170.52, 170.43, 170.34, 169.57 (4 × CH_3**C**O), 159.80 (Ar−C), 157.35 (Ar−C), 150.22 (Ar−C), 120.91−13.93 (m, Ar−C), 101.36 (C-1), 68.33 (C-2), 70.66 (C-3), 67.03 (C-4), 71.49 (C-5), 61.51 (C-6), 21.28, 21.15, 21.10, 20.91 (4 × **C**H_3CO); HRMS, $[M + Na]^+$, $C_{20}H_{22}O_{10}F^{79}BrNa$, calcd 543.0279, found 543.0266; $C_{20}H_{22}O_{10}F^{81}BrNa$, calcd 545.0259, found 545.0205; $[M + K]^+$, $C_{20}H_{22}O_{10}F^{79}BrK$, calcd 559.0043, found 559.0043; $C_{20}H_{22}O_{10}F^{81}BrNa$, calcd 560.9997, found 560.9892.

*2-Chloro-4-fluorophenyl 2,3,4,6-tetra-O-acetyl-β-D-galactopyranoside **15**:* 0.48 g, 99%; R_f 0.46 (3:2 cyclohexane−EtOAc); δ_H 7.21 (1H, dd, J = 4.8, 8.8 Hz, Ar−H), 7.13 (1H, dd, J = 3.2, 8.0 Hz, Ar−H), 6.92 (1H, m, Ar−H), 4.90 (1H, d, $J_{1,2}$ = 8.0 Hz, H-1), 5.54 (1H, dd, $J_{2,3}$ = 10.8 Hz, H-2), 5.12 (1H, dd, $J_{3,4}$ = 3.2 Hz, H-3), 5.46 (1H, d, $J_{4,5}$ = 3.6 Hz, H-4), 4.04 (1H, m, H-5), 4.26 (1H, dd, $J_{5,6a}$ = 6.8 Hz, $J_{6a,6b}$ = 11.4 Hz, H-6a), 4.16 (1H, dd, $J_{5,6b}$ = 6.4 Hz, H-6b), 2.19, 2.11, 2.06, 2.02 (12H, 4s, 4 × CH_3CO); δ_C 170.40, 170.32, 170.21, 169.49 (4 × CH_3**C**O), 159.72 (Ar−C), 157.25 (Ar−C), 149.14 (d, J_{F-C} = 3.1 Hz, Ar−C), 125.55 (d, J_{F-C} = 9.9 Hz, Ar−C), 120.62−114.34 (m, Ar−C), 101.46 (C-1), 68.29 (C-2), 70.51 (C-3), 66.97 (C-4), 71.38 (C-5), 61.40 (C-6), 20.99, 20.87, 20.77, 20.66 (4 × **C**H_3CO); HRMS, $[M + Na]^+$, $C_{20}H_{22}O_{10}F^{35}ClNa$, calcd 499.0783, found 499.0761; $C_{20}H_{22}O_{10}F^{37}ClNa$, calcd 501.0754, found 501.0701; $[M + K]^+$, $C_{20}H_{22}O_{10}F^{35}ClK$, calcd 515.0523, found 515.0495; $C_{20}H_{22}O_{10}F^{37}ClK$, calcd 517.0494, found 517.0488.

Fluoroaryl β-D-Galactopyranosides 16−22. *General Procedure.* A solution of fluorophenyl 2,3,4,6-tetra-*O*-acetyl-β-D-galactopyranoside (**9**−**15**) (0.4 g) in anhydrous MeOH (15 mL) containing 0.5 M NH_3 was vigorously stirred from 0 °C to room temperature overnight until

TLC showed complete reaction. Following solvent removal in vacuo, chromatography on silica gel (EtOAc/MeOH) afforded the free galactopyranosides **16**−**22** in nearly quantitative yield, as white crystalline materials.

*2-Nitro-4-fluorophenyl β-D-galactopyranoside **16**: R_f* 0.40 (1:9 MeOH−EtOAc), δ_H 7.84 (1H, dd, J = 2.8, 8.0 Hz, Ar−H), 7.53 (1H, ddd, J = 1.6, 1.0, 2.8 Hz, Ar−H), 7.43 (1H, dd, J = 4.4, 9.2 Hz, Ar−H), 4.96 (1H, d, $J_{1,2}$ = 7.6 Hz, H-1), 3.60 (1H, dd, $J_{2,3}$ = 10.6 Hz, H-2), 3.51 (1H, dd, $J_{3,4}$ = 5.2 Hz, H-3), 3.47 (1H, d, $J_{4,5}$ = 5.6 Hz, H-4), 3.43 (1H, m, H-5), 3.67 (2H, m, H-6), 5.16 (1H, d, $J_{H-2,OH-2}$ = 5.2 Hz, HO-2), 4.67 (1H, d, $J_{H-3,OH-3}$ = 4.4 Hz, HO-3), 4.90 (1H, d, $J_{H-4,OH-4}$ = 6.0 Hz, HO-4), 4.67 (1H, t, $J_{H-6,OH-6}$ = 5.2, 5.4 Hz, HO-6); δ_C 155.41 (d, J_{F-C} = 239.6 Hz, Ar−C), 146.19 (d, J_{F-C} = 3.1 Hz, Ar−C), 140.17 (d, J_{F-C} = 9.1 Hz, Ar−C), 120.91 (d, J_{F-C} = 22.1 Hz, Ar−C), 119.03 (d, J_{F-C} = 7.7 Hz, Ar−C), 111.89 (d, J_{F-C} = 27.5 Hz, Ar−C), 101.65 (C-1), 70.07 (C-2), 73.37 (C-3), 68.06 (C-4), 75.87 (C-5), 60.33 (C-6); HRMS, $[M + Na]^+$, $C_{12}H_{14}NO_8FNa$, calcd 342.0601, found 342.0589; $[M + K]^+$, $C_{12}H_{14}NO_8FK$, calcd 358.0341, found 358.0328.

*2-Fluorine-4-nitrophenyl β-D-galactopyranoside **17**: R_f* 0.45 (1:9 MeOH−EtOAc); δ_H 7.58 (1H, dd, J = 3.3, 8.0 Hz, Ar−H), 7.42 (1H, dd, J = 4.2, 8.7 Hz, Ar−H), 7.28 (1H, m, Ar−H), 5.16 (1H, d, $J_{1,2}$ = 7.8 Hz, H-1), 4.60 (1H, dd, $J_{2,3}$ = 8.8 Hz, H-2), 3.70 (1H, dd, $J_{3,4}$ = 3.2 Hz, H-3), 3.63 (1H, d, $J_{4,5}$ = 3.1 Hz, H-4), 3.60 (1H, m, H-5), 3.50 (2H, m, H-6), 4.98 (1H, d, $J_{H-2,OH-2}$ = 7.2 Hz, HO-2), 4.66 (1H, d, $J_{H-3,OH-3}$ = 4.0 Hz, HO-3), 4.80 (1H, d, $J_{H-4,OH-4}$ = 5.0 Hz, HO-4), 4.90 (1H, t, $J_{H-6,OH-6}$ = 5.5, 5.8 Hz, HO-6); δ_C 156.80 (d, J = 160.4 Hz, Ar−C), 146.55 (Ar−C), 140.68 (d, J = 5.5 Hz, Ar−C), 123.44 (d, J = 4.2 Hz, Ar−C), 121.33 (d, J = 18.2 Hz, Ar−C), 114.80 (d, J = 17.9 Hz, Ar−C), 101.73 (C-1), 68.33 (C-2), 70.86 (C-3), 66.90 (C-4), 71.47 (C-5), 61.77 (C-6); HRMS, $[M + Na]^+$, $C_{12}H_{14}NO_8FNa$, calcd 342.0601, found 342.0585; $[M + K]^+$, $C_{12}H_{14}NO_8FK$, calcd 358.0341, found 358.0320.

*2-Nitro-6-fluorophenyl β-D-galactopyranoside **18A**: R_f* 0.40 (1:9 MeOH−EtOAc); δ_H 7.73 (1H, ddd, J = 1.6, 3.2, 8.4 Hz, Ar−H), 7.63 (1H, ddd, J_{HH} = 1.2, 4.0, 8.4 Hz, J_{HF} = 19.2 Hz, Ar−H), 7.46 (1H, ddd, J_{HH} = 5.2, 8.4 Hz, J_{HF} = 16.8 Hz, Ar−H), 5.00 (1H, d, $J_{1,2}$ = 7.6 Hz, H-1), 3.88 (1H, dd, $J_{2,3}$ = 9.2 Hz, H-2), 3.82 (1H, dd, $J_{3,4}$ = 4.0 Hz, H-3), 3.70 (1H, dd, $J_{4,5}$ = 3.2 Hz, H-4), 3.66 (1H, m, H-5), 4.00 (2H, m, H-6), 3.80 (1H, d, $J_{H-2,OH-2}$ = 4.2 Hz, HO-2), 3.69 (1H, d, $J_{H-3,OH-3}$ = 3.0 Hz, HO-3), 3.86 (1H, d, $J_{H-4,OH-4}$ = 1.6 Hz, HO-4), 3.62 (1H, dd, $J_{H-6,OH-6}$ = 4.6, 5.0 Hz, HO-6); δ_C 156.66 (d, J_{F-C} = 246.2 Hz, Ar−C), 145.78 (Ar−C), 138.54 (d, J_{F-C} = 12.2 Hz, Ar−C), 125.83 (d, J_{F-C} = 8.4 Hz, Ar−C), 121.65 (d, J_{F-C} = 19.9 Hz, Ar−C), 120.80 (d, J_{F-C} = 3.8 Hz, Ar−C), 106.06 (d, J_{F-C} = 3.8 Hz, C-1), 70.59 (C-2), 74.48 (C-3), 69.30 (C-4), 77.00 (C-5), 61.73 (C-6); HRMS, $[M + Na]^+$, $C_{12}H_{14}NO_8FNa$, calcd 342.0601, found 342.0599; $[M + K]^+$, $C_{12}H_{14}NO_8FK$, calcd 358.0341, found 358.0337.

*2-Nitro-6-fluorophenyl α-D-galactopyranoside **18B**: R_f* 0.47 (1:9 MeOH−EtOAc); δ_H 7.76 (1H, ddd, J = 1.6, 2.8, 8.4 Hz, Ar−H), 7.62 (1H, ddd, J_{HH} = 0.4, 4.8, 8.4 Hz, J_{HF} = 12.0 Hz, Ar−H), 7.40 (1H, ddd, J_{HH} = 4.8, 8.4 Hz, J_{HF} = 13.2 Hz, Ar−H), 5.85 (1H, d, $J_{1,2}$ = 3.2 Hz, H-1), 4.01 (1H, dd, $J_{2,3}$ = 8.9 Hz, H-2), 4.03 (1H, dd, $J_{3,4}$ = 3.6 Hz, H-3), 4.11 (1H, dd, $J_{4,5}$ = 3.6 Hz, H-4), 3.74 (1H, m, H-5), 3.63 (2H, m, H-6), 3.92 (1H, d, $J_{H-2,OH-2}$ = 3.2 Hz, HO-2), 3.74 (1H, d, $J_{H-3,OH-3}$ = 3.6 Hz, HO-3), 3.83 (1H, d, $J_{H-4,OH-4}$ = 2.0 Hz, HO-4), 3.80 (1H, t, $J_{H-6,OH-6}$ = 5.6, 6.0 Hz, HO-6); δ_C 157.06 (d, J_{F-C} = 248.7 Hz, Ar−C), 146.05 (Ar−C), 139.20 (d, J_{F-C} = 13.8 Hz, Ar−C), 124.59 (d, J_{F-C} = 8.4 Hz, Ar−C), 122.05 (d, J_{F-C} = 19.9 Hz, Ar−C), 121.37 (d, J_{F-C} = 3.0 Hz, Ar−C), 104.14 (d, J_{F-C} = 7.6 Hz, C-1), 70.23 (C-2), 70.59 (C-3), 69.94 (C-4), 74.21 (C-5), 62.03 (C-6); HRMS, $[M + Na]^+$, $C_{12}H_{14}NO_8FNa$, calcd 342.0601, fouz342.0590; $[M + K]^+$, $C_{12}H_{14}NO_8FK$, calcd 358.0341, found 358.0333.

*2-Fluorophenyl β-D-galactopyranoside **19**: R_f* 0.48 (1:9 MeOH−EtOAc); δ_H 7.26 (1H, m, Ar−H), 7.21 (1H, ddd, J = 1.2, 3.6, 8.0 Hz, Ar−H), 7.11 (1H, ddd, J_{HH} = 1.2, 7.2, J_{HF} = 14.4 Hz, Ar−H), 6.98 (1H, m, Ar−H), 4.91 (1H, d, $J_{1,2}$ = 7.6 Hz, H-1), 3.41 (1H, dd, $J_{2,3}$ = 9.6 Hz, H-2), 3.47 (1H, dd, $J_{3,4}$ = 4.0 Hz, H-3), 3.71 (1H, d, $J_{4,5}$ = 3.2 Hz, H-4), 3.54 (1H, m, H-5), 3.60 (2H, m, H-6), 3.58 (1H, d, $J_{H-2,OH-2}$ = 4.0 Hz, HO-2), 3.48 (1H, d, $J_{H-3,OH-3}$ = 3.1 Hz, HO-3), 3.57 (1H, d, $J_{H-4,OH-4}$ = 2.2 Hz, HO-4), 3.54 (1H, t, $J_{H-6,OH-6}$ = 4.0, 5.2 Hz, HO-6); δ_C 152.28 (d, J_{F-C} = 242.7 Hz, Ar−C), 145.50 (d, J_{F-C} = 9.9 Hz, Ar−C), 125.10 (d, J_{F-C} = 3.8 Hz, Ar−C), 122.60 (d, J_{F-C} = 6.9 Hz, Ar−C), 117.73 (Ar−C), 116.66 (d, J_{F-C} = 18.3 Hz, Ar−C), 101.53 (C-1), 70.59 (C-2), 73.81 (C-3), 68.52 (C-4), 76.04 (C-5), 60.74 (C-6); HRMS, $[M + Na]^+$, $C_{12}H_{15}O_6FNa$, calcd 297.0750, found 297.0739; $[M + K]^+$, $C_{12}H_{15}O_6FK$, calcd 313.0490, found 313.0486.

*4-Fluorophenyl β-D-galactopyranoside **20**: R_f* 0.40 (1:9 MeOH−EtOAc); δ_H 7.14−7.03 (4H, m, Ar−H), 4.74 (1H, d, $J_{1,2}$ = 7.6 Hz, H-1), 3.54 (1H, dd, $J_{2,3}$ = 10.6 Hz, H-2), 3.50 (1H, dd, $J_{3,4}$ = 3.6 Hz, H-3), 3.72 (1H, d, $J_{4,5}$ = 3.2 Hz, H-4), 3.43 (1H, m, H-5), 3.58 (2H, m, H-6), 5.30−4.4 (4H, br, HO-2,3,4,6); δ_C 157.25 (d, J_{F-C} = 235 Hz, Ar−C), 153.98 (Ar−C), 117.93−115.69 (Ar−C), 101.88 (C-1), 70.40 (C-2), 73.32 (C-3), 68.30 (C-4), 75.60 (C-5), 60.46 (C-6); HRMS, $[M + Na]^+$, $C_{12}H_{15}O_6FNa$, calcd 297.0750, found 297.0731.

*2-Bromo-4-fluorophenyl β-D-galactopyranoside **21**: R_f* 0.52 (1:9 MeOH−EtOAc); δ_H 7.54 (1H, dd, J = 2.4, 8.0 Hz, Ar−H), 7.22 (2H, m, Ar−H), 4.90 (1H, d, $J_{1,2}$ = 7.6 Hz, H-1), 3.41 (1H, dd, $J_{2,3}$ = 9.6 Hz, H-2), 3.47 (1H, dd, $J_{3,4}$ = 4.0 Hz, H-3), 3.71 (1H, d, $J_{4,5}$ = 3.2 Hz, H-4), 3.54 (1H, m, H-5), 3.60 (2H, m, H-6), 5.11 (1H, d, $J_{H-2,OH-2}$ = 5.6 Hz, HO-2), 4.58 (1H, d, $J_{H-3,OH-3}$ =4.8 Hz, HO-3), 4.89 (1H, d, $J_{H-4,OH-4}$ = 5.2 Hz, HO-4), 4.67 (1H, t, $J_{H-6,OH-6}$ = 5.2, 5.2 Hz, HO-6); δ_C 157.38 (d, J_{F-C} = 240.4 Hz, Ar−C), 151.09 (Ar−C), 120.79−121.32 (m, Ar−C), 101.96 (C-1), 70.87 (C-2), 73.78 (C-3), 68.84 (C-4), 76.13 (C-5), 61.13 (C-6); HRMS, $[M + Na]^+$, $C_{12}H_{14}O_6F^{79}BrNa$, calcd 374.9855, found 374.9851; $C_{12}H_{14}O_6F^{81}BrNa$, calcd 376.9835, found 376.9665; $[M+K]^+$, $C_{12}H_{14}O_6F^{79}BrK$, calcd 390.9595, found 390.9803; $C_{12}H_{14}O_6F^{81}BrK$, calcd 392.9575, found 392.9687.

*2-Chloro-4-fluorophenyl β-D-galactopyranoside **22**: R_f* 0.45 (1:9 MeOH−EtOAc); δ_H 7.42 (1H, dd, J = 2.8, 8.4 Hz, Ar−H), 7.28 (1H, dd, J = 5.2, 9.6 Hz, Ar−H), 7.17 (1H, m, Ar−H), 4.90 (1H, d, $J_{1,2}$ = 7.6 Hz, H-1), 3.57 (1H, dd, $J_{2,3}$ = 11.6 Hz, H-2), 3.52 (1H, dd, $J_{3,4}$ = 5.2 Hz, H-3), 3.72 (1H, m, H-4), 3.17 (1H, m, H-5), 3.60 (1H, dd, $J_{5,6a}$ = 8.8 Hz, $J_{6a,6b}$ = 12.4 Hz, H-6a), 3.45 (1H, dd, $J_{5,6b}$ = 6.0 Hz, H-6b), 5.17 (1H, d, $J_{H-2,OH-2}$ = 4.0 Hz, HO-2), 4.59 (1H, d, $J_{H-3,OH-3}$ = 3.2 Hz, HO-3), 4.89 (1H, d, $J_{H-4,OH-4}$ = 7.0 Hz, HO-4), 4.69 (1H, br, HO-6); δ_C 156.38 (d, J_{F-C} = 238.80 Hz, Ar−C), 149.62 (Ar−C), 122.55 (d, J_{F-C} = 10.7 Hz, Ar−C), 117.45−114.54 (m, Ar−C), 101.45 (C-1), 70.25 (C-2), 73.47 (C-3), 68.23 (C-4), 75.75 (C-5), 60.39 (C-6); HRMS, $[M+Na]^+$, $C_{12}H_{14}O_6F^{35}ClNa$, calcd 331.0361, found 331.0349; $C_{12}H_{14}O_6F^{37}ClNa$, calcd 333.0331, found 333.0249.

Kinetic Experiments. Relative substrate efficacies of **16**−**22** were compared using ^{19}F NMR. Enzyme reactions were conducted at 37 °C in PBS (0.1 M, pH 7.4) using β-gal (E801A, Promega, Madison, WI). Fluorophenyl β-D-galactopyranosides **16**−**22** (15 mmol) were dissolved in PBS (600 μL, pH 7.4) and β-gal (20 μL, 1 unit/

μL E801A in PBS) was added, followed by immediate ^{19}F NMR data acquisition at 37 °C with subsequent spectra every 101 s providing a kinetic curve over 51 min.

Substrate efficacy relative to traditional indicators was assessed by spectrophotometry. PFONPG **16** and ONPG (2.5 μmol/mL), respectively, were dissolved in buffer (pH 4.5, 10 mM sodium hydrogen phosphate, 5 mM citric acid). A solution of β-gal [G5160 from *Aspergillus oryzae* (Aldrich), 95 μg in 10 μL of buffer] was added and the absorption ($\lambda = 420$ nm) measured every 30 s for 10 min at room temperature.

Cell Culture and Cell Proliferation Assay. Dunning R3327-MAT-Lu rat prostate cancer cells (isolated for growth in culture by us from solid tumor tissues originally provided by Dr. Peter Peschke of the DKFZ, Heidelberg, Germany) and MTLn3 rat breast cancer cells (ATCC, Manassas, VA) were maintained in RPMI-1640 medium supplemented with 100 units/mL penicillin, 100 μg/mL streptomycin, and 10% fetal bovine serum (FBS) at 37 °C, with 5% CO_2 and 95% humidified air. Using TransFast transfection reagent (Promega), MAT-Lu and MTLn3 cells were cotransfected with pCMVβ (Clontech, Palo Alto, CA) comprising the *Escherichia coli lacZ* gene located under the human cytomegalovirus (CMV) immediate-early enhancer/promoter region and pCI-neo (Promega) carrying the neomycin phosphotransferase gene and were selected in growth medium containing 400 μg/mL G418 (Cellgro, Merndon, VA). Cells were harvested, trypsinized and resuspended in PBS, pH 7.4. **17** (1.9 mg, 100 μL) was added to cell suspension in PBS (10^8 cells in 600 μL), and ^{19}F NMR spectra were acquired immediately at 37 °C and again at various times up to 72 h. The β-gal activity of MAT-Lu-LacZ cells was 196 milliunits/10^7 cells and that for MTLn3-LacZ cells, 67 milliunits/10^7 cells.

The toxicity of aglycons and conjugates was assessed in both wild-type and LacZ-transfected MAT-Lu cells using a colorimetric CellTiter 96 Aqueous Nonradioactive MTS Cell Proliferation Assay (Promega). Assays were performed in triplicate using 24-well plates seeded with 10^3 cells per well in 500 μL of RPMI-1640 without phenol red and supplemented with 10% FCS and 2 mM glutamine. After 24 h of incubation, the medium was replaced with fresh medium. To determine IC_{50}, cells were incubated (72 h) with molecules **2**−**8** (0−1.6 mM) and **16**−**22** (0−4.5 mM), followed by the MTS assay. In each case successive dilutions were 2-fold. In some cases maximum tested doses were lower because some molecules showed poor solubility.

RESULTS

The methodology presented by Yoon et al. (*30*) to synthesize phenyl fluorogalactoside tetraacetates using potassium salts of the phenol produced mediocre yields for the fluorophenyl analogues **9** and **10**. By contrast, the phase-transfer approach using TBAB produced fluorophenyl β-D-galactopyranoside tetraacetates **9**−**15** in nearly quantitative yields. The anomeric β-D-configuration of compounds **9**−**15** in the $^4C_1$ chair conformation was unambiguously established on the basis of the observed ^{1}H NMR chemical shifts (δ_H 5.00−5.25) of the anomeric protons and the $J_{1,2}$ ($J \sim 8$ Hz) and $J_{2,3}$ ($J \sim 10$ Hz) coupling constants (*34*). The signals of the ^{13}C NMR spectra of **9**−**15** were assigned by comparison with the chemical shifts of *p*-nitrophenyl β-D-galactopyranoside (*30*). As expected, the anomeric carbon resonances appeared at ~100 ppm in accord with the β-D-configuration.

Deacetylation of **9**−**15** gave the free galactopyranosides **16**−**22** in nearly quantitative yields. ^{1}H NMR spectra of

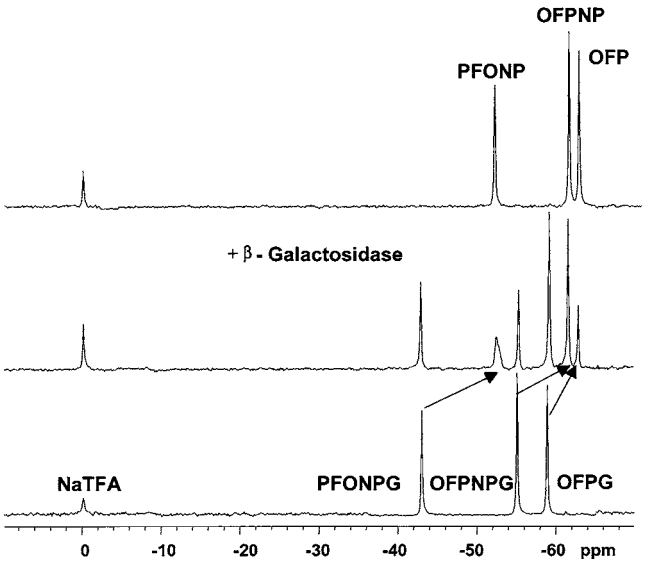


Figure 2. ^{19}F NMR spectra of β-D-galactopyranosides **16** (PFONPG), **17** (OFPNPG), and **19** (OFPG) in PBS at 37 °C (a) and following addition of β-gal [2 min) (b) and 34 min (c)].

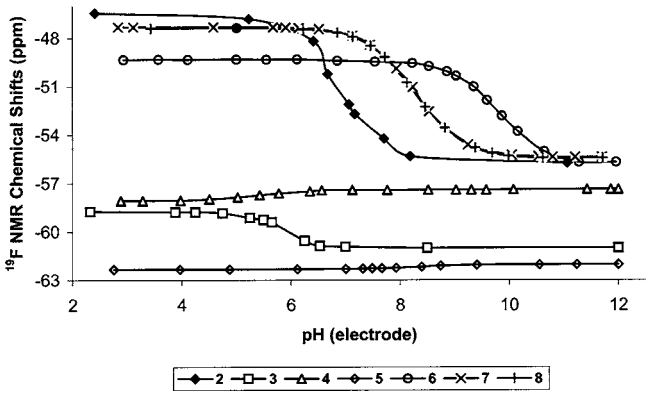


Figure 3. ^{19}F NMR chemical shift pH titration curves of **2**−**8** in saline at 25 °C.

16−**22** were assigned by ^{1}H−^{1}H COSY spectra and D_2O exchange. The ^{1}H NMR chemical shifts (δ_H 4.91−5.85) of the anomeric protons and the coupling constants ($J_{1,2} \sim 8$ Hz; $J_{2,3} \sim 10$ Hz) showed that the free galactopyranosides **16**−**22** (except **18**) retained the anomeric β-D-configuration with the $^4C_1$ chair conformation. The synthesis of **18** was more complex with the isolation of two distinct and separable isomers **18A** and **18B** in a 1:1 ratio, which also gave distinct ^{19}F NMR spectra. The downfield shifts of **18B** δ_{H1} at 5.85 with $J_{1,2} = 3.2$ Hz and δ_C at 104.14 compared to those of **18A** at 5.00 ppm with $J_{1,2} = 7.6$ Hz and δ_C at 106.06 suggest α and β isomers, respectively (*35*−*38*). Further evidence supporting the structural assignment of **18B** is that the α anomer resists activity of β-gal (Figure 4). Epimerization likely occurs during removal of the acetyl groups, possibly via a carbocation pathway due to the excellent leaving group ability of the 2-fluoro-6-nitrophenol anion group.

All except **18A** were stable in saline (0.9%), PBS (0.1 M), and fresh whole rabbit blood, at 25 and 37 °C, for extended periods showing no breakdown by ^{19}F NMR even after 1 week. **18A** hydrolyzed completely within 2 h in 0.1 M PBS buffer solution (pH 7.4) at 25 °C. By contrast, **18B** was stable even at 60 or 100 °C. As expected, the more polar substituted phenyl β-D-galactopyranosides **16**−**18** were most soluble and **19**−**21** quite

Table 1. ^{19}F Chemical Shifts (Parts per Million) of 16−22 before and after Hydrolysis by β-gal[a]

	compound							
	16	**17**	**18A**	**18B**	**19**	**20**	**21**	**22**
$\delta_{F(substrate)}$	−42.87	−54.93	−50.67	−49.37	−58.74	−45.87	−43.56	−43.82
$\delta_{F(product)}$	−52.71	−61.04	−58.67	−58.67	−62.30	−49.59	−48.13	−48.24
observed $\Delta\delta_F$	9.84	6.11	8.00	9.30	3.56	3.72	4.57	4.42
min $\Delta\delta_F$	1.57	3.84	6.72	8.7	3.3	3.46	3.76	3.58
max $\Delta\delta_F$	12.89	6.11	8.1	9.4	3.59	11.85	11.84	11.63

[a] β-gal (E801A, 20 units at 37 °C in 0.1 M PBS, pH 7.4).

Table 2. ^{19}F NMR pH Characterization of Aglycons at 25 °C

	compound						
	2	**3**	**4**	**5**	**6**	**7**	**8**
pK_a	6.87	6.03	5.44	8.33	9.80	8.31	8.28
$\delta_{(acid)}$	−46.44	−58.77	−58.07	−62.33	−49.33	−47.32	−47.40
$\delta_{(base)}$	−55.76	−61.01	−57.39	−62.04	−57.72	−55.40	−55.45
$\Delta\delta$	9.3	2.24	0.68	0.29	6.39	8.08	8.05

soluble in water, buffer, and whole blood, but 2-bromo-4-fluorophenyl β-D-galactopyranoside **22** was poorly soluble.

^{19}F NMR. Compounds **16**−**22** each gave a single, narrow ^{19}F NMR signal essentially invariant ($\Delta\delta \leq 0.03$) in rabbit whole blood, 0.9% saline, and PBS in the pH range 3−12 and at various temperatures ranging from 25 to 37 °C. The liberated aglycons display a chemical shift range of ∼16 ppm (Table 1; Figure 2). Addition of β-galactosidase (E801A) in PBS (0.1 M, pH 7.4) at 37 °C caused each substrate to hydrolyze, releasing the pH sensitive aglycons **2**−**8** appearing also as a single narrow ^{19}F NMR signal (Figure 2; Table 1), consistent with the titration curves of **2**−**8** (Figure 3; Table 2). The minimum ^{19}F NMR chemical shift response observed was 3.56 ppm for **19** and maximum was 9.84 ppm for **16** at pH 7.4 (Table 1).

The various substrates **16**−**22** exhibited differential sensitivity to β-galactosidase in PBS (pH 7.4), and kinetics were monitored by changes in the integration of the ^{19}F NMR signals (Figures 2 and 4). The shapes of the kinetic curves suggest straightforward first-order kinetics for all substrates. The best substrate was **18A**, with an initial rate of 0.74 mM/min/unit, although this molecule hydrolyzed spontaneously within 2 h. **16**, **17**, and **19** also showed rapid cleavage, whereas **20**−**22** were somewhat slower and **18B** resisted enzyme action (as expected for an α anomer). By colorimetric assay **16** was essentially equivalent to ONPG as a substrate (Figure 5).

Several of the aglycons (**2**, **3**, **6**−**8**) exhibit a large ^{19}F NMR chemical shift in response to pH with $\Delta\delta$ reaching 9.3. However, **4** and **5** showed little response (Figure 3). The observed pK_a values were found to be in the range of 5.4−9.8 (Table 2). There was a strong linear correlation between initial rate of enzymatic hydrolysis of the substrates and pK_a of the aglycon (Figure 6).

When **17** was incubated with wild-type MAT-Lu rat prostate cancer cells (4 h, PBS, 37 °C under air−5% CO_2 with 95% humidity), ^{19}F NMR spectra showed no changes. When **17** was incubated with MAT-Lu-LacZ cells (92 ×

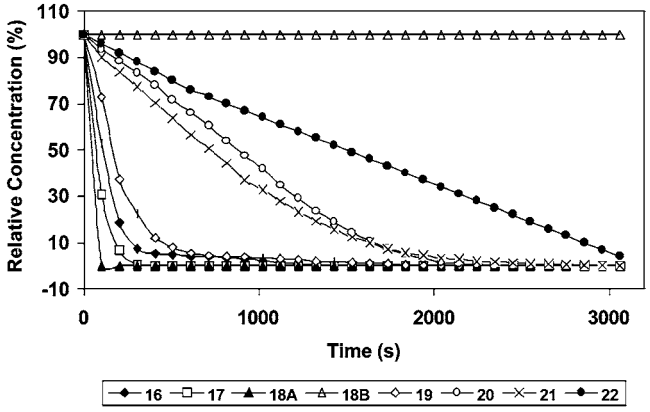


Figure 4. Hydrolysis time courses of **16**−**22** (15 mmol) by β-gal (E801A, 20 units) in PBS (0.1 M, 0.6 mL) at 37 °C.

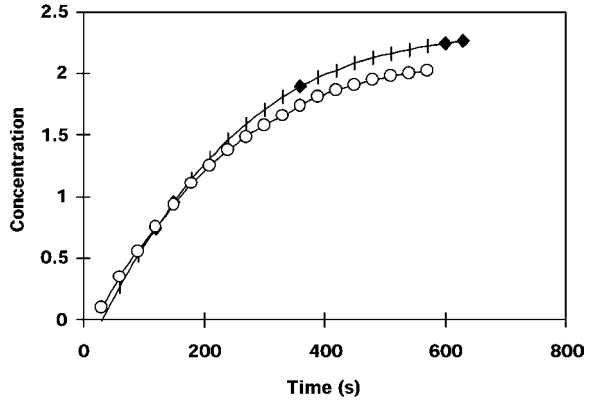


Figure 5. Colorimetric comparison of enzyme (G5160, pH 4.5) sensitivity for **16** and ONPG.

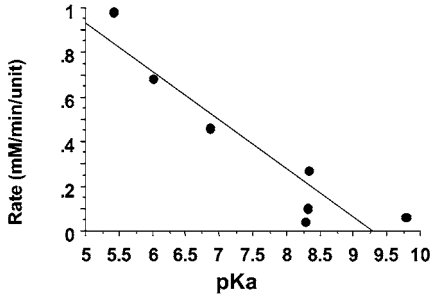


Figure 6. Brønsted plot of substrate susceptibility to β-gal (E801A, pH 7.4) versus of pK_a of liberated aglycon ($r^2 > 0.85$).

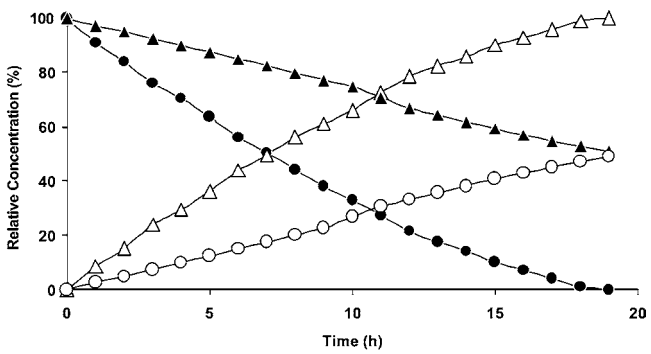


Figure 7. Hydrolysis of **17** (open symbols) to **3** (solid symbols) by stably transfected Dunning prostate R3327 MAT-Lu-*lacZ* cells (△, 92 × 10^6) and MTLn3-*lacZ* (○, 9.8 × 10^6) suspended in PBS at 37 °C.

Table 3. Toxicity of 2−8 and 16−22 to MAT-Lu -WT and -*LacZ* Cells (PBS, pH 7.4)

		molecule												
		2	**3**	**4**	**5**	**6**	**7**	**8**	**16**	**17**	**18A/B**	**19**	**20**	**21**	**22**
IC_{50} mM	MAT-Lu	<0.4	>1.6[a]	>1.3	<0.003	<1.6	<0.003	>0.9	>3.6[a]	<3	<4.5	>4.5	>4.5	>4.5[a]	>0.3[a]
	MAT-Lu-LacZ	<0.8	>1.6[a]	>1.3[a]	<0.003	< 0.8	<0.003	>0.9	>3.6[a]	>6	>4.5	>4.5	>4.5	>4.5[a]	>0.3[a]

[a] Greater than 90% survival at the highest dose tested.

10^6, 1803 milliunits of β-gal) in PBS, cleavage proceeded in a smooth monotonic manner with hydrolysis complete after 19 h (Figure 7). MTLn3-*LacZ* breast cancer cells (9.8×10^6, 67 milliunits of β-gal) hydrolyzed ~50% of **17** in 19 h.

Toxicity was evaluated for both aglycons and conjugates using both wild-type and lacZ expressing MAT-Lu cells (Table 3). **5** and **7** were severely cytotoxic, **2** was somewhat toxic (IC_{50} < 0.4 mM), and the other aglycons, **3**, **4**, **6**, and **8**, were less toxic (IC_{50} > 1 mM), making them more suitable for in vivo NMR investigations. Most conjugates were much less toxic; in particular, the toxicity of the aglycons was masked in **19** and **21**.

DISCUSSION

We have presented a method to efficiently and stereoselectively synthesize a series of fluorophenyl β-D-galactopyranosides **16**−**22** as potential ^{19}F NMR-based gene reporter molecules. We previously demonstrated that **16** could be used to assess β-gal activity in transiently transfected human prostate cancer cells (*27*). We have now assessed the relative substrate efficacy of a series of analogues and demonstrated the utility of **17** to assess β-gal activity in stably transfected rat breast and prostate tumor cells.

^{19}F NMR provides a large chemical shift response to small changes in molecular structure or microenvironment (*25*, *26*). Here, hydrolysis provided a minimum $\Delta\delta$ 3.56 between the substrate and the aglycon at pH 7.4, although depending on the pH, it could range from 1.6 to 12.9 ppm. Significantly, because of the chemical shift range of the ^{19}F signals of the aglycons **2**−**8** (up to 9.3 ppm), several substrates and aglycons can be detected simultaneously, allowing direct comparison of substrate efficacy (Figure 2). Preliminary data suggest that the approach used here could also be applied to glucosidases and glucoronides. Indeed, Schmidt and Monneret (*39*) presented ^{19}F NMR analysis of a fluorine-tagged nitrogen mustard pro-drug activated by glucuronidase. ^{19}F NMR spectroscopy lacks the spatial resolution of ^{1}H MRI, but the chemical shift accompanying substrate cleavage by β-gal unequivocally reveals enzyme activity. Comparing the substrates shows a 10-fold range in rate of substrate reaction at pH 7.4, the optimal pH for activity of β-gal derived from *Escherichia coli*. The observed initial rates were found to have a strong linear correlation with the pK_a of the aglycon (Figure 6), consistent with previous work by Richard et al. (*40*), who examined a series of alkyl β-galactosides. At pH 4.5—the optimal pH for β-gal derived from *Aspergillus oryzae*—**16** showed very similar activity in comparison with the traditional colorimetric indicator ONPG.

Substrates **16** and **17** share many attributes with similar sensitivity to β-gal at pH 7.4 (Figure 4), a large chemical shift range, and effective response to cells expressing β-gal (Figure 7) (*27*). All of the aglycons are electronically similar to the classic biochemical uncoupler dinitrophenol, raising potential concerns of toxicity. We have found extensive cell lysis upon direct exposure to the product aglycon **2** (IC_{50} < 0.4 mM), but **16** has allowed us to assess β-gal expression in culture (*27*). Other aglycons, **3**, **4**, **6**, and **8**, are less toxic, making them more suitable for in vivo NMR investigations, although **5** and **7** are severely cytotoxic. The conjugates are generally much less toxic, and indeed **19** and **21** showed essentially no toxicity up to the highest concentrations tested in wild-type or lacZ-expressing cells. Intriguingly, the conjugate **17** was more toxic that its aglycon. Similar toxicity was observed for all materials in wild-type or LacZ cells. Release of the less toxic, pH-sensitive aglycons suggests a novel approach to measuring pH at the site of enzyme activity. Moreover, noting the broad specificity of β-gal, we have synthesized an alternative galactoside with the ^{19}F NMR pH indicator fluoropyridoxol (*25*), as the aglycon and preliminary data show that it is also sensitive to enzyme activity (*41*).

We believe that noninvasive detection of gene reporter molecules will become increasingly important in biomedicine. It will be important to have diverse agents, genes, and modalities for specific applications. Fluorophenyl β-D-galactosides offer a novel approach for addressing β-gal activity. Moreover, we believe the concept of using ^{19}F NMR to monitor gene transfection, together with the molecular approach presented here, can serve as a platform technology with widespread application to many diverse genes and enzymes.

ACKNOWLEDGMENT

Supported in part by DOD Breast Cancer Initiative IDEA Award BC022001 DAMD17-03-1-0343-01, a DOD Prostate Cancer Initiative Postdoctoral Award W81XWH-04-10331 (L.L.), and the Cancer Imaging Program, NCI Pre-ICMIC P20 CA086354. NMR experiments were conducted at the Mary Nell and Ralph B. Rogers NMR Center, an NIH BTRP facility (P41-RR02584).

LITERATURE CITED

(1) Bronstein, I., Fortin, J., Stanley, P. E., Stewart, G. S., and Kricka, L. J. (1994) Chemiluminescent and bioluminescent reporter gene assays. *Anal. Biochem. 219*, 169−181.

(2) Contag, C. H., Jenkins, D., Contag, P. R., and Negrin, R. S. (2000) Use of reporter genes for optical measurements of neoplastic disease in vivo. *Neoplasia 2*, 41−52.

(3) Hoffman, R. (2002) Green fluorescent protein imaging of tumour growth, metastasis, and angiogenesis in mouse models. *Lancet Oncol. 3*, 546−556.

(4) Contag, C. H., and Ross, B. D. (2002) It's not just about anatomy: In vivo bioluminescence imaging as an eyepiece into biology. *J. Magn. Reson. Imag. 16*, 378−387.

(5) Herschman, H. R. (2002) Non-invasive imaging of reporter genes. *J. Cell. Biochem. 39*, 36−44.

(6) Tjuvajev, J. G., Doubrovin, M., Akhurst, T., Cai, S., Balatoni, J., Alauddin, M. M., Finn, R., Bornmann, W., Thaler, H., Conti, P. S., and Blasberg, R. G. (2002) Comparison of radiolabeled nucleoside probes (FIAU, FHBG, and FHPG) for PET imaging of HSV1-tk gene expression. *J. Nucl. Med. 43*, 1072−1083.

(7) Haberkorn, U., Altmann, A., Jiang, S., Morr, I., Mahmut, M., and Eisenhut, M. (2001) Iodide uptake in human anaplastic thyroid carcinoma cells after transfer of the human thyroid peroxidase gene. *Eur. J. Nucl. Med. 28*, 633−638.

(8) Weissleder, R., Simonova, M., Bogdanova, A., Bredow, S., Enochs, W. S., and Bogdanov, A. J. (1997) MR imaging and

scintigraphy of gene expression through melanin induction. *Radiology 204*, 425−429.
(9) Moore, A., Josephson, L., Bhorade, R. M., Basilion, J. P., and Weissleder, R. (2001) Human transferrin receptor gene as a marker gene for MR imaging. *Radiology 221*, 244−250.
(10) Stegman, L. D., Rehemtulla, A., Beattie, B., Kievit, E., Lawrence, T. S., Blasberg, R. G., Tjuvajev, J. G., and Ross, B. D. (1999) Noninvasive quantitation of cytosine deaminase transgene expression in human tumor xenografts with in vivo magnetic resonance spectroscopy. *Proc. Natl. Acad. Sci. U.S.A. 96*, 9821−9826.
(11) Beckwith, J. R., and Zipser, D. (1970) in *The Lactose Operon*, Cold Spring Harbor, Cold Spring Harbor, NY.
(12) Serebriiskii, I. G., and Golemis, E. A. (2000) Uses of lacZ to study gene function: evaluation of β-galactosidase assays employed in the yeast two-hybrid system. *Anal. Biochem. 285*, 1−15.
(13) Kruger, A., Schirrmacher, V., and Khokha, R. (1999) The bacterial lacZ gene: An important tool for metastasis research and evaluation if new cancer therapies. *Cancer Metastasis Rev. 17*, 285−294.
(14) Pulvin, S., Friboulet, A., and Thomas, D. (1990) Substrate inhibition or activation kinetics of the β-galactosidase from the extreme thermoacidophile archaebacterium *Caldariella acidophila*. *Biochim. Biophys. Acta 1041*, 97−100.
(15) Pocsi, I., Taylor, S. A., Richardson, A. C., Smith, B. V., and Price, R. G. (1993) Comparison of several new chromogenic galactosides as substrates for various β-D-galactosidases. *Biochim. Biophys. Acta 1163*, 54−60.
(16) James, A. L., Perry, J. D., Ford, M., Armstrong, L., and Gould, F. K. (1996) Evaluation of cyclohexenoesculetin-β-D-galactoside and -hydroxyquinoline-β-D-galactoside as substrates for the detection of β-galactosidase. *Appl. Environ. Microbiol. 62*, 3868−3870.
(17) James, A. L., Perry, J. D., Chilvers, K., Robson, I. S., Armstrong, L., and Orr, K. E. (2000) Alizarin-β-D-galactoside: a new substrate for the detection of bacterial β-galactosidase. *Lett. Appl. Microbiol. 30*, 336−340.
(18) Manafi, M., Kneifel, W., and Bascomb, S. (1991) Fluorogenic and chromogenic substrates used in bacterial diagnostics. *Microbiol. Rev. 55*, 335−348.
(19) Buller, C. J., Zang, X. P., Howard, E. W., and Pento, J. T. (2003) Measurement of β-galactosidase tissue levels in a tumor cell xenograft model. *Methods Findings Exp. Clin. Pharmacol. 25*, 713−716.
(20) Youngman, P., Zuber, P., Perkins, J. B., Sandman, K., Igo, M., and Losick, R. (1985) New ways to study developmental genes in spore-forming bacteria. *Science 228*, 285−290.
(21) Alam, J., and Cook, J. L. (1990) Reporter genes: Application to the study of mammalian gene transcription. *Anal. Biochem. 188*, 245−254.
(22) Horwitz, J. P., Chua, J., Curby, R. J., Tomson, A. J., DaRooge, M. A., Fisher, B. E., Mauricio, J., and Klundt, I. (1964) Substrates for cytochemical demonstration of enzyme activity. I. Some substituted 3-indolyl-β-D-glycopyranosides. *J. Med. Chem. 7*, 574−575.
(23) Heuermann, K., and Cosgrove, J. (2001) S-Gal: an autoclavable dye for color selection of cloned DNA inserts. *Biotechniques 30*, 1142−1147.
(24) Louie, A. Y., Huber, M. M., Ahrens, E. T., Rothbacher, U., Moats, R., Jacobs, R. E., Fraser, S. E., and Meade, T. J. (2000) In vivo visualization of gene expression using magnetic resonance imaging. *Nat. Biotechnol. 18*, 321−325.
(25) Mason, R. P. (1999) Transmembrane pH gradients in vivo: measurements using fluorinated vitamin B6 derivatives. *Curr. Med. Chem. 6*, 481−499.
(26) Mason, R. P., Ran, S., and Thorpe, P. E. (2002) Quantitative assessment of tumor oxygen dynamics: molecular imaging for prognostic radiology. *J. Cell. Biochem. 87S*, 45−53.
(27) Cui, W., Otten, P., Li, Y., Koeneman, K., Yu, J., and Mason, R. P. (2004) A novel NMR approach to assessing gene transfection: 4-fluoro-2-nitrophenyl-β-D-galactopyranoside as a prototype reporter molecule for β-galactosidase. *Magn. Reson. Med. 51*, 616−620.
(28) Hwang, D. R., and Scott, M. E. A. (1988) Chromogenic Substrates for β-Galactosidase, Eur. Pat. Appl. EP 88-304173 19880509.
(29) Guder, H. J., Herrmann, R. Z., and Zdunek, D. (1992) Preparation of Nitrophenyl β-D-Galactopyranosides as β-Galactosidase Substrates for Cloned Enzyme Donor Immunoassay (CEDIA), DE 4021063 A1 19920109; assignee: Boehringer Mannheim G.m.b.H.
(30) Yoon, S., Kim, H. G., Chun, K. H., and Shin, J. E. N. (1996) 4-deoxy-analogs of *p*-nitrophenyl β-D-galactopyranosides for specificity study with β-galactosidase from *Escherichia coli*. *Bull. Korean Chem. Soc. 17*, 599−604.
(31) Garegg, P. I. (1997) Thioglycosides as glycosyl donors in oligosaccharide synthesis. *Adv. Carbohydr. Chem. Biochem. 52*, 179−205.
(32) Ernst, B., Hart, G. W., and Sinäy, P. (2000) in *Chemistry of Saccharides; Chemical Syntheses of Glycosides and Glycomimetics*, Wiley-VCH, Weinheim, Germany.
(33) Lam, S. N., and Gervay-Hague, J. (2002) Solution-phase hexasaccharide synthesis using glucosyl iodides. *Org. Lett. 4*, 2039−2042.
(34) Dushin, R. G., and Danishefsky, S. J. (1992) Stereospecific synthesis of aryl β-glucosides: an application to the synthesis of a prototype corresponding to the aryloxy carbohydrate domain of vancomycin. *J. Am. Chem. Soc 114*, 3471−3475.
(35) Ding, Y. L., and Liu, Y. T. (1991) Stereoselective syntheses of acetylated *o*-tolyl 1-thioglycosides. *Carbohydr. Res. 209*, 306−310.
(36) Mizutani, K., Kasai, R., and Tanaka, O. (1980) 13C-NMR spectroscopy of α- and β-anomeric series of alkyl L-arabinopyranosides. *Carbohydr. Res. 87*, 19−26.
(37) Kasai, R., Okihara, M., Asakawa, J., Mizutani, K., and Tanaka, O. (1979) 13C-NMR study of a- and b-anomeric pairs of D-mannopyranosides and L-rhamnopyranoside**s**. *Tetrahedron 35*, 1427−1432.
(38) Duus, J. O., Gotfredsen, C. H., and Bock, K. (2000) Carbohydrate structural determination by NMR spectroscopy: modern methods and limitations. *Chem. Rev. 100*, 4589−4614.
(39) Schmidt, F., and Monneret, C. (2002) In vitro fluorine-19 nuclear magnetic resonance study of the liberation of antitumor nitrogen mustard from prodrugs. *J. Chem. Soc., Perkin Trans 1* 1302−1308.
(40) Richard, J. P., Westerfeld, J. G., and Lin, S. (1995) Structure−reactivity relationships for β-galactosidase (*Escherichia coli*, lac Z). 1. Bronsted parameters for cleavage of alkyl β-D-galactopyranosides. *Biochemistry 34*, 11703−11712.
(41) Yu, X., and Mason, R. P. (2003) Novel in vivo gene reporter molecule using fluorinated vitamin B6 as ^{19}F NMR indicator. In *Proceedings of the International Society for Magnetic Resonance in Medicine*, Toronto, Canada, p 675 ISMRM, Berkeley, CA.

BC049936D

DNA Complexing Lipopolythiourea

Isabelle Tranchant, Nathalie Mignet, Estelle Crozat, Jeanne Leblond, Christian Girard, Daniel Scherman, and Jean Herscovici*

Laboratoire de Pharmacologie Chimique et Génétique CNRS-UMR 8115, INSERM-U640, ENSCP 11 rue Pierre et Marie Curie 75231 Paris Cedex 05, France, and Faculté des Sciences Pharmaceutiques Biologiques 4, avenue de l'Observatoire 75270 Paris Cedex 06, France. Received March 31, 2004; Revised Manuscript Received October 1, 2004

We present a neutral lipopolythiourea (DTTU) as a potential DNA-binding agent. Light scattering experiments showed that mixing a lipopolythiourea with dipalmitoylphosphatidylcholine (DPPC/DTTU) led to small particles with sizes ranging from 100 to 150 nm at optimum conditions. Setting a fixed DNA amount, an increasing amount of DTTU/DPPC or DPPC lipids was added. Particle size increased only with DTTU/DPPC, indicating that interaction occurred between the DTTU/DPPC particles and DNA. In the same way, only DTTU/DPPC limited the ethidium bromide accessibility to plasmid DNA. These data suggest that DTTU/DPPC liposomes associate to DNA, which was confirmed by agarose gel experiments. To prove the active part of the DTTU lipid itself in DNA compaction, pegoylated-lipid was used. Cholesterol-PEG_{2000} alone was not able to condense DNA. In contrast, DTTU/PEG-cholesterol was able to retain plasmid DNA on an agarose gel. In vivo injection of DTTU/DPPC/ complexes was studied. Circulation time increase for noncationic particles as compared to cationic. More obvious was the lack of nonspecific accumulation in the lung, where a gain of 3 to 40 fold was measured.

INTRODUCTION

Among the many constructs that have been used to facilitate oligonucleotides, RNA, and plasmids intracellular delivery, cationic lipids and cationic polymers have received the greatest attention (*1*). Over the course of the past several years, it has become clear that the use of cationic lipids for nucleic acid in vivo delivery is compromised by substantial problems such as interaction with negatively charged extracellular components, complement activation, platelet aggregation, and related toxicity (*2*, *3*)

To overcome these hurdles, PEG-lipid was added to cationic lipoplexes aiming at reducing their blood clearance (*4*, *5*) as was previously shown for conventional liposomes (*6*). Unexpectedly, the coating providing a steric barrier against opsonising proteins did not necessarily extend blood circulation time (*7*, *8*).

The necessity of new nonviral delivery methods prompted us and others to investigate nucleic acid complexation by noncationic systems. Efficient encapsulation of DNA plasmids inside small, neutral liposomes was achieved by the addition of optimized amounts of ethanol and calcium chloride to an aqueous mixture of small unilamellar vesicles (SUVs) and plasmid (*9*). High plasmid confinement into neutral lamellar phase was shown to be possible, without electrostatic interactions, at high lipid/DNA weight ratios (*10*).

In the present approach, we present a neutral lipopolythiourea as a potential nucleic acid binding agent. The relatively acidic thiourea NH protons (*11*), with a strong hydrogen-bond donor capability, can establish multipoint hydrogen-bonded patterns with complementary acceptor groups in a specific and predictable manner. Moreover, bis-thiourea moieties selectively bind to dihydrogenphosphate via multitopic hydrogen bonding, giving stronger complexes with $H_2PO_4^-$ than any synthetic neutral receptor known so far (*12*). Finally, thioureas show a lower tendency to self-associate than the corresponding urea analogues (*11*).

All these data prompted us to prepare and study the physicochemical properties of lipopolythiourea/DNA complexes. To compare these complexes to cationic lipoplexes, we based the design on lipopolyamine the previously reported RPR 122766 (*13*). We chose the same hydrophobic anchor connected to a trithiourea by a succinic linker to obtain a comparable size for the two lipids (Figure 1).

MATERIALS AND METHODS

All solvents were purchased from SDS (Peypin France). Dichloromethane was distilled from P_2O_5. DMF was dried over 3 Å molecular sieves and pyridine over KOH. All chemicals were purchased from Sigma-Aldrich-Fluka or Lancaster. Other solvents and products were used without further purification. Reactions were monitored by thin-layer chromatography using Merck precoated 60 F_{254} silica gel plates. Column chromatography was performed over SDS (Peypin France) 35−70 μm silicagel according to the method of Still, Khan, and Mitra (*14*). ^1H and ^{13}C NMR spectra were recorded on a BRUKER Avance DRX-300 spectrometer at 300.13 MHz for the proton and 75.47 MHz for the carbon. NMR spectra were processed using xwinnmr (Bruker) or SwaN-MR (*15*). MS and elemental analysis were carried out at the Analysis Department of Aventis, Vitry sur Seine France. Dipalmytoylphosphatidylcholine (DPPC), egg phosphatidylcholine (EPC), and phosphatidylethanolamine-lissamine rhodamine were purchased from Aventi Polar Lipids (Alabaster Alabama). All in-vivo experiments were performed with distilled water for injection. Size measurements were performed

* To whom correspondence should be addressed. E-mail: herscovi@ext.jussieu.fr.

10.1021/bc049920n CCC: $27.50 © 2004 American Chemical Society
Published on Web 10/22/2004

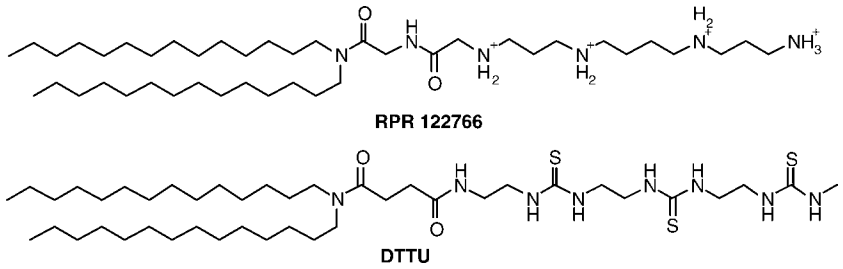


Figure 1. RPR 122766 and DTTU.

by dynamic light scattering (HPPS, Malvern Intruments). Ethidium Bromide assays were performed in a fluorospectrophotometer (Fluoromax2, Jobin Yvon).

Synthetic Procedures. *[2-(3-Ditetradecylcarbamoyl-propionylamino)-ethyl]-carbamic Acid tert-Butyl Ester (**4**).* PyBop (4.6 g, 8.84 mmol), (2-amino-ethyl)-carbamic acid *tert*-butyl ester (**3**) (1.56 g, 9.72 mmol), and diisopropylethylamine (4.24 mL, 24.31 mmol) were added successively to a stirred solution of *N,N*-ditetradecyl-succinamic acid (**2**) in dichloromethane (88 mL) at room temperature. After 4 h the solution was filtrated and evaporated to dryness. The resulting oil was purified by chromatography (heptane/ethyl acetate 1:1 then 2:8) to yield 3.79 g of **4** (66%).

^{1}H NMR ($CDCl_3$): δ (ppm) 0.87 (t, 6H, J = 6.6 Hz, H-14′), 1.25 (m, 44H, H-4′-H-11′), 1.43 (s, 9H, $(CH_3)_3$), 1.48 (m, 4H, H-2′), 2.56 (t, 2H, J = 6.7 Hz, H-2), 2.69 (t, 2H, J = 6.2 Hz, H-3), 3.28 (m, 4H, H-1′), 3.3 (m, 4H, H-5 and H-6).

^{13}C NMR ($CDCl_3$): δ (ppm) 14.07 (C-14′), 22.56 (C-13′), 26.99 ($(CH_3)_3$), 27.73 (C-3′), 28.29 (C-2), 28.59 (C-2′), 29.27 (C-4′-C-11′), 29.55 (C-3), 31.41 (C-12′), 39.85 (C-5), 40.39 (C-6), 46.21 et 47.98 (C-1′), 78.77 (C-8), 156.33 (C-7), 171.46 (C-1), 173.14 (C-4).MS (IS) calcd. for $C_{39}H_{77}N_3O_4$ 652,05, found 653.05 (MH^+), Anal. Calcd. C = 71.84; H = 11.90; N = 6.44, found C = 70.42; H = 12.45; N = 6.49.

*2-(3-Ditetradecylcarbamoyl-propionylamino)-ethylammonium Trifluoroacetate (**5**).* The carbamate **4** (1.59 g, 2.44 mmol) was dissolved in trifluoroacetic acid then the solution was stirred for 4 h. The acid was removed by evaporation then the residue was coevaporated twice with cyclohexane at room temperature. The resulting oil was dried overnight over NaOH pellets under vacuum to afford **5** (100%)

^{1}H NMR ($CDCl_3$): δ (ppm) 0.91 (t, 6H, J = 6.6 Hz, H-14′), 1.29 (m, 44 H, H-4′-H-11′), 1.51 (m, 4H, H-2′), 2.59 (t, 2H, J = 6.7 Hz, H-2), 2.71 (t, 2H, J = 6.2 Hz, H-3), 3.29 (m, 4H, H-1′), 3.31 (m, 4H, H-5 and H-6).

^{13}C NMR ($CDCl_3$): δ (ppm) 14.00 (C-14′), 22.67 (C′-13′), 27.35 (C-3′), 27.95 (C-2), 28.53 (C-2′), 29.65 (C-4′-C-11′), 30.70 (C-3), 31.94 (C-12′), 37.83 (C-5), 40.08 (C-6), 47.85 et 49.42 (C-1′), 171.72 (C-1), 173.26 (C-4).

*(2-{3-[2-(3-Ditetradecylcarbamoyl-propionylamino)-ethyl]-thioureido}-ethyl)-carbamic Acid tert-Butyl Ester (**7**).* The amine **5** (1.62 g, 2.44 mmol) was treated by triethylamine (1.36 mL, 9.76 mmol) for 15 min then the mixture was dissolved in dichloromethane (24.4 mL) and **6** was added (0.59 g, 2.92 mmol). The reaction mixture was stirred at room temperature for 12 h then the solvent was removed. The resulting oil was purified by chromatography (ethyl acetate/heptane 6:4 then pure ethyl acetate) to give 1.34 g of the thiourea **7** (yield 73%).

^{1}H NMR ($CDCl_3$): δ (ppm) 0.67 (t, 6H, J = 6.4 Hz, H-14′), 1.05 (m, 44 H, H-4′-H-11′), 1.26 (s, 9H, $CH_3)_3$), 1.35 (m, 4H, H-2′), 2.31 (m, 2H, H-2), 2.49 (m, 2H, H-3), 3.06 (m, 4H, H-1′), 3.11 (m, 4H, H-5 and H-9), 3.47 (m, 4H, H-6 and H-8), 7.14 (2H, H thiourea).

^{13}C NMR ($CDCl_3$): δ (ppm) 13.95 (C-14′), 22.57 (C-13′), 26.92 ($(CH_3)_3$), 27.07 (C-3′), 27.78 (C-2), 28.39 (C-2′), 28.82 (C-4′-C-11′), 29.55 (C-3), 31.83 (C-12′), 39.45 (C-5, C-9), 43.63 (C-6 et C-8), 46.39 and 48.16 (C-1′), 79.24 (C-11), 156.53 (C-10), 171.72 (C-1), 173.71 (C-4), 182.97 (C-7).

*2-{3-[2-(3-Ditetradecylcarbamoyl-propionylamino)-ethyl]-thioureido}-ethylammonium Trifluoroacetate (**8**).* The carbamate **7** (1.5 g, 9.86 mmol) was reacted with trifluoroacetic acid (0.76 mL, 9.86 mmol) for 3 h, and then the mixture worked-up as for **5** afforded the amine **8** (100%).

^{1}H NMR ($CDCl_3$): δ (ppm) 0.67 (t, 6H, J = 6.4 Hz, H-14′), 1.05 (m, 44 H, H-4′-H-11′), 1.31 (m, 4H, H-2′), 2.31 (m, 2H, H-2), 2.49 (m, 2H, H-3), 3.06 (m, 4H, H-1′), 3.11 (m, 4H, H-5 and H-9), 3.44 (m, 4H, H-6 and H-8), 7.10, (2H, H thiourea).

^{13}C NMR ($CDCl_3$): δ (ppm) 13.85 (C-14′), 22.49 (C-13′), 27.01 (C-3′), 27.72 (C-2), 28.29 (C-2′), 28.79 (C-4′-C-11′), 29.49 (C-3), 31.77 (C-12′), 39.42 (C-5, C-9), 43.75 (C-6 and C-8), 46.29 and 48.09 (C-1′), 171.72 (C-1), 173.71 (C-4′), 182.97 (C-7).

*(2-{3-[2-(2-{3-[2-(3-Ditetradecylcarbamoyl-propionylamino)-ethyl]-thioureido}-ethylamino)-ethyl]-thioureido}-ethyl)-carbamic Acid tert-Butyl Ester (**9**).* The amine **8** (1.47 g, 1.98 mmol) was treated by triethylamine (1.1 mL, 7.92 mmol) for 15 min then the mixture was dissolved in dichloromethane (20 mL) and **6** was added (0.46 g, 2.38 mmol). The reaction mixture was stirred at RT for 12 h, and then the solvent was removed. The resulting oil was purified by chromatography (ethyl acetate/heptane 6:4 then pure ethyl acetate/methanol 98:2) to give 1.14 g of the di-thiourea **9** (yield 67%).

^{1}H NMR ($CDCl_3$): δ (ppm) 0.74 (t, 6H, J = 6.6 Hz, H-14′), 1.12 (m, 44 H, H-4′-H-11′), 1.30 (s, 9H, $CH_3)_3$), 1.45 (m, 4H, H-2′), 2.41 (m, 2H, H-2), 2.58 (m, 2H, H-3), 3.12 (m, 4H, H-1′), 3.25 (m, 4H, H-5 and H-12), 3.56 (m, 8H, H-6, H-8, H-9, H-11), 7.14 (4H, H thiourea).

^{13}C NMR ($CDCl_3$): δ (ppm) 14.06 (C-14′), 22.57 (C-13′), 27.11 (C-3′), 26.93 ($(CH_3)_3$), 27.79 (C-2), 28.38 (C-2′), 28.81 (C-4′-C-11′), 29.56 (C-3), 31.83 (C-12′), 39.55 (C-5, C-12), 43.66 (C-6, C-8, C-9, C-11), 46.49 and 48.23 (C-1′), 79.28 (C-14), 156.61 (C-13), 171.96 (C-1), 173.72 (C-4), 182.93 (C-7, C-10). ms (IS), Anal. Calcd. for $C_{45}H_{89}N_7O_4S_2$ 856.38, found 857.38 (MH^+).

*2-{3-[2-(2-{3-[2-(3-Ditetradecylcarbamoyl-propionylamino)-ethyl]-thioureido}-ethylamino)-ethyl]-thioureido}-ethylammonium Trifluoroacetate (**10**).* The carbamate **9** (1 g, 1.15 mmol) was reacted with trifluoroacetic acid (0.45 mL, 5.84 mmol) for 3 h, and then the mixture worked-up as for **5** afforded the amine **10** (100%).

^{1}H NMR ($CDCl_3$): δ (ppm) 0.85 (t, 6H, J = 6.6 Hz, H-14′), 1.25 (m, 44 H, H-4′-H-11′), 1.48 (m, 4H, H-2′), 2.65 (m, 2H, H-2), 2.77 (m, 2H, H-3), 3.26 (m, 4H, H-1′), 3.43 (m, 4H, H-5, H-12), 3.85 (m, 8H, H-6, H-8, H-9, H-11), 7.44 (4H, H thiourea).

^{13}C NMR ($CDCl_3$): δ (ppm) 14.05 (C-14′), 22.68 (C-13′), 27.05 (C-3′), 27.58 (C-2), 28.71 (C-2′), 29.36 (C-4′-C-11′), 29.67 (C-3), 31.94 (C-12′), 40.49 (C-5), 43.49 (C-6, C-8, C-9, C-11), 47.40 and 49.07 (C-1′), 172.16 (C-1), 174.00 (C-4), 182.73 (C-7, C-10).

*N-(2-{3-[2-(2-{3-[2-(3-Methyl-thioureido)-ethyl]-thioureido}-ethylamino)-ethyl]-thioureido}-ethyl)-N′,N′-ditetradecyl-succinamide (**11**).* The amine **10** (0.24 g, 0.28 mmol) was treated by triethylamine (1.1 mL, 7.92 mmol) for 15 min, and then the mixture was dissolved in dichloromethane (3 mL) and methyl isothiocyanate was added (0.024 g, 0.34 mmol). The reaction mixture was stirred at RT for 12 h, and then the solvent was removed. The resulting oil was purified by chromatography (ethyl acetate/heptane 6:4 then pure ethyl acetate/methanol 98:5) to yield the tri-thiourea **11** (0.12 g, 51%).

^{1}H NMR ($CDCl_3$): δ (ppm) 0.86 (t, 6H, J = 6.7 Hz, H-14′), 1.24 (m, 44 H, H-4′-H-11′), 1.44 (m, 4H, H-2′), 2.52 (m, 2H, H-2), 2.67 (m, 2H, H-3), 3.05 (m, 3H, H-14), 3.21 (m, 4H, H-1′), 3.32 (m, 2H, H-5), 3.75 (m, 10H, H-6, H-8, H-9, H-11, H-12), 7.14 (6H, H thiourea).

^{13}C NMR ($CDCl_3$): δ (ppm) 14.09 (C-14′), 22.69 (C-13′), 27.24 (C-3′), 27.89 (C-2′), 28.87 (C-2), 29.38 (C-4′ C-11′), 29.67 (C-3), 31.26 (C-14), 31.94 (C-12′), 39.71 (C-5), 43.63 (C-6, C-8, C-9, C-11, C-12), 46.67 and 48.40 (C-1′), 172.16 (C-1), 174.00 (C-4), 182.73 (C-7, C10, C-13). MS (IS) calcd. for $C_{42}H_{84}N_8O_2S_3$ 829.38, found 830.38 (MH^+). Anal. Calcd. for $C_{42}H_{84}N_8O_2S_3$ C = 60.82; H = 10.21; N = 13.51; S = 11.60, found C = 60.73; H = 11.16; N = 12.47; S = 9.38.

Preparation of the Liposomes DTTU/DPPC by the Film/Hydration Method. Compound **11** (2 mg, 2.4 μmol) and DPPC (3.5 mg, 4.8 μmol) were dissolved in 500 μL of $CHCl_3$. After solvent removal under vacuum, the film obtained was hydrated with 240 μL of H_2O at 4 °C to give a 30 mM multilamellar liposome. Liposomes were successively heated at 45 °C and sonicated (Branson) during 10 min to form a polydisperse population of liposomes with a mean diameter of 142 ± 41 nm.

Preparation of the Liposomes DTTU/DPPC by the Ethanolic Injection Method. Compound **11** (2 mg, 2.4 μmol) and DPPC (3.5 mg, 4.8 μmol) were dissolved in 500 μL of a 1/1 mixture of acetone/ethanol. This mixture was dropped on stirred water (5 mL). Most of the solvents were removed under vacuum to obtain a fairly concentrated suspension (580 μL of H_2O, 12.4 mM) of liposomes exhibiting a mean diameter of 101 ± 34 nm.

Preparation of the Liposomes DTTU/PEG-Cholesterol. Compound **11** (2 mg, 2.4 μmol) and cholesterol-PEG_{2000} (0.12 μmol) were dissolved in 500 μL of $CHCl_3$. After solvent removal under vacuum, the film obtained was hydrated with 250 μL of H_2O at 4 °C to give a 10 mM multilamellar liposome. Liposomes were successively warmed and sonicated (Branson) during 10 min to form a polydisperse population of liposomes with a mean diameter of 200 ± 45 nm.

Preparation of the Complexes DPPC/DTTU/DNA. Plasmid DNA (pXL3031, from Gencell S.A) (400 μL, 0.02 g/L in Hepes 40 mM, pH 7.4; NaCl 300 mM) was added to various amounts of DPPC/DTTU liposomes (400 μL, 5 mM total lipids, H_2O) at RT, and the mixture was vortexed during 10 s and left at RT for 2 h before size measurements, which were performed on a HPPS (Malvern Intruments), using water viscosity and refractive index.

Ethidium Bromide Displacement Assays. A Jobin-Yvon Spex Fluoromax-2 spectrofluorometer (Longjumeau, France) was used to measure ethidium bromide fluorescence (Excitation 260 nm, emission 590 nm) at 25 °C. EtBr (3 μL, 1 mg/mL) was added to the complex suspension (800 μL, 10 μg/mL DNA). Values are expressed as a fluorescence percentage of ethidium bromide with free plasmid DNA, taken as a 100%.

Agarose Gel Electrophoresis. Samples were prepared as described above (20 μL) and 5 μL of 30% glucose was added. The mixtures were loaded into 0.8% (w/v) agarose gel at 70 V/cm in TBE buffer (1 M Tris, 0.9 M boric acid, 0.01 M EDTA). DNA was revealed with EtBr and visualized under UV light.

Zeta Potential Analysis. The zeta potential was determined using a ZetaSizer 3000HS (Malvern Instruments, Southborough, MA). The system was calibrated using a −50 ± 5 mV standard (DTS 50/50 Standard; Malvern Instruments). Complex samples prepared as described above in 20 mM NaCl subjected to 3 × 30 s (1000 Hz, no field correction) measurement.

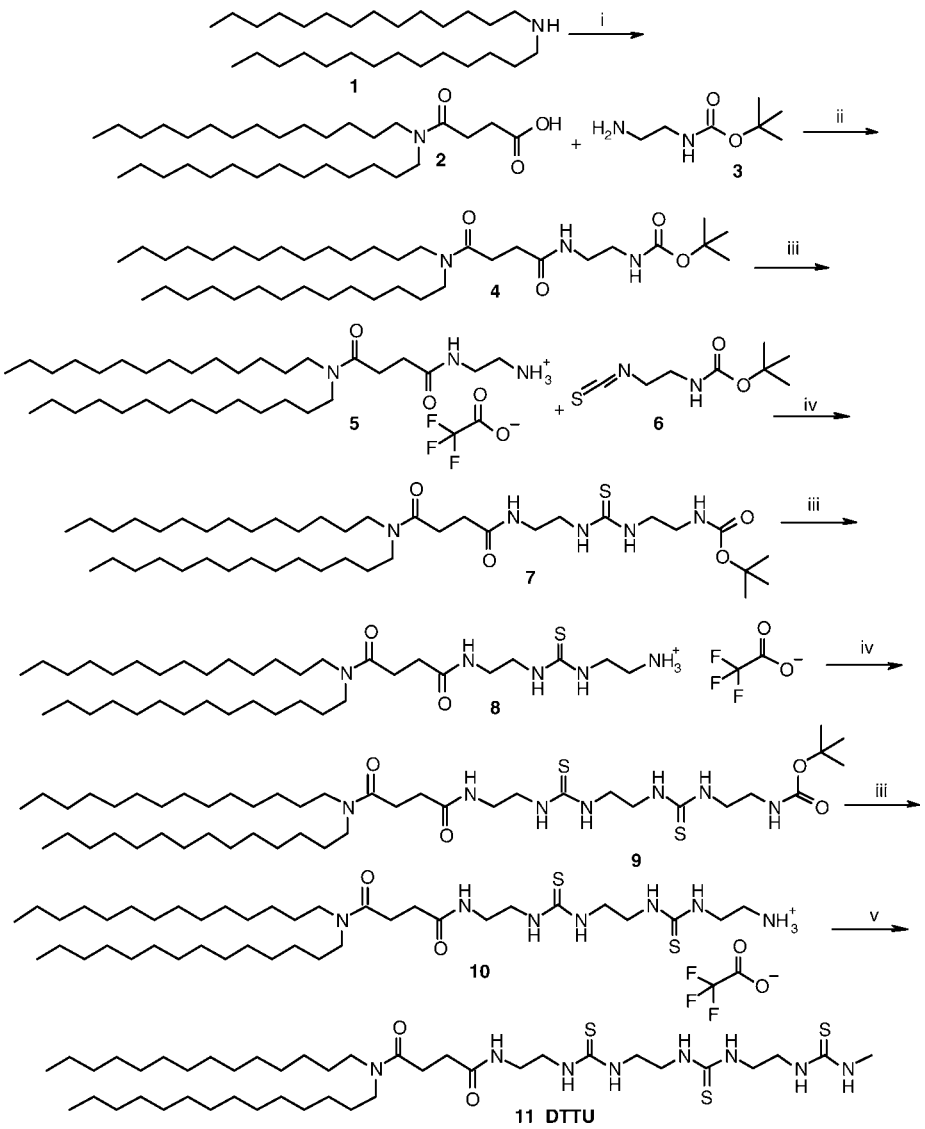
DNA Stability in Mouse Serum. A solution of complexes was prepared in 5% glucose, [DNA] = 0.25 g/L, with a total lipid/DNA charge ratio = 40 or 60 nmol/μg. For each complex tested, 50 μL of lipoplexes was incubated for 30 min at 37 °C/5% CO_2 in 1 mL serum diluted or not in 150 mM NaCl. Phenol/chloroform (1/1, v/v, 200 μL) and a solution of TRIS-EDTA (100 μL; 100 mM−10 mM, pH 8) were added to the lipoplex mixture in serum (200 μL). The mixture was vortexed and then centrifuged (Jouan MR 18 22, 12 000 rpm, 5 min, 4 °C) in microtubes. The aqueous phase was isolated and washed with a same volume of $CHCl_3$, and then centrifuged (Jouan MR 18 22, 12 000 rpm, 5 min, 4 °C). A solution of AcONa (10 μL, 3M) and EtOH (300 μL) was added in aqueous phase and stored at −20 °C. After 30 min, the mixture was centrifuged (Jouan MR 18 22, 12 000 rpm, 20 min, 4 °C), and the solvent was delicately removed. DNA was resuspended in H_2O and 1 μg was loaded on 1% agarose gel in 1% TBE buffer and electrophorized for 2 h at 70 V/cm in TBE buffer. DNA was revealed with ethidium bromide and visualized under UV light.

In Vivo Distribution in Tumor-Bearing Mice. Lewis Lung carcinoma tumors were implanted subcutaneously in the right flank of 6-week-old female C57Bl/6 mice (Charles River), and 10−14 days after biodistribution studies were undertaken as previously described.

Six-week-old female C57Bl/6 mice (Charles River) were anesthetized by intraperitoneal injection of a mix of ketamine (85.8 mg/kg; Merial) and xylazine (3.1 mg/kg; Bayer) diluted in 150 mM NaCl. Two hundred microliters of rhodamine-labeled complexes (10 μg of DNA, 400 nmol lipids in 5% glucose) were injected into the mouse tail vein. Blood was collected by cardiac puncture at appropriate intervals (30 min, 1, 2, 4, and 6 h after injection) and mice were euthanized at the end of the experiment. In the distribution study, mice were sacrificed at 30 min and 8 h after injection and the liver, spleen, lungs, and tumors were removed, weighed, and homogenized in pH 7.4 PBS (5 mL/g tissue). Experiments were conducted following the NIH recommendation for animal experimentation and Aventis local ethic committee on animal care and experimentation.

Rhodamine-labeled lipids were extracted from 100 μL of blood or tissue homogenates with 3 mL of $CHCl_3$/MeOH (1/1, v/v) by vigorously mixing during 30 min for blood and 40 min for tissue homogenates, followed by centrifugation (3000 rpm, 10 min). The fluorescence intensity was assayed on the supernatant with a fluorospectrophotometer (Fluoromax 2, Jobin Yvon). The amount of lipoplexes in the blood or tissue homogenates

Scheme 1. Preparation of the Lipopolythiourea[a]



[a] Reagents and conditions: (i) succinic anhydride, DMAP, pyridine, CH_2Cl_2, 98%; (ii) PyBop, diisopropylethylamine, RT, 66%; (iii) trifluoroacetic acid, RT, 100%; (iv) triethylamine, 67−72%; (v) triethylamine, methyl isothiocyanate, 51%.

was evaluated with a calibration curve and expressed as the remaining percentage of injected dose.

RESULTS

The lipopolythiourea was prepared as shown in Scheme 1. First, ditetradecylamine was reacted with succinic anhydride in the presence of DMAP and pyridine to give the succinate **2** in 98% yield. Reaction of **2** with the monoprotected diethylamine **3** in the presence of PyBop afforded **4** in 66% yield. After removal of the *tert*-butoxy carbamate, using trifluoroacetic acid, the resulting amine **5** was treated with the isothiocyanate **6** (*16*) to yield the thiourea **7** (73%).

Deprotection of **7**, then condensation with **6**, led to the amino thiourea **9**. Repetition of the same sequence on **9** afforded the di-thiourea **10**. Finally, removal of the protecting group then treatment with methyl isothiocyanate gave the ditetradecyl amino trithiourea **11** (DTTU) in 51% yield.

Formulation Study. The ability of lipopolythiourea (DTTU) **11** to form micellar or liposomal particles was then evaluated. The DTTU hydrophobicity prevents its solubilization in H_2O and particle formation. We added phosphatidylcholine (PC) as an amphiphilic co-lipid because of its high hydration potency and its zwitterionic nature. We evaluated the association to DTTU of EPC and of DPPC. Both EPC and DPPC formed mixed vesicles with DTTU. A ratio DTTU/DPPC of 1/2 is optimal to obtain a stable lipidic suspension. Energy gained by sonication to reduce particle size resulted in particles exhibiting a 142 ± 41 nm size distribution, as found by dynamic light scattering experiments. The potential primary amine containing lipid due to DTTU degradation was checked before and after sonication using the fluorescamine test (*17*) and zeta potential measurements ($\zeta = +7.1 \pm 2.8$ mV before sonication, $\zeta = +8.8 \pm 3.4$ mV after sonication).

The formation of liposomes by ethanol injection, which does not require any energy gain by sonication, was also performed with the same ratio DTTU/DPPC and spontaneously gave smaller particles (diameter 101 ± 34 nm; $\zeta = +5.4 \pm 4.3$ mV).

Interaction of DTTU/DPPC with DNA. The capacity of the DTTU/DPPC particles to associate to plasmid DNA was then studied and compared to DPPC/DNA association. Setting a fixed DNA amount, we added an increasing amount of DTTU/DPPC or DPPC lipids and measured the size of the particles obtained by dynamic

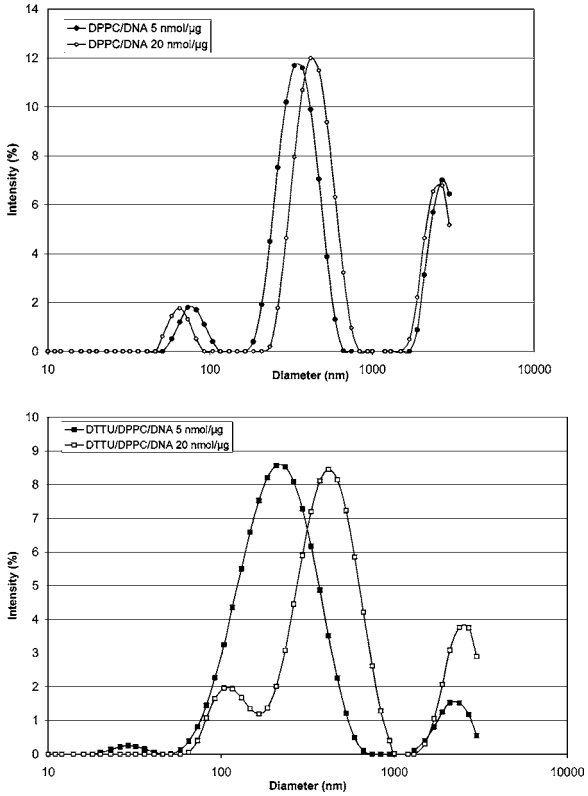


Figure 2. Diameter of the (a) DPPC/DNA particles and (b) DTTU/DPPC/DNA particles measured by dynamic light scattering. Plasmid DNA (8 μg) was added to various amounts of total lipid.

light scattering. Increasing the amount of DPPC from 5 to 20 nmol/μg DNA did not lead to any particle size modification (Figure 2). In contrast, above a ratio of 5 nmol of DTTU/DPPC lipids/μg of DNA, particle size increase was observed, leading to micrometer-range particles (Figure 2). This diameter change clearly indicated that in the conditions used an interaction occurred between the DTTU/DPPC particles and DNA and not between DPPC and DNA.

Interestingly, by increasing the amount of total lipid (over 20 nmol of lipid/μg of DNA), we observed stabilized particles with a size distribution of 170 $\pm$ 45 nm. We had previously observed such an interaction profile with a cationic lipid, by increasing the ratio lipid over DNA ratio (*18*), aggregation then stabilization.

We observed that addition of DPPC to DNA did not alter significantly ethidium bromide intercalation into DNA. In contrast, DTTU/DPPC presence limited the ethidium bromide accessibility to plasmid DNA, reducing the ethidium bromide fluorescence by a factor of 4 when the ratio lipid/DNA was increased from 0 to 20 nmol/μg. The observed decrease of ethidium bromide fluorescence reveals a lower DNA intercalation. It suggests that DTTU/DPPC liposomes associate to DNA, leading to a DNA compacted state preventing ethidium bromide access to DNA.

Agarose gel electrophoresis of the liposome/DNA complexes confirmed that plasmid DNA associates to DTTU/DPPC liposomes, with a decreasing amount of DNA migrating in the gel. In contrast, mixing the same lipid amount of DPPC alone with DNA did not retain DNA in the wells (Figure 4). The signal UV active in the wells might indicate that part of the nonmigrating DNA, which is associated to DTTU/DPPC liposomes, is accessible to ethidium bromide intercalation. Addition of cations such as Ca^{2+} instead of Na^{+} did not modify DNA retention on an agarose gel under the same conditions (not shown).

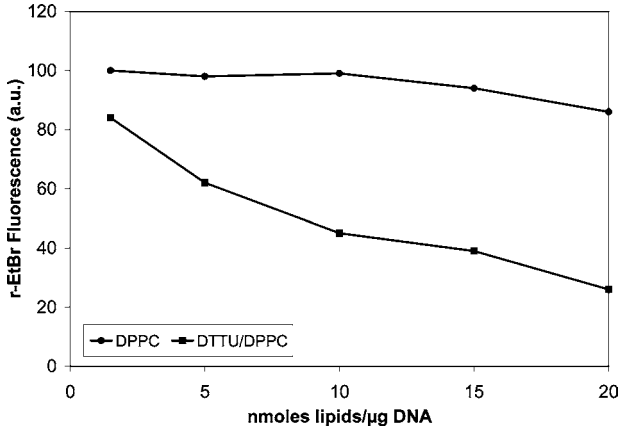


Figure 3. DNA was mixed with various amounts of DTTU/DPPC (1/2) liposomes. Ethidium bromide was then added and fluorescence was monitored at 590 nm.

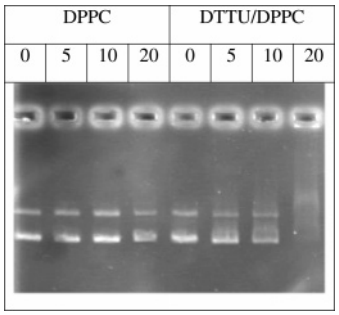


Figure 4. Migration of the DPPC/DNA and DTTU/DPPC/DNA complexes on a 0.8% agarose gel in TBE (1×). Complexes were revealed with ethidium bromide staining. From left to right, the lanes correspond to 0, 5, 10, 20 nmol of lipid/μg of DNA.

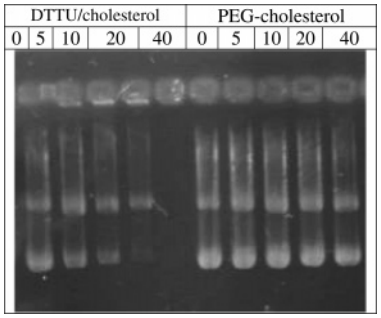


Figure 5. Complexes DTTU/cholesterol-PEG_{2000}/DNA and cholesterol-PEG_{2000}/DNA were loaded on a 0.8% agarose gel in TBE (1×) and revealed with EtBr staining. Total amount of lipids used is indicated (nmol of lipid/μg of DNA).

To prove the active part of the DTTU lipid itself in DNA compaction, we used a pegoylated-lipid (*7*) (cholesterol-PEG_{2000}) neutral as a co-lipid for DTTU lipid. We then checked by agarose gel electrophoresis the ability of this lipid mixture to associate with plasmid DNA. As observed in Figure 5, within the amount of lipid used, cholesterol-PEG_{2000} alone was not able to condense DNA and allowed DNA electrophoresis in the gel. In contrast, the mixture DTTU/PEG-cholesterol was able to retain plasmid DNA in deposit wells at 10, 20, and particularly 40 nmol of lipid/μg of DNA. This experiment confirms the active role played by the DTTU lipid in DNA association.

Zeta potential of the mixture DTTU/DPPC $\pm$ DNA was compared to the one obtained for lipopolyamine/DPPC $\pm$ DNA. Addition of DNA to DTTU/DPPC induced a

Table 1. Zeta Potential (mV) of DTTU/DPPC ± DNA, DTTU/Cholesterol-PEG$_{2000}$ ± DNA Complexes and RPR209120/DPPC/DNA Complexes Measured in 20 mM NaCl on a Malvern Instruments 3000HS[a]

	method	20 mM NaCl	+DNA/ 20 mM NaCl
lipopolyamine (L/D 5)	ethanolic injection	+60.1 ± 2.4	+30 ± 3.5
DTTU/DPPC 1/2 (L/D 20)	film + hydration	+8.8 ± 3.4	−20.3 ± 3.5
DTTU/DPPC 1/2 (L/D 20)	ethanolic injection	+5.4 ± 4.3	−16.6 ± 2.5
DTTU/CholPEG (L/D 20)	film + hydration	+1.8 ± 4.2	−0.2 ± 3.2

[a] L/D = ratio lipid/DNA in nmol of lipid/μg of DNA.

negatively charged zeta potential of −20.3 ± 3.5 mV for the DTTU/DPPC particles prepared by the film hydration method and −16.6 ± 2.5 mV for the particles prepared by the ethanolic injection method (Table 1).

Zeta potentials obtained by the two methods are quite comparable (with or without DNA) and far below the one obtained for the lipopolyamine control and other previously described cationic lipids (*19*). As expected, addition of 10% cholesterol-PEG$_{2000}$ to the DTTU lipid gave a zeta potential close to neutrality in the presence and absence of DNA. To explain the slightly positive value of potential zeta obtained for the DTTU/DPPC formulation in 20 mM NaCl, we searched for a potential amine contamination in each formulation using the fluorescamine test. Reaction of fluorescamine with alanine was taken as the calibration curve for amine quantification. We found 0.2% mol of amine in the DTTU/DPPC liposome prepared by the film method after sonication. This amount of amine could be responsible for the slightly positive zeta potential obtained, although this amount of amine could undeniably not be responsible for the DNA retention on an agarose gel or lipoplex size increase. Indeed, the amount of DTTU/DPPC used for DNA association: 20 nmol/μg lipid would represent 0.013 nmol of amine content/nmol of DNA phosphate, which is clearly not enough to account for the association effect observed.

DNA Protection toward Serum Enzymatic Degradation. DNA protection toward serum degradation was investigated in 20 and 100% serum in the absence and presence of DTTU/DPPC. After 30 min incubation at 37 °C, DNA was extracted by a phenol/chloroform process and loaded onto an agarose gel (Figure 6). In these two conditions, free DNA is fully degraded (lanes 4 and 7), while DNA integrity is conserved in 20% serum and partially maintained in 100% serum when associated to DTTU/DPPC (40 and 60 nmol/μg).

In Vivo Injection of DTTU/DPPC/DNA Complexes. Our interest in DTTU as complexing agent lies in the passive accumulation into tumor that could arise from longer circulation time, as previously reported with PEG-coated liposome (*20*). Indeed, reducing the charge of the lipid/DNA complexes should result in less protein interaction. Complexes including 5% PEG-cholesterol for stability and 1% DOPE-rhodamine for detection were injected into mice subcutaneously implanted with a Lewis lung carcinoma model. The lipids were extracted from the organs and treated for rhodamine recovery as described (Figure 7) (*12*).

Circulation time increase for noncationic particles as compared to cationic particles was noticeable after 30 min; 34 versus 17% was recovered in the blood. More obvious was the lack of nonspecific accumulation in the lung, where a gain of 3−40 was measured for noncationic

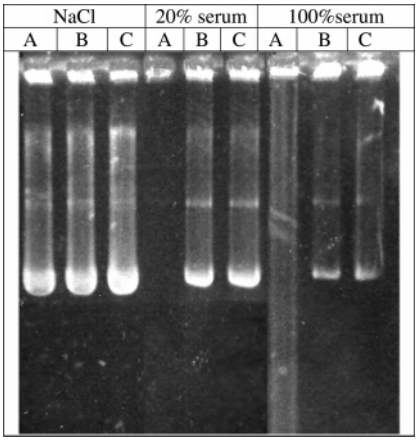


Figure 6. Integrity of plasmid DNA after complex exposure to mouse serum. DNA (A), DTTU/DPPC/DNA, 40 nmol/μg (B), and 60 nmol/μg (C) were incubated at 37 °C for 30 min in 150 mM NaCl, 20% serum or 100% serum. Plasmid was then extracted with phenol/$CHCl_3$ and its integrity was analyzed on a 0.8% agarose gel.

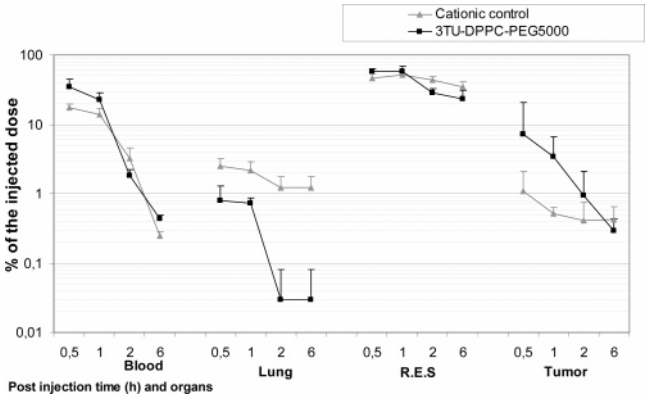


Figure 7. Biodistribution of fluorescently labeled particles. Cationic particles RPR209120/DPPC/cholesterol-PEG$_{2000}$/PE-rhodamine (triangles) used for the control were prepared via the ethanolic injection method as DTTU/DPPC/cholesterol-PEG$_{2000}$/PE-rhodamine particles (squares). Each point is an average of 5 mice + SD.

particles with regard to the cationic controls. Noncationic particles were also recovered in the reticuloendothelial system (liver + spleen) even at the early times. Passive accumulation seems to have occurred since a factor of 6.5 increase was found in the tumor at 30 min postinjection and was maintained after 1 h for noncationic particles versus cationic controls. No increase in transgene expression was found associated to the lipid accumulation, despite the co-injection of lipids/DNA where the plasmid-DNA expressed chloramphenicol acetyl transferase. It has to be noted that a low amount of DNA was injected (10 μg) per mouse.

DISCUSSION

The above data show that the lipopolythiourea DTTU can associate with plasmid DNA and protect it from degradation in serum. To date, this is the first report of a noncationic lipid able to associate to polyanionic DNA at low lipid concentration (*10*) and without addition of divalent cationic ions (*21*). DNA was shown to bind to DPPC zwitterionic lipid bilayers strongly enough to perform AFM studies (*9*, *22*). However, in our conditions, the DPPC binding is not sufficient to retain DNA on agarose wells, compete with ethidium bromide intercalation between DNA base pairs, nor induce a DPPC particle

size increase. The active part played by the lipopolythiourea in the interaction between DNA and DTTU/DPPC was evidenced by formulating DTTU with a cholesterol-PEG instead of DPPC.

Several processes could explain how DNA interaction occurs with DTTU/DPPC particles. The slightly positive zeta potential observed with DTTU/DPPC particles might be explained by the strong polarization of the NH linkage in the thiourea functions, which might be involved in the hydrogen bonds with DNA phosphates. As hypothesized, hydrogen bonds between the DNA phosphate groups and the thiourea headgroups might occur (*23*).

An alternative hypothesis to explain DNA association to neutral lipopolythiourea is to consider the polarization of the lipopolythiourea moiety. One can assume that the negatively polarized sulfur interacts with cationic monovalent or divalent cations from the solution. Such an interaction might account for the positive zeta potential of the DTTU/DPPC liposomes. It might also account for the DNA complexation effect. The involvement of cations has been demonstrated in the case of cochleates which are delivery particles composed of anionic lipids (*20*).

In conclusion, we describe here a new "noncationic" DNA interacting self-assembling system. Because of their very low zeta potential precluding nonspecific binding to plasmatic membrane and adsorption mediated endocytosis, we did not expect DTTU/DPPC/DNA particles to display high transfection efficiency. Indeed, preliminary experiments led to very weak transfection. Targeting DTTU/DPPC/DNA particles to membrane receptor and receptor-mediated transfection might represent the most suitable way to use these new DNA complexing particles for gene transfer. This lipid family might prove to be better tolerated in vivo than cationic DNA delivery vectors. Its ultimate capacity to efficiently deliver plasmid DNA in vitro and in vivo through the use of targeting moieties as well as the study of new polythiourea structures (*24*) is under investigation.

ACKNOWLEDGMENT

This work was supported by CNRS, ENSCP, and Gencell S. A. I.T. thanks Aventis Pharma for a graduate fellowship. We thank Dr. Michel Bessodes for providing us the pegoylated cholesterol.

LITERATURE CITED

(1) Miller, A. D. (1998) Cationic liposomes for gene therapy. *Angew. Chem., Int. Ed. 37*, 1768−1785.

(2) Zelphati, O., Uyechi, L. S., Barron, L. G., and Szoka R. C., Jr. (1998) Effect of serum components on the physico-chemical properties of cationic lipid/oligonucleotide complexes and on their interactions with cells. *Biochim. Biophys. Acta 1390*, 119−133.

(3) Tousignant, J. D., Gates, A. L., Ingram, L. A., Johnson, C. L., Nietupski, J. B., Cheng, S. H., Eastman, S. J., and Scheule, R. K. (2000) Comprehensive analysis of the acute toxicities induced by systemic administration of cationic lipid: plasmid DNA complexes in mice. *Hum. Gene Ther. 11*, 2493−2513.

(4) Wheeler, J., Palmer, L., Ossanlou, M., MacLachlan, M., Graham, R., Zhang, Y., Hope, M., Scherrer, P., and Cullis, P. (1999) Stabilized plasmid-lipid particles: construction and characterization. *Gene Ther. 6*, 271−281.

(5) Hofland, H. E., Masson, C., Iginla, S., Osetinsky, I., Reddy, J. A., Leamon, C. P., Scherman, D., Bessodes, M., and Wils, P. (2002) Folate-targeted gene transfer in vivo. *Mol. Ther. 6*, 739−744.

(6) Papahadjopoulos, D., Allen, T, Gabizon, A., Mayhew, E., Matthay, K., Huang, S., Lee, K., Woodle, M., Lasic, D., Redemann, C., and Martin, F. (1991) Sterically stabilized liposomes: improvements in pharmacokinetics and antitumor therapeutic efficacy. *Proc. Natl. Acad. Sci. U.S.A. 88*, 11460−11464.

(7) Nicolazzi, C., Mignet, N., De la Figuera, N., Cadet, M., Torero-Ibad, R., Seguin, J., Scherman, D., and Bessodes, M. (2003) Anionic polyethylene glycol lipids added to cationic lipoplexes increase their plasmatic circulation time. *J. Controlled Release 88*, 429−443.

(8) Oupicky, D., Ogris, M., Howard, K. A., Dash, P. R., Ulbrich, K., and Seymour, L. W. (2002) Importance of lateral and steric stabilization of polyelectrolyte gene delivery vectors for extended systemic circulation *Mol. Ther. 5*, 463−472.

(9) Bailey, A. L., and Sullivan, S. M. (2000) Efficient encapsulation of DNA plasmids in small neutral liposomes induced by ethanol and calcium. *Biochim. Biophys. Acta 1468*, 239−252.

(10) Pott, T., and Roux, D. (2002) DNA intercalation in neutral multilamellar membrane. *FEBS Lett. 5*, 150−154.

(11) Bordwell, F. G., Algrim, D. J., and Harrelson, J. A., Jr. (1988) The relative ease of removing a proton, a hydrogen atom, or an electron from carboxamides versus thiocarboxamides. *J. Am. Chem. Soc. 110*, 5903−5904.

(12) Buhlmann, P., Nishizawa, S., Xiao, K. P., and Umezawa, Y. (1997) Strong hydrogen bond-mediated complexation of H_2PO_4- by neutral bis-thiourea hosts. *Tetrahedron 53*, 1647−1654.

(13) Byk, G., Dubertret, C., Escriou, V., Frederic, M., Jaslin, G., Rangara, R., Pitard, B., Crouzet, J., Wils, P., Schwartz, B., and Scherman, D. (1998) Synthesis, Activity, and Structure−Activity Relationship Studies of Novel Cationic Lipids for DNA Transfer. *J. Med. Chem. 41*, 224−235.

(14) Still, W. C., Kahn, M., and Mitra, A. *J. Org. Chem.* **1978**, *43*, 2923−2926.

(15) Balacco, G. *J. Chem. Inf. Comput. Sci.* **1994**, *34*, 1235−1241.

(16) Kneeland, D. M., Ariga, K., Lynch, V. M., Huang, C. Y., Anslyn, E. V. (1993) Bis(alkylguanidinium) receptors for phosphodiesters: effect of counterions, solvent mixtures, and cavity flexibility on complexation. *J. Am. Chem. Soc. 115*, 10042−10055.

(17) Stocks, S. J., Jones, A. J., Ramey, C. W., and Brooks, D. E. (1986) A fluorometric assay of the degree of modification of protein primary amines with polyethylene glycol. *Anal. Biochem. 154*, 232−234.

(18) Pitard, B., Aguerre, O., Airiau, M., Lachagès, A. M., Boukhnikachvili, T., Byk, G., Dubertret, C., Herviou, C., Scherman, D., Mayaux, J. F., and Crouzet, J. (1997) Virus-sized self-assembling lamellar complexes between plasmid DNA and cationic micelles promote gene transfer. *Proc. Natl. Acad. Sci. U.S.A. 94*, 14412−14417.

(19) Son, K., Patel, D., Tkach, D., and Park, A. (2000) Cationic liposome and plasmid DNA complexes formed in serum-free medium under optimum transfection condition are negatively charged. *Biochim. Biophys. Acta 1466*, 11−15.

(20) Tam, P., Monck, M., Lee, D., Ludkovski, O., Leng, E., Clow, K., Stark, H., Scherrer, P., Graham, R., and Cullis, P. (2000) Stabilized plasmid-lipid particles for systemic gene therapy. *Gene Ther. 7*, 1867−1874.

(21) Tilcock, C., Bally, M., Farren, S., Cullis, P., and Gruner, S. (1984) Cation-dependent segregation phenomena and phase behavior in model membrane systems containing phosphatidylserine: influence of cholesterol and acyl chain composition. *Biochemistry 23*, 2696−2703.

(22) Malghani, M., and Yang, J. (1998) Stable binding of DNA to zwitterionic lipid bilayers in aqueous solutions. *J. Phys. Chem. B 102*, 8930−8933.

(23) Erkang, F., Scott, A., Van, Arman, S., Kincaid, S., and Hamilton, A. (1993) Molecular recognition: hydrogen-bonding receptors that function in highly competitive solvents. *J. Am. Chem. Soc. 115*, 369−370.

(24) Girard, C., Tranchant, I., Gorteau, V., Potey, L., and Herscovici, J. (2004) Development of a DNA interaction test with small molecules still grafted on solid phase. *J. Comb. Chem. 6*, 275−278.

BC049920N

Synthesis and Biological Activity of Water-Soluble Maleimide Derivatives of the Anticancer Drug Carboplatin Designed as Albumin-Binding Prodrugs

André Warnecke,[†] Iduna Fichtner,[‡] Dirk Garmann,[#] Ulrich Jaehde,[#] and Felix Kratz*,[†]

Tumor Biology Center, Breisacher Strasse 117, 79106 Freiburg, Germany, Max-Delbrück Centrum, Robert-Rössle-Strasse 10, 13122 Berlin, Germany, and Institute of Pharmacy, University of Bonn, An der Immenburg 4, 53121 Bonn, Germany. Received July 15, 2004; Revised Manuscript Received September 27, 2004

Four platinum (II) complexes (**13**−**16**) were synthesized by reacting either [Pt *trans*-DACH]$(NO_3)_2$ with a 6-maleimidocaproic acid, a 15-maleimido-4,7,10,13-tetroxapentadecanoic acid, and a 6-maleimido-4-oxacaproic ester derivative of cyclobutane-1,1-dicarboxylic acid (CDBA) or [Pt$(NH_3)_2$]$(NO_3)_2$ with a 6-maleimido-4-oxacaproic ester derivative of CBDA. Both complexes containing the 6-maleimido-4-oxacaproic ester (**15**, **16**) showed good water solubility (≥8 mg/mL) and CE experiments revealed rapid binding to human serum albumin and the formation of biadducts with dGMP and dAMP. In the MaTu xenograft model in nude mice, both complexes showed an improved antitumor effect at their maximum tolerated dose (2 × 50 mg/kg carboplatin equivalents) compared to therapy with carboplatin at equimolar dose or at its optimal dose (2 × 75 mg/kg).

INTRODUCTION

Carboplatin is a potent antineoplastic metal complex in the treatment of ovarian, cervix, and lung carcinoma as well as tumors of the head and neck (*1*). However, therapy with carboplatin causes several side effects such as myelotoxicity, nephrotoxicity, ototoxicity, stomatis, nausea, and vomiting (*1*).

Due to our interest in the role that human plasma proteins play in the in vivo distribution of anticancer metal complexes (*2*, *3*), we set out to develop albumin-binding carboplatin analogues considering that carboplatin shows a low degree of plasma protein-binding and fast renal clearance (*2*). Endogenous albumin is a potential drug carrier because it accumulates in solid tumors due to the pathophysiology of tumor tissue, characterized by angiogenesis, hypervasculature, a defective vascular architecture, and an impaired lymphatic drainage (*4*, *5*).

Recently, we have shown that maleimide derivatives of the anticancer drugs doxorubicin and camptothecin bind rapidly to the cysteine-34 position of circulating albumin after intravenous administration (*6*−*8*). Such designed prodrugs have shown enhanced antitumor efficacy in vivo compared to the respective free drug. An acid-sensitive (6-maleimidocaproyl)hydrazone derivative of doxorubicin, which demonstrated superior antitumor efficacy in several animal models and a significantly improved toxicity profile compared to the clinical standard doxorubicin (*7*), is currently being investigated in a phase I clinical trial.

In this work we synthesized strict analogues of carboplatin containing the bidendate ligand cyclobutane-1,1-dicarboxylic acid (CBDA)[1] that—once bound to human serum albumin (HSA)—would retain or improve the antitumor efficacy of the parent complex. The general structure of such compounds is depicted in Figure 1. The maleimide group was selected as the thiol-binding group owing to its specific and selective reaction with the cysteine-34 position of endogenous albumin. In contrast to our previous design of albumin-binding prodrugs, we did not specifically introduce an acid-sensitive or enzymatically degradable bond in the linker (*7*, *9*), considering that the platinum diammino moiety is released through hydrolysis from the CBDA ligand as the active agent in the tumor cell (*10*, *11*). To date, maleimide derivatives and polymer conjugates containing a diamino-dichloroplatinum(II) moiety (*12*−*14*) or a malonato-diammineplatinum(II) moiety (*15*−*17*) have been developed, but no reports of platinum polymer conjugates with a CBDA ligand have yet appeared in the literature.

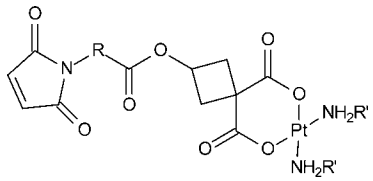


Figure 1. General structure of an albumin-binding carboplatin analogue. R is the backbone of the linker (alkyl or alkoxyalkyl chain). R′ is H or 1,2-cyclohexyl.

In this paper, we report on the synthesis, characterization, and in vitro as well as in vivo efficacy of albumin-binding platinum complexes incorporating cyclobutane-1,1-dicarboxylate and either 1,2-diaminocyclohexane (DACH) or diammine as the amine ligand.

* To whom correspondence should be addressed: Dr. Felix Kratz, Tumor Biology Center, Department of Medical Oncology, Clinical Research, Breisacher Strasse 117, D-79106 Freiburg, Federal Republic of Germany; Tel.: 0049-761-2062176; fax: 0049-761-2061899; e-mail: kratz@tumorbio.uni-freiburg.de.

[†] Tumor Biology Center.

[‡] Max-Delbrück Centrum.

[#] University of Bonn.

[1] Abbreviations: CBDA, cyclobutane-1,1-dicarboxylic acid; DACH, 1,2-diaminocyclohexyl; DCM, dichloromethane; EMC, 6-maleimidocaproic acid; EtOAc, ethyl acetate; HSA, human serum albumin; MeCN, acetonitrile; PMB, 4-methoxybenzyl.

10.1021/bc049829j CCC: $27.50 © 2004 American Chemical Society
Published on Web 10/26/2004

EXPERIMENTAL PROCEDURES

General. Chemicals and solvents were purchased from Sigma-Aldrich, Fluka, and Merck and were used without further purification except for methylene chloride, which was dried over calcium hydride and freshly distilled prior to use. Potassium tetrachloroplatinate was a gift from Degussa (Frankfurt, FRG). Bis(4-methoxybenzyl) malonate was prepared according to the literature (*18*). All organic reactions were carried out under a nitrogen atmosphere. Elemental analysis was performed on a Perkin-Elmer Elemental analyzer 240. HSA (20% solution) was purchased from Dessau Pharma, FRG that contained approximately 35% free thiol groups as assessed with the Ellmann's test. The buffers used were vacuum-filtered through a 0.2 μm membrane (Sartorius, FRG) and thoroughly degassed with argon or nitrogen prior to use. Human blood plasma was obtained from healthy volunteers. Cell culture media, supplements (L-glutamine, antibiotics, trypsin versene/EDTA) and fetal calf serum (FCS) were purchased from Bio Whittaker (Serva, Heidelberg, FRG). All culture flasks were obtained from Greiner Labortechnik (Frickenhausen, FRG).

Spectral Analyses. ^{1}H and ^{13}C NMR spectra were recorded on a Bruker ARX 300. Chemical shifts are expressed as parts per million using tetramethylsilane as the internal standard ($\delta = 0.0$ ppm) or acetone in case of the spectra measured with D_2O. The ^{195}Pt NMR spectrum was recorded on a Varian and refers to K_2PtCl_4 as a standard. Mass spectra were obtained on a Finnigan MAT 312 with associated MAT SS 200 data system using electron spray ionization at 4.0 kV. The infrared spectrum was recorded on a Bruker Vector-22-FTIR.

Chromatography. All organic reactions were monitored by TLC. Column chromatographic separations were carried out as flash chromatography using silica gel 60 from Merck with a particle size of 0.040−0.063 mm. HPLC for the determination of purity of the compounds was performed on a Nucleosil C18 column (100-5, 250 × 4 mm) from Macherey-Nagel using a HPLC pump 590 from Waters (flow: 1 mL/min) and a LKB Bromma UV Detector ($\lambda = 220$ nm). The same HPLC system was also used for the purification of **14**. For incubation studies with albumin or blood plasma, HPLC was performed with a Waters System (pump: Waters 616, detector: Waters 996 Photodiode Array detector and a Merck F-1050 Fluorescence spectrophotometer; controller: Waters 600S, auto sampler: Waters 717; software: Millenium Vers. 2.10; column: Waters, 300 Å, symmetry C18 [4.6 × 250 mm] with precolumn; chromatographic conditions: flow: 1.2 mL/min, mobile phase: 15% CH_3CN, 85% 20 mM potassium phosphate (pH 7.0), mobile phase B: CH_3CN, gradient: 0−25 min 100% mobile phase; 25−40 min increase to 70% CH_3CN, 30% 20 mM potassium phosphate; 40−50 min 70% CH_3CN, 30% 20 mM potassium phosphate; 50−60 min decrease to initial mobile phase; injection volume: 50 μL.

Capillary Electrophoresis. CE for the investigation of albumin binding was performed using a P/ACE 5510 instrument controlled by the P/ACE Station software version 1.21 (Beckman Coulter, USA). An uncoated capillary (37 μm ID, effective separation length 30 cm) was assembled in the P/ACE cartridge. Detection was performed on-line by UV absorption at 214 nm. The following conditions were used: running buffer: 20 mM sodium phosphate, pH 7.4; capillary temperature: 25 °C; separation voltage: 7 kV; injection: pressure 5 psi, 5 s; rinse prior to each analysis: separation buffer 2 min; rinse after each analysis: 0.1 M NaOH 2 min, water 1 min.

The same CE system was also used to study the reaction toward nucleotides. An uncoated capillary (57 μm ID, effective separation length 50 cm) was assembled in the P/ACE cartridge. Detection was performed on-line by UV absorption at 254 nm. The following conditions were used: running buffer: 400 mM borate, pH 9.1; capillary temperature: 18 °C; separation voltage: 25 kV; injection: pressure 5 psi, 5 s; rinse prior to each analysis: separation buffer 1 min; rinse after each analysis: 0.1 M NaOH 1 min, water 1 min.

1,3-Dibromo-2-(*tert*-butyldimethylsiloxy)propane (1). A solution of 1,3-dibromo-2-propanol (50.6 g, 221 mmol) in 25 mL of anhydrous DMF was added dropwise within 10 min to a solution of *tert*-butyldimethylchlorosilane (41.1 g, 265 mmol) and imidazole (33.0 g, 485 mmol) in 200 mL of anhydrous DMF. After stirring of the sample for 16 h at ambient temperature, the mixture was taken up in 800 mL of water and extracted with DCM. The combined organic layers were washed with 3 × 400 mL of water and dried over $MgSO_4$ and the volatiles were removed in vacuo. Purification of the crude product by silica column chromatography (isohexane) yielded 73.4 g (100%) of **1** as a colorless oil. ^{1}H NMR ($CDCl_3$): δ 0.13 (s, 6H, Si(CH_3)$_2$), 0.91 (s, 9H, C(CH_3)$_3$), 3.46 (dd, J_1 = 10.6 Hz, J_2 = 4.9 Hz, 2H, CH_2Br), 3.49 (dd, J_1 = 10.6 Hz, J_2 = 5.3 Hz, 2H, CH_2Br), 4.00 ('p', J = 5.1 Hz, 1H, CHOTBS). ^{13}C NMR ($CDCl_3$): δ −4.63 (Si(CH_3)$_2$), 18.06 (C(CH$_3$)$_3$), 25.68 (C(CH_3)$_3$), 35.45 (CH_2Br), 71.25 (CHOTBS). Anal. ($C_9H_{20}Br_2OSi$) C, H, Br.

Bis(4-methoxybenzyl) 3-(*tert*-Butyldimethylsiloxy)-cyclobutane-1,1-dicarboxylate (2). Bis(4-methoxybenzyl) malonate (6.00 g, 17.4 mmol) was added dropwise within 30 min to a suspension of potassium hydride (35% in mineral oil) (2.10 g, 18.3 mmol) in 20 mL of anhydrous dioxane and stirring was continued for 15 min at ambient temperature. Then **1** (6.08 g, 18.29 mmol) was added and the mixture was heated under reflux for 16 h. After cooling of the sample to room temperature, potassium hydride (35% in mineral oil) (2.10 g, 18.3 mmol) suspended in 10 mL of dioxane was added within 1 h and the reaction mixture was heated under reflux for a further 3 days. The hot mixture was filtered over Celite and the solvent was removed in vacuo. Purification of the crude product by silica column chromatography (EtOAc/isohexane 1:10) yielded 2.78 g (31%) of **2** as a colorless oil. ^{1}H NMR ($CDCl_3$): δ 0.01 (s, 6H, Si(CH_3)$_2$), 0.85 (s, 9H, C(CH_3)$_3$), 2.41−2.51 (m, 2H, CH_2CHOTBS), 2.74−2.84 (m, 2H, CH_2CHOTBS), 3.79 (s, 6H, ArOCH_3), 4.32 ('p', J = 7.3 Hz, 1H, CHOTBS), 5.04/5.06 (s, 4H, CH_2-Ar), 6.82/6.83 (d, J = 8.7 Hz, 4H, Ar-H), 7.17 (d, J = 8.7 Hz, 4H, Ar-H). ^{13}C NMR ($CDCl_3$): δ −4.86 (Si(CH_3)$_2$), 17.92 (C(CH_3)$_3$), 25.75 (C(CH_3)$_3$), 40.84 (CH_2CHOTBS), 45.90 (C(COOPMB)$_2$), 55.23 (ArOCH_3), 62.02 (CHOTBS), 66.95/67.09 (CH_2Ar), 113.85/113.88, 127.57/127.65, 129.81/129.92, 159.61/159.64 (Ar), 170.80/171.74 (C=O). Anal. ($C_{28}H_{38}O_7Si$) C, H.

Bis(4-methoxybenzyl) 3-Hydroxycyclobutane-1,1-dicarboxylate (3). To a solution of **2** (2.69 g, 5.23 mmol) in 25 mL of anhydrous THF was added TBAF (2.47 g, 7.85 mmol). After stirring of the sample for 15 min at ambient temperature, the volatiles were removed in vacuo. Purification of the crude product by silica column chromatography (EtOAc/isohexane 1:1) yielded 1.85 g (88%) of **3** as a colorless oil which slowly crystallizes. ^{1}H NMR ($CDCl_3$): δ 2.28−2.51 (m, 3H, CH_2CHOH), 2.80−2.91 (m, 2H, CH_2CHOH), 3.78 (s, 6H, ArOCH_3), 4.33 ('p', J = 7.4 Hz, 1H, CHOH), 5.05 (s, 4H, CH_2Ar), 6.82 (d, J = 8.5 Hz, 4H, Ar-H), 7.16/7.17 (d, J = 8.5 Hz, 4H, Ar-H). ^{13}C NMR ($CDCl_3$): δ 40.27 (CH_2CHOH), 46.02 (C-

(COOPMB)$_2$), 55.24 (ArOCH$_3$), 62.22 (CHOH), 67.18 (CH$_2$Ar), 113.92, 127.50, 129.91/129.95, 159.67 (Ar), 171.18/171.42 (C=O). Anal. ($C_{22}H_{24}O_7$) C, H.

***tert*-Butyl 6-Hydroxy-4-oxacaproate (4).** Sodium (65 mg, 2.9 mmol) was added to a solution of ethylene glycol (40.0 mL, 715 mmol) in 100 mL of anhydrous THF, and the mixture was stirred until the sodium dissolved completely. Subsequently, *tert*-butyl acrylate (21.0 mL, 143 mmol) was added dropwise within 2 min to the reaction mixture. After stirring of the sample for 4 days at ambient temperature, the reaction mixture was neutralized with 1 M HCl and the volatiles were removed in vacuo. The oily residue was taken up in 100 mL of water and extracted with 3 × 60 mL of Et_2O. The combined organic layers were dried over $MgSO_4$ and the solvent was removed in vacuo. Purification of the crude product by silica column chromatography (EtOAc/isohexane 1:1) yielded 16.1 g (59%) of **4** as a colorless oil. ^{1}H NMR ($CDCl_3$): δ 1.46 (s, 9H, C(CH$_3$)$_3$), 2.51 (t, J = 6.2 Hz, 2H, CH$_2$C(O)O^{t}Bu), 2.81 (bs, 1H, OH), 3.59 (t, J = 4.7 Hz, 2H, OCH$_2$), 3.71 (t, J = 4.7 Hz, 2H, OCH$_2$), 3.73 (t, J = 6.2 Hz, 2H, OCH$_2$). ^{13}C NMR ($CDCl_3$): δ 28.09 (C(CH$_3$)$_3$), 36.15 (CH$_2$C(O)O^{t}Bu), 61.56 (HOCH$_2$), 66.44, 70.28 (OCH$_2$), 80.60 (C(CH$_3$)$_3$), 171.26 (CH$_2$C(O)O^{t}Bu). Anal. ($C_9H_{18}O_4$) C, H.

***tert*-Butyl 6-Maleimido-4-oxacaproate (5).** A stirred solution of **4** (12.3 g, 64.5 mmol) and triphenyl phosphine (12.4 g, 47.3 mmol) in 250 mL of anhydrous THF was cooled to 0 °C. Finely ground maleimide (4.3 g, 43.0 mmol) followed by DIAD (9.7 g, 47.3 mmol) were added and the mixture was kept for 5 min at 0 °C. The cooling bath was removed and stirring was continued for 3 h at room temperature. The volatiles were removed in vacuo and the oily residue was purified by silica column chromatography (EtOAc/isohexane 1:3) yielding 8.0 g (69%) of **5** as a colorless oil which slowly crystallizes. ^{1}H NMR ($CDCl_3$): δ 1.43 (s, 9H, C(CH$_3$)$_3$), 2.43 (t, J = 6.6 Hz, 2H, CH$_2$C(O)O^{t}Bu), 3.51−3.79 (m, 6H, NCH$_2$, OCH$_2$), 6.69 (s, 2H, CH=CH). ^{13}C NMR ($CDCl_3$): δ 28.09 (C(CH$_3$)$_3$), 36.16 (CH$_2$C(O)O^{t}Bu), 37.24 (NCH$_2$), 66.43, 67.55 (OCH$_2$), 80.56 (C(CH$_3$)$_3$), 134.13 (CH=CH), 170.62 (C(O)CH=CHCO), 170.70 (CH$_2$C(O)O^{t}Bu). Anal. ($C_{13}H_{19}NO_5$) C, H, N.

6-Maleimido-4-oxacaproic Acid (6). A solution of **5** (7.09 g, 26.3 mmol) in 20 mL of anhydrous DCM was treated with 20 mL of trifluoroacetic acid and the reaction mixture was stirred for 1 h at ambient temperature. The volatiles were removed in vacuo and the residue was recrystallized from EtOAc/PE 60/80 1:2 yielding 4.90 g (87%) of **6** as a colorless solid. ^{1}H NMR ($CDCl_3$): δ 2.57 (t, J = 6.0 Hz, 2H, CH$_2$COOH), 3.60−3.75 (m, 6H, NCH$_2$, OCH$_2$), 6.72 (s, 2H, CH=CH), 10.56 (bs, 1H, COOH). ^{13}C NMR ($CDCl_3$): δ 34.81 (CH$_2$COOH), 37.11 (NCH$_2$), 65.76, 67.67 (OCH$_2$), 134.18 (CH=CH), 170.74 (C(O)CH=CHCO), 177.16 (COOH). Anal. ($C_9H_{11}NO_5$) C, H, N.

General Procedure for the Esterification of Maleimidocarboxylic Acids with 3. To a solution of **3** (1.97 g, 4.91 mmol), the maleimidocarboxylic acid (7.37 mmol), and triethylamine (2.04 mL, 8.64 mmol) in 30 mL of anhydrous DCM was added 2-chloro-1-methylpyridinium iodide (1.88 g, 7.37 mmol) as a finely ground solid. Stirring was continued for 2 h at room temperature during which the initially cloudy mixture turned into a yellow solution. The mixture was diluted with 140 mL of DCM and washed with 2 × 80 mL of 1 M HCl, 2 × 80 mL of water, and 80 mL of brine. The organic layer was dried over $MgSO_4$, the solvent was removed in vacuo and the residue was purified as described below.

Bis(4-methoxybenzyl) 3-(6-Maleimidohexanoyl)-cyclobutane-1,1-dicarboxylate (7) (from the reaction with EMC). Purification of the crude product by silica column chromatography (chloroform) afforded 2.16 g (74%) of **7** as a colorless oil which slowly crystallizes. ^{1}H NMR ($CDCl_3$): δ 1.22−1.36 (m, 2H, CH$_2$), 1.52−1.74 (m, 4H, CH$_2$), 2.24 (t, J = 7.2 Hz, CH$_2$COO), 2.53−2.64 (m, 2H, CH$_2$CHOR), 2.88−2.99 (m, 2H, CH$_2$CHOR), 3.50 (t, J = 7.4 Hz, 2H, NCH$_2$), 3.80 (s, 6H, ArOCH$_3$), 4.97−5.10 (m, 5H, CHOR, CH$_2$Ar), 6.67 (s, 2H, C(O)CH=CHCO), 6.83 (d, J = 8.3 Hz, 4H, Ar-H), 7.18 (d, J = 8.3 Hz, 4H, Ar-H). ^{13}C NMR ($CDCl_3$): δ 24.24 (CH$_2$), 26.22 (CH$_2$), 28.18 (CH$_2$), 33.84 (CH$_2$COO), 37.17 (CH$_2$CHOR), 37.60 (NCH$_2$), 47.12 (C(COOPMB)$_2$), 55.26 (ArOCH$_3$), 63.77 (CHOR), 67.22/67.35 (CH$_2$Ar), 113.91/113.95, 127.37/127.47, 129.97/130.06 (Ar), 134.07 (C(O)CH=CHCO), 159.70/159.73 (Ar), 170.44, 170.82, 170.89, 172.62 (C(O)-CH=CHCO, C(COOPMB)$_2$, CH$_2$COO). Anal. ($C_{32}H_{35}NO_{10}$) C, H, N.

Bis(4-methoxybenzyl) 3-(15-Maleimido-4,7,10,13-tetroxapentadecanoyl)cyclobutane-1,1-dicarboxylate (8) (from the reaction with 15-maleimido-4,7,10,13-tetroxapentadecanoic acid). Purification of the crude product by silica column chromatography (EtOAc) afforded 3.29 g (92%) of **8** as a colorless oil. ^{1}H NMR ($CDCl_3$): δ 2.55 (t, J = 6.4 Hz, 2H, CH$_2$COO), 2.56−2.66 (m, 2H, CH$_2$CHOR), 2.89−2.99 (m, 2H, CH$_2$CHOR), 3.57−3.77 (m, 18H, NCH$_2$, OCH$_2$), 3.80 (s, 6H, ArOCH$_3$), 5.00−5.13 (m, 1H, CHOR), 5.06/5.07 (s, 4H, CH$_2$Ar), 6.69 (s, 2H, C(O)CH=CHCO), 6.83 (d, J = 8.7 Hz, 4H, Ar-H), 7.18 (d, J = 8.7 Hz, 4H, Ar-H). ^{13}C NMR ($CDCl_3$): δ 34.87 (CH$_2$COO), 37.11 (NCH$_2$, CH$_2$CHOR), 47.04 (C(COOPMB)$_2$), 55.24 (ArOCH$_3$), 63.92 (CHOR), 66.57 (OCH$_2$), 67.20/67.34 (CH$_2$Ar), 67.80, 70.04, 70.42, 70.46, 70.53, 70.57, 70.61 (OCH$_2$), 113.89/113.92, 127.33/127.42, 129.97 (Ar), 134.14 (C(O)CH=CHCO), 159.68/159.70 (Ar), 170.38, 170.65, 170.75, 170.86 (C(O)CH=CHCO, C(COOPMB)$_2$, CH$_2$COO).

Bis(4-methoxybenzyl) 3-(6-Maleimido-4-oxacaproyl)cyclobutane-1,1-dicarboxylate (9) (from the reaction with **6**). Purification of the crude product by silica column chromatography (chloroform/MeOH 200:1) afforded 2.89 g (99%) of **9** as a colorless oil. ^{1}H NMR ($CDCl_3$): δ 2.47 (t, J = 6.4 Hz, 2H, CH$_2$COO), 2.54−2.65 (m, 2H, CH$_2$CHOR), 2.88−2.98 (m, 2H, CH$_2$CHOR), 3.55−3.75 (m, 6H, NCH$_2$, OCH$_2$), 3.80 (s, 6H, ArOCH$_3$), 4.97−5.13 (m, 1H, CHOR), 5.06/5.07 (s, 4H, CH$_2$Ar), 6.67 (s, 2H, C(O)CH=CHCO), 6.83 (d, J = 8.7 Hz, 4H, Ar-H), 7.26 (d, J = 8.7 Hz, 4H, Ar-H). ^{13}C NMR ($CDCl_3$): δ 34.84 (CH$_2$COO), 37.13 (NCH$_2$, CH$_2$CHOR), 47.06 (C(COOPMB)$_2$), 55.26 (ArOCH$_3$), 63.97 (CHOR), 65.94 (OCH$_2$), 67.22/67.36 (CH$_2$Ar), 67.68 (OCH$_2$), 113.90/113.94, 127.35/127.45, 129.98/130.00 (Ar), 134.13 (C(O)CH=CHCO), 159.69/159.72 (Ar), 170.39, 170.58, 170.61, 170.91 (C(O)-CH=CHCO, C(COOPMB)$_2$, CH$_2$COO). Anal. ($C_{31}H_{33}NO_{11}$) C, H, N.

General Procedure for the Cleavage of the PMB Protective Groups. A solution of the PMB protected dicarboxylic acid (4.63 mmol) and anisole (7.57 mL, 69.5 mmol) in 50 mL of anhydrous DCM was treated with 10 mL of trifluoroacetic acid at 0 °C. After stirring of the sample for 2 h at 0 °C, the volatiles were removed in vacuo and the residue was purified as described below.

3-(6-Maleimidohexanoyl)cyclobutane-1,1-dicarboxylic Acid (10) (from the reaction with **7**). Purification of the crude product by silica column chromatography (chloroform/MeOH 10:1) afforded 577 mg (35%) of **10** as a colorless sirup. ^{1}H NMR (DMSO-d_6): δ 1.13−1.27 (m, 2H, CH$_2$), 1.41−1.58 (m, 4H, CH$_2$), 2.26 (t, J = 6.8 Hz, CH$_2$COO), 2.35−2.47 (m, 2H, CH$_2$CHOR), 2.70−2.83 (m, 2H, CH$_2$CHOR), 3.38 (t, J = 7.4 Hz, 2H, NCH$_2$), 4.90 ('p',

J = 7.4 Hz, 1H, CHOR), 7.00 (s, 2H, C(O)CH=CHCO), 12.97 (bs, 2H, COOH). ^{13}C NMR (DMSO-d_6): δ 23.67 (CH_2), 25.37 (CH_2), 27.48 (CH_2), 32.99 (CH_2COO), 36.52 (CH_2CHOR), 36.77 (NCH_2), 46.29 (C(COOH)$_2$), 63.18 (CHOR), 134.34 (C(O)CH=CHCO), 170.96, 171.80, 172.08, 172.42 (C(O)CH=CHCO, C(COOH)$_2$, CH_2COO).

3-(15-Maleimido-4,7,10,13-tetroxapentadecanoyl)-cyclobutane-1,1-dicarboxylic Acid (11) (from the reaction with **8**). Purification of the crude product by silica column chromatography (chloroform/MeOH 10:1) afforded 2.00 g (89%) of **11** as a colorless sirup. ^{1}H NMR (DMSO-d_6): δ 2.35−2.56 (m, 4H, CH_2CHOR, CH_2COO), 2.68−2.83 (m, 2H, CH_2CHOR), 3.32−3.66 (m, 18H, NCH_2, OCH_2), 4.92 ('p', J = 7.3 Hz, 1H, CHOR), 7.02 (s, 2H, C(O)CH=CHCO). ^{13}C NMR (DMSO-d_6): δ 34.40 (CH_2COO), 36.49 (CH_2CHOR), 36.73 (NCH_2,), 46.32 (C(COOH)$_2$), 63.33 (CHOR), 65.80, 66.86, 69.33, 69.58, 69.68, 69.71 (OCH_2), 134.46 (C(O)CH=CHCO), 170.45, 170.82, 171.79, 172.42 (C(O)CH=CHCO, C(COOH)$_2$, CH_2COO). ESI-MS (4.0 kV, MeOH): m/z (%) 510.2 ([M+Na]$^+$, 100).

3-(6-Maleimido-4-oxacaproyl)cyclobutane-1,1-dicarboxylic Acid (12) (from the reaction with **9**). Purification of the crude product by silica column chromatography (chloroform/MeOH 20:1) afforded 1.28 g (78%) of **12** as a colorless sirup. ^{1}H NMR ($CDCl_3$): δ 2.53 (t, J = 6.2 Hz, 2H, CH_2COO), 2.64−2.79 (m, 2H, CH_2CHOR), 2.95−3.10 (m, 2H, CH_2CHOR), 3.57−3.77 (m, 6H, NCH_2, OCH_2), 5.05−5.19 (m, 1H, CHOR), 6.74 (s, 2H, C(O)-CH=CHCO), 10.01 (bs, 2H, COOH). ^{13}C NMR ($CDCl_3$): δ 34.83 (CH_2COO), 37.19, 37.30 (NCH_2, CH_2CHOR), 46.78 (C(COOH)$_2$), 64.08 (CHOR), 66.00 (OCH_2), 67.71 (OCH_2), 134.25 (C(O)CH=CHCO), 170.97, 171.09 (C(O)-CH=CHCO, CH_2COO), 174.81, 175.51 (COOH). Anal. ($C_{15}H_{17}NO_9$) C, H, N.

***trans-(R,R/S,S)*-Cyclohexane-1,2-diaminoplatinum(II)-[3-(6-maleimidohexanoyl)cyclobutane-1,1-dicarboxylate] (13).** [Pt *trans*-DACH]$(NO_3)_2$ (263 mg, 607 μmol) was dissolved at 50 °C in 30 mL of water. The solution was cooled to room temperature and **10** (236 mg, 668 μmol) dissolved in 5 mL of 0.01 M KOH was added. The pH was adjusted to pH 5.5 using 0.1 M KOH and the reaction mixture was stirred in the dark for 3 h. After cooling of the sample to 0 °C, the white precipitate was centrifuged, washed two times with 5 mL of water and dried in vacuo yielding 269 mg (67%) of **13** as a colorless powder. ^{1}H NMR (CD_3OD): δ 1.11−1.41 (m, 6H, CH_2, cyclohexyl-H), 1.50−1.70 (m, 6H, CH_2, cyclohexyl-H), 1.93−2.06 (m, 2H, cyclohexyl-H), 2.19−2.40 (m, 4H, CH_2-COO, cyclohexyl-H), 2.70−2.81 (m, 2H, CH_2CHOR), 3.36−3.46 (m, 2H, CH_2CHOR), 3.50 (t, J = 7.4 Hz, 2H, NCH_2), 6.81 (s, 2H, C(O)CH=CHCO). ^{13}C NMR (CD_3-OD): δ 25.44, 25.55, 27.17, 29.18 (CH_2, cyclohexyl), 33.25 (cyclohexyl), 34.78 (CH_2COO), 38.34, 39.94, 40.07 (CH_2-CHOR, NCH_2, cyclohexyl), 51.27 (C(COOH)$_2$), 63.86 (CHOR), 135.38 (C(O)CH=CHCO), 172.64, 174.83 (C(O)-CH=CHCO, CH_2COO), 180.50, 180.78 (C(COOH)$_2$). ESI-MS (4.0 kV, MeOH):

m/z (%) 1343.5 ([2*M+Na]$^+$, 100), 1321.6 ([2*M]$^+$, 22), 683.3 ([M+Na]$^+$, 35), 661.3 ([M]$^+$, 30). Anal. ($C_{22}H_{31}N_3O_8$-Pt) calculated: C: 40.00%, H: 4.73%, N: 6.36%, found: C: 39.45%, H: 4.56%, N: 5.91%. Purity determined by HPLC (water/MeCN 70:30 + 0.05% TFA) >93%.

***trans-(R,R/S,S)*-Cyclohexane-1,2-diaminoplatinum (II)-[3-(15-maleimido-4,7,10,13-tetroxapentadecanoyl-)cyclobutane-1,1-dicarboxylate] (14).** [Pt *trans*-DACH]-$(NO_3)_2$ (175 mg, 405 μmol) was dissolved at 50 °C in 30 mL of water. The solution was cooled to room temperature and **11** (217 mg, 445 μmol) dissolved in 5 mL of water was added. The pH was adjusted to pH 5.5 using 0.1 M KOH and the reaction mixture was stirred in the dark for 3 h. After the solution was concentrated in vacuo to a volume of 5 mL, the yellowish precipitate was removed by centrifugation and the supernatant was purified by preparative HPLC [*Nucleosil* 100−7-C18 column (250 × 15 mm), water/MeCN 80:20 + 0.05% TFA, flow: 20 mL/min, retention time: approximately 20 min]. The eluent was removed in vacuo and the oily product was crystallized by adding 1 mL of 2-propanol yielding 60 mg (19%) of **14** as a colorless solid. ^{1}H NMR (D_2O): δ 0.98−1.35 (m, 4H, cyclohexyl-H), 1.44−1.62 (m, 2H, cyclohexyl-H), 1.94−2.06 (m, 2H, cyclohexyl-H), 2.28−2.48 (m, 2H, cyclohexyl-H), 2.66 (t, J = 6.0 Hz, CH_2COO), 2.80−2.93 (m, 2H, CH_2CHOR), 3.34−3.50 (m, 2H, CH_2-CHOR), 3.54−3.84 (m, 18H, NCH_2, OCH_2), 4.93 ('p', J = 7.1 Hz, 1H, CHOR), 6.85 (s, 2H, C(O)CH=CHCO). ^{13}C NMR (D_2O): δ 24.30 (cyclohexyl), 32.22 (cyclohexyl), 34.91 (CH_2COO), 37.37, 38.54, 38.72 (CH_2CHOR, NCH_2, cyclohexyl), 50.71 (C(COOH)$_2$), 63.05 (CHOR), 65.37, 66.52, 68.02, 69.73, 69.97, 70.01 (OCH_2), 134.86 (C(O)-CH=CHCO), 173.39, 174.11 (C(O)CH=CHCO, CH_2COO), 180.30, 180.47 (C(COOH)$_2$). ^{195}Pt−NMR (D_2O): δ −311. IR (KBr): ν = 3448 (ss, b), 2934 (w, b), 1709 (ss), 1627 (s), 1353 (m), 1094 (ss, b), 696 (w) cm^{-1}. ESI-MS (4.0 kV, MeOH): m/z (%) 816.9 ([M+Na]$^+$, 100). Anal. ($C_{27}H_{41}N_3O_{12}$-Pt*H_2O) C, H, N. Purity determined by HPLC (water/MeCN 80:20 + 0.05% TFA) >94%.

***trans-(R,R/S,S)*-Cyclohexane-1,2-diaminoplatinum(II)-[3-(6-maleimido-4-oxacaproyl)cyclobutane-1,1-dicarboxylate] (15)** [Pt *trans*-DACH]$(NO_3)_2$ (300 mg, 692 μmol) was dissolved at 50 °C in 60 mL of water. The solution was cooled to room temperature and **12** (271 mg, 762 μmol) dissolved in 5 mL of water was added. The pH was adjusted to pH 5.5 using 0.1 M KOH and the reaction mixture was stirred in the dark for 3 h. After the solvent was removed in vacuo, the crude product was purified by silica column chromatography (ethanol) yielding 291 mg (61%) of **15** as a colorless powder. ^{1}H NMR (CD_3OD): δ 0.97−1.29 (m, 4H, cyclohexyl-H), 1.38−1.56 (m, 2H, cyclohexyl-H), 1.81−1.96 (m, 2H, cyclohexyl-H), 2.19−2.36 (m, 2H, cyclohexyl-H), 2.42 (t, J = 5.9 Hz, CH_2-COO), 2.60−2.79 (m, 2H, CH_2CHOR), 3.27−3.41 (m, 2H, CH_2CHOR), 3.46−3.66 (m, 6H, NCH_2, OCH_2), 4.67−4.86 (m, 1H, CHOR), 6.76 (s, 2H, C(O)CH=CHCO). ^{13}C NMR (CD_3OD): δ 25.51, 33.30 (cyclohexyl), 35.92 (CH_2COO), 38.17 (NCH_2), 39.80/40.09 (CH_2CHOR), 51.35 (C(COOH)$_2$), 63.81/63.86 (cyclohexyl-NH_2), 65.66 (CHOR), 67.22, 68.65 (OCH_2), 135.50 (C(O)CH=CHCO), 172.52, 172.80 (C(O)-CH=CHCO, CH_2COO), 180.41, 180.61 (C(*C*OOH)$_2$). ESI-MS (4.0 kV, MeOH): m/z (%) 663.0 ([M+1]$^+$, 100). Anal. ($C_{21}H_{29}N3O_9Pt$) C, H, N. Purity determined by HPLC (water/MeCN 70:30 + 0.05% TFA) >97%.

Diammineplatin(II)-[3-(6-maleimido-4-oxacaproyl)-cyclobutane-1,1-dicarboxylate] (16) *cis*-$[Pt(NH_3)_2]$-$(NO_3)_2$ (485 mg, 1.37 mmol) was dissolved at 50 °C in 60 mL of water. The solution was cooled to room temperature and **12** (538 mg, 1.51 mmol) dissolved in 5 mL of water was added. The pH was adjusted to pH 5.5 using 0.1 M KOH and the reaction mixture was stirred in the dark for 3 h. After the solvent was removed in vacuo, the crude product was purified by silica column chromatography (ethanol) yielding 263 mg (33%) of **16** as a colorless powder. ^{1}H NMR (CD_3OD): δ 2.55 (t, J = 5.9 Hz, CH_2COO), 2.77−2.88 (m, 2H, CH_2CHOR), 3.32−3.44 (m, 2H, CH_2CHOR), 3.63−3.77 (m, 6H, NCH_2, OCH_2), 4.79−4.91 (m, 1H, CHOR), 6.87 (s, 2H, C(O)CH=CHCO). ^{13}C NMR (CD_3OD): δ 35.02 (CH_2COO), 37.52 (NCH_2), 38.70 (CH_2CHOR), 50.67 (C(COOH)$_2$), 65.33 (CHOR),

Table 1. IC_{50} Values [μM][a] for Carboplatin, 15+HSA, and 16+HSA in LXFL 529 Lung Tumor Cells and MaTu Breast Tumor Cells as Determined with the MTT Assay

	IC_{50} [μM][a]	
compound	LXFL 529	MaTu
carboplatin	3.9 ± 0.7	6.4 ± 0.9
15+HSA	21.0 ± 1.6	49.0 ± 2.0
16+HSA	38.0 ± 1.6	41.0 ± 1.8

[a] IC_{50} values (50% inhibitory concentration) represent the mean ± standard deviation (n = 4); similar results were obtained in a further independent experiment.

66.32, 67.90 (OCH_2), 134.81 (C(O)CH=*C*HCO), 173.32, 174.00 (C(O)CH=CHCO, $CH_2CO\overline{O}$). ESI-MS (4.0 kV, MeOH): *m/z* (%) 581.8 ([M]$^+$, 100). Anal. ($C_{15}H_{21}N_3O_9$-Pt) C, H, N. Purity determined by HPLC (water/MeCN 70:30 + 0.05% TFA) >95%.

Albumin-Binding Experiments. 15 and **16** (150 μM) were each incubated with HSA (600 μM) at 37 °C (incubation buffer 4 mM sodium phosphate, pH 7.4). The samples were directly analyzed using capillary electrophoresis after an incubation time of 1, 5, 10, 15, and 20 min. The free compounds and albumin were detected at 214 nm. The linearity of the free compounds was shown between 3 and 300 μM. Blocking of sulfhydryl groups was achieved by preincubating HSA with an excess of EMC for 10 min at 37 °C.

Reactivity of 15 and 16 toward dAMP and dGMP. 15 or **16** (150 μM) was incubated with the nucleotides dAMP and dGMP (150 μM) at 37 °C (incubation buffer 4 mM sodium phosphate, 4 mM sodium chloride pH 7.4). dAMP and dGMP were quantified and the adduct formation was monitored up to 72 h with capillary electrophoresis. Separately incubated oxaliplatin and cisplatin solutions were co-injected to identify the formed adducts.

Cell Culture. The MTT assay was performed in analogy to a literature protocol (*19*). Briefly, approximately 5000 cells were plated in each well of a 96-well tissue culture plate. Medium supplemented with 10% FCS was added and cells were allowed to adhere for 24 h. Subsequently, cells were preincubated with various drug concentrations (0.1−300 μM) for 72 h and then labeled by adding sterile-filtered MTT (5 mg/mL PBS). Cultures were incubated at 37 °C for 2 h. Subsequently, the supernatant was removed and 100 μL of DMSO added to each well. After an incubation time of 10 min, the extinction of the samples was quantified with an ELISA reader (Dynatech Laboratories Inc., Sullyfield, UK) at a wavelength of 570 nm. IC_{50} values (50% inhibitory concentration) were calculated using GraphPad Prism and represent the mean ± standard deviation (n = 4); similar results were obtained in a further independent experiment. For cell culture experiments, a 3 mM stock solution of carboplatin in 10 mM sodium phosphate, 5% D-(+)-glucose, pH 6.4 was prepared. Albumin conjugates with **15** and **16** were prepared by preincubating **15** and **16** (750 μM) with HSA (3000 μM) for 30 min at 37 °C.

In Vivo Efficacy of 15 and 16. For the in vivo testing of **15** and **16** in comparison with carboplatin female NMRI: nu/nu mice (M&B A/S, Ry, Denmark) were used. The mice were held in laminar flow shelves under sterile and standardized environmental conditions (25 ± 2 °C room temperature, 50 ± 10% relative humidity, 12 h light-dark-rhythm). They received autoclaved food and bedding (ssniff, Soest, Germany) and acidified (pH 4.0) drinking water ad libitum. All animal experiments were performed under the auspices of the German Animal Protection Law.

10^7 cells of MaTu cells from in vitro culture were transplanted subcutaneously (s.c.) into the left flank region of anaesthetized (40 mg/kg i.p. Radenarkon, Asta Medica, Frankfurt, Germany) mice on day zero. Mice were randomly distributed to the experimental groups (8 mice per group). When the tumors were grown to a palpable size, treatment was initiated (see Figure 7 and Table 2). Mice were treated intravenously at day 7 and 14 or 7, 14, and 21, respectively, with either glucose phosphate buffer (10 mM sodium phosphate, 5% D-(+)-glucose, pH 6.4), carboplatin, **15** or **16** dissolved in glucose phosphate buffer; for doses see Table 2 and Figure 7. The injection volume was 0.2 mL/20 g body weight.

Tumor size was measured twice weekly with a calliper-like instrument in two dimensions. Individual tumor volumes *(V)* were calculated by the formula V = (length + [width]^2)/2 and related to the values on the first day of treatment (relative tumor volume, RTV). Statistical analysis was performed with the U-test (Mann and Whitney) with $p < 0.05$. The body weight of mice was determined every 3 to 4 days and the change in body weight (BWC) after initiation of treatment is presented in Figure 8.

RESULTS AND DISCUSSION

Chemistry. For developing water-soluble platinum complexes with CBDA ligands and an albumin-binding maleimide group, the following aspects were considered: (1) The maleimide group is sensitive to base and should therefore be introduced at a late stage of synthesis. (2) The base-sensitivity of the maleimide requires the use of acid-cleavable protection for the carboxylic groups of the CBDA ligand. (3) The synthetic approach should be flexible enough to incorporate different types of spacers (varying in length and number of solubilizing ether groups) between the protein-binding and platinum-binding unit to fine-tune the water solubility of the platinum complexes.

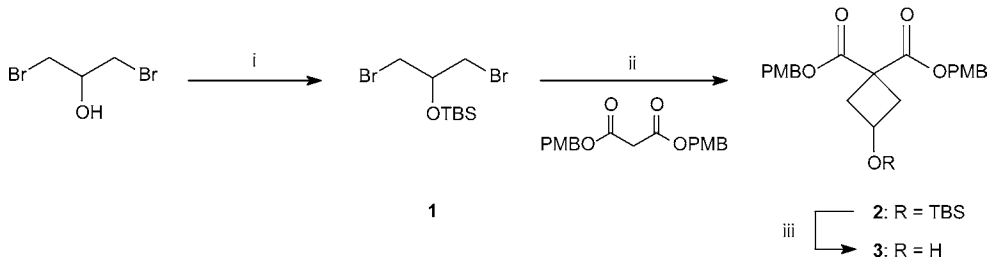
Considering the benefit of a functionalized CBDA ligand that can serve as a universally applicable platinum-binding precursor (e.g., for the development of other macromolecular platin prodrugs), our synthetic route began with the preparation of a hydroxy functionalized

Table 2. Treatment Schedule, Antitumor Activity, and Toxicity Data for Carboplatin, 15, and 16 in Nude Mice Bearing Human Breast Xenografts (MaTu)

compound	days of treatment	dose[a] [mg/kg] per inj	total dose[a] [mg/kg]	toxic deaths (d)	BWC [%] (d)	optimum T/C [%] (d)
buffer	7,14,21			0	0 (14)	
carboplatin	7,14	75	150	0	−8 (14)	50 (28)
carboplatin	7,14	50	100	0	−6 (10)	88 (21)
carboplatin	7,14,21	25	75	0	−6 (17)	63 (28)
15	7,14	50	100	0	−15 (17)	45 (28)[b]
16	7,14	50	100	0	−8 (17)	50 (31)[b]
16	7,14,21	25	75	0	−6 (17)	67 (35)

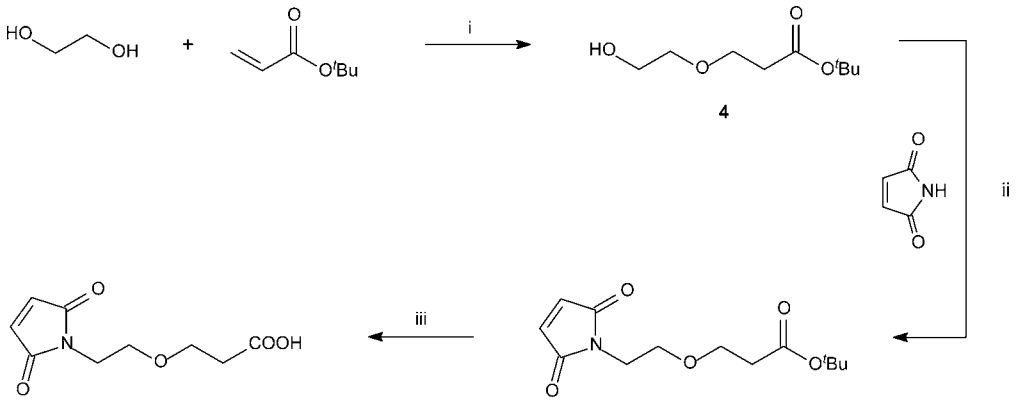
[a] Doses refer to carboplatin equivalents. [b] Significant to saline ($p < 0.05$).

Scheme 1 [a]



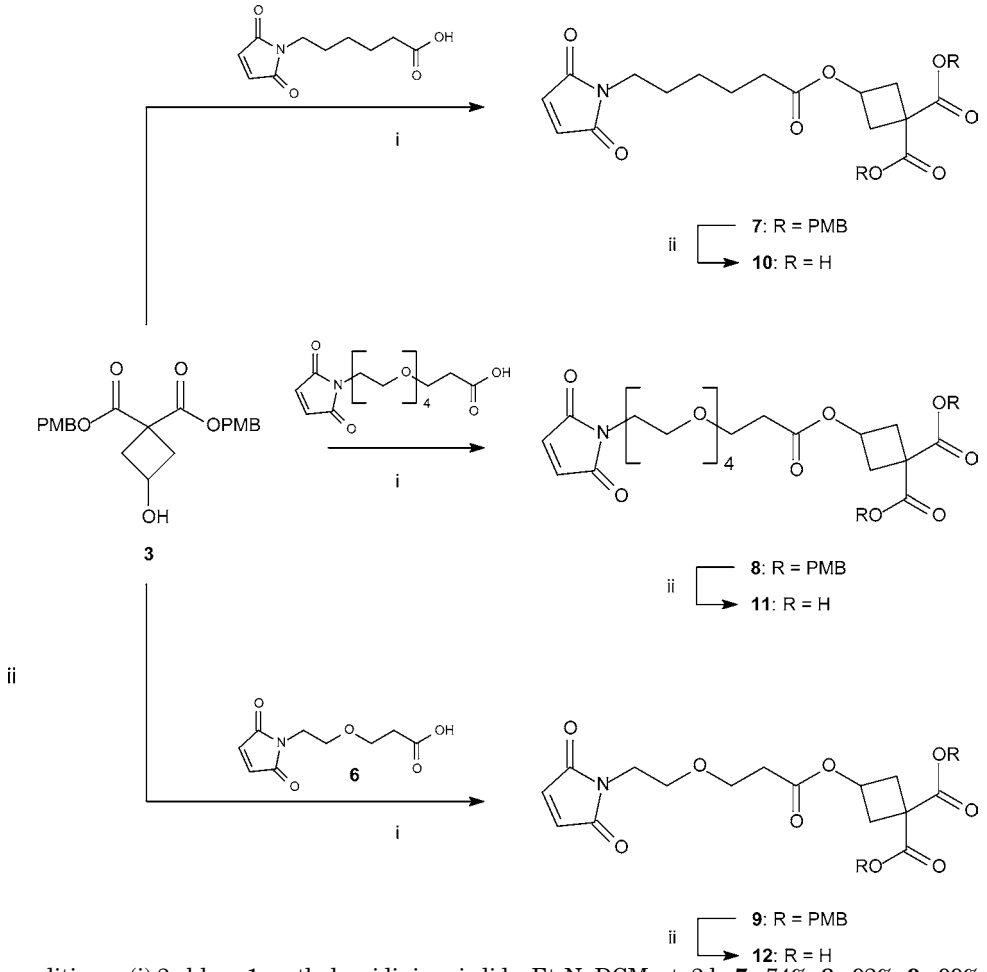
[a] Reagents and conditions: (i) TBSCl, imidazole, DMF, rt, 16 h, 100%; (ii) KH, dioxane, 120 °C, 4 days, 31%; (iii) TBAF, THF, rt, 15 min, 88%.

Scheme 2 [a]



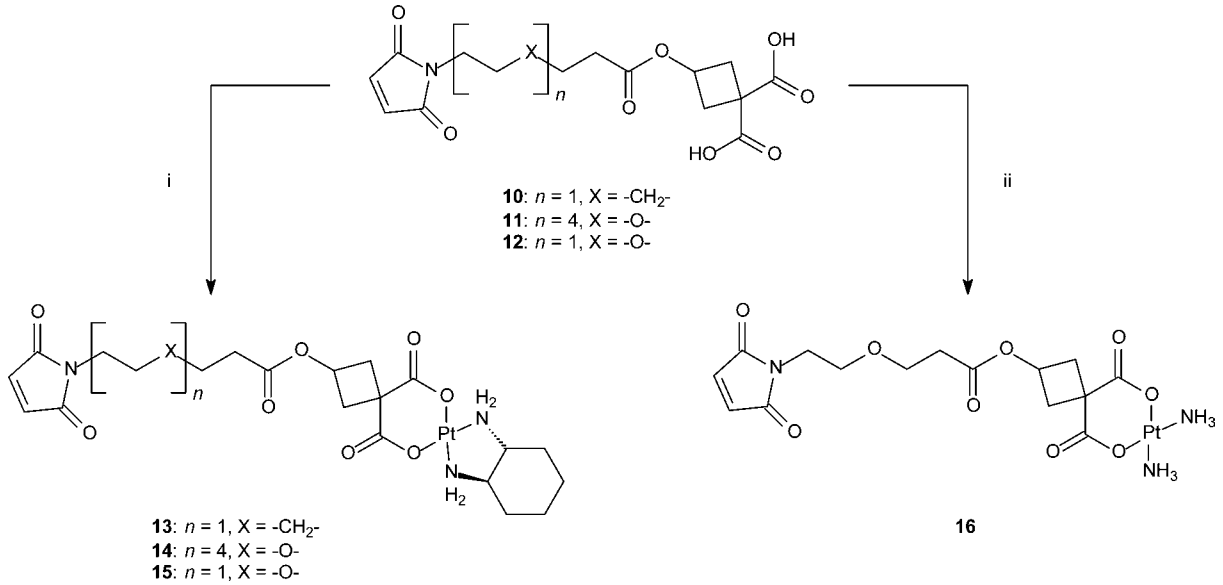
[a] Reagents and conditions: (i) Na, THF, rt, 4 days, 59%; (ii) Ph_3P, DIAD, THF, 0 °C, 3 h, 69%; (iii) TFA, DCM, rt, 1 h, 87%.

Scheme 3 [a]



[a] Reagents and conditions: (i) 2-chloro-1-methylpyridinium iodide, Et_3N, DCM, rt, 2 h, **7**: 74%, **8**: 92%, **9**: 99%; (ii) TFA, anisole, DCM, 0 °C, 2 h, **10**: 35%, **11**: 89%, **12**: 78%.

Scheme 4 [a]



[a] Reagents and conditions: (i) [Pt *trans*-DACH]$(NO_3)_2$, water, pH 5.5, rt, 3 h, **13**: 67%, **14**: 19%, **15**: 61%; (ii) *cis*-[Pt$(NH_3)_2$]$(NO_3)_2$ water, pH 5.5, rt, 3 h, 33%.

CBDA ligand as depicted in Scheme 1. 1,3-Dibromo-2-propanol was TBS protected in a first step and subsequently reacted with bis(4-methoxybenzyl) [bis(PMB)] protected malonic acid forming the four-membered ring under the conditions of a malonic ester synthesis. In the past, acid-cleavable PMB protective groups have proved useful for the synthesis of a carboplatin−cephalosporin conjugate (*18*). Deprotection of the hydroxy group yielded the bis(PMB) protected CBDA derivative **3**, which was further reacted with different maleimidocarboxylic acids as shown in Scheme 3. Our first attempt of preparing albumin-binding carboplatin analogues was to esterify **3** with the commercially available 6-maleimidocaproic acid (EMC). The ligand **10** was obtained after deprotection of the carboxylic acid groups and then further reacted to a first albumin-binding platinum prodrug (**13**) as depicted in Scheme 4. Due to the base-sensitive properties of the maleimide group, we chose a method for complex formation that is carried out in weak acid solution (pH 5.5) employing nitrato complexes of platinum. The precursors with *trans*-DACH and diammine ligands were prepared according to the literature (*20*). **13** with a *trans*-DACH ligand turned out to be poorly water soluble (<1 mg/mL) and precipitation occurred spontaneously during complex formation. To increase water solubility of the complexes that is suitable for intravenous administration, 15-maleimido-4,7,10,13-tetroxapentadecanoic acid with a highly hydrophilic oligo(ethylene glycol) backbone was selected as a linker. In our previous work, the introduction of 3−4 oligo(ethylene glycol) units in the maleimide linker had significantly enhanced water solubility for maleimide derivatives of doxorubicin (*9*), but not for albumin-binding prodrugs of camptothecin (*8*). Using this linker, we prepared a *trans*-DACH complex (**14**) in analogy to **13** (see Schemes 3 and 4). Substituting the hydrophobic EMC for the tetraethylene glycol derivative **9** resulted in a dramatic increase in water solubility (>100 mg/mL). Due to its hydrophilic properties, complex **14** had to be purified by preparative HPLC, which is not practical for large-scale synthesis. Furthermore, molecular modeling of the covalent interaction of maleimide spacers with the cysteine-34 position of HSA suggested that the optimal length of an aliphatic maleimide spacer consists of five to seven carbon atoms

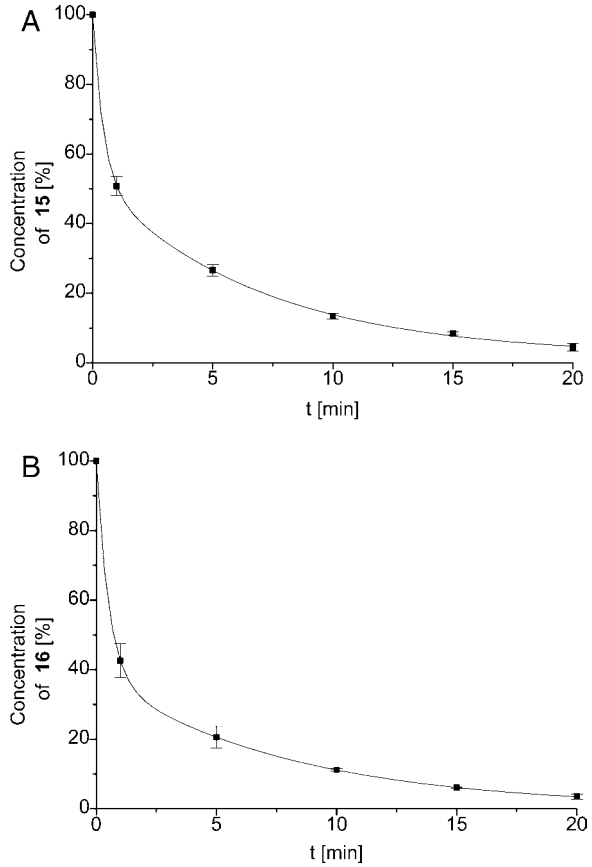


Figure 2. Decrease of free (a) **15** and (b) **16** after incubation with human serum albumin at 37 °C and pH 7.4 ($n = 3$).

(*7*). Therefore, we prepared a maleimide-functionalized linker with a shorter ethylene glycol chain that contained only one ether group (see Scheme 2). Starting with a monoalkylation of ethylene glycol using *tert*-butyl acrylate, the maleimide group was introduced under Mitsunobu conditions. Cleavage of the *tert*-butyl protective group afforded the linker **6**, which was further reacted with compound **3** (see Scheme 3). After removal of the PMB protective groups, ligand **12** was used for complex formation with [Pt *trans*-DACH]$(NO_3)_2$ and *cis*-[Pt$(NH_3)_2$]-

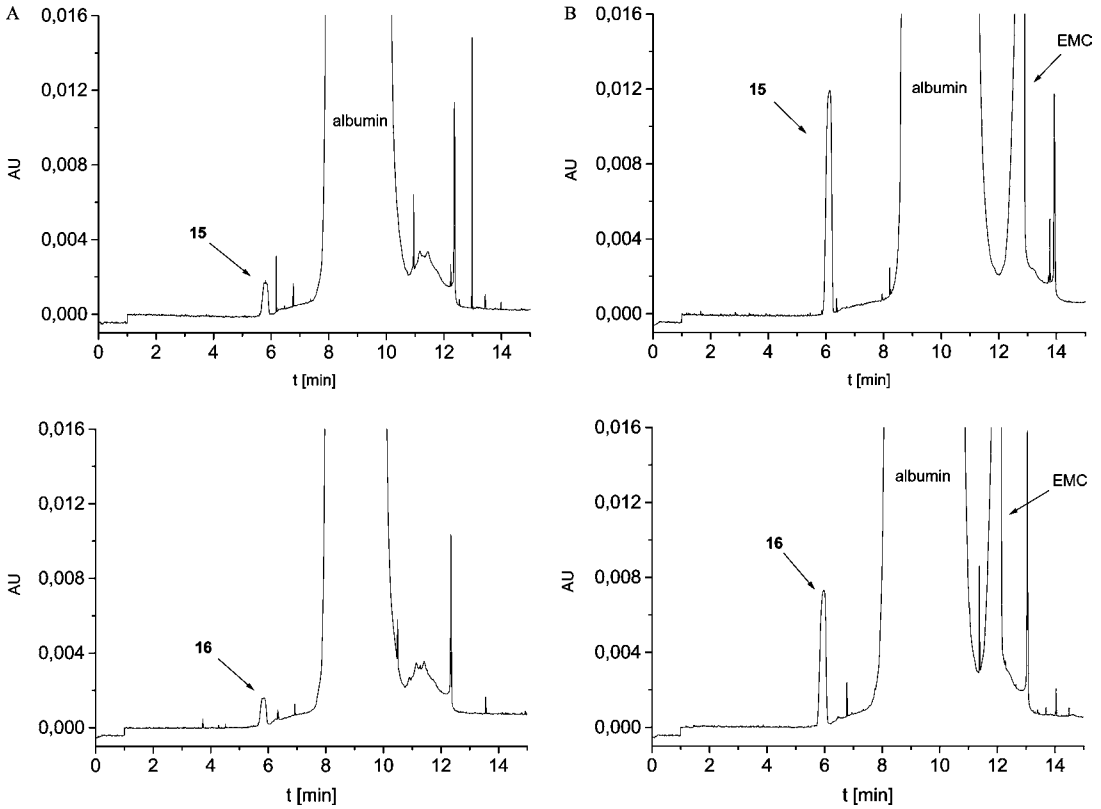


Figure 3. Electropherograms after a 10 min incubation of **15** and **16** (150 μM) with human serum albumin (600 μM) (A) and after a 10-min incubation with EMC-blocked human serum albumin (B).

$(NO_3)_2$ affording **15** and **16**, respectively, in moderate yields (see Scheme 4). **15** and **16** were obtained as colorless solids which were characterized by NMR spectroscopy, mass spectrometry, elemental analysis, and HPLC (see Experimental Section). It is a noteworthy finding that both complexes could be purified by column chromatography on silica gel with ethanol as an eluent, which represents a convenient and previously unknown method for the workup of platinum complexes. Although the water solubility of **15** and **16** was reduced when compared to complex **14**, both were adequately water soluble for assessing their biological activity in animal models (solubility in water was determined to be ~50 mg/mL for **15** and ~8 mg/mL for **16**). It is remarkable that compounds **13** and **15**, which merely differ in one oxygen atom in the chain of the linker, exhibit such dissimilar water solubilities. Substituting a methylene group for an oxygen atom increases the solubility by a factor of approximately 50, in contrast to our recently published work on albumin-binding prodrugs of camptothecin (*8*).

Albumin-Binding Properties of 15 and 16. In our previous work, we could show by mass spectrometry that the maleimide group of doxorubicin derivatives reacts specifically and selectively with the cysteine-34 group of exo- and endogenous HSA (*21*).

To investigate binding of **15** and **16** to albumin, the complexes (150 μM) were incubated at 37 °C with HSA (600 μM), which is a mixture of mercaptalbumin (~35%) and nonmercaptalbumin (~65%) in which the cysteine-34 position is oxidized by sulfhydryl compounds such as cysteine, homocysteine, glutathione, or nitric oxide (*22*–*24*). The samples were directly analyzed by capillary electrophoresis after an incubation time of 1, 5, 10, 15, and 20 min. The decrease in concentration of the platinum complexes **15** and **16** is depicted in Figure 2. Electropherograms recorded 10 min after incubation with HSA are shown in Figure 3.

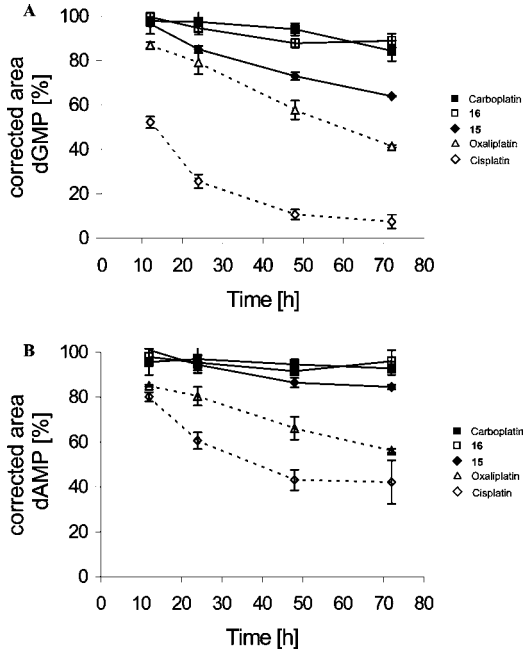


Figure 4. Decrease of dGMP (150 μM, A) and dAMP (150 μM, B) after incubation with **15**, **16**, carboplatin, oxaliplatin, and cisplatin (150 μM).

Approximately 50% of **15** or **16** are bound to albumin within the first minute and after 15 min less than 10% of the free complexes remained. To show that the maleimide group binds to the cysteine-34 position of HSA, experiments were carried out in which the thiol group was blocked by preincubating HSA with an excess of EMC prior to incubation with **15** or **16**. In these experiments, essentially no reaction of **15** or **16** could be

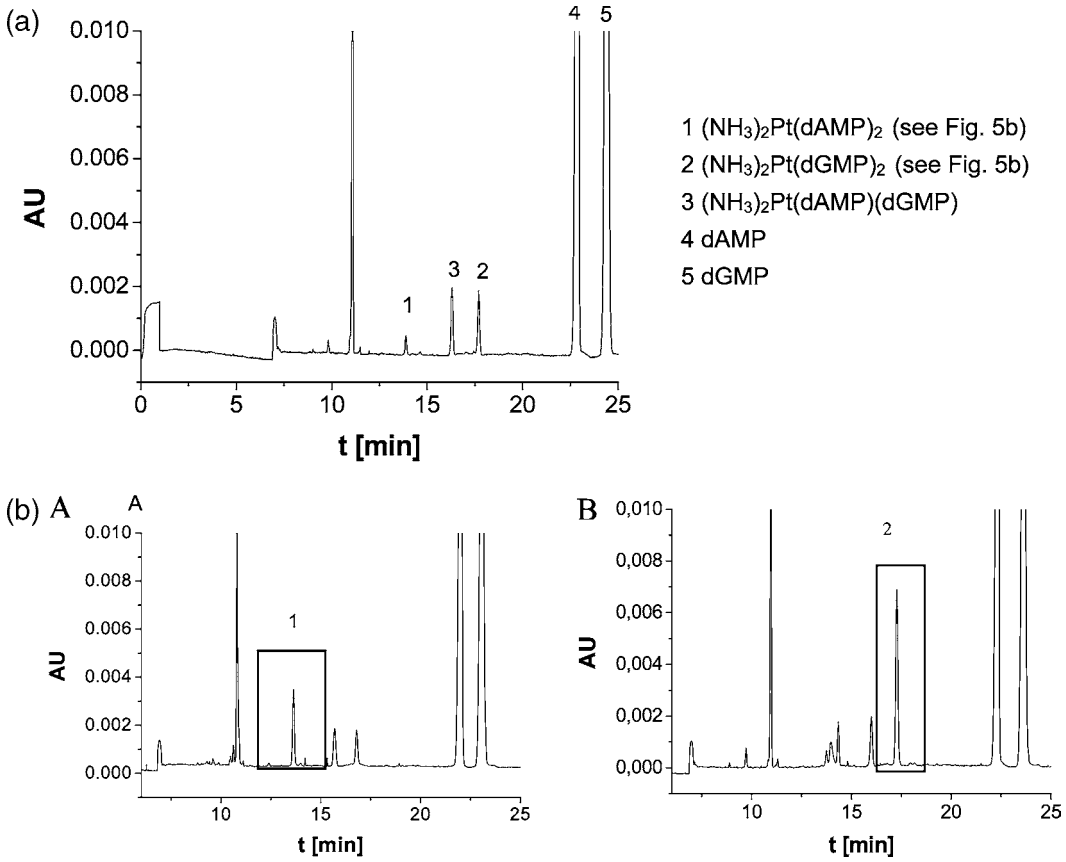


Figure 5. (a) Electropherogram obtained 48 h after incubation of dAMP and dGMP (150 μM each) with **16** (150 μM). (b) Electropherogram obtained 48 h after incubation of dAMP and dGMP (150 μM each) with **16** (150 μM) and co-injection of separately incubated cisplatin with dAMP (A) and dGMP (B).

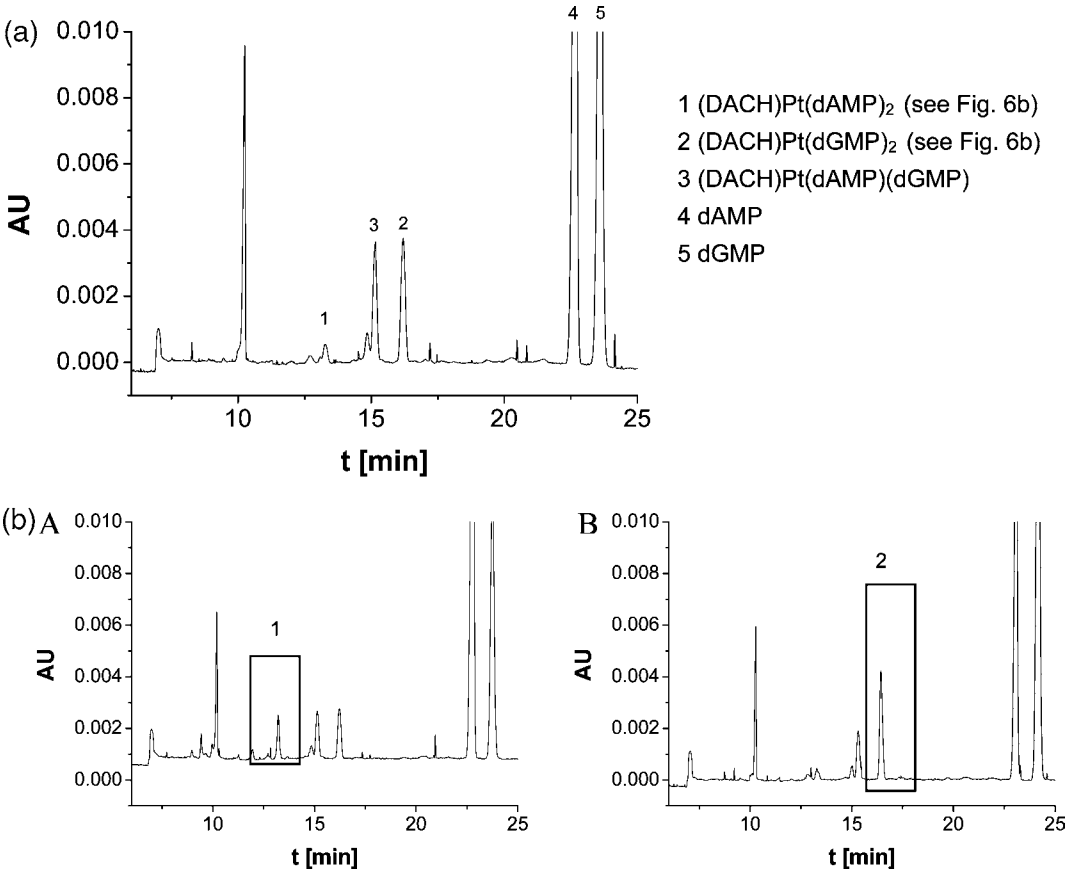


Figure 6. (a) Electropherogram obtained 48 h after incubation of dAMP and dGMP (150 μM each) with **15** (150 μM). (b) Electropherogram obtained 48 h after incubation of dAMP and dGMP (150 μM each) with **15** (150 μM) and co-injection of separately incubated oxaliplatin with dAMP (A) and dGMP (B).

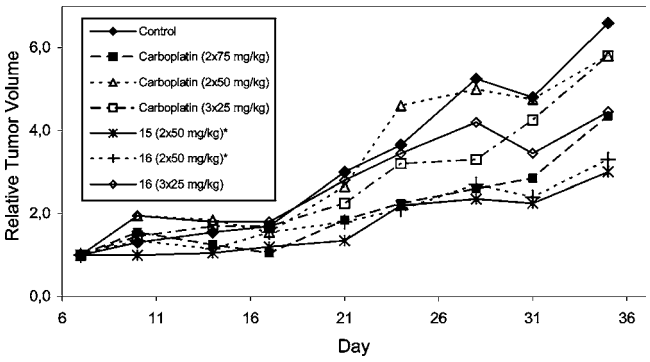


Figure 7. Curves depicting tumor growth inhibition of subcutaneously MaTu xenografts under therapy with carboplatin, **15**, and **16**. *significant to saline ($p < 0.05$).

observed after incubating the complexes for 10 min with the blocked albumin (see Figure 3B).

In Vitro Reactivity toward the Nucleotides dAMP and dGMP. To characterize the reactivity of **15** and **16** with DNA nucleotides, the two compounds (150 μM) were incubated each with dAMP and dGMP (150 μM) for 72 h. dAMP and dGMP were quantified up to 72 h using capillary electrophoresis. A higher reactivity of **15** compared to **16** and carboplatin was observed (Figure 4). The formed adducts were identified by co-injection of separately incubated solutions of oxaliplatin (for **15**) or cisplatin (for **16**) since these complexes should form identical adducts. Only biadducts were detected over the period of 72 h (Figures 5a,b and 6a,b).

Antiproliferative Activity against Two Tumor Cell Lines. The antiproliferative activity of the albumin conjugates of the platinum complexes **15** and **16** and of free carboplatin was assessed in the following two tumor cell lines using the MTT assay: LXFL 529 human lung carcinoma and MaTu human mamma carcinoma. The IC_{50} values that were obtained after a 72 h cell exposure are summarized in Table 1. Carboplatin is cytotoxic in both cell lines with IC_{50} values of 3.9 and 6.4 μM, respectively. The albumin conjugates of **15** and **16** are less active in both cell lines (IC_{50} values are 5−8-fold higher), but still showed cytotoxicity compared to controls. These results are in accordance with our experience with albumin conjugates of doxorubicin that were found to be approximately 10-fold less active than the parent compound (*7*).

In Vivo Efficacy against Human MaTu Breast Carcinoma. The two platinum complexes **15** and **16** were evaluated in xenografted nude mice (human MaTu breast carcinoma) in comparison to carboplatin. Both prodrugs were assessed at a dose of 2 × 50 mg/kg and 3 × 25 mg/kg (i.v.) carboplatin equivalents. These doses were selected based on preliminary toxicity studies at a dose of 1 × 50 mg/kg and 1 × 100 mg/kg carboplatin equivalents. Carboplatin was tested at the same doses and additionally at a dose of 2 × 75 mg/kg (i.v.), which is the MTD for carboplatin in nude mice models. Figure 7 shows the results of this experiment (dose schedules are summarized in Table 2, Figure 8 depicts body weight change). Treatment with carboplatin produced low antitumor effects at 3 × 25 mg/kg and 2 × 50 mg/kg with only a marginal reduction in tumor size compared to untreated animals after 35 days. A moderate activity was only observed at the high dose (2 × 75 mg/kg) with a 4-fold increase in tumor size at the end of the experiment compared to controls (optimum T/C value of 50%). Prodrug **16** at the low dose (3 × 25 mg/kg, 75 mg/kg total dose) showed a similar antitumor response compared to therapy with carboplatin at its optimal dose (i.e., twice the dose 2 × 75 mg/kg, 150 mg/kg total dose). (Complex **15** was also evaluated at 3 × 25 mg/kg (i.v.) carboplatin equivalents. However, this dose proved to be above the MTD producing two toxic deaths.) At the higher dose (2 × 50 mg/kg) treatment with **15** and **16** achieved the best efficacy, which resulted in a 2.5−3-fold increase in tumor size at the end of the experiment (optimum T/C values of 45 and 50%, respectively). This antitumor effect was significant to untreated animals ($p < 0.05$), whereas the effects achieved with carboplatin were not found to be significant at any dose. The carboplatin derivative (**16**) shows a change in body weight that is similar to the parent compound (BWC between −6 to −8% at all doses). In contrast, platinum complex **15** with the DACH ligand exhibited a higher toxicity (BWC: −15%).

CONCLUSIONS

This work focused on the development of novel albumin-binding derivatives of carboplatin analogues consisting of a thiol-binding maleimide group attached through a spacer molecule to a derivatized CBDA ligand as the platinum-complexing unit. We established a convenient synthesis for the ligand based on the esterification of a maleimidocarboxylic acid with a hydroxy functionalized bis(PMB) protected CBDA derivative (**3**) that could be readily prepared in a three-step procedure starting with 1,3-dibromo-2-propanol and including a malonate synthesis to form the four-membered ring. The number of

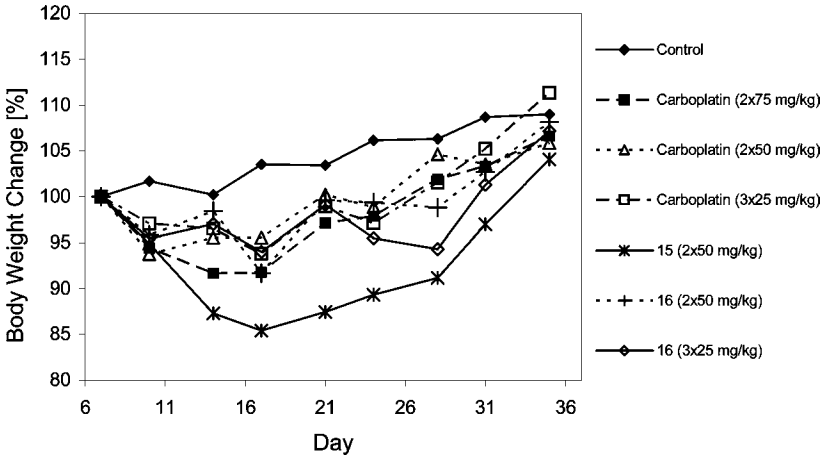


Figure 8. Curves depicting body weight change (BWC) of mice bearing subcutaneous MaTu xenografts under therapy with carboplatin, **15**, and **16**.

ethylene glycol units present in the spacer had a pronounced influence on water solubility of the developed platinum complexes, and one ether bond rendered good water solubility that was sufficient for preclinical assessment.

Both **15** and **16** were as or more effective than carboplatin in reducing the tumor size of nude mice bearing MaTu human breast tumors. **16**, the strict analogue of carboplatin, proved to be less toxic than **15** containing the DACH ligand and has been selected for further studies with respect to its mode of action on the cellular level and its antitumor efficacy in other preclinical models.

ACKNOWLEDGMENT

The support by the Deutsche Forschungsgemeinschaft is gratefully acknowledged. Furthermore, we thank Peter Lazar, Cornelia Stockmar, and Petra Stettner for their excellent technical assistance.

LITERATURE CITED

(1) Heim, M. E. (1993) Platinum and non-platinum complexes in clinical trials. Current status and new developments. *Metal Complexes in Cancer Chemotherapy* (Keppler, B. K., Ed.) pp 9−24, Verlag Chemie, Weinheim.

(2) Kratz, F. (1993) Interactions of antitumour metal complexes with serum proteins. Perspectives for anticancer drug development. A review. *Metal Complexes as Antitumour Agents*, Keppler, B. K. Verlag Chemie, Weinheim.

(3) Kratz, F., Hartmann, M., Keppler, B. K., and Messori, L. (1994) The binding properties of two antitumor ruthenium-(III) complexes to apotransferrin. *J. Biol. Chem. 269*, 2581−2588.

(4) Kratz, F., and Beyer, U. (1998) Serum proteins as drug carriers of anticancer agents: a review. *Drug Delivery 5*, 281−299.

(5) Maeda, H., Wu, J., Sawa, T., Matsumura, Y., and Hori, K. (2000) Tumor vascular permeability and the EPR effect in macromolecular therapeutics: a review. *J. Controlled Release 65*, 271−284.

(6) Kratz, F., Mueller-Driver, R., Hofmann, I., Drevs, J., and Unger, C. (2000) A novel macromolecular prodrug concept exploiting endogenous serum albumin as a drug carrier for cancer chemotherapy. *J. Med. Chem. 43*, 1253−1256.

(7) Kratz, F., Warnecke, A., Scheuermann, K., Stockmar, C., Schwab, J., Lazar, P., Drückes, P., Esser, N., Drevs, J., Rognan, D., Bissantz, C., Hinderling, C., Folkers, G., Fichtner, I., and Unger, C. (2002) Probing the cysteine-34 position of endogenous serum albumin with thiol-binding doxorubicin derivatives: improved efficacy of an acid-sensitive doxorubicin derivative with specific albumin-binding properties compared to that of the parent compound. *J. Med. Chem. 45*, 5523−5533.

(8) Warnecke, A., and Kratz, F. (2003) Maleimide-oligo(ethylene glycol) derivatives of camptothecin as albumin-binding prodrugs: synthesis and antitumor efficacy. *Bioconjugate Chem. 14*, 377−387.

(9) Mansour, A. M., Drevs, J., Esser, N., Hamada, F. M., Badary, O. A., Unger, C., Fichtner, I., and Kratz, F. (2003) A new approach for the treatment of malignant melanoma: enhanced antitumor efficacy of an albumin-binding doxorubicin prodrug that is cleaved by matrix metalloproteinase 2. *Cancer Res. 63*, 4062−4066.

(10) Allsopp, M. A., Sewell, G. J., Rowland, C. G., Riley, C. M., and Schowen, R. L. (1991) The degradation of carboplatin in aqueous solutions containing chloride or other selected nucleophiles. *Int. J. Pharm. 69*, 197−210.

(11) Lippard, S. J., Ushay, H. M., Merkel, C. M., and Poirier, M. C. (1983) Use of antibodies to probe the stereochemistry of antitumor platinum drug binding to deoxyribonucleic acid. *Biochemistry 22*, 5165−5168.

(12) Schütte, M. T., Schumacher, P., Unger, C., Mülhaupt, R., and Kratz, F. (1998) Synthesis of two maleimide derivatives of *cis*-configurated platinum(II) complexes for the preparation of chemoimmunoconjugates. *Inorg. Chim. Acta 267*, 133−136.

(13) Gianasi, E., Wasil, M., Evagorou, E. G., Keddle, A., Wilson, G., and Duncan, R. (1999) HPMA copolymer platinates as novel antitumour agents: in vitro properties, pharmacokinetics and antitumour activity in vivo. *Eur. J. Cancer 35*, 994−1002.

(14) Schütte, M. T., Mülhaupt, R., and Kratz, F. (2000) Development of acid-sensitive platinum(II) complexes with protein-binding properties. *Met.-Based Drugs 7*, 89−100.

(15) Ohya, Y., Masunaga, T., Baba, T., and Ouchi, T. (1996) Synthesis and cytotoxic activity of dextran-immobilizing platinum(II) complex through chelate-type coordination bond. *J. Macromol. Sci., Pure Appl. Chem. A33*, 1005−1016.

(16) Ohya, Y., Shirakawa, S., Matsumoto, M., and Ouchi, T. (2000) Design of poly(ethylene glycol) immobilizing complex through chelate-type coordination bond. *Polym. Adv. Technol. 11*, 635−641.

(17) Stewart, D. R., Callahan, E. H., Jacob, J. E., Rice, J. R., Shannon, K. F., St. John, J. V., and Nowotnik, D. P. Preclinical development of the polymer platinate AP 5280. *Proceedings of the 4th International Symposium on Polymer Therapeutics*: London, UK, 2000; p 57.

(18) Hanessian, S., and Wang, J. (1993) Design and synthesis of a cephalosporin-carboplatinum prodrug activatable by a β-lactamase. *Can. J. Chem. 71*, 896−906.

(19) Cole, S. P. (1986) Rapid chemosensitivity testing of human lung tumor cells using the MTT assay. *Cancer Chemother. Pharmacol. 17*, 259−263.

(20) Pasini, A., Caldirola, C., Spinelli, S., and Valsecchi, M. (1993) Comments on different synthetic methods for the preparation of diammine and bis(amine) organodicarboxylatoplatinum(II) complexes. *Synth. React. Inorg. Met.-Org. Chem. 23*, 1021−1060.

(21) Kratz, F., Drevs, J., Bing, G., Stockmar, C., Scheuermann, K., Lazar, P., and Unger, C. (2001) Development and in vitro efficacy of novel MMP2 and MMP9 specific doxorubicin albumin conjugates. *Bioorg. Med. Chem. Lett. 11*, 2001−2006.

(22) Sogami, M., Era, S., Nagaoka, S., Kuwata, K., Kida, K., Shigemi, J., Miura, K., Suzuki, E., Muto, Y., Tomita, E., et al. (1985) High-performance liquid chromatographic studies on non-mercapt in equilibrium with mercapt conversion of human serum albumin. II. *J. Chromatogr. 332*, 19−27.

(23) Etoh, T., Miyazaki, M., Harada, K., Nakayama, M., and Sugii, A. (1992) Rapid analysis of human serum albumin by high-performance liquid chromatography. *J. Chromatogr. 578*, 292−296.

(24) Era, S., Hamaguchi, T., Sogami, M., Kuwata, K., Suzuki, E., Miura, K., Kawai, K., Kitazawa, Y., Okabe, H., Noma, A., et al. (1988) Further studies on the resolution of human mercapt- and nonmercaptalbumin and on human serum albumin in the elderly by high-performance liquid chromatography. *Int. J. Pept. Protein Res. 31*, 435−442.

BC049829J

Design of Metalloporphyrin−Carbohydrate Conjugates for a New Superoxide Dismutase Mimic with Cellular Recognition

Shoichiro Asayama,* Kaori Mizushima, Shoji Nagaoka, and Hiroyoshi Kawakami

Department of Applied Chemistry, Tokyo Metropolitan University, 1-1 Minami-Osawa, Hachioji, Tokyo 192-0397, Japan. Received June 11, 2004; Revised Manuscript Received August 18, 2004

Metalloporphyrin−carbohydrate conjugates have been synthesized as superoxide dismutase (SOD) mimics with cellular recognition. To synthesize the conjugates, aliphatic primary amino groups for conjugation were introduced, with the cationic pyridyl groups for the SOD activity of porphyrin preserved. The reductive amination between introduced amino groups and the reducing end of lactose was then carried out. The resulting conjugates consisting of manganese (Mn)-porphyrin surrounded by several lactose molecules possessed significant SOD activity and low cytotoxicity. Compared with metalloporphyrins having no lactose molecule, the recognition of the resulting conjugates by human hepatoma HepG2 cells increased. The cellular recognition was inhibited by competitors of β-galactose. These results suggest that the Mn-porphyrin−lactose conjugates recognized the hepatic lectin on the cell surface.

INTRODUCTION

Reactive oxygen species (ROS[1]) are considered to be implicated in the pathogenesis of a number of diseases, such as atherosclerosis, cancer, and Alzheimer's disease (*1*−*3*). Their toxic effects are amplified by pathological events including neutrophil activation, hyperoxia, metabolism of redox-active drugs, radiation exposure, and ischemia/reperfusion. Subsequently, the overproduced ROS, such as superoxide radical anion ($O_2^{\bullet-}$), cause the membrane damage resulting from lipid peroxidation, as well as the attack on proteins and nucleic acids. Therefore, antioxidant enzymes are useful for the therapy of ROS-mediated injuries and diseases.

Superoxide dismutase (SOD) catalyzing the reduction from $O_2^{\bullet-}$ to H_2O_2 is the key enzyme for the protection from oxidative stress. As a defense mechanism against microorganisms and various exogenous compounds (*4*), on the other hand, phagocytic cells, i.e., neutrophils, monocytes, and macrophages, generate ROS during the respiratory burst by membrane-bound NADPH oxidase (*5*). These merits and demerits of ROS have led us to create a drug delivery system using SOD to reduce oxidative stress.

Fridovich and co-workers have reported that manganese porphyrins (Mn-porphyrins) are promising compounds as SOD mimics with chemical versatility (*6*). Subsequently, we have synthesized a macromolecular Mn-porphyrin for enhancing half-life in the blood circulation (*7*). However, these Mn-porphyrins lack the ability to target cells that overproduce $O_2^{\bullet-}$, although the selective delivery of SOD mimics into every particular cell is promising for a radical approach (*8*) to various therapies.

In this study, we have synthesized a new SOD mimic with the carbohydrate to facilitate receptor binding and hence active targeting. Carbohydrates are known as various ligands of cell surface lectins (*9*, *10*). In particular, the triantennary carbohydrate containing three terminal β-galactose residues is a high affinity ligand for a hepatic lectin, asialoglycoprotein receptor (ASGP-R) (*11*). Therefore, the Mn-porphyrin with several β-galactose residues is expected to be recognized by the ASGP-R expressed on hepatocytes or hepatoma cells, so we have designed new SOD mimic Mn-porphyrin−lactose (4-*O*-β-D-galactopyranosyl-D-glucose) conjugates with cellular recognition.

EXPERIMENTAL PROCEDURES

Materials. Pyridine-4-aldehyde and pyrrole were purchased from Tokyo Kasei Kogyo Co. Propionic acid, acetic anhydride, 3-bromopropylamine hydrobromide, lactose monohydrate, sodium cyanoborohydride ($NaBH_3CN$), and $Mn(OAc)_2{\cdot}4H_2O$ were from Kanto Chemical Co. 4-(2-Hydroxyethyl)-1-piperazinylethanesulfonic acid (HEPES) and dimethyl sulfoxide (DMSO) were purchased from Nacalai Tesque Inc. Potassium superoxide (KO_2) was purchased from Aldrich Chemical Co., and asialofetuin was from Sigma Chemical Co.

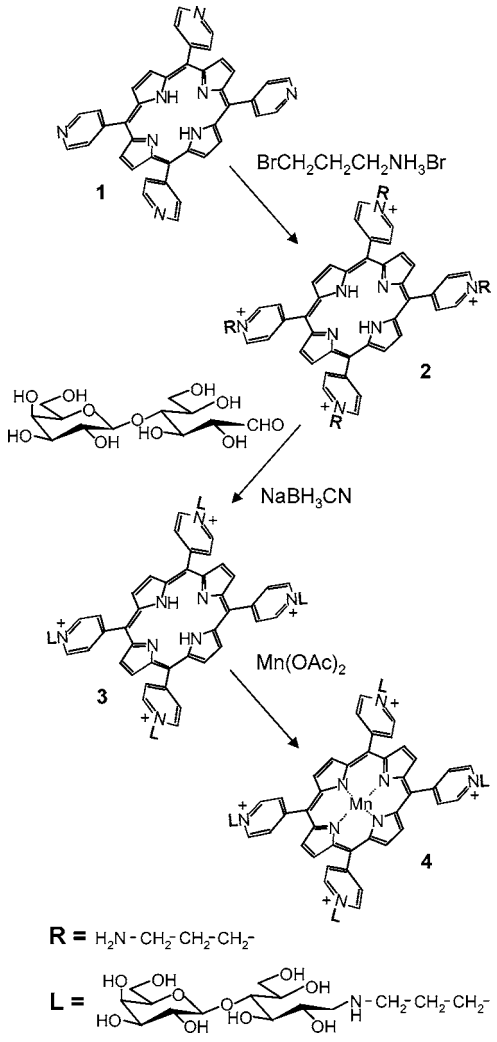
Synthesis of Mn-Porphyrin−Lactose Conjugates. The synthetic route of the conjugates is shown in Scheme 1. 5,10,15,20-Tetrakis(4-pyridyl)porphine (**1**) was synthesized, as reported in the literature (*12*). The typical procedure for the synthesis of Mn-porphyrin−lactose conjugates is as follows: the hydrophobic **1** (0.3 g, 0.5 mmol) was reacted with 3-bromopropylamine hydrobromide (3 g, 14 mmol) in DMF for 3 days under refluxing conditions. After the reaction, the mixture was dried on a rotary evaporator, followed by the extraction with water in methylene chloride. The PF_6^- salt of the porphyrin **2** was precipitated by the addition of a concentrated aqueous solution of NH_4PF_6. The compound was then dissolved in acetone, and a concentrated acetone solution of tetraethylammonium chloride was added, until the majority of the porphyrin **2** had precipitated in the form of its chloride salt. The precipitate was washed thoroughly with acetone, dissolved in methanol, and dried in vacuo. **2**: ^{1}H NMR (DMSO-d_6, 270 MHz) δ −3.0 (s,

* To whom correspondence should be addressed. Telephone: +81-426-77-1111 (ext.) 4975. Fax: +81-426-77-2821. E-mail: asayama-shoichiro@c.metro-u.ac.jp.

[1] Abbreviations: ROS, reactive oxygen species; SOD, superoxide dismutase; ASGP-R, asialoglycoprotein receptor; HEPES, 4-(2-hydroxyethyl)-1-piperazinylethanesulfonic acid; DMSO, dimethyl sulfoxide.

10.1021/bc049865i CCC: $27.50 © 2004 American Chemical Society
Published on Web 11/02/2004

Scheme 1. Synthesis of Mn-Porphyrin–Lactose Conjugates



2H, inner H), 3.5 (CH_2N), 5.0 (8H, N^+CH_2), 9.0 (8H, pyridinium), 9.3 (s, 8H, β-pyrrole), 9.7 (8H, pyridinium); λ_{max} (H_2O) 422, 519, 586, 643 nm.

The resulting water-soluble porphyrin **2** (0.04 g, 0.04 mmol) and lactose monohydrate (0.4 g, 1.1 mmol) were preincubated at 40 °C for 3 days in 4 mL of sodium borate buffer (0.1 M, pH 8.5). Then, a reducing agent, $NaBH_3CN$, was added to the mixture of **2** and lactose at a final concentration of 0.3 M. The reaction mixture was incubated at 40 °C for 4 days, followed by dialysis against distilled water using a Spectra/Por CE (cellulose ester) membrane (molecular weight cutoff = 500) to remove unreacted lactose. The resulting conjugate **3** was obtained by freeze-drying. **3**: ^{1}H NMR (DMSO-d_6, 270 MHz) δ −3.1 (s, 2H, inner H), 3.2–5.1 (CH protons of lactose), 9.0–9.6 (CH protons of porphyrin); λ_{max} (H_2O) 422, 519, 582, 640 nm.

The resulting porphyrin **3** and an equivalent amount of $Mn(OAc)_2{\cdot}4H_2O$ were incubated in H_2O at 40 °C for 24 h. The reaction was monitored by UV–visible spectroscopy and was stopped when the Soret band shift was completed (from 422 to 464 nm). The reaction mixture was dialyzed again against distilled water (molecular weight cutoff = 500). The resulting metalloporphyrin **4** was obtained by freeze-drying. **4**: λ_{max} (H_2O) 378, 400, 464, 561, 678 nm.

Stopped-Flow Kinetic Analysis. The rate constant (k_c) of the $O_2^{\bullet-}$ dismutation was measured with an SX.18MV stopped-flow spectrometer purchased from Applied Photophysics Ltd., UK, according to the literature (*13*). A DMSO solution of KO_2 was rapidly mixed with a HEPES buffer solution at pH 8.1 and 36 °C to give $O_2^{\bullet-}$ (*14*). The decay of $O_2^{\bullet-}$ was spectrophotometrically monitored at 245 nm (*15*). In the experimental runs, the points of 1000 data were acquired using a time basis of 1 s for monitoring the reaction. The absorbance data were processed to obtain an observed rate constant (k_{obs}) which was calculated from the slop of the plot of ln(absorbance at 245 nm) versus time. The k_c was determined from the slop of a plot of k_{obs} versus the concentration of the metalloporphyrins. The rate constants were determined from the mean of at least 20 experiments.

Cell Viability Assay. HepG2 cells (a gift from the Japan Health Sciences Foundation), human hepatoma cell line, were cultured in tissue culture flasks containing EMEM supplemented with 10% heat-inactivated fetal bovine serum. The cells were seeded at 5×10^3 cells/well in a 96-well plate and incubated overnight at 37 °C in a 5% CO_2 incubator. The cells were treated with each metalloporphyrin (0–100 μM) and incubated for 18 h at 37 °C. By further incubation for 5 h (approximately total 24 h), the cell viability was measured using the Alamar Blue assay (*16*) in quadruplicate.

Recognition of Mn-Porphyrin–Lactose Conjugates by HepG2 Cells. HepG2 cells were incubated in 75-cm^2 tissue culture flasks containing EMEM supplemented with 10% heat-inactivated fetal bovine serum. After confluent growth, each metalloporphyrin (100 μM) was added to the adherent cells, followed by the incubation for 24 h at 37 °C. For the competition assay, the Mn-porphyrin–lactose conjugates were incubated for 24 h at 37 °C in the presence of 4 mM lactose or 1 mg/mL of asialofetuin. The resulting cells were detached, counted, and washed with PBS (−) to remove free metalloporphyrins. Then, the cell lysis was obtained by adding 4 mL of 0.5 N HNO_3. The manganese in the lysis was determined by atomic absorption spectrometry at 403 nm using a Varian SpectraAA-640 (Varian Australia Pty., Ltd., Australia).

RESULTS AND DISCUSSION

Synthesis of Mn-Porphyrin–Lactose Conjugates. To deliver SOD mimics into hepatoma cells, we have designed a Mn-porphyrin–lactose conjugate, as shown in Scheme 1. For SOD activity, cationic pyridyl groups are necessary. Furthermore, for the conjugation of biomolecules, aliphatic primary amino groups are selected, due to the ease of chemical modification (*17*), e.g., ϵ-amino groups of lysine residues of a protein. To introduce cationic pyridyl groups and primary amino groups at once, we have reacted the hydrophobic porphyrin **1** with 3-bromopropylamine. The resulting water-soluble porphyrin **2** was subjected to reductive amination (*18*) between the introduced amino groups and the reducing end of lactose using $NaBH_3CN$ as a reducing agent. As shown in Figure 1, the spectrum of the freebase porphyrin **3** shifted completely after Mn introduction; namely, the Soret band was completely shifted from 422 to 464 nm. The resulting spectrum of the metalloporphyrin **4** exhibited no turbidity, which suggested that the Mn-porphyrin–lactose conjugate **4** was water-soluble. On average, the lactose content of the purified conjugate was estimated to be about 2.5 molecules per metalloporphyrin backbone by the phenol–sulfuric acid method (*19*), with lactose as the standard.

SOD Activity of Mn-Porphyrin–Lactose Conjugates. The resulting Mn-porphyrin–lactose conjugate

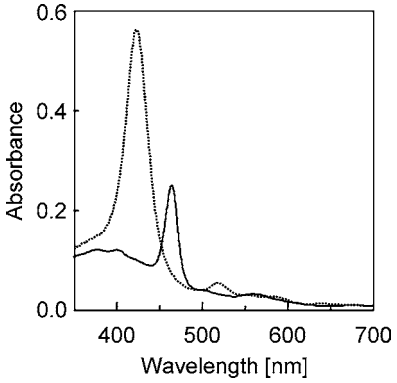


Figure 1. Optical spectra of the porphyrin−lactose conjugate before (dotted line) and after (solid line) Mn introduction. Both spectra were obtained at 5 μM porphyrin concentration in H_2O.

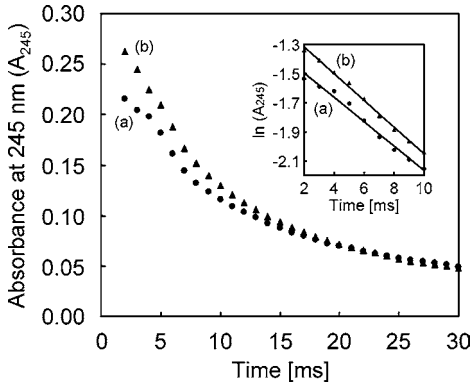


Figure 2. Stopped-flow traces of the conjugate-catalyzed decay of superoxide. The decay of superoxide was monitored spectrophotometrically at 245 nm and 37 °C. Inset: the first-order decay of superoxide. The concentration of the Mn-porphyrin−lactose conjugate was (a) 0 μM and (b) 0.5 μM.

Table 1. SOD Activity of Mn-Porphyrins

porphyrin	k_c, 10^6 M^{-1} s^{-1}
Mn-MPyP[a]	14(±1.6)
Mn-LacAPPyP[b]	5.6(±1.6)

[a] L = CH_3 in Scheme 1. [b] **4** in Scheme 1.

consists of a SOD mimic surrounded by several targeting ligands. To examine the SOD activity of the conjugate, we used the stopped-flow kinetic analysis technique developed for detecting and quantifying the dismutation of $O_2^{\bullet-}$. The decay of $O_2^{\bullet-}$ was spectrophotometrically monitored at 245 nm, the absorbance maximum for superoxide, with a stopped-flow spectrometer. Figure 2 shows the conjugate-induced decay of $O_2^{\bullet-}$. An observed rate constant (k_{obs}) was obtained from the slope of a plot of ln(absorbance at 245 nm) versus time (Figure 2, inset). Finally, the catalytic rate constant (k_c) was determined from the slope of a plot of k_{obs} versus conjugate concentration (0−4 μM). As shown in Table 1, the k_c value for the conjugate was 5.6(±1.6) × 10^6 M^{-1} s^{-1}, while that for Mn-porphyrin (L = CH_3 in Scheme 1) was 14(±1.6) × 10^6 M^{-1} s^{-1} under these conditions. It can be said that the Mn-porphyrin−lactose conjugate showed significant SOD activity despite the chemical modification of the metalloporphyrin. The native SOD enzymes react with $O_2^{\bullet-}$ at rate in the range 10^8 M^{-1} s^{-1} for mitochondrial Mn-SOD (*20*) and at the near-diffusion-limited rate of 2 × 10^9 M^{-1} s^{-1} for Cu,Zn-SOD (*21*). These metalloenzymes are, however, found at micromolar intracellular concentrations (*22*). If the new SOD mimics are concentrated at an intracellular site, the apparent activity of the enzyme is expected to increase.

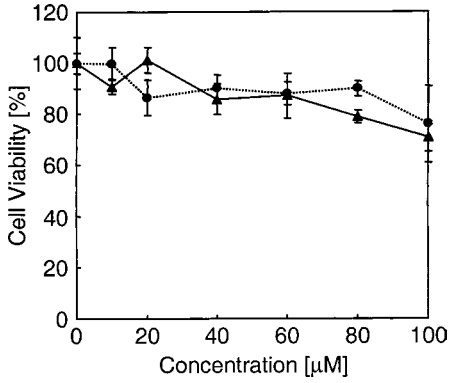


Figure 3. Effect of Mn-porphyrin derivatives on the viability of HepG2 cells after 1 day incubation: (●) Mn-porphyrin (L = CH_3 in Scheme 1); (▲) Mn-porphyrin−lactose conjugate. Symbols and error bars represent the mean and standard deviation of the measurements made in quadruplicate wells.

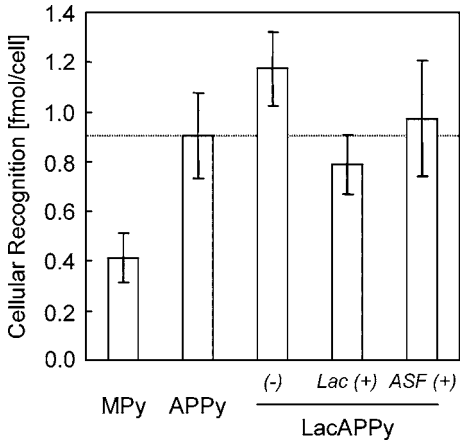


Figure 4. Cellular recognition of Mn-porphyrin derivatives by HepG2 cells. HepG2 cells were incubated with 100 μM normal Mn-porphyrin (L = CH_3 in Scheme 1; MPy), Mn-porphyrin precursor without lactose (L = R in Scheme 1; APPy), or Mn-porphyrin−lactose conjugate (LacAPPy). For competition, the Mn-porphyrin−lactose conjugates were incubated in the presence of 4 mM lactose (*Lac*(+)) or 1 mg/mL of asialofetuin (*ASF*(+)). Error bars represent the mean and standard deviation of the measurements made in at least triplicate.

Cellular Recognition of Mn-Porphyrin−Lactose Conjugates. To confirm the required property as antioxidant, we first carried out a cytotoxicity assay. Figure 3 shows the effect of the Mn-porphyrin−lactose conjugates on the viability of HepG2 cells after 1 day incubation. The cell viability did not significantly decrease when the conjugates were added up to the concentration of 100 μM. The control metalloporphyrin exhibited the almost same tendency as the conjugate. These results suggest that the Mn-porphyrin−lactose conjugates with no apparent cytotoxicity promised effective antioxidative activity.

As a result of no apparent cytotoxicity, we finally examined whether the Mn-porphyrin−lactose conjugates were specifically recognized by HepG2 cells. HepG2 cells are a human hepatoma cell line, so that ASGP-Rs are expressed on the cell surface (*23*). Figure 4 shows the recognition of Mn-porphyrin derivatives by HepG2 cells. The amount of Mn-porphyrin−lactose conjugates recognized by the cells was 1.2 ± 0.15 fmol/cell, which was approximately thrice greater than that of normal Mn-porphyrin (L = CH_3 in Scheme 1; 0.4 ± 0.10 fmol/cell). In the presence of approximately 10 equiv of free lactose molecules (4 mM), however, the recognition of Mn-porphyrin−lactose conjugates significantly (P < 0.01)

decreased up to 0.8 ± 0.16 fmol/cell, which was the almost same level of the Mn-porphyrin precursor without lactose (L = R in Scheme 1; 0.9 ± 0.17 fmol/cell). Furthermore, an asialoglycoprotein, asialofetuin (1 mg/mL), also inhibited the recognition between the Mn-porphyrin−lactose conjugate and HepG2 cells. These results suggest that the cellular recognition of the conjugates was inhibited by the competition of lactose molecules with β-galactose. The inhibition up to nonspecific interaction level (see Figure 4, dotted line) led us to consider that the conjugate recognized the HepG2 cells via asialoglycoprotein receptors on cell surface.

CONCLUSION

We have synthesized a new SOD mimic Mn-porphyrin−lactose conjugate. The resulting conjugate showed significant SOD activity, negligible cytotoxicity, and cellular recognition. From a practical point of view, the protective effects of the targeted conjugate against oxidative stress are important, so the protective experiments are now in progress. We expected that the new SOD mimic synthesized in this study would be the first step in targeting the various cells that overproduce $O_2^{\bullet-}$, through the interaction with carbohydrate-binding receptors.

ACKNOWLEDGMENT

This work was partially supported by a Grant-in-Aid (No. 14380409) from Japan Society for the Promotion of Science.

LITERATURE CITED

(1) Halliwell, B., and Gutteridge, J. M. (1990) Role of free radicals and catalytic metal ions in human diseases: An overview. *Methods Enzymol. 186*, 1−85.

(2) Cerutti, P. A. (1991) Oxidant stress and carcinogenesis. *Eur. J. Clin. Invest. 21*, 1−5.

(3) Simonian, N. A., and Coyle, J. T. (1996) Oxidative stress in neurodegenerative diseases. *Annu. Rev. Pharmacol. Toxicol. 36*, 83−106.

(4) Babior, B. M., Kipnes, R. S., and Curnutte, J. T. (1973) Biological defense mechanisms: The production by leukocytes of superoxide, a potential bactericidal agent. *J. Clin. Invest. 52*, 741−744.

(5) Rossi, F. (1986) The $O_2^{\bullet-}$- forming NADPH oxidase of the phagocytes: nature, mechanisms of activation and function. *Biochim. Biophys. Acta 853*, 65−89.

(6) Batinić-Haberle, I., Benov, L., Spasojević, I., and Fridovich, I. (1998) The *ortho* effect makes manganese(III) *meso*-tetrakis(*N*-methylpyridinium-2-yl)porphyrin a powerful and potentially useful superoxide dismutase mimic. *J. Biol. Chem. 273*, 24521−24528.

(7) Kawakami, H., Ohse, T., Kawano, M., and Nagaoka, S. (1999) Superoxide dismutase activity of a novel macromolecular manganese porphyrin. *Polym. Adv. Technol. 10*, 270−274.

(8) McCulloch, J., and Dewar, D. (2001) A radical approach to stroke therapy. *Proc. Natl. Acad. Sci. U.S.A. 98*, 10989−10991.

(9) Wu, G. Y., and Wu, C. H. (1988) Receptor-mediated gene delivery and expression in vivo. *J. Biol. Chem. 263*, 14621−14624.

(10) Varki, A. (1994) Selectin ligands. *Proc. Natl. Acad. Sci. U.S.A. 91*, 7390−7397.

(11) Chiu, M. H., Tamura, T., Wadhwa, M. S., and Rice, K. G. (1994) In vivo targeting function of *N*-linked oligosaccharides with terminating galactose and *N*-acetylgalactosamine residures. *J. Biol. Chem. 269*, 16195−16202.

(12) Kalyanasundaram, K. (1984) Photochemistry of water-soluble porphyrins: Comparative study of isomeric tetrapyridyl- and tetrakis(*N*-methylpyridiniumyl)porphyrins. *Inorg. Chem. 23*, 2453−2459.

(13) Riley, D. P., Rivers, W. J., and Weiss, R. H. (1991) Stopped-flow kinetic analysis for monitoring superoxide decay in aqueous systems. *Anal. Biochem. 196*, 344−349.

(14) Nilsson, R., and Kearns, R. D. (1974) Role of singlet oxygen in some chemiluminescence and enzyme oxidation reactions. *J. Phys. Chem. 78*, 1681−1683.

(15) Rabani, J., and Nielsen, S. O. (1969) Absorption spectrum and decay kinetics of O_2^- and HO_2 in aqueous solutions by pulse radiolysis. *J. Phys. Chem. 73*, 3736−3744.

(16) Unsworth, J. M., Rose, F. R. A. J., Wright, E., Scotchford, C. A., and Shakesheff, K. M. (2003) Seeding cells into needled felt scaffolds for tissue engineering applications. *J. Biomed. Mater. Res. 53*, 617−620.

(17) Asayama, S., Nogawa, M., Takei, Y., Akaike, T., and Maruyama, A. (1998) Synthesis of novel polyampholyte comb-type copolymer consisting of a poly(L-lysine) backbone and hyaluronic acid side chains for a DNA carrier. *Bioconjugate Chem. 9*, 476−481.

(18) Shen, T., Bogdanov, A., Bogdanova, A., Poss, K., Brady, T. J., and Weissleder, R. (1996) Magnetically labeled secretin retains receptor affinity to pancreas acinar cells. *Bioconjugate Chem. 7*, 311−316.

(19) Dubois, M., Giles, K., Hamilton, J. K., Rebers, P. A., and Smith, F. (1956) Colorimetric method for determination of sugars and related substrates. *Anal. Chem. 28*, 350−356.

(20) Gray, B., and Carmichael, A. J. (1992) Kinetics of superoxide scavenging by dismutase enzymes and manganese mimics determined by electron spin resonance. *Biochem. J. 281*, 795−802.

(21) Fridovich, I. (1989) Superoxide dismutases: An adaptation to a paramagnetic gas. *J. Biol. Chem. 264*, 7761−7764.

(22) Lee, J., Hunt, J. A., and Groves, J. T. (1998) Manganese porphyrins as redox-coupled peroxynitrite reductases. *J. Am. Chem. Soc. 120*, 6053−6061.

(23) Wu, G. Y., and Wu, C. H. (1988) Evidence for targeted gene delivery to HepG2 hepatoma cells in vitro. *Biochemistry 27*, 887−892.

BC049865I

In Vitro Cytotoxicity and in Vivo Distribution after Direct Delivery of PEG–Camptothecin Conjugates to the Rat Brain

Alison B. Fleming,[†] Kraig Haverstick,[†] and W. Mark Saltzman*,[†,‡]

School of Chemical and Biomolecular Engineering, Cornell University, 120 Olin Hall, Ithaca, New York 14853, and Department of Biomedical Engineering, Yale University, 227 Becton Center, New Haven, Connecticut 06511. Received September 30, 2003; Revised Manuscript Received September 2, 2004

Low water solubility and rapid elimination from the brain inhibits local delivery via implants and other delivery systems of most therapeutic drugs to the brain. We have conjugated the chemotherapy drug, camptothecin (CPT), to poly(ethylene glycol) (PEG) of molecular weight 3400 using previously established protocols. These new conjugates are very water-soluble and hydrolyze at a pH-dependent rate to release the active parent drug. We have studied the uptake of these conjugates by cells in vitro and quantified their cytotoxicity toward gliosarcoma cells. These conjugates were loaded into biodegradable polymeric controlled-release implants, and their release characteristics were studied in vitro. We implanted similar polymeric disks into rat brains and used a novel sectioning scheme to determine the concentration profile of CPT in comparison to conjugated CPT in the brain after 1, 7, 14, and 28 days. We have found that PEGylation greatly increases the maximum achievable drug concentration and greatly enhances the distribution properties of CPT, compared to corelease of CPT with PEG. Although only one percent of CPT in the conjugate system was found in the hydrolyzed, active form, drug concentrations were still significantly above cytotoxic levels over a greater distance for the conjugate system. On the basis of these results, we believe that PEGylation shows great promise toward increasing drug distribution after direct, local delivery in the brain for enhanced efficacy in drug treatment.

INTRODUCTION

Camptothecin, first isolated from the Chinese tree *Camptotheca acuminata* in the 1960s (*1*), is a potent anticancer agent that targets the DNA-unwinding enzyme topoisomerase I in the cell nucleus. Due to camptothecin's extremely low aqueous solubility, there has been much interest in the synthesis of more water-soluble derivatives. This effort has resulted in FDA approval of two small molecule analogues, topotecan and irinotecan, and also in the creation of CPT[1]–polymer conjugates. Camptothecin has been conjugated to several polymers including poly(ethylene glycol) (*2*), dextran (*3*), poly(L-glutamic acid) (*4*), and *N*-(2-hydroxypropyl)methacrylamide (*5*).

Camptothecin is a planar molecule composed of five rings (see Figure 1A). Of these rings, the α-hydroxy-δ-lactone moiety (ring E) is thought to be critical for cytotoxic activity. This lactone ring is subject to reversible hydrolysis to an open carboxylate form in aqueous solution with the dominant form at equilibrium depending on the pH of the solution. More specifically, it has been shown that the majority of camptothecin will be in the lactone form at pH <5, whereas the carboxylate form

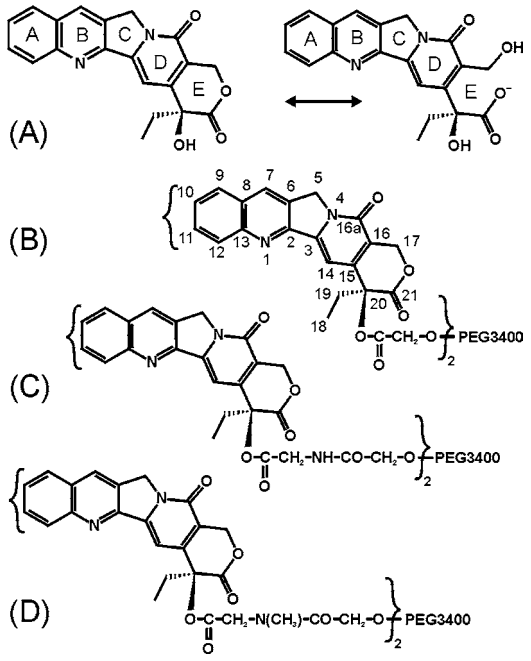


Figure 1. Camptothecin and camptothecin conjugates. (A) Chemical structure of camptothecin lactone and carboxylate forms. (B) Direct ester bond: CM-PEG–CPT. (C) Ester bond through a glycine residue: CM-PEG-Gly–CPT. (D) Ester bond through a sarcosine residue: CM-PEG-Sar–CPT.

* To whom correspondence should be addressed. Phone: (203) 432-4262. Fax: (203) 432-0030. Mail: Yale University, P.O. Box 208284, New Haven, CT 06520. E-mail: mark.saltzman@yale.edu.

[†] Cornell University.

[‡] Yale University.

[1] Abbreviations: AUC, area under the concentration–time curve; CM-PEG–CPT, carboxymethyl-poly(ethylene glycol) 3400–camptothecin; CM-PEG-Gly–CPT, carboxymethyl-poly(ethylene glycol) 3400-glycyl–camptothecin; CM-PEG-Sar–CPT, carboxymethyl-poly(ethylene glycol) 3400-sarcosinyl–camptothecin; CPT, camptothecin; DIC, differential interference contrast; DMEM, Dulbecco's Modified Eagle Medium; ELISA, enzyme-linked immunosorbent assay; MTS [3-(4,5-dimethylthiazol-2-yl)-5-(3-carboxymethoxyphenyl)-2-(4-sulfophenyl)-2*H*-tetrazolium; PBS, phosphate-buffered saline; p(CPP:SA), poly(1,3-bis(p-carboxy phenoxy)-propane: sebacic acid; PEG, poly(ethylene glycol); PNPA, *p*-nitrophenyl acetate.

10.1021/bc034180o CCC: $27.50 © 2004 American Chemical Society
Published on Web 11/02/2004

predominates at pH >8 (*6*). This has important implications for the efficacy of delivered camptothecin, since the open-ring carboxylate (i.e. the inactive form) will be favored at physiological pH.

Most attempts to increase the solubility of CPT have focused on stable substitutions at rings A and B (*7*). Although such substitutions may solve the problem of solubility, they have no effect on the rate of lactone hydrolysis (*8*). An alternative strategy is to modify the lactone moiety reversibly in order to create a water-soluble "prodrug" capable of releasing active-lactone CPT via hydrolysis or enzyme-mediated processes. The success of such PEG conjugates has been recently reviewed (*9*). This approach has been utilized in the creation of PEG−CPT conjugates for systemic administration (*1*, *7*, *10*, *11*). In these studies, attachment to PEG of molecular weight 40 000 (PEG40000) achieved water solubility, an increased residence time in the circulation, and stabilization of the essential lactone ring. CPT was linked to PEG40000 via a water-labile ester bond, and it was found that employing different spacer groups could alter the hydrolysis rate of the resulting conjugate (*12*).

In previous work, we showed that local controlled delivery of anticancer compounds could provide cytotoxic levels of agents in the brain tissue for prolonged periods of time (*13*, *14*); however, the volume of treatment is limited by the ability of drug molecules to penetrate into the local tissue before they are eliminated (*13*). We hypothesized that optimal local delivery requires agents that are both water-soluble, to prevent rapid clearance through capillary permeation, and stable in the brain extracellular space (*15*); conjugates of active drugs with inert polymers may provide these features (*16*). Therefore, we sought to synthesize PEG−CPT conjugates appropriate for local delivery to the brain using modifications of a previously published chemical approach (*12*).

PEG−camptothecin conjugates theoretically meet basic requirements for a successful polymeric carrier system for localized, direct drug delivery to the brain. Previously reported promising PEGylated drug conjugates relied on high molecular weight PEG to increase the circulation time of the conjugate during systemic delivery (*9*). In the present case of local delivery to the brain by diffusion from a polymeric implant, the molecular weight of the PEG must be optimized. Although increasing the molecular weight of the PEG increases the solubility of the drug, it decreases the rate of diffusion of the conjugate, which is the primary means of distribution of the conjugate in the brain. We expected conjugation to PEG3400 to solubilize CPT and increase the effective molecular weight beyond the theoretical threshold for blood−brain barrier penetration (*17*); these PEG3400 conjugates should also diffuse readily through the extracellular space (*18*). In addition, these conjugates should be capable of releasing free, active CPT upon ester hydrolysis. Three different PEG3400−CPT conjugates were synthesized. All conjugates were linked via an ester bond, either directly or through a single amino acid (Figure 1B−D). The variation in the nature of the linkage chemistry resulted in conjugates with different stabilities in aqueous solutions.

The primary objectives of this study were to measure solubility and stability of CPT conjugates in biological fluids, to determine if CPT released from our synthesized conjugates was capable of inducing cell death in culture, and to determine the drug distribution in vivo from a controlled release device implanted in the rat brain. Since it is known that large water-soluble polymers do not generally diffuse across cell membranes (*19*), these conjugates are likely taken up actively by endocytosis. It was thus of interest to determine if PEG−CPT conjugates release drug via hydrolysis outside of cells or if it is possible for the conjugate to enter the cell and release drug closer to its nuclear target.

EXPERIMENTAL PROCEDURES

Materials. (*S*)-(+)-Camptothecin (CPT) and poly(ethylene glycol), average M_n 3400 (PEG3400) were purchased from Aldrich Chemical Co. (Milwaukee, WI). Stock solutions of CPT were created by dissolving drug in dimethyl sulfoxide (DMSO; Sigma Chemical Company, St. Louis, MO), and the solutions were stored at 4 °C. Carboxymethyl-PEG3400 was purchased from Shearwater Polymers (now Nektar Therapeutics, Huntsville, AL). The MTS [3-(4,5-dimethylthiazol-2-yl)-5-(3-carboxymethoxyphenyl)-2-(4-sulfophenyl)-2*H*-tetrazolium, inner salt] assay reagent kit was purchased from Promega (CellTiter 96 Aqueous Non-Radioactive Cell Proliferation kit; Madison, WI). The LysoTracker Red probe for acidic organelles was purchased from Molecular Probes (Eugene, OR). Poly-L-lysine, type VI-S acetylcholinesterase from electric eel, crude esterase from porcine liver (liver esterase), type I protease from porcine pancreas, and *p*-nitrophenyl acetate were purchased from Sigma Chemical Company (St. Louis, MO). Poly(1,3-bis(*p*-carboxyphenoxy)propane: sebacic acid) 20:80 (p(CPP:SA)) was donated by Guilford Pharmaceuticals. The Coomassie Protein Reagent was purchased from Pierce Biotechnology (Rockford, IL).

Methods. Analysis of Conjugates. MALD/I TOF mass spectrometry was done at the Biotechnology Resource Center at Cornell University on a Bruker Daltonics Biflex III with α-cyano-4-hydroxycinnamic acid (ACCA) as the matrix. The raw MALD/I data and the list of major MALD/I peaks are shown in the Supporting Information. ^{1}H and ^{13}C nuclear magnetic resonance spectroscopy was done on an INOVA 500 MHz spectrometer at the NMR Facility at Cornell University. $CDCl_3$ was the solved used, and CPT peaks were correlated to published results for CPT in DMSO (*20*).

Synthesis of Camptothecin−Poly(ethylene glycol) Conjugates. These procedures were modified for PEG3400 from previously published protocols (*12*). The structures of the three conjugates appear in Figure 1. NMR peaks are labeled using the atom numbering shown for CPT in Figure 1B.

CM-PEG−CPT. Carboxymethyl-PEG3400 (244 mg, 0.068 mmol) was dried by azeotroping in 75 mL of toluene for 2 h. Remaining toluene was removed under vacuum, and the PEG and CPT (50 mg, 0.144 mmol) were dissolved in 100 mL of methylene chloride under stirring. The solution was cooled to 0−5 °C in an ice bath. 2-Chloro-1-methylpyridinium iodide (65 mg, 0.253 mmol) and 4-(dimethylamino)pyridine (67 mg, 0.547 mmol) were added. The solution was allowed to warm to room temperature, and the reaction was continued for 48 h. The organic solution was then washed with 0.5 M HCl (2 × 25 mL) and dried over $MgSO_4$. Solvent was removed under vacuum. The product was redissolved in 1−2 mL of methylene chloride and precipitated upon addition of 200 mL of 2-propanol. The precipitate was collected by filtration and dried under vacuum. The product was redissolved in 1−2 mL of methylene chloride and precipitated upon addition of 200 mL of ether. The precipitate was collected by filtration and dried under vacuum. The product was tested for purity by TLC with 5% dimethylformamide in chloroform. Yield = 90% CM-PEG−CPT. ^{1}H NMR ($CDCl_3$): δ(ppm) = 0.97 (t, 6, C(18)-

H_3), 2.17, 2.28 (mm, 4, C(19)H_2), 3.63 (m, >300, PEG), 4.34 (q, 4, OCH_2CO), 5.29 (t, 4, C(5)H_2), 5.41, 5.68 (dd, 4, C(17)H_2), 7.21 (s, 2, =C(14)*H*), 7.67 (t, 2, =C(10)*H*), 7.83 (t, 2, =C(11)*H*), 7.94 (d, 2, =C(9)*H*), 8.20 (d, 2, =C(12)-*H*), 8.40 (s, 2, =C(7)*H*). ^{13}C NMR ($CDCl_3$): δ(ppm) = 7.83 (C18), 32.02 (C19), 50.23 (C5), 67.45 (C17), 68.36−71.27 (PEG), 76.60 (C20), 96.19 (C14), 120.59 (C16), 128.35 (C10), 128.45 (C8), 128.50 (C9), 128.68 (C12), 129.86 (C6), 130.99 (C11), 131.53 (C7), 145.64 (C3), 146.64 (C13), 149.10 (C15), 152.49 (C2), 157.57 (C16a), 167.50 (*C*OO-CPT), 169.95 (C21). MALD/I TOF: [CM-PEG3400−CPT + 2ACCA +H]$^+$ predicted *m/z*: [CM-PEG3400 + 2ACCA +H]$^+$ + 660.69, observed: + 662.94.

CM-PEG-Gly-CPT. H-Gly−CPT·TFA was synthesized using a previously established protocol (*12*). Carboxymethyl-PEG3400 (200 mg, 0.056 mmol) was dried by azeotroping in 100 mL of toluene for 2 h. The volume of toluene was reduced to 20 mL, and the solution was cooled to room temperature. H-Gly−CPT·TFA (140 mg, 0.27 mmol), 2-ethoxy-1-ethoxycarbonyl-1,2-dihydroquinoline (62 mg, 0.25 mmol), and DMAP (110 mg, 0.90 mmol) were added. The solution was stirred at 55−60 °C for 16 h. Solvent was removed under vacuum, and the product was isolated by recrystallizing in 100 mL of 2-propanol, filtering, washing with ice-cold ether, and drying under vacuum. A second recrystallization was done when necessary to improve purity. Yield = 85% CM-PEG-Gly−CPT. ^{1}H NMR ($CDCl_3$): δ(ppm) = 0.96 (t, 6, C(18)H_3), 2.14, 2.25 (mm, 4, C(19)H_2), 3.61 (m, >300, PEG), (q, 4, OCH_2CO), 3.97 (m, 4, NHCH_2CO), 4.15, 4.46 (dd, 4, COCH_2O), 5.25 (t, 4, C(5)H_2), 5.37, 5.65 (dd, 4, C(17)H_2), 7.31 (s, 2, =C(14)*H*), 7.63 (d, 2, =C(10)*H*), 7.66 (q, 2, CON*H*), 7.80 (t, 2, =C(11)*H*), 7.90 (d, 2, =C(9)*H*), 8.22 (d, 2, =C(12)*H*), 8.38 (s, 2, =C(7)*H*). ^{13}C NMR ($CDCl_3$): δ(ppm) = 7.82 (C18), 32.02 (C19), 40.66 (CO*C*H_2NH), 50.22 (C5), 67.32 (C17), 70.27−71.32 (PEG), 76.96 (C20), 96.52 (C14), 120.25 (C16), 128.32 (C10), 128.38 (C8), 128.40 (C9), 128.67 (C12), 129.92 (C6), 130.95 (C11), 131.52 (C7), 145.78 (C3), 146.62 (C13), 149.00 (C15), 152.44 (C2), 157.55 (C16a), 167.37 (*C*OO-CPT), 169.16 (NH*C*O), 171.09 (C21). MALD/I TOF: [CM-PEG3400-Gly−CPT + 2ACCA +H]$^+$ predicted *m/z*: [CM-PEG3400 + 2ACCA +H]$^+$ + 774.79, observed: + 774.15.

CM-PEG-Sar-CPT. H-Sar−CPT·TFA was synthesized using a previously established protocol (*12*). Carboxymethyl-PEG3400 (239 mg, 0.067 mmol) was dried by azeotroping in 100 mL of toluene for 2 h. Remaining toluene was removed under vacuum, and the PEG was dissolved in 20 mL of methylene chloride under stirring. The solution was cooled to 0−5 °C in an ice bath. H-Sar−CPT·TFA (150 mg, 0.28 mmol), diisopropylcarbodiimide (42 μL, 0.27 mmol), and DMAP (33 mg, 0.27 mmol) were added. The solution was allowed to warm to room temperature, and the reaction was continued for 16 h. Solvent was removed under vacuum, and the product was isolated by recrystallizing in 100 mL of 2-propanol, filtering, washing with 2-propanol, and drying under vacuum. A second recrystallization was done when necessary to improve purity. Yield = 70% CM-PEG-Sar−CPT. ^{1}H NMR ($CDCl_3$): δ(ppm) = 0.97 (t, 6, C(18)H_3), 2.13, 2.24 (mm, 4, C(19)H_2), 3.04 (s, 6, N(CH_3)), 3.61 (m, >300, PEG), 4.03, 4.64 (dd, 4, COCH_2N(CH$_3$)), 4.20 (q, 4, OCH_2CO), 5.24 (t, 4, C(5)H_2), 5.37, 5.66 (dd, 4, C(17)-H_2), 7.31 (s, 2, =C(14)*H*), 7.64 (t, 2, =C(10)*H*), 7.80 (t, 2, =C(11)*H*), 7.90 (d, 2, =C(9)*H*), 8.23 (d, 2, =C(12)*H*), 8.37 (s, 2, =C(7)*H*). ^{13}C NMR ($CDCl_3$): δ(ppm) = 7.84 (C18), 31.96 (C19), 35.64 (N(**C**H$_3$)), 49.27 (CO*C*H$_2$N(CH$_3$)), 50.22 (C5), 67.36 (C17), 70.07−70.78 (PEG), 77.06 (C20), 96.57 (C14), 120.06 (C16), 128.30 (C10), 128.38 (C8), 128.38 (C9), 128.66 (C12), 129.98 (C6), 130.90 (C11), 131.47 (C7), 145.80 (C3), 146.65 (C13), 149.01 (C15), 152.45 (C2), 157.54 (C16a), 167.60 (*C*OO−CPT), 168.58 (N(CH$_3$)-*C*OCH$_2$), 170.31 (C21). MALD/I TOF: [CM-PEG3400-Sar−CPT + 2ACCA +H]$^+$ predicted *m/z*: [CM-PEG3400 + 2ACCA +H]$^+$ + 802.84, observed: + 804.96.

Stability of Conjugates in Neutral and Acidic Conditions. The hydrolysis rate of conjugates was determined in phosphate-buffered saline (PBS) at pH 7.4 and in citrate-phosphate buffer solutions at pH 5.5 and pH 6.0. Conjugates were dissolved at a concentration of 10 μg/mL and incubated at 37 °C. For HPLC analysis (Waters 2690 HPLC with photodiode array detector, Milford, MA), at each time point 10−40 μL of sample was injected and eluted on a 40-min, 80:0:20 to 0:80:20 (water: acetonitrile:water/0.5%TFA) gradient. Free CPT eluted at 12.9 min on a Zorbax 300SB−CN column (Phenomenex, Torrance, CA). Areas of absorbance peaks at 254, 354, and 369 nm were compared to CPT standards to determine concentrations. For extraction analysis, at specified time points, 250 μL was removed from each of the conjugate solutions and subjected to a modified extraction procedure (*21*). Since ethyl acetate preferentially extracts free CPT out of solutions containing free and conjugated drug, this procedure provided a rapid method to isolate free CPT. Briefly, each 250-μL sample was acidified to pH 3.0 with 1 M HCl. Water-saturated ethyl acetate (500 μL) was added to extract out CPT, and the sample was vortexed for 10 s. The sample was then centrifuged at 8160*g* for 5 min. Half of the ethyl acetate layer (250 μL) was transferred to a clean tube, while the remaining ethyl acetate was transferred to waste. An additional 500 μL of ethyl acetate was added to the aqueous sample, and the extraction procedure was repeated, with 250 μL of the organic phase retained. The combined ethyl acetate extracts (500 μL) were evaporated to dryness under a gentle stream of nitrogen, reconstituted in 95% ethanol (1 mL) and the fluorescence intensity of CPT was determined at an emission wavelength of 434 nm after excitation at 370 nm.

Stability of Conjugates in Simulated Biological Fluids. Conjugate stability studies were carried out at 37 °C and pH 7.4 in simulated biological fluids. Conjugates were present at a concentration of approximately 10 μg/mL in all cases. At specified time points, 250-μL samples were removed from the conjugate solutions and free CPT was quantified after preferentially extracting out the drug. The extraction procedure was the same as used for neutral and acidic stability experiments (see above), with the following changes. Ice cold citrate-phosphate buffer was used to reduce the pH to 3, and centrifugation was for 10 rather than 5 min.

Six in vitro solutions were tested: PBS, acetylcholinesterase in PBS, liver esterase in PBS, pancreatic protease in PBS, 9L lysates in PBS, and brain homogenate in PBS. To create the test solutions, acetylcholinesterase, esterase, and protease proteins were dissolved in PBS at 15 U/mL of enzymatic activity, based on activity reported by the vendor. Cell lysate solutions were created from 9L gliosarcoma cells in culture. Six 75-cm^2 flasks of cells were trypsinized at confluence, washed twice in PBS, and resuspended in 20 mL of PBS. Cells were lysed with sonication (TEKMAR Soni Disruptor, TM300) on ice at 40% power for 2 min. The lysate was centrifuged at 1070*g* for 10 min. The supernatant was diluted with approximately 30 mL of PBS to create a total volume of 50 mL, and the resulting lysate was diluted 1:1 with PBS to create the final solution used in the release study. Brain homogenate solutions were created by homogeniz-

ing (PowerGen Homogenizer, Fisher Scientific, Pittsburgh, PA) the brain of an adult female rat (Harlan Sprauge-Dawley) at a concentration of 50 mg/mL in PBS.

Total protein content in the cell lysate solution and brain homogenate was determined using the Coomassie Protein Reagent Kit. For the total protein assay, 100 μL of serially diluted samples and standards prepared from liver esterase were placed into the wells of a 96-well plate, followed by 100 μL of the Coomassie Protein Reagent. Absorbance was measured at 595 nm on a microplate reader (Molecular Devices, Sunnyvale, CA). Total protein content was based on comparison to a BSA standard provided with the assay kit. The esterase activity of brain homogenate and cell lysate solutions was measured using *p*-nitrophenyl acetate (PNPA) as a model substrate. PNPA was dissolved in DMSO to create a 100 mg/mL stock solution which was stored at −20 °C. From this stock, an assay solution of 0.1 mg/mL PNPA in PBS was made. Serially diluted 100-μL brain homogenate samples and standards prepared from liver esterase were placed into the wells of a 96-well plate, followed by 100 μL of the PNPA assay solution. Absorbance was measured at 405 nm using a microplate reader after 10 min of incubation at room temperature. Esterase activity was based on comparison to the liver esterase standards in PBS.

Cell Line. The 9L gliosarcoma cell line (9L) was kindly provided by Dr. Henry Brem of Johns Hopkins University (Baltimore, MD). The cell line was maintained in DMEM media (with L-glutamine) supplemented with 10% fetal bovine serum (FBS) and 1% penicillin/streptomycin at 37 °C and 5% CO_2 in a humidified environment. All tissue culture reagents were purchased from Gibco, BRL (Grand Island, NY). Cells were subcultured every 3−4 days at a relative cell density of 1:8.

In Vitro Cytotoxicity. The cytotoxicity of CPT conjugates and free CPT was measured against 9L cells in monolayer culture. Cells were plated in 96-well plates (200 cells/well) and allowed to attach. Drug was serially diluted in cell culture media; CPT conjugates were dissolved directly into media whereas CPT was added from a stock solution in DMSO (1 mg/mL). Plated cells were incubated in media containing free or conjugated drug for 24, 72, or 120 h. In the case of the 24 and 72-h time points, the free drug- or conjugate-containing media was removed and replaced with fresh media, and the cells were returned to the incubator. After 120 h, cell viability was determined in all wells using an MTS assay and a microplate reader. The fraction of cells surviving was calculated by dividing mean optical density produced by treated cells by the mean optical density from untreated control cells.

Cellular Uptake in Monolayer Culture. Glass slides were placed in six-well tissue culture plates and coated with a solution of poly-L-lysine in PBS (25 μg/mL) for 1 h at 37 °C. After the slides were rinsed with PBS, 9L cells were seeded at a density of 1.5×10^4 cells/cm^2 and allowed to attach overnight. The cells were then incubated in medium containing conjugated drug or free drug (100 μg/mL) for 5 h. In some cases a fluorescent marker for acidic organelles (LysoTracker Red) was added during the final 30 min of incubation at a concentration of 50 nM. After incubation, cells were rinsed three times with cold PBS and fixed with 4% paraformaldehyde for 15 min at room temperature. The resulting cell preparations were studied by fluorescence microscopy using an Olympus BX-50 fluorescence/DIC microscope with a mercury lamp excitation source. Camptothecin and LysoTracker fluorescence were visualized using UV and red filters, respectively.

Fabrication of Controlled-Release p(CPP:SA) Implants. Controlled-release devices containing CPT conjugates at 20 wt % were prepared by first codissolving 50 mg of each conjugate and 200 mg of p(CPP:SA) in methylene chloride (2 mL). Each solution was thoroughly vortexed and, after complete dissolution, placed under vacuum at room temperature for 24 h. The resulting material was crushed into a homogeneous powder consisting of relatively uniform particles. To produce implantable disks approximately 1 mm in thickness, 10 mg of the powder was placed in a stainless steel die (3 mm diameter) and 0.25 tons of pressure was applied with a Carver press for 20 s. Disks to release unmodified CPT were prepared containing CPT plus unconjugated PEG3400 (20 wt % total loading). CPT and free PEG were combined in methylene chloride at a CPT:PEG ratio of 1:6.14 to match the drug content of conjugated material. Unlike the CPT conjugates, CPT did not completely dissolve in methylene chloride.

Measurement of Drug Release into Phosphate-Buffered Saline. The in vitro release characteristics of matrixes made into disks were determined in continuously stirred phosphate-buffered saline (pH 7.4) at 37 °C. Three identical disks from each group were incubated in individual aliquots of 1.5 mL of PBS in test tubes. At various time points the entire volume of each tube was removed and replaced with fresh buffer. The amount of CPT released was quantified in the resulting samples by measurement of the intrinsic fluorescence of the drug. Individual samples were diluted with PBS to a total volume of 700 μL and acidified with 7 μL of 1 M hydrochloric acid to convert any free CPT in the carboxylate form back to the lactone. A 10% SDS solution was then added (100 μL) to break up any aggregation of CPT conjugates, the mixture was thoroughly vortexed, and bubbles were allowed to dissipate. The fluorescence of the samples was measured at 428 nm (excitation at 370 nm). In some cases the samples were briefly centrifuged at 8160*g* for 1 min to remove undegraded p(CPP:SA) wafer remnants prior to analysis. No significant change in the fluorescence of CPT conjugate solutions with time was detected, and it was assumed that CPT conjugates and the CPT released from the conjugates had the same fluorescence yield.

Implantation of p(CPP:SA) Matrixes into the Normal Rat Brain. Male Fischer 344 rats (200 g, Harlan, Indianapolis, IN) were anesthetized by intraperitoneal injection of 0.6 mL of a solution containing 25 mL of ketamine hydrochloride (100 mg/mL, Abbott Laboratories, N. Chicago, IL), 2.5 mL of xylazine (100 mg/mL, Bayer Corporation, Shawnee Mission, KS), 14.2 mL of ethanol (95%), and 58 mL of physiological saline (The Butler Company, Columbus, OH). A 3-cm incision was made above the skull, and the bregma was exposed. An oval-shaped burr hole was drilled 1 mm anterior to the bregma and perpendicular to the midline. A slit 4 to 5 mm deep was made in the dura and brain parenchyma with the tip of a number-11 scalpel blade, and the polymer matrix was gently inserted into the tissue, until it was no longer visible. Once the bleeding had ceased, the skin was closed with surgical staples. All procedures were approved by the Institutional Animal Care and Use Committee at Cornell University.

Brain Tissue Analysis. Rats were sacrificed 1, 7, 14, or 28 days following implantation. At the time of sacrifice, the brains were frozen in hexanes over dry ice. On the day of analysis, brains were cut into three bulk sections,

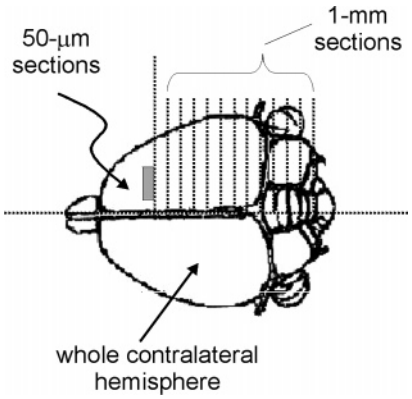


Figure 2. Implantation and sectioning scheme. The implant (grey rectangle) was placed 0.5−1 mm anterior to bregma. The frozen brain was first cut down the midline and then directly behind the polymer implant. The tissue posterior to the implant was sectioned into 1 mm slices. The tissue anterior to the implant was sectioned into 50 μm slices with a cryo-microtome.

first down the midline, and then directly behind the p(CPP:SA) implant (see Figure 2).

Posterior Sectioning. The portion of the brain behind the implant was sectioned in the coronal plane. Brains were placed in a chamber maintained at −20 °C, and razor blades, fastened at 1-mm intervals with screws and washers, were forced through the tissue under gentle pressure. The tissue was allowed to refreeze, and the 1-mm (thick) sections were weighed in tared vials. These tissue slices and the entire contralateral hemisphere were homogenized in citrate-phosphate buffer containing 1% SDS (pH 3.0) at a concentration of 20 mg tissue per mL buffer. One milliliter of each tissue sample was centrifuged at 16 000*g* for 5 min, and the supernatant (700 μL) was analyzed for the presence of CPT and conjugated CPT by spectrofluorimetry.

Anterior Sectioning. The frontal section of brain containing the polymer implant was placed on a cryostat chuck, embedded in OCT embedding medium, and cut into 50-μm (thin) sections using a cryomicrotome (Microm, Heidelberg, Germany) at −20 °C. Alternating sections were collected into separate tubes: one 50-μm section for total drug analysis, the next two 50-μm sections together for extraction of liberated CPT, one for total drug analysis, and so on. Thus total CPT levels (conjugated plus unconjugated) were measured in 50-μm sections of brain, whereas the fraction of drug in the free, liberated form was quantified in 100-μm sections (2, 50-μm sections).

Total Drug Levels in Thin Brain Slices. The total amount of CPT (in either conjugated or free form) was quantified in 50-μm sections of brain tissue. The sections were homogenized in citrate-phosphate buffer containing 1% SDS (pH 3.0) by sonication (Tekmar Soni Disrupter, microtip #4) on ice at 30% power for 10 s. The samples were centrifuged at 16 000*g* for 5 min, and the resulting supernatant (200 μL) was analyzed for the presence of CPT and conjugated CPT by spectrofluorimetry.

Amount of Liberated, Free CPT in Thin Brain Slices. Free drug in 100-μm sections of brain was quantified by an extraction method similar to that described for the simulated biological fluids with two alterations. After the solution was acidified to pH 3, the sample was homogenized by sonication at 30% power for 20 s on ice, and as the final step, 200 mL of ethanol was used to reconstitute the CPT residue. We expected that in brains implanted with p(CPP:SA) matrixes releasing unmodified CPT, procedures to measure the amount of total drug (conjugated plus free) and the amount of free drug would yield equivalent values since all drug was released from p(CPP:SA) in the free form. Since this was, in fact, the case for the first several animals studied, subsequent brains were grouped into 100-μm slices and subjected only to the extraction procedure.

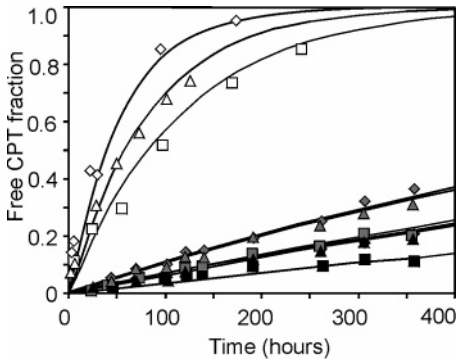


Figure 3. Stability of PEG-camptothecin conjugates in water at 37 °C. Experiments were done at pH 7.4 (white), at pH 6.0 (grey), and at pH 5.5 (black) for CM-PEG−CPT (◇), CM-PEG-Gly−CPT (△), and CM-PEG-Sar−CPT (□). The presence of free CPT was monitored as a function of time. Data at pH 7.4 was acquired by HPLC analysis and corroborated by extraction technique. Data at pH 6.0 and 5.5 were obtained by extraction.

Table 1. Conjugate Hydrolysis Half-Lives per Hour at Different pHs

	pH 7.4	pH 6.0	pH 5.5
CM-PEG−CPT	38.5	603	1000
CM-PEG-Gly−CPT	57.8	630	1050
CM-PEG-Sar−CPT	81.5	924	1820

RESULTS

In Vitro Experiments. Conjugates were first placed in aqueous solutions that simulated biological fluids, and the rates of hydrolysis were measured either by HPLC analysis or an extraction procedure with fluorescence detection. The stability of the CPT conjugates was determined in buffered solutions at pH 7.4, pH 6, and pH 5.5 to simulate the cytoplasmic/extracellular space, the endosome, and the lysosome, respectively (*22*). The resulting hydrolysis data appear in Figure 3. Independent measurements by HPLC and extraction at pH 7.4 gave identical results. The curves in Figure 3 represent best first-order fits to the data, and the half-lives for these curves are given in Table 1. All conjugates were much more stable at pH 6.0 and 5.5 than at pH 7.4, with the trend in hydrolysis rates for the three conjugates remaining the same (CM-PEG-Sar−CPT<CM-PEG-Gly−CPT<CM-PEG−CPT). The hydrolysis half-lives of the conjugates were increased 10-fold at pH 6.0 and 20-fold at pH 5.5 over pH 7.4 values.

Once a method of measuring free CPT was established for drug released from the newly synthesized CPT conjugates, it was necessary to confirm that the liberated drug maintained its cytotoxic activity. The response of 9L gliosarcoma cells was tested in vitro by seeding the cells and exposing them to various concentrations of conjugated or free CPT. Cells were exposed to drug for 24, 72, or 120 h and assayed for metabolic activity after a total of 120 h in all cases. Representative data for CPT and conjugate appear in Figure 4. The assay confirmed the cytotoxic nature of the conjugates, and it demonstrated that much more CPT-conjugate was required to achieve a level of cell death equivalent to that achieved by the parent compound, CPT. An effect of duration of

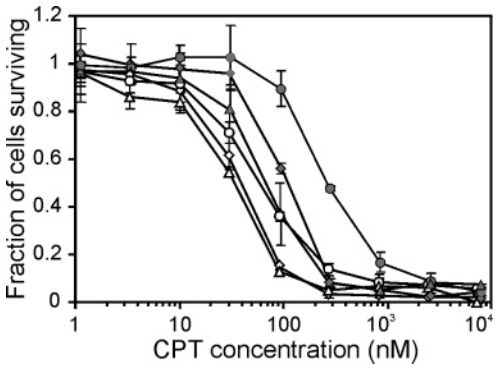


Figure 4. In vitro cytotoxicity of free CPT (white) and CM-PEG-Gly−CPT (grey) as a function of time of exposure. Cells were exposed to drug for 24 (○), 72 (◇), or 120 (△) hours and assayed for proliferation with a metabolic MTS assay after 120 h.

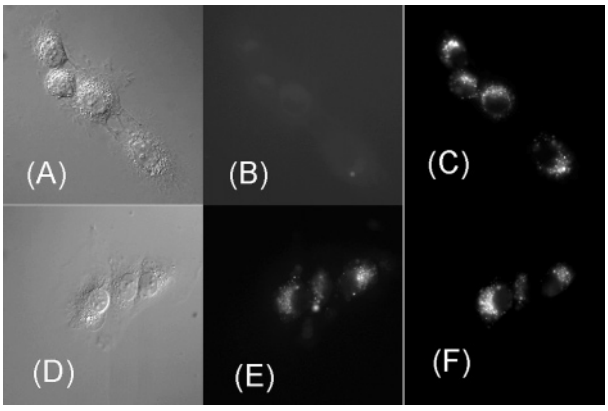


Figure 5. Uptake by 9L gliosarcoma cells counterstained with LysoTracker Red. Equivalent CPT concentration was 100 μg/mL for CM-PEG-Sar−CPT. Images shown at 38× magnification. Free CPT: (A) DIC image of cells, (B) CPT fluorescence with UV filter, (C) LysoTracker fluorescence with red filter. CM-PEG-Sar−CPT: (D) DIC image of cells, (E) CPT fluorescence with UV filter, (F) LysoTracker fluorescence with red filter.

exposure to drug or conjugate was also assessed. Increasing time of exposure to free drug or conjugate shifted the cytotoxicity curves toward a lower concentration, as anticipated for this cell cycle-specific drug. The shift was more dramatic for conjugate (as seen by the curves of dark-colored points in Figure 4) than for free drug, presumably because the amount of active drug in the medium being generated by conjugate hydrolysis was continually increasing with time during incubation.

Since CPT conjugates are relatively stable at physiological pH, it was of interest to determine if these compounds can enter cells and by what mechanism. CPT exhibits intrinsic fluorescence, and the uptake by 9L gliosarcoma cells was investigated qualitatively by fluorescence microscopy following incubation with conjugate or free drug. For all three conjugates, a punctate intracellular distribution pattern could be seen after a 5-h incubation period (see Figure 5E). This pattern of uptake is consistent with the sequestering of conjugate in intracellular compartments (endosomes and lysosomes) after the active uptake of the compound (*23*). The fluorescence exhibited by cells incubated with free drug was not any brighter than background (Figure 5B), and free drug distribution was clearly not limited to any intracellular compartments. To obtain further evidence that conjugate is taken up by endocytosis, CM-PEG-Sar−CPT was coincubated with LysoTracker Red, a fluorescent probe that labels lysosomes, endosomes, and other acidic cellular compartments. Colocalization of the CPT fluorescence pattern (blue excitation) with the pattern associated with LysoTracker Red (red excitation) suggests that CM-PEG-Sar−CPT was located within the acidic endosomal and lysosomal compartments (compare Figure 5E and 5F).

CPT conjugates and free CPT were next incorporated into biodegradable disks of p(CPP:SA) matrixes in order to create implantable devices capable of releasing these compounds in a sustained manner. Matrixes containing each of the three CPT conjugates were loaded at 20 wt %. Since conjugated material was comprised of approximately 14% CPT and 86% PEG by weight, free-CPT-releasing matrixes were created by combining CPT and PEG3400 in this ratio to obtain a final (free CPT + free PEG) loading of 20%. The in vitro release of CPT from the resulting devices was monitored for 25 days in continuously stirred PBS at 37 °C (Figure 6). Under these conditions all three types of CPT conjugates exhibited similar release kinetics. CPT conjugates were released from the devices over a period of 12−14 days. The conjugate release curve is characterized by a burst of 50% of the total dose in the first 3 h followed by a linear release over the next 11 days (Figure 6A). The total amount of CPT conjugates (Figure 6B) released from the devices differed due to the fact that the three conjugate forms had different loadings of CPT. The release of free CPT was very different from conjugated drug, presumably because free CPT is so much less water-soluble. Free CPT was slowly released in a linear fashion over the entire 25-day study, and even at that point only 60% of the drug had been released. On the basis of this result, it is clear that coreleasing CPT and PEG3400 is not sufficient to enhance the solubility of CPT and, further-

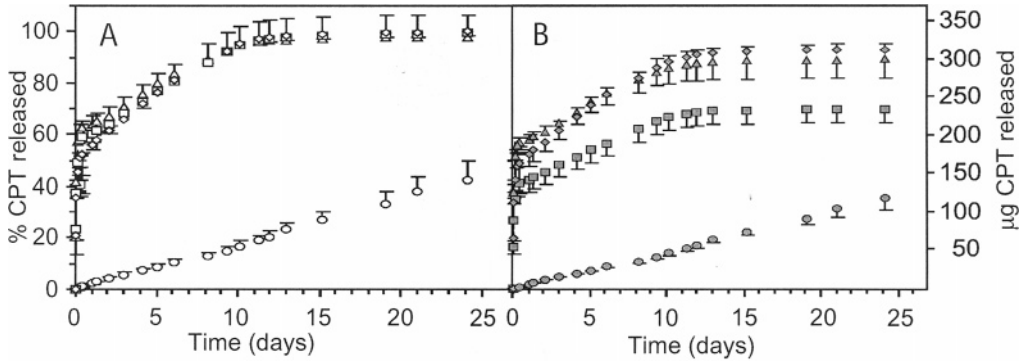


Figure 6. Controlled release of free CPT (○), CM-PEG-Sar−CPT (□), CM-PEG-Gly−CPT (△) and CM-PEG−CPT (◇) from 20%-loaded p(CPP:SA) matrixes in vitro. (A) Release as "percent of loading". (B) Release as "weight of CPT released" are indicated from the same experiments. Three identical 10-mg matrixes were incubated in continuously stirred PBS at 37 °C. Error bars represent the standard deviation in measurement for three matrixes.

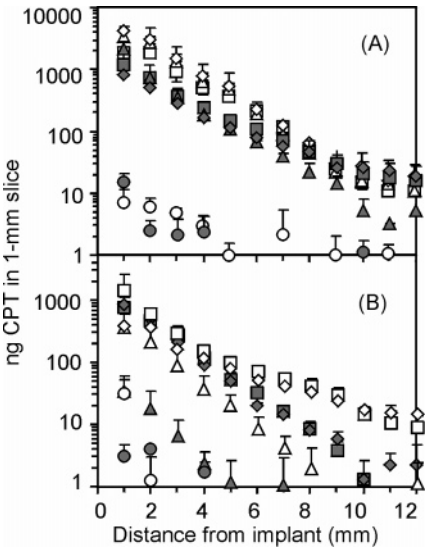


Figure 7. Total CPT found in 1-mm slices posterior (see Figure 2) to implants releasing free CPT (○), CM-PEG-Sar−CPT (□), CM-PEG-Gly−CPT (△), or CM-PEG−CPT (◇) at various time points. Animals were sacrificed for analysis at (A) 1 day (white), 7 days (grey), (B) 14 days (white), and 28 days (grey) following implantation. Error bars represent standard deviation of measurements made in three animals.

more, that a covalent attachment dramatically alters the controlled release kinetics of the drug.

Distribution of Drug in the Rat Brain. Similar p(CPP:SA) disks loaded with drug or conjugate were implanted in the brains of male Fischer rats (see Figure 2). To compare the extent of distribution of CPT conjugates to free CPT, we quantified the total amount of CPT (conjugated and unconjugated) in 1-mm slices posterior to the implant site at various time points (Figure 7). Conjugates were clearly distributed throughout the implant hemisphere at 1, 7, and 14 days following implantation. CPT delivered as free drug, on the other hand, was present in much lower levels and was only found in slices within 4 mm of the implant. The tissue levels of the three conjugate forms are similar up to one week following implantation, but at later time points (Figure 7B) the CM-PEG-Gly−CPT conjugate levels are significantly lower than CM-PEG-Sar−CPT and CM-PEG−CPT. In fact, almost all of the CM-PEG-Gly−CPT conjugate was eliminated from the brain by 28 days.

The analysis of 1-mm tissue (Figure 7) slices revealed the enhanced distribution of CPT conjugates as compared to free CPT. However, the gross resolution of this approach does not give detailed information about the distribution close to the polymer (0−2 mm). Thus, to gain more resolution, the brain anterior to the implant was cut into fine (50-μm) sections. Total levels of CPT (conjugated plus unconjugated) were determined in these 50-μm slices for the three conjugate forms, CM-PEG-Sar−CPT (Figure 8A), CM-PEG-Gly−CPT (Figure 8B), and CM-PEG−CPT (Figure 8C). Representative concentration profiles for the conjugates in the 50-μm slices are shown in Figure 8 at various time points after implantation of 20%-loaded p(CPP:SA) matrixes. The results of the more detailed thin slice analysis are in qualitative agreement with the data from thick (1-mm) slice sections. The three conjugate types exhibit similar distributions at early times (as shown in Figure 8), whereas at later times CM-PEG-Gly−CPT seems to be present at lower concentrations than both CM-PEG-Sar−CPT and CM-PEG−CPT. It is also of interest to note that while the penetration distance appears to be reduced in the thin slice data compared to the 1-mm slice data, this is most likely due to the relatively short distance from the polymer edge to the front tip of the brain (4 mm, see Figure 2).

It was also possible to determine concentration profiles close to the polymer disk in brain tissue following implantation of 20%-loaded free CPT matrixes (Figure 9). The interfacial concentration achieved by free CPT (25 ng/mg) was much lower than that achieved by conjugated drug (500 ng/mg, see Figure 8). The profiles for CPT were fairly constant throughout the treatment period (Figure 9) and, at all times, dropped off to background levels at 1−1.5 mm from the tissue/matrix interface. In contrast, measurable concentrations of CPT were found at 4 mm from the implant for all three CPT conjugates as early as 24 h after implantation (Figure 8).

Regarding the distributions in Figure 8, some experimental assumptions must be noted. For all of the conjugate forms, the p(CPP:SA) matrix had degraded substantially after one week, making it difficult to identify visually the polymer edge, which was used as a reference in measuring distribution distances. The distribution samples gathered for delivery of free CPT from the p(CPP:SA) disk, however, did not have this ambiguity, because the matrix remained fairly intact for the entire 28-day study. Also, because the concentrations in Figure 8 were calculated assuming semi-one-dimensional diffusion from the p(CPP:SA) matrix, the amount of drug

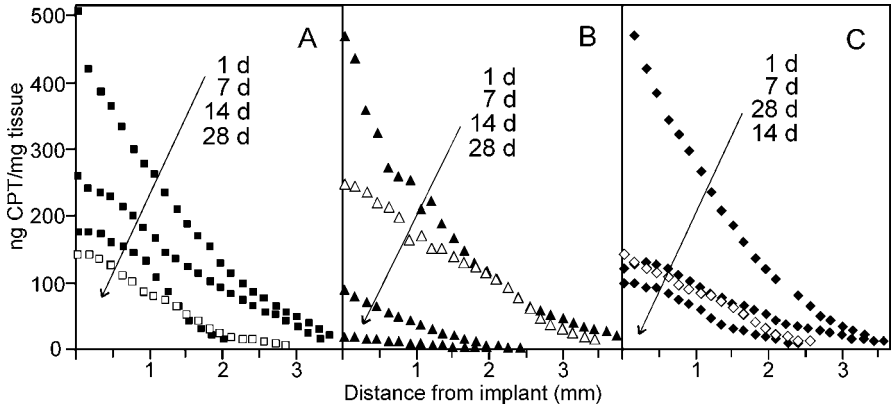


Figure 8. Anterior (see Figure 2) concentration profiles of Total CPT at 1, 7, 14, and 28 days following implantation of20%-loaded p(CPP:SA) matrixes containing (A) CM-PEG-Sar−CPT (□) [day 28 in gray for clarity], (B) CM-PEG-Gly−CPT (△) [day 7 in gray], and (C) CM-PEG−CPT (◇) [day 28 in gray]. Tissue anterior to the implant was sliced into 50-μm sections and total CPT was quantified by fluorescence. The C_0 values decreased with time for all cases except CM-PEG−CPT, where C_0 increased from day 14 to day 28.

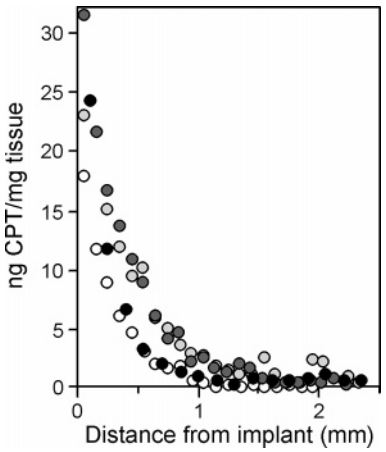


Figure 9. Anterior concentration profiles of Free CPT following release from 20%−CPT-loaded p(CPP:SA) matrixes on day 1 (white), 7 (light gray), 14 (grey), or 28 (black) following implantation. Errors were generally less than 10% of the mean value for plotted data points. Tissue anterior to the implant was sliced into 50 μm, and two slices were combined to make a 100 μm section. CPT was quantified by fluorescence following an extraction procedure of the combined slices.

in the 50-μm slices was normalized with a fixed volume of tissue based on the diameter of the implant source and the thickness of the slice. In reality, however, some drug diffused radially, resulting in this method overestimating concentrations close to the source.

An acceleration of hydrolytic release of drug in blood plasma has been reported for PEG40000−CPT compounds with the same linkage chemistry as ours. It was suggested in that study that an esterase for ester-bonded conjugates or protease for amino acid-linked conjugates mediates an acceleration of conjugate hydrolysis (*2*). As a test of our CM-PEG−CPT conjugates in the presence of such enzymes, several buffer solutions with different biological constituents were prepared and the release of CPT from conjugates in these environments was monitored over time by preferential extraction of free CPT. No increase in the hydrolysis rate was observed for CM-PEG−CPT, CM-PEG-Gly−CPT, or CM-PEG-Sar−CPT in any of the esterase, protease, lysate, or homogenate solutions tested.

Our distribution data (Figures 7 and 8) obtained in both gross and fine sections of brain tissue suggest that there may be a stability difference in vivo between the different conjugate forms. Furthermore, the observation that CM-PEG−CPT and CM-PEG-Sar−CPT remain in the brain up to two weeks after the p(CPP:SA) source would be exhausted indicates that these compounds are more stable in the brain than one would anticipate on the basis of their in vitro half-lives. Some of the reduction in CPT recovery, seen when enzymatic proteins are present in solution, may be due to the binding of proteins to unconjugated CPT. It is also possible that protein can bind and stabilize the conjugated compounds to slow the hydrolysis. The amount of CPT recovery was inversely dependent on the amount of protein present in the solution. No significant difference in the fraction of CPT recovered for each of the three types of conjugate compounds was detected for any of the solutions tested. Thus, there was no notable difference in the level of protein binding were it to occur between the three conjugate forms.

Having demonstrated that PEGylated forms of CPT produce an enhanced distribution in the rat brain, we wanted to determine the concentration of free, active CPT in the rat brain for the PEGylated system. We expected that hydrolysis of the ester between PEG and CPT must occur in order for the CPT to exert a toxic effect on cancer cells. Such an assumption is supported by previously reported results with PEGylated small molecule conjugates. When paclitaxel, methotrexate, and doxorubicin were permanently modified with PEG, the toxicity of the conjugates was found to be lower than the toxicity of the free drugs by a factor of 50 to 1000 (*24*). It was therefore of interest to determine what fraction of the measured total CPT was in the unconjugated, active form. Thin (50-μm) sections proved useful in answering this question, since alternating sections could be analyzed with different assays. More specifically, brains containing CPT conjugates were analyzed by measuring total drug in 50-μm sections and also by performing an extraction on alternating 100-μm sections to remove and quantify unconjugated CPT. By this extraction technique, the amount of free CPT in tissue was found to be low and often close to the detection limit of 1 ng/mg of the assay for all three conjugate forms. On samples from days 1 and 7, fluorescence levels above background could be detected only within 1 mm of the p(CPP:SA) source in all animals. After 7 days, levels consistently above background were not found. When compared to total drug levels measured in alternating slices, it was noted that roughly 1% or less of the dose in each section corresponded to liberated drug, and that a significant difference in the free drug fraction between the three types of conjugates was not measured.

DISCUSSION

The characteristic distribution profiles created by controlled release delivery from polymeric devices in brain tissue have been demonstrated both experimentally (*13*−*15, 25*) and theoretically (*26*). For most compounds, including several chemotherapy drugs, the concentration drops off exponentially with distance from the surface of the device and significant concentrations do not normally penetrate more than 3 mm into the tissue. A high-resolution method is necessary to capture the fine details of this type of distribution. Quantitative autoradiography, a technique in which autoradiographic films are exposed to thin sections (10−20 μm) of tissue containing radiolabeled drug and subsequently digitized for quantification, has been employed several times for this purpose (*13*−*15*). Autoradiography achieves very high spatial resolution and has therefore been useful to characterize steep concentration profiles. This type of analysis was used to validate a mathematical model for local delivery (*26*). The drawbacks of this technique, however, are a difficulty in confirming that the radiolabel corresponds to actual drug and an inability to quantify total levels of drug within tissue.

A more macroscopic approach is to quantify the total amount of drug in the implant and contralateral hemispheres with an analytical method such as spectrofluorimetry (*27*). This technique allows for accurate quantification of total drug levels with time, but there is a complete loss of spatial information. A reasonable compromise in resolution between analysis of 20-μm slices and the whole brain was met in a method demonstrated in this lab to study the delivery of nerve growth factor (NGF) to the brain (*28*). In these studies, brains were sliced into 1-mm thick sections and subsequently analyzed by a sensitive ELISA assay, thus obtaining gross spatial information rapidly.

Since it was anticipated that CPT conjugates could be present throughout the brain, a method capable of

Table 2. Cytotoxicity and Distribution Properties of CPT and PEGylated CPT (a = data from anterior brain sections; b = data from posterior brain section)

		k/D		
	IC_{50} (72 h) nM	(1 d)[a] mm^{-2}	(1 d)[b] mm^{-2}	(7 d)[c] mm^{-2}
camptothecin	43	12.25		
CM-PEG−CPT	84	0.64	0.36	0.27
CM-PEG-Gly−CPT	124	0.49	0.30	0.53
CM-PEG-Sar−CPT	163	0.42	0.25	0.23

[a] 1 day anterior (50-μm slices). [b] 1 day posterior (1-mm slices). [c] 7 days posterior (1-mm slices).

elucidating the full extent of distribution was desired to analyze conjugate-containing brains. The method of quantification of the intrinsic fluorescence of drug in 1-mm sections seemed appropriate to meet this goal. On the other hand, since higher resolution information is of interest, especially in the measurement of free CPT, a new brain-sectioning scheme was used. In this scheme, the drug-releasing source was implanted near the front portion of the brain and the implanted hemisphere was sectioned into 1-mm slices posterior to the implant and 50-μm slices anterior to the implant (see Figure 2). The intrinsic fluorescence of CPT was used to quantify drug in both gross and fine sections, providing information about the overall distribution of conjugate as well as more detailed concentration profiles from the same brain sample.

In the synthesized CPT conjugates, the polymer is linked to the drug on its active pharmacore, the lactone ring. Thus, we expected hydrolytic cleavage of the ester bond to occur before the drug can exert a significant cytotoxic effect (*24*). Hydrolysis studies (see Figure 3) demonstrated that free CPT is released from CPT conjugates in PBS, with the hydrolysis rate strongly dependent on pH. Figure 4 illustrates that CPT conjugates are capable of releasing drug in order to kill tumor cells in culture. To compare the potency of the compounds, the concentration of drug it takes to kill 50% of the cells (LC_{50}) was estimated from survival curves, including the curves in Figure 4, obtained from replicate experiments. The concentration of conjugated CPT required to kill half of the cells in culture (LC_{50}) was greater for all CPT conjugate forms than for free drug (Table 2, column 1). Time of exposure was more important for conjugates. For example, as exposure time increased from 24 to 72 to 120 h, LC_{50} dropped from 325 to 124 to 80 nM for CM-PEG-Gly−CPT compared to 62 to 43 to 36 for CPT. Also, the LC_{50} of the conjugates correlated with the hydrolytic stabilities of the compounds in PBS, suggesting that more conjugate was needed to kill an equivalent fraction of cells, because the conjugates released CPT over time whereas incubation with free drug resulted in a bolus dose.

If the predominant mechanism of cytotoxicity of the CPT conjugates is the hydrolysis of CPT conjugate in the medium followed by diffusion of free CPT into the cell, taking the release kinetics into account, one would expect the potency of the conjugate to be equivalent to free drug. To test this notion, the area under the concentration−time curve (AUC) was calculated based on the experimentally determined hydrolysis half-life for each conjugate in PBS at 37 °C. The calculation of AUC allows the release of free drug to be taken into account, and thus the AUC represents a time-weighted free CPT concentration in the media. Cytotoxicity data, such as from Figure 4, was then plotted versus AUC rather than total CPT concentration to produce Figure 10. This analysis is

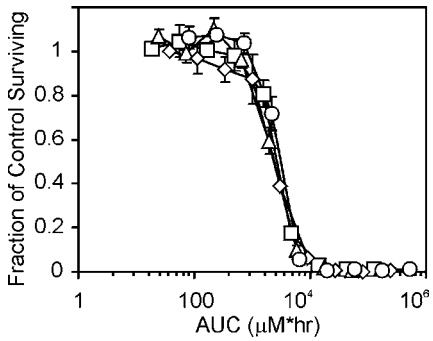


Figure 10. Fraction of cells surviving in vitro after 72 h of exposure as a function of AUC for CM-PEG-Sar−CPT (□), CM-PEG-Gly−CPT (△), CM-PEG−CPT (◇), and free CPT (○). In the calculation of AUC, the release rate of CPT from PEG−CPT conjugates was assumed to be the same as in PBS, at pH 7.4. When the cell survival is plotted in a way that takes into account the release kinetics of the conjugates, the potency of all compounds tested is equivalent.

oversimplified in that it does not account for the conversion of the lactone form of CPT to the carboxylate, but it does give an estimate of the quantitative effect of controlled CPT delivery as compared to a bolus dose. Once the cytotoxicity data was reanalyzed in this manner, little difference could be discerned in the potency of free drug and conjugates (Figure 10), further supporting the premise that drug liberation from the PEG precedes drug activity. A further discussion of calculation of AUC is given in the Supporting Information.

Polymer−drug conjugates are generally thought to enter cells by endocytosis rather than passive diffusion due to their large size (*19*). Since the CPT conjugates do not contain a targeting moiety, internalization will probably occur by a specific type of endocytosis known as pinocytosis, which involves nonspecific fluid phase uptake by the cell (*29*). Following internalization, conjugates will be transported to intracellular compartments, first to endosomes where the pH drops to 6 and then to lysosomes, which have an internal pH of 5.5 (*22*). Fluorescence microscopy of conjugate uptake was consistent with this mechanism of entry into the cell (Figure 5). Some form of endocytosis was assumed based on the punctate distribution pattern of CPT conjugate within the cell (Figure 5E) as well as the colocalization of intrinsic CPT fluorescence with a marker for endosomes and lysosomes (Figure 5F).

Since internalization by cells can potentially localize drug in perinuclear lysosomes, endocytosis could be an important mechanism in facilitating delivery of the lactone form of CPT to its site of action in the nucleus. Unfortunately, however, the stability of CPT conjugates was greatly enhanced in pH conditions that simulated the endosomal and lysosomal compartments (Figure 3). It is therefore likely that the release of free CPT from conjugates within the endosomes and lysosomes occurs very slowly. Extracellular release of free drug from the conjugate followed by free diffusion of CPT into the cell may thus be the dominant mechanism of cytotoxicity in culture, rather than free drug liberation within the acidic intracellular compartments. More detailed future studies of drug and conjugate concentration in the endosome versus free drug concentration in the cytoplasm are needed to answer this question completely.

Unlike conjugated CPT, free drug should be capable of diffusing across the cell membrane to the nucleus. Microscopy of cells following exposure to free CPT showed only a level of intracellular fluorescence close to back-

ground forcing us to conclude that in our experiment we could not detect free CPT in the cells (Figure 5B). The lack of signal above background level across the cells does indicate, however, that the CPT is not sequestered in any intracellular organelles. This is not entirely surprising given previous reports regarding CPT accumulation in cells. It has been demonstrated that uptake occurs rapidly within 10 min of incubation, followed by a gradual loss of drug over the next hour, and washing of cells with PBS following incubation was shown to remove a large fraction of the CPT from the cells (*30*).

The distribution of PEGylated and free CPT in the rat brain was characterized in thin sections of tissue at various time points following the implantation of 20%-drug-loaded p(CPP:SA) matrixes. The distribution data clearly demonstrate the superiority of the conjugates in penetrating tissue in high concentrations, but since there was such a disparity in the release kinetics between free CPT and conjugated CPT at 20% loading, the distribution difference could simply be the result of enhanced release of conjugate. A more complete analysis of the distribution data, however, does suggest that the difference results from a large change in transport properties in vivo in addition to a difference in release kinetics from p(CPP:SA). The 1-day data in Figures 8 and 9 was found to fit a previously established pharmacokinetic model for drug distribution in the brain (*26*). This model at steady-state reduces to the following equation in rectangular coordinates:

$$C(x) = C_0 e^{-x(k/D)^{1/2}} \quad (1)$$

where C is drug concentration at a distance x from the brain/implant interface, C_0 is drug concentration at the brain/implant interface, k is the first-order rate of elimination in the brain, and D is the effective diffusion coefficient in the brain. Equation 1 is appropriate for the case of a semi-infinite slab releasing into an infinite, homogeneous space.

The natural logarithm of the concentration data was found to vary linearly with distance, as predicted by this model, and a linear fit was used to extrapolate to $x = 0$ to estimate the interfacial concentration. The concentration at a distance from the implant was divided by the interfacial concentration to get the data points in Figure 11. The curves in Figure 11 represent best fits of the model to the experimental data. For our conjugate data derived from slices anterior to the implant, the logarithm of concentration deviates from linearity as the brain boundary at 4 mm is approached, and the data points past 2.5 mm were ignored in determining C_0 and k/D. The k/D values obtained by fitting Equation 1 to the Figure 11 data appear in column 2 of Table 2 and represent upper limit values of k/D. The k/D value is reduced more than 20-fold as a result of higher values of k/D resulting from PEGylation of CPT. A further explanation of determining k/D is given in the Supporting Information.

It is important to note that, although the distributions for the conjugates in the direction anterior to the matrix were significantly enhanced over free CPT (Figure 11), the penetration distances shown in Figure 8 are likely an underestimate of what could be achieved. In this experiment the polymer implant was located approximately 4 mm from the front tip of the brain, and on day-one after implantation, conjugate could be detected at a concentration of 10−30 ng/mg in slices close to the edge of the brain. Thus transfer of conjugate from the brain into the cerebrospinal fluid (CSF) likely occurred at the

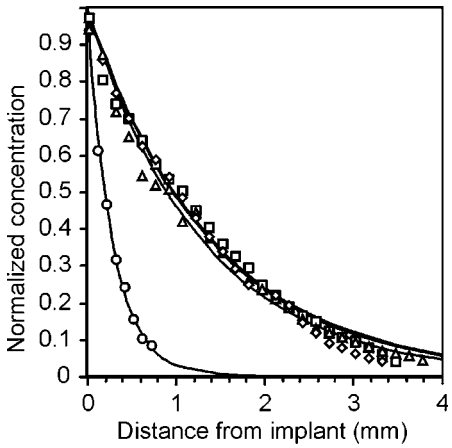


Figure 11. Normalized concentration profiles at distances anterior to the implants of CM-PEG-Sar−CPT (□), CM-PEG-Gly−CPT (△), CM-PEG−CPT (◇), and free CPT (○), fit to an established pharmacokinetic model (eq 1) 1 day following implantation of 20%-loaded p(CPP:SA) matrixes. Profiles were normalized with the concentration at the matrix/tissue interface that was estimated by extrapolating the experimental concentration data to the origin. Normalized data suggest that, in addition to the solubility and release kinetics, the transport properties of CPT in the brain have been changed by conjugation.

brain/CSF interface, effectively accelerating the apparent elimination of the compounds from the brain. Without the physical boundary at 4 mm, we would expect the drop-off to be slower, giving lower k/D values. Data from 1-mm slices posterior to the brain (Figure 7) showed the presence of high concentrations of conjugate more than 4 mm from the polymer, supporting the notion that greater penetration can be achieved by the conjugates in the absence of anatomical boundaries.

To determine the effect of the brain boundary, we have taken the rough 1-mm posterior distribution data, normalized it in the same way as for the thin-slice data, and fit it to the same steady-state distribution equation. No deviation from linearity was seen with these data, and data out to 10 mm was used for curve-fitting. Figure 12 shows the resulting data and curve fits for conjugates for both the 1-day and 7-day time points. A comparison of the k/D values in columns 3 and 4 to column 2 of Table 2 shows that the k/D value is similar for CM-PEG−CPT and CM-PEG-Sar−CPT in all three cases. The k/D is lower for the posterior data, indicating greater distribution is achieved once the anatomical boundary is removed. CM-PEG-Gly−CPT is an anomaly, in that the k/D value is always higher than for the other two conjugates and does not decrease between 1 and 7 days in the posterior sections. The k/D values for CM-PEG-Gly−CPT are consistent with our observation that total CPT concentrations are significantly lower for CM-PEG-Gly−CPT at later time points compared to the other two conjugate systems. Either the direct ester and sarcosine conjugates are stabilized by a mechanism not available to the glycine conjugate, or an additional route eliminates the glycine conjugate, yet to be identified, that is not available for the other two conjugates.

The distributions of CM-PEG-Sar−CPT, CM-PEG-Gly−CPT, and CM-PEG−CPT were characterized in 1-mm sections of tissue at various time points following the implantation of 20%-drug-loaded p(CPP:SA) matrixes (Figure 7). From data at 28 days after implantation, CM-PEG-Gly−CPT is present in lower concentrations than CM-PEG−CPT and CM-PEG-Sar−CPT despite their relatively similar rates of hydrolysis in vitro (see Figure

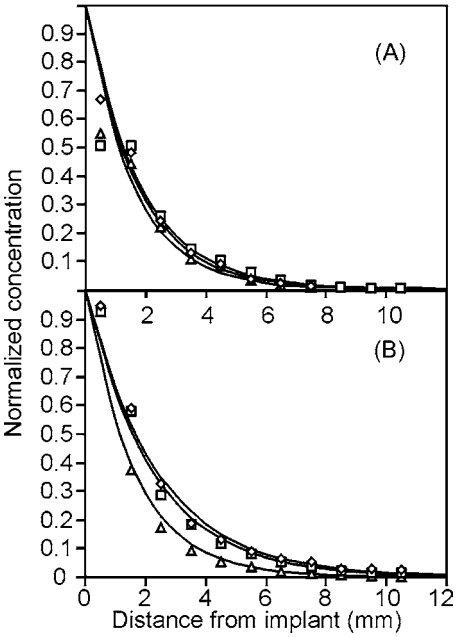


Figure 12. Normalized concentration profiles posterior to implant of CM-PEG-Sar−CPT (□), CM-PEG-Gly−CPT (△), and CM-PEG−CPT (◇): (A) 1 day following implantation and (B) 7 days following implantation of 20%-loaded p(CPP:SA) matrixes. Profiles are normalized with the concentration at the matrix/tissue interface. The interfacial concentration was estimated by extrapolating concentration data to the origin.

1). Furthermore, since we anticipate that the conjugate-releasing source is exhausted by two weeks following implantation, we would expect to see a large decrease in the concentration of conjugates in vivo between 14 and 28 days. Figure 7 shows that although this anticipated decrease was observed for CM-PEG-Gly−CPT, the concentrations of CM-PEG−CPT and CM-PEG-Sar−CPT stayed relatively high. On the basis of this reasoning, it seems that CM-PEG-Sar−CPT and CM-PEG−CPT may be stabilized in vivo by a mechanism that does not affect CM-PEG-Gly−CPT. For example, CM-PEG-Sar−CPT and CM-PEG−CPT may be specifically bound in a way that reduces or stops their hydrolysis to a greater extent than CM-PEG-Gly−CPT. Others have previously shown that when incubated in human plasma, only 25% of CPT was recovered from CM-PEG40000−CPT as compared to a 65% recovery of free drug for CM-PEG40000-Gly−CPT (*12*). This finding supports the idea that interactions with biological molecules can stabilize these conjugates in a manner dependent on their linkage chemistries. However, despite the fact that CM-PEG-Gly−CPT seems to be eliminated from the rat brain more rapidly than CM-PEG−CPT or CM-PEG-Sar−CPT, the levels of liberated drug measured for the three conjugate forms were similar. Since it is not known if the reduced retention of CM-PEG-Gly−CPT correlates with an increase in the amount of CPT liberated in vivo, it is not possible to conclude whether CM-PEG-Gly−CPT performs better or worse than the other conjugate forms based solely on the retention data.

If drug is eliminated at brain boundaries into the CSF as we expect, it is possible for compounds to enter back into brain tissue in distant locations. This mechanism may contribute to the noted presence of drug in the cerebellum following the delivery of CPT conjugates. The cerebellum was located approximately 10 mm from the implant site. Figure 7 shows levels of CPT above background in sections corresponding to this brain region for all conjugate forms up to one week after delivery. This was unexpected, since, although the cerebrum and the cerebellum are in contact, they are discrete regions of tissue and, intuitively, it would seem that the anatomical boundary between them would be a barrier for diffusion. Thus, this observation may indicate that convection in the CSF, which bathes the entire brain, may play a role in disseminating conjugate to distant regions of the brain.

In addition to measuring total CPT levels in thin sections of brain, alternating tissue slices were used to measure the fraction of total CPT in the unconjugated form. For all conjugates, only low levels of unconjugated drug, less than 1% of total CPT, could be detected. If we look at accumulation of CPT in our system:

$$\frac{dC_{CPT}}{dt} = k_h C_{conj} - k_e C_{CPT} \quad (2)$$

where k_h is the conjugate hydrolysis rate and k_e is the CPT elimination rate, the maximum ratio of CPT-to-conjugate would be found at steady-state, where $0 = k_h C_{conj} - k_e C_{CPT}$, or

$$\frac{C_{CPT}}{C_{conj}} = \frac{k_h}{k_e} \quad (3)$$

We have shown a k_h value of 0.012 h^{-1} for the sarcosine conjugate, and a k_e value of 1.2 h^{-1} for CPT are good estimates which would give a steady-state ratio of about 1-to-100. Our experimental finding of 1% or less free CPT is therefore not surprising. However, in comparing the detection limit of our assay (1 ng/mg) with the concentration of free drug required to kill cells in culture (LC_{50} = 0.015 ng/mg for a 3-day exposure), we see that it is not possible to predict the potential efficacy of the conjugates based on these free drug measurements, since even though concentrations are below the detection limit, they may be sufficient to kill tumor cells.

In summary, the synthesized CPT conjugates have pH-dependent hydrolysis rates similar to those reported for conjugates of PEG40000 (*2*). The conjugates were shown to be cytotoxic in cell culture. Fluorescence microscopy studies demonstrated that conjugate can be endocytosed by cells, but the conjugates were shown to be highly stable in acidic conditions, suggesting that this mechanism for toxicity may not make a large contribution to the overall cell kill. On the basis of LC_{50} data, the potency of the conjugates appears to be lower than for free drug, but in considering the dynamics of drug release from the conjugates, the shift in LC_{50} can be accounted for by release of drug over time rather than an irreversible loss of potency of the camptothecin molecule upon conjugation. Comparison of the distributions of CPT conjugates and unmodified CPT in rat brains demonstrated the capacity of conjugation to alter the transport properties of small molecules in brain tissue. When CPT was delivered in the conjugated form, the ratio of elimination to diffusion decreased, much higher concentrations of drug could be achieved within tissue, and drug could be detected at a greater distance from the source. These findings suggest that drug conjugation would be a useful adjunct to localized drug delivery in the brain.

ACKNOWLEDGMENT

This work was supported by National Institutes of Health Grant CA52857. Kathryn Feldman conducted the lysate experiments. Matthew Sklar performed most of the in vitro cytotoxicity work. Dr. Camille Solbrig provided invaluable editorial advice and assistance.

Supporting Information Available: MALDI-TOF data, calculations for AUC used in Figure 10, and a determination of *k/D* and its use in eq 1 are available free of charge via the Internet at http://pubs.acs.org/BC.

LITERATURE CITED

(1) Wall, M. E., Wani, M. C., Cook, C. E., Palmer, K. H., McPhail, A. T., and Sim G. A. (1966) Plant antitumor agents. I. Isolation and structure of camptothecin a novel alkaloidal leukemia and tumor inhibitor from *Camptotheca acuminata*. *J. Am. Chem. Soc. 88*, 3888−3890.

(2) Greenwald, R. B., Pendri, A., Conover, C., Gilbert, C., Yang, R., and Xia, J. (1996) Drug delivery systems 0.2. Camptothecin 20-O-poly(ethylene glycol) ester transport forms. *J. Med. Chem. 39*, 1938−1940.

(3) Harada, M., Sakakibara, H., Yano, T., Suzuki, T., and Okuno, S. (2000) Determinants for the drug release from T-0128, camptothecin analogue-carboxymethyl dextran conjugate. *J. Controlled Release 69*, 399−412.

(4) Singer, J. W., Bhatt, R., Tulinsky, J., Buhler, K. R., Heasley, E., Klein, P., and de Vries, P. (2001) Water-soluble poly-(l-glutamic acid)-gly camptothecin conjugates enhance camptothecin stability and efficacy in vivo. *J. Controlled Release 74*, 243−247.

(5) Caiolfa, V. R., Zamai, M., Fiorino, A., Frigerio, E., Pellizzoni, C., d'Argy, R., Ghiglieri, A., Castelli, M. G., Farao, M., Pesenti, E., Gigli, M., Angelucci, F., and Suarato, A. (2000) Polymer-bound camptothecin: Initial biodistribution and antitumour activity studies. *J. Controlled Release 65*, 105−119.

(6) Rivory, L. P. and Robert, J. (1995) Molecular, cellular, and clinical aspects of the pharmacology of 20(S) camptothecin and its derivatives. *Pharmacol. Ther. 68*, 269−296.

(7) Conover, C. D., Pendri, A., Lee, C., Gilbert, C. W., Shum, K. L., and Greenwald, R. B. (1997) Camptothecin delivery systems: The antitumor activity of a camptothecin 20-O-poly-(ethylene glycol) ester transport form. *Anticancer Res. 17*, 3361−3368.

(8) Garcia-Carbonero, R. and Supko, J. G. (2002) Current perspectives on the clinical experience, pharmacology, and continued development of the camptothecins. *Clin. Cancer Res. 8*, 641−661.

(9) Greenwald, R. B., Choe, Y. H., McGuire, J., and Conover, C. D. (2003) Effective drug delivery by PEGylated drug conjugates. *Adv. Drug Delivery Rev. 55*, 217−250.

(10) Conover, C. D., Greenwald, R. B., Pendri, A., Gilbert, C. W., and Shum, K. L. (1998) Camptothecin delivery systems: Enhanced efficacy and tumor accumulation of camptothecin following its conjugation to poly(ethylene glycol) via a glycine linker. *Cancer Chemother. Pharm. 42*, 407−414.

(11) Conover, C. D., Greenwald, R. B., Pendri, A., and Shum, K. L. (1999) Camptothecin delivery systems: The utility of amino acid spacers for the conjugation of camptothecin with poly(ethylene glycol) to create prodrugs. *Anti-Cancer Drug Des.14*, 499−506.

(12) Greenwald, R. B., Pendri, A., Conover, C. D., Lee, C., Choe, Y. H., Gilbert, C., Martinez, A., Xia, J., Wu, D. C., and Hsue, M. (1998). Camptothecin-20-PEG ester transport forms: The effect of spacer groups on antitumor activity. *Bioorg. Med. Chem. 6*, 551−562.

(13) Fung, L. K., Shin, M., Tyler, B., Brem, H., and Saltzman, W. M. (1996) Chemotherapeutic drugs released from polymers: Distribution of 1,3-bis (2-chloroethyl)-1-nitrosourea in the rat brain. *Pharm. Res. 13*, 671−682.

(14) Fung, L. K., Ewend, M. G., Sills, A., Sipos, E. P., Thompson, R., Watts, M., Colvin, O. M., Brem, H., and Saltzman, W. M. (1998) Pharmacokinetics of interstitial delivery of carmustine, 4-hydroperoxycyclophosphamide, and paclitaxel from a biodegradable polymer implant in the monkey brain. *Cancer Res. 58*, 672−684.

(15) Strasser, J., Fung, L. K., Eller, S., Grossman, S. A., and Saltzman, W. M. (1995) Distribution of 1,3-bis (2-chloroethyl)-1-nitrosourea and tracers in the rabbit brain after interstitial delivery by biodegradable polymer implants. *J. Pharmacol. Exp. Ther. 275*, 1647−1655.

(16) Dang, W. B., Colvin, O. M., Brem, H., and Saltzman, W. M. (1994) Covalent coupling of methotrexate to dextran enhances the penetration of cytotoxicity into a tissue-like matrix. *Cancer Res. 54*, 1729−1735.

(17) Levin, V. A. (1980) Relationship of octanol/water partition coefficient and molecular weight to rat brain capillary permeability. *J. Med. Chem. 23*, 682−684.

(18) Patlak, C. S., Hospod, F. E., Trowbridge, S. D., and Newman, G. C. (1998) Diffusion of radiotracers in normal and ischemic brain slices. *J. Cereb. Blood Flow Metab. 18*, 776−802.

(19) Soukos, N. S., Hamblin, M. R., and Hasan, T. (1997) The effect of charge on cellular uptake and phototoxicity of polylysine chlorin (e6) conjugates. *Photochem. Photobiol. 65*, 723−729.

(20) Ezell, E. L., and Smith, L. L. (1991) ^{1}H and ^{13}C NMR spectra of camptothecin and derivatives. *J. Nat. Prod.* 54, 1645−1650.

(21) Hart, L. G., Call, J. B., and Oliverio, V. T. (1969) A fluorometric method for determination of camptothecin in plasma and urine. *Cancer Chemother. Rep. 1 53*, 211−214.

(22) Duncan, R., Dimitrijevic, S., and Evagorou, E. G. (1996) The role of polymer conjugates in the diagnosis and treatment of cancer. *STP Pharma Sci. 6*, 237−263.

(23) Omelyanenko, V., Kopeckova, P., Gentry, C., and Kopecek, J. (1998) Targetable HPMA copolymer-adriamycin conjugates. Recognition, internalization, and subcellular fate. *J. Controlled Release 53*, 25−37.

(24) Pendri, A., Gilbert, C. W., Soundararajan, S., Bolikal, D., Shorr, R. G. L., and Greenwald, R. B. (1996) PEG modified anticancer drugs: Synthesis and biological activity. *J. Bioact. Compat. Polym. 11*, 122−135.

(25) Mahoney, M. J., and Saltzman W. M. (1999) Millimeter-scale positioning of a nerve-growth-factor source and biological activity in the brain. *P. Natl. Acad. Sci. U.S.A. 96*, 4536−4539.

(26) Saltzman W. M., and Radomsky, M. L. (1991) Drugs released from polymers − Diffusion and elimination in brain-tissue. *Chem. Eng. Sci. 46*, 2429−2444.

(27) Dang, W. B., and Saltzman, W. M. (1992) Dextran retention in the rat brain following release from polymer implant. *Biotechnol. Prog. 8*, 527−532.

(28) Krewson, C. E., Klarman, M. L., and Saltzman, W. M. (1995) Distribution of nerve growth-factor following direct delivery to brain interstitium. *Brain Res. 680*, 196−206.

(29) Cartlidge, S. A., Duncan, R., Lloyd, J. B., Rejmanova, P., and Kopecek, J. (1986) Soluble, crosslinked N-(2-hydroxypropyl)methacrylamide copolymers as potential drug carriers. 1. Pinocytosis by rat visceral yolk sacs and rat intestine cultured *in vitro*. Effect of molecular weight on uptake and intracellular degradation. *J. Controlled Release 3*, 55−66.

(30) Gabr, A., Kuin, A., Aalders, M., ElGawly, H., and Smets, L. A. (1997) Cellular pharmacokinetics and cytotoxicity of camptothecin and topotecan at normal and acidic pH. *Cancer Res. 57*, 4811−4816.

BC034180O

REVIEWS

Multimodality in Vivo Molecular-Genetic Imaging

Michael Doubrovin, Inna Serganova, Philipp Mayer-Kuckuk, Vladimir Ponomarev, and Ronald G. Blasberg*

Departments of Neurology and Radiology, Memorial Sloan-Kettering Cancer Center, New York, New York 10021. Received June 18, 2004

Multimodality imaging is increasingly being used in molecular-genetic studies in small animals. The coupling of nuclear and optical reporter genes represents the beginning of a far wider application of this technology. Optical imaging and optical reporter systems are cost-effective and time-efficient, they require less resources and space than PET or MRI, and they are particularly well suited for small animal imaging and for in vitro assays to validate different reporter systems. However, optical imaging techniques are limited by depth of light penetration and scatter and do not yet provide optimal quantitative or tomographic information. These issues are not limiting for PET- or MRI-based reporter systems, and PET- and MRI-based animal studies are more easily generalized to human applications. Many of the shortcomings of each modality alone can be overcome by the use of dual- or triple-modality reporter constructs that incorporate the opportunity for PET, fluorescence and bioluminescence imaging. We optimistically expect that some form of tomographic, small animal optical imaging capability will be developed soon, and that this will provide the opportunity for the colocalization of optical signals to anatomical structures provided by tomographic CT and MR imaging.

INTRODUCTION

As this was the first presentation at the Symposium on Chemistry and Biological Applications of Imaging Agents and Molecular Beacons, and is the initial article in this series of reviews, it might be advantageous to provide some background on the origins and development of "molecular imaging". The past several decades have witnessed an astonishing increase in our knowledge and understanding of the genetics and molecular biology of human disease. Significant progress has been made in our understanding of the molecular-genetic mechanisms of many diseases, and this has been achieved with the advent of the modern molecular-biological assays. In parallel with the developments in genetics and molecular biology, the imaging sciences have also made remarkable advances in technology for visualizing tissue structure and function. This progress includes the development of new instruments (e.g., microPET, microCT, high-field strength magnets, and novel optical and ultrasound technology) for imaging small animals with improved image resolution and sensitivity (*1*–*5*). There have been corresponding improvements in clinical imaging instrumentation as well. The molecular/cellular and imaging disciplines rarely interacted until the 1990s. In the mid 1990s, several investigators and the NCI began to promote "cellular and molecular imaging", and this convergence of the "molecular" and "imaging" sciences was nurtured by Richard Klausner, then director of the NCI. Molecular imaging–cancer imaging was designated as one of six "Extraordinary Scientific Opportunities for Investment" in 1997, and this initiative was strongly supported by two imaging-based NCI programs (the Small Animal Imaging Resource Program, SAIRP, and the In Vivo, Cellular and Molecular Imaging Centers, ICMIC). More recently, other NIH institutes and the Department of Energy (DOE) have also developed "molecular imaging" program support.

The convergence of molecular biology and noninvasive imaging was timely and addresses several experimental objectives. For example, ex vivo molecular assays in animal models of disease and in transgenic animals require invasive sampling procedures. Tissue sampling may not always adequately represent the biochemical or pathological process under investigation due to tissue heterogeneity, which is especially characteristic of cancer. Furthermore, time-course studies require large numbers of animals that are sacrificed at specific time points in order to achieve a statistically significant temporal profile. The development of versatile and sensitive assays to monitor molecular-genetic and cellular processes in vivo would be of considerable value in human subjects, as well as in experimental animal models of different diseases. Noninvasive imaging of molecular-genetic and cellular processes would compliment existing ex vivo molecular-biological assays and can provide a spatial as well as a temporal dimension to our understanding of various diseases.

At this point it may be helpful to provide the readership of this series on "molecular imaging" with a definition of this newly emerging and rapidly evolving field. We developed the following definition several years ago: "the visualization of cellular processes in space and time at a molecular or genetic level of function". Other

* To whom correspondence should be addressed. E-mail: blasberg@neurol.mskcc.org.

10.1021/bc0498572 CCC: $27.50 © 2004 American Chemical Society
Published on Web 11/02/2004

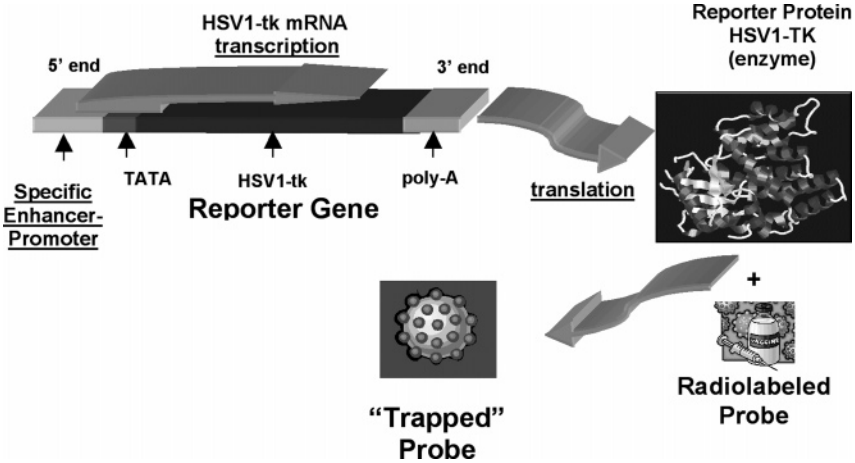


Figure 1. HSV1-*tk* reporter construct and the indirect reporter imaging paradigm. The basic structure of a reporter gene complex is shown, in this case herpes simplex virus type 1 thymidine kinase (HSV1-*tk*). The control and regulation of gene expression is performed through promoter and enhancer regions that are located at the 5′ end ("upstream") of the reporter gene. These promoter/enhancer elements can be "constitutive" and result in continuous gene expression ("always on"), or they can be "inducible" and sensitive to activation by endogenous transcription factors and promoters. Following the initiation of transcription and translation, the gene product, a protein, accumulates. In this case the reporter gene product is an enzyme (HSV1-TK). HSV1-TK will phosphorylate selected thymidine analogues (e.g., FIAU or FHBG), whereas these probes are not phosphorylated by endogenous mammalian TK1. The phosphorylated probe does not cross the cell membrane readily; it is "trapped" and accumulates within transduced cells. Thus, the magnitude of probe accumulation in the cell (level of radioactivity) reflects the level of HSV1-TK enzyme activity and level of HSV1-tk gene expression.

definitions of "molecular imaging" abound and include variations on the theme and some emphasize different aspects to explain the advent, development, and evolution of this new discipline.

The readers of this chapter are urged to consult other reviews of imaging transgene expression and molecular-biological reporter gene imaging that have been written (*6*−*13*), and other perspectives on molecular imaging (*14*−*20*). In addition, there are two new journals that are specifically serving the molecular imaging community: Molecular Imaging (MIT Press; the official journal of the Society of Molecular Imaging, www.molecularimaging-.com) and Molecular Imaging and Biology (Elsevier, the official journal of the Academy of Molecular Imaging, (http://149.142.143.206/index.html).

Molecular Imaging Strategies. Three imaging strategies have been described: "direct", "indirect", and "biomarker". Direct imaging strategies are based on imaging the target directly, usually with a target-specific probe. This strategy has been established using nuclear, optical, and MR imaging technology. The resultant image of probe localization and concentration (signal intensity) is directly related to its interaction with the target. Imaging cell surface specific antigens with radiolabeled antibodies and genetically engineered antibody fragments (e.g., minibodies) are examples of direct molecular imaging that has evolved over the past 30 years. In vivo imaging of receptor density/occupancy using small radiolabeled ligands has also been widely used, particularly in neuroscience research, over the past two decades. These examples represent some of the first "molecular imaging" applications used in clinical nuclear medicine research. More recent research has focused on chemistry and the synthesis of small radiolabeled or fluorescent probes (and paramagnetic nanoparticles) that target specific receptors (e.g, the estrogen or androgen receptors) and florescent probes that are activated by endogenous proteases (*21*). For example, the alpha(v)beta3 integrin is highly expressed on tumor vasculature and plays an important role in metastasis and tumor-induced angiogenesis; initial studies targeting and imaging of the alpha(v)beta3 integrin with radiolabeled glycosylated RGD-containing peptides are very encouraging (*22*). The development of other novel direct-imaging probes and ligands will be discussed by other contributors to this series, including C. Meares, R. Pandrey, D. Bornhop, J. Katzenellenbogen, W. Eckelman, D. Hnatowich, W. Welsh, and others.

Indirect molecular imaging strategies are a little more complex. One example of indirect imaging that is now being widely used is "reporter gene imaging". It requires "pretargeting" (delivery) of the reporter gene to the target tissue (by transfection/transduction), and it usually includes transcriptional control components that function as "molecular-genetic sensors" and initiate reporter gene expression. Reporter gene imaging may also require a specific probe that must interact with the reporter gene product in order to produce an image. In this case, the "target" molecule (or the activity of a specific intracellular signal transduction pathway) is not imaged directly. A simplified description and cartoon of a reporter gene is shown in Figure 1, and a representation of different reporter genes for imaging transduced cells is shown in Figure 2. The resultant image reflects multiple processes that include the transfer of the reporter gene into the target cells, followed by the initiation of reporter gene transcription and subsequent translation of the reporter protein (the reporter gene product). These issues and others related to the intracellular or membrane localization and the degradation or ubiquination of the reporter protein, the biodistribution and clearance of reporter probes, and the optimal conditions for fluorescence and bioluminescence imaging are more fully addressed below.

Biomarker or surrogate marker imaging can be used to assess downstream effects of one or more endogenous molecular-genetic processes. This approach is particularly attractive for potential translation into clinical studies in the near-term, because existing radiopharmaceuticals and imaging paradigms may be useful for monitoring downstream effects of changes in specific molecular-genetic pathways in diseases such as cancer. A recent example of clinically useful biomarker imaging for "early" assessment of treatment response is FDG PET imaging of gastrointestinal stromal tumors (GIST) pre- and post-

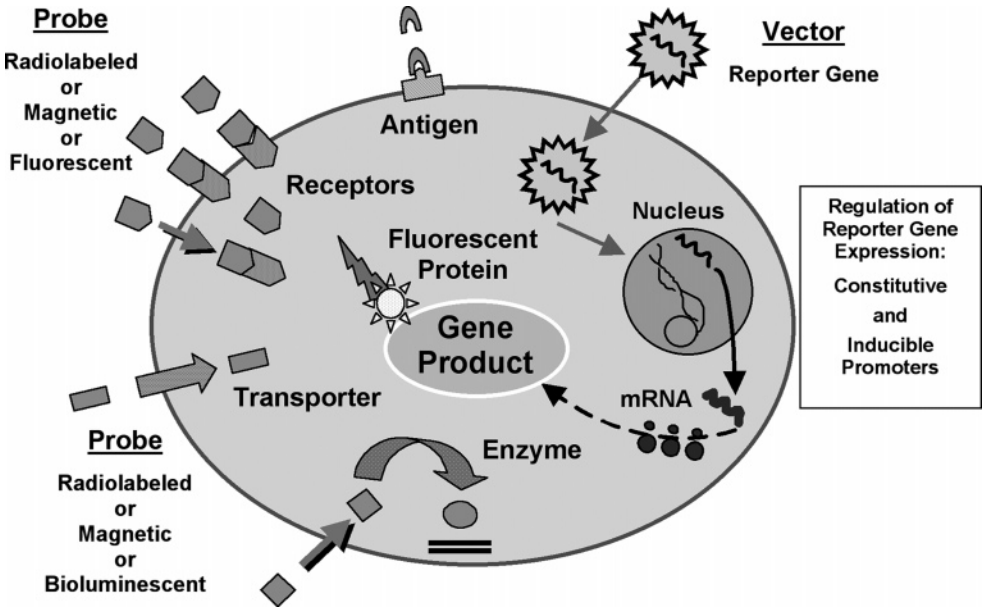


Figure 2. Different reporter systems. The reporter gene complex is transfected into target cells by a vector (e.g., a virus). Inside the transfected cell, the reporter gene may or may not be integrated into the host-cell genome; transcription of the reporter gene to mRNA is initiated by "constitutive" or "inducible" promoters, and translation of the mRNA to a protein, occurs on the ribosomes. The reporter gene product can be a cytoplasmic or nuclear enzyme, a transporter in the cell membrane, a receptor at the cell surface or part of cytoplasmic or nuclear complex, an artificial cell surface antigen, or a fluorescent protein. Often, a complimentary reporter probe (e.g, a radiolabeled, magnetic, or bioluminescent molecule) is given, and the probe concentrates (or emits light) at the site of reporter gene expression. The level of probe concentration (or intensity of light) is usually proportional to the level of reporter gene expression and can reflect several processes, including the level of transcription, the modulation and regulation of translation, protein−protein interactions, and posttranslational regulation of protein conformation and degradation.

Table 1. The Most Widely Used Imaging Modalities

- optical (fluorescence, bioluminescence, spectroscopy, optical coherence tomography)
- magnetic resonance (contrast, diffusion-weighted imaging, spectroscopy)
- radionuclide (PET, SPECT, gamma camera, autoradiography)

STI571 (Gleevec) treatment (*23*, *24*). Although glucose uptake and glycolytic enzyme activity is homeostatically regulated, glucose metabolism has been shown to be regulated by extracellular signals mediated by cell surface receptors. Receptor-mediated regulation of glucose uptake is thought to involve activation of PI 3-kinase, Akt, mTOR, and S6 kinase. A likely explanation for the dramatic effect of STI571 (Gleevec) on glucose uptake in GIST is that Kit receptor signaling regulates glucose uptake as well as glucose metabolism.

Imaging Modalities. The most widely used imaging modalities are listed in Table 1, although other modalities, such as ultrasound and CT, are seeing increasing application and could be included. The convergence of these different modalities to support current molecular imaging efforts is largely based on the development of multimodality reporter systems for both optical and radionuclide imaging (see below). A number of different strategies are also being developed for magnetic resonance reporter gene imaging, and they are being combined with other reporter systems to broaden the range of biological applications (*25*−*28*). MR spectroscopy can detect and measure the concentration of specific molecules such as 5FU. MR spectroscopy was used in combination with 5FC and yeast cytosine deaminase (yCD) in suicide gene therapy protocol and was shown to be effective (*29*). The interaction of several disciplines, including molecular-cell biology and chemistry with different imaging modalities, is illustrated by the Ven diagram (Figure 3) and illustrates the theme of this presentation. Namely, a mutimodality, mutidisciplinary approach to molecular imaging provides distinct advantages. Several of the imaging modalities (fluorescence, bioluminescence, and nuclear) will be illustrated in the following paragraph, and their combined advantage will be highlighted.

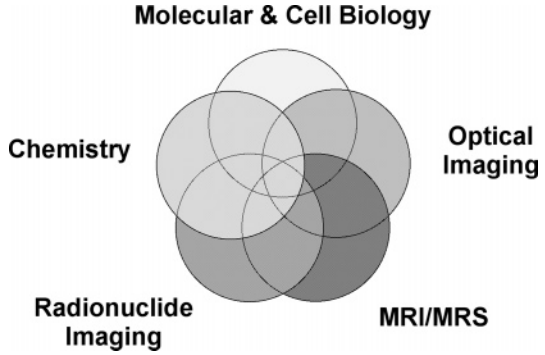


Figure 3. Mutidisciplinary approach to molecular imaging. Molecular and cell biology, along with chemistry, provide the foundation and resources for developing novel in vivo molecular constructs and imaging paradigms. Three imaging modalities currently dominate the field, but this will soon expand to include other modalities. The Ven diagram emphasizes the interaction between disciplines and different imaging modalities; it is this interaction that provides a broad new approach to the field.

Reporter Gene Imaging. This report will focus on noninvasive multimodality nuclear and optical reporter imaging in small animals. It will highlight the application and advantages of a multimodality imaging approach, as well as discuss the potential limits of reporter-gene imaging and its translation into clinical studies. It is important to note at the outset of this discussion that imaging transgene expression requires transfection/transduction of a reporter gene construct into target cells.

This is usually accomplished with a vector that is capable of transfecting/transducing the target tissue (cells), and several currently available vector types can be used (e.g., plasmid, retrovirus, adenovirus, adeno-associated virus, lentivirus). The reporter transgene can encode for an enzyme, (e.g., *HSV1-tk* (*30*) or *luciferase* (*31*)), a receptor (e.g., *hD2R* (*32*)) or *hSSTR2* (*33*)), or a transporter (e.g., *hNIS*) (*34*)), or it can encode for a fluorescent protein (e.g., *eGFP* (*35*)) (Figure 2).

The paradigm for quantitative imaging of transgene expression involves several key steps, including the transfer of the reporter construct into target tissue or cells, the initiation of transcription (that can be controlled by specific promoter/enhancer elements), the process of DNA transcription, and subsequent translation of mRNA into the gene product. As outlined below, recent studies have demonstrated that all these key events can be specifically visualized in vivo by utilizing reporter gene imaging. A general paradigm for gene imaging using radiolabeled probes was initially described in 1995 (*30*) and our first in vivo (autoradiographic) imaging study using herpes simplex virus type 1 thymidine kinase (HSV1-*tk*) as a reporter gene and 5-iodo-2′-fluoro-2′deoxy-1-β-D-arabino-furanosyl-uracil (FIAU) as a reporter probe is shown in Figure 4B. Subsequent imaging was performed with [^{131}I]FIAU (*36*) and a gamma camera (Figure 4C) and then with [^{124}I]FIAU (*37*) and PET (Figure 4D).

A common feature of all reporter constructs is the cDNA expression cassette containing the reporter gene(s) of interest (e.g., HSV1-*tk*) which can be placed under the control of specific promoter-enhancer elements. The versatility of reporter gene imaging results in part from the flexibility to tailor the expression cassette to an individual need. In most cases, standard molecular biology techniques are sufficient to design a suitable expression cassette. Using specific expression cassettes, reporter genes can be "always turned on" by constitutive promoters (such as LTR, RSV, CMV, PGK, EF1, etc.) and used to monitor cell trafficking by identifying the location, migration, targeting, and proliferation of stably transduced cells. Alternatively, the promoter/enhancer elements can be constructed to be "inducible" and "sensitive" to activation in selected cell types and regulation by specific endogenous pathways. Promoter activation can be tissue specific, where promoter/enhancer elements are activated by transcription factors that are overexpressed in specific tissue, e.g. the PSMA promoter shows significant activity in prostate cancer cells (*38*), the albumin promoter is expressed in liver (*39*), and the CEA promoter is highly expressed in colorectal cancer (*40*). Inducible reporter genes can also be constructed to be sensitive to specific endogenous molecular processes, including the regulation of endogenous gene expression (*41*), the activity of specific signal transduction pathways (*42*), and specific protein−protein interactions (*43*, *44*), and post-transcriptional regulation of protein expression (*45*).

Another example of the versatility of reporter systems is the ability to create multimodality reporter constructs. For example, a fusion gene containing cDNA from two or three different reporter genes can be constructed, where the gene product yields a single fusion protein that retains functionality of each of the composite gene products (*46*) (Figure 5). A second strategy links two reporter genes by a type II internal ribosomal entry site (IRES) sequence, where the IRES element enables translation initiation within the bicistronic mRNA, thus permitting gene coexpression by cap-dependent translation of the first cistron and cap-independent, IRES-mediated translation of the second cistron (*47*, *48*). A third strategy uses one vector containing two different promoters and two different reporter genes. A fourth strategy uses multiple vectors, where one or more vectors carry a therapeutic gene and other vectors carry the reporter genes (*49*). All four strategies are based on demonstrating a proportional and constant relationship in the coexpression of two or more transgenes over a wide range of expression levels.

Radionuclide-Reporter Gene Imaging. Wild-type *HSV1-tk* (*37*) and a mutant *HSV1-tk* gene, *HSV1-sr39tk* (*50*), are the reporter genes most commonly used in current molecular imaging studies using radiolabeled probes and PET imaging. The *HSV1-tk* and *HSV1-sr39tk* gene products are enzymes that have less substrate specificity than mammalian thymidine kinase 1 (TK1) and can phosphorylate a wider range of compounds. The viral kinases can phosphorylated acycloguanosines (e.g., acyclovir, ACV; ganciclovir, GCV; 9-[4-fluoro-3-(hydoxymethyl)butyl]guanine, FHBG) and 2′-fluoro-nucleoside analogues of thymidine (e.g., 5-iodo-2′-fluoro-2′deoxy-1-β-D-arabino-furanosyl-uracil, FIAU), whereas mammalian TK1 has limited or no ability to phosphorylate these compounds (*51*). This difference between mammalian and viral TK enzymes permits the development and use of radiolabeled probes that are selectively phosphorylated by HSV1-TK or HSV1-sr39TK. The advantages and disadvantages of different radiolabeled probes for imaging viral TK expression have been compared and extensively discussed in the literature (*52*, *53*). It is most likely that [^{124}I]FIAU (*54*) and [^{18}F]FHBG (*55*) will be the radiolabeled probes that will be first introduced into the clinic for imaging HSV1-tk gene expression. As noted above, other radionuclide-based reporter systems have been developed. Several of these reporter systems have distinct benefits with respect to initiating molecular/reporter imaging in human subjects, since the reporters are derived from human genes.

Optical-Reporter Gene Imaging. Optical-based (bioluminescence and fluorescence) reporter systems are receiving increased attention because of their efficiency for sequential imaging, operational simplicity, and substantial cost benefits. Bioluminescence reporter genes are being widely used for whole body imaging in small animals (Figures 5 and 6). The most commonly used bioluminescence reporter systems include the *Firefly* (FLuc) or *Renilla* (RLuc) luciferase genes (*56*). As with nuclear and magnetic resonance reporter systems, bioluminescence imaging depends on the delivery of a specific substrate to the reporter gene expressing cells. Further, the light emitting bioluminescence reaction catalyzed by luciferases depends on the presence of oxygen (*57*) and for example in the case of FLuc additionally on the cofactor ATP. The *Firefly* and *Renilla luciferase* reporter systems, in combination with their corresponding luminescent substrates (luciferin and coelenterazine), have several advantages for imaging small living animals. Autobioluminescence in most cases is essentially nonexistent and results in very low background light emission; this contributes to the very high sensitivity and specificity of this optical imaging technique (*58*, *59*). Semiquantitative accuracy and reproducibility requires that the luciferin, ATP, and oxygen levels are *not* rate determining, but rather are in excess. Under these conditions, the photon emission flux (light intensity) is directly related to reporter gene expression and the level of reporter gene product, namely, luciferase. Another potential concern is the fact that the substrate for *Renilla luciferase*, coelenterazine, is a substrate for the MDR1 transporter.

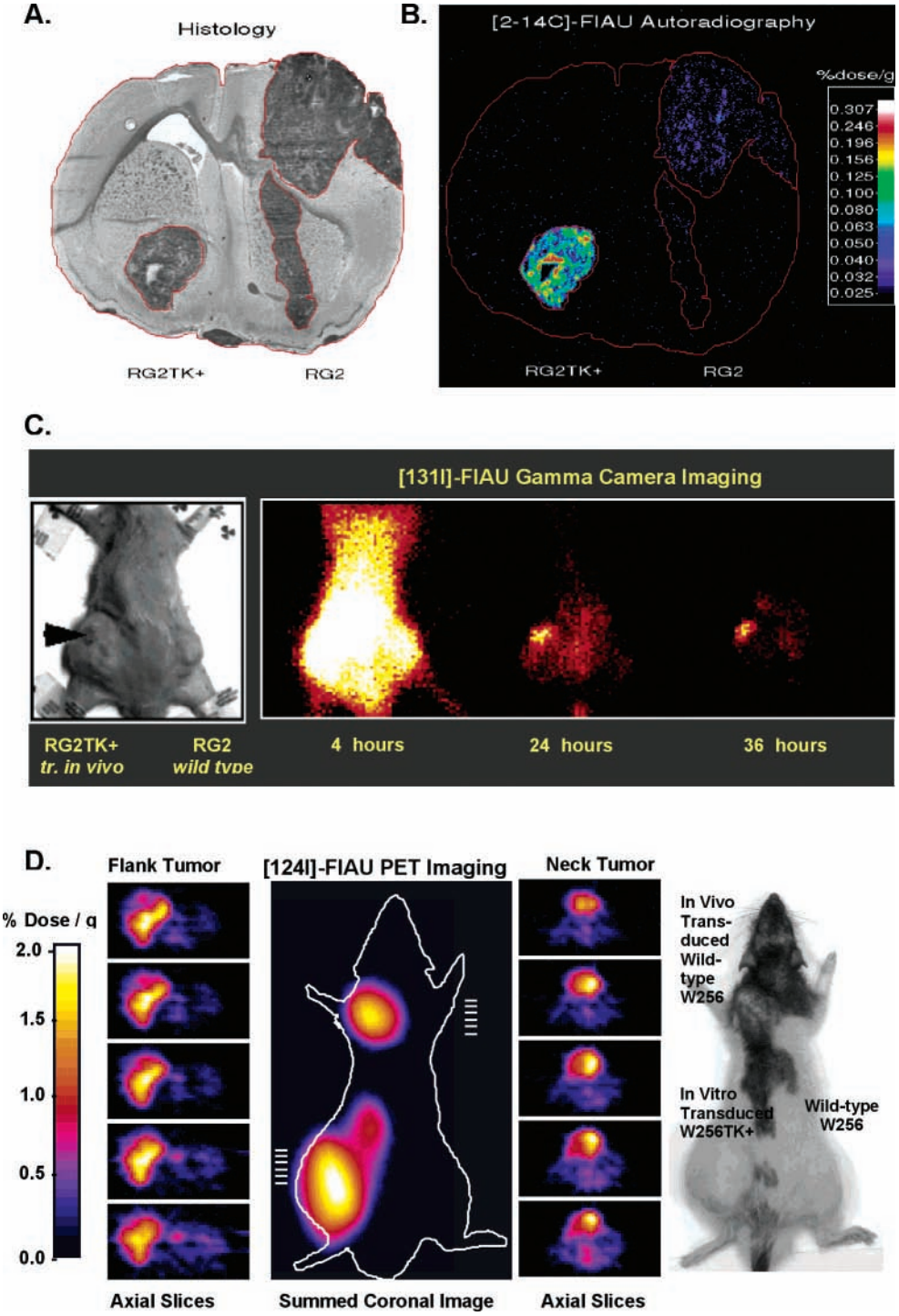


Figure 4. *Autoradiographic imaging HSV1-tk expression*. An animal with a stably transduced RG2TK+ xenograft in the left hemisphere and a wild-type (nontransduced) RG2 xenograft in the right hemisphere was studied. The histology and autoradiographic images were generated from the same tissue section (panels A and B). Both xenografts in the brain of this rat are clearly seen in the toluidine blue stained histological section (panel A). Twenty four hours after iv administration of [^{14}C]FIAU, the RG2TK+ tumor is clearly visualized in the autoradiographic image (panel B), whereas the RG2 tumor is barely detectable; the surrounding brain is at background levels. Figure adapted from ref 30. *Gamma camera imaging HSV1-tk expression* (panel C). Gamma camera imaging was performed at 4, 24, and 36 h after [^{131}I]FIAU injection in an animals bearing bilateral RG2 flank xenografts; the images have been normalized to a reference standard (not shown in the field of view). The site of inoculation of HSV1-*tk* retroviral vector producer cells (gp-STK-A2) into the left flank xenograft is indicated by the arrow. The sequential images demonstrate washout of radioactivity from the body, with specific retention of activity in the area of gp-STK-A2 cell inoculation and transduction of RG2 tumor cells with the HSV1-*tk* reporter (see the 24 and 36 h images). The nontransduced contralateral xenograft (right flank) and other tissues did not show any retention of radioactivity. Figure adapted from ref 36. *PET imaging HSV1-tk expression* (panel D). Three xenografts were produced in rnu Sprague Dawley R-Nu rats. A W256TK+ (positive control) xenograft was produced from stably transduced W256TK+ cells and is located in the left flank, and a wild-type W256 (negative control) xenograft was produced in the dorsum of the neck and in the right flank. The neck tumor (wild-type) was inoculated with 10^6 gp-STK-A2 vector-producer cells (retroviral titer: 10^6-10^7 cfu/mL) to induce HSV1-*tk* transduction of the tumor in vivo. Fourteen days after gp-STK-A2 cell inoculation, no-carrier-added [^{124}I]FIAU (25 μCi) was injected iv and PET imaging (GE Advance) was performed 30 h later. Localization of radioactivity is clearly seen in left flank tumor (positive control) and in the in vivo transduced neck tumor (test), but only low background levels of radioactivity were observed in the right flank tumor (negative control). Figure adapted from ref 37.

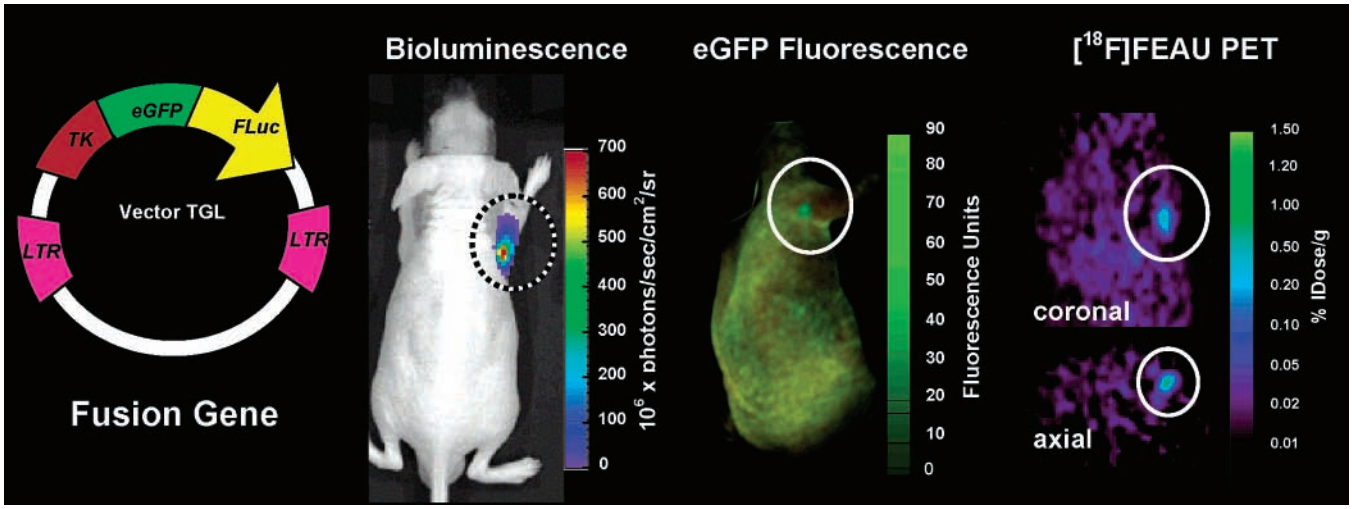


Figure 5. Multimodality triple-reporter system. Schematic structure of a retroviral vector (TGL) for mammalian expression of a triple-fusion reporter gene (HSV1-thymidine kinase, *TK*; enhanced green fluorescent protein, *eGFP*; firefly luciferase, *FLuc*) driven by an LTR promoter (left panel). Noninvasive, multimodality imaging of mice bearing subcutaneous xenografts produced from HSV1-tk/eGFP-cmvFluc transduced U87 cells (right shoulder) and wild-type (nontransduced) U87 cells (left shoulder). The xenografts were 4−5 mm in diameter. Whole-body fluorescence imaging (A), whole-body bioluminescence imaging (B), and axial and coronal microPET images of [^{18}F]FEAU accumulation are shown for the same mouse. Figure adapted from ref 77.

It has recently been shown that coelenterazine is rapidly exported from cell lines that express MDR1, and this could impact on the photon emission flux from the coelenterazine−*Renilla luciferase* reporter system in these cells (*60*). In vivo bioluminescence imaging has been successfully applied to many novel reporter systems and is rapidly expanding in the molecular and cell biology communities.

Fluorescent protein-based reporter gene systems started with different spectral shifted variants of *Aequorea victoria* green fluorescent protein (*GFP*), including an enhanced GFP (*eGFP*) (*61*−*67*). A number of red fluorescent proteins including *Discosoma species* (ds*Red1* and *dsRed2*) (*68*, *69*) and *Heteractis crispa* (HcRed) (*70*) have also been described. Fluorescence imaging has been shown to be very useful for in vitro applications such as (1) tracking the translocation of proteins within cells, (2) identifying and selecting transduced cells using FACS, and (3) cost-effective in vitro assays to validate the function and sensitivity of specific-inducible reporter systems. The development of whole body transcutaneous fluorescent imaging technology provides for (1) imaging reporter gene expression in small living animals (Figures 5 and 6), and (2) localizing transduced cells and/or the expression of inducible reporter systems (e.g., expression of p53, Figure 7) in tissue sections at the microscopic level by in situ fluorescence imaging (*16*, *71*). Limitations of fluorescence reporter imaging include the requirement of an external source of light and the exponentially decreasing intensity of light with increasing depth of the target. However, a new class of red fluorescent proteins and near-infrared dyes are providing better deep tissue imaging characteristics (*68*−*70*) and are a focus of current research development.

Endogenous autofluorescence of tissues frequently results in substantial background emissions that limit the sensitivity and specificity of this imaging technique, and this contributes to an important advantage of bioluminescence over fluorescence reporters. However, the use of selective filters or the application of spectral analysis can significantly reduce the contribution of autofluorescence to the acquired images. Nevertheless, in vivo bioluminescence reporter imaging remains more sensitive than in vivo fluorescence reporter imaging.

Luciferase may be well suited to monitor transcription due to its relatively fast induction (*72*) and to the considerable short biological half-life of luciferin and luciferase (*73*). This is an advantage compared to the longer-lived *eGFP*. However, short-lived (rapidly degradable) variants of *eGFP* have been recently developed, and *eGFP* can be used for higher resolution imaging in cells in vitro. Combining these reporter genes into a single gene could provide additional tools for the analysis of cancer cells in vivo and ex vivo. Such a dual-function reporter gene was created and the single encoded protein was shown to be fluorescent and bioluminescent (*74*).

Multimodality Nuclear and Optical Reporter Imaging. The coupling of a nuclear reporter gene (e.g. *HSV1-tk*) with an optical reporter gene (e.g., *eGFP*) has been reported (*75*). More recently a series of *TKeGFP* mutants were developed with altered nuclear localization and better cellular enzymatic activity to optimize the sensitivity for imaging HSV1-tk/eGFP reporter gene expression (*46*). The *TKeGFP* reporter gene has been introduced into several different reporter systems to assess different molecular-biological pathways (*41*, *42*). A mutant thymidine kinase (HSV1-sr39tk)−Renilla luciferase (RL) fusion reporter construct ($tk_{20}rl$) was recently developed for both nuclear and optical imaging (*76*). This study demonstrated the specificity and sensitivity of bioluminescence imaging and showed a good correlation between the nuclear (microPET) and optical (CCD camera) readouts of the dual reporter system.

More recently, a triple-fusion reporter construct, TKeGFPLuc (TGL), has been developed (*77*, *78*), and representative images are shown in Figure 5 and 6. A single reporter construct (vector) with a gene product that can be assayed by three different imaging technologies (fluorescence, bioluminescence, and nuclear or magnetic resonance) provides the benefits of each modality. It will facilitate the development, validation, and testing of new reporter systems in small animals, as well as provide preliminary data that will facilitate the translation of such studies into humans.

Although optical imaging does not yet provide optimal quantitative or tomographic information, these issues are not limiting for PET-based reporter systems, and PET

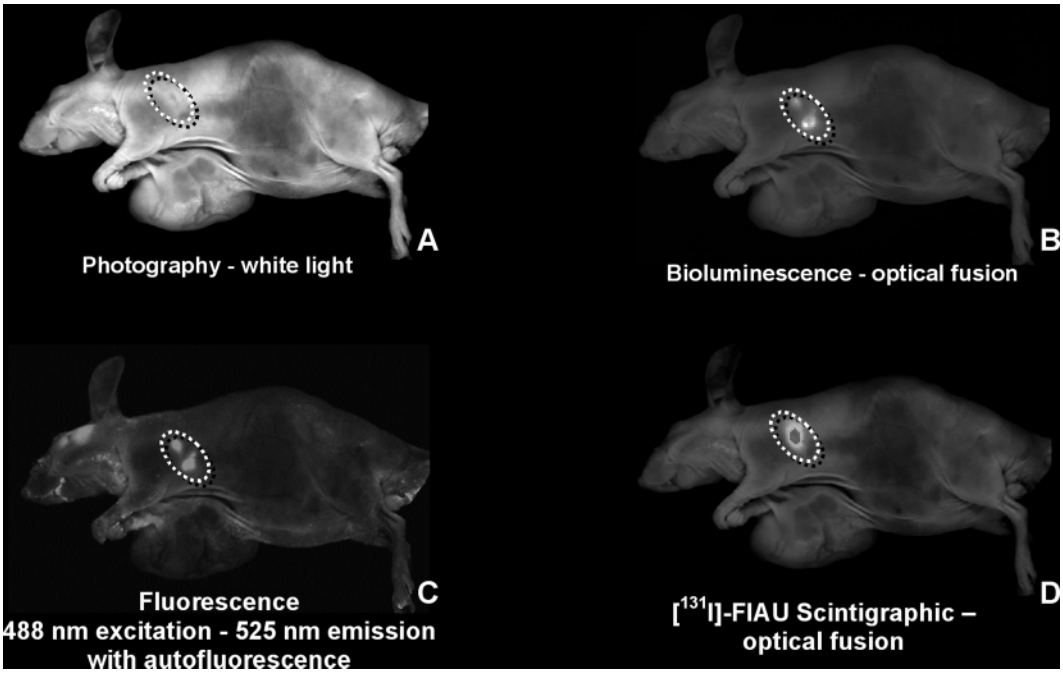


Figure 6. Multimodality imaging system. Multimodality imaging of a mouse bearing two xenografts: a small left shoulder xenograft (dashed oval outline) produced from 2×10^6 U87 cells transduced with the TK-eGFP−FLuc triple-modality reporter, and a large nontransduced U87MG xenograft located in the right shoulder and extending beneath the animal. A white light photograph is initially obtained (A), followed by whole-body fluorescence imaging − without correction for autofluorescence (B), followed by whole-body bioluminescence imaging (C), followed by whole-body scintigraphic imaging of [^{131}I]radioactivity, 24 h after iv [^{131}I]FIAU administration (D). All images were obtained from the same mouse at the same imaging session, and the mouse remained stationary between each imaging session. Note that panels C and D include optical fusion with the white-light photograph shown in panel A. Images were obtained on a Kodak R2000MM multimodal imaging system.

animal studies are more easily generalized to human applications. Using dual or triple modality reporter constructs (PET, fluorescence, and bioluminescence) overcomes many of the shortcomings of each modality alone. Multimodality reporters have been shown to facilitate the development, validation, and testing of new reporter systems in small animals (*41*, *42*), as well as provide preliminary data that will facilitate the translation of such studies into humans.

Imaging Biological Processes. Reporter-gene imaging is being used to address biological issues at the cellular and molecular level, even though our imaging resolution is at macroscopic levels. Within the past 5 years, proof-of-principle experiments in small animals have shown that it is possible to noninvasively image tissue-specific gene expression and the activity of several signal transduction pathways, and many of these studies involved multimodality imaging techniques. In addition, feasibility studies have shown that it is possible to image the endogenous regulation of transcription (*41*, *42*), posttranscriptional modulation of translation (*45*), specific protein−protein interactions (*43*, *44*, *79*), protein degradation and the activity of the proteosomal pathway (*80*), apoptosis (*81*), etc. Also, noninvasive imaging of viral (*82*, *83*), bacterial (*84*), and cell trafficking (*85*) studies have been published. Reporter gene labeling provides the opportunity for repetitive imaging and sequential monitoring of the tumor growth rate and response to treatment (*86*), as well as imaging metastases (*71*).

Imaging Transcriptional Regulation of Endogenous Genes. Noninvasive imaging of transcriptional regulation in living animals (and potentially in human subjects) will provide a clearer understanding of normal and cancer-related biological processes. A recent paper from our group (*42*) was the first to show that p53-dependent gene expression can be imaged in vivo with PET and by in situ fluorescence using a retroviral vector containing a *Cis*-p53/*TKeGFP* dual-reporter gene under control of a p53-specific response element (Figure 7). DNA damage-induced upregulation of p53 transcriptional activity was demonstrated and correlated with the expression of p53-dependent downstream genes (including p21). These findings were observed in U87 (p53 +/+) cells and xenografts, but not in SaOS (p53 −/−) cells. This was the first demonstration that a *Cis*-activated dual reporter system (*Cis*-p53/TKGFP) was sufficiently sensitive to image endogenous gene expression using noninvasive nuclear (PET) imaging. The PET images corresponded with up-regulation of genes in the p53 signal transduction pathway in response to DNA damage induced by BCNU chemotherapy. PET imaging of p53 transcriptional activity in tumors using the *Cis*-p53TKGFP reporter system could be used to assess the effects of new drugs or other novel therapeutic paradigms that are mediated through p53-dependent pathways. For example, specific p53 gene therapy strategies that are based on p53 overexpression could be monitored by noninvasive imaging.

The dual reporter construct (*TKeGFP*−fusion gene) provides the opportunity for multimodality (both nuclear and optical imaging) imaging of endogenous p53-dependent gene expression, in vivo. The *TKeGFP* reporter gene could be introduced into other reporter assay systems to assess other molecular-biological pathways. It should also be possible to use the *TKeGFP* reporter gene in transgenic animals; this will facilitate the monitoring and assessment of newly cloned genes or novel signal transduction pathways. Another advantage of the dual reporter system is the ability to compare the images of reporter gene expression obtained with PET, gamma camera, or autoradiography with corresponding in situ GFP fluorescence images. The comparison between GFP

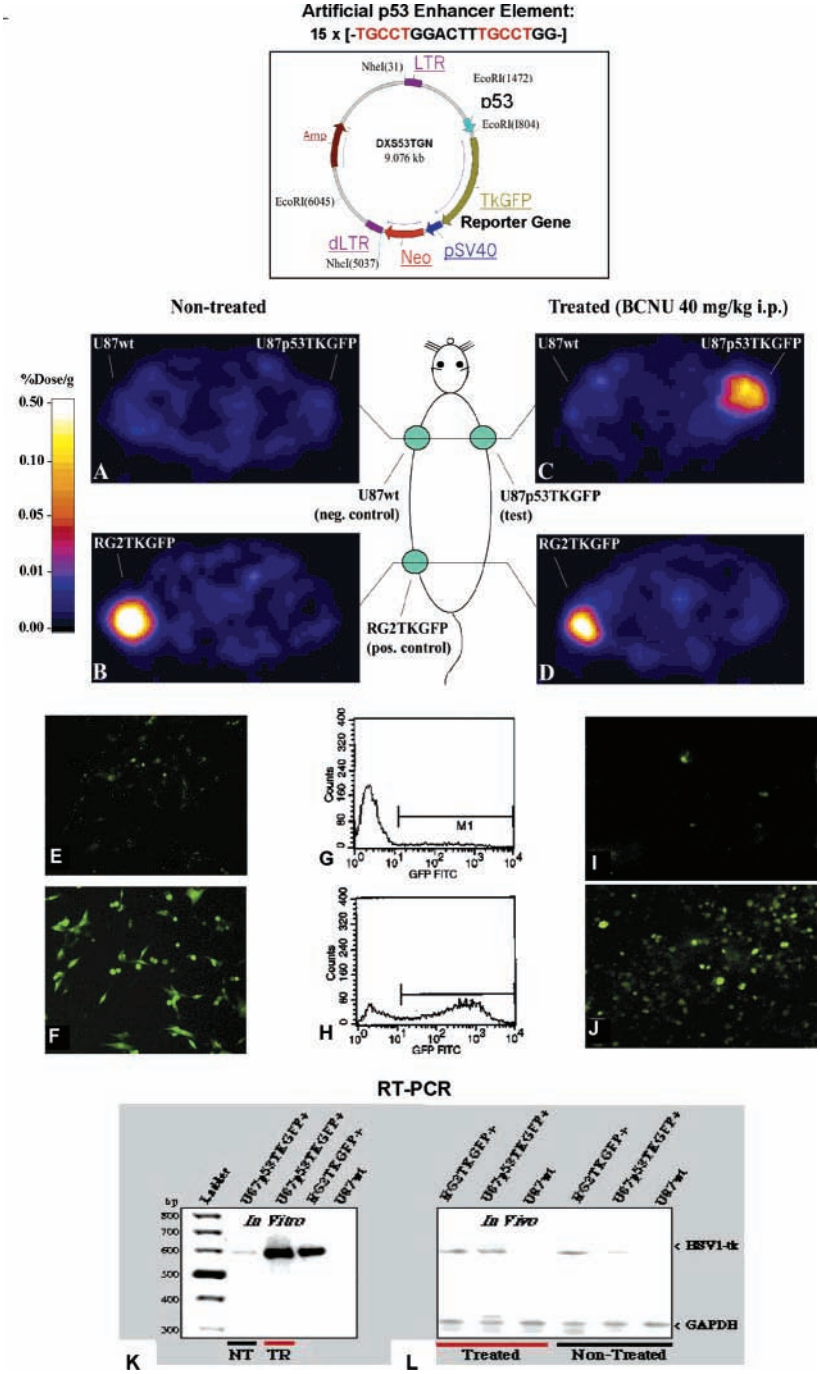


Figure 7. The p53-sensitive, dual-modality reporter vector (top panel) contains an artificial p53 specific enhancer element that activates expression of the *TKeGFP* reporter gene. A constitutively expressed neomycin selection gene is also included in the retroviral vector construct. Transaxial PET images (GE Advance tomograph) through the shoulder (A, C) and pelvis (B, D) of two rats are shown (second panel); the images are color-coded to the same radioactivity scale (%dose/g). An untreated animal is shown on the left (A, B), and a BCNU-treated animal, which is known to activate the p53 pathway, is shown on the right (C, D). Both animals have three sc xenografts: a U87p53TKGFP (test) in the right shoulder, a U87 wild-type (negative control) in the left shoulder, and a RG2TKGFP (positive control) in the left thigh. The nontreated animal on the left shows localization of radioactivity only in the positive control tumor (RG2TKGFP); the test (U87p53TKGFP) and negative control (U87wt) xenografts are at background levels. The BCNU-treated animal on the right shows significant radioactivity localization in the test tumor (right shoulder) and in the positive control (left thigh), but no radioactivity above background in the negative control (left shoulder). Fluorescence microscopy and FACS analysis (third panel) of a transduced U87p53/TKGFP cell population in the noninduced (control) state (E, G), and 24 h after a 2 h treatment with BCNU 40 mg/mL (F, H) are shown. Fluorescence microscopic images of post-motem U87p53/TKGFP sc tumor samples obtained from nontreated rats (I) and rats treated with 40 mg/kg BCNU ip (J) are also shown. These results (F−J) demonstrate a corresponding activation of the reporter system (increased fluorescence) due to p53 induction by BCNU treatment. RT-PCR blots from in vitro (K) and in vivo (L) experiments (lower panel) show very low HSV1-*tk* expression in nontreated U87p53TKGFP transduced cells and xenografts-bearing animals, respectively, and no HSV1-*tk* expression in wild-type U87 cells and tumor tissue, respectively. When U87p53TKGFP transduced cells and xenografts-bearing animals are treated with BCNU, there is a marked increase in HSV1-*tk* expression comparable to that in constitutively HSV1-*tk* expressing RG2TK+ cells and xenografts. Figure adapted from ref 42.

fluorescence and autoradiographic images, coupled with histology of corresponding tissue sections provides for spatial and quantitative assessments of reporter gene expression at the microscopic as well as macroscopic level.

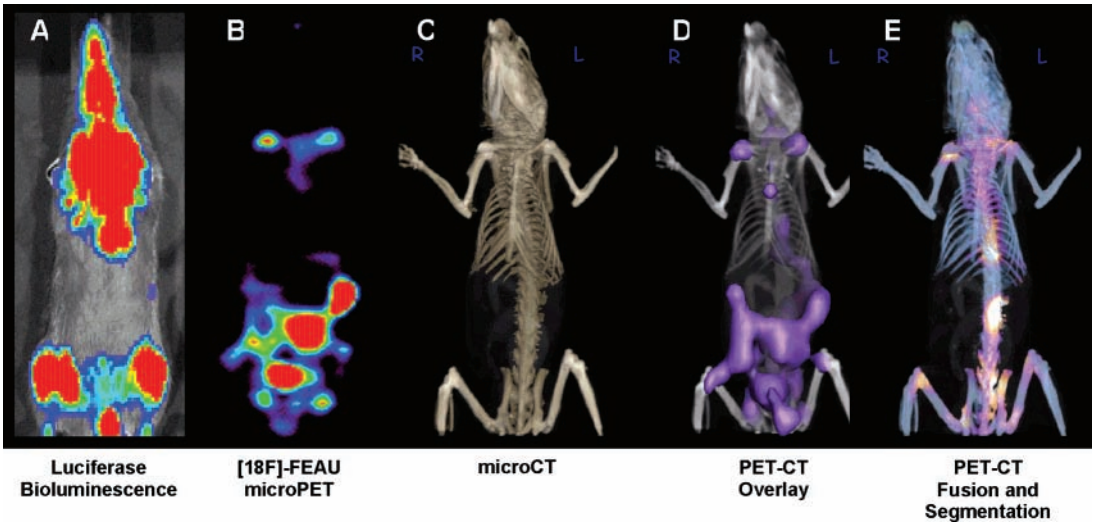


Figure 8. Multimodality imaging of autologous bone marrow-derived cells targeting bone. Multimodality imaging: bioluminescence (A); microPET (B); microCT (C); microPET-CT overlay (D); microPET-CT registration, segmentation, and fusion (E). Bone marrow-derived cells were transduced with a constitutively expressing triple-modality reporter (Figure 5) The images show targeting of bone 6 days after iv administration. Note that the tomographic display (E) confirms the targeting of transduced cells to bone; a future objective is to perform microPET-MR acquisitions and a similar tomographic microPET-MR registration and fusion to identify soft tissue structures that are targeted or are involved in trafficking of transduced reporter cells. It is also expected that some time in the near-future that tomographic bioluminescence and fluorescence images can be obtained, and that these images will be registered with currently available CT, MR, and PET tomographic images. The image fusion and segmentation was performed by Dr. Luc Bidault, MSKCC.

Imaging the Trafficking of T-Lymphocytes. T cells are an important component of the immune response and participate in the elimination of abnormal cells and infectious agents. Imaging the trafficking of T-lymphocytes has been performed using optical, MR, and PET-based imaging studies. Passive (ex vivo) labeling of T-cells with radioactive isotopes can be unstable and does not account for proliferation of activated T-cells in the body. An objective of ongoing studies in our laboratory is to image the in vivo targeting and the accumulation of EBV-lymphoma specific cytotoxic T-cells in allogeneic HLA-matched EBV B-lymphomas using PET and optical imaging modalities. Cytotoxic T-cells (CTL) specific for autologous EBV-transformed B-lymphocytes were obtained and stably transduced with a constitutively expressing dual reporter gene (*HSV1tk/egfp* fusion gene). Specific accumulation and localization of radioactivity was observed only in the autologous EBV(+) lymphoma, in the allogeneic HLA-matched EBV(+) lymphoma, and in the spleen; no localization was seen in the allogeneic HLA-matched non-EBV lymphoma and the HLA-mismatched EBV(+) lymphoma (*85*). Sequential imaging over 72 h in another set of animals showed trafficking as well as targeting of the transduced and radiolabeled CTLs. These preliminary studies indicate that it may be feasible to isolate and transduce CTLs (and other immune-specific cells) with reporter constructs and then monitor their targeting and proliferation in the donor or HLA-matched recipient using noninvasive reporter gene PET imaging.

Imaging the Trafficking of Bone Marrow-Derived Cells. Multimodality optical-, MR- and PET-based imaging studies can be performed. The use of PET for monitoring bone marrow and progenitor (stem) cell transplantation has lagged behind optical and MR techniques (*87*, *88*). In most cases, PET imaging has been applied to monitoring bone marrow transplantation (BMT), to assess for residual disease (*89*), or BMT conditioning regime-related toxicities (*90*). Monitoring the fate of bone marrow stem cells with PET following direct labeling with [^{18}F]fluorobenzoate and transplantation was first reported by Olasz et al. (*91*). Direct labeling of bone marrow-derived cells is limited by the half-life and quantity of isotope used in the labeling. Reporter gene technology precludes this limitation and allows for extended monitoring of stem cell engraftment. Recently, Cao et al. reported luciferase bioluminescence imaging of hematopoietic stem cells following transplantation into irradiated recipient mice (*92*). Donor stem cells were derived either from a luciferase or luciferase/GFP transgenic mouse and purified through cell sorting. After systemic administration, repeated optical imaging was used to detect the sites and kinetics of hematopoietic stem cell engraftment. The data suggests that the stem cells initially home to the bone marrow or spleen, while little specificity for a particular bone marrow compartment exists. Interestingly, different subsets of progenitor cells, such as short or long term repopulating cells, showed comparable homing profiles but differences in their proliferative potential. The potential of bioluminescence imaging to monitor engraftment of hematopoietic progenitor cells was previously shown in a mouse model of xenotransplantation of human hematopoietic stem cell populations (*93*). We have applied reporter gene technology to image the trafficking and distribution of bone marrow cells using a multiple-modality reporter gene approach (*94*). Coregistration of microPET and microCT images facilitated interpretation of the PET signal and allowed localization radioactive foci to specific anatomical structures (Figure 8). Others have studied effects of the bone marrow transplanted cells on the reconstruction of the ischemic myocardium (*95*, *96*).

COMMENTS

Multimodality imaging is increasingly being used in molecular-genetic studies in small animals. Fluorescence and bioluminescence imaging provides an efficient, rapid and low cost imaging alternative to more expensive and time-consuming microPET and MR imaging modalities. Optical reporter genes, including luciferase and eGFP, have unique properties that make each useful for particular experimental applications as described above.

Combining these reporter genes into a single fusion or bicistronic gene provides additional advantages. Nevertheless, optical imaging techniques are limited by depth of light penetration and scatter of emitted light photons, and optical imaging does not yet provide optimal quantitative or tomographic information. These issues are not limiting for PET- or MR-based reporter systems. In addition, PET and MR animal studies are more easily generalized to human applications. The use of dual-modality reporters has proven very successful in our laboratory, and this utility has been expanded by the development of a triple reporter system. Advantages of each separate imaging modality include the following: (1) fluorescence reporters provide for shorter development and validation times of new reporter systems by rapid and cost-effective real-time readout of cell-based in vitro assays and by in situ imaging of transduced cells in tissue samples; (2) bioluminescence reporters also provide for rapid, cost-effective real-time reporter imaging in small animals that is particularly useful for generating sequential time-dependent image profiles; (3) nuclear (and magnetic resonance) reporters provide the opportunity to obtain tomographic as well as quantitative measures of reporter gene expression. Since PET and MR are now well developed for imaging in human subjects as well as small animals, they provide a translational link from animal to human studies.

Thus, a single reporter construct (vector) with a gene product that can be assayed by three different imaging technologies (fluorescence, bioluminescence, and nuclear or magnetic resonance) would provide the benefits of each modality. It will facilitate the development, validation, and testing of new reporter systems in small animals, as well as provide preliminary data that will facilitate the translation of such studies into humans. In this respect, the triple modality reporter will be substantially greater than the sum of its individual parts.

ACKNOWLEDGMENT

A special acknowledgment is given to our friend and colleague, Juri Gelovani-Tjuvajev, who joined our group in 1991. He has recently accepted a well-deserved appointment as Chairman, Department of Experimental Diagnostic Imaging at M.D. Anderson Cancer Center in Houston. He was a leading investigator in our group and initiated many of the projects in our laboratory, including the development of noninvasive multimodality reporter transgene imaging.

LITERATURE CITED

(1) Jacobs, R. E., and Cherry, S. R. (2001) Complementary emerging techniques: high-resolution PET and MRI. *Curr. Opin. Neurobiol. 5*, 621−9.

(2) Weissleder, R. (2002) Scaling down imaging: molecular mapping of cancer in mice. *Nat. Rev. Cancer 1*, 11−8.

(3) Cherry, S. R. (2004) In vivo molecular and genomic imaging: new challenges for imaging physics. *Phys. Med. Biol. 3*, R13−48.

(4) Jones, T. The imaging science of positron emission tomography. (1996) *Eur. J. Nucl. Med. 7*, 807−13.

(5) Phelps, M. E. (2000) PET: the merging of biology and imaging into molecular imaging. *J. Nucl. Med. 4*, 661−81.

(6) Blasberg, R., and Tjuvajev, J. (1997) In Vivo Monitoring of Gene Therapy by Radiotracer Imaging, in *Ernst Shering Research Foundation Workshop 22: Impact of Molecular Biology and New Technical Developments on Diagnostic Imaging*, pp 161−189, Berlin-Heidelberg, Springer-Verlag,

(7) Gambhir, S. S., Herschman, H. R., Cherry, S. R., Barrio, J. R., Satyamurthy, N., Toyokuni, T., Phelps, M. E., Larson. S. M., Balatoni, J., Finn, R., Sadelain, M., Tjuvajev, J., and Blasberg, R. (2000) Imaging transgene expression with radionuclide imaging technologies. *Neoplasia 2*, 118−138.

(8) Tavitian, B. In vivo antisense imaging. (2000) *Q. J. Nucl. Med. 3*, 236−55.

(9) Ray. P, Bauer, E., Iyer, M., Barrio, J. R., Satyamurthy, N., Phelps, M. E., Herschman, H. R., and Gambhir, S. S. (2001) Monitoring gene therapy with reporter gene imaging. *Semin. Nucl. Med. 4*, 312−20.

(10) Blasberg, R. G., and Gelovani, J. (2002) Molecular-genetic imaging: a nuclear medicine-based perspective. *Mol Imaging 3*, 280−300.

(11) Luker, G. D., Sharma, V., and Piwnica-Worms, D. (2003) Visualizing protein−protein interactions in living animals. *Methods 1*, 110−22.

(12) Weissleder, R., and Ntziachristos, V. (2003) Shedding light onto live molecular targets. *Nat. Med. 1*, 123−8.

(13) Gelovani Tjuvajev, J., and Blasberg, R. G. (2003) In vivo imaging of molecular-genetic targets for cancer therapy. *Cancer Cell 4*, 327−32.

(14) Berger, F., and Gambhir, S. S. (2001) Recent advances in imaging endogenous or transferred gene expression utilizing radionuclide technologies in living subjects: applications to breast cancer. *Breast Cancer Res.* 1, 28−35.

(15) Contag, C. H., and Ross, B. D. (2002) It's not just about anatomy: in vivo bioluminescence imaging as an eyepiece into biology *J. Magn. Reson. Imaging 16*, 378−87.

(16) Gambhir, S. S. (2002) Molecular imaging of cancer with positron emission tomography. *Nat Rev Cancer 2*, 683−93.

(17) Blasberg, R. G., and Tjuvajev, J. G. (2003) Molecular-genetic imaging: current and future perspectives. *J. Clin. Invest. 11*, 1620−9.

(18) Weissleder, R., and Ntziachristos, V. (2003). Shedding light onto live molecular targets. *Nat. Med. 9*, 123−8.

(19) Min, J. J., and Gambhir, S. S. (2004) Gene therapy progress and prospects: noninvasive imaging of gene therapy in living subjects. *Gene Ther. 2*, 115−25.

(20) Shah, K., Jacobs, A., Breakefield, X. O., and Weissleder, R. (2004) Molecular imaging of gene therapy for cancer. *Gene Ther. 11* (15), 1175−1187.

(21) Jaffer, F. A., Tung, C. H., Gerszten, R. E., and Weissleder, R. (2002) In vivo imaging of thrombin activity in experimental thrombi with thrombin-sensitive near-infrared molecular probe. *Arterioscler Thromb Vasc. Biol. 22*, 1929−35.

(22) Haubner, R., Wester, H. J., Weber, W. A., Mang, C., Ziegler, S. I., Goodman, S. L., Senekowitsch-Schmidtke, R., Kessler, H., and Schwaiger, M. (2001) Noninvasive imaging of alpha(v)beta3 integrin expression using 18F-labeled RGD-containing glycopeptide and positron emission tomography. *Cancer Res. 61,* 1781−5.

(23) Demetri, G. D., von Mehren, M., Blanke, C D., Van den Abbeele, A. D., Eisenberg, B., Roberts, P. J., Heinrich, M. C., Tuveson, D. A., Singer, S., Janicek, M., Fletcher, J. A., Silverman, S. G., Silberman, S. L., Capdeville, R., Kiese, B., Peng, B., Dimitrijevic, S., Druker, B. J., Corless, C., Fletcher, C. D. M., and Joensuu, H. (2002) Efficacy and Safety of Imatinib Mesylate in Advanced Gastrointestinal Stromal Tumors. *N. Engl. J. Med. 347*, 472−480.

(24) Van den Abbeele A. D., (2001) The GIST Collaborative PET Study Group(Dana-Farber Cancer Institute, Boston, Massachusetts; OHSU, Portland, Oregon, Helsinki University Central Hospital, Turku University Central Hospital, Finland, Novartis Oncology). F18−FDG-PET provides early evidence of biological response to STI571 in patients with malignant gastrointestinal stromal tumors (GIST). *Proc. Am. Soc. Clin. Oncol. 20*: 362a.

(25) Bogdanov, A., and Weissleder, R. (1998) The development of in vivo imaging systems to study gene expression. *Trends Biotechnol. 16*, 5−10.

(26) Weissleder, R., and Mahmood, U. (2001) Molecular imaging. *Radiology 219*, 316−333.

(27) Rudin, M., and Weissleder, R. (2003) Molecular imaging in drug discovery and development. *Nat. Rev. Drug Discovery 2*, 123−131.

(28) Stegman, L. D., Rehemtulla, A., Beattie, B., Kievit, E., Lawrence, T. S., Blasberg, R. G., Tjuvajev, J. G., and Ross, B. D. (1999) Noninvasive quantitation of cytosine deaminase

transgene expression in human tumor xenografts with in vivo magnetic resonance spectroscopy. *Proc. Natl. Acad. Sci. U. S. A. 96*, 9821−9826.

(29) Hackman, T., Doubrovin, M., Balatoni, B., Beresten, T., Ponomarev, V., Beattie, B., Finn, R., Bornmann, W., Blasberg, R., and Tjuvajev, J. G. (2002) Imaging expression of cytosine deaminase-herpes virus thymidine kinase fusion gene (CD/TK) expression with [124I]FIAU and PE. *Mol. Imaging 1*, 36−42.

(30) Tjuvajev, J. G., Stockhammer, G., Desai, R., Uehara, H., Watanabe, H., Gansbacher, B., and Blasberg, R. G. (1995) Imaging the expression of transfected genes in vivo. *Cancer Res. 55*, 6126−6132.

(31) Contag, C. H., Spilman, S. D., Contag, P. R., Oshiro, M., Eames, B., Dennery, P., Stevenson D. K., and Benaron, D. A. (1997) Visualizing gene expression in living mammals using a bioluminescent reporter. *Photochem. Photobiol. 4*, 523−31.

(32) Liang, Q., Satyamurthy, N., Barrio, J. R., Toyokuni, T., Phelps, M. P., Gambhir, S. S., and Herschman, H. R. (2001) Noninvasive, quantitative imaging in living animals of a mutant dopamine D2 receptor reporter gene in which ligand binding is uncoupled from signal transduction. *Gene Ther. 8*, 1490−1498.

(33) Rogers, B. E., Zinn K. R., and Buchsbaum, D. J. (2000)-Gene transfer strategies for improving radiolabeled peptide imaging and therapy. *Q J. Nucl. Med. 3*, 208−223.

(34) Haberkorn, U. (2001) Gene therapy with sodium/iodide symporter in hepatocarcinoma. *Exp. Clin Endocrinol. 1*, 60−62.

(35) Chishima, T., Miyagi, Y., Wang, X., Yamaoka, H., Shimada, H., Moossa, A. R., and Hoffman, R. M. (1997) Cancer invasion and micrometastasis visualized in live tissue by green fluorescent protein expression. *Cancer Res. 10*, 2042−7.

(36) Tjuvajev, J. G., Finn, R., Watanabe, K., Joshi, R., Oku, T., Kennedy, J., Beattie, B., Koutcher, J., Larson, S., and Blasberg, R. G. (1996) Noninvasive imaging of herpes virus thymidine kinase gene transfer and expression: A potential method for monitoring clinical gene therapy. *Cancer Res. 56*, 4087−4095.

(37) Tjuvajev, J. G., Avril, N., Oku, T., Sasajima, T., Miyagawa, T., Joshi, R., Safer, M., Beattie, B., DiResta, G., Daghighian, F., Augensen, F., Koutcher, J., Zweit, J., Humm, J., Larson, S. M., Finn, R., and Blasberg, R. (1998) Imaging herpes virus thymidine kinase gene transfer and expression by positron emission tomography. *Cancer Res. 58*, 4333−4341.

(38) Zhang, L., Adams, J. Y., Billick, E., Ilagan, R., Iyer, M., Le, K., Smallwood, A., Gambhir, S. S., Carey, M., and Wu, L. (2002) Molecular Engineering of a Two-Step Transcription Amplification (TSTA) System for Transgene Delivery in Prostate Cancer. *Mol. Ther. 3*, 223−32.

(39) Green, L. A., Nguyen, K., Bauer, E., Barrio, J. R., Namavari, M., Satyamurthy, N., Tokokuni, T., Phelps, M. E., Sandgren, E. P., Herchmann, H. R., and Gambhir, S. S. (2000) Indirect Monitoring of Endogenous Gene Expression by Imaging PET Reporter Gene Expression in Transgenic Mice. *J. Nucl. Med. 5*, 81S.

(40) Qiao, J., Doubrovin, M., Sauter, M. V., Huang, Y., Guo, Z. S., Balatoni, J., Akhurst, T., Blasberg, R, Gelovani-Tjuvajev, J., Chen S. H., and Woo, S. L. C. (2002) Tumor-Specific Transcriptional Targeting of Suicide Gene Therapy. *Gene Ther. 9*, 168−175.

(41) Ponomarev, V., Doubrovin, M., Lyddane, C., Beresten, T., Balatoni, J., Bornmann, W., Finn, R., Akhurst, T., Larson, S., Blasberg, R., Sadelian, M., and Tjuvajev, J. G. (2001) Imaging TCR-Dependent NFAT-Mediated T-Cell Activation with Positron Emission Tomography In Vivo. *Neoplasia 3*, 480−488.

(42) Doubrovin, M., Ponomarev, V., Beresten, T., Balatoni, J., Bornmann, W., Finn, R., Humm, J., Larson, S., Sadelain, M., Blasberg, R., and Gelovani Tjuvajev, J. (2001) Imaging transcriptional regulation of p53-dependent genes with positron emission tomography in vivo. *Proc. Natl. Acad. Sci. U. S. A. 16*, 9300−9305.

(43) Ray, P., Pimenta, H., Paulmurugan, R., Berger, F., Phelps, M. E., Iyer, M., and Gambhir, S. S. (2002) Noninvasive quantitative imaging of protein−protein interactions in living subjects. *Proc. Natl. Acad. Sci. U. S. A. 5*, 3105−3110.

(44) Luker, G. D., Sharma, V., Pica, C. M., Dahlheimer, J. L., Li, W., Ochesky, J., Ryan, C. E., Piwnica-Worms, H., and Piwnica-Worms, D. (2002) Noninvasive imaging of protein−protein interactions in living animals. *Proc. Natl. Acad. Sci. U. S. A. 10*, 6961−6.

(45) Mayer Kuckuk, P., Banerjee, D., Malhotra, S., Doubrovin, M., Iwamoto, M., Akhurst, T., Balatoni, J., Bornmann, W., Finn, R., Larson, S., Fong, Y., Gelovani Tjuvajev, J., Blasberg, R., and Bertino, J. R. (2002) Cells exposed to antifolates show increased cellular levels of proteins fused to dihydrofolate reductase: a method to modulate gene expression. *Proc. Natl. Acad. Sci. U. S. A. 6*, 3400−3405.

(46) Ponomarev, V., Doubrovin, M., Serganova, I., Beresten, T., Vider, J., Sharvin, A., Ageyeva, L., Balatoni, J., Blasberg, R., and Tjuvajev, J. G. (2003) Cytoplasmically retargeted HSV1-tk/GFP reporter gene mutants for optimization of noninvasive molecular-genetic imaging. *Neoplasia 3*, 245−54.

(47) Pelletier, S. (1988) Internal initiation of translation of eukaryotic mRNA directed by a sequence derived from poliovirus RNA. *Nature 334*, 320−5.

(48) Sachs, A. B., Sarnow, P., and Hentze, M. W. (1997) Starting at the Beginning, Middle, and End: Translation Initiation in Eukaryotes. *Cell 89*, 831−838.

(49) Yaghoubi, S. S., Wu, L., Liang, Q., Toyokuni, T., Barrio, J. R., Namavari, M., Satyamurthy, N., Phelps, M. E., Herschman, H. R., and Gambhir, S. S. (2001) Direct correlation between positron emission tomographic images of two reporter genes delivered by two distinct adenoviral vectors. *Gene Ther. 14*, 1072−80.

(50) Gambhir, S. S., Bauer, E., Black, M. E., Liang, Q., Kokoris, M. S., Barrio, J. R., Iyer, M., Namavari, M., Phelps, M. E., and Herschman, H. R. (2000) A mutant herpes simplex virus type 1 thymidine kinase reporter gene shows improved sensitivity for imaging reporter gene expression with positron emission tomography. *Proc. Natl. Acad. Sci. U. S. A. 97*, 2785−2790.

(51) Wang, J., Su, C., Neuhard, J., and Eriksson, S. (2000) "Expression of human mitochondrial thymidine kinase in *Escherichia coli*: correlation between the enzymatic activity of pyrimidine nucleoside analogues and their inhibitory effect on bacterial growth. *Biochem Pharmacol. 53*, 1583−1588.

(52) Tjuvajev, J. G., Doubrovin, M., Akhurst, T., Cai, S., Balatoni, J., Alauddin, M. M., Finn, R., Bornmann, W., Thaler, H., Conti, P. S., and Blasberg, R. G. (2002) Comparison of radiolabeled nucleoside probes (FIAU, FHBG, and FHPG) for PET imaging of HSV1-tk gene expression. *J. Nucl. Med. 43*, 1072−1083.

(53) Min, J. J., Iyer, M., and Gambhir, S. S. (2003) Comparison of [18F] FHBG and [14C] FIAU for imaging of HSV1-tk reporter gene expression: adenoviral infection vs stable transfection. *Eur. J. Nucl. Med. Mol. Imaging 30*, 1547−1560.

(54) Jacobs, J., Voges, R., Reszka, M., Lercher, A., Gossmann, L., Kracht, C., Kaestle, R., Wagner, K., Wienhard, and Heiss, W. D. (2001) Positron-emission tomography of vector-mediated gene expression in gene therapy for gliomas. *Lancet 358*, 727−729.

(55) Yaghoubi, S., Barrio, J. R., Dahlbom, M. Iyer, M., Namavari, M., Satyamurthy, N., Goldman R., Herschman H. R., Phelps, M. E., and Gambhir. S. S. (2001) Human pharmacokinetic and dosimetry studies of [^{18}F]FHBG: a reporter probe for imaging herpes simplex virus type-1 thymidine kinase reporter gene expression. *J. Nucl. Med. 42*, 1225−1234.

(56) Yu, Y. A., Timiryasova, T. Zhang, Q., Beltz, R., and Szalay, A. A. (2003) Optical imaging: bacteria, viruses, and mammalian cells encoding light-emitting proteins reveal the locations of primary tumors and metastases in animals. *Anal. Bioanal. Chem. 377*, 964−972.

(57) Wilson, T., and Hastings, J. W. (1998) Bioluminescence. *Annu. Rev. Cell. Dev. Biol. 14*, 197−230.

(58) Wu, J. C., Inubushi, M., Sundaresan, G., Schelbert, H. R., and Gambhir, S. S. (2002) Optical imaging of cardiac reporter gene expression in living rats. *Circulation 105*, 1631−1634.
(59) Bhaumik, S., and Gambhir, S. (2002) Optical imaging of renilla luciferase reporter gene expression in living mice. *Proc. Natl. Acad. Sci. U.S.A. 99*, 377−382.
(60) Pichler, A., Prior, J. L., and Piwnica-Worms, D. (2004) Imaging reversal of multidrug resistance in living mice with bioluminescence: MDR1 P-glycoprotein transports coelenterazine. *Proc. Natl. Acad. Sci. U. S. A. 6*, 1702−7.
(61) Levy, J. P., Muldoon, R. R., Zolotukhin, S., and Link, C. J., Jr. (1996) Retroviral transfer and expression of a humanized, red-shifted green fluorescent protein gene into human tumor cells. *Nat. Biotechnol. 14*, 610−614.
(62) Lalwani, A. K., Han, J. J., Walsh, B. J., Zolotukhin, S., Muzyczka, N., and Mhatre, A. N. (1997) Green fluorescent protein as a reporter for gene transfer studies in the cochlea. *Hear. Res. 114*, 139−147.
(63) Ellenberg, J., Lippincott Schwartz, J., and Presley, J. F. (1999) Dual-colour imaging with GFP variants. *Trends Cell Biol. 9*, 52−56.
(64) Matz, M., Matz, M. V., Fradkov, A. F., Labas, Y. A., Savitsky, A. P., Zaraisky, A. G., Markelov, M. L., and Lukyanov SA. (1999) Fluorescent proteins from nonbioluminescent Anthozoa species. *Nat. Biotechnol. 17*, 969−973; Erratum in: *Nat. Biotechnol. 17*, 1227.
(65) Falk, M. M., and Lauf, U. (2001) High resolution, fluorescence deconvolution microscopy and tagging with the autofluorescent tracers CFP, GFP, and YFP to study the structural composition of gap junctions in living cells. *Microsc. Res. Technol. 52*, 251−262.
(66) Hadjantonakis, A. K., and Nagy, A. (2001) The color of mice: in the light of GFP-variant reporters. *Histochem Cell Biol. 115*, 49−58.
(67) Labas, Y. A., Gurskaya, N. G., Yanushevich, Y. G., Fradkov, A. F., Lukyanov, K. A., Lukyanov, S. A., and Matz, M. V. (2002) Diversity and evolution of the green fluorescent protein family. *Proc. Natl. Acad. Sci. U. S. A. 99*, 4256−4261.
(68) Campbell, R. E., Tour, O., Palmer, A. E., Steinbach, P. A., Baird, G. S., Zacharias, D. A., and Tsien, R. Y. (2002) A monomeric red fluorescent protein. *Proc. Natl. Acad. Sci. U.S.A. 99*, 7877−7882.
(69) S. Mathieu, S., and El-Battari, A. (2003) "Monitoring E-selectin-mediated adhesion using green and red fluorescent proteins. *J. Immunol Methods 272*, 81−92.
(70) Gurskaya, N. G., Fradkov, A. F., Terskikh, A., Matz, M. V., Labas, Y. A., Martynov, V. I., Yanushevich, Y. G., Lukyanov, K. A., and Lukyanov, S. A. (2001) GFP-like chromoproteins as a source of far-red fluorescent proteins. *FEBS Lett. 507*, 16−20.
(71) Yang, M., Baranov, E., Jiang, P., Sun, F., Li, X. M., Li, L. N., Hasegawa, S., Bouvet, M., Al Tuwaijri, M., Chishima, T., Shimada, H., Moossa, A. R., Penman, S., and Hoffman, R. M. (2000) Whole-body optical imaging of green fluorescent protein expressing tumors and metastases. *PNAS 97*, 1206−1211.
(72) Kolb, V. A., Makeyev, E. V., and Spirin, A. S. (2000) Co-translational folding of an eukaryotic multidomain protein in a prokaryotic translation system. *J. Biol. Chem. 275*, 16597−601.
(73) Thompson, J. F., Hayes, L. S., and Lloyd, D. B. (1991) Modulation of firefly luciferase stability and impact on studies of gene regulation. *Gene 103*, 171−177.
(74) Day, R. N., Kawecki, M., and Berry, D. (1998) Dual function reporter protein for analysis of gene expression in living cells. *Biotechnology 25*, 852−854.
(75) Jacobs, A., Doubrovin, M., Hewett, J., Sena-Esteves, M., Tan, C. W., Slack, M., Sadelain, M., Breakefield, X. O., and Tjuvajev, J. G. (1999) Functional coexpression of HSV-1 thymidine kinase and green fluorescent protein: implications for noninvasive imaging of transgene expression. *Neoplasia 1*, 154−161.
(76) Ray, P., Wu, A. M., and Gambhir, S. S.(2003) Optical bioluminescence and positron emission tomography imaging of a novel fusion reporter gene in tumor xenografts of living mice. *Cancer Res. 63*, 1160−1165.
(77) Ponomarev, V., Doubrovin, M., Serganova, I., Vider, J., Shavrin, A., Beresten, T., Ivanova, A., Ageyeva, L., Tourkova, V., Balatoni, J., Bornmann, W., Blasberg, R., and Gelovani Tjuvajev, J**.** (2004) A Novel Triple Modality Reporter Gene for Whole Body Fluorescent, Bioluminescent and Nuclear Noninvasive Imaging. *Eur. J. Nucl. Med. 5*, 740−51.
(78) Ray, P., De, A., Min, J. J., Tsien, R. Y., and Gambhir, S. S. (2004) Imaging tri-fusion multimodality reporter gene expression in living subjects. *Cancer Res. 64*, 1323−30.
(79) Luker, G. D., Sharma, V., Pica, C. M., Prior, J. L., Li, W., and Piwnica-Worms, D. (2003) Molecular imaging of protein−protein interactions: controlled expression of p53 and large T-antigen fusion proteins in vivo. *Cancer Res. 63*, 1780−1788.
(80) Luker, G. D., Pica, C. M., Song, J., Luker, K. E., and Piwnica-Worms, D. (2003) Imaging 26S proteasome activity and inhibition in living mice. *Nat. Med.* 9, 969−973.
(81) Laxman, B., Hall, D. E., Bhojani, M. S., Hamstra, D. A., Chenevert, T. L., Ross, B. D., and Rehemtulla, A. (2002) Noninvasive real-time imaging of apoptosis. *Proc. Natl. Acad. Sci. U. S. A. 99*, 16551−16555.
(82) Gambhir, S. S., Barrio, J. R., Phelps, M. E., Iyer, M., Namavari, M., Satyamurthy, N., Wu, L., Green, L. A., Bauer, E., MacLaren, D. C., Nguyen, K., Berk, A. J., Cherry, S. R., and Herschman, H. R. (1999) Imaging adenoviral-directed reporter gene expression in living animals with positron emission tomography. *Proc. Natl. Acad. Sci. U. S. A. 96*, 2333−2338.
(83) Tjuvajev, J. G., Chen, S. H., Joshi, A., Joshi, R., Guo, Z. S., Balatoni, J., Ballon, D., Koutcher, J., Finn, R., Woo, S. L., and Blasberg, R. G. (1999) Imaging adenoviral-mediated herpes virus thymidine kinase gene transfer and expression in vivo. *Cancer Res. 59*, 5186−5193.
(84) Tjuvajev, J., Blasberg, R., Luo, X., Zheng, L. M., King, I., and Bermudes D. (2001) Salmonella-based tumor-targeted cancer therapy: tumor amplified protein expression therapy (TAPET) for diagnostic imaging. *J. Controlled Release 74*, 313−315.
(85) Koehne, G., Doubrovin, M., Doubrovina, E., Zanzonico, P., Gallardo, H. F., Ivanova, A., Balatoni, J., Teruya-Feldstein, J., Heller, G., May, C., Ponomarev, V., Ruan, S., Finn, R., Blasberg, R. G., Bornmann, W., Riviere, I., Sadelain, M., O'Reilly, R. J., Larson, S. M., and Tjuvajev, J. G. (2003) Serial in vivo imaging of the targeted migration of human HSV-TK-transduced antigen-specific lymphocytes. *Nat. Biotechnol. 21*, 405−413.
(86) Rehemtulla, A., Stegman, L. D., Cardozo, S. J., Gupta, S., Hall, D. E., Contag, C. H., and Ross, B. D. (2000) Rapid and quantitative assessment of cancer treatment response using in vivo bioluminescence imaging. *Neoplasia 2*, 491−495.
(87) Wang, X., Rosol, M., Ge, S., Peterson, D., McNamara, G., Pollack, H., Kohn, D. B., Nelson, M. D., and Crooks, G. M. (2003) Dynamic tracking of human hematopoietic stem cell engraftment using in vivo bioluminescence imaging. *Blood 102*, 3478−82.
(88) Hill, J. M., Dick, A. J, Raman, V. K., Thompson, R. B., Yu, Z. X., Hinds, K. A., Pessanha, B. S., Guttman, M. A., Varney, T. R., Martin, B. J., Dunbar, C. E., McVeigh, E. R., and Lederman, R. J. (2003) Serial cardiac magnetic resonance imaging of injected mesenchymal stem cells. *Circulation 108*, 1009−1014.
(89) Vose, J. M., Bierman, P. J., Anderson, J. R., Harrison, K. A., Dalrymple, G. V., Byar, K., Kessinger, A., and Armitage, J. O. (1996) Single-photon emission computed tomography gallium imaging versus computed tomography: predictive value in patients undergoing high-dose chemotherapy and autologous stem-cell transplantation for non-Hodgkin's lymphoma. *J. Clin. Oncol. 14,* 2473−2479.
(90) Gardner, S. F., Lazarus, H. M., Bednarczyk, E. M., Creger, R. J., Miraldi, F. D., Leisure, G., and Green, J. A. (1993) High-dose cyclophosphamide-induced myocardial damage during BMT: assessment by positron emission tomography. *Bone Marrow Transplant 12*, 139−144.

(91) Olasz, E. B., Lang, L., Seidel, J., Green, M. V., Eckelman, W. C., and Katz, S. I. (2002) Fluorine-18 labeled mouse bone marrow-derived dendritic cells can be detected in vivo by high-resolution projection imaging. *J Immunol. Methods 260*, 137−48.

(92) Cao, Y. A., Wagers, A. J., Beilhack, A., Dusich, J.; Bachmann, M. H., Negrin, R. S., Weissman, I. L., and Contag, C. H. (2004) Shifting foci of hematopoiesis during reconstitution from single stem cells. *Proc. Natl. Acad. Sci. U.S.A. 101* (1), 221−226.

(93) Wang, X., Rosol, M., Ge, S., Peterson, D., McNamara, G., Pollack, H., Kohn, D. B., Nelson, M. D., and Crooks, G. M. (2003) Dynamic tracking of human hematopoietic stem cell engraftment using in vivo bioluminscence imaging. *Blood 102* (10), 3478−3482.

(94) Mayer-Kuckuk, P., Doubrovin, M., Budak-Alpdogan, T., Ponomarev, V., Blasberg, R., D. Banerjee, D., and Gelovani Tjuvajev, J. (2003) Noninvasive imaging of the transplanted bone marrow progenitor cells transfected with a triple gene reporter system in fusion with methotrexate resistant DHFR in vivo. (Presented at the 50th Annual Meeting of The Society of Nuclear Medicine, New Orleans, LA, Abstract no. 93) *J. Nucl. Med*. *44*, 29p.

(95) Tomita, S., Mickle, D. A., Weisel, R. D., Jia, Z. Q., Tumiati, L. C., Allidina, Y., Liu, P., and Li, R. K. (2002) Improved heart function with myogenesis and angiogenesis following autologous porcine bone marrow stromal cell transplantation. *J. Thorac. Cardiovasc. Surg*. *123*, 1132−1140.

(96) Stamm, C., Westphal, B., Kleine, H. D., Petzsch, M., Kittner, C., Klinge, H., Schumichen, C. Nienaber, C. A., Freund, M., and Steinhoff, G. (2003) Autologous bone-marrow stem-cell transplantation for myocardial infarction. *Lancet 361*, 45−46.

BC0498572

COMMUNICATIONS

Converting Weak Binders into Infinite Binders

Todd M. Corneillie, Paul A. Whetstone, Kelvin C. Lee, Jeremy P. Wong, and Claude F. Meares*

Department of Chemistry, University of California, Davis, California 95616. Received July 22, 2004

Monoclonal antibody 2D12.5 binds DOTA chelates of all the rare earths with $K_d \approx 10^{-8}$ M, making it useful for the capture of probe molecules with a variety of properties. To make 2D12.5 even more useful for biological applications, we have engineered a single cysteine residue at position 54 of the heavy chain, a site proximal to the protein's binding site, so that weakly electrophilic metal complexes of (*S*)-2-(4-acrylamidobenzyl)-DOTA (AABD) may bind and form permanent linkages. At 37 °C, pH 7.5, all of the rare earth−AABD complexes bind permanently to the 2D12.5 G54C mutant within 5 min, in yields that correlate with their relative binding affinities. Surprisingly, indium−AABD also binds permanently in >50% yield within 5 min, despite the fact that changing the metal to indium reduces the affinity ≈100×; even copper−AABD, which has ≈10 000× lower binding affinity than the rare earths, binds permanently in >70% yield within 2 h. However, acrylamido compounds with no measurable affinity do not bind permanently. The important practical implication is that the G54C mutant of 2D12.5 may be used for applications that include not only the rare earths, but also an unexpected range of other elements as well. This infinite binding system can exhibit selective and permanent attachment with a remarkable range of structurally related ligands, albeit at slower rates as affinities decrease.

A ligand−receptor system that permanently forms a specific complex may have a number of applications in the delivery or sequestration of the ligand. The purposeful development of such systems is a new endeavor, and a number of basic questions remain to be answered. So far, the most promising results in combining specificity with permanent attachment have involved engineering a reactive cysteine side chain at a position proximal to the ligand-binding site of a protein, accompanied by synthesis of a ligand bearing an appropriate complementary reactive group such as acryl (*1*−*3*). The reactivity of the protein side chain is modulated by its surface accessibility and location, while the reactivity of the ligand may be tuned with the tools of synthetic chemistry; attachment can occur within minutes, so that complexes form permanently in good yield when ligand and receptor first associate (*1*). Two acryl compounds that irreversibly target specific cysteines on human epidermal growth factor receptors are now in clinical trials (*4*). Recently Chen et al. explored ligands that bind permanently to a specific histidine (*5*), and Pollack et al. previously exploited reversible binding to attach a nucleophile that introduced catalytic activity near an antibody binding site (*6*); both attachments occurred at slower rates.

Monoclonal antibody 2D12.5 binds DOTA chelates of all the rare earths with $K_d \approx 10^{-8}$ M, making it useful for the capture of probe molecules for imaging and therapy (*7*−*9*). To make 2D12.5 even more useful for biological applications, we have engineered single cysteine residues near the protein's binding site so that acryl-DOTA chelates may bind and form permanent linkages (*10*). Three consecutive glycine residues that do not contact the ligand are located in a loop of the heavy chain, near the ligand p-substituent (Figure 1). We anticipated that mutating a single glycine to cysteine would not alter the loop conformation drastically: the other glycines could flexibly adjust their conformation to maintain the geometry required for binding. We prepared the three mutants and selected G54C for more extensive study because it had the best expression level and activity. The G54C mutant binds reversible ligands such as Y−NBD[1] with affinities comparable to the native protein (Supporting Information).

Formation of a permanent link between the engineered ligand and receptor requires specific binding, which increases the effective local concentration, accelerating an otherwise slow bond-forming reaction. We chose a weak Michael acceptor for the ligand so that permanent attachment is specific even in mixtures containing a variety of competing nucleophiles (*1*−*3*). We synthesized Y−AABD (Figure 2) as a candidate irreversible ligand and found that this yttrium complex bound reversibly to native 2D12.5 with $K_d \approx 4 \times 10^{-9}$ M, comparable to the reversible ligand Y−NBD.

We prepared ^{90}Y−AABD and tested it for permanent binding to the G54C mutant. The results in Figure 2B show that at 37 °C, pH 7.5, ^{90}Y−AABD permanently and specifically attaches to the G54C mutant. Under these conditions, the half-time for attachment is ≈13 min.

* Address correspondence to this author. Telephone: 530-752-0936. Fax: 530-752-8938. E-mail: cfmeares@ucdavis.edu.

[1] Abbreviations: AABD, (*S*)-2-(4-acrylamidobenzyl)-DOTA, see Figure 2; HETD, (*S*)-2-(4-(2-(2-hydroxyethylthio)acetamido)-benzyl)-DOTA; NBD, (*S*)-2-(4-nitrobenzyl)-DOTA.

10.1021/bc049825e CCC: $27.50 © 2004 American Chemical Society
Published on Web 10/06/2004

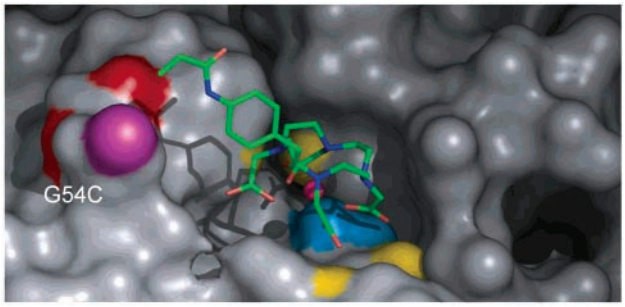


Figure 1. Site-directed cysteine mutations were designed (*10*) using the crystal structure of 2D12.5 Fab bound to the Y-DOTA derivative, Y−HETD[1], which was modified in silico to the electrophilic acryl derivative, Y−AABD (the p-substituent does not contact the protein). The native glycine residues 54, 55, and 56 in complementarity determining region 2 of the heavy chain appeared to be best suited for replacement with cysteine. The G54C mutant (cysteine sulfur colored purple) is shown (Cα's for G55 and G56 are colored red).

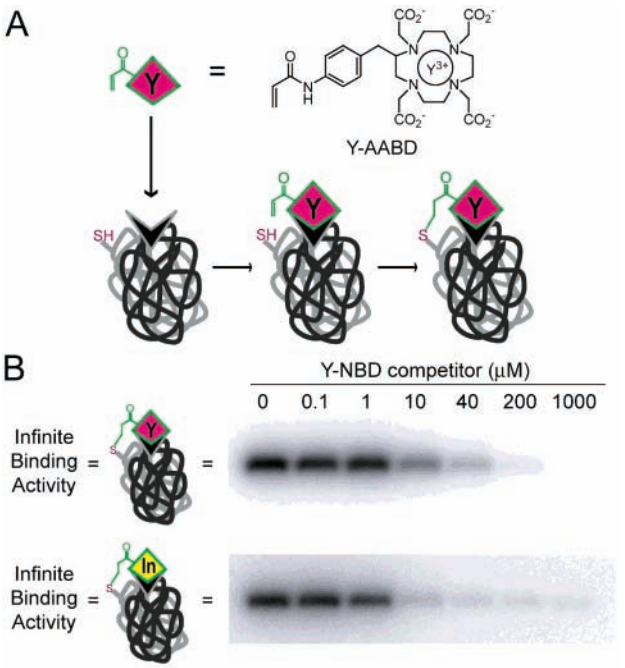


Figure 2. (A) Scheme describing the permanent binding pair. (B) Permanent binding is observed not only for ^{90}Y−AABD but also for ^{111}In−AABD, assayed by SDS−PAGE under denaturing conditions where only permanently bound complexes remain attached to the antibody. Increasing the concentration of unlabeled Y−NBD, a reversibly binding competitor, increasingly inhibits permanent attachment by preventing ^{90}Y−AABD or ^{111}In−AABD from accessing the binding site.

In addition, we discovered a new aspect of infinite binding: the reversible In−NBD chelate binds only weakly, but the acryl ligand ^{111}In−AABD binds permanently to the G54C mutant. Figure 2B shows that ^{111}In−AABD binds specifically to G54C, with a yield similar to the stronger ligand ^{90}Y−AABD. An important practical implication is that the G54C mutant of 2D12.5 may be used for applications that include not only radiotherapy with ^{90}Y, but also imaging with ^{111}In. The range of metals with useful probe properties thus extends beyond the rare earths ($K_d \approx 10^{-8}$ M for reversible binders) to scandium and indium, whose complexes do not have useful affinities as reversible binders ($K_d \approx 10^{-6}$ M), and perhaps beyond.

We were curious to see if an even weaker binder such as a copper chelate ($K_d \approx 10^{-4}$ M for Cu−NBD) would

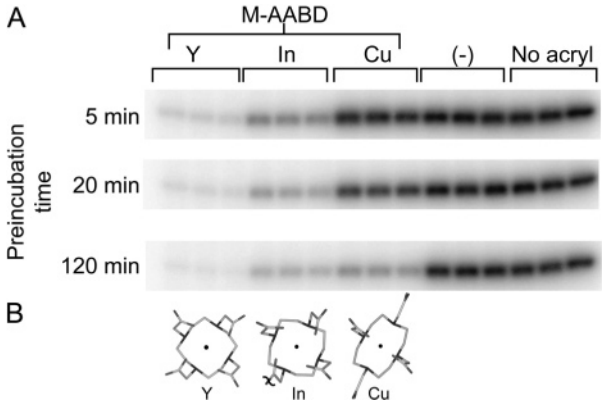


Figure 3. The G54C mutant was preincubated in triplicate with 10 μM AABD complexes of Y^{3+}, In^{3+}, or Cu^{2+}, a negative control *N*-(1-carbamoyl-2-(4-nitrophenyl)ethyl)acrylamide or *N*-(4-carboxymethylphenyl)acrylamide, or just buffer, for 5, 20, or 120 min at 37 °C, pH 7.5. At the stated times, ^{90}Y−AABD (1 μM) was added to each solution to compete for free G54C. Permanent binding was assayed by measuring band intensities after SDS−PAGE. (A) Phosphorimage of gel. The fainter the bands, the greater the permanent binding by the unlabeled ligand. (B) Crystal structures of Y−DOTA, In−DOTA-mono(*p*-aminoanilide) (some atoms removed for clarity) and Cu−DOTA.

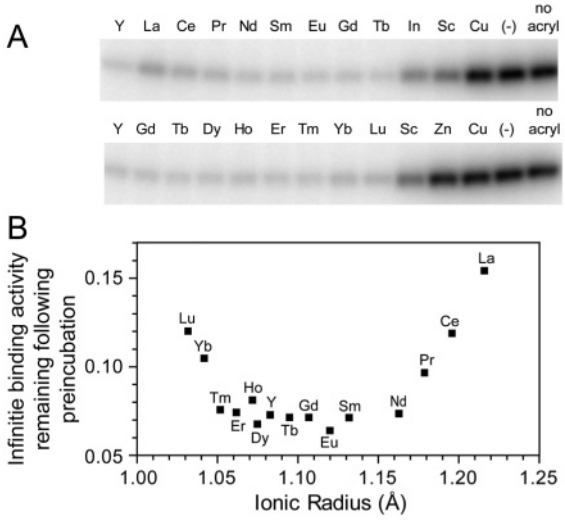


Figure 4. (A) Metal−AABD (10 μM) complexes were preincubated separately with aliquots of G54C for 5 min, followed by addition of 1 μM ^{90}Y−AABD, which competes for free G54C, and SDS−PAGE analysis. (B) From quantitative phosphorimaging, the highest-affinity AABD complexes form permanent bonds with G54C with higher yields than more weakly binding rare earth−AABD complexes whose ionic radii are slightly smaller (Lu^{3+}, Yb^{3+}) or larger (Ce^{3+}, La^{3+}) than ideal.

bind irreversibly under ordinary conditions. We tested this by comparing the permanent binding of Y^{3+}−, In^{3+}−, and Cu^{2+}−AABD, using competitive ^{90}Y−AABD attachment as an indicator (Figure 3). The positive control Y−AABD does not allow a significant amount of ^{90}Y−AABD to attach to the G54C: as expected, ^{90}Y−AABD is blocked from >90% of the sites after preincubation with Y−AABD. Weaker binding In−AABD blocks >50% of the sites after 5 min preincubation and even more at later times. Very weakly binding Cu−AABD initially occupies only about 10% of the G54C sites under these conditions, but it has permanently attached to G54C in good yield after 2 h, blocking >70% of the sites. In accord with their K_d values, evidence from crystal structures shows significant differences in preferred coordination geometry between the DOTA complexes of Y, In, and Cu (Figure 3B) (*11*−*15*). Control experiments with two acrylamido

compounds having no measurable affinity for 2D12.5 show no permanent attachment to G54C, indicating that ligand binding is required for the covalent bond-forming reaction to occur.

DOTA complexes of all the trivalent rare earth ions bind to 2D12.5 with similar affinities (*7*). Upon careful examination, the free energies of binding the rare earth−DOTA complexes to the antibody show a parabolic dependence on the ionic radius of the metal, with Gd at the bottom and La and Lu at the extremes. Figure 4 shows that the rare earth−AABD complexes bind permanently to G54C in yields that correlate with their relative affinities.

These results demonstrate that an infinite binding system can exhibit selective and permanent attachment with a surprising range of structurally related ligands, albeit at slower rates as affinities decrease. Separately engineering the reactivities of both ligand and receptor provides a direct route to the capture of a set of similar molecules, with unsurpassed affinity.

ACKNOWLEDGMENT

We thank Nathan Butlin, Sean Gay, Mark McCoy, and Susan Lee for helpful discussions, and NIH Research Grant CA16861 (C.F.M.) for support.

Supporting Information Available: Syntheses and additional experimental details and results. This material is available free of charge via the Internet at http://pubs.acs.org.

LITERATURE CITED

(1) Chmura, A. J., Orton, M. S., and Meares, C. F. (2001) Antibodies with infinite affinity. *Proc. Natl. Acad. Sci. U.S.A. 98*, 8480−8484.

(2) Chmura, A. J., Schmidt, B. D., Corson, D. T., Traviglia, S. L., and Meares, C. F. (2002) Electrophilic chelating agents for irreversible binding of metal chelates to engineered antibodies. *J. Controlled Release 78*, 249−258.

(3) Levitsky, K., Ciolli, C. J., and Belshaw, P. J. (2003) Selective inhibition of engineered receptors via proximity-accelerated alkylation. *Org. Lett. 5*, 693−696.

(4) Grunwald, V., and Hidalgo, M. (2003) Developing inhibitors of the epidermal growth factor receptor for cancer treatment. *J. Natl. Cancer Inst. 95*, 851−867.

(5) Chen, G., Heim, A., Riether, D., Yee, D., Milgrom, Y., Gawinowicz, M. A., and Sames, D. (2003) Reactivity of functional groups on the protein surface: development of epoxide probes for protein labeling. *J. Am. Chem. Soc. 125*, 8130−8133.

(6) Pollack, S. J., Nakayama, G. R., and Schultz, P. G. (1988) Introduction of nucleophiles and spectroscopic probes into antibody combining sites. *Science 242*, 1038−1040.

(7) Corneillie, T. M., Whetstone, P. A., Fisher, A. J., and Meares, C. F. (2003) A rare earth-DOTA-binding antibody: probe properties and binding affinity across the lanthanide series. *J. Am. Chem. Soc. 125*, 3436−3437.

(8) Corneillie, T. M., Fisher, A. J., and Meares, C. F. (2003) Crystal structures of two complexes of the rare-earth-DOTA-binding antibody 2D12.5: ligand generality from a chiral system. *J. Am. Chem. Soc. 125*, 15039−15048.

(9) Goodwin, D. A., Meares, C. F., Watanabe, N., McTigue, M., Chaovapong, W., Ransone, C. M., Renn, O., Greiner, D. P., Kukis, D. L., and Kronenberger, S. I. (1994) Pharmacokinetics of pretargeted monoclonal antibody 2D12.5 and 88Y-Janus-2-(*p*-nitrobenzyl)-1,4, 7,10-tetraazacyclododecanetetraacetic acid (DOTA) in BALB/c mice with KHJJ mouse adenocarcinoma: a model for 90Y radioimmunotherapy. *Cancer Res. 54*, 5937−5946.

(10) Corneillie, T. M., Lee, K. L., Whetstone, P. A., Wong, J. P., and Meares, C. F. (2004) Irreversible engineering of the multielement-binding antibody 2D12.5 and its complementary ligands. *Bioconjugate Chem. 15*, 1392−1402.

(11) Liu, S., He, Z., Hsieh, W. Y., and Fanwick, P. E. (2003) Synthesis, characterization, and X-ray crystal structure of In(DOTA-AA) (AA = *p*-aminoanilide): a model for ^{111}In-labeled DOTA-biomolecule conjugates. *Inorg. Chem. 42*, 8831−8837.

(12) Chang, C. A., Francesconi, L. C., Malley, M. F., Kumar, K., Gougoutas, J. Z., Tweedle, M. F., Lee, D. W., and Wilson, L. J. (1993) Synthesis, characterization, and crystal structures of M(DO3A) (M = Fe, Gd) and Na[M(DOTA)] (M = Fe, Y, Gd). *Inorg. Chem. 32*, 3501−3508.

(13) Parker, D., Pulukkody, K., Smith, F. C., Batsanov, A., and Howard, J. A. K. (1994) Structures of the yttrium complexes of 1,4,7,10-tetraazacyclododecane-N,N′,N″,N‴-tetraacetic acid (H-4 DOTA) and N, N″-bis(benzylcarbamoylmethyl)diethylene-triamine-N,N′,N″-triacetic acid and the solution structure of a zirconium complex of H-4 DOTA. *J. Chem. Soc., Dalton Trans.* 689−693.

(14) Riesen, A., Zehnder, M., and Kaden, T. A. (1986) Metal complexes of macrocyclic ligands. Part XXIII. Synthesis, properties, and structures of mononuclear complexes with 12- and 14-membered tetraazamacrocycle-N,N′,N″,N‴-tetraacetic acids. *Helv. Chim. Acta 69*, 2067−2073.

(15) Cosentino, U., Villa, A., Pitea, D., Moro, G., Barone, V., and Maiocchi, A. (2002) Conformational characterization of lanthanide(III)-DOTA complexes by ab initio investigation in vacuo and in aqueous solution. *J. Am. Chem. Soc. 124*, 4901−4909.

BC049825E

ARTICLES

Irreversible Engineering of the Multielement-Binding Antibody 2D12.5 and Its Complementary Ligands

Todd M. Corneillie, Kelvin C. Lee, Paul A. Whetstone, Jeremy P. Wong, and Claude F. Meares*

Department of Chemistry, University of California, Davis, California 95616. Received July 22, 2004

Engineering the permanent formation of a receptor−ligand complex has a number of potential applications in chemistry and biology, including targeted medical imaging and therapy. Starting from the crystal structure of the rare-earth-DOTA binding antibody 2D12.5 (Corneillie, T. M., Fisher, A. J., and Meares, C. F. (2003) *J. Am. Chem. Soc. 125*, 15039−15048), we used the site-directed incorporation of cysteine nucleophiles at the periphery of the antibody's binding site, paired with the chemical design of a weakly electrophilic ligand, to produce a receptor−ligand pair that associates efficiently and permanently. Protein residues proximal to the ligand's side chain were identified for engineering cysteine mutants. Fab fragments incorporating a cysteine at position 54, 55, or 56 of the heavy chain (complementarity determining region 2) were designed from the structure and then cloned, expressed in *Drosophila* S2 cells, and tested for reactivity with mildly electrophilic DOTA−yttrium ligands. All showed permanent binding activity, indicating that there is some tolerance for the location of the reactive mutant on the protein surface near the binding site. The G54C Fab mutant displayed the highest expression levels and permanent binding activity in initial experiments and was produced in high yield for further study. Upon examining the behavior of the G54C mutant with a small set of electrophilic ligands, differences in reactivity were observed which indicated that the substituents near the electrophilic atom can be important determinants of permanent binding. The G54C mutant permanently attaches to Y^{3+} complexes of (*S*)-2-(4-acrylamidobenzyl)-DOTA with a half-time of ≈13 min at 37 °C, making it potentially useful for in vivo pretargeting applications.

INTRODUCTION

For pretargeted imaging and therapy applications, achieving efficient capture of a small-molecule ligand by a protein-based receptor, as well as a long lifetime on the target, is essential. This is particularly true for radioactive ligands, which require a long residence time at a cancer cell to maximize treatment efficacy. Often a radionuclide suitable for in vivo use has a half-life that ranges from several hours to several days; if the nuclide is bound at the tumor for only a fraction of that period, the majority of radiation events will occur off target.

Antibodies are among the most heavily manipulated protein scaffolds and can be developed to bind a variety of natural and unnatural ligands (*1*). For applications where cell-surface antigens are targeted with bivalent antibodies, the bound lifetime can be extended due to the avidity of the antibody (*2*). However, because the binding interaction between antibodies and soluble small-molecule ligands is monovalent and gains no avidity advantage, the bound lifetime of the pair becomes a limiting factor in antibody-based probe capture schemes.

The half-life for ligand dissociation from a typical antibody with nanomolar affinity is likely to be on the order of 1 h at most (*3*−*6*). To improve the bound lifetime for ligands, either the valency or affinity of the system can be manipulated. Karacay et al. enhanced the bound lifetime of an antibody against an In−DTPA[1] derivative by using bivalent ligands to cross-link antibodies at cell surfaces (*7*). Others have used advances in combinatorial selection or directed evolution to produce affinities much stronger than nanomolar, into the picomolar or even femtomolar range, with half-lives for dissociation up to several days (*8*−*12*).

A different approach to improving the stability of the complex between a receptor and its ligand is to engineer infinite affinity (*13, 14*). This unconventional strategy for developing high affinity ligand−receptor pairs exploits chemical complementarity and reactivity novel to biology. Complementary reactive groups are designed and placed in the ligand and receptor such that their individual reactivities are negligible in a biological environment; however, upon complex formation, their mutual reactivity is remarkably enhanced by proximity, efficiently making association permanent.

Several groups have recently described the permanent coupling of a weakly electrophilic ligand to a nucleophilic amino acid—often cysteine, but also histidine or tyrosine—that is located near the ligand binding site of a protein (*13*−*17*). In the case of cysteine, which incorporates the most reactive nucleophile, there seems to be some practical tolerance in its location relative to the electrophilic ligand. Electrophilic species that have the requisite weak electrophilicity and stability in complex biological environments include acryl-based Michael acceptors, epoxides, and thioesters.

* Address correspondence to this author. Telephone: 530-752-0936. Fax: 530-752-8938. E-mail: cfmeares@ucdavis.edu.

10.1021/bc049824m CCC: $27.50 © 2004 American Chemical Society
Published on Web 11/02/2004

Recently we discovered a surprising aspect of infinite affinity: even ligands with modest affinity for reversible binding to a parent antibody can be converted to bind permanently (*18*). Acryl-DOTA−metal complexes that bind reversibly to antibody 2D12.5 with an affinity as low as 10^{-4} M can attach irreversibly to a 2D12.5 mutant in reasonable yield. Thus a family of probe molecules with structures that are similar can bind to a single receptor with infinite affinity. The basis of this effect appears to be that as long as a weak electrophile can be closely juxtaposed to a complementary nucleophile for a sufficient time, a permanent bond can be formed. We expect that as long as the bound lifetime of a weak ligand is at least comparable to the time required for reaction, the bond will be formed with good efficiency. This contrasts with the basis of combinatorial selection, which seeks complementary surfaces in ligand and receptor, enhancing affinity for a single structure without regard to others.

Here we describe the engineering and characterization of a new infinite binding antibody-based capture system, based on antibody 2D12.5 and metal−DOTA complexes (*19, 20*). A collection of chimeric Fab antibody fragments incorporating site mutations were designed in silico (Figure 1) and then cloned, expressed, and tested for attachment to complementary electrophilic yttrium-DOTA derivatives that were chosen to have low reactivities suited for use in vivo (Figure 2).

[1] Abbreviations: AABD, (*S*)-2-(4-acrylamidobenzyl)-DOTA; AABD-tBu, (*S*)-2-(4-acrylamidobenzyl)-DOTA tetra-*tert*-butyl ester; ABD, (S)-2-(4-aminobenzyl)-DOTA; ABD-tBu, (*S*)-2-(4-aminobenzyl)-DOTA tetra-*tert*-butyl ester; AMU, atomic mass units; BAD, (*S*)-2-(4-bromoacetamidobenzyl)-DOTA; CDR, complementarity determining region; C_{H1} and C_L, regions of the heavy chain and light chain comprising the constant domains of the Fab; CPM, 7-(diethylamino)-3-(4′-maleimidylphenyl)-4-methylcoumarin; DIEA, diisopropylethylamine; DMF, *N*,*N*-dimethylformamide; DMSO, dimethyl sulfoxide; DOTA, 1,4,7,10-tetraazacyclododecane-*N*,*N*′,*N*″,*N*‴-tetraacetic acid; DTPA, diethylenetriamine-*N*,*N*,*N*′,*N*″,*N*″-pentaacetic acid; DTT, dithiothreitol; FCS, fetal calf serum; ELISA, enzyme-linked immunosorbent assay; ESI-MS, electrospray ionization mass spectrometry; Fab, antigen-binding fragment of an antibody; FABD, (*S*)-2-(4-(*trans*-3-carboxyacrylamido)benzyl)-DOTA; HC, heavy chain; HCIC, hydrophobic charge-induction chromatography; HETD, (*S*)-2-(4-(2-(2-hydroxyethylthio)acetamido)benzyl)-DOTA; HRP, horseradish peroxidase; HSA−2IT−Y−BAD, human serum albumin conjugated to Y−BAD through a 2-iminothiolane linker; IMAC, immobilized metal affinity chromatography; IDA, iminodiacetic acid; $IMAC_{10}$ buffer, 20 mM sodium phosphate, 500 mM NaCl, 10 mM imidazole, pH 7.4; $IMAC_{20}$ buffer, 20 mM sodium phosphate, 500 mM NaCl, 20 mM imidazole, pH 7.4; $IMAC_{300}$ buffer, 20 mM sodium phosphate, 500 mM NaCl, 300 mM imidazole, pH 7.4; LC, light chain; mAb, monoclonal antibody; MABD, (*S*)-2-(4-(*cis*-3-carboxyacrylamido)benzyl)-DOTA; MEA, 2-mercaptoethylamine-HCl; MEP, 4-mercaptoethylpyridine; MOPS, EDTA buffer, 25 mM MOPS, 100 mM NaCl, 10 mM EDTA, pH 7.5; MWCO, molecular weight cutoff; NBD, (*S*)-2-(4-nitrobenzyl)-DOTA); PMSF, phenylmethanesulfonyl fluoride; SAB, nonreducing SDS−PAGE sample application buffer: 2% lithium dodecyl sulfate, 10% glycerol, 62.5 mM Tris, 5 mM EDTA, pH 6.8 (reducing SAB contains 1% 2-mercaptoethanol in addition to these components); SDS−PAGE, sodium dodecyl sulfate polyacrylamide gel electrophoresis (lithium dodecyl sulfate was used here); TBST, TBS (24.8 mM Tris, 137 mM NaCl, 0.269 mM KCl, pH 7.4) supplemented with 0.05% Tween-20 (v/v); TEA, triethylamine; TFF, tangential flow ultrafiltration; TLC, thin-layer chromatography; TMB, 3,3′,5,5′−tetramethylbenzidine; V_H and V_L, variable domains of an antibody heavy chain and light chain, respectively; Y−NBD, yttrium−NBD.

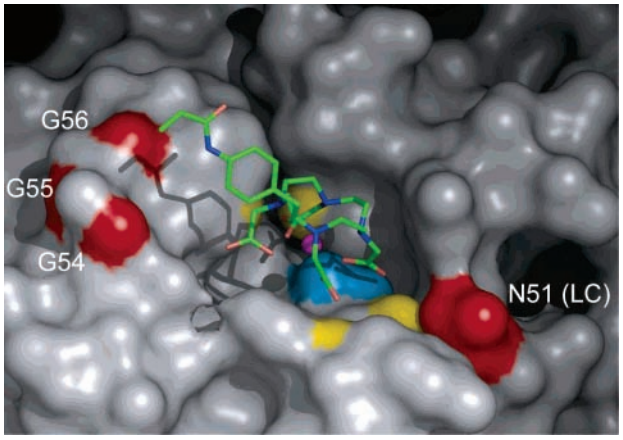


Figure 1. Native glycine residues 54, 55, and 56 (Kabat numbering) in CDR2 of the heavy chain (C_α atoms colored red) were selected as candidates for site-directed single-cysteine mutations. A fourth site, N51 (light chain, side chain colored red), was selected as a negative control (see text). The original Y−HETD ligand in the 2D12.5 Fab crystal structure was remodeled to Y−AABD to aid in the identification of preferable sites for mutagenesis. The theoretical G54C mutant positions the nucleophilic sulfur approximately 4.3 Å from the electrophilic acryl carbon. Protein atoms making noncovalent binding contacts with the HETD ligand carboxylates are colored yellow, and an arginine side chain that forms a stabilizing salt-bridge with a HETD carboxylate is colored blue.

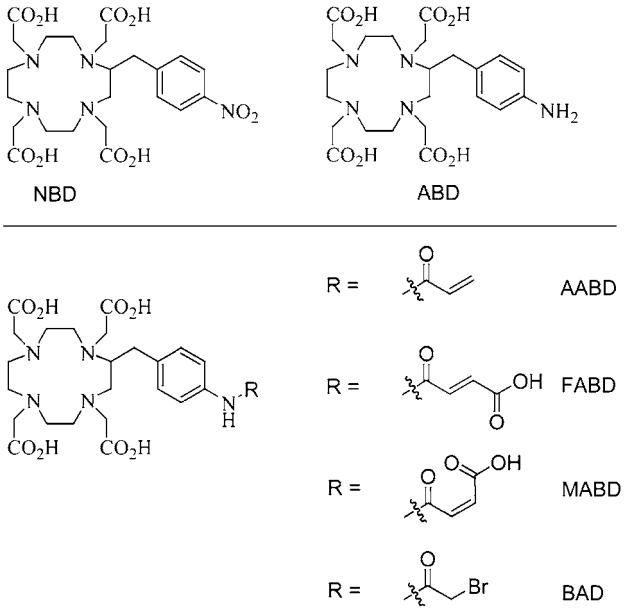


Figure 2. DOTA derivatives used to explore the permanent binding behavior of engineered 2D12.5 Fab mutants. The reversibly binding ligands, NBD and ABD, were used as negative controls and as competitors to characterize the permanent bond-forming capability of the Michael acceptor ligands AABD, FABD and MABD. The bromoacetamide DOTA derivative, BAD, was used as a positive control.

MATERIALS AND METHODS

Materials. Vent DNA polymerase, restriction enzymes, and T4 ligase were purchased from New England BioLabs, Beverly, MA. Taq DNA polymerase was purchased from Promega, Madison, WI. S2 cells, the inducible cloning vector pMTBiP/V5-His A, hygromycin-B, and anti-V5-AP and HRP conjugates were purchased from Invitrogen, Carlsbad, CA. Goat anti-human κ-AP conjugate was purchased from Southern Biotechnology Associates, Inc., Birmingham, AL. Schneider insect media

was supplied by Cambrex, Baltimore, MD. FCS (heat-inactivated, gamma-irradiated) and EX-CELL 420 serum-free media were purchased from JRH Biosciences, Lenexa, KS. MEP Hypercel resin was supplied by Ciphergen, Freemont, CA, and Chelating Sepharose Fast Flow resin and a Tricorn 10/300 column were purchased from Amersham Biosciences, Piscataway, NJ. Empty Econo-Pac columns were purchased from Bio-Rad, Hercules, CA. Sephadex G50 was purchased from Sigma, St. Louis, MO. 2-Mercaptoethylamine-HCl was purchased from Pierce Biotechnology, Rockford, IL. A Fluostar fluorescence microplate reader (BMG LabTechnologies, Durham, NC) and the CPM reagent (Molecular probes, Eugene, OR) were used for free thiol quantitation. Ultrafree centrifugal protein concentrators (10 000 MWCO) were obtained from Millipore, Bedford, MA. Analytical and preparative reversed phase HPLC was performed on an Altima 5 μm, 4.6 $\times$ 250 mm C_{18} column and an Altima 5 μm, 22 $\times$ 250 mm C_{18} column (Alltech Associates, Inc., Deerfield, IL), respectively. Hexahydrate chloride salts of yttrium and gadolinium were purchased from Sigma Aldrich (St. Louis, MO) and were obtained in their highest available purity. An Atlantis 3 μm, 2.1 $\times$ 100 mm dC_{18} column (Waters, Milford, MA) was used for LC/MS separation of peptide samples on a Thermo Finnigan LCQ Deca electrospray ion trap mass spectrometer. $^{90}YCl_3$ and $^{111}InCl_3$ solutions in 0.05 M HCl were purchased from PerkinElmer Life Sciences, Boston, MA. Pure water (18 MΩ cm) was used throughout.

Construction of Chimeric 2D12.5 Fab Heavy and Light Chain Genes for Expression in S2 Cells. Variable domain sequences of 2D12.5 heavy and light chains were obtained from total mRNA that was isolated from 2D12.5 hybridoma cells using Novagen's Ig Prime kit. Chimeric constructs of the murine 2D12.5 variable domains and human anti-tetanus toxoid antibody C_L and C_{H1} domains were assembled by two-step overlap extension (*21*). Bgl II and Xba I restriction sites were introduced into the 5′ and 3′ ends, respectively, of both the heavy and light chain genes during overlap extension, and were used to introduce each gene construct into the pMTBiP/V5-His A plasmid cassette for propagation in *E.coli* and expression in *Drosophila* S2 cells, which have been demonstrated to efficiently express whole antibodies, antibody Fab fragments, and single-chain antibodies (*13, 22*−*24*). The heavy and light chain genes were inserted into separate plasmids. Because light chains are generally overexpressed relative to heavy chains (*25, 26*), the heavy chain was placed in frame to include V5 and His tags at the C-terminus, while the light chain was cloned to prevent inclusion of the tags in the final expressed light chain product. Fab molecules incorporating a light chain paired with a heavy chain could then be selectively separated (using the His tag on the heavy chain) from improperly paired light chains lacking a His tag. Four cysteine mutants were constructed. Each site-directed mutation was prepared using four primers and two stages of PCR. Vent and Taq polymerases were used in stages one and two, respectively (*27*).

Transfection and Expression of Chimeric 2D12.5 Fab Genes in Drosophila S2 Cells. S2 cells were split to a density of 1 $\times$ 10^6 cells/mL in six-well microplates and cultured overnight in Schneider media containing 10% FCS at 27 °C in a humidified incubator. Transient expression of heavy and light chain plasmids was accomplished by cotransfecting *Drosophila* S2 cells the following day using precipitating calcium phosphate. Cells were induced after 3 days using 500 μM $CuSO_4$, and samples were taken to assay for gene expression by noncompetitive ELISA. Cotransfection of a plasmid containing the hygromycin B phosphotransferase gene with the heavy and light chain plasmids produced stable cell lines. Stable cell line selection proceeded for 3−4 weeks posttransfection with 300 μg/mL hygromycin B. Once cell populations reached approximately 0.8−1 $\times$ 10^7 cells/mL, cells were transferred to T25 flasks. Stable cell lines were induced with $CuSO_4$ for 3−4 days, and the presence of functional Fab was determined by noncompetitive ELISA of media that had been separated from cells.

Large-Scale Expression. S2 cells in T75 flasks were cultured to a density of approximately 1 $\times$ 10^7 cells/mL in Schneider media supplemented with 10% FCS before adapting to growth in Erlenmeyer and Fernbach shake flasks containing modified serum-free EX-CELL 420 medium. EX-CELL 420 was supplemented with 18 mM L-glutamine (90 mL of 200 mM L-glutamine added to 1 L EX-CELL 420). To transfer cells from serum-containing medium, cells were centrifuged at 1000*g* for 5 min and washed once with a small volume of EX-CELL 420 and centrifuged a second time before resuspending in fresh EX-CELL 420. 200 mL cultures were grown in 500 mL Erlenmeyer flasks at 130 rpm, 27 °C for 3−4 days (density increased from approximately 1 $\times$ 10^6 to 1 $\times$ 10^7 cells/mL). Cultures were pelleted by centrifugation, resuspended in 800 mL modified EX-CELL 420, and grown for 1 day at 27 °C (density $\approx$ 4 $\times$ 10^7 cells/mL). Media was exchanged again after pelleting cells and resuspending in fresh media. 500 μM $CuSO_4$ was added immediately, and cell density was monitored over several days. After 2.5 days, D-(+)-glucose was added to a final concentration of 0.2% (*28*). At days 2 and 4 of induction, the cell density was stable at approximately 4−6 $\times$ 10^7 cells/mL. Gene expression was monitored by ELISA; the highest expression levels were observed 3−4.5 days postinduction. Generally, the media was harvested when protein expression reached levels >5 mg/L.

Assaying 2D12.5 Chimeric Fab Expression and Activity. S2 cells transfected with chimeric 2D12.5 genes, adapted to growth in EX-CELL 420 media, were induced with 500 μM $CuSO_4$ for several days. Media containing Fab, separated from cells by centrifugation and filtration, was serially diluted in microtiter plates containing immobilized HSA−2IT−Y−BAD (*20, 29*). Following incubation for 1 h at 37 °C, wells were washed with TBST. Anti-V5-HRP antibody, which binds a C-terminal V5 tag expressed on the heavy chain, and a TMB substrate were used to quantify binding.

First Stage Purification of Chimeric 2D12.5 Fab Expressed in S2 Cells by MEP Hypercel HCIC. A two-step purification method was developed for the isolation of purified chimeric 2D12.5 Fab from S2 cell expression media. MEP Hypercel, which is reported to have high affinity for antibody Fc domains and somewhat weaker affinity for Fab domains (*30, 31*), was evaluated for chimeric 2D12.5 Fab purification. Previously reported methods provided initial guidance for method development (*26, 32*). Approximately 24 mL of MEP Hypercel gel resin was packed into a Tricorn 10/300 column and equilibrated at a flow rate of 2 mL/min (50 mM sodium phosphate, pH 7.2). Media containing Fab was separated from S2 cells by centrifugation and adjusted to pH 7.2 with Na_2CO_3. EDTA was added to a final concentration of 5 mM, and the solution was then sterile filtered and stored at 4 °C until further use. Before MEP resin purification, the media containing Fab was immediately filtered (0.2 μm) and allowed to warm to room temperature. Approximately 700−800 mL of media was then

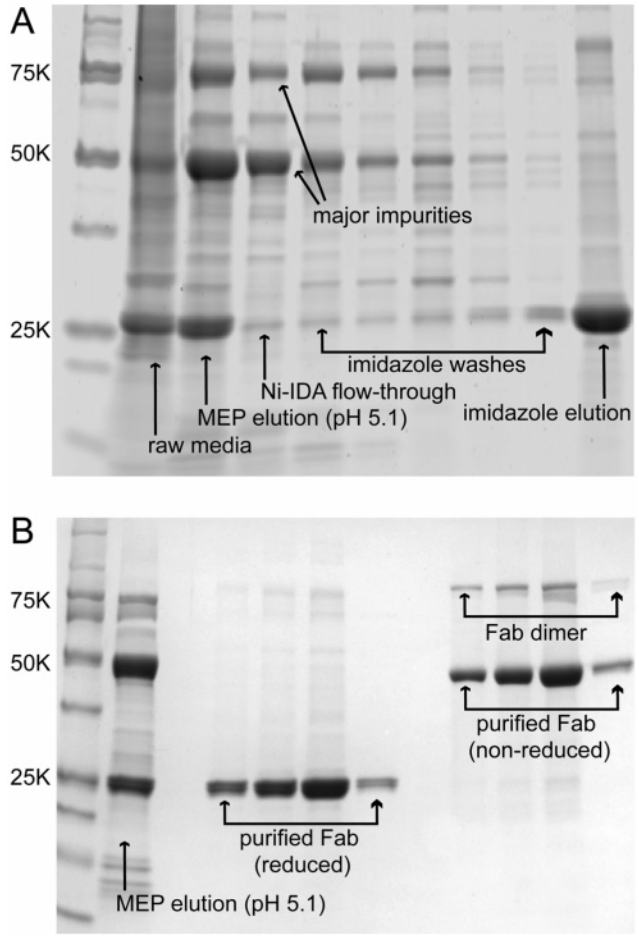


Figure 3. Purification of 2D12.5 G54C Fab from *Drosophila* S2 cell culture in serum-free expression media. (A) First stage MEP Hypercel purification yielded a partially purified Fab (SDS−PAGE, Sypro Ruby, lane 3). Second stage IMAC purification using Ni−IDA removed most of the remaining impurities including unpaired light chains that were cloned without a His tag (rightmost lane). (B) Purified Fab samples of different concentrations were analyzed for purity by SDS−PAGE (Coomassie Blue). Samples were either reduced to identify the separated light chain and heavy chains (lanes 4−7) or not reduced (lanes 9−12) to determine that the majority of the Fab was indeed monomeric. A small percentage of the purified Fab was isolated as a disulfide-linked dimer, indicating that the engineered cysteines of two Fab molecules had likely paired with each other.

loaded onto the MEP column at a flow rate of 2 mL/min. The column was washed with approximately five column volumes of phosphate buffer, and the Fab-containing fraction was isolated using a single step elution (50 mM sodium acetate, pH 5.1). The isolated fraction was then mixed 1:1 with 100 mM sodium phosphate, 1 M NaCl, 20 mM imidazole, pH 7.4, and stored overnight at 4 °C. All samples were analyzed by SDS−PAGE.

Second Stage IMAC Purification of Chimeric 2D12.5 Fab Expressed in S2 Cells. Chelating Sepharose Fast Flow (IDA) was loaded with Ni^{2+} ions by incubating washed gel with an excess of $NiSO_4$ according to the manufacturer's instructions. Ni^{2+}-charged resin was stored at 4 °C until use. An approximate working capacity of 2 mg Fab per mL IMAC gel was determined experimentally. MEP purified Fab solutions were warmed to room temperature and diluted 1:1 with 2× $IMAC_{10}$ load buffer. One milliliter of IMAC gel equilibrated in $IMAC_{10}$ buffer per 2 mg Fab was added to the Fab-containing solution, and the mixture was incubated with end-over-end rocking for 30 min. The mixture was then poured into an empty, capped Econo-Pac column equipped with a glass frit filter, and the gel was allowed to settle by gravity. A top frit was placed on the column, and the solution was allowed to flow through the column. The gel was washed with 10 column volumes of $IMAC_{10}$ buffer followed by an additional 10 column volumes of $IMAC_{20}$ buffer. Next, two column volumes of $IMAC_{300}$ were applied to the column, and the solution was allowed to flow into the gel and to incubate for 5 min. An additional three column volumes of $IMAC_{300}$ were added to the column, and allowed to flow through the column. All five column volumes of $IMAC_{300}$ were collected; the $IMAC_{300}$ solution eluted 90% of the bound Fab with high purity. A second $IMAC_{300}$ elution released the remaining 10% of bound Fab molecules. Samples were analyzed for purity by SDS−PAGE (Figure 3) and dialyzed into MOPS, EDTA buffer before storing at 4 °C. Purified yields of the 2D12.5 G54C Fab mutant approached 8−10 mg/L.

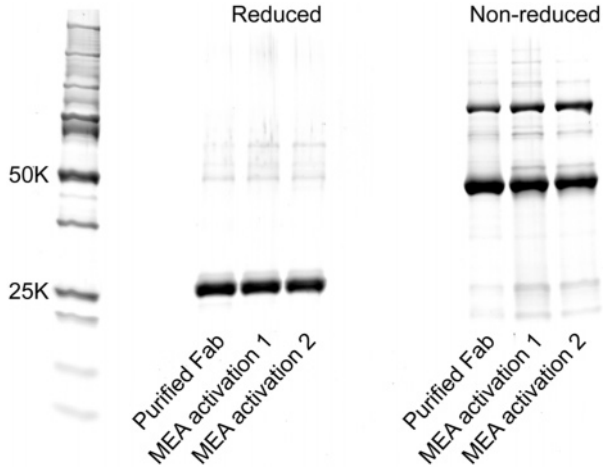


Figure 4. Purified G54C Fab was treated with MEA to remove blocking groups on the engineered cysteine. Samples were analyzed by reducing and nonreducing SDS−PAGE and stained with Sypro Ruby protein stain to confirm that no significant Fab reduction or change in dimerization occurred during the incubation with MEA.

Activation of Blocked Engineered Cysteine Residues with MEA. Fab isolated and purified from S2 cell expression was concentrated to 20−35 μM by centrifugal ultrafiltration. A 100 mM stock solution of MEA was dissolved into MOPS, EDTA buffer and added to the Fab solution to a final concentration of 10 mM. The solution was incubated overnight at room temperature and buffer exchanged using two consecutive Penefsky gel filtration columns to remove the MEA (*33*). The protein solution was assayed for free thiol activity using the fluorescent maleimide-containing compound CPM and stored at 4 °C (*34*). A standard curve was constructed using 2-mercaptoethanol. Free thiol activity for the G54C mutant ranged from a low of 5% to a high of 65% before and after activation of the site-directed cysteine mutant, respectively. Nonreducing SDS−PAGE analysis confirmed that the interchain disulfide between the light and heavy chains of the Fab remained intact following treatment with MEA (Figure 4).

Chelate Synthesis. *(S)-2-(4-Aminobenzyl)-1,4,7,10-tetraazacyclododecane-N,N′,N″,N‴-tetraacetic acid tetra-tert-butyl ester* (ABD-tBu, see Figure 2) was prepared according to previously published methods (*35*−*38*). ^{1}H NMR (300 MHz, $CDCl_3$) δ 1.0−5.0 (m, 63H), 6.39 (d, J = 8.7 Hz, 2H), 6.73 (d, J = 8.7 Hz, 2H).

(S)-2-(4-Acrylamidobenzyl)-1,4,7,10-tetraazacyclododecane-N,N′,N″,N‴-tetraacetic acid tetra-tert-butyl ester

(AABD-tBu) was prepared as follows: ABD-tBu (0.27 mmol) was dissolved in CH_2Cl_2 (2 mL) under Ar. Acryloyl chloride (1.5 equiv) and DIEA (2 equiv), each separately dissolved in CH_2Cl_2 (2 mL), were added dropwise through addition funnels over 15 min, and the resulting solution was allowed to stir for 10 min at room temperature. The solution was washed with 1% TEA in H_2O until the aqueous fractions remained basic. The CH_2Cl_2 layer was then dried over Na_2SO_4 and filtered, and solvent was removed under reduced pressure to yield AABD-tBu as a crude yellow solid. (ESI-MS *m/z* calcd (MNa^+): 810.51. Found: 810.53.

(S)-2-(4-Acrylamidobenzyl)-1,4,7,10-tetraazacyclododecane-N,N′,N″,N‴-tetraacetic Acid (AABD). The crude AABD-tBu product was dissolved in neat CF_3COOH at 4 °C under an Ar atmosphere, stirred overnight, and allowed to warm to room temperature. The CF_3COOH was removed under reduced pressure, and a portion of the resulting solid was purified by preparative reverse phase chromatography to yield a white solid after lyophilization. HPLC gradient: solvent A, water with 0.1% CF_3COOH; solvent B, CH_3CN with 0.075% CF_3COOH, 0−5 min, 5% B, 5−15 min, 5−30%, 15−45 min, 30−50% linear solvent B, 6 mL/min. (ESI-MS *m/z* calcd (MH^+): 564.26. Found: 564.28. ^{1}H NMR (300 MHz, DMSO-d_6) δ 1.0−5.0 (m, 25H), 5.74 (d, J = 10.2 Hz, 1H), 6.24 (d, J = 16.8 Hz, 1H), 6.43 (d,d, J = 16.8 Hz, 10.2 Hz, 1H), 7.18 (d, J = 7.8 Hz, 2H), 7.60 (d, J = 7.8 Hz, 2H), 10.12 (s, 1H).

(S)-2-(4-(cis-3-Carboxyacrylamido)benzyl)-1,4,7,10-tetrazacyclododecane-N,N′,N″,N‴-tetraacetic Acid (MABD). ABD-$(HCl)_4$ (0.030 mmol) was dissolved in 100 μL of water. To this solution, maleic anhydride (0.122 mmol, 4 equiv) dissolved in 100 μL of DMF was added and stirred at room temperature for 1 h. Solvent was removed under reduced pressure, and the resulting solid was redissolved in water and purified by reverse-phase HPLC to yield a yellow solid. HPLC gradient: solvent A, water; solvent B, methanol, 0−5 min, 5% 5−35 min, 5−55%, 4 mL/min. (ESI-MS *m/z* calcd (MH^+): 608.26. Found: 608.26. NMR (300 MHz, D_2O) δ 1.0−5.0 (m, 25H), 6.20 (d, J = 12.3 Hz, 1H), 6.43 (d, J = 12.3 Hz, 1H), 7.29 (d, J = 8.4 Hz, 2H), 7.47 (d, J = 8.4 Hz, 2H).

(S)-2-(4-(trans-3-Carboxyacrylamido)benzyl)-1,4,7,10-tetrazacyclododecane-N,N′,N″,N‴-tetraacetic Acid (FABD). ABD-$(HCl)_4$ (0.030 mmol) and DIEA (0.122 mmol, 20 μL) were dissolved in 100 μL of water and 100 μL of CH_3CN and added dropwise over 5 min to a 10 mL round-bottom flask containing fumaryl chloride (0.122 mmol) dissolved in 100 μL of acetonitrile. The solvent was removed under vacuum, and the resulting solid was redissolved in water and purified by reverse-phase HPLC. The HPLC purification method was identical to that used for MABD. ESI-MS *m/z* calcd (MH^+): 608.26. Found: 608.26. NMR (300 MHz, DMSO-d_6) δ 1.0−5.0 (m, 25H), 6.64 (d, J = 15.3 Hz, 1H), 7.13 (d, J = 15.3 Hz, 1H), 7.21 (d, J = 8.4 Hz, 2H), 7.61 (d, J = 8.4 Hz, 2H), 10.49 (s, 1H).

Metalation of Chelates. ^{90}Y and ^{111}In were received as solutions in 0.05 M HCl. Approximately 50 μCi of ^{90}Y or ^{111}In was incubated with a 0.5 mM solution of the indicated DOTA derivative in a total volume of 25 μL 0.1 M triethylammonium acetate buffer for 45−60 min at 70 °C. TLC confirmed completion of the complexation reaction. Solutions were stored at −20 °C prior to use. Metalation of chelates with nonradioactive metal ions was accomplished as described previously (*19, 29*).

Initial Evaluation of 2D12.5 Fab Proteins for the Ability to Bind Irreversibly to ^{90}Y−AABD. The heavy-chain CDR2 single-cysteine mutants (G54C, G55C, and G56C) were studied as unpurified protein samples, concentrated from the serum-free expression media used to support S2 cells, and dialyzed into buffer. Briefly, cells were grown in suspension (spinner flask) to an approximate density of 1×10^7 cells/mL and induced with 500 μM $CuSO_4$ for 3 days. Media (600−800 mL) was concentrated by TFF to approximately 50 mL and dialyzed into 10 mM MOPS, 100 mM NaCl, 1 mM EDTA, pH 7.2. The protein solutions were stored at 4 °C and used without further purification. These protein solutions demonstrated affinity for reversibly binding Y−NBD complexes by noncompetitive ELISA.

2D12.5 Fab solutions were estimated to be approximately 100 nM; carrier-free ^{90}Y complexes were <1 nM. The radioactive metal complex solutions and protein solutions were mixed in 100 mM MOPS, 100 mM NaCl, pH 7.4, and incubated at 37 °C for 3 h. Samples were denatured, and disulfides were reduced with reducing SAB containing 1% 2-mercaptoethanol. Samples were boiled for 5 min, flash frozen in liquid N_2, and stored at −20 °C prior to analysis by SDS−PAGE (~50 nCi per lane). Gels were fixed, rinsed, and exposed to a phosphor plate sensitive to radioactive decay for 20−90 min.

Characterizing 2D12.5 G54C Fab Reactivity with Various ^{90}Y Chelates. Solutions containing 2D12.5 G54C Fab (1 μM) and carrier-free ^{90}Y complexes (final DOTA concentration 1 μM) were mixed in 100 mM MOPS, 100 mM NaCl, 10 mM EDTA, pH 7.5, and allowed to incubate for 37 °C for 2 h. Aliquots were withdrawn after 2 h and immediately denatured with nonreducing or reducing SAB and analyzed by SDS−PAGE.

Labeling, LC/MS, and MS^2 Analysis of G54C Fab Labeled with Tb−AABD and Tm−AABD. Equivalent aliquots of MEA-activated G54C Fab (1.3 nmol dissolved in 60 μL MOPS, EDTA buffer) were incubated separately with either Tb−AABD or Tm−AABD (100 μM) at 37 °C for 2.5 h. The two aliquots were combined, and buffer was exchanged according to the method of Penefsky (*33*) prior to digestion with chymotrypsin. Tris, urea, and DTT were added to final concentrations of 125 mM, 5 M and 28.1 mM, respectively, and the resulting solution was incubated at 55 °C for 45 min. Iodoacetamide (dissolved to 500 mM in water) was added to a final concentration of 56 mM and incubated at room temperature for 20 min in the dark. Chymotrypsin (6 μg, 2.4 μL, 1/20 w/w, dissolved in 1 mM HCl) was added; the digestion mixture was allowed to incubate at room temperature for 14 h, whereupon PMSF was added to a final concentration of 1 mM. The resulting solution was diluted 1:1 in 25 mM triethylammonium acetate, pH 7, and purified by 2D12.5 affinity chromatography (*39*). A fraction (1/5) of the elution (0.4% CF_3COOH, 1:1 CH_3CN:H_2O) was concentrated under reduced pressure and injected onto a Thermo Finnigan LCQ Deca electrospray ion trap mass spectrometer equipped with an Atlantis dC_{18} column. HPLC gradient: solvent A, H_2O with 0.2% HCOOH; solvent B, CH_3CN with 0.175% HCOOH, 0−5 min, 5% B, 5−50 min, 5−25% B, 50−65 min, 25−55% B, 65−70 min 55−100% linear solvent B, 250 μL/min. ESI-MS *m/z* calcd (SC(Tb−AABD)GGTAY, MH^+): 1377.41. Found: 1377.39; *m/z* calcd (SC(Tm−AABD)GGTAY, MH^+): 1387.42. Found: 1387.41.

Kinetics of Permanent Bond Formation between 2D12.5 G54C Fab and Y−AABD. Two separate solutions were prepared as follows: ^{90}Y−AABD (^{90}Y, 0.24 nM) was mixed with 10 μM nonradioactive Y−AABD in MOPS, EDTA buffer preincubated at 37 °C. MEA-activated 2D12.5 G54C Fab (1 μM) was added to each tube, and the resulting solution incubated at 37 °C. Nonradioactive

Table 1. Cloned and Expressed Chimeric 2D12.5 Fabs

name	heavy chain	light chain
native	native	native
N85D	N85D	native
G54C	G54C, N85D	native
G55C	G55C, N85D	native
G56C	G56C, N85D	native
N51C (LC)	N85D	N51C

Y−NBD competitor (1 mM) was added to one of the tubes after 6 min. Aliquots were removed from each stock solution at indicated time points, denatured, and reduced by addition to a 5× SAB solution containing 5% 2-mercaptoethanol (1% 2-mercaptoethanol following sample addition), boiled for 5 min, flash frozen in liquid N_2, and stored at −20 °C for SDS−PAGE analysis.

RESULTS AND DISCUSSION

The crystal structures of antibody 2D12.5 bound to DOTA complexes of Y^{3+} and Gd^{3+} were solved to identify preferred residues on the protein for engineering single-cysteine mutants capable of forming a permanent bond with a captured rare earth-DOTA ligand (*20*). Two binding modes for the ligand (differing by a 90° rotation of the DOTA) are observed, as a consequence of the DOTA ligand's symmetry and the orientation in the binding pocket.

An ideal single-cysteine mutant would place the reactive cysteine at a site on the protein surface close enough to the binding site to react with a weakly electrophilic metal−DOTA complex such as AABD, yet at a position that does not interfere with binding of the ligand to the protein. Analysis of the crystal structure indicated that the CDR2 loop of the heavy chain best met these requirements: three glycine residues positioned at the top of the loop did not interact in any way with the ligand. We expect that these three consecutive glycines add flexibility to this segment of the polypeptide chain and hypothesized that a Gly to-Cys mutation at any one of these positions would not meaningfully alter the loop's shape. The remaining two glycines might adjust their conformations if necessary to maintain the binding ability of the native protein.

The 2D12.5 Fab crystal structures indicated that the heavy-chain CDR2 loop mutants were best positioned to interact with a derivatized ligand bound in one of the two possible binding modes (see Figure 1, which shows the binding mode for Y−HETD (*20*)). The other binding mode orients the para-substituent of the ligand over CDR3 of the heavy chain, a domain that plays a crucial role in ligand binding (see the binding mode displayed for Gd-NBD (*20*)); this second binding mode also orients the electrophilic domain of the para-substituted ligand away from the general surface of the protein. In case this turned out to be the preferred mode in solution, a fourth site for a single-cysteine mutation (light-chain CDR2 residue N51, see Figure 1) was identified as a possible reactive site for the second ligand binding mode. For para-substituted ligands such as AABD, it was expected that light chain mutant N51C would behave as a negative control; new ligands with the electrophile in different positions would be required to attach to N51C.

In all, six different chimeric Fab molecules were constructed, expressed, and assayed (Table 1). The first contained the native heavy chain, composed of the 2D12.5 mAb's variable domain fused with the C_{H1} of a human anti-tetanus toxoid antibody (*40*). The native variable domain of the heavy chain contained a N-linked glycosylation site at position 85 in framework 3. This glycosylation site was removed by incorporating a N85D mutation, because glycosylated recombinant proteins often exhibit heterogeneity due to differences in glycosylation. Also, different eukaryotes glycosylate proteins differently and may elicit an undesirable immune response when used in vivo *(41, 42)*. The N85D mutant was used as a heavy chain template to construct three heavy chain single-cysteine mutants (G54C, G55C, and G56C); therefore, the heavy chain cysteine mutants incorporated both the N85D mutation and the desired cysteine mutation. The native chimeric light chain and a single light chain cysteine mutant (N51C) were also constructed (Table 1). Each of the heavy chains was cotransfected with the native light chain in *Drosophila* S2 cells. The N85D heavy chain was cotransfected with the N51C light chain mutant.

Stably transfected *Drosophila* S2 cells were induced, and the media was assayed for protein expression by means of nonreducing SDS−PAGE separation followed by western blot analysis. Noncompetitive ELISA was used to assay binding activity of each of the chimeric Fabs (data not shown). In general, the native and N85D Fabs exhibited the highest expression levels, followed by the G54C and G56C heavy chain mutants. The G55C (HC) and N51C (LC) mutants yielded the lowest expression levels.

To assess the ability of the recombinant 2D12.5 Fab mutants to bind permanently to weakly electrophilic ligands, unpurified cell culture media containing each single-cysteine mutant in low concentration was concentrated and dialyzed into MOPS, EDTA buffer, and incubated with 10 μM ABD (negative control), 10 μM AABD, or 10 μM BAD (positive control) complexes containing ^{90}Y at 37 °C, pH 7.5 (Figure 5). After 2.5 h incubation, we investigated whether a permanent bond had formed between each engineered 2D12.5 single-cysteine Fab mutant and ^{90}Y−AABD. AABD incorporates a weakly electrophilic acryl functionality that has been shown to be unreactive with nucleophilic species naturally present in vivo *(13, 14)*. Following the incubation, protein samples were denatured and reduced, which destroys the binding site and breaks any reversible binding interactions between the protein and ligand. Permanent bonds are not broken by the sample treatment and analysis. Therefore, protein bands permanently tagged by the radioactive ligand are visible by autoradiography or phosphor plate. ABD, AABD, or BAD complexes of ^{90}Y that are not permanently bound migrate with the dye-front at the bottom of the gel.

All of the mutants incorporating the cysteine on CDR2 of the heavy chain showed permanent binding activity with ^{90}Y−AABD, and the Fab was the only protein labeled in cell culture media mixture (indicating high specificity). The G54C sample exhibited the highest concentration of protein with permanent binding activity. The N51C (LC) mutant showed no permanent attachment to ^{90}Y−AABD (data not shown). All of the cysteine mutants (including the N51C (LC) mutant) also formed permanent bonds with ^{90}Y−BAD, which incorporates a much more reactive electrophile. The higher background signal in the ^{90}Y−BAD containing lanes indicates that the ^{90}Y−BAD is less specific for its target and reacts with other proteins in the mixture. The N85D HC mutant showed no permanent bond-forming activity, as expected since a nucleophilic amino acid has not been engineered near the binding pocket. Negative controls incubated with the nonelectrophilic ^{90}Y−ABD also showed no attachment, as expected.

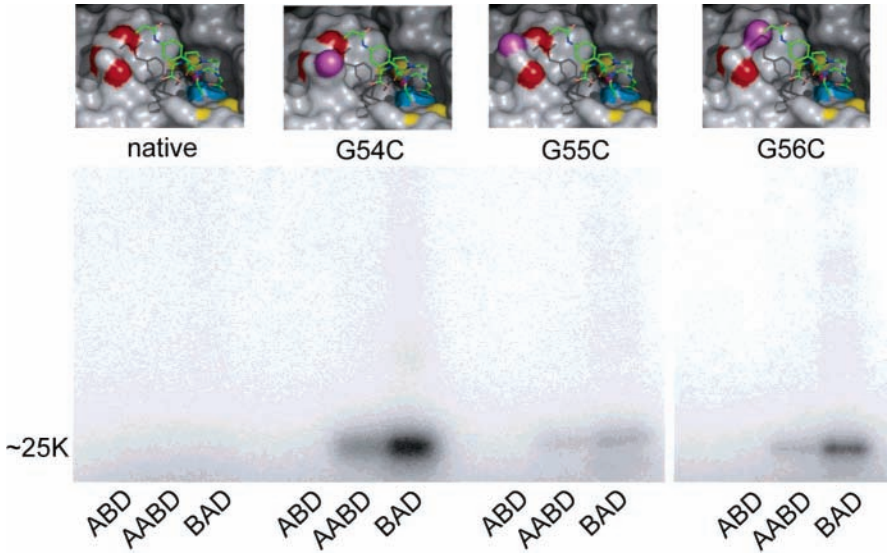


Figure 5. The single-cysteine mutants in CDR2 of the heavy chain were incubated with three DOTA ligands (ABD, AABD, and BAD) to evaluate their ability to form a permanent covalent bind with ^{90}Y−AABD. Raw media containing expressed protein was concentrated and dialyzed into a buffer for evaluation. Samples were adjusted to the same total protein concentration, so they contained different concentrations of Fab. All of the CDR2 (HC) mutants successfully formed a permanent covalent bind with ^{90}Y−AABD, but the G54C, N85D (HC) mutant appeared to be the most abundant and was selected for further study. All of the single-cysteine mutants reacted with ^{90}Y−BAD as expected. The ^{90}Y−AABD is highly selective for the Fab in dialyzed media containing significant amounts of other proteins, while the ^{90}Y−BAD reacts with other proteins in the mixture as well (background signal in BAD gel lanes).

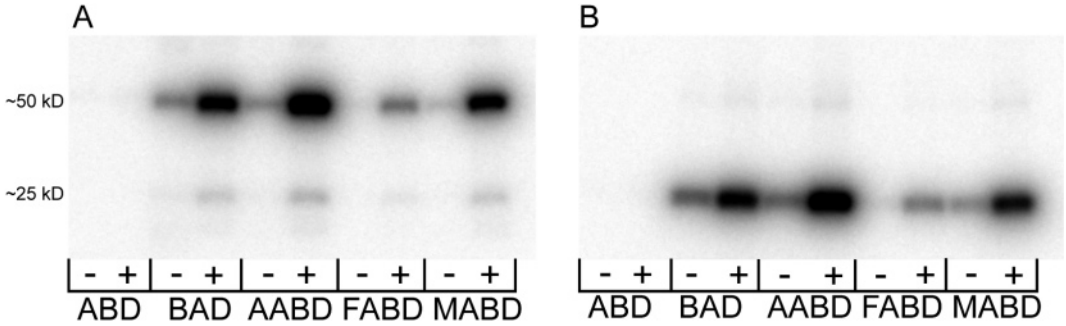


Figure 6. Several different carrier-free ^{90}Y−DOTA derivatives were evaluated for their ability to form a permanent covalent complex with purified G54C Fab. It is known that engineered cysteines often are blocked reversibly through heterogeneous disulfides formed with glutathione or cysteine. The G54C Fab was treated with MEA to activate the reversibly blocked cysteine; the Fab was evaluated for its capability to form a permanent covalent bond with indicated ^{90}Y−DOTA derivatives pre (−) and post (+) activation with MEA. The permanent bond-forming capacity of the G54C Fab improves dramatically with all tested electrophilic ^{90}Y−DOTA complexes following activation with MEA. MABD and FABD display markedly differing reactivities, with the cis-orientation of MABD considerably more favorable for permanent bond formation, while ^{90}Y−AABD, which lacks the carboxyl at the other end of the Michael acceptor, is more reactive than the ^{90}Y complex of either MABD and FABD. Samples were boiled and prepared for SDS−PAGE analysis without a reducing agent (A) and in the presence of 1% 2-mercaptoethanol (B). The nonreduced gel demonstrates that the interchain disulfide of the Fab is intact in almost all of the Fab molecules following treatment with MEA.

It is not clear from this experiment whether the higher infinite binding activity observed for the G54C mutant is due simply to its higher expression level or to the Cys location on the protein. Although analysis of the crystal structure indicates that the G54C mutant may be best positioned to form a permanent link with Y−AABD, experimental challenges make it difficult to assess the relative reactivity of each mutant. For example, engineered cysteines may be reversibly blocked with glutathione or cysteine when recombinant proteins are isolated from eukaryotic expression systems (*43, 44*). The percentage of cysteines that are blocked may vary with their surface accessibility.

Having developed a method for isolating purified chimeric Fab in high yield, we investigated whether the G54C mutant's engineered cysteine was reversibly blocked. Commonly, a mild reducing agent such as MEA may be used to preferentially reduce solvent-exposed disulfides while sparing buried ones (*43, 45*). Others have reported using stronger reducing agents such as DTT (*46*). Treatment of purified G54C Fab with 10 mM MEA overnight at room temperature, pH 7.5, significantly enhanced the permanent bond-forming capacity of the engineered Fab (Figure 6). MEA treatment of the Fab increased the free thiol activity by approximately an order of magnitude and was confirmed using a CPM thiol assay (*34*). Purified Fab samples always consisted of both monomer and a minor amount of Fab dimer (Figure 3). No significant change in the amount of Fab dimer was observed immediately following MEA activation of the cysteine mutant. Also, no significant reduction of the Fab's interchain disulfide was observed (Figure 4 and Figure 6A (nonreduced gel)). The disulfide linking the Fab dimer is apparently protected from solvent, similar to the interchain disulfide that covalently links the light and heavy chains, protecting the dimer from reduction by MEA. The Fab dimers present in solution showed no permanent bond-forming activity, as expected.

We compared the permanent binding activity of untreated and MEA-activated G54C Fab using ^{90}Y−AABD

and yttrium complexes of two other Michael acceptors, MABD and FABD (Figure 6). The experiment clearly shows that permanent binding capacity is significantly enhanced following MEA activation for each of the electrophiles. The smaller AABD shows higher reactivity than MABD or FABD, and apparently the cis-conformation of MABD is preferable to the trans-conformation of FABD. MABD may be interesting for further study because it is nearly as active as AABD, but may exhibit improved in vivo pharmacokinetic properties such as improved blood clearance because of its additional negative charge and overall higher hydrophilicity.

To be certain that we were labeling the G54C mutant specifically at the engineered cysteine site, we sought to further characterize the permanent bond formation between the G54C mutant and rare earth complexes of AABD. To simplify identification of the labeled site, ECAT methodology was used (*39*). Briefly, we incubated equal aliquots of MEA-activated G54C Fab with either Tb− or Tm−AABD, removed unlabeled AABD complexes by gel filtration and mixed the two protein samples. The combined sample was then digested with chymotrypsin, as the trypsin fragment would have been too large to identify conveniently with our MS instrumentation. Any peptides incorporating a metal−AABD tag were separated from untagged peptides using an immobilized 2D12.5 affinity column. The masses of any peptides tagged with Tb−AABD or Tm−AABD differ by 10 amu, a mass differential not commonly found in proteins. A search of the LC data identified only a single peptide that showed a pair of *m/z* peaks with a mass differential of 10 amu. MS^2 confirmed that the sequence of the peptide was SCGGTAY, and the cysteine was labeled with either Tb−AABD or Tm−AABD (Figure 7). This peptide incorporates the G54C mutation.

The LC/MS labeling experiments demonstrate that the covalent link between the G54C Fab mutant and metal−AABD complexes is specific to residue G54C. Further evidence for the specificity of permanent bond formation was collected through kinetics experiments, one of which incorporated the reversibly binding competitor Y−NBD (Figure 8). In the first experiment ^{90}Y-labeled 10 μM Y−AABD was added to purified G54C Fab (1 μM) at 37 °C, pH 7.5. Samples were withdrawn at various time points and were immediately boiled and reduced under denaturing conditions to effectively destroy the binding site and halt any further permanent bond formation. Samples were then analyzed by SDS−PAGE, and the extent of permanent bond formation was determined by measuring the relative radioactivity of bands using a phosphor screen sensitive to radioactive decay. The $t_{1/2}$ for permanent bond formation was ≈13 min.

In a second experiment performed in parallel, conditions were identical to the first except that after 6 min the unlabeled reversible competitor Y−NBD was added in great excess (1 mM) relative to [^{90}Y]Y−AABD (10 μM), effectively preventing rebinding of any [^{90}Y]Y−AABD that dissociated from the G54C Fab. Recall that there are two possible binding modes for Y−AABD to antibody 2D12.5 (*20*). If neither binding mode is favored over the other, the Y−AABD ligand should distribute evenly between them. Since only one of these modes is positioned to react with the G54C mutant, we expect to gain some insight into events in the binding site by adding the Y−NBD competitor at a time when all the sites are expected to be filled but few of the Y−AABD molecules are expected to have dissociated. Because it is in large excess, the Y−NBD should block any Y−AABD that may have initially been bound in the unreactive orientation from rebinding after dissociation. However, the Y−NBD should not affect rearrangements of Y−AABD within the binding site that do not involve dissociation.

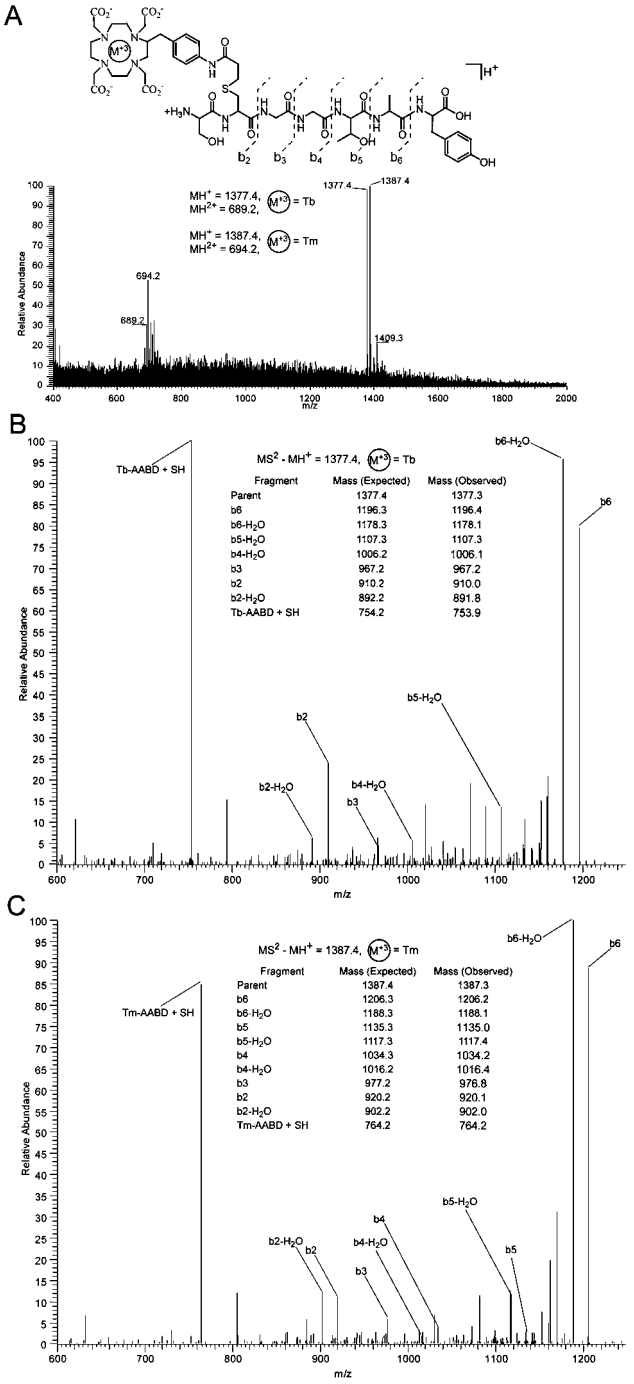


Figure 7. (A) LC/MS and LC/MS^2 analysis of (B) Tb−AABD and (C) Tm−AABD labeled G54C Fab subjected to enzymatic digestion with chymotrypsin. Equivalent aliquots of MEA-activated G54C Fab were incubated separately with either Tb−AABD or Tm−AABD and combined prior to digestion with chymotrypsin. Only the peptide containing the G54C engineered cysteine was labeled, and the ratio of Tb− and Tm−AABD labeled peptide was approximately equal as expected. MS^2 analysis confirmed the sequence of the peptide and presence of either the Tb−AABD or Tm−AABD label. The labeled peptide was affinity purified with an immobilized 2D12.5 column prior to LC/MS analysis as described previously (*39*). The Tb^{3+} and Tm^{3+} labels act as useful mass tags; the unnatural difference of 10 mass units between the Tb− and Tm−AABD labeled peptides simplifies peptide identification.

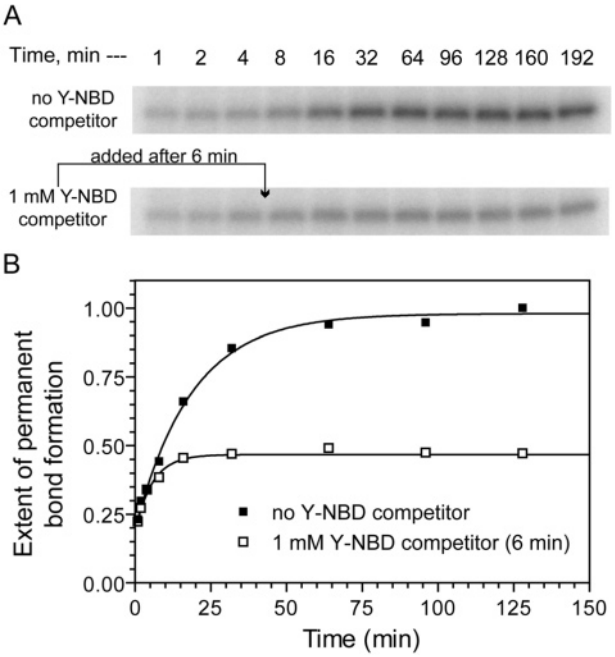


Figure 8. Kinetics of permanent bond formation between G54C Fab (1 μM) and ^{90}Y−AABD (including 10 μM Y−AABD carrier). The addition of a high concentration of Y−NBD, a reversibly binding competitor, after 6 min blocks the rebinding of Y−AABD after dissociation. The experiment containing no competitor, on the other hand, allows any Y−AABD molecules initially bound in an unreactive mode to dissociate and rebind in an orientation favorable for permanent covalent bond formation until a maximum is reached.

The experiment containing no competitor allows Y−AABD molecules to sample both binding orientations; those initially bound in the mode disfavored for permanent bond formation may dissociate and redistribute between the two orientations until all reactive sites are filled and permanent binding reaches a maximum. The overall $t_{1/2}$ of 13 min observed in the absence of competitor includes the time required for dissociation of unproductive complexes and rebinding of the Y−AABD ligand in the binding pocket. A much shorter $t_{1/2}$ for permanent binding (≈4 min) was observed in the presence of competitor, along with a yield ≈45%. A simple interpretation of these results is that the 4-min half-life measured in the latter experiment approximates the half-life for permanent bond formation for Y−AABD ligands bound in only the favored orientation, and that binding in the favored orientation occurs with at least 45% probability. While the kinetic scheme will not be fully understood without extensive study, it seems clear that a significant fraction of the G54C mutant attaches to the Y−AABD ligand in a short time under physiological conditions.

CONCLUSIONS

We have developed an artificial receptor system that binds irreversibly to its engineered ligands, using the general strategy first reported by Chmura et al. (*13*). In contrast to the earlier work, this system is notable for permanently binding a collection of structurally similar electrophilic ligands (*18*). Because the G54C mutant of 2D12.5 reacts quickly and with high specificity with both rare earth-AABD ligands and AABD complexes of other metals, it should be well suited for future applications that may place the receptor at cell surfaces for pretargeting applications.

The observed differences in reactivity between Y^{3+} complexes of MABD and FABD and the 2D12.5 G54C Fab mutant indicate that the steric bulk and conformation of atoms near the electrophilic site of the ligand can be important determinants of permanent binding. Initial experiments with the G55C and G56C mutants of 2D12.5 indicate that cysteines placed at these sites also exhibit permanent binding activity. Similar to the conclusions drawn by Levitsky et al. *(15)*, there seems to be some tolerance for the location of the reactive nucleophile on the protein surface near the binding site. Further work including the other 2D12.5 mutants introduced here should help delineate the importance of general surface location and ligand substitution and how these variables correlate with reactivity.

The tolerance for location coupled with the extension of permanent binding to ligands with weak affinity significantly enhances the general applicability of the infinite affinity concept and should lead to other examples. Recently, proximity accelerated coupling of ligand to protein and ligand to ligand has been applied to the identification of weakly binding ligand scaffolds for new combinatorial leads (*47, 48*). Proteins and/or ligands incorporating complementary reactive functional groups that are suitable for use in vivo may expand pharmaceutical design by offering alternative approaches to combating drug resistance or to target a family of similar molecules. In addition, the purposeful development of artificial receptor systems to produce binding pairs that exceed the affinity of even the avidin−biotin pairing should create a wealth of new possibilities for systems where high affinity has been difficult to attain.

ACKNOWLEDGMENT

We thank Nathan Butlin, Sean Gay, Mark McCoy, Susan Lee, and Saul Datwyler for helpful discussions, and NIH Research Grant CA16861 (C.F.M.) for support. The LCQ mass spectrometer was purchased with support from NIH Shared Instrumentation Grant RR014701.

LITERATURE CITED

(1) Hudson, P. J., and Souriau, C. (2003) Engineered antibodies. *Nat. Med. 9*, 129−34.

(2) Rheinnecker, M., Hardt, C., Ilag, L. L., Kufer, P., Gruber, R., Hoess, A., Lupas, A., Rottenberger, C., Pluckthun, A., and Pack, P. (1996) Multivalent antibody fragments with high functional affinity for a tumor-associated carbohydrate antigen. *J. Immunol. 157*, 2989−2997.

(3) Northrup, S. H., and Erickson, H. P. (1992) Kinetics of protein−protein association explained by Brownian dynamics computer simulation. *Proc. Natl. Acad. Sci. U.S.A. 89*, 3338−3342.

(4) Foote, J., and Eisen, H. N. (1995) Kinetic and affinity limits on antibodies produced during immune responses. *Proc. Natl. Acad. Sci. U.S.A. 92*, 1254−1256.

(5) Meyer, D. L., Fineman, M., Unger, B. W., and Frincke, J. M. (1990) Kinetics of the dissociation of indium-(p-substituted-benzyl)ethylenediaminetetraacetic acid hapten analogues from the monoclonal anti-hapten antibody CHA255. *Bioconjugate Chem. 1*, 278−284.

(6) Silbey, R. J., Alberty, R. A., and Bawendi, M. G. (2005) *Physical Chemistry*, 4th ed., p 646, Chapter 18, John Wiley & Sons, Hoboken, NJ, in press. ($t_{1/2} = (\ln 2/k_{off})$, and $10^{-3} < k_{off} < 10^{-4}$ s^{-1}, given that maximum association rate constants k_{on} are usually of the order 10^5−10^6 M^{-1} s^{-1}).

(7) Karacay, H., McBride, W. J., Griffiths, G. L., Sharkey, R. M., Barbet, J., Hansen, H. J., and Goldenberg, D. M. (2000) Experimental pretargeting studies of cancer with a humanized anti-CEA x murine anti-[In-DTPA] bispecific antibody construct and a (99m)Tc-/(188)Re-labeled peptide. *Bioconjugate Chem. 11*, 842−854.

(8) Boder, E. T., Midelfort, K. S., and Wittrup, K. D. (2000) Directed evolution of antibody fragments with monovalent

femtomolar antigen-binding affinity. *Proc. Natl. Acad. Sci. U.S.A. 97*, 10701−10705.

(9) Graff, C. P., Chester, K., Begent, R., and Wittrup, K. D. (2004) Directed evolution of an anti-carcinoembryonic antigen scFv with a four-day monovalent dissociation half-time at 37-{degrees}C. *Protein Eng. Des. Sel. 17*, 293−304.

(10) Yang, W. P., Green, K., Pinz-Sweeney, S., Briones, A. T., Burton, D. R., and Barbas, C. F., 3rd. (1995) CDR walking mutagenesis for the affinity maturation of a potent human anti-HIV-1 antibody into the picomolar range. *J. Mol. Biol. 254*, 392−403.

(11) Schier, R., McCall, A., Adams, G. P., Marshall, K. W., Merritt, H., Yim, M., Crawford, R. S., Weiner, L. M., Marks, C., and Marks, J. D. (1996) Isolation of picomolar affinity anti-c-erbB-2 single-chain Fv by molecular evolution of the complementarity determining regions in the center of the antibody binding site. *J. Mol. Biol. 263*, 551−567.

(12) Pini, A., Viti, F., Santucci, A., Carnemolla, B., Zardi, L., Neri, P., and Neri, D. (1998) Design and use of a phage display library. Human antibodies with subnanomolar affinity against a marker of angiogenesis eluted from a two-dimensional gel. *J. Biol. Chem. 273*, 21769−76.

(13) Chmura, A. J., Orton, M. S., and Meares, C. F. (2001) Antibodies with infinite affinity. *Proc. Natl. Acad. Sci. U.S.A. 98*, 8480−8484.

(14) Chmura, A. J., Schmidt, B. D., Corson, D. T., Traviglia, S. L., and Meares, C. F. (2002) Electrophilic chelating agents for irreversible binding of metal chelates to engineered antibodies. *J. Controlled Release 78*, 249−258.

(15) Levitsky, K., Ciolli, C. J., and Belshaw, P. J. (2003) Selective inhibition of engineered receptors via proximity-accelerated alkylation. *Org. Lett. 5*, 693−696.

(16) Chen, G., Heim, A., Riether, D., Yee, D., Milgrom, Y., Gawinowicz, M. A., and Sames, D. (2003) Reactivity of functional groups on the protein surface: development of epoxide probes for protein labeling. *J. Am. Chem. Soc. 125*, 8130−8133.

(17) Viljanen, J., Tegler, L., and Broo, K. S. (2004) Combinatorial chemical reengineering of the alpha class glutathione transferases. *Bioconjugate Chem. 15*, 718−727.

(18) Corneillie, T. M., Whetstone, P. A., Lee, K. L., Wong, J. W., and Meares, C. F. (2004) Converting weak binders into infinite binders. *Bioconjugate Chem. 15*, 1389−1391.

(19) Corneillie, T. M., Whetstone, P. A., Fisher, A. J., and Meares, C. F. (2003) A rare earth-DOTA-binding antibody: probe properties and binding affinity across the lanthanide series. *J. Am. Chem. Soc. 125*, 3436−3437.

(20) Corneillie, T. M., Fisher, A. J., and Meares, C. F. (2003) Crystal structures of two complexes of the rare-earth-DOTA-binding antibody 2D12.5: ligand generality from a chiral system. *J. Am. Chem. Soc. 125*, 15039−15048.

(21) Pont-Kingdon, G. (1994) Construction of chimeric molecules by a two-step recombinant PCR method. *BioTechniques 16*, 1010−1011.

(22) Ivey-Hoyle, M. (1991) Recombinant gene expression in cultured Drosophila melanogaster cells. *Curr. Opin. Biotechnol. 2*, 704−707.

(23) Kirkpatrick, R. B., Ganguly, S., Angelichio, M., Griego, S., Shatzman, A., Silverman, C., and Rosenberg, M. (1995) Heavy chain dimers as well as complete antibodies are efficiently formed and secreted from Drosophila via a BiP-mediated pathway. *J. Biol. Chem. 270*, 19800−19805.

(24) Reavy, B., Ziegler, A., Diplexcito, J., Macintosh, S. M., Torrance, L., and Mayo, M. (2000) Expression of functional recombinant antibody molecules in insect cell expression systems. *Protein Expr. Purif. 18*, 221−228.

(25) Skerra, A. (1994) A general vector, pASK84, for cloning, bacterial production, and single-step purification of antibody Fab fragments. *Gene 141*, 79−84.

(26) Willems, A., Leoen, J., Schoonooghe, S., Grooten, J., and Mertens, N. (2003) Optimizing expression and purification from cell culture medium of trispecific recombinant antibody derivatives. *J. Chromatogr. B Anal. Technol. Biomed. Life. Sci. 786*, 161−176.

(27) Ito, W., Ishiguro, H., and Kurosawa, Y. (1991) A general method for introducing a series of mutations into cloned DNA using the polymerase chain reaction. *Gene 102*, 67−70.

(28) Barinka, C., Rinnova, M., Sacha, P., Rojas, C., Majer, P., Slusher, B. S., and Konvalinka, J. (2002) Substrate specificity, inhibition and enzymological analysis of recombinant human glutamate carboxypeptidase II. *J. Neurochem. 80*, 477−487.

(29) Meares, C. F., McCall, M. J., Reardan, D. T., Goodwin, D. A., Diamanti, C. I., and McTigue, M. (1984) Conjugation of antibodies with bifunctional chelating agents: isothiocyanate and bromoacetamide reagents, methods of analysis, and subsequent addition of metal ions. *Anal. Biochem. 142*, 68−78.

(30) Guerrier, L., Girot, P., Schwartz, W., and Boschetti, E. (2000) New method for the selective capture of antibodies under physiological conditions. *Bioseparation 9*, 211−221.

(31) Schwartz, W., Judd, D., Wysocki, M., Guerrier, L., Birck-Wilson, E., and Boschetti, E. (2001) Comparison of hydrophobic charge induction chromatography with affinity chromatography on protein A for harvest and purification of antibodies. *J. Chromatogr. A 908*, 251−263.

(32) Schoonjans, R., Willems, A., Schoonooghe, S., Leoen, J., Grooten, J., and Mertens, N. (2001) A new model for intermediate molecular weight recombinant bispecific and trispecific antibodies by efficient heterodimerization of single chain variable domains through fusion to a Fab-chain. *Biomol. Eng. 17*, 193−202.

(33) Penefsky, H. S. (1979) A centrifuged-column procedure for the measurement of ligand binding by beef heart F1. *Methods Enzymol. 56*, 527−530.

(34) Parvari, R., Pecht, I., and Soreq, H. (1983) A microfluorometric assay for cholinesterases, suitable for multiple kinetic determinations of picomoles of released thiocholine. *Anal. Biochem. 133*, 450−456.

(35) Moi, M. K., Meares, C. F., and DeNardo, S. J. (1988) The peptide way to macrocyclic bifunctional chelating agents: synthesis of 2-(*p*-nitrobenzyl)-1,4,7,10-tetraazacyclododecane-*N*,*N*′,*N*",*N*‴-tetraacetic acid and study of its yttrium(III) complex. *J. Am. Chem. Soc. 110*, 6266−6267.

(36) Renn, O., and Meares, C. F. (1992) Large-scale synthesis of the bifunctional chelating agent 2-(*p*-nitrobenzyl)-1,4,7,-10-tetraazacyclododecane-*N*,*N*′,*N*″,*N*‴-tetraacetic acid, and the determination of its enantiomeric purity by chiral chromatography. *Bioconjugate Chem. 3*, 563−569.

(37) Takenouchi, K., Tabe, M., Watanabe, K., Hazato, A., Kato, Y., Shionoya, M., Koike, T., and Kimura, E. (1993) Novel pendant-type macrocyclic bifunctional chelating agents: (carboxymethyl)amino derivatives of 2-(4-nitrobenzyl)-1,4,7,10-tetraazacyclododecane-*N*,*N*′,*N*″,*N*‴-tetraacetic acid and their complex formation with yttrium(III). *J. Org. Chem. 58*, 6895−6899.

(38) Corson, D. T., and Meares, C. F. (2000) Efficient multigram synthesis of the bifunctional chelating agent (S)-1-p-isothiocyanatobenzyl-diethylenetriaminepentaacetic acid [correction of diethylenetetraminepentaacetic acid]. *Bioconjugate Chem. 11*, 292−299.

(39) Whetstone, P. A., Butlin, N. G., Corneillie, T. M., and Meares, C. F. (2004) Element-coded affinity tags for peptides and proteins. *Bioconjugate Chem. 15*, 3−6.

(40) Barbas, C. F., 3rd, Kang, A. S., Lerner, R. A., and Benkovic, S. J. (1991) Assembly of combinatorial antibody libraries on phage surfaces: the gene III site. *Proc. Natl. Acad. Sci. U.S.A. 88*, 7978−7982.

(41) Sheeley, D. M., Merrill, B. M., and Taylor, L. C. (1997) Characterization of monoclonal antibody glycosylation: comparison of expression systems and identification of terminal alpha-linked galactose. *Anal. Biochem. 247*, 102−110.

(42) Chargelegue, D., Vine, N. D., van Dolleweerd, C. J., Drake, P. M., and Ma, J. K. (2000) A murine monoclonal antibody produced in transgenic plants with plant-specific glycans is not immunogenic in mice. *Transgenic Res. 9*, 187−194.

(43) Stimmel, J. B., Merrill, B. M., Kuyper, L. F., Moxham, C. P., Hutchins, J. T., Fling, M. E., and Kull, F. C., Jr. (2000) Site-specific conjugation on serine right-arrow cysteine variant monoclonal antibodies. *J. Biol. Chem. 275*, 30445−30450.

(44) Lyons, A., King, D. J., Owens, R. J., Yarranton, G. T., Millican, A., Whittle, N. R., and Adair, J. R. (1990) Site-specific attachment to recombinant antibodies via introduced surface cysteine residues. *Protein Eng. 3*, 703−708.

(45) Karacay, H., Sharkey, R. M., McBride, W. J., Griffiths, G. L., Qu, Z., Chang, K., Hansen, H. J., and Goldenberg, D. M. (2002) Pretargeting for cancer radioimmunotherapy with bispecific antibodies: role of the bispecific antibody's valency for the tumor target antigen. *Bioconjugate Chem. 13*, 1054−1070.

(46) Yang, K., Basu, A., Wang, M., Chintala, R., Hsieh, M. C., Liu, S., Hua, J., Zhang, Z., Zhou, J., Li, M., Phyu, H., Petti, G., Mendez, M., Janjua, H., Peng, P., Longley, C., Borowski, V., Mehlig, M., and Filpula, D. (2003) Tailoring structure−function and pharmacokinetic properties of single-chain Fv proteins by site-specific PEGylation. *Protein Eng. 16*, 761−770.

(47) Erlanson, D. A., Braisted, A. C., Raphael, D. R., Randal, M., Stroud, R. M., Gordon, E. M., and Wells, J. A. (2000) Site-directed ligand discovery. *Proc. Natl. Acad. Sci. U.S.A. 97*, 9367−9372.

(48) Kolb, H. C., Finn, M. G., and Sharpless, K. B. (2001) Click chemistry: diverse chemical function from a few good reactions. *Angew. Chem., Int. Ed. Engl. 40*, 2004−2021.

BC049824M

Developing a Peptide-Based Near-Infrared Molecular Probe for Protease Sensing

Wellington Pham, Yongdoo Choi, Ralph Weissleder, and Ching-Hsuan Tung*

Center for Molecular Imaging Research, Massachusetts General Hospital, Harvard Medical School, Charlestown, Massachusetts 02129. Received March 25, 2004; Revised Manuscript Received May 3, 2004

Recently near-infrared (NIR) molecular probes have become important reporter molecules for a number of types of in vivo biomedical imaging. A peptide-based NIR fluorescence probe consisting of a NIR fluorescence emitter (Cy5.5), a NIR fluorescence absorber (NIRQ820), and a protease selective peptide sequence was designed to sense protease activity. Using a MMP-7 model, we showed that NIRQ820 efficiently absorbs the emission energy of Cy5.5 resulting in a low initial signal. Upon reacting with its target, MMP-7, the fluorescence signal of the designed probe was increased by 7-fold with a K_{cat}/K_m of 100 000 M^{-1} s^{-1}. The described synthetic strategy should have wide application for other NIR probe preparations.

INTRODUCTION

To identify promising drug candidates, reliable assays, which could truly report drug efficacy, are critical to initial screening and further evaluation. Many proteolytic assays have been reported and applied in vitro, but direct imaging of the therapeutic effect of drugs in vivo was not available until recently (*1*). A matrix metalloproteinase (MMP)-activatable near-infrared (NIR) fluorescence probe was developed to report inhibitor effect on proteolytic activity in animals (*1*). On each probe molecule, multiple NIR fluorochromes were anchored, via an MMP-selective peptide spacer. This probe is optically silent in its native (quenched) state and becomes highly fluorescent after the proteolysis of MMP substrate peptide linkers by the enzyme. Although this approach works well, it is reasonable to think of a simpler and more defined probe for in vivo assay.

For detecting enzymatic activity in vivo and for the imaging of deeper tissues in vivo, the use of near-infrared (NIR) light is required because hemoglobin and water, which are the major absorbers of visible and infrared light, respectively, have their lowest absorption coefficient in the NIR region around 650−900 nm (*2*). Although many fluorescence enzyme substrates have been reported and widely used, for example, coumarin, *p*-nitrophenol, and other analogues, most of these fluorochromes are in the visible range. The challenge of moving from visible into NIR window is to find a good matching pair of fluorescence donor and acceptor. The underlying principle of designing a NIR probe relies on fluorescence resonance energy transfer (FRET) between a fluorescent donor and a fluorescent or a nonfluorescent acceptor molecule linked via a protease substrate peptide linker. We reported this type of design previously for caspase-3 enzyme detection, using a synthesized nonfluorescence azulene quencher (abs = 750 nm) pairing with a commercial available fluorochrome (em = 700) (*3*). More than 4-fold increase in fluorescence signal was observed when treated with its target enzyme. Lately, we found that a previously synthesized NIR fluorochrome, NIRQ820 (*4*), served as a better acceptor for the fluorochromes with emission around 700 nm.

MMPs are known to be important in normal tissue remodeling, but also known to play critical roles in many diseases, such as lung diseases, atherosclerosis, and cancer (*5*−*7*). Elevated level of MMPs have been found in tumors and shown to correlate well with their invasive and metastatic profiles in both experimental cancer models and in human malignancies (*8*, *9*). The presence of extracellular and membrane-bound MMPs in tumors not only aids the degradation of extracellular matrix by neoplastic cells, but also facilitates their motility and directs cell invasion (*10*). Thus, MMPs have long been of interest as pharmaceutical targets (*11*−*13*). Among those MMPs, MMP-7 has been an important target, because it was overexpressed in pancreatic, colon, and breast cancers *(14, 15)*, In this report, we describe the design of a new type of well-defined low molecular weight peptide-based NIR fluorescence probe, designed primarily for sensing of tumor-associated MMP-7 activity.

EXPERIMENTAL PROCEDURES

Unless otherwise stated, reagents and solvents were obtained from commercial sources without further purification. All moisture or air-sensitive reactions were carried out under a static argon atmosphere. Standard Fmoc-amino acids, *N*-hydroxybenzotriazole (HOBt), and 2-(1*H*-benzotriazole 1-yl)-1,1,3,3-tetramethyluronium hexafluorophosphate (HBTU) (Applied Biosystem, Foster City, CA), Rink amide resin (100−200 mesh) (Novabiochem, San Dieago, CA), Cy5.5 mono maleimide (Amersham, Piscataway, NJ), and active human recombinant MMP-9 and MMP-7 enzymes (Calbiochem, San Diego, CA) were used.

Reverse phase HPLC purification was performed on a Hitachi Model D-7000 incorporated with Diode Array Detector L-7455 using Vydac 218TP1010 C_{18} column (Hesperia, CA) at a flow rate of 4.0 mL/min. The elution gradient was set from 0 to 50% of buffer B (10% of A in acetonitrile) in 45 min where buffer A was 0.1% TFA in

* To whom correspondence should be addressed. Ching H. Tung, Ph.D., Center for Molecular Imaging Research, Massachusetts General Hospital, 149 13th St., Rm. 5406, Charlestown, MA 02129. (tel): (617) 726−5779. (fax): (617) 726-5708. e-mail: tung@helix.mgh.harvard.edu.

10.1021/bc049924s CCC: $27.50 © 2004 American Chemical Society
Published on Web 09/24/2004

deionized water. Detection was monitored from 200 to 800 nm range and MALDI-TOF mass spectra were determined (Tufts Core Mass Spectrometry Facility, Boston, MA). Absorption and emission spectra were determined using Hitachi U-3000 Spectrophotometer and F-4500 Fluorescence Spectrophotometer, respectively.

Probe Synthesis. MMP-7 substrate, GVPLSLTMGC−NH_2, with glycine and cysteine at both ends for conjugation was synthesized on an automatic synthesizer (433A Peptide Synthesizer, Applied Biosystem) by Fmoc chemistry (0.1 mmol) using Rink amide resin (0.43 mmol/g) and HBTU/HOBt as the activating reagents. After the completion of the peptide synthesis, the fluorescence quencher, NIRQ820, was coupled to the N-terminus (*4*). NIRQ820 (0.4 mmol, 326.16 mg) was first activated with HBTU (0.2 mmol, 75.86 mg) and HOBt (0.2 mmol, 27.02 mg) in DMF in the presence of argon for 3 h and then reacted overnight. The NIRQ820-labeled peptide **3**, NIRQ820-GVPLSLTMGC−NH_2, was cleaved by a cocktail of TFA/thioanisole/ethandithiol/anisole (90/5/3/2), and purified by C18 reversed-phase HPLC to afford green-colored product. MALDI-TOF MS calcd (M + H)$^+$ 1774.57, found 1774.83.

The fluorescence donor, Cy5.5 mono maleimide (1 mg, 0.87 μmol), was reacted with the previously purified compound **3** (1.5 μmol) in 400 μL buffer (1:1 acetonitrile/50 mM sodium acetate, pH = 7.4) at room temperature in the dark with random shaking for 2 h. The final produce **4**, NIRQ820-GVPLSLTMGC(Cy5.5)-NH_2, was purified by reversed- phase HPLC. MALDI-TOF MS (M + H)$^+$ calcd. 2814.76, found 2814.99.

A control probe **5**, NIRQ820-GSMLPVTLGC(Cy5.5)-NH_2, was synthesized using the same approach.

Stern−Volmer Plot (*16*). A Stern−Volmer plot was obtained at room temperature where a fixed concentration of Cy5.5 (13 μM) was treated with an increasing amount of NIRQ820 (6.0−24 μM) in deionized water. The emission intensity was measured at 690 nm and the relative emission efficiencies of Cy5.5 in the absence and in the presence of NIRQ820 provided a straight line in the concentration range. The following equation was used to derive the Stern−Volmer quenching constant:

$$F_0/F = 1 + K_{sv}[\text{NIRQ820}]$$

where F_0 is the unquenched fluorescence intensity of Cy5.5, F is the fluorescence intensity at [NIRQ820], and K_{sv} is the Stern−Volmer quenching constant.

In vitro probe activation. Peptide-based probes were dissolved in deionized water and the concentration was determined by Beer's law: [C] = A/ϵ where A is the absorbance at 674 nm and ϵ is the molar extinction coefficient (250 000 M^{-1} cm^{-1}) of Cy5.5. The activation of the probes (10μM) was commenced with the addition of MMP-7 or MMP-9 enzymes (30 nM) in a buffer consisting of a 50 mM Tris (pH = 7.6), 200 m NaCl, 5 mM $CaCl_2$, and 1 μM $ZnCl_2$. The fluorescence signal was monitored using 667 nm excitation and 690 nm emission at room temperature for 3 h by SPECTRAmax Gemini (Molecular Devices, Sunnyvale, CA). The plate was set to stir 5 s prior to measurement.

Tumor Extraction. Human fibrosarcoma cell line (HT1080, ATCC, Manassas, VA) was grown in Dulbecco's medium (DMEM, Cellgro, Mediatech, Washington, DC) containing 10% (v/v) fetal bovine serum (FBS, Cellgro) and 1% penicillin/streptomycin at 37 °C in a humidified 5% CO_2 atmosphere. To induce solid tumors, 2×10^6 cells in DMEM media were injected subcutaneously into the mammary fat pad of athymic nude mice (6−7 weeks old)

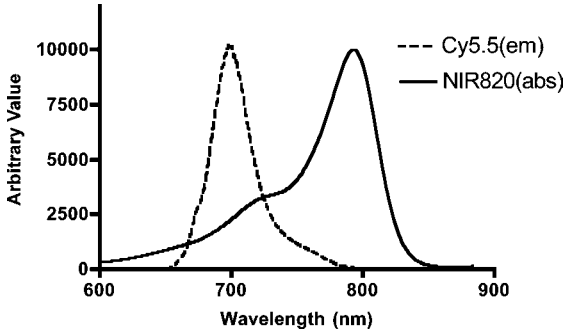


Figure 1. Normalized spectral overlap between the absorption of NIRQ820 (—) and emission of Cy5.5 (- - -). The spectra were obtained in water at room temperature.

(Charles River, Wilmington, MA). When the tumors were grown to 6−9 mm in diameter, the mice were anesthetized by means of intraperitoneal injection of ketamine (90 mg/kg body weight) and xylazine (10 mg/kg body weight). The tumor tissues were carefully dissected and reserved in a buffer solution (pH = 7.4, 50 mM Tris-HCl, 0.15 M NaCl, and 10 mM $CaCl_2$) followed by homogenization and centrifugation at 4 °C. The supernatant was collected and stored at −80 °C for future analysis. All procedures using the animals were conducted in compliance with state and federal guidelines and approved by institutional Animal Care.

Casein Zymography. To confirm the presence of active MMP-7 in tumor tissue, zymography using casein-loaded SDS-polyacrylamide gel was performed as described previously (*17*). Briefly, a 12% SDS-polyacrylamide gel was copolymerized with bovine β-casein (final concentration: 0.5 mg/mL), and then the prepared gel was pre-run at room temperature. Tumor tissue extract (20 μL) and the control MMP-7 enzyme (6 ng) were treated with mercaptoethanol-free Laemmli buffer followed by electrophoresis at 4 °C. SDS was removed from the gel by washing twice with 50 mM Tris-HCl (pH 7.5), 2.5% Triton X-100 for 30 min, and twice more for 10 min with 50 mM Tris-HCl (pH 7.5). The degradation of β-casein in the gel was started by incubating the gel overnight at 37 °C with 50 mM Tris-HCl (pH 7.5), 0.15 M NaCl, 10 mM $CaCl_2$, 0.1% Triton X-100, and 0.02% NaN_3. The staining was performed for 1 h at room temperature with 0.5% Coomassie brilliant blue R-250 in 10% acetic acid and destaining with 10% acetic acid. Caseinolytic activity was visualized as clear bands at 19 kDa of lysis against the dark background.

Probe Activation in Tumor Extract. For the fluorescence assay using tumor extract, 50 μL of tumor extracts were added into 96-well plate and mixed with 150 μL of the buffer solutions (pH = 7.6, 50 mM Tris, 200 m NaCl, 5 mM $CaCl_2$, and 1 μM $ZnCl_2$) containing probe **4** or **5** (10 μM). The solutions containing only probe **4** or probe **5** were also tested as controls. The fluorescence signal was monitored simultaneously for 3 h as described above.

RESULTS AND DISCUSSION

NIRQ820, a cyclohepta polymethine fluorochrome, ex/em = 790/820 nm, is a water soluble NIR fluorochrome with great chemical stability, and a good NIR fluorochrome for protein labeling (*4*). By studying NIRQ820 with a shorter wavelength commercial available fluorochrome, Cy5.5 (ex/em = 675/694 nm, Figure 1), it was found that NIRQ820 acted as an efficient quencher for Cy5.5. To assess the quenching efficiency of this FRET pair, a Stern−Volmer plot was obtained where the

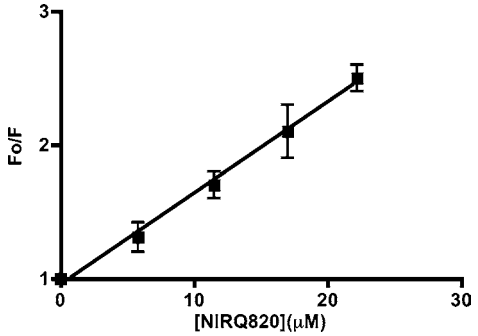


Figure 2. Stern−Volmer plot for determining quenching efficiency of NIRQ820 toward Cy5.5 in water. F_0 and F are fluorescence intensity of Cy5.5 (13 μM) in the absence and in the presence of NIRQ820, respectively. Values are means from two assays.

fluorescence intensity of the donor, Cy5.5, was measured with or without the acceptor, NIRQ820 (Figure 2). There was a decrease in the fluorescence intensity of Cy5.5 (1.32×10^{-5} M) with the increasing concentration of NIRQ820 (0.59×10^{-5} to 2.22×10^{-5} M). A nearly perfect linear line with a steep slope intercepting at 1 implied an effective dynamic diffusion control quenching effect (*18*, *19*).

Previously we have demonstrated that NIRQ820 can be conveniently synthesized in large quantity and is compatible with Fmoc solid-phase peptide synthesis (SPPS) (*4*). We thus chose to couple NIRQ820 quencher onto a MMP-7 selective peptide on solid support and label the peptide with the fluorescence donor, Cy5.5, later in solution (Figure 3).

The core specific peptide substrate, VPLSLTMG, for MMP-7 was selected from a combinatory peptide library (*20*). It has been shown that it is at least 10 to 100 times more selective for MMP-7 than for MMP-1, -2, -3, -9, and MT1-MMP. To the core MMP-7 substrate sequence, glycine and cysteine residues were incorporated at N- and C-termini, respectively, as handles for fluorochromes labeling. The peptide (GVPLSLTMGC) was synthesized on a Rink amide resin by Fmoc chemistry using SPPS. Upon complete synthesis of the peptide sequence, the N-terminal Fmoc group was removed and the sole active amino group was confirmed by ninhydrin test (*21*). NIRQ820 was preactivated by HOBt/HBTU in anhydrous DMF under the presence of argon for 2 h. The intermediate was then coupled to the peptide catalyzed by pyridine for 4 h. The green solid supports were washed with DMF, followed by methanol, before being subjected to standard cleavage conditions.

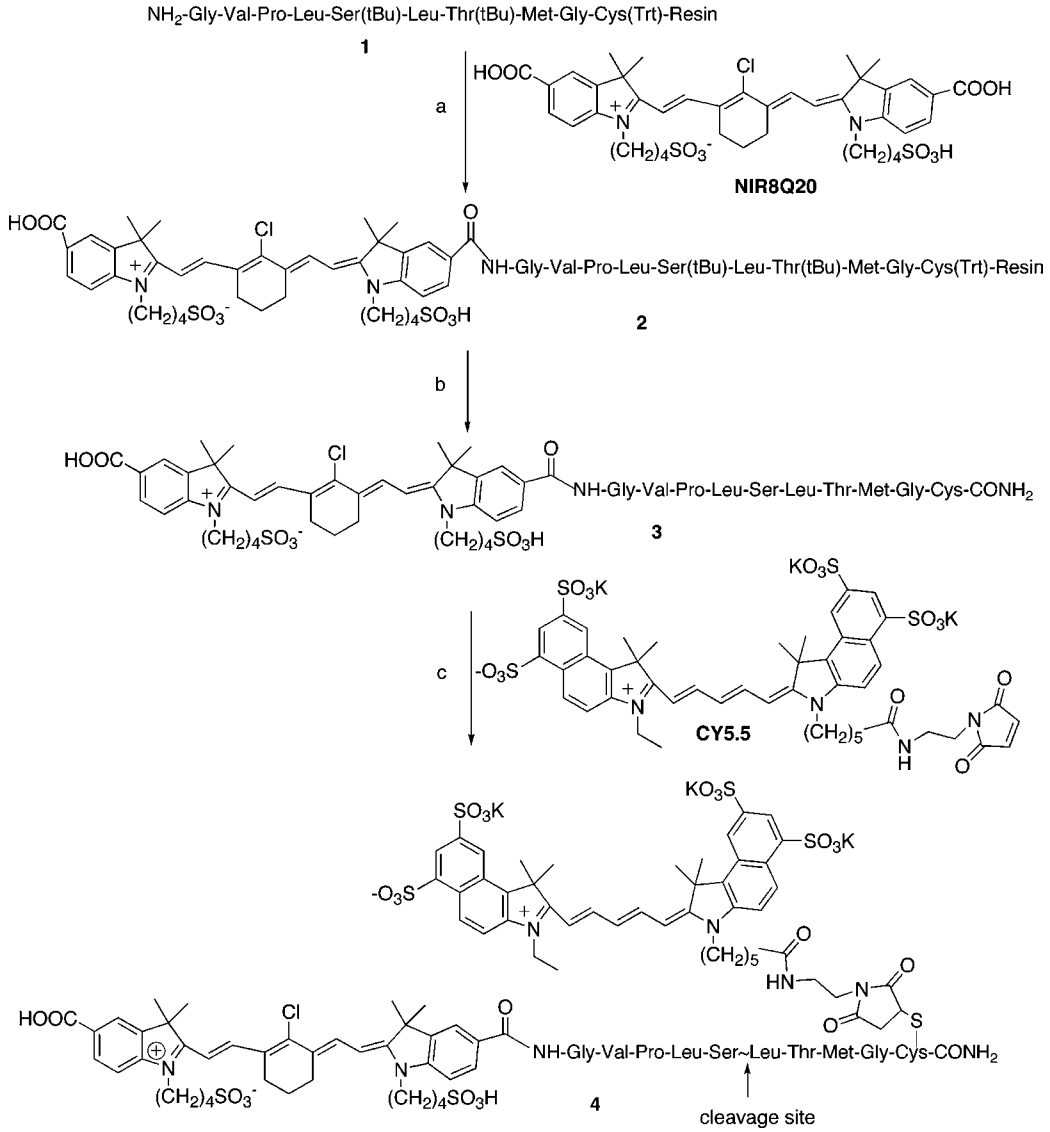


Figure 3. Synthesis of peptide-based MMP-7 probe **4**. Reagents and conditions: (a) HOBt/HBTU, pyridine, DMF, 6 h; (b) TFA and scavengers of thioanisole, anisole, and ethanedithiol, 3 h; (c) sodium acetate buffer (50 mM, pH = 7.4), 2 h.

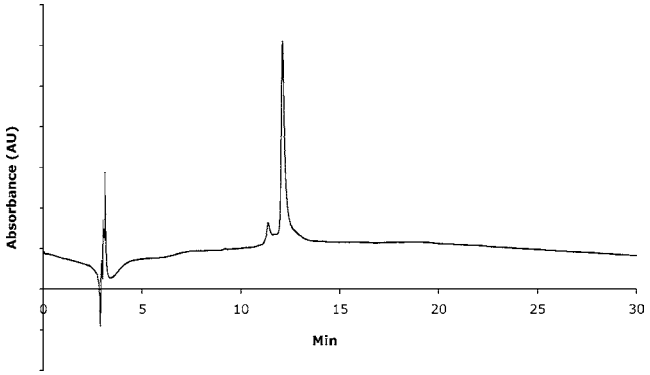


Figure 4. Analytical HPLC traces of probe **4**, NIRQ820-GVPLSLTMGC(Cy5.5)-NH_2.

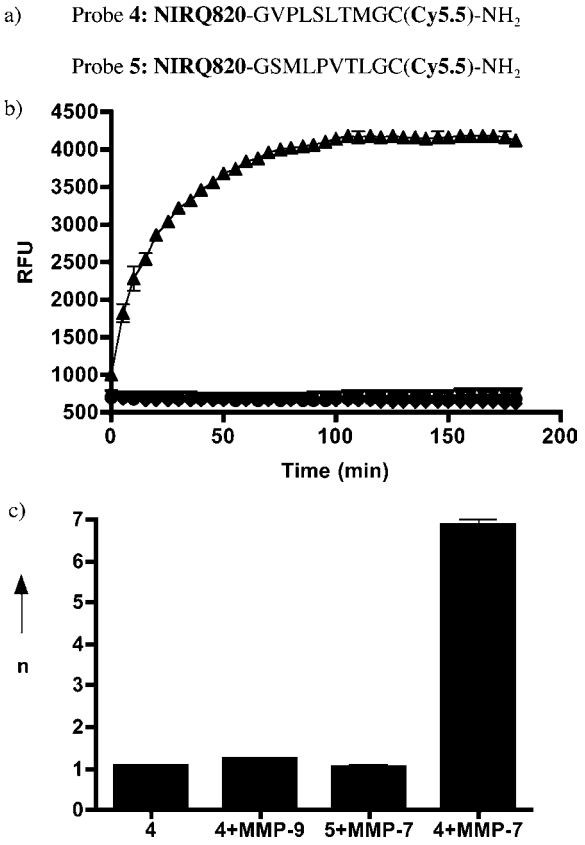


Figure 5. Activation of peptide-based NIR probes with MMPs. (a) Sequence of MMP-7 probe **4** and control scramble probe **5**. (b) Fluorescence signals change upon incubation with **4** alone (◆), **4** + MMP-9 (▼), **5** + MMP-7 (●), and **4** + MMP-7 (▲) in a 50 mM Tris (pH = 7.6), 200 M NaCl, 5 mM $CaCl_2$, and 1 μM $ZnCl_2$ buffer. (c) Fold increase of fluorescence signal at 100 min. Values are means of two assays.

After precipitation and washing with *tert*-butyl methyl ether at 4 °C, the labeled green peptide **3** was purified by HPLC and the product was stored at −78 °C for several months without trace of decomposition. Excess unreacted NIRQ820 was recovered by recrystallization in methanol/water. The thio-reactive maleimide moiety of Cy5.5 was further incorporated into the peptide sequence via the C-terminal cysteine residue in sodium acetate for 2 h following by HPLC purification to provide the MMP-7 probe **4** quantitatively (Figure 4).

The enzyme selectivity of the probes was studied with different controls in an optimal buffer condition using 50 mM Tris (pH = 7.6), 200 mM NaCl, 5 mM $CaCl_2$, and 1 μM $ZnCl_2$ (Figure 5). To follow the proteolytic reaction,

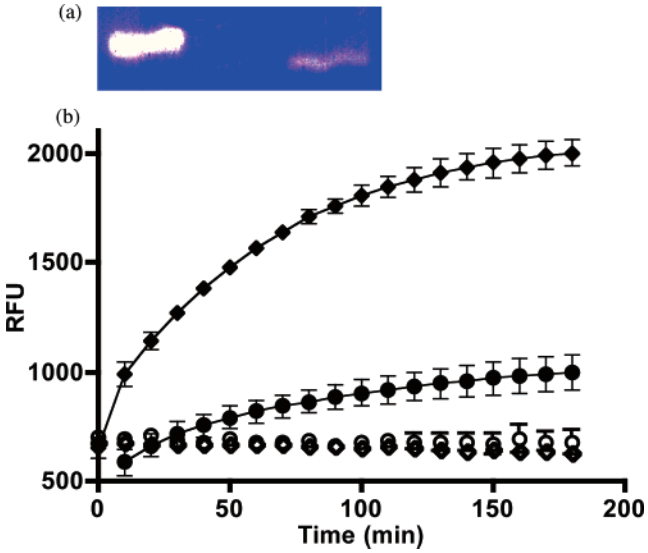


Figure 6. Activation of MMP-7 probe using tumor extract. (a) Casein zymography of HT1080 tumor extract. The 19 kDa bands indicate the active MMP-7 from standard (left) and from tumor extract (right). (b) Activation of NIR probes (10 μM) with tumor extract in a 50 mM Tris, 200 M NaCl, 5 mM $CaCl_2$, and 1 μM $ZnCl_2$ buffer or buffer only. Probe **4** plus tumor extract (solid diamond), scrambled probe **5** plus tumor extract (solid circle), probe **4** in buffer only (open diamond), scrambled probe **5** in buffer only (open circle).

fluorescence changes of Cy5.5 at 690 nm (excitation at 667 nm) were accessed by a fluorescence plate reader. Within 100 min, the Cy5.5 fluorescence signal of probe **4** increased 7-fold with MMP-7 as compared to the control enzyme, MMP-9, or when the probe **4** was incubated without MMP-7 (Figure 5). To further prove the specificity of this probe, a scrambled control probe **5**, SMLPVTLG, was synthesized (Figure 5a). There was no increase in the fluorescence intensity when MMP-7 was incubated with scrambled probe. The enzyme kinetics of probe **4** with MMP-7 was determined using the Michaelis−Menten equation. To obtain accurate initial rate of substrate cleavage, the inner filter effect was corrected according to a previously reported method (*22*). The determined k_{cat}/K_m was 100 000 M^{-1} s^{-1}. This result is consistent with the kinetics of the originally reported peptide sequence, k_{cat}/K_m = 120 000 M^{-1} s^{-1} (*20*). It suggests that chemical attachment of the fluorescence donor and acceptor did not significantly alter enzymatic reactivity and selectivity.

To evaluate the usage of probe **4** in detecting MMP-7 activity in biological systems, a HT1080 human fibrosarcoma tumor model was selected. It has been demonstrated previously that HT1080 has the overexpression of MMP-7 enzyme (*23*). The tumors were dissected when they were about 6−9 mm in size, and the tumor-associated enzymes were extracted by gradient centrifugation. The presence of active 19 kDa MMP-7 in the tumor extract was first confirmed using casein zymography (Figure 6). The fluorescence signal of probe **4** increased by 4-fold after incubating with the tumor extract in 3 h; however, the control probe **5** also gave a 2-fold increase in signal. In the previous experiment, it has been demonstrated that the control probe **5** could not be activated by recombinant MMP-7 (Figure 5C), thus the signal increase has to be caused by other proteases which were extracted from the whole tumor. This result suggests that nonspecific activation of the probe could be expected in the future in vivo imaging of MMP-7 activity.

In summary, we described a rational design of a peptide-based NIR probe. Efficient quenching effect between NIR fluorochrome at 700 nm and NIRQ820 was demonstrated. In the MMP-7 model, the probe is able to release fluorescence signal by 7-fold after enzymatic degradation. This probe design could be applied to assay enzyme activity in vitro, for example high-throughput screening of various inhibitors, and potentially can be used for in vivo imaging of tumor-associated enzyme activity.

ACKNOWLEDGMENT

This research was supported by NIH RO1-CA99385, DOD DAMD17-02-1-0693, and NSF BES-0119382.

LITERATURE CITED

(1) Bremer, C., Tung, C. H., and Weissleder, R. (2001) In vivo molecular target assessment of matrix metalloproteinase inhibition. *Nat. Med. 7*, 743−8.
(2) Weissleder, R., and Ntziachristos, V. (2003) Shedding light onto live molecular targets. *Nat Med. 9*, 123−8.
(3) Pham, W., Weissleder, R., and Tung, C. H. (2002) An azulene dimer as a near-infrared quencher. *Angew Chem., Int. Ed. 41*, 3659−3662.
(4) Pham, W., Lai, W. F., Weissleder, R., and Tung, C. H. (2003) High efficiency synthesis of a bioconjugatable near-infrared fluorochrome. *Bioconjugate Chem. 14*, 1048−51.
(5) Ohbayashi, H. (2002) Matrix metalloproteinases in lung diseases. *Curr. Protein Pept. Sci. 3*, 409−21.
(6) Thompson, R. W., and Baxter, B. T. (1999) MMP inhibition in abdominal aortic aneurysms. Rationale for a prospective randomized clinical trial. *Ann. N. Y. Acad. Sci. 878*, 159−78.
(7) McCawley, L. J., and Matrisian, L. M. (2000) Matrix metalloproteinases: multifunctional contributors to tumor progression. *Mol. Med. Today 6*, 149−56.
(8) Moses, M. A., Wiederschain, D., Loughlin, K. R., Zurakowski, D., Lamb, C. C., and Freeman, M. R. (1998) Increased incidence of matrix metalloproteinases in urine of cancer patients. *Cancer Res. 58*, 1395−9.
(9) Stearns, M. E., and Wang, M. (1993) Type IV collagenase (M(r) 72, 000) expression in human prostate: benign and malignant tissue. *Cancer Res. 53*, 878−83.
(10) Brooks, P. C., Stromblad, S., Sanders, L. C., von Schalscha, T. L., Aimes, R. T., and Stetler-Stevenson, W. G., et al. (1996) Localization of matrix metalloproteinase MMP-2 to the surface of invasive cells by interaction with integrin alpha v beta 3. *Cell 85*, 683−93.
(11) Freije, J. M., Balbin, M., Pendas, A. M., Sanchez, L. M., Puente, X. S., and Lopez-Otin, C. (2003) Matrix metalloproteinases and tumor progression. *Adv. Exp. Med. Biol. 532*, 91−107.
(12) Coussens, L. M., Fingleton, B., and Matrisian, L. M. (2002) Matrix metalloproteinase inhibitors and cancer: trials and tribulations. *Science 295*, 2387−92.
(13) Whittaker, M., Floyd, C. D., Brown, P., and Gearing, A. J. (1999) Design and therapeutic application of matrix metalloproteinase inhibitors. *Chem. Rev. 99*, 2735−76.
(14) Shiomi, T., and Okada, Y. (2003) MT1-MMP and MMP-7 in invasion and metastasis of human cancers. *Cancer Metastasis Rev. 22*, 145−52.
(15) Crawford, H. C., Scoggins, C. R., Washington, M. K., Matrisian, L. M., and Leach, S. D. (2002) Matrix metalloproteinase-7 is expressed by pancreatic cancer precursors and regulates acinar-to-ductal metaplasia in exocrine pancreas. *J. Clin. Invest. 109*, 1437−44.
(16) Lakowicz, J. R. (1999) *Principles of fluorescence spectroscopy*, 2nd ed., Kluwer, New York.
(17) Fernandez-Resa, P., Mira, E., and Quesada, A. R. (1995) Enhanced detection of casein zymography of matrix metalloproteinases. *Anal. Biochem. 224*, 434−5.
(18) Amao, Y., Asai, K., and Okura, I. (2000) Fluorescence quenching oxygen sensor using an aluminum phthalocyanine-polystyrene film. *Anal. Chim. Acta 407*, 41−44.
(19) Weber, C., Durr, H., and Bonneau, R. (1999) Calixochromes. Syntheses, structure, and supramolecular effects of biphotochromic calix[4]arenes. *Synthesis* 1005−1012.
(20) Turk, B. E., Huang, L. L., Piro, E. T., and Cantley, L. C. (2001) Determination of protease cleavage site motifs using mixture-based oriented peptide libraries. *Nat. Biotechnol. 19*, 661−7.
(21) Kaiser, E., Colescott, R. L., Bossinger, C. D., and Cook, P. I. (1970) Color test for detection of free terminal amino groups in the solid-phase synthesis of peptides. *Anal. Biochem. 34*, 595−8.
(22) Liu, Y., Kati, W., Chen, C. M., Tripathi, R., Molla, A., and Kohlbrenner, W. (1999) Use of a fluorescence plate reader for measuring kinetic parameters with inner filter effect correction. *Anal. Biochem. 267*, 331−5.
(23) Giambernardi, T. A., Grant, G. M., Taylor, G. P., Hay, R. J., Maher, V. M., McCormick, J. J., et al. (1998) Overview of matrix metalloproteinase expression in cultured human cells. *Matrix Biol. 16*, 483−96.

BC049924S

Synthesis and Characterization of Poly(L-glutamic acid) Gadolinium Chelate: A New Biodegradable MRI Contrast Agent

Xiaoxia Wen,[†] Edward F. Jackson,[‡] Roger E. Price,[‡] E. Edmund Kim,[†] Qingping Wu,[†] Sidney Wallace,[†] Chusilp Charnsangavej,[†] Juri G. Gelovani,[†] and Chun Li*,[†]

Department of Experimental Diagnostic Imaging and the Department of Imaging Physics, The University of Texas M. D. Anderson Cancer Center, Houston, Texas 77030. Received April 12, 2004; Revised Manuscript Received August 10, 2004

Most currently evaluated macromolecular contrast agents for magnetic resonance imaging (MRI) are not biodegradable. The goal of this study is to synthesize and characterize poly(L-glutamic acid) (PG) gadolinium chelates as biodegradable blood-pool MRI contrast agents. Two PG chelates of gadolinium diethylenetriaminepentaacetic acid (Gd-DTPA) were synthesized through the use of difunctional and monofunctional DTPA precursors. The conjugates were characterized with regard to molecular weight and molecular weight distribution, gadolinium content, relaxivity, and degradability. Distributions of the polymeric MRI contrast agents in various organs were determined by intravenous injection of ^{111}In-labeled polymers into mice bearing murine breast tumors. MRI scans were performed at 1.5 T in mice after bolus injection of the polymeric chelates. PG-Hex-DTPA-Gd, obtained from aminohexyl-substituted PG and DTPA-dianhydride, was partially cross-linked and was undegradable in the presence of cathepsin B. On the other hand, PG-Bz-DTPA-Gd synthesized directly from PG and monofunctional *p*-aminobenzyl-DTPA(acetic acid-*tert*-butyl ester) was a linear polymer and was degradable. The relaxivities of the polymers at 1.5 T were 3−8 times as great as that of Gd-DTPA. Both polymers had high blood concentrations and were primarily accumulated in the kidney. However, PG-Bz-DTPA-Gd was gradually cleared from the body and had significantly less retention in the blood, the spleen, and the kidney. MRI with PG-Bz-DTPA-Gd in mice showed enhanced vascular contrast at up to 2 h after the contrast agent injection. The ability of PG-Bz-DTPA-Gd to be degraded and cleared from the body makes it a favorable macromolecular MRI contrast agent.

INTRODUCTION

Noninvasive imaging of the intravascular compartment is of critical importance in clinical medicine. Many diseases, e.g., infection, ulcer, cardiovascular diseases, solid tumors, involve gross hemorrhage, abnormal vascular growth, or vascular occlusion (*1, 2*). With the help of blood-pool contrast agents, imaging using computed tomography (CT), ultrasonography, gamma scintigraphy, and magnetic resonance imaging (MRI)[1] can provide minimally invasive angiography, assess angiogenesis, quantify the number and spacing of blood vessels, and measure blood volume and blood flow. MRI blood-pool agents are often paramagnetic gadolinium chelates of high-molecular-weight polymers that are largely retained within the intravascular space during the time frame of an MRI examination (*3*). For example, blood-pool agents for contrast-enhanced magnetic resonance angiography allow prolonged imaging times for higher contrast and resolution. Imaging may be performed during the steady state when the contrast agent is distributed through the complete vascular system (*4*). Recent studies have shown that tumor vascular permeability measurements, derived from polymeric contrast agents enhanced dynamic MRI, correlate with tumor microvessel density counts, suggesting that MRI may be used to characterize tumor angiogenic activity (*5, 6*). Furthermore, polymeric MRI contrast agents may permit more accurate grading of tumor invasiveness than do small-molecular-weight contrast agents, e.g., Gd-DTPA (*7, 8*).

One approach toward clinically acceptable blood-pool MRI agents takes advantage of a small-molecular-weight Gd^{3+}-based agent (i.e., MS-325) that binds strongly but reversibly to human serum albumin (*9, 10*). MS-325 is designed in such a way that an equilibrium between free and protein-bound compound exists, ensuring efficient renal excretion. An alternative approach is to develop macromolecular MRI contrast agents. Various polymeric MRI contrast agents, including human serum albumin (*11*), polylysine (*12, 13*), dendrimers (*16*−*19*), polyamide (*15, 20*), and grafted copolymers (*21*), have been synthesized and evaluated as blood-pool imaging agents. Although most of these agents fulfill the criteria of long blood circulation time and high relaxivity, the safety of these agents has yet to be established. The clinical applications of many current macromolecular contrast agents are limited by slow excretion from the body and potential toxicity of free Gd^{3+} ions released by the metabolism of the contrast agents (*12*−*14, 22, 23*). For an albumin-based product, the possibility of immunogenic response makes the use of serum proteins less attractive. Dendrimer-based blood-pool MRI agents have the ad-

* To whom correspondence should be addressed: Chun Li, Ph.D., Department of Experimental Diagnostic Imaging, Box 59, The University of Texas M. D. Anderson Cancer Center, 1515 Holcombe Blvd., Houston, TX 77030. Phone: (713) 792-5182. Fax: (713) 794-5456. E-mail: cli@di.mdacc.tmc.edu.

[†] Department of Experimental Diagnostic Imaging.

[‡] Department of Imaging Physics.

[1] Abbreviations: MRI, magnetic resonance imaging; PG, poly(L-glutamic acid); DTPA, diethylenetriaminepentaacetic acid; Gd, gadolinium.

10.1021/bc049910m CCC: $27.50 © 2004 American Chemical Society
Published on Web 10/08/2004

vantage of extremely narrow molecular weight distribution. However, these agents are not biodegradable.

Ideally, a polymeric MRI contrast agent will reside in the blood long enough to allow for thorough MRI examinations and then be degraded and cleared from the body after completion of the imaging procedures. Poly(L-glutamic acid) (PG) is a synthetic polyamino acid that can be readily degraded by lysosomal enzymes to its basic component, L-glutamic acid, a nontoxic natural compound (*24*). The polymer contains a large number of carboxyl functional groups for drug attachment. Conjugation of paclitaxel to PG has resulted in a water-soluble paclitaxel conjugate with reduced systemic toxicity and enhanced antitumor efficacy (*25*). In various studies in rodents, PG used alone as a control agent at doses from 200 to 800 mg/kg did not cause apparent toxic effects. Phase III clinical trials of PG−paclitaxel (Xyotax) as a chemotherapeutic agent are now in progress, underscoring the safety of this polymeric carrier. Recently, Lu et al. (*26*) reported a PG-based MRI agent using cystamine as the cleavable spacer. Gd^{3+} chelates were cleaved from the polymer backbone through a disulfide−thiol exchange reaction. However, potential interaction of the polymer with endogenous thiol-containing biomolecules raises concerns over the safety of this type of agents. Also, it appears that the release and clearance of DTPA−Gd from the polymer backbone through in vivo disulfide−thiol exchange reaction is a rapid process, which may limit its application in steady-state MRI applications.

In this study, we describe the synthesis, characterization, and preliminary evaluation of Gd^{3+}-chelated PG polymers for blood-pool imaging applications. We demonstrate that the resulting polymeric conjugate is cleared from the body as a result of polymer backbone degradation.

EXPERIMENTAL PROCEDURES

Materials. PG sodium salt, *N-tert*-butoxycarbonyl-1,6-diaminohexane hydrochloride (*t*-Boc-Hex-NH_2), 1,3-diisopropylcarbodiimide, pyridine, 4-(dimethylamino)pyridine, trifluoroacetic acid (TFA), diethylenetriaminepentaacetic acid (DTPA) dianhydride, gadolinium(III) chloride hexahydrate, 2,4,6-trinitrobenzenesulfonate (TNBS), 4-(2-pyridylazo)resorcinol, PBS (0.01 M phosphate-buffered saline containing 138 mM NaCl and 2.7 mM KCl, pH 7.4), cathepsin B, and all the other reagents and solvents were purchased from Sigma-Aldrich (St. Louis, MO). *p*-Aminobenzyldiethylenetriaminepenta(acetic acid *tert*-butyl ester) was obtained from Macrocyclics (Dallas, TX). $^{111}InCl_3$ was obtained from Perkin-Elmer Life Sciences (Boston, MA). Spectra/Pro 7 dialysis tubing with molecular weight cutoff (MWCO) of 10 000 and Centricon Plus-20 centrifugal filters were purchased from Fisher Scientific (Pittsburgh, PA). PD-10 columns came from Amersham-Pharmacia Biotech (Piscataway, NJ).

Analytical Methods. Gel permeation chromatography (GPC) was performed on a Waters (Milford, MA) high-performance liquid chromatography (HPLC) system consisting of a 600 controller, a 717 plus auto sampler, and a Viscotek E-Z^{pro} triple detector (Viscotek, Houston, TX) that records refractive index, viscosity, and light-scattering signals. The samples were separated using an TSK-G4000PW 4.6 mm × 30 cm column (TosoHaas, Montgomeryville, PA) eluted with PBS containing 0.1% LiBr at a flow rate of 1.0 mL/min. Number-average molecular weights of the polymer conjugates were calculated using Viscotek TriSEC GPC software. Radio-GPC was performed with a HPLC unit equipped with a LDC pump (Laboratory Data Control, Rivera Beach, FL) and a LUDLUM radiometric detector (Measurement Inc., Sweetwater, TX). The samples were separated using a Phenomenex Biosep SEC-S3000 7.8 mm × 30 cm column eluted with PBS containing 0.1% LiBr at a flow rate of 1.0 mL/min. ^1H NMR was recorded at 300 MHz on a Bruker Avance 300 spectrometer (Billerica, MA) using D_2O as a solvent. Elemental analysis was performed by Galbraith Laboratories, Inc. (Knoxville, TN). Free amino groups in the polymer conjugates were quantified using a TNBS assay following a reported protocol (*27*).

Synthesis of 6-Aminohexyl Poly(L-glutamine) [PG-NH(CH_2)$_6$$NH_2$]. The aqueous solution of sodium salt of poly-L-glutamic acid (number-average molecular weight M_n, 17 500; degree of polymerization, 116) was converted to its acid form by acidifying with 1 N HCl to pH 3−4. The polymer precipitate was collected by centrifugation, washed with deionized water, and lyophilized. Into a solution of PG (0.66 g, 5 mmol [COOH]) in 15 mL of anhydrous dimethylformamide were added *t*-Boc-Hex-NH_2 hydrochloride (1.28 g, 5 mmol), 1,3-diisopropylcarbodiimide (0.76 g, 6 mmol), 0.5 mL of pyridine, and a trace amount of 4-(dimethylamino)pyridine. The reaction mixture was stirred at room-temperature overnight. The precipitate was filtered off, and the solvent was removed under vacuum. The residue was dissolved in 10 mL of trifluoroacetic acid in an ice bath and stirred at 4 °C overnight. Excess of trifluoroacetic acid was removed under vacuum. After dissolving of the residual solid in ice−water followed by neutralization with 1 N NaOH, the solution was dialyzed against PBS followed by deionized water (MWCO 10 000). The dialysate was lyophilized to yield 0.65 g (66%) of a spongelike solid. About 75% (87 of 116) of the glutamic acid residues in PG were converted to 6-aminohexyl glutamine based on the ratio of the integrals of 6-CH_2 protons adjacent to the amine in the 6-aminohexyl group (δ = 2.88 ppm, t) to the α-CH proton in the PG backbone (δ = 4.17 ppm, s).

Synthesis of PG-NH(CH_2)$_6$NH-DTPA-Gd (PG-Hex-DTPA-Gd). DTPA-dianhydride (1.43 g, 4 mmol) was added in portions over a period of 30 min into a solution of PG-NH(CH_2)$_6$$NH_2$ (500 mg, ∼1.1 mmol [NH_2]) in 15 mL of 0.1 M $NaHCO_3$. The pH of the reaction solution was adjusted to 8 by adding aliquots of 0.1 N NaOH solution. After being stirred at room temperature for 2 h, the reaction mixture was dialyzed against PBS and deionized water (MWCO 10 000). The resulting solution was concentrated to 5 mL on a centrifugal filter (MWCO 10 000) and stored at 4 °C for future use. The amount of DTPA attached to PG-NH(CH_2)$_6$$NH_2$ was determined by quantifying unreacted amino groups with the TNBS assay. Approximately 60% (52 of 87) of the amino groups in PG-NH(CH_2)$_6$$NH_2$ were conjugated to DTPA.

To chelate with Gd^{3+}, a solution of $GdCl_3$·$6H_2O$ in water (100 mg/mL) was added dropwise to the aqueous solution of PG-NH(CH_2)$_6$NH-DTPA (PG-Hex-DTPA). The presence of trace amounts of unchelated Gd^{3+} ion in the mixture was monitored with a Gd^{3+} indicator 4-(2-pyridylazo)resorcinol. The reaction solution was dialyzed against water (MWCO 10 000) until no free gadolinium was detected in the receiving medium. The product was further purified by gel filtration on a PD-10 column. Fractions that showed only a single polymer peak on GPC were pooled and lyophilized to give 1.0 g of product (91% yield based on PG-Hex-NH_2). The compound contained 11.9% (w/w) of gadolinium as determined by elemental analysis.

Synthesis of PG-Benzyl-DTPA (PG-Bz-DTPA). PG (M_n, 42 000; 130 mg, 1.0 mmol of carboxylic unit) and *p*-aminobenzyldiethylenetriaminepenta(acetic acid *tert*-butyl ester) (281 mg, 0.36 mmol) were dissolved in 5 mL of anhydrous DMF, followed by the addition of 1,3-diisopropylcarbodiimide (52 mg, 0.4 mmol), 0.16 mL of pyridine, and a trace amount of 4-(dimethylamino)-pyridine. The reaction mixture was stirred at 4 °C overnight. To remove the protecting groups, the reaction mixture was treated with TFA at 4 °C overnight. After removal of TFA under vacuum, 10 mL of ice-cold 1 M $NaHCO_3$ was added into the residual solid. The pH of the solution was brought up to 7.5 with 1 M NaOH, and the solution was dialyzed against PBS and water sequentially (MWCO 10 000). The resulting solution was filtered through 0.2 μm membrane filters and lyophilized to yield 230 mg of spongelike powder (yield 88%). About 55 of 278 glutamic acid residues were coupled to benzyl-DTPA, determined by measurement of UV/Vis absorbance of Bz-DTPA at 250 nm.

Synthesis of PG-Bz-DTPA-Gd. Into a PG-Bz-DTPA (110 mg) solution in 10 mL of sodium acetate-buffered aqueous solution (0.1 M, pH 5.5) was added 0.37 mL of $GdCl_3 \cdot 6H_2O$ (100 mg/mL, 0.1 mmol) in 0.1 M sodium acetate solution in small fractions. The solution was dialyzed against water (MWCO 10 000) until no free Gd^{3+} was detectable in the receiving vessel. The solution was lyophilized to yield 100 mg of white powder (yield of polymer 81%). The number-average molecular weight of Gd^{3+}-chelated polymeric conjugate was about 101 200 as measured by GPC. The compound contained 12.3% (w/w) of gadolinium. Approximately 24% of Glu repeating units contained Gd.

Determination of Relaxivity. Solutions of PG-Hex-DTPA-Gd and PG-Bz-DTPA-Gd were prepared in water at gadolinium concentrations of 0.005, 0.01, 0.02, 0.04, 0.08, and 0.16 mM. Spin lattice (T_1) and spin−spin (T_2) relaxivities were measured at 1.5 T on a GE Signa LX scanner (Milwaukee, WI) using inversion recovery and mutiecho pulse sequences, respectively. Relaxivities (R_1 or R_2 in $mM^{-1}\ s^{-1}$) were obtained from linear least-squares determination of the slopes of $1/T_1$ vs [Gd] or $1/T_2$ vs [Gd] plots.

Biodegradation of Gd-Chelated PG Polymers. Gadolinium chelated PG polymers were dissolved in PBS buffer (pH 5) at a concentration of 5.3 mg/mL. Cathepsin B was added to the solutions to a final concentration of 10 units/mL. The solutions were incubated at 37 °C. At predetermined time intervals, aliquots of the polymer solution were removed for GPC analysis.

^{111}In-Labeling of Gd-Chelated PG Polymers. An aqueous solution of either PG-Hex-DTPA-Gd or PG-Bz-DTPA-Gd (10−15 mg) in 1 M sodium acetate buffer (pH 5.5) was incubated with 300 μCi of $^{111}InCl_3$ at room temperature for 15 min. Free ^{111}In was removed by gel filtration on a PD-10 column eluted with PBS. The purity of the radiolabeled compounds was analyzed by radio-GPC.

Biodistribution Studies. Female C3Hf/Kam mice (20−25 g) were bred and maintained in a specific pathogen-free mouse colony in the Department of Experimental Radiation Oncology at the University of Texas M. D. Anderson Cancer Center. All experiments involving animals were performed in accordance with the guidelines of the Institutional Animal Care and Use Committee. Solid murine MCa-4 tumors were generated in the muscles of the right thigh of mice by inoculating 5×10^5 viable tumor cells in suspension in PBS. When tumors had grown to 8 mm in average diameter, mice were randomly allocated into groups, with each group consisting of 3−4 mice. Mice in each group were injected intravenously with either ^{111}In-labeled PG-Hex-DTPA-Gd (0.5 mg, 2 μCi per mouse) or ^{111}In-labeled PG-Bz-DTPA-Gd (0.4 mg, 15 μCi per mouse). Animals were killed at 5 min, 2 h, 24 h and 48 h after injection. Blood, liver, spleen, kidney, muscle, and tumor tissues were removed, weighed, and counted for radioactivity with a gamma counter (Packard, Downers Grove, IL). Uptakes of contrast agent in various tissues were calculated as the percentage of the injected dose per gram of tissue. Student's *t* test was used to compare differences in tissue uptakes between the two agents, with *p* values less than 0.05 considered significant.

Magnetic Resonance Imaging. For MRI studies, mice were anesthetized with 1−2% isoflurane in a 1 L/min O_2 flow and placed prone within a custom sled. A custom catheter made from 2 Fr silicon tubing and a 27 gauge needle was inserted in the tail vein of the mice. Gd-DTPA (0.1 mmol Gd/kg), PG-Hex-DTPA-Gd (0.008 mmol Gd/ml, 0.04 mmol Gd/kg), or PG-Bz-DTPA-Gd (0.008 mmol Gd/ml, 0.04 mmol Gd/kg) was injected through the catheter and the catheter flushed with normal saline. Two-dimensional coronal section spin−echo images were obtained before and at 10 min, 2 h, and 24 h after contrast agent injection using a 2.5 cm quadrature birdcage coil on a 1.5 T Signa LX MR scanner (GE Medical Systems, Milwaukee, WI). Six 1.5 mm contiguous sections were obtained using a 6 cm field-of-view, a 256 × 192 acquisition matrix, and four averages.

A dynamic T1-weighted image set was acquired using a custom multiphase fast spin−echo sequence with an echo train length of 4, echo time of 15 ms, and repetition time of 400 ms with a temporal resolution of 13.6 s/imaging set. After baseline images were acquired, polymeric contrast agent (0.04 mmol/kg) was rapidly injected through a tail vein catheter and followed by a saline flush. The total scan time for the dynamic sequence was 600 s.

RESULTS

Synthesis and Characterization of Gd-Chelated PG Polymers. Two methods were used to synthesize Gd-chelated PG polymers. The synthetic schemes for both synthetic routes were shown in Figure 1. In the first method, DTPA was conjugated to PG through 6-aminohexyl linkers previously introduced to the side chains of PG. Thus, *t*-Boc-Hex-NH_2 was coupled to the side chains of PG using carbodiimide-mediated coupling reaction, followed by removal of *t*-Boc protecting groups and subsequent reaction of the resulting PG-$NH(CH_2)_6NH_2$ with DTPA-dianhydride to give PG-Hex-DTPA (Figure 1). About 87 of the 116 carboxyl groups in PG were converted to 6-aminohexyl glutamine based on ^{1}H NMR analysis. Sixty percent of these 87 aminohexyl groups were further coupled to DTPA when reacted with DTPA-dianhydride on the basis of consumption of NH_2. Thus, the degree of DTPA substitution on the PG polymer was about 0.45 mol DTPA/mol of COOH (Table 1). On the basis of elemental analysis, the Gd content in PG-Hex-DTPA-Gd was 11.9%, indicating that about 0.28 mol COOH in PG was substituted with Gd-DTPA for each mole of COOH units (Table 1).

In the second method, monofunctional, *tert*-butyl ester-protected *p*-aminobenzyldiethylenetriaminepenta(acetic acid) was directly reacted with carboxylic groups of PG, followed by a deprotection step to yield PG-Bz-DTPA (Figure 1). Fifty-five out of 278 glutamic acid units, or

Table 1. Physicochemical Properties of Gd-DTPA-Bound Poly(L-glutamic acid)

property	PG-Hex-DTPA-Gd	PG-Bz-DTPA-Gd	DTPA-Gd
M_n			
calculated[a]	53700	77000	560
measured[b]	144600	101200	
polydispersity[b]	3.34	1.23	
degree of substitution (mol/mol of COOH)			
NH_2[c]	0.75	N/A	
DPTA	0.45[d]	0.20[e]	
Gd content, % (w/w)[f]	11.9	12.3	28.5
relaxivity,[g] (mM^{-1} s^{-1})			
R_1	12	21	4.1[g]
R_2	18	27	5.2[g]

[a] Calculated on the basis of degree of substitution and the molecular weight of parent PG. For PG-Hex-DTPA-Gd and PG-Bz-DTPA-Gd, the number-average molecular weights (M_n) of parent PG were 17 500 Da and 42 000 Da, respectively. [b] Measured by gel permeation chromatography with a Viscotek E-Z^{pro} triple detector system as described in Materials and Methods section. Polydispersity = M_w/M_n. [c] Measured by ^1H nuclear magnetic resonance. [d] Determined by quantifying [NH_2]. [e] Determined by UV/Vis measurement of Bz-DTPA attached to PG. [f] Measured by elemental analysis. [g] All data were obtained at 1.5T in phosphate-buffered saline. Data for Gd-DTPA were taken from ref 20.

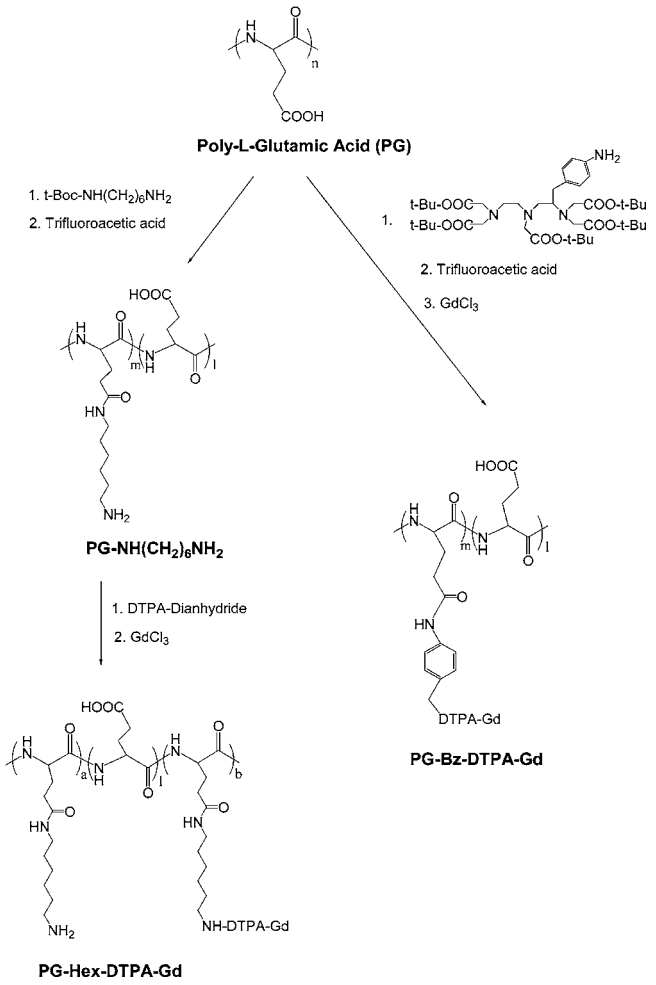


Figure 1. Reaction scheme for the synthesis of PG-Hex-DTPA-Gd and PG-Bz-DTPA-Gd.

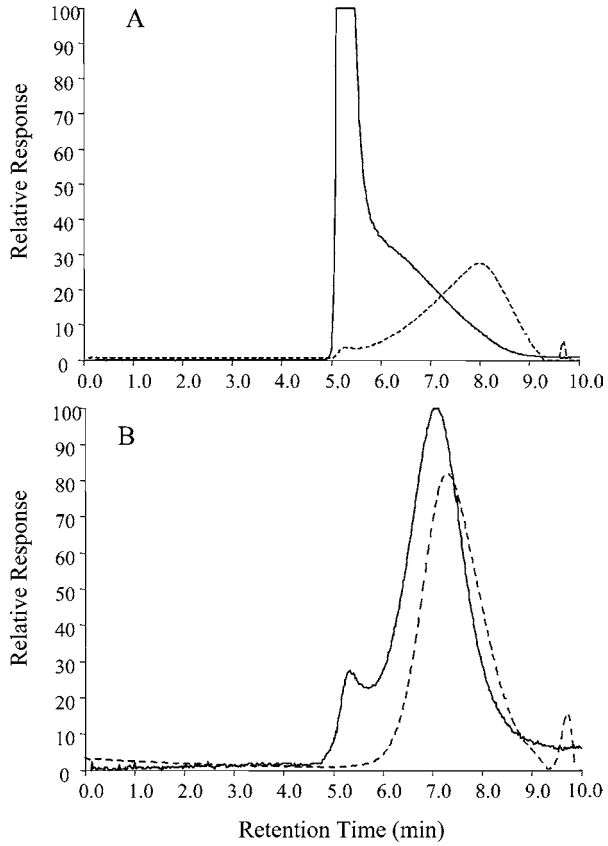


Figure 2. GPC profiles of PG-Hex-DTPA-Gd (A) and PG-Bz-DTPA-Gd (B) revealed by refractive index (- - -) and light scattering (—). The viscosity profile is not shown for reasons of clarity. The chromatography was run on an TSK-G4000PW column eluted with PBS containing 0.1% LiBr at a flow rate of 1.0 mL/min.

0.20 mol/mol of COOH, were attached to benzyl-DTPA as measured by UV absorbance of benzyl-DTPA at 248 nm. The degree of Gd-DTPA substitution based on Gd content in PG-Bz-DTPA-Gd (12.3%) was calculated to be 0.22 mol/mol COOH (Table 1).

Other physicochemical properties of the Gd^{3+}-chelated PG polymers are also summarized in Table 1. The reported number average molecular weights were estimated from GPC analyses. For comparison, the theoretical number-average molecular weights calculated on the basis of starting molecular weight of PG and the degree of substitution are also listed. The polydispersity of PG-Hex-DTPA-Gd (M_w/M_n = 3.34) was much greater than that of the starting PG polymer (M_w/M_n = 1.2) and PG-Bz-DTPA-Gd (Mw/Mn = 1.23) (Table 1). Both Gd^{3+}-chelated PG polymers had greater relaxivities than that of small molecular weight DTPA-Gd.

GPC chromatograms of PG-Hex-DTPA-Gd and PG-Bz-DTPA-Gd are presented in Figure 2. A strong peak from the light-scattering profile was observed in the GPC chromatogram of PG-Hex-DTPA-Gd (Figure 2A).

Biodegradation. The degradation of Gd-chelated PG polymers in the presence of cathepsin B was studied by analyzing changes in polymer molecular weights at various time intervals. PG-Bz-DTPA-Gd degraded rap-

Table 2. Biodistribution of Gd^{3+}-Chelated PG Polymers[a]

time	blood	liver	spleen	kidney	muscle	tumor
			PG-Hex-DTPA-Gd			
5 min	27.19 ± 4.11	4.33 ± 1.01	6.35 ± 1.67	15.54 ± 4.92	0.39 ± 0.04	1.08 ± 0.44
2 h	16.36 ± 1.61	8.09 ± 0.60	9.36 ± 1.13	53.39 ± 7.47	0.43 ± 0.08	3.04 ± 0.32
24 h	4.85 ± 1.26	7.24 ± 1.54	7.68 ± 1.68	44.60 ± 4.28	0.44 ± 0.09	3.44 ± 1.12
48 h	2.19 ± 0.28**	7.67 ± 1.50	8.88 ± 1.59	44.53 ± 3.80	0.48 ± 0.11	3.45 ± 0.59
			PG-Bz-DTPA-Gd			
5 min	28.50 ± 1.66	5.14 ± 0.29	6.59 ± 0.13	8.40 ± 0.37	0.64 ± 0.01	0.73 ± 0.14
2 h	7.72 ± 0.28	8.30 ± 1.47	5.09 ± 0.46	20.77 ± 4.70	0.83 ± 0.07	2.42 ± 0.77
24 h	0.96 ± 0.12	11.10 ± 1.72	5.19 ± 0.73	17.54 ± 2.70	0.55 ± 0.09	1.74 ± 0.54
48 h	0.53 ± 0.06	9.36 ± 0.43	4.03 ± 0.50	10.07 ± 0.61	0.39 ± 0.10	2.27 ± 0.22

[a] All data (other than time) are presented as percentage of injected dose per gram of tissue. Each value represents mean ± standard derivation ($n = 3$ or 4).

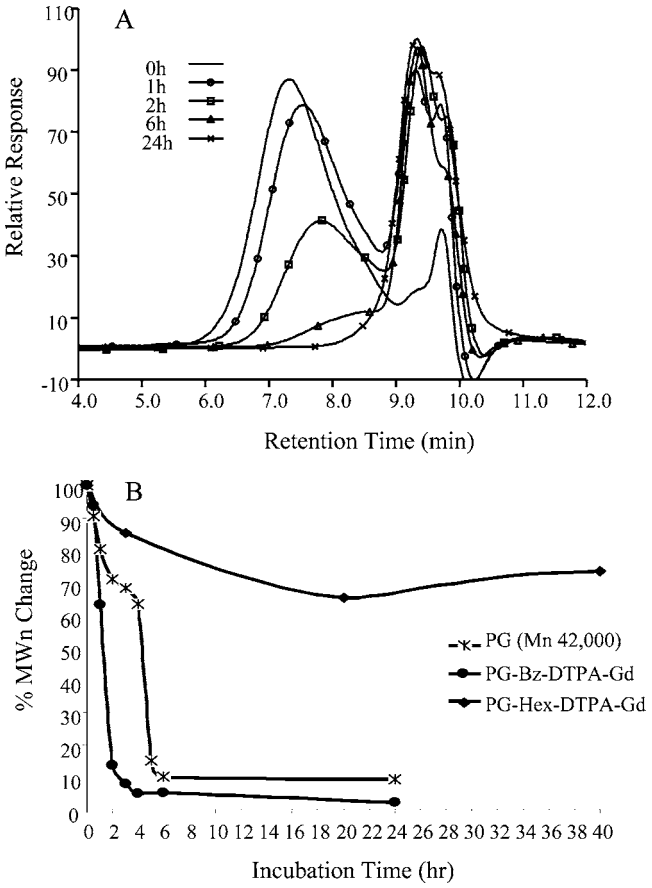


Figure 3. Degradation of Gd^{3+}-chelated PG polymers in the presence of cathepsin B. The polymers were incubated with a PBS solution (pH 5) of cathepsin B (10 units/ml) at 37 °C. GPC chromatograms of PG-Bz-DTPA-Gd at various time intervals revealed rapid degradation of the polymer (A). A comparison of changes in the number-average molecular weights for PG, PG-Bz-DTPA-Gd, and PG-Hex-DTPA-Gd is presented in B.

idly, with the main polymeric peak disappeared completely within 24 h (Figure 3A). On the other hand, the molecular weight of PG-Hex-DTPA-Gd only decreased 30% over a 48-h period (Figure 3B).

Biodistribution. Both Gd^{3+}-chelated polymers were successfully labeled with ^{111}In as demonstrated by the absence of small-molecular-weight ^{111}In-DTPA (retention time, 9.34 min) in the GPC chromatograms of the radiolabeled polymers (data not shown). Biodistribution data for ^{111}In-labeled Gd^{3+}-chelated polymers are summarized in Table 2. Both contrast agents had high blood activity (~28% injected dose per gram of blood, IND/g) at 5 min after contrast injection. By 2 h after contrast injection, substantial activities were still found in the blood, being 16.4% IND/g and 7.7% IND/g for mice injected with ^{111}In-labeled PG-Hex-DTPA-Gd and PG-Bz-DTPA-Gd, respectively. The highest uptakes at 2−48 h period for both ^{111}In-labeled PG-Hex-DTPA-Gd and PG-Bz-DTPA-Gd were found in the kidney. However, the activity of ^{111}In-labeled PG-Bz-DTPA-Gd in the kidney had decreased to 10.07%IND/g by 48 h postinjecition, while that of ^{111}In-labeled PG-Hex-DTPA-Gd remained at 44.6% IND/g. Interestingly, markedly increased uptake in tumors between 5 min and 2 h was observed with both polymers (PG-Hex-DTPA-Gd, 2.8-fold increase; PG-Bz-DTPA-Gd, 3.3-fold increase). At 48 postinjection, significantly lower activities were found in the blood ($p < 0.001$), the spleen ($p < 0.05$), the kidney ($p < 0.001$), and the tumor in mice injected with ^{111}In-labeled PG-Bz-DTPA-Gd than in mice injected with ^{111}In-labeled PG-Hex-DTPA-Gd (Table 2). No difference was found between their uptakes in the liver ($p = 0.1$). While the uptakes of ^{111}In-labeled PG-Hex-DTPA-Gd in the liver, the spleen, the kidney, and the muscle did not have significant change over the period of 24−48 h, the uptakes of ^{111}In-labeled PG-Bz-DTPA-Gd in these organs had decreased 15.7%, 22.4%, 42.6%, and 29.1%, respectively, over the same time period.

MRI Findings. Representative normalized MR signal intensity in the major blood vessel (e.g., IVC) and the muscle over time obtained immediately after the injection of PG-Bz-DTPA-Gd is shown in Figure 4. Figure 5 presents MR images obtained at 10 min, 2h, and 24 h after injection of PG-Bz-DTPA-Gd. Blood vessels such as the vena cava as well as myocardial, hepatic, lung, and renal perfusion were clearly visualized at 2 h after contrast injection at an injected dose of 0.04 mmol Gd/kg (Figure 5). By 24 h after contrast injection, the blood-pool activity had largely returned to the precontrast level. Interesting, the contrast in certain regions of the tumors was clearly enhanced at 24 h after contrast injection, reflecting enhanced permeability and retention of macromolecules in solid tumors. Similar findings were also observed in mice injected with PG-Hex-DTPA-Gd (data not shown).

DISCUSSION

The purpose of this study was aimed at development of biodegradable polymeric MRI contrast agents as blood-pool imaging agents. PG was chosen as the polymeric carrier for Gd^{3+}-chelates owing to its degradability and biocompatibility. Two methods were used to conjugate DTPA to the side chains of PG, resulting in two distinctly different Gd^{3+}-chelated PG polymers: PG-Hex-DTPA-Gd and PG-Bz-DTPA-Gd (Figure 1).

The two polymers differ in the way in which the metal chelator DTPA is introduced to PG. In PG-Hex-DTPA, DTPA was conjugated to PG through hexylamine spacers previously introduced to the side chains of PG. During

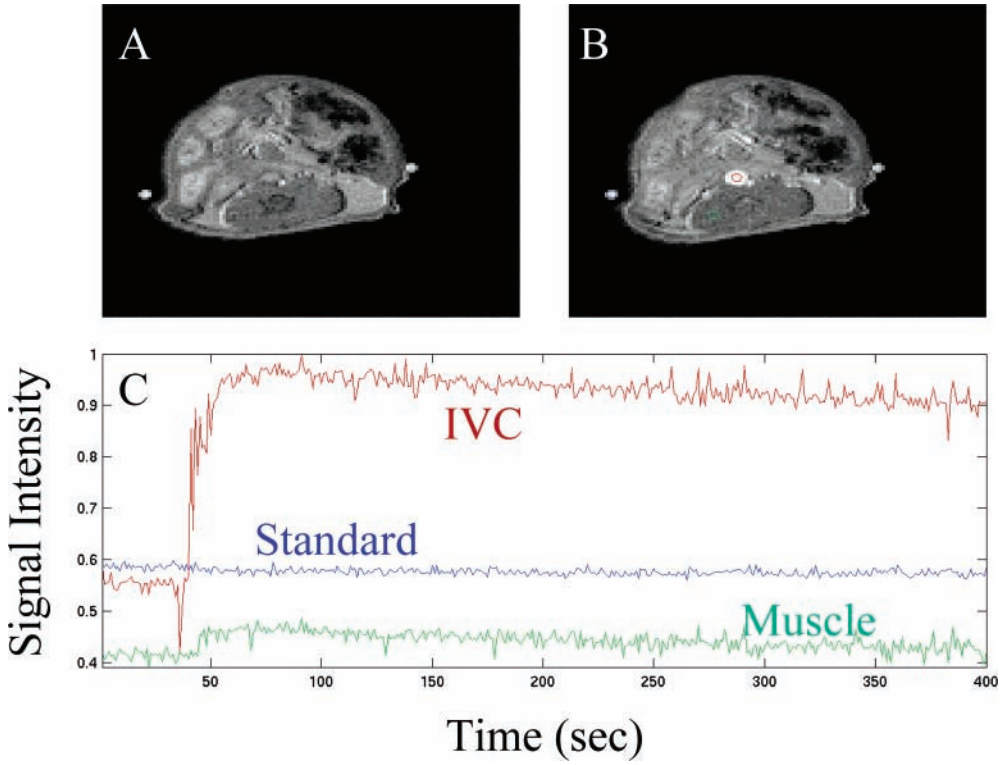


Figure 4. Precontrast (A) and postcontrast (B) of T_1-weighted images from the dynamic MRI series acquired after bolus injection of PG-Bz-DTPA-Gd. Time course of normalized MR signal intensity from regions indicated in B represents signals obtained from inferior vena cava (IVC) (red), muscle (green), and a standard (blue) (C).

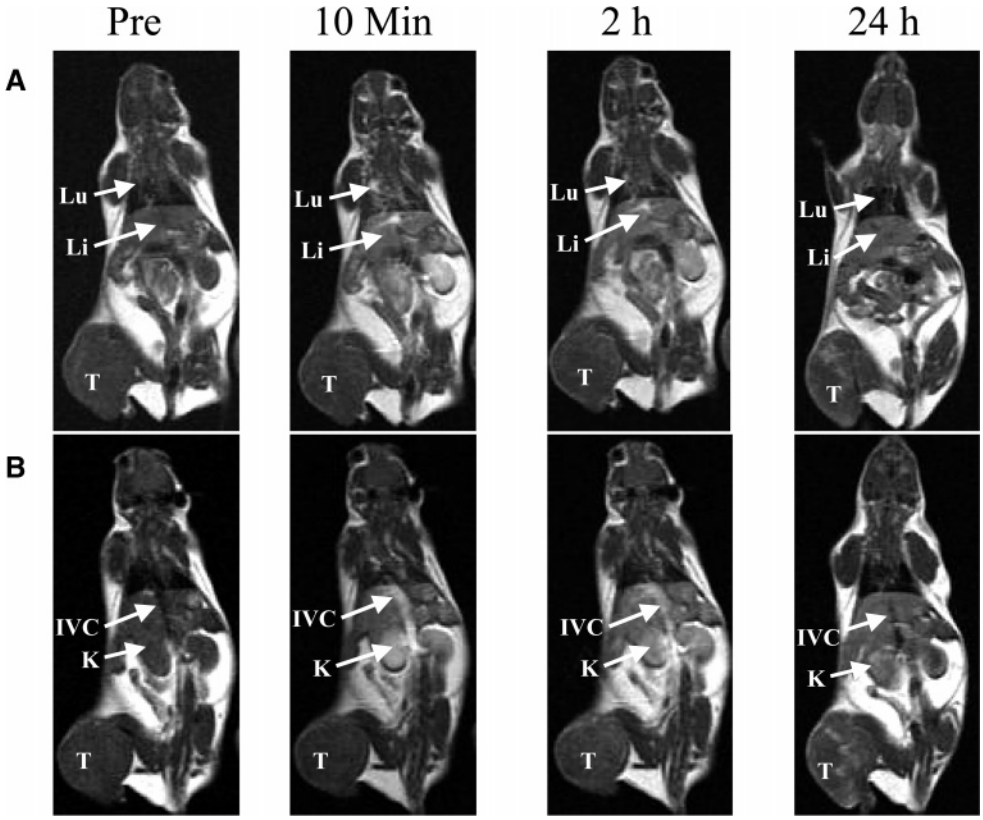


Figure 5. Whole body images of mice before and at 10 min, 2 h, and 24 h after intravenous injection of PG-Bz-DTPA-Gd at a dose of 0.04 mmol Gd/kg. (A) Selected anterior coronal image after injection of contrast agent demonstrates pulmonary and hepatic perfusion. (B) Selected posterior coronal image after injection of contrast agent demonstrates renal perfusion as well as persistent enhancement of the vena cava. Note enhancement of tumor at 24 h postinjection. Lu: lung; Li: liver; IVC, inferior vena cava; K, kidney; T: tumor.

conjugation of DTPA-dianhydride with PG-Hex-NH_2, some cross-linking reactions took place. This is supported by the following observations: (1) The measured molecular weight of PG-Hex-DTPA-Gd was much higher than its corresponding to theoretical molecular weights calculated on the basis of degree of substitution. (2) PG-

Hex-DTPA-Gd had much wider molecular weight distribution than the parent PG polymer. (3) The GPC profile of PG-Hex-DTPA-Gd showed a large peak at the dead volume of the column when light scattering signal was monitored, although this peak only represented a small fraction of polymer mass as shown by the GPC chromatogram of refractive index (Figure 2A). Cross-linking reactions occurred because bifunctional DTPA-dianhydride was used to introduce DTPA to PG-Hex-NH_2. To minimize cross-linking reaction, DTPA-dianhydride was added into a dilute solution of PG-Hex-NH_2 in multiple fractions over a prolonged period. The resulting PG-Hex-DTPA-Gd conjugate remained water-soluble and could be given safely to mice at a dose of up to 0.32 mmol Gd/kg. Doses higher than 0.32 mmol Gd/kg could not be given because of the limitation on injection volume.

In PG-Bz-DTPA-Gd, a monofunctional DTPA precursor *p*-aminobenzyldiethylenetriaminepenta(acetic acid *tert*-butyl ester) was directly conjugated to the carboxyl groups on the side chains of PG (Figure 1). This resulted in a linear polymer, as evidenced by its relatively narrow molecular weight distribution, by the close agreement between calculated molecular weight and GPC-measured molecular weight (Table 1), and by the lack of a fraction of cross-linked molecules (Figure 2B). Compared to PG-Hex-DTPA-Gd, PG-Bz-DTPA-Gd had much higher relaxivity. The reason for this phenomenon is not clear at this time. It is plausible that linear PG-Bz-DTPA-Gd may be more readily accessible to water molecules than cross-linked PG-Hex-DTPA-Gd polymer.

Several studies used isolated tissue lysosomal enzymes to investigate the degradability of PG and its derivatives (*28, 29*). PG was found to be more susceptible to lysosomal degradation than poly(L-aspartic acid) and poly(D-glutamic acid) (*29*). Recent results by Singer and his colleagues prove that monomeric L-glutamic acid is formed in the lysosomal degradation of PG (*30*). Evidence obtained from these studies suggests that cystein proteases, particularly cathepsins B, play key roles in the lysosomal degradation of PG (*28, 30*). Our results show that the difference in the linker groups (hexyl vs benzyl) and perhaps more importantly the presence/absence of polymer cross-link had profound effect on the biodegradability and distribution of Gd-chelated PG polymers. While PG-Hex-DTPA-Gd was essentially not degradable in the presence of cathepsin B, PG-Bz-DTPA-Gd degraded rapidly within 24 h (Figure 3). In vivo, PG-Bz-DTPA-Gd was cleared from the blood, spleen, and kidney faster than PG-Hex-DTPA-Gd. Significantly less uptakes in these tissues were found in mice injected with PG-Bz-DTPA-Gd than in mice injected with PG-Hex-DTPA-Gd at 48 h postinjection. (Table 2). It is noted that although the cross-linked polymer PG-Hex-DTPA-Gd had a high level of uptake in the kidney, the kidney uptake of the linear polymer PG-Bz-DTPA-Gd, on the other hand, was only about one-fourth of that of PG-Hex-DTPA-Gd at 48 h after contrast injection. Unlike PG-Hex-DTPA-Gd, the uptake of PG-Bz-DTPA-Gd in the kidney decreased steadily over a period of 48 h. Therefore, PG-Bz-DTPA-Gd, but not PG-Hex-DTPA-Gd, warrants further development for potential clinical applications.

Dynamic MR images obtained with PG-Bz-DTPA-Gd confirm that the agent markedly enhanced vascular contrast without causing significant loss of signal because of its limited diffusion into intravascular fluid space (Figure 4). MR imaging of mice bearing MCa-4 mammary tumors before and at various time points after the injection of PG-Bz-DTPA-Gd revealed significant contrast enhancement of blood vessels at up to 2 h after their intravenous injection. Indeed, vena cava and pulmonary, myocardial, hepatic, and renal perfusion of mice were clearly visualized (Figure 5). The signal intensities in the blood vessels gradually decreased over the time. By 24 h postinjection, the signal intensities in the blood pool had returned to the preinjection level, suggesting degradation and gradual clearance of the contrast agent from the body. Interestingly, the signal intensity in the tumor had increased during the same time period. These results indicate that PG-Bz-DTPA-Gd was retained in the MCa-4 tumors, possibly a result of the increased permeability and retention effect of macromolecules.

In summary, we have demonstrated that the degradability and biodistribution pattern of Gd^{3+}-chelated PG polymers are strongly affected by the way Gd^{3+} chelators are coupled to PG carrier. PG-Bz-DTPA-Gd and its ability to be cleared from the body make it a favorable macromolecular MRI contrast agent. The dose of PG that would need to be introduced into the body to obtain an equivalent Gd dose of 0.04 mmol/kg is estimated to be less than 52 mg PG/kg. These doses are 10- to 20-fold less than the dose of PG given to rodents without causing apparent toxic effect (*25*). Detailed studies are necessary to fully assess the toxicity of PG-Bz-DTPA-Gd before it is introduced into clinical applications. Further evaluation of both PG-Hex-DTPA-Gd and PG-Bz-DTPA-Gd is ongoing.

ACKNOWLEDGMENT

We would like to thank the National Institutes of Health (grant U54 CA90810), the Department of Defense Breast Cancer Research Program (grant DAMD17-00-1-0314), and the John S. Dunn Foundation for financial support of this work.

LITERATURE CITED

(1) Kroft, L. J. and de Roos, A. (1999) Blood pool contrast agents for cardiovascular MR imaging. *J. Magn. Reson. Imaging 10*, 395−403.

(2) Bogdanov Jr., A. A., Lewin, M., and Weissleder, R. (1999) Approaches and agents for imaging the vascular system. *Adv. Drug Delivery Rev. 37*, 279−293.

(3) Brasch, R. C. (1992) New directions in the development of MR imaging contrast media. *Radiology 183*, 1−11.

(4) van Bemmel, C. M., Wink, O., Verdonck, B., Viergever, M. A., and Niessen, W. J. (2003) Blood pool contrast-enhanced MRA: Improved arterial visualization in the steady state. *IEEE Trans. Med. Imaging 22*, 645−652.

(5) Su, M. Y., Muhler, A., Lao, X., and Nalcioglu, O. (1998) Tumor characterization with dynamic contrast-enhanced MRI using MR contrast agents of various molecular weights. *Magn. Reson. Med. 39*, 259−269.

(6) van Dijke, C. F., Brasch, R. C., Roberts, T. P., Weidner, N., Mathur, A., Shames, D. M., Mann, J. S., Demsar, F., Lang, P., and Schwickert, H. C. (1996) Mammary carcinoma model: Correlation of macromolecular contrast-enhanced MR imaging characterizations of tumor microvasculature and histologic capillary density. *Radiology 198*, 813−818.

(7) Gossmann, A., Okuhata, Y., Shames, D. M., Helbich, T. H., Roberts, T. P. L., Wendland, M. F., Huber, S., and Brasch, R. C. (1999) Prostate cancer tumor grade differentiation with dynamic contrast-enhanced MR imaging in the rat: Comparison of macromolecular and small-molecular contrast media-preliminary experience. *Radiology 213*, 265−272.

(8) Daldrup, H., Shames, D. M., Wendland, M., Okuhata, Y., Link, T. M., Rosenau, W., Lu, Y., and Brasch, R. C. (1998) Correlation of dynamic contrast-enhanced MR imaging with histologic tumor grade: Comparison of macromolecular and small-molecular contrast media. *Am. J. Roentgenol. 171*, 941−949.

(9) Lauffer, R. B., Parmelee, D. J., Dunham, S. U., Ouellet, H. S., Dolan, R. P., Witte, S., McMurry, T. J., and Walovitch, R. C. (1998) Ms-325: Albumin-targeted contrast agent for MR angiography. *Radiology 207*, 529−538.

(10) Adzamli, K., Yablonskiy, D. A., Chicoine, M. R., Won, E. K., Galen, K. P., Zahner, M. C., Woolsey, T. A., and Ackerman, J. J. (2003) Albumin-binding MR blood pool agents as MRI contrast agents in an intracranial mouse glioma model. *Magn. Reson. Med. 49*, 586−590.

(11) Schmiedl, U., Ogan, M., Paajanen, H., Marotti, M., Crooks, L., Brito, A., and Brasch, R. (1987) Albumin labeled with Gd-DTPA as an intravascular, blood pool-enhancing agent for MR imaging: Biodistribution and imaging studies. *Radiology 162*, 205−210.

(12) Schuhmann-Giampieri, G., Schmitt-Willich, H., Frenzel, T., Press, W. R., and Weinmann, H. J. (1991) In vivo and in vitro evaluation of Gd-DTPA-polylysine as a macromolecular contrast agent for magnetic resonance imaging. *Invest. Radiol. 26*, 969−974.

(13) Bogdanov, J., Alexei A., Weissleder, R., and Brady, T. J. (1995) Long-circulating blood pool imaging agents. *Adv. Drug Delivery Rev. 16*, 335−348.

(14) Wang, S. C., Wikstrom, M. G., White, D. L., Klaveness, J., Holtz, E., Rongved, P., Moseley, M. E., and Brasch, R. C. (1990) Evaluation of Gd-DTPA-labeled dextran as an intravascular MR contrast agent: Imaging characteristics in normal rat tissues. *Radiology 175*, 483−488.

(15) Rebizak, R., Schaefer, M., and Dellacherie, E. (1997) Polymeric conjugates of Gd(3+)-diethylenetriaminepentaacetic acid and dextran. 1. Synthesis, characterization, and paramagnetic properties. *Bioconjugate Chem. 8*, 605−610.

(16) Wiener, E. C., Brechbiel, M. W., Brothers, H., Magin, R. L., Gansow, O. A., Tomalia, D. A., and Lauterbur, P. C. (1994) Dendrimer-based metal chelates: A new class of magnetic resonance imaging contrast agents. *Magn. Reson. Med. 31*, 1−8.

(17) Adam, G., Neuerburg, J., Spuntrup, E., Muhler, A., Scherer, K., and Gunther, R. W. (1994) Gd-DTPA-cascade-polymer: Potential blood pool contrast agent for MR imaging. *J. Magn. Reson. Imaging 4*, 462−466.

(18) Kobayashi, H. and Brechbiel, M. W. (2003) Dendrimer-based macromolecular mri contrast agents: Characteristics and application. *Mol. Imaging 2*, 1−10.

(19) Kim, Y. H., Choi, B. I., Cho, W. H., Lim, S., Moon, W. K., Han, J. K., Weinmann, H. J., and Chang, K. H. (2003) Dynamic contrast-enhanced MR imaging of vx2 carcinomas after X irradiation in rabbits: Comparison of gadopentetate dimeglumine and a macromolecular contrast agent. *Invest. Radiol. 38*, 539−549.

(20) Unger, E. C., Shen, D., Wu, G., Stewart, L., Matsunaga, T. O., and Trouard, T. P. (1999) Gadolinium-containing copolymeric chelates—a new potential MR contrast agent. *Magma 8*, 154−162.

(21) Gupta, H., Wilkinson, R. A., Bogdanov, A. A., Jr., Callahan, R. J., and Weissleder, R. (1995) Inflammation: Imaging with methoxy poly(ethylene glycol)-poly-l-lysine-DTPA, a long-circulating graft copolymer. *Radiology 197*, 665−669.

(22) Rebizak, R., Schaefer, M., and Dellacherie, E. (1998) Polymeric conjugates of Gd(3+)-diethylenetriaminepentaacetic acid and dextran. 2. Influence of spacer arm length and conjugate molecular mass on the paramagnetic properties and some biological parameters. *Bioconjugate Chem. 9*, 94−99.

(23) Franano, F. N., Edwards, W. B., Welch, M. J., Brechbiel, M. W., Gansow, O. A., and Duncan, J. R. (1995) Biodistribution and metabolism of targeted and nontargeted protein-chelate-gadolinium complexes: Evidence for gadolinium dissociation in vitro and in vivo. *Magn. Reson. Imaging 13*, 201−214.

(24) Li, C. (2002) Poly(l-glutamic acid)- -anticancer drug conjugates. *Adv. Drug Delivery Rev. 54*, 695−713.

(25) Li, C., Yu, D. F., Newman, R. A., Cabral, F., Stephens, L. C., Hunter, N., Milas, L., and Wallace, S. (1998) Complete regression of well-established tumors using a novel water-soluble poly(l-glutamic acid)-paclitaxel conjugate. *Cancer Res. 58*, 2404−2409.

(26) Lu, Z. R., Wang, X., Parker, D. L., Goodrich, K. C., and Buswell, H. R. (2003) Poly(L-glutamic acid) Gd(iii)-DOTA conjugate with a degradable spacer for magnetic resonance imaging. *Bioconjugate Chem. 14*, 715−719.

(27) Hermanson, G. T. (1996) *Bioconjugate Techniques*, pp 112−113, Academic press, San Diego.

(28) Chiu, H. C., Kopeckova, P., Deshmane, S. S., and Kopecek, J. (1997) Lysosomal degradability of poly(alpha-amino acids). *J. Biomed. Mater. Res. 34*, 381−392.

(29) Kishore, B. K., Lambricht, P., Laurent, G., Maldague, P., Wagner, R., and Tulkens, P. M. (1990) Mechanism of protection afforded by polyaspartic acid against gentamicin-induced phospholipidosis. Ii. Comparative in vitro and in vivo studies with poly-l-aspartic, poly-l-glutamic and poly-d-glutamic acids. *J. Pharmacol. Exp. Ther. 255*, 875−885.

(30) Singer, J. W., Baker, B., De Vries, P., Kumar, A., Shaffer, S., Vawter, E., Bolton, M., and Garzone, P. (2003) Poly-(l)-glutamic acid-paclitaxel (ct-2103) [Xyotax], a biodegradable polymeric drug conjugate: Characterization, preclinical pharmacology, and preliminary clinical data. *Adv. Exp. Med. Biol. 519*, 81−99.

BC049910M

A New High Affinity Technetium Analogue of Bombesin Containing DTPA as a Pharmacokinetic Modifier

Kuo-Shyan Lin,[†] Andrew Luu,[†] Kwamena E. Baidoo,*[,†] Hossein Hashemzadeh-Gargari,[†] Ming-Kai Chen,[†] Roberto Pili,[‡] Martin Pomper,[§] Michael Carducci,[‡] and Henry N. Wagner, Jr.[†]

Department of Environmental Health Sciences, The Johns Hopkins Medical Institutions, 615 North Wolfe Street, Room E6632, Baltimore, Maryland 21205, The Sidney Kimmel Comprehensive Oncology Center, The Johns Hopkins Medical Institutions, Cancer Research Building 1650 Orleans Street, Baltimore, Maryland 21231, and Department of Radiology, The Johns Hopkins Medical Institutions, 600 North Wolfe Street, Baltimore, Maryland 21287. Received July 20, 2004; Revised Manuscript Received August 27, 2004

The bombesin (BN)/gastrin-releasing peptide (GRP) receptor is expressed in high density on the cell surface of a variety of tumors. This makes the receptors accessible as a molecular target for the detection of lesions in which they are expressed. In this study, we describe a high affinity hydrophilic ^{99m}Tc-labeled BN analogue, [DTPA^1, Lys^3(^{99m}Tc-Hx-DADT), Tyr^4]BN, having diethylenetriaminepentaacetic acid (DTPA), as a build-in pharmacokinetic modifier, to direct its excretion through the urinary system in order to lower abdominal background activity. In vitro binding studies using [^{125}I-Tyr^4]BN (K_d, 0.1 nM) and human prostate cancer PC-3 cell membranes showed that the inhibition constant (K_i) of [DTPA^1, Lys^3(^{99}Tc-Hx-DADT), Tyr^4]BN was 19.9 ± 8.0 nM. Biodistribution studies in normal mice showed fast blood clearance (0.15 ± 0.01% ID/g, 4 h postinjection), low intestinal accumulation (9.16 ± 2.35% ID/g, 4 h postinjection), and significant uptake in BN/GRP receptor rich tissues such as the pancreas (21.83 ± 2.88% ID/g, 15 min postinjection). The pancreas/blood, pancreas/muscle, and pancreas/liver ratios were highest at 2 h postinjection at 23, 74, and 8.4, respectively. The uptake in the pancreas could be blocked by BN (11.96 ± 1.17 vs 0.65 ± 0.16% ID/g), partially blocked by neuromedin B (11.96 ± 1.17 vs 6.66 ± 0.51% ID/g), but not affected by somatostatin (11.96 ± 1.17 vs 12.91 ± 2.53% ID/g), indicating that the binding of [DTPA^1, Lys^3(^{99m}Tc-Hx-DADT), Tyr^4]BN to the receptors was specific. Scintigraphic imaging of human PC-3 prostate cancer xenografts in SCID mice gave a high target to nontarget ratio on the image. Thus, [DTPA^1, Lys^3(^{99m}Tc-Hx-DADT), Tyr^4]BN has the potential for imaging BN/GRP receptor-positive lesions.

INTRODUCTION

Bombesin (BN), an amphibian tetradecapeptide originally isolated from frog skin (*1*), and its mammalian analogue, gastrin-releasing peptide (GRP), share the same C-terminal heptapeptide, Trp-Ala-Val-Gly-His-Leu-Met-NH_2, and bind with high affinity to the BN/GRP receptor. BN-like peptides have a wide range of physiological activities including stimulation of the release of numerous gastrointestinal hormones (*2*), stimulation of pancreatic enzyme secretion (*3*, *4*), effects on the central nervous system such as thermoregulation (*5*), and inhibition of thyroid-stimulating hormone (*6*).

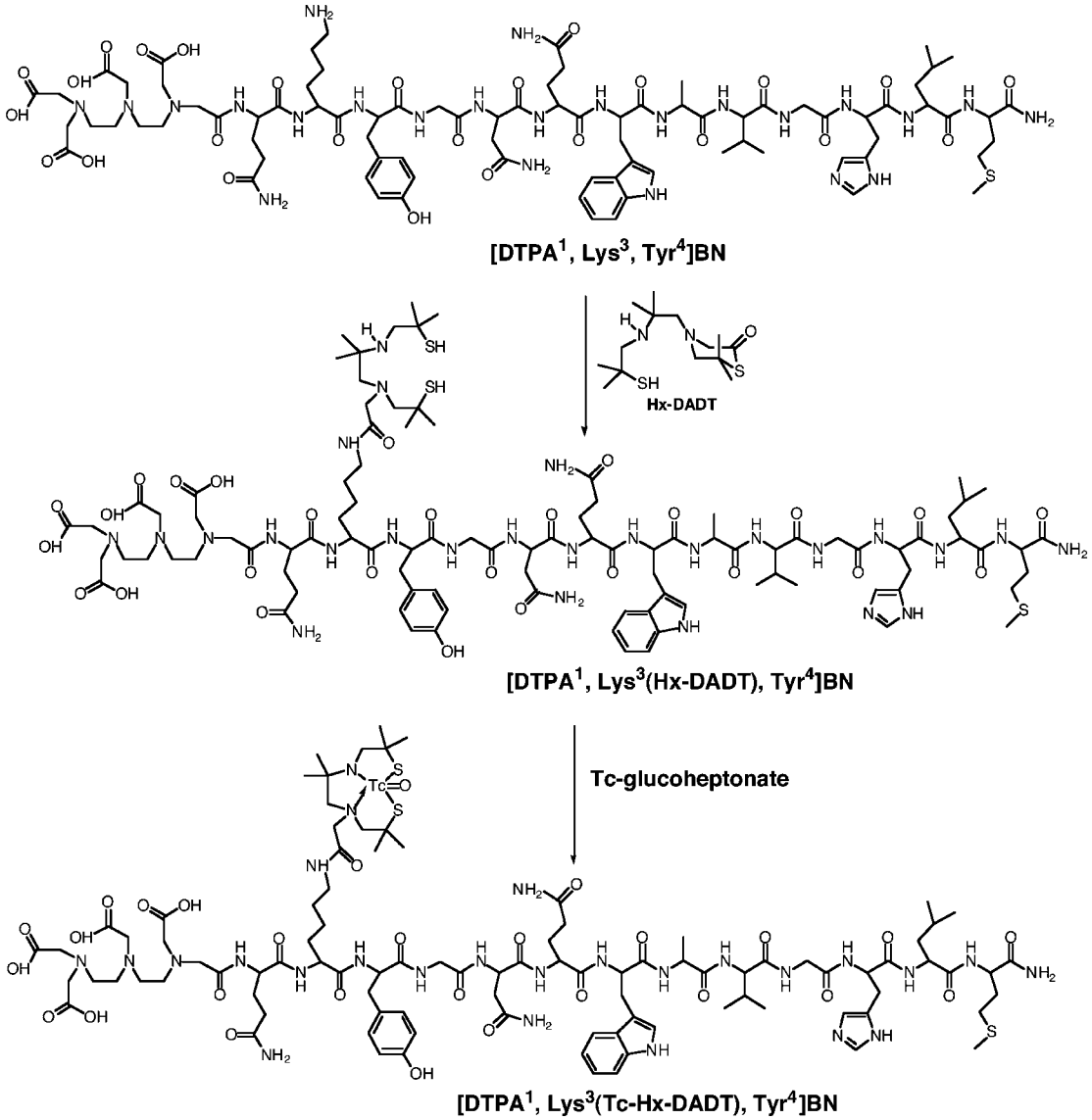
The BN/GRP receptor has also been shown to be overexpressed on many cancer cells including small cell lung cancer, glioblastoma, gastric, pancreatic, prostate, breast, and colon cancer (*7*−*14*) as well as premalignant cells in the case of prostate, gastric, and lung cancers (*13*−*15*). BN/GRP receptor expression could be used as a potential marker for early diagnosis as well as the staging of BN/GRP receptor-positive cancers and their metastasis if suitable tracers could be developed for in vivo scintigraphy of the receptors. Radionuclides, such as ^{111}In, ^{125}I, and ^{105}Rh (*16*−*18*), have been used to label BN/GRP analogues for in vivo scintigraphy of BN/GRP receptor-bearing tumors. However, due to the advantages of ^{99m}Tc, such as ready availability, low cost, excellent imaging properties (141 keV photon energy and 89% photon flux), favorable dosimetry, and high specific activity, the development of ^{99m}Tc-labeled BN/GRP analogues for cancer imaging would be even more promising. For his reason several investigators have investigated ^{99m}Tc-labeled analogues of bombesin for imaging cancer (*19*−*25*).

To label biomolecules with ^{99m}Tc, it is necessary to provide a site on the substrate for the chelation of the radiometal. The diaminodithiol (DADT) chelating system forms one of the most stable complexes with Tc. Tc complexes of this system, however, tend to be highly lipophilic. Therefore, upon the use of the ligand system to label substrates with ^{99m}Tc, the resultant tracers tend to be excreted primarily through the hepatobiliary system. For example, in a previous study (*19*), we reported a ^{99m}Tc-labeled BN analogue, Lys^3(^{99m}Tc-Hx-DADT)BN in which the diaminedithiol bifunctional chelating agent, Hx-DADT (Scheme 1) was used to chelate the Tc. This technetium analogue showed high affinity for the BN/GRP receptor. However, due to its lipophilicity, the radioactivity was excreted mainly through the hepatobiliary pathway as indicated by the high percent injected dose (% ID) in the liver and intestines (96% ID) at 1 h

* To whom correspondence should be addressed. Telephone: (410)-955-7706. Fax: (410) 955-6222. E-mail: kbaidoo@jhsph.edu.
[†] Department of Environmental Health Sciences.
[‡] The Sidney Kimmel Comprehensive Oncology Center.
[§] Department of Radiology.

10.1021/bc0498267 CCC: $27.50 © 2004 American Chemical Society
Published on Web 10/22/2004

Scheme 1. Synthesis of [DTPA^1, Lys^3(Tc−Hx-DADT), Tyr^4]BN



postinjection. This high accumulation of radioactivity in the liver and intestines would jeopardize the imaging of BN/GRP receptor-positive cancers and their metastases in the abdominal area. Since radiotracers with higher hydrophilicity tend to be excreted through the urinary system (*26*−*28*), different strategies, such as the use of a water-soluble bifunctional chelating agent (*29*), more hydrophilic coligands (*30*), or cleavable linkers (*31*), have been investigated as ways to increase the hydrophilicity of ^{99m}Tc-labeled peptides. In this study, we report the design, synthesis, and initial evaluation of a high affinity, hydrophilic ^{99m}Tc-labeled BN/GRP analogue, [DTPA^1, Lys^3(^{99m}Tc-Hx-DADT), Tyr^4]BN (Scheme 1), modified with a build-in pharmacokinetic modifier, diethylenetriaminepentaacetic acid (DTPA), at the N-terminus to direct its clearance through the urinary system.

EXPERIMENTAL PROCEDURES

Materials and General Methods. BN, neuromedin B, somatostatin, 1,3-diisopropylcarbodiimide (DIC), hydroxybenzotriazole (HOBt), Boc-L-methionine-*p*-methylbenzhydrylamine resin, and Boc-protected amino acids were purchased from Advanced ChemTech (Louisville, KY). [^{99}Tc]NH_4TcO_4 and [^{125}I-Tyr^4]BN were purchased from PerkinElmer Life Science (Boston, MA). [^{99m}Tc]-$NaTcO_4$ was purchased as a solution in physiologic saline from Syncor (Timonium, MD). The Glucoscan kit was purchased from the Du Pont Radiopharmaceutical Division (Billerica, MA). All other chemicals were obtained from either the Aldrich Chemical Co. (Milwaukee, WI) or Sigma Chemical Company (St. Louis, MO). Solvents and chemicals were reagent grade and used as received without further purification. The DADT bifunctional chelating agent, Hx-DADT (Scheme 1), was synthesized according to our previously published procedures (*31*).

Male CD-1 mice were purchased from the Charles River Laboratories (Charles River, MA). All in vivo studies on mice were approved by the Institutional Animal Care and Use Committee. The PC-3 cell line was obtained from the American Type Culture Collection (Rockville, MD) and grown in the Cell Culture Laboratory, School of Medicine, The Johns Hopkins University (Baltimore, MD). Amino acid analyses and MALDI mass spectroscopy were performed by AnaSpec, Inc. (San Jose, CA). FAB mass spectroscopy was performed by the Mass Spectrometry Service Laboratory of the University of Minnesota (Minneapolis, MN).

HPLC was performed with a Waters Chromatography Division (Milford, MA) HPLC System equipped with two

model 510EF pumps, a model 680 automated gradient controller, a model 490 UV absorbance detector, and a Bioscan NaI scintillation detector connected to a Bioscan Flow-count System (Bioscan, Inc., Washington, DC). The output from two channels of the UV detector and the output from the Flow-count system were fed into a Gateway 2000 P5−133 computer fitted with an IN/US System, Inc. (Tampa, FL) computer card. HPLC acquisition and analysis were performed with the Winflow software from IN/US. The semipreparative column (C18 Novapak cartridge, 25 mm × 10 cm, 6 μm), the analytical column (C18 Novapak cartridge, 8 mm × 10 cm, 4 μm), and the C18 Light Sep-Pak cartridges were purchased from Waters Chromatography Division. The G3000SW size exclusion column (7.5 mm × 30 cm, particle size 10 μm, pore size 25 nm) was purchased from TosoHaas (Montogomeryville, PA). Reversed phase HPLC solvents consisted of acetonitrile containing 0.1% trifluoroacetic acid (solvent A) and water containing 0.1% trifluoroacetic acid (solvent B). Liquid scintillation counting for quantification of ^{99}Tc activity was performed on an LKB Wallac instrument model 1219 Rackbeta using Ecolume (ICN Pharmaceuticals, Inc., Costa Mesa, CA) as cocktail. Filtration of in vitro assay mixtures was performed on a BRANDEL, 48M Harvester (Biomedical Research and Development Laboratories Inc., Gaithersburg, MD). ^{125}I activity on filters from in vitro assays and ^{99m}Tc activity of tissues from biodistribution and blocking studies were counted on an automated gamma counter (Pharmacia-Wallac model 1282). Analyses of in vitro binding assay results were performed using the EBDA/LIGAND programs from Biosoft (Milltown, NJ). ^{99m}Tc activity for synthetic reactions and doses for biodistribution were measured in a Capintec (Pittsburgh, PA) CRC-7 Dose Calibrator.

Synthesis of [DTPA^1, Lys^3, Tyr^4]BN. [DTPA^1, Lys^3, Tyr^4]BN was synthesized in an Advanced ChemTech 90 Tabletop Peptide Synthesizer using the *tert*-butyloxycarbonyl (Boc) protocol starting with Boc-L-methionine-*p*-methylbenzhydrylamine resin (3 g, 1 mmol/g). Each coupling step was performed with DIC (9 mmol), HOBt (9 mmol), and the appropriate Boc-protected amino acid (9 mmol) including N^{im}-tosyl His, N^{in}-formyl Trp, *N*-γ-xanthyl Gln, *N*-β-xanthyl Asn, *O*-2,6-dichlorobenzyl Tyr, and N^{ϵ}-2-chlorobenzyloxycarbonyl Lys in methylene chloride/dimethylformamide (1:1). The coupling reaction was usually complete in 30 min and was repeated if the nynhydrin test was positive. Trifluoroacetic acid (25%) in methylene chloride was used for Boc group deprotection during each cycle. DTPA was conjugated as the last step using the method of Mokotoff et al. (*32*). After assembly, peptide cleavage and side chain deprotection were performed using anhydrous hydrogen fluoride (14 g) at 0 °C for 1.5 h in the presence of anisole (19.7 mmol). After drying, the peptide was extracted into 5% aqueous acetic acid (50 mL) and purified by HPLC with a linear gradient from solvent A (15%)/solvent B (85%) to solvent A (40%)/solvent B (60%) over the course of 50 min at a flow rate of 6 mL/min using the semipreparative column monitored on-line for UV absorption at 220 nm. Eluates containing the product with a retention time of 26.0 min were collected, pooled, and lyophilized. The purity of [DTPA^1, Lys^3, Tyr^4]BN was >95% as assessed by analytical HPLC. The yield of [DTPA^1, Lys^3, Tyr^4]BN was 968 mg (17%). Amino acid analysis gave the expected amino acid ratio; calcd/found Asn (1/0.98), His (1/1.01), Val (1/1.00), Leu (1/1.00), Lys (1/1.02), Gln(2/1.96), Gly (2/2.03), Ala (1/1.02), Tyr (1/0.96), Met (1/1.00). MALDI MS: calcd MW for [DTPA^1, Lys^3, Tyr^4]BN 1904.9, found $[M + H]^+$ 1905.8.

Coupling of Hx-DADT to [DTPA^1, Lys^3, Tyr^4]BN. Hx-DADT was coupled to [DTPA^1, Lys^3, Tyr^4]BN according to Scheme 1. Hx-DADT·2HCl (3.6 mg, 9.1 μmol) and [DTPA^1, Lys^3, Tyr^4]BN (3.3 mg, 1.73 μmol) were dissolved in a mixture of borate buffer (0.4 mL, 0.1 M, pH 9) and acetonitrile (0.4 mL), and the pH was adjusted to 9 with triethylamine. The mixture was incubated at room temperature for 2 h and then extracted with ether (3 × 2 mL). The aqueous fraction was chromatographed by HPLC with a linear gradient from solvent B (100%) to solvent A (80%)/solvent B (20%) over the course of 60 min at a flow rate of 6 mL/min using the semipreparative column monitored on-line for UV absorption at 220 nm. The product with a retention time of 33.0 min was collected and then lyophilized. The yield of [DTPA^1, Lys^3(Hx-DADT), Tyr^4]BN was 1.7 mg (44%). Amino acid analysis gave the expected amino acid ratios; calcd/found Asn (1/0.88), His (1/1.02), Val (1/1.04), Leu (1/1.04), Lys (1/0.99), Gln(2/1.87), Gly (2/2.18), Ala (1/1.01), Tyr (1/1.00), Met (1/0.87). MALDI MS: calc MW for [DTPA^1, Lys^3(Hx-DADT), Tyr^4]BN 2209.1, found $[M + H]^+$ 2211.3.

^{99m}Tc Labeling of the [DTPA^1, Lys^3(Hx-DADT), Tyr^4]BN. ^{99m}Tc labeling of [DTPA^1, Lys^3(Hx-DADT), Tyr^4]BN was performed as depicted in Scheme 1. A glucoheptonate kit (Glucoscan) was reconstituted with water (1.0 mL). From this solution, [^{99m}Tc]glucoheptonate was prepared by addition of an aliquot (200 μL) to a [^{99m}Tc]pertechnetate solution (500 μL, 10−20 mCi). The mixture was vortexed for 1 min and allowed to stand at room temperature for 15 min. An aliquot of the [^{99m}Tc]-glucoheptonate solution (300 μL) was added to a solution of the [DTPA^1, Lys^3(Hx-DADT), Tyr^4]BN (0.5 μmol) in water (500 μL), and the mixture was vortexed for 1 min and incubated at room temperature for 10 min. The labeling reaction was followed by reversed phase HPLC using a linear gradient from solvent A (25%)/solvent B (75%) to solvent A (55%)/solvent B (45%) over the course of 60 min at a flow rate of 2 mL/min on the analytical column. HPLC was monitored on-line for UV absorption at 220 nm and scintillation for radioactivity. A single product designated as [DTPA^1, Lys^3(^{99m}Tc-Hx-DADT), Tyr^4]BN with a retention time of 37.0 min was obtained. The yield of the product was >90%.

Preparation of the ^{99}Tc Analogue of [DTPA^1, Lys^3(Hx-DADT), Tyr^4]BN. To a solution of [DTPA^1, Lys^3(Hx-DADT), Tyr^4]BN (2.6 mg, 1.18 μmol) in a methanol/water mixture (1:1, 800 μL) was added a solution of [^{99}Tc]glucoheptonate in water (60 μL, 20 mM). The mixture was stirred at room temperature for 1 h. A similar product was obtained as described above for the ^{99m}Tc analogue. The product was isolated by HPLC using the same conditions above for the purification of the ^{99m}Tc analogue. The yield of the product was 43%. MALDI MS: calcd MW for [DTPA^1, Lys^3(^{99}Tc-Hx-DADT), Tyr^4]BN 2321.0, found $[M + H]^+$ 2321.0.

Stability Test of [DTPA^1, Lys^3(^{99m}Tc-Hx-DADT), Tyr^4]BN in Human Serum. The purified ethanolic solution (300 μL) of [DTPA^1, Lys^3(^{99m}Tc-HX-DADT), Tyr^4]BN was diluted with saline (3 mL), and then 100 μL of this diluted solution was mixed with 900 μL of human serum. The mixture was incubated in a 37 °C water bath. After 2, 4, and 6 h, an aliquot (100 μL) was removed and analyzed by isocratic size exclusion HPLC.

The HPLC eluent flow rate was 1 mL/min using the size exclusion column monitored on-line for UV absorption at 220 and 280 nm and scintillation for radioactivity.

The eluent consisted of 10% acetonitrile in 0.2 M phosphate buffer (pH 7.15) containing 0.05% sodium azide. The serum proteins eluted at retention time ranging from 5 to 10 min, and [DTPA^1, Lys^3(^{99m}Tc-Hx-DADT), Tyr^4]BN eluted at the retention time of 15.8 min.

Competition of Hydrolyzed Hx-DADT with DTPA for ^{99m}Tc. Hx-DADT·2HCl (2 mg, 5.3 μmol) was dissolved in water (400 μL) and then hydrolyzed by the addition of 2.5 N NaOH (100 μL). After 10 min incubation, the pH was adjusted to 7 with 1 N HCl. DTPA (104 mg, 264 μmol) was added to the mixture, and the pH was readjusted to 7 with 2.5 N NaOH.

^{99m}Tc-glucoheptonate (300 μL, ~10 mCi) was added to the mixture, vortexed for 1 min, and then incubated at room temperature for 20 min. For comparison another reaction was set up with all the reagents except DTPA. The reactions were followed by reversed phase HPLC. The HPLC conditions used were the same as described above for the purification of [DTPA^1, Lys^3(^{99m}Tc-Hx-DADT), Tyr^4]BN. Both reaction mixtures showed similar HPLC spectra with two products, at retention time of 12.2 min (minor) and 24.8 min (major). The total labeling yield was >95% and the ratio of major/minor product was ~5.

^{99}Tc complexes of hydrolyzed Hx-DADT were similarly prepared using [^{99}Tc]glucoheptonate (1.05 μmol). Two products were obtained as described above for the ^{99m}Tc analogues. The total labeling yield was 56% and the ratio of major/minor product was ~1.5. FAB MS: calcd MW for ^{99}Tc-Hx-DADT 416.1, found $[M + H]^+$ 417.2 for both major and minor products.

In Vitro Binding Assay of BN Analogues. The binding studies were performed using a modified method of Reile et al. (*33*). Briefly, 10 μg membrane protein was incubated at 25 °C for 35 min with 100 pM [^{125}I-Tyr^4]BN in the presence or absence of various concentrations of BN, somatostatin, [DTPA^1, Lys^3, Tyr^4]BN, [DTPA^1, Lys^3(Hx-DADT), Tyr^4]BN or [DTPA^1, Lys^3(^{99}Tc-Hx-DADT), Tyr^4]BN ranging from 10 pM to 1 μM in the assay buffer (50 mM Tris-HCl buffer, pH 7.4, containing 1 mg/mL bovine serum albumin (BSA) and 2 μg/mL bacitracin, 125 μL total volume). Nonspecific binding was determined in the presence of 1 μM bombesin. The reaction was terminated by rapid filtration through Whatman GF/B glass fibers presoaked for 30 min in the wash buffer (50 mM Tris-HCl buffer, pH 7.4, containing 1 mg/mL BSA). The filter was washed 3 × 5 mL with ice-cold wash buffer. Radioactivity on the filters was counted in the automated gamma counter. The results of the assay were analyzed by the EBDA/LIGAND computer programs (*34*). The assays were performed in duplicate and the whole experiment was repeated 3 times.

Biodistribution of [DTPA^1, Lys^3(^{99m}Tc-Hx-DADT), Tyr^4]BN in Normal Mice. The HPLC-purified [DTPA^1, Lys^3(^{99m}Tc-Hx-DADT), Tyr^4]BN was isolated from the HPLC eluate by solid-phase extraction using the C18 Light Sep-Pak cartridge. The Sep-Pak cartridge was first washed with ethanol (5 mL) followed by a solution of ammonium acetate (0.05 M, 5 mL). The HPLC eluate containing [DTPA^1, Lys^3(^{99m}Tc-Hx-DADT), Tyr^4]BN was diluted five times with ammonium acetate (0.05 M) and then passed through the Sep-Pak cartridge. The Sep-Pak cartridge was washed with an ammonium acetate solution (0.05 M, 5 mL) followed by elution of the [DTPA^1, Lys^3(^{99m}Tc-Hx-DADT), Tyr^4]BN with ethanol (300 μL). The ethanolic solution was diluted with physiologic saline to make a final injectate (10 μCi/mL) containing <0.5% ethanol.

Normal male CD-1 mice weighing 23.6 ± 1.1 g were used for biodistribution studies. [DTPA^1, Lys^3(^{99m}Tc-Hx-DADT), Tyr^4]BN (2 μCi, 200 μL) was injected into mice via the tail vein. At 15 min, 1, 2, and 4 h postinjection, four mice for each time point were sacrificed by cervical dislocation. Major organs were dissected, weighed, and counted in an automated gamma counter with aliquots of the injectate (as standards) counted at the same time. The percent injected dose per organ (% ID/organ), and the percent injected dose per gram (% ID/g) was calculated. The % ID in blood was estimated with the assumption that the total blood volume is 6.5% of the body weight.

In blocking studies, each mouse received a subcutaneous injection of a suspension containing 700 μg of BN, neuromedin B, or somatostatin in saline (100 μL) 35 min before the injection of [DTPA^1, Lys^3(^{99m}Tc-Hx-DADT), Tyr^4]BN. Control (unblocked) mice received an injection of saline (100 μL) 35 min prior to the injection of [DTPA^1, Lys^3(^{99m}Tc-Hx-DADT), Tyr^4]BN. One hour after the injection of the tracer, the mice were euthanized and major organs were dissected, weighed, and counted as described above.

Imaging of Human Prostate Cancer PC-3 Tumor in Mice. Male SCID mice (24.0−32.6 g) were injected subcutaneously with 10^6 PC-3 human prostate cancer cells in matrigel (0.3 mL) in one flank. The mice having palpable tumors (0.5−1.2 g) after 8 weeks were used for imaging studies. HPLC purified [DTPA^1, Lys^3(^{99m}Tc-Hx-DADT), Tyr^4]BN (200 μCi) was injected through the tail vein. At 6 h postinjection, the mice were anesthetized with urethane and placed directly on the face of one crystal head of a Phillips IRIX VT camera fitted with a low energy high resolution parallel hole collimator and planar static images acquired for 15 min using a 512 × 512 matrix. Image analysis was performed using the Odyssey FX 8.9C software. Image contrast was adjusted in order to see the outlines of the mouse and the target to nontarget ratio on the image was calculated from regions of interest drawn over the tumor area (target) and the contralateral region (nontarget) of the image.

RESULTS AND DISCUSSION

It is becoming increasingly evident that the BN/GRP receptor becomes expressed early in the process of carcinogenesis in a number of cancers that have been investigated. For example, pulmonary BN/GRP receptor levels in adult lung are extremely low or nonexistent under normal conditions (*35*, *36*). However, prolonged tobacco exposure, transformed cells, and lung cancer result in marked increases in pulmonary BN/GRP levels and the expression of their receptors (*7*, *15*, *37*−*39*). In prostate tissue, a massive BN/GRP receptor overexpression has been demonstrated in prostatic intraepithelial proliferative lesions, a premalignant condition and in prostate carcinoma but not in normal tissues or other prostate hyperplasias (*13*). Similar results have also been reported for gastric cancer where a high density of receptors is present in gastric cancer and Menetrier's disease, a mucosal disorder known to be premalignant, but absent in the surrounding normal tissues (*14*). Such data are not only of biological significance but also provide a molecular basis for potential applications such as BN/GRP-receptor scintigraphy for early tumor detection if suitable radiotracers were available.

To label peptides with ^{99m}Tc, we have been investigating DADT ligands derivatized as bifunctional chelating agents. DADT ligands have been shown to be one of the

most promising chelators for Tc labeling. Having the advantages of stable Tc complexation, well characterized Tc-complex structures, and mild conditions for Tc labeling, DADT ligands have been used to label both proteins and peptides with ^{99m}Tc for applications such as cancer and inflammation imaging (*19*, *40*−*42*). In previous studies (*19*), we reported a ^{99m}Tc-labeled BN analogue, Lys^3(^{99m}Tc-Hx-DADT)-BN, using Hx-DADT as the bifunctional chelating agent and Lys^3-BN as the bombesin analogue. The Tc-chelate core of Hx-DADT is neutral and highly lipophilic. Therefore, while Lys^3(^{99m}Tc-Hx-DADT)-BN showed high affinity ($K_i = 5.2 \pm 1.5$ nM) for the BN/GRP receptor, the high lipophilicity conferred by the Tc-DADT chelate core resulted in most of the radioactivity being excreted through the hepatobiliary pathway (>96% ID). As a result, Lys^3(^{99m}Tc-Hx-DADT)BN would not be suitable for imaging BN/GRP receptor-positive tumors and their metastases in the abdominal area. To increase the hydrophilicity of ^{99m}Tc-labeled BN analogues, we have synthesized this new BN/GRP analogue, [DTPA^1, Lys^3, Tyr4]BN with a built-in pharmacokinetic modifier, DTPA, at the N-terminus so as to direct tracer clearance through the urinary system. To test the utility of this approach, we chose the highly lipophilic ^{99m}Tc-Hx-DADT chelate for labeling.

In the design of [DTPA^1, Lys^3, Tyr^4]BN we sought minimal modification of the structure of BN in order to preserve high affinity binding to the BN/GRP receptor. All modifications were restricted to the N-terminal region in order not to interfere with the C-terminal octapeptide binding site of the peptide. Pyr at the N-terminus was replaced by DTPA, which serves as the pharmacokinetic modifier. The assumption for using DTPA was that, as constructed, the four carboxylic groups introduced to the peptide after coupling DTPA to the peptide would be negatively charged at physiologic pH. Therefore, the peptide would be highly charged, aiding urinary excretion preferentially over hepatobiliary excretion. Arg at the third position of BN was replaced by Lys to provide an ϵ-amino group for coupling to the Tc-coordinating moieties such as Hx-DADT. Leu, the fourth residue, was also replaced by Tyr to allow the potential direct iodination of the resulting analogue. The binding site of BN was retained unaltered in the new analogue. The product, [DTPA^1, Lys^3, Tyr^4]BN, was purified by semipreparative reversed phase HPLC to a single species and characterized by both mass spectrometry and amino acid analysis. It is noteworthy that as constructed, the peptide can potentially be labeled with radionuclides other than ^{99m}Tc such as ^{111}In, $^{123/125/131}$I, ^{18}F and $^{186/188}$Re.

Coupling of the bifunctional chelating agent, Hx-DADT, to [DTPA^1, Lys^3, Tyr^4]BN was performed at pH 9 using a Hx-DADT:[DTPA^1, Lys^3, Tyr^4]BN ratio of 5:1 (Scheme 1). No side chain protection was necessary since the indole and imidazole groups of Trp and His, respectively, are weak nucleophiles under the coupling conditions. The purified adduct was also characterized by both mass spectrometry and amino acid analysis.

We have prepared both no-carrier-added (^{99m}Tc) and milligram quantities (^{99}Tc) of the Tc-labeled BN analogue, [DTPA^1, Lys^3(Tc-Hx-DADT), Tyr^4]BN (Scheme 1). Only one product was obtained in both cases. The yield of ^{99m}Tc product was >90% after a 10 min incubation at room temperature as determined by HPLC. The ^{99}Tc product with 43% isolated yield was characterized by mass spectrometry.

DTPA is capable of coordinating Tc. Therefore, a pertinent issue in the design of [DTPA^1, Lys^3(^{99m}Tc-Hx-DADT), Tyr^4]BN was whether the Tc was chelated by DTPA, DADT or both. The result from mass spectrometry of [DTPA^1, Lys^3(^{99}Tc-Hx-DADT), Tyr^4]BN indicated that only one technetium-oxo (TcO) group was chelated to [DTPA^1, Lys^3(Hx-DADT), Tyr^4]BN. Proteins labeled with Tc using DTPA as the bifunctional chelate usually show poor stability both in vitro and in vivo (*43*) whereas the use of DADT based chelates result in stable products. Results of the stability test of [DTPA^1, Lys^3(^{99m}Tc-Hx-DADT), Tyr^4]BN in human serum showed that less than 6% of radioactivity was transferred to serum proteins after 6 h incubation at 37 °C. This indicates strong binding of Tc in this product and suggests DADT chelation. In the competition study, identical products (^{99m}Tc-Hx-DADT) were obtained in the presence or absence of excess DTPA confirming that DTPA is unable to compete with DADT for Tc. The products had the same mass expected for Tc-Hx-DADT, indicating isomeric forms of this product as expected for Tc-DADT complexes. The combination of these facts strongly suggests that Tc is chelated to [DTPA^1, Lys^3(Hx-DADT), Tyr^4]BN via the DADT core rather than DTPA.

Table 1. Results of in Vitro Binding Studies of Bombesin Analogues to PC-3 Cell Membranes

compound	K_i [a] (nM)
BN	1.7 ± 0.6
[DTPA^1, Lys^3, Tyr^4]BN	3.1 ± 1.3
[DTPA^1, Lys^3(Hx-DADT), Tyr^4]BN	11.2 ± 5.4
[DTPA^1, Lys^3(^{99}Tc−Hx-DADT, Tyr^4]BN	19.9 ± 8.0
somatostatin	>10000

[a] Values represent the mean ± SD ($n = 3$).

Table 2: Biodistribution (% ID/organ)[a] of [DTPA^1, Lys^3(^{99m}Tc-Hx-DADT), Tyr^4]BN in normal Mice

	15 min	1 h	2 h	4 h
blood[b]	7.26 ± 1.27	1.38 ± 0.27	0.53 ± 0.14	0.23 ± 0.01
brain	0.10 ± 0.01	0.02 ± 0.01	0.02 ± 0.02	0.00 ± 0.00
heart	0.19 ± 0.02	0.03 ± 0.01	0.01 ± 0.00	0.01 ± 0.00
lung	0.63 ± 0.13	0.22 ± 0.03	0.08 ± 0.02	0.06 ± 0.04
kidneys	5.82 ± 0.94	2.90 ± 0.47	1.71 ± 0.06	0.85 ± 0.15
spleen	0.15 ± 0.04	0.06 ± 0.03	0.02 ± 0.01	0.01 ± 0.00
pancreas	2.74 ± 0.45	1.69 ± 0.54	1.16 ± 0.29	0.34 ± 0.07
intestines	14.3 ± 0.63	19.0 ± 0.49	22.1 ± 2.13	20.3 ± 4.33
stomach	1.26 ± 0.10	1.06 ± 0.21	0.66 ± 0.10	0.42 ± 0.03
liver	9.21 ± 1.67	2.41 ± 0.37	1.45 ± 0.13	1.04 ± 0.29

[a] Values represent the mean ± SD ($n = 4$). [b] The blood volume was estimated to be 6.5% of the body weight.

As a first step in the evaluation of the biological activity of [DTPA^1, Lys^3(Tc-Hx-DADT), Tyr^4]BN, we investigated the ability of [DTPA^1, Lys^3(Tc-Hx-DADT), Tyr^4]BN to bind to the BN/GRP receptor on human prostate cancer PC-3 cell membranes. These studies involved competitive binding experiments using the authentic BN receptor ligand [^{125}I-Tyr^4]BN. Results of analysis of the binding data with the EBDA/LIGAND computer programs are shown in Table 1. The apparent affinity, K_i, of [DTPA^1, Lys^3, Tyr^4]BN for the BN receptor was comparable to that of BN itself (3.1 ± 1.3 vs 1.7 ± 0.6 nM). Coupling of Hx-DADT to [DTPA^1, Lys^3, Tyr^4]BN and the subsequent labeling of Tc resulted in products, [DTPA^1, Lys^3(Hx-DADT), Tyr^4]BN and [DTPA^1, Lys^3(^{99}Tc-Hx-DADT), Tyr^4]BN, with slightly lower affinity ($K_i = 11.2 \pm 5.4$ and 19.9 ± 8.0 nM, respectively).

Results of the biodistribution studies of [DTPA^1, Lys^3(^{99m}Tc-Hx-DADT), Tyr^4]BN in normal mice are summarized in Tables 2 and 3. [DTPA^1, Lys^3(^{99m}Tc-Hx-DADT), Tyr^4]BN showed fast clearance from the blood (0.23 ± 0.01 ID, 0.15 ± 0.01%ID/g, 4 h postinjection) and nontarget tissues. The radioactivity excreted through the hepatobiliary system (liver plus intestines, ∼21% ID,

Table 3. Results of the Biodistribution (% ID/g)[a] of [DTPA[1], Lys[3](99mTc-Hx-DADT), Tyr[4]]BN in normal Mice at Different Time Points

organ	15 min	1 h	2 h	4 h
blood	4.68 ± 0.56	0.89 ± 0.19	0.35 ± 0.10	0.15 ± 0.01
brain	0.22 ± 0.02	0.05 ± 0.02	0.04 ± 0.04	0.009 ± 0.001
heart	1.74 ± 0.19	0.31 ± 0.06	0.12 ± 0.02	0.05 ± 0.01
lung	3.54 ± 0.16	1.05 ± 0.22	0.49 ± 0.19	0.28 ± 0.08
kidneys	18.10 ± 3.28	8.54 ± 1.25	5.44 ± 0.83	2.66 ± 0.70
spleen	1.90 ± 0.24	0.62 ± 0.34	0.30 ± 0.06	0.11 ± 0.03
pancreas	21.83 ± 2.88	12.8 ± 2.97	8.10 ± 1.88	2.62 ± 0.37
intestines	5.65 ± 0.41	7.74 ± 0.67	8.70 ± 1.34	9.16 ± 2.35
stomach	1.45 ± 0.56	1.64 ± 0.56	1.05 ± 0.25	1.16 ± 0.05
liver	5.97 ± 0.66	1.73 ± 0.21	0.97 ± 0.11	0.83 ± 0.23
muscle	0.98 ± 0.19	0.20 ± 0.07	0.11 ± 0.03	0.05 ± 0.01

[a] Values represent the mean ± SD ($n = 4$).

4 h postinjection) was much lower compared to the results of Lys[3](99mTc-Hx-DADT)BN (>96% ID, 3 h postinjection) in our previous studies (*19*), indicating the success of the pharmacokinetic modifier, DTPA, in reducing the radioactivity in the gut even with the use of the highly lipophilic 99mTc-Hx-DADT chelate for labeling. Only small amounts of activity remained in the kidneys, stomach and liver at 4 h postinjection (2.66 ± 0.70, 1.16 ± 0.05 and 0.83 ± 0.23% ID/g, respectively). The pancreas, which expresses BN receptors (*39*), has been used as a target by other investigators (*25*, *45*) for the biological evaluation of newly developed radiolabeled BN analogues. In this study, a significant uptake (21.83 ± 2.88% ID/g, 15 min postinjection) of the radioactivity was found in the pancreas. This demonstrates the ability of [DTPA[1], Lys[3](99mTc-Hx-DADT), Tyr[4]]BN to target BN/GRP receptor expressing cells in vivo. The pancreas/blood and pancreas/muscle ratios were highest at 2 h postinjection at 23 and 74, respectively. These ratios are similar to the ratios (22 and 80, 4 h postinjection) obtained by Karra et al. (*25*) using 99mTc-P_2S_2−$BN^{(7-14)}$, a BN analogue labeled with 99mTc by the use of a hydrophilic dithiadiphospine-based bifunctional chelating agent. However, compared to 99mTc-P_2S_2−$BN^{(7-14)}$, [DTPA[1], Lys[3](99mTc-Hx-DADT), Tyr[4]]BN showed less radioactivity excreted through the hepatobiliary pathway (liver plus intestines, 21 vs 35% ID, 4 h postinjection) and therefore higher pancreas/liver ratio (8.4, 2 h postinjection vs 2.1, 4 h postinjection). Since the hydrophilic dithiadiphospine-based bifunctional chelating agent also reduced the accumulation of radioactivity in the gut compared to [Lys[3](99mTc-Hx-DADT)]BN from our previous study (*19*), it will be interesting to combine both the built-in pharmacokinetic modifier with a hydrophilic bifunctional chelating agent in the same peptide to investigate the effect on hepatobiliary excretion.

Results of the receptor blocking studies with BN, neuromedin B, and somatostatin (Table 4) confirmed the specificity of [DTPA[1], Lys[3](99mTc-Hx-DADT), Tyr[4]]BN toward the BN/GRP receptors. The difference in the uptake of [DTPA[1], Lys[3](99mTc-Hx-DADT), Tyr[4]]BN with and without subcutaneous injection of 700 μg of BN are significant in the pancreas (0.65 ± 0.16 vs 11.96 ± 1.17% ID/g), intestines (4.23 ± 0.46 vs 6.90 ± 0.68% ID/g) and stomach (0.64 ± 0.24 vs 1.40 ± 0.47% ID/g). Acini cells of the pancreas, submucosal layer of the small intestine, circular muscle, and submucosal layer of the colon as well as the circular muscle of the gastric fundus and antrum all have been shown to express BN/GRP receptors (*44*, *46*). Neuromedin B (*47*), another mammalian analogue of BN, which shows moderate affinity (K_i, 150−350 nM against [125I-Tyr[4]]BN toward BN/GRP receptors in acini cells of rat pancreas) partially blocked the uptake of

Table 4. Blocking (% ID/g)[a] of [DTPA[1], Lys[3](99mTc-Hx-DADT), Tyr[4]]BN Distribution in normal Mice by Bombesin,[b] Neuromedin B and Somatostatin

	control	bombesin	neuromedin b	somatostatin
blood	0.85 ± 0.16	1.17 ± 0.16	1.08 ± 0.03	1.16 ± 0.17
heart	0.26 ± 0.05	0.44 ± 0.06	0.41 ± 0.02	0.62 ± 0.25
lung	0.59 ± 0.09	0.96 ± 0.09	1.04 ± 0.22	1.17 ± 0.15
kidneys	7.86 ± 1.72	10.56 ± 1.47	8.55 ± 0.78	10.94 ± 2.86
spleen	0.44 ± 0.06	0.35 ± 0.04	0.60 ± 0.27	0.49 ± 0.04
pancreas	11.96 ± 1.17	0.65 ± 0.16	6.66 ± 0.51	12.94 ± 2.53
intestines	6.90 ± 0.68	4.23 ± 0.46	6.72 ± 0.83	6.56 ± 0.50
stomach	1.40 ± 0.47	0.64 ± 0.24	1.28 ± 0.21	2.13 ± 0.64
liver	1.24 ± 0.16	1.64 ± 0.46	1.39 ± 0.16	1.72 ± 0.24
muscle	0.20 ± 0.03	0.31 ± 0.02	0.24 ± 0.02	0.25 ± 0.04

[a] Values represent the mean ± SD ($n = 4$). The animals were sacrificed 1 h after the injection of [DTPA[1], Lys[3](99mTc−Hx-DADT), Tyr[4]]BN. [b] 700 μg (in 100 μL saline) BN, neuromedin B or somatostatin was injected subcutaneously 30 min before the injection of [DTPA[1], Lys[3](99mTc−Hx-DADT), Tyr[4]]BN.

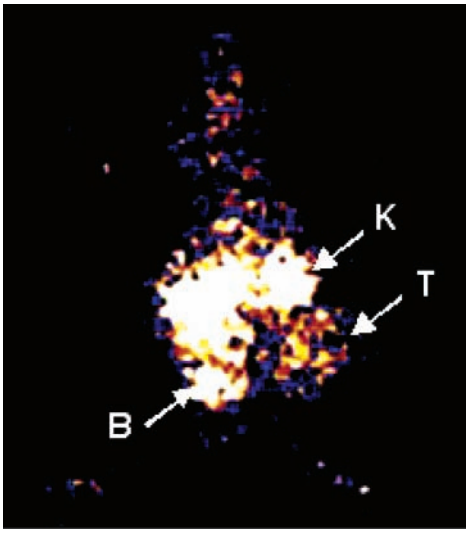


Figure 1. Image of a mouse carrying a human prostate PC-3 xenograft 6 h postinjection with [DTPA[1], Lys[3](99mTc-Hx-DADT), Tyr[4]]BN. Tumor, T; kidney, K; bladder, B.

radioactivity in pancreas (6.66 ± 0.51 vs. 11.96 ± 1.17% ID/g). In contrast, somatostatin with very low affinity for BN/GRP receptor showed no effect on the biodistribution of [DTPA[1], Lys[3](99mTc-Hx-DADT), Tyr[4]]BN. These results suggest that the uptake of [DTPA[1], Lys[3](99mTc-Hx-DADT), Tyr[4]]BN in receptor rich areas in vivo is specific.

In a preliminary study, we investigated the capability of using [DTPA[1], Lys[3](99mTc-Hx-DADT), Tyr[4]]BN for imaging prostate cancer using the PC-3 xenograft model in SCID mice. A representative image is shown in Figure 1. The site of the tumor could be differentiated in the 6 h image. The target to nontarget ratio on the image was 8:1, suggesting that the labeled peptide has potential for imaging prostate cancer and its metastases.

In summary, we have described a new hydrophilic peptide, [DTPA[1], Lys[3], Tyr[4]]BN, whose 99mTc-chelate-labeled product [DTPA[1], Lys[3](99mTc-Hx-DADT), Tyr[4]]BN showed greatly reduced accumulation of radioactivity in the liver and intestines compared with an analogue lacking the pharmacokinetic modifier. It may be possible to use [DTPA[1], Lys[3](99mTc-Hx-DADT), Tyr[4]]BN for imaging BN/GRP receptor-positive tumors. Since DADT ligands are also capable of forming highly stable complexes with Re, the congener of Tc, the 186Re and 188Re analogues of [DTPA[1], Lys[3](Hx-DADT), Tyr[4]]BN could be directly applicable for the radiotherapy of many cancers on account of the energetic beta emissions from these radionuclides.

The study demonstrates successful modification of in vivo pharmacokinetics using DTPA even when the highly lipophilic ^{99m}Tc chelate core, ^{99m}Tc-Hx-DADT, was used for labeling.

ACKNOWLEDGMENT

This work was supported by PHS Research Grant numbers CA32845, CA096817, SAIRP grant CA92871, and Training Grant CA09199 support for A.L. and H.H.G. from the National Cancer Institute.

LITERATURE CITED

(1) Anastasi, A., Erspamer, V., and Bucci, M. (1971) Isolation and structure of bombesin and alytesin, two analogous active peptides from the skin of the European amphibian. *Bombina Alytes*. *Experientia 27*, 166−167.

(2) Ghatei, M. A., Jung, R. T., Stevenson, J. C., Hillyard, C. J., Adrian, T. E., Lee, Y. C., Christtofides, N. D., Sarson, D. L., Mashiter, K., MacIntyre, I., and Bloom, S. R. (1982) Bombesin: action on gut hormones and calcium in man. *J. Clin. Endocrinol. Metab*. *54*, 980−985.

(3) Kaneto, A., Kaneko, T., Nakaya, S., Kajinuma, H., and Kasaka, K. (1978) Effect of bombesin infused intrapancreatically on glucagon and insulin secretion. *Metabolism 27*, 549−553.

(4) Jensen, R. T., Coy, D. H., Saeed, Z. A., Heinz-Erian, P., Mantey, S., and Gardner, J. D. (1988) Interaction of bombesin and related peptides with receptors on pancreatic acinar cells. *Ann. N. Y. Acad. Sci. 547*, 138−149.

(5) Brown, M. R., Carver, K., and Fisher, L. A. (1988) Bombesin: central nervous system actions to affect the autonomic nervous system. *Ann. N. Y. Acad. Sci. 547*, 174−182.

(6) Rettori, V., Pazos-Moura, C. C., Moura, E. G., Polak, J., and McCann, S. M. (1992) Role of neuromedin B in control of the release of thyrotropin in hypothyroid and hyperthyroid rats. *Proc. Natl. Acad. Sci. U.S.A. 89*, 3035−3039.

(7) Moody, T. W., Carney, D. N., Cuttitta, F., Quattrocchi, K., and Minna, J. D. (1985) High affinity receptors for bombesin/GRP-like peptides on human small cell lung cancer. *Life Sci. 37*, 105−113.

(8) Moody, T. W., Mahmoud, S., Staley, J. S., Naldini, L., Cirillo, D., South, V., Felder, S., and Kris, R. (1989) Human glioblastoma cell lines have neuropeptide receptors for bombesin/GRP. *J. Mol. Neurosci*. *1*, 235−242.

(9) Farre, A., Ishizuka, J., Gomez, G., Parekh, D., Koo, J. Y., Townsend, C. M., and Thompson, J. C. (1993) Bombesin stimulates growth of colon cancer in mice and decreases their survival. *Surg. Oncol. 2*, 169−173.

(10) Qin, Y., Ertl, T., Cai, R. Z., Halmos, G., and Schally, A. V. (1994) Inhibitory effect of bombesin receptor antagonist RC-3095 on the growth of human pancreatic cancer cells in vivo *and in vitro*. *Cancer Res. 54*, 1035−1041.

(11) Qin, Y., Halmos, G., and Cai, R. Z. (1994) Bombesin antagonist inhibit in vitro and in vivo growth of human gastric cancer and binding of bombesin to its receptors. *J. Cancer Res. Clin. Oncol. 120*, 519−528.

(12) Yano, T., Pinski, J., Szepeshazi, K., Groot, K., and Schally, A. V. (1992) Stimulation by bombesin and inhibition by bombesin/gastrin releasing peptide antagonist RC-3095 of growth of human breast cancer cell lines. *Cancer Res*. *52*, 4545−4547.

(13) Markwalder, R., and Reubi, J. C. (1999) Gastrin-releasing peptide receptors in the human prostate: relation to neoplastic transformation. *Cancer Res. 59*, 1152−1159.

(14) Preston, S. R., Woodhouse, L. F., Jones-Blackett, S., Wyatt, J. I., and Primrose, J. N. (1993) High affinity binding sites for gastrin releasing peptide on human gastric cancer and ménétrier's mucosa. *Cancer Res*. *53*, 5090−5092.

(15) Shriver, S. P., Bourdeau, H. A., Gubish, C. T., Tirpak, D. L., Davis, A. L. G., Luketich, J. D., and Siegfried, J. M. (2000) Sex-specific expression of gastrin-releasing peptide receptor: relationship to smoking history and risk of lung cancer. *J. Natl. Cancer Inst. 92*, 24−33.

(16) Breeman, W. A., De Jong, M., Bernard, B. F., Kwekkeboom, D. J., Srinivasan, A., van der Pluijm, M. E., Hofland, L. J., Visser, T. J., and Krenning, E. P. (1999) Pre-clinical evaluation of [(111)In-DTPA-Pro(1), Tyr(4)]bombesin, a new radioligand for bombesin-receptor scintigraphy. *Int. J. Cancer 83*, 657−663.

(17) Li, N., Struttman, M., Higginbotham, C., Grall, A. J., Skerlj, J. F., Vollano, J. F., Bridger, S. A., Ochrymowycz, L. A., Ketring, A. R., Abrams, M. J., and Volkert, W. A. (1997) Biodistribution of model 105Rh-labeled tetradentate thiamacrocycles in rats. *Nucl. Med. Biol. 24*, 85−92.

(18) Mantey, S., Frucht, H., Coy, D. H., and Jensen, R. T. (1993) Characterization of bombesin receptors using a novel, potent, radiolabeled antagonist that distinguishes bombesin receptor subtypes. *Mol. Pharmacol*. *43*, 762−774.

(19) Baidoo, K. E., Lin, K−S., Zhan, Y., Finley, P., Scheffel, U., and Wagner, H. N, Jr. (1998) Design, synthesis, and initial evaluation of high-affinity technetium bombesin analogues. *Bioconjugate Chem. 9*, 218−225.

(20) Nock, B., Nikolopoulou, A., Chiotellis, E., Loudos, G., Maintas, D., Reubi, J. C., and Maina, T. (2003) (99m)Tc]-Demobesin 1, a novel potent bombesin analogue for GRP receptor-targeted tumor imaging. *Eur. J. Nucl. Med. Mol. Imaging 30*, 247−58.

(21) Scopinaro, F., Varvarigou, A., Ussof, W., De Vincentis, G., Sourlingas, T. G., Evangelatos, G. P., Datsteris, J., and Archimandritis, S. C. (2002) Technetium labeled bombesin-like peptide: preliminary report on breast cancer uptake in patients. *Cancer Biother. Radiopharm. 17*, 327−335.

(22) La Bella, R., Garcia-Garayoa, E., Langer, M., Blauenstein, P., Beck-Sickinger, A. G., and Schubiger, P. A. (2002) In vitro and in vivo evaluation of a 99mTc(I)-labeled bombesin analogue for imaging of gastrin releasing peptide receptor-positive tumors. *Nucl. Med. Biol. 29*, 553−560.

(23) Gali, H., Hoffman, T. J., Sieckman, G. L., Owen, N. K., Katti, K. V., and Volkert, W. A. (2001) Synthesis, characterization, and labeling with 99mTc/188Re of peptide conjugates containing a dithia-bisphosphine chelating agent. *Bioconjugate Chem. 12*, 354−363.

(24) Van de Wiele, C., Dumont, F., Vanden Broecke, R., Oosterlinck, W., Cocquyt, V., Serreyn, R., Peers, S., Thornback, J., Slegers, G., and Dierckx, R. A. (2000) Technetium-99m RP527, a GRP analogue for visualisation of GRP receptor-expressing malignancies: a feasibility study. *Eur. J. Nucl. Med. 27*, 1694−1699.

(25) Karra, S. R., Schibli, R., Gali, H., Katti, K. V., Hoffman, T. J., Higginbotham, C., Sieckman, G. L., and Volkert, W. A. (1999) 99mTc-labeling and in vivo studies of a bombesin analogue with a novel water-soluble dithiadiphosphine-based bifunctional chelating agent. *Bioconjugate Chem. 10*, 254−260.

(26) Decristoforo, C., and Mather, S. J. (1999) 99m-Technetium -labeled peptide-HYNIC conjugates: effects of lipophilicity and stability on biodistribution. *Nucl. Med., Biol. 26*, 389−396.

(27) Trejtnar, F., Laznicek, M., Laznickova, A., and Mather, S. J. (2000) Pharmacokinetics and renal handling of 99mTc-labeled peptides. *J. Nucl. Med. 41*, 177−182.

(28) Marmion, M. E., Woulfe, S. R., Neumann, W. L., Nosco, D. L., and Deutsch, E. (1999) Preparation and characterization of technetium complexes with Schiff base and phosphine coordination. 1. Complexes of technetium-99g and −99m with substituted $acac_2$en and trialkyl phosphines (where $acac_2$en = N, N′- ethylenebis[acetylacetone iminato]). *Nucl. Med. Biol. 26*, 755−770.

(29) Edwards, D. S., Liu, S., Barrett, J. A., Harris, A. R., Looby, R. J., Ziegler, M. C., Heminway, S. J., and Carroll, T. R. (1997) New and versatile ternary ligand system for technetium radiopharmaceuticals: water soluble phosphines and tricine as coligands in labeling a hydrazinonicotinamide-modified cyclic glycoprotein IIb/IIIa receptor antagonist with ^{99m}Tc. *Bioconjugate Chem. 8*, 146−154.

(30) Bridger, G. J., Abrams, M. J., Padmanabhan, S., Gaul, F., Larsen, S., Henson, G. W., Schwartz, D. A., Longley, C., Burton, C. A., and Ultee, M. E. (1996) A comparison of cleavable and noncleavable hydrazinopyridine linkers for the ^{99m}Tc labeling of Fab′ monoclonal antibody fragments. *Bioconjugate Chem. 7*, 255−264.

(31) Baidoo, K. E., Lever, S. Z., and Scheffel, U. (1994) Bifunctional chelator for facile preparation of neutral technetium complexes. *Bioconjugate Chem. 5*, 114−118.

(32) Mokotoff, M., Swanson, D. P., Jonnalagadda, S. S., Epperly, M. W., and Brown, M. L. (1997) Evaluation of laminin peptide fragments labeled with indium-111 for the potential imaging of malignant tumors. *J. Pept. Res. 49*, 510−516.

(33) Reile, H., Armatis, P. E., and Schally, A. V. (1994) Characterization of high-affinity receptors for bombesin/gastrin releasing peptide on the human prostate cancer cell lines PC-3 and DU-145: Internalization of receptor bound [^{125}I-Tyr^{4}]bombesin by tumor cells. *The Prostate 25*, 29−38.

(34) McPherson, G. A. (1985) Analysis of radioligand binding experiments. A collection of computer programs of the IBM PC. *J. Pharmacol. Methods 14*, 213−228.

(35) Gosney, J. R., Sissons, M. C. J., and Allibone, R. O. (1988) Neuroendocrine cell populations in normal human lungs: a quantitative study. *Thorax 43*, 878−882.

(36) Cutz, E., Chan, W., and Track, N. S. (1981) Bombesin, calcitonin and leu-enkephalin immunoreactivity in endocrine cells of human lung. *Experientia 37*, 765−767.

(37) Siegfried, J. M., DeMichele, M. A. A., Hunt, J. D., Davis, A. G., Vohra, K. P., and Pilewski, J. M. (1997) Expression of mRNA for gastrin-releasing peptide receptor by human bronchial epithelial cells. *Am. J. Respir. Crit. Care Med*. *156*, 358−366.

(38) Aguayo, S. M., King, T. M., Jr., Kane, M. A., Sherritt, K. M., Silvers, W., Nett, L. M., Petty, T. L., and Miller, Y. E. (1992) Urinary levels of bombesin-like peptides in asymptomatic cigarette smokers: a potential risk marker for smoking-related diseases. *Cancer Res*. *52(suppl)*, 2727s−2731s.

(39) ToiScott, M., Jones, C. L. A., and Kane, M. A. (1996) Clinical correlates of bombesin-like peptide receptor subtype expression in human lung cancer cells. *Lung Cancer 15*, 341−354.

(40) Baidoo, K. E., and Lever, S. Z. (1990) Synthesis of a diaminedithiol bifunctional cheating agent for incorporation of technetium-99m into biomolecules. *Bioconjugate Chem*. *1*, 132−137.

(41) Baidoo, K. E., Scheffel, U., and Lever, S. Z. (1990) ^{99m}Tc labeling of proteins: initial evaluation of a novel diaminedithiol bifunctional cheating agent. *Cancer Res. 50(suppl.)*, 799s−803s.

(42) Baidoo, K. E., Scheffel, U., Stathis, M., Finley, P., Lever, S. Z., Zhan, Y., and Wagner, H. N., Jr. (1998) High-affinity no-carrier-added ^{99m}Tc-labeled chemotactic peptides for studies of inflammation in vivo. *Bioconjugate Chem. 9*, 208−217.

(43) Childs, R. L., and Hnatowich, D. J. (1985) Optimum conditions for labeling of DTPA-coupled antibodies with technetium-99m. *J. Nucl. Med. 26*, 293−299.

(44) Singh, P., Draviam, E., Guo, Y. S., and Kurosky, A. (1990) Molecular characterization of bombesin receptors on rat pancreatic AR42J cells. *Am. J. Physiol. 258*, G803−G809.

(45) Breeman, W. A. P., Hofland, L. J., De Jong, M., Bernard, B. F., Srinivasan, A., Kwekkeboom, D. J., Visser, T. J., and Krenning, E. P. (1999) Evaluation of radiolabeled bombesin analogues for receptor-targeted scintigraphy and radiotherapy. *Int. J. Cancer 81*, 658−665.

(46) Moran, T. H., Moody, T. W., Hostetler, A. M., Robinson, P. H., Godrich, M., and McHugh, P. R. (1988) Distribution of bombesin binding sites in the gastrointestinal tract. *Peptide 9*, 643−649.

(47) Von Schrenck, T., Heinz-Erian, P., Moran, T., Mantey, S. A., Gardner, J. D., and Jensen, R. T. (1989) Neuromedin B receptor in esophagus: evidence for subtypes of bombesin receptors. *Am. J. Physiol. 256*, G747−758.

BC0498267

PEG-*g*-poly(GdDTPA-*co*-L-cystine): A Biodegradable Macromolecular Blood Pool Contrast Agent for MR Imaging

Aaron M. Mohs,[†] Xinghe Wang,[†] K. Craig Goodrich,[‡] Yuda Zong,[†] Dennis L. Parker,[§] and Zheng-Rong Lu*,[†]

Department of Pharmaceutics and Pharmaceutical Chemistry, University of Utah, Salt Lake City, Utah 84112, Department of Radiology, LDS Hospital, Salt Lake City, Utah 84112, and Department of Radiology, University of Utah, Salt Lake City, Utah 84112. Received July 16, 2004

Biodegradable PEGylated Gd-DTPA L-cystine copolymers, PEG-*g*-poly(GdDTPA-*co*-L-cystine), were prepared and tested as a blood pool contrast agent in mice. The biodegradable macromolecular agent was designed to be broken down into smaller Gd complexes by endogenous thiols via the disulfide−thiol exchange reaction to facilitate the clearance of Gd complexes after the contrast-enhanced MRI examination. Gd-DTPA L-cystine copolymers were synthesized by condensation polymerization of L-cystine and DTPA-dianhydride in water followed by chelating with $Gd(OAc)_3$. MPEG-NH_2 (MW = 2000) was then conjugated to the polymeric backbone in different ratios. The macromolecular contrast agent was readily degraded with the incubation of L-cysteine. It also demonstrated superior contrast enhancement in the heart and blood vessels as compared to a low molecular weight control agent, Gd-(DTPA-BMA). At 1 h postcontrast, the PEGylated macromolecular agent still showed prominent enhancement, while little contrast enhancement was detectable in the blood pool by the control agent. PEG-*g*-poly(GdDTPA-*co*-L-cystine) shows promise as an MR blood pool imaging agent.

INTRODUCTION

Gadolinium complexes, Gd-DTPA, GD-DOTA, or their derivatives, are routinely used as extracellular MRI contrast agents in the detection and diagnosis of various cardiovascular pathological conditions by enhancing the morphology and functionality of the condition. Albeit these low molecular weight agents have low toxicity, their inherent pharmacokinetic properties, including transient blood pool retention time, do not render them ideal for cardiovascular imaging. These agents can rapidly extravasate out of blood vessels into the extracellular matrix, introducing difficulties for a quantitative diagnosis that force the application of complex mathematical models (*1*). In addition, the relaxation time of these molecules is relatively slow, necessitating a higher dose of extravascular contrast agent to achieve signal enhancement comparable to that of a macromolecular agent (*2*).

In order for macromolecular Gd complexes to be safe and effective it must be large enough to remain in the blood stream, yet small enough to be excreted after the exam. Previous attempts in the design of macromolecular blood pool agents have been hampered by the potential toxicity of the agents due to the slow clearance of the Gd complexes. Current blood pool agents based on macromolecular Gd(III) complexes from polymers, dendrimers, polypeptides, and polysaccharides have a less complete elimination than their low molecular weight counterparts, resulting in the possible accumulation of toxic metabolic byproducts (*3*−*6*).

The size limitation to macromolecular Gd(III) complexes presents a significant barrier for their application. In response, polymeric Gd(III) chelate conjugates with a cleavable disulfide spacer or polydisulfide-based biodegradable macromolecular Gd complexes were introduced to circumvent the problem of long-term toxic Gd^{3+} accumulation (*7*, *8*). The disulfide bond is cleaved by endogenous or exogenous thiols via the disulfide−thiol exchange reaction to release Gd(III) chelates from the conjugates or break down the macromolecular complexes into smaller complexes to facilitate the clearance of Gd(III) complexes. The plasma concentration of free thiols in humans is approximately 15 μM, allowing for gradual, yet sufficient breakdown of the macromolecules into smaller Gd complexes for complete elimination of the agent after the MRI examination (*9*, *10*).

Previously, we reported the first polydisulfide-based macromolecular Gd(III) complexes, Gd-DTPA cystamine copolymers. This agent resulted in more significant and prolonged blood pool contrast enhancement than a low molecular weight control, Gd-(DTPA-BMA). The agent was then rapidly degraded and extravasated from the blood pool (*8*). Further structural modification of the agent is needed to optimize its physicochemical and pharmacokinetic properties. Here we report a modified biodegradable polydisulfide-based macromolecular Gd(III) complex, poly(GdDTPA-*co*-L-cystine) grafted with monomethoxy-poly(ethylene glycol)amine (MPEG-NH_2), PEG-*g*-poly(GdDTPA-*co*-L-cystine). Poly(ethylene glycol) is a nontoxic, nonantigenic and biocompatible polymer that has a large hydrodynamic radius rendering itself ideal for biomedical applications. With respect to MRI, PEG has been used to stabilize paramagnetic vesicles (*11*), used in formulation with an oral contrast agent to enhance the distal ileum (*12*), incorporated into the

* To whom correspondence should be addressed. Dr. Zheng-Rong Lu, 421 Wakara Way, Suite 318, Salt Lake City, UT 84108. Phone: 801 587-9450. Fax: 801 585-3614. E-mail: zhengrong.lu@utah.edu.

[†] Department of Pharmaceutics and Pharmaceutical Chemistry, University of Utah.

[‡] Department of Radiology, LDS Hospital.

[§] Department of Radiology, University of Utah.

10.1021/bc049828r CCC: $27.50 © 2004 American Chemical Society
Published on Web 09/29/2004

backbone of copolymeric contrast agents (*13*−*15*), and grafted onto polymeric contrast agents (*16*, *17*). Preliminary results show significant contrast enhancement in the blood pool of mice for a longer period of time with the PEGylated polydisulfide agent compared to the clinically used low molecular weight agent, Gd-(DTPA-BMA), while still showing acceptable clearance.

EXPERIMENTAL PROCEDURES

DTPA was purchased from J. T. Baker (Phillipsburg, NJ). L-Cystine was purchased from Sigma (St. Louis, MO). $Gd(OAc)_3$ was purchased from Alfa Aesar (Ward Hill, MA). Monomethoxy-poly(ethylene glycol)-amine ($MPEG\text{-}NH_2$, MW = 2000) was synthesized according to the literature (*18*) as was DTPA dianhydride (*19*).

Synthesis of Poly(GdDTPA-*co*-L-cystine). Poly-(DTPA-*co*-L-cystine) (**I**) was first synthesized with the following procedure. L-Cystine (2.40 g, 10 mmol), deionized water (10 mL), and Na_2CO_3 (4.2 g) were stirred for 15 min. DTPA-dianhydride (3.93 g, 11 mmol) was then added in portions to the mixture with stirring, and the mixture was stirred overnight at room temperature. The copolymers were dialyzed against deionized water for 24 h using a regenerated cellulose membrane (MWCO = 6000−8000 Da) and were then concentrated in vacuo to dryness. The molecular weights of the copolymers were determined by size exclusion chromatography (SEC) on an AKTA FPLC system with a Superose 12 (10/300 GL) column and UV and refractive index detectors. The molecular weights were calibrated with poly[*N*-(2-hydroxypropyl)methacrylamide] standards. The number average (M_n) and weight average (M_w) molecular weights of the copolymers were 10.2 and 11.4 kDa, respectively. Proton NMR (ppm, D_2O): 2.94 (m, 8H, N*CH*$_2$*CH*$_2$N), 3.18 (s, 4H, N*CH*$_2$CONH), 3.25 (d, 2H, NHCH*CH*$_2$S), 3.32 (s, 4H, N*CH*$_2$COOH), 3.48 (s, 2H, N*CH*$_2$COOH), 4.42 (m, 1H, NH*CH*CH_2S).

Complexation was achieved by reacting poly(DTPA-*co*-L-cystine) with $Gd(OAc)_3$ in 8 mL of deionized water. Xylenol orange indicator was added and 1 N HCl was added dropwise until pH 5−5.5 was reached. Gd(III) acetate was added to the mixture until the color became pink, indicating an excess of free Gd^{3+} ions. Excess $Gd(OAc)_3$ was removed by eluting the solution through a Sephadex G-25 desalting column (Pharmacia). The purified poly(GdDTPA-*co*-L-cystine) (**II**, GDCP) was concentrated to dryness in vacuo and the molecular weights of the copolymers were determined by SEC, M_n = 10.0 kDa, M_w = 10.1 kDa. Gd content was 862 μmol Gd/g polymer as determined by ICP-OES (Perkin-Elmer, Norwalk, CT, Optima 3100XL).

Synthesis of PEG-*g*-poly(GdDTPA-*co*-L-cystine) (A). Poly(GdDTPA-*co*-L-cystine) (200 mg, 0.26 mmol cystine) was dissolved in 4 mL deionized water, and *N*-hydroxysuccinimide (270 mg, 2.4 mmol) was then added with stirring. An excess of 1-ethyl-3-(3-dimethylaminopropyl) carbodiimide hydrochloride (700 mg, 3.65 mmol) was slowly added, and the resulting yellow solution was stirred for 15 min. $MPEG\text{-}NH_2$ (MW = 2000 Da, 262 mg) was added in portions, and the reaction mixture was stirred overnight. White precipitate was removed by filtration. Unreacted PEG and salts were removed by ultrafiltration using a Centricon-10 concentrator (membrane MWCO = 10 000 Da). The resulting PEGylated poly(GdDTPA-*co*-L-cystine) (PEG_a-GDCP) was characterized by SEC and ICP-OES as described above. PEG_a-GDCP: M_n = 21.0 kDa, M_w = 24.5 kDa; 720 μmol Gd/g polymer.

Synthesis of PEG-*g*-poly(GdDTPA-*co*-L-cystine) (B). PEG-*g*-poly(GdDTPA-*co*-L-cystine) (PEG_b-GDCP) with high PEG content was prepared similarly with a high PEG to poly(GdDTPA-*co*-L-cystine) ratio. Briefly, poly-(GdDTPA-*co*-L-cystine) (200 mg, 0.26 mmol cystine) was dissolved in 4 mL deionized water, and *N*-hydroxysuccinimide (270 mg, 2.4 mmol) and 1-ethyl-3-(3-dimethylaminopropyl) carbodiimide hydrochloride (700 mg, 3.65 mmol) were then added with stirring. $MPEG\text{-}NH_2$ (524 mg) was added to the reaction and the mixture was stirred overnight. Unreacted PEG and salts were removed by ultrafiltration using a Centricon-10 concentrator (membrane MWCO = 10 000 Da). PEG_b-GDCP: M_n = 19.9 kDa kDa, M_w = 22.9 kDa; 449 μmol Gd/g polymer.

Relaxivity of PEG-*g*-poly(GdDTPA-*co*-L-cystine). The T_1 of different PEGylated complexes was determined on a Siemens Trio 3T scanner. T_1 relaxation times for three concentrations of the polymeric contrast agents were determined, along with reference values for water and Gd-(DTPA-BMA) by sequential application of a standard inversion−recovery (IR) pulse sequence with TR = 5000 ms, TE = 17 ms for inversion times TI = 22, 25, 30, 35, 40, 50, 100, 200, 300, 400, 500, 600, 700, and 800 ms. Net magnetization amplitude data for each sample were determined from the appropriate ROI and fit using the Marquardt−Levenberg algorithm for multiparametric nonlinear regression analysis to simultaneously determine T_1 and M_0. Regressions were individually inspected for convergence. Parameters and standard errors were determined using ANOVA as provided in the Mathematica Statistics Toolbox. Slope of the plot of $1/T_1$ vs [Gd(III)] then gave the relaxivity R_1.

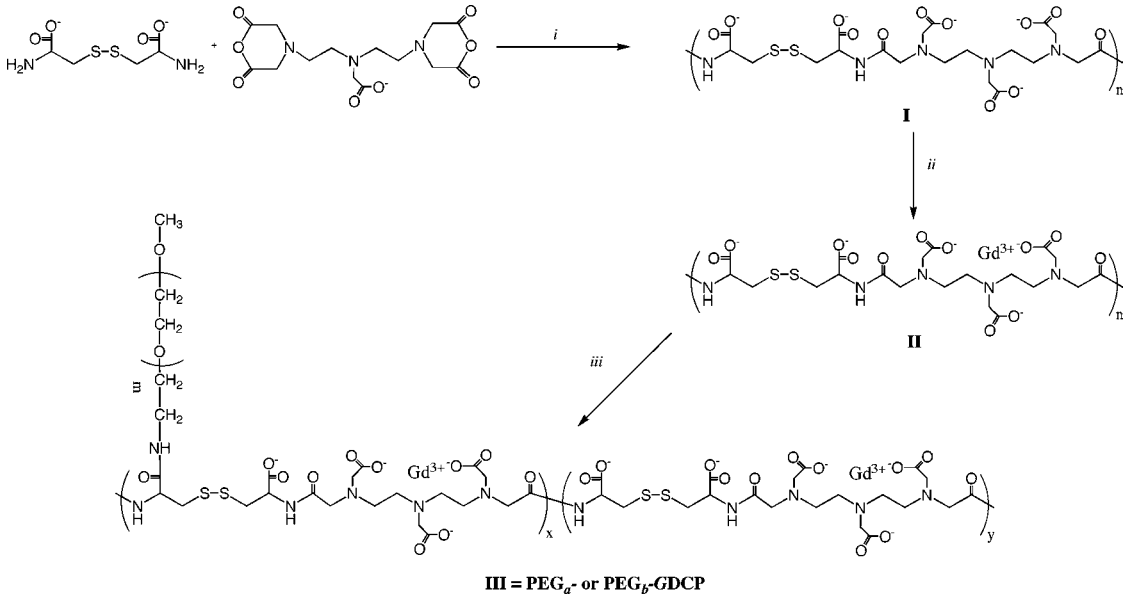
Degradation of PEG-*g*-poly(GdDTPA-*co*-L-cystine). PEGylated polymers PEG_a-GDCP and PEG_b-GDCP and un-PEGylated GDCP were separately incubated in an aqueous cysteine solution (100 μM) at 37°C. SEC was performed on the samples at 0, 3, and 24 h after incubation to demonstrate the time dependent degradation of the disulfide bonds by looking at the molecular weight change of the copolymers. MALDI-TOF mass spectrometry was then performed on the reaction mixture to observe the degradation products of PEG_a-GDCP, PEG_b-GDCP, and GDCP.

In Vivo MR Imaging. In vivo contrast enhanced MR imaging with the macromolecular agents was investigated in CD-1 mice (Charles River Laboratories). The animals were cared for under an approved protocol and the guidelines of the University of Utah Institutional Animal Care and Use Committee. The mice were anesthetized by the intramuscular administration of a mixture of ketamine (80 mg/kg) and xylazine (12 mg/kg). Contrast-enhanced images of mice were obtained on a Siemens Trio 3T MR scanner with a wrist coil pre- and postcontrast using the following imaging parameters: TE = 1.74 ms, TR = 4.3 ms, 25° RF tip angle, 3D acquisition with 128 slices/slab, 120 mm FOV, and 1.6 mm coronal slice thickness. Either Gd-(DTPA-BMA) (0.1 mmol Gd/kg) or a polymeric agent GDCP, PEG_a-GDCP, or PEG_b-GDCP (0.03 mmol Gd/kg for all polymeric agents) was injected via a tail vein into anesthetized mice and images were acquired at 1, 5, 15, 30, and 60 min postinjection of contrast agent. Each agent was investigated in a group of four mice.

RESULTS

Synthesis of PEG-*g*-poly(GdDTPA-*co*-L-cystine). The synthetic procedure of PEG-*g*-poly(GdDTPA-*co*-L-cystine) is described in Scheme 1. Poly(DTPA-*co*-L-

Scheme 1. Synthesis of PEG-*g*-poly(GdDTPA-*co*-L-cystine)[a]



[a] (i) Na_2CO_3, H_2O, rt, overnight; (ii) $Gd(OAc)_3$, pH 5.0−5.5, rt, 2 h; (iii) NHS, EDC, MPEG-NH_2, H_2O, pH 7−8, rt, overnight

cystine) was first synthesized by the copolymerization of DTPA dianhydride with L-cystine. L-Cystine is sparingly soluble in organic solvents and the copolymerization was performed in Na_2CO_3 aqueous conditions. The weak base Na_2CO_3 was used to maintain a relatively basic pH and to minimize the hydrolysis of the dianhydride. The molecular weight of poly(DTPA-*co*-L-cystine) was relatively low due to partial hydrolysis of the dianhydride, limiting chain growth of the copolymers.

The monomethoxy-PEG amine with an average molecular weight of approximately 2000 Da was used in the modification of GDCP. The content of PEG in PEG-*g*-poly(GdDTPA-*co*-L-cystine) was controlled by the molar ratio of MPEG-NH_2 and GDCP. PEG-*g*-poly(GdDTPA-*co*-L-cystine) with two different degrees of PEG modification were prepared. The molar ratio of PEG to the Gd-DTPA monomer was 0.33 and 0.76 for conjugates PEG$_a$-GDCP and PEG$_b$-GDCP, respectively, calculated from the Gd content per gram of polymer sample before and after PEGylation as determined by ICP-OES. The ratio of PEG grafted to cystine residues in the GDCP backbone is lower than the stoichiometric ratios used in the reaction, possibly due to the spatial restriction caused by the large hydrodynamic radius of PEG blocking the conjugation of more PEG molecules to the adjacent cystine residues. PEGylation increased the hydrodynamic volume of the copolymers. However, the increasing PEG content did not result in further increase of the hydrodynamic volume of the copolymers when comparing PEG$_a$-GDCP (M_w = 24.5 kDa) with PEG$_b$-GDCP (M_w = 22.9 kDa).

In Vitro Degradation. The in vitro degradation study was performed by incubating the macromolecular agent with L-cysteine to verify the degradability of the agents via the disulfide−thiol exchange reaction. The results showed the expected decrease for the high molecular weight fraction and an increase in PEGylated degradation products of the agents in the incubation mixture. SEC analysis of the incubation mixtures showed that there was a significant shift of molecular weight distribution to lower molecular weight, representing a breakdown in the most prominent polymer species. The time-dependent molecular weight distribution of PEG$_a$-GDCP in the incubation is shown as an example in Figure 1. The initial polymer peak at 27.4 min completely disappeared after 24 h of incubation. Consequently, there is a rise in signal intensity at 31.4 and 34.8 min over the same time period representing an increase in the PEGylated and unPEGylated degradation units, respectively. The low molecular weight degradation complexes **IV**, **V**, and **VI** in Scheme 2 were identified in the MALDI-TOF mass spectrum acquired on the reaction mixture at the end of the incubation period.

Relaxivity. Both PEGylated polymers, PEG$_a$-GDCP and PEG$_b$-GDCP, had a higher relaxivity than GDCP (5.5 mM^{-1} s^{-1}), while PEG$_a$-GDCP had a higher relaxivity than PEG$_b$-GDCP, 16.3 and 12.7 mM^{-1} s^{-1}, respectively. It is likely that PEG offers some steric limitation to the movement of the polymer, which increases the rotational correlation coefficient of the copolymers and in turn the relaxivity (*20*). However, PEG$_b$-GDCP with high PEG content possessed lower relaxivity than PEG$_a$-GDCP with low PEG content.

In Vivo MR Imaging. Figure 2 shows the coronal MR images of the heart of mice contrast enhanced with PEG$_a$-GDCP, PEG$_b$-GDCP, GDCP, and Gd-(DTPA-BMA) at various time points. Strong contrast enhancement was observed in the heart with the macromolecular agents at a dose of 0.03 mmol-Gd/kg 1 min postcontrast and the signal intensity gradually decreased over the period of observation. Significant contrast enhancement was still visible in the heart at 60 min for the polymeric agents. The low molecular weight control agent, Gd-(DTPA-BMA), produced visible contrast enhancement at a dose of 0.1 mmol/kg 1 min postinjection and little to no enhancement afterward.

The macromolecular agents also resulted in significant contrast enhancement in mouse blood vessels with the same trend. Figure 3 shows the coronal images of the descending aorta and common iliac arteries at various time points. The macromolecular agents clearly revealed the blood vessels 1 min post-contrast while little contrast enhancement was observed with the control agent. The blood vessels with PEGylated agents were more visible 5 min postinjection than those with the un-PEGylated polymeric agent. This demonstrates that PEGylation contributes to increased vascular retention, possibly by increasing the size of the agent.

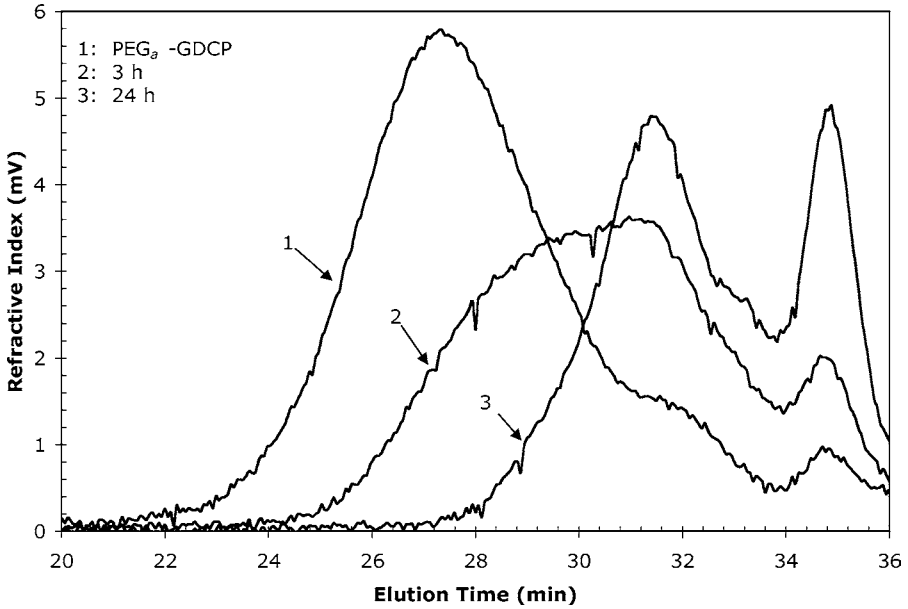
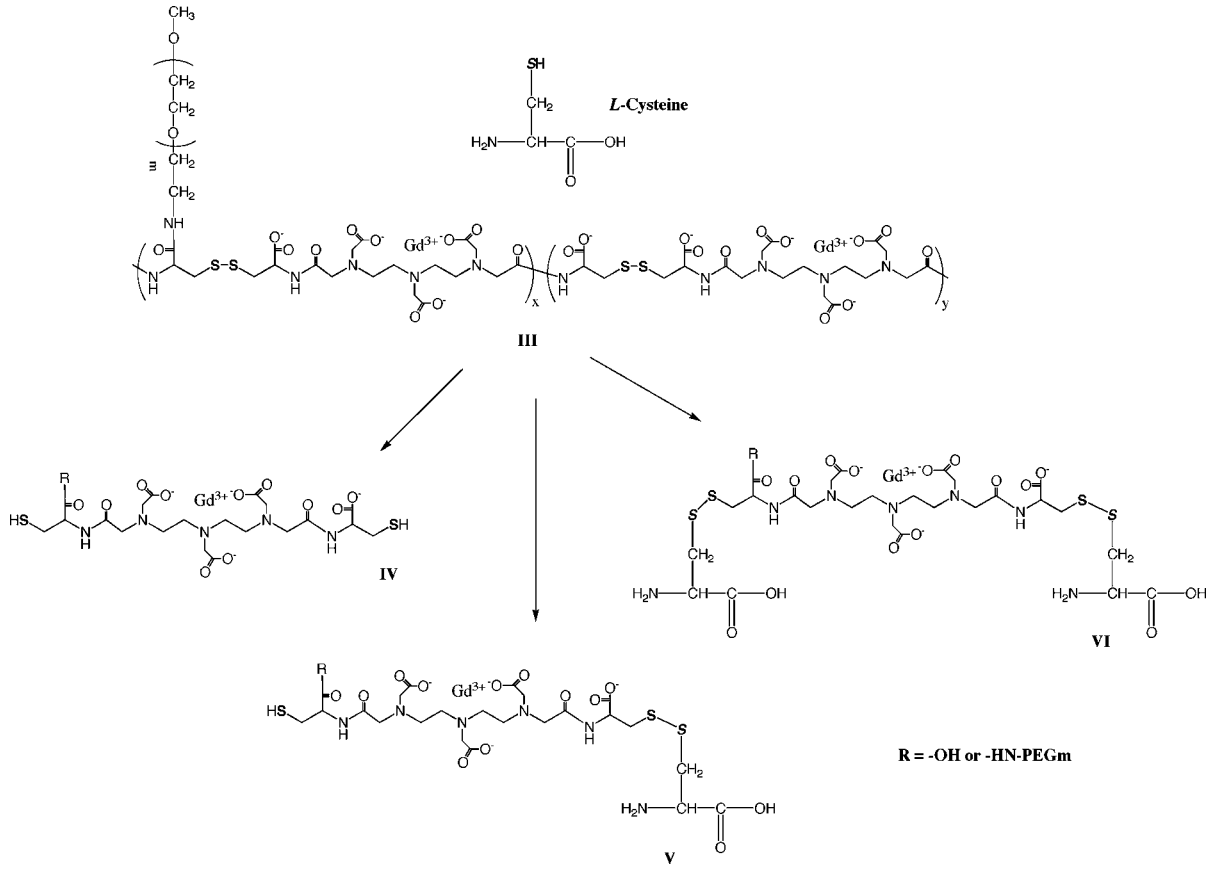


Figure 1. The effect on the molecular weight distribution of PEG$_a$-GDCP with incubation of L-cysteine in H_2O at 37 °C.

Scheme 2. Degradation Products from the Incubation of PEG-*g*-poly(GdDTPA-*co*-L-cystine) by the Incubation of L-Cysteine



DISCUSSION

Polydisulfide-based macromolecular Gd complexes have been designed to facilitate the clearance of Gd complexes after the MRI examination. Previously, we have demonstrated the feasibility of contrast-enhanced MRI with the first polydisulfide-based contrast agent, (Gd-DTPA)-cystamine copolymers (*8*). The copolymers resulted in significant blood pool contrast enhancement in rats in the early period postcontrast, approximately 2 min at a high dose (0.1 mmol-Gd/kg). However, less significant blood pool contrast enhancement was observed with the agent at a low dose (0.03 mmol-Gd/kg). PEGylated GDCP was designed and prepared to modify the physicochemical properties and in vivo contrast enhancement of biodegradable macromolecular agents.

PEGylation increased the molecular weight and hydrodynamic size of the macromolecular agent. It is interesting to note that the amount of MPEG-NH_2 grafted on the GDCP did not significantly affect on the hydrodynamic volume of the grafted agent. The increase of

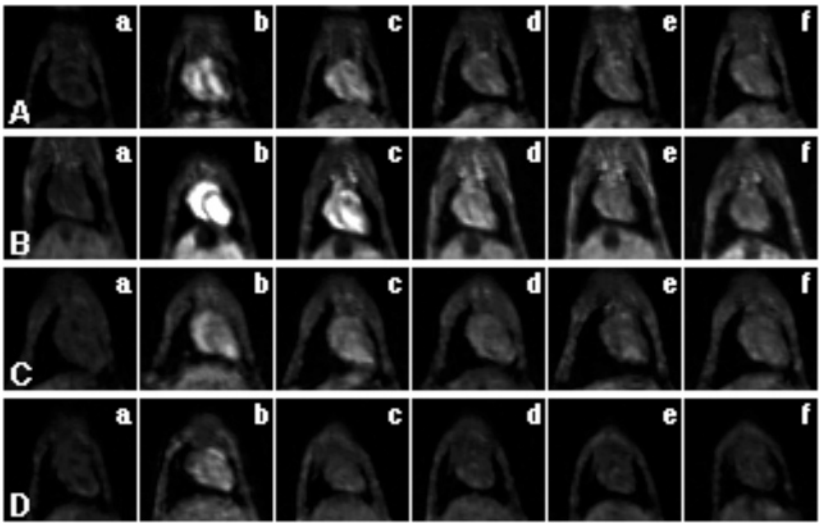


Figure 2. Coronal MR images of mouse heart preinjection (a) and 1 (b), 5 (c), 15 (d), 30 (e), and 60 min (f) postintravenous injection of PEG_a-GDCP (A), PEG_b-GDCP (B), GDCP (C), and Gd(DTPA-BMA) (D). Polymeric agents were given at a dose of 0.03 mmol-Gd/kg, and Gd(DTPA-BMA) was given at the standard clinical dose of 0.1 mmol/kg.

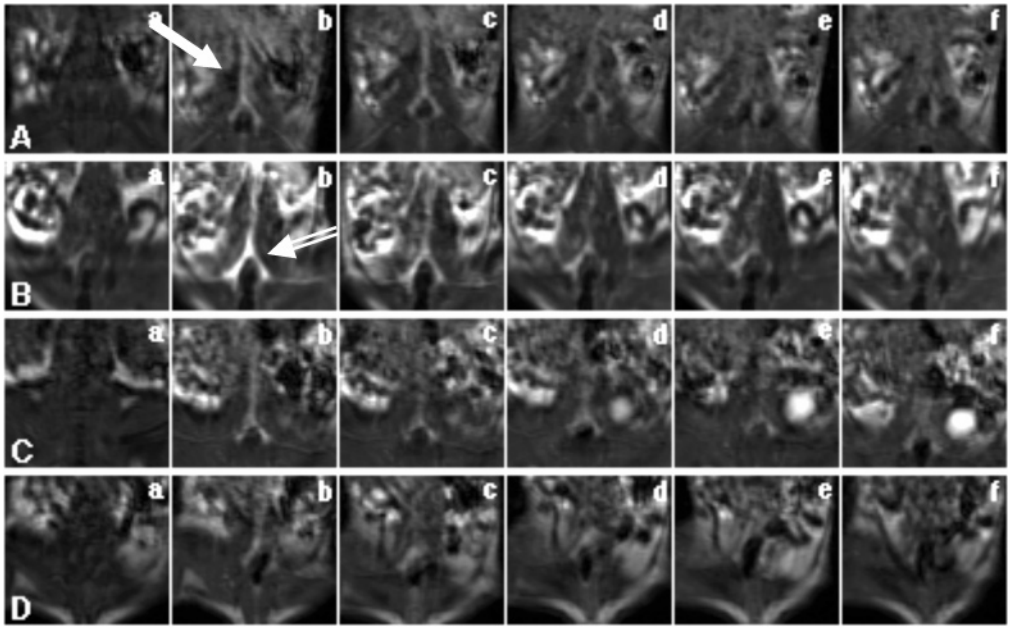


Figure 3. Coronal MR images of descending aorta (solid arrow) and common iliac arteries (hollow arrow) of the mouse preinjection (a) and 1 (b), 5 (c), 15 (d), 30 (e), and 60 min (f) postintravenous injection of PEG_a-GDCP (A), PEG_b-GDCP (B), GDCP (C), and Gd(DTPA-BMA) (D). Polymeric agents were given at a dose of 0.03 mmol-Gd/kg, and Gd(DTPA-BMA) was given at the standard clinical dose of 0.1 mmol/kg.

hydrodynamic volume of PEG_b-GDCP with a high PEG to Gd ratio (approximately 0.76:1) was less appreciable than that of PEG_a-GDCP with a low ratio (approximately 0.33:1). Although this seems counterintuitive because of PEG's large hydrodynamic radius, it is plausible that when more PEG is added, the density of PEG molecules on the polymer chain with a fixed length increases and it does not extend the length of the copolymers. The higher PEG density along the polymer chain may increase intermolecular interaction between the PEG chains and, probably, diminish their contribution to the hydrodynamic volume of the macromolecules.

The graft of PEG also increased the relaxivity of GDCP, most likely due to steric limitation on the rotational movement of the polymer increasing the rotational correlation coefficient and in turn the relaxivity (*20*). However, a further increase of PEG in PEG_b-GDCP resulted in decreased relaxivity. These results are consistent with the literature. Raymond et al. suggested that this is due to the possible association of water to PEG (*21*). As more PEG is added, more water is associated to PEG via hydrogen bonding, effectively reducing the local concentration of water proximal to the Gd^{3+} ions. This causes a probable decrease in the water−ion exchange rate, which increases the residence time of the coordinated water, τ_M, resulting in a decreased relaxivity, as shown in the following equation:

$$R_{1p}^{is} = \frac{c \times q}{55.6} \times \frac{1}{T_{1M}^{H} + \tau_M}$$

where R_{1p}^{is} is the inner coordination sphere relaxation of bulk water surrounding the paramagnetic ion, c is the concentration of the ion, q is the number of coordinated water molecules to the metal ion, and T_{1M}^{H} is the longitudinal relaxation time of the coordinated water (*22*).

In addition to increased relaxivity, the other advantage of PEGylation is the reduced tissue uptake of the macromolecular agents by the reticuloendothelial system (RES) and nonspecific binding. PEG is commonly used in the modification of biological and physiochemical properties of biological systems to minimize bioadhesion and immunological response (*23*). The incorporation of PEG in drug delivery systems significantly reduces the liver uptake of the systems and prolongs their circulation half-life. Kobayashi and co-workers have also reported that when the PEG content is increased on dendrimeric contrast agents, less contrast agent accumulates in the liver, spleen and kidneys leaving a larger percent in the blood pool, accounting for the increased signal intensity (*17*).

The PEGylation of polydisulfide-based biodegradable macromolecular Gd complexes, GDCP, resulted in high relaxivity and relatively large size of the modified agent and improved blood pool contrast enhancement in mice at a relatively low dose. The size of GDCP was relatively small due to the limitation of the current synthetic method. The blood pool contrast enhancement with the PEGylated agent may be further improved if GDCP with a larger size is used. Detailed investigations on the novel biodegradable macromolecular agents with different sizes are ongoing. The studies are focusing on the size impact of the PEGylated biodegradable macromolecular agent with respect to its physicochemical properties and in vivo contrast enhancement, pharmacokinetics, clearance, and long-term tissue Gd(III) accumulation.

CONCLUSION

Biodegradable PEGylated macromolecular Gd(III) complexes, PEG-*g*-poly(GdDTPA-*co*-L-cystine), were prepared and tested as a blood pool contrast agent in mice. The PEGylated macromolecular contrast agent demonstrated superior contrast enhancement in the heart and blood vessels as compared to the low molecular weight agent, Gd-(DTPA-BMA). An in vitro study demonstrated the time-dependent and complete degradation of PEG-*g*-poly(GdDTPA-*co*-L-cystine). MALDI-TOF mass spectrometry confirmed the degradation products. PEG-*g*-poly(GdDTPA-*co*-L-cystine) shows promise as a blood pool MRI contrast agent because of its increased signal intensity and retention time as well as its controllable degradation characteristics.

ACKNOWLEDGMENT

This research is supported in part by NIH grant EB00489. We thank Dr. Matthias Schabel for technical assistant in T_1 measurement and MR image acquisition. Mass spectral data were acquired at the University of Utah Mass Spectrometry Facility.

LITERATURE CITED

(1) Paetsch, I., Gebker, R., Fleck, E., and Nagel, E. (2003) Cardiac magnetic resonance (CMR) imaging: A noninvasive tool for functional and morphological assessment of coronary artery disease. *J. Interven. Cardiol. 16*, 457−463.

(2) Li, D., Zheng, J., and Weinmann, H.-J. (2001) Contrast-enhanced MR imaging of coronary arteries: comparison of intra- and extravascular contrast agents in swine. *Radiology 218*, 670−678.

(3) Bogdanov, A. A., Weissleder, R., Frank, H. W., Bogdanova, A. V., Nossif, N., Schaffer, B. K., Tsai, E., Papisov, M. I., and Brady, T. J. (1993) A new macromolecule as a contrast agent for MR angiography: Preparation, properties, and animal studies. *Radiology 187*, 701−706.

(4) Wang, S. C., Wikstrom, M. G., White, D. L., Klaveness, J., Holtz, E., Rongved, P., Moseley, M. E., Brasch, R. C. (1990) Evaluation of Gd-DTPA-labeled dextran as an intravascular MR contrast agent: Imaging characteristics in normal rat tissues. *Radiology 175*, 483−488.

(5) Franano, F. N., Edwards, W. B., Welch, M. J., Brechbeil, M. W., Gansow, O. A., and Duncan, J. R. (1995) Biodistribution and metabolism of targeted and nontargeted protein-chelate-gadolinium complexes: Evidence for gadolinium dissociation in vitro and in vivo. *Magn. Reson. Imaging 13*, 201−214.

(6) Kobayashi, H., Satomi, K., Jo, S.-K., Bryant, H. L., Brechbiel, M. W., and Star, R. A. (2003) Macromolecular MRI contrast agents with small dendrimers: pharmacokinetic differences between sizes and cores. *Bioconjugate Chem. 14*, 388−394.

(7) Lu, Z.-R., Wang, X., Parker, D. L., Goodrich, K. C., and Buswell, H. R. (2003) Poly(L-glutamic acid) Gd(III)-DOTA conjugate with a degradable spacer for magnetic resonance imaging. *Bioconjugate Chem. 14*, 715−719.

(8) Lu, Z.-R., Parker, D. L., Goodrich, K. C., Wang, X., Dalle, J. G., and Buswell, H. R. (2004) Extracellular biodegradable macromolecular gadolinium(III) complexes for MRI. *Magn. Reson. Med. 51*, 27−34.

(9) Andersson, A., Lindgren, A., Hultberg, B. (1995) Effect of thiol oxidation and thiol export from erythrocytes on determination of redox status off homocysteine and other thiols in plasma from healthy subjects and patients with cerebral infarction. *Clin. Chem. 41*, 361−366.

(10) Deneke, S. M., (2000) Thiol based antioxidants. *Curr. Top. Cell. Regul. 36*, 151−180.

(11) Luciani, A., Olivier, J.-C., Clement, O., Siauve, N., Brillet, P.-Y., Bessoud, B., Gazeau, F., Uchegbu, I. F., Kahn, E., Frija, G., and Cuenod, C. A. (2004) Glucose-receptor MR imaging of tumors: Study in mice with PEGylated paramagnetic niosomes. *Radiology 231*, 135−142.

(12) Laghi A., Paolantonio, P., Iafrate, F., Borrelli, O., Dito, L., Tomei, E., Cucchiara, S., and Passariello, R. MR of the small bowel with a biphasic oral contrast agent (polyethylene glycol): technical aspects and finding in patients affected by Crohn's disease. *Radiol. Med. 106*, 18−27.

(13) Shen, D., Fritz, T., Wu, G.-L., Kulik, B., Palestrant, D., and Unger, E. (1994) Block co-polymeric magnetic resonance contrast agents. *Invest. Radiol. 29*, S217−S219.

(14) Ladd, D. L., Hollister, R., Peng, X., Wei, D., Wu, G., Delecki, D., Snow, R. A., Toner, J. L., Keller, K., Eck, J., Desai, V. C., Raymond, G., Kinter, L. B., Desser, T. S., and Rubin, D. L. (1999) Polymeric gadolinium chelate magnetic resonance imaging contrast agents: Design, synthesis, and properties. *Bioconjugate Chem. 10*, 361−370.

(15) Unger, E. C., Shen, D., Wu, G., Stewart, L., Matsunaga, T. O., and Trouard, T. P. (1999) Gadolinium-containing copolymeric chelates − a new potential MR contrast agent. *Magn. Reson. Mater. Phys., Biol. Med. (MAGMA) 8*, 154−142.

(16) Weissleder, R., Bogdanov, A., Tung, C. H., and Weinmann, H.-J. (2001) Size optimization of synthetic graft copolymers for in vivo angiogenesis imaging. *Bioconjugate Chem. 12*, 213-219.

(17) Kobayashi, H., Kawamoto, S., Saga, T., Sato, N., Hiraga, A., Ishimori, T., Konishi, J., Togashi, K., Brechbeil, M. W., (2001) Positive effects of poly ethylene glycol conjugation to generation-4 polyamidoamine dendrimers as macromolecular MR contrast agents. *Magn. Reson. Med. 46*, 781−788.

(18) Zalipsky, S., Gilon, C., and Zilkha, A. (1983) Attachment of drugs to polyethylene glycols. *Eur. Polym. J. 19*, 1177−1183.

(19) Hnatowich, D. J., Friedman, B., Clancy, B., Novac, M. (1981) Labeling of preformed liposomes with Ga-67 and Tc-99m by chelation. *J. Nucl. Med. 22,* 810−814.

(20) Tóth, E., van Uffelen, I., Helm, L., Merbach, A. E., Ladd, D., Briley-Sæbø, K., Kellar., K. E. (1998) Gadolinium-based linear polymer with temperature-independent proton relaxivities: A unique interplay between the water exchange and rotational contributions. *Magn. Reson. Chem. 36*, S125−S134.

(21) Doble, D. M. J., Botta, M., Wang, J., Aime, S., Barge, A., and Raymond, K. N. (2001) Optimization of the relaxivity of MRI contrast agents: Effect of poly(ethylene glycol) chains on the water-exchange rates of Gd^{III} complexes. *J. Am. Chem. Soc. 123*, 10758−10759.

(22) Aime, S., Botta, M., Fasano, M., and Terreno, E. (1998) Lanthanide(III) chelates for NMR biomedical applications. *Chem. Soc. Rev. 27*, 19−29.

(23) Veronese, F. M., Monfardini, C., Caliceti, P., Schiavon, O., Scrawen, M. D., and Beer, D. (1996) Improvement of pharmacokinetic, immunological and stability properties of asparaginase by conjugation to linear and branched monomethoxy poly(ethylene glycol). *J. Controlled Release 40*, 199−209.

BC049828R

Cyclen-Based Phenylboronate Ligands and Their Eu^{3+} Complexes for Sensing Glucose by MRI

Robert Trokowski,[†] Shanrong Zhang,[§] and A. Dean Sherry[†,§,*]

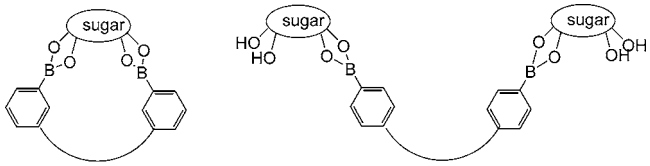
Department of Chemistry, The University of Texas at Dallas, P.O. Box 830688, Richardson, Texas 75083-0688, and The Rogers Magnetic Resonance Center, Department of Radiology, University of Texas Southwestern Medical Center, 5323 Harry Hines Boulevard, Dallas, Texas 75390-9085. Received April 25, 2004; Revised Manuscript Received August 4, 2004

Novel cyclen-based phenylboronate ligands and their corresponding Eu^{3+} complexes have been examined as glucose sensors using chemical exchange saturation transfer (CEST) MR imaging for detection. Two isomeric bis-phenylboronate complexes, Eu(**4**) and Eu(**10**), and a mono-phenylboronate complex, Eu(**12**), had been prepared and characterized by UV and circular dichroism spectroscopy, mass spectrometry, and CEST imaging. Both the free ligands and their Eu^{3+} complexes bind to simple sugars, but their selectivity and binding affinities vary with sugar structure. Interestingly, the free ligands, **4** and **10**, are selective for fructose over glucose, but this selectivity order switches in the respective Eu^{3+} complexes. Of the complexes examined, Eu(**4**) shows the highest selectivity and binding affinity for glucose ($2275 \pm 266\ M^{-1}$ at pH 10.2 and $339 \pm 29\ M^{-1}$ at pH 7). Glucose acts as a "capping" moiety in the Eu(**4**)·glucose binary complex and modulates water exchange between a single Eu^{3+}-bound water molecule and bulk water, an effect that can be detected by CEST imaging. Thus, Eu(**4**) represents a new class of metabolite-specific imaging agents that may allow mapping of metabolites by MRI of the bulk water signal.

INTRODUCTION

Sugars play important roles in energy production and storage in living organisms so methods to access their concentration and distribution in vivo are becoming increasingly important. A variety of techniques have been reported for quantification of glucose, the most abundant sugar in mammalian cells, but few provide information about its distribution in tissues (*1*). Among the detection methods, the most common are based on the enzymatic detection by glucose oxidase (*2*) or chemical sensors based on complexation of *cis*-hydroxy groups of sugars by phenylboronic acids. Such binding interactions have been detected by using a variety of spectroscopic techniques, including UV, fluorescence, or circular dichroism (CD) or electrochemical methods (*3*−*7*). Unfortunately, most of these methods cannot be applied to detect sugars in vivo (*8*). Magnetic resonance imaging (MRI) or spectroscopy (MRS) techniques have been used to obtain maps of common metabolites such as lactate, creatine, and *N*-acetylaspartate by ^{1}H detection and high energy metabolites by ^{31}P detection (*9*). Free glucose has been measured in brain by ^{1}H NMR (*10*, *11*) and by ^{13}C NMR (*12*) although ^{1}H detection is complicated by the numerous overlapping resonances in the 2−4 ppm range from other endogenous molecules. Recently, a ^{13}C-edited ^{1}H T-SEDOR technique had been used to image glucose in brain of living mice (*13*) but this requires double resonance techniques not commonly available on clinical MR scanners and the infusion of a high cost tracer (^{13}C-enriched glucose). Thus, a simple method for mapping this common metabolite in vivo, especially from tissues deep within the body, remains an important goal.

Scheme 1



a **b**

It is known that simple phenylboronic acids form reversible, cyclic ester bonds with *cis*-diols in a variety of sugars (*14*) and that the binding constants for these 1:1 complexes is highly dependent upon the orientation of the *cis*-diol groups in the sugar, typically decreasing in the order of D-fructose ≫ D-galactose > D-mannose > D-glucose (*15*, *16*). Sensors having two phenylboronic acid functionalities in juxtaposition form intramolecular 1:1 complexes with both "ends" of a sugar molecule (Scheme 1a) and often show a different stability order related to the specific spatial position of two boronic acid groups. In such complexes, a sugar can be selectively captured by appropriate positioning two phenylboronic acids in the same sensor molecule. The goal of this work was to create a sensor for glucose that might be used to image this important metabolite in tissues by magnetic resonance imaging (MRI). On the basis of prior experience with paramagnetic chemical exchange saturation transfer (PARACEST) agents (*17*), we anticipated that lanthanide complexes derived from tetraaza-tetraamide ligands with two appended phenylboronic acid groups might capture a glucose by forming a "bridge" above a single Ln^{3+}-bound water molecule and, in doing so, the encapsulated glucose might slow the rate at which the Ln^{3+}-bound water molecule exchanges with bulk water. In prototype experiments reported elsewhere (*18*), we demonstrated that upon binding of glucose to Eu(**4**) (see structure of ligand

* To whom correspondence should be addressed: Phone: (972) 883 2907. E-mail: sherry@utdallas.edu.

[†] The University of Texas at Dallas.

[§] University of Texas Southwestern Medical Center.

10.1021/bc0498976 CCC: $27.50 © 2004 American Chemical Society
Published on Web 10/12/2004

4 in Scheme 2), water exchange is indeed about 2-fold slower and this was sufficient to image glucose in vitro by MRI. Here, we describe details of the synthesis and characterization of two isomeric bis-phenylboronate sensors, Eu(**4**) and Eu(**10**), and a mono-phenylboronate sensor, Eu(**12**). The binding constants between various sugars and these sensors were determined by UV and CD spectroscopy, and their potential as PARACEST imaging agents were compared.

EXPERIMENTAL PROCEDURES

Instrumental Methods. Column chromatography was performed using Mallinckrodt Silicar silica gel-150 (60−200 mesh). Hydrogenations were performed on a Parr hydrogenation apparatus. ECI and MALDI TOF mass spectral analyses were obtained from HT Laboratories in San Diego. FAB mass spectral analyses were obtained from University of Kansas Mass Spectrometry Lab. CD spectra were recorded on AVIV Circular Dichroism Spectrometer Model 202. NMR spectra were recorded on JEOL Eclipse 270 MHz. UV−vis spectra were recorded on Hewlett-Packard 8453 UV−vis spectrophotometer. MRI images were recorded on a 4.7T Varian imager. A 2.5 cm surface coil was used to excite and to receive the magnetic resonance signal. A spin−echo pulse sequence was modified by adding a frequency-selective a presaturation pulse before the imaging pulses. Typically, a presaturation period of 1 s was used. The saturation power was set to 36 db (corresponding to B_1 field of 1020 Hz). The saturation frequency was set to 50 ppm (on the Eu^{3+}-bound water resonance), 30 ppm (between the Eu^{3+}-bound water and the bulk water), and −50 ppm (opposite to the Eu^{3+}-bound water), respectively. The CEST images were obtained by pixel by pixel subtraction the image at 50 ppm from that at 30 ppm, respectively. All other imaging parameters were presented in the corresponding figure captions.

Data Analysis. Data fitting was performed by using the commercial software, PSI-PLOT version 7.5, Poly Software International, Inc.. Binding constants were obtained by nonlinear fitting the experimental data to a 1:1 binding model (*28*).

$$A_{exp} = \frac{A_0 + A_{lim}K_a[\text{sugar}]}{1 + K_a[\text{sugar}]} \quad (1)$$

where K_a is the binding constant, A_0, A_{lim}, and A_{exp} are the initial, equilibrium, and experimental values, either the relative UV, CD signal intensities, or MRI CEST ratios.

Reagents. 1,4,7,10-Tetraazacyclododecane was purchased from Strem Chemicals, Inc. (Newburyport, MA); phenylboronic acid and 10% Pd/C were purchased from Aldrich Chemical Co. (Milwaukee, WI). All other reagents used were of analytical grade.

Syntheses. 3-Nitrophenylboronic acid and 3-aminophenylboronic acid was prepared as described by Seaman and Johnson (*26*) and Groziak et al. (*49*), respectively. 2-Bromo-*N*-methylacetamide was prepared by the method of Valtancoli et al. (*50*) and 1,7-bis(benzyloxycarbonyl)-1,4,7,10-tetraazacyclododecane was prepared by methods described by Kovacs and Sherry (*21*, *22*).

3-Bromoacetylaminophenylboronic Acid. To a mixture of 3-aminophenylboronic acid (1.77 g; 12.19 mmol) and sodium carbonate (2.74 g; 24.38 mmol) in THF (85 mL) cooled in an ice bath was added bromoacetyl bromide (3.4 mL; 36.57 mmol). The mixture was stirred at 0 °C for 30 min and at 25 °C for 1 h. The solution was filtered and the filtrate was evaporated under vacuum. Water (10 mL) was added to the residue, and the solid was filtered, washed with water (10 mL), and dried to yield 2.63 g (79%) of white solid. ^{1}H NMR (CD_3OD); δ (ppm): 3.95 (s; 1H); 7,29 (t; 1H; J = 7.9); 7,47 (b.s; 1H); 7.62 (d; 1H; J = 7.9); 7,80 (s; 1H); ^{13}C NMR (CD_3OD); δ (ppm): 28.46; 121.95; 125.39; 127.85; 129.89; 137.29; 166.36; ECI mass spectrum: 719 ($M - H^+$; anhydrous trimer).

1,7-Bis(benzyloxycarbonyl)-4,10-bis(methyl(carbamoylmethyl))-1,4,7,10-tetraazacyclododecane (2). To a solution of 1,7-bis(benzyloxycarbonyl)-1,4,7,10-tetraazacyclododecane (2,0 g; 4,54 mmol) and 2-bromo-*N*-methylacetamide (1,8 g; 11,48 mmol) in acetonitrile (70 mL) was added sodium carbonate (0.96; 9.05 mmol). The mixture was refluxed for 18 h. The remaining solids were removed by filtration, and filtrate was rotary evaporated in a vacuum. The residue was loaded on silica gel column (250 g), and the product was eluted with chloroform: methanol (5:0,2). The fractions containing the product were combined, and the solvent was removed in a vacuum to give 2.24 g (84%) of colorless oil. ^{1}H NMR ($CDCl_3$); δ (ppm): 2.58−2.85 (m; 14H); 3.12 (br.s; 4H); 3.39 (br.s; 8H); 5.07 (s; 4H); 7.29−7.31 (m; 10H); ^{13}C NMR ($CDCl_3$); δ (ppm): 25.58; 48.9; 55.4; 67.56; 128.32; 128.46; 128.73; 136.48; 157.05; 171.5.

1,7-Bis(methyl(carbamoylmethyl))-1,4,7,10-tetraazacyclododecane (3). A mixture of 1,7-bis(benzyloxycarbonyl)-4,10-bis(methyl(carbamoylmethyl))-1,4,7,-10-tetraazacyclododecane (2.24 g; 3.85 mmol) and 10% Pd/C (0.51 g) in absolute ethanol (60 mL) was shaken under 45 psi of H_2 for 3 days. The catalyst was removed by filtration, and the filtrate was rotary evaporated to dryness in a vacuum to give 1.18 g (98%) of white solid. ^{1}H NMR (CD_3OD); δ (ppm): 2.79 (s; 6H); 2.84−2.89 (m; 8H); 2.97−3.03 (m; 8H); 3.35 (s; 4H); ^{13}C NMR (CD_3OD); δ (ppm): 25.19; 44.10; 51.10; 57.35; 172.74.

1,7-Bis((*m*-dihydroxyborylphenyl)carbamoylmethyl)-4,10-bis(methyl(carbamoylmethyl))-1,4,7,-10-tetraazacyclododecane (4). To a solution of 1,4-bis-(methyl(carbamoylmethyl))-1,4,7,10-tetraazacyclododecane (1.18 g; 3.77 mmol) and 3-bromoacetylaminophenylboronic acid (2.04 g; 7.99 mmol) in methanol:acetonitrile (25:25 mL) was added sodium carbonate (0.80 g; 7.54 mmol). The mixture was refluxed overnight. The solvent was removed by rotary evaporation in a vacuum, and the remaining residue was dissolved in 0.5 M HCl (60 mL) and subsequently extracted with ethyl acetate (3 × 50 mL). The aqueous layer was neutralized with 2 M NaOH to pH 7, and the solid that precipitated at this point was filtered and dried to yield 2.01 g (80%) of a white solid. ^{1}H NMR (CD_3OD); δ (ppm): 2.25−2.45 (m; 14H); 2.66 (br.s; 8H); 3.05 (br.s; 4H); 3.27 (br.s; 4H); 7.22 (t; 1H; J = 8.1 Hz); 7.42 (br.s; 1H); 7.69 (d; 1H; J = 8.1 Hz); 7.79 (br.s; 1H); ^{13}C NMR (CD_3OD); δ (ppm): 25.10; 50.68; 56.55; 57.59; 125.35; 127.77; 129.49; 137.79; 170.98; 173.05; Fab mass spectrum: 781.4 ($M + H^+$; glycerol complex).

11,12-dioxo-1,4,7,10-tetraazabicyclo[8.2.2]-tetradecane (5); **4,7-bisbenzyl-1,4,7,10-tetraaza bicycle[8.2.2]-tetradecane-11,12-dione (6)** and **1,4-dibenzyl-1,4,7,10-tetraazacyclododecane (7)** were prepared according to the method of Handel at al. (*23*).

1,4-Bisbenzyl-7,10-bis(methyl(carbamoylmethyl))-1,4,7,10-tetraazacyclododecane (8). To a solution of 1,4-dibenzyl-1,4,7,10-tetraazacyclododecane (3.5 g; 9.94 mmol) and 2-bromo-*N*-methylacetamide (3.5 g; 23.02 mmol) in acetonitrile (300 mL) was added sodium carbonate (2.1 g; 19.81 mmol). The mixture was refluxed overnight. The remaining solid was filtered and the

solvent removed by rotary evaporation in a vacuum. The residue was dissolved into chloroform, loaded onto silica gel column (270 g), and eluted with chloroform:methanol (5:0.4). The fractions containing the product were combined, and the solvent was removed in a vacuum to give 4.06 g (83%) of a colorless oil. ^{1}H NMR ($CDCl_3$); δ (ppm): 2.54 (br.s; 8H); 2.71−2.79 (m; 14H); 3.1 (s; 4H); 3.55 (s; 4H); 7.12−7.33 (m; 10H); ^{13}C NMR ($CDCl_3$); δ (ppm): 26.09; 51.73; 53.41; 53.55; 54.53; 58.98; 59.90; 127.32; 128.35; 129.27; 137.7; 172.11.

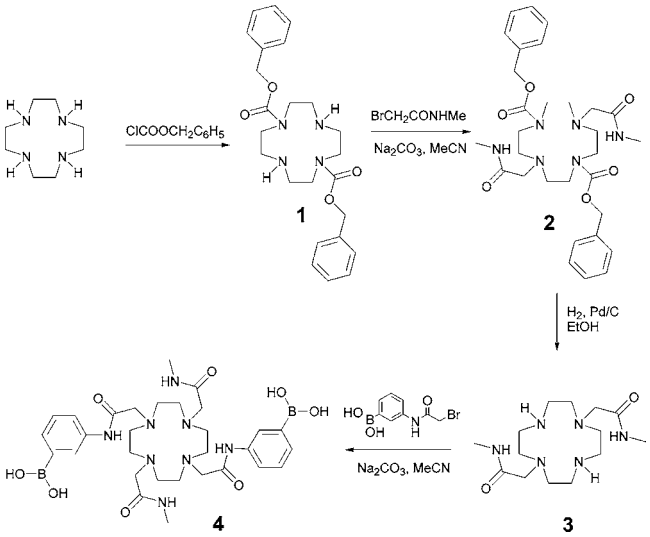
1,4-Bis(methyl(carbamoylmethyl))-1,4,7,10-tetraazacyclododecane (9). A mixture of 1,4-bis-benzyl-7,10-bis(methyl(carbamoylmethyl))-1,4,7,10-tetraazacyclododecane (2.55 g; 5.16 mmol) and 10% Pd/C (0.7 g) in absolute ethanol (60 mL) was shaken under 45 psi of H_2 for 3 days. The catalyst was removed by filtration and the solvent removed by rotary evaporation in a vacuum to give 1.5 g (92.5%) of a yellow oil. ^{1}H NMR ($CDCl_3$); δ (ppm): 2.51−2.57 (m; 8H); 2.63−2.72 (m; 10H); 2.81 (s; 4H); 3.06 (s; 4H); ^{13}C NMR ($CDCl_3$); δ (ppm): 18.25; 25.84; 44.91; 46.32; 52.33; 53.92; 58.06; 58.51; 171.88.

1,4-Bis((*m*-dihydroxyborylphenyl)carbamoylmethyl)-7,10-bis(methylcarbamoylmethyl)-1,4, 7,10-tetraazacyclododecane (10). To a solution of 1,4-bis-(methyl(carbamoylmethyl))-1,4,7,10-tetraazacyclododecane (0.95 g; 3.02 mmol) and (*m*-dihydroxyborylphenyl) bromo acetylamide (1.7 g; 6.6 mmol) in methanol:acetonitrile (25:25 mL) was added sodium carbonate (0.64 g; 6.04 mmol). The mixture was refluxed overnight. The solvent was removed by rotary evaporation in a vacuum, and the residue was dissolved in 0.5 M HCl (50 mL) and extracted with ethyl acetate (3 × 50 mL). The aqueous layer was neutralized with 2 M NaOH to pH 7, and the precipitate that formed was filtered and dried to yield 1.27 g (64%) of a white solid. ^{1}H NMR (CD_3OD); δ (ppm): 2.20−2.65 (m; 14H); 2.70−2.85 (m; 8H); 3.1 (br.s; 4H); 3.25 (br.s; 4H); 7.08 (d; 1H; J = 8 Hz); 7.27 (br.s; 1H); 7.56 (t; 2H; J = 8 Hz); ^{13}C NMR (CD_3OD); δ (ppm): 24.96; 50.47; 56.57; 57.22; 124.93; 127.56; 129.14; 137.64; 170.58; 172.75. Fab mass spectrum: 781.3 ($M + H^+$; glycerol complex).

1-(*m*-Dihydroxyborylphenyl)carbamoylmethyl)-1,4,7,10-tetraazacyclododecane (11). 3-Bromoacetylaminophenylboronic acid (1.0 g; 3.87 mmol) in methanol (150 mL) was added dropwise to a solution of 1,4,7,10-tetraazacyclododecane (4.8 g; 27.86 mmol) in acetonitrile (350 mL) over 2 days at room temperature. The reaction mixture was stirred for an additional day at room temperature. The solvent was removed by rotary evaporation in a vacuum. Acetonitrile as added to the remaining residue and the precipitate that formed was filtered, washed twice with acetonitrile, and dried to yield 1.0 g (60%) of a hydrobromide salt. ^{1}H NMR (CD_3OD); δ (ppm): 2.76−2.99 (m; 16H); 3.43 (s; 2H); 7.15 (t; ^{1}H; J = 7.4 Hz); 7.31 (d; ^{1}H; J = 7.4 Hz); 7.41 (s; ^{1}H); 7.61 (d; ^{1}H; J = 7.4 Hz). ^{13}C NMR (CD_3OD); δ (ppm): 44.15; 44.36; 45.29; 51.85; 57.88; 118.19; 124.82; 126.75; 129.38; 136.48; 170.87.

1-((*m*-Dihydroxyborylphenyl)carbamoylmethyl)-4,7,10-tris(methylcarbamoylmethyl)-1,4,7,10-tetraazacyclododecane (12). To a solution of 1-(*m*-dihydroxyborylphenyl)carbamoyl methyl)-1,4,7,10-tetraazacyclododecane (1.0 g; 2.32 mmol) and 2-bromo-*N*-methylacetamide (2.12 g; 13.95 mmol) in methanol:acetonitrile (25:25 mL) was added sodium carbonate (1.48 g; 13.95 mmol). The mixture was refluxed 2 days. The remaining solids were removed by filtration, and solvent was removed by rotary evaporation in a vacuum. The resulting residue was extracted first with chloroform:methanol

Scheme 2



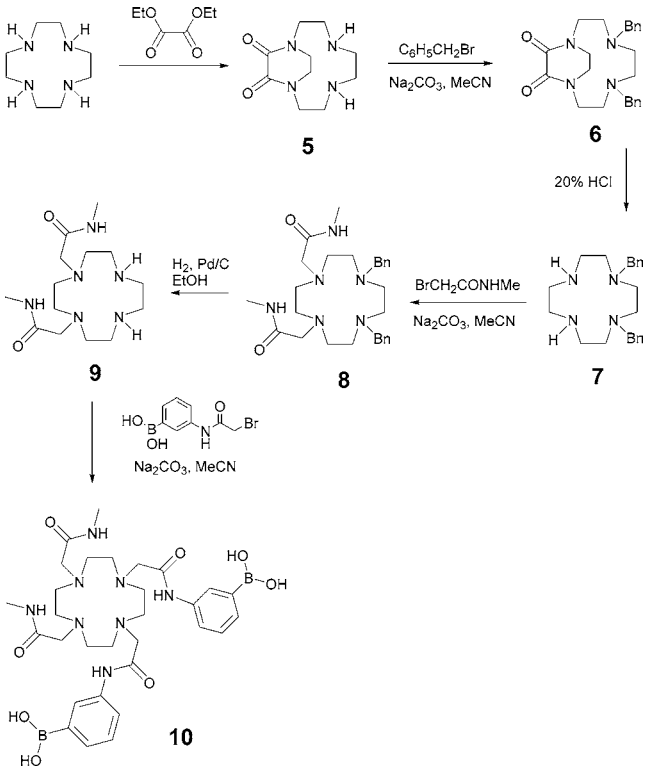
(50:0.5) and then by acetonitrile and finally removed by filtration, washed with cold water, washed twice with acetonitile, and dried to yield 0.9 g (69%) of a white solid. ^{1}H NMR (CD_3OD); δ (ppm): 2.31−2.49 (m; 4H); 2.68−2.81 (m; 15H); 3.05−3.14 (m; 6H); 3.35 (s; 8H); 7.11 (t; 1H; 7.7 Hz); 7.22−7.36 (m; 2H); 7.69 (d; 1H; 7.7 Hz). ^{13}C NMR (CD_3OD); δ (ppm): 25.04; 50.54; 56.66; 56.89; 57.53; 117.78; 124.52; 126.42; 129.33; 136.57; 170.29; 172.66; 172.74. Fab mass spectrum: 619.3 ($M + H^+$; glycerol complex).

Eu(4), Eu(10), and Eu(12) Preparation. Typically, ligand (10% excess) was added to an aqueous solution of $EuCl_3$ (0.2 M), and the resulting solution was stirred at room-temperature overnight to ensure full complexation. If necessary, a small amount of concentrated NaOH was added to maintain the pH near 7 until free Eu^{3+} could no longer be detected using xylenol orange as colorimetric indicator (in 1 M NaAc/HAc buffer solution at pH 5.3). Excess free ligand was filtrated, and the residue was freeze-dried.

RESULTS

Synthesis and Characterization of Phenylboronic Acid-Appended Macrocycles. Lanthanide cyclen complexes with amide pendant arms exhibit high kinetic inertness even in very acidic condition (*19*) and consequently have been found to have very important application as MRI contrast agents via a novel route based on chemical exchange saturation transfer (CEST) mechanism (*20*). We therefore focused on preparing new ligands based on tetramide derivatives of cyclen with phenylboronic acids groups as pendant arms. For bis-substitutions, two possibilities exist: one where the phenylboronic acids are trans to one another across the cyclen ring (ligand **4**) and another where they are cis to one another (ligand **10**). 1,7-Substituted cyclen was achieved by following a procedure reported by Kovacs and Sherry (*21*, *22*) through protection of *trans*-amines in cyclen by using benzyl chloroformate (Scheme 2). Treatment of **1** with 2-bromo-*N*-methylacetamide and sodium carbonate in MeCN followed by hydrogenolysis afforded **3** with methyl amide arms selectively substituted at positions 1 and 7. In the final step, reaction of **3** with 3-bromoacetylaminophenylboronic acid in MeCN:MeOH/sodium carbonate afforded the target ligand **4**. As these phenylboronate products have low solubility in water at pH 7 in water, they were easily purified by precipitation. Solid **4** was isolated in 80% yield.

Scheme 3



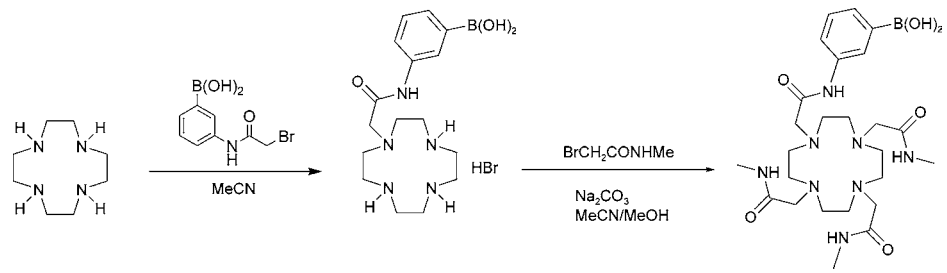
Selective protection of adjacent nitrogens of the cyclen ring was achieved following the procedure reported by Handel and co-workers (*23*) through formation of the oxamide by condensation with diethyl oxalate. This was followed by alkylation with benzyl bromide and deprotection by selective hydrolysis of the bicyclic diamide to afford **7** (Scheme 3). Reaction of **7** with 2-bromo-*N*-methylacetamide in MeCN/sodium carbonate yielded **8** and hydrogenolysis afforded the 1,4 methyl diamide derivative **9** in 92% yield. The reaction of **9** with 3-bromoacetylaminophenylboronic acid in MeCN:MeOH/sodium carbonate followed by precipitation from water at pH 7 yielded the cis-ligand **10** in 64% yield.

Finally, selective monoalkylation of cyclen can be run using two main strategies, either direct alkylation of excess of cyclen with the appropriate alkyl halide (*24*) or selective N-functionalization followed by alkylation−deprotection steps (*25*). We found that the best experimental conditions to perform the monoalkylation of cyclen required the use of 7 equiv of cyclen in MeCN in room temperature. In this way, we could isolate compound **11** in satisfactory yield (60%) without using chromatography (Scheme 4). Once the monoalkylated product **11** was isolated, conversion to the corresponding *N*-monophenylboronate compound **12** was accomplished by reaction of **11** with 2-bromo-*N*-methylacetamide in MeCN:MeOH/sodium carbonate. **12** was isolated as a white solid from water at pH 7 in 69% yield. All compounds were characterized by ^{1}H and ^{13}C NMR and mass spectroscopy. Elemental analyses of these boron-containing products were unsuccessful due to formation of incombustible residues (*26*) and the possibility of existences of mixture of acids and anhydrides that are common moieties of boronic acids. Europium complexes were formed by reaction with $EuCl_3$ at pH 7 and room temperature. The complexes were conveniently purified by filtering off the excess ligand from water at pH 7.

pH Titrations. The UV absorption spectra of phenylboronic acids undergo characteristic changes along with the sample pH that reflect conversion of neutral $B(OH)_2$ to anionic $B(OH)_3^-$ species. Typical absorption spectra of Eu(**4**) at various pH values are shown in Figure 1. Even though Eu(**4**) has two boronic acids, the single isobestic point near 253 nm indicates that the two groups titrate independently and have identical pK_a values. For this reason, plots of A_{271} versus pH for Eu(**4**), Eu(**10**), and Eu(**12**) were fit to a single protonation step to give the pK_a values shown in Table 1. Upon addition of excess sugar (D-fructose in this case), there is a shift in apparent pK_a of these systems to lower values that reflects a decreased boron−oxygen bond angle in the $-B(OR)_2$-$(OH)^-$ species and an increase in acidity of the boron center. D-Fructose was chosen as the reference sugar in this experiment because it has been reported that this sugar provides the largest pK_a shift upon binding to boronic acids (*14*, *27*). The UV spectra of Eu(**4**), Eu(**10**), and Eu(**12**) collected as a function of pH in the presence of excess D-fructose shows that all three phenylboronate derivatives form complexes with sugar and experience a similar pK_a shift upon binding to D-fructose.

Sugar Titrations. Changes also occur in the UV spectrum of phenylboronic acid upon addition of sugars (at constant pH) and these may be monitored to determine a conditional binding constant characteristic of that pH value (*28*). Initial binding experiments for Eu(**4**), Eu(**10**), and Eu(**12**) were performed at pH 10.2 (well above the pK_a of the boronic acids in these systems) with the three most abundant monosaccharides in human plasma, D-glucose (∼5 mM), D-fructose (∼0.05 mM), and D-galactose (∼0.05 mM) (*29*). Although D-fructose is known to display the highest affinity among these monosaccharides for mono-phenylboronic acid derivatives, some bis-phenylboronic acid derivatives bind selectively with D-glucose, providing that the phenylboronic acid functionalities are appropriately positioned (*30*−*33*). Typical changes in absorbance of Eu(**4**) upon addition of D-fructose and D-glucose are shown in Figure 2. In most experiments with monosaccharides, a general increase in absorbance such as that shown here for D-fructose is observed but an opposite behavior was observed upon

Scheme 4



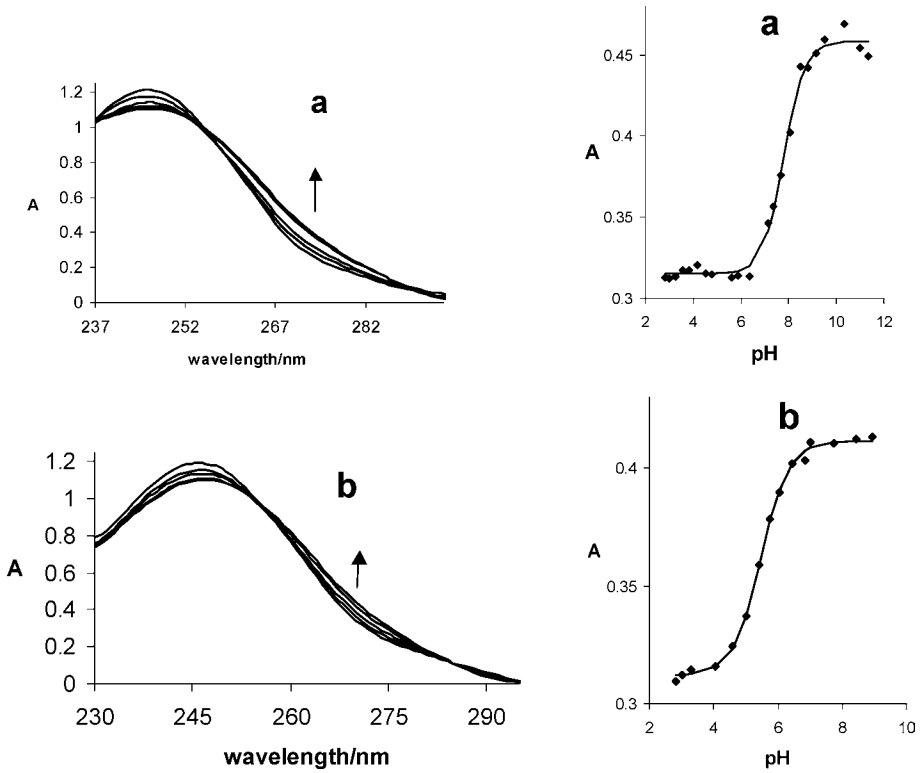


Figure 1. Absorption spectra of Eu(**4**) (5.64×10^{-5} M) as a function of pH. The changes in A_{271} are shown plotted as a function of pH in the absence (a) and presence (b) of 50 mM D-fructose.

Table 1. pK_a Values of Eu(4), Eu(10), and Eu(12) in the Absence and Presence of Excess D-Fructose As Measured by UV Spectroscopy

complex	pK_a (without D-fructose)	pK_a (with D-fructose)	ΔpK_a
Eu(**4**)	7.81	5.47	2.34
Eu(**10**)	8.03	5.71	2.32
Eu(**12**)	8.03	5.50	2.53

binding of D-glucose to Eu(**4**). Plots of these absorbance changes as a function of added sugar are shown in Figure 2. The solid lines represent the best fit of these data to 1:1 binding model for all systems. Fitting of the Eu(**4**) and Eu(**10**) data to a 1:2 binding model yielded rather poor agreement with the experimental values. Hence, a 1:1 binding model was assumed to hold for all combinations of Eu^{3+} complexes and sugars (more evidence is provided below for formation of 1:1 complexes). The resulting values are summarized in Table 2.

These data reveal a marked difference in stability between the three Eu^{3+} complexes and these sugars. The data for Eu(**12**) is typical of mono-phenylboronic acid−sugar interactions with the stability order of D-frucose > D-galactose > D-glucose (*15*, *16*). Eu(**10**) also displays the highest affinity for D-fructose but has an approximate 2-fold greater affinity for D-glucose than D-galactose. Eu(**4**), however, shows a completely different binding trend with these same sugars. This complex, the 1,7-*trans*-bis-phenylboronate, displays the highest affinity for D-glucose followed by D-fructose, D-galactose, and the other sugars. This indicates that the distance and positioning of the two phenylboronates in Eu(**4**) is most favorable for a bridging a single glucose molecule between the two complexing centers.

Binding of Eu^{3+} in the macrocyclic cavity of ligands such as these likely alters the geometry of the ligand side-chains and this in turn could have a profound effect upon the phenylboronate−sugar binding. To test this hypothesis, binding studies were also carried out between the free ligands and these same sugars (Table 3). It should be noted that free ligand **4** binds to D-fructose with such high affinity that it became difficult to arrive at a true equilibrium situation at the concentrations required for the spectroscopic measurement, i.e., essentially all of the fructose is bound at even the lowest ratio of D-fructose to ligand **4**. Hence, the K_a listed in Table 3 for this system (8325 ± 2192 M^{-1}) has a rather large error. Nonetheless, the experiment does prove that free ligand **4** does have the highest binding affinity for D-fructose among the sugars examined. Interestingly, in the absence of Eu^{3+}, **10** shows greater selectivity toward glucose than does **4**, a result just opposite from that seen with the corresponding Eu^{3+} complexes. The stability of the complex formed between **4** and glucose is ~8-fold lower than the stability of the complex formed between Eu(**4**) and glucose. This indicates that the selectivity of bis-phenylboronic acid derivatives for sugars is quite dependent on the distance separating the two phenylboronic acid moieties, consistent with other bis-phenylboronates (*29*, *34*, *35*). This also suggests that it may be possible to modulate the affinity of such cyclen-based systems for glucose by other factors that may influence the distance between the phenylboronates such as bulkiness of the other two amide side-chains or perhaps even the size of the lanthanide cation.

CD Spectroscopy. Sugar binding can also be conveniently monitored by changes in the chirality as detected by CD spectroscopy. Molecules containing bis-phenylboronic acid receptors typically become CD active when sugars form cyclic 1:1 complexes such as those illustrated by Scheme 1a while 1:2 complexes are less rigid (Scheme 1b) and are typically CD-silent (*36*−*39*). This makes CD spectroscopy a very convenient tool for differentiating between these two possible structural patterns. The CD spectra of Eu(**4**) and Eu(**10**) are silent in the absence of sugars but become active in the presence of all sugars examined here except D-fructose. The ketose, D-fructose, appears to be unique in this regard for reasons that are

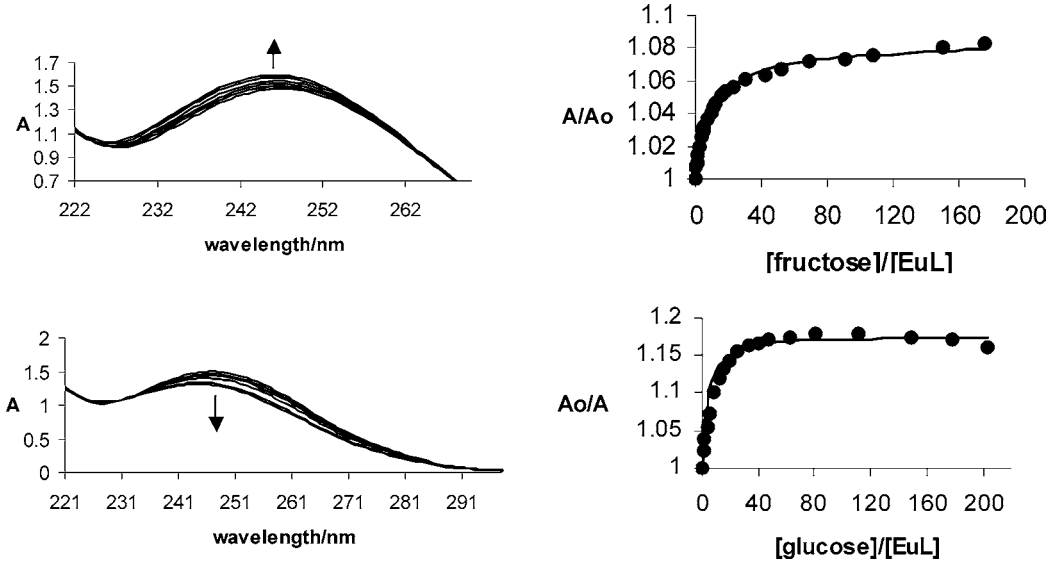


Figure 2. Absorption spectra of Eu(**4**) (7.52×10^{-5} M) as a function of added D-fructose (top row) or D-glucose (bottom row) at a constant pH = 10.2 (48 mM carbonate buffer). [D-fructose] was varied from 0; 1.8; 4.4; 11.3; 41.9; 108.3 mM while [D-glucose] was varied from 0; 0.9; 1.8; 5.6; 15.4; 24.9; 80.7 mM.

Table 2. Binding Constants (K_a, M^{-1}) for Formation of 1:1 Complexes between Eu(4), Eu(10), and Eu(12) and Various Saccharides at pH 10.2

saccharides	Eu(**4**)	Eu(**10**)	Eu(**12**)
glucose	2275 ± 266	319 ± 48	73 ± 13
galactose	198 ± 20	124 ± 15	118 ± 14
fructose	1259 ± 106	1503 ± 130	820 ± 124
lactose	110 ± 24	63 ± 9	159 ± 27

Table 3. Binding Constants (K_a, M^{-1}) between Free Ligands, 4 and 10, and Various Sugars at pH 10.2

saccharides	**4**	**10**
glucose	243 ± 32	1165 ± 106
galactose	671 ± 54	274 ± 54
fructose	8325 ± 2192	831 ± 208
lactose	137 ± 47	25 ± 54

not entirely clear. This same behavior has been observed for many other bis-phenylboronate systems that have been studied using CD spectroscopy (*3*, *16*, *40*, *41*). The CD spectra of Eu(**4**) and Eu(**10**) in the presence of excess D-glucose are shown in Figure 3. Clearly, both the *cis*-phenylboronate complex (Eu(**10**)) and the *trans*-phenylboronate complex (Eu(**4**)) form bridging 1:1 complexes with glucose but with opposite chirality. As a check, spectra of Eu(**4**) and Eu(**10**) with also run in the presence of excess L-glucose (data not shown) and the CD spectra of these were the mirror images of those shown in Figure 3. This lends support to the opposite chirality of Eu(**4**)·D-glucose and Eu(**10**)·D-glucose.

Binding constants between Eu(**4**) were also measured by CD spectroscopy at pH 10.2 (to compare with the UV results) and again at pH 7 (Figure 4). A fitting of the CD binding data at pH 10.2 gave a binding constant, K_a = 2280 M^{-1}, identical to the value determined in the UV titration. The titration performed at pH 7 gave a binding constant, K_a = 339 M^{-1}, again identical to the value determined previously in a CEST titration (383 M^{-1}) (*18*). This binding constant is in a reasonable range for using Eu(**4**) to detect physiological levels of glucose (~5 mM) by MRI.

Verification of Eu(4)·sugar stoichiometry by MALDI TOF Mass Spectrometry. To verify that glucose indeed binds to Eu(**4**) in a bridging manner as suggested by CD spectroscopy, mass spectroscopy was also performed on aqueous samples containing 10 mM Eu(**4**) plus either D-fructose or D-glucose at 1:1 and 1:2 ratios. For both glucose and fructose at pH 7, a mass peak at 1065 Da corresponding to a 1:1 complex was observed. For a sample recorded at pH 10 where the binding affinity is much higher, again a mass peak at 1066 Da dominated the spectrum. Only very small amounts of the 1:2, Eu(**4**)·$(sugar)_2$, complexes were detected at either pH value. This result verified the fits of the binding data and the CD active spectrum observed for Eu(**4**)·sugars described above.

MR Images of Phantoms Containing Eu(4) or Eu(12) Plus Simple Monosaccharides or Glycated HSA. To test whether these new sensors might be used to detect sugars by MRI based upon a CEST mechanism (*20*), phantoms consisting of four tubes (I.D. 4 mm) each containing 10 mM Eu(**4**) or Eu(**12**) and different amounts of monosaccharides were prepared in 100 mM PIPES

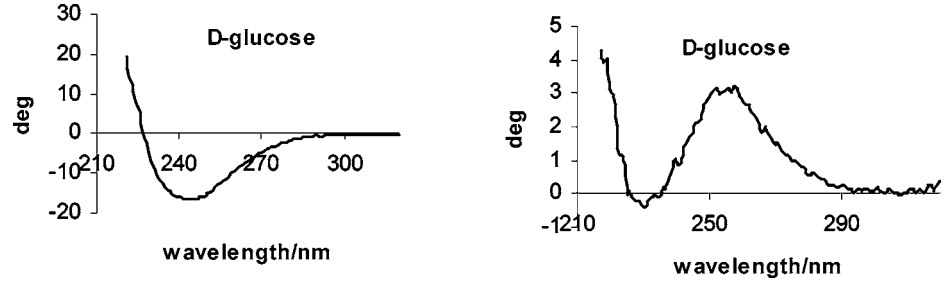


Figure 3. CD spectral changes of Eu(**4**) (left) and Eu(**10**) (right) in the presence of 50-fold excess D-glucose (24 mM carbonate buffer, pH 10.2; the concentrations of Eu(**10**) and Eu(**4**) were 7.52×10^{-5} M).

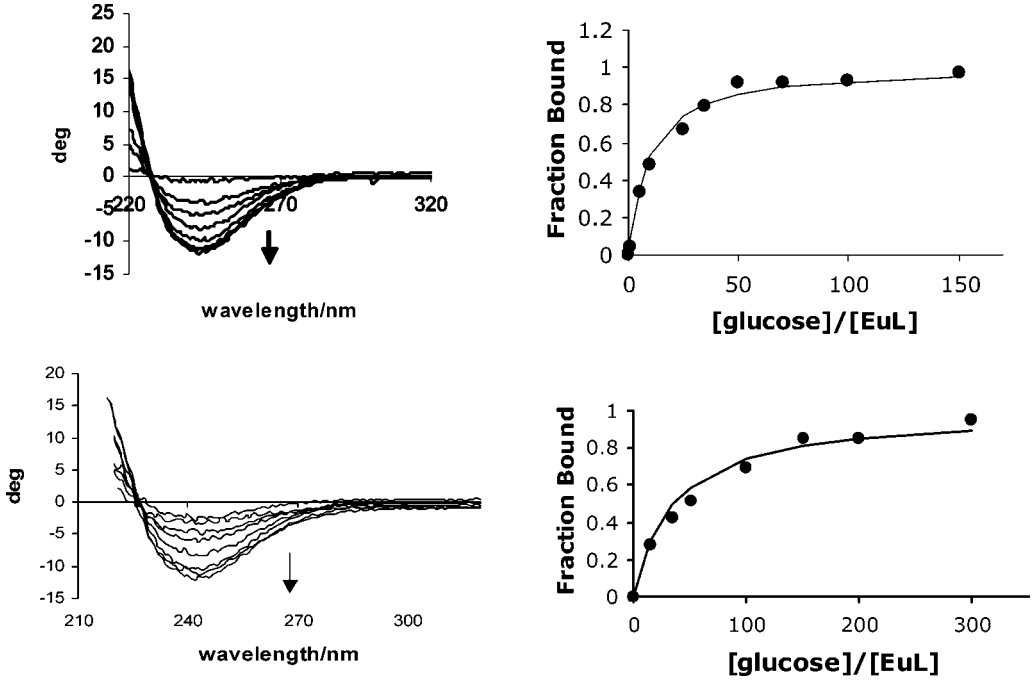


Figure 4. CD intensity changes of Eu(**4**) (5.26×10^{-5} M) in the presence of increasing concentrations of D-glucose. The top row is data collected at pH 10.2 (24 mM carbonate buffer) while the bottom row is data collected at pH 7.2 (24 mM phosphate buffer).

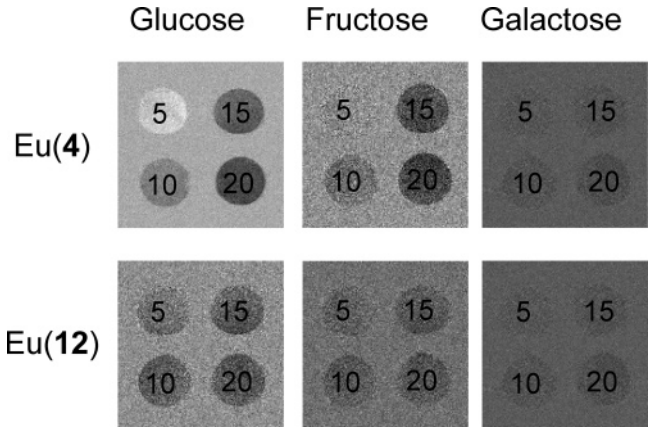


Figure 5. CEST images of phantoms containing 10 mM Eu(**4**) or Eu(**12**) and 0, 5, 10, and 20 mM sugar, respectively. PIPES (100 mM) was used to buffer the pH at 7.0. The image parameters were as follows: TR/TE = 3000/18 ms, FOV = 40 × 40 mm, coronal thickness 2 mm, data matrix 256 × 256, saturation duration time of 2 s at a power of 1020 Hz at a frequency offset of 50 and 30 ppm. The CEST images were obtained by pixel by pixel subtraction of the image at 50 ppm from that at 30 ppm, respectively.

buffer at pH 7.0. Eu(**4**) was selected because it has the highest binding ability to glucose, while Eu(**12**) was imaged simply for comparison. Images were acquired after alternatively applying identical presaturation pulses at 50 ppm (bound water) versus 30 ppm (between the bound and bulk water peaks) (*18*). Although the intensities of these individual images were visually similar, the difference images (referred to as a CEST image) show clear intensity gradations that parallel the sugar concentrations. Typical CEST images for Eu(**4**) or Eu(**12**) in the presence of different amounts of glucose, fructose, and galactose were shown in Figure 5. For example, using a gray scale of 0−255 (from the darkest to the brightest), the image intensities were 208, 148, 112, and 96 for samples containing 10 mM Eu(**4**) and either 0, 5, 10 and 20 mM glucose, respectively, while they were 134, 114, 110, and 106 for Eu(**12**) phantom. This demonstrates that Eu(**4**) may be used to quantitatively image glucose near physiological concentrations (∼5 mM). A comparison of the CEST images of Eu(**4**) in the presence of glucose or fructose suggests that fructose would likely interfere with detection of glucose if both sugars were presented at similar concentrations. This is consistent with the ∼2-fold lower binding constant for Eu(**4**) and fructose versus glucose (Table 2). However, the concentration of fructose in tissues is typically about 100-fold lower than glucose so one would anticipate that fructose would not interfere with quantitative imaging of glucose. Galactose binding is weak for both Eu^{3+} complexes, and the corresponding CEST images are little affected by this sugar.

CEST imaging experiments were also performed on samples containing glycated human serum albumin (HSA) to determine whether Eu(**4**) could be used as a sensor of sugars bound to proteins. Figure 6 shows images of phantoms containing 10 mM Eu(**4**) plus increasing amounts of glycated HSA (with an average of five hexose units per albumin). Assuming that Eu(**4**) binds to each of the five fructosamine moieties with equal binding affinity, a binding constant of 791 ± 301 M^{-1} was estimated from the limited CEST image intensity data of Figure 6. Although this binding constant has a rather large error, the value found is the same order of magnitude as the constants found for Eu(**4**) binding to simple sugars at this same pH. This indicates that amidation of fructose does not destroy recognition by Eu(**4**). However, the amounts of glycated proteins, such as albumin and hemoglobin, are proportional to the level of blood glucose with albumin glycated to an extent of about 10% at normal plasma levels (*42*). Thus, at a plasma concentration of 10% × 0.6 or ∼0.06 mM, the amount of glycated HSA present in plasma of a normal individual should not interfere with using Eu(**4**) as a sensor for glucose in tissue. On the other hand, this binding property could be useful as a rapid throughput analysis of the extent of glycation of HSA in vitro after separation of excess simple sugars. Glycation of proteins has been implicated in the development of diabetic complications and the aging process (*43*).

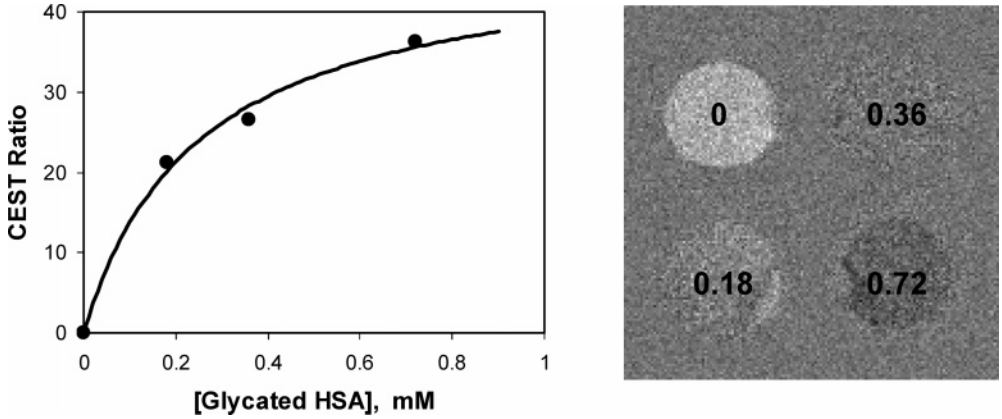


Figure 6. CEST images of phantoms containing 10 mM Eu(**4**) and 0, 0.18, 0.36, and 0.72 mM glycated HSA, respectively. PIPES (100 mM) was used to buffer the pH at 7.0. The image parameters are identical to those shown in Figure 5.

DISCUSSION

Three new cyclen-based tetraamide ligands containing either mono- and bis-phenylboronate extended arms were synthesized and their Eu^{3+} (europium) complexes characterized by UV, circular dichroism, mass spectrometry, and CEST imaging. The Eu^{3+} complexes of **4**, **10**, and **12** display quite different binding behavior with glucose, fructose, and galactose. The initial binding experiments were carried out at pH 10.2 (well above the physiological pH range) because it is well-known that phenylboronates have a much higher affinity for sugars at pH values above the pK_a of the boronic acid. Given that the affinity of many phenylboronates for sugars is too low to detect at pH values near 7, most binding studies are carried out first at pH values near 10 to ensure adequate binding. The design of bis-phenylboronic acid molecules as sensors specific for glucose assumes that bis-phenylboronic acids will be positioned at the proper distance and orientation to bind glucose with high affinity and selectivity. Although this has been demonstrated previously for several fluorescent molecules containing two phenylboronate groups (*29*, *44*−*46*), the degree of selectivity and binding affinity remains rather empirical. The goal of this project at the onset was to create a glucose sensor using MRI as the readout device. It has been shown recently that water exchange in cyclen-based Eu^{3+}-tetraamide complexes is quite sensitive to the identity of the appended amine side-chains (*17*, *47*) so it was reasonable to assume that one might be able to modulate water exchange in such systems by using glucose as a "capping" moiety over a Eu^{3+}-bound water molecule. Hence, the *trans*-1,7-bis-phenylboronate ligand (**4**) became the target ligand of choice while the *cis*-1,4-bis-phenylboronate ligand (**10**) was designed as a control. While simple mono-phenylboronic acids typically display a much higher affinity for fructose over glucose (for example, phenylboronic acid has a K_a of 162 M^{-1} for fructose and 5 M^{-1} for glucose (*48*)), bis-phenylboronic acids systems tend to become more selective for glucose. As anticipated, the mono-phenylboronic acid system, Eu(**12**) displayed an ∼11-fold selectivity for fructose over glucose and even had a greater affinity for galactose than glucose. Surprisingly, free ligand **4** also had an ∼34-fold binding selectivity for fructose over glucose and an unusually high affinity for fructose, comparable to some of the more favorable bis-phenylboronate systems that have been reported (*34*), while free ligand **10** slightly favored glucose in preference to fructose (more typical of over bis-phenylboronate systems). This indicates that the exact positioning of the two phenylboronate moieties not only determines sugar selectivity but also substantially impacts binding affinity. It is quite interesting and again surprising that formation of Eu^{3+} complexes with these same ligands has a much more dramatic impact in the case of Eu(**4**) than Eu(**10**). Now, Eu(**4**) favors glucose over fructose by ∼2-fold, a nearly 40-fold switch in binding selectivity upon going from free ligand **4** to Eu(**4**). This rather dramatic effect must be ascribed to a repositioning of the two phenylboronate side-chains upon entry of Eu^{3+} into the cyclen cavity and suggests that the ionic radius of the central metal ion might be used as an adjustable parameter for fine-tuning glucose selectivity and affinity. Conversely, a comparison of free ligand **10** with Eu(**10**) shows an opposite effect with free ligand **10** favoring glucose and Eu(**10**) favoring fructose. Here, the switch in binding affinity is less dramatic but nonetheless ∼7-fold. As predicted a priori, water exchange between the Eu^{3+}-bound water molecule in Eu(**4**) is indeed slower when glucose is bound, and this feature can be detected by CEST imaging (*18*). The images shown in Figure 5 indicate that water exchange is also slowed upon binding of fructose to Eu(**4**), but the effect is smaller in this system due to a combination of lower binding affinity and perhaps lower modulation of water exchange (the exchange rate has not been measured in this system). Addition of galactose to Eu(**4**) or addition of any monosaccharides to Eu(**10**) does not initiate a CEST effect. The later observation is not surprising since binding of sugars to the later *cis*-1,4-bis-phenylboronate complex would like not disturb the Eu^{3+}-bound water site.

Compared to other organic-based bis-phenylboronate glucose sensors, Eu(**4**) has a reasonably high binding affinity for glucose (2275 ± 266 M^{-1} at pH 10.2 and 339 ± 29 M^{-1} at pH 7) but only a modest selectivity for glucose over fructose. Sensor Eu(**4**) represents an improvement of about 455-fold in affinity and about 60-fold improvement in selectivity for glucose over fructose compared with simple phenylboronic acid. Although fructose and glycated HSA have similar binding affinities as glucose with Eu(**4**), it is unlikely that these sugars will interfere with imaging of glucose in tissues because the plasma concentrations of fructose and glycated HSA are much lower than that of glucose. Thus, Eu(**4**) is an important advance toward an optimal agent for imaging the tissue distribution of glucose by MRI.

ACKNOWLEDGMENT

This work was supported in part by grants from the Robert A. Welch Foundation (AT-584), the National Institutes of Health (CA-84697 and RR-02584), and the Texas Advanced Technology Program. Authors thank Dr

G. R. Dieckmann and Dr J. Sibert for access to their CD and UV spectrometers.

LITERATURE CITED

(1) Striegler, S. (2003) Selective carbohydrate recognition by synthetic receptors in aqueous solution. *Curr. Org. Chem. 7*, 81−102.

(2) Freckmann, G., Kalatz, B., Pfeiffer, B., Hoss, U., and Haug, C. (2001) Recent advances in continuous glucose monitoring. *Exp. Clin. Endocrinol. Diabetes 109*, 347−357.

(3) James, T. D., Sandanayake, K. R. A. S., and Shinkai, S. (1995) Recognition of sugars and related compounds by "reading-out"-type interfaces. *Supramol. Chem. 6*, 141−157.

(4) James, T. D., Linnane, P., and Shinkai, S. (1996) Fluorescent saccharide receptors: a sweet solution to the design, assembly and evaluation of boronic acid derived PET sensors. *Chem. Commun.* 281−288.

(5) James, T. D., Sandanayake, K. R. A. S., and Shinkai, S. (1996) Saccharide sensing with molecular receptors based on boronic acid. *Angew. Chem., Int. Ed. Engl. 35*, 1911−1922.

(6) Mizuno, T., Takeuchi, M., Hamachi, I., Nakashima, K., and Shinkai, S. (1997) Chiroselective transcription of the sugar structure to D- or L-$[CoIII(bpy)_3]^{3+}$ using a boronic acid-sugar template interaction. *Chem. Commun.* 1793−1794.

(7) Shinmori, H., Takeuchi, M., and Shinkai, S. (1998) A novel light-gated sugar receptor, which shows high glucose selectivity. *J. Chem. Soc., Perkin Trans. 2*, 847−852.

(8) Wang, W., Gao, X., and Wang, B. (2002) Boronic acid-based sensors. *Curr. Org. Chem. 6*, 1285−1317.

(9) Ross, B., and Bluml, S. (2001) Magnetic resonance spectroscopy of the human brain. *Anat. Rec. 265*, 54−84.

(10) Gruetter, R., Rothman, D. L., Novotny, E. J., Shulman, G. I., Prichard, J. W., and Shulman, R. G. (1992) Detection and Assignment of the Glucose Signal in H^1 NMR Difference Spectra of the Human Brain. *Magn. Reson. Med. 27*, 183−188.

(11) Seaquist, E. R., Damberg, G. S., Tkac, I., and Gruetter, R. (2001) The effect of insulin on in vivo cerebral glucose concentrations and rates of glucose transport/metabolism in humans. *Diabetes 50*, 2203−2209.

(12) Gruetter, R., Novotny, E. J., Boulware, S. D., Rothman, D. L., Mason, G. F., Shulman, G. I., Shulman, R. G., and Tamborlane, W. V. (1992) Direct Measurement of Brain Glucose-Concentrations in Humans by C-13 Nmr-Spectroscopy. *Proc. Natl. Acad. Sci. U.S.A. 89*, 12208−12208.

(13) Testa, C., Casieri, C., Canese, R., Carpinelli, G., Podo, F., and De Luca, F. (2001) In vivo detection of C-13-enriched glucose metabolites in mouse brain by T-SEDOR imaging. *Magn. Reson. Imaging 19*, 739−743.

(14) Lorand, J. P., and Edwards, J. O. (1959) Polyol complexes and structure of the benzeneboronate ion. *J. Org. Chem. 24*, 769−774.

(15) Murakami, H., Nagasaki, T., Hamachi, I., and Shinkai, S. (1993) Sugar sensing utilizing aggregation properties of a boronic-acid-appended porphyrin. *Tetrahedron Lett. 34*, 6273−6276.

(16) Arimori, S., Takeuchi, M., and Shinkai, S. (1996) Sugar-sensing by chiral orientation of dimeric boronic-acid-appended porphyrins which show selectivity for glucose and xylose. *Chem. Lett.* 77−78.

(17) Zhang, S. R., Merritt, M., Woessner, D. E., Lenkinski, R. E., and Sherry, A. D. (2003) PARACEST agents: Modulating MRI contrast via water proton exchange. *Acc. Chem. Res. 36*, 783−790.

(18) Zhang, S., Trokowski, R., and Sherry, A. D. (2003) A Paramagnetic CEST Agent for Imaging Glucose by MRI. *J. Am. Chem. Soc. 125*, 15288−15289.

(19) Wu, K., Zhang, S., Kovacs, Z., and Sherry, A. D. (2000) Dota-amide derivatives with extended arms form lanthanide complexes with unusual kinetic inertness. *J. Nucl. Med. 41*, 1085.

(20) Zhang, S., Winter, P., Wu, K., and Sherry, A. D. (2001) A novel europium(III)-based MRI contrast agent. *J. Am. Chem. Soc. 123*, 1517−1518.

(21) Kovacs, Z., and Sherry, A. D. (1995) General-Synthesis of 1,7-Disubstituted 1,4,7,10-Tetraazacyclododecanes. *J. Chem. Soc., Chem. Commun.* 185−186.

(22) Kovacs, Z., and Sherry, A. D. (1997) pH-controlled selective protection of polyaza macrocycles. *Synthesis* 759−763.

(23) Bellouard, F., Chuburu, F., Kervarec, N., Toupet, L., Triki, S., Le Mest, Y., and Handel, H. (1999) Cis-diprotected cyclams and cyclens: a new route to symmetrically or asymmetrically 1,4-disubstituted tetraazamacrocycles and to asymmetrically tetrasubstituted derivatives. *J. Chem. Soc., Perkin Trans. 1*, 3499−3505.

(24) Anelli, P. L., Murru, M., Uggeri, F., and Virtuani, M. (1991) Highly regioselective synthesis of 1,7-diprotected 1,4,7,10-tetraazacyclododecane derivatives. *J. Chem. Soc., Chem. Commun.* 1317−1318.

(25) Baker, W. C., Choi, M. J., Hill, D. C., Thompson, J. L., and Petillo, P. A. (1999) Synthesis of Lipophilic Paramagnetic Contrast Agents. *J. Org. Chem. 64*, 2683−2689.

(26) Seaman, W., and Johnson, J. R. (1931) Derivatives of phenylboric acid, their preparation and action upon bacteria. *J. Am. Chem. Soc. 7*, 711−723.

(27) Yoon, J., and Czarnik, A. W. (1992) Fluorescent Chemosensors of Carbohydrates − a Means of Chemically Communicating the Binding of Polyols in Water Based on Chelation-Enhanced Quenching. *J. Am. Chem. Soc. 114*, 5874−5875.

(28) Valeur, B., Pouget, J., Bourson, J., Kaschke, M., and Ernsting, N. P. (1992) Tuning of Photoinduced Energy-Transfer in a Bichromophoric Coumarin Supermolecule by Cation Binding. *J. Phys. Chem. 96*, 6545−6549.

(29) Eggert, H., Frederiksen, J., Morin, C., and Norrild, J. C. (1999) A new glucose-selective fluorescent bisboronic acid. First report of strong alpha-furanose complexation in aqueous solution at physiological pH. *J. Org. Chem. 64*, 3846−3852.

(30) Tsukagoshi, K., and Shinkai, S. (1991) Specific complexation with mono- and disaccharides that can be detected by circular dichroism. *J. Org. Chem. 56*, 4089−4091.

(31) Nakashima, K., and Shinkai, S. (1995) Diaza-18-crown-6-based sugar receptor bearing two boronic acids. Possible communication between bound sugars and metal cations. *Chem. Lett. 6*, 443−444.

(32) James, T. D., Sandanayake, K. R. A. S., and Shinkai S. (1994) A glucose-specific molecular fluorescence sensor. *Angew. Chem., Int. Ed. Engl. 106*, 2287−2289.

(33) Takeuchi, M., Mizuno, T., Shinmori, H., Nakashima, M., and Shinkai, S. (1996) Fluorescence and CD spectroscopic sugar sensing by a cyanine-appended diboronic acid probe. *Tetrahedron 52*, 1195−1204.

(34) Karnati, V. V., Gao, X., Gao, S., Yang, W., Ni, W., Sankar, S., and Wang, B. (2002) A glucose-selective fluorescence sensor based on boronic acid-diol recognition. *Bioorg. Med. Chem. Lett. 12*, 3373−3377.

(35) Hartley, J. H., James, T. D., and Ward, C. J. Synthetic receptors. (2000) *J. Chem. Soc., Perkin Trans. 1*, 3155−3184.

(36) Shiomi, Y., Saisho, M., Tsukagoshi, K., and Shinkai, S. (1993) Specific complexation of glucose with a diphenylmethane-3,3′-diboronic acid derivative: correlation between the absolute configuration of mono- and disaccharides and the circular dichroic-activity of the complex. *J. Chem. Soc., Perkin Trans. 1*, 2111−2117.

(37) Suenaga, H., Mikami, M., Sandanayake, K. R. A. S., and Shinkai, S. (1995) Screening of fluorescent boronic acids for sugar sensing which show a large fluorescence change. *Tetrahedron Lett. 36*, 4825−4828.

(38) Kondo, K., Shiomi, Y., Saisho, M., Harada, T., and Shinkai, S. (1992) Specific complexation of disaccharides with diphenyl-3,3′-diboronic acid that can be detected by circular dichroism. *Tetrahedron 48*, 8239−8252.

(39) Sandanayake, K. R. A. S., James, T. D., and Shinkai, S. (1995) Two-dimensional photoinduced electron transfer (PET) fluorescence sensor for saccharides. *Chem. Lett.* 503−504.

(40) Takeuchi, M., Yoda, S., Imada, T., and Shinkai, S. (1997) Chiral sugar recognition by a diboronic-acid-appended binaphthyl derivative through rigidification effect. *Tetrahedron 53*, 8335−8348.

(41) James, T. D., and Shinkai, S. (2002) Artificial receptors as chemosensors for carbohydrates. *Top. Curr. Chem. 218*, 159−200.

(42) Garlick, R. L., and Mazer, J. S. (1983) The Principal Site of Non-Enzymatic Glycosylation of Human-Serum Albumin In vivo. *J. Biol. Chem. 258*, 6142−6146.

(43) Sakaue, R., and Kajiyama, N. (2003) Thermostabilization of bacterial fructosyl-amino acid oxidase by directed evolution. *Appl. Environ. Microb. 69*, 139−145.

(44) Bielecki, M., Eggert, H., and Norrild, J. C. (1999) A fluorescent glucose sensor binding covalently to all five hydroxy groups of alpha-D-glucofuranose. A reinvestigation. *J. Chem. Soc., Perkin Trans. 2*, 449−455.

(45) Norrild, J. C., and Eggert, H. (1995) Evidence for Monodentate and Bisdentate Boronate Complexes of Glucose in the Furanose Form − Application of $^1J_{C-C}$-Coupling-Constants as a Structural Probe. *J. Am. Chem. Soc. 117*, 1479−1484.

(46) Yang, W., He, H., and Drueckhammer, D. G. (2001) Computer-guided design in molecular recognition: Design and synthesis of a glucopyranose receptor. *Angew. Chem., Int. Ed. 40*, 1714−1718.

(47) Zhang, S., and Sherry, A. D. (2003) Physical characteristics of lanthanide complexes that act as magnetization transfer (MT) contrast agents. *J. Solid State Chem. 171*, 38−43.

(48) Springsteen, G., and Wang, B. H. (2002) A detailed examination of boronic acid-diol complexation. *Tetrahedron 58*, 5291−5300.

(49) Groziak, M. P., Ganguly, A. D., and Robinson, P. D. (1994) Boron Heterocycles Bearing a Peripheral Resemblance to Naturally-Occurring Purines − Design, Syntheses, Structures, and Properties. *J. Am. Chem. Soc. 116*, 7597−7605.

(50) Bazzicalupi, C., Bianchi, A., Berni, E., Calabi, L., Giorgi, C., Mariani, P., Losi, P., and Valtancoli, B. (2002) Complexation properties of a new macrocyclic polyaminic ligand (L) containing amidic pendant arms: crystal structure of [PbL]-$(ClO_4)_2$. *Inorg. Chim. Acta 329*, 93−99.

BC0498976

Preparation and Properties of $^{99m}Tc(CO)_3^+$-Labeled *N*,*N*-Bis(2-pyridylmethyl)-4-aminobutyric Acid

Guozheng Liu,* Shuping Dou, Jiang He, Jean-Luc Vanderheyden, Mary Rusckowski, and Donald J. Hnatowich*

Department of Radiology, Division of Nuclear Medicine, University of Massachusetts Medical School, Worcester, Massachusetts 01655. Received June 10, 2004; Revised Manuscript Received August 5, 2004

Labeling biomolecules with $^{99m}Tc(CO)_3^+$ (^{99m}Tc tricarbonyl) is attracting increasing attention. Although histidine is often considered an ideal bifunctional chelator for ^{99m}Tc (or ^{188}Re) tricarbonyl, the family of dipicolylamine carboxylate chelators may be a useful alternative because of the expected ease of synthesis and because the structure provides a pendent carboxylate for potential conjugation to biomolecules. The dipicolylamine chelator *N*,*N*-bis(2-pyridylmethyl)-4-aminobutyric acid (BPABA) was synthesized using 4-aminobutyric acid in place of glycine or aminopropionic acid in the literature, to avoid possible involvement of the carboxylate in the complex formation process by forming five- or six-membered chelation rings. Using a commercial tricarbonyl kit (Mallinckrodt), the complex formation properties of both BPABA and commercial histidine with ^{99m}Tc tricarbonyl were investigated, and the in vitro complex stabilities in saline and in serum were compared. Stability in vivo was also examined following i.v. administration to normal mice. BPABA was synthesized simply and quantitatively by reacting picolyl chloride with aminobutyric acid in one step. On RP HPLC, the product eluted essentially in one peak and the structure was confirmed by ESI-MS. After labeling, both BPABA and histidine were shown by RP HPLC to form tricarbonyl complexes. In both cases, after incubation at 100 °C for 20 min, only one predominant peak of $^{99m}Tc(CO)_3^+$−histidine or $^{99m}Tc(CO)_3^+$−BPABA was apparent, and both complexes were stable at room temperature in saline for at least 24 h. After incubation for 24 h in 37 °C serum, by SE HPLC, 20% of the $^{99m}Tc(CO)_3^+$−histidine was bound to serum protein compared to less than 10% for $^{99m}Tc(CO)_3^+$−BPABA. A 5000 molar excess of histidine at 100 °C for 6 h was unable to dissociate $^{99m}Tc(CO)_3^+$−BPABA. By contrast, BPABA easily dissociated $^{99m}Tc(CO)_3^+$−histidine under the same conditions. Both complexes were stable in vivo in mice, and $^{99m}Tc(CO)_3^+$−BPABA showed rapid and specific hepatobiliary clearance while $^{99m}Tc(CO)_3^+$−histidine was cleared through the kidneys. In conclusion, BPABA was easily synthesized and was shown to possess properties comparable to histidine for labeling of biomolecules with ^{99m}Tc tricarbonyl. However, it was found that the chelator concentration required for quantitative ^{99m}Tc tricarbonyl labeling with both BPABA and histidine were 2 orders higher than that required with more conventional labeling using MAG_3. Finally, the complex $^{99m}Tc(CO)_3^+$−BPABA itself was found to clear exclusively via the hepatobiliary pathway and may have value as a potential hepatobiliary imaging agent.

INTRODUCTION

We have been investigating tumor imaging by pretargeting with antibodies conjugated with phosphodiamidate morpholino oligomers (MORFs) along with ^{99m}Tc-radiolabeled complementary MORFs as effector using MAG_3 as chelator (*1*−*4*). Our overall objective is to perform ^{188}Re radiotherapy using this MORF pretargeting approach. While MAG_3 performs well as a chelator for ^{99m}Tc, it falls short of ideal for the chelation of ^{188}Re. Preliminary studies showed that, when using MAG_3 as a chelator for ^{188}Re in the labeling of MORF, oxidization to $^{188}ReO_4^-$ during preparation was excessive (*5*). Since more suitable chelators for ^{188}Re are therefore still needed, the ^{188}Re-tricarbonyl core was investigated as an alternative labeling strategy because of the predicted kinetic inertness of these complexes (*6*−*8*). Initially, the ^{188}Re tricarbonyl labeling was achieved with Hynic-MORF (*9*). Evaluation showed improved stability of the label to oxidation but with kidney levels high enough to be problematic with ^{188}Re (or ^{99m}Tc). We suspected that the tricarbonyl complexes (*10, 11*) was binding to robust groups such as imidazole in kidney tissue proteins possibly through interaction of the open position of the tricarbonyl complex of the bidentate Hynic chelator.

Numerous ligands have now been recommended as chelators for labeling biomolecules with technetium or rhenium tricarbonyl cores, and it now seems clear that bidentate chelators are not ideal because of the remaining open position (*10, 11*). Of the tridentates considered, those containing the basic formula of [aromatic N-heterocycle]−[amine]−[carboxylate] have received the most attention (*8, 10*−*14*), although the tridentates [aromatic N-heterocycle]−[amine]−[thiol] (*15*) and [thioether]−[thioether]−[carboxylate] (*16*) have also been tested. Examples of rhenium tridentate tricarbonyl complexes are shown in Figure 1. Recently, when *N*,*N*-dipicolylglycine or *N*,*N*-di(imidazolylmethyl)glycine was allowed to react with $Re(CO)_3^+$, the complex with the two

* To whom correspondence should be addressed: Donald J. Hnatowich. Ph.D., Department of Radiology, Division of Nuclear Medicine, University of Massachusetts Medical School, 55 Lake Ave. North, Worcester, MA 01655-0243. Phone: (508) 856-4256. Fax: (508) 856-4572. E-mail: Donald.hnatowich@umassmed.edu.

10.1021/bc049866a CCC: $27.50 © 2004 American Chemical Society
Published on Web 10/08/2004

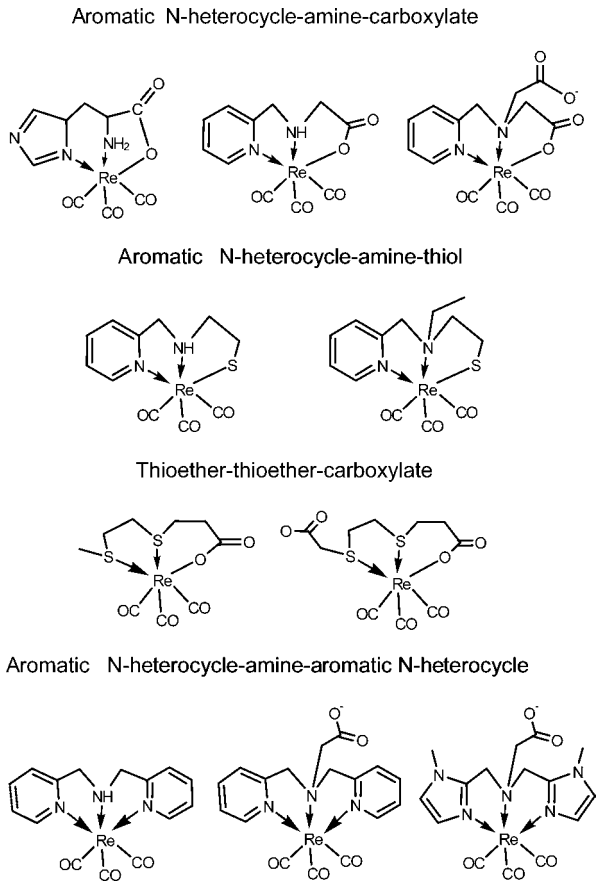


Figure 1. Examples of chemical structures between Re tricarbonyl and tridentates of different classes.

aromatic N-hetercyclic nitrogens and the amine in coordination was obtained leaving the carboxylate free (*17*). This suggested that tridentates with the formula of [aromatic N-heterocycle]−[amine]−[aromatic N-heterocycle] might be preferable for technetium or rhenium tricarbonyl labeling over [aromatic N-heterocycle]−[amine]−[carboxylate].

Lately we have become particularly interested in tridentates of *N*,*N*-dipicolyl-ω-amino acids. Besides providing the [aromatic N-heterocycle]−[amine]−[aromatic N-heterocycle] chelation site, these molecules have a pendent carboxylate group suitable for conjugation to the amines on biomolecules. They can be synthesized in one step simply by reacting picolyl chloride with the corresponding ω-amino acid (*17*).

We report herein on the labeling with $^{99m}Tc(CO)_3^+$ of a new dipicolylamino acid and the properties of the complex. While our ultimate goal is to develop a chelation strategy for $^{188}Re(CO)_3^+$, in this investigation $^{99m}Tc(CO)_3^+$ was used instead because of the ready availability of ^{99m}Tc and its tricarbonyl kit with a recognition of the structural similarities between rhenium and technetium.

MATERIALS AND METHODS

Bis(2-pyridylmethyl)-4-aminobutyric acid (BPABA), also called dipicolylaminobutyric acid, was synthesized in house while histidine was purchased from Aldrich (St. Louis, MO). The MS analysis was performed by the UMMS Proteomics and Mass Spectometry Facility. The Isolink kits for synthesizing $^{99m}Tc(CO)_3^+$ were gifts from Mallinckrodt Medical (St Louis, MO). Each lyophilized kit contained 8.5 mg of sodium tartrate, 2.85 mg of $Na_2B_4O_7{\cdot}10H_2O$, 7.15 mg of sodium carbonate, and 4.5 mg of sodium boranocarbonate. The $^{99m}TcO_4^-$ was eluted from a ^{99}Mo-^{99m}Tc generator (Bristol-Myers Squibb MedicalImaging, Inc., North Billerica, MA). All other chemicals were reagent grade and were used without purification.

Synthesis of Bis(2-pyridylmethyl)-4-aminobutyric Acid (BPABA). The reaction was achieved essentially according to a reported procedure (*17*) with a modification in separation method. The 2-chloromethylpyridine hydrochloride (33.7 g, 196 mmol) and 4-aminobutyric acid (8.3 g, 80 mmol) were dissolved in 100 mL of water, and the pH was adjusted to 10 and maintained in the range of 8−10 for 4 d by adding 5 M NaOH at intervals (total ~18 g, 450 mmol). The black reaction mixture was washed with $CHCl_3$ (70 mL × 4), followed by pH adjustment to 8 and concentration of the aqueous phase via evaporation. Toward the end of the evaporation, concentrated HCl was added to facilitate removal of as much NaCl as possible. The product was characterized by ESI-MS and HPLC.

HPLC Analysis. Reverse phase HPLC (RP HPLC) with an YMC-Pack C-18 column (system 1) was used for separation and analysis during synthesis of BPABA, while a Vydac C-18 column (system 2) was used for analysis during the ^{99m}Tc tricarbonyl labeling. Size exclusion HPLC (SE HPLC) was also used for in vitro and in vivo stability investigations of the ^{99m}Tc tricarbonyl complexes (system 3).

System 1: Semipreparative YMC-Pack C-18 column (250 × 10 mm, 5 μm, 323 Å); 10 mM HCl as solvent A and acetonitrile as solvent B; flow 2.0 mL/min. Gradient table: 0-15 min, 90% A; 15−20 min, 90−70% A; 20−23 min, 70−90% A, and 23−35 min, 90% A.

System 2: The Vydac C-18 column (5 μm, 250 × 4.6 mm); 0.05 M TEAP (triethylamine phosphate, pH 2.0) as solvent A and methanol as solvent B; 1.0 mL/min. Gradient table: 1-3 min, 100% A; 3−6 min, 100%-75% A; 6−9 min, 75% −66% A; 9−20 min, 66%-0% A; 20−27 min, 0% A; 27−40 min, 0%-100% A; 40−50 min, 100% A.

System 3: The Superose-12 size-exclusion column; 0.10 M pH 7.2 phosphate buffer; isocratic flow 0.6 mL/min.

Formation of $^{99m}Tc(CO)_3^+$ Complexes. The $^{99m}Tc(CO)_3^+$ core was prepared fresh daily by introducing 1 mL of $^{99m}TcO_4^-$ saline solution into a kit and heating in boiling water. An incubation time of 20 min was routinely used. After neutralization with 120 μL of 1 N HCl, an equal volume of aliquot was added to a vial containing either 1 mM BPABA or 1 mM histidine of pH 7.0 and heated in a boiling water bath normally for 20 min. Both the labeled compounds of $^{99m}Tc(CO)_3^+$−BPABA or $^{99m}Tc(CO)_3^+$−histidine were characterized by RP HPLC (system 2) and SE HPLC.

In Vitro Stability of $^{99m}Tc(CO)_3^+$-Labeled BPABA and Histidine. The stabilities of both complexes were tested by diluting the labeled solution 100 fold in saline or human serum, incubating at 37 °C, and analyzing at intervals using SE HPLC.

The affinity of $^{99m}Tc(CO)_3^+$ for BPABA relative to histidine was also measured by mixing $^{99m}Tc(CO)_3^+$−BPABA in 100 mM histidine at a molar ratio of BPABA to histidine of 1:5000 and incubating either at 37 °C for 24 h or in a boiling water bath 6 h. The identical procedure was also performed starting with $^{99m}Tc(CO)_3^+$−histidine in 100 mM BPABA.

In Vivo Stability and Biodistribution of ^{99m}Tc Tricarbonyl-Labeled BPABA. A group of four normal CD-1 mice (35−45 g) were each injected with 70 μCi of $^{99m}Tc(CO)_3^+$−BPABA or $^{99m}Tc(CO)_3^+$−histidine via a tail vein. After 35 min, the mice were sacrificed under

halothane anesthesia. Selected organs were harvested and rinsed, and their radioactivity was measured in a Cobra II auto-gamma counter (Packard, Downers Grove, IL). To provide an estimate of in vivo stability, plasma, urine, and an extract from small intestine contents were analyzed by SE HPLC. Plasma was obtained by adding 0.5 mL of blood from each mouse into a tube containing 0.068 mL of 7.5% K_3EDTA followed by centrifugation at 650−700 *g* for 10 min. The small intestine extract was obtained by washing with 4 mL of water and centrifuging the wash at 2500*g* for 20 min.

RESULTS

Characterization of BPABA. Analysis by RP HPLC (System 1) reveals one major peak at 7.8 min with over 90% of peak area and a small peak at 8.7 min, presumably due to $(PyCH_2)_2N(CH_2)_3COOH$ and $(PyCH_2)_3N^+(CH_2)_3$-COOH. The broad peak at 29 min is due to the solvent.

The ESI-MS analysis of BPABA shows a product peak attributed to $[(PyCH_2)_2NH^+(CH_2)_3COOH$ [MH^+: 286.2 *m/z*, abundance 100%; corresponding isotope peak at 287.2 *m/z*, abundance 17%] and a byproduct peak due to the quaternary ammonium salt $(PyCH_2)_3N^+(CH_2)_3COOH$ [M^+: 377.2 *m/z*, abundance 43%; corresponding isotope peak at 378.2 *m/z*, abundance 11%]. All other peaks are lower than 10% (data not presented). Confirmation of structure is apparent in that fragmentation of the molecular ion peak 286.2 *m/z* provide a series of fragment peaks: $(PyCH_2)_2NH^+(CH_2)_3COOH$, *m/z* 286.2, abundance 15.5%; $(PyCH_2)_2N(CH_2)_3CO^+$, *m/z* 268.2, abundance 25%; $(PyCH_2)_2NH_2^+$, *m/z* 200.2, abundance 13%; Py-CH=$NH^+(CH_2)_3COOH$ *m/z* 193.1, 25.0%; Py-CH=$N(CH_2)_3CO^+$ *m/z* 175.1, 16%.

Formation Kinetics of ^{99m}Tc(CO)$_3^+$−BPABA vs ^{99m}Tc(CO)$_3^+$−Histidine. On RP HPLC (System 2) the $^{99m}Tc(CO)_3^+$ core elutes at 4 min (Figure 2A) as described by the manufacturer and forms complexes with both BPABA and histidine (Figures 2B and 2C), resulting in single peaks and indicating a radiochemical purity of over 90%. Reaction times over 5−40 min in boiling water makes no difference in complex formation as shown by HPLC profiles identical to that of Figure 2B or 2C (data not presented). However, heating more than 60 min considerably increases the impurity peaks with both $^{99m}Tc(CO)_3^+$−BPABA and $^{99m}Tc(CO)_3^+$−histidine (data not presented). It was therefore judged safe in this study to employ a routine heating time of 20 min for complex formation.

In Vitro Stability of ^{99m}Tc(CO)$_3^+$−BPABA vs ^{99m}Tc(CO)$_3^+$−Histidine. Both $^{99m}Tc(CO)_3^+$−BPABA and $^{99m}Tc(CO)_3^+$−histidine are unaffected by 24 h incubation in 37 °C saline, but both show serum protein binding after 24 h incubation in 37 °C human serum (data not presented). The percentage of serum binding with $^{99m}Tc(CO)_3^+$−histidine is higher than that with $^{99m}Tc(CO)_3^+$−BPABA (20 vs 9.5% at 24 h), indicating that $^{99m}Tc(CO)_3^+$−histidine may be less stable against transchelation to proteins than $^{99m}Tc(CO)_3^+$−BPABA under these conditions.

Ligand exchange between BPABA and histidine was also investigated by SE HPLC (system 3). In this system, the $^{99m}Tc(CO)_3^+$ core itself does not elute probably due to interaction of the core with the cross-linked agarose matrix. The HPLC chromatograms of $^{99m}Tc(CO)_3^+$−histidine and $^{99m}Tc(CO)_3^+$−BPABA are shown in Figure 3 A and 3D, respectively. Incubation of $^{99m}Tc(CO)_3^+$−histidine with a 5000 molar excess of BPABA pH 7 at 37 °C over 1 d shows minimal replacement of histidine by BPABA (Figure 3 B); however, heating of the same mixture in a boiling water bath for 6 h induces almost total replacement of histidine by BPABA (Figure 3C). In contrast, incubation of $^{99m}Tc(CO)_3^+$−BPABA with a 5000 molar excess of histidine shows no replacement of BPABA (Figure 3 E) even at 100 °C for 6 h (Figure 3F). The capability of BPABA to replace histidine in its $^{99m}Tc(CO)_3^+$ complex, but not vice versa, reflect a higher affinity of BPABA for ^{99m}Tc tricarbonyl.

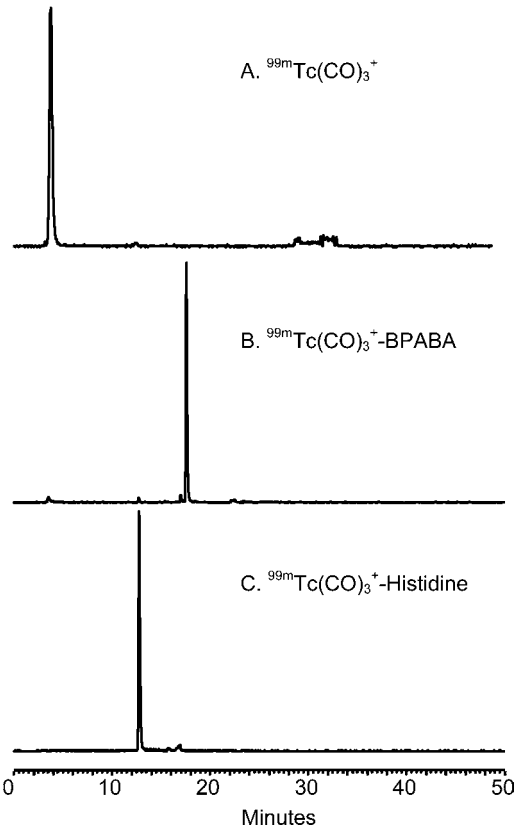


Figure 2. Radiochromatograms by RP HPLC (System 2) of $^{99m}Tc(CO)_3^+$ core (panel A) and $^{99m}Tc(CO)_3^+$−BPABA and $^{99m}Tc(CO)_3^+$−histidine following incubation at 37 °C for 40 min or less (panels B and C, respectively).

Biodistribution and In Vivo Stability of ^{99m}Tc(CO)$_3^+$−BPABA vs ^{99m}Tc(CO)$_3^+$−Histidine. Table 1 presents the biodistribution in normal mice at 35 min postadministration of $^{99m}Tc(CO)_3^+$−BPABA and $^{99m}Tc(CO)_3^+$−histidine. The biodistribution of $^{99m}Tc(CO)_3^+$−BPABA shows rapid hepatobiliary excretion with 57% in the small intestine, 5% in the large intestine, and 15% in liver including gall bladder at 35 min. Less than 8% was excreted into urine at this time. By SE HPLC analysis, only 30% (2.4%ID) of the radioactivity in urine was present as $^{99m}Tc(CO)_3^+$−BPABA. The remaining urine radioactivity was due to the approximately 5% radiochemical impurities in the $^{99m}Tc(CO)_3^+$−BPABA injectate. While clearance of these impurities via the kidneys was rapid and quantitative, the excretion of $^{99m}Tc(CO)_3^+$−BPABA via the kidney was largely negligible. By contrast, $^{99m}Tc(CO)_3^+$−histidine is predominantly excreted through kidney as reported previously (*10*, *11*) with 50% of $^{99m}Tc(CO)_3^+$−histidine in urine in 35 min. Though rapid, the kidney excretion is not as rapid as typical kidney imaging agents such as ^{99m}Tc−BPHA (*18*), ^{99m}Tc−DTPA (*19*), and ^{99m}Tc−MAG_3 (*20*).

The in vivo stabilities of $^{99m}Tc(CO)_3^+$−BPABA and $^{99m}Tc(CO)_3^+$−histidine were evaluated by comparing the SE HPLC radiochromatograms of the injectates with that

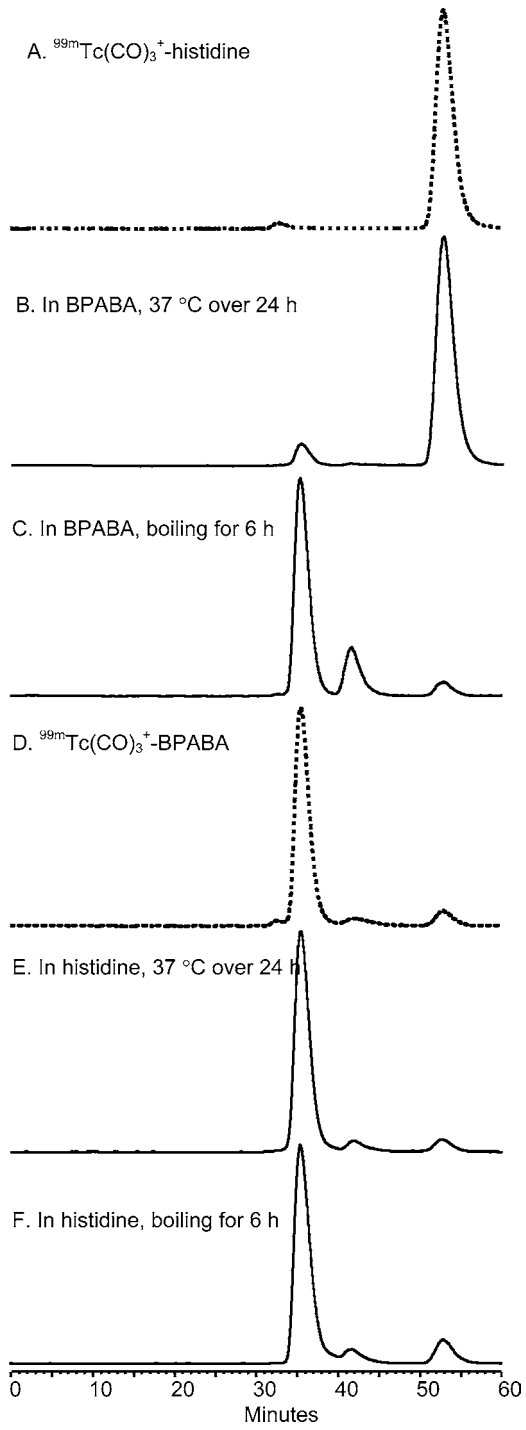


Figure 3. Radiochromatograms by SE HPLC (System 3) of $^{99m}Tc(CO)_3^+$−histidine alone (panels A) and after incubation with a 5000-fold molar excess of BPABA for 24 h at 37 °C (panel B) and 6 h at 100 °C (Panel C). Also presented are radiochromatograms of $^{99m}Tc(CO)_3^+$−BPABA alone (panels D) and after incubation with a 5000-fold molar excess of histidine for 24 h at 37 °C (panel E) and 6 h at 100 °C (Panel F).

of urine, plasma, and extracts of small intestine obtained from animals administered the complexes 35 min earlier. As shown in Figure 4, $^{99m}Tc(CO)_3^+$−BPABA is still intact in plasma as well as in the wash from the small intestines. Because of the negligible urinary excretion of $^{99m}Tc(CO)_3^+$−BPABA (less than 8% ID) the HPLC profile of urine is not presented. Like $^{99m}Tc(CO)_3^+$−BPABA, $^{99m}Tc(CO)_3^+$−histidine is also intact in plasma and in urine. Because of the negligible hepatobilliary excretion of $^{99m}Tc(CO)_3^+$−histidine, an HPLC profile of small intestine wash was not obtained in this case. These results show that both $^{99m}Tc(CO)_3^+$−BPABA and $^{99m}Tc(CO)_3^+$−histidine are "stable" in vivo.

Table 1. Biodistribution in Normal Mice of $^{99m}Tc(CO)_3^+$−BPABA and $^{99m}Tc(CO)_3^+$−Histidine at 35 min[a]

	BPABA		histidine	
organ	mean	SD	mean	SD
	(a) %ID/g			
liver	8.72	2.38	2.77	0.27
heart	0.29	0.08	0.69	0.07
kidneys	4.27	1.72	6.65	1.32
lungs	0.55	0.10	1.94	0.11
spleen	0.40	0.15	0.83	0.12
muscle	0.13	0.05	0.38	0.02
blood	0.73	0.16	1.54	0.16
	(b) %ID/organ			
liver	14.95	3.23	5.49	1.05
heart	0.05	0.01	0.14	0.03
kidneys	2.78	1.11	5.27	1.25
lungs	0.12	0.02	0.43	0.04
spleen	0.04	0.01	0.09	0.03
stomach	1.08	0.15	0.65	0.12
sm. intestines	57.35	8.78	3.35	0.28
lg. intestines	5.14	1.19	0.57	0.07
muscle	1.83	0.64	6.90	0.63
blood	1.87	0.29	4.85	0.74
whole body	92.5	1.7	50.6	4.0

[a] Mean of %ID or %ID/g with standard deviation (SD), $n = 4$.

DISCUSSION

In this investigation, BPABA has been chosen as a model compound because of its ease of synthesis and the presence of a pendent carboxylate group for conjugation to biomolecules. In addition, the molecule was selected to avoid five- or six-membered chelation rings with the ^{99m}Tc tricarbonyl core. Thus free BPABA should exhibit similar labeling properties to conjugated BPABA and therefore should serve as a reliable model for the behavior of BPABA-conjugated biomolecules. The result of this investigation show that the properties of complex formation and stability of BPABA are comparable, if not superior to, that of histidine, often considered a model compound for ^{99m}Tc tricarbonyl labeling (*10, 11, 14*).

Our interest in tricarbonyl labeling is in connection with phosphodiamidate morpholino (MORF) pretargeting in which it will eventually be necessary to radiolabel MORF with ^{188}Re and in a manner that avoids unacceptably large reoxidation to $^{188}ReO_4^-$. Because of the recognized kinetic inertness of these complexes (*6*−*8*), tricarbony labeling of biomolecules via BPABA is expected to avoid the oxidation problem at least to a greater degree than experienced in this laboratory with a more conventional labeling method for ^{188}Re using MAG_3 as a chelator (*5*). However, a drawback to the use of the tricarbonyl strategy resulting from kinetic inertness is "high" chelator concentration required for quantitative labeling (*10, 11*), a phenomenon verified in this research. A chelator concentration of 10^{-4} or 10^{-5} M was required for a labeling efficiency of 90%, even with histidine. By contrast, the concentration of MAG_3 can be reduced to below 10^{-6} M when labeling MAG_3-conjugated MORF or phosphorothioate DNA while still achieving a labeling efficiency of over 90% (*21*).

Parenthetically, it may be worth mentioning that the results presented here on the properties of $^{99m}Tc(CO)_3$−BPABA suggest that this complex may have utility for imaging the hepatobiliary system. The ^{99m}Tc-labeled hepatobiliary imaging agents include ^{99m}Tc−IDAs (*22,*

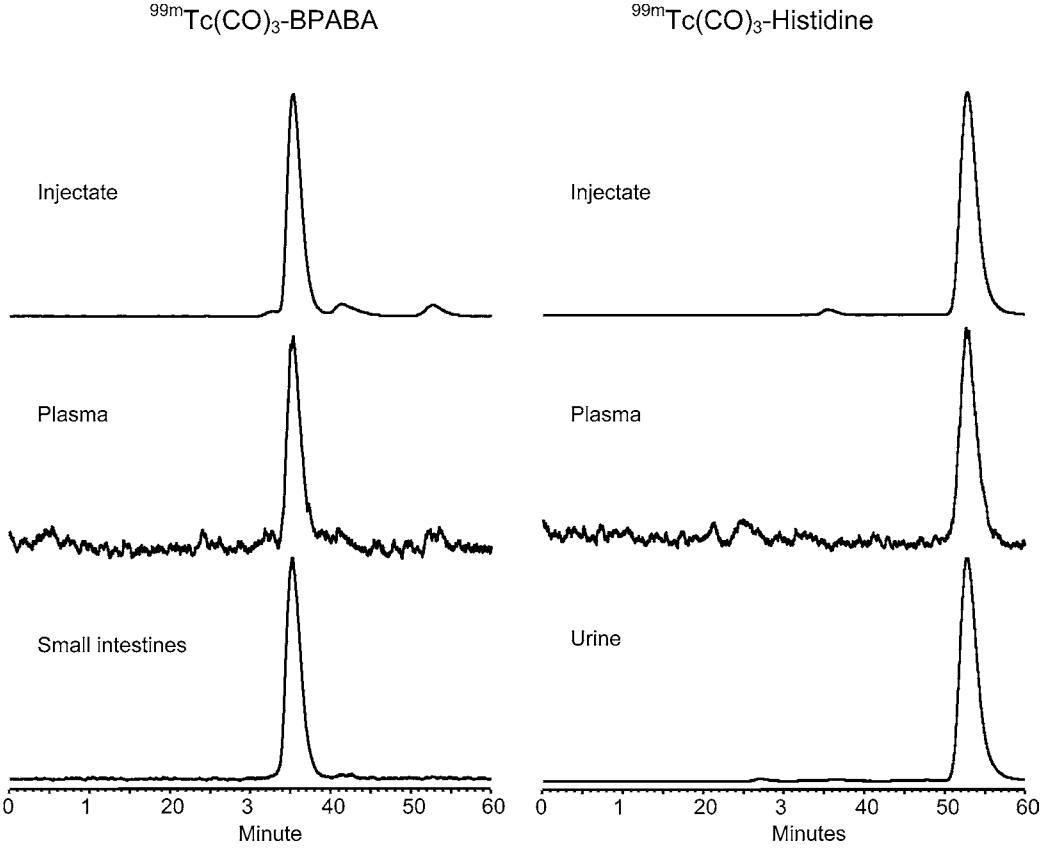


Figure 4. Radiochromatograms by SE HPLC (System 3) of ^{99m}Tc(CO)$_3^+$−BPABA injectate (top left panel) and ^{99m}Tc(CO)$_3^+$−histidine injectate (top right panel) and analysis of plasma (middle row), extract from the small intestines (in the case of ^{99m}Tc(CO)$_3^+$−BPABA) (left bottom panel), and urine (in the case of ^{99m}Tc(CO)$_3^+$-hisidine) (right bottom panel) from an animal injected 35 min earlier.

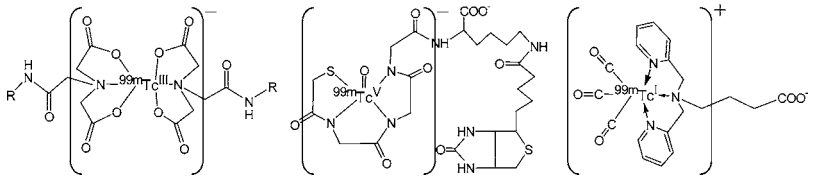


Figure 5. Structures of reported hepatobiliary specific imaging agents. (A) ^{99m}Tc−IDAs, (B) ^{99m}Tc−MAG$_3$−biocytin, and (C) ^{99m}Tc(CO)$_3^+$−BPABA.

23), ^{99m}Tc−pyridoxylidine glutamate (*24*), ^{99m}Tc−penicillamine (*25*), and ^{99m}Tc−MAG$_3$−biocytin (*26, 27*), with ^{99m}Tc−IDAs being the most extensively investigated. Both ^{99m}Tc−IDAs and ^{99m}Tc−MAG$_3$−biocytin are excreted exclusively via the hepatobiliary pathway in contrast to both ^{99m}Tc−pyriddoxylidine glutamate and ^{99m}Tc−penicillamine. Similar to the ^{99m}Tc−IDAs (<97% ID) and ^{99m}Tc−MAG$_3$−biocytin (>90%ID), ^{99m}Tc(CO)$_3$−BPABA is also cleared exclusively via the hepatobiliary pathway (97%ID).

The mechanism of hepatobiliary processing is reported to be different among these agents. As shown in Figure 5, the structures of the ^{99m}Tc−IDAs, ^{99m}Tc−MAG$_3$-biocytin and ^{99m}Tc(CO)$_3$−BPABA are fundamentally different and, as a result, each is expected to clear by a different mechanisms of hepatobiliary excretion. For example, ^{99m}Tc−IDAs and ^{99m}Tc−MAG$_3$-biocytin must clear by different mechanisms since only the former can be blocked by endogenous bilirubin (*26*) with the result that hepatobiliary function in patients with high serum bilirubin levels can be evaluated only with ^{99m}Tc−MAG$_3$-biocytin. Since ^{99m}Tc(CO)$_3$−BPABA possesses a different structure to those of ^{99m}Tc−IDAs and ^{99m}Tc−MAG$_3$-biocytin, the mechanism by which ^{99m}Tc(CO)$_3$−BPABA clears through the liver may be different as well. Therefore, should ^{99m}Tc(CO)$_3$−BPABA be investigated as a potential imaging agent for the hepatobiliary system, it may be shown to be cleared via a unique transporter, the function of which could then be evaluated.

CONCLUSION

The tridentate chelator *N*,*N*-bis(2-pyridylmethyl)-4-aminobutyric acid (BPABA) is easily synthesized and forms a "stable" complex with ^{99m}Tc(CO)$_3^+$. The property of stability might apply to radiorhenium as well for use in radiotherapy studies. Further development efforts are needed to improve the labeling recipes for high specific activity. Finally, the ^{99m}Tc(CO)$_3$−BPABA complex itself is hepatobiliary specific and might be useful in imaging malfunction of specific transporter in liver.

ACKNOWLEDGMENT

The authors are grateful to Mary Dyszlewski (Mallinckrodt Medical, St. Louis, MO) for providing the technetium tricarbonyl kits. Financial support for this investigation was provided in part by the National Institutes of Health (CA94994, CA107360, and CA79507).

LITERATURE CITED

(1) Liu, G.; Mangera, K.; Liu, N.; Gupta, S.; Rusckowski, M.; Hnatowich, D. J. (2002) Tumor pretargeting in mice using technetium-99m labeled morpholinos, a DNA analogue. *J. Nucl. Med*. *43*, 384−391.

(2) Liu, G.; Zhang, S.; He, J.; Liu, N.; Gupta, S.; Rusckowski, M.; Hnatowich, D. J. (2002) The Influence of Chain Length and Base Sequence on the Pharmacokinetic behavior of ^{99m}Tc−Morpholinos in Mice. *Q. J. Nucl. Med. 46*, 233−243.

(3) Liu, G.; Liu, C.; Zhang, S.; He, J.; Liu, N.; Gupta, S.; Rusckowski, M.; Hnatowich, D. J. (2003) Investigations of Technetium-99m Morpholino Pretargeting in Mice. *Nucl. Med. Commun*. *24*, 697−705.

(4) Liu, G.; He, J.; Dou, S.; Gupta, S.; Vanderheyden, J. L.; Rusckowski, M.; Hnatowich, D. J. (2004) Pretargeting in tumored mice with radiolabeled morpholino oligomer showing low kidney uptake. *Eur. J. Nucl. Med. Mol. Imaging. 31*, 417−424.

(5) Liu, C. B.; Liu, G. Z.; Liu, N.; Zhang, Y. M.; He, J.; Rusckowski, M.; Hnatowich, D. J. (2003) Radiolabeling morpholinos with ^{90}Y, ^{111}In, ^{188}Re and ^{99m}Tc. *Nucl. Med. Biol. 30*, 141−149.

(6) Alberto, R. (2003) $[Tc(CO)_3]^+$ chemistry: a promising new concept for SPET? For. *Eur. J. Nucl. Med. Mol. Imaging 30*, 1299−1302.

(7) Welch, M. J.; Lewis, J. S. (2003) $[Tc(CO)_3]^+$ chemistry: a promising new concept for SPECT? Against. *Eur. J. Nucl. Med. Mol. Imaging 30*, 1302−1304.

(8) Ballinger, J. R.; Cooper, M. S.; Mather, S. J. (2004) Re: Controversies-$[Tc(CO)_3]^+$ chemistry: a promising new concept for SPET? *Eur. J. Nucl. Med. Mol. Imaging 31*, 304−305 (letter).

(9) He, J.; Liu, C. B.; Vanderheyden, J-L.; Liu, G.; Dou, S.; Rusckowski, M.; Hnatowich, D. J. (2004) Radiolabeling morpholinos with ^{188}Re tricarbonyl provides improved in vitro and in vivo stability to reoxidation. *Nucl. Med. Commun*. *25*, 731−736.

(10) Egli, A.; Alberto, R.; Tannahill, L.; Schibli, R.; Abram, U.; Schaffland, A.; Waibel, R.; Tourwe, D.; Jeannin, L.; Iterbeke, K.; Schubiger, P. A. (1999) Organometallic ^{99m}Tc-aquaion labels peptide to an unprecedented high specific activity. *J. Nucl. Med*. *40*, 1913−1917.

(11) Schibli, R.; La Bella, R.; Alberto, R.; Garcia-Garayoa, E.; Ortner, K.; Abram, U.; Schubiger, P. A. (2000) Influence of the denticity of ligand systems on the in vitro and in vivo behavior of ^{99m}Tc(I)−tricarbonyl complexes: a hint for the future functionalization of biomolecules. *Bioconjugate Chem*. *11*, 345−351.

(12) Alberto, R.; Schibli, R.; Egli, A.; Schubiger, A. P. (1998) A novel organometallic aqua complex of technetium for the labeling of biomolecules: Synthesis of $[^{99m}Tc(OH_2)_3(CO)_3]^+$ from $[^{99m}TcO_4]^-$ in aqueous solution and its reaction with a bifunctional ligand. *J. Am. Chem. Soc*. *120*, 7987−7988.

(13) Stichelberger, A.; Waibel, R.; Dumas, C.; Schubiger, P. A.; Schibli, R. (2003) Versatile synthetic approach to new bifunctional chelating agents tailor-made for labeling with the fac-$[M(CO)_3]^+$ core (M = Tc, ^{99m}Tc, Re): synthesis, in vitro, and in vivo behavior of the model complex $[M(APPA)(CO)_3]$ (APPA = [(5-amino-pentyl)-pyridin-2-yl-methyl-amino]-acetic acid). *Nucl. Med. Biol*. *30*, 465−470.

(14) Pak, J. K.; Benny, P.; Spingler, B.; Ortner, K.; Alberto, R. (2003) N(epsilon) functionalization of metal and organic protected L-histidine for a highly efficient, direct labeling of biomolecules with $[Tc(OH_2)_3(CO)_3]^+$. *Chemistry 9*, 2053−2061.

(15) Kramer, D. J.; Davison, A.; Davis, W. M.; Jones, A. G. (2002) N−(2-Mercaptoethyl)picolylamine as a diaminomonothiolate ligand for the "fac-$[Re(CO)_3]^+$" core. *Inorg Chem*. *41*, 6181−6183.

(16) Pietzsch, H. J.; Gupta, A.; Reisgys, M.; Drews, A.; Seifert, S.; Syhre, R.; Spies, H.; Alberto, R.; Abram, U.; Schubiger, P. A.; Johannsen, B. (2000) Chemical and biological characterization of technetium(I) and rhenium(I) tricarbonyl complexes with dithioether ligands serving as linkers for coupling the $Tc(CO)_3$ and $Re(CO)_3$ moieties to biologically active molecules. *Bioconjugate Chem*. *11*, 414−424.

(17) Banerjee, S. R.; Levadala, M. K.; Lazarova, N.; Wei, L.; Valliant, J. F.; Stephenson, K. A.; Babich, J. W.; Maresca, K. P.; Zubieta, J. (2002) Bifunctional single amino acid chelates for labeling of biomolecules with the $[Tc(CO)_3]^+$ and $[Re(CO)_3]^+$ cores. Crystal and molecular structures of $[ReBr(CO)_3(H_2NCH_2C_5H_4N)]$, $[Re(CO)_3[(C_5H_4NCH_2)_2NH]]Br$, $[Re(CO)_3[(C_5H_4NCH_2)_2NCH_2CO_2H]]Br$, $[Re(CO)_3[X(Y)NCH_2CO_2CH_2CH_3]]Br$ (X = Y = 2-pyridylmethyl; X = 2-pyridylmethyl, Y = 2-(1-methylimidazolyl)methyl; X = Y = 2-(1-methylimidazolyl)methyl), $[ReBr(CO)_3[(C_5H_4NCH_2)NH(CH_2C_4H_3S)]]$, and $[Re(CO)_3[(C_5H_4NCH_2)N(CH_2C_4H_3S)(CH_2CO_2)]]$. *Inorg Chem*. *41*, 6417−6425.

(18) Liu, G.; Zhang, C.; Liu, F.; Wang, R.; Fu, Z.; Li, G.; Miao, Z. (2002) ^{99m}Tc-N,N′-bis(aminoethyl)propanediamine hexaacetic acid (BPHA): a glomerular filtration agent similar to ^{99m}Tc-DTPA. *Nucl. Med. Biol*. *29*, 399−404.

(19) Liu, G.-Z.; Liu, F.; Yang, T.; Miao, Z.-X.; Fang, J.-D. (2000) Structural consideration of divalent ion complexes of BPHA for fast renal excretion of ^{99m}Tc−BPHA. *J. Labelled Compd., Radiopharm*. *43*, 493−503.

(20) Fritzberg, A. R.; Kasina, S.; Eshima, D.; Johnson, D. L. (1986) Synthesis and biological evaluation of technetium-99m MAG_3 as a hippuran replacement. *J. Nucl. Med*. *27*, 111−116.

(21) Liu, G.; Zhang, S.; He, J.; Zhu, Z.; Rusckowski, Z.; Hnatowich, D. J. (2002) Improving the Labeling of *S*-Acetyl NHS-MAG_3-Conjugated Morpholino Oligomers. *Bioconjugate Chem. 13*, 893−897.

(22) Nunn, A. D.; Loberg, M. D.; Conley, R. A. (1983) A structure-distribution-relationship approach leading to the development of Tc-99m mebrofenin: an improved cholescintigraphic agent. *J. Nucl. Med*. 24, 423−430.

(23) Krishnamurthy, S.; Krishnamurthy, G. T. (1989) Technetium-99m-iminodiacetic acid organic anions: review of biokinetics and clinical application in hepatology. *Hepatology 9*, 139−153.

(24) Baker, R. J.; Bellen, J. C.; Ronai, P. M. (1975) Technetium-99m-pyridoxylideneglutamate: a new hepatobiliary radiopharmaceutical. I. Experimental aspects. *J. Nucl. Med*. *16*, 720−727.

(25) Tubis, M.; Krishnamurthy, G. T.; Endow, J. S.; Blahd, W. H. (1972) ^{99m}Tc-penicillamine, a new cholescintigraphic agent. *J. Nucl. Med*. *13*, 652−654.

(26) Kim, M.; Seidel, J.; Le, N.; Kim, I. S.; Yoo, T. M.; Barker, C.; Kobayashi, H.; Green, M. V.; Carrasquillo, J. A.; Paik, C. H. (1999) Evaluation of ^{99m}Tc-mercaptoacetyltriglycine-biocytin as a new hepatobiliary imaging agent in mice co-injected with bilirubin. *Nucl. Med. Biol*. *26*, 43−49.

(27) Jeong, J. M.; Kinuya, S.; Paik, C. H.; Saga, T.; Sood, V. K.; Neumann, R. C.; Reynolds, J. C.; Carrasquillo, J. A. (1993) Synthesis of a Tc-99m MAG_3-biotin conjugate as a biliary agent. *J. Labelled Compd. Radiopharm. 32*, 88−89.

BC049866A

^{18}F-Fluorothiols: A New Approach To Label Peptides Chemoselectively as Potential Tracers for Positron Emission Tomography†

Matthias Glaser,*,‡ Hege Karlsen,§ Magne Solbakken,§ Joseph Arukwe,§ Frank Brady,‡ Sajinder K. Luthra,‡ and Alan Cuthbertson§

Hammersmith Hospital, Hammersmith Imanet Ltd., Du Cane Road, London W12 0NN, U.K., and Medicinal Chemistry, Medical Diagnostics, GE Healthcare Bio-Sciences, P.O. Box 4220, Nydalen, N-0401 Oslo, Norway. Received May 26, 2004; Revised Manuscript Received August 31, 2004

[^{18}F]Fluorothiols are a new generation of peptide labeling reagents. This article describes the preparation of suitable methanesulfonyl precursors and their use in no-carrier-added radiosyntheses of ^{18}F-fluorothiols. The preparations of (3-[^{18}F]fluoropropylsulfanyl)triphenylmethane, (2-{2-[2-(2-[^{18}F]-fluoroethoxy)ethoxy]ethoxy}ethylsulfanyl)triphenylmethane, and 4-[^{18}F]fluoromethyl-*N*-[2-triphenylmethanesulfanyl)ethyl]benzamide starting from the corresponding methanesulfonyl precursors were investigated. Following the removal of the triphenylmethane protecting group, the ^{18}F-fluorothiols were reacted with the N-terminal chloroacetylated model peptide $ClCH_2C(O)$-LysGlyPheGlyLys. The corresponding radiochemical yields of ^{18}F-labeled isolated model peptide, decay-corrected to ^{18}F fluoride, were 10%, 32%, and 1%, respectively. These results indicate a considerable potential of ^{18}F-fluorothiols for the chemoselective labeling of peptides as tracers for positron emission tomography (PET).

INTRODUCTION

Radiolabeled peptides are important imgaging agents for nuclear medicine in general and for positron emission tomography (PET) in particular. This is reflected by the number of review articles (*1*−*5*). The positron emitter fluorine-18 ($T_{1/2}$ = 110 min) as a widespread positron emitter has been widely used to radiolabel peptides and proteins of medical interest. Although there are reports on direct incorporation of ^{18}F into peptides (*6*, *7*), the most promising approach still relies on the use of prelabeled ^{18}F reagents.

The majority of known ^{18}F reagents for peptide and protein labeling are targeting primary amino groups such as the N-terminus or lysine side chains. This is achieved through active esters (*8*−*10*), aldehydes (*11*), imidate (*12*), or azido functionalities (*2*). Fluorine-18-labeled amine was also coupled to a peptide with a prelabeled *N*-succinimidyl moiety (*13*). However, these peptide-coupling reactions are often low yielding, which is usually due to hydrolysis side reactions of the activated ^{18}F reagent. In addition, the synthesis of the ^{18}F prosthetic groups usually requires the time-consuming preparation and purification of multiple radioactive intermediates, reducing the available amount of ^{18}F at the end of synthesis. For instance, the production of the established *N*-succinimidyl *p*-[^{18}F]fluorobenzoate comprises three steps dealing with synthesis and purification of radioactive intermediates (*8*, *14*). More recently, efficient radiohalogenation was achieved by condensation of *p*-[^{18}F]fluorobenzaldehyde with aminooxy-modified peptide (*15*).

Alkylation reactions have only rarely been used for peptide labeling with fluorine-18-containing prosthetic groups. For example, one report mentions *p*-[^{18}F]fluorophenacyl bromide to label several proteins (*12*). However, there was no control on the binding site of the labeling reagent.

Alternatively, it is possible to take advantage of the high nucleophilicity of thiolates to couple an ^{18}F containing molecule with activated peptides. Here, we wish to describe the preparation of ^{18}F-prelabeled thiols and their chemoselective alkylation reaction with a chloroacetyl-modified model peptide.

RESULTS AND DISCUSSION

Precursors and [^{19}F]Fluoro Standard Compounds. Methanesulfonic acid 3-tritylsulfanyl-propyl ester **1** was prepared from 3-mercapto-1-propanol by reacting with trityl chloride and mesyl chloride (Scheme 1). The *S*-trityl-protected fluoro product **2** was obtained by fluoro demesylation of **1** using the KF−Kryptofix complex.

The PEG derivative **3** was designed in order to have a prosthetic group with potentially better pharmacologic properties available. Tetra(ethylene glycol) was thiolated by reacting its monotosylate with thiourea followed by hydrolysis of the resulting uronium salt. Reaction with trityl chloride and mesyl chloride gave mesylate precursor **3**. Reaction of **3** with tetrabutylammonium fluoride (TBAF) formed **4**.

The benzamide precursor **5** was devised as a reagent with improved UV−visiblity during chromatography. In the synthesis of **5**, cysteamine was S-tritylated using triphenylmethanol in trifluoroacetic acid (TFA). After coupling with 4-hydroxymethylbenzoic acid pentafluorophenyl ester, the hydroxymethyl function was mesy-

* Corresponding author. E-mail: mglaser@csc.mrc.ac.uk; Tel. +44(0) 20 8383 3162; Fax +44(0) 20 8383 3738.

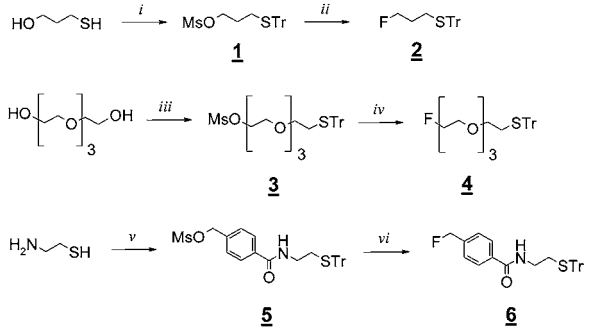
† A preliminary account of this work was presented at the 15th International Symposium on Radiopharmaceutical Chemistry in Sydney, Australia, August 10−14, 2003 [M. Glaser et al. (2003) *J. Labelled Compd. Radiopharm*. *46* S16].

‡ Hammersmith Imanet Ltd.

§ GE Healthcare Bio-Sciences.

10.1021/bc0498774 CCC: $27.50 © 2004 American Chemical Society
Published on Web 10/21/2004

Scheme 1. Preparation of the Trityl-Protected Fluorothiols 2, 4, and 6 from the Corresponding Mesylates 1, 3, and 5[a]



[a] Reagents and conditions: (*i*) 1. TrCl, NEt_3, 6 h; 2. MsCl, NEt_3, 30 min; (*ii*) KF, Kryptofix, 80 °C, 90 min; (*iii*) 1. TsCl, NEt_3, 17 h; 2. thiourea, EtOH, reflux, 24 h; 3. NaOH, reflux, 2.5 h; 4. TrCl, NEt_3, 7 h; 5. MsCl, NEt_3, 2 h; (*iv*) TBAF, 90 °C, 30 min; (*v*) 1. TrOH, TFA, NEt_3, 30 min; 2. 4-hydroxymethylbenzoic acid pentafluorophenyl ester, NMM, 36 h; 3. MsCl, NMP, 48 h; (*vi*) KF, Kryptofix, 65 °C, 10 min.

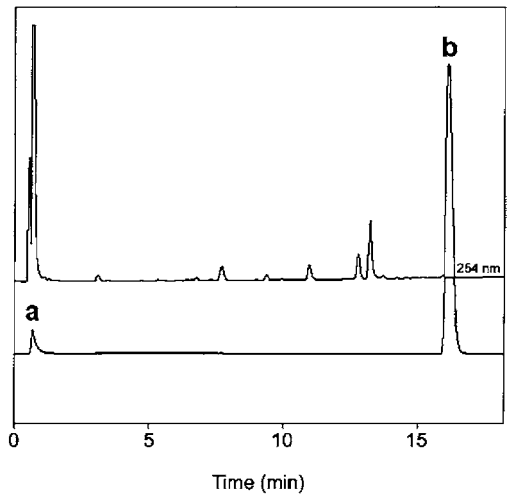


Figure 1. HPLC analysis of a reaction mixture of an ^{18}F-**2** preparation showing ^{18}F-**2** (b) (coeluted with standard **2**), and unreacted [^{18}F]fluoride (a).

lated. The fluoro standard **6** was prepared by reaction of **5** with KF−Kryptofix.

[^{18}F]Fluorothiols. The mesylate **1** gave only moderate yields of ^{18}F-**2** (24%) after a 5 min reaction with [^{18}F]KF−Kryptofix carbonate in acetonitrile at 80 °C as analyzed by HPLC. A plateau of 60% was reached after 30 min. DMF as solvent under identical conditions showed an improvement (72% after 30 min). However, DMSO proved to be the optimal solvent resulting in 79 ± 10% (n = 6) after already 5 min reaction time (Figures 1 and 2a).

The PEG-type mesylate **3** did react in DMSO somewhat slower using the above conditions. The maximum incorporation was observed after 15 min (77% of ^{18}F-**4**, Figure 2b). The yields in acetonitrile and DMF after 30 min were relatively low with 30% and 41%, respectively. The slower kinetics might be explained by the larger size of mesylate **3** compared with the small propyl compound **1**.

The benzamide mesylate **5** was tested using the experimental settings described. Here, the best yields of ^{18}F-**6** were obtained after reacting in acetonitrile for 5 min (25%, Figure 2c). The use of DMF and DMSO resulted only in yields of 7% and 17%, respectively (after 5 min), suggesting that the choice of solvent may have little impact on labeling efficiency. The benzyl mesylate

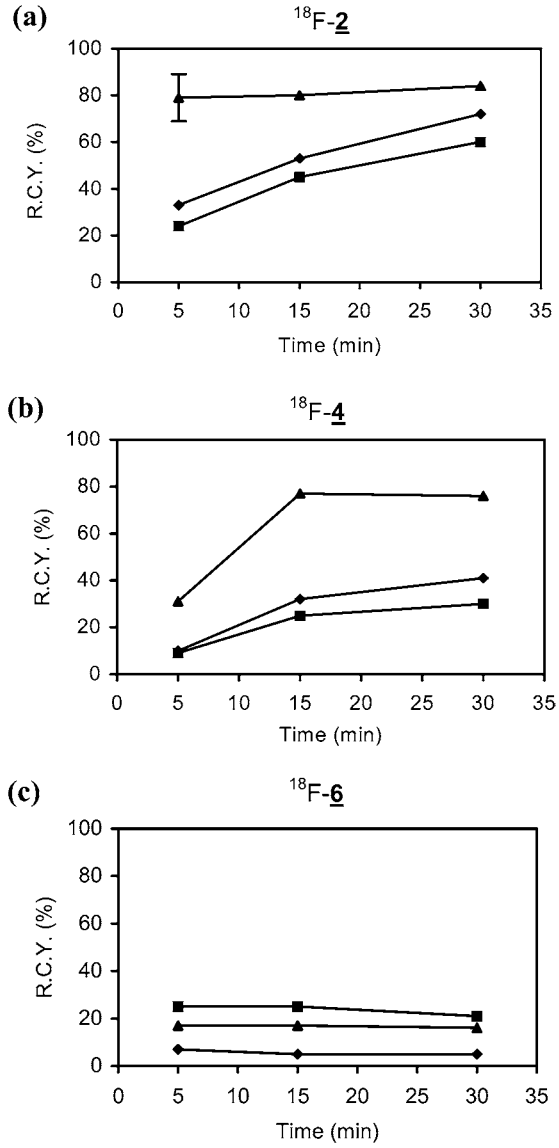


Figure 2. Radiolabeling yields of (a) ^{18}F-**2**, (b) ^{18}F-**4**, and (c) ^{18}F-**6** in DMSO (▲), DMF (◆), or MeCN (■) as obtained from HPLC analysis.

group is highly activated toward nucleophilic displacements as it was already observed during the ^{19}F labeling work. In those studies the mesylate **5** HPLC signal quickly degraded as a new peak appeared instead. This compound was identified as 4-hydroxymethyl-*N*-[2-(tritylsulfanyl)ethyl]benzamide. A similar behavior could be seen in the synthesis of ^{18}F-**6**. At the present this effect is not fully understood as the reaction was carried out in a strictly anhydrous environment. The ^{18}F-fluorodemesylation of **5** was also investigated at lower temperatures. The reaction occurred already at room temperature forming 22% of ^{18}F-**6** after 7 min. After that time, HPLC analysis revealed complete consumption of **5**. Cooling to −17 °C followed by warming up to room temperature gave no ^{18}F-**6** but only the hydrolysis product mentioned above. In an experiment without potassium carbonate neither hydroxy product or ^{18}F-**6** were detected after 5 min at room temperature and heating for 15 min at 80 °C. Obviously, the yields of ^{18}F-**6** might be still improved either by testing some alternative bases with the ^{18}F−Kryptofix complex or by using higher substrate concentrations of **5**.

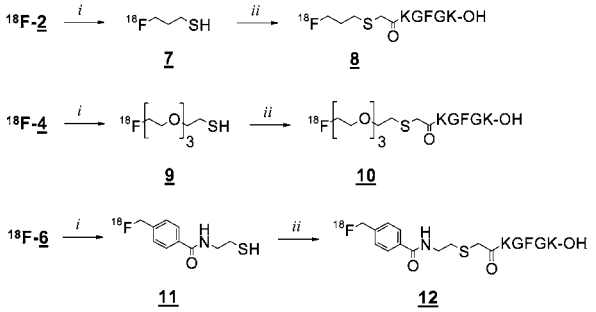
Further, our experiments indicated some degradation of already formed ^{18}F-**6** in all three solvent systems after

Table 1. Radiochemical Yields (rcy) of [^{18}F]Fluoropeptides 8, 10, and 12 Including Intermediates

mesylate precursor	**1**	**3**	**5**
S-Tr protected ^{18}F-reagent[a]	79 ± 10%[c] (^{18}F-**2**)	77% (^{18}F-**4**)	21% (^{18}F-**6**)
^{18}F-fluorothiol[a]	88% (^{18}F-**7**)	95% (^{18}F-**9**)	74% (^{18}F-**11**)
^{18}F-fluoropeptide[a]	93% (^{18}F-**8**)	41% (^{18}F-**10**)	86% (^{18}F-**12**)
rcy of ^{18}F-fluoropeptide[b]	10% (^{18}F-**8**)	32% (^{18}F-**10**)	1% (^{18}F-**12**)

[a] Yields based on analytical HPLC, referring to individual steps. [b] Yields of isolated ^{18}F-fluoropeptide, based on [^{18}F]fluoride and corrected for decay. [c] $n = 6$.

Scheme 2. Preparation [^{18}F]Fluorothiols 7, 9, and 11 as Labeling Reagents for the Corresponding [^{18}F]Fluoropeptides 8, 10, and 12[a]



[a] Reagents and conditions: (*i*) 1. ^{t}C18-SepPak-plus; 2. TFA/TIS/H_2O; (*ii*) $ClCH_2C(O)$-KGFGK-OH, pH 9−10, 70−80 °C, 30 min.

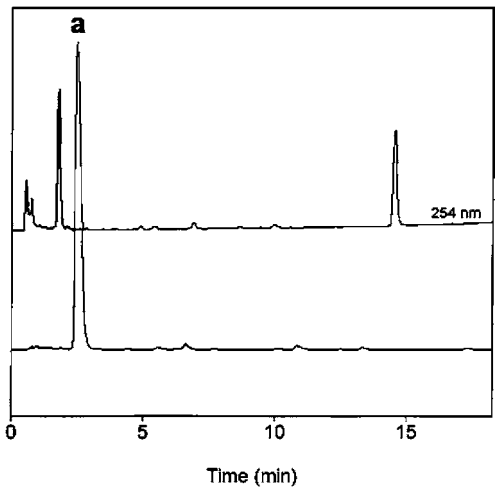


Figure 3. HPLC analysis of the reaction mixtures of the deprotection product ^{18}F-**7** (a).

5−15 min heating. In fact, the stability of ^{18}F-fluorobenzyl derivatives has been recently studied by others (*16*).

Peptide Labeling with [^{18}F]Fluorothiols. After its preparation, the *S*-trityl compound ^{18}F-**2** could be quantitatively transferred from DMSO into acetonitrile using a C18 SepPak cartridge. The radiochemical purity of ^{18}F-**2** was >99%. The trityl protecting group was removed with TFA in the presence of triisopropylsilane (TIS) to form **7** in good yield (Scheme 2, Figure 3, Table 1). The *N*-chloroacetylated model peptide $ClCH_2C(O)$-KGFGK-OH could be labeled in excellent yield. An analytical HPLC trace of the labeling mixture is shown in Figure 4.

Following identical protocols, the [^{18}F]fluorothiol compounds ^{18}F-**4** and ^{18}F-**6** were deprotected to react with the chloroacetyl peptide to form **9** and **11**, respectively. The efficiencies of the single steps are summarized in Table 1.

An investigation to test the stability of deprotected thiol **7** was carried out. This experiment suggested poor stability of the ^{18}F-thiol at pH 9−10 at room temperature.

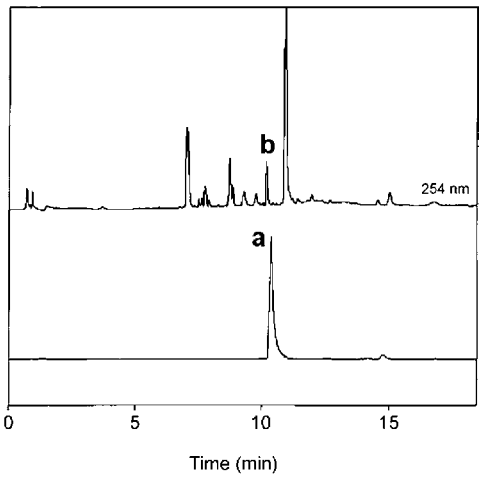


Figure 4. HPLC analysis of the reaction mixture of the labeled peptide ^{18}F-**8** (a) with spiked standard **8** (b).

After 1 h the HPLC signal of **7** was completely degraded. The use tris(2-carboxyethyl)phosphine (TCEP) as stabilizer was considered. TCEP as a selective reductant for disulfides has been described to be superior to dithiothreitol (*17*, *18*). Thiol **7** showed high stability in the presence of TCEP. Therefore, an additive of this stabilizer was used in the subsequent peptide labeling work.

The isolated radiochemical yields of [^{18}F]fluoropeptides **8**, **10**, and **12** are listed in Table 1. Both the reduced thermal stability of the ^{18}F-fluorobenzyl group and loss of radiolabeled peptide during the final HPLC purification possibly led to a decreased radiochemical yield of peptide **12**.

Only low levels of radioactivity of ^{18}F have been used for this study, and therefore, specific radioactivities have not been measured.The total synthesis time was 2−3 h.

CONCLUSIONS

[^{18}F]Fluorothiols have been introduced as a new group of no-carrier-added ^{18}F-reagents to label peptides as tracers for PET. The chloroacetyl function was used to chemoselectively enable the binding of the prosthetic ^{18}F-group to a model peptide. The protocol simplifies peptide labeling because the reagent is prepared in only two steps that involved handling of ^{18}F. In addition, there was also no need to purify the ^{18}F-compound. The radiochemistry should be easily amenable to automation.

MATERIALS AND METHODS

Preparation of Precursors and Standards. Chemicals. Fmoc amino acids, the Fmoc-Lys(Boc)-Sasrin resin, and peptide coupling reagents were purchased from Novabiochem, Bachem, and Applied Biosystems, respectively. 4-Hydroxymethylbenzoic acid pentafluorophenyl ester was obtained from MilliGen. All other reagents and solvents were purchased from Acros, Aldrich, or Fluka.

Mass spectra were recorded on a Finnigan LCQ system using electrospray ionization (ESI). MALDI-TOF mass spectra were measured on a Finnigan Lasermat 2000

instrument. Accurate mass spectra (HRMS) were measured on a Micromass Q-Tof Ultima machine coupled with a nano-LC system using Mass Lynx 3.5 software. NMR spectra were obtained from a Varian Unity Inova 500 instrument at 25 °C using a 5 mm $^1H\{^{15}N-^{31}P\}$ indirect detection pfg probe. Analytical and semipreparative reversed-phase HPLC using different gradients [solvent A: water (0.1% TFA), solvent B: acetonitrile (0.1% TFA)], and UV detection at 214 and 254 nm were performed on Shimadzu, Beckman, or Waters chromatography systems.

Cl-Ac-Lys-Gly-Phe-Gly-Lys-OH. Assembly of the amino acid sequence Lys-Gly-Phe-Gly-Lys-OH was done using fully automated synthesis (ABI 433A synthesis machine) with Fmoc-Lys(Boc)-Sasrin resin (0.25 mmol) using the Fastmoc Single Couple procedure with HBTU activation. Chloroacetic acid was coupled manually using chloroacetic anhydride (1.25 mmol). Simultaneous removal of the peptide from the resin and deprotection of side-chain protecting groups were carried out in trifluoroacetic acid containing triisopropylsilane and water (95: 2.5:2.5 v/v/v). After filtration, the solution was concentrated under reduced pressure and the residue was washed with diethyl ether. The crude product was purified by reversed-phase preparative chromatography (Phenomenex Luna C18(2) column, 250 × 50 mm, 10 μm; gradient 0−30% solvent B over 60 min; flow rate 50 mL/minute), affording 128 mg (83%) of pure compound. The product was analyzed by HPLC [Phenomenex Luna C18-(2), 50 × 4.6 mm, 5 μm; gradient 0−30% solvent B over 10 min; flow rate 2 mL/min; t_R = 5.1 min] and MS, *m/z* = 612.8 $(M + H)^+$; HRMS: found *m/z* = 612.2936 $(M + H)^+$ for $C_{27}H_{42}N_7O_7Cl$ calcd *m/z* = 612.2907.

Methanesulfonic Acid 3-Tritylsulfanylpropyl Ester 1. A solution of triphenylmethanol (391 mg, 1.50 mmol) in trifluoroacetic acid (10 mL) was added dropwise to a stirred solution of 3-mercaptopropyl alcohol (127 μL, 1.50 mmol) in trifluoroacetic acid (10 mL). The trifluoroacetic acid was evaporated under reduced pressure immediately after mixing of the reagents. The crude product was purified by reversed-phase preparative chromatography (Phenomenex Luna C18(2) column, 250 × 50 mm, 10 μm; gradient 70−80% solvent B over 60 min; flow rate 50 mL/min), affording 372 mg (74%) of pure compound (mp 122−125 °C). ^1H NMR (chloroform-*d*, 500 MHz): 7.40−7.44 (m, 6H, trityl *o*-H); 7.26−7.31 (m, 6H, trityl *m*-H); 7.19−7.24 (m, 3H, trityl *p*-H); 3.56 (t, 2H, $^3J_{HH}$ = 6.2 Hz, CH_2O); 2.28 (t, 2H, $^3J_{HH}$ = 7.2 Hz, CH_2S); 1.62 (t of t, 2H, $^3J_{HH}$ = 6.2 Hz, $^3J_{HH}$ = 7.2 Hz, $OCH_2CH_2CH_2S$).

To a solution of 3-tritylsulfanylpropan-1-ol (372 mg, 1.11 mmol) in tetrahydrofuran (10 mL) were added triethylamine (209 μL, 1.50 mmol) and methanesulfonyl chloride (117 μL, 1.50 mmol). The precipitate was filtered off after stirring at room temperature for 1 h. Tetrahydrofuran was evaporated under reduced pressure, and the crude product was purified by reversed-phase preparative chromatography (Phenomenex Luna C18(2) column, 250 × 50 mm, 10 μm; gradient 80−100% solvent B over 60 min; flow rate 50 mL/min), affording 318 mg (69%) of pure compound (mp 122−125 °C). ^1H NMR (chloroform-*d*, 500 MHz): 7.39−7.44 (m, 6H, trityl *o*-H); 7.26−7.32 (m, 6H, trityl *m*-H); 7.19−7.24 (m, 3H, trityl *p*-H); 4.13 (t, 2H, $^3J_{HH}$ = 6.4 Hz, CH_2O); 2.92 (s, 3H, CH_3S); 2.29 (t, 2H, $^3J_{HH}$ = 7.1 Hz, CH_2S); 1.71 (t of t, 2H, $^3J_{HH}$ = 6.4 Hz, $^3J_{HH}$ = 7.1 Hz, $OCH_2CH_2CH_2S$).

(3-Fluoropropylsulfanyl)triphenylmethane 2. Potassium fluoride (1.4 mg, 0.024 mmol) and Kryptofix (9 mg, 0.024 mmol) were dissolved in acetonitrile (0.2 mL) with heating. A solution of mesylate **1** (5 mg, 0.012 mmol) in acetonitrile (0.2 mL) was added. The mixture was heated at 80 °C for 90 min. The crude product was purified by HPLC (Vydac 218TP column, C18, 250 × 22 mm, 10 μm; gradient 40−90% B in 40 min; flow rate 10 mL/min; λ = 254 nm). The yield of **2** was 2 mg (50%). The product was analyzed by HPLC [Phenomenex Luna C18(2) column, 50 × 4.6 mm, 3 μm; gradient 40−80% solvent B in 10 min; flow rate 1 mL/min; t_R = 7.12 min, λ = 254 and 214 nm] and ^1H NMR (chloroform-*d*, 500 MHz): 7.39−7.44 (m, 6H, trityl *o*-H); 7.26−7.31 (m, 6H, trityl *m*-H); 7.19−7.24 (m, 3H, trityl *p*-H); 4.36 (d of t, 2H, $^2J_{HF}$ = 47.2 Hz, $^3J_{HH}$ = 5.9 Hz, CH_2F); 2.28 (t, 2H, $^3J_{HH}$ = 7.3 Hz, CH_2S); 1.72 (d of t of t, 2H, $^3J_{HF}$ = 25.4 Hz, $^3J_{HH}$ = 5.9 Hz, $^3J_{HH}$ = 7.3 Hz, $FCH_2CH_2CH_2S$).

Methanesulfonic Acid 2-{2-[2-(2-Tritylsulfanylethoxy)ethoxy]ethoxy}ethyl Ester 3. Triethylamine (13 mL, 93 mmol) was added to a stirred solution of *p*-toluenesulfonyl chloride (9.82 g, 51.5 mmol) in tetra(ethylene glycol) (20.0 g, 103 mmol) at 0 °C. The suspension was stirred at 0 °C for 1 h and at room temperature for 16 h. After adding of dichloromethane (350 mL), the solution was extracted with hydrochloric acid (1 M, 2 × 100 mL) and water (200 mL). The organic phase was dried ($MgSO_4$). After concentration, the product was purified by flash chromatography (ethyl acetate, first fraction: tetra(ethylene glycol) ditosylate) to give *p*-toluenesulfonic acid 2-{2-[2-(2-hydroxyethoxy)ethoxy]-ethoxy}ethyl ester as a colorless oil (8.9 g, 49%). ^1H NMR (chloroform-*d*, 500 MHz): 7.78−7.83 (m, 2H, $CH_3C_6H_4S$); 7.32−7.37 (m, 2H, $CH_3C_6H_4S$); 4.15−4.19 (m, 2H, $SOCH_2CH_2$); 3.58−3.74 (m, 14H, OCH_2CH_2); 2.45 (s, 3H, $CH_3C_6H_4S$).

A solution of thiourea (0.94 g, 12 mmol) and *p*-toluenesulfonic acid 2-{2-[2-(2-hydroxyethoxy)ethoxy]ethoxy}-ethyl ester (4.09 g, 11.8 mmol) in absolute ethanol (32 mL) was heated at reflux for 24 h under argon. The reaction mixture was cooled and a solution of sodium hydroxide (1.23 g, 30.8 mmol) in ethanol/water (9:1 v/v, 15 mL) was added. The mixture was refluxed under argon for 2.5 h, cooled to room temperature and acidified to pH 2 (concentrated HCl). After concentration the residue was purified by flash chromatography (ethyl acetate/ethanol, 10:1 v/v) to give 2-{2-[2-(2-mercaptoethoxy)ethoxy]ethoxy}-ethanol as a colorless oil (1.6 g, 66%).

^1H NMR (chloroform-*d*, 500 MHz): 3.72−3.76 (m, 2H, OCH_2CH_2O); 3.60−3.71 (m, 12H, OCH_2CH_2); 2.71 (d of t, 2H, $^3J_{HH}$ = 8.1 Hz, $^3J_{HH}$ = 6.6 Hz, $HSCH_2CH_2O$); 2.41 (broad s, 1H, $HOCH_2CH_2O$); 1.63 (t, 1H, $^3J_{HH}$ = 8.1 Hz, $HSCH_2CH_2O$).

To 2-{2-[2-(2-mercaptoethoxy)ethoxy]ethoxy}ethanol (310 mg, 1.47 mmol) and trityl chloride (452 mg, 1.62 mmol) under argon was added simultaneously triethylamine (2.1 mL, 14.7 mmol) and tetrahydrofuran (25 mL). After stirring for 7 h, methanol (6 mL) was added and stirring was continued for 5 min. The product was isolated by flash chromatography (ethyl acetate) to give 2-{2-[2-(2-tritylsulfanylethoxy)ethoxy]ethoxy}ethanol as a colorless oil (550 mg, 83%). ^1H NMR (chloroform-*d*, 500 MHz): 7.39−7.43 (m, 6H, trityl *o*-H); 7.25−7.30 (m, 6H, trityl *m*-H); 7.18−7.23 (m, 3H, trityl *p*-H); 3.68−3.72 (broad m, 2H, CH_2OH); 3.61−3.67 (m, 4H, OCH_2CH_2O); 3.57−3.60 (m, 2H, OCH_2CH_2OH); 3.56−3.59 (m, 2H, OCH_2CH_2O); 3.43−3.47 (m, 2H, OCH_2CH_2O); 3.30 (t, 2H, $^3J_{HH}$ = 6.9 Hz, OCH_2CH_2S); 2.44 (t, 2H, $^3J_{HH}$ = 6.9 Hz, OCH_2CH_2S); 2.40 (broad t, 1H, $^3J_{HH}$ = 5.8 Hz, OCH_2CH_2OH).

Methanesulfonyl chloride (47 μL, 0.60 mmol) was added to a stirred solution of tetrahydrofuran (12 mL),

2-{2-[2-(2-tritylsulfanylethoxy)ethoxy]ethoxy}ethanol (227 mg, 0.500 mmol), and triethylamine (139 μL, 1.00 mmol). After stirring for 2 h, the mixture was filtered and concentrated. The residue was purified by flash chromatography (ethyl acetate) affording **3** as a colorless oil (238 mg, 90%). ^{1}H NMR (chloroform-*d*, 300 MHz): 7.38−7.45 (m, 6H, trityl *o*-H); 7.17−7.32 (m, 9H, trityl *m*-H and *p*-H); 4.33−4.37 (m, 2H, S(O)$_2$O*CH*$_2$CH$_2$O); 3.71−3.77 (m, 2H, S(O)$_2$OCH$_2$*CH*$_2$O); 3.58−3.68 (m, 4H, O*CH*$_2$*CH*$_2$O); 3.41−3.58 (m, 4H, O*CH*$_2$*CH*$_2$O); 3.3 (t, 2H, O*CH*$_2$CH$_2$S, $^3J_{HH}$ = 6.9 Hz); 2.99 (s, 3H, CH$_3$S); 2.42 (t, 2H, OCH$_2$*CH*$_2$S, $^3J_{HH}$ = 6.9 Hz).

(2-{2-[2-(2-Fluoroethoxy)ethoxy]ethoxy}ethyl)trityl Sulfide 4. A stirring solution of **3** (71.7 mg, 0.14 mmol) and tetrabutylammonium fluoride (1.1 M in tetrahydrofuran, 127 μL, 0.14 mmol) was heated at 90 °C for 30 min. The solvent was evaporated, and the residue was purified by flash chromatography (ethyl acetate/hexane, 1/1) to give **4** as a colorless oil (45 mg, 70%). ^{1}H NMR (chloroform-*d*, 500 MHz): 7.40−7.45 (m, 6H, trityl *o*-H); 7.25−7.31 (m, 6H, trityl *m*-H); 7.25−7.31 (m, 3H, trityl *p*-H); 4.47−4.60 (d of m, 2H, $^2J_{HF}$ = 47.8 Hz, F*CH*$_2$CH$_2$O); 3.68−3.78 (d of m, 2H, $^3J_{HF}$ = 29.6 Hz, FCH$_2$*CH*$_2$O); 3.62−3.68 (m, 4H, O*CH*$_2$*CH*$_2$O); 3.44−3.60 (m, 4H, O*CH*$_2$*CH*$_2$O); 3.31 (t, 2H, $^3J_{HH}$ = 6.9 Hz, O*CH*$_2$-CH$_2$S); 2.44 (t, 2H, $^3J_{HH}$ = 6.9 Hz, OCH$_2$*CH*$_2$S); HRMS: found *m/z* = 472.2333 (M + NH$_4$)$^+$ for C$_{27}$H$_{31}$O$_3$SF calcd *m/z* = 472.2316.

Methanesulfonic Acid 4-[2-(Tritylsulfanyl)ethylcarbamoyl]benzyl Ester 5. To a stirred solution of cysteamine (3.85 g, 50.0 mmol) in trifluoroacetic acid (50 mL) was added triphenylmethanol (13.0 g, 50.0 mmol). The mixture was stirred at room temperature for 30 min and concentrated. After addition of diethyl ether (250 mL), the precipitate was filtered off and washed with diethyl ether (2 × 50 mL). The trifluoroacetic acid salt was partitioned between aqueous KOH solution (1 M, 150 mL) and diethyl ether (150 mL). The organic phase was dried (MgSO$_4$) and *S*-tritylcysteamine was crystallized from diethyl ether/*n*-hexane to give a white solid (9.2 g, 58%). ESI-MS: *m/z* = 243 (M − Ph)$^{\bullet+}$; ^{1}H NMR (chloroform-*d*, 500 MHz): 7.41−7.44 (m, 6H, trityl *o*-H); 7.25−7.30 (m, 6H, trityl *m*-H); 7.19−7.23 (m, 3H, trityl *p*-H); 2.60 (t, 2H, $^3J_{HH}$ = 6.6 Hz, CH$_2$N); 2.32 (t, 2H, $^3J_{HH}$ = 6.6 Hz, CH$_2$S); 1.07 (broad s, 2H, NH$_2$).

To a solution of *S*-trityl cysteamine (1.6 g, 5.0 mmol) and 4-hydroxymethylbenzoic acid pentafluorophenyl ester (1.5 g., 5.0 mmol) in dichloromethane (40 mL) was added *N*-methylmorpholine (0.55 mL, 5.0 mmol). After stirring at room temperature for 36 h, the precipitate was filtered off, washed with dichloromethane (3 × 5 mL), and dried to give 4-hydroxymethyl-*N*-[2-(tritylsulfanyl)-ethyl]benzamide as a white solid (1.3 g, 57%). ESI-MS: *m/z* = 476 (M + Na$^+$); ^{1}H NMR (DMSO-d_6, 500 MHz): 8.53 (t, 1H, $^3J_{HH}$ = 5.7 Hz, NH); 7.75−7.79 (m, 2H, OCH$_2$*C*$_6$*H*$_4$CO); 7.36−7.40 (m, 2H, OCH$_2$*C*$_6$*H*$_4$CO); 7.29−7.35 (m, 12H, trityl *o*-H and *p*-H); 7.22−7.28 (m, 3H, trityl *p*-H); 5.29 (t, 1H, $^3J_{HH}$ = 5.6 Hz, OH); 5.54 (d, 2H, $^3J_{HH}$ = 5.6 Hz, CH$_2$O); 3.23 (d of t, 2H, $^3J_{HH}$ = 5.7 Hz, $^3J_{HH}$ = 7.1 Hz, CH$_2$N); 2.33 (t, 2H, $^3J_{HH}$ = 7.1 Hz, CH$_2$S).

To a solution of 4-hydroxymethyl-*N*-[2-(tritylsulfanyl)-ethyl]benzamide (226 mg, 0.50 mmol) in anhydrous tetrahydrofuran (8 mL) were added *N*-methyl-2-pyrrolidinone (61 μL, 0.55 mmol) and methanesulfonyl chloride (85 μL, 1.1 mmol). The reaction mixture was stirred for 48 h at room temperature and filtered through silica. Purification by column chromatography (silica, 1% methanol in chloroform) gave **5** as an oil that solidified slowly on storage (213 mg, 80%). ^{1}H NMR (chloroform-*d*, 500 MHz): 7.72−7.76 (m, 2H, OCH$_2$*C*$_6$*H*$_4$CO); 7.46−7.50 (m, 2H, OCH$_2$*C*$_6$*H*$_4$CO); 7.40−7.44 (m, 6H, trityl *o*-H); 7.24−7.30 (m, 6H, trityl *m*-H); 7.19−7.24 (m, 3H, trityl *p*-H); 6.23 (broad t, 1H, $^3J_{HH}$ = 5.7 Hz, NH); 5.28 (s, 2H, CH$_2$O); 3.30 (d of t, 2H, $^3J_{HH}$ = 5.7 Hz, $^3J_{HH}$ = 6.2 Hz, CH$_2$N); 2.55 (t, 2H, $^3J_{HH}$ = 6.2 Hz, CH$_2$S); 2.97 (s, 3H, CH$_3$S).

4-Fluoromethyl-*N*-[2-(tritylsulfanyl)ethyl]benzamide 6. A solution of Kryptofix (15 mg, 40 μmol) in anhydrous acetonitrile (0.2 mL) was added to solid potassium fluoride (2.3 mg, 80 μmol). The mixture was shaken for 5 min and added to **5** (21 mg, 40 μmol) in acetonitrile (0.4 mL) followed by heating at 65 °C for 10 min. Product **6** was isolated by preparative HPLC [Phenomenex Luna C18 (2) column, 250 × 21.2 mm, 5 μm; gradient 40−80% solvent B over 10 min; flow rate 10 mL/min] as a white solid (4.5 mg, 25%). ^{1}H NMR (chloroform-*d*, 500 MHz): 7.71−7.75 (m, 2H, FCH$_2$*C*$_6$*H*$_4$CO); 7.42−7.44 (m, 2H, FCH$_2$*C*$_6$*H*$_4$CO); 7.40−7.44 (m, 6H, trityl *o*-H); 7.24−7.29 (m, 6H, trityl *m*-H); 7.19−7.23 (m, 3H, trityl *p*-H); 6.23 (broad t, 1H, $^3J_{HH}$ = 5.8 Hz, NH); 5.44 (d, 2H, $^2J_{HF}$ = 47.4 Hz, CH$_2$F); 3.65 (d of t, 2H, $^3J_{HH}$ = 5.8 Hz, $^3J_{HH}$ = 6.5 Hz, CH$_2$N); 2.55 (t, 2H, $^3J_{HH}$ = 6.5 Hz, CH$_2$S); HRMS: found *m/z* = 478.1624 (M + Na)$^+$ for C$_{29}$H$_{26}$OSF calcd *m/z* = 478.1611.

6-Amino-2-{2-[2-(2-{6-amino-2-[2-(3-fluoropropylsulfanyl)acetylamino]hexanoylamino}acetylamino)-3-phenylpropionylamino]acetylamino}hexanoic Acid (^{19}F-8). The trityl compound **2** (1 mg, 3 μmol) was deprotected with a mixture of trifluoroacetic acid (25μL), triisopropylsilane (5 μL), and water (5μL) at room temperature for 5 min. The mixture was cooled to 0 °C, a solution of ClAc-KGFGK-OH (3.6 mg, 6 μmol) in water (1 mL) added, followed by adjusting the pH to 9 (25% ammonia), and heating for 30 min at 60 °C. Product ^{19}F-**8** was isolated by preparative HPLC [Phenomenex C18(2) column, 250 × 10 mm, 10 μm; gradient 0−30% solvent B in 30 min; flow rate 5 mL/min; λ = 254 nm] with 0.5 mg (20%) yield. The labeled peptide was characterized by LC-MS [Phenomenex Luna C18(2) column, 50 × 4.6 mm, 3 μm, gradient 0−30% solvent B in 30 min; flow rate 1 mL/min; λ = 214 and 254 nm, R_f = 6.88 min, *m/z* = 670.35 (M + H)$^+$]; HRMS: found *m/z* = 670.3410 (M + H)$^+$ for C$_{30}$H$_{48}$N$_7$O$_7$FS calcd *m/z* = 670.3393.

6-Amino-2-{2-[2-(2-{6-amino-2-[2-(2-{2-[2-(2-fluoroethoxy)ethoxy]ethoxy}ethylsulfanyl)acetylamino]-hexanoylamino}acetylamino)-3-phenylpropionylamino]acetylamino}hexanoic Acid (^{19}F-10). To a vial containing trityl compound ^{19}F-**4** (1.2 μmol) was added a trifluoroacetic acid/triisopropylsilane/water mixture (95:2.5:2.5 v/v/v, 130 μL). After gentle agitating for 5 min, the mixture was concentrated in vacuo and sodium carbonate/bicarbonate buffer (0.1 M, pH 9.1, 0.1 mL) was added followed by a solution of ClAc-KGFGK-OH (3.6 mg, 6.0 μmol) in sodium carbonate/bicarbonate buffer (0.1 M, pH 9.1, 0.15 mL). The coupling product ^{19}F-**10** was purified by preparative HPLC [Phenomenex Luna C18(2) column, 250 × 10 mm, 10 μm; gradient 40−80% solvent B over 30 min; flow rate 5 mL/min] giving a yield of 4.0 mg (42%). The labeled peptide ^{19}F-**10** was characterized by MALDI-MS, *m/z* = 788 (M + H)$^+$; HRMS: found *m/z* = 788.4061 (M + H)$^+$ for C$_{35}$H$_{58}$N$_7$O$_{10}$FS calcd *m/z* = 788.4023.

6-Amino-2-(2-{2-[2-(6-amino-2-{2-[2-(4-fluoromethylbenzoylamino)ethylsulfanyl]acetylamino}hexanoylamino)acetylamino]-3-phenylpropionylamino}-acetylamino)hexanoic Acid (^{19}F-12). The labeled peptide ^{19}F-**12** was synthesized using the protocol for the preparation of ^{19}F-**10**.

The coupling product ^{19}F-**12** was purified by preparative HPLC [Phenomenex Luna C18(2) column, 250 × 21.2

mm, 5 μm; gradient 5−60% acetonitrile over 60 min; flow rate 10 mL/min] yielding 2 mg (42%) of a white solid. The labeled peptide was characterized by LC-MS [Phenomenex Luna C18(2) column, 50 × 4.6 mm, 3 μm; gradient 5−60% acetonitrile over 10 min; flow rate 0.3 mL/min, t_R = 4.3 min, m/z = 789.4 ($M + H^+$)]; HRMS: found m/z = 789.3743 $(M + H)^+$ for $C_{37}H_{53}N_8O_8SF$ calcd m/z = 789.3764.

Radiochemistry. Chemicals. Chemicals including anhydrous solvents were purchased from Sigma-Aldrich (Gillingham, UK). HPLC solvents were received from Fisher Scientific (Loughborough, UK).

Production of ^{18}F. Fluorine-18 was produced by a Scanditronix MC 40 cyclotron using the $^{18}O(p,n)^{18}F$ reaction. Enriched [^{18}O]H_2O (10−30% ^{18}O) was irradiated by protons (19 MeV) with an integrated beam current of 5−10 μAh.

HPLC. The HPLC system was a Beckman System Gold instrument equipped with a gamma detector (Bioscan Flow-count). A Phenomenex Luna C18(2) column (50 × 4.6 mm, 3 μm; flow rate 1 mL/min) was used for analytical HPLC. A semipreparative column [Phenomenex Luna C18(2), 250 × 10 mm, 5 μm; flow rate 4 mL/min] was used for the final purification of labeled peptides. The following mobile phase/gradient systems were used: solvent A: water (0.1%) TFA, solvent B: acetonitrile (0.1% TFA).

gradient 1: 1 min 40% B, 40−80% B in 15 min

gradient 2: 1 min 30% B, 30−80% B in 10 min

gradient 3: 1 min 30% B, 5−30% B in 20 min, 30−80% B in 5 min

gradient 4: 1 min 0% B, 0−30% B in 10 min

3-[^{18}F]Fluoro-1-mercaptotritylpropane (^{18}F-2). Fluorine-18 containing water (370 MBq, 1 mL) was added to a Wheaton vial (2 mL), charged with Kryptofix 222 (10 mg, 27 μmol), potassium carbonate (1 mg, 7 μmol, dissolved in 50 μL water), and acetonitrile (0.8 mL). The solvent was removed by heating at 110 °C for 1 h under a stream of nitrogen. Anhydrous acetonitrile (0.5 mL) was added and again evaporated as before. This step was repeated twice. The vial was cooled to room temperature followed by injecting a solution of **1** (1 mg, 2.4 μmol) in anhydrous DMSO (0.2 mL). The reaction mixture was stirred at 80 °C for 5 min and analyzed by HPLC (gradient 1, t_R = 16.2 min).

The reaction mixture was diluted with DMSO/water (1:1 v/v, 0.15 mL) and loaded onto a SepPak-Plus cartridge (^{t}C18, Waters) that had been conditioned (10 mL acetonitrile, 20 mL water). The cartridge was washed with water (10 mL) and the ^{18}F-**2** eluted using acetonitrile.

2-{2-[2-(2-[^{18}F]Fluoroethoxy)ethoxy]ethoxy}mercaptotritylethane (^{18}F-4). This preparation was carried out from **3** as described for ^{18}F-**2**. The reaction mixture was analyzed by HPLC (gradient 2, t_R = 12.6 min).

3-[^{18}F]Fluoromethyl-*N*-(2-mercaptotritylethyl)-benzamide (^{18}F-6). Again, ^{18}F-**6** was prepared as described for ^{18}F-**2**. The mesylate precursor **5** was stirred at room temperature for 15 min to give ^{18}F-**6** as analyzed by HPLC (gradient 1, t_R = 13.6 min).

6-Amino-2-{2-[2-(2-{6-amino-2-[2-(3-[^{18}F]fluoropropylsulfanyl)acetylamino]hexanoylamino}acetylamino)-3-phenylpropionylamino]acetylamino}hexanoic Acid (^{18}F-8). A solution of ^{18}F-**2** in acetonitrile (72 MBq, 0.5 mL) was evaporated to dryness using a stream of nitrogen and heating at 100 °C. A mixture of trifluoroacetic acid (0.05 mL), triisopropylsilane (0.01 mL), and water (0.01 mL) was added followed by heating for 10 min at 80 °C. The resulting thiol ^{18}F-**7** was not isolated (analytical HPLC: gradient 1, t_R = 2.5 min,). After the vial was cooled to 0 °C, ammonia (28% in water, 0.1 mL, Aldrich), TCEPxHCl (38 mg, 1.3 μmol, Aldrich) and peptide precursor ClAc−KFGFK−OH (2 mg, 3.2 μmol) in water (0.05 mL) were added. The mixture was stirred for 30 min at 80 °C. After diluting with 0.2 mL of water/MeCN/TFA (95:5:0.1 v/v/v), the mixture was purified on a semipreparative HPLC (gradient 3, t_R = 19.2 min) and analyzed by analytical HPLC (gradient 4, t_R = 10.3 min).

6-Amino-2-{2-[2-(2-{6-amino-2-[2-(2-{2-[2-(2-[^{18}F]-fluoroethoxy)ethoxy]ethoxy}ethylsulfanyl)acetylamino]hexanoylamino}acetylamino)-3-phenylpropionylamino]acetylamino}hexanoic Acid (^{18}F-10). The preparation of ^{18}F-**10** was carried out from ^{18}F-**4** following the method described for ^{18}F-**8**. The labeled peptide ^{18}F-**10** was isolated by semipreparative HPLC (gradient 3, t_R = 19.8 min).

6-Amino-2-(2-{2-[2-(6-amino-2-{2-[2-(4-[^{18}F]fluoromethylbenzoylamino)ethylsulfanyl]acetylamino}-hexanoylamino)acetylamino]-3-phenylpropionylamino}acetylamino)hexanoic Acid (^{18}F-12). The labeled peptide ^{18}F-**12** was synthesized from ^{18}F-**6** using the protocol for the preparation of ^{18}F-**8**. The product ^{18}F-**12** was obtained from semipreparative HPLC (gradient 3, t_R = 22.8 min).

Stability Test of ^{18}F-7. ^{18}F-**2** was deprotected as described above and dispensed in two conical vials A and B (1 MBq in 20 μL each). A yield of 70% deprotection product ^{18}F-**7** was established by HPLC analysis. A solution of TCEP × HCl (10 μL, 2.7 μmol) was added to vial A, followed by ammonia (50 μL, 28%). Ammonia (50 μL, 28%) was also added to vial B. After 1 h at room temperature, aliquots (10 μL) of both vials were analyzed by HPLC. Vial A showed 43% of thiol ^{18}F-**7** preserved with an increased peak at the solvent front. Numerous radioactive products but no signal for ^{18}F-**7** were found in vial B.

ACKNOWLEDGMENT

We would like to thank Colin Steel and the cyclotron operators of Hammersmith Imanet Ltd. for providing us with fluorine-18.

LITERATURE CITED

(1) Okarvi, S. M. (2001) Recent progress in fluorine-18 labeled peptide pharmaceuticals. *Eur. J. Nucl. Med. 28*, 929−938.

(2) Wester, H.-J., Hamacher, K., and Stoecklin, G. (1996) A comparative study of N. C. A. Fluorine-18 labeling of proteins via acylation and photochemical conjugation. *Nucl. Med. Biol. 23*, 365−372.

(3) Wilbur, D. S. (1992) Radiohalogenation of proteins: An overview of radionuclides, labeling methods, and reagents for conjugate labeling. *Bioconjugate Chem. 3*, 433−470.

(4) Lundqvist, H., and Tolmachev, V. (2002) Targeting peptides and positron emission tomography. *Biopolymers (Pept. Sci.) 66*, 381−392.

(5) Heppeler, A., Froidevaux, S., Eberle, A. N., and Maecke, H. R. (2000) Receptor targeting for tumor localisation and therapy with radiopeptides. *Curr. Med. Chem. 7*, 971−994.

(6) Jelinski, M., Hamacher, K., and Coenen, H. H. (2001) Direct ^{18}F-substitution of hydroxy groups in peptides using nonofluorobutane-1-sulfonyl[^{18}F]fluoride. *J. Labelled Compd. Radiopharm. 44*, S151−153.

(7) Ogawa, M., H. K., Oishi, S., Miyake, Y., Kawasumi, Y., Ito, K., Fujii, N., and Iida, H. (2002) Direct single step ^{18}F fluorination of peptides. *J. Nucl. Med. (suppl.) 43*, 137P.

(8) Vaidyanathan, G., and Zalutsky, M. R. (1992) Labeling proteins with fluorine-18 using N-succinimidyl 4-[^{18}F]fluorobenzoate. *Nucl. Med. Biol. 19*, 275−281.

(9) Lang, L., and Eckelman, W. C. (1994) One-step synthesis of ^{18}F labeled [^{18}F]-*N*-succinimidyl 4-(fluoromethyl)benzoate for protein labeling. *Appl. Radiat. Isot. 45*, 1155−1163.

(10) Guhlke, S., Wester, H.-J., Bruns, C., and Stoecklin, G. (1994) (2-[^{18}F]Fluoropropionyl-(D)phe^{1})-octreotide, a potential radiopharmaceutical for quantitative somatostatin receptor imaging with PET: Synthesis, radiolabeling, In Vitro validation and biodistribution in mice. *Nucl. Med. Biol. 21*, 819−825.

(11) Herman, L. W., Fischman, A. J., Tompkins, R. G., Hanson, R. N., Byon, C., Strauss, H. W., and Elmaleh, D. R. (1994) The use of pentafluorophenyl derivatives for the ^{18}F labelling of proteins. *Nucl. Med., Biol. 21*, 1005−1010.

(12) Kilbourn, M. R., Dence, C. S., Welch, M. J., and Mathias, C. J. (1987) Fluorine-18 labeling of proteins. *J. Nucl. Med. 28*, 462−470.

(13) Shai, Y., Kirk, K. L., Channing, M. A., Dunn, B. B., Lesniak, M. A., Eastman, R. C., Finn, D., Roth, J., and Jacobson, K. A. (1989) ^{18}F-Labeled insulin: A prosthetic group methodology for incorporation of a positron emitter into peptides and proteins. *Biochemistry 28*, 4801−4806.

(14) Wüst, F., Hultsch, C., Bergmann, R., Johannsen, B., and Henle, T. (2003) Radiolabelling of isopeptide N-ϵ-(γ-glutamyl)-L-lysine by conjugation with N-succinimidyl-4-[^{18}F]fluorobenzoate. *Appl. Rad. Isot. 59*, 43−48.

(15) Poethko, T., Schottelius, M., Thumshirn, G., Hersel, U., Herz, M., Henriksen, G., Kessler, H., Schwaiger, M., and Wester, H.-J. (2004) Two-step methodology for high-yield routine radiohalogenation of peptides: ^{18}F-labeled RGD and Octreotide analogs. *J. Nucl. Med. 45*, 892−902.

(16) Magata, Y., Lang, L., Kiesewetter, D. O., Jagoda, E. M., Channing, M. A., and Eckelman, W. C. (2000) Biologically stable [^{18}F]-labeled benzylfluoride derivatives. *Nucl. Med., Biol. 27*, 163−168.

(17) Burmeister-Getz, E., Xiao, M., Chakrabarty, T., Cooke, R., and Selvin, P. R. (1999) A comparison between the sulfhydryl reductants tris(2-carboxyethyl)phosphine an dithiothreitol for use in protein biochemistry. *Anal. Biochem. 273*, 73−80.

(18) Burns, J. A., Butler, J. C., Moran, J., and Whitesides, G. M. (1991) Selective reduction of disulfides by tris(2-carboxyethyl)phosphine. *J. Org. Chem. 56*, 2648−2650.

BC0498774

Streptavidin in Antibody Pretargeting. 4. Site-Directed Mutation Provides Evidence That Both Arginine and Lysine Residues Are Involved in Kidney Localization

D. Scott Wilbur,*,† Donald K. Hamlin,† James Sanderson,† and Yukang Lin§

Department of Radiation Oncology, University of Washington, Seattle, Washington 98195, and Fred Hutchinson Cancer Research Center, Seattle Washington 98109. Received June 5, 2004;
Revised Manuscript Received October 4, 2004

The in vivo application of the protein streptavidin is limited by its propensity to localize to kidney, particularly when it is used as a carrier of radionuclides in Targeted Radionuclide Therapy. Our previous studies demonstrated that modification of recombinant "core" streptavidin (rSAv) by reaction of lysine residues with succinic anhydride and arginine residues with 1,2-cyclohexanedione dramatically decreases the kidney concentrations over that obtained with wild-type rSAv. In this investigation, we explored the role of lysine and arginine residues in kidney localization further by evaluating site-directed mutants of rSAv. In the five mutants studied, the four lysine residues found in each subunit of rSAv were replaced (independently) with an alanine (K80A, K121A, K132A, K134A), and a specific arginine was replaced with a histidine (R59H). The rSAv mutants were prepared from a "core" rSAv construct produced by expression in *E. coli* that had 124 amino acids (residues 13−136). Another rSAv construct that had 127 amino acids (residues 13−139), used in most of our previous studies, was also included for comparison. As an additional comparison, succinylated rSAv was prepared and evaluated. The rSAv proteins were radioiodinated and injected into athymic mice that were on a biotin-free diet for 5−7 days prior, and biodistribution data were obtained (for most proteins) at 1, 4, 24, and 48 h postinjection. The data obtained show large differences in kidney localizations of the wild-type rSAv and some rSAv mutants. The largest difference in the kidney concentration was noted for the rSAv-K134A mutant (1.90 ± 0.22%ID/g; 24 h pi) as compared to the wild-type rSAv (31.83 ± 5.26%ID/g) at the same time point. The concentration of rSAv-K134A mutant in kidney was slightly lower than that obtained with succinylated rSAv. At the 24 h time point, the kidney concentrations of the rSAv-R59H mutant (8.95 ± 2.94%ID/g) and the rSAv-K121A mutant (11.86 ± 1.61%ID/g) were lower than wild-type rSAv, but the rSAv mutants rSAv-K80A (27.95 ± 1.82%ID/g) and rSAv-K132A (32.50 ± 10.09%ID/g) were essentially the same. The data suggests that specific lysine and arginine residues are involved in kidney localization. Possible mechanisms for the observed kidney localization are discussed.

INTRODUCTION

The very high binding affinity (10^{13}−10^{15} M^{-1}) of the egg white protein avidin (Av)[1] (*2*) and the bacterial protein streptavidin (SAv) (*3*) with biotin make them valuable chemical tools for a wide variety of applications. While most of the applications developed thus far are in vitro assays (*4*−*10*), in vivo applications are also being developed. For in vivo applications, protease resistant "core" recombinant SAv (rSAv) is being used (*11*). An inherent problem for use of the proteins Av and rSAv in vivo is their propensity to localize to kidney and liver. Importantly, there is a marked difference in the in vivo characteristics of the two proteins. Av clears rapidly from blood and is localized in both kidney and liver, whereas rSAv clears from blood more slowly and localizes primarily in kidney (*12*, *13*). The difference in pharmacokinetics and tissue localization of these similar proteins comes from Av being glycosylated and having a much higher pI than SAv (i.e. pI ∼10 vs 6−7). Deglycosylation of Av makes it more homogeneous (*3*) and results in blood clearance that is similar to rSAv, but the high pI can cause nonspecific interaction with tissues. Therefore, SAv is often considered more attractive for in vivo applications.

The natural propensity for SAv to localize to kidney is problematic for its use in vivo, except perhaps in some unique applications (*14*). We are investigating the use of SAv in an approach to cancer therapy termed "pretargeting" (*15*−*18*). In those studies, SAv is radiolabeled and injected into mice bearing human prostate tumor xenografts, which have been pretargeted with a biotinylated antibody or antibody fragment (*19*). While we demonstrated that an equal molar quantity of radiolabeled rSAv can bind with the biotinylated antibody on the tumor, a majority of the radiolabeled rSAv localizes to kidney. In this situation, the high concentration of

* Address correspondence to D. Scott Wilbur, Ph.D., Department of Radiation Oncology, University of Washington, Box 359658, 325 Ninth Ave., Seattle, WA 98104-2499. Phone: 206-341-5437. Fax: 206-341-5438. E-mail: dswilbur@u.washington.edu.

† University of Washington.

§ Fred Hutchinson Cancer Research Center.

[1] Abbreviations: Av, avidin; biotin-Rhd, biotin derivative containing a rhodamine moiety; biotin-CNCbl, biotin derivative containing a cyanocobalamin moiety; ChT, chloramine-T; cpm, counts per minute; IEF, isoelectric focusing; mAb, monoclonal antibody; %ID/g, percent injected dose per gram; PBS, phosphate-buffered saline; pi, postinjection; rSAv, recombinant streptavidin; rt, room temperature, Sav, streptavidin; sSAv, succinylated recombinant streptavidin.

10.1021/bc049869n CCC: $27.50 © 2004 American Chemical Society
Published on Web 10/26/2004

radioactivity in the kidney precludes administration of an adequate quantity of a radionuclide to kill the tumor due a dose-limiting toxicity in the kidney. For this reason, we are investigating methods for alleviating the kidney localization of rSAv. In prior studies, we demonstrated that chemical modification of lysine amines by reaction with succinic anhydride (*20*) and modification of arginine guanidine groups by reaction with 1,2-cyclohexanedione (*21*) on rSAv resulted in decreased kidney concentrations with minimal affect on biotin binding.

An alternative method for modifying lysine and arginine residues in rSAv is to conduct site-directed mutations in which lysine and arginine residues are replaced with other amino acids. Indeed a large number of site-directed mutations of rSAv have been conducted with truncated or "core" SAv (*11*, *22*) to probe interactions in the biotin-binding pocket (*23*−*28*) and produce mutants with desirable properties for specific applications (*29*−*36*). As rSAv is made up of four identical subunits (*3*), site-directed mutation of one amino acid results in changing four amino acids in the tetrameric intact molecule. Importantly, decreased kidney concentrations were observed in previous studies involving high specific activity (i.e. very low concentration) acylation of lysine residues with the reagent, *p*-[^{125}I]iodobenzoate *N*-hydroxysuccinimide ester, suggesting that modification of only one lysine residue per subunit might be required to decrease the kidney localization (*13*). It was reasoned that site-directed mutations which replace only one of the four lysines at a time could provide information as to whether this observation was correct, and if it were, identify which residue was responsible for kidney localization. Additionally, it had been postulated that kidney localization may be due to the ^{59}RYD^{61} sequence in SAv (*37*). As previously mentioned, modification of arginine residues with 1,2-cyclohexanedione demonstrated that kidney localization was dramatically decreased (*21*). Thus, site-directed mutation of that specific arginine[2] (R59) might also provide confirmation that arginine was involved in kidney localization of rSAv. On the basis of these considerations, we have conducted an investigation in which the four lysine residues in each streptavidin subunit (K80, K121, K132, K134) were replaced with alanine residues, and the arginine residue of interest (R59) was replaced with a histidine residue. Following production of the rSAv mutants, they were radioiodinated and injected into athymic mice, and their concentrations in tissues (including kidney) were assessed at selected times (e.g. 1, 4, 24, and 48 h) postinjection (pi). The experimental methods used, and results obtained, in that investigation are described herein.

EXPERIMENTAL PROCEDURES

General. All chemicals purchased from commercial sources were analytical grade or better and were used without further purification. Chloramine-T (ChT) and phosphate-buffered saline (PBS) were obtained from Sigma (St. Louis, MO). Recombinant streptavidin was obtained from Boehringer Mannheim (Indianapolis, IN). Iminobiotin affinity matrix was obtained from Pierce Chemical (Rockford, IL). Solvents for HPLC analyses were obtained as HPLC grade and were filtered (0.2 μm) prior to use. The biotin derivative containing the cyanocobalamin chromophore (biotin-CNCbl) was obtained[3] as previously described (*38*). Rhodamine-derivatized biotin (biotin-Rhd) was prepared as previously described (*39*). Biotin deficient diet chow with 10% egg white solids (TD 96343) was obtained from Harlan Teklad (Madison, WI, www.harlan.com). Centricon-10 and -30 centrifugation concentrators were obtained from Amicon (Beverly, MA). PD-10 and NAP-10 (Sephadex G-25) size-exclusion columns were obtained from Amersham Pharmacia Biotech AB (Uppsala, Sweden).

Na[^{125}I]I and Na[^{131}I]I were purchased from Perkin-Elmer Life and Analytical Sciences (formerly NEN/Dupont, Billerica, MA) as high concentration/high specific activity radioiodide in 0.1 N NaOH. Measurement of ^{125}I and ^{131}I was accomplished on the Capintec CRC-15R. Tissue samples were counted in a Wallac 1480 Wizard gamma counter with the following window settings: 15−85 keV for I-125 and 260 to 430 keV when ^{125}I and ^{131}I are counted together. The ^{125}I counts are compensated for spillover counts from the ^{131}I in the calculations.

Chromatography. FPLC purifications of the rSAv's were performed on a Pharmacia 2000 FPLC system fitted with a 280 nm detector. Expression level and purification recovery were determined using biotin-Rhd binding (*39*) in conjunction with size exclusion separation on a Zorbax GF-250 column (Dupont) run at 1.0 mL/min using a mobile phase of 20 mM sodium phosphate, pH 7, containing 15% DMSO, 1 mM sodium azide, and 500 mM sodium chloride. The effluent was monitored at 547 nm using a Varian Dynamax PDA-2 detector, and the peak area corresponding to the rSAv elution was determined using a Varian Dynamax HPLC Data System (Walnut Creek, CA).

HPLC separations of the modified rSAv were conducted on a Hewlett-Packard isocratic system consisting of a Model 1050 pumping system and a Model 1050 Multiple Wavelength Detector (280 nm). Proteins were evaluated on a Protein Pak 300 SW glass size-exclusion column (10 μm, 8 mm × 30 cm, Waters Corporation, Milford, MA) run at 1.0 mL/min eluting with 50 mM sodium phosphate buffer (pH 6.8) which contained 300 mM NaCl, 1 mM EDTA, and 1 mM sodium azide. Analyses of the HPLC data were conducted on Hewlett-Packard HPLC ChemStation software.

Radiolabeled Proteins. Size-exclusion chromatography was also used to evaluate radioiodinated rSAv. HPLC separations of radioiodinated proteins were conducted on a system that consisting of a Model 1050 pumping system, a Waters Lambda-Max 481 UV detector, and a Beckman model 170 radioisotope detector. The detectors were connected to a computer through a Hewlett-Packard Model 35900 interface, and data from the chromatograms was obtained on a computer running Hewlett-Packard ChemStation Software. The same size-exclusion column and elution conditions were used for the radiolabeled proteins as unlabeled proteins.

Mass Spectral Analyses. Electrospray mass spectra were obtained by atmospheric pressure chemical ionization on a Micromass Quattro II Tandem Quadrupole Mass Spectrometer (Micromass Ltd., Manchester, U.K.). The sample was introduced by direct injection. The mass spectral data was obtained on a PC running Windows NT based Micromass MaxEnt software. Prior to the mass spectral analyses, rSAv proteins were desalted. In the desalting procedure, 100 μL of a SAv in PBS solution was placed on a NAP-10 column that was equilibrated with deionized water. The column was eluted with deionized water, and the protein fractions were combined. The combined fractions were placed in a Centricon-30 ultrafiltration apparatus, concentrated, and washed three times with 1 mL of deionized water. The filtered solution was then concentrated to yield approximately 1 mg/mL of protein.

Preparation of Streptavidin Mutants. Preparation of wild-type rSAv, rSAv mutants[2] R59H, K80A, K121A, K132A, and K134C was accomplished in four steps: (1) construction of the rSAv mutant gene, (2) expression of rSAv mutant in *E. coli*, (3) refolding of rSAv proteins, and (4) purification. The procedures used in each step follow.

(1) The site-directed mutagenesis was performed using the QuickChange kit (Stratagen, La Jolla, CA). Plasmid A140−9, which contains the wild-type of core SAv gene in a pET3a vector (Novagen, Madison, WI) was the starting construct. The reactions were carried out in 50 μL of supplied reaction mixture containing 400 nM of each oligonucleotide primer and 100 ng of plasmid DNA. Reactions were performed on a PTC-100 thermal cycler (MJ Reaction, Waltham, MA) with 1 cycle of 95 °C for 30 s and 17 cycles of the following profile: 95 °C for 30 s; 55 °C for 1 s; 68 °C for 12 min. The reaction mixture (3 μL) was used to transform *E. coli* XL-1 Blue competent cells (60 μL, Statagene). Plasmid DNA were prepared from cultures of the transformants using a QIAprep Spin Miniprep kit (Qiagen, Valencia, CA). The sequences were confirmed using a Big Dye terminator cycle sequencing kit (Applied Biosystems, Foster City, CA).

(2) Cultures of the plasmid-containing *E. coli* BL21 (DE3) pLysS (Novagen) were grown in shake flasks overnight at 37 °C in Terrific broth (40 mL; Invitrogen, Carlsbad, CA) containing 50 μg/mL of carbenicillin (Sigma Chemical, St. Louis, MO). The cultures were diluted ~100-fold into fresh media (8 × 500 mL) contained in 2 L shake flasks and were grown until the cultures reached an optical density of 0.3−0.6 at 600 nm. At that point, isopropyl β-D-thiogalactopyranoside (Amersham Pharmacia Biotech Inc., Piscataway, NJ) was added to a final concentration of 0.5 mM. Incubation was continued for an additional 16 h. Cells were harvested by centrifugation at 4000*g* for 10 min at 10 °C and then washed twice with PBS (7 mM Na_2HPO_4, 150 mM NaCl, pH 7.0) before processing.

(3) Cell pellets were resuspended in ice-cold TE (30 mM Tris, 1 mM EDTA at pH 8.0) at 25% w/v. The cells were disrupted through two cycles of microfluidization (M-110S, Microfluidics International, Newton, MA). The inclusion bodies were recovered by centrifuging the suspension at 15 000*g* for 90 min at 10 °C, and then the supernatant was discarded. Recovery of the mutants from the pelleted inclusion bodies was performed as described in the literature (*35*). Briefly, a microfluidized pellet was resuspended in 8 mL of ice-cold 8 M guanidine-HCl at pH 1.5 per liter of cell culture. The resuspension was dialyzed at 5−10 °C against 6 M guanidine-HCl at pH 1.5 to remove endogenous biotin. The dialysate was centrifuged at 10 000*g* for 20 min, and then the supernatant was added dropwise to vigorously stirred, ice-cold refolding buffer (4 mM KH_2PO_4, 16 mM Na_2HPO_4, 115 mM NaCl at pH 7.0) using a volume of at least 31× that of the supernatant volume. The suspension was incubated at 4 °C overnight without stirring, and spun at 7000*g* for 5 min at 10 °C. The pellet was discarded.

(4) Prior to loading on the iminobiotin affinity column, the supernatant (from above) was adjusted to 50 mM glycine, 500 mM NaCl at pH 9.6, using concentrated stock. Conductivity was adjusted to 46−48 mSiemens/cm with deionized water, and the solution was filtered through a 2 μm membrane overlaid with a thin film of Cell Pure P-100 diatomaceous earth. The iminobiotin matrix was packed in a column and was equilibrated in 50 mM glycine, 500 mM NaCl at pH 9.6. The capacity for rSAv was >2 mg/mL bed volume under a flow of 3 mL/cm^2/min. The refolded rSAv mutant was loaded at room temperature onto a column which contained 150 mL of matrix bed volume per 75 g of cells. After washing with 20-bed volumes of 50 mM glycine, 500 mM NaCl at pH 9.6, the rSAv was eluted using 0.2 M sodium acetate, 0.1 M NaCl at pH 4.0. The eluate was neutralized to pH 7 with 300 mM Tris buffer (pH 8.0) and then exhaustively dialyzed in PBS at 4 °C. It was subsequently sterile filtered for refrigerated storage at 4 °C. Samples from the refolding and purification steps were run on 4−20% SDS−PAGE gels (Invitrogen, Carlsbad, CA) to qualitatively assess the rSAv expression levels and recovery of the tetrameric rSAv mutants. Quantitative assessment was performed using biotin-Rhd by size-exclusion chromatography. The final concentration of rSAv was calculated by comparison with a rSAv standard analyzed under the same conditions.

Succinylation of Streptavidin. The succinylation reactions were conducted in a manner similar to that previously described (*20*). Briefly, a 200 μL aliquot of a 5 mg/mL solution of rSAv (1 mg, 1.9×10^{-2} μmol) was added to 370 μL of 50 mM $NaHCO_3$ buffer (pH 8.5). To this solution was added either 50 equiv (94 μg; 0.94 μmol) or 100 equiv (188 μg; 1.88 μmol) of succinic anhydride in 20 μL DMSO. After 30 min at room temperature, the contents were transferred to a Centricon-10 and concentrated to approximately 50 μL. PBS (500 μL) was added and the solution was again concentrated to 50 μL. This wash step was repeated five times. The final concentrations of protein (e.g. 3.2 mg/mL) and recovery yields (80−85%) were determined for each succinylation reaction.

Isoelectric Focusing. IEF were obtained on a Novex PowerEase 500 instrument with the XCell II chamber using Invitrogen (Novex) precast gels, pH 3−10 or pH 3−7 (1.0 mm × 12 well) running under the standard IEF Program. The protein was stained with GelCode Blue Stain (Pierce). IEF standards were from Serva Electrophoresis GmbH: pI = 10.7 − cytochrome C; 9.5 − ribonuclease A; 8.3, 8.0, 7.8 − lectin; 7.4, 6.9 − myoglobin; 6.0 − carbonic anhydrase; 5.3, 5.2 − β-lactoglobulin; 4.5 − trypsin inhibitor; 4.2 − glucose oxidase; 3.5 − amyloglucosidase.

Biotin-Binding Studies. Biotin binding studies were conducted using biotin-CNCbl[3] as previously described (*38*). Briefly, to 300 μL of a 1 mg/mL solution (300 μg; 5.65 nmol) of wild-type rSAv or a rSAv mutant in a plastic microcentrifuge vial was added a freshly prepared solution containing approximately 4 equiv (22.6 nmol) of biotin-CNCbl dissolved in 30 μL of 10% aqueous DMSO. The rSAv/biotin derivative mixture was incubated for 1 h at room temperature and 100 μL of the solution was assayed on the HPLC. To the remaining rSAv/biotin derivative solution was added 40 μL of a 1 mg/mL

[2] Single letter designations for amino acids are used for simplification. Some single letter designations used in this paper include the following: R, arginine; K, lysine; A, alanine; H, histidine; G, glycine; D, aspartic acid; Y, tyrosine. Single letter designations for amino acids can be found in biochemistry text books (*1*). Site-directed mutations are designated by the one letter code for the amino acid that was originally present, followed by the residue number of that amino acid and then the single letter designation for the replacement amino acid. For example the abbreviation R59H designates that the arginine residue at amino acid 59 was replaced with a histidine residue.

[3] The biotin-CNCbl reagent is commercially available from Quanta BioDesign (Powell, OH, www.quantabiodesign.com) as biotin-dPEG$_4$-cyanocobalamin.

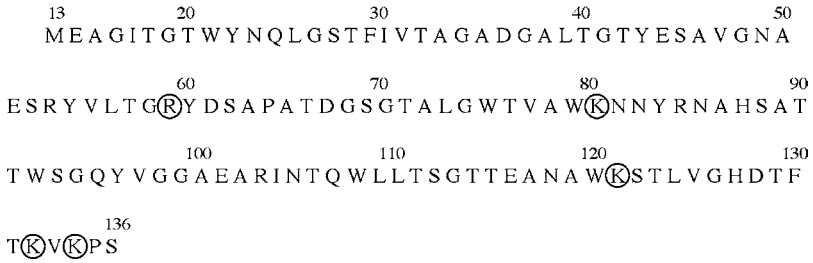


Figure 1. Amino acid sequence of the "core" streptavidin used. Wild-type rSAv (residues 13−136) has the sequence shown, with the exception that residue number 13, which is an alanine in native SAv, was replaced with a methionine to initiate translation. The amino acid residues where site-directed mutations were performed (R59H, K80A, K121A, K132A, K134A) are circled in the sequence.

solution (40 μg; 164 nmol) of biotin in 10% aqueous DMSO. That solution was incubated for 4 h and 100 μL was removed for analysis by HPLC. Areas under the peaks for bound and unbound biotin derivative were evaluated to determine if a change in the percent bound had occurred. Due to difficulties in assessing the quantity of rSAv mutant present, in some examples there was a slight excess (<10%) of the biotin-CNCbl that was not bound. The percent dissociation was adjusted for that material. Biotin binding capacity was additionally determined by incubation of the proteins with a 9-fold molar excess of [^{3}H]biotin [New England Nuclear/Sigma]. After the removal of unbound biotin using a PD-10 column, the amount of radioactivity associated with the protein was determined by liquid scintillation using a Hewlett-Packard beta counter.

Radioiodination of Proteins. Radioiodination reactions were conducted using chloramine-T as previously described (*13*). Radioiodination yields of ^{131}I-labeled rSAv (13−136) and of ^{131}I-labeled succinylated SAv ranged from 45 to 81%. Radioiodination yields for the rSAv mutants ranged from 28 to 72%.

Biodistributions. *General.* Animal use and procedures were approved by the University of Washington's Institutional Animal Care and Use Committee (IACUC). Animal care and use was conducted in accordance with the NIH guidelines.[4] Male athymic mice (BALB/c nu/nu), 4−5 weeks of age were obtained from Charles River Laboratories (Hollister, CA). All injections of reagents were administered to mice in a total volume of approximately 100 μL (injectate weighed) via the lateral tail vein. Injections and sacrifice of the animals were done at predetermined times. Tissues excised included muscle, lung, kidney, spleen, liver, intestine, neck (including thyroid), and stomach. A blood sample was obtained by cardiac puncture immediately before sacrifice. A urine sample was obtained by syringe bladder tap at the time the tissues were excised. Excised tissues were blotted free of blood, weighed, and counted. Calculation of the percent injected dose (%ID) and percent injected dose per gram (% ID/g) in the tissues was based on internal standards containing 1 μL of the injected dose. Total blood volume was estimated to be 8% of body weight for the calculations (*40*).

In the experiments, mice were placed on biotin-free diets for 5−7 days prior to beginning the study. Each mouse was injected with a mixture containing 15 μg of succinylated [^{131}I]rSAv and 15 μg of wild-type SAv or [^{125}I]-rSAv mutant, to result in a total of 30 μg protein per injection. The times for sacrifice, quantity of radioactivity injected for the mice, and experiment that the data was obtained from are described in the legend of Tables S1−S8 in the Supporting Information.

[4] NIH guidelines are described in NIH Publication 86-23: "Guide for the Care and Use of Laboratory Animals".

Molecular Modeling. The locations of, and distances between, the amino acid residues R59, K80, K121, K132, and K134 in core rSAv were modeled using ChemDraw 3D (version 8.0; CambridgeSoft, Cambridge, MA), and Swiss-PdbViewer/Deepview for OSX v3.71b1 (GlaxoSmithKline R&D and Swiss Institute of Bioinformatics, Geneva, Switzerland; http://www.expasy.org/spdbv/). The rSAv crystal structure used in the modeling came from the file 1SWE.pdb, which was obtained from the Research Collaboratory for Structural Bioinformatics (http://www.rcsb.org/pdb/). As the terminal amino acids were not observed in the crystal structure, the last three amino acids of both the N- and C-termini were added for illustration purposes. The ribbon/molecular structures provided as Figures S17 and S18 in the Supporting Information were prepared using the program iMol (v.0.30 www.pirx.com/iMol).

RESULTS

Modification of rSAv. Most previous studies in this laboratory employed rSAv purchased from Boehringer Mannheim (Indianapolis, IN). That "core" rSAv has 127 amino acids, which represent the amino acids that are found in residues 13−139 of the native SAv molecule. In this study, the rSAv (13−139) was used for comparison, but a slightly shorter rSAv construct of 124 amino acids was used to prepare the rSAv mutants. In the construct, the amino acid sequence is the same as found in residues 13−136 of the wild-type SAv molecule, except the amino terminal alanine was replaced with a translation-initiating methionine residue (A13M) as previously described (*35*). The shorter rSAv (13−136) was used in the site-directed mutagenesis to form the targeted rSAv mutants. The amino acid sequence of the rSAv (13−136) construct is shown in Figure 1.

Site-directed mutations of rSAv (13−136) were conducted by expression in *E. coli* using the standard techniques. All *E. coli* cultures produced between 66 and 90 g of cells per 4 L of media when grown overnight under the described shake flask conditions. Upon solubilization of inclusion bodies and subsequent refolding, wild-type rSAv expressed at 3 mg/g of cells (assessed by biotin-Rhd assay) were comparable to the levels reported in an earlier site-directed mutagenesis to reduce immunogenicity (*35*). Both rSAv-R59H and rSAv-K134A expressed at this same level while the rSAv mutants K80A, K121A, and K132A expressed at 39%, 59%, and 33% of wild-type, respectively. All mutant rSAv's bound and subsequently eluted from the iminobiotin affinity matrix in similar fashion, with comparable recoveries of 60−70%. Using the biotin-Rhd assay, no rSAv was detected in either the flow-thru or the wash. All of the purified rSAv preparations displayed a single band of molecular weight appropriate for tetrameric rSAv on SDS−PAGE. Upon boiling, all migrated as monomer.

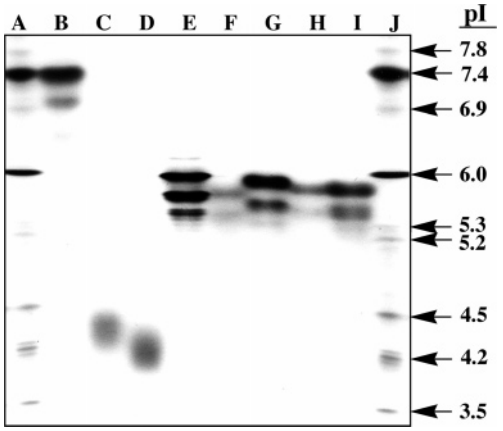


Figure 2. Digitized image of IEF gel comparing pI of unmodified rSAv, succinylated rSAv, and rSAv mutants. Lanes A and J: IEF standards (Serva IEF markers 3−7); Lane B: unmodified rSAv (control); Lane C: succinylated rSAv (50 equiv); Lane D: succinylated rSAv (100 equiv); Lane E: SAv mutant R59H; Lane F: SAv mutant K80A; Lane G: SAv mutant K121A; Lane H: SAv mutant K132A; Lane I: SAv mutant K134A.

Succinylated rSAv was prepared for comparison with the rSAv mutants. Previous studies demonstrated that succinylation of rSAv obtained from Boehringer Mannheim, when reacted with 50 equiv of succinic anhydride for 30 min at room temperature, had dramatically lower concentrations in kidney than the unmodified rSAv (*20*). In this investigation, an initial preparation of succinylated rSAv as previously described resulted in kidney concentrations considerably higher than expected. Evaluation of IEF and mass spectral data from that succinylated rSAv indicated that less modification of the lysines had occurred in the preparations than was obtained in previous studies (data not shown). Further investigation led to the finding that use of succinic anhydride which had been on the shelf for a long time (unknown period) did not give adequate reaction under the conditions employed to fully modify the lysine amines (unreported IEF data). Conducting the conjugation reaction of rSAv with newly obtained succinic anhydride under the standard reaction conditions provided a much higher percentage of lysine modification. Due to a concern about having the variances in the succinylated rSAv prepared, another preparation was made in which 100 equiv of succinic anhydride were reacted. Comparison of the pI values (Figure 2, lanes C and D) and mass spectra (Figures S15 and S16) of the rSAv modified with either 50 or 100 equiv of succinic anhydride clearly indicated that a higher percentage of lysines were modified using the larger quantity of succinic anhydride.

Characterization of Modified rSAv. Once isolated and purified, the rSAv, rSAv mutants, and succinylated rSAv were characterized by size-exclusion HPLC, mass spectral analyses, and isoelectric focusing (IEF) analyses. Size-exclusion HPLC chromatograms of rSAv(13−136) and the rSAv mutants R59H, K80A, K121A, K132A, and K134A all displayed single peaks that eluted with the same retention time (t_R = 10.3−10.4 min; Figures S1−S6 in Supporting Information). These data indicated that the tetrameric protein was formed and was likely to be the desired material. As previously noted (*21*), rSAv succinylated with 50 equiv of succinic anhydride eluted as a single peak with an earlier retention time (t_R = 9.84 min; Figure S7) than unmodified rSAv or its mutants, and rSAv succinylated with 100 equiv of succinic anhydride eluted at an even earlier retention time (t_R = 9.77 min; Figure S8).

Electrospray mass spectral analyses provided masses for monomeric subunits of rSAv (25% of molecular mass). The mass spectral data for the wild-type rSAv and rSAv mutants indicated that the correct compounds had been obtained (see Figures S9−S14 in Supporting Information). Mass spectral data obtained for rSAv succinylated using 50 equiv of succinic anhydride (Figure S15; Supporting Information) indicated that most subunits had three lysines modified, but that there were more protein subunits with only two lysines modified than there were with all four lysines modified. In contrast, when 100 equiv of fresh succinic anhydride was reacted with rSAv, the majority of rSAv subunits had three lysines modified, but a large number had four lysines modified and only a few subunits had just two lysines modified (Figure S16; Supporting Information).

IEF analyses were conducted on rSAv, succinylated rSAv, and rSAv mutants. A digitized scan of an IEF gel (pH 3−7) is shown in Figure 2. The wild-type rSAv (lane B) has a pI range 7.0−7.4. Succinic anhydride reacts with the ϵ-amines of lysine residues, resulting in a change from a positive ammonium ion to an anionic carboxylate ion. Since there are four lysine amines in each of the four subunits, complete succinylation can change rSAv by 32 charge units. As previously observed, the pI of succinylated rSAv varied with the quantity of succinic anhydride reacted. When 50 equiv of succinic anhydride were reacted, the pI range is 4.3−4.5 (lane C) and decreased to a pI range of 4.1−4.4 (lane D) when 100 equiv were reacted. This result is consistent with the mass spectral data that indicates more of the lysine amines react when 100 equiv of succinic anhydride is used. Replacement of an arginine residue with a histidine residue or a lysine residue with an alanine changes the charge on each subunit by one (positive) unit. Therefore, a smaller change in charge on the rSAv is expected (4 positive units) when a mutation is made. In fact, a smaller change in pI is noted, as all of the rSAv mutants, rSAv-R59H (lane E), rSAv-K80A (lane F), rSAv-K121A (lane G), rSAv-K132A (lane H) and rSAv-K134A (lane I) have pI in the range of 5.5−5.9.

Assessment of biotin binding capacity of the rSAv mutants using saturating levels of ^{3}H-biotin indicated that all mutants bound the full complement of four biotins per tetrameric moiety. To compare biotin-binding affinity among the mutants, the degree of dissociation of a biotin-CNCbl, when challenged with a large excess of biotin, was determined. While only providing a qualitative assessment, this assay has been previously used to determine if modifications of biotin derivatives alters their binding with rSAv (*38*, *41*). No (or insignificant) differences were observed at 4 h post addition of the large excess of biotin (data not shown), indicating that all of the rSAv mutants retained high binding affinities.

Comparative Tissue Distribution Studies. Five biodistribution studies (A−E) were conducted in athymic mice to compare the tissue distributions of the site-directed rSAv mutants with the two "core" rSAv (13−136 and 13−139) and succinylated rSAv. An initial biodistribution study was conducted in which the unmodified wild-type [^{131}I]rSAv (13−136), succinylated [^{125}I]-rSAv (13−136), and the rSAv mutants ([^{125}I]rSAv-R59H; [^{125}I]rSAv-K80A; [^{125}I]rSAv-K121A; [^{125}I]rSAv-K132A; [^{125}I]-rSAv-K134A) were evaluated in athymic mice at 4 h pi. The purpose of the experiment (study A) was to determine if any of the rSAv mutants could be eliminated from further study by comparing the concentration of radioiodinated rSAv in kidney at the 4 h sacrifice time. While the data (Figure 3, 4 h) did not indicate that any of the

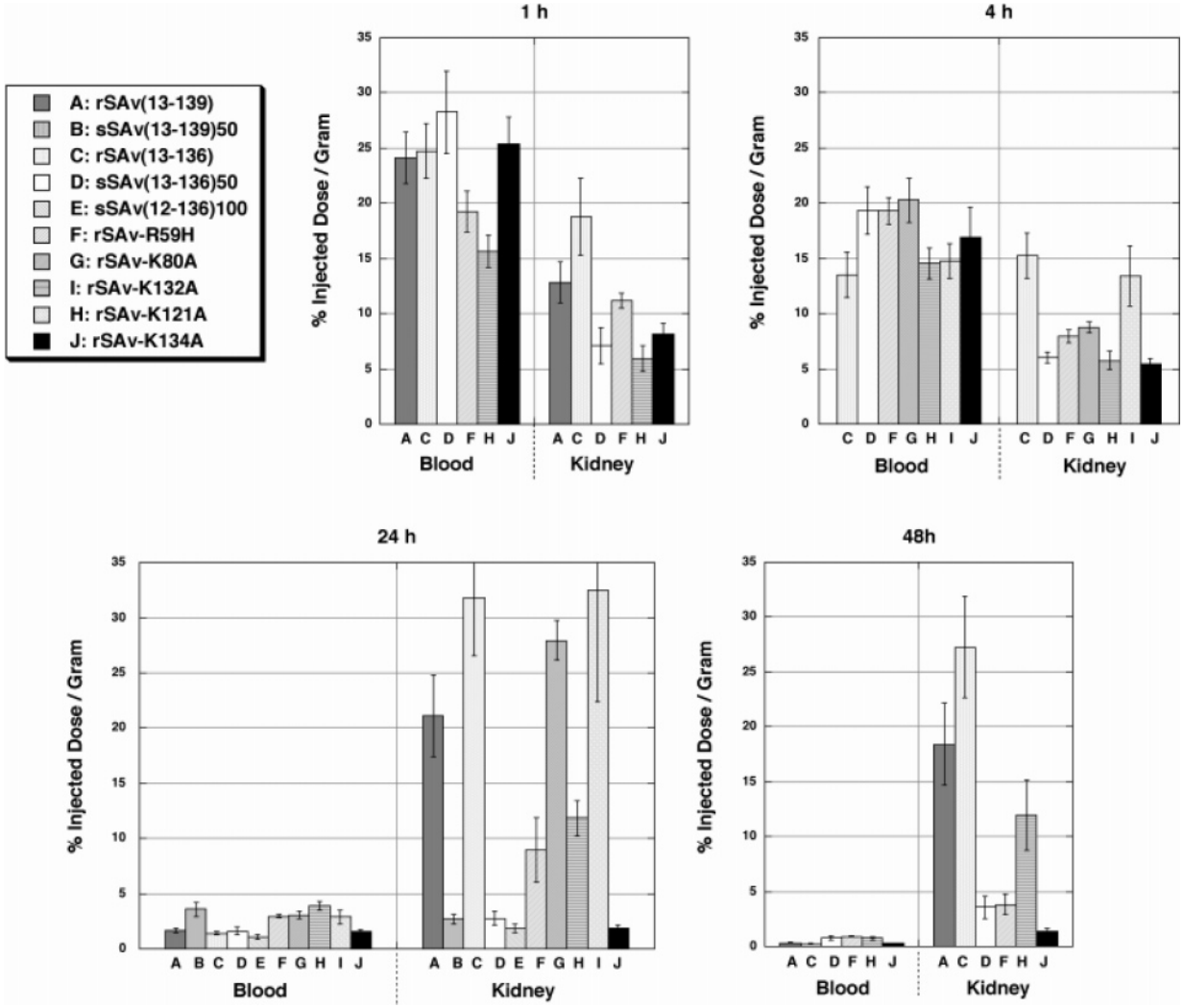


Figure 3. Bar graphs representing data obtained in biodistribution studies at 1, 4, 24, and 48 h after administration of reagents to athymic mice. Reagents studied are depicted as capital letters under the individual bars. The data plotted are for: (A), rSAv (13−139 from Boehringer Mannheim); (B), rSAv (13−139) succinylated with 50 equiv; (C), rSAv (13−136, expressed from *E. coli*); (D), rSAv(13−136) succinylated with 50 equiv; (E), rSAv(13−136) succinylated with 100 equiv; (F), rSAv-R59H; (G), rSAv-K80A; (H), rSAv-K121A; (I), rSAv-K132A; (J), rSAv-K134A. Data for some reagents (i.e. B, E, G, I) were obtained at only one or two time points, therefore the graphs do not have complete sets of reagents. All data were obtained from groups of five mice, except data obtained for G at 24 h and J at 48 h pi had four mice per group. Percent injected dose/gram data for all tissues excised are provided in Tables S1−S8 in Supporting Information.

rSAv mutants could be eliminated, we chose to evaluate [^{125}I]rSAv-K121A and [^{125}I]rSAv-K134A versus succinylated [^{131}I]rSAv next, as these rSAv mutants appeared to have the lowest concentrations in kidney at the 4 h pi time point. In that experiment (study B), the proteins were evaluated at 1, 24, and 48 h pi (4 h data was available from experiment A). In a subsequent experiment (study C) the mutant [^{125}I]rSAv-R59H was compared with succinylated [^{131}I]rSAv at the 1, 24, and 48 h time points. Due to obtaining higher than expected values for the succinylated rSAv in some experiments, an additional study comparing succinylated rSAv was conducted. In that experiment (study D), the biodistribution of succinylated [^{131}I]rSAv (13−139, from Boehringer Mannheim) was compared at 24 h pi with succinylated [^{125}I]rSAv (13−136; 50 and 100 equiv) along with the rSAv mutants [^{125}I]rSAv-K80A and [^{125}I]rSAv-K132A. In a further experiment (study E), the biodistribution of [^{131}I]rSAv (13−136) and [^{125}I]rSAv (13−139) were compared at 1, 24, and 48 h pi time points.

The data obtained from the biodistribution studies is provided in Tables S1−S8 in the Supporting Information, and the blood and kidney concentrations (%ID/g) at the four time points have been plotted in Figure 3. The bar graphs in Figure 3 (1, 4, 24, and 48 h panels) show clear differences in blood clearance and kidney localization between some of the rSAv proteins studied. Because the kidney concentration data obtained for rSAv-K80A and rSAv-K132 at 24 h pi (study D) was not different from unmodified rSAv, their biodistributions were not determined at 1 and 48 h pi. While blood concentrations of all the rSAv proteins studied decreased with time, kidney localization of unmodified rSAv (bars A and C) and rSAv mutants rSAv-K80A (bar G), rSAv-K121A (bar H), and rSAv-K132A (bar I) increased with time. However, it should be noted that the rSAv-K121A mutant reached only about half of the kidney concentration of the unmodified rSAv. In contrast, the kidney concentration of succinylated rSAv (bars B, D, E) and mutants rSAv-R59H (F) and rSAv-K134A (J) decreased with time.

It is readily apparent from the 24 and 48 h panels in Figure 3 that succinylated rSAv (bars D, E) and rSAv mutant K134A (bar J) provide the lowest concentrations in kidney over the time frame studied. Succinylated rSAv was included in this investigation as a coinjected dual-labeled control (^{131}I) since this modification had previ-

ously shown to dramatically decrease the kidney localization of rSAv. However, unexpectedly high concentrations observed in kidney in some biodistribution studies resulted in succinylation of rSAv becoming part of the study. To investigate this further, an animal study was conducted to compare the in vivo distributions of rSAv from Boehringer Mannheim (13−139) modified by reaction with 50 equiv of fresh succinic anhydride with the shorter rSAv (13−136) that had been modified by reaction with 50 or 100 equiv of succinic anhydride. The data obtained at 24 h pi indicate that there is no significant difference in kidney localization between the two rSAv proteins when both are modified with 50 equiv of succinic anhydride, but that use of 100 equiv decreases the concentration in kidney slightly (Table S4, Supporting Information). Interestingly, the shorter succinylated rSAv (13−136) appears to have a significantly lower blood concentration at the 24 h time point. On the basis of these data, we now use 100 equiv of succinic anhydride in modifications of rSAv to ensure that conjugation is sufficient to alleviate most of the kidney localization.

DISCUSSION

The propensity for rSAv to localize in kidney is a serious problem if it is to be used in vivo as a carrier for radionuclides in Targeted Radionuclide Therapy. While chemical linker methods have been developed for releasing the radioactivity postkidney localization (*42*), the fact that core rSAv is very resistant to protease degradation (*11*, *43*) makes this approach questionable as the linkers are often cleaved postdegradation of the protein. Lack of in vivo degradation is observed for the radioiodinated rSAv, which contrary to most radioiodinated proteins has an extended residence time (i.e. residualization) of the radioactivity in the kidney. Due to our interest in using rSAv as a carrier molecule for α-emitting radionuclides in pretargeting approaches to cancer therapy (*19*), we have investigated methods for reducing the high kidney concentrations of radiolabeled rSAv. We based previous investigations on literature reports that (1) infusion of basic amino acids diminished renal clearance of proteins (*44*−*50*), (2) lysine modification in proteins, including avidin and SAv, can decrease kidney localization (*12*, *51*−*54*), and (3) a report that a specific arginine (R59) may be involved in kidney localization as the RYD sequence in rSAv might bind with the RGD receptor on renal cells (*37*). The results obtained in our prior studies demonstrated that kidney localization can be diminished by using any of these three approaches. However, the results did not provide information on whether the specific arginine residue (R59) in the RYD sequence, or whether a specific lysine residue of the four present in each subunit of rSAv, was responsible for kidney localization. Preparation and evaluation of the site-directed rSAv mutants (R59H, K80A, K121A, K132A, K134A) allowed us to probe that question.

The question of whether a specific arginine or lysine is responsible for the high kidney concentrations of rSAv is not readily answered by inspection of the bar graphs in Figure 3. The fact that three of the rSAv mutants studied (R59H, K121A, K134A) appear to affect kidney localization, albeit to varying degrees, seems to indicate that no single amino acid residue is responsible for kidney localization. Since it is likely that kidney localization of rSAv occurs via the same mechanism(s) as other proteins, it is important to consider the possible mechanisms involved to interpret the results obtained. It is known that there are several mechanisms that cause protein localization in kidney (*55*). One mechanism is simple filtration through the glomerular wall. It has been shown that molecular size, shape, and charge influence filtration of macromolecules across the glomerular capillary wall (*56*). In those studies, it was shown that neutral macromolecules (e.g. dextrans) that have molecular radii smaller than 20 Å have no restriction to glomerular filtration, and that the fraction of a macromolecule filtered through the glomerular wall progressively decreases as its molecular radii increases from 20 Å to about 44 Å. In a more recent review, it is indicated that the glomerular filtration membrane has pores of about 75 Å size, allowing proteins of up to 60 kDa to pass (size not discussed). From molecular modeling using crystal structures of recombinant core streptavidin the shape and size of the molecule can be fit into a cube with dimensions of 55 Å × 55 Å × 55 Å. On the basis of the literature report that any molecule over 44 Å is excluded from glomerular filtrations (*56*), this size might be expected to be restricted from filtration. However, if the pore size is 75 Å, perhaps some molecules larger than 44 Å will filter. We previously hypothesized that the high anionic character of the succinylated rSAv would not allow it to pass through the glomerular pores due to the repulsion by the anionic membrane. This may be the correct explanation, but there are other plausible explanations as well.

In these studies we evaluated the size-exclusion chromatograms obtained when rSAv was succinylated with 50 and 100 equiv of succinic anhydride and found that higher degree of succinylation resulted in a faster column transit time. While the size of a protein cannot be accurately measured from the elution times on a size exclusion HPLC column, differences in elution times of modified rSAv can provide information on what might be considered their "effective size". Indeed, the highly acidic rSAv produced with 100 equiv of succinic anhydride has an elution time by size-exclusion HPLC (t_R = 9.8 min) that is between an antibody Fab′ (t_R = 9.0 min) and a F(ab′)$_2$ (t_R = 10.3 min) on the same column. Considering that Fab′ is about the same size (e.g. ∼50 kDa) as rSAv and F(ab′)$_2$ is twice that size (∼100 kDa), the effective size would be somewhere between these values. Thus, an alternative explanation for the lack of filtration of succinylated rSAv is that its effective size is too large for passing through the pores. However, other mechanisms for renal localization are required for the rSAv mutants, as their (effective) size is the same as unmodified rSAv.

A hypothesis that has been forwarded in the literature is that the ^{59}RYD^{61} (Arg-Tyr-Asp) sequence in rSAv (Figure 1) is "RGD-like" resulting in binding to the cell surface adhesion receptors by a "RGD mimicry" (*37*, *57*). Our previous studies involving chemical modification of arginine residues provided results that were consistent with that hypothesis (*21*). However, the results obtained when rSAv was succinylated (*20*) were not consistent with the hypothesis, unless another mechanism such as the size or charge effect noted above is operative. The fact that the results obtained in this investigation indicate that mutation of the lysine residue 134 has more of an effect on kidney localization than mutation of the arginine residue 59 in the RYD sequence seems contrary to the RGD-mimicking receptor hypothesis. While the RYD binding hypothesis was a plausible explanation due to the fact that fibronectin was found to efficiently displace rSAv from chinese hamster ovary cells (*37*), at present it does not appear that there is any conclusive evidence that a RYD sequence will bind specifically with the RGD receptors. Indeed, binding of the RGD sequence

with integrins is very specific, even involving a specific conformation and stereochemistry of the sequence (*58*, *59*). It seems unlikely that this high specificity would accommodate the large steric difference between having a glycine and a tyrosine, particularly in that it has been previously shown that small changes in the sequence, such as substitutions of lysine for the arginine, alanine for the glycine, or aspartic acid for the glutamic acid, eliminated the RGD binding (*60*). More recently, investigators have conducted site-directed mutagenesis altering the RYDS sequence to RYES and found that this very small change resulted in greatly diminished binding with (Lewis) kidney (NRK) cells in vitro (*61*). Unfortunately, no in vivo evaluations were conducted with the rSAv mutant. In contrast, other investigators have engineered the RGD sequence into rSAv and found a dose-dependent specific binding with rat aortic endothelial cells and human melanoma cells, whereas wild-type rSAv had no specific binding with these cells (*62*). While not disproved by the results obtained in this or our prior studies, the data seem to indicate that it is unlikely the RYD sequence plays a major role in the in vivo localization of rSAv to kidney.

The data obtained in this investigation indicate that both lysine and arginine residues participate in the kidney localization of rSAv. Both of these residues have positive charges in aqueous media. It has been previously demonstrated that alteration of the charge on proteins is very important in kidney localization. Although it is apparent that the charge on rSAv can contribute to the rate of filtration, it cannot be a major factor for the rSAv mutants, as they all have the same charge but are sequestered by the kidney to varying degrees. Rather than simply changing the charge, it may be that modification of rSAv alters specific arginine and lysine residues involved in binding with renal cells. Uptake of proteins by renal cells is accomplished by an endocytic process after adsorption on the luminal membrane (*63*). The uptake process is thought to be dependent on interaction of the protein with anionic sites on the surface of renal cells, resulting in anionic molecules being filtered more slowly and cationic molecules being filtered more rapidly than neutral molecules (*51*, *64*). Studies involving the cationic protein lysozyme demonstrated that absorption was a saturable process, which had a high capacity and low affinity (*64*). The fact that it is saturable may help explain why infusions of the basic amino acids lysine and arginine can decrease the kidney localization of proteins, but quickly come back to normal after stopping the administration of amino acids. The results suggest that the endocytic process (*65*) may be dependent on specific interactions with arginine and lysine residues in rSAv. rSAv-K134A (Figure 3, bar J) has the largest decrease in kidney localization relative to the corresponding wild-type rSAv (bar C) or any of the rSAv mutants studied. This amino acid residue is near the carboxyl terminus and has more freedom for interaction with renal cells, as it can move some distance from the bulky rSAv structure.

Computer-aided molecular modeling was conducted to determine if anything unusual could be noted about the locations of the mutated amino acids that might account for the differences in kidney localization. An interesting observation was made from the molecular modeling. The observation that lysine and arginine residues which have an effect on the kidney concentration of rSAv (R59, K121, K134) are paired, or can be paired,[5] in close proximity of each other. When paired in close proximity there are less than 16 Å between the lysine amines or arginine guanidine groups. In contrast, the lysine residues that do not have an effect on the kidney localization are distant from one another (e.g. >30 Å). The pairing effect of arginine and lysine residues is due to the symmetrical nature of the tetrameric rSAv molecule. Graphical depictions of the proximity of lysines 121, 134, and arginine 59 to one another are provided as Figures S17 and S18 in the Supporting Information. Molecular modeling using space filling views also show the positive charges of these residues to be surface exposed. While it is apparent from the results of these studies that arginine 59 and lysine 121 have an influence on the kidney localization of rSAv, we have not provided evidence that the nature of their location, and/or distance between residues of two positive charges, is important in the renal cell endocytosis process. Further studies will be required to answer such questions.

Summary. It is apparent from this investigation that some lysine residues affect the kidney localization of rSAv more than others. In particular, the most accessible lysine (K134) near the carboxyl terminus of each subunit has the largest effect on kidney localization when it is replaced with alanine. This may indicate that it is essential in the initial recognition/binding in kidney. Another lysine residue (K121) has an effect on kidney localization, but it is much less. This may indicate that it is also involved in the binding/internalization process, but it only occurs if the terminal lysine (K134) binds first. The arginine residue studied (R59) also has an effect on the kidney localization that appears to be secondary to the binding of the terminal lysine (K134), although the overall effect of its replacement with a histidine is comparable to that observed with succinylated rSAv. No data was obtained for other arginine residues, but these may also contribute to the kidney localization. These data do not provide a proof of the mechanism of kidney localization, but the location of the arginine and lysine residues within the rSAv structure appears to have a significance effect regarding kidney localization. Most importantly, we have found that mutation of only one lysine residue (per subunit) can provide a rSAv molecule that has a very low sequestration in the kidney.

ACKNOWLEDGMENT

We thank Janna Quinn and Dr. Robert Vessella for their contributions to the biodistribution studies. We thank NeoRx Corporation for their contribution to these studies. The rSAv mutants were prepared at NeoRx Corporation when two authors (J.S., Y.L.) were employed in the company. We are grateful for the financial support provided by the Department of Energy, Medical Applications and Biophysical Research Division, Office of Health and Environmental Research under grant number DE-FG03-98ER62572.

Supporting Information Available: Complete biodistribution data for wild-type rSAv, succinylated rSAv, and rSAv mutants (Tables S1−S8); size-exclusion HPLC and mass spectra for rSAv, rSAv mutants and succinylated rSAv (Figures S1−S16); and graphical representations of the proximity of paired lysines 121/134 and arginine

[5] The lysine amines in K134 have free movement so a close proximity can be attained; however, the groups are not held in that configuration. The location of the amines shown in Figure 17 (Supporting Information) are not established, as those amino acids were added to the crystal structure data for molecular modeling purposes.

59 (Figures S17 and S18). This material is available free of charge via the Internet at http://pubs.acs.org/BC.

LITERATURE CITED

(1) Nelson, D. L., and Cox, M. M. (2000) Tables 5-1: Properties and Conventions Associated with the Standard Amino Acids. *Lehninger Principles of Biochemistry*, pp 118, Worth Publishers, New York.

(2) Green, N. M. (1975) Avidin. *Adv. Prot. Chem. 29*, 85−133.

(3) Green, N. M. (1990) Avidin and Streptavidin. *Methods Enzymol. 184*, 51−67.

(4) Bayer, E. A., and Wilchek, M. (1980) The Use of the Avidin−Biotin Complex as a Tool in Molecular Biology, in *Methods of Biochemical Analysis* (Glick, D., Eds.) pp 1−45, John Wiley & Sons, New York.

(5) Wilchek, M., and Bayer, E. A. (1988) The Avidin−Biotin Complex in Bioanalytical Applications. *Anal. Biochem. 171*, 1−32.

(6) Wilchek, M., and Bayer, E. A. (1990) *Avidin−Biotin Technology*, Academic Press, Inc., San Diego.

(7) Savage, M. D., Mattson, G., Desai, S., Nielander, G. W., Morgensen, S., and Conklin, E. J. (1992) *Avidin−Biotin Chemistry: A Handbook*, Pierce Chemical Company, Rockford, IL.

(8) Diamandis, E. P., and Christopoulos, T. K. (1991) The Biotin-(Strept)Avidin System: Principles and Applications in Biotechnology. *Clin. Chem. 37*, 625−636.

(9) Bayer, E. A., and Wilchek, M. (1996) The Avidin−Biotin System. *Immunoassay* (Diamandis, E. P., and Christopoulos, T. K., Eds.) pp 237−267, Academic Press, San Diego.

(10) Schetters, H. (1999) Avidin and streptavidin in clinical diagnostics. *Biomol. Eng. 16*, 73−78.

(11) Sano, T., Pandori, M. W., Chen, X., Smith, C. L., and Cantor, C. R. (1995) Recombinant Core Streptavidins. A Minimum-Sized Core Streptavidin Has Enhanced Structural Stability and Higher Accessibility to Biotinylated Macromolecules. *J. Biol. Chem. 270*, 28204−28209.

(12) Rosebrough, S. F., and Hartley, D. F. (1996) Biochemical Modification of Streptavidin and Avidin: In Vitro and In Vivo Analysis. *J. Nucl. Med. 37*, 1380−1384.

(13) Wilbur, D. S., Stayton, P. S., To, R., Buhler, K. R., Klumb, L. A., Hamlin, D. K., Stray, J. E., and Vessella, R. L. (1998) Streptavidin in Antibody Pretargeting. Comparison of a Recombinant Streptavidin with Two Streptavidin Mutant Proteins and Two Commercially Available Streptavidin Proteins. *Bioconjugate Chem. 9*, 100−107.

(14) Schechter, B., Arnon, R., Colas, C., Burakova, T., and Wilchek, M. (1995) Renal accumulation of streptavidin: Potential use for targeted therapy of the kidney. *Kidney Int. 47*, 1327−1335.

(15) Paganelli, G., Malcovati, M., and Fazio, F. (1991) Monoclonal Antibody pretargetting techniques for tumour localization: the avidin−biotin system. *Nucl. Med. Commun. 12*, 211−234.

(16) Theodore, L. J., Fritzberg, A. R., Schultz, J. E., and Axworthy, D. B. (2000) Evolution of a Pretarget Radioimmunotherapeutic Regimen. *Radioimmunotherapy of Cancer* (Abrams, P. G., and Fritzberg, A. R., Eds.) pp 195−221, Marcel Dekker, New York.

(17) Chinol, M., Grana, C., Gennari, R., Cremonesi, M., Geraghty, J. G., and Paganelli, G. (2000) Pretargeted Radioimmunotherapy of Cancer. *Radioimmunotherapy of Cancer* (Abrams, P. G., and Fritzberg, A. R., Eds.) pp 169−193, Marcel Dekker, New York.

(18) Boerman, O. C., van Schaijk, F. G., Oyen, W. J., and Corstens, F. H. (2003) Pretargeted radioimmunotherapy of cancer: progress step by step. *J. Nucl. Med. 44*, 400−411.

(19) Wilbur, D. S., Hamlin, D. K., Vessella, R. L., Stray, J. E., Buhler, K. R., Stayton, P. S., Klumb, L. A., Pathare, P. M., and Weerawarna, S. A. (1996) Antibody fragments in tumor pretargeting. Evaluation of biotinylated Fab′ colocalization with recombinant streptavidin and avidin. *Bioconjugate Chem. 7*, 689−702.

(20) Wilbur, D. S., Hamlin, D. K., Buhler, K. R., Pathare, P. M., Vessella, R. L., Stayton, P. S., and To, R. (1998) Streptavidin in antibody pretargeting. 2. Evaluation of methods for decreasing localization of streptavidin to kidney while retaining its tumor binding capacity. *Bioconjugate Chem. 9*, 322−330.

(21) Wilbur, D. S., Hamlin, D. K., Meyer, D. L., Mallett, R. W., Quinn, J., Vessella, R. L., and Press, O. W. (2002) Streptavidin in Antibody Pretargeting. 3. Comparison of Biotin Binding and Tissue Localization of 1,2-Cyclohexanedione and Succinic Anhydride Modified Recombinant Streptavidin. *Bioconjugate Chem. 13*, 611−620.

(22) Pahler, A., Hendrickson, W. A., Kolks, M. A. G., Argarana, C. E., and Cantor, C. R. (1987) Characterization and Crystallization of Core Streptavidin. *J. Biol. Chem. 262*, 13933−13937.

(23) Sano, T., and Cantor, C. R. (1995) Intersubunit contacts made by tryptophan 120 with biotin are essential for both strong biotin binding and biotin-induced tighter subunit association of streptavidin. *Proc. Natl. Acad. Sci. U.S.A. 92*, 3180−3184.

(24) Chilkoti, A., Tan, P. H., and Stayton, P. S. (1995) Site-directed mutagenesis studies of the high-affinity streptavidin−biotin complex: contributions of tyrosine residues 79, 108, and 120. *Proc. Natl. Acad. Sci. U.S.A. 92*, 1754−1758.

(25) Klumb, L. A., Chu, V., and Stayton, P. S. (1998) Energetic roles of hydrogen bonds at the ureido oxygen binding pocket in the streptavidin−biotin complex. *Biochemistry 37*, 7657−7663.

(26) Stayton, P. S., Freitag, S., Klumb, L. A., Chilkoti, A., Chu, V., Penzotti, J. E., To, R., Hyre, D., Le-Trong, I., Lybrand, T. P., and Stenkamp, R. E. (1999) Streptavidin−biotin binding energetics. *Biomolecular Engineering 16*, 39−44.

(27) Hyre, D. E., Le Trong, I., Freitag, S., Stenkamp, R. E., and Stayton, P. S. (2000) Ser45 plays an important role in managing both the equilibrium and transition state energetics of the streptavidin−biotin system. *Protein Sci. 9*, 878−885.

(28) Le Trong, I., Freitag, S., Klumb, L. A., Chu, V., Stayton, P. S., and Stenkamp, R. E. (2003) Structural studies of hydrogen bonds in the high-affinity streptavidin−biotin complex: mutations of amino acids interacting with the ureido oxygen of biotin. *Acta Crystallogr. D Biol. Crystallogr. 59*, 1567−1573.

(29) Sano, T., Smith, C. L., and Cantor, C. R. (1993) A Streptavidin Mutant Containing a Cysteine Stretch That Facilitates Production of a Variety of Specific Streptavidin Conjugates. *Biotechnology 11*, 201−206.

(30) Reznik, G. O., Vajda, S., Smith, C. L., Cantor, C. R., and Sano, T. (1996) Streptavidins with intersubunit cross-links have enhanced stability. *Nature Biotechnology 14*, 1007−1011.

(31) Sano, T., Vajda, S., Smith, C. L., and Cantor, C. R. (1997) Engineering Subunit Association of Multisubunit Proteins: A Dimeric Streptavidin. *Proc. Natl. Acad. Sci. U.S.A. 94*, 6153−6158.

(32) Stayton, P. S., Nelson, K. E., McDevitt, T. C., Bulmus, V., Shimoboji, T., Ding, Z., and Hoffman, A. S. (1999) Smart and biofunctional streptavidin. *Biomol. Eng. 16*, 93−99.

(33) Bulmus, V., Ding, Z., Long, C. J., Stayton, P. S., and Hoffman, A. S. (2000) Site-specific polymer-streptavidin bioconjugate for pH-controlled binding and triggered release of biotin. *Bioconjugate Chem. 11*, 78−83.

(34) Reznik, G. O., Vajda, S., Cantor, C. R., and Sano, T. (2001) A streptavidin mutant useful for directed immobilization on solid surfaces. *Bioconjugate Chem. 12*, 1000−1004.

(35) Meyer, D. L., Schultz, J., Lin, Y., Henry, A., Sanderson, J., Jackson, J. M., Goshorn, S., Rees, A. R., and Graves, S. S. (2001) Reduced antibody response to streptavidin through site-directed mutagenesis. *Protein Sci. 10*, 491−503.

(36) Hamblett, K. J., Kegley, B. B., Hamlin, D. K., Chyan, M. K., Hyre, D. E., Press, O. W., Wilbur, D. S., and Stayton, P. S. (2002) A streptavidin−biotin binding system that minimizes blocking by endogenous biotin. *Bioconjugate Chem. 13*, 588−598.

(37) Alon, R., Bayer, E. A., and Wilchek, M. (1990) Streptavidin Contains an RYD Sequence Which Mimics the RGD Receptor Domain of Firbronectin. *Biochem. Biophys. Res. Comm. 170*, 1236−1241.

(38) Wilbur, D. S., Pathare, P. M., Hamlin, D. K., Frownfelter, M. B., Kegley, B. B., Leung, W. Y., and Gee, K. R. (2000) Evaluation of biotin-Dye conjugates for use in an HPLC assay To assess relative binding of biotin derivatives with avidin and streptavidin. *Bioconjugate Chem. 11*, 584−598.
(39) Schultz, J., Lin, Y., Sanderson, J., Zuo, Y., Stone, D., Mallett, R., Wilbert, S., and Axworthy, D. (2000) A tetravalent single-chain antibody-streptavidin fusion protein for pretargeted lymphoma therapy. *Cancer Res. 60*, 6663−6669.
(40) Fritzberg, A. R., Beaumier, P. L., Bottino, B. J., and Reno, J. M. (1994) Approaches to improved antibody- and peptide-mediated targeting for imaging and therapy of cancer. *J. Controlled Release 28*, 167−173.
(41) Wilbur, D. S., Chyan, M.-K., Pathare, P. M., Hamlin, D. K., Frownfelter, M. B., and Kegley, B. B. (2000) Biotin Reagents for Antibody Pretargeting. 4. Selection of Biotin Conjugates for in Vivo Application Based on Their Dissociation Rate from Avidin and Streptavidin. *Bioconjugate Chem. 11*, 569−583.
(42) Akizawa, H., and Arano, Y. (2002) Altering pharmacokinetics of radiolabeled antibodies by the interposition of metabolizable linkages. Metabolizable linkers and pharmacokinetics of monoclonal antibodies. *Quart. J. Nucl. Med. 46*, 206−223.
(43) Bayer, E. A., Hen-Hur, H., Hiller, Y., and Wilchek, M. (1989) Postsecretory modifications of streptavidin. *Biochem. J. 259*, 369−376.
(44) Mogensen, C. E., and Sølling, K. (1977) Studies on Renal Tubular Protein Reabsorption: Partial and Near Complete Inhibition by Certain Amino Acids. *Scand. J. Clin. Lab. Invest. 37*, 477−486.
(45) Mogensen, C. E., Vittinghus, E., and Sølling, K. (1979) Abnormal Albumin Excretion After Two Provocative Renal Tests in Diabetes: Physical Exercise and Lysine Injection. *Kidney Int. 16*, 385−393.
(46) Rustom, R., Maltby, P., Grim, J. S., Stockdale, H. R., Critchley, M., and Bone, J. M. (1992) Effects of Lysine Infusion on the Renal Metabolism of Aprotinin (Trasylol) in Man. *Clin. Sci. 83*, 295−299.
(47) Bernard, B. F., Krenning, E. P., Breeman, W. A., Rolleman, E. J., Bakker, W. H., Visser, T. J., Macke, H., and de Jong, M. (1997) D-Lysine Reduction of Indium-111 Octreotide and Yttrium-90 Octreotide Renal Uptake. *J. Nucl. Med. 38*, 1929−1933.
(48) Behr, T. M., Goldenberg, D. M., and Becker, W. (1998) Reducing the renal uptake of radiolabeled antibody fragments and peptides for diagnosis and therapy: present status, future prospects and limitations. *Eur. J. Nucl. Med. 25*, 201−212.
(49) Carrasquillo, J. A., Lang, L., Whatley, M., Herscovitch, P., Wang, Q.-c., Pastan, I., and Eckelman, W. C. (1998) Aminosyn II Effectively Blocks Renal Uptake of ^{18}F-labeled Anti-Tac Disulfide-stabilized Fv. *Cancer Res. 58*, 2612−2617.
(50) Hamilton, S., Odili, J., Wilson, G. D., and Kupsch, J. M. (2002) Reducing renal accumulation of single-chain Fv against melanoma-associated proteoglycan by coadministration of L-lysine. *Melanoma Res. 12*, 373−379.
(51) Rennke, H. G., Patel, Y., and Venkatachalam, M. A. (1978) Glomerular filtration of proteins: Clearance of anionic, neutral, and cationic horseradish peroxidase in the rat. *Kidney Int. 13*, 324−328.
(52) Jeong, J. M., Kinuya, S., Paik, C. H., Saga, T., Sood, V. K., Carrasquillo, J. A., Neumann, R. D., and Reynolds, J. C. (1994) Application of High Affinity Binding Concept to Radiolabel Avidin with Tc-99m Labeled Biotin and the Effect of pI on Biodistribution. *Nucl. Med. Biol. 21*, 935−940.
(53) Kobayashi, H., Le, N., Kim, I. S., Kim, M. K., Pie, J. E., Drumm, D., Paik, D. S., Waldmann, T. A., Paik, C. H., and Carrasquillo, J. A. (1999) The pharmacokinetic characteristics of glycolated humanized anti-Tac Fabs are determined by their isoelectric points. *Cancer Res. 59*, 422−430.
(54) Kim, I., Kobayashi, H., Yoo, T. M., Kim, M.-k., Le, N., Han, E.-s., Wang, Q. C., Pastan, I., Carrasquillo, J. A., and Paik, C. H. (2002) Lowering of pI by acylation improves the renal uptake of ^{99m}Tc-labeled anti-Tac dsFv: effect of different acylating reagents. *Nucl. Med. Biol. 29*, 795−801.
(55) Trejtnar, F., and Laznicek, M. (2002) Analysis of renal handling of radiopharmaceuticals. *Quart. J. Nucl. Med. 46*, 181−194.
(56) Brenner, B. M., Hostetter, T. H., and Humes, H. D. (1978) Glomerular permselectivity: barrier function based on discrimination of molecular size and charge. *Am. J. Physiol. 234*, F455−F460.
(57) Alon, R., Bayer, E. A., and Wilchek, M. (1992) Cell-adhesive properties of streptavidin are mediated by the exposure of an RGD-like RYD site. *Eur. J. Cell Biol. 58*, 271−279.
(58) Ruoslahti, E., and Pierschbacher, M. D. (1987) New perspectives in cell adhesion: RGD and integrins. *Science 238*, 491−497.
(59) Pierschbacher, M. D., and Ruoslahti, E. (1987) Influence of stereochemistry of the sequence Arg-Gly-Asp-Xaa on binding specificity in cell adhesion. *J. Biol. Chem. 262*, 17294−17298.
(60) Pierschbacher, M. D., and Ruoslahti, E. (1984) Variants of the cell recognition site of fibronectin that retain attachment-promoting activity. *Proc. Natl. Acad. Sci. U.S.A. 81*, 5985−5988.
(61) Murray, S., Maraveyas, A., Dougan, T., and Chu, A. C. (2002) Reduction of streptavidin RYDS-mediated renal adhesion by site-directed mutagenesis. *Biochim. Biophys. Acta 1570*, 81−88.
(62) McDevitt, T. C., Nelson, K. E., and Stayton, P. S. (1999) Constrained cell recognition peptides engineered into streptavidin. *Biotechnol. Prog. 15*, 391−396.
(63) Nielsen, S. (1994) Endocytosis in renal proximal tubules. Experimental electron microscopical studies of protein absorption and membrane traffic in isolated, in vitro perfused proximal tubules. *Dan. Med. Bull. 41*, 243−263.
(64) Sumpio, B. E., and Maack, T. (1982) Kinetics, Competition, and Selectivity of Tubular Absorption of Proteins. *Am. J. Physiol. 243*, F379−F392.
(65) Mukherjee, S., Ghosh, R. N., and Maxfield, F. R. (1997) Endocytosis. *Physiol. Rev. 77*, 759−803.

BC049869N

Radiopharmaceuticals for Assessment of Multidrug Resistance P-Glycoprotein-Mediated Drug Transport Activity

Vijay Sharma*

Molecular Imaging Center, Mallinckrodt Institute of Radiology, Washington University Medical School, St. Louis, Missouri 63110. Received June 30, 2004; Revised Manuscript Received October 5, 2004

Multidrug resistance (MDR) mediated by overexpression of *MDR1* P-glycoprotein (Pgp) is one of the best characterized transporter-mediated barriers to successful chemotherapy in cancer patients. Thus, noninvasive interrogation of Pgp-mediated transport activity in vivo would be beneficial in guiding therapeutic choices. Both small organic medicinals as well as metal complexes characterized as transport substrates for Pgp are amenable to incorporation of PET or SPECT radionuclides and may enable noninvasive imaging of Pgp in cancer patients. Toward this objective, clinically approved agents, exemplified by ^{99m}Tc-Sestamibi and ^{99m}Tetrofosmin, have already shown promise for the functional evaluation of Pgp-mediated transport activity in human tumors in vivo. In addition, selected agents from an upcoming class of substituted Schiff-base gallium(III) complexes containing an N_4O_2 donor core in their organic scaffold and capable of generating both SPECT and PET radiopharmaceuticals have also been shown to be promising for noninvasive assessment of Pgp activity in vitro and in vivo.

INTRODUCTION

Resistance to chemotherapy represents a major obstacle in the treatment of cancer. Many tumors are intrinsically resistant to chemotherapy, whereas others initially respond to treatment, but acquire resistance to selected cytotoxic drugs during chemotherapy. Multidrug resistance (MDR) can be broadly defined as a phenomenon by which cultured cells in vitro and tumor cells in vivo show resistance simultaneously to a variety of structurally and functionally dissimilar cytotoxic and xenobiotic compounds *(1−6)*. While several different genes have been shown to be associated with a multidrug resistance phenotype *(7−9)*, MDR mediated by overexpression of the *MDR1* gene product, P-glycoprotein (Pgp), represents one of the best characterized barriers to chemotherapeutic treatment in cancer *(6, 10)*. Pgp, a 170 kD plasma membrane protein, is predicted by sequence analysis to comprise two symmetrical halves that share both homology with a family of ATP-binding cassette (ABC) membrane transport proteins and a common ancestral origin with bacterial transport systems *(5, 11)*. Characterized by 12 transmembrane domains and two nucleotide-binding folds *(3, 5)*, the protein is thought to hydrolyze ATP to affect outward transport of substrates across or off the cell surface membrane *(5, 12)*. Although the specific protein domains and amino acids involved in substrate recognition continue to be characterized, genetic and biochemical evidence has conventionally been interpreted to show putative membrane-associated domains interacting directly with selected cytotoxic agents to affect transport *(10, 13−15)*. Regardless of mode of interaction, the net effect is that Pgp reduces the intracellular concentration of substrates in Pgp-expressing multidrug resistant cells compared with non-Pgp-expressing cells.

* To whom correspondence should be addressed. Vijay Sharma, Ph.D., Mallinckrodt Institute of Radiology, Washington University Medical School, Box 8225, 510 S. Kingshighway Blvd., St. Louis, MO 63110. Tel: 314-362-9358. Fax: 314-362-0152. E-mail: sharmav@mir.wustl.edu.

PROBABLE MECHANISM(S) FOR *MDR1* PGP-MEDIATED DRUG TRANSPORT

Commonly, *MDR1* Pgp has been postulated to act as an ATP-dependent efflux transporter of xenobiotics and chemotherapeutic drugs (*6*). In addition, several studies provide evidence supporting alternative mechanisms for the diminished Pgp-mediated drug accumulation in MDR cells. For example, a flippase model has been proposed for Pgp *(16)*. This model suggests that Pgp flips hydrophobic cytotoxic compounds from the inner to outer leaflet of the lipid bilayer wherein the agents can diffuse away. Alternatively, Pgp acts as a phospholipid flippase altering membrane permeability, thereby accounting for diminished intracellular concentration of drug and accounting for the broad specificity of Pgp toward its recognized substrates. In addition, cells expressing *MDR1* may have intracellular compartments that are more acidic than non-Pgp expressing cells *(17, 18)*, altered intracellular distribution of drug *(19)*, or altered membrane permeability resulting in decreased drug influx *(20)*. For example, Piwnica-Worms and co-workers have shown sustained expression of Pgp without use of chemotherapeutic drugs in a line of stable transfectants, MCF-7/*MDR1,* using a bicistronic vector for selection of cells *(21)*. Electrical current and drug transport experiments demonstrated insignificant variations in membrane potential or membrane conductance between parental MCF-7 and MCF-7/*MDR1* cells, but reduced unidirectional influx and steady-state cellular content of Pgp substrates. There was no change in unidirectional efflux of substrates from cells. These authors concluded that the dominant effect of *MDR1* Pgp in this system was reduction of drug influx, possibly through an increase in intramembranous dipole potential *(21)*. Finally, *MDR1* Pgp may interfere with or

10.1021/bc0498469 CCC: $27.50 © 2004 American Chemical Society
Published on Web 11/02/2004

alter pathways of apoptosis (programmed cell death) *(22, 23)*, therefore offering protection from cytotoxic compounds.

Thus, although the exact mechanism remains to be biochemically elucidated, the observed combined net effect is a decreased intracellular concentration of cytotoxic drugs that results from overexpression of *MDR1* Pgp, thereby rendering chemotherapeutic treatment ineffective in cancer.

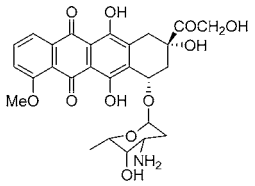
ROLE OF *MDR1* PGP IN PHARMACOKINETICS

In addition to its overexpression in tumors, *MDR1* Pgp is normally located in several tissues involved in excretory functions, including the brush border of proximal tubule cells in the kidney, the biliary surface of hepatocytes, and the apical surface of mucosal cells in the small intestine and colon *(24, 25)*. *MDR1* Pgp also is located on the luminal surface of endothelial cells lining capillaries in the brain and in the testis *(26−28)* as well as on the apical surface of choroid plexus epithelial cells *(27)*. However, despite its widely disseminated expression, the function of *MDR1* Pgp in normal physiology has not been clearly defined, although Pgp may have a role in protection from xenobiotics *(29)*. Piwnica-Worms and co-workers have also suggested a role for *MDR1* Pgp in intracellular cholesterol trafficking *(30)*. Furthermore, inhibition of Pgp with an MDR modulator could provide an effective means for increasing oral absorption of drugs and reducing drug excretion, resulting in decreased dosing requirements for treatment of cancer and infectious diseases. For example, Pgp modulation is currently under evaluation as a means to improve oral absorption of chemotherapeutics and HIV-1 protease inhibitors such as indinavir, nelfinavir, saquinavir, and rotonavir *(31, 32)*. Similarly, use of *MDR1* Pgp inhibitors (commonly known as MDR modulators or reversal agents) could allow drug penetration into Pgp protected sites in the body, such as the brain and selected hematopoietic cells, as has been shown for penetration of protease inhibitors into the central nervous system *(32)*. In addition, transgenic expression of the *MDR1* gene has been explored for hematopoietic cell protection in the context of cancer chemotherapy *(33−35)*, wherein Pgp could protect hematopoietic progenitor cells from chemotherapy-induced myelotoxicity. Hematopoietic cells transduced via retroviral-mediated transfer of the *MDR1* gene have shown preferential survival in vivo after treatment with MDR drugs *(35)* and data from pilot clinical studies support this approach *(36)*.

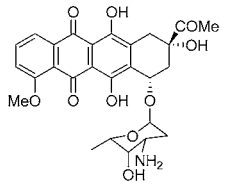
Thus, a noninvasive method of determining Pgp-mediated drug transport activity could be important in the use of new modulators, applications of gene therapy to chemotherapeutic protocols, and predicting oral absorption, pharmacokinetics, and penetrance of MDR drugs into target tissues and brain.

MDR1 PGP-MEDIATED DRUG TRANSPORT IN CHEMOTHERAPY

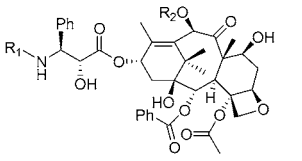
Compounds recognized by Pgp are typically characterized as modestly hydrophobic (octanol/water partitioning coefficient, log $P > 1$), often contain titratable protons with a net cationic charge under physiological conditions, and are predominately "natural products" with an aromatic moiety *(37, 38)*. In addition, incorporation of methoxy functionalities has been shown to enhance *MDR1* Pgp recognition. Among an extensive list of conventional cytotoxic compounds, anthracyclines (doxorubicin **1**, daunorubicin **2**), taxanes (paclitaxel **3**, docetaxel **4**), *Vinca* alkaloids (vincristine **5**, vinblastine **6**, vindesine **7**), and etoposides **8** (VP-16) are examples of



1

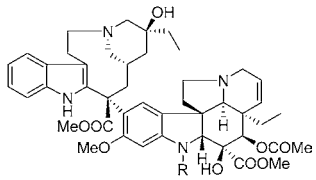


2



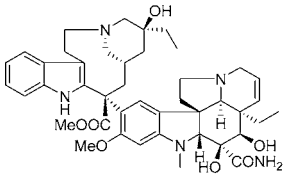
3 R_1 = COC_6H_5, R_2 = $COCH_3$ (Paclitaxel)

4 R_1 = $COOC(CH_3)_3$, R_2 = H (Docetaxel)

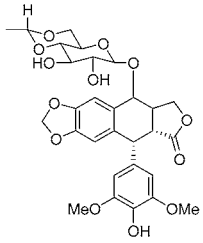


5 R = CHO (Vincristine)

6 R = Me (Vinblastine)

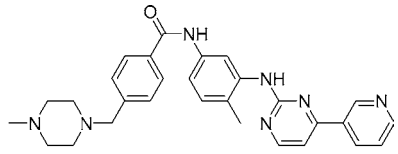


7



8

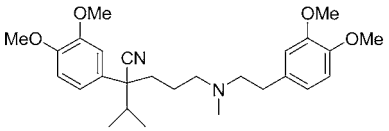
clinically important chemotherapeutic drugs recognized by *MDR1* Pgp (*6, 7, 37, 39*). The broad diversity in the scaffolds of these agents emphasizes the key characteristic feature of multidrug resistance, i.e., the apparent capacity of Pgp to recognize a large group of cytotoxic compounds sharing little or no structural or functional similarities. Furthermore, even targeted drugs have encountered MDR in clinics *(40)*. For example, Gleevec, **9**, a 2-phenylaminopyrimidine derivative *(41, 42)*, while



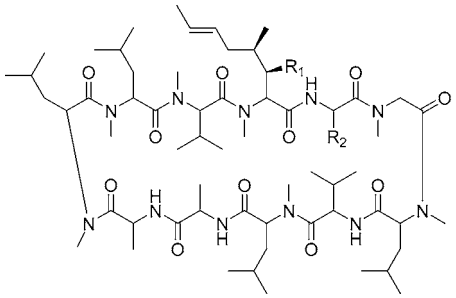
9

a highly potent inhibitor of receptor tyrosine kinases, such as BCR-Abl and PDGF−R, is also recognized and transported by *MDR1* Pgp *(6, 43)*. Thus, it would appear that even novel targeted therapeutics will remain susceptible to broad-specificity transporter-mediated resistance mechanisms.

Because clinical studies have documented the poor outcomes associated with *MDR1* Pgp expression in tumors *(39, 44)*, reversal of multidrug resistance by nontoxic agents that block the transport activity of *MDR1* Pgp has been an important target for pharmaceutical development. When coadministered with a cytotoxic agent, these nontoxic compounds (MDR reversal agents) enhance net accumulation of relevant cytotoxic drugs within the tumor cells. Many compounds known to have other pharmacological sites of action initially were used to reverse MDR in cancer cells grown in culture and several underwent pilot clinical trials *(37)*. These compounds included verapamil **10**, cyclosporin A **11**, quinidine **12**, trifluoperazine **13**, and their derivatives *(37)*.

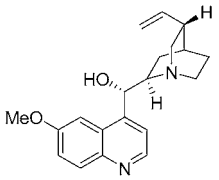


10

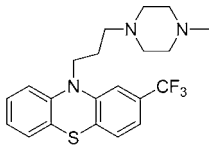


11 R_1 = OH, R_2 = CH_2CH_3 (Cyclosporin A)

14 R_1 = =O, R_2 = $CH(CH_3)_2$ (PSC 833)

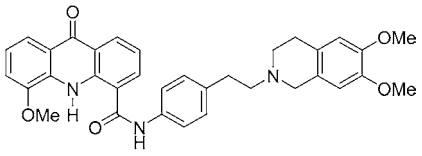


12



13

However, these agents had limited clinical utility because of unacceptable toxicities at serum levels of drug needed to modulate *MDR1* Pgp *(39)*. Second generation modulators, such as dexverapamil, an optically pure verapamil *(45)*, and PSC 833 (Valspodar) **14**, a cyclic undecapeptide analogue of cyclosporin A (*46*) were soon developed with improved efficacy. These were followed by third generation modulators, such as GF120918, **15**, a substituted isoquinolinyl acridonecarboxamide *(47)*, LY335979, **16**, a difluorocyclopropyl dibenzosuberane *(48)*, VX710 (biricodar) **17**, an amido-keto-pipecolinate *(49)*, XR9576 (tariquidar) **18**, an analogue of anthranilamide pharmacophore *(50−52),* and MS209, **19**, a quinoline-derivatized



15

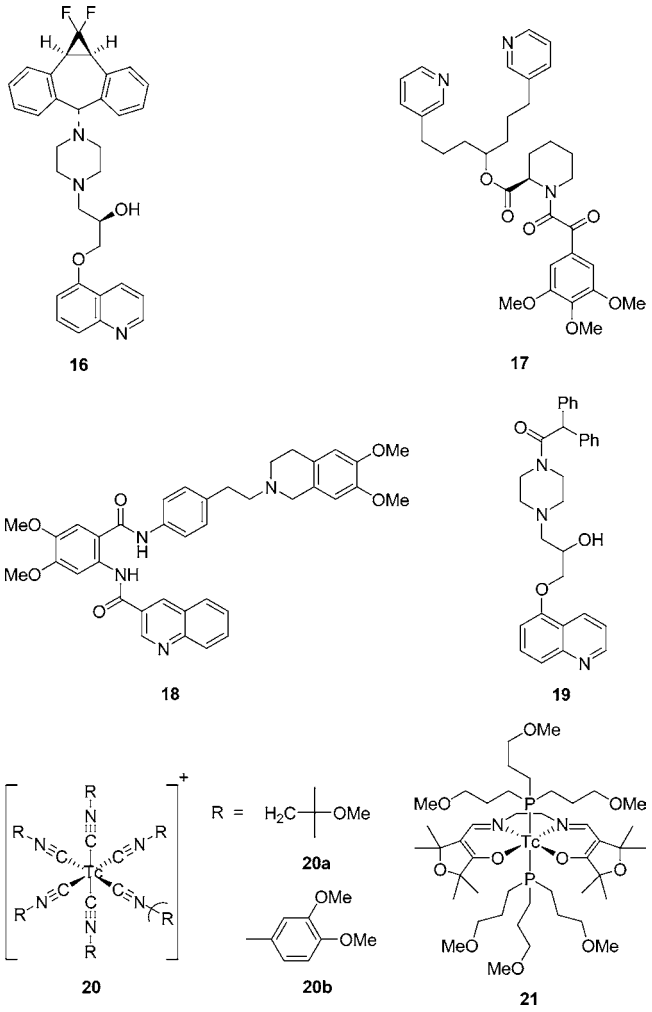
analogue *(53, 54)*, that have been developed more recently. Thus, the MDR phenotype may be modulated more effectively with these more selective reversal agents to improve the efficacy of chemotherapeutic agents by delivering an appropriate dose at the targeted site.

SPECT RADIOPHARMACEUTICALS FOR EVALUATION OF P-GLYCOPROTEIN-MEDIATED TRANSPORT ACTIVITY

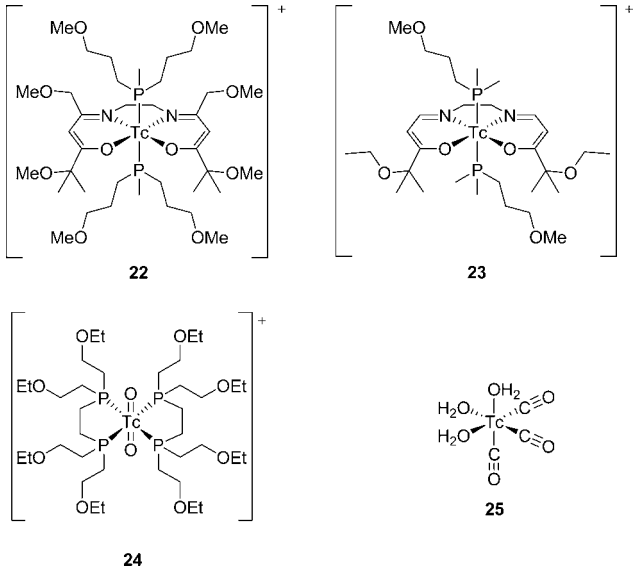
Increasingly, the choice of systemic therapy for cancer is based on a priori analysis of tumor markers to assess the presence or absence of a molecular pathway or target (such as a key receptor or enzyme activity) for a given therapeutic agent. Identification of tumor markers with diagnostic agents assists in the proper selection of patients most likely to benefit from targeted therapy. Measurement of MDR is one potentially important marker in planning systemic therapy. However, expression of *MDR1* Pgp, as detected at the level of messenger RNA or protein, does not always correlate with the functional assessment of Pgp-mediated transport activity. Because Pgp transport activity is affected by specific mutations as well as the phosphorylation state of the protein (*5, 55, 56*), altered or less active forms of Pgp may be detected by polymerase chain reaction (PCR) or immunohistochemistry which do not accurately reflect the status of tumor cell resistance. Thus, methods for functionally interrogating Pgp transport activity have been sought *(57)*. Imaging with a radiopharmaceutical that is transported by *MDR1* Pgp may identify noninvasively those tumors in which the transporter is not only expressed, but functional. Thus, significant effort has been directed toward the noninvasive detection of transporter-mediated resistance using planar scintigraphy or single-photon emission computed tomography (SPECT) employing radiolabeled metal complexes characterized as transport substrates for *MDR1* Pgp.

Hexakis(2-methoxyisobutylisonitrile)technetium-99m (commonly known as [^{99m}Tc]Sestamibi) **20a**, although originally developed as a radiopharmaceutical for myocardial perfusion imaging *(58, 59)*, subsequently was the first metal complex shown to be a Pgp transport substrate *(60)*. Characterized by octahedral geometry around the central technetium(I) core *(58, 61)*, the radiopharmaceutical possesses a cationic charge and modest hydrophobicity similar to many chemotherapeutic agents in the MDR phenotype. In the absence of Pgp expression, this ^{99m}Tc-isonitrile complex accumulates within the interior of cells in response to the physiologically negative mitochondrial and plasma membrane potentials maintained within cells *(62, 63)*. However, in Pgp-expressing multidrug resistant tumor cells, net cellular accumulation levels of [^{99m}Tc]Sestamibi are inversely proportional to the level of *MDR1* Pgp expression *(60, 64−67)*. Furthermore, complete reversal of the Pgp-mediated exclusion of [^{99m}Tc]Sestamibi has been affected by treatment with conventional *MDR1* Pgp inhibitors such as verapamil **10**, cyclosporin A **11**, and quinidine **12** or newer more potent reversal agents such as PSC 833 **14**, GF120918 **15**, LY335979 **16**, or VX710 **17** (*30, 38, 60, 64, 65, 68−73*), and more recently, XR-9576 **18** *(6, 50)*. Furthermore, to optimize the transport and Pgp-targeting characteristics of [^{99m}Tc]isonitrile complexes, several studies investigating structure−activity relationship (SAR) have been performed. In one study, the alkyl chains in [^{99m}Tc]-Sestamibi were replaced with longer chain ether functionalities. The hexakis(2-ethoxy-isobutylisonitrile)[^{99m}Tc] complex ([^{99m}Tc]EIBI) was shown to be a transport substrate recognized by Pgp, but with slightly greater nonspecific cell binding than [^{99m}Tc]Sestamibi *(74)* that would result in inferior target/background ratios compared with [^{99m}Tc]Sestamibi. Piwnica-Worms and coworkers have also explored substituted aromatic isonitriles *(75)*. A series of substituted arylisonitrile analogues were obtained from their corresponding amines through a reaction with dichlorocarbene under phase transfer-catalyzed conditions, and non-carrier-added hexakis-(arylisonitrile)-Tc-99m complexes were produced by reaction with pertechnetate in the presence of sodium dithionite. SAR studies resulted in a lead compound, **20b**, which demonstrated an overall encouraging transport profile in Pgp expressing cells, but significant nonspecific adsorption to hydrophobic compartments was identified. Nevertheless, results suggested that methoxy substituents, compared with other functionalities, preferentially contributed to enhanced Pgp recognition for this class of

compounds. However, none of these radiolabeled complexes exceeded [^{99m}Tc]Sestamibi in their Pgp-targeting properties.

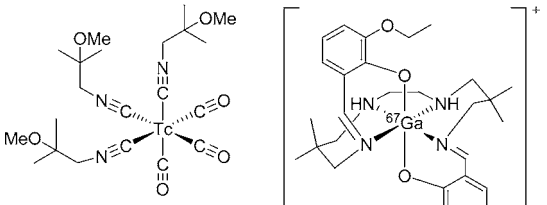


In addition, several entirely different classes of technetium-complexes have been identified as Pgp transport substrates. Using a planar Schiff-base moiety and hydrophobic phosphines, nonreducible Tc(III) monocationic compounds known as "Q-complexes" were developed for applications in myocardial perfusion imaging *(76, 77)*. The lead complex for clinical development was *trans*-[(1,2-bis(dihydro-2,2,5,5-tetramethyl-3(2*H*)furanone-4-methyleneimino)ethane)bis(tris(3-methoxy-1-propyl)phosphine)]Tc(III), known as [^{99m}Tc]Furifosmin **21** *(78)*. Because the hydrophobicity and Pgp-targeting properties of these complexes could be readily adjusted by varying functionalities on the Schiff base or phosphine moieties independently, a variety of novel ^{99m}Tc-Q-complexes with subtle structural variations were synthesized *(68, 79)*. This approach allowed the coordination environment of the Tc(III) metal core to be maintained while altering the overall electronic environment, thereby enabling evaluation of structural features conferring Pgp-mediated transport properties. Ether functionalities can be incorporated into the equatorial Schiff base ligand by condensation of ethylenediamines with ether-containing β-dicarbonyl compounds *(80)*. The presence of *gem*-dimethyl groups sterically hinders the attack of diamine at the adjacent carbonyl and the strategy results in regioselective condensation at the less hindered carbonyl. Preparation of the tertiary phosphines was accomplished in a two-step, one-pot reaction involving treatment of 1-chloro-3-methoxypropane with magnesium in tetrahydrofuran and subsequent reaction of the reagent with dimethylchlorophosphines or dichloromethylphosphines to provide the necessary substituted phosphines with overall yield of 50−70% *(79)*. The desired ^{99m}Tc-Q-complexes were then obtained by a two-step synthetic approach using the phosphines as both reductants and ligands *(81)*. From MDR transport assays in vitro, the *trans*-[2,2′-(1,2-ethanediyldiimino)bis(1,5-methoxy-5-methyl-4-oxohexenyl)]-bis[methyl-bis(3-methoxy-1-propyl)phosphine]Tc(III) complex **22** and the *trans*-[5,5′-(1,2-ethanediyldiimino)bis(2-ethoxy-2-methyl-3-oxo-4-pentenyl)]-bis[dimethyl(3-methoxy-1-propyl)phosphine]Tc(III) complex **23** were discovered. These complexes mimic [^{99m}Tc]Sestamibi for their Pgp recognition properties in vitro *(68, 79)*. In addition, a Tc(V) complex known as [^{99m}Tc]Tetrofosmin *(82)*, bis-[1,2-bis{bis(2-ethoxyethyl)phosphino}ethane]Tc(V) **24**, has been identified as another ^{99m}Tc-complex with highly favorable *MDR1* Pgp-mediated transport properties *(79, 83)*. While these metal complexes do not share any



obvious structural homology, they do share the common features of a delocalized cationic charge and modest hydrophobicity. Overall, which of these selected ^{99m}Tc-complexes would be most clinically useful in evaluation of the Pgp status of tumors by single photon emission computed tomography (SPECT) imaging continues to be rigorously investigated.

Another class of technetium based-radiopharmaceuticals has emerged on the basis of pioneering work done on the development of an air- and water-stable organometallic aqua complex [^{99m}Tc(OH$_2$)$_3$(CO)$_3$]$^+$ **25** obtained from reaction of pertechnetate in saline under 1 atm of CO *(84)*. Because it was shown that the coordinated water molecules were labile, thus exchangeable with other ligands, complexes with heterogeneous ligands could be generated. Upon the basis of these observations, these water molecules were substituted with methoxyisobutylisonitrile ligands to obtain another novel class of Pgp-targeted radiopharmaceuticals, tris(carbonyl)tris(2-methoxyisobutylisonitrile)technetium(I); [^{99m}Tc(CO)$_3$(MIBI)$_3$]$^+$ **26** *(85)*. Cellular accumulation of **26** in human epidermal carcinoma KB 3-1 (−Pgp) and KB 8-5 (+Pgp) cells demonstrated uptake profiles inversely proportional to Pgp expression indicating it to be recognized as a transport substrate *(86)*.



26 27

Organic scaffolds capable of coordinating other metals have also been explored. Multidentate ligands with an N_4O_2 donor core have the ability to form stable monomeric, monocationic, hydrophobic complexes with a variety of main group *(87, 88)* and transition metals *(89−91)*. Schiff-base Ga(III) complexes were previously reported as potential PET (positron emission tomography) radiopharmaceuticals with utility as myocardial perfusion imaging agents *(92, 93)*. These complexes, exemplified by the lead compound **27**, demonstrated pharmacological profiles consistent with their potential utility as PET probes of *MDR1* Pgp activity in tumors *(94−96)*. Substituted salicylaldehydes were obtained by ortho-formylation of phenols, and substituted linear tetramine was obtained through a reaction of dibromoethane and 2,2-dimethylpropane-1,3-diamine at room temperature. The triaryl precursors containing a central imidazolidine ring were synthesized by condensation of an appropriate substituted linear tetramine with substituted salicylaldehydes. The desired metal(III) complexes were obtained by cleavage of the imidazolidine ring via transmetalation reactions using appropriate metal(III) acetylacetonates. For evaluation of *MDR1* Pgp-targeting properties, these compounds were screened for their cytotoxicity in Pgp expressing tumor cells and their appropriate control (−Pgp) cells (Figure 1). Selected metal(III) complexes were able to differentiate between human epidermal carcinoma KB-3-1 (−Pgp) and KB-8-5 (+Pgp) cells through

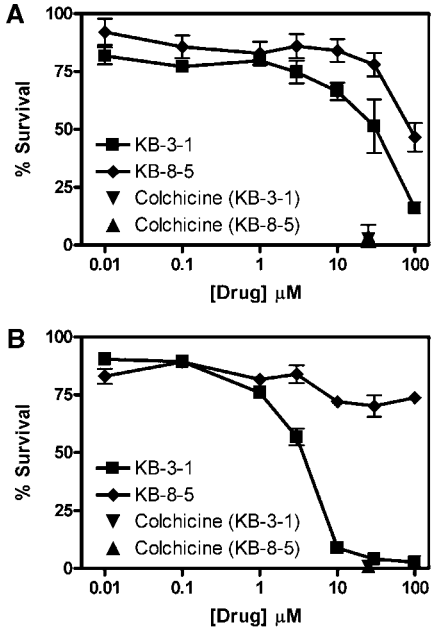


Figure 1. Cell survival studies in parental KB-3-1 (−Pgp) and multidrug resistant KB-8-5 (+Pgp) cells at increasing concentrations of R-ENBPI gallium(III) [R= 3-methoxy (A); 4,6-dimethoxy (B)] complexes, colchicine (25 μM, positive control). Each point represents the mean of triplicate determinations; bars represent ± SEM when larger than symbol; solid lines are a spline presentation of the data.

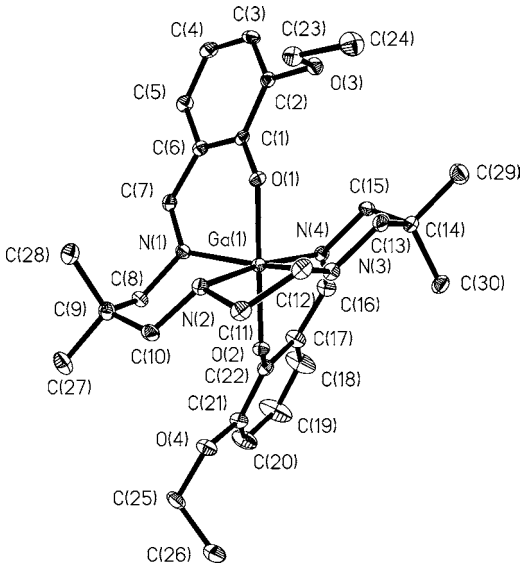


Figure 2. ORTEP drawing of Ga-ENBDMPI$^+$ cation in [(3-ethoxy-ENBDMPI)Ga]$^+$[ClO_4]$^-$ showing the crystallographic numbering scheme. Atoms are represented by thermal ellipsoids (20% probability).

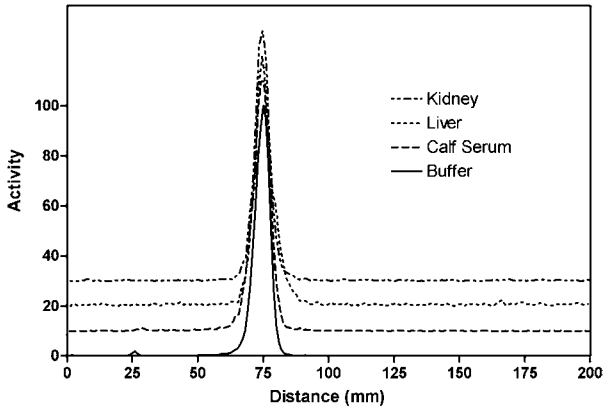


Figure 3. Radio-TLC analysis of ^{67}Ga-ENBDMPI (**27**) preincubated in buffer calf-serum, or extracted from mouse-liver and mouse-kidney postinjection.

differential cytotoxicity profiles indicating *MDR1* Pgp-mediated transport *(95)*. The active metal complexes containing 4,6-dimethoxy-substituted aromatic rings (Figure 1B) were more potent than their corresponding 3-methoxy analogues (Figure 1A). SAR studies led to discovery of a lead compound, [{bis(3-ethoxy-2-hydroxybenzylidene)-*N*,*N*′-bis(2,2-dimethyl-3-aminopropyl)ethylenediamine}gallium(III)], [Ga-ENBDMPI]$^+$ **27**. The crystal structure provided direct evidence that gallium is coordinated symmetrically and simultaneously to the N_4O_2 donor core of the ligand. The structure revealed that the central gallium is hexacoordinated, involving two phenoxy oxygens (O1 and O2), two secondary amine nitrogens (N2 and N3), and two imine nitrogens (N1 and N4) with overall trans-pseudooctahedral geometry (Figure 2). For biochemical studies, the ligand was labeled with gallium-67/68 through a simple transmetalation reaction of $^{67/68}$Ga(acetylacetonate)$_3$ and ligand dissolved in ethanol. The radiolabeled compound was purified through a C-18 sep-pack. For analysis of metabolites, the lead SPECT radiotracer, ^{67}Ga-ENBDMPI, was incubated in buffer and calf serum at 37 °C for 2 h. In addition, the radiopharmaceutical was extracted from mouse tissues (liver and kidney) 15 min after tail-vein injection. Radio-TLC analysis of the radiotracer in buffer,

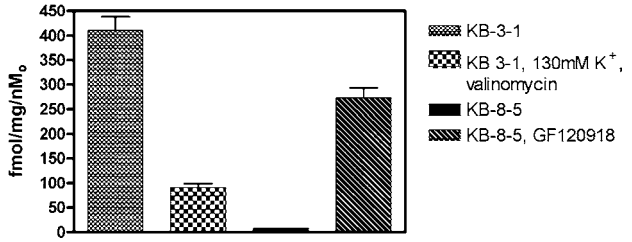


Figure 4. Accumulation of ^{67}Ga-ENBDMPI (**27**) in KB-3-1 cells (−Pgp) and MDR KB-8-5 cells (+Pgp) as indicated. Shown is net uptake [fmol/mg protein/nM$_o$] at 30 min. Each bar represents the mean of 4 determinations; line above the bar denotes +SEM.

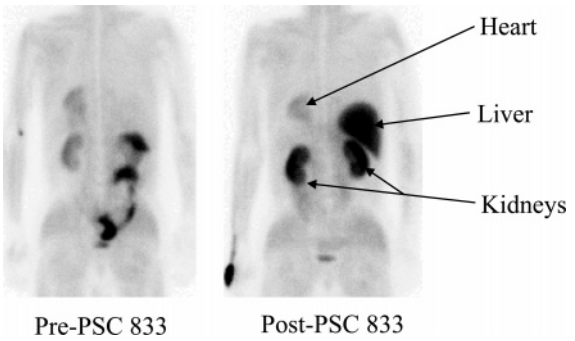


Figure 5. Effect of the *MDR1* Pgp inhibitor, PSC 833 on pharmacokinetics of ^{99m}Tc-Sestamibi in vivo: Whole body posterior planar image obtained at 2h postinjection of radiopharmaceutical. Left Panel: The pharmacokinetics demonstrated decreased retention of the radiotracer in the liver and kidney, 2h postinjection of the radiotracer in the absence of PSC 833. Right Panel: Following 24h treatment with PSC 833, image was obtained 2h postinjection of radiotracer. Because PSC 833 blocks Pgp, considerable amount of radioactivity was retained in the liver and kidney (right panel). Note that heart, being a Pgp (−ve) organ, retains the same amount of activity in both cases (Pre-PSC 833 and Post-PSC 833; left and right panels).

calf-serum, and tissue extracts indicated primarily a nonmetabolized agent (Figure 3). Because, net cell contents of hydrophobic and cationic radiopharmaceuticals transported by Pgp are a function of both passive potential-dependent influx and transporter-mediated efflux. Therefore, favorable cationic ^{67}Ga complexes would likely penetrate KB-3-1 cells as result of the inwardly directed electrochemical driving forces. Furthermore, membrane potential-dependent influx in KB-3-1 cells in 120 mM K^+/20 mM Cl^- buffer containing the potassium ionophore valinomycin (1 μg/mL) was shown to collapse mitochondrial and plasma membrane potentials toward zero and reduce net tracer uptake of membrane potential-responsive hydrophobic cations *(94, 96)*. Resultantly, net accumulation of the ^{67}Ga-complexes would be reduced in high K^+/valinomycin buffer, and furthermore, tracer levels greater than that expected from equilibrium distribution into the water spaces under these conditions would provide one measure of nonspecific adsorption to intracellular hydrophobic compartments. Conversely, *MDR1* Pgp-mediated outward transport of ^{67}Ga complexes would be expected to decrease net cellular accumulation in KB-8-5 cells compared with KB-3-1 cells. Following these criteria, ^{67}Ga-ENBDMPI accumulated in cells showing profiles inversely proportion to Pgp expression (Figure 4). While residual uptake in control KB-3-1 cells in the presence of high K^+/valinomycin buffer indicated modest nonspecific interaction, the inhibitor GF120918 induced uptake in MDR KB-8-5 cells (Figure 4) demonstrated target specificity *(94, 97)*. These results suggested that radiolabeled analogues of these Ga(III) complexes also could provide templates for ^{68}Ga-PET radiopharmaceuticals to probe Pgp transport activity in tumors *(96)*.

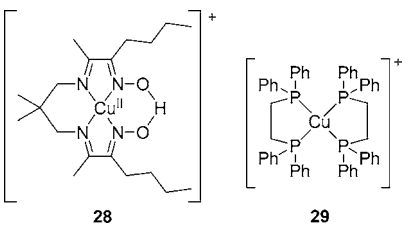
While gallium(III) radiopharmaceuticals are undergoing preclinical evaluation, technetium-99m based radiotracers have been clinically evaluated for assessment of the Pgp-mediated transport activity. Toward this objective, validation of successful inhibition of the transport function is necessary to evaluate the effects of Pgp inhibitors on patient outcomes. Initial clinical data indicates that [^{99m}Tc]Sestamibi can be used to detect inhibition of Pgp-meditated transport function in patients (Figure 5). Overall, pharmacokinetic studies demonstrated retention of activity in the liver and kidney (Pgp positive tissues) of patients treated with PSC 833, 2 h postinjection of the radiopharmaceutical (Figure 5) *(70, 71)*. In addition, the heart a Pgp negative tissue, acting as an internal control tissue, displayed no difference in retention of activity in either pre-PSC 833 (left panel, Figure 5) or post-PSC 833 (right panel, Figure 5). Overall, results indicated the potential of [^{99m}Tc]Sestamibi to serve as an efficient diagnostic probe of Pgp-mediated transport activity in vivo.

PET AGENTS FOR ASSESSMENT OF P-GLYCOPROTEIN-MEDIATED TRANSPORT ACTIVITY

Positron emission tomography (PET) radiopharmaceuticals offer enhanced spatial resolution and quantification capabilities compared to SPECT agents. To probe Pgp transport activity, PET-based radiopharmaceuticals have been actively investigated on three fronts: (a) employing SPECT organic ligands capable of accommodating PET radionuclides, (b) bioinorganic radiolabeled complexes, and, (c) conventional PET organic medicinals.

Among organic scaffolds that coordinate both SPECT and PET radionuclides, two validated examples make use of the PET radionuclides ^{94m}Tc and ^{68}Ga. Thus, the radiosynthesis and biochemical validation of ^{94m}Tc-Sestamibi and ^{68}Ga-ENBPI complexes have been reported *(94, 98)*. As expected chemically, the highly favorable Pgp-targeting properties of these metal complexes were retained upon transformation from SPECT agents to PET imaging agents.

On another front, organic scaffolds capable of accommodating PET radionuclides that generate novel metallopharmaceuticals through short synthetic routes have been reported. Thus, based upon rigorous prior contributions (*99*, *100*), a stable, monocationic radiolabeled complex of copper(II) **28** was obtained as a potential ^{64}Cu PET radiopharmaceutical for targeting Pgp *(101)*. The desired diiminedioxime ligand was synthesized from 2,3-dimethyl-propane-1,2-diamine and heptane-2,3-dione-3-oxime. Cellular accumulation in MES-SA (−Pgp) and MES-SA (+Pgp) cells demonstrated uptake profiles inversely proportional to Pgp expression. Furthermore, an inhibitor-induced accumulation was observed in Pgp (+) cells.



28 **29**

Bidentate tertiary phosphine ligands have the ability to generate stable copper(I) complexes through a one step synthesis in quantative yields (*102, 103*) and represent another class of potential ^{64}Cu PET radiopharmaceuticals

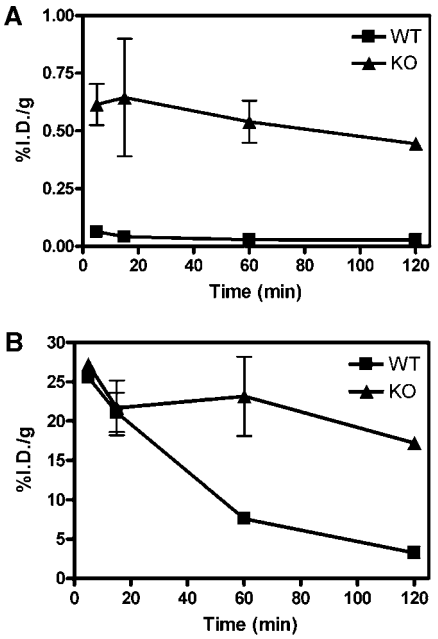


Figure 6. Pharmacokinetics of ^{67}Ga-ENBDMPI (**27**) in brain (A) and liver (B) of FVB mice. Wild-type [WT] and *mdr1a/1b* (-/-) [KO] *(123)* mice were administered **27** by bolus injection into a lateral tail vein and organs harvested at the indicated times for analysis. Data are expressed as percent of injected dose of radioactivity per gm tissue at each respective time point. Data points represent the mean of 2−4 determinations each; bars represent ± SEM when larger than the symbol.

targeting Pgp. These complexes previously demonstrated potent antitumor properties compared with their free ligands alone (*104, 105*). As with ^{99m}Tc-Q-complexes, herein phosphines were exploited as both ligands and reducing agents to generate cationic, hydrophobic, and tetrahedral copper(I) complexes **29** with 1,2-bis(diphenylphosphino)ethane. These potential PET radiopharmaceuticals show evidence of Pgp-targeting properties (*106, 107*). Although several leads exist for a ^{64}Cu-based radiopharmaceutical for interrogation of Pgp by PET, these radiopharmaceuticals show only modest Pgp-targeting properties compared with ^{94m}Tc-Sestamibi or ^{68}Ga-ENBDMPI.

To demonstrate the potential use of radiolabeled probes as imaging markers of Pgp-mediated transport in vivo, quantitative pharmacokinetic analysis in mice was performed following intravenous injection of tracers. Mice have two isoforms of Pgp (*mdr1a* and *mdr1b*) which confer multidrug resistance *(108)*. Drug-transporting *mdr1a* Pgp isoform is expressed in capillary endothelial cells of the brain wherein the protein is a major component of the blood−brain barrier *(109)*. Here, Pgp limits entry of a variety of amphipathic compounds into the central nervous system *(108)*. Drug-transporting Pgp isoforms are also expressed along the biliary cannalicular surface of hepatocytes wherein the transporters function to secrete substrates into the bile *(108)*. In this regard, *mdr1a/1b* (-/-) gene disrupted (KO) mice, which have no drug-transporting Pgp, are a robust model for evaluation of candidate MDR agents by interrogating net tracer accumulation into brain and liver tissues *(68)*. Therefore, analysis of initial tissue uptake and retention of ^{67}Ga-ENBDMPI **27** in *mdr1a/1b* (-/-) mice in comparison to wild-type (WT) FVB mice was performed (Figure 6). Relative to WT, the KO mice showed 10-fold more radiotracer **27** in brain parenchyma 5 min after injection of the complex (Figure 6A). Furthermore, the AUC_{5-120} of **27** in *mdr1a/1b* (-/-) brain was 62.5 ± 16.1 μCi (injected μCi)$^{-1}$ (g tissue)$^{-1}$ × 100 × minute (n = 8), a value 17-fold greater than wild-type mice ($p < 0.005$). While comparing to FDA approved radiopharmaceuticals for noninvasive imaging, ^{67}Ga-ENBDMPI showed 3- to 5-fold greater differences in brain AUC_{5-120} between WT and KO mice than ^{99m}Tc-Sestamibi *(110)* and ^{99m}Tc-Tetrofosmin *(111)*, further documenting its potential superiority for imaging Pgp activity in vivo. In addition, the liver showed twice the retained activity of ^{67}Ga-ENBDMPI **27** in KO mice compared with WT mice (Figure 6B). Thus, the data further validated **27** as a substrate for Pgp in vivo and showed its potential as a molecular imaging probe of transporter function and inhibition in the living organism.

A third focus has been directed toward incorporation of conventional PET radionuclides ^{11}C or ^{18}F into small organic medicinals characterized as substrates or inhibitors known to interact with Pgp (*112−114*). Employing this strategy, various labeled PET agents, including ^{11}C-colchicine, ^{11}C-verapamil, ^{11}C-daunomycin, and ^{11}C/^{18}F-paclitaxel, have been reported (*114−122*). While promising, some of these PET agents suffer from modest radiochemical yields and others from complex pharmacokinetics in vivo mediated, at least in part, by rapid metabolism of the radiolabeled compounds. In addition, these ^{11}C/^{18}F-radiopharmaceuticals are obtained in custom-designed, dedicated facilities located near cyclotrons that produce these isotopes, thereby imposing potential restrictions in their widespread distribution.

CONCLUSION

In summary, *MDR1* Pgp recognizes and outwardly transports a wide variety of bioinorganic complexes with a broad diversity of scaffolds in their chelation cores as well as conventional anticancer drugs. Both small organic medicinals as well as coordination compounds are amenable to incorporation of PET or SPECT radionuclides that may enable diagnostic imaging for functional interrogation of the MDR phenotype in cancer patients. In particular, clinically approved ^{99m}Tc-complexes have already shown to be beneficial in the evaluation of functional *MDR1* Pgp transport activity in human tumors in vivo. Therefore, contributions of bioinorganic radiochemistry and conventional organic radiochemistry are rapidly growing to enhance the existing armamentarium of targeted agents that would be capable of functionally analyzing the presence of Pgp in vivo.

ACKNOWLEDGMENT

The author is grateful to Prof. David Piwnica-Worms for inspiring and helpful discussions and co-workers (both past and present) for their contributions that led to successful execution of this review. This educational project was funded by DOE FG02 94ER61885 and NIH P50 CA94056.

LITERATURE CITED

(1) Ling, V., and Thompson, L. H. (1974) Reduced permeability in CHO cells as a mechanism of resistance to colchicine. *J. Cell. Physiol. 83*, 103−111.

(2) Gerlach, J. H., Endicott, J. A., Juranka, P. F., Henderson, G., Sarangi, F., Deuchars, K. L., and Ling, V. (1986) Homology between P-glycoprotein and a bacterial haemolysin transport protein suggests a model for multidrug resistance. *Nature 324*, 485−489.

(3) Gros, P., Ben Neriah, Y., Croop, J. M., and Housman, D. E. (1986) Isolation and expression of a complementary DNA that confers multidrug resistance. *Nature 323*, 728−731.

(4) Endicott, J. A., and Ling, V. (1989) The biochemistry of P-glycoprotein-mediated multidrug resistance. *Annu. Rev. Biochem. 58*, 137−171.
(5) Gottesman, M. M., and Pastan, I. (1993) Biochemistry of multidrug resistance mediated by the multidrug transporter. *Annu. Rev. Biochem. 62*, 385−427.
(6) Gottesman, M., Fojo, T., and Bates, S. (2002) Multidrug resistance in cancer: role of ATP-dependent transporters. *Nat. Rev. Cancer 2*, 48−58.
(7) Bosch, I., and Croop, J. (1996) P-glycoprotein multidrug resistance and cancer. *Biochim. Biophys. Acta 1288*, F37−F54.
(8) Borst, P., Evers, R., Kool, M., and Wijnholds, J. (2000) A family of drug transporters: the multidrug resistance-associated proteins. *J. Natl. Cancer Inst. 92*, 1295−1302.
(9) Kruh, G., and Belinsky, M. (2003). The MRP family of drug efflux pumps. *Oncogene 22*, 7537−7552.
(10) Ambudkar, S., Dey, S., Hrycyna, C., Ramachandra, M., Pastan, I., and Gottesman, M. (1999) Biochemical, cellular, and pharmacological aspects of the multidrug transporter. *Annu. Rev. Pharmacol. Toxicol. 31*, 361−398.
(11) Ames, G. (1986) Bacterial periplasmic transport systems: structure, mechanism and evolution. *Annu. Rev. Biochem. 55*, 397−425.
(12) Gros, P., Dhir, R., Croop, J., and Talbot, F. (1991) A single amino acid substitution strongly modulates the activity and substrate specificity of the mouse *mdr1* and *mdr3* drug efflux pumps. *Proc. Natl. Acad. Sci. U.S.A. 88*, 7289−7293.
(13) Bruggemann, E. P., Germann, U. A., Gottesman, M. M., and Pastan, I. (1989) Two different regions of phosphoglycoprotein are photoaffinity-labeled by azidopine. *J. Biol. Chem. 264*, 15483−15488.
(14) Yoshimura, A., Kuwazuru, Y., Sumizawa, T., Ichikawa, M., Ikeda, S., Uda, T., and Akiyama, S. (1989) Cytoplasmic orientation and two-domain structure of the multidrug transporter, P-glycoprotein, demonstrated with sequence-specific antibodies. *J. Biol. Chem. 264*, 16282−16291.
(15) Raviv, Y., Pollard, H., Bruggemann, E., Pastan, I., and Gottesman, M. (1990) Photosensitized labeling of a functional multidrug transporter in living drug-resistant tumor cells. *J. Biol. Chem. 265*, 3975−3980.
(16) Higgins, C. F., and Gottesman, M. M. (1992) Is the multidrug transporter a flippase? *Trends Biochem. Sci. 17*, 18−21.
(17) Altan, N., Chen, Y., Schindler, M., and Simon, S. (1998) Defective acidification in human breast tumor cells and implications for chemotherapy. *J. Exp. Med. 187*, 1583−1598.
(18) Hurwitz, S., Terashima, M., Mizunuma, N., and Slapak, C. (1997) Vesicular anthracycline accumulation in doxorubicin-selected U-937 cells: participation of lysosomes. *Blood 89*, 3745−3754.
(19) Lautier, D., Canitrot, Y., Deeley, R., and Cole, S. (1996) Multidrug resistance mediated by the multidrug resistance protein (*MRP*) gene. *Biochem. Pharmacol. 52*, 967−977.
(20) Stein, W. D., Cardarelli, C., Pastan, I., and Gottesman, M. M. (1994) Kinetic evidence suggesting that the multidrug transporter differentially handles influx and efflux of its substrates. *Mol. Pharmacol. 45*, 763−772.
(21) Luker, G. D., Flagg, T. P., Sha, Q., Luker, K. E., Pica, C. M., Nichols, C. G., and Piwnica-Worms, D. (2001) MDR1 P-glycoprotein reduces influx of substrates without affecting membrane potential. *J. Biol. Chem. 276*, 49053−49060.
(22) Robinson, L., Roberts, W., Ling, T., Lamming, D., Sternberg, S., and Roepe, P. (1997) Human MDR1 protein overexpression delays the apoptotic cascade in Chinese hamster ovary fibroblasts. *Biochemistry 36*, 11169−11178.
(23) Smyth, M. J., Krasovskis, E., Sutton, V. R., and Johnstone, R. W. (1998) The drug efflux protein P-glycoprotein additionally protects drug-resistant tumor cells from multiple forms of caspase-dependent apoptosis. *Proc. Natl. Acad. Sci. U.S.A. 95*, 7024−7029.
(24) Thiebaut, F., Tsuruo, T., Hamada, H., Gottesman, M. M., Pastan, I., and Willingham, M. C. (1987) Cellular localization of the multidrug-resistance gene product P-glycoprotein in normal human tissues. *Proc. Natl. Acad. Sci. U. S. A. 84*, 7735−7738.
(25) Hitchins, R. N., Harman, D. H., Davey, R. A., and Bell, D. R. (1988) Identification of a multidrug resistance associated antigen (P-glycoprotein) in normal human tissues. *Eur. J. Cancer Clin. Oncol. 24*, 449−454.
(26) Cordon-Cardo, C., OBrien, J., Casals, D., Rittman, G., Biedler, J., Melamed, M., and Bertino, J. (1989) Multidrug-resistance gene (P-glycoprotein) is expressed by endothelial cells at blood-brain barrier sites. *Proc. Natl. Acad. Sci. U.S.A. 86*, 695−698.
(27) Rao, V., Dahlheimer, J., Bardgett, M., Snyder, A., Finch, R., Sartorelli, A., and Piwnica-Worms, D. (1999) Choroid plexus epithelial expression of MDR1 P-glycoprotein and multidrug resistance-associated protein contribute to the blood-cerebrospinal fluid drug-permeability barrier. *Proc. Natl. Acad. Sci. U.S.A. 96*, 3900−3905.
(28) Croop, J. M., Raymond, M., Haber, D., Devault, A., Arceci, R. J., Gros, P., and Housman, D. E. (1989) The three mouse multidrug resistance (*mdr*) genes are expressed in a tissue-specific manner in normal mouse tissues. *Mol. Cell Biol. 9*, 1346−1350.
(29) Schinkel, A., Mayer, U., Wagenaar, E., Mol, C., van Deemer, L., Smit, J., van der Valk, M., Voordouw, A., Spits, H., van Tellingen, O., Zijlmans, J., Fibbe, W., and Borst, P. (1997) Normal viability and altered pharmacokinetics in mice lacking mdr1-type (drug-transporting) P-glycoproteins. *Proc. Natl. Acad. Sci. U.S.A. 94*, 4028−4033.
(30) Luker, G., Nilsson, K., Covey, D., and Piwnica-Worms, D. (1999) *MDR1* P-glycoprotein enhances esterification of plasma membrane cholesterol. *J. Biol. Chem. 274*, 6979−6991.
(31) van Asperen, J., van Tellingen, O., van der Valk, M., Rozenhart, M., and Beijnen, J. (1998) Enhanced oral absorption and decreased elimination of paclitaxel in mice cotreated with cyclosporin A. *Clin. Cancer Res. 4*, 2293−2297.
(32) Kim, R. B., Fromm, M. F., Wandel, C., Leake, B., Wood, A. J. J., Roden, D. M., and Wilkinson, G. R. (1998) The drug transporter P-glycoprotein limits oral adsorption and brain entry of HIV-1 protease inhibitors. *J. Clin. Invest. 101*, 289−294.
(33) Sorrentino, B., Brandt, S., Bodine, D., Gottesman, M., Pastan, I., Cline, A., and Nienhuis, A. (1992) Selection of drug-resistant bone marrow cells in vivo after retroviral transfer of human MDR1. *Science 257*, 99−103.
(34) Podda, S., Ward, M., Himelstein, A., Richardson, C., de la Flor-Weiss, E., Smith, L., Gottesman, M., Pastan, I., and Bank, A. (1992) Transfer and expression of the human multiple drug resistance gene into live mice. *Proc. Natl. Acad. Sci. U.S.A. 89*, 9676−9680.
(35) Hanania, E., Fu, S., Roninson, I., Zu, Z., Gottesman, M., and Deisseroth, A. (1995) Resistance to taxol chemotherapy produced in mouse marrow cells by safety-modified retroviruses containing a human MDR-1 transcription unit. *Gene Ther. 2*, 279−284.
(36) Moscow, J., Huang, H., Carter, C., Hines, K., Zujewsi, J., Cusack, G., Chow, C., Venzon, D., Sorrentino, B., Chiang, Y., Goldspiel, B., Leitman, S., Read, E., Abati, A., Gottesman, M., Pastan, I., Sellers, S., Dunbar, C., and Cowan, K. (1999) Engraftment of MDR1 and NeoR gene-transduced hematopoietic cells after breast cancer chemotherapy. *Blood 94*, 52−61.
(37) Ford, J. M., and Hait, W. N. (1990) Pharmacology of drugs that alter multidrug resistance in cancer. *Pharmacol Rev. 42*, 155−199.
(38) Pichler, A., Prior, J., and Piwnica-Worms, D. (2004) Imaging reversal of multidrug resistance in living mice with bioluminescence: *MDR1* P-glycoprotein transports coelenterazine. *Proc. Natl. Acad. Sci. U.S.A. 101*, 1702−1707.
(39) Sandor, V., Fojo, T., and Bates, S. (1998) Future perspectives for the development of P-glycoprotein modulators. *Drug Resist. Updates 1*, 190−200.
(40) Luo, J., Manning, B., and Cantley, L. (2003) Targeting the PI3K-Akt pathway in human cancer: rationale and promise. *Cancer Cell 4*, 257−262.
(41) Buchdunger, E., Zimmermann, J., Mett, H., Meyer, T., Muller, M., Druker, B. J., and Lydon, N. B. (1996) Inhibition

of the Abl protein-tyrosine kinase in vitro and in vivo by a 2-phenylaminopyrimidine derivative. *Cancer Res. 56*, 100−104.

(42) Schindler, T., Bornmann, W., Pellicena, P., Miller, W. T., Clarkson, B., and Kuriyan, J. (2000) Structural mechanism for STI-571 inhibition of Abelson tyrosine kinase. *Science 289*, 1938−1942.

(43) Mahon, F. X., Deininger, M. W. N., Schultheis, B., Chabrol, J., Reiffers, J., Goldman, J. M., and Melo, J. V. (2000) Selection and characterization of BCR-ABL positive cell lines with differential sensitivity to the tyrosine kinase inhibitor STI571: diverse mechanisms of resistance. *Blood 96*, 1070−1079.

(44) Trock, B., Leonessa, F., and Clarke, R. (1997) Multidrug resistance in breast cancer: a meta-analysis of MDR1/gp170 expression and its possible functional significance. *J. Natl. Cancer Inst. 89*, 917−931.

(45) Wilson, W., Jamis-Dow, C., Bryant, G., Balis, F., Klecker, R., Bates, S., Chabner, B., Steinberg, S., Kohler, D., and Wittes, R. (1995) Phase I and pharmacokinetic study of the multidrug resistance modulator dexverapamil with EPOCH chemotherapy. *J. Clin. Oncol. 13*, 1985−1994.

(46) Gaveriaux, C., Boesch, D., and Jachez, B. (1991) PSC 833 a nonimmunosuppressive cyclosporin analogue, is a very potent multidrug-resistance modifier. *J. Cell Pharmacol. 2*, 225−234.

(47) Hyafil, F., Vergely, C., Du Vignaud, P., and Grand-Perret, T. (1993) In vitro and in vivo reversal of multidrug resistance by GF120918, an acridonecarboxamide derivative. *Cancer Res. 53*, 4595−4602.

(48) Dantzig, A., Shepard, R., Cao, J., Law, K., Ehlhardt, W., Baughman, T., Bumol, T., and Starling, J. (1996) Reversal of P-glycoprotein-mediated multidrug resistance by a potent cyclopropyldibenzosuberane modulator, LY335979. *Cancer Res. 56*, 4171−4179.

(49) Germann, U., Ford, P., Schlakhter, D., Mason, V., and Harding, M. (1997) Chemosensitization and drug accumulation effects of VX-710, verapamil, cyclosporin A, MS-209, and GF120918 in multidrug resistant HL60/ADR cells expressing the multidrug resistance-associated protein MRP. *Anticancer Drugs 8*, 141−155.

(50) Agrawal, M., Abraham, J., Balis, F., Edgerly, M., Stein, W., Bates, S., Fojo, T., and Chen, C. (2003) Increased Tc-99m-Sestamibi accumulation in normal liver and drug-resistant tumors after the administration of the glycoprotein inhibitor, XR9576. *Clin. Cancer Res. 9*, 650−656.

(51) Mistry, P., Stewart, A., Dangerfield, W., Okiji, S., Liddle, C., Bootle, D., Plumb, J., Templeton, D., and Charlton, P. (2001) In vitro and in vivo reversal of P-glycoprotein-mediated multidrug resistance by a novel potent modulator, XR9576. *Cancer Res. 61*, 749−758.

(52) Martin, C., Berridge, G., Mistry, P., Higgins, C., Charlton, P., and Callaghan, R. (1999) The molecular interaction of the high affinity reversal agent XR9576 with P-glycoprotein. *Br. J. Pharmacol. 128*, 403−411.

(53) Suzuki, T., Fukazawa, N., and San-nohe, K. (1997) Structure activity relationship of newly synthesized quinoline derivatives for reversal of multidrug resistance in cancer. *J. Med. Chem. 40*, 2047−2052.

(54) Suzuki, T., Mabuchi, K., and Fukazawa, N. (1999) Synthesis of glucuronides of multidrug resistance reversing drug MS209. *Biorg. Med. Chem. Lett. 9*, 659−662.

(55) Germann, U. A., Willingham, M. C., Pastan, I., and Gottesman, M. M. (1990) Expression of the human multidrug transporter in insect cells by a recombinant baculovirus. *Biochemistry 29*, 2295−2303.

(56) Ahmad, S., Safa, A. R., and Glazer, R. I. (1994) Modulation of P-glycoprotein by protein kinase Cα in a baculovirus expression system. *Biochemistry 33*, 10313−10318.

(57) Homolya, L., Hollo, Z., Germann, U. A., Pastan, I., Gottesman, M. M., and Sarkadi, B. (1993) Fluorescent cellular indicators are extruded by the multidrug resistance protein. *J. Biol. Chem. 268*, 21493−21496.

(58) Abrams, M. A., Davison, A., Jones, A. G., Costello, C. E., and Pang, H. (1983) Synthesis and characterization hexakis-(alkyl isocyanide) and hexakis-(arylisocyanide) complexes of technetium(I). *Inorg. Chem. 22*, 2798−2800.

(59) Wackers, F. J., Berman, D., Maddahi, J., Beller, G., Straus, H., Boucher, C., Picard, M., Holman, B., and Fridrich, R. (1989) Tc-99m-hexakis 2-methoxy isobutylisonitrile: human biodistribution, dosimetry, safety and preliminary comparison to thallium-201 for myocardial perfusion imaging. *J. Nucl. Med. 30*, 301−309.

(60) Piwnica-Worms, D., Chiu, M., Budding, M., Kronauge, J., Kramer, R., and Croop, J. (1993) Functional imaging of multidrug-resistant P-glycoprotein with an organotechnetium complex. *Cancer Res. 53*, 977−984.

(61) Kronauge, J. F., Davison, A., Roseberry, A. M., Costello, C. E., Maleknia, S., and Jones, A. G. (1991) Synthesis and identification of monocation $Tc(CPl)_6^+$ in $Tc(CNC(CH_3)_2COOCH_3)_6Cl$ and its hydrolysis products. *Inorg. Chem. 30*, 4265−4271.

(62) Piwnica-Worms, D., Kronauge, J., and Chiu, M. (1990) Uptake and retention of hexakis (2-methoxy isobutyl isonitrile) technetium(I) in cultured chick myocardial cells: mitochondrial and plasma membrane potential dependence. *Circulation 82*, 1826−1838.

(63) Backus, M., Piwnica-Worms, D., Hockett, D., Kronauge, J., Lieberman, M., Ingram, P., and LeFurgey, A. (1993) Microprobe analysis of Tc-MIBI in heart cells: calculation of mitochondrial potential. *Am. J. Physiol. (Cell) 265*, C178−C187.

(64) Piwnica-Worms, D., Rao, V., Kronauge, J., and Croop, J. (1995) Characterization of multidrug-resistance P-glycoprotein transport function with an organotechnetium cation. *Biochemistry 34*, 12210−12220.

(65) Ballinger, J., Hua, H., Berry, B., Firby, P., and Boxen, I. (1995) ^{99m}Tc-Sestamibi as an agent for imaging P-glycoprotein-mediated multi-drug resistance: in vitro and in vivo studies in a rat breast tumour cell line and its doxorubicin-resistant variant. *Nucl. Med. Commun. 16*, 253−257.

(66) Ballinger, J. R., Sheldon, K. M., Boxen, I., Erlichman, C., and Ling, V. (1995) Differences between accumulation of Tc-99m-MIBI and Tl-201-thallous chloride in tumor cells: Role of P-glycoprotein. *Q. J. Nucl. Med. 39*, 122−128.

(67) Cordobes, M., Starzec, A., Delmon-Moingeon, L., Blanchot, C., Kouyoumdjian, J.-C., Prevost, G., Caglar, M., and Moretti, J. L. (1996) Technetium-99m-Sestamibi uptake by human benign and malignant breast tumor cells: correlation with *mdr* gene expression. *J. Nucl. Med. 37*, 286−289.

(68) Luker, G., Rao, V., Crankshaw, C., Dahlheimer, J., and Piwnica-Worms, D. (1997) Characterization of phosphine complexes of technetium (III) as transport substrates of the multidrug resistance (MDR1) P-glycoprotein and functional markers of P-glycoprotein at the blood-brain barrier. *Biochemistry 36*, 14218−14227.

(69) Bosch, I., Crankshaw, C., Piwnica-Worms, D., and Croop, J. (1997) Characterization of functional assays of P-glycoprotein transport activity. *Leukemia 11*, 1131−1137.

(70) Luker, G. D., Fracasso, P. M., Dobkin, J., and Piwnica-Worms, D. (1997) Modulation of the multidrug resistance P-glycoprotein: detection with Tc-99m-Sestamibi *in vivo. J. Nucl. Med. 38*, 369−372.

(71) Chen, C., Meadows, B., Regis, J., Kalafsky, G., Fojo, T., Carrasquillo, J., and Bates, S. (1997) Detection of in vivo P-glycoprotein inhibition by PSC 833 using Tc-99m-Sestamibi. *Clin. Cancer Res. 3*, 545−552.

(72) Barbarics, E., Kronauge, J., Cohen, D., Davison, A., Jones, A., and Croop, J. (1998) Characterization of P-glycoprotein transport and inhibition *in vivo. Cancer Res. 58*, 276−282.

(73) Peck, R., Hewett, J., Harding, M., Wang, Y., Chaturvedi, P., Bhatnagar, A., Ziessman, H., Atkins, F., and Hawkins, M. (2001) Phase I and pharmacokinetic study of the novel MDR1 and MRP1 inhibitor biricodar administered alone and in combination with doxorubicin. *J. Clin. Oncol. 19*, 3130−3141.

(74) Piwnica-Worms, D., and Kronauge, J. (1994) Tc-99m-EIBI is a transport substrate for the multidrug resistance (MDR) P-glycoprotein. *J. Nucl. Med. 35*, 230P.

(75) Herman, L. W., Sharma, V., Kronauge, J. F., Barbarics, E., Herman, L. A., and Piwnica-Worms, D. (1995) Novel

hexakis(areneisonitrile)technetium(I) complexes as radioligands targeted to the multidrug resistance P-glycoprotein. *J. Med. Chem. 38*, 2955−2963.

(76) Jurisson, S., Berning, D., Jia, W., and Ma, D.-S. (1993) Coordination compounds in nuclear medicine. *Chem. Rev. 93*, 1137−1156.

(77) Deutsch, E., Vanderheyden, J.-L., Gerundini, P., Libson, K., Hirth, W., Colombo, F., Savi, A., and Fazio, F. (1987) Development of nonreducible technetium-99m(III) cations as myocardial perfusion imaging agents: initial experience in humans. *J. Nucl. Med. 28*, 1870−1880.

(78) Rossetti, C., Vanoli, G., Paganelli, G., Kwiatkowski, M., Zito, F., Colombo, F., Bonino, C., Carpinelli, A., Casati, R., Deutsch, K., Marmion, M., Woulfe, S. R., Lunghi, F., Deutsch, E., and Fazio, F. (1994) Human biodistribution, dosimetry and clinical use of technetium(III)-99m−Q12. *J. Nucl. Med. 35*, 1571−1580.

(79) Crankshaw, C., Marmion, M., Luker, G., Rao, V., Dahlheimer, J., Burleigh, B., Webb, E., Deutsch, K., and Piwnica-Worms, D. (1998) Novel Tc(III)-Q-complexes for functional imaging of the multidrug resistance (*MDR1*) P-glycoprotein. *J. Nucl. Med. 39*, 77−86.

(80) Woulfe, S., Dunn, T., Marmion, M., MacDonald, J., Rogic, M., and Deutsch, E. (1991) The synthesis of analogous N_2O_2, N_2OS and diamide dimercapto Schiff base ligands for use in radiopharmaceutical inaging agents. *J. Nucl. Med. 32*, 1101.

(81) Jurisson, S. S., Dancey, K., McPartlin, M., Tasker, P. A., and Deutsch, E. (1984). Synthesis, characterization, and electrochemical properties of technetium complexes containing both tetradentate Schiff base and monodentate tertiary phosphine ligands: single-crystal structure of trans-(N,N′-ethylenebis(acetylacetone iminato))bis(triphenylphosphine)-technetium(III) hexafluorophosphate. *Inorg. Chem. 23*, 4743−4749.

(82) Kelly, J., Forster, A., Higley, B., Archer, C., Booker, F., Canning, L., Chiu, K., Edwards, B., Gill, H., McPartlin, M., Nagle, K., Latham, I., Pickett, R., Storey, A., and Webbon, P. (1993) Technetium-99m-tetrofosmin as a new radiopharmaceutical for myocardial perfusion imaging. *J. Nucl. Med. 34*, 222−227.

(83) Ballinger, J. R., Bannerman, J., Boxen, I., Firby, P., Hartman, N. G., and Moore, M. J. (1996) Technetium-99m-Tetrofosmin as a substrate for P-glycoprotein: in vitro studies in multidrug-resistant breast tumor cells. *J. Nucl. Med. 37*, 1578−1582.

(84) Alberto, R., Schibli, R., Egli, A., and Schubiger, A. (1998) A novel organometallic aqua complex of technetium for the labeling of biomolecules: synthesis of $[^{99m}Tc(OH_2)_3(CO)_3]^+$ from $[^{99m}TcO_4]^-$ in aqueous solution and its reaction with a bifunctional ligand. *J. Am. Chem. Soc. 120*, 7987−7988.

(85) Marmion, M., and MacDonald, J. (2000) Preparation and biodistribution of ^{99m}Tc(I)-tricarbonyl complexes containing isonitrile and phosphine ligands. *J. Nucl. Med. 41*, 40P.

(86) Dyszlewski, M., Blake, H., Dalheimer, J., Pica, C., and Piwnica-Worms, D. (2002) Characterization of a novel Tc-99m-carbonyl complex as a functional probe of *MDR1* P-glycoprotein transport activity. *Mol. Imaging 1*, 24−35.

(87) Wong, E., Liu, S., Lugger, T., Hahn, F. E., and Orvig, C. (1995) Hexadentate N_4O_2 amine phenol complexes of gallium and indium. *Inorg. Chem. 34*, 93−101.

(88) Yang, L. W., Liu, S., Wong, E., Rettig, S. J., and Orvig, C. (1995) Complexes of trivalent metal ions with potentially heptadentate N_4O_3 Schiff base and amine phenol ligands of variable rigidity. *Inorg. Chem. 34*, 2164−2178.

(89) Sarma, B. D., and Bailar, J. C. (1955) The stereochemistry of metal complexes with polydentate ligands. Part I. *J. Am. Chem. Soc. 77*, 5476−5480.

(90) Sarma, B. D., Ray, K. R., Sievers, R. E., and Bailar, J. C. (1964) The stereochemistry of metal chelates with multidentate ligands. Part II. *J. Am. Chem. Soc. 86*, 14−16.

(91) Tweedle, M. F., and Wilson, L. J. (1976) Variable spin iron-(III) chelates with hexadentate ligands derived from triethylenetetramine and various salicyaldehydes. *J. Am. Chem. Soc. 98*, 4824−4834.

(92) Tsang, B., Mathias, C., and Green, M. (1993). A gallium-68 radiopharmaceutical that is retained in myocardium: ^{68}-Ga-$[(4,6\text{-MeO})_2\text{sal})_2\text{BAPEN}]^+$. *J. Nucl. Med. 34*, 1127−1131.

(93) Tsang, B., Mathias, C., Fanwick, P., and Green, M. (1994) Structure-distribution relationship for metal-labeled myocardial imaging agents: Comparison of a series of cationic gallium(III) complexes with hexadentate bis(salicylaldimine) ligands. *J. Med. Chem. 37*, 4400−4406.

(94) Sharma, V., Beatty, A., Wey, S.-P., Dahlheimer, J., Pica, C., Crankshaw, C., Bass, L., Green, M., Welch, M., and Piwnica-Worms, D. (2000) Novel gallium(III) complexes transported by *MDR1* P-glycoprotein: potential PET imaging agents for probing P-glycoprotein-mediated transport activity *in vivo*. *Chem. Biol. 7*, 335−343.

(95) Sharma, V., Crankshaw, C., and Piwnica-Worms, D. (1996) Effects of multidrug resistance (*MDR1*) P-glycoprotein expression levels and coordination metal on the cytotoxic potency of multidentate (N_4O_2) ethylenediamine-bis[propyl-(R-benzylimino)]metal(III) cations. *J. Med. Chem. 39*, 3483−3490.

(96) Sharma, V., Wey, S. P., Bass, L., Crankshaw, C. L., Green, M. A., Welch, M. J., and Piwnica-Worms, D. (1996) Monocationic N_4O_2 Schiff-Base phenolate complexes of gallium(III): novel PET imaging agents of the human multidrug resistance (*MDR1*) P-glycoprotein. *J. Nucl. Med. 37*, 51P.

(97) Sharma, V., Prior, J., Belinsky, M., Kruh, G., and Piwnica-Worms, D. (2004) Characterization of a gallium-67/gallium-68 radiopharmaceutical for SPECT and PET imaging of MDR1 P-glycoprotein transport activity in vivo: Validation in multidrug resistant tumors and at the blood-brain barrier. *J. Nucl. Med*., in press.

(98) Bigott, H., McCarthy, D., Wust, F., Dahlheimer, J., Piwnica-Worms, D., and Welch, M. (2001) Production, processing and uses of 94m-Tc. *J. Labelled Compd. Radiopharm. 44*, S119−S121.

(99) Anderson, O., and Packard, A. (1980) Structure variations in macrocyclic copper(II) complexes: crystal and molecular structure of cyano(difluoro-3,3-(trimethylenedinitrilo)bis(2-butanone oximato)borato)copper II-methanol[Cu(cyclops)CN]. CH_3OH. *Inorg. Chem. 19*, 2941−2945.

(100) Anderson, O., and Packard, A. (1979) Structural variations in macrocyclic copper(II) complexes: Crystal and molecular structures of $[Cu(cyclops)H_2O](ClO_4)$ and $[Cu(PreH)H_2O](ClO_4).H_2O$. *Inorg. Chem. 18*, 1940−1947.

(101) Packard, A., Kronauge, J., Barbarics, E., Kiani, S., and Treves, S. (2002). Synthesis and biodistibution of a lipophilic ^{64}Cu-labeled monocationic copper(II) complex. *Nucl. Med. Biol. 29*, 289−294.

(102) Lewis, J., Zweit, J., Dearling, J., Rooney, B., and Blower, P. (1996). Copper(I) bis diphosphine complexes as basis for radiopharmaceuticals for positron emission tomography and targeted radiotherapy. *Chem. Commun*. 1093−1094.

(103) Blower, P. (1998) Small coordination compounds as radiopharmaceuticals for cancer targeting. *Transition Met. Chem. 23*, 109−112.

(104) Camus, A., Marsich, N., Nardin, G. and Randaccio, L. (1976) The crystal and molecular structure of bis[1, 2 bis-(diphenylphosphino)ethane]copper(I)-trifluoroacetate toluene solvate. *Transition Met. Chem. 1*, 205−206.

(105) Berners-Price, S., Johnson, R., Mirabelli, C., Faucette, L., McCabe, F., and Sadler, P. (1987) Copper(I) complexes with bidentate tertiary phosphine ligands: solution chemistry and antitumor activity. *Inorg. Chem. 26*, 3383−3387.

(106) Zweit, J., Lewis, J., Dearling, J., Rooney, B., Coley, H., and Kelland, L. (1997) Copper-64-diphosphine complexes: potential PET tracers for the assessment of multidrug resistance in tumors [abstract]. *J. Nucl. Med. 38*, 133P.

(107) Lewis, J., Dearling, J., Sosabowski, J., Zweit, J., Carnochan, P., Kelland, L., Coley, H., and Blower, P. (2000) Copper bis(diphosphine)complexes: radiopharmaceuticals for detection of multidrug resistance in tumors by PET. *Eur. J. Nucl. Med. 27*, 638−646.

(108) Schinkel, A. H., Mol, C. A. A. M., Wagenaar, E., van Deemter, L., Smit, J. J. M., and Borst, P. (1995) Multidrug resistance and the role of P-glycoprotein knockout mice. *Eur. J. Cancer 31A*, 1295−1298.

(109) Schinkel, A., Smit, J., van Tellingen, O., Beijnen, J., Wagenaar, E., van Deemter, L., Mol, C., van der Valk, M., Robanus-Maandag, E., te Riele, H., Berns, A., and Borst, P. (1994) Disruption of the mouse *mdr1a* P-glycoprotein gene leads to a deficiency in the blood-brain barrier and to increased sensitivity to drugs. *Cell 77*, 491−502.

(110) Slapak, C., Dahlheimer, J., and Piwnica-Worms, D. (2001) Reversal of multidrug resistance with LY335979: functional analysis of P-glycoprotein-mediated transport activity and its modulation *in vivo. J. Clin. Pharmacol. 41*, 29S-38S.

(111) Chen, W., Luker, K., Dahlheimer, J., Pica, C., Luker, G., and Piwnica-Worms, D. (2000). Effects of *MDR1* and *MDR3* P-glycoproteins, MRP1 and BCRP/MXR/ABCP on transport of Tc-99m-Tetrofosmin. *Biochem. Pharmacol. 60*, 413−426.

(112) Mehta, B. M., Rosa, E., Fissekis, J. D., Bading, J. R., Biedler, J. L., and Larson, S. M. (1992) In-vivo identification of tumor multidrug resistance with tritum-3-colchicine. *J. Nucl. Med. 33*, 1373−1377.

(113) Mehta, B., Rosa, E., Biedler, J., and Larson, S. (1994) In vivo uptake of carbon-14-colchicine for identification of tumor multidrug resistance. *J. Nucl. Med. 35*, 1179−1184.

(114) Elsinga, P. H., Franssen, J. F., Hendrikse, N. H., Fluks, L., Weemaes, A.-M. A., van der Graaf, W. T. A., de Vries, E. G. E., Visser, G. M., and Vaalburg, W. (1996) Carbon-11-labeled daunorubicin and verapamil for probing P-glycoprotein in tumors with PET. *J. Nucl. Med. 37*, 1571−1575.

(115) Hendrikse, N., Franssen, E., van der Graaf, W., Vaalburg, W., and de Vries, E. (1999) Visualization of multidrug resistance in vivo. *Eur. J. Nucl. Med. 26*, 283−293.

(116) Hendrikse, N., EGE, d. V., Eriks-Fluks, L., van der Graaf, W., Hospers, G., Willemsen, A., Vaalburg, W., and Franssen, E. (1999) A new in vivo method to study P-glycoprotein transport in tumors and the blood-brain barrier. *Cancer Res. 59*, 2411−2416.

(117) Levchenko, A., Mehta, B., Lee, J.-B., Humm, J., Augensen, F., Squire, O., Kothari, P., Finn, R., Leonard, E., and Larson, S. (2000) Evaluation of ^{11}C-colchicine for PET imaging of multiple drug resistance. *J. Nucl. Med. 41*, 493−501.

(118) Luurtsema, G., Molthoff, C., Windhorst, A., Smit, J., Keizer, R., Boellaard, R., Lammertsma, A., and Franssen, E. (2003) (R)- and (S)-[11C] Verapamil as PET-tracers for measuring P-glycoprotein function: in vitro and in vivo evaluation. *Nucl. Med. Biol. 30*, 747−751.

(119) Hendrikse, N., and Vaalburg, W. (2002) Imaging of P-glycoprotein function in vivo with PET. *Novartis Found Symp. 243*, 137−145.

(120) Ravert, H., Klecker, R., Collins, J., Mathews, W., Pomper, M., Wahl, R., and Dannals, R. (2002) Radiosynthesis of [C-11]-paclitaxel. *J. Labelled Compd. Radiopharm. 45*, 471−477.

(121) Kiesewetter, D., and Eckelman, W. (2001) Radiochemical synthesis of [18F]fluoropaclitaxel [abstract]. *J. Labelled Compd. Radiopharm. 44*, S903−S905.

(122) Kiesewetter, D., Jagoda, E., Kao, C., Ma, Y., Ravasi, L., Shimoji, K., Szajek, L., and Eckelman, W. (2003) Fluoro-, bromo-, and iodopaclitaxel derivatives: synthesis and biological evaluation. *Nucl. Med. Biol. 30*, 11−24.

(123) Hrycyna, C. A., Ramachandra, M., Ambudkar, S. V., Ko, Y., Pedersen, P., Pastan, I., and Gottesman, M. M. (1998) Mechanism of action of human P-glycoprotein ATPase activity. Photochemical cleavage during a catalytic transition state using orthovandate reveals cross talk between two ATP sites. *J. Biol. Chem. 273*, 16631−16634.

BC0498469

TECHNICAL NOTES

Evidence of Antisense Tumor Targeting in Mice

K. Nakamura,[†] C. Fan,[‡,§] G. Liu,[‡] S. Gupta,[‡] J. He,[‡] S. Dou,[‡] A. Kubo,[†] M. Rusckowski,[‡] and D. J. Hnatowich*[,‡]

Department of Radiology, Keio University School of Medicine, Tokyo, Japan, Department of Radiology, University of Massachusetts Medical School, Worcester, Massachusetts 01655, and Department of Nuclear Medicine, West China Hospital, Sichuan University, Chengdu, China.
Received April 13, 2004; Revised Manuscript Received May 27, 2004

Even though increased accumulations of radiolabeled antisense DNAs compared to control DNAs are becoming a routine observation in cultured tumor cells, trustworthy evidence of tumor targeting in vivo by an antisense mechanism remains elusive. The goal of this study was to obtain convincing evidence of antisense tumor targeting in nude mice by using two different tumors and both intratumoral (i.t.) and intravenous (i.v.) administration of radiolabeled antisense and control sense DNAs. Both the MDR++ cell line KB-G2 and its parent MDR+ cell line KB-31 were used in this study. The antisense (AS) DNA was directed against the AUG start codon of the MDR1 mRNA and, along with the sense (S) control DNA, was a uniform phosphorothioate administered naked. In previous cell culture studies from our laboratories, the accumulation of this AS DNA was strikingly high in KB-G2 cells and only average in KB-31 cells, a fact we attribute to the 1000-fold higher expression by RT-PCR of MDR1 mRNA in the former cell line. In this study, both DNAs were radiolabeled with ^{99m}Tc via MAG3 and administered i.t. or i.v. at 1 μg (100 μCi) per animal 24 h prior to sacrifice and dissection in mice bearing thigh tumors of about 1 g. Following i.t. administration, no statistically significant differences (Student's t test, $p < 0.05$, $N = 4$) between the AS and S DNA biodistributions in normal tissues were observed except in the KB-G2 mice in which muscle levels were lower for the S control. In contrast, tumor levels in the KB-G2 animals were significantly higher for the AS DNA vs S DNA (14.7 vs 8.5% ID/g) while this difference (8.6 vs 4.3% ID/g) was insignificant in the KB-31 animals. The whole body images obtained just prior to sacrifice clearly show improved targeting of AS DNA vs S DNA in the KB-G2 but not the KB-31 animals. Calculations based on these results show that about 60 000 AS DNAs accumulated specifically (i.e. AS DNA − S DNA) per KB-G2 tumor cell following i.t. administration. When administered i.v. rather than i.t., higher tumor levels in KB-G2 animals compared to KB-31 were not observed, most likely because of the lower dosage reaching the tumors. When the KB-G2 and KB-31 results are combined, no statistically significant differences between the AS and S DNA biodistributions in normal tissues were observed except in blood in which S DNA levels were higher and in spleen in which they were lower. In contrast, tumor levels were significantly higher for the AS DNA vs S DNA (0.100 vs 0.063% ID/g). Calculations based on these results show that about 400 AS DNAs accumulated specifically per tumor cell following i.v. administration. Therefore evidence for tumor targeting in vivo by an antisense mechanism has been obtained in that statistically higher tumor accumulations of the ^{99m}Tc-AS DNA were observed compared to the control ^{99m}Tc-S DNA both following i.t. and i.v. administrations. The successful localization of AS DNA in tumor demonstrates that in vivo AS targeting of tumor is feasible although improvements in tumor delivery and normal tissue clearance are needed for practical antisense imaging.

INTRODUCTION

Before radiolabeled antisense (AS) oligomers merit serious consideration as targeting modalities for tumor and other tissues, it must first be demonstrated to the greatest possible extent that localization follows an antisense mechanism. To prove an antisense mechanism may be extremely difficult especially in the case of phosphorothioate DNAs that show high binding affinities for proteins. One obvious concern is the possibility of binding by an aptameric mechanism in which the AS oligomer, but not its control oligomer, assumes a particular configuration that encourages binding to cellular proteins by a sequence-specific but non-antisense mechanism (*1*). If increased accumulations compared to control DNAs are observed for a variety of DNAs, radiolabeled by different methods, with antisense base sequence against different messenger RNA (mRNA) targets and

* Corresponding author: D. J. Hnatowich, Ph.D., Professor of Radiology, Division of Nuclear Medicine, Department of Radiology, H2-579, University of Massachusetts Medical School 55 Lake Ave. North, Worcester, MA 01655. Tel: (508) 856-4256. Fax: (508) 856-4572. E-mail: donald.hnatowich@umassmed.edu.
[†] Keio University School of Medicine.
[‡] University of Massachusetts Medical School.
[§] Sichuan University

10.1021/bc0499073 CCC: $27.50 © 2004 American Chemical Society
Published on Web 10/05/2004

in different cell types with irrelevant base sequences (e.g. sense, random, scrambled), then an aptameric mechanism for the increased accumulations may be largely excluded. Since oligomers with different base sequences will show differences in behavior, a large number of such studies with positive accumulations compared to controls will be necessary to exclude aptameric effects as a plausible mechanism.

In general, to help establish an antisense mechanism by a different means, at a minimum, four criteria should be met: (1) higher accumulations must be demonstrated for the AS oligomer in comparison to a control oligomer designed to be as identical as possible to that of the study DNA but with restricted or nonexistent hybridization affinities for the mRNA target; (2) higher accumulations compared to controls should be demonstrated for the AS oligomer in a variety of cell types, hopefully with accumulations in proportion to the estimated mRNA target concentrations of each cell type; (3) the higher accumulations should be demonstrated for different AS oligomers directed against different mRNA targets as evidence against aptameric effects; and (4) the higher accumulations of the AS oligomer should be shown to decrease with increasing AS DNA concentrations as evidence of specific binding.

While a direct demonstration of an antisense mechanism remains elusive even in cell culture, indirect evidence of this mechanism is now common. We have observed statistically significant increased accumulation of radioactivity in LS174T colon cancer cells and ACHN kidney cancer cells with endogenously labeled ^{35}S as well as ^{99m}Tc-radiolabeled uniform phosphorothioate MAG3-DNA against the regulatory subunit I alpha (RIα) mRNA of protein kinase A (PKA) compared to sense and random DNA controls but not in HC2 cells with irrelevant murine RIα mRNA (*2*). An increased accumulation of radioactivity in MDA-MB-231 breast cancer cells with ^{99m}Tc-labeled Hynic-DNA antisense to the c-myc oncogene compared to the S DNA control has also been observed (*3*). Recently a statistically significant increased accumulation was also observed in targeting of multidrug resistance mRNA in epidermal carcinoma cells KB-G2 and KB-31 with ^{99m}Tc-labeled AS MAG3-DNA compared to the S DNA control (*4*). Should an AS oligomer assume a particular configuration that encourages increased cellular accumulation by an aptameric effect, this would be extremely unlikely to be the case for each of the large variety of base sequences, labeling methods, mRNA targets and cell types described in the above studies.

Another test of specific mechanism of localization is to demonstrate that accumulation decreases with increasing dosage as binding becomes saturated. When ACHN cells were incubated with ^{99m}Tc-labeled AS DNA with increasing concentrations of unlabeled AS DNA in the range 7 to 100 nM and compared to the accumulations of ^{99m}Tc-labeled S DNA with increasing concentrations of unlabeled S DNA in the same range, the difference in AS compared to S DNA accumulations decreased and became statistically insignificant as the concentration increased (*2*). More definitive results have recently been observed for ^{99m}Tc-labeled AS and control S DNAs in the KB-G2 and KB-31 cells as well as TCO-1 cells, another multidrug resistance positive cell type (*4*).

These studies in cell culture therefore generally satisfy the above four conditions necessary to claim evidence of an antisense mechanism. The more important remaining challenge is therefore to demonstrate evidence of an antisense mechanism in vivo. Herein we report on the first results from these laboratories of in vivo antisense targeting of tumor in mice. The MDR++ cell line KB-G2 and its parent MDR+ cell line KB-31 were again used along with the same AS and control S DNAs used previously with these cell types. The expression of MDR1 has been reported to be 1000-fold higher by RT-PCR for KB-G2 cells compared to KB-31 cells (*4*). In that investigation, the increased expression of MDR in the KB-G2 cells compared to KB-31 cells and the specificity of the AS DNA for its target were both confirmed in cell culture using ^{99m}Tc-sestamibi, a substrate of MDR. Because delivery is an important issue in antisense targeting, especially when oligomers are to be administered naked as in this case, intratumor (i.t.) as well as intravenous (i.v.) administrations were performed.

MATERIALS AND METHODS

Uniform phosphorothioate DNAs were obtained for this investigation with a primary amine on the 5′-end via a six-carbon alkyl linker (Qiagen, Alameda, CA). All DNAs were 20-mer and all were HPLC purified by the supplier. The base sequence of the AS DNA was 5′-CCA-TCC−CGA-CCT-CGC-GCT-CC while that of the S control was 5 '-GGA-GCG-CGA-GGT-CGG-GAT-GG (*5*). S-Acetyl NHS-MAG3 was synthesized in house (*6*) and its structure confirmed by elemental analysis, proton nuclear magnetic resonance, and mass spectroscopy. The P4 medium for separation was purchased (Bio-Rad Laboratories Inc., Hercules, CA). The ^{99m}Tc-pertechnetate was eluted from a $^{99}Mo-^{99m}Tc$ generator (Bristol-Myers Squibb Medical Imaging, Inc., North Billerica, MA, or Daiichi Radioisotopes, Tokyo, Japan). The two cell lines were a generous gift from Dr. I. Sugawara, Research Institute of Tuberculosis, Tokyo, Japan. Other chemicals were obtained from various suppliers and used without purification.

DNA Conjugation and Radiolabeling. Both DNAs were conjugated with *S*-acetyl NHS-MAG3 via the 5′-derivatized amine as previously described (*7*). A solution of 1 mg (about 0.15 μmol) of DNA in 200 μL of 0.2 M pH 8.0 HEPES buffer was added to a vial containing 1.7−2.0 mg (about 4.5 μmol) *S*-acetyl NHS-MAG3. The vial was vortexed immediately and incubated for 1 h at room temperature. The DNA was then purified on a 0.7 × 20 cm P4 column with either 0.25 M pH 5.2 NH_4OAc buffer or 0.05 M PBS pH 7.2 buffer as eluant. The peak fractions were pooled and the DNA concentration quantitated by UV absorbance at 265 nm.

Radiolabeling of the DNAs was achieved by introducing about 1 mCi (20−40 μL) of ^{99m}Tc-pertechnetate generator eluate into a combined solution consisting of 50 μL (about 10 μg) MAG3-conjugated DNA in either buffer, 25 μL of 50 μg/μL Na_2tartrate·$2H_2O$ in a pH 9.2 buffer, and 5 μL of fresh 4 μg/μL $SnCl_2$·$2H_2O$ in 10 mM HCl. The final pH was about 7.8. After vortexing and then heating for 20 min in boiling water, the labeling was confirmed by C18 SepPak (Waters, Milford, MA) in which the first elution with PBS removes radiolabeled pertechnetate and tartrate, the second elution with 40% acetonitrile removes radiolabeled DNA and the SepPak retained radiolabeled colloids. In most cases, the radiochemical purity exceeded 90% without purification, and the specific radioactivity was about 100 μCi/μg.

Biodistribution Studies. All animal studies at UMMS were performed with the approval of the UMMS Institutional Animal Care and Use Committee while all animal studies at Keio University School of Medicine were performed with the approval of The Laboratory Animal Care and use Committee.

For the i.t. studies, the cells were grown in D-MEM supplemented with 10% fetal bovine serum (FBS), 100

Table 1. Biodistribution of ^{99m}Tc-Labeled Antisense and Sense DNA Obtained 24 h Postintratumoral Administration to Nude Mice Bearing KB-G2 Tumors (% ID/g (SD) $N = 4$)

tissue	antisense	sense	P value
blood	0.018 (0.003)	0.021(0.005)	0.377
heart	0.016 (0.002)	0.018 (0.003)	0.415
lung	0.023 (0.005)	0.030 (0.013)	0.319
liver	0.215 (0.080)	0.301 (0.200)	0.455
spleen	0.052 (0.024)	0.083 (0.056)	0.354
small intestines	0.247 (0.070)	0.493 (0.389)	0.260
large intestines	3.01 (0.43)	5.27 (2.76)	0.158
kidney	0.243 (0.018)	0.323 (0.083)	0.107
muscle	0.027 (0.007)	0.015 (0.005)	0.027[a]
tumor	14.74 (3.24)	8.52 (3.45)	0.039[a]

[a] Difference statistically significant (Student's t test).

Table 2. Biodistribution of ^{99m}Tc-Labeled Antisense and Sense DNA Obtained 24 h Postintratumoral Administration to Nude Mice Bearing KB-31 Tumors (% ID/g (SD) $N = 4$)

tissue	antisense	sense	P value
blood	0.019 (0.005)	0.023 (0.011)	0.546
heart	0.018 (0.006)	0.020 (0.015)	0.847
lung	0.025 (0.006)	0.053 (0.057)	0.369
liver	0.230 (0.120)	0.291 (0.245)	0.695
spleen	0.057 (0.016)	0.079 (0.059)	0.497
small intestines	0.189 (0.081)	0.156 (0.121)	0.663
large intestines	2.86 (0.89)	3.70 (3.07)	0.619
kidney	0.200 (0.009)	0.276 (0.164)	0.389
muscle	0.014 (0.006)	0.063 (0.039)	0.050
tumor	8.65 (5.00)	4.30 (3.38)	0.199

Table 3. Biodistribution of ^{99m}Tc-Labeled Antisense and Sense DNA Obtained 24 h Postintravenous Administration to Tumor Bearing Nude Mice. Results for KB-31 and KB-G2 Combined (% ID/g (SD) $N = 5-6$)

tissue	antisense	sense	P value
blood	0.022 (0.003)	0.017 (0.002)	0.018[a]
heart	0.055 (0.012)	0.049 (0.012)	0.433
lung	0.106 (0.021)	0.081 (0.024)	0.108
liver	2.58 (0.18)	2.46 (0.19)	0.155
spleen	0.688 (0.060)	1.00 (0.12)	0.003[a]
small intestines	0.151 (0.083)	0.098 (0.024)	0.189
large intestines	0.519 (0.212)	0.376 (0.217)	0.302
kidney	0.778 (0.086)	0.699 (0.145)	0.324
muscle	0.016 (0.004)	0.018 (0.006)	0.719
tumor	0.100 (0.011)	0.063 (0.009)	4.8×10^{-8} [a]

[a] Difference statistically significant (Student's t test).

units/mL penicillin, and 100 μg/mL streptomycin (Gibco-Invitrogen, Carlsbad, CA). Cells were maintained as monolayers in a humidified 5% carbon dioxide atmosphere, normally in T75 flasks (Falcon, Becton Dickinson, Lincoln Park, NJ). The cells were trypsinated in the T75 flasks at 80−90% confluence using 0.05% trypsin/0.02% EDTA and were then suspended in MEM with 10% FBS.

For the i.v. studies, the cells were grown in RPMI medium (RPMI 1640, Gibco BRL Products, Gaithersburg, MD) with 2.0 mg/L sodium bicarbonate, supplemented with 10% FBS. The cells were trypsinated in the T75 flasks at 80−90% confluence using 0.5% trypsin and were then suspended in PBS.

Nude mice (i.t. studies: NIH Swiss, Taconic Farms, Germantown, NY, 30−40 g; i.v. studies: BALB/c AnNCrj-nu male, Oriental, Tokyo, 25−30 g) were each injected subcutaneously in the left thigh with a 0.1 mL suspension containing 10^7 KB-G2 or KB-31 tumor cells with greater than 95% viability. Animals were used 10 days (KB-31) or14 days (KB-G2) later when the tumors were about 1.0 cm in any dimension. Each tumored nude mouse was injected with 1.0 μg of DNA (100 μCi) in 100 μL i.v. via a tail vein or with 50 μL i.t. Animals were sacrificed under halothane anesthesia at 24 h, blood and other organs were removed, weighed, and counted in a NaI(Tl) well counter along with a standard of the injectate. Statistical significance between tissue radioactivity levels in animals receiving AS vs S DNA was established by the Student's t test two-tailed distribution and paired.

In the case of animals receiving radiolabeled DNA by i.t. administration, prior to sacrifice, the animals were imaged simultaneously in groups of four while resting on the collimator of an Elscint APEX 409 M large view gamma camera (Hackensack, NJ).

RESULTS

The biodistribution results obtained 24 h post i.t. administration of radiolabeled AS and S DNAs to nude mice bearing KB-G2 and KB-31 tumors are presented in Tables 1 and 2, respectively. The only normal tissues showing statistically significant differences in radioactivity accumulation of AS DNA compared to S DNA are in the KB-G2 animals in which muscle levels were lower for the S DNA. Possibly because of differences in pharmacokinetic properties of the DNAs resulting from the different base sequence, tissue levels tend to be higher in general following administration of the S DNA when administered i.t. That this difference was not seen following i.v. administration may be due to pharmacokinetic differences following delivery into the vasculature compared to the lymphatics.

While the tumor accumulations were higher in both animal models following administration of the AS DNA compared to S DNA, this difference was significant only in the KB-G2 case. The absence of significance in the KB-31 case may be related to the large standard deviations of the tumor values resulting from the i.t. administrations. That the accumulations of AS DNA in KB-G2 tumor compared to KB-31 were significantly higher ($P = 0.047$) may be related to the higher expression levels of the target MDR1 mRNA in the former tumor type. The higher accumulation of S DNAs in KB-G2 tumors compared to KB-31 tumors failed to reach significance ($P = 0.13$).

These biodistribution results are faithfully reflected in the whole body radioactivity images obtained at 22 h postadministration as shown in Figures 1 and 2. Each figure is a composite in which scintigraphic whole body images have been superimposed on a photographic image taken during imaging to provide accurate registration. In each image, two animals receiving the AS DNA have been imaged simultaneously with two animals receiving the S DNA, as indicated in the figures. The higher radioactivity levels in tumor (left thighs) in animals receiving the AS DNA compared to animals receiving the S DNA is readily apparent in Figure 1 for KB-G2 tumored mice. The higher levels are less evident in Figure 2 for KB-31 animals.

From the specific radioactivity of the labeled DNAs, the dosage administered, the percent accumulating in each gram of tumor and under the assumption of 10^8 tumored cells per gram, a simple calculation will show that about 66 000 AS DNAs accumulated specifically (i.e. AS DNA accumulation − S DNA accumulation) per KB-G2 cell while for KB-31, this value was 53 000 per cell.

Table 3 presents biodistribution results obtained in the identical fashion to that of Tables 1 and 2 except that administration was intravenous rather than intratumoral. This study was performed separately for both KB-G2 and KB-31 animals. However, unlike the i.t. study, no differences were apparent between the biodistributions obtained in KB-G2 and KB-31 animals following

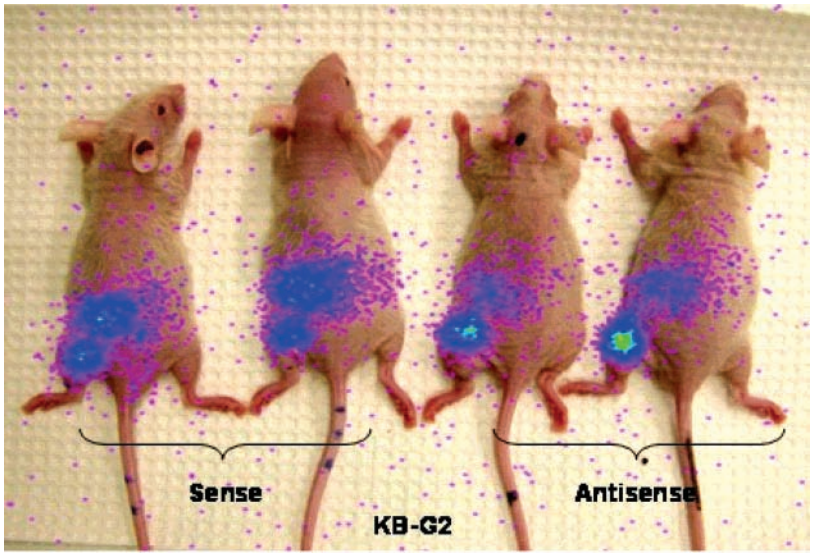


Figure 1. A composite obtained at 22 h postadministration in KB-G2 tumored mice. The scintigraphic whole body image has been superimposed on a photographic image taken during imaging to provide accurate registration. Two animals receiving the AS DNA are on the right while two identical animals receiving the control S DNA are on the left. In all cases, the tumor is in the left thigh.

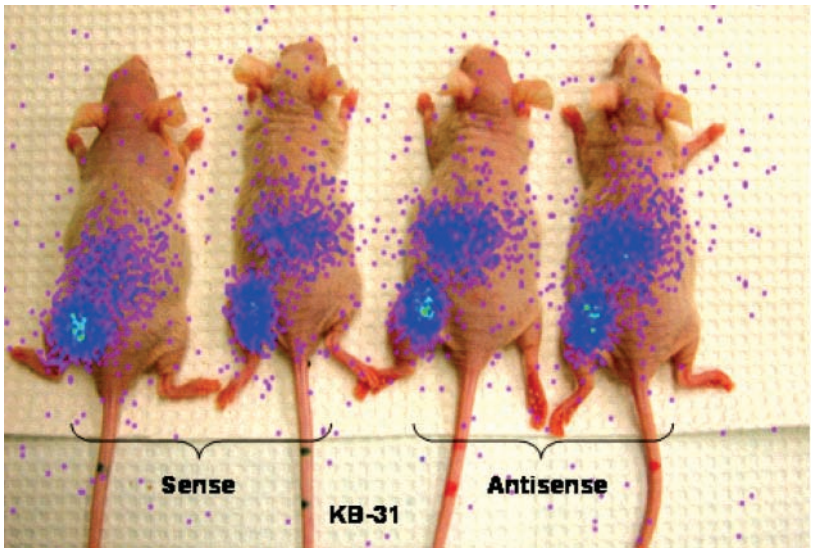


Figure 2. A composite obtained at 22 h postadministration in KB-31 tumored mice. The scintigraphic whole body image has been superimposed on a photographic image taken during imaging to provide accurate registration. Two animals receiving the AS DNA are on the right while two identical animals receiving the control S DNA are on the left. In all cases, the tumor is in the left thigh.

i.v. administration (data not presented). Whereas tumor levels for both DNAs were higher in KB-G2 compared to KB-31 animals following i.t. administration, tumor levels were identical following i.v. administration. This may be due to the much smaller dosage of DNA reaching the tumor following i.v. administration compared to i.t. such that the difference in the number of mRNA targets between the two tumors may be immaterial under the i.v. conditions. The KB-G2 and KB-31 results have therefore been combined in Table 3 to improve the estimate of statistical significance.

Among the normal tissues considered, only blood and spleen showed statistically significant accumulations between AS and S DNAs with the former showing lower levels and the latter higher levels for the S DNA. The accumulation of AS DNA was higher in most normal organs as shown in Table 3 although these differences are not significant. Since the mouse MDR1 gene is reported to be expressed in most mouse organs such as liver, kidney, lung, and heart and since there is reported to be homology in the mouse and human gene (*8*), some of the observed increased accumulations of AS DNA in normal tissues may be specific.

Possibly because the variability in tumor accumulations was much smaller following i.v. vs i.t. administration, the higher accumulation of the AS DNA in tumor compared to S DNA following i.v. administration is considerably more statistically significant compared to that of the KB-G2 tumors following i.t. administration. The identical calculation applied to animals administered i.v. as that described above for animals receiving i.t. injections show that about 400 AS DNAs accumulated specifically in each tumor cell.

DISCUSSION

An evaluation of studies in cell culture with AS oligomers permits the conclusion that, thus far, results have been very positive (*2*). Accumulations have been observed by what appears to be an antisense mechanism, and the magnitude of these accumulations have been much greater than that predicted on the basis of estimated steady-state mRNA levels (*9*). The more difficult

challenge that remains is now to demonstrate that AS oligomers will accumulate in target tissues in vivo by an antisense mechanism. Among the factors that will make this challenge difficult is insufficient delivery of AS DNA into tumor cells when administered i.v. While in culture, cellular accumulations are at levels that would certainly provide adequate nuclear medicine images; the barriers to in vivo cellular accumulations will reduce these levels considerably. Another factor contributing to the difficulties ahead may be nonspecific accumulations of radiolabeled DNAs in nontarget tissues leading to high background radioactivity levels.

An impression that antisense imaging may not be achievable has been reinforced by the general absence of positive results thus far in the limited number of published studies of in vivo antisense targeting (*10*, *11*). Recently positive images were reported in mouse xenografts in which the target mRNA could be upregulated by epidermal growth factor (*12*). Superior images were obtained following ^{111} In-labeled DNA administration in mice bearing the tumor following upregulation. However, since no significant differences were observed between the AS DNA and its random control DNA, the improvement in imaging with upregulation may not be due to an antisense mechanism. The possibility that the intratumor administration of epidermal growth factor has altered tumor phenotype to explain the increased accumulations cannot be excluded. Recently, several other in vitro and/or in vivo studies have been reported using control tumors (*13*−*15*). While useful in other ways, the results of these investigations shed little light on whether accumulations were by an antisense mechanism since control oligomers were not used. Convincing evidence of an antisense mechanism in the in vivo targeting of firefly luc gene in the brain of transgenic mice was obtained using a ^{125}I-labeled peptide nucleic acid (PNA) and quantitative autoradiography. Higher accumulations of the antisense oligomer was reported compared to control oligomer (*16*). Autoradiography had also earlier been used to show higher in vivo accumulations of a ^{11}C-labeled AS DNA against a target mRNA expressed in rat tumor compared to a mismatched control DNA (*17*). A more recent report presents whole body images of tumored rats obtained with ^{68}Ga-AS DNA directed against the K-ras mRNA (*18*). While a control tumor not expressing the target mRNA was used and accumulation of labeled AS DNA compared to the study tumor, a control DNA was apparently not used in the imaging studies. In another study, a careful investigation of antisense targeting of c-myc mRNA in mice using ^{99m}Tc-labeled PNAs showed a significantly higher accumulation in tumor of the AS compared to mismatched control oligomer at 4 h but not 24 h post i.v. administration (*19*). Despite the encouraging results of this study, a positive biodistribution in a tumored animal that may be attributed to antisense targeting has not yet been reported. In a pioneer study, Dewanjee et al. reported surprisingly positive results in a mouse tumor model using an AS DNA of unspecified sequence complementary to the initiation codon site of the c-myc oncogene mRNA (*20*). However, these favorable results have yet to be reproduced elsewhere.

The results obtained in this in vivo investigation are encouraging. In the absence of additional studies, it is not possible to claim that the mechanism of tumor accumulation observed herein involved in vivo antisense targeting. However, the significantly higher levels of AS DNA compared to control S DNA accumulated in tumor both following i.t. and i.v. administrations in a well characterized AS DNA/tumor cell system *(4)* provides what may be convincing, albeit not yet definitive, evidence for antisense tumor targeting. These results would appear to satisfy two of the four criteria described above that may be necessary and sufficient to claim evidence of an antisense mechanism. First, tumor accumulation of AS DNA reached higher levels compared to control DNA. Second, tumor accumulation appeared to increase with increasing target mRNA levels in that the accumulations in Pgp++ KB-G2 tumors exceeded that of Pgp+ KB-31 tumor following i.t. administration. That no difference between tumor types was observed following i.v. administration may be attributed to the low dosage of DNAs delivered via this route that may have been so far below saturation levels that differences in mRNA target concentrations became irrelevant.

In conclusion, evidence for tumor targeting in vivo by an antisense mechanism has been obtained. The successful localization of AS DNA in tumor demonstrates that in vivo antisense targeting of tumor is feasible although improvements in tumor delivery and clearance from normal tissues are needed for practical antisense imaging.

ACKNOWLEDGMENT

The preparation of this report was supported in part by the Office of Science (BER), U.S. Department of Energy, Grant Nos. DE-FG02-99ER62781 and DE-FG02-03ER63602. One of us (K.N.) was supported by a Grant-in-Aid for Scientific Research (13670965) from the Japanese Ministry of Education, Science, Sports and Culture.

LITERATURE CITED

(1) Hnatowich, D. J. (1999) Antisense and Nuclear Medicine. *J. Nucl. Med. 40*, 693−703.
(2) Zhang, Y. M., Wang, Y., Liu, N., Zhu, Z. H., Rusckowski, M., and Hnatowich, D. J. (2001) In vitro investigations of tumor targeting with ^{99m}Tc-labeled antisense DNA. *J. Nucl. Med. 42*, 1660−1669.
(3) Zhang, Y., Rusckowski, M., Liu, N., Liu, C., and Hnatowich, D. J. (2001) Cationic liposomes enhance cellular/nuclear localization of ^{99m}Tc-antisense oligonucleotides in target tumor cells. *Cancer Biother. Radiopharm. 16*, 411−419.
(4) Nakamura, K., Liu, G., Zhang, Y., Kubo, A., and Hnatowich, D. J. (2003) Antisense targeting of P-glycoprotein MDR expression in tissue culture. *J. Nucl. Med. 44*, 304 (Abstract).
(5) Alahari, S. K., DeLong, R., Fisher, M. H., Dean, N. M., Viliet, P., and Juliano, R. L. (1998) Novel chemically modified oligonucleotides provide potent inhibition of P-glycoprotein expression. *J. Pharm. Exp. Ther. 286,* 419−428.
(6) Winnard, P., Jr., Chang, F., Rusckowski, M., Mardirossian, G., and Hnatowich, D. J. (1997) Preparation and use of NHS-MAG_3 for technetium-99m labeling of DNA. *Nucl. Med. Biol. 24*, 425−432.
(7) Liu, G., Zhang, S., He, J., Zhu, Z., Rusckowski, M., and Hnatowich, D. J. (2002) Improving the labeling of *S*-acetyl NHS-MAG_3-conjugated morpholino oligomers. *Bioconjugate Chem. 13*, 893−897.
(8) Chen, C., and Smith, B. J. (2003) Utility of Mdr1-gene deficient mice in assessing the impact of P-glycoprotein on pharmacokinetics and pharmacodynamics in drug discovery. *Curr. Drug Metab. 4*, 272−291.
(9) Hnatowich, D. J. (2000) Antisense and Nuclear Medicine. Where are we now? *Cancer Biother. Radiopharm. 15*, 447−457.
(10) Lewis, M. R., and Jia, F. (2003) Antisense imaging: and miles to go before we sleep? *J. Cell Biochem. 90*, 464−474.
(11) Younes, C. K., Boisgard, R., and Tavitian, B. (2002) Labeled oligonucleotides as radiopharmaceuticals: pitfalls, problems and perspectives. *Curr. Pharm. Des. 8*, 1451−1466.
(12) Wang, J., Chen, P., Mrkobrada, M., Hu, M., Vallis, K. A., and Reilly, R. M. (2003) Antisense imaging of epidermal growth factor-induced $p21^{WAF-1/CIP-1}$ gene expression in MDA-

MB-468 human breast cancer xenografts *Eur. J. Nucl. Med. Mol. Imaging 30,* 1273−1280.

(13) Lewis, M. R., Jia, F., Gallazzi, F., Wang, T., Zhang, J., Shenoy, N., Lever, S. Z., and Hannink, M. (2002) Radiometal-labeled peptide-PNA conjugates for targeting bcl-2 expression: preparation, characterization, and in vitro mRNA binding. *Bioconjugate Chem. 13*, 1176−1180.

(14) Sato, N., Kobayashi, H., Saga, T., Nakamoto, Y., Ishimori, T., Togashi, K., Fujibayashi, Y., Konishi, J., and Brechbiel, M. W. (2001) Tumor targeting and imaging of intraperitoneal tumors by use of antisense oligo-DNA complexed with dendrimers and/or avidin in mice. *Clin. Cancer Res. 7*, 3606−3612.

(15) Wang, L., Prakash, R. H., Stein, C. A., Koehn, R. K., and Ruffner, D. E. (2003a) Progress in the delivery of therapeutic oligonucleotides: Organ/cellular distribution and targeted delivery of oligonucleotides in vivo. *Antisense Nucleic Acid Drug Dev. 13*, 169−189.

(16) Lee, H. J., Boado, R. J., Braasch, D. A., Corey, D. R., and Partridge, W. M. (2002) Imaging gene expression in the brain in vivo in a transgenic mouse model of Huntington's disease with an antisense radiopharmaceutical and drug-targeting technology. *J. Nucl. Med. 43*, 948−956.

(17) Kobori, N., Imabori, Y., Mineura, K., Ueda, S., and Fujii, R. (1999) Visualization of mRNA expression in CNS using ^{11}C-labeled phosphorothioate oliogdeoxynucleotide. *Neuroreport. 10*, 2971−2974.

(18) Roivainen, A., Tolvanen, T., Salomake, S., Lendvai, G., Velikyan, I., Numminen, P., Valila, M., Sipila, H., Bergstrom, M., Harkonen, P., Lonnberg, H., and Langstrom, B. (2004) ^{68}Ga-labeled oligonucleotides for in vivo imaging with PET *J. Nucl. Med. 45*, 347−355.

(19) Rao, P. S., Tian, X., Ojn, W., Aruva, M. R., Sauter, E. R., Thakur, M. L., and Wickstrom, E. (2003) ^{99m}Tc-peptide-peptide nucleic acid probes for imaging oncogene mRNAs in tumors. *Nuc. Med. Commun. 24*, 857−863.

(20) Dewanjee, M. K., Ghafouripour, A. K., Kapodvanjwala, M., Dewanjee, S., Sarafini, A. N., Lopez, D. M., and Sfakianakis, G. N. (1994) Noninvasive imaging of c-myc oncogene messenger RNA with indium-111-antisense probes in a mammary tumor-bearing mouse model. *J. Nucl. Med. 35*, 1054−1063.

BC0499073

Synthesis and Properties of Fluorescent NF-κB-Recognizing Hairpin Oligodeoxyribonucleotide Decoys

Valeri Metelev,† Ralph Weissleder, and Alexei Bogdanov, Jr.*

Center for Molecular Imaging Research, Massachusetts General Hospital, Charlestown, Massachusetts 02129, and Department of Radiology, Harvard Medical School, Boston, Massachusetts 02129. Received April 6, 2004; Revised Manuscript Received May 27, 2004

Intramolecular fluorescence quenching of cyanine dyes was investigated using a model hairpin oligonucleotide decoy encoding a NF-κB p50 subunit binding site. Two types of hairpin oligonucleotides were synthesized: (1) 5′-(6-aminohexyl)- and 3′-(3-aminopropyl)-linked (**I**); (2) 5′-(6-aminohexyl)- and 3′-[3-(3-hydroxypropyldithio)propyl]-linked (**II**). Oligonucleotide **I** was covalently modified using monofunctional either Cy3- or Cy5.5-*N*-hydroxysuccinimide esters. Using reverse-phase HPLC, mono- and dicyanineamide derivatives of **I** were isolated. Mono-Cy3-modified derivatives of **I**, but not the mono-Cy5.5-modified derivatives, showed a 2-fold higher Cy3 fluorescence intensity compared to the free dye. There was no detectable difference in fluorescence between the di-Cy3 derivative of **I** and the free dye at the same concentration. However, there was a 4-fold quenching of fluorescence in the case of the di-Cy5.5 derivative of the same hairpin oligonucleotide. The quenching of Cy5.5 fluorescence could not be explained by the interaction of Cy5.5 with nucleotide bases as demonstrated by incubating free Cy5.5 dye with oligonuclotides. The quenching effect was further investigated using an oligonucleotide bearing a cleavable 3′-amino-terminated linker bearing an S−S bond (**III**). After modification of the 5′- and 3′-end of oligonucleotide **III** with a Cy5.5 monofunctional hydroxysuccinimide ester, a 70−75% quenching of fluorescence was observed. Fluorescence was 100% dequenched after the reduction of S−S bond. The obtained result unequivocally demonstrates that the formation of intramolecular Cy5.5 dimers is the dominant mechanism of fluorescence quenching in symmetric dye−dye hairpin decoy beacons.

INTRODUCTION

The ability to attenuate the level of target gene expression in living cells allows individual biochemical pathways to be dissected (*1*) as well as alteration of the phenotype and, potentially, enables the attenuation of gene expression in vivo (*2*−*6*). The "knockdown" of gene expression could be achieved at transcription and post-transcription. In the first case, oligonucleotide hairpin decoys could be used (reviewed in ref 7). In the second case, siRNA (small interfering) (*8*, *9*) and antisense oligonucleotides have been proven to be effective. The inhibitive effect of both DNA-based and RNA-based constructs depends to a large extent on their ability to penetrate into the cellular interior and on the rate of intracellular catabolism of short oligo deoxy- or ribonucleotides. Both endo- and exonuclease degradation severely limits the half-life of oligodeoxyribo- or oligoribonucleotides in vitro and in vivo. Nevertheless, the stability of oligonucleotides can be modified by applying a variety of synthetic strategies (*10*, *11*), reviewed in refs 12−14). While recent research has proved that antisense oligoribonucleotides (especially siRNAs) are undoubtedly efficacious in vitro, they are susceptible to rapid degradation prior to interaction with target mRNA in vivo (*15*). Small interfering RNAs are also known to activate interferon-mediated pathways resulting in a broad interferon-mediated gene upregulation (*16*, *17*).

Hairpin oligonucleotide decoys are designed to block the transcription of a target gene by competing with genomic DNA for relevant transcription factors. For example, decoys bearing a NF-κB recognition sequence, which binds the p50 subunit of a transcription factor, were amenable to modifications with reactive nucleotide analogues that enabled trapping of NF-κB on the decoy and resulted in apoptosis (*18*−*20*). To assess the efficacy of intracellular penetration and to track their intracellualr fate, oligonucleotides can be labeled with molecular probes to make them detectable by imaging techniques, either microscopic, or macroscopic for in vivo work (*21*−*24*). The goal of this work was to synthesize and characterize far-red fluorochrome-labeled decoys. Indocyanine far red fluorescent dyes have excellent photostability, are pH insensitive, and potentially could be detected in vivo. We anticipate that such labeled oligonucleotides will prove useful in elucidating mechanisms of hairpin decoy penetration into cells and imaging interactions between the decoy and target transcription activators.

MATERIALS AND METHODS

Materials. Oligodeoxyribonucleotides with 3′,5′-diaminoalkyl linkers were synthesized at MGH Department of Molecular Biology, DNA Oligonucleotide Synthesis Core (Dr. Jay Klaren) and supplied in ammonia solution.

Triethylammonium acetate solution (2 M, TEAA), pH 7.0, was purchased from Glen Research (Sterling VA), 2-aminoethyl-2′-aminoethanethiosulfonate from Pierce-

* Corresponding author: Center for Molecular Imaging Research, Massachusetts General Hospital, Building 149, 13th St., 5420, Charlestown MA 02129. Tel.: (617) 726-5784. Fax: (617) 726-5708. E-mail: abogdanov@helix.mgh.harvard.edu.

† Present address: Division of Chemistry of Natural Compounds; Department of Chemistry, M. V. Lomonosov Moscow State University, Moscow 119992, Russia.

10.1021/bc049916b CCC: $27.50 © 2004 American Chemical Society
Published on Web 10/16/2004

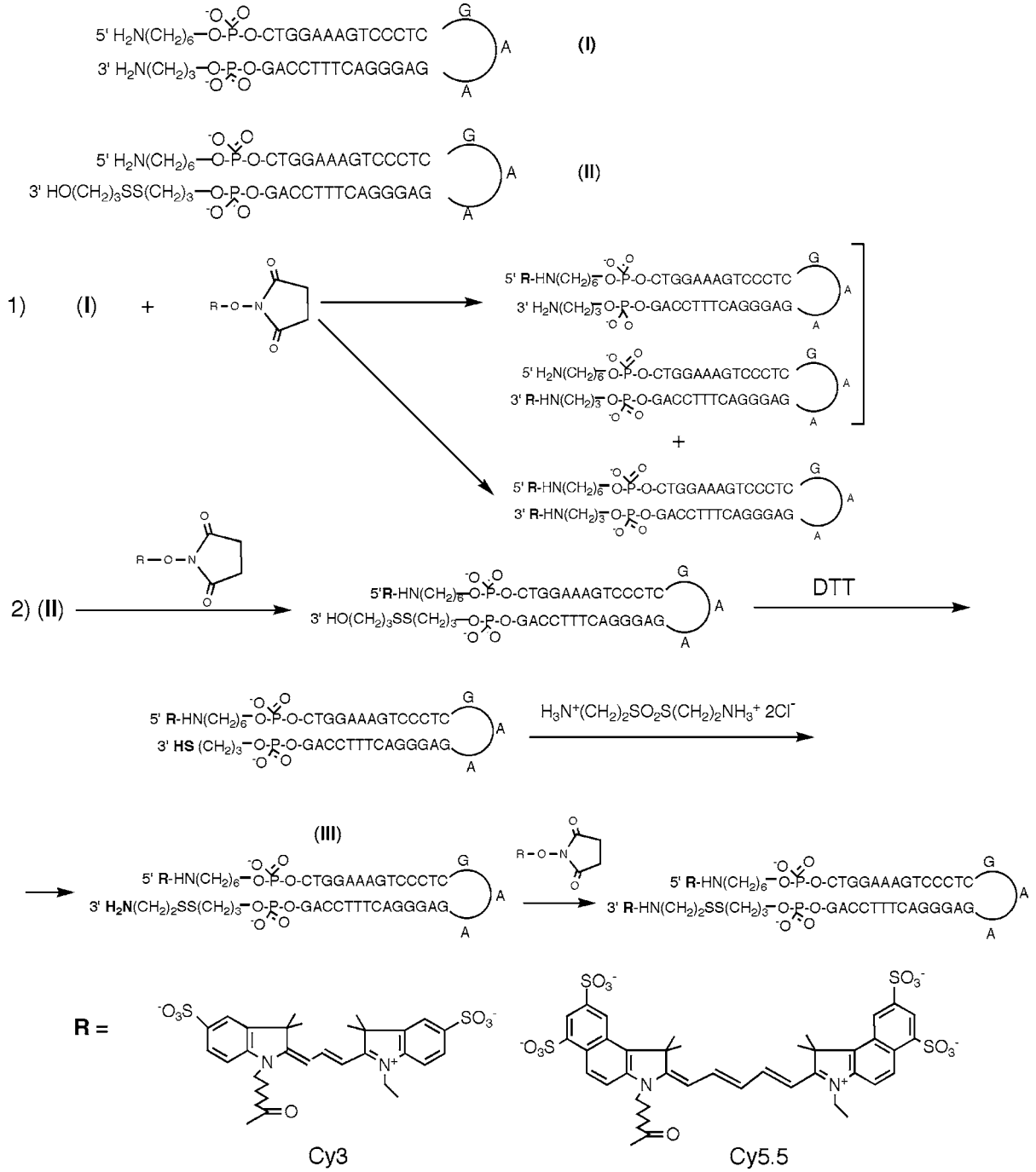


Figure 1. Scheme of fluorescently labeled hairpin oligonucleotide decoy synthesis. **I**, precursor (noncleavable, diamino terminated) oligonucleotide; **II**, oligonucleotide with a 3′-dithio linker; **III**, monomodified oligonucleotide with an amino-terminated dithio linker.

Endogen (Rockford, IL), Cy5.5 mono-*N*-hydroxysuccinimide ester (NHS) and Cy3 NHS from Amersham Biosciences (Piscataway, NJ). Micro Bio-Spin 6 columns (SSC buffer, pH 7.0) were obtained from Bio-Rad (Hercules CA). All other chemicals were from Sigma-Aldrich (St. Louis, MO).

Initial Purification of Oligonucleotides. The ion-pair reversed-phase HPLC method was used for the isolation and purification of modified oligodeoxyribonucleotides on a C18 column (Zorbax ODS 4.6 × 25 mm, DuPont). For HPLC linear gradient the following buffers were used: A, 2% acetonitrile in 0.1 M TEAA, pH 7; B, 50% acetonitrile in 0.1 M TEAA, pH 7. The column was eluted at 1 mL/min at room temperature. Purified oligonucleotides were concentrated in a centrifugal vacuum concentrator (SpeedVac, Savant).

Modification of Oligodeoxyribonucleotides Bearing 3′- and 5′-Aminoalkyl Linkers (Figure 1, Reaction 1). Ten nanomoles of the oligonucleotide d(pCTG-GAAAGTCCCTCGAAGAGGGACTTTCCAGp) bearing 3′- and 5′-aminoalkyl linkers was dissolved in 15 μL of 0.1 M $NaHCO_3$. To this was added 7 μL of 62 mM Cy3-NHS (or 49 mM Cy5.5-NHS in DMSO), and the mixture was incubated at room temperature for 6−16 h in the dark. Then 40 μL of water was added, and the modified oligonucleotide was separated from excess dye by two consecutive separations on Micro Bio-Spin 6 columns according to the manufacturer's recommendations. After the second spin-chromatography, oligonucleotides were precipitated by standard ethanol−sodium acetate treatment and purified by HPLC as described above. The chromatography showed complete absense of free dyes

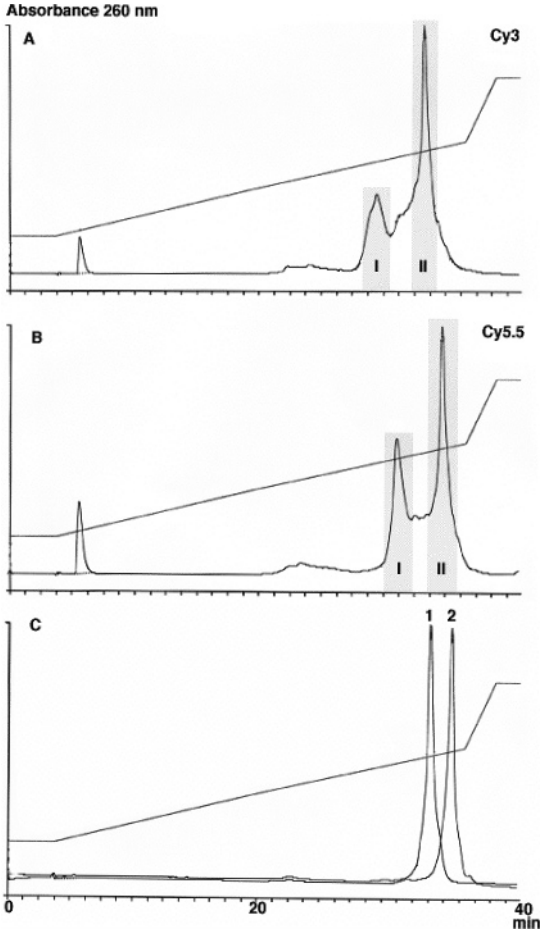


Figure 2. Preparative HPLC of Cy3 (A) and Cy5.5 (B) modified oligonucleotide **I**. Shaded peaks corresponding to mono (I) and di- (II)- modified oligonucleotides were collected for further analysis; (C) superimposed elution profiles of purified dicyanine-modified oligonucleotides: 1, Cy3-modified; 2, Cy5.5-modified oligonucleotide **I**.

and a disappearance of the peak corresponding to the nonlabeled oligonucleotide. Fractions corresponding to mono- and dimodified oligonucleotides were collected (Figure 2) and concentrated by evaporation using a centrifugal vacuum concentrator (final volume about 50−100 μL). Oligonucleotides were precipitated in ethanol−sodium acetate by adding a 0.1 volume of 3 M sodium acetate, pH 5.5, followed by 5 volumes of cold ethanol. Labeled oligonucleotides were characterized using MALDI-mass spectrometry (Integrated DNA Technologies, Coralville, IA) and yielded for di-Cy3-labeled (**I**) ($M + H^+$) 11195.8 (calculated, 11207.0) and for di-Cy5.5 labeled (**I**) ($M+H^+$) 11775.1 (calculated, 11796.5). In calculations we assumed that acetate anion served as a counterion of the quarternized nitrogen in Cy dye residues.

Synthesis of Fluorescent Oligonucleotide Decoy Probes Bearing a Dithio Bond (Figure 1, Reaction 2). The initial compound used for the synthesis of dual-labeled probes was 5′-N-MeOTr-**II**, i.e. oligonucleotide d(pCTGGAAAGTCCCTCGAAGAGGGACTTTCCAGp) bearing asymmetric 5′-(6-MeOTr-aminohexyl)- and 3′-[3-(3-hydroxypropyldithio)propyl] linkers (Figure 1). 5′-N-MeOTr-**II** was purified by HPLC on an octadecyl silica column (Zorbax ODS 5 μm, DuPont) using a linear gradient of buffers A and B (10−100% B, 30 min) and was detritylated using 80% acetic acid for 1 h. Further synthesis included the following steps: (1) reacting the purified oligonucleotide with NHS esters of Cy5.5 or Cy3 dyes as described above; (2) isolating the monolabeled oligonucleotide on the HPLC column and reducing the 3′-disulfide bond with dithiotreitol, resulting in the formation of an oligonucleotide bearing a 3′-(3-mercaptopropyl) linker. Briefly, 10 μL of 1 M DTT was added to the monolabeled oligonucleotide dissolved in 100 μL of 0.02 M $NaHCO_3$. After a 1 h incubation at room temperature, the reduced oligonucleotide was precipitated by using ethanol−sodium acetate treatment; (3) reacting the above oligonucleotide with 2-aminoethyl-2′-aminoethane thiosulfonate. The reaction yielded oligonucleotide **III**, containing a 3′-[3-(2-aminoethyldithio)propyl] linker (Figure 1). Briefly, the oligonucleotide was dissolved in 50 μL of 0.2 M $NaHCO_3$, the solution was cooled to 4 °C, mixed with 15 μL of 0.15 M 2-aminoethyl-2′-aminoethanethiosulfonate and incubated for 1 h at 4° C followed by separation on a Micro Bio-Spin 6 column; (4) modifying oligonucleotide **III** with an *N*-hydroxysuccinimide ester of the reporter dye (Cy5.5 or Cy3); (5) isolating dual-labeled oligonucleotide by HPLC. Oligonucleotides were precipitated by adding 2% lithium perchlorate in acetone and redissolved in water. By MALDI-mass spectrometry the ($M+H^+$) was 11905.6 (calculated − 11893.8).

Interaction of Hydrolyzed Cyanine NHS-esters with Oligonucleotide Containing 3′,5′-Diaminoalkyl Linkers. Three nanomoles of the oligonucleotide was dissolved in 25 μL of solution containing hydrolyzed Cy5.5-NHS, and the resulting mixture was incubated at the same conditions as the standard Cy5.5-NHS oligonucleotide reaction mixture. To obtain hydrolyzed Cy5.5-NHS ester, 7 μL of 49 mM Cy5.5-NHS in DMSO was dissolved in 18 μL of 0.2 M $NaHCO_3$, and the mixture was incubated for 36 h in the dark at room temperature.

Interaction of Hydrolyzed Cy5.5 NHS with DTT or Glutathione. To 35 μL of hydrolyzed Cy5.5 were added 10 μL of 1 M DTT (or 0.5 M reduced glutathione) and 10 μL, 0.2 M $NaHCO_3$, and the solution was incubated in the dark overnight.

The Reduction of Disulfide Bond in Dual-Labeled Oligonucleotides. To reduce the dithio bond in the oligonucleotide and to achieve dequenching of fluorescence, dual-labeled probes were diluted in 1−1.5 mL of PBS buffer (pH 7.5) and subjected to fluorimetry, followed by mixing with 15 μL of 1 M DTT or with 30 μL of 0.5 M reduced glutathione. The solutions were incubated overnight at room temperature followed by fluorimetry as described above.

DNAse Digestion of Labeled Probes. Solutions of the oligonucleotides were prepared in magnesium-containing Dulbecco's PBS, pH 7, at the concentration of 20−100 μM. Each solution was divided into aliquots. For each oligonucleotide, a half of the samples was treated with DNAse I (10 U/mL, Stratagene, La Jolla CA) for 6 h at 37 °C. Control samples were not treated with DNAse. Absorbance and fluorescence at appropriate wavelengths were measured in DNAse-treated samples and compared to the control samples.

Spectral measurements were performed at room temperature using a U-3000 and F-4500 Hitachi spectrophotometer and spectrofluorometer, respectively. The cyanine dyes and labeled oligonucleotides were diluted in 2 mL of PBS, pH 7.5, and absorbance and fluorescence spectra were recorded sequentially in quartz cuvettes.

RESULTS AND DISCUSSION

Tagging oligonucleotides with imaging probes provides a means of tracking these molecules in living cells and ultimately in vivo. For example, labeling of oligonucle-

otides with radioactive isotopes has been used for noninvasive tracking of oligonucleotide biodistribution. This approach potentially enables localizing sites of target gene expression (reviewed in (*25*, *26*)). Conjugation of oligonucleotides with cyanine dyes could result in highly useful "beacons" based on the effect of fluorescence quenching between the labeled proximal 3′- and 5′-termini. The quenching effect is abrogated by the dequenching of fluorescence upon the interaction with in vitro targets in structurally constrained stem-loop beacons as well as stemless beacons (reviewed in 27, 28). Moreover, it has been demonstrated that enzyme-specific dequenching of cyanine-labeled macromolecules can be imaged in vivo (*29*). In this report we investigated quenching and dequenching effect in hairpin oligonucleotide decoys using two commercially available cyanine dyes.

Purification of Initial Oligonucleotides. To obtain a first generation of quenched oligonucleotide decoy probes, we used d(pCTGGAAAGTCCCTCGAAGAGGGACTTTCCAGp) as a precursor for synthesis of dye-labeled probes. This oligonucleotide was prepared to enable asymmetric modifications at the 3′- and 5′-termini using a protected 5′-(6-MeOTr-aminohexyl)-linker as well as a free amino group-containing 3′-(3-aminopropyl) linker (Figure 1). We assumed that above linkers would provide a means of conjugating the first dye (reporter or quencher) specifically to the 3′-amino group. The synthesis would be followed by (1) the isolation of the 3′ mono Cy-dye labeled 5′-N-MeOTr-**I** fraction by HPLC; (2) detritylation of **I** by 80% acetic acid. Deprotected compound would then be used to attach the second dye (quencher or reporter) to the free 5′-amino group followed by HPLC purification. Contrary to our expectations, we found that the 5′-MeOTr-NH bond is unstable and hydrolyzes rapidly during the purification of **I** by HPLC in 0.1 M TEAA, pH 7.0, or by using the Poly-Pack cartridge method. Since partial (10−30%) detritylation of the 5′-amino group took place, oligonucleotide **I** could not be used for synthesis of probes dually labeled by two different dyes. Therefore, after HPLC isolation from the reaction mixture, oligonucleotide **I** was detritylated by 80% acetic acid, and the obtained oligonucleotide (HPLC elution time, 18.5 min) was used to synthesize probes dually labeled by Cy3 or Cy5.5 cyanine dyes.

Purification of dye-modified oligonucleotides from nonreacted dyes was attempted using three approaches: (a) by repeated ethanol−sodium acetate precipitation of oligonucleotide; (b) by gel filtration on NAP-10 cartridges; (c) by separating on Micro Bio-Spin 6 columns. We found that the particular dyes and oligonucleotides used in this work could not be efficiently separated using size-exclusion chromatography on a Sephadex G-25 column (NAP-10). A procedure involving separations on Micro Bio-Spin 6 columns followed by ethanol−sodium acetate precipitation of the oligonucleotides was clearly superior over other purification strategies. The mono- and dimodified derivatives could then be easily separated using a C18 HPLC column Figure 2 (A,B, peaks I and II). The isolated fluorescent dimodified oligonucleotides showed a very high purity (Figure 2, C) suitable for further spectral analysis and mass-spectrometry. Elution times on HPLC column were 27.0 min for the di-Cy3-modified oligonucleotide and 28.3 min for the di-Cy5.5-modified one.

Spectral Properties of Modified Oligonucleotide I. To investigate spectral properties of cyanine dye-modified oligonucleotides, we initially performed a modification of hairpin oligonucleotide **I** with Cy3-NHS and Cy5.5-NHS followed by the isolation of mono- and dicyanine derivatives of **I** using HPLC. The above dyes were chosen because of the advantageous photostability of Cy3 and the near-infrared "in vivo imaging" fluorescence range of Cy5.5 (*29*, *30*). The initial experiments showed that the attachment of dyes to hairpin oligodeoxyribonucleotides with 3′-(3-aminopropyl), 5′-(6-aminohexyl)-linkers resulted in significant changes in the visible range of cyanine dye absorption when spectras of nonconjugated dyes were compared to the cyanine-modified oligonucleotides. First, we observed an increase of absorbance in the range of 500−525 nm in the case of Cy3 (Figure 3A) and in the range of 600−650 nm in the case of Cy5.5 after the conjugation (Figure 3B). Such spectral changes were previously attributed to a formation of dimers in Cy-modified proteins (*31*). In our case, such spectral changes were detectable only in the case of dimodified oligonucleotides as opposed to its mono-Cy derivative. There was no evidence of the formation of J-aggregates that absorb light at longer wavelengths. The increase of absorption at shorter wavelengths was especially prominent in the case of Cy5.5 and was less prominent for Cy3 derivatives (Figure 3). In addition, there was a small but detectable 3−5 nm-"red" shift of the fluorescence emission maximum. We also observed that covalent linking of a single Cy3 group to **I** causes a 100% increase of the fluorescence intensity. In the case of Cy5.5 fluorescence in the mono-derivatized oligonucleotide did not change appreciably whereas dimodified **I** showed a substantial quenching of Cy5.5 fluorescence which could be reliably measured using extensive enzymatic degradation of the oligonucleotide. As a result of DNAse-mediated cleavage, fluorescence increased approximately 13 times. Additional control experiments that included incubating hydrolyzed cyanine dye esters with the oligonucleotide showed that the above fluorescence effects were specific for conjugated dyes and could not be explained by simple interaction of cyanine moiety with nucleotides (e.g. partial intercalation of cyanine group between the nucleotide pairs).

Experiments with Derivatives of Oligonucleotide II Containing a Cleavable Bond. To prove that the observed self-quenching effects were caused by the interaction of two cyanine dye residues positioned in close proximity to each other (i.e. that hairpin conformation induces the dimerization of Cy5.5 dye), we designed a hairpin oligonucleotide **II** (HPLC elution time, 19.1 min) with a nucleotide sequence identical to that of **I** but containing a dithio bond at the 3′-terminus of the molecule (Figure 1). We hypothesized that the bond could be reduced and that the formed 3′-sulfhydryl could then react with 2-aminoethyl-2′-aminoethanethiosulfonate to form a 3′-amino linker bearing a dithio bond. The amino group could be then used for further modification of **II** with a second fluorophore or other probe to yield oligonucleotide **III** (Figure 2, HPLC elution time, 28.0 min). In oligonucleotide **III** that bears two Cy5.5 modifications, the 3′-dithio bond could be reduced using a 10−15 mM dithiotreitol (or glutathione). First, we excluded potential quenching of Cy dyes as a result of chemical interaction with DTT or glutathione. Second, we tested whether the reduction that cleaves the S−S bond results in the dissociation of the dimer and resultant dequenching of fluorescence. As expected, after DTT or glutathione treatment, we observed a change in absorbance in the range of 600−650 nm (Figure 4 A) and a dequenching of the Cy5.5 fluorescence (Figure 4B and 4C). The ratio of fluorescence intensities measured after and before the treatment with DTT was in the range of 3.5 to 4. The latter quenching factor was close to that measured using

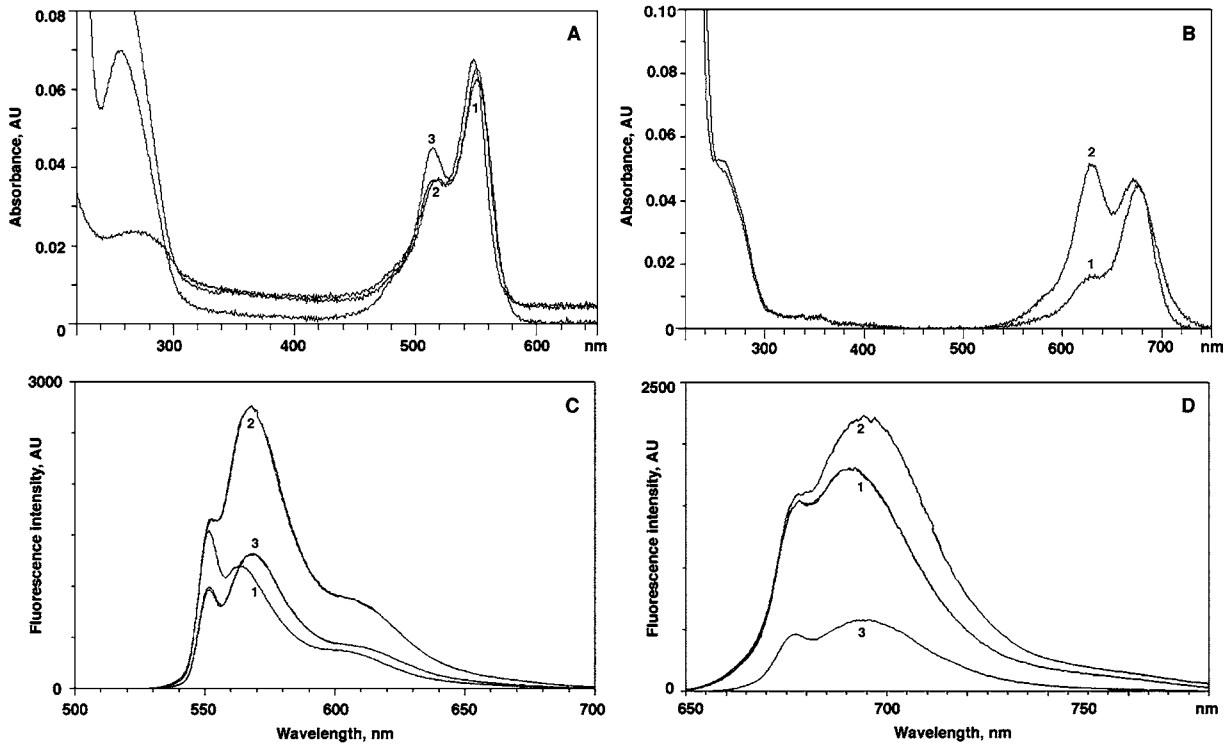


Figure 3. (A) Absorption and (C) emission spectra of 1, Cy3 dye; 2, mono-Cy3 derivative; and 3, di-Cy3 derivative of oligonucleotide **I**. (B) Absorption spectras of 1, mono-Cy5.5; 2, di-Cy5.5 derivative of oligonucleotide **I**, (D) Emission spectra of 1, Cy5.5; 2, mono-Cy5.5 derivative; and 3, di-Cy5.5 derivative of oligonucleotide **I**. The spectrum of di-Cy5.5 oligonucleotide **I** shows strong absorption at 629 nm due to the dye dimerization and no absorption due to J-aggregates.

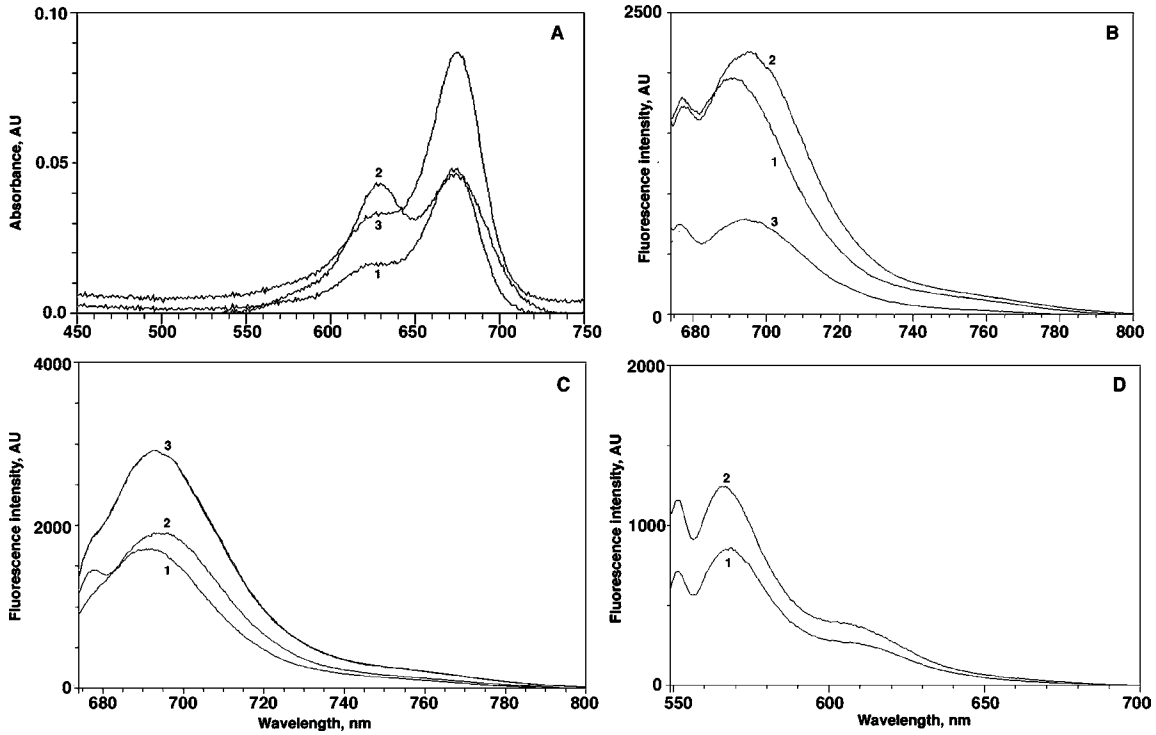


Figure 4. (A) Absorption spectra: 1, Cy5.5 in PBS; 2, dimodified oligonucleotide **III** before disulfide bond reduction with DTT; 3, after DTT treatment. (B) Emission spectra before DTT treatment: 1, Cy5.5; 2, mono-Cy5.5-modified oligonucleotide **III**; 3, di-Cy5.5-modified oligonucleotide **III**. (C) Emission spectra after disulfide bond reduction with DTT: 1, Cy5.5; 2, mono-Cy5.5-modified oligonucleotide **III**; 3, di-Cy5.5-modified oligonucleotide **III**. (D) Emission spectra of di-Cy3-modified oligonucleotide **III** : 1, before; and 2, after DTT treatment.

extensive DNAse I-mediated degradation (5.4 times, Table 1). The absorbance spectrum reverted to the typical Cy5.5 shape following the reduction with a concomitant 1.8- fold increase at the maximum of absorbance because of the transition of 50% of the dimerized, blue-shifted Cy5.5 molecules into the noninteracting pool of molecules. Interestingly, dye quenching in non-DTT-cleavable di-Cy5.5 decoy was more efficient than that of in a cleavable one (Table 1). The observed difference in quenching factors (12.9 for 3′-Cy5.5-**I**-5′-Cy5.5 vs 5.6 for 3′-Cy5.5-

Table 1. Some Fluorescent Properties of Cyanine Dyes and Labeled Oligonucleotide Hairpin Probes

fluorophore/labeled oligonucleotide	excitation, nm	emission max., nm	quenching factor[a]
Cy3	548	563	1.0
Cy5.5	674	692	1.0
Cy3-**I**	548	568	—[b]
Cy3-**I**-Cy3	548	568	5.4
Cy5.5-**I**	674	695	1.1
Cy5.5-**I**-Cy5.5	674	695	12.9
Cy3-**II**	548	568	ND[c]
Cy3-**III**-Cy3	548	567	ND
Cy5.5-**II**	674	695	1.2
Cy5.5-**III**-Cy5.5	674	695	5.6

[a] Quenching factor was calculated as a ratio of fluorescence intensities measured in a sample containing 20−100 μM of labeled hairpin oligonucleotide decoy without DNAse I to that of containing DNAse I. [b] Fluorescence of oligonucleotide-conjugated Cy3 was higher than that of the free Cy3 by a factor of 2. [c] ND, not done.

III-5′-Cy5.5, Table 1) could be a result of differences in both linker length and structure in above constructs. Alternatively, thiol−disulfide exchange catalyzed by minute amounts of free thiols in oligonucleotide **III** dimodified preparation could result in partial dequenching of Cy5.5 dye.

The DTT treatment of di-Cy3-modified oligonucleotide lead only to a modest increase of fluorescence (1.4 times, Figure 4D). However, as noted before, in the case of Cy3 it is problematic to estimate the degree of true quenching of Cy3 conjugated to a hairpin nucleotide since the monomodified Cy3-oligonucleotide had higher fluorescence than free Cy3 dye at the same molar concentration (see Figure 4C). In the case of a monomodified oligonucleotide (i.e. Cy3-NH-oligonucleotide-S−S−CH_2CH_2-CH_2OH) disulfide reduction did not result in any appreciable changes of probe fluorescence (not shown).

In conclusion, we synthesized and tested fluorescent hairpin oligonucleotides bearing one or two fluorophores at their termini. Our results demonstrate that (1) there is a dimerization of cyanine dyes both in the case of dimodified Cy5.5 and dimodified Cy3-labeled oligonucleotides, (2) dimerization of the Cy5.5 fluorophore results in strong self-quenching, and (3) fluorescence quenching in dimodified Cy5.5 oligonucleotides could be reversed by dissociating one of the linkers between the oligonucleotide and one of the dyes. The observed effects and developed synthetic approaches are instrumental in further design of hairpin oligonucleotide beacons that would have reversible, quenched near-infrared fluorescence. We are currently refining the developed synthetic strategy for achieving highly termini-specific labeling with fluorescent probes and fluorescence quenchers.

ACKNOWLEDGMENT

This work was supported in part by the NCI (P50 Center for Molecular Imaging Grant).

LITERATURE CITED

(1) Xu, J., Wu, Y., He, L., Yang, Y., Moore, S. A., and Hsu, C. Y. (1997) Regulation of cytokine-induced iNOS expression by a hairpin oligonucleotide in murine cerebral endothelial cells. *Biochem. Biophys. Res. Commun. 235*, 394−397.

(2) Nakamura, T., Morishita, R., Asai, T., Tsuboniwa, N., Aoki, M., Sakonjo, H., Yamasaki, K., Hashiya, N., Kaneda, Y., and Ogihara, T. (2002) Molecular strategy using cis-element 'decoy' of E2F binding site inhibits neointimal formation in porcine balloon-injured coronary artery model. *Gene Ther. 9*, 488−494.

(3) Kume, M., Komori, K., Matsumoto, T., Onohara, T., Takeuchi, K., Yonemitsu, Y., and Sugimachi, K. (2002) Administration of a decoy against the activator protein-1 binding site suppresses neointimal thickening in rabbit balloon-injured arteries. *Circulation 105*, 1226−1232.

(4) Buchwald, A. B., Wagner, A. H., Webel, C., and Hecker, M. (2002) Decoy oligodeoxynucleotide against activator protein-1 reduces neointimal proliferation after coronary angioplasty in hypercholesterolemic minipigs. *J. Am. Coll. Cardiol. 39*, 732−738.

(5) Novina, C. D., Murray, M. F., Dykxhoorn, D. M., Beresford, P. J., Riess, J., Lee, S. K., Collman, R. G., Lieberman, J., Shankar, P., and Sharp, P. A. (2002) siRNA-directed inhibition of HIV-1 infection. *Nat Med. 8*, 681−686.

(6) Cullen, B. R. (2002) RNA interference: antiviral defense and genetic tool. *Nat. Immunol. 3*, 597−599.

(7) Cho-Chung, Y. S., Park, Y. G., and Lee, Y. N. (1999) Oligonucleotides as transcription factor decoys. *Curr. Opin. Mol. Ther. 1*, 386−392.

(8) Xia, H., Mao, Q., Paulson, H. L., and Davidson, B. L. (2002) siRNA-mediated gene silencing in vitro and in vivo. *Nat Biotechnol. 20*, 1006−1010.

(9) Lewis, D. L., Hagstrom, J. E., Loomis, A. G., Wolff, J. A., and Herweijer, H. (2002) Efficient delivery of siRNA for inhibition of gene expression in postnatal mice. *Nat. Genet. 32*, 107−108.

(10) Rapaport, E., Levina, A., Metelev, V., and Zamecnik, P. C. (1996) Antimycobacterial activities of antisense oligodeoxynucleotide phosphorothioates in drug-resistant strains. *Proc. Natl. Acad. Sci. U.S.A. 93*, 709−713.

(11) Barker, R. H., Jr., Metelev, V., Rapaport, E., and Zamecnik, P. (1996) Inhibition of Plasmodium falciparum malaria using antisense oligodeoxynucleotides. *Proc. Natl. Acad. Sci. U.S.A. 93*, 514−518.

(12) Alama, A., Barbieri, F., Cagnoli, M., and Schettini, G. (1997) Antisense oligonucleotides as therapeutic agents. *Pharmacol. Res. 36*, 171−178.

(13) Agrawal, S., and Iyer, R. P. (1997) Perspectives in antisense therapeutics. *Pharmacol. Ther. 76*, 151−160.

(14) Nielsen, P. E. (1999) Peptide nucleic acids as therapeutic agents. *Curr. Opin. Struct. Biol. 9*, 353−357.

(15) Kurreck, J. (2003) Antisense technologies. Improvement through novel chemical modifications. *Eur. J. Biochem. 270*, 1628−1644.

(16) Bridge, A. J., Pebernard, S., Ducraux, A., Nicoulaz, A. L., and Iggo, R. (2003) Induction of an interferon response by RNAi vectors in mammalian cells. *Nat. Genet. 34*, 263−264.

(17) Sledz, C. A., Holko, M., de Veer, M. J., Silverman, R. H., and Williams, B. R. (2003) Activation of the interferon system by short-interfering RNAs. *Nat. Cell Biol. 5*, 834−839.

(18) Lesage, D., Metelev, V., Borisova, O., Dolinnaya, N., Oretskaya, T., Baran-Marszak, F., Taillandier, E., Raphael, M., and Fagard, R. (2003) Specific covalent binding of a NF-kappaB decoy hairpin oligonucleotide targeted to the p50 subunit and induction of apoptosis. *FEBS Lett. 547*, 115−118.

(19) Metelev, V. G., Kubareva, E. A., Vorob'eva, O. V., Romanenkov, A. S., and Oretskaya, T. S. (2003) Specific conjugation of DNA binding proteins to DNA templates through thiol-disulfide exchange. *FEBS Lett. 538*, 48−52.

(20) Metelev, V. G., Borisova, O. A., Volkov, E. M., Oretskaya, T. S., and Dolinnaya, N. G. (2001) New chemically reactive dsDNAs containing single internucleotide monophosphoryldithio links: reactivity of 5′-mercapto-oligodeoxyribonucleotides. *Nucl. Acids. Res. 29*, 4062−4069.

(21) Thierry, A. R., Vives, E., Richard, J. P., Prevot, P., Martinand-Mari, C., Robbins, I., and Lebleu, B. (2003) Cellular uptake and intracellular fate of antisense oligonucleotides. *Curr. Opin. Mol. Ther. 5*, 133−138.

(22) Hu, Q., Bally, M. B., and Madden, T. D. (2002) Subcellular trafficking of antisense oligonucleotides and down-regulation of bcl-2 gene expression in human melanoma cells using a fusogenic liposome delivery system. *Nucl. Acids. Res. 30*, 3632−3641.

(23) Islam, A., Handley, S. L., Thompson, K. S., and Akhtar, S. (2000) Studies on uptake, sub-cellular trafficking and efflux of antisense oligodeoxynucleotides in glioma cells using self-assembling cationic lipoplexes as delivery systems. *J. Drug Target. 7*, 373−382.

(24) Marcusson, E. G., Bhat, B., Manoharan, M., Bennett, C. F., and Dean, N. M. (1998) Phosphorothioate oligodeoxyribonucleotides dissociate from cationic lipids before entering the nucleus. *Nucl. Acids. Res. 26*, 2016−2023.

(25) Hnatowich, D. J. (1996) Pharmacokinetics of 99mTc-labeled oligonucleotides. *Quart. J. Nucl. Med. 40*, 202−208.

(26) Tavitian, B. (2000) In vivo antisense imaging. *Quart. J. Nucl. Med. 44*, 236−255.

(27) Broude, N. E. (2002) Stem-loop oligonucleotides: a robust tool for molecular biology and biotechnology. *Trends Biotechnol. 20*, 249−256.

(28) Johansson, M. K., and Cook, R. M. (2003) Intramolecular dimers: a new design strategy for fluorescence-quenched probes. *Chemistry Eur. J. 9*, 3466−3471.

(29) Weissleder, R., Tung, C. H., Mahmood, U., and Bogdanov, A., Jr. (1999) In vivo imaging of tumors with protease-activated near-infrared fluorescent probes. *Nat. Biotechnol 17*, 375−378.

(30) Neri, D., Carnemolla, B., Nissim, A., Leprini, A., Querze, G., Balza, E., Pini, A., Tarli, L., Halin, C., Neri, P., Zardi, L., and Winter, G. (1997) Targeting by affinity-matured recombinant antibody fragments of an angiogenesis associated fibronectin isoform. *Nat. Biotechnol. 15*, 1271−1275.

(31) Mujumdar, S., Mujumdar, R., Grant, C., and Waggoner, A. (1995) Cyanine-labeling reagents: sulfobenzindocyanine succinimidyl esters. *Bioconjugate Chem. 7*, 356−362.

BC049916B

Targeted Molecular Imaging Agents for Cellular-Scale Bimodal Imaging

H. Charles Manning,[†] Timothy Goebel,[‡] Reid C. Thompson,[§] Ronald R. Price,[||] Haakil Lee,[||] and Darryl J. Bornhop*[,†]

Department of Chemistry, Vanderbilt University, Nashville, Tennessee 37232, Department of Chemistry, Texas Tech University, Lubbock, Texas 79409, Section of Neurosurgical Oncology, Vanderbilt University, Nashville, Tennessee 37232, and Department of Radiology, Vanderbilt University Medical Center, Nashville, Tennessee 37232. Received April 16, 2004; Revised Manuscript Received June 28, 2004

Molecular imaging is a powerful tool that has the ability to elucidate biochemical mechanisms and signal the early onset of disease. Overexpression of the peripheral benzodiazepine receptor (PBR) has been observed in a variety disease states, including glioblastoma, breast cancer, and Alzheimer's disease. Thus, the PBR could be an attractive target for molecular imaging. In this paper, the authors report cellular uptake and multimodal (MRI and fluorescence) imaging of PBR-overexpressing C6 glioblastoma (brain cancer) cells using a cocktail administration approach and a new PBR targeted lanthanide chelate molecular imaging agent.

INTRODUCTION

Recent discoveries in molecular imaging (MI) are certain to play a vital role in the early detection, diagnosis, and treatment of disease, as well as aid in the study of biological and biochemical mechanisms, immunology, and neuroscience (*1*−*7*). The ubiquitous clinical agent, Magnevist, is a perfusion agent that can give vascularity and fluid transport information, but has the limitation of lacking the ability to target specific tissues. Generally, targeted MI agents consist of a targeting functionality such as an antibody, peptide (*8*), sugar (*9*), or a ligand such as a peripheral benzodiazepine receptor (PBR) ligand (*10*) combined with a signaling moiety (a fluorophore, radioisotope, or Gd^{3+} ion, etc.). In some cases, the signal can be activated by a species found in the target environment such as an enzyme or high Ca^{2+} concentration (*11*−*13*). Targeted fluorescent MI agents show great promise for following gene therapy/delivery (*14*), for elucidating signaling pathways (*1*), and for performing disease diagnosis at the molecular level (*6*). Magnetic resonance MI agents have also been developed that provide unique insights on system physiology (*11*) and allow effective tumor imaging (*5, 12*).

While existing MI agents have been functional, another limitation of most existing MI agents is that they provide a single signature. Multimodal agents have the potential to enhance visualization of diseased tissue by generating more than one signature from a single biological matrix. Two-signature integrated molecules for bimodal imaging have been used by Meade and coworkers to follow cell lineage in *Xenopus laevis* (*15*) and even stem cell migration (*16*). Figure 1 shows the result obtained when a *X. laevis* embryo was injected with Gd−(DTPA)-tetramethylrhodamine-hydroxypropylpoly-(D-lysine) ($GRIP_c$, Figure 1A) into a marginal blastomere (*15*) and subsequently imaged with confocal microscopy (Figure 1B) and MRI (Figure 1C). Both MR and fluorescence signatures seem to colocalize in similar regions of the embryo.

More recently, Josephson, Weissleder, and co-workers have reported an activatable polymeric agent that combines NIR fluorescence and MR properties (*17*). The agent, shown in Figure 2, utilizes a protease cleavable carrier that can be labeled with Cy5.5 and cross-linked iron oxide particles (CLIO). Two dye-arginyl peptide nanoparticle conjugates were reported, Cy5.5-R4-SS-CLIO and Cy5.5-R4-SC-CLIO, where "SS" denotes a disulfide linkage between the peptide and the iron oxide while "SC" denotes a thioether linkage, while R4 stands for four L-arginyl peptides. As reported, the primary amine of a dextran-coated CLIO was reacted with one of two activating agents, either *N*-succinimidyl 3-(2-pyridyldithio)propionate (SPDP) or succinimdyl iodoacetate (SIA), to produce two reactive forms of the CLIO as shown in Figure 2. The L-arginyl peptide is attached to the activated CLIO through a C-terminal cysteine residue while the *N*-hydroxysuccinimide ester of Cy5.5 is attached via the terminal amine, yielding the bifunctional species. Upon in vivo administration of Cy5.5-R4-SC-CLIO, MR and fluorescence signals were observed to be colocalized in lymph nodes (Figure 2A−D). While both of these imaging strategies show promise, the aforementioned contrast agents are of a nontargeted (perfusion) nature. Bimodal *targeted* imaging using a PBR ligand would be particularly attractive due to the importance of this receptor in cell physiology (*18*).

Thus, an alternate approach to bimodal imaging using "cocktails" of the PBR targeted fluorescent Eu-PK11195 and the MR active Gd-PK11195 complex is demonstrated for the first time. Multiple signature moieties could facilitate development of practical methodologies for correlating intraoperative in vivo fluorescence detection with MRI, thereby enhancing tumor resection and subsequently improving patient outcome.

* To whom correspondence should be addressed. E-mail: darryl.bornhop@vanderbilt.edu.

[†] Department of Chemistry, Vanderbilt University.

[‡] Department of Chemistry, Texas Tech University.

[§] Section of Neurosurgical Oncology, Vanderbilt University.

[||] Department of Radiology, Vanderbilt University Medical Center.

10.1021/bc049904q CCC: $27.50 © 2004 American Chemical Society
Published on Web 10/30/2004

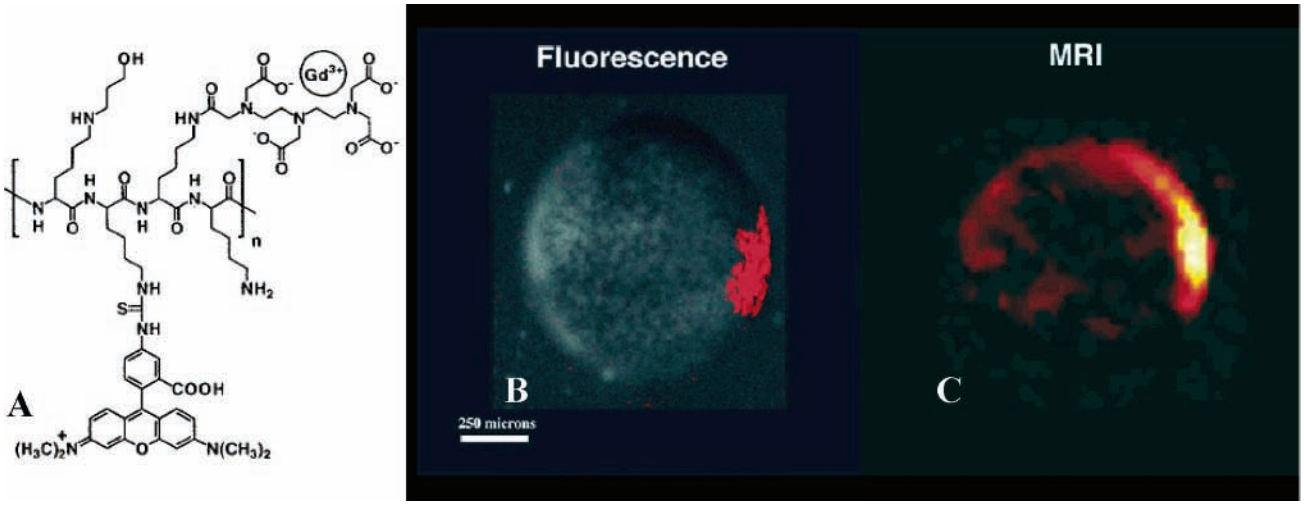


Figure 1. *X. laevis* embryo (stage 8) with $GRIP_c$ injected into the marginal blastomere at 16-cell stage. (A) Chemical structure of $GRIP_c$. (B) Confocal fluorescence image. (C) MRI image show both signals propagate from the same population of cells. Image courtesy Tom Meade (*42*).

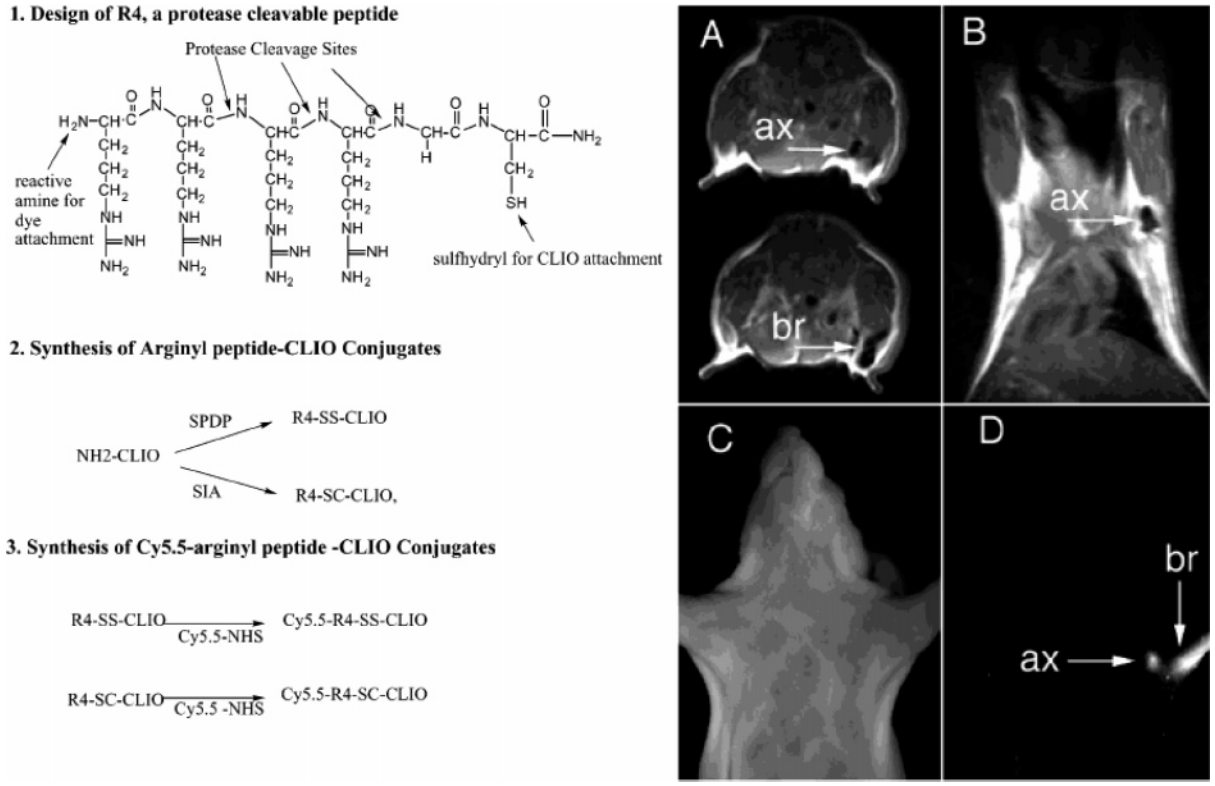
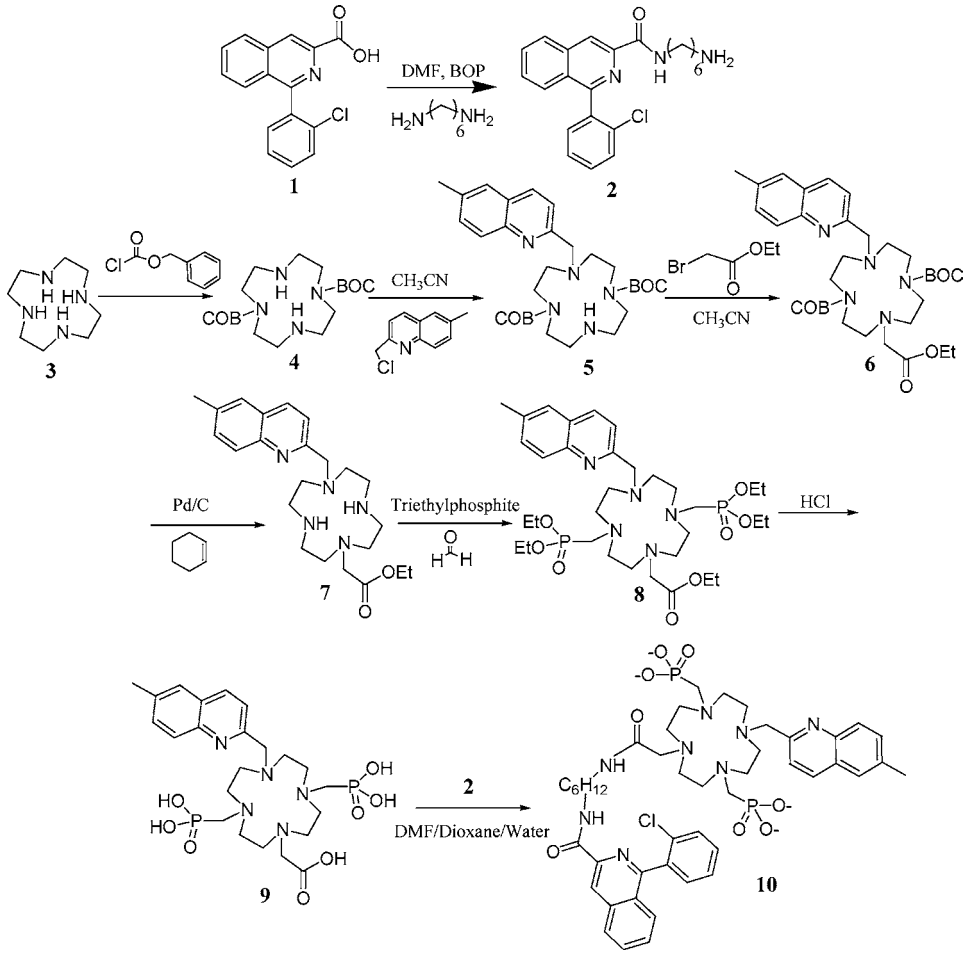


Figure 2. Synthesis and MR/NIRF images from animals injected with Cy5.5-R4-SC-CLIO. (A) Contrast-enhanced MR image of lymph nodes where ax = axillary and br = brachial. (B) Contrast-enhanced coronal image of axillary node. (C and D) White light and NIRF images, respectively, showing NIRF emission from the axillary and brachial nodes. Figure adapted from Josephson et al. (*17*).

Numerous targets exist for molecular imaging, including the sigma 2 (*19*), EGFr (*20*), and peripheral benzodiazepine receptor (PBR) (*18, 21, 22*). The 18 kDa protein, PBR, located in the mitochondria, has been demonstrated to be associated with numerous biological functions including regulation of cellular proliferation, immunomodulation, porphyrin transport, heme biosynthesis, anion transport, regulation of steroidogenesis, and even apoptosis (*18, 23, 24*). PBR density changes have important implications when acute and chronic human neurodegenerative pathologies are present. For example, temporal cortex obtained from Alzheimer's patients showed an increase in PBR (*25*). Additionally, correlations with Huntington's disease (*26*), multiple sclerosis (*27, 28*), and gliosis (*29, 30*) have been observed. Combined with evidence that PBRs play a major role in proliferation of aggressive tumor cells (*31*), overexpression of PBR in these cells creates an excellent target for study of diseased human tissues and represents a potential tool for improving detection, diagnosis, prevention, and, very likely, treatment of certain cancers.

Because PBR overexpression in diseased tissue has been suggested as an effective target for glioma and CNS disease (*32*), a number of ligands have been developed for targeting this receptor (*10, 22, 33*). Even though PBRs are expressed throughout the body (*18*), their density in the CNS is primarily limited to the ependymal cells and glia (*25*). Thus, compounds based on the well-character-

Scheme 1. Synthesis of Conjugable PBR Ligand (2) and PBR-Targeted Ligand (10)



ized, high affinity PBR ligand (*33*) PK11195 have been tested as PET agents for visualizing rat and human glia (*22*) and as a targeted therapeutic agent when conjugated to the drug gemcitabine (*34*). Furthermore, the ^{11}C PET version is currently being tested in the clinic to study acute brain injury and neuroinflammation (*35*).

Here we describe the first PBR-targeted MI agent that could facilitate MR imaging and, when delivered as a cocktail (Eu^{3+} and Gd^{3+}) of a Ln-PK11195 complex, produces cellular-scale bimodal (MR and fluorescence) imaging. The MI agent described is a PK11195 (nanomolar binding PBR ligand) analogue conjugated to a trifunctional lanthanide chelate (Ln-QM-CTMC) (*36*−*38*). When prepared as the Eu^{3+}complex, Eu-QM-CTMC-PK11195 (Eu-PK11195), exhibited visibly bright fluorescence (*38*). By substitution with Gd^{3+}, Gd-PK11195 then acts as a MRI agent with molar relaxivity comparable to Magnevist. This new MI agent could be useful for numerous applications in molecular imaging including disease mapping, surgical resection guidance through in vivo imaging, and the further elucidation of PBR function in cell biology.

EXPERIMENTAL PROCEDURES

Uptake Experiments. C6 glioblastoma cells were cultured in Dulbecco's Modified Eagle Medium (DMEM)-F12 medium (Gibco/Invitrogen) supplemented with 15% horse serum (ATCC), 2.5% FBS (Gibco/Invitrogen), and 0.1% 50 mg/mL gentamicin sulfate (Biowhittaker). Standard medium pH was between 7.2 and 7.4. Cells were maintained in a Forma Scientific incubator at 37 °C in a sterile air environment containing 5% CO_2 and were plated for imaging on glass coverslips just prior to confluency. Next, cells were dosed with 1 mL of the contrast agent in 0.9% saline (25 μM Eu-PK11195) and allowed to incubate at either 37 °C (or 4 °C, cold study) for various times, including 35 min, 45 min, 60 min, and beyond. At the end of the incubation time, the cells were thoroughly rinsed with saline and imaged in white light and fluorescence directly using a standard epi-illumination fluorescence microscope (Carl Zeiss, Axioskop). The microscope was configured to facilitate the imaging of our complex. The optical train consisted of a UG11 filter inserted into the excitation path. The subsequent light was reflected onto a dosed sample using a 400 nm cutoff dichroic mirror. Finally, fluorescence was collected through a 40× objective (NA = 0.5), passed through a 612 × 25 nm emission filter, and directed onto a Sinsys CCD camera. Images were collected and stored on a pc.

Displacement Experiments. C6 glioblastoma cells were plated out on glass coverslips and incubated at 37 °C until just prior to confluency. Next, cells were dosed with 1 mL of contrast agent in 0.9% saline (25 μM Eu-PK11195) and allowed to incubate at 37 °C for 60 min. At the end of the incubation time, the cells were thoroughly rinsed with saline and imaged in white light and fluorescence directly using a standard epi-illumination fluorescence microscope (Carl Zeiss, Axioskop). Next, a 6-fold molar excess of PK11195 was allowed to incubate with the fluorescing cells at 37 °C for 1 h. At the appropriate time, the cells were again rinsed with saline and imaged directly under the fluorescence microscope. To calculate the change in fluorescence intensity between the dosed and displaced experiments, the total gray scale

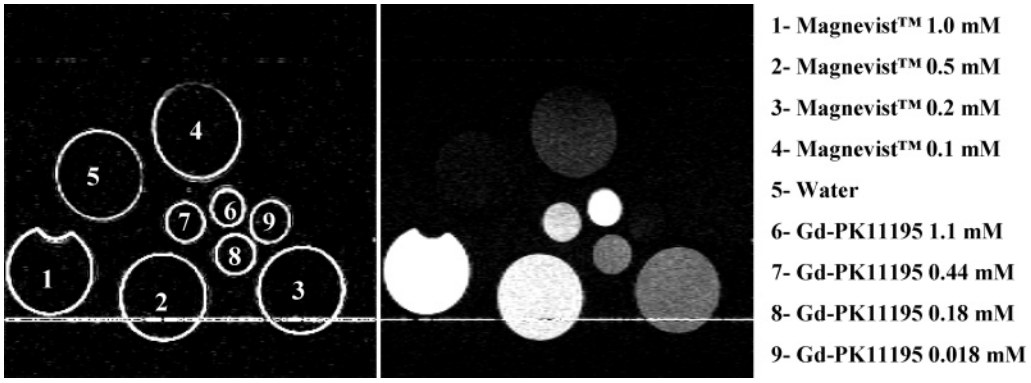
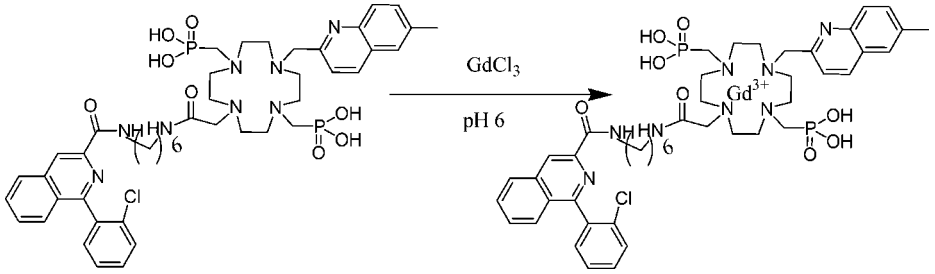


Figure 3. Comparison of MR contrast between a commercially available agent and Gd-PK11195. Note, unlike the former agent (Magnevist), the latter compound affords the ability to utilize *both* fluorescence and MR signatures as diagnostic tools.

Scheme 2. Complexation of Ln-PK11195 Facilitating the Preparation of a PBR-Targeted MR Agent



intensity was integrated over both pictures (same integration times) using Adobe Photoshop. Values were recorded, and the displaced intensity was compared to the dosed intensity to give the percent fluorescence change [100 − (displaced/dosed) × 100].

MR Imaging. Sample solutions (Magnevist and Gd-PK11195) were prepared in water and imaged via a T_1-weighted Spin−Echo pulse sequence in a standard 4.7 T instrument where TE was kept constant and TR was varied 100−3000 ms.

Cocktail Imaging. Approximately 10^6 C6 glial cells were inoculated with a 40−60 cocktail (1 mM total Ln-PK11195 concentration) of the Eu-PK11195 and the Gd-PK11195 complexes. Directly after 60-min incubation time, fluorescence microscopy was performed on a small number of cell cultures that were flash frozen for subsequent MR imaging. Images of thawed cells (in μL centrifuge tubes) were acquired using a 4.7 T instrument (Figure 8, TE/TR = 11/1000 ms, FOV = 4 cm, slice thickness = 1 mm). The data matrix was 256 × 128, extrapolated to 256 × 256 for the final images.

RESULTS AND DISCUSSION

Initially, we prepared the PBR targeted ligand by coupling our conjugable form of PK11195 to a trifunctional lanthanide chelate (*38*) (Scheme 1). The conjugable PBR ligand was realized by first synthesizing 1-(2-chlorophenyl)isoquinoline-3-carboxylic acid using established procedures (*39*). We completed the conjugable molecule by appending the carboxylic acid residue with a diamine linker (*38*). Previously, we have reported the synthetic methodology leading to the trifunctional lanthanide chelator {Griffin, 2001 #48; Manning, 2004 #46}. Briefly, cyclen is first selectively di-protected with benzyloxycarbonyl groups at low pH (*40*). Next, the 1, 7-diprotected macrocycle can then be mono-alkylated with an antenna to later be used for lanthanide sensitization. The macrocycle is then fitted with a pendant carboxylic ester residue for conjugation (*36*). The protecting groups are removed under mild hydrogenation conditions using cyclohexene and Pd/C, and complexation arms are then added. Initially, we chose to alkylate the remaining cyclen nitrogen atoms with phosphonate acid-ester pendant arms, which, upon hydrolysis have very good chelation ability (*41*). After hydrolysis, the completed trifunctional lanthanide chelator was coupled to the conjugable form of PK11195 in mixed aqueous organic solvent (*38*). Complexation of the ligand with europium resulted in a fluorescent derivative that gave the expected lanthanide luminescence (*38*).

The Gd^{3+} derivative was prepared as shown in Scheme 2. While the substitution may seem trivial, simply exchanging the metal ion in the complex results in another agent with an entirely different signature. In this way, one scaffold offers multiple facets of imaging opportunity. For example, aside from fluorescence (M = Tb or Eu) and MRI (Gd), additional metal substitution (M = Ga, Cu, Ho, etc.) can facilitate applications for PET imaging and ultimately, targeted therapeutic dose delivery.

Next, we evaluated the magnetic resonance signature of this new PBR-targeted compound (Gd-PK11195) by correlation to the clinical MRI agent Magnevist. A series of dilutions of each contrast agent at similar concentrations was used to measure the molecular relaxivity at 4.7 T. From the linear calibration plot ($r^2 = 0.999$, data not shown), $r1_{Gd\text{-}PK_{11195}} = 5.94\ s^{-1}\ mM^{-1}$ and $r1_{Magnevist} = 6.45\ s^{-1}\ mM^{-1}$. These data show that the new PBR targeted MI has a T_1 relaxivity value comparable to a commonly used perfusion agent.

To evaluate functional contrast, the same solutions were imaged as phantoms in a standard MR imaging system, again at 4.7 T. Figure 3 shows the result of this experiment, the T_1 weighted phantom images of Gd-PK11195 and Magnevist solutions over a range of concentrations. As the images demonstrate, Gd-PK11195 gives similar MR contrast to Magnevist. Therefore, Gd-PK11195 delivered to the specific target, PBR, results in contrast comparable with an accepted agent. Such specificity for PBR-overexpressing cells or tissues could

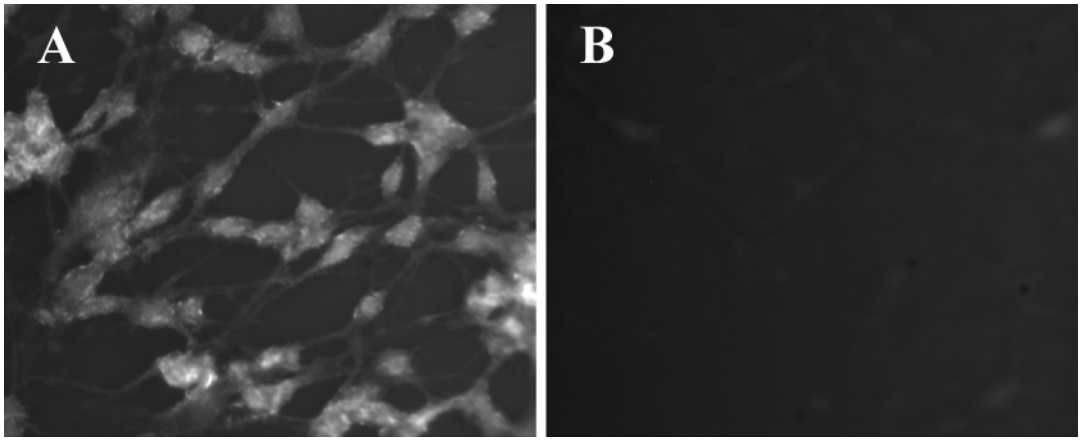


Figure 4. (A) C6 glioblastoma cells incubated with Eu-PK11195 for 60 min. (B) Blank, undosed C6 cells.

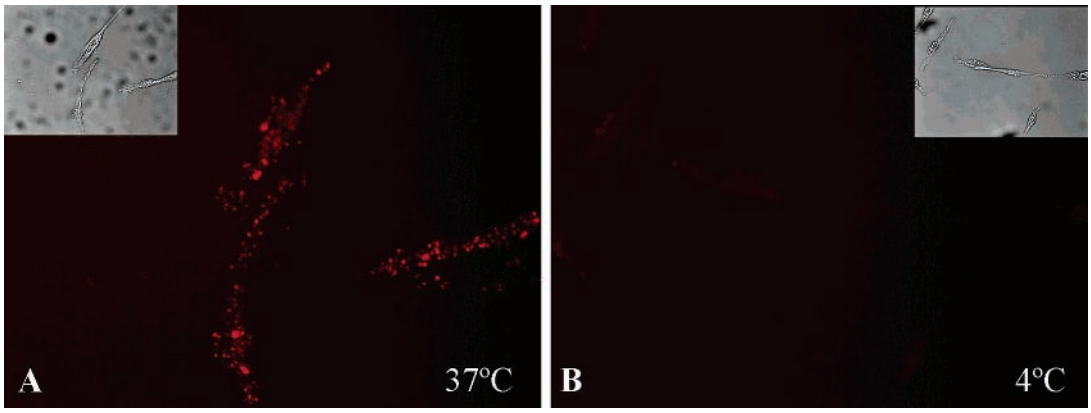


Figure 5. (A) C6 glioma cells incubated with Eu-PK11195 at 37 °C, demonstrating appreciable uptake and fluorescence. (B) C6 cells incubated with Eu-PK11195 at 4 °C, demonstrating minimal fluorescence.

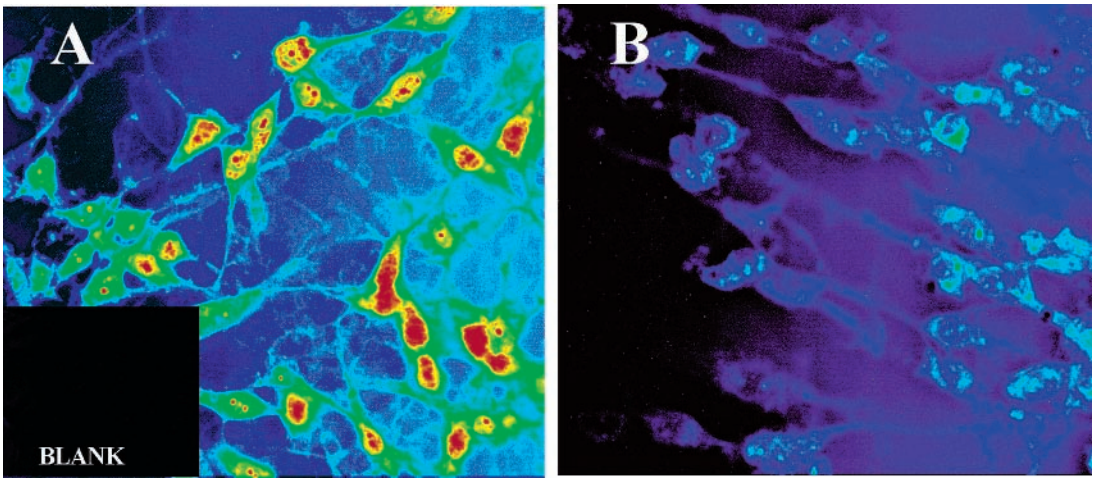


Figure 6. (A) C6 glioblastoma cells after 60-min incubation with Eu-PK11195 and viewed in fluorescence mode (False Colorized). Inset: undosed (blank) C6 glioblastoma cells. (B) C6 culture first incubated 60 min with Eu-PK11195, then counter-incubated with PK11195 for 60 min.

prove useful in elucidating the critical functions of PBR, dealing with reactive oxygen species (*31*), and even improved detection of mitochondrial misfunction diseases (*21*).

To evaluate Ln-PK11195-targeted delivery, we performed uptake and displacement studies. PBR-overexpressing C6 glioma cells (*10, 22*) were dosed with Eu-PK11195 at concentrations of 10 μM to 1.0 mM for times ranging from 20 to 60 min. Quinoline-sensitized fluorescence from the Eu^{3+} complex (*38*) was readily detectable in the cells at all incubation times and concentrations using a modified epi-illumination fluorescence microscope affixed with a CCD camera. For 10−500 μM concentrations of the agent, the optimum dosage time was found to be between 45 min and 1 h. As illustrated in Figure 4A, there is substantial uptake of Eu-PK11195 by C6 glioma cells, with fluorescence being associated with distinct internal structures, suggesting specific organelle location of the protein. PBRs are in fact known to be expressed in the outer mitochondrial membrane (*18, 42*). Preliminary coregistration studies indicate that Ln-PK11195 is localized in the same region of the cell as the mitochondrial dye JC-1 (*43*). Figure 4B presents the control, an undosed population of C6 cells of comparable

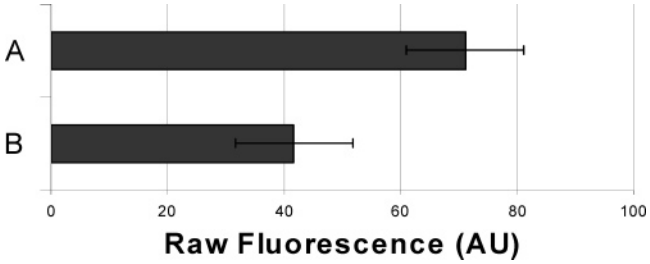


Figure 7. Average raw fluorescence of agent-dosed C6 glioblastoma cells. Bar A is the raw fluorescence after dosing with Eu-PK11195. Bar B is the raw fluorescence after PK11195 displacement of contrast agent from PBR. Error bars represent the standard deviation of triplicate experiments.

density, which is relatively devoid of fluorescence. To demonstrate that the Eu-PK11195 molecule was being transported into the cells as opposed to simply adhering to the surface, we performed a standard biological cold-uptake mechanism study where C6 glioma cells were incubated with the same concentration of Eu-PK11195 at both 37 °C and 4 °C. As seen in Figure 5A, the cells incubated with the contrast agent at 37 °C show appreciable fluorescence, while those incubated at 4 °C (Figure 5B) show very little. These data suggests that the molecule is labeling the cell internally, consistent with endocytosis, although the exact transport mechanism remains unknown (*44*). Next, a preliminary displacement study to obtain an estimate for the binding affinity of Ln-PK11195 for PBR relative to the high affinity ligand PK11195 was undertaken. Utilizing procedures similar to Pramanik (*45*), we labeled cells with our agent and quantified the binding via fluorescence intensity. We then treated the same cells with a 6-fold excess of the native, nonlabeled PBR ligand, PK11195. The reduction in fluorescence intensity was used to give an estimate of ligand displacement (*45*). One result of these experiments is displayed in Figure 6. The false colorized image in Figure 6A is of cells dosed with Eu-PK11195, while Figure 6B shows the cells after 60-min competition with excess PK11195. Cell repositioning, due to rinsing procedures, accounts for the differences in appearance of the images. The average reduction in fluorescence intensity (triplicate determinations) after displacement of Eu-PK11195 with PK11195 was 37% (Figure 7), indicating that Eu-PK11195 functions as a PBR ligand. Yet, there is still appreciable fluorescence remaining in the cells after the displacement dosage of a 6-fold excess of the native PK11195, suggesting that our complex is binding to the PBR with substantial affinity as desired (*10*). Additional studies are currently underway to quantify binding affinity, with nanomolar K_d values expected.

Next, cocktail mixtures were prepared in varying ratios (20:80, 30:70, 40:60, and 50:50, Eu^{3+}:Gd^{3+}) and used for examination of C6 glioma cell colonies in order to demonstrate the "cocktail" approach. All ratios gave both signatures, with Figure 8 illustrating that the 40% Eu^{3+}: 60% Gd^{3+} cocktail has readily quantifiable fluorescence and MR contrast from the *same* population of C6 cells. A cursory evaluation of these preliminary data indicates contrast enhancement (signal-to-background ratio) by the MI agent to be 9:1 for fluorescence and 1.7:1 for MR. Of particular intrigue is the observation of significant MR contrast using Gd-PK11195 given the controversy surrounding quantitative receptor imaging using Gd^{3+} complexes. To be sure, MR imaging of receptors is only possible if the receptor of interest is expressed at a sufficiently high rate, and if the agent of interest can be delivered and retained in sufficient concentration. Tweedle and co-workers have estimated that at least 10^6 receptor-bound Gd^{3+} agents are required per cell to achieve approximately 2:1 S/N in a conventional 2T MR imager (*46*). Thus, assuming a 1:1 receptor−contrast agent pair, there would have to be on the order of 10^6 PBR in a cell to observe MR contrast. In fact, Papadopoulos has indeed reported PBR concentrations in cancer cells on the order of 10^6 receptors/cell, assuming 10^{10} cells/g (*42, 47*). Therefore, given the expression profile reported for PBR, in conjunction with our experiments being performed at high field (4.7 T), it would appear that PBR can be imaged in cells with Gd-PK11195.

In conclusion, we have demonstrated targeted delivery of Ln-PK11195 to PBR-overexpressing C-6 glioma cells. Bright, localized fluorescence of the Eu-PK11195 was observed with standard microscopy and displacement studies indicated PBR ligand functionality. Furthermore, it was shown that the Gd^{3+} complex of Ln-PK11195 has a relaxivity and an MR signature comparable in brightness to the clinical agent Magnevist but with the benefit of specificity. Through internalization and association with the PBR within the mitochondria, we can now use MRI to study expression, identify up-regulating cells, and further elucidate PBR functions, including its association with apoptosis (*48*). Finally, bimodal cellular-scale contrast−enhancement was afforded using a cocktail of Eu-PK11195 and Gd-PK11195.

These investigations demonstrate that both fluorescence and MRI signatures are possible and were observed in C6 glioma cells using a PBR ligand-based MI agent. To expand on these findings, experiments are underway to determine if PBR expression can be imaged in real-time using Ln-PK11195. Other investigations with this new MI agent include both relaxivity determination (contrast enhancement) in PBR-overexpressing tissues and quantification of K_d for PBR. Other variations of the metal-PK11195 complex could potentially facilitate targeted imaging with PET (M = Ga, Cu, etc.) and eventu-

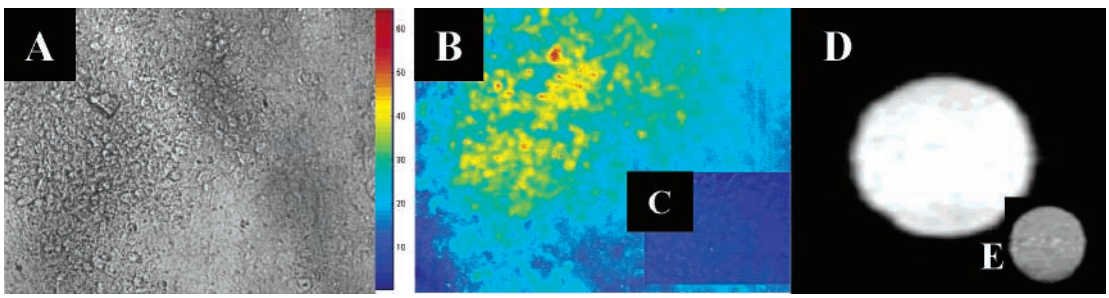


Figure 8. (A) White-light image of C6 glioma cells (40×) dosed with a cocktail of Ln-PK11195 (40% Eu:60% Gd). (B) Cocktail-dosed C6 glioma cells from A imaged in fluorescence mode. (C) Undosed (blank) C6 glioma cells. (D) MRI image of cocktail-dosed C6 glioma cells. (E) MRI image of undosed (blank) cells.

ally site-directed therapy delivery of a radioactive isotope (M = ^{166}Ho, ^{177}Lu). We envision that Eu-PK11195 can be useful as a histopathological stain, and that this unique strategy of integrating optical imaging with the specificity of a targeted delivery could ultimately facilitate intraoperative multimodal imaging, impacting diagnosis and treatment of malignant brain cancer and other neurological dysfunctions.

ACKNOWLEDGMENT

The authors would like to recognize financial contributions from NSF and the Whitaker Foundation.

LITERATURE CITED

(1) www.MolecularProbes.com.

(2) Ntziachristos, V., and Chance, B. (2001). Probing physiology and molecular function using optical imaging: applications to breast cancer. *Breast Cancer Res. 3*, 41−46.

(3) Licha, K., Riefke, B., Ntziachristos, V., Becker, A., Chance, B., and Semmler, W. (2000). Hydrophilic cyanine dyes as contrast agents for near-infrared tumor imaging: Synthesis, photophysical properties and spectroscopic in vivo characterization. *Photochem. Photobiol. 72*, 392−398.

(4) Hawrysz, D. J., and Sevick-Muraca, E. M. (2000). Developments toward diagnostic breast cancer imaging using near-infrared optical measurements and fluorescent contrast agents. *Neoplasia 2*, 388−417.

(5) Weissleder, R., and Mahmood, U. (2001). Molecular imaging. *Radiology 219*, 316−333.

(6) Gaietta, G., Deerinck, T. J., Adams, S. R., Bouwer, J., Tour, O., Laird, D. W., Sosinsky, G. E., Tsien, R. Y., and Ellisman, M. H. (2002). Multicolor and electron microscopic imaging of connexin trafficking. *Science 296*, 503−507.

(7) Louie, A. Y., Huber, M. M., Ahrens, E. T., Rothbacher, U., Moats, R., Jacobs, R. E., Fraser, S. E., and Meade, T. J. (2000). In vivo visualization of gene expression using magnetic resonance imaging. *Nature Biotechnol. 18*, 321−325.

(8) Wolfe, H. R., Mendizabal, M., Lleong, E., Cuthbertson, A., Desai, V., Pullan, S., Fujii, D. K., Morrison, M., Pither, R., and Waldman, S. A. (2002). In vivo imaging of human colon cancer xenografts in immunodeficient mice using a guanylyl cyclase C-specific ligand. *J. Nuclear Med. 43*, 392−399.

(9) Lemieux, G. A., Yarema, K. J., Jacobs, C. L., and Bertozzi, C. R. (1999). Exploiting differences in sialoside expression for selective targeting of MRI contrast reagents. *J. Am. Chem. Soc. 121*, 4278−4279.

(10) Kozikowski, A. P., Kotoula, M., Ma, D. W., Boujrad, N., Tuckmantel, W., and Papadopoulos, V. (1997). Synthesis and biology of a 7-nitro-2,1,3-benzoxadiazol-4-yl derivative of 2-phenylindole-3-acetamide: A fluorescent probe for the peripheral-type benzodiazepine receptor. *J. Med. Chem. 40*, 2435−2439.

(11) Li, W. H., Fraser, S. E., and Meade, T. J. (1999). A calcium-sensitive magnetic resonance imaging contrast agent. *J. Am. Chem. Soc. 121*, 1413−1414.

(12) Weissleder, R., Tung, C. H., Mahmood, U., and Bogdanov, A. (1999). In vivo imaging of tumors with protease-activated near-infrared fluorescent probes. *Nature Biotechnol. 17*, 375−378.

(13) Moats, R. A., Fraser, S. E., and Meade, T. J. (1997). A ″smart″ magnetic resonance imaging agent that reports on specific enzymatic activity. *Angew. Chem.-Int. Ed. Engl. 36*, 726−728.

(14) Mahmood, U., Tung, C. H., and Weissleder, R. (1999). Optical imaging of gene expression using enzyme-specific activatable contrast agents. *Radiology 213P*, 102−102.

(15) Huber, M. M., Staubli, A. B., Kustedjo, K., Gray, M. H. B., Shih, J., Fraser, S. E., Jacobs, R. E., and Meade, T. J. (1998). Fluorescently detectable magnetic resonance imaging agents. *Bioconjugate Chem 9*, 242−249.

(16) Modo, M., Cash, D., Mellodew, K., Williams, S. C. R., Fraser, S. E., Meade, T. J., Price, J., and Hodges, H. (2002). Tracking transplanted stem cell migration using bifunctional, contrast agent-enhanced, magnetic resonance imaging. *Neuroimage 17*, 803−811.

(17) Josephson, L., Kircher, M. F., Mahmood, U., Tang, Y., and Weissleder, R. (2002). Near-infrared fluorescent nanoparticles as combined MR/optical imaging probes. *Bioconjugate Chem 13*, 554−560.

(18) Casellas, P., Galiegue, S., and Basile, A. S. (2002). Peripheral benzodiazepine receptors and mitochondrial function. *Neurochem. Int. 40*, 475−486.

(19) Wheeler, K. T., Wang, L. M., Wallen, C. A., Childers, S. R., Cline, J. M., Keng, P. C., Mach, R. H., and Department of Radiology, W. F. U. S.o. M. W.-S. N. C. U.S.A. (2000). Sigma-2 receptors as a biomarker of proliferation in solid tumours. *Br. J. Cancer 82 (6)*, 1223−1232.

(20) Carlsson, J., Blomquist, E., Gedda, L., Liljegren, A., Malmstrom, P. U., Sjostrom, A., Sundin, A., Westlin, J. E., Zhao, Q. H., Tolmachev, V., and Lundqvist, H. (1999). Conjugate chemistry and cellular processing of EGF-Dextran. *Acta Oncologica 38*, 313−321.

(21) Szewczyk, A., and Wojtczak, L. (2002). Mitochondria as a pharmacological target. *Pharmacol. Rev. 54*, 101−127.

(22) Starosta-Rubinstein, S., Ciliax, B., Penney, J., McKeever, P., and Young, A. (1987). Imaging of a glioma using peripheral benzodiazepine receptor ligands. *Proc. Natl. Acad. Sci. U.S.A. 84*, 891−895.

(23) Garnier, M., Boujrad, N., Oke, B. O., Brown, A. S., Riond, J., Ferrara, P., Shoyab, M., Suarezquian, C. A., and Papadopoulos, V. (1993). Diazepam Binding Inhibitor Is a Paracrine Autocrine Regulator of Leydig-Cell Proliferation and Steroidogenesis − Action Via Peripheral-Type Benzodiazepine Receptor and Independent Mechanisms. *Endocrinology 132*, 444−458.

(24) Alho, H., Varga, V., and Krueger, K. E. (1994). Expression of Mitochondrial Benzodiazepine Receptor and Its Putative Endogenous Ligand in Cultured Primary Astrocytes and C-6 Cells − Relation to Cell-Growth. *Cell Growth Differ. 5*, 1005−1014.

(25) Papadopoulos, V. (2003). Peripheral benzodiazepine receptor: structure and function in health and disease. *Ann. Pharm. Fr. 61*, 30−50.

(26) Messmer, K., and Reynolds, G. P. (1998). Increased peripheral benzodiazepine binding sites in the brain of patients with Huntington's disease. *Neurosci. Lett. 241*, 53−56.

(27) Vowinckel, E., Reutens, D., Becher, B., Verge, G., Evans, A., Owens, T., and Antel, J. P. (1997). PK11195 binding to the peripheral benzodiazepine receptor as a marker of microglia activation in multiple sclerosis and experimental autoimmune encephalomyelitis. *J. Neurosci. Res. 50*, 345−353.

(28) Reutens, D. C., Vowinckel, E., Owens, T., Evans, A. C., and Antel, J. (1997). In vivo and in vitro binding of the peripheral benzodiazepine receptor ligand PK11195 in active lesions of multiple sclerosis and experimental allergic encephalomyelitis. *Neurology 48*, 2071−2071.

(29) Broaddus, W. C., Bennett, J. P., Jr., and Department of Neurosurgery, U.o. V. H. S. C. C. (1990). Peripheral-type benzodiazepine receptors in human glioblastomas: pharmacologic characterization and photoaffinity labeling of ligand recognition site. *Brain Res. 518 (1−2)*, 199−208.

(30) Brown, R. C., Degenhardt, B., Kotoula, M., and Papadopoulous, V. (2000). Location-dependent role of the human glioma cell peripheral-type benzodiazepine receptor in proliferation and steroid biosynthesis. *Cancer Lett. 156*, 125−132.

(31) Delavoie, F., Li, H., Hardwick, M., Robert, J., Giatzakis, C., Peranzi, G., Yao, Z., Maccario, J., Lacapere, J., and Papadopoulos, V. (2003). In vivo and in vitro peripheral-type benzodiazepine receptor polymerization: functional significance in drug ligand and cholesterol binding. *Biochemistry 42*, 4506−4519.

(32) Miettinen, H., Kononen, J., Haapasalo, H., Helen, P., Sallinen, P., Harjuntausta, T., Helin, H., and Alho, H. (1995). Expression of Peripheral-Type Benzodiazepine Receptor and

Diazepam-Binding Inhibitor in Human Astrocytomas − Relationship to Cell-Proliferation. *Cancer Res. 55*, 2691−2695.
(33) Campiani, G., Cappelli, A., Nacci, V., Anzini, M., Vomero, S., Hamon, M., Cagnotto, A., Fracasso, C., Uboldi, C., Caccia, S., Consolo, S., and Mennini, T. (1997). Novel and highly potent 5-HT3 receptor agonists based on a pyrroloquinoxaline structure. *J. Med. Chem 40*, 3670−3678.
(34) Guo, P. G., Ma, J. G., Li, S. L., Guo, Z. W., Adams, A. L., and Gallo, J. M. (2001). Targeted delivery of a peripheral benzodiazepine receptor ligand-gemcitabine conjugate to brain tumors in a xenograft model. *Cancer Chemother. Pharmacol. 48*, 169−176.
(35) Menon, D. K. (personal communication, 2003).
(36) Griffin, J. M. M., Skwierawska, A. M., Manning, H. C., Marx, J. N., and Bornhop, D. J. (2001). Simple, high yielding synthesis of trifunctional fluorescent lanthanide chelates. *Tetrahedron Lett. 42*, 3823−3825.
(37) Manning, C. H., Skwierawska, A., Marx, J. N., and Bornhop, D. J. (2003). Rapid removal of benzyloxycarbonyl groups from 1, 4, 7, 10-tetraazacyclododecane derivatives by catalytic transfer hydrogenation. *Synth. Commun. 33*, 457−461.
(38) Manning, H. C., Goebel, T., Marx, J. N., and Bornhop, D. J. (2002). Facile, efficient conjugation of a trifunctional lanthanide chelate to a peripheral benzodiazepine receptor ligand. *Org. Lett. 4*, 1075−1078.
(39) Goodman, M. M. (1999). US Patent 5,998,624.
(40) Kovacs, Z., and Sherry, A. D. (1995). A General-Synthesis of 1,7-Disubstituted 1,4,7,10-Tetraazacyclododecanes. *J Chem Soc., Chem. Commun.* 185−186.
(41) Caravan, P., Ellison, J. J., McMurry, T. J., and Lauffer, R. B. (1999). Gadolinium(III) chelates as MRI contrast agents: Structure, dynamics, and applications. *Chem. Rev. 99*, 2293−2352.
(42) Hardwick, M., Fertikh, D., Culty, M., Li, H., Vidic, B., and Papadopoulos, V. (1999). Peripheral-type benzodiazepine receptor (PBR) in human breast cancer: Correlation of breast cancer cell aggressive phenotype with PBR expression, nuclear localization, and PBR-mediated cell proliferation and nuclear transport of cholesterol. *Cancer Res. 59*, 831−842.
(43) Reers, M., Smith, T. W., and Chen, L. B. (1991). J-Aggregate Formation of a Carbocyanine as a Quantitative Fluorescent Indicator of Membrane-Potential. *Biochemistry 30*, 4480−4486.
(44) Dokka, S., Toledo-Velasquez, D., Shi, X. L., Wang, L. Y., and Rojanasakul, Y. (1997). Cellular delivery of oligonucleotides by synthetic import peptide carrier. *Pharm. Res. 14*, 1759−1764.
(45) Pramanik, A., Olsson, M., Langel, U., Bartfai, T., and Rigler, R. (2001). Fluorescence correlation spectroscopy detects galanin receptor diversity on insulinoma cells. *Biochemistry 40*, 10839−10845.
(46) Nunn, A. D., Linder, M. F., Tweedle, M. F. (1997). Can receptors be imaged with MRI. *Quart. J. Nuclear Med. 41*, 155−162.
(47) Hardwick, M., Rone, J., Han, Z. Q., Haddad, B., and Papadopoulos, V. (2001). Peripheral-type benzodiazepine receptor levels correlate with the ability of human breast cancer MDA-MB-231 cell line to grow in SCID mice. *Int. J. Cancer 94*, 322−327.
(48) Sutter, A. P., Maaser, K., Hèopfner, M., Barthel, B., Grabowski, P., Faiss, S., Carayon, P., Zeitz, M., Scherèubl, H., and Medical Clinic I, B. F. U. H. F. U.o. B. B. G. (2002). Specific ligands of the peripheral benzodiazepine receptor induce apoptosis and cell cycle arrest in human esophageal cancer cells. *Int. J. Cancer. 102 (4)*, 318−327.

BC049904Q

Estimating the Number of Bound Waters in Gd(III) Complexes Revisited. Improved Methods for the Prediction of *q*-Values

Benjamin P. Hay,*,† Eric J. Werner,§ and Kenneth N. Raymond§

Chemical Sciences Division, Pacific Northwest National Laboratory, P.O. Box 999, Richland, Washington 99352, and Department of Chemistry, University of California, Berkeley, California 94720-1460. Received July 9, 2004; Revised Manuscript Received September 27, 2004

Two literature computational methods for the prediction of the number of inner-sphere aqua ligands, *q*, have been applied to a test set of seven Gd(aminocarboxylate) complexes. The first method is based on the hypothesis that *q* should be proportional to the solvent-accessible surface area of the ligand-complexed Gd ion (Castonguay, L. A., Treasurywala, A. M., Caulfield, T. J., Jaeger, E. P., and Kellar, K. E. (1999) Prediction of *q*-Values and Conformations of Gadolinium Chelates for Magnetic Resonance Imaging. *Bioconjugate Chem. 10*, 958). The second method is based on the hypothesis that *q*-values can be deduced by examining series of steric energy versus ionic radii plots as a function of coordination number (Reichert, D. E., Hancock, R. D., and Welch, M. J. (1996) Molecular Mechanics Investigation of Gadolinium(III) Complexes. *Inorg. Chem. 35*, 7013). This study identifies deficiencies in these methods and, with respect to the first method, describes some apparent errors. Although neither method was reliable at predicting *q*, two alternate approaches based on either molecular mechanics strain thresholds or exposed Gd surface area thresholds are shown to predict observed *q*-values for all Gd aminocarboxylate complexes in the test set.

INTRODUCTION

Magnetic resonance imaging (MRI) has become an important tool in modern medicine, providing high-quality three-dimensional images without the use of harmful ionizing radiation (*1*). Signal intensity in MRI stems mainly from the relaxation rate of in vivo water protons and is enhanced by the administration of a contrast agent prior to the scan. Such agents include a paramagnetic metal ion that decreases the relaxation times of nearby water protons. Contrast media often employ gadolinium(III) due to its high magnetic moment and slow electronic relaxation rate. As free Gd(III) is toxic (*2*), the design of ligands that form stable Gd(III) complexes for MRI application remains a significant area of research (*2*−*4*).

The efficacy of Gd-based contrast agents is determined by the extent to which the relaxation rate of water protons is increased, in other words, relaxivity. Agent design focuses mainly on attaining higher inner-sphere, longitudinal relaxivity, r_1, from protons of water molecules directly coordinated to the metal. Theory reveals the need to maximize *q*, the number of inner-sphere water molecules, to obtain optimal relaxivity (*2*, *3*). Simply decreasing the number of binding sites in the ligand will lead to higher *q*-values, but may weaken the Gd-ligand binding and possibly release free Gd(III) in vivo. Therefore, one design goal for MRI contrast agents is to increase the *q*-value without significantly decreasing the binding affinity of the ligand (*2*−*4*).

The ability to predict *q* prior to synthesis and testing would facilitate the design of improved contrast agents. Molecular dynamics simulations of Gd−ligand complexes in aqueous solution have been shown to predict correctly the number of bound waters in several cases (*5*). However, such simulations require a significant amount of computational resources and are not suitable for the evaluation of large numbers of candidate structures. This situation has prompted the development of simpler methods for estimating *q* from static structures that have been optimized with molecular mechanics models. One approach is based on the hypothesis that *q* should be proportional to the solvent-accessible surface area of the ligand-complexed Gd ion (*6*). Another approach is based on the hypothesis that *q*-values can be deduced by examining a series of steric energy versus ionic radii plots as a function of coordination number (*7*).

Our interest in these methods originated from a desire to apply them to a new family of potential MRI agents that are based on catecholate and hydroxypyridinonate donor groups (*8*). As the first step toward this goal, we chose to test the predictive capability of these methods on known compounds. Since the reported methods were tested primarily on aminocarboxylates, we selected a set of aminocarboxylate ligands for this verification. The test set, shown in Figure 1, was chosen for two reasons. First, *q*-values in aqueous solution, which span a range of 0 to 3, have been determined for these structures either via experimental measurement with the similar sized Eu(III) ion (*2*) and/or by MD simulation with the Gd(III) ion (*5*). Second, with the exception of NOTA, crystal structure data are available for Gd complexes with these ligands in which bound water is the only other inner-sphere ligand (*9*, *10*). It is interesting to note that, in all cases where comparison is possible, the *q*-values in aqueous solution are in agreement with the number of bound waters observed in the crystal structures.

After extending the MM3 model to treat Gd(III) complexes with aminocarboxylate and aqua ligands, we evaluated the ability of the "Connolly surface area" method (*6*) and the "coordination scan" method (*7*) to

* To whom correspondence should be addressed. E-mail: ben.hay@pnl.gov.
† Pacific Northwest National Laboratory.
§ University of California, Berkeley.

10.1021/bc0498370 CCC: $27.50 © 2004 American Chemical Society
Published on Web 10/26/2004

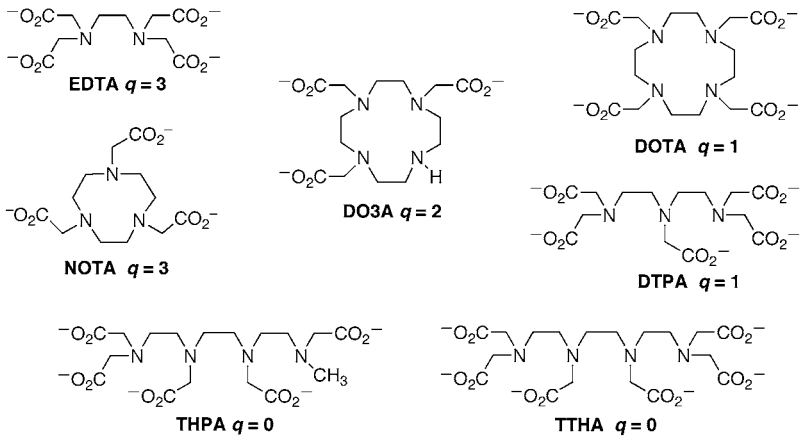


Figure 1. Test set of aminocarboxylate ligands.

predict q-values for the ligand test set (Figure 1). Neither approach was entirely successful. The "Connolly surface area" method, which we find to be misnamed, fails to predict q-values for two out of the seven cases. The "coordination scan" method systematically underestimates q-values for all cases. Although the reported methods fail, the evaluation of optimized geometries for Gd(ligand)$(O)_n$ complexes, where $n = 0$ to $q + 1$, yields alternative approaches that allow q-value predictions to be made for all seven cases using either Gd surface areas or strain energies.

COMPUTATIONAL DETAILS

Force Field Model. Molecular mechanics calculations were carried out using the MM3 program (*11*), which has been modified to support POS metal atom types (*12*). In the POS approach (*13*), all "bound" ligand atoms are formally connected to the metal ion requiring the definition of M−L stretch, M−L−X bend, and M−L−X−X torsion potentials (M = metal, L = donor atom, X = any other atom). All L−M−L angles are omitted, and van der Waals interactions between the L groups attached to the metal are added. In a recent study of steric interactions in U(IV) complexes, we have shown that the aqua ligand can be modeled as a neutrally charged oxygen atom (*14*), and the same approximation was used in this study. Prior parameter sets for Gd(III) complexes with aminocarboxylate and aqua ligands have been developed for POS force fields and shown to reproduce the geometries of these complexes with a fair degree of accuracy (*7*, *15*, *16*). Using these prior parametrizations as a starting point, we optimized geometries for Gd(EDTA)$(O)_3$, Gd(DO3A)$(O)_2$, Gd(DOTA)(O), Gd(DTPA)(O), Gd(THPA), and Gd(TTHA) complexes starting from their X-ray structure coordinates (*10*). The parameter set was then adjusted to minimize the sum of the rmsd values for superposition of calculated and experimental structures. The final parameter set and input files for all complexes are available as Supporting Information.

Surface Area Calculations. Connolly surface areas and exposed van der Waals (VDW) surface areas for Gd were calculated with GEPOL (*17*). Tripose VDW radii used for the organic atoms were as follows: H, 1.500 Å; C, 1.700 Å; N, 1.555 Å; O, 1.520 Å (*18*). VDW radii for Gd were assigned based on the 53 Å^2 surface area reported for the bare Gd ion (*6*). For the Connolly surface area calculations with a default probe radius of 1.40 Å, this surface area is achieved with a Gd radius of 0.65 Å. For exposed VDW surface area calculations this surface area is achieved with a Gd radius of 2.05 Å.

Calibration curves to establish the relationship between Gd surface area and q-value were prepared using the $Gd(OH_2)_9$ X-ray structure (*19*) with strict adherence to the published method (*6*). Gd surface areas were calculated for the structures obtained after removal of 0 to 9 water molecules from this crystal structure *without any optimization*. When there was more than one way to remove the water, all ways were examined subject to the following restriction. For $n = 2$ to 8, only sets of contiguous waters were removed. A plot of surface area versus q-value was generated from the results. A second calibration curve was prepared for $n = 0$ to 9 by plotting the Gd surface areas obtained from the model complex $Gd(O)_n$ where the complex was optimized with the MM3 model after the addition of each oxygen atom.

Exposed VDW surface areas for the metal ion in Gd(ligand) complexes were obtained from MM3 optimized geometries. Initial geometries for these optimizations were taken from X-ray coordinates (*10*). For each complex investigated, the number of added oxygen atoms was varied from 0 to $q+1$. In cases where there was more than one possible placement for the oxygen atoms, all placements were tried and the lowest energy geometry was retained.

Coordination Scan Calculations. Initial geometries for Gd(ligand)$(O)_n$ complexes were prepared as described above for $n = 0$ to q. The size of the metal was varied by systematically altering the M−N and M−O equilibrium bond length parameters in the following manner: M−N bond length = ionic radius + 1.7 Å; M−O bond length = ionic radius + 1.4 Å. Scans were performed by varying the ionic radius from 0.5 to 1.5 Å in 0.1 Å intervals with the stretching force constant kept at a constant value of 0.695 mdyn/Å (equivalent to the 100 kcal/mol·Å^2 force constants used in the prior study) (*7*). Plots of steric energy versus metal radius were then generated for each coordination number and superimposed on the same graph. The results were interpreted with the following ionic radii for Gd(III): 0.94 Å for six-coordinate, 1.00 Å for seven-coordinate, 1.05 Å for eight-coordinate, and 1.11 Å for nine-coordinate environments (*20*).

Strain Threshold Calculations. Initial geometries for each Gd(ligand)$(O)_n$ complex were prepared as described above for $n = 0$ to $q+1$. After geometry optimization, the strain energy associated with adding the ith oxygen atom to the inner-sphere was taken as the difference $U_i - U_{i-1}$, where U_i is the steric energy of the complex with the ith oxygen atom present and U_{i-1} is the steric energy of the complex before the ith oxygen atom was added.

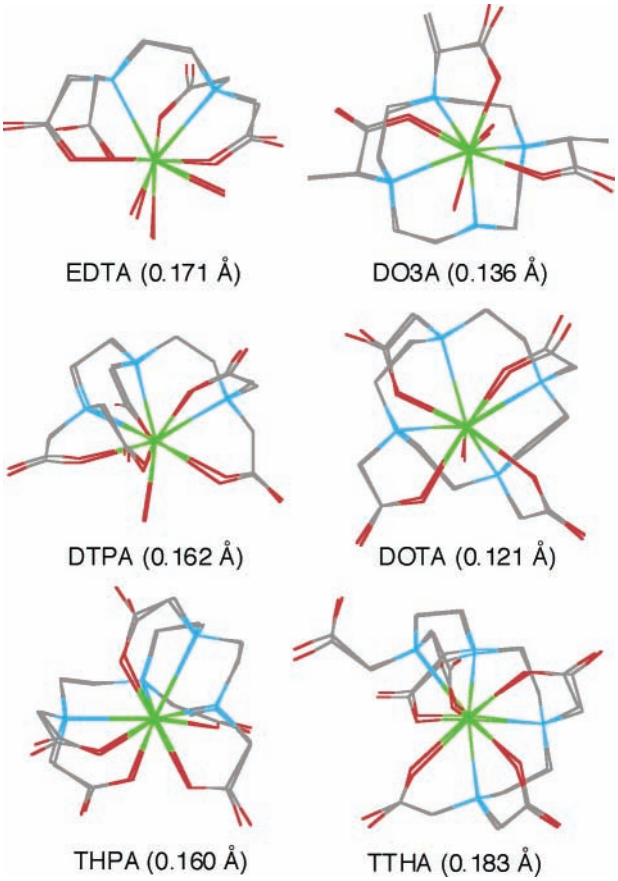


Figure 2. Superposition of calculated and X-ray geometries. The rmsd value for each structure is given in parentheses.

RESULTS AND DISCUSSION

Force Field Model Validation. Application of q prediction methods requires a molecular model to compute geometries for the Gd(ligand) complexes. The MM3 force field was extended to treat Gd(III) complexes with aminocarboxylate and aqua ligands. A model capable of reproducing the metal complex geometries observed in the solid state was obtained after adjusting parameters taken from prior POS force field models (*7*, *15*, *16*) to yield the best overall fit to crystal structure data (*10*). The root-mean-squared deviation (rmsd) between the calculated and experimental atom positions for all non-hydrogen atoms provides a measure of the accuracy of the model. In this instance the superposition of calculated and experimental structures, shown in Figure 2, yields an average rmsd of 0.156 Å. This level of accuracy is as least as good or better than that of the models used in prior q predictions (*6*, *7*).

"Connolly Surface Area" Method. A Connolly surface, also known as a solvent-accessible surface, is the surface traced out by the center of a test probe as it is rolled over a molecule (*21*). The Connolly surface for a single atom in a molecule can be computed as the surface traced out by the test probe center while the probe remains in direct contact with the atom. It was reported that the Connolly surface area for the Gd(III) ion in a Gd(ligand) complex can be used to predict the q-value for that complex (*6*). The stated method involves (1) optimization of a geometry for the Gd(ligand) complex, (2) calculation of the Connolly surface area for the Gd(III) ion, and (3) comparison of this surface area with a calibration curve relating surface area to the number of bound water molecules. The calibration curve was purportedly generated by rolling a test probe of radius 1.4 Å over $Gd(OH_2)_n$ structures, where $n = 0$ to 9, to yield a linear correlation running from ~53 Å^2 for the bare Gd(III) ion to 0 Å^2 for the nonaaqua ion. The reported relationship is depicted in Figure 3. Error bars on the points reflect the degree of variation resulting from removal of different sets of contiguous water molecules.

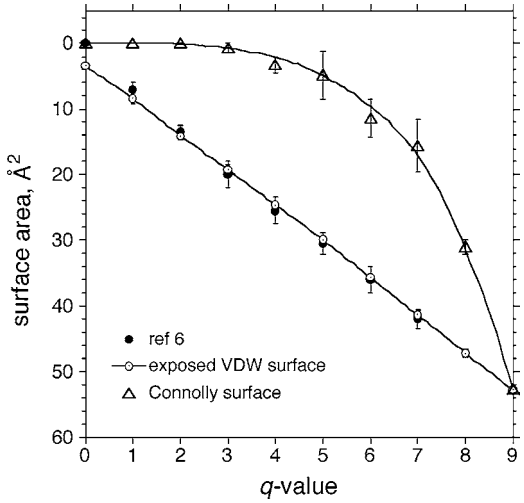


Figure 3. Relationship between various Gd surface areas and q, where $q = 9 -$ number of bound aqua ligands. Literature values were taken from Figure 1 in ref 6.

We attempted to reproduce the calibration curve using atomic coordinates from the same $Gd(OH_2)_9$ X-ray structure used in the prior study. Default Sybyl force field VDW radii were used for the oxygen and hydrogen atoms. To calculate a Connolly surface area of ~53 Å^2 for the bare Gd(III) using a test probe radius of 1.40 Å, it is a mathematical requirement that the Gd(III) radius be set to a value near 0.65 Å. A plot of the Connolly surface area for Gd(III) versus the number of bound water molecules is also shown in Figure 3. Comparison of the Connolly surface areas to the surface areas reported in the prior study reveals a large difference in behavior, establishing that the reported values were not obtained by the Connolly method.

Further calculations showed that computing a different geometric property, the exposed VDW surface area for the Gd(III) ion could largely reproduce the reported surface areas. This surface corresponds to the surface of the metal ion that would be visible in a space-filling model of the complex. Our calibration curve was not linear, however, showing a slight curvature at the higher coordination numbers (see Figure 3). Even with nine bound water molecules, 3.5 Å^2 or 6.6% of the metal ion surface remains exposed. Another difference was a significantly smaller extent of area fluctuation as a function of the choice of contiguous water molecules removed. Where the literature calibration curve suggests fluctuations as large as ±1.5 Å^2 about the mean, our range of area values was less than ±1.0 Å^2 at any given coordination number.

A second calibration curve was generated by computing the exposed VDW surface area for Gd(III) in a series of MM3 optimized model complexes, $Gd(O)_n$, where $n = 0$ to 9. Comparison with the average surface areas obtained by removing sets of contiguous water molecules from the $Gd(OH_2)_n$ X-ray structure revealed that the Gd(III) surface areas differed by less than 1.0 Å^2 at all coordination numbers. Thus, an exposed VDW surface area versus q plot essentially identical to that shown in Figure 3 is obtained by using (1) oxygen atoms to model aqua ligands

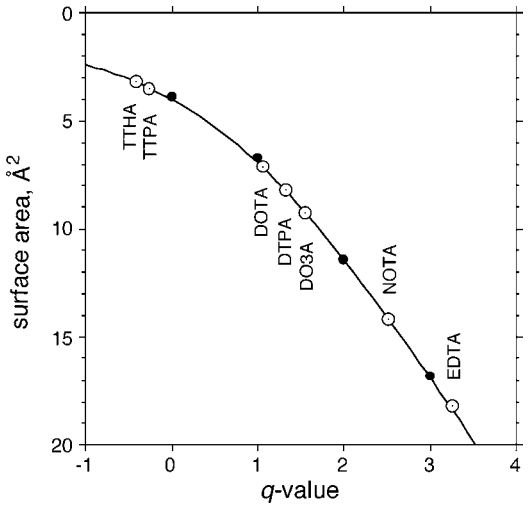


Figure 4. Interpolation of q-values for Gd(ligand) complexes from a plot of exposed VDW surface versus q generated from $Gd(O)_n$ complexes.

Table 1. Exposed Gd VDW Surface Areas in Gd(ligand) Complexes and Predicted *q*-Values Interpolated from the Calibration Curve (Figure 4)

ligand	surface area, Å^2	q-value (calcd)	q-value (obsd)
EDTA	18.2	3.26	3
NOTA	14.2	2.52	3
DO3A	9.3	1.56	2
DTPA	8.2	1.33	1
DOTA	7.1	1.06	1
TTPA	3.5	-0.26	0
TTHA	3.2	-0.41	0

and (2) a single optimized geometry to calculate the surface area at each coordination number.

This second calibration curve was used to predict q-values based on the exposed Gd VDW surface areas in MM3 optimized Gd(ligand) complexes (see Figure 4). The surface areas and predicted q-values are given in Table 1. The method successfully predicts q-values for five of the test cases, but leads to ambiguous predictions for DO3A, which lies midway between $q = 1$ and 2, and NOTA, which lies midway between $q = 2$ and 3. Thus, while there exists a definite trend between the exposed surface area of the metal ion in a nonhydrated Gd(ligand) complex and the number of water molecules that will bind, the method fails as an accurate predictor of q-value in two out of seven cases.

There is an issue with using the exposed VDW surface areas obtained from Gd(ligand) structures that have been optimized in the absence of any bound water. Metal−ligand distances generally increase with increasing coordination number. Thus, the inner sphere will swell in size as more oxygen atoms are added. As the bound atoms move outward, more metal ion surface will be exposed. Therefore, the surface areas calculated for Gd(ligand) complexes will at best represent a lower limit to the actual area that is allowed by the ligand under consideration. This effect is observed by comparing the Gd surface area in the optimized Gd(ligand) geometry to that in an nonoptimized Gd(ligand) geometry created by removing the water molecules from the X-ray structure. For example, Gd(EDTA) exhibits18.2 Å^2 in the optimized geometry versus 20.5 Å^2 in the X-ray geometry and Gd(DTPA) exhibits 8.2 Å^2 in the optimized geometry versus 10.1 Å^2 in the X-ray geometry.

"Coordination Scan" Method. This method involves calculation of the steric energy of the metal complex as a function of both metal ion size and coordination number (*7*, *22*). These plots are superimposed to yield a family of curves. The curves exhibit intersection points that define zones of preferred coordination number as a function of metal ion size. By comparing the ionic radii of a metal ion in different coordination states to this family of curves it is possible to determine which coordination number is sterically favored for that metal ion.

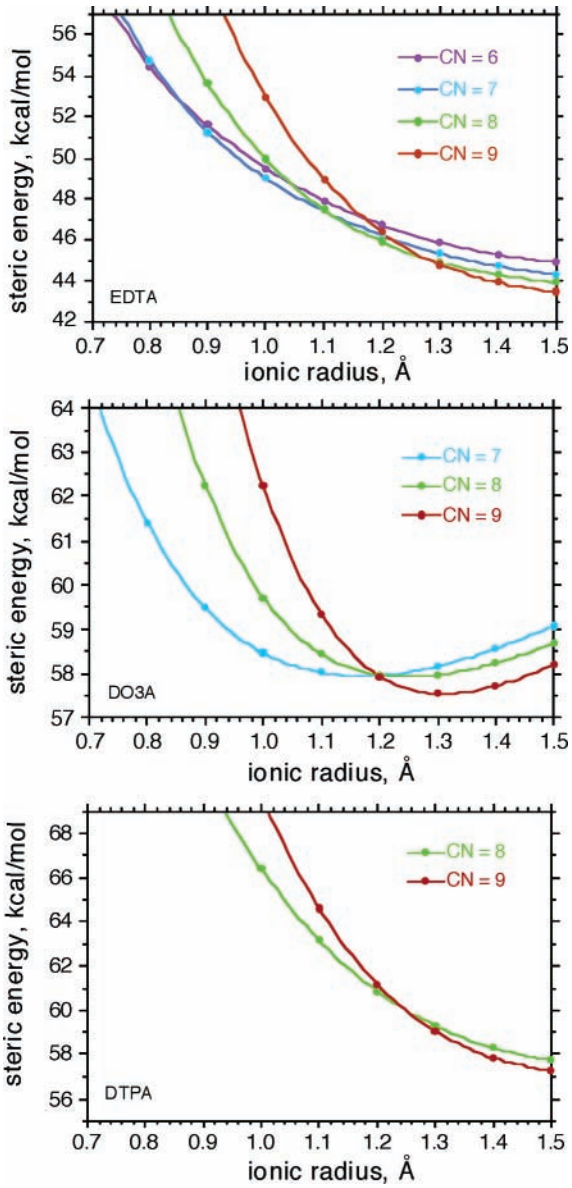


Figure 5. Coordination scan plots for EDTA (top), DO3A (middle), and DTPA (bottom).

Using the extended MM3 model, coordination scans were performed on EDTA, NOTA, DO3A, DTPA, and DOTA. As illustrated by the examples shown in Figure 5, a series of intersecting curves are obtained on superposition of the scans. The EDTA plot shows that a six-coordinate environment is preferred for metals with ionic radii below 0.85 Å, a seven-coordinate environment is preferred for ionic radii between 0.85 and 1.11 Å, an eight-coordinate environment is preferred for ionic radii between 1.11 and 1.28 Å, and a nine-coordinate environment is preferred for radii above 1.28 Å. Comparison with the ionic radii for Gd in different coordination states (0.94 Å, CN = 6; 1.00 Å, CN = 7; 1.05 Å, CN = 8; 1.11 Å CN = 9) predicts that Gd(EDTA) complex has a steric preference for a seven coordinate environment, thereby

predicting $q = 1$. Performing this analysis for the other ligands also predicts q-values that are too low: NOTA, $q = 1$; D03A, $q = 0$; DOTA, $q = 0$; DTPA, $q = 0$.

These results are in disagreement with the prior application of this method (*7*) in which the correct q-values were obtained for these same ligands using a modified Tripose force field model, TAFF (*18*). We suspect the discrepancy between the results arises from differences in the TAFF and MM3 force fields. With the POS metal ion treatment used in both studies, the shape of the steric energy versus metal ionic radius curves will depend strongly on the VDW radii assigned to atoms attached directly to the metal ion. The VDW radii used in the TAFF model (nitrogen 1.555 Å, oxygen 1.520 Å) are significantly smaller than those used in MM3 model (nitrogen radius 1.93 Å, oxygen radius 1.82 Å). In addition, different functional forms are used for VDW interactions in these two models, TAFF (Leonard−Jones 12-6) and MM3 (Buckingham exp-6).

It is clear that the coordination scan method underestimates q-values in the current application. Although the method may work with other force field models, we note that there is a fundamental flaw with the approach. The method relies on the use of a model in which the inner-sphere atoms are formally connected to the metal. In such models, each metal−ligand bond stretch interaction is treated with a potential function that has an interaction energy of zero when the bond is at its equilibrium length. These models are useful for predicting structures and examining conformational potential surfaces, but they do not address completely the energetics of bond formation. Thus, while the "coordination scan" method may indicate which coordination number is *sterically* favored as a function of metal ion radius, it ignores any compensating stabilization that might result from $Gd-OH_2$ bonding interactions.

"Strain Threshold" and "Surface Area Threshold" Methods. To overcome the inherent deficiency in the "coordination scan" approach, we chose an alternate way of interpreting the steric energies for a series of $Gd(ligand)(O)_n$ complexes. The method is based on the concept that adding a water molecule to the coordination sphere in the absence of any steric hindrance will result in a bonding interaction with a stabilizing energy. If the destabilizing strain energy for adding the next water molecule exceeds an intrinsic stabilization energy threshold, then the water will not be bound. An analogous threshold concept can be applied to the interpretation of Gd surface area data. In other words, there is a minimal space requirement for adding another oxygen atom to the inner sphere. If there is insufficient space, then the water will not be bound.

To test these concepts, we optimized a series of $Gd(ligand)(O)_n$ complexes, where $n = 1$ to $q+1$, for each ligand in the test set. Incremental strain energies for the sequential addition of oxygen atoms and exposed Gd surface areas are summarized in Table 2. It can be seen that the strain for adding an oxygen atom to the inner sphere gradually increases as the coordination number increases (*23*). The strain energies for forming the $n = q$ species range from 5.3 to 7.8 kcal/mol. The strain energies for forming the $n = q+1$ species are significantly higher, 11.3 to 23.5 kcal/mol. Thus, there is a threshold energy that lies somewhere between 8 and 11 kcal/mol. Setting a threshold in the middle of this range yields the following criterion that correctly predicts q for all structures in the test set: if the strain energy for adding the next oxygen atom exceeds 9.5 ± 1.5 kcal/mol, then the next oxygen atom will not bind.

Table 2. Strain Energies for the Addition of O Atoms and Exposed Gd VDW Surface Areas Used To Predict q-Values via Threshold Methods

complex	strain energy, kcal/mol	Gd surface area, Å	predicted q-value	observed q-value
Gd(EDTA)(O)	0.4	12.4		
$Gd(EDTA)(O)_2$	2.2	7.7		
$Gd(EDTA)(O)_3$	5.3	4.5	3	3
$Gd(EDTA)(O)_4$	11.3	2.9		
Gd(NOTA)		14.2		
Gd(NOTA)(O)	1.2	9.6		
$Gd(NOTA)(O)_2$	7.1	6.5		
$Gd(NOTA)(O)_3$	6.1	4.5	3	3
$Gd(NOTA)(O)_4$	20.4	3.4		
Gd(DO3A)		9.3		
Gd(DO3A)(O)	4.0	6.3		
$Gd(DO3A)(O)_2$	6.4	3.9	2	2
$Gd(DO3A)(O)_3$	17.1	2.9		
Gd(DTPA)		8.2		
Gd(DTPA)(O)	7.8	5.8	1	1
$Gd(DTPA)(O)_2$	13.3	4.1		
Gd(DOTA)		7.1		
Gd(DOTA)(O)	5.8	4.2	1	1
$Gd(DOTA)(O)_2$	21.9	4.8		
Gd(TTHA)		3.5	0	0
Gd(TTHA)(O)	23.4	3.6		
Gd(TTPA)		3.2	0	0
Gd(TTPA)(O)	23.5	3.1		

Similarly, as the number of atoms in the inner sphere increases the surface area decreases. At $n = q - 1$, where there should be sufficient space to allow another bound oxygen atom, Gd surface areas range from 6.3 to 8.2 Å^2. At $n = q$, where there should not be sufficient space to allow another bound oxygen atom, the Gd surface areas range from 3.2 to 5.8 Å. Thus, there is a threshold surface area that lies near 6.0 Å^2. Interestingly, this is exactly the surface area consumed when a single oxygen atom is bound to a bare Gd(III) ion. These observations lead to a second criterion that also correctly predicts q for all structures in the test set: if the exposed Gd surface area is less than 6.0 Å^2, then the next oxygen atom will not bind.

SUMMARY AND CONCLUSIONS

The reported "Connolly surface area" method (*6*) is based on the exposed VDW, rather than the Connolly, surface of the Gd ion. We find that while there exists a definite trend between the exposed surface area of the metal ion in a nonhydrated Gd(ligand) complex and the number of water molecules that will bind, the method fails as an accurate predictor of q-value in two out of seven test cases. We have presented a modified approach, the "surface area threshold" method, which predicts all q values in the test set using exposed Gd VDW surface areas from geometry optimized $Gd(ligand)(O)_n$ complexes.

The "coordination scan" method is force field dependent and systematically underestimates q with our extended MM3 model. Efforts to compensate for an inherent deficiency in the "coordination scan" approach led us to develop an alternate method to apply POS force fields to q prediction. In the "strain threshold" method, q is predicted by evaluating the increase in strain that accompanies successive addition of oxygen atoms to the inner sphere. A water molecule will not be bound when this increase exceeds a threshold energy. Calibration of this method on the test set yields a threshold value that correctly predicts q in all cases. With the MM3 model used here, this value is 9.5 ± 1.5 kcal/mol. Although this threshold will depend on the parameter set, the "strain threshold" method should be applicable with other force

fields. Calibration with a set of known compounds must be performed to establish the appropriate threshold for the force field used.

Finally, this study demonstrates that simple approaches based on steric hindrance can be used to predict observed q values for Gd aminocarboxylate complexes. The predictions are based on thresholds for surface area and strain. These thresholds, which reflect a competition between steric and electronic effects, may vary as a function of the binding sites that are present in the ligand. Binding sites that are more electron donating than amine nitrogen atoms and carboxylate oxygen atoms might make it more difficult to add an inner sphere aqua ligand. This situation would be expected to increase the surface area threshold and decrease the strain energy threshold. It remains to be seen whether the thresholds derived from this set of aminocarboxylate ligands are transferable to complexes bearing other classes of ligands.

ACKNOWLEDGMENT

This research was performed at the Pacific Northwest National Laboratory, operated by Battelle for the U.S. Department of Energy (DOE) under contract DE-AC06-76RLO 1830 and supported (PNNL) by Grant No. 73759 of the Environmental Management Science Program of the Office of Science, DOE, and (UCB) NIH Grant HL69832. The authors would like to thank Profs. R. D. Hancock and D. E. Reichert for their helpful comments and suggestions.

Supporting Information Available: The extended MM3 parameter set and input files for the Gd−aminocarboxylate complexes. This material is available free of charge via the Internet at http://pubs.acs.org/BC.

LITERATURE CITED

(1) Lauffer, R. B. (1987) Paramagnetic Metal-Complexes as Water Proton Relaxation Agents for NMR Imaging − Theory and Design. *Chem. Rev. 87*, 901.

(2) Caravan, P., Ellison, J. J., McMurry, T. J., and Lauffer, R. B. (1999) Gadolinium(III) Chelates as MRI Contrast Agents: Structure, Dynamics, and Applications. *Chem. Rev. 99*, 2293.

(3) Merbach, A. E., and Toth, E., Eds. (2001) *The Chemistry of Contrast Agents in Medical Magnetic Resonance Imaging,* Wiley, Chichester.

(4) Reichert, D. E., Lewis, J. S., and Anderson, C. J. (1999) Metal Complexes as Diagnostic Tools. *Coord. Chem. Rev. 184*, 3.

(5) (a) Fossheim, R., and Dahl, S. G. (1990) Molecular Structure and Dynamics of Aminopolycarboxylates and their Lanthanide Ion Complexes. *Acta Chem. Scand. 44*, 696. (b) Fossheim, R., Dugstad, H., and Dahl, S. G. (1991) Structure−Stability Relationships of Gd(III) Ion Complexes for Magnetic Resonance Imaging. *J. Med. Chem. 34*, 819. (c) Tan, Y. T., Judson, R. S., Melius, C. F., Toner, J., and Wu G. (1996) Using Molecular Dynamics to Predict Factors Affecting Binding Strength and Magnetic Relaxivity of MRI Contrast Agents. *J. Mol. Model. 2,* 160. (d) Durand, S., Dognon, J.-P., Guilbaud, P., Rabbe, C., and Wipff, G. (2000) Lanthanide and Alkaline-Earth Complexes of EDTA in Water: A Molecular Dynamics Study of Structures and Binding Selectivities. *J. Chem. Soc., Perkin 2* 705. (e) Chang, C. A., Liu, Y.-L., Chen, C.-Y., and Chou, X.-M. (2001) Ligand Preorganization in Metal Ion Complexation: Molecular Mechanics/Dynamics Kinetics, and Laser-Excited Luminescence Studies of Trivalent Lanthanide Complex Formation with Macrocyclic Ligands TETA and DOTA. *Inorg. Chem. 40,* 5448.

(6) Castonguay, L. A., Treasurywala, A. M., Caulfield, T. J., Jaeger, E. P., and Kellar, K. E. (1999) Prediction of q-Values and Conformations of Gadolinium Chelates for Magnetic Resonance Imaging. *Bioconjugate Chem. 10*, 958.

(7) Reichert, D. E., Hancock, R. D., and Welch, M. J. (1996) Molecular Mechanics Investigation of Gadolinium(III) Complexes. *Inorg. Chem. 35*, 7013.

(8) (a) Thompson, M. K., Botta, M. Nicolle, G., Helm, L, Aime, S., Merbach, A. E., and Raymond, K. N. (2003) A Highly Stable Gadolinium Complex with a Fast, Associative Mechanism of Water Exchange. *J. Am. Chem. Soc. 125*, 14274. (b) Doble, D. M. J., Melchior, M., O'Sullivan, B., Siering, C., Xu, J. D., Pierre, V. C., and Raymond, K. N. (2003) Toward Optimized High-Relaxivity MRI Agents: The Effect of Ligand Basicity on the Thermodynamic Stability of Hexadentate Hydroxypyridonate/Catecholate Gadolinium(III) Complexes. *Inorg. Chem. 42*, 4930. (c) O'Sullivan, B., Doble, D. M. J., Thompson, M. K., Siering, C., Xu, J. D., Botta, M., Aime, S., and Raymond K. N. (2003) The Effect of Ligand Scaffold Size on the Stability of Tripodal Hydroxypyridonate Gadolinium Complexes. *Inorg. Chem. 42*, 2577.

(9) Allen, F. H. (2002) The Cambridge Structural Database: A Quarter of a Million Crystal Structures and Rising. *Acta Crystallogr., B 58*, 380.

(10) (a) Templeton, L. K., Templeton, D. H., Zalkin, A., and Ruben, H. W. (1982) Anomalous Scattering by Praseodymium, Samarium, and Gadolinium and Structures of Their Ethylenediaminetetraacetate (EDTA) Salts. *Acta Crystallogr., B 38*, 2155. (b) Sakagami, N., Yamada, Y., Konno, T., and Okamoto, K. (1999) Crystal Structures and Stereochemical Properties of Lanthanide(III) Complexes with Ethylenediamine-N,N,N′,N′-tetraacetate. *Inorg. Chim. Acta 288*, 7. (c) Kang, S. I., Ranganathan, R. S., Emswiler, J. E., Kumar, K., Gougoutas, J. Z., Malley, M. F., and Tweedle, M. F. (1993) Synthesis, Characterization, and Crystal Structure of the Gadolinium(III) Chelate of (1*R*,4*R*,7*R*)-alpha,alpha′,alpha″-Trimethyl-1,4,7,10-tetraazacyclododecane-1,4,7-triacetic acid (DO3MA). *Inorg. Chem. 32*, 2912. (d) Chang, C. A., Francesconi, L. C., Malley, M. F., Kumar, K., Gougoutas, J. Z., Malley, M. F., and Tweedle, M. F. (1993) Synthesis, Characterization, and Crystal Structures of M(DO3A) (M = Fe, Gd) and Na[M(DOTA)] (M = Fe, Y, Gd). *Inorg. Chem. 32*, 3501. (e) Dubost, J. P., Leger, J.-M., Langlois, M.-H., Meyer, D., Schaefer, M., and Seances, C. R. (1991) Structure of a Magnetic-Resonance-Imaging Agent − The Gadolinium-DOTA Complex $C_{16}H_{24}N_4O_8NaGd{\cdot}5H_2O$. *Acad. Sci., Ser. 2 312*, 349. (f) Ruloff, R., Gelbrich, T., Hoyer, E., Sieler, J., and Beyer, L. *Z.* (1998) Controlled Crystallization of the Gadolinium(III) Complex of Diethylenetriamine-pentaacetate: Monomeric and Dimeric Structure. *Naturforsch, Teil B 53*, 955. (g) Ruloff, R., Gelbrich, T., Sieler, J., Hoyer, E., and Beyer, L. (1997) Structures of Two Isomeric Gadolinium(III) Polyamino Polycarboxylates − Relation to their Significant Differences in H^1 NMR Relaxation. *Z. Naturforsch., Teil B 52*, 805. (h) Wang, R.-Y., Zhang, H.-J., Jin, T.-Z., Zhou, Z.-Y., and Zhou, X.-G. (1999) Synthesis and Crystal Structure of Gadolinium Mononuclear Complex with Triethylenetetraaminehexaacetic Acid. *Chem. J. Chin. Uni. 20*, 176. (i) Wei, P.-R., Jin, T.-Z., Gao, S., Xu, G.-X., and Jin, Z.-S. (1993) Synthesis and Crystal Structure of alpha,alpha′,alpha″-Trimethyl-1,4,7-Triazacyclononane-N,N′,N″-triacetic Acid. *Chin. Sci. Bull. 38*, 467.

(11) (a) Allinger, N. L., Yuh, Y. H., and Lii, J.-H. (1989) Molecular Mechanics − The MM3 Force-Field for Hydrocarbons. 1. *J. Am. Chem. Soc. 111*, 8551. (b) Lii, J.-H and Allinger, N. L. (1989) Molecular-Mechanics − The MM3 Force-Field for Hydrocarbons. 2. Vibrational Frequencies and Thermodyanmics. *J. Am. Chem. Soc. 111*, 8566. (c) Lii, J.-H. and Allinger, N. L. (1989) Molecular Mechanics − The MM3 Force-Field for Hydrocarbons. 3. The van der Waals Potentials and Crystal Data for Aliphatic and Aromatic Hydrocarbons. *J. Am. Chem. Soc. 111*, 8576.

(12) (a) Hay, B. P., Yang, L., Allinger, N. L., and Lii, J.-H. (1998) An Extended MM3(96) Force Field for Complexes of the Group 1A and 2A Cations with Ligands Bearing Conjugated Ether Donor Groups. *J. Mol. Struct. (THEOCHEM) 428*, 203. (b) Hay, B. P., Clement, O., Sandrone, G., and Dixon, D. A.

(1998) A Molecular Mechanics (MM396) Force Field for Metal-Amide Complexes. *Inorg. Chem. 37*, 5887.
(13) Hay, B. P. (1993) Methods for Molecular Mechanics Modeling of Coordination Compounds. *Coord. Chem. Rev. 126*, 177.
(14) Hay, B. P., Uddin, J., and Firman, T. K. (2004) Eight-coordinate Stereochemistries of U(IV) Catecholate and Aqua Complexes. *Polyhedron 23*, 145.
(15) Hay, B. P. (1991) Extension of Molecular Mechanics to High-Coordinate Metal Complexes. Calculation of the Structures of Aqua and Nitrato Complexes of Lanthanide(III) Metal Ions. *Inorg. Chem. 30*, 2876.
(16) Cundari, T. R., Moody, E. W., and Sommerer, S. O. (1995) Computer-Aided Design of Metallopharmaceuticals: A Molecular Mechanics Force Field for Gadolinium Complexes. *Inorg. Chem. 34*, 5989.
(17) (a) Pascual-Ahuir, J. L. and Silla, E. (1990) GEPOL: An Improved Description of Molecular Surfaces. I. Building the Spherical Surface Set. *J. Comput. Chem. 11*, 1047. (b) Silla, E., Tunon, I., and Pascual-Ahuir, J. L. (1991) GEPOL: An Improved Description of Molecular Surfaces. II. Computing the Molecular Area and Volume. *J. Comput. Chem. 12*, 1077. (c) Pascual-Ahuir, J. L., Tunon, I., and Silla, E. (1994) GEPOL: An Improved Description of Molecular Surfaces. III. A New Algorithm for the Computation of a Solvent-Excluding Surface. *J. Comput. Chem. 15*, 1127.
(18) Clark, M., Cramer, R. D., III., and van Opdenhosch, N. (1989) Validation of the General Purpose Tripose 5.2 Force Field. *J. Comput. Chem. 10*, 982.
(19) Chatterjee, A., Maslen, E. N., and Watson, K. J. (1988) The Effect of the Lanthanoid Contraction on the Nonaaqualanthanoid(III) Tris(trifluoromethanesulfonates. *Acta Crystallogr., B 44*, 381.
(20) Shannon, R. D. (1976) Revised Effective Ionic Radii and Systematic Studies of Interatomic Distances in Halides and Chalcogenides. *Acta Crystallogr., A32*, 751.
(21) (a) Connolly, M. L. (1983) Solvent-Accessible Surfaces of Proteins and Nucleic Acids. *Science 221*, 709. (b) Connolly, M. L. (1983) Analytical Molecular Surface Calculation. *J. Appl. Crystallogr. 16*, 548.
(22) Hegetschweiler, K., Hancock, R. D., Ghisletta, M., Kradolfer, T., Gramlich, V., and Schmalle, H. W. (1993) 1,3,5-Triamino-1,3,5-trideoxy-cis-inosotol, a Ligand with a Remarkable Versatility for Metal Ions. 5. Complex Formation with Magnesium(II), Calcium(II), Strontium(II), Barium(II), and Cadmium(II). *Inorg. Chem. 32*, 5273.
(23) The only exception is with NOTA where the addition of the third oxygen atom occurs with 1.0 kcal/mol less strain than the addition of the second oxygen atom.

BC0498370